Optimizing Senior Living with Robots: A User Study on Social and Architectural Integration*

M. Sartorius, P. von Both, *Karlsruhe Institute of Technology*

***Abstract*— This research investigates the integration of Humanoid Assistance Robots into senior living environments to enhance independence and reduce the burden on caregivers. The user study of this paper was conducted to identify the housing needs of seniors and their openness to assistive technology, focusing on their technical competence and preferences for daily task assistance. The findings show a general openness towards technology that is intuitive and easily accessible. The participants strongly favored robotic assistance for physically demanding and repetitive chores but preferred human support for tasks requiring physical and emotional closeness. The results also highlight the need for ergonomic and accessible design. In the context of our Project JuBot at Karlsruhe Institute of Technology, the survey is relevant for the development of our humanoid robot ARMAR and a user-centered living typology. The project aims to enhance safety, independence, and autonomy by balancing technological assistance with human interaction.**

I. Introduction

Demographic changes and an aging population require modern solutions that enhance the quality of life in old age while also relieving the burden on caregivers and relatives. Extending independence in old age has been proven to affect aging positively [1] [2] and is one of the six main elements of the Active Aging Model [3]. It should also be supported "through suitable housing and infrastructure" [3]. However, some form of assistance is essential to make independent living as safe as possible despite physical limitations [4].

A. Motivation

Technical devices offer the option to compensate for physical limitations without depending on caregivers. Advancements in technology bring the vision of personal assistant robots closer to reality — robots capable of delivering breakfast, cleaning the kitchen, compensating for motor impairments, and handling heavy household items are already under development. To optimally integrate such assistance technology into future users' lives and living environments, it is essential to consider their attitudes, desires, and concerns.

Research questions to be asked are: Who can benefit most from such assistance? What requirements come from the users' side, and what reservations might they have?

The interdisciplinary project JuBot at the Karlsruhe Institute of Technology (KIT) investigates the integration of humanoid robots and assistive technologies for a senior-friendly living environment to maximize their independence and support caregivers without replacing interpersonal contact. The JuBot team brings together researchers "from robotics, artificial intelligence, human-machine interfaces, IT security, engineering and sports sciences, and architecture and technology assessment" [5]. Our work (at the Building Lifecycle Management professorship) concerns the architecture research area. As part of our work in JuBot, we conducted a user study with the following research questions: What residential needs do senior citizens have? Can they imagine using assistive technology (including assistive robotics) as a solution to maximize their independence? How competent do people over 50 currently consider themselves in technology? Which everyday tasks are mainly requested for assistance technology?

In this paper, we analyze and interpret the findings of this study and compare findings with the results of other studies. During the JuBot project, this information will be incorporated into further development of our humanoid assistant Robot ARMAR at the Institut für Anthropomatik und Robotik (IAR) [5] and, in addition, the optimization strategies for user-centered housing typologies.

The survey covered the following areas:

Part 1: Demographics and physical condition
Part 2: Technical affinity, openness, and everyday tasks
Part 3: Residential needs

The User Study was reviewed by the ethics committee and data protection officer of the KIT and has been conducted in accordance with their principles [6].

B. Methodology

The study was conducted in Germany. All participant quotes and survey content were originally in German and have been translated into English for this paper.

The Questions are aimed at the aging population. The option of reading and writing support allowed us to reach a group of participants with very different cognitive and physical abilities. In addition, the survey was divided into three parts to adapt the number of questions to the attention span of each individual. Participation in the study was voluntary and without monetary compensation. Each person was informed beforehand that they could withdraw at any time, even after receiving the questionnaire, without providing a reason or

* We would like to express our sincere recognition to the Carl-Zeiss-Stiftung, which generously supports the JuBot project and thus provides the basis for this research.

Marie P. Sartorius is with the Professorship of Building Lifecycle Management of Karlsruhe Institute of Technology, 76131 Karlsruhe, Germany (phone: 0049 – 151 556 429 14; e-mail: marie.sartorius@kit.edu).

Petra von Both is with the Professorship of Building Lifecycle Management of Karlsruhe Institute of Technology, 76131 Karlsruhe, Germany

facing any disadvantages. The results were anonymized to prevent any identification of our participants. In the questionnaire, we used Likert scales to ensure comparability. In addition, respondents were also given the option to express further thoughts in open-text fields for each question.

C. Demographics and physical condition

Part 1 of the study provides information on the demographic characteristics of the respondents. A total of 8 residents of the "Alte Mälzerei" nursing home in Karlsruhe, Germany and 13 individuals living independently participated in the study. The sample group consisted predominantly of persons over 50 without significant cognitive limitations. Most volunteers are from southern and western Germany. Twice as many women as men took part in the survey.

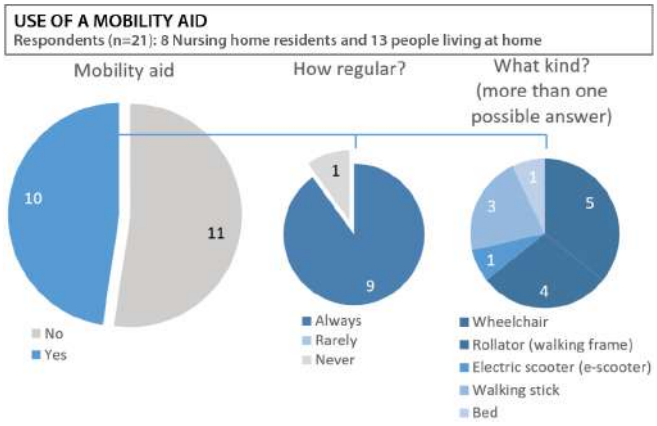


Figure 1. Use of mobility aid of interviewees

More than half of the respondents held a university entrance qualification or a master's degree as their highest level of education. The professional backgrounds were diverse. Slightly more than half of the respondents used a mobility aid. (Figure 1)

II. RESULTS: TECHNOLOGY

A. Technical affinity and openness to technology

While respondents generally viewed themselves as technically skilled and recognized the benefits of innovations, nearly half expressed reluctance to engage with new technologies if they can avoid it. A similar number reported that they do not enjoy exploring new technologies.

Contrary to previous statements, the majority of the 21 participants could still imagine getting help from a humanoid assistant robot for the following tasks:

- Reminders for meals, medication, and doctor's appointments (16 are positive, and two were unsure)
- Helping with directions in buildings (16 were positive, and three were unsure)
- Walking stabilization or pushing the wheelchair (13 are positive, and five were unsure)
- Transfer in and out of the wheelchair or use them as a stand-up aid (14 are positive, and two are not sure)

When asked, "Would you let a robot help you get up or transfer you out of bed, into a wheelchair and back?", most participants said they would be happy to accept such help. Only 4 out of the 21 surveyed did not want to use any technical assistance. These contrasting attitudes towards assistant technology suggest that technical devices are generally well-received as long as they are intuitive, easily accessible, and require minimal effort to learn how to operate them. Since robots are known for their easy access through speech recognition capabilities, this enhances acceptance even among individuals who don't enjoy learning to operate new technology.

B. Openness to Assistive Robotics

The responses to questions about opportunities and concerns regarding technical assistance in the home (Figure 2) were generally positive. Participants identified key opportunities in increased independence, enhanced safety (such as the ability to contact help in emergencies), reduced physical strain, and the potential to live at home longer.

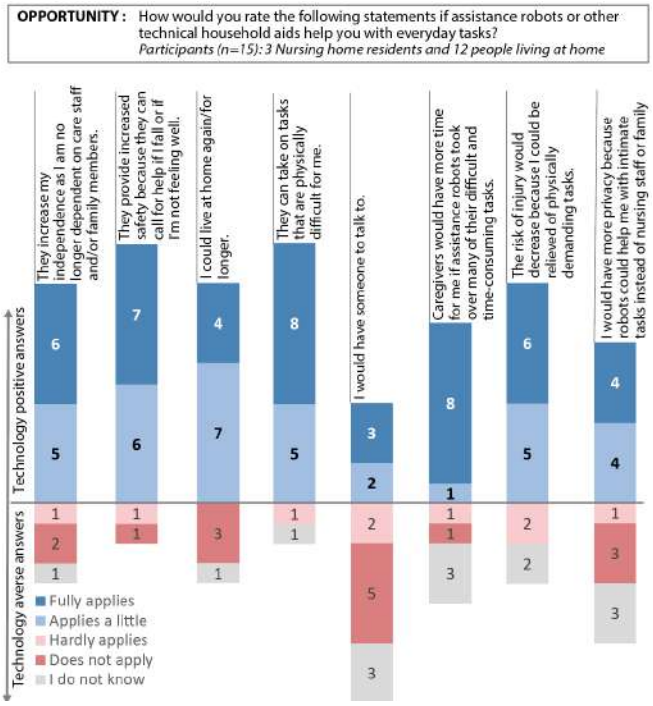


Figure 2. Opportunities towards technology

Notably, there was strong agreement that robots and assistive technologies should handle physically demanding tasks. One respondent emphasized this in the open comments, stating: "Assistance robots don't have a bad mood or get sick. - They are more reliable than humans".

The strong agreement that caregivers would gain more time for human interaction with robots highlights the value of human connection in old age. In line with this, most respondents disagreed with the statement, "I would have someone to talk to" (Figure 2), indicating that they do not perceive social benefits from social robotic interaction.

C. Concerns with Assistive Robotics

When asked about reservations, participants expressed concerns about dependence on technology, security risks, and potential privacy breaches. Despite providing primarily positive feedback, one respondent remarked, "Unless it gets

hacked". Addressing these issues will be essential to building and strengthening trust and encouraging the use of assistive devices in the daily lives of senior citizens. Possible approaches are discussed in Chapter III.

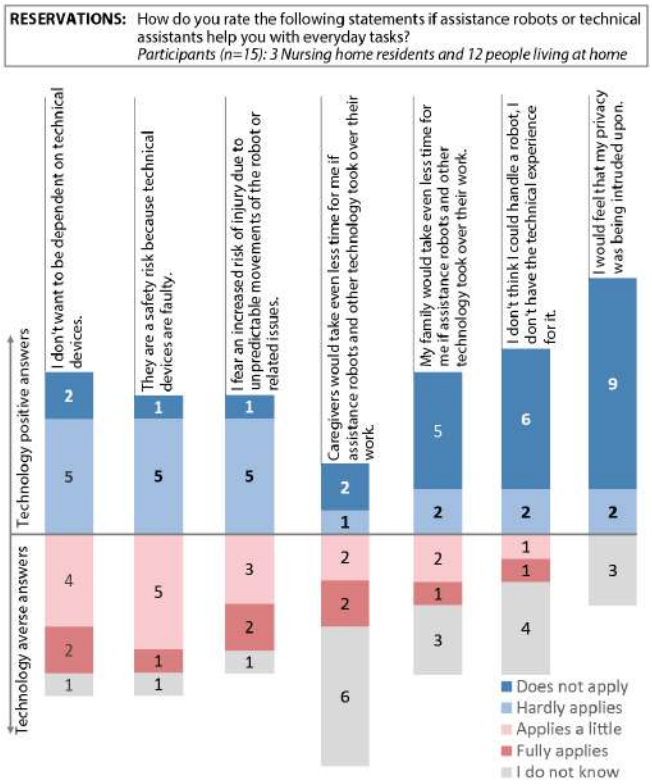


Figure 3. Reservations towards technology

D. *Preferences for Assistance Tasks*

The questions evaluating the acceptance of technical household aids for various daily tasks and activities are categorized into Household, Body care, Healthcare, and Leisure Activities.

The set of daily activities was already collected in an earlier project stage for a function-based analysis of user scenarios for assistive technology and can be found in [4]. The current user study now evaluates the potential distribution of stakeholders within the care setting.

Figure 4 presents the revised study results, with tasks arranged from left (high acceptance of technical support) to right (low acceptance of technical support). The answer option "equal" (indicating no preference) was interpreted as positive feedback towards technology, as the aim of this analysis is to identify growth potential for technical aids and pinpoint the task areas where caregivers and family members can be most effectively relieved.

The blue and purple areas of the graph indicate a preference for technical support. The upper boundary of the blue area reflects the combined responses for: "only technology," "rather technology," and "equal" preference. In contrast, the red line represents answers in favor of human support, comprising the responses: "only human" and "rather human".

The overall graphs show strong positive feedback for technical support in physically demanding and time-consuming tasks, such as carrying heavy objects, retrieving items, cleaning windows, refrigerators, and kitchens. Repetitive chores also benefit from technical assistance, especially when familiar technical aids are available. Key tasks in this category include remembering appointments, vacuuming, mopping floors, ironing clothes, and dusting.

In contrast, tasks involving emotional significance or physical contact are generally preferred to be handled by humans. These tasks include setting the table, washing dishes by hand, storing dishes, administering healthcare, or treating wounds. These findings align with the attitudes towards technology observed in earlier questions.

E. *Growth potential of Assistance Tasks*

The area where technology acceptance decreases and the preference for human support increases (the "narrowing gap of preferences") represents a key growth potential for technical solutions. Since there is no clear preference for human or technical support, the cautious openness can be further directed towards technology. Developing strategies that build trust and address the reservations highlighted in Chapter II, Sections B, and C are essential to increase acceptance and implementation areas. Since each use case combines its own set of benefits and concerns, the next chapter serves as an orientation to allocate those to design appropriate individual strategies for each use case.

III. Discussion: Empathising Technology Acceptance

The study results allowed us to allocate key factors that influence technology acceptance. The following topics are presented and compared with findings from other published studies. In our project, this information serves to weigh which tasks can be taken over by our assistant robot and find an appropriate implementation strategy. In addition, specific tasks can be identified that intentionally do not need to be further elaborated since the hurdles are too great, while the need for human contact in the care context cannot be surpassed in any case.

A. *Physical strain*

Due to motor limitations, physical straining tasks are often challenging or even painful for older adults. Previous studies have confirmed that physical relief benefits the acceptance of household technologies [7]. Additionally, as noted in earlier research, "seniors want to remain independent and not be a burden to anyone" [8] (German translation); another study reports that older adults strive for greater independence and autonomy to minimize their impact on family members [9].

B. *Familiarity with existing technical household aids*

Existing technical household aids, even those only seen through advertising, positively influence technology acceptance due to familiarity. In our study, this was strongly perceived in the context of appointment reminders (in the form of digital Calendars) and vacuuming. While most of the respondents themselves did not own a vacuum robot, they were very open to the idea. One respondent pointed out the positive feedback from friends as the reason.

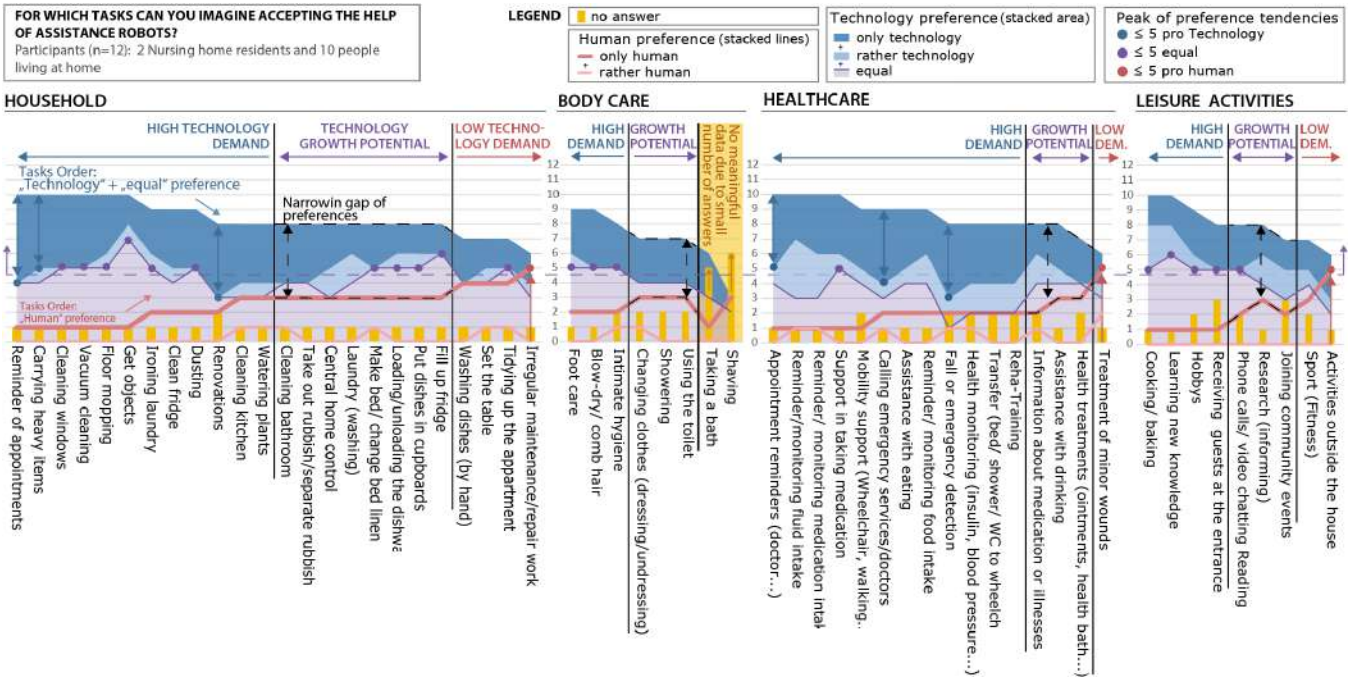


Figure. 4. Technology preference for everyday tasks

In addition to that, a study explores this topic, demonstrating that seniors' understanding and acceptance of technology increase after receiving training and using smartphones [10]. This suggests that technology acceptance is dynamic and can be positively influenced. As a consequence, future technology will always benefit from its predecessors due to already-learned functions. Therefore, the aging "digital natives" generation will continue to increase the acceptance of new technology, although according to a study, they also prefer easy-to-use interfaces [11].

C. *Emotional Significance*

Tasks with high emotional significance, such as setting the table, tidying up (organizing), or cooking and baking, reveal mixed preferences regarding technical support. While some respondents are open to technical assistance, others prefer human support. These tasks often carry social and emotional elements difficult for technical aids to replicate. The mixed responses indicate that a combination of human and technical support may be most appropriate for these activities. Studies also highlight the importance of emotional attachment and social interaction in accepting assistance [12].

D. *Physical Contact*

Most respondents expressed a clear human assistance preference for tasks requiring close physical proximity, such as intimate care, toileting, and showering, where trust, security, and empathy — qualities currently beyond the capabilities of robots — are crucial. One respondent commented, "I wouldn't allow an intimate wash, but I'd be fine with freshening up below (preparing panty liners would be okay)." Comments such as "If I were to fall in the process, I'd rather have a real person to help me up again" and "I'd like to see someone else do it first, to know how they handle patients and see how it works" show that the reasons for rejection are based on concerns around the physical proximity.

The study "Domestic Robots for Older Adults: Attitudes, Preferences, and Potential" [13] reflects a similar pattern, with an even stronger inclination toward human assistance in personal care. The tasks in this category include "shaving, washing/combing hair, bathing, eating/feeding, dressing, brushing teeth, and walking" [13].

There are hardly any studies that deal with specific strategies for increasing acceptance in this field. One study explored the "effective interaction method of robots in the functional intimate zone" [14] and came to the conclusion that intimate interactions via indirect "non-physical contact" will be more accepted [14].

E. *Complexity*

As tasks become more complex and motor-intensive, the preference for human versus technological assistance becomes less distinct in our study. Examples include making the bed, washing dishes by hand, putting dishes away, and performing repair work. These activities typically require a high degree of precision and skill, which respondents may associate with human assistance, or they may be uncertain about the capabilities of technical aids in handling such tasks. However, no additional evidence supports this hypothesis, and the study "Domestic Robots for Older Adults: Attitudes, Preferences, and Potential" [13] even contradicts this assumption.

F. *Data Security*

Security in the digital world is a sensitive topic that every technology must address. Although the majority of our respondents did not feel that their privacy was being invaded by assistance technology, there was the additional comment that this only applies if the assistance technology cannot be hacked.

This challenge is not new and already affects widespread technologies such as smartphones and their access to sensitive data (e.g. through banking apps), which can be protected by multi-factor authentication. Another solution is the integration

of blockchain technologies that are used successfully to secure data in other sensitive areas such as healthcare [15].

In order to strengthen user trust, it is necessary to develop secure data processing methods in addition to functional applications.

IV. RESULTS: ARCHITECTURAL NEEDS AND PREFERENCES

The survey's Architectural questions focus on senior citizens' housing needs. The results indicate that respondents place high importance on accessibility, ergonomic design, and privacy.

Participants were first asked which rooms they occasionally find challenging to navigate independently. The bathroom was mentioned most, followed by the kitchen, living room, and hallway. Common reasons included insufficient space (e.g., for wheelchairs), obstacles like door thresholds, and limitations related to medical conditions such as multiple sclerosis.

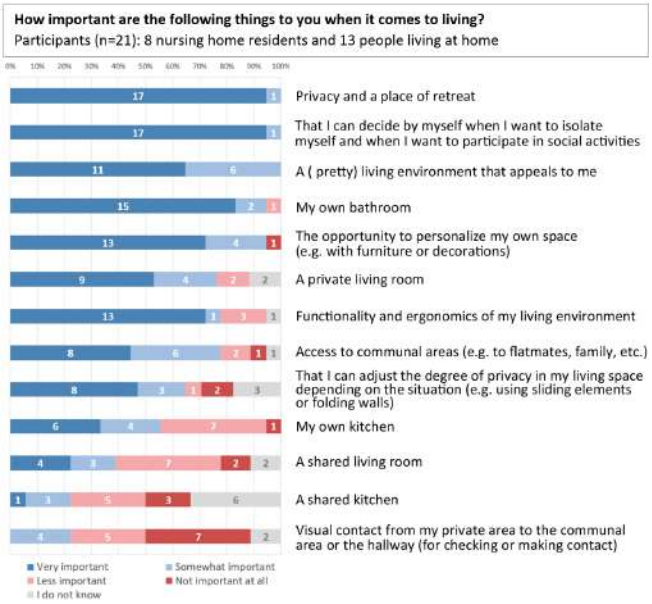


Figure 5. Living space preferences

In response to the question "Where would you prefer to live?" (with multiple answers allowed), 12 participants clearly preferred living in their own apartment or house. This was followed by the preference for multi-generational housing (with four votes) and living with family (with three votes). Retirement homes and private residential communities with other senior citizens were even less favored.

When asked about the importance of different aspects of living (Figure 5), 17 of the 21 participants rated privacy and the ability to retreat from shared spaces as "very important." The ability to choose between privacy and social interaction was also highly valued. Participants placed similar importance on having an aesthetically pleasing living environment, a private bathroom, and the freedom to personalize their space.

The survey also explored preferences for specific living area features. A floor-level shower with no steps or thresholds was considered "very important" (by 15 participants). Additionally, many respondents preferred natural lighting, direct outdoor views from the bedroom, access to outdoor spaces from both private and communal areas, ergonomic kitchen designs, and a seating option in the shower.

V. DISCUSSION: USER-ORIENTED LIVING

The results clearly show that even in old age, people are very attached to their private residence and that alternative forms of housing are generally only considered if circumstances leave no other choice. In addition, German care homes, for example, currently do not even have sufficient capacity for a quarter of all senior citizens [16]. This underlines the particularly high importance of a safe living environment and support with everyday tasks.

A diverse range of services is, therefore, the most promising approach to finding a suitable solution for each individual in old age. In addition to the various established living and care concepts, these services should increasingly include technical support options.

VI. CONCLUSION

The positive feedback regarding assistive technology opens up the possibility of rethinking the provision of care and expanding existing structures.

Applying the universal design strategy [17] [18], which emphasizes inclusivity across varying abilities, ages, needs, and social backgrounds, can expand this acceptance further. This philosophy posits that design "can be understood and used without additional technology or special adaptations" (German translation) [17]. According to [18] [19], these design principles can be extended beyond everyday objects to encompass architectural contexts as well.

At the same time, the architectural results underscore the desire for accessibility, privacy, and individual design options, which play just as important a role in the acceptance of assistive technologies. The study results show that the desire for privacy is not compromised by using a robot. Rather, the robot is perceived as a supportive element that strengthens independence and autonomy without interfering with personal space. Therefore, the combination of assistive robots with senior-friendly architecture offers a sustainable solution for age-appropriate living.

However, technical aids involving close physical contact will likely be accepted only under predominantly human control (such as orthoses). This underscores our aim not to replace care entirely with technology but to deploy it specifically for physically demanding and time-consuming tasks, while emotional and care-related activities should remain the preserve of human support.; our study confirms that technological support should not be seen as a substitute for social interaction but as a targeted supplement to create more time for personal care.

Our survey helps us to optimize our future studies in this context so that we can ask more targeted questions.

A. Outlook

Based on the Study findings, specific areas of application for the humanoid assistant robot ARMAR will be further developed and optimized during the JuBot project.

The most frequently requested areas of robot application will be an important basis for analyzing the robot's motion sequences (using navigation cost maps) in a residential context and for determining space requirements for the built environment. In collaboration with our project partner, the Anthropomatics and Robotics (IAR), this "navigation cost map" can be generated to ensure safe and reliable navigation, allowing the robot to maintain appropriate distances from obstacles [20].

The apartment modules developed from previous research, "Rule-Based Design for the Integration of Humanoid Assistance Robotics into the Living Environment of Senior Citizens" [4], can then be further enhanced to accommodate new robot tasks with requirements for increased space needs or specific furniture arrangements.

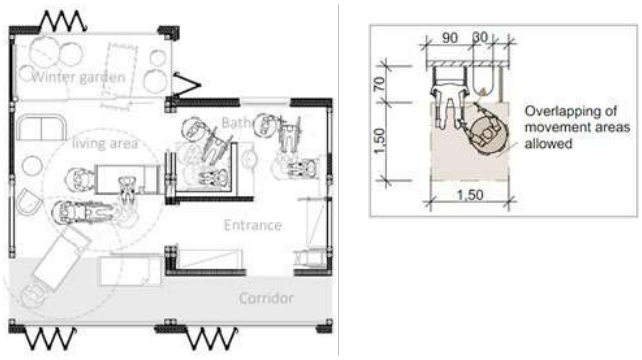


Figure 6. Development of an optimized senior apartment module

The long-term aim is to establish a closer link between Building Information Modeling (BIM) and robot simulation. Developing efficient technical interfaces, the integrated planning and construction process of buildings and robotics enhances the integrated planning process. This integration requires specific modeling standards for digital building models to provide all necessary information for robot navigation. Parametric mapping methods are ideal for modeling motion sequences like opening doors or drawers. Moreover, semantic information on furnishing properties, door types, and opening directions can be beneficial. As a result, the project will focus on creating a comprehensive model and interface concept to bridge BIM and robotics simulation. Initial investigations suggest that Industry Foundation Classes (IFC) are suitable for cross-platform data exchange.

Our Project partner will continue to focus on increasing the acceptance of assistance technologies through user-centered education strategies and accessible operating concepts in order to further enhance acceptance of Assistance Technology amongst seniors, relatives, and caregivers.

ACKNOWLEDGMENT

Special thanks go to the senior citizens of the nursing home "Alte Mälzerei" in Karlsruhe (Germany) for participating in the study and giving us an insight into their lives.

REFERENCES

[1] J. Secker, R. Hill, L. Villeneau und S. Parkman, Promoting independence: but promoting what and how?, Ageing & Society 23, 2003, p. 375–391.

[2] European Commission, "Green Paper on Ageing: Fostering Solidarity and Responsibility Between Generations, "Brussels:, 2021.

[3] A. Boushra und W. Gregor, "Analysis of Newspaper Coverage of Active Aging through the Lens of the 2002 World Health Organization Active Ageing Report: A Policy Framework and the 2010 Toronto Charter for Physical Activity: A Global Call for Action, "2013.

[4] M. P. Sartorius und P. v. Both, "Rule-Based Design for the integration of Humanoid Assistance Robotics into the Living Environment of Senior Citizens, "Belgium, 2022.

[5] F. Mescoli, "Staying young in old age with assistance robots, "2020. [Online]. Available: https://www.informatik.kit.edu/11147_11625.php. [Zugriff am 3 July 2024].

[6] K. I. o. Technology, "Applications to the Ethics Committee, "[Online]. Available: https://www.ethik.kit.edu/english/applications.php. [Zugriff am 14 February 2025].

[7] C. A. Smarr, A. Prakash, J. M. Beer, T. L. Mitzner, C. C. Kemp und W. A. Rogers, "Older adults' preferences for and acceptance of robot assistance for everyday living tasks, "in Proceedings of the Human Factors and Ergonomics Society Annual Meeting, 2014.

[8] G. Kaiser, Bauen für ältere Menschen, Köln: Rudolf Müller, 2014.

[9] J. F. Coughlin, L. A. D'Ambrosio, B. Reimer und M. R. Pratt, "Older Adult Perceptions of Smart Home Technologies: Implications for Research, Policy & Market Innovations in Healthcare., "in Conference Proceedings of the IEEE Engineering in Medicine and Biology Society, 2007.

[10] C.-C. Yang, C. Liu und Y.-S. Wang, "The acceptance and use of smartphones among older adults: differences in UTAUT determinants before and after training., "in Library Hi Tech, 2023.

[11] A. D. T. Hamelmann, Impacts of Digital Natives on Technology Acceptance: A Conceptual Analysis, Sydney, USA: Australasian Conference on Information Systems, 2018.

[12] T. L. Mitzner, J. B. Boron, C. B. Fausset, A. E. Adams, N. Charness, S. J. Czaja, K. Dijkstra, A. D. Fisk, W. A. Rogers und J. Sharit, "Older adults talk technology: Technology usage and attitudes., "in Computers in Human Behavior, 2010.

[13] C. Smarr, T. L. Mitzner, J. M. Beer, A. Prakash, T. L. Chen, C. C. Kemp und W. A. Rogers, "Domestic Robots for Older Adults: Attitudes, Preferences, and Potential, "in Int J of Soc Robotics 6, 2014.

[14] D. Kang, S. K. Kim und a. S. S. Kwak, The Effects of the Physical Contact in the Functional Intimate Distance on User's Acceptance toward Robots, New York, USA: ACM/IEEE International Conference on Human-Robot Interaction (HRI '18). Association for Computing Machinery, 2018.

[15] A. A. Khan, S. Bourouis, M. M. Kamruzzaman, M. Hadjouni, Z. A. Shaikh, A. A. Laghari, H. Elmannai und S. Dhahbi, "Data Security in Healthcare Industrial Internet of Things With Blockchain, "Bde. %1 von %2vol. 23, no. 20, EEE Sensors Journal, 2023, pp. 25144-25151.

[16] S. Bundesamt, „Anzahl der zu Hause sowie in Heimen versorgten Pflegebedürftigen in Deutschland in den Jahren 1999 bis 2021 (in 1.000),“ Online, 2022.

[17] B. Dietz, Demenzsensible Architektur, Stuttgart: Frauenhofer IRB Verlag, 2018.

[18] O. Herwig, Universal Design. Lösungen für einen barrierefreien Alltag, Basel: De Gruyter, 2012.

[19] B. R. Connell, M. Jones, Mace, Ron, J. Mueller, A. Mullick, E. Ostroff, J. Sanford, E. Steinfeld, M. Story and G. Vanderheiden, "The principles of Universal Design," NC State University, The Center for Universal Design, 04 January 1997. [Online]. Available: https://projects.ncsu.edu/ncsu/design/cud/about_ud/udprinciplestext.htm. [Accessed 17 May 2021].

[20] F. Reister, M. Grotz und T. Asfour, "Combining Navigation and Manipulation Costs for Time-Efficient Robot Placement in Mobile Manipulation Tasks, "in IEEE Robotics and Automation Letters, 2022.

Characterizing expert exoskeleton-assisted gait: insights to accelerate ankle exoskeleton mastery

Ava Lakmazaheri
Department of Mechanical Engineering
Stanford University
Stanford, USA
avalak@stanford.edu

Steven H. Collins
Department of Mechanical Engineering
Stanford University
Stanford, USA
stevecollins@stanford.edu

***Abstract*—Exoskeletons can make walking easier, but extensive training is needed to fully benefit from them, potentially hindering device adoption. Coaching new exoskeleton users to walk with energetically beneficial gait patterns might accelerate motor learning, but these target patterns have yet to be established. In this study, we characterized changes in gait biomechanics between healthy young adults' first exposure to ankle exoskeletons and after 7+ hours of training when they demonstrated full motor adaptation. We observed consistent markers of adaptation in ankle kinematics and spatial gait features; expert exoskeleton users exhibited greater ankle dorsiflexion before a powerful and concentrated push-off while walking with narrower and longer steps. Adaptations in muscle coordination patterns were more varied, but generally involved reducing co-contraction throughout the leg. By the end of training, non-propulsive exoskeleton-assisted gait features approached those of unassisted walking. Our results suggest that effective exoskeleton use involves selectively avoiding most disruptions to typical gait while accommodating energetically beneficial changes around push-off. All reported gait features can be monitored and targeted in real-time, facilitating the application of these results to reduce the time burden for novice users to maximally benefit from ankle exoskeletons.**

Keywords—exoskeletons, motor learning, gait, biomechanics

I. Introduction

Exoskeletons are promising tools to address losses in mobility, such as those arising from age, stroke, or neurodegenerative disorders. Exoskeletons can offload assisted muscle activity and augment biological joint power, reducing the energetic cost of walking [1–3]. Making walking easier for those who struggle with mobility could promote physical activity, increasing independence, social participation, and well-being [4]. Ankle exoskeletons have particular promise for real-world use, as they can be relatively lightweight, easy to don and doff, and have been shown experimentally to provide the largest reduction in energy cost of walking of any lower-limb joint [5].

This work was supported by the National Science Foundation (1828993 and DGE-1656518) and the Gabilan Stanford Graduate Fellowship.

The timescale of learning to effectively use exoskeletons is slow. Healthy young adults extract full metabolic benefit of ankle exoskeletons after approximately two hours of training [6], and they continue to explore varied motor control strategies for two additional hours before achieving steady-state gait [7]. This timescale is likely to be significantly longer as people age or experience neurologically-based gait changes, given slowed or impaired motor learning [8–11]. New training approaches should be explored to ensure that the time burden of learning how to comfortably and effectively use exoskeletons is not prohibitively high.

Coaching people to walk with efficient gait patterns might expedite exoskeleton training. Prompting low-cost gait patterns for even short periods of time can aid the nervous system in identifying relevant dimensions of energy optimization in a new motor context [12]. Neither natural gait variability nor open-ended prompts to explore new coordination strategies has reliably produced initiation of energy optimization within a comparable time scale [12]. While exploration is a critical component of motor learning [6,13], insufficient knowledge about the relevant dimensions to explore could unnecessarily slow the learning process. Identifying low-cost gait patterns, in order to strategically expose people to these behaviors, could be fruitful before deploying new assistive devices.

Existing characterizations of exoskeleton-assisted gait may be insufficient to accelerate exoskeleton mastery. Lower-limb biomechanics while walking with an ankle exoskeleton have primarily been characterized after 20-30 minute training sessions. These studies found reductions in both plantarflexor activity and co-contraction of antagonist muscles, while ankle kinematics, step width, and stride time remained unchanged due to training [14–17]. Notably, motor adaptation was not characterized in these studies, and may have been ongoing. Assessing biomechanical gait changes before and after complete motor adaptation would better indicate the most relevant gait dimensions for energy optimization.

Gait biomechanics of fully adapted exoskeleton users have only been characterized for a small number of gait features selected *a priori*. In one study of users who trained extensively with exoskeletons, expertise was demonstrated by an exponential decay of gait variability to steady-state values, corresponding to a final metabolic benefit triple that of initial

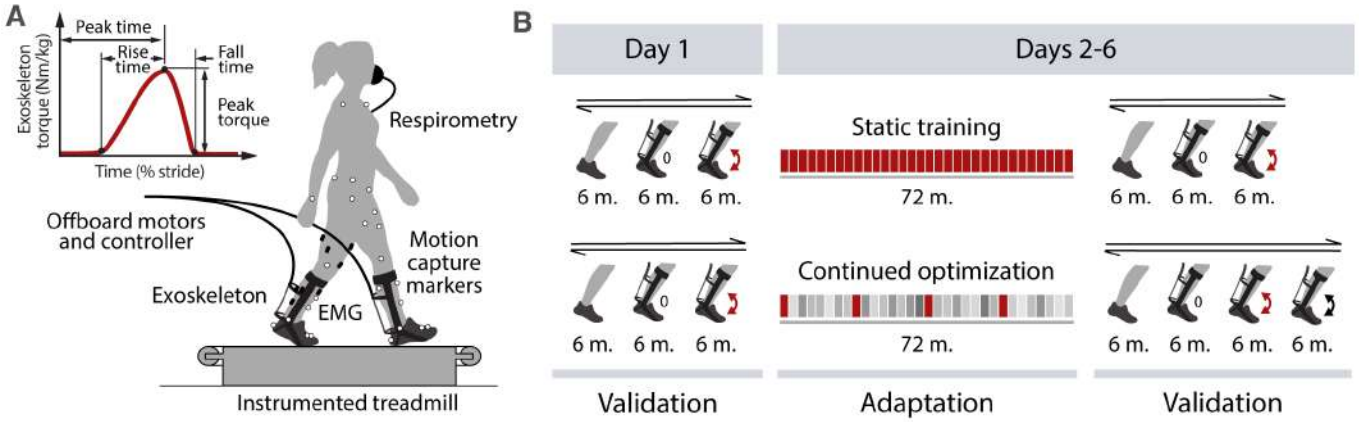


Fig. 1. (A) Schematic of the experimental setup. Respirometry, motion capture, electromyography, and ground reaction force data were recorded. Exoskeleton torque was applied by off-board motors and parameterized by the magnitude and timing of peak torque, rise time, and fall time. (B) Schematic of the experimental protocol. Validation trials were performed in a double-reversal order: wearing running shoes only, exoskeletons applying zero torque, and exoskeletons applying generic assistance. In adaptation trials, the static training group (n = 5) experienced generic assistance (red) and the continued optimization group (n = 5) underwent human-in-the-loop optimization, with generic assistance tested periodically. The continued optimization group also tested optimized assistance during validation.

exposure, and the largest benefit thus far reported for use of ankle exoskeletons [6,7]. Gait adaptations reported in this study included reduced step frequency, reduced ankle angle range over the gait cycle, and reduced total plantarflexor activity [6].

In this study, we performed a broader exploration of changes in gait biomechanics as the same participants—initially naïve to exoskeleton use—became expert at walking with plantarflexion assistance. We considered nine healthy young adults that trained with ankle exoskeletons over 7+ hours, and analyzed biomechanical gait data that can be monitored in real-time on a step-by-step basis: sagittal plane ankle kinematics, spatial gait features, and peak activity of lower-limb muscles. We compared changes between novices and experts, walking with and without plantarflexion assistance, to assess the relevant gait dimensions of energy optimization. We expect that this analysis can inform future work using biofeedback to guide first-time exoskeleton users toward beneficial gait patterns, expediting motor learning and improving perception of human-exoskeleton interaction.

II. Methods

A. Data Collection

Data for this study were taken from [7], with relevant details repeated here. The experimental protocol was approved by the Stanford Institutional Review Board (IRB-48749) and all participants provided written consent before participating. Healthy young adults naïve to exoskeleton use (N = 9; 3 females; age: 24 ± 3 years; body mass: 69.4 ± 10.6 kg; height: 1.73 ± 0.08 m) underwent a six-day protocol during which they walked with bilateral ankle exoskeletons at 1.25 m/s (Fig. 1). Each exoskeleton was controlled by an off-board motor, enabling the application of various high-magnitude plantarflexion torque profiles while remaining lightweight (0.88 kg). Torque profiles were parameterized by peak magnitude, peak time, rise time, and fall time (Fig. 1A).

In order to capture "novice" performance, participants first underwent six-minute pre-test trials of walking without exoskeletons, walking with exoskeletons tracking the ankle joint so as to apply negligible torque, and walking with exoskeletons applying an assistive plantarflexion torque once per step. This torque profile ("generic assistance") was set by parameters found to be widely beneficial in pilot testing: a peak magnitude of 0.54 times body weight at 52.9% stride with a rise time of 26.2% stride and a fall time of 9.8% stride. Each six-minute condition was then repeated in a double-reversal order (Fig. 1B).

Ten participants, comprising two experimental groups, were considered. Both groups experienced the same pre-test trials. The "static training" group (n = 5) then walked with generic assistance for 72 minutes in the remaining five experimental sessions. For the same duration, the "continued optimization" group (n = 5) underwent human-in-the-loop optimization [18], with a new torque profile tested every two minutes to minimize energy cost of walking. For this group, generic assistance was applied every 16 minutes to track learning (Fig. 1B). The six-minute double-reversal validation trials of no exoskeleton, unassisted, and generically-assisted walking were repeated at the end of each day for both groups. The continued optimization group also walked with optimized assistance in the end-of-day validation trials. Participants each accrued 7.4 to 8.4 hours of experience with assisted walking and 8.4 to 9.4 total hours of walking while wearing the exoskeletons. Throughout the study, data were collected from an indirect calorimetry device (Cosmed Quark CPET), motion capture system (Vicon), instrumented treadmill (Bertec), and eight electromyography electrodes per leg (Delsys). One participant from the continued optimization group was excluded from our analysis due to incomplete data recording on the first day of the study.

B. Data Analysis

The distinction between novice and expert exoskeleton use was made by comparing matched validation trials between the first and last experimental session. Expert status was conferred by participants tripling their initial metabolic benefit by the end of the study [7] and by gait variability

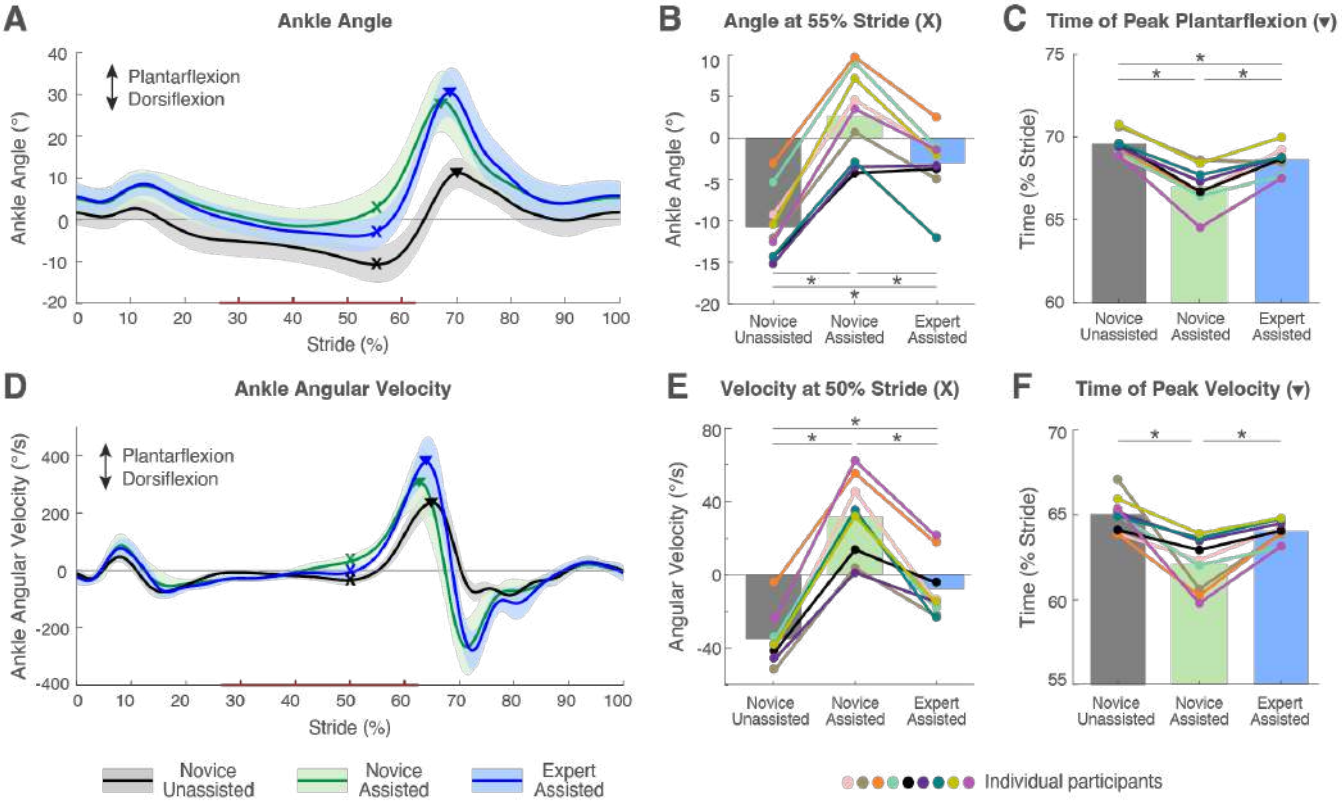


Fig. 2. Adaptations in ankle kinematics. Average (A) ankle angle and (D) ankle angular velocity profiles, measured from exoskeleton encoder. Key features of (B-C) ankle angle and (E-F) ankle angular velocity profiles across trial types. Shaded regions represent 95% confidence intervals. Red portion of axes denote when exoskeleton torque is non-zero. X denotes magitude at 50% or 55% stride and inverted triangle denotes peak magnitude. Individual participants are represented by distinct colored circles. Asterisk signifies $p < 0.05$.

exponentially regressing to that of walking without an exoskeleton, indicating acquisition of stable motor skill [6]. Both the static training and continued optimization groups were indistinguishable by these measures. Therefore, all strides from final validation sessions were treated as instances of expert behavior with no additional comparisons made between experimental groups. A significant difference between novice and expert gait outcomes was assessed using analysis of variance and post-hoc paired t-tests with the Bonferroni adjustment for multiple comparisons and an alpha value of 0.05.

Stride-by-stride trajectories of exoskeleton ankle angle and angular velocity were acquired through measurement from an on-board encoder. Step length and width were calculated from the position of the foot center of pressure at heel strike, measured from force plate data via the split-belt treadmill. Changes in stride duration were captured from analysis of changes in stride length given the fixed treadmill speed. Muscle activity was acquired from electromyography signals after high pass filtering at 30 Hz, rectifying, low pass filtering at 6 Hz, and normalizing to the peak activity calculated from no-exoskeleton trials in the same session. Trials with poor electromyography signal quality were excluded from analysis. Respirometry and motion capture data were not analyzed in this study, but were available for reference from this dataset.

All biomechanical profiles were normalized to percent stride, averaged across the final three minutes of each six-minute validation trial, and averaged across legs. We used visual inspection to identify features in kinematic profiles that consistently changed between novices and experts. If multiple features reflected the same gait behavior, we selected and reported one that appeared most robust to inter-subject and inter-session variability. To ensure a rigorous assessment of timing-related features, we report these analyses for biomechanical profiles both with and without normalization to stride duration.

Results

Ankle kinematics differed significantly between novice and expert exoskeleton users (Fig. 2). Experts dorsiflexed more mid-stride, evidenced by increased peak dorsiflexion, increased dorsiflexion at 50-55% stride, and decreased plantarflexion velocity at 50-55% stride. Natural variations in the curvature of ankle angle profiles made calculations based on peak dorsiflexion timing less consistent. Therefore, we focused our analysis on features at fixed points in the gait cycle.

Ankle angle at 55% stride was 5.7° more dorsiflexed by the end of training (Fig. 2A-B, Table 1, $p = 0.01$). With expertise, assisted ankle angle at this time approached that of unassisted walking (Fig. 2A-B). Novice users were 13.4° more plantarflexed when assisted than when unassisted ($p =$

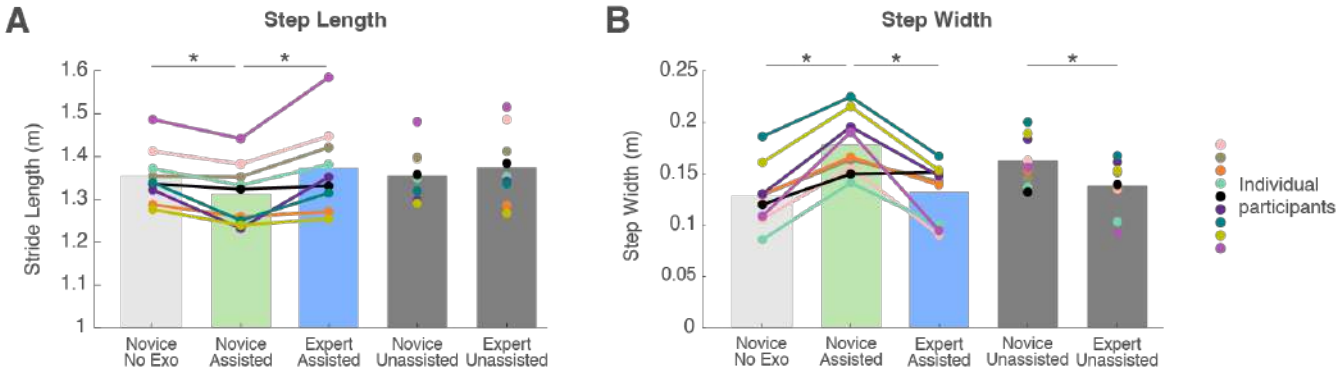


Fig. 3. Adaptations in spatial gait features. (A) Stride length and (B) step width for novice versus expert exoskeleton users across relevant trial types. Individual participants are represented by distinct colors. Asterisk signifies $p < 0.05$.

8e-7). Expert users were 7.7° more plantarflexed when assisted than when unassisted (p = 6e-4). In general, the application of plantarflexion torque from 26.7% to 62.7% stride resulted in greater ankle plantarflexion throughout the gait cycle (Fig. 2A). Unassisted ankle angle at 55% stride did not significantly change with expertise (p = 0.4).

All experts slowed their mid-stride ankle angular velocity (Fig. 2D-E). Expert walking with assistance corresponded to an angular velocity at 50% stride that was 39.2°/s slower than that of novices (p = 6e-4). With training, assisted angular velocity at 50% stride approached that of unassisted walking (Fig. 2D-E). Assistance resulted in a 66.2°/s speed increase during initial exposure (p = 2e-6) and 27.0°/s increase from baseline during final exposure (p = 2e-4). Expert ankle angular velocity without assistance was also 12.7°/s increased from baseline (p = 0.01).

Experts also shifted ankle kinematics to delay timing of toe-off. This shift was reflected in the later timing of peak plantarflexion and dorsiflexion angles, peak plantarflexion velocity, and transition times between plantarflexion and dorsiflexion for both angle and velocity profiles. In addition to the inconsistencies in peak dorsiflexion timing described previously, the transition from plantarflexion to dorsiflexion could not be reliably reported as differences in exoskeleton fitting across sessions caused artificial shifts in ankle angle at heel strike for some participants. Therefore, we focused analysis on the timing of peak plantarflexion angle and peak plantarflexion velocity.

Peak plantarflexion angle shifted later in stride as participants adapted to exoskeleton assistance (Fig. 2C, Table 1). Expertise corresponded to a peak plantarflexion angle 1.5% or 40 ms later in stride (p = 0.01 and p = 4e-4, respectively). Changes in peak plantarflexion timing approached participants' unassisted baseline with training (Fig. 2C): from 3.0% or 50 ms earlier on initial exposure (p = 0.003 and p = 3e-6, respectively) to 1.5% or 6 ms earlier on final exposure (p = 0.02 and p = 1, respectively). Peak plantarflexion timing during unassisted walking did not significantly change with expertise (p = 0.7 and p = 0.06 with and without stride normalization, respectively).

Peak ankle angular velocity also consistently shifted later in stride as people adapted to assistance, by an average of 1.2% stride or 46 ms (Fig. 2F, Table 1, p = 0.01 and p = 5e-4, respectively). As users adapted, their peak velocity timing during assisted gait approached their baseline timing during unassisted gait: from 2.0% or 53 ms earlier on initial exposure to 0.8% or 7 ms earlier on final exposure (Fig. 2F, p = 0.004, p = 4e-4, p = 0.3, p = 0.9, respectively). Peak velocity timing during unassisted walking did not significantly change with expertise (p = 0.1 and p = 0.09 with and without stride normalization, respectively).

All experts increased their stride length such that, on average, assisted strides were 6.0 cm longer after training (Table 1, Fig. 3A, p = 0.02). Compared to walking in normal shoes, assistance resulted in a 4.1 cm shortening of stride for novices and a 1.9 cm lengthening of stride for experts (Fig. 3A, p = 0.01, p = 0.9, respectively).

Step width decreased significantly with training. Expertise resulted in a 4.6 cm narrowing of step width when walking with assistance (Table 1, Fig. 3B, p = 0.005). Expertise also corresponded to a 2.4 cm narrowing of step width when walking without assistance (Fig. 3B, p = 0.04). After sufficient

TABLE I. BIOMECHANICAL GAIT FEATURES (MEAN ± STANDARD DEVIATION) DURING ASSISTED WALKING PRE- AND POST- ADAPTATION.

Gait Features	Novice	Expert	*p*
Ankle angle at 55% stride (°)	2.7 ± 5.4	-3.0 ± 4.0	0.01
Peak ankle angle time (% stride)	67.0 ± 1.3	68.7 ± 0.8	0.01
Ankle angular velocity at 50% stride (°/s)	31.5 ± 21.6	-7.7 ± 16.6	6e-4
Peak ankle angular velocity time (% stride)	62.1 ± 1.2	64.0 ± 0.6	0.01
Stride length (m)	1.31 ± 0.07	1.37 ± 0.10	0.02
Step width (m)	0.18 ± 0.03	0.13 ± 0.03	0.005
Peak med. gastroc. activity (%)	102.5 ± 14.1	100.4 ± 14.8	0.6
Peak lat. gastroc. activity (%)	83.0 ± 24.8	77.5 ± 18.5	0.5
Peak soleus activity (%)	65.7 ± 10.0	66.0 ± 10.8	0.9
Peak tib. ant. activity (%)	127.3 ± 29.7	110.6 ± 14.5	0.03
Peak rectus fem. activity (%)	122.8 ± 31.0	97.7 ± 8.9	0.02
Peak vastus med. activity (%)	92.2 ± 21.5	95.9 ± 9.5	0.7
Peak biceps fem. activity (%)	130.3 ± 40.7	112.4 ± 46.9	0.1
Peak semiten. activity (%)	91.6 ± 22.5	93.2 ± 14.8	0.7

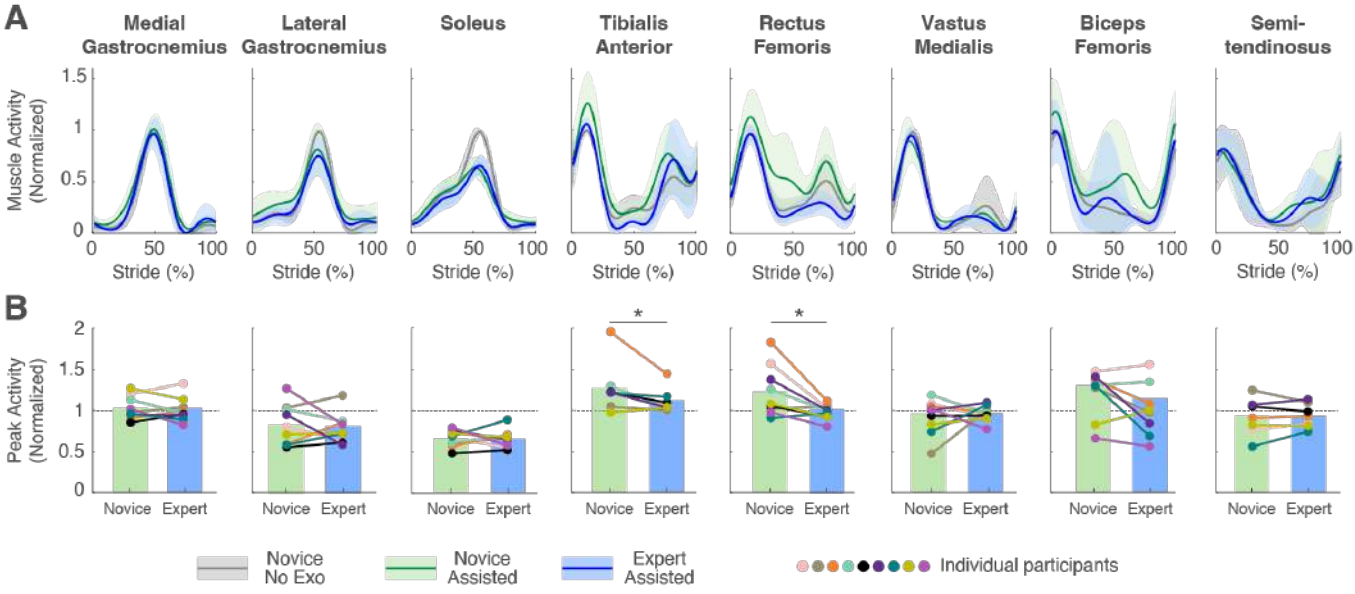


Fig. 4. Changes in muscle activity between novice and expert exoskeleton users. (A) Profiles of recorded muscle activity, averaged across subjects and between legs. All profiles are normalized to values from walking without exoskeletons. Green and blue graphs represent novice and expert exoskeleton-assisted trials, respectively. Gray curves represent novices walking with no exoskeleton. Shaded regions show 95% confidence interval. (B) Changes in peak magnitude of normalized muscle activity with expertise. Individual participants are represented by distinct colors.

training, assisted step width approached baseline values of walking in normal shoes. Initially, assisted steps were 5.0 cm wider than in no-exoskeleton gait ($p = 1e\text{-}4$) and, ultimately, only 0.3 cm wider ($p = 1$).

Some differences in muscle coordination patterns were observed between novice and expert exoskeleton users. The strategy to reduce energy consumption by offloading muscles assisted by the exoskeleton was not unique to experts, reflecting results from prior short duration studies [6,14–17]. In this dataset, peak muscle activity was similar between novices and experts for the medial gastrocnemius, lateral gastrocnemius, soleus, vastus medialis, and semitendinosus (Fig. 4, Table 1). Novices had relatively high activation in the tibialis anterior, rectus femoris, and biceps femoris compared to walking without an exoskeleton, indicating high stiffness throughout the leg. Experts generally reduced this stiffness via lowered activity of the rectus femoris (122.8% vs. 97.7%, $p = 0.02$) and tibialis anterior (127.4% vs. 110.6%, $p = 0.03$). Activity in the biceps femoris also decreased, though this effect was not statistically significant (130.3% vs. 112.4%, $p = 0.1$). Inter-subject variability of muscle coordination patterns was high overall, and trends of changing peak activity were not consistent across participants (Fig. 4B).

Discussion

We identified several biomechanical gait changes that occurred as novice exoskeleton users adapted to plantarflexion assistance. Changes in ankle kinematics and spatial gait features were highly consistent across participants. Changes in muscle coordination patterns were more variable, but the tendency for experts to decrease co-contraction throughout the leg appeared meaningful. Most reported changes emerged later in training than has previously been tested [14,16,17], indicating the importance of sufficient exposure to capture behaviors emerging over long or unknown timescales. The gait features we identified can be monitored and targeted in real time using wearable sensors and biofeedback, making them promising tools to elicit energetically efficient gait behaviors in new exoskeleton users.

Kinematic adaptations appeared to improve the efficiency of push-off. Novices generated positive plantarflexion velocity as exoskeleton torque was rising, causing plantarflexor muscles and tendons to shorten before significant power was needed for toe-off. In contrast, experts actively dorsiflexed, generating negative work, during this portion of stride (Fig. 2). Experts' lower metabolic cost is likely explained in part by eccentric muscle contractions generating force more efficiently than concentric contractions, and lengthening Achilles tendons enabling greater elastic energy storage and release [2,19].

Changes in step length and width throughout training could reflect task priorities shifting from maintaining balance to minimizing energy cost. Optimization of foot placement typically accounts for several objectives, including energy cost, stability, and maneuverability [20,21]; each objective may progress with a unique timescale [6,22]. For these participants, adaptations in step frequency variability—an indicator of dynamic balance [23]—occurred twice as quickly as adaptations in step frequency [6]. Participants may have initially responded to torque-induced perturbations of their typical gait by placing their feet further apart mediolaterally and closer to their base of support anteroposterially [21,24]. Once balance was more easily maintained, participants may have reduced step width to minimize the energetic cost of redirecting center of mass velocity during step-to-step transitions [21] and increased step length to mitigate the high energetic penalty of swing [25].

With experience, most gait features shifted toward participants' baseline values from unassisted or no-exoskeleton walking. Expert exoskeleton users reduced disruptions to gait where no energetic benefit was provided: increased plantarflexion throughout stride, wider stance, shorter steps, and greater co-contraction for stabilization. Simultaneously, experts preserved exoskeleton-induced gait changes that provided energetic benefits, namely offloading plantarflexor activity and stretching the plantarflexor muscle-tendon units before a powerful push-off. It should be further explored if this trend persists for groups other than healthy young adults, whose baseline gait patterns may be less energetically optimal.

Our findings suggest that short bouts of walking may be sufficient for individualization of desired exoskeleton-assisted gait behaviors. For each participant, step length and width generally returned to values observed during no-exoskeleton pre-test trials (Fig. 3). Experts' step lengths consistently exceeded baseline values by an average of 2 cm, likely due to the increased penalty of swing with the exoskeleton's added distal mass and medial envelope. Kinematic features did not revert to participants' initial values from unassisted walking, but did consistently progress toward the approximate average of unassisted and assisted baseline values (Fig. 2). Supplemental analysis showed that kinematic changes plateaued before the final experimental session, suggesting that these values would change minimally with additional training, and that the remaining offset is due to limits created by human-exoskeleton interaction. Given the high inter-subject variability of absolute gait outcomes and the consistency of trends across trial types (Fig. 2-3), we believe that prompting changes toward one's own unassisted or no-exoskeleton baseline will likely be more effective than trying to induce any absolute gait outcome.

A portion of the observed gait changes were attributed to learning to walk while wearing the exoskeletons alone. Gait compensations to the added medial envelope and mass of the device presented in both unassisted and assisted walking trials (Fig. 3). This suggests that training to adapt to wearing a new device is partially separable from training to adapt to assistance. Beginning with unassisted training might prove more tractable for novices learning to use exoskeletons that are particularly large, heavy, or restrictive of typical joint kinematics.

This study is limited by high inter-subject variability and a relatively small sample size. Findings may vary with additional or demographically distinct participants. We could not reliably calculate an ideal magnitude of change for each gait outcome, if such an absolute measure exists. However, the consistency of trends across participants strongly indicates that these are important dimensions for people to adapt along. Analyzing motion capture data could provide more detailed insights into adaptations occurring throughout the leg, and reveal more about the complex mechanisms underlying reduced metabolic cost of walking with exoskeletons.

Further research is needed to evaluate the generalizability of these findings. The observed trends reflect behavior from one lightweight, torque-controlled ankle exoskeleton assisting plantarflexion. Use of an ankle exoskeleton with a different mechanical design and control will likely affect the magnitude of changes between novices and experts. However, we expect the direction of the observed trends to remain consistent for other ankle exoskeletons given the similarity between early behavior in this study and outcomes of prior ankle exoskeleton research [6,14–17]. The spatial gait changes observed in this study were also consistent with the metabolic determinants of step length and width in simple walking models when accounting for the added penalty of distal mass and medial obstructions [21,25], suggesting that similar effects may occur during adaptation to other types of wearable robots.

Our future work will coach novice exoskeleton users to exhibit the expert gait biomechanics identified in this study. Kinematic, spatiotemporal, electromyographic, and metabolic changes co-occurred throughout the experimental protocol, but an immediate metabolic benefit from adopting the identified gait changes has not been demonstrated. Differences in timescales between neuromechanical and metabolic adaptations in this dataset [6,7] and others [22,26] suggest complex mechanisms of reducing whole-body metabolic cost. If it is shown that large energetic benefits can be extracted without extensive self-guided gait exploration, this could prove an effective technique for expediting required exoskeleton training times. Future work can additionally apply this approach to characterize biofeedback targets for expert use of a wide range of assistive devices.

Conclusions

There are consistent biomechanical differences in how people walk with ankle exoskeletons at the beginning and end of motor adaptation. Identified changes included dorsiflexing more preceding a later push-off, taking narrower and longer steps, and mitigating high levels of co-contraction throughout the leg. This study reveals that relatively subtle changes in human-exoskeleton interaction can correspond to large changes in energy cost of walking. However, these improvements take a long time for healthy young adults to discover when only subject to natural gait variability. Leveraging our results to coach new exoskeleton users toward the identified gait changes could reduce the time needed for people to extract maximum benefit from exoskeletons. Improving human-device interaction during training may increase user acceptance of exoskeletons for those who could benefit from them most.

Acknowledgment

We thank K. L. Poggensee for her open-source data sharing of this biomechanical dataset.

References

[1] L. M. Mooney and H. M. Herr, "Biomechanical walking mechanisms underlying the metabolic reduction caused by an autonomous exoskeleton," *Journal of NeuroEngineering and Rehabilitation*, vol. 13, no. 1, p. 4, Jan. 2016, doi: 10.1186/s12984-016-0111-3.

[2] R. W. Jackson, C. L. Dembia, S. L. Delp, and S. H. Collins, "Muscle-tendon mechanics explain unexpected effects of exoskeleton assistance on metabolic rate during walking," *J Exp Biol*, vol. 220, no. 11, pp. 2082–2095, Jan. 2017, doi: 10.1242/jeb.150011.

[3] K. L. Poggensee and S. H. Collins, "Lower limb biomechanics of fully trained exoskeleton users reveal complex mechanisms behind the reductions in energy cost with human-in-the-loop

optimization," *Front. Robot. AI*, vol. 11, p. 1283080, Jan. 2024, doi: 10.3389/frobt.2024.1283080.

[4] A. Crawford, H. H. Hollingsworth, K. Morgan, and D. B. Gray, "People with mobility impairments: Physical activity and quality of participation," *Disability and Health Journal*, vol. 1, no. 1, pp. 7–13, Jan. 2008, doi: 10.1016/j.dhjo.2007.11.004.

[5] P. W. Franks, G. M. Bryan, R. M. Martin, R. Reyes, A. C. Lakmazaheri, and S. H. Collins, "Comparing optimized exoskeleton assistance of the hip, knee, and ankle in single and multi-joint configurations," *Wearable Technol.*, vol. 2, p. E16, 2021, doi: 10.1017/wtc.2021.14.

[6] S. J. Abram *et al.*, "General variability leads to specific adaptation toward optimal movement policies," *Current Biology*, vol. 32, no. 10, pp. 2222–2232, May 2022, doi: 10.1016/j.cub.2022.04.015.

[7] K. L. Poggensee and S. H. Collins, "How adaptation, training, and customization contribute to benefits from exoskeleton assistance," *Science Robotics*, vol. 6, no. 58, pp. 1–13, Sep. 2021, doi: 10.1126/scirobotics.abf1078.

[8] J. M. VanSwearingen and S. A. Studenski, "Aging, Motor Skill, and the Energy Cost of Walking: Implications for the Prevention and Treatment of Mobility Decline in Older Persons," *J Gerontol A Biol Sci Med Sci*, vol. 69, no. 11, pp. 1429–1436, Nov. 2014, doi: 10.1093/gerona/glu153.

[9] A. Lakmazaheri, S. Song, B. B. Vuong, B. Biskner, D. M. Kado, and S. H. Collins, "Optimizing exoskeleton assistance to improve walking speed and energy economy for older adults," *J NeuroEngineering Rehabil*, vol. 21, no. 1, p. 1, Jan. 2024, doi: 10.1186/s12984-023-01287-5.

[10] M. Olson, T. E. Lockhart, and A. Lieberman, "Motor Learning Deficits in Parkinson's Disease (PD) and Their Effect on Training Response in Gait and Balance: A Narrative Review," *Front. Neurol.*, vol. 10, p. 62, Feb. 2019, doi: 10.3389/fneur.2019.00062.

[11] C. Sampaio-Baptista, Z.-B. Sanders, and H. Johansen-Berg, "Structural Plasticity in Adulthood with Motor Learning and Stroke Rehabilitation," *Annu. Rev. Neurosci.*, vol. 41, no. 1, pp. 25–40, Jul. 2018, doi: 10.1146/annurev-neuro-080317-062015.

[12] J. C. Selinger, J. D. Wong, S. N. Simha, and J. M. Donelan, "How humans initiate energy optimization and converge on their optimal gaits," *Journal of Experimental Biology*, vol. 222, no. 19, Oct. 2019, doi: 10.1242/jeb.198234.

[13] D. Sternad, "It's not (only) the mean that matters: variability, noise and exploration in skill learning," *Current Opinion in Behavioral Sciences*, vol. 20, pp. 183–195, Apr. 2018, doi: 10.1016/j.cobeha.2018.01.004.

[14] K. E. Gordon and D. P. Ferris, "Learning to walk with a robotic ankle exoskeleton," *Journal of Biomechanics*, vol. 40, no. 12, pp. 2636–2644, Jan. 2007, doi: 10.1016/j.jbiomech.2006.12.006.

[15] G. S. Sawicki and D. P. Ferris, "Mechanics and energetics of level walking with powered ankle exoskeletons," *Journal of Experimental Biology*, vol. 211, no. 9, pp. 1402–1413, May 2008, doi: 10.1242/jeb.009241.

[16] S. Galle, P. Malcolm, W. Derave, and D. De Clercq, "Adaptation to walking with an exoskeleton that assists ankle extension," *Gait & Posture*, vol. 38, no. 3, pp. 495–499, Jul. 2013, doi: 10.1016/j.gaitpost.2013.01.029.

[17] S. Song, C. A. Haynes, and J. Cortney Bradford, "Novice users' brain activity and biomechanics change after practicing walking with an ankle exoskeleton," *IEEE Trans. Neural Syst. Rehabil. Eng.*, pp. 1–1, 2024, doi: 10.1109/TNSRE.2024.3423696.

[18] J. Zhang *et al.*, "Human-in-the-loop optimization of exoskeleton assistance during walking," *Science*, vol. 356, no. 6344, pp. 1280–1284, Jun. 2017, doi: 10.1126/science.aal5054.

[19] T. J. Roberts, "The integrated function of muscles and tendons during locomotion," *Comparative Biochemistry and Physiology Part A: Molecular & Integrative Physiology*, vol. 133, no. 4, pp. 1087–1099, Dec. 2002, doi: 10.1016/S1095-6433(02)00244-1.

[20] H. J. Huang and A. A. Ahmed, "Tradeoff between Stability and Maneuverability during Whole-Body Movements," *PLoS ONE*, vol. 6, no. 7, p. e21815, Jul. 2011, doi: 10.1371/journal.pone.0021815.

[21] J. M. Donelan, R. Kram, and A. D. Kuo, "Mechanical and metabolic determinants of the preferred step width in human walking," *Proc Biol Sci*, vol. 268, no. 1480, pp. 1985–1992, Oct. 2001, doi: 10.1098/rspb.2001.1761.

[22] S. A. Brinkerhoff *et al.*, "The dual timescales of gait adaptation: Initial stability adjustments followed by subsequent energetic cost adjustments," *Journal of Experimental Biology*, p. jeb.249217, Oct. 2024, doi: 10.1242/jeb.249217.

[23] C. K. Balasubramanian, R. R. Neptune, and S. A. Kautz, "Variability in spatiotemporal step characteristics and its relationship to walking performance post-stroke," *Gait & Posture*, vol. 29, no. 3, pp. 408–414, Apr. 2009, doi: 10.1016/j.gaitpost.2008.10.061.

[24] L. Hak, H. Houdijk, P. J. Beek, and J. H. Van Dieën, "Steps to Take to Enhance Gait Stability: The Effect of Stride Frequency, Stride Length, and Walking Speed on Local Dynamic Stability and Margins of Stability," *PLoS ONE*, vol. 8, no. 12, p. e82842, Dec. 2013, doi: 10.1371/journal.pone.0082842.

[25] J. Doke, J. M. Donelan, and A. D. Kuo, "Mechanics and energetics of swinging the human leg," *Journal of Experimental Biology*, vol. 210, no. 13, pp. 2399–2399, Jul. 2007, doi: 10.1242/jeb.006767.

[26] F. L. Haufe, A. M. Kober, P. Wolf, R. Riener, and M. Xiloyannis, "Learning to walk with a wearable robot in 880 simple steps: a pilot study on motor adaptation," *J NeuroEngineering Rehabil*, vol. 18, no. 1, p. 157, Dec. 2021, doi: 10.1186/s12984-021-00946-9.

Implementation and Validation of a Data-Driven Variable Impedance Controller on the Össur Power Knee

T. Kevin Best[1], C. Andrew Seelhoff[2], and Robert D. Gregg[1,2]

***Abstract*—While prototype prostheses and control algorithms have demonstrated compelling clinical benefits in research laboratories, studies with commercially-available robotic prostheses have often failed to demonstrate similar benefits for users, limiting their adoption into mainstream clinical practice. This work is a step towards addressing this shortcoming by presenting the implementation of a phase-based variable impedance controller on the commercially-available Össur Power Knee™ for walking and sit/stand tasks. We show that, through preliminary experiments with N=4 high-mobility above-knee prosthesis users, the Power Knee under our controller can produce clear clinical benefits compared to the users' prescribed prostheses. In sitting and standing, users demonstrated generally increased leg-loading symmetry and speed with the Power Knee, indicating easier motions with less over-use of the sound limb. In walking, users demonstrated improved gait with the Power Knee, including increases in toe clearance and early-stance knee flexion. These positive results are similar to our previous work on prototype hardware, demonstrating our controller's hardware generalization and its potential for generating clinical benefits with commercial prostheses. These results are a step towards a promising future in which commercially-available robotic prostheses provide users with concrete clinical benefits.**

I. Introduction

Robotic knee prostheses have been slow to gain widespread adoption in clinical practice, despite their many promised benefits [1], [2]. In research laboratories, prototype robotic knee-ankle prostheses have been shown to enable more normative joint biomechanics [3]–[5], improve inter-limb symmetry [3], [6]–[8], reduce energy expenditure [9], [10], and, in some cases, improve user endurance [11]. However, translating these technologies into clear clinical benefits with commercialized robotic knee prostheses, such as the Össur Power Knee™ (Reykjavík, Iceland), has historically been a challenge [12]–[14].

In addition to energy, weight, noise, and cost concerns, the limited adoption of robotic knees in clinical practice is likely due to challenges in designing their control systems. A commercial prosthesis must be extremely robust, predictable, and easy to use, often leading manufacturers to elect to use simple and conservative discrete control approaches, such as the seminal finite state machine (FSM) impedance controller [15]. An FSM impedance controller uses distinct impedance parameters in a sequence of discrete gait phases, which are uniquely defined for each discrete activity mode. While these types of controllers can be quite effective in their intended conditions, optimal performance often requires extensive tuning by trained experts [16]. This poses a problem for clinical deployment, as clinicians often lack both the time and technical expertise to optimally configure these controllers, potentially resulting in sub-optimal configurations and subsequent user outcomes. It is likely that, even with the same hardware, better user outcomes could be more consistently achievable either through automated parameter tuning [17], [18], or by using alternative control strategies with lesser tuning requirements. Additionally, better outcomes may be achievable with controllers that can automatically adapt to continuous variations in the user's activity (*e.g.,* walking speed or ground incline).

Our research group has worked towards addressing these challenges through the development of a continuous, data-driven control framework known as hybrid kinematic impedance control (HKIC). These controllers encode information from large biomechanics datasets of able-bodied (AB) individuals performing various activities of daily living (ADLs) [19]–[21], utilizing continuous gait phase and task estimates to synchronize with the user and to adapt prosthesis behavior to suit the current terrain. We have applied this control framework for walking at variable speeds and inclines [5], [22], stair ascent and descent at different step heights [23], [24], and transitioning to/from sitting with different chair heights [8]. When deployed on our high-torque, low-inertia prototype powered knee-ankle prosthesis [25], these controllers have been shown to produce clinical benefits such as biomimetic joint mechanics [5], [8], [23], improved symmetry [8], reduced toe stubbing [26], and improved endurance [11].

This data-driven control approach is attractive for use in clinical settings, as it would, in theory, allow users to realize these clinical benefits across a continuum of ambulation tasks without imposing a tuning burden on the clinician. It must be shown, however, that the controller's benefits persist when deployed on a clinically-ready robotic prosthesis rather than on our prototype prosthesis. The translation of benefits is not guaranteed, as commercially-available robotic prostheses have many more practical design constraints than research prototypes, such as cost, weight, reliability, manufacturability, and more. These opposing constraints often result in a device that is more difficult to control due to more limited sensing and more complicated drivetrain dynamics. Further, robotic knee prostheses are most often paired with passive ankle/foot prostheses. The lack of an actuated ankle joint likely affects the overall behavior of the prosthesis during some activities, potentially affecting the efficacy of our controller.

This material is based on work supported by the National Institute of Child Health & Human Development of the National Institutes of Health under Award R01HD094772 and by the National Science Foundation under the Graduate Research Fellowship DGE 1841052. Prosthetic hardware and initial financial support were provided by Össur hf (Reykjavík, Iceland).

[1]Department of Robotics and [2]Department of Mechanical Engineering, University of Michigan, Ann Arbor, MI 48109. Contact: {tkbest, rdgregg}@umich.edu.

Therefore in this work, we detail and validate the deployment of our phase-based data-driven HKIC controller on the latest generation Össur Power Knee (PKA01) for sit/stand and level-ground walking tasks. After reviewing the Power Knee hardware and our HKIC controller from [5], [8], [11], we describe the updates made to the controller that account for the Power Knee's lack of ankle actuation and its non-negligible actuator dynamics. We then describe a series of experiments with N=4 high-mobility above-knee prosthesis users that highlight the clinical benefits of our controller on Power Knee compared with the users' prescribed passive devices in a series of stand-walk-sit experiments. Our preliminary results show that, despite different hardware properties compared to our research prosthesis, many of our controller's benefits persist across devices. Specifically, we demonstrate an increase in sit/stand speed and loading symmetry, similar to [8]. We also show improved walking gaits with increased early stance knee flexion and toe clearance. However, we also highlight instances in which the lack of an actuated ankle adversely affects the controller's biomimicry, such as in sit/stand. Overall, our results indicate our controller's ability to generalize to commercially-viable prostheses while retaining most of its clinical benefits.

II. Related Work

Previous research has tested the clinical benefits of commercially-available robotic prostheses, including earlier generations of the Össur Power Knee. Highsmith et al. presented a case study investigating sitting, standing, and walking on the first generation Power Knee [12]. The authors found that, for their participant, the Power Knee increased hip moment symmetry while sitting down compared to a C-Leg. However, no substantial symmetry improvement was observed at the knee joint or at all during standing. Wolf et al. similarly investigated the biomechanical differences in sit/stand when using the second generation Power Knee and the C-Leg, but observed "few differences between components and no effect on the intact limb" [13].

Most recently, Hafner et al. compared clinical outcomes between mechanical, microprocessor (Össur Rheo Knee™ II), and powered (second generation Össur Power Knee) prosthetic knees in an extensive 14 month randomized crossover trial with 12 participants [14]. The authors found that the Rheo Knee significantly improved the participants' mobility compared to mechanical knees and all of the participants elected to keep their Rheo Knee after the study. With the Power Knee, however, users demonstrated worse performance in the laboratory-based outcomes and the authors noted "high attrition of subjects", suggesting that users were unhappy with the powered device.

These three studies were unable to demonstrate compelling clinical benefits with the early models of the Power Knee, perhaps due to limitations in the prosthetic hardware, control software, or both. New, lighter and more compact commercialized robotic knees are now available, which may enable stronger clinical benefits. In this work therefore, we aim to again investigate the potential clinical benefits of commercialized robotic knees, but this time with modern hardware and a fundamentally different control approach that has previously shown benefits on a prototype prosthesis.

III. Prosthesis and Control System

A. Hardware Overview

In this study, we utilize the latest generation Power Knee from Össur (model PKA01), which is a commercialized robotic knee prosthesis. The drivetrain of the Power Knee consists of a brushless DC motor, a harmonic drive transmission, and a compliant linkage that connects the transmission output to the knee joint. The torque-angle relationship of the compliant linkage is nonlinear, stiffening under increasing deflection. The knee assembly weighs 2.7 kg (including battery) and the joint has a 120 deg range of motion. The removable lithium ion battery powers the motor and the embedded control electronics. The sensing suite includes joint and motor position encoders, a shank-mounted inertial measurement unit, and an array of ground reaction force (GRF) hall-effect sensors [27].

Based on the manufacturer's recommendations, we paired the Power Knee with the Pro-Flex® carbon fiber ankle-foot prosthesis. We used the Low Profile (LP) variety for all participants in order to maximize compatibility with different user heights and limb geometries. The appropriate size and category foot was used for each participant based on the sizing guidelines in the Pro-Flex LP Catalog. For a representative participant with average height and weight, the entire prosthesis, including the Power Knee, pylon, foot, shoe, and other hardware components, weighed 3.9 kg.

B. HKIC Controller Overview

In place of the Power Knee's stock control software, we also deployed a simplified version of our multi-activity phase-based HKIC controller [11], [28] for sit/stand and walking on the Power Knee (Fig. 1). This controller integrates the sit/stand and walk controllers from our research group's prior work [5], [8], using continuous, data-driven models of joint impedance and kinematics to produce biomimetic joint behavior for various activities. Our controller comprises two high-level modes: $\mu \in \{\text{Sit/Stand, Walk}\}$, which are automatically selected via a Finite State Machine (FSM). Simple, explainable transition rules based on the user's thigh motion control the transitions between modes (see Fig. 1 in [8] for further detail). A time-based interpolation between modal torque commands is used to smooth transitions between control modes over 100 ms.

In addition to the discrete mode μ, the controller calculates a continuous task variable χ and a continuous phase variable ϕ to evaluate the kinematic and impedance models (Fig. 1). In this initial translation to the Power Knee, we only include walking speed in the task variable χ, though other variables such as ground incline could be included in future iterations [5]. The phase variable $\phi \in [0, 1]$ quantifies the user's progression through either a walking gait cycle [5] or sitting and standing motions [8]. We calculate ϕ based on algebraic mappings of the user's thigh angle θ_{th}, giving

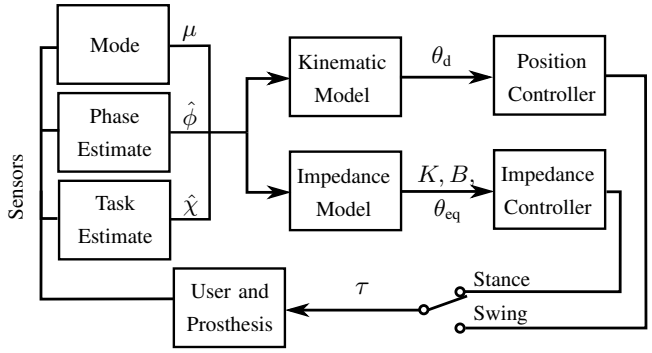


Fig. 1. A block diagram of the Hybrid Kinematic Impedance Controller used in this work. Real-time estimates of gait phase $\hat{\phi}$, task variation $\hat{\chi}$ (*i.e.* walking speed), and control mode μ (*i.e.* Walk vs. Sit/Stand) define desired joint impedance parameters K, B, θ_{eq} and joint angles θ_d using data-driven models. The torque commands τ are calculated using an impedance controller during stance or a position controller during swing.

them indirect volitional control over the prosthesis's behavior. The parameters used to calculate the phase variables adjust to the current task, allowing ϕ to appropriately parameterize the motion regardless of the varying thigh kinematics associated with different speeds and chair heights [19], [20].

While the user is in stance (which includes the entirety of Sit/Stand mode), the knee torque set point τ is calculated based on the joint angle θ_j and velocity $\dot{\theta}_j$ using impedance control:

$$\tau = K(\phi, \chi, \mu)\,[\theta_{eq}(\phi, \chi, \mu) - \theta_j] - B(\phi, \chi, \mu)\dot{\theta}_j, \quad (1)$$

where the stiffness K, damping B, and equilibrium angle θ_{eq} are functions of the phase variable ϕ, task variable χ, and mode μ. These parametric functions are fit offline to able-bodied training datasets [19], [21] such that (1) produces biomimetic joint torques when subjected to biomimetic joint kinematics. Details on the impedance model can be found in [5], [8].

Similarly, we use position control during the swing phase, where the desired joint angle θ_d and velocity $\dot{\theta}_d$ are modeled as functions of ϕ, χ, and μ. This kinematic model is likewise generated based on able-bodied kinematic data via convex optimization, with details in [29]. The knee torque is calculated through a proportional-derivative position controller as

$$\tau = k_p[\theta_d(\phi, \chi, \mu) - \theta_j] + k_d[\dot{\theta}_d(\phi, \chi, \mu) - \dot{\theta}_j], \quad (2)$$

where k_p and k_d are proportional and derivative gains, respectively. These gains are held constant across users.

C. HKIC Modifications for the Power Knee

In our previous work, our controllers have been mainly developed and evaluated using a prototype quasi-direct drive knee-ankle prosthesis [25]. While the Power Knee is distinct from this prototype prosthesis in many ways, there are two differences that are most relevant for control: 1) the Power Knee's drivetrain dynamics are more complex, and 2) the Power Knee does not have an actuated ankle joint. These differences impact how the knee joint should be controlled. We detail the modifications we made to our HKIC controller in response to each of these distinctions in turn below.

1) Low-Level Drivetrain Dynamics Compensation: Historically, the simple drivetrain dynamics of our original prototype prosthesis have allowed us to accurately control the joint impedance by assuming a proportional relationship between motor current and joint torque via the gear ratio and the motor's torque constant [25]. These assumptions are invalid on the Power Knee, as the design's high gear ratio and nonlinear series elasticity add substantial complexity to the drivetrain dynamics. For similar devices with these complex dynamics, such as the second generation Open-Source Leg [30], it has been shown that the motor inertia, series elasticity, and friction effects can introduce errors in the rendered joint impedance and ultimately errors in the produced joint torque [31], [32]. Further, it is well known in control theory that series elasticity can introduce stability problems when attempting to directly control joint position via non-collocated joint feedback [33]. Therefore, modifications to our original implementation are necessary in order to ensure accurate and stable impedance control on the Power Knee.

We utilize the approach presented in [32] to calculate optimal motor feedback gains that account for the drivetrain dynamics and minimize the rendered impedance error. Instead of calculating a motor torque setpoint using (1) and (2) directly, we use a collocated motor-space controller of the form

$$\tau = K_1(\theta_{eq,m} + \theta^* - \theta_m) - B_1\dot{\theta}_m, \quad (3)$$

where K_1 and B_1 are feedback gains that depend on the desired impedance K and B, the system parameters (inertia, viscous damping, etc.), and the transmission stiffness at the current transmission deflection. The motor states θ_m and $\dot{\theta}_m$ are decoupled from the joint states θ_j and $\dot{\theta}_j$ via the transmission elasticity. An offset angle θ^* is included to account for the transmission's nonlinear torque-angle relationship. Details on the calculation of K_1, B_1 and θ^* can be found in [32].

2) Unactuated Ankle Joint: Our previous work was performed using a prosthesis with an actuated ankle joint, allowing the ankle to behave biomimetically during all tasks. In contrast, the Pro-Flex foot used in conjunction with the Power Knee has fixed elastic properties that relate its ankle kinematics to ankle torques, constraining the space of producible behaviors. For level-ground walking, this added biomechanical constraint has comparatively little effect, as the Pro-Flex LP prosthesis is designed to primarily emulate level-ground walking biomechanics. For other activities however, normative ankle biomechanics deviate from this constraint curve in the torque-angle space, making it impossible for the passive prosthetic foot to replicate them.

One such activity in which the ankle biomechanics deviate substantially from the constraint curve is sit/stand. Average able-bodied seated data shows a moderately dorsiflexed ankle joint with zero ankle torque [21] (Fig. 2a). With a passive foot prosthesis and an unarticulated ankle joint however, the user cannot reach this low-torque, dorsiflexed configuration. They must instead choose between either a flat foot configuration with a vertical shank (Fig. 2b) or a non-flat foot configuration with an inclined shank (Fig. 2c).

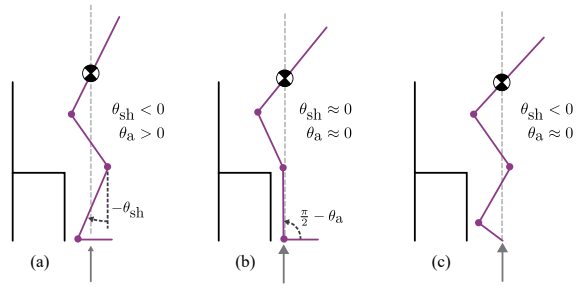


Fig. 2. A planar model of a person's foot, shank, thigh, and torso during the sit-to-stand motion in three possible configurations. The ground reaction force (gray arrow) is applied at the CoP, coinciding with the user's center of mass based on a quasi-static assumption. Tile (a) shows the nominal joint configurations used by able-bodied individuals, with $\theta_{sh} < 0, \theta_a > 0$, and the CoP located posterior to the knee joint center. Tiles (b) and (c) show the possible sit-to-stand configurations for a person using an above-knee prosthesis with a passive foot ($\theta_a \approx 0$), with either (b) a vertical shank ($\theta_{sh} \approx 0$) or (c) a non-flat foot ($\theta_{sh} < 0$).

Of the three configurations, the dorsiflexed configuration (Fig. 2a) is the most advantageous, as it allows the user to locate their center of pressure (CoP) posterior to the knee joint center. Assuming minimal anterior/posterior forces, it can be shown that the posterior separation of the CoP relative to the knee joint center prevents the foot/ankle complex from rotating off the ground (*i.e.* pivoting about the heel of the foot) when substantial knee torques are applied. The dorsiflexed configuration also helps prevent foot slipping, as the knee moment is opposed primarily by normal ground reaction forces rather than only by friction.

Of the two configurations available with a passive ankle, the inclined shank configuration (Fig. 2c) is most advantageous, as it does allow the CoP to be posterior to the knee joint, though only briefly. However, it requires the user to balance on the toe of the prosthesis during the motion, which may feel unstable. In our experience, most participants habitually use the configuration in Fig. 2b with their prescribed prostheses.

With a powered knee prosthesis, there is a risk of the applied knee extension torque producing negative consequences when the user elects to use the vertical shank configuration (Fig. 2b). If the CoP is too far anterior, the foot will rotate about the heel, sending the knee center backwards and potentially making the user lose their balance. Additionally, insufficient ground reaction force in this configuration may cause the knee torque to produce foot slipping rather than body weight support.

In response to this limitation caused by the unarticulated ankle joint, we modified our original sit/stand controller to prevent applying knee torques when the user elects to sit with a vertical shank (Fig. 2b). We scale the sit/stand knee stiffness and damping references with a unit logistic function of the user's shank angle θ_{sh}. The logistic mapping is defined as

$$\xi(\theta_{sh}) = \frac{1}{1 + e^{1.5(\theta_{sh}+2)}}, \tag{4}$$

where the angle constants have units of degrees. To prevent closed-loop oscillations that can occur from the interaction between the torque command and θ_{sh}, we low-pass filter θ_{sh} prior to (4). Since users typically adjust their posture slowly before standing, a 1 Hz cutoff frequency is sufficient to filter the signal without causing noticeable delays or response lag. As θ_{sh} increases above 0, the stiffness and damping asymptotically scale to 0, resulting in no knee joint torque. Conversely, as θ_{sh} decreases beyond 0, the logistic function approaches 1 and the stiffness and damping commands remain unchanged.

IV. Experimental Validation

To validate our controller's implementation on the Power Knee and to test for its clinical benefits, we recruited four participants with unilateral above-knee amputations (Table 1) to participate in our study. All participants were strong community ambulators (K4) and did not require mobility aids. The experimental protocol was approved by the University of Michigan Institutional Review Board (HUM00230065) and each participant provided informed consent.

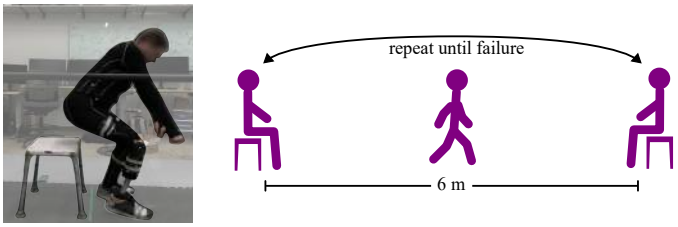
A. Methods

We tested two conditions in this experiment over three sessions, with the participants using either 1) their prescribed prostheses (PRES), or 2) the Power Knee running our HKIC controller (PKNE). Each condition was tested on a separate day to mitigate fatigue effects, and the testing order was randomized to prevent procedural bias. Prior to the experiments, an acclimation day was provided during which the Power Knee prosthesis was fit and aligned to the participant by a certified prosthetist. The appropriate Pro-Flex LP foot was used for each participant based on their weight, activity level, and shoe size. The participant was taught how to use the Power Knee with the novel controller, and provided ample time to practice sitting, standing, and walking. The research team also provided coaching on how to best leverage the device's capabilities. This acclimation session lasted up to four hours.

The remaining two visits were identical aside from the prosthesis used (either PRES or PKNE). First, the participants were allowed to practice sitting, standing, and walking to warm up and re-familiarize themselves with the prosthesis.

TABLE 1
Enrolled Participant Details

Participant	Sex	Age (yrs)	Mass (kg)	Prescribed Prosthesis (Knee/Ankle)	Etiology	Amputation Type	Time Since Amputation (yrs)
TF01	M	23	79	Genium/Triton	Dysvascular Disease	Above Knee	10
TF02	M	25	84	Rheo/Proflex XC	Congenital	Knee Disartic.	24
TF03	M	20	75	Quattro/Shockwave	Cancer	Above Knee	2
TF04	F	42	66	X3/Triton LP	Trauma	Knee Disartic.	6



(a) (b)

Fig. 3. (a) A photo of participant TF01 standing from the first stool during the PKNE condition. (b) A graphical depiction of the incremental shuttle walk test protocol, depicting the participants walking between two stools approximately 6 m apart. Participants repeated walking between the stools until they could no longer keep up with the slowly increasing cued pace.

Visual feedback during sit-stand was provided to allow the participants to practice symmetric limb loading, similar to [8]. This feedback was removed after the warm up period.

Next, the participants completed the main experiment, which involved completing repeated laps of an ambulation circuit consisting of two stools (45 cm tall) located approximately 6 m apart (Fig. 3). The protocol was inspired by the incremental shuttle walk test used to assess fitness in other domains [34], [35]. Handrails were provided along the walkway for safety, but their use was discouraged unless required to prevent a fall. Upon an auditory cue, participants stood up from a stool, walked to the opposite stool, turned around, and sat down to wait until the next cue. The cues were automated and followed this schedule: four cues at 65-second intervals, six at 43.3-second intervals, and eight at 32.5-second intervals, and so on, gradually increasing the minimum average walking pace from 0.1 m/s to 0.15 m/s and 0.2 m/s, respectively. The number of repetitions was chosen such that the total time at each pace was 260 s. Participants were allowed to choose their walking speed, but needed to reach the opposite stool before the next cue. The test ended if a participant failed to reach the stool on time for two consecutive laps.

During the experiments, motion capture and ground reaction force data were recorded (Vicon, Oxford, UK). These data were processed in OpenSim 4.5 (Stanford, CA, USA) using the model from Rajagopal et. al [36] with appropriate modifications made to the prosthetic side inertial properties, similar to [37]. Forceplates were located at each stool, allowing individual measurements of each leg's ground reaction force and inverse dynamics calculations. The walkway was not instrumented, and thus no walking joint kinetics were calculated.

In this work, we are only concerned with the non-rushed portions of the experiment (before the time between cues decreased substantially), as these are most similar to how our controller was previously tested on our prototype hardware. Therefore, we limit our analysis to the first 70 laps of the experiment. These early laps correspond to minimum average walking paces of ≤ 0.4 m/s and thus allow for "leisurely" activity completions without time pressure. Future work will analyze the latter portions of the experiment to investigate how performance changed under time pressure and with fatigue.

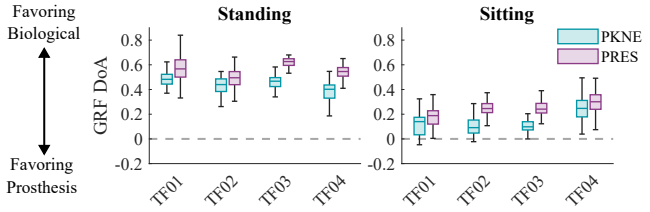


Fig. 4. Boxplots of the mean vertical GRF degree of asymmetry during sitting (left) and standing (right) for each participant. Values closer to zero indicate better GRF symmetry, whereas ± 1 indicate complete asymmetry.

We segmented the experiment data from the first 70 laps into sitting, standing, transitioning, walking, and resting periods based on kinematic and force thresholds. We further divided the walking data into individual gait cycles based on the marker positions using methods from [38]. To examine whether the prosthesis condition had a statistically significant effect on the biomechanical measures of interest, we utilized linear mixed-effects models (LMMs). LMMs were chosen for their ability to include both fixed and random effects, allowing us to account for inter-participant variability. We treated the prosthesis condition (PRES or PKNE) as a fixed effect and the participant as a random intercept. Our null hypothesis posited that there would be no significant difference in these biomechanical measures between the prosthesis conditions, and our significance threshold was set to $\alpha = 0.05$.

B. Results

All participants were able to complete over 100 laps of the circuit with both their prescribed prostheses and the Power Knee, demonstrating the baseline functionality of our HKIC controller. The following subsections present results for the sitting/standing and walking portions of the circuit. For clarity in the presented boxplots, we excluded data points that are considered outliers, specifically those below Q1-1.5×IQR and above Q3+1.5×IQR.

1) Sitting and Standing: On the prototype hardware, our controller previously produced improved ground reaction force (GRF) symmetry [8]. We define the GFR degree of asymmetry DoA as

$$DoA = (F_\mathrm{b} - F_\mathrm{p})/(F_\mathrm{b} + F_\mathrm{p}), \tag{5}$$

where F_b and F_p are the vertical GRFs on the biological and prosthetic limbs, respectively. $DoA = 0$ indicates perfect GRF symmetry, whereas $DoA = 1$ and $DoA = -1$ indicate all force on the biological and prosthetic limbs, respectively. Similar to what was observed with the prototype hardware in [8], the mean GRF loading symmetry was improved in the PKNE condition compared to PRES condition for all participants (Fig. 4). The fit LMM showed an average DoA improvement of 11.6% for standing ($p < 0.001$) and 9.5% in sitting ($p < 0.001$) by the PKNE condition. Both conditions showed better sitting symmetry than standing symmetry.

We also calculated the time the participants took to perform the standing and sitting motions in each lap (Fig. 5). These timings only include the duration of the actual motions, excluding

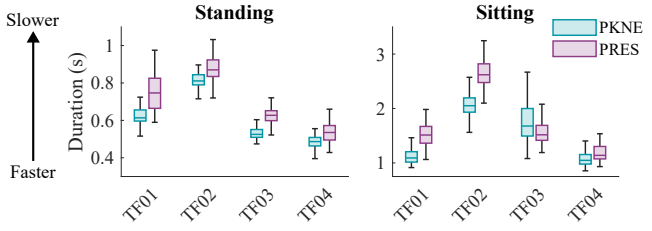


Fig. 5. Boxplots of the average duration of the sitting and standing motions during the experiment for each participant. The PKNE condition was significantly faster on average than the PRES condition.

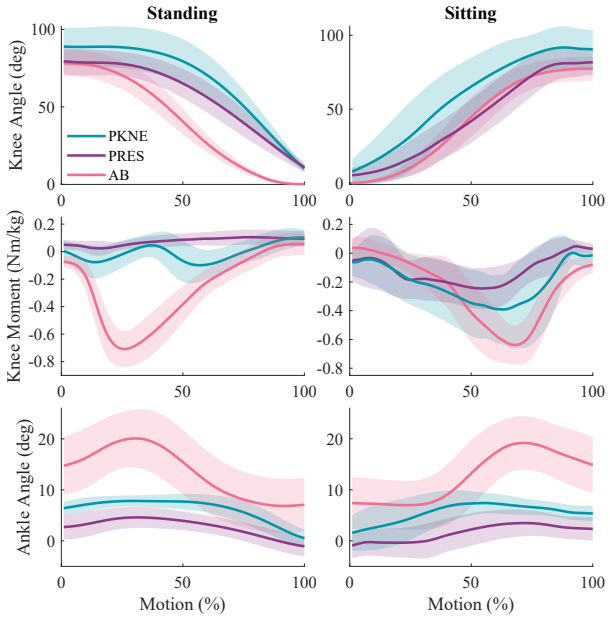


Fig. 6. Inter-participant average prosthetic-side joint kinematics and kinetics while sitting (left) and standing (right). Normative trajectories (AB) from [21] are shown as well for context. Ankle moments are excluded for brevity. Shaded regions represent ± 1 standard deviation.

transitions. On average, the PKNE condition produced faster motions than the PRES condition, with 11.9% ($p < 0.001$) and 13.0% ($p < 0.001$) reductions in standing and sitting times, respectively. Larger variance was observed in sitting, with some participants showing similar speed in both conditions.

We then compared the mean prosthetic knee and ankle kinematics and kinetics during sit/stand with normative able-bodied trajectories (Fig. 6). We did not plot the ankle moments, as they were small and their shape can be inferred from the kinematics due to the elastic nature of the prosthetic foot. Both conditions produced knee kinematics that are similar to able-bodied, with the PRES condition being the most similar in sitting. However, the ankle kinematics produced by either condition's passive feet differ substantially from the normative trajectories, likely impacting the knee's behavior. The knee moments in sitting are more similar to able-bodied for the PKNE condition than for the PRES condition. While the standing knee moments for PKNE are also closer to able-bodied than the PRES condition, they are still not as biomimetic as what was observed in [8], likely due to the

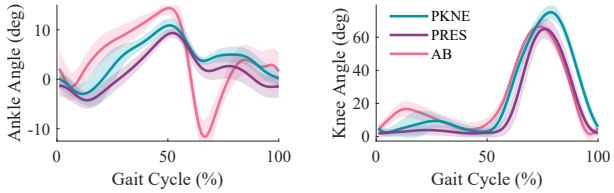


Fig. 7. Inter-participant average kinematic trajectories of the prosthetic joints during the overground walking portions of the experiment. Mean able-bodied trajectories (AB) of 1.0 m/s walking from [19] are also plotted for reference. Shaded regions represent ± 1 standard deviation.

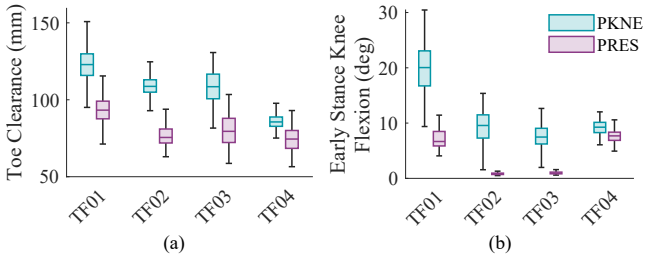


Fig. 8. Boxplots of the average kinematic features during the overground walking portions of the experiments. Tile (a) shows the minimum toe clearance during swing and tile (b) shows the peak early stance knee flexion.

configuration mismatch caused by the passive ankle and our control modification to taper knee torque as $\theta_{sh} \to 0$.

2) Overground Walking: Like in sit/stand, we compared the mean prosthetic knee and ankle kinematics with normative able-bodied trajectories (Fig. 7), as previous experiments with the prototype hardware demonstrated improved biomimicry [5]. Qualitatively, the kinematics at both joints were reasonably similar to able-bodied for both conditions, with a few notable differences in key kinematic features. The PKNE condition showed slightly larger peak ankle dorsiflexion angles, suggesting more energy storage in the prosthetic foot available for push off. The PKNE condition also showed increased peak swing knee flexion angles (mean $\approx$ 76 deg). The peak knee flexion angle in the HKIC controller's kinematic model is $\approx$ 68 deg, indicating that the observed extra flexion was caused by natural swing dynamics rather than explicit control effort. Though less biomimetic, the increased knee flexion was likely beneficial in increasing the toe clearance during swing (Fig. 8a). We calculated this toe clearance based on the minimum position of the 1st and 5th metatarsal markers during mid-swing. On average, the PKNE condition produced 25.5 mm (31.4%) more toe clearance than the PRES condition ($p < 0.001$). An increase in early stance knee flexion was also observed in the PKNE condition (Fig. 8b), with one participant approaching the average able-bodied amount of 16.5 deg. On average, the PKNE condition produced 7.4 deg (172.8%) more early stance knee flexion than the PRES condition ($p < 0.001$).

Finally, we calculated the step length symmetry index for each stride and condition, defined as ratio between the prosthetic and the subsequent biological leg step lengths. A step length symmetry index of 1 corresponds to perfectly symmetric step lengths, while values greater than 1 indicate

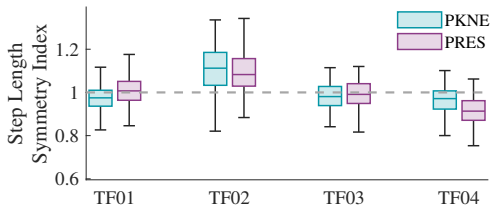


Fig. 9. Mean step length symmetry index for each participant and condition during the overground walking portions of the experiment. Perfectly equal step lengths would result in a symmetry index of 1, whereas values greater than 1 indicate longer steps with the prosthesis.

longer steps with the prosthesis. Shown in Fig. 9, no significant relationship between the prosthesis condition and step length symmetry was observed ($p = 0.54$).

V. Discussion

Many, but not all, of the clinical benefits observed on the prototype hardware in [5], [8] transferred with the HKIC to the Power Knee. The improved GRF symmetry during sit/stand observed in the PKNE condition is an important clinical result, as the better sharing of the GRF between limbs will likely reduce overuse injuries over time. Further, while the speed increase is not directly clinically relevant, it is likely indicative of the sit/stand motions being easier to perform with the PKNE condition than the PRES condition.

However, these effects are not as large as they were previously in [8], likely due to configuration mismatches caused by the passive ankle (Fig. 2). In particular, the standing knee moments produced by the PKNE condition were not as biomimetic as they had been previously (Fig. 6). We hypothesize that this is due, in part, to the difficulty of maintaining the Fig. 2c configuration. Participants often reverted to the vertical shank configuration, in which our controller does not apply knee torque in order to avoid slipping. Systematically characterizing the effects of a non-articulated ankle in sit/stand is an interesting avenue for future work.

In the overground walking portions of the experiment, we observed improvements in key kinematic gait features. The increased toe clearance in the PKNE condition (Fig. 8a), which likely resulted from the increased peak swing knee flexion (Fig. 7), is beneficial for real-world use, as mid-swing trips are a common source of falls [39]. Importantly, the participants did not note any disadvantages of the increased toe clearance or swing knee flexion. The PKNE condition also created more early stance knee flexion than the PRES condition, though not quite to the extent of normative able-bodied gait. Early stance knee flexion is desirable, as it can absorb heelstrike impacts and allow individuals to better maintain forward momentum [40]. Although the prescribed MPKs used by the participants all support early stance knee flexion, the participants did not appear to leverage this feature in the PRES condition.

Though promising, this initial study is not without limitations. First, our study cohort represents only a limited segment of the population, which restricts the generalizability of our findings. The participants were all high-activity (K4) ambulators, and it is possible that our results are unique to this demographic. For instance, related work in robotic ankle prostheses found that higher mobility groups benefited more from the robotic assistance compared to those with lower mobility [41]. Future work is required to understand the PKNE condition's effects across broader populations.

Furthermore, our experiments did not capture all aspects of everyday prosthesis use. For example, we tested only a portion of the activities that occur in real-world ambulation, neglecting activities such as stair traversal. Experiments testing the generalization of our stairs controller [23] should be performed as well. Additionally, we provided limited training and acclimation to the novel device, whereas the participants were extremely acclimated to their PRES prostheses. In real-world use, the acclimation levels across conditions would be more balanced. As our controller matures and becomes appropriate for take-home use, a more comprehensive experiment with longer acclimation and testing horizons should be performed, similar to [14].

Finally, the extent to which the HKIC control methodology independently influenced the observed outcomes was not tested in our experiments. Future work should compare results between the Power Knee under HKIC control to those created with its default control behavior to isolate these effects.

VI. Conclusion

In this article, we presented the first implementation of a phase-variable impedance controller on the Össur Power Knee, utilizing data-driven impedance and kinematic models in place of FSM control. In preliminary experiments involving walking and sit/stand, we showed that many of the clinical benefits that we observed with the same control approach on prototype hardware generalized to the Power Knee. By demonstrating compelling evidence of clinical benefits on commercially-viable prosthesis hardware such as the Power Knee, we aim to help accelerate the adoption of robotic knee-ankle prostheses into mainstream clinical practice.

Acknowledgments

The authors would like to thank Jeffrey Wensman, CPO for providing clinical support, Atli Örn Sverrisson and David Langlois for assistance with the Power Knee hardware, Dr. Ryan Posh for providing valuable feedback on the manuscript, and our dedicated participants for making this work possible.

Conflict of Interest Disclosure

TKB and RDG have applied for patents related to the HKIC control method.

This research received initial funding from Össur ehf (Reykjavík, Iceland), which may have a financial interest in the outcomes of this study. The authors independently conducted the research and analysis, and the results and conclusions presented in this paper are those of the authors alone. These findings do not necessarily reflect the views or positions of Össur ehf, the National Science Foundation, or the National Institutes of Health.

REFERENCES

[1] R. Gehlhar, M. Tucker, A. J. Young, and A. D. Ames, "A review of current state-of-the-art control methods for lower-limb powered prostheses," *Annu. Rev. Control.*, vol. 55, pp. 142–164, 2023.

[2] I. Fagioli, A. Mazzarini, C. Livolsi, E. Gruppioni, N. Vitiello, S. Crea, and E. Trigili, "Advancements and Challenges in the Development of Robotic Lower Limb Prostheses: a Systematic Review," *IEEE Trans. Med. Robot. and Bionics*, vol. PP, no. 99, pp. 1–1, 2024.

[3] C. Jayaraman, S. Hoppe-Ludwig, S. Deems-Dluhy, M. McGuire, C. Mummidisetty, R. Siegal, A. Naef, B. E. Lawson, M. Goldfarb, K. E. Gordon, and A. Jayaraman, "Impact of Powered Knee-Ankle Prosthesis on Low Back Muscle Mechanics in Transfemoral Amputees: A Case Series," *Frontiers in Neuroscience*, vol. 12, p. 134, 2018.

[4] M. Tran, L. Gabert, S. Hood, and T. Lenzi, "A lightweight robotic leg prosthesis replicating the biomechanics of the knee, ankle, and toe joint," *Science Robotics*, vol. 7, no. 72, p. eabo3996, 2022.

[5] T. K. Best, C. G. Welker, E. J. Rouse, and R. D. Gregg, "Data-driven variable impedance control of a powered knee–ankle prosthesis for adaptive speed and incline walking," *IEEE Trans. Robot.*, vol. 39, no. 3, pp. 2151–2169, 2023.

[6] A. M. Simon, N. P. Fey, K. A. Ingraham, S. B. Finucane, E. G. Halsne, and L. J. Hargrove, "Improved Weight-Bearing Symmetry for Transfemoral Amputees during Standing Up and Sitting Down with a Powered Knee-Ankle Prosthesis," *Arch. of Phys. Med. and Rehab.*, vol. 97, pp. 1100–1106, 2016.

[7] G. Hunt, S. Hood, and T. Lenzi, "Stand-Up, Squat, Lunge, and Walk with a Robotic Knee and Ankle Prosthesis under Shared Neural Control," *IEEE Open J. Eng. Med. Biol.*, vol. 2, pp. 267–277, 2021.

[8] C. G. Welker, T. K. Best, R. D. Gregg, and C. G. Welker, "Improving Sit/Stand Loading Symmetry and Timing Through Unified Variable Impedance Control of a Powered Knee-Ankle Prosthesis," *IEEE Trans. Neural Syst. Rehabil. Eng.*, vol. 31, pp. 4146–4155, 2023.

[9] E. C. Martinez-Villalpando, L. Mooney, G. Elliott, and H. Herr, "Antagonistic Active Knee Prosthesis. A Metabolic Cost of Walking Comparison With a Variable-Damping Prosthetic Knee," *Conf. Proc. IEEE Eng. Med. Biol. Soc.*, vol. 2011, pp. 8519–8522, 2011.

[10] E. D. Ledoux and M. Goldfarb, "Control and evaluation of a powered transfemoral prosthesis for stair ascent," *IEEE Trans. Neural Syst. Rehabilitation Eng.*, vol. 25, 2017.

[11] T. K. Best, C. A. Laubscher, R. J. Cortino, S. Cheng, and R. D. Gregg, "Improving amputee endurance over activities of daily living with a robotic knee-ankle prosthesis: A case study," in *IEEE/RSJ Int. Conf. Intell. Robots Syst.*, 2023, pp. 2101–2107.

[12] M. J. Highsmith, J. T. Kahle, S. L. Carey, D. J. Lura, R. V. Dubey, and W. S. Quillen, "Kinetic Differences Using a Power Knee and C-Leg While Sitting Down and Standing Up: A Case Report," *J. Prosthetics and Orthotics*, vol. 22, no. 4, pp. 237–243, 2010.

[13] E. J. Wolf, V. Q. Everding, A. A. Linberg, J. M. Czerniecki, and C. J. M. Gambel, "Comparison of the Power Knee and C-Leg during step-up and sit-to-stand tasks," *Gait & Posture*, vol. 38, no. 3, pp. 397–402, 2013.

[14] B. J. Hafner and R. L. Askew, "Physical performance and self-report outcomes associated with use of passive, adaptive, and active prosthetic knees in persons with unilateral, transfemoral amputation: Randomized crossover trial," *J. Rehabil. Res. Dev.*, vol. 52, no. 6, pp. 677–700, 2015.

[15] F. Sup, A. Bohara, and M. Goldfarb, "Design and control of a powered transfemoral prosthesis," *The Int. J. of Robotics Research*, vol. 27, no. 2, pp. 263–273, 2008.

[16] A. M. Simon, K. A. Ingraham, N. P. Fey, S. B. Finucane, R. D. Lipschutz, A. J. Young, and L. J. Hargrove, "Configuring a powered knee and ankle prosthesis for transfemoral amputees within five specific ambulation modes," *PLoS One*, vol. 9, no. 6, 2014.

[17] H. Huang, D. L. Crouch, M. Liu, G. S. Sawicki, and D. Wang, "A Cyber Expert System for Auto-Tuning Powered Prosthesis Impedance Control Parameters," *Ann. Biomed. Eng.*, vol. 44, no. 5, pp. 1613–1624, 2016.

[18] R. Wu, M. Li, Z. Yao, W. Liu, J. Si, and H. Huang, "Reinforcement learning impedance control of a robotic prosthesis to coordinate with human intact knee motion," *IEEE Robotics and Automation Letters*, vol. 7, no. 3, pp. 7014–7020, 2022.

[19] E. Reznick, K. R. Embry, R. Neuman, E. Bolívar-Nieto, N. P. Fey, and R. D. Gregg, "Lower-limb kinematics and kinetics during continuously varying human locomotion," *Sci. Data*, vol. 8, 2021.

[20] J. Camargo, A. Ramanathan, W. Flanagan, and A. Young, "A comprehensive, open-source dataset of lower limb biomechanics in multiple conditions of stairs, ramps, and level-ground ambulation and transitions," *J. Biomech.*, vol. 119, p. 110320, 2021.

[21] J. Vantilt *et al.*, "Model-based control for exoskeletons with series elastic actuators evaluated on sit-to-stand movements," *J. NeuroEng. Rehabil.*, vol. 16, no. 65, Jun. 2019.

[22] T. K. Best, K. Embry, E. J. Rouse, and R. D. Gregg, "Phase-variable control of a powered knee-ankle prosthesis over continuously varying speeds and inclines," *IEEE Int. Conf. Intelli. Robot. Sys.*, 2021.

[23] R. J. Cortino, T. K. Best, and R. D. Gregg, "Data-driven phase-based control of a powered knee-ankle prosthesis for variable-incline stair ascent and descent," *IEEE Trans. Med. Robot. Bionics*, vol. 6, no. 1, pp. 175–188, 2024.

[24] S. Cheng, C. A. Laubscher, and R. D. Gregg, "Controlling Powered Prosthesis Kinematics over Continuous Inter-Leg Transitions Between Walking and Stair Ascent/Descent," *IEEE Trans. Neural Syst. Rehabil. Eng.*, vol. PP, no. 99, pp. 1–1, 2024.

[25] T. Elery, S. Rezazadeh, C. Nesler, and R. D. Gregg, "Design and validation of a powered knee-ankle prosthesis with high-torque, low-impedance actuators," *IEEE Trans. Robot.*, vol. 36, no. 6, pp. 1649–1668, 2020.

[26] S. Cheng, C. A. Laubscher, R. D. Gregg, and S. Cheng, "Automatic Stub Avoidance for a Powered Prosthetic Leg Over Stairs and Obstacles," *IEEE Trans. Biomed. Eng.*, vol. 71, no. 5, pp. 1499–1510, 2024.

[27] S. Gudjonsson, Á. Einarsson, H. I. Thorsteinsdottir, and D. Langlois, "Ground contact sensor array for lower-limb prosthetic and orthotic devices," U.S. Patent Application US20 220 401 236A1, 2022.

[28] S. Cheng, C. A. Laubscher, T. K. Best, and R. D. Gregg, "Ambilateral activity recognition and continuous adaptation with a powered knee-ankle prosthesis," *IEEE Transactions on Robotics*, pp. 1–17, 2025.

[29] K. Embry, D. J. Villarreal, R. L. Macaluso, and R. D. Gregg, "Modeling the Kinematics of Human Locomotion over Continuously Varying Speeds and Inclines," *IEEE Trans. Neural Syst. Rehabil. Eng.*, vol. 26, no. 12, pp. 2342–2350, 2018.

[30] S. Ayyappan and E. Rouse. (2023) The Open Source Leg. [Online]. Available: https://www.opensourceleg.org/build

[31] A. F. Azocar and E. J. Rouse, "Characterization of Open-loop Impedance Control and Efficiency in Wearable Robots," *IEEE Robot. Autom. Lett.*, vol. 7, no. 2, pp. 4313–4320, 2022.

[32] T. K. Best, G. C. Thomas, S. R. Ayyappan, R. D. Gregg, and E. J. Rouse, "A Compensated Open-Loop Impedance Controller Evaluated on the Second-Generation Open-Source Leg Prosthesis," *Under Review.*, 2024.

[33] M. W. Spong, S. Hutchinson, and M. Vidyasagar, *Robot Modeling and Control (2nd Edition)*. Wiley, 2020.

[34] F. J. Morales, A. Martínez, M. Méndez, A. Agarrado, F. Ortega, J. Fernández-Guerra, T. Montemayor, and J. Burgos, "A shuttle walk test for assessment of functional capacity in chronic heart failure," *Am. Heart J.*, vol. 138, no. 2, pp. 291–298, 1999.

[35] M. T. Mahar, A. M. Guerieri, M. S. Hanna, and C. D. Kemble, "Estimation of Aerobic Fitness from 20-m Multistage Shuttle Run Test Performance," *Am. J. Preventive Medicine*, vol. 41, no. 4, pp. S117–S123, 2011.

[36] A. Rajagopal, C. L. Dembia, M. S. DeMers, D. D. Delp, J. L. Hicks, and S. L. Delp, "Full-body musculoskeletal model for muscle-driven simulation of human gait," *IEEE Trans. Biomed. Eng.*, vol. 63, no. 10, pp. 2068–2079, 2016.

[37] V. Raveendranathan, V. G. M. Kooiman, and R. Carloni, "Musculoskeletal model of osseointegrated transfemoral amputees in OpenSim," *PLOS ONE*, vol. 18, no. 9, p. e0288864, 2023.

[38] J. Zeni, J. Richards, and J. Higginson, "Two simple methods for determining gait events during treadmill and overground walking using kinematic data," *Gait & Posture*, vol. 27, no. 4, pp. 710–714, 2008.

[39] J. Kim, C. L. McDonald, B. J. Hafner, and A. Sawers, "Fall-related events in people who are lower limb prosthesis users: the lived experience," *Disabil. Rehabil.*, vol. 44, no. 15, pp. 3897–3908, 2022.

[40] J. Perry, J. Burnfield, and L. Cabico, *Gait Analysis: Normal and Pathological Function*, 2nd ed. Thorofare, NJ: Slack, 2010.

[41] E. S. Gardinier, B. M. Kelly, J. Wensman, and D. H. Gates, "A controlled clinical trial of a clinically-tuned powered ankle prosthesis in people with transtibial amputation," *Clinical Rehabilitation*, vol. 32, no. 3, pp. 319–329, 2017.

Real-time Prediction of Leg Joint Kinematics during Steady-State Walking and Task Transitions*

Louis Devillez[1,3] and Renaud Ronsse[1,2]

***Abstract*— Amputations and other impairments heavily impact human locomotion. To compensate for these disabilities, advanced devices such as active orthoses and prostheses are being developed with the aim of restoring locomotor function. To achieve this goal, the control of such technologies has been identified as a key research challenge. A reference kinematic profile for the affected or missing joints is often useful for device control. This paper introduces a novel method for estimating reference kinematics of leg joints from kinematic signals of the contralateral leg. This method leverages fusion of two different estimators – i.e. Complementary Limb Motion Estimation and Adaptive Oscillators – which are combined through the use of a logistic function. The method is then applied to estimate the kinematics of a hip joint, and the performance is compared with that of each individual estimator during walking. The correlation between the estimated signal and the ground truth is assessed on a cycle-by-cycle basis. During transitions, our new method behaves similarly to Complementary Limb Motion Estimation. After a few cycles, the method shifts towards Adaptive Oscillators to achieve a better correlation during quasi-steady-state locomotion.**

I. Introduction

There are many neuromusculoskeletal disorders impacting lower limb functions. Examples include Parkinson's disease, stroke, or amputation, and each of them leads to serious locomotion disabilities. Advanced technologies have been developed to alleviate the effects of these disorders, such as powered orthoses [1], [2] or prostheses [3], [4]. A key challenge that remains to be solved is the control of such technologies. A particularly emerging approach consists in governing the device behavior through bio-inspired control principles, mainly through descending activation patterns, feedback-driven reflexes, and/or motor primitives [5]. Implementation of such control can be divided into two key steps. First, reference kinematics of affected joints need to be generated. Then, the device behavior is regulated as a function of these reference kinematics, either through a stiff PID controller [6], or by computing assist-as-needed force profiles in an impedance-based controller [7]. Finite-state machines can be used to sequence the controller behavior into a series of distinct phases synchronized with events — such as heel strike — to modulate gains or combine different control modes [8], [9].

In this paper, the focus is on the first step, i.e. generation of relevant reference kinematics. Since the corresponding joint is missing or no longer functional, its reference kinematics need to be estimated, for instance by measuring signals on the contralateral leg. Ideally, this reference kinematics should also adapt as a function of the executed task: leg joints do not follow the same pattern during overground walking and stair ascending/descending, and even during walking at two different speeds. These statements are particularly relevant for proximal joints, since they govern the whole leg rhythmicity [10]. For example, in the case of hip disarticulation, i.e. amputation of a whole leg, the reference kinematics of the hip prosthesis module could only be estimated from signals measured on the rest of the body [11].

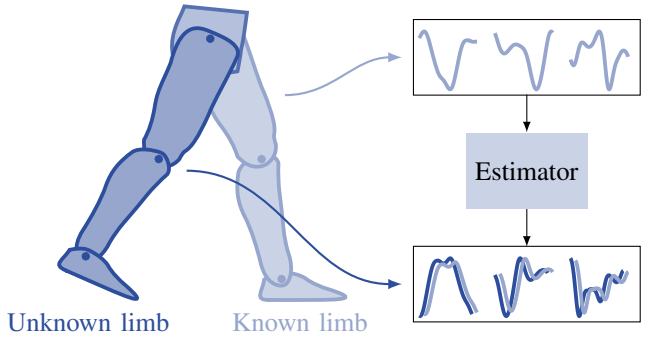


Fig. 1. Schematic representation of the problem statement. By measuring the kinematic signals of one leg, we aim at predicting the kinematics of at least one joint of the contralateral leg.

Human locomotion is a combination of rhythmic and discrete movements [12]. Walking and ascending stairs are examples of rhythmic movements — at least during their steady-state segments — while the transition from standing to walking or sitting are discrete movements. A large proportion of controllers for assistive locomotion devices rely on phase-based methods, i.e., real-time estimation of a continuously evolving gait phase between 0 % and 100 % [13] to generate reference kinematics. This implies that they only work during (quasi-)rhythmic tasks. For example, [14] used precomputed signals as reference kinematics, that varied with respect to the estimated gait phase. In echo control, the kinematic profile of one joint is recorded and replayed with some time delay to serve as a reference for the contralateral joint [15]. Adaptive Oscillators (AO) are dynamical systems capable of synchronizing with a quasi-periodic input by learning its features in state variables [16]. Since these methods require rhythmicity, they are not well adapted to discrete transitions. Other methods, such as Complementary Limb Motion Estimation (CLME), do not leverage the intrinsic

*This work was supported by the Belgian F.R.S.-FNRS (Aspirant #40011487 awarded to LD)

[1]Institute of Mechanics, Materials and Civil Engineering and Louvain Bionics, UCLouvain, 1348 Louvain-la-Neuve, Belgium

[2]Institute of Neuroscience, UCLouvain, 1200 Brussels, Belgium

[3]louis.devillez@uclouvain.be

rhythmicity of locomotion in their working principle. CLME infers the intended motion of the affected joints from the motion of the residual joints [17]. This method can handle transitions but requires specific parameter tuning for each task and potentially even for each user.

The methodology presented in this paper combines two methods, i.e. AO and CLME, in order to leverage their respective benefits. We strive to develop an estimator adapted to both discrete and rhythmic segments of walking, i.e. giving precedence to AO during rhythmic segments, and to CLME during discrete transitions. Additionally, this method can reduce the need for gain tuning. The article is structured as follows: Section II presents the problem statement. Section III overviews the algorithms of CLME and AO in detail. The mechanism to combine both methods is described in Section IV. Section V applies this combined estimator to our target application, i.e. estimating the kinematics of a missing hip joint. Results are compared and analyzed in Section VI. The paper ends with a discussion and a conclusion.

II. Problem statement

The problem addressed in the present paper consists in estimating in real-time the joint kinematics of one leg from measurements of kinematic signals taken from the other leg. A schematic representation is depicted in Fig. 1. Let $\boldsymbol{q}$ be a time-dependent vector with $3M$ components containing kinematic signals of M leg joints, such that for each joint i:

- $q_{3(i-1)+1}$ is the joint position
- $q_{3(i-1)+2}$ is the joint velocity
- $q_{3(i-1)+3}$ is the joint acceleration

The problem can thus be expressed as finding a function f such that:

$$\boldsymbol{q}_U[t] = f(\boldsymbol{q}_K[t]) \tag{1}$$

The subscripts K and U are used to denote the known limb and the unknown one.

III. Related work

In this section, we overview two existing methodologies providing a particular implementation of the function f. First, CLME augmented with a Kalman filter is presented; then AO are introduced.

A. Complementary limb motion estimation

CLME was developed by Vallery and colleagues in [17]–[20]. The principle behind this method is to leverage interjoint coordination [21] and, consequently, to find the best linear combination of known joint kinematic variables (position, velocity, and/or acceleration) to estimate similar variables of another joint.

To construct a CLME, data from both known and unknown joints are required. Moreover, this framework does not require to specify which kinematic variables are used to compose vectors $\boldsymbol{q}_U$ and $\boldsymbol{q}_K$ since it can be implemented with any combination of position, velocity, and acceleration signals.

The first step consists in normalizing the variables, i.e. computing normalized vectors $\boldsymbol{x}$ as:

$$\boldsymbol{S}_i = \text{diag}\left(\text{var}(\boldsymbol{q}_i)\right) \tag{2}$$

$$\boldsymbol{x}_i = \boldsymbol{S}_i^{-1}\left(\boldsymbol{q}_i - \bar{\boldsymbol{q}}_i\right) \tag{3}$$

with $\text{var}(\boldsymbol{q}_i)$ being the variance and $\bar{\boldsymbol{q}}_i$ the mean of $\boldsymbol{q}_i$, and the subscript i denoting both U and K. The best estimator is defined as the matrix $\boldsymbol{C}$ such that the expected error between the normalized vector of the unknown joint and the estimation is minimized, i.e.:

$$\text{argmin}\left(\sum(||\boldsymbol{x}_U - \boldsymbol{C}\boldsymbol{x}_K||)\right) \tag{4}$$

Importantly, since this problem is linear, it has an exact solution, that can be computed as:

$$\boldsymbol{C}_{\text{opt}} = \left(\text{cov}^{-1}(\boldsymbol{x}_K, \boldsymbol{x}_K) * \text{cov}(\boldsymbol{x}_K, \boldsymbol{x}_U)\right)^T \tag{5}$$

with $\text{cov}(\cdot,\cdot)$ denoting the covariance function. An estimator of the unknown joint kinematics can then be constructed as:

$$\boldsymbol{q}_U^{\text{CLME}} = \boldsymbol{A}\boldsymbol{q}_K + \boldsymbol{b} \tag{6}$$

$$\boldsymbol{A} = \boldsymbol{S}_U\boldsymbol{C}\boldsymbol{S}_K^{-1} \tag{7}$$

$$\boldsymbol{b} = \boldsymbol{A}\bar{\boldsymbol{q}}_K + \bar{\boldsymbol{q}}_U \tag{8}$$

This approach computes estimates of the kinematic variables independently of each other, i.e. without accounting for the fact that one might be the derivative of another. In other words, following the problem statement, it does not guarantee that the derivative of $q_{3(i-1)+1}$ is equal to $q_{3(i-1)+2}$ and that the derivative of $q_{3(i-1)+2}$ is equal to $q_{3(i-1)+3}$.

However, there are many reasons why satisfying these constraints between position, velocity, and/or acceleration is essential. For instance, if the position estimate is used as a reference signal for a controller, its dynamics can benefit greatly from having an estimate of the reference velocity, as long as it is the actual derivative of the position [22].

To solve this problem, this correlation-based CLME measurement can be coupled with a model-based prediction that takes into account the derivative relationship between variables. This can be achieved by coupling a Kalman filter [17], thus combining a predictor based on an internal model with a series of integrators, to the CLME-based estimation [23]. Therefore, we define the following variables:

- $\boldsymbol{q}_U^*$: the prediction from the internal model of the filter
- $\boldsymbol{q}_U^{\text{KF}}$: the output from the Kalman filter, combining the model-based prediction and CLME-based estimation
- $\boldsymbol{K}$: the Kalman gain matrix

The internal model estimate is expressed as a chain of Euler-explicit integrators, i.e.:

$$\boldsymbol{q}_U^*[t+1] = \begin{bmatrix} \boldsymbol{F} & & \\ & \ddots & \\ & & \boldsymbol{F} \end{bmatrix} \boldsymbol{q}_U^{\text{KF}}[t] \tag{9}$$

where

$$\boldsymbol{F} = \begin{bmatrix} 1 & \Delta t & 0 \\ 0 & 1 & \Delta t \\ 0 & 0 & 1 \end{bmatrix} \tag{10}$$

The output of the whole filter is then obtained as:

$$\boldsymbol{q}_U^{\text{KF}}[t+1] = \boldsymbol{q}_U^*[t+1] + \boldsymbol{K}\left(\boldsymbol{q}_U^{\text{CLME}}[t] - \boldsymbol{q}_U^*[t]\right) \quad (11)$$

The principle of a Kalman filter is to find the best gain matrix $\boldsymbol{K}$ that minimizes the error of the combined estimates. Several references explain how to compute $\boldsymbol{K}$, as a function of the covariance of the process noise (here the variance of the acceleration, i.e. var $\left(q_{U,3(i-1)+3}\right)$) and the observation noise (here, the variance of the measurement error, i.e. var $\left(q^{\text{CLME}}_{U,3(i-1)+1} - q_{U,3(i-1)+1}\right)$) [24].

B. Adaptive oscillators

Any periodic signal can be decomposed into an infinite sum of sinusoidal signals, as captured by Fourier's theorem. An estimate of this signal can be constructed by truncating this sum to its first N terms. Such an estimation can be applied to the position of the known leg and is thus expressed as:

$$q^{\text{AO}}_{K,3(i-1)+1}(t) = \alpha_0 + \sum_{j=1}^{N} \alpha_j \sin\left(\phi_j(t)\right) \quad (12)$$

$$\dot{\phi}_j(t) = j\omega \quad (13)$$

with the following parameters: α_0 the offset, α_j the amplitude of the j-th harmonic, ω the frequency of the fundamental harmonic, and ϕ_j the phase of the j-th harmonic.

AO are a mathematical tool specifically developed in order to estimate these parameters [25]. The estimation error, ϵ is computed as the difference between the periodic signal to be estimated and its estimation. Here we assume the signal to be estimated is the measured joint angular position of the known leg, i.e.:

$$\epsilon(t) = q_{K,3(i-1)+1}(t) - q^{\text{AO}}_{K,3(i-1)+1}(t) \quad (14)$$

The dynamics governing the learning of the estimation state variables are given as follows:

$$\dot{\alpha}_0(t) = \epsilon(t)\ \eta \quad (15)$$

$$\dot{\alpha}_j(t) = \epsilon(t)\ \eta \sin\left(\phi_j(t)\right) \quad (16)$$

$$\dot{\omega}(t) = \epsilon(t)\ \nu_\omega \frac{\cos\left(\phi_1(t)\right)}{\sum_{j=1}^{N} \alpha_j(t)} \quad (17)$$

$$\dot{\phi}_j(t) = \epsilon(t)\ \nu_\phi \frac{\cos\left(\phi_j(t)\right)}{\sum_{j=1}^{N} \alpha_j(t)} + j\omega(t) \quad (18)$$

with η, ν_ω and ν_ϕ being the learning gains for, respectively, the amplitude, frequency and phase. Note that the state equations (15)-(18) should be discretized in order to be solved in real-time. This can be done through classical explicit integration schemes like Euler or Runge-Kutta. In [16], a method to tune the learning gains gave the following rules:

$$\eta = \frac{2}{\tau_\alpha} \qquad \nu_\omega = \frac{20}{\tau_\omega^2} \qquad \nu_\phi = \frac{22}{\tau_\omega} \quad (19)$$

with τ_α and τ_ω being the time constants of the amplitude and frequency dynamics, respectively.

Assuming that both legs are in antiphase during walking, the estimation of the unknown leg can be built based on the state variables learned from the known leg, yet with an extra phase shift of $j\pi$. The estimation of the unknown angular position can then be expressed as:

$$q^{\text{AO}}_{U,3(i-1)+1}(t) = \alpha_0(t) + \sum_{j=1}^{N} \alpha_j(t) \sin\left(\phi_j(t) + j\pi\right) \quad (20)$$

The velocity and acceleration can be obtained by analytically differentiating (20), i.e.:

$$q^{\text{AO}}_{U,3(i-1)+2}(t) = \sum_{j=1}^{N} \alpha_j(t) j\omega(t) \cos\left(\phi_j(t) + j\pi\right) \quad (21)$$

$$q^{\text{AO}}_{U,3(i-1)+3}(t) = -\sum_{j=1}^{N} \alpha_j(t) j^2 \omega(t)^2 \sin\left(\phi_j(t) + j\pi\right) \quad (22)$$

Since AO build a kind of real-time Fourier series, it only works during (quasi-)rhythmic movements, i.e. steady-state walking. During transients, its performance degenerates to that of a low-pass filter.

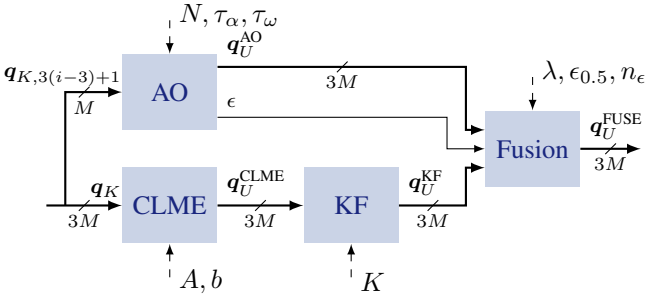


Fig. 2. Block diagram of the various components of the fused estimator. Each block has its own parameters, represented by the vertical arrows. The input of both CLME and AO are kinematics signals. The CLME output is filtered with a Kalman filter (KF). Fusion of both estimators is governed by the AO error ϵ.

IV. Fusing the estimators

In the previous section, we introduced CLME and AO, two methods to estimate the unknown leg kinematics from the known one. In this section, both estimators are fused together to obtain a more robust estimation of the unknown side. Fig. 2 illustrates the relationship between the different blocks.

Both methods have their advantages and disadvantages. CLME is time-invariant and provides a time-independent optimal estimation, in the least-squares sense. However, the quality of this estimation depends on the dataset on which the gains have been optimized and does not exactly satisfy relationships between position, velocity, and acceleration signals. AO can provide an estimation that is exactly in antiphase with respect to the known leg and that satisfies relationships between kinematic derivatives. However, it is governed by its intrinsic dynamics and thus needs time to reach a new (quasi) steady-state after each transition. As a consequence, it is preferable to use the estimation from CLME during transient phases, and to give more weight to

the estimation provided by AO once steady-state locomotion has been reached.

A fixed weighted average between both estimators would not take into account the temporal dynamics of the AO-based estimation. Yet, the quality of this AO-based estimation is directly provided by the error signal ϵ. For large ϵ, when the estimation does not match the measurement, state variables evolve rapidly (15-18), indicating that AO have not converged. In contrast, small ϵ indicates a slow evolution of state variables, capturing that AO have converged.

In order to hide high-frequency variations in both the measured signal and its estimate, we chose to use the moving average of ϵ, denoted, ϵ_{MA}, as the convergence metric of AO. Its window size is denoted by n_ϵ. The weight that should be given to the estimation provided by AO is then defined by the following logistic function, bounded between 0 and 1:

$$W(\bar{\epsilon}) = 1 - \frac{1}{1 + \exp\left(\lambda\left(\epsilon_{0.5} - \epsilon_{\text{MA}}\right)\right)} \tag{23}$$

with $\epsilon_{0.5}$ being a parameter equal to the value of ϵ_{MA} corresponding to a weight of 0.5, and λ being another parameter capturing the function steepness. The nonlinear profile of (23) allows a rapid shift between CLME and AO. The output of the fused estimator is eventually computed as:

$$\boldsymbol{q}_U^{\text{FUSE}} = W(\epsilon_{\text{MA}}) \cdot \boldsymbol{q}_U^{\text{AO}} + (1 - W(\epsilon_{\text{MA}})) \cdot \boldsymbol{q}_U^{\text{CLME}} \tag{24}$$

V. Application for an Active Hip Prosthesis

The previous section showed how to fuse CLME- and AO-based estimations into a single estimate, giving more weight to AO when it has converged, i.e. during steady-state locomotion. In this section, this algorithm is applied to estimate the position and velocity of a hip joint. These estimates could be used directly to control a hip prosthesis, like the one we developed in [11]. In the remainder of this section, the position of the unknown hip will be denoted θ and its velocity $\dot{\theta}$.

A. Dataset

Two pre-existing datasets were used to train, test and evaluate the estimators. The position and velocity of both legs were extracted as well as their decomposition into gait cycles. The first dataset is taken from [26] and contains data from 12 subjects performing different cyclic or non-cyclic locomotion-related tasks. Only walking trials with speeds ranging from $0.6\,\text{m}\,\text{s}^{-1}$ to $1.8\,\text{m}\,\text{s}^{-1}$ were kept for analysis. The second dataset is taken from [27] and contains data from 22 subjects who also performing different locomotion tasks. Only the level-ground and treadmill trials were kept for all subjects, with walking speeds ranging from $0.5\,\text{m}\,\text{s}^{-1}$ to $1.85\,\text{m}\,\text{s}^{-1}$. Trials with fewer than 5 cycles were excluded. This resulted in a total of 329 trials and 1,974 cycles. We arbitrarily chose the right leg as the known leg and the left leg as the unknown leg for each trial.

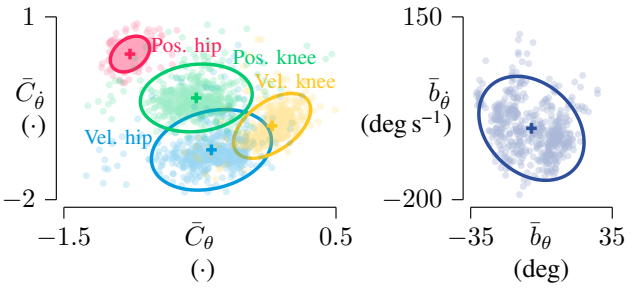


Fig. 3. Normalized gains of CLME trained on all available trials. Left: $\boldsymbol{C}$ matrix; right: $\boldsymbol{b}$ vector. The color represents the different input signals of CLME and each axis captures its magnitude for estimating both the position and velocity of the hip. Ellispses capture the normalized distribution of these points.

B. Generic CLME implementation

The CLME implementation is very similar to that of [17], where the authors showed that using acceleration signals to estimate position and velocity was of little interest. Therefore, we also decided to use only the position and velocity signals of the known leg to build the estimate. Furthermore, only hip and knee signals are used and not ankle ones, with the aim of keeping requirements for body instrumentation as low as possible, given our target application.

Data from both the known and unknown joints are required to compute the gains of CLME. Using data from the same user for both learning and estimation leads to an individualized CLME, i.e. with user-dependent gains $\boldsymbol{A}$ and $\boldsymbol{b}$. This yields the optimal CLME that can be designed for a given individual and task. However it is not always possible to have access to these data for each and every user. For instance, no data exist for the unknown joint kinematics of an individual with an amputation.

On the other hand, it is possible to use generic gains for CLME, providing a kind of "one-size-fits-all" estimator. This degrades individual estimations but removes the need for learning data for each user. To compute these generic gains, matrix $\boldsymbol{A}$ (7) and $\boldsymbol{b}$ (8) are averaged over all available trials. A representation of the distribution of the best individual gains, along with their mean value, is shown in Fig. 3. Note that the $\boldsymbol{C}$ matrix is displayed in Fig. 3 instead of the $\boldsymbol{A}$ matrix, as it captures normalized gains. As pictured in Fig. 3, each indiviual gain is distributed in signal-dependent dense clusters. This suggests that averaging may be a valid approach, at least when it is not possible to compute individualized gains.

For the used datasets, numerical values for $\bar{\boldsymbol{A}}$ and $\bar{\boldsymbol{b}}$ are the following:

$$\bar{\boldsymbol{A}} = \begin{pmatrix} -0.987 & -0.063\,\text{s} & -0.439 & 0.003\,\text{s} \\ 2.47\,\text{s}^{-1} & -1.15 & -1.79\,\text{s}^{-1} & -0.473 \end{pmatrix} \tag{25}$$

$$\bar{\boldsymbol{b}} = \begin{pmatrix} -4.95\,\text{deg} \\ -63.3\,\text{deg}\,\text{s}^{-1} \end{pmatrix} \tag{26}$$

The Kalman gain matrix is also averaged over all trials, and

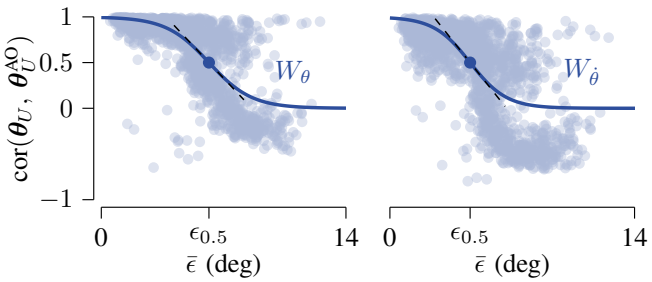


Fig. 4. Correlation between the AO-based estimation and ground-truth signals from the dataset, as a function of the time-averaged AO error $\bar\epsilon$, for the position (left) and velocity (right) signals. Each dot represents one walking cycle for the datasets. The solid lines represent the best possible fit of the weighting function (23), eventually used as weight given to the AO-based estimation. The dashed line captures the slope of the logistic function at $(\epsilon_{0.5}, 0.5)$.

we obtained the following optimal gains:

$$\bar{\boldsymbol{K}} = \begin{pmatrix} 0.049 & 0.004\,\mathrm{s} \\ 0.179\,\mathrm{s}^{-1} & 0.446 \end{pmatrix} \tag{27}$$

C. AO implementation

AO parameters were selected as follows: $N = 3$, $\tau_\alpha = \tau_\omega = 3\,\mathrm{s}$. At the beginning of each trial, the initial parameters of AO were set to the following values: $\alpha_0 = \alpha_i = 1\,\mathrm{deg}$, $\omega = 5\,\mathrm{rad\,s^{-1}}$ and $\phi_i = 0\,\mathrm{rad}$.

A useful pragmatic addition to the generic AO is to prevent the learned frequency ω to go below a certain threshold. This facilitates convergence during steady-state locomotion. Here, we set a threshold to 0.3 Hz, i.e. well below a typical walking frequency.

D. Merging function

In the fused estimator, a window size n_ϵ = 100 was used, which corresponds to a time frame of 0.5 s, given the signal sampling rate. The parameters of the logistic function (23), i.e. λ and $\epsilon_{0.5}$, were fitted using values from the whole datasets. For each cycle of each trial, the correlation between the AO-based estimation and the actual signal was computed as a function of the time-averaged AO error $\bar\epsilon$. The logistic function was then fitted to this data cloud using a least-squares method (Fig. 4).

Note that the value of the correlation may be negative (when the AO-based estimate is poor), but not the logistic function. This forces the logistic function to remain close to 0 for negative correlations. This behavior is desired when the correlation is close to 0 or negative, CLME should be preferred over AO. The values for the best-fit parameters are: $\lambda = 0.82$ and $\epsilon_{0.5} = 6.2\,\mathrm{deg}$ for the position estimate, and $\lambda = 0.96$ and $\epsilon_{0.5} = 4.6\,\mathrm{deg}$ for the velocity estimate. Note that the transition from CLME to AO is steeper for velocity estimation and occurs for a smaller value of ϵ_{MA}.

VI. Kinematic estimation results

Fig. 5 provides a typical estimation result obtained with CLME, using both individualized and generic gains. The individualized CLME produces a good estimation for the

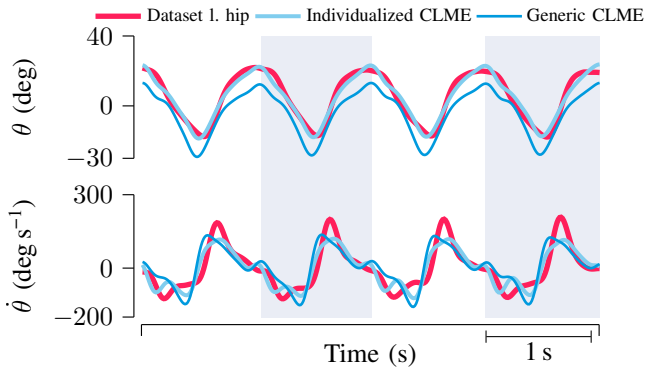


Fig. 5. Time evolution of the left hip angular position (top) and velocity (bottom) from subject 08 walking at $1.2\,\mathrm{m\,s^{-1}}$ (first four cycles). Red lines are taken from [26], light blue lines are the estimates from the individualized CLME and dark blue lines from the generic CLME. Different shades of grey in the background separate successive cycles.

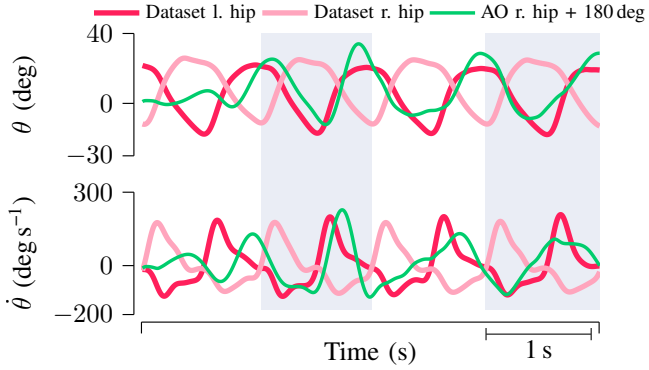


Fig. 6. Time evolution of both hips angular position (top) and velocity (bottom) from subject 08 walking at $1.2\,\mathrm{m\,s^{-1}}$ (first four cycles). Red lines are taken from [26], green lines are estimations from AO. Different shades of grey in the background separate successive cycles.

position. It is less performant for velocity as it cannot capture all signal variations. The generic CLME performs similarly well, but with a significant offset in its position estimation.

The same trial is used as a typical trial for AO (Fig. 6). It clearly shows that AO need time to converge to their best estimate, since their quality improves over time. In fact, AO cannot estimate the left leg position well in the first cycle. During the following cycles, the shape and amplitude of the signal converge to those of the actual signals. The estimation convergence is similar for position and velocity.

An example of the fused estimator is depicted in Fig. 7. It is compared to the CLME- and AO-based estiamtors for the same trial as above. Initially, the fused estimator follows the CLME estimation. As ϵ_{MA} decreases, the weight given to AO, W, increases. The AO contributions are not the same for position and velocity, with velocity using more of the CLME estimation. Importantly, the error of the fused estimator is never larger than the largest error of either the CLME- or AO-only estimates. This highlights the interest of the proposed fusion technique, which exploits both approaches during their most favorable epochs.

Finally, we performed a global analysis of all trials com-

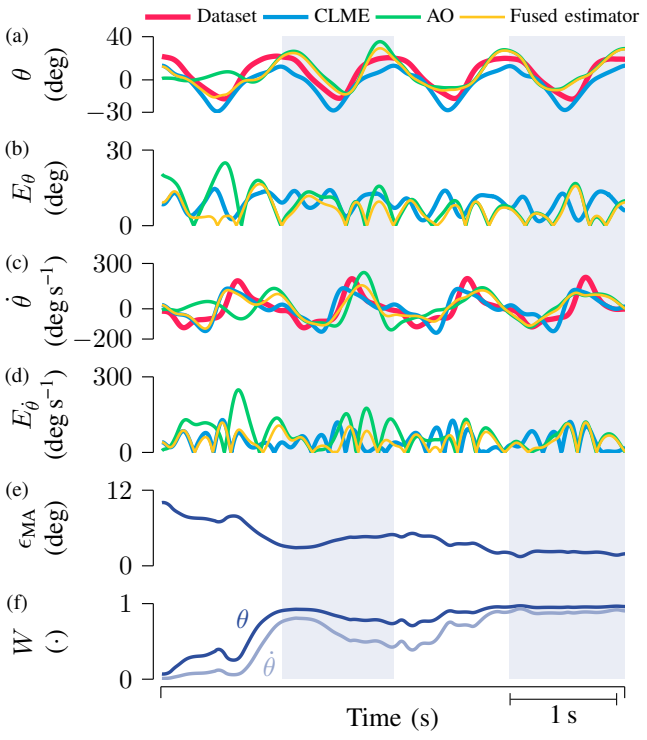


Fig. 7. Time evolution of left hip angular position (a) and velocity (c) from subject 08 walking at 1.2 m s^{-1} (first four cycles). The different lines represent actual data from [26] (red), estimation from CLME after Kalman filter (blue), estimation from AO (green), and estimation from fused estimator (yellow). The position and velocity errors are given in panels (b) and (d), respectively. The evolution of the window-averaged mean error of the AO is given in panel (e), and the corresponding weights of AO in panel (f). Different shades of grey in the background separate successive cycles.

paring the correlation between each of the three estimators (CLME only, AO only, fused) over each cycle and the actual kinematic signals from the whole dataset (Fig. 8). We decided to focus on the first five cycles of each trial, as this is the epoch where the transition between both estimators is most valuable. As expected, CLME provides consistent estimates across cycles for both position and velocity, given that it is time-invariant. Also, the position correlation is higher than the velocity correlation, i.e. about 0.81 for position as compared to 0.14 for velocity. AO obey a dynamic learning trend: their performance is poor during the first cycle, and improves together with their convergence (correlation of about 0.30 in position, and even negative in velocity). They eventually reach a correlation of 0.96 in position and 0.86 in velocity, indicating that they provide a high quality estimate after convergence. As captured by the inter-trial standard deviation, the variability of the AO-based estimate also decreases over time. This variability is equal to 0.28 for the first cycle, and decreases to 0.03 for the fifth one. The fused estimator starts with a performance close to the CLME estimator, and then shifts towards the AO. This holds for both mean and standard deviation.

VII. Conclusion and Discussion

This paper presents a novel method to predict the kinematics of missing leg joint(s) based on corresponding kinematic

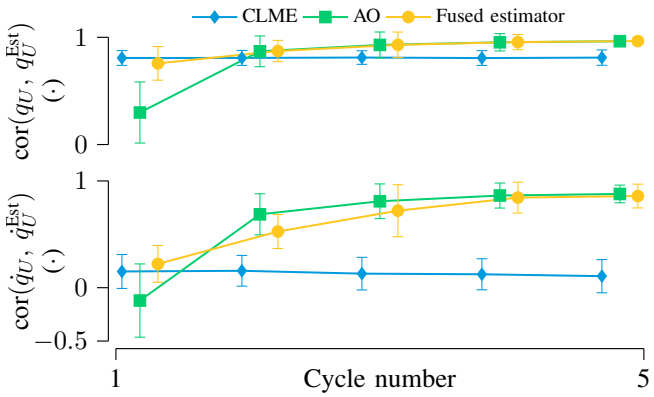


Fig. 8. Correlation between the ground-truth kinematic signals from the datasets and the corresponding estimation provided by the three estimators: CLME only, AO only, and fused one. Values are given for the first five cycles of each trials. Error bars capture the inter-trials standard deviation.

signals measured on the other leg. The method is designed for both steady-state walking and task transitions, and is based on two estimators of kinematic signals: CLME, a correlation-based approach that works during both transients and steady-state locomotion, and AO, which exploits the rhythmicity of the task and therefore works only during steady-state epochs. First, both methods were presented, and then the fusion approach was explained. We applied the fused estimator to estimate hip kinematic signals from two different datasets. The parameters of the different estimators were computed in a way that they could be used for a generalized population, although this brought some issues for the CLME-based estimation, especially with respect to the position offset. As expected, our new method takes the best of both individual approaches, favoring CLME when AO have not yet converged, and AO otherwise.

We observed that CLME is not robust to position offset. This is expected since its gains are computed on normalized data. Note that this does not degrade the performance metric shown in Fig. 8, i.e. correlation, since it is not sensitive to offset. However, poor offset estimation would be critical in an actual application, such as controlling an orthosis or prosthesis. In our future work, we will investigate the possibility of using the offset estimated by AO, i.e. the state variable α_0, to mitigate this error in the CLME-based estimator, even when AO have not yet converged. Indeed, preliminary results suggest that α_0 converges faster than the other AO state variables.

In the present paper, the performance of our estimator is evaluated only during steady-state walking. However, our method is also designed to handle sharp transients as well. During transitions, e.g. between standing still and walking, we would expect CLME to quickly supersede AO, since the AO error would increase rapidly. Other datasets include such transitions (e.g. [28]) and could be used to assess our method. Preliminary results indicate a good correlation between the CLME-based estimation and the hip signal during such transitions, as well as for other transitions, such as from

walking to standing and between different walking speeds. The correlation analysis showed that the contribution of the CLME to our fused estimator is larger in the first cycle, where the convergence of the AO is low. Effective control of powered devices requires accurate estimation for each cycle, including the very first one, thus highlighting the necessary contribution of CLME in our method, even if limited to few cycles. Moreover, we expect that locomotion in an ecological environment – i.e. out of the treadmill – would contain much more walking speed variations and transitions between tasks, thus providing a larger role to the CLME.

Our newly developed method is well suited for real-time applications, since neither CLME nor AO require large computational power. Instead, both rely on a minimal amount of code. Furthermore, input signals can be acquired in real-time, for example using IMUs.

Our future work will focus in implementing the proposed estimator for the control of our designed hip prosthesis [11] and evaluating its performance in generating reference signals for this device.

REFERENCES

[1] Y. Fang and Z. F. Lerner, "Bilateral vs. Paretic-Limb-Only Ankle Exoskeleton Assistance for Improving Hemiparetic Gait: A Case Series," *IEEE Robot. Autom. Lett.*, vol. 7, no. 2, pp. 1246–1253, Apr. 2022. DOI:10.1109/lra.2021.3139540

[2] B. Kalita, J. Narayan, and S. K. Dwivedy, "Development of Active Lower Limb Robotic-Based Orthosis and Exoskeleton Devices: A Systematic Review," *Int J of Soc Robotics*, vol. 13, no. 4, pp. 775–793, July 2021. DOI:10.1007/s12369-020-00662-9

[3] F. Heremans, J. Evrard, D. Langlois, and R. Ronsse, "A Lightweight and Compact Lockable Parallel Spring Enhances the Performance of a Powered Ankle-Foot Prosthesis," in *2024 10th IEEE RAS/EMBS International Conference for Biomedical Robotics and Biomechatronics (BioRob)*, Sept. 2024, pp. 407–412. DOI:10.1109/biorob60516.2024.10719808

[4] I. Fagioli, A. Mazzarini, C. Livolsi, E. Gruppioni, N. Vitiello, S. Crea, and E. Trigili, "Advancements and Challenges in the Development of Robotic Lower Limb Prostheses: A Systematic Review," *IEEE Transactions on Medical Robotics and Bionics*, vol. 6, no. 4, pp. 1409–1422, Nov. 2024. DOI:10.1109/tmrb.2024.3464126

[5] H. Laloyaux and R. Ronsse, "Extraction of simple monophasic motor primitives towards bio-inspired locomotion assistance," in *2019 IEEE International Conference on Cyborg and Bionic Systems (CBS)*, Sept. 2019, pp. 253–260. DOI:10.1109/cbs46900.2019.9114458

[6] T. K. Best, K. R. Embry, E. J. Rouse, and R. D. Gregg, "Phase-Variable Control of a Powered Knee-Ankle Prosthesis over Continuously Varying Speeds and Inclines," in *2021 IEEE/RSJ International Conference on Intelligent Robots and Systems (IROS)*, Sept. 2021, pp. 6182–6189. DOI:10.1109/iros51168.2021.9636180

[7] A. Mohammadi and R. D. Gregg, "Variable Impedance Control of Powered Knee Prostheses Using Human-Inspired Algebraic Curves," *Journal of Computational and Nonlinear Dynamics*, vol. 14, no. 101007, Sept. 2019. DOI:10.1115/1.4043002

[8] S. K. Au, J. Weber, and H. Herr, "Powered Ankle–Foot Prosthesis Improves Walking Metabolic Economy," *IEEE Trans. Robot.*, vol. 25, no. 1, pp. 51–66, Feb. 2009. DOI:10.1109/tro.2008.2008747

[9] T. K. Best, C. G. Welker, E. J. Rouse, and R. D. Gregg, "Data-Driven Variable Impedance Control of a Powered Knee–Ankle Prosthesis for Adaptive Speed and Incline Walking," *IEEE Transactions on Robotics*, vol. 39, no. 3, pp. 2151–2169, June 2023. DOI:10.1109/tro.2022.3226887

[10] F. Dzeladini, J. van den Kieboom, and A. Ijspeert, "The contribution of a central pattern generator in a reflex-based neuromuscular model," *Front Hum Neurosci*, vol. 8, p. 371, 2014. DOI:10.3389/fnhum.2014.00371

[11] L. Devillez, B. Herman, and R. Ronsse, "Design of a Compact Active Hip Prosthesis with Human-Like Range of Motion and Torque," in *2024 10th IEEE RAS/EMBS International Conference for Biomedical Robotics and Biomechatronics (BioRob)*, Sept. 2024, pp. 160–166. DOI:10.1109/biorob60516.2024.10719919

[12] N. Hogan and D. Sternad, "Dynamic primitives in the control of locomotion," *Front. Comput. Neurosci.*, vol. 7, June 2013. DOI:10.3389/fncom.2013.00071

[13] M. R. Tucker, J. Olivier, A. Pagel, H. Bleuler, M. Bouri, O. Lambercy, J. d. R. Millán, R. Riener, H. Vallery, and R. Gassert, "Control strategies for active lower extremity prosthetics and orthotics: A review," *Journal of NeuroEngineering and Rehabilitation*, vol. 12, no. 1, p. 1, Jan. 2015. DOI:10.1186/1743-0003-12-1

[14] A. H. Hansen and D. S. Childress, "Investigations of roll-over shape: Implications for design, alignment, and evaluation of ankle-foot prostheses and orthoses," *Disability and Rehabilitation*, vol. 32, no. 26, pp. 2201–2209, Jan. 2010. DOI:10.3109/09638288.2010.502586

[15] W. J. Wang, J. Li, W. D. Li, and L. N. Sun, "An Echo-Based Gait Phase Determination Method of Lower Limb Prosthesis," *Advanced Materials Research*, vol. 706–708, pp. 629–634, 2013. DOI:10.4028/www.scientific.net/amr.706-708.629

[16] R. Ronsse, S. M. M. De Rossi, N. Vitiello, T. Lenzi, M. C. Carrozza, and A. J. Ijspeert, "Real-Time Estimate of Velocity and Acceleration of Quasi-Periodic Signals Using Adaptive Oscillators," *IEEE Trans. Robot.*, vol. 29, no. 3, pp. 783–791, June 2013. DOI:10.1109/tro.2013.2240173

[17] H. Vallery and M. Buss, "Complementary limb motion estimation based on interjoint coordination using Principal Components Analysis," in *2006 IEEE International Conference on Control Applications*, Oct. 2006, pp. 933–938. DOI:10.1109/cacsd-cca-isic.2006.4776770

[18] H. Vallery, R. Ekkelenkamp, M. Buss, and H. van der Kooij, "Complementary Limb Motion Estimation based on Interjoint Coordination: Experimental Evaluation," in *2007 IEEE 10th International Conference on Rehabilitation Robotics*, June 2007, pp. 798–803. DOI:10.1109/icorr.2007.4428516

[19] H. Vallery, E. H. F. van Asseldonk, M. Buss, and H. van der Kooij, "Reference Trajectory Generation for Rehabilitation Robots: Complementary Limb Motion Estimation," *IEEE Trans. Neural Syst. Rehabil. Eng.*, vol. 17, no. 1, pp. 23–30, Feb. 2009. DOI:10.1109/tnsre.2008.2008278

[20] H. Vallery, R. Burgkart, C. Hartmann, J. Mitternacht, R. Riener, and M. Buss, "Complementary limb motion estimation for the control of active knee prostheses," *Biomedical Engineering / Biomedizinische Technik*, vol. 56, no. 1, pp. 45–51, Feb. 2011. DOI:10.1515/bmt.2010.057

[21] N. St-Onge and A. G. Feldman, "Interjoint coordination in lower limbs during different movements in humans," *Exp Brain Res*, vol. 148, no. 2, pp. 139–149, Jan. 2003. DOI:10.1007/s00221-002-1212-8

[22] A. Kiffe, C. Graf, and J. Maas, "Feed forward control concept for electric drives," in *2012 IEEE/ASME (AIM)*, July 2012, pp. 332–337. DOI:10.1109/aim.2012.6266046

[23] D. Simon, *Optimal State Estimation: Kalman, H Infinity, and Nonlinear Approaches*. John Wiley & Sons, June 2006.

[24] A. Kelly, "A 3D State Space Formulation of a Navigation Kalman Filter for Autonomous Vehicles:," Defense Technical Information Center, Fort Belvoir, VA, Tech. Rep., May 1994. http://www.dtic.mil/docs/citations/ADA282853

[25] L. Righetti, J. Buchli, and A. J. Ijspeert, "Dynamic Hebbian learning in adaptive frequency oscillators," *Physica D: Nonlinear Phenomena*, vol. 216, no. 2, pp. 269–281, Apr. 2006. DOI:10.1016/j.physd.2006.02.009

[26] K. Scherpereel, D. Molinaro, O. Inan, M. Shepherd, and A. Young, "A human lower-limb biomechanics and wearable sensors dataset during cyclic and non-cyclic activities," *Sci Data*, vol. 10, no. 1, p. 924, Dec. 2023. DOI:10.1038/s41597-023-02840-6

[27] J. Camargo, A. Ramanathan, W. Flanagan, and A. Young, "A comprehensive, open-source dataset of lower limb biomechanics in multiple conditions of stairs, ramps, and level-ground ambulation and transitions," *Journal of Biomechanics*, vol. 119, p. 110320, Apr. 2021. DOI:10.1016/j.jbiomech.2021.110320

[28] A. Sharma, V. Rai, M. Calvert, Z. Dai, Z. Guo, D. Boe, and E. Rombokas, "A Non-Laboratory Gait Dataset of Full Body Kinematics and Egocentric Vision," *Sci Data*, vol. 10, p. 26, Jan. 2023. DOI:10.1038/s41597-023-01932-7

PLEXUS Hand: Lightweight Four-Motor Prosthetic Hand Enabling Precision–Lateral Dexterous Manipulation

Yuki Kuroda[1], Tomoya Takahashi[1], Cristian C. Beltran-Hernandez[1], Masashi Hamaya[1] and Kazutoshi Tanaka[1]

***Abstract*— Electric prosthetic hands should be lightweight to decrease the burden on the user, shaped like human hands for cosmetic purposes, and have motors inside to protect them from damage and dirt. In addition to the ability to perform daily activities, these features are essential for everyday use of the hand. In-hand manipulation is necessary to perform daily activities such as transitioning between different postures, particularly through rotational movements, such as reorienting cards before slot insertion and operating tools such as screwdrivers. However, currently used electric prosthetic hands only achieve static grasp postures, and existing manipulation approaches require either many motors, which makes the prosthesis heavy for daily use in the hand, or complex mechanisms that demand a large internal space and force external motor placement, complicating attachment and exposing the components to damage. Alternatively, we combine a single-axis thumb and optimized thumb positioning to achieve basic posture and in-hand manipulation, that is, the reorientation between precision and lateral grasps, using only four motors in a lightweight (311 g) prosthetic hand. Experimental validation using primitive objects of various widths (5–30 mm) and shapes (cylinders and prisms) resulted in success rates of 90–100% for reorientation tasks. The hand performed seal stamping and USB device insertion, as well as rotation to operate a screwdriver.**

I. INTRODUCTION

Electric prosthetic hands are used by people who cannot perform hand functions because of congenital conditions or acquired causes such as accidents. These prostheses should be shaped similar to a biological human hand for cosmetic purposes, be lightweight (maximum acceptable weight is around 500 g [1]) to decrease the burden on the user, have motors inside the hand due to protect them from damage and dirt, and be capable of performing activities of daily living (ADLs) [2], [3], [4]. ADLs include fundamental tasks necessary for daily self-care, including housework and communication, which involve grasping and manipulating various objects such as tableware, writing implements, cash, and tools. As currently used prosthetic hands can only provide grasping functions [5], [6], [7], we focus on incorporating in-hand manipulation capabilities to move objects between different grasping postures.

As the complex movements for in-hand manipulation require multiple motors, maintaining a lightweight design for daily use is challenging. A modular prosthetic limb is a sophisticated prosthetic hand that can perform in-hand manipulation [8]. Although its 10 motors afford this capability, its weight of 1315 g makes it too heavy for daily use.

[1]OMRON SINIC X Corporation, Tokyo, Japan. yuki.kuroda@sinicx.com

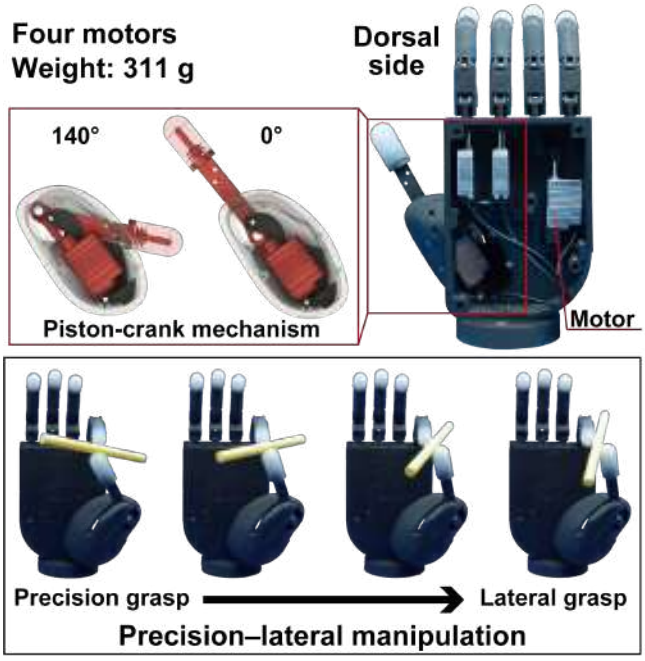


Fig. 1: Configuration of PLEXUS hand and images of precision–lateral manipulation.

In this study, we develop an electric prosthetic hand that can perform in-hand manipulation and basic hand postures with a minimal number of motors (NoM) for a lightweight design. Our approach enables rotational movements between different grasp types. To this end, we focus on the transition between precision and lateral grasps, which we refer to as precision–lateral manipulation, as illustrated in Fig. 1. This rotational capability enables performing essential daily tasks (e.g., reorienting objects such as cards before slot insertion and operating screwdrivers and other tools that require rotational manipulation) while minimizing compensatory movements.

We combined a single-axis thumb design at the carpometacarpal (CM) joint with optimized positioning. Liu et al. [9] reported that, although the human thumb is anatomically capable of movement along more than five axes, it primarily rotates around a single axis at the CM joint during daily grasping tasks, particularly during distal grasping, such as when using fingertips. Inspired by these findings, we propose a prosthetic hand design that enables in-hand manipulation in addition to basic hand postures by optimizing the position of the CM joint rotation axis in the thumb. This optimization maximizes the range of object widths for precision–lateral manipulation while ensuring the

TABLE I: Related works

	Hand	Weight (g)	Motor position	NoM (thumb)	Five basic postures	Manipulation
Prosthetic hands	**PLEXUS hand (proposed)**	**311**	Interior	**4 (1)**	5	**precision–lateral**
	BIT Hand [10], [11]	330	Interior	5 (1)	4	
	i-limb quantum [7]	454–628	Interior	6 (2)	5	
	Bebionic [6]	495–529 [5]	Interior	5 (1)	5	
	TUAT/Karlsruhe humanoid hand [12]	125	Interior	1	4	
	F hand [13]		Interior	1	4	
	SoftHand Pro [14]	520	Interior	1	4	
	Belter and Dollar 2013 [15]	350	Interior	1	4	
	Hannes hand [16]	480	Interior	1	4	
	Modular prosthetic limb [8]	1315	Interior	10 (4)	5	rolling
Robotic Hands	Shadow dexterous hand [17]	4000	Exterior	20 (5)	5	precision–lateral + reposition
	Twendy-one hand [18]		Interior	13 (4)	5	precision–lateral + reposition
	Allegro hand [19]	1500	Interior	16 (4)	5	precision–lateral + reposition
	EthoHand [20]		Exterior	7 (3)	5	precision–lateral
	Proposal by Kontoudis et al. [21]	650	Exterior	4 (2)	4	slight rolling + slight reposition

capability of basic hand postures.

We evaluated the performance of the prosthetic hand by testing the rotation of cylinders and square prisms with widths ranging from 5 to 30 mm and other objects in daily life. The results indicated high success rates for rotating cylinders, prisms, cards, personal seals, spoons, and screwdrivers. Practical applications included using personal seals, inserting USB devices, and turning screws using a screwdriver, suggesting the high potential effectiveness of the proposed prosthetic hand in ADLs.

The main contribution of this study is the development of a lightweight (311 g) prosthetic hand that enables both basic hand postures and precision–lateral manipulation using only four motors.

II. RELATED WORK

Two categories of hands, that is, practical electric prosthetic hands and anthropomorphic robotic hands capable of in-hand manipulation, are discussed. Table I summarizes related work. We analyze the characteristics of available solutions based on existing studies and demonstrations focusing on total NoM, NoM in the thumb, weight, motor placement, capabilities in five basic hand postures (i.e., power, precision, tripod, and lateral grasps, as well as index pointing) [22], [23] and manipulation. Table I defines slight rolling and repositioning as minimal in-hand manipulations that do not enable transitions between static grasp postures.

A. Anthropomorphic Robotic Hands with the Capability of Daily Life In-Hand Manipulation

In-hand manipulation can be achieved through two approaches: high-NoM designs (e.g., 13 motors [18], 16 motors [19], and 20 motors [17]) and mechanical solutions with fewer motors. Notable examples of the latter include EthoHand (seven motors) [20], which employs a tendon-driven ball joint for the thumb to reproduce human-like movements, and the design by Kontoudis et al., which achieves thumb abduction, adduction, and flexion using a tendon-driven differential mechanism with only two motors [21]. Although these mechanical solutions achieve in-hand manipulation with fewer actuators, their mechanisms occupy space on the palm, impeding internal motor placement, which is crucial to ensure durability and space efficiency when attached to the residual limb of the user [3]. Consequently, existing solutions either became too heavy (exceeding 1500 g) because of the large NoM or required palm space for their mechanisms. Our prosthetic hand addresses these limitations with a four-motor design weighing 311 g, which can perform five basic postures and in-hand manipulation while maintaining all mechanisms inside the hand.

B. Lightweight Prosthetic Hand with Low NoM

A modular prosthetic limb (10 motors) was developed as a prosthetic hand and can perform object rotation. However, its large NoM makes it too heavy (1315 g) for typical prosthesis users [8]. To date, several practical electrical prosthetic hands have been proposed. Among them, the two widely adopted electric prosthetic hands in clinical use are bebionic (five motors) [6] and i-Limb (six motors) [7]. Most practical hands weigh approximately 500 g, which is the minimum weight of prosthetic hands mentioned in previous studies [1]. However, further weight reduction is necessary to minimize the burden on the users.

Recently, electric prosthetic hands that incorporate adaptive grasp mechanisms (e.g., differential mechanisms) have been developed for achieving a lighter weight while enabling diverse grasping motions with a low NoM. The TUAT/Karlsruhe humanoid hand, which combines compound four-bar linkages with differential mechanisms, achieves four basic hand postures and all 14 types of Kamakura's grasp taxonomy with only one motor [12]. Several other studies have achieved coordinated finger movements using differential mechanisms, enabling various hand postures with minimal actuation [13]–[16].

Although the abovementioned developments represent a significant progress in static grasping, technical challenges

TABLE II: Parameters of PLEXUS Hand.

Grasp range requirements	
Radius for precision grasp [R_{Gmin}, R_{Gmax}]	[0, 60] mm
Radius for lateral grasp [R_{Gmin}, R_{Gmax}]	[0, 30] mm
Radius for tripod grasp [R_{Tmin}, R_{Tmax}]	[10, 80] mm
Width for in-hand manipulation [W_{min}, W_{max}]	[0, 30] mm
Common geometric parameters	
δ_m (maximum fingertip deformation)	4.87 mm
θ_{min} (minimum grasp angle)	110°
α_{perm} (permitted contact angle)	30°

related to in-hand manipulation persist because the mechanically linked adaptive mechanism that connects all finger movements is incompatible with the independent finger control required for object manipulation [24]. Existing advanced anthropomorphic hands require from two to four motors [20], [21] for thumb rotation and two motors [17], [18], [19] for each non-thumb finger for translational operations, thereby making implementation challenging in prosthetic hands that must be lightweight and have internal actuators. In contrast, our hand achieves in-hand manipulation with a single motor for the thumb by combining a single-axis thumb design at the CM joint with optimized positioning.

III. HAND DESIGN OPTIMIZATION

A. Design Requirements

1) Grasping Requirements: Cipriani et al. claimed that a hand should be able to perform five basic postures: power, precision, tripod, and lateral grasps, as well as index pointing [22], [23]. The range of graspable object widths is based on the inter-fingertip distance, and only fingertip-based grasping postures (i.e., precision, tripod, and lateral grasps) are considered because palm-based grasping (i.e., power grasp) has uncertain contact positions, hindering range definition. Unlike human-enveloping grasps, prosthetic hands achieve a power grasp by adding palm contact to fingertip-based grasping. Therefore, satisfying the geometric requirements for precision grasping ensures power grasping. Based on daily object grasping analysis [25] and considering contact position uncertainty, we set the grasp range to approximately three times the average grasping width, as indicated in Table II.

2) In-Hand Manipulation Requirements: The hand must handle flat and curved surfaces to accommodate the manipulation of objects with different geometries. Based on daily object-grasping analysis studies [25], the average object width for lateral and precision grasps is approximately 20 mm. We set the requirement to 30 mm for providing a margin above this average to perform in-hand manipulation.

3) Implementation Requirements: Actuators should be placed inside the hand for durability and space limitations [3]. In addition, actuation must enable independent control of the thumb, index, and middle fingers for basic postures, with a synergistic ring–little finger actuation for achieving a power grasp using a minimal NoM. The selected prosthetic hand dimensions are based on the 50th percentile of the Japanese anthropometric data [26]. Moreover, the prosthesis employs actuators equivalent to those in clinically validated hands [10], [11] to ensure sufficient grasping force, and they should achieve a significantly lower weight (under 350 g, excluding electronics) than common electric prostheses [6], [7].

Algorithm 1 Optimize thumb configuration for grasping and manipulation

Require: Four-finger configuration, search ranges, grasp constraints, manipulation parameters
Ensure: Optimal thumb configuration ω_{opt} (x, y, z, roll, pitch, yaw)
function FINDOPTIMALTHUMBCONFIGURATION
  $\Omega_{valid} \leftarrow \emptyset$ ▷ Valid configurations
  for each thumb configuration ω in search space **do**
    if ISVALIDGRASP(ω) **then**
      $\Omega_{valid} \leftarrow \Omega_{valid} \cup \{\omega\}$
    end if
  end for
  $\omega_{opt} \leftarrow$ null, $w_{max} \leftarrow 0$ ▷ Best configuration and its range
  for each $\omega \in \Omega_{valid}$ **do**
    $W(\omega) \leftarrow$ CALCULATEMANIPULATIONRANGE(ω)
    if $|W(\omega)| > w_{max}$ **then**
      $\omega_{opt} \leftarrow \omega$, $w_{max} \leftarrow |W(\omega)|$
    end if
  end for
  return ω_{opt}
end function

B. Optimization Method

We aim to maximize the range of precision–lateral manipulation through optimal thumb positioning to achieve better manipulation capabilities for common objects while satisfying the requirements described in Sec. III-A. A manual search is impractical because even small position errors can lead to manipulation failures. This challenge explains why conventional prosthetic hands, in which thumb positioning is predominantly based on anatomical structures [27], struggle with precision–lateral manipulation. Hence, we employ optimization to determine the position using the parameters defined in Table II.

We propose a two-stage optimization process to find the optimal thumb axis configuration, ω_{opt} (x, y, z, roll, pitch, and yaw). First, we identify configurations that satisfy all grasp requirements to reduce the search space and then select the configuration that enables the largest range of object widths for precision–lateral manipulation.

For simplicity, we model the fingertips and grasped objects as spheres. The grasped object is assumed to be sufficiently light such that its mass can be neglected. Let $\boldsymbol{c}_{\text{T}}$, $\boldsymbol{c}_{\text{I}}$, and $\boldsymbol{c}_{\text{M}}$ represent the position vectors of the thumb, index, and middle fingers, respectively, and $\boldsymbol{c}_{\text{O}}$ represent the position of the grasped object. Their radii are r_{T}, r_{I}, r_{M}, and R.

The following sections describe the grasp requirements and manipulation range calculations implemented in ISVALIDGRASP and CALCULATEMANIPULATIONRANGE. The complete optimization process is summarized in Algorithm 1.

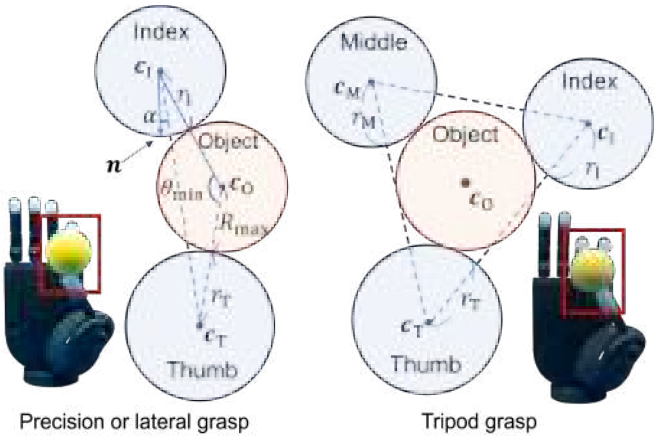


Fig. 2: Geometric definitions of fingers and object to calculate grasp requirements. In precision and lateral grasps, the orientation of reference vector $\boldsymbol{n}$ differs. This vector defines the grasping direction of the object.

1) Grasp Validation: Function IsValidGrasp in Algorithm 1 evaluates whether a given thumb configuration satisfies the requirements for precision, lateral, and tripod grasps. For thumb configuration ω to be valid, all three grasp types must be achievable within their respective object size ranges.

For precision and lateral grasps, we consider the relative positions between thumb position $\boldsymbol{c}_{\mathrm{T}}(\omega)$ determined by configuration parameters ω and index finger position $\boldsymbol{c}_{\mathrm{I}}$. A configuration is considered valid if it satisfies the following geometric range requirements:

- The maximum graspable distance, R_{max}, calculated as shown in Fig. 2, must satisfy $R_{\mathrm{max}} \geq R_{\mathrm{Gmax}}$. This limit is determined by θ_{min} (illustrated in Fig. 2), which represents the minimum angle between vectors $\boldsymbol{c}_{\mathrm{T}}(\omega) - \boldsymbol{c}_{\mathrm{O}}$ and $\boldsymbol{c}_{\mathrm{I}} - \boldsymbol{c}_{\mathrm{O}}$ required for stable grasping considering friction.
- The minimum distance between fingertips, R_{min}, occurs when $\boldsymbol{c}_{\mathrm{T}}(\omega)$, $\boldsymbol{c}_{\mathrm{I}}$, and $\boldsymbol{c}_{\mathrm{O}}$ are colinear, and it must satisfy $R_{\mathrm{min}} \leq R_{\mathrm{Gmin}}$.

Grasping is established when the following conditions are satisfied:

- As illustrated in Fig. 2, angle α between reference vector $\boldsymbol{n}$ (normal to the optimal contact surface of the index finger) and the grasp direction must satisfy $-\alpha_{\mathrm{perm}} \leq \alpha \leq \alpha_{\mathrm{perm}}$, where α_{perm} is empirically determined due to the lack of standardized angular definitions for grasp types.
- The force-applying digit (i.e., index finger for precision grasp and thumb for lateral grasp) must maintain its motion direction at an angle less than 45° relative to vector $\boldsymbol{c}_{\mathrm{T}}(\omega) - \boldsymbol{c}_{\mathrm{I}}$ and $\boldsymbol{c}_{\mathrm{I}} - \boldsymbol{c}_{\mathrm{T}}(\omega)$, respectively, to maintain the appropriate force direction.

For the tripod grasp, we evaluate the triangle formed by the thumb ($\boldsymbol{c}_{\mathrm{T}}(\omega)$), index finger ($\boldsymbol{c}_{\mathrm{I}}$), and middle finger ($\boldsymbol{c}_{\mathrm{M}}$). The object center, $\boldsymbol{c}_{\mathrm{O}}$, must lie within this triangle, and the achievable grasp radii, $[R_{\mathrm{min}}, R_{\mathrm{max}}]$, must encompass the specified range ($R_{\mathrm{min}} \leq R_{\mathrm{Tmin}}$ and $R_{\mathrm{max}} \geq R_{\mathrm{Tmax}}$).

2) Manipulation Range Analysis: Function CalculateManipulationRange analyzes the precision–lateral transition path where the thumb moves from the lateral to the precision grasp position to determine the range of object sizes that can be manipulated. Let $i \in I$ and $j \in J$ be discretized steps along the motion ranges of the index finger and thumb, respectively. For each index finger position $\boldsymbol{c}_{\mathrm{I}}(i)$ and corresponding thumb position $\boldsymbol{c}_{\mathrm{T}}(\omega, j)$ determined by configuration ω, we identify two critical points: $j_{i,\mathrm{L}} \in J$ (i.e., the last position allowing lateral grasp, Sec. III-B.1) and $j_{i,\mathrm{P}} \in J$ (i.e., the first position permitting precision grasp, Sec. III-B.1). The manipulation interval is $J_m = \{j \in J \mid j_{i,\mathrm{L}} \leq j \leq j_{i,\mathrm{P}}\}$.

For each index position i, the maximum and minimum distances during the transition are calculated as $d_{\mathrm{max}}(\omega, i) = \max_{j \in J_m} |\boldsymbol{c}_{\mathrm{I}}(i) - \boldsymbol{c}_{\mathrm{T}}(\omega, j)|$ and $d_{\mathrm{min}}(\omega, i) = \min_{j \in J_m} |\boldsymbol{c}_{\mathrm{I}}(i) - \boldsymbol{c}_{\mathrm{T}}(\omega, j)|$.

The range of manipulatable object widths $W_i(\omega)$ at each index position i for thumb configuration ω is defined as

$$W_i(\omega) = [d_{\mathrm{max}}(\omega, i) - (r_{\mathrm{T}} + r_{\mathrm{I}}), d_{\mathrm{min}}(\omega, i) - (r_{\mathrm{T}} + r_{\mathrm{I}}) + 2\delta_m], \tag{1}$$

where δ_m represents the allowable deformation of the flexible fingertip, calculated as $\delta_m = \sqrt{F/(\pi E)}$ [28] with an assumed pinch force $F = 10$ N based on a prosthetic hand using equivalent actuators [10], and Young's modulus E given in Table III. The lower bound is determined by subtracting the fingertip radii from the maximum distance, whereas the upper bound considers the additional grasp range enabled by fingertip deformation.

The overall manipulation range, $W(\omega)$, for the configuration is calculated as the intersection of the ranges across the set of all index finger positions I.

$$W(\omega) = \bigcap_{i \in I} W_i(\omega) \tag{2}$$

This ensures that objects within range $W(\omega)$ can be stably manipulated throughout the precision–lateral transition.

Among all valid thumb configurations Ω_{valid} found by IsValidGrasp, we select optimal configuration ω_{opt} that maximizes the manipulation range.

$$\omega_{\mathrm{opt}} = \arg\max_{\omega \in \Omega_{\mathrm{valid}}} |W(\omega)| \tag{3}$$

IV. PLEXUS Hand

Based on the optimization described in Sec. III, we engineered a prototype of the PLEXUS hand (Precision–Lateral dEXteroUS manipulation hand), incorporating the optimal thumb axis position as determined by our optimization algorithms. The PLEXUS hand achieves both precision–lateral manipulation and the basic hand postures required for prosthetic applications (Fig. 3) while maintaining a simple design with only four motors, including a single motor for the thumb. Table III lists the specifications of the PLEXUS hand and optimization conditions.

The PLEXUS hand features distinct actuation mechanisms for different digit groups. All digits are driven by linear actuators to simplify the control system integration.



Fig. 3: Execution of basic postures using PLEXUS hand. Index pointing was omitted because the index finger can clearly move independently.

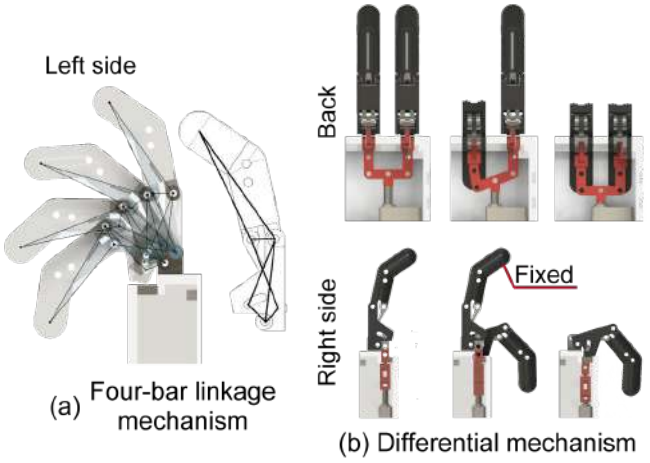


Fig. 4: (a) Actuation and structure of four-bar linkage mechanism. (b) Differential mechanism that distributes motion between the fingers. When one finger is constrained, the displacement is redirected entirely to the unconstrained finger. Without constraints, motion is distributed to both fingers equally.

i) Thumb: Driven by a LAS16-023D linear motor (Beijing Inspire Robots Technology, China) and utilizing a piston–crank mechanism [10] as the simplest solution for linear-to-rotary motion conversion, as shown in Fig. 1.

ii) Index and middle fingers: Actuated via four-bar linkage mechanisms [10], as shown in Fig. 4(a). Each mechanism transforms the linear motion of LAS10-023D actuators (Beijing Inspire Robots Technology) into natural curling movements, enabling multiple contact points with objects for stable grasping.

iii) Ring and little fingers: Sharing a single LAS10-023D actuator through a differential mechanism [13], as shown in Fig. 4(b). The differential mechanism automatically distributes the displacement of the actuator between both fingers. When one finger encounters an object, the other can continue to move, enabling adaptive grasping while reducing the number of actuators needed.

TABLE III: Specifications of PLEXUS hand.

Physical specifications	
Dimensions (W × D × H)	130 × 30 × 210 mm
Weight	311 g
NoM (thumb)	4 (1)
Main material	Nylon (3D printed)
Fingertip silicone	
Type	TSG-E10 (TANAC, Japan)
Young's modulus	134.3 kPa [29]
Optimization	
Optimization method	Grid search
Number of axis positions explored	19,200,000

V. EXPERIMENT AND RESULTS

We conducted a quantitative evaluation using primitive and common objects to verify the capability of the proposed prosthetic hand to perform precision–lateral manipulation across a range of object sizes and shapes and a preliminary demonstration of practical applications for validating the effectiveness of the hand in real-world scenarios.

A. Experiment 1: Quantitative Evaluation with Primitive and Common Objects

1) Objects Used: The following two object categories were used for Experiment 1:

- **Primitive objects:** Square prisms and cylinders with height of 120 mm. Both types varied in width/diameter from 5–30 mm in 5 mm increments, totaling six variations per object. These objects allowed us to evaluate performance on flat and curved surfaces.
- **Common objects of daily living:** Business card, light pen, heavy pen, seal stamp, spoon, and precision screwdriver [30]. These objects were chosen as representative examples of objects requiring precision–lateral manipulation in everyday situations.

2) Experimental Procedure: Sec. III-B.2 determines the optimization target range between the thumb positions corresponding to trajectory elements $j_{i,\mathrm{P}}$ and $j_{i,\mathrm{L}}$ for object manipulation. We implemented the following setup to experimentally validate the manipulation capability in this range. Considering mechanical errors and calibration constraints,

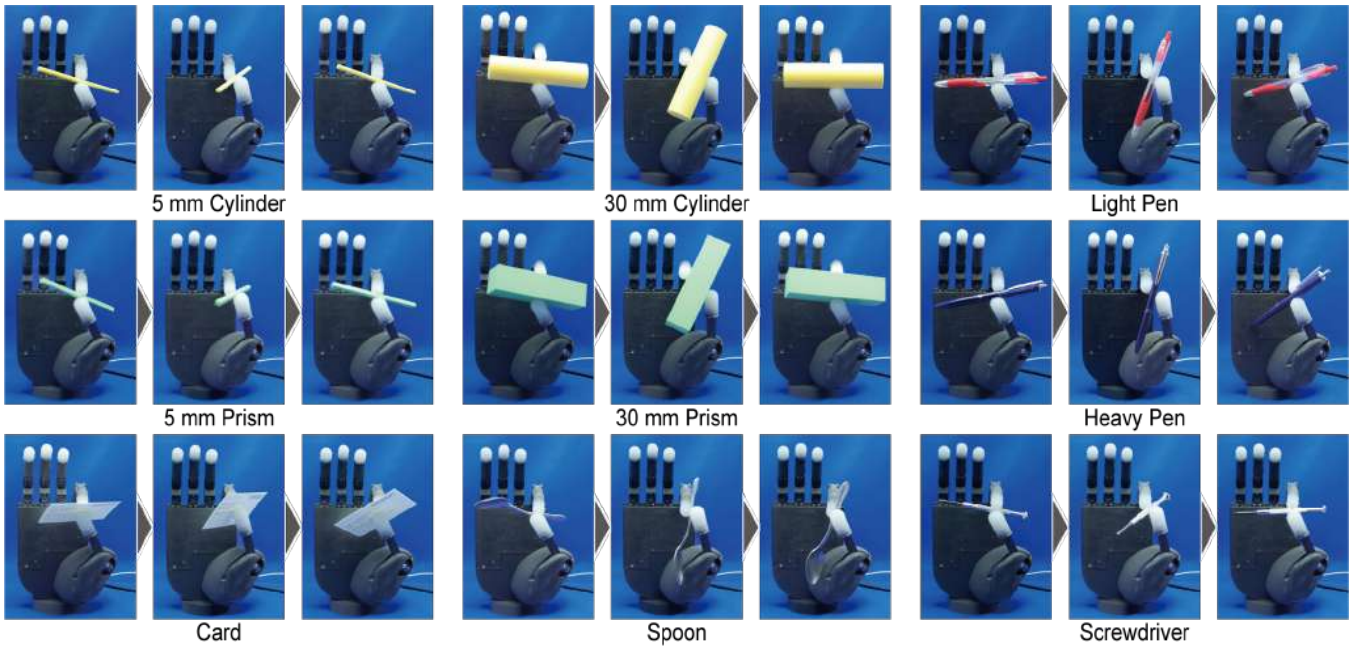


Fig. 5: Precision–lateral manipulation experiments for each object.

we prioritized achieving the target position for lateral grasp (corresponding to $j_{i,\mathrm{L}}$) because precise positioning is crucial owing to its dependence on geometric constraints. For precision grasping, we adopted an initial position with the thumb directly below the index finger. The index finger position was adjusted for each object to enable secure holding in a precision grasp and remained fixed throughout manipulation, while only the thumb moved. This setup resulted in a validation over an extended range, including the position corresponding to $j_{i,\mathrm{P}}$.

For each object, we performed the following steps 10 times:

i) The object was grasped near its center using a precision grasp, and its stability was manually confirmed by slightly moving the object.
ii) The manipulation from precision to lateral grasp was executed over 2.5 s, with the thumb moving to the position corresponding to $j_{i,\mathrm{L}}$ optimized for each object width.
iii) The grasp was maintained at the lateral position for 2 s to confirm stability.
iv) The manipulation from lateral back to precision grasp was executed over 2.5 s.

Manipulation was considered successful if the object was grasped during both transitions.

3) Results: The success rates for precision–lateral manipulation are listed in Table IV. Images of the experiment are shown in Fig. 5.

B. Experiment 2: Demonstration of Practical Applications

1) Experimental Setup: Although comprehensive testing with users wearing a prosthetic hand remains a key objective for future work, we conducted preliminary demonstrations in three practical scenarios to illustrate the potential real-world applications of our approach and developed prosthesis.

TABLE IV: Success rates for precision–lateral manipulation.

Width (mm)	Primitive type	Weight (g)	Success rate (%)
5	Cylinder	2.79	100
	Square prism	2.49	100
10	Cylinder	5.04	90
	Square prism	6.20	100
15	Cylinder	9.90	100
	Square prism	11.59	100
20	Cylinder	14.58	100
	Square prism	18.03	100
25	Cylinder	20.80	100
	Square prism	24.65	100
30	Cylinder	28.34	100
	Square prism	34.34	100
0.3	Card	1.16	100
10.3	Heavy pen	23.45	60
10.2	Light pen	9.75	50
9.9	Seal	4.68	100
1.7	Spoon	15.48	100
6.2	Screwdriver	21.22	80

i) **Precision screwdriver operation:** This task demonstrated turning screws with a precision screwdriver. The PLEXUS hand lacked the flexibility afforded by a human hand with a flexible palm for stabilization. This hindered steady handling of the screwdriver. Therefore, guides were used to maintain the position of the screwdriver. Developing a flexible palm for better object manipulation will be part of future work.
ii) **Seal (hanko) usage:** We also demonstrated the ability to pick up, manipulate, and apply a seal to a document. This task addressed a common need in Japan, particularly for package receipt confirmation.
iii) **USB device insertion:** Finally, we demonstrated the capability of the prosthetic hand to pick up, manipu-

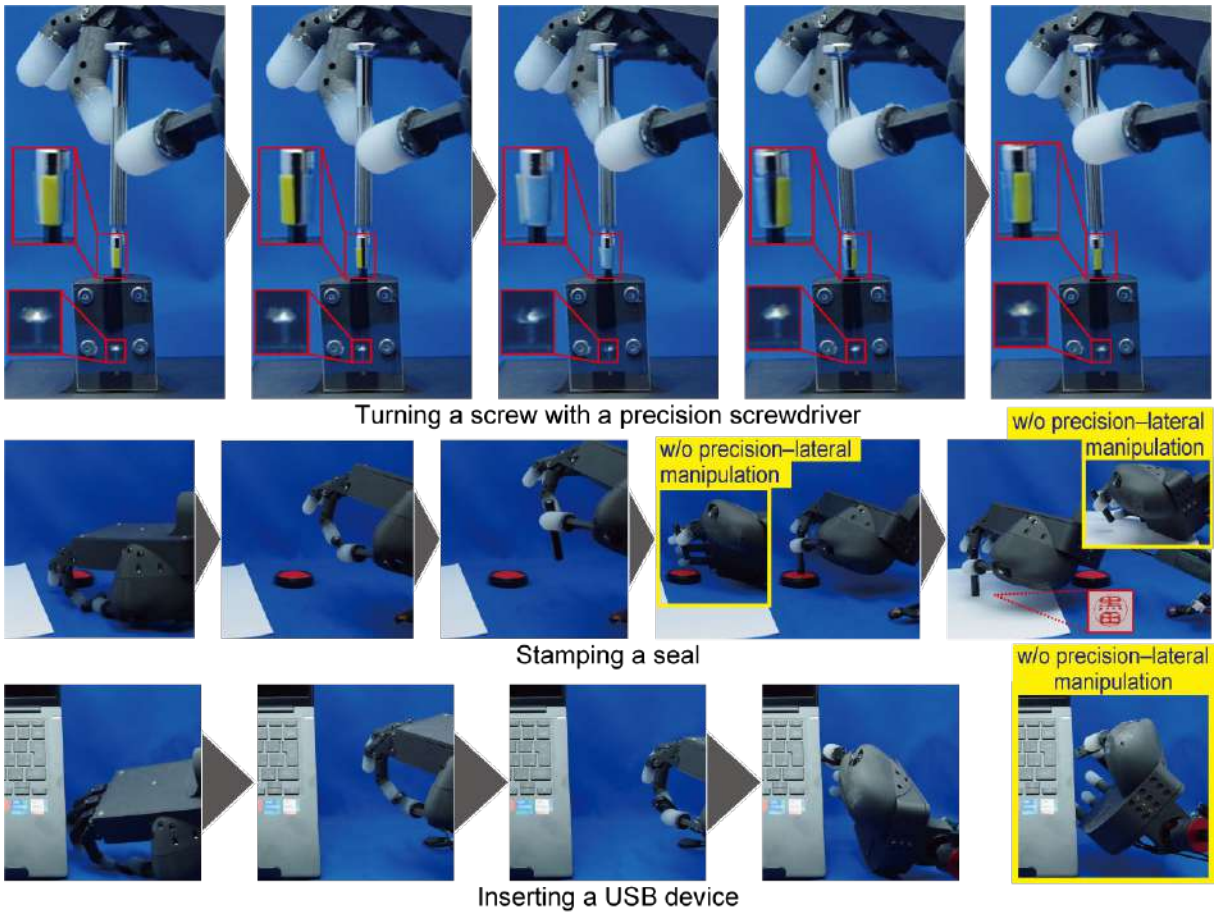


Fig. 6: Precision–lateral manipulation and its applications. Without precision–lateral manipulation (yellow frame), the palm blocks the movement.

late, and insert a USB device into a laptop port.

2) Results: Images of the practical demonstrations are shown in Fig. 6. The "w/o precision–lateral manipulation" condition refers to cases without precision–lateral manipulation, where palmar interference prevented successful task execution.

VI. DISCUSSION

A. Experimental Results

1) Primitive Objects: Experiments with primitive objects generally achieved high success rates. However, narrower objects with smaller contact areas tended to be less stable, particularly cylinders. This instability resulted from the reduced elastic force and friction caused by a low compression of the flexible tissue of the fingertip on small cross-sectional areas.

2) Common Objects of Daily Living: Experiments with common objects of daily living revealed instability when handling heavy items relative to their width and cylindrical shape, such as a pen or screwdriver, making it difficult to secure an adequate contact area. The primary challenge was the insufficient pinch force to manipulate or hold heavy objects. This limitation stemmed from our fixed-finger control approach. Although precision grasps achieved a proper force direction where the thumb trajectory intersected the motion path of the index finger, lateral grasps were limited because the fixed index finger could not be positioned along the motion path of the thumb. Future improvements should involve repositioning the index finger during manipulation, which may require advanced control systems with touch sensors for adaptive adjustments. Furthermore, a spherical finger shape decreased the contact area with cylindrical objects, making finger shape optimization another challenge for future work.

B. Practical Use

Conventional practical prosthetic hands cannot be used to perform rotational movements essential for tasks such as turning screws. Furthermore, they often require non-disabled hands to reposition objects or force users to adopt physically demanding postures [31], [32], [33]. Our developed prosthetic hand may increase the number of achievable ADLs while reducing the burden on the user by enabling in-hand manipulation using only the prosthetic hand.

VII. CONCLUSIONS

We present a novel approach to design a four-motor lightweight electric prosthetic hand that can perform five basic hand postures and precision–lateral manipulation. Our

PLEXUS hand demonstrates the ability to manipulate objects of various widths and common objects of daily living with high success rates. Our study and findings provide insights into improving the performance of electric prosthetic hands, potentially enhancing the quality of life of people with upper limb deficiencies.

ACKNOWLEDGMENT

This work was supported by JSPS KAKENHI Grant Number JP24KJ0248.

REFERENCES

[1] R. Vinet, Y. Lozac, N. Beaudry, and G. Drouin, "Design methodology for a multifunctional hand prosthesis," *Department Veterans Affairs Journal of Rehabilitation Research and Development*, vol. 32, pp. 316–324, 1995.

[2] Áine M Carroll and N. Fyfe, "A comparison of the effect of the aesthetics of digital cosmetic prostheses on body image and well-being," *Journal of Prosthetics and Orthotics*, vol. 16, pp. 66–68, Apr. 2004.

[3] A. Mohammadi, J. Lavranos, H. Zhou, R. Mutlu, G. Alici, Y. Tan, P. Choong, and D. Oetomo, "A practical 3d-printed soft robotic prosthetic hand with multi-articulating capabilities," *PLoS ONE*, vol. 15, p. e0232766, May 2020.

[4] J. T. Belter and A. M. Dollar, "Performance characteristics of anthropomorphic prosthetic hands," in *2011 IEEE International Conference on Rehabilitation Robotics (ICORR)*. IEEE, Jun. 2011, pp. 1–7.

[5] J. T. Belter, J. L. Segil, A. M. Dollar, and R. F. Weir, "Mechanical design and performance specifications of anthropomorphic prosthetic hands: A review," *Journal of Rehabilitation Research and Development*, vol. 50, pp. 599–618, 2013.

[6] Ottobock US, "bebionic," accessed: Nov. 21, 2024. [Online]. Available: https://www.ottobockus.com/prosthetics/upper-limb-prosthetics/solution-overview/bebionic-hand/#video-2

[7] Össur, "i-limb quantum," accessed: Nov. 21, 2024. [Online]. Available: https://www.ossur.com/en-us/prosthetics/arms/i-limb-quantum

[8] M. Johannes, J. Bigelow, J. Burck, S. Harshbarger, M. Kozlowski, and T. Doren, "An overview of the developmental process for the modular prosthetic limb," *Johns Hopkins APL Technical Digest (Applied Physics Laboratory)*, vol. 30, pp. 207–216, Oct. 2011.

[9] Y. Liu, B. Zeng, L. Jiang, H. Liu, and D. Ming, "Quantitative investigation of hand grasp functionality: Thumb grasping behavior adapting to different object shapes, sizes, and relative positions," *Applied Bionics and Biomechanics*, vol. 2021, pp. 1–17, Nov. 2021.

[10] Y. Wang, Y. Tian, H. She, Y. Jiang, H. Yokoi, and Y. Liu, "Design of an effective prosthetic hand system for adaptive grasping with the control of myoelectric pattern recognition approach," *Micromachines*, vol. 13, Feb. 2022.

[11] Y. Kuroda, T. Tsujimoto, T. Shimada, Y. Yabuki, D. Bai, Y. Yamanoi, Y. Jiang, J. Zhu, and H. Yokoi, "Development and clinical evaluation of a five-fingered myoelectric prosthetic hand with pattern recognition," in *2022 IEEE 4th Global Conference on Life Sciences and Technologies (LifeTech)*. IEEE, 2022, pp. 235–236.

[12] N. Fukaya, S. Toyama, T. Asfour, and R. Dillmann, "Design of the tuat/karlsruhe humanoid hand," in *2000 IEEE/RSJ International Conference on Intelligent Robots and Systems (IROS)*, vol. 3. IEEE, 2000, pp. 1754–1759.

[13] N. Fukaya and Y. Ogasawara, "Development of humanoid hand with cover integrated link mechanism for daily life work," in *2017 IEEE 6th Global Conference on Consumer Electronics (GCCE)*, vol. 2017-Janua, Oct. 2017, pp. 1–4.

[14] S. B. Godfrey, K. D. Zhao, A. Theuer, M. G. Catalano, M. Bianchi, R. Breighner, D. Bhaskaran, R. Lennon, G. Grioli, M. Santello, A. Bicchi, and K. Andrews, "The softhand pro: Functional evaluation of a novel, flexible, and robust myoelectric prosthesis," *PLOS ONE*, vol. 13, p. e0205653, Oct. 2018.

[15] J. T. Belter and A. M. Dollar, "Novel differential mechanism enabling two dof from a single actuator: Application to a prosthetic hand," in *2013 IEEE 13th International Conference on Rehabilitation Robotics (ICORR)*. IEEE, Jun. 2013, pp. 1–6.

[16] M. Laffranchi, N. Boccardo, S. Traverso, L. Lombardi, M. Canepa, A. Lince, M. Semprini, J. A. Saglia, A. Naceri, R. Sacchetti, E. Gruppioni, and L. D. Michieli, "The hannes hand prosthesis replicates the key biological properties of the human hand," *Science Robotics*, vol. 5, p. 467, Sep. 2020.

[17] Shadow Robot Company, "Dexterous hand series," accessed: Sep. 15, 2024. [Online]. Available: https://www.shadowrobot.com/dexterous-hand-series/

[18] S. Funabashi, A. Schmitz, T. Sato, S. Somlor, and S. Sugano, "Versatile in-hand manipulation of objects with different sizes and shapes using neural networks," in *2018 IEEE-RAS 18th International Conference on Humanoid Robots (Humanoids)*. IEEE, Nov. 2018, pp. 1–9.

[19] K. Or, M. Tomura, A. Schmitz, S. Funabashi, and S. Sugano, "Position-force combination control with passive flexibility for versatile in-hand manipulation based on posture interpolation," in *2016 IEEE/RSJ International Conference on Intelligent Robots and Systems (IROS)*. IEEE, Oct. 2016, pp. 2542–2547.

[20] C. Konnaris, C. Gavriel, A. A. Thomik, and A. A. Faisal, "Ethohand: A dexterous robotic hand with ball-joint thumb enables complex in-hand object manipulation," in *2016 6th IEEE International Conference on Biomedical Robotics and Biomechatronics (BioRob)*. IEEE, Jun. 2016, pp. 1154–1159.

[21] G. P. Kontoudis, M. Liarokapis, and K. G. Vamvoudakis, "An adaptive, humanlike robot hand with selective interdigitation: Towards robust grasping and dexterous, in-hand manipulation," in *2019 IEEE-RAS 19th International Conference on Humanoid Robots (Humanoids)*. IEEE, Oct. 2019, pp. 251–258.

[22] C. Cipriani, F. Zaccone, S. Micera, and M. C. Carrozza, "On the shared control of an emg-controlled prosthetic hand: Analysis of user-prosthesis interaction," *IEEE Transactions on Robotics*, vol. 24, pp. 170–184, Feb. 2008.

[23] C. Cipriani, M. Controzzi, and M. C. Carrozza, "Objectives, criteria and methods for the design of the smarthand transradial prosthesis," *Robotica*, vol. 28, pp. 919–927, Oct. 2010.

[24] M. Ciocarlie and P. Allen, "A design and analysis tool for underactuated compliant hands," *2009 IEEE/RSJ International Conference on Intelligent Robots and Systems (IROS)*, pp. 5234–5239, Oct. 2009.

[25] T. Feix, I. M. Bullock, and A. M. Dollar, "Analysis of human grasping behavior: Object characteristics and grasp type," *IEEE Transactions on Haptics*, vol. 7, pp. 311–323, Jul. 2014.

[26] M. Kouchi, "Aist nihonjin no te no sunpo data (aist dimension data of japanese hand)," 2012. [Online]. Available: https://www.airc.aist.go.jp/dhrt/hand/index.html

[27] J. Andrés-Esperanza, J. L. Iserte-Vilar, I. Llop-Harillo, and A. Pérez-González, "Effect of the thumb orientation and actuation on the functionality and performance of affordable prosthetic hands: Obtaining design criteria," *Biomimetics*, vol. 7, Dec. 2022.

[28] I. K. Amin Fakhari, Mehdi Keshmiri and S. H. Jazi, "Slippage control in soft finger grasping and manipulation," *Advanced Robotics*, vol. 30, no. 2, pp. 97–108, 2016.

[29] Y. Yabuki, "Superelastomer glove for emg prosthetic hand (published in japanese)," Ph.D. dissertation, The University of Electro-Communications, 2020. [Online]. Available: https://uec.repo.nii.ac.jp/records/9562

[30] C. Owsley, G. McGwin, M. E. Sloane, B. T. Stalvey, and J. Wells, "Timed instrumental activities of daily living tasks: Relationship to visual function in older adults," *Optometry and Vision Science*, vol. 78, pp. 350–359, May 2001.

[31] A. Chadwell, L. Kenney, M. H. Granat, S. Thies, J. Head, A. Galpin, R. Baker, and J. Kulkarni, "Upper limb activity in myoelectric prosthesis users is biased towards the intact limb and appears unrelated to goal-directed task performance," *Scientific Reports*, vol. 8, p. 11084, Jul. 2018.

[32] H. E. Williams, C. S. Chapman, P. M. Pilarski, A. H. Vette, and J. S. Hebert, "Myoelectric prosthesis users and non-disabled individuals wearing a simulated prosthesis exhibit similar compensatory movement strategies," *Journal of NeuroEngineering and Rehabilitation*, vol. 18, May 2021.

[33] A. J. Spiers, L. Resnik, and A. M. Dollar, "Analyzing at-home prosthesis use in unilateral upper-limb amputees to inform treatment & device design," in *2017 International Conference on Rehabilitation Robotics (ICORR)*. IEEE, Jul. 2017, pp. 1273–1280.

Optimization of an exosuit design for elbow and shoulder joints considering comfort and safety

Pierre Garnault[1] Yannick Aoustin[1] Vigen Arakelian[2]

***Abstract*—To ensure comfort and safety in the design of wearable robots, a multi-objective optimization method is defined for shoulder and elbow assistance. This optimization method is evaluated with a simulation platform implemented on Matlab integrating biomechanical features from the software OpenSim. Thus, the interaction forces between skin and cuffs and the metabolic cost could be estimated during design phase. Finally a drinking task trajectory is carried out to validate the efficiency of wearing an exosuit reducing the fatigue by 32%.**

***Index Terms*—exosuit, design, multi-objective optimization, OpenSim, human in the loop, biomechanics**

I. Introduction

For assistance and rehabilitation a new type of wearable device called "exosuit" is developed since a decade [1]. These devices are lightweight, with compliant materials and soft actuators like cables or pneumatic actuators. As the motors are no longer located directly at the joints, unlike exoskeletons, this reduces the mass and inertia of the limbs. Another advantage is that there are no rigid links to constrain the movement of the joints [2]. Elbow flexion is not a pure rotation and the revolute joint axis undergoes a slight translation. But a cable driven exosuit raises new issues, in particular how to place these cables and define a suitable path for them. Indeed, the actuators must assist the user during the movement effectively, while complying with safety and comfort objectives, particularly at skin-cuff contact [3]. In literature design optimization algorithms are synthetized considering force distribution, following or ensuring human workspace [2]. Then, energy saving is estimated after prototyping. All these approaches are mechanical without taking into account human with muscles and its contribution during an assisted movement. From this point of view, developing a simulation platform that couples a musculoskeletal model and its exosuit is of great potential. First, Thelen et al, 2003 [4] proposed steps to implement computed muscle control algorithm and simulate human movement. Recently Sambhav et al, 2022 [5] presented a framework to integrate simulation with ©OpenSim and ©Matlab on a very simple model for elbow flexion. In this paper, a simulation platform is set with a full upper limb model using OpenSim biomechanical model and Matlab simulation environment. This platform will be used for two purposes: optimize the cable routing for an active upper limb exosuit considering safety and comfort and estimate metabolic savings offered by the new design. The method is described as follows. A musculoskeletal model is built and an exosuit design is added. A platform, including the model, simulates a daily life task (drinking task), the computed trajectory and the energy gain. Then a multi-objective optimization based on NSGA-II [6] and safety objectives lead to design of cable path. Three cable paths are optimized following three clinical motions: shoulder abduction, shoulder flexion, and elbow flexion.

[1]Pierre Garnault and Yannick Aoustin are with Nantes Université, Centrale Nantes, LS2N UMR CNRS 6004 1, rue de la Noë BP 92101 44321 NANTES Cedex 3, Pierre.Garnault@ls2n.fr; Yannick.Aoustin@univ-nantes.fr

[2] Vigen Arakelyan is with Nantes Université, Centrale Nantes, INSA Rennes, LS2N UMR CNRS 6004, Rennes 35000 Vigen.Arakelyan@insa-rennes.fr

II. Human in the loop simulation platform

The simulation is implemented in Matlab using OpenSim features. OpenSim [7] is a software developed by Stanford University and commonly used in biomechanical modeling and movement analysis.

A. Musculoskeletal model

The chosen model is 'MoBL-ARMS.osim' updated [8] from Holzbaur et al, 2005 [9]. It is a full upper limb model with seven degrees of freedom (DoF), 50 muscles, ligaments and model of the scapula sliding along the thorax (passive DoF).

To measure the effort, a metabolic probe (*'Umberger2010MuscleMetabolicsProbe'*) derivating from Umberger et al, 2003 [10] is added. Metabolic cost is based on thermodynamic principle where it is the sum of the heat and mechanical work delivered by muscles during contractions:

$$\dot{E} = \dot{B} + \dot{A} + \dot{M} + \dot{S} + \dot{W} \tag{1}$$

Where $\dot{E}$ is the effort, $\dot{B}$ is basal rate to satisfy essential physiological needs (breathing, functioning of vital organs), $\dot{A}$ is the heat produced to activate the muscle, $\dot{M}$ is the heat resulting from maintaining position which appears during tetanic efforts, $\dot{S}$ depends on the speed of contraction $\dot{W}$ is mechanical work rate. These six physical variables involved in (1) are defined in Watt as functions of intern parameters of muscle (mass, density, fiber length...) but also from the twitch fibers ratio. Indeed, there are two types of fibers: fast twitch fibers (FTF) and slow twitch fibers (STF). FTF are recruited for short but intense contractions more energy-consuming than STF used during endurance efforts. By default the ratio is 50/50, but to be consistent in our modeling the ratio is determined for each muscle according to biomechanical literature ([11], [12], [13], [14], [15], [16], [17], and [18]). From these papers, STF or FTF ratio is extracted for all 50 muscles described in our musculoskeletal model. When

a muscle is depicted in several papers, the ratio is the mean of values weighted by the number of samples. These papers do not provide ratio estimations for supinator and brachialis. However estimated values about these missing ratios can be found in [19] on a monkey species *Macaca mulatta*.

Then rigid bodies are added to model user and exosuit. First, there are a skull and a spine for aesthetic reasons and next three cuffs to match the design of commercialised orthoses : a shoulder cuff, an arm cuff and a forearm cuff. Shoulder cuff dimensions are $r_1 = 0.058\,\mathrm{m}$; $r_2 = 0.073\,\mathrm{m}$; $h = 0.120\,\mathrm{m}$ (Figure 1). Arm and forearm cuffs are both cylinder with dimensions: $r_{arm} = r_{forearm} = 0.041\,\mathrm{m}$; $l_{arm} = l_{forearm} = 0.120\,\mathrm{m}$. Because the wearable device is lightweight, we assume them massless.

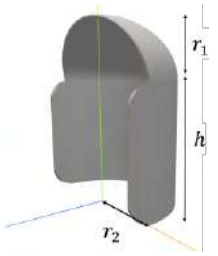


Fig. 1. Shoulder cuff dimensions.

Finally, *'wrap'* objects are added to avoid collision between cables and bone meshes and make an organic cable routing. Three *'wrap'* have been added to the existing ones: a sphere and a cylinder for the shoulder cuff and an ellipse for the scapula (Figure 2).

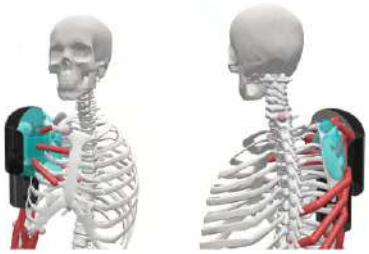


Fig. 2. Biomechanical model with key components highlighted cuffs (black), new *'wrap'* objects (cyan), muscles (red).

B. Simulation platform

The OpenSim API can be used on MATLAB to work with our biomechanical model, solvers and functions integrated into OpenSim. The aim is to run a simulation with a closed control loop (Figure 3). The input is a reference trajectory, i.e. the position, velocity, and angular acceleration of each joint, and the outputs are the simulated trajectory, the metabolic cost and the forces in the cable. The simulator is made up of four blocks.

1) Inverse Dynamics: Generalized forces τ_h are determined knowing angular position q, angular velocity $\dot{q}$ and angular acceleration $\ddot{q}$ with dynamic model :

$$\tau_h = M\ddot{q} + C(q,\dot{q}) + G(q) + \Upsilon \tag{2}$$

Where M is the positive definite inertia matrix of the system, C is the vector of centrifugal and Corriolis forces, G is the gravity vector and Υ is the vector of external forces applied to the system. In the OpenSim API, the function *InverseDynamicsSolver* is used to solve this equation. According to Thelen et al, 2003 [4], $\ddot{q}$ is the sum of $\ddot{q}_{des}$ and the corrected errors in velocity and position such that:

$$\ddot{q} = \ddot{q}_{des} + k_v(\dot{q}_{des} - \dot{q}) + k_p(q_{des} - q) \tag{3}$$

The gains k_p and k_v are chosen so that the error $e = q_{des} - q$ asymptotically converges to zero without overshoot and oscillation, i.e., it is governed by the equation $\ddot{e} + k_v\dot{e} + k_p e = 0$ with $k_v = 2\sqrt{k_p}$ for a given k_p.

2) Static Optimization: Optimizing muscular activity is necessary to determine the strength and contribution of each muscle. The contribution J of muscular activation a must be optimized and minimized because it is directly linked to energy expenditure. This means that only the muscles useful for the movement will be activated. A static optimization problem, i.e., independent of time, can be defined as follows for m muscles:

$$\begin{cases} \arg\min_{a_i} J = \sum_{i=1}^{m} a_i^2 \\ \\ 0 \leq a_i \leq 1 \end{cases} \tag{4}$$

Such as the torque τ_j applied by a muscle i in joint j is equal to

$$\tau_j = \sum_{i=1}^{m} d_{i,j} F_i \tag{5}$$

Here $d_{i,j}$ is the moment arm of muscle i with respect to joint j, a_i the activation of muscle i and F_i is the muscle force. For a muscle its force F is calculated using the activation a and biomechanical parameters according to the Hill model [20]:

$$F = \left(a\tilde{f}_a(l^m)\tilde{f}_v(\dot{l}^m) + \tilde{f}_p(l^m)\right) f_{iso}\cos\alpha \tag{6}$$

Here l^m is the length of the muscle, $\dot{l}^m$ is the speed of the muscle elongation, $\tilde{f}_a$ is the active force normalized in relation to the maximum isometric force (f_{iso}), $\tilde{f}_p$ is the normalized passive force, $\tilde{f}_v$ a coefficient derived from the force-velocity relationship. All these parameters can be obtained using the API with the functions *getMaxIsometricForce*, *getActiveForceLengthMultiplier*, *getForceVelocityMultiplier*, *getPassiveForceMultiplier*, *getCosPennationAngle* and the moment arms are determined using *computeMomentArm*. This static optimization problem is solved using the *fmincon* function in the MATLAB toolbox *Optimization Toolbox*.

3) Gravity Compensation Controller: The control law is defined to compensate the weight of arm, forearm or hand. It is possible to add a known external load in the hand.

$$\tau_{exo} = m_{limb} g l \sin(q_{joint}) + m_{load} g L \sin(q_{joint}) \tag{7}$$

With m_{limb} the mass of limb, l the length between joint and center of mass of the limb, m_{load} the mass of external load, g is the gravity constant and L the length between joint and

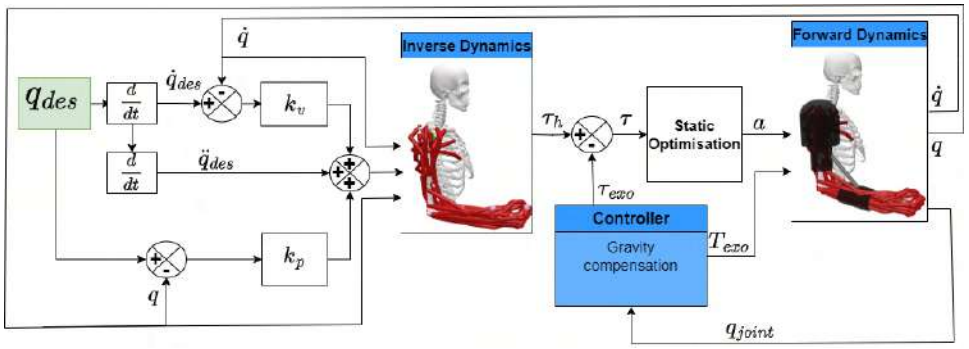


Fig. 3. Block diagram of the simulation platform.

center of mass of the load. Then knowing d_{cable} the moment arm, the tension is:

$$T_{exo} = \frac{\tau_{exo}}{d_{cable}} \tag{8}$$

4) Forward Dynamics: A group of actuators is created with muscles and cables and the function *PrescribedController* is used to activate actuators. The activation a follows a dynamic transformation into excitations according to Thelen et al, 2003 [21]:

$$\frac{\mathrm{d}a}{\mathrm{d}t} = \frac{u-a}{\delta_a(a,u)} \tag{9}$$

Where u is the excitation, δ_a is a time constant depending on activation level:

$$\delta_a(a,u) = \begin{cases} \delta_{act}(0.5+1.5a); u > a \\ \delta_{deact}/(0.5+1.5a); u \leq a \end{cases} \tag{10}$$

With $\delta_{deact} \approx 40$ms and $\delta_{act} \approx 10$ms.

With Runge-Kutta algorithm the following inverse model is solved to get $\dot{q}$ and q :

$$\ddot{q} = M^{-1}(\tau + \tau_{exo} - C(q,\dot{q}) - G(q) - \Upsilon) \tag{11}$$

C. Drinking task trajectory

To illustrate and validate our method, a daily life task is computed. The chosen task is a drinking task during four seconds which involves all of the DoF of the arm at the same time. The arm and hand are along the body, then the hand reaches the mouth in one second and the arm and hand return along the body in one second. The musculoskeletal model shoulder joints are defined following ISB recommendations [22]. For elbow, it is a flexion/extension from 0° to 130° and for the shoulder there are an elevation plane rotation from 0° to 53°, a shoulder elevation from from 0° to 75° and an internal/external rotation from from 0° to 34°. These DoF are different from the clinical description: abduction, flexion and rotation. It is because clinical movements are described in planes, and composing a movement with these definitions would make the arm position dependent on the angular sequence (Paradox of Codman). Flexion or abduction are both movement of elevation, only the plane in which the elevation takes place changes. This is why an elevation plane is constructed. When the angle of the plane of elevation is 0° (respectively 90°), it coincides with the coronal plane (respectively sagittal plane). According to Figures 4 and 5, the simulated angular trajectory is consistent with the reference. The RMSE is calculated in Table I and supports the accuracy of the simulation. At 0.2s, the shoulder rotation briefly deviates but stabilises, without significantly affecting the task.

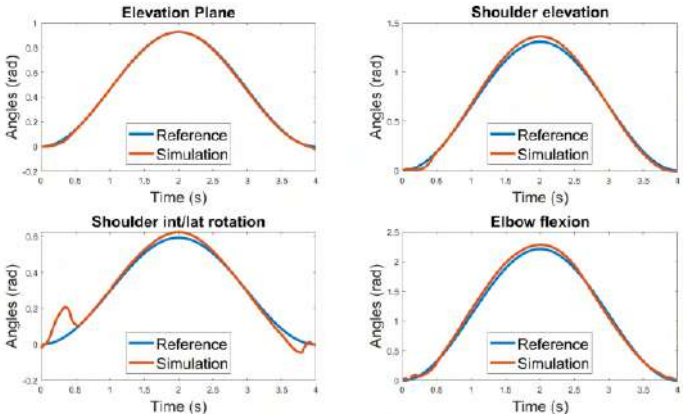


Fig. 4. Angular trajectory at each joint for a drinking task. The reference is in blue and the simulation results in red.

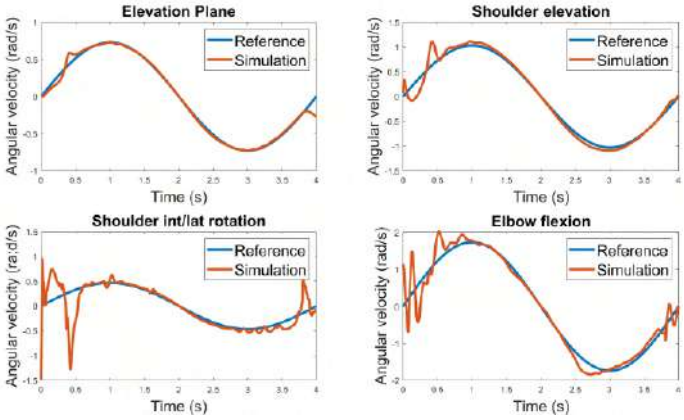


Fig. 5. Angular velocity at each joint for a drinking task. The reference is in blue and the simulation results in red.

TABLE I
RMSE BETWEEN THE REFERENCE AND THE COMPUTED TRAJECTORY

RMSE	Angle (rad)	Angular velocity (rad/s)
Elevation plane	0.007	0.044
Shoulder elevation	0.032	0.106
Int/Lat. rotation	0.043	0.261
Elbow flexion	0.057	0.258

III. Design Optimization

A. Interaction force constraints

Comfort and safety are expressed through force constraints based on pain tolerance thresholds.

1) No pain condition: According to algometry research, humans experience discomfort and pain at circumferential compression levels around 25 kPa [23]. Given that the cable is limited to pulling forces, the pressure is concentrated on the side of the cuffs opposite the pulling direction. Maximal peak of normal force $||\vec{F}_N||$ is constrained such as:

$$||\vec{F}_N|| \leq P_{pain}(\pi r_{cuff} l_{cuff}) \tag{12}$$

2) No slipping condition: When a cuff applies continuous pressure on human body, the threshold pressure is at 30mmHg i.e. 4kPa [3]. 3.5kPa is a comfortable compression level. Assuming well-distributed forces, the tangential force must satisfy Coulomb's friction criterion to prevent slipping on the skin.

$$\begin{cases} ||\vec{F}_T|| \leq ||\vec{F}_{cuff}||\mu \\ \\ \quad \text{with } ||\vec{F}_{cuff}|| = P_{lim}(2\pi r_{cuff} l_{cuff}) \end{cases} \tag{13}$$

$||\vec{F}_{cuff}||$ is the force required to hold the cuff and μ is the coefficient of friction between skin and cuff, equal to 0.6 [24].

B. Geometric constraints

Cables are defined by via points and anchors points. Each point is localized in a frame of parent body. Some geometric constraints are set to limit exosuit volume, avoid collision between cables and the user and to guarantee that the final anchor points are on the cuffs.

1) elbow flexion: The cable is straight with an anchor point on each cuff.

- P_1: Point on arm cuff. Should stay at the surface of the cuff on the anterior side
- P_2: Point on forearm cuff. Should stay at the surface of the cuff on the anterior side.

2) shoulder flexion: Five points are considered to avoid collision with bones and keep consistent the cable path during a movement from 0° to 90° in one second.

- P_1: Fixed point along the spine.
- P_2: Point located at the back of the shoulder between the scapula and the glenohumeral joint. Its frame is the thorax, so it is immobile during shoulder movement.
- P_3: Point located around the spherical part of the cuff, around the glenohumeral joint with maximal height of 5 cm above the cuff.
- P_4: Point along anterior side of the cuff with maximal height of 5 cm above the cuff.
- P_5: Point along anterior side, on the cuff's surface.

3) shoulder abduction: For the same reason as shoulder flexion, four points are built according to abduction from 0° to 120° in one second.

- P_1: Fixed point along the spine.
- P_2: Point located around the spherical part of the cuff, around the glenohumeral joint with maximal height of 5 cm above the cuff.
- P_3: Point along sagittal side of the cuff with maximal height of 5 cm above the cuff.
- P_4: Point along sagittal side, on the cuff's surface.

C. Multi-Objective Optimization: NSGA-II

In a previous work [25], we showed that cable placement influences force distribution more than metabolic cost. The results indicate that energy consumption, used in cost function, depends more on the level of assistance than on cable routing. Since assistance is determined by joint torque and thus cable path, we optimise using normal and tangential forces to ensure safety and comfort, then evaluate energy consumption separately. For multi-objective optimization, NSGA-II [6] is set up on Matlab. The optimization will be done cable by cable according to the actuated DoF with all the range of motion of the movement as described section III-B.

1) Cost function: The cost functions are defined in function of the mean norm of normal forces ($\vec{F}_N$) and shear forces ($\vec{F}_T$).

$$\begin{cases} f_{1,T} = \frac{1}{n}\sum_{i=1}^{n} \left\|\vec{F}_{T,i}\right\| \\ \\ f_{2,N} = \frac{1}{n}\sum_{i=1}^{n} \left\|\vec{F}_{N,i}\right\| \end{cases} \tag{14}$$

2) Algorithm parameters: The population is composed of 50 individuals and each individual has three coordinates for each point as parameters. The genes are evaluated with simulation platform, the best 10 solutions are selected, made 7 children, 10 genes are from mutations of this population and 23 are from new random genes. During mutation or random phases, the gene parameters have to respect geometric constraints defined section III-B and after evaluation if a solution does not respect force constraints defined section III-A, it is penalized. The optimization is performed over 100 generations.

IV. Results

A. Pareto front

For shoulder movements, the placement of the cables can lead to a completely normal or completely tangent force distribution. The most limiting constraint for comfort relates to shear forces, however, taking a solution that has no shear would be unrealistic as forces will be exerted by the anchor point supports. Since constraints are set on the forces and solutions that don't respect them are eliminated, all Pareto-front solutions are viable. To make a trade-off for each cable,

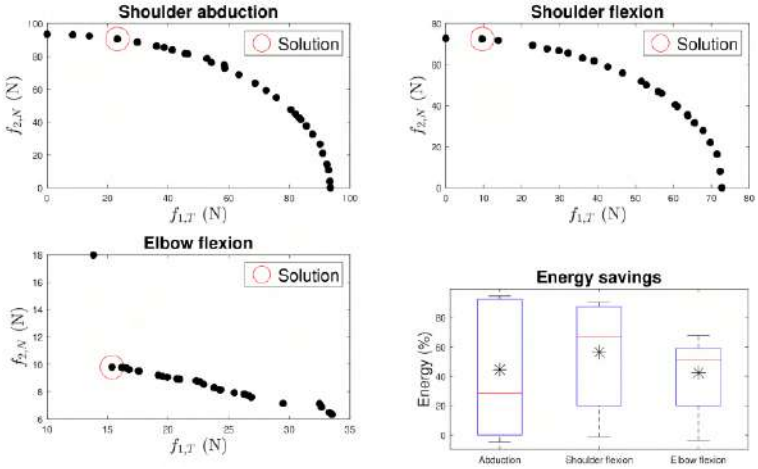


Fig. 6. Pareto front of each cable optimization and metabolic savings due to exosuit during clinical movements. * is the mean.

the selected solution (circled on Figure 6), is the solution with minimal norm tension where normal effort is than higher tangent effort. In terms of metabolic cost, the gain is calculated by taking into account the metabolic rate of muscles expending the most energy. For example, for abduction, it is the intermediate part of the deltoid muscle, which is recruited, and it consumes a lot of energy. The cable compensates for this effort by almost 45% on average, and even more than 90% in few phases of the movement. For shoulder flexion, it is the anterior part of the deltoid which is activated and for the elbow there are three flexors: the biceps, the brachialis, and the brachioradialis. As depicted on Figure 6, there is no saving at some points. It happens when the arm is along the body, with gravity compensation law there is no tension in cable at this phase.

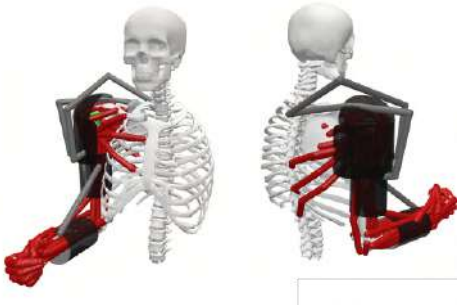


Fig. 7. Biomechanical model with fully optimized exosuit design.

The proposed solution (Figure 7) found by the genetic algorithm follows a simple principle: position the attachment points to maximize the moment arm and stay in the plane of the movement. It is particularly visible on the cable for elbow flexion. Then, to reduce frictional forces, the cable should be connected to the cuff as normal as possible.

B. Drinking task trajectory

To illustrate the efficiency of wearing an exosuit, the drinking task is simulated with and without the device. According to the results (Figure 8), the exosuit reduces fatigue in the movement to reach the mouth by 32%. As explained above,

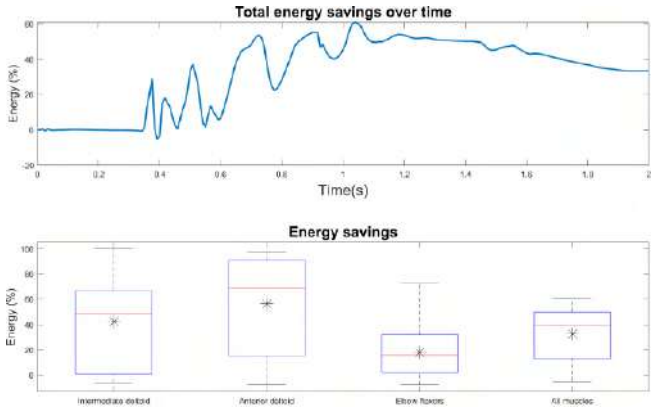


Fig. 8. Comparison of metabolic expenditure with and without exosuit. (1) total energy savings (%) over time, (2) distribution of saved energy across muscle groups (mean shown *).

in the first phase the exosuit provides very small assistance to the user, but as the movement progresses, the user is increasingly assisted. On a movement with several DoF, the average saving is no longer around 50%. Actually, in this task, there is non assistive internal rotation, so bi-articular muscles are recruited in at least two DoF. Furthermore, the combination of movements leads to the combination and synchronization of activations between several muscles.

V. Discussion & Perspectives

In this work, a platform is implemented following guidelines to simulate a user and its musculoskeletal model with a cable driven exosuit. Designed to follow a reference movement, the outputs are the simulated trajectory, energy expenditure and cable tensions. With this new tool, the cable routing of an

exosuit for shoulder and elbow assistance is optimized considering the force distribution to ensure safety and comfort. These requirements are guaranteed by limits on shear and normal forces and multi-objective problem is solved by NSGA-II. The results show a maximization of the moment arm and an energy saving of more than 32% when wearing the exosuit. The advantage is that the simulation method can be reused for other limbs and other musculoskeletal models, weight can easily be put on to simulate load lifting and new control laws can be tested. In addition, different exosuit designs can be evaluated, and passive elements can be added to the design to help the prototyping phase. However, the cable placement appears straight, lacking a organic flow because we do not develop a detailed design to propose a simplified one. The results presented in this study depend on the geometry of the cuffs, the number of points, models, the control laws, the joints and motions. These parameters can be customized in OpenSim or in the simulation platform as well as in the definition of the population and constraints within the genetic algorithm. A future project would be to propose a real prototype based on these results, perhaps incorporating more attachment points and technical solutions for routing cables (pulleys, sheaths, etc). Another point is that OpenSim does not have a finite element calculation tool to estimate exactly the pressure applied to the skin and its distribution. Our assumptions are that the force is homogeneously distributed and that the tension in the cable is ideal (no friction, no backlash). In addition, the model is a closed chain and cannot interact with an external environment to perform more complex simulations.

REFERENCES

[1] Elena Bardi, Marta Gandolla, Francesco Braghin, Ferruccio Resta, Alessandra LG Pedrocchi, and Emilia Ambrosini. Upper limb soft robotic wearable devices: a systematic review. Journal of NeuroEngineering and Rehabilitation, 19(1):87, 2022.

[2] Michele Xiloyannis, Ryan Alicea, Anna-Maria Georgarakis, Florian L Haufe, Peter Wolf, Lorenzo Masia, and Robert Riener. Soft robotic suits: State of the art, core technologies, and open challenges. IEEE Transactions on Robotics, 38(3):1343–1362, 2021.

[3] E Rocon, AF Ruiz, R Raya, A Schiele, Jose L Pons, JM Belda-Lois, R Poveda, MJ Vivas, and JC Moreno. Human-robot physical interaction. Wearable robots: Biomechatronic exoskeletons, pages 127–163, 2008.

[4] Darryl G. Thelen, Frank C. Anderson, and Scott L. Delp. Generating dynamic simulations of movement using computed muscle control. Journal of Biomechanics, 36(3):321–328, March 2003.

[5] Ratna Sambhav, Shreeshan Jena, Ankit Chatterjee, Shubhendu Bhasin, Sushma Santapuri, Lalan Kumar, Suriya Prakash Muthukrishnan, and Sitikantha Roy. An integrated dynamic closed loop simulation platform for elbow flexion augmentation using an upper limb exosuit model. Frontiers in Robotics and AI, 9:768841, 2022.

[6] Kalyanmoy Deb, Amrit Pratap, Sameer Agarwal, and TAMT Meyarivan. A fast and elitist multiobjective genetic algorithm: Nsga-ii. IEEE transactions on evolutionary computation, 6(2):182–197, 2002.

[7] Scott L Delp, Frank C Anderson, Allison S Arnold, Peter Loan, Ayman Habib, Chand T John, Eran Guendelman, and Darryl G Thelen. Opensim: open-source software to create and analyze dynamic simulations of movement. IEEE transactions on biomedical engineering, 54(11):1940–1950, 2007.

[8] Katherine R Saul, Xiao Hu, Craig M Goehler, Meghan E Vidt, Melissa Daly, Anca Velisar, and Wendy M Murray. Benchmarking of dynamic simulation predictions in two software platforms using an upper limb musculoskeletal model. Computer methods in biomechanics and biomedical engineering, 18(13):1445–1458, 2015.

[9] Katherine RS Holzbaur, Wendy M Murray, and Scott L Delp. A model of the upper extremity for simulating musculoskeletal surgery and analyzing neuromuscular control. Annals of biomedical engineering, 33:829–840, 2005.

[10] Brian R Umberger, Karin GM Gerritsen, and Philip E Martin. A model of human muscle energy expenditure. Computer methods in biomechanics and biomedical engineering, 6(2):99–111, 2003.

[11] M_A Johnson, J Polgar, Dorothy Weightman, and D Appleton. Data on the distribution of fibre types in thirty-six human muscles: an autopsy study. Journal of the neurological sciences, 18(1):111–129, 1973.

[12] GC Elder, K Bradbury, and RJJoAP Roberts. Variability of fiber type distributions within human muscles. Journal of Applied Physiology, 53(6):1473–1480, 1982.

[13] Peter Schantz, Emily RANDALL-FOX, Wallace Hutchison, Anders Tydén, and P-O Åstrand. Muscle fibre type distribution, muscle cross-sectional area and maximal voluntary strength in humans. Acta Physiologica Scandinavica, 117(2):219–226, 1983.

[14] S Le Bozec and B Maton. Differences between motor unit firing rate, twitch characteristics and fibre type composition in an agonistic muscle group in man. European journal of applied physiology and occupational physiology, 56:350–355, 1987.

[15] Cliff S Klein, Greg D Marsh, Robert J Petrella, and Charles L Rice. Muscle fiber number in the biceps brachii muscle of young and old men. Muscle & Nerve: Official Journal of the American Association of Electrodiagnostic Medicine, 28(1):62–68, 2003.

[16] Raja Dahmane, Srdjan Djordjevič, Bostjan Šimunič, and Vojko Valenčič. Spatial fiber type distribution in normal human muscle: Histochemical and tensiomyographical evaluation. Journal of biomechanics, 38(12):2451–2459, 2005.

[17] Ramesh C Srinivasan, Matthew P Lungren, Joseph E Langenderfer, and Richard E Hughes. Fiber type composition and maximum shortening velocity of muscles crossing the human shoulder. Clinical Anatomy: The Official Journal of the American Association of Clinical Anatomists and the British Association of Clinical Anatomists, 20(2):144–149, 2007.

[18] Morten Kjaer Ravn, Trine Ivarsen Ostergaard, Henrik Daa Schroeder, Jens Randel Nyengaard, Kate Lykke Lambertsen, and Lars Henrik Frich. Supraspinatus and deltoid muscle fiber composition in rotator cuff tear conditions. JSES international, 4(3):431–437, 2020.

[19] Kan Singh, Ellen H Melis, Frances JR Richmond, and Stephen H Scott. Morphometry of macaca mulatta forelimb. ii. fiber-type composition in shoulder and elbow muscles. Journal of morphology, 251(3):323–332, 2002.

[20] Archibald Vivian Hill. The heat of shortening and the dynamic constants of muscle. Proceedings of the Royal Society of London. Series B-Biological Sciences, 126(843):136–195, 1938.

[21] Darryl G. Thelen. Adjustment of Muscle Mechanics Model Parameters to Simulate Dynamic Contractions in Older Adults. Journal of Biomechanical Engineering, 125(1):70–77, February 2003.

[22] Ge Wu, Frans CT Van der Helm, HEJ DirkJan Veeger, Mohsen Makhsous, Peter Van Roy, Carolyn Anglin, Jochem Nagels, Andrew R Karduna, Kevin McQuade, Xuguang Wang, et al. Isb recommendation on definitions of joint coordinate systems of various joints for the reporting of human joint motion—part ii: shoulder, elbow, wrist and hand. Journal of biomechanics, 38(5):981–992, 2005.

[23] Tjaša Kermavnar, Valerie Power, Adam de Eyto, and Leonard O'Sullivan. Cuff pressure algometry in patients with chronic pain as guidance for circumferential tissue compression for wearable soft exoskeletons: a systematic review. Soft robotics, 5(5):497–511, 2018.

[24] Joan E Sanders, Joan M Greve, Stuart B Mitchell, and Santosh G Zachariah. Material properties of commonly-used interface materials and their static coefficients of friction with skin and socks. Journal of rehabilitation research and development, 35:161–176, 1998.

[25] Pierre Garnault, Yannick Aoustin, and Vigen Arakelian. Optimising elbow flexion exosuit design: Considering metabolic cost and interaction forces. Multidisciplinary Biomechanics Journal, (49), 2024.

A Geometric Approach for the Comparison of Kinematic Synergy Postures

Federico Tessari
Dept. of Mechanical Engineering
MIT
Cambridge, MA, USA
ftessari@mit.edu

A. Michael West Jr.
Dept. of Mechanical Engineering
Johns Hopkins University
Baltimore, MD, USA
awest36@jh.edu

Neville Hogan
Dept. of Mechanical Engineering
MIT
Cambridge, MA, USA
neville@mit.edu

***Abstract*—The analysis of human movements has highlighted the presence of stereotyped coordination patterns among the different joints of the human body. These patterns are commonly referred to as kinematic synergies. Synergies have been used to both elucidate the underlying neuromotor control strategies adopted by humans during coordinated motion and inform the design and control of assistive and rehabilitative devices such as prostheses and exoskeletons. A particularly thorny problem in the analysis of synergies is the comparison of the synergy postures i.e., the hyper-dimensional vectors containing the contribution of each analyzed feature (e.g., joint angles) to the considered synergies. Often, synergy postures are compared using cosine similarity, which is sensitive to the dimensionality of the input data and does not offer an intuitive understanding of the synergies' similarities and differences. In this study, we introduce a new geometric method, Geometric Configuration Similarity (GCS), specifically designed to compare kinematic synergy postures, with a particular emphasis on hand kinematic synergies. GCS provides a more intuitive geometric understanding of how these postures relate to one another. We demonstrate its advantages over cosine similarity through experimental and numerical results, offering the human motor control and rehabilitation robotics communities a new tool for analyzing kinematic hand synergies and improving the design and control of assistive systems.**

***Index Terms*—synergies, kinematics, hand, manipulation, dexterity, similarity**

I. Introduction

The fine and dexterous control of the hand requires the coordination of a large number of joint degrees of freedom (20+) (i.e., hand joints), and more than double that number of intrinsic and extrinsic muscles of the hand [1], [2]. Given this complexity, the question arises: how do humans seamlessly control their hands without incurring the control limitations associated with the curse of dimensionality [3]? One of the leading theories assumes that humans might take advantage of lower-dimensional and sufficiently stereotyped commands to simplify the motor control problem. Such commands are often referred to as motor synergies, and depending on the considered physiological nature of the signals, they are usually classified as neural [4], [5], muscular [6] or kinematic synergies [7]–[10].

The seminal work by Santello et al. [4], [7] showed that a few kinematic synergies - typically extracted by means of dimensionality reduction techniques such as principal component analysis (PCA) [11] or singular value decomposition (SVD) [12] - accounted for most of the variance in the data of healthy humans performing a variety of reaching and grasping movements. Subsequent work has found similar results in tasks that involve object manipulation [8], [13], [14] the American sign language [6], and even piano playing [10], [15]. For review see [16]. Moreover, some research has highlighted how such synergies are both the results of biomechanical constraints (e.g., tendons and ligaments), as well as descending neural commands [8], [17]. Additionally, research indicates that the reduction of the operational degrees of freedom of the hand may facilitate more straightforward control [18]–[22]. Prior work by the authors showed how humans need to recruit a growing number of synergies in order to perform more advanced dexterous manipulation tasks such as wire-harnessing or playing a musical instrument [10]. A recent theoretical framework highlighted how the number of synergies that humans can employ to perform a given motor task may exceed the number of controlled features, such as joint angles or muscle contractions [23]. Moreover, substantial efforts have been made to refine mathematical methods for extracting synergies [9], [24], [25] through various dimensionality reduction techniques [11], [12], [26].

However, a particularly thorny problem is represented by the difficulty of comparing the synergy vectors resulting from these reduction techniques. The synergy vectors or hyper-points are often high dimensional - with dozens if not hundreds of elements - which limits our capability to visualize and, consequently, get a profound insight on their relation to each other. A common approach to compare synergy vectors, specifically termed 'synergy postures' for kinematic synergies, is to compute the cosine similarity between them. The most widely used formulation computes the positive angle between two vectors, returning 0 if the vectors are orthogonal and 1 if the vectors are collinear.

Recent work by Tessari and Hogan highlighted how the cosine similarity metric is sensitive to the number of dimensions [27]. Specifically, for increasing dimensions the cosine similarity between any 2 random vectors will tend to converge to a value of about 0.75, with decreasing variance. This represents a substantial limitation to the use and interpretability of such a metric. An alternative approach would be to use a dimension-insensitive metric, such as the dimension insensitve Euclidian

metric (DIEM) [27]. This metric is unaffected by the number of dimensions, enabling robust statistical analysis and hypothesis testing—areas where cosine similarity falls short. However, DIEM relies on comparing synergy vectors that are not of unit length. This can be the case for muscular synergies extracted through Non-Negative Matrix Factorization [26], [28], [29], but not for kinematic synergies obtained through PCA or SVD. Moreover, most distance metrics still do not provide an intuitive way to visualize and internalize the similarity between kinematic synergies. To address the limitations of cosine similarity and DIEM, we propose a new geometric approach to compare kinematic hand synergies, called "Geometric Configuration Similarity". This method, which maps kinematic synergies to task-space motion, enables users to quantitatively compare and visualize pairs of kinematic hand synergy postures. In the following sections, we demonstrate the shortcomings of cosine similarity while contrasting it with our proposed approach. Additionally, we provide a library for future researchers to implement the Geometric Configuration Similarity in their work.

II. Materials and Methods

A. Synergy Extraction through SVD

Consider a matrix $X \in \mathbb{R}^{n \times m}$ containing the kinematic data of the joint trajectories recorded across n observations (e.g., the time evolution of each degree of freedom) and m number of features (e.g., the number of analyzed degrees of freedom, DoF) for a given set (one or more) of experiments.

According to West et al. [9], prior to synergy extraction the data should be centered i.e., the mean value of each column - which represents the average angular value for that DoF - needs to removed. This is done to prevent the first synergy from incorrectly 'aiming' toward the center of the offset data distribution.

$$X^* = X - mean(X) \tag{1}$$

Then, synergies can be extracted using SVD — the most adopted algorithm for kinematic synergy extraction [7], [8] — on the mean-removed data set:

$$X^* = U \cdot S \cdot V^T \tag{2}$$

where $U \in \mathbb{R}^{n \times n}$ is an orthonormal matrix whose columns denote the temporal evolution of a given synergy, $S \in \mathbb{R}^{n \times m}$ is diagonal matrix of singular values which give an estimate of the Variance-Accounted-For (VAF) in a given synergy, and $V \in \mathbb{R}^{m \times m}$ is an orthonormal matrix whose columns represent the synergy vectors $V = [\mathbf{v_1}, \mathbf{v_2}, ..., \mathbf{v_m}]$. The elements of each synergy vector represent the contribution of each DoF to that synergy $\mathbf{v_i} = [\theta_1, \theta_2, ..., \theta_m]^T$. The synergy vectors $\mathbf{v_i}$ are of unitary length. For a geometrical interpretation of this, see [9]. In the specific case of hand joint kinematic synergies, the elements of $\mathbf{v_i}$ represent the proportion by which each joint of the hand contributes to that synergy.

B. Limitations of Cosine Similarity

Comparing a pair of synergy vectors $\mathbf{v_i}, \mathbf{v_j}$ fundamentally requires establishing a distance metric between these two hyper-dimensional quantities. As briefly mentioned in the Introduction, this is often done by computing the cosine similarity between them:

$$cos(\phi) = \frac{|\mathbf{v_i}^T \cdot \mathbf{v_j}|}{||\mathbf{v_i}|| \cdot ||\mathbf{v_j}||} \tag{3}$$

However, Tessari et al. showed that this metric is **sensitive to the number of dimensions** and, thus, is not able to provide statistically reliable comparisons [27]. Specifically, as the number of dimensions grows the cosine similarity of two randomly generated vectors tends toward 0.75. Moreover, the resulting computation does **not provide an intuitive geometrical understanding** of how the posture of the hand differs between the two synergy vectors.

C. Geometric Configuration Similarity

To address the limitations of the cosine similarity metric—namely (i) dimension-sensitivity, and (ii) geometric interpretability—the authors propose a new approach coined 'Geometric Configuration Similarity' (GCS), to compute the degree of similarity or difference between any two pairs of kinematic synergy vectors $\mathbf{v_i}$, and $\mathbf{v_j}$. The approach is showcased for hand kinematic synergies, but its application extends to any form of kinematic synergies at every level of the human body.

The core idea of the GCS is to map the synergy vectors from the joint-space to the task-space. This mapping is biomechanically informed through direct kinematics. Given a specific geometry of the hand (i.e., link lengths and joint types) the mapping of any point $\mathbf{p}$ on the hand with respect to a set of joint coordinates—assumed here to be the relative angles between successive links—is unique and well defined as:

$$\mathbf{p} = \mathcal{L}(\Theta) = \mathcal{L}(\theta_1, ..., \theta_m) \tag{4}$$

where $\mathcal{L}$ describes the forward kinematics.

To map a synergy vector $\mathbf{v_i}$ to a hand task-space configuration, we need to (i) multiply it by an activation coefficient u—which could also be a function, $u(t)$, if the intention is to reconstruct the entire motion—and (ii) add back the previously subtracted average posture of the original dataset $\mathbf{\Theta}_{avg} = mean(X)$:

$$\mathbf{\Theta_i} = u \cdot \mathbf{v_i} + \mathbf{\Theta}_{avg} \tag{5}$$

Together, Equations 4 and 5, allow for the mapping of a synergy vector to any point of the considered geometry (e.g., the hand).

In the proposed case (i.e., hand kinematic synergies), we considered a 20 DoFs hand model characterized by 4 DoFs per finger. For the index, middle, ring and little fingers, we included flexion-extension of the metacarpophalangeal (MCP), proximal interphalangeal (PIP), and distal interphalangeal

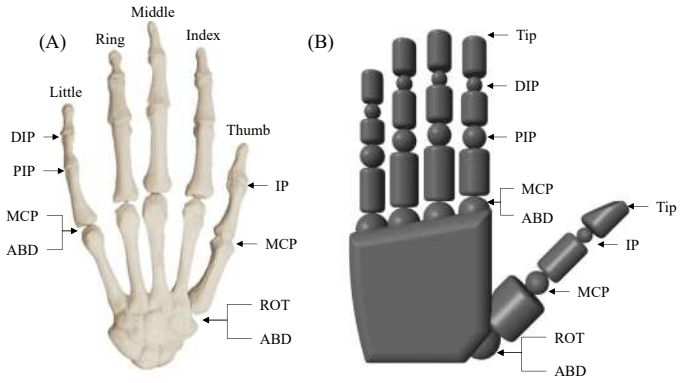


Fig. 1. Adopted hand model. Panel (A) shows the considered human anatomical joints. Panel (B) presents the reconstructed rigid link model.

(DIP) joints, and abduction-adduction (ABD) of the metacarpophalangeal joint. For the thumb, we included rotation (ROT) and abduction-adduction (ABD) at the carpometacarpal and flexion-extension at the metacarpophalangeal (MCP), and interphalangeal (IP) joints. Figure 1A provides a schematic representation of the considered anatomical hand joint.

A rigid-link model (Figure 1B), based on the aforementioned 20 DoFs, was developed considering the following two assumptions. First, the PIP and DIP joints of the index, middle, ring, and little fingers, along with the MCP and IP joints of the thumb, were modeled as perfect rotational joints. Second, the MCP and ABD joints of the index, middle, ring, and little fingers, as well as the ROT and ABD joints of the thumb, were modeled as universal joints (U-joints or Cardan joints).

The link lengths were sized considering the 50th percentile male hand size [30]. However, we want to emphasize that the proposed metric is not influenced by the size of the considered hand. Additional details are provided in the Discussion.

Considering the presented hand model and the mapping from joint-space to task-space using Equations 4 and 5, the 'Geometric Configuration Similarity' fundamentally computes the Euclidean distance between a pair of hand configurations from two synergy vectors $\mathbf{v_i}, \mathbf{v_j}$. The Euclidian distance is computed at 3 different key-points for each finger. Specifically, for the index, middle, ring and little fingers the Cartesian coordinates of the PIP joint, DIP joint and tip of the finger are considered; for the thumb, the MCP joint, IP joint and tip of the thumb are considered. These distances are normalized by the maximum distance that each key-point can assume considering the biomechanical range of motion (ROM) limits of each joint of the hand. The ROM for each joint were extracted from the works of: Bain et al. for the index, middle, ring and little MCP, DIP, and PIP joints [31], Gracia-Ibanez et al. for the ROT, MCP, and IP joints of the thumb [32], and from available online data sheets for the ABD joints [33].

This normalization provides two advantages: (i) it ensures that the size of the hand will not influence the proposed metric, (ii) it guarantees a finite range for the metric, namely 0 to 100.

Mathematically, the Geometric Configuration Similarity between two task-space mapped synergy vectors Θ_i, Θ_j is formulated as:

$$GCS(f) = \frac{1}{3}\sum_{k=1}^{3} 100 \cdot \left(1 - \frac{||\mathbf{p_k}(\mathbf{\Theta_i}) - \mathbf{p_k}(\mathbf{\Theta_j})||_2^2}{max(d(k,f))}\right) \quad (6)$$
$$with\ f = 1, ..., 5$$

Where f represents the finger index, and k is the key-point index. $\mathbf{p_k}(\mathbf{\Theta_i})$, and $\mathbf{p_k}(\mathbf{\Theta_j})$ are, respectively, the task-space Cartesian positions of the k-th key-point for the synergy vector $\mathbf{v_i}$ and $\mathbf{v_j}$. $max(d(k,f))$ is the maximum Euclidean distance that the k-th key-point of the f-th finger can assume considering the human physiological ROM [31]–[33]. Note, GCS produces a similarity measure for each of the five fingers.

Intuitively, for a given finger f, if the two synergy vectors map to the exact same position, their distance will be $||\mathbf{p_k}(\mathbf{\Theta_i}) - \mathbf{p_k}(\mathbf{\Theta_j})||_2^2 = 0\,\forall k$, and therefore the Geometric Configuration Similarity will be 100. Alternatively, if the two synergy vectors map to the maximum possible biomechanical distance $||\mathbf{p_k}(\mathbf{\Theta_i}) - \mathbf{p_k}(\mathbf{\Theta_j})||_2^2 = max(d(k,f))\,\forall k$, then the Geometric Configuration Similarity will be 0.

To provide a unique scalar macroscopic description of the similarity between two synergy vectors, we can use the arithmetic mean of the Geometric Configuration Similarities of the five fingers:

$$mean(GCS) = \frac{1}{5}\sum_{f=1}^{5} GCS(f) \quad (7)$$

D. The Selection of the Activation Coefficients

Particular attention must be given to the selection of the activation coefficient u. As presented in Equation 5, the activation coefficient is necessary to map the synergy vector to a given joint configuration or trajectory. In fact, without an activation coefficient, the synergy vectors just inform us of the proportionality ratio between features but not the extent to which such synergies are employed. Several options for the selection of u are possible. However, for the sake of comparing synergies, two main approaches are considered here.

The first approach consists in using the maximum and minimum activation coefficients found in the columns of the matrix product $U \cdot S = T$, found in Equation 2. The resulting matrix $T = [\mathbf{t_1}, \mathbf{t_2}, ..., \mathbf{t_m}]$ will have as columns the temporal evolutions of each synergy vector based on the input data X^*. Consequently, the $min(\mathbf{t})$ and $max(\mathbf{t})$ values of each temporal evolution represent the maximum and minimum values that a given synergy assumed based on the input data.

This approach is data-driven and, therefore, eliminates the risk of over-activating a synergy vector with respect to another one. Moreover, it will always generate physiologically reasonable movements - assuming no errors during data acquisition.

However, one should remember that by using PCA or SVD, the synergies are extracted in decreasing order of variance-accounted-for. Therefore, higher order synergies will have smaller activation coefficients, and this will influence the comparability of synergy vectors with different orders.

Moreover, if interested in reconstructing the entire motion, you can use these activation coefficients to craft a personalized temporal evolution. In the provided software package, a 4^{th} order polynomial (sine-wave like) starting at 0 and stopping at 0 and passing through $max(\mathbf{t})$ and $min(\mathbf{t})$ was adopted.

The second approach is instead driven by biomechanics. Instead of using the activation coefficients extracted through PCA/SVD, these can be modeled so that a synergy vector spans the maximum range of motion of a certain feature. A reasonable choice is to select the largest element of a synergy vector i.e., the largest contributing joint DoF in the hand case, and scale it such that its value will reach the minimum and maximum ROM of that hand joint. In this case, the activation functions for higher order synergies will not be limited by the lower variance-accounted-for synergies. However, it is not guaranteed that the resulting hand posture will represent a physiological configuration.

The authors think the selection of the appropriate activation function is context dependent. In the case of comparison with experimental data, the first approach i.e., using the columns of T, seems more appropriate, and that is what is used in the Results of this work. In the case of using synergies for design or control purposes, the second approach i.e., extending the synergy to the ROM limits, might be the right choice.

E. The three Geometric Configuration Similarities

Considering two synergy vectors $\mathbf{v_i}$, and $\mathbf{v_j}$ extracted from dataset having average postures $\mathbf{\Theta_{i_{avg}}}$, and $\mathbf{\Theta_{j_{avg}}}$, and with minimum and maximum activation coefficients u_{max_i}, u_{max_j}, u_{min_i}, and u_{min_j}, three different, Geometric Configuration Similarities are computed. These represent the average posture, maximum posture and minimum posture conditions:

$$GCS(f)_{avg}|\mathbf{\Theta_i} = \mathbf{\Theta}_{i_{avg}} \wedge \mathbf{\Theta_j} = \mathbf{\Theta}_{j_{avg}} \tag{8}$$

$$GCS(f)_{max}|\mathbf{\Theta_i} = u_{max_i} \cdot \mathbf{v_i} + \mathbf{\Theta}_{i_{avg}} \wedge \quad \mathbf{\Theta_j} = u_{max_j} \cdot \mathbf{v_j} + \mathbf{\Theta}_{j_{avg}} \tag{9}$$

$$GCS(f)_{min}|\mathbf{\Theta_i} = u_{min_i} \cdot \mathbf{v_i} + \mathbf{\Theta}_{i_{avg}} \wedge \quad \mathbf{\Theta_j} = u_{min_j} \cdot \mathbf{v_j} + \mathbf{\Theta}_{j_{avg}} \tag{10}$$

The $GCS(f)_{avg}$ provides information on how much the average postures of the considered datasets are similar to each other. This parameter is independent of the considered synergy vectors and it is always equal to 100 when the comparison is performed between synergies extracted from the same dataset i.e., $\mathbf{\Theta_i} = \mathbf{\Theta_j}$. $GCS(f)_{max}$ and $GCS(f)_{min}$ quantify the geometric difference between the maximum or minimum postures between the considered synergy vectors.

Two different applications of the Geometric Configuration Similarity are reported in the following. The first presents a numerical example involving two biomechanically relevant, artificially synthesized hand postures that yield a GCS close to the minimum. This example highlights a disparity between GCS and cosine similarity. The second provides an experimental example, consisting of two case studies, and applies the GCS to the kinematic hand synergies extracted from the authors' previously reported work on piano playing [10].

A software package to run GCS and reproduce the experimental results presented in this work can be found at the following GitHub repository: https://github.com/ftessari23/GCS.

III. Results

The hand model was calibrated on the 50th percentile male hand, and the resulting maximum distances $max(d(k,f))$ for each key-point (PIP,DIP,Tip) and each finger are reported in Table III.

$max(d(k,f))$ $[m]$	Joints		
	Tip	**DIP (IP)**	**PIP (MCP)**
Thumb	0.195 ± 0.003	$0.159 \pm < 0.001$	$0.083 \pm < 0.001$
Index	0.176 ± 0.003	0.126 ± 0.002	$0.071 \pm < 0.001$
Middle	0.193 ± 0.003	0.144 ± 0.003	$0.085 \pm < 0.001$
Ring	0.194 ± 0.002	0.149 ± 0.002	$0.086 \pm < 0.001$
Little	0.170 ± 0.003	0.126 ± 0.002	$0.076 \pm < 0.001$

TABLE I

Maximum Euclidean distance plus-minus the numerical measurement tolerance at each key-point (PIP, DIP, Tip) in each finger. In brackets you can find the name of the thumb joints.

A. Numerical Example: Joints Limit Hand Configurations

In this first example, we aimed to compare the most biologically distinct hand postures. Thus, we chose two hand configurations in which the first has all the joints at the maximum ROM and, the second has all the joints at the minimum ROM:

$$\mathbf{\Theta_1} = [\theta_{1_{max}}, ..., \theta_{20_{max}}] \tag{11}$$

$$\mathbf{\Theta_2} = [\theta_{1_{min}}, ..., \theta_{20_{min}}] \tag{12}$$

The cosine similarity between these biomechanically distinct hand postures is 0.71, which corresponds to an angular difference of about $44.6°$. This suggests a non-negligible similarity between the vectors.

However, when the vectors are mapped to the task-space and the GCS is computed, we observe (Figure 2) that the 2 postures have very poor similarity - as expected - with an average GCS of 8.7% across the five fingers. It is worth emphasizing that, despite the very small value, the GCS did not converge completely to 0%. This is expected, since the maximum and minimum ROM do not always represent the condition of maximum Euclidean distance for each of the different finger key-points.

B. Experimental Example: Piano Playing

Next, we compare kinematic synergies extracted on a group of healthy individuals while performing a series of piano pieces. All subjects were right-handed, received a comprehensive briefing on the experimental procedures, and signed a consent form approved by MIT's Institutional Review Board. We invite readers to refer to the work by West et al. for details on the experimental data acquisition and processing [10]. Here, two case studies are considered to highlight the benefits of the Geometric Configuration Similarity.

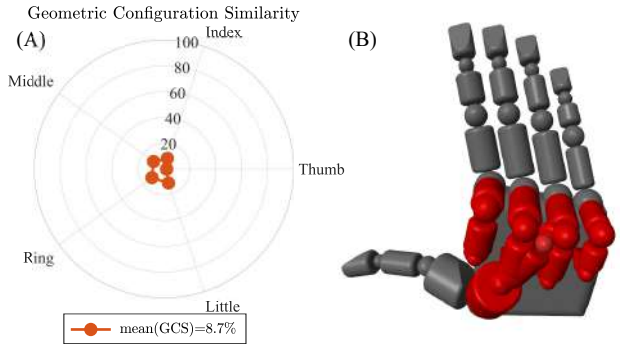


Fig. 2. Geometric Configuration Similarity between two synthetic synergy vectors $\mathbf{v_1}$ and $\mathbf{v_2}$ obtained by having the hand joints at their maximum and minimum ROM, respectively. In panel (A), the orange, dotted polygon represents the comparison between the two hand configuration postures $GCS(f)$. In panel (B), the maximum hand postures $\mathbf{\Theta_{1_{max}}(v_1)}$ and $\mathbf{\Theta_{2_{max}}(v_2)}$ are reported in the 3D hand model in gray and red, respectively.

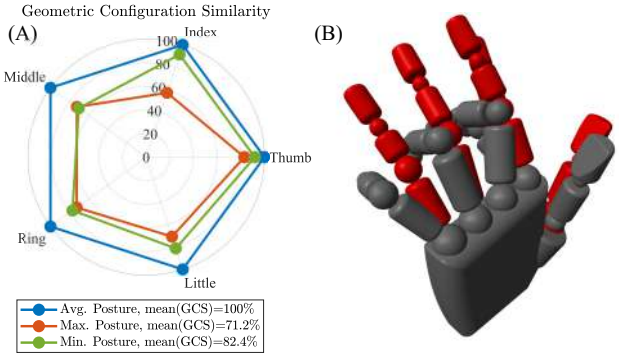


Fig. 3. Geometric Configuration Similarity between the first two synergy vectors, $\mathbf{v_1}$ and $\mathbf{v_2}$, of a representative subject playing the piano piece Bach Prelude in C Major. In panel (A), the blue, dotted polygon represents the comparison between average postures $GCS(f)_{avg}$, the orange, dotted polygon is the comparison between maximum postures $GCS(f)_{max}$, and the green, dotted polygon is the comparison between minimum postures $GCS(f)_{min}$. In panel (B), the maximum hand postures $\mathbf{\Theta_{1_{max}}(v_1)}$ and $\mathbf{\Theta_{2_{max}}(v_2)}$ are reported in the 3D hand model in gray and red, respectively.

1) Within-Subject - Different Order Synergies: In the first case study, we present a comparison of the first 2 kinematic synergies of a representative subject (nr. 2) performing the Bach Prelude in C Major by J.S. Bach. The synergies were extracted using the approach presented in Section II.A; they represent the first 2 columns of matrix V (i.e., $\mathbf{v_1}$ and $\mathbf{v_2}$). They account, respectively, for 44% and 25% of the Variance-Accounted-For (VAF). By computing the cosine similarity of these two synergies, we observe that such synergies are perfectly orthogonal:

$$cos(\theta) = \frac{|\mathbf{v_1}^T \cdot \mathbf{v_2}|}{||\mathbf{v_1}|| \cdot ||\mathbf{v_2}||} = 0 \tag{13}$$

This follows directly from SVD, as the columns of V are orthonormal, meaning they are mutually orthogonal.

However, when using the Geometric Configuration Similarity, we observe (Figure 3) that the two synergies - despite their orthogonality - present substantial similarities. Specifically, the maximum and minimum postures of the first 2 synergies show an average Geometric Configuration Similarity across the five fingers of 71.2% and 82.4%, respectively. The average posture $\mathbf{\Theta_{avg}}$ presents, instead, a GCS of 100%. This is a natural consequence of the fact that both synergies were extracted from the same dataset, thus they must have the same average posture.

2) Between-Subjects - Same Order Synergies: In the second case study, we compare the first synergies of two different subjects (nr. 2 and nr. 5) performing the same piano piece (i.e., Bach Prelude in C Major). These two synergies account, respectively, for 44% and 42% of the Variance-Accounted-For. Their cosine similarity is equal to 0.19, which represents an angular difference of about $79°$. Once more, the synergies appear close to orthogonality, and thus would typically be considered very *different postures*.

However, when the synergies are compared with the Geometric Configuration Similarity, we observe (Figure 4) that the average postures present an average GCS of 89.4% indicating that the two subjects had a similar - but not identical - average hand configuration while playing the same piano piece. Moreover, the maximum and minimum hand postures - dictated by each subjects' first synergy - show an average GCS of 64.5% and 78%, respectively. These values provide a geometrically intuitive understanding of how *similar* the two synergies between the subjects are. Moreover, this tool enables us to observe that the index and little fingers are actually the ones that were used most differently between the subjects (see Figure 4).

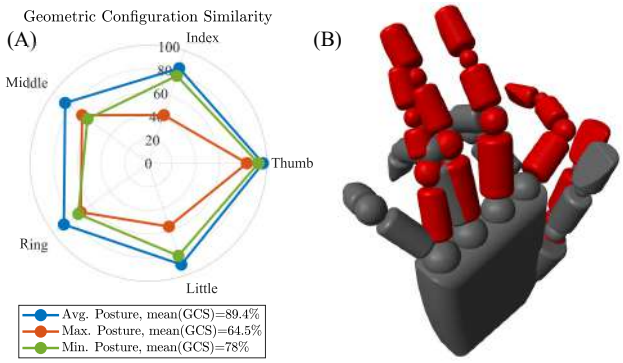


Fig. 4. Geometric Configuration Similarity between the first synergy vectors $\mathbf{v_{1_{s2}}}$ and $\mathbf{v_{1_{s5}}}$ of two representative subjects (nr.2 and nr. 5) performing the same piano playing task i.e., Bach Prelude in C Major. In panel (A), the blue, dotted polygon represents the comparison between average postures $GCS(f)_{avg}$, the orange, dotted polygon is the comparison between maximum postures $GCS(f)_{max}$, and the green, dotted polygon is the comparison between minimum postures $GCS(f)_{min}$. In panel (B), the maximum hand postures $\mathbf{\Theta_{1_{max}}(v_{1_{s2}})}$ and $\mathbf{\Theta_{1_{max}}(v_{1_{s5}})}$ are reported in the 3D hand model respectively in gray and red, respectively.

IV. Discussion

In this paper, we addressed the limitations of cosine similarity by proposing a novel geometric approach for comparing kinematic hand synergies, termed Geometric Configuration Similarity (GCS). GCS utilizes MATLAB's multibody simulation, Simscape, and forward kinematics to map joint space

synergies to a task-space hand configuration. This mapping enables both visual and analytical comparison of kinematic synergies. Through numerical and experimental comparisons, we demonstrate that GCS provides valuable insights overlooked by cosine similarity. Looking ahead, we believe that the publicly available GCS framework will assist researchers in conducting more thorough analyses of hand kinematics.

A. Geometric Interpretability

1) Numerical Example: In our numerical example, we compared two biologically distinct hand configurations: one with all joints at their maximum range of motion (ROM) and another with all joints at their minimum ROM. The Geometric Configuration Similarity (GCS) metric revealed a stark contrast between these two postures, yielding a low similarity score of 8.7% across the five fingers (Fig. 2). This finding highlights the significant differences in hand kinematics that are present, despite the similarity suggested by the cosine similarity score of 0.71. Such a high cosine similarity value implies significant similarity, which is misleading given that the two configurations are functionally and anatomically disparate.

This discrepancy underscores the limitations of relying solely on cosine similarity for evaluating hand postures. While cosine similarity may indicate a non-negligible relationship between the two synergy vectors, it fails to capture the true geometric differences that GCS effectively elucidates. By mapping the synergy vectors to task-space configurations, GCS provides a more intuitive representation of the distinct hand postures, thereby enhancing our understanding of the complex mechanics involved in hand manipulation.

It is important to note that in this numerical example, the GCS did not reach a minimum value of zero; instead, it was 8.7% (Fig. 2). While it may be theoretically possible to achieve a lower GCS, attaining a value of zero is unlikely. As outlined in Eq. 6, the Cartesian distance between each pair of keypoints is normalized by its theoretical maximum, which considers the biomechanical range of motion. For the GCS to equal zero, all keypoints would need to be positioned at points of maximum distance simultaneously. However, due to the interconnected nature of finger joints in our multibody model, the position of each keypoint is influenced by the configuration of the distal joints. Consequently, a configuration that maximizes the distance between the PIP and DIP joints may not necessarily maximize the distance at the TIP. This issue becomes even more pronounced when considering movements such as abduction and adduction. Nevertheless, Fig. 2 provides a useful reference for understanding the range of GCS values achievable under different configurations.

2) Experimental Example: In our first experimental example (*Within-Subject - Different Order Synergies*), we examined the kinematic synergies of a subject performing the Bach Prelude in C Major, focusing on the first two synergy vectors extracted via Singular Value Decomposition. While cosine similarity indicates that these two vectors are orthogonal, signifying that they span completely different hyperspaces—a result of the SVD design—Geometric Configuration Similarity reveals significant kinematic similarities in the configuration space. This distinction is crucial, and it, again, underscores the limitations of relying solely on cosine similarity to evaluate hand postures. Moreover, GCS allows for a more intuitive interpretation of the data, enabling us to easily identify which fingers exhibit higher or lower similarity between the synergies. For example, in Fig. 3 we can see that the largest discrepancy lies in the motion of the index finger, whose maximum posture GCS is 57%, while there is high similarity in the thumb whose minimum and maximum posture GCS are 92% and 83%, respectively. Such insights are vital when discussing the functional roles of each synergy in hand movements. Consequently, one could argue that GCS serves as a valuable proxy measure for assessing the similarity of kinematic synergies as they relate to function, providing a deeper understanding of the intricacies of hand manipulation.

In our second experimental example (*Between-Subjects - Same Order Synergies*), we compared the first synergy vectors of two different subjects performing the same piano piece, the Bach Prelude in C Major. Notably, the cosine similarity for these vectors was measured at 0.19, indicating a relatively higher degree of similarity compared to the first example, where cosine similarity was 0 for within-subject comparisons of different order synergies. However, the Geometric Configuration Similarity tells a different story. In this case, the GCS for the maximum posture scenario decreased from 71.2% in the within-subject example to 64.5% when comparing between subjects, and similarly dropped from 82.4% to 78% in the minimum posture scenario. This juxtaposition highlights the limitations of cosine similarity and shows that GCS provides a more nuanced understanding of the functional similarities and differences in hand configurations. Moreover, GCS intuitively highlights that index and little finger motion might be the root of this cause; their maximum posture GCS reduced from 57%, index, and 71%, little, (Fig. 3) to 43% and 56% (Fig. 4), respectively. Such insights are critical for assessing how different individuals may employ similar synergies in varied ways during complex motor tasks.

B. Methodological Considerations

We want to highlight that the choice to utilize three key points per finger in measuring configuration was intentional and is crucial for eliminating discrepancies that may arise from redundancy in joint movements. For instance, if we were to measure only the distance at the Tip of each finger, that position could be achieved through multiple joint configurations. Specifically, the fingertip is described by three Cartesian degrees of freedom (DOF), while the finger possesses 4 (three flexion + 1 ab/addcution) DOFs, resulting in a one-dimensional null space. This means that different combinations of joint angles could yield the same TIP position, leading to ambiguity in interpreting movement. By selecting three key points—namely the PIP, DIP, and TIP, we increase the number of task-space DOFs relative to joint-space DOFs. This approach effectively eliminates the potential for errors due to

redundancy, and enhances the reliability of the GCS metric in capturing the complexities of hand movements.

The current version of the GCS is implemented in Matlab 2023b by using the multibody library available in Simulink/Simscape. However, alternatives exist. The first is to use Exp[licit], a recently released robotic control library, which has demonstrated better computational efficiency compared to standard robotic control toolboxes [34]. A second alternative is represented by advanced physics simulators such as Mujoco [35]. It is worth emphasizing that GCS is independent of the adopted software framework and is only a function of the considered hand geometry.

C. Limitations

One limitation of this study lies in the geometric assumptions regarding the hand model used for analyzing kinematic synergies. The model was based on a rigid-link representation of a 20-degree-of-freedom hand, incorporating four degrees of freedom per finger. However, more detailed mechanical models could be used to include the hand's remaining degrees of freedom [36]. Additionally, the current model may not adequately account for individual anatomical variations among subjects (e.g., larger or smaller hands, as well as different proportions between the phalanges), which could influence the accuracy of the Geometric Configuration Similarity (GCS) measurements. To help mitigate these limitations, we have open-sourced the GCS framework, allowing future researchers to utilize the metric and customize the hand model to better fit the specific anatomical characteristics of their study populations. Moreover, we are planning to parameterize the GCS model so that users will be able to input the hand percentile and automatically scale the GCS to the size of interest.

Another limitation of this study is the inability of GCS to provide statistical measures. In this regard, cosine similarity also falls short. As noted in our previous study [27], cosine similarity tends to converge toward 0.75, as the number of dimensions increases. DIEM addresses this issue [27], but requires non-unitary length vectors. Therefore, DIEM can be applied to either the reconstructed joint configurations (Equation 5) or the task-space positions (Equation 4). Future work should investigate the statistical properties of GCS and DIEM to enhance reliability and interpretability.

D. Impact

The discrepancies observed between cosine similarity and Geometric Configuration Similarity (GCS) can be attributed to the inherent differences in what each metric measures. Cosine similarity evaluates the angle between vectors, providing insight into their orientation rather than their geometric relationship in configuration space. This can lead - as shown in this paper - to misleading interpretations that fail to capture the intricate functional differences that exist between hand configurations, potentially obscuring the understanding of how specific movements contribute to overall hand function.

In contrast, GCS is inherently linked to the function of hand movements, as it assesses geometric distances between mapped configurations in task space. This metric provides insights into how individual joint positions relate to functional outcomes in hand manipulation. By focusing on spatial configurations, GCS reveals critical kinematic similarities and differences essential for understanding motor control. For instance, it allows researchers to identify which fingers demonstrate higher or lower similarity in their movements, thus connecting the analysis of synergies to their functional roles.

This relationship highlights the utility of GCS in rehabilitation and motor control research, offering a more meaningful understanding of how hand movements serve specific functional objectives. For example, the GCS could be used as an input for the design of exoskeletal or prosthetic devices [37], [38] that aim to reconstruct specific hand motions e.g., piano playing or tool-use. Often times synergy orthogonality (observed through cosine similarity) is used to introduce a new DOF in assistive or rehabilitative devices. GCS offers a much more direct intuition of the geometric consequences of adding a new synergy to a certain hand configuration, thus enabling more adequate design choices. Additionally, GCS could be used as a metric to assess the recovery of hand motor function when computed between healthy and impaired individuals.

Finally, it is important to underline that the Geometric Configuration Similarity approach can be extended beyond hand kinematics to other parts of the human body such as upper-limb or lower-limb kinematic synergies.

Comparing GCS and cosine similarity offers an interesting parallel to a classic question in motor control: do humans plan and execute motion using intrinsic or extrinsic coordinates [39]–[41]? Cosine similarity, by comparing synergy vectors based on joint configurations, inherently reflects comparisons in intrinsic coordinates. This perspective has been used to discuss how humans may simplify the highly redundant motor control problem when planning an action. On the other hand, GCS compares synergies after projecting them into task-space, which corresponds to the end-effector positions and represents the extrinsic coordinates in which actions are typically executed. A substantial body of evidence suggests that humans often plan motion in extrinsic coordinates [39]–[41], where the focus is on achieving goals in the environment rather than coordinating individual joints. Therefore, future work using GCS could provide valuable insights into how humans simplify path planning in extrinsic coordinates, shedding light on how synergies are organized for task-level control.

V. Conclusions

The human hand, with its high degrees of freedom and ability to perform a vast array of complex tasks, poses significant challenges for studying its kinematics and motor control [36]. To simplify this analysis and enhance understanding, researchers have turned to the concept of synergies [16]. Cosine similarity has traditionally been the go-to method for comparing these synergies. However, as highlighted in this paper, cosine similarity has notable limitations, particularly when it comes to its interpretability and capturing the true

geometric relationships between hand configurations. To address these shortcomings, we introduced the Geometric Configuration Similarity (GCS) metric, a tool designed to provide researchers with a more intuitive and meaningful way to compare kinematic synergies. GCS can help researchers gain a deeper understanding of hand function, ultimately advancing the study of hand motor control in both healthy and impaired populations.

ACKNOWLEDGMENT

This work was funded by the Eric P. and Evelyn E. Newman fund, Takeda Fellowship, Accenture Fellowship, and the Johns Hopkins University Provost's Postdoctoral Fellowship.

REFERENCES

[1] E. J. Alpenfels, "The anthropology and social significance of the human hand," *Artificial Limbs*, vol. 2, pp. 4–21, 1955.

[2] C. L. Taylor and R. J. Schwarz, "The anatomy and mechanics of the human hand," *Artificial Limbs*, vol. 2, pp. 22–35, 1955.

[3] R. Bellman, "Dynamic programming," *Science*, vol. 153, pp. 34–37, 7 1966.

[4] M. Santello, G. Baud-Bovy, and H. Jörntell, "Neural bases of hand synergies," *Frontiers in Computational Neuroscience*, vol. 7, p. 42740, 3 2013.

[5] V. C. Cheung and K. Seki, "Approaches to revealing the neural basis of muscle synergies: A review and a critique," *Journal of Neurophysiology*, vol. 125, pp. 1580–1597, 5 2021.

[6] E. J. Weiss and M. Flanders, "Muscular and postural synergies of the human hand," *Journal of Neurophysiology*, vol. 92, pp. 523–535, 7 2004.

[7] M. Santello, M. Flanders, and J. F. Soechting, "Postural hand synergies for tool use," *Journal of Neuroscience*, vol. 18, pp. 10 105–10 115, 12 1998.

[8] E. Todorov and Z. Ghahramani, "Analysis of the synergies underlying complex hand manipulation," *Annual International Conference of the IEEE Engineering in Medicine and Biology - Proceedings*, vol. 26 VI, pp. 4637–4640, 2004.

[9] A. M. West, F. Tessari, and N. Hogan, "The study of complex manipulation via kinematic hand synergies: The effects of data pre-processing," *IEEE ... International Conference on Rehabilitation Robotics : [proceedings]*, vol. 2023, pp. 1–6, 9 2023.

[10] ——, "The study of dexterous hand manipulation: A synergy-based complexity index," *IEEE Transactions of Medical Robotics and Bionics*, 2024.

[11] K. Pearson, "Principal components analysis," *The London Edinburgh and Dublin Philosophical Magazine and Journal of Science*, vol. 6, p. 559, 1901.

[12] G. W. Stewart, "On the early history of the singular value decomposition," *SIAM review*, vol. 35, pp. 551–566, 7 2006.

[13] A. M. West, "Towards a non-invasive measurement of human motion, force, and impedance during a complex physical-interaction task : wire-harnessing," 2020.

[14] A. M. West Jr, "All Models are Wrong , Simple Models Provide Insight : A Study of Human Manipulation," Ph.D. dissertation, Massachusetts Institute of Technology, 2024.

[15] S. Furuya, M. Flanders, and J. F. Soechting, "Hand kinematics of piano playing," *Journal of Neurophysiology*, vol. 106, pp. 2849–2864, 12 2011.

[16] M. Santello, M. Bianchi, M. Gabiccini, E. Ricciardi, G. Salvietti, D. Prattichizzo, M. Ernst, A. Moscatelli, H. Jörntell, A. M. Kappers, K. Kyriakopoulos, A. Albu-Schäffer, C. Castellini, and A. Bicchi, "Hand synergies: Integration of robotics and neuroscience for understanding the control of biological and artificial hands," pp. 1–23, jul 2016.

[17] M. H. Schieber and M. Santello, "Hand function: peripheral and central constraints on performance," *Journal of applied physiology*, vol. 96, pp. 2293–2300, 6 2004.

[18] T. Flash and B. Hochner, "Motor primitives in vertebrates and invertebrates," pp. 660–666, dec 2005.

[19] J. N. Ingram, K. P. Körding, I. S. Howard, and D. M. Wolpert, "The statistics of natural hand movements," *Experimental Brain Research*, vol. 188, no. 2, 2008.

[20] S. A. Overduin, A. D'Avella, J. Roh, and E. Bizzi, "Modulation of muscle synergy recruitment in primate grasping," *Journal of Neuroscience*, vol. 28, no. 4, 2008.

[21] S. A. Overduin, A. D'Avella, J. M. Carmena, and E. Bizzi, "Microstimulation Activates a Handful of Muscle Synergies," *Neuron*, vol. 76, no. 6, 2012.

[22] S. A. Overduin, A. D'Avella, J. Roh, J. M. Carmena, and E. Bizzi, "Representation of muscle synergies in the primate brain," *Journal of Neuroscience*, vol. 35, no. 37, 2015.

[23] F. Tessari, A. West, and N. Hogan, "On human motor coordination: The synergy expansion hypothesis," *bioRxiv*, p. 2024.04.10.588877, 4 2024.

[24] N. Lambert-Shirzad and H. F. V. D. Loos, "Data sample size needed for analysis of kinematic and muscle synergies in healthy and stroke populations," *IEEE International Conference on Rehabilitation Robotics*, pp. 777–782, 8 2017.

[25] K. Zhao, Z. Zhang, H. Wen, and A. Scano, "Number of trials and data structure affect the number and components of muscle synergies in upper-limb reaching movements," *Physiological Measurement*, vol. 43, p. 105008, 10 2022.

[26] Y. X. Wang and Y. J. Zhang, "Nonnegative matrix factorization: A comprehensive review," *IEEE Transactions on Knowledge and Data Engineering*, vol. 25, pp. 1336–1353, 6 2013.

[27] F. Tessari and N. Hogan, "Surpassing cosine similarity for multidimensional comparisons: Dimension insensitive euclidean metric (diem)," *arXiv*, 7 2024.

[28] M. F. Rabbi, C. Pizzolato, D. G. Lloyd, C. P. Carty, D. Devaprakash, and L. E. Diamond, "Non-negative matrix factorisation is the most appropriate method for extraction of muscle synergies in walking and running," *Nature Scientific Reports*, 2020.

[29] M. W. Berry, M. Browne, A. N. Langville, V. P. Pauca, and R. J. Plemmons, "Algorithms and applications for approximate nonnegative matrix factorization," *Computational Statistics Data Analysis*, vol. 52, pp. 155–173, 9 2007.

[30] C. C. Gordon, T. Churchill, C. E. Clauser, B. Bradtmiller, J. T. McConville, I. Tebbetts, and R. A. Walker, "1988 anthropometric survey of u.s. personnel: Summary statistics interim report," 1988.

[31] G. I. Bain, N. Polites, B. G. Higgs, R. J. Heptinstall, and A. M. McGrath, "The functional range of motion of the finger joints," *Journal of Hand Surgery: European Volume*, vol. 40, pp. 406–411, 5 2015.

[32] V. Gracia-Ibáñez, M. Vergara, J. L. Sancho-Bru, M. C. Mora, and C. Piqueras, "Functional range of motion of the hand joints in activities of the international classification of functioning, disability and health," *Journal of Hand Therapy*, vol. 30, pp. 337–347, 7 2017.

[33] Physiotutors. (2024) Wrist/hand active range of motion (arom) — basic assessment.

[34] J. Lachner, M. C. Nah, S. Stramigioli, and N. Hogan, "Exp[licit] an educational robot modeling software based on exponential maps," *IEEE/ASME International Conference on Advanced Intelligent Mechatronics, AIM*, pp. 1359–1366, 2024.

[35] E. Todorov, T. Erez, and Y. Tassa, "Mujoco: A physics engine for model-based control," *IEEE International Conference on Intelligent Robots and Systems*, pp. 5026–5033, 2012.

[36] E. R. Kandel, J. D. Koester, S. H. Mack, and S. A. Siegelbaum, *Principles of Neural Science, Sixth Edition*. McGraw Hill, 2021.

[37] M. G. Catalano, G. Grioli, E. Farnioli, A. Serio, C. Piazza, and A. Bicchi, "Adaptive synergies for the design and control of the pisa/iit softhand," *International Journal of Robotics Research*, vol. 33, pp. 768–782, 4 2014.

[38] M. Laffranchi, N. Boccardo, S. Traverso, L. Lombardi, M. Canepa, A. Lince, M. Semprini, J. A. Saglia, A. Naceri, R. Sacchetti, E. Gruppioni, and L. De Michieli, "The Hannes hand prosthesis replicates the key biological properties of the human hand," *Science Robotics*, vol. 5, no. 46, p. 467, 2020.

[39] P. Morasso, "Spatial control of arm movements," *Experimental Brain Research*, vol. 42, pp. 223–227, 4 1981.

[40] J. R. Flanagan and A. K. Rao, "Trajectory adaptation to a nonlinear visuomotor transformation: evidence of motion planning in visually perceived space," *Journal of Neurophysiology*, vol. 74, no. 5, pp. 2174–2178, 1995, pMID: 8592205.

[41] P. Dizio and J. R. Lackner, "Motor adaptation to coriolis force perturbations of reaching movements: endpoint but not trajectory adaptation transfers to the nonexposed arm," *Journal of neurophysiology*, vol. 74, pp. 1787–1792, 1995.

Differentiable Biomechanics Unlocks Opportunities for Markerless Motion Capture

1st R. James Cotton
Department of Physical Medicine and Rehabilitation, Northwestern University
Shirley Ryan AbilityLab
Chicago, IL
rcotton@sralab.org

***Abstract*—Recent developments have created differentiable physics simulators designed for machine learning pipelines that can be accelerated on a GPU. While these can simulate biomechanical models, these opportunities have not been exploited for biomechanics research or markerless motion capture. We show that these simulators can be used to fit inverse kinematics to markerless motion capture data, including scaling the model to fit the anthropomorphic measurements of an individual. This is performed end-to-end with an implicit representation of the movement trajectory, which is propagated through the forward kinematic model to minimize the error from the 3D markers reprojected into the images. The differential optimizer yields other opportunities, such as adding bundle adjustment during trajectory optimization to refine the extrinsic camera parameters or meta-optimization to improve the base model jointly over trajectories from multiple participants. This approach improves the reprojection error from markerless motion capture over prior methods and produces accurate spatial step parameters compared to an instrumented walkway for control and clinical populations.**

I. Introduction

Markerless motion capture (MMC), using multiple synchronized cameras to capture and reconstruct movement using computer vision, can greatly expand access to movement analysis in rehabilitation and movement science research and clinical practice. In recent years several open and proprietary systems have emerged and been validated for this purpose [1]–[4]. However, existing approaches are limited by the lack of biomechanical body models designed for integration into machine learning pipelines. OpenSim is a widely used open-source biomechanical modeling framework [5], [6], for which there are many models including for the whole body and focused models of the arm [7]–[9]. However, simulation in this environment is slow and not easily integrated into GPU-accelerated frameworks. Although the NimblePhysics biomechanical simulator is faster it still cannot be parallelized and or accelerated on a GPU [10].

Mujoco [11] is another simulator that supports biomechanical models, including muscle-actuated models. Recently, GPU acceleration was integrated into Mujoco as Mujoco-MJX, based on the physics simulator from Brax [12]. Mujoco has enabled the development of multiple biomechanically oriented frameworks designed integration with machine learning and reinforcement learning, including MyoSuite [13], [14], which includes a tool for converting OpenSim models into Mujoco, and LocoMujoco [15], a locomotion imitation benchmark suite.

In addition to performance, a benefit of simulators like Brax and Mujoco-MJX is that they are differentiable, which opens up the opportunities that we explore in this work. We previously showed that implicit representations for movement trajectories, where a function is learned that maps for time to a coordinate space, $f_\theta : t \rightarrow \mathbf{x}$, recover smoother and more anatomically consistent trajectories from markerless motion capture while having better convergence properties [16]. We then perform inverse kinematic fits of a biomechanical to these marker trajectories to recover joint angles [17]. This was done using a bilevel optimization approach that jointly estimates the skeleton scaling and the inverse kinematics across multiple trajectories [18]. We were forced into this two-stage approach because we could not propagate gradients from the reprojected marker location errors through the kinematic model and into the learned implicit representation, which is straightforward to do with differentiable, GPU-accelerated simulators.

However, a barrier to this is that, to the best of our knowledge, scaling the models to fit the anthropomorphic measurements of an individual is not supported with current platforms using Mujoco. Furthermore, there are many different human pose estimation (HPE) algorithms for detecting keypoints from images, that are trained on a diversity of datasets, each having different idiosyncracies. To obtain accurate fits, the model must have marker locations that are optimized for the keypoint set used. Differentiable biomechanical models allow the marker locations on the base model to be optimized end-to-end with the reconstructions from a population of individuals with a range of anthropomorphic measurements. Differentiability also allows marker offsets and skeleton scaling for each individual to integrate naturally into the optimization process. In this work, we selected the MOVI keypoints outputs from the MetrABs-ACAE algorithm [19], which our prior work found are some of the most accurate and anatomically consistent when varying viewpoints. Full differentiability also means that we can perform bundle adjustment [20] by computing the derivatives with respect to the extrinsic camera parameters. Thus the biomechanically constrained observations of the movement can even improve the calibration.

In short, our contributions are:

- We enable personalized model scaling and inverse kinematic fitting with bilevel optimization using a GPU-accelerated, fully differentiable biomechanical model using Mujoco.
- Implement this using an end-to-end differentiable bilevel optimization with an implicit representation of pose trajectories propagated through the forward kinematic biomechanical model to minimize the error from the 3D markers reprojected into the images.
- Perform bundle adjustment to refine the extrinsic camera parameters during this optimization.
- Implement a trilevel optimization process that meta-optimizes the base biomechanical model marker locations over a dataset of trajectories from multiple participants.

II. Methods

A. Participants

This study was approved by the Northwestern University Institutional Review Board. Participants performed several activities, with the majority performing multiple walking trials, often at different speeds or using different assistive devices. These were performed while participants walked along an instrumented walkway that recorded foot contact and toe-off timing and locations [21], [22]. Some participants performed additional tasks like the timed-up-and-go and the four-square-step-test [23]. Our dataset contains a mixed population with able-bodied controls and participants with a history of neurologic conditions, predominantly stroke but some traumatic brain injury, spinal cord injury, peripheral neuropathy, as well as lower limb prosthesis users. There are also several participants with a history of knee osteoarthritis and pediatric participants. For quantifying and comparing performance, we focus on the set of trials that were fit using our previously described biomechanical pipeline [16], [17].

B. Markerless Motion Capture

Multicamera data was collected with a custom system we developed using 8 to 12 FLIR BlackFly S GigE cameras with F1.4/6mm lens [16], [17]. This system acquires 2048 $\times$ 1536 images at 30 fps that are synchronized using the IEEE1558. Extrinsic and intrinsic calibration was performed using the anipose library [24] using a checkerboard. These fitted parameters produce a function for each camera i that projects points in the 3D space of the acquisition volume onto the 2D image plane of each camera:

$$\Pi_i : \mathbf{x} \rightarrow y,\ \mathbf{x} \in \mathbb{R}^3,\ y \in \mathbb{R}^2 \tag{1}$$

We used the previously described user interface to select the person of interest from an initial scene reconstruction, which is used to compute the bounding box for that individual across all of the cameras and frames. Keypoints were estimated independently for each frame using an algorithm trained on numerous 3D datasets that outputs the superset of all these formats (MeTRAbs-ACAE) [19]. We used a subset from this output that are the 87 keypoints from the MOVI dataset [25], which correspond to those often used in biomechanical analysis and that we used in our prior reconstruction methods [16], [17]. MeTRAbs-ACAE also directly outputs 3D joint locations from each camera, but we only use the 2D outputs. In our prior work, we have found the keypoints from this algorithm are more geometrically consistent when varying perspectives than other algorithms [17], likely due to the unique training on extensive 3D datasets. It does not provide confidence intervals for each keypoints, so we approximated them by measuring the standard deviation of each 3D joint location estimated from 10 different augmented versions of each video frame. This was converted to a confidence estimate using a sigmoid function with a half maximum at 30mm and a width of 10mm. This is different than the value we previously used (200 and 50 respectively) [16], as we discovered these prior values provided more of a binary "detected" signal than a continuous score.

C. Implicit representation

When reconstructing biomechanics from multiple synchronized cameras, we previously found an implicit representation that uses a function to map from time to virtual marker positions, $f_\phi(t) \rightarrow \mathbf{x}$ with $\mathbf{x} \in J \times 3$, outperforms optimizing an explicit trajectory for $\mathbf{x}(t)$ or using a robust triangulation [16]. This learnable function is instantiated as a multi-layer perceptron (MLP) and time is input using sinusoidal positional encoding after scaling the time inputs from 0 to π to prevent aliasing in the encoding [26]. In this work, we modified the implicit representation from directly outputting 3D joint locations to outputting pose parameters that are input to a forward kinematics model implemented in Mujoco. The pose parameters corresponding to joint angles were constrained to the joint range limits through a `tanh` nonlinearity.

D. Mujoco model

We used a biomechanically grounded, forward kinematic implemented in Mujoco [11]. We based our model on LocoMujoco [15], which in turn is based on the OpenSim model Hamner, Seth, and Delp [8]. We modified the LocoMujoco model by removing collisions other than on the feet, which significantly accelerated the forward kinematics, and we also added a neck joint with 3 degrees of freedom. In our prior work, we optimized marker locations compatible with the MOVI keypoints on a similar biomechanical model in the OpenSim format using the nimblephysics simulator [10]. We ported these marker locations to the model used in this work using the site Mujoco element, which corresponds to a virtual marker rigidly attached to a component of the model.

To the best of our knowledge, model scaling, and marker offset calculation have not been implemented using Mujoco and MJX. LocoMujoco implements a similar process by modifying the model specification in the XML before instantiating it, but this does not allow these parameters to be changed dynamically in the GPU or to compute the derivatives or trajectories with respect to scaling and offsets. We implemented a wrapper for the forward kinematics that allows passing in scaling parameters as well as marker offsets in

addition to the joint angles. The base model is then modified in memory before computing the forward kinematics. The scaling was implemented using a matrix that maps from a set of scale parameters to scaling individual body segments isotropically. We included 8 scale parameters: an overall size, the pelvis, left thigh, left leg and foot, right thigh, right leg and foot, the left arm, and the left leg. This could be naturally extended to allow separate scales on more body segments or anisotropic scaling, but we did not explore that in this work. Following notation used by the popular skinned multi-person linear model (SMPL)[27], we can thus represent our GPU-accelerated, biomechanical forward kinematic equation as:

$$\mathbf{x} = \mathcal{M}(\theta, \beta) \tag{2}$$

Where $\theta \in \mathbb{R}^{40}$ are the inputs to the skeleton model, $\beta \in \mathbb{R}^{8+87*3}$ are the set of 8 scaling parameters are the offsets for each of the marker locations, and $\S \in \mathbb{R}^{87\times 3}$ are the predicted marker locations. The forward kinematic model also can provide the location and orientation of each of the 21 body components along the kinematic tree as well as the mesh geometry locations and orientations, neither of which we use in this work. Finally, the model includes dynamics, with each component having linear and rotational velocities that respond to torques from the joints, which we also do not use in this work.

E. MyoSkeleton model

We were also kindly granted early access to a new model being developed for MyoSuite [13], [14], called the MyoSkeleton. This has many more degrees of freedom (152), such as all the degrees of freedom in the spine at many vertebral levels, a fully articulated hand, and even an articulated patella. These additional degrees of freedom are governed by 66 equality constraints corresponding to typical movement, such as how the flexion at L4-5 should be related to the flexion at L3-4. MJX allows computing an error function for how much these constraints are violated [11], $\boldsymbol{\epsilon} = \mathrm{err}(\boldsymbol{\theta})$. When fitting the MyoSkeleton model, in addition to having the implicit function output 152 degrees of freedom, we included an additional loss term that penalized the violation of these constraints,$\mathcal{L}_\epsilon = \lambda_\epsilon \frac{1}{66}\sum_i \epsilon_i^2$. We used $\lambda_\epsilon = 0.01$ based on initial experiments showing this drove the constraint violations to very low levels, and leave further optimization of this to future work. Otherwise, fitting the MyoSkeleton used identical code and settings to the LocoMujoco model.

F. Bilevel optimization

We followed the bilevel optimization approach of Werling, Raitor, Stingel, *et al.* [18], jointly solving for the skeleton scaling, marker offsets, and joint angle trajectories over multiple movement sequences. This approach was developed for precomputed 3D marker trajectories, either from traditional optical marker-based motion capture and then adopted in our recent work to virtual 3D marker trajectories from markerless motion capture [17]. In this work, we make two critical modifications: 1) we represent the pose trajectory over time, θ_t, with an implicit representation instead of using this function to predict virtual marker locations, $\mathbf{x}_t$, and 2) we minimize the error between the detected joint locations in the image plane and the marker locations in 3D space after reprojecting the coordinates through the calibrated camera function, Π_i, for camera i. Thus, this approach directly optimizes the joint angles that control the biomechanical model to produce marker locations consistent with keypoints detected in the image plane. This is possible because our entire model is end-to-end differentiable and accelerated on the GPU.

More formally, we have a set of N recordings, each of which has keypoints detected for each joint, j, per timestep, t, and per camera, c: $\left\{y^{(n)}_{t,j,c}\right\}_{n=1...N}$. The modeled 3D virtual marker locations are produced from the learned implicit function learned separately for each trajectory, which is then passed through the forward kinematic model using a common β parameter for all trajectories:

$$\mathbf{x}^{(n)}_t = \mathcal{M}(f_{\phi_n}(t), \beta) \tag{3}$$

The parameters for the set of trajectories, $\{\phi_0, ..., \phi_N, \beta\}$, are jointly optimized by minimizing the reprojection loss between the detected 2D keypoints and the reprojected 3D marker locations:

$$\mathcal{L}_\Pi = \frac{1}{T \cdot J \cdot C} \sum_{T,J,c\in C} w_{c,t,j}\, g\left(||\Pi_c \mathbf{x}_{t,j} - y_{t,j,c}||\right) \tag{4}$$

Where $g(\cdot)$ is the Huber loss and $w_{c,t,j}$ is the confidence of the detected keypoint. We also include an L2 regularization on the components of β corresponding to the site markers to prevent them from shifting too far from the default location:

$$\mathcal{L}_\beta = \frac{1}{87\times 3} \sum_{i=8...8+87*3} \beta_i^2 \tag{5}$$

The total loss is then:

$$\mathcal{L} = \mathcal{L}_\Pi + \lambda_\beta \mathcal{L}_\beta + \lambda_\epsilon \mathcal{L}_\epsilon \tag{6}$$

We did not find any additional regularization for temporal smoothness was necessary, although this could be an opportunity for future improvements. We only included the constraint violation loss, $\mathcal{L}_\epsilon$, when fitting the MyoSkeleton model.

1) Bundle adjustment: Because the entire system, including the camera parameters, is end-to-end differentiable, we can also perform bundle adjustment to further refine the calibration parameters. Specifically, we allowed the translation and rotation parameters of Π_c from (4) to be learnable parameters, while performing the optimization. We used a learning rate schedule that only allowed these parameters to start adjusting later during the optimization process.

2) Implementation and Optimization details: Our implicit representations were implemented in Jax using the Equinox framework [28]. We used an MLP with layer sizes of 128, 256, 512, 1024, 2048, 2048, 4096. Time was scaled to not exceed π and was positionally encoded, using an encoding dimension

of 29. We performed optimization with the AdamW optimizer from Optax [29], [30], using $\beta_1 = 0.8$ and weight decay of $1e-5$. The learning rate used included an exponential decay from an initial value of $1e-4$ to an end value of $1e-7$. We used 40k optimization steps with bundle adjustment enabled at the 30k step using a separate Adam optimizer with a learning rate of $1e-5$. We typically performed this on an A6000 and found it could perform more than 500 iterations a second for a single trajectory of 10 seconds. For typical sessions with 10 trials, this optimization took several minutes. Because Jax operates more efficiently on fixed array sizes (new array sizes trigger tracing and recompiling the code), when training on multiple trajectories with different lengths we would randomly sample a set of 300 time points from each trajectory per iteration.

G. Trilevel optimization

One challenge is placing all of the markers on the biomechanical model in a location that is consistent with the marker locations produced by the model. When developing our prior method using nimblephysics, we iteratively optimized many separate runs and then applied the mean marker offsets to the original unscaled model. Several rounds of this process did improve our results [17]. However, this process required repeatedly correcting some of the marker locations that shifted too far and did not necessarily produce the optimal locations.

We took advantage of the fact that our framework is fully differentiable and runs extremely quickly to jointly optimize the default marker locations by fitting the model to 31 different individuals from our dataset with 2 trials per individual, which we found could be performed on a single 80GB A100. This optimization included multiple of the 31 independent models similar to the one described under bilevel optimization. However, the marker offset for the base model was also made learnable, with the models from the 31 individuals each being independently scaled $\mathcal{L}_\beta$ applied to their independent site offsets. To prevent the markers from shrinking inward, which we had initially observed, we froze the position of the bilateral heel markers on the base model. We performed this process once at the beginning of this work and then used this optimized base model to fit all of the trajectories for each individual using a bilevel optimization approach, which then scaled the model and learned individualized marker offsets with regularization from (5) to prevent the markers moving much beyond this.

H. Baseline biomechanics

We compare the biomechanics results against our prior methodology, which decomposes this into two steps equivalent to a typical biomechanics pipeline [16], [17]. Specifically, it uses an implicit representation to reconstruct the 3D marker trajectories over time, which we found produced better results than optimizing explicit marker trajectories directly or robust triangulation. It then uses the nimblephysics library for bilevel optimization, which fits the model scaling and marker offsets while performing inverse kinematics for each trial. However, in contrast to the approach proposed in this paper, this prior approach is not end-to-end differentiable so the nimblephysics model results are optimized against the reconstructed marker trajectories instead of the raw image observations. We hypothesized this decomposition would limit performance.

I. Performance metrics

1) Geometric Consistency: We measured the geometric consistency between the model-based marker trajectories and the detected keypoints, based on the distance between the reprojected model-based markers and the detected keypoints. To quantify this, we computed the fraction of the points below a threshold number of pixels, conditioned on being greater than a specified confidence interval.

$$\delta_{t,j,c} = ||\Pi_c \mathbf{x}_{t,j} - y_{t,j,c}|| \tag{7}$$

$$q(d, \lambda) = \frac{\sum(\delta_{t,j,c} < d)(w_{t,j,c} > \lambda)}{\sum w_{t,j,c} > \lambda} \tag{8}$$

Below, we report $GC_d = q(d, 0.5)$ with $d = 5$ pixels.

2) GaitRite comparison: We compared the heel marker position from the forward kinematics to those measured by the GaitRite to measure the error of each step length, stride length, and step width. We report the width of the error distribution as normalized IQR, $\sigma_{IQR} = 0.7413 \cdot IQR(x)$. We use this in place of the standard deviation because it is more robust to the few outliers we observe, and we also show the histogram of errors in the results.

III. Results

A. Visualizations

We first visually confirmed the quality of the reconstructions by creating videos comparing the reprojected model-based markers reprojected into each of the image planes to the 2D keypoint detections. Figure 1 shows an example frame from 10 cameras acquired simultaneously, showing close alignment between the reconstructed and detected keypoints.

We also used the Mujoco renderer videos of the walking trajectories, which replicated the movements seen in the videos. Figure 2 shows example frames from a walking trial, reconstructed with both skeletons. Note that the fully articulated MyoSkeleton hand is not properly constrained by the 87 keypoints used.

B. Samples waveforms

Figure 3 shows sample waveforms from a single trial from a control participant reflecting a stable, symmetric, periodic gait pattern. Figure 4 shows a sample waveform from a participant with a history of stroke which captures the spatiotemporal asymmetry and greater step-width variability.

C. Reprojection loss

We also compared the error in the camera reprojections between our prior approach and the new approach, measured by the fraction of sites that reproject within a specific number of pixels, GC_x. We found that the end-to-end optimization approach with differentiable biomechanics had a better GC_5 for almost every trial. When comparing the GC_5 for trials

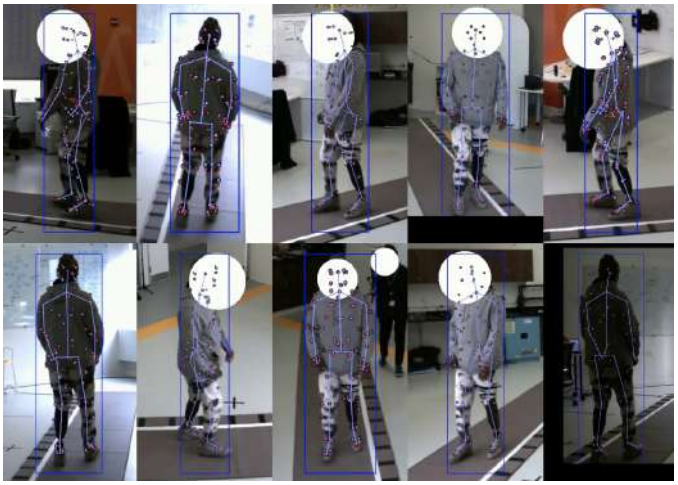


Fig. 1. Visualization of reprojection errors. Each panel is a zoomed in crop from the image around the detected bounding box from a different view. The red dots are the 87 detected keypoints in each frame and the blue dots are the reprojected model-based markers, with the drawn skeleton connecting a subset of these keypoints.

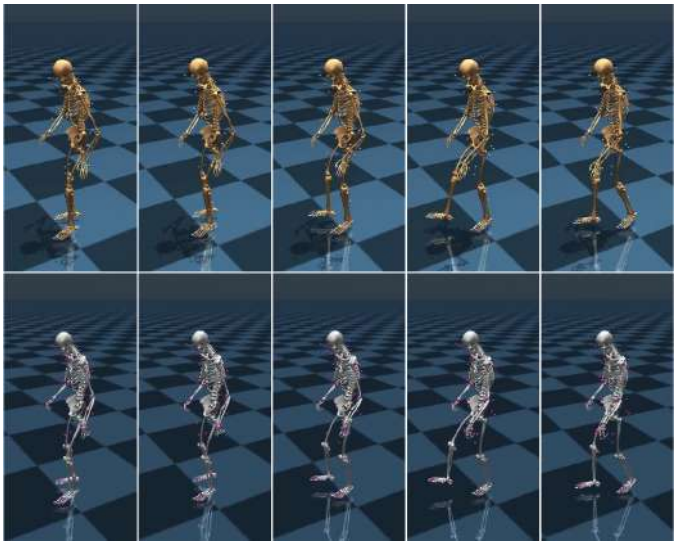


Fig. 2. Sample rendered frames from a walking trial fit from an individual with a history of stroke using a cane on the left side. The top row is the modified LocoMujoco skeleton and the bottom row is the MyoSkeleton.

using differentiable biomechanics without and with bundle adjustment enabled, we also saw a performance improvement. The average GC_x curve for differentiable biomechanics with calibration exceeded the other approach for all x values (Figure 5).

We quantified this difference by performing an ANOVA with method as the main factor and GC_5 as the dependent variable. This was highly significant ($p < 1{\times}10^{-5}$, $F = 4418$) and a post-hoc Tukey test showed a significant difference between all conditions. This included the small 1.9% increase in GC_5 when enabling bundle adjustment. Note, that this analysis only included 851 of the trials in our dataset, as we do not routinely run reconstruction with Nimblephysics anymore.

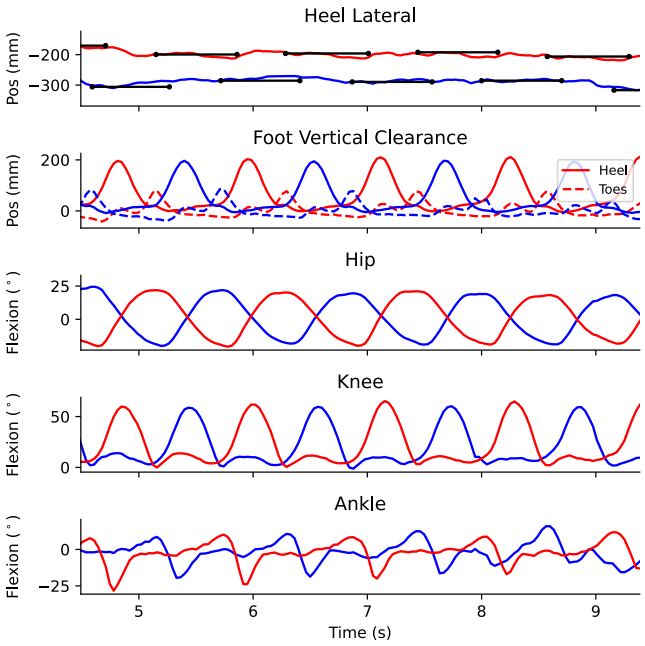


Fig. 3. Sample waveforms from a control participant. The left leg is shown in blue and the right leg is shown in red. The top row shows the lateral position of the heel with the positions detected from the instrumented walkway shown in black. The next row shows the vertical clearance from the heel and toes. The last three rows show the flexion angles for the hip, knee, and ankle, respectively.

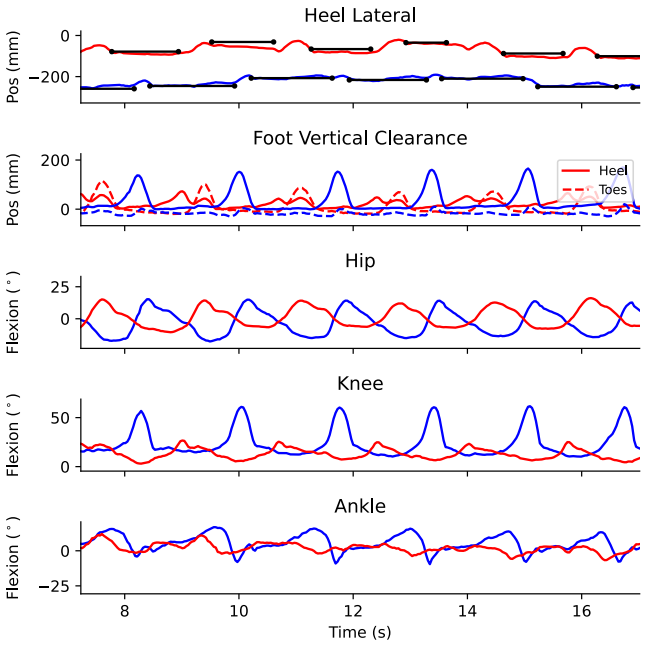


Fig. 4. Sample waveforms from a participant with a history of stroke, corresponding to the visualization from Figure 2. This captures the reduced range of motion on the right hemiparetic side, particularly with reduced knee flexion.

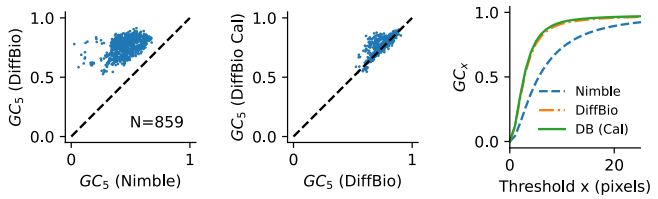


Fig. 5. Reprojection losses for reconstruction with two-stage approach using implicit representation followed by nimblephysics versus end-to-end approach with implicit representation and forward kinematic biomechanical model in mujoco. The left panel compares the GC_5 between our prior two-stage approach using nimble physics (horizontal axis) with differentiable biomechanics (vertical axis) for a number of trials. The middle panel compares trials with and without bundle adjustment to refine calibration. The right panel shows the average GC_x as a function of the pixel threshold for those trials.

D. Step parameter errors

We also compare the errors in the spatial step parameters computed between the GaitRite and the heel marker from the fitted model. The process of aligning the reference frame spatially and temporally between the two systems was the same as our prior work [16], with an affine transformation and temporal offset computed to minimize the error over a set of trials. Note this marker location does not precisely correspond to the same anatomic location as the center of pressure from the heel measured by the instrumented walkway, but provides a rough estimate of accuracy. Figure 6 shows the distribution of errors for each of these parameters.

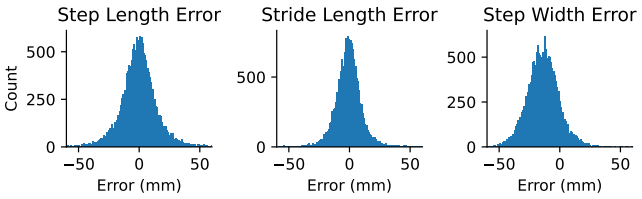


Fig. 6. Histogram of step length, stride length, and step width errors comparing the GaitRite and biomechanical reconstruction.

Table I shows the σ_{IQR} for each of these parameters broken down by several clinical populations. We see for control participants, the error is about 8-10 mm across the parameters but is slightly higher for some of the clinical populations. In particular, for some of the clinical populations, the step length error increases more than the stride length error. We hypothesize this may arise due to asymmetries in weight loading that are measured differently from the instrumented walkway than from the location of heel markers. This may also be due to reduced keypoint detection accuracy of HPE algorithms in some clinical populations, which we have shown for lower limb prosthesis users (LLPUs), particularly those with more proximal or bilateral amputations [31]. Finally, the error may also arise from keypoints detected on physical therapists who are often walking closely to the participant for safety, which are then misattributed to the participant, although our Huber loss is generally robust to this [16].

TABLE I
σ_{NIQR} FOR GAIT METRICS BROKEN DOWN BY CLINICAL POPULATION, AS WELL AS THE NUMBER OF SUBJECTS AND TRIALS IN EACH CATEGORY.

Population	Step Width	Stride Length	Step Length	Subjects	Trials
Controls	10.6	8.1	7.9	29	622
LLPU	10.6	9.0	15.1	46	431
Neurologic	12.4	10.2	19.1	37	333
Orthopedic	15.3	8.5	7.9	5	37
Pediatric	16.2	13.1	15.1	5	34

TABLE II
GAIT METRICS OVER ALL TRIALS FOR DIFFERENT MODELS AND OPTIMIZATION APPROACHES.

Model	Bund Adj	Step Width	Stride Length	Step Length	GC_5
LocoMujoco	False	12.31	9.97	13.00	0.70
LocoMujoco	True	12.19	9.05	12.57	0.72
MyoSkeleton	False	12.33	9.91	13.17	0.69
MyoSkeleton	True	12.18	9.07	12.73	0.72

We also computed this for the LocoMujoco model and the MyoSkeleton model, both with and without bundle adjustment. We found that both models perform well, despite the MyoSkeleton having higher degrees of freedom. Errors in the spatial gait parameters were similar to our prior work, although here we computed on a large sample [17].

IV. DISCUSSION

Having a fully differentiable biomechanical model that can be accelerated on a GPU is an extremely powerful tool for rehabilitation and movement science research. Here, we showed we can drive this forward kinematic with implicit representation for movement trajectories and optimize them to get accurate movement reconstructions. The trajectories from multiple trials can be jointly optimized with the skeleton scaling and marker offsets in a consistent end-to-end framework, providing a straightforward implementation of bilevel optimization [18].

Our model also allows trilevel optimization, where multiple individuals' trajectories and skeleton scaling are fit simultaneously while also optimizing the base model marker offsets. This is a powerful tool for integrating biomechanics into different computer-vision pipelines, as in our experience, inconsistencies between marker conventions are a source of error. Now, these markers can be roughly initialized and attached to the right body component and then fine-tuned on an entire dataset. This will be convenient for creating new models for new HPE algorithms, such as detailed hand tracking or other commonly used markersets. We did note some limitations from our trilevel approach. The first limitation was that only 31 individuals with 2 trials each were used due to limitations in GPU memory, and this many people might not be sufficiently representative. This limitation arose as all trials were processed for each iteration. In the future, we will implement mini-batching over subsets to allow jointly optimizing parameters over many participants. We are also experimenting with manually setting and anchoring additional

markers that are anatomically well-defined in addition to the heel, as we saw that the elbow site location was displaced more anterior than we believe it should be. Thus, the current model risks introducing a biased offset in the joint angles compared to ground truth.

Our results show that end-to-end optimization produces fits that are more geometrically consistent with the detected keypoints than a two-stage optimization approach, as measured through the GC_x of the reprojected fit results. This is fairly unsurprising, as decomposing the problem does not allow the initial trajectories to be directly constrained by the biomechanical model. Our prior work with the implicit representation included explicit regularization to keep the bone lengths consistent over the trajectory for certain keypoints [16], but for many keypoints, such as those in the foot or the middle of a limb, it was less clear how to structure those constraints. In our fully differentiable implicit reconstruction approach, these constraints and others, such as joint limits, arise naturally from the biomechanical model fit for each individual over multiple trials. In the case of the MyoSkeleton, this also extended to the joint equality constraints to allow fitting the many degrees of freedom over the spine with anatomically valid values.

We exploited differentiability through the camera model to incorporate bundle adjustment into the later iterations of optimization, to refine extrinsic camera parameters. This step made a small but significant improvement in the reprojection errors and the step parameter errors. This is despite us already performing a rigorous calibration with anipose before each experiment [24]. While we are not ready to skip the calibration step yet, removing this need is another useful step to making MMC even easier to use. This also suggests a path to optimizing other differentiable meta-parameters for a session, such as how we account for the keypoint confidence scores.

Optimizing how we account for keypoint uncertainty is another opportunity to improve the reconstructions we have not yet explored. Our current approach does not produce confidence bounds on the joint angles, which will vary across a trial based on the number of cameras viewing certain markers and their relative geometry. Reliable confidence estimates are critical for wider usage, particularly in clinical settings, as knowing when you can trust the data is essential. In the context of lifting from 2D to 3D keypoints, we have shown that fitting probabilistic models and optimizing the negative log-likelihood (NLL) instead of minimizing a point estimate of error can produce these calibrated uncertainty estimates [32]. Our recent work demonstrates that we can expand the implicit representations over joint angles to a probability distribution and optimize it using variational inference to accomplish this aim [33].

Computing confidence over joint angles will also benefit approaches where obtaining ground truth information is hard. This includes large-scale data collection on representative clinical populations, as in our current work. This also includes tracking the hand, where placing markers on individual joints is impractical and alters the visual appearance and function of the hand. The MyoSkeleton [13], [14] includes a fully articulated hand, and we have also ported the MoBL-ARMS biomechanical model [34] to MuJoCo. The end-to-end optimization approach we demonstrate here can be extended to full hand tracking with only a few millimeters of error [35]. We have also validated our end-to-end approach for multiview video reconstructions against marker-based motion capture of arm kinematics during a drinking task and find agreement within a few degrees [36].

It is reassuring that our model produces high-quality fits for a range of clinical populations, including lower-limb prosthesis users, those with neurologic conditions, pediatric patients, and people with musculoskeletal conditions. The step parameters do increase in some populations, with the noise in the step length increasing to as high as 2cm for individuals with neurologic conditions often walk with an accompanying therapist, where keypoints from the wrong individual may be mis-associated. This suggests opportunities for improving the geometric scene understanding and using multi-person tracking to improve the results further. Stride length remains 1cm in this condition, which may also suggest this relates to systematic differences between measuring weight pressure locations versus computer vision.

While multiview markerless motion capture is a powerful tool that produces accurate results, it has limitations. This includes substantial amounts of processing power and time to analyze the results. Furthermore, our optimization approach is fit to the full trajectory, precluding any attempt to make it run in realtime. Another limitation is the requirement of multiple cameras. Thus, we are excited about our recent results demonstrating this technique can be extended to smartphone video, showing a close correspondence to results from multiview video [37].

GPU-accelerated biomechanical models offer additional opportunities. We are currently extending the implicit representation to include actions, allowing optimization of dynamic rollouts with ground reaction forces and joint torques. We also recently showed that using reinforcement learning (RL) to train an imitation learning policy driven by monocular computer vision improves gait analysis from single camera views [38], which can be further improved by using the more accurate biomechanical models in MuJoCo. Finally, MyoSuite is building a community and set of tools around neuromuscular and biomechanical modeling using Mujoco, and the work we described here will enable the creation of large-scale datasets of movements from real people compatible with their tools [13]. This hybridizes well with recent advances such as the SKEL and OSSO model [39], [40], which map biomechanical models to the body models more typically used in computer vision research, such as SMPL [27].

V. Conclusion

Fully differentiable biomechanical models that can be accelerated on a GPU are a promising tool for rehabilitation and movement science. Here, we demonstrate an end-to-end bilevel optimization algorithm to scale biomechanical models, compute inverse kinematics over multiple trials, and even

perform bundle adjustment of the camera calibration. This end-to-end optimization approach can both improve the accuracy of biomechanics from multiview markerless motion capture and open up new avenues.

REFERENCES

[1] N. Nakano, T. Sakura, K. Ueda, *et al.*, "Evaluation of 3d Markerless Motion Capture Accuracy Using OpenPose With Multiple Video Cameras," *Frontiers in Sports and Active Living*, vol. 2, p. 50, May 2020.

[2] S. D. Uhlrich, A. Falisse, Ł. Kidziński, *et al.*, "Opencap: 3d Human Movement Dynamics from Smartphone Videos," p. 2022.07.07.499061, Jul. 2022.

[3] R. M. Kanko, E. K. Laende, E. M. Davis, W. S. Selbie, and K. J. Deluzio, "Concurrent Assessment of Gait Kinematics Using Marker-Based and Markerless Motion Capture," *Journal of Biomechanics*, vol. 127, p. 110 665, Oct. 2021.

[4] A. Cherian, P. Queen, W. Trent, I. Endurance, and J. S. Matthis, *Freemocap: A Free, Open Source Markerless Motion Capture System*, 2024.

[5] C. L. Dembia, N. A. Bianco, A. Falisse, J. L. Hicks, and S. L. Delp, "Opensim Moco: Musculoskeletal Optimal Control," *PLOS Computational Biology*, vol. 16, no. 12, K. S. Campbell, Ed., e1008493, Dec. 2020.

[6] A. Seth, J. L. Hicks, T. K. Uchida, *et al.*, "Opensim: Simulating Musculoskeletal Dynamics and Neuromuscular Control to Study Human and Animal Movement," *PLoS Computational Biology*, vol. 14, no. 7, e1006223, Jul. 2018.

[7] A. Rajagopal, C. L. Dembia, M. S. DeMers, D. D. Delp, J. L. Hicks, and S. L. Delp, "Full-Body Musculoskeletal Model for Muscle-Driven Simulation of Human Gait," *IEEE Transactions on Biomedical Engineering*, vol. 63, no. 10, pp. 2068–2079, 2016.

[8] S. R. Hamner, A. Seth, and S. L. Delp, "Muscle Contributions to Propulsion and Support during Running," *Journal of Biomechanics*, vol. 43, no. 14, pp. 2709–2716, Oct. 2010.

[9] D. C. McFarland, B. I. Binder-Markey, J. A. Nichols, S. J. Wohlman, M. de Bruin, and W. M. Murray, "A Musculoskeletal Model of the Hand and Wrist Capable of Simulating Functional Tasks," *IEEE transactions on bio-medical engineering*, vol. 70, no. 5, pp. 1424–1435, May 2023.

[10] K. Werling, *Nimblephysics*, https://github.com/keenon/nimblephysics, 2022.

[11] E. Todorov, T. Erez, and Y. Tassa, "Mujoco: A Physics Engine for Model-Based Control," in *2012 IEEE/RSJ International Conference on Intelligent Robots and Systems*, Oct. 2012, pp. 5026–5033.

[12] C. D. Freeman, E. Frey, A. Raichuk, S. Girgin, I. Mordatch, and O. Bachem, "Brax – A Differentiable Physics Engine for Large Scale Rigid Body Simulation," Jun. 2021.

[13] V. Caggiano, H. Wang, G. Durandau, M. Sartori, and V. Kumar, *Myosuite – A Contact-Rich Simulation Suite for Musculoskeletal Motor Control*, http://arxiv.org/abs/2205.13600, May 2022.

[14] H. Wang, V. Caggiano, G. Durandau, M. Sartori, and V. Kumar, "Myosim: Fast and Physiologically Realistic MuJoCo Models for Musculoskeletal and Exoskeletal Studies," in *2022 International Conference on Robotics and Automation (ICRA)*, May 2022, pp. 8104–8111.

[15] F. Al-Hafez, G. Zhao, J. Peters, and D. Tateo, *Locomujoco: A Comprehensive Imitation Learning Benchmark for Locomotion*, http://arxiv.org/abs/2311.02496, Nov. 2023.

[16] R. J. Cotton, A. Cimorelli, K. Shah, S. Anarwala, S. Uhlrich, and T. Karakostas, "Improved Trajectory Reconstruction for Markerless Pose Estimation," in *45th Annual International Conference of the IEEE Engineering in Medicine and Biology Society*, Sydney, Mar. 2023.

[17] R. J. Cotton, A. DeLillo, A. Cimorelli, *et al.*, "Optimizing Trajectories and Inverse Kinematics for Biomechanical Analysis of Markerless Motion Capture Data," in *IEEE International Consortium for Rehabilitation Robotics*, arXiv, Mar. 2023.

[18] K. Werling, M. Raitor, J. Stingel, *et al.*, "Rapid Bilevel Optimization to Concurrently Solve Musculoskeletal Scaling, Marker Registration, and Inverse Kinematic Problems for Human Motion Reconstruction," p. 2022.08.22.504896, Aug. 2022.

[19] I. Sárándi, A. Hermans, and B. Leibe, "Learning 3d Human Pose Estimation from Dozens of Datasets Using a Geometry-Aware Autoencoder to Bridge Between Skeleton Formats," in *IEEE/CVF Winter Conference on Applications of Computer Vision (WACV)*, arXiv, 2023.

[20] R. Hartley and A. Zisserman, *Multiple View Geometry in Computer Vision*. Cambridge University Press, 2003.

[21] A. L. McDonough, M. Batavia, F. C. Chen, S. Kwon, and J. Ziai, "The Validity and Reliability of the GAITRite System's Measurements: A Preliminary Evaluation," *Archives of Physical Medicine and Rehabilitation*, vol. 82, no. 3, pp. 419–425, Mar. 2001.

[22] B. Bilney, M. Morris, and K. Webster, "Concurrent Related Validity of the GAITRite Walkway System for Quantification of the Spatial and Temporal Parameters of Gait," *Gait and Posture*, vol. 17, no. 1, pp. 68–74, Feb. 2003.

[23] Shirley Ryan AbilityLab, *Rehabilitation Measures*, https://www.sralab.org/rehabilitation-measures, Feb. 2025.

[24] P. Karashchuk, K. L. Rupp, E. S. Dickinson, *et al.*, "Anipose: A Toolkit for Robust Markerless 3d Pose Estimation," *bioRxiv*, p. 2020.05.26.117325, May 2020.

[25] S. Ghorbani, K. Mahdaviani, A. Thaler, *et al.*, "Movi: A Large Multi-Purpose Human Motion and Video Dataset," *PLOS ONE*, vol. 16, no. 6, e0253157, Jun. 2021.

[26] A. Vaswani, N. Shazeer, N. Parmar, *et al.*, "Attention Is All You Need," 2017.

[27] M. Loper, N. Mahmood, J. Romero, G. Pons-Moll, and M. J. Black, "Smpl: A Skinned Multi-Person Linear Model," *ACM Transactions on Graphics*, vol. 34, no. 6, pp. 1–16, Oct. 2015.

[28] P. Kidger and C. Garcia, "Equinox: Neural Networks in JAX via Callable PyTrees and Filtered Transformations," Oct. 2021.

[29] I. Loshchilov and F. Hutter, *Decoupled Weight Decay Regularization*, http://arxiv.org/abs/1711.05101, Jan. 2019.

[30] DeepMind, I. Babuschkin, K. Baumli, *et al.*, *The DeepMind JAX Ecosystem*, http://github.com/google-deepmind, 2020.

[31] A. Cimorelli, A. Patel, T. Karakostas, and R. J. Cotton, "Portable In-Clinic Video-Based Gait Analysis: Validation Study on Prosthetic Users," *medRxiv : the preprint server for health sciences*, 2022.

[32] P. A. Pierzchlewicz, M. Bashiri, R. J. Cotton, and F. H. Sinz, "Optimizing MPJPE Promotes Miscalibration in Multi-Hypothesis Human Pose Lifting," in *ICLR 2023 Affinity Workshop*, Apr. 2023.

[33] R. J. Cotton and F. Sinz, *Biomechanical Reconstruction with Confidence Intervals from Multiview Markerless Motion Capture*, http://arxiv.org/abs/2502.06486, Feb. 2025.

[34] K. R. S. Holzbaur, W. M. Murray, and S. L. Delp, "A Model of the Upper Extremity for Simulating Musculoskeletal Surgery and Analyzing Neuromuscular Control," *Annals of Biomedical Engineering*, vol. 33, no. 6, pp. 829–840, Jun. 2005.

[35] P. Firouzabadi, W. Murray, A. R. Sobinov, *et al.*, "Biomechanical Arm and Hand Tracking with Multiview Markerless Motion Capture," in *2024 10th IEEE RAS/EMBS International Conference for Biomedical Robotics and Biomechatronics (BioRob)*, Sep. 2024, pp. 1641–1648.

[36] T. Unger, A. S. Moslehian, J. D. Peiffer, *et al.*, "Differentiable Biomechanics for Markerless Motion Capture in Upper Limb Stroke Rehabilitation: A Comparison with Optical Motion Capture," in *IEEE International Consortium for Rehabilitation Robotics*, 2025.

[37] J. Peiffer, K. Shah, S. Anarwala, K. Abdou, and R. J. Cotton, "Fusing Uncalibrated IMUs and Handheld Smartphone Video to Reconstruct Knee Kinematics," in *2024 10th IEEE RAS/EMBS International Conference for Biomedical Robotics and Biomechatronics (BioRob)*, Sep. 2024, pp. 1275–1282.

[38] N. Smyrnakis, T. Karakostas, and R. J. Cotton, *Advancing Monocular Video-Based Gait Analysis Using Motion Imitation with Physics-Based Simulation*, http://arxiv.org/abs/2402.12676, Feb. 2024.

[39] M. Keller, K. Werling, S. Shin, *et al.*, "From Skin to Skeleton: Towards Biomechanically Accurate 3d Digital Humans," *ACM Transactions on Graphics*, vol. 42, no. 6, 253:1–253:12, Dec. 2023.

[40] M. Keller, S. Zuffi, M. J. Black, and S. Pujades, "Osso: Obtaining Skeletal Shape from Outside," in *2022 IEEE/CVF Conference on Computer Vision and Pattern Recognition (CVPR)*, Jun. 2022, pp. 20 460–20 469.

Assessment of motion sickness associated with motor amplification in a low-cost virtual reality rehabilitation system

Aidan Fisk
Department of Psychology
Acadia University
Wolfville, NS
aidanfiskvr@gmail.com

Summer Fox
Department of Psychology
Acadia University
Wolfville, NS
summerfox@acadiau.ca

Jenna Floyd
Department of Psychology
Acadia University
Wolfville, NS
jennadawnfloyd@gmail.com

Daniel Blustein
Department of Psychology
Acadia University
Wolfville, NS
blustein.neuro@gmail.com

***Abstract*— Effective rehabilitation is critical for individuals with motor deficits, such as following a stroke or brain injury. Although high doses of intensive motor rehabilitation can provide maximal benefit, several barriers can prevent attaining necessary therapy levels, including cost, physical access, clinical resource availability, and patient disengagement. Virtual Reality (VR) offers a potential solution to overcome these challenges and enable home-based, self-directed therapy. Here we present custom software that runs on the low-cost Meta Quest 2 headset to deliver immersive rehabilitation exercises. The system uses movement amplification to virtually reduce motor deficits, enabling successful task completion even in individuals with severe disabilities. This approach leverages reinforcement learning to maintain patient engagement during rehabilitation. The system capitalizes on recent advances in VR technology, including inside-out hand tracking, voice recognition, and a responsive virtual coach, to create a more accessible environment for users with no prior VR experience. We present the custom virtual rehabilitation implementation and test whether motor amplification leads to an increase in visually induced motion sickness experienced by individuals without disabilities. We find that motor amplification does not elevate reported motion sickness levels, suggesting that low-cost VR systems may enable increased access to individualized and guided motor rehabilitation.**

Keywords—motor rehabilitation, virtual reality, assistive technology, accessible healthcare

I. Introduction

Emerging medical treatments have improved survival rates for many conditions, including stroke [1] and neurodevelopmental disabilities [2], with the consequence of increased disability rates. For example, over the past 30 years, stroke has led to a steady increase in disability-adjusted life-years lost, especially in lower and lower-middle-income countries [1]. Motor, sensory, and cognitive deficits associated with stroke, traumatic brain injuries and neurodegenerative disorders contribute to a loss of function that makes daily life challenging, often requiring intensive and expensive assistive care. Motor disabilities often lead to a reinforcing cycle – the more difficult it is to use an affected limb, the less it will be used, and the more quickly remaining function will be lost. Overcoming this process of learned non-use, such as in the approximately 70% of stroke patients with upper limb motor deficits [3], is a key focus of efforts to improve access to motor rehabilitation.

Higher doses of therapy following an acute loss of function – including physical therapy, occupational therapy, and speech and language therapy – lead to better recovery outcomes [4], [5], [6]. For example, using and moving a limb affected by a stroke is critical to leveraging the brain's natural neuroplasticity in regaining lost motor and sensory function, and ultimately improving daily life functionality. Many effective treatments capitalize on this principle including constraint-induced movement therapy [7] and emerging robot-assisted systems [8].

There are numerous impediments to providing high volumes of motor rehabilitation therapy, which means patients often receive less care than they should [9]. Access to treatment can be limited by cost. For example, a best practice stroke rehabilitation protocol, constraint-induced movement therapy, spans 10 to 15 days with up to 6 hours of therapy per day [10], costing thousands of dollars [11]. Other emerging rehabilitation technologies such as robot-assisted therapy also require high costs and significant clinician oversight [8].

Physical access to rehabilitation services is another barrier patients face. Long distances to clinics in areas with limited transportation options can be difficult to overcome, especially for patients that often suffer from limited mobility. Barriers to travel to seek rehabilitation services are exacerbated in rural areas [12].

Some of these barriers to accessing treatment can be reduced by prescribing home exercises which have been shown effective in reducing disability, improving quality of life, and increasing patient self-efficacy [13]. However, at-home therapies face their own barriers to maximal

This work was supported by ResearchNS under the New Health Investigator Grant program.

effectiveness. Rates of exercise completion are low with about 60% of patients not fully adhering to at-home physiotherapy programs [13], [14], and even compliant patients incorrectly executing 10-20% of exercises after clinician instruction [13], [15]. Patients often struggle to incorporate exercises into their daily lives [14]. Memory issues, especially in older adults, contribute to noncompliance [16]. Increased clinician-patient interaction improves compliance with home exercise programs [17] yet resource constraints and access barriers limit this option.

Virtual Reality (VR) solutions have the potential to expand patient access to therapy and ultimately improve rehabilitation outcomes. Immersive VR rehabilitation has shown significant benefit compared to conventional rehabilitation, particularly with improvements in activities of daily living and gross motor function [18], [19]. For example, stroke patients receiving VR rehabilitation therapy as a supplement [20] or instead of [21] conventional rehabilitation therapy have shown significant improvements on the Box & Block Test and Fugl-Meyer Upper Extremity Scale, respectively.

Several recent efforts [22], [23] have implemented gamified rehabilitation exercises on the Meta Quest 2, an affordable commercially-available system that supports controller-free hand tracking. Gamified exercises have consistently been shown to boost motivation and engagement [24], [25].

One approach to boost engagement is to artificially reduce motor deficits in the virtual environment, leading to more consistent task completion that leverages positive reinforcement to encourage ongoing system use. When a stroke-affected limb's real-world movements are amplified in the virtual space, stroke patients are more likely to use their motor deficient limb, suggesting a way to counteract learned non-use [26]. On the Meta Quest 2, others have attempted to diversify the range of grasps in VR for those with motor deficits [27] or to use relocation algorithms to adapt the virtual world to a user's range of motion [28].

One key concern with virtual reality-based rehabilitation systems is the potential for induced motion sickness [29]. In previous work, VR users have demonstrated sometimes debilitating motion sickness, an effect more pronounced in women [30]. The expectation is that emerging VR technologies may reduce visually-induced motion sickness (e.g. [31]), but this has not been systematically tested with the latest technology. A key step in determining the initial feasibility of a low-cost VR rehabilitation system is to assess levels of motion sickness in its users, particularly when motor amplification is applied.

Here we describe a novel virtual reality rehabilitation system that addresses some of the systemic and individual patient barriers to treatment, namely limited location flexibility, high costs, and the need for constant clinician oversight. For an initial assessment, younger adults without disability tested our novel rehabilitation program to determine if motor amplification leads to increased visually-induced motion sickness in users.

II. Technology development

We developed a software program in which participants could engage in 12 gamified tasks, three of which were tested in this work. Tasks were designed to either emulate activities of daily living, such as pouring water into a glass, or serve as immersive games in which the hand becomes a controller in a classic game like Pong or Snake. Each task focused on one category of movement: 1) Gross reaching; 2) Reach and grasp; or 3) Precision Grasping. In this study, all tasks involved Gross reaching as this has been shown to be a motor skill most sensitive to immersive VR rehabilitation [19].

A. Virtual reality system

The VR setup used a Meta Quest 2 Head Mounted Display (HMD) connected to a Windows PC via a USB tether cable. The software used to develop this program was Unity3D with the use of the Oculus Integration Kit for VR interactions, including simulating the user's position in the virtual environment and capturing their inputs to drive actions like picking up an object. The headset can be used as a wireless standalone system to support eventual at home use.

B. Hand tracking and user input

The Meta Quest 2 HMD utilizes four infrared (IR) cameras built into the headset to facilitate positional tracking of the user in their environment, as well as to track hand positions for interactions in the program. This standalone headset enables the potential for future at home use with minimal setup, unlike typical VR headsets that require external IR cameras to be physically mounted in the environment around the user. Users can interact with the system by touching virtual buttons, manipulating objects, and using voice commands detected with an onboard microphone.

C. Physics interactions

The virtual environment presented to participants simulates the physics of gravity and normal forces in the real-world using engines built into the Unity environment. Due to the lack of touch feedback with hand tracking, interactions with virtual objects rely on visual changes in VR. When the hand hovers over an object that it can interact with, the hand changes color from gray to yellow. When the first finger and thumb are pinched together while overlapping the object, the hand turns blue indicating that the object is being grasped. Now the object will move as the hand moves and can be moved to a different part of the virtual world. Users are given a demonstrative tutorial at the beginning of their VR experience to learn the nuances of interacting with a virtual environment.

D. Motor amplification

For users with limited range of motion, physical movements can be amplified in the virtual space, increasing their functional range of motion in VR [26]. The motor amplification algorithm works similarly to how a computer mouse's sensitivity can be adjusted on a desktop computer. A "rest" or center position is determined during calibration, and the position of the amplified hand relative to that center point is multiplied by an amplification factor. For example, a user sitting with their arm on a chair's armrest would have their rest position at that point in the world. Lifting the arm up 20cm from that point, with an amplification factor of 2, would mean

that the virtual hand appears in VR to be 40cm above the starting rest position. We accomplish this by taking the amplification factor and multiplying it by the position vector (the *x,y,z* value) of the amplification target. In the Unity3D environment, the *x* is the horizontal axis relative to the subject, the *y* is the vertical axis, and *z* is the depth (or the axis that extends directly out in front of the user).

The amplification factor is determined through a software-guided calibration process which measures the range of motion for both upper limbs and for hand grasp apertures. At the start of each session, participants complete a Calibration Task in which they are guided to reach to four targets in the virtual space: 1) straight ahead with full arm extension (arms parallel to table), 2) 45 degrees laterally left, 3) 45 degrees laterally right, and 4) 45 degrees above the horizon and straight ahead. Hand location (*x, y, z* position), rotation (*x, y, z*) and grip aperture (*fingerCurl* parameter in Unity) are continuously tracked throughout the Calibration Task. For positional amplification, the range of movement (maximum minus minimum position away from the body) in each of the three environmental axes is computed for both hands. The hand with lower movement extent in at least two axes is automatically selected to be amplified and is used as the target hand during virtual rehabilitation exercises. The proportional difference between the hand with greater range of motion and the hand with lesser range of motion is averaged across all three axes and that value is used to multiply the positions when motor amplification is applied.

Since the tasks tested in this study involved only gross reaching, wrist rotation and grip aperture amplification were not enabled. Nevertheless, the respective amplification factors are computed similarly to that of positional amplification.

E. Motor smoothing

Noise in the IR camera tracking system due to factors like lighting condition and the system's confidence in localizing hand positions can cause jitter in a visually displayed hand. In typical unamplified movements, this is not an issue as the positional noise is nearly imperceptible, but when amplified, it becomes apparent. To resolve this issue, the program uses a spring-damper function to adjust the hand's position proportional to the amount of amplification applied (i.e., the more a hand is amplified, the stronger the smoothing function becomes). This approach could theoretically introduce some lag in the graphics display, which is part of the reason why assessing visually induced motion sickness is important. However, it is unlikely for the delay to have a noticeable impact; amplification of at least 150% is necessary for the delay to equal the framerate of the headset, and there is a delay maximum of 300ms which would occur with amplification factors over 800%.

III. Assessment of Visually-induced motion Sickness

After the initial development of the VR software, we tested a sample VR rehabilitation session in younger adults without disability. All study protocols were conducted with the approval and oversight of the Acadia University Research Ethics Board (File #22-07). Sixty participants were recruited from the Acadia University student population using an online study recruitment platform. Students were enrolled in psychology courses and received course credit for their participation. Demographic information was collected from each participant including gender identity [M/F/other], handedness [L/R/other], and age.

A. Study setup

A Meta Quest 2 HMD connected to a desktop computer, as described in Section II.A., was used to implement the VR exercises (Fig. 1(a)). The experimenter could watch the participant's view of the virtual environment on a separate screen and provide assistance when needed. Including the Calibration Task and coach-guided instructions, the VR exercises lasted approximately 10-15 minutes. This was enough time to observe motion sickness as VR-induced nausea often occurs quickly, with mean onset times of 62 seconds reported for a VR rollercoaster experience [32]. Immediately following the VR session, participants completed a motion sickness survey. Other data were collected to generate a normative motor performance dataset and are not reported here. Half of the participants were randomly assigned to receive motor amplification of hand position; the other half served as a baseline control with no amplification.

B. VR tasks

All participants first completed a Calibration Task (see Section II.D.), after which amplification was enabled for the experimental group, and then all participants played the Bubble Pop game (Fig. 1(b)) (see below for detailed descriptions of each task). The Bubble Pop game was always played first as it was the simplest game, enabling users to engage most easily, and this provided consistency in the initial experience for participants. Participants then completed two more tasks, a Pong Paddle game (Fig. 1(c)) and an Animal Feeding game (Fig. 1(d)). The order of the last two tasks was counterbalanced: half of the participants within each group completed the Pong Paddle game first, while the other half completed the Animal Feeding task first. Here is a description of each task in the VR session:

Calibration Task: During this task, participants reach towards different locations in the room indicated by colored cubes. The software logs the minimum and maximum extent of points reached by the left and right hands to calculate the range of motion for each. In the Amplification group, the hand with the smaller movement extent is selected to be amplified by the proportional difference between the sides. The range of motion is also used to set the boundary area for object interaction in the tasks that follow. See Section II.D. for more details about the Calibration Task.

Bubble Pop Task: The user pops as many bubbles as possible within one minute. Bubbles appear one at a time and only appear within the participant's field of view within the headset. During this period the user's hand positions are recorded every 20ms to map their movements in the space.

Pong Paddle Game: While seated at a table, the user controls a paddle by moving their hand forward or backward. The hand with the lower range of motion is assigned to control the paddle, with this hand amplified in the Amplification condition. A small ball bounces across the board which is oriented from left to right. On the side opposite the user's

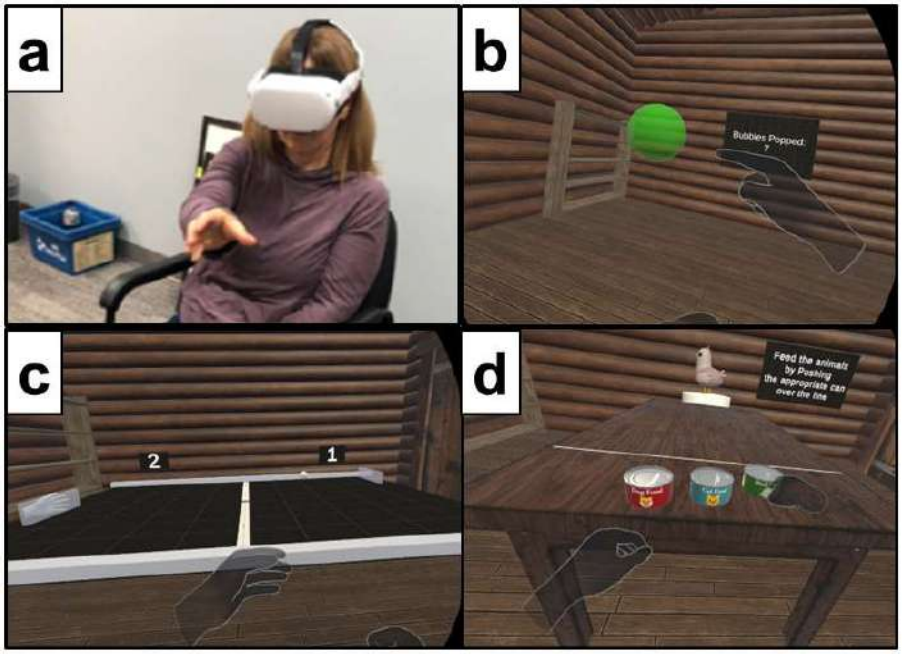


Fig. 1. Low-cost VR system overview. (a) User operating the system. (b) Screenshot of the Bubble Pop game. (c) Screenshot of the Pong Paddle game. (d) Screenshot of the Animal Feeding game.

paddle is a paddle controlled by the computer. A point is earned if the ball passes by the paddle of the opposing player. Participants practice the task for one minute and then complete a two-minute game.

Animal Feeding Game: The participant is seated at the end of a long table with an animal visualized at the far end of the table. The participant pushes forward one of three cans sitting on the table until it crosses a white line to "feed" the animal, with the line's distance calibrated to the user's range of motion. Each can is labeled as a food for one of three animals (a dog, cat, and bird) and users must push the can that matches the visualized animal. Once the can has crossed the line, the animal will change its appearance into one of the other available options and play a sound clip (a bark for a dog, a meow for a cat, and a tweet for a bird). Participants practice the task for one minute and then complete a two-minute game.

C. *Visually induced motion sickness survey*

Following the VR exercises, an abbreviated motion sickness symptom assessment was administered consisting of 5 of 9 items from the Virtual Reality Sickness Questionnaire (VRSQ) [33]: General Discomfort, Fatigue, Eyestrain, Difficulty Focusing, Headache. The mean score across the five items was used to indicate visually induced motion sickness immediately following the VR experience.

D. *Analysis plan*

To determine if motion sickness levels exceeded minimal levels following the VR experience, a Wilcoxon signed rank test was conducted (on the medians) with the alternative hypothesis that the true location is greater than 1 (median > 1). Wilcoxon rank sum tests were run for comparisons between groups for reported motion sickness levels. Medians (and thus the nonparametric Wilcoxon tests) were selected due to non-normally distributed zero-inflated data. Analysis scripts in the R programming language, along with all data, are available at OSF [https://osf.io/45kad/].

IV. Results

Sixty younger adults without disability completed VR rehabilitation exercises, with or without motor amplification. 47 participants identified as women, 10 as men, and 3 as non-binary. Participants ranged in age from 18 to 39 years old (mean age = 19.7 years, SD = 3.22 years). Three self-reported as left-handed.

Across all participants in both conditions there was a mean motion sickness score of 0.57 immediately following the VR experience (Fig. 2) (SD = 0.44, median = 0.4). Note that three participants did not complete all of the questions on the motion sickness survey and their data have been omitted from these results. As a motion sickness score below 1 indicates less than a mild response on the VRSQ [34], a Wilcoxon signed rank test with continuity correction rejected the alternative hypothesis that $u > 1$ ($V = 95.5$, $p = 1$).

Amplified group participants, with an average of 4.4% amplification applied, showed slightly higher motion sickness scores (mean = 0.64, median = 0.6) compared to control participants (mean = 0.50, median = 0.4), but a Wilcoxon rank sum test with continuity correction indicated that this was not a statistically significant difference ($W = 326$, $p = .20$) (Fig. 3).

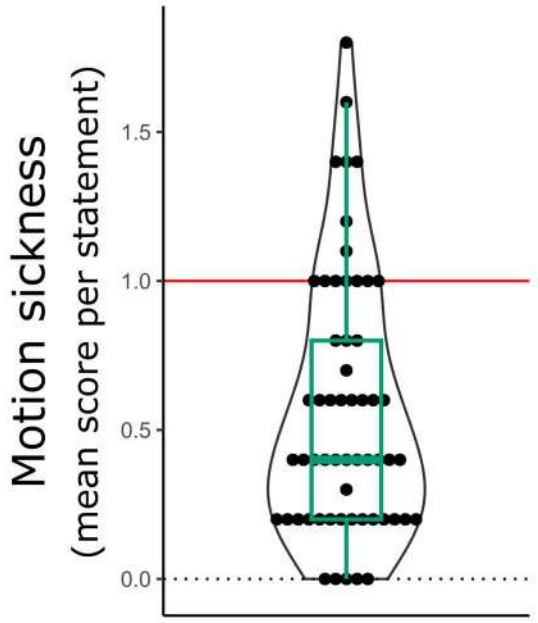


Fig. 2. Average motion sickness scores for all participants following the VR session. Dots represent individual participant mean scores, the box plot indicates the group median.

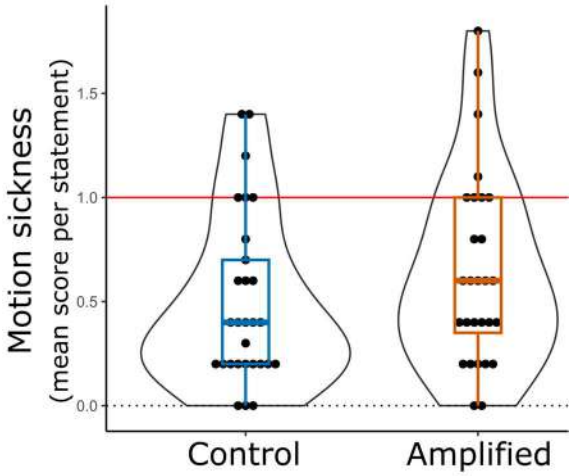


Fig. 3. Average motion sickness scores by amplification status during the VR session. Dots represent individual participant mean scores, the box plots indicate the group medians.

V. Discussion

We developed a virtual reality motor rehabilitation platform using a low-cost commercially available headset, the Meta Quest 2. In younger adults without disability tested in this work, we observed low levels of reported motion sickness, though slightly higher motion sickness levels were observed in the motor amplification group. Although this was not a statistically significant difference, it could indicate potential issues with the greater amplification factors required in clinical populations. Careful study with participants with reduced ROM requiring increased amplification is necessary to further investigate this.

Seven out of 60 participants did present average motion sickness scores above 1, suggesting that there is room for improvement in the VR system. However, no baseline motion sickness data were collected, so it is possible that other factors could have contributed to the feelings of motion sickness data reported. Nevertheless, more recently released low-cost headsets with improved graphics and hand tracking, like the Meta Quest 3, may organically reduce experienced motion sickness. Lessons learned from this study have led to subsequent software improvements, including a more standardized testing environment, improved virtual coach instructions and demonstrations, and more stringent task constraints to reduce head movements.

One key benefit of the system presented is its accessibility, which increases its potential for widespread implementation. By using a commercially available low-cost HMD, costs are reduced, thus increasing its availability to potential users. The calibration process enabling motor amplification allows for use by patients with a wide range of motor deficits. As this process is automated, unlike with other currently available software solutions [35], the need for clinician oversight is reduced. A virtual coach guiding participants through the exercises further supports standalone use at home. User-friendly interaction options make the technology more approachable for novice users, including hand tracking (i.e. the patients do not hold anything) and multiple interaction options (e.g. an option to speak commands to the virtual coach). Ultimately, the assistive motor amplification in gamified tasks demonstrated in this work enables more consistent task completion and more positive task engagement, supporting those with severe motor deficits.

The low level of reported motion sickness we observed indicates the potential for the use of low-cost off-the-shelf HMDs to deliver rehabilitation therapies. We are currently testing the system in older adults without disability and stroke survivors of all ages. With these additional results, we will continue exploring the platform's potential to deliver widespread access to evidence-based rehabilitation interventions, supporting motor recovery following brain damage.

Acknowledgment

We thank Sam Churchill and Ansaar Khadaroo for assistance with data collection. We thank Saif Miskin for assistance with figure graphics.

References

[1] V. L. Feigin *et al.*, "World Stroke Organization (WSO): Global Stroke Fact Sheet 2022," *International Journal of Stroke*, vol. 17, no. 1, pp. 18–29, Jan. 2022, doi: 10.1177/17474930211065917.

[2] D. Wilson-Costello, H. Friedman, N. Minich, A. A. Fanaroff, and M. Hack, "Improved survival rates with increased neurodevelopmental disability for extremely low birth weight infants in the 1990s," *Pediatrics*, vol. 115, no. 4, pp. 997–1003, Apr. 2005, doi: 10.1542/peds.2004-0221.

[3] H. Nakayama, H. S. Jørgensen, H. O. Raaschou, and T. S. Olsen, "Recovery of upper extremity function in stroke patients: the Copenhagen Stroke Study," *Arch Phys Med Rehabil*, vol. 75, no. 4, pp. 394–398, Apr. 1994, doi: 10.1016/0003-9993(94)90161-9.

[4] H. Wang, M. Camicia, J. Terdiman, M. K. Mannava, S. Sidney, and M. E. Sandel, "Daily treatment time and functional gains of stroke patients during inpatient rehabilitation," *PM R*, vol. 5, no. 2, pp. 122–128, Feb. 2013, doi: 10.1016/j.pmrj.2012.08.013.

[5] T. Imura, Y. Nagasawa, H. Fukuyama, N. Imada, S. Oki, and O. Araki, “Effect of early and intensive rehabilitation in acute stroke patients: retrospective pre-/post-comparison in Japanese hospital,” *Disabil Rehabil*, vol. 40, no. 12, pp. 1452–1455, Jun. 2018, doi: 10.1080/09638288.2017.1300337.

[6] E. J. Schneider, N. A. Lannin, L. Ada, and J. Schmidt, “Increasing the amount of usual rehabilitation improves activity after stroke: a systematic review,” *J Physiother*, vol. 62, no. 4, pp. 182–187, Oct. 2016, doi: 10.1016/j.jphys.2016.08.006.

[7] E. Taub, G. Uswatte, D. K. King, D. Morris, J. E. Crago, and A. Chatterjee, “A Placebo-Controlled Trial of Constraint-Induced Movement Therapy for Upper Extremity After Stroke,” *Stroke*, vol. 37, no. 4, Art. no. 4, Mar. 2006, doi: 10.1161/01.STR.0000206463.66461.97.

[8] J. W. Krakauer *et al.*, “Comparing a Novel Neuroanimation Experience to Conventional Therapy for High-Dose Intensive Upper-Limb Training in Subacute Stroke: The SMARTS2 Randomized Trial,” *Neurorehabilitation and Neural Repair*, vol. 35, no. 5, pp. 393–405, 2021, doi: 10.1177/1545968321100007.

[9] R. Stockley, R. Peel, K. Jarvis, and L. Connell, “Current therapy for the upper limb after stroke: a cross-sectional survey of UK therapists,” *BMJ Open*, vol. 9, no. 9, p. e030262, Sep. 2019, doi: 10.1136/bmjopen-2019-030262.

[10] R. Viana and R. Teasell, “Barriers to the Implementation of Constraint-Induced Movement Therapy Into Practice,” *Topics in Stroke Rehabilitation*, vol. 19, no. 2, pp. 104–114, Mar. 2012, doi: 10.1310/tsr1902-104.

[11] L. J. Christie, N. Fearn, A. McCluskey, M. Lovarini, R. Rendell, and A. Pearce, “Cost-Effectiveness of Constraint-Induced Movement Therapy Implementation in Neurorehabilitation: The ACTIveARM Project,” *PharmacoEconomics Open*, vol. 6, no. 3, pp. 437–450, May 2022, doi: 10.1007/s41669-022-00323-9.

[12] H. Jia, D. C. Cowper, Y. Tang, E. Litt, and L. Wilson, “Postacute Stroke Rehabilitation Utilization: Are There Differences Between Rural-Urban Patients and Taxonomies?: Stroke Rehabilitation and Rural-Urban taxonomy,” *The Journal of Rural Health*, vol. 28, no. 3, pp. 242–247, Jun. 2012, doi: 10.1111/j.1748-0361.2011.00397.x.

[13] K. Peek, R. Sanson-Fisher, L. Mackenzie, and M. Carey, “Patient adherence to physiotherapist prescribed self-management strategies: A critical review,” *International Journal of Therapy and Rehabilitation*, vol. 22, no. 11, pp. 535–543, Nov. 2015, doi: 10.12968/ijtr.2015.22.11.535.

[14] R. Campbell, “Why don’t patients do their exercises? Understanding non-compliance with physiotherapy in patients with osteoarthritis of the knee,” *Journal of Epidemiology & Community Health*, vol. 55, no. 2, pp. 132–138, Feb. 2001, doi: 10.1136/jech.55.2.132.

[15] A. M. M. Schoo, M. E. Morris, and Q. M. Bui, “The effects of mode of exercise instruction on compliance with a home exercise program in older adults with osteoarthritis,” *Physiotherapy*, vol. 91, no. 2, pp. 79–86, Jun. 2005, doi: 10.1016/j.physio.2004.09.019.

[16] M. Rastall, B. Brooks, M. Klarneta, N. Moylan, W. McCloud, and S. Tracey, “An Investigation into Younger and Older Adults’ Memory for Physiotherapy Exercises,” *Physiotherapy*, vol. 85, no. 3, pp. 122–128, Mar. 1999, doi: 10.1016/S0031-9406(05)65691-X.

[17] K. Reilly, B. Lovejoy, R. Williams, and H. Roth, “Differences between a supervised and independent strength and conditioning program with chronic low back syndromes,” *J Occup Med*, vol. 31, no. 6, pp. 547–550, Jun. 1989, doi: 10.1097/00043764-198906000-00012.

[18] P. Kiper *et al.*, “Effects of Immersive Virtual Reality on Upper-Extremity Stroke Rehabilitation: A Systematic Review with Meta-Analysis,” *JCM*, vol. 13, no. 1, p. 146, Dec. 2023, doi: 10.3390/jcm13010146.

[19] M. Soleimani, M. Ghazisaeedi, and S. Heydari, “The efficacy of virtual reality for upper limb rehabilitation in stroke patients: a systematic review and meta-analysis,” *BMC Med Inform Decis Mak*, vol. 24, no. 1, p. 135, May 2024, doi: 10.1186/s12911-024-02534-y.

[20] S. Ikbali Afsar, I. Mirzayev, O. Umit Yemisci, and S. N. Cosar Saracgil, “Virtual Reality in Upper Extremity Rehabilitation of Stroke Patients: A Randomized Controlled Trial,” *Journal of Stroke and Cerebrovascular Diseases*, vol. 27, no. 12, pp. 3473–3478, Dec. 2018, doi: 10.1016/j.jstrokecerebrovasdis.2018.08.007.

[21] P. Kiper *et al.*, “Virtual Reality for Upper Limb Rehabilitation in Subacute and Chronic Stroke: A Randomized Controlled Trial,” *Archives of Physical Medicine and Rehabilitation*, vol. 99, no. 5, pp. 834-842.e4, May 2018, doi: 10.1016/j.apmr.2018.01.023.

[22] F. Amin *et al.*, “Effectiveness of Immersive Virtual Reality-Based Hand Rehabilitation Games for Improving Hand Motor Functions in Subacute Stroke Patients,” *IEEE Trans. Neural Syst. Rehabil. Eng.*, vol. 32, pp. 2060–2069, 2024, doi: 10.1109/TNSRE.2024.3405852.

[23] B. Zhang *et al.*, “Handy Juice Bar: a Hand Rehabilitation Game using Immersive VR and Finger Tracking,” in *2022 IEEE 10th International Conference on Serious Games and Applications for Health(SeGAH)*, Aug. 2022, pp. 1–6. doi: 10.1109/SEGAH54908.2022.9978599.

[24] M. Bressler *et al.*, “A Virtual Reality Serious Game for the Rehabilitation of Hand and Finger Function: Iterative Development and Suitability Study,” *JMIR Serious Games*, vol. 12, p. e54193, Aug. 2024, doi: 10.2196/54193.

[25] A. Mc Kittrick, M. R. Desselle, A. Padilha Lanari Bo, B. Zhang, S. Laracy, and G. Tornatore, “Patient Experience in Adjunct Controller-Free Hand Tracking Virtual Reality Tasks for Upper-Limb Occupational Therapy Rehabilitation,” *Journal of Patient Experience*, vol. 10, p. 23743735231211983, Jan. 2023, doi: 10.1177/23743735231211983.

[26] B. R. Ballester *et al.*, “The visual amplification of goal-oriented movements counteracts acquired non-use in hemiparetic stroke patients,” *J NeuroEngineering Rehabil*, vol. 12, no. 1, p. 50, Dec. 2015, doi: 10.1186/s12984-015-0039-z.

[27] V. Herrera *et al.*, “Rehab-Immersive: A framework to support the development of virtual reality applications in upper limb rehabilitation,” *SoftwareX*, vol. 23, p. 101412, Jul. 2023, doi: 10.1016/j.softx.2023.101412.

[28] V. Herrera, J. Albusac, S. Schez-Sobrino, A. Reyes-Guzmán, and C. Glez-Morcillo, “Dynamic Adjustment of Interactive Objects in Virtual Environments for Upper Limb Rehabilitation: A Patient-Centred Solution,” *Spanish Computer Graphics Conference (CEIG)*, 2024, doi: 10.2312/CEIG.20241142.

[29] M. E. McCauley and T. J. Sharkey, “Cybersickness: Perception of Self-Motion in Virtual Environments,” *Presence: Teleoperators and Virtual Environments*, vol. 1, no. 3, pp. 311–318, Aug. 1992, doi: 10.1162/pres.1992.1.3.311.

[30] K. Stanney, C. Fidopiastis, and L. Foster, “Virtual Reality Is Sexist: But It Does Not Have to Be,” *Front. Robot. AI*, vol. 7, Jan. 2020, doi: 10.3389/frobt.2020.00004.

[31] K. Carnegie and T. Rhee, “Reducing Visual Discomfort with HMDs Using Dynamic Depth of Field,” *IEEE Computer Graphics and Applications*, vol. 35, no. 5, pp. 34–41, Oct. 2015, doi: 10.1109/MCG.2015.98.

[32] A. Mazloumi Gavgani, F. R. Walker, D. M. Hodgson, and E. Nalivaiko, “A comparative study of cybersickness during exposure to virtual reality and ‘classic’ motion sickness: are they different?,” *Journal of Applied Physiology*, vol. 125, no. 6, pp. 1670–1680, Dec. 2018, doi: 10.1152/japplphysiol.00338.2018.

[33] H. K. Kim, J. Park, Y. Choi, and M. Choe, “Virtual reality sickness questionnaire (VRSQ): Motion sickness measurement index in a virtual reality environment,” *Applied Ergonomics*, vol. 69, pp. 66–73, May 2018, doi: 10.1016/j.apergo.2017.12.016.

[34] R. S. Kennedy, N. E. Lane, K. S. Berbaum, and M. G. Lilienthal, “Simulator Sickness Questionnaire: An Enhanced Method for Quantifying Simulator Sickness,” *The International Journal of Aviation Psychology*, vol. 3, no. 3, pp. 203–220, Jul. 1993, doi: 10.1207/s15327108ijap0303_3.

[35] “WalkinVR,” Accessed: Feb. 21, 2025. [Online]. Available: https://www.walkinvrdriver.com/

Balance Assistance without Mechanical Support using a Virtual Cane with Haptic Feedback

Sindhu Reddy Alluri, Sambad Regmi, Fazlur Rashid, Devin Burns, Yun Seong Song, *Member, IEEE*

***Abstract*—Light Touch (LT) has been known to improve standing balance without mechanical support by providing sensory information about the movement of the body. Inspired by this, this work developed a Virtual Cane (VC) which gives no physical support but provides other sensory information that a physical cane would. The VC is developed with a distance sensor and vibration actuators to provide cane tip-to-ground distance information to the user. The extent to which this haptic feedback improves standing balance was assessed in a human experiment. 10 healthy young participants underwent a standing balance experiment with tandem stance and eyes closed, using VC with No Feedback (NF) as the baseline, VC with feedback, and with physical cane (PC). Center-of-Pressure (CoP) metrics as well as Sway-density metrics were analyzed to study the effect of these conditions on standing balance. It was found that the CoP metrics in VC were significantly improved compared to baseline (NF) and approaching the benefit of a full physical cane (PC). Sway-density metrics showed no difference between the conditions. This shows that simple, binary feedback from VC on the position of the body and cane was sufficient to positively affect standing balance without significantly altering the biomechanical strategy of standing balance. This is also a demonstration of an assistive device with a complete absence of mechanical support that can provide substantial benefit to balance.**

I. Introduction

Falls are the second leading cause of accidental or unintentional injury deaths worldwide, where each year an estimated 684,000 individuals die from falls globally according to the World Health Organization (WHO) [1]. In particular, falls are one of the major causes of life-threatening injuries in older adults [2, 3]. Passive assistive devices such as canes, crutches, or walkers, can help improve balance and reduce the risk of falls, especially for populations who require substantial physical assistance [4].

*Research supported by the National Science Foundation (NSF), grant CMMI-1843892.

S. Reddy Alluri was with Missouri University of Science and Technology, Rolla, MO 65409, USA. She is now with Amazon Global Robotics, Boston, MA 01864, USA (email: sindhualluri94@gmail.com).

S. Regmi was with Missouri University of Science and Technology, Rolla, MO 65409, USA. He is now with ASML, Wilton, CT 06851, USA (e-mail: sambadregmi@mst.edu).

F. Rashid was with Missouri University of Science and Technology, Rolla, MO 65409, USA. He is now with the Department of Mechanical Science & Engineering, University of Illinois Urbana Champaign, Urbana, IL 61801, USA (e-mail: fazlurr2@illinois.edu).

D. Burns is an Associate Professor with the Department of Psychological Science, Missouri University of Science and Technology, Rolla, MO 65409 (email: burnsde@mst.edu).

Y. S. Song is an Associate Professor with the Department of Mechanical and Aerospace Engineering, Missouri University of Science and Technology, Rolla, MO 65409, USA (corresponding author, phone: 573-341-4371, email: songyun@mst.edu).

Light interaction forces, or light touch (LT), may help improve balance while allowing users to use their functional muscles. Without relying on substantial physical support, it was shown by Jeka [5] that light contact of the fingertip on a rigid surface was enough to reduce the Center-of-Pressure (CoP) sway of healthy individuals during quiet standing. That is, a simple application of a small force onto one of the most distal parts of the human body (fingertip) was sufficient for the human participant to outperform his/her own best effort to stand as still as possible. Such improvement was observed in a wide range of populations, including healthy young adults [5, 6], healthy older adults [9], stroke patients [8, 9], peripheral neuropathy patients [10], Parkinson's Disease patients [11] and anterior cruciate ligament (ACL) injury patients [12]. LT was also shown to affect balance during treadmill walking [13]. Interestingly, this improvement in the balance due to LT is not due to mechanical support. Indeed, the LT magnitude is too small (often below 1 N) to provide any meaningful physical assistance [4, 5, 14, 15]. Instead, it is suggested that the additional sensory information about the body movement with respect to a fixed reference, which is provided through LT, helps improve balance [5, 14, 16]. This was demonstrated in [16] using virtual LT, where the information about the position of one's body provided through vibrations could improve standing balance. However, the device in [16] required an indoor motion capture system which cannot be deployed in everyday outdoor activities.

Inspired by the balance improvement from LT, our goal is to understand the effect of providing sensory information about body movement on standing balance and to investigate the potential of a new type of balance assistive device that does not provide mechanical support, which also shows potential for practical use. For this, we investigated the balance assistance by one of the most widely used items, a cane. While the physical contact between a typical cane handle and the hand of the user may not be considered an LT, the contact of the cane to the ground and the subsequent sensory information through the hands could resemble the information provided by LT, thereby improving balance. In this work, an instrumented cane (hereon called the Virtual Cane, or VC), is developed that can provide information about the hand position with respect to the ground surface. This VC, however, does not make any contact with the ground and therefore does not provide mechanical support that physical canes do. We hypothesized that, if the hand position information can be provided to the user of VC without making physical contact with the ground, then balance improvement would be observed. We further hypothesized that this improvement would be less than the total benefit provided by a physical cane that makes contact with the ground and provides mechanical support in addition to sensory information.

II. METHODS

A. Apparatus

The VC was designed to allow the testing of the above-mentioned hypothesis such that it is capable of delivering information through the hand and assisting in improving human body balance. In this view, the VC should feel like a physical cane in its weight and inertia, except for the inevitable difference in the sensation of contact with the ground. To ensure as similar a mechanical feel as possible, we developed VC apparatus - a foldable cane with a sensor that measures the distance between the cane and the ground, and a glove that provides this information to the user in the form of vibration. The trifold physical cane (Figure 1) is height adjustable (83 cm ~ 93 cm). At 21 centimeters from the bottom of the shaft of the physical cane, an Ultrasonic sensor (HC-SR04; measurement range of 2 ~ 500 cm, resolution of 0.3 cm) is mounted. This is used to measure the distance between the bottom tip of the folded cane and the ground. This information is monitored by an Arduino Uno microcontroller which modulates the vibration actuators on the instrumented glove (Figure 1). If the distance measured is 21±2.5 cm, there is no vibration. If the change in distance is more than 2.5 cm from the nominal distance of 21 cm, the vibration actuators are turned on to inform the user of this deviation. The vibration "dead zone" of 5 cm was selected to be more than 10 times the sensor resolution, but less than 10% of the length of the cane. The glove consists of three bend sensors/ short flex sensors (ID:1070, Adafruit.com) and four vibration actuators (ID:1201, Adafruit.com). Bend sensors are placed along the top sides of the thumb, middle finger, and little finger of the glove, and are used to detect if the hand is making a grip while holding the cane. This was to prevent the vibration actuators from unnecessarily turning on during experiment trials. Vibration actuators were attached to the outer side of the glove at the fingertips.

B. Experiment Procedure

Ten healthy young participants were recruited for standing balance experiments (5 males, 19-30 years of age). All the participants were physically active and healthy with no self-reported history of neurological disorders or musculoskeletal injuries. The protocol was approved by the Missouri S&T Institutional Review Board (IRB). All participants provided written consent.

The participant was asked to stand on the force plate (Optima OPT400600HF, Advanced Material Technology Inc., sampling frequency of 1 kHz) without shoes with the tandem stance (right foot forward [17]) with their eyes closed, as depicted in Figure 2. This provided challenges to standing balance which would otherwise be trivial for the study population. To ensure the same foot position in all the trials for all participants, the anterior-posterior axis was marked on the center of the force plate using adhesive tape. The participants were given two minutes to get accustomed to the pose. Their right hand with the instrumented glove held the handle of the cane to a comfortable height while their left hand rested freely on the side. This pose was maintained throughout the trials. After the 2-minute accustomation. The participant was instructed to stand as still as possible during trials with one of the three conditions:

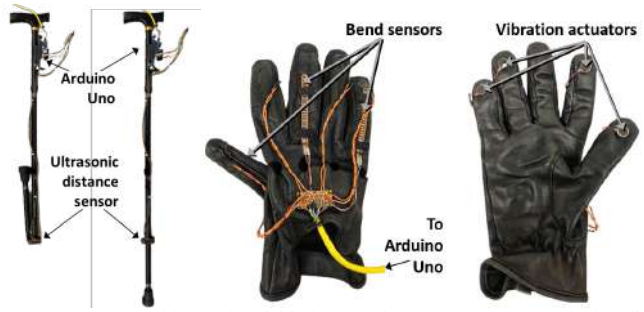


Figure 1. (Left) Folded and unfolded VC with an Arduino Uno at the handle and an ultrasonic sensor at the bottom fold of the cane's shaft. (Right) Instrumented glove. The outer side has the bend sensors on the thumb, middle, and little fingers. The inner side of the glove shows the vibration actuators.

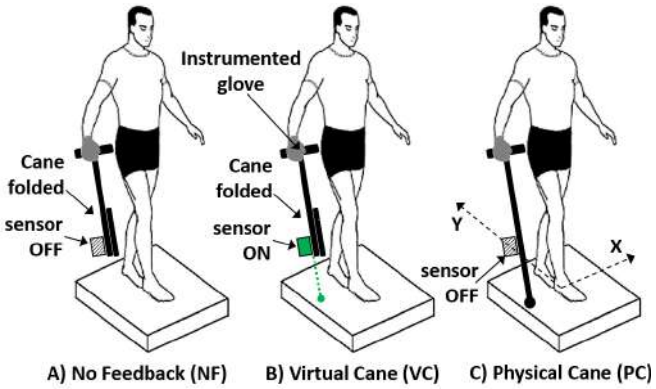


Figure 2. A participant standing on the force plate in tandem stance, with eyes closed, right foot in front of the left in three control conditions. A) No Feedback, B) Virtual Cane, and C) Physical Cane.

i. No Feedback (NF) – In this control condition, the participant held the physical cane whose bottom quarter of the shaft was folded, and the instrumented glove with the vibration actuators was turned off for the entire length of the trial. They held the cane to a height that an unfolded cane would have touched the ground. This condition preserved the sense of mechanical grip on the handle as well as the sense of the inertia of the physical cane (weight and rotational inertia) but did not provide mechanical support or the sense of the cane touching the ground.

ii. Virtual Cane (VC) – In this condition, the cane remained folded, but the instrumented glove was powered on. The ultrasonic sensor on the cane pointed to the surface of the force plate (note that the participants were able to maintain the VC to point on a surface on the force plate). The distance between the sensor and the ground (force plate surface) was constantly measured. Whenever this distance deviated from the expected distance of 21 cm by more than a 2.5 cm threshold in either direction (providing a 5 cm thickness of no vibration zone), feedback was provided to the participant's fingertips by turning on the vibration actuators. The amplitude of the vibration was constant and did not depend on the distance measured by the sensor. This condition provided no physical assistance from the cane but provided information to the user on the distance between the sensor and the ground, similar to what a normal cane would provide.

iii. Physical Cane (PC) – In this condition, the glove was powered off and the participant was given physical support

by resting the end of the unfolded cane shaft on the surface of the force plate. The participants were free to exhibit their desired amount of force through the cane as they would with any ordinary cane.

Each participant performed three blocks of 12 trials (36 trials total), with four of each condition whose order is randomized in each block. The duration of each trial was 20 seconds. A 5-minute break was given to the participant after each block. In each trial, the force plate measured the ground reaction forces and torques.

C. Analysis

Data from blocks 1 & 2 were not analyzed to help mitigate learning effects. The third blocks of all 10 participants were analyzed using MATLAB (MathWorks) to derive the center of pressure (CoP) during the trials. This data was then smoothed with a moving average filter with a 100 ms window. The standing balance was analyzed in terms of the variability metrics of the static (CoP) and dynamic (velocity of CoP) aspects commonly used in standing balance studies that involves haptics and/or LT [14, 18, 19]. From the CoP of each trial, the mediolateral (CoPx) and the anterior-posterior (CoPy) CoP, as well as their time derivatives (vCoPx, vCoPy) were obtained. The standard deviations of these values, SD-CoPx, SD-CoPy, SD-vCoPx, and SD-vCoPy, were then obtained for each trial. As the distributions were reasonably normal (Figures 3 and 4), each metric of balance was then analyzed with 2-way ANOVA using SPSS (IBM, version 23) with participants and conditions (NF, VC, or PC) as fixed effects. Tukey HSD was used to test the significance at $p < 0.05$.

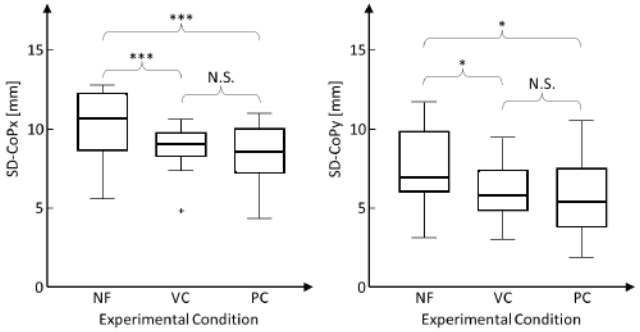


Figure 3. Box plots of SD-CoPx and SD-CoPy of all participants by experimental condition. *denotes $p < 0.05$, ***denotes $p<0.001$, N.S. denotes not significant ($p > 0.05$).

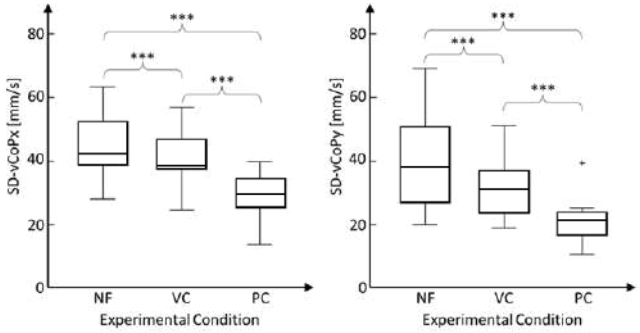


Figure 4. Box plots of SD-vCoPx and SD-vCoPy of all subjects by experimental condition. ***denotes $p<0.001$.

TABLE I. SWAY-DENSITY METRICS

	MeanP	MeanT	MeanD
Condition	$p = 0.733$	$p = 0.711$	$p = 0.642$
Participant	$p = 0.008$**	$p = 0.0004$***	$p = 0.094$
Condition x Participant	$p = 0.785$	$p = 0.223$	$p = 0.646$

** denotes p<0.01, *** denotes p<0.001

In addition to the CoP-derived balance metrics, sway density was calculated to analyze possible modifications in the postural stabilization process between experimental conditions [20]. From the 2-dimensional CoP trajectories of each trial, the mean value of the peaks (meanP), the mean value of the time interval between successive peaks (meanT), and the mean value of the distance between successive peaks (meanD) were calculated. These three metrics were then analyzed with ANOVA using R (R Foundation) with participants and conditions (NF, VC, or PC) as fixed effects.

III. RESULTS

Comparisons between conditions are provided in Figures 3 and 4 (all F-tests resulted in $p < 0.001$). As expected, CoP metrics were always significantly lower with PC than with NF. Both SD-CoPx and SD-CoPy were significantly lower with VC than NF ($p < 0.001$ and $p = 0.038$, respectively). These metrics were not significantly different between VC and PC ($p > 0.05$). Also, both SD-vCoPx and SD-vCoPy were significantly lower with VC than NF ($p < 0.001$). These metrics were also significantly lower with PC than VC ($p < 0.001$).

The statistical analysis results for the sway-density metrics are shown in Table I. While there were individual differences between participants, there were no statistical differences in all three metrics (meanP, meanT, meanD) between experimental conditions. There was also no significant interaction between participants and experimental conditions.

IV. DISCUSSION

The only other device that the authors are aware of, that provides balance assistance with LT without mechanical support, is in [16]. There are functional as well as practical differences between this work and [16]. In [16], the users must lift their arm and constantly 'tap' the finger attached to the biofeedback actuator to 'feel' the virtual boundary (or virtual wall) around the participant. This virtual boundary is implemented using the indoor precision motion capture system that constantly acquires the finger position on the global coordinate. This makes the system in [16] difficult to deploy in practical scenarios where precise and continuous monitoring of finger locations is nearly impossible. On the other hand, the VC in this works very similar to a physical cane in that no continuous movement of the hand/finger nor a sophisticated portable measurement unit is required. The VC is fully portable, lightweight, and cost-effective to develop.

The four CoP-based balance metrics used in this study all show significantly lower values in PC than in NF, implying that the lower these metrics, the better performance in standing balance the participants showed. In this view, participants were better in standing balance with the Virtual

Cane as compared to the no-cane condition (NF). Since the only difference between VC from NF was the existence of the vibration feedback, it can be inferred that the distance feedback provided by VC was key to balance improvement - supporting our first hypothesis. Nonetheless, the level of balance improvement with VC was not as good as with physical cane (PC) in the SD-vCoP metrics. This supports our second hypothesis that the distance feedback alone cannot account for the total improvement in balance due to PC. This was expected since the mechanical support in PC was absent with VC.

The CoP position metrics (SD-CoPx and SD-CoPy) were not significantly different between VC and PC, whereas the velocity metrics (SD-vCoPx and SD-vCoPy) were significantly different between the two conditions. This may be interpreted as the position-dependent feedback provided by VC acting to more effectively reduce position-based balance metrics. This interpretation is comparable to the work in [19] where velocity-dependent feedback provided by the robot arm acted to more effectively reduce velocity-based balance metrics. While this work did not specifically investigate the relationship between the nature of feedback and the corresponding CoP-based metric improvements, this work and [19] together suggest that specific aspects of balance (sway or velocity of sway) could be targeted by biofeedback devices for patient-specific balance assistance.

Analysis of Sway Density Curves (SDC) is often used to study the postural stabilization mechanism [20]. Changes in the parameters in meanP, meanT, and/or meanD indicated modifications of motor control strategy in quiet standing in various populations, including patients with low back pain [21], obese children [22], obese adults [23], and in older adults [24]. In this regard, there being no significant differences in these metrics in this study between all three conditions implies that using VC did not compel participants to modify their balancing strategy. This may be viewed as normal since there were no physiological changes such as body weight [22, 23] within any participant during the experiment. Nonetheless, this result shows that, at least to the healthy young participants in this study, using VC did not require a substantially different strategy than using PC or even NF.

This work provides notable observations regarding the mechanism underlying balance improvement from LT experiments. While it is widely accepted that LT provides sensory feedback and not mechanical support [5, 14], this idea was not explicitly tested in the pure absence of mechanical support and in comparable experimental settings. Since light 'touch' assumed humans make physical contact with an external reference, mechanical support, although very small, could not be completely removed in previous LT experiments. In this regard, this work provided an experimental setup (using VC) that removes mechanical support entirely but still provides feedback similar to that by LT. And because of this unique setup, this work was able to provide an experimental verification of pure sensory feedback through hands providing balance improvements.

Another notable observation in relation to LT is that, according to our results, very low-bit information such as the binary feedback in this study is sufficient to improve balance. Without providing more high-fidelity feedback (e.g. modulating the intensity of vibration according to the distance error), a simple on-off scheme with as much as 5 cm dead zone led to balance improvements. Because the dead zone was not small, some participants did not feel the vibration in certain trials and wondered if the device was working properly. Furthermore, our vibration feedback scheme simply informed the participant whether or not the 'virtual tip' left the dead zone, but did not inform if the dead zone was crossed at the upper or lower boundary. These observations suggest that even small information can be used by the human body for significant modulation of balance and that a low-cost, simple-design assistive device like VC may be more useful than it first appears.

The haptic feedback in this work was provided at the hand in the form of vibration. This choice was made because the study aimed to mimic the haptic information that the user would receive when using a physical cane. Nonetheless, if the design was to harness the benefit of sensory feedback while not necessarily constrained to mimic a physical cane, opportunities may exist where the feedback can be provided in a different way. For example, it can be provided visually or through audio, or through a vibration actuator attached further away from the hand, to free the hand from having to hold the cane.

In this specific setup of VC, we provide not only the lower boundary but the upper boundary of no-vibration zone. This choice was made for the VC to provide haptic feedback that represents the 'correct distance' between the hand and the ground, similar to PC. That is, when using PC, the distance between the hand and the ground is maintained constant. Anything less (cane piercing the ground) or more (cane being off the ground) is deemed undesirable in standing balance with a PC. Hence, the vibration actuators would turn on to signal these scenarios to the user. If there was only a lower bound to the no-vibration zone, then a substantial increase in the distance between the tip of the cane to the ground would not be communicated to the user.

This work aimed at studying whether haptic information could provide balance assistance in the complete absence of mechanical support. That is, the goal of this work was not to train the users to have better balance through VC – but rather a cross-sectional behavioral study to analyze the effect of haptic feedback in standing balance. This led us to omit blocks 1 and 2 and analyze only the last block (block 3) of the experiment. However, if the study goal was to analyze the learning effect and retention of such effect using VC, a longitudinal study is recommended in the future.

While walkers, canes, or crutches help with balance, they may provide more-than-needed assistance by providing extensive mechanical support. This could cause reduced usage of weak yet functional muscles and may prevent recovery and accelerate dependence on these assistive devices. In this regard, LT-motivated balance assistive devices such as the VC in this work can provide an alternative solution which allows usage of functional muscles while providing subtle yet effective balance assistance.

V. Conclusion

The benefit in standing balance provided by the proposed Virtual Cane highlights the potential for using LT-inspired

assistive devices. This is especially promising given the simplistic nature of the feedback provided by Virtual Cane. This allows the development of portable and affordable balance assistive devices, specifically for population whose balance can be assisted without a strict mechanical support.

REFERENCES

[1] World Health Organization, Fact Sheet, "Falls," http://www.who.int/mediacentre/factsheets/fs344/en/, 2021 (accessed 14 September 2023).

[2] J.A. Stevens, P.S. Corso, E.A. Finkelstein, T.R. Miller, The costs of fatal and non-fatal falls among older adults, Inj. Prev. 12(2006) 290-295. doi: 10.1136/ip.2005.011015.

[3] K.D. Kochanek, S.L. Murphy, J. Xu, B. Tejada-Vera, Deaths: Final Data for 2014, Natl. Vital Stat. Rep., 65(2016) 1-122.

[4] J.J. Jeka, Light Touch Contact as a Balance Aid, Phys. Ther., 77(1997) 476-487.

[5] J.J. Jeka, J.R. Lackner, Fingertip contact influences human postural control, Exp. Brain Res. 100(1994) 495-502. https://doi.org/10.1007/BF00229188.

[6] M.A. Riley, T.A. Stroffregen, M.J. Grocki, M.T. Turvey, Postural stabilization for the control of touching, Hum. Mov. Sci., 18(1999) 795-817. https://doi.org/10.1016/S0167-9457(99)00041-X.

[7] M. Baccini, L.A. Rinaldi, G. Federighi, L. Vannucchi, M. Paci, G. Masotti, Effectiveness of fingertip light contact in reducing postural sway in older people, Age and Ageing, 36(2007) 30-35. https://doi.org/10.1093/ageing/afl072.

[8] Boonsinsukh R, Panichareon L, Phansuwan-Pujito P. Light touch cue through a cane improves pelvic stability during walking in stroke. Arch Phys Med Rehabil. 2009;90: 919-926. https://doi.org/10.1016/j.apmr.2008.12.022.

[9] B.P. Cunha, S.R. Alouche, I.M.G. Araujo, S. Freitas, Individuals with post-stroke hemiparesis are able to use additional sensory information to reduce postural sway, Neurosci. Lett., 513(2012) 6-11. https://doi.org/10.1016/j.neulet.2012.01.053.

[10] R. Dickstein, C.L. Shupert, F.B. Horak, Fingertip touch improves postural stability in patients with peripheral neuropathy, Gait posture, 14(2001) 238-247. https://doi.org/10.1016/S0966-6362(01)00161-8.

[11] E. Franzen, C. Paquette, V. Gurfinkel, F. Horak, Light and Heavy Touch Reduces Postural Sway and Modifies Axial Tone in Parkinson's Disease, Neurorehabil. Neural Repair., 26(2012) 1007-1014. https://doi.org/10.1177/1545968312437942.

[12] T.R. Bonfim, D.B. Grossi, C.A.J. Paccola, J.A. Barela, Additional sensory information reduces body sway of individuals with anterior cruciate ligament injury, Neurosci. Lett., 441(2008) 257-260. https://doi.org/10.1016/j.neulet.2008.06.039.

[13] T. IJmker, C.J. Lamoth, H. Houdijk, M. Tolsma, L.H.V. van der Woude, A. Daffertshofer, P.J. Beek, Effects of handrail hold and light touch on energetics, step parameters, and neuromuscular activity during walking after stroke, J. NeuroEng. Rehab. 12(2015). https://doi.org/10.1186/s12984-015-0051-3.

[14] F. Verite, W. Bachta, G. Morel, Closed loop kinesthetic feedback for postural control rehabilitation, IEEE Trans. Haptics, 7(2014) 150-160. doi: 10.1109/TOH.2013.64.

[15] J. Ventura, J.R. Lackner, M. Holden, Stabilization of posture by precision contact of the index finger, J. Vestib. Res., 4(1994) 285-301.

[16] K. Shima, K. Shimatani, A. Sugie, Y. Kurita, R. Kohno, T. Tsuji, Virtual light touch contact: A novel concept for mitigation of body sway, 7th International Symposium on Medical Information and Communication Technology (ISMICT), 2013. doi:10.1109/ismict.2013.6521710.

[17] A.M. Wing, L. Johannsen, S. Endo, Light touch for balance: influence of a time-varying external driving signal, Philos. Trans. R. Soc. Lond. B. Biol. Sci., 366(2011) 3133-3141. https://doi.org/10.1098/rstb.2011.0169.

[18] L. Johannsen, E. McKenzie, M. Brown, M.S. Redfern, A.M. Wing, Deliberately Light Interpersonal Touch as an Aid to Balance Control in Neurologic Conditions, Rehabilitation Nursing, (2014) 1–10. https://doi.org/10.1002/rnj.197.

[19] A. Saini, D. Burns, D. Emmett, Y.S. Song, Trunk velocity-dependent Light Touch reduces postural sway during standing, PLoS One, 14(2019). https://doi.org/10.1371/journal.pone.0224943.

[20] M. Jacono, M. Casadio, P.G. Morasso, V. Sanguineti, The sway-density curve and the underlying postural stabilization process, Motor Control, 8(2004), 292-311. https://doi.org/10.1123/mcj.8.3.292.

[21] T. Popa, M. Bonifazi, R. Della Volpe, A. Rossi, R. Mazzocchio, Adaptive changes in postural strategy selection in chronic low back pain, Exp. Brain Res. 177(2007), 411-418. dio: 10.1007/s00221-006-0683-4.

[22] I. Villarrasa-Sapiña, X. García-Massó, P. Serra-Añó, C. Garcia-Lucerga, L.M. Gonzalez, E. Lurbe, Differences in intermittent postural control between normal-weight and obese children, Gait and Posture, 49(2016), 1-6. doi: https://doi.org/10.1016/j.gaitpost.2016.06.012.

[23] N. Teasdale, O. Hue, J. Marcotte, F. Berrigan, M. Simoneau, J. Doré, P. Marceau, S. Marceau, A. Tremblay, Reducing weight increases postural stability in obese and morbid obese men, International Journal of Obesity, 31(2007), 153–160. https://doi.org/10.1038/sj.ijo.0803360.

[24] T.M.M. Vieira, L.F. de Oliveira, J. Nadal, An overview of age-related changes in postural control during quiet standing tasks using classical and modern stabilometric descriptors, J. Eletromyography and Kinesiology, 19(2009), e513-e519. doi:10.1016/j.jelekin.2008.10.007.

Can Learning from Demonstration Approaches Encode and Generalise Human Movements for Neurorehabilitation?

Jia Quan Loh, Vincent Crocher, Denny Oetomo, Ying Tan

***Abstract*—The use of robotic systems in Upper-Limb (UL) neurorehabilitation typically involves semi-standardised, simple movement exercises controlled by the robot. However, alternative approaches aim to support more complex movements that align with Activities of Daily Living (ADLs) and offer greater customisation of interactions tailored to individual patients by clinicians. These approaches, however, require increased therapist involvement, which underscores the need for methods that allow clinicians to teach a set of exercises to the robot. This has led to the development of various Learning by Demonstration (LfD) algorithms. These algorithms require the ability to encode the movements demonstrated by the clinician and generalise them across various task variations. Towards this goal, this study compares two existing LfD algorithms, Task-Parameterised Gaussian mixture models (TPGMM) and Dynamic Movement Primitives (DMP), in their capacity to generalise UL movements required for ADLs. The study then extends the best performing algorithm — TPGMM — to encode movements from both healthy and post-stroke participants performing a drinking task. TPGMM shows better performance in generalising healthy human movements for tasks and environments of increasing complexity when compared to a model-based approach and DMPs. TPGMM further shows that it better encodes movements of individuals post-stroke compared to ones of healthy individuals.**

***Index Terms*—Neurorehabilitation, Upper-Limb, Learning from Demonstration, Generalisation, Movement Quality.**

I. Introduction

Although rehabilitation robotic approaches in Upper-Limb (UL) therapy often aim for a high-level of automation and standardisation of therapy [1], another approach consists of enabling the clinician to customise rehabilitation exercises and possibly orient patients towards more functional practice. In this later approach, as attempted by Johnson or Timmermans with the Haptic Master [2], [3] or by the authors [4], the robotic device is used as an adjunct for clinicians to provide high intensity and consistent feedback to the patient. Thus, the presence of the therapist is required at all times to redemonstrate movement when task variations are introduced, which in turn leads to decreased robot autonomy and limits the possible cost and intensity benefit of robots.

In this scenario, it is thus desirable to allow a clinician to demonstrate examples of a (potentially complex) rehabilitation exercise, customised to a given patient, and allow the robot to guide the patient through this exercise and associated variations in the next therapy episode. It is expected that the robot can capture the "essence" of the exercise demonstrated — and the associated therapist action — and that the robot can then autonomously guide the patient through the exercise and its variations.

The *encoding*, *reproduction* and *generalisation* of an action — or a set of actions — demonstrated by a user to a robot is the objective of Learning from Demonstration (LfD) approaches encountered in classic robotic applications including pick-and-place or complex object manipulation [5], [6].

In a neurorehabilitation scenario, we assume that the patient's movements are more important than the robot's, shifting the focus towards learning actual human movement. This requires LfD algorithms to be applied in a larger dimensional space representing UL joints compared to the 3-DoF wrist position or robot joints classically used in LfD. The learning can then be extended towards human-on-human demonstration during therapy rather than relying on the rehabilitation robot's parameters during kinaesthetic teaching.

Reviewing existing literature on LfD in neurorehabilitation, Najafi et al. [7], Luciani et al. [8] and Lauretti et al. [9] employed Gaussian Mixture Models (GMM), Hidden Markov Models and Dynamic Movement Primitives (DMP) respectively to encode the joint kinematics of rehabilitation robots.

Noticeably, most LfD approaches constrain their learning space within the robot parameters, though one could argue that [8], [9] provides an UL approximation using their exoskeleton. Only Liu et al. [10] attempted to encode actual UL joints of humans using Kernel Movement Primitives. Furthermore, only [9] thoroughly evaluated the generalisability of deterministic LfD algorithms to tasks variations (*i.e.* new task points), which is essential to quantify the level of autonomy a rehabilitation robot can achieve. More importantly, to date, only [11] proposed a formal comparison of human movement quality preserved from each algorithm's reconstruction.

In this work, we extend Luciani's work [11] by investigating how well existing LfD algorithms generalise UL movement for unimanual daily activities (*e.g.* pick-place and drinking tasks) used in rehabilitation sessions. Specifically, this work proposes implementations of Task-Parameterised Gaussian Mixture Models (TPGMM) and DMP applied to UL joint trajectories (see Section II) and compares their performances on experimental data to a purely model-based representation of UL kinematics (using minimum jerk trajectories and inverse kinematics). The comparison is specifically evaluated on

The authors are with the Human Robotics Laboratory, Department of Mechanical Engineering and the Graeme Clark Institute, The University of Melbourne.
Correspondence: jqloh@student.unimelb.edu.au

kinematic metrics relevant to human movement analysis and rehabilitation (see Section III). In addition, we tested whether the best performing algorithm is able to capture the specificity of the movements of stroke patients compared to those of people without impairment for a classic drinking task from an existing datatset [12].

II. Objective and LfD algorithms evaluated

A. Upper-limb kinematics modelling and encoding objective

In this work, we propose to compare how well existing LfD algorithms are able to encode UL joint trajectories for common ADLs and generalise these trajectories to task variations (*i.e.* different starting, final or intermediate — via — points). Due to the importance of varying task points, we chose algorithms that explicitly address varying task points within their mathematical formulation to ensure convergence towards specified points.

The UL is modelled as a two links serial manipulator, connected with four DoFs: three coaxial revolute joints representing the gleno-humeral joint and a revolute joint for the elbow flexion-extension. This model references the MVN Biomechanical model for ease of comparison with datasets captured using XSENS (Xsens Technologies, Enschede, Netherlands).

B. LfD algorithms evaluated

The objective of the LfD algorithms is to encode a demonstrated kinematic trajectory $\Xi \in \mathcal{R}^{T\times 5}$, made of T vectors $\boldsymbol{\xi}_t = [\sigma_t, q_{1,t}, q_{2,t}, q_{3,t}, q_{4,t}]$ with $q_{1-4,t}$ the UL joint angles and σ_t the sampled time at each timestep $t \in [1, \dots, T]$.

Both TPGMM and DMP algorithms are adapted as follows to encode UL joint movements rather than the conventional task space movement.

1) Task-Parameterised Gaussian Mixture Model and Regression (TPGMM + GMR): In contrast to stochastic policies (*e.g.* ProMPs, HMM) that generalise distributions in a single reference frame (*e.g.* inertial frame or the trajectory starting point or end point), TPGMM adapts the distribution to multiple different start, final or via-points by superposing different reference frames relevant for a task [13].

For each task demonstration, the joint trajectory Ξ is observed from P reference frames, each assigned to the start, via and final points of the demonstration. Each p^{th} reference frame is characterised by a rotation matrix $A_p \in \mathcal{R}^{N\times N}$ and a displacement vector $\boldsymbol{b}_p \in \mathcal{R}^{1\times 5}$, referenced from an inertial frame. The kinematic profile at time step t in the p^{th} reference frame, denoted as $\boldsymbol{\xi}_t^{(p)}$, can be expressed as

$$\boldsymbol{\xi}_t^{(p)} = A_p^{-1}(\boldsymbol{\xi}_t - \boldsymbol{b}_p), \quad p = 1, ..., P, \tag{1}$$

where $\boldsymbol{\xi}_t$ is the t^{th} row vector of Ξ. Adapting this to joint space, A_p is set to the identity matrix and $\boldsymbol{b}_p$ is the joint displacement from the origin pose when the UL is at the p^{th} reference frame. Here, the displacement $\boldsymbol{b}_p$ represents the full transformation from one reference UL posture to another.

M demonstrations of P trajectories with T time steps each are concatenated demonstration by demonstration.

From these observations, K Gaussian kernels are identified, with each k^{th} kernel parameterised to P multivariate Gaussian distributions $\mathcal{N}(\boldsymbol{\mu}_k^{(p)}, \Sigma_k^{(p)})$ and their associated weight π_k. $\boldsymbol{\mu}_k^{(p)}$ and $\Sigma_k^{(p)}$ are respectively the mean vector and covariance matrix of the k^{th} Gaussian kernel in the p^{th} reference frame.

The number of Gaussian kernels K required to represent the task is optimised using the Bayesian Information Criterion test [14]. The $\boldsymbol{\mu}_k^{(p)}$ and $\Sigma_k^{(p)}$ of each Gaussian distribution are identified by an Expectation-Maximisation algorithm which maximises the likelihood of the demonstrated trajectories to lie within the identified Gaussian distributions [13].

To reconstruct a movement for new start, via and final UL postures, a new GMM and its corresponding Gaussian kernels $\mathcal{N}(\hat{\boldsymbol{\mu}}_k, \hat{\Sigma}_k)$ is obtained by conditioning the learned $\mathcal{N}(\boldsymbol{\mu}_k^{(p)}, \Sigma_k^{(p)})$ to the new reference frames defined by $\boldsymbol{b}_p$ (*i.e.* the joint configurations required at the new task points):

$$\hat{\boldsymbol{\mu}}_k = \Sigma_k \sum_{p=1}^{P} {\Sigma_k^{(p)}}^{-1} \hat{\boldsymbol{\mu}}_k^{(p)}, \quad \hat{\Sigma}_k = \left(\sum_{p=1}^{P} {\Sigma_k^{(p)}}^{-1} \right)^{-1} with \tag{2}$$

$$\hat{\boldsymbol{\mu}}_k^{(p)} = \boldsymbol{\mu}_k^{(p)} + \boldsymbol{b}_p. \tag{3}$$

The conditioned GMM is then used to generate a new motion plan with the sampled time, σ_t as the input, via Gaussian Mixture Regression, which calculates the conditional probability and expectation of the output for this given input.

Note: The conditioning of the new GMM (Eq. 2 and 3) is simplified compared to the common $\mathcal{R}^3$ case given the absence of rotation A_p in the joint configuration space.

2) Dynamic Movement Primitives: Dynamic Movement Primitives formulate a movement as a dynamical model (*e.g.* a spring-damper system) that modulates its non-linear forcing term after a desired attractor behaviour, usually an ideal demonstrated trajectory [15]. For each DoF of the UL model, the equation of the point attractor system is given by:

$$\tau \ddot{q}_n(t) = \alpha_n(\beta_n(g_n - q_n(t)) - \dot{q}_n(t)) + f_n(x), \tag{4}$$

where $q_n(t)$, $\dot{q}_n(t)$ and $\ddot{q}_n(t)$ are the n^{th}-DoF trajectory and its time derivatives, τ is the duration of the demonstrated movement and $g_n = q_n(t = \tau)$ is the corresponding joint angle of the final UL posture. α_n and β_n are positive constants selected such that the system is critically damped (*e.g.* $\beta_n = \alpha_n/4$). $f_n(x)$ is the forcing term expressed as:

$$f_n(x) = \frac{\sum_{k=1}^{K} \Psi_k(x_n)\omega_k}{\sum_{k=1}^{K} \Psi_k(x_n)} x_n(g_n - s_n), \tag{5}$$

where K is the chosen number of Gaussian kernels, $s_n = q_n(t = 0)$ is the starting posture of the trajectory, and ω_k are the DMP weights that will be learned from the demonstration(s) [15]. $\Psi_k(x_n)$ are Gaussian kernels expressed as:

$$\Psi_k(x_n) = \exp\left(-\frac{1}{2\sigma_k^2}(x_n - \mu_k)^2 \right), \tag{6}$$

where σ_k and μ_k are the selected widths and centers of the Gaussian kernels.

(5) and (6) are dependent on state variable x_n, expressed as a decaying canonical system to inhibit time dependence of the system:

$$\tau \dot{x}_n = -\gamma_n x_n, \tag{7}$$

where γ_n is set as a positive constant. Recommended values for α_n, μ_k, σ_k and γ_n were obtained from [16]. As there are no formal optimisation process for the exact number of K, a linear search up to 250 kernels was performed, with K kernels providing lowest RMSE when reconstructing the training dataset.

DMP weights ω_k are learned through the Locally Weighted Regression algorithm [17]. Given a demonstration of T time steps indexed by $t \in [1, ..., T]$, the recorded DoF and their derivatives, $q_n(t)$, $\dot{q}_n(t)$ and $\ddot{q}_n(t)$, are inserted into (4) to obtain T forcing terms f_n at each timestep:

$$f_n(t) = \tau \ddot{q}_n(t) - \alpha_n(\beta_n(g_n - q_n(t)) - \dot{q}_n(t)). \tag{8}$$

To learn ω_k, the locally weighted quadratic error is minimised for each Gaussian kernel using the following cost function, J_k:

$$J_k = \sum_{t=1}^{T} \Psi_k(x)(f_n(t) - \omega_k \epsilon(x))^2 \quad with \tag{9}$$

$$\epsilon(x) = x_n(t)(g_n - s_n). \tag{10}$$

An independent DMP is learned for each DoF of the UL model. As proposed by Lauretti et al. [9] to overcome the potential limitation of encoding a complex task with a single set of DMPs, a task is divided into sub-movements (each corresponding to a part of the movement stopping at a via-point and with a zero-velocity crossing) for which the above DMP approach is applied, effectively creating a dictionary of DMPs for different sub-movements. To reconstruct each new sub-movement, the start and final posture, s_n and g_n are adjusted to the desired postures and inserted into (4) and (5) of the corresponding DMP for said sub-movement. The q_n trajectory is obtained via forward integration.

Given the DMP approach does not explicitly learn from multiple demonstrations; when required, the ideal learning trajectory is taken from the average of multiple demonstrations aligned in time.

3) Model-based comparison: In addition to the two LfD algorithms above, a purely model-based approach is used as a comparison point in this work. Namely, the hand trajectory for each sub-movement is represented by a point-to-point minimum jerk function [18].

A numerical inverse kinematics using the Moore-Penrose inverse and Gauss-Newton algorithm is then applied onto each sampling point to define the corresponding UL posture. For the first point of each sub-movement the actual UL posture is used as the initial guess of the optimisation.

The joint space trajectories obtained with this model-based methods are then evaluated the same way as the trajectories obtained from the LfD algorithms.

III. Experimental evaluations

Two distinct experimental evaluations of these LfD algorithms were performed to evaluate if these methods could be used in neurorehabilitation: one to assess the ability of LfD algorithms to generalise healthy human movements to new task variations; and a second one to evaluate if the best of these algorithms can encode the specificity of participants with UL impairment after stroke. Both experiments rely on the evaluation of reconstructed movements (by LfD algorithms and model) against the original human movements. This comparison is here performed thanks to dedicated kinematic metrics.

A. Evaluation metrics and analysis

The set of metrics selected aims to cover the human likeness aspect of movements both at the end-effector and joints level and their temporal and spatial aspects:

1) *Joints Trajectory Dynamic Time Warping (Joints DTW)*: DTW aligns two signals by optimizing the distance value between points of the signals at current and previous time steps [19]. Its associated alignment cost is used as a temporal similarity measure for human action recognition [20]. DTW is used to evaluate the temporal similarity of the UL joints trajectories.
2) *Swivel Angle Trajectory DTW (Swivel DTW)*: Considering a 4-DoF UL model, a reaching movement contains a redundant DoF which can be parameterised by the swivel angle [21]. The swivel angle is defined as the angle between the the arm-plane and the vertical direction, with 0° when the arm-plane is parallel to the sagittal plane and 90° when parallel to the transverse plane. DTW is applied separately to the swivel angle trajectory to evaluate similarity of the encoded movement's redundancy.
3) *Mean Absolute Relative Phase Difference ($\Delta MARP$)*: Continuous Relative Phase (CRP) quantifies inter-joint coordination. It extracts phase angles between joint position and velocity, then compares it between different joints. A joint trajectory, $q(t)$ is decomposed into a complex signal, $\zeta(t)$ using the Hilbert Transform, $H(q(t))$ as described in [22]:

$$\zeta(t) = H(q(t)) = q(t) + iH(t). \tag{11}$$

The phase trajectory $\phi(t)$ is calculated by

$$\phi(t) = \arctan\left(\frac{H(t)}{q(t)}\right). \tag{12}$$

The CRP trajectory, $CRP(t)$ between two joints $q_1(t)$ and $q_2(t)$ is obtained by subtracting the phase angles

$$CRP(t) = \phi_1(t) - \phi_2(t). \tag{13}$$

where $\phi_1(t)$ and $\phi_2(t)$ is the phase angles of the two joints respectively.
Since CRP is a time series, the mean absolute value over the trajectory called Mean Absolute Relative Phase (MARP) is used to quantify the average phase of a movement [23]. To capture the extent of how the LfD algorithms encode joints coordination, the maximum difference in MARP between movements is reported in this study (*i.e.* the worst change among the six inter-joint pairs).

4) *Hand Trajectory Hausdorff Distance (Hand HD)*: The minimum Hausdorff Distance is the minimum value of the greatest of all the distances from a point in one trajectory to the closest point in the other trajectory [24]. HD is used to evaluate spatial similarity between hand movements, independently of time.
5) *Smoothness Difference (ΔSAL)*: Spectral Arc Length (SAL) defines movement smoothness as introduced in [25]. SAL is always negative with a value closer to zero corresponding to a smoother movement. The difference ΔSAL between the SAL of recorded and reconstructed sub-movements is calculated.
6) *Time-to-Peak-Speed Difference (ΔTTP)*: The speed profile of each sub-movement is calculated on the hand trajectory using a first-order Euler approximation. The peak speed and time-to-peak-speed refer to the largest value in the profile and corresponding time stamp relative to the start of the sub-movement. For each sub-movement, TTP is normalised to the sub-movement duration [26] and the difference ΔTTP between these normalised TTP is calculated. The average ΔTTP across all sub-movements is reported.

For all these metrics, a smaller value corresponds to a better, more faithful, movement reconstruction.

B. Experiment 1 - Standardised ADLs generalisation

In the first experiment, participants without movement impairment were recruited to perform ADLs tasks. The study was approved by the University of Melbourne HREC ($\#2024-31144-60078-3$).

1) Setup: Participant's joint angles were recorded using Vive Inertial Trackers (HTC, Taiwan) providing 6-DoF position and orientation measurements at the shoulder, the end of the humerus, and the wrist as shown on Fig. 1-a and recording at 90Hz. The trackers are interfaced with a custom C# program and a Unity UI (Unity Technologies, USA).

2) Task protocol: Participants were asked to sit at a table in front of a custom setup (see Fig. 1-b) and to perform a series of physical tasks while wearing the Vive Trackers.

Four tasks of increasing complexity associated with ADLs were selected: T1-Planar Pick-Place, T2-Elevated Pick-Place, T3-Obstructed Planar Pick-Place and T4-Pick-Drink. For each task, six configurations corresponding to a different picking or placing locations were recorded (see Fig. 2 and Table I). The placement of the task points were normalised based on the participant's forearm length, shoulder width and furthest diagonal reach.

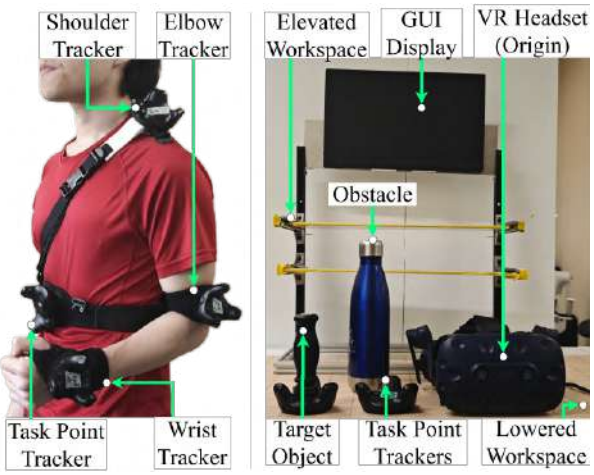


Fig. 1. Motion capture sensors (a) and experimental bench (b) and used for standardised ADLs movements recording. Note that the VR headset is only used here as a reference frame and not worn by the participants.

TABLE I
TASK DESCRIPTION

Task	Sub-task	Description
1	1-1	Move wrist from home position to TP1.
	1-2	Move object from TP1 to TP2 on a low level.
	1-3	Release object on TP2 and return to home position.
2	2-1	Move wrist from home position to TP1.
	2-2	Move object from TP1 to TP2 on an elevated level.
	2-3	Release object on TP2 and return to home position.
3	3-1	Move wrist from home position to TP1.
	3-2	Move object from TP1 to TP2 on a low level avoiding the obstacle in the middle.
	3-3	Release object on TP2 and return to home position.
4	4-1	Move wrist from home position to TP1.
	4-2	Move object from TP1 to mouth.
	4-3	Return to home position.

For each task, participants were asked to perform three demonstrations for each configuration using their dominant hand. They were then given a ten-minute rest, before repeating the experiment with their non-dominant hand. The overall session consisted in a total of 144 tasks repetitions.

3) Data post-processing and analysis: A fourth-order, low-pass Butter-worth filter with a cut-off frequency of 5Hz [27] was applied on joint angle signals. The filtered signal is then down-sampled to 50Hz to reduce model computation. To align multiple demonstrations in time, each joint trajectory was then normalised to unit time.

For each Task and each Participant, two non contiguous configurations were randomly selected for generalisation evaluation whereas the remaining four configurations were used for LfD training. The reconstructed trajectories from the generalisation set were compared to their corresponding recorded movements using the six kinematic metrics.

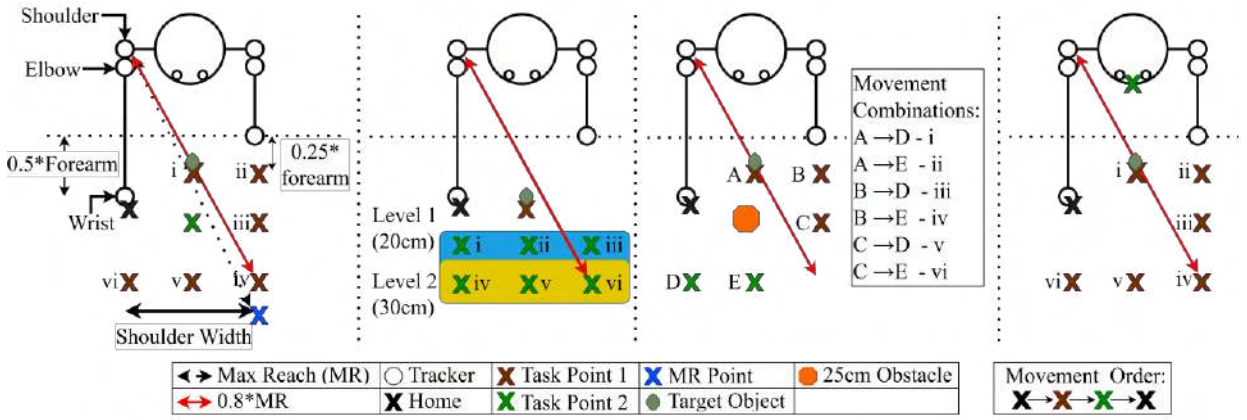


Fig. 2. Schematic of setup and Tasks configurations i / vi. Overall motion consists of moving from the home position (black cross) to grasp the object at TP1 (red cross), transporting it to TP2 (green cross) and returning to the home position. From left to right: 1) Lowered Pick-Place, 2) Elevated Pick-Place, 3) Obstructed Pick-Place, 4) Pick-Drink.

Distribution of each metric outcome for each LfD Algorithm and each Task were tested for normality (Shapiro–Wilk test, $p < 0.05$), followed by a repeated ANOVA / Friedman test and corresponding post-hoc paired t-test / Wilcoxon signed-rank test to evaluate differences between the three reconstructions.

C. Experiment 2 - Impaired movements encoding

To further evaluate the capability of LfD algorithms to encode movements for a rehabilitation context, the best performing algorithm was further applied to encode movements of five participants with stroke (51 to 74 years, FMA-UE: 21 to 61) and five control healthy participants (42 to 78 years) performing a drinking task. Movements were selected from the UL-ADL dataset by Schwarz et al. [12]. Only participants with a right-dominant-impaired side were selected for better comparison with the group of non-impaired individuals (all right handed). TPGMM as described in Section II was used to encode each task for each participant (using three repetitions).

Movement reconstructions were then compared to the three recorded repetitions using the same set of kinematic metrics. The distribution of the metrics difference for each group are reported for comparison.

This analysis specifically aims to test if the encoding of movements preserve the specificity of movements with participants with stroke compared to the encoding of individuals without neurological injury (*i.e.* are movements of individuals with stroke reconstructed as well or worse as those of healthy individuals).

IV. Results

A. Experiment 1 - Standardised ADLs generalisation

Five naive, healthy participants (28.4 ± 3.36 years old) were recruited. According to the Edinburgh Handedness Inventory [28], three participants were predominantly right-handed, 1 ambidextrous, and 1 predominantly left-handed.

Fig. 3 shows an example of an Obstructed Pick-place task (Task 3) and corresponding reconstruction by the LfD algorithms.

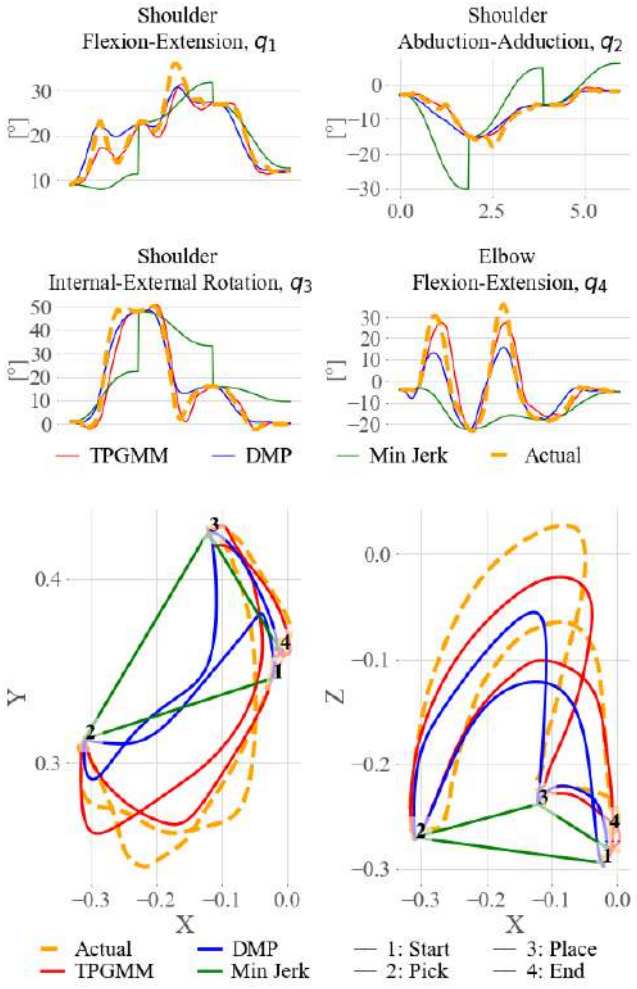


Fig. 3. Example of actual and reconstructed UL joint trajectories (a) and hand trajectories (b) (left: Top View, Right: Front View) between actual and reconstructed joints for Task 3 - Obstructed pick-place task.

Table II presents the mean difference (and post-hoc significance level) between the different approaches for each metric for each task. Metrics for which methods are not statistically different are omitted.

TABLE II
METRIC COMPARISON BETWEEN LFD ALGORITHMS AND MINIMUM JERK

Metric	**Mean Difference** i / j			**Best**
	TPGMM -Min Jerk	DMP -Min Jerk	TPGMM -DMP	
Task 1 – Planar Pick-Place				
Joints DTW (rad)	-1.807***	-1.743***	-	-
Swivel DTW (rad)	-0.231***	-0.219***	-	-
ΔMARP	-0.106**	-	-	-
Hand HD (m)	-0.018*	-	-	-
ΔSAL	-	-	-	-
ΔTTP	-	-	-	-
Task 2 – Elevated Pick-Place				
Joints DTW (rad)	-3.695***	-3.850***	-	-
Swivel DTW (rad)	-0.681**	-0.719**	-	-
ΔMARP	-0.194**	-0.209**	-	-
Hand HD (m)	-0.075***	-0.077***	-	-
ΔSAL	-0.364***	-0.393***	-	-
ΔTTP	-0.033*	-0.076***	0.043***	DMP
Task 3 – Obstructed Pick-Place				
Joints DTW (rad)	-3.150***	-2.244***	-0.906***	TPGMM
Swivel DTW (rad)	-0.369***	-0.236**	-0.133**	TPGMM
ΔMARP	-0.247**	-0.124*	-	-
Hand HD (m)	-0.056**	-0.023**	-0.033**	TPGMM
ΔSAL	-	-	-	-
ΔTTP	-	-0.061***	0.037*	DMP
Task 4 – Pick-Drink				
Joints DTW (rad)	-5.855***	-5.857***	-	-
Swivel DTW (rad)	-	-	-	-
ΔMARP	-0.232***	-0.192*	-	-
Hand HD (m)	-0.056***	-0.043***	-0.013*	TPGMM
ΔSAL	-0.404*	-0.333*	-	-
ΔTTP	-0.056**	-0.095***	0.039*	DMP

$^{*}p < 0.05$, $^{**}p < 0.01$, $^{***}p < 0.001$.

B. Experiment 2 - Impaired movements encoding

Fig. 4 compares the distribution of the metrics obtained from TPGMM reproductions between healthy and post-stroke participants.

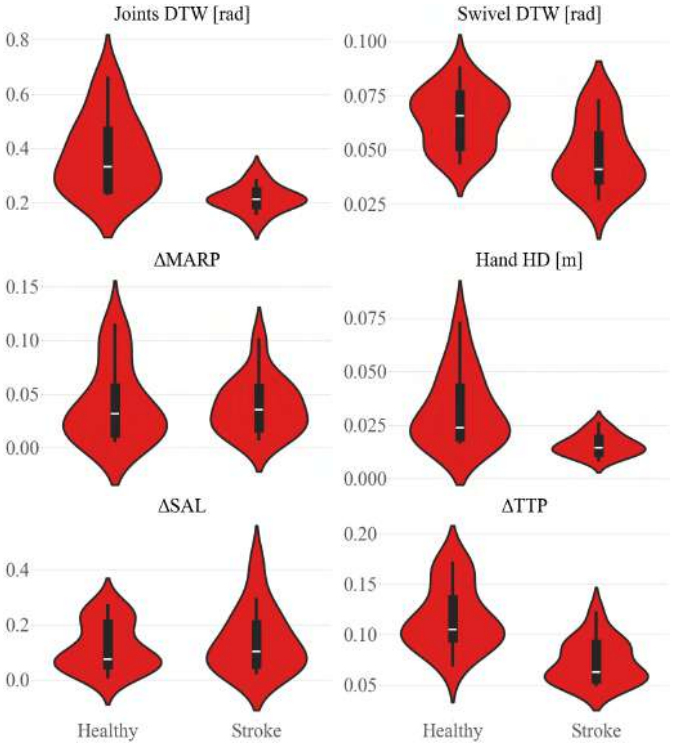


Fig. 4. Violin plots showing the metric distribution of TPGMM reconstruction for healthy and stroke participants.

V. DISCUSSION

A. Generalisation over increasing task complexity

The purely model-based approach is able to generate simple planar point-to-point movements of the hand equally well to the LfD policies but already failed to capture as good a representation in joints space. As task complexity increases and divert from a simple point-to-point reaching, the LfD algorithms perform significantly better than the simple model, even in reproducing the hand trajectory.

Although DMPs and TPGMM did not show significant difference in maintaining human likeness for its generalisation during T1, T2 and T4; of which a similar behaviour was observed in [11]'s work for reproducing pick-place and pick-drink joint movement; TPGMM significantly better generalises to new task parameters than DMPs when both task and environment becomes more complex, demonstrated by the addition of obstacles in T3. While not visible for all metrics, this is clear for both hand space (as shown by the Hand HD) and joints space (as shown by the Joints DTW and Swivel angle DTW) for T3 as presented on Table II. This better generalisation of complex tasks might be due to TPGMM's formulation that explicitly observes the joints distribution from multiple coordinate frames.

Importantly, the advantage of TPGMM is clearly visible in joint space (Joints and Swivel DTW). This is an important point for neuro-rehabilitation given the specificity of joint synergies and compensatory behaviour observed post-stroke which are desirable to capture.

In addition, the complexity (*i.e.* number of kernels) of LfD techniques can significantly influence their performance and, despite using optimisations approaches in this work, the choice made may have influenced the results. Still, it is to note that TPGMM outperforms DMPs in the current work while requiring a lower number of kernels with 118 on average compared to 280 for DMPs.

B. Encoding of movements specificity of participants with stroke

It is well documented that following a stroke, UL movements are impaired and the execution of classic tasks differs in

multiple way from one of healthy individuals. Thus, evaluating how TPGMM, which shows the best ability in more complex tasks, can capture this specificity does provide an indication on how well it could encode rehabilitation movements (*i.e.* assuming that those movements lie somewhere in between those of healthy individuals and natural ones of the stroke patient). Interestingly, the evaluation performed on a drinking task reveals that TPGMM produces a more faithful and consistent encoding of stroke participants' movements compared to ones of healthy individuals. This is the case for all metrics except for ΔSAL (see Fig. 4). This encoding performance comes at the expense of an increased modelling complexity: healthy participants movements required between 20 and 63 kernels, whereas stroke participants movements required between 38 and 92 kernels.

C. Limitations and future work

It is to note that the UL model used is limited to only four DoFs and does not include any scapula or trunk motion. This is an important limitation for rehabilitation applications where patients tend to compensate for limited elbow and shoulder flexion/extension using trunk and scapula motions [29]. Such motions should thus ideally be encoded and reconstructed by the LfD policies.

While this first analysis provides insights on the two LfD algorithms to encode human movements that could be used in neurorehabilitation, the two experiments presented do not truly represent actual rehabilitation exercise prescribed by therapists. While the results indicate that TPGMM is the best candidate for such scenario, a formal evaluation in real conditions should still be conducted.

ACKNOWLEDGEMENT

This work was supported by the Australian Research Council (#LP220100417).

REFERENCES

[1] P. J. Mahdieh Babaiasl, Seyyed Hamed Mahdioun and M. Yazdani, "A review of technological and clinical aspects of robot-aided rehabilitation of upper-extremity after stroke," *Disability and Rehabilitation: Assistive Technology*, vol. 11, no. 4, pp. 263–280, 2016.

[2] M. Johnson, K. Wisneski, J. Anderson, D. Nathan, and R. Smith, "Development of ADLER: The Activities of Daily Living Exercise Robot," in *The First IEEE/RAS-EMBS International Conference on Biomedical Robotics and Biomechatronics*, 2006, pp. 881–886.

[3] A. A. A. Timmermans, R. J. M. Lemmens, M. Monfrance, R. P. J. Geers, W. Bakx, R. J. E. M. Smeets, and H. A. M. Seelen, "Effects of task-oriented robot training on arm function, activity, and quality of life in chronic stroke patients: a randomized controlled trial," *J. NeuroEng. Rehabil.*, vol. 11, p. 45, Mar. 2014.

[4] V. Crocher, K. Brock, J. Simondson, M. Klaic, and M. P. Galea, "Robotic task specific training for upper limb neurorehabilitation: a mixed methods feasibility trial reporting achievable dose," *Disabil. Rehabil.*, pp. 1–9, 2024.

[5] H. Ravichandar, A. S. Polydoros, S. Chernova, and A. Billard, "Recent advances in robot learning from demonstration," *Annu. Rev. Control Robot. Auton. Syst.*, vol. 3, no. Volume 3, 2020, pp. 297–330, 2020.

[6] A. Correia and L. A. Alexandre, "A survey of demonstration learning," *Robot. Auton. Syst.*, vol. 182, p. 104812, 2024.

[7] M. Najafi, K. Adams, and M. Tavakoli, "Robotic learning from demonstration of therapist's time-varying assistance to a patient in trajectory-following tasks," in *2017 International Conference on Rehabilitation Robotics (ICORR)*. IEEE, 2017, pp. 888–894.

[8] B. Luciani, L. Roveda, F. Braghin, A. Pedrocchi, and M. Gandolla, "Trajectory learning by therapists' demonstrations for an upper limb rehabilitation exoskeleton," *IEEE Robot. Autom. Lett.*, vol. 8, no. 8, pp. 4561–4568, 2023.

[9] C. Lauretti, F. Cordella, E. Guglielmelli, and L. Zollo, "Learning by demonstration for planning activities of daily living in rehabilitation and assistive robotics," *IEEE Robot. Autom. Lett.*, vol. 2, no. 3, pp. 1375–1382, 2017.

[10] Z. Liu, Q. Ai, H. Liu, W. Meng, and Q. Liu, "Human-like trajectory planning based on postural synergistic kernelized movement primitives for robot-assisted rehabilitation," *IEEE Trans. Hum.-Mach. Syst.*, 2024.

[11] B. Luciani, S. Costante, F. Braghin, A. Pedrocchi, and M. Gandolla, "Imitation learning using gaussian mixture models and dynamic movement primitives for rehabilitation exoskeletons: A comparison," in *2024 10th IEEE RAS/EMBS International Conference for Biomedical Robotics and Biomechatronics (BioRob)*, 2024, pp. 122–127.

[12] A. Schwarz, J. P. O. Held, and A. R. Luft, "Post-stroke Upper Limb Kinematics of a set of Daily Living Tasks," Mar. 2020.

[13] S. Calinon, "A tutorial on task-parameterized movement learning and retrieval," *Intell. Serv. Robot.*, vol. 9, no. 1, p. 1–29, Jan. 2016.

[14] T. Hastie, R. Tibshirani, J. Friedman, and J. Franklin, "The elements of statistical learning: data mining, inference and prediction," *Math. Intell.*, vol. 27, no. 2, pp. 83–85, 2005.

[15] A. J. Ijspeert, J. Nakanishi, H. Hoffmann, P. Pastor, and S. Schaal, "Dynamical movement primitives: Learning attractor models for motor behaviors," *Neural Comput.*, vol. 25, no. 2, pp. 328–373, 2013.

[16] A. Fabisch, "movement_primitives: Imitation learning of cartesian motion with movement primitives," *Journal of Open Source Software*, vol. 9, no. 97, p. 6695, 2024.

[17] S. Schaal and C. G. Atkeson, "Constructive incremental learning from only local information," *Neural Comput.*, vol. 10, no. 8, p. 2047–2084, Nov. 1998.

[18] T. Flash and N. Hogan, "The coordination of arm movements: an experimentally confirmed mathematical model," *J. Neurosci.*, vol. 5, no. 7, pp. 1688–1703, 1985.

[19] M. Müller, *Information Retrieval for Music and Motion*. Berlin, Heidelberg: Springer-Verlag, 2007.

[20] S. Sempena, N. U. Maulidevi, and P. R. Aryan, "Human action recognition using dynamic time warping," in *Proceedings of the 2011 International Conference on Electrical Engineering and Informatics*, 2011, pp. 1–5.

[21] D. Tolani, A. Goswami, and N. I. Badler, "Real-time inverse kinematics techniques for anthropomorphic limbs," *Graph. Models*, vol. 62, no. 5, pp. 353–388, 2000.

[22] P. F. Lamb and M. Stöckl, "On the use of continuous relative phase: Review of current approaches and outline for a new standard," *Clin. Biomech. (Bristol)*, vol. 29, no. 5, pp. 484–493, Mar. 2014.

[23] A. K. Galgon and P. A. Shewokis, "Using mean absolute relative phase, deviation phase and Point-Estimation relative phase to measure postural coordination in a serial reaching task," *J. Sports. Sci. Med.*, vol. 15, no. 1, pp. 131–141, Feb. 2016.

[24] D. P. Huttenlocher, K. Kedem, and J. M. Kleinberg, "On dynamic voronoi diagrams and the minimum hausdorff distance for point sets under euclidean motion in the plane," in *Proceedings of the Eighth Annual Symposium on Computational Geometry*, ser. SCG '92. New York, NY, USA: Association for Computing Machinery, 1992, p. 110–119.

[25] S. Balasubramanian, A. Melendez-Calderon, A. Roby-Brami, and E. Burdet, "On the analysis of movement smoothness," *J. NeuroEng. Rehabil.*, vol. 12, no. 1, p. 112, Dec. 2015.

[26] M. A. Murphy, C. Willén, and K. S. Sunnerhagen, "Kinematic variables quantifying upper-extremity performance after stroke during reaching and drinking from a glass," *Neurorehabilit. Neural Repair*, vol. 25, no. 1, pp. 71–80, 2011.

[27] R. C. G. Diego Álvarez, Juan C. Alvarez and A. M. López, "Upper limb joint angle measurement in occupational health," *Comput. Methods Biomech. Biomed. Eng.*, vol. 19, no. 2, pp. 159–170, 2016.

[28] J. F. Veale, "Edinburgh handedness inventory–short form: a revised version based on confirmatory factor analysis," *Laterality: Asymmetries of Body, Brain and Cognition*, vol. 19, no. 2, pp. 164–177, 2014.

[29] S. K. Subramanian, J. Yamanaka, G. Chilingaryan, and M. F. Levin, "Validity of movement pattern kinematics as measures of arm motor impairment poststroke," *Stroke*, vol. 41, no. 10, pp. 2303–2308, Sep. 2010.

Instructions From an Active Robotic Hand Increase Body Ownership and Task Clarity

1st Sweder van Dipten
DTU Electro
Danmarks Tekniske Universitet
Kgs. Lyngby, Denmark
swedervandipten@gmail.com

2nd John Paulin Hansen
Department of Technology, Management and Economics
Danmarks Tekniske Universitet
Kgs. Lyngby, Denmark

***Abstract*—This study introduces a novel approach to home rehabilitation exercise instructions, utilizing a 3D-printed robotic hand that can mimic the patient's hand movements and follow pre-programmed instructions. This robotic hand, made from inexpensive 3D printed components and hobbyist equipment, is controlled by open source computer vision tracking.**

Two within-subject crossover studies were conducted with 30 healthy participants. The first study assessed the participants' sense of embodiment, while the second compared their ability to remember movement exercises when instructed by the robotic hand versus video clips.

The results showed that the participants experienced a higher sense of embodiment with the robotic hand in its active mode. Furthermore, they demonstrated significantly better short-term memory retention of medium and difficult finger movement sequences when instructed by the robotic hand compared to video instruction ($F_{1,56}$ = 4.047, p $<$ .05) and ($F_{1,56}$ = 19.463, p $<$ .05). These findings suggest that this innovative method could improve remote therapy and strengthen bodily ownership, which is essential in stroke rehabilitation.

***Index Terms*—Body Ownership Illusion, Embodiment, Human-Robot Interaction, Rubber Hand Illusion, Stroke Rehabilitation**

I. Introduction

Rehabilitating finger and grip movements at home is relevant for several patient groups, for example, stroke survivors. Stroke can cause paralysis or reduced muscle control in the hand, which requires rehabilitation to regain strength and coordination. According to the World Health Organization, approximately 15 million people suffer strokes annually worldwide [1]. A significant proportion of stroke survivors experience hand weakness or motor deficits, indicating a substantial number of patients who need hand rehabilitation services. Furthermore, stroke is one of the leading causes of long-term severe disabilities, underscoring the need for effective rehabilitation strategies. Despite the availability of therapeutic interventions that can ameliorate post-stroke disabilities, a significant proportion of survivors continue to face chronic physical or cognitive impairments. For example, approximately 65% of the survivors struggle to reintegrate their affected hand into daily activities after completing conventional therapy [2]. This scenario is set against a backdrop of increasing costs, with stroke-related expenses in the European Union expected to grow significantly from an estimated 45 billion euros in 2017 [3].

In addition, hand rehabilitation is commonly needed after surgeries. Patients recovering from hand injuries, such as fractures, dislocations, or severe sprains, require rehabilitation to regain strength and dexterity. As the aging population increases, so does the prevalence of age-related hand problems. Conditions such as osteoarthritis and rheumatoid arthritis, both known to impact hand movement, are relatively common; consequently, a significant number of older adults are likely to seek hand rehabilitation services. Parkinson's disease can also affect hand function, necessitating ongoing rehabilitation. Finally, age-related weakness and loss of dexterity in the hands are common among the elderly, making exercises crucial to maintaining joint mobility and reducing pain.

The primary objective of this paper is to support the rehabilitation of late-stage stroke, carried out within the home environment. This phase lacks a clear end point and may last for years, relying heavily on the motivation, effort, and set goals of the survivor [4]. We relate to mirror therapy, since our robotic hand acts as a direct alternative to mirror therapy with the added benefit of being able to personalize the rehabilitation of the patient by having them interact with their therapist remotely.

The rubber hand illusion (RHI) [5] is an important method in investigating body ownership and agency and plays a crucial role in the effectiveness of mirror therapy. In this experiment, we successfully elicited the RHI using a robotic hand, demonstrating a key component to leverage mirror therapy techniques.

Rehabilitation robotics offers promising prospects for improving therapeutic interventions and addressing the challenges of teletherapy. By allowing therapists to remotely interact with patients through the robotic hand, our goal is to improve the personalization and effectiveness of home rehabilitation. The development of a 3D robotic hand instructor that is controlled by stroke patients and accessible remotely to therapists exemplifies this approach, aiming to surpass the limitations of conventional therapy [12] [13].

Our study investigates the potential for a 3D printed robotic hand to induce a sense of embodiment in participants, similar to the illusion of a rubber hand [5], and explores its effects



Fig. 1. The Robotic Hand connected to an Arduino Uno, alongside an Intel RealSense D435 Stereovision Camera.

on performance in memorizing task instructions. In this way, we focus on developing user-friendly teletherapy support systems that provide clear instructions, ensuring accessibility for individuals with limited digital literacy.

II. Related work

The rubber hand illusion demonstrates how sensory information can manipulate the feeling of body ownership, where participants come to accept a rubber hand as part of their own body through a combination of visual, tactile, and proprioceptive stimuli. This illusion is induced by simultaneously stroking both the participant's hidden real hand and a visible rubber hand, leading to an altered perception of self-ownership over the artificial limb. Investigating the limits of self-perception via the rubber hand illusion and body ownership illusions allows researchers to uncover significant insights into the brain's adaptable representation of self. Research has extended the RHI to virtual bodies [6] and explored the use of robotic hands to induce similar illusions [7] [8]. The relationship between ownership and agency in these illusions has been investigated [9], with findings suggesting that these are distinct but interacting cognitive processes. Furthermore, the embodiment of robotic or virtual hands has been explored in the field of psychology and robotics [10] [11]. These studies highlight the potential for technology to manipulate body perception and create novel rehabilitation strategies.

Mirror therapy is a therapeutic technique used to alleviate sensory and motor deficits, particularly in the affected limb, by employing the principle of visual illusion. A mirror is strategically placed to reflect the image of the unaffected limb, creating the illusion that the affected limb is moving without difficulty [14]. Mirror therapy capitalizes on neuroplasticity in the brain, promoting the re-wiring of neural pathways associated with motor function and sensory perception [15]. By visualizing the affected limb in a normal state, the brain is encouraged to restore connections and improve motor control, which has shown promise in improving motor function of the limb, reducing pain perception, and improving overall recovery of the upper limb [16] [17]. However, therapy success depends on the patient's ability to perform exercises correctly, which, in some cases, requires guidance and practice under the supervision of a skilled healthcare professional [18]. This required guidance ensures that patients engage in mirror therapy with precision, optimizing its potential benefits, while mitigating the risk of incorrect execution. Furthermore, the applicability of mirror therapy may vary from person to person. Some people do not respond as well as others to mirror therapy [19]. Consequently, the utility and generalizability of mirror therapy in the context of hand stroke rehabilitation remain subject to review and ongoing investigation [20].

Teletherapy serves as a powerful conduit to transcend geographical barriers that have historically restricted access to expert stroke rehabilitation services [21]. The ability to receive therapy remotely ensures that people residing in remote or underserved areas, often far away from specialized rehabilitation centers, can access the specialized care they require. This geographical inclusivity addresses a disparity in healthcare access, promoting equity and ensuring that stroke survivors from various locations can benefit from the latest advances in upper limb stroke rehabilitation [22]. In addition, teletherapy offers the flexibility of scheduling sessions at times convenient to the patient, further enhancing adherence and overall therapeutic results. Despite its considerable advantages, teletherapy faces a series of challenges in the context of upper limb stroke rehabilitation, the most notable being the limited physical interaction it provides. The absence of physical interaction in teletherapy poses a fundamental limitation, particularly in cases where personalized tactile interventions are crucial to rehabilitation success [23].

The effectiveness of teletherapy is intricately intertwined with technological prerequisites. Patients must have access to suitable equipment and possess a degree of digital literacy to participate effectively in remote therapy sessions. Although advancements in technology have made these prerequisites increasingly accessible, disparities persist, potentially hindering certain individuals' participation. The digital divide, compounded by socioeconomic disparities, can exacerbate healthcare inequalities, raising relevant ethical concerns [24].

III. Material and Methods

The robotic hand is constructed using open source 3D prints from the InMoov project [25] and Parallax Inc 4 servomotors.

The robotic hand is operated by implementing computer vision, using the OpenCV library (Version 4.8.1), to detect hand movement, which is then translated into binary finger movement (i.e., open or closed) in the robotic hand. The script, developed in Python, utilizes an Intel D435 camera along with MediaPipe for hand tracking and palm detection, selected for its superior image quality and speed, making it well-suited for tracking rapidly moving fingers. It detects 21 hand landmarks to identify open or closed fingers based on their positions. Finger counting is performed using a skeletal mesh model, and the status of fingers is determined by comparing the positions of the fingertips and phalanges. The script then sends a string to an Arduino script to represent the hand's state, with each digit in the string representing a finger's status (open or closed).

The script imports libraries for computer vision and hand tracking, including 'cv2' for image processing, and custom modules from 'cvzone' (Version 1.6.1) for hand detection and tracking. It initializes video capture, sets parameters for hand detection, and uses a loop to capture frames, detect hands, and count open fingers. The hand detection results are used to control an Arduino Uno via serial communication, displaying the video feed in real-time with overlaid hand landmarks and the detected hand contours.

The Arduino script controls the servomotors based on the data received from the hand-tracking script. It reads serial data, identifies commands for finger positions, and adjusts the servomotors accordingly. The setup includes an Arduino Uno, Parallax servomotors, and an Adafruit servo shield, chosen for their cost-effectiveness, quality, and capability to handle multiple servomotors with an external power supply. The system translates digital instructions into motion, controlling servomotors to replicate hand gestures. The total cost of the components amounts to approximately €525, with the Intel D435 stereo camera being the most financially significant component at around €390. However, a basic webcam can be implemented as a viable substitute, reducing the total cost to €150. Although this cost reduction slightly compromises image quality, it still enables satisfactory finger tracking and movement detection, making it a practical and cost-effective alternative. This approach is significantly more affordable than virtual reality mirror therapy sets, which range from $252 [26] to considerably higher prices depending on technological complexity [27]. In particular, the system achieves a minimal latency of 90 milliseconds, significantly below the 300-millisecond threshold beyond which visuomotor delays become perceptible to users [28].

The research comprises two controlled within-subject crossover studies aimed at assessing the participants' sense of embodiment and their memorization performance when interacting with the robotic hand. All participants were recorded as right-hand dominant. Before starting the experiments, participants were asked about their gender and age group, 22 participants being male (73%) and the other 8 female (27%). Most of the participants belonged to the 18-24 age group (53%), the rest was made up of the 25-34 age group (37%), the 35-44 age group (7%) and the 45-54 age group (3%). All participants were university students, except for one. Before participation, all participants filled out a signed consent form. This research work was exempted from ethical approval by the Danish Research Ethics Committee because data was collected solely for technical purposes and were not intended for use in a clinical setting.

The methodology involved dividing participants into two groups, each undergoing a test and control study in both experiments, with the order of participation reversed between the groups. The two experiments were conducted successively, starting with the first experiment.

Experiment 1 sought to determine whether participants experienced a sense of embodiment with the robotic hand. Participants were seated with their hands on a table in front of them, but unlike the usual procedure their hands were facing upwards, not downwards. A divider and a long-sleeved shirt worn backward were used to obscure their right hand and replace its visual position with the robotic hand (Figure 2). This setup was aimed at minimizing distractions and maintaining the illusion. An Intel RealSense D435 camera captured the movements of the participants' hands, allowing them to control the robotic hand. The experiment consisted of one control phase and one test phase, each lasting 5 minutes. In the control phase, both the participant's right hand and the robotic hand were simultaneously stroked with a paintbrush to elicit the rubber hand illusion, and in the test phase, participants had full control over the robotic hand's movements. The order of the control and test phases was counterbalanced between the participants to minimize order effects. Half of the participants performed the control phase first, followed by the test phase, while the other half performed the test phase first, followed by the control phase. Both phases were followed by a questionnaire based on the questionnaire used by Botvinick and Cohen [5] to capture the participant's experience. Questionnaire responses were collected using a 7-point Likert scale, with answers numerically translated such that 7 represented 'strongly agree' and 0 represented 'strongly disagree'. A Wilcoxon Signed-Rank test was used to analyze the data from Experiment 1. In the control study, the robotic hand is referred to as ***passive***, since the participant is stimulated by touch administered by the researcher through paintbrushes. For the test study, the robotic hand is referred to as ***active***, since the participant is stimulating the robotic hand themselves by movement of the fingers of their right hand (Figure 2).

Experiment 2 focused on assessing whether interaction with the robotic hand improved participants' memorization task performance compared to observing a prerecorded video of a human hand. The setup included an iPad with video clips for the control study and the robotic hand for the test study, both displaying sequences of finger movements classified into easy, medium, and difficult instructions. The robotic hand was operated by the researcher. A task of easy complexity encompassed three to four distinct operations, while tasks of medium and difficult complexity comprised six and nine



Fig. 2. Front view (left) and top view (right) of the setup of Experiment 1. Following the standard rubber hand illusion procedure, a divider hides their right hand, replacing it with the robotic hand.

operations, respectively. Participants were exposed to a total of 15 sequences across these categories and asked to remain still (no finger movements) during observation in both video and robotic hand conditions. They were then requested to replicate each sequence with their right hand after observing the demonstrated sequence. For each sequence in Experiment 2, a participant's score was calculated as the percentage of correctly replicated finger movements out of the total number of movements in that sequence. The sequence presentation order was randomized using a Latin Square design to avoid order effects. An ANOVA was used to analyze the data from Experiment 2.

IV. Results

Before the analysis of data from Experiment 1, participants were first screened for 'responders' and 'rejecters' based on the work of Kalckert and Ehrsson [29]. Rejectors are classified according to the criteria that they did not answer a single individual question on the positive spectrum of the Likert scale. Although some strong and mild responders were found, no rejecters were found in the data. All 30 participants were used in the analysis. The results indicated a significant sense of embodiment with the active robotic hand in three aspects: feeling of having an additional hand or arm (Passive: Mean = 3.5, SD = 1.77; Active: Mean = 4.5, SD = 1.7), sensation of the hand becoming 'mechanical' or 'artificial' (Passive: Mean = 3.6, SD = 1.65; Active: Mean = 4.7, SD = 1.7), and the resemblance of the robotic hand to the participant's own hand (Passive: Mean = 2.7, SD = 1.3; Active: Mean = 3.1, SD = 1.6). Furthermore, 20 of the 30 participants felt that the active robotic hand was more integrated into their body image compared to the passive robotic hand.

Data from Experiment 2 underwent variance analysis (ANOVA) to assess performance in a memorization task with either video instructions from the iPad or robotic hand guidance. No significant differences were observed in the easy tasks between mediums (iPad: 97.47%, Robotic Hand: 98.62%; $F_{1,56}$ = 1.373, ns). However, significant differences were observed in medium (iPad: 83.56%, Robotic Hand: 89.04%; $F_{1,56}$ = 4.047, p $<$ .05) and difficult tasks (iPad: 67.18%, Robotic Hand: 79.89%; $F_{1,56}$ = 19.463, p $<$ .05), indicating enhanced performance with the robotic hand. No significant training effect was found.

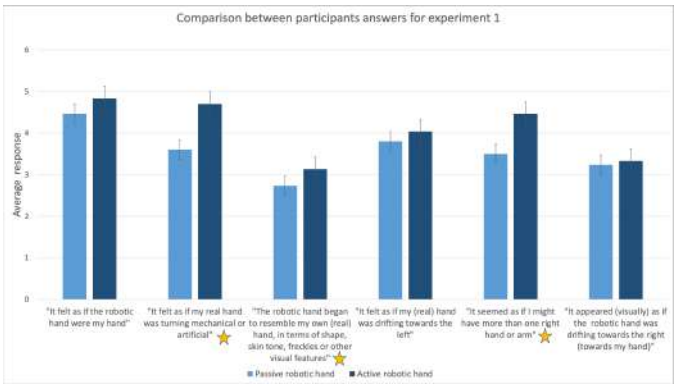


Fig. 3. Answers for 6 questions from the questionnaire proposed by Botvinick and Cohen [5]. A star marks results with a significant difference (p $<$ .05) between the passive (light blue) and active (dark blue) version of the robot hand.

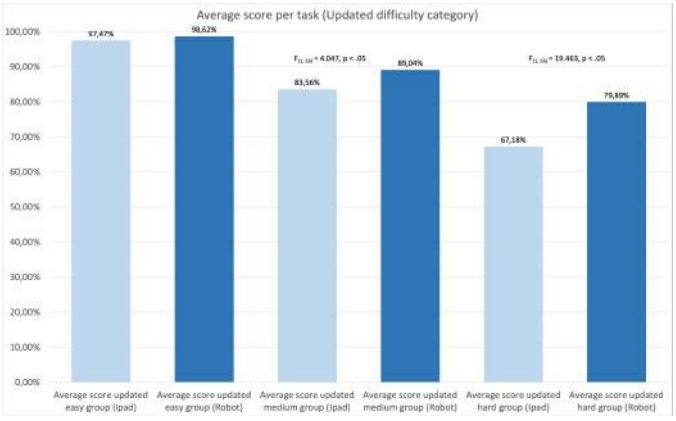


Fig. 4. Average correct replications of finger movement instructions per task (easy, medium, difficult) are shown. Light blue columns represent video clip instructions, and dark blue columns represent robotic hand instructions.

V. Discussion

Experiment 1's findings align with the foundational rubber hand illusion experiments by Botvinick and Cohen [5], demonstrating that the active robotic hand fosters a greater sense of embodiment and immersion compared to its passive counterpart. Participants reported a heightened sense of embodiment with the active robotic hand, in particular, noting its more convincing appearance and the sensation of having an additional limb. These results suggest that active interaction with the robotic hand not only reinforces the illusion of ownership, but also enhances the sensory integration necessary for a convincing experience of body ownership.

Qualitative feedback from participants further underscores the illusion's efficacy, with reports of the active hand feeling like a part of their body, indicating a strong sense of embodiment. However, discrepancies in timing and mechanical feedback occasionally disrupted this illusion, highlighting areas for improvement in the robotic hand's design.

Arata et al. [8] also demonstrated the RHI using a robotic hand, further validating this approach. However, while Arata et al.'s robotic hand was limited to tapping the index finger, our system allows simultaneous and individual movement of all five fingers, potentially contributing to a more complex and robust illusion. Furthermore, although both studies employed the Botvinick and Cohen questionnaire, our study yielded higher scores, particularly for questions 3 ('I felt as if the rubber hand were my hand') and 4 ('It seemed as if I might have more than one right hand or arm'), compared to those reported by Arata et al. This difference may be attributed to the increased dexterity and realism afforded by our five-fingered robotic hand, which more closely mimics natural human hand movements and coordination.

The results of Experiment 2 indicate that the participants performed better in the memorization tasks with the robotic hand, compared to passively watching a video instruction, suggesting that physical interaction and embodiment effects contribute to cognitive engagement and learning efficiency. This aligns with existing research on active learning, which shows that physical involvement and sensory integration can improve memory and learning outcomes [30].

The study highlights the importance of agency in enhancing the sense of ownership and embodiment. Active control over the robotic hand not only deepened the illusion but also introduced a dynamic element to the participants' experience, merging sensory feedback with motor control to reinforce the integration of the robotic hand into the body schema. This suggests a promising avenue for rehabilitation technologies, emphasizing the importance of user control and interaction in designing effective assistive devices. Furthermore, the robotic hand provides an alternative to virtual reality for patients who are uncomfortable with or unable to use headsets [31].

VI. Future work

While the study provides valuable information on the effects of embodiment and technology on perception and learning, it is subject to limitations. The use of a predominantly student sample and the reliance on subjective measures of embodiment highlight the need for further research across diverse populations and with more objective measurement techniques.

Given the promising results in the implementation and performance of motor tasks, future work should prioritize clinical translation and patient-centered design. Although our study provided initial information using a brief experimental setup, conducting long-term impact studies with stroke patients in real-world rehabilitation settings is essential. These trials can provide valuable data on the effectiveness, safety, and user experience of the robotic hand in diverse patient populations, and would help evaluate the sustainability of the improvements achieved through robotic-assisted rehabilitation.

Researchers and therapists can track patient progress over long periods to assess the durability of motor recovery and functional improvements. Crucially, these clinical trials should incorporate detailed patient feedback on usability, comfort, and perceived benefits of the robotic hand. Understanding patient needs and preferences will be essential to tailor technology to individual rehabilitation goals.

Future studies should also explore the impact of personalized ergonomic design on user experience and adherence to rehabilitation protocols. Patient feedback can be used to inform design iterations, ensuring that the robotic hand is comfortable, intuitive to use, and effectively supports individual motor impairments.

Furthermore, involving therapists and medical experts can lead to a deeper understanding of the clinical implications and practical challenges associated with robotic-assisted rehabilitation. For example, therapists could provide insights into how the robotic hand can be best integrated into existing rehabilitation workflows and used to augment traditional therapy techniques.

To enhance connection and embodiment, both mechanical and cosmetic improvements are necessary. In particular, applying soft robotics could offer more natural movements and a lifelike appearance, potentially improving user experience and the illusion's effectiveness.

The insights gained from clinical trials and patient feedback can then be used to guide future technological development, ensuring that improvements are driven by real-world needs and lead to tangible benefits for stroke survivors. This iterative process of clinical evaluation, patient feedback, and technological refinement will be critical to realizing the full potential of robotic embodiment in stroke rehabilitation.

VII. Conclusion

During this study, a successful prototype robotic hand was built using inexpensive 3D-printed parts and appliances. The hand was able to mimic the opening and closing of fingers of a human hand with a latency of only 90ms, making it suitable to be used as a tool to research embodiment with active versus passive stimuli, as well as memory retrieval.

The results indicate that the active version of the robotic hand created a higher sense of embodiment than the passive version. Additionally, the robotic hand yields significantly higher accuracy in memorization tasks compared to video clip instructions.

In conclusion, the results of this study suggest that the robotic hand could be a valuable and useful tool for stroke patients during their rehabilitation process, adding a personalized experience with the help of active stimulation combined with low costs.

References

[1] WHO EMRO, "Stroke, Cerebrovascular accident — Health topics," *World Health Organization Eastern Mediterranean Regional Office*, 2024. [Online]. Available: https://www.emro.who.int/health-topics/stroke-cerebrovascular-accident/index.html

[2] G. Kwakkel, B. J. Kollen, J. V. Van Der Grond, and A. J. H. Prevo, "Probability of regaining dexterity in the flaccid upper limb," *Stroke*, vol. 34, no. 9, pp. 2181–2186, Sep. 2003. DOI: 10.1161/01.str.0000087172.16305.cd. [Online]. Available: https://doi.org/10.1161/01.str.0000087172.16305.cd

[3] H. Wafa, C. Wolfe, E. Emmett, G. A. Roth, C. O. Johnson, and Y. Wang, "Burden of stroke in Europe," *Stroke*, vol. 51, no. 8, pp. 2418–2427, Aug. 2020. DOI: 10.1161/strokeaha.120.029606. [Online]. Available: https://doi.org/10.1161/strokeaha.120.029606

[4] L. Preede, H. L. Soberg, H. Dalen, A. Nyquist, R. Jahnsen, M. Saebu, E. Bautz-Holter, and C. Røe, "Rehabilitation goals and effects of goal achievement on outcome following an Adapted Physical Activity-Based Rehabilitation intervention," *Patient Preference and Adherence*, vol. 15, pp. 1545–1555, July 2021. DOI: 10.2147/PPA.S311966. [Online]. Available: https://doi.org/10.2147/ppa.s311966

[5] M. Botvinick and J. Cohen, "Rubber hands 'feel' touch that eyes see," *Nature*, vol. 391, no. 6669, p. 756, Feb. 1998. DOI: 10.1038/35784. [Online]. Available: https://doi.org/10.1038/35784

[6] Slater, Mel and Slater, Mel and Marcos, Daniel Pérez and Ehrsson, Henrik and Sanchez-Vives, Maria V and Sanchez-Vives, Maria V, *Inducing illusory ownership of a virtual body*, Frontiers in Neuroscience, month = 9, number = 2, pages = 214–220, volume = 3, year = 2009, doi = 10.3389/neuro.01.029.2009, url = https://doi.org/10.3389/neuro.01.029.2009,

[7] Daniele Romano and Elisa Caffa and Alejandro Hernandez-Arieta and Peter Brugger and Angelo Maravita, *The robot hand illusion: Inducing proprioceptive drift through visuo-motor congruency*, Neuropsychologia, volume = 70, pages = 414-420, year = 2015, issn = 0028-3932, doi = https://doi.org/10.1016/j.neuropsychologia.2014.10.033, url = https://www.sciencedirect.com/science/article/pii/S0028393214003935

[8] Arata, Jumpei and Hattori, Masashi and Ichikawa, Shohei and Sakaguchi, Masamichi,*Robotically Enhanced Rubber Hand Illusion*, IEEE Transactions on Haptics, year=2014, volume=7, number=4, pages=526-532, doi=10.1109/TOH.2014.2304722

[9] Kalckert, Andreas and Ehrsson, H. Henrik, *Moving a Rubber Hand that Feels Like Your Own: A Dissociation of Ownership and Agency*, Frontiers in Human Neuroscience, month = 1, volume = 6, year = 2012, doi = 10.3389/fnhum.2012.00040, url = https://doi.org/10.3389/fnhum.2012.00040

[10] Ma, Ke and Hommel, Bernhard, *The virtual-hand illusion: effects of impact and threat on perceived ownership and affective resonance*, Frontiers in Psychology, month = 1, volume = 4, year = 2013, doi = 10.3389/fpsyg.2013.00604, url = https://doi.org/10.3389/fpsyg.2013.00604

[11] Hara, Masayuki and Sugata, Hisato and Otsuru, Naofumi and Takasaki, Masaya and Ishino, Yuji and Mizuno, Takeshi and Miki, Masahito and Kanayama, Noriaki, *Effect of a Body Part Action on Body Perception of the Other Inactive Body Part*, IEEE Transactions on Cognitive and Developmental Systems, volume = PP, year = 2022, month = 01, pages = 1-1, volume = PP,
doi = 10.1109/TCDS.2022.3210659

[12] S. S. Kuys, T. Edwards, and N. R. Morris, "Effects and adherence of mirror therapy in people with chronic upper limb hemiparesis: A preliminary study," *International Scholarly Research Notices*, vol. 2012, 2012. Hindawi.

[13] L. M. Weber, D. M. Nilsen, G. Gillen, J. Yoon, and J. Stein, "Immersive virtual reality mirror therapy for upper limb recovery following stroke: A pilot study," *American Journal of Physical Medicine & Rehabilitation*, vol. 98, no. 9, p. 783, 2019. NIH Public Access.

[14] Holm Thieme, Nadine Morkisch, Jan Mehrholz, Marcus Pohl, Johann Behrens, Bernhard Borgetto, Christian Dohle, *Mirror therapy for improving motor function after stroke*, *The Cochrane Library*, vol. 2018, no. 7, Elsevier BV, July 2018, DOI: 10.1002/14651858.cd008449.pub3, URL: https://doi.org/10.1002/14651858.cd008449.pub3.

[15] Elisheva R Coleman, Rohitha Moudgal, Kathleen Lang, Hyacinth Idu Hyacinth, Oluwole O. Awosika, Brett M. Kissela, Wuwei Feng, *Early Rehabilitation After Stroke: A Narrative review*, *Current Atherosclerosis Reports*, vol. 19, no. 12, Springer Science+Business Media, November 2017, DOI: 10.1007/s11883-017-0686-6, URL: https://doi.org/10.1007/s11883-017-0686-6.

[16] Luca Mirela Cristina, Daniela Matei, Bogdan Ignat, Cristian D. Popescu, *Mirror therapy enhances upper extremity motor recovery in stroke patients*, *Acta Neurologica Belgica*, vol. 115, no. 4, pp. 597–603, April 8, 2015, DOI: 10.1007/s13760-015-0465-5, URL: https://doi.org/10.1007/s13760-015-0465-5.

[17] Hamza Y. Madhoun, Botao Tan, Yali Feng, Yi Zhou, Cuijuan Zhou, Lehua Yu, *Task-based mirror therapy enhances the upper limb motor function in subacute stroke patients: a randomized control trial*, *European Journal of Physical and Rehabilitation Medicine*, vol. 56, no. 3, Edizioni Minerva Medica, July 2020, DOI: 10.23736/s1973-9087.20.06070-0, URL: https://doi.org/10.23736/s1973-9087.20.06070-0.

[18] Josefa Gonzalez-Santos, Raul Soto-Camara, Paula Rodriguez-Fernández, Maria Jimenez-Barrios, Jeronimo Gonzalez-Bernal, Carla Collazo-Riobo, Maha Jahouh, Yolanda Bravo-Anguiano, Jose M Trejo-Gabriel-Galan, *Effects of home-based mirror therapy and cognitive therapeutic exercise on the improvement of the upper extremity functions in patients with severe hemiparesis after a stroke: A protocol for a pilot randomised clinical trial*, *BMJ open*, vol. 10, no. 9, pages e035768, British Medical Journal Publishing Group, 2020.

[19] Maddalena Brunetti, Nadine Morkisch, Claire Fritzsch, Jan Mehnert, Jens Steinbrink, Michael Niedeggen, Christian Dohle, *Potential determinants of efficacy of mirror therapy in stroke patients–A pilot study*, *Restorative Neurology and Neuroscience*, vol. 33, no. 4, pages 421–434, IOS Press, 2015.

[20] Saragih, Ita Daryanti and Priyanti, Ratna Puji and Batubara, Sakti Oktaria and Lee, Bih-O, *Effects of mirror therapy on upper limb motor function of patients with stroke: A systematic review and meta-analysis of randomized controlled trials*, Clinical Rehabilitation, month = 1, year = 2025, doi = 10.1177/02692155241299211, url = https://doi.org/10.1177/02692155241299211,

[21] Fred Stephen Sarfo, Sheila Adamu, Dominic Awuah, Osei Sarfo-Kantanka, Bruce Ovbiagele, *Potential role of tele-rehabilitation to address barriers to implementation of physical therapy among West African stroke survivors: A cross-sectional survey*, *Journal of the Neurological Sciences*, vol. 381, month = 10, pages = 203–208, Elsevier BV, 2017, DOI: 10.1016/j.jns.2017.08.3265, URL: https://doi.org/10.1016/j.jns.2017.08.3265.

[22] Daniel T. Gillespie, Crystal L. MacLellan, Martin Ferguson-Pell, Andrea Taeger, Patricia J. Manns, *Balancing Access with Technology: Comparing In-Person and Telerehabilitation Berg Balance Scale Scores among Stroke Survivors*, *Physiotherapy Canada*, vol. 73, no. 3, month = 8, pages = 276–285, University of Toronto Press, 2021, DOI: 10.3138/ptc-2019-0095, URL: https://doi.org/10.3138/ptc-2019-0095.

[23] Parisa Arzani, Minoo Khalkhali Zavieh, Khosro Khademi Kalantari, Alireza Akbarzadeh Baghban, *Opportunities and barriers for telerehabilitation during Coronavirus outbreak*, *Medical journal of the Islamic Republic of Iran*, month = 4, Iran University of Medical Sciences, 2021, DOI: 10.47176/mjiri.35.100, URL: https://doi.org/10.47176/mjiri.35.100.

[24] Hanna Vollbrecht, Vineet M. Arora, Sebastian Otero, Kyle Carey, David O. Meltzer, Valerie G. Press, *Evaluating the need to address digital literacy among hospitalized patients: Cross-Sectional Observational study*, *Journal of Medical Internet Research*, vol. 22, no. 6, month = 6, pages = e17519, JMIR Publications, 2020, DOI: 10.2196/17519, URL: https://doi.org/10.2196/17519.

[25] InMoov, "InMoov - home - InMoov," Nov. 2022. [Online]. Available: https://inmoov.fr/

[26] Morris, Colin and Fu, Yuxin and McCormick, Scott and Wachter, Bradley and Devasia, Santosh, *Low-cost assistive robot for mirror therapy rehabilitation*, 2017 IEEE International Conference on Robotics and Biomimetics (ROBIO), year = 2017, month = 12, pages = 2057-2062, doi = 10.1109/ROBIO.2017.8324722

[27] Darbois, Nelly and Guillaud, Albin and Pinsault, Nicolas, *Do robotics and virtual reality add real progress to mirror therapy rehabilitation? A scoping review*, Rehabilitation Research and Practice, month = 8, pages = 1–15, volume = 2018, year = 2018, doi = 10.1155/2018/6412318, url = https://doi.org/10.1155/2018/6412318

[28] S. Shimada, K. Fukuda, and K. Hiraki, "Rubber Hand Illusion under Delayed Visual Feedback," *PLOS ONE*, vol. 4, no. 7, e6185, Jul. 2009. DOI: 10.1371/journal.pone.0006185. [Online]. Available: https://doi.org/10.1371/journal.pone.0006185

[29] A. Kalckert and H. H. Ehrsson, "The moving rubber hand illusion revisited: Comparing movements and visuotactile stimulation to induce illusory ownership," *Consciousness and Cognition*, vol. 26, pp. 117–132, May 2014. DOI: 10.1016/j.concog.2014.02.003. [Online]. Available: https://doi.org/10.1016/j.concog.2014.02.003

[30] Kontra, Carly and Lyons, Daniel J and Fischer, Susan M and Beilock, Sian L. "Physical experience enhances science learning." *Psychological Science*, 26(6):737–749, 2015. Sage Publications Sage CA: Los Angeles, CA.

[31] Höhler, Chiara and Rasamoel, Nils David and Rohrbach, Nina and Hansen, John Paulin and Jahn, Klaus and Hermsdörfer, Joachim and Krewer, Carmen, *The impact of visuospatial perception on distance judgment and depth perception in an Augmented Reality environment in patients after stroke: an exploratory study*, Journal of neuroengineering and rehabilitation, volume=18, number=1, pages=127, year=2021, publisher=Springer

Lower-Limb Motor Imagery-based Brain-Computer Interface to Control Treadmill Velocities

Aura Ximena González-Cely *Graduate Student member, IEEE*[1], Surjo R. Soekadar[2], Denis Delisle-Rodriguez[3], and Teodiano Bastos-Filho[1]

***Abstract*— Lower-limb rehabilitation traditionally relies on physical therapy, but motor imagery(MI)-based brain- computer interfaces (BCIs) promise to facilitate neuroplasticity and adaptation by closing the perception-action cycle. Here, we present a BCI system based on kinesthetic MI that enables treadmill velocity control, establishing a closed-loop feedback mechanism. The system was tested in a healthy participant translating mu (8-12 Hz) and high-beta (18-24 Hz) rhythm modulation into treadmill velocity control commands. Feature extraction techniques, including power spectral density (PSD) and Riemannian geometry (RG), were used for MI- and resting state classification. Additionally, Logistic Regression (LR), k-nearest neighbors, support vector machine, and Linear Discriminant Analysis (LDA) were employed and optimized for accuracy. The results showed increased mu and high-beta activation modulation at the vertex. The online RG+LDA classifier achieving an average accuracy of 72%, while the pseudo-online RG+LR reached 95%. The study's novelty lies in combining kinesthetic MI with treadmill control and employing RG for feature extraction, demonstrating its potential to enhance cortical modulation during rehabilitation. Future work will have to validate the system in poststroke patients for clinical applicability.**

I. INTRODUCTION

Stroke is one of the leading causes of locomotor impairments worldwide, commonly resulting in clinical conditions, such as hemiparesis and hemiplegia. Common symptoms are muscle weakness, impaired coordination, abnormal muscle tone, and posture, which can significantly hinder stroke survivors' mobility. As a consequence, 50% of stroke survivors use assistive devices as wheelchairs, with only 15% being independent while walking, 10% going outdoors, and 5% going upstairs from the total population [1]. Effective physical rehabilitation is therefore essential for restoring lower-limb functions toward independence and enabling stroke survivors to engage in Activities of the Daily Living (ADL) [1].

Motorized and electrical devices such as treadmills, exoskeletons, mini-motorized exercise bikes for movement execution, and Functional Electrical Stimulation (FES) to induce muscle contractions [1]–[10], have been used in MI-based Brain-Computer Interface (BCI) rehabilitation to assist movement. These brain controlled devices offer a feedback considering the brain signals, typically recorded via Electroencephalography (EEG). By detecting the user's Motor Imagery (MI), which is the action of imagining a limb's movement [1], [5], [11], EEG-based Brain-Computer Interface (BCI) converts these patterns into electrical commands to trigger a device, changing the ongoing interactions, with the opportunity of recovering patient's motor skills [1], [2], [12].

BCIs commanding treadmills has shown promise for activating the sensorimotor cortex and improving gait in post-stroke patients [1]. Moreover, EEG power-based analyses, such as Power Spectral Density (PSD) and Event-Related Synchronization/Desynchronization (ERD/ERS), have been used to track brain responses and to provide brain-signal related feedback during rehabilitation [3], [6], [7], [10].

A BCI is commonly composed of a first stage, called in this study Condition 1, which acquires EEG data for subsequent system calibration. Following, there is an operation stage, called in this study Condition 2 which uses the calibrated BCI to modulate cortical rhythms and provide feedback. The system calibration uses classification algorithms to discriminate between different mental tasks, very often MI and resting [4], [10], [11], while in the lower-limb area, walking speeds [13], [14]. Additionally, classifiers such as Linear Discriminant Analysis (LDA) [4], [7], [11], Support Vector Machine (SVM) [10], k-Nearest Neighbors (kNN) [14], and Logistic Regression (LR), among others classifiers, have been employed in BCIs. These classifiers use power-based analysis, such as PSD, ERD/ERS or powerful techniques based on covariance matrices as Common Spatial Patterns (CSP) [3], [7], and Riemannian Geometry (RG) [4], [14].

Previous research has primarily focused on discriminating motor imagery (MI) tasks, but little studies have integrated Neurofeedback (NF) with MI classification to dynamically adjust treadmill speed in real-time. The key challenge lies in accurately classifying walking-based MI while simultaneously applying Kinesthetic Neurofeedback (KNF), where treadmill velocities are modulated according to the user's MI performance. This approach has the potential to enhance the user's engagement, and promote cortical activation during MI tasks. To address this gap, our study proposes a NF system that leverages power changes in the central motor cortex to enable control of treadmill speed, providing real-time feedback based on the user's MI performance.

[1]Aura Ximena González-Cely and Teodiano Freire Bastos-Filho are with the Postgraduate Program in Electrical Engineering, Federal University of Espírito Santo, Vitoria, Brazil aura.cely@edu.ufes.br

[2]Surjo R. Soekadar is with the Department of Psychiatry and Neurosciences, Charité Campus Mitte (CCM), Charité - Universitätsmedizin Berlin, Berlin, Germany surjo.soekadar@charite.de

[3]Denis Delisle-Rodriguez are with the Postgraduate Program in Neuroengineering, Edmond and Lily Safra International Institute of Neuroscience, Macaiba, Brazil denis.rodriguez@isd.org.br

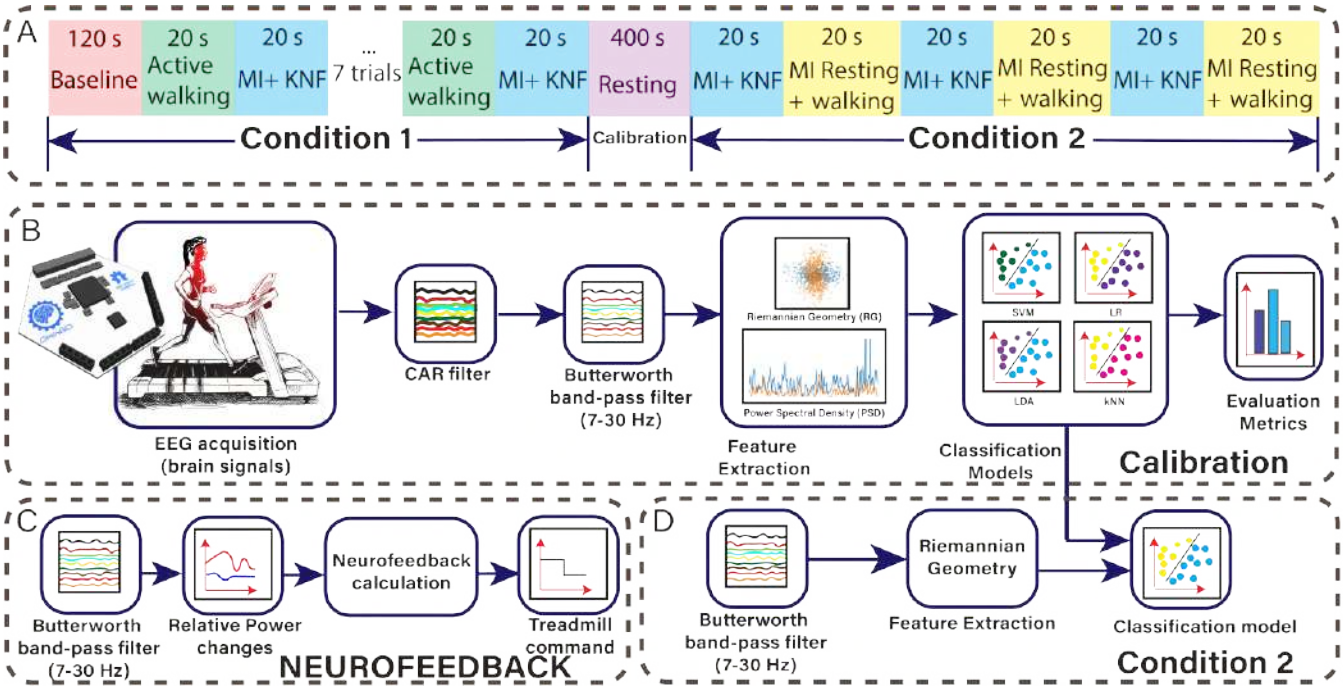


Fig. 1: MI-based BCI methodology. (A) Protocol implemented in Condition 1, system calibration and Condition 2 of the MI-based BCI; (B) System calibration since EEG data acquisition to model generation; (C) Neurofeedback stage calculating relative power changes to control the treadmill; (D) Condition 2 implemented based on the classification model and KNF parameters generated in the system calibration.

II. PROPOSED BRAIN-COMPUTER INTERFACE

A. Treadmill setup

An electric-powered treadmill (from Usilever Equipamentos, Brazil) was used in this study, with its circuit modified to allow for speed control via brain signal classification. The treadmill's circuit has a potentiometer to manually control its speed by adjusting voltages in range from 0 to 12 V DC, which is now linked through an in-house electronic circuit built to control the treadmill velocity. An ESP32 generates Pulse Width Modulation (PWM) signals between 0 and 3.3 V, which are converted into DC through a resistor-capacitor (RC) filter and amplified to match the treadmill's voltage range (0-12 V). This setup enables precise, real-time treadmill speed control in response to EEG signals.

The control system communicates with the treadmill wirelessly through User Datagram Protocol (UDP), which was chosen for its low latency and reliability in sending commands [11], in addition to provide safety to the patient. The main control unit processes EEG data, classifies MI, and conveys speed commands to the treadmill. The BCI pipeline, which consists of EEG acquisition, MI recognition, and treadmill command transmission, ensuring seamless feedback to the user during the task.

B. Participant

A healthy subject (26 years old, male) voluntarily participated in this study, without previous experience with MI. Ethical approval was obtained from the Research and Ethical Committees of the Federal University of Espirito Santo, Brazil (registry number CAAE: 46099421.9.0000.5542), and the study followed the Declaration of Helsinki.

C. EEG acquisition

EEG signals were acquired using a 16-channel Cyton board (OpenBCI, US), at a 125 Hz sampling rate. This board was selected for its compatibility with OpenViBE software, which supports seamless integration with custom electronic control systems through Python [4], [8], [13]. EEG electrodes were positioned on the motor cortex and sensorimotor area associated with lower-limb movement, according to [5], [6], [11], [15]. The EEG channels recorded were FP1, FP2, F3, F4, FC1, FCz, FC2, C3, C1, Cz, C2, C4, CP1, CP2, and Pz, followed by ground (GND) and reference (REF) electrodes.

D. Experimental protocol

Fig. 1A shows the protocol performed while using the BCI composed of three stages called Condition 1, calibration, and Condition 2. Condition 1 started with 120-s baseline, where the participant remained in rest state. This was followed by seven trials, each one consisting of 20-s of active walking followed by 20-s of walking-based MI. During MI, the treadmill was controlled by a KNF model, providing changes in treadmill speed based on brain power relative changes using three speeds considered as high, moderate, and low velocity. These velocities are linked to MI perfomance. The participant had a 400-s rest period to prevent mental fatigue, in which EEG data acquired during Condition 1 were used to calibrate the system. After calibration, Condition 2 allowed the system to discriminate between MI and resting.

The participant performed three trials, each with alternating intervals of 20-s of MI and KNF, which was activated while MI was classified, followed by 20-s of mental rest and active walking.

E. Condition 1 and system calibration

Fig. 1B shows the pipeline implemented in the system calibration using the EEG dataset acquired during Condition 1, as an input to recognize between MI and resting, where the period of baseline is considered as the resting class. The system's calibration considers the use of a 5-fold cross-validation to avoid overfitting, data leaking, and generalize better the system, as done in [3], [4], [14]. This stage generates the classification model and KNF parameters to be used in Condition 2.

1) Pre-processing stage: The pre-processing stage started with a segmentation to split the dataset into 80% for training, and 20% for testing. From the previous 80%, a new split was performed to obtain new training and validation datasets. With each segment of data, a 1-second sliding window (with 50% overlap) was applied to segment the data for processing, as performed in [4], [7], [11]. Using each window of data, a Butterworth zero-phase band-pass filter was used between 7 to 30 Hz to isolate mu and beta bands [3].

2) Feature extraction and Classification: RG based on covariance matrices that are projected in the tangent space was used for feature extraction [4], [14]. LDA was chosen for classification due to its use in similar studies related to lower-limb BCIs [4]. Accuracy (ACC) was used as metric to determine the best classifier performance. This way, ACC was obtained from each fold, using a 5-fold cross-validation, and the respective classification model was stored and implemented in Condition 2.

F. Neurofeedback Technique

The NF pipeline shown in Fig. 1C was implemented to provide treadmill speed adjustments based on MI power levels in both Conditions 1 and 2, while the participant imagined performing the walking task. It is worth mentioning that treadmill velocities were not classified in our study, which means that only MI and resting were classified, which were used to trigger KNF.

In Condition 1, EEG signals were processed using a 1-s window, calculating the Relative power changes (R) as shown in (1), for mu and beta bands, using a Laplacian filter around Cz, as suggested in [4], [6]. These power changes are based on the difference between Active Walking (AW) and MI, as shown in (1). Based on these values, interpolation of 25, 50, and 75% were used to generate three velocities levels: low, moderate, and high, which are based on the participant's performance. Brain power changes were mapped to speed levels, providing the participant with immediate feedback. This strategy is applied to guide the modulation of cortical rhythms of interest, with a focus on achieving the highest velocity.

$$R(\%) = \left| \frac{R_{MI} - \overline{R}_{AW}}{\overline{R}_{AW}} \right| \times 100 \ , \qquad (1)$$

In Condition 2, MI classification activates KNF to provide treadmill velocity changes, also considering previous KNF parameters obtained from Condition 1, which are related to the closer patterns between MI and AW. These parameters were calculated as shown in [4].

G. Condition 2

Fig. 1D shows the pipeline that starts filtering EEG data windows and feature extraction stage, followed by the use of the classification model (obtained in the system's calibration), which discriminates between subject's resting and MI. Whether MI is classified, the NF calculation is performed, and the treadmill is commanded. The participant was verbally guided to focus on walking MI, not related to the velocity, but with the aim to increase the treadmill velocity.

III. PSEUDO-ONLINE ANALYSIS

A. Feature Extraction

Two types of features were analyzed in this study to enhance the system in future implementations. 1) PSD based on the brain signals power using the Fast Fourier Transform (FFT) in mu (8-12 Hz) and beta (18-24 Hz) bands [3], [10], [16], 2) RG. It is worth mentioning that PSD used pre-processed data considering a Common Average Reference (CAR) filter to remove common interference [6], as well as a Butterworth band-pass filter. However, RG features were obtained only considering the Butterworth band-pass filter [4], [14].

B. Classification

LR, SVM, kNN, and LDA are used in this study, due to their good performance in binary classification problems [2], [11], [14], [16]. LR and LDA do not use a hyperparameter stage because both classifiers are linear, whereas kNN and SVM implemented a hyperparameter tuning. The hyperparameters studied here for kNN were "k" neighbors (1,3,5,7,9). For SVM, the analysis was focused on the type of kernel (linear, polynomial, rbf, or sigmoid).

C. Evaluation metrics

The classification model's performance was evaluated using ACC and Area Under the Curve (AUC). Latency was also assessed, measuring the delay between EEG signal acquisition and treadmill activation to ensure real-time response capability. In addition, R changes were calculated based on (1). In the cortical activation analysis, R_{MI} represented in (1) was changed for MI data of each condition, which were represented in topographic maps considering a mean of all trials.

IV. RESULTS AND DISCUSSION

A. Cortical Activation Patterns

The cortical activation results demonstrate distinct patterns between MI and resting across frequency bands. As shown in Fig. 2, higher R appeared in the mu band in the lateral and parietal areas, and lower R in the low-beta and high-beta band. In addition, lower R are focused around Cz in the

mu band, in Condition 2, compared with Condition 1. This behavior is similar in the low-beta with a increased R around Cz and C2 channels. This negative R changes in the mu band are aligned with studies associating this cortical activity with motor tasks, suggesting the potential utility of focusing feedback on central regions to enhance MI performance [7].

Condition 2 is more focused on the central part of the brain, specifically in the Cz electrode location, in the mu band as shown in [1], [4], [7], [16]. Higher activation was presented in the mu band, focusing on the parietal and lateral brain regions, also related to attention levels, which agrees with other outcomes [7], [9]. Other studies have shown parietal and lateral activations while performing walking-based MI tasks [1], [4].

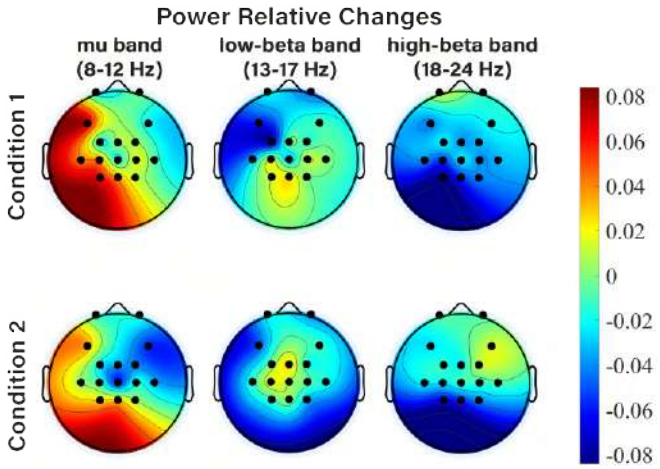


Fig. 2: Topographic maps based on R in three stages: Condition 1, system calibration, and Condition 2 in the mu, low-beta, and high-beta bands.

B. BCI performance

In our study, in Condition 2, RG+LDA obtained a mean ACC close to 0.72 whereas the literature has implemented the same combination using an exoskeleton with Spinal Cord Injury (SCI) survivors with ACC higher than 0.7 [4]. For this reason, we implemented in this preliminary study the same combination of RG+LDA due to some similarities in terms of the walking task, ACC outcomes, and KNF principle.

Our system was tested offline and online whereas other approaches implemented only offline or pseudo-online analysis [3]. Studies employing other feature extraction or classification techniques, such as the use of Filter Bank Common Spatial Patterns (FBCSP)+LDA using a treadmill with a mean ACC of 0.68 [2], CSP+LDA with ACC close to 0.75 [7], and Hjorth parameters with ACC close to 0.68 [3], suggested that our results are promising for enhancing ACC outcomes with post-stroke patients, providing a more reliable basis for motor rehabilitation using BCIs.

In terms of time response, the system's calibration was processed in 10 s to obtain the classification model and parameters for Condition 2, guaranteeing a low calibration time for clinical use. The latency since EEG data are acquired to trigger the treadmill was close to 250 ms while pre-processing data windows, extracting features, classifying data, and sending the output classifier translated into a velocity command to the treadmill. Such responsiveness is crucial for MI-based immediate feedback to help participants sustain MI and enhances engagement. Other studies in the literature have shown calibrations with higher time responses [17] or the inability to control the end-effector [4].

C. Pseudo-online analysis

The pseudo-analysis was performed to enhance the BCI in future implementations, and these outcomes indicate that RG features outperformed PSD in terms of ACC and AUC, with mean ACC values exceeding 0.8 for RG features as shown in Fig. 3. LR and SVM achieved the highest ACC, with 0.95 and 0.94, respectively, while implementing RG features, indicating that these combinations are particularly suitable for distinguishing MI from resting states. These results corroborate findings from previous BCI studies that also found higher accuracies with RG as a feature [13], [14]. In contrast, PSD features yielded lower performance, with ACC values for LDA and kNN reaching 0.72 and 0.71, respectively. Compared to other BCI implementations, our results with RG+LR and RG+SVM combinations show a promising improvement in classifier performance, especially for real-time applications in rehabilitation.

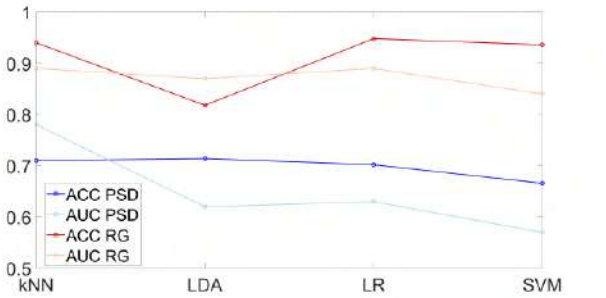


Fig. 3: ACC and AUC outcomes per classifier and feature extraction technique.

Our findings support the use of treadmill-based MI neurofeedback for lower-limb rehabilitation, with potential benefits over stationary or restricted systems, such as cycling and exoskeletons. Walking tasks have demonstrated muscle strengthen as well as improvement of physical condition, which are vital for post-stroke patients, potentially enhancing neuroplasticity through active participation and MI practice. Furthermore, controlling treadmill speed through MI provides a form of interactive feedback that can better maintain the user's participation over static feedback types, which can lead to muscle or mental fatigue [1]. Other systems such as pedaling bicycles or exoskeletons cannot perform the same process, even demonstrating relevant outcomes and the advantage of being implemented for both SCI survivors and/or impaired post-stroke patients.

In terms of physical limitations, we avoided the use of exoskeletons, and focused on a comfortable system to use,

whereas other studies lack in the use of skin electrodes, [10], [18] as well as wearable exoskeletons, which delay the preparation time and could generate fatigue [6], [11]. Our system utilizes velocity changes as a way of NF to assist the modulation of EEG bands of interest, whereas other studies implement vibrotactile feedback [10] or visual NF [4], which could generate visual or muscle fatigue.

It is worth noting that our NF system is designed to increase treadmill velocities in response to MI execution during Condition 2. It is worth mentioning that triggering the treadmill was not the primary objective of this proposed MI-based BCI, but rather the increase in velocity served as a key goal. Additionally, KNF is implemented in both conditions, to first guide and train users in modulating the targeted cortical rhythms, and second, to increase the task difficulty using the calibrated system, thereby promoting improved MI performance. This approach ensures both muscle activation, comparable to conventional physiotherapy, and modulation of cortical rhythms to enhance neuroplasticity.

As a limitation of this research, our study lacks in the number of healthy subjects that tested the system and the number of sessions achieved, which restricts generalizability. In addition, there was not implementation in real-time of the combination of RG+LR which achieved the highest offline performance. It is worth commenting that our treadmill also has a body-weight support that could be used for SCI survivors, and also implementing FES to generate a virtual gait. Future studies will expand the participation pool, including healthy subjects, post-stroke and SCI survivors, to assess the broader applicability of this approach. Furthermore, collaboration with clinical professionals will help refine the BCI, ensuring that it meets rehabilitation goals effectively.

V. CONCLUSION

This study implemented a real-time MI-based BCI that adjusts treadmill speeds as a way of neurofeedback, showing promise for lower-limb rehabilitation. By focusing on changes in cortical activation at the Cz electrode, the system can increase or decrease treadmill velocity based on MI, allowing for dynamic, responsive interaction. With Riemannian Geometry and Linear Discriminant Analysis, a mean ACC of 0.72 was achieved, while recognizing MI and resting classes.

Despite these positive findings, the study was limited by its single-participant sample and preliminary classifier configurations. Future implementations will expand participant diversity, particularly including SCI and post-stroke survivors, to evaluate generalizability. We will also explore additional classifier combinations, such as Riemannian geometry with logistic regression, and integrate body-weight support, enhancing system adaptability for individuals with severe motor impairments. We believe that these developments could make MI-based BCI valuable tools in clinical rehabilitation settings, potentially improving motor recovery and quality of life for patients with mobility challenges.

ACKNOWLEDGMENT

Aura Ximena González-Cely acknowledges the financial support from (CAPES) (001), Brazil. Surjo R. Soekadar received support by the European Research Council (ERC) under the projects NGBMI (759370) and TIMS (101081905), Deutsche Forschungsgemeinschaft (DFG) under the project SO932/7-1, the Federal Ministry of Research and Education (BMBF) under the projects SSMART (01DR21025A), NEO (01DR21025A) QHMI (03ZU1110DD) and NeuroQ (13N16486), and the Einstein Foundation Berlin (ESB). Denis Delisle-Rodriguez acknowledges the financial support from Santos Dumont Institute, CAPES (001), CNPq (301233/2018-7), Brazil. Bastos-Filho T. acknowledges the financial support from CNPq (301233/2018-7), and FAPES, Brazil.

REFERENCES

[1] E. Bobrova, V. Reshetnikova, A. Frolov, and Y. P. Gerasimenko, "Use of imaginary lower limb movements to control brain–computer interface systems," *Neuroscience and Behavioral Physiology*, vol. 50, pp. 585–592, 2020.

[2] L. Ferrero, V. Quiles, M. Ortiz, E. Iáñez, and J. M. Azorín, "Bci based on lower-limb motor imagery and a state machine for walking on a treadmill," in *2021 10th International IEEE/EMBS Conference on Neural Engineering (NER)*. IEEE, 2021, pp. 1–4.

[3] V. Quiles, L. Ferrero, E. Iáñez, M. Ortiz, Á. Gil-Agudo, and J. M. Azorín, "Brain-machine interface based on transfer-learning for detecting the appearance of obstacles during exoskeleton-assisted walking," *Frontiers in Neuroscience*, vol. 17, p. 1154480, 2023.

[4] C. F. Blanco-Diaz, E. R. d. S. Serafini, T. Bastos-Filho, A. F. O. d. A. Dantas, C. C. d. E. Santo, and D. Delisle-Rodriguez, "A gait imagery-based brain-computer interface with visual feedback for spinal cord injury rehabilitation on lokomat," *IEEE Transactions on Biomedical Engineering*, pp. 1–10, 2024.

[5] J. Choi, K. T. Kim, J. H. Jeong, L. Kim, S. J. Lee, and H. Kim, "Developing a motor imagery-based real-time asynchronous hybrid bci controller for a lower-limb exoskeleton," *Sensors*, vol. 20, no. 24, p. 7309, 2020.

[6] E. López-Larraz, F. Trincado-Alonso, V. Rajasekaran, S. Pérez-Nombela, A. J. Del-Ama, J. Aranda, J. Minguez, A. Gil-Agudo, and L. Montesano, "Control of an ambulatory exoskeleton with a brain–machine interface for spinal cord injury gait rehabilitation," *Frontiers in neuroscience*, vol. 10, p. 359, 2016.

[7] M. Ortiz, L. de la Ossa, J. Juan, E. Iáñez, D. Torricelli, J. Tornero, and J. M. Azorín, "An eeg database for the cognitive assessment of motor imagery during walking with a lower-limb exoskeleton," *Scientific Data*, vol. 10, no. 1, p. 343, 2023.

[8] M. A. Romero-Laiseca, D. Delisle-Rodriguez, V. Cardoso, D. Gurve, F. Loterio, J. H. Posses Nascimento, S. Krishnan, A. Frizera-Neto, and T. Bastos-Filho, "A low-cost lower-limb brain-machine interface triggered by pedaling motor imagery for post-stroke patients rehabilitation," *IEEE Transactions on Neural Systems and Rehabilitation Engineering*, vol. 28, no. 4, pp. 988–996, 2020.

[9] L. Storzer, M. Butz, J. Hirschmann, O. Abbasi, M. Gratkowski, D. Saupe, A. Schnitzler, and S. Dalal, "Bicycling and walking are associated with different cortical oscillatory dynamics. front. hum. neurosci. 10," 2016.

[10] S. Ren, W. Wang, Z.-G. Hou, X. Liang, J. Wang, and W. Shi, "Enhanced motor imagery based brain-computer interface via fes and vr for lower limbs," *IEEE Transactions on Neural Systems and Rehabilitation Engineering*, vol. 28, no. 8, pp. 1846–1855, 2020.

[11] M. Ortiz, L. Ferrero, E. Iáñez, J. M. Azorín, and J. L. Contreras-Vidal, "Sensory integration in human movement: A new brain-machine interface based on gamma band and attention level for controlling a lower-limb exoskeleton," *Frontiers in Bioengineering and Biotechnology*, vol. 8, p. 735, 2020.

[12] BCI Society. (2023) Bci definition. Accessed: 2025-02-05. [Online]. Available: https://bcisociety.org/bci-definition/

[13] A. Gonzalez-Cely, C. Blanco-Diaz, D. Delisle-Rodriguez, and T. Bastos-Filho, "Eeg-based multi-class classification for recognizing pedaling velocities: A promising approach for brain-computer interface-enhanced lower-limb robotic rehabilitation," in *2024 10th IEEE RAS/EMBS International Conference for Biomedical Robotics and Biomechatronics (BioRob)*, 2024, pp. 223–228.

[14] F. Lotte, L. Bougrain, A. Cichocki, M. Clerc, M. Congedo, A. Rakotomamonjy, and F. Yger, "A review of classification algorithms for eeg-based brain–computer interfaces: a 10 year update," *Journal of neural engineering*, vol. 15, no. 3, p. 031005, 2018.

[15] V. Quiles, L. Ferrero, E. Iáñez, M. Ortiz, J. M. Cano, and J. M. Azorín, "Detecting the speed change intention from eeg signals: From the offline and pseudo-online analysis to an online closed-loop validation," *Applied Sciences*, vol. 12, no. 1, p. 415, 2022.

[16] M. Tariq, P. Trivailo, and M. Simic, "Eeg-based bci control schemes for lower-limb assistive-robots. front hum neurosci 12: 312," 2018.

[17] S. Nakagome, T. P. Luu, Y. He, A. S. Ravindran, and J. L. Contreras-Vidal, "An empirical comparison of neural networks and machine learning algorithms for eeg gait decoding," *Scientific reports*, vol. 10, no. 1, p. 4372, 2020.

[18] C. E. King, P. T. Wang, C. M. McCrimmon, C. C. Chou, A. H. Do, and Z. Nenadic, "The feasibility of a brain-computer interface functional electrical stimulation system for the restoration of overground walking after paraplegia," *Journal of neuroengineering and rehabilitation*, vol. 12, pp. 1–11, 2015.

Muscle Activation and Postural Sway in Response to Task Complexity: A Study of Balance Control in Older Adults

Longbin Zhang[1,2,3], Ananda Sidarta[2], Yu Chin Lim[2], Carol Er[2], Xiaoyue Yan[2,3], Tsung-Lin Wu[2,3], and Wei Tech Ang[2,3]

***Abstract*— In this study, we investigate muscle activation patterns and postural sway in older adults across different stance conditions with varying challenges. Muscle activity from lower limb and trunk muscles was recorded in seven older adults during four stance tasks: double stance, tandem stance, tandem stance with a cognitive task, and tandem stance with combined cognitive and motor tasks (TSCM). We analyzed CoP (centre of pressure) features, EMG (electromyography) patterns, and the coherence between EMG-CoP, to gain insights into neuromuscular coordination and balance control. Our findings indicate that task complexity significantly impacts postural stability, with tandem stances—particularly TSCM—leading to increased instability along the anterior-posterior axis. Key stabilizing muscles, such as the gastrocnemius medialis and tibialis anterior, showed heightened activation and strong EMG-CoP coherence under complex tasks, highlighting their essential role in counteracting gravitational forces to maintain balance. A lateral asymmetry in muscle activation was also observed, with left-side muscles consistently showing greater activity than right-side counterparts, suggesting lateralized contributions to postural control. These results emphasize the importance of specific muscles for stability in challenging postural tasks and may offer valuable insights for designing targeted interventions, including robotic rehabilitation systems and assistive technologies, to enhance balance and reduce fall risk in older adults.**

I. Introduction

Postural control is a complex function that involves maintaining the vertical projection of the center of gravity within the base of support, ensuring stability during both static and dynamic activities [1]. Falls, the most severe consequence of postural control disorders, pose a significant threat to the independence of older adults and are an escalating public health concern, often resulting in severe injuries, diminished quality of life, and reduced mobility [2]–[4]. This highlights the critical need to study postural control in this population. Maintaining postural control requires intricate coordination between the sensory systems (visual, vestibular, and proprioceptive), the central nervous system, and the musculoskeletal system [5]. Kinematic measures such as the base of support (BoS), center of mass (CoM), and center of pressure (CoP) are crucial for evaluating postural control, with the CoP frequently acting as a key indicator. [6]. Recently, growing interest has focused on exploring the neural mechanisms underlying postural control using tools like electroencephalography and electromyography (EMG), which provide valuable insights into cortical and muscular activities involved in maintaining stability [3], [7]. Understanding these processes is crucial for diagnosing and treating balance disorders and enhancing assistive technologies such as neuroprosthetics and rehabilitation robotics.

EMG-CoP coherence has been studied in older adults to assess how muscle strength affects balance. Skeparianos et al. [8] found that stronger ankle muscles, particularly plantar flexors and dorsiflexors, are associated with reduced postural sway, especially in challenging stances such as tandem and one-legged standing. Sozzi et al. [9] further examined leg muscle activity during tandem stance and highlighted that while the soleus muscle maintains upright posture with tonic activity, the tibialis anterior and peroneus longus muscles contribute to balance control through reciprocal actions in the medio-lateral direction. Their findings suggest that muscular strength and coordination are critical for maintaining postural stability in older adults. These studies highlight the importance of muscular-postural sway coherence in understanding postural control in older adults, suggesting the potential for training interventions, particularly given the differences in athletes. Indirectly, such a measure may reflect the balance ability of older adults while doing tasks of varying complexity. Therefore, it is essential to investigate muscular-postural sway coherence in older adults during balance tasks.

Cognitive decline, a natural consequence of aging, further complicates balance control by impairing memory, attention, decision-making, and executive functions, all of which are crucial for daily activities [10]. Cognition plays a vital role in postural control by integrating sensory information, facilitating decision-making, and enabling motor planning, allowing older adults to assess risks, maintain attention, and adapt movements based on past experiences. Increased cognitive load, such as when multitasking, can compromise balance. Effective cognitive processes are thus essential for maintaining stability and preventing falls [11].While many studies have examined interventions to slow cognitive decline, limited research has explored how muscular-postural sway coherence interacts during dual-task activities that combine cognitive and motor demands. Understanding how cognitive and motor tasks jointly influence balance control is vital for identifying early markers of decline and developing interventions to maintain stability in older adults.

*The authors would like to thank the sponsorship of Nanyang Technological University, the Agency for Science Technology and Research (A*STAR), the National Healthcare Group (NHG). (Corresponding author: Ananda Sidarta.)

[1]School of Robotics, Hunan University, Changsha, China

[2]Rehabilitation Research Institute of Singapore, Lee Kong Chian School of Medicine, Nanyang Technological University, Singapore

[3]School of Mechanical and Aerospace Engineering, Nanyang Technological University, Singapore

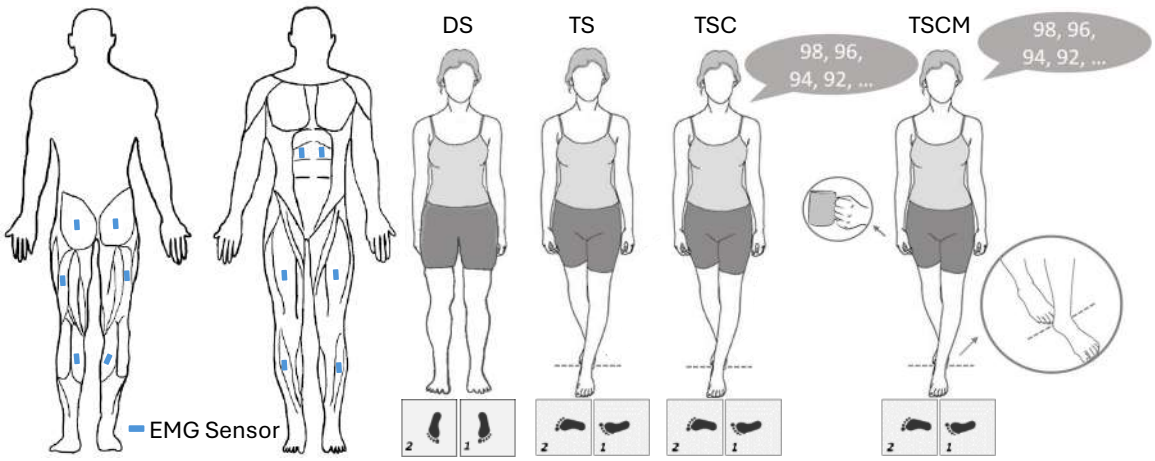


Fig. 1. Experimental setup for assessing stance stability. Electromyography signals were recorded from lower limb and trunk muscles along with center of pressure data during four stance tasks: double-leg stance (DS), tandem stance (TS), tandem stance with a cognitive task (TSC), and tandem stance with combined cognitive and motor tasks (TSCM).

The objective of this study is to examine how different stance tasks with varying difficulty impact muscle activation patterns, postural sway characteristics, and EMG-CoP coherence in older adults. This involves analyzing the role of lower limb and trunk muscles, as well as center of pressure features, across different stance conditions that include cognitive and motor demands.

II. Methods

A. Experimental Setup

Seven sedentary older adults (sex: 2F/5M; age: 64.7 $\pm$ 4.0 years; weight: 62.3 $\pm$ 11.3 kg; height: 163.7 $\pm$ 9.2 cm) were recruited. All participants provided informed written consent. Data collection was conducted at the Rehabilitation Research Institute of Singapore, with the study approved by the Nanyang Technological University Institutional Review Board (IRB-2022-382). Participants were instructed to perform a series of static balance tasks, comprising double-leg stance (DS), tandem stance (TS), tandem stance with a cognitive task (TSC), and tandem stance with both cognitive and motor tasks (TSCM), with a pseudorandomized sequence across participants. In all tasks, participants had to maintain an upright steady posture as much as possible, with eyes open looking at a fixation cross in front of them. They stood with each foot occupying a force platform (9260AA6, Kistler Instruments AG, Winterthur, Switzerland) embedded underneath the ground. The force platforms recorded the time-varying CoP of the participants with a sampling frequency of 2000 Hz. All participants were right-hand and right-leg dominant.

In the DS task, participants were asked to stand quietly and maintain their posture for 60 s. During the TS task, the individual stood in a tandem position, i.e. their dominant foot was positioned in front of the other, with both feet pointing forward, and arms resting at their sides. Each foot was placed on each square (Fig. 1). The TSC task was essentially a tandem stance with an additional memory test. Here, they were asked to do a tandem stance as before, while memorizing a series of numbers presented to them throughout the task. After the task completion, they had to verbally recall the numbers presented earlier. Finally, in the TSCM, participants were asked to do TSC with an additional motor task in the form of holding a cup filled with water with the dominant hand. The TS, TSC, and TSCM consisted of 2 repetitions of 40 s each, and the average of the results was used for representation. A short demonstration was given by the experimenter and each participant was allowed to practice the posture once. All participants were able to complete every task within the required duration.

EMG recordings were obtained using 12 wireless surface EMG electrodes (Cometa Systems, Italy). After appropriate skin preparation, electrodes were placed bilaterally on the muscle bellies of eight muscle groups, aligned parallel to the direction of muscle fibers. The muscle groups tested included the Gastrocnemius Medialis (GM), biceps femoris (BF), gluteus maximus (GluM), tibialis anterior (TA), rectus femoris (RF), and Rectus Abdominis (RA). EMG signals were recorded at a sampling frequency of 2000 Hz. Electrode placement was conducted following SENIAM (Surface EMG for Non-Invasive Assessment of Muscles) project recommendations. The EMG data were band-pass filtered (5–400 Hz) to isolate relevant frequencies, and then rectified using full-wave rectification, a process that has been shown to enhance information about the temporal patterns of grouped motor unit firing [12]. To obtain the muscle activation envelope, the rectified EMG was further low-pass filtered at 6 Hz and normalized to the maximum EMG value across all movement trials [13]–[15].

B. CoP Sway Features

The anterior-posterior (AP) and mediolateral (ML) CoP signals, derived from force and moment data, were low-pass filtered at 15 Hz using a fourth-order, zero-phase lag Butterworth filter. We then calculated the CoP area and mean

frequency for the whole body, as well as the mean distance, the range of maximum deviation, mean velocity in AP and ML directions, and power frequency dispersion in both directions [16]. These CoP features were analyzed and compared across all tasks. Shapiro-Wilk tests were applied to assess the normality of CoP features. For group comparisons, paired t-tests were used for features with normal distributions, while Wilcoxon signed-rank tests were applied for non-normally distributed features. Statistical significance was determined at $p < 0.05$ with Bonferroni correction applied for multiple comparisons.

C. EMG-CoP Muscular-postural Sway Coherence

To assess the coherence between EMG signals and CoP sway, we calculated the EMG-CoP coherence for each muscle with respect to the postural sway of the corresponding foot. For example, coherence between the GM on the left side was analyzed in relation to the CoP of the left foot across the frequency spectrum. Coherence, a measure of the linear association between two signals across frequencies, was calculated using the following formula:

$$Coh_{S1,S2}(f) = \frac{|P_{S1,S2}(f)|^2}{|P_{S1}(f)| \times |P_{S2}(f)|} \quad (1)$$

$$P_{S1,S2}(f) = \frac{1}{n}\sum_{i=1}^{n} S1_i(f) \cdot S2_i^*(f) \quad (2)$$

where $Coh_{S1,S2}(f)$ represents the coherence between EMG ($S1$) and CoP ($S2$) at frequency f; $P_{S1,S2}(f)$ is the cross-spectrum density of the signal, $P_{S1}(f)$ and $P_{S2}(f)$ are the auto-spectral densities of the EMG and CoP signals, respectively. Coherence values are normalized and bounded between 0 and 1, where a value of 1 indicates a perfect correlation between EMG and CoP at a given frequency, and a value of 0 indicates no correlation.

III. Results

A. CoP sway measures

In the ML direction, the mean distance significantly increased in TS compared to DS ($p < 0.01$). In the AP direction, the mean distance was significantly higher in TS ($p = 0.03$), TSC ($p = 0.02$), and TSCM ($p = 0.02$) than in DS. Additionally, mean distance values in the AP direction were larger than those in the ML direction across TS, TSC, and TSCM (Fig. 2).

The range, defined as the distance between maximum deviations, was significantly greater in TS, TSC, and TSCM compared to DS in both the ML and AP directions (all $p < 0.01$). Notably, the range values in the AP direction exceeded those in the ML direction across TS, TSC, and TSCM.

Similarly, in mean velocity, the data showed significantly higher values in TS, TSC, and TSCM than in DS for both directions. Mean velocity in the AP direction was also consistently higher than in the ML direction across these stances. Compared to DS, power in the AP direction was significantly higher in TSC ($p = 0.04$) and TSCM ($p = 0.02$), and was also elevated, though not significantly, in TS ($p = 0.06$). In the ML direction, power was significantly greater in TS compared to DS ($p = 0.03$). Additionally, power magnitude in the AP direction was consistently larger than in the ML direction across TS, TSC, and TSCM.

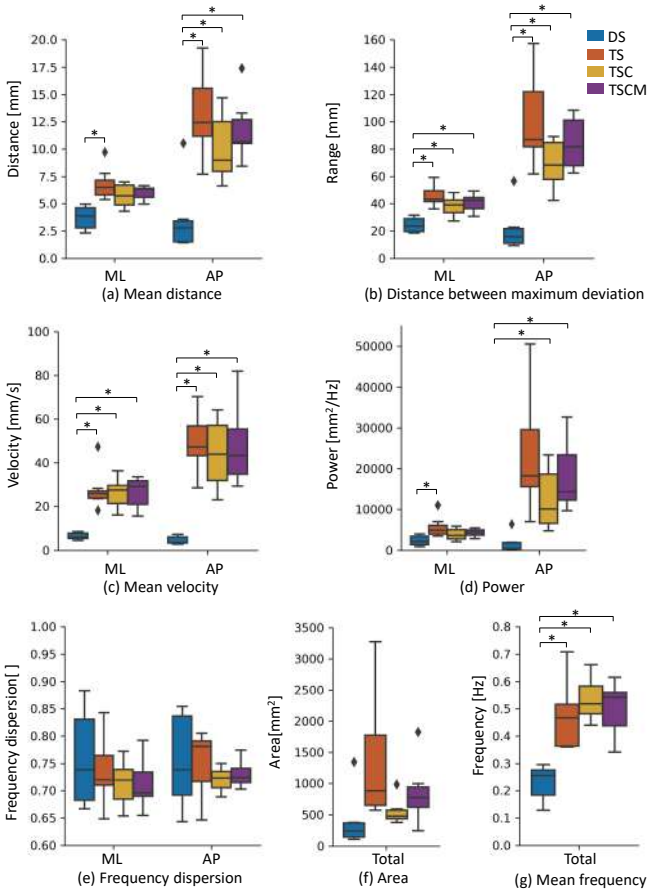


Fig. 2. Center of pressure (CoP) features for all subjects across four tasks: DS (double stance), TS (tandem stance), TSC (tandem stance with cognitive task), and TSCM (tandem stance with cognitive and motor tasks). The features displayed are: (a) mean distance in anterior-posterior (AP) and mediolateral (ML) directions, (b) range of maximum deviation in ML and AP, (c) mean velocity in ML and AP, (d) power in ML and AP, (e) frequency dispersion in ML and AP, (f) area, and (g) mean frequency. Asterisks (*) indicate statistically significant differences between the two groups, determined using paired t-tests for normally distributed data or Wilcoxon signed-rank tests for non-normally distributed data, with Bonferroni correction applied.

The area was larger in TS, TSC, and TSCM compared to DS. Interestingly, the sway area in TSC and TSCM was lower than in TS. The mean frequency of postural sway was significantly higher in TS, TSC, and TSCM compared to DS (All $p < 0.01$). Furthermore, mean frequency followed an ascending pattern, with TSC being higher than TS and TSCM being higher than TSC. No significant differences were observed in frequency dispersion across the stance conditions.

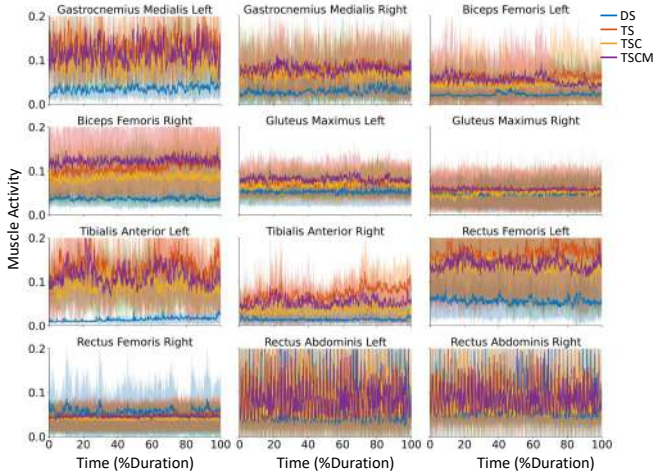


Fig. 3. Muscle activities (normalized to maximal value across all trials) across all subjects for four tasks: DS (Double Stance), TS (Tandem Stance), TSC (Tandem Stance with Cognitive Task), and TSCM (Tandem Stance with Cognitive and Motor Tasks). Results were presented as mean ± standard deviation for each muscle across all subjects.

B. Muscle patterns

Muscle activity patterns were generally similar across the TS, TSC, and TSCM conditions in the GM, TA and BF on both the left and right sides, as well as in the RF and GluM on the left side. However, these muscles exhibited notably higher activity in the TSCM condition compared to the DS condition (Fig.3).

Differences in muscle activity across conditions were minimal in the RF and GluM on the right side and the RA on both sides, with only slight variations observed across the conditions.

An asymmetry in muscle activity was also observed, where the left-side muscles—particularly the GM, TA, and RF—exhibited higher activity levels than their counterparts on the right side under the TS, TSC, and TSCM conditions.

C. EMG-CoP muscular-postural sway Coherence

The EMG-CoP coherence of lower limb muscles was found up to around 20 Hz across all tasks: DS, TS, TSC, and TSCM. Among the muscles, the GM consistently demonstrated the highest coherence with CoP, followed by the TA and RF (Fig. 4).

In the GM, coherence with CoP was generally higher in the TS, TSC, and TSCM conditions compared to DS. On the left side, coherence was highest in TSCM compared to TS and TSC, whereas on the right side, coherence in TSCM was lower than in TS and TSC. Coherence of BF and GluM with CoP was slightly higher on the left side compared to the right. Minimal coherence was observed in the RA across all tasks.

IV. Discussion

In this study, we explored the relationship between postural sway, activation patterns of lower limb and trunk muscles, and EMG-CoP coherence in older adults during various stance tasks: double stance, tandem stance, tandem stance with a cognitive task, and tandem stance with combined cognitive and motor tasks. Our findings revealed that postural sway measures—including mean distance, range, mean velocity, sway area, and mean frequency—were generally higher in TS, TSC, and TSCM compared to DS, reflecting the increased challenge of maintaining stability on a narrow base of support. In line with this increase in sway, muscle activity in most lower limb muscles was also elevated in TS, TSC, and TSCM relative to DS, suggesting greater neuromuscular demand to stabilize the body under more challenging conditions. Furthermore, EMG-CoP coherence analysis indicated that lower limb muscles exhibited coherence with CoP up to around 20 Hz across all tasks, with the GM demonstrating the highest coherence. This suggests that the GM plays a key role in coordinating muscular responses to maintain postural stability. These findings provide valuable insights into the roles of different muscles in stabilizing posture under varied conditions and emphasize the potential importance of task-specific muscle activation for postural control. Such insights could inform injury prevention strategies and rehabilitation programs by identifying muscles that are crucial for maintaining balance, particularly under challenging conditions like narrow stances or multitasking.

Task complexity and stance type substantially influence postural control, leading to increased instability and more frequent postural adjustments, particularly along the AP axis. However, no significant effect of concurrent motor or cognitive tasks on balance parameters was observed. Both mean distance and range increase notably in TS, TSC, and TSCM tasks, particularly in the AP direction, suggesting that tandem positioning, with its restricted base of support, presents greater stability challenges along this axis. Similarly, mean velocity rises across TS, TSC, and TSCM, indicating a heightened need for postural corrections as task demands increase. The higher power in the AP direction under TSC and TSCM further highlights the additional balance control demands imposed by complex task conditions. Interestingly, while sway area peaks in TS, it slightly decreases in TSC and TSCM, suggesting that additional tasks may lead to a more concentrated, yet still broad, sway pattern. The lack of a significant effect of concurrent motor or cognitive tasks on balance parameters is consistent with the findings of Xu et al. [17], who examined balance ability and prefrontal cortex activation under single- and dual-task conditions. Their results similarly indicate that dual-tasking does not significantly impact balance performance in healthy older adults, suggesting that balance control may operate implicitly, even when additional cognitive tasks are introduced. This aligns with the Task Prioritization Model [18], which posits that as postural threat increases, older adults prioritize postural stability over cognitive performance. We acknowledge that the small sample size may limit the ability to detect finer differences among TS, TSC, and TSCM. Further research with larger cohorts is necessary to confirm these trends and explore potential subtleties in task-dependent balance control mechanisms.

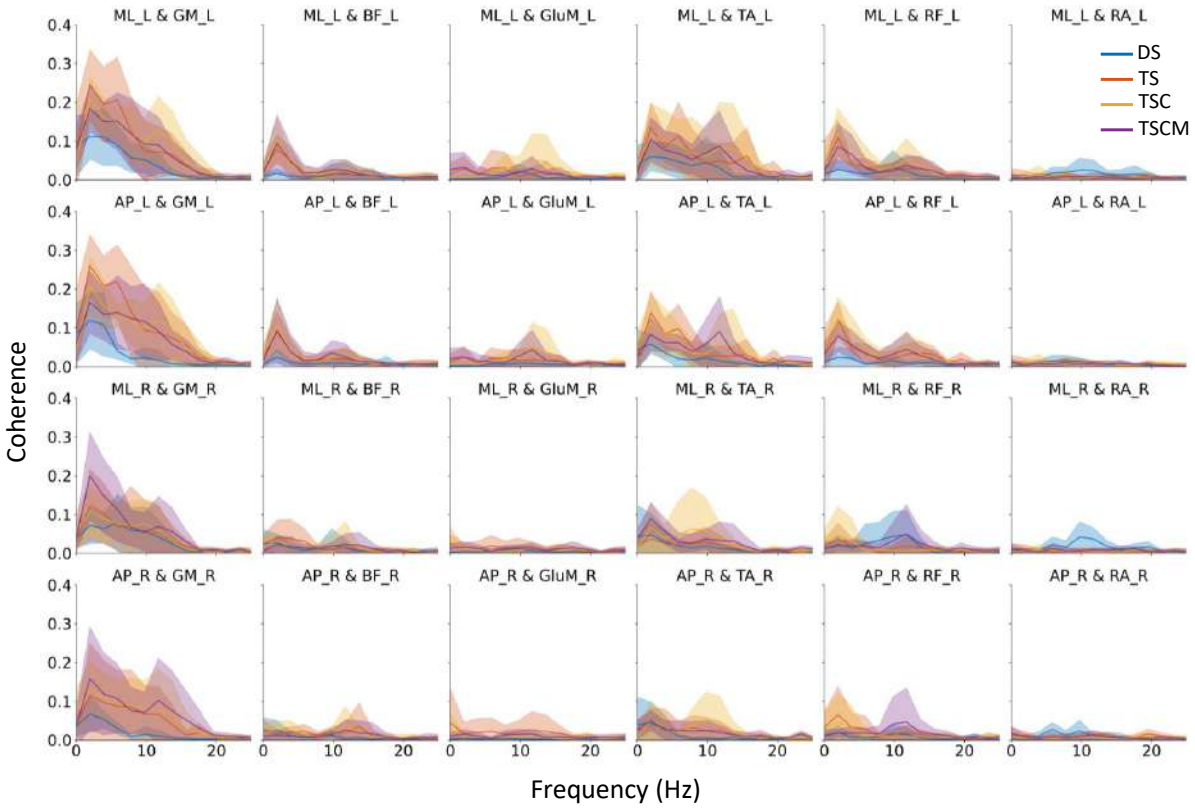


Fig. 4. Coherence between electromyography (EMG) and center of pressure (CoP) data across all subjects for four tasks: Double Stance (DS), Tandem Stance (TS), Tandem Stance with Cognitive Task (TSC), and Tandem Stance with Cognitive and Motor Tasks (TSCM). Results were presented as mean $\pm$ standard deviation across all subjects. ML_L and ML_R represent the mediolateral directions of CoP on the left and right sides, respectively; similarly, AP_L and AP_R indicated the anteroposterior directions. Muscle activity was represented by GM_L and GM_R for Gastrocnemius Medialis on the left and right sides, and corresponding labels for Biceps Femoris (BF), Gluteus Maximus (GluM), Tibialis Anterior (TA), Rectus Femoris (RF), and Rectus Abdominis (RA).

Muscle activity levels vary with task complexity, with greater engagement noted in the TSCM condition compared to DS, especially in the GM, TA, and BF on both sides and in the left RF and GluM. This pattern indicates that more complex tasks requiring both cognitive and motor coordination (TSCM) demand increased muscle activation to maintain postural stability. The minimal differences in activity across conditions in the bilateral RA, along with the low EMG-CoP coherence, suggest that the RA may be less responsive to changes in task complexity. The moderately high normalized values observed in the bilateral RA may be attributed to normalization relative to the maximum value across all trials, as RA activity remained generally low and stable. Additionally, asymmetry in muscle activity was observed, with left-side muscles (non-dominant leg), particularly the GM, TA, and RF, showing consistently higher activation than their right-side counterparts during TS, TSC, and TSCM. This asymmetry may reflect inherent lateral dominance or compensatory strategies, suggesting that the non-dominant side plays a more active role in stabilizing posture under complex conditions, such as tandem stance. These findings are consistent with Sozzi et al. [9], who reported higher EMG activity in the non-dominant leg, indicating that it serves as the primary stabilizer in tandem stance, thereby assuming a greater postural load.

A notable coupling between muscle activation and postural sway was observed, especially in the GM, with coherence up to approximately 20 Hz across all tasks. In a related study, Watanabe et al. [12] investigated the coordination of plantar flexor muscles—specifically the medial and lateral gastrocnemius and soleus—and their relationship with postural stability during bipedal and unipedal stances, finding coherence levels up to about 10 Hz in elderly adults. Our study expands upon this by including additional muscles to provide a more comprehensive analysis of the relationship between muscular activation and postural sway coherence. In this study, the GM displayed the highest EMG-CoP coherence among the lower limb muscles, underscoring its critical role in postural adjustments. This finding aligns with previous research suggesting that the gastrocnemius is a primary contributor to modulating AP sway, particularly during challenging balance tasks [19]–[21]. Both the GM and TA demonstrated higher coherence levels than other muscles, indicating their prominent involvement in stabilizing posture under increased task demands. This is consistent with studies that reported elevated EMG amplitudes in the GM and TA compared to the RF and BF across balance tasks. The greater activation in the ankle muscles may be due to the reliance

on an ankle strategy to counteract gravitational torque in an upright stance, an essential mechanism in maintaining balance [22]–[24]. Notably, a task-related asymmetry emerges in the GM, with left-side coherence peaking in TSCM, while right-side coherence is lower in TSCM than in TS and TSC, suggesting potential lateralized differences in muscle-sway coordination under high task demands. Other muscles, like BF and GluM, exhibit slightly higher coherence on the left side, pointing to a subtle lateral asymmetry in postural sway synchronization, while the RA shows minimal coherence across all tasks, indicating a limited role in postural sway regulation. These findings suggest that while GM is central to postural control across tasks, asymmetric coherence patterns may reflect compensatory strategies or task-specific muscle contributions to stability.

V. Conclusion

We investigated how different stance tasks affect postural sway, lower limb and trunk muscle activation, and EMG-CoP coherence in older adults, highlighting the distinct roles of muscle activation patterns and muscle-postural sway coherence in maintaining balance under varying levels of task complexity. The findings indicate that tandem stances, especially when coupled with cognitive and motor tasks (TSCM), significantly challenge postural stability, demanding higher activation in key stabilizing muscles like the GM and TA. These muscles, particularly the GM, demonstrated high coherence with CoP sway, reflecting their importance in counteracting gravitational forces and stabilizing posture. Notable asymmetries were observed, with left-side muscles showing heightened activation, suggesting lateralized contributions to balance. The lack of differences in sway with the additional cognitive task may suggest that balance control is implicit. The coherence analysis further underscores the reliance on the ankle strategy for AP sway control, particularly under challenging conditions. Together, these results emphasize the critical contributions of specific muscles in stabilizing posture, particularly in complex tasks, offering insights for targeted interventions and training focused on enhancing balance in populations at risk of instability.

References

[1] T. Paillard, "Effects of general and local fatigue on postural control: a review," *Neuroscience & Biobehavioral Reviews*, vol. 36, no. 1, pp. 162–176, 2012.

[2] G. C. Ang, S. L. Low, and C. H. How, "Approach to falls among the elderly in the community," *Singapore Medical Journal*, vol. 61, no. 3, p. 116, 2020.

[3] S. A. Stehle, R. Aubonnet, M. Hassan, M. Recenti, D. Jacob, H. Petersen, and P. Gargiulo, "Predicting postural control adaptation measuring eeg, emg, and center of pressure changes: Biovrsea paradigm," *Frontiers in Human Neuroscience*, vol. 16, pp. 1–12, 2022.

[4] N. B. Alexander, "Postural control in older adults," *American Geriatrics Society*, vol. 42, no. 1, pp. 93–108, 1994.

[5] J. Wang, Y. Li, G.-Y. Yang, and K. Jin, "Age-related dysfunction in balance: a comprehensive review of causes, consequences, and interventions," *Aging and Disease*, 2024.

[6] S. L. Pavão, A. N. dos Santos, M. H. Woollacott, and N. A. C. F. Rocha, "Assessment of postural control in children with cerebral palsy: a review," *Research in Developmental Disabilities*, vol. 34, no. 5, pp. 1367–1375, 2013.

[7] A. Hua, G. Wang, J. Bai, Z. Hao, J. Liu, J. Meng, and J. Wang, "Nonlinear dynamics of postural control system under visual-vestibular habituation balance practice: evidence from eeg, emg and center of pressure signals," *Frontiers in Human Neuroscience*, vol. 18, pp. 1–10, 2024.

[8] A. Skeparianos, I. G. Amiridis, P. Violaris, Z. Tsampalaki, T. M. Kannas, C. Sahinis, K. Salonikidis, F. Negro, V. Hatzitaki, and R. M. Enoka, "Association between ankle muscle strength and postural sway in older adults," *Journal of Physical Education and Sport*, vol. 23, no. 10, pp. 2592–2600, 2023.

[9] S. Sozzi, J.-L. Honeine, M.-C. Do, and M. Schieppati, "Leg muscle activity during tandem stance and the control of body balance in the frontal plane," *Clinical Neurophysiology*, vol. 124, no. 6, pp. 1175–1186, 2013.

[10] J. G. van Uffelen, M. J. C. A. Paw, M. Hopman-Rock, and W. van Mechelen, "The effects of exercise on cognition in older adults with and without cognitive decline: a systematic review," *Clinical Journal of Sport Medicine*, vol. 18, no. 6, pp. 486–500, 2008.

[11] K. Hauer, M. Pfisterer, C. Weber, N. Wezler, M. Kliegel, and P. Oster, "Cognitive impairment decreases postural control during dual tasks in geriatric patients with a history of severe falls," *Journal of the American Geriatrics Society*, vol. 51, no. 11, pp. 1638–1644, 2003.

[12] T. Watanabe, K. Saito, K. Ishida, S. Tanabe, and I. Nojima, "Coordination of plantar flexor muscles during bipedal and unipedal stances in young and elderly adults," *Experimental Brain Research*, vol. 236, pp. 1229–1239, 2018.

[13] C. Pizzolato, M. Reggiani, L. Modenese, and D. Lloyd, "Real-time inverse kinematics and inverse dynamics for lower limb applications using opensim," *Computer Methods in Biomechanics and Biomedical Engineering*, vol. 20, no. 4, pp. 436–445, 2017.

[14] L. Zhang, Z. Li, Y. Hu, C. Smith, E. M. G. Farewik, and R. Wang, "Ankle joint torque estimation using an emg-driven neuromusculoskeletal model and an artificial neural network model," *IEEE Transactions on Automation Science and Engineering*, 2020.

[15] L. Zhang, D. Soselia, R. Wang, and E. M. Gutierrez-Farewik, "Lower-limb joint torque prediction using lstm neural networks and transfer learning," *IEEE Transactions on Neural Systems and Rehabilitation Engineering*, vol. 30, pp. 600–609, 2022.

[16] F. Quijoux, A. Nicolaï, I. Chairi, I. Bargiotas, D. Ricard, A. Yelnik, L. Oudre, F. Bertin-Hugault, P.-P. Vidal, N. Vayatis *et al.*, "A review of center of pressure (cop) variables to quantify standing balance in elderly people: Algorithms and open-access code," *Physiological reports*, vol. 9, no. 22, pp. 1–32, 2021.

[17] G. Xu, M. Zhou, Y. Chen, Q. Song, W. Sun, and J. Wang, "Brain activation during standing balance control in dual-task paradigm and its correlation among older adults with mild cognitive impairment: a fnirs study," *BMC Geriatrics*, vol. 24, no. 1, pp. 1–11, 2024.

[18] M. Lacour, L. Bernard-Demanze, and M. Dumitrescu, "Posture control, aging, and attention resources: models and posture-analysis methods," *Neurophysiologie Clinique/Clinical Neurophysiology*, vol. 38, no. 6, pp. 411–421, 2008.

[19] L. Li-Liang and C. Fu-Chen, "Effects of kinesio taping on static balance performance and muscle activity in children with developmental coordination disorder: a single-group pretest-posttest study," *Journal of Rehabilitation mMedicine*, vol. 55, 2023.

[20] F. Borg, M. Finell, I. Hakala, and M. Herrala, "Analyzing gastrocnemius emg-activity and sway data from quiet and perturbed standing," *Journal of Electromyography and Kinesiology*, vol. 17, no. 5, pp. 622–634, 2007.

[21] I. D. Loram, C. N. Maganaris, and M. Lakie, "Paradoxical muscle movement in human standing," *The Journal of Physiology*, vol. 556, no. 3, pp. 683–689, 2004.

[22] D. B. Murillo, R. S. Solana, F. J. Vera-Garcia, N. G. Fuertes, and F. J. Moreno, "Effect of increasing difficulty in standing balance tasks with visual feedback on postural sway and emg: complexity and performance," *Human Movement Science*, vol. 31, no. 5, pp. 1224–1237, 2012.

[23] D. A. Winter, A. E. Patla, F. Prince, M. Ishac, and K. Gielo-Perczak, "Stiffness control of balance in quiet standing," *Journal of Neurophysiology*, vol. 80, no. 3, pp. 1211–1221, 1998.

[24] D. A. Winter, A. E. Patla, S. Rietdyk, and M. G. Ishac, "Ankle muscle stiffness in the control of balance during quiet standing," *Journal of Neurophysiology*, vol. 85, no. 6, pp. 2630–2633, 2001.

Design and benchmarking of a two degree of freedom tendon driver unit for cable-driven wearable technologies

Adrian Esser[1,*], Chiara Basla[1], Peter Wolf[1], Robert Riener[1,2]

***Abstract*—Exosuits have recently been developed as alternatives to rigid exoskeletons and are increasingly adopted for both upper and lower limb therapy and assistance in clinical and home environments. Many cable-driven exosuits have been developed but little has been published on their electromechanical designs and performance. Therefore, this paper presents a comprehensive design and performance analysis of a two degree of freedom tendon driver unit (TDU) for cable-driven wearable exosuits. Detailed methodologies are presented to benchmark the functionality of the TDU. A static torque output test compares the commanded and measured torques. A velocity control test evaluates the attenuation and phase shift across velocities. A noise test evaluates how loud the TDU is for the wearer under different speeds. A thermal stress test captures the cooling performance of the TDU to ensure safe operation at higher loads. Finally, a battery endurance test evaluates the runtime of the TDU under various loading conditions to inform the usable time. To demonstrate these tests, a modular TDU system for cable-driven applications is introduced, which allows components such as motors, pulleys, and sensors to be adapted based on the requirements of the intended application. By sharing detailed methodologies and performance results, this study aims to provide a TDU design that may be leveraged by others and resources for researchers and engineers to better document the capabilities of their TDU designs.**

***Index Terms*—wearable robots, exosuits, cable-driven, tendon driver unit, assistive devices**

I. Introduction

In the past decade, exosuits have emerged as a technology to support individuals with partial motor functions, enhancing their ability to participate in daily activities. Unlike traditional rigid exoskeletons, exosuits offer a lighter, more flexible, and affordable solution that prioritizes user comfort and accessibility for everyday use. These qualities make exosuits versatile tools with potential for broad adoption across multiple applications. Based on actuation methodologies, exosuits are classified into cable-driven, pneumatic, twisted strings, and shape-memory alloy systems [1]. Recent advances in electric motor control and the flexible routing of cables have expanded cable-driven exosuits, which are currently the most widely adopted form [1].

This work was supported as a part of NCCR Robotics, a National Centre of Competence in Research, funded by the Swiss National Science Foundation (grant number 51NF40_185543).

[1] Sensory-Motor Systems Lab, Institute of Robotics and Intelligent Systems (IRIS), ETH Zurich, Switzerland

[2] Spinal Cord Injury Center, Balgrist University Hospital, Medical Faculty, University of Zürich, Switzerland

[*] Corresponding author: adrian.esser@hest.ethz.ch

Exosuits have been developed for both lower and upper limb assistance. Lower limb devices often actuate single joints, like the ankle [2], [3] or hip [4]–[6], and can also integrate multi-joint actuation for comprehensive support, such as hip-ankle [7] or hip-knee systems [8]–[10]. For upper limbs, exosuits typically have one or two actuated joints with a range of configurations to support various arm movements effectively. Examples include elbow flexion [11], shoulder-elbow flexion [12], [13], wrist support [14], and shoulder elevation [15], [16]. Each of these examples has one or two degrees of freedom (DOF), referring to the number of actuators embedded in the exosuit. Each actuator can affect multiple joints and facilitate multidirectional movement based on tendon routing along the limb (Fig. 1).

All portable cable-driven exosuits include an actuation system, referred to as tendon driver unit (TDU). This commonly houses electronics, motors, batteries, and one or more cables routed to flexible joint attachments. Despite notable progress, documentation and transparent sharing of exosuit TDU design, performance metrics, and benchmarks remain limited. This lack of detail impedes researchers and engineers from replicating existing systems, refining devices, and building on shared knowledge within the field.

To address this gap, we outline benchmarking tests to evaluate performance. In addition to standard performance metrics, such as torque and velocity, we recommend further tests to assess noise, battery life, and thermal management, all critical considerations for portable exosuit applications suited for clinic or home use. Factors such as torque and velocity performance are important to evaluate because they fundamentally determine the range of anthropometrics that can be supported by the device (i.e., how heavy or tall the user is) and what types of movements may be performed (i.e. how fast one can lift the arm or walk). Factors such as noise, battery life, and thermal management are included as well as they are often overlooked, but also are necessary for device usability and acceptance. By sharing these methodologies, we aim to foster performance transparency and comparability within the exosuit field, facilitating improved design choices, accelerated advancements, and enriched technical documentation through accessible research and open-source repositories.[1]

Alongside the methodologies, we present a lightweight,

[1] All design files and scripts for testing and data processing are available publicly: https://bitbucket.org/AdrianJEsser/icorr_2025_tdu/src/main/

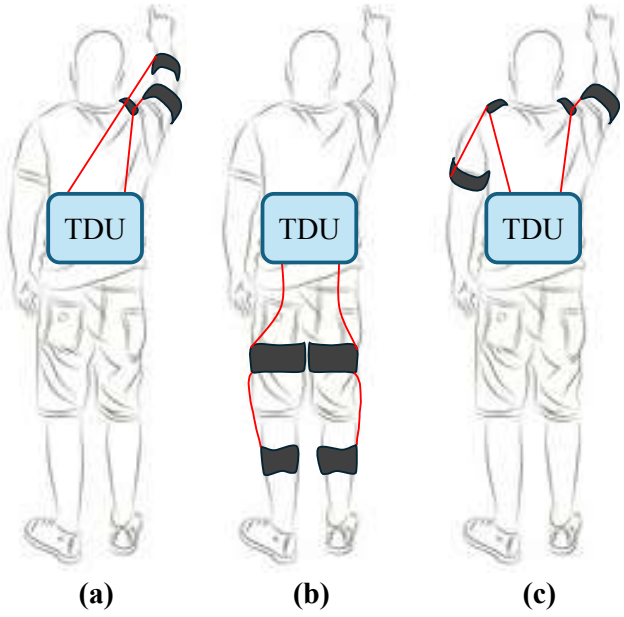


Fig. 1. Three conceptual designs demonstrating examples of how a two DOF TDU may support multiple joints: **(a)** shoulder and elbow on one arm, **(b)** hip and/or knee on the legs, or **(c)** shoulder elevation on both arms.



Fig. 2. An example of how the TDU can be mounted on the body in real life. In this application, the TDU is used, along with a textile interface, to support the right and left shoulder joints against gravity during shoulder elevation.

adaptable TDU design with two DOF. This TDU supports multiple configurations, making it suitable for both upper and lower limb exosuits. It can be customized to accommodate different applications and user needs through modular features that enable the swapping of components to adjust battery capacity, voltage, and output torque, along with a flexible programming interface to support diverse performance and sensor requirements.

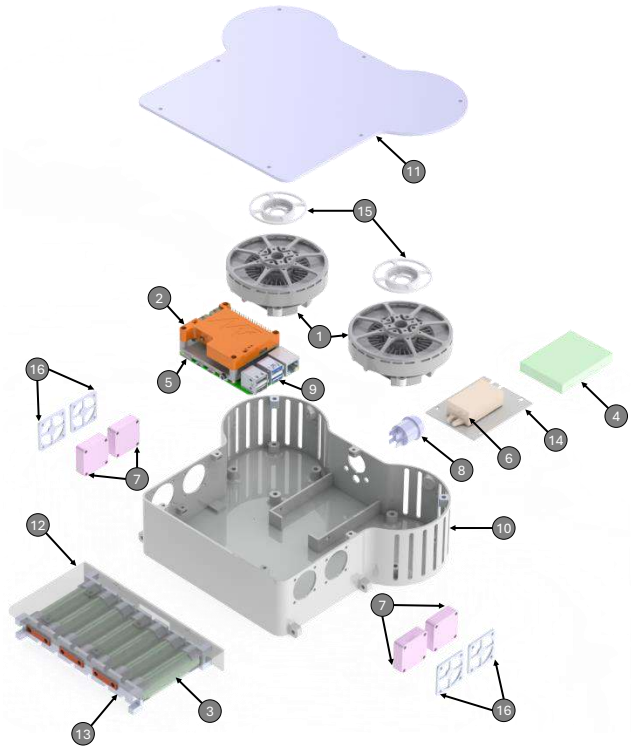


Fig. 3. Rendering of an exploded view of the TDU. The numbers correspond to the system components in Table I.

II. Tendon Driver Unit Design

A. Description of Components

The main body of the TDU was 3D printed (Prusa MK4S) out of black polylactic acid (PLA) (Fig. 3 and Tab. I). Other custom designed printed parts include the protective covers for the fans, the 30mm cable pulleys, the cover for the battery management system (BMS), and the cover for the battery module. The cover for the TDU was laser cut (Trotec Speedy 400) with 3mm thick transparent acrylic. The 7S1P battery pack (24V. nominal) is custom assembled from LG MJ1 18650 battery cells (3500mAh) and a 24V. 7S BMS (Vruzend). Controlling the TDU is a Raspberry Pi 4B (8Gb RAM) with a RTL881cu USB WiFi network card (PiShop.ch), allowing the TDU to simultaneously connect to a Wifi network and broadcast an independent access point. Power is provided to the microcontroller with a 5V 3A step down buck converter module (PiShop.ch). The regulated 5V module also powers the four PWM HighPi brushless fans (1.4CFM per fan, PiShop.ch), which pull in air from the side of the case, and expel it near the top by the motors. The TDU houses two U8 Lite L KV95 direct drive motors (1.5Nm rated torque, 3Nm peak torque, from MAB Robotics) which are controlled with MD80 brushless motor controller drives (MAB Robotics). Communication to the motors is performed over a controller area network (CAN) protocol with a CANdle hat for the Raspberry Pi (MAB Robotics).

TABLE I
MASS BREAKDOWN FOR ALL MAJOR COMPONENTS OF THE TDU. THE NUMBERING IN THE ID COLUMN CORRESPONDS TO THE LABELS IN THE EXPLODED VIEW PRESENTED IN FIG. 3.

ID	Components	Weight (g)
	Actuation	-
1	2x U8 Lite L KV95 + MD80	636
2	CANdle Hat	28
	Hardware and wiring	52
	Subtotal Actuation	**716**
	Battery	-
3	7x LG INR18650MJ1 Cells	343
4	24V 7S BMS	80
	Hardware and wiring	28
	Subtotal Battery	**447**
	Electronics	-
5	Raspberry Pi 4B	46
6	5V converter module	32
7	Cooling fans	20
8	Power button	5
9	USB Wifi card	3
	Hardware and wiring	24
	Subtotal Electronics	**134**
	Printed Parts	-
10	Main housing	237
11	Acrylic cover	118
12	Battery cell cover	42
13	Battery cell holders	26
14	BMS cover	11
15	2x 30mm pulleys	6
16	Fan covers	5
	Hardware	32
	Subtotal Printed Parts	**477**
	Grand Total	**1774**



Fig. 4. Aerial view of the assembled TDU

III. PERFORMANCE TESTING METHODOLOGIES

The protocols for all performance tests are detailed in the subsections below. The left and right motors are referred to as Motor 1 and Motor 2 respectively, when viewing Fig. 4.

The open-loop torque controllers and close-loopthe mea velocity controllers used in the following performance tests were not developed by the authors, but used directly from the manufacturers of the motor and controllers, available here: https://mabrobotics.github.io/MD80-x-CANdle-Documentation/intro.html

A. Open-Loop Static Torque Performance

This test evaluates the precision and accuracy of the motors when producing static torques. Actuator torque is not directly measured using the MD80 controller, but rather estimated by measuring the motor phase currents. This can be a suitable proxy for the torque of the drive when a low gear ratio is used (i.e. the motor is backdrivable) [17]. For this test, a pulley with a diameter of 3cm was printed and fixed on the rotor of the TDU motor. The TDU was fixed horizontally, and connected to a digital crane scale (ZW 5.0 force gauge from HKM Messtechnik, 500N nominal, 0.1N step) via a cable (1.5mm Dyneema, extremtextil). A series of increasing fixed torques were commanded (0.25Nm to 2.0Nm in 0.25Nm increments), the system was given 30s to settle, and the load on the scale was recorded. Five repetitions were performed for each condition to ascertain the repeatability of the system. The measured tensile load from the crane scale was converted to the actual output torque of the motor given the pulley diameter of 3cm, and this was compared to the commanded torque of the motor. The protocol was repeated twice, once for each motor in the TDU.

B. Closed-Loop Velocity Control

This test evaluates the attenuation and phase shift of the motor when tracking velocity reference signals with varying frequencies and amplitudes. This is an important test to understand if a particular actuator can meet the requirement speeds and frequencies of the intended application. Sinusoidal velocity reference signals were commanded to the drives while in velocity PID control. The signals had amplitudes ranging from 5rad/s up to 30rad/s in 5rad/s increments and 20 frequencies ranging from 0.1Hz to 10Hz in even log-space increments. For each commanded signal 10 full cycles of the motor response velocity were collected. Then the gain and phase shift of the actual motor velocity was computed relative to the reference velocity signal and averaged between both motors. The tests were done without the pulleys attached to the rotors.

C. Thermal Cooling

This test evaluates the thermal cooling effect of the fans in the TDU. Thermal management is essential for safe continued operation of motors under higher loads and for longer times. The TDU was fixed flat on a table, and both motors were connected to each other outside of the TDU with a re-direct

pulley. The left motor was controlled in torque to a constant 1.5Nm (rated torque from the manufacturer), while the right motor was controlled in position executing a sinusoidal profile with an amplitude of 2πrad and a period of 4s. The test was performed dynamically to ensure even heating of all motor windings. The motor stator temperature was recorded with a NTC100K thermistor integrated with MD80 controller. The TDU was turned on with all four fans running (100% duty cycle), and given 5min for the motor temperature to stabilize with the airflow. Then the system was held dynamically under tension until the first of the two motors hit 80°C, then the tension was released from the system and the motors were allowed to cool. Then the fans were disabled, and the test was repeated again without the cooling airflow.

D. Noise

This test evaluates the noise level of the TDU in various dynamic conditions. Noise level can impact usability and comfort if too loud by obstructing conversations, and in extreme cases lead to gradual hearing loss. Noise level testing was done in a sound isolated room using a NTI XL2 audio analyzer. The microphone was placed horizontally on a table, with the head of the microphone 50cm away from the top of the TDU, and centered between the two motors. The TDU was lying flat on the table with the acrylic cover facing up. Both the microphone and TDU were set on a thin piece of foam to prevent vibrations from passing through the table. All tests were triggered remotely from outside of the isolated room.

For all tests, the equivalent continuous sound pressure level was recorded over a 20 second window. First, the sound floor of the room was captured with the TDU off. Second, the noise level was captured with the TDU on with fans (100% duty cycle) but both motors disabled and stationary. Finally, the noise level was recorded for both motors, individually and together, over the set of speeds: 5, 10, 15, 20, 25 and 30 rad/s.

For all measurements the sound floor of the room with the TDU off (L_{room}) was subtracted from the noise level of the TDU in its respective operating condition (L_{meas}) using the following equation:

$$L_{meas} - L_{room} = 10 \cdot \log_{10}(10^{\frac{L_{meas}}{10}} - 10^{\frac{L_{room}}{10}}) \quad (1)$$

E. Battery Life

Evaluating the battery life under different loading conditions can give developers better guidance in specifying motors and battery cells in TDU design. The runtime of the TDU was tested for four different conditions: idle, 2kg, 4kg, and 6kg dynamic loading. The three loading conditions correspond to theoretical average motor torques of 0.29Nm, 0.59Nm, and 0.88Nm respectively, spanning the usable torque range of the motors. For the idle condition, the TDU was left on with the microcontroller and fans running, but the two motors disabled. For the dynamic loading conditions, the TDU raised and lowered the weights according to a sinusoidal position profile with an amplitude of 2πrad and a period of 6s. The TDU was fixed horizontally on a table, and the weights were lifted vertically, using a re-direct pulley mounted on the edge of the table to convert the horizontal pulling force to a vertical force. For all tests, the TDU was first fully charged (29.1V) and then we measured the time it took to discharge until the BMS hit the low voltage cutoff (17.5V) after which the TDU would shut off to protect the cells from over-discharge.

IV. Results and Discussion

All tests were done with the TDU in a horizontal orientation, but as Figure 1 and 2 suggest, when the TDU is in use it would likely have a vertical mounting on the body (so that the tendons exit either towards the legs or the shoulders). In general, loads were applied to the motors using redirect pulleys so that the loads could be moved against gravity, but the TDU could be mounted and secured on the table in a horizontal orientation (for practicality of performing the test in a controlled environment). It is likely that the re-direct pulleys introduced a small amount of friction to the test setup, so the true performance of the TDU might be slightly better than these test results suggest (across all tests that involved loading the TDU motors). Despite this, the additional friction that would be introduced to the cable transmission system, for example in Figure 2 where the tendons are routed from the back all the way over the shoulders, should be much greater than the friction introduced by a single re-direct pulley used for these tests. Thus it is anticipated that these results still present an upper bound on the performance of the TDU unit (for this configuration of batteries and motors), and the general methodologies still provide a meaningful method to bound the performance of the TDU and understand for what scenarios and applications it could be used for.

In order to present a complete TDU in this paper, certain design choices (like the choice of motor, battery cells) had to be fixed. For example, ungeared U8 Lite L KV95 direct drive motors controlled with MD80 brushless motor controller drives (MAB Robotics). For applications with higher torque requirements, one could instead spec the AK60-6 V1.1 CubeMars motor from MAB Robotics (3Nm rated / 9Nm peak torque). This would only involve re-sizing the case, modifying the mounting points, and potentially designing a pulley with a different radius if necessary. Designers can in principle use any motor / controller combination that communicates with a CANBUS, with the addition of a CAN transceiver between the Raspberry Pi and the motor controllers, so one would not be limited to motors and controllers from MAB Robotics as well.

A. Open-Loop Static Torque Performance

The static torques delivered by the drive are consistent and repeatable, albeit under-deliver consistently (Fig. 5). There was a high goodness of fit for both motors, with coefficients of determination of 0.99984 and 0.99975 for the left and right motors, respectively. These correspond to the following relationships:

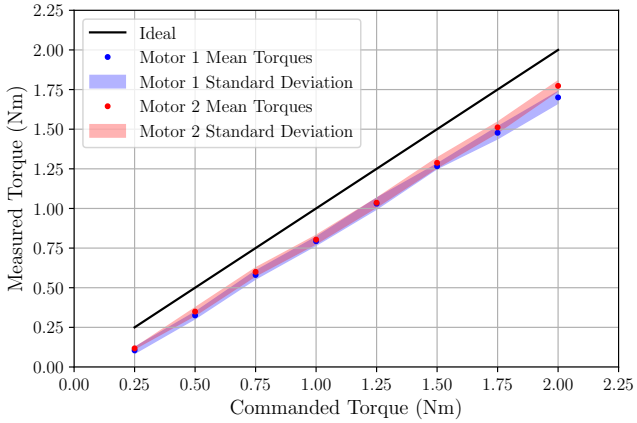


Fig. 5. Static torque test results demonstrating the relationship between commanded motor torque and measured output torque based on cable tension measurements.

$$\tau_{act} = \begin{cases} 0.915 \cdot \tau_{cmd} - 0.120, \text{left motor} \\ 0.938 \cdot \tau_{cmd} - 0.120, \text{right motor} \end{cases} \quad (2)$$

where τ_{act} is the measured motor torque (Nm) and τ_{cmd} is the commanded motor torque (Nm). This indicates that an inverse linear model may be used to correct the commanded torque depending on the desired output rotor torque, especially if a distal load sensor will not be used to measure cable tension. The offset may come from rotor stiction (since the measurements were made at stall) or from modelling errors on the MD80 controllers.

B. Closed-Loop Velocity Control

For a fixed signal frequency, higher peak rotor speeds had lower attenuation and phase shift (Fig. 6 and 7). This is likely a result of using a direct-drive motor and thus the cogging torque acts as a disturbance at lower speeds. For shoulder elevation, Georgarakis and colleagues estimated a minimum movement bandwidth requirement of 0.67Hzm and that elevating the arm to 68° at a peak speed of $171\frac{^\circ}{s}$ would take 0.4s [18]. Assuming that an implementation requires 20cm of cable travel (with a 30mm diameter pulley) to elevating the arm in this time, the required rotor speed would be $5.3\frac{rad}{s}$. At this frequency and speed, the motors perform with almost no signal attenuation, and a phase shift of between 5 and 10 degrees. For lower-limb applications, sources estimate that step frequencies can range between 0.3Hz (incidental stepping) and 2.0Hz (brisk walking) in both healthy and impaired adult populations [19], [20]. Within this range of frequencies, the phase shift does not exceed 15° across all peak rotor speeds, but for the higher range of walking speeds, amplitude attenuation starts to drop off for the lower range of peak rotor speeds. Ultimately, these results also need to be considered in the context of the final exosuit design, as it depends on the kinematics of the cable routing, supported joints, and the anticipated application.

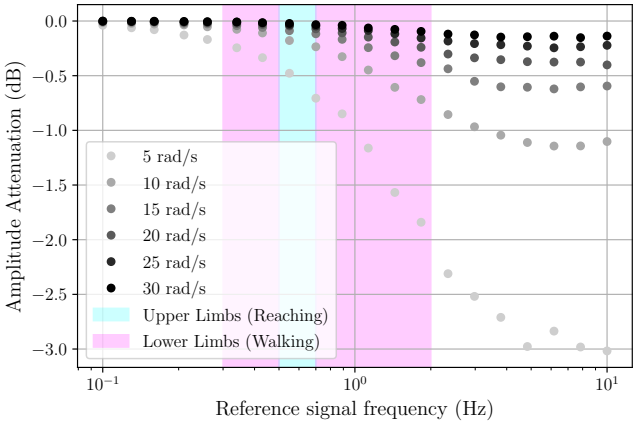


Fig. 6. Magnitude Bode plot demonstrating the velocity amplitude attenuation with increasing frequency, across a range of velocity amplitudes.

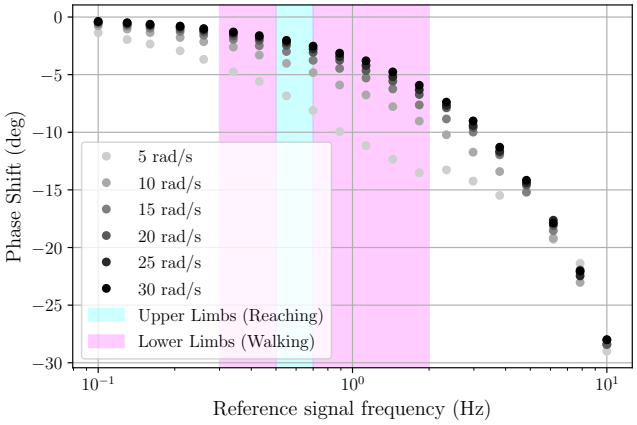


Fig. 7. Phase-shift Bode plot demonstrating the increasing lag with increasing driving frequency, across a range of velocity amplitudes.

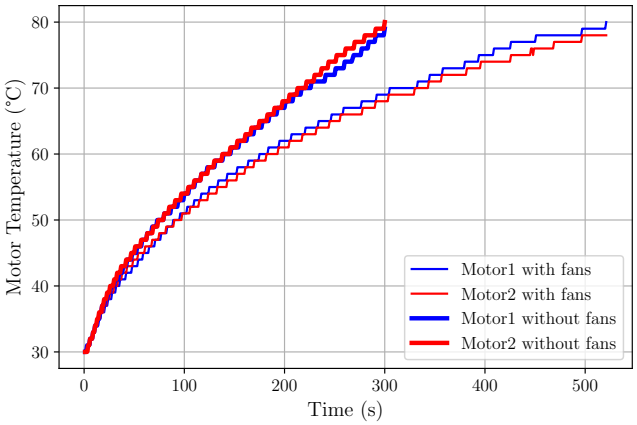


Fig. 8. Temperature rise curves for both TDU motors while under a constant dynamic load, with and without the cooling airflow from the side-mounted fans.

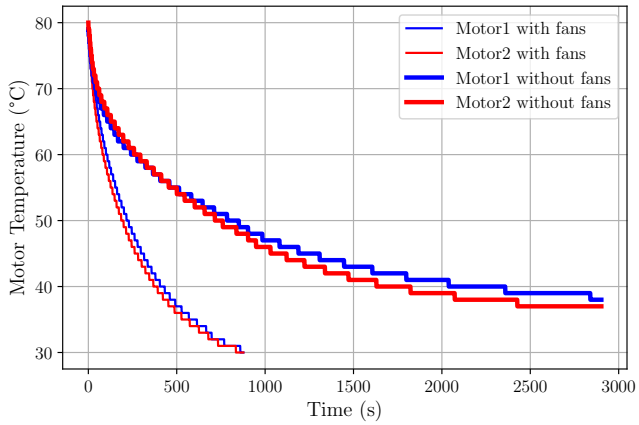


Fig. 9. Temperature fall curves for both TDU motors after heated under a constant dynamic load, with and without the cooling airflow from the side-mounted fans.

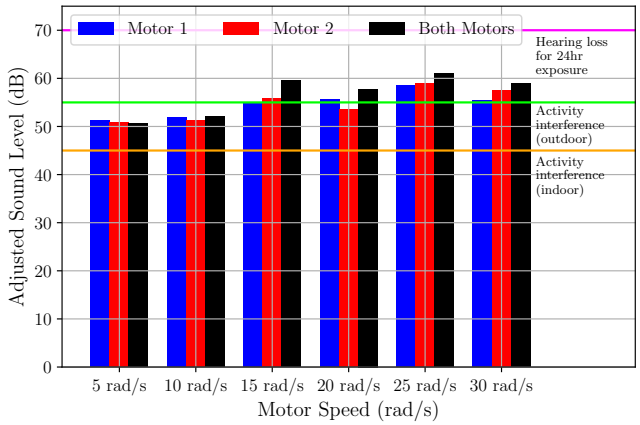


Fig. 10. Noise test results for the individual and combined motors across different operating speeds.

C. Thermal Cooling

The cooling effect of the fans is demonstrated in the temperature rise and fall times (Fig. 8 and 9). During the tests, the ambient air temperature was measured at 23°C. Without the fans enabled it took only 300s for the stator temperature to rise from 30°C to 80°C, while with the fans enabled it took 520s for the same change in temperature. The effect of convective cooling is also apparent during the cooling phase, as the fans could bring the stator temperature from 80°C back down to 30°C in 850s, whereas with only conductive cooling it took approximately 2000-3000s for the temperatures to fall back down below 40°C. These results in absolute terms depend on the ambient air temperature, how much heat is allowed to develop in the stator of the motor, and how fast the fans are controlled. For this particular test, the cutoff was set to 80°C, since PLA has a glass transition temperature of approximately 60°C (to avoid the case yielding or failing during the test).

Based on the thermal results from this test, it is clear that if the device will be used continuously at torques around 1.5Nm, a combination of active cooling (with fans) and perhaps controlled thermal throttling would be necessary for safe, long-term use (exceeding 10 minutes). This could be done by specifying stronger fans to improve airflow (and thus cooling), but this could come at the cost of increased noise during high-torque performance. Alternatively, one could implement a thermal throttling / rollback of the applied torque when the temperatures exceed a certain threshold (i.e. linearly reduce the output torque from 100% of commanded torque to 50% of commanded torque when the temperature is between 80 deg C and 120 deg C respectively). The specific implementation of such a the thermal control law would have to be researched and tested in further detail, but the general idea would be to trade-off performance for thermal management if the system overheats.

D. Noise

With the TDU on and only the fans running, the system had a noise level of 43.7dB. Across all active conditions tested, the TDU demonstrated sound levels ranging from 50.7dB up to 61.1dB. The US EPA identifies a constant 70dB over 24h as the upper level of environmental noise which will not cause any measurable hearing loss over ones life. Furthermore, levels of 55dB outdoors and 45dB indoors are identified as preventing activity interference and annoyance (ie these levels of noise permit spoken conversation and other activities such as sleeping, working and recreation) [21]. Thus the current design of this TDU should not over time cause any permanent hearing loss due to use, although during faster movements, the sound produced by the motors might hinder / obstruct conversations.

TABLE II
TDU RUN-TIME UNDER DIFFERENT LOADING CONDITIONS.

Condition	Mean Motor Torque (Nm) ± Standard Deviation (Nm)	Runtime (HH:MM:SS)
Idle	$8.16 \cdot 10^{-6} \pm 0.00128$	11:20:23
2kg	0.306 ± 0.0634	08:06:11
4kg	0.627 ± 0.0743	04:39:34
6kg	0.943 ± 0.0941	02:38:20

E. Battery Life

The battery life of the TDU depended greatly on the average external load imposed on it (Table II), ranging from over 11hr of idle / standby time, down to just over 2.5hr with a constant load of 0.943Nm on both motors. Ultimately, the battery life of the TDU in an exosuit application will also depend on other factors, such as the intended support levels, the user anthropometrics, the transmission efficiency, frequency of use, battery cell chemistry, or if the voltage range is padded. Future designs could also explore custom flat Lipo packs arranged in series and parallel to achieve the desired voltage and capacity.

V. Conclusion

This study presents a series of benchmarking tests that may be used to document the performance capabilities of cable-driven TDUs. The proposed tests capture static torque control, bandwidth of velocity control, thermal management, noise, and

battery life. As well, we present a lightweight and customizable TDU designed for cable-driven wearable applications, showcasing a modular design that allows flexibility in motor selection, pulley configuration, and sensor integration. The modularity of this TDU enables it to be easily adapted for various applications in upper and lower limb exosuits.

Our results reveal that the TDU provides accurate and repeatable torque control. Velocity control has a very high bandwidth, well covering the range of speeds required for upper and lower-limb movements. The cooling system proved effective, with fans extending operational duration under higher loads. Noise measurements indicate that, while the TDU is mostly unobtrusive, improvements could be made to reduce motor sound during high-speed operations. Furthermore, the battery tests confirm adequate runtime for practical, day-long use under moderate loading conditions.

The open sharing of our TDU's design and testing methodologies contributes to a collaborative approach within the exosuit research community. By making these resources publicly available we seek to promote advancements in assistive wearable technologies.

ACKNOWLEDGMENTS

The authors would like to thank Michael Herold-Nadig for his continuous support with debugging and integration of the electronics in the TDU. We thank fellow colleagues Alexander Breuss and David Rode for their support with the software and programming, and students Kai Stewart and Matthias Jammot for their contributions to the project. Finally, we acknowledge the constant emotional support of our lab dog Copper.



REFERENCES

[1] Xiloyannis, M., Alicea, R., Georgarakis, A. M., Haufe, F. L., Wolf, P., Masia, L., & Riener, R. (2021). Soft robotic suits: State of the art, core technologies, and open challenges. IEEE Transactions on Robotics, 38(3), 1343-1362.

[2] Bae, J., Siviy, C., Rouleau, M., Menard, N., O'Donnell, K., Geliana, I., ... & Walsh, C. J. (2018). A lightweight and efficient portable soft exosuit for paretic ankle assistance in walking after stroke. In 2018 IEEE international conference on robotics and automation (ICRA) (pp. 2820-2827). IEEE.

[3] Awad, L. N., Bae, J., O'donnell, K., De Rossi, S. M., Hendron, K., Sloot, L. H., ... & Walsh, C. J. (2017). A soft robotic exosuit improves walking in patients after stroke. Science translational medicine, 9(400), eaai9084.

[4] Asbeck, A. T., Schmidt, K., & Walsh, C. J. (2015). Soft exosuit for hip assistance. Robotics and Autonomous Systems, 73, 102-110.

[5] Kim, J., Lee, G., Heimgartner, R., Arumukhom Revi, D., Karavas, N., Nathanson, D., ... & Walsh, C. J. (2019). Reducing the metabolic rate of walking and running with a versatile, portable exosuit. Science, 365(6454), 668-672.

[6] Panizzolo, F. A., Freisinger, G. M., Karavas, N., Eckert-Erdheim, A. M., Siviy, C., Long, A., ... & Walsh, C. J. (2019). Metabolic cost adaptations during training with a soft exosuit assisting the hip joint. Scientific reports, 9(1), 9779.

[7] Asbeck, A. T., De Rossi, S. M., Holt, K. G., & Walsh, C. J. (2015). A biologically inspired soft exosuit for walking assistance. The International Journal of Robotics Research, 34(6), 744-762.

[8] Schmidt, K., Duarte, J. E., Grimmer, M., Sancho-Puchades, A., Wei, H., Easthope, C. S., & Riener, R. (2017). The myosuit: Bi-articular anti-gravity exosuit that reduces hip extensor activity in sitting transfers. Frontiers in neurorobotics, 11, 57.

[9] Park, H., Lan, J., Zhang, J., Chen, K., & Fu, C. (2019). Design of a soft wearable device for hip and knee extension assistance. In 2019 5th International Conference on Control, Automation and Robotics (ICCAR) (pp. 798-801). IEEE.

[10] Chen, C., Zhang, Y., Li, Y., Wang, Z., Liu, Y., Cao, W., & Wu, X. (2020). Iterative learning control for a soft exoskeleton with hip and knee joint assistance. Sensors, 20(15), 4333.

[11] Nycz, C. J., Delph, M. A., & Fischer, G. S. (2015). Modeling and design of a tendon actuated soft robotic exoskeleton for hemiparetic upper limb rehabilitation. In 2015 37th annual international conference of the IEEE engineering in medicine and biology society (EMBC) (pp. 3889-3892). IEEE.

[12] Pont, D., Contreras, A. F., Samper, J. L., Sáez, F. J., Ferre, M., Sánchez, M. Á., ... & García, Á. (2019). Exoflex: An upper-limb cable-driven exosuit. In Iberian Robotics Conference (pp. 417-428). Cham: Springer International Publishing.

[13] Samper-Escudero, J. L., Gimenez-Fernandez, A., Sánchez-Urán, M. Á., & Ferre, M. (2020). A cable-driven exosuit for upper limb flexion based on fibres compliance. IEEE Access, 8, 153297-153310.

[14] Choi, H., Kang, B. B., Jung, B. K., & Cho, K. J. (2019). Exo-wrist: A soft tendon-driven wrist-wearable robot with active anchor for dart-throwing motion in hemiplegic patients. IEEE Robotics and Automation Letters, 4(4), 4499-4506.

[15] Georgarakis, AM., Xiloyannis, M., Wolf, P. et al. A textile exomuscle that assists the shoulder during functional movements for everyday life. Nat Mach Intell 4, 574–582 (2022). https://doi.org/10.1038/s42256-022-00495-3

[16] Bardi, E., Esser, A., Wolf, P., Gandolla, M., Ambrosini, E., Pedrocchi, A., & Riener, R. (2024). Sensorless model-based tension control for a cable-driven exosuit. arXiv preprint arXiv:2406.18412.

[17] Lee, U. H., Pan, C. W., & Rouse, E. J. (2019). Empirical characterization of a high-performance exterior-rotor type brushless DC motor and drive. In 2019 IEEE/RSJ International Conference on Intelligent Robots and Systems (IROS) (pp. 8018-8025). IEEE.

[18] Georgarakis, A. M., Song, J., Wolf, P., Riener, R., & Xiloyannis, M. (2020). Control for gravity compensation in tendon-driven upper limb exosuits. In 2020 8th IEEE RAS/EMBS International Conference for Biomedical Robotics and Biomechatronics (BioRob) (pp. 340-345). IEEE.

[19] Tudor-Locke, C., Han, H., Aguiar, E. J., Barreira, T. V., Schuna Jr, J. M., Kang, M., & Rowe, D. A. (2018). How fast is fast enough? Walking cadence (steps/min) as a practical estimate of intensity in adults: a narrative review. British journal of sports medicine, 52(12), 776-788.

[20] Bohannon, R. W. (1986). Strength of lower limb related to gait velocity and cadence in stroke patients. Physiotherapy Canada, 38(4), 204-206.

[21] EPA Press Release, Version: 1974-04-02, Accessed: 05.11.2024, Available: https://www.epa.gov/archive/epa/aboutepa/epa-identifies-noise-levels-affecting-health-and-welfare.html

Towards a real-time, interactive, incremental learning algorithm for prosthetic myocontrol

Michele Canepa
Rehab Technologies Lab
Istituto Italiano di Tecnologia
Open University (ARC@IIT)
Genoa, Italy
michele.canepa@iit.it

Lorenzo Marucchi
Rehab Technologies Lab
Istituto Italiano di Tecnologia
Genoa, Italy
Politecnico di Milano, Italy
lorenzo.marucchi@iit.it

Nicolò Boccardo
Rehab Technologies Lab
Istituto Italiano di Tecnologia
Open University (ARC@IIT)
Genoa, Italy
nicolo.boccardo@iit.it

Andrea Marinelli
Rehab Technologies Lab
Istituto Italiano di Tecnologia
Genoa, Italy
andrea.marinelli@iit.it

Dario Di Domenico
Rehab Technologies Lab
Istituto Italiano di Tecnologia
Genoa, Italy
DET, Politecnico di Torino, Italy dario.didomenico@iit.it

Marta Gandolla
Dept. Mechanical Engineering
Politecnico di Milano, Italy
Milano, Italy
marta.gandolla@polimi.it

Matteo Laffranchi
Rehab Technologies Lab
Istituto Italiano di Tecnologia
Genoa, Italy
matteo.laffranchi@iit.it

Claudio Castellini
Assistive Intelligent Robotics Lab (AIROB)
Friedrich-Alexander-Universität
Erlangen, Germany
claudio.castellini@fau.de

***Abstract*— Myocontrol based upon machine learning usually requires a large initial labeled dataset to build its model and prescribes that said model will never change in the course of time. This approach has several limitations, e.g., the difficulty of building such a proper dataset and the low generalization power of the obtained model against the variety of situations encountered by the user in daily life. In this work we introduce an interactive, incremental learning method for intention detection in real-time, along with some optimization techniques. The method enables users to quickly update the myocontrol system on demand, reducing the impact of the non-stationarity of input signals, improving the generalization power and providing an interactive experience to the user.**

Keywords—Prosthetic control, incremental learning, EMG intent detection

Research and commercial efforts in upper-limb prosthetics strive to create highly functional replacements for missing limbs. These advanced prostheses, often equipped with multiple motors and designed for various levels of amputation, exhibit advanced dexterity and prehensile abilities. They can replicate a significant portion of the mechanical performance of natural limbs, offering, in principle, high biomimicry [1]. What is still missing is an effective way to volitionally control complex, multi-motor prostheses in a *natural* fashion (accurately, simultaneously and proportionally), due to the lack of a suitable method of extracting enough independent motor commands from the residual user biosignals [2]. In practice, a user's intended movement triggers contractions in residual muscles, which can be recorded and interpreted by surface electromyography (sEMG) sensors. Early control strategies, such as dual-site direct control or methods based on finite state machine, rely on the sequential selection of motors or grips through brief co-contractions of antagonist muscles. Despite their utility, these methods lack intuitive and simultaneous control capabilities. To address this, pattern recognition (PR) techniques based on machine learning (ML) have been largely employed, mapping specific movements to distinct muscle activation patterns and enable multi-joint control [3]. However, as most systems use classifiers, they do not allow simultaneous control of multiple actions. To address this issue, regression-based approaches have been used, since these algorithms do not map discrete movements to muscular patterns, but rather estimate a proportional activation for each degree of freedom, providing the user with a continuous, physiologically acceptable manifold of actions [4]. Another limitation is that both classification and regression-based control systems typically use "monolithic" training approaches. They require a comprehensive, labeled dataset covering all desired actions to be gathered in the beginning, thus keeping the trained model fixed in the course of time. This approach severely limits the generalization power of the underlying ML model over time. Indeed, in real-life scenarios, multiple disturbances, deriving from the variability of sEMG signals over time, seriously affect the pre-trained model accuracy [5, 6]. In contrast to monolithic learning, an alternative, less explored class of algorithms, involves the usage of regressors in combination with incremental learning techniques [7]. Incremental learning allows ML models to be updated and downdated on demand, i.e., to quickly adapt the model to novel data distributions, avoiding the training from scratch. In myoelectric control, the effectiveness of incremental training to counter non-stationarity in the data distribution has been shown in [8, 9] [10, 11] and more recently on high-density sEMG configuration in [12]. These works show that both intact and limb-absent users benefit from on-demand updates, showing better acceptance, faster task completion times and higher trajectory quality on both lab-designed and daily living tasks. However, these approaches still do not explore the possibility of dynamically labeling new set of input data on-the-fly and adapt the model weights as needed; moreover, a serious analysis of the computational requirements of incremental learning approaches versus the traditional ones is missing. In Castellini 2016 [7], it is suggested the concept of *interactive learning*, in which the user can trigger the adaptation of the underlying ML model, notifying to the

This work was supported by the Istituto Nazionale Assicurazione Infortuni sul Lavoro, under grant agreement PR23-PAS-P1 DexterHand and by the German Federal Ministry of Education and Research (BMBF) under the Robotics Institute Germany (RIG). The Open University Affiliated Research Centre at Istituto Italiano di Tecnologia (ARC@IIT) is part of the Open University, Milton Keynes MK7 6AA, United Kingdom.

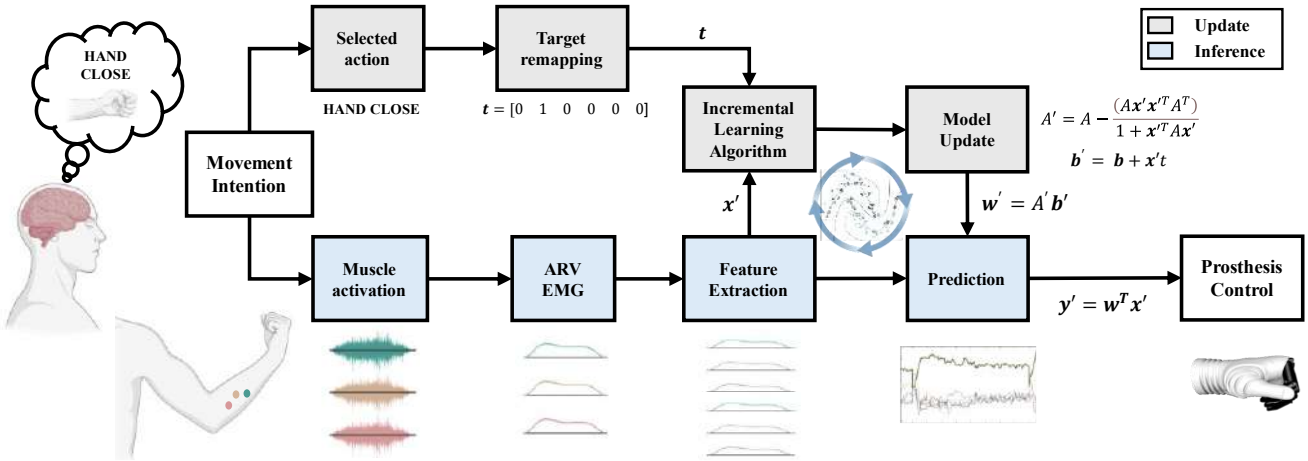


Figure 1 Interactive Incremental Learning Algorithm concept: whenever training is needed, the user, according to its movement intention, simultaneously executes the muscle activation pattern and communicates the selected action to the algorithm. After target remapping, the target vector t is sent to the incremental learning algorithm. At the same time, ARV of EMG signals are measured by the sensors. Features are extracted from signals, to obtain the input vector x'. The incremental learning algorithm updates the model weights w and updates the predictions y' accordingly. During normal operation, predictions are made using last model weights and prosthesis is controlled to execute the required action.

system the action to be mapped to the current muscular pattern. The author suggested also a set of requirements that the system should respect, being adaptive, quickly calibrated, bounded in memory and time, and, of course, incrementally trainable. This study aims to provide a starting point towards the design of an adaptive, real-time, interactive, incremental learning system usable in a real prosthetic scenario. To this end, we collected EMG data from able-bodied and trans-radial amputees during hand and wrist movements, implementing an offline simulation of an *interactive incremental learning algorithm* (I2LA) pipeline (Figure 1). Beginning with an empty model, we simulated user interactions for real-time labeling to identify best algorithm configurations. We compared different approaches to feature extraction and target remapping, proposing a methodology to explore sensitivity to hyperparameters tuning. We assess performance through standard regression metrics, demonstrating the algorithm ability to adapt model weights in real-time to new EMG data and accurately remap predictions to previously unseen patterns, with the final goal of controlling an advanced hand and wrist [13] trans-radial prostheses.

I. Materials and Methods

A. Participants

We recruited 20 healthy participants (ages 22–33, mean age 27.1 ± 3.2) and 10 individuals with unilateral trans-radial amputation of the dominant limb, all experienced in using active prostheses. Each participant provided written informed consent prior to the study, which followed the principles of the Declaration of Helsinki and received approval from the Bologna-Imola ethics committee (CP-PPRAS1/1-01).

B. Experimental Setup

Figure 2 illustrates the experimental setup. Six pre-amplified bipolar EMG sensors (13E200=50 AC Ottobock or equivalent IIT miniature circular sensors [11]) were positioned approximately 5 cm below the olecranon around the forearm or stump. These sensors, which are commonly used in prosthetic applications, recorded averaged, rectified, and amplified muscle activity (ARV) during hand open-close (HOC), wrist pronation-supination (WPS), and wrist flexion-extension (WFE) movements. The muscles monitored were identified through manual and visual inspection, (Figure 2B) targeting Extensor Carpi Radialis Longus (E0), Extensor Digitorum (E2), Extensor Carpi Ulnaris (E4), Palmaris Longus and Flexor Carpi Ulnaris (E1), Flexor Carpi Radialis (E3), and Brachioradialis (E5). Participants performed 10 repetitions for each of the 6 movements, with 2-second intervals of recorded muscle activity. Movement cues were displayed on a PC interface that presented an animated Hannes prosthetic hand [1], guiding each movement. The EMG signals were sampled at 1 kHz with a 12-bit resolution using a custom microcontroller board, also used to control the prosthetic arm. Additionally, we recorded 16 repetitions of a resting state (2 seconds each) interspersed with gesture repetitions to introduce rest periods after each contraction. The data was wirelessly transferred to a PC via Bluetooth and labeled according to the task performed.

C. Interactive Incremental Learning Algorithm for Prosthetic Control

This study investigates a scenario where the user can update the control model in real-time, sending feedback to the machine, via a human machine interface, labeling new actions as they are performed. Therefore, we are looking for an algorithm which can be incrementally trained and updated, i.e. which can quickly adapt its weights according to a new $(\boldsymbol{x}, \boldsymbol{t})$ pair, with $\boldsymbol{x}$ the input vector of dimensionality d and $\boldsymbol{t}$ the target vector of dimensionality m. To this end, we implemented an incremental version of the Ridge Regressor algorithm (RR), a regularized variant of least-squares regression. In the monolithic general form, for a single action $(m = 1)$, with a training set of N samples and input vector of dimension d, we define the matrix $X \in \mathbb{R}^{N\,x\,d}$ representing the training set, and the targets vector $\boldsymbol{t} \in \mathbb{R}^N$.
The RR model $\boldsymbol{w}$ is then defined by:

$$\boldsymbol{w} = (X^TX + \lambda I)^{-1}X^T\boldsymbol{t} \qquad (1)$$

A prediction $y' \in \mathbb{R}$ associated to a new sample of the input vector $x' \in \mathbb{R}^d$, is then given by the formula:

$$y' = w^T x' \qquad (2)$$

To transform the monolithic RR model in an incremental one, we exploit a very simple solution (rank-1 update method), in which the arrival of a new pair of input sample and target (label) is considered as a perturbation of the inverse matrix $(X^T X + \lambda I)^{-1}$. In fact, Equation (1) can be rewritten as

$$w = (X^T X + \lambda I)^{-1} X^T t := Ab \qquad (3)$$

Where $A = (X^T X + \lambda I)^{-1}$ and $b = X^T t$.
Given a new sample and target pair (x', t), the updated model $w' = A'b'$ is given by applying the Sherman-Morrison formula [14]

$$A' = A - \frac{(Ax' x'^T A^T)}{1 + x'^T A x'} \qquad (4)$$

$$b' = b + x' t \qquad (5)$$

The initial matrix is set to obtain the empty model at the beginning of time $w_{t0} = 0$, therefore $A_{t0} = \frac{1}{\lambda} I$ and $b_{t0} = 0$. Figure 1 illustrates the algorithm's operation: during use, the model predicts movement intention based on the latest model weights, w, through Equation (2). The model updates with new sample-target pairs (new data stream) as needed, recalculating w' via Equation (4) and (5). For multiple actions, *m* independent instances of the RR model are trained for each action. The algorithm was implemented and analyzed using Matlab R2024b (Natick, MA, USA) on a desktop with an Intel i5-9400 CPU.

D. Model training and validation

Starting from the dataset of each subject, we define an empty model and simulate the effect of communicating to the algorithm the selected action during muscle activation, sample by sample. For each action, participants performed 10 repetitions, with 5 used for training and 5 for validation. The training and validation repetitions were randomized. During the training phase, the model adjusts its coefficients in real-time with new EMG data samples. In the validation phase, the model uses the latest weights to make predictions, which are then compared to target values to assess accuracy.

E. Interactive Incremental Learning Algorithm Pipeline

We tailored our pipeline to meet specific needs for computational efficiency and real-time processing, relying on only the (x', t) pairs available at each time instant. Then, we analyzed the impact of combining different feature extraction methods with various *target remapping* strategies, i.e., different ways of delivering information about the selected actions to the algorithm. For what concerns feature extraction, after normalizing EMG signals to the range [0.0, 1.0], we compared various methods (linear, quadratic, cubic, and Random Fourier Features (RFF) [15]). RFF projects input data into a higher dimensionality feature space, enabling the usage of linear methods, such as the incremental learning algorithm, to solve non-linear problems. We chose polynomial methods and RFF because they are fast to compute with limited resources. We also tested the sensitivity of feature dimensionality parameter D on RFF up to 300. TABLE II lists the methods investigated and the complexity obtained with 6 EMG sensors as input. As for target remapping, we explored also different target value assignment strategies. In *single action* variant, only the regressor for the selected action was trained, with target value of 1.0. In *all actions* variant, we train all regressors simultaneously, by assigning 1.0 to the selected action and 0.0 to the other actions. In *antagonist compensation* variant we set the target value to 1.0 for the selected action and -1.0 for the antagonist action, 0.0 to the others.

F. Best algorithm variant search and hyperparameters tuning

To optimize RFF feature extraction, we tuned two hyperparameters: γ (controlling the locality of Radial Basis Function kernel approximation, with high values leading to more localized features) and D (feature dimensionality). Using 5-fold cross-validation over the training set (5 of the 10 repetitions), we optimized γ over a coarse search range $\gamma \in [2^{-8}, 2^{-7}, \dots, 2^{7}]$ and refining the search over $\gamma \in [2^{0}, 2^{0.3}, \dots, 2^{4}]$. We determine the optimal γ values separately for able-bodied (AB) and limb different (LD)

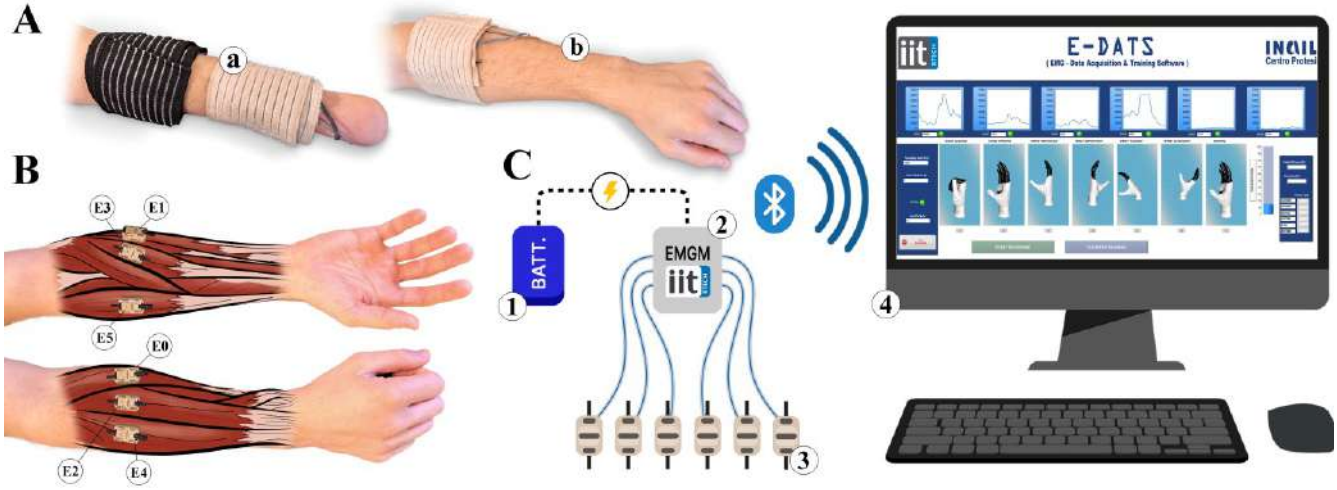


Figure 2 Experimental Setup: (A) LD (a) and AB (b) subjects wore 6 ARV EMG sensors targeting 6 main muscles (B). (C) Signals are sampled via a custom microcontroller board (2) and streamed to the PC via Bluetooth. A custom GUI (4) was used to record signals and synchronize the 6 actions plus rest.

subjects to account for the variability of the EMG signals between the two groups. The performance of each feature extraction and target remapping method was then assessed under these optimal γ values. The prediction accuracy is affected by dimensionality of the input data. However, the complexity, computing time and memory footprint needed to run the algorithm in real-time increases quadratically with *D*, and a careful tradeoff is needed to avoid wasting precious computational resources. To this end, we report the performances with different values of *D* up to 300 (21, 27, 83, 100, 300), using the best γ_{AB} , γ_{LD} value for the two populations, respectively. D values up to 83 are selected to ensure a fair comparison between RFF and the polynomial variants, maintaining the same output features dimensionality (see TABLE II).

G. Regularization parameter optimization (λ)

For final optimization, we adjusted the Ridge Regression regularization parameter λ through 5-fold cross-validation on the training set, using the best pipeline configuration.

H. Accuracy Evaluation Metrics

We evaluated model accuracy with adjusted R^2 and Bayesian Information Criterion (BIC), which are typically used to assess regressor performance.

II. Results

A. RFF hyperparameters tuning

TABLE I illustrates the results of the RFF hyperparameter optimization, including the optimal γ values, average adjusted R^2, and standard deviation across different feature dimensionalities (D) for both able-bodied and limb-different groups. Figure 3 shows an example of the grid search output for D=83: we observe that performance varies substantially with γ and reaches a global maximum within the fine-tuning interval. Accuracy was generally higher and with lower variability for able-bodied participants compared to limb-different participants. In TABLE I is reported the relationship between prediction accuracy and D, showing that increasing D enhances accuracy, as expected. However, beyond D=83, further increases in D yield no statistically significant

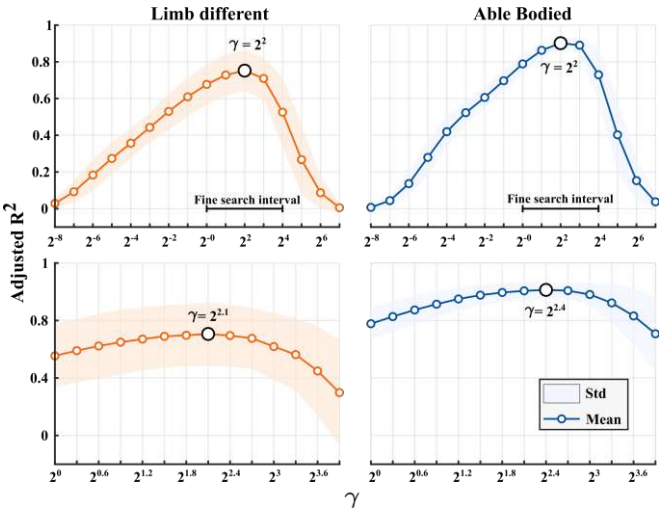


Figure 3 Random Fourier Features hyperparameters optimization. Accuracy for LD and AB subjects vs. γ parameter for D=83. Solid lines are the mean value among subjects; shaded area is the standard deviation.

TABLE I Optimal gamma values and accuracy of random fourier features variants

RFF D	γ_{LD}	γ_{AB}	R^2adj_{LD}	R^2adj_{AB}
21	$2^{1.2}$	$2^{1.5}$	0.6571 (±0.1140)	0.8090 (±0.0343)
27	$2^{1.2}$	$2^{1.8}$	0.6883 (±0.1109)	0.8245 (±0.0397)
83	$2^{2.1}$	$2^{2.4}$	0.7532 (±0.1108)	0.9065 (±0.0297)
100	$2^{2.1}$	$2^{2.4}$	0.7542 (±0.1122)	0.9130 (±0.0242)
300	$2^{2.4}$	$2^{2.7}$	0.7755 (±0.1121)	0.9343 (±0.0202)

improvement (p-value > 0.05), suggesting that additional complexity could result in unnecessary computational costs without accuracy gains.

B. Best feature extraction and target remapping combination

Figure 4 shows the combined analysis of feature extraction and target remapping strategies, with results separated for able-bodied and limb-different participants. Box plots display the adjusted R^2 and BIC metrics. The single action target remapping strategy yielded low accuracy across all feature extraction methods. In many cases, the adjusted R^2 mean was negative, indicating the model performed worse than a simple average of the outcome variable. In contrast, methods that assigned target values to all actions simultaneously significantly improved performance, supporting the hypothesis that muscle activation patterns for different actions interfere with one another. Thus, each incremental RR model must be trained in parallel across all actions with each (x', t) input sample to obtain useful results. We observed no significant difference in performance between assigning zeros to non-selected actions (all actions) and assigning a negative value to antagonistic actions (antagonist compensation). Adjusted R^2 and BIC metrics revealed similar qualitative trends across methods, underscoring their consistency in highlighting the most effective approaches. To compare polynomial methods with Random Fourier Features, we matched D values between RFF and polynomial feature extraction techniques. Figure 4 demonstrates that RFF consistently outperformed polynomial methods, showing statistically significant differences in accuracy (1-way ANOVA, p-value<0.001 in AB). Based on these findings, we identified the best model configuration that minimizes computational complexity and memory use while maintaining high predictive accuracy. This configuration uses the RFF feature extraction method with *D*=83, $\gamma_{LD}=2^{2.1}$, $\gamma_{AB}=2^{2.4}$, and *all actions* target remapping method.

C. Regularization parameter cross-validation (λ)

Regarding the cross validation of λ parameter, we found similar performances for a broad range of values, spanning from 2^{-12} to 2^{-3}. It is convenient to choose the higher λ value maintaining acceptable performances to prevent overfitting.

D. Model real-time update

Figure 5 illustrates the algorithm's operation using the best model configuration with RFF feature extraction (D=83, all-actions target remapping) on a training dataset from a limb different participant. Figure 5B shows the evolution of model weights for each action, where each color represents a distinct weight. At the starting point (t = 0s), all model weights are set to zero, so no action is predicted, regardless of the EMG

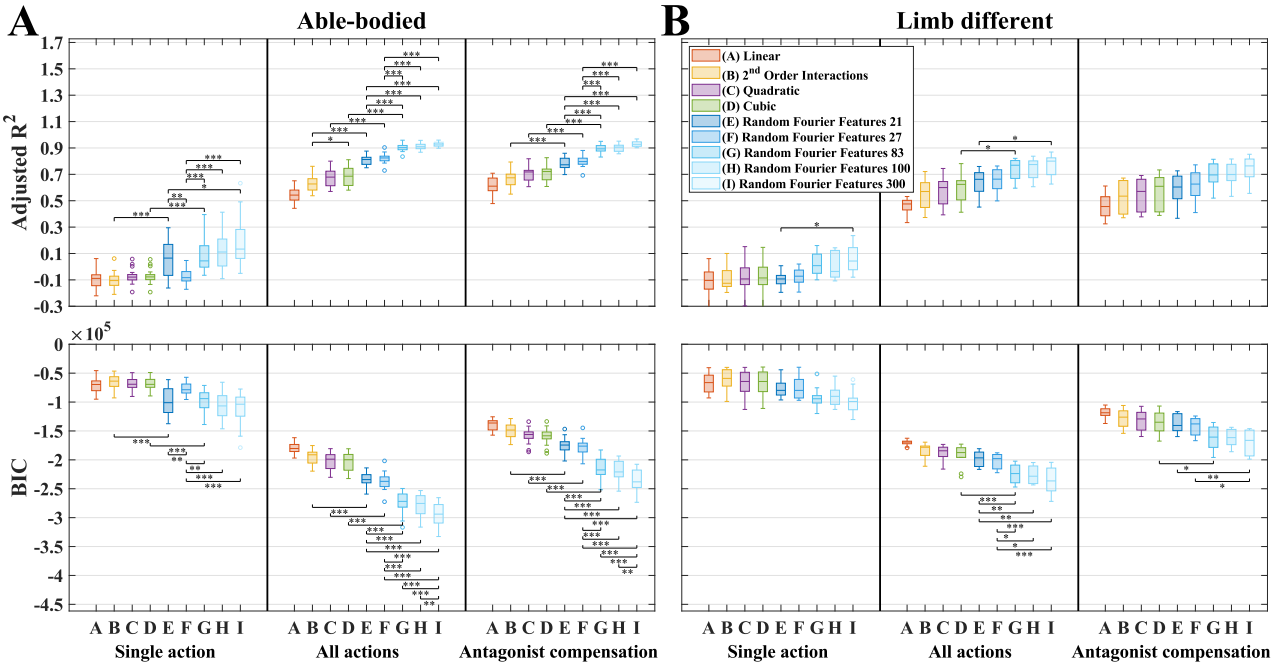


Figure 4 Algorithm performance vs feature extraction and target remapping methods: whisker plots of adjusted R^2 and BIC are represented separately for AB (A) and LD (B) population. (* p-value<0.05, ** p-value<0.01, *** p-value<0.001)

inputs. From t = 0s to t = 10s, the hand close action is incrementally trained based on EMG inputs, causing the weights to adjust almost immediately and stabilize into a reliable prediction. Between t = 10s and t = 20s, training for the hand open action begins with a target value of 1.0. The model modifies weights to establish a stable hand open prediction, while simultaneously realigning weights for the previously learned hand close action (now with a target of zero) to distinguish between the two learned actions. In each subsequent 10-second interval, the remaining actions are trained similarly. This progressive adjustment of model weights demonstrates how the model adapts in real time to new targets and muscular patterns.

III. Discussions

Results demonstrate the effectiveness of using RFF for feature extraction, showing significant performance improvements over polynomial feature extraction methods, both in able-bodied and limb-different participants. The superior performance of RFF over polynomial features suggests its capacity to approximate non-linear relationships in myoelectric data providing a robust basis for enhancing control accuracy. The influence of the gamma (γ) parameter on RFF performance was significant, highlighting the importance of tuning this parameter to maximize model accuracy. Our findings indicate that once the best γ is identified for a given D (dimensionality), this parameter generalizes well across users with similar characteristics, such

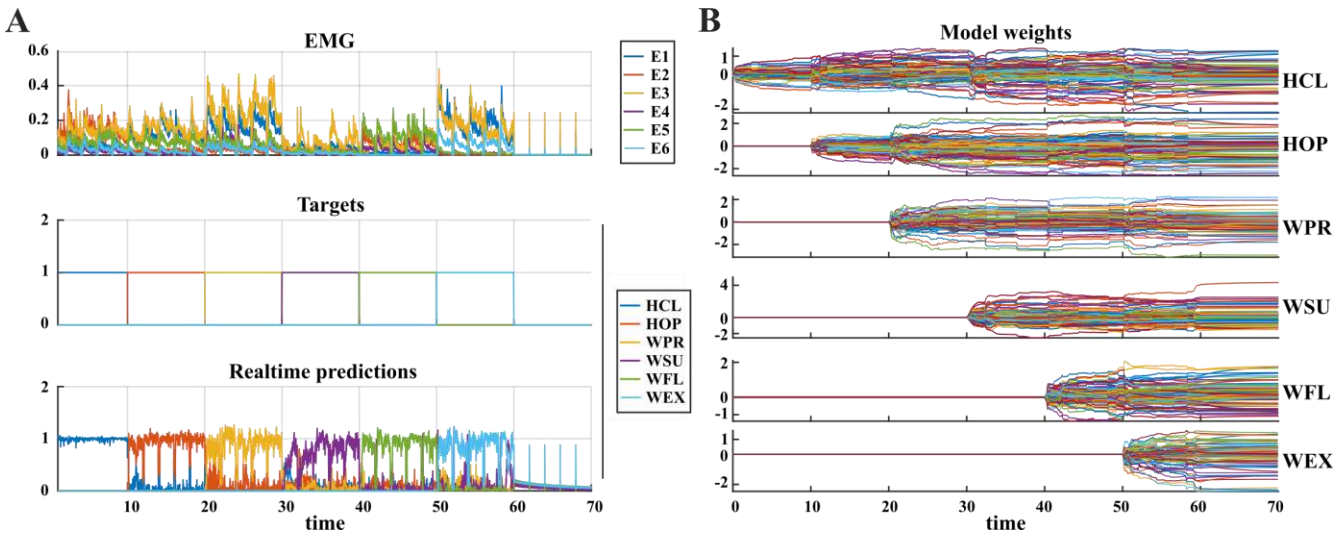


Figure 5 Incremental Learning Algorithm real-time prediction: (A) EMG signals, targets and actions prediction in real-time; (B) model weights evolution for each action. The model dynamically evolves its weights according to the prescribed action and updates the prediction simultaneously.

TABLE II FEATURE EXTRACTION METHODS AND COMPLEXITY

Feature type	d(n)	d(6)
Linear	n+1	7
Interaction 2*nd* order	C(n+2,2) - n	22
Quadratic	C(n+2,2)	28
Cubic	C(n+3,3)	84
RFF (D=21)	D+1	22
RFF (D=27)	D+1	28
RFF (D=83)	D+1	84
RFF (D=100)	D+1	101
RFF (D=300)	D+1	301

as able-bodied or limb-different groups, and for similar task demands. This generalizability reduces the need for repeated, individualized parameter tuning while still supporting a high level of accuracy and user-specific adaptation. While increasing the D value generally improved performance, this effect stabilized after specific D value corresponding to 83 yielding diminishing returns on accuracy. Higher D values will result in increased computational complexity, longer processing times, and higher memory requirements, which could limit real-time application feasibility in prostheses. Therefore, a balance must be established, selecting the best D value that achieves robust performance. Our study indicates that D = 83 is an efficient tradeoff, making it well-suited for embedded processing in low-power environments. A comparative analysis of results from able-bodied and limb-different subjects revealed similar accuracy trends, although able-bodied participants consistently achieved higher prediction accuracies and less variability. This discrepancy reflects the differences in muscle physiology and signal quality between able-bodied and limb-different users, particularly in terms of muscle mass and EMG signal consistency. However, the similar trends observed in both groups suggest that the incremental learning algorithm and selected feature extraction techniques can be applied effectively across a range of users with appropriate parameter adjustments. The target remapping strategy was also a critical factor in model performance. Our results indicate that training all regressors simultaneously and assigning positive target values for the selected action, combined with null targets for other actions, produced more accurate predictions than exclusive remapping for each action separately. The main limitation to the generalization of the results is the usage of gestures obtained from a single stationary position of the limb, without the prosthesis weight: this will be addressed in future works applied to the prosthetic scenario.

IV. CONCLUSIONS

In conclusion, this work presents an innovative approach to incrementally training intention-detection models for prosthetic control, which could empower users to personalize the internal intention detection model with minimal or no assistance. By embedding this incremental learning algorithm in a prosthetic device and designing an intuitive interface for selecting actions, users could independently train their prostheses to recognize and respond accurately to their specific EMG signal patterns. This would mean each model could be tailored to the individual's unique muscle responses and configurations, while being easily and quickly retrained by the user. This on-the-fly adjustment would enable near-instantaneous updates to the model, potentially requiring minimal computational power and memory. By offering real-time adaptability, this approach addresses one of the biggest challenges in myoelectric control: maintaining stable, responsive prosthetic performance adapting to the variable nature of the EMG control interface. Moreover, the usage of regression can enable simultaneous and proportional control, when associated with an appropriate prosthesis control strategy. In essence, this approach could significantly enhance the usability and effectiveness of myoelectric prostheses, providing a path for users to take control of their own customization and fine-tuning. With the ability to refine and update their prosthesis's functionality in response input variations, users could experience a higher level of control and precision in everyday prosthetic use, without the need for lengthy recalibration sessions or reliance on external support. Future work will implement these algorithms in real-time on a realistic prosthetic device, exploring the capability of an interactive retrain system to align muscular patterns to user intention incrementally and almost instantaneously.

REFERENCES

[1] M. Laffranchi *et al.*, "The Hannes hand prosthesis replicates the key biological properties of the human hand", *Science Robotics,* 2020.

[2] D. Farina *et al.*, "Toward higher-performance bionic limbs for wider clinical use", *Nature Biomedical Engineering,* pp. 1-13, 2021.

[3] A. Marinelli *et al.*, "Active upper limb prostheses: A review on current state and upcoming breakthroughs", *Progress in Biomedical Engineering,* 2022.

[4] J. M. Hahne *et al.*, "Simultaneous control of multiple functions of bionic hand prostheses: performance and robustness in end users", *Science Robotics,* 2018.

[5] A. Radmand *et al.*, "A characterization of the effect of limb position on EMG features to guide the development of effective prosthetic control schemes", *Annu Int Conf IEEE Eng Med Biol Soc,* pp. 662-7, 2014.

[6] I. Kyranou *et al.*, "Causes of performance degradation in non-invasive electromyographic pattern recognition in upper limb prostheses", *Frontiers in Neurorobotics,* vol. 12, Sep 2018.

[7] C. Castellini, "Incremental learning of muscle synergies: from calibration to interaction", *Human and Robot Hands: Sensorimotor Synergies to Bridge the Gap Between Neuroscience and Robotics*, Springer International Publishing, 2016, pp. 171-193.

[8] A. Gigli *et al.*, "Feedback-aided data acquisition improves myoelectric control of a prosthetic hand", *Journal of Neural Engineering,* vol. 17, no. 5, p. 056047, 2020.

[9] I. Strazzulla *et al.*, "Online bimanual manipulation using surface electromyography and incremental learning", *IEEE Trans Neural Syst Rehabil Eng,* vol. 25, no. 3, pp. 227-234, Mar 2017.

[10] M. Nowak *et al.*, "Simultaneous assessment and training of an upper-limb amputee using incremental machine-learning-based myocontrol: a single-case experimental design", *Journal of NeuroEngineering and Rehabilitation,* vol. 20, no. 1, p. 39, 2023.

[11] M. Nowak *et al.*, "Applying radical constructivism to machine learning: a pilot study in assistive robotics", *Constructivist Foundations,* vol. 13, no. 2, pp. 250-262, 2018.

[12] D. Di Domenico *et al.*, "Long-term upper-limb prosthesis myocontrol via high-density sEMG and incremental learning", *IEEE Robotics and Automation Letters,* pp. 1-8, 2024.

[13] N. Boccardo *et al.*, "Development of a 2-DoFs actuated wrist for enhancing the dexterity of myoelectric hands", *IEEE Transactions on Medical Robotics and Bionics,* vol. 6, no. 1, pp. 257-270, 2024..

[14] W. W. Hager, "Updating the inverse of a matrix", *SIAM Review,* vol. 31, no. 2, pp. 221-239, 1989.

[15] A. Rahimi and B. Recht, "Random features for large-scale kernel machines", *Neural Information Processing Systems*, 2007.

Machine Learning-Based Estimation of Upper Extremity Function in Stroke Rehabilitation Using Body-Worn Inertial Sensors

Shusuke Okita[1,2], Jared Berry[3], Rushmin Khazanchi[4], Francesco Lanotte[1,2], Megan K. O'Brien[1,2], and Arun Jayaraman[1,2,5,*]

***Abstract*— Neurological injuries such as stroke are a leading cause of disability, significantly impairing upper extremity (UE) function. Standardized clinical assessments are essential to evaluate patient function, monitor progress, and tailor interventions; however, these assessments are time-consuming to administer and require specialized training, limiting their accessibility. We developed a machine learning model to estimate Action Research Arm Test (ARAT) scores with wearable inertial sensors, aiming to reduce patients' and clinicians' workloads in rehabilitation. Twenty-three patients with chronic stroke performed the ARAT with ActiGraph sensors on their wrists and waist. Models used these data to predict the total ARAT score from a minimal set of UE tasks, selecting one item from each ARAT sub-test (grasp, grip, pinch, and gross movement). A nested cross-validation was used to optimize item selection, feature selection, and hyperparameters. The optimized model achieved a median absolute error of 3.81 points, and a coefficient of determination of 0.93 to estimate the total ARAT score. SHapley Additive exPlanations (SHAP) values identified key contributors to the predictions in each ARAT sub-test. The proposed approach demonstrates the potential of combining wearable sensor data with machine learning to facilitate more frequent and efficient monitoring of rehabilitation progress throughout the care continuum.**

I. Introduction

Neurological conditions, such as stroke, are a major cause of disability worldwide [1]. The high prevalence of motor impairments following stroke highlights the critical need for effective rehabilitation strategies [2], and emphasizes the importance of accurate and efficient assessment tools to guide treatment and monitor patient progress throughout the rehabilitation [3]. Clinical assessment of motor function traditionally relies on standardized, manually administered tests by clinicians [2], [4]. These assessments evaluate motor function through a series of motor movements, with clinicians scoring each component individually [5]. While frequent and continuous assessments are indispensable for monitoring recovery and tailoring rehabilitation programs [6], their time-intensive nature contributes to clinician burnout [7] and reduces the time available in the clinic for therapy or other care. Furthermore, these assessments require specialized training, making them less accessible in research or non-clinical settings.

Recent advances in wearable technology and machine learning algorithms have opened new avenues for automating measuring clinical assessments [8]. The Automate-Illuminate-Predict (AIP) framework, proposed by O'Brien et al., offers a comprehensive approach for extracting meaningful healthcare analytics from wearable sensors [9], encompassing three key processes: (1) automate traditional clinical measures, (2) illuminate novel correlates of disease and impairment, and (3) predict future outcomes (e.g., at discharge). To enhance the accessibility of functional assessments while saving time, the AIP framework recommends monitoring patients through brief, simple movements using a minimal set of sensors.

When considering this framework in the analytics for upper extremity (UE), several studies have demonstrated the feasibility of automating clinical outcomes using wearable inertial sensors [10], [11]. However, these studies exhibit limitations when it comes to directly applying the AIP framework. First, existing research often leverages sensor data collected across all items of a standardized clinical assessment to evaluate functional status [11]. This is unlikely to reduce clinicians' workload, as it still necessitates conducting the full assessment, with the addition of placing sensors. Second, the most informative sensor data for accurate functional outcome estimation remains unclear. Utilizing multiple sensor units affects model complexity and time to set-up, hindering the perceived usability by both clinicians and patients. Determining the optimal activities and sensor placement is key, both for minimizing data requirements without compromising accuracy [12], and for guiding additional illuminative or predictive measures to enhance clinical insights.

Our study addresses these limitations by training and validating machine learning algorithms to estimate scores for the most common UE clinical assessment in stroke, the Action Research Arm Test (ARAT) [5]. Following the "automate" component of the AIP framework, we used body-worn inertial sensors to collect input data for training a machine learning algorithm, and then identified the optimal item to automatically estimate scores from each ARAT sub-test (i.e., grasp, grip, pinch, and gross movement). Specifically, we aimed to: (1) utilize single items to estimate scores from each sub-test, (2) identify the most informative ARAT items for automated assessment, and (3) conduct feature importance

This work was supported by the National Institute on Disability, Independent Living, and Rehabilitation Research (90REGE0010).

[1]Max Näder Center for Rehabilitation, Technologies and Outcomes Research, Shirley Ryan AbilityLab, Chicago, IL, USA.

[2]Department of Physical Medicine and Rehabilitation, Northwestern University, Chicago, IL, USA.

[3]Department of Mechanical Engineering, McCormick School of Engineering, Northwestern University, Chicago, USA.

[4]Feinberg School of Medicine, Northwestern University, Chicago, USA.

[5]Department of Physical Therapy and Human Movement Sciences, Northwestern University, Chicago, IL, USA.

*Corresponding author: ajayaraman@sralab.org.

analysis to determine the most meaningful sensor-derived features for model construction.

II. Methods

A. Participants

We recruited 23 individuals with chronic stroke at the Shirley Ryan AbilityLab in Chicago, Illinois (Table I). Inclusion criteria required participants to safely walk for 10 meters with or without assistance. Exclusion criteria included pregnancy, nursing, or skin allergies that would prevent safe sensor use. The study was approved by the Institutional Review Board of Northwestern University (STU00216350), and all participants provided written informed consent.

TABLE I
Participant Demographics

	n=23
Age (years)	60.9 ± 9.9
Sex (Male/Female)	11/12
Height (cm)	169.0 ± 10.3
Weight (kg)	87.0 ± 23.1
Years since Stroke	9.7 ± 6.4
Stroke Type (Ischemic/Hemorrhagic)	12/11
Paretic Side (Left/Right)	13/10

B. Experimental Protocol

Participants completed the ARAT test with their impaired arm only during a single study visit. The test comprises 19 items across four sub-tests: grasp, grip, pinch, and gross arm movement (Table II). A clinician administered and scored each item (0–3) using standardized procedures [13]. They used their impaired hand while wearing ActiGraph GT9X Link IMUs (ActiGraph LLC, Pensacola, Florida), recording data at 100 Hz. The IMUs were attached with straps on both wrists and around the waist. If participants were unable to perform a specific item due to motor impairment, that item was skipped and no sensor data were recorded. Table II shows the completion rates (CRs) for each ARAT item, with rates ranging from 52.2% to 100%. The gross movement sub-test had the highest CRs (95.7-100%), while the pinch sub-test showed the lowest (52.2-69.6%).

C. Data processing

Raw data from IMUs were downloaded, and manually segmented according to ARAT item timestamps. To avoid explicit directionality, we computed the Euclidean norm of triaxial accelerometer and gyroscope signals [14]. Magnetometer data were excluded since these readings can be affected by ambient ferrous materials. Features were extracted from both time and frequency domains, supplemented by clinical information (Table III), following IMU analysis protocols in existing studies [11], [15].

TABLE II
ARAT Items and Completion Rate (CR)

Sub-Test (pts)	**Test #**	**Item Description**	**CR[a] (%)**
Grasp (18 pts)	1	Block, 10 cm^3	91.3
	2	Block, 2.5 cm^3	95.7
	3	Block, 5 cm^3	73.9
	4	Block, 7.5 cm^3	69.6
	5	Cricket ball	65.2
	6	Sharpening stone	69.6
Grip (12 pts)	7	Pour water from one glass to another	82.6
	8	Move 2.25-cm tube across table	91.3
	9	Move 1-cm tube across table	82.6
	10	Place washer over bolt	65.2
Pinch (18 pts)	11	Ball bearing, ring finger and thumb	56.5
	12	Marble, index finger and thumb	69.6
	13	Ball bearing, middle finger and thumb	52.2
	14	Ball bearing, index finger and thumb	56.5
	15	Marble, ring finger and thumb	52.2
	16	Marble, middle finger and thumb	56.5
Gross[b] (9 pts)	17	Hand to behind the head	95.7
	18	Hand to top of head	95.7
	19	Hand to mouth	100.0

[a]Based on 23 participants per item; [b]Gross Movement.

D. Model Development (Figure 1)

Our modeling approach focused on developing separate models specific to each ARAT sub-test (i.e., grasp, grip, pinch, and gross movement), while optimizing various sensor configurations, including impaired wrist only, both wrists, and impaired wrist with waist sensor. For each configuration, we analyzed 19 items and identified the item yielding minimum error against ground truth scores per sub-test. Then, we combined the predictions from these optimized sub-test models to estimate total ARAT scores.

To validate the model, we implemented a Leave-One-Subject-Out-Cross-Validation (LOSOCV) pipeline. To handle missing data from uncompleted items (Table II), we used multivariate iterative imputation through the scikit-learn IterativeImputer (version 1.2.0) with Python 3.11 [16]. This approach estimates missing values by modeling each feature with missing values as a function of other features in a round-robin fashion. After imputation, features were processed using robust scaling. These processing steps were conducted exclusively on the training data in each loop. Then, feature selection was conducted in two stages: first, using unsuper-

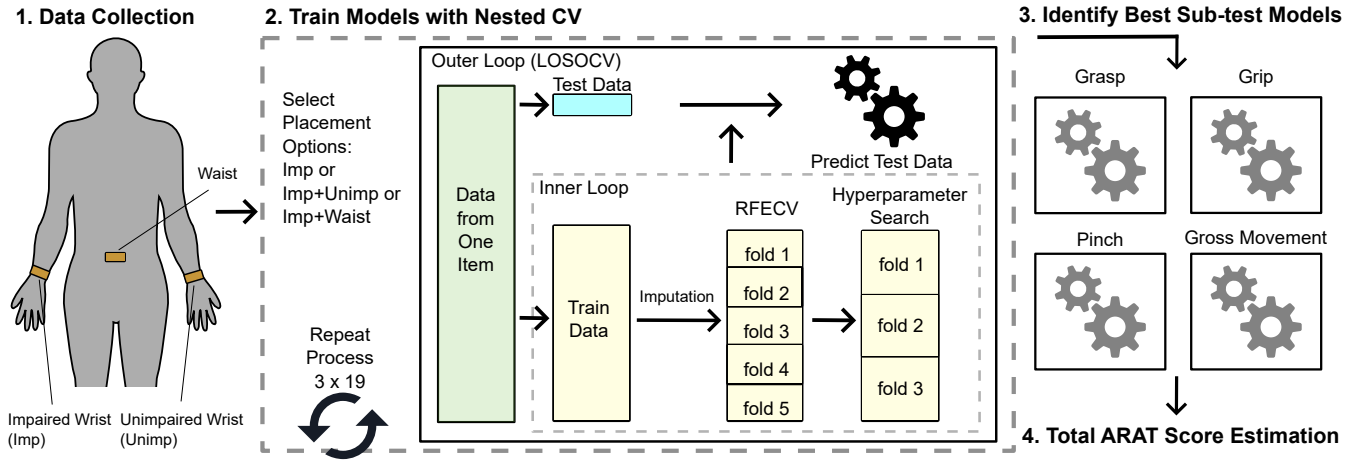


Fig. 1. Data processing pipeline for ARAT score estimation. The pipeline consists of four main steps: (1) Data collection from IMU sensors placed on impaired wrist, unimpaired wrist, and waist; (2) Model training using nested cross-validation, incorporating recursive feature elimination (RFECV) and hyperparameter optimization with Optuna; (3) Model selection identifying optimal performing items for each sub-test; and (4) Total ARAT score estimation by combining sub-test predictions.

TABLE III
EXTRACTED FEATURES [15] (25 FEATURES IN TOTAL)

Domain	Features
Time	Mean, Variance, MAD[a], RMS[b], ZCR[c], IQR[d], 75th Percentile, Kurtosis, SMA[e], Absolute Range
Frequency	Spectral Centroid, Principal Frequency, Energy & Entropy (0-25 Hz in 5 Hz bands)
Other	Age, Paretic Side, Dominant Side

[a]MAD: Mean Absolute Deviation; [b]RMS: Root Mean Square
[c]ZCR: Zero-Crossing Rate; [d]IQR: Interquartile Range.
[e]SMA: Signal Magnitude Area.

TABLE IV
A LIST OF HYPERPARAMETERS

Parameter	Search Space
Number of Trees	50–300
Tree Depth	5–30
Minimum Samples Split	2–10
Minimum Samples Leaf	1–10

vised methods including correlation matrices and variance thresholds, and second, through supervised recursive feature elimination with nested 5-fold cross-validation (RFECV).

Model optimization was achieved through 3-fold cross-validation hyperparameter tuning using Optuna [17]. We chose the Random Forest algorithm for its ability to capture non-linear relationships and robust performance with high-dimensional feature spaces [10], [18]. The hyperparameter search spaces are detailed in Table IV.

Based on the LOSOCV performance, we identified optimal configurations for hyperparameters, item selection, and feature elimination across the entire dataset. To investigate feature importance patterns comprehensively, we trained a final model using the complete dataset, allowing us to leverage all available data to understand feature contributions. For this final model, we conducted recursive feature elimination to identify the optimal feature subset yielding the minimum Mean Absolute Error (MAE) for each sub-test. We then analyzed feature importance on these optimized models using SHapley Additive exPlanation (SHAP) values [19]. All developments were conducted on a workstation running Ubuntu 24.04.1 LTS with an NVIDIA TITAN V GPU, and a CUDA version of 12.4.

E. Evaluation Metrics

Model performance was evaluated using MAE and Median Absolute Error (MedAE) to quantify the average magnitude of prediction errors, while the Coefficient of Determination (R^2) measured the proportion of variance explained by the model.

III. RESULTS

ARAT scores among participants varied widely (mean = 25.91, SD = 22.44), with grasp and pinch sub-tests showing the highest variability (SD = 7.95 and 7.39), and gross movement the least (SD = 2.78) (Table V). The nested CV yielded optimized random forest models across sub-tests (Table VI).

TABLE V
SUMMARY STATISTICS OF ARAT SCORES

Statistic	Grasp	Grip	Pinch	Gross[a]	Total
Mean	8.30	5.26	6.57	5.78	25.91
SD[b]	7.95	5.08	7.39	2.78	22.44
Median	7.00	4.00	4.00	5.00	27.00
Minimum	0.00	0.00	0.00	1.00	1.00
Maximum	18.00	12.00	18.00	9.00	57.00

[a]Gross Movement; [b]Standard Deviation.

TABLE VI

OPTIMIZED HYPERPARAMETERS BY THE NESTED CV

Hyperparameter	Grasp	Grip	Pinch	Gross
Number of Estimators	211	248	223	218
Maximum Depth of Tree	17	13	16	20
Minimum Samples Split	2	4	4	3
Minimum Samples Leaf	1	1	1	1

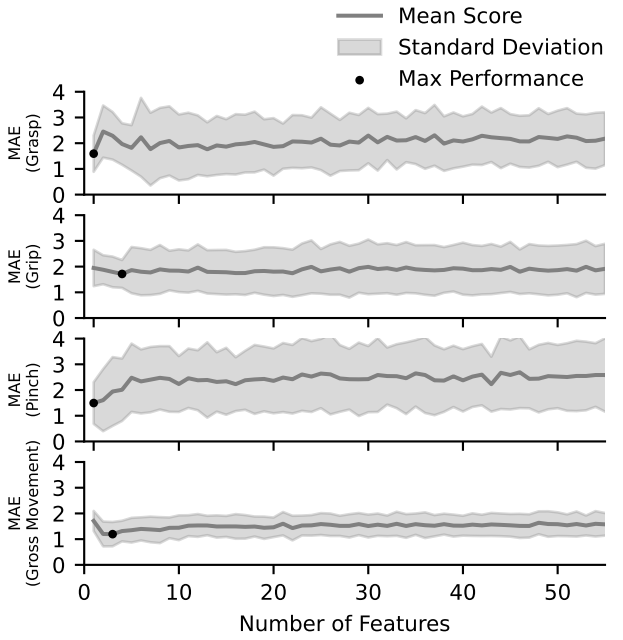


Fig. 2. Relationship between MAE and the number of features. Maximum performance for each sub-test is determined by the lowest mean MAE.

TABLE VII

MAES FOR ARAT ITEMS UNDER THREE SENSOR CONFIGURATIONS

Sub-test	Item	Imp[a] + Unimp[b]	Imp[a] + Waist	Imp[a]
Grasp	1	3.10	5.40	6.27
	2	5.42	5.93	5.90
	3	3.56	3.55	6.26
	4	2.66	3.69	6.88
	5	**2.43**	2.69	7.00
	6	2.99	5.14	6.02
Grip	7	3.09	3.29	3.51
	8	2.33	1.80	1.87
	9	1.71	**1.53**	1.83
	10	3.18	2.59	3.32
Pinch	11	4.45	5.42	4.35
	12	4.26	3.73	5.69
	13	1.70	1.85	1.81
	14	**1.64**	3.31	4.22
	15	3.83	2.74	3.01
	16	2.07	2.01	2.21
Gross[c]	17	1.79	1.36	1.64
	18	**1.23**	1.92	2.53
	19	1.77	2.10	2.09

[a]Impaired Wrist; [b]Unimpaired Wrist; [c]Gross Movement.

TABLE VIII

ESTIMATION PERFORMANCE FOR SUB-TESTS AND FULL ARAT

Metric	Grasp	Grip	Pinch	Gross[a]	Full ARAT
MAE	2.4	1.48	1.16	1.25	**4.55**
MedAE	1.70	0.66	0.44	0.91	**3.81**
R^2	0.80	0.77	0.93	0.64	**0.93**

[a]Gross Movement.

A. Model Performance

Model performance varied across ARAT items and sensor configurations (Table VII). For the grasp sub-test, Item 5 using both impaired and unimpaired wrist sensors achieved the lowest MAE (2.43 points). In the grip sub-test, Item 9 with both wrist sensors performed best (MAE = 1.71 points). Pinch sub-test optimization occurred with Item 14 (MAE = 1.64 points), and gross movement performed best with Item 18 (MAE = 1.23 points). These items were selected as representative tasks for their sub-tests.

The aggregated model estimated the full ARAT score with an MAE of 4.55 points, MedAE of 3.81 points, and an R^2 of 0.93 (Table VIII). Sub-test performances varied, with the pinch sub-test showing the highest accuracy (MAE = 1.16, R^2 = 0.93), followed by gross movement (MAE = 1.25, R^2 = 0.64), grip (MAE = 1.48, R^2 = 0.77), and grasp (MAE = 2.4, R^2 = 0.80).

B. Feature Selection and Importance

Figure 2 shows stable performance across number of features; thus, we selected minimal sets achieving the lowest MAE: grasp – one feature (absolute range), grip – four features (spectral centroid, absolute range, principal frequency, kurtosis), pinch – one feature (spectral entropy), and gross movement – three features (mean angular velocity, IQR, ZCR). SHAP analysis (Figure 3) revealed key features: grasp – unimpaired wrist's absolute range of normalized angular velocity during Item 5; grip – features from both wrists during Item 9; pinch – impaired wrist's spectral entropy during Item 14; gross movement – unimpaired wrist's mean angular velocity, IQR, and ZCR during Item 18.

IV. DISCUSSION

We developed machine learning models to estimate ARAT scores for individuals with stroke using a minimal sensor configuration; with additional model training, we expect this approach can be used to estimate UE function in other clinical populations as well (e.g., Parkinson's disease). Accurate ARAT estimation is possible using one item per sub-test, and adding sensors (unimpaired wrist or waist) further improves performance (Table VII). The MAE of 3.8 points in full score estimation is comparable to existing studies [10], [11] and falls below the minimally clinically important difference (MCID) of the ARAT (6 points) [5], validating our approach for assessment while minimizing required test items; as long as the estimation error remains within the MCID, the

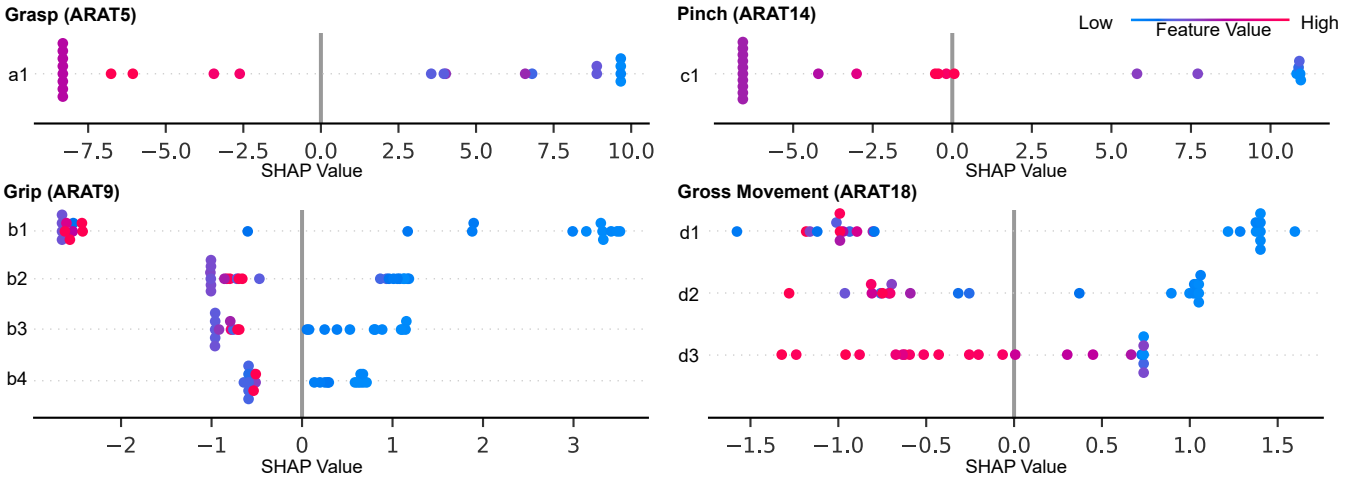


Fig. 3. SHAP analysis across ARAT sub-tests. Each point represents a SHAP value, with color gradient from blue (low) to pink (high) indicating feature values. (a1-d3) correspond to features specific to each item. a1: Absolute Range of Normalized Angular Velocity (Unimpaired Wrist); b1: Spectral Centroid of Normalized Acceleration (Impaired Wrist); b2: Absolute Range of Normalized Angular Velocity (Impaired Wrist); b3: Principal Frequency of Normalized Angular Velocity (Impaired Wrist); b4: Kurtosis of Normalized Angular Velocity (Unimpaired Wrist); c1: Spectral Entropy of Normalized Angular Velocity (Impaired Wrist); d1: Mean of Normalized Angular Velocity (Unimpaired Wrist); d2: IQR of Normalized Acceleration (Unimpaired Wrist); d3: ZCR of Normalized Angular Velocity (Unimpaired Wrist).

assessment is unlikely to affect clinical interpretation.

An unexpected finding was the enhanced model performance when including sensor data from the unimpaired wrist, particularly in the grasp sub-test (Table VII). While the ARAT in our study only scored the impaired arm's performance, this improvement suggests the model may consider compensatory movements during task execution in estimating the score. The SHAP analysis showed that decreased feature values generally corresponded to improvement of SHAP values. However, as this analysis was conducted on the final model after optimization, these patterns require validation on external datasets.

In the grasp model, the absolute range of angular velocities in the unimpaired wrist likely indicates compensatory movements, such as increased trunk rotation when patients struggle with grasping objects [20]. The grip model's reliance on spectral centroid, absolute range, and principal frequency from the impaired wrist sensor may reflect less controlled motions, movement stability, and compensatory behaviors. For the pinch model, spectral entropy likely measures movement complexity and smoothness on the unimpaired wrist [21], with higher values indicating motor control issues such as tremors that impair pinch tasks. The gross movement model's features (mean angular velocity, IQR, and ZCR of acceleration) appear to capture wrist movement variability [22].

While we focused on task-agnostic features that could be computed across any UE task being performed, incorporating task-specific features (e.g., forearm elevations, wrist orientations, finger movements [10], [23]–[25]) could enhance model performance and provide deeper insights into movement patterns. Additionally, exploring sensor placement on the shoulder, or chest could offer valuable information about compensatory movements, potentially improving ARAT score estimates. However, adding sensors introduces additional administration time and complexity. Future research should investigate optimal sensor placement while maintaining minimal setup requirements, similar to the study in LE function using three sensors [14].

The relatively small sample size (n=23) and uneven representation across ARAT score ranges, particularly in the grasp sub-test, may have affected model performance. A larger, more diverse sample could improve model robustness and generalization. Furthermore, our focus on chronic stroke patients, whose movement patterns may differ from acute cases, suggests the need to investigate this approach with acute stroke populations. While previous research has demonstrated predictive performance with acute stroke participants [11], verification with a larger acute stroke patient cohort is essential for implementation through the care continuum.

Acknowledgment

This data was collected as part of the Center for Smart Use of Technologies to Assess Real World Outcomes (C-STAR), which is funded by the National Institutes of Health (Grant #P2C HD101899) supported by NICHD and NINDS. We extend our gratitude to all the participants who contributed to the data collection process.

References

[1] V. L. Feigin, T. Vos, E. Nichols, M. O. Owolabi, W. M. Carroll, M. Dichgans, G. Deuschl, P. Parmar, M. Brainin, and C. Murray, "The global burden of neurological disorders: translating evidence into policy," *The Lancet Neurology*, vol. 19, no. 3, pp. 255–265, Mar. 2020.

[2] M. Taylor-Rowan, A. Wilson, J. Dawson, and T. J. Quinn, "Functional Assessment for Acute Stroke Trials: Properties, Analysis, and Application," *Frontiers in Neurology*, vol. 9, Mar. 2018, publisher: Frontiers.

[3] S. M. Hatem, G. Saussez, M. della Faille, V. Prist, X. Zhang, D. Dispa, and Y. Bleyenheuft, "Rehabilitation of Motor Function after Stroke: A Multiple Systematic Review Focused on Techniques to Stimulate Upper Extremity Recovery," *Frontiers in Human Neuroscience*, vol. 10, Sep. 2016, publisher: Frontiers.

[4] G. Kwakkel, E. Van Wegen, J. Burridge, C. Winstein, L. van Dokkum, M. Alt Murphy, M. Levin, and J. Krakauer, "Standardized measurement of quality of upper limb movement after stroke: Consensus-based core recommendations from the Second Stroke Recovery and Rehabilitation Roundtable," *International Journal of Stroke*, vol. 14, no. 8, pp. 783–791, Oct. 2019, publisher: SAGE Publications.

[5] C. E. Lang, M. D. Bland, R. R. Bailey, S. Y. Schaefer, and R. L. Birkenmeier, "Assessment of upper extremity impairment, function, and activity after stroke: foundations for clinical decision making," *Journal of Hand Therapy*, vol. 26, no. 2, pp. 104–115, Apr. 2013.

[6] M. A. French, R. T. Roemmich, K. Daley, M. Beier, S. Penttinen, P. Raghavan, P. Searson, S. Wegener, and P. Celnik, "Precision Rehabilitation: Optimizing Function, Adding Value to Health Care," *Archives of Physical Medicine and Rehabilitation*, vol. 103, no. 6, pp. 1233–1239, Jun. 2022.

[7] C. P. West, L. N. Dyrbye, and T. D. Shanafelt, "Physician burnout: contributors, consequences and solutions," *Journal of Internal Medicine*, vol. 283, no. 6, pp. 516–529, 2018.

[8] S. Patel, H. Park, P. Bonato, L. Chan, and M. Rodgers, "A review of wearable sensors and systems with application in rehabilitation," *Journal of NeuroEngineering and Rehabilitation*, vol. 9, no. 1, p. 21, Apr. 2012.

[9] M. K. O'Brien, K. Hohl, R. L. Lieber, and A. Jayaraman, "Automate, Illuminate, Predict: A Universal Framework for Integrating Wearable Sensors in Healthcare," *Digital Biomarkers*, vol. 8, no. 1, pp. 149–158, Aug. 2024.

[10] C. Adans-Dester, N. Hankov, A. O'Brien, G. Vergara-Diaz, R. Black-Schaffer, R. Zafonte, J. Dy, S. I. Lee, and P. Bonato, "Enabling precision rehabilitation interventions using wearable sensors and machine learning to track motor recovery," *npj Digital Medicine*, vol. 3, no. 1, pp. 1–10, Sep. 2020, publisher: Nature Publishing Group.

[11] C. Werner, J. G. Schönhammer, M. K. Steitz, O. Lambercy, A. R. Luft, L. Demkó, and C. A. Easthope, "Using Wearable Inertial Sensors to Estimate Clinical Scores of Upper Limb Movement Quality in Stroke," *Frontiers in Physiology*, vol. 13, May 2022, publisher: Frontiers.

[12] L. Lonini, A. Dai, N. Shawen, T. Simuni, C. Poon, L. Shimanovich, M. Daeschler, R. Ghaffari, J. A. Rogers, and A. Jayaraman, "Wearable sensors for Parkinson's disease: which data are worth collecting for training symptom detection models," *npj Digital Medicine*, vol. 1, no. 1, pp. 1–8, Nov. 2018, number: 1 Publisher: Nature Publishing Group.

[13] N. Yozbatiran, L. Der-Yeghiaian, and S. C. Cramer, "A Standardized Approach to Performing the Action Research Arm Test," *Neurorehabilitation and Neural Repair*, vol. 22, no. 1, pp. 78–90, Jan. 2008, publisher: SAGE Publications Inc STM.

[14] M. K. O'Brien, F. Lanotte, R. Khazanchi, S. Y. Shin, R. L. Lieber, R. Ghaffari, J. A. Rogers, and A. Jayaraman, "Early Prediction of Poststroke Rehabilitation Outcomes Using Wearable Sensors," *Physical Therapy*, vol. 104, no. 2, p. pzad183, Feb. 2024.

[15] J. Suto, S. Oniga, and P. P. Sitar, "Feature Analysis to Human Activity Recognition," *INTERNATIONAL JOURNAL OF COMPUTERS COMMUNICATIONS & CONTROL*, vol. 12, no. 1, pp. 116–130, Dec. 2016, number: 1.

[16] F. Pedregosa, G. Varoquaux, A. Gramfort, V. Michel, B. Thirion, O. Grisel, M. Blondel, P. Prettenhofer, R. Weiss, V. Dubourg, J. Vanderplas, A. Passos, D. Cournapeau, M. Brucher, M. Perrot, and Duchesnay, "Scikit-learn: Machine Learning in Python," *J. Mach. Learn. Res.*, vol. 12, no. null, pp. 2825–2830, Nov. 2011.

[17] T. Akiba, S. Sano, T. Yanase, T. Ohta, and M. Koyama, "Optuna: A Next-generation Hyperparameter Optimization Framework," in *Proceedings of the 25th ACM SIGKDD International Conference on Knowledge Discovery & Data Mining*, ser. KDD '19. New York, NY, USA: Association for Computing Machinery, Jul. 2019, pp. 2623–2631.

[18] S. Campagnini, P. Liuzzi, A. Mannini, B. Basagni, C. Macchi, M. C. Carrozza, and F. Cecchi, "Cross-validation of predictive models for functional recovery after post-stroke rehabilitation," *Journal of NeuroEngineering and Rehabilitation*, vol. 19, no. 1, p. 96, Sep. 2022.

[19] S. M. Lundberg and S.-I. Lee, "A unified approach to interpreting model predictions," in *Proceedings of the 31st International Conference on Neural Information Processing Systems*, ser. NIPS'17. Red Hook, NY, USA: Curran Associates Inc., Dec. 2017, pp. 4768–4777.

[20] M. J. Major, R. L. Stine, C. W. Heckathorne, S. Fatone, and S. A. Gard, "Comparison of range-of-motion and variability in upper body movements between transradial prosthesis users and able-bodied controls when executing goal-oriented tasks," *Journal of NeuroEngineering and Rehabilitation*, vol. 11, no. 1, p. 132, Sep. 2014.

[21] S. Balasubramanian, A. Melendez-Calderon, A. Roby-Brami, and E. Burdet, "On the analysis of movement smoothness," *Journal of NeuroEngineering and Rehabilitation*, vol. 12, no. 1, p. 112, Dec. 2015.

[22] I. S. Howard, J. N. Ingram, K. P. Körding, and D. M. Wolpert, "Statistics of Natural Movements Are Reflected in Motor Errors," *Journal of Neurophysiology*, vol. 102, no. 3, pp. 1902–1910, Sep. 2009, publisher: American Physiological Society.

[23] K. Leuenberger, R. Gonzenbach, S. Wachter, A. Luft, and R. Gassert, "A method to qualitatively assess arm use in stroke survivors in the home environment," *Medical & Biological Engineering & Computing*, vol. 55, no. 1, pp. 141–150, Jan. 2017.

[24] S. Okita, D. Schwerz de Lucena, and D. J. Reinkensmeyer, "Movement Diversity and Complexity Increase as Arm Impairment Decreases After Stroke: Quality of Movement Experience as a Possible Target for Wearable Feedback," *IEEE Transactions on Neural Systems and Rehabilitation Engineering*, vol. 32, pp. 2961–2970, 2024.

[25] D. Schwerz de Lucena, J. Rowe, V. Chan, and D. J. Reinkensmeyer, "Magnetically Counting Hand Movements: Validation of a Calibration-Free Algorithm and Application to Testing the Threshold Hypothesis of Real-World Hand Use after Stroke," *Sensors*, vol. 21, no. 4, p. 1502, Jan. 2021, number: 4 Publisher: Multidisciplinary Digital Publishing Institute.

The Role of Muscle Property Changes in Identifying Motor Adaptation Stages for Myoelectric Control

Johanna Happold[1,2], Patricia Capsi-Morales[1,2] and Cristina Piazza[1,2]

***Abstract*— Despite technological advancements in assistive robotics, patients still face considerable challenges in their control, with proficiency varying widely among individuals. While training programs include task-related performance metrics to evaluate individuals' skill levels, these may overlook critical adaptations at the muscle. This study explores neuromuscular adaptations in forearm antagonist muscles during a 3-degree-of-freedom myoelectric control task. Participants completed a 45-minute training session and were categorized as rapid learners or plateau learners based on their performance evolution. We then evaluated changes in muscle properties within groups, including stability, antagonistic co-contraction, and neural synchronization. Rapid learners showed lower initial proficiency and improved task performance metrics, with reduced muscle variability and increased co-contraction, suggesting greater movement consistency. In contrast, plateau learners achieved a higher baseline performance with minimal improvements. These individuals reported decreased co-contraction levels and phase locking between antagonistic muscles, indicating task endurance and more fine motor control over time. These findings highlight differences in neuromuscular adaptations among individuals, possibly aiding clinicians in assessing therapy effectiveness.**

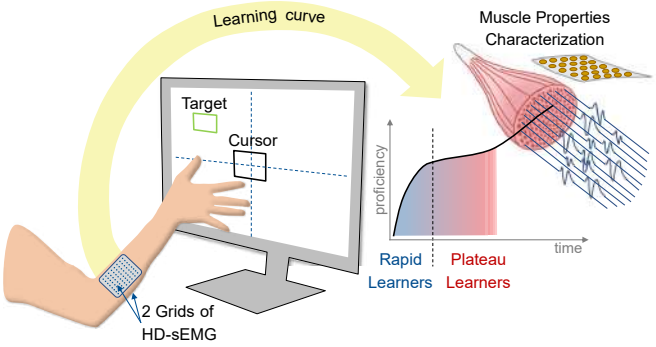


Fig. 1. Schematics of the experimental setup and study concept. Two HD-sEMG sensors were placed on the extensor and flexor muscles of the forearm. Participants were tasked to move a cursor to reach to different targets by simultaneous control of three DoFs involving wrist (extension, flexion, abduction, adduction) and hand (open, close) movements. After the experiment, participants were divided into *rapid* and *plateau learners* based on proficiency evolution, and underlying muscle properties were analyzed.

I. INTRODUCTION

Modern rehabilitation therapies offer a wide range of specialized and personalized care for patients with motor impairments or limb loss [1], [2]. These therapies leverage man-machine interfaces and biofeedback systems to stimulate neural pathways, supporting the recovery of motor function and adaptation to assistive devices like robotic aids or prosthetics. Among control options, muscle interfacing using surface electromyography (sEMG) is widely used for decoding motor intention into actionable control data [3]. However, direct control strategies often rely on simplistic methods, restricting users to a small set of predefined actions [4], [5]. A promising alternative is the application of machine learning techniques, such as classification and regression [6]–[9]. Among various applications, the field of prosthetics has been a primary driver for the development of more sophisticated motor intention decoders. Classification approaches map sEMG signals into discrete movement classes, enabling the execution of a larger variety of actions [4]. However, this results in a sequential control structure, reducing the fluidity of transitions between movements [10], [11]. Regression-based techniques offer more dynamic solutions, enabling proportional and simultaneous activation of multiple but fewer degrees-of-freedom (DoFs), mimicking the coordinated control of human motor behavior [10], [11].

Despite technical advancements in controllers, effective use of assistive devices requires comprehensive user training, particularly in the early stages of device adoption [12], [13]. Evidence shows considerable differences in the acquisition of new motor skills among individuals [14], [15]. This is also reflected in the variability in baseline myoelectric capacity and the rate of improvement observed during training [16], [17]. Standard methods to assess proficiency involve task-specific performance metrics [18], [19]. However, they may overlook critical aspects such as changes in muscle coordination, long-term task endurance, and neuromuscular adjustments required for effective myoelectric control.

In this study, we investigate neuromuscular control changes and their relationship with task performance during a 3-DoFs regression-based training program (Fig. 1). We evaluated 10 able-bodied participants, executing a goal-reaching task for 45 minutes. Based on performance evolution, we split them into two groups and analyzed differences in neuromuscular adaptation regarding contraction stability, antagonistic co-contraction, and neural synchronization, inspired by [20], [21]. With this, we aim to enhance understanding of training progression and skill acquisition at the muscular level, supporting more targeted training assessments.

This research work was supported by TUM AGENDA 2030, funded by the Federal Ministry of Education and Research (BMBF) and the Free State of Bavaria under the Excellence Strategy of the Federal Government and the Länder as well as by the Hightech Agenda Bavaria.

[1]School of Computation, Information and Technology, Technical University of Munich (TUM), Munich, Germany

[2]Munich Institute of Robotics and Machine Intelligence (MIRMI), TechnicalUniversity of Munich (TUM), Munich, Germany

* Corresponding author: johanna.happold@tum.de

II. Material and Methods

A. Study Procedure

The study involved 10 able-bodied participants (7 male, 3 female), with a mean age of 26.7 $\pm$ 3.4 years. All participants were right-handed and had little to no prior experience with myoelectric control. The study protocol was approved by the Ethics Committee of the Technical University of Munich (ref. number 2023-223-S-KH), and all participants gave consent.

The experiment started with an initial phase of data collection to train the control algorithm, followed by a real-time goal-reaching task involving 3-DoF control over wrist and hand gestures. Participants were comfortably seated with their elbows resting on a table. Myoelectric activity of the forearm's extensor and flexor muscles was recorded using high-density sEMG (HD-sEMG) electrodes (Fig. 1).

1) *Calibration Session*: the session started with a 5s recording of resting muscle activity, followed by a 5s recording to measure the maximum voluntary contraction (MVC) during wrist extension. Subsequently, participants performed six distinct gestures: wrist extension, flexion, abduction, adduction, and hand opening and closing. Each gesture followed a trapezoid-shaped target of 2s rest, a 5s ramp-up, a 5s plateau phase at 60% of MVC, a 5s ramp-down, and another 2s rest phase, with visual feedback on their median sEMG activity on a monitor. Each gesture was recorded three times. A regressor was trained for real-time control of the cursor.
2) *Familiarization Session*: participants had two minutes to familiarize themselves with the user interface and trained controller.
3) *Assessment Session*: participants were tasked with moving a cursor to match a series of targets. Each target remained visible for 15s, during which participants had to reach the target and maintain a stable posture until the end of the trial. A total of ten targets were used: six for 1-DoF movements (each gesture) and four requiring activation of 2 or 3 DoFs (Fig. 2 bottom left). The targets can be reached at 30% of the MVC, with a bar displaying real-time mean sEMG levels for consistent effort.
4) *Training Session*: participants were asked to match and hold the targets for 2s within a 20s window. A trial was considered successful if the cursor's deviation was within 10% of the target size in all three dimensions. The first two training sessions consisted of nine targets, while the third and fourth sessions included 18 targets each. The task space was divided into nine sections, corresponding to nine targets, to ensure complete coverage of the reaching space (Fig. 2 bottom right). The target locations were kept consistent across training sessions, though the order was randomized for each session and identical for all participants.

A total of five assessment and four training sessions were conducted alternately (Fig. 2 upper panel), with the entire experiment lasting approximately 90 minutes.

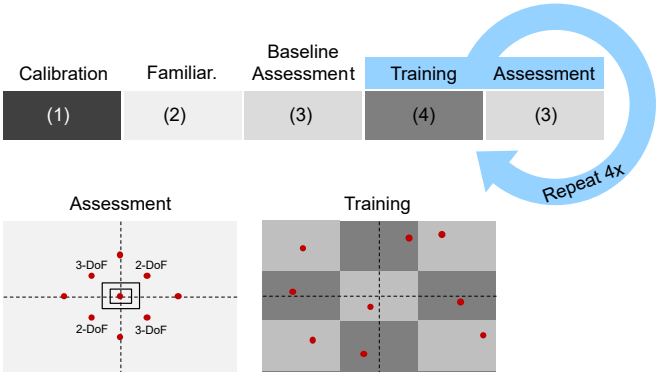


Fig. 2. Study procedure and schematic representation of task space. The study pipeline is illustrated in the top panel, with numbered steps corresponding to the sessions detailed in Section II-A. Participants began with a calibration session to collect data for calibrating the control algorithm, followed by multiple session of a 3-DoF goal-reaching task. The bottom panel shows target placement for both session types. Assessment sessions included ten targets: six 1-DoF, two 2-DoF, and two 3-DoF targets, with example target visualization shown for opening and closing of the hand. Training session targets were distributed across nine regions of the task space to ensure full coverage.

B. High-Density sEMG Recordings

Muscle signals were recorded using HD-sEMG electrodes to ensure full muscle coverage and achieve greater spatial resolution compared to traditional single-channel electrodes. This reduces the risk of electrode placement errors, effectively capturing activity across the targeted muscle regions. HD-sEMG signals were recorded using two 2D adhesive grids of 64 electrodes (HD10MM0808; OT Bioelettronica) placed on the extensor and flexor muscle group of the forearm. Monopolar sEMG signals were recorded via a multichannel amplifier system (2 Muovi+, OT Bioelettronica), amplified, and bandpass filtered at source prior to offline analysis. Reference electrodes were placed on the participants' wrists, and signals were sampled at 2000 Hz.

C. Motion Estimation and Control Algorithm

A multi-output regressor was designed to predict the activation levels of 3 DoFs simultaneously using a Support Vector Regression (SVR) model with radial basis function (RBF) and C = 5, ε = 0.01. These hyperparameters were optimized through a grid search strategy based on a separate dataset that included one repetition of all six gestures from an individual not involved in the main study.

We initially selected 22 features based on [22], comprising 17 time-domain features and five frequency-domain features. To reduce redundancy, we computed the correlation between the extracted features and eliminated those with a correlation coefficient exceeding 0.9. A permutation importance analysis on the remaining subset identified the four most important features. These features included Integral Absolute Value (IAV), Slope Sign Change (SSC), Willison Amplitude (WAMP), and Power Spectrum Deformation (OHM). This feature selection process was performed on the same dataset used for hyperparameter tuning.

D. Generation of Training Data

To ensure robust training samples for the regressor, initial preprocessing involved the removal of noisy channels. Channels were evaluated for outliers in RMS values and low-frequency drift, and discarded if identified as such. Only 1-DoF movements were recorded as training data to reduce time requirements in the study. However, concurrent activation of multiple DoFs is essential for effective simultaneous control. To simulate simultaneous activation, we employed data augmentation inspired by [23]. The generation of multi-DoF data was performed as described in Eq. 1 and Eq. 2.

$$X_{ij} \approx \alpha_1 * X_i + \alpha_2 * X_j \tag{1}$$

$$X_{ijk} \approx \alpha_1 * X_i + \alpha_2 * X_j + \alpha_3 * X_k \tag{2}$$

Here, $\{X_i, X_j, X_k\} \in \mathbb{R}^{nxd}$ represent the sEMG signals corresponding to 1-DoF activations, where $\{i, j, k\} \in \{wrist_extension, wrist_flexion, wrist_abduction, wrist_adduction, hand_open, hand_close\}$. The parameters d and n denote the number of sEMG electrodes and data samples, respectively. $\alpha_x \in \{0.3, 0.7\}$ with $x \in \{1, 2, 3\}$ denote the weighting factors of the signals. The resulting mixtures X_{ij} and X_{ijk} represent the generated multi-DoF signals. Note that only movements from different DoFs were combined for data augmentation. Combinations involving opposite movements within the same DoF (e.g., extension and flexion) were excluded, as such combinations are physiologically implausible. Recordings were synthetically labeled to indicate the performed gestures and estimated force (no kinematics or kinetics were captured). The resting state was labeled y = 0, while the plateau phase of the trapezoid-shape target (60% of MVC) was labeled y = 1 or y = -1, according to the DoF direction. For example, a synthetic combination of extension and abduction with weights $\alpha_1 = 0.3$ and $\alpha_2 = 0.7$ was labeled [0.3, 0.7, 0]. The labels were scaled according to the force level of the ramp-up and ramp-down phases of the trapezoid. The signals of the augmented dataset were segmented into non-overlapping windows of 250ms to maintain a processing delay under the 300ms threshold, considered undetectable by humans [8]. Each segment was bandpass filtered using a 3rd-order Butterworth filter with cutoff frequencies between 5 and 500 Hz, and powerline interference was removed using a notch filter. Following this, the four selected features were computed for each channel within each window.

E. Task Performance Analysis and Subject Grouping

To evaluate participants' performance, we computed three performance metrics, including success rate (SR), path efficiency (PE), and success time (ST). PE and ST were analyzed only for successfully matched targets. Participants were categorized as either *rapid* or *plateau learners* based on their performance evolution within the training period recorded. *Rapid learners* are characterized by a marked improvement in task-related performance metrics, typically observed during the initial phase of adaptation. In contrast, *plateau learners* demonstrate steadier performance levels, indicative of the plateau phase often linked with already higher proficiency. We defined a performance evolution measure (PEM) (Eq. 3) to quantify overall changes. To ensure comparability, each performance metric was normalized to $[0, 1]$ across all participants. PE and ST were averaged across all targets within a training session. The PEM score was computed by summing the changes across the different performance metrics, with ST included as a negative term since lower values indicate better performance.

$$PEM = mean(\Delta PE) - mean(\Delta ST) + \Delta SR \tag{3}$$

where $\Delta(metric) = metric_{tf} - metric_0$, with $metric \in \{PE, ST, SR\}$. Here, $metric_0$ and $metric_{tf}$ represent the values from the first and last training sessions, respectively.

F. Muscle Property Analysis

For the analysis of muscle properties, the raw sEMG data was first checked for noisy channels by assessing outliers in RMS values and low-frequency drift. The remaining channels were filtered using a 3rd-order Butterworth bandpass filter with cutoff frequencies at 5Hz and 500Hz. A notch filter was used to remove powerline interference. For the analysis, we used the last 10s of each target, assuming that stable postures were achieved after the first 5s. To evaluate changes in muscle properties during motor adaptation, we computed three different sEMG metrics:

- Standard deviation (STD) of the sEMG signals: reflects movement stability, with higher values indicating greater variability. STD was calculated for each sEMG channel and averaged across all channels.
- sEMG signal correlation: was assessed between sEMG signals within (PCC_flex, PCC_ext) and between (PCC_aa) antagonistic muscle groups using the Pearson correlation coefficient (PCC). Correlations were computed for all channel combinations, and the resulting values were averaged.
- Phase locking value (PLV): offers insights into muscle synchronization. PLVs were computed for the beta band (15-30 Hz), strongly linked to voluntary movement and corticospinal activity, coordinating rhythmic interactions between the motor cortex and muscles [21], [24]. PLVs were computed for all channel combinations between antagonistic muscles with values ranging from 0 (no synchrony) to 1 (perfect synchrony).

III. Results

A. Performance Evaluation

As introduced in section II-E, participants were divided into two equally sized groups based on their PEM scores. The five participants with the highest PEM score were classified as *rapid learners*, while the five participants with the lowest PEM score were categorized as *plateau learners*. Individual PEM scores and group assignments are presented in Table I. A two-sample t-test showed a significant group difference in

PEM ($p = 0.007$) and PE ($p = 0.047$). Moreover, one-way ANOVA for baseline performance (session 0) with group as the factor indicated that *rapid learners* demonstrated significantly lower PE scores compared to *plateau learners* ($p = 0.002$) and significantly longer ST ($p < 0.001$). By session 4, however, an equivalent test showed no significant difference between groups.

TABLE I
PERFORMANCE EVOLUTION SCORES AND ASSOCIATED GROUPS

Subject	PEM	Group
P1	0.56789	Rapid Learner
P2	0.77133	Rapid Learner
P3	1.62351	Rapid Learner
P4	-0.45312	Plateau Learner
P5	-0.42903	Plateau Learner
P6	0.48756	Rapid Learner
P7	1.78246	Rapid Learner
P8	0.37628	Plateau Learner
P9	-0.04786	Plateau Learner
P10	0.15456	Plateau Learner

Within the *rapid learners* group, RM-ANOVA with factor training session indicates significant differences across training sessions for SR ($p = 0.045$), PE ($p = 0.019$), and ST ($p = 0.010$). However, post-hoc pairwise t-tests with Bonferroni correction did not reveal significant differences within session pairs. Correlation analysis was conducted through PCC to identify trends in participants' performance. Training sessions demonstrated a significant positive correlation with PE ($p = 0.002, Pearson - Coeff = 0.226$) and a significant negative correlation with ST ($p < 0.001, Pearson - Coeff = -0.250$) (Fig. 3 left). For *plateau learners*, an RM-ANOVA did not reveal differences across training sessions for any of the performance metrics. Likewise, training sessions did not show a significant correlation with any performance metric (SR $p = 0.659$, PE $p = 0.898$, ST $p = 0.944$) (Fig. 3 right).

B. Muscle Properties Characterization

Changes in muscle properties were analyzed for *rapid* and *plateau learners* separately and are reported in Fig 4. First, fatigue over the assessment trials was evaluated by computing the mean frequencies of the sEMG signals [25], with both groups showing no evidence of fatigue. The *rapid learners* exhibited a baseline average mean frequency of 108 Hz, which remained stable throughout the training ($\Delta F = 0.7Hz, Pearson - Coeff = 0.03, p = 0.659$). *Plateau learners* had an initial mean frequency of 106 Hz, with $\Delta F = 3Hz$ ($Pearson - Coeff = 0.06, p = 0.347$). Since no signs of fatigue were detected in either group, its impact on muscle property analysis is considered negligible.

Two-sample t-test was performed to identify group differences in muscle property metrics. Significance were revealed between the two groups for PCC_flex ($p < 0.001$), PCC_aa ($p < 0.001$), and PLV ($p < 0.001$). In the *rapid learner* group, RM-ANOVA did not show significant differences across sessions. However, a significant negative correlation between the STD of sEMG signals with assessment sessions was revealed ($p = 0.031$, Pearson-Coeff = -0.139), indicating

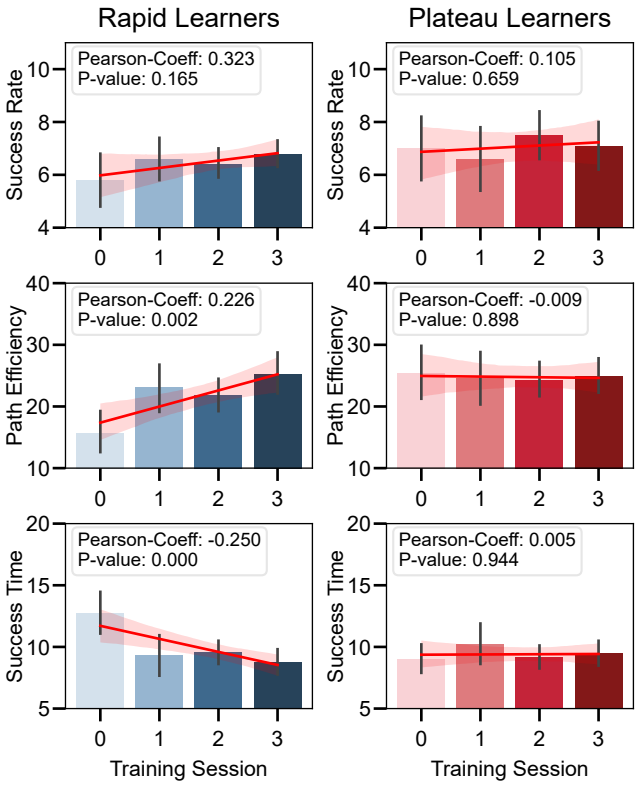


Fig. 3. Task performance metrics. The number of samples in each bar will be noted as $N_{session}$. SR, PE, and ST across training sessions are visualized for *rapid learners* (left column, SR: $N_{all} = 5$, PE/ST: $N_0 = 29, N_1 = 33, N_2 = 64, N_3 = 68$) and *plateau learners* (right column, SR: $N_{all} = 5$, PE/ST: $N_0 = 35$, $N_1 = 33$, $N_2 = 75$, $N_3 = 71$).

improved stability over time. The correlation between sEMG signals across electrodes within a single grid - whether placed over extensor or flexor arm muscles - remained stable, with no significant correlation across sessions (PCC_flex $p = 0.061$, PCC_ext $p = 0.202$). However, PCC_aa showed a significant positive correlation with assessment sessions ($p = 0.002$, Pearson-Coeff = 0.192), indicating increased co-contraction by the end of the experiment. The PLVs exhibited a weak correlation with assessment sessions ($p = 0.050$).

In the *plateau learner* group, RM-ANOVA did not reveal significant differences across testing sessions for any metric. Similarly, no significant correlation across assessment sessions and the STD of sEMG signals ($p = 0.347$) or the correlation of sEMG signals within the grids (PCC_flex $p = 0.682$, PCC_ext $p = 0.947$) was revealed. In contrast to the *rapid learner* group, PCC_aa is significantly negatively correlated with assessment sessions ($p < 0.001$, Pearson-Coeff = -0.409). Likewise, PLVs showed a significant negative correlation with assessment sessions ($p < 0.001$, Pearson-Coeff = -0.289).

IV. DISCUSSION & CONCLUSION

This study examined changes in forearm antagonist muscle properties in relation to task-specific performance metrics in a 3-DoF goal-reaching task, centering on three key characteristics: stability, co-contraction, and neural synchronization.

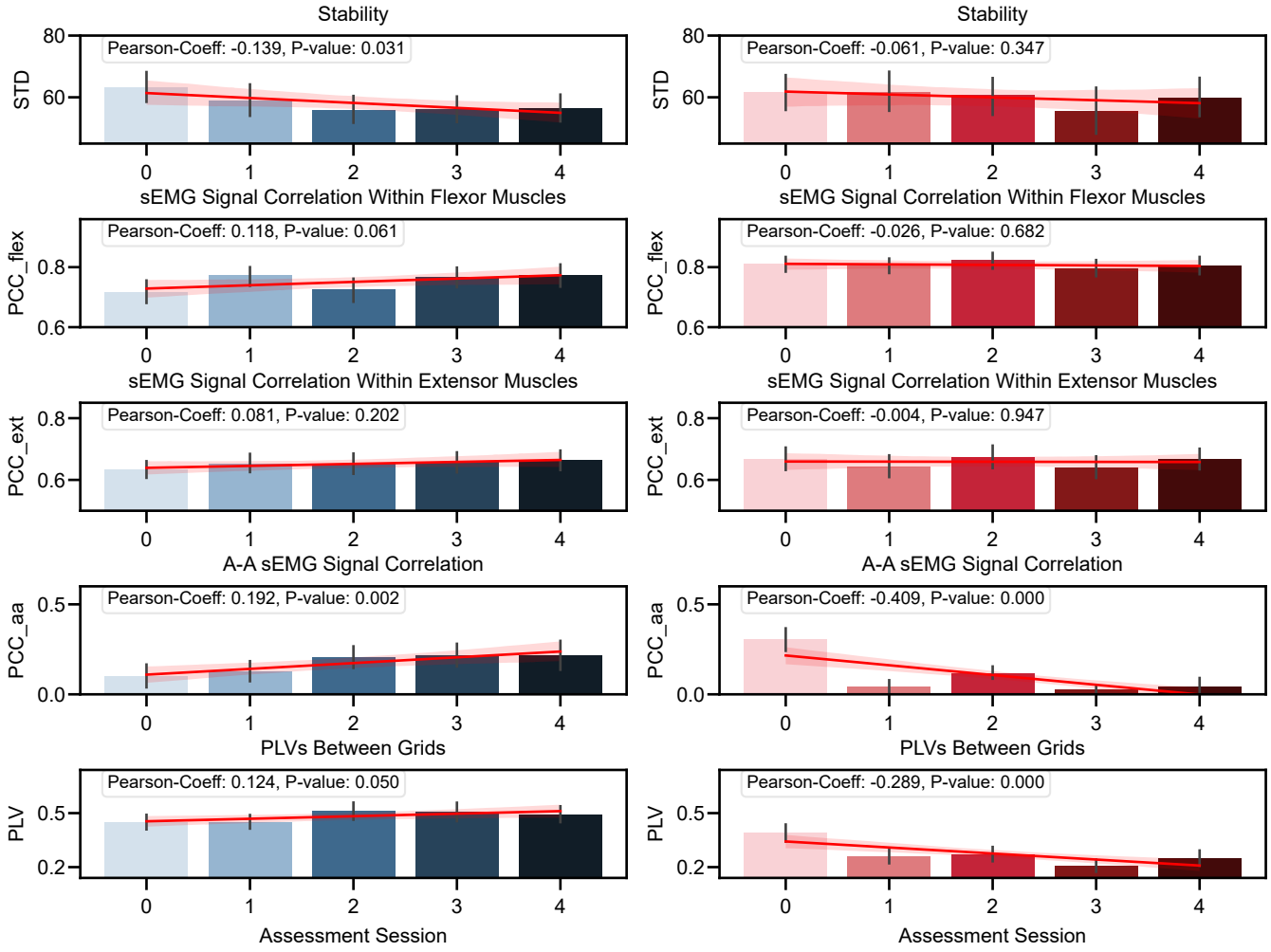


Fig. 4. Analysis of muscle properties across assessment sessions. Evaluated muscle properties included the STD of sEMG signals (row 1), intra-grid sEMG signal correlations (PCC_flex row 2 and PCC_ext row 3), inter-grid sEMG correlations (PCC_aa row 4), and PLVs between grids (row 5). The left column shows results for *rapid* and the right for *plateau learners*. Each bar includes 50 datapoints.

To account for individual differences in training responses [17], participants were categorized as *rapid* and *plateau learners*, based on their PEM score. Significant differences in PE/ST baseline and PE evolution across training sessions between groups highlight the need for subject-specific clustering in assessing myoelectric control and motor adaptation. The positive correlation in PE and negative correlation in ST across sessions for *rapid learners* indicate that training effectively improved task-specific metrics for this cohort. In contrast, the *plateau learner* group showed no significant changes in task-specific performance metrics. While task-level evaluations alone might indicate insufficient adaptation for this group, motor adaptations primarily occur at the muscular level rather than in immediate performance metrics.

Muscle property analysis in *rapid learners* reveals a negative correlation for the STD of sEMG signals across assessment sessions, demonstrating increased stability in muscle contractions and more consistent movement patterns by the end of the 45-minute training period. While no significant relationship in PCC_flex and PCC_ext with sessions was observed, a significant positive correlation was revealed in PCC_aa across assessment sessions. This suggests increased co-contraction, leading to greater joint stiffness [26], which can enhance stability and thereby improve overall task performance [27]. In contrast, PLVs observed across sessions indicate that participants rely on an almost consistent coordination of neural pattern over time, reflecting a neuromuscular approach that prioritizes stability over fine-tuning control.

Muscle property analysis in *plateau learners* reveals no significant correlation between the STD of sEMG signals and training sessions, consistent with the stability in performance. Although *rapid learners* rely on increased co-contraction for stability, this can reduce individual muscle activation in tasks requiring fine control. *Plateau learners* start with higher task performance, potentially needing less co-contraction to stabilize movements, suggested by a negative correlation of PCC_aa across sessions. This, combined with the decrease in PLVs over training, suggests greater independence in

activating antagonistic muscles, resulting in smoother and still precise movements but reducing the risk of fatigue.

Despite both groups reached similar performance by the end of the experiment, they seem to represent distinct motor adaptation stages. *Rapid learners* prioritize stable muscle activation for movement consistency, helping them reach a solid level of task performance. In contrast, *plateau learners* start with higher baseline performance, making further improvements in performance metrics more challenging. Nonetheless, we demonstrated that their progress is observable at the muscular level, where they refine control strategies to possibly enhance endurance and independence in muscle contractions for finely tuned control. These differences should be carefully considered when evaluating adaptation and learning effects, as some individuals may not exhibit task-specific improvements yet still benefit from training in terms of muscle conditioning and control strategies.

Note that in this preliminary investigation the sample size was limited to 10 participants, which might influence statistical power. Additionally, the training duration was restricted to 45 minutes, which does not capture the long-term effects of training. This study focused on one type of controller and a single task modality, limiting the generalizability of the findings. Therefore, future research should incorporate these factors to better understand motor adaptation strategies across various settings and populations. Furthermore, it should investigate whether *rapid learners* eventually reach a phase where task performance stabilizes and adaptation shifts toward finer neuromuscular changes or if this group represents a fundamentally different adaptation behavior. To further deepen the understanding of neuromuscular reorganization during motor adaptation, future studies should incorporate motor neuron activity into the analysis to validate how neural drive adapts over time in response to training demands. Our insights could inform the design of tailored training protocols and assessment methods for assistive devices involving myoelectric control and help clinicians to better evaluate the depth and efficacy of the training provided.

REFERENCES

[1] C. L. Toledo-Peral, G. Vega-Martínez, J. A. Mercado-Gutiérrez, G. Rodríguez-Reyes, A. Vera-Hernández, L. Leija-Salas, and J. Gutiérrez-Martínez, "Virtual/augmented reality for rehabilitation applications using electromyography as control/biofeedback: systematic literature review," *Electronics*, vol. 11, no. 14, p. 2271, 2022.

[2] G. Stucki, "Advancing the rehabilitation sciences," p. 617749, 2021.

[3] D. Farina and M. Sartori, "Surface electromyography for man-machine interfacing in rehabilitation technologies," *Surface Electromyography: Physiology, Engineering, and Applications*, pp. 540–560, 2016.

[4] E. Scheme and K. Englehart, "Electromyogram pattern recognition for control of powered upper-limb prostheses: state of the art and challenges for clinical use." *Journal of Rehabilitation Research & Development*, vol. 48, no. 6, 2011.

[5] I. Moon, M. Lee, J. Chu, and M. Mun, "Wearable emg-based hci for electric-powered wheelchair users with motor disabilities," in *Proceedings of the 2005 IEEE international conference on robotics and automation*. IEEE, 2005, pp. 2649–2654.

[6] B. Cesqui, P. Tropea, S. Micera, and H. I. Krebs, "Emg-based pattern recognition approach in post stroke robot-aided rehabilitation: a feasibility study," *Journal of neuroengineering and rehabilitation*, vol. 10, pp. 1–15, 2013.

[7] A. Phinyomark, P. Phukpattaranont, and C. Limsakul, "A review of control methods for electric power wheelchairs based on electromyography signals with special emphasis on pattern recognition," *IETE Technical Review*, vol. 28, no. 4, pp. 316–326, 2011.

[8] M. A. Oskoei and H. Hu, "Myoelectric control systems—a survey," *Biomedical signal processing and control*, vol. 2, no. 4.

[9] C. Piazza, M. Rossi, M. G. Catalano, A. Bicchi, and L. J. Hargrove, "Evaluation of a simultaneous myoelectric control strategy for a multi-dof transradial prosthesis," *IEEE Transactions on Neural Systems and Rehabilitation Engineering*, vol. 28, no. 10, pp. 2286–2295, 2020.

[10] Y. Cho, P. Kim, and K.-S. Kim, "Estimating simultaneous and proportional finger force intention based on semg using a constrained autoencoder," *IEEE Access*, vol. 8, pp. 138 264–138 276, 2020.

[11] Y. Yu, C. Chen, X. Sheng, and X. Zhu, "Multi-dof continuous estimation for wrist torques using stacked autoencoder," *Biomedical Signal Processing and Control*, vol. 57, p. 101733, 2020.

[12] S. Salminger, H. Stino, L. H. Pichler, C. Gstoettner, A. Sturma, J. A. Mayer, M. Szivak, and O. C. Aszmann, "Current rates of prosthetic usage in upper-limb amputees–have innovations had an impact on device acceptance?" *Disability and Rehabilitation*, vol. 44, no. 14, pp. 3708–3713, 2022.

[13] J. Happold, D. Morais, P. Capsi-Morales, and C. Piazza, "Preliminary validation of an immersive virtual reality framework for prosthetic embodiment quantification," in *2024 10th IEEE RAS/EMBS International Conference for Biomedical Robotics and Biomechatronics (BioRob)*. IEEE, 2024, pp. 68–74.

[14] D. I. Anderson, K. R. Lohse, T. C. V. Lopes, and A. M. Williams, "Individual differences in motor skill learning: Past, present and future," *Human Movement Science*, vol. 78, p. 102818, 2021.

[15] K. C. Tse, P. Capsi-Morales, and C. Piazza, "Learning dynamics of muscle synergies during non-biomimetic control maps," *Wearable Technologies*, vol. 6, p. e1, 2025.

[16] A. Chadwell, L. Kenney, S. Thies, A. Galpin, and J. Head, "The reality of myoelectric prostheses: understanding what makes these devices difficult for some users to control," *Frontiers in neurorobotics*.

[17] E. Campbell, J. Chang, A. Phinyomark, and E. Scheme, "A comparison of amputee and able-bodied inter-subject variability in myoelectric control," in *Myoelectric Controls Symposium*, 2020.

[18] H. Bouwsema, C. K. van der Sluis, and R. M. Bongers, "Changes in performance over time while learning to use a myoelectric prosthesis," *Journal of neuroengineering and rehabilitation*, vol. 11.

[19] M. Dyson, S. Dupan, H. Jones, and K. Nazarpour, "Learning, generalization, and scalability of abstract myoelectric control," *IEEE Transactions on Neural Systems and Rehabilitation Engineering*, vol. 28, no. 7, pp. 1539–1547, 2020.

[20] P. L. Gribble, L. I. Mullin, N. Cothros, and A. Mattar, "Role of cocontraction in arm movement accuracy," *Journal of neurophysiology*, vol. 89, no. 5, pp. 2396–2405, 2003.

[21] M. Camara, M. de Carvalho, T. Araújo, H. Gamboa, and C. Quintao, "Coherence and phase locking disruption in electromyograms of patients with amyotrophic lateral sclerosis," in *International Conference on Bio-inspired Systems and Signal Processing*.

[22] A. Phinyomark, F. Quaine, S. Charbonnier, C. Serviere, F. Tarpin-Bernard, and Y. Laurillau, "Emg feature evaluation for improving myoelectric pattern recognition robustness," *Expert Systems with applications*, vol. 40, no. 12, pp. 4832–4840, 2013.

[23] M. Nowak and C. Castellini, "The let procedure for prosthetic myocontrol: towards multi-dof control using single-dof activations," *PLoS One*, vol. 11, no. 9, p. e0161678, 2016.

[24] S. Suwansawang and D. Halliday, "Time-frequency based coherence and phase locking value analysis of human locomotion data using generalized morse wavelets," in *International Conference on Bio-inspired Systems and Signal Processing*, vol. 5.

[25] N. Daniel, J. Małachowski, K. Sybilski, and D. Siemiaszko, "Quantitative assessment of muscle fatigue during rowing ergometer exercise using wavelet analysis of surface electromyography (semg)," *Frontiers in Bioengineering and Biotechnology*, vol. 12, p. 1344239, 2024.

[26] P. Capsi-Morales, C. Piazza, M. G. Catalano, A. Bicchi, and G. Grioli, "Exploring stiffness modulation in prosthetic hands and its perceived function in manipulation and social interaction," *Frontiers in Neurorobotics*, vol. 14, p. 33, 2020.

[27] A. A. Blank, A. M. Okamura, and L. L. Whitcomb, "Task-dependent impedance and implications for upper-limb prosthesis control," *The International Journal of Robotics Research*, vol. 33, no. 6, pp. 827–846, 2014.

Neural Network Sparsity in Brain-Body-Machine Interfaces

Laura C. Petrich[1,4,*], Samuel Neumann[1,4,*], Patrick M. Pilarski[1,2,4], and Alona Fyshe[1,3,4]

***Abstract*— Brain-body-machine interfaces acquire, process, and translate brain signals for individuals with severe motor impairments to communicate and control the assistive technology that supports their daily life activities. Electroencephalography (EEG) is a standard approach for acquiring such brain signals due to its low cost and high temporal resolution. EEG signals can be thought of as a proxy for the user's intent. One established method for translating this intent into inferences and actions are neural networks. However, densely connected neural networks can be computationally expensive—a problem for real-time, deployed brain-body-machine interface systems. In this paper we investigate the use of *sparsity* in neural networks for EEG-based motor classification, with the goal of reducing the number of neuronal connections without sacrificing a system's performance. We compare two sparsity-inducing algorithms, weight pruning and sparse evolutionary training, with a dense neural network under three experimental conditions. Overall, our results show that sparse neural networks can achieve higher performance accuracy and generalization than their densely-connected counterparts for an EEG-based classification task. We found that sparse evolutionary training achieves the highest and most stable performance across all experiments. Introducing sparsity into the network is a viable option for efficient EEG-based control, with promising applications in a range of related rehabilitation and assistive technologies. This brings us closer to helping individuals with severe motor impairments reclaim independence through more computationally realizable methods of interacting with their technology and the world around them.**

I. Introduction

Brain-body-machine interfaces (BBMIs) are an emerging technology aimed at enabling the control of external devices via acquired brain signals and other signals from the human body [1]. BBMIs have improved the quality of life for individuals with physical disabilities by increasing their personal autonomy [2]. The overarching goal of a BBMI system is to offer an alternative means of communication in order for the user to interact with their environment. A BBMI system is composed of three components: signal acquisition, signal processing (involving feature extraction, classification, and translation), and the control application [1]. The overall performance and success of a BBMI relies on the quality of signals acquired from the brain or body as these are used to interpret the user's intent. In this work we compare the performance of three neural network training regimes, shown in Fig. 1, on a BBMI task.

This work was supported by the Alberta Machine Intelligence Institute (Amii), the National Science and Engineering Research Council (NSERC), Alberta Innovates, and in part through the Canada CIFAR AI Chairs Program. [1]Dept. of Computing Science, [2]Dept. of Medicine, and [3]Dept. of Psychology, University of Alberta, Edmonton, AB, Canada; [4]Alberta Machine Intelligence Institute (Amii), Edmonton, AB, Canada.

* These authors contributed equally to this work. Please direct all correspondence to laurapetrich@ualberta.ca

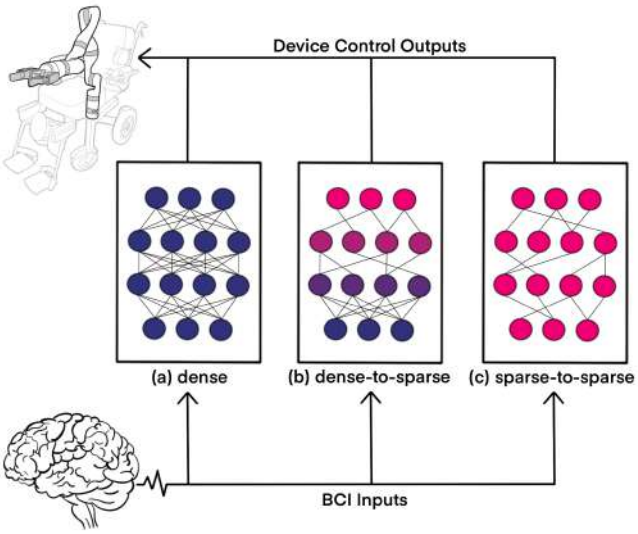


Fig. 1: Sparsity can be dynamically introduced into (a) *densely* connected neural networks by either starting with a dense layer and pruning network connections, known as (b) *dense-to-sparse* training, or initializing a sparse topology and iteratively pruning and regrowing connections, i.e., (c) *sparse-to-sparse* training. In this work we compare the performance of these three training regimes on a brain-computer interface task mapping electroencephalography signals (BBMI inputs) to upper limb motion events (device control outputs).

Electroencephalography (EEG) is a method of capturing the brain's electrical activity (i.e., signal acquisition) through wet or dry electrodes placed on the scalp [3]. It is popular for real-time control as EEG systems are relatively low-cost, non-invasive, and portable [4]. EEG signals have a high temporal resolution, however, they are inherently noisy and have poor spatial resolution [5]. Signal processing extracts a clean signal from a noisy EEG recording and then generates a mapping to the user's intent [6]. First, a preprocessing step is performed, involving channel selection (i.e., determine features relevant to the task of interest), signal frequency filtering (i.e., what filters should we apply to remove noise), and artifact removal (i.e., identify and remove irrelevant noise artifacts) [7]. Once the relevant features are extracted they can be classified and translated into motor commands to send to an external device (i.e., the control application), e.g., to control a smart wheelchair or robotic arm [1].

Due to the high-dimensionality, non-stationarity, and complexity of EEG data, dense neural networks are often used

for classification [8]. However, these networks can be computationally expensive and have large memory requirements. For practical control with EEG-based BBMI systems, low memory and computation requirements are necessary. The deployed system will need to be portable for improved usability, particularly for applications that do not have a local computer or internet connection. BBMI systems should be able to predict the user's intent accurately and react quickly to a user's input or feedback. Sparse neural networks are an emerging research area in machine learning that address both of these constraints [9], making them particularly well suited for BBMI control.

In a sparse neural network, each neuron is connected to a subset of neurons in the proceeding layer. This is in contrast to dense neural networks where each neuron is connected to all of the neurons in the proceeding layer. Sparse neural networks can be more energy efficient than dense neural networks, using a fraction of the memory and compute while reaching higher levels of performance and generalization [9]–[12]. In a recent survey on sparsity in deep learning, Hoefler et al. [13] found "that today's sparsification methods can lead to a 10-100x reduction in model size, and to corresponding theoretical gains in computational, storage, and energy efficiency, all without significant loss of accuracy" (p. 2–3). Furthermore, sparse neural networks may be more resistant to interference and catastrophic forgetting than their fully connected counterparts [14]–[16]. Finally, dense neural networks generally require large amounts of training data to generalize well, an important consideration in the application of BBMI systems where training datasets are usually small [8].

In this work *we investigate how sparsity affects the performance and generalization capabilities of neural networks in a classification task with EEG data.* Our key contribution is an empirical comparison of two techniques for adding sparsity to neural networks used for EEG-based classification, specifically examining their performance in the presence of variability both within individual participants and across different participants. We hypothesize that, when training and testing on a fixed pool of participants, with fewer neuronal connections sparse neural networks can attain higher levels of prediction accuracy and generalization compared to a dense neural network.

II. Sparsity in neural networks

Sparsity can be introduced into neural networks either *statically* or *dynamically*. Static sparse networks have fixed sparse connections between neurons and are not adapted during training [17]. Sparsity in these networks is due to deliberate architecture choices. In contrast, dynamic sparse networks have sparse connections that are learned through a gradual prune-and-regrow procedure [13]; it is this class of sparse networks we consider in the present study, due to their experimentally suggested utility within the animal brain. For example, Barth and Poulet [18] provide empirical evidence that the brain exhibits sparse firing of neocortical neurons, allowing for efficient representation of sensory information.

Algorithm 1: Sparse Evolutionary Training

Input: prune fraction ζ, prune frequency n, sparsity level ε, optimiser $\mathcal{O}$, loss $\mathscr{L}$
Initialize network with Erdős-Rényi topology with sparsity level ε
for *each training epoch* e **do**
  Train network parameters using $\mathcal{O}$ on $\mathscr{L}$
  if $e \equiv 0 \pmod{n}$ **then**
    Remove $\frac{100\zeta\%}{2}$ smallest positive weights
    Remove $\frac{100\zeta\%}{2}$ largest negative weights
    if e *is not the last epoch* **then**
      Add random new connections (weights) between consecutive layers equal to the amount removed
    end
  end
end

Algorithm 2: Weight Pruning

Input: prune fraction ε, prune epoch n, optimiser $\mathcal{O}$, loss $\mathscr{L}$, final network topology $\mathcal{T}$
for *each training epoch* e **do**
  Train network parameters using $\mathcal{O}$ on $\mathscr{L}$
  if $e = n$ **then**
    Remove $100\varepsilon\%$ of weights of lowest magnitude, ensuring that the resulting network has topology $\mathcal{T}$
  end
end

Dynamic sparse networks have also been argued to be more biologically plausible than static sparse networks, given the way that the animal brain is known to dynamically adjust its neuronal connections [19]–[21].

Dynamic Sparse Training (DST) refers to the simultaneous optimization of a dynamic sparse network's weights and neuronal connections. The Sparse Evolutionary Training (SET) algorithm of Mocanu et al., shown in Algorithm 1, is one of the seminal works in the DST line of research [10]. SET follows a *sparse-to-sparse* training regime (e.g., Fig. 1c), meaning that it initializes a neural network with a sparse Erdős-Rényi random graph topology [22] with sparsity level $\varepsilon \in (0, 1)$ and subsequently learns the weights and connections. Every n epochs, SET prunes and re-grows the connections. To do so, it first removes the $\frac{100\zeta\%}{2}$ smallest positive and largest negative weights (i.e., weights closest to zero) for $\zeta \in (0, 1)$. Next, an equal number of random connections are added back into the network, preserving the Erdős-Rényi topology. Conventional training then continues until the next pruning epoch. Mocanu et al. [10] show that networks trained with SET can match the performance of densely connected networks with a fraction of the number of neurons and far less memory and computation.

In contrast, *dense-to-sparse* training algorithms (e.g., Fig. 1b) begin by initializing a dense network then introduce sparsity by pruning network connections during training [23]–[26]. Such methods generally follow a three stage process. In the first stage, a densely connected network is

trained following conventional training procedures. During this stage, the learned network weights are considered to represent the importance of each connection where the importance of a weight is measured by its magnitude. In the second stage, the $100\varepsilon\%$ of unimportant connections are pruned at epoch n for $\varepsilon \in (0, 1)$. Finally, the pruned, sparse network is re-trained from either the current weight values or after re-initializing the weights. A typical weight pruning algorithm (WP) adapted from Han et al. [24], and the one we consider in this work, is shown in Algorithm 2.

III. Methods

A. Data characteristics and considerations

For this study work with the upper-limb prosthesis WAY-EEG-GAL dataset collected by Luciw et al. [27]. This dataset is well established in the community and has been used in classification tasks to achieve a high classification accuracy [28]–[30]. It was gathered with the intent of evaluating whether EEG signals can be used for upper-limb prosthetic device control. The data was collected with twelve right-handed participants and contains a total of 3,936 grasp and lift trials (328 trials per participant). Each participant completed ten series consisting of approximately 30 trials within each series. For each trial the participant reached out, grasped an object, lifted the object, and held it in the air for a few seconds before placing it back down and releasing the object. A hand motion event label was assigned to an EEG recording by Luciw et al. [27] using a combination of velocity and force data to determine the event onset. A subset of the original dataset was then extracted for a Kaggle competition where an event label was also assigned to an EEG sample if it was within 150 ms of the event onset [31]; it is this subset that we used for our study. For detailed information on the data collection protocol we refer the reader to the original article by Luciw et al. [27].

Since the events occur sequentially (i.e., time-series data), each EEG sample may be labelled with multiple events. In order to better isolate the effect of introducing sparsity, we extracted four event classes that did not have overlapping event labels for training our classifiers: HandStart (class 0), LiftOff (class 1), Replace (class 2), and BothReleased (class 3). The class label, class number, and number of samples for each class are summarized in Table I. Each sample (i.e., model input) contains 32 channels of raw EEG data from wet electrodes collected at a 500 Hz sampling rate with a corresponding event label (i.e., there is a signal-label sample every 0.002 seconds).

TABLE I: Class details for the dataset used in our multi-class classification problem. A weighted cross-entropy loss function was used to help address the class imbalance.

Class Label	Class Number	Number of Samples
HandStart	0	468000
LiftOff	1	388279
Replace	2	321905
BothReleased	3	321905

B. Data pre-processing

EEG data is known to be noisy and requires filtering in order to be sure that artifacts are not interfering with model predictions [32]. Head or wire movements as well as perspiration can cause low frequency noise artifacts. High frequency artifacts can be caused by muscle contractions in the vicinity of the EEG recording sites (electromyography artifacts), eye blinking or movement (electrooculography artifacts), and electromagnetic interference. During data collection for the original WAY-EEG-GAL dataset, no pre-processing (e.g., artifact rejection) steps were applied to the EEG signals other than the removal of "unneeded or extra samples at the beginning and end of each series" (p. 5) [27]. In line with standard practices, e.g., Janapati et al. [33], we applied a bandpass filter with a low frequency cutoff of 0.2 Hz and a high frequency cutoff of 50 Hz. The frequency cutoff of 0.2 Hz will remove low frequency movement artifacts, while the 50 Hz cutoff will remove high frequency noise artifacts from muscle contractions, eye movements, and electromagnetic interference.

C. Algorithms and hyperparameter tuning

To better understand how sparse neural networks can perform on an EEG-based classification task, we studied the learning process of two dynamic sparse training (DST) algorithms. The first algorithm is sparse evolutionary training (SET), shown in Algorithm 1. The second is a weight pruning (WP) algorithm, shown in Algorithm 2, similar to those used by Frankle and Carbin [26] and Han et al. [24]. Following the advice of Han et al. [24] who found that retraining pruned layers from the surviving parameters resulted in better performance; we did not re-initialize weights after pruning, rather training continued from the current weight values.

We compared these two DST algorithms with two baselines. The first baseline is a small densely connected network, which we denote as DN. The second baseline randomly predicted class labels according to their relative occurrence frequency in the dataset. This baseline served as a sanity check to ensure that each algorithm learned reasonable behaviour. All algorithms were implemented in `Flax` [34] using the `jaxpruner` library [35].

Due to the nature of our study, we were not interested in attaining state-of-the-art performance, rather, we wanted to characterize the learning processes of sparsity-inducing algorithms. For all experiments to remain interpretable, all neural networks were composed of two hidden layers. We performed a sweep of hidden layer sizes in $\{128, 256, 512, 1024\}$ and found that all networks performed best with hidden layers of size 1024 and that the computation time for all network sizes was similar. We constrained ourselves to hidden layers of 1024 and below to keep our study focused on relatively small computational loads that are deployable on embedded systems. For the rest of the experiments we set the hidden layers to size 1024. Each network predicted a softmax distribution over class labels. All neural networks were trained using the Adam

optimizer [36] from the `Optax` library [37] with default hyperparameters, except for the stepsize.

To tune the stepsize and sparsity specific hyperparameters, we conducted a grid search for multiple runs with three random seeds for Experiments 1 and 2, and fifteen random seeds for Experiment 3. We selected the tuned hyperparameters based on the highest average prediction accuracy achieved throughout training. For all experiments we swept stepsizes in $\{0.01, 0.001, 0.0001\}$. In our preliminary experiments, we evaluated the prediction accuracy of SET and WP for sparsity levels $\varepsilon \in \{0.25, 0.5, 0.75\}$ and percentage of dropped weights (SET) $\zeta \in \{0.15, 0.3, 0.5\}$. For both the sparsity level and percentage of dropped weights, we found that prediction accuracy was highest for the lowest two values and swept over those values for the final experiments. We further performed a sweep of batch sizes and found that full-batch updating resulted in highest prediction accuracy across all algorithms. However, in a number of experiments, full-batch updating was not possible due to the immense size of the training data. We therefore used a large batch size of 8192. We tested pruning weights every $\{1, 2, 5\}$ epochs for SET (since this algorithm prunes many times during training) and once at epoch $\{167, 333, 400\}$ for WP (i.e., pruning once $\frac{1}{3}$ $\frac{2}{3}$, or $\frac{4}{5}$ of the way through the total number of epochs).

For all experiments we used a weighted cross-entropy loss to help address the class imbalance, similar to that in the `scikit-learn` library [38]. The loss term for each class y was weighted by $\frac{N}{Cn_y}$, where N is the total number of data samples in the dataset, C is the number of classes, and n_y is the number of data points with label y. We used a stratified 80/10/10 train, test, and validation split for each experiment.

D. Experiment details

We conducted three different experiments to test the efficacy of sparsity in different settings. First, each algorithm was evaluated when training and testing data came from the same pool of participants. Next, we evaluated how each algorithm performed when classifying out-of-distribution data, where the training and testing datasets came from different pools of participants. Finally, we investigated how increasing amounts of training data from a single participant affected each algorithm's predictions on the same participant.

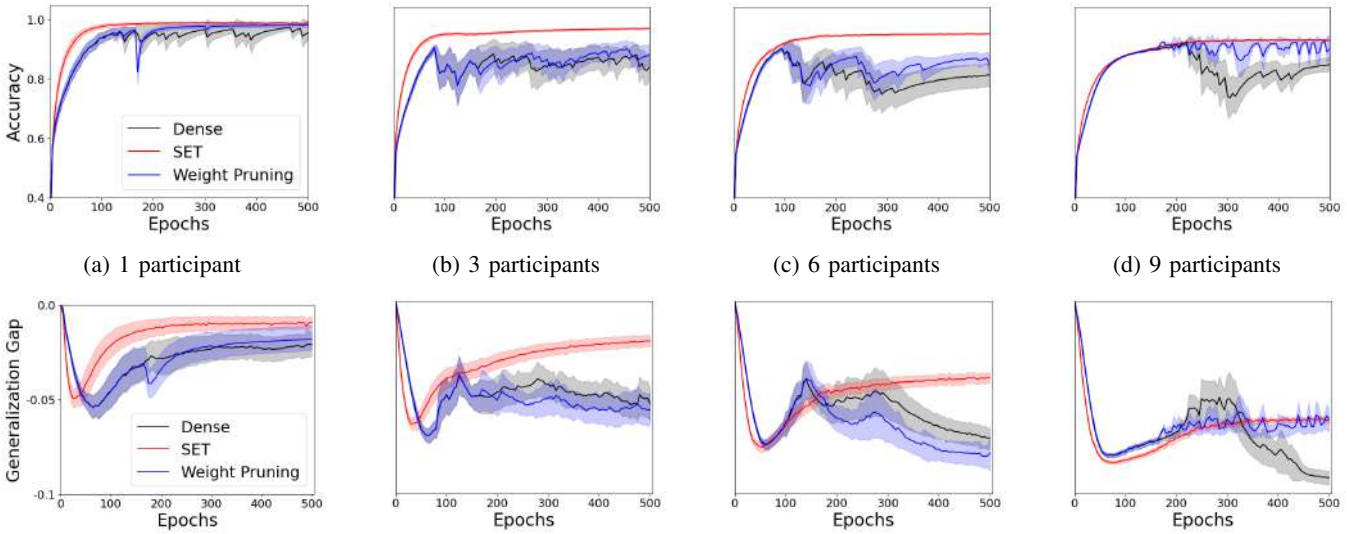
a) Experiment 1: Our first experiment addressed the question *how does each model perform within the participant pool it was trained on?* To answer this question, we trained and tested each algorithm on data from $N \in \{1, 3, 6, 9\}$ participants out of the first ten participants. The N participants were randomly sampled without replacement. We tuned hyperparameters over three random seeds. We then conducted an additional 20 experimental runs using the tuned hyperparameters and report performance metrics for these final 20 independent runs.

Due to the nature of the EEG data, we expected that increasing the number of participants in the training dataset would decrease prediction accuracy. This is because the model needs to account not only for variability that exists within an individual participant but also for variability between different participants. We were interested to see whether sparsity can help to counteract this effect. Indeed, for many of the highest performing submissions in the Kaggle competition, a separate network was trained for each participant [31]. Nevertheless, a BBMI system should be capable of being trained on multiple participants data in order to reduce the amount of training data required per individual.

b) Experiment 2: Our second experiment addressed the question *can each model efficiently generalize to the data of new, held-out participants?* For this experiment we took the tuned-and-trained models from Experiment 1 and tested how they performed on data from the two held-out participants 11 and 12. We expected each model to perform worse in this setting compared to Experiment 1, but we were interested in determining if sparsity helps to negate it (e.g., via improved generalization or reduced loss in prediction accuracy). This study allowed us to better understand how training data should be collected for real-world BBMI systems—from the end user or other participants. Improving generalization to new participants would be of great benefit to BBMI systems, as it is often challenging to have the end-user come in for multiple training sessions.

c) Experiment 3: Our final experiment sought to address the question *how does each algorithm perform with differing levels of training data for a single participant?* This experiment allowed us to better understand how each algorithm may behave in a real-world setting where the system could potentially learn and adapt to the behaviour of the end-user during deployment. For this experiment, data from a single randomly sampled participant from the first ten participants was split into training, validation, and test sets. The training set was composed of $p \in \{10\%, 20\%, 30\%, 50\%, 70\%, 80\%\}$ of the participant's data. The validation set was composed of 10% of the training set, and the test set was composed of the remaining data. Note that when the training data reaches 80% of the data this is equivalent to the 1 participant setting in Experiment 1. An increasing amount of training data should improve the performance of each algorithm, with diminishing returns. A well-performing algorithm, especially one suited for a deployable BBMI system, should reach reasonable performance with a moderate amount of training data. We repeated this experiment 15 times with different random seeds, tuning hyperparameters and reporting performance over all 15 seeds.

d) Evaluation metrics: Model performance was evaluated by prediction accuracy. Similar to Novak et al. [39] and Liu et al. [40], generalization is quantified as the *generalization gap*—the difference in prediction accuracy between the testing and training datasets. The generalization gap is expected to be less than zero, as it is unlikely that the test accuracy is greater or equal to the training accuracy. If a model were to perfectly generalize to unseen data, the generalization gap would be zero. We report mean evaluation metrics across runs with bootstrap confidence intervals. We used 10k resamples, batch sizes of 10, and 5% significance to construct confidence intervals, unless otherwise specified.



(a) 1 participant (b) 3 participants (c) 6 participants (d) 9 participants

(e) 1 participant (f) 3 participants (g) 6 participants (h) 9 participants

Fig. 2: Sparse Evolutionary Training (SET) displays consistently high accuracy and better generalization than other algorithms in Experiment 1, where both train and test data are from the same pool of participants. **Top Row**: Test accuracy over 20 independent runs. As more participants are added to the training dataset, the performance of SET stays consistently high with low variance. **Bottom Row**: Generalization gap (i.e., difference between the test and train accuracy) over 20 independent runs. SET is able to generalize more efficiently than either the dense network (DN) or weight pruning (WP). **Both**: Solid lines denote mean performance with shaded regions denoting 95% bootstrapped confidence intervals.

IV. Results

A. Experiment 1: Pooling participant's data

The top row of Fig. 2 shows the test accuracy for each algorithm over 20 independent runs with training/test data from 1, 3, 6, and 9 randomly sampled participants. WP performed similarly to DN in terms of prediction accuracy. In contrast, SET generally improved prediction accuracy compared to DN and learned noticeably faster than both DN and WP. Accuracy decreased for all algorithms when more participants were added into the training data. We hypothesize that this is because each algorithm had to better generalize among all participant's conditional data distributions.[1]

Whereas SET exhibited low variance in prediction accuracy with tight confidence intervals, DN and WP exhibited severe degradation in prediction accuracy at differing intervals throughout training as seen in the top row of Fig. 2. Notably, these dips are not apparent when using full-batch updating and happen across all classes (that is, the dips are not due to poor prediction accuracy for a single class). Such a phenomenon reduces the utility of both these algorithms to real-life BBMI systems.

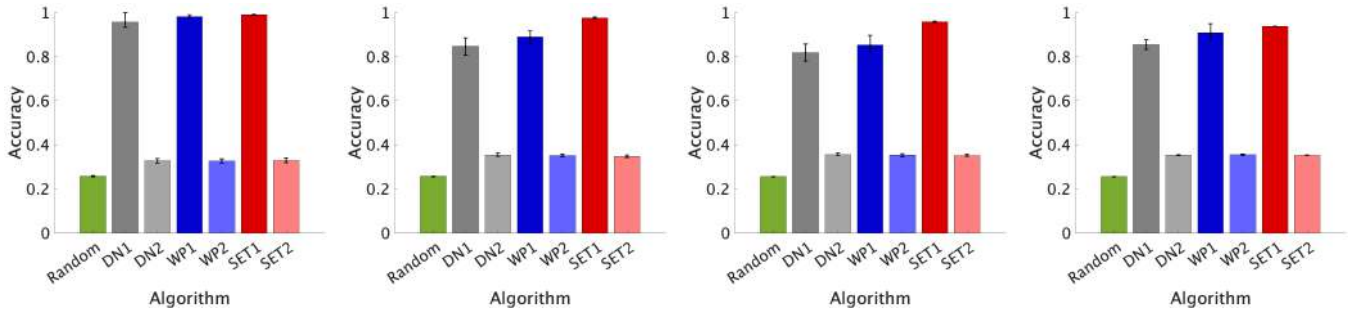
The bottom row of Fig. 2 outlines the generalization gap for each algorithm. SET often exhibited a significantly lower magnitude generalization gap than either DN or WP (note where the confidence intervals do not overlap). WP and DN exhibited a similar-magnitude generalization gap, except when training on 9 participants. For all algorithms, the generalization gap increased with an increasing number of participants. Overall, SET obtains the best prediction accuracy and performance stability across all settings suggesting that it is a helpful training regime when adding more participants data into the training pool.

B. Experiment 2: Generalizing to held-out participants

For this experiment we took the tuned-and-trained models from Experiment 1 and tested how well they performed on data from held-out participants 11 and 12. Fig. 3 shows the test accuracy of random predictions, DN, WP, and SET over 20 random seeds for both Experiment 1 and Experiment 2. Overall, we see a steep decline in accuracy when making predictions on held-out participant data, with algorithms performing only marginally better than the random baseline. For the 1-participant case, we see a $\sim 66\%$ decrease in prediction accuracy for all algorithms (comparing the Experiment 1 bars with corresponding Experiment 2 bars in Fig. 3).

Notably, this decline in prediction accuracy is not due to the held-out participants having poor quality data. We verified that each algorithm could learn on these participants' data, each reaching over 90% prediction accuracy. Overall, DN, SET, and WP each performed approximately equally when predicting on held-out participant data, with a slight increase in accuracy moving from the 1 to 3 participant setting (approximately 32% to 35%). This is unsurprising as EEG signals have been used for person recognition systems, suggesting there is sufficient variation in the signals between different people for classification. Considering these results in tandem with those of Experiment 1, we conclude that it

[1]Denote the theoretical distribution of EEG data (X) and labels (y) on this grasp-and-lift task as $p(X, y)$. Then the distribution of EEG data from a single participant S is $p(X, y \mid S)$.



(a) 1 participant (b) 3 participants (c) 6 participants (d) 9 participants

Fig. 3: The deep coloured bars (DN1, WP1, and SET1) show the Experiment 1 results while the faded bars (DN2, WP2, and SET2) show the Experiment 2 results. All network architectures show a steep decline in accuracy from the Experiment 1 results when making predicts based on out-of-distribution data from held-out participants. Bars show the accuracy of random predictions, dense network (DN1/DN2), weight pruning (WP1/WP2), and sparse evolutionary training (SET1/SET2) algorithms for Experiments 1 and 2, respectively, over 20 random seeds. Error bars denote 95% bootstrapped confidence intervals with 10,000 resamples.

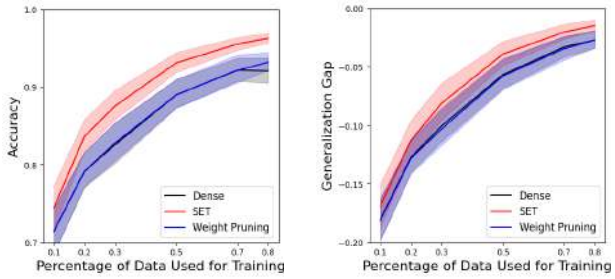
might be beneficial to include *data from the end-user when training a BBMI control system in order to help reduce the loss in model performance.*

C. Experiment 3: Single-participant models

A successful BBMI system should be able to continually learn and adapt to the dynamic nature of its user. This experiment allowed us to quantify the gains in performance with increasing data from the end-user. Ideally, a BBMI system would be useful even with a low amount of training data, although what defines a model as *useful* will ultimately depend on the end application.

Fig. 4a shows the accuracy during learning for increasing amounts of training data. Even with a low amount of data, all algorithms attained reasonable performance. With just 10% of the training data (approximately 27 grasp and lift trials), all algorithms reached a prediction accuracy around 75%. As more training data was introduced, the accuracy of all algorithms continued to increase, as expected. The prediction accuracy of SET increased more quickly than that of DN and WP and was significantly higher for datasets composed of more than 10% of a participant's data (note how the accuracy confidence intervals do not overlap). For the largest dataset sizes, SET attained significantly higher levels of precision and recall than DN (with a significance level of 0.1); table omitted for concision.

Fig. 4b shows the generalization gap for DN, SET, and WP. Overall, the gap shrinks with increasing training data, indicating that all algorithms can better generalize with more training data. When 10% of the data was used for training, the generalization gap was around 20% across algorithms—indicating overfitting. When more than 70% of the data was used for training, the generalization gap was less than 5%, indicating that the algorithms could generalize to unseen data effectively. All three algorithms exhibited a similar generalization gap for increasing dataset sizes.



(a) (b)

Fig. 4: The amount of participant data used in training impacts both accuracy and generalization, as shown via Experiment 3 results with train and test data from a single participant. Prediction (a) accuracy and (b) generalization gap when trained on increasing amounts of training data. Solid lines denote mean performance with shaded regions denoting 95% bootstrap confidence intervals. (a) SET attained the highest accuracy for increasing dataset sizes; (b) each algorithm exhibited a similar generalization gap.

V. Discussion

An open question in the BBMI community is *from whom should data be collected* in order to reduce the effects of intra- and inter-participant variability when training a BBMI control model [41]. We showed how the algorithms under consideration were able to make accurate predictions for participant data on which each algorithm was trained. But, when testing on held-out participant data, each algorithm exhibited a significant, and considerably large, drop in prediction accuracy, precision, and recall. This suggests that such computational models should include some training data from the end-user. Pre-trained models should be either fine-tuned to the end-user prior to deployment, for example through transfer learning [42], or include data from the end-user while training the model. For best performance, we suggest training a model on as much data as possible from solely the end-user, although we do acknowledge this may

not always be a viable option. When training on data from multiple participants, SET could help to minimize the decline in prediction accuracy.

Overall, our empirical study suggests that sparsifying a neural network is a viable option for reducing the number of neuronal connections when training an EEG-based model without significant loss of performance. As suggested by Lasby et al. [9], selective reduction may support the active alignment of network architectures to deployed computational hardware. Our study also indicates that sparse neural networks have the ability to adapt more quickly during training than their densely connected counterparts. This brings us one step closer towards making a *direct impact on the lives of people living with severe motor impairments through the use of machine learning models trained on brain data.*

A. Ethical considerations

As machine learning models become more prevalent in every day life, they are being used to make decisions that affect not only individuals but also society as a whole. Thus, it is important to understand the potential sources of harm that could arise during different stages of the machine learning life cycle. Suresh and Guttag [43] present a framework for identifying seven sources of harm, three of which we take into consideration for this study. The first is *representation bias*, which we note in the participant pool recruitment of the WAY-GAL-EEG dataset [27]; the population that would end up requiring and using a model such as this for BBMI control is underrepresented and models trained on this set could fail to generalize well for an assistive rehabilitation technology user population. The second is *measurement bias*. By oversimplifying a complex motor action recorded via EEG signals into four simple labels, we run the risk of a trained model being a poor reflection of user intent as measured from the whole brain. The third is *deployment bias*. A key goal of this work is to develop efficient and accurate prediction models for use in a real-world BBMI control system. Such a system would involve a human user controlling a neuroprosthetic device via real-time EEG signals. Thus, it is important that future work consider the match between the prediction problem that the model solves and how it is being used during deployment. Reproducibility and transparency are also an important part of ethical research practices. To this end, we open-sourced all of our code for dataset loading, model training, and evaluation.[2]

B. Limitations and future work

Our empirical analysis contained factors that limit the immediate transferability of our findings to deployed environments. One choice made in our data pre-processing step was to remove all samples with overlapping or no event labels. While making evaluation more straightforward, this choice makes it more difficult to transfer the approach verbatim to a real-time control system as there will be a significant amount of out-of-distribution EEG signals being fed into the trained model. One intermediary step before moving to a BBMI application could therefore be to re-train these models using the full set of original event labels to see if our conclusions still hold. Future work should ideally focus on studying sparse neural network algorithms on a variety of larger BBMI datasets. Many of our conclusions are a direct consequence of training on a small dataset of twelve participants with a reduced number of class labels, and it is unclear if these conclusions will consistently present in larger, more diverse or contextual datasets. Future work should also consider systematic hyperparameter sensitivity analyses of these algorithms, to understand better how they would perform in real-world scenarios where tuning is impossible.

[2] https://github.com/lpetrich/SparsEEG

VI. Conclusion

In this work we evaluated the performance of two sparse neural network algorithms for an EEG-based upper-limb motion classification task. It is well-known that sparse neural networks can reduce the computational and memory requirements of deep-learning systems [9], [13], and our goal was to determine whether such networks are viable for adaptive BBMI systems. Our results show how sparse neural networks can achieve higher performance and generalization than dense neural networks on one EEG dataset. Furthermore, our experiments provide evidence that sparse neural networks can achieve high accuracy with low variance during learning, making these networks candidates for real-time BBMI systems which adapt to the end-user during deployment. For example, improvements in the performance and stability of EEG-based control for wheelchair-mounted robotic arms could help empower individuals to perform everyday tasks such as eating, drinking, and grasping objects independently. In addition to their use in rehabilitation and assistive robotics, we expect these insights into sparsity to inform the development of other non-medical biomechatronic and bio-inspired systems with limited on-board computational resources. We hope that the present research has therefore laid the groundwork necessary for conducting ambitious future studies into the intuitive and computationally efficient user control of BBMI systems such as robotic arms and other assistive technologies.

Acknowledgment

The authors would like to thank Johannes Günther, Matthew E. Taylor, and Alex Murphy for many helpful discussions and feedback on this paper. Special thanks to Shaylee Lorrain for graphical design assistance.

References

[1] B. Maiseli, A. T. Abdalla, L. V. Massawe, M. Mbise, K. Mkocha, N. A. Nassor, M. Ismail, J. Michael, and S. Kimambo, "Brain–computer interface: Trend, challenges, and threats," *Brain Informatics*, vol. 10, no. 1, p. 20, 2023.

[2] A. N. Belkacem, N. Jamil, J. A. Palmer, S. Ouhbi, and C. Chen, "Brain computer interfaces for improving the quality of life of older adults and elderly patients," *Frontiers in Neuroscience*, vol. 14, p. 692, 2020.

[3] A. Biasiucci, B. Franceschiello, and M. M. Murray, "Electroencephalography," *Current Biology*, vol. 29, no. 3, pp. R80–R85, 2019.

[4] M. S. Al-Quraishi, I. Elamvazuthi, S. A. Daud, S. Parasuraman, and A. Borboni, "EEG-based control for upper and lower limb exoskeletons and prostheses: A systematic review," *Sensors*, vol. 18, no. 10, p. 3342, 2018.

[5] M. Bamdad, H. Zarshenas, and M. A. Auais, "Application of BCI systems in neurorehabilitation: A scoping review," *Disability and Rehabilitation: Assistive Technology*, vol. 10, no. 5, pp. 355–364, 2015.

[6] E. H. T. Shad, M. Molinas, and T. Ytterdal, "Impedance and noise of passive and active dry EEG electrodes: A review," *IEEE Sensors Journal*, vol. 20, no. 24, pp. 14 565–14 577, 2020.

[7] H. Altaheri, G. Muhammad, M. Alsulaiman, S. U. Amin, G. A. Altuwaijri, W. Abdul, M. A. Bencherif, and M. Faisal, "Deep learning techniques for classification of electroencephalogram (EEG) motor imagery (MI) signals: A review," *Neural Computing and Applications*, vol. 35, no. 20, pp. 14 681–14 722, 2023.

[8] F. Lotte, M. Congedo, A. Lécuyer, F. Lamarche, and B. Arnaldi, "A review of classification algorithms for EEG-based brain–computer interfaces," *Journal of Neural Engineering*, vol. 4, no. 2, p. R1, 2007.

[9] M. Lasby, A. Golubeva, U. Evci, M. Nica, and Y. Ioannou, "Dynamic sparse training with structured sparsity," *Proceedings of the 12th International Conference on Learning Representations*, 2024.

[10] D. C. Mocanu, E. Mocanu, P. Stone, P. H. Nguyen, M. Gibescu, and A. Liotta, "Scalable training of artificial neural networks with adaptive sparse connectivity inspired by network science," *Nature Communications*, vol. 9, no. 1, p. 2383, 2018.

[11] G. Bellec, D. Kappel, W. Maass, and R. Legenstein, "Deep rewiring: Training very sparse deep networks," in *Proceedings of the 6th International Conference on Learning Representations*, 2018.

[12] S. Liu, "Learning sparse neural networks for better generalization," in *Proceedings of the Twenty-Ninth International Joint Conference on Artificial Intelligence, IJCAI-20*, pp. 5190–5191, 2020.

[13] T. Hoefler, D. Alistarh, T. Ben-Nun, N. Dryden, and A. Peste, "Sparsity in deep learning: Pruning and growth for efficient inference and training in neural networks," *The Journal of Machine Learning Research*, vol. 22, no. 1, pp. 10 882–11 005, 2021.

[14] V. Liu, R. Kumaraswamy, L. Le, and M. White, "The utility of sparse representations for control in reinforcement learning," in *Proceedings of the AAAI Conference on Artificial Intelligence*, vol. 33, no. 01, pp. 4384–4391, 2019

[15] S. Ghiassian, B. Rafiee, Y. L. Lo, and A. White, "Improving performance in reinforcement learning by breaking generalization in neural networks," in *Proceedings of the 19th International Conference on Autonomous Agents and MultiAgent Systems*, 2020.

[16] Y. Pan, K. Banman, and M. White, "Fuzzy tiling activations: A simple approach to learning sparse representations online," in *Proceedings of the 9th International Conference on Learning Representations*, 2021.

[17] B. Grooten, G. Sokar, S. Dohare, E. Mocanu, M. E. Taylor, M. Pechenizkiy, and D. C. Mocanu, "Automatic noise filtering with dynamic sparse training in deep reinforcement learning," in *Proceedings of the 2023 International Conference on Autonomous Agents and Multiagent Systems*, 2023.

[18] A. L. Barth and J. F. Poulet, "Experimental evidence for sparse firing in the neocortex," *Trends in Neurosciences*, vol. 35, no. 6, pp. 345–355, 2012.

[19] A. J. Holtmaat, J. T. Trachtenberg, L. Wilbrecht, G. M. Shepherd, X. Zhang, G. W. Knott, and K. Svoboda, "Transient and persistent dendritic spines in the neocortex in vivo," *Neuron*, vol. 45, no. 2, pp. 279–291, 2005.

[20] D. D. Stettler, H. Yamahachi, W. Li, W. Denk, and C. D. Gilbert, "Axons and synaptic boutons are highly dynamic in adult visual cortex," *Neuron*, vol. 49, no. 6, pp. 877–887, 2006.

[21] A. R. Chambers and S. Rumpel, "A stable brain from unstable components: Emerging concepts and implications for neural computation," *Neuroscience*, vol. 357, pp. 172–184, 2017.

[22] P. Erdős and A. Rényi, "On random graphs I," *Publicationes Mathematicae Debrecen*, vol. 6, no. 18, pp. 290–297, 1959.

[23] S. A. Janowsky, "Pruning versus clipping in neural networks," *Physical Review A*, vol. 39, no. 12, pp. 6600–6603, Jun. 1989.

[24] S. Han, J. Pool, J. Tran, and W. Dally, "Learning both weights and connections for efficient neural network," *Proceedings of the 28th International Conference on Neural Information Processing Systems*, vol. 28, 2015.

[25] M. Zhu and S. Gupta, "To prune, or not to prune: Exploring the efficacy of pruning for model compression," in *Proceedings of the 6th International Conference on Learning Representations Workshop Track*, 2018.

[26] J. Frankle and M. Carbin, "The lottery ticket hypothesis: Finding sparse, trainable neural networks," in *Proceedings of the 7th International Conference on Learning Representations*, 2019.

[27] M. D. Luciw, E. Jarocka, and B. B. Edin, "Multi-channel EEG recordings during 3,936 grasp and lift trials with varying weight and friction," *Scientific Data*, vol. 1, no. 1, pp. 1–11, 2014.

[28] N. Yahya, H. Musa, Z. Y. Ong, and I. Elamvazuthi, "Classification of motor functions from electroencephalogram (EEG) signals based on an integrated method comprised of common spatial pattern and wavelet transform framework," *Sensors*, vol. 19, no. 22, p. 4878, 2019.

[29] T. Liu and D. Yang, "A three-branch 3D convolutional neural network for EEG-based different hand movement stages classification," *Scientific Reports*, vol. 11, no. 1, p. 10758, 2021.

[30] S. Li and H. Feng, "EEG signal classification method based on feature priority analysis and CNN," in *2019 International Conference on Communications, Information System and Computer Engineering (CISCE)*, pp. 403–406, 2019.

[31] B. Edin, K. Greff, and W. Cukierski, "Grasp-and-lift EEG detection," 2015. [Online]. Available: https://kaggle.com/competitions/grasp-and-lift-eeg-detection

[32] X. Jiang, G.-B. Bian, and Z. Tian, "Removal of artifacts from EEG signals: A review," *Sensors*, vol. 19, no. 5, p. 987, Feb. 2019.

[33] R. Janapati, V. Dalal, and R. Sengupta, "Advances in modern EEG-BCI signal processing: A review," *Materials Today: Proceedings*, vol. 80, pp. 2563–2566, 2023.

[34] J. Heek, A. Levskaya, A. Oliver, M. Ritter, B. Rondepierre, A. Steiner, and M. van Zee, "Flax: A neural network library and ecosystem for JAX," 2023. [Online]. Available: http://github.com/google/flax

[35] J. H. Lee, W. Park, N. Mitchell, J. Pilault, J. S. Obando-Ceron, H.-B. Kim, N. Lee, E. Frantar, Y. Long, A. Yazdanbakhsh, S. Agrawal, S. Subramanian, X. Wang, S.-C. Kao, X. Zhang, T. Gale, A. J. C. Bik, W. Han, M. Ferev, Z. Han, H.-S. Kim, Y. Dauphin, K. Dziugaite, P. S. Castro, and U. Evci, "JaxPruner: A concise library for sparsity research," 2023.

[36] D. P. Kingma and J. Ba, "Adam: A method for stochastic optimization," *Proceedings of the 3rd International Conference on Learning Representations*, 2014.

[37] DeepMind, I. Babuschkin, K. Baumli, A. Bell, S. Bhupatiraju, J. Bruce, P. Buchlovsky, D. Budden, T. Cai, A. Clark, I. Danihelka, A. Dedieu, C. Fantacci, J. Godwin, C. Jones, R. Hemsley, T. Hennigan, M. Hessel, S. Hou, S. Kapturowski, T. Keck, I. Kemaev, M. King, M. Kunesch, L. Martens, H. Merzic, V. Mikulik, T. Norman, G. Papamakarios, J. Quan, R. Ring, F. Ruiz, A. Sanchez, L. Sartran, R. Schneider, E. Sezener, S. Spencer, S. Srinivasan, M. Stanojević, W. Stokowiec, L. Wang, G. Zhou, and F. Viola, "The DeepMind JAX ecosystem," 2020. [Online]. Available: http://github.com/google-deepmind

[38] F. Pedregosa, G. Varoquaux, A. Gramfort, V. Michel, B. Thirion, O. Grisel, M. Blondel, P. Prettenhofer, R. Weiss, V. Dubourg, J. Vanderplas, A. Passos, D. Cournapeau, M. Brucher, M. Perrot, and Édouard Duchesnay, "Scikit-learn: Machine learning in Python," *Journal of Machine Learning Research*, vol. 12, no. 85, pp. 2825–2830, 2011.

[39] R. Novak, Y. Bahri, D. A. Abolafia, J. Pennington, and J. Sohl-Dickstein, "Sensitivity and generalization in neural networks: An empirical study," in *Proceedings of the 6th International Conference on Learning Representations*, 2018.

[40] S. Liu, D. C. Mocanu, and M. Pechenizkiy, "On improving deep learning generalization with adaptive sparse connectivity," *ICML 2019 Workshop on Understanding and Improving Generalization in Deep Learning*, 2019.

[41] S. Saha and M. Baumert, "Intra- and inter-subject variability in EEG-based sensorimotor brain computer interface: A review," *Frontiers in Computational Neuroscience*, vol. 13, p. 87, 2020.

[42] F. Fahimi, Z. Zhang, W. B. Goh, T.-S. Lee, K. K. Ang, and C. Guan, "Inter-subject transfer learning with an end-to-end deep convolutional neural network for EEG-based BCI," *Journal of Neural Engineering*, vol. 16, no. 2, p. 026007, Jan. 2019.

[43] H. Suresh and J. Guttag, "A framework for understanding sources of harm throughout the machine learning life cycle," in *Equity and Access in Algorithms, Mechanisms, and Optimization*, pp. 1–9, Oct. 2021.

Strategic User Identification Increases the Impact of Wearable Airbags in High-Fall Risk Populations with Neurological Disease

Kyle R. Embry, PhD
Center for Bionic Medicine
Shirley Ryan AbilityLab
Chicago, USA
Department of Physical Medicine and Rehabilitation,
Northwestern University
Chicago, USA
kembry@sralab.org

Katelyn Aragon, BS
Max Näder Rehabilitation Technologies and Outcomes Lab
Shirley Ryan AbilityLab
Chicago, USA
karagon@sralab.org

Sajjad Daneshgar, PhD
Max Näder Rehabilitation Technologies and Outcomes Lab
Shirley Ryan AbilityLab
Chicago, USA
sdaneshgar@sralab.org

Arun Jayaraman, PT, PhD
Max Näder Rehabilitation Technologies and Outcomes Lab
Shirley Ryan AbilityLab
Chicago, USA
Department of Physical Medicine and Rehabilitation,
Northwestern University
Chicago, USA
ajayaraman@sralab.org

***Abstract*—Falls are a major health concern among older adults, particularly those with neurological conditions such as Parkinson's disease or stroke. Wearable airbags are a promising new technology that may help mitigate fall-related injuries. These devices use motion sensors, pre-impact fall detection algorithms, and CO_2-powered airbags to cushion the impact of a fall. However, this technology is only needed for people with a high risk of falls, and it is only useful if the pre-impact fall detection algorithm successfully detects the fall. Our prior work showed that some individuals benefit more from one pre-impact fall detection algorithm than another due to their unique movement characteristics and biomechanics. This study aims to determine who may be suitable users for this technology by predicting future fall risk and categorizing users as 'responders' or 'non-responders' based on their predicted algorithm performance. We recruited 22 participants with neurological conditions in a six-month study design. Using baseline physical assessments, survey scores, and principal component analysis, we trained a logistic regression model that distinguished high-risk 'fallers' from 'non-fallers' with an average F1 score of 0.76. The model also identified 'responder' individuals, whose fall patterns were accurately detected, achieving an F1 score of 0.75. These findings suggest that identifying high fall risk users whose falls are best identified by a fall detection algorithm can enhance device effectiveness and maximize benefits for users.**

Keywords—Fall Detection, Wearable Device, Machine Learning, Stroke, Parkinson's disease, Fall Risk

This study was funded by the Department of Health and Human Services, National Institute on Disability, Independent Living, and Rehabilitation (NIDILRR), RERC Grant # 90REGE0003-03-00 and The Michael J. Fox Foundation Grant # 16696

I. INTRODUCTION

Fall-related injuries are a prominent issue for older adults, not only in the United States, but also the world, with approximately 37.3 million falls requiring emergency medical care worldwide each year [1]. As the global population of older adults continues to grow, with an anticipated increase from 1 billion adults aged 60 and over in 2020 to 1.4 billion by 2030 [2], the number of falls and fall-related injuries will continue to increase. Today, one in four adults over 65 experience a fall throughout the year in the United States [3], resulting in an estimated $50 billion spent on medical costs related to non-fatal fall injuries and $754 million on costs related to fatal falls [4]. Falls can have lasting physical and psychological consequences, such as chronic pain, reduced mobility, fear of falling, social isolation, and depression [5], [6]. Around 50% of hospitalizations after a fall are due to hip fractures, making them a critical problem to address [7]. The risk of falling increases as individuals are diagnosed with neurological conditions such as Parkinson's disease (PD) or stroke. Individuals with PD are twice as likely to fall compared to other neurological disorders [8]. Older adults with stroke are also at high risk, as they have a 1.5-4 times higher risk for falls in comparison to age matched peers [9]. Existing strategies to prevent falls, such as exercise and medication, have not been proven to be fully effective in the PD and stroke populations [10], [11]. As a result, methods to reduce fall injury are of interest. Hip pads are the most common method of fall injury protection, but most are uncomfortable and have low compliance rates [12]. An alternative is wearable airbags, which use pre-impact fall detection algorithms to determine when a person is falling and deploy airbags before the individual comes into contact with the ground. One commercially-available device that utilizes this type of system is the WOLK Hip Airbag (Wolk De Heupairbag; Wolk Company, Netherlands). The device was used in a pilot study across 11 long-term care facilities and

more than 900 individuals. While there was a limited number of devices available, the group with access to the wearable airbag experienced fewer hip fractures than the group without [13].

Our prior work has shown that fall detection algorithms can be more effective when trained for a specific patient population [14]. People with neurological conditions have differing biomechanics, even during a fall. This can be seen in individuals with stroke, as they have delayed postural reflex onset latencies, longer intra limb coupling durations [15], and various gait deficits [16]. This suggests that fall detection models should be specialized to the population using it to optimize its effectiveness, and that some individuals may get more benefit from certain algorithms. For this paper, we developed and tested a fall detection algorithm specialized to detect falls of individuals with neurological conditions.

In order to utilize this technology most effectively, we aim to first identify potential users with a high risk of falling in the near future. While most fall detection systems have focused on optimizing algorithm performance by adjusting biosensor locations, task types, or the algorithm design [17], disease-related gait and balance differences within study cohorts are often underestimated. For instance, fall risk factors in neurological conditions are associated with measures of balance [18], [19] and abilities related to activities of daily living (ADL) [20]. These gait and balance factors can be used to group individuals into two groups of high-fall and low-fall risk in the next six months, also known as 'faller' and 'non-faller' groups [21]. Identifying future fall risk groups can help identify appropriate users.

Moreover, fall patterns can vary among neurological conditions and severities [14], [22], [23] and some individuals may experience better performance from specific fall detection algorithms. This variation allows us to categorize and define users into 'responders' (those for whom the given algorithm is highly effective) and 'non-responders' (those for whom the algorithm is less effective) [24]. By understanding baseline measures in balance, quality of life, activities of daily living, we can predict which users will benefit most from the device.

The purpose of this study is to assess future fall risk and optimize the use and benefit of wearable airbag devices for individuals at high risk of falls. We aim to develop classification algorithms that utilize baseline physical assessments and survey scores to: 1) distinguish between 'faller' users–defined as those with at least one expected fall in the next six months–and 'non-faller' users, and 2) further stratify fallers into two subgroups: 'responders', who demonstrate clear differentiation of fall patterns from non-fall activities by the given fall detection algorithm, and 'non-responders', whose fall patterns are less differentiable by the given fall detection algorithm.

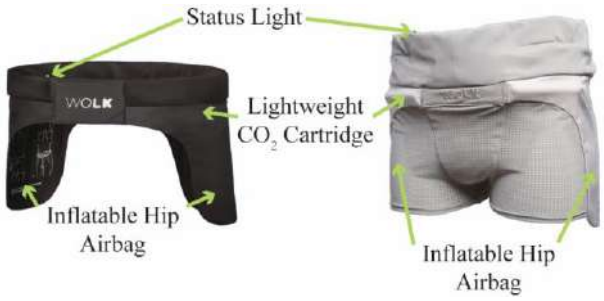


Fig. 1. **Airbag System Hardware**. The WOLK Active Airbag System is used in two models, a belt (left) or shorts (right). Both Systems deploy hip mounted airbags to protect the hips when a fall is detected.

II. METHODS

A. Participants

Individuals with Parkinson's disease (N = 10, Average age 72.4 ± 3.4 Standard deviation, 4 female) and chronic stroke (at least six months from diagnosis; N = 12, Average age 64.9 ± 14.5, 7 female) were recruited in the **community deployment pilot study**. Inclusion criteria included ages 18-85, with at least one self-reported fall in the last six months, homebound or community ambulators, with a waist circumference of 84-125 cm (due to the airbag device sizing). Individuals using a wheelchair for mobility in both indoor and outdoor areas, as well as individuals with colorblindness that would affect their ability to perceive the light status on the device were excluded from this study. Informed consent was obtained from all participants prior to participation, in accordance with guidelines from the Northwestern University IRB (NUIRB, IL, USA).

B. Device

The WOLK Hip Airbag (Wolk De Heupairbag; Wolk Company, Netherlands) was used in this study (Figure 1). This wearable airbag device can be worn discreetly under clothing, while offering hip protection. It uses three fixed Inertial Measurement Unit (IMU) sensors located on the lateral sides

TABLE I. LIST OF FALL AND NON-FALL EVENTS REPORTED OR COMPLETED BY PARTICIPANTS IN THE COMMUNITY DEPLOYMENT AND IN-LABORATORY STUDIES

Community Deployment Pilot Study		**In-Laboratory Study**	
Fall (All lost balance and landed on hip or rear)	**Non-Fall**	**Fall** (All landed on hip or rear)	**Non-Fall**
Walking Putting on clothing Reaching for an item Transitioning between positions Turning	Sit to stand Sit (static) Lying on back Jumping in place Picking up an object from floor Functional Gait Assessment items Mini Balance Evaluation System Test items	Sit to stand / Stand to sit Slipping Tripping Pushed over, with arms crossed	Sit to stand Walking Sitting (static) Lying on back Jumping in place Picking up an object from floor

of the hips and on the lower back (at the L3 vertebrae). The IMU sensors each contain an accelerometer and gyroscope sensor that collect data in the x, y, and z axes, with a sampling rate of 500 Hz. The two embedded CO_2 cartridges deploy the airbags after receiving commands from the embedded pre-impact fall detection algorithm. If a fall is detected, the IMU data is recorded and saved in an output file. For in-laboratory activities, individuals wore a modified WOLK device that records IMU data continuously.

C. Experimental Setup

This study collected data from real-world participants and incorporated previously collected data from simulated in-laboratory falls for analysis (Figure 2A). The two datasets involved different individuals and all fall and non-fall activities are listed in Table I.

1) Community Deployment Pilot Study:

The real-world falls data **was collected during the community deployment pilot study.** This pilot study was designed to capture six months of data for each participant, with a laboratory visit on the first day. During the laboratory visit, participants completed a series of physical assessments and surveys (Table II). During these physical assessments, individuals wore the modified WOLK device to record their movement data, and the assessment items were recorded and time stamped with a smartphone. These activities were used as replications of activities of daily living (ADLs). For the remainder of the six-month period, participants were provided with a wearable airbag device and instructed to use it as consistently as possible during daily life activities. Fall incidents at home or in the community were tracked by both the airbag device and self-reported during bi-weekly phone calls. The falls were specifically defined as events in which the participant lost balance, and their hip or rear made direct contact with the ground. These events will be referred to as "falls" in this study. "Non-fall" events included any false activations caused by dropping the device or other ADLs, as well as the replications of ADLs from the physical assessments.

2) In-Laboratory Study:

The in-laboratory dataset [14] was recorded with a separate cohort of individuals with PD (N = 19) and chronic stroke (N = 20), but only in the laboratory environment. Each participant was equipped with protective gear (e.g., helmet, neck/knee/elbow guards) and performed non-fall and fall tasks. "Fall" events were defined in the same way as the community deployment study. However, non-fall events were independent of the activation of the wearable device but still included ADLs (e.g., walking, sitting, picking an item off the floor) and near-falls (e.g., slips, trips, loss of balance that does not result in hitting the ground). All of the in-laboratory data were collected using the modified WOLK belt. We processed and integrated the community deployment pilot study data, and the in-laboratory fall data into the fall prediction algorithm.

D. Data Processing

1) IMU Data:

To identify the risk of falling and responder status of each participant, features were calculated from the baseline clinical measures, survey scores and IMU signals. Subsequently, three predictive machine learning classifiers were trained on those features. To minimize the number of features and increase the generalizability of the prediction models, only signals from the lower back IMU were used, and lateral sensors were removed. The IMU data collected from the real-world falls and in-laboratory assessment items were processed as described in [14]. In summary, each real-world fall event and in-laboratory assessment item was labeled with an event ID, fall status (Fall or Non-Fall), fall specification (activity of daily living (ADL), side, anterior/posterior (AP)), and a fall description (e.g. "subject lost balance standing, hip or rear impact"). The raw data was band-pass Butterworth filtered (0.1-50 Hz) before generating three moving windows (100 ms duration with 50% overlap), starting 300 ms before the impact, as this would allow at least 100 ms for the device to deploy the airbags. The impact time was defined as the peak acceleration of the fall event. For non-falls, the three windows were selected that lead up to the maximum acceleration magnitude of the event. On each window, twelve features were calculated for both the accelerometer and gyroscope in each direction (x, y, and z). These features included minimum, maximum, absolute minimum, absolute maximum, root mean

TABLE III. PHYSICAL ASSESSMENTS AND QUESTIONNAIRES COMPLETED BY PARTICIPANTS DURING THE LABORATORY VISIT

Physical Assessment	Surveys
10-Meter Walk Test (10MWT) Functional Gait Assessment (FGA) Mini-Balance Evaluation Systems Test (BESTest)	Modified Falls Efficacy Scale (mFES) Mini-Mental Status Exam (MMSE) World Health Organization Quality of Life-BREF (WHOQOL-BREF) Customer User Satisfaction Survey

TABLE II. PRINCIPAL COMPONENT ANALYSES (PCA) AND ASSOCIATED FEATURES. EACH PCA WAS RUN SEPARATELY AND THE FIRST PRINCIPAL COMPONENT WAS SELECTED AS THE OUTCOME VARIABLE. FEATURES OF EACH PRINCIPAL COMPONENT WERE SELECTED BASED ON THE CORRELATION THRESHOLD > 85%.

Principal Component Analysis	Variables
PCA 1	10-meter walking speed at normal, slow and fast speeds
PCA 2	Quality of Life in Physical, Psychological, Social, and Overall domains
PCA 3	10-meter walking speed at normal, slow, and fast speeds and Mini Mental Examination Test
PCA 4	All domains of the Mini Balance Evaluation System Test
PCA 5	Gait with horizontal and vertical head turn items from the Functional Gait Assessment.
PCA 6	Gait on a level surface and change in gait speed items from the Functional Gait Assessment.

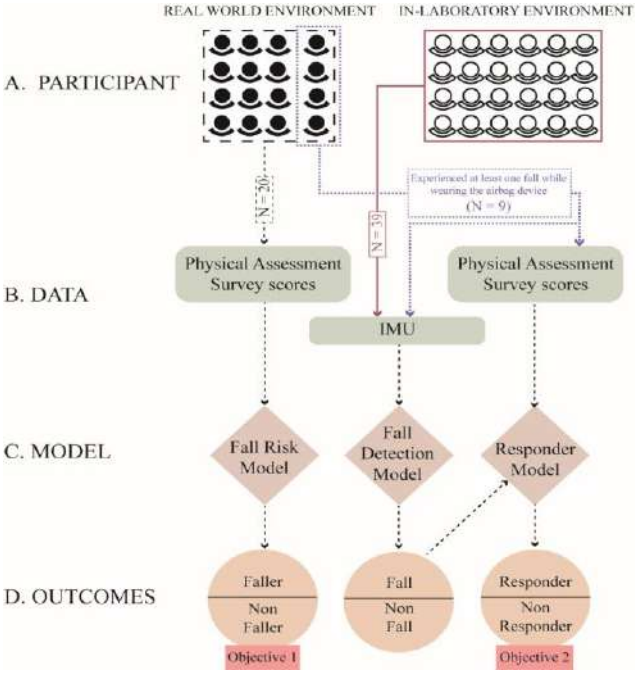


Fig. 3. The overall flowchart of data collection, processing, and machine learning models. (A) shows the data collection environment and number of participants for each model. (B) Specific features from each data were calculated and (C) trained in separate machine learning models. (D) These models were able to predict the risk of falling, pre-impact fall patterns, and responder status.

squared, median, standard deviation, skewness, kurtosis, velocity, jerk, and interquartile range. The calculated features were used as input to develop a machine learning classifier for pre-impact fall detection algorithms (Figure 2B).

2) Clinical Data:

The correlation among physical assessment subcategories and survey's sub-scores recorded at the initial visit in the community deployment pilot study were evaluated using a Pearson correlation matrix. Principal component analysis (PCA) was then applied to combine highly correlated standardized scores and surveys into single-dimensional principal component variables. To ensure maximal preservation of variability among baseline measures, only principal components explaining over 85% of the variance were included in subsequent analysis. All principal components were positively correlated with their variables and listed in Table III.

E. Machine Learning Models

To achieve both objectives of this study, three binary classification machine learning algorithms were trained to evaluate 1) the falling risk, 2) performance of the fall detection algorithm and 3) responder status of participants (Figure 2C). Four outcomes of F1 score, precision, recall and accuracy were reported separately for each logistic regression model.

1) Fall Risk Machine Learning Model:

The first machine-learning model, called the "Fall Risk Model" aimed to predict the risk of future falls over a six-month period. Of the recruited participants, those who did not complete the full duration of the study (N = 2) were excluded from this model. Participants who experienced at least one fall during the study were labeled as 'fallers' (N = 14; PD = 8, stroke = 6), while those with no experienced falls were labeled as 'non-fallers' (N = 6; PD = 2, Stroke = 4). A logistic regression model, with 1,000 iterations and L2 regularization, was trained using only the data from the clinical data from the first visit, including physical assessment, survey scores and their principal components, to predict the participants' faller status (Faller/ Non-faller; Figure 2D). To maintain balanced training, the dataset was limited to all unique combinations of six fallers paired with the six non-fallers. The model was validated using a leave-one-out cross-validation approach with the average F1 score, recall, and precision reported as measures of performance. In this model, recall is the average measure of the proportion of actual "fallers" or "non-fallers" that were correctly identified by the model. It reflects how well the model captures each class, whether it is "fallers" or "non-fallers." Precision measures the ratio of correctly predicted "fallers" or "non-fallers" to all instances predicted as that class. The F1 score and accuracy are measures that evaluate the model's performance across both "fallers" and "non-fallers." F1 score is more elaborated in (1) and accuracy is the total number of correct predictions over the total number of predictions made in the model.

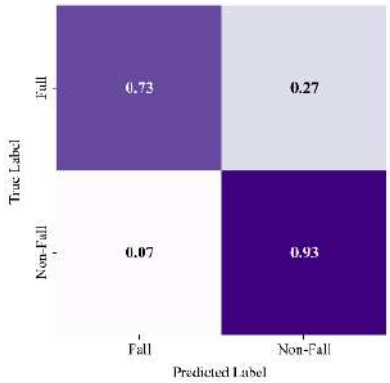


Fig. 2. Confusion matrix demonstrating the prediction performance of the fall detection algorithm (Table IV, model 2) on detecting fall and non-fall windows. Values in the top row represent the proportions of correctly and incorrectly predicted fall incidents, while values in the bottom row represent the proportions for correctly and incorrectly predicted non-fall incidents.

$$F1\ Score = 2 \times \frac{Precision \times Recall}{Precision + Recall} \quad (1)$$

2) Fall Detection Machine Learning Model:

The second machine learning model called the "Fall Detection Model" was developed to evaluate the performance of the pre-impact fall detection algorithm for each participant (Figure 2D). IMU features were calculated from 2436 fall windows and 3004 non-fall windows in the in-laboratory dataset [14]. These features were then used to train a logistic regression classification model with class weighting, a 70%-30% train-test split, and 10-fold stratified cross-validation grouped by participants. This trained model was then tested on data from community deployment participants who

experienced real-world falls while wearing the airbag device (N = 9; PD = 5, stroke = 4), with IMU features calculated from 96 fall windows and 48 non-fall windows. To address the low number of reported real-world non-fall ADLs and maintain label balance in the test dataset, non-fall ADLs from participants' first in-lab visit (1231 samples) were incorporated into the test data. These non-fall samples were randomly under-sampled across participants to reach the 96 non-fall ADL samples and combined with their real-world fall samples in the test set. The predicted labels of the model were grouped by participants and recall and precision rate for each participant were calculated separately. In this model, recall is the average measure of the proportion of actual "fall" or "non-fall" windows that were correctly identified and precision measures the ratio of correctly predicted "fall" or "non-fall" windows to all instances predicted as that class.

3) Responder Machine Learning Model:

The third machine learning model, called the "Responder Model" was developed to predict if the fall Detection Model would work well for each individual participant. To begin, we used the F1 scores calculated for each participant to categorize them into responder and non-responder groups (Figure 2D). This score is a measure of how accurately the fall detection algorithm performed for each individual. To set a classification threshold for responder and non-responder status, we used the median performance (F1 score = 0.90) across all participants, with those scoring above or equal the median labeled as responders (N = 5) and those below as non-responders (N = 4). The third logistic regression model was trained on the physical assessments, survey scores (Table II), and their principal component variables to predict the responder status of each participant. A leave-one-out cross-validation approach was used to validate the results, with the F1 score, recall and precision metrics reported as performance measures of the model. All IMU features, machine learning and PCA analyses were developed and processed in Python (3.10.11).

III. Results

Twenty of our participants successfully finished the study period and were included in the fall risk prediction model. Nine of our participants experienced at least one fall while wearing the wearable airbag device and were included in the responder prediction model.

A. Fall Risk Prediction

A total of 3003 logistic regression models were run, each using a unique combination of four fallers and all three non-faller participants. Performance metrics and the most important predictors were averaged across these iterations. The logistic regression algorithm achieved a high performance in distinguishing fallers from non-fallers (Table IV). The four most significant predictors of faller status were 1) a lower PCA 1 score (Table III; non-faller: 0.42 ± 1.07, faller: -0.12 ± 1.03; values represent average ± standard deviation), 2) higher FGA scores in the stairs task (non-faller: 1.2 ± 0.7, faller: 1.6 ± 0.6), 3) lower scores in postural control domain of the Balance Evaluation System assessment (non-faller: 3.0 ± 2.4, faller: 1.9 ± 2.1), and 4) higher scores in sensory orientation domain of the Balance Evaluation System assessment (non-faller: 3.2 ± 1.8, faller: 3.9 ± 2.3).

B. Fall Detection Prediction

The calculated features from 192 real-world fall and non-fall windows were tested in a pre-trained logistic regression model on the in-laboratory collected data from [14]. The model effectively distinguished fall event windows from non-fall event windows (Table IV). The confusion matrix of all 196 windows is demonstrated in Figure 3. We calculated F1 scores for each participant separately based on the proportion of true and false predictions.

C. Responder Prediction

Using the median performance threshold (F1 score = 0.90), we grouped F1 score of individuals into four participants as non-responders (F1 score < 0.90; PD = 2, stroke = 2) and five as responders (F1 score ≥ 0.90; PD = 3, stroke = 2). A logistic regression model was trained on clinical features including physical assessments, survey scores (Table II), and their principal component variables (Table III) to distinguish responder from non-responder participants. This model achieved a high performance in distinguishing responders from non-responders (Table IV) and four key predictors: 1) lower PCA 2 scores (responders = -0.27 ± 1.03, non-responders = 0.33 ± 0.98), 2) higher scores in gait and pivoting as assessed by the FGA (responders = 1.6 ± 1.5, non-responders = 0.5 ± 0.6), 3) higher PCA 5 scores (responders = 0.36 ± 0.95, non-responders = -0.46 ± 0.98), and 4) higher PCA 3 scores (responders = 0.3 ± 1.3, non-responders = -0.4 ± 0.2).

IV. Discussion

The objective of this pilot study was to enhance the effectiveness of pre-impact fall detection wearable airbag devices in patients with neurological diseases by identifying individuals with high risk of falling and predicting the likelihood they will respond well to the fall detection algorithm. Our results show that baseline clinical measures and survey scores can predict the future fall risk and differentiate those who may receive the greatest benefit from various wearable devices in patients with Parkinson's disease and stroke. This approach allows for selecting responders–

TABLE IV. Performance Outcomes of the Machine Learning Algorithms

Model	Target labels	F1 Score	Precision	Recall	Accuracy
Fall Risk	"Faller" - "Non-faller"	0.76 ± 0.13[a]	0.75 ± 0.15[a]	0.79 ± 0.14[a]	0.77 ± 0.12[a]
Fall Detection	"Fall" - "Non-fall"	0.83	0.83	0.84	0.83
Responder	"Responder" - "Non-responder"	0.75	1.00	0.60	0.78

[a.] Data represent average ± standard deviation

those who have higher fall risk and benefit most from the device–and maximizing hip injury mitigation.

A. Fall Risk Prediction

Our pilot results indicate subtle differences in baseline physical assessments and clinical survey scores that can help identify individuals with a high risk of falling. Consistent with the previous studies, our findings show gait and balance outcomes as key predictors of fall risk [25], [26]. Our results showed that patients with Parkinson's disease or chronic stroke who exhibit less impairment in gait and balance abilities appear to have higher fall risk, possibly due to increased level of physical activity and greater chance of experiencing falls. This idea was also supported by two of our non-faller participants who showed a greater step count in the 10-meter walking tasks and a much lower daily step count, suggesting low balance confidence and a possible tendency to adopt a more cautious gait and sedentary lifestyle.

B. Responder Prediction

Further analysis of high fall risk patients with Parkinson's disease or stroke showed distinct differences in fall and non-fall patterns as captured by the IMU. Our fall detection algorithm was trained on in-laboratory fall data and tested on real-world fall data and could distinguish fall and non-fall patterns with a F1 score $\geq$ 0.90 for almost half of our participants. Based on the previous findings on variations in fall patterns among stroke patients with different impairment sides and severities [19], we suggested that different fall detection algorithms on wearable devices should be prescribed for different users to maximize their effectiveness. Our developed responder identification algorithm identified users for whom the fall detection algorithm performs above 0.90 with an F1 score of 0.75 and accuracy of 0.78. Participants with PD or stroke were distributed almost equally within each group. The average walking velocities for responders and non-responders are 0.6 m/s and 0.7 m/s, respectively, categorizing stroke patients as limited community ambulators in both groups [27]. Although walking speed fluctuates over time in PD, these responder and non-responder velocities are often categorized as below the threshold for community ambulation in the PD population as well [28].

The responder group reported less impairment in gait and balance scores (measured by FGA scores). Despite showing less impairment in gait and balance, they showed lower quality of life scores (WHOQOL) across four out of five life domains. This finding may show an increased awareness of one's own risk of falling, which could affect quality of life [29]. It also aligns with the previous fall risk prediction model, where less impairment correlated with a higher fall risk, likely due to increase physical activity and associated fall risks. In general, we expect that the more typical fall patterns experience by the responder group allowed the pre-trained fall detection algorithm to better distinguish falls from non-fall incidents.

This pilot study has some limitations. First, all three models presented in Table IV were developed using a limited sample size, due to both a small number of participants, and the fact we were only able to record data from real falls that were detected by the wearable system. These limitations create bias in the system, as the models were only validated on the data available from our subjects. It is important to note that the relations between important predictors of the models may not be linear and depend on the sample size. To enhance fall risk prediction and optimize wearable device prescriptions for specific neurological conditions, future studies should include larger and more diverse participant groups with varying collected data from demographics, impairment levels, physical, and cognitive abilities, and may consider a specialized detection algorithm with a very high recall rate (even at the cost of lowered precision). Second, due to the small sample size and the range of expected falls and near-fall incidents among participants in the real-world environment, we had to combine some in-laboratory ADL data with real-world non-fall incidents. It is unclear to what extent ADLs (such as walking or sit to stand) differ across laboratory and real-world settings [30], [31], and therefore future studies should aim to collect more near-fall or non-fall ADL data in a real-world environment for better representation. We believe that the results shown here demonstrate the potential for this technique to predict both fallers and responders, making us optimistic that addressing the limitations above will help to create a more generalizable model.

As a further limitation, recording falls in the real-world is challenging. To increase the chance of recording falls, we recruited subjects with an increased risk of falls by using at least one self-reported fall in the past six months as an inclusion criteria. This study primarily focused on demonstrating the approach of classifying wearable airbag users based on future fall likelihood and response rate. In addition to optimizing user classification, it is also important to consider how consistently individuals will use the device (compliance). While we believe the increased performance of the fall detection algorithm will increase the compliance rates of users, compliance will still be a challenge with any wearable device. Therefore, it is crucial that future studies work to address this issue to capture and protect from as many falls as possible. Lastly, both the responder classification and fall risk prediction algorithms were trained using six months of participant collected data and treat all outcomes as binary. Future studies should aim to explore these categorizations as continuous spectrum–ranging from very low to very high fall risk–and evaluate the device's responsiveness across varying fall types and risk levels to better adjust interventions.

V. Conclusion

By integrating physical, cognitive, and social factors prior to utilizing the fall detection algorithms, we could identify users who are likely to fall, and for whom the fall detection algorithm may perform better than others. This approach allows for designing neurological-specific algorithms, and maximizing the benefits of wearable airbag devices by focusing on 'responders' whose fall patterns can easily be detected and utilizing alternative fall detection algorithms on 'non-responders'. This strategic identification not only enhances device effectiveness but also supports more targeted fall detection algorithms and efficient fall prevention strategies.

ACKNOWLEDGMENT

We would like to greatly appreciate Kavya Sudhir, Jonathan Mendley, and Olivia K. Botonis for helping us through this project, the Wolk Company for their hardware and firmware support and all our participants for their time and help.

REFERENCES

[1] World Health Organization, "Falls." Accessed: Nov. 05, 2024. [Online]. Available: https://www.who.int/news-room/fact-sheets/detail/falls

[2] World Health Organization, "Ageing and health." Accessed: Nov. 05, 2024. [Online]. Available: https://www.who.int/news-room/fact-sheets/detail/ageing-and-health

[3] Center for Disease Control and Prevention, "Older Adult Falls Data | Older Adult Fall Prevention | CDC." Accessed: Nov. 06, 2024. [Online]. Available: https://www.cdc.gov/falls/data-research/index.html

[4] Center for Disease Control and Prevention, "Cost of older adult falls." Accessed: Nov. 05, 2024. [Online]. Available: https://stacks.cdc.gov/view/cdc/122747

[5] R. Vaishya and A. Vaish, "Falls in Older Adults are Serious," *Indian J Orthop*, vol. 54, no. 1, p. 69, Feb. 2020, doi: 10.1007/S43465-019-00037-X.

[6] A. A. Schmid et al., "Circumstances and consequences of falls among people with chronic stroke," *J Rehabil Res Dev*, vol. 50, no. 9, pp. 1277–1286, 2013, doi: 10.1682/JRRD.2012.11.0215.

[7] C. S. Rau et al., "Geriatric hospitalizations in fall-related injuries," *Scand J Trauma Resusc Emerg Med*, vol. 22, no. 1, pp. 1–8, Nov. 2014, doi: 10.1186/S13049-014-0063-1/TABLES/4.

[8] H. Stolze et al., "Prevalence of gait disorders in hospitalized neurological patients," *Mov Disord*, vol. 20, no. 1, pp. 89–94, Jan. 2005, doi: 10.1002/MDS.20266.

[9] M. S. Dennis, K. M. Lo, M. McDowall, and T. West, "Fractures after stroke: frequency, types, and associations," *Stroke*, vol. 33, no. 3, pp. 728–734, 2002, doi: 10.1161/HS0302.103621.

[10] N. E. Allen et al., "Interventions for preventing falls in Parkinson's disease," *Cochrane Database Syst Rev*, vol. 6, no. 6, Jun. 2022, doi: 10.1002/14651858.CD011574.PUB2.

[11] S. Denissen et al., "Interventions for preventing falls in people after stroke," *Cochrane Database Syst Rev*, vol. 10, no. 10, Oct. 2019, doi: 10.1002/14651858.CD008728.PUB3.

[12] N. M. Van Schoor, W. L. Devillé, L. M. Bouter, and P. Lips, "Acceptance and compliance with external hip protectors: A systematic review of the literature," *Osteoporosis International*, vol. 13, no. 12, pp. 917–924, Dec. 2002, doi: 10.1007/S001980200128/METRICS.

[13] B. Nemeth, M. van der Kaaij, R. Nelissen, J. K. van Wijnen, K. Drost, and G. J. Blauw, "Prevention of hip fractures in older adults residing in long-term care facilities with a hip airbag: a retrospective pilot study," *BMC Geriatr*, vol. 22, no. 1, pp. 1–7, Dec. 2022, doi: 10.1186/S12877-022-03221-1/TABLES/3.

[14] O. K. Botonis et al., "Wearable airbag technology and machine learned models to mitigate falls after stroke," *J Neuroeng Rehabil*, vol. 19, no. 1, pp. 1–14, Dec. 2022, doi: 10.1186/S12984-022-01040-4/FIGURES/4.

[15] D. S. Marigold and J. J. Eng, "Altered timing of postural reflexes contributes to falling in persons with chronic stroke," *Exp Brain Res*, vol. 171, no. 4, pp. 459–468, Jun. 2006, doi: 10.1007/S00221-005-0293-6.

[16] V. Weerdesteyn, M. de Niet, H. J. R. van Duijnhoven, and A. C. H. Geurts, "Falls in individuals with stroke.," *J Rehabil Res Dev*, vol. 45, no. 8, pp. 1195–213, 2008.

[17] J. Liu et al., "A review of wearable sensors based fall-related recognition systems," *Eng Appl Artif Intell*, vol. 121, p. 105993, May 2023, doi: 10.1016/J.ENGAPPAI.2023.105993.

[18] J. Jonsdottir, F. G. Mestanza Mattos, A. Torchio, C. Corrini, and D. Cattaneo, "Fallers after stroke: a retrospective study to investigate the combination of postural sway measures and clinical information in faller's identification," *Front Neurol*, vol. 14, p. 1157453, Apr. 2023, doi: 10.3389/FNEUR.2023.1157453/BIBTEX.

[19] D. S. Marigold and J. J. Eng, "Altered timing of postural reflexes contributes to falling in persons with chronic stroke," *Exp Brain Res*, vol. 171, no. 4, pp. 459–468, Jun. 2006, doi: 10.1007/S00221-005-0293-6/FIGURES/4.

[20] D. Hyndman, A. Ashburn, and E. Stack, "Fall events among people with stroke living in the community: circumstances of falls and characteristics of fallers," *Arch Phys Med Rehabil*, vol. 83, no. 2, pp. 165–170, 2002, doi: 10.1053/APMR.2002.28030.

[21] Y. Zhou et al., "Classification of Neurological Patients to Identify Fallers Based on Spatial-Temporal Gait Characteristics Measured by a Wearable Device," *Sensors*, Vol. 20, no. 4, p. 4098, vol. 20, Jul. 2020, doi: 10.3390/S20154098.

[22] S. F. H. Mackintosh, K. Hill, K. J. Dodd, P. Goldie, and E. Culham, "Falls and injury prevention should be part of every stroke rehabilitation plan," *Clin Rehabil*, vol. 19, no. 4, pp. 441–451, Jun. 2005, doi: 10.1191/0269215505CR796OA.

[23] R. Dickstein and N. Abulaffio, "Postural sway of the affected and nonaffected pelvis and leg in stance of hemiparetic patients," *Arch Phys Med Rehabil*, vol. 81, no. 3, pp. 364–367, Mar. 2000, doi: 10.1016/S0003-9993(00)90085-6.

[24] J. Padilla, E. Leary, and J. K. Limberg, "Identifying responders versus non-responders: Incorporation of controls is required for sound statistical interference," *Exp Physiol*, vol. 106, no. 2, pp. 375-376, Feb. 2021, doi: 10.1113/EP089142

[25] S. J. Winser, P. Kannan, U. M. Bello, and S. L. Whitney, "Measures of balance and falls risk prediction in people with Parkinson's disease: a systematic review of psychometric properties," *Clin Rehabil*, vol. 33, no. 12, p. 1949, Dec. 2019, doi: 10.1177/0269215519877498.

[26] K. Bower et al., "Dynamic balance and instrumented gait variables are independent predictors of falls following stroke," *J Neuroeng Rehabil*, vol. 16, no. 1, Jan. 2019, doi: 10.1186/S12984-018-0478-4.

[27] M. G. Bowden, C. K. Balasubramanian, A. L. Behrman, and S. A. Kautz, "Validation of a Speed-Based Classification System Using Quantitative Measures of Walking Performance Poststroke," *Neurorehabilitation and Neural Repair*, vol. 22, no. 6, pp. 672-675, Oct. 2008, doi: 10.1177/1545968308318837.

[28] R. Elbers, E. Wegen, J. Verhoef, and G. Kwakkel, "Is gait speed a valid measure to predict community ambulation in patients with Parkinson's disease?," *Journal of Rehabilitation Medicine*, vol. 45, no. 4, pp. 370–375, 2013, doi: 10.2340/16501977-1123.

[29] D. Schoene, C. Heller, Y.N. Aung, C.C. Sieber, W. Kemmler, and E. Freiberger, "A systematic review on the influence of fear of falling on quality of life in older people: is there a role for falls?," *Clinical Interventions in Aging*, vol 14, no. 14, pp. 701-719, Apr. 2019, doi: 10.2147/cia.s197857.

[30] H. Gaßner et al., "Clinical Relevance of Standardized Mobile Gait Tests. Reliability Analysis Between Gait Recordings at Hospital and Home in Parkinson's Disease: A Pilot Study," *J Parkinsons Dis*, vol. 10, no. 4, pp. 1763–1773, 2020, doi: 10.3233/JPD-202129.

[31] C. Bottari, É. Dutil, C. Dassa, and C. Rainville, "Choosing the most appropriate environment to evaluate independence in everyday activities: Home or clinic?," *Aust Occup Ther J*, vol. 53, no. 2, pp. 98–106, Jun. 2006, doi: 10.1111/J.1440-1630.2006.00547

MyoBack: A Musculoskeletal Model of the Human Back with Integrated Exoskeleton

Rohan Walia*[1], Morgane Billot*[1], Kevin Garzon-Aguirre*[1],
Swathika Subramanian[2], Huiyi Wang[1,3], Mohamed Irfan Refai[2], Guillaume Durandau[1,3]

***Abstract*— Given the challenges of real-life experimentation, musculoskeletal simulation models could become essential in biomedical research. This is especially critical for the human back, a key structure involved in daily movements, where modeling and simulation could streamline design and support the development of treatments and robotic rehabilitation techniques, such as exoskeletons. However, musculoskeletal simulation engines are computationally demanding and lack contact dynamics, restricting current models' use in studying prolonged behaviors or optimizing system design while maintaining physiological accuracy. To overcome this limitation, this work proposes MyoBack, a human back model part of the MyoSuite framework relying on the physics engine MuJoCo. This model is derived from a physiologically accurate model built in the state-of-the-art musculoskeletal simulation software OpenSim and replicates the latter's kinematic properties accurately, with some discrepancies regarding muscle dynamics stemming from engine differences. The MyoBack model was also validated empirically by integrating a passive back exoskeleton in simulation and comparing forces exerted on the back with values from experimental trials. Over different tasks, the model reproduced measured force progressions well, resulting in RMSE = 11% for a stoop and RMSE = 16% for a squat motion pattern relative to peak forces. The MyoBack model can be accessed here: https://github.com/rohwalia/MyoBack**

I. INTRODUCTION

Human biomechanics is a rapidly growing field that attempts to understand the intricate interplay between biology and mechanics in human movement, structure, and function. In particular, modeling the back presents significant challenges due to its complex anatomy and the delicate balance required to maintain posture and mobility. The back contributes to everyday movements such as running or lifting objects [1], [2], [3], [4]. Exactly these kinds of common tasks are affected by musculoskeletal disorders (MSDs) prevalent in around 20% of the global population [5], much of it work-related [6], [7] and occurring primarily in the lower back [8]. These issues, in turn, can lead to other complications such as gait disorders, particularly in the elderly [9], limiting quality of life notably.

To alleviate these problems, assistance systems such as exoskeletons are becoming increasingly widespread and hold significant potential to enhance human mobility [10]. However, their development is human resource-intensive and time-consuming [11], [12], [10]. Integrating design and testing environments through modeling and simulation can significantly enhance efficiency, reducing time and hardware costs [13], [14]. Simulation also enables diverse and repeatable testing for optimal system performance. Hence, reliable human body models are essential to better understand musculoskeletal dynamics, identify the causes of MSDs, assess risks of repetitive or prolonged actions, and aid in the customization of medical devices for patient-specific treatment solutions.

Currently, a wide variety of human models are available. For instance, a relatively simple representation of the human body is the Human Dynamic Model [15] which simulates movements based on motion capture data. This model incorporates sufficient degrees of freedom to reproduce complex movements and approximate mechanical energy expenditure during tasks. On the other hand, there are physics-based musculoskeletal simulation engines such as OpenSim [16], AnyBody [17], and SIMM [18] which focus on making detailed and physiologically accurate models of the musculoskeletal system. These tools are extensively used in human neuromechanical control, human-robot interaction, and rehabilitation. Several of these human body models already include the back and have been used in a variety of research projects, for example, to study the effect of unilateral knee extension restriction on the back during gait [19] or to analyze the biomechanical effects of different bag-carrying styles on the back region [20], among others [21], [22], [23].

These musculoskeletal simulation engines are computationally intensive and offer limited support for complex contact interactions. Consequently, most current human body models are impractical for long-term simulations or high-frequency task repetitions while maintaining physiological accuracy. As a result, they are unsuitable for studying long-term behavior or for optimization purposes in system design. Notably, the proprietary software Hyfydy [24] provides a valid approach to this problem. Still, since it is not open-source, using it for custom use cases (e.g., testing personal exoskeleton) in different settings, such as research and industrial, might be difficult. To meet the needs of physiological accuracy, contact dynamics, speed, and accessibility, the use of MuJoCo (Multi-Joint dynamics with Contact) [25] is particularly relevant. MuJoCo is a state-of-the-art open-source physics engine designed for model-based control, offering efficient computational capabilities for multi-joint dynamics and contact mechanics. Importantly,

*These authors contributed equally to this manuscript.
[1]Department of Mechanical Engineering, McGill University, Canada guillaume.durandau@mcgill.ca
[2]Department of Biomechancial Engineering, University of Twente, Netherlands m.i.mohamedrefai@utwente.nl
[3]CRIR, Jewish Rehabilitation Hospital, Canada

it has the capacity to simulate muscle dynamics while supporting contact-rich interactions. In particular, MyoSuite [26], a software framework based on MuJoCo, is more than two orders of magnitude faster than state-of-the-art musculoskeletal models. This advantage is particularly crucial for highly detailed musculoskeletal models, including our model which features a tenfold increase in muscle patterning and joint degrees of freedom complexity with 210 actuators [27]. To date, various models have been implemented (e.g., arm, leg) but not yet a model of the back. Integrating a back model into MyoSuite would, therefore, enable complex human movements involving the back to be simulated quickly and accurately. This has huge potential in the testing and development of exoskeletons and could be beneficial in rehabilitation, ergonomic design, and personalized healthcare solutions.

Therefore, we developed MyoBack, a back model part of the MyoSuite framework based on an existing OpenSim model [28]. Section II details how the MyoBack model is created and validated by comparing the OpenSim and the derived MuJoCo model with respect to kinematics and dynamics. Furthermore, a passive exoskeleton was developed within the simulation to validate the back model against empirical data. Section III explores the impact of the passive exoskeleton on various back-involved movements by integrating it with the back model and comparing the simulation outputs to experimental results.

II. METHODS

This section first describes the musculoskeletal model conversion tool [27], MyoConverter, that was used to convert the back model from Opensim to MuJoCo. Then, the manual tuning performed with the output of the conversion tool to complete the final MyoSuite back model is explained. Finally, it is outlined how a passive exoskeleton is added to the back model. This is the basis for experimental validation following the setup and protocol developed in section III.

A. MyoConverter

We derive our MyoSuite back model (.xml) from an OpenSim model (.osim) [28] using MyoConverter. This conversion tool optimizes muscle kinematics and kinetics and has been tested extensively on other musculoskeletal models such as neck, lower limb and arm [27]. The OpenSim model contains 210 muscle-tendon units (MTUs) and 18 joints. The model can be controlled by 3 "virtual" DoFs that map to the real joints: flexion extension, lateral bending and axial rotation. It has also been incorporated into a full-body lumbar spine model [29] with a general validation regarding model parameters and muscle output. In addition, a slightly adapted model [30] was explicitly validated for lifting motions, demonstrating its suitability to evaluate changes in lumbar loading during lifting. Given its extensive validation, particularly in terms of muscle activation and joint moments, the OpenSim model is regarded as the state-of-the-art reference, and the goal of MyoConverter is to align the MuJoCo model to it as closely as possible.

The conversion tool consists of three steps:

- Step 1 – Geometry Conversion: parse multi-body kinematic tree containing the fundamental elements of musculoskeletal models (body segments, joints, muscles, wrapping bodies, etc.) from OpenSim into MuJoCo.
- Step 2 – Wrapping optimization: optimize wrapping constraints to guarantee that the muscle pathways in MuJoCo are physiologically reasonable like in OpenSim while accounting for the fact that MuJoCo's wrapping surfaces are simple geometric objects (e.g., spheres, cylinders), which prevents an exact replication of OpenSim muscle pathways but enhances computational efficiency, and check the resulting moment arms exerted by each muscle.
- Step 3 – Force property optimization: optimize muscle force parameters in MuJoCo to approximate the OpenSim model's force curves and check the force-length-activation.

The conversion tool needed to be modified to convert the back model. Mainly, the handling of edge cases occurring in the OpenSim model that had not been implemented in MyoConverter, e.g., coupled constraints of the *PiecewiseLinearFunction* type, was added.

B. MuJoCo: MyoBack

The output model from MyoConverter had a few issues. The wrapping pathways of some muscles around a geometric body for specific joint configurations were discontinuous, leading to discrete jumps in muscle-tendon length (Fig.1a). Also, MyoConverter did not parse some geometries correctly from the OpenSim model (Fig.1c). The mapping of the 3 "virtual" DoFs to the real joints of the model had to be fixed as well (Fig.1b,d) by changing the equality constraints [31].

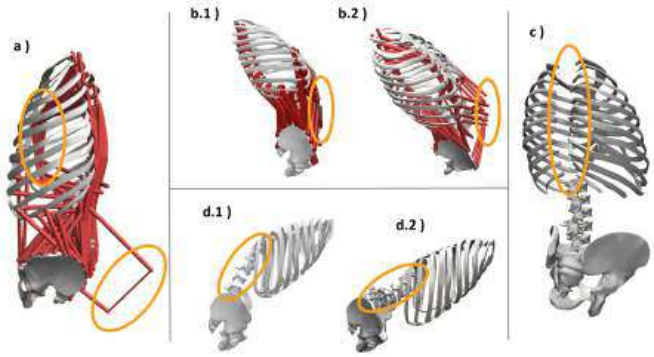
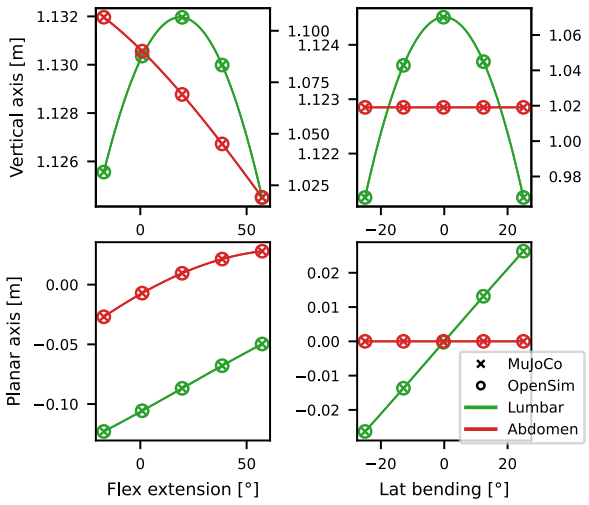
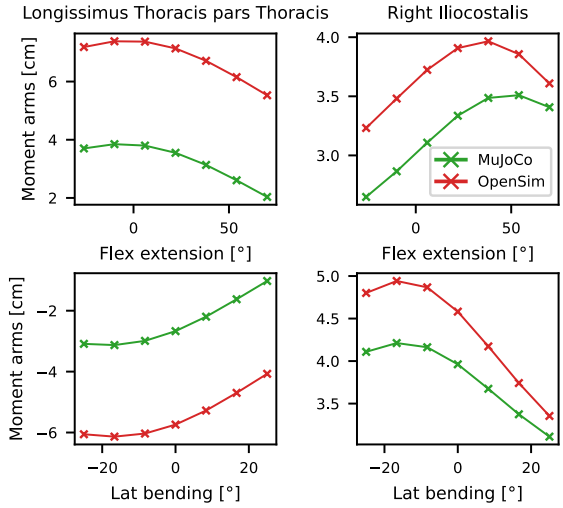


Fig. 1: Model problems after conversion a) Jumping muscles b) Immobile abdomen 1) Opensim 2) MuJoCo c) Non-curved spine 1) Opensim 2) MuJoCo d) Absent thoracic vertebrae.

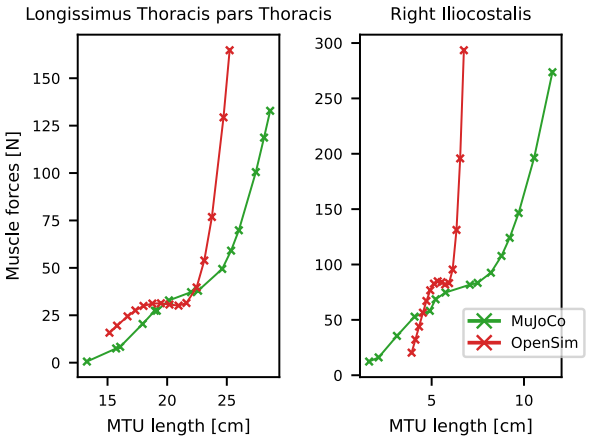
This back model was compared to the OpenSim model with respect to kinematics by observing end point positions (Fig.2a), moment arms exerted by muscles on joints (Fig.2b) and force-length-activation (Fig.2c). The results of this comparison are shown for relevant geometric bodies in the kinematic chain for the former and representative back muscles for the latter two.



(a) Comparing the position of lumbar vertebrae and abdomen for a full range of the DoFs flexion extension and lateral bending.



(b) Simulating muscle dynamics of the Longissimus Thoracis pars Thoracis and Right Iliocostalis for a full range of the DoFs flexion extension and lateral bending.



(c) Observing force-length activation curves for the Longissimus Thoracis pars Thoracis and Right Iliocostalis.

Fig. 2: Comparative analysis of the MyoSuite back model and the reference OpenSim model.

C. MuJoCo: MyoBack + exoskeleton

We validated the MyoBack model by conducting trials with a passive exoskeleton. The aim was to compare the forces exerted by the exoskeleton in simulation and experiments for lifting tasks. We modeled the passive exoskeleton, the Auxivo Liftsuit 1.0 (Auxivo, Schwerzenbach, Switzerland) [32], in MuJoCo. A simple model of the passive exoskeleton was implemented respecting the mass distribution and elastic properties of the exoskeleton. For the latter, the two main elastic bands on the back were considered. The elastic bands of the passive exoskeleton were modeled as tendons [33] attached at the level of the 5th thoracic rib and the posterior superior iliac spine (see Figure 3), corresponding to the actual Auxivo elastic band positions. The tendons' stiffness was calculated to produce an equivalent force to that of the elastic bands. The Auxivo Liftsuit has previously been experimentally benchmarked, where the stiffness of its elastic bands was measured. Nonlinear relationships were identified between the force exerted by the elastic bands and their elongation during lifting and lowering [34]. However, in MuJoCo, only a constant stiffness can be implemented. The nonlinear functions were thus approximated to a unique linear function with stiffness $K_{Auxivo} = F/\Delta L$ determined to be $K_{Auxivo} = 1527.5N/m$. Due to the different resting lengths of the elastic band in the Auxivo Liftsuit and the tendons in the back model, the value for K_{Auxivo} had to be scaled accordingly and the stiffness obtained for the tendons is $K_{MuJoCo} = 526.4N/m$.

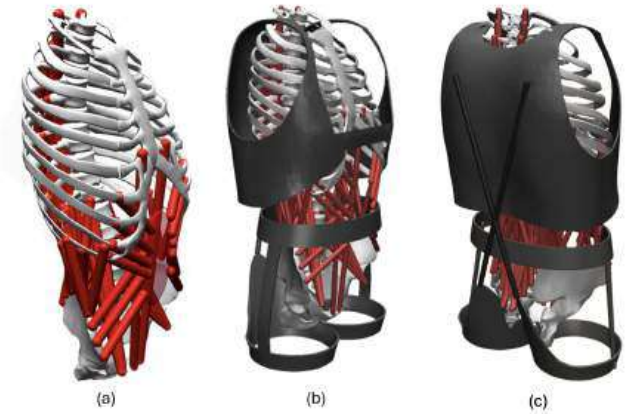


Fig. 3: (a) Back model in OpenSim. (b) MyoBack model with exosuit in MuJoCo. (c) Backward view of MyoBack model with exosuit.

The visual meshes of the exoskeleton were built using 3D modeling software separately and then added to the model. The complete MyoBack model is shown in Figure 3. For wider application, a separate version of the MyoBack model is available, with legs incorporated from the MyoLegs model of the MyoSuite framework [35], [36].

III. EXPERIMENTS

The Auxivo Liftsuit [32] was used to validate the back model. This device, designed to support lifting tasks by

reducing strain on the back and hip muscles, helps users handle loads between 5 and 20 kg with less physical stress. Users reported noticeable reductions in muscle strain and an overall improvement in lifting ease while wearing the LiftSuit [37]. Although not unique in the market—other devices like the Darwing Hakobelude (Daiya Industry Co., Ltd., Okayama, Japan) [38] offer similar support—the LiftSuit has been studied in several research contexts. User reports remain promising for its effectiveness, among other settings, in industrial applications [39], [40], [41].

A. Sensoring the exosuit

First, load cells were integrated into the elastic bands of the Auxivo to measure the actual forces applied by the exosuit onto the user, as shown in Figure 4. One end of the load cell was attached to the metal part of the elastic band and the other to the straps.



Fig. 4: a) Load cell attached in series to one end of the elastic band situated in Auxivo b) Auxivo exosuit with 2 load cells attached to each of the elastic bands. The red arrows on the elastic bands indicate the line of action of stretch force and the red dots indicate the positions of markers at the anchoring points of the elastic bands on the exosuits.

The load cells, placed in series with the elastic bands, measured the deformation of these bands as voltages. These were amplified and digitized before being processed by an Arduino microcontroller. A mapping between the forces exerted and the amplified voltages was known through prior calibration.

B. Participants

A sample of 9 participants (height in cm: 173.8 ± 11.1, weight in kg: 73.4 ± 16.5, age in years: 23.5 ± 1.4) with no previous experience with exosuits and with no history of back injuries were recruited for the study. All participants provided informed consent. The study was approved by the University of Twente's ethical review board (Ref. number: 240424).

C. Apparatus

For this study, data from load cells, reflective markers (Qualisys Medical AB, Gothenburg, Sweden), and IMUs (Movella, Enschede, Netherlands) were used. 63 optical markers were placed on the participant. 56 markers on bony landmarks and body segments and 7 on the exosuit as in [34]. 17 full-body IMU sensors were placed on the subject. Data from IMUs was visualized to examine flexion extension and knee joint angles during static hold trials. Marker data was sampled at 128 Hz and load cell data at 80 Hz. The data from markers was synchronized with the Qualisys Track Manager. This was then manually synchronized with the load cells using a switch during the trials.

D. Experimental protocol

First, the subjects performed a maximum voluntary contraction (MVC) trial to establish a baseline measurement of each muscle strength. To acquire the MVC for back muscles, the participants were asked to lie on their stomachs and perform reverse crunches against resistance, and vocal motivation was used to ask the participants to contract their muscles as much as possible. Following this, exosuits were worn by the participants and adjusted according to individual user specifications. The participants were asked to perform the following tasks commonly linked with industrial tasks [42].

1) *Static hold trials:* Participants were asked to maintain stoop posture at predefined flexion extension angles of 40°, 60°, and 80° for 3 seconds before returning to an upright posture. Then, participants were asked to perform squats at predefined knee flexion angles of 70°, 90°, and 110°, holding the position for 3 seconds before returning to the initial upright position. Both squatting and stooping movements were repeated three times each. The participants used data from IMUs as visual feedback to maintain the required joint angles.
2) *Dynamic trials*: Participants were instructed to stoop by flexing their trunk to lift an empty box from a table in front of them, then return to an upright posture. They then stooped again to place the box back on the table. Both the squatting and stooping movements were performed at a pace of 40 beats per minute using a metronome, with five repetitions for each movement.

E. Data analysis

The load cell data was filtered by a zero-lag second-order Butterworth low pass filter of 6Hz. Forces from load cells on both sides of the exosuits were averaged across all 9 participants. To obtain the resultant force acting on the trunk of the user, the measured interaction forces of the right and left elastic bands were summed.

Raw marker data was filtered by a zero-lag second-order Butterworth low pass filter of 6Hz. Marker data was used to compute the stretch forces of elastic bands and joint angles of flexion extension and knee. The previous approach described in [34] for the estimation of forces using markers on the exosuits, as shown in Figure 4, was implemented. In doing so, the change in distance between the markers placed on either end of each elastic band from when the participant was upright was considered band elongation. This value was fed to two polynomial equations representing the loading (flexion) and unloading (extension) phase of a task cycle to

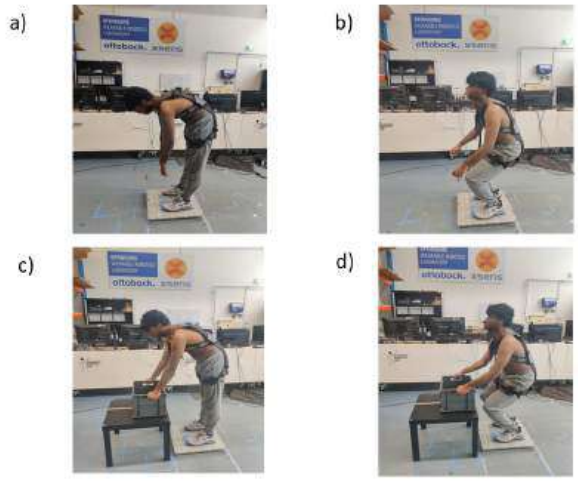


Fig. 5: a) Static stoop: Subject performing forward bend with minimal knee flexion b) Static squat: Subject performing squat with minimal trunk flexion. c) Dynamic stoop: Subject performing stoop lifting technique with a box d) Dynamic squat: Subject performing squat lifting technique with a box.

estimate forces for each exosuit. The estimated forces from the two elastic bands were summed and averaged across all participants for both exosuits. This conventional marker-based method for determining stretch forces was employed alongside the original sensor-based approach of integrating load cells into an exosuit for verification.

The flexion extension and knee joint angles were computed using marker trajectories in the 2-D sagittal plane. For flexion extension, the angle between the vector joining the markers C7 vertebra and right posterior superior iliac and an arbitrary vector perpendicular to the ground was measured. Similarly, knee flexion angles were computed using the two vectors joining right anterior superior iliac-right lateral femoral epicondyl and right lateral femoral epicondyl-right lateral malleolus.

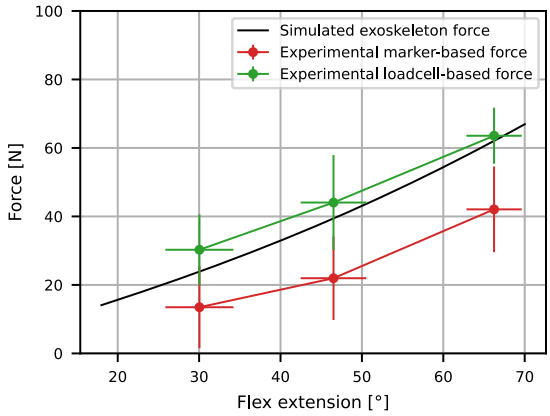
F. Simulation

The motion patterns of the experimental trials were replicated in simulation using the MyoBack model with the exoskeleton. For the static hold trials, a sweep was done over the two relevant parameters: flexion extension angle and knee flexion angle. The latter needs to be mapped to the appropriate model joints using marker data to achieve a realistic squat position with the subject leaning forward. For the dynamic trials, marker data was again employed to obtain the joint angles and simulate the complete motion cycle of the stoop/squat.

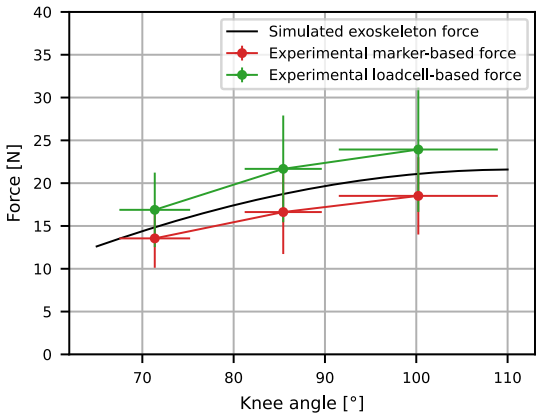
IV. Results

A. Static hold trials

In the static stoop results (Fig.6a), the flexion extension angles executed by participants ($\overline{\mathrm{SD}} = 3.9°$) were consistently lower than the predefined values. The MyoBack model with the exoskeleton shows a good reproduction of exoskeleton forces exerted on the human body, notably better with force data derived directly from the load cell sensors ($\mathrm{RMSE_{lc}} = 4.7\mathrm{N}$ with $\overline{\mathrm{SD}}_{\mathrm{lc}} = 10.8\mathrm{N}$) than the marker data ($\mathrm{RMSE_m} = 16.4\mathrm{N}$ with $\overline{\mathrm{SD}}_{\mathrm{m}} = 12.2\mathrm{N}$). In the case of static squat (Fig.6b), the knee flexion angles match more accurately with the intended ones. However, the uncertainty increases for a deeper squat regarding the knee flexion angle ($\widehat{\mathrm{SD}} = 8.7°$) and the measured forces ($\widehat{\mathrm{SD}}_{\mathrm{lc}} = 7.3\mathrm{N}$, $\widehat{\mathrm{SD}}_{\mathrm{m}} = 4.9\mathrm{N}$). Also, here the simulated exoskeleton forces follow the experimental trend well ($\mathrm{RMSE_{lc}} = 2.6\mathrm{N}$, $\mathrm{RMSE_m} = 2.1\mathrm{N}$).



(a) Static stoop.



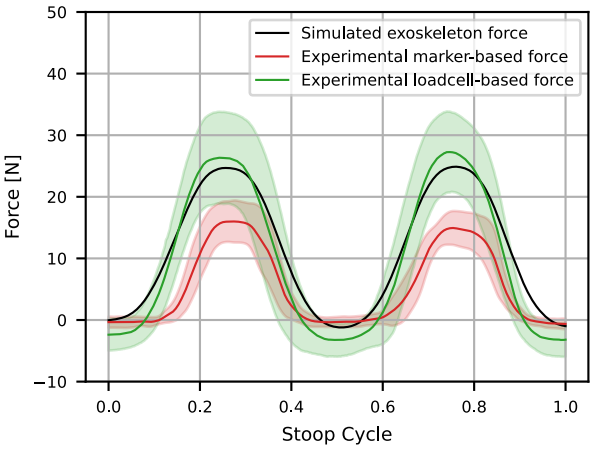
(b) Static squat.

Fig. 6: Comparison of experimental static trial exoskeleton force data for stoop and squat motion patterns, derived from load cells and indirectly from markers, with simulation data.

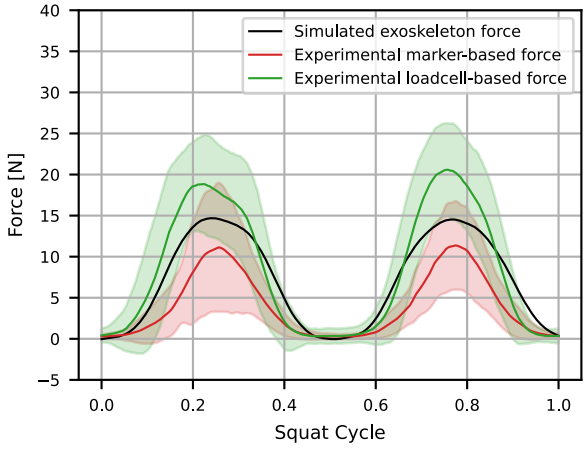
B. Dynamic trials

To allow for a better comparison, the data was normalized to the percentage of a stoop/squat cycle. For the stoop cycle (Fig.7a), the force data derived from the load cells ($\overline{\mathrm{SD}}_{\mathrm{lc}} = 5.6\mathrm{N}$) and the markers ($\overline{\mathrm{SD}}_{\mathrm{m}} = 2.3\mathrm{N}$) shows similar behavior to the static trials with the latter being consistently lower than the former and the simulated exoskeleton forces matching the former better ($\mathrm{RMSE_{lc}} = 2.8\mathrm{N}$, $\mathrm{RMSE_m} = 7.2\mathrm{N}$). Resembling the static trials, the squat cycle (Fig.7b) shows high uncertainties ($\overline{\mathrm{SD}}_{\mathrm{lc}} = 4.2\mathrm{N}$, $\overline{\mathrm{SD}}_{\mathrm{m}} = 2.7\mathrm{N}$). When the squat cycle is simulated using the MyoBack model with the exoskeleton, the reproduced force progressions correlate

well with the experimental ones ($RMSE_{lc} = 2.9N$, $RMSE_{m} = 3.8N$).



(a) Dynamic stoop.



(b) Dynamic squat.

Fig. 7: Comparison of experimental dynamic trial exoskeleton force data for stoop and squat motion patterns, derived from load cells and indirectly from markers, with simulation data.

V. Discussion and Conclusions

This study introduced the MyoBack model, a human back model part of the MyoSuite framework, derived from a physiologically accurate OpenSim model. The two models were compared with respect to kinematics, moment arms exerted by the muscles depending directly on the muscle pathways and the force-length-activation of muscles to ensure the accuracy of the derived model. No discrepancies were observed for the former, suggesting that the geometries and joint relations have been transferred successfully to the MyoBack model. However, regarding the latter two deviations can be seen. This is consistent with OpenSim models of other body parts with similar complexity (number of muscles and DoFs) converted using the MyoConverter, such as the neck model (72 MTUs and 6 joints) [27].

The observed differences stem from the fundamental disparities in how MuJoCo and OpenSim handle physical constraints, such as wrapping surfaces and geometry. OpenSim provides a detailed approach to muscle pathway constraints through specialized wrapping surfaces, while MuJoCo is limited to simple geometries and constraint handling methods. Hence, although MyoConverter facilitated the model conversion, it reached its optimization limit for muscle pathways, leaving some differences unaddressed. Importantly, the direction and trend of the moment arms match well between the two models and the fact that there are no discrete jumps. Also, the muscles themselves are modeled differently in MuJoCo and OpenSim. The possible MTU length may vary for the force-length activation, given that the muscle pathways are different in the two models. But notably, the force exerted at the relative length of the muscle is the same, and the maximum muscle force matches well. This allows for simulation with the MyoBack model with reasonably accurate results.

For empirical validation, the Auxivo Liftsuit, a passive exoskeleton, was modeled in MuJoCo and added to the MyoBack model. Force data derived from load cells and marker information were successfully compared with simulated exoskeleton forces acting on the human body in the context of stoop/squat movements. However, the study's major weaknesses include a small sample size of nine participants and the use of a standard-sized exosuit, which did not account for individual differences in body size. This led to variable exosuit forces across participants. Additionally, variations in measured flexion-extension angles could be attributed to potential misplacement or slippage of IMU sensors on the lumbar region during repeated or maximum forward bending. Furthermore, the placement of pelvis markers on the exosuit rather than on bony landmarks could have contributed to inaccuracies in computed angles.

Variations in knee flexion angles might also result from offsets in the IMUs placed on the thigh and shank. The significant discrepancies between forces derived from load cells and markers requires further investigation. Notably, load cell data, which directly measures force within the system, is likely to be more reliable. In contrast, markers are prone to slippage over the duration of trials and may be placed inconsistently among participants with varying anatomies.

Future work involves the analysis of EMG data collected from experimental trials, which will enable a more comprehensive validation of muscle activation levels within the MyoBack model. Currently, the validation considers only kinematics and muscle pathways. Still, exploring whether a reinforcement learning (RL) agent trained to perform specific static and dynamic tasks will exhibit activation patterns similar to those observed in human trials will be informative. The MyoBack model has the potential to extend its applications to various aspects of human locomotion and agility, including object lifting, balancing, and running, which remain unexplored in the current study. Additionally, integrating this model with both active and passive exoskeletons across the full body could further be used for rehabilitation and industrial design purposes and benefit populations such as the elderly and workers.

REFERENCES

[1] D. G. Behm, D. Cappa, and G. A. Power, "Trunk muscle activation during moderate- and high-intensity running," *Applied Physiology, Nutrition, and Metabolism*, vol. 34, no. 6, p. 1008–1016, Dec. 2009. [Online]. Available: http://dx.doi.org/10.1139/H09-102

[2] R. Müller, T. Ertelt, and R. Blickhan, "Low back pain affects trunk as well as lower limb movements during walking and running," *Journal of Biomechanics*, vol. 48, no. 6, p. 1009–1014, Apr. 2015. [Online]. Available: http://dx.doi.org/10.1016/j.jbiomech.2015.01.042

[3] M. Masaki, T. Aoyama, T. Murakami, K. Yanase, X. Ji, H. Tateuchi, and N. Ichihashi, "Association of low back pain with muscle stiffness and muscle mass of the lumbar back muscles, and sagittal spinal alignment in young and middle-aged medical workers," *Clinical Biomechanics*, vol. 49, p. 128–133, Nov. 2017. [Online]. Available: http://dx.doi.org/10.1016/j.clinbiomech.2017.09.008

[4] C. Larivière, D. Gagnon, and P. Loisel, "A biomechanical comparison of lifting techniques between subjects with and without chronic low back pain during freestyle lifting and lowering tasks," *Clinical Biomechanics*, vol. 17, no. 2, p. 89–98, Feb. 2002. [Online]. Available: http://dx.doi.org/10.1016/S0268-0033(01)00106-1

[5] A. Cieza, K. Causey, K. Kamenov, S. W. Hanson, S. Chatterji, and T. Vos, "Global estimates of the need for rehabilitation based on the Global Burden of Disease study 2019: a systematic analysis for the Global Burden of Disease Study 2019," *The Lancet*, vol. 396, no. 10267, pp. 2006–2017, Dec. 2020. [Online]. Available: https://linkinghub.elsevier.com/retrieve/pii/S0140673620323400

[6] National Research Council (US) and Institute of Medicine (US) Panel on Musculoskeletal Disorders and the Workplace, "Dimensions of the Problem," in *Musculoskeletal Disorders and the Workplace: Low Back and Upper Extremities*. National Academies Press (US), 2001. [Online]. Available: https://www.ncbi.nlm.nih.gov/books/NBK222425/

[7] J. Jacquier-Bret and P. Gorce, "Prevalence of Body Area Work-Related Musculoskeletal Disorders among Healthcare Professionals: A Systematic Review," *International Journal of Environmental Research and Public Health*, vol. 20, no. 1, p. 841, Jan. 2023. [Online]. Available: https://pmc.ncbi.nlm.nih.gov/articles/PMC9819551/

[8] European Agency for Safety and Health at Work., IKEI., and Panteia., *Work-related musculoskeletal disorders: prevalence, costs and demographics in the EU*. LU: Publications Office, 2019. [Online]. Available: https://data.europa.eu/doi/10.2802/66947

[9] W. Pirker and R. Katzenschlager, "Gait disorders in adults and the elderly," *Wiener klinische Wochenschrift*, vol. 129, pp. 81–95, 10 2016.

[10] S. Luo, M. Jiang, S. Zhang, J. Zhu, S. Yu, I. Dominguez Silva, T. Wang, E. Rouse, B. Zhou, H. Yuk, X. Zhou, and H. Su, "Experiment-free exoskeleton assistance via learning in simulation," *Nature*, vol. 630, no. 8016, p. 353–359, Jun. 2024. [Online]. Available: http://dx.doi.org/10.1038/s41586-024-07382-4

[11] S. Qiu, Z. Pei, C. Wang, and Z. Tang, "Systematic review on wearable lower extremity robotic exoskeletons for assisted locomotion," *Journal of Bionic Engineering*, vol. 20, no. 2, p. 436–469, Oct. 2022. [Online]. Available: http://dx.doi.org/10.1007/S42235-022-00289-8

[12] S. Luo, G. Androwis, S. Adamovich, E. Nunez, H. Su, and X. Zhou, "Robust walking control of a lower limb rehabilitation exoskeleton coupled with a musculoskeletal model via deep reinforcement learning," *Journal of NeuroEngineering and Rehabilitation*, vol. 20, no. 1, Mar. 2023. [Online]. Available: http://dx.doi.org/10.1186/S12984-023-01147-2

[13] M. Dodgson, D. M. Gann, and A. Salter, "The Impact of Modelling and Simulation Technology on Engineering Problem Solving," *Technology Analysis & Strategic Management*, vol. 19, no. 4, pp. 471–489, Jul. 2007. [Online]. Available: http://www.tandfonline.com/doi/abs/10.1080/09537320701403425

[14] T. Lu and C. Chang, "Biomechanics of human movement and its clinical applications," *The Kaohsiung Journal of Medical Sciences*, vol. 28, no. 2S, Feb. 2012. [Online]. Available: https://onlinelibrary.wiley.com/doi/10.1016/j.kjms.2011.08.004

[15] L. Liu, J. L. Cooper, and D. H. Ballard, "Computational modeling: Human dynamic model," *Frontiers in Neurorobotics*, vol. 15, 09 2021.

[16] A. Seth, J. L. Hicks, T. K. Uchida, A. Habib, C. L. Dembia, J. J. Dunne, C. F. Ong, M. S. DeMers, A. Rajagopal, M. Millard, S. R. Hamner, E. M. Arnold, J. R. Yong, S. K. Lakshmikanth, M. A. Sherman, J. P. Ku, and S. L. Delp, "OpenSim: Simulating musculoskeletal dynamics and neuromuscular control to study human and animal movement," *PLOS Computational Biology*, vol. 14, no. 7, p. e1006223, Jul. 2018. [Online]. Available: https://dx.plos.org/10.1371/journal.pcbi.1006223

[17] M. Damsgaard, J. Rasmussen, S. T. Christensen, E. Surma, and M. De Zee, "Analysis of musculoskeletal systems in the AnyBody Modeling System," *Simulation Modelling Practice and Theory*, vol. 14, no. 8, pp. 1100–1111, Nov. 2006. [Online]. Available: https://linkinghub.elsevier.com/retrieve/pii/S1569190X06000554

[18] "W04-(5) SIMM(Software for Interactive Musculoskeletal Modeling)," *The Reference Collection of Annual Meeting*, vol. VII.01.1, no. 0, pp. 325–326, 2001. [Online]. Available: https://www.jstage.jst.go.jp/article/jsmemecjsm/VII.01.1/0/VII.01.1_325/_article/-char/ja/

[19] S. Nakatsuji, M. Kawada, Y. Takeshita, Y. Matsuzawa, K. Hata, S. Araki, and R. Kiyama, "Effect of Unilateral Knee Extension Restriction on the Lumbar Region during Gait," *Journal of Healthcare Engineering*, vol. 2022, p. 1151753, Aug. 2022. [Online]. Available: https://pmc.ncbi.nlm.nih.gov/articles/PMC9424019/

[20] G. Zhao, H. Wang, L. Wang, Y. Ibrahim, Y. Wan, J. Sun, S. Yuan, and X. Liu, "The Biomechanical Effects of Different Bag-Carrying Styles on Lumbar Spine and Paraspinal Muscles: A Combined Musculoskeletal and Finite Element Study," *Orthopaedic Surgery*, vol. 15, no. 1, pp. 315–327, Jan. 2023.

[21] M. Abdullah, A. A. Hulleck, R. Katmah, K. Khalaf, and M. El-Rich, "Multibody dynamics-based musculoskeletal modeling for gait analysis: a systematic review," *Journal of Neuroengineering and Rehabilitation*, vol. 21, no. 1, p. 178, Oct. 2024.

[22] S. Zhang, H. Kui, X. Liu, and Z. Zhang, "Analysis of Musculoskeletal Biomechanics of Lower Limbs of Drivers in Pedal-Operation States," *Sensors (Basel, Switzerland)*, vol. 23, no. 21, p. 8897, Nov. 2023.

[23] A. Dallaway, M. Duncan, C. Griffen, D. Renshaw, J. Tallis, and J. Hattersley, "Age-Related Differences in the Functional Demand Placed on the Lumbar Spine during Walking in Healthy Older versus Younger Men," *Geriatrics (Basel, Switzerland)*, vol. 9, no. 5, p. 108, Aug. 2024.

[24] T. Geijtenbeek, "The Hyfydy simulation software," 11 2021, https://hyfydy.com. [Online]. Available: https://hyfydy.com

[25] E. Todorov, T. Erez, and Y. Tassa, "Mujoco: A physics engine for model-based control," in *2012 IEEE/RSJ International Conference on Intelligent Robots and Systems*, 2012, pp. 5026–5033.

[26] V. Caggiano, H. Wang, G. Durandau, M. Sartori, and V. Kumar, "MyoSuite – A contact-rich simulation suite for musculoskeletal motor control," May 2022, arXiv:2205.13600 [cs]. [Online]. Available: http://arxiv.org/abs/2205.13600

[27] H. Wang, V. Caggiano, G. Durandau, M. Sartori, and V. Kumar, "Myosim: Fast and physiologically realistic mujoco models for musculoskeletal and exoskeletal studies," *2022 International Conference on Robotics and Automation (ICRA)*, 05 2022.

[28] M. Christophy, N. A. Faruk Senan, J. C. Lotz, and O. M. O'Reilly, "A musculoskeletal model for the lumbar spine," *Biomechanics and Modeling in Mechanobiology*, vol. 11, pp. 19–34, 02 2011.

[29] M. E. Raabe and A. M. W. Chaudhari, "An investigation of jogging biomechanics using the full-body lumbar spine model: Model development and validation," *Journal of Biomechanics*, vol. 49, no. 7, pp. 1238–1243, May 2016.

[30] E. Beaucage-Gauvreau, W. S. P. Robertson, S. C. E. Brandon, R. Fraser, B. J. C. Freeman, R. B. Graham, D. Thewlis, and C. F. Jones, "Validation of an OpenSim full-body model with detailed lumbar spine for estimating lower lumbar spine loads during symmetric and asymmetric lifting tasks," *Computer Methods in Biomechanics and Biomedical Engineering*, vol. 22, no. 5, pp. 451–464, Apr. 2019. [Online]. Available: https://www.tandfonline.com/doi/full/10.1080/10255842.2018.1564819

[31] "XML Reference - MuJoCo Documentation." [Online]. Available: https://mujoco.readthedocs.io/en/stable/XMLreference.html#equality-joint

[32] "LiftSuit." [Online]. Available: https://www.auxivo.com/de/liftsuit

[33] "XML Reference - MuJoCo Documentation." [Online]. Available: https://mujoco.readthedocs.io/en/stable/XMLreference.html#tendon-spatial

[34] M. I. Mohamed Refai, A. Moya-Esteban, L. van Zijl, H. , and M. Sartori, "Benchmarking commercially available soft and rigid passive back exoskeletons for an industrial workplace," *Wearable Technologies*, vol. 5, p. e6, 2024. [Online]. Available: https://www.cambridge.org/core/journals/wearable-technologies/article/benchmarking-commercially-available-soft-

and-rigid-passive-back-exoskeletons-for-an-industrial-workplace/FE5D724EF59E482DCD2B6BBCD80ADB29

[35] V. Caggiano, H. Wang, G. Durandau, M. Sartori, and V. Kumar, "Myosuite – a contact-rich simulation suite for musculoskeletal motor control," arXiv.org, 05 2022. [Online]. Available: https://arxiv.org/abs/2205.13600

[36] A. Rajagopal, C. L. Dembia, M. S. DeMers, D. D. Delp, J. L. Hicks, and S. L. Delp, "Full-body musculoskeletal model for muscle-driven simulation of human gait," *IEEE Transactions on Biomedical Engineering*, vol. 63, no. 10, pp. 2068–2079, 2016.

[37] P. G. Arauz, G. Chavez, V. Reinoso, P. Ruiz, E. Ortiz, C. Cevallos, and G. Garcia, "Influence of a passive exoskeleton on kinematics, joint moments, and self-reported ratings during a lifting task," *Journal of Biomechanics*, vol. 162, p. 111886, 01 2024. [Online]. Available: https://www.sciencedirect.com/science/article/abs/pii/S0021929023004578

[38] "DARWING Hakobelude | Daiya Industry Co., Ltd." [Online]. Available: https://www.daiyak.co.jp/work_en/item/darwing-hakobelude.html

[39] M. Goršič, Y. Song, B. Dai, and V. D. Novak, "Short-term effects of the auxivo liftsuit during lifting and static leaning," *Applied Ergonomics*, vol. 102, p. 103765, 07 2022.

[40] V. Van Harmelen, J. Schnieders, and S. Wagemaker, "Measuring the amount of support of lower back exoskeletons," *Laevo White Paper*, 2022.

[41] R. M. van Sluijs, D. Rodriguez-Cianca, C. B. Sanz-Morère, S. Massardi, V. Bartenbach, and D. Torricelli, "A method to quantify the reduction of back and hip muscle fatigue of lift-support exoskeletons," *Wearable Technologies*, vol. 4, p. e2, 2023.

[42] J. H. van Dieën, M. J. Hoozemans, and H. M. Toussaint, "Stoop or squat: a review of biomechanical studies on lifting technique," *Clinical Biomechanics*, vol. 14, pp. 685–696, 12 1999.

Gait Adaptations Under Functional Asymmetry: Exploring the Role of Step Width, Step Length, and CoM in Lateral Stability

Tomislav Bačeк
Department of Mechanical Engineering
The University of Melbourne
Melbourne, Australia
tomislav.bacek@unimelb.edu.au

Denny Oetomo
Department of Mechanical Engineering
The University of Melbourne
Melbourne, Australia
doetomo@unimelb.edu.au

Ying Tan
Department of Mechanical Engineering
The University of Melbourne
Melbourne, Australia
yingt@unimelb.edu.au

***Abstract*—Bipedal gait is inherently unstable, requiring a complex interplay between foot placement and centre of mass (CoM) movement to maintain balance. While various factors are known to impact walking balance, few studies have explored the specific effects of functional asymmetry on lateral stability. This study investigates how step length, step width, and CoM adaptations impact lateral gait stability in healthy young adults walking with and without a functional asymmetry induced by fully extending the left knee. The results show that step length remains unaffected by functional asymmetry regardless of speed, while step width increases under the constraint. This adjustment increases the base of support; however, the concurrent increase in lateral CoM movement reduces overall lateral stability. These findings offer valuable insights into fundamental gait adaptation and stability mechanisms, with potential implications for designing rehabilitation strategies for individuals with gait asymmetry.**

***Index Terms*—functional gait asymmetry, margin of stability, step length, step width, centre of mass.**

I. Introduction

The ability to maintain stability (i.e., avoid falling) is fundamental to human walking. This requires humans to keep their centre of mass (CoM) within a stable base of support (BoS) formed by the contact with the ground. Due to our CoM being located high above a relatively narrow BoS, bipedal gait is inherently unstable, necessitating multiple strategies to control balance during walking [1].

Precise foot placement has been identified as the primary mechanism for maintaining bipedal stability [2]. Foot placement control uses different mechanisms in the sagittal and frontal planes, but operates simultaneously and seemingly with a degree of interaction [2]–[4]. In the sagittal plane, anterior-posterior (AP) foot placement (i.e., step length, SL) primarily drives forward progression and contributes less directly to stability [4]. In contrast, medio-lateral (ML) stability in the frontal plane requires active control [3], which can be achieved either by modulating lateral foot placement (i.e., step width, SW) during the swing phase to adjust the next step's BoS [5], [6] or by managing CoM during the stance phase [7].

This work was supported by the Australian Research Council's Discovery Project scheme (DP190100916).

While often studied separately, SW modulation and CoM movement are closely linked. Variations in CoM kinematics influence variations in SW [8], and the CoM trajectory during stance reliably predicts the next foot position variance [9]. This intricate interaction extends beyond lateral balance, as increased balance control – such as through enforced gait patterns – was shown to impose its own metabolic penalty [10], independent of costs associated with non-preferred SWs [11] or fluctuations in CoM energy [12]. Furthermore, the *bow-tie* CoM trajectory, characteristic of healthy walking, changes uniformly with walking speed [13]. In contrast, SW changes with speed have shown conflicting trends: decreasing [14], remaining unchanged [15], following a U-shape [16], or exhibiting a reverse J-curve [17] as speed increases.

The interplay between SW and CoM dynamics becomes particularly relevant in the presence of functional asymmetry, which is common in neurologically impaired populations. Functional asymmetry often results in a disrupted *bow-tie* CoM trajectory [18] and consistently wider SW across speeds [19]–[21], with falls, common during walking, often attributed to poor balance control [22]. However, studies in patient populations make it difficult to isolate the underlying biomechanical adaptations due to varying levels of impairment and individual-specific constraints. Comparing patients to healthy controls matched by speed or age provides only partial insights, as inherent biomechanical and dynamic differences persist irrespective of these factors. A notable attempt to address this gap is McCain et al. [23], who induced asymmetry in healthy individuals using knee and ankle bracing. However, the study was limited to walking only at 0.8 m/s, leaving functional asymmetry's broader implications unexplored.

This study addresses these gaps by investigating gait adaptations under functional asymmetry in healthy young adults across three speeds, focusing on the interplay between SL, SW, and CoM dynamics. A unilateral knee constraint was used to emulate biomechanical challenges faced by individuals with impaired gait, such as stroke survivors, while allowing isolation of specific gait adaptations. Stability was quantified using Hof et al.'s concept of the extrapolated CoM (xCoM) [24] and

the margin of stability (MoS). We hypothesised that functional asymmetry would lead to significant adjustments in lateral and fore-aft foot placement to counter altered CoM dynamics. We also hypothesised that walking with a knee constraint would increase MoS to compensate for the heightened demands imposed by the asymmetry. This within-subject design provides new insights into biomechanical and stability strategies under functional asymmetry, with implications for both clinical and robotic gait interventions.

II. Methodology

A. Walking dataset

We used human gait dataset published by Baček et al. [25]. The dataset contains data of 21 neurotypical young adults who walked on a dual-belt instrumented treadmill over two sessions (days). In this study, data of only 17 participants are used since two dropped out after the first session (*Sub7* and *Sub12* in [25]) and two have poor lateral-medial ground reaction force (GRF) data (*Sub9* and *Sub10* in [25]). The 17 participants analysed herein include 5 females, with the following anthropometry: age 31±8 years, body mass 72.8±13.2 kg, height 1.71±0.09 m (mean ± standard deviation).

All participants were free of any lower-extremity injury. Walking trials took five minutes each and include walking at three speeds (0.4, 0.8, and 1.1 m/s) and five cadences per speed (preferred, as well as two lower and two higher than preferred). All speed-cadence combinations were repeated twice: without constraints (i.e., *free*) and with a left knee joint extended using a passive knee brace (i.e., *constrained*), emulating hemiparetic compensatory gait. In this analysis, only tests at the participants' preferred cadence from [25] are used: *T3*, *T8*, and *T13* for free walking, and *T18*, *T23*, and *28* for constrained walking at 0.4, 0.8, and 1.1 m/s, respectively.

B. Gait variables

All gait variables were extracted and calculated in Matlab 2024a using custom-written scripts. GRF data were collected at 1 kHz and filtered using low-pass Butterworth filter with a 6 Hz cut-off frequency [26]. The vertical GRF component was used to segment walking data into gait cycles (time between two subsequent heel strikes of the same leg), with 5% of the peak amplitude used as a threshold (i.e., for a 70 kg person, the threshold is 70×9.81×0.05 = 34 N). All data represent the last 60-second average of a 5-minute trial, as gait variables of interest stabilise within 4 minutes before the analysis [27].

We define step length (SL) as the fore-aft and step width (SW) as the medio-lateral distance between the two calcaneous (heel) markers at the time of the leading leg's heel strike. Margin of stability (MoS) is calculated using the concept of extrapolated centre of mass (xCoM) [24]. Centre of mass (CoM) was calculated using the double integration method [28]; to calculate xCoM (1), CoM's medio-lateral position ($pCoM_{ml}$) was summed up with its corresponding velocity ($vCoM_{ml}$) times a factor $\sqrt{l/g}$, where l is the person's leg length and g gravity acceleration. Medio-lateral MoS (2) was calculated as the smallest lateral distance between the centre of pressure's (CoP's) measured lateral position ($pCoP_{ml}$) and the lateral xCoM position ($xCoM_{ml}$) during the stance phase. Leg length was measured as the distance between the anterior superior iliac spine (ASIS) and the ipsilateral medial malleolus in a standing position during static calibration (see [25] for details). Positive MoS values indicate laterally stable gait (the higher the value, the more stable the gait is).

$$xCoM_{ml} = pCoM_{ml} + vCoM_{ml} \cdot \sqrt{l/g}, \quad (1)$$

$$MoS_{ml} = min(pCoP_{ml} - xCoM_{ml}). \quad (2)$$

The medio-lateral CoM range of motion (ROM) is the distance between two furthest CoM positions in the lateral direction (frontal plane) during a gait cycle. A projection of the 3D CoM movement onto a transverse plane, i.e., the movement in the medio-lateral (ML) and anterior-posterior (AP) directions, makes a well-known shape resembling number eight [29]. We define the area enclosed by each of the number eight's halves (*ellipses*) as CoM Area, and CoM Area Symmetry as a ratio between the left CoM Area divided by the sum of the left and right CoM Area (50% = symmetric).

C. Statistical analysis

Statistical data analysis has been carried out in Python 3.10.10 using *scipy* package. The effects of speed and condition (free vs. constrained) on gait variables per leg were analysed using a two-way repeated measures ANOVA (RMANOVA) and a significance level of $p = 0.05$. Where statistically significant differences were found, Tukey's Honestly Significant Difference (HSD) tests were conducted for pairwise post-hoc analysis, with Bonferroni corrections applied to account for multiple comparisons. Tukey's HSD tests were also used to compare the difference between the two legs where applicable (Left vs. Right) for each speed-condition combination (e.g., free walking at 0.8 m/s). We define three levels of statistical significance: weak ($0.01<p\leq0.05$), moderate ($0.001<p\leq0.01$), and strong ($p\leq0.001$).

III. Results

In all boxplot graphs, three walking speeds are separated by vertical dashed lines, and two conditions labeled with *F* for free and *C* for constrained walking. In boxplots, box represents interquartile range (IQR, 25th to 75th percentile), middle line is median, whiskers are 1.5IQR, and (red) crosses are outliers. Data are average across all 17 participants, with full bars representing mean and error bars standard deviation of the population data.

A. Foot placement – step length (SL) and width (SW)

Increasing gait speed increases SL on both legs (Fig. 1, top row), with significant effect of speed (strong effect, $p<0.001$) during both free (blue bars) and constrained (red bars) walking. SL symmetry (not visualised), calculated as the ratio of the left SL to the sum of the two SLs (50%=symmetric), remains consistent and strongly symmetric – free vs. constrained, on average: 50.2% vs. 49.3% at 0.4 m/s, 50.1% vs. 51.1% at 0.8

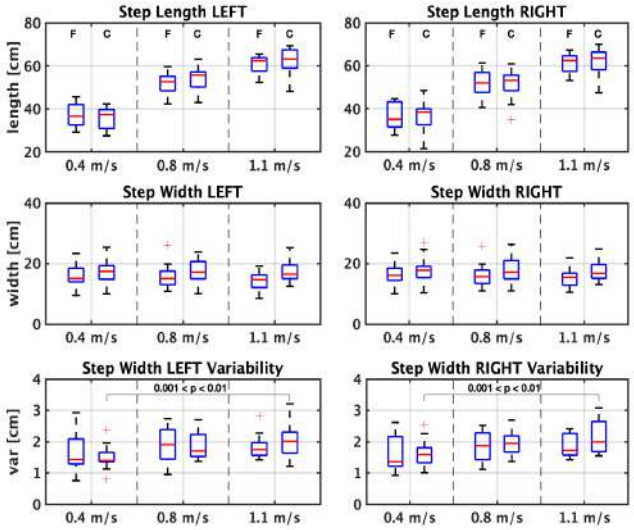


Figure 1. Step length (SL), Step width (SW), and SW variability. Note the same y-axis in each row. SW variability is calculated by averaging individual variability across participants. *F* is free, and *C* is constrained walking.

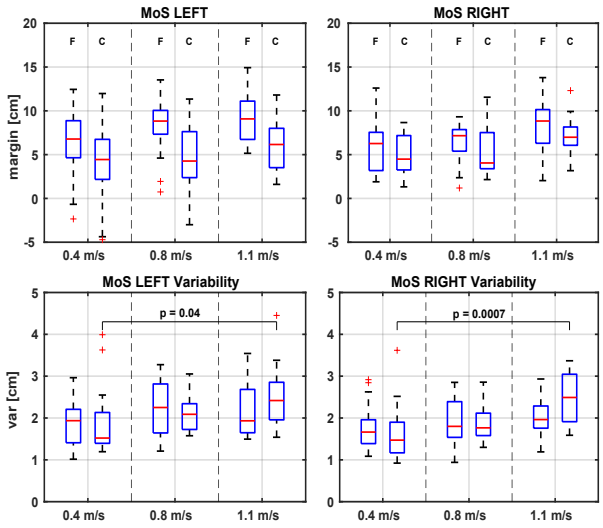


Figure 2. Medio-lateral margin of stability (MoS) and its variability across conditions. Note the same y-axis limits in each row. Positive values indicate stable gait. *F* is free, and *C* is constrained walking.

m/s, and 49.9% vs. 50.4% at 1.1 m/s. Consequently, across all speeds and conditions, there are no significant differences in SL symmetry, or in free vs. constrained SL (p>0.85).

Increasing walking speed has little effect on SW irrespective of the walking condition (Fig. 1, middle row); on both legs and in both conditions (free, constrained), the effect of speed is insignificant (p>0.95). Adding a passive knee brace increases SW by about 2 cm (≈12%) on both legs, but the increase is not significant (p>0.12). Similarly, there are no differences in SW between Left and Right legs in any of the speed-constraint combinations (p>0.99).

A different trend is observed in SW variability (Fig. 1, bottom row). During free walking, there is no significant effect of speed (p>0.49) or side (Left vs. Right; p>0.99) on repeatability of lateral foot positioning. When a knee constraint it added, walking speed only has a significant effect when comparing 1.1 to 0.4 m/s on both legs (moderate effect, 0.001<p<0.01). SW variability remains similar across the two legs (p>0.93), and added constraint does not significantly change it on either leg.

Overall, knee constraint does not affect SL or SL asymmetry, indicating a disassociation from SW modulation. SW is unaffected by the speed but increases during constrained walking, suggesting SW was used to control lateral stability.

B. Margin of stability (MoS)

Increasing walking speed increases lateral MoS in both free (Fig. 2, top row, blue bars) and constrained walking (Fig. 2, top row, red bars), albeit without statistical significance (p>0.21). Similarly, no statistically significant differences exist when comparing MoS between the two legs at any of the six speed-constraint combinations (p>0.59). Adding a knee brace on the left leg reduces average MoS on both legs and across all three speeds (Fig. 2, top row, blue vs. red) albeit with no significance (p>0.17). The exception is the left leg at 0.8 m/s, which exhibited a decrease as big as 35% (or 3 cm; p=0.07). Note that, on average, participants always walk with a stable gait (MoS>0); individually, two participants had MoS<0 on their left leg during free walking at 0.4 m/s; during constrained walking, the same two participants had MoS<0 on their left leg at 0.4 and 0.8 m/s, and one more participant at 0.4 m/s.

MoS variability remained fairly consistent across speeds, conditions, and legs (Fig. 2, bottom row). There is no significant effect of speed in either leg during free walking (p>0.28); during constrained walking, speed only significantly changes MoS variability when comparing 1.1 to 0.4 m/s on the left (weak effect, p=0.04) and right leg (strong effect, p=0.0007). There are no Left vs. Right differences in either constrained or free walking (p>0.54), and adding constraint to the left knee introduces no significant changes to MoS variability in either leg (p>0.42; notably, p=0.06 on the right leg at 1.1 m/s).

Overall, MoS slightly increased with speed but decreased on both legs under knee constraint, though without statistical significance. Trends in MoS variability suggest that participants found it more challenging to control MoS during constrained walking only at 1.1 m/s, and equally so on both legs.

C. Centre of Mass (CoM) movement

As walking speed increases, lateral CoM movement tends to decrease significantly in both free and constrained walking (strong effect, p<0.001; Fig. 3, top left). Notably, despite an increase in the lateral CoM movement when walking with constraints, the change is not significant at any speed compared to free walking (p>0.67). In contrast, CoM Area Symmetry notably changes (Fig. 3, top right). During free walking (blue bars), participants maintained near-perfect symmetry across speeds (p>0.98), as illustrated by the CoM path in the transverse plane (Fig. 3, bottom, full lines). Under constraints,

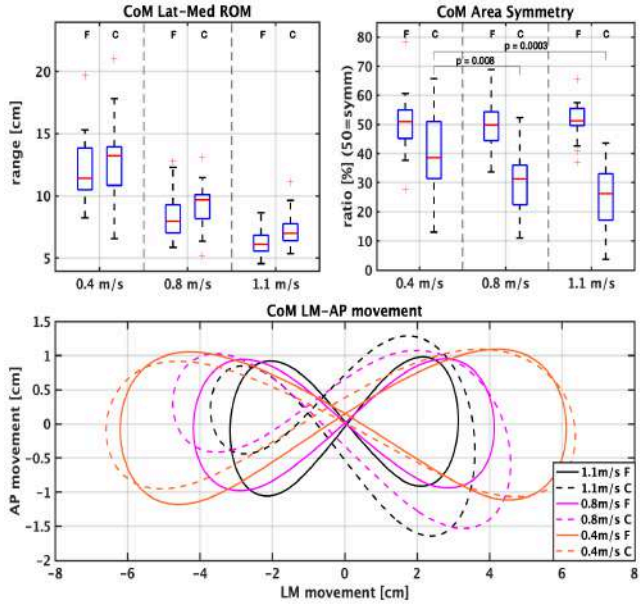


Figure 3. Centre of mass (CoM) movement in the frontal plane (ROM) and projected onto the transverse plane (Area Ratio, LM-AP movement). Top row: *F* is free, and *C* constrained walking. Bottom row: walking speeds are colour-coded and the two conditions visualised using full (free; F) and dashed (constrained; C) lines.

CoM Area Symmetry dropped below 50%, indicating greater reliance on the right (unconstrained) leg. The effect of speed on CoM Area Symmetry during constrained walking leads to significant difference between 0.4 and 1.1 m/s (strong effect, p=0.0003), and 0.4 and 0.8 m/s (moderate effect, p=0.008), and between free and constrained walking at 0.8 and 1.1 m/s (strong effect, p<0.001).

Dashed lines in Fig. 3 (bottom) illustrate the impact of a knee brace on CoM. At 0.8 and 1.1 m/s, functional asymmetry increases both lateral and fore-aft movement of the CoM on the right side, while only lateral movement increases on the left side. At 0.4 m/s, lateral CoM movement increases slightly on the right side, with reduced fore-aft and increased lateral movement on the left side. The constraint-induced changes are less pronounced at 0.4 m/s, explaining the smaller free vs. constrained CoM Area Symmetry difference at this speed compared to the two faster speeds (Fig 3, top right).

Overall, lateral CoM movement decreases with speed during both free and constrained walking, with the constraint having the greatest impact in the fore-aft direction. Constrained walking also results in marked asymmetry in the CoM Area Symmetry, reflecting a compensatory reliance on the right (unconstrained) leg to control lateral stability.

IV. Discussion

This study investigated human gait adaptations under functional asymmetry across a range of speeds relevant to healthy young adults (1.1 m/s, [30]) and hemiparetic patients (0.8 and 0.4 m/s, [31]). By having participants serve as their own control, we isolated these adaptations from other factors often present in patients or between-group comparisons. The primary focus was on the interplay between step length (SL), step width (SW), and centre of mass (CoM) movement and their combined effects on lateral gait stability. Our first hypothesis was partially confirmed: participants modulated SW but not SL to counteract CoM impacts on lateral stability. Conversely, our second hypothesis was rejected, as MoS decreased, rather than increased, during constrained walking.

A. Walking dataset

Human gait adaptations are often studied by comparing different groups, such as through speed- or age-matching designs [32], [33]. However, these approaches cannot fully account for biomechanical differences that are independent of speed or age, especially in patient populations [34]. The within-subject design of the walking study used herein [25], where participants act as their own control, offers a unique advantage by isolating gait adaptations solely due to functional asymmetry, free from other factors (e.g., muscle weakness). In the study, participants wore a passive knee brace that restricted left knee flexion, limiting ankle plantarflexion during push-off and inducing propulsive asymmetry [35] as well as compensatory gait adjustments [36]. As gait speed increased, propulsive asymmetry did too [35], reflecting the natural demands of higher speeds on joint mobility [37]. Despite a metronome guidance, participants were free to make slight adjustments to their step length and step time (and their symmetries) as long as the resulting gait speed (i.e., *stride* length / *stride* time) matched that imposed by the treadmill.

B. Fore-aft foot placement

During free walking, participants increased their SL with speed (Fig.1, top row, blue bars), consistent with the well-documented positive correlation between gait speed and SL [38]. This adaptation was observed symmetrically across both legs, resulting in strong SL symmetry at all three speeds, concurrent with the speed-agnostic propulsive symmetry reported by [35]. These findings reinforce the critical role of SL in forward progression and its assumed influence on the mechanical and metabolic costs of walking [11], [39].

Interestingly, introducing a left knee constraint had no measurable effect on SL or its symmetry (Fig.1, top row, red bars), even in the presence of pronounced propulsive asymmetries at 0.8 and 1.1 m/s [35] (similar to those observed in stroke patients classified as having *mild* to *moderate* impairments [40]). These results align with findings by McCain et al. [23], who similarly used knee brace to externally induce propulsive asymmetry and reported minimal impact on SL symmetry (and metabolic cost) during walking at 0.8 m/s. Importantly, this consistency holds despite differences in our experimental protocols, as McCain et al. did not employ metronome guidance.

A notable observation is that their participants prioritised SL over step time (ST) symmetry during constrained walking. Although ST symmetry is beyond the scope of this paper, we note that our participants exhibited similar adaptations. This behavior contrasts with findings from free walking, where ST,

rather than SL asymmetry, has been shown to significantly influence the metabolic cost of walking [12], [41]. The underlying mechanisms driving this prioritisation during constrained walking remain unclear and warrant further investigation.

C. Lateral foot placement and medio-lateral stability

In the walking study used herein [25], participants on average maintained a consistent SW and SW variability across different speeds during free walking, with similar values observed for both legs (Fig. 1, middle and bottom rows, blue bars). This stability in SW across speeds aligns with findings from [6] and [15], though it contrasts with studies like [14], [16], [17], likely due to differences in experimental designs and speed ranges tested. Additionally, our results support the finding in [4] of an independent SW-SL control at self-selected speeds, extending it across a wider range of speeds.

Generally, higher walking speeds during free walking result in reduced CoM movement in 3D space [29], as there is less time to execute step-to-step transitions. When this decrease is decoupled from SW modulations, as was the case here – SW remained consistent across speeds (Fig. 1, middle row, blue bars) – lateral stability, as defined by MoS, would be expected to increase. As shown in Fig. 2, this was indeed the case. Using MoS at 1.1 m/s, a speed close to the preferred metabolically efficient gait speed for healthy young adults, as a reference for stability, the reduction in MoS at 0.4 m/s, despite participants reporting feeling *less stable* and disliking the speed, suggests that lateral stability may not be prioritised at slower speeds.

This is likely due to the metabolic penalty associated with wider steps. While taking wider steps at a given speed enhances lateral stability in both healthy individuals and hemiparetic patients [32], [33], [42], it also increases metabolic cost [11]. Furthermore, wider steps are typically more constrained at higher speeds, where longer steps are preferred [42], suggesting that participants could have taken wider steps at lower speeds to increase their MoS. The fact that they didn't – in fact, quite the opposite – suggests that a combination of having more time to correct for potential disturbances at slower speeds and the intrinsic metabolic penalty of walking slowly takes precedence over maximising lateral stability, which is instead maintained at a *sufficient* level during free walking.

Adding a knee constraint impacted SW, MoS, and CoM, but to different degrees. Walking with propulsive asymmetry, particularly at 0.8 and 1.1 m/s [35], led to significant asymmetry in CoM Area (Fig. 3, top right), indicating increased reliance on the right (unconstrained) leg. The fully extended left knee prevented participants from performing *natural* weight acceptance following heel strike or push-off after toe-off, resulting in reduced CoM movement in the AP and increased in the LM directions (Fig. 3). The apparent effect of increased lateral CoM movement at a given speed is comparable to reducing speed, which typically allows more time to manage potential disturbances. This increased need for lateral stabilisation was accompanied by an increase in SW across speeds, as expected, and is consistent with the literature [7], [33], [43].

The increase in SW during constrained walking was consistent across speeds, mirroring the trend observed during free walking. This could be specific to our group of participants, whose preference for a consistent SW across conditions may not have been significantly challenged by the constraint or the range of tested speeds. As a result, they may have defaulted to habitual motor patterns developed during free walking, potentially trading MoS at slower walking speeds. However, this does not fully explain why participants walked with decreased MoS across all speeds compared to free walking.

At 1.1 m/s, it's conceivable that their SW was near its max value, making it mechanically difficult to walk wider. This hypothesis is supported by the increased variability in SW and MoS compared to other conditions (Fig. 1 and 2). At 0.8 and 0.4 m/s, however, this explanation seems unlikely. Instead, altered CoM dynamics during constrained walking (Fig. 3), also common in neurologically-impaired patients [18], combined with the metabolic penalties associated with increased SW and lateral stabilisation, suggests that the trade-off landscape between lateral stability and metabolic cost was shifted by the constraint. If true, participants may still have been minimising their metabolic cost, even at the expense of reducing their stability margin. This hypothesis, though, is beyond the scope of this paper and warrants further investigation.

D. Limitations

This study has several limitations. First, the participant pool of young, healthy adults limits the generalisability of the findings to broader populations. Second, it focused on SL, SW, and CoM dynamics, excluding variables like step time symmetry and metabolic cost. Lastly, using MoS as the sole metric for lateral stability, while valuable, may not fully capture the complexity of dynamic balance recovery strategies.

V. Conclusion

This paper examines gait adaptations in young, healthy adults walking with and without propulsive asymmetry, focusing on how step length, step width, and lateral centre of mass (CoM) movement interact to influence lateral margin of stability. Results indicate that humans prioritise step length symmetry even under propulsive asymmetry, while maintaining consistent step width across speeds. This results in a slight increase in lateral stability with higher speeds, suggesting humans prioritise a trade-off that ensures *sufficient* gait stability. Functional asymmetry significantly changes gait dynamics, including CoM movement and stability margins. These adaptations highlight a complex interplay between lateral balance, preferred motor patterns, and potentially metabolic efficiency. Overall, this underscores the importance of targeting propulsive asymmetry and CoM dynamics in correcting gait, rather than focusing on, e.g. reducing step length asymmetry.

Acknowledgment

The authors would like to thank Mr. Yufan Xu and his supervisor, Dr. Liuhua Peng of The University of Melbourne's Faculty of Science, for providing their expertise in running statistical analysis and preparing results.

REFERENCES

[1] H. Reimann, T. Fettrow, and J. J. Jeka, "Strategies for the control of balance during locomotion," *Kinesiology Review*, vol. 7, pp. 18–25, 2018.

[2] M. Vlutters, E. H. F. van Asseldonk, and H. van der Kooij, "Center of mass velocity-based predictions in balance recovery following pelvis perturbations during human walking," *Journal of Experimental Biology*, vol. 219, pp. 1514–1523, 5 2016.

[3] C. E. Bauby and A. D. Kuo, "Active control of lateral balance in human walking," *Journal of Biomechanics*, vol. 33, pp. 1433–1440, 2000.

[4] S. H. Collins and A. D. Kuo, "Two independent contributions to step variability during over-ground human walking," *PLOS ONE*, vol. 8, pp. e73 597–, 8 2013.

[5] J. Perry and M. Srinivasan, "Walking with wider steps changes foot placement control, increases kinematic variability and does not improve linear stability," *Royal Society Open Science*, vol. 4, p. 160627, 9 2017.

[6] K. H. Stimpson, L. N. Heitkamp, J. S. Horne, and J. C. Dean, "Effects of walking speed on the step-by-step control of step width," *Journal of Biomechanics*, vol. 68, pp. 78–83, 2018.

[7] M. Arvin, J. V. Dieen, and S. Bruijn, "Effects of constrained trunk movement on frontal plane gait kinematics," *Journal of Biomechanics*, vol. 49, 7 2016.

[8] C. P. Hurt, N. Rosenblatt, J. R. Crenshaw, and M. D. Grabiner, "Variation in trunk kinematics influences variation in step width during treadmill walking by older and younger adults," *Gait Posture*, vol. 31, pp. 461–464, 2010.

[9] Y. Wang and M. Srinivasan, "Stepping in the direction of the fall: The next foot placement can be predicted from current upper body state in steady-state walking," *Biology letters*, vol. 10, 9 2014.

[10] D. Wezenberg, A. de Haan, C. A. M. van Bennekom, and H. Houdijk, "Mind your step: Metabolic energy cost while walking an enforced gait pattern," *Gait Posture*, vol. 33, pp. 544–549, 2011.

[11] J. M. Donelan, R. Kram, and A. D. Kuo, "Mechanical and metabolic determinants of the preferred step width in human walking." *Proc. R. Soc. B Biol. Sci.*, vol. 268, pp. 1985–1992, 10 2001.

[12] J. Stenum and J. T. Choi, "Disentangling the energetic costs of step time asymmetry and step length asymmetry in human walking," *Journal of Experimental Biology*, vol. 224, p. jeb242258, 6 2021.

[13] L. Tesio, V. Rota, C. Chessa, and L. Perucca, "The 3d path of body centre of mass during walking on force treadmill," *Journal of biomechanics*, vol. 43, pp. 938–944, 12 2009.

[14] M. Orendurff, A. D. Segal, G. K. Klute, J. S. Berge, E. Rohr, and N. J. Kadel, "The effect of walking speed on center of mass displacement." *Journal of rehab research and development*, vol. 41, pp. 829–34, 2004.

[15] H. G. Kang and J. B. Dingwell, "Effects of walking speed, strength and range of motion on gait stability in healthy older adults," *Journal of Biomechanics*, vol. 41, pp. 2899–2905, 2008.

[16] J. L. Helbostad and R. Moe-Nilssen, "The effect of gait speed on lateral balance control during walking in healthy elderly," *Gait Posture*, vol. 18, pp. 27–36, 2003.

[17] S. A. Brinkerhoff, W. M. Murrah, and J. A. Roper, "The relationship between gait speed and mediolateral stability depends on a person's preferred speed," *Scientific Reports*, vol. 13, p. 6056, 2023.

[18] H. Iida and T. Yamamuro, "Kinetic analysis of the center of gravity of the human body in normal and pathological gaits," *Journal of Biomechanics*, vol. 20, pp. 987–995, 1987.

[19] A. L. Hof, R. M. van Bockel, T. Schoppen, and K. Postema, "Control of lateral balance in walking: Experimental findings in normal subjects and above-knee amputees," *Gait Posture*, vol. 25, pp. 250–258, 2007.

[20] L. Hak, H. Houdijk, P. van der Wurff, M. R. Prins, A. Mert, P. J. Beek, and J. H. van Dieën, "Stepping strategies used by post-stroke individuals to maintain margins of stability during walking," *Clinical Biomechanics*, vol. 28, pp. 1041–1048, 2013.

[21] M. D. Lewek, C. E. Bradley, C. J. Wutzke, and S. M. Zinder, "The relationship between spatiotemporal gait asymmetry and balance in individuals with chronic stroke," *Journal of Applied Biomechanics*, vol. 30, pp. 31–36, 2014.

[22] K. Hill, P. Ellis, J. Bernhardt, P. Maggs, and S. Hull, "Balance and mobility outcomes for stroke patients: A comprehensive audit," *Australian Journal of Physiotherapy*, vol. 43, no. 3, pp. 173–180, 1997.

[23] E. M. McCain, M. E. Berno, T. L. Libera, M. D. Lewek, G. S. Sawicki, and K. R. Saul, "Reduced joint motion supersedes asymmetry in explaining increased metabolic demand during walking with mechanical restriction." *Journal of Biomechanics*, vol. 126, 2021.

[24] A. L. Hof, M. G. J. Gazendam, and W. E. Sinke, "The condition for dynamic stability," *Journal of Biomechanics*, vol. 38, pp. 1–8, 2005.

[25] T. Baček, M. Sun, H. Liu, Z. Chen, C. Manzie, E. Burdet, D. Kulić, D. Oetomo, and Y. Tan, "A biomechanics and energetics dataset of neurotypical adults walking with and without kinematic constraints," *Scientific Data*, vol. 11, p. 646, 2024.

[26] D. Winter, *Biomechanics and Motor Control of Human Movement.*, 4th ed. Wiley, 9 2009.

[27] C. Meyer, T. Killeen, C. S. Easthope, A. Curt, M. Bolliger, M. Linnebank, B. Zörner, and L. Filli, "Familiarization with treadmill walking: How much is enough?." *Sci. Rep.*, vol. 9, p. 5232, 2019.

[28] G. A. Cavagna, "Force platforms as ergometers," *Journal of Applied Physiology*, vol. 39, pp. 174–179, 7 1975.

[29] L. Tesio and V. Rota, "The motion of body center of mass during walking: A review oriented to clinical applications," *Frontiers in Neurology*, vol. 10, 2019.

[30] C. A. Fukuchi, R. K. Fukuchi, and M. Duarte, "Effects of walking speed on gait biomechanics in healthy participants: a systematic review and meta-analysis." *Systematic reviews*, vol. 8, p. 153, 6 2019.

[31] J. Perry, M. Garrett, J. Gronley, and S. J. Mulroy, "Classification of walking handicap in the stroke population." *Stroke*, vol. 26, pp. 982–989, 1995.

[32] J. C. Dean, N. B. Alexander, and A. D. Kuo, "The effect of lateral stabilization on walking in young and old adults," *IEEE Transactions on Biomedical Engineering*, vol. 54, pp. 1919–1926, 2007.

[33] H. B. Frame, C. Finetto, J. C. Dean, and R. R. Neptune, "The influence of lateral stabilization on walking performance and balance control in neurologically-intact and post-stroke individuals," *Clinical Biomechanics*, vol. 73, pp. 172–180, 2020.

[34] S. J. Ali, A. N. Ansari, A. Rahman, S. Imtiyaz, and B. Rashid, "Post-stroke hemiplegic gait: A review," *Pharma Innov.*, vol. 3, pp. 36–41, 2014.

[35] T. Baček, Y. Xu, L. Peng, D. Oetomo, and Y. Tan, "Gait adaptations in step length and forward propulsion during walking with functional asymmetry," *Frontiers in Bioengineering and Biotechnology*, 2024, submitted for review.

[36] T. Baček, M. Sun, H. Liu, Z. Chen, D. Kulić, D. Oetomo, and Y. Tan, "Varying joint patterns and compensatory strategies can lead to the same functional gait outcomes: A case study," in *2022 International Conference on Rehabilitation Robotics (ICORR)*, 2022, pp. 1–6.

[37] B. F. Mentiplay, M. Banky, R. A. Clark, M. B. Kahn, and G. Williams, "Lower limb angular velocity during walking at various speeds," *Gait Posture*, vol. 65, pp. 190–196, 2018.

[38] M. B. Yanez, S. A. Kettlety, J. M. Finley, N. Schweighofer, and K. A. Leech, "Gait speed and individual characteristics are related to specific gait metrics in neurotypical adults," *Scientific Reports*, vol. 13, p. 8069, 2023.

[39] J. M. Donelan, R. Kram, and A. D. Kuo, "Mechanical work for step-to-step transitions is a major determinant of the metabolic cost of human walking," *J. Exp. Biol.*, vol. 205, pp. 3717–3727, 2002.

[40] M. G. Bowden, C. K. Balasubramanian, R. R. Neptune, and S. A. Kautz, "Anterior-posterior ground reaction forces as a measure of paretic leg contribution in hemiparetic walking," *Stroke*, vol. 37, pp. 872–876, 2006.

[41] R. Ellis, K. Howard, and R. Kram, "The metabolic and mechanical costs of step time asymmetry in walking," *Proceedings. Biological sciences / The Royal Society*, vol. 280, p. 20122784, 4 2013.

[42] P. M. M. Young and J. B. Dingwell, "Voluntary changes in step width and step length during human walking affect dynamic margins of stability," *Gait Posture*, vol. 36, pp. 219–224, 2012.

[43] S. Bruijn and J. V. Dieen, "Control of human gait stability through foot placement," *Journal of The Royal Society Interface*, vol. 15, 6 2018.

Independent Donning and Doffing Robotic Hand System: An Innovative Solution for Stroke Home-Rehabilitation

Garam Lee, Hyun-Ji Kim, Won Kee Chang, Nam-Jong Paik*

***Abstract*—Stroke often results in spastic or clenched hands, which presents a considerable obstacle to the independent donning of robotic hand systems. To address these issues, we developed a novel robotic hand system comprising a Hand Setup Station and a Pneumatic Robotic Hand. The system was designed with the objective of facilitating efficient and independent donning and doffing. The Hand Setup Station incorporates a finger extension mechanism to safely extend clenched fingers during the process, ensuring secure and comfortable attachment. The user-friendly controls allow for precise adjustments tailored to individual needs. In a randomized evaluation involving five participants wearing a glove to simulate stroke-like hand rigidity, the system-assisted donning significantly reduced task completion time compared to manual donning (Manual 98.68 $\pm$ 7.68 sec vs. Proposed 68.89 $\pm$ 7.33 sec, $p < 0.05$). Participants reported higher ratings for ease of use (Manual 4.4 vs. Proposed 2) and experienced lower pain levels (2.2 vs. 3.8) compared to the manual process, which was noted for its physical strain and inefficiency. These findings demonstrate the system's potential to enhance usability and accessibility for stroke rehabilitation, particularly in remote or home-based settings. Future work will focus on optimizing actuator positioning, personalized control, and compatibility with various robotic hand designs for broader application.**

I. INTRODUCTION

Stroke is a leading cause of long-term disability worldwide and the second leading cause of death globally [1]. It occurs when a cerebral blood vessel is either obstructed or ruptured, resulting in localized brain cell damage [2]. This damage manifests in various neurological deficits, including hemiparesis, impaired consciousness, and speech disorders [3]. Among these, post-stroke upper limb dysfunction represents a significant challenge, as it significantly impairs patients' ability to independently perform essential activities of daily living (ADLs), including eating, dressing, and personal hygiene [4]. Consequently, restoring hand functionality is recognized as a pivotal objective in the rehabilitation process for stroke survivors [5]–[7].

The manual facilitation of hand joint movements by physical therapists is beset with significant challenges, largely due to the hand's complex biomechanical structure and the extensive range of motion it exhibits. These factors demand considerable time and effort to address [8]. To overcome these limitations, a variety of robotic systems have been developed to deliver precise and repetitive hand rehabilitation training. Compared to conventional manual therapy, robot-assisted rehabilitation offers more intensive and repetitive training within a constrained time frame, demonstrating substantial efficacy in promoting motor function recovery [9]–[12]. Furthermore, these systems are designed to incorporate the patient's motor intentions, enabling natural and intuitive interaction [13], [14]. This not only increases patient engagement but also enhances the overall rehabilitation outcome.

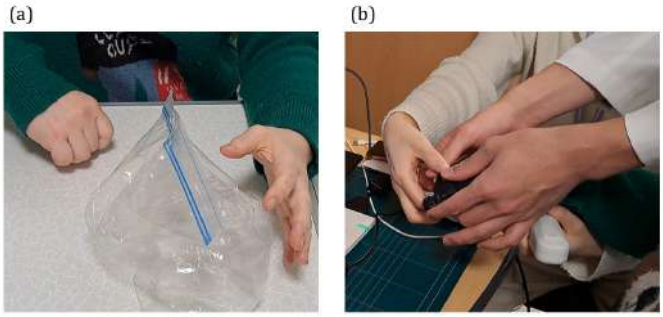


Fig. 1. The appearance of a stroke patient and the preparation process for robotic hand rehabilitation. (a) The spastic hand of a stroke patient. (b) Pretreatment to prepare the patient's hand for robotic hand donning.

However, for chronic stroke patients, spasticity or paralysis causes the hand remaining in a clenched position, as illustrated in Fig. 1. This presents a significant challenge in the direct application of a robotic hand device. For the hand extension, a therapist is required to manually extend the patient's hand, a process that is both labor-intensive and time-consuming [8], [15], [16]. This dependency precludes patients from utilizing robotic hand systems independently, thereby imposing a significant constraint on their practical application. Consequently, many patients are excluded from the benefits of such devices due to the difficulty in donning and doffing them without external assistance. To address this issue, there is a growing demand for a novel robotic hand system that enables patients to independently wear and remove the device without requiring manual intervention.

Recently, the COVID-19 pandemic has highlighted the

Garam Lee and Hyun-Ji Kim are with the Department of Health Science and Technology, Graduate School of Convergence Science and Technology, Seoul National University, Seoul, 08826, Korea (garamlee@snu.ac.kr, hyunjikim.official@gmail.com)

Won Kee Chang and Nam-Jong Paik are with the Department of Rehabilitation Medicine, Seoul National University Bundang Hospital, Seoul National University College of Medicine, Seongnam, 13620, Korea (wonkee.chang@gmail.com, njpaik@snu.ac.kr)

critical need for remote rehabilitation, as hospital visits were often restricted or entirely unfeasible. Furthermore, the shortage of physical therapists and caregivers, combined with the geographical isolation of many patients in areas with limited healthcare access, exacerbates the difficulties in providing adequate rehabilitation therapy [17], [18]. These limitations underscore the necessity for innovative solutions to address the growing demand for accessible rehabilitation. A robotic hand system that stroke survivors can independently don and operate offers a promising approach to enhance accessibility. In particular, a system optimized for remote use could provide continuous and effective rehabilitation opportunities, significantly improving outcomes for patients unable to attend conventional therapy sessions.

Against this backdrop, this study aims to develop a robotic hand system that stroke patients can use independently, without external assistance. The proposed system is designed to enhance patient autonomy, improve accessibility to rehabilitation, and enable effective utilization in remote rehabilitation environments. By addressing these challenges, the system has the potential to significantly improve the quality of life for chronic stroke patients and establish a new paradigm in rehabilitation therapy.

The following sections of this paper provides an overview of the proposed system, followed by details on the development and operating principles of the proposed robotic hand system in Section II. Section III presents the experiments of the proposed system. Section IV provides the experimental results, and discussions are drawn in Section V.

II. PROPOSED ROBOTIC HAND SYSTEM

The proposed robotic hand system is designed to enable stroke patients to independently don and doff the device without external assistance. As shown in Fig. 2, the system comprises two main components: the Hand Setup Station and the Pneumatic Robotic Hand.

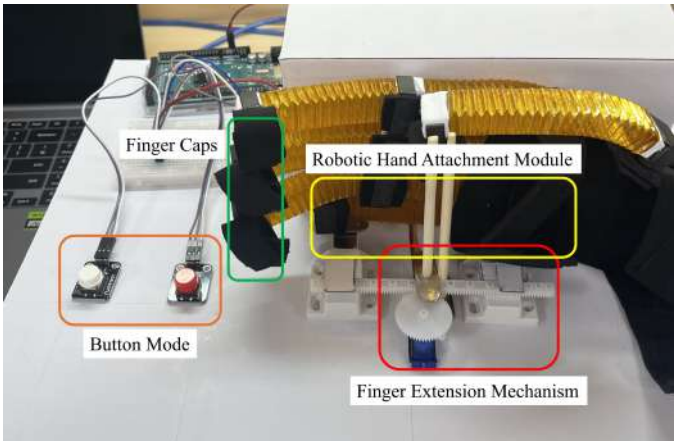


Fig. 2. A robotic hand system for independent donning and doffing of robotic hands by patients. This system is designed to allow the unaffected hand to fully assist in donning the robotic hand onto the affected hand. The station is operated simply by pressing buttons. After doffing, the system returns to its initial state, enabling the same conditions for the next donning process.

A. Hand Setup Station

The Hand Setup Station is designed to gently open the stiff, spastic hands of chronic stroke patients, preparing them for the application of the robotic hand system [19]. Chronic stroke patients, particularly those with prolonged symptoms, often exhibit persistent hand clenching, which complicates the donning of the robotic hand and limits finger mobility. To address this, the station securely stabilizes the patient's hand in a comfortable position while facilitating finger extension through the following components:

1) The Finger Extension Mechanism utilizes two thin actuators, which facilitate the gradual extension of clenched fingers. This design is inspired by findings from the BeBiTT test [20]. This test was conducted with six chronic stroke patients (3F/3M; average age 48.5 $\pm$ 16 years; average onset 3.8 $\pm$ 2.1 years). During the test, patients performed ADL tasks using common household objects, and the activity scores for the affected hand were evaluated. All procedures related to the experiment were approved by the Institutional Review Board of Seoul National University Bundang Hospital (IRB No. B-2205-756-003). Results showed that ADL tasks involving thin cylindrical objects, such as holding a toothpaste tube, had the highest activity scores as shown in Table I.

TABLE I
RESULTS OF THE BEBITT TEST FOR STROKE PATIENTS PERFORMED BY 6 PARTICIPANTS (3F/3M, AVERAGE AGE: 48.5 ± 16 YRS, ONSET: 3.8 ± 2.1 YRS) USING POWER GRASP, CYLINDRICAL GRASP, LATERAL PINCH, AND PRECISION PINCH FOR DAILY LIVING TASKS (2 REPETITIONS EACH, 5-POINT SCALE).

Participant	Spherical Grasp	Cylindrical Grasp	Lateral Pinch	Precision Pinch
1	2	3	0	0
2	1.5	3	1.5	2
3	3.5	4	1.5	2
4	1	3	0	0.5
5	2.5	5	2	2.5
6	2	4.5	3	3

Building on this, the mechanism leverages the paretic hand's adaptability to cylindrical shapes, allowing controlled finger extension through a motor-driven rack-and-pinion system. The second actuator operates the robotic hand attachment module, enabling vertical displacement for secure locking and unlocking. This dual-actuator design ensures precise, adjustable extension tailored to each patient's needs while maintaining safety and comfort.

2) The Button Mode provides an intuitive interface for controlling the Finger Extension Mechanism, featuring two distinct buttons for precise and user-friendly operation. The red button controls the actuator's vertical movement, enabling the system to position the hand in a ready posture for extension or to facilitate the safe and comfortable removal of the hand from the system. The white button allows for linear extension and retraction of the fingers, ensuring precise adjustments during the flexion or extension process based on the patient's needs.

B. Pneumatic Robotic Hand

The Pneumatic Robotic Hand utilizes Pneumatic Origami Muscle Actuators (POMA) to achieve controlled and adaptive finger movements [21]. This design enables seamless integration after the hand preparation phase, allowing patients to perform rehabilitation exercises with improved comfort and natural motion. The robotic hand comprises the following components:

1) The Robotic Hand Attachment Module enables stable attachment of the robotic hand to the Hand Setup Station during the donning process. A latch system secures the robotic hand in place, preventing unwanted movement and ensuring precise alignment during application.

2) The Finger Caps are soft, thimble-like covers placed at the ends of the robotic hand to ensure a secure and comfortable fit for each finger [22]. These caps are designed to minimize discomfort and provide stability during rehabilitation tasks, accommodating varying finger shapes and sizes.

C. Control Design

The control system of the proposed robotic hand optimizes finger extension through kinematic calculations. The cylindrical actuator extends and stabilizes the fingers while considering hand biomechanics. In stroke patients, paralysis affects the metacarpophalangeal (MCP), proximal interphalangeal (PIP), and distal interphalangeal (DIP) joints, making sudden extension risky [23]. Finger kinematics show that MCP movement initiates hand opening or closing, followed by PIP and DIP motion [24]. To prevent strain, the system restricts extension to the MCP joint while stabilizing the PIP and DIP joints, as illustrated in Fig. 3. The cylindrical actuator is fixed at the PIP joint, keeping the middle and distal phalanges immobile during extension.

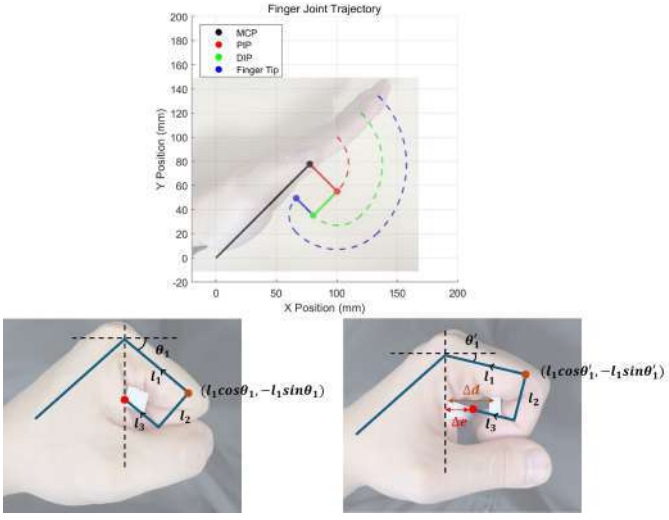


Fig. 3. Finger kinematics during hand flexion and extension.

The finger kinematic analysis is crucial to determining the minimum movement range required for the MCP joint to allow the robotic hand to be securely attached at the fingertips. Initially, the hand posture follows Eq. (1) while in a clenched state, and once the hand is extended, it follows Eq. (2).

$$l_1 cos\theta_1 - l_2 sin\theta_2 - l_3 cos\theta_3 = 0 \quad (1)$$

$$l_1 cos\theta_1' - l_2 sin\theta_2' - l_3 cos\theta_3' = \Delta e \quad (2)$$

where l_1, l_2, and l_3 represent the lengths of the Proximal Phalanx, Middle Phalanx, and Distal Phalanx. θ_1, θ_2, and θ_3 denote the flexion angles of the MCP, PIP, and DIP joints. θ_1', θ_2', and θ_3' represent the angles of the joints after the hand is extended. After finger flexion, Δe indicates the distance traveled by the fingertip from the initial pose.

The minimum linear displacement of the cylindrical actuator Δe, which is powered by the rack-and-pinion system introduced in the Finger Extension Mechanism, is set to 35 mm to accommodate fingertip attachment. Using Eq. (1) and Eq. (2), once θ_1' is determined, the desired displacement Δd can be calculated as follows Eq. (3).

$$\sqrt{(l_1 cos\theta_1' - l_1 cos\theta_1)^2 + (l_1 sin\theta_1 - l_1 sin\theta_1')^2} = \Delta d \quad (3)$$

D. General Operating Procedure

The donning process follows the sequence in Fig. 4. The user presses the red button to lock the cylindrical actuator (Fig. 4a). Using their non-affected hand, the stroke patient slightly opens the affected fingers, grasps the actuator, and wraps the wrist strap (Fig. 4b, 4c). Pressing the white button extends the actuator (Fig. 4d), guiding the clenched hand to a position where the robotic hand can attach at the fingertips (Fig. 4e). Finally, the robotic hand is secured, and pressing the red button again releases the hand from the system (Fig. 4f).

III. EXPERIMENTS

An experimental evaluation was conducted to comprehensively assess the efficiency and usability of the proposed robotic hand system during the donning process. The evaluation aimed to achieve two primary objectives: (1) to compare the time required for donning the robotic hand system with that of manual donning performed without assistance, and (2) to evaluate the level of comfort experienced by participants throughout the donning process.

The study involved five healthy participants (3 males, 2 females), each simulating the spasticity typically observed in stroke patients by wearing a custom-designed finger rigidity control glove, as illustrated in Fig. 5. The glove's adjustable cable stiffness was calibrated based on previous studies on stroke-related hand rigidity [25], [26]. As stroke severity increases, hand rigidity also intensifies, with stiffness values ranging from 0.4 to 0.9 N/mm depending on the level of spasticity. To replicate severe spasticity, the glove incorporated a spring with an average stiffness coefficient of 0.8 N/mm, ensuring that the resistance closely matched that of stroke patients with moderate to severe rigidity. By replacing the spring, the resolution of rigidity simulation can be refined,

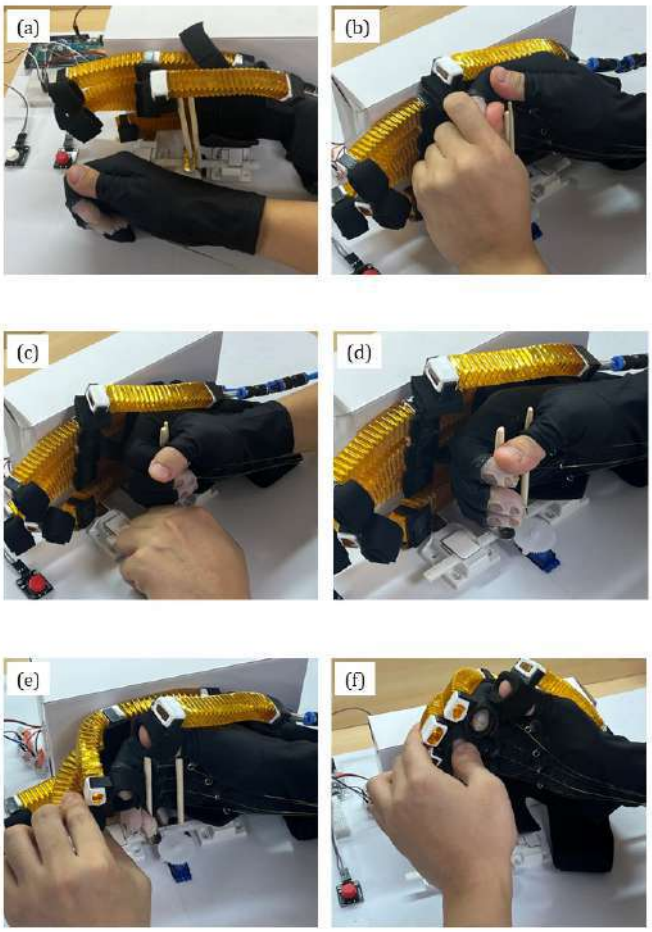


Fig. 4. Donning process of the robotic hand using the robotic hand system.

allowing for a more precise replication of varying spasticity levels.

The experiment was conducted with two conditions:

1) **Manual Donning:** Participants donned the robotic hand manually without any robotic assistance.
2) **System-Assisted Donning:** Participants donned the robotic hand using the proposed robotic system.

In both conditions, the time required to fully wear the robotic hand on the simulated affected hand was recorded. For Manual Donning, the recorded time refers to the duration required to wear the robotic hand completely. In contrast, for proposed System-Assisted Donning, the recorded time includes both the time to don the robotic hand using the system and the time required to detach the system afterward. Participants were instructed to minimize any voluntary finger movements in the simulated affected hand to replicate the limited mobility characteristic of spastic hands. To ensure reliability, participants were given sufficient time to familiarize themselves with the robotic system and the donning procedure prior to the trials. After completing the experiments, participants evaluated their perceived pain and convenience for each condition using a Likert-scale [27].

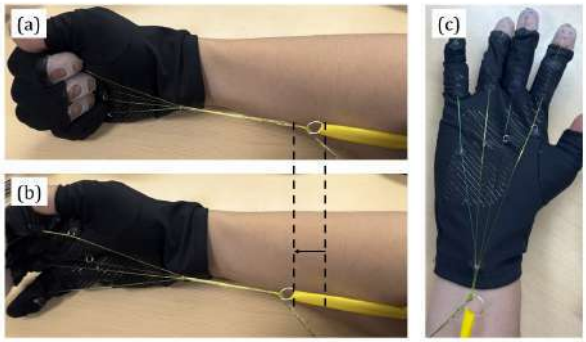


Fig. 5. A glove simulating the spasticity of a stroke patient's hand. Each finger joint is connected to a tensioner via wiring, with the tensioner stiffness adjustable to mimic varying levels of spasticity.

IV. RESULTS

A. Task Completion Time

All participants successfully completed the tasks in two randomized conditions, Manual Donning and System-Assisted Donning. For Manual Donning, the time required to fully attach the robotic hand was recorded. For System-Assisted Donning, the time to complete each step was measured according to Table II. In this setup, the timer continuously ran from the beginning, and lap times were recorded at the completion of each step.

TABLE II
SYSTEM-ASSISTED DONNING TASK ORDER AND DESCRIPTIONS

Task Step	Description
1	Extend the paralyzed hand fingers and grasp the cylindrical actuator.
2	Attach the wrist strap of the robotic hand.
3	Press the button to expand the hand.
4	Attach the robotic hand's fingertip caps to the fingers of the paralyzed hand.
5	Press the button and detach the hand wearing the robotic hand from the system.

Manual Donning required an average time of 98.68 ± 7.68 seconds. For System-Assisted Donning, the average completion times for each step were as follows: Step 1: $11.61 \pm 2.31s$, Step 2: $13.37 \pm 3.69s$, Step 3: $4.68 \pm 0.37s$, Step 4: $27.77 \pm 4.12s$, and Step 5: $9.45 \pm 0.63s$, with an overall completion time of $68.89 \pm 7.33s$ (Fig. 6). The difference in total completion time between the two conditions was an average of $98.68 \pm 7.68s$, demonstrating that System-Assisted Donning is more efficient than Manual Donning as shown in Fig. 7. A paired t-test was conducted between the two conditions (N=5, df=4), yielding a $p-value < 0.05, (T-statistic = 14.307)$, indicating a statistically significant difference between the conditions.

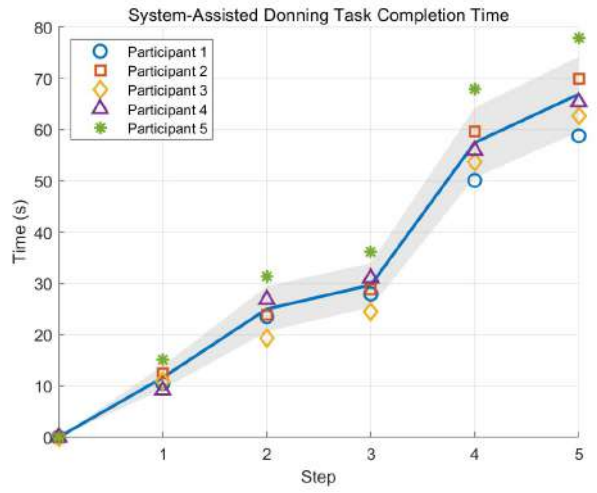


Fig. 6. Measured step-by-step task completion times for participants during System-Assisted Donning.

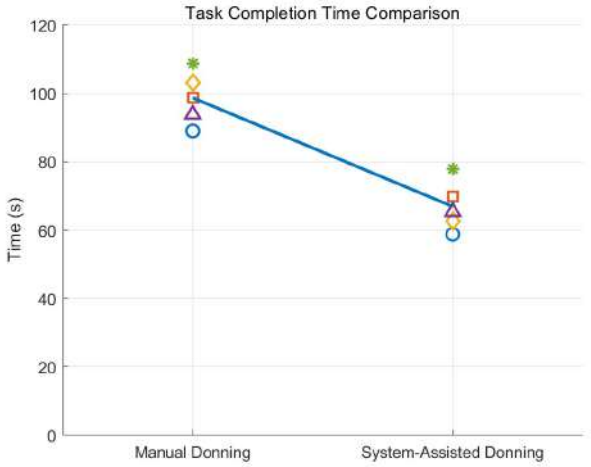


Fig. 7. Comparison of task completion times between Manual Donning and System-Assisted Donning. System-Assisted Donning significantly reduced overall task completion time compared to Manual Donning, as supported by statistical analysis ($p < 0.05$).

B. Usability Evaluation

After completing both conditions, participants evaluated the usability and pain level of the robotic hand donning process using a Likert scale questionnaire (Table. III).

For Manual Donning, the usability was rated at an average of 2 points, while the pain level was rated at 3.8 points. Participants reported difficulties due to the lack of a fixed mechanism to stabilize the robotic hand, which made it challenging to attach the hand to the participant's wrist. Furthermore, even when the fingers were extended, they tended to flex again, resulting in prolonged time and effort to insert the fingers into the robotic hand.

In contrast, for System-Assisted Donning, the usability was rated at an average of 4.4 points, with all participants providing scores of 4 or higher, and the pain level was rated at 2.2 points.

TABLE III
AVERAGE RATINGS FROM PARTICIPANTS (BLUE: MANUAL DONNING, RED: SYSTEM-ASSISTED DONNING) ON THEIR PERCEPTION OF THE ROBOTIC HAND DONNING PROCESS (PARTICIPANTS N = 5).

	1	2	3	4	5	
Difficult		2			4.4	Easy
No pain		2.2	3.8			Extreme pain

Participants highlighted that the system-assisted process was significantly easier and more comfortable compared to the manual method. They also noted that the automated assistance reduced physical strain on the wrist and fingers, making the process more effortless and less painful.

V. CONCLUSION AND DISCUSSION

This paper presents the effectiveness of the proposed system-assisted donning and doffing approach for a robotic hand. Statistical analysis revealed a significant reduction in task completion time ($p < 0.05$) for system-assisted donning compared to manual methods. A detailed analysis of Fig. 6 reveals that Task 3 in the system-assisted donning process required the shortest completion time. This suggests that the system effectively facilitates the extension and maintenance of clenched fingers, which is the most time-consuming step in manual donning. Conversely, Tasks 2 and 4 required the longest completion times. These steps involved securing the wrist strap and fitting the finger caps. This indicates potential areas for improvement, where modifications to the materials or the structural design of the robotic hand could further reduce task completion times and enhance overall efficiency. Additionally, The automated alignment during the doffing process ensures optimal positioning for subsequent use, thereby enhancing operational efficiency in iterative donning sessions. This improvement is particularly salient for users with impaired hand function, such as stroke survivors, where prolonged or complex donning procedures may induce fatigue or discomfort. User evaluation data indicated higher scores for ease of use (mean difference = 2.4) and lower reported pain levels (mean difference = -1.6) with the system-assisted approach. These findings suggest that the proposed system not only accelerates the donning process but also enhances user experience, presenting a viable solution for rehabilitation applications.

The proposed system has the potential to address critical challenges in the rehabilitation of stroke patients. By enabling independent donning of robotic devices, it reduces the need for caregiver assistance, thereby increasing accessibility and usability in home settings. A simple and straightforward donning process minimizes the need for patient training and external assistance, enabling immediate and independent use of the robotic system. This is especially valuable in remote or resource-limited areas where access to professional therapists may be restricted. Additionally, the reduction in physical strain and improved user satisfaction observed in this study suggest

that the system could alleviate some of the psychological and physical barriers associated with rehabilitation, encouraging patients to engage more consistently in therapy.

While this study showed promising results, the small sample size (N=5) included only healthy participants simulating stroke conditions, with occasional unintended muscle use potentially affecting results. Despite instructions to avoid using the muscles of the simulated paretic hand, participants occasionally relied on it for assistance, potentially influencing the results. Testing with real stroke survivors may pose challenges such as spasticity variability, cognitive impairments, and difficulties in independent donning. Addressing these factors is crucial for real-world usability. Additionally, the system's impact on long-term functional rehabilitation remains unassessed, requiring further investigation.

Future research should focus on integrating the system with advanced robotic functionalities, such as adaptive control mechanisms tailored to individual needs. Currently, the finger extension mechanism is fixed in a single position. To accommodate the variability in patients' affected hands—whether left or right—and their specific positioning, the actuator will be redesigned to adapt dynamically, ensuring optimal alignment for donning. Additionally, the extension speed and range of motion will be customized through user feedback, enabling personalized control for each patient.

Exploring the system's use in conjunction with task-specific training protocols could further enhance its rehabilitation outcomes. Longitudinal studies focusing on motor recovery and quality of life over extended periods are essential to comprehensively evaluate the system's therapeutic potential. Finally, efforts will be made to generalize the system beyond the POMA glove, creating a modular design compatible with a wide range of robotic hands. This integration will expand the system's applicability, allowing it to support diverse rehabilitation devices and scenarios effectively.

ACKNOWLEDGMENT

This work was supported by the Technology Innovation Program (Grant Number: 20014480) funded by the Ministry of Trade, Industry, and Energy (MOTIE, Korea). The 2024 Engineering-Medical interdisciplinary research program of Seoul National University (Grant # 800-20240492) The robotic hand POMA is provided by the Soft Robotics and Bionics Lab, Seoul National University, Seoul, Korea.

REFERENCES

[1] V. L. Feigin, B. Norrving, and George A. Mensah. "Global burden of stroke," Circulation research 120.3 (2017): 439-448.

[2] European Stroke Organisation (ESO) Executive Committee, and ESO Writing Committee. "Guidelines for management of ischaemic stroke and transient ischaemic attack 2008," Cerebrovascular diseases, 25.5, 2008, pp.457-507.

[3] J. Bamford et al., "Classification and natural history of clinically identifiable subtypes of cerebral infarction," The Lancet, 337.8756, 1991, pp.1521-1526.

[4] G. Kwakkel et al., "Effects of intensity of rehabilitation after stroke: a research synthesis," Stroke, 28.8, 1997, pp.1550-1556.

[5] P. Langhorne et al., "Early supported discharge services for stroke patients: a meta-analysis of individual patients' data," The Lancet, 365.9458, 2005, PP.501-506.

[6] S. M. Hatem, G. Saussez, M. Della Faille, V. Prist, X. Zhang, D. Dispa, and Y. Bleyenheuft, "Rehabilitation of motor function after stroke: a multiple systematic review focused on techniques to stimulate upper extremity recovery," Frontiers in human neuroscience, 10, 2016, p. 442.

[7] R. Kabir, M. S. H. Sunny, H. U. Ahmed, and M. H. Rahman, "Hand rehabilitation devices: A comprehensive systematic review," Micromachines, 13.7, 2022, p. 1033.

[8] B. Sheng, J. Zhao, Y. Zhang, S. Xie, and J. Tao, "Commercial device-based hand rehabilitation systems for stroke patients: State of the art and future prospects," Heliyon, 9.3, 2023.

[9] M. F. Bruni, et al., "What does best evidence tell us about robotic gait rehabilitation in stroke patients: a systematic review and meta-analysis," Journal of Clinical Neuroscience, 48, 2018, pp. 11-17.

[10] F. Vanoglio, et al., "Feasibility and efficacy of a robotic device for hand rehabilitation in hemiplegic stroke patients: a randomized pilot controlled study," Clinical rehabilitation, 31.3, 2017, pp. 351-360.

[11] R. Ranzani, et al., "Neurocognitive robot-assisted rehabilitation of hand function: a randomized control trial on motor recovery in subacute stroke," Journal of neuroengineering and rehabilitation, 17, 2020 pp. 1-13.

[12] C. Y. Chu and R. M. Patterson, "Soft robotic devices for hand rehabilitation and assistance: a narrative review," Journal of neuroengineering and rehabilitation, 15, 2018, pp. 1-14.

[13] A. Mohebbi, "Human-robot interaction in rehabilitation and assistance: a review," Current Robotics Reports, 1.3, 2020, pp. 131-144.

[14] P. D. E. Baniqued, et al., "Brain–computer interface robotics for hand rehabilitation after stroke: a systematic review," Journal of neuroengineering and rehabilitation, 18, 2021, pp. 1-25.

[15] R. Rätz, F. Conti, I. Thaler, R. M. Müri,and L. Marchal-Crespo, "Enhancing stroke rehabilitation with whole-hand haptic rendering: development and clinical usability evaluation of a novel upper-limb rehabilitation device," Journal of NeuroEngineering and Rehabilitation, 21(1), 2024, p. 172.

[16] C. E. Proulx, J. Higgins, and D. H. Gagnon, "Occupational therapists' evaluation of the perceived usability and utility of wearable soft robotic exoskeleton gloves for hand function rehabilitation following a stroke," Disability and Rehabilitation: Assistive Technology, 18.6, 2023, pp. 953-962.

[17] B. F. Kocyigit, M. I. Assylbek, and M. Yessirkepov, "Telerehabilitation: lessons from the COVID-19 pandemic and future perspectives," Rheumatology International, 44.4, 2024, pp. 577-582.

[18] J. Prvu Bettger, and L. J. Resnik, "Telerehabilitation in the age of COVID-19: an opportunity for learning health system research," Physical therapy, 100.11, 2020, pp. 1913-1916.

[19] Z. Zhang, et al., "Immediate effect of dry needling at myofascial trigger point on hand spasticity in chronic post-stroke patients: a multicenter randomized controlled trial," Frontiers in neurology, 12, 2021, p. 745618.

[20] C. Angerhöfer, et al., "The Berlin Bimanual Test for Tetraplegia (BeBiTT): development, psychometric properties, and sensitivity to change in assistive hand exoskeleton application," Journal of neuroengineering and rehabilitation, 20.1, 2023, p. 17.

[21] T. H. Hong, S. H. Park, J. H. Park, N. J. Paik, and Y. L. Park, "Design of pneumatic origami muscle actuators (POMAs) for a soft robotic hand orthosis for grasping assistance," In 2020 3rd IEEE International Conference on Soft Robotics (RoboSoft), 2020, pp. 627-632.

[22] Y. Lee and H. S. Park, "Design Optimization of a Soft Robotic Rehabilitation Glove Based on Finger Workspace Analysis," Biomimetics, 9.3, 2024, p. 172.

[23] H. C. Fischer, et al., "Hand rehabilitation following stroke: a pilot study of assisted finger extension training in a virtual environment," Topics in stroke rehabilitation, 14.1, 2007, pp. 1-12.

[24] I. Carpinella, J. Jonsdottir, and M. Ferrarin, "Multi-finger coordination in healthy subjects and stroke patients: a mathematical modelling approach," Journal of neuroengineering and rehabilitation, 8, 2011, pp. 1-20.

[25] F. Pisano, et al., "Quantitative measures of spasticity in post-stroke patients," Clinical Neurophysiology, 111.6, 2000, pp. 1015-1022.

[26] Ranzani, Raffaele, et al., "An online method to monitor hand muscle tone during robot-assisted rehabilitation," Frontiers in Robotics and AI, 10, 2023, 1093124.

[27] G. M. Sullivan and A. R. Artino Jr, "Analyzing and interpreting data from Likert-type scales," Journal of graduate medical education, 5.4, 2013, pp. 541-542.

Simultaneous Recognition of Locomotion Mode, Phase, and Phase Progression Using Deep Learning Models

Yekwang Kim
Department of Biomedical Engineering
Korea University College of Medicine
Seoul, Republic of Korea
yekwang@korea.ac.kr

Jaewook Kim
Department of Biomedical Engineering
Korea University College of Medicine
Seoul, Republic of Korea
jaewook_kim@korea.ac.kr

Juhui Moon
Department of Biomedical Engineering
Korea University College of Medicine
Seoul, Republic of Korea
answn520@korea.ac.kr

Mun-Taek Choi
School of Mechanical Engineering
Sungkyunkwan University
Suwon, Republic of Korea
mtchoi@skku.edu

Seung-Jong Kim
Department of Biomedical Engineering
Korea University College of Medicine
Seoul, Republic of Korea
sjkim586@korea.ac.kr

***Abstract*—Despite advances in gait-assist wearable robots, application in real-world scenarios remains limited, largely due to challenges in developing an effective user intention recognition algorithm. These algorithms are crucial as they enable the robot to move harmoniously with the user by predicting their intent during various locomotion activities such as level walking, stair ascent, stair descent, and sit-to-stand. It is essential to not only identify these locomotion modes but also their phases and progression for real-time assistance. Traditional classification methods often require extensive manual feature extraction from signals like those from inertial measurement units (IMU), electromyography, and plantar force sensors. Recent machine learning, particularly deep learning approaches, have simplified this process through automatic feature extraction. However, no existing method simultaneously predicts locomotion modes, phases, and phase progression, which is significant for personalized assistance. This study introduces a deep learning framework that classifies locomotion modes and phases and estimates the phase progressions using IMU data from sensors placed on the sternum and limbs. Results from five participants show that our model effectively classifies the locomotion phase and well estimates the phase progression percentage. The model was evaluated using a leave-one-subject-out approach, ensuring generalizability across different users.**

Keywords—Gait intention recognition, gait, deep learning, biomechanics, human computer interface

I. INTRODUCTION

Despite promising research, seldom are gait-assist wearable robots observed in real-world environments. One of the main challenges is identified to be the development of well-working user intention recognition algorithms. In order to appropriately assist the user, the robot must work in accordance with user's movements during locomotion which requires the prediction of the user's intent. Level walking (LW), stair ascent (SA), stair descent (SD), and sit-to-stand (StS), are composed of a series of biomechanically distinct phases that must be successfully executed in order to properly complete the task. Thus, the robots' control system must be able to accurately recognize not only the locomotion mode but also its phases and progression in order to generate optimal real-time assistance.

The classification of locomotion modes and estimation of gait cycle percentages, crucial for developing effective gait assistive technologies, have been extensively researched [1]–[8]. Numerous studies have introduced innovative classifiers tailored to various environments, focusing on distinguishing locomotion modes and phases. Traditional approaches often rely on feature extraction from signals obtained via sensors like inertial measurement units (IMUs), electromyography (EMG), and plantar force (PF) sensors [9]–[12]. These methods typically estimate joint trajectories and heel contacts but require significant manual intervention, making the process labor-intensive. Recent advancements in machine learning, particularly deep learning, have transformed this field. These models automatically extract relevant features, which simplifies the classification process. For instance, Huang et al. developed a support vector machine (SVM) model using EMG, PF, and IMU signals to classify five distinct locomotion modes: LW, SA, SD, ramp ascent, and ramp descent [3]. Studies by Kang and Zhu also explored classification using fewer signal modalities, such as only IMU data or a combination of IMU and encoder signals within CNN frameworks [2], [5]. These methods reduce system complexity and enhance practicality. Additionally, Wang et al. utilized long short-term memory (LSTM) models to StS

This research was supported by a grant of the Korea Health Technology R&D Project through the Korea Health Industry Development Institute (KHIDI), funded by the Ministry of Health & Welfare, Republic of Korea (grant number: RS-2022-KH129263).

activities and divide the gait cycle into distinct phases [13]–[15]. Despite these advancements, no current approach simultaneously predicts locomotion modes, phases, and phase progression percentages. Predicting phase percentage progression is significant because phase duration can vary due to individual differences, aging, and gait abnormalities, which can impact safety due to assistance that is not in phase with the user [16]–[20].

In this study, we introduce a deep learning model capable of classifying locomotion modes (LW, SA, SD, and StS) and their respective phases while also predicting phase progression. Our model utilizes data from five IMU sensors placed on the sternum and both thighs and shanks. The algorithm was evaluated on two fronts: the classification of locomotion modes and their phases, as well as phase progression regression. Results from five participants demonstrated the model's effectiveness in recognizing individual phases and their progression. Our algorithm has the potential to enhance the performance of wearable gait-assistive robots, ultimately improving user safety and comfort.

II. Materials and Methods

A. Participants

five healthy males (age: 32±5.2 years, height: 178.4±4.4cm, and weight: 86.2±3.2kg) that participated in this study had no prior history of lower limb injuries (previous 6 months). All participants provided a written informed consent and research ethics of human experiments was ensured by conducting the sessions in accordance with the contents approved by the Institutional Review Board of Korea University College of Medicine (IRB No. KUIRB-2024-0206-01). All experiments adhered to the approved guidelines and complied with the Declaration of Helsinki. The raw data supporting the findings of this study are available upon request to the corresponding author.

B. Activity Dataset Collection

In this investigation, we utilized a set of five IMU sensors (Trigno™ wireless system, Delsys Inc., Natick, MA, USA), positioned on both lower limbs as well as the sternum of each participant. The sensors were affixed to the lateral mid-thigh, mid-shank, and at the lower end of the sternum. Once the sensors were secured, participants were instructed to perform a series of locomotion tasks, including LW, SA, SD, and StS activities.

During the LW trials, participants executed 50 consecutive gait bouts, which began from a stationary standing posture, progressed four steps, and concluded to a complete stop. For the SA and SD trials, participants began from the same idle standing position and approached the staircase with several LW steps, then ascended or descended a set of 12 steps based on the specific trial, followed by additional LW steps before concluding to a complete stop. This LW-(SA/SD)-LW cycle was repeated 20 times for each subject. Additionally, participants undertook 100 iterations of the StS task, which comprised of sitting in a chair for 3 seconds, standing up, holding a stationary position for another 3 seconds, and then returning to a seated posture. There were no restrictions regarding the pace at which these activities were carried out.

C. Ground Truth Labeling

To ensure accurate ground truth labels for the time-series IMU data, we incorporated five additional 3-axis orientation sensors alongside pressure-sensitive insoles (Pedar-X™, Novel GmbH, Munich, Germany) during the experiments. The phases of LW, SA, and SD were identified via analysis of the PF patterns (Fig. 1). Knee joint angles, obtained via 3-axis orientation sensors affixed to the thighs and shanks, were used to label the phases of standing, sitting, sit-down, and stand-up (Fig. 1). Both the orientation sensors and pressure-sensitive insoles recorded data at a frequency of 100 Hz.

For data segmentation, we applied a sliding window approach of 500 msec (50 frames) with a stride length of 10 msec (1 frame) to create input datasets for the proposed deep learning model. Each data segment received a phase label along with a progression percentage. Because predicting the phase progression is crucial for safe and comfortable assistance in gait assistive robot control it is imperative that we are able to properly label the phase progression percentages. For static activities such as idle standing and sitting, where progression is not applicable, a phase progression of 0% was assigned. For dynamic phases, the beginning was labeled as 0% and the conclusion as 100% with intermediate frames proportionately divided. During gait initiation and termination, the phases and progressions were tagged as either SS 50% or SW 50%, depending upon which limb was used to initiate or terminate the locomotion (Fig. 1). For instance, if the left leg was in the swing phase at termination, the segment was labeled as SS 50%, while a right leg in the swing phase was marked SW 50%. Since the right limb was defined as the ipsilateral limb, SS was indicative of the SW phase for the left limb. The 50% progression designation was based on the observation that, upon initiating gait, the limb's lifted position aligns closely with the midway point of the swing phase. This holds true at the end of the locomotion cycle as well. The ground truth label for each input segment was thus determined from the phase and progression of the final frame within the 500 msec segment. The data segments were also categorized into 16 distinct phases, which include two idle phases (standing and sitting), as well as the sit-down, stand-up, and four phases each for LW, SA, and SD. Specifically, the phases for LW, SA, and SD were designated as DS1, SS, DS2, and SW, including the right limb as the ipsilateral limb. These classifications were guided by established literature that delineates the biomechanical criteria necessary for executing each locomotion phase[13]–[15], [21]–[23].

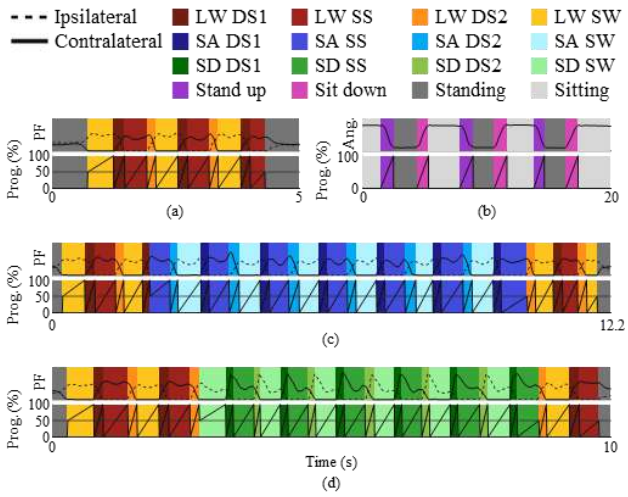


Fig. 1. Ground truth labeling. The locomotion modes, phases, and the phase progression percentages were labeled by assessing the PF for LW, SD, and SA, and the knee joint angles for StS. (a) Top row shows the PF for LW. As seen below, the gait phases are differentiated by the different shades. Also, the black line depicts the ground truth phase progression percentages. (b) The StS activity is shown. The different shaded areas depict the different phases: sitting, stand-up, standing, and sit-down. The phases were divided according to the knee angles shown in the upper row. (c) and (d) The SA and SD gait sessions are shown. For both cases, the upper rows show the PF patterns. The data shows that several LW steps were taken prior to SA or SD and a few LW steps were taken afterwards. The phases were divided according to the PF patterns, and phase progression percentages were assigned accordingly.

D. Deep Learning Model and Training

Our novel deep learning framework is designed as a two-stage sequential system, drawing inspiration from the framework previously proposed by Yu et al. [6]. In the first stage, a Bidirectional LSTM (Bi-LSTM) model is utilized to concurrently identify the locomotion type and its corresponding phases (Fig. 2a). The model processes inputs of the dimension (50, 30) and includes two Bi-LSTM layers, each with 50 units. These are followed by Dense layers with 50 and 32 units, activated via ReLU. The final layer, with 16 units, implements a softmax activation function to categorize the data into 16 distinct phases, capturing each unique combination of locomotion type and phase (Fig. 2b). Depending on which locomotion mode and phase are classified, if the locomotion mode is not idle (i.e., standing and sitting), the system selects one of 14 independent Bi-LSTM-based models to handle the input in order to perform phase percentage regression. The input is the same as the input that was fed to the model in the first stage (refer to Fig. 2c). These networks also receive inputs of size (50, 30) and are comprised of two Bi-LSTM layers, each with 50 units. The output layer is a single unit activating using a sigmoid function, while ReLU activation is applied throughout the preceding layers. Importantly, all 14 networks share consistent hyperparameters. This stage focuses on predicting the phase progression percentage using the model corresponding to the phase determined in the initial stage.

Development and training of the model were performed using TensorFlow (version 2.10.0) and Python (version 3.9.18). The Adam optimizer, with a batch size of 128 and for 50 epochs, was employed in all models. To mitigate overfitting, early stopping was implemented, and TensorFlow's hyperparameters were decided using a random search method.

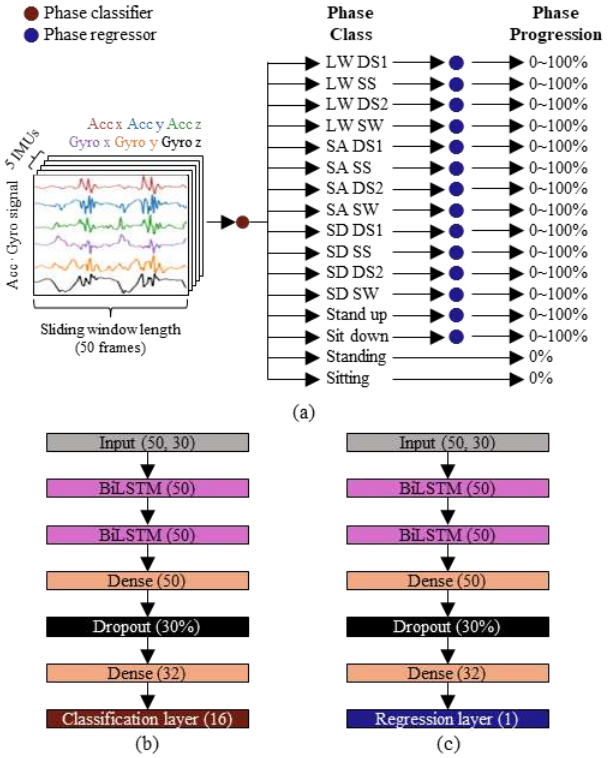


Fig. 2. Schematic of the proposed two-stage deep learning model for classifying locomotion mode and phase and predicting the phase progression percentage. (a) The input data is first fed to a phase classifier (red circle) which classifies the input data into 16 individual classes. For the 14 dynamic classes, the input data are used to estimate the phase progression percentage via a Bi-LSTM-based regressor (blue circle). (b) A Bi-LSTM-based model for phase classification. (c) A Bi-LSTM-based deep learning model for phase progression regression.

E. Evaluation Metrics

When dealing with the different nature of classification and regression outputs, it is essential to use appropriate evaluation metrics. For the classification of locomotion mode and phase, accuracy is a commonly used metric. Accuracy is the ratio of correctly predicted instances to the total number of instances. Nevertheless, relying solely on accuracy may be insufficient for assessing a model's performance. To gain deeper insights, metrics such as precision, recall, and F1-score are also employed. Precision indicates the proportion of true positive predictions among all positive predictions. Recall reflects the proportion of actual positive instances that were correctly identified by the model. The F1-score, which is the harmonic mean of precision and recall, offers a balanced evaluation of classification performance. The formulas for accuracy (A), precision (P), recall (R), and F1-score ($F1$) are as follows:

$$A = \frac{N_{tp}+N_{tn}}{N_{tp}+N_{tn}+N_{fp}+N_{fn}} \quad (1)$$

$$P = \frac{N_{tp}}{N_{tp}+N_{fp}} \quad (2)$$

$$R = \frac{N_{tp}}{N_{tp}+N_{fn}} \quad (3)$$

$$F1 = \frac{2PR}{P+R} \quad (4)$$

where N_{tp}, N_{tn}, N_{fp}, and N_{fn} are the number true positives, false positives, and false negatives, respectively.

Unlike binary classification problems, multiclassification problems require the use of macro-precision (P_{macro}), macro-recall (R_{macro}), and macro-F1 ($F1_{macro}$) metrics because there are multiple true positives. This also circumvents any biases that can occur due to data imbalances. The indices are calculated as shown below:

$$P_{macro} = \frac{1}{n}\sum_{1}^{n}\frac{N_{tp}}{N_{tp}+N_{fp}} \quad (5)$$

$$R_{macro} = \frac{1}{n}\sum_{1}^{n}\frac{N_{tp}}{N_{tp}+N_{fn}} \quad (6)$$

$$F1_{macro} = \frac{2P_{macro}R_{macro}}{P_{macro}+R_{macro}} \quad (7)$$

Where n is the number of classes. We additionally present the normalized confusion matrix, in which the columns correspond to predicted labels and the rows to actual labels. Consequently, the diagonal elements illustrate the probabilities of true positives, while the off-diagonal elements indicate the probabilities of misclassification. Furthermore, we evaluate the model's ability to identify transitions between phases of locomotion modes. This is measured using $\Delta t_{transition}$, as defined in Eq. 8, which denotes the average of the absolute time delays between the estimated and actual phase transition points. Various types of misclassifications such as negative delay, positive delay, and non-adjacent errors are illustrated in Fig. 3.

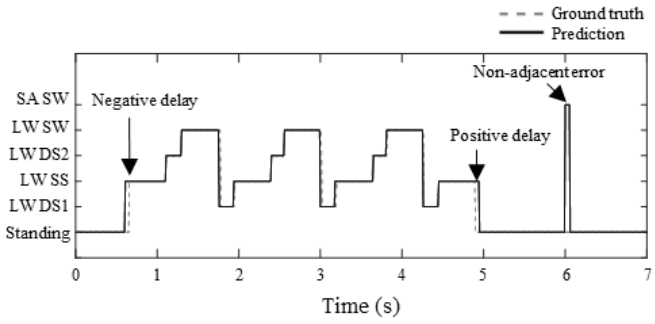


Fig. 3. Transient depiction of ground truth phases and predicted phases. The solid and dashed lines represent the predicted and ground truth phases, respectively. A negative delay is defined as instances where the subsequent phase is estimated in the current input, such that the prediction leads to the ground truth. Positive delays are the opposite, where the estimated class corresponds to the previous phase.

$$\Delta t_{transition} = \frac{1}{N_{transition}}\sum_{i=1}^{N_{transition}}|\hat{t_i} - t_i| \quad (8)$$

Where, $N_{transition}$ denotes the total number of phase transitions, and $\hat{t_i}$ and t_i represent the time of the estimated and ground truth transition, respectively. Also, phase percentage regressor was evaluated via root mean square error ($RMSE_{phase}$).

The evaluation techniques outlined above are suitable for analyzing individual subjects. To evaluate the model's performance across the entire group, we utilized a leave-one-subject-out strategy. This method allows for the assessment of the model's effectiveness on previously unseen subjects by setting aside one subject as the test sample while using data from the other subjects for training the model. This process was repeated for each of the 10 participants. Subsequently, median and quartile values were calculated to provide a comprehensive summary of the model's performance across all subjects.

III. Result

A. Classification Results

A total of 1,967,176 input data samples were evaluated in this study with 117,210 misclassifications leading to a median accuracy of 94.01%. The median P_{macro}, R_{macro}, and $F1_{macro}$ of the entire group was 88.19%, 90.96%, and 89.38%, respectively. The median $\Delta t_{transition}$ was 0.11 seconds and the confusion matrix for subject 1 is shown in Fig. 4. When we analyze the confusion matrix, we can observe that most of the misclassifications are adjacent to the diagonal line, which suggests that most misclassifications were due to negative or positive delays. This observation is further supported by the infrequent occurrence of non-adjacent errors that which were noted in less than 0.15% of instances (Fig. 5).

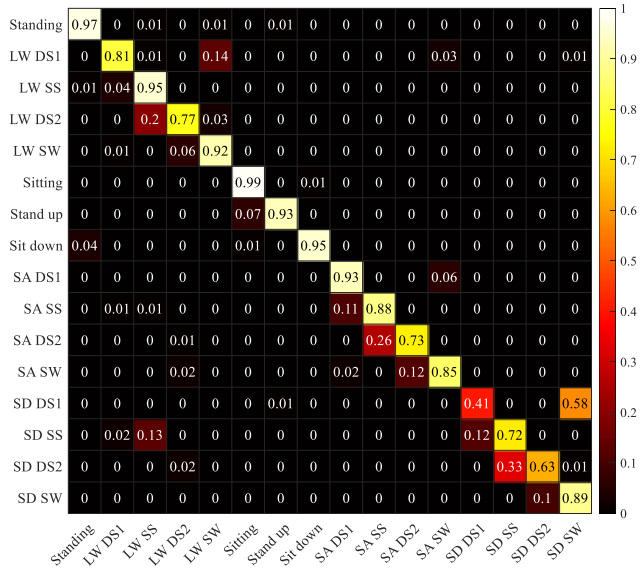


Fig. 4. Confusion matrix for all 16 activity phases for subject 1. The diagonal elements represent the probability of true positives.

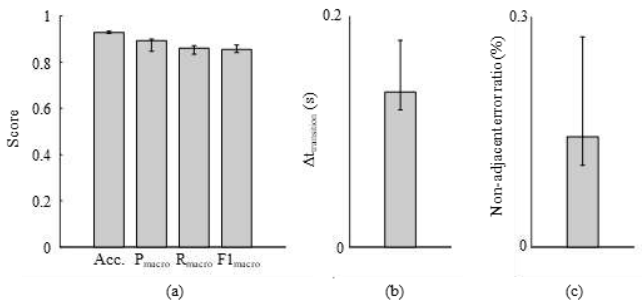


Fig. 5. Group analysis for activity phase classification. The accuracy, P_{macro}, R_{macro}, and $F1_{macro}$ are shown in (a), the $\Delta t_{transition}$ and non-adjacent error ratio are shown in (b) and (c), respectively. The data are represented as median and quartiles.

B. *Phase progression regression results*

To assess the performance of our model in predicting phase progression, we compared the regression trajectories against the ground truth, represented as red and black lines in Fig. 6, respectively. The trajectories for both the predicted and actual phases of LW, StS, SA, and SD are illustrated in Fig. 6a-d. It is evident that the red lines closely follow the black lines, indicating a strong regressor model. For a more quantitative evaluation, we computed the $RMSE_{phase}$ between our predictions and the ground truth values. The results indicated a median $RMSE_{phase}$ of 9.6% across all samples and 7.6% for only those that were correctly classified (Fig. 7). Although our model demonstrated reasonably good performance, we noted that the $RMSE_{phase}$ values for the DS phases of LW, SA, and SD were higher when compared to other phases. We previously categorized the phase progression for gait initiation and termination as either SW 50% or SS 50%, based on which limb initiated or concluded the locomotion mode. The findings presented in Fig. 6 and Fig. 7 suggest that our model effectively estimates phase progression in line with this classification.

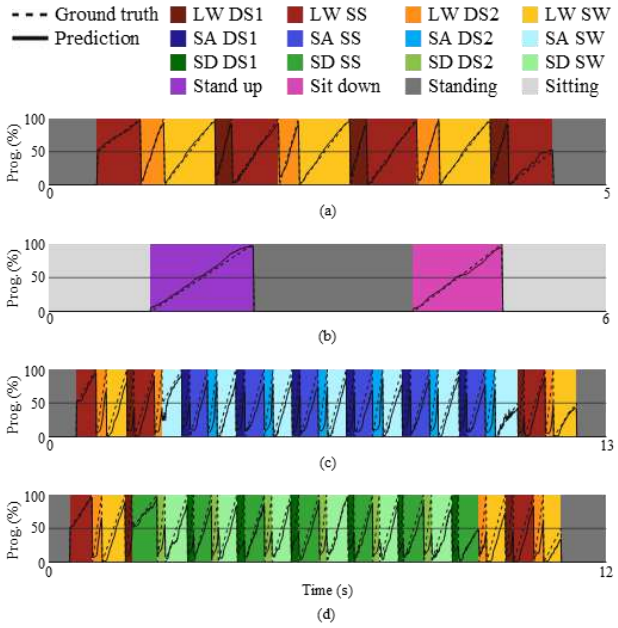


Fig. 6. Phase progression percentage regression results for subject 1. The solid and dashed lines represent the estimated phase progression percentage and ground truth, respectively. The results are shown from top to bottom for LW, StS, SA, and SD.

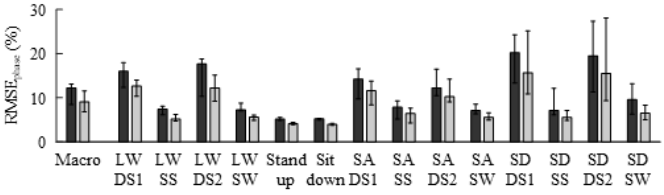


Fig. 7. Group analysis for phase progression percentage regression. The median $RMSE_{phase}$ all 14 dynamic locomotion mode phases for all sample data and only the correctly classified data are shown as black and grey bars, respectively. The error bars represent the quartiles.

IV. Discussion

In this study, we present a novel two-stage deep learning framework that employs a Bi-LSTM architecture for classifying locomotion phases, specifically focusing on locomotion with LW, SA, SD, StS actions. Additionally, we incorporate a 1-D CNN model to estimate phase progression percentages. The system processes kinematic data obtained from IMU sensors strategically placed on the thighs, shanks, and sternum of participants. Our experimental results, drawn from a study involving five subjects, indicate that our approach effectively classifies 16 distinct phases across the four locomotion modes while predicting their progression percentages. This assessment is supported by various performance metrics such as accuracy, P_{macro}, R_{macro}, $F1_{macro}$, and $RMSE_{phase}$. Notably, the model demonstrates low $\Delta t_{transition}$, highlighting its potential for integration into gait-assistive robotics, which require prompt actuator responses.

To elaborate, our phase classification algorithm achieved commendable median performance ratings, recording an accuracy of 94.01%, P_{macro} of 88.19%, R_{macro} of 90.96%, $F1_{macro}$ of 89.38%, along with a $\Delta t_{transition}$ of just 0.11 seconds. A thorough examination of the confusion matrix revealed patterns in classification errors; for instance, while phases involving sitting, standing, sit-down, and stand-up movements were predominantly accurate, certain dynamic segments (DS phases) occasionally faced misclassification into adjacent phases. This suggests that while our classification model operates effectively, transitional errors primarily emerge during phase transitions. In addition, our regression model for phase progression displayed robust performance, underscored by a low $RMSE_{phase}$ value of 7.6%.

However, our study has its set of limitations. The participant pool was restricted to five healthy individuals, excluding those requiring assistive support for gait tasks or individuals with gait abnormalities, who represent the intended audience for our model. Moreover, the locomotion mode classification and phase progression models have yet to undergo real-time testing. For future application in practical settings, the system must efficiently process input from five IMU sensors with data dimensions of (50, 30) on a mobile platform. Furthermore, although the model is intended for gait intention recognition in wearable robotics, it has not yet been deployed on actual robotic systems. Additionally, it may be pointed out that our deep learning model may not be optimal, considered that it has not been compared to state-of-the-art deep learning models such as attention mechanisms and transformers. Finally, to suit gait assistive robots, the system should operate free of positive delays, fostering timely assistance prior to robotic actuation. We propose that a possible solution lies in adjusting label shifts in the dataset to reflect predictive outcomes rather than exact ground truths.

Future investigations will aim to assess the model's efficacy across a broader demographic, including the elderly and individuals with anomalous gait patterns or disabilities. Additional focus will be placed on expanding the dataset to encapsulate a wider array of activities and corresponding

phases. For certain intricate movements, the deployment of five IMU sensors may prove inadequate, thus requiring supplementary sensors or a multimodal approach encompassing varied sensor technologies. Moreover, we will explore the model's real-time operational capabilities using IMUs in conjunction with single-board computers, paving the way for applications in health monitoring, diagnostic procedures, and the enhancement of gait-assistive robotic technologies.

REFERENCES

[1] C. Wang, X. Wu, Y. Ma, G. Wu, and Y. Luo, 'A flexible lower extremity exoskeleton robot with deep locomotion mode identification', *Complexity*, vol. 2018, 2018, doi: 10.1155/2018/5712108.

[2] L. Zhu et al., 'A novel motion intention recognition approach for soft exoskeleton via IMU', *Electronics (Switzerland)*, vol. 9, no. 12, pp. 1–18, Dec. 2020, doi: 10.3390/electronics9122176.

[3] H. Huang, F. Zhang, L. J. Hargrove, Z. Dou, D. R. Rogers, and K. B. Englehart, 'Continuous locomotion-mode identification for prosthetic legs based on neuromuscular - Mechanical fusion', *IEEE Trans Biomed Eng*, vol. 58, no. 10 PART 1, pp. 2867–2875, Oct. 2011, doi: 10.1109/TBME.2011.2161671.

[4] J. Wang et al., 'Integral Real-time Locomotion Mode Recognition Based on GA-CNN for Lower Limb Exoskeleton', *J Bionic Eng*, vol. 19, no. 5, pp. 1359–1373, Sep. 2022, doi: 10.1007/s42235-022-00230-z.

[5] I. Kang, D. D. Molinaro, G. Choi, J. Camargo, and A. J. Young, 'Subject-Independent Continuous Locomotion Mode Classification for Robotic Hip Exoskeleton Applications', *IEEE Trans Biomed Eng*, vol. 69, no. 10, pp. 3234–3242, Oct. 2022, doi: 10.1109/TBME.2022.3165547.

[6] S. Yu et al., 'Artificial Neural Network-Based Activities Classification, Gait Phase Estimation, and Prediction', *Ann Biomed Eng*, vol. 51, no. 7, pp. 1471–1484, Jul. 2023, doi: 10.1007/s10439-023-03151-y.

[7] I. Kang, D. D. Molinaro, S. Duggal, Y. Chen, P. Kunapuli, and A. J. Young, 'Real-Time Gait Phase Estimation for Robotic Hip Exoskeleton Control during Multimodal Locomotion', *IEEE Robot Autom Lett*, vol. 6, no. 2, pp. 3491–3497, Apr. 2021, doi: 10.1109/LRA.2021.3062562.

[8] A. Narayan, F. A. Reyes, M. Ren, and Y. Haoyong, 'Real-Time Hierarchical Classification of Time Series Data for Locomotion Mode Detection', *IEEE J Biomed Health Inform*, vol. 26, no. 4, pp. 1749–1760, Apr. 2022, doi: 10.1109/JBHI.2021.3106110.

[9] M. Hassan, H. Kadone, K. Suzuki, and Y. Sankai, 'Wearable gait measurement system with an instrumented cane for exoskeleton control', *Sensors (Switzerland)*, vol. 14, no. 1, pp. 1705–1722, Jan. 2014, doi: 10.3390/s140101705.

[10] W. Huo, S. Mohammed, J. C. Moreno, and Y. Amirat, 'Lower Limb Wearable Robots for Assistance and Rehabilitation: A State of the Art', Sep. 01, 2016, *Institute of Electrical and Electronics Engineers Inc*. doi: 10.1109/JSYST.2014.2351491.

[11] D. Wang, X. Gu, and H. Yu, 'Sensors and algorithms for locomotion intention detection of lower limb exoskeletons', Mar. 01, 2023, Elsevier Ltd. doi: 10.1016/j.medengphy.2023.103960.

[12] O. Mounir Alaoui, 'Developing a Human-Machine Control Interface for the Detection of Motion Intentions in a Self-Balanced Lower-Limb Exoskeleton'. [Online]. Available: https://theses.hal.science/tel-03866856v1

[13] H. Jeon and D. Lee, 'Bi-Directional Long Short-Term Memory-Based Gait Phase Recognition Method Robust to Directional Variations in Subject's Gait Progression Using Wearable Inertial Sensor', *Sensors*, vol. 24, no. 4, Feb. 2024, doi: 10.3390/s24041276.

[14] Z. Zhang, Z. Wang, H. Lei, and W. Gu, 'Gait phase recognition of lower limb exoskeleton system based on the integrated network model', *Biomed Signal Process Control*, vol. 76, Jul. 2022, doi: 10.1016/j.bspc.2022.103693.

[15] K. Liu, Y. Liu, S. Ji, C. Gao, S. Zhang, and J. Fu, 'A Novel Gait Phase Recognition Method Based on DPF-LSTM-CNN Using Wearable Inertial Sensors', *Sensors*, vol. 23, no. 13, Jul. 2023, doi: 10.3390/s23135905.

[16] E. Watelain, F. Barbier, P. Allard, A. Thevenon, and J. C. Angué, 'Gait pattern classification of healthy elderly men based on biomechanical data', *Arch Phys Med Rehabil*, vol. 81, no. 5, pp. 579–586, 2000, doi: 10.1053/mr.2000.4415.

[17] M. S. Kwon, Y. R. Kwon, Y. S. Park, and J. W. Kim, 'Comparison of gait patterns in elderly fallers and non-fallers', in *Technology and Health Care, IOS Press*, May 2018, pp. S427–S436. doi: 10.3233/THC-174736.

[18] I. N. Afiah, H. Nakashima, P. Y. Loh, and S. Muraki, 'An exploratory investigation of changes in gait parameters with age in elderly Japanese women', *Springerplus*, vol. 5, no. 1, Dec. 2016, doi: 10.1186/s40064-016-2739-7.

[19] J. Kim et al., 'Gait patterns of chronic ambulatory hemiplegic elderly compared with normal Age-Matched elderly', *International Journal of Precision Engineering and Manufacturing*, vol. 16, no. 2, pp. 385–392, Feb. 2015, doi: 10.1007/s12541-015-0051-z.

[20] A. R. Den Otter, A. C. H. Geurts, T. Mulder, and J. Duysens, 'Abnormalities in the temporal patterning of lower extremity muscle activity in hemiparetic gait', *Gait Posture*, vol. 25, no. 3, pp. 342–352, Mar. 2007, doi: 10.1016/j.gaitpost.2006.04.007.

[21] Jacquelin. Perry, J. M. . Burnfield, and L. M. . Cabico, Gait analysis : normal and pathological function. CRC Press, 2024.

[22] A. Kharb, V. Saini, Y. K. Jain, and S. Dhiman, 'A review of gait cycle and its parameters', 2011. [Online]. Available: www.IJCEM.orgIJCEMwww.ijcem.org

[23] X. Wu, Y. Yuan, X. Zhang, C. Wang, T. Xu, and D. Tao, 'Gait Phase Classification for a Lower Limb Exoskeleton System Based on a Graph Convolutional Network Model', *IEEE Transactions on Industrial Electronics*, vol. 69, no. 5, pp. 4999–5008, May 2022, doi: 10.1109/TIE.2021.3082067.

Introducing V-Soft Pro: a Modular Platform for a Transhumeral Prosthesis with Controllable Stiffness

Giuseppe Milazzo, Giorgio Grioli, Antonio Bicchi, and Manuel G. Catalano

***Abstract*— Current upper limb prostheses aim to enhance user independence in daily activities by incorporating basic motor functions. However, they fall short of replicating the natural movement and interaction capabilities of the human arm. In contrast, human limbs leverage intrinsic compliance and actively modulate joint stiffness, enabling adaptive responses to varying tasks, impact absorption, and efficient energy transfer during dynamic actions. Inspired by this adaptability, we developed a transhumeral prosthesis with Variable Stiffness Actuators (VSAs) to replicate the controllable compliance found in biological joints. The proposed prosthesis features a modular design, allowing customization for different residual limb shapes and accommodating a range of independent control signals derived from users' biological cues. Integrated elastic elements passively support more natural movements, facilitate safe interactions with the environment, and adapt to diverse task requirements. This paper presents a comprehensive overview of the platform and its functionalities, highlighting its potential applications in the field of prosthetics.**

I. Introduction

Limb loss brings profound challenges to individuals, affecting not only their motor capabilities but also their emotional well-being and social lives. Prosthetic devices help bridge this gap by restoring the natural appearance of the human body and some functional capabilities of human limbs. However, current prostheses fall short of replicating the complex functionality of natural limbs, focusing mainly on enabling users to achieve a basic level of self-sufficiency with essential motor functions.

Myoelectric upper-limb prostheses represent the current frontier in human-like limb restoration and natural motor control. However, robotic prostheses often rely on rigid joints, which lack the fluid, adaptive behavior that human limbs exhibit in motion and interaction with the environment. Humans voluntarily adjust the impedance of their limbs by coactivating antagonistic muscles. This adaptive strategy provides flexible and responsive limb behavior: a compliant approach reduces applied force during constrained tasks and allows safe exploration in unfamiliar environments, while high stiffness enables precision tasks and counters external forces effectively [1]–[4]. Inspired by this capability, it is clear that upper-limb prosthetic devices should incorporate mechanisms for users to actively control impedance, which would enhance both versatility and task performance [4], [5]. Unlike human limbs, rigid joints lack the adaptability provided by passive compliance and controllable stiffness. Rigid devices are also less suitable for safe interaction in unstructured and dynamic environments, where humans frequently face unpredictable conditions in daily life. Unable to absorb shocks, these devices increase the risk of harm to people and objects during unintended collisions, which are common due to a lack of proprioceptive feedback. Furthermore, rigid prostheses are limited in their ability to apply low interaction forces, making delicate interactions with fragile objects challenging.



Fig. 1. Two configurations of the V-Soft Pro transhumeral prosthesis, customized to meet diverse user needs. Panel (a) illustrates a V-Soft Pro configuration designed to achieve a human-like weight distribution for proximal transhumeral amputations. Panel (b) shows a version of the V-Soft Pro platform adapted for users with longer residual limbs.

Impedance control has revolutionized robotic applications that require physical interaction with the environment and cooperation with humans [6]–[9], enabling robots to follow planned paths during free motion and supervise interaction forces when encountering obstacles along the path. Impedance control can be implemented in standard torque-controlled robots simply via software. However, it relies on high-performance sensors, actuators, and computing, making it well-suited for most industrial applications but difficult to integrate into portable robotic devices with limited battery life and performance, such as prostheses [10]. An alternative approach is to embed variable impedance characteristics directly into the robot hardware design [11]–[13]. On one hand, Variable Impedance Actuators (VIAs) involve complex hardware implementations, as they require dedicated mechanisms to alter the physical properties of the joint. On the other hand, they often rely on simple software control

This work was supported by the European Union's ERC Synergy Natural BionicS under Grant ID 810346. The content of this publication is the sole responsibility of the authors. The European Commission or its services cannot be held responsible for any use that may be made of the information it contains.

Corresponding author: Giuseppe Milazzo. email: giuseppe.milazzo@iit.it

All the authors are with Soft Robotics for Human Cooperation and Rehabilitation, Istituto Italiano di Tecnologia, Genova 16163, Italy.

G. Grioli and A. Bicchi are also with the Research Center "Enrico Piaggio" & Department of Information Engineering, University of Pisa, Pisa 56126, Italy.

This article has supplementary downloadable material available at `https://ieeexplore.ieee.org`, provided by the authors.

and are intrinsically robust and versatile, as joint impedance is dictated passively by the physical properties of the joint. Among VIAs, VSAs integrate redundant actuation and non-linear elastic transmissions into their mechanical design, allowing them to adjust output stiffness by controlling the active deflection of elastic elements, akin to antagonistic muscle coactivation.

This paper introduces V-Soft Pro (V-SP), a modular platform for an active transhumeral prosthesis with user-controllable stiffness. The platform consists of two elbow modules, three wrist modules, and two hand modules, which can be combined to create a transhumeral prosthesis tailored to the user's limb morphology and the available biosignals for control. While some of the V-SP modules have been previously presented and characterized in our past works [14], [15], this paper focuses on their integration into a customizable transhumeral prosthesis with variable stiffness (VS). Section II provides an overview of the state of the art in transhumeral prostheses and VS prosthetic joints. Section III details the V-SP hardware design and the implementation of its submodules. Section IV presents the hardware integration of two different configurations of the V-SP platform and demonstrates the functionality of the VS transhumeral prostheses. Section V discusses potential applications and limitations of the system, and conclusions are provided in Section VI.

II. Related Work

Robotic upper limb prostheses typically feature rigid actuation and fixed impedance properties. However, some elbow and wrist prostheses offer a transition between two discrete stiffness levels (locked or unlocked) by activating a locking mechanism through electromyographic (EMG) control or with the contralateral arm. For instance, elbow prostheses[1,2] can be locked to support external weights or unlocked to swing freely during walking [16]. Similarly, spring-loaded flexion wrists[3] can be unlocked to exploit environmental constraints during grasping or locked to resist perturbations [17]. While these locking mechanisms provide some degree of task adaptability, they lack the natural ability to smoothly and accurately control joint stiffness. VSAs have recently been applied in prosthetics due to their similarity to the human musculoskeletal system in terms of interaction and joint stiffness regulation. Recent studies report applications of VSAs in standalone VS prosthetic joints, including ankle-foot [18]–[20], hand [21], wrist [15], and elbow [14], [22] prostheses. However, multiple VS joints have never been integrated into a single transhumeral prosthesis.

Wrist prostheses are often significantly streamlined to reduce overall complexity. These prosthetic wrists are typically passive and usually feature a limited number of degrees of freedom (DoFs), prioritizing wrist pronation/supination (wPS), occasionally implementing wrist flexion/extension (wFE), and rarely incorporating radial/ulnar deviation (RUD) [23]–[25].

Developing human-like bionic hands has been a longstanding challenge in upper limb prosthetics research. Due to the remarkable complexity and versatility of human hands, artificial hands inevitably require a trade-off between functionality and complexity. Polyarticulated hand prostheses are sophisticated devices that typically include a set of pre-installed standard grips, each designed for a specific task [26]–[29]. However, these dexterous devices are often abandoned due to their increased weight, cognitive load, and the frustration of selecting the desired grasping strategy [30], [31]. In contrast, soft hands are easier to use, as their compliant designs allow passive adaptation to object shapes. Additionally, some can modulate stiffness to enhance precision and grasp strength, utilizing technologies such as pneumatic actuators, shape memory alloys, or cable-driven actuation [32].

Bionic limb replacement becomes more challenging as the level of amputation grows, and prosthetic devices must implement a higher number of motor functions while respecting strict morphological (i.e., size and weight) and functional (i.e., range of motion, torque, speed, and battery life) requirements [14], [15], [33], [34]. Consequently, transhumeral prostheses often omit some biological DoFs and leave small space for user-centered customizations due to restrictive design constraints [16], [35]–[38].

III. The V-Soft Pro Platform

The V-SP platform features a modular design, outlined in Fig. 2, allowing users to select the most suitable configuration based on their individual residual limb morphology, number of independent control channels, and daily needs. The platform includes the VS-Elbow, presented in [14], which offers two different layouts designed to optimize ergonomics and biomimicry for both distal and proximal transhumeral amputations. Additionally, users can choose from three prosthetic wrists, depending on their ability to control numerous DoFs. The V-SP platform includes the VS-Wrist [15], a prosthetic wrist with 3 active DoFs and controllable stiffness, along with two commercial wrists: the Ottobock Wrist Rotator[4] and the Ottobock Quick Disconnect Wrist[5]. Additionally, the V-SP platform is compatible with two prosthetic hands: the SoftHand Pro and SoftHand 2. This flexibility allows the user to choose from terminal devices with varying levels of dexterity, depending on their myoelectric control skills and daily needs.

A. Elbow Module

The VS-Elbow is a prosthetic elbow featuring redundant actuation and non-linear elastic transmission, which allows for decoupled control of elbow stiffness and position. The VS-Elbow features a single kinematic DoF that actuates elbow flexion/extension (eFE). However, the device incorporates two DC motors, which drive the elbow shaft through an open timing belt. Belt tension is adjusted via a lever arm

[1]Fillauer Utah Arm U3
[2]Ottobock Dynamic Arm
[3]Touch Bionics Flexion Wrist
[4]Ottobock Wrist Rotator
[5]Ottobock Quick Disconnect Wrist

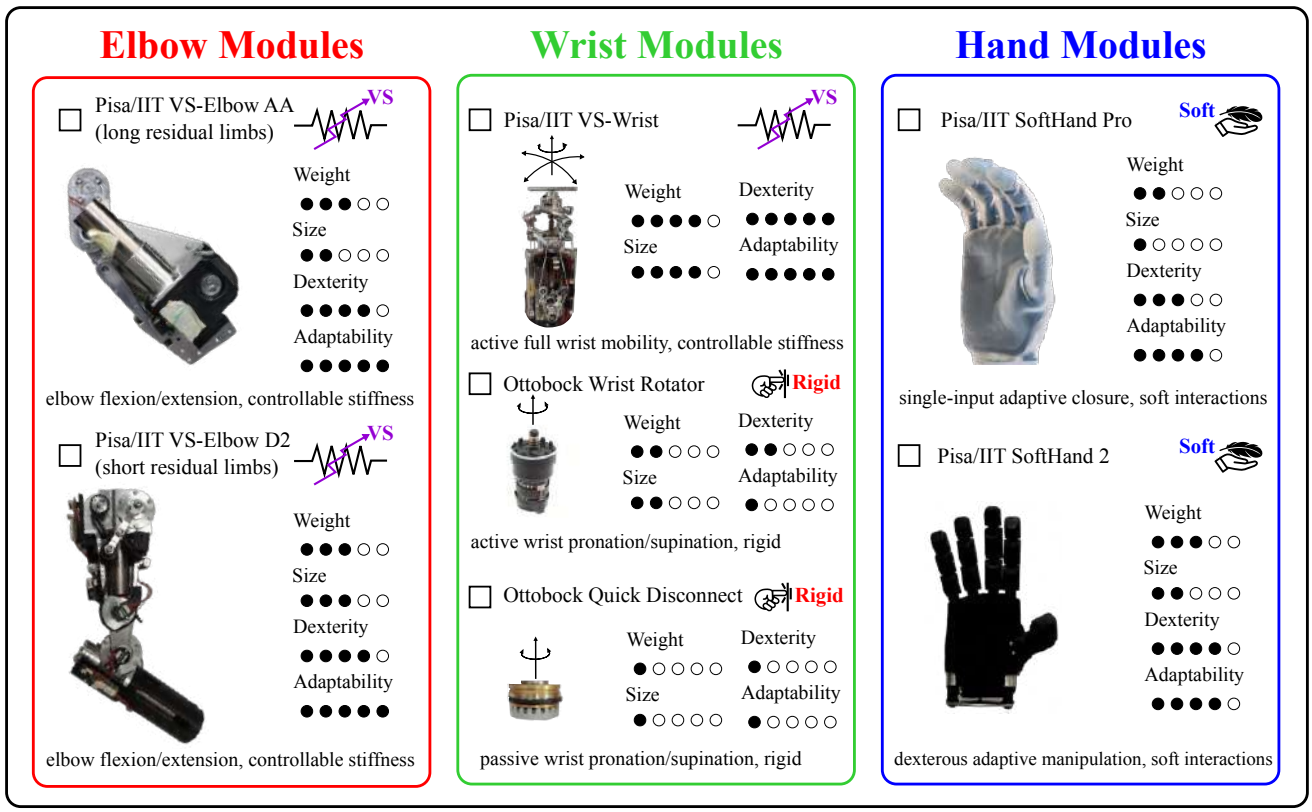


Fig. 2. The V-Soft Pro platform. The V-Soft Pro transhumeral prosthesis supports a modular design that can be customized to meet the diverse needs of end-users, including residual limb morphology, required dexterity, comfort with device weight, and available control inputs.

mechanism that affects the active deflection of extension springs. By leveraging redundant actuation, the VS-Elbow adjusts the active length of the transmission belts, thereby modifying the preload on the elastic transmission and regulating elbow stiffness. This mechanism of stiffness regulation is analogous to the coactivation of agonist-antagonist (AA) muscle groups, such as the biceps and triceps brachii. Each DC motor is equipped with a planetary gearbox and a worm gear to amplify output torque, ensuring sufficient performance for standard activities of daily living, such as actively lifting payloads of up to 3 kg. The motor transmission is designed to be non-backdrivable, enabling the VS-Elbow to support payloads and maintain high stiffness passively, which in turn improves battery efficiency. The output joint is decoupled from the motor shaft, ensuring compliant behavior and maintaining the imposed stiffness even when the system is powered off.

The VS-Elbow is available in two different layouts to accommodate the diverse morphologies of residual limbs. The VS-Elbow AA adopts a VSA with an AA configuration, where one elastic actuator represents the triceps brachii and the other represents the biceps brachii. Thus, the net torque generated by one branch relative to the other produces elbow flexion or extension, while their magnitudes determine the joint stiffness. The AA design results in a compact form factor that can be fully contained within the forearm segment of the bionic limb. Due to this feature, the VS-Elbow can be adapted to fit proximal transhumeral amputations while meeting the restrictive functional and morphological requirements of upper limb prostheses, and it can achieve symmetry with the contralateral elbow axis of rotation. However, since the weight of the elbow prosthesis is concentrated in the forearm, the VS-Elbow AA may not offer optimal comfort for individuals with distal transhumeral amputations, as it leaves unused space in the upper limb segment.

Addressing individuals with short residual limbs, V-Soft Pro features the VS-Elbow D2, a prosthetic elbow that evenly distributes its mass and volume between the upper limb and forearm. This unique design ensures a human-like mass distribution, enhancing ergonomics and promoting natural movement for distal transhumeral amputees [14]. The VS-Elbow D2 is a VSA with an Explicit Stiffness Variation layout, where the two DC motors operate independently to control either the position or the stiffness of the joint. The stiffness motor is located in the upper limb segment and modulates joint stiffness by adjusting the preload of two elastic transmission mechanisms. These non-linear springs are configured to function as an AA system, ensuring symmetry of joint stiffness during both flexion and extension. Conversely, the position motor is located in the forearm segment and drives eFE by rotating the forearm around the fixed elbow shaft.

B. Wrist Module

The wrist module of V-Soft Pro can be customized to accommodate the final user's available control channels and daily needs. The VS-Wrist is the most advanced wrist module in the platform, featuring 3 active DoFs and user-controllable stiffness. It is the first prosthetic wrist designed to actively restore all human wrist DoFs while providing decoupled stiffness control across a continuous range through modulation of non-linear spring preload. Typically, a 3-DoF VSA requires 6 motors, resulting in significant bulk and weight that would hinder prosthetic applications. However, the VS-Wrist utilizes a hybrid parallel-serial architecture to achieve 3 kinematic DoFs and user-controllable stiffness within a compact design, requiring only 4 motors. The parallel manipulator (PM) offers a hemispherical range of motion, enabling wrist flexion/extension (wFE) and radial/ulnar deviation (RUD). Although it has two DoFs, the PM is redundantly actuated by three DC motors through a non-linear elastic transmission. This architecture allows modulation of internal forces to the PM, thereby adjusting the preload on the non-linear springs without affecting the wrist equilibrium position, and enabling decoupled stiffness and position control. Similar to the VS-Elbow, each motor transmission incorporates a planetary gearbox and a worm drive, achieving non-backdrivability to maintain static loads without power consumption. Furthermore, the VS-Wrist includes a dedicated motor unit that actuates wrist pronation/supination (wPS) through two opposed universal joints, positioned at the center of the PM.

V-Soft Pro is also compatible with two simpler commercial prosthetic wrists, offering options for users with fewer control inputs or those preferring a lighter device, although at the expense of some functionalities. The Ottobock Wrist Rotator is a commercial myoelectric wrist that supports EMG control of wPS, while wFE and RUD are blocked. The Ottobock Quick Disconnect Wrist is more compact but allows only passive wPS, which the user can actuate using the contralateral arm.

C. Hand Module

The SoftHand Pro [39] uses a single motor to actuate 19 DoFs, replicating the kinematics and morphology of a human hand. Each finger consists of three rigid modules, similar to phalanges, with the thumb comprising only two segments. These phalange modules are 3D-printed and available in various sizes. Elastic joints connect consecutive phalanges, ensuring robust and safe interaction with the environment. In this way, rigid links, representing bones, are connected by elastic bands that function like ligaments. A differential transmission evenly distributes contact forces across all fingers, enabling the hand to grasp objects of various shapes. Thanks to the mechanical intelligence inherent in its design, the SoftHand Pro is intuitive to use, allowing users to execute a variety of grasping strategies that passively adapt to different shapes with a single closing command. For users with advanced EMG control skills, the SoftHand 2 introduces an additional synergistic actuator, expanding the range of grasping, manipulation, and fine gesture capabilities [40]. The SoftHand also features a silicone glove or rubber pads, enhancing grasp stability and offering a customizable cosmetic appearance.

IV. Experiments

We present the integration of the V-SP platform in two distinct configurations. The first configuration includes the VS-Elbow D2, the VS-Wrist, and the SoftHand Pro, providing a total of 5 DoFs for kinematics and 2 DoFs for stiffness control. The second configuration utilizes the VS-Elbow AA, the Ottobock Wrist Rotator, and the SoftHand 2, offering 4 kinematic DoFs and 1 DoF to control elbow stiffness.

Each motor position is regulated by a dedicated PID controller operating at 200 Hz, which modulates the duty cycle of a 20 kHz PWM signal. The system is powered by a single 24 V commercial battery. An external laptop, running a Matlab Simulink graphic user interface, enables the user to set position and stiffness references for each prosthetic joint, as well as to monitor encoder and EMG signals in real-time.

We report preliminary lab tests demonstrating the varying degrees of prosthesis functionality achievable through customization of the modular V-SP platform. A comprehensive technical characterization of the V-SP platform submodules can be found in [14], [15], [39], [40]. Fig. 3 presents photo sequences extracted from the multimedia material accompanying this paper. Fig. 3a illustrates the first configuration of the V-SP system during coordinated active motion of all prosthetic joints, highlighting its high wrist mobility. Fig. 3b depicts the second configuration of the V-SP system, where the prosthesis adjusts its elbow stiffness to adapt to different tasks. This adaptability suggests the enhanced versatility of V-SP prostheses in unstructured environments. The V-SP transhumeral prosthesis can reduce elbow stiffness to accommodate obstacles along its path and comply with external forces, enabling gentle interactions. Conversely, it increases elbow stiffness to reject disturbances and support precision tasks.

V. Discussion

Current robotic prostheses significantly enhance the quality of life for upper limb amputees. However, they typically incorporate simplified motor functions and lack the natural compliance of human limbs. Replicating the controllable stiffness of the human musculoskeletal system in a prosthetic device would enable more human-like interactions, thus increasing acceptance and social integration. Moreover, compliant bionic limbs improve safety by absorbing unintended impacts that can arise from the absence of proprioceptive feedback or from errors in the operation of the prosthetic limb. Furthermore, VS prostheses can adapt their behavior to various tasks encountered in daily life. As shown in Fig. 3b, soft joints enable the exploitation of environmental constraints, ensuring safe interactions in cluttered environments by adapting to obstacles and preventing damage. Meanwhile, high elbow stiffness is crucial for rejecting disturbances during precision tasks. While this preliminary experiment suggests that VS prosthetic limbs may improve users' quality

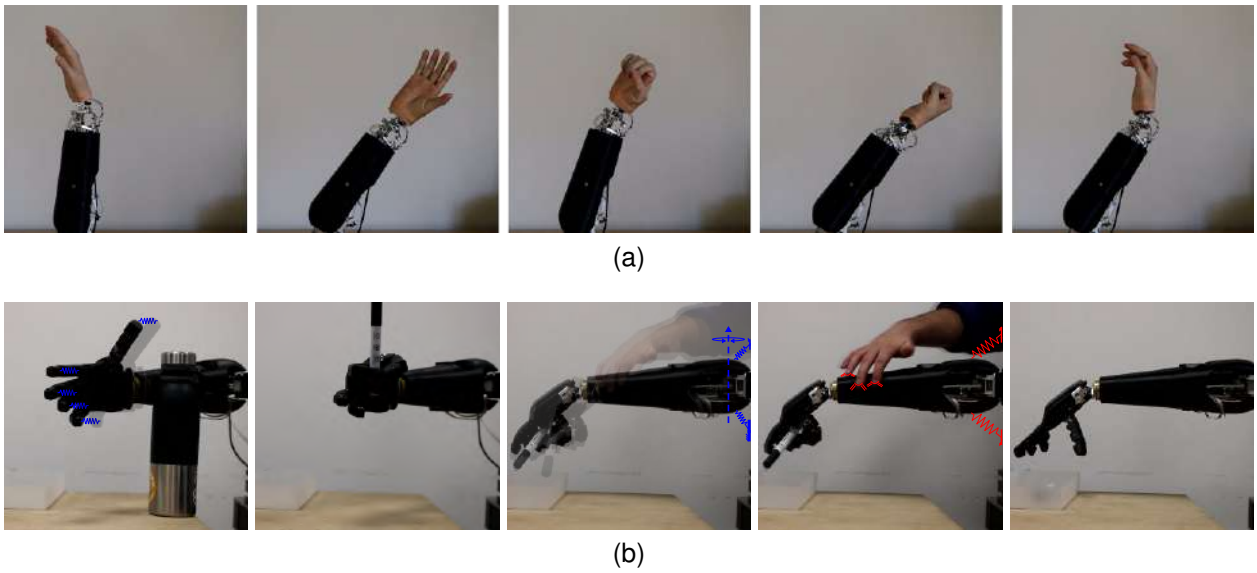


Fig. 3. Functional demonstration of two configurations of the V-Soft Pro system. Sequence (a) shows the V-SP platform performing active, simultaneous motion across all its submodules. Sequence (b) demonstrates the benefits of variable stiffness actuation within the transhumeral prosthesis. In the first scene, the prosthesis uses low joint stiffness to navigate an unstructured environment, allowing gentle contact with nearby objects without knocking them over. It then performs a tripod grasp (second scene) followed by wrist pronation. With low elbow stiffness, the prosthesis adapts to external forces without resisting (third scene). However, the V-SP system can increase its stiffness to counter external disturbances (fourth scene) and perform precision tasks (fifth scene).

of life, further testing with prosthesis users is necessary to evaluate their real-world functionality.

The V-SP platform offers a customizable transhumeral prosthesis that meets diverse user specifications, considering both ergonomics and the number of controllable motions. Future work will focus on tailoring the EMG control of the V-SP system to the individual user. One possibility is to adopt existing EMG-based VS controllers from the literature, which regulate the stiffness and position of single-DoF joints [41]–[43], and extend these approaches to sequential control, commonly used in multi-DoF prostheses. In this scenario, the user utilizes a switching signal to toggle control between different prosthetic joints, such as rapid coactivations, signals from auxiliary EMG recording sites, or even a physical switch activated by the contralateral arm. While sequential control is easy to implement, it may result in unnatural motion and unintuitive control as the number of DoFs increases, limiting the usability of advanced prostheses. Key enablers of this technology may include surgical procedures that increase the number of independent biosignals (e.g., Targeted Muscle Reinnervation and Regenerative Peripheral Nerve Interfaces), cutting-edge EMG recording technologies (such as high-density EMG and implantable electrodes), and advanced neural decoding algorithms [26], [44]–[46].

VI. Conclusion

Current robotic prostheses lack the innate compliance and variable stiffness of human limbs, leading to unnatural interactions with people and objects, while compromising versatility and social engagement. To address these issues, this paper presents V-Soft Pro, a modular platform for a transhumeral prosthesis with user-controllable stiffness. V-Soft Pro features a user-centered design, enabling customization of its components based on the user's level of amputation, daily needs, and myoelectric control skills. Recognizing the diversity among users, the modular design offers various configurations to optimize comfort and usability for each individual. The prosthetic joints integrate VSAs to replicate the adaptive behavior of human limbs, providing human-like dynamics and continuous joint stiffness regulation. The V-Soft Pro system has the potential to significantly enhance the user experience by improving the natural feel of bionic limbs and offering customized prosthetic solutions to individual needs. However, further research is necessary to accurately decode user intent, enabling more natural operation of the prosthesis and maximizing its capabilities. Clinical trials with prosthesis users are needed to assess the functionality of user-controllable stiffness in prosthetic devices during ADLs and social interactions.

Acknowledgment

The authors would like to thank Manuel Barbarossa, Vinicio Tincani, Mattia Poggiani, Marina Gnocco, Cristiano Petrocelli, Emanuele Sessa, and Octavie Somoza for their fundamental work on the hardware implementation of the prototypes.

References

[1] R. Osu, N. Kamimura, H. Iwasaki, E. Nakano, C. M. Harris, Y. Wada, and M. Kawato, "Optimal impedance control for task achievement in the presence of signal-dependent noise," *Journal of Neurophysiology*, vol. 92, no. 2, pp. 1199–1215, 2004.

[2] D. Borzelli, B. Cesqui, D. J. Berger, E. Burdet, and A. d'Avella, "Muscle patterns underlying voluntary modulation of co-contraction," *PLoS One*, vol. 13, no. 10, p. e0205911, 2018.

[3] G.-H. Phan, C. Hansen, P. Tommasino, A. Budhota, D. M. Mohan, A. Hussain, E. Burdet, and D. Campolo, "Estimating human wrist stiffness during a tooling task," *Sensors*, vol. 20, no. 11, p. 3260, 2020.

[4] A. A. Blank, A. M. Okamura, and L. L. Whitcomb, "Task-dependent impedance and implications for upper-limb prosthesis control," *The International Journal of Robotics Research*, vol. 33, no. 6, pp. 827–846, 2014.

[5] N. Hogan, "Prostheses should have adaptively controllable impedance," in *Control Aspects of Prosthetics and Orthotics*. Elsevier, 1983, pp. 155–162.

[6] ——, "Impedance control: An approach to manipulation: Part ii—implementation," *Journal of Dynamic Systems Measurement and Control-transactions of The Asme*, vol. 107, pp. 8–16, 1985. [Online]. Available: https://api.semanticscholar.org/CorpusID:85508543

[7] S. Haddadin and E. Shahriari, "Unified force-impedance control," *The International Journal of Robotics Research*, vol. 43, no. 13, pp. 2112–2141, 2024.

[8] X. Zhao, Y. Chen, L. Qian, B. Tao, and H. Ding, "Human–robot collaboration framework based on impedance control in robotic assembly," *Engineering*, vol. 30, pp. 83–92, 2023.

[9] Z. Liao and Y. Wang, "Trust-based variable impedance control of human–robot cooperative manipulation," *Robotics and Computer-Integrated Manufacturing*, vol. 88, p. 102730, 2024.

[10] C. English and D. Russell, "Mechanics and stiffness limitations of a variable stiffness actuator for use in prosthetic limbs," *Mechanism and machine theory*, vol. 34, no. 1, pp. 7–25, 1999.

[11] M. Howard, D. J. Braun, and S. Vijayakumar, "Transferring human impedance behavior to heterogeneous variable impedance actuators," *IEEE Transactions on Robotics*, vol. 29, no. 4, pp. 847–862, 2013.

[12] N. L. Tagliamonte, F. Sergi, D. Accoto, G. Carpino, and E. Guglielmelli, "Double actuation architectures for rendering variable impedance in compliant robots: A review," *Mechatronics*, vol. 22, no. 8, pp. 1187–1203, 2012.

[13] M. Tiboni, A. Borboni, F. Vérité, C. Bregoli, and C. Amici, "Sensors and actuation technologies in exoskeletons: A review," *Sensors*, vol. 22, no. 3, p. 884, 2022.

[14] G. Milazzo, S. Lemerle, G. Grioli, A. Bicchi, and M. G. Catalano, "Design, characterization, and validation of a variable stiffness prosthetic elbow," *IEEE Transactions on Robotics*, pp. 1–14, 2024.

[15] G. Milazzo, M. G. Catalano, A. Bicchi, and G. Grioli, "Modeling and control of a novel variable stiffness three dofs wrist," *The International Journal of Robotics Research*, p. 02783649241236204, 2024.

[16] D. A. Bennett, J. E. Mitchell, D. Truex, and M. Goldfarb, "Design of a myoelectric transhumeral prosthesis," *IEEE/ASME Transactions on Mechatronics*, vol. 21, no. 4, pp. 1868–1879, 2016.

[17] P. Capsi-Morales, C. Piazza, G. Grioli, A. Bicchi, and M. G. Catalano, "A three degrees of freedom switchable impedance myoelectric prosthetic wrist," *The International Journal of Robotics Research*, p. 02783649241231298, 2024.

[18] M. K. Shepherd and E. J. Rouse, "The vspa foot: A quasi-passive ankle-foot prosthesis with continuously variable stiffness," *IEEE Transactions on Neural Systems and Rehabilitation Engineering*, vol. 25, no. 12, pp. 2375–2386, 2017.

[19] E. M. Glanzer and P. G. Adamczyk, "Design and validation of a semi-active variable stiffness foot prosthesis," *IEEE Transactions on Neural Systems and Rehabilitation Engineering*, vol. 26, no. 12, pp. 2351–2359, 2018.

[20] E. Rogers-Bradley, S. H. Yeon, C. Landis, and H. M. Herr, "Design and evaluation of a quasi-passive variable stiffness prosthesis for walking speed adaptation in people with transtibial amputation," *IEEE/ASME Transactions on Mechatronics*, vol. 29, no. 1, pp. 335–346, 2023.

[21] E. Hocaoglu and V. Patoglu, "Design, implementation, and evaluation of a variable stiffness transradial hand prosthesis," *Frontiers in neurorobotics*, vol. 16, p. 789210, 2022.

[22] M. Baggetta, G. Berselli, G. Palli, and C. Melchiorri, "Design, modeling, and control of a variable stiffness elbow joint," *The International Journal of Advanced Manufacturing Technology*, vol. 122, no. 11-12, pp. 4437–4451, 2022.

[23] H. Fan, G. Wei, and L. Ren, "Prosthetic and robotic wrists comparing with the intelligently evolved human wrist: A review," *Robotica*, vol. 40, no. 11, pp. 4169–4191, 2022.

[24] N. M. Bajaj, A. J. Spiers, and A. M. Dollar, "State of the art in artificial wrists: A review of prosthetic and robotic wrist design," *IEEE Transactions on Robotics*, vol. 35, no. 1, pp. 261–277, 2019.

[25] R. Damerla, K. Rice, D. Rubio-Ejchel, M. Miro, E. Braucher, J. Foote, I. Bourai, A. Singhal, K. Yang, H. Guang, *et al.*, "Design and testing of a novel, high-performance two dof prosthetic wrist," *IEEE Transactions on Medical Robotics and Bionics*, vol. 4, no. 2, pp. 502–519, 2022.

[26] V. Mendez, F. Iberite, S. Shokur, and S. Micera, "Current solutions and future trends for robotic prosthetic hands," *Annual Review of Control, Robotics, and Autonomous Systems*, vol. 4, no. 1, pp. 595–627, 2021.

[27] C. Piazza, G. Grioli, M. G. Catalano, and A. Bicchi, "A century of robotic hands," *Annual Review of Control, Robotics, and Autonomous Systems*, vol. 2, no. 1, pp. 1–32, 2019.

[28] A. Saikia, S. Mazumdar, N. Sahai, S. Paul, D. Bhatia, S. Verma, and P. K. Rohilla, "Recent advancements in prosthetic hand technology," *Journal of medical engineering & technology*, vol. 40, no. 5, pp. 255–264, 2016.

[29] N. Lan, M. Hao, C. M. Niu, H. Cui, Y. Wang, T. Zhang, P. Fang, and C.-h. Chou, "Next-generation prosthetic hand: from biomimetic to biorealistic," *Research*, 2021.

[30] L. C. Smail, C. Neal, C. Wilkins, and T. L. Packham, "Comfort and function remain key factors in upper limb prosthetic abandonment: findings of a scoping review," *Disability and rehabilitation: Assistive technology*, vol. 16, no. 8, pp. 821–830, 2021.

[31] F. Cordella, A. L. Ciancio, R. Sacchetti, A. Davalli, A. G. Cutti, E. Guglielmelli, and L. Zollo, "Literature review on needs of upper limb prosthesis users," *Frontiers in neuroscience*, vol. 10, p. 209, 2016.

[32] M. Li, A. Pal, A. Aghakhani, A. Pena-Francesch, and M. Sitti, "Soft actuators for real-world applications," *Nature Reviews Materials*, vol. 7, no. 3, pp. 235–249, 2022.

[33] NASA, "Man-systems integration standards - volume i." https://msis.jsc.nasa.gov/Volume1.htm. Last Accessed: November 2023, November 1995.

[34] A. R. Tilley, *The measure of man and woman: human factors in design*. John Wiley & Sons, 2001.

[35] T. Lenzi, J. Lipsey, and J. W. Sensinger, "The ric arm—a small anthropomorphic transhumeral prosthesis," *IEEE/ASME Transactions on Mechatronics*, vol. 21, no. 6, pp. 2660–2671, 2016.

[36] R. A. M. Abayasiri, D. K. Madusanka, N. Arachchige, A. Silva, and R. Gopura, "Mobio: A 5 dof trans-humeral robotic prosthesis," in *2017 International Conference on Rehabilitation Robotics (ICORR)*. IEEE, 2017, pp. 1627–1632.

[37] K. B. Fite, T. J. Withrow, K. W. Wait, and M. Goldfarb, "A gas-actuated anthropomorphic transhumeral prosthesis," in *Proceedings 2007 IEEE International Conference on Robotics and Automation*. IEEE, 2007, pp. 3748–3754.

[38] M. S. Johannes, E. L. Faulring, K. D. Katyal, M. P. Para, J. B. Helder, A. Makhlin, T. Moyer, D. Wahl, J. Solberg, S. Clark, *et al.*, "The modular prosthetic limb," in *Wearable robotics*. Elsevier, 2020, pp. 393–444.

[39] S. B. Godfrey, K. D. Zhao, A. Theuer, M. G. Catalano, M. Bianchi, R. Breighner, D. Bhaskaran, R. Lennon, G. Grioli, M. Santello, *et al.*, "The softhand pro: Functional evaluation of a novel, flexible, and robust myoelectric prosthesis," *PloS one*, vol. 13, no. 10, p. e0205653, 2018.

[40] C. Della Santina, C. Piazza, G. Grioli, M. G. Catalano, and A. Bicchi, "Toward dexterous manipulation with augmented adaptive synergies: The pisa/iit softhand 2," *IEEE Transactions on Robotics*, vol. 34, no. 5, pp. 1141–1156, 2018.

[41] J. W. Sensinger *et al.*, "User-modulated impedance control of a prosthetic elbow in unconstrained, perturbed motion," *IEEE Transactions on biomedical engineering*, vol. 55, no. 3, pp. 1043–1055, 2008.

[42] P. Capsi-Morales, C. Piazza, M. G. Catalano, A. Bicchi, and G. Grioli, "Exploring stiffness modulation in prosthetic hands and its perceived function in manipulation and social interaction," *Frontiers in Neurorobotics*, p. 33, 2020.

[43] L. Ferrante, M. Sridharan, C. Zito, and D. Farina, "Toward impedance control in human-machine interfaces for upper-limb prostheses," *IEEE Transactions on Biomedical Engineering*, 2024.

[44] H. Huang, L. J. Hargrove, M. Ortiz-Catalan, and J. W. Sensinger, "Integrating upper-limb prostheses with the human body: Technology advances, readiness, and roles in human–prosthesis interaction," *Annual Review of Biomedical Engineering*, vol. 26, 2024.

[45] D. Farina, I. Vujaklija, R. Brånemark, A. M. Bull, H. Dietl, B. Graimann, L. J. Hargrove, K.-P. Hoffmann, H. Huang, T. Ingvarsson, *et al.*, "Toward higher-performance bionic limbs for wider clinical use," *Nature biomedical engineering*, vol. 7, no. 4, pp. 473–485, 2023.

[46] K. Jyothish and S. Mishra, "A survey on robotic prosthetics: Neuroprosthetics, soft actuators, and control strategies," *ACM Computing Surveys*, vol. 56, no. 8, pp. 1–44, 2024.

Assessing Repeatability of CLEVERArm Exoskeleton Using Healthy Subjects: A Pilot Study

Adib H. Laskar
Department of Mechanical Engineering
Texas A&M University
College Station, TX, United States
adiblaskar@tamu.edu

Reza Tafreshi
Department of Mechanical Engineering
Texas A&M University
College Station, TX, United States
rtafreshi@tamu.edu

Muhammad Bin Mughees
Department of Electrical Engineering
Texas A&M University
College Station, TX, United States
muhammadbinmughees@tamu.edu

Khaled Al-Halabi
Department of Mechanical Engineering
Texas A&M University
College Station, TX, United States
khaled.alhalabi@tamu.edu

Reza Langari
Department of Mechanical Engineering
Texas A&M University
College Station, TX, United States
rlangari@tamu.edu

Md Ferdous Wahid
Department of Mechanical Engineering
Texas A&M University
College Station, TX, United States
wahid@tamu.edu

***Abstract*—Upper extremity (UE) impairments resulting from non-communicable diseases continue to rise annually across the globe. Robotic devices offer promising solutions for mitigating the long-term logistical challenges and limited recovery outcomes associated with short-term, one-to-one rehabilitation sessions. This study presents a repeatability analysis of CLEVERArm (compact, lightweight, ergonomic, VR/AR-enhanced rehabilitation arm), an eight-degrees-of-freedom (DOF) robotic exoskeleton for treating patients with UE impairments, focusing on validating both single-DOF (sDOF) and multi-DOF (mDOF) trajectories produced by the device. Eighteen healthy subjects performed tasks ranging from simple to complex UE movements associated with activities of daily living. The device then autonomously repeated the movements made by the participants. Across all tasks, CLEVERArm demonstrated low root mean square deviation ($< 3.42^{\circ}$), and high correlations (> 0.99) between reference and repetition trajectories recorded by absolute encoders. High intra-class coefficient values (> 0.9) further constitute the system's consistency and accuracy in UE movement over time. These results suggest that CLEVERArm can reliably replicate input trajectories, providing consistent and positive outcomes in rehabilitation settings. Future work will utilize the device's ability to accurately replicate trajectories for designing personalized rehabilitation regimens, monitoring patient progress, and tailoring exercises to individual needs, ultimately enhancing long-term recovery for patients with UE impairments.**

***Index Terms*—Rehabilitation, Exoskeleton, Upper-limb impairment, Repeatability, Activities of Daily Living.**

I. Introduction

The prevalence of neurological and neurodegenerative disorders, including spinal cord injury (SCI), traumatic brain injuries (TBI), Parkinson's Disease (PD), Multiple Sclerosis (MS), and stroke, is now affecting a billion people in the world [1]. Projected increases in the incidence of each disorder will lead to higher rehabilitation costs and treatment of each condition. However, the projected growth of professionals with the appropriate training is considerably lower than the incidence rate [2]. Consequently, these conditions pressure healthcare providers for treatment, rehabilitation, and support services. Thus, an autonomous intervention can mitigate the effects of logistical constraints and provide intensive, repetitive, and task-oriented rehabilitation that is needed for effective recovery in the long term [3].

The inherent capabilities of robotic systems in producing high-intensity, repeatable, and precisely controllable motions make them a desirable candidate for upper extremity (UE) rehabilitation [4]. Two types of robotic systems exist: end-effectors and exoskeletons. End-effector robots tend to focus rehabilitation on the distal part of the UE. In contrast, exoskeletons focus heavily on the entire UE by aligning them with the anatomical axes of the patient [5]. Due to the limitations of end-effector control of the proximal aspects of the UE, researchers have focused on exoskeletons, as they enable patients to perform movements that typically span a broader range of the UE workspace. These movements range from single-degree-of-freedom (sDOF) to multi-degree-of-freedom (mDOF) tasks, assessing the patient's ability to perform activities of daily living (ADL) movements that replicate those commonly performed in everyday life [6]. Despite this advantage, achieving kinematic compatibility between the exoskeleton and the human arm remains a challenge, making trajectory assessment and control difficult across a wide range of movements [2], [7].

With the use of robotic exoskeletons, robotic devices can provide more reliable quantifiable metrics that can track patient improvement in trajectories compared to existing clinical measures such as the Fugl-Meyer Assesment (FMA) and Modified Ashworth Scale (MAS) that rely on ordinal scales to track rehabilitation progress [8]. Previous forms of robotic assessments have relied on metrics quantifying trajectory tracking and speed in point-to-point reaching tasks [9], [10] while ADL tasks limited to a singular aspect of the UE workspace [11]. However, while the metrics for each trajectory are validated, the motions themselves are not complex enough to transfer to real-life situations where patient improvement

would be noticeable [12], [13]. Additionally, many of the assessment methods rely on trajectory characteristics [14], [15] and patient capability [16], depending on control measures to account for errors when trajectories are repeated [17], [18]. They do not consider the consistency of robotic controllability when trajectories are reproduced on multiple attempts based on the reference path lines.

This study aims to validate the CLEVERArm (compact, lightweight, ergonomic, VR/AR-enhanced rehabilitation arm) exoskeleton, developed by our research team [2], [19], in accurately reproducing various movements. The device is designed to automatically provide repetitive rehabilitation and offer 0-100% weighted support during various UE motions. A large cohort of subjects was used to statistically validate the device's repeatability (i.e. carrying out a trajectory multiple times) and reliability (i.e. consistency in replicating the inputted trajectory) across tasks of varying complexity. The validation process includes visual inspection, quantitative measurements, and statistical analysis, ensuring the system's robustness and performance.

II. Materials and Methods

The following subsections detail the CLEVERArm specifications and validation methodology employed in this study.

A. CLEVERArm Exoskeleton System

The CLEVERArm (see Fig. 1) has eight DOFs supporting the motion of the shoulder girdle, glenohumeral (GH) joint, elbow, and wrist. Out of the eight DOFs, six DOFs are active (Maxon EC brushless motors), while the other two are passive. An active DOF is used to assist in flexion/extension of the elbow joint, while three active DOFs are used to support shoulder motion. Two additional active DOFs, one prismatic and one revolute, are used to account for scapulohumeral rhythms during shoulder motion. Robotic configuration is determined using joint angle measurements from absolute rotary encoders (AksIM™ Off-Axis Rotary Absolute Magnetic Encoder) situated at each of the revolute joints.

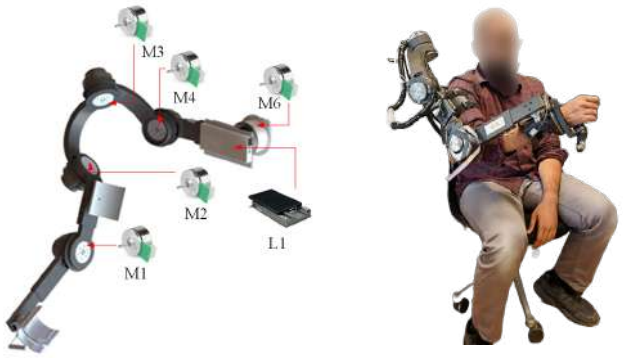
The overall control architecture of the CLEVERArm involves baseline gravitational compensation with the appropriate inertial parameters calculated by the CAD model in SolidWorks [2].The exoskeleton currently operates within a user-friendly interface on LabVIEW. For the passive therapy module, the subject performs the motion while the pathline is recorded. The recorded pathline is interpolated into 100 equally spaced points, appended with its reverse to form a complete movement, and repeated as required by the desired number of iterations for the robotic trajectory. A uniform PID controller (K_p = 1.5, K_i = 0.03, K_d = 0.002) is applied to each actuator at every point, with baseline controllers running concurrently. The passive therapy module has been optimized using parallelization strategies to minimize delays in the long-term during execution of the desired trajectories.

TABLE I: Rehabilitation Tasks

Name	DOF	Task Description	Configuration
Task 1	Single	Elbow Flexion-Extension	0-140°
Task 2	Single	Shoulder Abduction-Adduction	0-90°
Task 3	Single	Shoulder Flexion-Extension	0-90°
Task 4	Multiple	Reaching to Head	As needed
Task 5	Multiple	Eating Activity	As needed
Task 6	Multiple	Combing Activity	As needed

B. Experimental Protocol

The Institutional Review Board (IRB) granted ethical approval (IRB2018-0016DQ, QU-IRB 1884-EA/23, MRC-02-22-164), ensuring adherence to established research standards. We recruited 18 healthy subjects (age range 18-35) to determine the repeatability of the CLEVERArm device. All participants had no history of UE injuries or musculoskeletal disorders. All tasks were exclusively performed using their right limbs. Each subject executed a set of six tasks, repeating each task five times, resulting in a total of 30 experiments per participant. Upon wearing the exoskeleton, subjects initially executed each task themselves, constituting the reference data for subsequent evaluations. The CLEVERArm device then replicated the motion for each task five times, denoted as repetitions. The arm's starting position was fully extended for all task scenarios. Joint angle data for actuators 1 to 4, where actuator 1 corresponds to the elbow and 2 to 4 to the shoulder, were measured using the built-in absolute encoders (Fig. 1a). The sampling rate was 100 Hz. Subjects engaged in three sDOF and three ADL, referred to as mDOF, including reaching towards the head, combing, and eating (Table I). This comprehensive study design ensures a thorough exploration of the CLEVERArm's repeatability across various simple to complex activities, providing valuable insights for future developments and applications.



(a) (b)

Fig. 1: (a) Schematic of the CLEVERArm with active DOF labeled: M = rotary motor/encoder, L = prismatic motor/encoder [19] (b) Subject wearing the CLEVERArm Exoskeleton preparing for movement

C. Repeatability Analysis

The repeatability assessment of CLEVERArm was carried out employing a comprehensive array of methodologies, each aimed at providing an in-depth understanding of its performance characteristics. These methodologies included visual inspection, correlation analysis, computation of root mean square deviation (RMSD) between reference and repetition signals, analysis of variance (ANOVA), and computation of intraclass correlation coefficients (ICCs).

1) Visual Inspection and Quantitative Measurement: Both the reference and repetition tasks were plotted for each actuator to qualitatively assess the similarity and consistency between the two signals, allowing for the identification of any observable discrepancies or patterns. To quantify the differences, the RMSD was computed for each task:

$$d_t = \sqrt{\frac{1}{n}\sum_{i=1}^{n}(y_i - \hat{y}_i)^2}, \tag{1}$$

where y_i and $\hat{y}_i$ denote the i-th sample of the reference and repetition signals, respectively, n represents the total number of samples and d_t represents the RMSD for the *t*-th task. Additionally, the Pearson correlation coefficient (r) was computed to quantitatively evaluate the relationship between the reference and repetition signals as follows:

$$r = \frac{\sum_{i=1}^{n}(y_i - \bar{y})\left]\hat{y}_i - \bar{\hat{y}}\right)}{\sqrt{\sum_{i=1}^{n}(y_i - \bar{y})^2 \sum_{i=1}^{n}\left]\hat{y}_i - \bar{\hat{y}}\right)^2}}, \tag{2}$$

where n is the total number of samples, y_i and $\hat{y}_i$ are the reference and repetition signals for the i-th sample, and $\bar{y}$ and $\bar{\hat{y}}$ are the mean values of the reference and repetition signals, respectively.

2) Analysis of Variance (ANOVA): A two-way within-within repeated measure ANOVA was conducted to assess differences across tasks, repetitions, and their interactions. In this design, subjects were considered random effects to account for individual variability, while tasks and repetitions were analyzed as fixed effects to explore their impact on RMSD values. The generalized eta squared (η^2) was used to calculate effect sizes, providing insight into the practical significance of the findings. The effect size can be interpreted as negligible when $\eta^2 < 0.01$, small $0.01 <= \eta^2 < 0.06$, medium $0.06 <= \eta^2 < 0.14$, and large $\eta^2 >= 0.14$ [20]. This approach enabled a comprehensive investigation, shedding light on the performance and repeatability of the CLEVERArm exoskeleton system.

3) Intraclass Correlation Coefficient (ICC): ICCs were computed to assess the test-retest reliability of the CLEVERArm exoskeleton system across tasks and repetitions. ICC(3,1), a two-way mixed effect for consistency, was chosen for its ability to capture systematic differences and random errors within each repetition, making it suitable for evaluating the device's reliability. The test-retest reliability value can be interpreted as follows: <0.5 = poor reliability, 0.5-0.75 = moderate reliability, 0.75-0.9 = good reliability, and >0.90 = excellent reliability [21].

III. Results and Discussion

The repeatability of CLEVERArm was analyzed using a multifaceted approach, including visual inspection, quantitative analysis, and statistical analysis. As shown in Fig. 2, the alignment between repetition and reference signals across various tasks showcased a clear consistency in the system performance. Complementing this qualitative assessment, Table II presents quantitative measurements, including RMSD and correlation values between reference and repetition signals for all tasks. The results consistently demonstrate values below 3.42° and above 0.99 for RMSD and correlations, respectively, underscoring the system's remarkable stability and fidelity in executing synchronous movements across tasks. The RMSD values across actuators show generally low deviation, with most tasks demonstrating less than 1° of variation for sDOF and less than 2° for mDOF tasks. Only in shoulder flexion-extension did actuator 4 exceed 3° (3.41°), while actuator 2, the key responsible actuator, showed less than 1° of deviation. This discrepancy is likely due to external forces from subject movement or slight posture changes. The mDOF movements showed a slight increase in variation compared to sDOF, as expected, due to their inherent complexity. Overall, the system's performance remains stable, with deviations within acceptable limits, confirming its robustness for rehabilitation applications.

Despite minor fluctuations, the average RMSD remained consistently below 2° (Fig. 3), indicating high repeatability across tasks and trials. It should be noted that the marginally moved actuators produced minimal variations (see Fig. 3), which resulted in low correlations, although both signals aligned. This occurs because the small differences between data points and the mean reduce the numerator in the correlation coefficient calculation. In essence, even though the signals visually align, the lack of significant movement variation limits the extent of their linear relationship, resulting in lower correlation values. Nevertheless, both of these qualitative and quantitative analyses provide a holistic understanding of CLEVERArm's repeatability.

The two-way repeated measure ANOVA revealed significant effects for both task ($F(5, 85) = 9.262, p < 0.01$) and repetition ($F(4, 68) = 8.321, p < 0.01$). Effect sizes, represented by generalized eta squared (η^2), indicated that the task had a relatively large effect size ($\eta^2 = 0.340$), suggesting that differences between tasks accounted for a substantial proportion of the variability in the data. This outcome was anticipated due to the higher complexity of tasks involving mDOF compared to those with sDOF, where multiple actuators move simultaneously, resulting in significant differences. This reaffirms the effectiveness of the task complexity design in evaluating CLEVERArm's repeatability. In contrast, repetition had a smaller effect size ($\eta^2 = 0.007$), indicating a lesser and negligible impact on the outcomes and consistent performance irrespective of repetition. While the first repetition consistently yielded lower RMSD values compared to other repetitions, the difference was less than 0.2°, as reflected in the effect size

TABLE II: CLEVERArm's Repeatability Analysis

Metric	Actuator	Elbow Flexion-Extension		Shoulder Abduction-Adduction		Shoulder Flexion-Extension		Reaching to Head		Eating Activity		Combing Activity	
		Mean	STD	Mean	STD	Mean	STD	Mean	STD	Mean	STD	Mean	STD
RMSD	Actuator 1	2.03	1.14	0.54	0.54	0.18	0.39	0.69	0.53	2.51	0.86	2.27	0.84
	Actuator 2	0.89	0.40	2.64	0.74	0.87	0.78	2.77	0.90	1.78	0.62	2.07	0.82
	Actuator 3	0.51	0.30	1.81	0.85	0.93	0.81	1.96	0.65	1.29	0.42	1.38	0.51
	Actuator 4	0.61	0.48	1.54	0.72	3.41	1.11	1.49	0.98	0.98	0.51	1.20	0.58
Correlations	Actuator 1	1.00	0.00	0.37	0.48	0.09	0.32	0.61	0.46	1.00	0.00	1.00	0.00
	Actuator 2	0.76	0.42	1.00	0.00	0.53	0.50	1.00	0.00	0.99	0.00	1.00	0.00
	Actuator 3	0.39	0.54	0.98	0.02	0.27	0.66	0.99	0.02	0.66	0.01	0.97	0.11
	Actuator 4	0.38	0.44	0.78	0.40	0.99	0.00	0.78	0.36	0.54	0.46	0.73	0.48

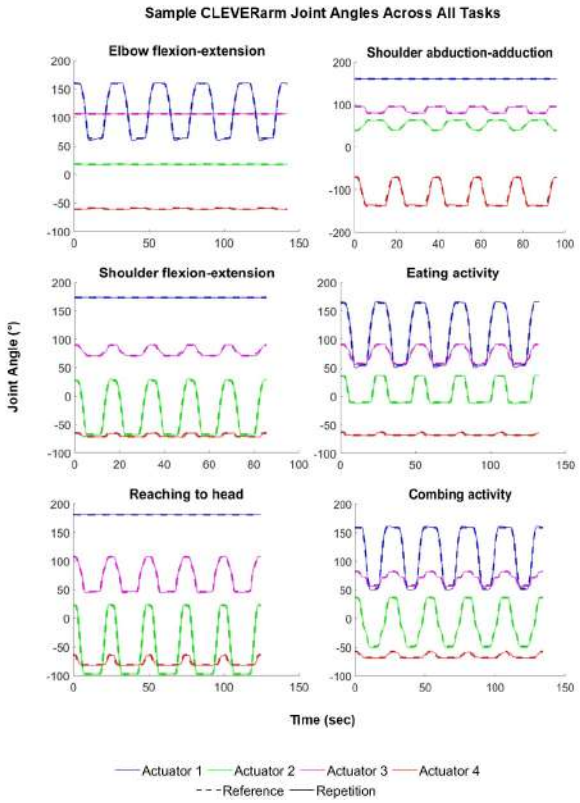


Fig. 2: Illustration of CLEVERArm joint angles across all tasks for all actuators, with dashed lines representing reference signals and solid lines indicating repetitions. Plots depict data for one subject.

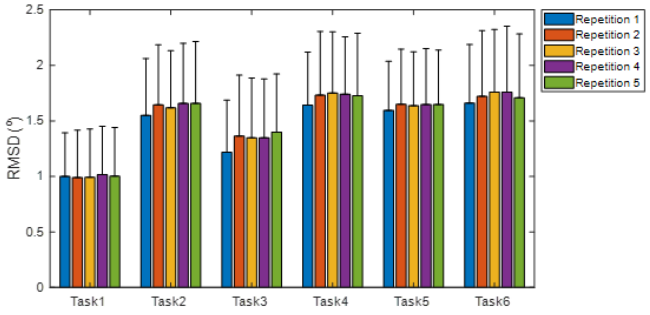


Fig. 3: Bar plot of RMSD values across all repetitions and tasks for all subjects

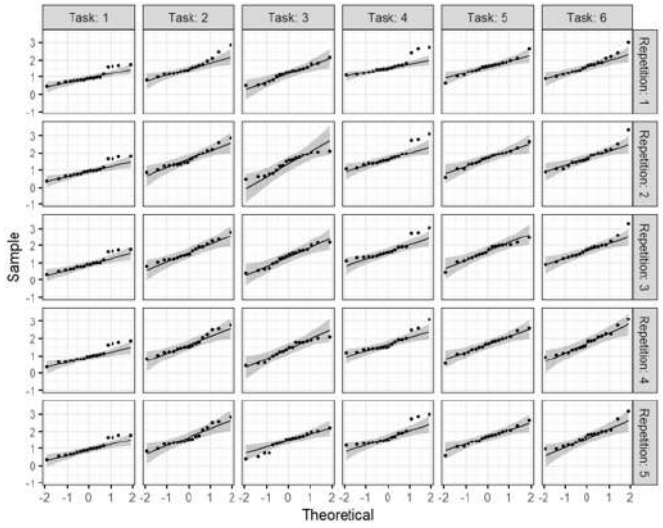


Fig. 4: Q-Q plots for the two-way repeated measure ANOVA

calculation of 0.007, indicating negligible significance.

These findings collectively affirm the robust repeatability of the CLEVERArm system, demonstrating its ability to replicate movements across various repetitions consistently. Moreover, adherence to statistical assumptions of homogeneity, independence, and sphericity ensures the validity and reliability of the ANOVA results. While normality tests using the Shapiro-Wilk test indicated that the residuals from the ANOVA were not normally distributed ($W = 0.971$, $p < 0.001$), the Quantile-Quantile (Q-Q) plot (Fig. 4), which compares sample quantiles with theoretical normal distribution, visually affirms that the deviation is marginal. In the Q-Q plot, if the points fall along a straight 45-degree line, it indicates that the sample follows the theoretical distribution; however, deviations from this line suggest departures from normality, such as skewness or the presence of outliers. As shown in the figure, since the residual errors were not highly skewed, the reliability of the ANOVA results can be considered acceptable, as suggested by [22].

Table III presents the ICC values for each task, ranging from 0.93 to 0.99, along with corresponding 95% confidence intervals. The high ICC values indicate excellent test-retest reliability of the CLEVERArm exoskeleton device across different tasks. The consistency and stability of measurements across repetitions underscore the device's ability to produce consistent outcomes, which is essential for its clinical utility.

TABLE III: Intra-class correlation coefficient for various tasks performed by CLEVERArm

Task	ICC	95% CI	
		Lower	Upper
1	0.99	0.97	0.99
2	0.97	0.94	0.99
3	0.93	0.87	0.97
4	0.96	0.93	0.98
5	0.97	0.95	0.99
6	0.97	0.94	0.99

These findings suggest that clinicians and researchers can depend on the CLEVERArm exoskeleton to reliably and accurately assess UE movement parameters across diverse tasks.

The robust repeatability demonstrated by the CLEVERArm exoskeleton system holds significant clinical implications for rehabilitation practices and patient care. The system's ability to consistently replicate movements across various tasks and repetitions underscores its potential as a reliable tool for therapeutic interventions targeting UE impairments. Clinicians can leverage the system's precision and stability to design personalized rehabilitation protocols tailored to individual patient needs. By incorporating the CLEVERArm into rehabilitation regimens, therapists can track patients' progress accurately, monitor movement patterns, and adjust treatment strategies accordingly. In future work, we aim to integrate electromyography (EMG) signals into CLEVERArm's controller algorithm to enhance assistance, as EMG signals reflect muscle activation and provide critical insights into patient participation. We have developed machine learning algorithms to classify movement types [23] and predict joint angles [24] based on EMG data, which will be incorporated into the control system. This approach aligns with previous recommendations to combine muscular activity analysis with kinematic measures for developing more effective, patient-specific neurorehabilitation paradigms [25].

IV. Conclusion

The analyses of the repeatability and efficacy demonstrated that the CLEVERArm is a valuable exoskeleton system in UE rehabilitation. We verified the system's robust performance and reliability across various tasks and repetitions comprehensively through visual inspection, quantitative measurements, and statistical analysis. The consistently high intraclass correlation coefficients (ICCs) ($>$0.9) obtained for each task further reinforce the system's ability to produce consistent outcomes and accurately capture changes in UE movement over time. Additionally, the low RMSD values ($< 3.42°$) and high correlations ($>$0.99) between reference and repetition signals attest to the system's ability to reproduce desired movements accurately, which was further supported by the two-way repeated measures ANOVA analysis. This study lays the groundwork for further exploration into optimizing the system's functionality, expanding its clinical applications, and enhancing rehabilitation outcomes for individuals with UE impairments. The device's consistent performance across tasks of varying complexity highlights its versatility, addressing rehabilitation goals ranging from basic range-of-motion exercises to intricate functional movements mimicking ADL. By leveraging the insights gained from this investigation, future endeavors can continue to propel the field of exoskeleton-assisted rehabilitation forward, ultimately benefiting patients and clinicians alike.

V. Acknowledgment

This paper was made possible by a Qatar Technology and Development Fund (QTDF) project, award QTDF 03-1208-210012 from the Qatar National Research Fund (a member of The Qatar Foundation). The contents herein are solely the responsibility of the authors.

References

[1] N. Yanguas-Casás, "Sex Differences in Neurodegenerative Diseases," *SM Journal of Neurological Disorders and Stroke*, vol. 3, no. 1, 2017.

[2] A. Zeiaee, R. S. Zarrin, A. Eib, R. Langari, and R. Tafreshi, "CLEVER-arm: A Lightweight and Compact Exoskeleton for Upper-Limb Rehabilitation," *IEEE Robotics and Automation Letters*, vol. 7, no. 2, pp. 1880–1887, 2022.

[3] A. Basteris, S. M. Nijenhuis, A. H. Stienen, J. H. Buurke, G. B. Prange, and F. Amirabdollahian, "Training modalities in robot-mediated upper limb rehabilitation in stroke: a framework for classification based on a systematic review," *Journal of NeuroEngineering and Rehabilitation*, vol. 11, no. 1, p. 111, 2014.

[4] A. A. Blank, J. A. French, A. U. Pehlivan, and M. K. O'Malley, "Current Trends in Robot-Assisted Upper-Limb Stroke Rehabilitation: Promoting Patient Engagement in Therapy," *Current Physical Medicine and Rehabilitation Reports*, vol. 2, no. 3, pp. 184–195, 2014.

[5] W. H. Chang and Y.-H. Kim, "Robot-assisted Therapy in Stroke Rehabilitation," *Journal of Stroke*, vol. 15, no. 3, p. 174, 2013.

[6] H. S. Lo and S. Q. Xie, "Exoskeleton robots for upper-limb rehabilitation: State of the art and future prospects," *Medical Engineering & Physics*, vol. 34, no. 3, pp. 261–268, 2012.

[7] A. U. Pehlivan, D. P. Losey, and M. K. O'Malley, "Minimal Assist-as-Needed Controller for Upper Limb Robotic Rehabilitation," *IEEE Transactions on Robotics*, vol. 32, no. 1, pp. 113–124, 2016.

[8] H. I. Krebs, M. Krams, D. K. Agrafiotis, A. DiBernardo, J. C. Chavez, G. S. Littman, E. Yang, G. Byttebier, L. Dipietro, A. Rykman, K. McArthur, K. Hajjar, K. R. Lees, and B. T. Volpe, "Robotic Measurement of Arm Movements After Stroke Establishes Biomarkers of Motor Recovery," *Stroke*, vol. 45, no. 1, pp. 200–204, 2014.

[9] R. Colombo, I. Cusmano, I. Sterpi, A. Mazzone, C. Delconte, and F. Pisano, "Test–Retest Reliability of Robotic Assessment Measures for the Evaluation of Upper Limb Recovery," *IEEE Transactions on Neural Systems and Rehabilitation Engineering*, vol. 22, no. 5, pp. 1020–1029, 2014.

[10] J. M. Wagner, J. A. Rhodes, and C. Patten, "Reproducibility and Minimal Detectable Change of Three-Dimensional Kinematic Analysis of Reaching Tasks in People With Hemiparesis After Stroke," *Physical Therapy*, vol. 88, no. 5, pp. 652–663, 2008.

[11] R. M. Maura, S. Rueda Parra, R. E. Stevens, D. L. Weeks, E. T. Wolbrecht, and J. C. Perry, "Literature review of stroke assessment for upper-extremity physical function via EEG, EMG, kinematic, and kinetic measurements and their reliability," *Journal of NeuroEngineering and Rehabilitation*, vol. 20, no. 1, p. 21, 2023.

[12] Y. Choi, J. Gordon, H. Park, and N. Schweighofer, "Feasibility of the adaptive and automatic presentation of tasks (ADAPT) system for rehabilitation of upper extremity function post-stroke," *Journal of NeuroEngineering and Rehabilitation*, vol. 8, no. 1, p. 42, 2011.

[13] J. R. Carey, E. Bhatt, and A. Nagpal, "Neuroplasticity Promoted by Task Complexity," *Exercise and Sport Sciences Reviews*, vol. 33, no. 1, 2005.

[14] P. Culmer, A. Jackson, S. Makower, J. Cozens, M. Levesley, M. Mon-Williams, and B. Bhakta, "A novel robotic system for quantifying arm kinematics and kinetics: Description and evaluation in therapist-assisted passive arm movements post-stroke," *Journal of Neuroscience Methods*, vol. 197, no. 2, pp. 259–269, 2011.

[15] K. J. Wisneski and M. J. Johnson, "Quantifying kinematics of purposeful movements to real, imagined, or absent functional objects: Implications for modelling trajectories for robot-assisted ADL tasks**," *Journal of NeuroEngineering and Rehabilitation*, vol. 4, no. 1, p. 7, 2007.

[16] M. Goffredo, S. Mazzoleni, A. Gison, F. Infarinato, S. Pournajaf, D. Galafate, M. Agosti, F. Posteraro, and M. Franceschini, "Kinematic Parameters for Tracking Patient Progress during Upper Limb Robot-Assisted Rehabilitation: An Observational Study on Subacute Stroke Subjects," *Applied Bionics and Biomechanics*, vol. 2019, pp. 1–12, 2019.

[17] W. Tian, M. Xu, X. Zhang, X. Guo, L. Wang, and T. Huang, "Repeatability prediction of 6-DOF hybrid robot based on equivalent error model of actuated joint," *Measurement*, vol. 207, p. 112377, 2023.

[18] X. Zhang, W. Tian, L. Wang, and T. Huang, "Evaluation and prediction method of robot pose repeatability based on statistical distance," *Mechanism and Machine Theory*, vol. 179, p. 105122, 2023.

[19] A. Zeiaee, R. Soltani-Zarrin, R. Langari, and R. Tafreshi, "Kinematic Design Optimization of an Eight Degree-of-Freedom Upper-Limb Exoskeleton," *Robotica*, vol. 37, no. 12, pp. 2073–2086, 2019.

[20] J. Cohen, *Statistical power analysis for the behavioral sciences*. Hillsdale, N.J: L. Erlbaum Associates, 2nd ed ed., 1988.

[21] T. K. Koo and M. Y. Li, "A Guideline of Selecting and Reporting Intraclass Correlation Coefficients for Reliability Research," *Journal of Chiropractic Medicine*, vol. 15, no. 2, pp. 155–163, 2016.

[22] U. Knief and W. Forstmeier, "Violating the normality assumption may be the lesser of two evils," *Behavior Research Methods*, vol. 53, no. 6, pp. 2576–2590, 2021.

[23] M. F. Wahid, R. Tafreshi, and R. Langari, "A Multi-Window Majority Voting Strategy to Improve Hand Gesture Recognition Accuracies Using Electromyography Signal," *IEEE Transactions on Neural Systems and Rehabilitation Engineering*, vol. 28, no. 2, pp. 427–436, 2020.

[24] M. F. Wahid and R. Tafreshi, "Enhanced Joint Angle Estimation Using Support Vector Machine-Long Short-Term Memory Fusion with Electromyography Signals," in *2024 American Control Conference (ACC)*, (Toronto, ON, Canada), pp. 510–515, IEEE, 2024.

[25] A. Budhota, A. Hussain, C. Hughes, C. Hansen, S. Kager, D. A. Vishwanath, C. W. K. Kuah, K. Chua, and D. Campolo, "Role of EMG as a complementary tool for assessment of motor impairment," in *2016 6th IEEE International Conference on Biomedical Robotics and Biomechatronics (BioRob)*, (Singapore), pp. 692–697, IEEE, 2016.

Unsupervised robot-assisted therapy at home after stroke: a pilot feasibility study

Giada Devittori[1], Daria Dinacci[2], Claudio Petrillo[2], Paolo Rossi[2], Roger Gassert[1,3] and Olivier Lambercy[1,3]

***Abstract*— Unsupervised robot-assisted therapy could allow increasing upper limb therapy dose for stroke survivors with minimal additional burden on the healthcare system. Thanks to the ability to actively assist movement and dynamically adapt the assistance level, actuated devices can support individuals with a wide range of deficits. However, these devices are often complex to use, and their application in a fully unsupervised setting has rarely been explored. Here, we present a pilot study investigating the feasibility of unsupervised therapy with ReHandyBot, an actuated device for upper limb rehabilitation. The increase in therapy dose achieved during unsupervised training, device usability and user experience were evaluated. Stroke inpatients of a rehabilitation clinic learned how to use the device for two weeks with progressively decreasing levels of supervision. After discharge, they could take it home for two weeks of unsupervised therapy. Four of the five recruited participants learned how to use the device without supervision, and three completed the protocol. During the two weeks at home, on average they performed 518.3 minutes of therapy with ReHandyBot. Usability and user experience ratings show that the device was well accepted. These positive results support larger studies investigating unsupervised home therapy with ReHandyBot and suggest that active devices can be used by patients with no to mild cognitive impairments at home without the supervision of external persons.**

I. INTRODUCTION

Stroke is one of the leading causes of disability, and many stroke survivors are left with chronic upper limb impairments [1], which negatively affect quality of life. Giving stroke patients the opportunity to perform more upper limb therapy than offered during standard care may improve their functional outcomes and overall well-being [2]. However, increasing the dose of therapy (e.g., therapy time) for stroke patients, either during their stay in the clinic or at home after discharge, presents many challenges, mainly related to the high costs of rehabilitation and the limited number of available therapists for an increasing number of patients [3].

Unsupervised therapy is one approach holding the promise of giving stroke patients access to a higher dose of therapy with minimal additional burden on the healthcare system. In this setting, patients perform exercises without the supervision of any external person, ideally directly at their homes. Several tools for unsupervised therapy have been explored, e.g., exergames and sensor-based devices [4], [5]. Thanks to the ability to actively support movements, dynamically adapt the assistance level, and provide engaging exercises, active (i.e., actuated) robotic devices might be the most comprehensive solution to support a broad range of stroke patients during unsupervised upper limb therapy. However, most active robotic devices do not meet the requirements for fully unsupervised training. For instance, they are often difficult to use or do not have the ability to automatically tailor the difficulty of therapy to the evolving level of impairment. Therefore, some form of supervision is often still required also when deployed at home (e.g., remote by a therapist, onsite by caregivers [6]) and the fully unsupervised use of active robotic devices has rarely been explored.

Our group developed the ReHapticKnob, an active end-effector device for hand rehabilitation, focusing on its clinical benefit, usability, and adaptability [7], [8]. Recently, a clinical trial with 13 subacute stroke patients showed that unsupervised therapy with the ReHapticKnob in a clinical setting is feasible and can increase therapy dose compared to standard care [9]. Building on these promising results, we propose to evaluate a similar unsupervised rehabilitation concept in patients' homes, as outpatients have access to significantly fewer therapy sessions than inpatients and may benefit most from an increase in therapy dose. A portable version of the ReHapticKnob, named ReHandyBot, was thus developed. Despite the smaller dimensions, ReHandyBot has the same functionalities and therapy exercises as its previous version.

Here, we present a pilot study evaluating unsupervised therapy at home with ReHandyBot. The main goals of this pilot study are to investigate (i) the feasibility of unsupervised therapy with ReHandyBot within stroke patients' homes, (ii) the effect of unsupervised therapy with the device on therapy dose after discharge from the clinic, and (iii) the usability of ReHandyBot and user experience when training with it outside of clinical settings. This work will help define whether ReHandyBot, and potentially other similar active devices, can be used at home in a fully unsupervised way to provide novel solutions for increasing therapy dose for neurological patients without increasing therapists' workload.

II. METHODS

A. ReHandyBot

ReHandyBot (Fig. 1) is an actuated end-effector haptic device for hand sensorimotor therapy with two degrees of freedom [10]. Its exercises focus on grasping (i.e., finger flexion and extension) and forearm pronosupination movements and follow the neurocognitive therapy approach, which trains motor, sensory, and cognitive functions [11]. The therapy

Part of this project is supported by Suva via the ETH Zurich Foundation.

[1]Rehabilitation Engineering Laboratory (RELab), ETH Zurich, Switzerland (e-mail: giada.devittori@hest.ethz.ch)

[2]Clinica Hildebrand Centro di Riabilitazione Brissago, Switzerland

[3]Future Health Technologies program, Singapore-ETH Centre, Campus for Research Excellence and Technological Enterprise (CREATE), Singapore



Fig. 1. A stroke patient training with ReHandyBot at home. The hand is fixed to the handles with Velcro straps, and a hand cover hides the hand as the exercises require patients to focus on the somatosensory feedback from the impaired hand and not on the visual feedback [11]. The virtual environment of the exercises is shown on the monitor of the laptop and patients use a color-coded pushbutton keyboard to interact with it.

tasks mainly involve interacting with the objects rendered by the device and displayed in the virtual environment to identify their different mechanical properties (e.g., stiffness, length) based on the somatosensory feedback from the affected upper limb.

Therapy with ReHandyBot is tailored to each patient according to the following procedure. Before the first session with the device, therapists select therapy settings specific to the patients, such as which exercises suit them. During the first two sessions, patients perform assessments of hand function implemented in the device. ReHandyBot then combines therapy settings, assessment results, and patient's performance during the exercises (constantly monitored by the device) to automatically adapt therapy difficulty throughout the following sessions [8]. This ensures that, after the first session, no external intervention is needed to further tailor therapy difficulty.

To increase motivation to train, a simple gaming environment was integrated, where patients earn coins based on their training time. The coins can then be used in the context of a virtual traveling theme where patients can explore and get to know some interesting facts about different cities around the world. These facts (i.e., information and related picture) are presented at the end of each session only if the patient has trained for more than 15 minutes.

B. Study protocol

This study was approved by the Swiss authorities supervising clinical trials with medical devices (CE TI 4371, Swissmedic 102706281). The study protocol is adapted from [12], but with an unsupervised part at the patient's home.

To summarize, a target sample of 5 participants was selected, as it was considered sufficient for a pilot feasibility study. Participants were stroke inpatients of the Clinica Hildebrand Centro di Riabilitazione Brissago. Inclusion criteria were age between 18 and 90 years old, recruitment within 12 weeks from stroke onset, pre-stroke modified Rankin score [13] $\leq$ 1, National Institutes of Health Stroke Scale [14] $\geq$ 1 in at least one of the items regarding motor or

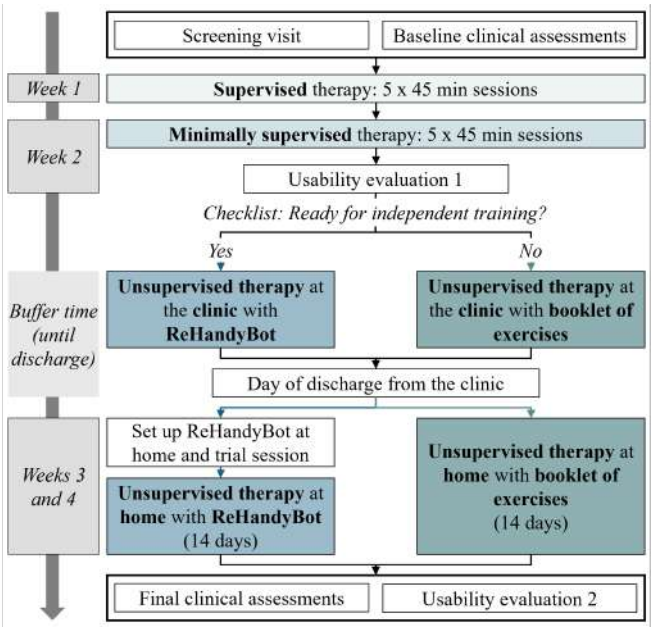


Fig. 2. Study protocol followed during this pilot feasibility study investigating the use of ReHandyBot in the home setting.

sensory function and ataxia, possibility (e.g., enough space) to set up the ReHandyBot at home, and signed informed consent form. Exclusion criteria were moderate to severe aphasia (Goodglass-Kaplan's scale [15] $<$ 3), moderate to severe cognitive deficits (levels of cognitive functioning-revised [16] $<$ 9), functional impairment of the upper limb due to other pathologies, severe pain in the affected arm (visual analogue scale for pain $\geq$ 5), other pathologies possibly interfering with the study, pacemakers and other active implants, discharge to an assisted living facility (e.g., care home), and modified Ashworth Scale (mAS) [17] $>$ 2 for one or more muscles of the impaired upper limb.

To enable patients to safely and comfortably learn how to use ReHandyBot, a progressive transition from supervised to unsupervised use of the device was implemented [12]. For each participant, the study protocol lasted around five to six weeks (Fig. 2). The first two weeks of the study, namely the familiarization phase, took place at the clinic. The first week included five sessions of 45 minutes of supervised therapy with ReHandyBot (one session per day, weekends excluded), where a supervisor (i.e., a therapist or an investigator) was present to explain how to use the device. The second week (five sessions of 45 minutes) was minimally supervised, i.e., participants tried to perform therapy with ReHandyBot by themselves. The supervisor was still present but helped only upon request.

At the end of the familiarization phase, the supervisor used a checklist to determine if the participant correctly learned how to use ReHandyBot and was ready to safely use it without supervision. If the participant was ready for independent therapy with ReHandyBot, they could take it home and continue to train with it unsupervised for two weeks, with the recommendation of performing at least one

therapy session per day (i.e., around 45 minutes). For ethical reasons, if the participants were not ready for independent therapy with the device, they were given the possibility to continue training at home unsupervised with a booklet of conventional exercises, which were explained by the therapist before discharge.

Ideally, the minimally supervised phase would have ended the day before discharge from the clinic so that the unsupervised phase could have directly started when the participant was back at home. However, estimating the exact day when a participant was discharged was difficult. Therefore, a buffer time was considered. The buffer time lasted from the first day after the minimally supervised phase to the day before discharge and was, thus, variable according to the different participants' schedules. During this buffer phase, the participant performed unsupervised therapy at the clinic, again with the recommendation of performing at least one therapy session per day. For participants who brought ReHandyBot home, one to three days after discharge, one of the investigators installed the device at their home and performed a minimally supervised session with the patient to ensure that everything was correctly set up and the patient felt comfortable with the new setting. The two weeks of unsupervised therapy at home started the day after.

At the beginning of the study, participants underwent a screening visit with a physician, where the eligibility criteria were checked and the Montreal Cognitive Assessment (MoCA) [18] was performed. At the beginning and at the end of the study, clinical assessments (e.g., the Fugl-Meyer Assessment of Upper Extremities (FMA-UE) [19]) were also performed. At the end of the minimally supervised phase, participants had to rate the usability of ReHandyBot and user experience when training with it (Usability 1). This evaluation was repeated at the end of the protocol (Usability 2).

During the unsupervised phase at home, therapists and investigators did not contact the participants to remind them to train or to adjust therapy parameters (i.e., fully unsupervised therapy). Any contacts made by participants to request assistance were recorded, together with the actions taken to address the issues.

C. Outcome measures

The feasibility of unsupervised therapy at home with ReHandyBot was measured as the number of subjects who could proceed to the unsupervised phase with the device, safety of use (i.e., number of adverse events and device deficiencies), and attendance during the unsupervised phase. Attendance is defined as the percentage of days the participant trained at least once with ReHandyBot (detected through the device data) out of the total number of offered days for unsupervised therapy at home. Parameters (e.g., age, cognitive deficit) possibly influencing the ability to train unsupervised were also evaluated.

The dose of unsupervised therapy at home with ReHandyBot was measured as therapy duration in minutes per day and total minutes over the two weeks of unsupervised therapy, number of task repetitions, and percentage increase in physical therapy time due to therapy with the device with respect to the conventional physical therapy time (i.e., upper limb and lower limb physio- and occupational therapy) performed as outpatients. When possible, conventional physical therapy time was precisely calculated for each participant based on their conventional therapy plan provided by the administration of the outpatient centers. Participants, however, were instructed to note in a journal the duration and type of conventional therapy performed during the unsupervised phase, and this data was used in the absence of more precise one.

The change in usability and user experience between the evaluations given during Usability 1 and Usability 2 was analyzed to define whether training at home without supervision negatively impacted usability and user experience. Usability questionnaires comprised the System Usability Scale (SUS) [20] and the Post-Study System Usability Questionnaire (PSSUQ) [21]. User experience was assessed with the net promoter score (NPS) [22], the customer satisfaction score (CSAT), the "interest/enjoyment" subscale of the intrinsic motivation inventory (IMI), and custom questions (e.g., relative to the gaming environment). The NPS reflected the probability on a scale ranging from 0 to 10 that a participant would recommend therapy with the ReHandyBot to another patient. The CSAT corresponded to the participant's level of satisfaction with the therapy with ReHandyBot on a 5-point scale ranging from "very unsatisfied" (i.e., 1) to "very satisfied." A semi-structured interview about ReHandyBot and unsupervised therapy was performed during the Usability 2 session.

The difference in the content of the therapy sessions performed with ReHandyBot in the three phases was evaluated to determine whether participants engaged in the exercises during the unsupervised phase. Therapy content was assessed by calculating intensity (i.e., number of task repetitions per minute), task performance (i.e., correct trials out of the total number of repetitions), and the ratio of effective therapy time (i.e., net therapy time without breaks) to total duration of a therapy session. For all three phases, we expected no significant difference in therapy content.

The changes in clinical assessment scores (i.e., functional recovery) were not analyzed as part of this pilot study focusing on feasibility.

D. Data analysis

Descriptive statistics (mean and range (min-max)) were used to characterize study population, attendance, therapy dose, user experience, device usability, and therapy content. The total dose of unsupervised therapy achieved in the unsupervised phase at home was calculated only for participants who completed the two weeks at home. The other dose-related metrics included data for all participants training without supervision.

The difference in the scores collected during Usability 1 and Usability 2 was computed to evaluate the impact of unsupervised therapy on the metrics related to usability

and user experience. Participants who did not perform the Usability 2 session were excluded from this analysis.

Given the low sample size, no statistical analysis was performed, and parameters possibly affecting the ability to train unsupervised with ReHandyBot were qualitatively analyzed.

III. RESULTS

Five participants were recruited for this feasibility study. Of these, three completed the entire protocol, one (P3) dropped out at the end of the minimally supervised phase without providing a specific reason, and one dropped out after 9 days of unsupervised therapy at home due to a second stroke. Participant's characteristics are reported in Table I.

TABLE I

CHARACTERISTICS OF THE STUDY PARTICIPANTS.

	Mean (range)	**Ratio**
Age (years)	67.2 (59.0-75.0)	
Gender (Female:Male)		0:5
Time after stroke onset (days)	16.2 (6.0-46.0)	
Stroke type (Ischemic:Hemorrhagic)		5:0
Impaired side (Left:Right)		1:4
MoCA (30 = minimum impairment)	23.8 (15.0-27.0)	
FMA-UE (66 = minimum impairment)	59.8 (52.0-64.0)	

A. Feasibility of unsupervised therapy with ReHandyBot

Four participants met the requirements defined by the checklist and could bring ReHandyBot home. For them, mean attendance during the unsupervised phase at home was 83.9% (57.1-100.0%). The participant who could not proceed to independent training at home with the device (i.e., P3) dropped out before starting the unsupervised phase. No adverse events related to the study protocol or device deficiencies were reported.

Age and level of impairment did not seem to affect the ability to train without supervision, as the oldest participant and the one with the lowest baseline FMA-UE score could train with ReHandyBot at home. In contrast, cognitive ability may be a relevant factor, as P3 had a lower MoCA score (i.e., 15) than the participants who could train without supervision with the device (MoCA $\geq$25).

During the unsupervised phase at home, one participant contacted one of the investigators once, as he could no longer turn on the device. After going to the participant's home, the investigator could solve the issue as it was not a technical problem, but the participant got confused and set the power switch to the wrong position.

B. Dose of unsupervised therapy and content of the therapy sessions performed with ReHandyBot

Over the two weeks of unsupervised therapy at home, on average, participants trained for a total of 518.3 (399.9-582.2) minutes with ReHandyBot. Considering only the days when the participants used the device, the mean daily therapy dose was 41.4 (36.4-46.8) minutes and the mean number of daily task repetitions was 146.3 (117.5-166.4). The increase in physical therapy time achieved by the participants thanks to training with ReHandyBot (compared to conventional therapy) was 177.5% (117.6-293.7%).

The content of the therapy sessions performed with ReHandyBot during the three phases of the study is reported in Table II.

TABLE II

CONTENT (MEAN (RANGE)) OF THE THERAPY SESSIONS PERFORMED WITH REHANDYBOT DURING THE SUPERVISED (SUP), MINIMALLY SUPERVISED (MIN), AND UNSUPERVISED (UNS) PHASES.

	SUP	**MIN**	**UNS**
Intensity (repetitions/minute)	2.0 (1.8-2.4)	3.3 (2.9-3.5)	3.5 (3.0-4.1)
Task performance (%)	59.3 (48.6-65.2)	69.0 (62.9-71.7)	67.4 (63.2-71.1)
Effective/total therapy time	0.6 (0.5-0.7)	0.8 (0.8-0.9)	0.8 (0.7-0.9)

C. Usability and user experience

The results of the usability and user experience questionnaires for participants who completed both usability evaluations (n=3) are reported in Table III and Table IV.

TABLE III

RESULTS (MEAN (RANGE)) FOR THE OUTCOME MEASURES RELATED TO THE USABILITY OF REHANDYBOT AND USER EXPERIENCE.

	Usability 1	**Usability 2**	**Difference**
SUS (0-**100**)	85.0 (80.0-95.0)	94.2 (90.0-97.5)	9.2 (2.5-15.0)
PSSUQ (**1**-7)	1.7 (1.2-2.1)	1.6 (1.0-1.9)	-0.1 (-0.3-0.2)
NPS (1-**10**)	9.0 (7.0-10.0)	9.0 (8.0-10.0)	0.0 (-2.0-3.0)
CSAT (1-**5**)	4.0 (4.0-4.0)	4.3 (4.0-5.0)	0.3 (0.0-1.0)
IMI (1-**7**)	6.0 (4.7-6.7)	6.2 (4.6-7.0)	0.2 (-0.1-0.4)

For each scale, the range of possible answers is indicated in brackets. The value corresponding to the best rating in terms of high usability and user experience is given in bold.

During the semi-structured interview, two participants mentioned that 45 minutes of therapy with ReHandyBot were very intense and tiring, and the break time between exercises should be increased or the overall session duration decreased.

When asked whether unsupervised therapy at home is helpful, participants agreed and said that they appreciated the possibility of training more. Furthermore, one stated that unsupervised therapy is a valid option only if persons are motivated to train and convinced that they are doing something beneficial for them. Another participant said, "A good occupational therapist is better than a robot. The combination of outpatient sessions with a therapist and the robot at home is good. Only having the robot is not."

Participants were also asked if they would consider paying to rent ReHandyBot, and they all answered that they probably would. Two participants mentioned that having evidence that a tool helps recover hand function is a crucial factor that would influence their decision on whether to pay for it or not.

TABLE IV

RESULTS (MEAN (RANGE)) FOR THE CUSTOM QUESTIONS (Q1-Q5) RELATED TO REHANDYBOT AND THE GAMING ENVIRONMENT.

		Usability 1	**Usability 2**	**Difference**
Q1.	The gaming environment motivated me to train more.	3.7 (1.0-7.0)	4.0 (2.0-5.0)	0.3 (-2.0-2.0)
Q2.	The gaming environment prevented me from focusing on the therapy exercises.	7.0 (7.0-7.0)	7.0 (7.0-7.0)	0.0 (0.0-0.0)
Q3.	If I could choose, I would remove the gaming environment from the therapy sessions.	7.0 (7.0-7.0)	7.0 (7.0-7.0)	0.0 (0.0-0.0)
Q4.	If I could choose, I would keep training with ReHandyBot at home.	N/A	2.7 (1.0-5.0)	N/A
Q5.	Reminders to do the unsupervised therapy sessions would have helped me to train more.	N/A	6.7 (6.0-7.0)	N/A

Possible answers ranged from 1 (i.e., completely agree) to 7 (i.e., strongly disagree). Q4-5 were only asked during Usability 2. N/A: not applicable.

Furthermore, one participant stated that if he could, he would have kept the device. Two others stated that their hand already recovered well. Therefore, they would have kept the device past the two weeks to continue training, but they mentioned that they would have likely not continued using it daily.

IV. DISCUSSION

The main goal of this pilot feasibility study was to determine whether people after a stroke could learn to independently use the active rehabilitation robot ReHandyBot while they were hospitalized in a rehabilitation clinic and then, once discharged, take it home to continue training without the supervision of any external person. Further goals were to investigate the increase in therapy dose achievable by training with the rehabilitation device at home compared to conventional care, as well as the usability of ReHandyBot and the user experience when training with it. The results presented here suggest that unsupervised therapy at home with ReHandyBot is feasible and can lead to an important increase in the dose of upper limb therapy performed by the patients. Furthermore, our study is one of the first to show the feasibility for stroke patients with mild to no cognitive impairments to use active, end-effector robotic devices for fully unsupervised home therapy.

A. Unsupervised therapy at home with ReHandyBot was feasible and allowed to increase therapy dose

The majority of the study participants were able to learn to operate the device independently, although they were part of one of the age groups that is expected to be less familiar with technology [23]. Participants who performed unsupervised therapy with ReHandyBot trained for more than 8 hours during the two weeks at home. The daily dose of unsupervised therapy achieved in this pilot study was higher than that reported in other studies evaluating the minimally supervised or unsupervised use of rehabilitation technologies by stroke patients or older adults. For example, the average daily use in [24] and [25] was 21 minutes over 4 weeks and 29 minutes over 8 weeks, respectively. Attendance (83.9%) and therapy dose (518 minutes) achieved here were also higher than the mean ones registered by patients training unsupervised at the clinic with the non-portable version of the ReHandyBot (i.e., ReHapticKnob) [9], which were 77% and 360 minutes, respectively. Since the protocol of the two studies was similar, this difference could be partly explained by the fact that, in the previous study, participants were inpatients already undergoing many conventional therapies, and we did not give precise recommendations on how much to train with the device.

As expected, the mean percentage increase in physical therapy time achieved in this pilot study thanks to unsupervised therapy with ReHandyBot is higher (around 4x) than that reported in [9], where the participants undergoing unsupervised robot-assisted therapy were inpatients of a rehabilitation clinic. This is mainly due to the drastic decrease in the dose of conventional therapy accessible to outpatients. These findings emphasize how unsupervised therapy with active devices at home is even more necessary than in a clinical setting when aiming to increase the therapy dose.

Although the increase in therapy dose achieved in this pilot study is important, the amount of additional upper limb therapy performed by the participants with ReHandyBot was still not as high as what seems necessary to lead to significant benefits (e.g., 25-30 hours per week [26], [2]). This suggests that, in the future, we should increase the recommended number of daily therapy sessions or recommend a number tailored to the individual patient's level of impairment. Another possibility would be to implement additional motivational strategies to encourage patients to train more. Indeed, although patients would not remove the gaming environment from the therapy sessions with ReHandyBot (Q3), its ability to boost motivation varies greatly between individuals (Q1).

Also worth noting is that the absence of the therapist did not negatively impact the therapy content, and consequently the therapy quality, between the different phases of the study. Indeed, intensity, task performance, and the ratio of effective to total therapy time during the unsupervised phase were similar to the minimally supervised phase and greater than during the supervised phase. Lower values for the supervised sessions can be explained by the fact that in this phase patients were unfamiliar with the device and the exercises, and more time was dedicated to instructions.

B. ReHandyBot showed good usability and user experience

The metrics tested in Usability 1 and Usability 2 remained stable or improved between the two time points, indicating that the home setting and the absence of the therapist did not negatively affect the perceived usability of ReHandyBot and the user experience.

The NPS, CSAT, and IMI ratings suggest that participants were satisfied, enjoyed training with the device, and would

recommend it to other patients. According to the mean SUS results ($\geq$85), the usability of ReHandyBot is good to excellent [27]. The mean SUS scores obtained here are higher than those obtained by other devices tested with minimal or no supervision. For example, the SUS score for the MERLIN (i.e., a passive device for the upper limbs) was 77 [28].

C. Limitations and future work

The number of participants included in this pilot feasibility study was low, and the unsupervised phase at home lasted only two weeks. Therefore, the results must be interpreted carefully, and more data is needed to draw conclusions, specifically with respect to the potential clinical benefits of this approach. Moreover, the patients enrolled in this study had mild upper limb impairment. While we know from previous work that our device can also be used by more severely impaired patients, it would still need to be verified how these preliminary results translate to this population. In fact, moderately and severely impaired patients are the ones who should benefit most from training with ReHandyBot and might be more motivated to increase their therapy dose.

However, the preliminary findings of this study are encouraging and support testing unsupervised training with ReHandyBot with more subjects and for a longer time (i.e., 6 weeks of unsupervised therapy at home) to verify if the increase in therapy dose and high attendance can be maintained.

ACKNOWLEDGMENT

The authors would like to thank the study participants and all the therapists and physicians of the Clinica Hildebrand Centro di riabilitazione Brissago who contributed to this study.

REFERENCES

[1] E. S. Lawrence et al., "Estimates of the Prevalence of Acute Stroke Impairments and Disability in a Multiethnic Population," Stroke, vol. 32, no. 6, pp. 1279–1284, 2001.

[2] N. S. Ward, F. Brander, and K. Kelly, "Intensive upper limb neurorehabilitation in chronic stroke: Outcomes from the Queen Square programme," J Neurol Neurosurg Psychiatry, vol. 90, no. 5, pp. 498–506, 2019.

[3] T. S. Jesus, M. D. Landry, G. Dussault, and I. Fronteira, "Human resources for health (and rehabilitation): Six Rehab-Workforce Challenges for the century," Hum Resour Health, vol. 15, no. 1, 2017.

[4] M. Broderick, L. Almedom, E. Burdet, J. Burridge, and P. Bentley, "Self-Directed Exergaming for Stroke Upper Limb Impairment Increases Exercise Dose Compared to Standard Care," Original Research Article Neurorehabilitation and Neural Repair, vol. 35, no. 11, pp. 974–985, 2019.

[5] F. Wittmann et al., "Self-directed arm therapy at home after stroke with a sensor-based virtual reality training system," J Neuroeng Rehabil, vol. 13, no. 75, 2016.

[6] F. Bressi et al., "Upper limb home-based robotic rehabilitation in chronic stroke patients: A pilot study," Front Neurorobot, vol. 17, p. 1130770, 2023.

[7] R. Ranzani et al., "Towards a Platform for Robot-Assisted Minimally-Supervised Therapy of Hand Function: Design and Pilot Usability Evaluation," Front Bioeng Biotechnol, vol. 9,2021.

[8] G. Devittori et al., "Automatic and Personalized Adaptation of Therapy Parameters for Unsupervised Robot-Assisted Rehabilitation: a Pilot Evaluation," IEEE International Conference on Rehabilitation Robotics, vol. 2022-July, 2022.

[9] G. Devittori et al., "Unsupervised robot-assisted rehabilitation after stroke: feasibility, effect on therapy dose, and user experience," J Neuroeng Rehabil, vol. 21, no. 1, pp. 1–11, 2024.

[10] R. Ranzani, G. Chiriatti, A. Schwarz, G. Devittori, R. Gassert, and O. Lambercy, "An online method to monitor hand muscle tone during robot-assisted rehabilitation," Front Robot AI, vol. 10, p. 14, 2023.

[11] J. C. Metzger et al., "Neurocognitive robot-assisted therapy of hand function," IEEE Trans Haptics, vol. 7, no. 2, pp. 140–149, 2014.

[12] G. Devittori et al., "Progressive Transition From Supervised to Unsupervised Robot-Assisted Therapy After Stroke: Protocol for a Single-Group, Interventional Feasibility Study," JMIR Res Protoc, vol. 12, no. 1, p. e48485, 2023.

[13] T. J. Quinn et al., "Pre-stroke modified Rankin Scale: Evaluation of validity, prognostic accuracy, and association with treatment," Front Neurol, vol. 8, no. JUN, p. 275, 2017.

[14] T. Brott et al., "Measurements of acute cerebral infarction: A clinical examination scale," Stroke, vol. 20, no. 7, pp. 864–870, 1989.

[15] W. Huber, G. Klingenberg, K. Poeck, and K. Willmes, "Die Supplemente zum Aachener Aphasie Test: Aufbau und Resultate der Validierung," Neurolinguistik: Zeitschrift für Aphasieforschung und -therapie, vol. 7, pp. 43–66, 1993.

[16] C. Hagen, "Rancho Levels of Cognitive Functioning-Revised," TBI rehabilitation in a managed care environment: An interdisciplinary approach to rehabilitation, Continuing Education Programs of America, San Antonio, TX, 2000.

[17] C. P. Charalambous, "Interrater reliability of a modified ashworth scale of muscle spasticity," Classic Papers in Orthopaedics, vol. 67, pp. 415–417, 2014.

[18] Z. S. Nasreddine et al., "The Montreal Cognitive Assessment, MoCA: A Brief Screening Tool For Mild Cognitive Impairment," J Am Geriatr Soc, vol. 53, no. 4, pp. 695–699, 2005.

[19] A. R. Fugl Meyer, L. Jaasko, and I. Leyman, "The post-stroke hemiplegic patient. 1. a method for evaluation of physical performance." Scand J Rehabil Med, vol. 7, no. 1, pp. 13–31, 1975.

[20] J. Brooke, "SUS-A quick and dirty usability scale," Usability Eval. Ind., vol. 189, 1996.

[21] J. R. Lewis, "Psychometric Evaluation of the PSSUQ Using Data from Five Years of Usability Studies," Int J Hum Comput Interact, vol. 14, no. 3–4, pp. 463–488, 2002.

[22] F. F. Reichheld, "The One Number You Need to Grow," Harvard Business Review, 2003. Accessed: Sep. 01, 2022. [Online]. Available: https://hbr.org/2003/12/the-one-number-you-need-to-grow

[23] J. Nicosia et al., "Bridging the Technological Divide: Stigmas and Challenges With Technology in Digital Brain Health Studies of Older Adults," Front Digit Health, vol. 4, p. 880055, 2022.

[24] B. Radder et al., "Home rehabilitation supported by a wearable soft-robotic device for improving hand function in older adults: A pilot randomized controlled trial," PLoS One, 2019.

[25] M. G. Lansberg et al., "Home-based virtual reality therapy for hand recovery after stroke," PM R, vol. 14, no. 3, pp. 320–328, 2022.

[26] J. McCabe, M. Monkiewicz, J. Holcomb, S. Pundik, and J. J. Daly, "Comparison of robotics, functional electrical stimulation, and motor learning methods for treatment of persistent upper extremity dysfunction after stroke: A randomized controlled trial," Arch Phys Med Rehabil, vol. 96, no. 6, pp. 981–990, 2015.

[27] A. Bangor, P. T. Kortum, and J. T. Miller, "An Empirical Evaluation of the System Usability Scale," Int J Hum Comput Interact, vol. 24, no. 6, pp. 574–594, 2008.

[28] S. G. Rozevink, C. K. van der Sluis, A. Garzo, T. Keller, and J. M. Hijmans, "HoMEcare aRm rehabiLItatioN (MERLIN): telerehabilitation using an unactuated device based on serious games improves the upper limb function in chronic stroke," J Neuroeng Rehabil, vol. 18, no. 1, 2021.

Motion Range and Control of an Escort-Type Upper Limb Rehabilitation Robot for Assisting Reaching Motion

Kiyoshi Nagai*, Muhammad Syahmi Tuan†, Hariz Akmal†, Fumiaki Amano‡, Yanming Zhou‡, Rui C. V. Loureiro§ and William S. H. Harwin¶

*College of Science and Engineering, Ritsumeikan University, Kusatsu, Japan, nagai@se.ritsumei.ac.jp

†College of Science and Engineering, Ritsumeikan University, Kusatsu, Japan

‡Graduate School of Science and Engineering, Ritsumeikan University, Kusatsu, Japan

§Aspire Centre for Rehabilitation Engineering and Assistive Technology, UCL, London, UK

¶Department of Bioengineering, University of Reading, Reading, UK

***Abstract*—To secure the amount of rehabilitation in motor function recovery training after stroke, it is important to realize a rehabilitation robot for the upper limb to guide the reaching motion of patients in the acute and convalescent phases of rehabilitation in hospitals and in the maintenance phase of rehabilitation at home without a therapist. Therefore, in this study, the escort-type rehabilitation robot, which has been proposed as a structure to guide the user's hand position and arm posture, is shown to have a motion range for the user's reaching motion including arm posture. In addition, it is shown that the escort-type rehabilitation robot can guide reaching motion for the arm posture as well as the hand position and can also guide functional reach in collaboration with the user's trunk motion, proven by simulation and experiment.**

I. Introduction

Many studies have suggested the effectiveness of robot-assisted therapy using upper limb rehabilitation robots for training the recovery of upper limb motor function after stroke [1] [2]. This robot-assisted therapy is based on brain plasticity [3], and assists repetitive motion and task-oriented training [1]. The upper limb rehabilitation robot are classified into end-effector type rehabilitation robots that hold the upper limb near the hand and exoskeleton type rehabilitation robots with a similar structure to the upper limb [4] [5].

Examples of endeffector-type rehabilitation robot development include MIT-MANUS which guides arm motions while supporting the hand and forearm with a planar arm [6], InMotion ARM which was developed as its successor [7], GENTLE/s which guides arm reaching motions with a 3-DOF arm [8] and Gentle/G which is also equipped with a mechanism to guide hand motions [9], and NeReBot which guides the arm by suspending it with wires [10] [11] which is guided by suspending the arm with a wire. Examples of exoskeletal rehabilitation robots include the T-WREX [12] [13], the ARMin-II [14], and the Harmony [15]. Comparing these two forms, endeffector-type robots are easier to precisely control the hand position, while exoskeleton robots are easier to support the arm posture [4]. The basic issue in the mechanical design of these rehabilitation robots is how to provide an upper limb motion guidance function.

Reaching motion of stroke patients targeted by such robots has been reported to produce characteristics that differ from those of healthy subjects [16]. In addition, it has been shown that the reaching motion of stroke patients is more dependent on compensatory movements than that of healthy subjects [17]. Based on the above, it would be desirable that the robot's reaching motion guidance of the upper limb described above suppress compensatory movements and provide a more natural motion pattern for the entire upper limb, including the hand position and arm posture.

On the other hand, for exoskeletal robots, to address the problem of misalignment between the robot's shoulder joint position and the patient's vulnerable shoulder joint position, the introduction of compliant actuation [18] and the automatic adjustment to decrease the misalignment [19] have been reported. However, considering that the trunk plays an important role in reaching motion, it is desirable to be able to perform a functional reach [20] that collaborates the upper limb motion and the shoulder position motion by the trunk.

To address this problem, the authors' research team has shown the usefulness of employing the rehabilitation robot structure that we call the escort-type [21]. This escort-type robot, like the end-effector type, is designed to be attached to the forearm of the patient's upper limb to guide the reaching motion. However, (1) it can provide arm posture guidance as well as hand position guidance, and (2) it does not constrain the shoulder joint position, thus allowing functional reach. In addition, a new escort-type rehabilitation robot structure has been proposed [22] [23], but the research is limited to basic kinematic analysis concerning the validity of the structure.

Therefore, the objective of this study is set to clarify that this escort-type rehabilitation robot is suitable for guiding reaching motion. The research subjects are set to clarify the motion range required for reaching motion in consideration of safety [24], and to clarify that this robot can guide reaching motion including arm posture and that it can tolerate functional reach.

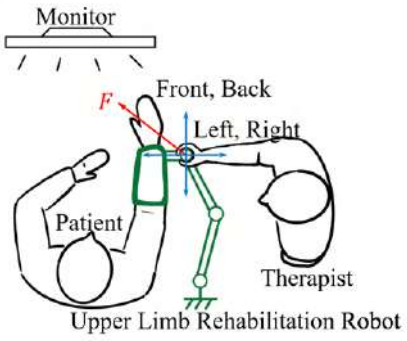


Fig. 1: Robot intervening in rehabilitation

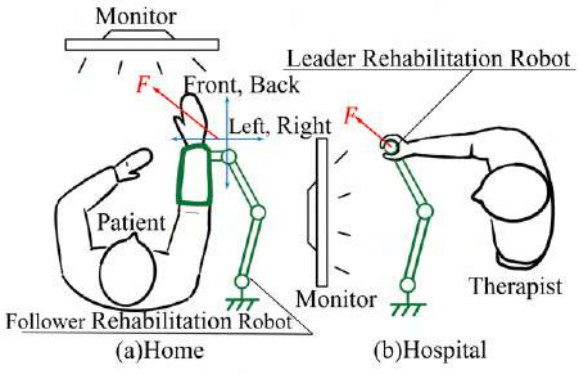


Fig. 2: Teleoperated rehabilitation robot

This paper is organized as follows. Section 2 describes the basic concept of the escort-type rehabilitation robot, the robot under discussion, and the problem statement. Section 3 clarifies how to calculate the motion range of the robot when it is attached to an upper limb dummy robot. In Section 4, simulation results show that the robot is capable of both hand position guidance and arm posture guidance, and that it can tolerate functional reach. In Section 5, experiments are described to examine the validity of the robot. In the concluding section, the findings of this study are presented.

II. Proposed Escort-type Rehabilitation Robot

A. Concept on Upper Limb Rehabilitation Robot

Fig.1 shows a conceptual diagram of a rehabilitation robot for upper limb that is used in the acute/convalescent phase of rehabilitation in hospitals for training the recovery of upper limb motor function. Here, the therapist applies manipulative force to the rehabilitation robot attached to the patient's forearm to guide the reaching motion of the patient whose upper limb has been paralyzed due to stroke. With this configuration, the rehabilitation robot can record changes in the position and posture of the patient's hand on the upper limb, changes in the force applied by the robot to the patient, and changes in the force applied by the therapist to the robot, if any. The recorded information could be used to assess the patient's recovery.

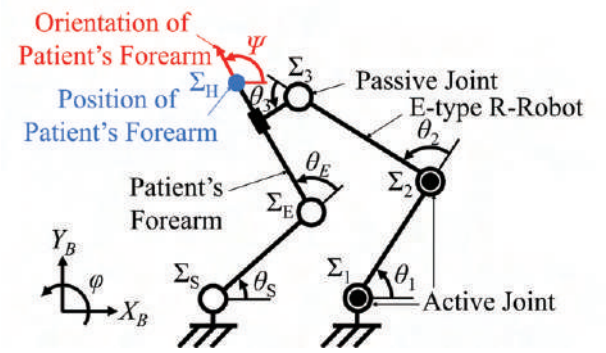


Fig. 3: Conceptual diagram of escort-type rehabilitation robot

Fig.2 shows a conceptual diagram of a teleoperated rehabilitation robot base on a leader-follower type rehabilitation robot for upper limbs to be used in convalescent phase rehabilitation in hospitals after acute phase rehabilitation and in maintenance phase rehabilitation at home. By using such a leader-follower type robot, not only can record changes in position and force as in the acute/convalescent phase rehabilitation, but also can guide the patient's reaching motion during the maintenance phase rehabilitation at home, where therapists are not present. Combined with the information recorded during the acute/convalescent phase of rehabilitation, this information can be used to assess the patient's level of recovery in a series of rehabilitation. The use of this rehabilitation robot in the hospital before the patient is discharged from the hospital will provide practice for the maintenance phase rehabilitation at home.

To design the robots shown in Fig.1 and Fig.2 so that they can be regarded as the same robot by patients and therapists is a useful way to secure the amount of rehabilitation in a series of acute, convalescent, and maintenance phases. For this reason, this idea can be stated as the design concept of this rehabilitation robot.

Fig.3 is a conceptual diagram of an escort-type upper limb rehabilitation robot that is attached to a patient's forearm to guide the reaching motion of the upper limb. The robot includes both active and passive joints. The active joints control the movement, while the passive joint allows flexibility when attached to the patient' s forearm. This setup ensures that both the patient's and the robot' s arm postures remain fixed during movement. However, the passive joint does not constrain the patient' s shoulder position. In the three-dimensional version of this robot described below, the robot can also guide the patient' s arm posture while assisting reaching motion.

B. Escort-Type Rehabilitation Robot

Fig.4 describes the structure for the escort-type upper limb rehabilitation robot attached to a dummy robot. The dummy robot acts as patient in upper-limb rehabilitation and the escort-type robot is attached at the patient forearm at the point O_A. This figure indicates the arm posture at the initial position, where the escort-type robot's joint angles θ_1 to θ_3 are set to 90° and θ_4 to θ_5 are set to 0°, while the dummy

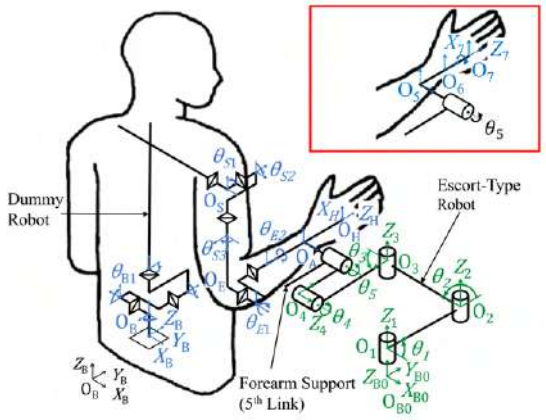


Fig. 4: Proposed escort-type rehabilitation robot [22] [23]

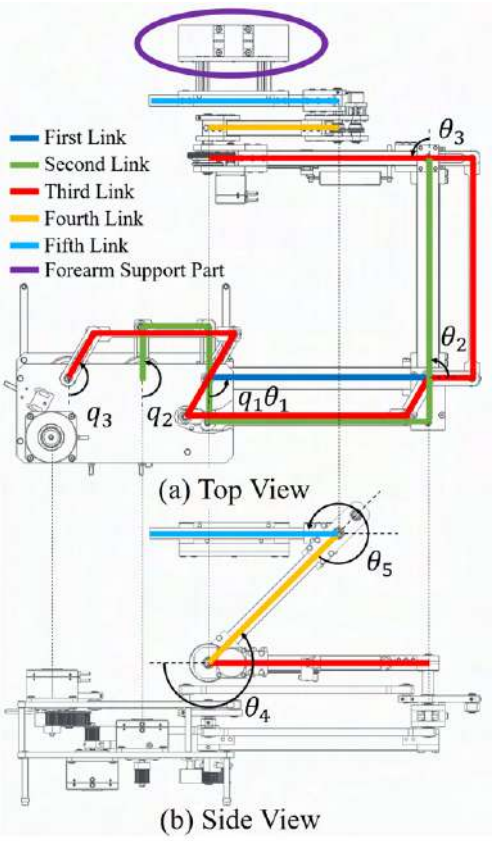


Fig. 5: Escort-type rehabilitation robot kinematic model

robot's arm adopts an L-shaped posture. This configuration is chosen because it provides a clear and structured reference pose, making it easier to analyze joint movements. When the escort-type robot attached to the dummy robot, inverse kinematics can be determined that will be explained clearly in the next subsection. The escort-type robot shown in Fig.5 has four active joints (joints 1 to 4) and a passive joint (joint 5), and a forearm support to be attached to the patient's forearm. These four active joints are used to guide the translational position x, y, z of the hand and the yaw angle ψ, which is

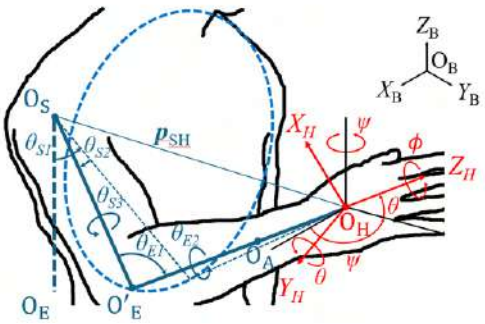


Fig. 6: Orientation of hand and arm posture

a part of the arm posture. The DH parameters of the escort-type upper limb rehabilitation robot and the dummy robot are described in the appendix.

C. Problem Statement

In this study, the following two problem statements are made in accordance with the research subject.

1) To clarify the method of deriving the motion range of the escort-type rehabilitation robot for the upper limb.
2) To clarify that the escort-type rehabilitation robot for the upper limb has a structure that (a) enables arm posture guidance as well as hand position guidance in guiding reaching motion, and (b) allows functional reach.

In 1), it should be noted that in the case of escort-type rehabilitation robots with passive joints, the arm posture of both the patient and the robot are determined when the robot is attached to the patient's arm (in this study, to the arm of the dummy robot). Therefore, when using inverse kinematics to derive the motion range, the arm posture of the robot is derived after the arm posture of the patient is derived for the condition in which the robot is attached to the patient's arm.

On the other hand, note that in 2) (a), different arm postures can be taken for the same hand position guidance in reaching motion. Also, in 2) (b), it is to be shown that the shoulder position can be shifted for functional reach while the escort-type rehabilitation robot is guiding the reaching motion.

III. Motion Range

A. Inverse Kinematics

To determine the motion range of an escort-type rehabilitation robot, we assume that the robot is attached to the forearm of the upper limb dummy robot described above. The position and posture of the hand are then given as grid points in the hand space, and each joint angle obtained by inverse kinematics is examined to judge whether it is within the range of each feasible joint angle.

Fig.6 shows that the hand posture can be represented by the roll angle ϕ, the pitch angle θ, and the yaw angle ψ. However, in the escort-type upper limb rehabilitation robot, ϕ is excluded from the target to be guided. Additionally, θ and ψ are not independent when the dummy robot's forearm is attached to the escort robot' s 5-th link at point $\mathrm{O_A}$, as no free motion

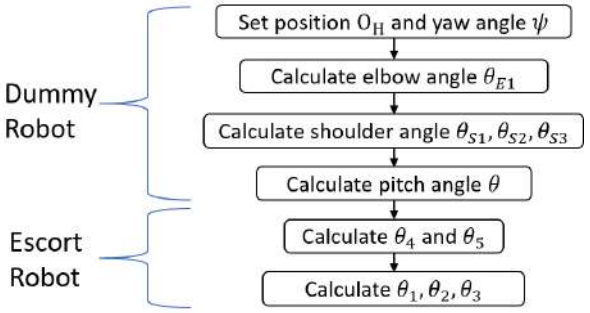


Fig. 7: Flow chart of inverse kinematics

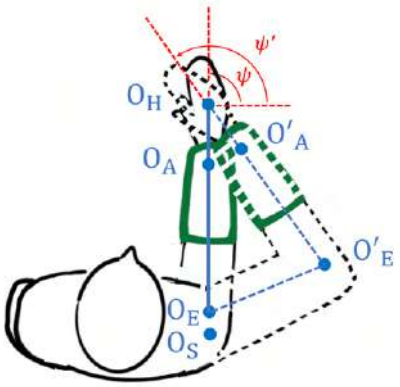


Fig. 8: Relation between yaw angle ψ and arm posture

remains. Once the yaw angle, ψ is set and the shoulder position O_S is fixed, the arm posture is reduced to a single degree of freedom (1-DOF). Therefore, in the inverse kinematics, the hand position and orientation are given by the total four components of x, y, z of the point O_H on the hand, and the yaw angle ψ. In the inverse kinematics explained below, the pitch angle θ is first obtained for the given hand position and posture based on the geometric relationship among the patient's shoulder position O_S, elbow position O_E and hand position O_H.

As shown in Fig.7, the procedure to calculate inverse kinematic for the attached escort and dummy robots begins by determining the dummy robot's angles based on the target hand position O_H and yaw angle ψ, followed by the escort robot's angles. The forearm twist angle θ_{E2} is set to $0°$ because torsional roll angle ϕ at hand shown at Fig.6 is not subject to induction as we assume no bending occurs at wrist since dummy robot is used instead of patient's hand. Next, we set shoulder position O_S as reference point to calculate elbow angle θ_{E1} in order to determine the elbow position at O_E. From all positions of O_H, O_E, and O_S, the shoulder angles θ_{S1}, θ_{S2}, and θ_{S3} are calculated to ensure the angles are within the constraints.

Next, the fourth joint angle θ_4 is calculated by focusing on the O_A and O_4 positions. Then, the fifth joint angle θ_5 is calculated from the obtained pitch angle θ and the fourth joint angle θ_4. The position of O_3 can be obtained from the positional relationship with O_4 because the third link L_3 is oriented toward the yaw angle ψ. L_1, L_2 are first obtained for the second joint angle θ_2, and then for the first joint angle θ_1. Finally, the third joint angle θ_3 is obtained from ψ, θ_1 and θ_2. By determining that these angles are within the constraints of the escort robot and dummy robot, it is possible to determine the range of motion. The described inverse kinematics is essential for using it both simulation and experiment.

B. Analysis of Motion Range

Motion range can be determined by constraints of escort robot and dummy robot which is can lead to define the forearm motion and the range that escort robot can be reach to guide patient's hand.

The folowing describes the robot's constraint ranges:

a) Joint constraints for escort robot
$\frac{\pi}{6} \leq \theta_1 \leq \frac{5\pi}{6}, \frac{\pi}{6} \leq \theta_2 \leq \frac{5\pi}{6}, \frac{\pi}{6} \leq \theta_3 \leq \frac{5\pi}{6}$
$\pi \leq \theta_4 \leq \frac{3\pi}{2}, -\frac{2\pi}{3} \leq \theta_5 \leq \frac{2\pi}{3}$

b) Joint constraints for dummy robot
$\frac{5\pi}{18} \leq \theta_{S1} \leq \frac{4\pi}{3}, 0 \leq \theta_{S2} \leq \pi, \frac{\pi}{6} \leq \theta_{S3} \leq \frac{8\pi}{9}$
$0 \leq \theta_{E1} \leq \frac{29\pi}{36}$

c) Rehabilitation-specific joints constrain
$\frac{\pi}{6} \leq \theta_1 \leq \frac{5\pi}{6}, \frac{\pi}{6} \leq \theta_2 \leq \frac{5\pi}{6}, \frac{\pi}{6} \leq \theta_3 \leq \frac{5\pi}{6}$
$\frac{17\pi}{18} \leq \theta_4 \leq \frac{3\pi}{2}, \frac{7\pi}{4} \leq \theta_5 \leq 2\pi$
$\frac{5\pi}{18} \leq \theta_{S1} \leq \pi, 0 \leq \theta_{S2} \leq \frac{\pi}{2}, \frac{\pi}{6} \leq \theta_{S3} \leq \frac{8\pi}{9}$
$0 \leq \theta_{E1} \leq \frac{29\pi}{36}$

The rehabilitation-specific joint constraints for the escort and dummy robots are designed to ensure safety and prevent strain to the patient, especially at the shoulder. For the escort robot, θ_4 is limited to at least $170°$ as the forearm starts from an initial position of π and may drop around $10°$ due to gravity, and θ_5 is restricted between $0°$ and $45°$ to prevent the elbow from moving above shoulder level. For the dummy robot, the shoulder's angles θ_{S1}, θ_{S2} are restricted to prevent hand movements above the shoulder and to accommodate the escort robot's link lengths. These constraints will determine the range of motion described in Fig.9 so that the motion range will be included in the safe range to avoid injury to the patient. The joint ranges also have been modified for inverse kinematics, ensuring the range boundaries remain within these real constraints to ensure safety during rehabilitation.

Fig.8 shows a topview image of the arm postures corresponding to the yaw angles ψ and ψ', when the shoulder position O_S and the hand position O_H are constant. The arm posture can be obtained using the inverse kinematics described above by specifying ψ or ψ'. This figure indicates the arm posture at initial position will be change according to the maximum value of yaw angle within robot constrain.

Fig.9 shows positions O_H are set with increments of 0.15 meters in the X or Y axis and 0.1 meters in the Z axis, allowing for a detailed analysis of forearm motion. The motion is calculated from the minimum of yaw angle ψ, from $\frac{\pi}{2}$ to the

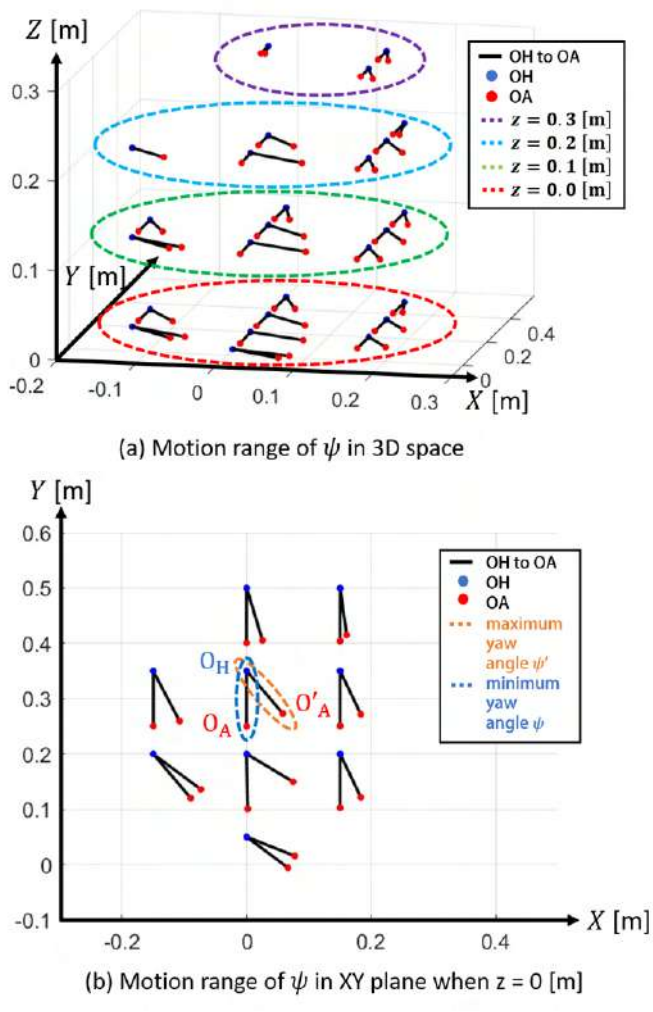


Fig. 9: Motion range of ψ at each translational position

maximum yaw angle. The initial position $\boldsymbol{p}_S = [0\ 0.35\ 0]^{\mathrm{T}}[\mathrm{m}]$ indicate at the Fig.8 and Fig.9(b) shows arm posture change reaching the maximum value of yaw angle 127°. This motion range of ψ can be determined by constrains of escort robot and dummy robot.

In order to ensure that the robot's motion range includes the motion range required for reaching motion and that the robot's footprint is small, it is necessary to design the mechanism using not only the setting of the robot's base position but also the setting of constraints on link lengths and joint angles.

IV. Simulation

A. Design Parameters

This subsection defines the design parameters for constructing the real escort-type upper limb rehabilitation robot and its simulation model. Despite having a parallel link mechanism, it is treated as a serial link robot, excluding the auxiliary link in discussions of hand characteristics.

The link lengths from the root of each i-th link to its center of mass are given by $L_{Ci} = [L_{C1}\, L_{C2}\, L_{C3}\, L_{C4}\, L_{C5}]^{\mathrm{T}} = \left[\frac{L_1}{2}\ \frac{L_2}{2}\ \frac{L_3}{2}\ \frac{L_4}{2}\ \frac{L_5}{2}\right]^{\mathrm{T}}$[mm]. The material density is defined as $\rho = 2.69 \times 10^{-3}$ [g/mm^3], while the mass of each link is computed using $m_i = \rho A_i B_i L_i$, where A_i and B_i represent the link height and width, respectively, with values $A_i = B_i = [30\ 30\ 30\ 20\ 15]^{\mathrm{T}}$ mm.

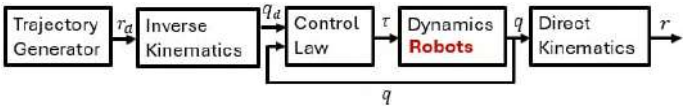


Fig. 10: Control system of escort-type rehabilitation robot

B. Control System and Issues for Investigation

This section simulates motion control for guiding the dummy robot' s reaching motion with the escort-type rehabilitation robot. The effectiveness of this guidance is shown from two perspectives.

1) Escort-type rehabilitation robot can provide arm posture guidance as well as hand position guidance.
2) Escort-type rehabilitation robots allow trunk movements to perform Functional Reach.

Fig.10 is the control system for guiding the reaching motion of the upper limb dummy robot by the escort-type rehabilitation robot. In this case, the handling of the hand position and posture is the same as in the motion range analysis in the previous section. That is, the target hand position $\boldsymbol{r}_d$ of the upper limb dummy robot is represented by four components: three components of the target hand translational position $\boldsymbol{p}_d$ and one component of the target hand posture angle ψ_d. The time function is used as the target hand trajectory. Inverse kinematics calculates the target value $\boldsymbol{\theta}_d$ of the joint angles $\boldsymbol{\theta}$ of the four active joints defined by the DH notation, and further calculates the target value $\boldsymbol{q}_d$ of the joint angle $\boldsymbol{q}$ defined according to the mechanical structure. The control input is determined using a PD control law, expressed as $\tau = K_p(q_d - q) - K_d(\dot{q}_d - \dot{q})$, where the proportional and derivative gains are set to $K_p = 1.2$ and $K_d = 0.8$. The dynamics of the escort-type rehabilitation robot used in the simulation is obtained by Simscape Multibody in MATLAB/Simulink. The monitoring of the hand position $\boldsymbol{r}$ in the simulation is calculated by applying forward kinematics to the joint angle $\boldsymbol{q}$.

C. Guiding Reaching Motion in Different arm Postures

The reaching motion was conducted to investigate whether the escort-type upper limb rehabilitation robot can assist the dummy robot in reaching its desired position, not only when the yaw angle remains constant throughout the rehabilitation but also while accommodating various yaw angles to adjust the arm posture. Fig.11 shows the arm postures of the dummy robot as the escort-type upper limb rehabilitation robot assists it in reaching $\boldsymbol{p}_{OH2} = [0\ 0.48\ 0]^{\mathrm{T}}[\mathrm{m}]$. Escort-type upper limb rehabilitation robot is being attached to the forearm of dummy robot on point $\mathrm{O_{A1}}$. Dummy robot's shoulder is fixed throughout the entire simulation on $\boldsymbol{p}_{OS} = [0\ 0\ 0.3]^{\mathrm{T}}[\mathrm{m}]$, and

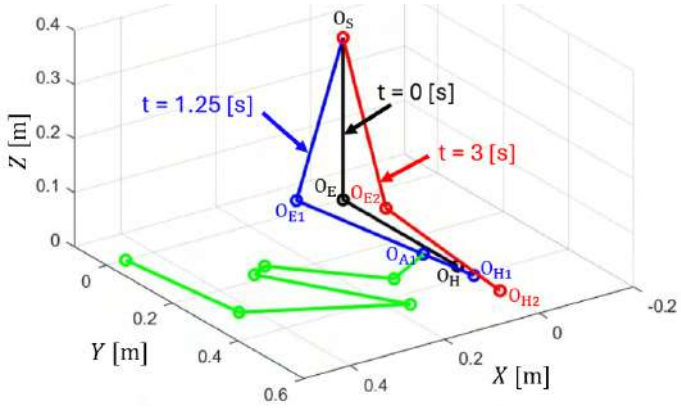


Fig. 11: Dummy robot arm posture when t = 0, 1.25 and 3[s]

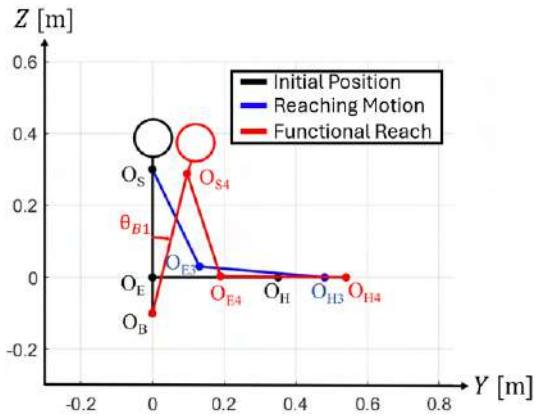


Fig. 13: Reaching motion (RM) and functional reach (FR)

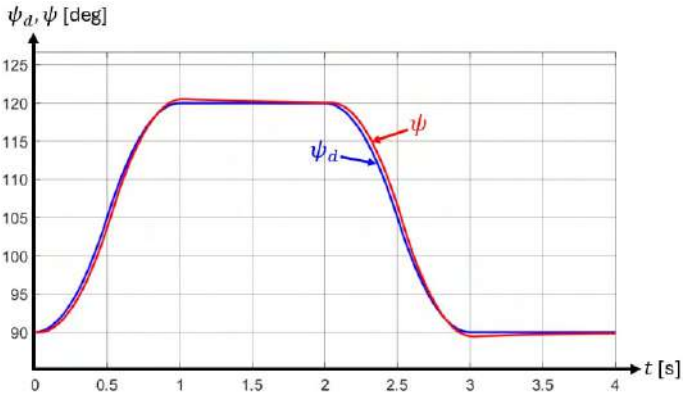


Fig. 12: Desired yaw angle ψ_d and its response ψ

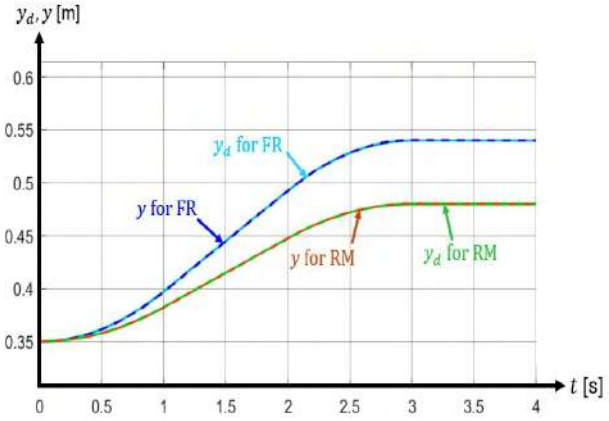


Fig. 14: Desired y position y_d and response y in RM and FR

the initial position of its hand is $\boldsymbol{p}_{OH} = [0\ 0.35\ 0]^{\mathrm{T}}[\mathrm{m}]$ on yaw angle 90° when t = 0 [s]. Then, the dummy robot will be assisted to reach $\boldsymbol{p}_{OH1} = [0\ 0.4\ 0]^{\mathrm{T}}[\mathrm{m}]$ when t = 1.25 [s] while changing the yaw angle from 90° to 120°. Lastly, the dummy robot will reach the desired position when t = 3 [s] and the yaw angle will be guided back from 120° to 90°. The proposed robot is able to guide the arm posture to achieve the desired yaw angles as shown in Fig.12. This tells that the escort-type upperlimb rehabiliation robot can help the patients to improve their arms mobility across all axes and not just on fixed yaw angle.

D. Allowing Trunk Movements for Functional Reach

This section describes the simulation of escort-type upper limb rehabilitation robot assisting dummy robot in two conditions which are reaching motion, RM (shoulder position is fixed) and functional reach, FR (shoulder position is not fixed). Fig.13 shows both conditions as the desired position for reaching motion is $\boldsymbol{p}_{OH3} = [0\ 0.48\ 0]^{\mathrm{T}}[\mathrm{m}]$ and functional reach is $\boldsymbol{p}_{OH4} = [0\ 0.54\ 0]^{\mathrm{T}}[\mathrm{m}]$. Both simulation using constant yaw angle throughout the simulation which is 90°. For functional reach, the proposed robot can be set to guide the dummy robot to reach a further position within the safe range as bending motion is allowed. In this case, the dummy robot's body will be assist to bend 14° to reach $\boldsymbol{p}_{OH4} = [0\ 0.54\ 0]^{\mathrm{T}}[\mathrm{m}]$. The actual trajectory for both conditions obtained from the simulation is close to the desired trajetoryas shown in Fig.14, which tells that the escort-type upper limb rehabilitation robot can also guide the body of dummy robot within safe range.

The above simulation results show that the proposed escort-type rehabilitation robot can simultaneously guide the arm posture while guiding the hand position for reaching motion, without fixing the shoulder joint position as an exoskeleton-type rehabilitation robot does.

When the proposed escort-type robot is deployed in actual clinical practice, we believe it will function effectively in a series of rehabilitation as described in Section 2.

V. Experiment

Fig.15 and Fig.16 show a photograph of the Escort-Type upper limb rehabilitation robot prototype attached to the forearm of an upper limb dummy robot, when we confirmed that the robot could take an arm posture to guide the reaching motion of the upper limb dummy robot. Torque control is used for this experiment same as simulation and input is determined the same way as simulation where the proportional and derivative gains are set to $K_p = 2.0$ and $K_d = 0.05$. In this prototype, a 70W DD motor is used as the drive motor for the first, second, and third joints, and is installed on the base. A pulley and a

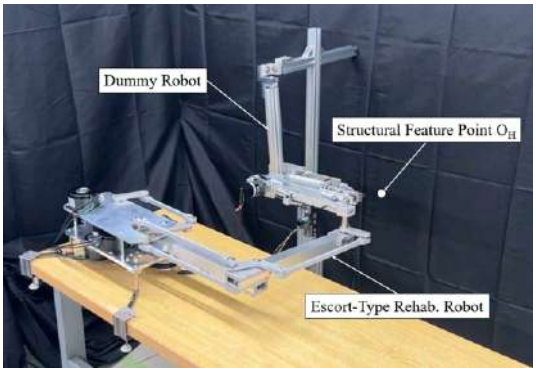


Fig. 15: Photo of escort-type robot during initial position

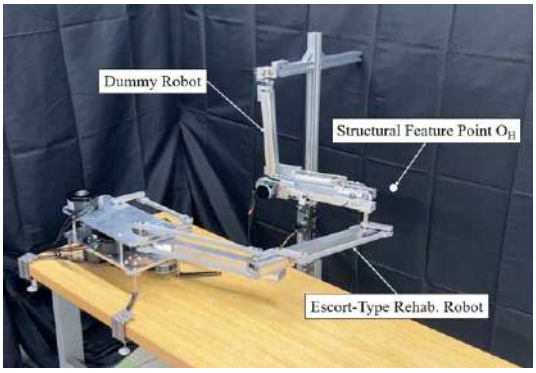


Fig. 16: Photo of escort-type robot during reaching motion

timing belt constitute the drive unit with the reduction ratio of 3. A 40W DD motor is used as the drive motor for the fourth joint, installed at the tip of the third link, and a gear is used to configure the drive unit with the reduction ratio of 5. Since the weight of the arm is added to the fourth joint, a gravity compensation mechanism using a spring is installed to generate the necessary driving force.

On the other hand, the upper limb dummy robot has a joint structure that resembles a human upper limb and upper body, all of which are non-driven joints, as described above. In addition, the shoulder position of the upper limb dummy robot is fixed by three joints in the waist that generate forward and backward tilting of the upper body, right and left tilting, and torsion.

In order to correspond to the aforementioned simulation, this prototype is planned to adopt a different arm posture when guiding the reaching motion of the upper limb dummy robot. The real-time control system for this prototype is based on Simulink Desktop Real-Time, which runs on a PC.

Fig.17 and Fig.18 show the experimental results of guiding hand with the same desired trajectory of hand position and yaw angle as described in the simulation section. During functional reach, the dummy robot's body bends because the shouder is not fixed, causing the shoulder position in the Y axis to increase as it moves forward, reaching a maximum at $\boldsymbol{p}_{OS} = [0\ 0.11\ 0.28]^{\mathrm{T}}[\mathrm{m}]$. Hence, the result shows that arm posture and hand can be guide when shoulder is fixed or not proven

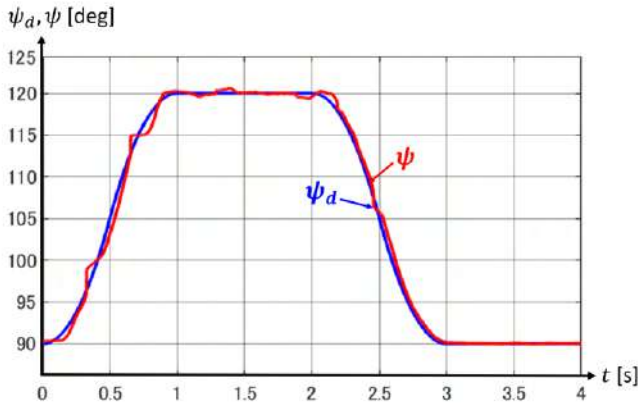


Fig. 17: Desire yaw angle ψ_d and its response ψ

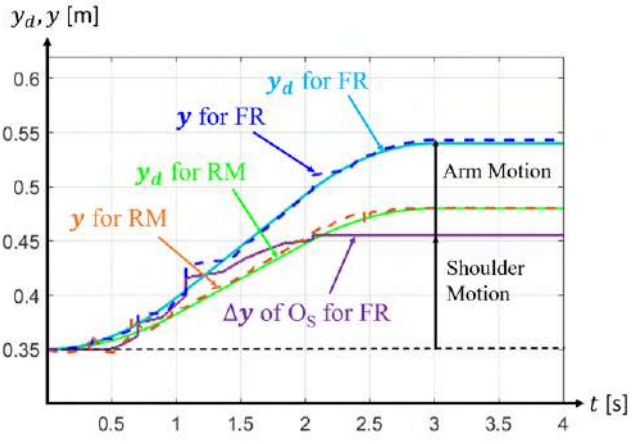


Fig. 18: y position and shoulder position in RM and FR.

by experiment as well as simulation.

VI. Conclusion

The findings obtained in this study are as follows.

1) The method for deriving the motion range of an escort-type rehabilitation robot for the upper limb was clarified. In the escort-type rehabilitation robot with passive joints, the arm postures of both the patient and the robot will be determined when the robot is attached to the patient's arm (or to the arm of a dummy robot in this study). Therefore, the inverse kinematics of the robot for deriving the range of motion is performed on the patient's arm, and the arm posture of the robot is derived after the arm posture of the patient is derived.
2) The escort-type rehabilitation robot for upper limbs was found to have the following two features: (1) The structure enables simultaneous hand position guidance and arm posture guidance in reaching motion, and (2) The structure allows functional reach because the shoulder position is not restrained during the reaching motion.

These features are unique and novel contributions of this research on rehabilitation robots for upper limbs.

Future research topics for the practical use of the escort-type upper limb rehabilitation robot include the measurement of not only the hand position and posture but also the force applied from the escort-type upper limb rehabilitation robot to the upper limb dummy robot during the guided reaching motion, and the establishment of an evaluation method for the degree of recovery during the rehabilitation process.

REFERENCES

[1] P. Maciejasz et al., "A survey on robotic devices for upper limb rehabilitation," *J. NeuroEng. Rehabil.*, vol. 11, no. 3, 2014.

[2] M. Babaiasl et al., "A review of technological and clinical aspects of robot-aided rehabilitation of upper-extremity after stroke," *Disabil. Rehabil.: Assist. Technol.*, vol. 11, no. 4, pp. 263–280, 2016.

[3] R. Nudo et al, "Use-dependent alterations of movement representations in primary motor cortex of adult squirrel monkeys," *J. Neurosci.*, vol. 16, no. 2, pp. 785–807, 1996.

[4] R. Gassert and V. Dietz, "Rehabilitation robots for the treatment of sensorimotor deficits: a neurophysiological perspective," *J. NeuroEng. Rehabil.*, vol. 15, no. 46, 2018.

[5] S. Lee et al., "Comparisons between end-effector and exoskeleton rehabilitation robots regarding upper extremity function among chronic stroke patients with moderate-to-severe upper limb impairment," *Sci. Rep.*, vol. 10, no. 1806, 2020.

[6] H. Krebs et al. "Robot-aided neurorehabilitation," *IEEE Trans. Neural Syst. Rehabil. Eng.*, vol. 6, no. 1, pp. 75–87, 1998.

[7] L. BIONIK, "Inmotion ® arm for neurological rehabilitation," https://bioniklabs.com/inmotion-arm/, 2024, (Accessed on 14/11/2024).

[8] R. Loureiro, "Upper limb robot mediated stroke therapy-gentle/s approach," *Auton. Robots*, vol. 15, pp. 35–51, 2003.

[9] R. C. V. Loureiro, W. S. Harwin et al., "Evaluation of reach and grasp robot-assisted therapy suggests similar functional recovery patterns on proximal and distal arm segments in sub-acute hemiplegia," *IEEE Trans. Neural Syst. Rehabil. Eng.*, vol. 22, no. 3, pp. 593–602, 2014.

[10] G. Rosati et al., "Design of a new 5 d.o.f. wire-based robot for rehabilitation," *Proc. of ICORR 2005*, 2005, pp. 430–433.

[11] G. Rosati et al, "Design, implementation and clinical tests of a wire-based robot for neurorehabilitation," *IEEE Trans. Neural Syst. Rehabil. Eng.*, vol. 15, no. 4, pp. 560–569, 2007.

[12] T. Rahman et al., "A body-powered functional upper limb orthosis," *J. Rehabil. Res. Dev.*, vol. 37 6, pp. 675–80, 2000.

[13] R. Sanchez et al., "Automating arm movement training following severe stroke," *IEEE Trans. Neural Syst. Rehabil. Eng.*, vol. 14, no. 3, pp. 378–389, 2006.

[14] M. Mihelj et al., "ARMin II - 7 dof rehabilitation robot: mechanics and kinematics," *Proc. of ICRA 2007*, 2007, pp. 4120–4125.

[15] B. Kim and A. Deshpande, "An upper-body rehabilitation exoskeleton harmony with an anatomical shoulder mechanism," *Int. J. Robot. Res.*, vol. 36, pp. 414–435, 2017.

[16] M. A. Murphy et al., "Kinematic variables quantifying upper-extremity performance after stroke during reaching and drinking from a glass," *Neurorehabilit. Neural Repair*, vol. 25, no. 1, pp. 71–80, 2011.

[17] H. Ota et al., "Movement component analysis of reaching strategies in individuals with stroke: Preliminary study," *JMIR Rehabil. Assist. Technol.*, vol. 10, p. e50571, Dec 2023.

[18] H. Vallery et al., "Compliant actuation of rehabilitation robots," *IEEE Robot. Autom. Mag.*, vol. 15, no. 3, pp. 60–69, 2008.

[19] A. H. A. Stienen et al., "Self-aligning exoskeleton axes through decoupling of joint rotations and translations," *T-RO*, vol. 25, no. 3, pp. 628–633, 2009.

[20] P. W. Duncan et al., "Functional reach: A new clinical measure of balance," *J. Gerontol.*, vol. 45, no. 6, pp. M192–M197, 11 1990.

[21] K. Nagai, K. Kitayama, K. Ito, R. C. Loureiro, and W. S. Harwin, "Structural analysis of an escort type rehabilitation robot (in JPN)," *J. Robot. Soc. Jpn.*, vol. 30, pp. 53–61, 2012.

[22] S. Li and K. Nagai, "Kinematical analysis of an upper limb rehabilitation robot to assist in reaching motions (in JPN)," *RSJ*, no. 1J3-02, 2021.

[23] —, "The role of the passive joints to ensure user safety in escort-type rehabilitation robots for upper limb (in JPN)," *RSJ*, no. 4D3-01, 2022.

[24] K. Nagai et al., "Development of an 8 dof robotic orthosis for assisting human upper limb motion," *Proc. ICRA 1998*, vol. 4, pp. 3486–3491.

APPENDIX

TABLE I: DH Parameters for Escort-type Rehabilitation Robot

i	a_{i-1}	α_{i-1}	d_i	θ_i
1	L_0	0	H_0	θ_1
2	L_1	0	H_1	θ_2
3	L_2	0	H_2	θ_3
4	L_3	$-\pi/2$	$-H_3$	θ_4
5	L_4	0	$-H_4-H_B$	θ_5
6	0	$\pi/2$	L_6	θ_6
7	0	0	L_7	0

Link length of the ith link$(i=1,2,3,4,5,6,7)$:

$$\begin{aligned}\boldsymbol{L}_i &= [L_1\, L_2\, L_3\, L_4\, L_5\, L_6\, L_7]^{\mathrm{T}} \\ &= [\,300\ \ 300\ \ 300\ \ 250\ \ 250\ \ 50\ \ 50]^{\mathrm{T}}[\mathrm{mm}]\end{aligned}$$

Distance between links:

$$\begin{aligned}\boldsymbol{H}_i &= [H_0\, H_1\, H_2\, H_3\, H_4\, H_B]^{\mathrm{T}} \\ &= [\,90.1\ \ 32.1\ \ 72.6\ \ 41.3\ \ 37.3\ \ 81.5]^{\mathrm{T}}[\mathrm{mm}]\end{aligned}$$

TABLE II: DH Parameters of Dummy Robot for Upper Limb

i	a_{i-1}	α_{i-1}	d_i	θ_i
0	0	0	d_0	θ_0
1	0	$\pi/2$	0	θ_{B1}
2	0	$-\pi/2$	0	θ_{B2}
3	0	$\pi/2$	d_3	θ_{B3}
4	0	$\pi/2$	d_4	θ_{S1}
5	0	$\pi/2$	0	θ_{S2}
6	0	$-\pi/2$	d_6	θ_{S3}
7	0	$\pi/2$	0	θ_{E1}
8	0	$\pi/2$	0	θ_{E2}
9	0	0	d_9	0
10	0	0	d_{10}	0
11	0	0	d_{11}	0

A Therapist-Inspired Approach to Stiffness Modulation in Rehabilitation Exoskeletons

Beatrice Luciani[1,2,*], Alessandra Pedrocchi[1,2], Francesco Braghin[1,2] and Marta Gandolla[1,2]

***Abstract*—In rehabilitation robotics, adapting exoskeleton behaviour to align with therapists' approach -where they intuitively vary their arm stiffness to provide tailored assistance to patients- is key for effective treatment and technology acceptance. Advanced robotic platforms have multiple setting parameters, but these often fail to precisely reflect therapists' desires. This work presents a novel framework to quantify and replicate therapists' stiffness when guiding arm movements, enabling its transfer to exoskeleton control. Using surface electromyography and torque sensors, we analyzed the relationship between muscle activity and joint torque to estimate stiffness, specifically focusing on the elbow joint. We tested our framework on the AGREE exoskeleton with three healthy participants simulating therapist roles and interacting with the robot under different conditions. Participants' activity was recorded and their elbow stiffness was then converted to robotic stiffness to control the elbow flexion-extension joint. Results show that our framework effectively captured participants' behavioural nuances and translated them into human-like robotic behaviours. When applied to AGREE, therapist-derived stiffness values generated trajectory-tracking errors similar to those observed when participants manually guided the robot. By mirroring therapists' adaptive support, this approach could enhance patient recovery and bridge the gap between human and robotic therapy in clinical settings.**

***Index Terms*—rehabilitation exoskeletons, stiffness modulation, therapist, learning from humans**

I. Introduction

When performing complex tasks, people naturally adapt the rigidity, or stiffness, of their arms to match the varying resistance of the environment. This adaptation aids in more effective interaction with the surroundings [1]. In robotics, this behaviour is implemented through the *variable impedance control* (VIC) [2]. VIC allows the mechanical behaviour of a robot to be altered by adjusting stiffness, damping and inertia. These alterations make the robot more suited to the demands of a task, especially when the external environment is unpredictable or not well known.

Taking a look at a classic therapy session of post-stroke rehabilitation, we would see a therapist manipulating the arm of the patient. This allows the therapist to perceive and understand the needs and level of motor capacity of the patient they are treating. At this point, the therapist can tune his/her support to the execution of the therapy exercise, on the basis of his/her experience, regulating the rigidity of his/her hand and arm. The rigidity of rehabilitation robots can also be tuned, specifically by acting on their joint-level stiffness parameters. The best values can be selected empirically by sampling the parameter space that guarantees stable robotic behaviour [3], or by acting mechanically on the joint if provided with a variable stiffness actuator [4]. This shapes the interaction between the robot and the user, ranging from full guidance to varying levels of assistance, to simple gravity support for the user's free movement[5]. Patient performances are evaluated by the therapist or through the use of sensors and a modality is chosen for the execution of the exercises, providing the desired level of assistance [3].

The above method, however, does not ensure that the different contributions provided by the robotic device correspond to the amount of support a therapist would apply for a specific patient condition, nor do they necessarily meet the therapist's expectations for the rehabilitation session. As a result, this can decrease the overall effectiveness of therapy, potentially causing "slacking" [6] and reducing clinicians' acceptance of rehabilitation robotics. To address this lack of correspondence, studies in the literature have investigated possibilities for rehabilitation robots to mimic therapists' support to be provided to the arm of the patient, focusing on the transfer of force profiles [7], [8]. To extrapolate force contributions from the therapist's actions, researchers have employed specific force sensors. Not every robotic device, anyway, is provided with the same sensors and literature approaches might not always be applicable. To overcome literature limitations concerning both the correspondence of robot and therapist behaviours and hardware availability, our project aims to develop a framework that records the therapist's support directly from a portable sensor to be positioned on the therapist's arm and extract stiffness values to be then transferred to the robot.

II. Related projects: translating human stiffness to robots

In the literature, various approaches to extracting the human arm's stiffness have been explored [9]. Traditional methods include **active evaluation** of end-point stiffness, where controlled perturbations are applied to the human hand, followed by measurements of resulting displacements and forces [10]. While precise, this technique can be challenging for real-time implementation in dynamic therapy settings [11]. Alternatively, **musculoskeletal models** of the arm [12] can be exploited to evaluate stiffness at different limb levels. Such models can provide detailed representations of joint

[1]WE-COBOT Laboratory, Polo Territoriale di Lecco, Politecnico di Milano, Via G.Previati, 1/c, 23900 Lecco, Italy.

[2]Department of Mechanical Engineering, Politecnico di Milano, Via La Masa 1, 20156, Milano, Italy.

[2]Department of Electronics, Information and Bioengineering, Politecnico di Milano, Via Ponzio 34/5, 20133 Milano, Italia

*Beatrice Luciani is the corresponding author: beatrice.luciani@polimi.it

AP, FB, MG hold shares in AGADE s.r.l., and AllyArm srl.

stiffness but are often computationally expensive, limiting their practicality for adaptive robotic applications. **Surface electromyography (sEMG)** based methods, on the other hand, have gained significant traction due to their ability to provide real-time tracking of muscle activity in an effective and non-invasive way. In particular, they can be used to evaluate the co-contraction activity of antagonist pairs of muscles, which is directly linked to joint torque profiles [13] and to the stiffness of the limb [14], [15].

In the industrial sector, EMG-based frameworks have been used for human-robot collaboration applications. In this context, real-time stiffness modulation can optimise the robotic response to human movements, enhancing both safety and efficiency in tasks that require precise manual control [11], while also improving robot performances. For example, Liang *et al.* [13] developed an electromyography-based stiffness evaluation framework designed to real-time adjust the tracking capabilities of an industrial robot, thus reducing the impact of external disturbances. They linked sEMG data from the biceps and triceps to the force exerted at the elbow level by a user, to then estimate custom parameters for the electromyography-stiffness transformation. In another work, Wu and colleagues [16] presented a framework for endpoint stiffness extraction for teleoperation and optimisation of industrial interactive tasks. sEMG signals are recorded with an armband and forearm angles are evaluated via an optical-marker system. From the collected data, their system evaluates the operator's stiffness and adjusts the corresponding stiffness of an industrial manipulator.

Stiffness estimation from EMG signals has also been exploited in the field of surgical robotics. The work presented by Arduini *et al.*[17], for instance, describes a Learning from Demonstrations framework that leverages electromyography and motion tracking to determine the endpoint stiffness of a surgeon while performing surgical blunt dissection tasks.

In rehabilitation, sEMG is a leading method for creating a natural interaction between humans and rehabilitation devices and is normally used for intention-detection purposes. Therefore, its use can be easily extended to stiffness estimation purposes. In their work, Ma *et al.* [18] proposed a neural-network-based framework to extract the endpoint stiffness of post-stroke patients from EMG data and elbow angle, and consequently adjust the control of the rehabilitation robot. Castellini and colleagues [19] implemented a hand-stiffness extraction framework to intuitively control the stiffness of a rehabilitation robot or prosthesis. They integrated it with force feedback, to create a rehabilitation system that regulates robotic contribution to patients' capacities and provides them with realistic feelings of natural control over the robotic device.

Although the applications developed thus far for rehabilitation have shown effective results, they primarily focus on adjusting robotic stiffness to match the patient's remaining abilities. To our knowledge, none have aimed at translating a therapist's stiffness into robotic behaviour.

III. Therapist's stiffness extraction framework

The framework we developed to extract arm stiffness values from therapists' demonstrations, similar to what Liang *et al.*[13] did for industrial applications, analyses the correlation between sEMG signals and joint torque. In fact, according to the literature, we can quasi-linearly correlate torques (τ) and muscular activity of antagonist pairs of muscles ($p_{agonist}$ and $p_{antagonist}$), according to the following general equation:

$$\tau_{joint} \approx A * p_{agonist} + B * p_{antagonist} \quad (1)$$

and then use A and B to extract stiffness values from co-contraction signals, as we will explain later. We specifically focused on the evaluation of the therapist's arm stiffness at the elbow-joint level.

A. Experimental setup

To extract the therapist's muscular activity and torque produced at the elbow joint, we decided to employ two main devices:

1) AGREE: AGREE [3] is an upper limb exoskeleton designed for arm neuro-rehabilitation. It is composed of four robotic joints and each joint actuation unit has a brushless motor, an incremental encoder for position information and a reaction torsional loadcell (TRT-50/200, Transducer Techniques, CA, USA) to provide torque data. Sensor data are recorded at 1 kHz.

2) Myo Armband: The Myo armband by Thalamic Labs is a wearable device equipped with eight electromyographic (EMG) electrodes and a 9-axis inertial measurement unit (IMU). The recording frequency for the EMG sensors is $f_{samp} = 200Hz$. The Myo armband transmits these signals via Bluetooth to possible connected devices, such as prosthetics or computers [20]. Even if we decided to use it for the analysis of the biceps-triceps complex, it can be worn both on the upper arm and forearm, according to the groups of muscles one wants to record.

B. Framework

The stiffness-extraction framework we developed can be divided into two subsequent phases: *Calibration* and *Stiffness extraction* (see Fig.1). At the start of the procedure (*Calibration* phase), the participant wears the Myo Armband on his/her upper arm, verifying that it adheres to the skin and is placed at the level of the midpoint of the bicep belly. The Armband needs to be left in position along all the steps.

1) Calibration:

Phase 1 - EMG peaks extraction: The participant is asked to execute three consecutive isometric contractions of the biceps, followed by three consecutive isometric contractions of the triceps, using a table as support and stopper. The Armband records the EMG signal coming from the eight channels and includes a 50 Hz notch filter to eliminate power-line noise. We elaborate the data through the following **EMG-analysis** steps:

- **Envelope extraction**: the sEMG signals are elaborated to extract the general muscle activation pattern. The magnitude of the analytic recorded signal is computed

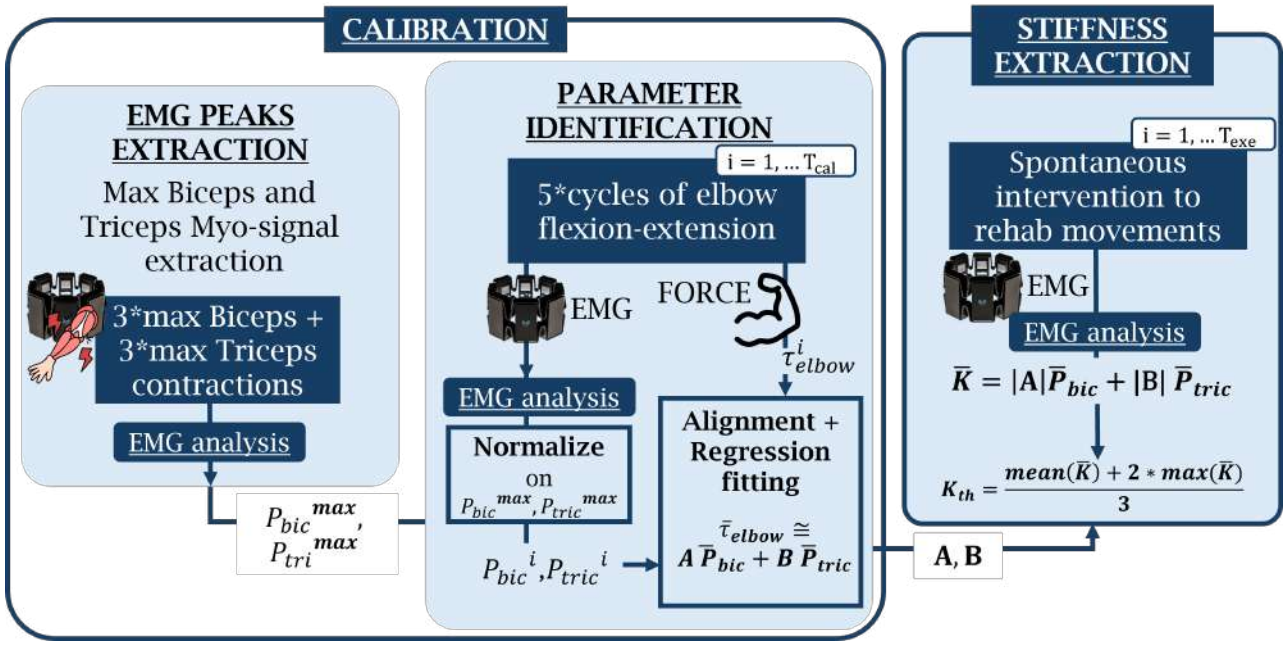


Fig. 1. Scheme of the therapist-stiffness extraction framework. With the calibration phase, we can extract the maximum values for Biceps and Triceps contraction, use them to normalise EMG data recorded while the therapist freely moves the arm wearing the Myo, and define the regression parameters that link the therapist's muscular activity and force exerted at the level of the elbow. We can then use such parameters, during therapist-patient interactions, to transform recorded EMG data into corresponding stiffness values to describe therapist's support.

via the *hilbert* MATLAB function and provides the envelope of the EMG.

- **Filtering**: the resulting signals are low-pass filtered ($f_{cut} = 2.5Hz$ - set experimentally to align with literature values [21]).
- **Main signals extraction**: since users can wear the bracelet without precise muscle alignment, the readings from each channel of the Myo reflect activity across multiple muscles. The sensors capture a mix of signals from various motor units, including those of both the muscles of interest. To address this, we apply Principal Component Analysis (PCA) to the data from all eight channels. PCA identifies and extracts two summarising signals (the two first principal components coming from the analysis) that represent the contraction activity of the biceps and triceps.

We then evaluate the maximum for the two resulting biceps and triceps components along the calibration signals, obtaining the sEMG values for the maximal contractions (p_{bic}^{max}, p_{tri}^{max}).

Phase 2 - Parameters identification: To estimate the parameters A and B presented in Eq.1, we need to study the correlation between the sEMG biceps and triceps signals and the torque produced at the elbow joint. To build such correlation, the participant (i.e. the therapist) is asked to wear the AGREE exoskeleton, always with the Myo Armband placed on the upper arm, and perform 5 full-range repetitions of an elbow flexion-extension movement. To minimise external forces and characterize the elbow parameters for the therapist, the movement is carried out with AGREE set in a gravity-compensating modality, allowing the participant to move without resisting gravity. Having to support the weight of the robotic arm when wearing it would, in fact, overload the patient's muscles and potentially alter stiffness results. The exoskeleton is adjusted so that the shoulder is elevated and the elbow flexion extensions are performed on a horizontal plane. During the movement execution, we record sEMG data and elaborate them as previously described, to extract their two main components. Biceps and triceps activities are then normalized with respect to, respectively, p_{bic}^{max} and p_{tri}^{max}. We obtain p_{bic}^{i} and p_{tri}^{i}, where $i = 1, ..., T_{cal}$ and T_{cal} is the time-length of the recording. EMG normalised data are then synchronized with torque data coming from the sensor of AGREE elbow joint (τ_{elbow}^{i}, with $i = 1, ..., T_{cal}$).
Adapting Eq.1 to our specific case, we obtain:

$$\overline{\tau}_{elbow} \approx A \cdot \overline{p}_{bic} + B \cdot \overline{p}_{tri} \tag{2}$$

where:

- $\overline{\tau}_{elbow} = (\tau_{1,elbow}, \tau_{2,elbow}, ..., \tau_{T_{cal},elbow})^T$,
- $\overline{p}_{bic} = (p_{bic,1}, p_{bic,2}, ..., p_{bic,T_{cal}})^T$,
- $\overline{p}_{tri} = (p_{tri,1}, p_{tri,2}, ..., p_{tri,T_{cal}})^T$.

we can perform a least squares fitting to define A and B parameters.

2) Stiffness extraction: Having modelled the stiffness behaviour of the participant's arm, we can now ask them to perform any desired movement, with only the Armband on to record their sEMG activity (as depicted in Fig.2). According to the aforementioned literature work by Liang *et al.*[13], we can exploit the parameters extracted during Calibration to

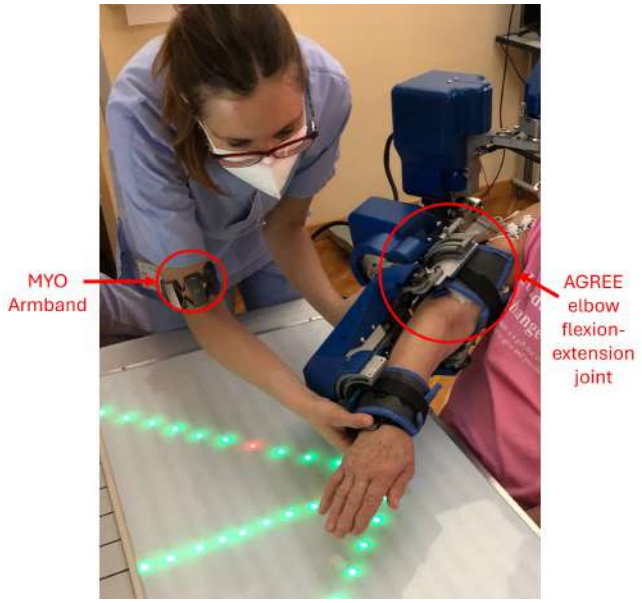


Fig. 2. The therapist can wear the Myo Armband on the upper arm while manipulating the robot along the desired movements. In this way, the co-contraction activity of the biceps and triceps are evaluated and can be used to obtain the therapist's stiffness values thanks to the A and B parameters previously extracted during the calibration.

transform the EMG data recorded in this phase into punctual elbow stiffness values:

$$\overline{K} = |A| \cdot \overline{p}_{bic} + |B| \cdot \overline{p}_{tri} \tag{3}$$

where $\overline{K} = (k_1, k_2, ..., k_{T_{exp}})^T$ and $|A|$ and $|B|$ are the absolute values of A and B. This time, $i = 1, ..., T_{exp}$, where T_{exp} is the time duration of the participant's movements. After the recording, we estimate a global stiffness value

$$K_{th} = \frac{mean(\overline{K}) + 2 \cdot max(\overline{K})}{3} \tag{4}$$

to describe the therapist's behaviour. The idea is that, according to the specific condition of interaction with the patient and to the therapist's approach towards the therapy execution, his/her EMG activity will change, and so will the corresponding stiffness. Eq.4 is defined experimentally to balance the mean and maximum stiffness, ensuring that transient peaks do not overly dominate the result while still capturing significant variations.

Conversion to AGREE stiffness values: The stiffness values estimated so far do not actually have a real measurement unit and are just meant to describe variations in human behaviour. To tune AGREE behaviour according to such variations, we rescale human stiffness values in AGREE joint stiffness value. Specifically, we know that K_{AGREE}, at the elbow joint, goes from $5\frac{Nm}{rad}$ to $60\frac{Nm}{rad}$ [3]. Given that K_{th}^{max} can be estimated from p_{bic}^{max} and p_{tri}^{max}, and that we evaluated K_{th}^{min} to be approximately zero, we can compute:

$$K_{AGREE} = (60 - 5)\frac{Nm}{rad} \cdot \frac{K_{th}}{K_{th}^{max}} + 5\frac{Nm}{rad} \tag{5}$$

By rescaling stiffness within AGREE's operational range, we ensure that variations in therapist stiffness are transferred to AGREE while maintaining system stability. Since AGREE has physical limitations, we need to avoid excessive stiffness that could induce vibrations or excessive compliance that could result in instability. This transformation is therefore necessary to ensure safe operation.

C. Testing

To prove the efficacy of our framework, we involved healthy volunteers in testing our system from the therapist's point of view, with two different experiments. Participants were required to have no history of neurological diseases and to have full upper-limb function. Tests were approved by the Ethical Committee of Politecnico di Milano (Application No. 8/2022 - 16.02.2022).

Experiment 1: For the first experiment, three volunteers were recruited and were asked to wear the Myo Armband on their upper arm and keep it in place throughout the entire experiment. First, they completed the two first steps of the framework, allowing us to identify their personal parameters. Then, we asked them to interact with AGREE in two different tests, manipulating the exoskeleton in the execution of an elbow flexion-extension exercise, and repeating the movement five times per test. During the **Test 1**, AGREE was set in a modality defined as *null-gravity*, where it does not compensate for its own weight and should, for our experiment, represent a patient who is unable to actively move or lift the arm. In **Test 2**, AGREE was set in *gravity-compensation* mode, where it does not actively move but compensates for its weight. In this case, it should represent the behaviour of a less-impaired patient.

The variable behaviours of AGREE should produce different behaviours in the subjects playing the therapist part, who are led to approach the exoskeleton with variable contributions for the execution of the same task. Specifically, we expect the arm stiffness obtainable from **Test 1** (i.e. severely-impaired patient) to be higher than the arm stiffness evaluated during **Test 2** (i.e. mildly-impaired patient).

Experiment 2: As an additional validation to our framework, we asked one of the three volunteers to manipulate AGREE. He physically supported it in the execution of a predefined trajectory (i.e., a reaching task from one point to another) and repeated the movement five times. During the manipulation, AGREE was set to a low-assistive modality (namely **A3** in [3]), and we measured the kinematic error at each joint, with respect to the desired trajectory. After assessing the stiffness of the therapist's arm along the manipulation, it was translated into AGREE stiffness values. Then, using the calculated robotic stiffness, AGREE independently executed the same trajectory, without any external intervention. We finally compared the kinematic error produced at the elbow joint when the participant assisted the trajectory with the error generated by AGREE's flexion-extension joint during its independent execution. AGREE kinematic performances, depending on the choice of stiffness and damping for each of its joints, can also be retrieved from its control-system analysis, presented in [3]. This experiment was repeated twice (Trial 1 and Trial 2).

IV. Results and Discussions

Experiment 1: Our framework was tested with three healthy participants acting as therapists, each performing stiffness modulation under different robotic assistance conditions. Table I summarizes the individual parameters and stiffness values derived from the two test conditions described in the previous paragraphs. In **Test 1**, where AGREE simulates a fully impaired patient, we observed notably higher arm stiffness values. This indicates high effort and rigidity from the participant to stabilize and guide the robot. In contrast, **Test 2** resulted in lower stiffness values, reflecting a more flexible approach from the participants. This reduction, which is coherent with our expectations, confirms that the framework can successfully modulate stiffness in response to varying conditions of therapist-patient interactions, thus mimicking therapist-driven adaptations during therapy sessions.

TABLE I
RESULTS OF THE TESTS PERFORMED WITH THE THREE PARTICIPANTS: A, B PARAMETERS OBTAINED THROUGH OUR FRAMEWORK, STIFFNESS VALUES IN THE DIFFERENT TESTING CONDITIONS, BOTH IN "MYO-SCALE " AND AGREE SCALE.

	A	B	Stiff Max	Stiff 1	Stiff 2
S1	2.80	1.41	1.65 (60 $\frac{Nm}{rad}$)	0.85 (33 $\frac{Nm}{rad}$)	0.49 (22 $\frac{Nm}{rad}$)
S2	1.73	2.17	1.27 (60 $\frac{Nm}{rad}$)	0.96 (46 $\frac{Nm}{rad}$)	0.63 (32 $\frac{Nm}{rad}$)
S3	1.57	4.00	1.29 (60 $\frac{Nm}{rad}$)	0.97 (46 $\frac{Nm}{rad}$)	0.67 (33 $\frac{Nm}{rad}$)

The stiffness values we extract can vary based on several factors. The therapist's decisions, such as how much support to provide or whether to grasp the patient's arm more proximally or distally, are part of the rehabilitation strategy and directly affect the recorded stiffness. External factors like the therapist's positioning or the physical distance between the patient and therapist, on the other side, can lead to variations in stiffness that are not directly tied to the clinician's intentions for executing the task. However, even if these factors do not explicitly define a rehabilitation strategy, they still influence the haptic interaction between the therapist and the patient's arm in a conventional therapy session. As a result, it is reasonable to replicate their effects in our framework, as they naturally shape the physical dynamics of therapist-guided movements.

Experiment 2: As previously described, in the second experiment we compared the kinematic error produced by the therapist's intervention to that produced by the robot while working with the corresponding stiffness parameter, to assess the fidelity of the system in transforming human behaviour into robotic. As shown in Fig.3 **A3** parameters would produce, without external interventions, a mean tracking error at elbow level of around 11 degrees.

With subject guidance to the movement of the robot, instead, we evaluated a mean error over the execution of the trajectory of 4.5 degrees for the first trial, and 5.9 degrees for the second. The extracted elbow stiffness values were converted, for the two trials, to AGREE stiffness values and coupled with the damping associated with the **A3** modality

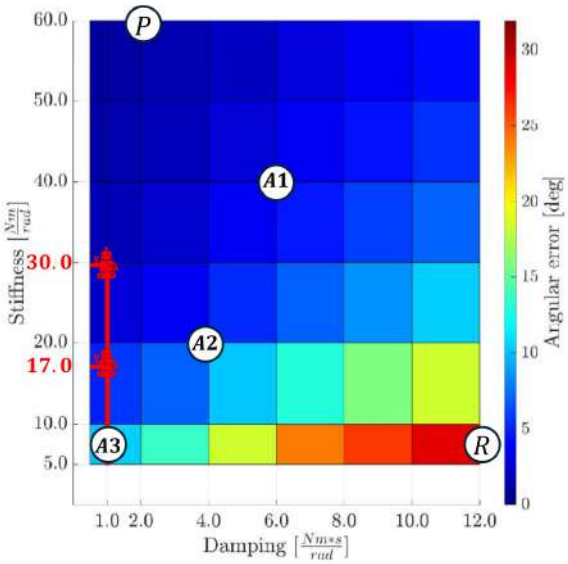


Fig. 3. Colour map of the kinematic error made by the robot, at the elbow joint, given the combination of all the possible values of stiffness and damping included in the stability range for the joint itself. We highlighted the pairs of parameters identified in our second experiment, with the indication of the corresponding errors. The references to the **P, A1, A2, A3** and **R** indicate the couples of parameters selected for the different working modalities presented in [3]. In those modalities, parameters were selected sampling the space of stable parameters.

($D = 1.0Nm * sec/rad$). Tab.II summarizes the results for the two trials of this second experiment. The mean trajectory-tracking errors for the AGREE elbow flexion-extension joint, as shown in Table II, are 4.0 degrees and 6.1 degrees, respectively. Considering the range of potential errors caused by varying the AGREE elbow joint parameters, we can conclude that both values are comparable to their corresponding manipulation errors. This finding confirms the reliability of the method in accurately replicating the therapist's approach to executing exercises.

TABLE II
RESULTS OF THE TWO TRIALS OF THE SECOND EXPERIMENT, INCLUDING THE HUMAN STIFFNESS EVALUATED AT ELBOW LEVEL, WITH THE ERROR PRODUCED BY HUMAN MANIPULATION, AND THE CORRESPONDING ROBOTIC STIFFNESS WITH THE ERROR AGREE ELBOW JOINT WOULD PRODUCE WITH SUCH A STIFFNESS.

	Therapist		AGREE	
	Stiffness	Error [deg]	Stiffness [Nm/rad]	Error [deg]
Trial 1	0.50	4.5	30	4.0
Trial 2	0.09	5.9	12	6.1

V. Conclusions and Future Perspectives

In this work, for the first time, we have developed a framework to translate therapist behaviours in terms of stiffness to a rehabilitation robot, overcoming the problem of defining the assistance through parameters. The results of the experiments we conducted demonstrate the potential of the framework to capture the individualised nature of therapist-patient interaction and translate it into robotic action.

The punctual stiffness values extracted during the teaching phase are then summarised with a single value to capture the "global" therapist's behaviour. The global stiffness is then transformed into robotic parameters to be applied during a whole rehabilitation session or, at the very least, during a specific exercise. Even if punctual stiffness values are surely more representative of the variations in the therapist's approach along with the execution of the therapy exercise, employing them at the current stage of this research would have strongly limited the applicability of the results, forcing us to re-apply the recorded stiffness along with the execution of the single recorded trajectory. By overcoming the strict link between a specific stiffness profile and its corresponding trajectory, and generalising the relationship between stiffness variations and kinematics through techniques like machine learning approaches, we can broaden the applicability of our system. We could, for instance, reproduce the vector-search-based approach we employed for force-based mimicking in one of our previous studies [7].

A fundamental future step for this research is presenting our framework to therapists and other clinicians in neurorehabilitation. Their feedback on the utility of this approach, related to its ability to accurately represent therapists' behaviours and intentions, along with an evaluation of usability, would add important insight. The involvement of clinicians would also help us understand how the extracted stiffness values change according to the individual approach therapists adopt when manipulating patients' arms.

ACKNOWLEDGMENT

This project was supported by the Italian Ministry of University and Research within the project HYBR-ID (Project number: 2022F3JPLY; CUP: D53D23001230006; Fundings: Next Generation EU).

REFERENCES

[1] E. Burdet, R. Osu, D. Franklin, T. Milner, and M. Kawato, "The central nervous system stabilizes unstable dynamics by learning optimal impedance," *Nature*, vol. 414, pp. 446–9, 12 2001.

[2] F. J. Abu-Dakka and M. Saveriano, "Variable impedance control and learning—a review," *Frontiers in Robotics and AI*, vol. 7, 2020.

[3] S. Dalla Gasperina, M. Gandolla, V. Longatelli, M. Panzenbeck, B. Luciani, F. Braghin, and A. Pedrocchi, "Agree: A compliant-controlled upper-limb exoskeleton for physical rehabilitation of neurological patients," *IEEE Transactions on Medical Robotics and Bionics*, vol. 5, no. 1, pp. 143–154, 2023.

[4] Y. Liu, S. Guo, H. Hirata, H. Ishihara, and T. Tamiya, "Development of a powered variable-stiffness exoskeleton device for elbow rehabilitation," *Biomedical Microdevices*, vol. 20, 08 2018.

[5] T. Proietti, V. Crocher, A. Roby-Brami, and N. Jarrassé, "Upper-limb robotic exoskeletons for neurorehabilitation: A review on control strategies," *IEEE Reviews in Biomedical Engineering*, vol. 9, pp. 4–14, 2016.

[6] D. Losey, C. McDonald, E. Battaglia, and M. O'Malley, "A review of intent detection, arbitration, and communication aspects of shared control for physical human–robot interaction," *Applied Mechanics Reviews*, vol. 70, 01 2018.

[7] B. Luciani, M. Sommerhalder, M. Gandolla, P. Wolf, F. Braghin, and R. Riener, "Therapists' force-profile teach-and-mimic approach for upper-limb rehabilitation exoskeletons," *IEEE Transactions on Medical Robotics and Bionics*, vol. 6, no. 4, pp. 1658–1665, 2024.

[8] Fabian Just, *Fusing Conventional and Robotic Rehabilitation Therapy [Doctoral Thesis]*. PhD thesis, Eidgenössische Technische Hochschule (ETH) Zurich, Zurich, 2020.

[9] J. Buzzi, G. Ferrigno, J. M. Jansma, and E. De Momi, "On the value of estimating human arm stiffness during virtual teleoperation with robotic manipulators," *Frontiers in Neuroscience*, vol. 11, 2017.

[10] F. Lacquaniti, M. Carrozzo, and N. Borghese, "Time-varying mechanical behavior of multijointed arm in man," *Journal of Neurophysiology*, vol. 69, no. 5, pp. 1443–64, 1993.

[11] A. Ajoudani, C. Fang, N. G. Tsagarakis, and A. Bicchi, "A reduced-complexity description of arm endpoint stiffness with applications to teleimpedance control," in *2015 IEEE/RSJ International Conference on Intelligent Robots and Systems (IROS)*, pp. 1017–1023, 2015.

[12] C. Fang, A. Ajoudani, A. Bicchi, and N. G. Tsagarakis, "Online model based estimation of complete joint stiffness of human arm," *IEEE Robotics and Automation Letters*, vol. 3, no. 1, pp. 84–91, 2018.

[13] P. Liang, C. Yang, N. Wang, and R. Li, "A discrete-time algorithm for stiffness extraction from sEMG and its application in antidisturbance teleoperation," *Discrete Dynamics in Nature and Society*, vol. 2016, pp. 1–11, 04 2016.

[14] S. Heitmann, N. Ferns, and M. Breakspear, "Muscle co-contraction modulates damping and joint stability in a three-link biomechanical limb," *Frontiers in neurorobotics*, vol. 5, p. 5, 01 2011.

[15] G. Li, M. Shourijeh, D. Ao, C. Patten, and B. Fregly, "How well do commonly used co-contraction indices approximate lower limb joint stiffness trends during gait for individuals post-stroke?," *Frontiers in Bioengineering and Biotechnology*, vol. 8, 01 2021.

[16] R. Wu, H. Zhang, and J. Zhao, "Robot variable impedance skill transfer and learning framework based on a simplified human arm impedance model," *IEEE Access*, vol. PP, pp. 1–1, 12 2020.

[17] R. Arduini, Y. Michel, H. Singh, J. Klodmann, and D. Lee, "Learning from demonstration of robot motions and stiffness behaviors for surgical blunt dissection," in *2024 33rd IEEE International Conference on Robot and Human Interactive Communication (ROMAN)*, pp. 1491–1496, 2024.

[18] Y. Ma, Q. Liu, H. Liu, and W. Meng, "sEMG-based estimation of human arm endpoint stiffness using long short-term memory neural networks and autoencoders," in *Intelligent Robotics and Applications* (H. Liu, Z. Yin, L. Liu, L. Jiang, G. Gu, X. Wu, and W. Ren, eds.), (Cham), pp. 699–710, Springer International Publishing, 2022.

[19] C. Castellini, A. Arquer, and J. Artigas, "sEMG-based estimation of human stiffness: Towards impedance-controlled rehabilitation," in *5th IEEE RAS/EMBS International Conference on Biomedical Robotics and Biomechatronics*, pp. 604–609, 2014.

[20] P. Visconti, F. Gaetani, G. Zappatore, and P. Primiceri, "Technical features and functionalities of myo armband: An overview on related literature and advanced applications of myoelectric armbands mainly focused on arm prostheses," *International Journal on Smart Sensing and Intelligent Systems*, vol. 11, pp. 1–25, 06 2018.

[21] F. Di Nardo and S. Fioretti, "Accuracy of emg linear envelope in identifying the peak of muscular activity during walking," *Gait & Posture*, vol. 111, pp. 185–190, 2024.

On the Impact of Proprioception in EEG Representations and Decoding during Human-Hand Exoskeleton Interaction

Qiang Sun, Eva Calvo Merino, Liuyin Yang, Axel Faes, and Marc M. Van Hulle

***Abstract*—Controlling a hand exoskeleton based on electroencephalogram (EEG)-based brain-computer interfacing (BCI) holds promise for human motor augmentation and neurorehabilitation. To achieve natural control, a critical step is to understand the impact of proprioception provided by the exoskeleton during interaction. In this study, we aim to approach the goal by quantifying EEG representations and BCI performance. We monitored 25 healthy subjects' full-scalp EEG while performing different finger movement tasks with a cable-driven hand exoskeleton. Each task involves three movement modalities, i.e., imagined (IM), passive (PM), and congruent imagined and passive (IPM) finger flexion. We found that alpha (8 - 13 Hz) and beta (13 - 30 Hz) band desynchronization in the sensorimotor area was significantly stronger for PM and IPM tasks compared to IM, with no significant difference between PM and IPM. Using machine learning models, we achieved a high accuracy in classifying exoskeleton-assisted movements from the rest condition (IPM vs. REST: 0.80 ± 0.07, PM vs. REST: 0.72 ± 0.10), with the IPM modality returning the highest accuracy. However, distinguishing between IPM and PM yielded only 0.61 ± 0.09, significantly lower than the condition of intention detection without the exoskeleton (IM vs. REST: 0.73 ± 0.08). Our findings suggest that sensorimotor EEG activity can track proprioceptive feedback induced by the hand exoskeleton. While this feedback is pronounced and distinguishable, detecting motor intention during exoskeleton movement remains highly challenging. This highlights the need for advanced decoders and control strategies for the future development of continuous BCI-actuated hand exoskeletons.**

***Index Terms*—brain-computer interfaces (BCIs), electroencephalogram (EEG), hand exoskeleton, motor intention, proprioception.**

I. Introduction

Brain-computer interfaces (BCIs) build a direct connection between the human brain and effectors, bypassing the normal neuromuscular pathway [1]. A promising field for BCI systems is human motor augmentation and neurorehabilitation, where the end users can rely on a brain-actuated exoskeleton to accomplish daily activities. For practical considerations, electroencephalogram (EEG) is recommended for recording brain activities as it is non-invasive, affordable, and offers relatively high temporal and spatial resolution compared to other non-invasive recording techniques. A successful demonstration has been realized by Soekadar *et al.* [2], where an individual with impaired hand function could accomplish different daily hand tasks with an EEG-controlled exoskeleton.

Exoskeletons are widely used in neurorehabilitation to encourage the patient's engagement which in turn promotes motor recovery [3]. A BCI-controlled exoskeleton is particularly useful in this case as the patient's active motor intentions can be decoded and translated into exoskeleton commands. For patients with limited motor control functions, their intentions are conveyed through imagined movement, a type of movement that motor-disabled individuals can do by imagining a given movement without actually performing it [2], [4]. Such a closed-loop active robot-assisted mode has been shown to improve post-stroke rehabilitation outcomes [4]. In this study, we focused on BCI-actuated hand exoskeletons, as they hold promise for restoring intuitive finger control in people with hand motor impairments.

A major feature of human-exoskeleton interaction, compared to human-robotic arm or avatar interaction, is the strong proprioceptive feedback provided by the device. Once the exoskeleton is activated, the user can sense body posture and limb movements during physical interaction, leading to the excitation of the sensorimotor cortex [5]–[7]. From ongoing EEG, this excitatory activity is characterized by a power decrease or increase in particular frequency bands, termed event-related desynchronization (ERD) and event-related synchronization (ERS), respectively [8]. Specifically, robot-assisted passive movement can elicit bilaterally distributed alpha (8 - 13 Hz) and beta (13 - 30 Hz) ERD during the movement, albeit stronger on the contralateral side [5], [7]. Once the movement is terminated, ERS in the beta band occurs centrally, partially reflecting an active inhibition of the motor cortex by somatosensory afferents [9].

From a control perspective, it is pivotal to develop asynchronous and, ideally, continuous BCI, as it attributes to the autonomy of the user and provides more natural control capabilities. An asynchronous BCI system allows the user to voluntarily decide when to initiate or terminate a task. In contrast, a continuous BCI system provides ongoing, real-time outputs that continuously map the user's brain activity

This work was supported in part by Horizon Europe's Marie Sklodowska-Curie Action (No. 101118964), Horizon 2020 research and innovation programme (No. 857375), the special research fund of the KU Leuven (C24/18/098), the Belgian Fund for Scientific Research - Flanders (G0A4118N, G0A4321N, G0C1522N), the Hercules Foundation (AKUL 043), and the China Scholarship Council. (Correspondence: Qiang Sun. qiang.sun@kuleuven.be).

Qiang Sun, Eva Calvo Merino, Liuyin Yang, and Marc M. Van Hulle are with the Laboratory for Neuro- and Psychophysiology, Department of Neuroscience, KU Leuven, Leuven, Belgium.

Axel Faes was with the Laboratory for Neuro- and Psychophysiology, Department of Neuroscience, KU Leuven, Leuven, Belgium. He is now with the BIOMED and DSI groups at UHasselt, Diepenbeek, Belgium.

to control parameters, such as movement or speed, reflecting their dynamic motor intentions. Both types of BCIs rely on real-time monitoring and decoding of the user's motor intentions. However, as the exoskeleton will produce proprioceptive afferents during interaction, the difficulty of motor intention decoding from EEG needs to be addressed. Indeed, a recent study reported that motor intention detection is more challenging during lower-limb exoskeleton interaction compared to a static case [10]. However, whether this phenomenon pertains to hand exoskeletons remains unexplored.

In this study, we designed an experimental paradigm combining a cable-driven hand exoskeleton and full-scalp EEG recordings. Our first objective is to compare the EEG representations of different movement modalities, including imagined (IM), passive (PM), and congruent imagined and passive (IPM) finger flexions, with a particular interest in comparing IPM and PM. The second objective is to assess motor intention detection performance in situations with and without exoskeleton assistance. Based on our findings, we highlight the key challenges of EEG decoding during human-hand exoskeleton interaction.

II. Materials and Methods

A. Subjects

We recruited 25 right-handed subjects (12 males and 13 females, 24.20 ± 3.29 years old). Each subject's handedness was evaluated using the Edinburgh Handedness Inventory[1]. All subjects participated in a single-session EEG experiment. This study was approved by the Ethical Committee of the University Hospital of KU Leuven (UZ Leuven) under reference number S6254. Before the experiment, all subjects were informed about the study details and gave their written consent.

B. Experimental setup and paradigm details

The experiment was conducted in a quiet recording room. Subjects sat on a comfortable chair wearing the EEG cap and a right-hand exoskeleton, as illustrated in Fig. 1a. We configured 62 EEG active electrodes (Easycap GmbH, Germany) covering the full scalp following the 10%-System. Additional reference and ground electrodes were placed at FCz and AFz, respectively. When preparing the electrodes, we kept the impedance below 5kΩ. For EEG recording, we used the Neuroscan SynAmps RT device (Compumedics, Australia) operating at 1000 Hz sampling rate. As for the exoskeleton, we used the Gloreha Sinfonia (renamed R-TOUCH by BTL Industries). This device enables one degree-of-freedom for each finger and controls its flexion and extension by an electric actuator-driven steel cable (Fig. 1b).

The paradigm instructions were shown on the screen (ViewPixx, Canada) in front of the subjects (Fig. 1a). We designed three movement modalities, namely, IM, PM, and IPM. Each modality had three finger tasks including thumb, index, and middle-ring-little finger flexion. The timing of an exemplary imagined thumb trial is shown in Fig. 1c. At the beginning of the trial, a cross was shown on the screen for 1.5s instructing the subject to stay focused. Later, a circle and tick marks, were shown, centered on the cross, as well as a word cue indicating the finger task to be performed. Upon the disappearance of the word cue (1s later), the circle started to shrink at a constant speed. Once the circle touched the tick marks(2s later), the subject performed the finger task, either by imaging finger flexion (IM and IPM conditions) or by refraining from any mental tasks but by undergoing (and feeling) the exoskeleton movement (PM condition). After 2.5s, the subject could relax for 2-3s. There was a homing-back action from the exoskeleton in the PM and IPM conditions. For IM and IPM, we asked our subjects to perform kinesthetic imagination, i.e., imagine they were moving their right-hand fingers at the same speed as the shrinking circle. For PM, we asked our subjects to avoid any mental tasks. The exoskeleton moved the fingers at the same speed. The experiment had 30-40 rounds with each round randomizing three modalities each one comprising three randomized finger tasks. The subjects could relax between rounds and were given a form to report the trials they did wrong in the past round. All subjects practiced the paradigm prior to the real experiment. A camera monitored the behavior of each subject's right hand during the entire experiment.

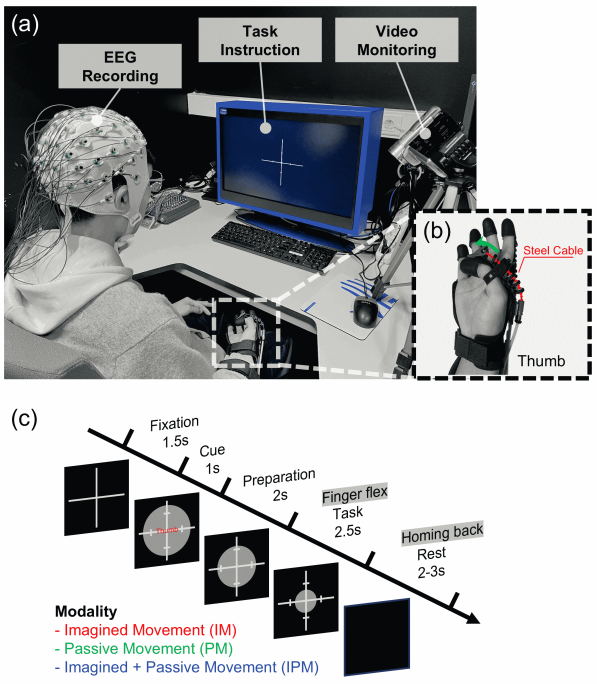


Fig. 1. Experimental paradigm. (a) Experimental setup. The subject wore a hand exoskeleton and performed the instructed tasks while the full-scalp EEG signals were recorded. (b) The exoskeleton made the thumb of the subject flex via a steel cable. (c) Timing of an exemplary imagined thumb movement trial.

C. EEG data preprocessing

Data preprocessing was done based on customized MATLAB code and scripts from the FieldTrip toolbox [11]. The recorded raw EEG data were downsampled to 250 Hz for ease

[1]https://www.brainmapping.org/shared/Edinburgh.php

of computation after applying an antialiasing filter. Then, two notch filters were applied to remove power line noise at 50 Hz and 100 Hz. Next, we filtered the continuous signals into 0.1 - 120 Hz. The mentioned filters were all 3-order Butterworth IIR filters. Before removing eye movement artifacts, we visually inspected and removed faulty channels noted during the recording. Then, we used independent component analysis (*runica* implemention in FieldTrip) to detect vertical and horizontal eye movement-related components and removed them. Common average referencing was implemented. Finally, we imputed the excluded noisy channel EEGs based on those of neighboring electrodes.

The cleaned EEGs were segmented into 9-s epochs according to trial markers, starting from trial onset (Fig. 1c). For each epoch, we detected the noisy channels based on features: kurtosis, mean value, and variance. Specifically, a channel was detected as noisy if any of its features exceeded three times the standard deviation of the mean for all channels. The noisy channels were interpolated. We also removed bad epochs when a third of the channels had an amplitude over ±100 μV.

D. EEG representations

We looked into event-related spectrum perturbation (ERSP) of the EEG signals, which reflects the spectra power changes relative to a baseline. The group-averaged ERSP for a given finger task at channel *c*, frequency *f*, and time *t* is calculated as:

$$ERSP(c,f,t) = \frac{1}{S}\sum_{s=1}^{S}\frac{1}{N}\sum_{n=1}^{N}\Big]F_{s,n,c}(f,t) - F_{s,n,c}^{baseline}(f)\Big) \tag{1}$$

where *S* and *N* represent the number of subjects and the number of trials in the current task, respectively. $F_{s,n,c}$ indicates the time-frequency representation (TFR) of the *c*-th channel and *n*-th trial from subject *s*. We calculated the averaged power from 0.5 to 1.5s with respect to the appearance of the cross during the fixation phase (Fig. 1c) as the baseline $F_{s,n,c}^{baseline}$. The TFRs were calculated based on Short-Time Fourier Transform (STFT) with a window of 1s and overlap of 1 sample. We took the logarithm for ERSP calculation.

EEG oscillatory activities in the alpha (8 - 13 Hz) and beta (13 - 30 Hz) bands were specifically analyzed, as these rhythms are characteristic of both active and passive finger movements [6], [12]. We first visualized the topographical distribution of alpha and beta ERSP on the scalp. Then, we looked into the TFR of the representative EEG channels.

E. Decoding models

We built four binary classification models based on the Fisher Geodesic Minimal Distance to Mean (FgMDM) classifier [13]. FgMDM works in the Riemannian space and shows exceptional decoding performance in many BCI tasks [14]. In the first model, we classified IM versus the resting state (IM vs. REST), representing motor intention detection without exoskeleton movement. The second and third models classified PM versus REST and IPM versus REST, respectively, to assess whether the exoskeleton induces distinguishable features. The final model classified IPM versus PM (IPM vs. PM), simulating a scenario to determine the presence of motor intention during exoskeleton interaction. We pooled all three finger tasks' epochs together for IM, PM, and IPM. The cleaned epochs were further bandpassed into 4 - 40 Hz. Considering the shorter displacement of thumb flexion and future online BCI applications, we opted for a 1-s data length to test decoding performance. Therefore, we extracted the first 1-second segment (time window: 4.5 – 5.5 s) from the task period for IM, PM, and IPM, respectively (Fig. 1c). For the resting state, a 1-second segment (time window: 0.5 – 1.5 s) was obtained from the fixation phase (Fig. 1c), which also served as the baseline for ERSP calculation. In the end, we obtained 105.25 ± 13.57, 105.08 ± 12.08, and 106.67 ± 11.94 segments for IM, PM, and IPM, respectively. The resting state contained the same number of segments as IM, PM, and IPM, respectively.

The FgMDM classifier was implemented using the Covariance toolbox[2] with the Riemannian mean and distance as model parameters. All models were trained and tested following a 10×5-fold (stratified) cross-validation procedure. The average accuracy (correct predictions out of all samples) is reported.

F. Statistical analysis

We compared the alpha and beta rhythm power changes at channels C3 and C4 via the Wilcoxon rank sum test. We used repeated measures Analysis of Variance (ANOVA) to test the difference of alpha and beta rhythm for different modalities. Once a significant effect was found, we performed multiple comparisons with Bonferroni correction. The classification accuracies from different models were tested in the same way. The normality of variable observations was examined based on the Shapiro-Wilk test. All statistical analyses used a significant level of 0.05.

III. Results

A. Exoskeleton-assisted finger movements induce strong EEG desynchronization in sensorimotor area

Figure 2 illustrates the evolution of EEG activities within the alpha and beta bands for three movement modalities. Each topoplot represents the averaged ERSP across all finger tasks, subjects, and the selected time window. During the preparation stage, IM and IPM exhibited relatively stronger power decreases (i.e., desynchronization or ERD) compared to PM in the contralateral central region, with IPM showing more widespread activation. Upon exoskeleton activation, stronger ERD occurred in the sensorimotor area, as observed in PM and IPM modalities during the task and rest stages. The proprioceptive feedback-induced ERD was bilaterally distributed, with the strongest effects observed contralaterally. It is worth noting that for PM and IPM in the rest stage, the exoskeleton is

[2]https://github.com/alexandrebarachant/covariancetoolbox/tree/master

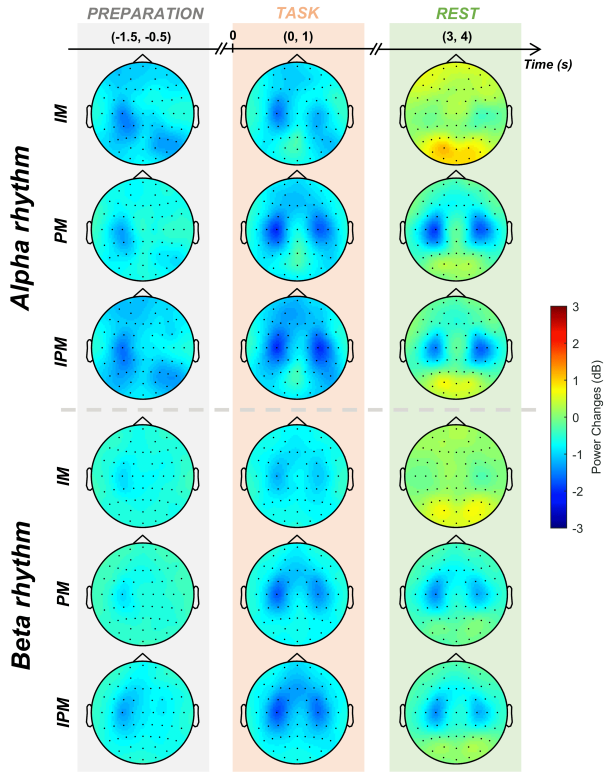


Fig. 2. Changes in alpha and beta rhythm power distribution over time for different movement modalities across three interaction stages: Preparation, Task, and Rest. Each column represents a distinct stage, with time = 0 s indicating the onset of the task. The color scale shows power changes in dB. EEG electrode locations were marked in black dots.

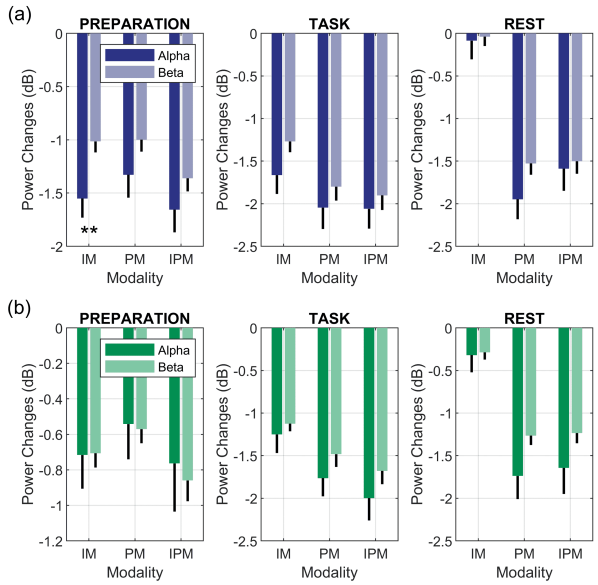


Fig. 3. Comparison between alpha and beta band power changes at channel (a) C3 and (b) C4. From left to right, each subfigure represents a different interaction stage similar to Fig. 2. The whisker on each bar corresponds to the standard error of the mean (SEM) power changes across subjects. The asterisk indicates a significant difference between alpha and beta was found via the Wilcoxon rank sum test (**: $p < 0.01$).

homing back at a faster speed, which partly explains why rest-stage ERD patterns differ from those of the task stage. Additionally, a strong ERS was observed in the occipital region for the IM modality during REST when the subject ceased motor imagery, with a similar but less pronounced effect for IPM and minimal occurrence in PM. For the distribution differences between alpha and beta rhythms, more brain regions engaged in alpha ERD, particularly for the preparation and task stages. The strength of each rhythm at the C3 (contralateral) and C4 (ipsilateral) EEG channel was statistically compared in Fig. 3. Generally, alpha rhythm showed stronger ERD compared to the beta rhythm for the EEG channels of both hemispheres, with the exception of the preparation stage in C4. However, a significant difference between alpha and beta was only found in C3 during the preparation stage of the IM modality (Fig. 3a).

B. Comparable alpha and beta ERD in exoskeleton-assisted movements regardless of motor intentions

Figure 4 presents the time-frequency representation of the C3 and C4 channels for three movement modalities. The 8-30 Hz frequency band activity was most pronounced in each modality, particularly when exoskeleton movement was involved (Fig. 4a and d). During exoskeleton-assisted movement (PM and IPM), stronger ERD was observed compared to

TABLE I
COMPARISON BETWEEN MOVEMENT MODALITIES IN ALPHA AND BETA BAND POWER CHANGES AT CHANNEL C3 AND C4. N.S. INDICATES NOT SIGNIFICANT

Channel	Rhythm	Comparison	P-value
C3	alpha	PM vs. IM	0.00044218
		IPM vs. IM	0.00086206
		IPM vs. PM	n.s.
	beta	PM vs. IM	3.234e-05
		IPM vs. IM	4.5419e-06
		IPM vs. PM	n.s.
C4	alpha	PM vs. IM	0.003176
		IPM vs. IM	5.6824e-05
		IPM vs. PM	n.s.
	beta	PM vs. IM	0.00098239
		IPM vs. IM	9.517e-06
		IPM vs. PM	n.s.

IM. A pronounced ERS was observed in the IM condition after the end of the task, whereas the exoskeleton-induced ERD persisted because of the device homing back. During the task, alpha and beta rhythms showed distinct behaviors, as illustrated in Fig. 4b-c and e-f. Notably, a steep decrease in alpha power was observed upon exoskeleton activation (Fig. 4b and e). In terms of modality differences, PM and IPM showed similar alpha and beta band desynchronization, with minimal variation during the pre- and post-task stages. Table I compares power changes across modalities in the alpha and beta bands during the task stage (time window: 5 - 6s), revealing significant differences for both PM and IPM compared to IM, while no significant difference was detected between PM and IPM.

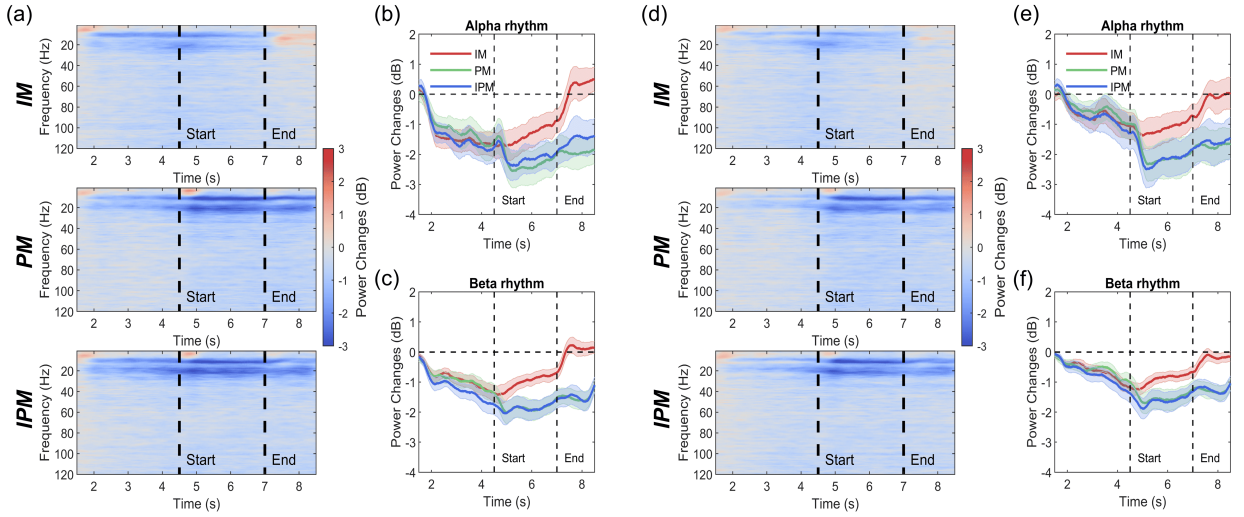


Fig. 4. Time-frequency representation of EEG activity in the C3 (a-c) and C4 (d-f) channels for different movement modalities. (a, d) Time-frequency spectra for IM, PM, and IPM modalities, illustrating power changes in dB over time. (b-c, e-f) Comparison of alpha (8-13 Hz) and beta (13-30 Hz) band power changes across movement modalities. 'Start' and 'End' denote the onset and offset of the task, respectively. Thick lines in (b-c) and (e-f) correspond to the average across trials, shaded regions to the 95% confidence interval.

C. Motor intention detection is more challenging with proprioceptive feedback

Figure 5 presents the binary classification results from four models. In general, distinguishing different movement modalities from the resting state is relatively easy, with the highest accuracy achieved 0.80 ± 0.07 (IPM vs. REST). The worst condition was IPM vs. PM, which obtained an accuracy of 0.61 ± 0.09, thus slightly above the chance level. It is interesting that the models IM vs. REST and PM vs. REST showed no significant difference, and a larger accuracy variation was found for PM vs. REST.

IV. Discussion

As growing attention is being dedicated to BCI-controlled hand exoskeletons, the challenges for advancing this BCI application should be addressed. In this study, we focused on a critical component, namely, motor intention decoding from brain activities during human-hand exoskeleton interaction. From continuous EEG recordings, we observed that exoskeleton-assisted passive movement introduced prominent bilateral ERD in alpha and beta bands, which is similar in frequency range but stronger in amplitude compared to imagined movement-induced neural correlates (Fig. 2 and Fig. 4). When the exoskeleton's movement was involved, it became difficult to discern motor intention-related EEG responses, as reflected by the statistical comparisons between PM and IPM modalities (Table I). This could partially explain why motor intention detection was quite difficult for IPM vs. PM (Fig. 5).

It is worth noting that our study focused specifically on the interaction between humans and a cable-driven hand exoskeleton. EEG correlates may vary across different exoskeleton systems. Our findings align with those reported in [6], where the same hand exoskeleton model was used,

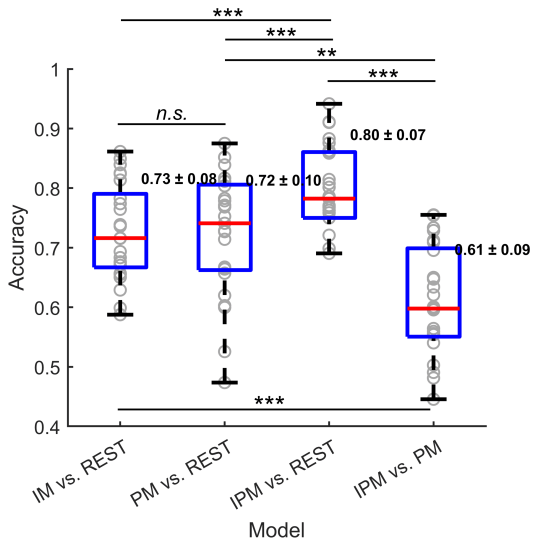


Fig. 5. Comparison between different binary classification models. Each box shows the distribution of each subject's accuracy (n = 25), with the middle red line representing the median. The whiskers correspond to 1.5 × IQR. The average accuracy and standard deviation are shown next to each box. P-values from post-hoc multiple comparisons are marked on the figure (***: $p < 0.001$, **: $p < 0.01$, n.s.: not significant)

and ERD patterns were observed in similar frequency ranges. Although the proprioceptive representation of the hand differs from that of proximal limb counterparts [15], similarities in EEG correlates are evident across the hand (our study and [6]), wrist [5], forearm [16], and lower limb [7]. Generally, passive movement elicits bilateral alpha and beta ERD, with a predominance on the contralateral side. On the other hand, factors such as movement speed and the type of exoskeleton motor will also impact EEG correlates. For example, Iwane

et al. reported that passive movement speed was correlated with the contralateral beta rebound and ipsilateral alpha ERD [16]. Mitra *et al.* observed a strong broadband synchronization coinciding with the robot movement [17], suggesting some exoskeletons (Harmony Exoskeleton used in their study) will likely introduce instrumental noise.

When comparing alpha and beta ERD, we found alpha rhythm had stronger desynchronization than beta rhythm (Fig. 3), particularly on the contralateral side, which is in line with observations in [5], [7], [18]. This supports earlier observations that alpha and beta rhythms would be related to different functional properties, i.e. somatosensory- and somatomotor cortical function, respectively [19]. Another finding in our study is that passive movement produced clear-cut modification of alpha band oscillations compared to beta band upon exoskeleton activation, as depicted in Fig. 4b-c. This could be partially explained by the sensitivity of alpha rhythm to attention and cognitive engagement [20]. During exoskeleton-assisted movements, the subject might pay more attention to the sensation of movement or the mechanical action of the exoskeleton.

We found a significant difference in motor intention detection with and without exoskeleton movement in Fig. 5. With exoskeleton movement, intention detection becomes more challenging (IPM vs. PM compared to IM vs. REST). This phenomenon was also reflected in Ferrero *et al.*'s study [10], where the authors found that it was more challenging to detect 'stop' intention when the lower-limb exoskeleton was activated compared to detecting 'start' intention without robot activation. Our experiment revealed that when the exoskeleton is activated, brain activations are similar regardless of whether the subject imagines a movement (IPM modality) or not (PM modality). In contrast, when the exoskeleton is not involved, the ERD induced by motor imagery (IM modality) can be clearly distinguished from REST. Therefore, extracting motor intention-related EEG features becomes more challenging in situations with exoskeleton activation. An interesting finding is that although both IPM and PM showed significantly different power changes compared to IM (Table I), PM vs. REST did not show as high accuracy as IPM vs. REST, nor IM vs. REST. One explanation is that we were classifying the covariance feature on the manifold space, not the power feature.

Although BCI-actuated hand exoskeletons hold great promise for neurorehabilitation, their current control strategies remain limited. Typically, a BCI decoder detects the user's motor intention and triggers the exoskeleton accordingly. However, once the exoskeleton is activated, the decoder struggles to function effectively, restricting the system to discrete control [21]. This means users can initiate movement but cannot continuously modulate or stop it. A key challenge for the next generation of BCI-exoskeleton systems is enabling continuous control, where motor intentions are dynamically monitored and executed in real-time. Our findings highlight this challenge: during exoskeleton interaction, the brain generates ERD patterns that are similar but stronger than those observed during motor imagery (Fig. 2, Fig. 4). Moreover, our decoding results suggest that detecting motor intention becomes significantly more difficult when the exoskeleton is moving (IPM vs. PM), with a classification accuracy only marginally above chance level. There is a trade-off between system stability and subject engagement. For stable control and better task completion, one may consider using a shared-control strategy [22] as it relies more on robot intelligence. For natural control and more subject engagement, we believe subject learning and advanced decoders are required. Indeed, although we asked the subject to avoid performing any movement imagination during PM, they reported that it was quite hard to finish the task. This suggested that subject learning is necessary in order to obtain task-differentiable data [23]. Our previous studies have shown the possibility of regressing fine finger movements from intracranial brain activity [24], [25], those explainable models can be particularly useful for continuous motor intention decoding during human-hand exoskeleton interaction.

V. Conclusion

We designed an experiment to investigate the impact of proprioception in EEG representations and decoding when interacting with a hand exoskeleton. We found when the exoskeleton was activated, strong alpha and beta ERDs were elicited due to proprioceptive afferents. However, EEG correlates were similar in situations with and without imagined motor intention upon the exoskeleton activation. Those findings explain why poor motor intention detection accuracy was observed when involving the exoskeleton. For future development of continuous BCI-actuated hand exoskeletons, we suggest using advanced decoders or control strategies considering the trade-off between system stability and subject engagement.

Acknowledgment

We would like to thank all subjects for their active participation of this study. We thank Idrogenet team for their technical support. We thank all funding agencies supporting this study.

References

[1] J. R. Wolpaw, N. Birbaumer, D. J. McFarland, G. Pfurtscheller, and T. M. Vaughan, "Brain–computer interfaces for communication and control," *Clinical neurophysiology*, vol. 113, no. 6, pp. 767–791, 2002.

[2] S. R. Soekadar, M. Witkowski, C. Gómez, E. Opisso, J. Medina, M. Cortese, M. Cempini, M. C. Carrozza, L. G. Cohen, N. Birbaumer, and N. Vitiello, "Hybrid EEG/EOG-based brain/neural hand exoskeleton restores fully independent daily living activities after quadriplegia," *Science Robotics*, vol. 1, no. 1, p. eaag3296, Dec. 2016.

[3] A. A. Blank, J. A. French, A. U. Pehlivan, and M. K. O'Malley, "Current trends in robot-assisted upper-limb stroke rehabilitation: promoting patient engagement in therapy," *Current physical medicine and rehabilitation reports*, vol. 2, pp. 184–195, 2014.

[4] A. A. Frolov, O. Mokienko, R. Lyukmanov, E. Biryukova, S. Kotov, L. Turbina, G. Nadareyshvily, and Y. Bushkova, "Post-stroke rehabilitation training with a motor-imagery-based brain-computer interface (BCI)-controlled hand exoskeleton: a randomized controlled multicenter trial," *Frontiers in neuroscience*, vol. 11, p. 400, 2017.

[5] E. Formaggio, S. F. Storti, I. Boscolo Galazzo, M. Gandolfi, C. Geroin, N. Smania, L. Spezia, A. Waldner, A. Fiaschi, and P. Manganotti, "Modulation of event-related desynchronization in robot-assisted hand performance: brain oscillatory changes in active, passive and imagined movements," *Journal of NeuroEngineering and Rehabilitation*, vol. 10, no. 1, p. 24, Dec. 2013.

[6] G. Tacchino, M. Gandolla, S. Coelli, R. Barbieri, A. Pedrocchi, and A. M. Bianchi, "EEG analysis during active and assisted repetitive movements: evidence for differences in neural engagement," *IEEE Transactions on Neural Systems and Rehabilitation Engineering*, vol. 25, no. 6, pp. 761–771, Jun. 2017.

[7] E. Formaggio, S. Masiero, A. Bosco, F. Izzi, F. Piccione, and A. Del Felice, "Quantitative EEG evaluation during robot-assisted foot movement," *IEEE Transactions on Neural Systems and Rehabilitation Engineering*, vol. 25, no. 9, pp. 1633–1640, Sep. 2017.

[8] G. Pfurtscheller and F. Lopes Da Silva, "Event-related EEG/MEG synchronization and desynchronization: basic principles," *Clinical Neurophysiology*, vol. 110, no. 11, pp. 1842–1857, Nov. 1999.

[9] F. Cassim, C. Monaca, W. Szurhaj, J. Bourriez, L. Defebvre, P. Derambure, and J. Guieu, "Does post-movement beta synchronization reflect an idling motor cortex?" *Neuroreport*, vol. 12, no. 17, pp. 3859–3863, Dec. 2001.

[10] L. Ferrero, P. Soriano-Segura, J. Navarro, O. Jones, M. Ortiz, E. Iáñez, J. M. Azorín, and J. L. Contreras-Vidal, "Brain–machine interface based on deep learning to control asynchronously a lower-limb robotic exoskeleton: a case-of-study," *Journal of NeuroEngineering and Rehabilitation*, vol. 21, no. 1, p. 48, 2024.

[11] R. Oostenveld, P. Fries, E. Maris, and J.-M. Schoffelen, "FieldTrip: open source software for advanced analysis of MEG, EEG, and invasive electrophysiological data," *Computational Intelligence and Neuroscience*, vol. 2011, no. 1, pp. 1:1–1:9, 2011.

[12] Q. Sun, E. C. Merino, L. Yang, and M. M. Van Hulle, "Unraveling EEG correlates of unimanual finger movements: insights from non-repetitive flexion and extension tasks," *Journal of NeuroEngineering and Rehabilitation*, vol. 21, no. 1, p. 228, 2024.

[13] A. Barachant, S. Bonnet, M. Congedo, and C. Jutten, "Riemannian geometry applied to bci classification," in *International conference on latent variable analysis and signal separation*. Springer, 2010, pp. 629–636.

[14] S. Chevallier, I. Carrara, B. Aristimunha, P. Guetschel, S. Sedlar, B. Lopes, S. Velut, S. Khazem, and T. Moreau, "The largest EEG-based BCI reproducibility study for open science: the MOABB benchmark," *arXiv preprint arXiv:2404.15319*, 2024.

[15] O. J. Lutz and S. J. Bensmaia, "Proprioceptive representations of the hand in somatosensory cortex," *Current Opinion in Physiology*, vol. 21, pp. 9–16, 2021.

[16] F. Iwane, G. Lisi, and J. Morimoto, "EEG sensorimotor correlates of speed during forearm passive movements," *IEEE Transactions on Neural Systems and Rehabilitation Engineering*, vol. 27, no. 9, pp. 1667–1675, Sep. 2019.

[17] K. Mitra, F. S. Racz, S. Kumar, A. D. Deshpande, and J. D. R. Millán, "Characterizing the onset and offset of motor imagery during passive arm movements induced by an upper-body exoskeleton," in *2023 IEEE/RSJ International Conference on Intelligent Robots and Systems (IROS)*. IEEE, 2023, pp. 3789–3794.

[18] E. Formaggio, S. F. Storti, I. Boscolo Galazzo, M. Gandolfi, C. Geroin, N. Smania, A. Fiaschi, and P. Manganotti, "Time–frequency modulation of ERD and EEG coherence in robot-assisted hand performance," *Brain topography*, vol. 28, pp. 352–363, 2015.

[19] A. Stolk, L. Brinkman, M. J. Vansteensel, E. Aarnoutse, F. S. Leijten, C. H. Dijkerman, R. T. Knight, F. P. de Lange, and I. Toni, "Electrocorticographic dissociation of alpha and beta rhythmic activity in the human sensorimotor system," *Elife*, vol. 8, p. e48065, 2019.

[20] J. A. Pineda, "The functional significance of mu rhythms: translating "seeing" and "hearing" into "doing"," *Brain research reviews*, vol. 50, no. 1, pp. 57–68, 2005.

[21] N. Rustamov, L. Souders, L. Sheehan, A. Carter, and E. C. Leuthardt, "IpsiHand brain-computer interface therapy induces broad upper extremity motor recovery in chronic stroke," *medRxiv*, pp. 2023–08, 2023.

[22] J. M. Catalán, E. Trigili, M. Nann, A. Blanco-Ivorra, C. Lauretti, F. Cordella, E. Ivorra, E. Armstrong, S. Crea, M. Alcañiz *et al.*, "Hybrid brain/neural interface and autonomous vision-guided whole-arm exoskeleton control to perform activities of daily living (adls)," *Journal of NeuroEngineering and Rehabilitation*, vol. 20, no. 1, p. 61, 2023.

[23] S. Perdikis, L. Tonin, S. Saeedi, C. Schneider, and J. d. R. Millán, "The Cybathlon BCI race: Successful longitudinal mutual learning with two tetraplegic users," *PLoS biology*, vol. 16, no. 5, p. e2003787, 2018.

[24] A. Faes, F. Camarrone, and M. M. Van Hulle, "Single finger trajectory prediction from intracranial brain activity using block-term tensor regression with fast and automatic component extraction," *IEEE Transactions on Neural Networks and Learning Systems*, 2022.

[25] A. Faes and M. Van Hulle, "Finger movement and coactivation predicted from intracranial brain activity using extended block-term tensor regression," *Journal of Neural Engineering*, vol. 19, no. 6, p. 066011, 2022.

Feasibility of a customised handgrip for a rehabilitation robot to meet specific needs

Lutong Li
School of Engineering
The University of Manchester
United Kingdom
lutong.li@manchester.ac.uk

Helen Dawes
Medical School, NIHR Exeter BRC
University of Exeter
United Kingdom
h.dawes@exeter.ac.uk

Sarah Tyson
School of Health Science
The University of Manchester
United Kingdom
sarah.tyson@manchester.ac.uk

Glen Cooper
School of Engineering
The University of Manchester
United Kingdom
glen.cooper@manchester.ac.uk

Andrew Weightman
School of Engineering
The University of Manchester
United Kingdom
andrew.weightman@manchester.ac.uk

***Abstract*—Stroke is a common healthcare problem, leading to disability and significantly impacting individuals' quality of life. A customised device was suggested to be used for robotic-assisted therapy to meet different stroke survivors' needs. However, most existing upper limb rehabilitation robots only offer a generic handgrip, which fails to meet the various needs of stroke survivors with different spastic patterns and levels of upper limb weakness. This study investigates the technical and clinical feasibility of customised handgrips to meet stroke survivors' needs through an online questionnaire with 25 therapists and parametric handgrip designs. One wrist support and two different handgrips were designed, and their size (e.g., length and width) can be adapted based on the individual anthropology data. By using the additive manufacturing method, the manufacturing cost of bespoke handgrip is reduced by up to 15%. Additionally, more than 90% of professionals (n=23) stated the positive impact of customised handgrip on rehabilitation outcomes and 72% (n=18) would like to use it with stroke survivors due to its high accessibility and variability. The results indicate that a customised handgrip has the potential to benefit the stroke rehabilitation from both technical and clinical perspectives.**

Keywords—customisation, stroke, rehabilitation, bespoke, additive manufacturing

I. INTRODUCTION

During the last few decades, the ability of robotics-assisted therapy to promote high intensity, high repetition, task-oriented exercise and quantifiable neurorehabilitation was identified, which is considered one of the most effective methods to restore upper limb function [1]. Evidence shows that post-stroke upper limb robotic-assisted therapy can significantly improve motor control ($P<0.05$) [2]. The majority of existing end-effector upper limb rehabilitation robots are limited in that they provide only a generic handgrip. The handgrip in this research is defined as the passive handle attached to an end-effector rehabilitation robot. However, a generic handgrip cannot meet the needs of all stroke survivors due to the various spastic patterns and upper limb weakness levels. The common spasticity patterns of the upper limb after a stroke are 'Flexed elbow', 'Bent wrist', 'Pronated forearm', 'Clenched fist', and 'Thumb in palm', and these different patterns limit their ability to grip a generic handgrip. From the designers' perspective, providing a customised upper limb rehabilitation handgrip (e.g., handgrip size, shape, and type) could be an effective solution to enhance access to rehabilitation and improve outcomes. Based on this, one research question was raised '*Would customised handgrip be beneficial for stroke rehabilitation?*'

Fu in 2019 [3] identified the four most frequent grip types that people use in activities of daily living: grasp grip (usage frequency 33.3%), pinch/key grip (66.7%), pencil grip (14.3%) and hook grip (4.8%). He conducted a review of 120 upper limb rehabilitation robots found that 52.5% (63/120) included handgrip, while only 8.7% (11/120) provided pinch grip. This indicated that the current rehabilitation robot cannot provide sufficient grip types to meet Activities in Daily Living (ADLs).

According to professionals' recommendations in the United Kingdom *National Clinical Guideline for Stroke* [4], customised rehabilitation devices such as individually fitted orthosis were suggested for use to meet different users' needs. However, most of the commercialised rehabilitation robots are developed for using in hospitals, often at a high cost [5]. Additive manufacturing (AM) is an ideal technology for customisation at a relatively low cost and has been widely used in bioengineering and medical devices in the last several decades such as implants, orthoses and rehabilitation robot [6]. With minimal design restrictions, AM enables medical institutions to produce customised, cost-effective, durable, and lightweight products with low labour input [7].

Customised rehabilitation devices can increase users' satisfaction and allow more users to receive better rehabilitation results. Chen et al in 2016 identified that the bespoken rehabilitation devices can meet specific requirements of prostheses and orthoses, which improve the satisfaction of both healthcare professionals and stroke survivors [8]. In 2019, Sarwar et al [9] highlighted that bespoken hand exoskeleton systems can be provided at a relatively low cost by using AM. In 2021, Ibrahim and Faller designed and developed a customised hand rehabilitation glove by using AM that can fit different individuals to avoid the secondary injury caused by misalignment [10]. However, the measurement method they used to obtain anthropology data was 3D scanning, which is not simple or convenient enough for both therapists and stroke survivors. Additionally, the rehabilitation glove requires stroke survivors can grasp, which limits the type and number of stroke survivors who can use the customised rehabilitation glove. However, most

customised upper limb rehabilitation robots limit the types of users due to complex structures and requirements for users' movement ability. Therefore, the customised handgrip for an upper limb rehabilitation robot which is easy to use and fit for more stroke survivors' needs is required. Although some research emphasises the importance and potential of customisation in stroke rehabilitation, most of them focus on the control algorithms or human-computer interaction, no relevant study focuses on design customisation and its feasibility [11].

To answer the research question, this research aims to identify the technical and clinical feasibility of a customised handgrip for a rehabilitation robot and how if they could benefit stroke survivors, therapists, and manufacturers. A two-stage research approach was undertaken. During the first stage, we determined and designed customised handgrips for the upper limb rehabilitation robot using parametric design. In the second stage, the clinical feasibility of customised handgrip was identified through an online questionnaire with healthcare professionals.

II. Methodology

A. Design and optimisation of customised rehabilitation robot handgrip

1) Identification of customisation rehabilitation robot handgrip type

We conducted a consultation with physiotherapists (PTs) and an online questionnaire with 11 PTs and 4 occupational therapists (OTs) to determine customised rehabilitation robot handgrip types and their priority for stroke survivors. Participants were asked to rank the four grip types (grasp, pinch, pencil and hook grip) according to the importance level for upper limb rehabilitation from high to low (1 to 4).

2) Conceptual design and parameters determination

Parameter determination: A consultation with an experienced therapist led to categorizing handgrip sizes into small, medium, large, and extra-large, based solely on anthropometric data (e.g., palm width, hand length, wrist circumference). The measurement method is introduced in Table I which was inspired by the Saebo glove selection method. If measurements were difficult to obtain, then the unaffected hand could be used or estimated from observation.
Conceptual design: CAD software (SolidWorks) as used for parametric 3D design and cost estimation. The SolidWorks costing tool was utilised automatically calculate the manufacturing cost according to the manufacturing geometry, manufacturing method, materials and labour setting [12]. The default setting in the SolidWorks costing was used including the material information and labour rate that was set as the UK average labour cost of manufacturing.

TABLE I. Method to determine the handgrip size

Anthropological data (mm)	Handgrip parameter (mm)
Palm width between the 1st and 5th metacarpophalangeal joints	Height (H) of vertical handgrip
Hand length (tip of the 3rd finger to the 1st wrist crease)	Diameter (D) of vertical/hemispheric handgrip
Wrist circumference	Width (W) of the wrist support is the 1/2 of wrist circumference

B. Questionnaire to determine professionals' view of customised rehabilitation robot handgrip

1) Design and distribution of the questionnaire

To identify the professionals' views on the customised upper limb rehabilitation robot handgrip, an online questionnaire was devised by our research team and piloted with 25 healthcare professionals in our clinical stroke research network. The first part was about the participants' background including work experience and experience using rehabilitation robots. The second section was professionals' views of the customised handgrip for upper limb rehabilitation robots. The questionnaire was distributed by email, through relevant research networks of our research team, and social media to professionals with previous or current experience in stroke rehabilitation in any clinical setting. Participants were provided the Participant Information Sheet (PIS) before starting the formal online questionnaire. They were free to opt for this online questionnaire anytime. Only the response with 100% completion was included in the final data analysis.

2) Questionnaire data analysis

Mann-Whitney test and descriptive statistics in IBM SPSS v25.0 was used to compare and describe quantitative data. The groups were categorised based on participants' experience of using rehabilitation robots. A general thematic analysis and was conducted to determine professionals' views of the customised handgrip for upper limb rehabilitation robots for qualitative data analysis. Participant statements were downloaded into Excel and categorised using a coding matrix. Descriptive statistics, including frequency counts and percentage distributions, were used to summarise key themes and the prevalence of specific responses. All questionnaire responses and collected data were anonymised and did not contain any sensitive data.

According to the ethical requirement of the University of Manchester and NHS Health Research Authority, this research does not require ethical approval.

III. Results

A. Design and optimisation of customised handgrip

1) Conceptual design of customised rehabilitation robot handgrip

Of the 15 therapists involved in the first stage of this study, 73% had more than 10 years' working experience. Table II illustrates the usage and importance level of four grips in daily living (grab grip, pinch grip, pencil grip and hook grip). The pinch grip was found to be the most commonly used (66.7%, 14/21 activities), followed by the grab grip (33.3%, 7/21 activities) [3]. However, according to the questionnaire results, the grasp grip was reported as the most important followed by the pinch grip.

According to the questionnaire results, the concept should be developed as a parametric modular handgrip. This design should guarantee the integration of essential sensors and allows the model to automatically adapt to the needs of different stroke survivors. This should ensure economic feasibility whilst also bespoke rehab. Thus, based on the therapists' suggestions and the postures of the four main grip types, hemispherical and vertical handgrips were selected for design. The hemispherical design was chosen for its ergonomics, stability, and manufacturability, while the vertical handgrip was selected for its widespread use. Both designs support four grip types and accommodate stroke survivors by allowing size adjustments. As shown in Table III, the wrist support was designed for stroke survivors having

mild-moderate, severe-very severe weakness or inability to grasp at all. The wrist support can work with either a hemispherical handgrip or a vertical handgrip as an extra support for the forearm. The hemispherical handgrip would be suitable for stroke survivors with mild to moderate weakness, finger stiffness, or the ability to perform hook or grasp grips. The vertical handgrip was designed for stroke survivors with mild to moderate weakness or those able to perform grasp, pinch, or hook grips. All handgrips featured Velcro for secure user attachment and a modular connector for an upper limb rehabilitation robot. Their size (length and width) was adjustable based on individual anthropometric data. Additionally, an optional force sensor was integrated to monitor grip strength, with a dedicated space ensuring sensor stability regardless of size or shape modifications. A two-step guideline was created to help therapists determine customised handgrips: 1) selecting the handgrip type based on the patient's condition (e.g. weakness level, hand characteristics), and 2) determining the size using anthropometric data (e.g., hand length, palm width) measured by therapists.

TABLE II. THE FREQUENCY OF HUMAN GRIPS IN ACTIVITES OF DAILY LIVING AND THE IMPORTANCE LEVEL OF REHABILITATION

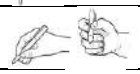
Type of grip	Illustration of grip	Frequency in daily life (%) [3]	Importance level[1]
Grasp grip		7 (33.3%)	1
Pinch grip		14 (66.7%)	2
Pencil grip		3 (14.3%)	3
Hook grip		1 (4.8%)	4
(***Note*** [1]: Results were obtained from the online questionnaire with 15 therapists; the importance level from high to low is from 1 to 4).			

TABLE III. CONCEPTUAL DESIGN OF CUSTOMISED HANDGRIPS FOR A REHABILITATION ROBOT

	Wrist support	Hemispherical handgrip	Vertical handgrip
Conceptual Design			
Target users	**1.** Severe or very severe weakness **2.** Wrist stiffness **3.** Cannot grasp at all	**1.** Mild to Moderate weakness **2.** Finger stiffness **3.** Can do some hook or grasp grip	**1.** Mild to Moderate weakness **2.** Can do some grasp, pinch, pencil or hook grip

2) Technical feasibility of customised rehabilitation handgrip

The SolidWorks 2020 costing tool was used to estimate manufacturing costs and assess the feasibility of a customised handgrip. All the parameters such as labour cost and materials were set to guarantee data consistency in different manufacturing methods. Fig.1 indicates the estimated cost of customised handgrips for various manufacturing methods when the total manufacturing quantity was 100. At 60% infill rate, the AM reduced cost by 5-15% across all handgrip types compared to traditional manufacturing at a low small manufacturing quantity.

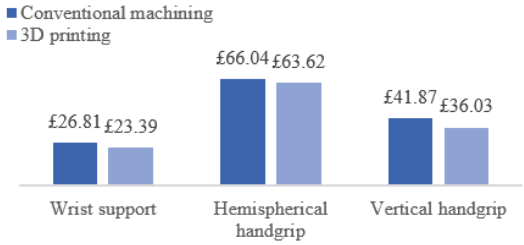


Fig. 1. Manufacturing cost estimation of per customised handgrip according to different manufacturing methods

B. The clinical feasibility and potential benefit of the customised handgrip

In total, 25 professionals participated in the online questionnaire, most from the UK (n=21, 84%) (Table IV). More than half were PTs (n=14, 56%); one-third were OTs (n=8, 32%). Most (n=19, 76%) had more than five years' work experience and worked in the local public health system—National Health Service (n=15, 60%). In-patient rehabilitation unit was the most common (n=18, 72%) work setting. Almost half (n=11, 44%) had the experience of using rehabilitation robots, all based in clinical settings.

In terms of the rehabilitation robot used by professionals in this research, most of them (10 of 11) provided a combination rehabilitation for both arm and hand, while only 5 of them provided customisation which was 'MIT-Manus', 'Re-o-Go', 'MyoPro', Motus Nove' and 'Amadeo'. While the professionals reported that these rehabilitation robots provided customised handgrips, most achieved customisation by adjusting the Velcro fixation or control system (e.g. resistance level), except the ReoGO and MyPro which provided multiple handgrip or support options. Although the features can be adjusted for these robots including the resistance of glove, different types of handgrips and finger position, professionals reported *"The glove is fiddly to fit the handgrips/gloves"*. Although the effectiveness of robotic-assisted therapy has been demonstrated, the adaptation rate is low which is compared with other common intervention, especially for the complexed hand rehabilitation. Table V indicates the current intervention for hand rehabilitation after a stroke. The repetitive task training / functional task practice mentioned frequency (MF) =17.02%) was the most used intervention followed by exercise (MF=20%) and splints or orthoses (MF=13.48%).

More than 90% of professionals (n=23) stated the positive impact of customised handgrip on rehabilitation outcomes and 72% (n=18) would like to use a customised handgrip with stroke survivors due to its high accessibility and variability. 'Accessibility' here is defined as the opportunity for stroke survivors to use rehabilitation robots. Few professionals (n=4, 16%) were reluctant to use customised handgrip due to the high cost, limited clinical evidence and required extra training. Stroke survivors with moderate upper limb weakness were regarded as the most suitable people (34%) to use customised handgrip, with approximately equal proportions of stroke survivors with mild or severe upper limb weakness (Table VI). Professionals with and without experience using rehabilitation robots had similar opinions on the type of stroke survivors who were suitable to use customised ($P>0.05$). Although some suggested using customised handgrip for stroke survivors having severe weakness, they also pointed out that more intense training and therapists' supervision may be required.

TABLE IV. DEMOGRAPHICS OF QUESTIONNAIRE PROFESSIONAL PARTICIPANTS

Characteristic		Number (%) of participants
Country United Kingdom		21 (84%)
	United States	2 (8%)
	United Arab Emirates	1 (4%)
	Prefer not to say	1 (4%)
Profession	Occupation therapists	8 (32%)
	Physiotherapists	14 (56%)
	Doctors	2 (8%)
	Others (Research associate)	1 (4%)
Work organization*	Local public health system/ NHS	15 (60%)
	Private practice	5 (20%)
	Other (University or rehabilitation product institution)	6 (24%)
Work setting*	Acute care	15 (60%)
	In-patient rehabilitation Unit	18 (72%)
	Long-term care	5 (20%)
	Outpatient Clinic	14 (56%)
	Community-based care	15 (60%)
	Other	4 (16%)
Career stage	< 1 year experience	1 (4%)
	1—5 year's experience	5 (20%)
	6—10 year's experience	5 (20%)
	> 10 year's experience	14 (56%)
Experience in using rehabilitation robots Have experience		11 (44%)
	Have no experience	14 (56%)
*(**Note**: * participants indicated all the areas in which they had experience, so totals exceed 100%)*		

TABLE V. THE RESULTS OF THE PREVALENCE OF HAND REHABILITATION INTERVENTIONS AFTER STROKE

Current intervention for hand rehabilitation	Frequency (%)
Repetitive task training / functional task practice	24 (17.02%)
Exercise	20 (14.8%)
Splints or orthoses	19 (13.48%)
Electrical stimulation	17 (12.06%)
Mental practice	15 (10.64%)
Mirror therapy	13 (9.22%)
Constraint-induced movement therapy (CIMT)	13 (9.22%)
Bobath	7 (4.96%)
Virtual reality	5 (3.55%)
Other (e.g. robotics, hydrotherapy or spasticity management)	8 (5.67%)

TABLE VI. SUITABILITY OF CUSTOMISED HANDGRIPS FOR DIFFERENT LEVELS OF UPPER LIMB WEAKNESS FROM QUESTIONNAIRE

Upper limb weakness level	Suitability (%)
Mild weakness (movement in all joints against gravity but limited range, strength, and dexterity).	13 (24.53%)
Moderate weakness (some movements in all joints but limited range against gravity and only a basic, weak grip grasp, little dexterity. Can use the arm as a 'helping hand').	18 (33.96%)
Severe weakness (can make movements in some joints but not against gravity, no functional grip).	11 (20.75%)
Very severe (complete paresis, no functional movement).	5 (9.43%)
Others	6 (11.32%)
*(**Note:** Participants can select multiple options, so suitability is calculated as the selection count for each option over the total selections)*	

IV. DISCUSSION

The results of this research identified the potential feasibility of a customised upper limb rehabilitation robot handgrip for stroke rehabilitation from both a manufacturing and rehabilitation perspective. The parametric design allows engineers to adapt the 3D design quickly according to stroke survivors' data (e.g., palm width and length). By using the AM method, users will be provided with more customised features such as the material, colour, and texture. The texture of a handgrip plays a crucial role in user preference and usability, as it directly affects comfort, grip stability, and tactile feedback. A well-designed texture can enhance user confidence, reduce fatigue, and improve overall interaction, particularly for individuals with limited hand function. The rehabilitation feasibility of a customised handgrip was identified by an online questionnaire with 25 professionals. Due to the variety of stroke survivors' weakness levels, the standard handgrip is always insufficient or uncomfortable to use. Professionals highlighted the potential of customised handgrips to increase the accessibility of upper limb rehabilitation robots and stroke survivors' motivation.

A. Technical feasibility of customised upper limb rehabilitation robot handgrip

The goals of the medical device industry are reducing costs, waste, energy use, and labour. AM has been recognised as a cost and labour-effective method for prototyping and manufacturing [13]. AM is not yet cost-competitive for high-volume manufacturing but is viable for small-scale or personalised medical devices, where traditional tooling is costly. For a production volume of 100, AM costs 85-95% of traditional methods, with cost reduction varying by design complexity. It enables affordable customization without additional tooling, tailoring products to stroke survivors' needs while reducing production cycles by eliminating machine changeovers and labour shifts [13].

Despite its benefits, AM adoption faces challenges, such as surface quality [14]. For medical devices like prostheses and orthoses, a key challenge, as highlighted by Ngo et al., is layer delamination and internal stress from non-uniform phase changes [15]. High AM usage increases plastic waste, which is difficult to recycle. Additionally, the lack of standards limits adoption. While AM shows promise for customised rehabilitation robots, most research remains in early stages due to technological barriers and concerns [10]. The concerns of using customised handgrip will be discussed in the next section.

B. Clinical feasibility of customised home-based rehabilitation robot handgrip

1) Benefits of customised home-based rehabilitation robot handgrip

Analysis of ADLs showed the most prevalent grip was the pinch grip, but rehabilitation robots also needed to accommodate a grasp grip. This indicates that a generic (grasp) handgrip cannot meet the needs of stroke survivors who need to facilitate more ADLs-based practice or who are unable to grip. Pencil and hook grips were a lower priority. This shows that single-grip robots (which are currently the norm) are not fit-for-purpose and limit access for those with severe disabilities. Most professionals showed positive attitudes toward using the customised rehabilitation robot grips due to the higher accessibility, and higher variability in patients.

Potential improvement in rehabilitation outcomes

Promoting improved clinical outcomes of rehabilitation has been reported as the biggest benefit of rehabilitation robots/technology (Fig. 2). To improve the normal pattern of

movement, the handgrip needs to be based on the individual for stroke survivors. Additionally, the individualised presentation of the stroke survivors and impairment levels makes customisation relevant to the rehabilitation of the individual. According to professionals' experience, high tone makes conventional grip (grasp grip) often difficult to achieve and changes in sensation and pain also make standard equipment difficult to use. Moreover, different grip functions are important for function transfer. A suitable handgrip allows progression and enables the rehabilitation robot to be used with a wide range of patient capabilities. Moreover, customised handgrips bring more practice variation to stroke survivors which may help them stay interested and practice more.

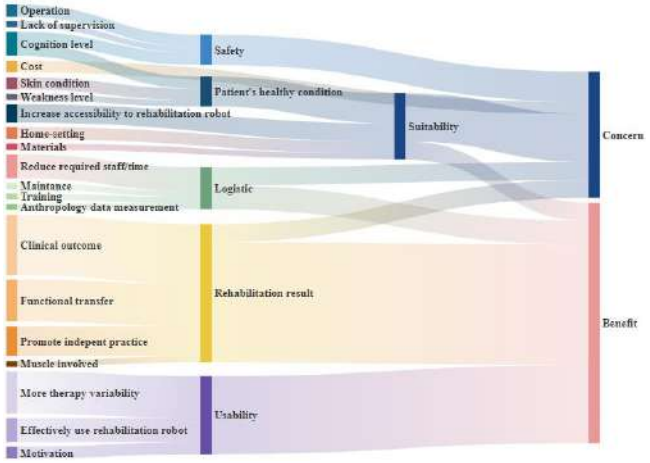


Fig. 2. Thematic analysis results: Sankey diagram illustrating the benefits and concerns of using a customised upper limb rehabilitation robot handgrip. The width of each theme represents its relative weight

Improve the usability and accessibility

Professionals raised that the rehabilitation robot handgrip in the current market is fiddly to fit for both therapists and stroke survivors. Ease of donning and doffing is a requirement for customised handgrip and upper limb rehabilitation robots. Compared to standard one-size-fits-all grips, the customised design offers better adaptability to individual hand shapes and impairments, as supported by insights from our questionnaire. While initial adaptation may require brief familiarization, both therapists and patients can easily adjust with minimal training. Apart from this, stroke survivors with poor grip strength or increased tone are difficult to maintain. Providing the adjustable Velcro tape can help to easily and safely fix stroke survivors' hands. As highlighted by professionals, every individual is unique in their grip and functioning pre- and post-condition events. A generic grip may fit a majority of service users, however, those who arguably need the support most would not be catered for without it. The customised handgrip provides more options of shapes, sizes, and materials for stakeholders (stroke survivors and therapists), which also increases the accessibility of rehabilitation robots for stroke survivors. Additionally, a parametric modular design supports sensor integration in a handgrip by offering flexibility and adaptability.

In addition to function-related characteristics such as shape and size, personal preference-related characteristics such as colour and texture were suggested as customisation options to appeal to stroke survivors by professionals. The personal preference has been emphasised for chronic disease rehabilitation and medical technology assessment [16]. In 2013, Centre for Devices and Radiological Health (CDRH) in the United States (US) conducted a project that identified the patient-centric assessment for medical technology has the potential to lead a better decision-making in healthcare [17]. Lewis et al emphasised that users' preference testing provided valuable information that can help to improve the design and development of a medical device, and users' acceptance in 2022 [18]. However, it still requires more standards to help put the personal preference in medical device design loop. In addition, AM customised handgrips presents several challenges, including ensuring biocompatibility and durability of materials to meet medical standards (e.g., ISO 13485 and IEC 60601). Regulatory approval for patient-specific designs can be complex, requiring thorough validation and compliance with medical device certification processes. Additionally, achieving consistent mechanical properties and surface finishes while maintaining cost-effectiveness remains a key hurdle for widespread clinical adoption. In addition, professionals want to use customised handgrip for an upper limb rehabilitation robot not only in clinical settings but also for users at home, a win-win strategy for therapists and stroke survivors. For the therapists, they are able to diagnose or supervise more patients; for the stroke survivors, they could reduce the time and cost of travelling between their homes and rehabilitation centres. Additionally, usability trials should be conducted to gather qualitative insights on user experience, ease of adaptation, and comfort. Additionally, feedback from healthcare professionals should be incorporated to refine the design and optimise its application. Further investigation into material preferences and grip textures will help improve user satisfaction and increase the likelihood of adoption. Future work should focus on refining personalisation methods based on patient-specific grip strength and dexterity levels to enhance functional outcomes.

2) Concerns and requirements of customised home-based rehabilitation robot handgrip

Although benefits and desire of using customised handgrip have been identified in this study, few professionals (n=4, 16%) raised concerns regarding the safety, suitability (e.g., upper limb weakness level), and logistics "*Not sure if the customised handgrip can be benefit to all users*". These concerns are highly consistent with our previous study *'Professionals' Views and Experiences of Using Rehabilitation Robotics With Stroke Survivors: A Mixed Methods Survey'[19]*, which indicates that similar concerns are raised by professionals when adopting new technology. As with other medical devices, safety is a paramount consideration for adopting a customised handgrip, which is often raised by professionals. Stroke survivors with cognitive or open wounds are not suitable for using customised handgrip. In addition, considering the degree of upper limb weakness and spasticity pattern to determine the handgrip can avoid secondary injury during the training. The potential extra training for device operation and the maintenance of handgrips were also raised as main concerns. The same concern was raised for rehabilitation robot adoption [19]. Staff shortages and heavy workloads in public healthcare may be a factor. The WHO reports a current shortage of 7.2 million healthcare workers, projected to reach 12.9 million by 2035

[20]. The easy-to-use and easy-to-maintain customised handgrips are desired to avoid extra training and workload.

Placement of fingers, especially for the thumb is helpful, but it is often difficult and not always possible with the robot. In addition to this, finger release and strength monitoring were also suggested for the customised handgrip. However, it is difficult to find the balance between the stakeholders' desires and the final function of products. More research and clinical trials are required to identify the balance between the product features and stakeholders' desires.

C. *Study limitations*

This study has some limitations. Stroke survivors were not involved in the questionnaire, and their feedback is essential to strengthen the research. Additionally, manufacturing costs varied depending on initial settings such as cost of materials and labour, requiring further detailed cost analysis in future studies.

V. CONCLUSION

Customisation of rehabilitation robots has attracted researchers' interest for its potential to improve clinical rehabilitation outcomes. However, there is no studies have specifically focused on customised handgrips. This research identified and demonstrated the clinical and technical feasibility of a customised handgrip for upper limb rehabilitation robot, demonstrating its potential to address different user needs effectively. The most significant outcome is that individuals who genuinely require rehabilitation can now access it through the use of upper limb rehabilitation robot with customised handgrip. This advancement not only enhances accessibility but also promotes user-centred rehabilitation by accommodating individual preferences and physical conditions. Moreover, the approach offers a substantial advantage in terms of cost-efficiency. By utilising parametric modular design and AM manufacturing, the proposed handgrip can be produced and customised economically (e.g., handgrip type, shape, size, and material customisation), making it suitable for widespread implementation. This combination of accessibility, adaptability, and affordability marks a meaningful step forward in the field of assistive robotics and rehabilitation, paving the way for improved outcomes and quality of life for users. Future research should focus on commercialization, and market adoption challenges. Additionally, refining the design based on patient feedback will enhance adaptability and accessibility in rehabilitation. More clinical research is also required to increase the new technology including the customised handgrip adoption for stroke rehabilitation.

REFERENCES

[1] G. Morone, I. Cocchi, S. Paolucci, and M. Iosa, "Robot-assisted therapy for arm recovery for stroke patients: state of the art and clinical implication," *Expert Review of Medical Devices,* vol. 17, no. 3, pp. 223-233, 2020/03/03 2020, doi: 10.1080/17434440.2020.1733408.

[2] J. M. Veerbeek, A. C. Langbroek-Amersfoort, E. E. Van Wegen, C. G. Meskers, and G. Kwakkel, "Effects of robot-assisted therapy for the upper limb after stroke: a systematic review and meta-analysis," *Neurorehabilitation neural repair,* vol. 31, no. 2, pp. 107-121, 2017.

[3] Q. Fu, "Design, implementation and analysis of a cost-effective rehabilitation robot for children with cerebral palsy," The University of Manchester (United Kingdom), 2021.

[4] I. S. W. Party, *National clinical guideline for stroke*. London: Royal College of Physicians, 2012.

[5] P. Chaiyawat and K. Kulkantrakorn, "Effectiveness of home rehabilitation program for ischemic stroke upon disability and quality of life: A randomized controlled trial," *Clinical Neurology and Neurosurgery,* vol. 114, no. 7, pp. 866-870, 2012/09/01/ 2012, doi: https://doi.org/10.1016/j.clineuro.2012.01.018.

[6] C. J. Nycz, T. Bützer, O. Lambercy, J. Arata, G. S. Fischer, and R. Gassert, "Design and Characterization of a Lightweight and Fully Portable Remote Actuation System for Use With a Hand Exoskeleton," *IEEE Robotics and Automation Letters,* vol. 1, no. 2, pp. 976-983, 2016, doi: 10.1109/LRA.2016.2528296.

[7] C. Weller and R. Kleer, "Economic Value of Digitized Manufacturing: Product Customization with 3D Printing," *Academy of Management Proceedings,* vol. 2015, no. 1, p. 11524, 2015/01/01 2015, doi: 10.5465/ambpp.2015.11524abstract.

[8] R. K. Chen, Y.-a. Jin, J. Wensman, and A. Shih, "Additive manufacturing of custom orthoses and prostheses—A review," *Additive Manufacturing,* vol. 12, pp. 77-89, 2016/10/01/ 2016, doi: https://doi.org/10.1016/j.addma.2016.04.002.

[9] W. Sarwar, W. Harwin, B. Janko, and G. Bell, "Multi-Compliance Printing Techniques for the Fabrication of Customisable Hand Exoskeletons," in *2019 IEEE 16th International Conference on Rehabilitation Robotics (ICORR)*, 24-28 June 2019 2019, pp. 488-493, doi: 10.1109/ICORR.2019.8779371.

[10] K. Ibrahim and L.-M. Faller, "Development of A Customized Rehabilitation Device Using Additive Manufacturing," in *The 14th Pervasive Technologies Related to Assistive Environments Conference*, 2021, pp. 354-358.

[11] G. Devittori *et al.*, "Automatic and Personalized Adaptation of Therapy Parameters for Unsupervised Robot-Assisted Rehabilitation: a Pilot Evaluation," in *2022 International Conference on Rehabilitation Robotics (ICORR)*, 25-29 July 2022 2022, pp. 1-6, doi: 10.1109/ICORR55369.2022.9896527.

[12] D. Systemes, "Solidworks. 2019," *Dessault Systemes: Vélizy-Villacoublay, France,* 2011.

[13] C. Weller, R. Kleer, and F. T. Piller, "Economic implications of 3D printing: Market structure models in light of additive manufacturing revisited," *International Journal of Production Economics,* vol. 164, pp. 43-56, 2015/06/01/ 2015, doi: https://doi.org/10.1016/j.ijpe.2015.02.020.

[14] M. Bhuvanesh Kumar and P. Sathiya, "Methods and materials for additive manufacturing: A critical review on advancements and challenges," *Thin-Walled Structures,* vol. 159, p. 107228, 2021/02/01/ 2021, doi: https://doi.org/10.1016/j.tws.2020.107228.

[15] T. D. Ngo, A. Kashani, G. Imbalzano, K. T. Q. Nguyen, and D. Hui, "Additive manufacturing (3D printing): A review of materials, methods, applications and challenges," *Composites Part B: Engineering,* vol. 143, pp. 172-196, 2018/06/15/ 2018, doi: https://doi.org/10.1016/j.compositesb.2018.02.012.

[16] M. Ho *et al.*, "A Framework for Incorporating Patient Preferences Regarding Benefits and Risks into Regulatory Assessment of Medical Technologies," *Value in Health,* vol. 19, no. 6, pp. 746-750, 2016/09/01/ 2016, doi: https://doi.org/10.1016/j.jval.2016.02.019.

[17] U. Food and D. Administration, "Guidance for industry and Food and Drug Administration staff—Factors to consider when making benefit-risk determinations in medical device premarket approvals and de novo classifications," *Silver Spring: Center for Devices and Radiological Health, Center for Biologics Evaluation and Research, Food and Drug Administration. Retrieved November,* vol. 3, p. 2017, 2012.

[18] A. Lewis *et al.*, "Preference Testing in Medical Devices: Current Framework and Regulatory Gaps," (in eng), *Med Devices (Auckl),* vol. 15, pp. 199-213, 2022, doi: 10.2147/mder.S368420.

[19] L. Li, S. Tyson, and A. Weightman, "Professionals' Views and Experiences of Using Rehabilitation Robotics With Stroke Survivors: A Mixed Methods Survey," (in English), *Frontiers in Medical Technology,* Original Research vol. 3, 2021-November-11 2021, doi: 10.3389/fmedt.2021.780090.

[20] A. U. Truth, "No health without a workforce," *World Health Organisation (WHO) Report,* pp. 1-104, 2013.

Towards Magnetically Induced Skin Stretch for Hand Proprioceptive Feedback

Eleonora Fontana*[1], Manuel G. Catalano[2], Giorgio Grioli[1,2], Matteo Bianchi[1], and Antonio Bicchi[1,2]

***Abstract*— Skin stretch feedback is increasingly recognized in rehabilitation and prosthetics for its ability to convey proprioceptive cues. Magnetically-induced skin stretch can offer interesting perspectives, not only for non-invasive stimulation but also for integration within the body. This study presents the first step towards the development of the MISS (Magnetically Induced Skin Stretch) device, a wearable system that uses magnetic interactions to provide proprioceptive feedback through skin stretch. By manipulating two magnets attached to the skin, the device aims to convey stretch sensations for hand proprioception. After preliminary Finite Element Method Magnetics simulations (FEMM), we came to the MISS design, which consists of a C-shaped ferromagnetic core with two solenoids at its ends. When the solenoids are powered, they generate a magnetic field that interacts with the magnets, causing controlled skin displacements to produce both stretch and pinch sensations. Psychophysical tests with the device positioned on the hand dorsum were performed to evaluate the skin deformations, whose outcomes support the device's potential application in proprioceptive feedback for prosthetics and hand rehabilitation.**

I. INTRODUCTION

Proprioception is fundamental for motor control, balance, and coordination in everyday tasks as well as in complex activities. In the context of human-computer interaction, robotics-enabled prosthetics, and rehabilitation, there is a growing interest in developing systems capable of restoring or enhancing proprioceptive feedback [1], [2]. Among the various methods for delivering this sensory information, one promising approach is the use of skin stretch, which involves the mechanical deformation of the skin to convey information about movement and forces applied to the body. Specifically, skin mechanoreceptors have been shown to play a significant role in the kinesthetic perception of finger and joint positions [3], [4], eventually inducing illusory sensations of movement. In previous research, we further explored this relationship between skin stretch and finger joints [5], confirming its fundamental role in proprioception.

Several approaches for delivering skin stretch have been explored in literature, with notable success in providing naturalistic feedback. Typically, these devices use mechanical actuators to pull or push the skin, aiming to convey feedback proportional to the hand level of aperture [6], [7], [8]. For example, Colella et al. [9] proposed the Stretch-Pro, a wearable device that provides proprioceptive feedback on artificial hand aperture using fixed actuated rollers to induce skin stretch. In addition to traditional proprioceptive feedback systems, recent research has explored magnetic field-based systems as alternatives to mechanical actuators to induce skin deformation. These systems can be employed in skin-integrated feedback solutions [10] or wearable devices [11], and offer promising non-invasive options. For instance, contactless devices use time-varying magnetic fields to stimulate mechanoreceptors through obstacles [12], [13], while others, such as the device described in [14], employ magnetic interactions between two magnets to generate tactile feedback. By adjusting the magnets' position, distance, and intensity, the magnetic field can be modulated to induce different skin sensations, such as vibrations, enhancing tactile feedback and perception.

Magnetically driven interfaces are appealing not only for their non-invasive nature but also for their potential for integration within the body. One example for bionic limb control is the Myokinetic Interface described in [15], [16], where external coils are used to track implanted permanent magnets inside the muscle. This system enables the detection of muscle contractions and translates them into control signals for a myoelectric prosthesis, facilitating a more fluid and natural interface. In their latest study [17], researchers demonstrated that, after just six weeks, the participant was able to complete a series of functional tasks, achieving performance scores comparable to those obtained with myoelectric controllers while maintaining similar physical and mental workloads.

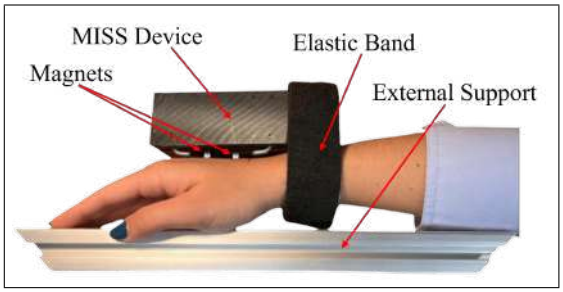


Fig. 1. Overview of the Magnetically Induce Skin Stretch (MISS) device worn on the hand dorsum, with the palm resting on external support to maintain a stable hand posture. The MISS device is secured with an elastic band around the wrist, and two permanent magnets are attached to the skin.

*Corresponding author.

This work was supported by the European Research Council Synergy Grant Natural BionicS (NBS) project (Grant Agreement No. 810346). This work was also supported in part by the Next Generation EU Project ECS00000017 'Ecosistema dell'Innovazione' Tuscany Health Ecosystem (THE, PNRR, Spoke 9: Robotics and Automation for Health), and in part by the Italian Ministry of Education and Research (MIUR) in the framework of the ForeLab project (Departments of Excellence).

[1]with the Department of Information Engineering and Centro di Ricerca "Enrico Piaggio", University of Pisa, Pisa, Italy. eleonora.fontana@phd.unipi.it

[2]with Soft Robotics for Human Cooperation and Rehabilitation, Istituto Italiano di Tecnologia, Genova, Italy.

While non-invasive systems are generally preferred, it is not always clear if the additional benefits of invasive technologies justify replacing non-invasive alternatives. Non-invasive methods face limitations such as bulk, daily application, and, in some cases, restricted sensory feedback. As implanted systems improve in safety, longevity, and biocompatibility, their clinical feasibility is expected to grow [18].

In this context, our goal is to explore, for the first time, the feasibility of using magnetic forces to induce skin stretch by moving magnets placed on the skin. While the focus is currently on non-invasive methods, this work may eventually open the possibility of implanting the magnets under the skin to enhance embodiment, which could contribute to the development of a new generation of high-performance bionic limbs [19]. This paper presents an initial step toward the development of the MISS (Magnetically Induced Skin Stretch) device. Worn on the hand dorsum as reported in Fig. 1, the MISS device utilizes magnetic interactions between coils and magnets affixed to the skin to generate different stretch sensations, i.e. stretch and pinch. We provided a comprehensive overview of the design process, including the optimization of the device's components and the results of preliminary simulations. Additionally, we conducted both physical and psychophysical characterizations with 12 able-bodied participants to assess the device's effectiveness in producing skin deformations. Specifically, we calculated the Just Noticeable Difference (JND) and Point of Subjective Equality (PSE) for both skin stretch and pinch conditions. The JND results indicate that participants were more sensitive to changes in pinch feedback than in stretch. However, the PSE values were nearly identical for both conditions, indicating that participants perceived both sensations as equally intense. These results demonstrate that the MISS device can reliably generate distinct stretch and pinch sensations, with good discrimination and precision, making it a promising solution for prosthetics and rehabilitation applications.

II. THE CONCEPT

Investigating the use of magnetic fields to generate controlled skin displacement remains a novel approach to inducing proprioceptive feedback via skin stretch. In our previous study [20], we investigated the feasibility of manipulating a single magnet using three solenoids positioned beneath a layer of artificial skin. The setup presented in [20] allowed for directional control of the magnet's movement. However, various limitations emerged during testing. In that configuration, the magnet was not constrained, allowing it to slide easily over the artificial skin. When we attached the magnet to the skin (to ensure that any movement would directly translate into skin displacement), the system struggled to achieve the same degree of movement. This was due not only to the increased resistance from the skin but also to the limited magnetic field generated by the solenoids. This limitation is intrinsic to solenoids, which primarily produce a strong magnetic field within their core, while the field strength outside remains minimal [21]. As a result, the magnet aligned with only a small portion of the field lines, leading to a weak magnetic interaction and insufficient force to effectively move it when affixed to the skin.

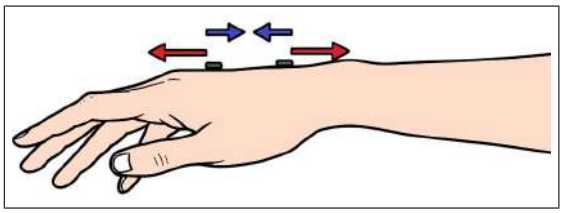


Fig. 2. Conceptual representation of the skin stretch (in red) and pinch (in blue) strategies achieved through the interaction of an external magnetic field with two magnets attached to the skin. By modulating the magnetic field, the magnets can be repelled (skin stretch) or attracted (pinch effects) to each other.

To address these challenges, we focused on optimizing the design to maximize the external magnetic field while maintaining a compact, wearable device. The core concept of this study is to apply forces at two different points on the skin to produce skin deformations, namely, *stretch* and *pinch*, along the longitudinal direction of the hand dorsum (see Fig. 2). When these points are drawn apart, the skin between them stretches, creating a stretch sensation; conversely, when the points are pushed closer together, the skin compresses, producing a pinch sensation. We selected the longitudinal direction based on prior evidence suggesting its enhanced efficacy for delivering skin stretch feedback [22]. To implement this principle, two magnets were attached to the skin at the designated points. By modulating an external magnetic field, we aimed to control the movement of these magnets along the longitudinal axis, ideally generating the desired stretch and pinch sensations. Therefore, our goal was to design a system capable of producing a sufficiently strong magnetic field in the region where the magnets were attached to the skin, ensuring they experienced enough force to achieve the desired skin displacements.

III. THE MISS DEVICE

A. Design Investigation

Starting from three different setups, we evaluated their effectiveness in enhancing the interaction between the magnets and the magnetic field generated by the coils.

All three experimental setups were designed utilizing a ferromagnetic core with a circular cross-section, having a diameter of 4 mm, around which a coil of 500 turns of 30 AWG (American Wire Gauge) frame wire was wound. The core is made of iron, selected for its favorable ferromagnetic properties, with an expected relative permeability μ_r of 2000. The core length is approximately 20 cm. The inductance L of each coil was estimated using the following equation:

$$L = \frac{\mu_0 \cdot \mu_r \cdot N^2 \cdot A}{l} \tag{1}$$

where $\mu_0 = 4\pi \times 10^{-7}$ H/m represents the permeability of free space, μ_r is the relative permeability of the iron core, $N = 500$ denotes the number of turns in the coil, $A = 1.257 \times 10^{-5}\,\mathrm{m}^2$ is the cross-sectional area of the core, and $l = 0.2\,\mathrm{m}$ is the length of the core. Based on these

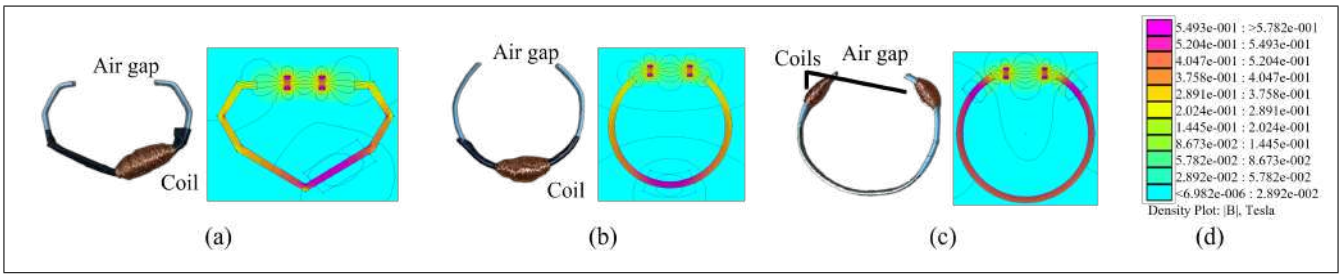


Fig. 3. Outline of the three setup configurations: (a) the initial design featuring a single coil and a ferromagnetic core, (b) a revised design with rounded core edges and a central coil, and (c) an optimized configuration with two coils positioned near the core ends. Next to each setup, the simulated magnetic field distribution is shown, computed using FEMM software with a current of 1 A through the coil windings. The color scale in (d) represents magnetic field strength, while variations in color and field line density highlight the progressively enhanced magnetic interaction.

parameters, the inductance of each coil was calculated to be approximately 39.5 mH. For the simulations, two cylindrical, axially magnetized neodymium permanent magnets (S-06-02-N, Supermagnete, Webcraft GmbH, Gottmadingen, Germany) were considered. These magnets have a diameter of 6 mm, a height of 2 mm, and a holding force of approximately 740 g. The presence of these magnets is crucial in shaping the magnetic field across the air gap, which significantly influences the overall flux and the current dynamics within the system. In simulations, we assumed that the magnets would be positioned on the skin aligned with opposite polarities at a 20 mm distance between them to avoid undesired migration due to their attractive forces, remaining above the two-point discrimination threshold for the hand dorsum [23]. Furthermore, all three setups were designed to be worn in such a way that there is a 10 mm distance between each end of the C-shaped core and the attached magnets. When the solenoid is powered, the core becomes magnetized, inducing distinct magnetic poles at its ends. The magnets then interact with the magnetic field in the air gap, experiencing either attraction or repulsion, depending on the direction of the current and the resulting polarity of the core.

To evaluate the effectiveness of these setups, we conducted simulations using the Finite Element Method Magnetics (FEMM) software, a widely-used open-source tool for 2-D finite element magnetic analysis and simulations [24], [25], [26]. The simulations allowed us to model the magnetic field distribution and assess the strength of the interaction between the coils, the ferromagnetic core, and the magnets placed on the skin. For the simulations, a current of 1 Ampere was assumed to flow through the coils. Fig.3 illustrates the setups and their corresponding simulations. Compared to the configuration in Fig.3(a), the device in Fig.3(b) incorporates rounded edges to reduce magnetic field dispersion caused by sharp core edges [27]. The setup in Fig.3(c) maintains the smoother core geometry while adding two coils closer to the core ends to further optimize the magnetic field distribution in the air gap. Simulations reveal that the third setup, with its dual-coil configuration and smoothed core, achieves the strongest magnetic interaction, as indicated by the darker core color. Additionally, the density of magnetic field lines between each end of the core and the magnets was notably higher in Fig. 3(c), indicating a more efficient interaction between the magnets and the coil-generated field. These results suggested that the third setup is predicted to generate the largest displacement of the magnets, which could lead to more pronounced skin stretch and pinch effects.

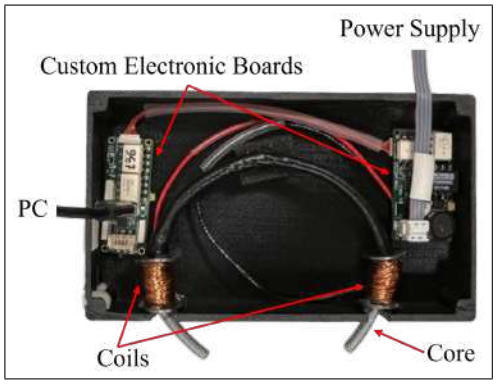


Fig. 4. Overview of the main components of the MISS device. An external case houses two custom electronic boards that control the current flowing through the coils wound around the ends of a ferromagnetic core. When powered, the device generates a magnetic field in the air gap, interacting with magnets attached to the skin to induce targeted skin deformations.

Based on these considerations, we decided to adopt the third setup to develop the MISS device for hand proprioceptive feedback.

B. Final Configuration

The final configuration of the MISS device is depicted in Fig. 4. It consists of a C-shaped ferromagnetic core with coils positioned at each end. The MISS device is worn on the hand dorsum, positioned so that two magnets on the skin are aligned within the air gap at a specified distance, as depicted in Fig. 5 and defined in previous sections. The magnets are securely attached with a skin-safe adhesive (Mastix Spirit Gum, Kryolan, Berlin, Germany). The device is controlled by two custom electronic boards based on a Cypress PSoC (Programmable System-on-Chip) microcontroller [28]. When activated, the coils magnetize the ferromagnetic core, establishing distinct north and south poles at the ends. The interaction between these poles and the magnets has the aim of producing targeted pinch and stretch sensations on the skin.

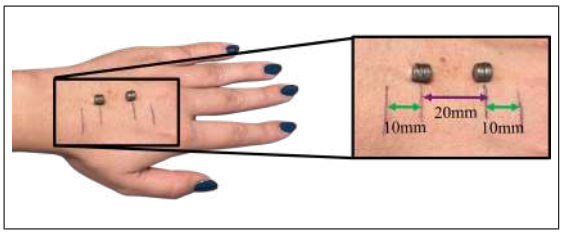


Fig. 5. Schematic representation of the magnets' position on the hand dorsum. The magnets are affixed to the skin with a mutual distance of 20 mm, each placed 10 mm from the ferromagnetic core ends of the device.

IV. DEVICE CHARACTERIZATION

The MISS device is designed to be worn on the dorsum of the user's right hand. To evaluate its functionality, we conducted both a Physical Characterization and a Psychophysical Characterization.

A. Participants

Twelve participants (4 female, 8 male; mean age 31) took part in both the physical and psychophysical experiments. Since skin displacement may be influenced by Body Mass Index (BMI), we selected individuals with BMIs within the average range for standard biometric tables (BMI range: 20–24.9) [29]. All participants were screened to ensure they had no physical limitations that could affect the experimental outcomes. They were comfortably seated in an office chair with their forearm in a neutral position (thumb facing upward) and their elbow resting on a table. To maintain this posture, each participant's hand was supported by an external support fixed to the table, allowing for a relaxed yet stable hand position. An elastic band was placed around the wrist to ensure the MISS device remained securely in position throughout the experiment. The experimenter verified that the magnets were securely attached in the correct position, ensuring the distances specified in the previous sections using a caliper. To eliminate visual and auditory distractions, they wore goggles with obscured lenses and noise-canceling headphones playing white noise. The experimental procedures were approved by the Committee on Bioethics of the University of Pisa - Review No. 68/2024, and all participants provided informed consent prior to participation.

B. Physical Characterization

To investigate the correlation between the magnetic field generated by the two coils and the resulting skin displacement produced by the interaction between the magnets and the field, we conducted a Physical Characterization of the MISS device. In this experiment, the objective was to determine the optimal voltage threshold for powering the device, balancing the maximum achievable displacement while staying within safety parameters. Starting from 0V, the voltage was incrementally increased until the displacement of the magnets reached a threshold, defined as the point at which no further significant increase in displacement was observed. To measure the displacement, we draw a marker on the skin, aligned with the center of each magnet. The movement of the marker, induced by skin stretch, was recorded with a camera, while graph paper was placed beneath the area of interest to facilitate displacement quantification throughout the characterization process.

C. Psychophysical Characterization

The Psychophysical Characterization aimed to assess the participant's ability to distinguish between varying levels of skin stretch or pinch induced by the MISS device, quantified in terms of the Just Noticeable Difference (JND). The JND represents the smallest change in a stimulus that can be detected by the participant [30]. To calculate the JND, we employed the method of constant stimuli [30], a widely used psychophysical method that involves presenting two stimuli to the participant—a reference stimulus (RS) and a comparison stimulus (CS)—and asking them to judge which stimulus feels stronger.

1) Experimental Session: During the experiment, participants received paired stimuli presented in a pseudorandom order. Each trial consisted of the presentation of the first stimulus, followed by a 1-second inter-stimulus interval, and then the second stimulus, after which participants were asked to indicate the one that felt stronger. The experiment consisted of two blocks, each corresponding to a direction of magnet displacement—pinch or stretch—with 100 trials in each block. The binary responses of the participants were recorded.

2) Data Analysis: To analyze participants' responses, we employed a Generalized Linear Mixed Model (GLMM)[31], which accounts for both the fixed effects of experimental variables and the random effects due to inter-participant variability. The GLMM framework allows for the modeling of binary response data while accommodating the hierarchical structure of repeated measures across participants. A probit link function was used to model the probability $P(Y_j = 1)$ that, in trial j, the participant judged the comparison stimulus to be more intense than the reference stimulus. The model is expressed as:

$$\phi^{-1}[P(Y_j = 1)] = \beta_0 + \beta_1 \cdot x_j \tag{2}$$

where ϕ^{-1} is the inverse of the cumulative normal distribution (probit transformation), and x_j represents the intensity of the comparison stimulus. The parameters β_0 and β_1 correspond to the intercept and slope, capturing the fixed effects.

This model was applied across all participants to estimate key psychometric parameters, including the JND and the Point of Subjective Equality (PSE), representing the comparison stimulus value at which participants were equally likely to perceive it as either stronger or weaker than the reference (corresponding to a response probability of 0.5). We derived 95% confidence intervals (CIs) for these estimates using a bootstrap method, ensuring robust estimates of precision and accuracy for each experimental condition. For further details on this analysis, please refer to [31].

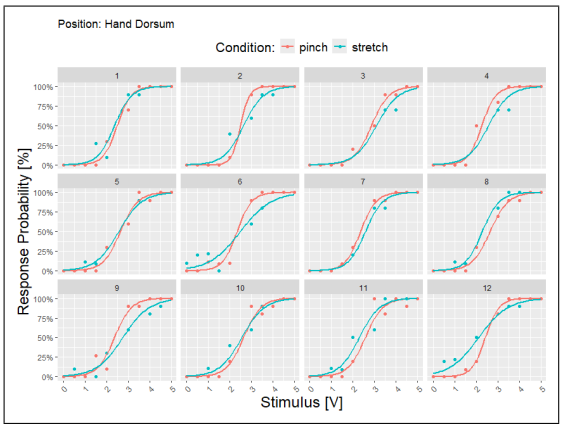


Fig. 6. Results of the psychophysical characterization, showing GLMM predictions for the stretch and pinch conditions across all subjects for the hand dorsum. The dots are data points corresponding to the individual predictions of the GLMM for each participant (labeled 1 - 12). Each box represents the model's predictions for the response probability under the stretch and pinch conditions, summarizing the trend across all subjects.

V. RESULTS

A. Physical Characterization

The maximum effective voltage identified in the first experiment was 5V. This threshold was established based on both safety and performance considerations: beyond 5V, further voltage increases did not result in significant displacement, indicating that the system had reached its effective operating capacity. Although modeling the relationship between voltage and skin stretch was not the goal of this study, we report here the skin stretch values observed at the maximum applied voltage. We plan to investigate such a relationship in depth in future work. Specifically, the mean displacement on the hand dorsum was 5.64 mm for skin stretch (standard deviation: 0.50 mm) and 6.18 mm for pinch (standard deviation: 0.75 mm). Additionally, the 5V limit is well below the threshold established by general electrical safety standards [32], ensuring that the current induced remained below levels associated with noticeable physiological effects [32]. Thus, this voltage was chosen to balance device efficacy in achieving targeted displacement with the safety and comfort of participants, minimizing any risk of discomfort or harm.

B. Psychophysical Characterization

For the JND calculation using the method of constant stimuli, we considered the range defined by the maximum voltage of 5V determined in the previous experiment. This range was divided into ten equally spaced intervals, from 0.5V to 5V, with a step size of 0.5V (0.5, 1, 1.5, 2, 2.5, 3, 3.5, 4, 4.5, 5V). The reference stimulus (RS) was set at 2.5V, while the remaining nine values served as comparison stimuli (CS). The results of the GLMM applied to each participant are shown in Fig. 6. The obtained JND and PSE values, along with their respective 95% CIs, are summarized in Table I for both stretch and pinch conditions.

TABLE I

SUMMARY OF JND AND PSE VALUES FOR STRETCH AND PINCH CONDITIONS ON THE HAND DORSUM.

	JND [V]	**95% CIs [V]**	**PSE [V]**	**95% CIs [V]**
Stretch	0.63	[0.58; 0.68]	2.53	[2.43; 2.63]
Pinch	0.37	[0.33; 0.41]	2.52	[2.42; 2.61]

VI. DISCUSSION AND CONCLUSION

In this study, we developed, designed, and evaluated the MISS (Magnetically Induced Skin Stretch) device, a novel wearable system that leverages magnetic forces to induce skin stretch and provide proprioceptive feedback. Three initial configurations were tested, with the dual-coil C-shaped core design ultimately selected based on simulation results. Psychophysical testing on able-bodied participants demonstrated that the device effectively generated distinct stretch and pinch sensations on the hand dorsum. Moreover, participants were able to reliably differentiate stimulus intensities, as indicated by the calculated Just Noticeable Differences (JNDs) and Points of Subjective Equality (PSEs) for both conditions.

The results summarized in Table I show that participants were more sensitive to variations in stimulus intensity during the pinch condition, as indicated by the lower JND (0.37V) compared to the stretch condition (0.63V). One possible explanation is that in the pinch condition, the magnets experience both the repulsive force from the coils and an increasing attractive force pulling them together, leading to greater displacement. Our measurements showed that the displacement of the magnets was significantly greater in the pinch condition compared to the stretch condition, with statistical analysis (t-test, $p < 0.05$) confirming the possibility of enhanced stimulus perceptibility. Regarding the PSE, values for both conditions were similar, suggesting that participants perceived comparable stimulus levels as equal across conditions. The associated 95% confidence intervals (CIs) also provide insight into response consistency. Although the CIs for both conditions significantly overlap, the slightly narrower CIs for the pinch condition suggest that responses were more consistent among participants.

Despite these promising results, our study has some limitations. First, testing was conducted exclusively on able-bodied participants and focused only on the hand dorsum. Further research is necessary to evaluate the effectiveness of the MISS device with prosthesis users and in other relevant body areas. Additionally, our sample was limited to younger participants, whereas age-related declines in skin elasticity and proprioception may influence displacement and detection thresholds. Future studies should include a broader age range to investigate these effects. While this study focused on binary stimulation, future work will explore continuous proprioceptive feedback by refining control strategies and graded stimulation patterns. We also aim to improve the design for greater compactness and seamless integration into prosthetic sockets. Moreover, we plan to extend testing to a larger and more diverse participant group, including prosthesis users,

to assess the device's potential in conveying proprioceptive feedback during active tasks. Finally, we will explore the integration of MISS with robotic supernumerary hands for rehabilitation applications [33].

ACKNOWLEDGMENT

The authors would like to thank Manuel Barbarossa and Marina Gnocco for contributing to the technical development of this work.

REFERENCES

[1] C. Antfolk, M. D'Alonzo, B. Rosén, G. Lundborg, F. Sebelius, and C. Cipriani, "Sensory feedback in upper limb prosthetics," *Expert Review of Medical Devices*, vol. 10, pp. 45 – 54, 2013. [Online]. Available: https://api.semanticscholar.org/CorpusID:18234259

[2] W. Semere, M. Kitagawa, and A. M. Okamura, "Methods for haptic feedback in teleoperated robot-assisted surgery," 2004. [Online]. Available: https://api.semanticscholar.org/CorpusID:195357205

[3] B. B. Edin and N. Johansson, "Skin strain patterns provide kinaesthetic information to the human central nervous system." *The Journal of Physiology*, vol. 487, 1995. [Online]. Available: https://api.semanticscholar.org/CorpusID:45336210

[4] D. F. Collins, K. M. Refshauge, G. Todd, and S. C. Gandevia, "Cutaneous receptors contribute to kinesthesia at the index finger, elbow, and knee." *Journal of neurophysiology*, vol. 94 3, pp. 1699–706, 2005. [Online]. Available: https://api.semanticscholar.org/CorpusID:12118989

[5] E. Fontana, V. Catrambone, M. Catalano, A. Bicchi, and M. Bianchi, "On the relation of skin stretch and finger joint angle evolution in human hand grasping tasks," pp. 331–345, 2025.

[6] K. Bark, J. W. Wheeler, P. B. Shull, J. Savall, and M. R. Cutkosky, "Rotational skin stretch feedback: A wearable haptic display for motion," *IEEE Transactions on Haptics*, vol. 3, pp. 166–176, 2010. [Online]. Available: https://api.semanticscholar.org/CorpusID:4845129

[7] E. Battaglia, J. P. Clark, M. Bianchi, M. G. Catalano, A. Bicchi, and M. K. O'Malley, "The rice haptic rocker: Skin stretch haptic feedback with the pisa/iit softhand," *2017 IEEE World Haptics Conference (WHC)*, pp. 7–12, 2017. [Online]. Available: https://api.semanticscholar.org/CorpusID:9591916

[8] M. Rossi, M. Bianchi, E. Battaglia, M. G. Catalano, and A. Bicchi, "Happro: A wearable haptic device for proprioceptive feedback," *IEEE Transactions on Biomedical Engineering*, vol. 66, pp. 138–149, 2019. [Online]. Available: https://api.semanticscholar.org/CorpusID:51611491

[9] N. Colella, M. Bianchi, G. Grioli, A. Bicchi, and M. G. Catalano, "A novel skin-stretch haptic device for intuitive control of robotic prostheses and avatars," *IEEE Robotics and Automation Letters*, vol. 4, pp. 1572–1579, 2019. [Online]. Available: https://api.semanticscholar.org/CorpusID:67872310

[10] W. Guo, Y. Hu, Z. Yin, and H. Wu, "On-skin stimulation devices for haptic feedback and human–machine interfaces," *Advanced Materials Technologies*, vol. 7, 2021. [Online]. Available: https://api.semanticscholar.org/CorpusID:238738584

[11] F. Pece, J. J. Zárate, V. Vechev, N. Besse, O. Gudozhnik, H. R. Shea, and O. Hilliges, "Magtics: Flexible and thin form factor magnetic actuators for dynamic and wearable haptic feedback," *Proceedings of the 30th Annual ACM Symposium on User Interface Software and Technology*, 2017. [Online]. Available: https://api.semanticscholar.org/CorpusID:3339695

[12] H. S. Kim, J.-H. Jo, J.-H. Lee, J. ju Jung, J.-S. An, M.-H. Choi, and S.-C. Chung, "Development of a tactile actuator with non-contact and trans-object characteristics using a time-varying magnetic field," *Actuators*, vol. 10, p. 106, 2021. [Online]. Available: https://api.semanticscholar.org/CorpusID:236378357

[13] X. Lu, Y. Yan, B. Qi, H. Qian, J. Sun, and A. Quigley, "Contactless haptic display through magnetic field control," *IEEE Transactions on Haptics*, vol. 15, pp. 328–338, 2022. [Online]. Available: https://api.semanticscholar.org/CorpusID:246902426

[14] F. AlShaibani, M. S. Thompson, and J. H. M. Bergmann, "Experimental analysis of a novel, magnetic-driven tactile feedback device," *Prosthesis*, 2020. [Online]. Available: https://api.semanticscholar.org/CorpusID:215925391

[15] M. Gherardini, F. Masiero, V. Ianniciello, and C. Cipriani, "The myokinetic interface: implanting permanent magnets to restore the sensory-motor control loop in amputees," *Current Opinion in Biomedical Engineering*, 2023. [Online]. Available: https://api.semanticscholar.org/CorpusID:258012035

[16] S. Tarantino, F. Clemente, D. Barone, M. Controzzi, and C. Cipriani, "The myokinetic control interface: tracking implanted magnets as a means for prosthetic control," *Scientific Reports*, vol. 7, 2017. [Online]. Available: https://api.semanticscholar.org/CorpusID:3305302

[17] M. G. et al., "Restoration of grasping in an upper limb amputee using the myokinetic prosthesis with implanted magnets," *Science Robotics*, vol. 9, no. 94, p. eadp3260, 2024. [Online]. Available: https://www.science.org/doi/abs/10.1126/scirobotics.adp3260

[18] S. J. Bensmaia, D. J. Tyler, and S. Micera, "Restoration of sensory information via bionic hands," *Nature Biomedical Engineering*, vol. 7, pp. 443–455, 2020. [Online]. Available: https://api.semanticscholar.org/CorpusID:227157003

[19] D. F. et al., "Toward higher-performance bionic limbs for wider clinical use," *Nature Biomedical Engineering*, vol. 7, pp. 473–485, 2021. [Online]. Available: https://api.semanticscholar.org/CorpusID:235268852

[20] E. Fontana, G. Giorgio, M. G. Catalano, M. Bianchi, and A. Bicchi, "A test-bench to investigate the use of magnetic fields for haptic feedback in prosthetics," Mar. 2024. [Online]. Available: https://doi.org/10.5281/zenodo.10722454

[21] C. Wei, W. Fancheng, Y. Zhiyong, H. Yuguo, and X. Junhui, "Analysis of solenoid magnetic field based on maxwell equation," , vol. 27, no. 12, p. 123201, 2015.

[22] J. P. Clark, S. Y. Kim, and M. K. O'Malley, "The rice haptic rocker: Comparing longitudinal and lateral upper-limb skin stretch perception," in *Haptics: Science, Technology, and Applications*, D. Prattichizzo, H. Shinoda, H. Z. Tan, E. Ruffaldi, and A. Frisoli, Eds. Cham: Springer International Publishing, 2018, pp. 125–134.

[23] S. Thube, M. R. Shah, and P. H. Kothari, "Assessment of two point discrimination on hand in adult population: An observational study," *International Journal of Health Sciences and Research*, vol. 10, pp. 60–63, 2020. [Online]. Available: https://api.semanticscholar.org/CorpusID:219437253

[24] M. Białek, P. Nowak, T. Lindner, and D. Wyrwal, "Femm examination of the gripper with magnetorheological cushion," *2020 International Conference Mechatronic Systems and Materials (MSM)*, pp. 1–5, 2020. [Online]. Available: https://api.semanticscholar.org/CorpusID:221916990

[25] Ubaidillah and B. W. Lenggana, "Finite element magnetic method for magnetorheological based actuators," 2020. [Online]. Available: https://api.semanticscholar.org/CorpusID:228967640

[26] D. C. Meeker, "Finite element method magnetics, version 4.2 (28feb2018 build)," https://www.femm.info, 2018, accessed: 2024-11-11.

[27] M. Puskarczyk, B. Jamieson, and W. Jurczak, "The influence of core shape and material nonlinearities to corner losses of inductive element," 2011. [Online]. Available: https://api.semanticscholar.org/CorpusID:55492315

[28] C. Della Santina, C. Piazza, G. M. Gasparri, M. Bonilla, M. G. Catalano, G. Grioli, M. Garabini, and A. Bicchi, "The quest for natural machine motion: An open platform to fast-prototyping articulated soft robots," *IEEE Robotics Automation Magazine*, vol. 24, no. 1, pp. 48–56, 2017.

[29] F. Q. Nuttall, "Body mass index: Obesity, bmi, and health: A critical review," *Nutrition Today*, vol. 50, pp. 117 – 128, 2015. [Online]. Available: https://doi.org/10.1097/NT.0000000000000092

[30] L. A. Jones and H. Z. Tan, "Application of psychophysical techniques to haptic research," *IEEE Transactions on Haptics*, vol. 6, pp. 268–284, 2013. [Online]. Available: https://api.semanticscholar.org/CorpusID:11024851

[31] A. Moscatelli, M. Mezzetti, and F. Lacquaniti, "Modeling psychophysical data at the population-level: the generalized linear mixed model." *Journal of vision*, vol. 12 11, 2012. [Online]. Available: https://api.semanticscholar.org/CorpusID:17437963

[32] International Electrotechnical Commission, "Iec 60479-1:2018, effects of current on human beings and livestock - part 1: General aspects," https://standards.iteh.ai/catalog/standards/sist/d1fa6359-af30-4e4f-8b86-79a01de41738/iec-60479-1-2018, 2018, accessed: 2024-11-11.

[33] C. Trompetto, M. Catalano, A. Farina, G. Grioli, L. Mori, A. Ciullo, M. Pittaluga, M. Rossero, L. Puce, and A. Bicchi, "A soft supernumerary hand for rehabilitation in sub-acute stroke: a pilot study," *Scientific Reports*, vol. 12, 12 2022.

Enhancing Hand Dexterity Assessment Through Protocol Revision and Pilot Evaluation of the Virtual Eggs Test

Lucia Angelini*, *Student Member, IEEE,* Michele Piazzini*, Robinson Guachi, Francesca Toso, Marco Baccini, Francesca Cecchi† and Marco Controzzi†, *Member, IEEE*

***Abstract*— Hand function assessment enables the therapist to select the proper rehabilitation therapy as well as to monitor the recovery progress. The Virtual Eggs Test (VET) stands out from the other tests for hand dexterity evaluation since evaluates both gross and fine dexterity. This is achieved by integrating measures of accuracy and speed in transporting objects with increasing fragilities. A clinical trial to validate VET was carried out with a population of amputees and a small group of healthy participants, showing promising results. To improve the resolution of the test, here we propose a revised version of the execution protocol without extending the duration. The new version has been preliminary evaluated by seven healthy participants of different ages. The results of this pilot study support test-retest reliability for the original formulation of the Fine Dexterity Index, while suggesting for a revision of the Gross Dexterity Index.**

I. Introduction

Hand assessment is the examination process used to evaluate the performance of the hand [1]. It enables therapists to select the appropriate rehabilitation process and monitor recovery over time [2]. Different methods can be used to evaluate the hand functions, such as the measurement of the range of motion (ROM) or handgrip strength [3]. Among those, the evaluation of hand dexterity plays a key role. Hand dexterity is considered a valid indicator of the residual function of the hand [4] and "the best predictor of independence during everyday activities" [5]. Hand dexterity can be defined as the ability to coordinate voluntary movements (and thus forces) to complete a functional task with accuracy, speed and efficiency [6]. It can be classified into fine and gross dexterity according to the precision of the movement required [7][8]. Hand dexterity is a skilled behavior that entails the coordination of multiple segments of the hand [9]. Consequently, assessing hand dexterity poses a significant challenge [5][9]. Hand dexterity is typically evaluated by observing patients as they perform simple tasks or by using standardized assessment tools [10]. These last must demonstrate validity and reliability prior to their use in a clinical context [2], [5]. In other words, assessment tools should be able to measure what they intend to measure (i.e. validity) and provide similar results under the same conditions (i.e. reliability) so that therapists can trust the outcome of the test [11][12]. Tools for the evaluation of the hand dexterity have been largely reviewed [2], [5], [13]. They can be grouped based on the assessment method (i.e., self-reported or performance-based), the type of evaluated dexterity (i.e., fine, gross or both) and the target population. Self-reported tests (i.e., questionnaires) rely on the subject's perception of his/her capability in real-life environments. In contrast, performance-based tests are objective tools that evaluate subjects' performance in standardized tasks [2]. Three frequently used and validated performance-based tests [5] are the Box and Block Test (BBT), the Minnesota Rate of Manipulation Test (MRMT), and the Purdue Pegboard Test (PPT). The first two tests are employed to assess gross dexterity, while the third focuses on the evaluation of fine dexterity. In the BBT, subjects are asked to transfer the larger number of rigid wooden blocks from one compartment of a box to another, one by one, within a time limit of 60 seconds. The outcome of the test is the total number of blocks successfully transferred [7]. The MRMT consists of five subtests in which subjects are asked to turn and/or place small pegs into a board. The score is computed as the sum of the time taken to complete all subsets [14]. Similarly, the PPT is composed of 4 subtests involving the insertion of pins, collars, and washers into predefined small holes. Both hands are assessed during the test, either individually or in a coordinated fashion. The score is the sum of elements correctly positioned within a predefined amount of time (30 or 60 seconds) [8]. The previously described tests, as well as most of the other non-validated tests, are time-based [2]: they provide outcome measures related to the completion rate of the task without considering other important factors, such as in-hand manipulation or dynamic force control [10]. Quite the opposite, the Strength-Dexterity test (SD) is a test that specifically focuses on dynamic force control. The test evaluates subjects' ability to regulate the force at their fingertips to compress springs avoiding their buckling [15]. We have proposed the Virtual Eggs Test (VET) to evaluate hand dexterity by merging those two approaches. The VET outcomes combine information related to the task completion rate (i.e., the speed of the task) and dynamic force control (i.e., the accuracy of the task) [16]. The VET assesses both fine and gross dexterity evaluating the ability of subjects to transport objects with different fragilities (doubled Virtual Egg – VE) from one side to the other of a barrier, without breaking them and as fast as they can. A preliminary version of the VET was successfully exploited in various studies

*Equal contribution first author. †Equal contribution senior author.

Project acronym: Fit4MedRob (Fit for Medical Robotics) - Piano Nazionale Complementare PNC - project code: PNC0000007.

L. A., R.G., M. C. are with The BioRobotics Institute, Scuola Superiore Sant'Anna, Pisa, Italy, and with the Department of Excellence in Robotics & AI, Pisa, Scuola Superiore Sant'Anna, Italy.

R.G. is also with Department of Mechatronics, Universidad Internacional del Ecuador, Quito, Ecuador.

M. B and F. C. are with IRCCS Fondazione don Carlo Gnocchi ONLUS, Firenze, Italia.

M. P., F. T. and F. C. are with Dipartimento di Medicina Sperimentale e Clinica, UniFi, Firenze, Italia

(Corresponding author M. C. phone: +39050881720; e-mail: marco.controzzi@santannapisa.it and Francesca Cecchi, +39 3388627184, fcecchi@dongnocchi.it)

involving amputees [17], [18], [19]. The first campaign devoted to the validation of the VET was conducted with 35 healthy individuals and 30 amputees using myoelectric prostheses [16]. The results proved construct validity (i.e., the capability of discriminate different groups) and test-retest reliability for the healthy population. However, test-retest reliability was achieved after an intense familiarization phase. Healthy participants performed the VET twice in each session and only comparisons between the last performed VET of each session showed test-retest reliability. Moreover, reliability was investigated only on healthy participants aged between 21 and 45 and using their dominant hand, without accounting for age or sex that are factors proved to influence hand dexterity [20], [21]. Results variability among subjects was low, for both the outcome measures of the VET (i.e., Fine Dexterity Index and Gross Dexterity Index). This low variability could be biased by a lack of age diversity among participants or/and by the poor resolution of the VET that may not be able to perceive existing differences. These considerations led us modify the protocol with the aim of increasing the usability and the resolution of the assessment tool, without affecting the overall duration of the test [22]. So, we increased the number of VEs comprising the kit from 11 to 20 and we changed their break threshold to simulate more fragile objects. We aim to exploit the new protocol to collect normative data for healthy participants and to validate the VET with different populations. Here, the new protocol was tested within a pilot study involving seven healthy participants with ages ranging from 29 to 83 years. Test-retest reliability and variation based on age were preliminary evaluated. This paper reports the results of this pilot, and it is organized as follows: Section II presents the experimental procedure describing the new protocol of the VET, the outcome measures of the test and the statistical analysis performed on the data. Results are reported in Section III and discussed in Section IV.

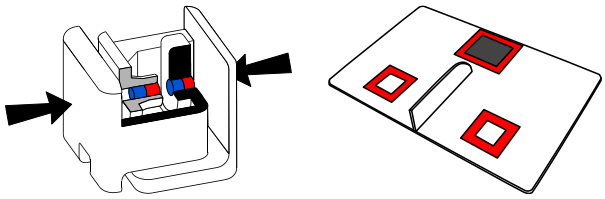
II. Materials and Methods

A. Participants

Seven participants were enrolled considering the inclusion and exclusion criteria listed in Table 1. Participants were distributed among seven different groups according to their age: 18-29, 30-39, 40-49, 50-59, 60-69, 70-79, >80 (Table 2). Four participants were right-handed according to the Oldfield questionnaire (see the Experimental Procedure).

Table 1 Inclusion and exclusion criteria

Inclusion Criteria	*Exclusion Criteria*
Participants of both sexes and any ethnicity aged ⩾ 18	Severe visual and oculomotor deficits
Absence of motor impairments	Neurological or musculoskeletal pathologies that impact upper limb function, clinical instability
Willingness to participate in the study and sign the consent form	Psychiatric comorbidities
	Lack of understanding of the Italian language
	Consumption of alcohol or diuretics before tests



(a) (b)

Figure 1 Setup of the Virtual Eggs Test. (a) Virtual Egg [16]; (b) platform.

Table 2 Participants enrolled for the pilot study

Group age	*Age*	*Sex*	*Dominant hand*
18 – 29	29	Female	Right
30 – 39	39	Male	Left
40 – 49	46	Female	Left
50 – 59	59	Female	Right
60 – 69	64	Male	Left
70 – 79	79	Female	Right
> 80	83	Female	Right

Participants carried out the experiment without compensation at the premises of the Fondazione Don Carlo Gnocchi (FI). The experiment was conducted in full compliance with international legislation and its national transposition concerning clinical trials and the principles of the Declaration of Helsinki. Participants signed the informed consent and read the information sheet of the study. The study was approved by the local ethical committee of the Area Toscana Centro, Italy (Approval number: 23327_spe.).

B. Experimental procedure

Prior to the experiment procedure, the laterality of the participant was assessed according to the Oldfield questionnaire [23]. Participants performed the Virtual Eggs Test (VET) in two different trials with both hands. The distance between the two trials was at least 14 days to decrease the possibility of learning effects [24]. The dominant hand was always tested first.

C. The Virtual Eggs Test

Setup. The setup of the Virtual Eggs Test (VET) comprised 20 Virtual Eggs, a platform and a software (Figure 1). The Virtual Egg (VE) is a custom fragile device (Figure 1 (a)). It is equipped with a magnetic fuse responsible for keeping the external wall in a pre-defined "non-collapsed" position. When the VE is grasped with a grip force greater than the break threshold (T_{break}) the external walls collapse and the VE "breaks". The break threshold of the magnetic fuse can be calibrated either by changing the magnetization of the magnets or their distance. Each VE is characterized by the normalized break threshold $\Phi = T_{break}/GF_{min}$. Where $GF_{min} = W/(2*\mu)$ is the minimum grip force necessary to lift it, W is the weight of the VE and μ is the coefficient of friction between the fingers and the graspable walls. We covered these walls with sandpaper

(grit 240) to decrease the variability among participants. The coefficient of friction was experimentally derived and equal to 1.44. The range and the step of the values of Φ within the 20 VEs comprising the kit were selected after a preliminary test phase. They range from 1, which corresponds to the minimum grip force required to lift the object without breaking it, to 10.5 with increasing steps of 0.5 (Table 3).

TABLE 3 BREAK THRESHOLDS AND NORMALIZED BREAK THRESHOLDS OF THE VES.

VE#	Weight (g)	Break threshold (N)	Φ
1	90.4	0.31	1
2	89.1	0.47	1.5
3	89.2	0.62	2
4	89.6	0.77	2.5
5	90.5	0.92	3
6	90.7	1.09	3.5
7	90.6	1.23	4
8	90.8	1.37	4.5
9	90.9	1.53	5
10	90.4	1.69	5.5
11	90.5	1.86	6
12	90.6	2.02	6.5
13	90.4	2.15	7
14	89.6	2.32	7.5
15	90.9	2.46	8
16	91.0	2.61	8.5
17	90.7	2.77	9
18	90.9	2.94	9.5
19	90.8	3.08	10
20	90.7	3.23	10.5

The platform (Figure 1 (b)) is placed on the table 10 cm away from the edge and wire-connected with the PC where the software is running. The platform hosts three distinct areas: the home position and two Egg placers divided by a 6 cm high barrier. Each area is highlighted with a red frame and is equipped with a sensor to record the time of the task. During the test, the platform collects the data, which are stored and visualized by the software that also supports the examiner during the execution of the VET allowing him/her to take notes of the broken VE.

Protocol. We here exploited an adaptive protocol comprising two consecutive phases: a familiarization phase and a testing phase. Before starting, the participant washes his/her hand and sits on an adjustable chair, the position of the chair is set so that when the hand lays on the platform the forearm is parallel to the floor. During the familiarization and the testing phase, the participant performs many trials with different VE. Each trial comprises the following sequence: (i) dip the thumb and index finger into the magnesite powder; (ii) voluntarily break the VE multiple times to test its fragility; (iii) place the VE on the starting Egg placer (i.e., the one on the side of the tested hand); (iv) perform seven repetitions. The movement of the VE over the platform is defined as repetition (Figure 2). Each repetition consists of the following steps: (i) put the hand in the home position; (ii) reach and grasp the VE from the starting Egg placer exploiting a pinch grasp; (iii) transport the VE over the barrier as fast as possible and without breaking it; (iv) place the VE in the ending Egg placer; (v) replace the hand over the home position. The ending Egg placer of the first repetition becomes the starting Egg placer in the second repetition and so on: the VE is moved once from right to left and once from left to right.

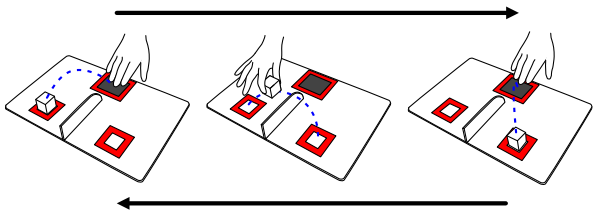


Figure 2 Repetition (movement of the VE over the platform). The movement can be performed from right to left or from left to right.

A repetition fails if the participant releases the VE in a wrong position or breaks it, while a trial fails if at least two of the seven repetitions fail. During the familiarization phase, the participant completes three trials with VE20 (the most robust one), VE10 and VE5, respectively. Instead, the testing phase comprises several trials with different VEs. The first trial is performed with VE20, then the subsequent number of the VE to be transported, and so its fragility, is chosen according to the performance of the participant following an Up/Down method [25] with a size of step down and up equal to 3 and 2 respectively (Figure 3 - left). If the subsequent VE number is less than 1 or exceeds 20, VE1 or VE20 is respectively selected. The test phase ends when the fifth reversal (i.e., a successful trial following one or more failed trials, or vice versa) occurs or if the participant has manipulated the VE20 or the VE1 for three trials consecutively.

Metrics. The VET returns as outcomes two different indexes: the Fine Dexterity Index (FDI) and the Gross Dexterity Index (GDI) [16]. The former index assesses the capability of transporting the most fragile VEs (and so the fine dexterity) while the latter describes the ability to move the most robust VEs as fast as possible but without breaking them. Together, the two indexes comprehensively described the performance of the participants considering the two trade-off factors during the task: the regulation of the grip force to not break the object and the time required to accomplish the task.

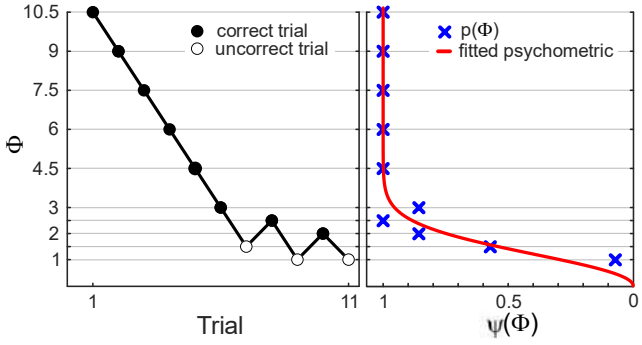


Figure 3 Example of a VET protocol following un up/down procedure (left) and the fitted psychometric curve (right).

More in detail, for each manipulated VE, the first factor is evaluated by the ratio of successful repetitions over the total ones. The collected data express the probability of correct transport of a VE with a specific normalized threshold, $p(\Phi)$. Following the high-threshold theory [25], $p(\Phi)$is fitted using

Weibull's psychometric function $\psi(\Phi)$ (1) (Figure 3 - right). The guessing rate γ was fixed to 0 since the data were derived from the performance of the participant, and the slope β was fixed to 2 based on previous experimental evaluation.

$$\psi(\Phi) = (1-\lambda)\left(1 - e^{\left(-\frac{\Phi}{\alpha}\right)^2}\right) \quad (1)$$

The outputs of the fitting are two parameters λ and α. The lapse rate λ is mostly associated with the performance of the most robust VEs. The threshold α varies according to the performance of the most fragile VEs. The lower the values of those two parameters the better the performance of the participant.

The time required to accomplish the task (b), which is the second trade-off factor, is calculated as mean of the best transport time of VE20 and VE19. Finally, by combining λ, α and b, we defined the Fine Dexterity Index FDI (2) and the Gross Dexterity Index GDI (3) as follows:

$$FDI = \alpha \quad (2)$$

$$GDI = \left(1 - \frac{b}{20}\right)(1-\lambda) \quad (3)$$

D. Statistical Analysis

Statistical analysis was performed using IBM® SPSS® and Matlab. We separately evaluated the test-retest reliability for each outcome measure (i.e., FDI and GDI) for the dominant and non-dominant hand. We followed a two-step procedure according to the CONSMIN guidelines [26][27]: (1) evaluate the stability of patients; (2) compute the Intraclass Correlation Coefficient (ICC) with the 95% Confidence Interval (CI) if data were stable. The stability of patients was evaluated by exploiting non-parametric tests since the small sample size (i.e., seven participants). We selected the T-Wilcoxon Signed Rank if the distribution of the difference between the two populations was symmetric ($|\gamma| < 1$, where γ is the skewness index), otherwise, we used the Sign test. The statistical significance of all the tests performed was defined by $p < 0.05$. The ICC coefficient was evaluated as two-way mixed effects absolute agreement single measurement [28] (also named ICC(A,1) [29]). According to Resnik et al. [13] we considered an excellent reliability when ICC ≥ 0.8, good reliability if 0.80 > ICC ≥ 0.6, and poor reliability if ICC < 0.6. In addition, we report Standard Error Measurement (SEM) (4), Minimal Detectable Change with a 95% CI (MDC_{95}) (5), and MDC95 percentage ($MDC_{\%}$) (6), where SD is the standard deviation of the score from all subjects [30] and $\bar{X}$ is the mean of the considered variable.

$$SEM = SD \times \sqrt{1 - ICC} \quad (4)$$

$$MDC_{95} = SEM \times 1.96 \times \sqrt{2} \quad (5)$$

$$MDC_{\%} = \frac{MDC_{95}}{\bar{X}} \times 100 \quad (6)$$

III. Results

The Fine Dexterity Index (FDI) and the Gross Dexterity Index of each participant are shown in Table 4 and Figure 4. FDI and GDI are reported according to the hand (dominant or non-dominant) and the sessions (test or retest). The mean distance between test and retest was 24 days (Table 4). Test-retest reliability was assessed for each Index and each hand separately. No statistical differences were found for the FDI both for the dominant and non-dominant hand (Wilcoxon signed-rank p-value = 0.237 and p-value = 0.612, respectively). For the dominant hand, the ICC was 0.95 (with 95% CI = 0.76 to 1.00), the SEM was 0.204, the MDC_{95} was 0.567 and the $MDC_{\%}$ was 28.0%. For the non-dominant hand, ICC was 0.91 (with 95% CI = 0.56 to 0.98), the SEM was 0.216, the MDC_{95} was 0.598 and the $MDC_{\%}$ was 29.5%. Regarding the GDI, no statistical differences were found for the dominant hand (Wilcoxon signed-rank p-value = 0.237) with ICC equal to 0.13 (with 95% CI = -0.39 to 0.73), SEM equal to 0.023, MDC_{95} equal to 0.064 and the $MDC_{\%}$ was 7.2 %. On the contrary, GDI shows statistical differences for the non-dominant hand (Wilcoxon signed-rank p-value = 0.018).

IV. Discussion

The VET aims to evaluate hand dexterity focusing on the capability of the participant to carry fragile objects without breaking them and as fast as possible. We improved the VET with respect to its first validation [16], by introducing a structured familiarization phase aiming to reduce the learning. In addition, we enlarged the number of the VEs (from 11 to 20) to have a finer discretization, keeping the execution time similar to the previous version by following an up/down procedure. To assess these changes and in the effort of extending the results of the previous study, we are currently running a clinical trial to collect normative data. Here we present a first evaluation of the modified protocol. The two-fold objective is to estimate test-retest reliability both for the dominant and non-dominant hand and preliminarily evaluate the influence of age on the results. Difference between performance of the dominant and non-dominant hand are not investigated in this pilot. Seven healthy participants, aged between 29 and 83 years, were involved in this pilot study. They performed the VET in two different sessions, distant no less than 14 days, with both hands. For each participant, performances were reported as Fine Dexterity Index (FDI) and Gross Dexterity Index (GDI). Test-retest reliability was statistically evaluated while the trend according to age was qualitatively assessed by looking at the trend of the data.

FDI, for both the dominant and non-dominant hand, shows excellent test-retest variability with an Intraclass Correlation Coefficient (ICC) equal to 0.95 and 0.91 respectively [13]. The new protocol proves to preserve the reliability of FDI without requiring the participant to perform the test twice [16]. However, the sample size should be increased including at least 30 participants to have more robust results [28], this is currently under investigation. The Standard Error Measurement (SEM) and Minimal Detectable Change (MDC_{95}) are similar for both hands. This suggests the VET can evaluate without bias both the dominant and non-dominant hands. The finding is coherent with the construct of the test. The VET is symmetrical, both in the setup and in the task, and

TABLE 4 OUTCOME MEASURE OF THE VIRTUAL EGGS TEST (VET) AND DISTANCE BETWEEN TEST-RETEST FOR EACH SUBJECT. THE FINE DEXTERITY INDEX (FDI) AND GROSS DEXTERITY INDEX (GDI) ARE REPORTED FOR THE DOMINANT AND NON-DOMINANT HAND FOR THE TWO DIFFERENT TRIALS (TEST AND RETEST).

	Distance between test and retest (days)	*FDI*				*GDI*			
		Dominant hand		*Non-dominant hand*		*Dominant hand*		*Non-dominant hand*	
Group age		*test*	*retest*	*test*	*retest*	*test*	*retest*	*test*	*retest*
18 – 29	42	1.67	1.41	1.75	1.41	0.92	0.91	0.89	0.91
30 – 39	15	1.63	1.41	1.68	1.42	0.91	0.90	0.90	0.91
40 – 49	24	1.34	1.47	1.71	1.26	0.85	0.89	0.86	0.88
50 – 59	14	1.49	1.29	1.29	1.32	0.89	0.89	0.87	0.88
60 – 69	36	2.00	2.38	2.29	2.46	0.90	0.90	0.89	0.90
70 – 79	19	2.30	2.14	2.90	2.85	0.85	0.90	0.85	0.89
> 80	19	4.20	3.66	2.77	3.30	0.83	0.90	0.87	0.89
Mean	24.1	2.09	1.97	2.06	2.00	0.88	0.90	0.88	0.90
Standard deviation	10.8	0.98	0.85	0.60	0.84	0.03	0.01	0.02	0.01

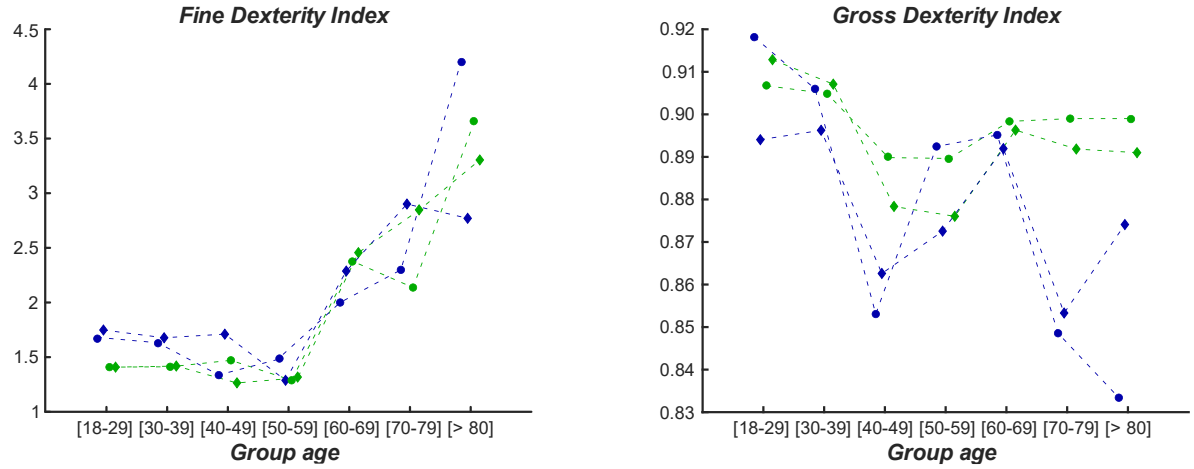


Figure 4 Outcome measure of the Virtual Eggs Test (VET), data associated with the test and retest are reported in blue and green respectively, data of the dominant and non-dominant hand are reported with circle and rhombus respectively. Fine Dexterity (FDI) (a), Gross Dexterity Index (GDI) (b).

does not change based on which hand the participant uses. By looking at the relationship between age and FDI we can observe an increase in FDI (i.e., a decreasing fine dexterity) with increasing age. This result is coherent with normative data of other hand dexterity assessment tools such as the Box and Block Test [7] or the Nine Hole Peg Test [31]. The variability of the values of FDI is higher with respect to our previous study [16]. In our opinion, this is caused by the heterogeneity of participants' ages but also by an increased resolution of the VET led by a finer discretization of the break threshold. On the contrary, GDI didn't prove test-retest reliability. In the case of the dominant hand, data didn't prove a statistical difference but showed a poor ICC. In the case of non-dominant hand, data showed a statistical difference. Usually, participants have a higher GDI (i.e., a better performance) during the retest session (Table 4). GDI is mainly affected by the performance associated with the most robust VEs. Those VEs are the first to be manipulated at the beginning of the testing phase, so the participant may be less confident in performing the test. In addition, GDI is computed considering the transport time of only two VEs (VE20 and VE19) and this could amplify the overmentioned problem. This result is in contrast with our findings in the first validation [16] where GDI proved test-retest reliability. One reason may lie in the fact that in [16] we used higher break thresholds (normalized force three times higher than the one used here). A new formulation of the GDI, an extension of the familiarization phase or an increase break threshold of the most robust VEs may be required to increase the reliability of GDI over time. We are confident that one or the combination of those possible improvements will make the GDI reliable. The variability of the GDI among participants is low, and so trends of the performance according to age are difficult to propose. As for the FDI, additional participants are needed to increase the power of the study. Results associated with SEM, MDC_{95} and $MDC_{\%}$, are reported for the sake of clarity of the procedure but not detailed discussed since the small sample size. Currently we are running an investigation involving

additional participants, and we will further analyze these values in a large population.

V. Conclusions and Future Works

The outcomes provided by this pilot study suggest that the new protocol can keep the reliability of the VET in terms of Fine Dexterity Index (FDI). On the contrary, results suggest for a revision of the Gross Dexterity Index (GDI) to increase its reliability and variability among different ages. In addition, more participants must be enrolled to increase the statistical power of the analysis and also to take into account other variables influencing the results such as the sex and the dominance of the hand [20], [21]. The new study, that is undergoing, involves both males and females for each age group and randomizes the order of the first-tested hand (i.e., dominant or non-dominant) among participants to investigate if the VET can highlight the difference between the two hands. Moreover, clinical trials involving participants with different pathologies will be carried out to continue the VET validation.

References

[1] J. Bear-Lehman and B. C. Abreu, "Evaluating the hand: Issues in reliability and validity," *Phys. Ther.*, vol. 69, no. 12, pp. 1025–1033, 1989, doi: 10.1093/ptj/69.12.1025.

[2] K. Schoneveld, H. Wittink, and T. Takken, "Clinimetric Evaluation of Measurement Tools Used in Hand Therapy to Assess Activity and Participation," *J. Hand Ther.*, vol. 22, no. 3, pp. 221–236, 2009, doi: 10.1016/j.jht.2008.11.005.

[3] L. A. Jones, "The assessment of hand function: A critical review of techniques," *J. Hand Surg. Am.*, vol. 14, no. 2 PART 1, pp. 221–228, 1989, doi: 10.1016/0363-5023(89)90010-5.

[4] F. Poirier, "Dexterity as a valid measure of hand function: A Pilot Study," *Hand Rehabil. Occup. Ther.*, pp. 69–84, 1988, doi: 10.1080/J003v04n03_07.

[5] K. E. Yancosek and D. Howell, "A Narrative Review of Dexterity Assessments," *J. Hand Ther.*, vol. 22, no. 3, pp. 258–270, 2009, doi: 10.1016/j.jht.2008.11.004.

[6] J. Yong, J. C. MacDermid, and T. Packham, "Defining dexterity—Untangling the discourse in clinical practice," *J. Hand Ther.*, vol. 33, no. 4, pp. 517–519, 2020, doi: 10.1016/j.jht.2019.11.001.

[7] J. Desrosiers, G. Bravo, R. Hébert, É. Dutil, and L. Mercier, "Validation of the Box and Block Test as a measure of dexterity of elderly people: Reliability, validity, and norms studies," *Arch. Phys. Med. Rehabil.*, vol. 75, no. 7, pp. 751–755, 1994, doi: 10.1016/0003-9993(94)90130-9.

[8] J. Desrosiers, R. Hébert, G. Bravo, and E. Dutil, "The purdue pegboard test: Normative data for people aged 60 and Over," *Disabil. Rehabil.*, vol. 17, no. 5, pp. 217–224, 1995, doi: 10.3109/09638289509166638.

[9] A. R. Sobinov and S. J. Bensmaia, "The neural mechanisms of manual dexterity," *Nat. Rev. Neurosci.*, vol. 22, no. 12, pp. 741–757, 2021, doi: 10.1038/s41583-021-00528-7.

[10] S. V. Duff, D. H. Aaron, G. R. Gogola, and F. J. Valero-Cuevas, "Innovative evaluation of dexterity in pediatrics," *J. Hand Ther.*, vol. 28, no. 2, pp. 144–150, 2015, doi: 10.1016/j.jht.2015.01.004.

[11] E. M. Andresen, "Criteria for assessing the tools of disability outcomes research," *Arch. Phys. Med. Rehabil.*, vol. 81, no. 12 SUPPL. 2, pp. 15–20, 2000, doi: 10.1053/apmr.2000.20619.

[12] L. G. Portney, *Foundations of clinical research: applications to evidence-based practice*, FA Davis. 2020.

[13] L. Resnik, M. Borgia, B. Silver, and J. Cancio, "Systematic Review of Measures of Impairment and Activity Limitation for Persons With Upper Limb Trauma and Amputation," *Arch. Phys. Med. Rehabil.*, vol. 98, no. 9, pp. 1863-1892.e14, 2017, doi: 10.1016/j.apmr.2017.01.015.

[14] S. S. Rane, A. Paul, and R. P. Mullerpatan, "Reference values of manual dexterity using minnesota rate of manipulation test for Indian adults," *Hand Ther.*, vol. 22, no. 2, pp. 79–85, 2017, doi: 10.1177/1758998317694474.

[15] E. L. Lawrence, I. Fassola, I. Werner, C. Leclercq, and F. J. Valero-Cuevas, "Quantification of dexterity as the dynamical regulation of instabilities: Comparisons across gender, age, and disease," *Front. Neurol.*, vol. 5 APR, no. April, pp. 1–13, 2014, doi: 10.3389/fneur.2014.00053.

[16] M. Controzzi *et al.*, "Assessing Hand Function in Trans-Radial Amputees Wearing Myoelectric Hands : The Virtual Eggs Test (VET)". Submitted to TNSRE and TechRxiv. July 15, 2024. DOI: 10.36227/techrxiv.172107404.47826209/v1

[17] F. Clemente, M. D'Alonzo, M. Controzzi, B. B. Edin, and C. Cipriani, "Non-Invasive, Temporally Discrete Feedback of Object Contact and Release Improves Grasp Control of Closed-Loop Myoelectric Transradial Prostheses," *IEEE Trans. Neural Syst. Rehabil. Eng.*, vol. 24, no. 12, pp. 1314–1322, 2016, doi: 10.1109/TNSRE.2015.2500586.

[18] E. Mastinu *et al.*, "Grip control and motor coordination with implanted and surface electrodes while grasping with an osseointegrated prosthetic hand," *J. Neuroeng. Rehabil.*, vol. 16, no. 1, pp. 1–10, 2019, doi: 10.1186/s12984-019-0511-2.

[19] F. M. Petrini *et al.*, "Six-Month Assessment of a Hand Prosthesis with Intraneural Tactile Feedback," *Ann. Neurol.*, vol. 85, no. 1, pp. 137–154, 2019, doi: 10.1002/ana.25384.

[20] Y. T. Prasetyo, "Factors Affecting Gross Manual Dexterity: A Structural Equation Modeling Approach," *ACM Int. Conf. Proceeding Ser.*, no. Hypothesis 1, pp. 304–308, 2020, doi: 10.1145/3396743.3396776.

[21] Y. T. Prasetyo, "Factors Affecting Fine Dexterity: A Structural Equation Modeling Approach," *ACM Int. Conf. Proceeding Ser.*, no. Hypothesis 1, pp. 304–308, 2020, doi: 10.1145/3396743.3396776.

[22] L. Angelini, R. Guachi, and M. Controzzi, "Improvements on The Virtual Eggs Test to assess Hand Dexterity," in *6th International Conference on NeuroRehabilitation (ICNR2024)*,

[23] R. C. Oldfield, "The assessment and analysis of handedness: The Edinburgh inventory," *Neuropsychologia*, vol. 9, no. 1, pp. 97–113, 1971, doi: 10.1016/0028-3932(71)90067-4.

[24] C. B. Terwee *et al.*, "Quality criteria were proposed for measurement properties of health status questionnaires," *J. Clin. Epidemiol.*, vol. 60, no. 1, pp. 34–42, 2007, doi: 10.1016/j.jclinepi.2006.03.012.

[25] F. A. A. Kingdom and N. Prins, *Psychophysics: A Practical Introduction*. 2017.

[26] L. B. Mokkink *et al.*, "COSMIN Risk of Bias tool to assess the quality of studies on reliability or measurement error of outcome measurement instruments: a Delphi study.," *BMC Med. Res. Methodol.*, 2020.

[27] J. E. Lexell and D. Y. Downham, "How to assess the reliability of measurements in rehabilitation," *Am. J. Phys. Med. Rehabil.*, vol. 84, no. 9, pp. 719–723, 2005, doi: 10.1097/01.phm.0000176452.17771.20.

[28] T. K. Koo and M. Y. Li, "A Guideline of Selecting and Reporting Intraclass Correlation Coefficients for Reliability Research," *J. Chiropr. Med.*, vol. 15, no. 2, pp. 155–163, 2016, doi: 10.1016/j.jcm.2016.02.012.

[29] K. O. McGraw and S. P. Wong, "'Forming inferences about some intraclass correlations coefficients': Correction.," *Psychol. Methods*, vol. 1, no. 4, pp. 390–390, 1996, doi: 10.1037//1082-989x.1.4.390.

[30] J. P. Weir, "Quantifying Test-Retest Reliability Using the Intraclass Correlation Coefficient and the SEM," *J. Strength Cond. Res.*, vol. 19, no. 1, pp. 231–240, 2005.

[31] V. Mathiowetz, K. Weber, N. Kashman, and G. Volland, "Adult norms for the nine hole peg test of finger dexterity," *Occup. Ther. J. Res.*, vol. 5, no. 1, pp. 24–38, 1985, doi: 10.1177/153944928500500102.

Beyond the Legs: Leveraging Trunk and Driving Muscle EMG to Improve Gait Model Predictions

Annika Guez, Sabine Baier, Nicolas Berberich, Ravi Vaidyanathan and Gordon Cheng

***Abstract*— Gait prediction models based on electromyography (EMG) have been extensively used for motion intent detection in lower-limb exoskeletons. Traditionally, gait prediction models tend to rely solely on lower-limb EMG signals. However, based on the importance of trunk muscles in clinical gait studies, we hypothesise that these could provide valuable information for the development of more accurate gait models. Furthermore, based on previous literature on muscle functionality during steady-state walking, we also hypothesise that focusing on muscle groups that are responsible for movement generation in gait (referred to as driving muscles, or "drivers") will lead to improved kinematics predictions compared to other muscle subsets. In this study, we examine the predictive value of EMG signals extracted from the trunk and driving muscles versus purely the lower-limbs in predictive gait models. We investigate prediction horizons of 0.05 ms (one time-step ahead), 100 ms, and 200 ms, and predict the angular output of the hip, knee and ankle joints, as well as the estimated gait cycle percentage. Our results show that models trained using trunk muscle EMG significantly outperform models trained only on lower-limb EMG, particularly for knee angle outputs with longer prediction horizons (p <0.05). Furthermore, training on selected driving muscles further improved model performance when predicting the knee and ankle joint kinematics, particularly with short prediction horizons (p <0.001). These findings support the hypothesis that including trunk muscles contributes significantly to the development of accurate gait models, and highlight the potential of targeting "drivers" to select more relevant EMG inputs for kinematic predictions.**

I. Introduction

In recent years, lower-limb exoskeletons (LLEs) have been gaining traction as a means for helping patients regain their independence and providing assistance through their rehabilitation process [1], [2]. Within this context, understanding the complex internal mechanisms of the user's neuromusculoskeletal function is crucial in developing effective user-centred devices [3]. Consequently, establishing reliable relationships between the user's intent and their corresponding limb movements has been a core focus in research. This effort involves in-depth gait analysis and advanced modelling techniques to generate the required kinematic information for accurate exoskeleton control [4]. Given that LLEs are robotic systems designed for human-in-the-loop control, correctly deciphering the user's motion intent is essential for the user's safety and rehabilitation effectiveness.

Electromyography (EMG) is a sensing modality that detects the electrical activity generated in muscle fibres prior to muscle contraction. In the domain of gait analysis and modelling, EMG signals have extensively been used as inputs for motion intent detection [5], and are currently the only clinically viable approach to interfacing with the subject's nervous system without surgery [3]. However, the translation of these EMG-based models to clinical environments, either within patient populations or in the development of LLEs, remains a challenge [6]; the non-stationary nature of EMG signals and their susceptibility to external factors limit their application in muscle-driven models [7], which is further exacerbated by inter-session and cross-subject inconsistencies [8]. Therefore, input optimisation is essential to ensure accurate predictions, and the reduction of redundant hardware could help improve computational efficiency and reduce cost for LLE applications.

Previous studies on EMG-driven models for lower-limb kinematics predictions have focused mainly on muscles from the lower-limbs [9], with a particular focus on the Gluteus (GT), Rectus Femoris (RF), Biceps Femoris (BF), Vastus Lateralis (VL), Tibialis Anterior (TA), and Soleus (SO) to predict the angular kinematics of the hip, knee and ankle. However, in addition to the lower-limbs, clinical gait research puts an emphasis on the role of the trunk during gait, and the relationship between trunk muscle activation and lower-limb movement [10]. Furthermore, the trunk has often been a point of focus in gait rehabilitation practices [11]. The trunk muscles play a dual role during steady-state walking, focused on both the maintenance of postural balance and the facilitation of lower-limb movement; the trunk is perceived as the centre of the functional kinematic chain during gait [12] as its muscle activation precedes those of the lower-limbs and pushes the Centre of Mass (CoM) forwards [10], therefore providing a stable basis for control and the generation of movement during gait.

Beyond the role of the trunk, this notion of task-specific muscle roles can be extended to the lower-limbs as well, as previous studies have made the distinction between muscles responsible for movement generation (also known as "drivers") and those that provide stability and balance to facilitate the motion (also known as "stabilisers") [13]. Whilst this distinction isn't yet clear for all the muscles involved in gait, the Multifidus (MF) and Erector Spinae (ES) muscles have been characterised in previous studies as "drivers" due to their clear phasic activation patterns [14], [15]. The RF

This work was supported by: The UKRI CDT in AI for Healthcare (Grant No. EP/S023283/1), the Joint Academy of Doctoral Studies (JADS) between Imperial College London and the Technical University of Munich, the UK Dementia Research Institute Care Research & Technology Centre (DRI-CR&T), and the European Research Council (ERC) (Grant No. 101098308).

Annika Guez and Prof. Ravi Vaidyanathan are with Department of Mechanical Engineering and DRI-CR&T, Imperial College London, London, United Kingdom. Sabine Baier, Nicolas Berberich and Prof. Gordon Cheng are part of the Institute of Cognitive Systems at the Technical University of Munich, Munich, Germany.

and SO have also been recognised as "drivers" in the lower-limbs [16]. Based on this information, we further hypothesise that using these "driving" muscles as inputs into our gait models would lead to better predictions, since they would have a more direct relationship with the resulting movement. In this study, we therefore investigate whether the use of trunk muscles and "driver" muscles as EMG signal inputs will improve gait model predictions, compared to using only leg muscles as previously done in literature.

II. Methods

A. Subjects

This study involved 5 able-bodied participants with no previous neurological or physiological conditions that could impact their gait (2 male, 3 female, with a mean age of 26 $\pm$ 5 years, a mean height of 171 $\pm$ 10 cm, and a mean weight of 62 $\pm$ 10 kg). The experiments used in this study were conducted in accordance with ethical guidelines approved by the Imperial College Research Ethics Committee (ICREC reference: 21IC7204).

B. Experimental procedure

To gather steady-state gait data across various walking speeds, the participants were asked to walk on a treadmill at speeds ranging from 0.40 $m{\cdot}s^{\propto l}$) to 0.80 $m{\cdot}s^{\propto l}$), with increments of 0.04 $m{\cdot}s^{\propto l}$), for a duration of 2 minutes per speed (this corresponds to an average of 75 strides per speed, so over 680 steady-state cycles per subject). Since this study focuses on the recruitment strategies of the subject's muscles to generate the cyclical movements at different speeds for efficient walking, overground walking or start-and-stop tasks were not investigated.

*1) **Delsys bipolar EMG**:* During walking, synchronous muscle activity data was collected using Delsys Avanti Trigno bipolar EMG sensors placed on 8 muscles from the trunk and the lower-limb based on the SENIAM [17] standards. Since gait is predominantly a combination of weight shifting in the transverse plane as well as movement from the lower-limbs, the trunk data was acquired bilaterally (from both sides) to capture the adjustments of the CoM [18] whilst the leg data was acquired unilaterally since we are only focusing on the joint angles of the investigated limb [9]. In particular, bilateral data were recorded from the MF and Erector Spinae Longissimus (ESL), in conjunction with lower-limb data of the dominant leg recorded from the RF, BF, TA and SO. The dominant leg was determined through a push test by selecting the leg with which the participant instinctively stepped forward.

*2) **Vicon Motion Capture**:* Using a Vicon Motion Capture system with ten 120 Hz Vicon Vero v2.2 cameras positioned around the workspace, the joint kinematics of the subjects' dominant leg were recorded as they walked. These encompass the joint angles from the hip, knee, and ankle joints, which have all previously been used for gait analysis and prediction [7]. The marker trajectory data was labelled using the Vicon Nexus software, and kinematics information was extracted using the Nexus Plug-In Gait Kinematics pipeline for lower-body modelling [19]. Since all the data acquisition was done simultaneously through the analogue-integrated version of the Delsys Avanti Trigno (EMG) and Vicon Nexus (motion capture), the two data streams were internally synchronised during recording. The motion data was then upsampled to align with the sampling frequency of the EMG signals.

C. Data preprocessing

To facilitate the analysis of the recorded EMG signals after having been standardised, these were band-pass filtered (20-400 Hz), rectified, and low-pass filtered at 10 Hz to extract the signal envelopes. Causal filtering was used to ensure that the temporal integrity of the data was maintained. To capture the sequential nature of the data, the signals were segmented into windows, with a duration of 250 ms (500 samples for a 2 kHz sampling frequency) and a step of 40 samples. To analyse the predictive power of the different muscle subsets, multiple prediction horizons (PHs) were investigated, i.e. the time between the end of the EMG input window and the predicted joint angle output. Each extracted EMG window was therefore paired with joint angle outputs corresponding to the following PHs: 0.5 ms (one time-step ahead of the window, also referred to as the "one-step-ahead" prediction), 100 ms, and 200 ms.

1) Muscle subsets: The majority of previous EMG-based gait studies focused on the RF, BF, TA and SO as inputs to their models, as they are perceived to be the main muscles responsible for the motion of the knee and ankle joints [16]. Our analysis further focuses on the inclusion of trunk muscles as inputs to gait prediction models, specifically comparing this commonly used lower-limb muscle subset with the following 2 subsets: one solely composed of trunk muscles, and one composed of a combination of trunk and leg muscles that are theorised to be the main "drivers" of motion during cyclic gait. The investigated subsets are shown in Table I, with the *Drivers* subset corresponding to muscles identified as "drivers" in literature. [14]–[16].

TABLE I: Muscle groups included in the investigated subsets. The suffix "-L" and "-R" refer to the left and right sides of the body. Trunk muscles were always included bilaterally.

	Muscle groups							
Subset	ESL-L	ESL-R	MF-L	MF-R	RF	SO	BF	TA
Trunk	✓	✓	✓	✓				
Leg					✓	✓	✓	✓
Drivers			✓	✓	✓	✓		

All the analysed muscle subsets in this study comprised of 4 muscle groups at a time to ensure that the results across the different muscle combinations weren't biased by the amount of available data.

2) The predicted outputs: Following previous studies on modelling joint kinematics in gait [9], this study employed all the lower-limb joints as outputs to the prediction, consisting of the recorded hip, knee, and ankle joints of the dominant leg. Since joint angle range of motion (RoM) is

dependent on the physiology of the subject, an additional, physiology-independent output was investigated to assess its viability; the gait cycle percentage (GC%) represents the user's progression through the gait cycle, as a percentage of the total cycle. This metric was designed using the knee angle's flexion peaks to segment the gait cycles, with the percentages linearly fitted to each extracted cycle.

D. Multi-Layer Perceptron

A regressive multi-layer perceptron (MLP) was implemented as the evaluation model, mapping the windowed EMG envelopes to the chosen predictive output (see Subsection II-C.2). The model architecture consisted of 7 fully connected layers with Rectified Linear Unit (ReLU) activation, trained using a Mean Squared Error loss function and an Adam optimizer. Although there exists more advanced architectures, MLPs are simpler and better suited for smaller datasets, whilst maintaining the ability to approximate temporal dependencies due to the use of windowed inputs [20]. To ensure that the extracted results were representative of the dataset and to minimise bias caused by the train-validation split, the models were trained using a 5-fold cross-validation scheme. The models using the muscle subsets outlined in Subsection II-C.1 were trained using a learning rate (LR) of $10^{\circ 4}$ and a weight decay of $10^{\circ 5}$ for a maximum of 100 epochs, with early stopping if the validation performance stagnated for more than 6 epochs. The reported validation performance in Section III is that of the best validation performance achieved before the model stopped training. To allow for a more meaningful comparison of the performances achieved, the recorded validation Root Mean Squared Error (RMSE) values were normalised based on the true range of the output; for the angular outputs, this corresponds to the RoM of the joint, whilst this was set to 100 for the GC%.

E. Analysis Outline

Models were trained for all the combinations of investigated muscle subsets (see Subsection II-C.1) and predicted outputs (see Subsection II-C.2), resulting in the training of 12 MLPs per subject for a given PH, and a total of 180 5-fold cross-validation models across all subjects and conditions for the 3 chosen PHs (see Subsection II-C).

To evaluate the statistical significance of the results, an independent two-sample t-test was conducted to compare the validation RMSE values (from the 5-fold cross-validation scheme) of the MLP models across the different investigated muscle subsets for all given output variables (only two models are compared at a time). Prior to conducting the statistical analysis, the normality of the RMSE distributions was assessed using a Shapiro-Wilk test. The results are reported in the performance figures using the following notations: ($* = p < 0.05$; $** = p < 0.01$; $*** = p < 0.001$; $**** = p < 0.0001$).

III. Results

A. Subset comparison in the one-step-ahead scheme

Figure 1 illustrates the normalised validation RMSE of the models across all subjects, trained on all combinations of muscle subsets and outputs for the one-step-ahead prediction scheme. As can be seen, for all predicted outputs, the *Trunk* subset consistently outperformed the *Leg* subset, with an average normalised RMSE decrease of 1.64% for the hip joint, 5.62% for the knee joint, 2.10% for the ankle joint, and 6.65% for the GC%. Whilst the performance of the *Trunk* and *Drivers* subsets was comparable in the case of the hip and the GC%, the *Drivers* outperformed the *Trunk* muscles when predicting the knee and ankle joints, with a normalised RMSE decrease of 6.60% and 3.10% respectively. Table II gives a more detailed description of the p-values for the individual subjects.

TABLE II: P-values comparing Trunk vs. Leg subsets (TL) and Leg vs. Combined subsets (LC) for all investigated subjects in the one-step-ahead MLP prediction scheme.

	Hip		**Knee**		**Ankle**		GC%	
Subjects	TL	LC	TL	LC	TL	LC	TL	LC
1	-	****	***	****	-	***	**	***
2	-	*	*	***	**	*	*	**
3	*	-	***	**	*	**	-	-
4	****	****	****	****	***	***	****	****
5	**	****	*	***	**	***	**	-

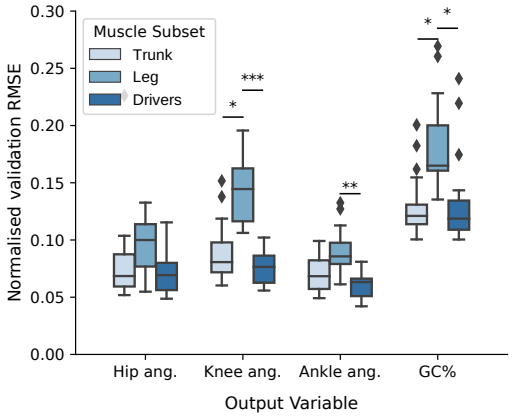
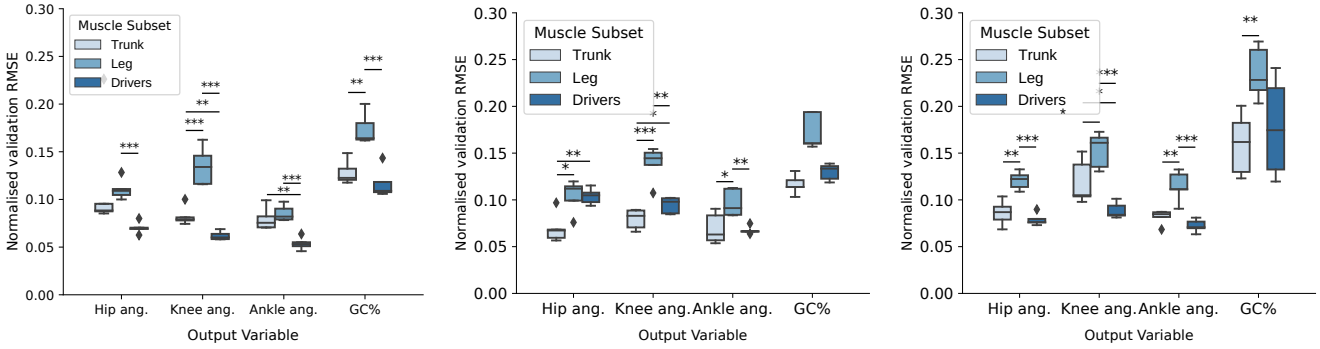


Fig. 1: Cross-subject performance of the investigated muscle subsets for the different predicted output variables in the one-step ahead scheme

At first glance, from Figure 1, the comparative performance of the *Trunk* and *Drivers* subsets could suggest that the MF is the main predictor for this joint as it is present in both subsets, and is therefore responsible for the improved model performance. However, the subject-specific visualisation in Figure 2 shows that the predictive power of these two subsets seems to alternate across subjects, thus alluding to more complex inter-subject variations in muscle recruitment strategies for hip movement. This could be related to the subjects' specific balancing strategies, as some will focus on the flexion and extension of the hip to maintain balance (known as *hip-strategy*, with an emphasis on trunk extension) while others will instead sway about their ankle joint (known as *ankle-strategy*) and therefore display less balance-focused hip movements [21].



(a) Subject 1 (b) Subject 3 (c) Subject 5

Fig. 2: The performance of the investigated muscle subsets when predicting the different outputs in a one-step-ahead scheme for 3 example subjects. Subjects 1, 3, and 5 were selected for this visualisation since they displayed a range of different significance levels during the significance analysis (see Table II).

B. The impact of prediction horizons on performance

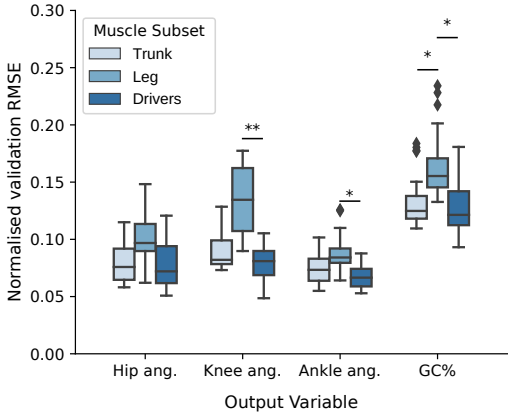


Fig. 3: Cross-subject performance of the investigated muscle subsets using a 100 ms prediction horizon.

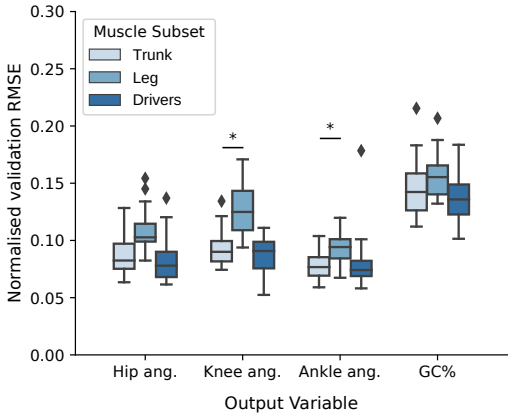


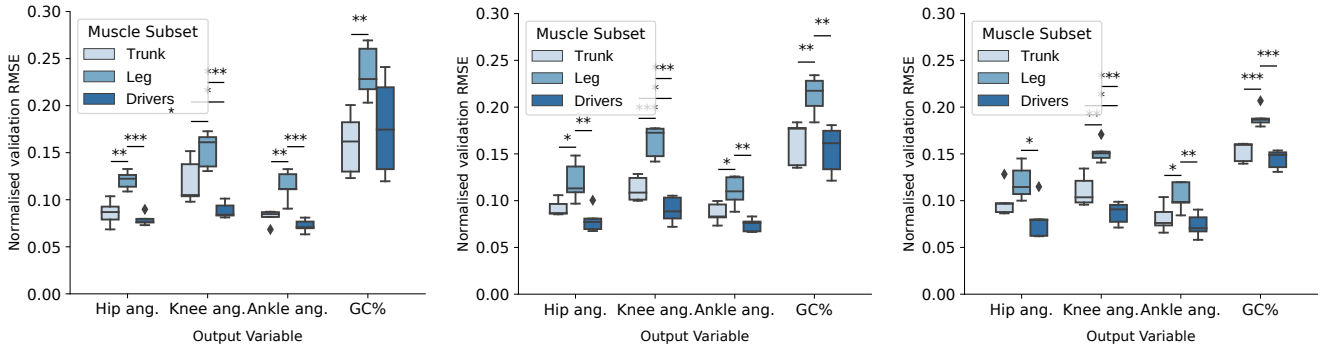
Fig. 4: Cross-subject performance of the investigated muscle subsets using a 200 ms prediction horizon.

As outlined in Subsection II-E, the prediction was repeated for PHs of 100 ms and 200 ms to assess their relationship to subset performance. Figures 3 and 4 illustrate the performance of the subsets on all investigated outputs for the 100 ms and 200 ms windows respectively. Surprisingly, the cross-subject prediction performance of the subsets remained largely unaffected by an increased PH, likely due to the cyclic nature of the motion. This suggests that differences between subsets are more influenced by signal quality than by time-based suitability. As can be seen, the *Trunk* and *Drivers* subsets consistently performed better than the *Leg* subset across all predicted outputs, with a normalised RMSE decrease of 5.63% between the *Leg* and *Drivers* subsets for the knee joint, and 2.50% for the ankle joint. However, the significance of these results decreased as the PH increased (the pairwise p-values between the *Drivers* and *Leg* subsets increased from $p < 0.001$ to $p < 0.01$ for the knee angle prediction, and $p < 0.01$ to $p < 0.05$ for the ankle angle). It should however be noted that, whilst there is a greater significance between the performances of the *Leg* and *Drivers* subsets for a 100 ms PH, the greater significance shifts to the *Leg* and *Trunk* pairs at 200 ms, suggesting that the trunk muscles' activation patterns become more important than the lower-limb's when attempting earlier predictions. This could be related to the importance of the trunk with regards to anticipatory postural adjustments, in preparation for the movement of the legs [22].

Figure 5 illustrates the change of subset performances across the investigated PHs for an example subject. Whilst the average performance values and their attributed pairwise significance varies across PHs, the trend remains the same for this subject, with the *Drivers* subset achieving the lowest validation RMSE values across all joint angles. The most noticeable change in this scenario, however, is the increasing performance for the prediction of the GC% as the PH increases, reinforcing the potential of gait cycle progression as a representative measure for gait-related outputs.

IV. Discussion

Across all subjects in the one-step-ahead prediction scheme, both the *Trunk* and *Drivers* subsets outperformed the *Leg* subset, particularly for the knee joint output. Whilst this general trend remained the same across all PHs, the *Drivers* subset displayed the strongest significance when comparing



(a) One-step-ahead (b) 100 ms horizon (c) 200 ms horizon

Fig. 5: Prediction performance of the investigated subset and output pairs for Subject 5, across different prediction horizons.

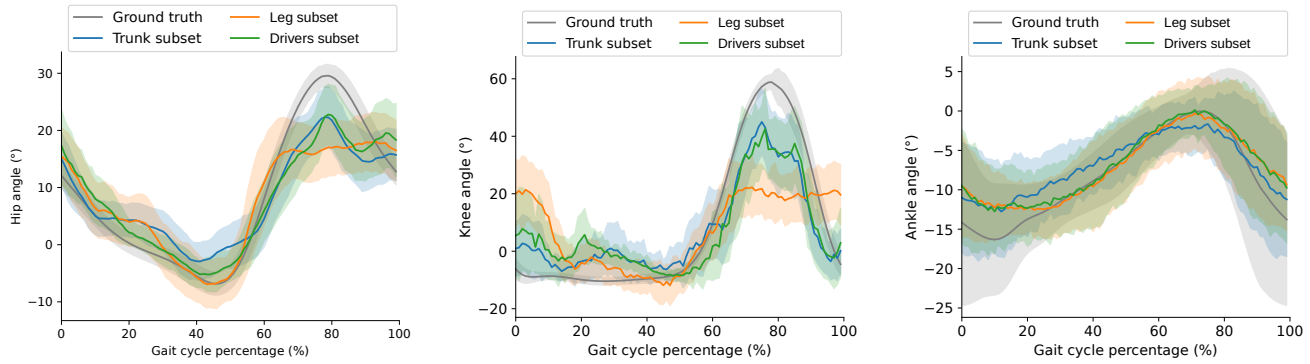
its performance to the *Leg* subset for both the knee and ankle joints when using a 100 ms PH, with p-values of $p < 0.001$ and $p < 0.01$ respectively. Despite lower p-values ($p < 0.01$ and $p < 0.05$ respectively), this suggests that "driving" muscles could provide valuable information for more accurate gait predictions relative to solely leg muscles. Interestingly, the strongest significance, when comparing against the performance of the *Leg* subset, shifted from the *Drivers* to the *Trunk* subset when employing a 200 ms PH. This could be due to the importance of the core muscles in performing anticipatory postural adjustments in preparation for lower-limb motion [22], highlighting the importance of including the trunk muscles in predictive gait modelling.

The notion that human movement results from the coordinated co-contraction of muscle synergies has been widely studied in gait analysis [23]. While gait prediction models often prioritise lower-limb muscles as inputs, other muscle groups - particularly the trunk - play a crucial role in leg mobilisation and can enhance model accuracy, as demonstrated by our results. Future EMG-based gait models should therefore incorporate trunk muscles to improve prediction performance. Furthermore, the increased performance when using "driving" muscles as inputs reveals that the understanding of task-specific muscle roles could also provide indications on which muscle groups to prioritise when selecting gait model inputs. This physiologically informed input selection is particularly relevant when analysing steady-state walking; due to the cyclical nature of gait, the central nervous system (CNS) aims to minimise cognitive effort by reducing the number of muscles that behave volitionally [24]. Therefore, whilst a large number of muscles from the trunk and lower-limbs activate during gait, only a fraction of these are responsible for the generation of movement ("drivers") whereas the others focus on providing stability and balance. The improved performance when using the *Drivers* subset in this study would suggest that the concentric contraction of these muscles provide a more reliable EMG input [25], and that their activation could be more directly linked to the kinematic outputs observed. Future research should therefore prioritise the deeper physiological understanding of the target task, including muscle recruitment strategies and functional roles, which would enable the selection of the most relevant muscles as inputs, and further enhance model performance.

Although the *Trunk* and *Drivers* subsets consistently outperformed the *Leg* subset across all subjects and PHs, Figures 1, 3, and 4 reveal noticeable cross-subject differences in the comparative performance of the *Trunk* and *Drivers* subsets, especially for the hip joint, which could stem from individual variations in balancing strategies. Figure 6 illustrates the predicted joint angles in the one-step-ahead scheme for one of the validation folds of an example subject. As can be seen, the predictions from the *Trunk* and *Drivers* subsets for the hip and knee joints are closer to the ground truth than that of the *Leg* subset. Whilst this isn't as evident for the ankle joint in this example fold, Figure 6.c does give us insights on the balancing strategy used by the subject: the noticeably higher variance of the ankle angle throughout the gait cycle would suggest the subject was heavily reliant on adapting the ankle's angular position to maintain posture (i.e. using *ankle strategy* for balance), which is further corroborated by the reduced knee flexion during the stance phase. Considering the impact of gait strategies on muscle activation patterns and joint trajectories, understanding and accounting for these inherent cross-subject variations could help group individuals with similar EMG patterns and kinematic profiles. This could facilitate the development of generalisable models and should be a focus of future research.

V. Conclusion

Due to their role in both postural balance and motion during gait, *Trunk* muscles were shown to be a reliable source of EMG inputs for gait prediction models compared to the *Leg*, with an average normalised RMSE decrease of 5.62% for the knee joint and 2.10% for the ankle joint in the one-step-ahead scheme, 4.49% and 1.31% for a 100 ms PH, and 3.40% and 1.53% for a 200 ms PH. The *Trunk*, however, exhibited a larger performance variability for the hip angle and GC%, which could be related to physiological balancing strategies that differ across subjects. On the other hand, selecting *Drivers* as inputs to the model led to consistently higher prediction performances for the knee and ankle joints, with the *Drivers* subset resulting in an average normalised RMSE decrease relative to the *Leg* subset of: 6.60% and 3.07% (one-step-ahead), 5.63% and 2.15% (100 ms horizon),



(a) Hip angle (b) Knee angle (c) Ankle angle

Fig. 6: An example prediction output for the (a) hip, (b) knee, and (c) ankle angles averaged across gait cycles. The results shown here are for Subject 4 and correspond to the validation output of one of the folds in the one-step-ahead scheme.

and 4.06% and 1.35% (200 ms horizon) for both joints respectively. This study demonstrates that incorporating trunk muscles enhances prediction performance, and highlights the importance of understanding muscle functionality (drivers vs. stabilisers) for developing accurate gait models. Such insights could facilitate the selection of more relevant EMG inputs for LLEs, improving safety and reliability while also reducing costs. Future research should therefore prioritise the inclusion of trunk muscles and the further exploration task-specific muscle roles.

References

[1] H. Ma, C. Zhong, B. Chen, K.-M. Chan, and W.-H. Liao, "User-adaptive assistance of assistive knee braces for gait rehabilitation," *IEEE Transactions on Neural Systems and Rehabilitation Engineering*, vol. 26, no. 10, pp. 1994–2005, 2018.

[2] G. Cheng, S. K. Ehrlich, M. Lebedev, and M. A. L. Nicolelis, "Neuroengineering challenges of fusing robotics and neuroscience," *Science Robotics*, vol. 5, no. 49, p. eabd1911, 2020.

[3] M. Sartori, D. G. Lloyd, and D. Farina, "Neural data-driven musculoskeletal modeling for personalized neurorehabilitation technologies," *IEEE Transactions on Biomedical Engineering*, vol. 63, no. 5, pp. 879–893, 2016, epub 2016 Mar 24.

[4] S. Sivolobov, A. Khoperskov, and V. Bumagin, "Human gait modeling method," *IOP Conference Series: Materials Science and Engineering*, vol. 828, p. 012024, 2020.

[5] E. Wentink, S. Beijen, H. Hermens, J. Rietman, and P. Veltink, "Intention detection of gait initiation using emg and kinematic data," *Gait Posture*, vol. 37, no. 2, pp. 223–228, 2013.

[6] G. Durandau, D. Farina, and M. Sartori, "Robust real-time musculoskeletal modeling driven by electromyograms," *IEEE Transactions on Biomedical Engineering*, vol. PP, pp. 1–1, 2017.

[7] A. Rajagopal, C. L. Dembia, M. S. DeMers, D. D. Delp, J. L. Hicks, and S. L. Delp, "Full-body musculoskeletal model for muscle-driven simulation of human gait," *IEEE Transactions on Biomedical Engineering*, vol. 63, no. 10, 2016, epub 2016 Jul 7.

[8] V. Agostini, M. Ghislieri, S. Rosati, G. Balestra, and M. Knaflitz, "Surface electromyography applied to gait analysis: How to improve its impact in clinics?" *Frontiers in Neurology*, vol. 11, Sep 2020.

[9] N. Amrani El Yaakoubi, C. McDonald, and O. Lennon, "Prediction of gait kinematics and kinetics: A systematic review of emg and eeg signal use and their contribution to prediction accuracy," *Bioengineering*, vol. 10, no. 10, 2023.

[10] J. D. Willson, C. P. Dougherty, M. L. Ireland, and I. M. Davis, "Core stability and its relationship to lower extremity function and injury," *Journal of the American Academy of Orthopaedic Surgeons*, vol. 13, no. 5, pp. 316–325, 2005.

[11] W. Mahmood, H. Burq, S. Ehsan, B. Sagheer, and T. Mahmood, "Effect of core stabilization exercises in addition to conventional therapy in improving trunk mobility, function, ambulation and quality of life in stroke patients: a randomized controlled trial," *BMC Sports Science, Medicine and Rehabilitation*, vol. 14, 2022.

[12] E.-J. Chung, J.-H. Kim, and B.-H. Lee, "The effects of core stabilization exercise on dynamic balance and gait function in stroke patients," *Journal of physical therapy science*, vol. 25, pp. 803–806, 2013.

[13] T. E. Flaxman, A. D. Speirs, and D. L. Benoit, "Joint stabilisers or moment actuators: The role of knee joint muscles while weight-bearing," *Journal of Biomechanics*, vol. 45, no. 15, pp. 2570–2576, 2012.

[14] C. Anders, H. Wagner, C. Puta, R. Grassme, A. Petrovitch, and H.-C. Scholle, "Trunk muscle activation patterns during walking at different speeds," *Journal of Electromyography and Kinesiology*, vol. 17, no. 2, pp. 245–252, 2007.

[15] G. Li, D. Ao, M. M. Vega, M. S. Shourijeh, P. Zandiyeh, S.-H. Chang, V. O. Lewis, N. J. Dunbar, A. Babazadeh-Naseri, A. J. Baines, and B. J. Fregly, "A computational method for estimating trunk muscle activations during gait using lower extremity muscle synergies," *Frontiers in Bioengineering and Biotechnology*, vol. 10, 2022.

[16] R. Chiba, K. Takakusaki, J. Ota, A. Yozu, and N. Haga, "Human upright posture control models based on multisensory inputs; in fast and slow dynamics," *Neuroscience Research*, vol. 104, pp. 96–104, 2016, body representation in the brain.

[17] H. J. Hermens, B. Freriks, R. Merletti, D. Stegeman, J. Blok, G. Rau, C. Disselhorst-Klug, and G. Hägg, "European recommendations for surface electromyography," *Roessingh research and development*, vol. 8, no. 2, pp. 13–54, 1999.

[18] D. Jarchi, J. Pope, T. K. M. Lee, L. Tamjidi, A. Mirzaei, and S. Sanei, "A review on accelerometry-based gait analysis and emerging clinical applications," *IEEE Reviews in Biomedical Engineering*, vol. 11, pp. 177–194, 2018.

[19] V. Nexus, *Plug-In Gait Reference Guide*, Vicon Motion Systems.

[20] J. Song, A. Zhu, Y. Tu, H. Huang, M. A. Arif, Z. Shen, X. Zhang, and G. Cao, "Effects of different feature parameters of sEMG on human motion pattern recognition using multilayer perceptrons and LSTM neural networks," *Applied Sciences*, vol. 10, no. 10, 2020.

[21] A. D. Kuo and F. E. Zajac, "Chapter 31 human standing posture: multi-joint movement strategies based on biomechanical constraints," in *Natural and Artificial Control of Hearing and Balance*, ser. Progress in Brain Research, J. Allum, D. Allum-Mecklenburg, F. Harris, and R. Probst, Eds. Elsevier, 1993, vol. 97, pp. 349–358.

[22] V. Farinelli, F. Bolzoni, S. M. Marchese, R. Esposti, and P. Cavallari, "A novel viewpoint on the anticipatory postural adjustments during gait initiation," *Frontiers in Human Neuroscience*, vol. 15, p. 709780, 2021.

[23] T. Wojtara, F. Alnajjar, S. Shimoda, and H. Kimura, "Muscle synergy stability and human balance maintenance," *Journal of neuroengineering and rehabilitation*, vol. 11, p. 129, 2014.

[24] E. B. Simonsen, "Contributions to the understanding of gait control." *Danish medical journal*, vol. 61 4, 2014.

[25] W. Kibler, J. Press, and A. Sciascia, "The role of core stability in athletic function," *Sports medicine (Auckland, N.Z.)*, vol. 36, pp. 189–98, 2006.

Egocentric Perception of Walking Environments using an Interactive Vision-Language System

Haining Tan, Alex Mihailidis, and Brokoslaw Laschowski

Abstract – **Large language models can provide detailed contextual understanding of a scene beyond what computer vision alone can provide, which has implications for robotics and embodied intelligence. In this study, we developed a novel multimodal vision-language system for egocentric visual perception, with an initial focus on real-world walking environments. We trained a number of state-of-the-art transformer-based vision-language models that use causal language modelling on our custom dataset of 43,055 image-text pairs for few-shot image captioning. We designed a new speech synthesis model and a user interface to convert the generated image captions into speech for audio feedback to users. Our system also uniquely allows for feedforward user prompts to personalize the generated image captions by incorporating human cognition in the decision making. Our system is able to generate detailed captions with an average length of 10 words while achieving a high ROUGE-L score of 43.9% and a low word error rate of 28.1% with an end-to-end processing time of 2.2 seconds. Overall, our new multimodal vision-language system can generate accurate and detailed descriptions of scenes, which can be further augmented by user prompts. This innovative feature allows our image captions to be personalized to the individual needs and preferences of the user, thus optimizing the closed-loop interactions between the human and generative AI models for understanding and navigating of real-world environments.**

I. Introduction

Vision plays a critical role in human locomotion by providing feedback about the environment, allowing individuals to navigate obstacles, maintain balance, and adapt their behavior accordingly. Visual information helps in the coordination of motor actions, such as stepping over obstacles or adjusting walking speed [1], by allowing the brain to predict and respond to changes in the terrain. Without vision, humans often struggle to move efficiently and safely in dynamic environments, highlighting the fundamental link between visual perception and movement. Inspired by this biological vision-locomotor control, computer vision systems, powered by deep learning, have likewise been developed for robotics [2]-[7]. However, language can provide a more detailed contextual understanding of a scene beyond what computer vision alone can provide.

The use of image captions for human-robot locomotion is a relatively unexplored area of research. By translating complex visual information into natural language, image captions could provide a high-level abstraction of the real-world (e.g., terrain types and obstacles), in addition to providing an intuitive user interface for human interaction. Textual information could be used by reinforcement learning algorithms to dynamically adapt the human and robot's walking strategy, allowing for real-time optimization based on the described scene [8]-[10]. Recent advances in generative AI and vision-language models [11] have opened new opportunities for this area of research. For example, [12] and [13] recently showed that vision-language models could interpret dynamic and unpredictable environments and execute complex navigational tasks from natural language instructions for robotics. Unlike traditional computer vision systems that focus on feature extraction, vision-language models can provide a richer understanding of scenes through textual abstraction. This enables detailed, user-personalized feedback, enhancing human-robot interaction.

Here we developed a new multimodal vision-language system for egocentric visual perception of real-world walking environments. We trained several transformer-based vision-language models [14]-[16], characterized by strong few-shot performance, which were pretrained on large vision datasets with natural language supervision [17]. Our system is able to generate accurate and detailed scene descriptions and identify obstacles, changes in terrain, and other critical navigational cues. We also developed a new speech synthesis model and a user interface to convert the generated text into audio feedback to users. Our system also uniquely allows for user prompts to tailor the generated image captions to the individual needs and preferences of the human user by incorporating human cognition in the decision making. Our system addresses key limitations in previous research, including dynamic scene interpretation beyond static object recognition, personalized user feedback for diverse navigation, and real-time closed-loop human-AI interaction for improved decision-making. To our knowledge, this is the first study to explore closed-loop human-AI interactions with vision-language models for real-world locomotion.

II. Methods

A. Image Dataset with Natural Language

We used the Microsoft COCO Captions dataset to finetune our vision-language models, a widely used benchmark dataset in computer vision and natural language processing [18]. The dataset contains over 200,000 images with human-generated captions. The images were collected from a wide range of contexts, including diverse settings such as urban environments and natural landscapes. For image captioning of walking environments, we adapted and manually curated a subset of the MSCOCO Captions dataset. We collected 43,055 image-text pairs based on the appearance of keywords. The average length of the captions in our new dataset was 10-15 words per cap-

*Research supported by the Schroeder Institute for Brain Innovation and Recovery and the Mitacs Accelerate Program, Canada.

H. Tan is with the Department of Computer Science, University of Toronto, Toronto, Canada (e-mail: haining.tan@mail.utoronto.ca).

A. Mihailidis is with the Institute of Biomedical Engineering, University of Toronto, Toronto, Canada, and the KITE Research Institute, Toronto Rehabilitation Institute, Toronto, Canada (e-mail: alex.mihailidis@utoronto.ca).

B. Laschowski is with the Department of Mechanical and Industrial Engineering, University of Toronto, Toronto, Canada, and the KITE Research Institute, Toronto Rehabilitation Institute, Toronto, Canada (e-mail: brokoslaw.laschowski@utoronto.ca).

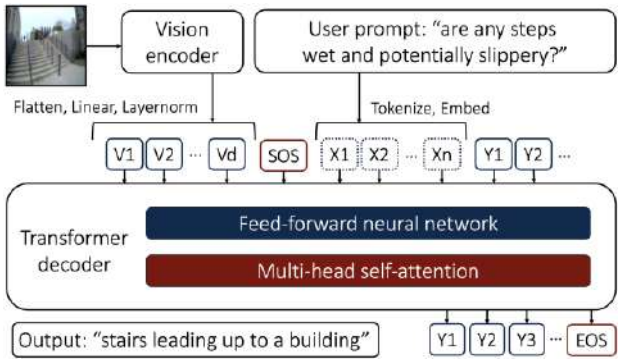


Fig. 1 Our transformer-based encoder-decoder network architecture used for few-shot image captioning of real-world walking environments, including optional user prompts to tailor the generated image captions to the individual needs and preferences of the user.

tion. Prior to model training, we standardized the images to RGB format and performed a random split, allocating 90% and 10% of the images for training and testing, respectively.

B. Vision-Language Models

Our image captioning module is used to generate detailed descriptions of the images using large vision-language models. We used an encoder-decoder framework (Fig. 1), which is common in state-of-the-art vision-language models, to translate images to text. The system extracts features from the initial input image and converts the 2D data structure into a sequence of visual tokens through a vision encoder. We then perform a sequence-to-sequence translation using our text decoder to produce contextually relevant captions corresponding to the visual environment.

This encoder-decoder framework was first proposed using a convolutional neural network as the vision encoder and a long short-term memory (LSTM) network as the text decoder [19] for real-world multimodal perception. To improve the quality of the text generation, we applied a transformer-based architecture to perform causal language modeling [20]. Causal language models can capture extensive context because they attend directly to any previous token to predict the next token through the attention mechanism. They have consistently demonstrated impressive capabilities since the inception of large language models like GPT2 [15], which can capture extensive context because they consider all previous tokens to predict the next token. The transformer architecture is designed for parallel processing of sequences and uses attention mechanism to capture relationships among tokens, leading to a more coherent and contextually relevant text generation. Given a sequence of tokens, the general loss of causal language models is computed by:

$$L_{CausalLM}(x) = \frac{1}{T}\sum_{i=1}^{T} log\ P(x_i|x_{<i})$$

We first encoded the visual information into a sequence of embeddings analogous to word embeddings in language models. We used the Vision Transformer (ViT) model, which segments the image into patches for encoding [14]. Following the visual tokens, our transformer decoder starts the image caption generation with a start-of-sentence (SOS) token. To handle the multimodal nature of our task, we used bifurcated multi-head self-attention to separately model the interactions between the word and visual embeddings and the relationships among word embeddings themselves. This dual aspect of self-attention allows our models to produce captions that are both visually congruent and linguistically coherent. To model sequentially dependent structures, we masked the self-attention such that each caption token only attends to the preceding caption tokens and the visual tokens.

As shown in Fig. 1, our model also has the inherent flexibility to integrate user prompts as additional features for our image caption generation. If a user prompt is introduced, we initialize the decoding sequence after the visual embeddings and the SOS token, directing the decoder to generate the subsequent responses based on the user prompt. This novel function enhances the performance and human interaction for our multimodal system. We used two generative vision-language models as the backbone of our image captioning module, building on recent advances in vision-language pre-training [17], including the ViT-GPT2 and the Generative Image-to-text Transformer (GIT) models.

We first experimented with the ViT model as our vision encoder and the GPT2 as our text decoder [14]-[15]. The ViT model, designed to process visual data like sentences [14], splits the input image into a series of patches. These patches are then linearly embedded, with positional encodings added to retain the locational context, resulting in a sequence of visual embeddings that serve as an input to our language model. For text generation, the GPT2 model uses a robust transformer architecture to interpret these visual embeddings and generate descriptive captions. The pre-trained GPT2 comes with an extensive understanding of language and allows for relevant text generation that is synched with the visual input when adapted through fine-tuning on our new image-text pairs of real-world walking environments.

We also experimented with the GIT model [16] for image captioning. This unified transformer-based architecture uses the CLIP vision encoder based on contrastive learning between the vision and language modalities [17], which embeds visual tokens in the same embedding space as the language tokens, leading to a more consistent decoding process. The GIT model is pre-trained on a vast dataset comprising billions of vision-language pairs and demonstrates a strong capability to interpret complex visual environments and recognize scene texts without relying on external optical character recognition systems. We optimized the GIT model to provide descriptive navigational information.

We fine-tuned both vision-language models on our new custom dataset using an NVIDIA Tesla A100 GPU for 5 epochs with a learning rate of 5e-5. To reduce the high GPU RAM requirement due to the large model size and to accelerate model training, we used 16-bit floating precision for the numerical optimization on GPU instead of the commonly used 32-bit precision.

C. Speech Synthesis Model

To convert the image captions from our vision-language models into speech for audio feedback to users, we developed a speech synthesis model building on state-of-the-art text-to-

speech models. We used the SpeechT5 transformer encoder-decoder model as our backbone network with a set of modality-specific (speech/text) pre-nets and post-nets [21]. We used the text encoder pre-net to handle text inputs and the speech decoder pre-net and post-net for speech outputs. We used the text encoder pre-net to map the word tokens of our generated captions into a sequence of embeddings as inputs to our encoder. After the encoding, our speech decoder performs a sequence-to-sequence transformation to generate a log mel spectrogram conditioned on the hidden representations from the speech decoder pre-net and refined by the speech decoder post-net. We converted the output log mel spectrogram into an audio waveform via an additional vocoder neural network.

The SpeechT5 model can also convert to diverse voices, with the speaker embeddings as decoder inputs that capture a speaker's unique voice characteristics [21]. We used X-Vector speaker embeddings, which are derived from deep neural networks and have shown to be superior in capturing contextual information from speech frames. Our speaker embeddings were sourced from the CMU ARCTIC speech synthesis database [22]. Our system provides users the ability to customize the output voice by substituting different speaker embeddings. The vocoder we used to generate the final audio waveform is an advanced generative adversarial network (GAN), which is designed to generate high-quality speech waveforms from spectrograms [23].

We designed a custom end-to-end pipeline to integrate our image captioning module with our speech synthesis module. The pipeline starts with our image captioning module, which takes visual input from the environment and extracts image features. Our vision encoder then transforms the features into visual tokens, followed by our text decoder to generate descriptive captions conditioned on an optional user prompt. This textual information is then rendered into speech waveforms by our speech synthesis model to provide users audio feedback of the outputs, allowing the user to interact bidirectionally with the generative AI models and improve system performance by incorporating human cognition in the decision making.

D. User Interface Design

To enable human interaction and real-world practical use, we deployed our new multimodal system on the Gradio platform powered by cloud compute [24]. We configured the virtual environment required to support our models and all necessary scripts to execute the system. Additionally, we embedded our system in a web app based on the Next.js framework and hosted on GitHub Pages. We developed this web app with an emphasis on human interaction and a minimalist user interface design to promote accessibility across diverse user populations. Fig. 2 shows several examples of our user interface in action.

E. Performance Evaluation

We evaluated the performance of our vision-language models using several well-established metrics for text generation, including the Recall-Oriented Understudy for Gisting Evaluation (ROUGE) score. The ROUGE score measures the similarity between the generated text and a set of reference texts, which are typically human annotated. We focused on two common variants: ROUGE-N and ROUGE-L. The ROUGE-N score evaluates the overlap of n-grams, bordering sequences of *n* words, between the generated candidate and the reference text. We also used the ROUGE-L score that measures the longest common subsequence between the candidate and the reference. A higher ROUGE score indicates a better quality of the generated caption in terms of its similarity to the reference image captions that are human annotated. We also used the Word Error Rate (WER), which measures the

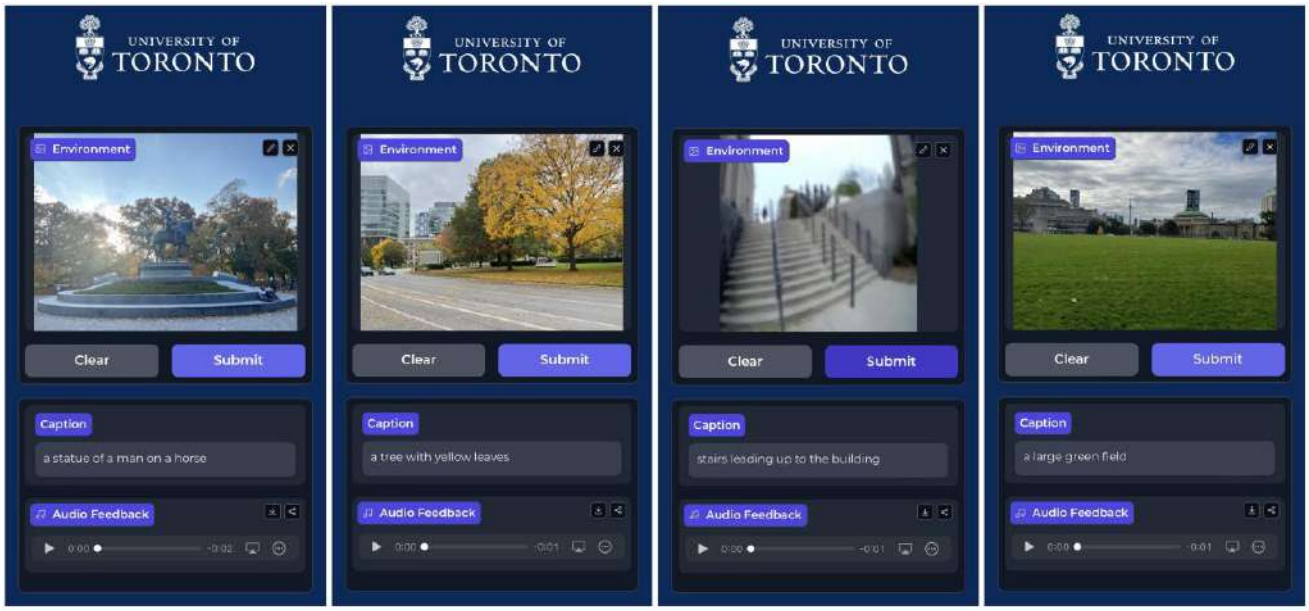


Fig. 2 Our custom-designed user interface to provide audio feedback to users describing the generated image captions by the vision-language models. Our interface also supports feedforward user prompts, allowing for closed-loop human-AI interactions and the ability to augment the decision making of the vision-language models with human cognition.

number of substitution, deletion, and insertion errors in the generated image captions compared to the reference text. It is calculated based on $WER = \frac{(S+D+1)}{N}$, where S is the number of substitutions, D is the number of deletions, and I is the number of insertions needed to transform the generated image captions into the reference text. A lower WER score indicates better system performance.

While our study mainly focused on algorithmic performance, practical usability is critical. To assess real-world applicability, we ran experiments to measure the system response times, user interaction efficiency, and overall reliability in dynamic environments. This strengthens the applicability of our research to robotics and human-computer interaction. We also tested the processing speed of our new system when deployed using cloud computing with different hardware for image captioning and feedback generation. We experimented with four different variants of our system: (1) text-only feedback generation, (2) text and audio feedback generation, (3) text-only feedback generation with user prompts, and (4) text and audio feedback generation with user prompts. We tested each of these four system variants with three different computing hardware configurations (Table 1).

III. Results

Our ViT-GPT2 vision-language model achieved a high ROUGE-1 score of 48.3%, a ROUGE-2 score of 21.8%, and a ROUGE-L score of 43.9% on the MSCOCO Captions dataset. Our GIT vision-language model achieved a low word error rate of 28.1%. In terms of deployed processing time (Table 2), our text-only feedback generation was the fastest across all computing devices, achieving speeds as fast as 2.2 seconds on the NVIDIA A10G GPU. Incorporating audio feedback led to slight increases in processing times (i.e., approximately 1 second). However, including user prompts significantly increased processing times, with average durations ranging from 11.3 to 15.3 seconds on GPU devices. The processing times varied depending on the computing hardware, with the NVIDIA A10G GPU consistently demonstrating faster information processing speeds compared to the Intel Xeon CPU and the NVIDIA T4 GPU. Processing times on the CPUs were approximately 2-3 times longer than those on GPUs.

IV. Discussion

In this study, we developed a novel multimodal vision-language system for egocentric visual perception, with an initial use case on understanding real-world walking environments. We trained a number of state-of-the-art transformer-based encoder-decoder models using 43,055 image-text pairs of scenes for few-shot image captioning. We also custom-designed a new speech synthesis model and a user interface to convert the generated text into speech for audio feedback to users. Most notably, our system uniquely allows for feedforward user prompts to personalize the generated image captions to the individual and immediate needs and preferences of the user (i.e., incorporating human cognition in the decision making), thus optimizing the closed-loop human-AI interactions for understanding and navigating real-world environments. Moving forward, this research has practical implications for robotics and embodied intelligence.

Table 1. The different computing hardware that we used to test our new multimodal vision-language system for image caption generation.

Computing	vCPUs	System RAM	GPU RAM
Intel Xeon CPU	2	16GB	0GB
Nvidia T4 GPU	4	15GB	16GB
Nvidia A10G GPU	4	15GB	24GB

Table 2. The average processing times for our system variants, including (1) text-only feedback generation, (2) text and audio feedback generation, (3) text-only feedback generation with user prompts, and (4) text and audio feedback generation with user prompts. Each system variant was tested with three different computing hardware.

System Variants	CPU	T4 GPU	A10G GPU
Text feedback	7.5s	2.4s	2.2s
Text and audio feedback	8.5s	3.0s	2.6s
Text feedback with user prompts	30.2s	12.5s	11.3s
Text and audio feedback with user prompts	31.1s	15.3s	12.4s

Our system is able to generate image captions with an average length of 10 words while achieving a high ROUGE-L score of 43.9% using the ViT-GPT2 model and a low word error rate of 28.1% using the GIT model. This is in comparison to previous image caption generation systems like [25], which score a bilingual evaluation understudy (BLEU) of 40.3% and a Metric for Evaluation of Translation with Explicit ORdering (METEOR) of 30.7%. One novelty of our system lies in fine-tuning the vision-language models on large-scale data specific to our application, which differs from previous research that simply applied pretrained models [13]. As mentioned by [26], fine-tuning can significantly improve the decision-making of vision-language models in tasks that require fine-grained visual recognition and visual semantic reasoning. These observations are in agreement with our study, which found that, after fine-tuning, the ROUGE score of the ViT-GPT2 model improved from 40.7% to 43.9%.

Regarding applications in robot control [27], our system uniquely includes the human in the loop by providing audio feedback as per the decision-making of the learning algorithm. While research in human-robot systems has included feedforward mechanisms for control [28]-[30], our system also provides feedback to the user. This integration can enhance user awareness compared to other systems, which could be beneficial for acceptance and trustworthiness of intelligent controllers. Our research increases the human interaction by including user prompts to tailor the generated image captions to the individual user needs and preferences, thus augmenting the vision-language models with human cognition. To our knowledge, this is the first study to develop and explore such capabilities for understanding and navigating real-world environments. As noted in [27] and [31], customizing robot behaviors to individual user preferences (e.g., while walking with a robotic prosthetic leg) is important for task performance and our new multimodal system provides a means by which the research community can explore such principles. Overall, a key innovation of our system is its integration of audio feedback and user prompts, enabling personalized captioning for individual needs and preferences. This feature improves the

adaptability for diverse tasks such as adjusting robot walking control strategies based on terrain descriptions.

Despite these developments, our study is not without limitations. For example, one major challenge of our system is the real-time processing requirements of the large vision-language models, with increased computational costs associated with the user prompts and audio feedback generation. Including the user prompts significantly increased processing times, with average durations ranging from 11.3 to 15.3 seconds on GPU devices. This can limit the practical deployment of our system in resource-constrained environments where GPU computational resources are not readily available.

Moving forward, further research is warranted to improve our system efficiency. Optimizing the large vision-language models to reduce computational demands could help broaden the applicability and impact of our research. Exploring the potential for edge computing to handle the information processing locally could decrease the latency and reliance on cloud computing, thus making our system more practical in diverse applications. Moreover, adding an automatic speech recognition model [32] would be beneficial, where the closed-loop human-AI interactions could be performed through conversational feedback. We are also especially interested in using this research to augment the decision-making of vision-language models with human cognition. In summary, here we developed a new multimodal, interactive vision-language system for egocentric visual perception, with an initial focus on understanding real-world walking environments. This system could be used to support research and development in robotics, embodied intelligence, and human-computer interaction.

ACKNOWLEDGMENT

This research study is dedicated to the people of Ukraine in response to Russia's ongoing invasion.

REFERENCES

[1] A. E. Patla, "Understanding the roles of vision in the control of human locomotion," *Gait & Posture*, Feb. 1997.

[2] A. G. Kurbis, D. Kuzmenko, B. Ivanyuk-Skulskiy, A. Mihailidis, and B. Laschowski, "StairNet: Visual recognition of stairs for human-robot locomotion," *BioMedical Engineering OnLine*, Feb. 2024.

[3] D. Kuzmenko, O. Tsepa, A. G. Kurbis, A. Mihailidis, and B. Laschowski, "Efficient visual perception of human-robot walking environments using semi-supervised learning," *IEEE International Conference on Intelligent Robots and Systems (IROS)*, Dec. 2023.

[4] O. Tsepa, R. Burakov, B. Laschowski, and A. Mihailidis, "Continuous prediction of leg kinematics during walking using inertial sensors, smart glasses, and embedded computing," *IEEE International Conference on Robotics and Automation (ICRA)*, Jul. 2023.

[5] B. Ivanyuk-Skulskiy, A. G. Kurbis, A. Mihailidis, and B. Laschowski, "Sequential image classification of human-robot walking environments using temporal neural networks," *IEEE International Conference for Biomedical Robotics and Biomechatronics (BioRob)*, Oct. 2024.

[6] D. Rossos, A. Mihailidis, and B. Laschowski, "AI-powered smart glasses for sensing and recognition of human-robot walking environments," *IEEE International Conference for Biomedical Robotics and Biomechatronics (BioRob)*, Oct. 2024.

[7] A. G. Kurbis, A. Mihailidis, and B. Laschowski, "Development and mobile deployment of a stair recognition system for human-robot locomotion," *IEEE Transactions on Medical Robotics and Bionics*, Jan. 2024.

[8] A. Dashkovets and B. Laschowski, "Reinforcement learning for control of human locomotion in simulation," *IEEE International Conference for Biomedical Robotics and Biomechatronics (BioRob)*, Oct. 2024.

[9] A. S. Chen et al., "Commonsense reasoning for legged robot adaptation with vision-language models," *arXiv*, Jul. 2024.

[10] Y. Hu et al., "Toward general-purpose robots via foundation models: A survey and meta-analysis," *arXiv*, Dec. 2023.

[11] F. Bordes et al., "An Introduction to Vision-Language Modeling," *arXiv*, May 2024.

[12] W. Chen et al., "Vision-language models provide promptable representations for reinforcement learning," *arXiv*, Feb. 2024.

[13] D. Shah, B. Osinski, B. Ichter, S. Levine, "LM-NAV: Robotic navigation with large pre-trained models of language, vision, and action," *Conference on Robot Learning (CoRL)*, 2022.

[14] A. Dosovitskiy, L. Beyer, A. Kolesnikov, D. Weissenborn, X. Zhai, T. Unterthiner, and N. Houlsby, "An image is worth 16x16 words: Transformers for image recognition at scale," *arXiv*, Oct. 2020.

[15] A. Radford, J. Wu, R. Child, D. Luan, D. Amodei, and I. Sutskever, "Language models are unsupervised multitask learners," *OpenAI blog*, 2019.

[16] J. Wang, Z. Yang, X. Hu, L. Li, K. Lin, Z. Gan, and L. Wang, "Git: A generative image-to-text transformer for vision and language," *arXiv*, May 2022.

[17] A. Radford, J. W. Kim, C. Hallacy, A. Ramesh, G. Goh, S. Agarwal, and I. Sutskever, "Learning transferable visual models from natural language supervision," *International Conference on Machine Learning (ICML)*, Feb. 2021.

[18] X. Chen, H. Fang, T. Y. Lin, R. Vedantam, S. Gupta, P. Dollár, and C. L. Zitnick, "Microsoft COCO captions: Data collection and evaluation server," *arXiv*, Apr. 2015.

[19] K. Xu, J. Ba, R. Kiros, K. Cho, A. Courville, R. Salakhudinov, and Y. Bengio, "Show, attend and tell: Neural image caption generation with visual attention," *International Conference on Machine Learning (ICML)*, 2015.

[20] E. Kıcıman, R. Ness, A. Sharma, and C. Tan, "Causal reasoning and large language models: Opening a new frontier for causality," *arXiv*, Apr. 2023.

[21] J. Ao, R. Wang, L. Zhou, C. Wang, S. Ren, Y. Wu, and F. Wei, "SpeechT5: Unified-modal encoder-decoder pre-training for spoken language processing," *arXiv*, Oct. 2021.

[22] J. Kominek and A. W. Black, "The CMU arctic speech databases," *ISCA Workshop on Speech Synthesis*, 2004.

[23] J. Kong, J. Kim, and J. Bae, "HiFi-GAN: Generative adversarial networks for efficient and high-fidelity speech synthesis," *Advances in Neural Information Processing Systems (NeurIPS)*, 2020.

[24] A. Abid et al., "Gradio: Hassle-free sharing and testing of ML models in the wild," *arXiv*, Jun. 2019.

[25] Z. Y. Dou et al., "Coarse-to-fine vision-language pre-training with fusion in the backbone," *Advances in Neural Information Processing Systems (NeurIPS)*, 2022.

[26] Y. Zhai et al., "Fine-tuning large vision-language models as decision-making agents via reinforcement learning," *arXiv*, May 2024.

[27] R. Gehlhar et al., "A review of current state-of-the-art control methods for lower-limb powered prostheses," *Annual Reviews in Control*, May 2023.

[28] J. B. Thomas and B. Laschowski, "Development of a real-time neural controller using an EMG-driven musculoskeletal model," *bioRxiv*, Dec. 2024.

[29] O. Shevchenko, S. Yeremeieva, and B. Laschowski, "Comparative analysis of neural decoding algorithms for brain-machine interfaces," *bioRxiv*, Dec. 2024.

[30] A. Dempster and B. Laschowski, "Domain adaptation for decoding brain dynamics using mixture models," *bioRxiv*, 2025.

[31] Y. J. Wang, B. Zhang, J. Chen, and K. Sreenath, "Prompt a robot to walk with large language models," *arXiv*, Sept. 2023.

[32] M. Benzeghiba et al., "Automatic speech recognition and speech variability: A Review," *Speech Communication*, Feb. 2007.

A Deep Learning Framework with Domain Generalization and Few-Shot Learning for Locomotion Mode Classification Across Users, Sessions, and Prostheses

Eugenio Anselmino
Department of Excellence in Robotics and AI, Scuola Superiore Sant'Anna, The BioRobotics Institute
Pisa, Italy
eugenio.anselmino@santannapisa.it

Ann M. Simon
Shirley Ryan AbilityLab
Department of PhysicalMedicine and Rehabilitation, Northwestern University
Chicago, USA
asimon@sralab.org

Levi J. Hargrove
Shirley Ryan AbilityLab
Departments of PhysicalMedicine and Rehabilitation and Biomedical Engineering, Northwestern University
Chicago, USA
ORCID: 0000-0002-1705-0050

***Abstract*— Transfemoral amputees don and doff their prostheses at least daily, making inter-session classification performance important for clinical implementation of locomotion mode classification algorithms. Here, we present a deep-learning framework based on domain-adversarial training and few-shot learning fine-tuning to classify locomotion modes in unseen sessions or subjects' data across different prosthesis models. We validated the approach with a leave-one-session-out analysis repeated five times and made comparisons to a prosthesis-specific classifier. The dataset was created by merging data from two different prosthesis models (Vanderbilt University, VU, Gen 2 and Gen 3 powered knee-ankle prostheses), for a total of 31 sessions acquired across multiple days from 11 subjects. Subjects performed five locomotion tasks: level walking, incline and decline walking, and stair ascent and descent. Since transitions between different locomotion modes happen at different gait events, the analyses have been repeated for both heel-strike (HS) and toe-off (TO) events. At HS events, the proposed approach achieves a median f1-score of 99.12% and 92.41% on VU Gen 2 and Gen 3 prostheses respectively. At TO events, the proposed approach reaches a median f1-score of 96.83% with VU Gen 2 and 94.36% with VU Gen 3. The proposed framework is a promising solution for locomotion classification on data of previously unseen sessions or subjects, allowing classification on multiple prosthesis models.**

Keywords—locomotion mode classification, intention decoding, lower limb prostheses, deep learning

I. INTRODUCTION

Lower limb amputations severely impact the quality of life of a person, reducing their independence and mobility [1]. Individuals with an amputation present a less efficient [2], slower, and less stable gait when compared to non-impaired people [3]. These deficits are often exacerbated during the execution of challenging tasks such as stairs and ramps ascent and descent [4]. Powered lower limb prostheses can improve amputees' mobility due to the device's ability to provide net mechanical energy, mimicking the biomechanical functionality of biological joints across different locomotion tasks [5], [6], [7], [8]. These devices effectively assist amputees with various movements, but the process of switching between modes is not seamless. Changing locomotion mode with a key-fob or via mechanical movements can help achieve reliable mode transitions, but it can be perceived as unnatural and cumbersome.

Machine learning (ML) and deep learning (DL) algorithms have shown promising results in locomotion mode classification. These algorithms predict users' intended movements by interpreting prosthesis sensor signals [9], [10]. Both ML and DL approaches have achieved high classification accuracies in laboratory settings when trained on subject-specific data[10], [11]. However, these approaches are limited by their need for properly labelled training datasets from each end user. This limitation is particularly significant because achieving robust performance requires data collection across all desired locomotion activities and the transitions between them, which can be burdensome to collect [12].

To mitigate large subject-dependent training datasets, domain-generalization (DG) and few-shot learning (FSL) strategies can be adopted. DG aims to learn from multiple related but distinct domains (e.g., subjects) in such a way that the model can generalize to a previously unseen domain (e.g., unseen sessions or subjects) [13]. FSL, instead, aims to maximize the learning with limited datasets by transforming the learning process into a similarity comparison with one or more data points from previously seen domains [14]. Recently, both DG and FSL approaches have gained popularity in upper-limb prosthesis control, especially with electromyographic (EMG) signals as they help mitigate EMG's intrinsic subject dependency and temporal instability. DG approaches outperform traditional DL methods in cross-subject hand gesture classification, reaching accuracies similar to subject-specific approaches [15]. Similarly, DG-based DL models have improved the robustness of hand gesture classifiers across sessions held on different days with the same subject[16]. FSL approaches have shown comparable success, achieving convergence with only 20

This work is supported by the NIH through Grant R01HD108554.

TABLE I. POSSIBLE TRANSITIONS ACCORDING TO THE GAIT EVENT AND CURRENT LOCOMOTION MODE.

		Locomotion mode				
		LW	***SA***	***SD***	***RA***	***RD***
Gait event	***HS***	LW, SD, RA, RD		LW, SD	LW, RA	LW, RD
	TO	LW, SA				
	FF		LW			

samples from the target dataset[17] and outperforming traditional methods when dealing with limited datasets [18]

Here, we present a DL approach for transfemoral powered prostheses to classify five locomotion modalities: level walking (LW), stair ascending (SA), stair descending (SD), ramp ascending (RA), and ramp descending (RD). The approach uses signals from onboard prosthesis sensors and combines both DG and FSL methods to improve inter-session accuracy. We validated the approach using a dataset comprising 31 sessions from 11 different subjects, collected using two different prosthesis models: the Vanderbilt University (VU) 2nd and 3rd-generation powered knee-ankle prostheses [19].

II. MATERIALS AND METHODS

A. Dataset

Detailed experimental protocols for data acquisition are described in [20] for the VU Gen 2 prosthesis and in [21] for the VU Gen 3 prosthesis. All subjects were unilateral transfemoral amputees and experienced prosthesis users. The subjects performed locomotion circuits including walking on level ground, ascending and descending a 10° incline, and ascending or descending a 5 or 6-step staircase. During level walking, subjects performed multiple starts and stops, turns, and shuffling to increase step variability. For both prosthesis models, an experimenter managed locomotion mode transitions using a key fob, with each transition occurring 90 ms after heel strike (HS), flat foot (FF), or toe-off (TO) events [22]. The possible transitions are shown in Table 1.

The dataset comprises 24 acquisition sessions from 4 subjects using the VU Gen 2 prosthesis and 7 acquisition sessions from 7 subjects using the VU Gen 3 prosthesis. Data from both prostheses were merged into two single datasets, one for TO and one for HS events. FF events were excluded since the prosthesis always transitions from SA to LW, eliminating the need for classification. To enable DL models to work with both prosthesis generations, we selected only common signals between them: knee and ankle joint angles, velocities, and currents; leg anteroposterior, mediolateral, and vertical accelerations and angular velocities; shank and thigh angles; knee and ankle reference torques; and vertical load.

Signals from 210 ms before to 90 ms after the relevant gait events were selected and downsampled from 1 kHz to 200 Hz for computational efficiency. Information regarding dataset composition before the data augmentation and balancing processes is shown in Table 2.

Before the model training phase, one session was removed from the dataset and used as test dataset. We adopted dataset augmentation techniques on the training dataset to reduce overfitting. We created 2 additional copies of the TO and HS datasets by temporally shifting the input window in a range of ±10 ms. We created 10 additional copies by scaling the original datasets and 8 additional copies by scaling the shifted datasets. During the scaling process, each channel was multiplied by a factor sampled from a uniform distribution between 0.95 and 1.05. Data have been normalized on a channel basis using robust scaling, with a scaling range between the 2^{nd} and 98^{th} percentiles.

To maintain balance during the training process, we selected 20,000 steps for each prosthesis model for SD, RA, and RD locomotion modes in the HS dataset. Since LW steps are more prevalent both in the dataset and in real-world scenarios, we selected 30,000 steps for the LW class for each prosthesis model. This approach helps retain more variability for the dominant class. Similarly, for the TO dataset, we selected 25,000 steps from the LW class and 20,000 from the SA class for each prosthesis model. If a class had fewer steps than the desired threshold, we generated additional copies by adding zero-centered Gaussian noise ($\sigma = 0.025$). During testing, data were scaled and normalized as per the training dataset. The fine-tune dataset is extracted from the test dataset according to the process presented in Section B.2). More than 50 steps were always present for SD, RD, and RA classes and more than 90 for the SA class. The LW class was dominant in both TO and HS datasets, with more than 1000 steps.

B. Classification approach

We leveraged both DG and FSL approaches to develop a neural network capable of working on multiple prosthesis models and generalizing on previously unseen acquisition sessions or subjects. The training approach is based on two sequential steps: the first one leverages DG to pre-train the neural network; the second adopts FSL to fine-tune the network using a small portion of the test dataset. The process is repeated to create two distinct neural networks, one for the classification at HS and one for classification at TO.

1) Pre-training network (DANN-VAE)

A neural network with a hybrid structure between Domain-Adversarial-Neural-Network (DANN) [23] and a Variational-Auto-Encoder (VAE) [24] was adopted to pretrain the network (Fig 1a.) The main objective of the DANN-VAE is

TABLE II. DATASET COMPOSITION.

Prosthesis	***Total steps***	***Transitions***	***Steady-state***	***LW***	***RA***	***RD***	***SA***	***SD***
HS, VU Gen 2	32990	1377	31613	27808	1664	1969		1549
HS, VU Gen 3	11780	1562	10218	10061	445	556		718
TO, VU Gen 2	43469	7115	36294	40283			3186	
TO, VU Gen 3	11051	1612	9434	10282			769	

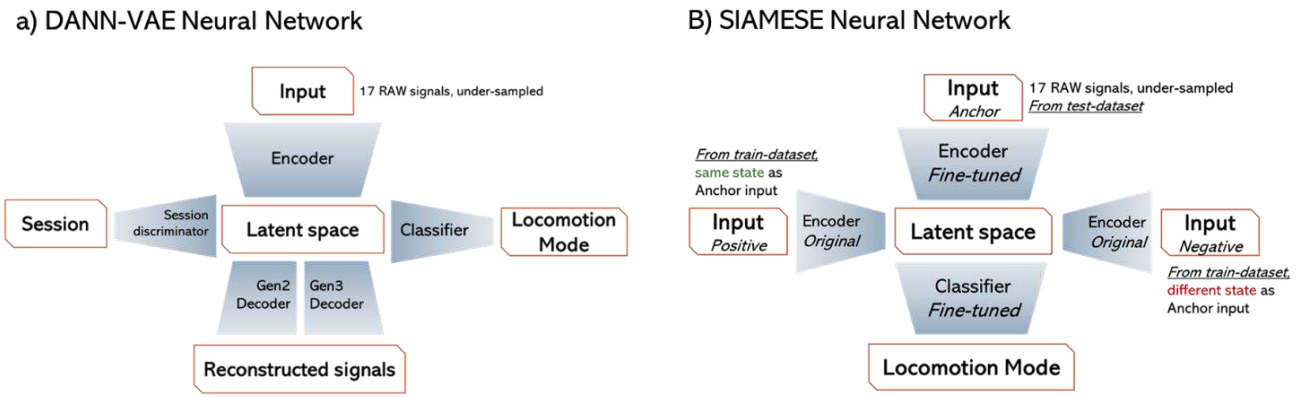


Fig. 1. Overview of the neural network structure used for the pre-training (a) and fine-tuning (b) processes.

to promote the Encoder sub-model to extract features from the input that allow the locomotion mode classification, via the Classifier sub-model, and the reconstruction of the input signals, via the Gen 2 and Gen 3 Decoders. Concurrently, the gradient from the Session discriminator is reversed to encourage the Encoder to extract session-independent features, as explained in [23].

The *Encoder sub-model* consists of an input layer for the time series, a corruptor layer that applies additive zero-centered Gaussian noise (σ=0.05), a sequence of three stride convolution layers with batch normalization and dropout, a flattening layer, and a latent encoder layer. In convolution layers, we used two-dimensional kernels to combine movement-related information across channels and temporal downsampling to encourage learning time-invariant features. Each convolutional layer used 256 filters, Leaky ReLU activations (α=0.2), and L2 normalization (λ=10-6). For the latent layer, we followed the implementation of [24], to map the extracted features to an 80-dimensional manifold.

The *Classifier and Session discriminator sub-models* have the same architecture. They consist of a corruptor layer (σ=0.05), a 64-neuron dense layer with batch normalization and Leaky ReLU activation (α=0.2), a dropout layer, and an output layer with softmax activation. Accordingly to [23], the loss of the Session discriminator is inverted for the training of the Encoder to promote the learning of session-invariant features.

Each *Decoder sub-model* consists of a corruptor layer (σ=0.05), a dense layer with batch normalization and Leaky ReLU activation (α=0.2), followed by a dropout layer and a reshape layer (features, 1, filters), and two stride transposed convolutional layers. The transposed convolutional layers are responsible for expanding the feature compressed by the Encoder to match the original input shape. Each transposed convolution layer uses 256 filters and two-dimensional kernels and is combined with batch normalization and dropout; the first layer uses a Leaky ReLU activation (α=0.2), and the second layer uses a Hyperbolic tangent activation. The hyperparameters σ, α, and λ of the sub-models have been selected in accordance with [25].

2) Fine-tuning network (SIAMESE)

To fine-tune the Encoder and Classifier sub-models, five samples from each prosthesis state are randomly selected from the test dataset. A prosthesis state is intended as the combination of locomotion modes before and after the gait event of interest (e.g., from LW to LW, from LW to RD, etc.). Next, the same dataset augmentation techniques adopted for the training dataset are applied to the fine-tune dataset. For the LW-to-LW state (i.e., steady-state level walking), 5 additional samples have been selected to retain the variability of the dominant class. The number of samples was selected to be low enough to be acquired with a very short calibration session; in this case, performing a circuit involving the desired locomotion modes 5 times.

The fine-tuning is a two-step process and the SIAMESE neural network used for it is shown in Fig. 1b. Firstly, the Encoder sub-model is finetuned using the approach described in [26]: an anchor sample from the fine-tune dataset is given as input to the Encoder, whose output is compared via the triplet loss with the output of two samples from the training dataset, one with the same and one with a different state. Secondly, the Classifier is fine-tuned on the fine-tune dataset only. Lastly, the fine-tuned DANN (DANN FT) is recompiled using the fine-tuned Encoder and Classifier sub-models.

C. Performed tests

Our approach is tested on the HS and TO datasets using a leave-one-session-out approach: one session is used for testing and the others for training. The testing protocol is repeated 5 times. The results of the performed tests are reported using the median f1-score and interquartile range (IQR). The Wilcoxon signed rank test (WSRT) was performed to compare different conditions. The approach is compared with a basic neural network composed of the Encoder, Decoder, and Classifier sub-model (VAE network). The models have been implemented in Keras v.3.4.1. Tests have been performed on a server (256 GB RAM, NVIDIA RTX A6000) using custom Python scripts (Python v.3.9.19).

During the *pretraining phase*, the DANN-VAE network is trained with a batch of 256 for 30 epochs, using the AdamW optimizer [27] with a learning rate of 0.0001 and an exponential decay rate for the 1st-moment estimates of 0.5. To promote training stability a warmup approach [28] has been adopted for the learning rate, starting from 0.00001 and reaching 0.0001 after 3 epochs.

During the *fine-tuning phase*, the Encoder is fine-tuned with a batch of 32 samples for 10 epochs, using the Adam optimizer with a learning rate of 0.0001 and an exponential decay rate for the 1st-moment estimates of 0.5. The Classifier

is fine-tuned for 10 epochs, using a 32-sample batch and the Adam optimizer with a learning rate of 0.00001 and an exponential decay rate for the 1st-moment estimates of 0.5.

The VAE network is trained for 50 epochs using data from a single prosthesis model, with a batch of 256. We used the

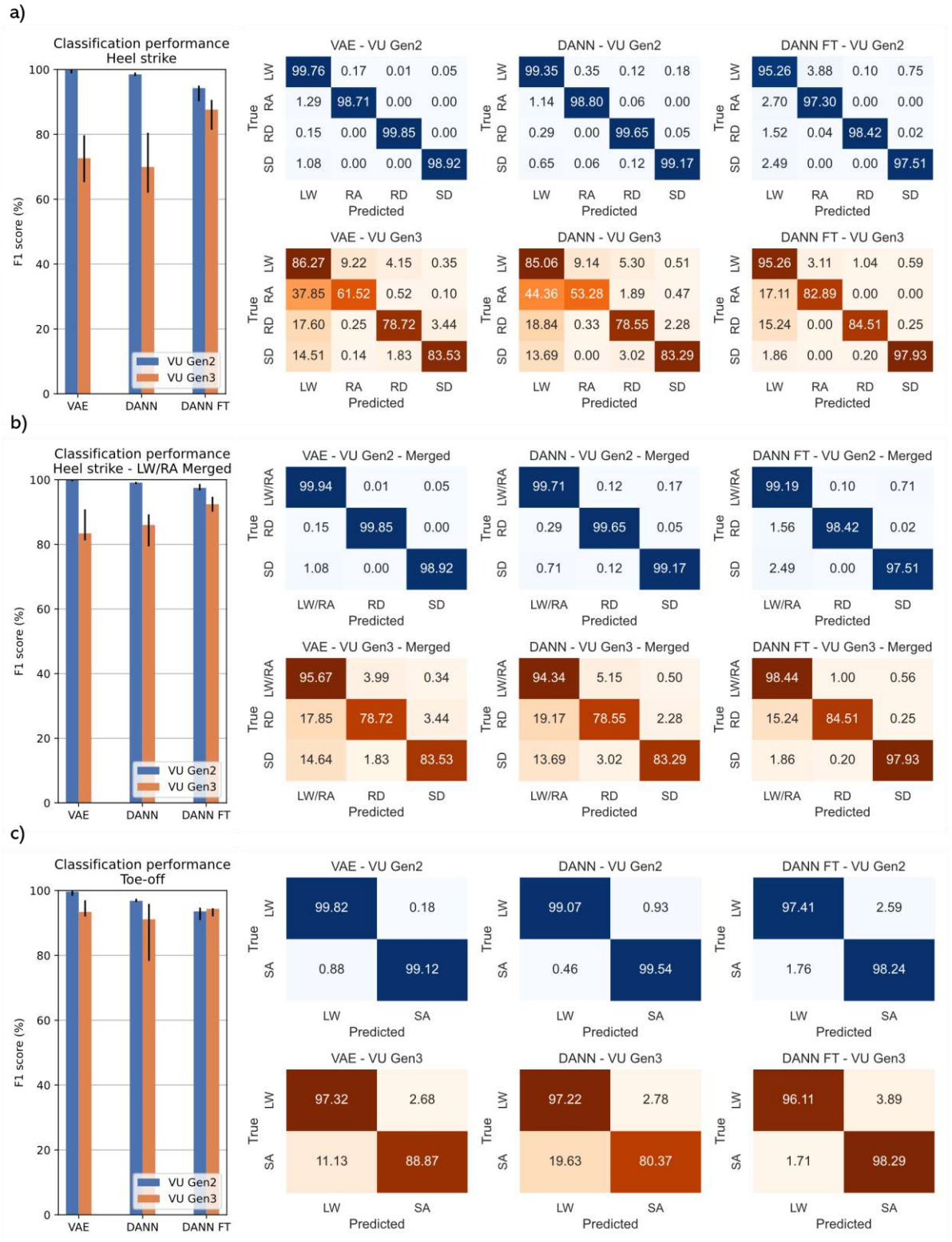


Fig. 2. Performance of VAE, DANN, and DANN FT on the HS dataset without merging LW and RA classes (a); the HS dataset merging LW and RA classes (b); the TO dataset (c). The bar plots show the median performance (F1-score, IQR) across the population. The confusion matrixes show the global accuracy on the population (i.e., each matrix is obtained by summing the population confusion matrixes and dividing by the total number of steps of the class).

Adam optimizer with a learning rate of 0.0001 and an exponential decay rate for the 1st-moment estimates of 0.5.

Notably, the prostheses used the same impedance parameters for the LW and RA activities. Therefore, despite the networks being trained on all the locomotion modes, it is possible to merge the LW and RA classes to improve the classification accuracy, without impacting the devices' usability [29]. Consequently, we present the results both with and without LW and RA classes merged.

III. Results

The accuracies of both the proposed and comparison approaches are different between prosthesis models, with lower accuracy and increased IQR with the VU Gen 3 (WSRT, $p < 0.05$) (Fig. 2). Additionally, on VU Gen 2 data, the tested models resulted in similar performances on steady-state and transition steps (WSRT, $p < 0.05$), while with VU Gen 3, the accuracy on transition steps is lower (WSRT, $p < 0.05$), except for DANN FT on TO dataset (Fig. 3).

Regarding the *VU Gen 2 results* on the HS dataset, if LW and RA classes are kept separated, VAE, DANN, and DANN FT reach median f1-scores above 94% (Fig. 2a, left). VAE and DANN show similar per-class accuracy, while DANN-FT shows a drop in classification performances, especially in the LW class (Figure 2a, right). If the LW and RA classes are merged (Fig. 2b, left), the f1-score of VAE, DANN, and DANN FT networks is above 96%, with the best performer being the VAE with 99.53% (WSRT, $p < 0.05$). The TO dataset results in a similar trend, with VAE, DANN, and DANN FT reaching median f1-scores above 94% (Fig. 2c, left) and VAE being the best performer with a median f1-score of 99.64% (WSRT, $p < 0.05$). The confusion matrixes show similar per-class accuracy between VAE and DANN (WSRT, $p > 0.05$), while DANN-FT shows a drop in classification performances (Fig. 2c, right).

Regarding the *VU Gen 3 results* on the HS dataset, the VAE and DANN approaches show no statistically significant differences in accuracy with and without LW/RA class merging (WSRT, $p > 0.05$). Median accuracies are above 70% with LW and RA separated and 83% with LW and RA merged. The DANN FT reaches a median accuracy of 87.63% without class merging and 92.41% with merging, overperforming both VAE and DANN networks (WSRT, $p < 0.05$) (Fig. 2a, b, left). In general, on VU Gen 3 data, all the proposed networks tend to misclassify RA, RD, and SD classes with LW. The issue is particularly prominent in the RA class. The per-class performance increases noticeably when adopting fine-tuning, especially in the SD class, where the accuracy reaches 97.93% (Fig. 2a, b, right). On the TO dataset, VAE, DANN, and DANN FT show no statistically significant differences in performances (WSRT, $p > 0.05$), reaching 93.40%, 91.14%, and 94.36% median f1-scores respectively (Fig. 2c, left). It is important to point out that DANN FT presents noticeably improved performances in classifying the SA class, reaching a 98.29% accuracy against 88.87% of VAE and 80.37% of DANN (Fig. 2c, right).

IV. Discussion

We developed and tested a DL approach using DG and FSL to classify locomotion intent across previously unseen acquisition sessions (or subjects) and multiple prosthesis models. This inter-session classification is crucial for clinical implementation, as users don and doff the prosthesis at least daily. Reducing the amount of data required for algorithm recalibration is essential to reduce the subject's burden and enhance usability of powered prostheses. Furthermore, the proposed approach's compatibility with multiple prosthesis models provides a strong foundation for further prosthesis-specific classification models.

Despite their similarity, data from the two prosthesis models present differences which are reflected in the results. At HS, the DANN FT network reached median f1-scores above 92% with VU Gen 3 prosthesis and above 97% with VU Gen 2. At TO, both VAE and DANN networks reach higher median f1-scores on VU Gen 2 data. HS results are consistent across the VAE, DANN, and DANN FT models on the VU Gen 2 dataset; DANN FT largely outperforms the

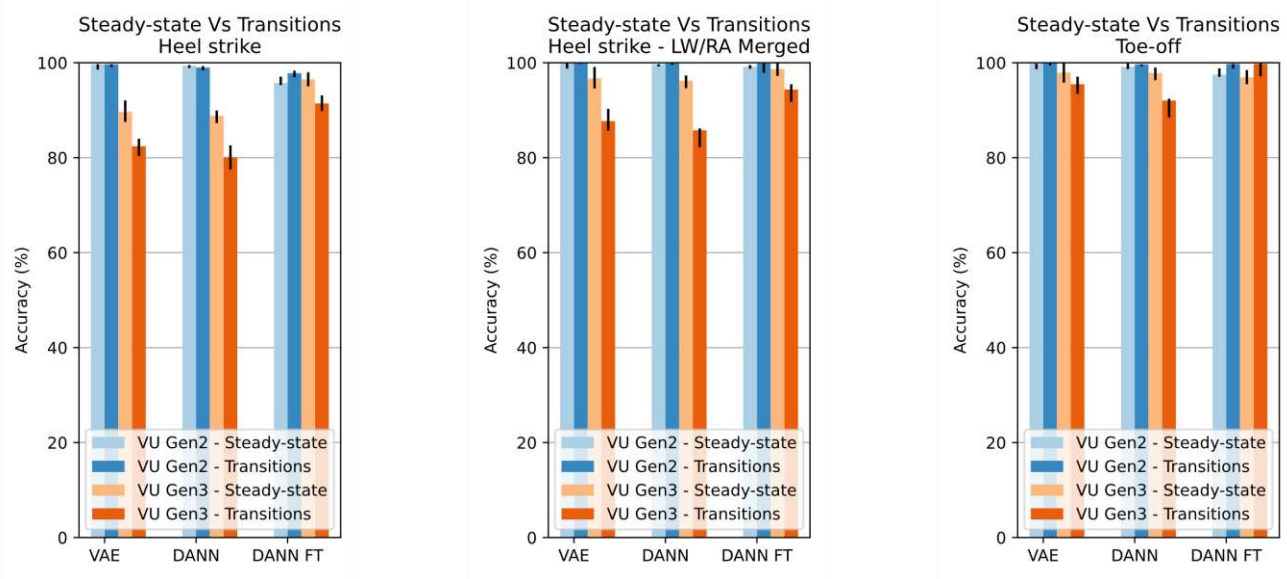


Fig. 3. Accuracy (median, IQR) of VAE, DANN, and DANN FT networks on steady-state and transition steps.

other two approaches with VU Gen 3 data instead. Similarly, DANN FT shows better accuracy in the SA class on the VU Gen 3 TO dataset, while performances drop slightly on the VU Gen 2 dataset. Such a different behavior may be traced to two factors: data quantity and data variability. The VU Gen 2 HS dataset is three times larger than the VU Gen 3 dataset but presents a comparable amount of transition steps, which are more complex to classify. Fig. 3 suggests that a larger dataset can help achieve higher accuracies on transition steps. Additionally, both HS and TO VU Gen 2 datasets contain multiple sessions per subject, promoting better inter-session accuracy since data from the tested subjects are present in the training dataset. Ultimately, session and prosthesis-specific approaches may achieve comparable performances when the dataset is large enough. Specifically, the VU Gen 2 data results suggest that fine-tuning may be avoided when multiple sessions per subject are available in large datasets. As suggested in the literature [18], fine-tuning can noticeably improve global and per-class accuracies when the dataset is smaller and more variable instead, as shown by the results on the HS and TO VU Gen 3 datasets.

The need for a common set of onboard sensors between the different prosthesis models represents the main limitation of the work, preventing the possibility of leveraging additional signals in newer prostheses. Additionally, differences in sensor placement and orientation require a fine inspection of data to ensure coherence and reduce possible errors. In a real-time scenario, signal transformation to match the neural network's expected input must be considered, potentially adding processing time.

In conclusion, the proposed approach successfully created a common base classifier for multiple prosthesis models, achieving accuracies above 92% and up to 99% on data from unseen sessions or subjects. This classifier can be further adapted via fine-tuning for small or highly variable datasets, enhancing both overall and per-class accuracies with only a limited fine-tuning dataset. Specifically, the fine-tuning samples used in this work can be acquired by performing a circuit including the target locomotion modes only five times. Additionally, the classifier's accuracies can be further improved by implementing prosthesis-aware constraints, which limit the possible classification outcomes based on the current prosthesis state.

We will next explore the real-time portability of the proposed approach, by assessing its classification and inference performances online with a powered prosthesis. Additionally, the approach will be tested on other prosthesis models to assess its generalizability.

REFERENCES

[1] F. Barberi, E. Anselmino, A. Mazzoni, M. Goldfarb, and S. Micera, "Toward the Development of User-Centered Neurointegrated Lower Limb Prostheses," *IEEE Rev Biomed Eng*, vol. 17, pp. 212–228, 2024, doi: 10.1109/RBME.2023.3309328.

[2] R. Waters, J. Perry, D. Antonelli, and H. Hislop, "Energy cost of walking of amputees," *J Bone Joint Surg*, vol. 58, no. 1, pp. 42–46, Jan. 1976, doi: 10.2106/00004623-197658010-00007.

[3] W. C. Miller, A. B. Deathe, M. Speechley, and J. Koval, "The influence of falling, fear of falling, and balance confidence on prosthetic mobility and social activity among individuals with a lower extremity amputation," *Arch Phys Med Rehabil*, vol. 82, no. 9, pp. 1238–1244, Sep. 2001, doi: 10.1053/apmr.2001.25079.

[4] L. Nolan, A. Wit, K. Dudziñski, A. Lees, M. Lake, and M. Wychowañski, "Adjustments in gait symmetry with walking speed in trans-femoral and trans-tibial amputees," *Gait Posture*, vol. 17, no. 2, pp. 142–151, Apr. 2003, doi: 10.1016/S0966-6362(02)00066-8.

[5] D. H. Gates, J. M. Aldridge, and J. M. Wilken, "Kinematic comparison of walking on uneven ground using powered and unpowered prostheses," *Clinical Biomechanics*, vol. 28, no. 4, pp. 467–472, 2013, doi: 10.1016/j.clinbiomech.2013.03.005.

[6] E. R. Esposito, J. M. A. Whitehead, and J. M. Wilken, "Step-to-step transition work during level and inclined walking using passive and powered ankle-foot prostheses," *Prosthet Orthot Int*, vol. 40, no. 3, pp. 311–319, Jun. 2016, doi: 10.1177/0309364614564021.

[7] A. M. Simon, N. P. Fey, K. A. Ingraham, S. B. Finucane, E. G. Halsne, and L. J. Hargrove, "Improved Weight-Bearing Symmetry for Transfemoral Amputees During Standing Up and Sitting Down With a Powered Knee-Ankle Prosthesis," *Arch Phys Med Rehabil*, vol. 97, no. 7, pp. 1100–1106, Jul. 2016, doi: 10.1016/j.apmr.2015.11.006.

[8] B. E. Lawson, H. A. Varol, A. Huff, E. Erdemir, and M. Goldfarb, "Control of Stair Ascent and Descent With a Powered Transfemoral Prosthesis," *IEEE Transactions on Neural Systems and Rehabilitation Engineering*, vol. 21, no. 3, pp. 466–473, May 2013, doi: 10.1109/TNSRE.2012.2225640.

[9] L. J. Hargrove *et al.*, "Intuitive control of a powered prosthetic leg during ambulation: A randomized clinical trial," *JAMA - Journal of the American Medical Association*, vol. 313, no. 22, pp. 2244–2252, Jun. 2015, doi: 10.1001/jama.2015.4527.

[10] F. Barberi *et al.*, "Early decoding of walking tasks with minimal set of EMG channels," *J Neural Eng*, Mar. 2023, doi: 10.1088/1741-2552/acc901.

[11] A. Vijayvargiya, B. Singh, R. Kumar, U. Desai, and J. Hemanth, "Hybrid Deep Learning Approaches for sEMG Signal-Based Lower Limb Activity Recognition," *Math Probl Eng*, vol. 2022, pp. 1–12, Nov. 2022, doi: 10.1155/2022/3321810.

[12] D. Xu and Q. Wang, "Noninvasive Human-Prosthesis Interfaces for Locomotion Intent Recognition: A Review," Jan. 01, 2021, *American Association for the Advancement of Science*. doi: 10.34133/2021/9863761.

[13] G. Blanchard, G. Lee, and C. Scott, "Generalizing from Several Related Classification Tasks to a New Unlabeled Sample."

[14] G. Koch, R. Zemel, and R. Salakhutdinov, “Siamese Neural Networks for One-shot Image Recognition.”

[15] E. Campbell, A. Phinyomark, and E. Scheme, “Deep Cross-User Models Reduce the Training Burden in Myoelectric Control,” *Front Neurosci*, vol. 15, May 2021, doi: 10.3389/fnins.2021.657958.

[16] P. Shi, X. Zhang, W. Li, and H. Yu, “Improving the Robustness and Adaptability of sEMG-Based Pattern Recognition Using Deep Domain Adaptation,” *IEEE J Biomed Health Inform*, vol. 26, no. 11, pp. 5450–5460, Nov. 2022, doi: 10.1109/JBHI.2022.3197831.

[17] S. Tam, M. Boukadoum, A. Campeau-Lecours, and B. Gosselin, “Siamese Convolutional Neural Network and Few-Shot Learning for Embedded Gesture Recognition,” in *20th IEEE International Interregional NEWCAS Conference, NEWCAS 2022 - Proceedings*, Institute of Electrical and Electronics Engineers Inc., 2022, pp. 114–118. doi: 10.1109/NEWCAS52662.2022.9901391.

[18] R. V. Godoy, B. Guan, F. Sanches, A. Dwivedi, and M. Liarokapis, “Electromyography Based Gesture Decoding Employing Few-Shot Learning, Transfer Learning, and Training From Scratch,” *IEEE Access*, vol. 11, pp. 104142–104154, 2023, doi: 10.1109/ACCESS.2023.3317956.

[19] F. Sup, H. A. Varol, J. Mitchell, T. J. Withrow, and M. Goldfarb, “Preliminary Evaluations of a Self-Contained Anthropomorphic Transfemoral Prosthesis,” *IEEE/ASME Transactions on Mechatronics*, vol. 14, no. 6, pp. 667–676, Dec. 2009, doi: 10.1109/TMECH.2009.2032688.

[20] A. M. Simon, E. A. Seyforth, and L. J. Hargrove, “Across-Day Lower Limb Pattern Recognition Performance of a Powered Knee-Ankle Prosthesis,” in *2018 7th IEEE International Conference on Biomedical Robotics and Biomechatronics (Biorob)*, IEEE, Aug. 2018, pp. 242–247. doi: 10.1109/BIOROB.2018.8487836.

[21] J. A. Spanias, A. M. Simon, S. B. Finucane, E. J. Perreault, and L. J. Hargrove, “Online adaptive neural control of a robotic lower limb prosthesis,” *J Neural Eng*, vol. 15, no. 1, p. 016015, Feb. 2018, doi: 10.1088/1741-2552/aa92a8.

[22] A. M. Simon *et al.*, “Delaying Ambulation Mode Transition Decisions Improves Accuracy of a Flexible Control System for Powered Knee-Ankle Prosthesis,” *IEEE Transactions on Neural Systems and Rehabilitation Engineering*, vol. 25, no. 8, pp. 1164–1171, Aug. 2017, doi: 10.1109/TNSRE.2016.2613020.

[23] Y. Ganin *et al.*, “Domain-Adversarial Training of Neural Networks,” 2016.

[24] D. P. Kingma and M. Welling, “Auto-Encoding Variational Bayes,” Dec. 2013, [Online]. Available: http://arxiv.org/abs/1312.6114

[25] B. H. Hu, “Applying Sensor Fusion and Deep Learning to Discover Robust Representations of Movement Intention for Powered Leg Prostheses,” Northwestern University, Evanston, 2019.

[26] X. Dong and J. Shen, “Triplet Loss in Siamese Network for Object Tracking.” [Online]. Available: http://github.com/shenjianbing/TripletTracking

[27] I. Loshchilov and F. Hutter, “Decoupled Weight Decay Regularization,” Nov. 2017, [Online]. Available: http://arxiv.org/abs/1711.05101

[28] D. S. Kalra and M. Barkeshli, “Why Warmup the Learning Rate? Underlying Mechanisms and Improvements,” Jun. 2024, [Online]. Available: http://arxiv.org/abs/2406.09405

[29] A. J. Young, A. Simon, and L. J. Hargrove, “An intent recognition strategy for transfemoral amputee ambulation across different locomotion modes,” in *2013 35th Annual International Conference of the IEEE Engineering in Medicine and Biology Society (EMBC)*, IEEE, Jul. 2013, pp. 1587–1590. doi: 10.1109/EMBC.2013.6609818.

Comparative Analysis of Neural Decoding Algorithms for Brain-Machine Interfaces

Olena Shevchenko, Sofiia Yeremeieva, and Brokoslaw Laschowski

Abstract – **Accurate neural decoding of brain dynamics remains an open challenge in brain-machine interfaces. While various signal processing, feature extraction, and classification algorithms have been proposed, a systematic comparison of these is lacking. Accordingly, here we conducted one of the largest comparative studies to evaluate different combinations of state-of-the-art algorithms for motor neural decoding in order to find the optimal combination. We studied three signal processing methods (i.e., artifact subspace reconstruction, surface Laplacian filtering, and data normalization), four feature extractors (i.e., common spatial patterns, independent component analysis, short-time Fourier transform, and no feature extraction), and four machine learning classifiers (i.e., support vector machine, linear discriminant analysis, convolutional neural networks, and long short-term memory networks). Using a large-scale EEG dataset, we optimized each combination for individual subjects (i.e., resulting in 672 total experiments) and evaluated performance based on classification accuracy. We also compared the computational and memory storage requirements, which are important for real-time embedded computing. Our comparative analysis provides novel insights that can help inform the design of next-generation neural decoding algorithms for brain-machine interfaces.**

I. Introduction

Brain-machine interfaces have potential to allow patients with physical disabilities to interact with and control robots and computers via neuroimaging techniques such as electroencephalography (EEG). EEG can capture the brain's neural dynamics associated with imagined limb movements, inducing specific oscillatory EEG processes such as desynchronisation of mu (8-12 Hz) and beta (16-30 Hz) rhythms, which reflect motor planning and execution. After task competition (i.e., resting state condition), these rhythms exhibit a synchronization, making EEG a powerful tool for decoding neural signals [1]. However, accurately decoding brain dynamics into control commands remains an open challenge. For example, EEG signals are prone to noise from eye movements and muscle activity [2]. Additionally, their low signal-to-noise ratio requires advanced signal processing and feature extraction to enhance data fidelity and extract meaningful neural information.

Different neural decoding algorithms for brain-machine interfaces have been proposed. For example, [3] developed a two-class neural decoder, comparing H∞ filters and artifact subspace reconstruction (ASR) with four different classifiers, including support vector machine (SVM), minimum distance to mean (MDM), MDM with filter, and linear discriminant analysis (LDA). In pseudo-online cross-validation experiments, they achieved accuracies of 66.2% for a generic model and 69.6% for a personalized model, with H∞ filter and MDM filter yielding the best neural decoding performance.

In terms of deep learning, [4] used recurrent long short-term memory (LSTM) neural networks, comparing them to LDA classifiers. After a two-step signal preprocessing using ASR and independent component analysis (ICA), the authors extracted neural correlates from 1-40 Hz frequency bands. The LSTM neural network outperformed their LDA model during online evaluation, achieving accuracies of 83.3%, 80.5%, and 75.3%. Similarly, [5] compared common spatial patterns (CSP) with LDA and a convolutional neural network (CNN) classifier, finding the CNN significantly outperformed CSP with an LDA model by 15-18%.

Our review of the literature revealed a wide variety of signal processing, feature extraction, and machine learning classification models used for motor neural decoding for brain-machine interfaces, with most studies creating their own algorithms. An unanswered question is: "what is the optimal combination of these algorithms to decode neural dynamics from the brain"? To help answer this question, here we conducted one of the largest comparative studies to develop and test different neural decoding algorithms (i.e., consisting of 48 combinations of state-of-the-art signal processing, feature extraction, and machine learning classifiers, each optimized for individual subjects) using a large-scale EEG dataset to determine the optimal combination for brain-machine interfaces (Fig. 1).

II. Methods

A. Brain Dataset

We used the open-source EEG dataset [6], which includes labels for gait events—"right heel strike" (190 ± 60 ms), "left heel strike" (180 ± 20 ms), "right toe off" (360 ± 20 ms), and "left toe off" (360 ± 20 ms)—from real-world walking experiments. We selected this dataset for its focus on short events, which require precise signal processing for accurate neural decoding. The brain data, recorded at 500 Hz from 26 healthy adults using 66 Ag/AgCl EEG electrodes in a custom 64-channel layout based on the 10-5 system, were referenced online to FCz. Foot movements were captured with 3D accelerometers, and EEG measurements were synchronized offline.

To maintain a large sample size while reducing experimental complexity, we used data from 14 subjects, with an average recording duration of 15 minutes per subject. We set aside the last two minutes of each recording as validation and

*Research supported by the Schroeder Institute for Brain Innovation and Recovery, Canada.

O. Shevchenko is with the Department of Computer Science, Ukrainian Catholic University, Lviv, Ukraine (e-mail: olena.shev4nko@gmail.com).

S. Yeremeieva is with the Department of Computer Science, National University of Kyiv-Mohyla Academy, Kyiv, Ukraine (e-mail: sofiia.yeremeieva@ukma.edu.ua).

B. Laschowski is with the Department of Mechanical and Industrial Engineering, University of Toronto, Toronto, Canada, and the KITE Research Institute, Toronto Rehabilitation Institute, Toronto, Canada (e-mail: brokoslaw.laschowski@utoronto.ca).

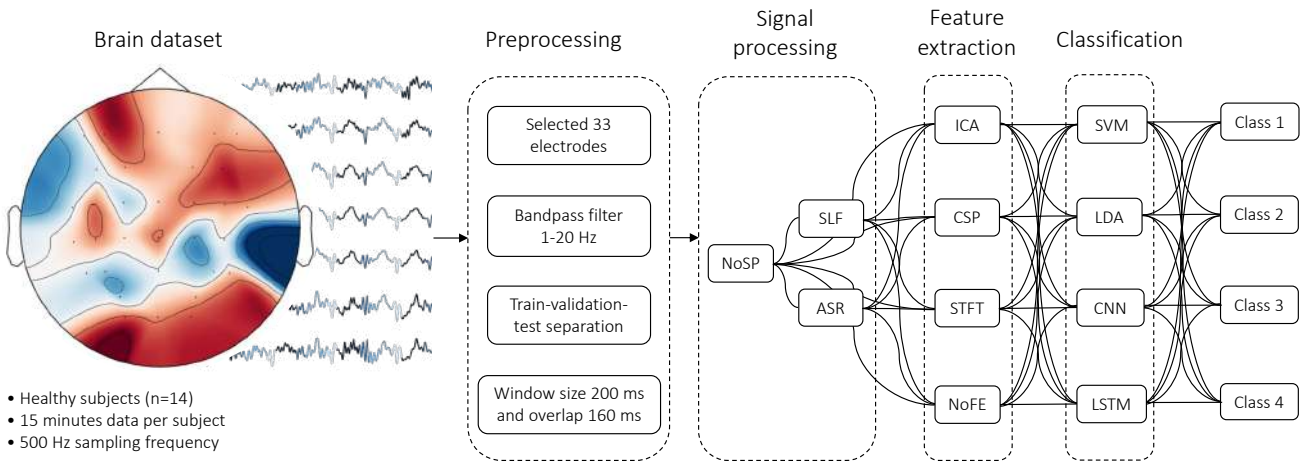


Fig. 1 Our experimental design. We tested different state-of-the-art signal processing, feature extraction, and classification algorithms to find the optimal combination for neural decoding of brain dynamics. Our baseline is no signal processing (NoSP) and no feature extraction (NoFE).

testing sets to prevent data leakage. We kept the sampling rate at 500 Hz. We experimented with several different electrode subsets for EEG channel selection, including a 24-electrode set designed for motor imagery and four custom sets targeting different cortical areas in the brain. Although we found no statistically significant difference in F1-score, the custom set, which included 33 electrodes (F5, F3, Fz, F4, F6, FC3, FC1, FC2, FC4, C5, C3, C1, Cz, C2, C4, C6, CP5, CP3, CP1, CPz, CP2, CP4, CP6, P5, P3, Pz, P4, P6, PO3, PO4, O1, Oz, O2), slightly outperformed the others with a 0.1 increase in F1-score.

For frequency filtering, we tested various combinations of high-pass (0.5–2.5 Hz) and low-pass (20–40 Hz) filters. We found that high-pass filters > 1.0 Hz significantly degraded classification accuracy, while low-pass filters > 20 Hz caused only a slight reduction. The optimal bandpass filter was 1–20 Hz, yielding the highest average F1-score across participants. We divided the data into windows, each labeled by the last element. We tested window lengths between 100-500 ms and overlaps of 20-160 ms. A window size of 200 ms with a 160 ms overlap provided one of the best F1-scores, generating fewer data points (i.e., 22,000 windows vs. 87,000 with a 150 ms window and 140 ms overlap) while ensuring enough data for training without exceeding the smallest class size (Fig. 2). Fewer windows helped reduce the memory storage and compute requirements.

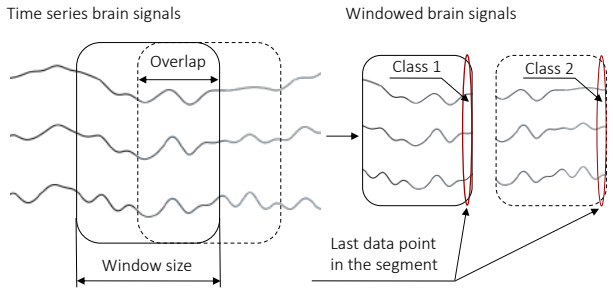


Fig. 2 Schematic of our dataset adaptation used for semi-real-time neural decoding, including segmenting the brain signals with fixed window size and overlap. We defined the class of an entire segment based on the class of the last data point within that segment, even if multiple classes exist in the same window.

Although each time series contains the same number of gait events, the duration of these events varies. Consequently, after sampling the data, as shown in Fig. 2, events with longer durations generated more windows, leading to an imbalanced final dataset. To address this, we evaluated two strategies: down sampling the overrepresented classes and retaining the original distribution. Up sampling was not considered due to the limited research on effective data augmentation techniques for EEG signals. Our analysis revealed that down sampling significantly reduced model performance. Therefore, we opted to retain the current class distributions to preserve the integrity of the neural data.

B. Signal Processing

Common artifact removal methods in brain-machine interface decoding range from simple thresholding to more advanced methods like blind source separation [1], improving signal-to-noise ratio and data quality. In our study, we compared two signal processing algorithms: 1) artifact subspace reconstruction (ASR), designed to handle non-stationary artifacts, and 2) surface Laplacian filter (SLF), which increases local information by estimating the radial current flow at the scalp. We also used normalized data as our baseline, centering values around the mean with unit standard deviation.

Artifact Subspace Reconstruction (ASR) is an automatic method for removing transient, large-amplitude artifacts with minimal computational effort. It learns artifact characteristics directly from data, thus increasing specificity. While ASR cannot completely eliminate all artifacts—such as those from eye movements, muscle activity, or poor electrode contact—it can significantly improve data quality, facilitating further processing like ICA decomposition [7].

Surface Laplacian Filter (SLF), or current source density, enhances neural data by emphasizing local brain dynamics and minimizing distant signal interference. It can improve spatial filtering, reduce noise, and highlight sensorimotor rhythms, by

calculating the second spatial derivative of scalp potentials, enhancing topographical localization and reducing volume-conduction effects. Its effectiveness depends on electrode density and spacing, and is independent of reference electrode choice. Positive estimates represent current flow from the brain to the scalp, while negative values indicate flow from the scalp to the brain [8].

C. Feature Extraction

Feature extraction is important to transform complex brain dynamics into discriminative representations. By reducing data dimensionality, it highlights subtle neural modulations related to movements, focusing on features such as event-related spectral perturbations and sensorimotor rhythms. This not only captures the spatial and temporal dynamics important for movement classification but also enhances the robustness and reliability of motor neural decoding.

We compared three state-of-the-art feature extraction methods used in brain-machine interfaces: common spatial patterns (CSP), which optimizes the spatial filters to distinguish brain dynamics; independent component analysis (ICA), which isolates the independent signals within the neural data; and short-time Fourier transform (STFT), which analyzes the frequency content of neural signals to capture both time and frequency information. We also used no feature extraction as our baseline for comparison.

Common Spatial Patterns (CSP), originally developed for binary classification, decompose signals into spatial patterns that maximize variance between two states. For multi-class classification, we used the "one-versus-rest" method [9], generating spatial filters for each class against the rest. We factorized covariance matrices from each segment to extract eigenvectors corresponding to the largest eigenvalues, forming spatial filters to improve the signal-to-noise ratio and capture discriminative features critical for motor neural decoding [10].

Independent Component Analysis (ICA), widely used in artifact removal and neural decoding, separates brain signals into independent sources. ICA finds an unmixing matrix based on component independence, enhancing the interpretability of brain data by isolating neural and non-neural sources. The independent components extracted serve as features, refining the representation of brain dynamics [11].

Short-Time Fourier Transform (STFT) applies Fourier transforms to windowed signal segments, providing time-localized frequency information. This method captures dynamic, time-specific brain activity, which is important for classifying event-related potentials, such as those associated with movement. In our study, we used a semi-real-time decoding approach with windowed brain signals.

D. Classification

The choice of classification algorithm is essential for motor neural decoding, influencing accuracy, computational efficiency, and real-time performance. We compared four classifiers: two deep learning models (i.e., convolutional neural network, CNN; and long short-term memory network, LSTM) and two classical machine learning models (i.e., support vector machine, SVM; and linear discriminant analysis, LDA).

Support Vector Machine (SVM) is a supervised machine learning algorithm that classifies data by finding the optimal hyperplane that maximizes the margin between classes, thus improving generalization. For non-linear classification, SVM uses a kernel function to map data into a higher-dimensional space where linear separation is possible.

Linear Discriminant Analysis (LDA) is a supervised method for classification and dimensionality reduction commonly used in neural decoding of brain dynamics [12]. The algorithm identifies a one-dimensional subspace such that a linear hyperplane best separates the classes while maximizing the difference in class means. It assigns larger weights to predictors that show greater class distinction.

Convolutional Neural Network (CNN) is a deep learning model that applies convolutions to capture spatial patterns. Increasingly used in brain-machine interfaces, CNNs are well-designed for neural decoding. We used EEGNet, which is the state-of-the-art CNN optimized for EEG neural decoding, which uses depthwise and separable convolutions to create an efficient deep learning model that captures key features while remaining lightweight [13].

Long Short-Term Memory (LSTM) networks are recurrent neural networks designed to process sequential data and capture temporal dynamics. We used the LSTM architecture by [4], which demonstrated over 80% accuracy in decoding human movements from brain signals. The network consists of two LSTM layers, where the output of the first layer serves as input to the second, followed by a fully-connected layer and a softmax activation function to return the class probabilities.

E. Experiments

We designed a new pipeline to compare the different signal processing, feature extraction, and classification algorithms for motor neural decoding. We conducted a total of 672 experiments, testing three signal processing methods, four feature extractors, and four machine learning classifiers, each of which were optimized for individual subjects. This resulted in 48 unique neural decoding algorithms per subject. Our experimental design is shown in Fig. 1. Our pipeline begins with preprocessing, including bandpass filtering (1–20 Hz), train-validation-test separation, and windowing with a fixed 200 ms rolling window size with a 160 ms overlap. The label "NoSP-NoFE" (i.e., no signal processing or feature extraction) served as our baseline for comparison.

We then applied signal processing per subject. For ASR, we trained the model on clean calibration data with a $K = 20$ cutoff, applying it to the train, validation, and test segments. The result was labeled ASR-NoFE. For SLF, we used the spherical spline method, calculating G and H matrices based on electrode distances and Legendre polynomial terms. This produced three datasets for each subject: NoSP-NoFE, ASR-NoFE, and SLF-NoFE.

We then applied the different feature extractors. Our preliminary tests revealed that CSP features caused significant accuracy drops in multiclass classification, so we used projected EEG signals instead for classification. CSP failed to converge with SLF-processed data for four subjects, so we also excluded this combination. For ICA, we used the FastICA algorithm (max_iter = 2000 and tol = 0.0001) fitting the model with the calibration dataset and applying it to the segmented train, validation, and test datasets. For STFT, we applied Fourier trans-

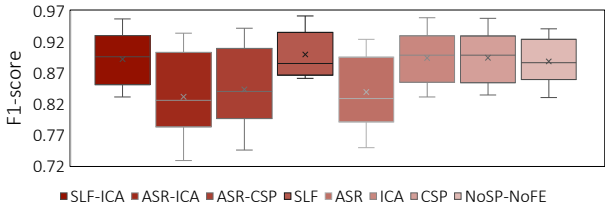


Fig. 3 Neural decoding performance (i.e., weighted F1-score) using our support vector machine (SVM) classifier across all 14 subjects for each combination of signal processing and feature extraction.

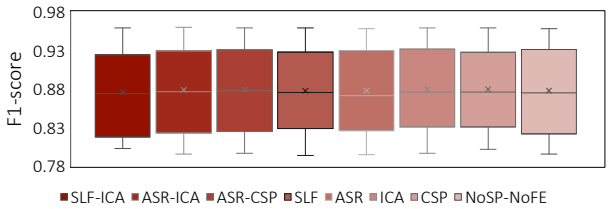


Fig. 4 Neural decoding performance (i.e., weighted F1-score) using our linear discriminate analysis (LDA) classifier across all 14 subjects for each combination of signal processing and feature extraction.

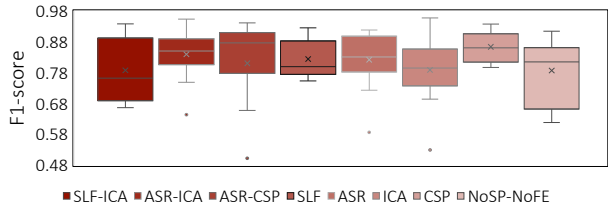


Fig. 5 Neural decoding performance (i.e., weighted F1-score) using our long short-term memory (LSTM) neural network across all 14 subjects for each combination of signal processing and feature extraction.

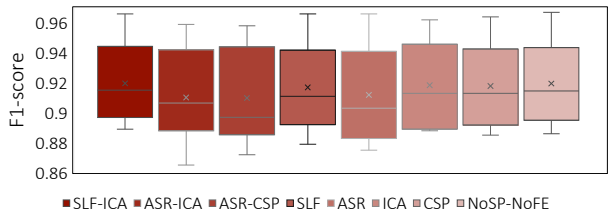


Fig. 6 Neural decoding performance (i.e., weighted F1-score) using our convolutional neural network (CNN) classifier across all 14 subjects for each combination of signal processing and feature extraction.

forms to each time window to obtain time-frequency representations for classifier input.

We then trained the four machine learning classifiers on each subject. We applied data normalization before the classification by standardizing each segment using the mean and standard deviation from the calibration train set. For SVM, we used the radial basis function kernel and optimized the regularization parameter C with cross-validation, testing values from 1 to 1000. For LDA, we used the shrinkage LDA, which regularizes class covariance matrices to prevent instability and overfitting. We selected the best shrinkage value via cross-validation, ranging from 0.01 to 1, using the least squares solver.

We trained our CNN model with hyperparameter optimization using four randomly selected subjects. We tuned batch size, number of temporal filters (F1), depth multiplier (D), and fully-connected (FC) size, with little variation in F1-scores (0.02). The final parameters were F1 = 8, D = 5, and batch size = 64. We also optimized the LSTM hyperparameters, although the results were less consistent than our CNN model. To address this, we used early stopping, scheduled learning rates, and fixed initial weights. The final parameters were batch size = 256, hidden size = 80, and FC size = 75. After training, we performed inference on the test set, calculating accuracy, precision, recall, and F1-score for each class, along with their weighted averages. Additionally, we measured compute time and memory usage. We carried out statistical comparisons using the Wilcoxon signed-rank test, with the null hypothesis that there is no significant difference in F1-scores between models. The NoSP-NoFE model served as our baseline. We ran all experiments on Google Colab with an NVIDIA T4 GPU and 50 GB of RAM. The full implementation of our experiments is available in our open-source repository at https://github.com/OlenaShev4nko/BMI-Decoder-Comparison.

III. Results

Our results are summarized in Table 1. We used weighted F1-score since it is the most representative metric for multiclass classification and can capture misclassification. For all our machine learning classifiers, adding STFT feature extraction significantly reduced neural decoding performance by up to 25%. Among all subjects, the highest-performing neural decoders used our CNN classifier. Data processing appeared to have a modest effect across the different classifiers, but additional processing slightly reduced the performance variability compared to using only data normalization.

For our SVM classifier, SLF produced the highest F1-score, with a Wilcoxon test p-value of 0.0063, indicating a statistically significant improvement over our baseline model.

Table 1. Average F1-scores across all 14 subjects for each neural decoding algorithm, including different combinations signal processing (i.e., SLF and ASR), feature extraction (i.e., ICA and CSP), and machine learning classification (i.e., SVM, LDA, LSTM, and CNN). NoSP means no signal processing and NoFE means no feature extraction.

Classifier	NoSP-NoFE	SLF-NoFE	ASR-NoFE	NoSP-ICA	NoSP-CSP	SLF-ICA	ASR-ICA	ASR-CSP
SVM	88.8±4	89.9±4	83.9±6	89.4±4	89.4±4	89.2±4	83.1±7	84.3±6
LDA	87.8±5	87.8±5	87.8±5	87.9±5	87.9±5	87.6±5	87.9±5	87.9±5
LSTM	78.7±10	82.4±6	82.2±9	78.9±10	86.3±10	78.8±10	83.9±8	81.0±15
CNN	91.9±3	91.7±3	91.2±3	91.8±3	91.8±3	92.9±3	91.0±3	90.9±3

Table 2. Example confusion matrix showing neural decoding accuracy (%) per class using our CNN model with NoSP and NoFE for one subject. The overall decoding accuracy was 95.5%.

	RightTO	RightHS	LeftTO	LeftHS
RightTO	97.1	2.38	0.31	0.21
RightHS	1.31	88.41	6.17	4.11
LeftTO	0.0	0.62	98.46	0.92
LeftHS	4.41	0.0	1.15	94.44

Table 3. Example confusion matrix showing neural decoding accuracy (%) per class using our CNN model with SLF and NoFE for one subject. The overall decoding accuracy was 95.7%.

	RightTO	RightHS	LeftTO	LeftHS
RightTO	97.62	1.86	0.1	0.41
RightHS	2.24	88.79	4.67	4.3
LeftTO	0.0	1.13	98.15	0.72
LeftHS	3.26	0.38	1.72	94.64

Table 4. Example confusion matrix showing neural decoding accuracy (%) per class using our CNN model with NoSP and ICA for one subject. The overall decoding accuracy was 95.4%.

	RightTO	RightHS	LeftTO	LeftHS
RightTO	97.72	1.66	0.1	0.52
RightHS	2.06	87.66	5.98	4.3
LeftTO	0.1	1.13	98.25	0.51
LeftHS	3.64	0.38	2.3	93.68

Table 5. Example confusion matrix showing neural decoding accuracy (%) per class using our CNN model with SLF and ICA for one subject. The overall decoding accuracy was 95.4%.

	RightTO	RightHS	LeftTO	LeftHS
RightTO	97.72	1.76	0.1	0.41
RightHS	1.87	87.85	6.36	3.93
LeftTO	0.0	0.92	98.56	0.51
LeftHS	4.02	0.96	2.11	92.91

ASR, in contrast, consistently decreased our neural decoding accuracy. The distribution of SVM results for each signal processing and feature extraction combination is shown in Fig. 3. For LDA, ICA typically produced the highest F1-score, but the Wilcoxon test (p-value = 0.3076) showed no statistically significant difference from our baseline. Fig. 4 shows the LDA results for each combination of signal processing and feature extraction.

For our LSTM classifier, CSP generally yielded the highest F1-score. The Wilcoxon test (p-value = 0.0001) confirmed a statistically significant improvement compared to our baseline. Fig. 5 shows the distribution of LSTM results across subjects. For our CNN classifier, the combination of SLF and ICA achieved the highest F1-scores, but the Wilcoxon test (p-value = 0.8597) showed no significant difference from our baseline. The CNN classification results are shown in Fig. 6. Tables 2-5 show several examples of confusion matrices using our CNN classifier for one subject.

Our model training took 2 minutes for CNN and LSTM, 2.5 minutes for LDA, and 6 minutes for SVM. Our smallest classification algorithm was the CNN model at 0.03 MB, while the LSTM model was 2 MB, and LDA and SVM models were 50.2 MB and 278.5 MB, respectively. Including signal processing and feature extraction increased processing times. The average time per data segment (100 data points, 33 features) was 4 ± 0.3 ms for ASR, 38 ± 3 ms for SLF, 0.3 ± 0.05 ms for ICA, 0.4 ± 0.06 ms for CSP, and 0.2 ± 0.05 ms for STFT.

IV. Discussion

In this study, we conducted one of the largest comparative analyses testing different state-of-the-art signal processing, feature extraction, and classification algorithms to determine the optimal combination for motor neural decoding of brain dynamics. Using a large-scale EEG dataset of human movements in real-world environments, we tested three signal processing algorithms, four feature extractors, and four machine learning classifiers, each of which were optimized for individual subjects, resulting in 672 total experiments (i.e., 48 unique neural decoders per subject). We evaluated the performance of each combination based on weighted F1-score, inference speed, and model size, which have practical implications for real-time embedded computing. The results of our analyses can help inform the design of next-generation neural decoding algorithms for brain-machine interfaces.

Our research showed that CNNs achieve the best neural decoding performance compared to classical machine learning algorithms and other deep learning models such as LSTMs. Our CNN significantly outperformed SVM, LDA, and LSTM models, with the highest F1-score observed when in combination with surface Laplacian filter (SLF) and independent component analysis (ICA) (93%). Although this improvement was not statistically significant compared to our baseline CNN model, it underscores the robustness of CNNs to different preprocessing. These results are consistent with previous research [5], which reported that CNNs optimized on raw EEG signals outperform the conventional CSP+LDA pipeline. Moreover, for neural decoding of human locomotion, we extended the application of LSTM models to four-class classification, exceeding the binary classification of previous research [4]. While [4] found that LSTM with ASR processing outperformed LDA with CSP, we observed the opposite. Our results showed that ASR processing increased performance variability and reduced decoding accuracy, suggesting that its utility requires careful evaluation. Our LSTM neural network achieved its best performance when combined with CSP signal processing, yielding statistically significant improvements over the other combinations.

We also found that SVM achieves its best performance when paired with SLF processing, a statistically significant improvement over filtered and normalized data. These findings align with previous research [3], which found that SVM outperformed LDA under similar conditions. Furthermore, while our LDA classifier demonstrated its highest accuracy when combined with ICA, the Wilcoxon test revealed no significant difference compared to filtered and normalized data. These results highlight how classical models, despite their simplicity, can achieve competitive performance with appropriate signal processing. By comparing these models and signal processing algorithms, our study provides a comprehensive evaluation that bridges gaps in prior literature, offering deeper insights into optimal neural decoder designs.

Despite these developments, our study has several limitations. Our evaluation was limited to pseudo-online experi-

ments aimed at developing and proving the feasibility of our decoding algorithms. However, brain-machine interfaces are real-time, closed-loop systems and thus need to be tested online to demonstrate real-world performance. While we observed trends in higher F1-scores for some algorithms over others, we cannot be certain that these trends will generalize to other datasets or online measurements of brain dynamics. Furthermore, although the two signal processing and three feature extraction algorithms that we studied are among the most popular in motor neural decoding, especially for leg movements, other methods exist and should be considered in future research [3].

To address these limitations, we plan to extend the number of datasets and subjects used to optimize our neural decoding algorithms, including data from more invasive recording technologies. Data from other sensors such as inertial sensors or egocentric vision could be integrated in a multimodal system together with brain data to improve accuracy in predicting human movements [14]-[19]. Furthermore, rather than optimizing neural decoders for individual subjects, as done in our study, future research could explore principles of transfer learning to develop a general model with the best combination of signal processing, feature extraction, and classification, trained on brain data from all subjects [20]. This general model could then be compared to our neural decoding algorithms optimized for individual subjects.

In addition to testing other signal processing and feature extraction algorithms, we also plan to expand the number of machine learning classifiers for comparison such as hybrid CNN-LSTM model, graph neural networks, unsupervised autoencoders and transformers, which have recently gained significant attention. Several studies have already demonstrated that transformers can outperform CNNs in EEG classification and prediction tasks [21]-[22]. A detailed comparison of these models using our new pipeline would be valuable. Combining multimodal signals in neural-machine interfaces could also offer more reliable input for diverse populations and applications [23]. We also plan to deploy our neural decoding algorithms to evaluate real-time embedded computing performance and extend our research to simulated environments [24]. In conclusion here we developed and tested dozens of neural decoding algorithms (i.e., consisting of different signal processing, feature extraction, and machine learning classifiers) using a large-scale EEG dataset to determine the optimal combination for brain-machine interfaces.

Acknowledgment

This research study is dedicated to the people of Ukraine in response to Russia's ongoing invasion.

References

[1] R. Abiri et al., "A comprehensive review of EEG-based brain–computer interface paradigms," *Journal of Neural Engineering*, Nov. 2018.

[2] I. Iturrate, R. Chavarriaga, and J. D. R. Millán, "General principles of machine learning for brain-computer interfacing," *Handbook of Clinical Neurology*, vol. 168, pp. 311-328, Mar. 2020.

[3] V. Quiles et al., "Decoding of turning intention during walking based on EEG biomarkers," *Biosensors*, vol. 12, pp. 555, Jul. 2022.

[4] S. Tortora et al., "Deep learning-based BCI for gait decoding from EEG with LSTM recurrent neural network," *Journal of Neural Engineering*, vol. 17, pp. 046011, Jul. 2020.

[5] N. Tibrewal, N. Leeuwis, and M. Alimardani, "Classification of motor imagery EEG using deep learning increases performance in inefficient BCI users," *Plos One*, vol. 17, pp. e0268880, Jul. 2022.

[6] N. S. J. Jacobsen, S. Blum, K. Witt, and S. Debener, "A walk in the park? Characterizing gait-related artifacts in mobile EEG recordings," *European Journal of Neuroscience*, vol. 54, pp. 8421-8440, Dec. 2021.

[7] C. Y. Chang, S. H. Hsu, L. Pion-Tonachini, and T. P. Jung, "Evaluation of artifact subspace reconstruction for automatic artifact components removal in multi-channel EEG recordings," *IEEE Transactions on Biomedical Engineering*, vol. 67, pp. 1114-1121, Jul. 2019.

[8] S. Deng, W. Winter, S. Thorpe, and R. Srinivasan, "Improved surface Laplacian estimates of cortical potential using realistic models of head geometry," *IEEE Transactions on Biomedical Engineering*, vol. 59, pp. 2979-2985, Nov. 2012.

[9] Z. Y. Chin, K. K. Ang, C. Wang, C. Guan, and H. Zhang, "Multi-class filter bank common spatial pattern for four-class motor imagery BCI," *Annual International Conference of the IEEE Engineering in Medicine and Biology Society*, Nov. 2009.

[10] H. Ramoser, J. Muller-Gerking, and G. Pfurtscheller, "Optimal spatial filtering of single trial EEG during imagined hand movement," *IEEE Transactions on Rehabilitation Engineering*, vol. 8, pp. 441-446, Dec. 2000.

[11] A. S. Oliveira, B. R. Schlink, W. D. Hairston, P. König, and D. P. Ferris, "A channel rejection method for attenuating motion-related artifacts in EEG recordings during walking," *Frontiers in Neuroscience*, vol. 11, pp. 225, Apr. 2017.

[12] D. Liu et al., "EEG-based lower-limb movement onset decoding: Continuous classification and asynchronous detection," *IEEE Transactions on Neural Systems and Rehabilitation Engineering*, vol. 26, pp. 1626-1635, Aug. 2018.

[13] V. J. Lawhern et al., "EEGNet: a compact convolutional neural network for EEG-based brain–computer interfaces," *Journal of Neural Engineering*, vol. 15, pp. 056013, Jul. 2018.

[14] O. Tsepa, R. Burakov, B. Laschowski, and A. Mihailidis, "Continuous prediction of leg kinematics during walking using inertial sensors, smart glasses, and embedded computing," *IEEE International Conference on Robotics and Automation (ICRA)*, May. 2023.

[15] H. Tan, A. Mihailidis, and B. Laschowski, "Egocentric perception of walking environments using an interactive vision-language system," *bioRxiv*, Dec. 2024.

[16] D. Kuzmenko, O. Tsepa, A. G. Kurbis, A. Mihailidis, and B. Laschowski, "Efficient visual perception of human-robot walking environments using semi-supervised learning," *IEEE International Conference on Intelligent Robots and Systems (IROS)*. Dec. 2023.

[17] B. Ivanyuk-Skulskiy, A. G. Kurbis, A. Mihailidis, and B. Laschowski, "Sequential image classification of human-robot walking environments using temporal neural networks," *IEEE International Conference for Biomedical Robotics and Biomechatronics (BioRob)*, Oct. 2024.

[18] A. G. Kurbis, D. Kuzmenko, B. Ivanyuk-Skulskiy, A. Mihailidis, and B. Laschowski, "StairNet: Visual recognition of stairs for human-robot locomotion," *BioMedical Engineering OnLine*, Feb. 2024.

[19] D. Rossos, A. Mihailidis, and B. Laschowski, "AI-powered smart glasses for sensing and recognition of human-robot walking environments," *IEEE International Conference for Biomedical Robotics and Biomechatronics (BioRob)*, Sept. 2024.

[20] A. Dempster and B. Laschowski, "Domain adaptation for decoding brain dynamics using mixture models," *bioRxiv*, 2025.

[21] W. Cui et al., "Neuro-GPT: Towards a foundation model for EEG," *arXiv*, Mar. 2024.

[22] Y. Song, X. Jia, L. Yang, and L. Xie, "Transformer-based spatial-temporal feature learning for EEG decoding," *arXiv*, Jun. 2021.

[23] J. Thomas and B. Laschowski, "Development of a real-time neural controller using an EMG-driven musculoskeletal model," *bioRxiv*, Dec. 2024.

[24] A. Dashkovets and B. Laschowski, "Reinforcement learning for control of human locomotion in simulation," *IEEE International Conference on Biomedical Robotics and Biomechatronics (BioRob)*, Oct. 2024.

Adapting Biomimetic Kinematics for Controlling a Powered-Knee, Passive-Ankle Prosthesis Across Inclines

C. Andrew Seelhoff[1], T. Kevin Best[2] , and Robert D. Gregg[1,2]

***Abstract*— Despite promising benefits for people with limb loss, powered multi-joint prostheses from the research field have not been translated into the clinical space. Commercial powered knee prostheses like the Össur Power Knee™ are paired with passive feet which lack the range of motion of biological ankle joints, especially on steep inclines. This discrepancy prevents the direct translation of emerging biomimetic control methods for powered knee-ankle prostheses, which implicitly assume both joints exhibit normative biomechanics. To enable commercial prostheses to benefit from biomimetic control methods on inclines, this paper adapts a continuous knee kinematic model to minimize the difference in global foot angle compared to able-bodied reference data, under the assumption that the ankle joint is locked. In a pilot experiment with an above-knee amputee participant, our adapted controller produced substantial benefits compared to a baseline controller that only tracks able-bodied knee trajectories. Level-ground walking performance is similar to existing methods despite the change of objective, and on steep inclines, prosthesis load-bearing and center of pressure progression are restored to near-normative levels. These results show a promising pathway towards translation of biomimetic control methods onto existing commercial hardware, allowing near-term impacts with tangible benefits for prosthesis users.**

I. Introduction

There are over two million people with limb loss in the United States [1], and this population is expected grow a further 150% by 2060 [2]. The limb loss population experiences reduced quality of life as most current prosthetic limbs are unable to replicate the joint torques normally provided by intact musculature, resulting in an increased metabolic cost of walking [3], [4]. Activities which require net-positive work, such as walking up ramps or stairs, further exacerbate these deficiencies. In response, the research field has made substantial progress developing multi-joint powered prostheses, which place motors at the knee and ankle joint to allow the limb to propel itself and assist the user during ambulation [5], leading to reductions in metabolic cost, increasing walking speed, and even reducing compensatory behaviors [6]–[8].

There has been limited, but growing, commercial development of powered prostheses, including one powered ankle, the Empower (Otto Bock, Duderstadt, Germany), and three powered knee prostheses: the Power Knee™ (Össur hf, Reykjavík, Iceland), the Intuy Knee (Reboocon, Delft, The Netherlands), and the Bio Leg (BionicM, Tokyo, Japan). The primary obstacles towards clinical adoption of powered prostheses are their bulkiness and complexity compared to existing passive solutions [5]. While commercial powered knees are typically heavier than passive counterparts, they occupy a similar form factor. Powered ankles, however, are much heavier and larger than passive Energy Storage and Return (ESR) feet, which consist of fiberglass or carbon fiber springs. Combining powered joints also presents a complex, interdependent control problem, often involving dozens of user-specific parameters [9]. As a result, commercially-available powered transfemoral prostheses primarily use a *powered-knee, passive-ankle* configuration to minimize distal mass and reduce complexity.

Although ESR feet lack a physical joint, they can emulate a limited ankle range of motion (RoM) through deformation of the elastic heel and keel. ESR feet are designed primarily to facilitate level walking, where able-bodied RoM is relatively limited [10], but in other activities, the prosthesis-side gait kinematics depart substantially from able-bodied data [11], [12]. As a result, prosthesis users experience reduced symmetry and stability [13], [14] and must make gait compensations on inclines, [15], declines [16], and stairs [17]. Effective RoM can be marginally increased by making the ESR foot less stiff, although this comes at a cost of lower energy-return, leading to further physical and perceptual changes to gait [18]–[20].

Because of these limitations of ESR feet, powered knee, passive-ankle prostheses have not yet achieved the versatility of powered knee-ankle prostheses, which can facilitate variable-speed/incline walking [21]–[23], variable-height stair climbing [24], [25], and continuous transitions between these activities [26]. Many multi-joint controllers are designed to reproduce able-bodied joint trajectories to promote more normative gait while reducing (or eliminating) hand-tuned parameters [27]–[29]. Able-bodied joint patterns are typically parameterized by a phase variable, which can be calculated using residual-limb thigh kinematics to synchronize the prosthesis to the user's movement [21], [22], [30]. Our group initially implemented position controllers using continuous-phase/task models of able-bodied joint kinematics [31], [32], although shortcomings in resultant gait kinetics led to the use of data-driven joint impedance during the stance phase [22]. These hybrid kinematic impedance controllers improved joint work [22], [24], symmetry [33], and endurance measures [34] when implemented on a prototype powered knee-ankle prosthesis [35]. However, these biomimetic controllers cannot be directly translated onto

This work was supported by the National Institute of Child Health & Human Development of the NIH under Award R01HD094772, by the University of Michigan Rackham Merit Fellowship, and by the National Science Foundation under the Graduate Research Fellowship DGE 1841052. Hardware was provided by Össur hf (Reykjavík, Iceland).

[1]Department of Mechanical Engineering, [2]Department of Robotics, University of Michigan, Ann Arbor, MI 48109, USA. Contact: {seelhoff, tkbest, rdgregg}@umich.edu

powered-knee, passive-ankle prostheses, as they implicitly expect biological ankle behavior which ESR feet cannot provide on uneven terrains. To have tangible short-term impact, we must adapt multi-joint prosthesis control methods for use with powered-knee, passive-ankle prostheses, especially for inclined walking.

In this work, we introduce a novel knee prosthesis controller designed to account for ESR foot behavior on inclines. As a proof-of-concept, we alter the knee kinematic model of a PD position controller by simulating the effects of an ESR foot on able-bodied foot kinematics. We describe the optimization process for generating continuous knee trajectories as a function of gait phase, walking speed, and incline, focusing on achieving more biomimetic foot angle kinematics in place of biomimetic knee angle kinematics. Pilot experiments with one transfemoral amputee subject suggest the proposed *ESR-Adapted* controller greatly mitigates gait alterations imposed by ESR feet on steep inclines without sacrificing level-ground performance when compared to a biomimetic kinematic control strategy. The results demonstrate the potential for our controller to be further refined and adapted to other gait tasks, improving mobility for users of powered-knee, passive-ankle prostheses and making the case for more widespread adoption of powered prostheses.

II. Methodology

A. Hardware Overview

In this study, we utilize the latest generation Power Knee from Össur (model PKA01). The drivetrain of the Power Knee consists of a brushless DC motor, a harmonic drive transmission, and a compliant linkage that connects the transmission output to the knee joint. The torque-angle relationship of the compliant linkage is nonlinear, stiffening under increasing deflection. The knee assembly weighs 2.7 kg with the battery, and the joint has a 120 deg RoM. The removable lithium ion battery powers the motor and the embedded control electronics.

The sensing suite includes joint and motor position encoders, a shank-mounted inertial measurement unit, and an array of ground reaction force hall-effect sensors [36]. Based on the manufacturer's recommendations, we paired the Power Knee with the Össur Pro-Flex LP carbon fiber ankle-foot prosthesis. We selected the appropriate size and category foot (size R28 category 5) for our participant based on the sizing guidelines in the Pro-Flex LP catalog. The entire prosthesis, including the Power Knee, pylon, foot, shoe, and other hardware components configured for our participant, weighed 3.9 kg.

B. Controller Overview

Previous work in our group has shown success with continuous parametrization of joint angles in walking as a function of gait phase, incline, and speed [31], [32]. We adapted this control architecture for use on powered-knee, passive-ankle prostheses by removing the ankle dependency, yielding a singular position controller for the knee (Fig. 1). We constructed and tested two kinematic models for this

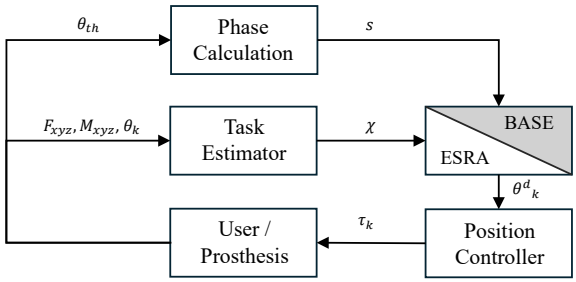


Fig. 1. Block diagram of the proposed control architecture, adapted from [32]. A phase estimate s and task estimate χ feed into either the baseline model (BASE) or the ESR-Adapted model (ESRA). While the BASE model generates a knee trajectory based on able-bodied reference data, the ESRA model described in this work accounts for ESR behavior. Both models produce a desired knee angle θ_k^d which is sent to the PD Position controller, driving the prosthesis. Interactions between the user, prosthesis, and environment generate external forces and moments F_{xyz}, M_{xyz} and alter the knee and thigh angles θ_k, θ_{th}.

controller. The *baseline* (BASE) model is similar to the model used in [31], [32], directly tracking biological knee kinematics assuming the ankle is also actuated within biological ranges of motion. The *ESR-Adapted* (ESRA) model was designed to account for ESR foot behavior.

Both models interfaced with the same PD position controller, which was parameterized by the gait phase s and task vector $\chi = (v, \gamma)$, where v represents the user's forward speed and γ represents the ground slope. The PD controller commanded a torque τ_k and was defined as

$$\tau_k(s,\chi) = k_p e(s,\chi) + k_d \dot{e}(s,\chi), \tag{1}$$

where $e(s,\chi)$ represents the error in knee position $\theta_k(s,\chi)$ compared to a desired position $\theta_k^d(s,\chi)$, and $\dot{e}$ is its derivative. The proportional and derivative gains k_p and k_d were set to values previously used by our group for PD position control of a multi-joint powered prosthesis. The *task space* spanned forward speeds within $v \in [0.8, 1.2]$ m/s and slopes within $\gamma \in [0, 10]$ deg.

C. Knee Kinematic Models

Following previous work from [31], we model the knee angle trajectory for a given task χ as a phase-dependent Fourier Series of degree k with the following equation:

$$\theta_k(s,\chi) = \alpha_0(\chi) + \sum_{n=1}^{k} (\alpha_n(\chi)\sin(2\pi n s) + \beta_n(\chi)\cos(2\pi n s)), \tag{2}$$

where $s \in \{0,1\}$ and the weights $w(\chi) = (\alpha_0, ..., \alpha_k, \beta_1, ..., \beta_k) \in \mathbb{R}^{2k+1}$ are used as decision variables for optimization. Selecting the degree $k = 5$ enables the Fourier Series to successfully replicate able-bodied knee kinematic trajectories without overfitting. With all terms being periodic, the Fourier Series ensures there is continuity between the end of one stride and the start of the next. We can also write (2) as

$$\theta_k(s,\chi) = A(s,\chi) w(\chi), \tag{3}$$

where $w(\chi) = (\alpha_0, ..., \alpha_5, \beta_1, ..., \beta_5) \in \mathbb{R}^{11}$. The matrix $A \in \mathbb{R}^{1500\times11}$ contains 10 concatenated sets of the basis functions 1, $\sin(2\pi s)$, $\cos(2\pi s)$, ..., $\sin(10\pi s)$, $\cos(10\pi s)$ evaluated at 150 discrete values of phase s, linearly spaced between 0 and 1, for the given task χ. Each $\mathbb{R}^{150\times11}$ set of basis functions corresponds to one of the $n = 10$ subjects in an able-bodied reference dataset collected by our group [37].

For both kinematic models, at each task, we aim to find the optimal weights $w_{\text{opt}}(\chi)$ to satisfy our control objective $J(s, \chi, w)$, which differs between the two models:

$$w_{\text{opt}}(s, \chi) = \arg\min_{w\in\mathbb{R}^{11}} J(s, \chi, w). \tag{4}$$

The specific objective functions and optimization methods used for each kinematic model are described below. For each model, we solve the optimization problem for a set of discrete tasks within our task space according to the able-bodied reference data from n = 10 subjects [37]. We include all available speeds ($v = \{0.8, 1.0, 1.2\}$ m/s) and all positive-slope inclines ($\gamma = \{0, +5, +10\}$ deg) from the dataset, resulting in $3 \times 3 = 9$ discrete tasks for evaluation. Then, using the fact that our function for θ_k is linear with respect to w, we perform bilinear interpolation in terms of speed and incline between these nine tasks to generate continuous kinematic surfaces.

1) Baseline Kinematic Model: The baseline kinematic model is created using the existing methodology in [31] for comparison with our proposed kinematic model. Our objective function is the error in knee trajectory:

$$J_{\text{BASE}}(s, \chi, w) = \|(A(s, \chi)w - \theta_k^{\text{ref}}(s, \chi)\|^2, \tag{5}$$

where $\theta_k^{\text{ref}}(s, \chi)$ is the able-bodied reference knee trajectory at phase s and task χ. Similar to A, the reference trajectories for each subject are concatenated vertically to allow for subject-average optimization. Substituting (5) into (4) yields a least-squares optimization problem with a known closed-form solution. Fig. 2 (left) shows the kinematic surface generated through optimization across all inclines at a fixed speed of 1 m/s.

2) ESR-Adapted Kinematic Model: Previous pilot testing revealed that our baseline kinematic model, which assumes the ESR foot behaves exactly as an able-bodied ankle, can result in unfavorable behaviors during activities with high ankle RoM. These shortcomings inform the design of a modified controller which accounts for ESR foot mechanics. This control method requires an objective function that allows the Power Knee to influence foot behavior while accounting for the ESR behavior itself.

First, we model the alterations to biological kinematics caused by an ESR foot. Setting the kinematic origin of the leg at the hip, forward kinematics define the position of each joint center progressing distally, ending with the (global) foot angle and position. An ideal model would simulate the deformation of the ESR foot through ground contact simulation, but the sheer variety of ESR feet in terms of stiffness, RoM, and size make this approach practically infeasible for generalization. As such, we elect to take the reduced RoM to its extreme, modeling the ankle as fixed at its neutral ankle, yielding the following equation for foot angle, defined with respect to the horizontal:

$$\theta_{\text{foot}}(s, \chi) = \theta_{\text{thigh}}^{\text{ref}} - \theta_k + \theta_{\text{ankle}}^{\text{f}} = \theta_{\text{thigh}}^{\text{ref}} - Aw, \tag{6}$$

where $\theta_{\text{thigh}}^{\text{ref}}$ is the reference global thigh angle angle from [37] with all ten subjects' trajectories concatenated vertically and $\theta_{\text{ankle}}^{\text{f}}$ is the fixed ankle angle, which is 0 deg with respect to vertical. All variables are dependent on the current phase s and task χ.

The ankle's rigidity results in an overly-plantarflexed foot throughout stance phase in simulation, which would result in improper loading on the keel of the prosthesis. A feasible optimization objective would be restoration of a biological foot angle trajectory through stance phase. Since there is no ground contact during swing phase, we use a biological knee angle tracking objective after toe-off to allow for biomimetic swing behavior. The first component of this modified objective function is

$$J_{\text{ESRA}}^1(s, \chi) = \begin{cases} \|\theta_{\text{foot}} - \theta_{\text{foot}}^{\text{ref}}\|^2 & \text{for } s \le s_{\text{TO}} \\ J_{\text{BASE}} & \text{otherwise} \end{cases} \tag{7}$$

with the toe-off threshold $s_{\text{TO}} = 0.64$ selected based on able-bodied reference data [37].

In preliminary testing, the foot angle objective alone caused rapid extension of the knee in early stance phase. To balance this behavior and make heel-strike and midstance smoother, we penalize the knee velocity $\dot{\theta}_k(s)$ during the first three-quarters of stance phase, giving the second objective component

$$J_{\text{ESRA}}^2(s, \chi) = \begin{cases} (4 - \frac{4s}{0.75 s_{\text{TO}}})\dot{\theta}_k(s)^2 & \text{for } s \le 0.75 s_{\text{TO}} \\ 0 & \text{otherwise} \end{cases} \tag{8}$$

where the coefficient on $\dot{\theta}_k(s)^2$ linearly decreases from 4 to 0 over the range $s \in [0, 0.75 s_{TO}]$. The knee velocity is given by

$$\dot{\theta}_k(s) = \frac{\partial A}{\partial s}\frac{\partial s}{\partial t}w, \tag{9}$$

where $\frac{\partial A}{\partial s}$ is the element-wise derivative of A with respect to phase, and $\frac{\partial s}{\partial t} = 1$ as we assume each stride has a duration of one second.

Due to the linearity of θ_k, θ_{foot}, and $\dot{\theta}_k$ with respect to w, our final objective function $J_{\text{ESRA}} = J_{\text{ESRA}}^1 + J_{\text{ESRA}}^2$ is also linear in terms of w, allowing us to once again approach this problem using least squares. However, since we do not explicitly command the knee angle, we must enforce joint limits to ensure the Power Knee stays within its RoM, $\theta_k \in [0, 120]$, yielding a constrained least squares problem which can be solved using a Quadratic Program. The resultant kinematic surface is shown in Fig. 2 (right) for a fixed speed of 1 m/s. Fig. 3 shows the simulated foot trajectories for both models in comparison to reference data.

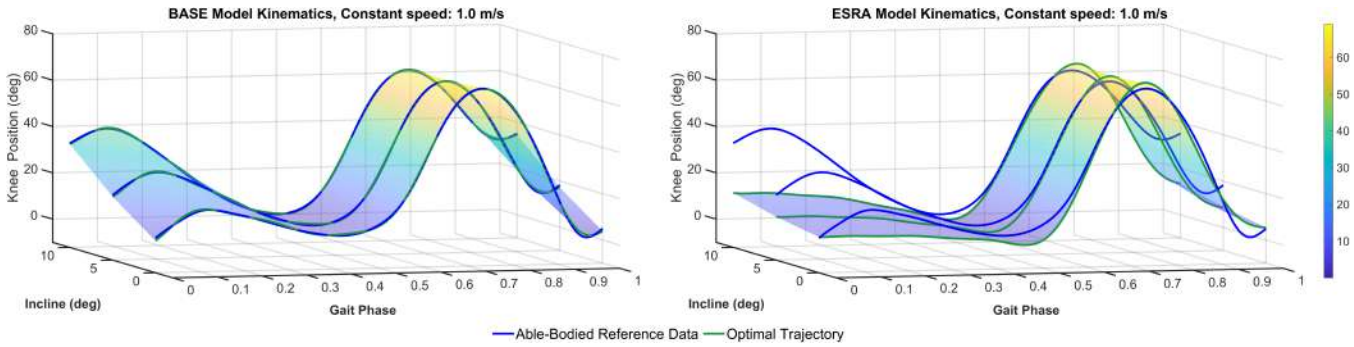


Fig. 2. Kinematic Surfaces for the baseline (BASE) and ESR-Adapted (ESRA) controllers for a constant walking speed of 1 m/s. Note the optimized and able-bodied reference trajectories from [37] overlap for the BASE controller but not for the ESRA controller.

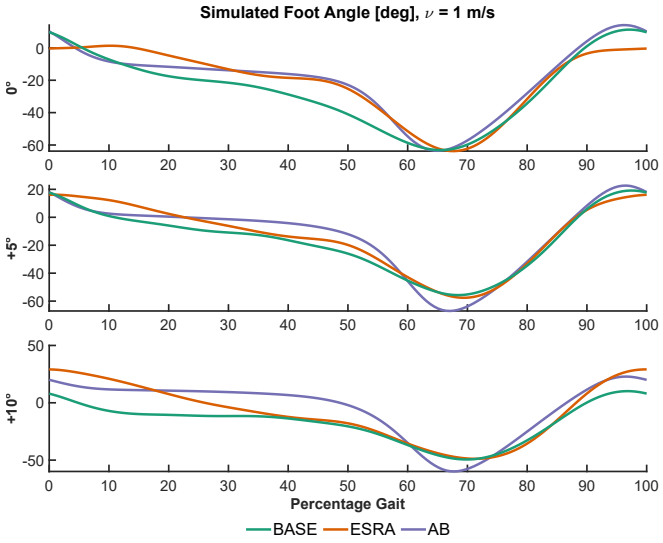


Fig. 3. Simulated optimal foot trajectories for the BASE and ESRA kinematic models, with Able-Bodied data (AB) as reference trajectories.

D. Experiment Design

One pilot transfemoral amputee subject (male, 23 years, 80 kg with prosthesis, 175 cm, activity level K4) was enrolled in our study and provided written informed consent in accordance with the Institutional Review Board of the University of Michigan (HUM00230065). The subject wore a motion capture suit and was equipped with a set of motion capture markers on the legs and torso. For each controller, the subject walked on an instrumented treadmill (Bertec Corporation, Columbus, OH) at a fixed 1.0 m/s speed for three inclines (0, 5, 10 deg) for 150 seconds each. Before each trial, the Power Knee was configured to use the correct controller, and the correct parameter set corresponding to the current incline was manually selected. Although previous work has enabled real-time incline estimation using this control framework [22], we manually set the incline estimate in this preliminary work to isolate the effects of our modified kinematic model.

The instrumented split-belt treadmill collected ground reaction force (GRF) data for each leg at 1000 Hz. A motion capture system (Vicon, Oxford, UK) was used to record 3D positions of all markers at 250 Hz. The first 30 seconds of data for each trial were excluded from processing to restrict our analysis to steady-state walking. We processed the steady-state data in OpenSim 4.5 (Stanford, CA, USA) using the model from Rajagopal et al. [38] with modifications made to account for the Power Knee's inertial properties, similar to [39].

III. Results

Figures 4 presents the average kinematic and GRF trajectories for each trial, along with reference able-bodied data. Table I presents normalized root mean square errors (NRMSE) for kinematics and GRF trajectories for each controller compared to able-bodied reference data, presented as a percentage of the range of each trajectory.

A. Kinematics

On level ground, the two controllers behaved similarly, as shown by similar NRMSE values compared to able-bodied gait (Table I). This result was expected as the ESR foot's RoM is closer to that of normative ankle motion in level walking. In fact, experimental foot angle trajectories only differed slightly, with the BASE controlled foot briefly plantarflexing then dorsiflexing in midstance while the ESRA controlled foot remained planted (Fig. 4, column 1). This deviation grew to 10 deg of excess plantarflexion on steeper inclines (see supplementary video). The corrective behavior by the ESRA controller remained across all three inclines, as NRMSE in foot angle remained approximately the same for the ESRA controller whereas the BASE controller's NRMSE steadily increased with incline (Table I).

Due to differences in their optimization objectives, the controllers exhibited distinct knee trajectories when compared to able-bodied data. The BASE controller was able to retain a near-normative level of stance phase knee flexion, although the peak flexion occurred later in stance, perhaps due to the position controller gains not being strong enough to counteract the ESR foot's limited deflection. The ESRA controller, on the other hand, had stance-phase knee flexion peaks aligned in phase but not in magnitude: the prioritization of foot-angle tracking combined with the fixed-ankle assumption resulted in reduced peak knee flexion and earlier extension of the knee during stance phase (Fig. 4, column 2). At 10 deg, both kinematic models exhibited worsened performance due to ESR feet being unable to replicate the

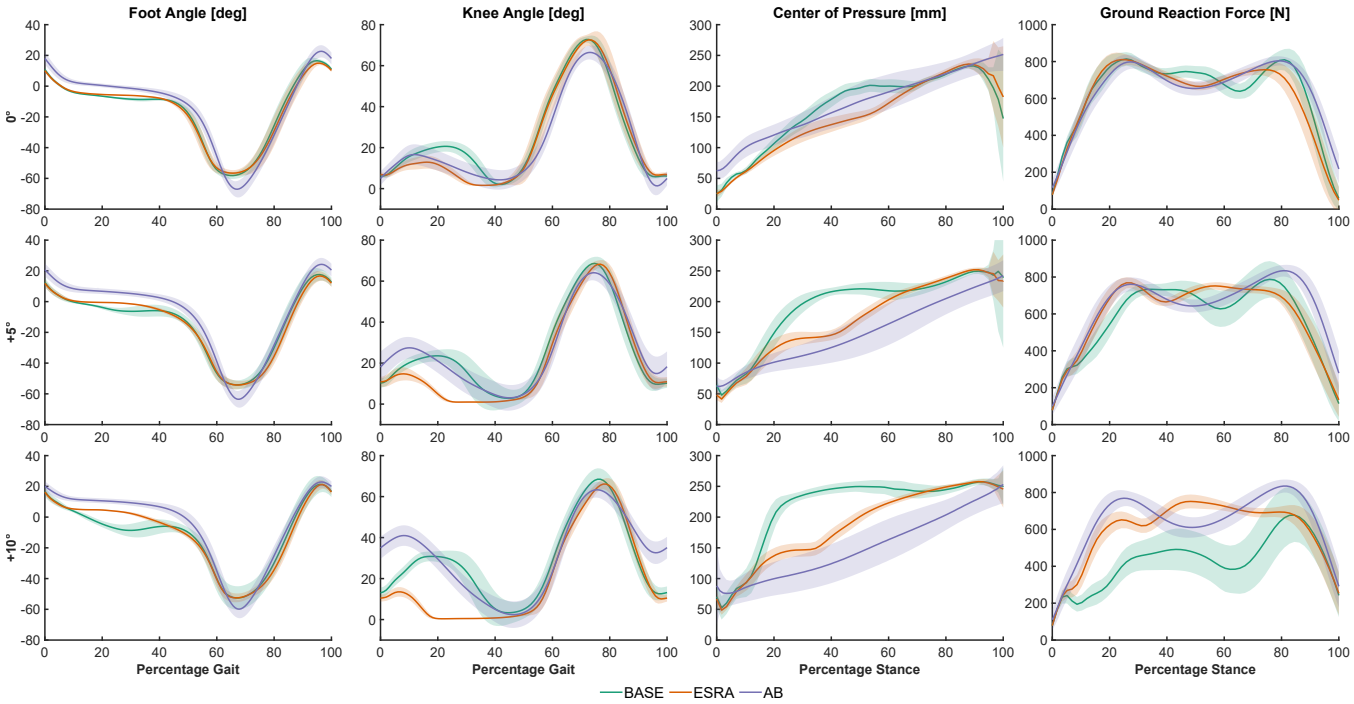


Fig. 4. Average experimental kinematic trajectories and ground reaction force data from both controllers. For able bodied reference data (AB) from [37], inter-subject averages are shown. Shaded regions represent ± 1 standard deviation of data. Note for Center of Pressure and Ground Reaction Force, only stance phase is shown ($s \leq s_{\text{TO}}$).

TABLE I
NORMALIZED ROOT MEAN SQUARE ERROR ACROSS INCLINES

	1.0 m/s, 0°		1.0 m/s, +5°		1.0 m/s, +10°	
	BASE	ESRA	BASE	ESRA	BASE	ESRA
θ_{foot} (%)	7.95	7.56	9.26	8.40	11.59	8.45
θ_k (%)	9.99	7.88	9.06	13.17	16.51	26.89
CoP (%)	25.96	19.80	23.40	11.70	29.72	16.38
GRF (%)	10.84	13.40	14.79	14.78	29.55	13.27

high biological ankle RoM observed at this incline. The reduced stance flexion commanded by the ESRA controller resulted in a substantial increase in knee angle NRMSE (13.17% at 5 deg and 26.89% at 10 deg) compared to the BASE controller, which has the sole objective of knee-angle tracking (9.06% at 5 deg and 16.51% at 10 deg). The periodicity requirement for the optimal trajectories resulted in these deviations from able-bodied gait in late swing phase, as the ESRA controller's heel strike target angle was substantially more extended than that of able-bodied data. We will see below that these deviations from able-bodied knee kinematics are a necessary tradeoff in pursuit of favorable ground contact with an ESR foot on inclines.

B. Ground Interactions

The kinematics results discussed above help explain the causes for changes in ground interaction between the two position controllers. Incorrect placement of the ESR foot throughout stance phase by the BASE controller prevented proper loading of the device, while the ESRA controller's corrected positioning substantially improved prosthesis loading and resultant ground interactions. To analyze these changes, we first examined Center of Pressure (CoP), which we defined as the distance between the heel marker and the point at which the net GRF acts on the foot. As seen in the representative able-bodied trajectories in Fig. 4 (column 3), CoP should smoothly progress through stance phase as the foot rolls over from heel to toe.

The BASE controller did not produce the smooth CoP progression we would expect and instead underwent rapid progression for the first half of stance phase (Fig. 4, column 3). On level ground, the prosthesis geometry allowed the heel to still take the majority of the user's weight, but on steeper inclines, this resulted in forefoot strikes rather than heel strikes. As a result, the foot visibly bounced as the keel unloaded in midstance, where the CoP regressed slightly and lost monotonicity. This trend can be seen through the NRMSE for CoP (Table I), for which the BASE values are substantially higher than those of the ESRA controller across inclines.

The ESRA controller significantly mitigated, but did not completely remove, this rapid progression. Proper foot placement allowed the heel to be loaded, delaying initial rollover making for a smoother stance phase progression. This loading on the ESRA controller was similar in magnitude to able-bodied GRF data, whereas the BASE controlled prosthesis was far under-loaded on steeper inclines (Fig. 4, column 4). While the ESRA controller allowed the user to properly bear weight with their prosthesis throughout stance phase, the loading profile still departed from the standard "M-shape" seen in able-bodied reference data. This trend was most noticeable at 10 deg, where the heel of the prosthesis could not be sufficiently loaded while using the BASE controller.

The user's confidence in the prosthesis lowered due to the resulting irregular foot behavior, leading to lower weight bearing and GRF throughout stance phase, as shown in Fig. 4 (Row 3, Column 4). The NRMSE compared to reference GRF data was 29.55% for the BASE controller and 13.27% for the ESRA controller (Table I).

IV. Discussion

By attempting to follow able-bodied trajectories at the knee, the BASE controller implicitly expects biological ankle behavior from the ESR foot. As the ESR foot cannot fully exhibit normative ranges of motion across steeper inclines, the foot is incorrectly loaded through stance phase, leading to departures from normative kinematics and kinetics. The ESRA controller is able to mitigate these issues rather well, even if the controller cannot completely return the prosthesis to able-bodied behavior.

Another observation is that these notable improvements from the ESRA controller are not a result of increased RoM, but rather shifting foot placement. The model for finding optimal trajectories, along with the controller itself, have no knowledge about the ESR foot or how it will behave: the performance changes emerge solely from the foot landing in a more favorable configuration which can better absorb and return energy through stance phase.

Ultimately, able-bodied gait may not be a proper objective choice for powered-knee, passive-ankle prostheses, since prostheses with ESR feet cannot perfectly replicate able-bodied movement in all tasks. Rather, perhaps a more fitting target for kinematics and kinetics is data from transtibial amputees, whose intact biological knees optimally adjust to using ESR feet. Future work for powered-knee, passive-ankle prostheses could incorporate transtibial amputee gait data for a more achievable reference trajectory set, although a dataset with sufficient data across a range of activities would need to be collected to enable this approach.

A. Limitations

The modeling assumption of a fixed ankle joint is a strong simplification which directly affects the extent of differences between the BASE and ESRA models. This is evident from the large deviations between the simulated (Fig. 3) and experimental (Fig. 4) foot trajectories, as the ESR foot bends enough such that the prosthesis is always more plantarflexed than representative able-bodied data. A foot-deflection model which relates GRF to ankle angle would allow for the limited ankle RoM of ESR feet to be taken into account, although the wide variety of ESR feet would make it difficult to generalize these results. If a generalized ESR foot deflection model could be developed, this would result in less extreme adjustments to knee trajectories for the ESRA controller.

Further, the incline setting in the controller was manually configured by a researcher in these experiments. Outside of the laboratory environment, we aim for these devices to automatically discern inclines as the user walks to allow for seamless adaptation between slopes. Future work will involve collecting data from the device's sensing suite in order to correlate existing signals with the current ground slope. While an additional, foot-mounted IMU sensor could trivialize this task, maintaining the existing sensor set on the Power Knee would be preferable for rapid translation of our control methods to clinical use.

Finally, the results in this work come from a pilot study with a single participant who had familiarity with the controller implemented on the Power Knee. As such, we are unable to generalize any claims about the trends and results observed. We intend to run a validation study with more participants in future work, which will also consider additional terrains such as declined ramps and uneven outdoor surfaces.

V. Conclusion

By indirectly controlling foot angle, as opposed to directly controlling the knee angle, the proposed control method allows for improved ground-contact behavior and proper loading of the ESR foot in a powered-knee, passive-ankle prosthesis. The effect is particularly evident while navigating steeper inclines. In a pilot subject experiment, our proposed controller results in substantial improvements in kinematics and ground interactions, showing that biomimicry can remain a feasible objective despite ESR feet's limited ability to mimic a biological ankle. This work serves as a step towards translation of versatile, biomimetic control methods from the research field onto commercially available clinical hardware, strengthening the case for widespread adoption of powered prostheses.

ACKNOWLEDGMENTS

The authors would like to thank Atli Örn Sverrisson and David Langlois for assistance with the Power Knee hardware and Jeffrey Wensman, CPO for clinical support.

Competing Interest Disclosures

The authors are listed on patents or patent applications related to the HKIC control method.

Hardware and related support was provided by Össur hf (Reykjavík, Iceland), which could have a financial interest in the results of this study. The results and conclusions in this work are entirely those of the authors and may not reflect the views of Össur hf or the National Institutes of Health.

References

[1] M. Caruso and S. Harrington, "Prevalence of Limb Loss and Limb Difference in the United States: Implications for Public Policy," 2024.

[2] J. A. Rivera, K. Churovich, A. B. Anderson, and B. K. Potter, "Estimating Recent US Limb Loss Prevalence and Updating Future Projections," *Archives of Rehabilitation Research and Clinical Translation*, p. 100376, Oct. 2024.

[3] R. L. Waters, J. Perry, D. Antonelli, and H. Hislop, "Energy cost of walking of amputees: the influence of level of amputation," *The Journal of Bone and Joint Surgery. American Volume*, vol. 58, no. 1, pp. 42–46, Jan. 1976.

[4] A. S. Göktepe, B. Cakir, B. Yilmaz, and K. Yazicioglu, "Energy expenditure of walking with prostheses: comparison of three amputation levels," *Prosthetics and Orthotics International*, vol. 34, no. 1, pp. 31–36, Mar. 2010.

[5] R. Gehlhar, M. Tucker, A. J. Young, and A. D. Ames, "A review of current state-of-the-art control methods for lower-limb powered prostheses," *Annual Reviews in Control*, vol. 55, pp. 142–164, Jan. 2023.

[6] S. K. Au, J. Weber, and H. Herr, "Powered Ankle–Foot Prosthesis Improves Walking Metabolic Economy," *IEEE Trans. Robotics*, vol. 25, no. 1, pp. 51–66, Feb. 2009.

[7] E. C. Martinez-Villalpando, L. Mooney, G. Elliott, and H. Herr, "Antagonistic active knee prosthesis. A metabolic cost of walking comparison with a variable-damping prosthetic knee," in *Annu. Int. Conf. of the IEEE Eng. in Med. and Biol. Soc.*, vol. 2011, 2011, pp. 8519–8522.

[8] E. D. Ledoux and M. Goldfarb, "Control and Evaluation of a Powered Transfemoral Prosthesis for Stair Ascent," *IEEE Trans Neural Syst Rehabil Eng*, vol. 25, no. 7, pp. 917–924, Jul. 2017.

[9] A. M. Simon, K. A. Ingraham, N. P. Fey, S. B. Finucane, R. D. Lipschutz, A. J. Young, and L. J. Hargrove, "Configuring a Powered Knee and Ankle Prosthesis for Transfemoral Amputees within Five Specific Ambulation Modes," *PLOS ONE*, vol. 9, no. 6, p. e99387, Jun. 2014, publisher: Public Library of Science.

[10] C. L. Brockett and G. J. Chapman, "Biomechanics of the ankle," *Orthop Trauma*, vol. 30, no. 3, p. 232, Jun. 2016.

[11] A. S. McIntosh, K. T. Beatty, L. N. Dwan, and D. R. Vickers, "Gait dynamics on an inclined walkway," *J. Biomechanics*, vol. 39, no. 13, pp. 2491–2502, Jan. 2006.

[12] N. T. Pickle, A. M. Grabowski, J. R. Jeffers, and A. K. Silverman, "The Functional Roles of Muscles, Passive Prostheses, and Powered Prostheses During Sloped Walking in People With a Transtibial Amputation," *J. Biomechanical Eng.*, vol. 139, no. 111005, Oct. 2017.

[13] F. B. Rodrigues, G. S. de Sá e Souza, E. de Mendonça Mesquita, R. de Sousa Gomide, R. R. Baptista, A. A. Pereira, A. O. Andrade, and M. F. Vieira, "Margins of stability of persons with transtibial or transfemoral amputations walking on sloped surfaces," *J. Biomechanics*, vol. 123, p. 110453, Jun. 2021.

[14] N. T. Pickle, J. M. Wilken, J. M. Aldridge Whitehead, and A. K. Silverman, "Whole-body angular momentum during sloped walking using passive and powered lower-limb prostheses," *Journal of Biomechanics*, vol. 49, no. 14, pp. 3397–3406, Oct. 2016.

[15] A. H. Vrieling, H. G. van Keeken, T. Schoppen, E. Otten, J. P. K. Halbertsma, A. L. Hof, and K. Postema, "Uphill and downhill walking in unilateral lower limb amputees," *Gait & Posture*, vol. 28, no. 2, pp. 235–242, Aug. 2008.

[16] D. C. Morgenroth, M. Roland, A. L. Pruziner, and J. M. Czerniecki, "Transfemoral amputee intact limb loading and compensatory gait mechanics during down slope ambulation and the effect of prosthetic knee mechanisms," *Clin. Biomechanics*, vol. 55, pp. 65–72, Jun. 2018, publisher: Elsevier.

[17] T. Schmalz, S. Blumentritt, and B. Marx, "Biomechanical analysis of stair ambulation in lower limb amputees," *Gait & Posture*, vol. 25, no. 2, pp. 267–278, Feb. 2007.

[18] W. L. Childers and K. Z. Takahashi, "Increasing prosthetic foot energy return affects whole-body mechanics during walking on level ground and slopes," *Scientific Reports*, vol. 8, no. 1, p. 5354, Mar. 2018.

[19] N. P. Fey, G. K. Klute, and R. R. Neptune, "The influence of energy storage and return foot stiffness on walking mechanics and muscle activity in below-knee amputees," *Clinical Biomechanics*, vol. 26, no. 10, pp. 1025–1032, Dec. 2011.

[20] B. J. Hafner, J. E. Sanders, J. Czerniecki, and J. Fergason, "Energy storage and return prostheses: does patient perception correlate with biomechanical analysis?" *Clin. Biomechanics*, vol. 17, no. 5, pp. 325–344, Jun. 2002.

[21] D. Quintero, D. J. Villarreal, D. J. Lambert, S. Kapp, and R. D. Gregg, "Continuous-Phase Control of a Powered Knee–Ankle Prosthesis: Amputee Experiments Across Speeds and Inclines," *IEEE Trans. Robotics*, vol. 34, no. 3, pp. 686–701, Jun. 2018.

[22] T. K. Best, C. G. Welker, E. J. Rouse, and R. D. Gregg, "Data-Driven Variable Impedance Control of a Powered Knee–Ankle Prosthesis for Adaptive Speed and Incline Walking," *IEEE Trans. Robotics*, vol. 39, no. 3, pp. 2151–2169, Jun. 2023.

[23] L. M. Sullivan, S. Creveling, M. Cowan, L. Gabert, and T. Lenzi, "Powered Knee and Ankle Prosthesis Control for Adaptive Ambulation at Variable Speeds, Inclines, and Uneven Terrains," *IEEE/RSJ Int. Conf. on Intell. Robot. and Syst.*, vol. 2023, pp. 2128–2133, Oct. 2023.

[24] R. J. Cortino, T. K. Best, and R. D. Gregg, "Data-Driven Phase-Based Control of a Powered Knee-Ankle Prosthesis for Variable-Incline Stair Ascent and Descent," *IEEE Trans. on Med. Robot. and Bionics*, vol. 6, no. 1, pp. 175–188, Feb. 2024.

[25] S. Hood, L. Gabert, and T. Lenzi, "Powered Knee and Ankle Prosthesis With Adaptive Control Enables Climbing Stairs With Different Stair Heights, Cadences, and Gait Patterns," *IEEE Trans. Robotics*, vol. 38, no. 3, pp. 1430–1441, Jun. 2022.

[26] S. Cheng, C. A. Laubscher, and R. D. Gregg, "Controlling Powered Prosthesis Kinematics Over Continuous Inter-Leg Transitions Between Walking and Stair Ascent/Descent," *IEEE Trans. Neural Syst. and Rehabil. Eng.*, vol. 32, pp. 3891–3901, 2024.

[27] M. A. Holgate, T. G. Sugar, and A. W. Bohler, "A novel control algorithm for wearable robotics using phase plane invariants," in *2009 IEEE Int. Conf. on Robot. and Automat.*, May 2009, pp. 3845–3850, iSSN: 1050-4729.

[28] R. D. Gregg, T. Lenzi, L. J. Hargrove, and J. W. Sensinger, "Virtual Constraint Control of a Powered Prosthetic Leg: From Simulation to Experiments with Transfemoral Amputees," *IEEE Trans. Robotics*, vol. 30, no. 6, p. 1455, Dec. 2014.

[29] N. Thatte, T. Shah, and H. Geyer, "Robust and Adaptive Lower Limb Prosthesis Stance Control via Extended Kalman Filter-Based Gait Phase Estimation," *IEEE Robotics and Automation Letters*, vol. 4, no. 4, pp. 3129–3136, Oct. 2019.

[30] S. Rezazadeh, D. Quintero, N. Divekar, E. Reznick, L. Gray, and R. D. Gregg, "A Phase Variable Approach for Improved Rhythmic and Non-Rhythmic Control of a Powered Knee-Ankle Prosthesis," *IEEE access: practical innovations, open solutions*, vol. 7, pp. 109 840–109 855, 2019.

[31] K. R. Embry, D. J. Villarreal, R. L. Macaluso, and R. D. Gregg, "Modeling the Kinematics of Human Locomotion Over Continuously Varying Speeds and Inclines," *IEEE Trans. Neural Syst. and Rehabil. Eng.*, vol. 26, no. 12, pp. 2342–2350, Dec. 2018.

[32] T. K. Best, K. R. Embry, E. J. Rouse, and R. D. Gregg, "Phase-Variable Control of a Powered Knee-Ankle Prosthesis over Continuously Varying Speeds and Inclines," in *2021 IEEE/RSJ Int. Conf. Intell. Robot. and Syst. (IROS)*, Sep. 2021, pp. 6182–6189, iSSN: 2153-0866.

[33] C. G. Welker, T. K. Best, and R. D. Gregg, "Improving Sit/Stand Loading Symmetry and Timing Through Unified Variable Impedance Control of a Powered Knee-Ankle Prosthesis," *IEEE Trans. Neural Syst. and Rehabil. Eng.*, vol. 31, pp. 4146–4155, 2023.

[34] T. K. Best, C. A. Laubscher, R. J. Cortino, S. Cheng, and R. D. Gregg, "Improving Amputee Endurance Over Activities of Daily Living with a Robotic Knee-Ankle Prosthesis: A Case Study," in *2023 IEEE/RSJ Int. Conf. Intell. Rob. and Syst. (IROS)*, Oct. 2023, pp. 2101–2107, iSSN: 2153-0866.

[35] T. Elery, S. Rezazadeh, C. Nesler, and R. D. Gregg, "Design and Validation of a Powered Knee–Ankle Prosthesis With High-Torque, Low-Impedance Actuators," *IEEE Trans. Robotics*, vol. 36, no. 6, pp. 1649–1668, Dec. 2020.

[36] S. Gudjonsson, A. Einarsson, H. I. Thorsteinsdottir, and D. Langlois, "Ground contact sensor array for lower-limb prosthetic and orthotic devices," US Patent 20 220 401 236A1, Dec., 2022.

[37] E. Reznick, K. R. Embry, R. Neuman, E. Bolívar-Nieto, N. P. Fey, and R. D. Gregg, "Lower-limb kinematics and kinetics during continuously varying human locomotion," *Scientific Data*, vol. 8, no. 1, p. 282, Oct. 2021.

[38] A. Rajagopal, C. L. Dembia, M. S. DeMers, D. D. Delp, J. L. Hicks, and S. L. Delp, "Full-Body Musculoskeletal Model for Muscle-Driven Simulation of Human Gait," *IEEE transactions on bio-medical engineering*, vol. 63, no. 10, pp. 2068–2079, Oct. 2016.

[39] V. Raveendranathan, V. G. M. Kooiman, and R. Carloni, "Musculoskeletal model of osseointegrated transfemoral amputees in OpenSim," *PloS One*, vol. 18, no. 9, p. e0288864, 2023.

Understanding the importance of feature groups for clinical outcome predictions with machine learning in post-stroke robotic-assisted rehabilitation

Anastasios Tzepkenlis[1*], Cristian Camardella[1], Daniele Leonardis[1], Stefano Mazzoleni[2,3,4], and Antonio Frisoli[1]

***Abstract*—Outcome predictions in post-stroke rehabilitation are a key element to personalize the treatment to the needs of the patient, finally enhancing effectiveness of the therapy. They can form the basis of Decision Support Systems, helping clinicians to progressively tune the therapy depending on patients' clinical status and progress. Diverse data sources, such as clinical, demographic, kinematic and time-related data in robotic-assisted rehabilitation, can provide different prediction results. Understanding which data source, or combination thereof, contains useful information for outcome predictions can improve the development of machine learning tools, Decision Support Systems, and even clinical setups designed to record these useful data. The presented work investigates different feature groups and machine learning methods, using data recorded within a robotic-assisted rehabilitation treatment including 44 stroke patients. Results highlight the effectiveness of using multi-dimensional feature groups to predict post-stroke rehabilitation. While clinical data alone can already achieve a solid basis for predictive modeling, the integration of kinematic and time-related data can significantly improve prediction accuracy of the patient outcome.**

***Index Terms*—Rehabilitation, Robotics, Stroke, Upper limb, Prediction, Machine Learning, Kinematics, Clinical Scale, Permutation Importance**

I. Introduction

Post-stroke rehabilitation plays a crucial role in improving functional recovery for patients, where personalized therapies can significantly enhance outcomes. However, current clinical approaches are often challenged by the heterogeneity of patients' characteristics, variability in clinicians' choices, and the lack of standardized decision-making frameworks. These challenges underscore the need for robust decision-support systems (DSS) to assist clinicians in tailoring therapies based on reliable predictions of recovery outcomes. Predictive models in rehabilitation have demonstrated their potential to reduce uncertainty, optimize treatment strategies, and even minimize costs by enabling adaptive and personalized interventions [1], [2]. Despite advancements in predictive systems, many existing models focus primarily on clinical and demographic features while overlooking the potential of instrumental kinematic and time-related data measured during robotic rehabilitation. To bridge these gaps, exploring the predictive power of diverse feature groups (e.g., clinical, demographic, kinematic, and time-related) is crucial to gain a comprehensive understanding of their individual and combined contributions to predicting post-stroke clinical outcomes such as the Fugl-Meyer Assessment (FMA), the Action Research Arm Test (ARAT) and the Motricity Index (MI). Recent studies have employed various machine learning (ML) techniques to predict motor recovery and functional scores [3]–[5]. Depending on the application and the amount of available data, some algorithms can show higher performance than others [6]. Among these, Decision-Tree based algorithms have often shown superior performance due to their ability to better leverage on small amount of data, which is more common in clinical contexts, also evaluating variable importance, offering insights into the underlying recovery processes [7]–[11]. Typically these algorithms are Random Forest, XGBoost, CatBoost, and LightGBM. Other algorithms often employed in predictive systems are K-Nearest Neighbors, Support Vector Machines, or Linear Regression based techniques [6], [12]. However, existing studies have rarely explored the distinct predictive capabilities of kinematic and time-related features derived from robot-assisted rehabilitation, which could provide clinicians with actionable insights to fine-tune therapy parameters in real time. The difficulty in this context is assessing the predictive capabilities of multiple algorithms having an input set that is always composed of different variables. In this sense, it is indeed difficult both to judge the absolute predictive performance of a certain algorithm, given a certain input set, and to understand how certain types of features can add more information on a general basis. The understanding of these relationships between data and predictive algorithms could be a breakthrough either in finding the optimal characteristics of a pre-existing clinical setup or in equipping modern rehabilitation systems with the appropriate tools. This paper aims to address these limitations by evaluating the predictive power of different feature groups (i.e., kinematic, clinical, demographic, and time-related) using various machine learn-

[1] The authors are with the Institute of Mechanical Intelligence, Scuola Superiore Sant'Anna, Pisa, Italy.

[2] The author is with the Department of Electrical and Information Engineering, Politecnico di Bari, Bari, Italy.

[3] The author is with IMT School for Advanced Studies Lucca, Italy.

[4] The author is with the BioRobotics Institute, Scuola Superiore Sant'Anna, Pisa, Italy.

[*] corresponding author:
cristian.camardella@santannapisa.it

ing algorithms. Specifically, we assess their ability to predict clinical scales at discharge for post-stroke patients undergoing robot-assisted upper limb rehabilitation. By integrating these diverse feature sets, we seek to identify the most informative predictors of recovery and determine whether combining these features enhances predictive performance. Furthermore, this study contributes to the growing body of evidence supporting the integration of machine learning tools in rehabilitation to facilitate data-driven, explainable, and adaptive interventions for improved patient outcomes [13], [14]. The results of this work have the potential to inform the design of next-generation DSS that prioritizes interpretability and clinical relevance, paving the way for more effective and standardized approaches in post-stroke rehabilitation.

II. Methodology

A. Data Collection and Processing

Forty-four stroke patients participated in an upper limb robot-assisted rehabilitation program using the MOTORE (Humanware Srl, Pisa, Italy) end-effector device. The study ("iMotore" project) was approved by the Ethics Committee Lazio 1 on December 29, 2021 (STS CE Lazio 1/N-873). Figure 1 illustrates the clinical robotic treatment setup. Four patients were excluded due to incomplete treatment, leaving no final clinical assessment. This dataset extends [15], comprising 71 features across four groups: Clinical, Demographics, Kinematics, and Time-Related (detailed in Table I). Clinical (28) and Demographic (16) features are collected at rehabilitation start. Kinematic features (20) derive from processed force and position data recorded by the robot during therapy, shared across seven rehabilitation game scenarios. These exercises assess range of motion, force exertion, trajectory precision, and task execution (e.g., object collection, simulated daily activities). Some also integrate cognitive tasks to enhance motor and mental agility. The system tracks applied forces, movement accuracy, and task completion—autonomous or assisted. Additionally, 7 time-related features indicate patient performance. Sessions performed entirely in autonomous mode, where the robot completed tasks without patient engagement, were excluded. The combined 71 features predict post-therapy clinical outcomes: motor capability scores (FMA, ARAT, MI).

B. Clinical Outcome Prediction Algorithms

The study employed various machine learning algorithms to predict clinical outcomes: Random Forest, XGBoost, CatBoost, HGBR, LightGBM, and KNN. Random Forest leverages an ensemble of decision trees to enhance robustness and reduce overfitting [16]. XGBoost [17] and CatBoost [18] utilize gradient boosting, with XGBoost excelling in efficiency and scalability, and CatBoost being optimized for categorical data handling. HGBR enhances gradient boosting by discretizing features into histograms for faster training and lower memory usage [19]. LightGBM [20], like XGBoost and CatBoost, is a gradient boosting framework, which optimizes training speed and efficiency by using a histogram-based approach, particularly suited for large datasets with many features. Finally, K-Nearest Neighbors (KNN) predicts outcomes based on the proximity of data points in feature space, making it straightforward and effective for smaller datasets [21].

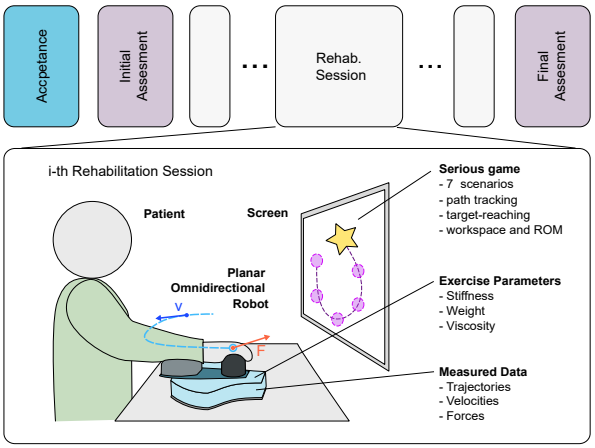


Fig. 1. Scheme of the rehabilitation treatment and setup used to collect the data.

C. Training and Evaluation

Regarding the training and evaluation of the networks, at first we separated the dataset into 80%/20% training/testing based on the number of patients, so 32 patients for training and 8 patients for testing and in total we performed 30 train/test folds. For each of these patients, each completed game session was mapped to the individual clinical outcome score (FMA, ARAT and MI) which was collected at the end of the therapy and the evaluation was calculated as the root-mean-square error between the predicted outcome at the given time against the true outcome at the end of the therapy as noticed in equation (1).

$$\text{RMSE} = \sqrt{\frac{1}{n}\sum_{i=1}^{n}(y - \hat{y}_i)^2} \tag{1}$$

where:

- n: The total number of data points for each patient.
- y_i: The true clinical outcome at the end of the therapy.
- $\hat{y}_i$: The predicted value at the i-th point.

D. Feature Group Analysis

To provide an accurate overview on how each group of features performs on the different networks, we performed an extended ablation study. There, we investigated all possible combinations between the aforementioned groups (Clinical, Demographics, Kinematics and Time-Related). Finally, we evaluated the groups by calculating the cumulative mean of the appearance of each group throughout the ablation study, as seen in Equation 2.

$$\text{Cumulative Mean}_G = \frac{\sum_{G=1}^{N_G} \text{RMSE}_G}{N_G} \tag{2}$$

where:

TABLE I
THE FOUR FEATURE GROUPS, CLINICAL, DEMOGRAPHICS, KINEMATICS AND TIME-RELATED WITH THE CORRESPONDING FEATURES AND DESCRIPTION

Feature Group	Feature Name	Feature Description
Clinical	FMA (fma_a, fma_b, fma_c, fma_d, fma_ul, fma_ul_sens), ARAT (arat_grasp_score, arat_grip_score, arat_pinch_score, arat_gross_score.t9, arat_tot), MI (motrocityindex), BB (bb_aff, bb_na) MAS (mas_sh1, mas_sh2, mas_elb), mas_wrist), MRC (mrc01, mrc02, mrc03) MBI, NRS, DN4, MOCA, PCS, MCS, FAT	Fugl-Meyer Assessment: Measures motor function recovery after stroke Action Research Arm Test: Evaluates upper limb function Motricity Index: Quantifies strength in specific muscle groups Box and Blocks Test: Measures manual dexterity Modified Ashworth Scale: Assesses muscle spasticity Medical Research Council Scale: Measures muscle strength in specific groups Modified Barthel Index, Numerical Rating Scale, Douleur Neuropathique 4, Montreal Cognitive Assessment, Physical Component Score, Mental Component Score, Fatigue Assessment Tool
Demographic	age, sex, height, weight, bmi, latency, laterality, education, smoke, first_event, stroke_type, hemiparesis, aphasia, sus, likert, bamford	age (years), sex (male, female), height (cm), weight (kg), bmi (kg/sq.m) latency: Time delay between stroke onset and assessment (years), laterality: side of the brain affected by the stroke, education (years), smoke (yes/no), first_event (yes/no), stroke_type (ischemic, hemorrhagic), hemipareses (yes/no), aphasia (yes/no), sus (System Usability Scale), likert (scale), bamford (scale)
Kinematic	game_type, userVelocityAvg, workUserTotal, precisionWork, distanceTask, autonomyDuration, workTanUserTotal, velocityNorm, durationUser, workTanRobot, workTanUserSelf, params, overall, calories, timeUser, smoothnessForce, smoothnessKin, weight, viscosity, stiffness	game_type: Selected game among seven available userVelocityAvg: Average robot speed during session workUserTotal: Total work done by user workTanUserTotal: Work along game-demanded direction precisionWork: Ratio of workTanUserTotal to workUserTotal distanceTask: Length completed by patient autonomyDuration: Percentage of self-mode time velocityNorm: Average speed relative to healthy subject durationUser: Total exercise duration workTanRobot: Robot's work to assist patient params: Timerate of precisionWork workTanUserSelf: Work in self-mode overall: Weighted final score calories: Estimated user energy consumption timeUser: Game duration in seconds smoothnessForce & smoothnessKin: Smoothness of force and position weight, viscosity, stiffness: Game difficulty parameters
Time-Related	date_diff, date_diff_session, total_sessions_day number_of_sessions, remainingDaysOfTherapy, total_sessions_incr, automode_sessions	date_diff: Difference between current and first session date_diff_session: Difference between current and previous session remainingDaysOfTherapy: Remaining days until therapy end number_of_sessions: Games completed in a session total_sessions_day & total_sessions_incr: Total games in a session automode_sessions: Games completed in automode

- G: Any of the four groups (Clinical, Demographics, Kinematics, Time-Related).
- N_G: The total number of combinations in which the group G appears.
- RMSE$_G$: The RMSE as noted in equation 1 for the combinations that include G.

E. Permutation Importance

We calculate the Permutation Importance (PI) [22], as implemented in sklearn, which is a model-agnostic method to measure feature significance. It works by randomly shuffling the values of a feature and observing the impact on model performance (e.g. RMSE). The decrease in performance indicates the importance of the shuffled feature, as a larger drop suggests a stronger dependence of the model on that feature.

III. RESULTS AND DISCUSSION

The results of the cumulative mean analysis illustrated in Figure 2 highlight the critical role of the Clinical feature group in increasing the accuracy of predictions. This result demonstrates how clinical data is a reliable foundation for model performance across a range of methods and scales. The Clinical group stands as the most influential feature set, achieving the lowest RMSE values and likely capturing key information directly associated with the target outcome. The observed ranking of groups, where Kinematic group follows the Clinical group, then the Time-Related group, and finally the Demographic group, provides insights of the relative importance of these feature sets. This hierarchy suggests that kinematic data may offer additional complementary predictive value, likely reflecting dynamic aspects of the subjects that clinical scales alone cannot fully capture. Time-Related features, while contributing less than Kinematic features, may represent temporal patterns that are less impactful but still relevant. Ranking last is the demographic group, which features' did lead to the least accurate predictions.

In Figure 3, we present the RMSE values across all algorithms and every possible combination of the three clinical scores. The key finding is that incorporating Kinematic features (Clinical + Kinematics), Time-Related features (Clinical + Time-Related), or both (Clinical + Kinematics + Time-Related) generally improves prediction accuracy for most algorithms and clinical scales. Specific combinations for each algorithm that result in an improvement over using

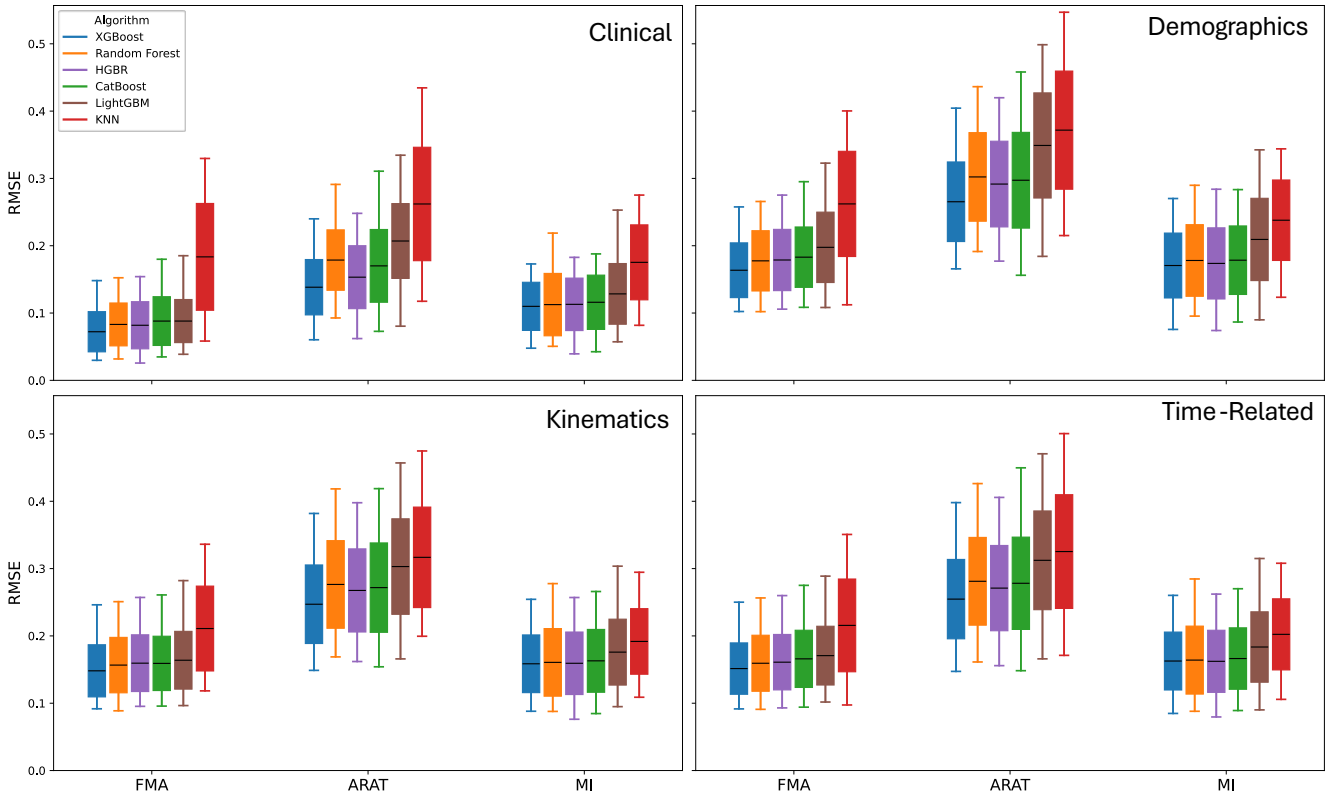


Fig. 2. Boxplot illustrations of the cumulative mean RMSE, calculated using Equation 2, for all the algorithms and for the four feature groups (a: Clinical, b: Demographics, c: Kinematics, d: Time-Related) across the three clinical scores (FMA, ARAT, and MI).

only clinical data are marked with an asterisk (*) above the corresponding boxplots. In most of the analyzed algorithms, it is more likely to find the lowest RMSE when adding kinematic and time-related features meaning that, on average, it is always a good choice employing instrumental data acquisition systems in the clinical setup. Another noteworthy observation is that for the HGBR algorithm, the inclusion of demographic features, either alone or in combination with kinematic and time-related features, consistently enhances prediction accuracy across all three clinical scales. It has to be noted that in literature, researchers often refer to the minimal clinical important differences (MCID) to determine if a significant change in the therapy has to be made, as the smallest change in scores that also are considered clinically important and meaningful in health status perceived by the patient: previous studies set this value around 10/15% of the maximum score [23], [24].

In Figure 4, we present the five most prominent features from each feature group, normalized to enhance visualization clarity. The normalization was applied within this subset by mapping the highest value to the maximum and the lowest to the minimum. As anticipated, the key features within the clinical group for the FMA and ARAT scales are the respective clinical scores at the start of therapy. For the MI scale, however, the most influential feature remains the FMA score at the beginning of therapy. Regarding the Demographic feature group, we observe similarity across all clinical scales and most algorithms that the patient's age and gender as well as the latency are predictors of high importance, leading to more accurate clinical outcome predictions: also height showed to be important, probably caused by a bias of the specific dataset used in this analysis and, thus, to be considered an artifact. Results of this study are also coherent with previous studies where some clinical features were listed as the most relevant one in predicting upper-limb motor recovery [9], [15]. Examining the Kinematic feature group, there is no obvious agreement on which features are more relevant across the algorithms and the three clinical scores. For example, the Duration of the game played by the user is highly relevant for most algorithms when predicting FMA and ARAT. Additionally, factors such as the accuracy in game execution and the user's total effort play crucial roles across all three clinical scales. Notably, the overall game performance feature, representing a total score for the completion of each serious game, is of high importance when predicting the MI clinical scale. Finally, for the Time-Related feature group, a consistent pattern is evident. Across all clinical scales and algorithms, features such as the time difference between the current therapy session and the start of therapy, the total number of serious games completed during a specific rehabilitation session, and the cumulative count of completed game sessions are consistently associated with more accurate predictions.

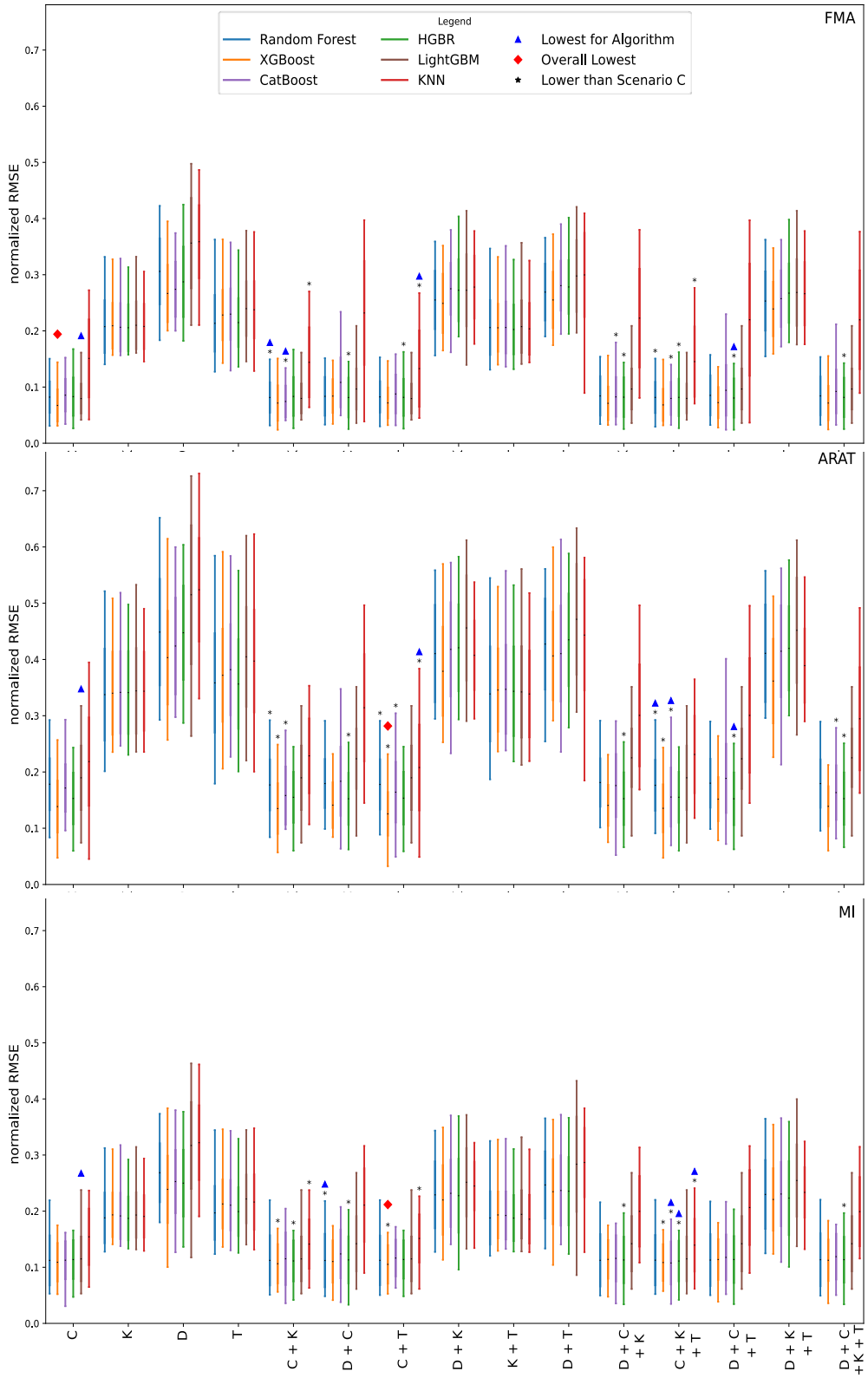


Fig. 3. Boxplot illustrations of all unique combinations of the feature groups (C: Clinical, D: Demographics, K: Kinematics, and T: Time-Related) are provided for the three clinical scores (a: FMA, b: ARAT, c: MI) and all algorithms. Boxplots marked with a star indicate scenarios that outperform the use of clinical information alone for the corresponding algorithm, while the blue triangle indicates the best performance of each algorithm and the red diamond the overall best performance for the clinical scale.

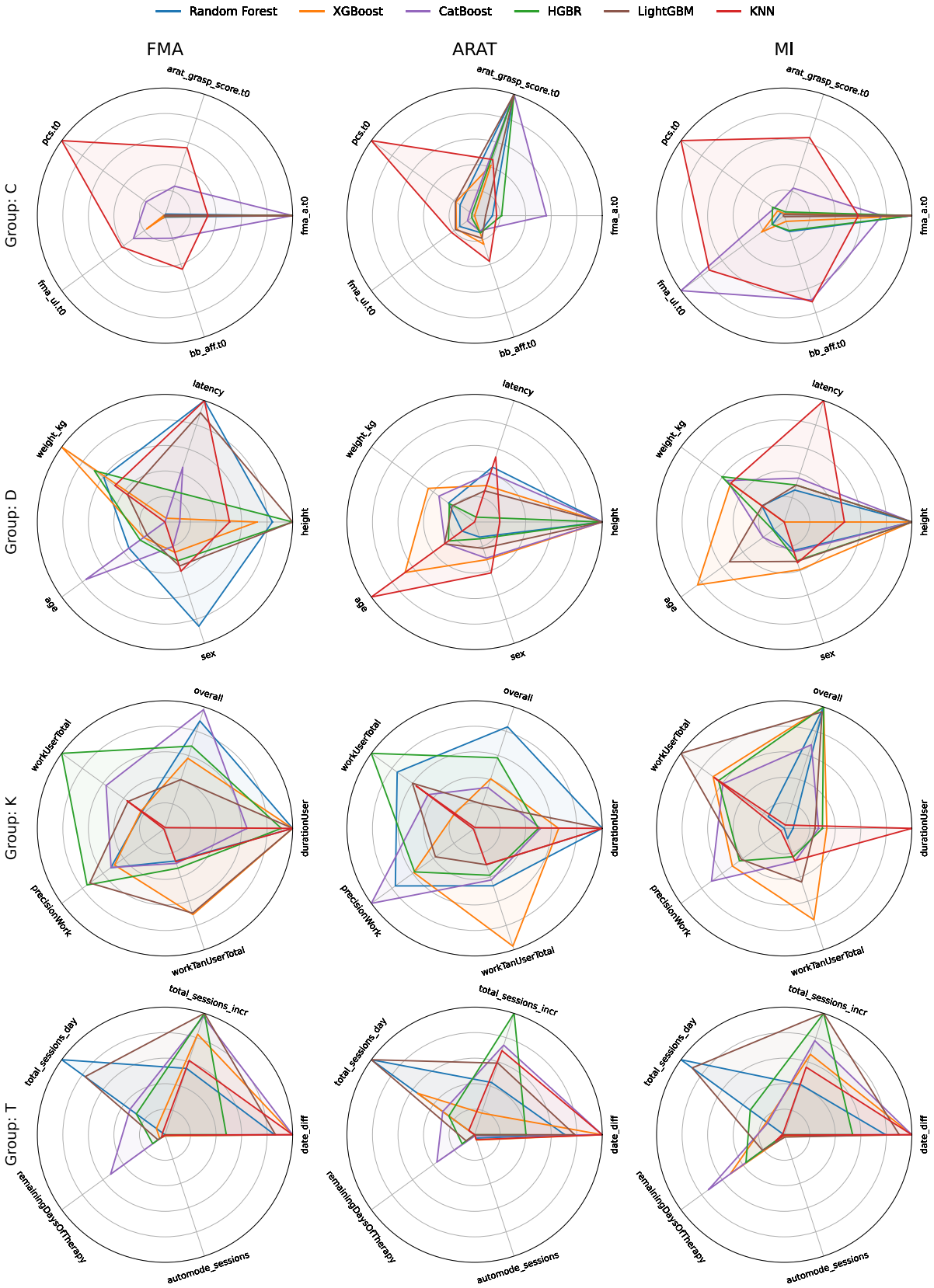


Fig. 4. Radar plots of the four feature groups (C: Clinical, D: Demographics, K: Kinematics, and T: Time-Related), displaying the five most important normalized features, considering both the algorithms and the clinical scales.

IV. Conclusion

This study evaluates the effectiveness of multi-dimensional feature groups in predicting outcomes in post-stroke, robotic-assisted rehabilitation. Clinical features had the most significant impact on reducing RMSE among the four groups (Clinical, Demographic, Kinematic, and Time-Related), constituting a strong foundation for predictive modeling. Kinematic and Time-Related features further improved accuracy, capturing dynamic and temporal aspects of patient performance.

Ablation studies showed that models combining clinical, kinematic, and time-related data outperformed those using clinical data alone, while demographic features were the least predictive. Consistent trends across algorithms indicate robustness. PI analysis revealed that initial FMA and ARAT scores were crucial predictors, while overall game performance influenced MI. Game time and execution accuracy were particularly relevant for FMA and ARAT. Time-Related features, such as the Number of Sessions and time since therapy initiation, were consistently important. Among demographics, patient's age and latency were the strongest predictors.

This study lays the groundwork for defining a minimal clinical setup for effective prediction systems, leveraging clinical assessments and robotic rehabilitation data. Further research is needed to assess the clinical impact of individual and correlated features on stroke recovery.

Acknowledgment

This work has been funded by the MNESYS project (A.F.) (European Union-NextGenerationEU. PNRR – 'MNESYS – A Multiscale integrated approach to the study of the nervous system in health and disease'. Cod. PE 00000006) and the CO-AIDER project (A.T.) which was funded by the Italian Ministry of Health under the "Ricerca Finalizzata" program through the project "Clinical validatiOn of an AI-based DEcision support system for Robotic upper limb rehabilitation in patients with Stroke. A CO-AIDER Study" (RF-2021-12375472).

References

[1] C. Stinear, "Prediction of recovery of motor function after stroke," *The Lancet Neurology*, vol. 9, no. 12, pp. 1228–1232, 2010.

[2] C. M. Stinear, W. D. Byblow, S. J. Ackerley, P. A. Barber, and M.-C. Smith, "Predicting recovery potential for individual stroke patients increases rehabilitation efficiency," *Stroke*, vol. 48, no. 4, pp. 1011–1019, 2017.

[3] R. van der Vliet, R. W. Selles, E.-R. Andrinopoulou, R. Nijland, G. M. Ribbers, M. A. Frens, C. Meskers, and G. Kwakkel, "Predicting upper limb motor impairment recovery after stroke: a mixture model," *Annals of Neurology*, vol. 87, no. 3, pp. 383–393, 2020.

[4] S. I. Lee, C. P. Adans-Dester, A. T. O'Brien, G. P. Vergara-Diaz, R. Black-Schaffer, R. Zafonte, J. G. Dy, and P. Bonato, "Predicting and monitoring upper-limb rehabilitation outcomes using clinical and wearable sensor data in brain injury survivors," *IEEE Transactions on Biomedical Engineering*, vol. 68, no. 6, pp. 1871–1881, 2021.

[5] W.-Y. Lin, C.-H. Chen, Y.-J. Tseng, Y.-T. Tsai, C.-Y. Chang, H.-Y. Wang, and C.-K. Chen, "Predicting post-stroke activities of daily living through a machine learning-based approach on initiating rehabilitation," *International journal of medical informatics*, vol. 111, pp. 159–164, 2018.

[6] G. Shtar, L. Rokach, B. Shapira, R. Nissan, and A. Hershkovitz, "Using machine learning to predict rehabilitation outcomes in postacute hip fracture patients," *Archives of physical medicine and rehabilitation*, vol. 102, no. 3, pp. 386–394, 2021.

[7] V. P. Gupta, A. L. Garton, J. A. Sisti, B. R. Christophe, A. S. Lord, A. K. Lewis, H.-P. Frey, J. Claassen, and E. S. Connolly Jr, "Prognosticating functional outcome after intracerebral hemorrhage: the ichop score," *World neurosurgery*, vol. 101, pp. 577–583, 2017.

[8] S. Campagnini, P. Liuzzi, A. Mannini, B. Basagni, C. Macchi, M. C. Carrozza, and F. Cecchi, "Cross-validation of predictive models for functional recovery after post-stroke rehabilitation," *Journal of NeuroEngineering and Rehabilitation*, vol. 19, no. 1, p. 96, 2022.

[9] C. Camardella, G. Cappiello, Z. Curto, M. Germanotta, I. Aprile, S. Mazzoleni, A. Scoglio, and A. Frisoli, "A random tree forest decision support system to personalize upper extremity robot-assisted rehabilitation in stroke: A pilot study," in *2022 International Conference on Rehabilitation Robotics (ICORR)*. IEEE, 2022, pp. 1–6.

[10] E. Zihni, V. I. Madai, M. Livne, I. Galinovic, A. A. Khalil, J. B. Fiebach, and D. Frey, "Opening the black box of artificial intelligence for clinical decision support: A study predicting stroke outcome," *Plos one*, vol. 15, no. 4, p. e0231166, 2020.

[11] G. Joo, Y. Song, H. Im, and J. Park, "Clinical implication of machine learning in predicting the occurrence of cardiovascular disease using big data (nationwide cohort data in korea)," *IEEE Access*, vol. 8, pp. 157 643–157 653, 2020.

[12] W.-W. Liao, Y.-W. Hsieh, T.-H. Lee, C.-l. Chen, and C.-y. Wu, "Machine learning predicts clinically significant health related quality of life improvement after sensorimotor rehabilitation interventions in chronic stroke," *Scientific Reports*, vol. 12, no. 1, p. 11235, 2022.

[13] K. Mouridsen, P. Thurner, and G. Zaharchuk, "Artificial intelligence applications in stroke," *Stroke*, vol. 51, no. 8, pp. 2573–2579, 2020.

[14] A. Bivard, L. Churilov, and M. Parsons, "Artificial intelligence for decision support in acute stroke—current roles and potential," *Nature Reviews Neurology*, vol. 16, no. 10, pp. 575–585, 2020.

[15] C. Camardella, M. Germanotta, I. Aprile, G. Cappiello, Z. Curto, A. Scoglio, S. Mazzoleni, and A. Frisoli, "A decision support system to provide an ongoing prediction of robot-assisted rehabilitation outcome in stroke survivors," in *2023 International Conference on Rehabilitation Robotics (ICORR)*. IEEE, 2023, pp. 1–6.

[16] L. Breiman, "Random forests," *Machine learning*, vol. 45, pp. 5–32, 2001.

[17] T. Chen and C. Guestrin, "Xgboost: A scalable tree boosting system," in *Proceedings of the 22nd acm sigkdd international conference on knowledge discovery and data mining*, 2016, pp. 785–794.

[18] L. Prokhorenkova, G. Gusev, A. Vorobev, A. V. Dorogush, and A. Gulin, "Catboost: unbiased boosting with categorical features," *Advances in neural information processing systems*, vol. 31, 2018.

[19] A. Guryanov, "Histogram-based algorithm for building gradient boosting ensembles of piecewise linear decision trees," in *Analysis of Images, Social Networks and Texts: 8th International Conference, AIST 2019, Kazan, Russia, July 17–19, 2019, Revised Selected Papers 8*. Springer, 2019, pp. 39–50.

[20] G. Ke, Q. Meng, T. Finley, T. Wang, W. Chen, W. Ma, Q. Ye, and T.-Y. Liu, "Lightgbm: A highly efficient gradient boosting decision tree," *Advances in neural information processing systems*, vol. 30, 2017.

[21] G. Guo, H. Wang, D. Bell, Y. Bi, and K. Greer, "Knn model-based approach in classification," in *On The Move to Meaningful Internet Systems 2003: CoopIS, DOA, and ODBASE: OTM Confederated International Conferences, CoopIS, DOA, and ODBASE 2003, Catania, Sicily, Italy, November 3-7, 2003. Proceedings*. Springer, 2003, pp. 986–996.

[22] A. Altmann, L. Toloşi, O. Sander, and T. Lengauer, "Permutation importance: a corrected feature importance measure," *Bioinformatics*, vol. 26, no. 10, pp. 1340–1347, 2010.

[23] O. Hägg, P. Fritzell, and A. Nordwall, "The clinical importance of changes in outcome scores after treatment for chronic low back pain," *European Spine Journal*, vol. 12, pp. 12–20, 2003.

[24] J. H. Van der Lee, R. C. Wagenaar, G. J. Lankhorst, T. W. Vogelaar, W. L. Devillé, and L. M. Bouter, "Forced use of the upper extremity in chronic stroke patients: results from a single-blind randomized clinical trial," *Stroke*, vol. 30, no. 11, pp. 2369–2375, 1999.

Utilizing Interlimb Coupling with Mirrored Deficit Fields for Enhanced Bilateral Arm Movement*

Won-Kyung Song†, *IEEE Member*
Department of Rehabilitative and Assistive Technology
National Rehabilitation Center
Seoul, Korea
wksong@nrc.go.kr

Seong-Hoon Lee
Department of Rehabilitative and Assistive Technology
National Rehabilitation Center
Seoul, Korea
lsh1799@korea.kr

***Abstract*—This study investigates mirrored deficit fields' effects on bimanual coordination in post-stroke rehabilitation using the NREH-Bimanual robotic platform. We tested our approach with eleven participants (six stroke, five able-bodied), deriving force field parameters from the affected/non-dominant arm's velocity distribution and mirroring them to the unaffected/dominant arm. Movement quality was assessed using Randomness Score, Cumulative Traveling Distance, and Workspace Area across four conditions: null field, unilateral deficit field on affected side, unilateral mirrored deficit field on unaffected side, and bilateral deficit fields. Results showed increased movement quality with deficit field application, particularly when applied bilaterally or to the unaffected arm. The stroke group's affected side improved in Randomness Score (17-24%) and workspace area (16-29%), with enhanced movement perception and speed (~20%) when deficit fields were applied to the unaffected side. These findings demonstrate mirrored deficit fields' potential as a novel rehabilitation strategy for improving bimanual coordination in stroke patients through interlimb coupling mechanisms.**

Keywords—Bimanual coordination, motor rehabilitation, deficit field, interlimb coupling, stroke rehabilitation, error augmentation, robotic rehabilitation, motor learning, velocity-dependent force field, movement exploration

I. INTRODUCTION

Stroke often leads to persistent motor deficits, significantly impacting individuals' ability to perform daily tasks and participate in society [1]. Among these deficits, impaired bimanual coordination is particularly debilitating, affecting tasks that require coordinated movements of both arms, such as dressing, eating, and manipulating objects [2]. Therefore, developing effective rehabilitation strategies to improve bimanual coordination in stroke patients is crucial.

Conventional rehabilitation approaches typically focus on repetitive movements and task-specific training. However, recent research has explored the potential of error augmentation (EA) techniques to enhance motor learning and recovery [3, 4, 5, 6, 7]. EA involves introducing perturbations or disturbances during movement, forcing the nervous system to adapt and learn new motor control strategies. Multiple systematic reviews have demonstrated that EA-based interventions can effectively improve upper extremity performance and recovery in stroke patients [5, 6, 7, 8], with recent evidence supporting its integration into robotic therapy approaches [9]. One method of implementing EA is through the application of deficit fields (DFs), which are force fields designed to exacerbate movement errors and promote increased exploration of the movement space [10].

Previous studies have primarily focused on applying DF to a single limb, demonstrating its potential for improving unilateral motor control [10, 11, 12]. However, these studies have not explored DF's effects on bimanual coordination, as they typically apply DF only to the affected limb. Our study introduces a novel approach by applying DF to both arms—using a conventional DF on the affected/non-dominant arm and a mirrored DF on the unaffected/dominant arm. This allows us to investigate the impact of bilateral force perturbations on interlimb coordination and movement exploration, which has not been previously examined. Mirror therapy, using visual feedback of the unaffected limb, has shown promise in stroke rehabilitation [13, 14]. Our approach extends beyond visual feedback by incorporating physical perturbations through deficit fields to engage multiple sensorimotor learning pathways.

We hypothesize that mirroring the DF parameters derived from the affected/non-dominant arm to the unaffected/dominant arm will lead to increased exploration and enhanced motor learning in both groups. This approach is based on the principle of interlimb coupling, which facilitates coordinated movement patterns between limbs through bilateral neural mechanisms [15, 16]. By applying mirrored DFs, we aim to induce interlimb coupling, which facilitates coordinated movement patterns between limbs through bilateral neural mechanisms.

Using the NREH-Bimanual robotic platform, we investigated mirrored deficit fields' effects on bimanual coordination. Participants generated personalized parameters through free exploration with their affected/non-dominant arm, which were then mirrored. Movement quality was assessed using three metrics (Randomness Score, Cumulative Traveling Distance, and Workspace Area) to evaluate this approach's potential as a novel stroke rehabilitation strategy.

II. METHODS

A. Participants

Eleven participants were recruited for this study: six individuals with chronic stroke (≥6 months post-stroke) and five able-bodied controls. Stroke patients exhibited mild to moderate upper limb impairment, with Fugl-Meyer

This project was supported by the Translational Research Program for Rehabilitation Robots, National Rehabilitation Center, Korea [NRCTR-IN23004, NRCTR-IN24004].

Assessment scores [17] > 20. Ethical approval was obtained from the Institutional Review Board (IRB No#: NRC-2020-06-040), and all participants provided written informed consent before participating in the study.

Included six stroke survivors (5 male, 1 female; average age: 67.00 ± 8.36 years; time since stroke: 17.83 ± 6.96 years; Fugl-Meyer Assessment (FMA) of motor function and joint range of motion, scored from 0-66 for the upper extremity: 47.00 ± 13.50; Box and Block Test (BBT) assessing hand dexterity and functional ability, measuring the number of blocks transferred in one minute: 12.17 ± 10.20; Action Research Arm Test (ARAT) providing a comprehensive assessment of arm and hand functional ability, scored from 0-57: 33.50 ± 21.57; Modified Barthel Index (MBI) assessing activities of daily living, scored from 0-100: 94.67 ± 3.90 and five able-bodied participants (3 male, 2 female; average age: 34.00 ± 5.58 years).

B. NREH-Bimanual robotic platform

The NREH-Bimanual robotic platform [18, 19] was employed to apply forces to the participants' arms during the experiment. This device allows for precise control of forces and accurate measurement of arm movements in two dimensions. Participants were seated comfortably facing the robot, with their arms supported by the robot arms. Visual feedback of hand position was provided on a display integrated into the NREH-Bimanual (Fig. 1).

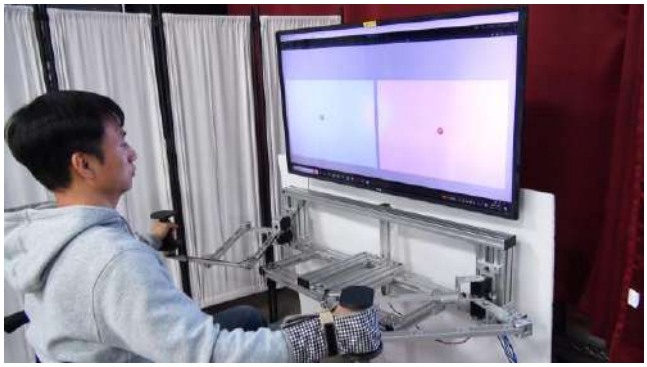


Fig. 1. NREH-Bimanual robotic platform.

C. Experimental Procedure

To generate the Deficit Field, participants first completed a Free Exploration task using their affected (or non-dominant) arm for 4 minutes within a 600×400 mm workspace. During this task, participants were instructed to explore freely in various directions and at different speeds. This task was used to customize the Deficit Field parameters for subsequent conditions. A 2-minute rest period was provided following this task. All experimental tasks were performed simultaneously with both arms to ensure bimanual coordination throughout the sessions.

Participants then performed the following experimental conditions, each lasting 2 minutes and followed by a 2-minute rest period:

- **Condition #1:** Null Field (NF). No force field was applied. This served as a baseline measure of exploratory behavior.
- **Condition #2:** Unilateral DF on Affected/Non-dominant Side. DF was applied only to the affected arm in stroke patients, or the non-dominant arm in able-bodied participants.
- **Condition #3:** Unilateral DF on Unaffected/Dominant Side with Mirrored DF. DF, with mirrored parameters from the affected/non-dominant arm, was applied only to the unaffected arm in stroke patients, or the dominant arm in able-bodied participants.
- **Condition #4:** Bilateral DF with Mirrored DF on Unaffected/Dominant Side. DF was applied to both arms. The affected/non-dominant arm received its individually tuned DF, while the unaffected/dominant arm received the mirrored DF.

Participants were instructed to maximize exploratory movements, covering as many directions and speeds as possible during each condition. In particular, Condition #2 and Condition #3 were applied in random order. The total training session concluded after completing the four conditions and their associated rest periods.

D. Deficit Field

The deficit field (DF) was implemented as a velocity-dependent force field [10, 11] that perturbed hand movements based on the velocity data collected from one arm using the NREH bimanual system. To analyze velocity distribution, a two-dimensional histogram was generated to discretize the distribution of velocity vectors. The histogram bin boundaries were created by equally dividing the velocity data range, defined by the minimum and maximum values of the measured data, into 20 bins. The histogram was then normalized to obtain the velocity density (defined as D), which represents the probability distribution of velocities in each bin.

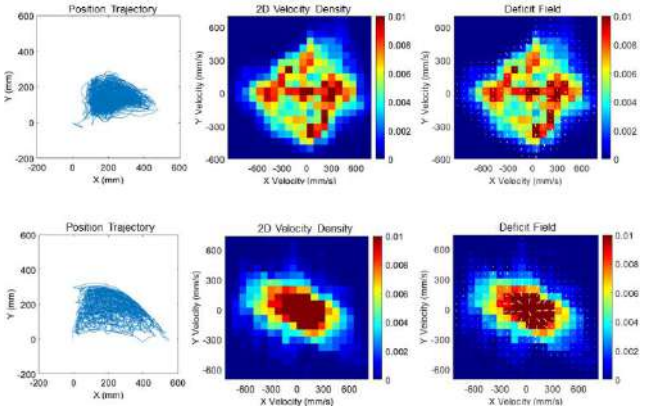


Fig. 2. Free exploration trajectories, normalized velocity density, and deficit fields derived from normalized velocity density using gradients for the affected right hands of two stroke participants. Top row: data from the first participant; bottom row: data from the second participant.

The force field was generated by calculating gradients (p_x, p_y) from the velocity density D. The gradient magnitude was calculated as $mag = sqrt(p_x^2 + p_y^2)$, and force vectors were defined as $F_x = -p_x/mag$ and $F_y = -p_y/mag$. The gradient direction was inverted to act from high to low velocity density regions, facilitating movement exploration into less frequently

visited areas. To prevent excessive force perturbations, a gradient threshold of 0.005 was applied, rescaling the gradient magnitude to a maximum of 0.005 when it exceeded this threshold. This normalization ensured smooth force transitions while preventing abrupt changes in force magnitude. Fig. 2 illustrates this process, showing the velocity density distribution, gradient computation, and resulting force field visualization.

The direction and magnitude of the force field were personalized based on each participant's individual motor characteristics [20, 21]. For stroke patients, parameters were derived from velocity data during free exploration of the affected arm, while for able-bodied participants, these were calculated from the non-dominant arm. In the mirroring condition, these parameters were mirrored and applied to the unaffected/dominant arm, following principles of interlimb coupling and motor learning [22, 23, 24, 25]. Using the Robotis XM540 actuator, the force field was limited to a maximum handle force of 30N, with a gradient threshold of 0.005 to ensure safe, comfortable interaction.

E. Metrics

To evaluate arm functionality during randomness movements performed using both hands to control the handles, the following metrics were used:

- **Randomness Score (RS)** [10, 11]: The RS quantifies exploratory behavior by assessing movement variability and distribution. To compute RS, position and velocity data from each arm were recorded in a 600 mm × 400 mm workspace. This workspace was divided into a 5 × 5 grid (25 zones). Within each zone, a velocity histogram was generated using horizontal and vertical velocity components ranging from -2.00 m/s to 2.00 m/s, with each axis discretized into 20 bins (bin size: 0.2 m/s). During the scoring process, a zone received a maximum score of 100 if all velocity histogram bins were filled, indicating a high degree of velocity diversity. The final RS was computed by averaging the scores across all 25 zones, with higher RS values reflecting greater movement diversity and exploration.
- **Cumulative Traveling Distance**: The cumulative distance traveled by the arms during the task is calculated as the sum of all movements. A greater total traveling distance indicates higher arm activity, reflecting increased effort. A larger distance is considered desirable as it implies more active movement. Since all conditions were performed for a fixed duration, an increase in cumulative traveling distance inherently suggests an increase in average speed.
- **Workspace Area**: Two robotic arms were positioned in a 2D plane where participants held the end-effectors. This metric quantifies changes in the convex hull area covered by arm movements.

Given our small sample size (stroke: n=6, able-bodied: n=5), we used descriptive statistics to analyze outcome trends and examined individual participant data to understand response patterns across conditions.

III. RESULTS

We analyzed three key metrics - Randomness Score (RS), Cumulative Traveling Distance (CTD), and Workspace Area - to evaluate the effectiveness of the Deficit Field (DF) conditions. These metrics were compared across all four experimental conditions for both stroke and able-bodied participants.

A. Randomness Score

Analysis of Fig. 3 shows that in the stroke group, the application of DF showed a clear trend of increasing RS. Unilateral DF applied to the affected arm (condition #2) led to an increase in RS compared to the null field condition (condition #1). Applying the mirrored DF to the unaffected arm (condition #3) also resulted in an increase in RS, highlighting the potential for interlimb coupling.

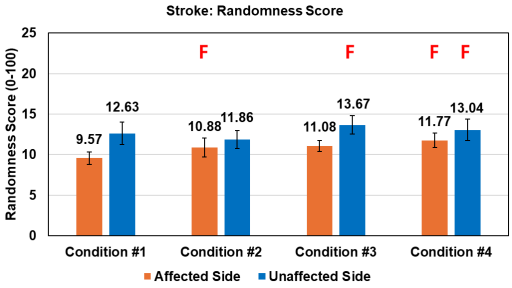


Fig. 3. Randomness Score across conditions in stroke patient (C1: Null Field, C2: Unilateral DF on Affected Side, C3: Unilateral Mirrored DF on Unaffected Side, C4: Bilateral DF). 'F' marks indicate the application of the Deficit Field (DF) on the corresponding arm. In Condition #4, DF was applied bilaterally, so 'F' appears on both arms.

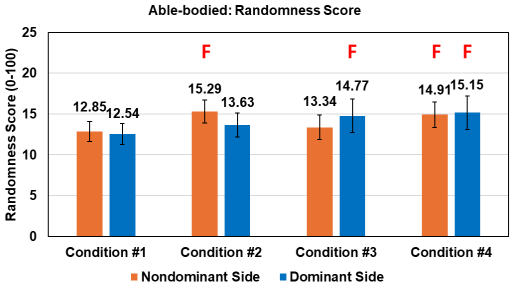


Fig. 4. Randomness Score across conditions in able-bodied patient (C1: Null Field, C2: Unilateral DF on Nondominant Side, C3: Unilateral Mirrored DF on Dominant Side, C4: Bilateral DF). Error bars show standard deviation. 'F' marks indicate the application of the Deficit Field (DF) on the corresponding arm. In Condition #4, DF was applied bilaterally, so 'F' appears on both arms.

As shown in Fig. 4, the able-bodied participants demonstrated similar increases in RS with DF application. Under unilateral DF conditions (conditions #2 and #3), RS was higher compared to the null field condition (condition #1), with the effect being more pronounced in the arm to which DF was applied. In the bilateral DF condition (condition #4), the RS difference between the nondominant and dominant sides was reduced, possibly due to the intact sensorimotor systems of able-bodied individuals.

Participants were instructed to explore the workspace freely for 2 minutes in each condition, varying their movement directions and speeds. Compared to baseline (Condition #1),

the mean Randomness Score (mean ± SD) increased for both groups. The stroke group's affected side showed improvements of 12.99±6.02% in Condition #2, 16.89±5.36% in Condition #3, and 24.30±9.43% in Condition #4. Similarly, the able-bodied group's nondominant side improved by 23.43±8.30%, 5.00±4.30%, and 14.52±7.45% in Conditions #2, #3, and #4, respectively.

B. Cumulative Traveling Distance

Analysis of Figs. 5 and 6 shows distinct patterns in both groups when DF was applied. In the stroke group, CTD increased progressively, with the highest values observed in bilateral DF condition (condition #4). Notably, DF application to the unaffected side promoted movement more effectively than to the affected side. The affected side showed improvements of 13.59±9.39%, 23.98±9.27%, and 34.52±10.72% in Conditions #2, #3, and #4 respectively, compared to baseline.

In the able-bodied group, unilateral DF conditions (#2 and #3) resulted in decreased CTD in the arm without DF, suggesting redistribution of sensorimotor resources. However, bilateral DF (condition #4) produced balanced engagement, with the nondominant side showing changes of 2.83±6.48%, -2.25±6.95%, and 6.01±4.97% in Conditions #2, #3, and #4 respectively. This demonstrates bilateral DF's potential for promoting symmetrical motor performance.

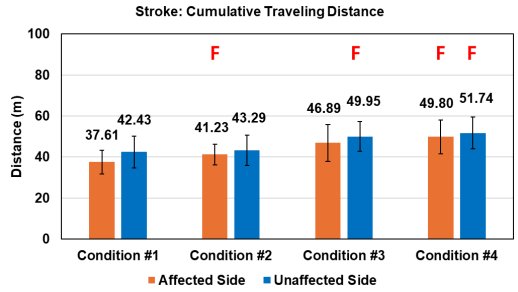


Fig. 5. Cumulative Traveling Distance in stroke patients for the same conditions as in Fig. 3.

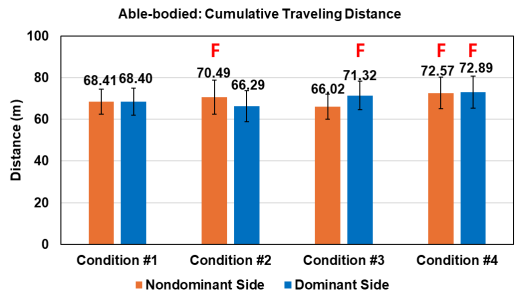


Fig. 6. Cumulative Traveling Distance in able-bodied patient for the same conditions as in Fig. 4.

C. Workspace Area

Analysis of Figs. 7 and 8 revealed distinct workspace patterns for both groups. In the stroke group, unilateral DF (Condition #2) increased the affected side's workspace while decreasing the unaffected side's area. When DF was applied to the unaffected side (Condition #3) or bilaterally (Condition #4), both arms showed increasing workspace. The affected side showed improvements of 10.36±2.92%, 15.70±9.82%, and 28.52±14.95% in Conditions #2, #3, and #4 respectively, with the largest increase under bilateral DF.

In the able-bodied group, unilateral DF produced opposing effects: when applied to one side, that side's workspace increased while the other decreased slightly. Bilateral DF (Condition #4) resulted in workspace expansion for both sides, particularly the dominant side. The nondominant side showed changes of 22.28±11.24%, -3.31±7.58%, and 19.52±11.80% in Conditions #2, #3, and #4 respectively. These results suggest able-bodied individuals adapt effectively to force conditions, achieving immediate and symmetric workspace expansions.

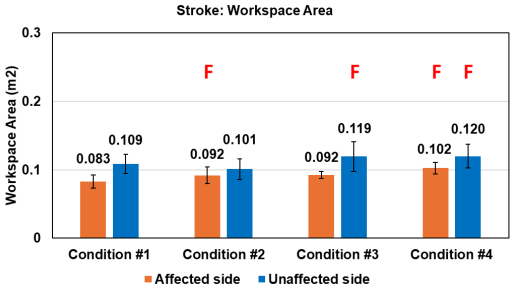


Fig. 7. Workspace Area in stroke patients for the same conditions as in Fig. 3.

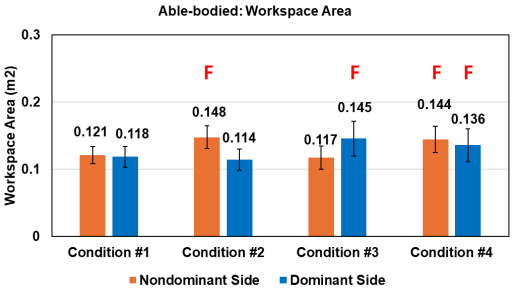


Fig. 8. Workspace Area in able-bodied patient for the same conditions as in Fig. 4.

D. Qualitative Observations

Qualitative observations during the experiment provided further insights into participants' behavior. When DF was applied to the affected side in Condition #2, the stroke group generally had difficulty recognizing the force exerted by the DF. However, when DF was applied to the unaffected side (Condition #3), participants were able to recognize the force more clearly. Notably, one stroke participant reported feeling that both hands moved noticeably faster when DF was applied to the unaffected side. Supporting this observation, the stroke group's average speed in Condition #3 increased by approximately 20% compared to Condition #1, suggesting a potential facilitation effect from applying DF to the unaffected side.

IV. Discussion

This study investigated the effects of mirrored deficit fields (DF) on bimanual coordination and exploration in both stroke patients and able-bodied individuals. Our findings demonstrate that applying DF, particularly with mirrored parameters, enhances exploratory behavior and motor performance, as evidenced by increased Randomness Scores

(RS) and workspace area. This effect was observed even when the DF was applied to the unaffected/dominant arm, suggesting the presence of interlimb coupling and its potential to facilitate motor learning in the affected limb.

While our small sample size (stroke n=6, able-bodied n=5) precludes statistical inference, the consistent trends observed across participants suggest potential benefits of the mirrored DF approach. The magnitude of improvements in both RS and workspace area, particularly in the bilateral DF condition, provides preliminary evidence for the effectiveness of this intervention. Individual participant data revealed that all stroke patients showed some degree of improvement in at least one outcome measure, with five out of six patients showing improvements across all measures in the bilateral DF condition. In the able-bodied group, all participants demonstrated consistent improvements in both RS and workspace area during bilateral DF application, suggesting the robustness of this approach across different populations.

The observed increase in RS with DF application can be attributed to the principles of error augmentation and motor adaptation [5, 6, 9]. By perturbing movements, DF creates a challenging environment that encourages the nervous system to actively explore new movement solutions and adapt to the imposed constraints [20, 21, 22]. This increased exploration, reflected in higher RS, may facilitate the discovery of more efficient and coordinated movement patterns, potentially leading to improved bimanual performance.

The significant increase in RS with mirrored DF on the unaffected/dominant arm (condition #3) is particularly noteworthy. This finding supports our hypothesis of interlimb coupling, where motor learning and adaptation in one limb can influence the motor control of the other limb [23, 24, 25]. By mirroring the DF parameters from the affected/non-dominant arm, we observed increased exploration in the unaffected/dominant arm, suggesting that force field parameters derived from one arm can effectively challenge movement patterns in the other arm. This suggests that interlimb coupling can be exploited to enhance motor learning and promote recovery in the affected limb, even without direct intervention.

The observed interlimb coupling effects can be explained through multiple mechanisms. At the neural level, interhemispheric interactions facilitate bilateral motor control through transcallosal pathways [26]. Biomechanically, force transmission through the trunk contributes to bilateral movement coordination. From a motor control perspective, the nervous system employs shared bilateral planning and movement synergies, while integrated proprioceptive and visual feedback provides crucial sensory information for coordinated movement [27]. These mechanisms collectively support the efficacy of bilateral approaches in rehabilitation and guide the development of advanced robotic rehabilitation strategies [28].

While mirror therapy utilizes visual feedback from the unaffected limb, our mirrored deficit field approach provides active force-based perturbations engaging both proprioceptive and motor learning pathways. This multi-modal engagement may explain our observed improvements. Our robotic assessment metrics (RS, CTD, Workspace Area) complemented traditional clinical scales like FMA and ARAT by providing detailed insights into movement quality and exploration patterns.

Furthermore, the bilateral DF condition (condition #4) resulted in the most significant improvements in both RS and workspace area for both groups. This highlights the potential of bilateral DF application to promote symmetrical motor performance and facilitate coordinated movement patterns between both limbs. The robust response to bilateral DF aligns with our understanding of interlimb coupling mechanisms and suggests that simultaneous bilateral training may be particularly effective in rehabilitation settings [12, 23]. By challenging both limbs simultaneously, bilateral DF may encourage the nervous system to develop more efficient and adaptive motor control strategies, leading to enhanced bimanual coordination.

The small sample size (six participants with stroke and five able-bodied participants) warrants caution in generalizing the findings to the broader stroke population. The long-term retention effects of mirrored DF training were not assessed. The transfer of improved motor performance to activities of daily living was not evaluated. The optimal parameters for DF application need to be further investigated through systematic parameter space exploration. Future studies with larger samples and longer follow-up periods are needed to address these limitations.

Despite these limitations, this study provides valuable insights into the potential of mirrored DF as a novel intervention strategy for enhancing motor learning and functional recovery in stroke. By promoting interlimb coupling and challenging bimanual coordination, mirrored DF may offer a unique opportunity to optimize rehabilitation programs and improve outcomes for individuals with stroke.

The clinical implications of this study demonstrate the potential of mirrored DF training to enhance bimanual coordination and motor learning in stroke rehabilitation. This approach offers several clinical benefits: enhanced motor learning through the promotion of motor learning in the affected limb by leveraging interlimb coupling and facilitating the transfer of learned strategies from the unaffected limb; improved bimanual coordination by challenging both limbs simultaneously to encourage the development of more coordinated and efficient movement patterns; and increased patient engagement through the novel and challenging nature of mirrored DF training. Future research should focus on larger-scale clinical trials to validate these findings and investigate the long-term benefits of this approach. Additionally, further exploration of optimal DF parameters and integration with other rehabilitation strategies will be crucial to maximize its therapeutic impact.

V. Conclusion

This study demonstrated the effectiveness of mirrored deficit fields in enhancing bilateral arm movements through interlimb coupling mechanisms. Using our novel NREH-Bimanual robotic platform, we implemented a velocity-dependent force field derived from free exploration data and investigated its effects across four distinct conditions in eleven participants (six stroke patients and five able-bodied individuals).

Our findings revealed three significant outcomes: (1) The application of deficit fields enhanced movement exploration, as evidenced by increased Randomness Scores (up to 24.30% improvement) and workspace areas (up to 28.52% expansion); (2) The mirrored application of DF parameters from the affected to the unaffected arm demonstrated particular effectiveness, suggesting successful utilization of interlimb coupling mechanisms; (3) Bilateral DF application showed the most substantial improvements in movement quality, with enhanced movement perception and increased average speed (approximately 20%) in stroke patients.

Future research directions should focus on: 1) Conducting larger-scale clinical trials with diverse stroke populations, 2) Developing algorithms for real-time optimization of individual DF parameters, 3) Investigating the long-term retention of motor improvements, and 4) Exploring the transfer effects to activities of daily living. This work provides promising evidence for the potential of mirrored DF as an effective rehabilitation strategy for enhancing bimanual coordination and motor recovery in clinical settings.

ACKNOWLEDGMENT

We want to thank Ms. Mi-Ran Hong, Mr. Jun-Yong Song, and Mr. Jae-Yeop Nam for their support.

REFERENCES

[1] S. M. Hatem et al., "Rehabilitation of motor function after stroke: a multiple systematic review focused on techniques to stimulate upper extremity recovery," Front. Hum. Neurosci., vol. 10, pp. 442, 2016.

[2] C. A. Potts and S. S. Kantak, "Post-stroke deficits in the anticipatory control and bimanual coordination during naturalistic cooperative bimanual action," J. NeuroEng. Rehabil., vol. 20, no. 1, pp. 153, 2023.

[3] J. L. Patton, M. E. Stoykov, M. Kovic, and F. A. Mussa-Ivaldi, "Evaluation of robotic training forces that either enhance or reduce error in chronic hemiparetic stroke survivors," Exp. Brain Res., vol. 168, pp. 368-383, 2006.

[4] L. Y. Liu, Y. Li, and A. Lamontagne, "The effects of error-augmentation versus error-reduction paradigms in robotic therapy to enhance upper extremity performance and recovery post-stroke: a systematic review," J. NeuroEng. Rehabil., vol. 15, pp. 1-25, 2018.

[5] S. Israely and E. Carmeli, "Error augmentation as a possible technique for improving upper extremity motor performance after a stroke–a systematic review," Top. Stroke Rehabil., vol. 23, no. 2, pp. 116-125, 2016.

[6] L. Y. Liu, Y. Li, and A. Lamontagne, "The effects of error-augmentation versus error-reduction paradigms in robotic therapy to enhance upper extremity performance and recovery post-stroke: a systematic review," J. NeuroEng. Rehabil., vol. 15, Art. no. 25, 2018.

[7] F. Abdollahi et al., "Error-augmented bimanual therapy for stroke survivors," NeuroRehabil., vol. 43, no. 1, pp. 51-61, 2018.

[8] F. Abdollahi et al., "Error augmentation enhancing arm recovery in individuals with chronic stroke: a randomized crossover design," Neurorehabil. Neural Repair, vol. 28, no. 2, pp. 120-128, 2014.

[9] E. Carmeli et al., "Robotically driven e rror augmentation training enhances post ‐ stroke arm motor recovery," Eng. Rep., Art. no. e12720, 2023.

[10] Z. A. Wright, J. L. Patton, F. C. Huang, and E. Lazzaro, "Evaluation of force field training customized according to individual movement deficit patterns," in Proc. IEEE Int. Conf. Rehabil. Robot. (ICORR), 2015, pp. 193-198.

[11] Z. A. Wright, E. Lazzaro, K. O. Thielbar, J. L. Patton, and F. C. Huang, "Robot training with vector fields based on stroke survivors' individual movement statistics," IEEE Trans. Neural Syst. Rehabil. Eng., vol. 26, no. 2, pp. 307-323, 2017.

[12] K. C. Stewart, J. H. Cauraugh, and J. J. Summers, "Bilateral movement training and stroke rehabilitation: a systematic review and meta-analysis," J. Neurol. Sci., vol. 244, no. 1-2, pp. 89-95, 2006.

[13] H. Thieme, J. Mehrholz, M. Pohl, J. Behrens, C. Dohle, and Mirror Therapy Review Group, "Mirror therapy for improving motor function after stroke," *Cochrane Database of Systematic Reviews*, no. 3, Art. no. CD008449, 2012.

[14] V. S. Ramachandran and E. L. Altschuler, "The use of visual feedback, in particular mirror visual feedback, in restoring brain function," *Brain*, vol. 132, no. 7, pp. 1693–1710, 2009.

[15] S. Hascher, A. Shuster, R. Mukamel, and O. Ossmy, "The power of multivariate approach in identifying EEG correlates of interlimb coupling," Front. Hum. Neurosci., vol. 17, Art. no. 1256497, 2023.

[16] K. N. Arya and S. Pandian, "Interlimb neural coupling: Implications for poststroke hemiparesis," Ann. Phys. Rehabil. Med., vol. 57, no. 9-10, pp. 696-713, 2014.

[17] A. R. Fugl-Meyer, L. Jääskö, I. Leyman, S. Olsson, and S. Steglind, "A method for evaluation of physical performance," Scand. J. Rehabil. Med., vol. 7, no. 1, pp. 13–31, 1975.

[18] W.-K. Song, "Upper extremity rehabilitation robot platform: From unilateral toward bimanual," in Proc. 18th Int. Conf. Intell. Auton. Syst., Suwon, Korea, 2023, pp. 1-6.

[19] S. H. Lee and W.-K. Song, "Bilateral arm movement enhancement: Robotic error augmentation insights from stroke and able-bodied participants," in Proc. 10th IEEE RAS/EMBS Int. Conf. Biomed. Robot. Biomechatron. (BioRob), 2024, pp. 705-710.

[20] J. L. Emken and D. J. Reinkensmeyer, "Robot-enhanced motor learning: accelerating internal model formation during locomotion by transient dynamic amplification," IEEE Trans. Neural Syst. Rehabil. Eng., vol. 13, no. 1, pp. 33-39, 2005.

[21] C. K. Williams and H. Carnahan, "Motor learning perspectives on haptic training for the upper extremities," IEEE Trans. Haptics, vol. 7, no. 2, pp. 240-250, 2014.

[22] L. Marchal-Crespo, L. Michels, L. Jaeger, J. López-Olóriz, and R. Riener, "Effect of error augmentation on brain activation and motor learning of a complex locomotor task," Front. Neurosci., vol. 11, Art. no. 526, 2017.

[23] J. W. Krakauer, "Motor learning: its relevance to stroke recovery and neurorehabilitation," Curr. Opin. Neurol., vol. 19, no. 1, pp. 84-90, 2006.

[24] M. Maier, B. R. Ballester, and P. F. M. J. Verschure, "Principles of neurorehabilitation after stroke based on motor learning and brain plasticity mechanisms," Front. Syst. Neurosci., vol. 13, Art. no. 74, 2019.

[25] R. Shadmehr and F. A. Mussa-Ivaldi, "Adaptive representation of dynamics during learning of a motor task," J. Neurosci., vol. 14, no. 5, pp. 3208-3224, 1994.

[26] J. H. Cauraugh and J. J. Summers, "Neural plasticity and bilateral movements: A rehabilitation approach for chronic stroke," Progress in Neurobiology, vol. 75, no. 5, pp. 309-320, 2005.

[27] S. McCombe Waller and J. Whitall, "Bilateral arm training: Why and who benefits?," NeuroRehabilitation, vol. 23, no. 1, pp. 29-41, 2008.

[28] R. L. Sainburg et al., "Effects of altering initial position on movement direction and extent," Journal of Neurology & Translational Neuroscience, vol. 1, no. 3, pp. 1025, 201.

General Purpose Haptic/Biometric-Based Dynamic Difficulty Adjustment for Post-stroke Upper-limb Rehabilitation Games

Yiyang Shang[1], Sasan Bahrami[2], Samuel Gaardsmoe[3], Alwyn Johnson[4], Michelle J. Johnson[5], Paul Diefenbach[6]

***Abstract*—Rehabilitation therapy can be more effective and engaging when interactive technologies are involved. To enhance this experience, we integrated a haptic/biometric-based (HBB) Dynamic Difficulty Adjustment (DDA) system into the enAblegames™ platform, which already uses body tracking for therapeutic gaming. This system adapts game and haptic difficulty in real time based on each patient's biometric data and performance, making therapy more personalized.**

We tested this system with 11 participants, comparing their experiences with and without DDA. The results were promising—36% preferred DDA-enhanced games, compared to just 7% for non-DDA, and in a single-game scenario, preference for DDA increased by 50%.

These early findings suggest that HBB-DDA can make rehabilitation more engaging and tailored to individual needs. While more research is needed to understand its full impact, this system has the potential to improve patient experience and therapy outcomes.

I. INTRODUCTION

Rehabilitation after stroke often requires a long recovery process [1], and patients may lose the motivation to continue to comply with exercise regimens from their clinical advisors, leading to diminished functional outcomes [2]. Wrapping rehabilitation exercises with games, often called exergames [3], can help maintain patient engagement during a therapy session and across a prescribed therapy period consisting of multiple sessions. [4] Recognizing the need to personalize these games to a patient's mental and physical function level, the idea of developing methods to promote the dynamic adjustment of exercise-based games has emerged as a promising approach to enhance user engagement and optimize training outcomes during rehabilitation [5], [6], [7], and [8]. Incorporating adaptive gameplay and dynamic difficulty adjustment (DDA) in serious games for rehabilitation shows promising results [9], and [10]. These strategies enhance patient engagement, motivation, and overall rehabilitation outcomes, contributing to more effective and personalized interventions across various rehabilitation domains. The continuous advancement of serious games in rehabilitation holds significant potential for transforming patient experiences and improving rehabilitation programs [11], [12], and [13]. Although prior studies have shown that there is a need for DDA in games used in rehabilitation robotics [14], [15], and [16], few games have been developed for this purpose. There is a need to develop a DDA package that can be applied to games of varied design structures to best address different therapy goals while having a multitude of distinct games to reduce boredom among patients [8], [17], [18], and [19]. Furthermore, since the application of rehabilitation robotic technologies varies in complexity and types of impairment profiles treated, there is a need for flexibility in a DDA system to leverage player biometric and robotic inputs (in addition to game performance data) to best determine adaptive game levels. In particular, when dealing with force-feedback technologies, the DDA system should provide both in-game dynamic feedback and haptic feedback to execute these adaptations. This paper details the development and use of a novel DDA algorithm called Haptic/Biometric-Based (HBB) Dynamic Difficulty Adjustment (DDA) HBB-DDA in therapy games, followed by a discussion of how this DDA approach compares to previous systems.

II. RELATED WORKS

With the aim of tailoring the gaming experience to each patient's particular talent and rehabilitation goals, methods for adopting dynamic difficulty adjustment (DDA) in therapeutic gaming have been investigated, [10], [20], and [21]. Several studies in [15], [16] ,and [22] highlighted the significance of personalization in therapeutic video games, aligning challenges with patients' abilities and rehabilitation goals, and enhancing patient engagement and compliance, which are crucial for effective rehabilitation programs. DDA models typically work by adjusting the difficulty levels of game tasks. According to the flow model, a task's difficulty should match the user's capabilities to prevent boredom from too few challenges and anxiety from too many challenges [23]. People exhibit various "flow zones" because

[1]Yiyang Shang is a PhD student at Drexel University in the Antoinette Westphal College of Media Arts and Design. rs3648@drexel.edu

[2]Sasan Bahrami is a PhD student at Drexel University in the Antoinette Westphal College of Media Arts and Design. sb4333@drexel.edu

[3]Samuel Gaardsmoe is the lead engineer at Recupero Robotics LLC.sgaards@gmail.com

[4]Alwyn Johnson is CTO at Recupero Robotics LLC.research@tecxet.com

[5]Michelle J. Johnson is an Associate Professor at the University of Pennsylvania with a primary appointment in Physical Medicine & Rehabilitation and secondary appointments in Bioengineering and Mechanical Engineering and Applied Mechanics. johnmic@pennmedicine.upenn.edu

[6]Paul Diefenbach is an Associate Professor at Drexel University, Director of RePlay Lab, and Co-Founder of enAbleGames. pjdief@drexel.edu

they have diverse preferences for the levels of challenge [23], and [24]. The concept of DDA has been expanded beyond conventional exercise games [6] to virtual reality exercise games for rehabilitation [8], a field tangential to our research. Huber et al. explored DDA through Experience-driven Procedural Content Generation in VR exergames, enhancing engagement by adapting challenges to player performance, which is critical for rehabilitation, and also focused on tailored challenges in rehabilitation exergames [7]. In addition, DDA has been used in robot-assisted therapy, a fast-developing method for recovering from stroke injuries [25], [26], [27], and [28]. Robots frequently use games to keep patients motivated during workouts [29], [29], and [30], and dynamic player modeling has proven to be an effective tool in this setting [31], and [32]. For example, in order to maximize the efficacy of rehabilitation, scientists [33] , and [14] investigated dynamic player modeling in therapeutic robotics games by continuously modifying game obstacles based on player skills. Evolutionary algorithms [14], [34], and [35] have also been used to continuously assess user performance and adjust the level of difficulty of the game in real-time, resulting in more customized and successful rehabilitation experiences. Ozkul [36] presented a fresh and creative approach that combined performance data with real-time emotion feedback as the input to their DDA algorithm, In addition to improving customized therapy, and this integration [35]. Engagement/participation in therapy sessions has a significant impact on how well a patient recovers [37]. Researchers have also investigated the use of physical games for stroke recovery, including digital components to improve therapy, using the digital box and Blocks Test [38], [39], and [40]. Their strategy focuses on blending physical and digital elements to produce enjoyable and efficient rehabilitation experiences [41], [42], [43], and [44].

Our paper describes a new DDA algorithm and a pilot study that examines power generation, game performance, and user preferences in the context of robotic therapy games. Although the focus of our study is mostly on digital therapy games with DDA, the general goal is to utilize technology to improve rehabilitation results.

III. Architecture

A. Design and implementation

This study is part of a multi-year project to design and evaluate a reconfigurable haptic robotics platform integrated with adaptive video games for use in rehabilitation therapy for stroke patients. During the first year, a prototype robot hardware [45] and software platform was developed to test the viability of this approach. The HBB-DDA integration leverages the traditional DDA design, extending it with novel biometric and haptic support. It will also be revised based on the findings presented in this paper.

The Haptic TheraDrive, a one-degree-of-freedom robotic device, enhances upper-limb rehabilitation through personalized adaptive resistance and feedback. It is integrated with therapy and assessment exergames designed to make rehabilitation engaging and effective by tailoring exercises to patient needs and significantly advancing stroke recovery strategies. Figure 1 shows a subject using the hardware of a robot in various configurations. The control algorithm is designed to permit the robot to apply varying levels of assistive or resistive forces to its end effector. Typically, users are seated in front of or on the side of the robot, with their dominant or non-dominant resting comfortably on the handle of the end-effector. The user must move the robot handle to interact with the icon in the game. The mapping of handle rotation to the game icon depends heavily on the game objectives.



Fig. 1: Patient using robot in all configurations

B. Therapy Games

Integrating the Haptic TheraDrive system with exergames for therapy or assessment allows personalization and affordable post-stroke upper limb rehabilitation. The assessment games were designed to assess motor and cognitive performance [46]. Therapy exergames, tailored to patient capabilities and therapeutic requirements, leverage adaptive difficulty settings to ensure optimal engagement and recovery outcomes (Fig. 2). This approach enhances patient motivation and fosters a personalized and effective rehabilitation experience.

C. Haptic Biometric-Based Dynamic Difficulty Adjustment

We integrated a novel haptic/biometric-based dynamic difficulty adjustment (HBB-DDA) system into the enAblegames™ platform to dynamically modify assistive/resistive forces and game difficulty based on user needs. This system adapts robotic force feedback, in-game difficulty, and player guidance in real time using motor and cognitive capabilities, performance metrics, and therapist-defined parameters.

The HBB-Dynamic Adjustment System (fig 3) of the game comprises two main subsystems: the Dynamic Difficulty Adjustment System (DDA) and the Dynamic Feedback System (DFS). These are informed by the Standard Difficulty Adjustment (SDA) system. The DDA adjusts the game's difficulty in real time according to the patient's performance and physiological data. The DFS uses the patient's profile to modify the feedback elements of the game, including text, user interface, and visual and sound effects. The System for Kinematic Input (SUKI) processes player inputs, whether kinematic, robotic,

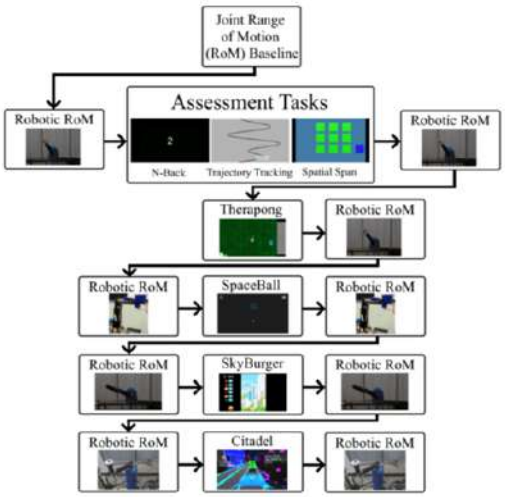


Fig. 2: Experimental workflow during robot-assisted exercise. Participants performed assessment tasks, therapy games, and standardized range of motion (ROM) [47] movements at each position shown in Figure 1 to determine their motor capability while operating the robot.

or biometric. A cloud-connected parameter system allows therapists to control the interaction of these systems, such as haptic feedback, ROM adaptation, and level count. A tracking system records game data, including robotic inputs, and saves it to the cloud for evaluation. The patient's haptic adjustments play a role in the DDA diagram. These subsystems modify the game to meet the patient's needs, providing appropriate challenges without overwhelming them.

DDA, a standalone unit, works with three systems within the enAblegames package: Static Difficulty Adjustment, Feedback, and SUKI:

1) SDA: The Standard Difficulty Adjustment (SDA) system manages fixed game settings, including cognitive difficulty and feedback preferences, using cloud-stored patient profiles that can be adjusted locally when needed.

2) Feedback: The customizable feedback system, guided by SDA settings, dynamically adjusts visual, audio, and text-based cues to indicate difficulty changes and encourage players, with intensity controlled by SDA data.

3) SUKI: The System for Unified Kinematic Input (SUKI) [48] was extended to integrate robotic and biometric inputs into a unified format, mapping data like robot angle, pinch angle, and heart rate to game controls while dynamically adjusting input ranges based on patient profiles stored and updated in the cloud.

The DDA receives data from SUKI and updates patient data and motor performance data, which is linked to game logic. Changes in difficulty are sent to a feedback system that includes text-based, sound-based, background-based, and visual effects. The DDA system used here is a modified version of the Partially Ordered Set Master algorithm suggested by Missura in 2011 [49] for DDA adjustment. This study offers a method for representing and adapting user flow zones within a game using physiological data analysis. To determine a patient's flow zone, we constantly altered the game's complexity by introducing the POSM algorithm, which dynamically adjusts the difficulty based on a 'harder than' relationship between levels. Each difficulty level has a belief vector that directs the prediction process. Further refinement of this vector based on observations and the patient's emotional state during a game session updates the game's difficulty. [37] [36].

Algorithm 1 Partially Ordered Set Master with Physiological Feedback

Require: A partial order $\succeq$ on K different levels, $\beta \in (0, 1)$

for t = 1, 2, ... **do**
  $\forall k \in K$: let $A_t(K) = \sum_{x \in K, x \geq k} w_t(x)$
  $\forall k \in K$: let $B_t(K) = \sum_{x \in K, x \leq k} w_t(x)$
  Decide $k_t^* = \arg\max_{k \in K} \min\{B_t(k), A_t(k)\}$
  Observe $o_t \in \{-2, -1, 0, 1, 2\}$
  Emotion State $e_t \in \{0, 1, 2, 3, 4\}$
  if $o_t = 2 \vee (e_t = 0 \wedge o_t \neq -2)$ **then**
    $\forall k \in K$: let $w_{t+1}(k) = \begin{cases} \beta w_t(k), & k \leq k_t^* \\ w_t(k), & \text{otherwise} \end{cases}$
  else if $o_t = -2 \vee (e_t = 5 \wedge o_t \neq 2)$ **then**
    $\forall k \in K$: let $w_{t+1}(k) = \begin{cases} \beta w_t(k), & k \geq k_t^* \\ w_t(k), & \text{otherwise} \end{cases}$
  end if
end for

Based on the observation O_t, the algorithm updates belief vectors for each difficulty level and predicts the difficulty level. Unlike the suggested study, HBB-DDA has more flexibility in updating belief vectors. First, variable β varies based on whether the difficulty level is harder or easier than the current one. If the patient is a hardcore player, β for harder difficulties will be larger. Second, the observation has five values: 1 for doing good, 0 for average, -1 for doing poorly, and 2 -2 for extreme performance. HBB-DDA can also take the game signal to indicate when the player is doing too well or too badly before the session ends and make changes immediately to prevent boredom or frustration.

In addition to regular performance observation, we added biological data to provide insight into the arousal value of the player's emotional state, including heart rate (HR) and Galvanic Skin Response (GSR). Baseline measurements of GSR and HR were obtained before the gaming sessions. During gameplay, deviations from the baseline indicated stress levels. We converted deviations to stress levels by comparing the size of the deviation to the baseline. Discrepancies between GSR and HR were resolved using GSR over HR data. When the indicators aligned, the DDA algorithm incorporated performance data to operate on GSR and HR values.

IV. Pilot Study

A pilot study was conducted to assess the effectiveness of our robotics and gaming platform for stroke rehabilitation using the Haptic TheraDrive system. Approval was obtained from the University of Pennsylvania IRB (IRB#849090).

Physiological measures, such as Galvanic Skin Response (GSR) and Heart Rate (HR), were integrated to assess

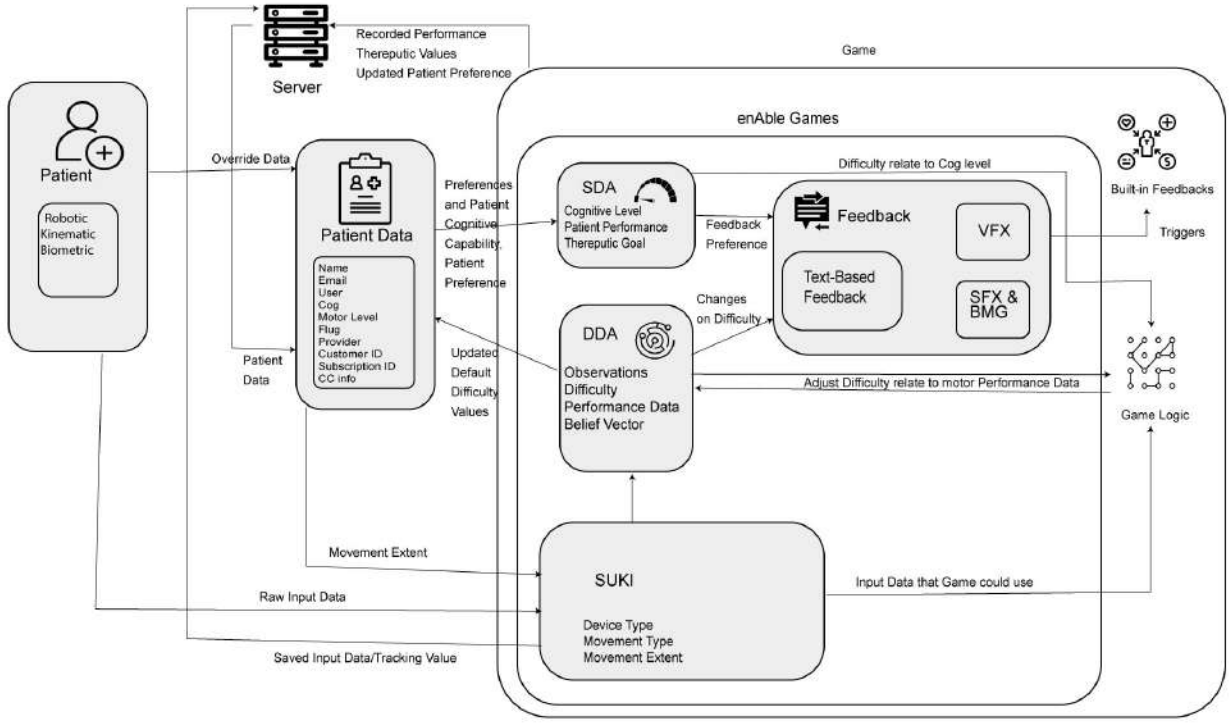


Fig. 3: DDA Diagram and its interaction with different modules

participants' engagement and stress levels. This approach explored the impact of adaptive technologies on rehabilitation outcomes, highlighting the potential benefits of customized game design for enhanced patient recovery and engagement.

Eleven stroke subjects tested the combined robot and gaming system. Informed consent was obtained from all patients. Upper limb motor and cognitive impairments varied from mild to moderate (UE-FM 23-66, MoCA score from 12-29). Subjects played one therapy game (TheraPong) without DDA and three therapy games (Citadel, SkyBurger, and SpaceBall) with and without the HBB-DDA system engaged while using the robot. The DDA adjusted game parameters and robot force feedback but not biological signals. Subjects completed surveys after each game and DDA conditions.

The result shows this system adapts the game's difficulty level in real-time using user performance and biometric feedback, enhancing patient engagement and potentially improving therapeutic outcomes. The use of haptic feedback and biometric data represents a significant innovation in rehabilitation technology, enhancing patient-therapy experiences. In a preference study, 36% preferred DDA game trials over 7% without DDA, with 57% having no preference. In the most difficult game, Spaceball, DDA preference reached 50% over 12% without DDA.

The HBB-DDA integration extends traditional DDA design with biometric and haptic support, and will be revised based on this paper's findings.

The study examined power, calculated as force times linear velocity, which changes during gameplay. Normalized to the maximum and lowest values, this power quantifies the physical labor performed by patients during therapeutic games.

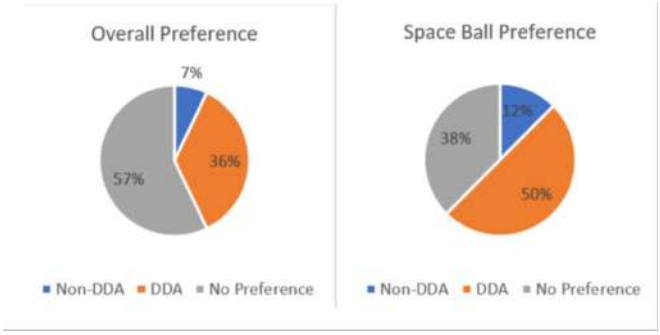


Fig. 4: Pie chart of user preference usage of DDA

The power score summary shows how participation correlates with improvements in motor control, as expressed by UE-FM scores. The research found a stronger relationship between exerted power and motor function than with cognitive performance, indicating that physical components of therapy games are more important for evaluating motor recovery. This is crucial for customizing treatment to maximize recovery.

V. Discussion

Our findings indicate that the HBB-DDA system, mixed with haptic power measures, has enhanced player engagement and personalized rehabilitation. This adaptability is crucial for long-term neuromotor disabilities, as maintaining interest impacts recovery. The system adjusts haptic feedback, game settings, and player interaction, making it versatile for therapists. Despite promising results, further research is needed with a larger sample and expanded biometric markers. Since the pilot, the system has supported eight exergames

TABLE I: Games used in the study

Game	About	How to Play	DDA Values
Citadel	Citadel is a futuristic driving simulator where you must hit arrow signs and avoid octagon signs to get the highest speed and score.	• Move the spaceship by rotating the handle. • Dodge the octagon signs, or else you will slow down. • Pass through the arrow signs to speed up and gain points. • The more arrow signs you collect, the more your speed increases.	• The Speed floor • The speed ceiling • Percentage of the green block
Skyburger	SkyBurger is a stacking game where the player must stack the listed ingredients to make a sandwich.	• Move the burger by rotating the handle. • Collect all ingredients that are shown on the list according to their labeled quantity. If you collect the wrong ingredient, you will lose points. • Avoid the top bun until you complete the recipe; otherwise, you will lose the round. • Once all ingredients in the recipe are collected and the bun is placed on top, you will win the round.	• Each level is based on DDA
Spaceball	Spaceball is a shooting game where you must shoot numbered circles until they read "zero".	• To start the game, press the button. • Aim the cursor toward the target by turning the handle. • Shoot the numbered shapes until the number goes to 0. • Avoid shooting the rotating shields around the circle.	• The range of position the target might spawn • Number of the shots the target needs • Number of shields on the target • Moving speed of the target

with ongoing improvements, including enhanced communication, expanded player profiles, and a new hierarchical game parameter system. These refinements position the HBB-DDA system as a potential benchmark for personalized rehabilitation.

VI. Conclusion

The enAblegames platform's introduction of the Haptic/Biometric-Based Dynamic Difficulty Adjustment (HBB-DDA) technology has demonstrated the system's potential to in rehabilitation therapy. Early findings show that participants clearly prefer games that use the DDA system, with a sizable portion expressing no preference. This suggests that the system's adaptability is successfully meeting the needs of different patients. By keeping patients motivated and involved in their recovery, this individualized approach not only improves therapeutic outcomes but also makes rehabilitation more pleasurable.

ACKNOWLEDGMENT

We thank the Rehab Robotics Lab at UPenn for data collection oversight, Enable Games LLC for software development, and Recupero Robotics LLC for robot development. Special thanks to Gary Lin for his dedication to force feedback programming. The views expressed are solely those of the authors and do not necessarily reflect those of the NIH.

References

[1] H. Hetherington and R. J. Earlam, "Rehabilitation after injury and the need for coordination," *Injury*, vol. 25, pp. 527–531, Oct. 1994.

[2] D. K. Chan, C. Lonsdale, P. Y. Ho, P. S. Yung, and K. M. Chan, "Patient motivation and adherence to postsurgery rehabilitation exercise recommendations: the influence of physiotherapists' autonomy-supportive behaviors," *Archives of Physical Medicine and Rehabilitation*, vol. 90, pp. 1977–1982, Dec. 2009.

[3] Y. Oh and S. Yang, *Defining exergames & exergaming*. Jan. 2010.

[4] I. Elkin, L. Falconnier, Y. Smith, K. E. Canada, E. Henderson, E. R. Brown, and B. M. McKay, "Therapist responsiveness and patient engagement in therapy," *Psychotherapy Research: Journal of the Society for Psychotherapy Research*, vol. 24, no. 1, pp. 52–66, 2014.

[5] M. Danousis, C. Goumopoulos, and A. Fakis, "Exergames in the GAME2AWE Platform with Dynamic Difficulty Adjustment," in *Entertainment Computing – ICEC 2022: 21st IFIP TC 14 International Conference, ICEC 2022, Bremen, Germany, November 1–3, 2022, Proceedings*, (Berlin, Heidelberg), pp. 214–223, Springer-Verlag, Nov. 2022.

[6] A. Darzi, S. M. McCrea, and D. Novak, "User Experience With Dynamic Difficulty Adjustment Methods for an Affective Exergame: Comparative Laboratory-Based Study," *JMIR Serious Games*, vol. 9, p. e25771, May 2021. Company: JMIR Serious Games Distributor: JMIR Serious Games Institution: JMIR Serious Games Label: JMIR Serious Games Publisher: JMIR Publications Inc., Toronto, Canada.

[7] T. Huber, S. Mertes, S. Rangelova, S. Flutura, and E. André, "Dynamic difficulty adjustment in virtual reality exergames through experience-driven procedural content generation," in *2021 IEEE Symposium Series on Computational Intelligence (SSCI)*, pp. 1–8, IEEE, 2021.

[8] M. Pezzera and N. A. Borghese, "Dynamic difficulty adjustment in exer-games for rehabilitation: a mixed approach," in *2020 IEEE 8th International Conference on Serious Games and Applications for Health (SeGAH)*, pp. 1–7, Aug. 2020. ISSN: 2573-3060.

[9] N. Hocine, A. Gouaïch, S. A. Cerri, D. Mottet, J. Froger, and I. Laffont, "Adaptation in serious games for upper-limb rehabilitation: an approach to improve training outcomes," *User Modeling and User-Adapted Interaction*, vol. 25, pp. 65–98, Mar. 2015.

[10] P. D. Paraschos and D. E. Koulouriotis, "Game Difficulty Adaptation and Experience Personalization: A Literature Review," *International Journal of Human–Computer Interaction*, vol. 39, pp. 1–22, Jan. 2023. Publisher: Taylor & Francis _eprint: https://doi.org/10.1080/10447318.2021.2020008.

[11] J. Wiemeyer and A. Kliem, "Serious games in prevention and rehabilitation—a new panacea for elderly people?," *European Review of Aging and Physical Activity*, vol. 9, pp. 41–50, Apr. 2012. Number: 1 Publisher: BioMed Central.

[12] P. Rego, P. M. Moreira, and L. P. Reis, "Serious games for rehabilitation: A survey and a classification towards a taxonomy," *5th Iberian Conference on Information Systems and Technologies*, June 2010.

[13] C. S. González-González, P. A. Toledo-Delgado, V. Muñoz-Cruz, and P. V. Torres-Carrion, "Serious games for rehabilitation: Gestural interaction in personalized gamified exercises through a recommender system," *Journal of Biomedical Informatics*, vol. 97, p. 103266, Sept. 2019.

[14] K. d. O. Andrade, G. Fernandes, G. A. Caurin, A. A. Siqueira, R. A. Romero, and R. d. L. Pereira, "Dynamic Player Modelling in Serious Games Applied to Rehabilitation Robotics," in *2014 Joint Conference on Robotics: SBR-LARS Robotics Symposium and Robocontrol*, pp. 211–216, Oct. 2014.

[15] O. Barzilay and A. Wolf, "Adaptive rehabilitation games," *Journal of Electromyography and Kinesiology*, vol. 23, pp. 182–189, Feb. 2013.

[16] J. F. Pinto, H. R. Carvalho, G. R. R. Chambel, J. Ramiro, and

A. Goncalves, "Adaptive gameplay and difficulty adjustment in a gamified upper-limb rehabilitation," in *2018 IEEE 6th International Conference on Serious Games and Applications for Health (SeGAH)*, pp. 1–8, May 2018. ISSN: 2573-3060.

[17] O. S. Ajani and R. Mallipeddi, "Pareto-based Dynamic Difficulty Adjustment of a competitive exergame for arm rehabilitation," *International Journal of Human-Computer Studies*, vol. 178, p. 103100, Oct. 2023.

[18] N. Robb and B. Zhang, "Performance-Based Dynamic Difficulty Adjustment and Player Experience in a 2D Digital Game: A Controlled Experiment," *Acta Ludologica*, vol. 5, no. 1, pp. 4–22, 2022. Publisher: Fakulta masmediálnej komunikácie Univerzita sv. Cyrila a Metoda.

[19] S. Jaferian and L. Farhadian, "Investigating health risk behavior disparities in the united states with finite mixture modeling. discover public health, 21 (1), 81," 2024.

[20] D. Ang and A. Mitchell, "Comparing Effects of Dynamic Difficulty Adjustment Systems on Video Game Experience," *Proceedings of the Annual Symposium on Computer-Human Interaction in Play*, pp. 317–327, Oct. 2017. Conference Name: CHI PLAY '17: The annual symposium on Computer-Human Interaction in Play ISBN: 9781450348980 Place: Amsterdam The Netherlands Publisher: ACM.

[21] M. Zohaib, "Dynamic Difficulty Adjustment (DDA) in Computer Games: A Review," *Advances in Human-Computer Interaction*, vol. 2018, p. e5681652, Nov. 2018. Publisher: Hindawi.

[22] S. Siegel and J. Smeddinck, "Adaptive Difficulty with Dynamic Range of Motion Adjustments in Exergames for Parkinson's Disease Patients," in *Entertainment Computing - ICEC 2012* (M. Herrlich, R. Malaka, and M. Masuch, eds.), Lecture Notes in Computer Science, (Berlin, Heidelberg), pp. 429–432, Springer, 2012.

[23] M. Csikszentmihalyi, *Flow: the psychology of optimal experience*. New York: Harper & Row, first edition ed., 1990.

[24] J. Chen, "Design Flow."

[25] J.-C. Metzger, O. Lambercy, A. Califfi, D. Dinacci, C. Petrillo, P. Rossi, F. M. Conti, and R. Gassert, "Assessment-driven selection and adaptation of exercise difficulty in robot-assisted therapy: a pilot study with a hand rehabilitation robot," *Journal of NeuroEngineering and Rehabilitation*, vol. 11, p. 154, Nov. 2014.

[26] M. Guidali, U. Keller, V. Klamroth-Marganska, T. Nef, and R. Riener, "Estimating the patient's contribution during robot-assisted therapy," *Journal of Rehabilitation Research and Development*, vol. 50, no. 3, pp. 379–394, 2013.

[27] N. Shirzad, *The use of physiological signals and motor performance metrics in task difficulty adaptation : improving engagement in robot-assisted movement therapy*. PhD thesis, University of British Columbia, 2013.

[28] K. Tsiakas, M. Papakostas, B. Chebaa, D. Ebert, V. Karkaletsis, and F. Makedon, "An Interactive Learning and Adaptation Framework for Adaptive Robot Assisted Therapy," in *Proceedings of the 9th ACM International Conference on PErvasive Technologies Related to Assistive Environments*, PETRA '16, (New York, NY, USA), pp. 1–4, Association for Computing Machinery, June 2016.

[29] J. Fasola and M. J. Matarić, "A socially assistive robot exercise coach for the elderly," *Journal of Human-Robot Interaction*, vol. 2, pp. 3–32, June 2013.

[30] E. Flores, G. Tobon, E. Cavallaro, F. I. Cavallaro, J. C. Perry, and T. Keller, "Improving patient motivation in game development for motor deficit rehabilitation," in *Proceedings of the 2008 International Conference on Advances in Computer Entertainment Technology*, (Yokohama Japan), pp. 381–384, ACM, Dec. 2008.

[31] H. I. Krebs, B. T. Volpe, D. Williams, J. Celestino, S. K. Charles, D. Lynch, and N. Hogan, "Robot-aided neurorehabilitation: a robot for wrist rehabilitation," *IEEE transactions on neural systems and rehabilitation engineering: a publication of the IEEE Engineering in Medicine and Biology Society*, vol. 15, pp. 327–335, Sept. 2007.

[32] L. Žlajpah, "Simulation in robotics," *Mathematics and Computers in Simulation*, vol. 79, pp. 879–897, Dec. 2008.

[33] K. d. O. Andrade, T. B. Pasqual, G. A. P. Caurin, and M. K. Crocomo, "Dynamic difficulty adjustment with evolutionary algorithm in games for rehabilitation robotics," in *2016 IEEE International Conference on Serious Games and Applications for Health (SeGAH)*, p. 1–8, May 2016.

[34] J. C. Lopes and R. P. Lopes, "A Review of Dynamic Difficulty Adjustment Methods for Serious Games," in *Optimization, Learning Algorithms and Applications* (A. I. Pereira, A. Košir, F. P. Fernandes, M. F. Pacheco, J. P. Teixeira, and R. P. Lopes, eds.), (Cham), pp. 144–159, Springer International Publishing, 2022.

[35] P. Sripian, M. N. A. M. Anuardi, T. Ito, Y. Tobe, and M. Sugaya, "Emotion-sensitive voice-casting care robot in rehabilitation using real-time sensing and analysis of biometric information," *Journal of Ambient Intelligence and Smart Environments*, vol. 13, pp. 413–431, Jan. 2021. Publisher: IOS Press.

[36] F. Ozkul, Y. Palaska, E. Masazade, and D. Erol-Barkana, "Exploring dynamic difficulty adjustment mechanism for rehabilitation tasks using physiological measures and subjective ratings," *IET Signal Processing*, vol. 13, p. 378–386, May 2019.

[37] F. Ozkul, "Dynamic difficulty adjustment of rehabilitation tasks throughreal-time emotion feedback and performance.," 2019.

[38] G. Alankus, A. Lazar, M. May, and C. Kelleher, "Towards customizable games for stroke rehabilitation," in *Proceedings of the SIGCHI Conference on Human Factors in Computing Systems*, CHI '10, (New York, NY, USA), pp. 2113–2122, Association for Computing Machinery, Apr. 2010.

[39] M. Ma and K. Bechkoum, "Serious games for movement therapy after stroke," in *2008 IEEE International Conference on Systems, Man and Cybernetics*, pp. 1872–1877, Oct. 2008. ISSN: 1062-922X.

[40] O. Mubin, F. Alnajjar, A. Al Mahmud, N. Jishtu, and B. Alsinglawi, "Exploring serious games for stroke rehabilitation: a scoping review," *Disability and Rehabilitation. Assistive Technology*, vol. 17, pp. 159–165, Feb. 2022.

[41] A. Elor, M. Teodorescu, and S. Kurniawan, "Project Star Catcher: A Novel Immersive Virtual Reality Experience for Upper Limb Rehabilitation," *ACM Transactions on Accessible Computing*, vol. 11, pp. 20:1–20:25, Nov. 2018.

[42] B. Ferreira and P. Menezes, "Gamifying Motor Rehabilitation Therapies: Challenges and Opportunities of Immersive Technologies," *Information*, vol. 11, p. 88, Feb. 2020. Number: 2 Publisher: Multidisciplinary Digital Publishing Institute.

[43] J. Luker, E. Lynch, S. Bernhardsson, L. Bennett, and J. Bernhardt, "Stroke Survivors' Experiences of Physical Rehabilitation: A Systematic Review of Qualitative Studies," *Archives of Physical Medicine and Rehabilitation*, vol. 96, pp. 1698–1708.e10, Sept. 2015.

[44] D. Mitchell, "Promoting enjoyment and self-belief through work rehabilitation," *Archives of Psychiatric Nursing*, vol. 12, pp. 344–350, Dec. 1998.

[45] M. J. Johnson, R. Rai, S. Barathi, R. Mendonca, and K. Bustamante-Valles, "Affordable stroke therapy in high-, low-and middle-income countries: From theradrive to rehab cares, a compact robot gym," *Journal of rehabilitation and assistive technologies engineering*, vol. 4, p. 2055668317708732, 2017.

[46] K. D. Bui, B. Lyn, M. Roland, C. A. Wamsley, R. Mendonca, and M. J. Johnson, "The impact of cognitive impairment on robot-based upper-limb motor assessment in chronic stroke," *Neurorehabilitation and neural repair*, vol. 36, no. 9, pp. 587–595, 2022.

[47] N. Y. Meng, E. L. Waters, G. Lin, S. Gaardsmoe, A. Johnson, L. A. Hallock, R. J. Mendonca, P. Z. Cacchione, , and M. J. Johnson, "Analysis of induced muscle activations by an affordable, reconfigurable robot for comprehensive post-stroke rehabilitation," in *2025 19th IEEE/RAS-EMBS International Conference on Rehabilitation Robotics (ICORR 2025)*, 2025.

[48] R. C. Gray, "Adaptive Game Input Using Knowledge of Player Capability: Designing for Individuals with Different Abilities - ProQuest."

[49] O. Missura and T. Gärtner, "Predicting Dynamic Difficulty," in *Advances in Neural Information Processing Systems*, vol. 24, Curran Associates, Inc., 2011.

Retrofitting Soft Assistive Robots with Sew-free Sensing Garments for Joint Motion Tracking and Kinematic Feedback

Anoush Sepehri[1], Michael T. Tolley[2], Tania K. Morimoto[3]

***Abstract*— Tracking human movement is essential during robot-assisted rehabilitation to provide kinematic feedback for monitoring range of motion, counting repetitions of a certain movement, or achieving closed-loop control. Current strategies for tracking and analyzing human motion, however, are costly, not easily accessible, or challenging to integrate with existing soft assistive robots. In this work, we present skin-tight sensing garments using commercial flex sensors that can be rapidly manufactured using a sew-free lamination strategy. We designed and fabricated sensing garments that can be worn underneath an existing soft robotic wrist orthosis to provide kinematic feedback on flexion and extension of the wrist. We conducted preliminary experiments and demonstrated that our sensing garment can track the position of the wrist with less than 5° of root mean squared error (RMSE) when compared to motion capture. We also demonstrated that our garment design and fabrication approach can be easily extended to other joints and rehabilitation devices to track uniaxial motions by developing a sensing garment for the index finger to provide kinematic feedback when used with a commercial soft rehabilitation glove. Our sensing garments are easy to manufacture, consist of inexpensive and readily available materials, and show promise as a method for providing real-time kinematic feedback of the user during robot-assisted rehabilitation activities.**

I. Introduction

Tracking and analyzing the movement of humans is essential in a variety of medical applications such as mobility tests, diagnosis of pathological movement, and monitoring activity during daily living [1], [2]. Over the last two decades, researchers have begun developing soft robots that can be worn to provide physical assistance to enhance rehabilitation treatment. Consequently, monitoring human movement while operating an assistive device has become necessary for closed-loop control [3], identifying the intention of the user [4] or estimating joint spasticity [5].

While providing kinematic feedback can increase the potential use-cases for soft assistive robots, these systems often use unconventional actuation methods (i.e., fluid-driven soft actuators) [6]. As a result, common sensing strategies seen in rigid robots (i.e., rotary encoders) are not suitable for these systems [7]. While researchers have been actively investigating new sensing strategies that can be integrated into soft robots [8], most soft assistive robots are initially developed without any form of kinematic sensing [9], [10], [11], thus limiting their practical use.

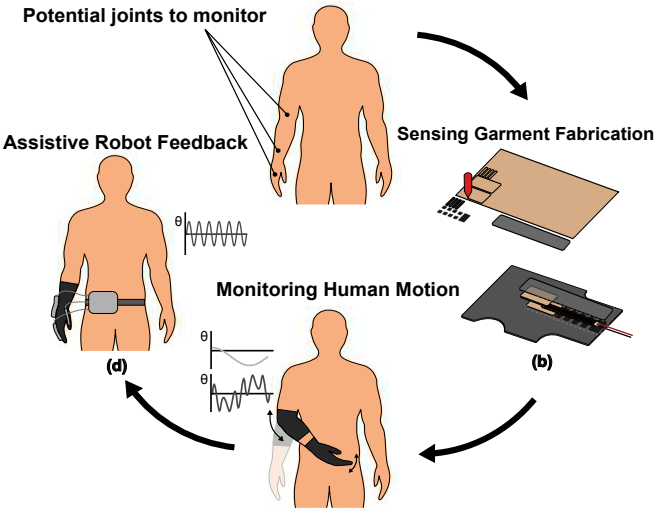


Fig. 1. We propose a simple and repeatable method to manufacture sensing garments for use with existing soft assistive robots. A sensing garment can be manufactured using a sew-free lamination strategy for the targeted joint and desired uniaxial motion to track. The sensing garment can then be used to track human movement and worn under a soft assistive robot to provide kinematic feedback for different purposes (e.g., monitoring or control).

A. Existing Motion Tracking Strategies

The clinical standard for tracking human movement is vision-based motion capture (e.g., VICON or Optitrack) [12]. While vision-based systems are capable of sub-millimeter accuracy and can be used for complex, full body motions, they require stationary cameras and can be expensive, thus limiting their use to clinical and laboratory environments. Furthermore, vision based tracking methods can suffer from occlusion, especially for tasks such as hand pose tracking [13].

Inertial measurement units (IMUs) are widely used for tracking human movement, both with and without an assistive device. While IMUs provide a minimally invasive way to track 3D motion, they suffer from drift, thus limiting their use to short-term experiments [14]. Previous work that has used IMUs for motion tracking [15] and for sensing kinematics of a wearable upper extremity soft robot [3] have reported drift of up to 0.8° RMSE per minute. Periodic re-calibration can help minimize drift over longer time horizons, however, this introduces extra steps that can complicate the tracking process.

Over the last 15 years, researchers have developed soft, stretchable sensors using liquid metal [8], textiles [16], and

[1]Anoush Sepehri is with the Department of Mechanical and Aerospace Engineering, University of California San Diego, La Jolla, CA 92093 USA.
[2]Michael T. Tolley is with the Department of Mechanical and Aerospace Engineering and the Materials Science and Engineering Program, University of California San Diego, La Jolla, CA 92093 USA.
[3]Tania K. Morimoto is with the Department of Mechanical and Aerospace Engineering and the Department of Surgery, University of California San Diego, La Jolla, CA 92093 USA.

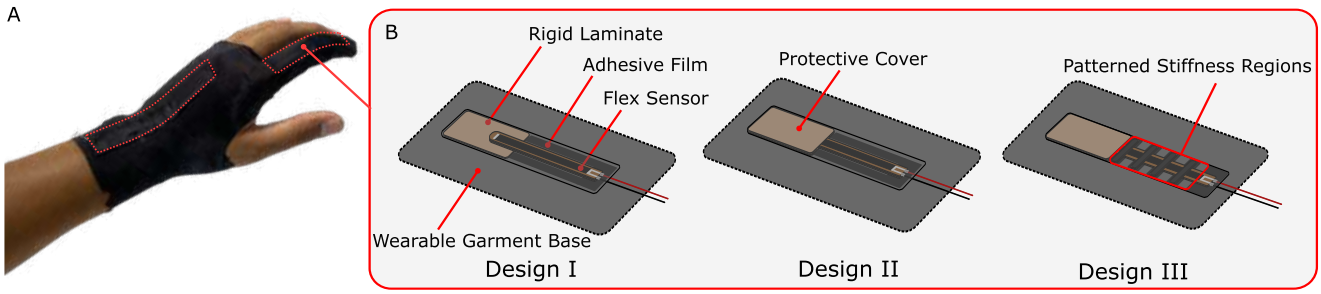


Fig. 2. The proposed sensing garments for tracking human motion. (A) Examples of the sensing garment for monitoring flexion and extension of the wrist and index finger. (B) Three proposed designs to integrate the flex sensor onto the joint. Design I included a rigid laminate that the sensor can slide along during motion. A stiffening layer (not shown here) was under the flex sensor to increase its buckling strength. Design II built upon Design I by adding a protective cover so that the sensor has a rigid groove to slide in. Design III built upon Design II by patterning the adhesive film and included rigid laminates along the sensor body to ensure uniform creasing of the fabric and to increase the contact pressure between the sensor and the joint.

conductive yarns [17]. While these sensors have been successfully integrated into wearable systems, several challenges are apparent. Isolating deformation modes is extremely challenging due to the compliance of the sensor [18]. As a result, interaction forces can lead to poor tracking performance when the sensor is mounted on the body. Menguc et al. [19] designed a soft sensing suit for gait measurement, but reported up to 15° RMSE that were likely due to slippage, forces, and deformation of the sensor when on the body. Integrating soft sensors into a wearable assistive device can pose new challenges because of the added components that can interact with the sensor. For example, Park et. al. had to use a specific shoe and ankle brace when designing a soft robotic ankle orthosis to ensure minimal interaction between the device and liquid metal sensors around the ankle [20]. In general, careful consideration is required when integrating the sensor into the assistive device, thus increasing the design and fabrication complexity of the entire system.

Commercial flex sensors are thin, lightweight laminates that change in resistance when bent. They are readily available, occupy a small footprint, and are robust to pressure and external forces, thus making them attractive for wearable applications. Currently, there is only limited work studying flex sensors as a method for tracking human movement. Existing work has typically focused on developing proof-of-concept gloves for monitoring flexion and extension of the fingers and were not used to retrofit existing assistive devices [21], [22], [23]. The fabrication of these gloves has also generally required a cut-and-sew process that is not only labor-intensive and time-consuming, but requires a skilled sewing machine operator as discussed in previous literature [9], [24]. Other work that used flex sensors with a rehabilitation device only used the sensors to activate discrete actions (i.e., using the tenodesis effect to open and close the fingers [25]). Being able to measure continuous variables, such as the angle of a joint during robot-assisted rehabilitation, would provide new opportunities for rehabilitation treatment, thus warranting further investigation.

B. Contributions

To help address the challenges in kinematic sensing during robot-assisted rehabilitation, we developed a method to rapidly manufacture sensing garments for tracking human motion (i.e., for tracking the user while they move their joints) and for providing kinematic feedback when used with a soft assistive robot (i.e., for tracking a robot while it moves the joints of a human; see Fig. 1). We used the term sensing garments throughout this work to describe a thin, skin-tight textile sleeve that is worn around the joint. We developed a simple and repeatable multi-layer heat lamination strategy to integrate commercial flex sensors onto textile sleeves to track uniaxial motions for different joints. A key requirement that we considered was that the sensing garments should be able to be worn underneath an existing soft assistive robot to act as a sensing "skin" to provide kinematic feedback without requiring modifications to the design or the operation of the device itself. We fabricated three different sensing garments for tracking flexion and extension of the wrist and evaluated the calibration results when used with and without a soft robotic wrist orthosis to identify design features that improved calibration accuracy. We then fabricated sensing garments for tracking flexion and extension of the wrist and fingers and validated the sensing accuracy in controlled motion tracking experiments with and without a soft assistive robot. The results in this work demonstrate that our sensing garments can be a simple and viable method for retrofitting soft assistive robots to provide kinematic feedback during robot-assisted rehabilitation activities.

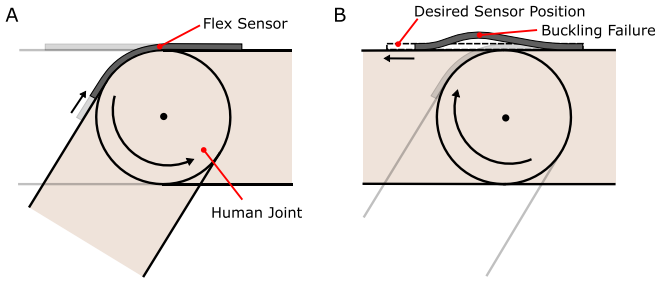


Fig. 3. Due to unavoidable misalignment between the neutral axis of the sensor and the joint, we found that the sensor must be able to slide freely within the sensing garment while conforming to the curvature of the joint. (A) During counterclockwise motion, the sensor is under tensile load and must slide backwards. (B) During clockwise motion, the sensor is under compressive load and must slide forwards. The sensor will buckle and fail if the compressive forces on the sensor exceeds its buckling strength.

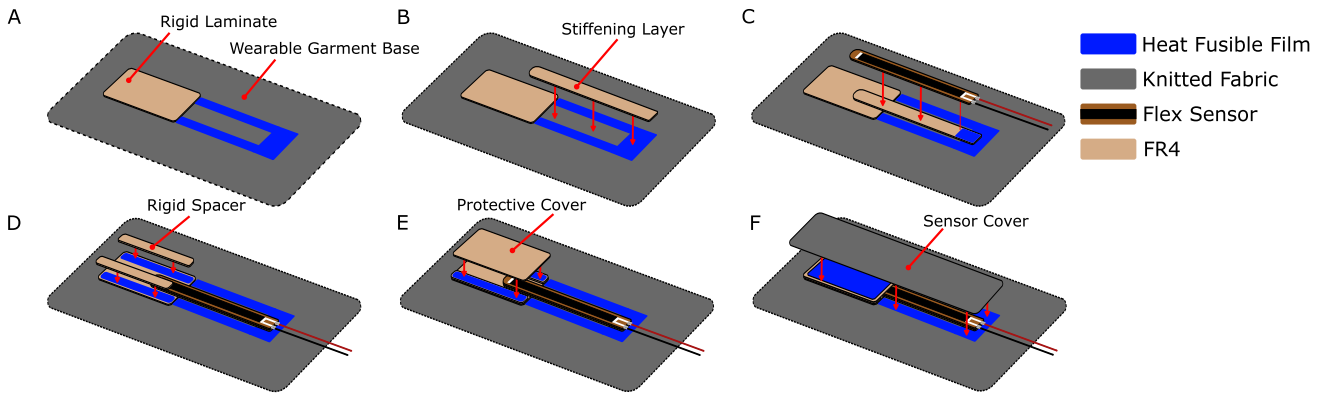


Fig. 4. Representative steps to fabricate Design II of the sensing garments. (A) The rigid laminate was first bonded to the garment base. (B) A stiffening layer was then bonded under the sensor to increase its buckling strength. (C) The flex sensor was attached to the stiffening layer. (D) 1 mm thick spacers were added to the rigid laminate. (E) A protective cover was attached to the top of the spacers to provide a low-friction groove for the sensor to slide through. (F) A sensor cover made from knitted fabric was attached over the laminated layers to hold the sensor against the skin.

II. Sensing Garment Design and Fabrication

A. Sensing Garment Designs

We used commercially available flex sensors (Bend Sensor, Flexpoint Sensor Systems, Inc), that have been previously used in soft wearable devices [5], [21], [22], [23], [25]. We selected the 2 inch bi-directional sensor with no protective laminate layer because previous literature suggested that the protective layer degraded tracking performance due to creep [21]. We wired the bi-directional flex sensor as a voltage divider and read the signal output using a microcontroller (UNO, Arduino) as suggested in the sensor manual.

One of the biggest challenges when using flex sensors to monitor human movement is that the sensor must slide to account for misalignment between the neutral axis of the joint and the sensor (see Fig. 3). We aimed to address this challenge by designing and evaluating three versions of the sensing garments that allowed for sliding of the sensor relative to the joint (see Fig. 2). We designed each sensing garment for monitoring flexion and extension of the wrist because it allowed us to evaluate our sensing garments when bending in both directions. The results from testing on the wrist therefore generalized to other joints for tracking uniaxial motions in one direction (e.g., elbow extension).

The simplest strategy to integrate a flex sensor onto the body is to place the sensor in a sleeve that is attached directly over the joint [22], [23]. We observed, however, that the flex sensor would frequently buckle (see Fig. 3). We addressed this issue in Design I of our sensing garment by bonding a rigid laminate to the wearable garment base to provide a smooth surface for the tip of the sensor to slide along. The rigid laminate was a 0.2 mm thick fiber-reinforced epoxy laminate material (FR4). We also added a 0.2 mm thick piece of FR4 directly under the flex sensor to act as a stiffening layer to increase the buckling strength of the sensor. We then used a piece of fabric to cover and hold the sensor against the joint.

When the sensor slid along the joint in Design I, we observed considerable friction between the sensor and the fabric. In Design II, we added a 1 mm rigid spacer and protective cover, both made from FR4, on top of the rigid laminate to allow the tip of the sensor to slide freely without being in contact with the fabric. We hypothesized that minimizing sliding friction between the sensor and the fabric would reduce the hysteresis when compared to Design I.

In Design III, we patterned the adhesive film along the length of the sensor to control the stiffness of the sensing garment for more uniform creasing of the fabric during motion. We also added strips of FR4 along the patterned adhesive film to increase the pressure holding the sensor in contact with the joint. We hypothesized that these modifications would further improve the hysteresis and reliability of the sensing garment in comparison to Design II.

B. Multi-layer Fabrication Procedure

We used a multi-layer lamination process to integrate the flex sensor into a skin-tight wearable garment around the wrist (see Fig. 4 for representative steps for Design II). A similar fabrication strategy was previously proposed to design a rehabilitative glove [9] and soft assistive robot for the shoulder [24]. Each sensing garment consisted of layers of knitted fabrics (24710, Darlington Fabrics) and FR4 bonded together using heat fusible thin films (Ultrahold Iron-on Adhesive, HeatnBond). We first used a CO_2 laser cutter to cut the FR4, heat fusible thin film, and fabric to the appropriate shapes prior to laminating. While any commercial sleeve that is compatible with the adhesive film can be used as the wearable garment base, we fabricated our own using the knitted fabric for faster design iteration across different joints. We chose a knitted fabric because the elastic properties of the material allowed the sensing garment to conform to the joint during motion. To bond the FR4 and knitted fabric together, we bonded one side of the adhesive film to the FR4 using a heat press for 4 s at 250°C. We then positioned the exposed side of the adhesive film directly on the knitted fabric and used the heat press for 12 s at 250°C to create a permanent bond. We used repositioning adhesive (Spray Mount Adhesive, 3M) to prevent the layers from moving relative to one another when using the heat press. We repeated these steps to bond the FR4, knitted fabric, and flex sensor together for each of the designs previously discussed.

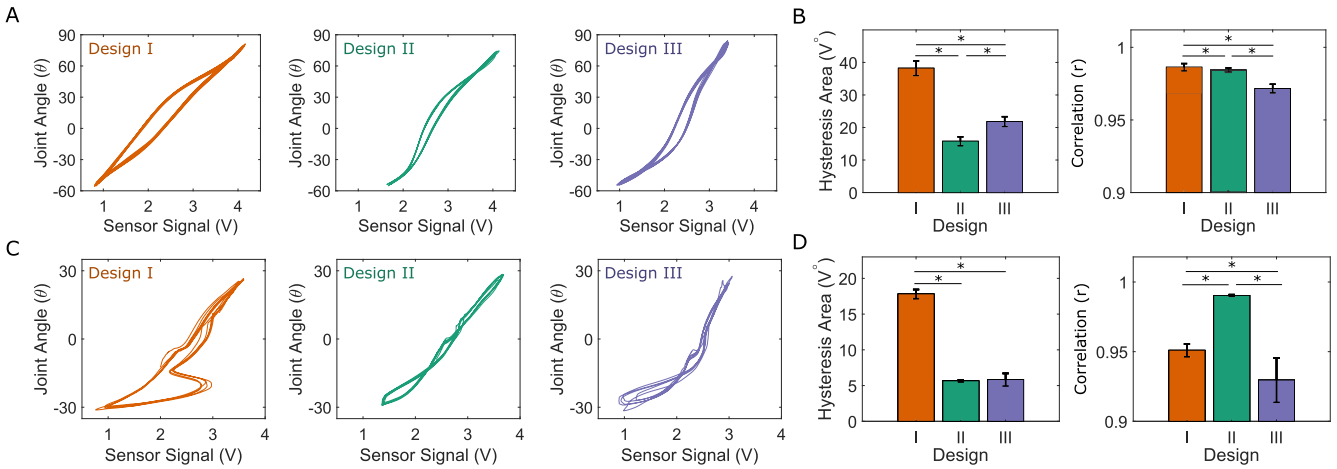


Fig. 5. Experimental results to compare the different sensing garment designs. (A) Characterization results without an assistive device. Positive and negative angles represent flexion and extension of the wrist respectively. (B) Hysteresis area and Pearson correlation coefficients for each of the calibration curves in (A). (C) Characterization results when the soft robotic wrist orthosis was worn over the sensing garments. (D) Hysteresis area and Pearson correlation coefficients for each of the calibration curves in (C). All bar plots include mean and standard deviation error bars. Statistical significance ($p < 0.05$) between different sensing garment designs was marked using an asterisk.

III. Sensing Garment Comparison

A. Characterization Procedure

We used an OptiTrack motion capture system to measure the true joint position when calibrating the sensing garments. First, the user donned the sensing garment and the reflective markers for the motion capture system. We generated two rigid body coordinate frames, one for the hand and one for the forearm, and calculated the homogeneous transformation matrix between them to estimate the angle of the wrist. Data was sampled at 60 Hz and synchronized with the flex sensor using a synchronization device (eSync 2, OptiTrack).

We conducted calibration experiments to identify which sensing garment design was best for tracking human motion and providing kinematic feedback when used with a soft assistive robot. Because the goal of this work was to evaluate the functionality of our sensing garments, all data was collected on the authors. For experiments without any assistive robot, the user moved their wrist through their active range of motion for approximately 45 seconds. We tested the sensing garment when used with a soft assistive robot by using a soft robotic wrist orthosis that we previously developed [26]. The device consisted of two textile pneumatic actuators that provided flexion and extension assistance for the wrist. The user first donned the sensing garment, then donned the assistive device as intended. While the user was completely relaxed, we programmed the device to move through a predefined range of motion for six full cycles, taking approximately 145 seconds to complete. We limited the range of motion to approximately 60 degrees of flexion and extension for all experiments when using the soft robotic wrist orthosis.

B. Results and Discussion

We first compared the calibration curves, which map the sensor signal to the joint angle, for each of the three sensing garment designs when no assistive device was used (see Fig. 5A). We calculated the hysteresis area and the Pearson correlation coefficient for each of the calibration curves to estimate the linearity (see Fig. 5B). We used the Shapiro-Wilk test to confirm normality in or data and conducted an unpaired, two-tailed T-test with a 0.05 significance threshold to compare each design. Design II had the lowest hysteresis area with only a 0.3% decrease in linearity in comparison to Design I. We attributed the reduction in hysteresis to the protective cover which minimized frictional losses as the sensor moved along the joint. Patterning the adhesive film and adding FR4 slots in Design III did not reduce

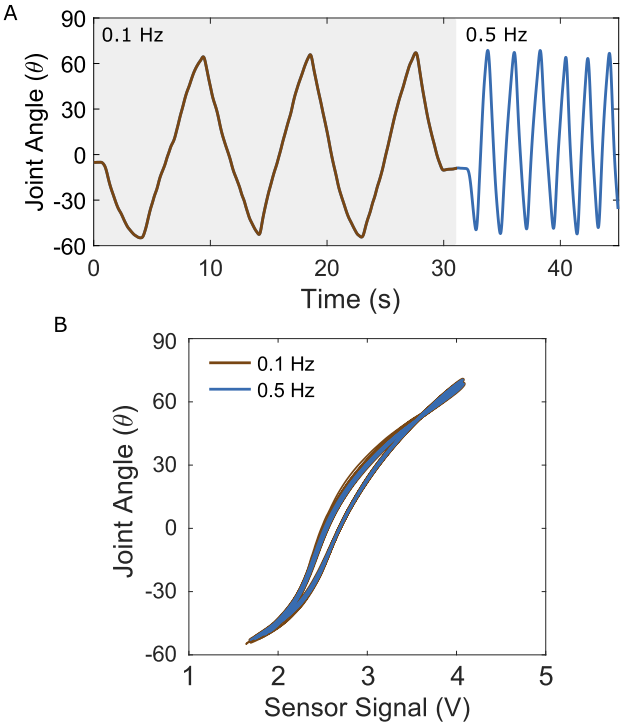


Fig. 6. Evaluating the tracking accuracy of our sensing garments for different joint velocities. (A) The raw kinematic data from the motion capture system. (B) Calibration curves corresponding to the data in (A). The calibration curves are nearly identical, thus suggesting our sensing garments are reliable over a range of speeds relevant for rehabilitation activities.

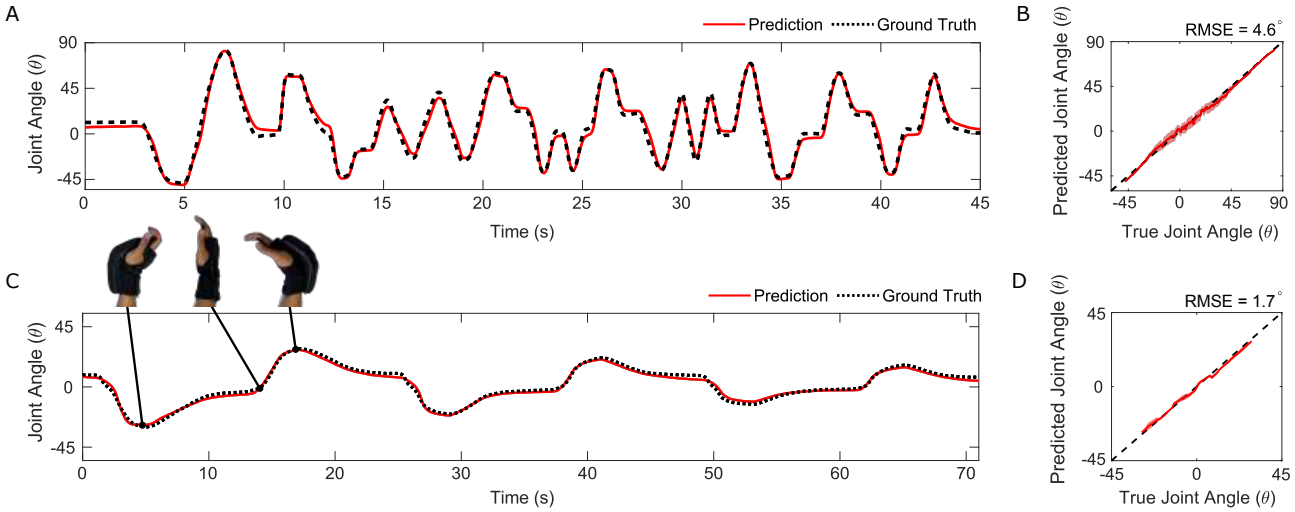


Fig. 7. Experimental results for tracking flexion and extension of the wrist. (A) Validation results for tracking motion of the wrist without the soft robotic wrist orthosis. The user moved their wrist through an arbitrary trajectory that covered their active range of motion. (B) Comparison between the predicted and true joint angles for the data in (A). The shaded area represents the standard deviation of the prediction. (C) Validation results when using the soft robotic wrist orthosis for continuous passive motion therapy. (D) Comparison between the predicted and true joint angles for the data in (C).

the hysteresis further, and instead, likely increased the non-linearity of the calibration results.

We then compared the calibration curves for each of the three sensing garments when used with the soft robotic wrist orthosis (see Fig. 5C and Fig. 5D). We used the Shapiro-Wilk test to confirm normality in our data and determined that the Pearson correlation coefficient estimates for Design III could not be assumed to be normally distributed. As a result, we used the Mann-Whitney test with a 0.05 significance threshold to compare the Pearson correlation score for Design III with the other two designs. For all other comparisons, we used the same unpaired T-test as before. During wrist extension, the flex sensor in Design I buckled, resulting in poor calibration results. We believe that this occurred because of the contact forces between the soft robotic wrist orthosis and the sensing garment that prevented the sensor from sliding along the wrist. Design II and Design III showed no signs of sensor buckling, likely due to the protective cover that prevented the soft robotic wrist orthosis from constraining the motion of the sensor. Design II had a higher linearity score when compared to Design III but there was no significant difference in the hysteresis. We decided to move forward with Design II for the rest of this work because it had the best performance in terms of hysteresis and linearity during calibration.

IV. Motion Tracking Characterization

A. Evaluating Calibration Accuracy at Different Speeds

We first investigated how the tracking accuracy of our sensing garment changed when the user moved at different speeds because previous literature has shown that faster movements can lead to larger tracking errors [19]. Given that the average dominant frequency of wrist movement is 1 Hz [27] and that rehabilitation activities are generally delivered in a slow, controlled manner (i.e., continuous passive motion therapy) we chose to evaluate the accuracy of our sensing garment for movements at 0.1 Hz and 0.5 Hz. The user first donned the sensing garment and moved their wrist through their full range of motion at approximately 0.1 Hz for 30 seconds. The user then moved their wrist through their full range of motion at approximately 0.5 Hz for 15 seconds (see Fig. 6A). We used the data collected at 0.1 Hz to fit a cubic spline to map the signal from the flex sensor to the joint position. We then evaluated the accuracy of the fitted spline against the data collected at both speeds.

When comparing the data collected at 0.1 Hz and the data collect at 0.5 Hz, the hysteresis area reduced by 21%. The Pearson correlation coefficient, however, only changed by 0.5% and the shape of the calibration curve stayed approximately the same (see Fig. 6B). Our spline calibration had an error of 5.2° and 3.7° RMSE for the data collected at 0.1 Hz and 0.5 Hz respectively, thus suggesting that our sensing garments can achieve high accuracy at different speeds that are relevant for rehabilitation activities.

B. Tracking Human Motion

We evaluated the tracking accuracy of our sensing garment in controlled motion tracking experiments with and without a soft assistive robot. We followed the calibration procedure outlined in Section III and fit the data using a cubic spline, as discussed in the previous section. We immediately collected the validation dataset after calibrating the sensing garment to minimize any effects garment shifting could have on the tracking performance. When collecting the validation dataset without an assistive device, the user moved their wrist through an arbitrary trajectory that covered their active range of motion for approximately 45 seconds. To collect the validation dataset with the soft robotic wrist orthosis, we programmed the device to simulate continuous passive motion therapy over different ranges of motion.

The tracking RMSE of our sensing garment was 4.6° over 45 seconds of self-directed motion by the user and 1.7° when used to provide kinematic feedback for the soft robotic wrist

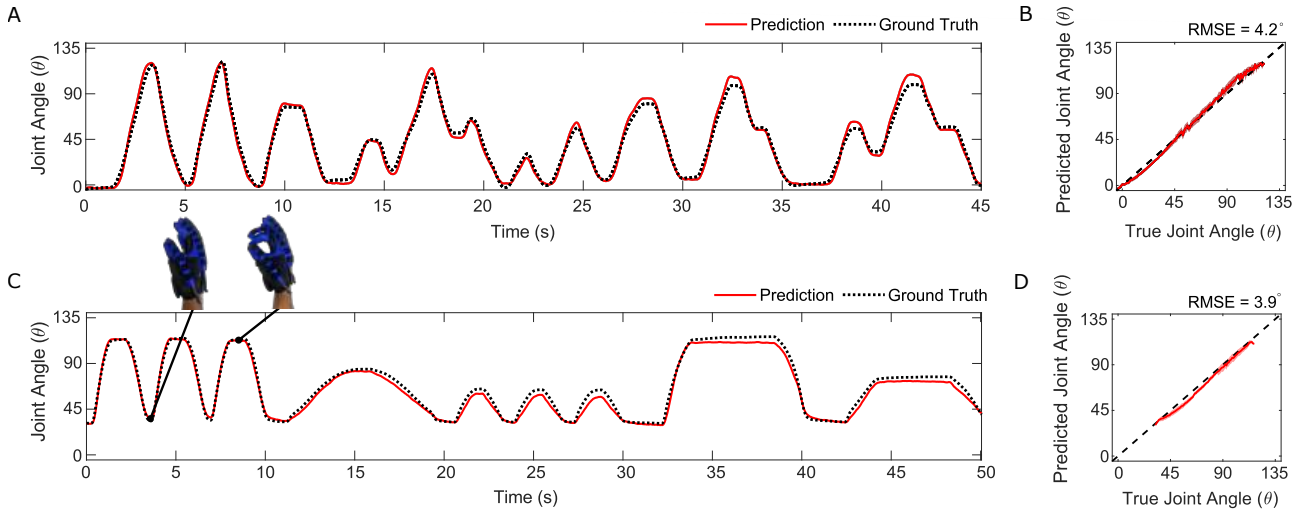


Fig. 8. Experimental results for tracking flexion and extension of the index finger. (A) Validation results for tracking motion of the finger without the rehabilitation glove. The user moved their finger through an arbitrary trajectory that covered their active range of motion. (B) Comparison between the predicted and true joint angles for the data in (A). The shaded area represents the standard deviation of the prediction. (C) Validation results when using the rehabilitation glove for flexion and extension assistance of the finger. (D) Comparison between the predicted and true joint angles for the data in (C).

orthosis (see (see Fig. 7A) and Fig. 7C). We also found that our sensing garment could predict the position of the joint with low variance over the full range of motion of the wrist (see Fig. 7B and Fig. 7D).

V. Generalization to Other Joints and Uniaxial Motions

In this section, we investigated how our design principles and fabrication method can be used to develop sensing garments for other joints and soft assistive robots to provide kinematic feedback for uniaxial motions. We fabricated a sensing garment for the index finger to monitor flexion and extension by tracking the angle of the proximal interphalangeal joint. We targeted the finger because hand impairment is one of the most common disabilities after a stroke [28] and because there are many commercially available soft assistive robots for the hand without integrated sensing that could benefit from our garments. We purchased a pneumatically actuated rehabilitation glove (Becggse, Amazon) that consisted of bellowed plastic actuators that flex when pressurized. We used the same electro-pneumatic regulators that we used for the soft robotic wrist orthosis to control the input pressure to the bellowed actuator on the index finger.

We followed the same procedure to collect the calibration and validation datasets that we used when evaluating the sensing garment for the wrist. The true angle of the finger was measured using motion capture and was based on the position of the distal tip relative to the base of the finger. We selected arbitrary pressure inputs that spanned a wide range of motions when collecting the validation dataset with the soft commercial rehabilitation glove. It should be noted that when the bellowed actuator on the rehabilitation glove was not pressurized and the user was relaxed, the fingers were flexed to approximately 30° due to the intrinsic stiffness of the glove. We only used positive pressure to operate the rehabilitation glove, hence we ignored all angles smaller than 30° in our experiments.

Our sensing garment could successfully track the position of the finger even when worn underneath the rehabilitation glove. The RMSE when compared to motion capture was approximately 4.2° and 3.9° when used with and without the rehabilitation device and once again had low variance over the entire range that we evaluated (see Fig. 8).

VI. Discussion

Our sensing garments can be worn underneath a soft assistive robot and can track human motion with less than 5° RMSE. Literature suggests that 5° RMSE is acceptable for many research and clinical applications, although requirements are dependent on the task [29]. We believe 5° RMSE is acceptable for tasks such as achieving closed-loop control for a soft assistive robot where tracking errors of the controller can range from 3° to 6° RMSE [3], [5].

Existing work that used flex sensors to track human motion generally focused on designing gloves to track flexion and extension of the fingers by placing the sensor inside a fabric sleeve sewn directly over the fingers [22], [23]. This method to integrate the sensor on the body, however, led to buckling failure when used for joints such as the wrist, most likely due to the larger discrepancy between the neutral axis of the sensor and the joint. In this work, we identified design features that can be created using FR4 that eliminated buckling failure, improved calibration accuracy, and ensured our sensing garments could be used for joints other than the finger and with existing soft assistive robots.

Existing sensing gloves that used flex sensors are also typically fabricated using a cut and sew method [22], [23]. We assembled our sensing garments using a sew-free heat lamination strategy,thus eliminating the need for a skilled sewing machine operator and complex cut-and-sew procedures that can lead to potential sources of error [9], [24].

It is well known that any shifting of the sensor on the body could lead to errors when tracking human motion [15], [30]. While we did not observe any shifting during our tests due

to the short duration of our experiments, future work should investigate features, such as high-friction layers between the sensing garment and the skin, to minimize shifting during extended use. Future work should also evaluate our garment design with the target population (e.g., stroke survivors) to consider constraints during donning and doffing. Lastly, since most soft assistive robots provide simple, single-degree-of-freedom assistance [4], [9], [11], [31], we focused on tracking uniaxial motions. Future work should explore ways to integrate the flex sensors onto the body to measure multi-degree-of-freedom motions to increase the potential use cases of our sensing garments.

VII. Conclusion

In this paper, we presented wearable sensing garments for monitoring human movement using commercial flex sensors. Our sensing garments are easy to manufacture, made from readily available materials, and are suitable for different joints for tracking uniaxial motions. They offer suitable accuracy for rehabilitation applications and can serve as a sensing "skin" for soft assistive robots without any form of integrated sensing. This work provides new opportunities for motion analysis during rehabilitation treatment that is accessible to a wide audience of researchers and users.

References

[1] F. Porciuncula, A. V. Roto, D. Kumar, I. Davis, S. Roy, C. J. Walsh, and L. N. Awad, "Wearable movement sensors for rehabilitation: a focused review of technological and clinical advances," *Pm&r*, vol. 10, no. 9, pp. S220–S232, 2018.

[2] C. P. Adans-Dester, C. E. Lang, D. J. Reinkensmeyer, and P. Bonato, *Wearable Sensors for Stroke Rehabilitation*. Cham: Springer International Publishing, 2022, pp. 467–507. [Online]. Available: https://doi.org/10.1007/978-3-031-08995-4_21

[3] T. Proietti, C. O'Neill, C. J. Hohimer, K. Nuckols, M. E. Clarke, Y. M. Zhou, D. J. Lin, and C. J. Walsh, "Sensing and control of a multi-joint soft wearable robot for upper-limb assistance and rehabilitation," *IEEE Robotics and Automation Letters*, vol. 6, no. 2, pp. 2381–2388, 2021.

[4] Y. M. Zhou, C. Hohimer, T. Proietti, C. T. O'Neill, and C. J. Walsh, "Kinematics-based control of an inflatable soft wearable robot for assisting the shoulder of industrial workers," *IEEE Robotics and Automation Letters*, vol. 6, no. 2, pp. 2155–2162, 2021.

[5] Z. Q. Tang, H. L. Heung, K. Y. Tong, and Z. Li, "Model-based online learning and adaptive control for a "human-wearable soft robot" integrated system," *The International Journal of Robotics Research*, vol. 40, no. 1, pp. 256–276, 2021.

[6] M. Pan, C. Yuan, X. Liang, T. Dong, T. Liu, J. Zhang, J. Zou, H. Yang, and C. Bowen, "Soft actuators and robotic devices for rehabilitation and assistance," *Advanced Intelligent Systems*, vol. 4, no. 4, p. 2100140, 2022.

[7] D. Rus and M. T. Tolley, "Design, fabrication and control of soft robots," *Nature*, vol. 521, no. 7553, pp. 467–475, 2015.

[8] Y.-L. Park, B.-R. Chen, and R. J. Wood, "Design and fabrication of soft artificial skin using embedded microchannels and liquid conductors," *IEEE Sensors journal*, vol. 12, no. 8, pp. 2711–2718, 2012.

[9] F. Connolly, D. A. Wagner, C. J. Walsh, and K. Bertoldi, "Sew-free anisotropic textile composites for rapid design and manufacturing of soft wearable robots," *Extreme Mechanics Letters*, vol. 27, pp. 52–58, 2019.

[10] J. Jeong, K. Hyeon, J. Han, C. H. Park, S.-Y. Ahn, S.-K. Bok, and K.-U. Kyung, "Wrist assisting soft wearable robot with stretchable coolant vessel integrated sma muscle," *IEEE/ASME Transactions On Mechatronics*, vol. 27, no. 2, pp. 1046–1058, 2021.

[11] H. Young, L. Gerez, T. Cole, B. Inirio, T. Proietti, B. Closs, S. Paganoni, and C. Walsh, "Air efficient soft wearable robot for high-torque elbow flexion assistance," in *2023 International Conference on Rehabilitation Robotics (ICORR)*. IEEE, 2023, pp. 1–6.

[12] H. Zhou and H. Hu, "Human motion tracking for rehabilitation—a survey," *Biomedical signal processing and control*, vol. 3, no. 1, pp. 1–18, 2008.

[13] W. Chen, C. Yu, C. Tu, Z. Lyu, J. Tang, S. Ou, Y. Fu, and Z. Xue, "A survey on hand pose estimation with wearable sensors and computer-vision-based methods," *Sensors*, vol. 20, no. 4, p. 1074, 2020.

[14] J. Zhao, "A review of wearable imu (inertial-measurement-unit)-based pose estimation and drift reduction technologies," in *Journal of Physics: Conference Series*, vol. 1087. IOP Publishing, 2018, p. 042003.

[15] P. Slade, A. Habib, J. L. Hicks, and S. L. Delp, "An open-source and wearable system for measuring 3d human motion in real-time," *IEEE Transactions on Biomedical Engineering*, vol. 69, no. 2, pp. 678–688, 2021.

[16] L. Sanchez-Botero, A. Agrawala, and R. Kramer-Bottiglio, "Stretchable, breathable, and washable fabric sensor for human motion monitoring," *Advanced Materials Technologies*, vol. 8, no. 17, p. 2300378, 2023.

[17] H. Souri and D. Bhattacharyya, "Highly stretchable and wearable strain sensors using conductive wool yarns with controllable sensitivity," *Sensors and Actuators A: Physical*, vol. 285, pp. 142–148, 2019.

[18] J. Jung, E. Lee, J. Kim, and Y.-L. Park, "Ultra-thin multi-modal soft sensor using liquid-metal thin-film deposition for enhanced human-robot interaction," *IEEE Robotics and Automation Letters*, 2024.

[19] Y. Mengüç, Y.-L. Park, H. Pei, D. Vogt, P. M. Aubin, E. Winchell, L. Fluke, L. Stirling, R. J. Wood, and C. J. Walsh, "Wearable soft sensing suit for human gait measurement," *The International Journal of Robotics Research*, vol. 33, no. 14, pp. 1748–1764, 2014.

[20] Y.-L. Park, B.-r. Chen, N. O. Pérez-Arancibia, D. Young, L. Stirling, R. J. Wood, E. C. Goldfield, and R. Nagpal, "Design and control of a bio-inspired soft wearable robotic device for ankle–foot rehabilitation," *Bioinspiration & biomimetics*, vol. 9, no. 1, p. 016007, 2014.

[21] L. K. Simone and D. G. Kamper, "Design considerations for a wearable monitor to measure finger posture," *Journal of neuroengineering and rehabilitation*, vol. 2, pp. 1–10, 2005.

[22] Y. Zheng, Y. Peng, G. Wang, X. Liu, X. Dong, and J. Wang, "Development and evaluation of a sensor glove for hand function assessment and preliminary attempts at assessing hand coordination," *Measurement*, vol. 93, pp. 1–12, 2016.

[23] G. Saggio, A. Calado, V. Errico, B.-S. Lin, and I.-J. Lee, "Dynamic measurement assessments of sensory gloves based on resistive flex sensors and inertial measurement units," *IEEE Transactions on Instrumentation and Measurement*, vol. 72, pp. 1–10, 2023.

[24] L. Campioni, G. Dimonte, G. Sciarrone, G. Righi, C. Walsh, M. Gandolla, G. Del Popolo, S. Micera, and T. Proietti, "Preliminary evaluation of a soft wearable robot for shoulder movement assistance," *IEEE Transactions on Medical Robotics and Bionics*, 2025.

[25] C. G. Rose and M. K. O'Malley, "Hybrid rigid-soft hand exoskeleton to assist functional dexterity," *IEEE Robotics and Automation Letters*, vol. 4, no. 1, pp. 73–80, 2018.

[26] A. Sepehri, S. Ward, M. T. Tolley, and T. K. Morimoto, "A soft robotic wrist orthosis using textile pneumatic actuators for passive rehabilitation," in *2024 IEEE 7th International Conference on Soft Robotics (RoboSoft)*. IEEE, 2024, pp. 284–290.

[27] K. A. Mann, F. W. Wernere, and A. K. Palmer, "Frequency spectrum analysis of wrist motion for activities of daily living," *Journal of Orthopaedic research*, vol. 7, no. 2, pp. 304–306, 1989.

[28] P. Raghavan, "The nature of hand motor impairment after stroke and its treatment," *Current treatment options in cardiovascular medicine*, vol. 9, no. 3, pp. 221–228, 2007.

[29] J. L. McGinley, R. Baker, R. Wolfe, and M. E. Morris, "The reliability of three-dimensional kinematic gait measurements: a systematic review," *Gait & posture*, vol. 29, no. 3, pp. 360–369, 2009.

[30] Y. Jin, C. M. Glover, H. Cho, O. A. Araromi, M. A. Graule, N. Li, R. J. Wood, and C. J. Walsh, "Soft sensing shirt for shoulder kinematics estimation," in *2020 IEEE International Conference on Robotics and Automation (ICRA)*. IEEE, 2020, pp. 4863–4869.

[31] S. Sridar, Z. Qiao, A. Rascon, A. Biemond, A. Beltran, T. Maruyama, C. Kwasnica, P. Polygerinos, and W. Zhang, "Evaluating immediate benefits of assisting knee extension with a soft inflatable exosuit," *IEEE Transactions on Medical Robotics and Bionics*, vol. 2, no. 2, pp. 216–225, 2020.

Biomechanical Effects of Modulating Pedaling Configurations on a Tilted-Plane Ergometer

Seonghyun Kang
Department of Biomedical Engineering
Korea University College of Medicine
Seoul, Republic of Korea
ss7186@korea.ac.kr

Jaewook Kim
Department of Biomedical Engineering
Korea University College of Medicine
Seoul, Republic of Korea
jaewook_kim@korea.ac.kr

Yekwang Kim
Department of Biomedical Engineering
Korea University College of Medicine
Seoul, Republic of Korea
yekwang@korea.ac.kr

Juhui Moon
Department of Biomedical Engineering
Korea University College of Medicine
Seoul, Republic of Korea
answn520@korea.ac.kr

Seung-Jong Kim
Department of Biomedical Engineering
Korea University College of Medicine
Seoul, Republic of Korea
sjkim586@korea.ac.kr

***Abstract*— Excessive coronal or axial plane moments in lower extremity joints are commonly linked to musculoskeletal injuries. However, deliberately inducing such moments can be advantageous in personalized rehabilitation by addressing specific biomechanical needs. The tilted-plane ergometer, designed to tilt the pedaling plane and adjust pedal orientation, facilitates desired limb alignment during pedaling. This study examined changes in joint dynamics, and muscle activity across various ergometer configurations using a musculoskeletal modeling approach. Five participants performed pedaling tasks under four distinct configurations, with data collected via a motion capture system and a force-torque sensor integrated into the pedal. Configurations favoring abducted pedaling planes reduced knee adduction moments and increased ankle abduction moments, while axial rotation moments were modulated through targeted pedal orientations. Conversely, adducted pedaling planes combined with inverted pedal orientations significantly increased internal rotation moments at the knee and ankle, alongside inducing posterior directional forces at the hip and ankle joints. Estimated muscle activity varied across configurations, demonstrating the device's adaptability in targeting specific biomechanics. These findings underscore the potential of the tilted-plane ergometer to effectively modulate joint biomechanics, positioning it as a promising tool for personalized rehabilitation interventions.**

Keywords—bicycle ergometer, biomechanics, tilted pedaling plane, musculoskeletal modeling, personalized rehabilitation

I. INTRODUCTION

In personalized rehabilitation, the primary goal is to tailor interventions to protect specific structures from excessive loading or, conversely, to stimulate recovery by applying targeted mechanical stress. Rehabilitation strategies should also focus on engaging muscles critical to functional recovery while minimizing adverse mechanical effects on the joints and surrounding structures. For instance, following total hip arthroplasty, rehabilitation should focus on strengthening the hip abductors while avoiding internal rotation and adduction moments to prevent dislocation [1]. For ACL injury recovery, restoring hamstring function is essential while minimizing anterior tibial forces to protect the ligament or graft [2].

Excessive coronal or axial plane moments in lower extremity joints are often implicated in musculoskeletal injuries [3]. However, deliberately inducing such moments can be beneficial in personalized rehabilitation when addressing specific biomechanical deficits [4]. In order to address this need, we developed a tilted-plane ergometer enabling movement across multiple pedaling planes (Fig. 1). The device offers dynamic control of joint loading by tilting the pedaling plane beyond a single degree of freedom (DoF) into a tilted orientation. Additionally, it enables precise adjustment of pedal-foot orientation to guide specific lower limb alignments, facilitating the desired load distribution across the joints [5].

Our previous research has demonstrated that the tilted-plane ergometer effectively alters muscle activation patterns and joint kinematics [6, 7]. However, its influence on joint kinetics remains insufficiently studied. Net joint forces and moments, or partial joint reaction forces (JRFs), can be calculated using inverse dynamics based on external force data and kinematic measurements. Estimating actual JRFs, which incorporate the contributions of muscles and ligaments, requires a more sophisticated approach using musculoskeletal modeling [8]. By leveraging multibody dynamics frameworks that integrate rigid body components, kinematic actuators, and muscle-based force and torque actuators, it is possible to accurately simulate muscle forces and actual JRFs [9].

In this study, we utilized a 6-axis force-torque sensor integrated into the pedal and a motion capture system to evaluate JRFs under various pedaling configurations using a

This research was supported by a grant from the MD-PhD/Medical Scientist Training Program and Korea Health Technology R&D Project (grant number: RS-2022-KH129263) through the Korea Health Industry Development Institute (KHIDI), funded by the Ministry of Health and Welfare, Republic of Korea.

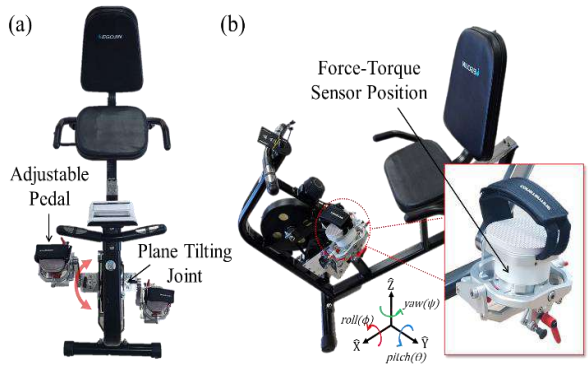


Figure 1. Image of Tilted-Plane Ergometer. (a) Anterior view showing the tilting direction of the pedaling plane. (b) Adjustable 3-DoF pedal equipped with a force-torque sensor. (*DoF: Degree of Freedom*).

musculoskeletal modeling approach. Our findings revealed that pedaling configurations with abducted planes (yaw = -30° for the right pedaling plane in Fig. 1(b)) reduced knee adduction moments (KAMs) and increased ankle abduction moments, while axial rotation moments were adjusted through specific pedal orientations. Conversely, configurations with adducted pedaling planes and inverted (roll = +15° for the right pedal in Fig. 1(b)) pedals significantly increased internal rotation moments at the knee and ankle and generated posterior directional forces at the hip and ankle joints. These results highlight the potential of the tilted-plane ergometer to serve as a highly adaptable tool for optimizing rehabilitation by enabling individualized biomechanical adjustments to target specific therapeutic goals.

II. Materials and Methods

A. Participants

Five participants (mean age: 30.8 ± 5.6 years, height: 1.70 ± 0.09 m, weight: 68.8 ± 10.0 kg), consisting of two females and three males, were enrolled in this study. All participants had no history of musculoskeletal injury within the past six months or major lower extremity surgery. Written informed consent was obtained from each participant, and the study adhered to ethical guidelines for human research. The experimental protocol was approved by the Institutional Review Board of Korea University College of Medicine (IRB number: KUIRB-2024-0015-01). Before the experiment, a physical therapist and an orthopedic surgeon conducted a general physical assessment to ensure that participants had no pain or mobility limitations that could interfere with their participation in the study.

B. Device and Experimental Design

The tilted-plane ergometer used in this study was developed by our team to facilitate multi-planar lower limb movements tailored for individual rehabilitation needs. The device allows adjustment of the pedaling plane in the XY plane by modifying the yaw angle of the plane-tilting joint (Fig. 1), corresponding to the abduction/adduction angle in the coronal plane. A universal joint ensures synchronized crank rotation while supporting tilted-plane pedaling. Figure 1b highlights the adjustable pedal mechanism, integrated with a 6-axis force-torque sensor (DynPick WEF-6A1000-30, WACOH_TECH Inc., Japan), capable of measuring forces and torques within ±1000 N and ±30 Nm, respectively, at a

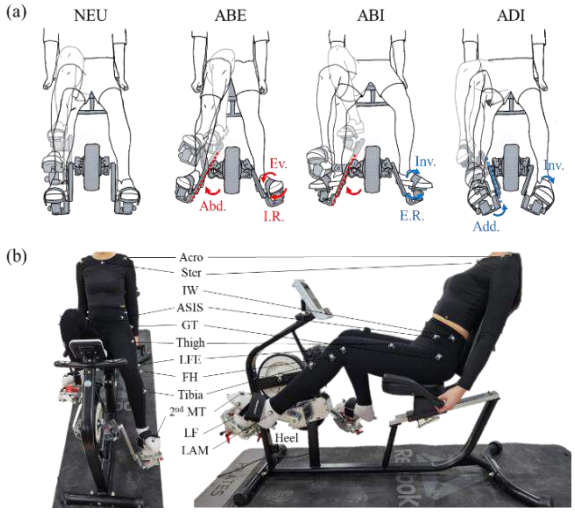


Figure 2. Experimental Setup. (a) The position of reflective markers. (b) Illustrations of 4 experimental configurations. (Abd/Add.: Abd/Adduction, Ev./Inv.: Ev/Inversion, I.R/E.R.: Internal/External rotation, Acro: Acromion, Ster: Sternum, IW: Iliac wing, ASIS: Anterior superior iliac spine, GT: Greater trochanter, LFE: Lateral femoral epicondyle, FH: Fibular head, LAM: Lateral ankle malleolus, LF: Lateral forefoot, MT: Metatarsal head).

sampling rate of 2000 Hz. The pedal design permits fine-tuning of roll, pitch, and yaw angles for customized foot positioning.

The pedaling conditions and experimental procedures followed the framework established in our previous studies, detailed in [6] and [7]. Four configurations (Fig. 2a) were evaluated: (1) NEU: a baseline setup with neutral pedaling, no tilt, and no pedal adjustments. (2) ABE: pedaling plane tilted -30° in the abduction direction (yaw, based on right side), with the pedal set to -5° eversion (roll) and +5° internal rotation (yaw). (3) ABI: an abducted pedaling plane with the pedal adjusted to +15° inversion and -30° external rotation. (4) ADI: a +15° adduction-direction tilt (yaw) combined with +15° pedal inversion (roll). Participants pedaled at level 8 intensity (of 14 levels), maintaining a speed of 15-17 km/h. After a brief calibration, each participant completed 25 cycles for each condition, with a 2-minute rest interval between trials to minimize fatigue. The sequence of conditions was randomized for each participant to reduce potential order effects.

Motion capture was performed using a Vicon motion capture system (Vicon, Oxford, UK) with eight cameras operating at 100 Hz. A total of 25 passive reflective markers were strategically placed on the participants, following established protocols with minor adjustments [10] (Fig. 2b). Anatomical landmarks near the joints were marked to identify joint centers, while additional markers were attached to well-visible areas like the anterior surfaces of the thigh and tibia to ensure accurate tracking. For the pelvis, the posterior superior iliac spine (PSIS) markers were obstructed by the backrest, so alternative tracking markers were positioned on the lateral upper iliac wing.

To synchronize the motion capture and force-torque data, an inertial measurement unit (IMU, WT901BLECL5.0, WIT Motion, China) was mounted on the anterior aspect of the right thigh. This IMU was pre-synchronized with the force-

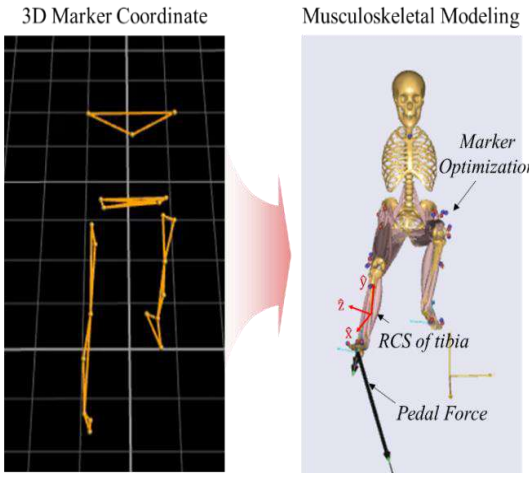


Figure 3. Musculoskeletal Modeling. The process of musculoskeletal modeling, starting from real-time data acquisition (left) to the integration of musculoskeletal modeling with external pedal force data (right). (*RCS: reference coordinate system*)

torque sensor. By aligning the sagittal plane angle data independently captured by the IMU with the motion capture system, both data streams were effectively synchronized, ensuring accurate integration of force-torque and motion data.

C. Musculoskeletal Modeling

The musculoskeletal model was created using AnyBody Modeling System 7.4 (AnyBody Technology, Aalborg, Denmark), a software designed to process 3D motion capture data with high precision and reliability [11]. We utilized a full-body template within the AnyBody Managed Model Repository but focused solely on the lower extremities, excluding upper body muscles and skeletal structures distal to the scapula. It incorporated 1 DoF for each knee joint, 3 for the ankle and hip joints, 6 for the pelvis, and 3 for the connection between the pelvis and thorax. To align with the study's experimental marker setup, the model's tracking marker positions were adapted from the basic template, originally based on the Plug-in-Gait model. The model was then scaled to match each participant's specific segment lengths and body weights, ensuring individual accuracy. Personalized models were driven by kinematic data obtained from 3D skin marker coordinates [9]. Unlike standard templates that typically rely on kinetic data from force plates, this model was customized to incorporate force-torque data from sensors placed at the middle plantar region of the foot. The model was further modified to apply these force-torque inputs directly to a designated node on the middle plantar side, making it more suitable for the experimental design (Fig. 3).

The force and moment axes were defined in a relative coordinate system for each body segment: the x-axis representing posterior-to-anterior, the y-axis distal-to-proximal, and the z-axis medial-to-lateral directions (Fig. 3 right panel). When calculating joint reaction forces and moments, the axes are referenced at the proximal end of the distal segment, meaning the reaction forces and moments are expressed relative to the reference frame of the distal segment. In this study, force-torque sensors were applied only to the right-side pedal; therefore, all data were collected exclusively from the right lower limb.

D. Data Prosseing and Analysis

Kinematic, kinetic, and estimated muscle activation data were segmented by the pedaling cycle, with the data normalized to a time axis spanning 0–100% of each cycle. The pedaling cycle was defined as beginning at the position of maximum hip flexion, consistent with our previous studies. The push phase (or power phase) was identified as the first half of the cycle, during which the hip and knee joints extended to apply pushing forces to the pedal, generating rotational motion. The pull phase (or recovery phase) was designated as the latter half of the cycle.

For each participant, mean values were calculated for each phase-frame, and the combined data across participants were summarized as means and standard deviations (SDs) to evaluate differences between ergometer conditions. Kinetic data, including net and actual JRFs, were normalized to each participant's body weight to facilitate group-level analysis. For statistical comparisons, a paired t-test or Wilcoxon signed-rank test was applied to compare each data between the baseline NEU condition and other configurations, based on the normality and homoscedasticity of the data. All data processing and analyses were conducted using MATLAB version R2024a (MathWorks, Inc., Natick, MA, USA).

III. Results

A. Kinematic Data

Figure 4 presents the kinematic results for hip and knee joint angles across different conditions, shown as mean values with SDs. The sagittal angles of the hip and knee joints, reflecting flexion/extension movements, exhibit similar patterns across all configurations. However, an offset of approximately 10˚ was noted in knee joint motion under the ADI condition. Compared to the baseline NEU condition, the hip joint showed slightly increased adduction in the ABE condition, while greater abduction angles were observed in the ABI and ADI conditions. Notably, the axial rotation pattern in the ABE condition differed significantly from NEU and ADI, with a reduced range of motion (ROM).

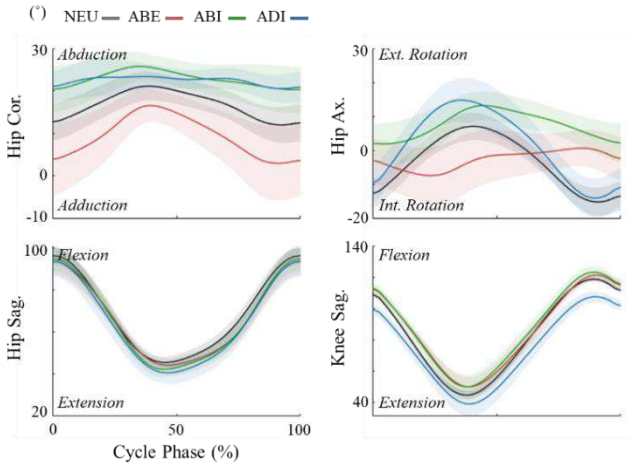


Figure 4. Joint angle. Lower extremity joint angles during the pedaling cycle are compared across different ergometer conditions. Lines represent the mean joint angles, and shaded areas indicate standard deviations. The results are averaged across all participants. (*Sag.: sagittal, Cor.: coronal, Ax.: axial, Ext.: external, Int.: internal*)

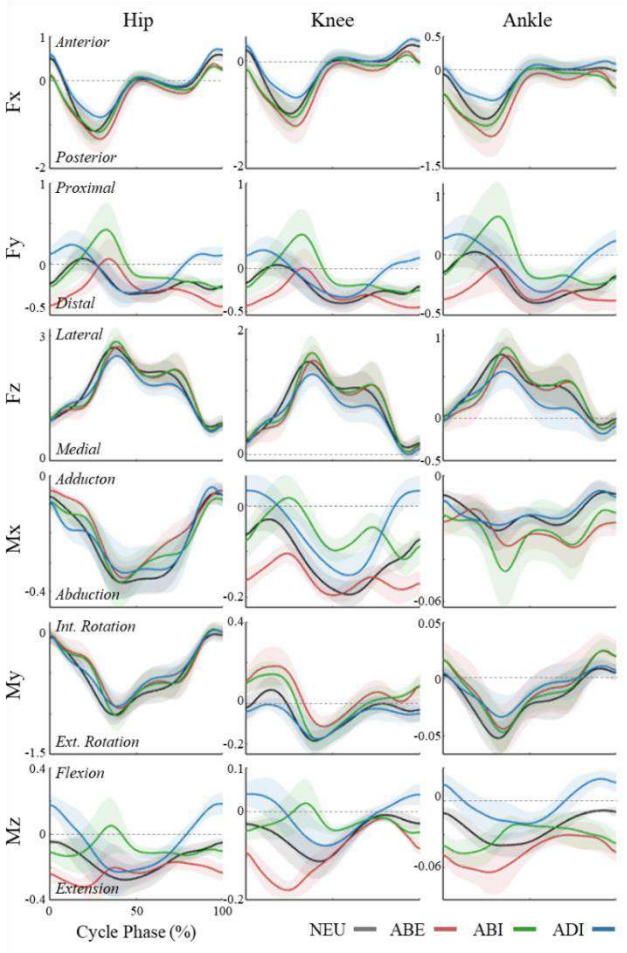


Figure 5. Net joint reaction force and moment. Net joint forces (N/kg) and moments (Nm/kg), normalized to each participant's body weight, are compared across different ergometer conditions throughout the pedaling cycle. (*Fx/y/z: force components along the x, y, and z axes; Mx/y/z: moment components about the x, y, and z axes*.)

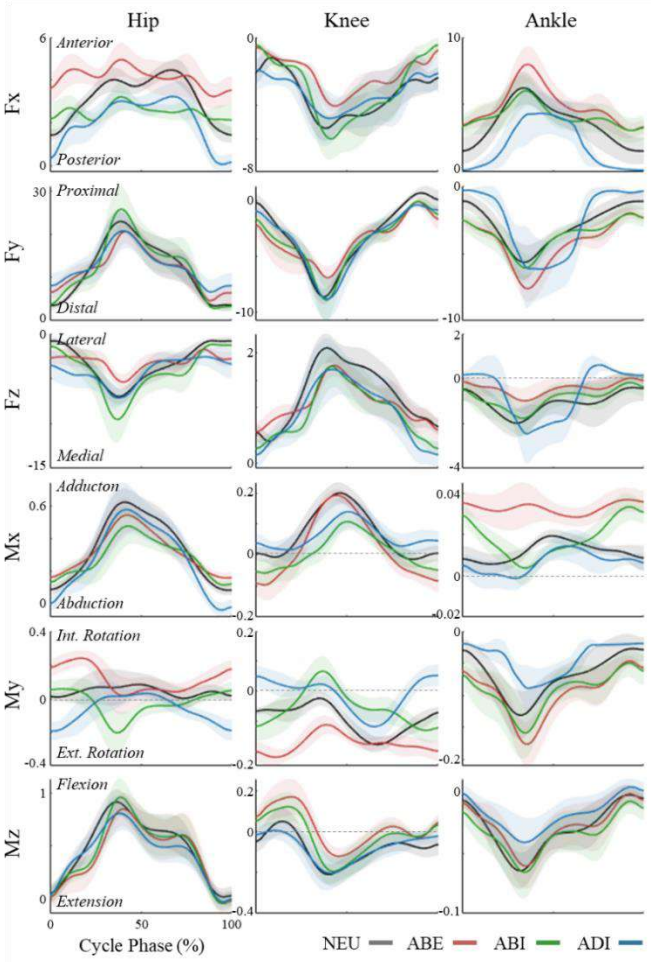


Figure 6. Actual joint reaction force and moment. Estimated actual joint reaction forces (N/kg) and moments (Nm/kg), normalized to each participant's body weight, are compared across different ergometer conditions throughout the pedaling cycle.

B. Kinetic Data

Figure 5 presents the net JRF results for the hip, knee, and ankle joints across the three axes. The x-axis and z-axis components of the net joint force (*nFx* and *nFz*) exhibited similar patterns across all three joints. However, the y-axis component (*nFy*) showed decreased proximal-directed forces in the ABE condition and increased values in the ABI and ADI conditions compared to NEU, consistently across the joints. For the x-axis component of the net joint moment (*nMx*), a reduction in KAM was observed in the ABE condition. Regarding the z-axis net joint moment (*nMz*), the ABE condition demonstrated increased extension moments, while the ABI and ADI conditions showed increased flexion moments across all three joints. The y-axis component of the net joint moment (*nMy*) exhibited a consistent pattern across all conditions, except for increased internal rotation moments observed in the knee joint under the ABE and ABI conditions.

Figure 6 presents the actual JRF results, which exhibited distinct patterns compared to the net JRF data. The x-axis actual joint reaction force (*aFx*) increased in the hip and ankle joints during the ABE condition but decreased in the ADI condition. When accounting for muscle forces, the KAM during the ABE condition increased during the latter push phase and initial pull phase, although the overall values remained lower than those in the NEU condition. Interestingly, the KAM in the ABI condition showed a reduction in the actual JRF analysis, in contrast to the increased values observed in the net JRF analysis. The ankle joint's x-axis actual joint reaction moment (*aMx*) increased in both the ABE and ABI conditions. For the axial rotation moment (y-axis actual joint reaction moment, *aMy*), the hip joint exhibited an increased internal rotation moment in the ABE condition, while the ABI and ADI conditions demonstrated increased external rotation moments. This pattern contrasted with the moment trends observed in the knee joint.

Statistical analysis revealed significant increases in *aFx* across all three joints during the ABE condition, contrasting with significant decreases in *aFx* in the ADI condition. KAM was significantly reduced in both the ABE and ADI conditions, indicating decreased medial contact forces. The *aMx* value showed a marked increase in the ABE condition. For the hip joint's *aMy*, an internal rotation moment was observed in the ABE condition, while external rotation moments were noted in the ABI and ADI conditions, which was opposite to the pattern observed in the knee joint (Fig. 7).

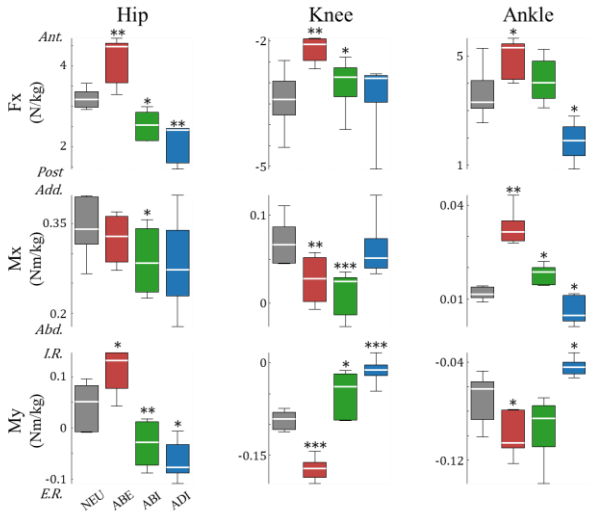


Figure 7. Box plots for actual joint reaction force and moment. The box plots show medians (white line), 25th–75th percentiles (box), and min–max values (whiskers). Statistical comparisons with baseline NEU are indicated by asterisks: $^{*}p < 0.05$, $^{**}p < 0.01$, $^{***}p < 0.001$. (*Lat.: lateral, Med.: medial, Add.: adduction, Abd.: abduction, I.R./E.R.: internal/external rotation*)

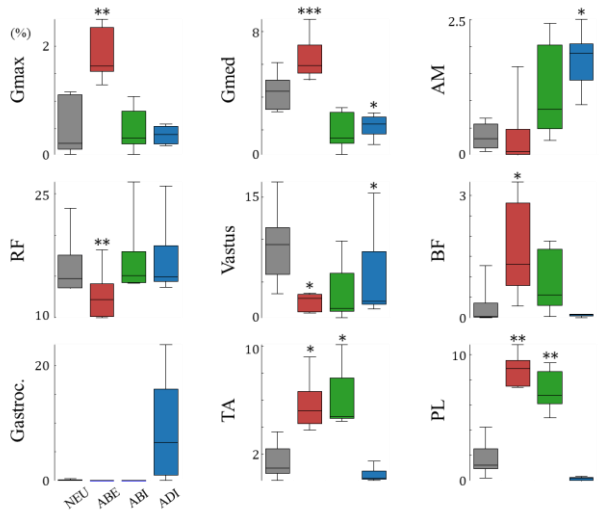


Figure 9. Box plots for muscle activity. The box plots depict the median (black line), interquartile range (25th–75th percentiles, box), and the full range (min–max, whiskers) of mean muscle activation levels for each participant. Statistical comparisons with the baseline NEU condition are denoted by asterisks: $^{*}p < 0.05$, $^{**}p < 0.01$, $^{***}p < 0.001$.

C. *Muscle Activation*

Figure 8 illustrates the muscle activation patterns, derived by normalizing the estimated muscle forces to the maximal force capacity of each muscle. The gluteus maximus (Gmax), a primary hip extensor, showed the highest activation during the latter pull phase to the middle push phase in the ABE condition. Similarly, gluteus medius (Gmed), a key hip abductor, exhibited greater activity in the ABE condition, peaking during the latter push phase. Conversely, the adductor magnus (AM), a hip adductor, was primarily activated in the ABI and ADI conditions, although the timing of activation varied between these conditions. While rectus femoris (RF) activity showed minimal changes, the vastus muscles demonstrated decreased activation across all three conditions. Biceps femoris (BF) activity increased in the ABE and ABI conditions but decreased in ADI. The gastrocnemius was exclusively activated in the ADI condition, whereas tibialis anterior (TA) and peroneus longus (PL) displayed increased activation in the ABE and ABI conditions.

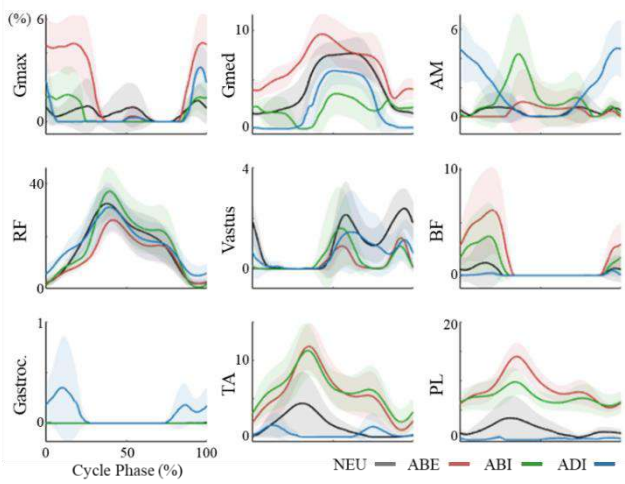


Figure 8. Estimated muscle activation. Estimated muscle activity, derived from normalized muscle force, are compared across different ergometer conditions throughout the pedaling cycle. (*Gmax: gluteus maximus, Gmed: gluteus medius, AM: adductor magnus, RF: rectus femoris, BF: biceps femoris, Gastroc.: gastrocnemius, TA: tibialis anterior, PL: peroneus longus*)

Statistical analysis was performed to compare mean muscle activities with the NEU condition, and the results are presented as box plots in Fig. 9. ABE condition showed a significant increase in the activity of the Gmax and Gmed, while the ADI condition demonstrated significantly higher activation of the AM. Knee extensor muscles (RF and vastus) exhibited significantly reduced activity in the ABE condition, whereas the knee flexor (BF) showed increased activation. TA and PL displayed significantly higher activity in the ABE and ABI conditions.

IV. Discussion

This study explored the biomechanical effects of tilted-plane ergometer, emphasizing kinematic, kinetic, and muscle activation changes under various pedaling configurations. A musculoskeletal modeling approach was employed, integrating motion capture data and force-torque profiles obtained from a sensor-equipped pedal.

Kinematic analysis revealed notable changes in joint alignment across configurations. The ABE condition increased hip adduction, in contrast to the hip abduction observed in the ABI and ADI conditions. Additionally, unique axial rotation patterns distinguished the ABE and ABI conditions from NEU and ADI. These findings are consistent with our prior study using inertial measurement units and RGB-D cameras, which also reported variations in joint angles under different conditions.

The kinetic results provided valuable insights into how the tilted-plane configurations affected net and actual JRFs. In the ABE condition, KAM was significantly reduced, consistent with kinematic changes inducing a dynamic valgus alignment, potentially beneficial for reducing medial knee loading [12]. Interestingly, while previous study associated the ABI

condition with a dynamic varus alignment and increased KAM, as reflected in the net JRF results, the actual JRF analysis revealed reductions in KAM. This discrepancy highlights the importance of incorporating muscle forces for more accurate estimations of joint loads. Additionally, the ABE condition demonstrated increased hip internal rotation moments, which may have implications for conditions requiring rotational load adjustments, such as femoro-acetabular impingement or labral tears [13].

Muscle activation analysis revealed that the ABE condition significantly increased activation of Gmax and Gmed, particularly during the push phase, emphasizing Gmed's crucial role in hip abduction and postural stability. In contrast, the ADI condition increased activation of AM, a hip adductor critical for pelvic and knee stability. Vastus muscle activity decreased under both ABE and ADI conditions, aligning well with previous findings from surface electromyography (EMG) studies. However, BF activity exhibited a notable increase in the ABE condition and a decrease in ADI. For muscles below the knee, gastrocnemius activation, while significantly elevated in experimental EMG data, was minimal in the modeling results except for the ADI condition. TA and PL demonstrated heightened activity in the ABE and ABI conditions, deviating from prior reports. As this study did not focus on a direct comparison of EMG and model-based results, discrepancies between the two approaches were not quantitatively assessed. Future research integrating detailed analyses of both methods could offer deeper insights into these variations.

This study highlights the applicability of the tilted-plane ergometer as a rehabilitation tool, enabling clinicians to address specific biomechanical deficits through dynamic adjustments to pedaling trajectories. For example, the reduction in KAM observed in the ABE and ABI conditions may alleviate medial knee joint loading in patients with osteoarthritis or cartilage injuries. Similarly, the increased external rotation moments in the ABI condition could support the management of patellar instability [14] or aid in early rehabilitation following total hip arthroplasty, potentially preventing hip dislocations.

Despite its promising results, the study has several limitations. The musculoskeletal model used represented the knee joint as a hinge joint with a single DoF in the sagittal plane, disregarding coronal and axial plane motions. However, actual knee movement involves small but meaningful coronal and axial rotations that vary with flexion angles [15]. Given that the knee was consistently flexed beyond 30˚ in this study's ergometer setup, these additional motions cannot be entirely ignored. As such, caution is necessary when interpreting the results, as the hinge joint constraint in the model may oversimplify actual knee mechanics. Additionally, the study's small sample size limits the generalizability of the findings. Future studies should aim to include a larger and more diverse participant pool. Long-term clinical trials are also needed to validate the therapeutic benefits of the tilted-plane ergometer in specific patient populations.

The tilted-plane ergometer demonstrated its potential as a customizable rehabilitation tool by effectively modulating joint kinetics and muscle activation patterns. Its ability to introduce multiple options for pedaling plane and limb alignment, even in a seated exercise setting, allows for tailored adjustments that promote desired targeted training while avoiding harmful loads. This study highlighted the device's capacity to induce significant kinetic and kinematic changes through angle modifications, providing a versatile platform for personalized rehabilitation. To maximize its clinical utility, the development of protocols that integrate these biomechanical adjustments into targeted treatment plans will be crucial, making the device a promising tool for individualized therapeutic strategies.

REFERENCES

[1] V. Colibazzi, A. Coladonato, M. Zanazzo, and E. Romanini, "Evidence based rehabilitation after hip arthroplasty," *Hip International*, vol. 30, no. 2_suppl, pp. 20–29, 2020.

[2] M. Buckthorpe, F. Danelon, G. La Rosa, G. Nanni, M. Stride, and F. Della Villa, "Recommendations for hamstring function recovery after ACL reconstruction," *Sports Medicine*, vol. 51, no. 4, pp. 607–624, 2021.

[3] J. A. Barrios, K. M. Crossley, and I. S. Davis, "Gait retraining to reduce the knee adduction moment through real-time visual feedback of dynamic knee alignment," *Journal of Biomechanics*, vol. 43, no. 11, pp. 2208–2213, Aug. 2010.

[4] A. O. Radzimski, A. Mündermann, and G. Sole, "Effect of footwear on the external knee adduction moment - A systematic review," *The Knee*, vol. 19, no. 3, pp. 163–175, Jun. 2012.

[5] J. Kim, S. Kang, and S.-J. Kim, "A smart insole system capable of identifying proper heel raise posture for chronic ankle instability rehabilitation," *Scientific Reports*, vol. 12, no. 1, p. 10796, 2022.

[6] S. Kang, J. Kim, Y. Kim, J. Moon, S. Park, and S.-J. Kim, "Feasibility of a new bicycle ergometer with adjustable pedaling configuration for personalized lower limb rehabilitation," *Scientific Reports*, vol. 14, no. 1, p. 25504, 2024.

[7] S. Kang, J. Kim, Y. Kim, J. Moon, S. Park, and S.-J. Kim, "A novel tilted-plane ergometer system for subject-specific rehabilitation," in *2023 International Conference on Rehabilitation Robotics (ICORR)*, IEEE, 2023, pp. 1–6.

[8] V. Baltzopoulos, "Inverse dynamics, joint reaction forces and loading in the musculoskeletal system: guidelines for correct mechanical terms and recommendations for accurate reporting of results," *Sports Biomechanics*, vol. 23, no. 3, pp. 287–300, 2024.

[9] S. Daroudi, N. Arjmand, M. Mohseni, M. El-Rich, and M. Parnianpour, "Evaluation of ground reaction forces and centers of pressure predicted by AnyBody Modeling System during load reaching/handling activities and effects of the prediction errors on model-estimated spinal loads," *Journal of Biomechanics*, vol. 164, p. 111974, Feb. 2024.

[10] T. D. Collins, S. N. Ghoussayni, D. J. Ewins, and J. A. Kent, "A six degrees-of-freedom marker set for gait analysis: repeatability and comparison with a modified Helen Hayes set," *Gait & Posture*, vol. 30, no. 2, pp. 173–180, Aug. 2009.

[11] H. Li, X. Wang, Z. Du, and S. Shen, "Analysis of technical characteristics of typical lower limb balance movements in Tai Chi: a cross-sectional study based on AnyBody bone muscle modeling," *PeerJ*, vol. 11, p. e15817, 2023.

[12] Á. Uhlár et al., "Kinect azure–based accurate measurement of dynamic valgus position of the knee—A corrigible predisposing factor of osteoarthritis," *Applied Sciences*, vol. 11, no. 12, p. 5536, 2021.

[13] J. D. Sampson and M. R. Safran, "Biomechanical implications of corrective surgery for FAI: an evidence-based review," *Sports Medicine and Arthroscopy Review*, vol. 23, no. 4, pp. 169–173, 2015.

[14] S. N. Parikh, M. G. Lykissas, and I. Gkiatas, "Predicting risk of recurrent patellar dislocation," *Current Reviews in Musculoskeletal Medicine*, vol. 11, pp. 253–260, 2018.

[15] B. Zarins, C. R. Rowe, B. A. Harris, and M. P. Watkins, "Rotational motion of the knee," *The American Journal of Sports Medicine*, vol. 11, no. 3, pp. 152–156, May–Jun. 1983.

Unilateral Compliant Surfaces in Post-Stroke Gait Retraining: Enhancing Symmetry and Stability

Vaughn Chambers and Panagiotis Artemiadis*, *IEEE Senior Member*

***Abstract*— Stroke is a leading cause of disability worldwide, frequently resulting in gait dysfunction characterized by asymmetries in kinematics and kinetics, reduced push-off force, and diminished muscle activity. These impairments contribute to slow, unstable, and energy-intensive walking, significantly lowering the quality of life and increasing fall risk. Current rehabilitation strategies often fail to deliver a lasting and comprehensive recovery. This study investigates the use of unilaterally compliant terrain as a novel intervention for post-stroke gait rehabilitation. A brief 3 to 4-minute exposure to unilateral low-stiffness terrain was tested on six stroke survivors, yielding statistically significant aftereffects that persisted for up to 5 to 6 minutes post-intervention. Improvements included increased vertical push-off force, reductions in asymmetry in vertical push-off force, and improved center of pressure symmetry, which is related to balance during walking. These promising results suggest that unilaterally compliant terrain may enhance the effectiveness of gait retraining and contribute to more lasting functional recovery for stroke survivors.**

I. Introduction

A stroke, caused by a blocked or ruptured blood vessel in the brain, is a leading cause of disability, particularly affecting gait. Up to 85% of stroke survivors experience hemiplegia, or partial paralysis on one side of the body, which disrupts interlimb coordination – long thought to be controlled at the spine but now attributed to the brain as well [1–4]. Post-stroke gait is marked by slower speeds, instability, and a higher risk of falls [5]. At the timing level, impairments include increased stance and swing times and altered support phases [6–8]. Kinematic deficits involve reduced dorsiflexion, hip and knee flexion, and hip extension [9]. Decreased propulsion [6] and overall lower-limb muscle activity [6, 8] are also evident, though muscle activity patterns are highly variable among individuals. The resulting asymmetry is the hallmark of post-stroke gait, leading to inefficient and unstable walking [10].

Post-stroke gait rehabilitation has long focused on strategies such as body-weight-supported treadmill walking, which enables patients to practice walking in a safer environment with reduced fear of falling and, in some cases, with partial weight offloading to ease movement [11]. Split-belt treadmills, where belts move at different speeds, have shown promise, producing aftereffects lasting up to 10 minutes in both healthy individuals and stroke patients [12–14]. One study demonstrated significant improvements in step length asymmetry and walking speed after a stroke survivor underwent a month-long split-belt treadmill intervention – 30-minute sessions, three times per week – with these gains persisting even one month post-training [15]. While these approaches show varying degrees of success, post-stroke gait rehabilitation remains far from addressing the full spectrum of challenges [16,17]. Expanding rehabilitation strategies by integrating novel physical approaches, targeting diverse neurological pathways, and interacting with patients in innovative ways is likely to enhance outcomes [18].

Integrating robotics into post-stroke gait rehabilitation represents a promising avenue for innovation. Although robots have been extensively explored for upper-limb rehabilitation over the past 25 years [19, 20], their application to gait retraining is still developing. Robots provide unmatched precision and repeatability, making them particularly suited for complex and repetitive tasks like walking [21]. Exoskeletons, orthoses, and other robotic assistive technologies have been investigated for post-stroke gait rehabilitation [22, 23]. However, these technologies often demonstrate limited effectiveness [18], suggesting that further innovation is needed to fully realize their potential.

Efforts to advance robot-assisted post-stroke gait rehabilitation have increasingly focused on low-stiffness environments, particularly unilaterally compliant environments. These terrains theoretically drive neural plasticity by targeting multiple neural pathways. Proprioception is challenged as one foot deflects below the typical ground level, requiring novel postural adjustments [24, 25]. Force feedback is perturbed as the ground reaction force profile is altered during key phases of gait [26, 27]. Additionally, asymmetric balance and interlimb coordination are disrupted, creating a unique stimulus to address gait asymmetry [4,28]. Traditionally, compliant environments have been explored through single or multiple steps on varied surfaces during overground walking [29]. Recently, the Variable Stiffness Treadmill (VST) was developed to provide repeated and precise, compliant surface conditions [30,31]. This split-belt treadmill adjusts stiffness via a linear actuator altering the moment arm of applied forces [30]. Using the VST, experiments with healthy individuals have demonstrated significant brain activity and contralateral muscle responses to unilateral perturbations [3, 4]. Notably, a study found that repeated unilateral stiffness perturbations in healthy subjects produced significant aftereffects, highlighting their potential for post-stroke rehabilitation [32].

This study utilizes a new device, the VST 2, an advanced robotic split-belt treadmill specifically designed to investigate

*This material is based upon work supported by the National Institutes of Health Grant No. 1R01HD111071-01

Vaughn Chambers and Panagiotis Artemiadis are with the Mechanical Engineering Department, at the University of Delaware, Newark, DE 19716, USA. vaughn@udel.edu, partem@udel.edu

*Corrresponding author

unilaterally reduced ground stiffness as a novel post-stroke gait rehabilitation intervention [33]. The VST 2 builds on its predecessor with significant enhancements, including a larger walking area, improved stiffness accuracy, vertical deflection capabilities, and the ability to independently adjust the stiffness of each belt, enabling precise and targeted perturbations. Using this device, the study evaluates the effects of a single 3-4 minute unilateral low-stiffness intervention on six hemiplegic stroke patients. The intervention produced statistically significant aftereffects lasting up to six minutes, including increased vertical push-off force, reductions in asymmetry in vertical push-off force, and improved center of pressure symmetry, which is related to balance during walking. These results suggest that unilateral low-stiffness walking has strong potential as an effective and innovative rehabilitation tool for restoring more natural and symmetric gait patterns in stroke survivors.

II. METHODS

This study investigated the short-term aftereffects of repeated unilateral stiffness perturbations on the gait of stroke survivors. Participants walked in a unilaterally compliant environment, and the effects on their gait were subsequently evaluated on rigid ground. Six stroke survivors participated in the study, including two males and four females, with an average age of 61.8 ± 7.8 years. Three had left-side hemiplegia, and three had right-side hemiplegia. All participants were relatively active and could walk without assistive devices, though one subject used a sling for arm support while walking. The treadmill's handrails were the only other form of assistance provided. A physical therapist, familiar with each subject's physical capabilities, supervised the experiments to ensure safety. All participants provided informed consent, and the study was approved by the University of Delaware Institutional Review Board (IRB ID# 2068278-1). The experimental setup is shown in Fig. 1.

A. Experiment Hardware Components

The primary device used in this study was the Variable Stiffness Treadmill (VST) 2, a robotic split-belt treadmill capable of independently adjusting the vertical stiffness of each belt across a range from 17 kN/m to rigid (5 MN/m) [33]. At its lowest stiffness, the treadmill allows for several inches of vertical deflection under an adult subject, with finer adjustments as the stiffness approaches rigid. The device offers precise control with an average stiffness resolution of 0.07 N/m. Adjustable handrails on either side provide support to subjects while maintaining visibility for motion capture markers. The treadmill also includes safety features, such as a body-weight support system (Litegait Inc.), which was used purely as a precaution without offloading any subject's weight.

During trials, each subject's movement was tracked using 22 reflective markers placed on their lower body, with an 8-camera motion capture system (Vicon Motion Systems Ltd.). Marker placement followed a previous study's protocol [32], and VICON Nexus software was used for data collection and processing. Additionally, force data was captured using Force mats (TekScan 3140 with VersaTek Cuffs, TekScan Inc.) located beneath the treadmill belts. These mats, equipped with 4224 force-sensing cells per belt, measured forces at a spatial resolution of 1 cm and a frequency of 65 Hz, enabling the calculation of total applied force and center of pressure location.



Fig. 1: The Variable Stiffness Treadmill (VST) 2 with the subject wearing motion capture markers, EMGs (under wraps), body-weight-support harness, and heart rate monitor (under harness). The left platform can be seen deflecting as the subject steps on it.

Muscle activity was recorded using Trigno electromyographic (EMG) electrodes (Delsys Inc.), placed on ten muscles across both legs following ISEK guidelines [34]. Targeted muscles included the tibialis anterior (TA), medial gastrocnemius (GA), vastus medialis (VA), rectus femoris (RF), and biceps femoris (BF). Heart rate monitoring was performed throughout the experiment using a Polar H10 chest strap, which recorded data at 1 Hz. The physical therapist present used the monitor to oversee subject safety and was prepared to halt the experiment if necessary; however, no interruptions occurred. Since most participants were on beta-blocker medication, the collected heart rate data were not analyzed for exertion levels.

B. Experiment Protocol

In this study, participants walked in an asymmetrically compliant environment where the treadmill's stiffness was adjusted to create an imbalance. The treadmill belt under the nonparetic leg was set to a lower stiffness, while the paretic leg remained on a rigid surface. This configuration was designed to perturb gait in a way that encouraged greater reliance on the paretic limb, aiming to promote rehabilitation through controlled asymmetry. The experiment consisted of three phases in series with no breaks in between: baseline (20%), adaptation (30%), and observation (50%). During the baseline and observation phases, both treadmill belts were rigid, while in the adaptation phase, the nonparetic

side experienced reduced stiffness. Subjects were informed of transitions with a one-minute warning and a five-second countdown to ensure preparedness. This setup was intended to challenge neural pathways without causing discomfort or fatigue.

Perturbing the nonparetic limb was chosen for several reasons. First, keeping the paretic limb on rigid ground ensured subject comfort, a priority for both participants and the supervising physical therapist. Second, perturbing the nonparetic side encouraged subjects to engage their paretic limb more actively, contrasting the typical assistive approach of exoskeletons. Most critically, prior research has shown that perturbing one limb activates the corresponding brain hemisphere responsible for the opposite limb [3], making this strategy particularly effective for engaging the brain areas controlling the paretic side.

Subjects selected a comfortable walking speed by incrementally testing speeds between 0.3 and 0.6 m/s, with input from the physical therapist. The stiffness level was similarly calibrated, testing values between 21 and 45 kN/m to achieve approximately 2–3 cm of deflection while maintaining comfort. Depending on the subject's capacity, the experiment duration was set to either 10 or 12 minutes. Finally, throughout the experiment, subjects reported perceived exertion every two minutes using the Borg Rating Scale (6–20) [35], with a threshold of 17 set for immediate termination. No subject reported values above 9, and heart rate monitoring by the physical therapist confirmed safety throughout.

C. Processing and Statistical Analysis of Collected Data

In this study, motion capture, muscle activity, and force data were synchronized using a trigger signal from the VICON Lock Lab system. This ensured the alignment of all data streams for accurate analysis. Heel strikes were identified via the force mats, with a strike detected when force rose from 0 to 5% of the subject's body weight. Toe-offs were determined kinematically by the most posterior position of the toe marker during a gait cycle. Gait cycles were defined based on heel strikes of the nonparetic leg. Force mat data, sampled initially at 65 Hz, was upsampled to 100 Hz using linear interpolation for alignment with motion capture data. The center of pressure (CoP) was calculated by translating force mat measurements to the motion capture frame and normalizing the anterior-posterior CoP relative to the subject's estimated center of mass, determined from the average position of four pelvic markers (left and right anterior and posterior superior iliac spines). Muscle activity data are not discussed in this paper.

All statistical analyses in this study were conducted using the Wilcoxon rank-sum test, a non-parametric alternative to the t-test that does not rely on assumptions about the data's distribution or shape [36]. An alpha level of 0.05 was used to determine statistical significance. The primary focus of this study was to evaluate aftereffects, so statistical comparisons were made between the observation phase and the baseline phase. Rather than analyzing responses during the intervention, the analysis targeted changes that persisted post-intervention, comparing these to pre-intervention behavior. Specifically, tests were performed between the last 30 gait cycles of the baseline phase and the first 30 gait cycles of the observation phase (early observation), as well as between the last 30 gait cycles of the baseline phase and the last 30 gait cycles of the observation phase (late observation). This approach aimed to identify both immediate and sustained aftereffects of the intervention, which was the main goal of the study.

III. Results

Figures 2 and 3 illustrate findings related to average vertical push-off ground reaction force (GRF) across all six subjects. This force, quantified as a percentage of body weight (PBW), was determined as the second peak of the vertical GRF during the stance phase. Significance lines at the top of the graph indicate the comparisons between data sets, with arrows showing the direction of change – upward for an increase and downward for a decrease. Blue lines represent the nonparetic limb, red lines indicate the paretic limb, and purple lines combine results from both limbs.

All subjects demonstrated a statistically significant aftereffect of increased vertical push-off force in both their paretic and nonparetic legs. On average, the nonparetic leg's push-off force increased from a baseline of 98.20 PBW to 100.20 PBW (a 2.04% increase) in early observation and 99.42 PBW (a 1.24% increase) in late observation. The paretic leg showed more substantial gains, rising from a baseline of 90.63 PBW to 97.42 PBW (a 7.49% increase) in early observation and 94.69 PBW (a 4.48% increase) in late observation. These results, illustrated in Fig. 2, not only indicate significant improvements on both sides but also suggest a shift toward greater symmetry, which is further explored in the subsequent discussion.

Although this study focused on vertical ground reaction forces, these forces are related to horizontal propulsive forces through kinematic interactions. Under consistent kinematics, an increase in vertical force would imply a corresponding increase in horizontal propulsion. In summary, the observed significant average increase of about 8% in vertical push-off force across all six subjects is an encouraging outcome, potentially contributing to improved step length and walking speed during overground locomotion.

A notable aftereffect also observed is the improvement in symmetry of vertical push-off forces between the paretic and nonparetic limbs. As highlighted earlier, while both limbs demonstrate increased push-off forces following the intervention, they also exhibit a shift toward greater symmetry. Before discussing the results, it is essential to clarify that asymmetry is always calculated by subtracting the paretic side's parameter value from the nonparetic side's parameter value. Therefore, a positive asymmetry value indicates that the nonparetic side's parameter is greater than that of the paretic side. On average, the baseline asymmetry in vertical push-off force among the six participants was 17.45 PBW. This asymmetry significantly decreased to 10.10 PBW (a

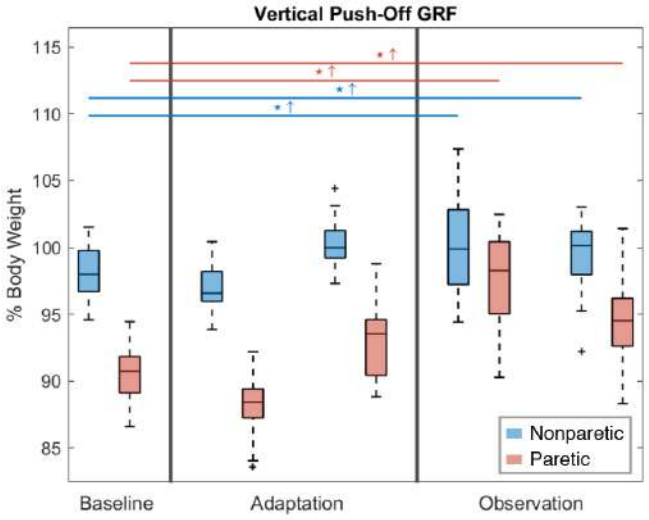


Fig. 2: Average vertical push-off ground reaction force (GRF) for all six subjects. The push-off force was calculated as the second peak of the vertical force during the stance phase. Significance lines are shown connecting the two data sets compared, with an arrow pointing to the direction of change.

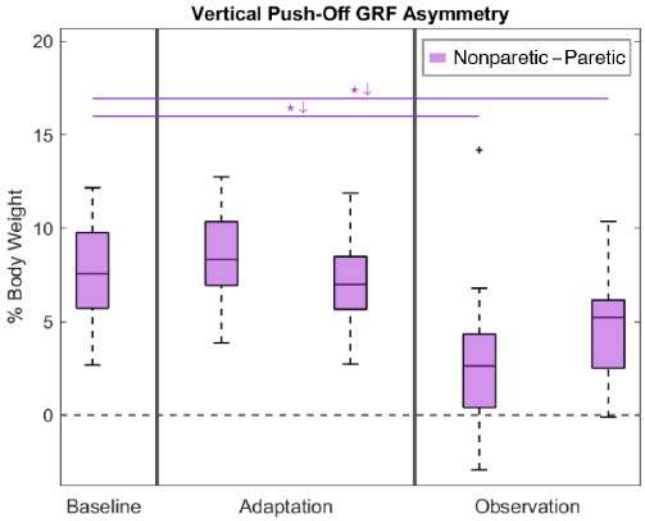


Fig. 3: Average vertical push-off ground reaction force asymmetry across all six subjects is shown. The push-off force was determined as the second peak of the vertical force during the stance phase. Asymmetry was determined by subtracting the paretic side's push-off force from the non-paretic side's push-off force. Significance lines connect the compared data sets, with arrows indicating the direction of change.

42.12% reduction) in early observation and $15.93\ PBW$ (an 8.71% reduction) in late observation, as shown in Fig. 3. These reductions in asymmetry are statistically significant and represent meaningful progress toward more balanced gait mechanics.

Improved symmetry in push-off force may indicate enhanced coordination and a more equal distribution of effort between the paretic and nonparetic limbs. This shift is crucial, as asymmetries in force production are often linked to inefficient and unstable walking patterns, increasing the risk of falls and energy expenditure. The observed improvements suggest that the intervention not only strengthens both limbs but also promotes more natural and efficient gait dynamics, a critical goal in post-stroke rehabilitation.

The total center of pressure (CoP) path also exhibited a more symmetric aftereffect following the intervention. The CoP was measured using force mats positioned beneath the treadmill belts, with normalization applied relative to the subject's center of mass in the anterior/posterior direction to account for drift. In Fig. 4, the orientation depicts the subject as if viewed from above, walking toward the top of the page.

As illustrated in Fig. 4 (top), five key parameters are derived from the CoP path plot. The anterior/posterior length of each lobe, corresponding to the time a limb is in single support, is represented by nonparetic and paretic Y1. The anterior/posterior distance between the front of one lobe and the back of the opposite lobe, referred to as Y2, relates to step length, with each parameter labeled according to the lobe being referenced. Lastly, lateral asymmetry measures the medial/lateral distance between the meeting point of the nonparetic and paretic lobes and the midpoint between their most lateral points. In a healthy, symmetric gait, nonparetic and paretic Y1 values would be equal, nonparetic and paretic Y2 values would match, and lateral asymmetry would measure zero, indicating balanced movement.

Subject 3 was selected as a representative example for discussion (see Fig. 4, bottom), while all subjects had similar results. As a reminder, asymmetry is calculated by subtracting paretic side values from the non-paretic side. During the baseline phase, Subject 3 exhibited a Y1 asymmetry of $-12\ mm$, which improved to a more symmetric $-3\ mm$ in early observation and $2\ mm$ in late observation. Similarly, the Y2 asymmetry decreased from $-88\ mm$ in the baseline phase to $-49\ mm$ in early observation and $-54\ mm$ in late observation, indicating a notable shift toward symmetry after the intervention.

IV. Conclusion

This study highlights the transformative potential of integrating unilateral compliant environments into post-stroke gait rehabilitation. By utilizing the Variable Stiffness Treadmill (VST) 2, designed to create asymmetrical terrain conditions, the research demonstrated statistically significant improvements in key gait metrics among stroke survivors. Notable aftereffects included increased vertical push-off force, reductions in asymmetry in vertical push-off force, and improved center of pressure symmetry, which is related to balance during walking. These improvements, observed after a brief 3-4 minute intervention, underline the immediate efficacy of this novel approach in promoting more symmetric and functional walking patterns.

This study introduced a novel use of unilateral low-stiffness terrain as a rehabilitation tool, offering a fresh approach to gait retraining. Unlike traditional methods such as body-weight-supported or split-belt treadmill training,

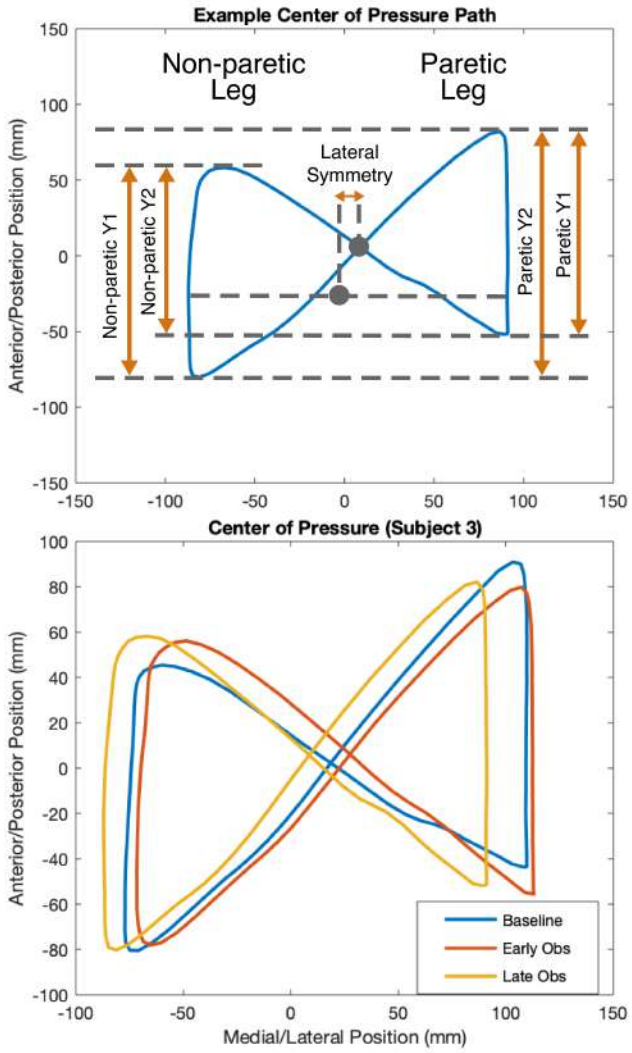


Fig. 4: Illustration of the center of pressure (CoP) path: an example path (top) and the CoP path for Subject 3 (bottom). CoP data was collected using force mats beneath the treadmill belts and normalized relative to the subject's center of mass in the anterior-posterior direction to compensate for drift. The plots are oriented as though viewed from above, with the subject appearing to walk toward the top of the page.

which provide broad benefits, this approach introduces targeted perturbations designed to engage neural plasticity and proprioceptive adaptation more effectively. By employing controlled asymmetry, the methodology aims to stimulate compensatory mechanisms and support neural reorganization, diverging from conventional symmetrical rehabilitation techniques. The integration of advanced robotic systems like the VST 2 ensures precision and consistency in delivering these interventions, enhancing their potential therapeutic impact. A future study that would benchmark this approach against traditional approaches is possible.

This study demonstrated that many after-effects persisted for the full 5-6 minute observation period following just a brief 2-3 minute intervention. This suggests that the induced changes may have had an even longer duration, had the experiment been extended. These findings are both exciting and promising, highlighting the potential for short, targeted interventions to produce lasting after-effects in stroke survivors. However, further research, with a larger sample size, is necessary to explore the longevity and mechanisms of these after-effects, as well as their implications for clinical applications and rehabilitation strategies.

The findings of this study open new avenues for robot-assisted gait rehabilitation. By introducing controlled instability through compliant surfaces, this approach directly addresses gait asymmetry – a hallmark challenge in post-stroke recovery. The results suggest that integrating this technology into clinical practice could foster faster, more robust recovery, reducing reliance on assistive devices and improving long-term mobility. Future research could expand on these findings, exploring the integration of such systems into personalized rehabilitation protocols, potentially transforming the standard of care for stroke survivors.

References

[1] B. H. Dobkin, *The Clinical Science of Neurologic Rehabilitation*. New York: Oxford University Press, Jan. 2003.

[2] S. P. Swinnen, J. Massion, H. Heuer, and P. Casaer, *Interlimb Coordination: Neural, Dynamical, and Cognitive Constraints*. San Diego, CA: Academic Press, Oct. 2013.

[3] J. Skidmore and P. Artemiadis, "Unilateral walking surface stiffness perturbations evoke brain responses: Toward bilaterally informed robot-assisted gait rehabilitation," in *Proceedings - IEEE International Conference on Robotics and Automation*, vol. 2016-June. Stockholm, Sweden: IEEE, May 2016, pp. 3698–3703.

[4] J. Skidmore and P. Artemiadis, "Unilateral Floor Stiffness Perturbations Systematically Evoke Contralateral Leg Muscle Responses: A New Approach to Robot-Assisted Gait Therapy," *IEEE Transactions on Neural Systems and Rehabilitation Engineering*, vol. 24, no. 4, pp. 467–474, Apr. 2016.

[5] P.-C. Kao, J. B. Dingwell, J. S. Higginson, and S. Binder-Macleod, "Dynamic instability during post-stroke hemiparetic walking," *Gait & Posture*, vol. 40, no. 3, pp. 457–463, July 2014.

[6] G. Chen, C. Patten, D. H. Kothari, and F. E. Zajac, "Gait differences between individuals with post-stroke hemiparesis and non-disabled controls at matched speeds," *Gait & Posture*, vol. 22, no. 1, pp. 51–56, Aug. 2005.

[7] S. Nadeau, "Understanding Spatial and Temporal Gait Asymmetries in Individuals Post Stroke," *International Journal of Physical Medicine & Rehabilitation*, vol. 02, no. 03, 2014.

[8] S. J. Olney and C. Richards, "Hemiparetic gait following stroke. Part I: Characteristics," *Gait & Posture*, vol. 4, no. 2, pp. 136–148, Apr. 1996.

[9] B. Balaban and F. Tok, "Gait Disturbances in Patients With Stroke," *PM&R*, vol. 6, no. 7, pp. 635–642, 2014.

[10] D. M. Mohan, A. H. Khandoker, S. A. Wasti, S. Ismail Ibrahim Ismail Alali, H. F. Jelinek, and K. Khalaf, "Assessment Methods of Post-stroke Gait: A Scoping Review of Technology-Driven Approaches to Gait Characterization and Analysis," *Frontiers in Neurology*, vol. 12, p. 650024, June 2021.

[11] M. Visintin, H. Barbeau, N. Korner-Bitensky, and N. E. Mayo, "A new approach to retrain gait in stroke patients through body weight support and treadmill stimulation," *Stroke*, vol. 29, no. 6, pp. 1122–1128, 1998.

[12] D. S. Reisman, R. Wityk, K. Silver, and A. J. Bastian, "Split-Belt Treadmill Adaptation Transfers to Overground Walking in Persons Poststroke," *Neurorehabilitation and Neural Repair*, vol. 23, pp. 735–744, 2009.

[13] J. T. Choi and A. J. Bastian, "Adaptation reveals independent control networks for human walking," *Nature neuroscience*, vol. 10, no. 8, pp. 1055–1062, Aug. 2007.

[14] K. V. Huynh, C. H. Sarmento, R. T. Roemmich, E. L. Stegemöller, and C. J. Hass, "Comparing aftereffects after split-belt treadmill walking and unilateral stepping," *Medicine and Science in Sports and Exercise*, vol. 46, no. 7, pp. 1392–1399, 2014.

[15] D. S. Reisman, H. McLean, and A. J. Bastian, "Split-belt treadmill training post-stroke: A case study," *Journal of Neurologic Physical Therapy*, vol. 34, no. 4, pp. 202–207, Dec. 2010.

[16] P. Langhorne, J. Bernhardt, and G. Kwakkel, "Stroke rehabilitation," *Lancet (London, England)*, vol. 377, no. 9778, pp. 1693–1702, May 2011.

[17] C. Beyaert, R. Vasa, and G. E. Frykberg, "Gait post-stroke: Pathophysiology and rehabilitation strategies," *Neurophysiologie Clinique/Clinical Neurophysiology*, vol. 45, no. 4, pp. 335–355, Nov. 2015.

[18] B. Hobbs and P. Artemiadis, "A Review of Robot-Assisted Lower-Limb Stroke Therapy: Unexplored Paths and Future Directions in Gait Rehabilitation," *Frontiers in Neurorobotics*, vol. 14, 2020.

[19] P. Poli, G. Morone, G. Rosati, and S. Masiero, "Robotic Technologies and Rehabilitation: New Tools for Stroke Patients' Therapy," *BioMed Research International*, vol. 2013, p. e153872, Nov. 2013.

[20] R. Gassert and V. Dietz, "Rehabilitation robots for the treatment of sensorimotor deficits: A neurophysiological perspective," *Journal of NeuroEngineering and Rehabilitation*, vol. 15, no. 1, p. 46, June 2018.

[21] R. S. Calabrò, G. Sorrentino, A. Cassio, D. Mazzoli, E. Andrenelli, E. Bizzarini, I. Campanini, S. M. Carmignano, S. Cerulli, C. Chisari, V. Colombo, S. Dalise, C. Fundarò, V. Gazzotti, D. Mazzoleni, M. Mazzucchelli, C. Melegari, A. Merlo, G. Stampacchia, P. Boldrini, S. Mazzoleni, F. Posteraro, P. Benanti, E. Castelli, F. Draicchio, V. Falabella, S. Galeri, F. Gimigliano, M. Grigioni, S. Mazzon, F. Molteni, G. Morone, M. Petrarca, A. Picelli, M. Senatore, G. Turchetti, and D. Bonaiuti, "Robotic-assisted gait rehabilitation following stroke: A systematic review of current guidelines and practical clinical recommendations," *European Journal of Physical and Rehabilitation Medicine*, vol. 57, no. 3, July 2021.

[22] A. Nilsson, K. S. Vreede, V. Häglund, H. Kawamoto, Y. Sankai, and J. Borg, "Gait training early after stroke with a new exoskeleton – the hybrid assistive limb: A study of safety and feasibility," *Journal of NeuroEngineering and Rehabilitation*, vol. 11, no. 1, p. 92, June 2014.

[23] L. W. Forrester, A. Roy, H. I. Krebs, and R. F. Macko, "Ankle Training With a Robotic Device Improves Hemiparetic Gait After a Stroke," *Neurorehabilitation and Neural Repair*, vol. 25, no. 4, pp. 369–377, May 2011.

[24] D. Rand, "Proprioception deficits in chronic stroke—Upper extremity function and daily living," *PLOS ONE*, vol. 13, no. 3, p. e0195043, Mar. 2018.

[25] J. C. Tuthill and E. Azim, "Proprioception," *Current Biology*, vol. 28, no. 5, pp. R194–R203, 2018.

[26] S. Preusser, S. D. Thiel, C. Rook, E. Roggenhofer, A. Kosatschek, B. Draganski, F. Blankenburg, J. Driver, A. Villringer, and B. Pleger, "The perception of touch and the ventral somatosensory pathway," *Brain*, vol. 138, no. 3, pp. 540–548, Mar. 2015.

[27] J. Perry, *Gait Analysis: Normal and Pathological Function*. New Jersey: Slack Incorporated, 1992.

[28] S. Handelzalts, I. Melzer, and N. Soroker, "Analysis of brain lesion impact on balance and gait following stroke," *Frontiers in Human Neuroscience*, vol. 13, Feb. 2019.

[29] K. Xie, Y. Lyu, X. Zhang, and R. Song, "How Compliance of Surfaces Affects Ankle Moment and Stiffness Regulation During Walking," *Frontiers in Bioengineering and Biotechnology*, vol. 9, no. October, pp. 1–10, 2021.

[30] A. Barkan, J. Skidmore, and P. Artemiadis, "Variable Stiffness Treadmill (VST): A novel tool for the investigation of gait," in *Proceedings - IEEE International Conference on Robotics and Automation*. Hong Kong, China: Institute of Electrical and Electronics Engineers Inc., Sept. 2014, pp. 2838–2843.

[31] J. Skidmore, A. Barkan, and P. Artemiadis, "Variable Stiffness Treadmill (VST): System Development, Characterization, and Preliminary Experiments," *IEEE/ASME Transactions on Mechatronics*, vol. 20, no. 4, pp. 1717–1724, Aug. 2015.

[32] V. Chambers and P. Artemiadis, "Using robot-assisted stiffness perturbations to evoke aftereffects useful to post-stroke gait rehabilitation," *Frontiers in Robotics and AI*, vol. 9, 2023.

[33] V. Chambers, B. Hobbs, W. Gaither, Z. Thé, A. Zhou, C. Karakasis, and P. Artemiadis, "The Variable Stiffness Treadmill (VST) 2: Development and Validation of a Unique Tool to Investigate Locomotion on Compliant Terrains [In Review]," *Journal of Mechanisms and Robotics*, vol. [Accepted], 2024.

[34] R. Merletti and d. T. Politecnico, "Journal of Electromyography and Kinesiology," *Journal of Electromyography and Kinesiology*, pp. 3–4, 1999.

[35] G. Borg, *Borg's perceived exertion and pain scales*. Champaign, IL: Human kinetics, 1998.

[36] W. Haynes, "Wilcoxon Rank Sum Test," in *Encyclopedia of Systems Biology*, W. Dubitzky, O. Wolkenhauer, K.-H. Cho, and H. Yokota, Eds. New York, NY: Springer New York, 2013, pp. 2354–2355.

Development of the Myoelectric Control Resolution Assessment: A Rapid and Device-Agnostic Outcome Measure for Upper-Limb Prostheses

Eric J. Earley, PhD
Bone-Anchored Limb Research Group
Department of Orthopedics
University of Colorado Anschutz Medical Campus
Aurora, CO, USA
ORCID: 0000-0002-1203-7316

***Abstract*— Myoelectric prosthetic hands and terminal devices are a standard of care for individuals with upper limb loss or congenital limb difference, typically controlled using surface electromyography electrodes. While numerous outcome measures exist to assess user performance with a myoelectric prosthesis, many are time-consuming and impractical for clinical settings. This paper introduces the Myoelectric Control Resolution Assessment (MCRA), a rapid and device-agnostic outcome measure requiring only a caliper, making it accessible even in low-resource settings. The MCRA evaluates the smallest volitional movements a user can generate with their myoelectric prosthesis, normalizing measurements to account for mechanical variability of the terminal device. Simulation results demonstrate the MCRA's ability to provide accurate, consistent, and unbiased control resolution estimates in as few as five measurements. The MCRA's simplicity and efficiency make it accessible to both prosthetic clinics and research organizations. It holds potential for clinical evaluation, myoelectric control algorithm comparison, training, and longitudinal studies, representing a novel advancement in the evaluation of myoelectric control fidelity and highlighting its potential for widespread clinical and research applications.**

Keywords—myoelectric control, pattern recognition, surface electromyography, prosthetic hands, outcome measures

I. Introduction

Myoelectric prosthetic hands and terminal devices represent a current standard of care for individuals with limb loss or congenital limb difference. These terminal devices come in a wide range of appearances and functions, from clamp-like grippers to simple single degree-of-freedom (DOF) hand to multi-articulating hands with isolated finger control [1-3]. Regardless of the design, nearly all commercially-available myoelectric prostheses are controlled using a direct control scheme, wherein surface electromyography (sEMG) electrodes located of a pair of agonist/antagonist muscles are used to proportionally control the opening or closing speed of the terminal device [4, 5]. Additionally, in recent years, machine learning approaches to myoelectric control are becoming more common in research and commercial applications [6-8], however proportional control is still typically applied to the speed, and not the position, of the terminal device. Although this control scheme is simple in concept, dual-site myoelectric control requires training and practice to learn and develop this skill.

For both clinical and research assessment purposes, numerous outcome measures have been proposed to characterize a user's performance when using an upper limb prosthesis [9]. Many outcomes involve the user's ability to complete a selection of activities of daily living (ADLs) using the prosthesis, however these often require specific or proprietary equipment to perform and can be very time-intensive, taking upwards of an hour to complete and thus rendering them infeasible for use within a clinical setting [10, 11]. Other outcome measures simplify the tasks observed during the evaluation, often only involving a single task. While these simpler outcomes can be useful for quickly characterizing performance during grasping tasks, it is only grossly capable of evaluating myoelectric control, differentiating only between adequate and inadequate control but unable to measure the ability to control the level of force applied to objects.

The ability to modulate grasping force is a frequent design priority for prosthesis users [12, 13], especially given the higher grasping forces possible with prosthetic hands compared to biological hands [14]. Similarly, many users have indicated an interest in artificial sensory feedback to aid in their grasp force perception [15-17]. This sensory feedback enhances the process of motor learning of new skills and motor adaptation of learned skills (such as prosthesis control) [18], which in turn improves muscle (and thereby myoelectric) control [19, 20]. Some outcome measures, like the Virtual Egg Test (VET) [21] or the Pick & Lift Test (PLT) [22], are able to evaluate this fine myoelectric control, however they also require specialized equipment, making them inaccessible for general clinical use.

The purpose of this paper is to propose and describe a rapid and device-agnostic outcome measure for myoelectric fidelity: the Myoelectric Control Resolution Assessment (MCRA). The MCRA requires only a caliper to perform and can be completed in as few as five measurements, making it accessible even to prosthetic clinics and research organizations in low-income or underserved areas. The mathematics behind the MCRA are detailed and a simulated proof-of-concept is presented to demonstrate feasibility of the assessment.

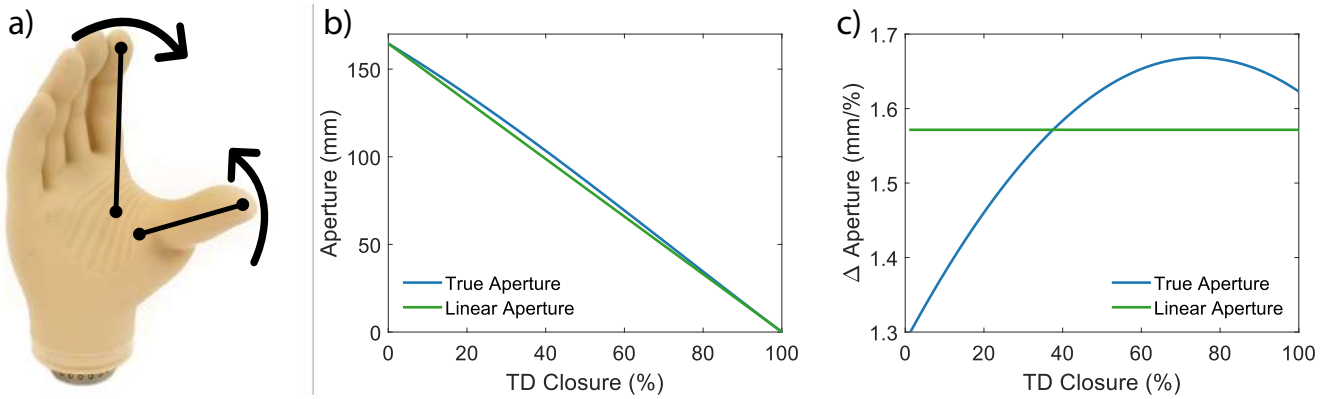


Fig. 1. (a) Because of the geometry of the terminal device (TD), the fingertips follow curvilinear trajectories between the open and closed postures. (b) As a result, the aperture between the fingertips follows a non-linear profile (blue) throughout the range of motion. (c) This non-linear profile means that the rate of change in aperture (i.e. the derivative of (b)) is non-uniform compared to a theoretical linear aperture closure (green). For this prosthetic hand, a given control signal will yield a smaller change in aperture while the hand is fully open (0%), compared to when it is nearly closed (100%). The MCRA aims to mitigate this variability arising purely from the geometry of the terminal device by transforming the measured aperture (blue) into a theoretical linearized closure (green), such that consistent results are given regardless of where in the range of motion aperture measurements are taken.

II. Methods

A. Development

Development of the MCRA builds upon an unvalidated test used in previous studies comparing the fidelity of myoelectric prosthetic hands using implanted EMG electrodes and surface EMG electrodes [23]. Briefly, the participant starts with their prosthetic hand fully open, and the aperture between the index finger and the thumb is measured using calipers. Next, the participant is instructed to close the prosthetic hand by the smallest margin possible. Once the participant has further closed the hand, the aperture is measured again. This process is repeated until the prosthesis is fully closed. The same process is repeated in the opposite direction – the aperture is measured, the hand is opened by the smallest margin possible, and the aperture measurement is repeated. The movement resolution is then calculated as the average of the changes in aperture between subsequent measurements – in other words, the average smallest volitional movement that the participant can generate. This protocol has been used to evaluate both aperture resolution as well as resolution of force generation [24].

This protocol has the advantage of being completed quickly, requiring only a matter of minutes to take several measurements. Furthermore, no special or expensive equipment is required to conduct the test, only a caliper (or even a ruler or tape measure) is required. However, a limitation of this approach is that, because of the mechanics of the hand (Fig. 1a), the rate of change of the aperture (the distance between the fingertips) is not constant across the range of motion of the hand (Fig. 1b). The aperture changes at a slower rate when the hand is fully open, and more quickly when the hand is nearly closed (Fig. 1c). As a result, evaluating control resolution will result in better performance with the fingers closer together than with the fingers apart, even if the underlying myoelectric control is identical.

The MCRA is proposed to account for this variability. The raw measurements are converted into a normalized measure based on the overall range of motion – in other words, yielding a *percentage* of range of motion As a result, identical myoelectric inputs will yield identical outcomes, and variability will be lower.

B. Derivation

Consider a conventional myoelectric prosthetic hand configured to perform only a palmar grasp (Fig. 1a). We define the aperture α as the linear distance (e.g. inches or millimeters) measured between the thumb and the index finger which contact when the hand is fully closed. The aperture of the prosthesis throughout its range of motion is determined by the mechanical design of the prosthesis – for example, the length of the fingers, offset between the flexion rotation axes, and actuation ratios between the fingers.

The aperture α can be said to change as a function of the normalized prosthesis closure x, such that:

$$\alpha(x) = B(x) \tag{1}$$

where x is the current hand closure compared to the overall range of motion (e.g. as a percentage of the range of motion) and B is the function describing the mechanical closing of the prosthetic hand. This closing function B can be determined by analyzing the mechanical design of the prosthesis, or approximated via a piecewise or polynomial fit function based on physical aperture measurements with repeated, consistent myoelectric (or simply electric) inputs.

Determining the normalized prosthesis closure x based on direct measurement of the aperture α is a simple matter of inverting the closing function:

$$x(\alpha) = B^{-1}(\alpha) \tag{2}$$

The Myoelectric Control Resolution MCR of any given measurement $\alpha(i)$, compared to the previous measurement $\alpha(i-1)$, is then calculated as:

$$MCR(i) = T \cdot \Big(x\big(\alpha(i)\big) - x(\alpha(i-1))\Big) \tag{3}$$

where T is the time required to fully actuate the terminal device, which serves here as a normalizing factor such that the

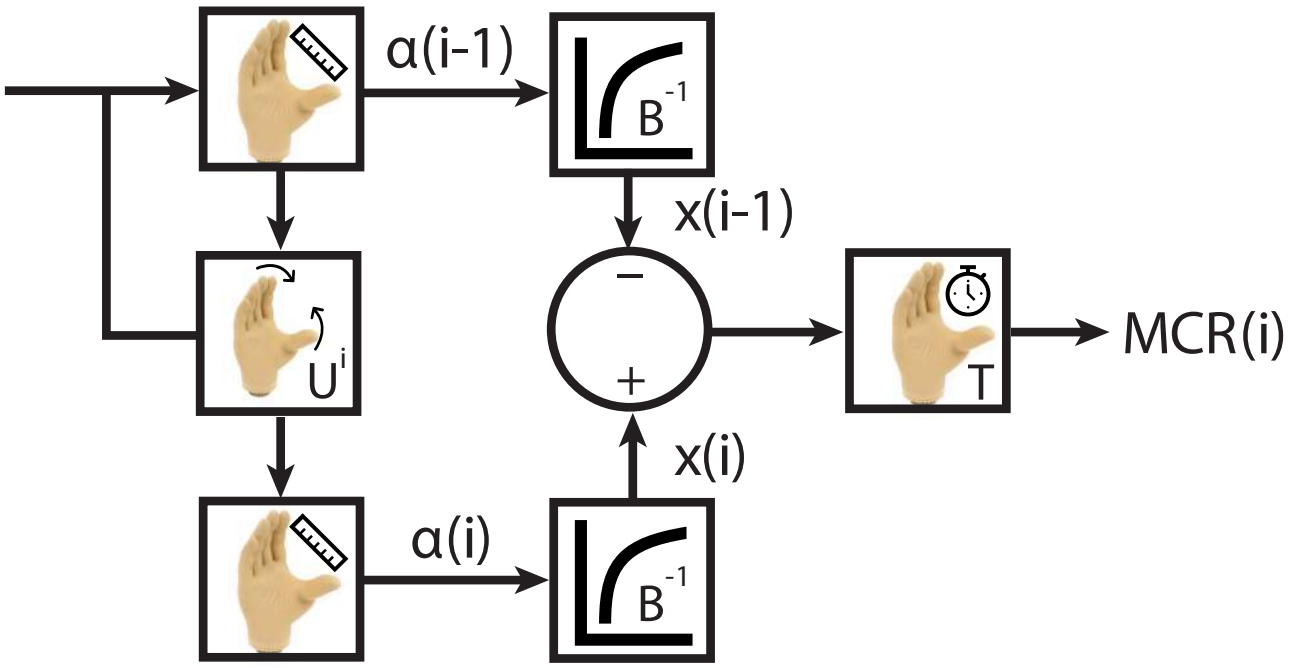


Fig. 2. The protocol for performing the MCRA is as follows. The aperture α of the terminal device is measured before and after the user actuates the terminal device according to motor command U^i. The apertures α are converted into a normalized closure x by means of the inverted closing function B^{-1}. After calculating the difference between the two normalized closures x, the myoelectric control resolution MCR is calculated by adjusting the difference by the closing time T.

MCR will be identical regardless of the maximum actuation speed of the terminal device and its control algorithm. This definition of MCR can be interpreted as an equivalent duration of maximum-speed prosthesis operation, where smaller durations indicate greater control over the prosthesis.

C. Protocol

The protocol for performing the MCRA (Fig. 2) is as follows:

1. Start with the terminal device in a fully-opened position. The experimenter measures the aperture of the terminal device using e.g. a caliper.
2. The experimenter instructs the participant to close the terminal device by the smallest amount possible. The terminal device must visually move – only hearing the sound of the motors activate is not sufficient.
3. Once the terminal device has completed its movement, the aperture of the terminal device is measured again.
4. Both aperture measurements are converted into normalized prosthesis closure using the inverse closing function, and the difference between them is calculated. This difference is then multiplied by the closing time to yield the MCR.
5. Repeat steps 2-4 until the terminal device is fully closed. MCR is averaged across all measurements.
6. Repeat steps 1-5 with the terminal device in the fully-closed position, where the participant is asked to volitionally open the terminal device by the smallest amount possible. This yields separate MCRs for terminal device closing and terminal device opening.

D. Simulation

To characterize the performance of the MCRA, the mechanical closing of a commercially-available prosthetic hand (SensorHand Speed; Ottobock SE & Co. KGaA, Duderstadt, Germany) was simulated based on physical measurements of the ungloved mechanism (Fig. 1b-c). The protocol described above was simulated for 1,000 participants as follows. Starting from a fully open position, the simulated participant would proceed to close the terminal device at an average of 5% increments of the total range of motion (e.g. their simulated average minimum actuation), with either 5%, 10%, or 15% variability in their movements (similar to EMG amplitude variability observed in previous research [25]). Caliper measurements were simulated to measure the aperture of the terminal device. This process was repeated until the terminal device was fully closed; any trials where the control signal would have extended the terminal device beyond its range of motion were discarded. The entire protocol was simulated for both closing and opening control.

The control resolution, as determined by both the raw aperture measurements and the MCR, is calculated as a cumulative average of the current and all previous measurements. For example, the second calculated control resolution would be the average of the first two differences in aperture or MCRs, the third calculated control resolution would be the average of the first three differences, and so on. This simulates the procedure as it would happen within a

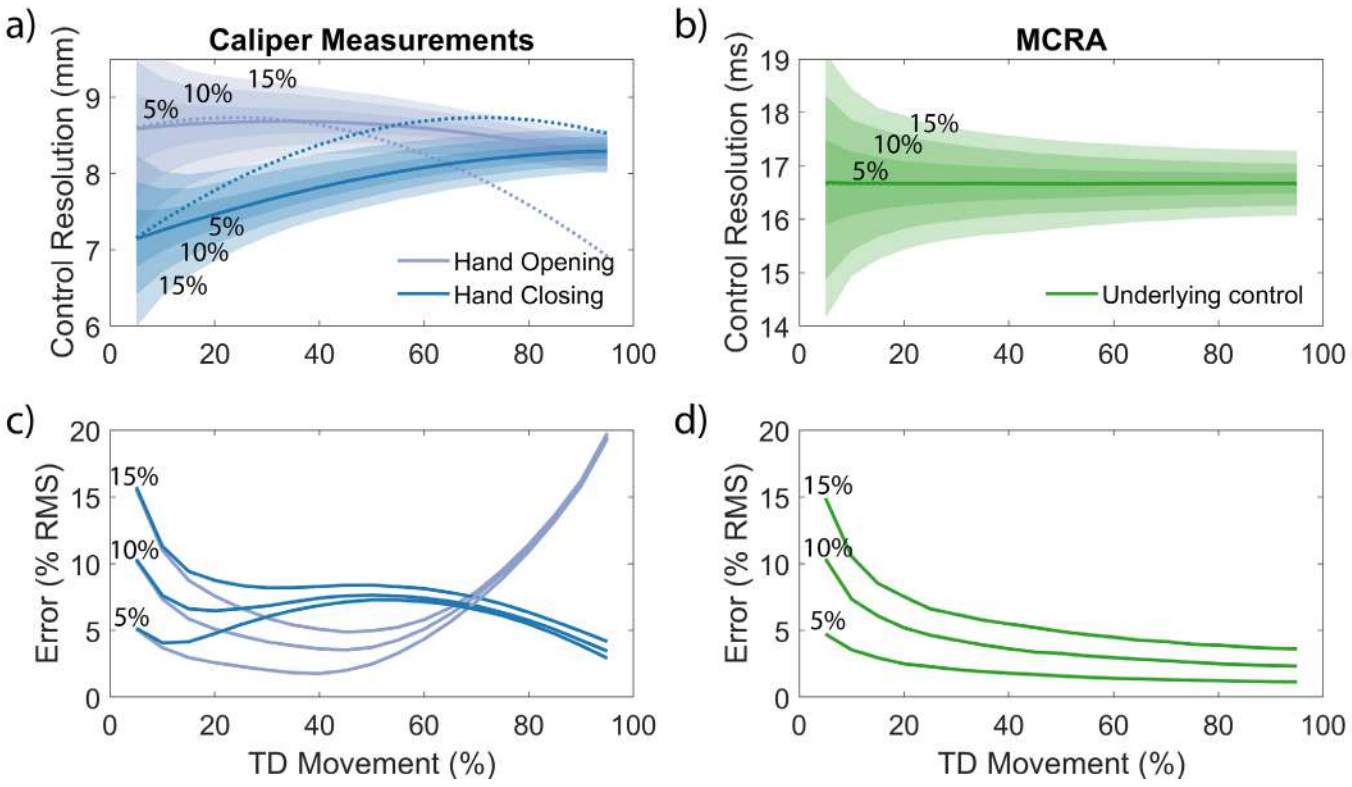


Fig. 3. (a) Measuring myoelectric control resolution directly using calipers yields biased results, even when the underlying motor commands are identical. Control resolution will be worse when opening the hand (violet) compared to closing the hand (blue) due solely to the geometry of the terminal device. (b) Applying a corrective factor to caliper measurements eliminates this bias and can provide more accurate and uniform estimates of both opening and closing control with fewer measurements. Dashed lines indicate the true resolution across the operating range, solid lines indicate the mean of all previous measurements that would be taken from the starting position, and shaded areas indicate standard deviation of measurements at different levels of movement. MCRA control resolution is measured in units of equivalent milliseconds of maximum-speed prosthesis operation. (c-d) The control resolution error from caliper measurements (c) starts the same as the MCRA (d) for the first measurement, but diverges due to the cumulative averaging of previous measurements. Expected MCR error consistently decreases with additional measurements, reaching half of the underlying control variability in only 5 measurements.

clinic, where the participant is continually closing or opening the prosthesis, and the previously-measured aperture is used as the reference for calculating the next control resolution.

III. Results

The outcomes from the simulated task are shown in Fig. 3. Directly estimating the control resolution using caliper measurements of the terminal device aperture (Fig. 3a) yields inconsistent outcomes depending on the direction of movement (closing or opening) and the current aperture (due to cumulative averaging). When measuring during closing (blue), aperture changes are smaller when the hand is more open, but the aperture changes at a faster rate as the fingers near closing. This results in an underestimation of the underlying control resolution (dashed lines) due to the cumulative averaging over the course of successive measurements (solid lines). The opposite phenomenon is observed when estimating opening control resolution (violet); changes in aperture are larger when the hand is fully closed, and gradually slow as it nears its full range of motion. As a result, control resolution using direct aperture measurements are biased towards larger resolution and worse performance. These biases are also observed in the expected error of the estimates (Fig. 3c) – measurement error does not always monotonically decrease with additional measurements, but can in fact increase because of the divergence between the cumulative averages and the true underlying control resolution.

When performing the MCRA (Fig. 3b), each measurement is corrected by the inverse closing function to translate directly to the underlying control; thus, there is no bias in control resolution estimates, regardless of whether the terminal device is opening or closing. Furthermore, the expected error of estimates (Fig. 3d) monotonically decreases when averaging across multiple measurements.

IV. Discussions

The purpose of this paper was to propose and describe a rapid and device-agnostic assessment for myoelectric control resolution. This assessment can be conducted using only a caliper, making it accessible to clinicians and researchers in low-income or underserved areas. Simulations show that the expected error of the MCR, compared to the true underlying control resolution, drops of half of the combined movement and measurement variability in as few as 5 trials. Assuming that each measurement takes approximately 10 seconds, the assessment can be completed in about one minute; although full opening or closure of the prosthesis is not required, additional measurements will further reduce this expected error in a monotonic fashion. The required number of assessments should be determined alongside validation of the MCRA compared to functional and quality-of-life outcomes.

The derivation of the MCRA, as proposed in this paper, estimates the underlying control resolution of the participant's myoelectric signals via measurements of the aperture of a terminal device. However, the underlying theory behind the MCRA can be extended to a number of other types of measurements. For example, the protocol upon which the MCRA is based has been used to evaluate both aperture resolution [23] as well as resolution of force generation [24]. It would be possible to develop a variation of the MCRA that uses prosthesis force as the measured variable instead of aperture; the only difference would be that a different closing function B would be required to properly calibrate the assessment. This could be especially useful if consistent device is used to measure force generation, as this opens the doors for at-home and longitudinal testing of MCR. Furthermore, despite the name of the assessment specifically indicating myoelectric control, other bioelectric control signals could be evaluated using the proposed assessment, including mechanomyography [26], electroneurography [27], and ultrasound [28] and myokinetic interfaces [29].

Although the protocol proposed in this study describes the use of a prosthetic hand or terminal device as the instrument of the MCRA, the MCRA can easily be extended to evaluate the control of any other prosthetic joint. For example, estimating the control resolution of a myoelectric prosthetic elbow could follow an identical protocol as for the hand simply by defining the "aperture" as the distance between the end of the terminal device and the shoulder; in such an instance, this distance would likely be measured using a tape measure instead of a caliper. Even a powered wrist control via myoelectric signals could be evaluated if the rotation angle is measurable. Regardless of the prosthetic joint being controlled and the variable being measured, the MCRA ensures that the true underlying myoelectric control resolution is being estimated, such that no differences should be observed between different measurement methods so long as the closing functions are accurate.

Because of the simplicity of the MCRA, there are some limitations that should be noted. Firstly, the control "resolution" evaluated as part of the MCRA is not expected to be consistent across all amplitudes of myoelectric signals. The MCR is, in essence, a measure of the minimum viable actuation; it does not speak to the smallest *change* in volitional myoelectric signal generation that a participant can generate. As a result, a change in the activation threshold of myoelectric control could affect the estimated control resolution by making small volitional movements easier or harder to control. Additionally, the MCRA assumes that the prosthesis only moves in a single direction during the assessment (e.g. only opening or only closing). This may present challenges to participants who are new to myoelectric control and have difficulty volitionally separating between antagonistic motions. This also may present challenges for myoelectric control schemes that are based on position control (as opposed to velocity or force control, where the prosthesis does not move when the user relaxes their muscles). Evaluating MCR for such a control may require calculations based on the rate of change of prosthesis operation, rather than trial-by-trial measurement, and would therefore require specialized equipment to accomplish.

Another limitation is that a different mechanical closing function is required for the MCRA to be generalizable. This would likely require a broad collaborative effort to define these closing functions for commercially-available prosthetic terminal devices, and to make these functions publicly available for clinicians to use. If a closing function is not available for a prosthesis but one desires to characterize MCR for a prosthesis user regardless, then the drawbacks of the raw caliper aperture measurement methods can be partially addressed by repeating measurements from the start of the range of motion (e.g. measuring closing resolution from the fully-opened position and measuring opening resolution from the fully-closed position). While this will mitigate the issue of bias from successive measurements, it should be noted that the opening and closing resolutions will no longer be directly comparable. MCR estimated in this way should only be used to make longitudinal comparisons for each movement separately.

Acknowledgment

I would like to thank Fabian Just and Enzo Mastinu for their feedback on this manuscript.

References

[1] C. Piazza, G. Grioli, M. G. Catalano, and A. Bicchi, "A Century of Robotic Hands," in *Annual Review of Control, Robotics, and Autonomous Systems* vol. 2, ed, 2019, pp. 1-32.

[2] C. Widehammar, A. Hiyoshi, K. Lidström Holmqvist, H. Lindner, and L. Hermansson, "Effect of multi-grip myoelectric prosthetic hands on daily activities, pain-related disability and prosthesis use compared with single-grip myoelectric prostheses: A single-case study," *Journal of Rehabilitation Medicine,* 2021, doi: 10.2340/jrm.v53.807.

[3] E. J. Earley, C. Piazza, and K. Turner, "A Taxonomy for Commercially Available Myoelectric Terminal Devices," presented at the Myoelectric Controls Symposium (MEC), Frederickton, NB, Canada, 2024.

[4] P. Herberts, "Myoelectric signals in control of prostheses," in *Acta Ortop. Scand. (suppl)* vol. 40, ed, 1969, p. 124.

[5] P. A. Parker and R. N. Scott, "Myoelectric control of prostheses," in *Crit Rev Biomed Eng* vol. 13, ed, 1986, pp. 283-310.

[6] B. Hudgins, P. Parker, and R. N. Scott, "A new strategy for multifunction myoelectric control," in *IEEE Trans Biomed Eng* vol. 40, ed, 1993, pp. 82-94.

[7] K. Englehart and B. Hudgins, "A robust, real-time control scheme for multifunction myoelectric control," in *IEEE Trans Biomed Eng* vol. 50, ed, 2003, pp. 848-854.

[8] C. Igual, L. A. Pardo, J. M. Hahne, and J. Igual, "Myoelectric Control for Upper Limb Prostheses," *Electronics,* vol. 8, no. 11, p. 1244, 2019, doi: 10.3390/electronics8111244.

[9] S. Wang *et al.*, "Evaluation of Performance-Based Outcome Measures for the Upper Limb: A

Comprehensive Narrative Review," *PM&R,* vol. 10, no. 9, pp. 951-962.e3, 2018/09/01/ 2018, doi: 10.1016/j.pmrj.2018.02.008.

[10] C. M. Light, P. H. Chappell, and P. J. Kyberd, "Establishing a standardized clinical assessment tool of pathologic and prosthetic hand function: Normative data, reliability, and validity," *Archives of Physical Medicine and Rehabilitation,* vol. 83, no. 6, pp. 776-783, 2002, doi: 10.1053/apmr.2002.32737.

[11] L. M. Hermansson, A. G. Fisher, B. Bernspång, and A. C. Eliasson, "Assessment of Capacity for Myoelectric Control: A new Rasch-built measure of prosthetic hand control," in *Journal of Rehabilitation Medicine* vol. 37, ed, 2005, pp. 166-171.

[12] E. Biddiss, D. Beaton, and T. Chau, "Consumer design priorities for upper limb prosthetics.," in *Disability and rehabilitation. Assistive technology* vol. 2, ed, 2007, pp. 346-357.

[13] F. Cordella *et al.*, "Literature review on needs of upper limb prosthesis users," in *Frontiers in Neuroscience* vol. 10, ed, 2016, pp. 1-14.

[14] A. Kargov, C. Pylatiuk, J. Martin, S. Schulz, and L. Döderlein, "A comparison of the grip force distribution in natural hands and in prosthetic hands," *Disability and Rehabilitation,* vol. 26, no. 12, pp. 705-711, 2004, doi: 10.1080/09638280410001704278.

[15] A. M. De Nunzio *et al.*, "Tactile feedback is an effective instrument for the training of grasping with a prosthesis at low- and medium-force levels," in *Experimental Brain Research* vol. 235, ed: Springer Berlin Heidelberg, 2017, pp. 2547-2559.

[16] S. Raspopovic, G. Valle, and F. M. Petrini, "Sensory feedback for limb prostheses in amputees," *Nature Materials,* vol. 20, no. 7, pp. 925-939, 2021, doi: 10.1038/s41563-021-00966-9.

[17] L. Jabban, S. Dupan, D. Zhang, B. Ainsworth, K. Nazarpour, and B. W. Metcalfe, "Sensory Feedback for Upper-Limb Prostheses: Opportunities and Barriers," in *IEEE Transactions on Neural Systems and Rehabilitation Engineering*, ed, 2022, pp. 1-1.

[18] R. Sigrist, G. Rauter, R. Riener, and P. Wolf, "Augmented visual, auditory, haptic, and multimodal feedback in motor learning: A review," in *Psychonomic Bulletin and Review* vol. 20, ed, 2013, pp. 21-53.

[19] D. M. Wolpert, J. Diedrichsen, and J. R. Flanagan, "Principles of sensorimotor learning," in *Nature Reviews Neuroscience* vol. 12, ed: Nature Publishing Group, 2011, pp. 1-13.

[20] R. E. Johnson, K. P. Kording, L. J. Hargrove, and J. W. Sensinger, "Does EMG control lead to distinct motor adaptation?," in *Frontiers in Neuroscience* vol. 8, ed, 2014, pp. 1-6.

[21] M. Controzzi *et al.*, "Assessing Hand Function in Trans-Radial Amputees Wearing Myoelectric Hands: The Virtual Eggs Test (VET)," Institute of Electrical and Electronics Engineers (IEEE), 2024.

[22] E. Mastinu *et al.*, "Neural feedback strategies to improve grasping coordination in neuromusculoskeletal prostheses," in *Scientific Reports* vol. 10, ed: Nature Publishing Group UK, 2020, pp. 1-15.

[23] M. Ortiz-Catalan, B. Håkansson, and R. Brånemark, "An osseointegrated human-machine gateway for long-term sensory feedback and motor control of artificial limbs," in *Science Translational Medicine* vol. 6, ed, 2014, pp. 257re6-257re6.

[24] M. Ortiz-Catalan *et al.*, "A highly integrated bionic hand with neural control and feedback for use in daily life," *Science Robotics,* vol. 8, no. 83, p. eadf7360, 2023, doi: doi:10.1126/scirobotics.adf7360.

[25] M. A. Schweisfurth, M. Markovic, S. Dosen, F. Teich, B. Graimann, and D. Farina, "Electrotactile EMG feedback improves the control of prosthesis grasping force," in *Journal of Neural Engineering* vol. 13, ed: IOP Publishing, 2016.

[26] C. Meagher *et al.*, "New advances in mechanomyography sensor technology and signal processing: Validity and intrarater reliability of recordings from muscle," *Journal of Rehabilitation and Assistive Technologies Engineering,* vol. 7, p. 205566832091611, 2020, doi: 10.1177/2055668320916116.

[27] B. Ahkami, E. Mastinu, E. J. Earley, and M. Ortiz-Catalan, "Extra-neural signals from severed nerves enable intrinsic hand movements in transhumeral amputations," *Scientific Reports,* vol. 12, no. 1, 2022, doi: 10.1038/s41598-022-13363-2.

[28] Z. Yin *et al.*, "A Wearable Ultrasound Interface for Prosthetic Hand Control," *IEEE Journal of Biomedical and Health Informatics,* vol. 26, no. 11, pp. 5384-5393, 2022, doi: 10.1109/jbhi.2022.3203084.

[29] M. Gherardini, F. Masiero, V. Ianniciello, and C. Cipriani, "The myokinetic interface: Implanting permanent magnets to restore the sensory-motor control loop in amputees," *Current Opinion in Biomedical Engineering,* vol. 27, p. 100460, 2023/09/01/ 2023, doi: 10.1016/j.cobme.2023.100460.

Assessing the Impact of Loading on Mobility and Physical Exertion of Manual Wheelchair Users Using Wearable Sensors

Grace McClatchey
Department of Biomedical Engineering
University of Wisconsin-Milwaukee
Milwaukee, WI, USA
gofasipe@uwm.edu

Maja Goršič
Department of Biomedical Engineering
University of Wisconsin-Milwaukee
Marquette University
Milwaukee, WI, USA
gorsic@uwm.edu

Erika V. Zabre
Department of Biomedical Engineering
University of Wisconsin-Milwaukee
Milwauke, WI, USA
ezabre@uwm.edu

Jacob R. Rammer
Department of Biomedical Engineering
University of Wisconsin-Milwaukee
Milwaukee, WI, USA
jrrammer@uwm.edu

***Abstract*—Manual wheelchair users face many physical and physiological demands when maneuvering and participating within their community. One aspect of daily life which has not been thoroughly examined is how carrying a load affects their mobility. This study presents data collected from 10 participants completing a short outdoor course. Each participant completed the course twice: with and without an additional backpack, carrying approximately 10% of their bodyweight. Inertial and heart rate data from wrist mounted sensors were analyzed to determine the effect of loading on manual wheelchair user mobility and cardiovascular strain. The results of the Wilcoxon sign-rank test showed that carrying a load significantly increased the travel time ($z = -2.035$, $p = 0.042$) and heart rate ($z = -2.073$, $p = 0.038$) of the participants. Furthermore, analysis of the propulsion data suggested different strategies were used by the participants to compensate for the loaded condition. This highlights the need for developing individualized rehabilitation strategies to address the unique needs of manual wheelchair users for improving their quality of life.**

Keywords—community mobility, physical exertion, manual wheelchair users, inertial sensors, heart rate.

I. Introduction

The physical demands of Manual Wheelchair Users (MWU) during mobility and participation in the community, and their ability to meet demands play a crucial role in shaping their overall quality of life [1], [2]. MWU are often faced with diverse challenges in navigating outdoor environments, particularly when encountering different terrains and loading conditions [3]. These environmental aspects can impose significant exertion on MWU, impacting their mobility and overall participation in daily activities. Understanding the effects of exertion is crucial for those seeking to improve wheelchair design, enhance rehabilitation strategies, and to support the independence and quality of life of MWU [4], [5], [6], [7].

One of the factors that can influence the mobility and participation of MWU in the community is the shoulder demands of manual wheelchair use across a spectrum of activities such as wheelchair propulsion, weight carrying, and terrain maneuverability [8]. Past research has explored the different physical demands faced by MWU and highlighted the significant biomechanical challenges they encounter [8], [9]. The incidence of shoulder injuries among MWU, primarily due to repetitive strain during wheelchair propulsion, plays a vital role in their mobility and participation [9], [10], [11]. Long-term wheelchair users often experience shoulder pain, which can be intensified by additional load carrying [11], [12], [13]. Load carrying, whether it be personal belongings, groceries or other necessities, can alter the dynamics of wheelchair propulsion by increasing the physical effort required and affecting the user's ability to maneuver effectively [14], [15], [16], [17], [18]. Despite the importance of load bearing, there has been limited research that specifically investigates its impact on the mobility and exertion of MWU, particularly in real-world, outdoor settings.

Studies have integrated the use of inertial measurement units (IMU) for assessing mobility and participation of MWU. Research has demonstrated the efficacy of IMUs in capturing detailed biomedical data [19], [20], [21], [22], [23]. The effect of different terrain on manual wheelchair propulsion is crucial to fully understand shoulder function and its impact in the real-world environment [3]. Studies have shown that rough terrain increases the effort of MWU, thereby increasing the risk of shoulder injuries [8]. The use of technology like IMUs not only aids in understanding the challenges faced by MWU, but also offers potential solutions to enhance their community participation by informing the design of more adaptive and supportive mobility aids.

The ability to navigate different environments safely and efficiently is crucial for social engagement [24]. While various studies have examined the general mobility and upper extremity demands of MWU [25], [26], [27], there is a need for further assessment of their ability to engage in community activities especially in environments where they might need to carry groceries, personal items or other external loads.

This work was supported in part by the US Department of Health and Human Services, Grant No. 90ARHF0006.

This study aims to assess the kinematic and heart rate response of MWUs when carrying a load on an outdoor course using IMUs and a heart rate monitor. By using these sensors, this research seeks to provide insight into how load carrying affects key aspects of wheelchair mobility and cardiovascular response, and its relationship to community mobility and participation in a real-world setting.

II. METHODS

A. Participants

The participants in this study were selected based on the following inclusion criteria: they were at least 18 years old, were experienced manual wheelchair users who relied on their wheelchair for daily mobility, were able to self-propel and transfer independently, and reported no shoulder injury or surgery within the last year.

A total of 10 participants were recruited for the study. The sample included 7 males and 3 females, with a mean age of 34 ± 9 years and BMI of 28.8 ± 7.1 kg/m2. Each participant provided written informed consent prior to participation. The study was approved by the University of Wisconsin-Milwaukee Institutional Review Board (protocol #24.059). A summary of participant demographic information is presented in Table I, including age, gender, BMI, level of injury, and wheelchair propulsion type based on visual observations made by the tester during data collection.

TABLE I. PARTICIPANT DEMOGRAPHICS; SCI – SPINAL CORD INJURY, BMI – BODY MASS INDEX

#ID	Gender	Age	Weight (lbs)	BMI	Injury Type	Propulsion Pattern
1	Male	41	160	23.6	SCI L3 incomplete	Semicircular[a]
2	Male	26	183	32.4	SCI T10 incomplete	Semicircular
3	Male	32	245	40.8	Sacral Spina Bifida, incomplete SCI	Arc[b]
4	Male	39	225	29.7	SCI T8 incomplete	Arc
5	Male	38	135	19.4	SCI T6 incomplete	Arc
6	Female	22	140	23.3	Neuromuscular autoimmune condition	Semicircular
7	Female	22	245	39.5	Spina Bifida L3-L5	Semicircular
8	Male	47	220	28.2	SCI C6/C7 incomplete	Arc
9	Female	43	150	28.3	Spina bifida T12	Semicircular
10	Male	30	155	22.9	SCI T10-T12 incomplete	Semicircular

[a] Hands follow the pushrim in a roughly half-circle motion, then drop below the pushrim during recovery

[b] Hands move in a short downard and backward motion along the pushrim

B. Equipement and Hardware

- **IMU**: In this study, IMUs were used to capture detailed data on the motion dynamics of the wheelchair and user. An IMU was secured to the participants' right wrists, and one on the frame of the wheelchair. The placement of the IMUs on the wrist and wheelchair (Fig. 1 – left) is described in a previous study [22]. The IMUs were triaxial Blue Trident IMUs (Vicon Motion Systems Ltd., Oxford, UK) and recorded linear acceleration and angular velocity.
- **Heart Rate Monitoring**: A commercially available Garmin Forerunner 735XT (Garmin Ltd., Olathe, KS, USA) wristwatch was used to record time and heart rate. The heart rate monitor with a photoplethysmography sensor was used to assess the cardiovascular effort during the test. The heart rate data were used to compare the physiological demand of the two test conditions and identify any significant increases in exertion when carrying an additional load.
- **Ramp and Course Description**: The study was conducted outdoors to simulate a real-world environment with conditions typically encountered by MWU. Cones were laid out to mark the course which included a ramp (with an incline, plateau, and decline) and a gravel surface representative of those found in urban settings. The ramp was constructed from a nonskid aluminum with a uniform surface to minimize variability in rolling resistance. The incline/decline had a slope of 8.33% to meet ADA ramp requirements, with a sloped length of 0.9 meters and a top plateau length of 1.8 meters. The gravel area consisted of loose uneven stones of varying sizes, and created a rough, unstable surface approximately 1.5 meters long. The course also included flat segments and turns around traffic cones to create a realistic and challenging environment for the participants, approximately 22 meters long (see Fig. 1 – right for a sketch of the course).

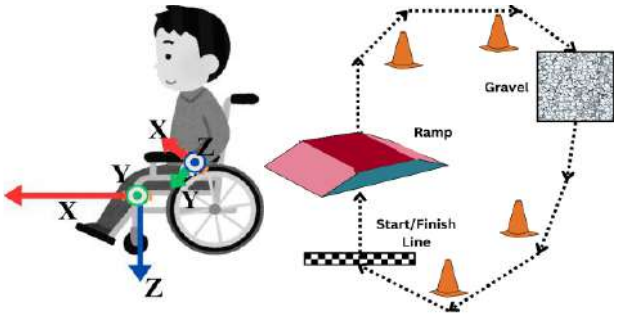


Fig 1. LEFT: Wheelchair user with two inertial sensors. Vector orientation of the IMU axes on the wrist and wheelchair is shown. RIGHT: Sketch of the course and all its elements.

C. Study Protocol

Before testing, the participants were given an explanation of the study's objectives and the steps they would follow. Each participant had the wristwatch and IMU secured to their right wrist and an IMU on their wheelchair. The study began with a familiarization phase, during which each participant went through the course once without data collection.

The study involved two testing conditions: the unloaded condition performed first, followed by the loaded condition, with a break in between for setup and rest. Participants did not report fatigue after the unloaded condition.

- **Unloaded Condition**: Participants were instructed to propel themselves around the course at a comfortable self-selected pace while maintaining safety on the ramp and other challenging sections.
- **Loaded Condition**: Participants were required to complete the same course while carrying an additional load equivalent to 10% of their body weight in a backpack, rounded to the nearest 5 pounds. The loaded condition was designed to simulate real-world scenarios in which wheelchair users might need to carry personal belongings or other items while navigating their local environment.

D. Data Processing

For each participant, Blue Trident IMU and Garmin wristwatch data were collected and processed for both conditions. IMU data were used to determine events of the individual's propulsion cycle from the y-axis acceleration of the wrist-mounted IMU (push rim-hand contact and release points, thus identifying the push and recovery phases) [22], as well as to calculate their cadence. The y-axis angular velocity from the gyroscope of the IMU on the wheelchair was used to detect sections in the course where sudden, sharp increases in angular velocity indicated wheelchair pitch rotations, such as when the front wheels were elevated to enter the ramp or gravel section. IMU data were filtered using a low pass Butterworth filter (6 Hz) to remove any noise and artifacts that might have resulted from vibrations or sudden movements not related to propulsion. Heart rate data were averaged across the entire course to provide a clear picture of the cardiovascular demand under each condition.

All statistical analyses were performed using SPSS software (version 28, SPSS Inc., Chicago, IL, USA). The analysis compared the participants' performance and physiological responses between the two testing conditions: loaded and unloaded. Missing heart rate data from participant 5 was excluded from the statistical analysis. A Shapiro-Wilk test for normality showed that the loaded completion time was not normally distributed ($p < 0.05$). As a result, a Wilcoxon signed-rank test was used to compare cadence, heart rate, and completion time differences between loaded and unloaded conditions across participants, with a p-value of less than 0.05 indicating significant differences. This non-parametric test assessed the impact of additional load on participants' mobility and exertion.

III. Results

Fig. 2 shows the y-axis angular velocity of the wheelchair-mounted IMU, with peaks indicating backward wheelchair tilt and valleys indicating forward tilt in the sagittal plane, which correspond to course obstacles such as going up and down the ramp and traversing the gravel. Descriptive statistics for the entire course, shown for all participants and averaged across them, are presented in Table II. The displayed time is how long the participant took to complete the course from start to finish during both the loaded and unloaded conditions, while mean heart rate is the average heart rate of the participant, measured during the course.

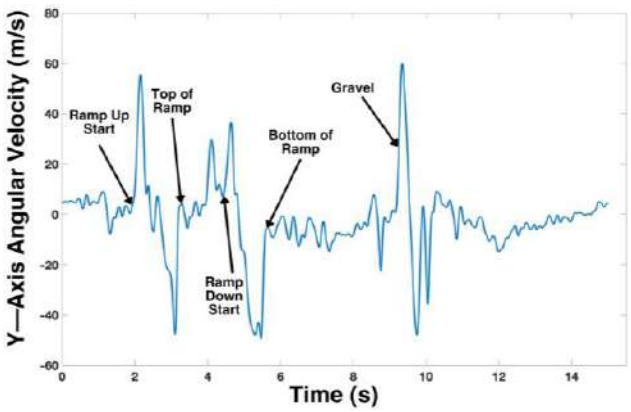


Fig 2. Wheelchair IMU y-axis angular velocity for Participant 1 for unloaded condition, with marked wheelchair pitching movements indicating different segments of the course.

TABLE II. TRIAL RESULTS; UD – UNLOADED, LD – LOADED, HR – HEART RATE

ID	UD Time (s)	LD Time (s)	UD Cadence (cycle/min)	LD Cadence (cycle/min)	UD Mean HR (bpm)	LD Mean HR (bpm)
1	15	15	60.0	52.0	95.9	99.6
2	16	17	56.2	45.9	93.3	109.4
3	13	15	50.8	52.0	115.4	113.8
4	10	16	88.4	86.2	104.3	101.4
5	16	22	45.0	57.3	-	-
6	18	34	63.3	40.9	80	90.4
7	19	17	37.9	45.9	106	110.4
8	18	25	60.0	59.1	78.9	97.5
9	11	11	70.9	65.4	93.1	96.3
10	10	11	72.0	87.3	121.1	116.4
$\bar{X}$ (σ)	14.6 (3.5)	18.3 (7.0)	60.5 (14.5)	59.2 (16.2)	97.5 (13.4)	104.1 (9.0)

Fig. 3 also shows the cadence during the ramp segment for the unloaded and loaded conditions for each participant, calculated from the y-axis acceleration of the wrist IMU. The calculated cadence exhibited distinct responses to the external load, varying among participants for both the entire course (Table II) and while traversing the ramp (Fig. 3). Some participants showed little to no change in cadence between loaded and unloaded conditions, while others increased or decreased their cadence in the loaded condition. There was no statistically significant difference in cadence across participants between the loaded and unloaded conditions for the entire course (Wilcoxon $z = -0.306$, $p = 0.760$). Conversely, there was a significant difference in the time taken to complete the course (Wilcoxon $z = -2.035$, $p =$

0.042) and the mean heart rate (Wilcoxon z = -2.073, p = 0.038) between the loaded and unloaded conditions.

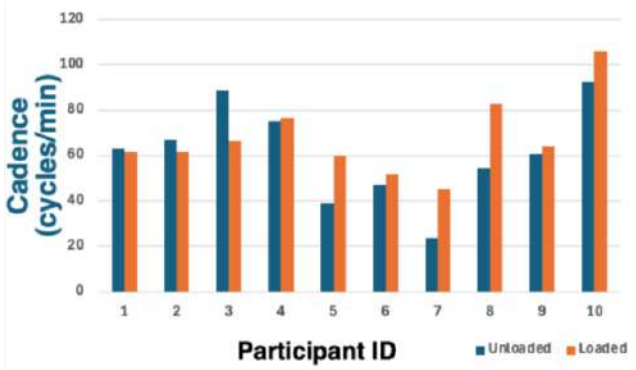


Fig 3. Unloaded and loaded cadence for each participant while traversing the ramp.

IV. Discussion

To gain a comprehensive understanding of the impact of load carrying on wheelchair propulsion, the quantitative data from the IMUs and heart rate monitor were analyzed. This approach allowed for the examination of how physical performance and physiological exertion varied between loaded and unloaded conditions and from person to person.

The increase in both the heart rate (p = 0.038) and the time to complete the course (p = 0.042) for the loaded condition underscores the dual impact of load carrying on both physical and cardiovascular performance. From a biomechanical perspective [11], [12], [13], the additional weight likely increased the force required to overcome course obstacles, resulting in a longer completion time and a greater cardiovascular exertion during the loaded condition.

A closer examination of the cadence data illustrated in Fig. 3 and listed in Table II revealed considerable variability in how each participant reacted to carrying the extra weight. This variability likely explains the lack of statistical significance in cadence between the loaded and unloaded conditions, potentially attributed to participants adopting different propulsion patterns when faced with the additional load. Some participants may have chosen to maintain or decrease their cadence by exerting more force per stroke, while others may have increased their cadence but applied less power into each stroke to manage the increased effort required for propulsion. This variability highlights individual differences in coping mechanisms and physical conditioning among MWU, emphasizing the need for effective methods of individualized assessment.

These findings have important implications for the assessment and training of MWU to improve their mobility and participation in their community. The significant increase in completion time and heart rate under the loaded condition supports the need for training and rehabilitation programs that specifically address physical fitness and the challenges of load carrying to build strength and endurance necessary to handle such conditions in the daily lives of MWU. The difference in the cadence responses also suggests that a one-size-fits-all approach for wheelchair training may not be appropriate. A personalized training program that considers the user's physical condition and preferred propulsion strategies may be more effective. This study also highlights the importance of regular cardiovascular monitoring, as the increased heart rate under the loaded condition suggests that even moderate loads can significantly stress the cardiovascular system. This also agrees with previous findings on the effect of loading on MWUs [14], [15], [16], [17], [18].

While this study provides valuable insights, there were limitations that must be acknowledged. Given the relatively small sample size, future studies with larger and more diverse populations could provide additional understanding of the impact of load carrying on different groups of wheelchair users. Additionally, as only one trial per condition was collected for each participant, future studies should include multiple trials and average the results. Future studies should consider varying the order of the conditions to avoid any effects of fatigue. Furthermore, future research can explore the long-term effects of regular load carrying on wheelchair users, particularly in relation to musculoskeletal health and the risk of overuse injuries. By investigating these questions, future research can continue to enhance our understanding of wheelchair mobility and contribute to the development of solutions that promote independence and well-being for MWU.

V. Conclusion

This study explored the impact of load carrying on mobility and physical exertion of MWU by comparing inertial and heart rate data under loaded and unloaded conditions. The findings illustrated the increased physical and cardiovascular strain associated with load carrying that could affect daily mobility and the overall well-being of MWU. Awareness of the potential for increased fatigue and the need for pacing during activities that involve carrying weight can help users make more informed decisions about managing their daily routines. Additionally, the variability in individual responses emphasizes the importance of personalized approaches in training and rehabilitation, where individual capabilities and techniques are taken into account. This study contributed valuable insights into the challenges faced by MWU when carrying loads, providing a foundation for further research and practical applications aimed at enhancing the mobility and quality of life of MWU.

References

[1] C. L. Flemmer and R. C. Flemmer, "A review of manual wheelchairs," Disability and Rehabilitation: Assistive Technology, vol. 11, no. 3, pp. 177–187, Nov. 2015.

[2] S. M. Hosseini, M. L. Oyster, R. L. Kirby, A. L. Harrington, and M. L. Boninger, "Manual Wheelchair Skills Capacity Predicts Quality of Life and Community Integration in Persons With Spinal Cord Injury," *Archives of Physical Medicine and Rehabilitation*, vol. 93, no. 12, pp. 2237–2243, Dec. 2012.

[3] T. Rouvier et al., "Manual wheelchair biomechanics while overcoming various environmental barriers: A systematic review," PLOS ONE, vol. 17, no. 6, p. e0269657, Jun. 2022.

[4] P. Requejo, S. Mulroy, L. L. Haubert, C. Newsam, J. Gronley, and J. Perry, "Evidence-Based Strategies to Preserve Shoulder Function in Manual Wheelchair Users with Spinal Cord Injury," *Topics in Spinal Cord Injury Rehabilitation*, vol. 13, no. 4, pp. 86–119, Apr. 2008.

[5] I. Madanhire, L. Gudukeya, and R. Mushonga, 'Development of a Rough Terrain Wheelchair Design', Public Health in Developing Countries - Challenges and Opportunities. IntechOpen, Sep. 09, 2020.

[6] J. W. Chow and C. E. Levy, "Wheelchair propulsion biomechanics and wheelers' quality of life: an exploratory review," *Disability and Rehabilitation: Assistive Technology*, vol. 6, no. 5, pp. 365–377, Oct. 2010.

[7] J. W. Rankin, W. M. Richter, and R. R. Neptune, "Individual muscle contributions to push and recovery subtasks during wheelchair propulsion," *Journal of Biomechanics*, vol. 44, no. 7, pp. 1246–1252, Apr. 2011.

[8] M. M. B. Morrow, W. J. Hurd, K. R. Kaufman, and K.-N. An, "SHOULDER DEMANDS IN MANUAL WHEELCHAIR USERS ACROSS A SPECTRUM OF ACTIVITIES," *Journal of electromyography and kinesiology : official journal of the International Society of Electrophysiological Kinesiology*, vol. 20, no. 1, pp. 61–67, Feb. 2010.

[9] F. Ambrosio, M. L. Boninger, A. L. Souza, S. G. Fitzgerald, A. Koontz, and R. A. Cooper, "Biomechanics and Strength of Manual Wheelchair Users," *The Journal of Spinal Cord Medicine*, vol. 28, no. 5, pp. 407–414, Jan. 2005, doi: https://doi.org/10.1080/10790268.2005.11753840.

[10] M. B. Warner, B. S. Mason, V. L. Goosey-Tolfrey, and N. Webborn, "Physical activity levels and shoulder pain in wheelchair users during COVID-19 restrictions," *Disability and Health Journal*, vol. 15, no. 3, p. 101326, Jul. 2022.

[11] Y.-S. Lin, M. Boninger, L. Worobey, S. Farrokhi, and A. Koontz, "Effects of Repetitive Shoulder Activity on the Subacromial Space in Manual Wheelchair Users," *BioMed Research International*, vol. 2014, pp. 1–9, 2014, doi: https://doi.org/10.1155/2014/583951.

[12] G. da Silva Bertolaccini, F. E. Sandnes, F. O. Medola, and T. Gjøvaag, "Effect of Manual Wheelchair Type on Mobility Performance, Cardiorespiratory Responses, and Perceived Exertion," *Rehabilitation Research and Practice*, vol. 2022, pp. 1–11, Jun. 2022.

[13] S. L. Walford, P. S. Requejo, S. J. Mulroy, and R. R. Neptune, "Predictors of shoulder pain in manual wheelchair users," *Clinical Biomechanics*, vol. 65, pp. 1–12, May 2019.

[14] H. E. J. Veeger, L. A. Rozendaal, and F. C. T. van der Helm, "Load on the shoulder in low intensity wheelchair propulsion," *Clinical Biomechanics*, vol. 17, no. 3, pp. 211–218, Mar. 2002.

[15] Ángel Gil-Agudo *et al.*, "Echographic and Kinetic Changes in the Shoulder Joint after Manual Wheelchair Propulsion Under Two Different Workload Settings," *Frontiers in bioengineering and biotechnology*, vol. 2, Dec. 2014.

[16] S. Sprigle and M. Huang, "Manual wheelchair propulsion cost across different components and configurations during straight and turning maneuvers," *Journal of Rehabilitation and Assistive Technologies Engineering*, vol. 7, p. 205566832090781, Jan. 2020.

[17] S. Sprigle and M. Huang, "Impact of Mass and Weight Distribution on Manual Wheelchair Propulsion Torque," *Assistive Technology*, vol. 27, no. 4, pp. 226–235, May 2015.

[18] R. Aissaoui and D. Gagnon, "Effect of Haptic Training During Manual Wheelchair Propulsion on Shoulder Joint Reaction Moments," *Frontiers in Rehabilitation Sciences*, vol. 3, Apr. 2022.

[19] E. Fortune *et al.*, "Estimation of manual wheelchair-based activities in the free-living environment using a neural network model with inertial body-worn sensors," *Journal of Electromyography and Kinesiology*, vol. 62, p. 102337, Feb. 2022.

[20] W. H. K. de Vries, R. M. A. van der Slikke, M. P. van Dijk, and U. Arnet, "Real-Life Wheelchair Mobility Metrics from IMUs," Sensors, vol. 23, no. 16, p. 7174, Jan. 2023.

[21] S. E. Sonenblum, S. Sprigle, and R. A. Lopez, "Manual Wheelchair Use: Bouts of Mobility in Everyday Life," Rehabilitation Research and Practice, vol. 2012, pp. 1–7, 2012.

[22] G. Fasipe, Maja Goršič, E. V. Zabre, and J. R. Rammer, "Inertial Measurement Unit and Heart Rate Monitoring to Assess Cardiovascular Fitness of Manual Wheelchair Users during the Six-Minute Push Test," *Sensors*, vol. 24, no. 13, pp. 4172–4172, Jun. 2024.

[23] B. Hordacre, C. Barr, and M. Crotty, "Use of an Activity Monitor and GPS Device to Assess Community Activity and Participation in Transtibial Amputees," *Sensors*, vol. 14, no. 4, pp. 5845–5859, Mar. 2014, doi: https://doi.org/10.3390/s140405845.

[24] G. Fasipe, M. Goršič, M. H. Rahman, and J. Rammer, "Community mobility and participation assessment of manual wheelchair users: a review of current techniques and challenges," Front. Hum. Neurosci., vol. 17, p. 1331395, 2024.

[25] S. E. Sonenblum, S. Sprigle, J. Caspall, and R. Lopez, "Validation of an accelerometer-based method to measure the use of manual wheelchairs," Medical Engineering & Physics, vol. 34, no. 6, pp. 781–786, Jul. 2012.

[26] A. Marco-Ahulló, L. Montesinos-Magraner, L.-M. Gonzalez, R. Llorens, X. Segura-Navarro, and X. García-Massó, "Validation of Using Smartphone Built-In Accelerometers to Estimate the Active Energy Expenditures of Full-Time Manual Wheelchair Users with Spinal Cord Injury," Sensors, vol. 21, no. 4, p. 1498, Feb. 2021.

[27] B. M. Goodwin et al., "Application and Reliability of Accelerometer-Based Arm Use Intensities in the Free-Living Environment for Manual Wheelchair Users and Able-Bodied Individuals," Sensors, vol. 21, no. 4, pp. 1236–1236, Feb. 2021.

Optimising continuous control of real-time brain-computer interfaces through trial length and feedback update interval selection

Malik Muhammad Naeem Mannan
Australian Centre for Precision Health and Technology (PRECISE),
Griffith University
Gold Coast, QLD, Australia
m.mannan@griffith.edu.au

David G. Lloyd
Australian Centre for Precision Health and Technology (PRECISE),
Griffith University
Gold Coast, QLD, Australia
david.lloyd@griffith.edu.au

Claudio Pizzolato
Australian Centre for Precision Health and Technology (PRECISE),
Griffith University
Gold Coast, QLD, Australia
c.pizzolato@griffith.edu.au

***Abstract*— Brain-computer interfaces (BCIs) offer promising potential to aid neurorehabilitation by transforming motor imagery (MI) signals into control commands, bypassing damaged neural pathways to support motor recovery. However, a key challenge in BCI research is achieving an effective balance between classification accuracy and real-time responsiveness, as both are critical for enhancing user embodiment and control for neurorehabilitation outcomes. This study investigates the impact of trial length and feedback update interval (FUI) on classification accuracy in an MI-based BCI system. Using EEG data from five subjects across 50 sessions, we evaluated classification performance across various trial length (1–5 seconds) and FUI (0.2–1 second) configurations. Results revealed that both trial length and FUI significantly influenced classification accuracy, with longer trial length (4–5 seconds) and FUI (0.4–1 seconds) yielding the highest accuracy. However, post-hoc analyses indicated a saturation effect, with no significant differences in the accuracy for these parameters. These findings underscore the importance of balancing signal stability with responsiveness for optimal BCI performance, providing insights into parameter settings that can enhance BCI usability in neurorehabilitation. Future work may explore adaptive approaches to dynamically adjust these parameters based on real-time requirements, potentially offering a more responsive and efficient BCI for clinical rehabilitation.**

Keywords*— Brain-computer interface, Real-time, Motor imagery, Virtual reality, Neurorehabilitation, Common spatial patterns, Linear discriminant analysis, Responsiveness, Feedback update interval

I. INTRODUCTION

Sensorimotor rehabilitation is critical in treating conditions such as spinal cord injury (SCI) and stroke, aiming to restore motor function and improve quality of life [1], [2]. Recent research highlights brain-computer interfaces (BCIs) as a promising technology to promote neuroplasticity, positioning BCIs as a potential adjunct to current rehabilitation interventions after neural trauma [1]. BCIs record brain activity and translate into control commands, bypassing peripheral nerves and muscles to control external devices [3]. Specifically, motor imagery (MI) BCIs use electroencephalography (EEG) to detect imagined movements—thoughts of motion without physical movement—enabling users with neurological impairments to interact within real or virtual environments despite disrupted motor pathways [1], [4]. EEG-based BCIs are particularly advantageous due to their non-invasive nature, portability, and high temporal resolution [5], [6]. Although advancements in BCI-driven rehabilitation have significantly improved the quality of life for individuals post-stroke or SCI [7], [8], BCIs are not yet widely adopted in clinical practice [9].

A core challenge in BCIs is achieving real-time responsiveness, which is essential for effective neurorehabilitation [10], [11]. For BCIs to be effective, they must rapidly and accurately transform neural signals into commands. Despite advancements, BCI research has often emphasized classification accuracy over real-time responsiveness, impacting users' perception of control [12]. In applications requiring immediate interaction, reducing processing delays is crucial to enhancing both user experience and system functionality [13]. Continuous BCI control relies on real-time feedback, and delays can disrupt users' perception of agency [12], [14], potentially hindering the relearning of motor skills. Conversely, timely feedback reinforces intended brain activity patterns, promoting effective motor learning and neuroplasticity in rehabilitation [11], [15].

Optimizing BCI responsiveness involves balancing trial length (EEG data segment used to produce one classification output) and feedback update interval (FUI; sliding window length used to generate subsequent classification outputs) (Fig. 1): shorter configurations may enhance responsiveness but risk signal instability and misclassification, while longer configurations provide more stable signals but may introduce delays [12]. A recent study has explored the effect of trial length on classification accuracy in offline BCI systems; however, they did not consider the influence of FUI, nor did they report results for continuous real-time BCI control [12]. Another study examined the impact of shorter FUIs on behavioural and neurophysiological measures following BCI training for a single stroke patient, but its effect on BCI accuracy was not addressed [11]. Moreover, longer trial length and FUI configurations may capture richer MI spatial patterns, enhancing classification accuracy, thus exploring the

This work was supported by the Queensland Motor Accident Insurance Commission (MAIC), Australia, as part of BioSpine research project.

trade-off between responsiveness and performance may improve neurorehabilitation outcomes.

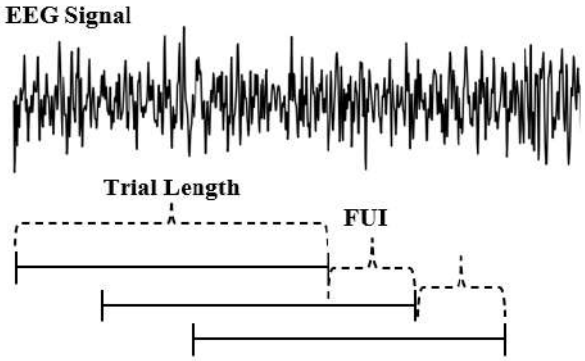


Fig. 1. Example of EEG signal partitioned into trial length and feedback update interval (FUI) using sliding window technique.

This study addresses this gap by analysing the relationship between trial length, FUI, and BCI classification accuracy. Our objective is to identify configurations that support both high accuracy and real-time feedback, enhancing BCI usability in neurorehabilitation. Using data from five subjects across 50 sessions, we evaluated classification accuracy across different trial length and FUI combinations. By identifying optimal settings for these parameters, our findings aim to contribute to the development of more responsive and robust BCI systems, ultimately improving rehabilitation outcomes for individuals relying on BCI technology..

II. Materials and Methods

A. Experimental Setup and Signal Processing

Fifty sessions 2-class MI EEG datasets from five healthy naïve subjects (2 females, aged 24-40 years) were used in this study [16] (Fig. 2). During each session, subjects sat on a comfortable chair wearing an OpenBCI EEG (USA) and Oculus VR headset (USA). Subjects were immersed via a virtual pathed environment designed in Unity 3D (Unity Technologies, USA). Continuous 16-channels (AFz, F4, Fz, F3, FC6, FC2, FC1, FC5, C4, Cz, C3, CP6, CP2, CP1, CP5, and Pz) dry EEG signals at 125 Hz were recorded for three phases: calibration, cued-online, and self-paced online BCI. Here, we only used calibration phase data to train the BCI model and cued-online data to simulate real-time feedback scenarios. A Zero-phase bandpass finite impulse response filter was used to filter the EEG data between 4–30 Hz [17]. Afterwards, common spatial patterns (CSP) was applied to extract discriminative features from the EEG data, enhancing the variance differences between two classes. CSP operates by maximizing the variance for one class while minimizing it for the other, producing a set of spatial filters that project the EEG signals into a feature space optimal for classification [18], [19]. Following feature extraction, linear discriminant analysis (LDA) was employed as the primary classifier. LDA is a widely used algorithm in BCI research due to its efficiency and simplicity. It operates by finding a linear combination of features that best separates the classes, which is particularly effective for MI-based BCI tasks. The CSP-derived features were input to the LDA model for classification, providing real-time feedback to the user [20]. The MI-BCI was implemented using Python (MNE and scikit-learn libraries) in the Robotic Operating System (ROS) to enable real-time EEG data acquisition and processing, as well as synchronisation with the VR environment [16]. An Intel Xeon 3.6GHz with 32GB RAM was used to implement the system and data collection. All the offline simulations were performed on Dell G3 laptop with an Intel Core i7 (8th Gen, 2.2 GHz) processor and 16 GB RAM. Using our EEG sampling rate of 125 Hz the processing times remained consistent across different conditions with an average model calibration time of 3.0±0.2s and real-time classification of 6.6±1.3ms. Notably, model calibration is conducted before real-time BCI control, ensuring it does not impact real-time classification performance.

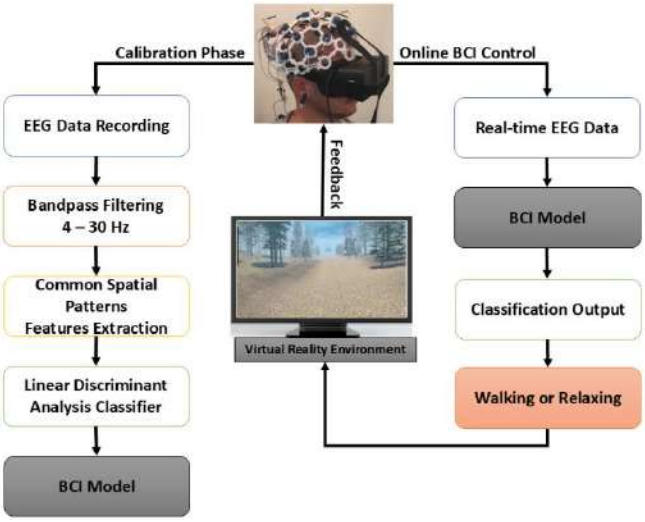


Fig. 2. Overview of the BCI data collection and processing framework. Each session began with a calibration phase, where individualised classification models were created based on the subject's EEG data. This was followed by a cued-online BCI phase, where participants performed motor imagery (MI) tasks while receiving real-time feedback through an immersive virtual reality (VR) interface.

B. Data Collection

During the calibration phase of each session, participants alternated between relaxation and walking MI with virtual reality (VR) feedback, while EEG data were recorded. In the VR environment, participants had a first-person view of their avatar walking during the walking MI task or no movement for the relaxation task. The calibration phase included five runs, with each run containing 10 trials per MI task (totalling 100 trials). Each trial lasted 12 seconds and followed a set sequence: a fixation cross from 0 to 2 seconds, followed by audio cues "relax" or "walk" from 2 to 4 seconds to prompt the participant to begin the MI task, which they performed from 4 to 10 seconds. At 10 seconds, participants heard "stop" as audio feedback, and a rest period continued from 10 to 12 seconds. After each run, participants had a one-minute break. They were instructed to minimize eye blinks and body movements, especially during the task period.

Following the calibration of the classification model, a cued-online phase was conducted to assess each participant's performance in real-time BCI control. This phase began with a welcome screen displayed from 0 to 10 seconds. The cued-online phase consisted of three 60-second trials for each MI task, during which the participants were prompted by an audio

cue to perform the specified MI task continuously for 60 seconds. During the data collection, real-time VR biofeedback was provided based on the decoded MI command using 5s trial length and 1s FUI, allowing participants to see immediate feedback on their performance. Unlike the calibration phase, the cued-online phase included no fixation crosses, cues, or rest periods between trials. In total, the cued-online phase lasted six minutes and ten seconds.

C. *Performance Analysis*

To evaluate the performance of BCI control, we simulated various real-time BCI scenarios using different combinations of trial length (1-5 seconds with increments of 1 second) and FUI (0.2-1 second with increments of 0.2 second) to determine the optimal balance between real-time feedback and classification accuracy. The CSP-LDA classifier was calibrated using offline data corresponding to each trial length, and classification accuracy was calculated for cued-online data. Classification accuracy, our primary metric, was calculated using true positives (TP: walking MI correctly classified as walking), false positives (FP: relaxing MI misclassified as walking), true negatives (TN: relaxing MI correctly classified as relaxing), and false negatives (FN: walking MI misclassified as relaxing). This accuracy metric is defined as

$$Classification\ Accuracy = \frac{TP + TN}{TP + TN + FP + FN}$$

By analysing these configurations, we determined optimal parameters that enhance the responsiveness and reliability of BCI systems for real-time applications, especially in neurorehabilitation settings where both accuracy and continuous control are essential.

D. *Statistical Analysis*

A two-way ANOVA was conducted to assess the main and interaction effects of trial length and FUI. This was followed by post-hoc comparisons to further analyse the impact of each parameter on classification accuracy.

III. RESULTS

Classification accuracy increased as both trial length and FUI increased (Fig. 3). For a 1-second trial length, average accuracy increased from 54.4±1.1% to 67.1±2.1% as FUI increased; for a 2-second trial, accuracy improved from 58.6±1.3% to 70.7±1.7%; for a 3-second trial, accuracy increased from 61.4±1.69% to 72.1±1.9%; for a 4-second trial, accuracy increased from 63.3±2.1% to 72.6±1.7%; and for a 5-second trial, accuracy increased from 65.42±2.5% to 72.8±1.9% with larger FUI.

ANOVA results indicated significant main effects for both trial length ($F = 236.29$, $p < 0.001$) and FUI ($F = 40.45$, $p < 0.001$), along with a significant interaction between them ($F = 14.60$, $p < 0.001$). Post-hoc tests ($p < 0.001$) confirmed that classification accuracy was highest for longer trial lengths (4–5 seconds) combined with FUI (0.4–1 second). These parameter settings exhibited a synergistic effect, achieving notable accuracy improvements compared to other configurations. However, no significant accuracy differences were observed between the longest trial lengths and FUI, indicating a possible saturation point in performance gains.

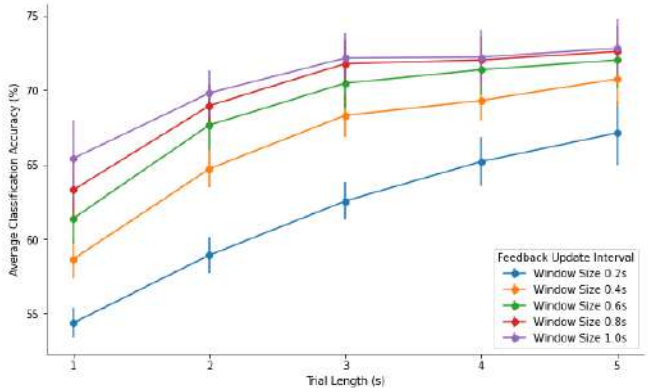


Fig. 3. Average classification accuracy (%) with standard deviation (error bars) across 50 sessions for different trial lengths (1–5 seconds) and feedback update interval (FUI; 0.2–1 second) combinations.

IV. DISCUSSION

This study highlights the importance of optimising trial length and FUI for effective MI-based BCIs in neurorehabilitation. Our findings demonstrated a consistent increase in classification accuracy with longer trial lengths and FUI, suggesting that these configurations may capture richer information from EEG signals associated with MI tasks. The highest accuracies were achieved with trial lengths of 4–5 seconds and FUI of 0.4–1 second, a combination that enabled stable classification by leveraging a broader temporal representation of MI signals. This outcome aligns with existing literature, which suggests that increased time windows provide better separation of EEG activity, thus enhancing BCI performance [12].

Despite the accuracy gains associated with larger time windows, a key consideration is the trade-off between accuracy and real-time responsiveness. For neurorehabilitation and other real-world applications, responsiveness is crucial to providing users with timely feedback, reinforcing motor relearning, and promoting neuroplasticity [10], [11], [15]. Extended processing times could diminish this experience by introducing delays, which could reduce users' perceived control over the BCI system and ultimately affect the efficacy of the rehabilitation process [12], [14]. Therefore, while longer configurations yield higher accuracy, they may not always be practical in scenarios requiring immediate interaction, such as neurofeedback-based rehabilitation for individuals recovering from SCI or stroke.

The significant interaction between trial length and FUI further emphasizes the need for a balanced parameter configuration to achieve optimal performance (Fig. 3). While a previous study has demonstrated the influence of trial length on offline classification accuracy, they did not consider FUI's impact or address results in the context of continuous real-time BCI control [12]. Our findings extend this understanding by showing that the benefit of a longer FUI is most pronounced at extended trial lengths, where sufficient signal information is available for accurate classification. Similarly, earlier research investigating shorter FUIs in stroke rehabilitation reported improvements in behavioral and

neurophysiological measures but did not explore their effect on classification accuracy [11]. Our results bridge this gap, revealing that while longer trial lengths and FUIs enhance accuracy by capturing richer MI spatial patterns, this improvement plateaus with no significant difference in classification accuracy beyond 4-second trial lengths and 0.4-second FUI, indicating a saturation effect. This finding suggests that increasing these parameters beyond a certain point does not substantially enhance accuracy and could introduce unnecessary delays, underscoring the need for careful parameter tuning to balance performance and user experience.

Recent clinical studies have aimed to validate the effectiveness of BCI-based rehabilitation in individuals with neurological impairments, with trials demonstrating functional improvements [25], [26], [27]. However, the widespread translation of BCI-based rehabilitation into real-world medical applications remains limited due to challenges in signal reliability, user variability, and long-term engagement [16]. To address these limitations, various strategies have been explored, including transfer learning approaches to reduce calibration time [24] and virtual reality (VR)-integrated BCIs to enhance user performance and engagement over longitudinal use [16]. Additionally, hybrid BCIs that integrate EEG with other physiological signals have been investigated to improve classification accuracy and robustness [21], [22], [23]. Despite these advancements, systematic investigations into fundamental system parameters such as trial duration and FUI are often overlooked in the design process [11], [12]. Our study systematically evaluated how these factors affect classification performance, informing design choices beyond arbitrary selection. Moreover, while no universal parameters apply to all applications, our findings offer valuable guidelines that can serve as a starting point for MI-BCI optimization. This contribution is particularly relevant for applications involving longitudinal training, where optimizing user adaptation and system responsiveness is crucial for long-term usability and performance improvement.

This study has several limitations that highlight opportunities for future research. The analysis was conducted on data from unimpaired individuals; replicating it with data from neurorehabilitation end-users could yield valuable insights, as their EEG signal characteristics and control strategies may differ significantly. We used consumer-grade dry EEG systems sampled at 125 Hz. Employing EEG systems with higher sampling rates could provide richer data, potentially enabling further reductions in FUI without compromising accuracy. This study focused on a two-class BCI; extending it to multi-class BCIs could explore whether similar trends persist and how trial length and FUI impact multi-class performance. While CSP-LDA was used for classification, advanced methods like deep learning could offer deeper insights and enhanced performance. Future work can expand on this foundation by exploring how different machine learning models, including deep learning architectures, interact with the identified optimal trial lengths and FUI. Incorporating more advanced classifiers may enhance system adaptability and improve classification accuracy, particularly for long-term BCI use. However, it is crucial to maintain a balance between model training and execution computational speed, classification accuracy, and real-time feasibility, especially in neurorehabilitation applications where system responsiveness is critical. Real-time feedback was provided exclusively in the 5s trial length and 1s FUI condition, while other configurations were assessed using offline simulations. This design choice allowed for controlled comparisons. However, as neurofeedback involves a learning process, participants may have optimized their cognitive strategies for the tested configuration, potentially influencing results. Future studies will address this by conducting real-time experiments across all trial length and FUI conditions, allowing participants to adjust their cognitive strategies dynamically. This approach will provide a more comprehensive understanding of how real-time neurofeedback modulates BCI performance under different settings. Finally, the limited sample size may restrict generalizability, and future studies with larger, more diverse participant pools could provide more robust findings.

In practical applications, such as virtual or real-time rehabilitation scenarios, adaptive parameter adjustments could be beneficial. For instance, during periods when high accuracy is required, the system could employ longer trial lengths and FUI, while shorter configurations could be used when immediate responsiveness is prioritized. Future work could explore adaptive BCI models that adjust trial length and FUI dynamically based on user performance or real-time feedback requirements. Such an approach could support a more flexible and responsive BCI system that meets both accuracy and responsiveness demands.

These findings contribute to our understanding of how parameter settings influence BCI performance, offering a pathway to develop more responsive and robust BCI systems for neurorehabilitation. By identifying optimal parameter configurations, this study provides valuable insights for advancing BCI usability, ultimately enhancing rehabilitation outcomes for individuals with motor impairments. Further research, potentially incorporating adaptive algorithms and testing in clinical settings, is recommended to refine these configurations and validate their effectiveness in diverse rehabilitation applications.

V. CONCLUSIONS

This study examined the effects of trial length and FUI on classification accuracy in a MI-based BCI system, aiming to identify optimal parameters for effective and responsive neurorehabilitation applications. Results demonstrated that both parameters significantly impact classification accuracy, with longer trial lengths (4–5 seconds) and larger FUI (0.4–1 second) producing the highest accuracy. However, accuracy gains reached a saturation point beyond these values, highlighting the need to balance responsiveness with signal stability for real-time BCI performance. These findings underscore that while longer configurations enhance accuracy, they may introduce delays incompatible with immediate interaction needs in neurorehabilitation. Future work could focus on adaptive parameter tuning that adjusts in real time, offering both precision and responsiveness. This approach may pave the way for more reliable and efficient BCIs, ultimately improving therapeutic outcomes and usability in clinical settings for individuals with motor impairments.

REFERENCES

[1] C. Pizzolato et al., "Non-invasive approaches to functional recovery after spinal cord injury: Therapeutic targets and multimodal device interventions," Exp Neurol, vol. 339, p. 113612, May 2021, doi: 10.1016/j.expneurol.2021.113612.

[2] A. R. C. Donati et al., "Long-Term Training with a Brain-Machine Interface-Based Gait Protocol Induces Partial Neurological Recovery in Paraplegic Patients," Sci Rep, vol. 6, no. 1, Sep. 2016, doi: 10.1038/srep30383.

[3] J. R. Wolpaw, N. Birbaumer, D. J. McFarland, G. Pfurtscheller, and T. M. Vaughan, "Brain–computer interfaces for communication and control," Clinical Neurophysiology, vol. 113, no. 6, Jun. 2002, doi: 10.1016/S1388-2457(02)00057-3.

[4] C. Pizzolato et al., "Neuromusculoskeletal Modeling-Based Prostheses for Recovery After Spinal Cord Injury," Front Neurorobot, vol. 13, Dec. 2019, doi: 10.3389/fnbot.2019.00097.

[5] M. M. N. Mannan, M. A. Kamran, and M. Y. Jeong, "Identification and removal of physiological artifacts from electroencephalogram signals: A review," IEEE Access, vol. 6, 2018, doi: 10.1109/ACCESS.2018.2842082.

[6] M. M. N. Mannan, M. A. Kamran, S. Kang, H. S. Choi, and M. Y. Jeong, "A Hybrid Speller Design Using Eye Tracking and SSVEP Brain–Computer Interface," Sensors, vol. 20, no. 3, Feb. 2020, doi: 10.3390/s20030891.

[7] U. Chaudhary, N. Birbaumer, and A. Ramos-Murguialday, "Brain–computer interfaces for communication and rehabilitation," Nat Rev Neurol, vol. 12, no. 9, Sep. 2016, doi: 10.1038/nrneurol.2016.113.

[8] J. J. Daly and J. R. Wolpaw, "Brain–computer interfaces in neurological rehabilitation," Lancet Neurol, vol. 7, no. 11, Nov. 2008, doi: 10.1016/S1474-4422(08)70223-0.

[9] S. Letourneau, E. T. Zewdie, Z. Jadavji, J. Andersen, L. M. Burkholder, and A. Kirton, "Clinician awareness of brain computer interfaces: a Canadian national survey," J Neuroeng Rehabil, vol. 17, no. 1, Dec. 2020, doi: 10.1186/s12984-019-0624-7.

[10] L. Pillette, F. Lotte, B. N'Kaoua, P.-A. Joseph, C. Jeunet, and B. Glize, "Why we should systematically assess, control and report somatosensory impairments in BCI-based motor rehabilitation after stroke studies," Neuroimage Clin, vol. 28, p. 102417, 2020, doi: 10.1016/j.nicl.2020.102417.

[11] S. Darvishi, M. C. Ridding, B. Hordacre, D. Abbott, and M. Baumert, "Investigating the impact of feedback update interval on the efficacy of restorative brain–computer interfaces," R Soc Open Sci, vol. 4, no. 8, p. 170660, Aug. 2017, doi: 10.1098/rsos.170660.

[12] A. Miladinović, A. Accardo, J. Jarmolowska, U. Marusic, and M. Ajčević, "Optimizing Real-Time MI-BCI Performance in Post-Stroke Patients: Impact of Time Window Duration on Classification Accuracy and Responsiveness," Sensors, vol. 24, no. 18, p. 6125, Sep. 2024, doi: 10.3390/s24186125.

[13] F. Lotte, F. Larrue, and C. Mühl, "Flaws in current human training protocols for spontaneous Brain-Computer Interfaces: lessons learned from instructional design," Front Hum Neurosci, vol. 7, 2013, doi: 10.3389/fnhum.2013.00568.

[14] W. Jin et al., "Electroencephalogram-based adaptive closed-loop brain-computer interface in neurorehabilitation: a review," Front Comput Neurosci, vol. 18, Sep. 2024, doi: 10.3389/fncom.2024.1431815.

[15] Á. Barbero and M. Grosse-Wentrup, "Biased feedback in brain-computer interfaces," J Neuroeng Rehabil, vol. 7, no. 1, p. 34, Dec. 2010, doi: 10.1186/1743-0003-7-34.

[16] M. M. N. Mannan et al., "Virtual reality mediated brain-computer interface training improves sensorimotor neuromodulation in unimpaired and post spinal cord injury individuals," medRxiv (Cold Spring Harbor Laboratory), Dec. 2024, doi: https://doi.org/10.1101/2024.12.18.24317160.

[17] A. Gramfort et al., "MEG and EEG data analysis with MNE-Python," Front Neurosci, vol. 7, 2013, doi: 10.3389/fnins.2013.00267.

[18] M. Lotze and L. G. Cohen, "Volition and Imagery in Neurorehabilitation," Cognitive and Behavioral Neurology, vol. 19, no. 3, pp. 135–140, Sep. 2006, doi: 10.1097/01.wnn.0000209875.56060.06.

[19] G. Pfurtscheller and C. Neuper, "Motor imagery and direct brain-computer communication," Proceedings of the IEEE, vol. 89, no. 7, pp. 1123–1134, Jul. 2001, doi: 10.1109/5.939829.

[20] F. Lotte, M. Congedo, A. Lécuyer, F. Lamarche, and B. Arnaldi, "A review of classification algorithms for EEG-based brain–computer interfaces," J Neural Eng, vol. 4, no. 2, Jun. 2007, doi: 10.1088/1741-2560/4/2/R01.

[21] H. Li *et al.*, "A sequential learning model with GNN for EEG-EMG-based stroke rehabilitation BCI," *Frontiers in Neuroscience*, vol. 17, Apr. 2023, doi: https://doi.org/10.3389/fnins.2023.1125230.

[22] M. U. Ali *et al.*, "Correlation-Filter-Based Channel and Feature Selection Framework for Hybrid EEG-fNIRS BCI Applications," *IEEE Journal of Biomedical and Health Informatics*, vol. 28, no. 6, pp. 3361–3370, Jun. 2024, doi: https://doi.org/10.1109/jbhi.2023.3294586.

[23] T. Xu *et al.*, "Motor Imagery Decoding Enhancement Based on Hybrid EEG-fNIRS Signals," *IEEE Access*, vol. 11, pp. 65277–65288, Jan. 2023, doi: https://doi.org/10.1109/access.2023.3289709.

[24] H. He and D. Wu, "Transfer Learning for Brain–Computer Interfaces: A Euclidean Space Data Alignment Approach," *IEEE Transactions on Biomedical Engineering*, vol. 67, no. 2, pp. 399–410, Feb. 2020, doi: https://doi.org/10.1109/TBME.2019.2913914.

[25] M. S. Kim *et al.*, "Efficacy of brain-computer interface training with motor imagery-contingent feedback in improving upper limb function and neuroplasticity among persons with chronic stroke: a double-blinded, parallel-group, randomized controlled trial," *Journal of NeuroEngineering and Rehabilitation*, vol. 22, no. 1, Jan. 2025, doi: https://doi.org/10.1186/s12984-024-01535-2.

[26] A. Wang *et al.*, "Rehabilitation with brain-computer interface and upper limb motor function in ischemic stroke: A randomized controlled trial," *Med*, vol. 5, no. 6, pp. 559-569.e4, Apr. 2024, doi: https://doi.org/10.1016/j.medj.2024.02.014.

[27] F. R. Willett et al., "A high-performance speech neuroprosthesis," Nature, vol. 620, no. 7976, pp. 1031–1036, Aug. 2023, doi: https://doi.org/10.1038/s41586-023-06377-x.

Design of a Rope-Driven Finger Exoskeleton System with a Universal Double Grooved Roller for Adaptive Rehabilitation

Wenqi Li, Le Bao, and Wansoo Kim*, *Member, IEEE*

***Abstract*— Impaired hand function caused by neurological conditions, such as stroke, severely limits individuals' ability to perform daily tasks, highlighting the importance of accessible rehabilitation devices. Although the double grooved roller design in existing rope-driven exoskeletons reduces weight and enhances compactness, the different amount of change in the upper and lower traction cords when the fingers are flexed and torsioned can easily lead to slack and slippage of the traction cords, which affects the accuracy of movement. To address these limitations, a rope-driven exoskeleton system with a universal double grooved roller is designed for assisting finger movement based on a study of the index finger. In order to enhance the universal performance of the exoskeleton, in this study, 40 groups of index finger flexion and extension movements with upward and downward stretching are collected and statistically analyzed to find out the universal ratio of double grooved rollers. The experiment tested the finger-driving capability of the exoskeleton device, achieving a range of motion up to 94% of unassisted natural motion, with stable performance during repetitive movements. Additionally, the finger-driving success rate for seven subjects with varying finger sizes reached 100%, and the test results were analyzed in detail. The designed system demonstrates feasibility, reliability, and universality, offering a viable new solution for adaptive hand rehabilitation.**

I. Introduction

Neurological diseases such as stroke often lead to impaired hand motor functions, severely reducing patients' quality of life by limiting their ability to perform daily activities independently [1], [2]. Hand rehabilitation is crucial for these patients to regain their ability to care for themselves in daily life [3].

The advancement of wearable robotic devices has significantly increased interest in rope-driven finger exoskeleton, which combine lightweight design and flexible actuation to provide a more natural and user-friendly rehabilitation experience [4], [5]. In addition, the rope-driven system has low noise, high safety, low cost, and can reduce joint loads by arranging the actuator in non-critical areas through long-distance transmission [6], [7]. These features make rope-driven exoskeletons highly suitable for applications in medical rehabilitation and industrial assistance.

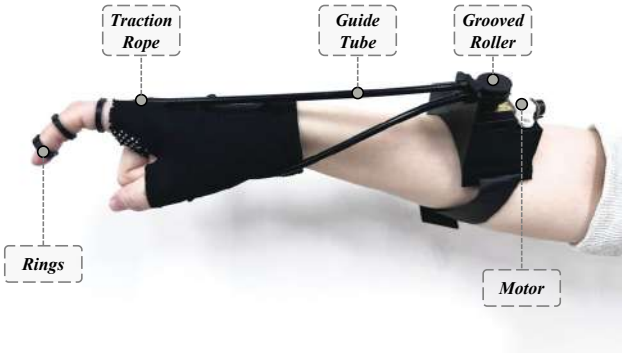


Fig. 1: The designed rope-driven finger exoskeleton system with double grooved roller.

Despite these advantages, existing rope-driven exoskeleton designs face significant challenges in addressing the variability of finger flexion and extension motions. In the study by Burns et al. each finger is equipped with two motors, one for flexion and one for extension [8]. While this can cope with the difference in the amount of change during finger flexion and extension, each finger is equipped with two motors, which increases the weight of the exoskeleton and takes up more installation space. Flexo-glove proposed by Mohammadi et al. is a lightweight and modular flexible exoskeleton glove [9]. Its drive system is designed to realize bi-directional movement of flexion and extension through the design of double grooved roller. However, traditional rope-driven devices often suffer from uneven force distribution, slack, or slippage due to the varying length changes in traction ropes during finger flexion and extension. This in turn affects the stability and accuracy of control and increases the patient's discomfort of use.

To address these limitations, this study proposes a novel double grooved roller design to accommodate the difference in length change of the traction rope when controlling finger flexion and extension. This design connects the traction rope for controlling flexion and extension by setting a large grooved and a small grooved, so as to ensure the tension of the traction line in motion and avoid slipping and slacking. The designed device can reduce the use of motors, thus reducing the cost, reducing the weight of the mechanical structure, and enhancing the user experience. This study provides new ideas for the design of low-cost, home-useable

This work was supported in part by the National Research Foundation of Korea(NRF) grant funded by the Korea government(MSIT) (No. 2022R1C1C1008306), and in part by the China Scholarship Council(CSC) (No. 202208260074).

Wenqi Li is with the Department of Mechatronics Engineering, Hanyang University, Ansan, Gyeonggi-do 15588, Republic of Korea.

Le Bao is with the Research Institute of Engineering & Technology, Hanyang University ERICA, Ansan, Gyeonggi-do 15588, Republic of Korea.

Wansoo Kim is with the Robotics Department, Hanyang University ERICA, Ansan, Gyeonggi-do 15588, Republic of Korea.

Wenqi Li and Le Bao are co-first authors.

* Corresponding author. (e-mail: wansookim@hanyang.ac.kr)

hand rehabilitation devices.

The main contributions of this study are:

- Sampled 40 sets of data, analyzed to a generic scaling ratio value, and designed a rope-driven finger exoskeleton with a universal double grooved roller by this ratio value.
- The designed rope-driven exoskeleton system was verified to be effective in driving fingers by testing the exoskeleton device's ability to drive fingers.
- The feasibility of the rope-driven exoskeleton and the versatility of the universal double grooved roller was experimentally verified through comparative experiments with multiple subjects of different sizes.

II. Methodology

In rehabilitation, the index finger is often trained individually as a focal point [10], because it requires special attention in terms of strength output, dexterity, and coordination. The muscles (e.g., flexor digitorum superficialis, flexor digitorum profundus) and nerves (median nerve, radial nerve) associated with the index finger are more sensitive than those of other fingers, which is an important indicator for monitoring the rehabilitation effect. Therefore, in this study, a finger rope-driven exoskeleton system is designed for flexion and extension rehabilitation maneuvers of the index finger and is planned to be extended to the rehabilitation control of other fingers.

A. System Overview

As shown in Fig. 1, the designed system is mainly composed of finger rings, traction ropes, double grooved roller, guide tubes and motor. Among them, the finger fixation ring is used to stabilize the finger joints and ensure that the force exerted by the rope can be directly converted into flexion and extension motions [11]. The rope-driven structure consists of two independent ropes, each responsible for either flexion or extension motions. These ropes are strategically arranged along the dorsal and palmar sides of the fingers to realize flexible finger control by stretching or relaxing.

However, during the stretching and relaxing of the leash, the flexion and contraction of the fingers require different lengths of leash retraction and release. In this regard, a roller with double grooves is designed to control the flexion and relaxation of the finger with the rope on the top and bottom of the roller, respectively. The large and small grooves of the roller are designed to provide different ratios in a single motor revolution based on the ratio of the rope changes, thus realizing the precise movement of the finger. Compared to existing studies, both flexion and extension movements of the fingers can be controlled using only a single motor [8]. In addition, the different radii of the double grooved rollers can reduce the slack of the traction rope during flexion and extension [9].

B. Sampling and Analysis

Since fingers stretch up and down differently during flexion and extension, 40 sets of data are collected in this study

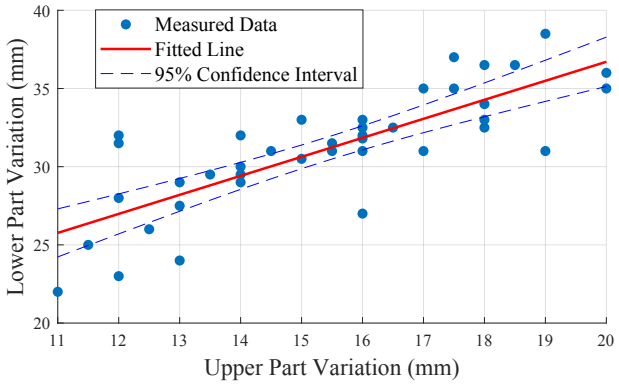


Fig. 2: Linear regression analysis of finger upper and lower extension variations.

in order to observe the changes in the fingers during flexion and extension. Finger fixation rings of different sizes are printed using 3D printing for stabilizing the finger joints during movement, ensuring that the force exerted by the rope could be directly translated into flexion and extension movements. The measurements were made by fixing finger rings on the distal phalanx, middle phalanx and proximal phalanx of the index finger of the subject and connecting the rings with a string on the upper and lower sides of the finger respectively. Attach the traction rope to the distal phalanx ring and record the displacement of the proximal phalanx ring along the traction rope during index finger flexion and extension.

Fig. 2 represents the measure data. To understand the relationship between the upper and lower rope length variations during finger flexion and extension, a linear regression analysis was conducted on the collected data. The resulting regression equation represents the line of best fit for the observed data as follows

$$\Delta L_1 = 1.22 \cdot \Delta L_2 + 12.39 \ , \tag{1}$$

where ΔL_1 is the lower rope-driven structure expansion and ΔL_2 is the upper rope-driven structure expansion. Most of the data in the figure lie within the 95% confidence interval.

In addition, the Pearson correlation coefficient [12], in Equation (2), can be used to analyze the correlation between ΔL_1 and ΔL_2.

$$r = \frac{\sum(\Delta L_{1,i} - \overline{\Delta L_1})(\Delta L_{2,i} - \overline{\Delta L_2})}{\sqrt{\sum(\Delta L_{1,i} - \overline{\Delta L_1})^2}\sqrt{\sum(\Delta L_{2,i} - \overline{\Delta L_2})^2}} \ , \tag{2}$$

$$t_{\text{statistic}} = r \cdot \sqrt{\frac{n-2}{1-r^2}} \ , \tag{3}$$

$$dof = n - 2 \ , \tag{4}$$

$$p = 2 \cdot (1 - F_t\left(|t_{\text{statistic}}|, dof\right)) \ . \tag{5}$$

where $\Delta L_{1,i}$ and $\Delta L_{2,i}$ denote different data points, respectively, $i = 1, 2, \cdots n$. $\overline{\Delta L_1}$ and $\overline{\Delta L_2}$ are the means of these data, respectively. The result is obtained r equal to 0.796, which indicates a strong positive linear correlation between

the two variables. The $t_{\text{statistic}}$ is 8.312 calculated through the r-value. The dof is degrees of freedom. The degree of freedom is 38, where n is the total sample size 40. The p-value is calculated as twice the probability that a t-distributed random variable with dof exceeds the absolute value of the t-statistic, as Equation (5). The p-value is 4.46×10^{-10}, which is further evidence of a strong correlation since the p-value is much less than 0.01.

To design a finger exoskeleton device suitable for the majority of people, this study uses data within the 95% confidence interval as representative sizes. These data are then analyzed to determine the generalizable ratio of flexion and extension. First, the ratio η_j of ΔL_1 and ΔL_2 is calculated for each set of data, as well as the mean value of all ratios $\overline{\eta}$:

$$\eta_j = \frac{\Delta L_{2,j}}{\Delta L_{1,j}} \quad (j = 1, 2, \cdots m) \ , \tag{6}$$

$$\overline{\eta} = \frac{1}{m} \sum_{j=1}^{m} \eta_j \ , \tag{7}$$

where m is the total amount of data and the mean value results is 0.488.

Finally, the standard deviation σ of the ratio is further calculated to assess the stability of the proportionality relationship in the data set. The standard deviation is calculated using the following equation:

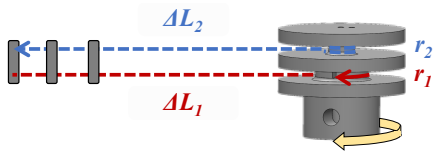
$$\sigma = \sqrt{\frac{1}{m-1} \sum_{j=1}^{m} (\eta_j - \overline{\eta})^2} \quad (j = 1, 2, \cdots m) \ . \tag{8}$$

As a result, the standard deviation σ is obtained as 0.146, indicating that the ratio is relatively stable and less fluctuating among different individuals. The linear regression analysis and Pearson's correlation coefficient calculation and mean ratio analysis showed that there is a significant linear relationship between ΔL_1 and ΔL_2, and the ratio between them is relatively stable. The above results provide a basis for further modeling the universal relationship between the upper and lower finger stretch.

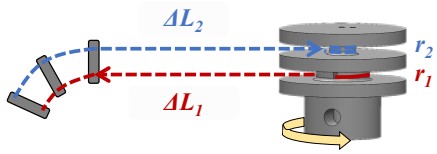
C. Grooved Roller Design for the Rope-Driven Exoskeleton

The double grooved roller design enables simultaneous control of flexion and extension movements by adapting to different rope length changes. As shown in Fig. 3, the dimensions of the two tracks of the roller wheel consist of circles with different radii to cope with the different amounts of up and down stretching when the finger flexes and extends. As the roller wheel rotates, the rope pulls the rings on the finger joints in different directions.

In order to realize the precise control of finger flexion and extension movements by the rope, the design of the double grooved roller needs to have two keys requirements. First, the paths above and below the rope-driven structure must be independent to avoid entanglement of the traction ropes and to ensure motion stability. Secondly, the size of the large and small grooves of the roller needs to adapt to the different



(a) Clockwise rotation causes finger flexion.



(b) Counterclockwise rotation causes finger extension.

Fig. 3: The principle of the double-grooved roller traction for finger flexion and extension.

lengths of the two traction ropes in the flexion and extension process to reduce the loss of driving force, and at the same time, the design of the roller disk has a strong versatility, which can meet the needs of most of the individuals, simplify the production process, and facilitate the promotion of large-scale.

In accordance with these design requirements, the double grooved roller has different sized grooves: the large groove connects to the lower part of the finger ring for controlling finger flexion and the small groove connects to the upper part of the finger ring for controlling finger extension. The upper traction rope is wrapped clockwise around the small groove and the lower traction rope is wrapped counterclockwise around the large groove. In this way, when the double groove roller turns clockwise, the traction rope on the small groove relaxes and the traction rope on the large groove tightens to achieve finger flexion. Conversely, when the double-grooved wheel is turned counterclockwise, finger flexion is achieved. The design of the double grooved rollers allows the traction ropes to run along different radial trajectories on the rollers so that the traction ropes not interfere with each other. By analyzing the data from several experiments, the length change ratio of the upper and lower traction lines is determined and used as the basis for the design of the double grooved roller dimensions, so that the rope-driven system can meet the demand for different amplitude of finger flexion and extension movements.

In this design, a rope-driven structure is used to control the flexion and extension movements of the fingers. In order to accurately describe the motion relationship of the system, the lengths of the ropes required for the upward and downward flexion and extension of the index finger are defined as ΔL_1 and ΔL_2 and the radii of the grooved rollers corresponding to the upward and downward movements of the index finger are defined as r_1 and r_2. Since the double grooved rollers shared a concentric axis, they maintain the equal number of revolutions n. This ensures a proportional relationship between the pulley radii r_1 and r_2 of the grooves and the rope lengths required for flexion and extension movements.

Hence, this relationship is expressed as follows:

$$n = \frac{\Delta L_1}{2\pi r_1} = \frac{\Delta L_2}{2\pi r_2} \ , \tag{9}$$

$$\frac{r_1}{r_2} = \frac{\Delta L_1}{\Delta L_2} \ . \tag{10}$$

The experimental analysis determined an optimum ratio $\overline{\eta} = 0.488$ from the previous section, representing the most suitable proportional relationship for the majority of users. We define 0.488 as the universal size ratio. When designing the double-grooved roller, it was necessary to balance this ratio with the material constraints of 3D printing. If the groove radius is too small, the strength of the structure of the roller may be compromised, leading to potential breakage or deformation during use. To ensure durability while maintaining the optimized ratio, the smaller radius r_1 was set to 2 mm, which resulted in a corresponding larger radius r_2 of 4.1 mm. This configuration provides a robust and universal design that accommodates diverse user requirements while ensuring mechanical stability.

III. Experiments and Analysis

A. Experimental Setup

The experimental portion of the study consisted of a single set of tests of the finger actuation ability of the exoskeleton device, as well as comparative tests on seven subjects with different hand sizes. The experiments are used to observe the trajectory of the fingers under rope-driven traction and to verify the reliability and versatility of the exoskeleton with double grooved roller. In this case, the experimental subjects were all healthy adults between the ages of 20 and 30. The study was reviewed by the Hanyang University Institutional Review Board under the number HYU-2024-100.

The scene of the experimental setup is shown in Fig. 4. The motor rotates forward and backward according to the signals from the buttons, ensuring that the index finger's range of motion remains within reasonable limits. A camera was utilized to record hand movements, specifically tracking

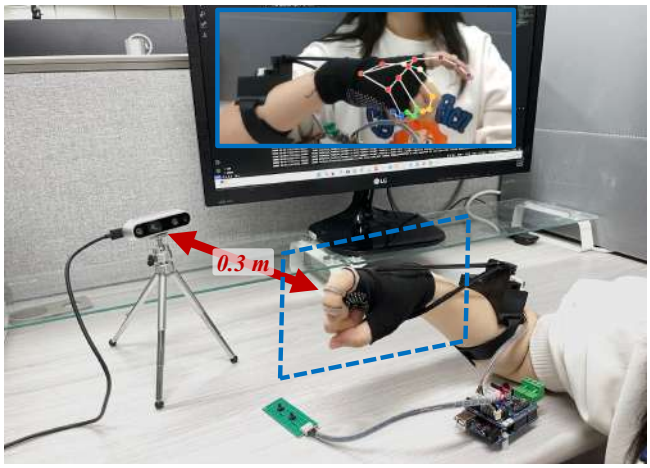


Fig. 4: The scene of the experimental setup.

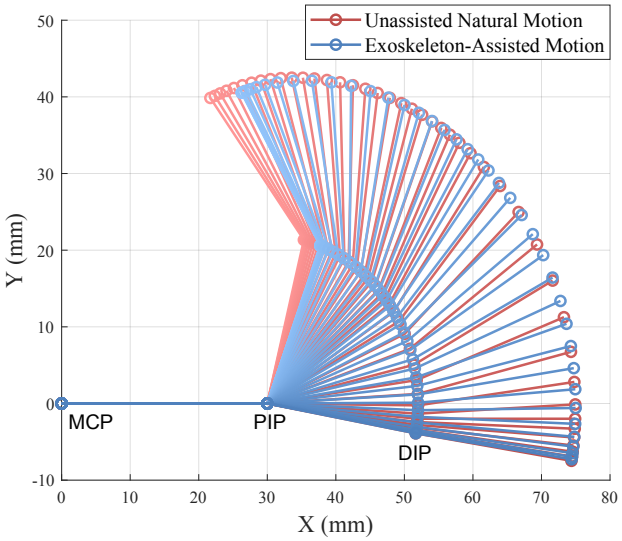


Fig. 5: Finger motion trajectories obtained through visual recognition.

changes in joint angles during flexion and extension. The Mediapipe framework was employed for its real-time skeletal tracking capabilities [13], with noise-reduction filters applied to enhance data accuracy. To ensure more effective data capture, the tester's index finger movement plane must be parallel to the camera, and maintained at a relative distance of 0.3 m. After obtaining the plane position information of the index finger joint, the angles of Distal Interphalangeal Joint (DIP) and Proximal Interphalangeal Joint (PIP) of the index finger are calculated by trigonometric functions [14].

B. Usability Validation of the Finger Exoskeleton

The range of motion of the index finger in unassisted natural state (without the exoskeleton) and when wearing the exoskeleton and being pulled by the rope-driven traction were recorded in the experiments.

As shown in Fig. 5, the MCP and PIP joint positions of the fingers were set to remain fixed (i.e., X-axis direction), and the changes in the angles of the PIP and DIP joints were recorded. When the exoskeleton rope-driven system provided assisted traction on the index finger, the trajectory of the finger was very close to the range of motion of the finger in its unassisted natural state. The active area of the finger under exoskeleton traction was calculated to be $1677.5\ mm^2$, and the active area of the finger in the unassisted natural state was $1576.8\ mm^2$, with an area overlap of approximately 94%. This indicates that the rope-driven exoskeleton did not affect the activity of the index finger while providing external support, verifying the effectiveness of the rope-driven structure.

With the exoskeleton on, the subject performed multiple flexion and extension movements of the index finger, during which the angle of the DIP and PIP joints changed as shown in Fig. 6. It can be seen that the flexion and extension movements of the finger driven by the exoskeleton remained

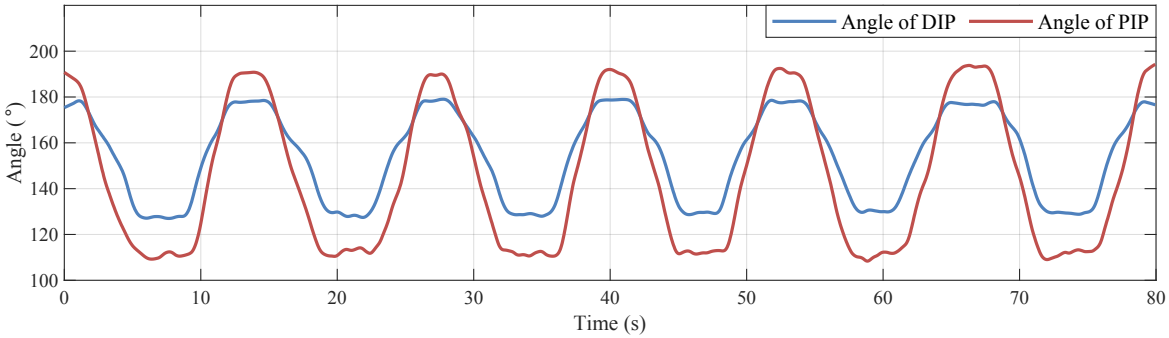


Fig. 6: Angle variation curves of the index finger's DIP and PIP joints while wearing the exoskeleton.

TABLE I: Experimental results of the exoskeleton on flexion and extension movements in subjects with different finger sizes.

No.	Position	Finger Size	DIP			PIP			Rotation Count	Tightness	Task Completion
			With Exoskeleton	Without Exoskeleton	Completion	With Exoskeleton	Without Exoskeleton	Completion			
1	OnLine	Medium	50°	45°	111.1%	80°	90°	88.9%	1.5	Suitable	Yes
2	In 95%CI	Small	45°	40°	112.5%	95°	100°	95%	1.4	Suitable	Yes
3	In 95%CI	Medium	50°	43°	116.3%	85°	90°	94.4%	1.5	Suitable	Yes
4	In 95%CI	Large	40°	35°	114.3%	70°	95°	73.7%	1.6	Suitable	Yes
5	Out 95%CI	Small	40°	45°	88.9%	80°	90°	88.9%	1.3	Suitable	Yes
6	Out 95%CI	Medium	42°	36°	116.7%	84°	90°	93.3%	2.1	Loose	Yes
7	Out 95%CI	Large	45°	38°	118.4%	90°	95°	94.7%	1.7	Slightly Loose	Yes

highly stable during multiple reciprocal movements. The magnitude of the angular changes of the DIP and PIP joints remained the same even in the case of multiple repetitive motions, indicating that the exoskeleton was able to provide stable assistive forces. This result suggests that the designed exoskeleton not only has reliable actuation ability, but also can maintain the stability of the motion during prolonged and high-frequency maneuvers.

C. Universality Validation of the Finger Exoskeleton

In order to purposefully verify the versatility and effectiveness of the designed double grooved roller, seven subjects with varying finger sizes (large, medium, and small) participated in the experiment to evaluate the exoskeleton's adaptability. The test results are shown in Table. I.

All the seven subjects wearing the exoskeleton device completed flexion and extension activities of the index finger in the experiment. Among them, the measured value of subject No. 1 is highly consistent with the fitting line and belonged to the medium finger size; subjects No. 2 to 4 are people with universal size, belonging to the large, medium, and small finger sizes; and subjects No. 5 to 7 are not people with universal size, belonging to the large, medium, and small finger sizes, respectively. The number of rotations of the motor, the looseness of the traction rope, and the completion of the bending maneuver while wearing the exoskeleton were recorded during the experiment to assess the assistive effect of the exoskeleton.

The results of the experiment showed that all seven subjects were able to perform the intended task while wearing the exoskeleton, while the tightness of the traction rope varied within a reasonable range. The four subjects with the universal size performed more consistently, meeting the reasonable range of variation set by the experiment, with the right amount of slack in the traction rope during movement. Of the three subjects who did not have the universal size, one subject's leash remained stable and accomplished the task well, suggesting that the elastic properties of the fingers allow for some error and that the exoskeleton was still able to assist effectively. The other two subjects showed a slight loosening of the leash in one and a significant loosening of the leash in the other during the course of the experiment, suggesting that the double grooved rollers were not perfectly sized, and that the number of motor revolutions increased, even though they both accomplished the flexion-distension task.

IV. Discussion

The usability of the designed rope-driven exoskeleton was demonstrated through hand trajectory recording experiments on a single subject. A universal size double grooved roller was validated through an experiment comparing test results from multiple groups of subjects. Through the experiment, it was shown that the double grooved roller can be designed to fit most people's sizes, but for those with large deviations may need to be individually sized. In addition, the joint angle ratios of the DIP and PIP were compared between wearing the exoskeleton and not wearing the exoskeleton. With the exoskeleton, the range of motion of the DIP of the index finger in most of the subjects exceeded the range of motion

of the index finger in its natural state. The range of motion of the PIP did not exceed the natural state, but there was not a great deal of difference, either. From this result, it is clear that the rope-driven exoskeleton system does not limit the range of motion of the fingers.

The double grooved roller with universal proportions designed in this study improve the common problem of traction rope loosening during finger flexion and extension of exoskeleton devices compared to the traditional double grooved roller with the same diameter [9]. By optimizing the ratio design of the rollers, it is more in line with the biomechanical characteristics of human hand movement, reducing the slackness of the traction rope at different stages of movement and improving the precision of the exoskeleton during finger flexion and extension. This improvement not only enhances user comfort and control precision during operation, but also helps to broaden the scope of application of the finger exoskeleton to meet the needs of different individuals in rehabilitation training or strength assistance.

V. Conclusion

In this paper, a rope-driven exoskeleton with a universal-size double grooved roller is proposed to improve the stability and adaptability of the system. Compared with conventional designs, the universal-size double grooved roller reduce the risk of rope slippage and provide a more stable trajectory by independently controlling the path of the upper and lower flexion ropes.

This study analysed the extension of the upper and lower traction ropes during index finger flexion in 40 subjects. Statistical analyses showed a strong positive linear relationship between them, and proportional means within 95% confidence intervals were used to determine the optimal size ratio of the double grooved ropes.

Experimental results showed that the exoskeleton-assisted index finger movement closely approximated the natural range with an overlap of 94%. The angular changes of the DIP and PIP joints were consistent over multiple cycles, indicating reliable and stable actuation. Moreover, comparative experiments with seven individuals with different finger sizes further confirmed the versatility of the dual-slot roller. The design adapted to differences in finger length and flexion/extension angles, improving the stability of the leash. When comparing assisted and unassisted movements, the angular variability of the DIP and PIP joints was 111.12% and 89.84%, respectively, indicating minimal effect on natural movement. The proposed roller design improves the stability and accuracy of the rope actuation system and reduces the risk of slipping and slackening of the haul rope, while improving user comfort.

Future study will expand from healthy subjects to individuals with impaired hand function and evaluate the effectiveness of the system. Additionally, the scope will be extended from traction on the index finger to other fingers, with the incorporation of pressure sensors to further optimize the control design of the hand exoskeleton.

Acknowledgment

This work was supported in part by the National Research Foundation of Korea(NRF) grant funded by the Korea government(MSIT) (No. 2022R1C1C1008306), and in part by the China Scholarship Council(CSC) (No. 202208260074).

References

[1] P. Tran, S. Jeong, K. Herrin, S. Bhatia, S. Kozin, and J. P. Desai, "Flexotendon glove-iii: Soft robotic hand rehabilitation exoskeleton for spinal cord injury," in *2021 IEEE International Conference on Robotics and Automation (ICRA)*, 2021, pp. 10 332–10 339.

[2] E. R. Triolo and B. F. Busha, "Design and experimental testing of a force-augmenting exoskeleton for the human hand," *Journal of NeuroEngineering and Rehabilitation*, vol. 19, no. 1, 2022.

[3] M. Sandison, K. Phan, R. Casas, L. Nguyen, M. Lum, M. Pergami-Peries, and P. S. Lum, "Handmate: Wearable robotic hand exoskeleton and integrated android app for at home stroke rehabilitation," *2020 42nd Annual International Conference of the IEEE Engineering in Medicine & Biology Society (EMBC)*, pp. 4867–4872, 2020.

[4] W. Chen, G. Li, N. Li, W. Wang, P. Yu, R. Wang, X. Xue, X. Zhao, and L. Liu, "Soft exoskeleton with fully actuated thumb movements for grasping assistance," *IEEE Transactions on Robotics*, vol. 38, no. 4, pp. 2194–2207, 2022.

[5] D. Popov, I. Gaponov, and J.-H. Ryu, "Portable exoskeleton glove with soft structure for hand assistance in activities of daily living," *IEEE/ASME Transactions on Mechatronics*, vol. 22, no. 2, pp. 865–875, 2017.

[6] A. W. A. Aziz, J. Jalani, A. S. Sadun, and M. Z. Hussin, "A low cost of an exoskeleton finger for stroke patient," *Journal of Advanced Research in Applied Sciences and Engineering Technology*, vol. 38, no. 2, p. 16–26, Jan. 2024.

[7] R. Conti, E. Meli, and A. Ridolfi, "A novel kinematic architecture for portable hand exoskeletons," *Mechatronics*, vol. 35, pp. 192–207, 2016.

[8] M. K. Burns, K. Van Orden, V. Patel, and R. Vinjamuri, "Towards a wearable hand exoskeleton with embedded synergies," in *2017 39th Annual International Conference of the IEEE Engineering in Medicine and Biology Society (EMBC)*, 2017, pp. 213–216.

[9] A. Mohammadi, J. Lavranos, P. Choong, and D. Oetomo, "Flexo-glove: A 3d printed soft exoskeleton robotic glove for impaired hand rehabilitation and assistance," in *2018 40th Annual International Conference of the IEEE Engineering in Medicine and Biology Society (EMBC)*, 2018, pp. 2120–2123.

[10] T. P. Valayil and T. K. Tanev, "Optimal design of a bilateral stand-alone robotic motion-assisted finger exoskeleton for home rehabilitation," *Machines*, vol. 12, no. 10, 2024.

[11] H.-J. Yoo, S. Lee, J. Kim, C. Park, and B. Lee, "Development of 3d-printed myoelectric hand orthosis for patients with spinal cord injury," *Journal of NeuroEngineering and Rehabilitation*, vol. 16, no. 1, 2019.

[12] E. I. Obilor and E. C. Amadi, "Test for significance of pearson's correlation coefficient," *International Journal of Innovative Mathematics, Statistics & Energy Policies*, vol. 6, no. 1, pp. 11–23, 2018.

[13] F. Zhang, V. Bazarevsky, A. Vakunov, A. Tkachenka, G. Sung, C. Chang, and M. Grundmann, "Mediapipe hands: On-device real-time hand tracking," *CoRR*, vol. abs/2006.10214, 2020. [Online]. Available: https://arxiv.org/abs/2006.10214

[14] T. Shahid, D. Gouwanda, T. Shahid, A. A. Gopalai, S. G. Nurzaman, and T. K. Kheng, "Joint angle control of a cable-actuated soft hand exoskeleton," in *2021 International Conference on Robotics and Automation in Industry (ICRAI)*, 2021, pp. 1–5.

Synchronicity: A Measure of Multi-Joint Movement Coordination in Device Assessment

Yuri Gloumakov*, Erin Y. Chang, and Hannah S. Stuart

***Abstract*— This work explores the concept of movement coordination over time; smooth multi-joint gestures are a hallmark of healthy and normative body function. Deviations from normative movement coordination are linked to various health conditions, such as stroke or injury, and can lead to further complications if not addressed. Identifying abnormal movement and quantifying its degree is therefore crucial. Although some quantitative assessments exist, final evaluations often require expert input from occupational or physical therapists. We investigate the characterization of joint movements using motion capture as an objective indicator of synchronous behavior and propose a new quantitative metric to assess device and rehabilitation interventions, *synchronicity*. We apply our metric to three studies with various populations that compare normative hand use to movement with wrist braces, transradial prostheses, and a wrist exoskeleton, revealing that synchronicity may be an indicator of device embodiment and function.**

I. Introduction

The musculoskeletal system is made of complex, though highly coordinated, series of interactions. While the upper-limb function is a perfect example of versatile motion [1], it nonetheless operates in a lower dimensional manifold [2], and therefore, much like gait [3], can be evaluated for normativity [4]. Physical injuries, stroke, or amputation disrupt these interactions, and can lead to compensatory movements [5] that could result in overuse injuries [6], impacting individuals' health, physical [7], and social functioning [8]. Both rehabilitation programs and robotic interventions (such as prosthetics or exoskeletons) aim to restore upper-limb function to normative levels while minimizing body compensation, however, the evaluation of a patient's rehabilitation progress or success of device intervention remains largely qualitative. In this work we explore a new quantitative perspective to movement coordination across different upper-limb interventions (Fig. 1).

Most common quantitative assessments involve measuring the time to complete a task [9], progress and success rate [10], or measuring joint range of motion [11]. More complex body compensation metrics have also been used, such as measuring the length of the Cartesian path a joint travels [12], as well as multi-modal measures that account for a set of metrics simultaneously [13]. And although these metrics are used to compare the performances between interventions and normative behavior, they do not directly observe whether the attribute of motion coordination is preserved. Data driven methods have additionally been explored to classify movement appearance of "natural human motion" [14], though human perception continues to be the ultimate arbiter in physically simulated characters [15]. Cosmeses – prosthetics or prosthetic coverings designed for the primary purpose of cosmetics – are popular but they typically do not enhance movement coordination. We wish to understand how motion coordination itself affects device appearance and acceptance, an idea we wish to coin "motion cosmesis."



Fig. 1. We quantify the coordination of the torso, shoulder, and elbow joints. In this work we explore how different upper-limb conditions, namely normative, braced, prosthesis, and exoskeleton use, impact the normativity of motion of the remaining joints, and whether we can capture this effect using the proposed *synchronicity* metric.

Unlike the morphological cosmesis of prosthetic devices, the appearance of *synchronicity* in movement, the coordinated appearance of motion, is also functional. In social robotics, greater multi-joint movement coordination can lead robots to better communicate through their movements,

Y. Gloumakov is with the RUKA Lab, Dept. of Electrical and Computer Engineering, University of Connecticut, Storrs, CT, USA. E.Y. Chang and H.S. Stuart are with the Embodied Dexterity Group, Dept. of Mechanical Engineering, University of California Berkeley, Berkeley, CA, USA.

This work involved human subjects in its research. Approval of all ethical and experimental procedures and protocols was granted by the Yale University Institutional Review Board under Application No. HSC 1610018511, and the University of California, Berkeley Institutional Review Board under Application No. 2020-02-12983.

* Corresponding author's email: yuri.gloumakov@uconn.edu

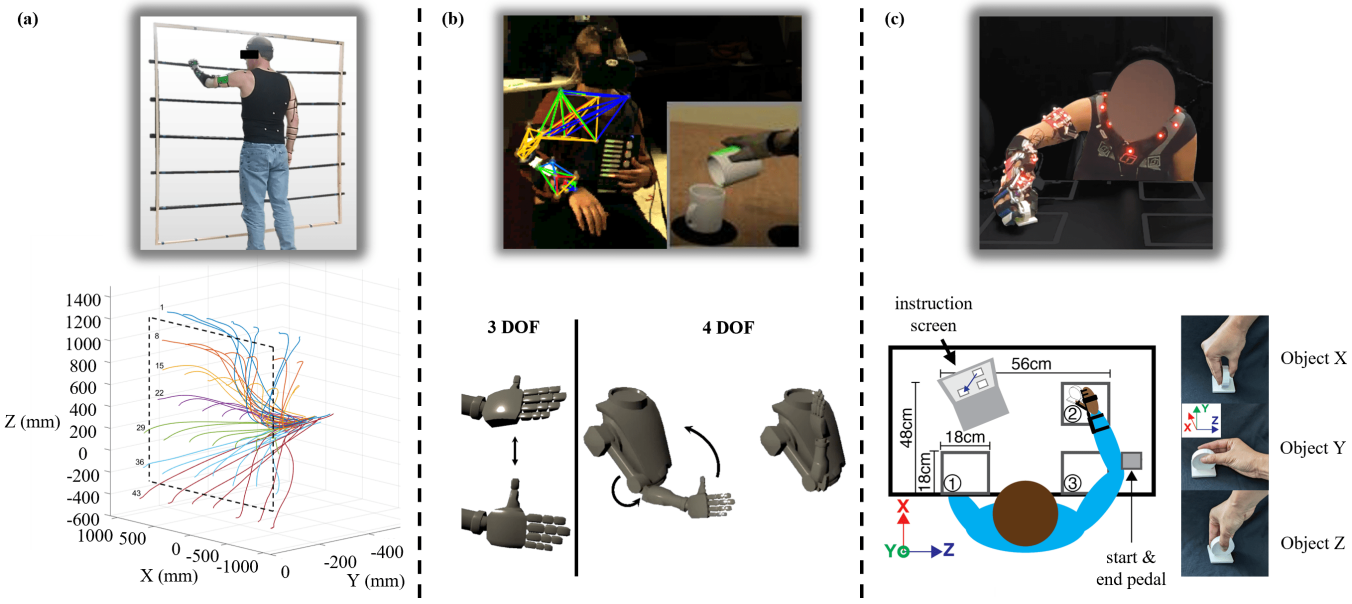


Fig. 2. Top row includes snapshots of the three experiments that generated the datasets while the bottom row offers further details of the experiment procedures. (a) Grid reaching experiment displays a prosthesis user reaching towards the grid. The bottom image demonstrates traces of the end-effector as the participant reached towards each of the 49 targets. (b) A screenshot of the virtual reality experiment is displayed next to the participant donning the virtual reality headset and keyboard controller. The participant visualizes the virtual prosthesis in pace of their own, with the wrist or elbow-wrist joints being operated with the participant's own joints or with one of three control modes. (c) An SCI participant is seen grasping an object in one of the three locations. The schematic depicts the dimensions of the test set up, including the three locations, the instruction screen, and the "start & end" pedal from which the participants initiate their movements. The three object grasp and release orientations are depicted on the right.

exhibit increased transparency, and improve synchronization with human teammates by aligning with their expectations [16], [17]. In contrast, optimized movements that do not consider natural human motion has been found to harm coordination, negatively impacting task efficiency and participants' perception of the collaboration [18]. In surveys conducted on upper-limb amputees, users of primarily functional prostheses, such as body-powered hooks, cited an ongoing desire to improve natural movement [19]. Today, morphological cosmesis plays a significant role in users choosing devices based on social acceptance [20], and the appearance of multi-joint synchronicity likely does as well.

Efforts to establish normative movement have involved minimizing jerk [21], minimizing variance [22], and studying human pose-to-target relationships [23]. Motion capture with human participants has also been used to generate human-like robot [24] and upper-limb prosthesis [25] motion by learning motor coordination, though timing is often neglected causing robot movement to occur at unrealistic and non-human velocities [26]. Translating these methods to evaluate movement coordination in humans is not clear, since people's joints by default exhibit human-like motion profiles.

To address this gap, we propose a metric called "*synchronicity*" to evaluate the degree of coordination among a set of body joints. Robotic movement is typically seen as the isolation of individual joints, and is precisely the opposite of synchronous movement, and is colloquially considered an impressive skill in people. Upper-limb myoelectric prosthetic devices that include a wrist or an elbow, as well as some robotic manipulators (e.g. [27]), are often operated by users controlling the joints sequentially, moving one joint at a time to position the end-effector. In addition to the cognitive load associated with operating multiple joints simultaneously, this limitation arises primarily from having access to very few control inputs, a particular challenge for those already missing portions of their limb. We hypothesize that operating a worn device, such as a brace, prosthesis, or exoskeleton, will cause residual joints to also become sequential as the user attempts to minimize the cognitive load associated with positioning the end-effector. We explore whether more coordinated conditions tend to score higher across these interventions. In the remainder of this paper, we describe the human subject datasets (Section II) used to test the proposed *synchronicity* metric, detailed in Section III. We then present the results (Section IV), comparing *synchronicity* scores across interventions, followed by a discussion of the metric and conclusions (Section V).

II. Datasets

In this work we used three datasets featuring reaching and manipulation movements of the upper-limb across a broad range of tasks and populations (Fig. 2), all of which were collected in an attempt to assess an intervention and its impact on body compensation. The datasets include three subject populations: normative subjects using their own hand with and without a wrist brace and using virtual prostheses, amputee subjects using either their intact hand or their own transradial prosthesis, and spinal cord injury (SCI) population using their own hands with and without the assistance of an exoskeleton device. In all cases, the data included the motion capture markers placed around the participants' hips

(if standing), torso, humerus, and forearm, from which joint angle data was extracted; for seated tasks, the pelvis was considered fixed to the chair. All subjects provided written and informed consent.

A. Dataset 1: Grid Reaching

The first dataset used in this study is the publicly available ROAG dataset [28], featuring a set of reaching motions performed by 7 normative (ages 24-56) and 2 transradial amputee participants (ages 23 and 53) [5]. A grid of vertical and horizontal cylindrical targets were placed in front of the participants 0.6 m away with the targets evenly spaced at 300 mm intervals across a 7×7 square grid, for a total of 49 locations (Fig. 2a). Each recording included a single reaching movement with participants' dominant arms starting at their sides and ending when they reached the target. Motion was captured using 27 retroreflective markers and 12 Bonita cameras (Vicon, Oxford, UK) recording at 100 Hz.

In addition to recording normative reaching, the normative participants reached for the targets under different braced conditions that limited their wrist degrees-of-freedom (DOF): 2-DOF brace (DonJoy ComfortFORM Wrist Support Brace, DJO Global, Vista, CA, USA) restricted flexion-extension movement and ulnar-radial deviation, herein referred to as *brace1*, and a 3-DOF brace, made by combining the 2-DOF brace with an elbow brace (Orthomen, Foothill Ranch, CA, USA), that additionally limited pronation-supination, herein referred to as *brace2*. The amputee participants performed the reaching tasks with both hands, once with their able hand and once with their prosthesis. Although both participants had wrist functionality in their prosthesis, they were instructed to pre-position their wrist prior to each recording. In total there were 2450 reaching motions: 49 targets × 2 orientations × (7 normative participants × 3 conditions + 2 amputee participants × 2 conditions).

B. Dataset 2: ADL in Virtual Reality

The second dataset includes 11 reaching and transferring movements made with objects related to Activities of Daily Living (ADL), detailed in Table I, by 12 right-handed normative participants (ages 18-53). These tasks were performed entirely in a virtual reality environment (VRE) (Fig. 2b) and included both standing and sitting tasks during which the participants sat on a real chair; no other physical props were used. Motion tracking was performed using the same system as the previous dataset.

The participants completed each task while operating various devices (3-DOF wrist or 4-DOF elbow-wrist) with various control modes (sequential, simultaneous, or trajectory) using a K-Mix MIDI keyboard (Keith McMillen Instruments, Berkeley CA, USA) worn on their torso using foam shoulder pads (Gait Gunner, Altamont, NY, USA), and operated with their unused hand. The virtual prostheses were overlaid on their right hand, so that they perceived and operated the device as if it were theirs. The participants also performed the tasks with their own hand and while wearing a 3-DOF wrist brace, same as in the previous dataset, that locked their wrist in place. When operating the wrist or elbow-wrist prostheses, they were instructed to operate it with one of three control methods, described as follows:

- **Sequential:** In this mode participants are provided with a single input that operates one joint at a time. Operation of different joints (including grasping) is switched between using an additional button.
- **Simultaneous:** In this mode, participants are given access to multiple inputs, each matching a different joint, allowing them to control the joints simultaneously.
- **Trajectory:** Similar to the sequential control mode, participants operate one trajectory at a time using a single input, switching between trajectories using a button. In this mode, trajectories are a fixed set of coordinated joints that move along predefined 1-DOF paths. 3-DOF trajectories refer to fixed prosthesis wrist movements, while 4-DOF trajectories involve a different set of coordinated elbow and wrist movements. The data used to generate the trajectories is publicly available online [29], with details found in our prior work [2].

Due to physical constraints, not all tasks were feasible for some of the participants, and the final dataset includes only 896 manipulation recordings out of 1056 attempts. This study protocol was approved by Yale University Institutional Review Board, HSC# 1610018511.

TABLE I
VIRTUAL REALITY TASKS

standing tasks[a]	
briefcase	reach towards the handle of briefcase resting on the floor
cell phone	transfer the cell phone to the ear
cook	reach towards the handle of a pan resting on a stove
cup	reach towards the cup on the counter
doorknob	reach towards the doorknob
can	reach towards a can on the top shelf
screwdriver	reach towards the screwdriver resting on the table
sitting tasks[a]	
cup	reach towards the cup on the table
fork	reach towards the fork resting next to the plate
spoon	reach towards the spoon resting next to the plate

[a]Standing tasks started and ended with the subjects' hands by their side while for sitting tasks the hands were to start on their laps.

C. Dataset 3: Wrist Orthosis for SCI

The third dataset includes four participants (Table II), all with SCI at the C5-C7 level (herein referred to simply as SCI) and similar American Spinal Injury Association Impairment Scale (AIS) scores, that completed a series of transfer tasks with or without motorized assistance while wearing the motorized wrist driven orthosis (MWDO) exoskeleton. The device is intended to augment existing tenodesis functionality [30], offering additional grasp security while reducing body compensation [12]. The device was donned in both *passive* (device unassisted) and *motorized* (device assisted) modes, toggled by the experimenters between tasks, to study the impacts of shared actuation. In the motorized condition, the device augmented the tenodesis grasp aperture using wrist angle, while in the passive mode the device merely

TABLE II
SCI PARTICIPANT DEMOGRAPHICS

	Subj 1	**Subj 2**	**Subj 3**	**Subj 4**
Sex	Female	Male	Male	Male
Age	64	35	33	35
Injury Level	C5-6	C5-6	C5-6	C5-6
Years Post-Injury	50+	16	12	19
AIS Score	A	A	A	B

supported existing tenodesis capability much like a non-motorized exoskeleton brace would.

Motion was captured using 32 active markers and 4 Impulse X2E cameras (PhaseSpace, San Leandro, California, USA) recording at 120 Hz. The active LEDs were attached to the participants using straps and the modified shoulder pads, and onto the MWDO using double-sided tape. The tasks required participants to grasp and release the same 3D-printed stamp-like object in three orientations, transferring it between three locations (Fig. 2c). The object was to be picked up by its large flat surfaces, 14 mm wide, using prehensile grasping. The participants completed the tasks seated at a comfortable distance from the table, adjusted to their preferred height, and were asked to reset their hands between transfers using the "start & end" pedal. In total, there were 432 transfers: 3 orientations × 6 transfer targets × 2 conditions × 3 repetitions × 4 participants. This study protocol was approved by the University of California, Berkeley Institutional Review Board #2020-02-12983.

III. METHOD

Synchronization of body segments occurs when a reaching movement involves all relevant body features moving simultaneously towards their target position. Over a single movement we can calculate *synchronicity S* as the dot product of the velocities $\mathbf{v}_n(t)$ of each time varying feature normalized by the number of features *N* and duration of the movement *t*:

$$S = \frac{\mathbf{v}_1 \cdot \mathbf{v}_2 \cdot \mathbf{v}_3 \cdot \ldots \cdot \mathbf{v}_N}{N * t} \tag{1}$$

The value of *S* is not informative on its own; it's value is derived relative to other test conditions. A larger *S* implies that joint movements are largely coordinated while a smaller *S* suggests that they are more sequential.

Body features can be represented in various ways. Cartesian representation is a precise method to track body segment positions over time, but it requires additional effort to identify morphological significance and makes data comparison across participants more difficult. On the other hand, Euler angle representation of each body joint is more commonly used in clinical settings and evaluations [11]. Despite the multiple ways to formulate Euler angles around a 3-DOF joint, efforts have been made to define joint definition standards that capture anatomical relevance [31]. Euler angles result in 3-DOF for the torso, 3-DOF for the shoulder, and 1-DOF for the elbow. However, two issues arise when using Euler angles to calculate *S*. First, torso and shoulder angles carry greater weight due to having additional DOF. Second, if shoulder movement occurs primarily along a single axis, the shoulder's two other DOF would zero-out the dot product. While the motion may still present normative movement, it would receive a lower *synchronicity* score.

To represent each joint with the same number of features, regardless of its DOF, we use quaternion representation; for our purposes, rotation matrix representation would be equally sufficient. Quaternions can be transformed into any other orientation using an axis-angle representation; there exists an axis around which a quaternion could rotate with some angle to reach any other quaternion. As a joint moves from one orientation to another during the reaching motion, the angle transformation represents its velocity over time. Therefore, each joint, whether a 3-DOF ball-and-socket joint or a 1-DOF hinge joint, can be represented by a single angular velocity. For a 1-DOF hinge joint, the quaternion angle transformation will be identical to the conventional angle measurement. Quaternion representation for each joint was made with respect to its parent joint: the elbow quaternion with respect to the shoulder, the shoulder with respect to the torso, the torso with respect to the pelvis, and the pelvis with respect to the global reference frame.

Synchronicity scores of the residual joints were calculated in three ways: using (1) all the residual joints, i.e. torso, shoulder, and elbow (referred to as torso-shoulder-elbow for simplicity), or a pair of residual joints, i.e. either (2) torso and shoulder joints (referred to as torso-shoulder), or (3) shoulder and elbow joints (referred to as shoulder-elbow). The second dataset, virtual reality prosthesis use, was the only one that included an elbow device, and therefore only the torso-shoulder score was calculated for those testing conditions. Distributions of *synchronicity* scores across conditions were tested for similarity using a two-tailed t-test. Calculations were performed in MATLAB 2023b.

IV. RESULTS

With the goal of comparing testing conditions, we primarily focus our evaluation on whether there are statistically significant differences between them rather than between participants or tasks. The *synchronicity* results for the grid reaching dataset can be seen in Fig. 3. Prosthesis scores significantly differed from other scores across all joint combinations. Additionally, *brace2* scores significantly differed from both *brace1* and normative scores in *synchronicity* measurements that included the elbow.

Synchronicity scores for the virtual reality dataset are displayed in Fig. 4. Rather than presenting the scores for each task separately, we only include the aggregate results across the whole study. *Synchronicity* between the elbow and the other joints was not calculated for the *seq4*, *sim4*, and *tra4* prosthesis control conditions, as they refer to the cases where subjects operated the elbow-wrist device; this left only the torso and shoulder as the residual joints. Across all joint combinations, normative scores significantly differed from scores calculated for 3 or more of the virtual prosthesis conditions. *Synchronicity* of the braced condition differed significantly from all other conditions across all

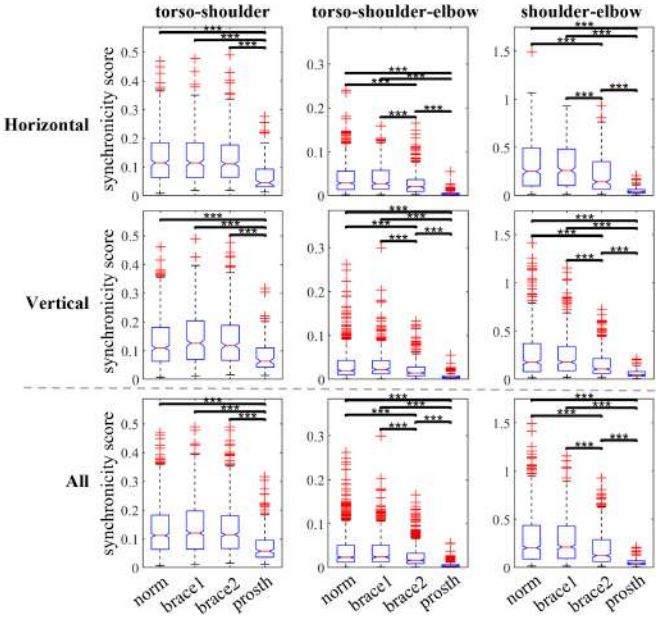


Fig. 3. *Synchronicity* scores for horizontal and vertical reachings, as well as the aggregate of the two, across each condition (*norm*: all normative participants, *brace1* and *brace2*: normative participants with each brace, *prosth*: amputee participants with transradial prosthesis). Column 1 contains scores for the torso and shoulder joints, column 2 contains scores for the torso, shoulder, and elbow joints, and column 3 contains scores for the shoulder and elbow joints. ***p<0.001

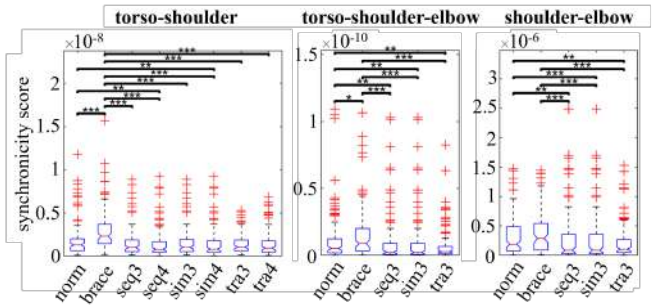


Fig. 4. *Synchronicity* scores from the virtual reality dataset, across each condition (*norm*: all normative participants, *brace*: normative participants with brace, *seq3* and *seq4*: sequential control with each DOF, *sim3* and *sim4*: simultaneous control with each DOF, *tra3* and *tra4*: trajectory control with each DOF). Column 1 contains scores for the torso and shoulder joints, column 2 contains scores for the torso, shoulder, and elbow joints, and column 3 contains scores for the shoulder and elbow joints. *p<0.05, **p<0.01, ***p<0.001

joint combinations, except for the normative condition when assessing the shoulder-elbow combination.

Due to large variability in participant performance, *synchronicity* scores for the SCI dataset is displayed separately for each participant (Fig. 5). While two tailed t-tests were performed between pairs of test conditions, none of the pairs were found to be significantly different at $\alpha = 0.05$.

V. Discussion

For the grid reaching dataset, we observe no major differences between the horizontal and vertical tasks. The primary aim was to determine if *brace2* (which fixes the 3-DOF of the wrist in place) effectively simulates the lack of wrist functionality faced by most prosthesis users. However, it

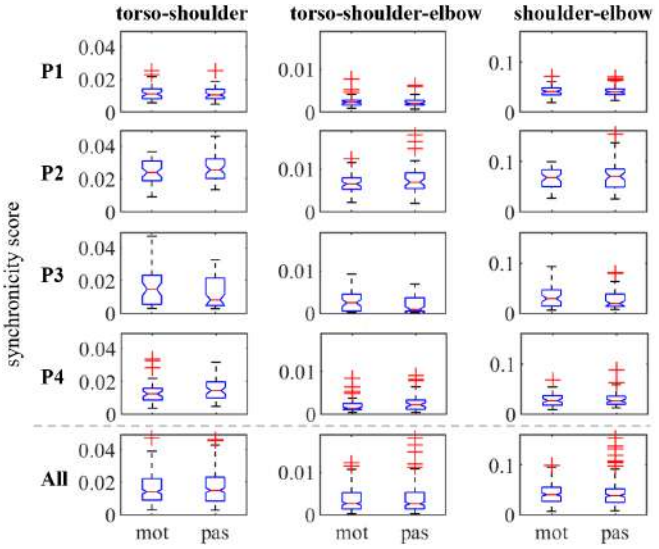


Fig. 5. *Synchronicity* scores for each participant with SCI and the participants aggregated, across both exoskeleton modes (*mot*: motorized, *pas*: passive). Column 1 contains scores for the torso and shoulder joints, column 2 contains scores for the torso, shoulder, and elbow joints, and column 3 contains scores for the shoulder and elbow joints.

appears *brace2* did not affect the residual limb in the same way, despite having identical DOF limitations. Instead, prosthesis users' *synchronicity* scores were significantly lower than those in other modes, even though the torso, shoulder, and elbow joints were unimpaired. *Synchronicity* between shoulder and elbow joints was lower for *brace2* than for the normative or *brace1* conditions, but higher than for prosthesis use. This suggests that there is likely additional cognitive load when the end effector is not embodied.

In the virtual reality dataset, we observe that the brace condition generally had a higher *synchronicity* score than even the normative condition. As before, we suspect that the embodiment of the hand does not diminish in the braced condition as it does with prosthesis use, so the *synchronicity* of the residual joints may not be affected. Higher scores seem to suggest that users may be performing larger movements to compensate for the lack of wrist mobility. We also observe that prosthesis use negatively impacts *synchronicity* scores. Torso-shoulder *synchronicity* did not appear to be significantly different between the two prosthesis conditions, regardless of the mode. This suggests that removing an additional normative joint does not reduce the coordination of the residual joints, indicating that the embodiment may be binary rather than gradual. Further testing with a greater resolution of controllable joints is required to confirm this.

In the SCI dataset involving the exoskeleton device, we observe no significant differences between device conditions. We hypothesized that device intervention would improve residual joint coordination, but found that, similar to the previous two datasets, embodiment appears to play a larger role in residual joint coordination. Since only hand closure is affected, we suspect that embodiment remains largely intact as participants continue using their own hand, which can be more intuitive to orient than another tool. If the device

required additional inputs, such as sequentially opening and closing the hand as with prosthetic devices, we would expect a reduction in coordination, similar to the previous dataset.

A. Conclusion

This work examines the concept of movement coordination, referring to the synchronous joint motion that is typical of normative movement, which we quantified and term *synchronicity*. *Synchronicity* is not only crucial for social interactions but also serves as a valuable quantitative metric in clinical evaluations. We analyzed three datasets of upper-limb motions, encompassing normative movement, wrist braces, transradial prostheses, and a wrist exoskeleton. Our results show that prosthesis use significantly reduces *synchronicity*, while braces and the exoskeleton do not. This suggests that device embodiment is the primary driver of residual joint movement coordination. Nonetheless, its clinical value requires further validation. Future research will involve studying pre- and post-rehabilitation patients, comparing outcomes with medical professionals' evaluations of movement coordination and quality, using data-driven computer vision methods to validate the new metric, and gathering observer feedback to deepen our understanding of normative movement and model-based movement behavior.

REFERENCES

[1] C. J. van Andel, N. Wolterbeek, C. A. Doorenbosch, D. H. Veeger, and J. Harlaar, "Complete 3d kinematics of upper extremity functional tasks," *Gait & posture*, vol. 27, no. 1, pp. 120–127, 2008.

[2] Y. Gloumakov, A. J. Spiers, and A. M. Dollar, "Dimensionality reduction and motion clustering during activities of daily living: Three-, four-, and seven-degree-of-freedom arm movements," *IEEE Transactions on Neural Systems and Rehabilitation Engineering*, vol. 28, no. 12, pp. 2826–2836, 2020.

[3] C. J. Hass, P. Malczak, J. Nocera, E. L. Stegemöller, A. Shukala, I. Malaty, C. E. Jacobson IV, M. S. Okun, and N. McFarland, "Quantitative normative gait data in a large cohort of ambulatory persons with parkinson's disease," 2012.

[4] L. Resnik, L. Adams, M. Borgia, J. Delikat, R. Disla, C. Ebner, and L. S. Walters, "Development and evaluation of the activities measure for upper limb amputees," *Archives of physical medicine and rehabilitation*, vol. 94, no. 3, pp. 488–494, 2013.

[5] A. J. Spiers, Y. Gloumakov, and A. M. Dollar, "Transradial amputee reaching: Compensatory motion quantification versus unaffected individuals including bracing," *IEEE Transactions on Medical Robotics and Bionics*, 2024.

[6] C. R. Gambrell, "Overuse syndrome and the unilateral upper limb amputee: consequences and prevention," *JPO: Journal of Prosthetics and Orthotics*, vol. 20, no. 3, pp. 126–132, 2008.

[7] P. Martinez-Martin, "What is quality of life and how do we measure it? relevance to parkinson's disease and movement disorders," *Movement Disorders*, vol. 32, no. 3, pp. 382–392, 2017.

[8] M. Jahanshahi and C. Marsden, "Body concept, disability, and depression in patients with spasmodic torticollis," *Behavioural neurology*, vol. 3, no. 2, pp. 117–131, 1990.

[9] C. M. Light, P. H. Chappell, and P. J. Kyberd, "Establishing a standardized clinical assessment tool of pathologic and prosthetic hand function: normative data, reliability, and validity," *Archives of physical medicine and rehabilitation*, vol. 83, no. 6, pp. 776–783, 2002.

[10] J. Desrosiers, G. Bravo, R. Hébert, É. Dutil, and L. Mercier, "Validation of the box and block test as a measure of dexterity of elderly people: reliability, validity, and norms studies," *Archives of physical medicine and rehabilitation*, vol. 75, no. 7, pp. 751–755, 1994.

[11] A. M. Oosterwijk, M. K. Nieuwenhuis, C. P. van der Schans, and L. J. Mouton, "Shoulder and elbow range of motion for the performance of activities of daily living: A systematic review," *Physiotherapy theory and practice*, vol. 34, no. 7, pp. 505–528, 2018.

[12] E. Y. Chang, A. I. McPherson, R. C. Adolf, Y. Gloumakov, and H. S. Stuart, "Modulating wrist-hand kinematics in motorized assisted grasping with c5-6 spinal cord injury," *IEEE Transactions on Medical Robotics and Bionics*, 2023.

[13] Q. Yang, Y. Gloumakov, and A. J. Spiers, "Multi-feature compensatory motion analysis for reaching motions over a discretely sampled workspace," in *2024 10th IEEE RAS/EMBS International Conference for Biomedical Robotics and Biomechatronics (BioRob)*. IEEE, 2024, pp. 284–290.

[14] L. Ren, A. Patrick, A. A. Efros, J. K. Hodgins, and J. M. Rehg, "A data-driven approach to quantifying natural human motion," *ACM Transactions on Graphics (TOG)*, vol. 24, no. 3, pp. 1090–1097, 2005.

[15] D. Wu, "Ad hoc meta-analysis of perceived error in physically simulated characters," in *Game Developers Convention. Microsoft Game Studios*, 2009.

[16] T. Fong, I. Nourbakhsh, and K. Dautenhahn, "A survey of socially interactive robots," *Robotics and autonomous systems*, vol. 42, no. 3-4, pp. 143–166, 2003.

[17] J. Cassell, "Embodied conversational agents: representation and intelligence in user interfaces," *AI magazine*, vol. 22, no. 4, p. 67, 2001.

[18] A. D. Dragan, S. Bauman, J. Forlizzi, and S. S. Srinivasa, "Effects of robot motion on human-robot collaboration," in *Proceedings of the tenth annual ACM/IEEE international conference on human-robot interaction*, 2015, pp. 51–58.

[19] P. J. Kyberd, C. Wartenberg, L. Sandsjö, S. Jönsson, D. Gow, J. Frid, C. Almström, and L. Sperling, "Survey of upper-extremity prosthesis users in sweden and the united kingdom," *JPO: Journal of Prosthetics and Orthotics*, vol. 19, no. 2, pp. 55–62, 2007.

[20] E. Biddiss, D. Beaton, and T. Chau, "Consumer design priorities for upper limb prosthetics," *Disability and rehabilitation: Assistive technology*, vol. 2, no. 6, pp. 346–357, 2007.

[21] T. Flash and N. Hogan, "The coordination of arm movements: an experimentally confirmed mathematical model," *Journal of neuroscience*, vol. 5, no. 7, pp. 1688–1703, 1985.

[22] M. J. Gielniak, C. K. Liu, and A. L. Thomaz, "Generating human-like motion for robots," *The International journal of robotics research*, vol. 32, no. 11, pp. 1275–1301, 2013.

[23] R. Tomovic, G. Bekey, and W. Karplus, "A strategy for grasp synthesis with multifingered robot hands," in *Proceedings. 1987 IEEE International Conference on Robotics and Automation*, vol. 4. IEEE, 1987, pp. 83–89.

[24] D. Oziem, N. Campbell, C. Dalton, D. Gibson, and B. Thomas, "Combining sampling and autoregression for motion synthesis," in *Proceedings Computer Graphics International, 2004.* IEEE, 2004, pp. 510–513.

[25] Y. Gloumakov, J. Bimbo, and A. M. Dollar, "Trajectory control–an effective strategy for controlling multi-dof upper limb prosthetic devices," *IEEE Transactions on Neural Systems and Rehabilitation Engineering*, vol. 30, pp. 420–430, 2022.

[26] T. Asfour, A. Ude, K. Berns, and R. Dillmann, "Control of armar for the realization of anthropomorphic motion patterns," in *The second IEEE-RAS International Conference on Humanoid Robots (HUMANOIDS 2001)*, 2001, pp. 22–24.

[27] A. Campeau-Lecours, V. Maheu, S. Lepage, H. Lamontagne, S. Latour, L. Paquet, and N. Hardie, "Jaco assistive robotic device: Empowering people with disabilities through innovative algorithms," in *Rehabilitation Engineering and Assistive Technology Society of North America (RESNA) Annual Conference*, 2016.

[28] Q. Yang, A. Spiers, Y. Gloumakov, and A. Dollar, "ROAG (Reaching Over A Grid): Dataset of Human Reaching Motions Over a Discretely Sampled Workspace." Zenodo, Oct. 2024.

[29] Y. Gloumakov, A. Spiers, and A. Dollar, "ADL human arm motion data." IEEE Dataport, 2021.

[30] A. I. McPherson, V. V. Patel, P. R. Downey, A. A. Alvi, M. E. Abbott, and H. S. Stuart, "Motor-augmented wrist-driven orthosis: Flexible grasp assistance for people with spinal cord injury," in *2020 42nd Annual International Conference of the IEEE Engineering in Medicine & Biology Society (EMBC)*. IEEE, 2020, pp. 4936–4940.

[31] G. Wu, F. C. Van der Helm, H. D. Veeger, M. Makhsous, P. Van Roy, C. Anglin, J. Nagels, A. R. Karduna, K. McQuade, X. Wang *et al.*, "Isb recommendation on definitions of joint coordinate systems of various joints for the reporting of human joint motion—part ii: shoulder, elbow, wrist and hand," *Journal of biomechanics*, vol. 38, no. 5, pp. 981–992, 2005.

Real-time Open Source Kinematic Estimation with Wearable IMUs

Chenquan Xu
State Key Laboratory of Mechanical System and Vibration
Shanghai Jiaotong University
Shanghai, China
xiaoqin@sjtu.edu.cn

Yuanshuo Tan
State Key Laboratory of Mechanical System and Vibration
Shanghai Jiaotong University
Shanghai, China
tanyuanshuo@sjtu.edu.cn

Zach Strout
SageMotion, LLC
Kalispell, MT
zach@sagemotion.com

Guoxing Liu
State Key Laboratory of Mechanical System and Vibration
Shanghai Jiaotong University
Shanghai, China
lgxing1900@sjtu.edu.cn

Kezhe Zhu
State Key Laboratory of Mechanical System and Vibration
Shanghai Jiaotong University
Shanghai, China
kezhe_zhu@sjtu.edu.cn

Peter Shull*
State Key Laboratory of Mechanical System and Vibration
Shanghai Jiaotong University
Shanghai, China
pshull@sjtu.edu.cn

Abstract—Despite the growing demand for healthcare services due to an aging population, patients may avoid traditional rehabilitation centers due to high costs, discomfort, and time constraints associated with in-person assessments. Home-based rehabilitation offers a promising alternative, but effective kinematic monitoring and assessment remain challenging, especially for real-time applications. To address this gap, we have developed real-time, full-body kinematic analysis and visualization based on 12 wearable inertial measurement units (IMUs). Full body real-time kinematics estimation (20Hz) was evaluated during walking, running, squatting, boxing, yoga, dance, badminton, and various seated extremity exercises and IMU estimations were compared with optical motion capture to determine accuracy. Results showed that walking was the most accurate with 5.4 deg median RMSE, and the overall median RMSE was 7.2 deg for all activities. A mean of 1.0 deg RMSE against offline computations (100Hz) was also demonstrated, with a mean latency of 44.1 ms from sensor data acquisition to kinematic output. This approach holds the potential to revolutionize rehabilitation by enabling rapid assessment and real-time biofeedback for motion performance in orthopedic and neurological conditions and could significantly enhance treatment outcomes and patient compliance.

Index Terms—inertial measurement unit, biomechanics, real-time, inverse kinematics, wearable sensors.

I. Introduction

Wearable systems have revolutionized rehabilitation by offering real-time data and personalized feedback for human physiological functions and performance across various activities. [1]–[3]. Traditional rehabilitation methods, often conducted in hospitals and healthcare centers, rely heavily on the expertise and availability of medical professionals. These methods are typically conducted in laboratories with specialized equipment, which can be uncomfortable and time-consuming for patients. Additionally, physiotherapy programs at home often suffer from patient non-compliance, particularly post-surgery, due to a lack of time, specialist feedback, and tangible benefits [2]. The integration of wearable systems in rehabilitation processes effectively mitigates these issues by providing convenient, patient-centric [3], sustainable, and comfortable rehabilitation assessments for the elderly and patients, which can substantially improve recovery outcomes and facilitate the monitoring of progress, reducing the intensified labor demands on healthcare providers.

Human kinematics analysis is crucial in professional research fields such as human-computer interaction [4], ergonomics, and biomechanics, and is essential for disease analysis [5]. It also holds significant potential for practical applications in everyday scenarios, such as rehabilitation assessment for patients with musculoskeletal impairment [6] [7] or neurological disorders like Parkinson's disease [8] [9], which are common among the aging population [10]. While kinematics analysis of human movement is generally conducted post-measurement using inverse kinematics (IK) algorithms, real-time kinematics solutions offer broader applicability in rehabilitation by enabling quick assessment and feedback for individual human movement. Real-time wearable-based kinematics can promote advancements in rapid diagnoses, correction of rehabilitation, and motion ability improvement. Real-time visual, haptic, or audio biofeedback about human motion can also enhance user engagement and enjoyment [11], leading to more effective movement execution and, consequently, the effectiveness of rehabilitation.

Optical motion capture (OMC) systems, which track retroreflective markers placed on the bony landmarks, are considered the gold standard in biomechanics research due to their ability to provide high-resolution, accurate 3D kinematic data [12]. However, OMC systems are expensive, typically confined to a small capture volume

in the lab, and need professional operators to operate the system and accurately find the anatomical landmarks. They also require a line of sight to each marker, making them susceptible to marker occlusion and displacement. Wearable systems overcome these limitations of OMC systems by their lightweight, portability, usability, and affordability, resulting in the growing interest in inertial motion analysis [13] [14]. Inertial measurement units (IMUs), typically consisting of accelerometers, gyroscopes, and magnetometers, which provide information about the motion of the sensor in space, are the most commonly used portable compact sensors in wearable systems. With sensor orientations obtained through various sensor fusion algorithms, wearable IMUs can commonly offer a portable solution for motion capture [15], enabling data collection in different daily living scenarios outside the laboratory. IMU-based real-time kinematics analysis facilitates home-based rehabilitation, reducing the labor intensity for medical staff and improving work efficiency.

The conversion from IMU orientation to joint angle is typically achieved by defining a general human skeletal model. OpenSim is a versatile open-source software platform for musculoskeletal modeling and simulation, developed to study the mechanics and control of movement [16]. It features a repository of pre-built musculoskeletal models that users can access and modify for specific needs and offers a powerful visualization tool for graphical representation of musculoskeletal structures and animation of simulations. OpenSim's IK tool can solve the inverse kinematics problem and determine the joint angles of a model by minimizing the sum of the weighted squared orientation errors, aligning the model's markings with experimental data [17]. The IMU IK Tool available in OpenSim 4.2, however, estimates the pose of an OpenSim model that best matches experimental IMU orientations using an optimization method [18].

II. Methods

A. Pipeline of Real-Time Kinematics Estimation

The workflow for real-time kinematics estimation involves the transmission of data from IMU nodes to the hub (SageMotion, Kalispell, MT, USA) and subsequently to a computer for processing (Fig. 1). The SageMotion hub wirelessly collects data from IMUs, specifically accelerometer and gyroscope readings, and transmits this information, along with timestamps and computed quaternions, to a computer via socket communication. The computer software then translates the quaternions from IMUs into human body kinematics, utilizing the IMU inverse kinematics and visualization tools from OpenSim version 4.5. To ensure accurate and stable IMU orientation data with less drift, the gyroscope offset is calibrated using SageMotion's built-in calibration application, requiring all sensors to remain stationary for 2 seconds.

Prior to inverse kinematics computation, OpenSim's IK solver is configured experimentally with a constraint variable of 10.0 and an accuracy of 0.01 following empirical optimization for a balance between speed and precision, and a musculoskeletal model from the OpenSim repository is selected. We chose model Rajagopal2015 [19], which is a commonly used full-body model for gait analysis, and modified it by removing all the muscles and releasing the clamp of all joints to accommodate a broader range of human movements beyond walking. The model is then calibrated by virtually placing IMUs on each segment, referencing their orientation differences relative to a base IMU attached to the pelvis during a static calibration process, which involves the user assuming the initial pose of the selected model. IMU orientations are determined by collecting data for 2 seconds and averaging the rotations of each sensor during this period. Given that OpenSim's IMU placement mechanism presupposes a shared world frame for all IMUs to calculate orientation differences against body segments [20], maintaining a uniform coordinate system across all IMUs is crucial. To achieve this uniformity and to circumvent magnetic field interference, the VRU sensor fusion algorithm is implemented, synchronizing the activation of all sensors in an identical orientation, with magnetometer data excluded from the process.

The real-time inverse kinematics pipeline is executed through two concurrent threads (Fig. 1). In the data acquisition thread, the computer constantly receives quaternions from the Raspberry Pi in the SageMotion hub and saves them into a buffer queue. In the IK processing thread, a temporary queue stores quaternions from the buffer queue in the event of data loss. The data drop is detected by comparing the current time stamp and the previous time stamp. Data drops are identified by comparing current and previous timestamps, and compensated by sending the last validated quaternions to the inverse kinematics process to fill any gaps. The thread prioritizes drawing quaternions from the temporary queue if it contains data, otherwise retrieves quaternions from the shared buffer queue. These quaternions are then either logged into a table for further analysis or discarded, based on the predefined frequency (20Hz) for inverse kinematics calculations. The IMU IK Tool of OpenSim calculates real-time kinematics from the quaternions table and outputs the joint angles, while the visualization tool simulates the real-time human movement by animating the selected skeletal model.

We also monitor the time delay from IMU data reception at the hub to joint angle computation and the time required to solve inverse kinematics. Timestamps for these intervals are recorded in accordance with the Network Time Protocol and saved for post-trial analysis. The computational hardware used in this experiment is a laptop (Windows 11 64-bit, AMD Ryzen 7 5800H with Radeon Graphics 3.20 GHz processor, 15.9 RAM).

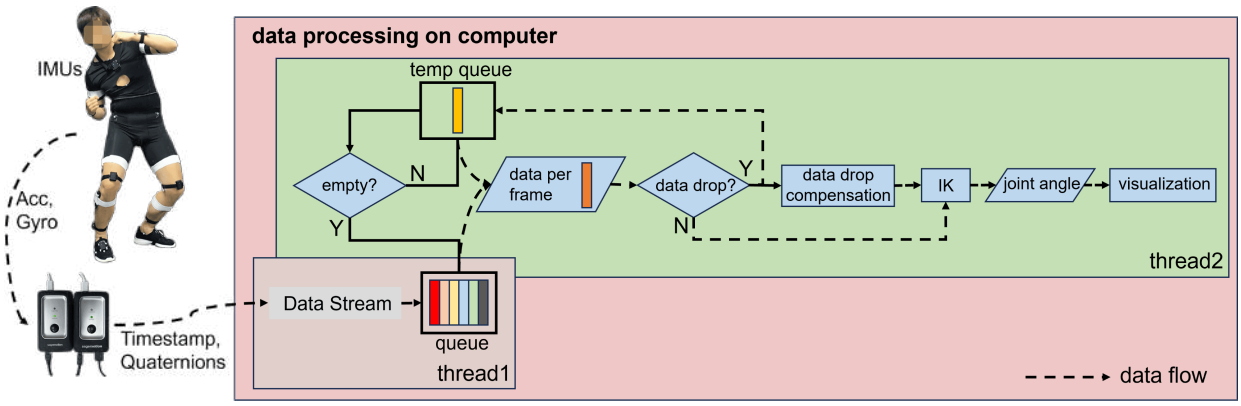


Fig. 1. Overview of the real-time analysis data flow and pipeline of real-time inverse kinematics (thread 1 represents data acquisition, thread 2 represents IK processing)

B. Experiment Protocol

1) Subjects: Seven subjects (all male; age: 21.9±1.1; height: 1.76±0.06m; mass: 71.1±13.8kg; BMI: 22.4±5.4kg/m²) with no history of musculoskeletal or neurological disorders volunteered to participate in this study. All subjects provided written informed consent before being tested, and the experimental protocol was reviewed and approved by the ethics committee of Shanghai Jiao Tong University (No. E2021013P).

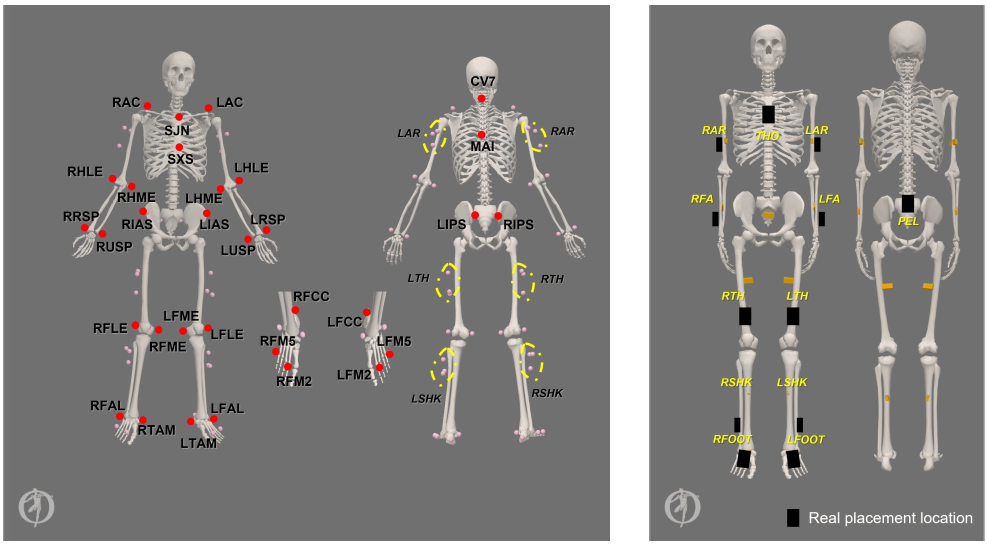
2) Marker Placement: Retroreflective markers were placed on 32 anatomical landmarks to determine the segments: posterior surface of the calcaneus (LFCC/RFCC), head of the second metatarsal (LFM2/RFM2), head of the fifth metatarsal (LFM5/RFM5), fibula apex of lateral and tibia apex of medial malleoli (LFAL/RFAL/LTAM/RTAM), lateral and medial femoral epicondyles (LFLE/RFLE/LFME/RFME), left and right anterior superior iliac spines (LIAS/RIAS), left and right posterior superior iliac spines (LIPS/RIPS), sternum jugular notch (SJN), left and right acromion (LAC/RAC), seventh cervical vertebra (CV7), sternum xiphisternal joint (SXS), midway between the inferior angles of most caudal points of the two scapula (MAI), lateral and medial humerus epicondyles (LHLE/RHLE/LHME/RHME), and radius-styloid and ulna-styloid processes (LRSP/RRSP/LUSP/RUSP). Eight clusters with three markers on each were placed on the segments of the shank (LSHK/RSHK), thigh (LTH/RTH), upper arm (LAR/RAR) and forearm (LFA/RFA) for stable optical tracking (Fig. 2(a)). Marker trajectories were recorded at 100 Hz with a twelve-camera optical motion capture system (Vicon, Oxford Metrics Group, Oxford, U.K.).

3) IMU Placement: Twelve IMU sensors with built-in real-time calibration and sampling rate of 100 Hz (SageMotion, Kalispell, MT, USA) were turned on in the same orientation and then securely strapped to each subject. Sensors were placed at the following locations to minimize soft tissue artifacts: dorsal foot, distal lateral shank, distal anterior thigh, middle lateral upper arm, distal dorsal forearm, sacrum, and sternum (Fig. 2(b)). For this experiment, a neutral pose (N-pose) with hands facing each other (Fig. 2(b)) was used for calibration, setting all joint angles to zero, except for forearm pronation and supination, which were set at 90 degrees.

4) Experimental Procedure: After proper attachment of markers and IMUs, subjects performed flexion for elbow and knee, rotation/flexion/adduction for hip and shoulder, flexion/dorsification for ankle to calibrate joint centers. Each trial began with a 2-second static N-pose, followed by a synchronization step where subjects swung their right shank three times while standing on their left foot. Subjects then completed eight trials of various activities, including walking, running, squatting, boxing, yoga, dance, badminton, and extremity exercises while sitting (Fig. 3). Activities were performed on a treadmill for walking and running at a self-selected comfortable speed. Squatting was performed 10 times in each trial with varying speeds and intensities. Boxing included a range of movements of jab, cross, hook, footwork, and defensive blocks, which were selected randomly by the subjects. Yoga (Dragon Pose, Phantom Chair Pose, Warrior II Pose, Warrior III Pose, and Warrior I Pose) involved holding each pose for at least 8 seconds and slowly changing the pose. The dance included a variety of fitness movements of sidesteps, jumps, arm swings, and hip rotations. Badminton trials consisted of performing familiar actions with a racket. Seated exercises focused on rehabilitation movements, including knee extension, elbow flexion, and hip flexion. All trials except squatting were performed for around 1.5 minutes. The gyroscope calibration of all IMUs was done approximately every 20 minutes.

C. Data Processing

1) Ground Truth Kinematics: The experimental optical motion capture data were converted from .c3d files to .trc format using a C3D file reader of the OpenSim library. The .trc file specifies the positions of markers in 3-dimensional



(a) Marker placement on anatomical landmarks and marker clusters placement on segments

(b) IMU placement calibration on N-pose model

Fig. 2. Illustration of marker placement, model calibration with IMU placement



Fig. 3. Activities: walking, running, squatting, boxing, yoga, dance, badminton and seated extremity exercises

space and is a standard format for subsequent import and analysis in OpenSim. For each subject, the musculoskeletal model was scaled to match the marker positions on anatomical landmarks identified during the static trial. Subsequently, inverse kinematics was applied to the scaled model to achieve the highest accuracy in marker tracking across each trial. The joint angles extracted during motion were recorded using OpenSim's analysis tools, establishing the ground truth kinematics.

2) Offline Predicted Kinematics: Raw data, comprising quaternions and timestamps, were captured at a 100 Hz sampling rate by the SageMotion hub. Any missing data points were linearly interpolated, and the complete dataset was then processed on the computer using the aforementioned software for offline inverse kinematics analysis.

3) Online Predicted Kinematics: After each trial, the timetable of the real-time output joint angles and associated time delay data were saved for further analysis.

4) Data Synchronization: To synchronize the three data sources—optical motion capture IK data, offline IMU IK data, and online IMU IK data—we utilized the right knee flexion angle values obtained during the initial three swings of each trial. Cross-correlation was applied to align these datasets.

The ground truth kinematics, offline predicted kinematics, and online predicted kinematics were compared to evaluate the accuracy and performance of the real-time wearable human inverse kinematics system. Additionally, the mean time delay and computation time for real-time IK were analyzed.

III. Results

We analyzed the real-time estimation accuracy for each joint's rotating angle across all subjects and trials (representative results in Fig. 4), and the estimation accuracy of each type of movement of human kinematics for all subjects (Fig. 5). The RMSE of the entire experiment prediction compared with OMC results had an average of 9.1° and a median of 7.2°. Walking had the highest accuracy of all activities with a 5.4° median RMSE. In addition, the RMSE for real-time estimations (20Hz) against offline results (100Hz) had an average of 1.0° and a median of 0.6° over all trials, with the highest RMSE of 2.4° observed during running trials. Fig. 4 illustrates the comparison of ground truth kinematics from OMC, offline predicted kinematics, and online predicted kinematics during a dance trial of one representative subject. The average time delay of the system is 44.7 ms and the average time for solving inverse kinematics is 15.5 ms on the laptop computer.

IV. Discussion

In this work, we developed a wearable system equipped with 12 IMUs capable of computing and visualizing full-body kinematics in real-time using OpenSim. We tested the system by assessing both human upper and lower body real-time kinematics for a diverse range of activities, including walking, running, squatting, boxing, yoga, dance, badminton, and seated extremity exercises. Results of the experiments demonstrated the system's accuracy in real-time kinematics estimation by achieving a mean RMSE of 9.1 degrees compared to optical motion capture systems and a mean RMSE of 1.0 degrees against offline calculation.

The discrepancies between our estimations and the ground truth were primarily attributed to the N-pose calibration process as the estimation of rotating angles proved more accurate than that of absolute joint angles. Factors contributing to the calibration error included the inaccuracy of marker placement on anatomical landmarks, nonstandard N-pose of the subject, and the inherent variability of the human skeleton. Notably, the hip flexion and lumbar extension angles deviated most significantly from the N-pose OpenSim model's default zero values, likely due to the challenges in identifying pelvic landmarks and individual differences in hip tilting habits while being told to stand straight. These joint angle offsets also came from differences between the subject's actual skeleton and the selected musculoskeletal model. The relatively poor estimation of arm flexion angle and arm rotation angle may be related to the ignored degree of freedom of the scapulae and clavicles [21] [22] in the model. Furthermore, the forearm's pronation and supination were not accurately predicted, primarily because of especially significant skin motion artifacts of the forearm. The IMU on the forearm, assumed to rigidly follow the radius, does not account for the non-rigid alignment between the skin and the radius or the IMU's movement relative to the skin. The accuracy of walking trials was the highest among all activities, presumably because the adopted Opensim musculoskeletal model was originally designed for human gait simulation. Despite the sacrifice of model extensive applicability, the design of activity-specific models has a high probability of improving the accuracy of kinematic estimations achieved utilizing this computing method.

The error between online and offline estimation is usually small, as some lines for online and offline prediction in Fig. 4 coincide. The error mainly arises from the difference in sampling rate. While offline prediction calculates IK at 100Hz, online prediction is computed at 20Hz, which can introduce errors especially during a sudden change of motion speed, such as when running and jumping, to have a peak prediction value difference. Additionally, consecutive data drops can affect estimation accuracy and increase the time delay in real-time visualization. The median RMSE of 0.6° indicates the small difference between sampling rates of 100Hz and 20Hz, suggesting that 20Hz of computational frequency is sufficient for real-time human IK in the selected activities.

Previous studies have employed the IMU IK Tool of OpenSim to develop wearable systems capable of estimating real-time human kinematics. Lavikainen et al. developed software capable of real-time inverse kinematics (IK) calculations at a rate of 45 Hz [23]. The software's performance was evaluated through walking tests involving varying numbers of IMUs, different computer systems, and different thread configurations. Real-time results were compared to offline computations to assess the efficacy of online processing. Slade et al. designed the hardware and software for a portable real-time wearable system [24] operating at 30 Hz. However, upper and lower body kinematics were only tested separately and all sensors of the system were connected to the microcontroller through cables, which could interfere with human movement and cause inconvenience to wear. While most wearable systems focus on gait analysis and have tests mainly on ambulation tasks [25] [26], the proposed system was tested across a broader range of activities to ensure its applicability in diverse rehabilitation scenarios for training and assessment. We also utilized the visualization tool

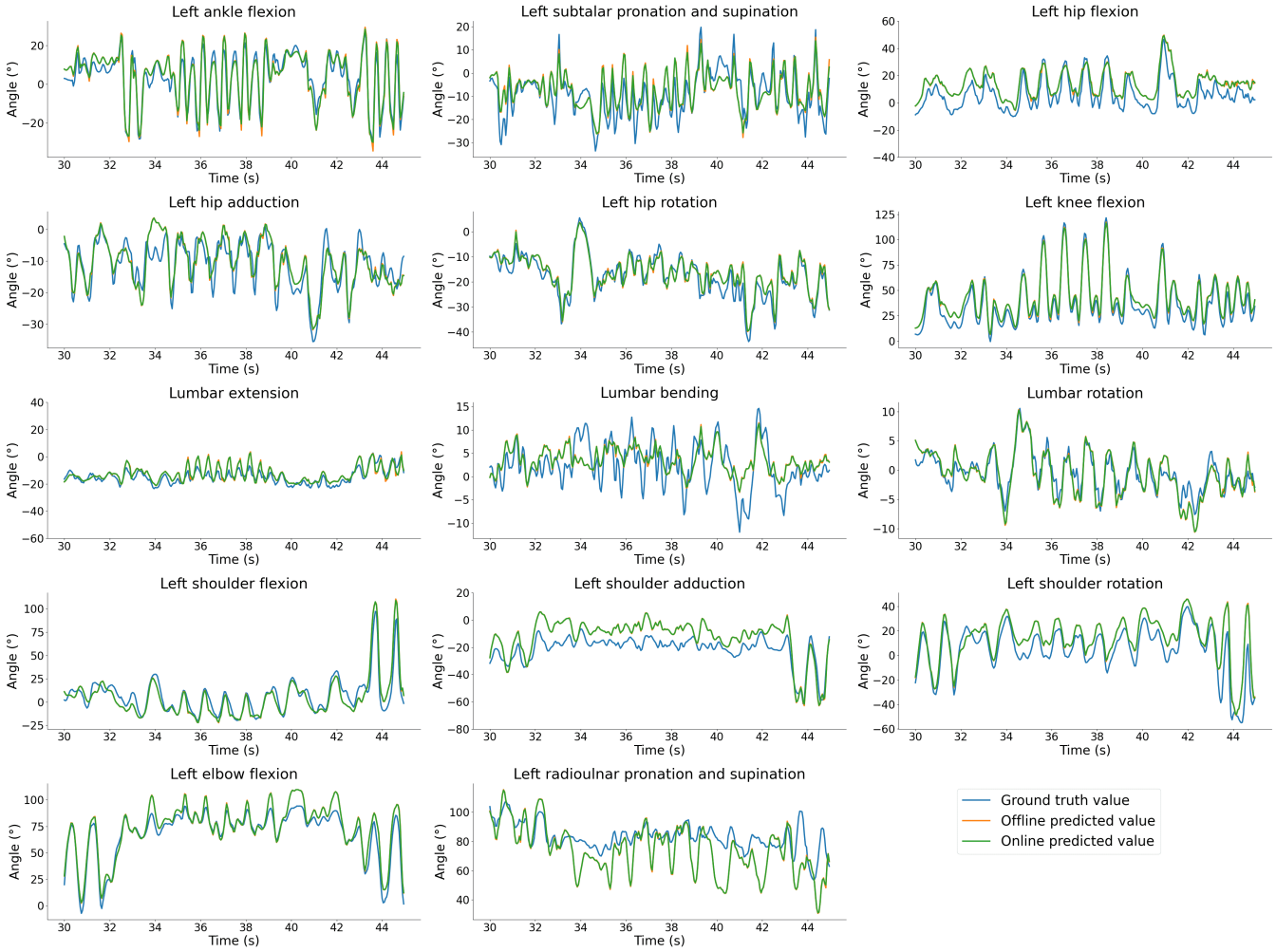


Fig. 4. Left side joint angle results of one representative subject during the dancing trial

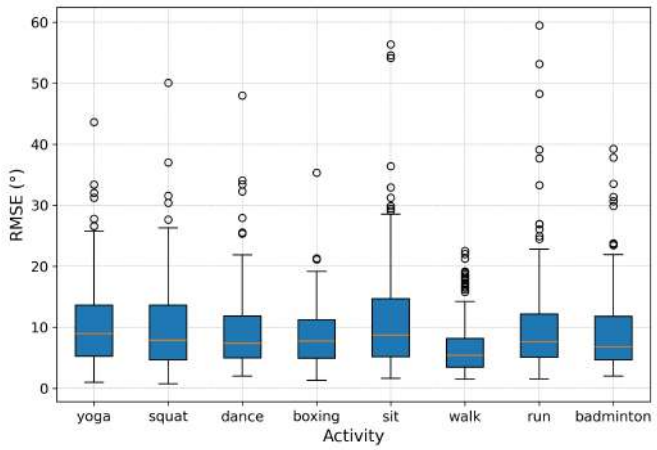


Fig. 5. Human body kinematics estimation RMSEs across all activities (circles refer to individual trials)

of OpenSim to provide real-time feedback on kinematics estimation performance and identify any sensor issues, which could enhance patient engagement if integrated into actual rehabilitation processes. The development of this wearable system offers the possibility of rapid rehabilitation assessment and real-time motion feedback for orthopedic and neurological conditions, alleviating the workload on medical professionals and facilities. It holds the potential to provide a more convenient and faster way of human movement assessment, increase patient engagement in rehabilitation training, and by further enhancing feedback features, provide personalized feedback and customized rehabilitation plans, thereby improving rehabilitation outcomes.

V. Acknowledgements

This work was supported by the National Natural Science Foundation of China under Grant W2441018.

VI. Conclusion

The paper presented a 12-IMU wearable system to track full-body kinematics in real time. Results demonstrated the robustness of our approach in accurately assessing human body joint angles across diverse activities of walking, running, squatting, boxing, yoga, dance, badminton, and extremity exercises while sitting. These findings indicate the potential of our wearable system for convenient, personalized, sustainable, and comfortable rehabilitation assessments.

Future research should focus on developing portable, wireless real-time human kinematics for broader rehabilitation applications. An accurate, flexible calibration method is needed, particularly for patient and elderly populations who may find standard calibration challenging. Extensive clinical trials with these groups are essential to validate the system's practicality in healthcare settings.

References

[1] S. Díaz, J. B. Stephenson, and M. A. Labrador, "Use of wearable sensor technology in gait, balance, and range of motion analysis," Applied Sciences, vol. 10, no. 1, p. 234, 2020.

[2] R. De Fazio, V. M. Mastronardi, M. De Vittorio, and P. Visconti, "Wearable sensors and smart devices to monitor rehabilitation parameters and sports performance: An overview," Sensors, vol. 23, no. 4, p. 1856, 2023.

[3] A. Haleem, M. Javaid, R. Pratap Singh, and R. Suman, "Medical 4.0 technologies for healthcare: Features, capabilities, and applications," Internet of Things and Cyber-Physical Systems, vol. 2, pp. 12–30, 2022.

[4] J. Zhang, P. Li, T. Zhu, W. A. Zhang, and S. Liu, "Human motion capture based on kinect and imus and its application to human-robot collaboration," in 2020 5th International Conference on Advanced Robotics and Mechatronics (ICARM), 2006, Conference Proceedings, pp. 392–397.

[5] J. L. McGinley, R. Baker, R. Wolfe, and M. E. Morris, "The reliability of three-dimensional kinematic gait measurements: A systematic review," Gait & Posture, vol. 29, no. 3, pp. 360–369, 2009.

[6] J.-S. Tan, S. Tippaya, T. Binnie, P. Davey, K. Napier, J. P. Caneiro, P. Kent, A. Smith, P. O'Sullivan, and A. Campbell, "Predicting knee joint kinematics from wearable sensor data in people with knee osteoarthritis and clinical considerations for future machine learning models," Sensors, vol. 22, no. 2, p. 446, 2022.

[7] J. N. Katz, K. R. Arant, and R. F. Loeser, "Diagnosis and treatment of hip and knee osteoarthritis: a review," Jama, vol. 325, no. 6, pp. 568–578, 2021.

[8] W. H. Organization, Neurological disorders: public health challenges. World Health Organization, 2006.

[9] V. L. Feigin, T. Vos, F. Alahdab, A. M. L. Amit, T. W. Bärnighausen, E. Beghi, M. Beheshti, P. P. Chavan, M. H. Criqui, and R. Desai, "Burden of neurological disorders across the us from 1990-2017: a global burden of disease study," JAMA neurology, vol. 78, no. 2, pp. 165–176, 2021.

[10] A. Cieza, K. Causey, K. Kamenov, S. W. Hanson, S. Chatterji, and T. Vos, "Global estimates of the need for rehabilitation based on the global burden of disease study 2019: a systematic analysis for the global burden of disease study 2019," The Lancet, vol. 396, no. 10267, pp. 2006–2017, 2020.

[11] V. Vasilyev, V. Borisov, and A. Syskov, "Biofeedback methodology: a narrative review," in 2019 International Multi-Conference on Engineering, Computer and Information Sciences (SIBIRCON). IEEE, 2019, Conference Proceedings, pp. 0011–0016.

[12] A. M. Valevicius, P. Y. Jun, J. S. Hebert, and A. H. Vette, "Use of optical motion capture for the analysis of normative upper body kinematics during functional upper limb tasks: A systematic review," Journal of Electromyography and Kinesiology, vol. 40, pp. 1–15, 2018.

[13] X. Robert-Lachaine, H. Mecheri, C. Larue, and A. Plamondon, "Validation of inertial measurement units with an optoelectronic system for whole-body motion analysis," Medical & Biological Engineering & Computing, vol. 55, no. 4, pp. 609–619, 2017.

[14] S. García-de Villa, D. Casillas-Pérez, A. Jiménez-Martín, and J. J. García-Domínguez, "Inertial sensors for human motion analysis: A comprehensive review," IEEE Transactions on Instrumentation and Measurement, vol. 72, pp. 1–39, 2023.

[15] C. Gu, W. Lin, X. He, L. Zhang, and M. Zhang, "Imu-based motion capture system for rehabilitation applications: A systematic review," Biomimetic Intelligence and Robotics, vol. 3, no. 2, p. 100097, 2023.

[16] S. L. Delp, F. C. Anderson, A. S. Arnold, P. Loan, A. Habib, C. T. John, E. Guendelman, and D. G. Thelen, "Opensim: Open-source software to create and analyze dynamic simulations of movement," IEEE Transactions on Biomedical Engineering, vol. 54, no. 11, pp. 1940–1950, 2007.

[17] J. L. Hicks, T. K. Uchida, A. Seth, A. Rajagopal, and S. L. Delp, "Is my model good enough? best practices for verification and validation of musculoskeletal models and simulations of movement," Journal of Biomechanical Engineering, vol. 137, no. 2, p. 020905, 2015, oA status: green_published.

[18] A. Seth, J. L. Hicks, T. K. Uchida, A. Habib, C. L. Dembia, J. J. Dunne, C. F. Ong, M. S. Demers, A. Rajagopal, M. Millard, S. R. Hamner, E. M. Arnold, J. R. Yong, S. K. Lakshmikanth, M. A. Sherman, J. P. Ku, and S. L. Delp, "Opensim: Simulating musculoskeletal dynamics and neuromuscular control to study human and animal movement," PLOS Computational Biology, vol. 14, no. 7, p. e1006223, 2018, oA status: green_published.

[19] A. Rajagopal, C. L. Dembia, M. S. Demers, D. D. Delp, J. L. Hicks, and S. L. Delp, "Full-body musculoskeletal model for muscle-driven simulation of human gait," IEEE Transactions on Biomedical Engineering, vol. 63, no. 10, pp. 2068–2079, 2016.

[20] M. Al Borno, J. O'Day, V. Ibarra, J. Dunne, A. Seth, A. Habib, C. Ong, J. Hicks, S. Uhlrich, and S. Delp, "Opensense: An open-source toolbox for inertial-measurement-unit-based measurement of lower extremity kinematics over long durations," Journal of NeuroEngineering and Rehabilitation, vol. 19, no. 1, 2022.

[21] R. Krishnan, N. Björsell, E. M. Gutierrez-Farewik, and C. Smith, "A survey of human shoulder functional kinematic representations," Medical & Biological Engineering & Computing, vol. 57, no. 2, pp. 339–367, 2019, oA status: green_published.

[22] Z. Fang, S. Woodford, D. Senanayake, and D. Ackland, "Conversion of upper-limb inertial measurement unit data to joint angles: A systematic review," Sensors, vol. 23, no. 14, p. 6535, 2023.

[23] J. Lavikainen, P. Vartiainen, L. Stenroth, and P. A. Karjalainen, "Open-source software library for real-time inertial measurement unit data-based inverse kinematics using opensim," PeerJ, vol. 11, p. e15097, 2023.

[24] P. Slade, A. Habib, J. L. Hicks, and S. L. Delp, "An open-source and wearable system for measuring 3d human motion in real-time," IEEE Transactions on Biomedical Engineering, vol. 69, no. 2, pp. 678–688, 2022.

[25] M. Sharifi-Renani, M. H. Mahoor, and C. W. Clary, "Biomat: An open-source biomechanics multi-activity transformer for joint kinematic predictions using wearable sensors," Sensors, vol. 23, no. 13, p. 5778, 2023.

[26] M. Moniruzzaman, Z. Yin, M. S. B. Hossain, H. Choi, and Z. Guo, "Wearable motion capture: Reconstructing and predicting 3d human poses from wearable sensors," IEEE Journal of Biomedical and Health Informatics, vol. 27, no. 11, pp. 5345–5356, 2023.

Investigation of delays and connection stability in teleoperation via VR capabilities for remote exoskeleton-aided physiotherapy

1st Piotr Falkowski
Łukasiewicz Research Network – Industrial Research Institute for Automation and Measurements PIAP
Warsaw, Poland
0000-0002-9436-5566

2nd Krzysztof Zawalski
Łukasiewicz Research Network – Industrial Research Institute for Automation and Measurements PIAP
Warsaw, Poland
0009-0001-0366-836X

3rd Kajetan Jeznach
Łukasiewicz Research Network – Industrial Research Institute for Automation and Measurements PIAP
Warsaw, Poland
0009-0000-4794-9051

4th Jan Oleksiuk
Łukasiewicz Research Network – Industrial Research Institute for Automation and Measurements PIAP
Warsaw, Poland
0009-0005-4453-0024

5thMehmet Emin Aktan
Bartin University
Bartin, Türkiye
0000-0001-7058-8362

6th Vasfi Emre Ömürlü
3LS
Istanbul, Türkiye
0000-0001-8918-558X

7th Paweł Niedbalski
Elmiko Biosignals
Warsaw, Poland

8th Erhan Akdoğan
Yildiz University
Istanbul, Türkiye
0000-0003-1223-2725

9th Piotr Kołodziejski
Łukasiewicz Research Network – Industrial Research Institute for Automation and Measurements PIAP
Warsaw, Poland
0009-0008-8274-5378

Abstract—The research paper examines the challenges of remote control delays in exoskeleton-aided physiotherapy. It focuses on the implications of telerehabilitation requirements for safe treatment. As the global share of disabled and elderly people increases, the demand for effective teleoperated physiotherapy solutions rises, necessitating precise control over robotic systems. The study utilizes a mixed-methods approach to assess delays in communication between a rehabilitation exoskeleton and the control system's based on the digital twin in VR (virtual reality) components at different stages. Moreover, additional delays coming from distant operations are assessed. Key findings reveal that the average latency for joint control on shorter distances remains below 300 ms - considered acceptable for comfortable manual teleoperation. The delays between setting the device's configuration and reaching it by a physical exoskeleton differ for particular joints and depend mainly on the torque-to-moment of inertia ratio. The total communication cycle should not exceed 400 ms, which can be further reduced by using a 6G network in the future or ADS (Automation Device Specification) communication protocol instead of the database. Ultimately, the study provides a foundation for developing algorithms that can mitigate delays and improve the efficacy of telehealth solutions with physically supportive devices.

Index Terms—control accuracy, data transmission, digital twin, exoskeleton, robot-aided physiotherapy, teleoperation

I. Introduction

Rehabilitation robots can physically support physiotherapists and automate their work, also considering patients' safety [1]–[4]. Thanks to the mechatronic devices, repetitive exercising trajectories can be looped and realised with high accuracy. Moreover, with the technology of the digital twin connected to wearable sensors, a single therapist can supervise multiple devices operating patients simultaneously [5]. This is also possible for the ones in different locations [6]. Once programmed, exercising trajectories can be repeated for single users with no time limitations. However, with the progress of the patient or appearing pain and discomfort, it can be necessary to shift the recorded paths [7], [8]. To make it more immersive and ensure the movements ar smooth and accurate, the process can be recorded with the digital twin operated in virtual reality as within the conventional treatment [5]. However, this is a significant challenge, especially when it comes to telerehabilitation [5].

During conventional onsite physiotherapy, a specialist supports or resists the patient's movements with their hands, which enables two contact points. This process can be transferred to the robotic setup. However, with the end-effector type rehabilitation robots, only one contact point is possible, as they are underconstrained for

physical therapy [9]. On the contrary to the end-effector robots, exoskeletons enable precise mobilisation of every joint degree of freedom separately with the correlated drive's torques [10]. Moreover, they monitor every joint separately as well. For this reason, they are superior for individualised telerehabilitation with limited visual observation possibilities.

While a change of exercising trajectory is required, immersive technologies can be used to mimic conventional interventions in the cyber-physical environment [11]. The physiotherapist can modify the motion in the virtual world, which is then reflected by the rehabilitation robot in a distant location [12]. To increase the immersion, virtual reality (VR) based digital twins are constructed [5]. They visualise the real-world operation of the device, which is physically interfacing with the extremity, and give the opportunity to interact with the patient remotely by interacting with the model. With such a technology, specialists can perform telerehabilitation as if they were performing conventional therapy onsite - simply by dragging the virtual representation of the patient with their two hands [5].

However, this method raises novel challenges. The local infrastructure must enable a stable internet connection and meet the cybersecurity medical standards [5]. Moreover, rehabilitation systems' control algorithms must be prepared for signal losses and limitations correlated with establishing a secure network connection to the robotic system and ping related to the distance. Furthermore, even if no of the mentioned hazards appear, the distant control over robots brings delays, which can control less accurate trajectory following [13]. In extreme cases, the lags can restrain the possibility of almost real-time control.

The presented study aims to investigate delays and accuracy obtained with international teleoperation over a rehabilitation exoskeleton. The trials are intended to assess the impact of every component in the communication chain on the delays and find the bottleneck of the process. Additionally, alternative solutions to the cloud databases typically used in current trials, and mainly suitable for setting parameters of the treatment, not teleoperating the device [14], [15], are proposed. Moreover, the correlation between receiving the desired point and the following accuracy is also analysed. The results should be the basis for building algorithms that meet the safety criteria and analysing risks for teleoperation in robot-aided physiotherapy.

II. Methodology

A. Experimental setup

The teleoperation experiments were conducted remotely in Warsaw (Poland), without involving any human participants. Therefore, no significant lag between master (computer with the digital twin) and slave (exoskeleton) devices occurred. Further delay tests were performed at a distance between Istanbul (Türkiye) and Warsaw (Poland). The controlled object was the SmartEx-Twin exoskeleton attached to the test frame, as presented in Fig. 1. It has four controllable degrees of freedom (DOFs), driven by the mentioned servomotors, which correspond to the following motions of a human lower extremity:

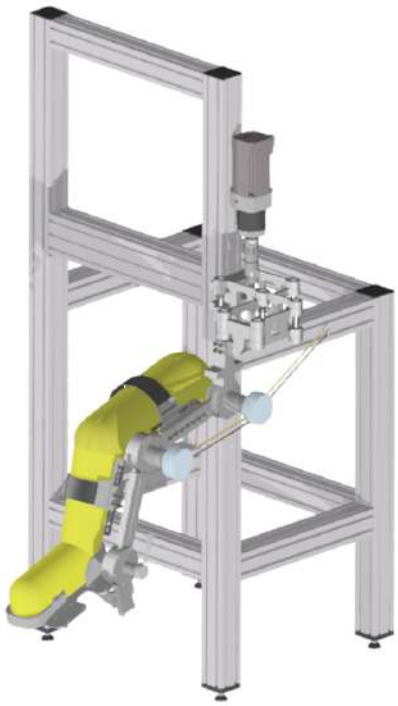


Fig. 1. Visual of the experimental setup with the SmartEx-Twin exoskeleton with the model of the extremity as attached during the planned physiotherapy (yellow model)

- DOF1: Hip abduction/adduction or internal/external rotation (dependent on the rotation of the DOF2; motor: Beckhoff AM8142-0NG0-0000; gearbox: Beckhoff AG2250-+PLE80-M02-32-0E1-F4);
- DOF2: Hip flexion/extension (motor: Maxon 607327; gearbox: Maxon 223089;
- DOF3: Knee flexion/extension (motor: Maxon 607327; gearbox: Maxon 223087);
- DOF4: Ankle flexion/extension (motor: Maxon 651613; gearbox: Maxon 166165).

These degrees of freedom are fully controllable with the DC motors with planetary gearboxes and integrated encoders via their dedicated position controllers. Their control signals include trajectory points which they follow. These data can be sent directly from the industrial computer (IPC), the master controller of the system, or the database server prepared within the robotic system. The trajectories in the database can be either modified manually by sending the point series from the computer database or registered with the interactive digital twin of the exoskeleton in virtual reality (see

TABLE I
Parameters of the exoskeleton DOFs (torque and velocity columns correspond to their peak values)

DOF	ROM min	ROM max	Torque	Velocity
1	-20 deg	40 deg	120 Nm	47 rpm
2	-30 deg	120 deg	31 Nm	38 rpm
3	0 deg	150 deg	21 Nm	64 rpm
4	-50 deg	20 deg	4.6 Nm	71 rpm

schematic communication flow in Fig. 2). A real-life possible implementation of the described system was visualised in the previous author's paper related to the topic [5].

Within the tests, the Exoskeleton is located in Poland and connected to the wireless network, simulating a possible home-like environment for telerehabilitation with the tested speed parameters as below:

- Latency: 24 ms;
- Download speed: 27.26 Mb/s;
- Upload speed: 33.13 Mb/s.

The DOFs of the exoskeleton have the available ranges of motion (ROMs), maximum torques of the corresponding motors and maximum rotation velocities of the corresponding motors, as presented in Table I.

B. Experimental routine

The experiments were run in three series of trials to determine three types of lags. These are:

1) Pre-loading the trajectory into the IPC (Beckhoff C6015) and controlling the drives simultaneously by setting the desired points into position controllers of the motors while measuring real-life rotations in every exoskeleton joint;
2) Downloading the trajectory point by point in real-time from the cloud database by the IPC and controlling the drives simultaneously by setting the desired points into position controllers of the motors while measuring real-life rotations in every exoskeleton joint;
3) Sending the trajectory point by point in real-time into the cloud database from the digital twin (visualized in VR and operatable by the physiotherapist) of the system, downloading the trajectory point by point in real-time from the cloud database by the IPC and controlling the drives simultaneously by setting the desired points into position controllers of the motors while measuring real-life rotations in every exoskeleton joint.

For every session, the realised joint trajectories were registered. Every time, the set desired trajectories were the same and consisted of continuous smooth trajectories within the whole range of a particular DOF with changing velocity. Based on the registered and desired trajectories, the delays and accuracy in realised trajectories were computed. The delays at the A-B loop were computed as the differences between the time of

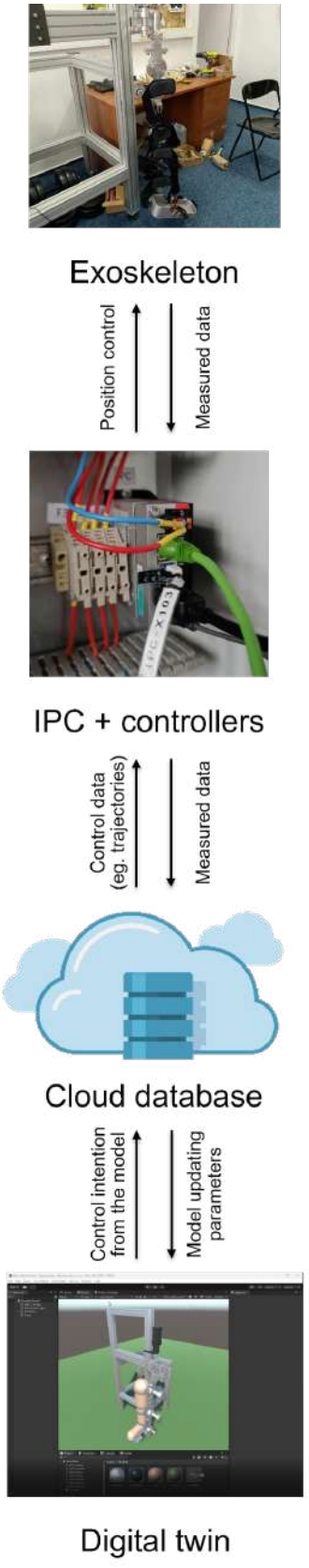


Fig. 2. Block graph of the remote control chain

sending the point by node A within the trajectory and visualizing reaching this point by node B, based on the smoothed registered trajectory. The inaccuracies values were compared based on the average square mean and the maximum absolute error.

Every trial session was repeated three times with sinusoidal trajectories of different periods (2-6 s) and amplitudes covering the whole range of joints (see Table I). The frequency of the data transfer was set to the maximum operatable by the bottleneck of the loop (typically cloud database, related to select/insert queries realisation times). The trajectories were registered at the different stages, including:

- data inserted by the digital twin to the database (Data Set 1),
- data selected by the IPC software from the database (Data Set 2).
- data recorded by the exoskeleton encoders (Data Set 3),
- data inserted to the database by the IPC software (Data Set 4),
- data selected from the database by the digital twin (Data Set 5).

An example of the registered interpolated signals is visualised in Fig. 3.

The teleoperation trials were followed with tests of additional delays for communication at the Poland-Türkiye distance. These included measuring digital twin-exoskeleton control commands execution times and assessing times for ping OS native program. Twenty series of 30-minute connection trials were carried out between Türkiye and Poland to measure delays and validate the stability of the connection.

The computer uploading data to the database directly or via the digital twin located in Turkiye was connected to the network with the tested speed parameters as below:

- Latency: 2 ms;
- Download speed: 32.9 Mb/s;
- Upload speed: 38.4 Mb/s.

III. Results and discussion

Results of the performed experiments are presented in Tables II and III. These include the times of transferring control commands from the digital twin or the database to the exoskeleton and the times for sending measurements from encoders back to the database and visualising them in the digital twin. Moreover, the times of that whole loop from control via the digital twin to visualising the desired position in the model and the loop from setting the desired position in the database to inserting information on reaching it were tested. Only flexion/extension motion was examined as being subject to gravity in passive therapy.

The latency was computed as the difference between setting a certain position and either reaching it by a physical component or getting the same value in the software. Therefore, it varies depending on the joint studied, especially while the physical object control is in the measuring cycle. The times differ mainly due to the ratios of maximum torques and velocities in the joints to the moments of inertia of the distal segments of the exoskeleton. As can be observed in Table II, the differences and times of transfer of the measured signals to the database (exoskeleton - cloud delay) are minimal. Furthermore, the differences in these can result from the order of measuring the angular positions in joints realised sequentially by IPC.

The ankle joint has the lowest delays overall, suggesting that this component is the least mechanically complex, as it is responsible for the last element in the kinematic chain. Hence, its moment of inertia is the smallest compared to the segments corresponding to medial joints. The knee joint has the highest latency in most cases, which may indicate problems with mechanical inaccuracies. That is proved in Table III, where degrees' inaccuracies are also the highest for the knee joint (0.606 deg) during teleoperation, which could be observed as visible vibrations during the experiment. Again, the lowest inaccuracies were measured for the ankle joint (0.188 deg).

The total time of the cycle from setting a position to the digital twin, through reaching it by a physical exoskeleton, to seeing it visualised in the digital twin does not exceed 211.6 ms for any joint (the highest value is for the knee joint). This does not include additional delays coming from the more distant connection, which is elaborated in the next part of the section. Therefore, compared to the values reached in the teleoperation of surgical devices (considered safe while remaining below 300 ms) [16], these are acceptable for manual control over rehabilitation devices.

Visibly, the motion inaccuracies result from the time differences between sending signals for setting a position and executing control commands based on these. These affect the smoothness of the motion process and result in small oscillations within the motion. Moreover, since the times from setting the position and obtaining it can differ for the joints, reaching the position is not possible with the accuracy of the industrial robots [17]. However, the obtained accuracy is outperforming the accuracy obtained for some rehabilitation robots accepted for practical application [18].

Fig. 3. Experimental set of registered experimental data for DOF 4

TABLE II
Average delays during teleoperation between the selected nodes of the system presented in Fig. 2 (digital twin - digital twin means a full loop from setting control via the digital twin to observing reaching the position via the digital twin; cloud - cloud means a loop from setting control via the cloud database to observing reaching the position via the cloud database)

Joint	Hip	Knee	Ankle
Digital twin - exoskeleton delay [ms]	133.14	156.95	98.94
Cloud - exoskeleton delay [ms]	74.69	98.51	40.50
Exoskeleton - cloud delay [ms]	13.66	7.09	8.65
Exoskeleton - digital twin delay [ms]	60.92	54.64	55.66
Cloud - cloud delay [ms]	88.34	105.60	49.14
Digital twin - digital twin delay [ms]	194.05	211.60	154.60

TABLE III
Average control inaccuracy during experimental trials

Joint	Hip	Knee	Ankle
Inaccuracy during PID control [deg]	0.006	0.014	0.008
Inaccuracy during teleoperation [deg]	0.462	0.606	0.188

Additional measurements of delays in communication at the Poland-Türkiye distance were performed in twenty 30-minute connection trials. The average ping value across all sessions is 51.29 ms, and the standard deviation is 1.85 ms. The device being pinged was an IPC computer (responsible for setting trajectories), and the pinging device was a laptop in Türkiye connected to the wireless network (as a representation of a digital twin device). Throughout the twenty sessions, 100% of the data packets sent were delivered, which proves the reliability and robustness of the created robotic system's network.

The observed delays are not significant and allow safe therapy, both from the patient and from a cybersecurity perspective. It can be expected that the total control process with the safe three-way handshake communication protocol should not exceed 400 ms, which is defined as acceptable but tiring for teleoperation [17]. Furthermore, continued development of the project and advancements in global technologies, such as 6G, could further improve these results, enhancing both system performance and safety.

IV. Conclusion

The performed investigation included short-distance teleoperation to assess delays occurring at the different communication stages, resulting from the performance of control systems and communication protocols. Moreover, the accuracy obtained with the exoskeleton controlled with this method was computed. These trials were followed by tests of additional delays coming from long-distance communication and assessment of such connection stability. These proved that telerehabilitation can be performed with the presented methodology. However, the delays can increase significantly while meeting safety requirements with multiple data exchange steps to send one position frame from the digital twin. For such applications, delays of up to one second can occur. With such, manual control over such a system is not possible, and the motion control system irregularity introduces vibrations.

Further investigation will focus on reducing delays and mitigating the effects of the minimum lags. Therefore, the presented trial will be repeated after the implementation of the ADS communication protocol to the system, which changes the way of communication between the IPC and the rest of the components in the network. This can improve the results by decreasing lags and providing comfortable control of the exoskeleton from Türkiye to Poland. Moreover, to ensure smoother movements, the position control will be changed into velocity control. Therefore, even the non-continued control signals will result in a continuous expected joint angle trajectory.

The presented methodology for controlling exoskeletons will be directly implemented into the SmartEx-Twin exoskeleton of the lower extremity. It will regularly operate based on pre-programmed motion routines with optimisation of treatment based on EMG and EEG tracking. However, in case of significantly improper activation of the muscular group regarding performed motions, the process will be stopped, and the physiotherapist will be able to overtake control remotely via a VR-based system. Thanks to this, the performed motion trajectories could be adjusted to the individual needs of a patient on the spot.

Nevertheless, the teleoperation methodology is applicable to other exoskeleton-based physiotherapy devices. Moreover, it can be also easily transferable to other medical devices with physical interactions with their users.

Acknowledgment

The paper is based on the results of the "Smart exoskeleton for remote rehabilitation with the digital twin technology" – SmartEx-Twin project, financed in 2023-2025 (265,800 EUR), in the scope of scientific research and development works by the National Center for Research and Development (funding programme 5^{th} Call for Proposals Poland-Turkey, contract number POLTUR5/2022/81/SmartEx-Twin/2023)."

References

[1] Piotr Falkowski, Krzysztof Zawalski, Jan Oleksiuk, Bazyli Leczkowski, Zbigniew Pilat, Mehmet Emin Aktan, Erhan Akdogan, Paweł Niedbalski, Vasfi Emre Omurlu, Michał Jarek, et al. Systematic review of mechanical designs of rehabilitation exoskeletons for lower-extremity. Archive of Mechanical Engineering, pages 621–644, 2024.

[2] Julia Wilk, Piotr Falkowski, and Tomasz Osiak. The overview of challenges in detecting patients' hazards during robot-aided remote home motor rehabilitation. Journal of Automation, Mobile Robotics and Intelligent Systems, 17(4):17–27, Mar. 2024.

[3] Piotr Falkowski. An optimisation problem for exoskeleton-aided functional rehabilitation of an upper extremity. In IOP Conference Series: Materials Science and Engineering, volume 1239, page 012012. IOP Publishing, 2022.

[4] Piotr Falkowski and Kajetan Jeznach. Simulation of a control method for active kinesiotherapy with an upper extremity rehabilitation exoskeleton without force sensor. 2023.

[5] Piotr Falkowski, Tomasz Osiak, Julia Wilk, Norbert Prokopiuk, Bazyli Leczkowski, Zbigniew Pilat, and Cezary Rzymkowski. Study on the applicability of digital twins for home remote motor rehabilitation. Sensors, 23(2):911, 2023.

[6] Deepti Aggarwal, Bernd Ploderer, Thuong Hoang, Frank Vetere, and Mark Bradford. Physiotherapy over a distance: The use of wearable technology for video consultations in hospital settings. ACM Transactions on Computing for Healthcare, 1(4):1–29, 2020.

[7] Matthew Buckthorpe, Antonio Tamisari, and Francesco Della Villa. A ten task-based progression in rehabilitation after acl reconstruction: from post-surgery to return to play–a clinical commentary. International journal of sports physical therapy, 15(4):611, 2020.

[8] Piotr Falkowski, Jan Oleksiuk, Kajetan Jeznach, and Mehmet Emin Aktan. Method of automatic biomedical signals interpretation for safety supervision and optimisation of the exoskeleton-aided physiotherapy of lower extremity. In Proceedings of the 2024 4th International Conference on Robotics and Control Engineering, pages 57–63, 2024.

[9] Jule Bessler, Gerdienke B Prange-Lasonder, Leendert Schaake, José F Saenz, Catherine Bidard, Irene Fassi, Marcello Valori, Aske Bach Lassen, and Jaap H Buurke. Safety assessment of rehabilitation robots: A review identifying safety skills and current knowledge gaps. Frontiers in Robotics and AI, 8:602878, 2021.

[10] Piotr Falkowski, Cezary Rzymkowski, and Zbigniew Pilat. Analysis of rehabilitation systems in regards to requirements towards remote home rehabilitation devices. Journal of Automation, Mobile Robotics and Intelligent Systems, pages 61–73, 2023.

[11] Johanna Pirker, Enrica Loria, Saeed Safikhani, Andreas Künz, and Sabrina Rosmann. Immersive virtual reality for virtual and digital twins: A literature review to identify state of the art and perspectives. In 2022 IEEE Conference on Virtual Reality and 3D User Interfaces Abstracts and Workshops (VRW), pages 114–115. IEEE, 2022.

[12] Li Gao, Li-Jie Zhao, Gui-Song Yang, and Chao-Jie Ma. A digital twin-driven trajectory tracking control method of a lower-limb exoskeleton. Control Engineering Practice, 127:105271, 2022.

[13] Chun-Ming Chang, Cheng-Hsin Hsu, Chih-Fan Hsu, and Kuan-Ta Chen. Performance measurements of virtual reality systems: Quantifying the timing and positioning accuracy. In Proceedings of the 24th ACM international conference on Multimedia, pages 655–659, 2016.

[14] Antonio Celesti, Aimé Lay-Ekuakille, Jiafu Wan, Maria Fazio, Fabrizio Celesti, Agata Romano, Placido Bramanti, and Massimo Villari. Information management in iot cloud-based telerehabilitation as a service for smart cities: Comparison of nosql approaches. Measurement, 151:107218, 2020.

[15] Hui-Jun Li and Ai-Guo Song. Architectural design of a cloud robotic system for upper-limb rehabilitation with multimodal interaction. Journal of Computer Science and Technology, 32:258–268, 2017.

[16] George Moustris, Costas Tzafestas, and Konstantinos Konstantinidis. A long distance telesurgical demonstration on robotic surgery phantoms over 5g. International journal of computer assisted radiology and surgery, 18(9):1577–1587, 2023.

[17] Zhibin Li, Shuai Li, and Xin Luo. An overview of calibration technology of industrial robots. IEEE/CAA Journal of Automatica Sinica, 8(1):23–36, 2021.

[18] Mingjie Dong, Yu Zhou, Jianfeng Li, Xi Rong, Wenpei Fan, Xiaodong Zhou, and Yuan Kong. State of the art in parallel ankle rehabilitation robot: a systematic review. Journal of NeuroEngineering and Rehabilitation, 18:1–15, 2021.

Position based camera-2D LiDAR fusion and person following for Mobile robots

Reinaldy Maslim
RRIS, NTU, Singapore
reinaldy.maslim@ntu.edu.sg

Manoj Ramanathan
RRIS, NTU, Singapore
mramanathan@ntu.edu.sg

Neha Priyadarshini Garg
RRIS, NTU, Singapore
priyadarshini.neha@gmail.com

Ang Wei Tech
RRIS, NTU, Singapore
wtang@ntu.edu.sg

***Abstract*—Person following is a crucial feature for mobile robots, with many using 2D LiDAR-based tracking due to its cost-effectiveness. However, such methods have limitations, such as tracking only from the front or back and being prone to false positives from environmental artifacts. More advanced tracking approaches combine position and appearance information. These can be classified into two categories: 1) position-based tracking, which fuses features from RGBD cameras and LiDARs, and 2) image-based tracking, which uses deep learning to match person appearances in images and then computes position via 3D de-projection. While position-based tracking has shown to be effective for short-term tracking, it has not been tested for person following application on a real robot. Image-based methods have been deployed on real robots but have not been compared to position-based tracking of target person for person following application, where consistent tracking without ID switching is crucial. This work presents a position-based target person tracking system tested on a real robot for person following application using deep learning for person detection, multi-sensor fusion (RGBD cameras and LiDAR), and UCMCtrack algorithm. We compare this with the SORT algorithms for image-based tracking. Our results show that position-based tracking is more suitable for person following, as image-based methods are prone to ID switching due to close proximity in images but distant in 3D space.**

***Index Terms*—Person tracking and following for mobile robots, Camera and LiDAR sensor fusion, Human Robot Interaction.**

I. Introduction

Person following is crucial for mobile robots working alongside humans, enabling applications like luggage-carrying and caregiver following wheelchair. A key challenge in person following is ensuring that the robot can reliably detect and track the target person in unstructured environments. Existing approaches such as [1]–[3] do back following using 2D lidar based person detection and tracking by detecting cross section of person's leg in 2D LiDAR scans. However, they are prone to a high rate of false positives, due to environmental artefacts such as chairs being mistaken for legs. Since, lidar scan area can be restricted for back following, 2D lidar based tracking is still effective.

However, for person following by a robotics wheelchair, in order to enable caregivers to maintain proper contact with the wheelchair user, ability to follow a person from front, side or back is important. Information in 2D lidar scans is not sufficient for reliable person detection and tracking in a wider field of view. For more robust tracking, it is important to use modalities like camera image which provide much more information about target person.

Existing approaches which utilize both lidar and camera sensors for person detection can be categorized into 2 main categories 1) position-based tracking 2) image-based tracking. Position-based tracking approaches [4]–[7] fuse inputs from different sensors to get an estimate of the position of the person in 3D space at every time step and then track the person using Extended Kalman Filter based trackers. Such approaches have been shown to work well for short term person tracking where motive is to avoid the tracked person and ID switching of tracked person after a short while is acceptable. For person following application, such approaches have not been tested on a real robot. Vision or image based tracking like SORT [8], [9] derive motion cues from image observations such as detection bounding boxes, their velocity profile, IOU etc to determine current state of tracked person. Even though they have shown good tracking performance on state-of-the-art datasets and have been deployed on real robots, they tend to restrict to a single camera and all computations are done in image space.

To best of our knowledge, no studies have compared position-based and image-based tracking for person following from front, side or back application where long term consistent tracking with less ID switching is crucial.

In this work, we implement a position-based tracking approach using deep learning for person detection, multi-sensor fusion and modified UCMCtrack [10] algorithm and deploy it on a real robotic wheelchair. Our sensor fusion approach integrates camera and LiDAR detections as probability distributions, considering both position (mean) and covariance matrix, which are essential for Kalman filter-based tracking. We extend the covariance matrix to polar coordinates, enabling fusion of detections from multiple sensors in 3D space, improving person detection and reducing false positives compared to 2D LiDAR tracking. Multiple cameras with overlapping fields of view are used to ensure better track initiation and to allow the user to be detected anywhere around the robot, alongside LiDAR.

Additionally, we modify UCMCtrack [10], which efficiently tracks objects by projecting detections onto the ground plane (obtained from image) as probability distributions and applying a Kalman filter with Mapped Mahalanobis Distance

Authors are from Rehabilitation Research Institute of Singapore (RRIS), Nanyang Technological University (NTU), Singapore

(MMD) for improved tracking accuracy. By combining UCMCtrack with our sensor fusion framework, we achieve robust human tracking in 3D space using multiple sensing modalities. To compare position-based tracking approach with image-based tracking, we also implement OCSORT [8] and Hybrid SORT [9] which use wheelchair robot's RGBD cameras. Our experimental results show that position-based tracking performs much better than baseline approaches in terms of consistent ID retention, association with fewer false positives.

The rest of the paper is organized as: Section II provides related work done in person tracking. Section III introduces our position based tracking framework including sensor fusion and tracking paradigms. In section IV, we show the experiments conducted and results in comparison to baseline approaches. In Section V, provide the conclusion and future works.

II. Related Work

2D LiDAR based person tracking is a very common approach in mobile robotics that aims to provide the position and velocity of the people being tracked. Detecting people's legs in laser scan points using feature based clustering [3] and deep learning [1], [2] have shown good performance, they depend on the training data used and do not generalize well in new environments and might require retraining, which is impractical for mobile robots. These methods also suffer from high false positive rate in crowded and cluttered environments as the amount of information in 2D LiDAR clusters is very limited.

To account for the lack of semantic information in LIDAR detections, vision based approaches are combined with them. [11] proposed a fusion approach for person following but it was not reliable in multiple people scenarios [3]. [4] evaluated a combination of 2D LiDAR, RGB-D person tracking, sensor fusion approaches in a crowded environment for guiding a person. [7] proposed multimodal person tracking algorithms in crowd with the aim of avoiding them. For assistive robots, [12], [13] proposed human perception and interaction frameworks based on leg detector [3] and RGB-D based upper body detections. But [12] had to add an extra thermal camera to handle the false positives. All these approaches focused on tracking persons around the robot to guide or avoid them and didn't focus on following a target person.

For small size robot platforms with a single monocular camera [14] or single RGB-Stereo-Depth camera [15] person following algorithms have been developed that assume the target is always in front of the camera. Similar to these approaches, we combine camera and 2D LiDAR to remove false positives and use both modalities for tracking continuously. Also, in contrast, we allow for the target person to be anywhere around the robot (not restricting to back following). For this purpose, we implement a sensor fusion algorithm that can account for multiple cameras and fuse detections of camera and LiDAR.

SORT based approaches [8], [9] are popular in multi-object tracking. Traditionally, these are vision-based motion model trackers that rely on cues extracted from 2D bounding boxes, their IOU etc for association. They are viable frameworks for combining 2D motion and camera's ReID appearance features as shown by [9]. But they perform motion tracking in a 2D image plane that restricts their ability to be used for multiple cameras and sensors. In contrast, we propose to use spatial information from LiDAR and combine them with camera person detections. For person tracking and following framework, we modify the UCMCtrack to work with final set of detections in a 3D space around the wheelchair.

III. Our Proposed Tracking Framework

A. Hardware Configuration

The proposed tracking framework is implemented, tested and verified in our wheelchair prototype shown in Figure 1. Our prototype includes 3 orbbec RGB-D cameras on the top to cover a field of view of close to 200 degrees in front of the wheelchair. Also, 3 LiDARs are included to provide laser scan of the environment around the wheelchair. All required modules such as mapping, navigation and localization etc are run in ROS framework. Given this wheelchair hardware, the aim is to develop a person/target tracking system that can track the person anywhere around the wheelchair robustly. The tracking framework aims to provide the position of the target with respect to a fixed world coordinate. It is necessary for the framework to provide a consistent tracking ID for the target being followed without losing him/her

.

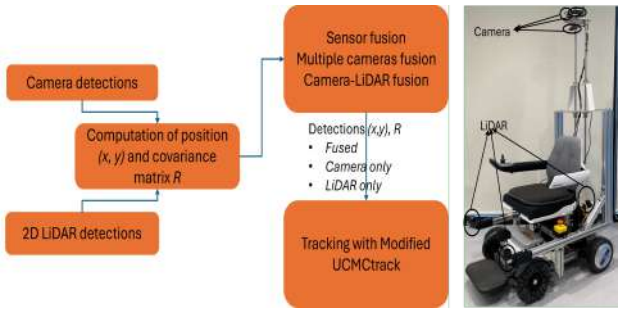


Fig. 1. (Left) Our approach computes the position and covariance matrix for both camera and 2D LiDAR detections, allowing the sensor fusion algorithm to decide whether to merge them. These fused detections are then input into a modified UCMCtrack for tracking and following a person in a wheelchair. (Right) Our Wheelchair prototype with multiple cameras and LiDARs

B. Overview of the proposed framework

As shown in Figure 1, the proposed framework could be divided into three components, namely, person detections from camera and LiDAR, sensor fusion to identify actual person and modified UCMCtrack that handles detections (fused and separate) to provide a consistent tracking ID for the people around the wheelchair.

For vision-based person detection, we use YOLO [16] to identify all persons in the cameras around the wheelchair, assigning each detection a bounding box and confidence score. Depth d_s is estimated using the bounding box coordinates in the depth frame, and the 3D world position is computed via

inverse projection using the centroid, depth, and the cameras' intrinsic and extrinsic parameters. The wheelchair's $base_link$ serves as the reference frame for the extrinsic matrix.

For LiDAR based person detection, we utilize the $leg_tracker$ package [3] which outputs the position $(x, y) \in \mathbb{R}^2$ for each detected pair of legs, a track ID and a confidence score for each detection. The position for each detection is again provided with respect to the wheelchair's $base_link$.

A key component of sensor fusion and tracking is the covariance matrix $R \in \mathbb{R}^{2\times2}$, which quantifies the uncertainty of each detection's position (x, y). Confidence scores from YOLO and $leg_tracker$ are retained for camera and LiDAR detections, respectively. Camera-camera detection association is first performed to match detections from neighboring cameras, followed by LiDAR-camera detection association.

Finally, all detections, which are represented in the form of position (x, y) in the bird's-eye view with an associated covariance matrix R defined with respect to the wheelchair's $base_link$ are provided as input to UCMCTrack. Here after, person tracking and following are performed relative to wheelchair's $base_link$. In the following subsections, we begin with the preliminaries related to representation of our fused person detections, computation of detection covariance matrices for each detections, proposed sensor fusion (camera-camera and camera-lidar), modifications within UCMCtrack.

C. Unified Representation for Person Detections

In our framework both camera and lidar detections are unified under a single representation $(x, y, R, conf, bbox : [bb_lt_x, bb_lt_y, w, h], cam_id, fuse_state_name, ID)$ that contains the position $(x, y) \in \mathbb{R}^2$ in 3D coordinates (z as height is omitted), covariance matrix $R \in \mathbb{R}^{2\times2}$, confidence score $conf \in (0, 1) \subset \mathbb{R}$, bounding box information: top left pixel coordinates $(bb_lt_x, bb_lt_y) \in \mathbb{Z}_{\geq0}$, width $w \in \mathbb{Z}_{\geq0}$, height $h \in \mathbb{Z}_{\geq0}$, camera ID $cam_id \in \mathbb{N}$ to distinguish between camera detections from different cameras, $fuse_state_name$ is the current fusion state of the detection e.g. *'camera', 'lidar', 'camera+lidar'*, and the track ID which is assigned once the detection has been through the tracker. Since the bounding box information and camera ID is applicable only to camera detections, for lidar detections, the bounding box information is filled with zeros i.e. $bbox : (0, 0, 0, 0)$ and cam_id with -1 i.e. cam_id: -1.

D. Computation of Detection Covariance Matrices

Covariances of detections are crucial for computing Mahalanobis distances which serve as the association metric employed in UCMCTrack. In the original UCMCtrack framework, the tracking is done in a single camera frame and define covariance matrices in terms of ground plane obtained from (u, v) pixel in 2D image space alone which might not be valid for the proposed use case, as we are dealing with both camera and 2D LiDAR detections.

A study on robot localization [17] observed that the pose distribution of a noisy two-wheeled robot moving in a plane follows a "banana-shaped" distribution, which is non-Gaussian in Cartesian coordinates. Most algorithms assume a Gaussian distribution in Cartesian space, leading to inconsistencies as uncertainty increases. To address this, [17] suggested using exponential coordinates (a more robust form of polar coordinates) for Gaussian fusion. Inspired by this approach, we apply a similar strategy to handle uncertainty in a person's position. For a generalized covariance matrix definition, we define a Gaussian distribution in polar coordinates that allows us to deal with both types of detection, compare their positions and fuse them if needed. Also this enables us to track in 3D space around the wheelchair.

We define the wheelchair coordinate axes $base_link$ (x', y'), with basis vectors $\hat{i}'$ and $\hat{j}'$, as the standard coordinate Cartesian coordinates (x, y), with basis vectors $\hat{i}$ and $\hat{j}$, rotated by 90^o counter-clockwise (CCW) around the z-axis. Here, the z-axis is defined as the direction perpendicular to the (x, y) plane in $\mathbb{R}^2$, corresponding to the positive z direction in a right-handed coordinate system.

Also polar coordinates (r, ϕ), with basis vectors $\hat{r}$ and $\hat{z}$ where $r \in \mathbb{R}_{\geq0}$ is the radial distance and the angle $\phi \in [-\pi, \pi] \subset \mathbb{R}$ is the angle measured from x' axis to the position vector $r\hat{r} = x'\hat{i}' + y'\hat{j}'$ positive CCW (following the right hand rule).

The covariance matrix of the Gaussian distribution can then be defined as:

$$\Sigma(r, \phi) = \begin{bmatrix} \sigma_{rr} & \sigma_{r\phi} \\ \sigma_{\phi r} & \sigma_{\phi\phi} \end{bmatrix} \in \mathbb{R}^{2\times2}$$

where

$$\sigma_{rr} = \frac{k_r}{r^2} \quad \sigma_{\phi\phi} = \frac{k_\phi^2}{r^2} \text{and} \quad \sigma_{r\phi} = \sigma_{\phi r} = \rho(\phi)\frac{\sqrt{k_r}k_\phi}{r^2}$$

$\sigma_{r\phi} = \sigma_{\phi r}$ since covariance matrices are required to be symmetric and positive definite. $k_r \in \mathbb{R}_{>0}$ and $k_\phi \in \mathbb{R}_{>0}$ are the scaling factors that affects how the radial distance r and angle ϕ are related. $\rho(\phi)$ is the correlation parameter that adjusts the covariance between variables r and ϕ.

To satisfy positive definiteness, the determinant of the covariance matrix should be greater than zero i.e. $\det\Sigma(r, \phi) > 0$. The condition,

$$\det\Sigma(r, \phi) = (1 - \rho(\phi)^2)\frac{k_r k_\phi^2}{r^4} > 0 \Rightarrow -1 < \rho(\phi) < 1$$

follows. Choosing $\rho(\phi) = \rho_0 \cos(2\phi) \in (-1, 1) \subset \mathbb{R}$, where ρ_0 being the correlation coefficient, $-1 < \rho_0 < 1$, and noting that $\cos(2\phi)$ is symmetric along the range $[-\pi, \pi]$, making it a suitable choice in consideration of the problem's geometry.

For our experiments ρ_0 is chosen to be 0.5, k_r is chosen to be 0.05 for lidar detections and 0.07 for camera detections and k_ϕ is chosen to be 0.25 for both camera and lidar detections.

As mentioned in subsection III-C, each of the detection contains position (x, y) in 3D coordinates as z (height) is omitted, which is equivalent to 2D tracking. Because tracking is done in the 2-dimensional Euclidean space $\mathbb{R}^2$, the covariance matrix should be transformed to the standard Cartesian coordinates (x, y). Given the relationship

$$x' = y, \quad y' = -x \quad \Rightarrow \quad x = -y', \quad y = x'$$

and

$$x' = r\cos\phi, \quad y' = r\sin\phi$$

the Jacobian matrix J of the transformation $(r, \phi) \rightarrow (x', y') \rightarrow (x, y)$ is given by

$$J_{x,y}(r,\phi) = J_{x,y}(x',y')J_{x',y'}(r,\phi)$$

$$= \begin{bmatrix} \frac{\partial x}{\partial x'} & \frac{\partial x}{\partial y'} \\ \frac{\partial y}{\partial x'} & \frac{\partial y}{\partial y'} \end{bmatrix} \begin{bmatrix} \frac{\partial x'}{\partial r} & \frac{\partial x'}{\partial \phi} \\ \frac{\partial y'}{\partial r} & \frac{\partial y'}{\partial \phi} \end{bmatrix} = \begin{bmatrix} -\sin\phi & -r\cos\phi \\ \cos\phi & -r\sin\phi \end{bmatrix}$$

Thus the covariance matrix $\Sigma(x, y)$ can be computed as:

$$\Sigma(x,y) = J_{x,y}(r,\phi)\Sigma(r,\phi)J_{x,y}(r,\phi)^T$$

this expression can then be calculated numerically by substituting, $r = \sqrt{x'^2 + y'^2}$ and $\phi = \text{atan2}(y', x')$

Therefore, each detection can be written as $\det \sim \mathcal{N}((x', y'), R)$, where (x', y') represents the mean and $R = \Sigma(x, y)$ denotes the covariance matrix. It is worth noting that $\Sigma(x, y)$ and $\Sigma(x', y')$ are related by a rotation about the z-axis. Specifically, $\Sigma(x, y)$ can be obtained by applying a $+\frac{\pi}{2}$ rotation to $\Sigma(x', y')$ and vice versa, $\Sigma(x', y')$ can be obtained by applying a $-\frac{\pi}{2}$ rotation to $\Sigma(x, y)$.

E. Sensor Fusion Algorithm

In this section, we brief on how we associate and merge camera-camera, camera-lidar detections using the position and covariance matrices.

1) Association of Camera-Camera Detections: From the hardware shown in Figure 1, we can clearly see that there are multiple cameras with overlapping FOV between neighboring cameras. First, we aim to associate detections of the same person, who might appear in two cameras due to the overlapping FOVs. We consider a general setup of $n \in \mathbb{N}$ cameras, $n > 1$ arranged radially facing outwards at distinct angles $\phi_k \in (-\pi, \pi)$, where k is the camera number, $k \in \{1, 2, \ldots, n\}$ and ϕ is the angle between the x'-axis and the vector resulting from the projection of camera optical axis z_c onto the 2D plane $\mathbb{R}^2$.

Now, define the sequence S of ordered pairs of consecutive camera IDs as follows:

$$S = \{(l, l+1) | l \in \{1, 2, \ldots, n-1\}\}$$

Each pair $(l, l+1) \in S$ represents the ordered pair of consecutive camera IDs in sorted order of angles ϕ of the corresponding cameras. The sequence S captures the adjacency of camera IDs in decreasing order of their angles ϕ.

The association process involves traversing the sequence S, where for each pair $(l, l+1)$, detections from camera ID l are matched with those from camera ID $l+1$ based on the position of the detection. For $n > 2$, each element $l \in \{2, 3, \ldots, n-1\}$ appears twice in S, once in $(l-1, l)$ and once in $(l, l+1)$. Thus, care must be taken when associating detections between consecutive camera IDs, as unmatched detections from $(l-1, l)$ may be matched with detections from $(l, l+1)$.

The distance metric used to construct the association cost matrix for detections between two adjacent cameras, det_a and det_b, is the Euclidean distance, $d_{\text{euclidean}}$:

$$d_{\text{euclidean}}(\text{det}_a, \text{det}_b) = \|\mu_a - \mu_b\| = \sqrt{(x_a - x_b)^2 + (y_a - y_b)^2}$$

, where (x_a, y_a) refers to a detection with $cam_id = l$ and (x_b, y_b) refers another detection with $cam_id = l + 1$. It is important to note that not all detections present in the camera pair are to be included in the association process but only detections with bounding boxes intersecting the left *or* right border of the camera image frame in the camera pair $(l, l+1)$.

2) Merging of Camera-Camera Detections: Merging of two camera detections, det_a and det_b, can be done by

$$\mu_{\text{fused}} = \left(\frac{x_a + x_b}{2}, \frac{y_a + y_b}{2}\right), \Sigma_{\text{fused}} = (R_a^{-1} + R_b^{-1})^{-1}$$

where μ_{fused} geometrically means taking the midpoint of the line segment connecting μ_a and μ_b as the combined mean. While Σ_{fused} is the covariance of the pdf resulting from the multiplication of two Gaussian pdfs.

3) Association of Camera-Lidar Detections: The resulting detections from the association of camera-camera detections (Section III-E1 and III-E2) are then used for camera-lidar detections association.

The association cost matrix for assignments of camera-lidar detections are constructed based on the expected squared distance between two Gaussian distributions. Given two Gaussian pdfs, one of camera detection $\text{det}_c \sim \mathcal{N}((x_c, y_c), R_c)$ and the other of lidar detection $\text{det}_d \sim \mathcal{N}((x_d, y_d), R_d)$ that are independent, the expected squared distance is given by

$$\begin{aligned} d_{\text{squared-distance}}(\text{det}_c, \text{det}_d) &= E(\|\text{det}_c - \text{det}_d\|^2) \\ &= \|\mu_c - \mu_d\|^2 + \text{Tr}(\Sigma_c + \Sigma_d) \\ &= \|(x_c, y_c) - (x_d, y_d)\|^2 + \text{Tr}(R_c + R_d) \end{aligned}$$

where the first term is the squared distance between the means and the second term is the trace of the sum of the covariance matrices.

4) Merging of Camera-Lidar Detections: Merging of camera and lidar detections can be performed either by using inverse-variance weighting of the pdfs of the camera and LiDAR, where the weights are modulated by its respective confidence scores, or by relying solely on the LiDAR pdf. Based on qualitative observations from our experiments, no significant difference were observed between the two approaches. Therefore, we choose to use only the LiDAR measurement, as it is also known to have higher positional accuracy compared to the camera.

F. Modified UCMCtrack

Our tracking framework utilizes fused *'camera + lidar'* as well as separate *'camera'* and *'lidar'* detections provided by sensor fusion that follow the representation in section III-C. Each detection comprises position x, y in 3D space around the wheelchair and covariance matrix R which UCMCtrack uses to compute MMD. Specifically, we have made changes in Initialization of tracks and track management.

1) Initialization of Tracks: In our implementation of UCM-CTrack, a detection is only initialized as a track when it is in the fused state or *'camera+lidar'*. This helps us to reduce the number of false positive tracks and contribute to better tracking performance in office environment where there is an abundant number of chairs. After initialization, while updating the tracks, we don't consider the $fuse_state_name$ of the detection. This is because when the person goes out of the camera frames or LiDAR range we still need to track them.

2) Track Management: Track management is an auxiliary tracker that maintains an internal list of Kalman tracks with IDs that of the output from our implementation of UCMC-Track. Its main purpose is to smoothen jaggy outputs from the tracker upstream, to manage tracks and transforming the known relative position and heading direction of the target to a fixed world coordinate for person following. The proposed method was implemented with our wheelchair prototype for successful target following.

IV. Experimental Results and Discussion

A. Dataset

For testing the efficiency of our position-based tracking framework in mobile robots, it is necessary to have a dataset that contains both multiple cameras and 2D LiDAR modalities. Also, it is required to have ground truth location of people around and actual target whom the mobile robot is following. Existing datasets [4], [6] provide multimodal data and ground truth people tracks but there is no target person that the robot follows from start to end. They were created for testing the efficiency of person tracking and for the robot to learn how to react in crowded scenarios. Existing person following dataset [15] provide only stereo depth camera images without any LiDAR information and couldn't be considered for our application. To the best of our knowledge, we couldn't find a dataset with camera, LiDAR modalities that also includes a target person. Thus, we collected our own dataset with multiple cameras and 2D LiDAR in our wheelchair prototype. For data collection, we collected rosbags with the required topics. The rosbags were recorded with various conditions like one person, multiple person and actual crowded scenarios in a university environment. The groundtruth bounding boxes were marked in each of the camera frames. During data collection, the wheelchair was manually controlled by an operator (using joystick) to follow the actual target. This was to ensure that our dataset is able to capture the person following mobile robot use case. A total $382.005596s$ of data was recorded.

B. Evaluation Metric

We employ the popular HOTA metrics [18] to evaluate the effectiveness of the proposed method. Whenever a person is available in the camera frame, the bounding box is annotated manually. HOTA [18] introduced a set of performance metrics that provided better understanding of tracker behavior in the Multi object Tracking (MOT) field. Using the metric, we can show the effectiveness of the tracking ID association and better ID retention. Specifically, we look at DetA (indicates detection performance), overall HOTA and AssA (indicates ID retention and association, important to person following use case). Also, we use false positive rate to compare our method and LiDAR-only tracking in terms of false positives.

TABLE I
Comparison of the HOTA metrics between proposed and baseline methods

Method	HOTA	DetA	AssA	False Positive Tracks
Our Method	74.753	75.537	73.977	0
LiDAR-only tracking [3]	73.643	76.039	71.323	23
OCSort	45.012	68.23	29.778	-
HybridSORT	44.566	47.765	42.787	-

C. Baseline

For baseline, we consider image based SORT approaches [8], [9] and position based LiDAR-only tracking [3]. Since, [3] deals only with LiDAR scan, we can't be directly estimate HOTA. Therefore, we perform sensor fusion with camera using the proposed method but instead of using the tracking ID provided by our method, we use the tracking ID provided by [3]. This way we would be able to test the ID association and retention capabilities of the baseline. For false positives, we just consider the tracks detected by the leg tracker [3] without any sensor fusion. We aim to provide rigorous evaluation of these approaches in person following application.

D. Results and Discussion

1) Better Tracking Performance: Table I shows that our method achieves better person tracking using both camera and 2D LiDAR. The HOTA metric [18], which evaluates trajectory alignment and penalizes mismatches, indicates superior performance compared to image-based SORT tracking approaches [8], [9]. Unlike SORT, which struggles with ID switching in crowded scenarios due to close proximity in image space, our method tracks in 3D space around the wheelchair, leading to better ID retention and association. Compared to LiDAR-only tracking [3], our method achieves higher HOTA and AssA scores, demonstrating improved ID retention while maintaining a comparable DetA. While LiDAR-only tracking reliably detects a single person despite false positives, it suffers from ID switching and target loss in crowded environments. As shown in Figure 2, our method significantly reduces ID switching, ensuring better target tracking even in dense crowds

2) Lower false positives: To evaluate false positives, we used rosbags with a single person walking in front of the wheelchair, ensuring only one valid track (for groundtruth). False positives were determined by counting extra initiated tracks. Table I shows our position-based tracking method eliminated false positives by leveraging the camera's semantic information, whereas LiDAR-only tracking detected 23 false positives due to environmental artifacts in the LiDAR scan (See Figure 3).

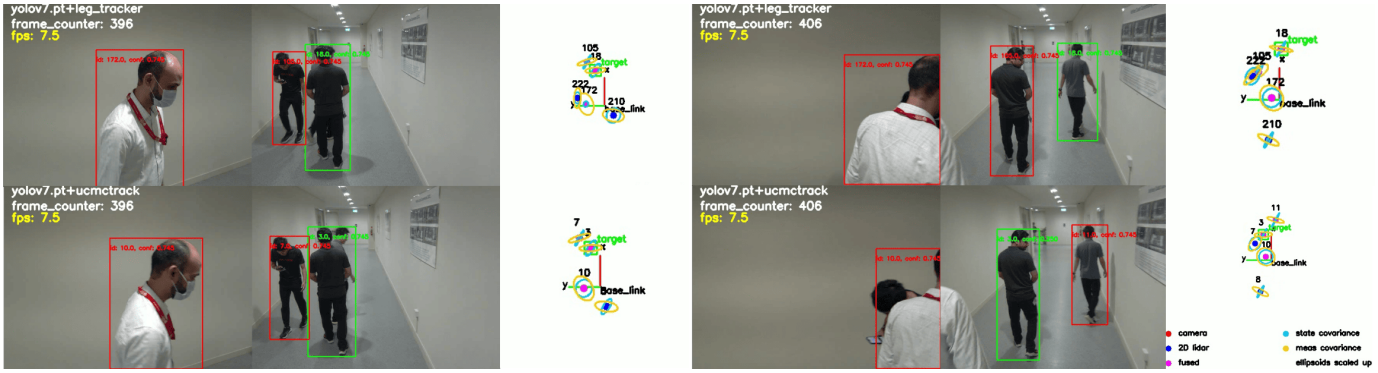


Fig. 2. Output of the target (in green) being followed using LiDAR-only tracking (top row) and proposed method (bottom row). The ID switches to another person with baseline where as the proposed method is still able track the original target with same ID.

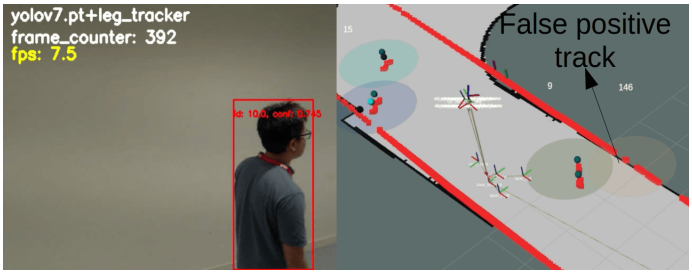


Fig. 3. False positive track detected on the wall with an assigned track ID (in white). LiDAR-only tracking detects a person's leg but also a false positive track on the wall as the pattern is very similar to legs.

V. Conclusion and Future Work

We develop a position-based person tracking framework for wheelchair robots, featuring a sensor fusion algorithm that incorporates position and covariance matrix information to integrate multiple cameras and LiDARs. By modifying the UCMCtrack framework to handle *'camera', 'lidar', 'fused'* detections, we enable person following around the wheelchair. Experimental results show position-based tracking performs better than image-based tracking for person-following applications. Also, we plan to test and collect a more diverse and bigger dataset in the future.

Acknowledgment

This research is supported by A*STAR under the National Robotics Programme (NRP) BAU grant, Assistive Robotics Programme (Award No: M22NBK0074). Also, Thanks to Mr. Neelkanth Jha and Mr. Cheng Yap for developing the wheelchair prototype and helping with testing.

References

[1] D. Jia, M. Steinweg, A. Hermans, and B. Leibe, "Self-Supervised Person Detection in 2D Range Data using a Calibrated Camera," in *ICRA*, 2021.

[2] D. Jia, A. Hermans, and B. Leibe, "DR-SPAAM: A Spatial-Attention and Auto-regressive Model for Person Detection in 2D Range Data," in *IROS*, 2020.

[3] A. Leigh, J. Pineau, N. Olmedo, and H. Zhang, "Person tracking and following with 2d laser scanners," in *ICRA*, 2015.

[4] T. Linder, S. Breuers, B. Leibe, and K. Arras, "On multi-modal people tracking from mobile platforms in very crowded and dynamic environments," in *ICRA*, 05 2016, pp. 5512–5519.

[5] T. Linder and K. O. Arras, *People Detection, Tracking and Visualization Using ROS on a Mobile Service Robot*. Cham: Springer International Publishing, 2016, pp. 187–213. [Online]. Available: https://doi.org/10.1007/978-3-319-26054-9_8

[6] D. Paez-Granados, Y. He, D. Gonon, L. Huber, and A. Billard, "3d point cloud and rgbd of pedestrians in robot crowd navigation: detection and tracking," 2021. [Online]. Available: https://dx.doi.org/10.21227/ak77-d722

[7] D. Gonon, D. Paez Granados, and A. Billard, "Reactive navigation in crowds for non-holonomic robots with convex bounding shape," *IEEE Robotics and Automation Letters*, vol. PP, pp. 1–1, 03 2021.

[8] J. Cao, J. Pang, X. Weng, R. Khirodkar, and K. Kitani, "Observation-centric sort: Rethinking sort for robust multi-object tracking," in *CVPR*, 2023.

[9] M. Yang, G. Han, B. Yan, W. Zhang, J. Qi, H. Lu, and D. Wang, "Hybrid-sort: Weak cues matter for online multi-object tracking," *arXiv preprint arXiv:2308.00783*, 2023.

[10] K. Yi, K. Luo, X. Luo, J. Huang, H. Wu, R. Hu, and W. Hao, "UCMCTrack: Multi-Object Tracking with Uniform Camera Motion Compensation," *Proc. of the AAAI Conf. on Artificial Intelligence*, vol. 38, no. 7, Mar. 2024.

[11] A. Cosgun, D. A. Florencio, and H. I. Christensen, "Autonomous person following for telepresence robots," in *ICRA*, 2013.

[12] S. Coşar, M. Fernández-Carmona, R. Agrigoroaie, J. Pages, F. Ferland, F. Zhao, S. Yue, N. Bellotto, and A. Tapus, "Enrichme: Perception and interaction of an assistive robot for the elderly at home," *International Journal of Social Robotics*, vol. 12, 07 2020.

[13] H. Kivrak, F. Cakmak, H. Kose, and S. Yavuz, "Social navigation framework for assistive robots in human inhabited unknown environments," *Engineering Science and Technology, an International Journal*, vol. 24, no. 2, pp. 284–298, 2021. [Online]. Available: https://www.sciencedirect.com/science/article/pii/S2215098620308727

[14] H. Ye, J. Zhao, Y. Pan, W. Chen, L. He, and H. Zhang, "Robot person following under partial occlusion," in *ICRA*. IEEE, 2023.

[15] B. X. Chen, R. Sahdev, and J. K. Tsotsos, "Integrating stereo vision with a cnn tracker for a person-following robot," in *Computer Vision Systems*, M. Liu, H. Chen, and M. Vincze, Eds. Cham: Springer International Publishing, 2017, pp. 300–313.

[16] C.-Y. Wang, A. Bochkovskiy, and H.-Y. M. Liao, "YOLOv7: Trainable bag-of-freebies sets new state-of-the-art for real-time object detectors," in *CVPR*, 2023.

[17] A. W. Long, K. C. Wolfe, M. Mashner, and G. S. Chirikjian, "The banana distribution is gaussian: A localization study with exponential coordinates," in *RSS*, 2012. [Online]. Available: https://api.semanticscholar.org/CorpusID:7470502

[18] J. Luiten, A. Osep, P. Dendorfer, P. Torr, A. Geiger, L. Leal-Taixé, and B. Leibe, "Hota: A higher order metric for evaluating multi-object tracking," *International Journal of Computer Vision*, vol. 129, no. 2, p. 548–578, Oct. 2020. [Online]. Available: http://dx.doi.org/10.1007/s11263-020-01375-2

Exploring Synergy Between Tactile Perception and Arm Usage

Yuhe Chen, Jonathan van Zanten, Michaël Wiertlewski, Arno Stienen[1]

***Abstract*—Stroke causes severe tactile deficiencies which affects motor control when grasping and lifting objects. Understanding the fundamental neural disorders associated with tactile deficits is crucial to developing rehabilitation and treatment plans correspondingly. Earlier studies have studied the dynamics between finger grasping behavior and arm muscle activation in stroke patients. However, the exact neuromuscular synergy of tactile perception and arm usage is left unexplored. Here we designed a comprehensive experiment platform and tested the potential synergy on 12 healthy young adults, serving as a control group to establish a foundation for future studies on stroke patients. The experimental platform consists of a lever arm on which torques can be applied to the subject's arm. The end effector is equipped with a special ultrasonic friction modulation plate that can reduce the apparent friction of the object by up to 63%, simulating real-world grasping tasks in a controlled setting. The experiments were performed under varying conditions of friction and arm usage. Results indicate significant effects of tactile stimulation on grasping force adaptation ($p < 0.05$ in 8 of 12 experimental conditions). In the meantime, arm usage did not show a significant synergy with tactile perception ($p = 0.44$ in grasping force adaptation amplitude, and $p = 0.73$ in reflex delay). These findings demonstrate that the experimental platform can provide insights into human tactile behaviors, which is critical for studying tactile sensory and motor control synergy. The results will lay the groundwork for future research on underlying pathologies and rehabilitation strategies for stroke patients.**

***Index Terms*—tactile perception, ultrasonic friction modulation, stroke, synergy**

I. Introduction

STROKE is the second-leading cause of death and the third-leading cause of disability and death combined, as a study has revealed in 2021 [1]. More than 50% stroke patients reported perceptual disorders [2], including deficiencies in somatosensation [3] and proprioception [4]. These deficiencies cause stress, loss of daily task functions, and reduction of quality of life among stroke patients [5]. Especially, impairment of tactile perception has a detrimental impact since patients have reported difficulty in sensing touch, pressure, and temperature, discriminating textures, and recognizing objects through tactile senses [6], as well as reduced or altered pain sensations [7]. To develop targeted treatment and rehabilitation strategies, it is crucial to understand the fundamental neural discrepancies associated with tactile deficits.

Tactile perception plays a fundamental role in manipulation tasks. Tasks as mundane as holding a cup or writing with a pen become tedious in the absence of touch. This is especially true when estimating the grip force necessary to securely grasp an object [8]. Stroke patients may use abnormally high forces to ensure the security of grasping, and studies have suggested that during object-lifting tasks, their grasping force fluctuates with the acceleration and deceleration of the object [9]. Accelerations and decelerations involve extensive activation of arm muscles, and the fluctuations of grasping force that occur at these moments are likely to be caused by tactile sensibility deficits [9]. Their correlation implies a neuromuscular synergy between tactile perception and arm muscle activation.

Despite increasing knowledge of the effect of friction on grasping [10], the effect of stroke on tactile functions or its effect on grasping is understudied [11]. Specifically, few studies have explored the dynamics of stroke patients' tactile perception deficits, and how they correlate with other neurological effects in complex tasks that involve the coordination of multiple neural inputs and outputs.

The absence of detailed knowledge of the impact of impaired touch on grasp is partially due to the difficulty of controlling tactile stimulation. Traditionally, changing tactile interaction is done by changing surface materials or using different gratings [12]. This method is tedious and it is often difficult to establish a general standard. But more importantly, it is impossible to study real-time responses to tactile stimulations.

In recent years, however, a new class of haptic devices, called surface haptics have emerged. These devices can modulate friction with the bare finger directly either via electroadhesive effect or using ultrasonic vibration, see [13] for a comprehensive review. Contrary to electroadhesive devices, ultrasonic friction modulation can change the coefficient of friction on a wide dynamic range. It works by physically reducing the friction between the human finger and the surface [14] and the friction coefficient can be modulated from about 1 all the way to 0 [15]. The wide dynamics range makes it ideal for simulating real-world dynamics of grasping tasks.

The ultrasonic method was first introduced in 1995 [16]. Its functional mechanism to reduce friction involves the squeeze film effect in which ultrasonic waves create an overpressure between the finger and the vibrating plate. The air between the skin and the plate is squeezed into a thin film, which slightly levitates the skin and reduces the number of asperities in contact, thus lowering friction [14, 15, 17].

We leverage ultrasonic friction modulation to study how human participants grasp objects. This marks our first attempt to understand whether stroke patients, suffering from

All authors are affiliated with Technical University of Delft. Corresponding author[1] email: a.h.a.stienen@tudelft.nl.

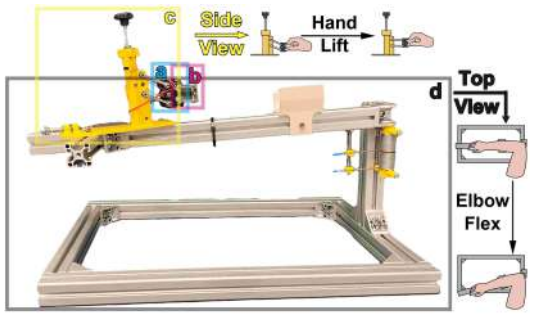


Fig. 1. The full assembly of the experimental setup. a) The grasping object. b) The friction-modulation plates. c) The constant force system. d) The elbow support.

neurological disorders, experience a synergy between arm usage and tactile perception. This pilot study, conducted on healthy subjects as a control group, serves as a preliminary step to develop an experimental platform that can be used for future studies involving stroke patients. The results of this study, while not directly conducted with stroke patients, will provide critical baseline data for understanding how tactile perception and arm usage may interact in individuals with stroke-related deficits.

II. Materials and Methods

A. Goal

The goal of this experiment is to mimic a casual lifting task: a person grabs an object with a certain weight, lifts it slightly with their hand and wrist, with or without activating arm muscles, and holds it for a short time. The person does these all without special focus on the task itself, to reflect real-life behaviors, where people also do not pay special attention when casually grasping objects. Specifically in this experiment, the friction level of the object is changed during a trial. The subject's grasping force and the object's angle are recorded and analyzed to evaluate the response to tactile stimulation.

B. Setup

The experiment setup (Fig. 1) consists of four distinct sections:

1) Grasping Object: The grasping object (Fig. 1a) mimics a general object to be gripped in everyday life. It is able to record the subject's grasping force with two load cells. The subjects' active grasping force represents how much force they think they need to secure the grasp, reflecting how slippery they perceive the object at hand to be. The width of the object is 50 mm, and the effective grasping area is 34 mm $\times$ 25.5 mm.

2) Friction Modulation Plates: Two glass-based friction modulation plates (Fig. 1b) provide tactile stimulation on both sides of the grasping object. When activated, the actuators vibrate the plates to an ultrasonic frequency (around 23 kHz), causing a 6.21 μm and a 5.72 μm displacement amplitude on the plates' centers respectively. This ultrasonic vibration provides the squeeze-film effect, greatly reducing the plates' surface friction.

3) Constant Force System: The constant force system (Fig. 1c) uses a pulley system and an extension spring to provide a constant vertical force on the grasping object. This system is designed to provide an adjustable vertical force from - 5 N to + 5 N, adjusted by turning the black knob on the lead screw.

4) Elbow Support: The elbow support (Fig. 1d) has a rotational stiffness. When the subject flexes their elbow to an angle, they have to use their arm muscles to counter this stiffness, thus this structure can mimic the use of the arm in the object-grasping task. When the subject is instructed to flex their elbow to a fixed angle (around 30 degrees), they will need to apply approximately 4.14 N·m of torque to counter this stiffness.

C. Controls and Data Acquisitions

Grasping force from the load cells and the object's angle from an angular sensor are gathered at 100 Hz. A Labview program visualizes the data in real time and automatically executes the progressions of each trial.

D. Experimental Protocols

The main experiment studies three controlled variables: the net vertical force of the object (-0.5 N, 0 N, 0.5 N), flexion of the elbow (yes, no), and friction perturbation (high to low, low to high). Before a trial, the constant force system is adjusted to the destination force level, and the subject is asked to relax or flex their elbow to the fixed angle. Note that when the vertical force of the object is 0 N, there is no actual need to change the grasping force when there is a change in friction. This group acts as a "placebo" control to account for factors like vibration, heat, and habitual behavior, excluding the effects of friction change on the results.

The participant task includes three program-controlled phases (Fig. 2):

1) Lifting phase. This phase has no time limit. The initial friction state is applied before the start of this phase. During this phase, the subject is asked to use their hand and wrist to move the object from its beginning position to the middle (see Fig. 2), using an optimal grasp effort. The optimal effort means applying the minimal grasping force necessary while ensuring grasp stability.
2) Holding phase 1. This phase lasts for 2 seconds. It is used to establish a steady baseline of the initial grasping force. Data from the beginning of this phase are used for further analysis.
3) Holding phase 2. This phase lasts for 8 seconds. Immediately at the start of this phase, the friction state switches to the opposite as a perturbation. The subject's goal is to maintain the object's position.

Fig. 3 depicts a typical trial. During the experiment, the subject is asked to wear a pair of active noise-canceling headphones to avoid any audio cues. In the meantime, a nature documentary is played to them to divert their attention and mimic a casual grasping task.

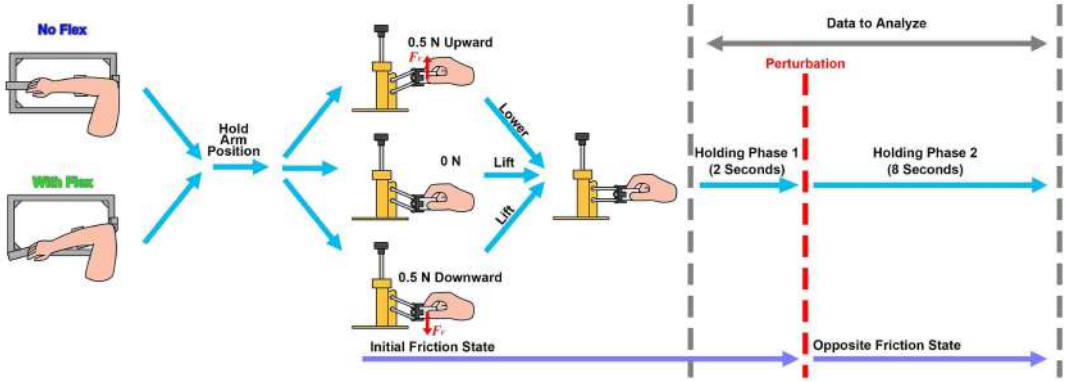


Fig. 2. Flowchart of the experimental protocol. Controlled variables are 1) Elbow position (no flex, with flex; illustrated by the elbow drawings on the left), the subject keeps their elbow position during the entirety of the trial; 2) Vertical force (0.5 N upward, 0 N, 0.5 N downward, illustrated by the hand drawings in the middle), the trial data used is the 10 seconds after they have lifted/lowered the object and stabilized; 3) Friction perturbation (high to low, low to high; shown by the purple arrows on the bottom), the initial friction state starts before the subject touches the object.

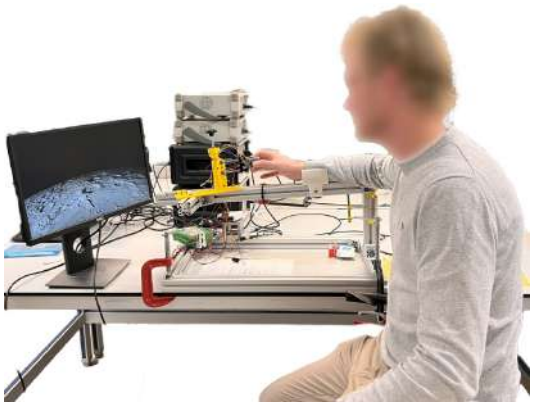


Fig. 3. A typical scene where a participant is performing the experiment. They are currently in the holding phase of a trial, not flexing their elbow, while watching the nature documentary.

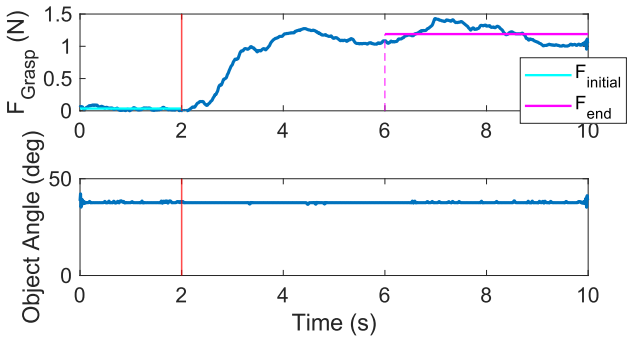


Fig. 4. A typical trial where the friction changes from high to low, and the object has a downward vertical force. The upper plot shows the grasping force over time, and the lower one shows the object's angle over time. The vertical red lines indicate the time of the friction change (2 s). The horizontal magenta lines show the initial force before the perturbation and the end force after the perturbation.

E. Friction Modulation Characterization

Before the main experiment, subjects were asked to perform a qualitative test to characterize the effectiveness of friction reduction. The object was adjusted to have a force of 0.5 N downwards. The subject would first squeeze the object with excessive force and lift it. Then, they would gradually reduce their grasping force, until the object starts to slip slowly. They were instructed to continue to release their grip until the object fully slipped from their fingers. They repeated this process with friction reduction either off (high friction) or on (low friction). Their grasping force and the object's position during the whole process were recorded and analyzed. Assuming a simple friction model, the minimum grasping force before the object slips provides a friction force equal to the object's vertical force.

F. Data Processing

1) Data Cleaning: Grasping force and object angle data were cleaned first before further analysis. First, their zero baselines were subtracted. Next, data were segmented into trials. The data acquisition rate was set to be 100 Hz; however, due to hardware limitations, the actual sampling was approximately 65 Hz, with a variable sampling rate. So, all segments were then resampled to 100 Hz by interpolation.

2) Data Exclusion: A threshold was used for detecting human errors in the trials. The value was determined by 10 times the minimum grasping force needed at the low friction condition (8.56 N in this case, as will be later shown in the results section). Further analysis excludes all trials with force exceeding this threshold. 12 trials were excluded in total among 432 trials.

3) Metric Extraction: Fig. 4 shows a typical trial where the friction changes from high to low on the two-second point (red lines), and the object has a downward vertical force. The object's position (angle) does not significantly change during a trial, and is not in the scope of this experiment, thus is not further studied.

3 metrics were extracted from each trial: the initial grasping force before the perturbation $F_{initial}$, the end force after full adaptation F_{end} (the cyan and magenta lines in Fig. 4), and the difference between them ΔF_{end}. They are calculated by:

$$\begin{cases} F_{initial} = mean(F(t < 2)) \\ F_{end} = mean(F(t > 6)) \\ \Delta F_{end} = F_{end} - F_{initial} \end{cases} \quad (1)$$

The reason F_{end} is not calculated directly after the perturbation is because there is a delay in the adaptation for grasping forces, especially in friction-increasing conditions (which will be shown in the next section). So the calculation uses the second half of the data (from 6 s to 10 s) after the perturbation.

G. Participants

This experiment recruited 12 participants, 7 males and 5 females. They are all healthy adults with no diagnosed tactile or arm usage deficiencies. Their age ranges from 24 to 30 (mean 26.4). Since the experiment setup is specifically designed for right-hand use, only right-handed individuals were recruited.

III. Results

A. Friction Modulation Effect

A paired t-test was performed for the mean values of each subject's minimum grasping force before slippage in the characterization test. It confirmed that friction modulation has a significant effect on the grasping force ($t_{12} = -3.3, p = 0.0069$). The average minimum force for the high friction condition is 0.32 N, while that of the low friction condition is 0.86 N. Assuming a simple friction model without viscosity, the ultrasonic friction effectively reduced the surface friction coefficient by 63%. Note that the actual friction model is more complex and depends on the subject [18], so this value is just for qualitative reference.

B. Data Overview

Fig. 5 plots the force data of all 12 conditions separately. The blue lines indicate when the subject does not flex their elbow, while the green lines indicate the opposite. Shaded areas are their standard deviations. The left column indicates when the friction changes from low to high, while the right one indicates otherwise. The rows from top to bottom indicate 0.5 N upward, 0 N, and 0.5 N downward force on the object respectively. Fig. 6 further illustrates the mean and standard deviations of the difference in force $\Delta\overline{F}$ over time. ΔF has a similar definition as ΔF_{end}:

$$\Delta F(t) = F(t) - F_{initial} \quad (2)$$

IV. Discussions

A. Experiment Validation

Before addressing the primary research question, it is essential to establish the validity of the experiment. This entails demonstrating that the results accurately reflect the participants' tactile perception and align with established findings in the field. Fig. 7 shows the confidence levels $(1-p)$ of paired t-tests ($N = 12$) between $\overline{F}_{initial}$ and $\overline{F}_{end}$ of each subject under different conditions. Since the confidence levels

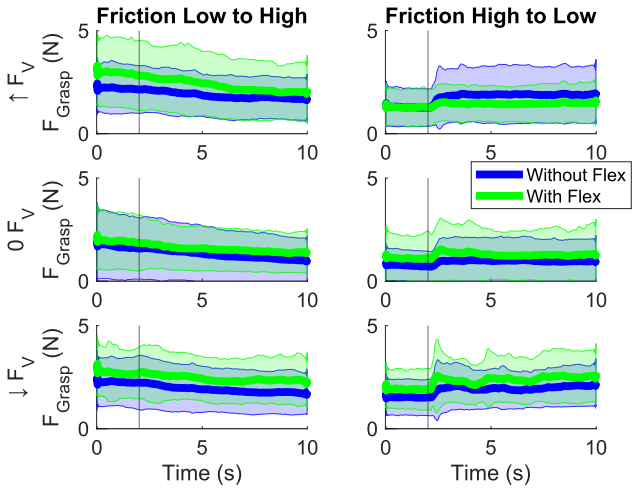


Fig. 5. Overview of the means of grasping force over time under 12 different conditions. The blue lines indicate when the subject does not flex their elbow, while the green lines indicate otherwise. Shaded areas are their standard deviations. The left column indicates when the friction changes from low to high, while the right one indicates otherwise. The rows from top to bottom indicate 0.5 N upward, 0 N, and 0.5 N downward force on the object respectively.

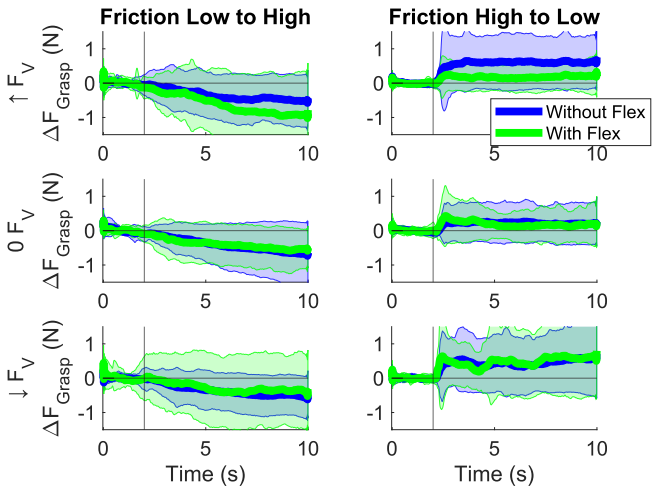


Fig. 6. Overview of the means of $\Delta\overline{F}$ over time under 12 different conditions. ΔF is the force data subtracted by $F_{initial}$. The blue lines indicate when the subject does not flex their elbow, while the green lines indicate otherwise. Shaded areas are their standard deviations. The left column indicates when the friction changes from low to high, while the right one indicates otherwise. The rows from top to bottom indicate 0.5 N upward, 0 N, and 0.5 N downward force on the object respectively.

are all above 85% and 8 out of 12 are above 95%, it is a clear indication that the friction perturbation has a significant impact on the participants' ability to regulate their grasping force.

Furthermore, there is no statistical difference when it comes to the direction of the vertical force ($t_{24} = -1.1, p = 0.3$, and $t_{24} = -0.96, p = 0.34$ for friction increasing and decreasing respectively). Thus, the upward force and downward force conditions can be combined as "with vertical force" experimental groups, with respect to "no vertical force" control groups.

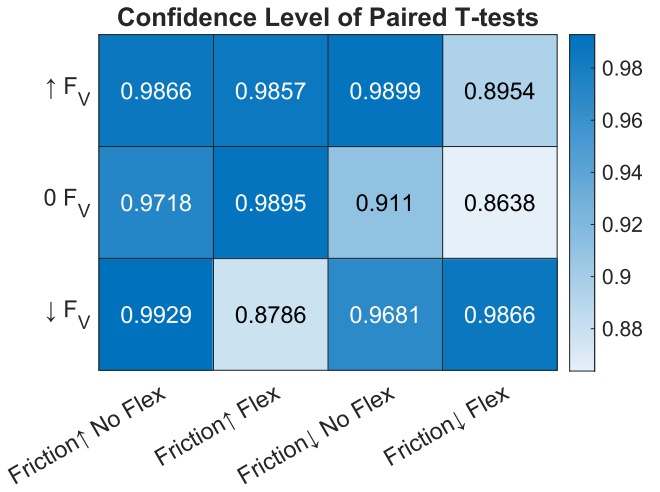


Fig. 7. Heatmap of confidence levels of paired t-tests between $\overline{F}_{initial}$ and $\overline{F}_{end}$ (as in Fig. 4) of each subject under different variable combinations. The higher the value, the deeper the color, and the more significant that the perturbation had an effect.

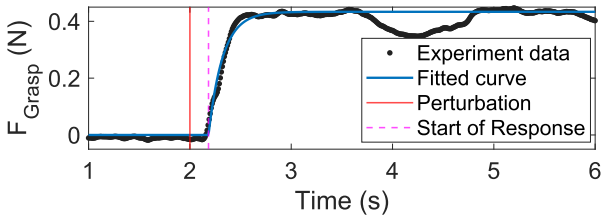


Fig. 8. Fitted curve of the mean of all trials with decreasing friction and non-zero vertical force. The black dots represent the experiment data points, while the blue line is the fitted curve. The red vertical line marks the start of the perturbation. The fitted time delay of the system is 184 ms, which is marked by the dashed magenta line.

However, it seems that the control groups (no vertical force but with friction perturbation) also demonstrated a significant effect of tactile stimulation on the grasping behaviors. So, paired t-tests of $\Delta\overline{F}_{end}$ comparing trials with and without a vertical force are performed. In these tests, all other conditions are combined except for the friction perturbation, because the difference in it affects the direction of ΔF_{end}. Results showed that there is no significant difference between the control groups and the group where friction increases ($t_{24} = 1.1, p = 0.3$). In contrast, when the friction decreases, the groups exhibit significantly larger effects ($t_{24} = -2.9, p = 0.0088$).

Taking all factors into account, it is clear that the subjects can perceive the change in friction and adapt accordingly, thus this experiment is able to reflect their tactile perceptions.

B. General Grasping Behavior

1) Decreasing Friction: Subjects increase their grasping force when the friction decreases and they sense an actual need to grip tighter. Their reactions can resemble a first-order system, where there is a small delay after the impulse (perturbation), and then the system output (grasping force) increases negative exponentially to a new steady state, as the lines on the right side of Fig. 6 suggest. In fact, the delay t_{delay} can be calculated if fitting the force curve with a piecewise function after the perturbation:

$$\begin{cases} \Delta\hat{F}(t < t_{delay}) = 0 \\ \Delta\hat{F}(t \geq t_{delay}) = A \times (1 - e^{\frac{-(t-t_{delay})}{\tau}}) \end{cases} \quad (3)$$

where A is the gain and τ is the time constant. Because individual trials often have very large deviations, the goodness of fit is not always satisfactory. As a consequence, only the average of every trial with decreasing friction and non-zero vertical force was fitted with the non-linear least squares method, as shown in Fig. 8. The resulting time delay is 184 ms. The delay is slightly larger than previous findings on friction-induced reflex response time [19], but still in the same magnitude. It is also consistent with the previous study [20]. This short delay implies that there is an intrinsic reflex pathway in humans to react to sudden grasp instability.

2) Increasing Friction: A decrease in grasping force is observed when the friction increases during a trial, but at a significantly slower rate than when friction decreases (Fig. 6). In both increasing and decreasing friction conditions, the amplitude of grasping force change is similar (comparing the left and right sides of Fig. 6). This means they adapt to the same level of friction change, no matter the direction, with the same level of grasping force change. Also, the F_{end} in increasing friction conditions is close to $F_{initial}$ in decreasing friction conditions (comparing the left and right sides of Fig. 5). This implies subjects adapted their grasping effort to their perceived optimal level. These similarities suggest that grasping forces are actively adapting to the level of friction to expend as little energy as possible while maintaining the stability of the grasp. The control groups, however, showed the same pattern of grasping force decrease as the experimental groups, despite that there is no actual need for the grasping force to change. This might be explained by: 1) Since the actual grasping forces are a lot higher than the minimum required grasping force, even in low friction conditions, the decrease in the grasping force is merely an attempt to optimize the grasping effort. 2) Since there is no actual grasping force needed in the control group, the subjects also felt the need to reduce their grasping force, as in situations where friction increases. However, the amplitude of this reduction happens to coincide with that in non-zero vertical force conditions, thus the results yield no statistical difference.

C. Effects of Arm Usage

1) Effects on Grasping Force: Fig. 5 suggests that there is a difference between the grasping force with and without arm usage, regardless of the perturbation. The control groups were not taken into account. A paired t-test between each subject's $\overline{F}_{initial}$ without and with arm usage under all other conditions confirmed there is a significant effect of arm usage on the level of force generated ($t_{48} = -3.8, p = 4.2 \times 10^{\circledast 4}$). The same test on their $\overline{F}_{end}$ yields similar results ($t_{48} = -3, p = 0.0039$), suggesting that when participants are using

their arms, they use a significantly higher grasping force both at the beginning of the grasping task and at the steady state where they have adapted to the new friction level.

2) Effects on Force Change: Since it is not confirmed that the friction-increase conditions reflect tactile perception, only friction-decrease conditions are used in this evaluation. A paired t-test between each subject's $\Delta\overline{F}_{end}$ without and with arm usage proved no significant difference ($t_{24} = 0.79, p = 0.44$). The subjects adapt to the same level of friction change with the same amplitude of force change, regardless of the usage of their arm.

3) Effects on Time Delay: Using the same function 3, response delay t_{delay} can be calculated for every subject under decreasing friction. However, due to the high deviations of each trial, this function was only successfully fitted to 8 subjects with meaningful results. A paired t-test between these subjects' t_{delay} without and with arm usage proved no significant difference ($t_{24} = -0.35, p = 0.73$). This possibly means that arm usage does not affect the time delay of response to tactile perception.

4) Is There a Synergy?: In conclusion, subjects tend to use a higher grasping force with arm usage whatever the condition; however, they respond to the same level of tactile perturbations with the same amplitude of force adaptation and likely the same level of time delay. Since several subjects reported that they involuntarily use their hand to assist in bending the elbow support (see the mechanism in Fig. 1), it is highly likely that the higher grasping force is just the additional hand pressure on the plates. With this factor accounted for, we can conclude that with healthy young adults, there is no significant neuromuscular synergy between arm usage and tactile perception.

V. Conclusions

We presented a pilot study that explores whether there is a neuromuscular synergy between humans' arm usage and their tactile perception of the object in hand. This study serves as a preliminary step, using healthy subjects as a control group, to develop an experimental platform that can be used for future research involving stroke patients. The results revealed a general grasping behavior that is consistent with earlier findings, confirming that this experiment is valid to reveal possible tactile perception discrepancies. In the end, we found no significant evidence that arm usage has a synergy with healthy subjects' tactile perception. This conclusion suggests that for healthy humans, the regulation of grasping force may function independently of general motor control. However, the findings from this study will lay the groundwork for future research on stroke patients, providing critical baseline data to explore how these dynamics interact in individuals with stroke-related deficits.

References

[1] V. L. Feigin *et al.*, "Global, regional, and national burden of stroke and its risk factors, 1990–2019: A systematic analysis for the Global Burden of Disease Study 2019," *The Lancet Neurology*, vol. 20, no. 10, pp. 795–820, Oct. 1, 2021.

[2] L. M. Carey and T. A. Matyas, "Frequency of discriminative sensory loss in the hand after stroke in a rehabilitation setting," *Journal of Rehabilitation Medicine*, vol. 43, no. 3, pp. 257–263, Feb. 2011.

[3] S. S. Kessner, U. Bingel, and G. Thomalla, "Somatosensory deficits after stroke: A scoping review," *Topics in Stroke Rehabilitation*, vol. 23, no. 2, pp. 136–146, Feb. 17, 2016.

[4] J. E. Aman, N. Elangovan, I.-L. Yeh, and J. Konczak, "The effectiveness of proprioceptive training for improving motor function: A systematic review," *Frontiers in Human Neuroscience*, vol. 8, Jan. 28, 2015.

[5] J. E. Sullivan and L. D. Hedman, "Sensory dysfunction following stroke: Incidence, significance, examination, and intervention," *Topics in Stroke Rehabilitation*, vol. 15, no. 3, pp. 200–217, May 1, 2008.

[6] L. M. Carey, "Somatosensory loss after stroke," *Critical Reviews™ in Physical and Rehabilitation Medicine*, vol. 7, no. 1, 1995.

[7] H. Klit, N. B. Finnerup, G. Andersen, and T. S. Jensen, "Central poststroke pain: A population-based study," *Pain*, vol. 152, no. 4, p. 818, Apr. 2011.

[8] R. S. Johansson and G. Westling, "Roles of glabrous skin receptors and sensorimotor memory in automatic control of precision grip when lifting rougher or more slippery objects," *Experimental Brain Research*, vol. 56, no. 3, pp. 550–564, Oct. 1, 1984.

[9] J. Hermsdörfer, E. Hagl, D. Nowak, and C. Marquardt, "Grip force control during object manipulation in cerebral stroke," *Clinical Neurophysiology*, vol. 114, no. 5, pp. 915–929, May 1, 2003.

[10] L. Willemet, F. Roël, D. Abbink, I. Birznieks, and M. Wiertlewski, "Grip force control under sudden change of friction," *Journal of Physiology*, in press.

[11] D. A. Nowak and J. Hermsdörfer, "Grip force behavior during object manipulation in neurological disorders: Toward an objective evaluation of manual performance deficits," *Movement Disorders*, vol. 20, no. 1, pp. 11–25, 2005.

[12] R. S. Johansson, "Sensory input and control of grip," in *Sensory Guidance of Movement*, G. R. Bock and J. A. Goode, Eds., vol. 218, 1998, pp. 45–63.

[13] C. Basdogan, F. Giraud, V. Levesque, and S. Choi, "A review of surface haptics: Enabling tactile effects on touch surfaces," *IEEE Transactions on Haptics*, vol. 13, no. 3, pp. 450–470, Jul. 2020.

[14] M. Biet, F. Giraud, and B. Lemaire-Semail, "Squeeze film effect for the design of an ultrasonic tactile plate," *IEEE Transactions on Ultrasonics Ferroelectrics and Frequency Control*, vol. 54, no. 12, pp. 2678–2688, Dec. 2007.

[15] M. Wiertlewski, R. F. Friesen, and J. E. Colgate, "Partial squeeze film levitation modulates fingertip friction," *Proceedings of the National Academy of Sciences of the United States of America*, vol. 113, no. 33, pp. 9210–9215, Aug. 16, 2016.

[16] T. Watanabe and S. Fukui, "A method for controlling tactile sensation of surface roughness using ultrasonic vibration," in *Nippon Telegraph & Telephone Corporation*, 1995, pp. 1134–1139.

[17] L. Winfield, J. Glassmire, J. E. Colgate, and M. Peshkin, "T-PaD: Tactile pattern display through variable friction reduction," in *Northwestern University*, 2007, pp. 421–+.

[18] N. Huloux, C. Bernard, and M. Wiertlewski, "Estimating friction modulation from the ultrasonic mechanical impedance," *IEEE Transactions on Haptics*, vol. 14, no. 2, pp. 409–420, Apr. 2021.

[19] R. S. Johansson and G. Westling, "Signals in tactile afferents from the fingers eliciting adaptive motor responses during precision grip," *Experimental Brain Research*, vol. 66, no. 1, pp. 141–154, Mar. 1, 1987.

[20] F. Roël, "A better grasp on the asymmetrical adaptation of grip force in response to friction perturbations," M.S. thesis, Delft University of Technology, 2022.

Mapping Encoder Values to Ankle Angles in a 3 DoF Parallel Ankle Exoskeleton

Miha Dežman*†, Charlotte Marquardt* and Tamim Asfour*†

***Abstract*— Accurate estimation of ankle joint angles is vital for advancing assistive technologies such as ankle exoskeletons. This study investigates whether three encoders within the parallel kinematics of a three degree of freedom (3-DoF) ankle exoskeleton can effectively estimate the three rotational movements of the ankle: plantar-/dorsiflexion (PF/DF), in-/eversion (IN/EV), and internal/external rotation (IR/ER). Performance was tested during walking, curve walking, and stair climbing with two healthy participants. Ankle motion was independently captured using a motion capture system, while encoder values from the exoskeleton were concurrently recorded. The root-mean-squared error (RMSE) for angle estimations ranged from 1° and 3°, indicating good accuracy, particularly for IN/EV and IR/ER, though challenges were noted in capturing peak dorsiflexion. The findings suggest that misalignment between the exoskeleton and the biological joint axis may have contributed to the observed inaccuracies, particularly for PF/DF, as evidenced by differing range of motion (RoM). Additionally, variability between the two participants may reflect the potential impact of individual anthropometry and alignment quality, which could inform future considerations for design and alignment protocols. Future model enhancements could incorporate dynamic effects and machine learning to generalize across diverse populations.**

I. INTRODUCTION

Exoskeletons have emerged as innovative assistive devices designed to enhance mobility, support rehabilitation, and improve the overall quality of life for individuals with various physical impairments. Among these, ankle exoskeletons specifically target the ankle joint, providing assistance to reduce the metabolic cost of walking. These systems enable users to regain or enhance movement patterns that may have been disrupted due to injury or disease [1], [2].

A critical aspect of optimizing ankle exoskeletons is the accurate estimation of ankle joint kinematics, which is essential for delivering customized assistance across the three degree of freedom (DoF) of the ankle: plantar-/dorsiflexion (PF/DF), in-/eversion (IN/EV), and internal/external rotation (IR/ER). However, determining the precise motion of the ankle joint is inherently complex due to the necessity of three-dimensional imaging techniques, which are vital for capturing the intricate movements of the ankle [3]–[5]. These imaging techniques provide valuable data but can be resource-intensive and not always accessible in all clinical or research settings.

This work has been supported by the Carl Zeiss Foundation through the JuBot project and the German Federal Ministry of Education and Research (BMBF) under the Robotics Institute Germany (RIG).

*High Performance Humanoid Technologies Lab, Institute for Anthropomatics and Robotics, Karlsruhe Institute of Technology (KIT), Germany
†Corresponding authors: {miha.dezman,asfour}@kit.edu

The integration of sensors into exoskeletons marks an advancement in the continuous monitoring and analysis of user data, particularly concerning motor performance [6]. These devices can provide real-time feedback, enhancing the understanding of joint kinematics and thereby improving rehabilitation protocols and performance assessments. However, most wearable exoskeleton designs primarily optimize for PF/DF motion, offering limited motion or assistance for IN/EV and IR/ER [7], [8]. A notable example is the wearable three DoF exoskeleton developed by Weerasingha et al. [9], which incorporates direct angle measurement via encoders and allows for assistance. However, this system is constrained by its considerable weight and limited torque assistance, highlighting the ongoing challenge of balancing functionality and portability in exoskeleton design. Another three DoF ankle exoskeleton mechanism by Hong et al. [10] uses a configuration of three encoders integrated into a spherical mechanism. These measure all rotations of the ankle joint. However, the proposed device does not include a method for actuation and active assistance. Lack of a rigid supportive three DoF structure requires multi-DoF measurement methods or external sensing systems to determine the accurate state of the exoskeleton. Such an example is the three DoF exoskeleton by Mooney et al. [11], which utilizes struts attached to a hiking boot for torque transmission, facilitating some IN/EV and IR/ER movements. Struts deformations were measured using motion capture (MOCAP) to estimate assistance torques, allowing for a simplified exoskeleton design but limiting its use to a laboratory setting.

Multidimensional DoF measurement of the ankle is also possible with systems exploiting magnetic fields for actuation and sensing [12]. However, the findings indicate that while magnetic fields can facilitate complex motion tracking, they require specialized calibration setups to ensure accuracy, showing the complexities involved in kinematic measurement within multi-DoF systems.

Soft exosuits allow minimally restrictive motion of user joints with structures relying on fabric materials and cables for force transmission. These exoskeletons represent a lightweight alternative with excellent adaptability to various postures and dynamic movements [13], [14]. However, their inherent compliance introduces challenges in achieving accurate kinematic assessments. This difficulty arises primarily from the non-rigid nature of their components and the lack of rigid attachment points, which complicates the use of conventional angular encoder measurements. Instead, novel sensor systems and technologies are proposed, including optoelectronic systems [15], stretchable sensors [16], and

capacitance-based bending sensors [17], to facilitate continuous monitoring of joint angles. To address these challenges, novel sensor systems and technologies have been proposed, including optoelectronic systems [15], stretchable sensors [16], and capacitance-based bending sensors [17], to facilitate continuous monitoring of joint angles despite the adaptability of exosuits. However, these novel sensors are not yet widely accessible.

Alternatively, inertial measurement unit (IMU) sensors are frequently employed for tracking motion in wearable devices, which includes both rigid and soft exoskeletons. Chapman et al. [18] validated IMU-based methods against optical MOCAP systems, demonstrating high accuracy for upper extremity movements. Similarly, Kim et al. [19] confirmed the reliability of IMU sensors in tracking ankle kinematics during running. The quality of measurements can be enhanced through sensor fusion techniques that integrate different modalities. For example, Arceo et al. [20] developed a robust system that combines force sensing resistor (FSR) and IMU sensors to measure both force myography (FMG) signals and limb motion. However, while IMU sensors offer practical solutions for motion tracking, they require extensive calibration to ensure accuracy, and there may be inherent limitations to the precision they can achieve due to factors such as drift and sensor misalignment [21], [22].

This study builds upon prior work to evaluate the feasibility of a 3-DoF ankle exoskeleton equipped with encoders for joint angle estimation [7]. The kinematic design of the ankle exoskeleton enables passive adaptation to IN/EV and IR/ER motion and assistance along PF/DF motion. It features a size adjustable frame and embedded encoders for angle measurement. Notably, the encoders are arranged in a parallel kinematics configuration, meaning that they do not directly represent the three rotations of the ankle joint. This study presents a simplified model to estimate the three ankle rotations based on the encoder values and their combinations. By testing the exoskeleton on two participants during walking, curve walking, and stair-climbing tasks, we examine the system's ability to capture 3-DoF ankle rotations and assess factors influencing its performance. The findings provide valuable insights into design and alignment improvements necessary for future iterations.

The remainder of this paper is structured as follows. Section II details the design of the exoskeleton device, the user study protocol, and the procedures for data collection, postprocessing, and optimization. Section III presents the experimental results, including an analysis of the system's performance in estimating 3-DoF ankle rotations. Section IV explores the implications of these findings, highlighting design considerations and future directions for improvement. Finally, Section V summarizes the contributions of this study and outlines potential avenues for further research.

II. METHODS

A. Exoskeleton

This paper builds on the exoskeleton presented in [7]. The exoskeleton consists of a rigid frame structure that includes a *shank* and a *foot* section, shown in Fig. 1 (left). A series of joints, including a parallelogram mechanism, link the two sections. The *shank* frame has a kinematic design that adjusts to the user's ankle movements. It incorporates 11 DoF, comprising multiple passive 1 DoF joints as well as two passive 3 DoF joints, as illustrated in Fig. 1(right). Additional

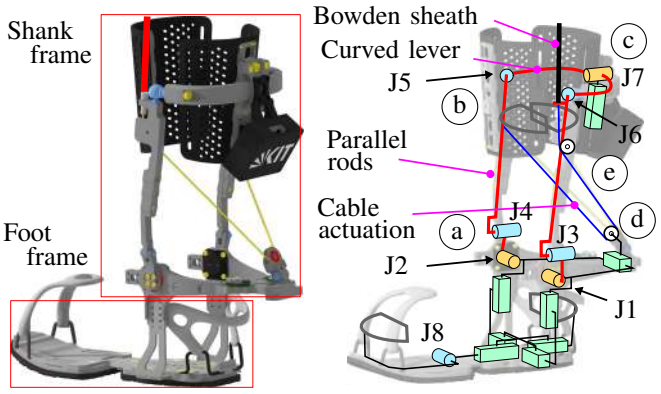


Fig. 1: Exoskeleton shown *left* and the kinematic representation shown *right*. The structure consists of several passive joints: "▭" 1 rotation DoF joint, "●" 3 DoF ball joint, "▭" 1 rotation DoF with an encoder and "▭" 1 DoF manually adjustable translation joint. (reused from [7])

aspects of the *shank* frame include: two cylindrical joints on both sides of the exoskeleton (J1, J2, J3, J4) illustrated in Fig. 1 ⓐ, are intentionally misaligned for a more compact integration of the magnetic encoder. The two ball joints (J5, J6) connect each parallel strut to the curved lever, as shown in Fig. 1 ⓑ, allowing for both IN/EV and IR/ER of the ankle. A cylindrical joint (J7) links the curved lever to the exoskeleton cuff, depicted in Fig. 1 ⓒ, and incorporates the third encoder. Altogether, three of the passive joints (J1, J2, J7) include an integrated absolute encoder (RMB20, RLS d.o.o.) to infer the ankle joint angles. The exoskeleton frame is designed to adjust in multiple dimensions for both the *shank* and *foot* frames, as illustrated in Fig. 1(right).

This passive joint configuration permits all three types of ankle rotation, as shown in Fig. 2. When joints J1 and J2 rotate in the same direction, PF/DF movement occurs. The combined rotation of joints J3 and J4 with joints J5 to J7 facilitates the IN/EV motion. Conversely, rotating joints J1 and J2 in opposite directions alongside joints J5 to J7 allows for the IR/ER. An additional foot frame DoF allows for forefoot rotation.

The *foot* frame design is rigid with one passive DoF for rotation of the forefoot, and several adjustable DoF to fit different shoe sizes. The shoe is secured using toe and heel bails adopted from crampons (Petzl, France).

B. User-study

This user study evaluates the proposed encoder model's effectiveness in estimating the three rotational movements of the ankle across three tasks. Effectiveness is assessed by comparing actual ankle motion, measured independently

TABLE I: Participant Information

Participant	Sex	Height (cm)	Weight (kg)	EU shoe size	Age (y)
pA	female	170	59	40	27
pB	male	178	65	42	22

via MOCAP technology, with ankle measurements from the exoskeleton's three encoders. Two healthy participants performed activities including straight-path walking, curved-path navigation, and stair ascent and descent. Their demographic and physical details are presented in Table I

Both participants provided written informed consent before the study, which followed the ethical guidelines of the Declaration of Helsinki. The experimental protocol was reviewed and approved by the Karlsruhe Institute of Technology (KIT) Ethics Committee as part of the JuBot project's ethical application.

The participants engaged in three distinct tasks: 1) *Normal walking*: This task involved walking along a straight path measuring 3 m in length, with two turnarounds that returned them to the starting position. 2) *Figure-eight walking*: In this task, participants maneuvered along a figure-eight path, designed to simulate slalom walking, measuring 3 m in length and 1.5 m in width, starting and ending at the center of the figure-eight. 3) *stair climbing/descending*: Participants ascended a flight of four steps, paused to turn at the top, and then descended back down the stairs before rotating to return to the starting position. These specific tasks were chosen because they represent common and functionally relevant movement patterns in daily activities and exoskeleton applications. The tasks were conducted in a randomized order, with each task repeated three times to ensure consistency in the data collection. Prior to the session, each participant underwent a 3 min familiarization phase, and resting pauses were provided between conditions and repetitions to minimize fatigue.

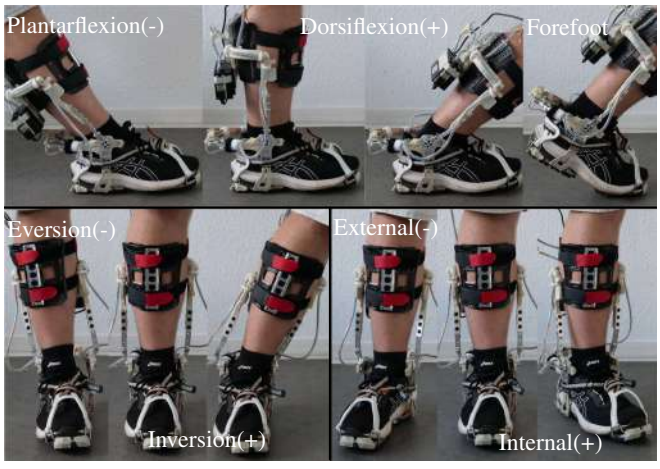


Fig. 2: A display of the exoskeleton's functionality, highlighting the three main ankle joint rotations: PF/DF, IN/EV, and IR/ER, in addition to the forefoot rotation of the foot frame. (reused from [7])

The ankle exoskeleton was fitted to the right leg of each participant and the *foot* frame was adjusted to accommodate the user's shoe size. During the donning process, the exoskeleton's PF/DF axis was aligned with the user's medial malleolus for accurate motion tracking.

The exoskeleton shank was then rotated to achieve symmetry with the sagittal plane and secured in place using adjustable straps. To account for the height of the exoskeleton's rubber sole, a separate *foot* segment was worn on the left leg, ensuring balanced support during the tasks.

C. Data Collection and Post-Processing

During the experiment, the motion of both the user and the exoskeleton was captured independently across all tasks. Passive markers were placed on the participant to track all three rotational movements of the ankle joint using an optical MOCAP system (Vicon Motion Systems, Ltd., UK). Additionally, the exoskeleton's internal sensors, including three encoders and a heel switch, were recorded on the exoskeleton side. A combined trigger signal was employed to synchronize the two data sources effectively. The encoders used are RMB14 (RLS d.o.o., Slovenia) that provide a 12-bit resolution. The MOCAP data was sampled at 100 Hz, while the exoskeleton data was collected at 200 Hz.

At the start of each recording, participants were asked to stand in a relaxed position to establish neutral marker positions and neutral positions of the encoders. After the measurements, the MOCAP data was processed to compute the ankle joint angles, as detailed in [7]. The resulting ankle angles calculated with MOCAP are henceforth named as α_{PFDF}, α_{INEV} and α_{IRER}, to denote ankle PF/DF, IN/EV and IR/ER, and present the ground truth for the subsequent analysis. In the same way, the exoskeleton encoder angles are named as $\varepsilon_{\text{LEFT}}$, $\varepsilon_{\text{RIGHT}}$ and $\varepsilon_{\text{BACK}}$, representing the encoders at position J1, J2 and J7, respectively, as shown in Fig. 1. To align with the exoskeleton's sampling frequency, α_{PFDF}, α_{INEV} and α_{IRER} were interpolated to 200 Hz using the *interp1* function in MATLAB® (R2023a, MathWorks, USA).

In all recordings, the mean of the first 100 data points from each of 6 parameters named above was used to calibrate the measurement to the neutral position. For each participant, all recordings related to a specific parameter were concatenated and used to optimize a personalized, user-specific model. To create the generalized model, recordings from all participants were combined. Finally, the distribution of all angles and encoder measurements was calculated using the MATLAB®function *ksdensity*. For visualization, the heel switch measurements marked the beginning of the right stride during straight and figure-eight walking, while MOCAP data was used to identify the start of stair steps.

D. Mathematical Model and Optimization

This section describes the mathematical model and optimization process used for estimation of ankle angles from encoder measurements. For the modeling, a 3D plane equation was used:

$$ax + by + cz = d, \tag{1}$$

where x, y and z represent the three spatial coordinates of the plane, and a, b, c and d are the plane parameters to be determined through optimization.

For easier interpretation and comparison of the plane parameters, Eq. (1) is rearranged into the following form:

$$z = -\frac{a}{c}x - \frac{b}{c}y - \frac{d}{c}. \tag{2}$$

To simplify the notation, we define the terms $-\frac{a}{c}$, $-\frac{b}{c}$, and $-\frac{d}{c}$ as P_1, P_2, and P_3, respectively. This transforms the equation into:

$$z = f_{\mathrm{i}}(x,y) = P_1 x + P_2 y + P_3, \tag{3}$$

where i is the respective plane fitting. The parameters P_1, P_2 and P_3 were optimized using the nonlinear programming solver *fmincon* in MATLAB®. An initial guess vector $x_0 = [1,1,1]$ was provided, and no bounds were imposed on the search space.

This paper assumes the following parameter relations:

$$\varepsilon_{\mathrm{DIFF}} = \varepsilon_{\mathrm{LEFT}} - \varepsilon_{\mathrm{RIGHT}}, \tag{4}$$

$$\tilde{\alpha}_{\mathrm{PFDF}} = \frac{\varepsilon_{\mathrm{LEFT}} + \varepsilon_{\mathrm{RIGHT}}}{2} + f_{\mathrm{CPFDF}}(\varepsilon_{\mathrm{BACK}}, \varepsilon_{\mathrm{DIFF}}), \tag{5}$$

$$\tilde{\alpha}_{\mathrm{INEV}} = f_{\alpha\mathrm{INEV}}(\varepsilon_{\mathrm{BACK}}, \varepsilon_{\mathrm{DIFF}}), \tag{6}$$

$$\tilde{\alpha}_{\mathrm{IRER}} = f_{\alpha\mathrm{IRER}}(\varepsilon_{\mathrm{BACK}}, \varepsilon_{\mathrm{DIFF}}), \tag{7}$$

where $f_{\mathrm{CPFDF}}(\varepsilon_{\mathrm{BACK}}, \varepsilon_{\mathrm{DIFF}})$ is a plane that estimates a correction factor to improve the $\tilde{\alpha}_{\mathrm{PFDF}}$ calculated using the average of $\varepsilon_{\mathrm{LEFT}}$ and $\varepsilon_{\mathrm{RIGHT}}$. And $\tilde{\alpha}_{\mathrm{INEV}}$ and $\tilde{\alpha}_{\mathrm{IRER}}$ are estimated directly from the corresponding planes $f_{\alpha\mathrm{INEV}}$ and $f_{\alpha\mathrm{IRER}}$, respectively.

III. Results and Analysis

A. Optimized Parameters

A simple plane fitting was conducted for both individual participants (personalized model) and for the combined data from both participants (generalized model). Table II displays the optimized parameters for the three planes: f_{CPFDF}, $f_{\alpha\mathrm{INEV}}$ and $f_{\alpha\mathrm{IRER}}$, which correspond to the ankle rotations α_{PFDF}, α_{INEV}, and α_{IRER}, respectively. While $f_{\alpha\mathrm{INEV}}$ and $f_{\alpha\mathrm{IRER}}$ directly represent the estimated ankle angles, f_{CPFDF} functions as a correction factor that is added to the average readings from the left and right encoders. This correction improves the estimation the PF/DF angle, as shown in Eq. (5).

The goodness of fit for each plane is assessed using the RMSE, with lower values indicating a closer alignment to the recorded data. Table II presents the RMSE values calculated for both the individualized models and the generalized model. The table comprises three rows: one for the individual models of participants pA and pB, and another for the generalized model (pAB). The parameters P_1, P_2, and P_3 define the orientation of each plane relative to the three axes, providing insight into how well the models represent the actual ankle movements. Normalized RMSE values from this table are presented in Table III to account for different range of motion (RoM).

Participant pB consistently demonstrates the lowest RMSE values across all three parameters (f_{CPFDF}, $f_{\alpha\mathrm{INEV}}$, $f_{\alpha\mathrm{IRER}}$), indicating the most accurate fit of the modeled planes. Notably, the RMSE values for participant pB are smaller for nearly 30% of those recorded for participant pA in both f_{CPFDF} and $f_{\alpha\mathrm{INEV}}$. This disparity suggests that participant pB's movement patterns align more closely with the modeled planes, resulting in a superior fit. In contrast, participant pA exhibits higher RMSE values for all parameters, underscoring a less precise correspondence between their motion and the fitted model.

The generalized model (pAB) yields root RMSE values that lie between those of the individual participants. This suggests that while the combined model captures overarching trends across both participants, it sacrifices some specificity achieved by the individualized models. Although the generalized model results in slightly higher RMSE values, the differences are relatively small, indicating that it could serve as a practical approximation. Nonetheless, its performance may still be enhanced through further fine-tuning for each participant to improve accuracy.

The plane parameters P_1, P_2, and P_3 provide valuable insights into the relative contributions of the encoders in estimating each plane. For f_{CPFDF}, parameters P_1 and P_2 consistently dominate across all cases, while P_3 remains close to zero, suggesting a negligible influence on the estimation. A similar pattern is observed for $f_{\alpha\mathrm{INEV}}$, where P_2 and P_3

TABLE II: Optimized Parameters for 3D Plane Fitting Across Ankle Rotations

	f_{CPFDF}				$f_{\alpha\mathrm{INEV}}$				$f_{\alpha\mathrm{IRER}}$			
Participant	P_1	P_2	P_3	RMSE	P_1	P_2	P_3	RMSE	P_1	P_2	P_3	RMSE
pA	0.295	-0.168	-0.952	2.945[1]	-0.053	1.009	0.706	1.433[1]	1.402	-0.047	0.380	1.846[1]
				2.962[2]				1.453[2]				1.890[2]
pB	0.407	0.033	-0.576	2.147[1]	-0.040	1.016	0.288	0.980[1]	1.706	-0.045	0.129	1.674[1]
				2.188[2]				0.995[2]				1.730[2]
pAB	0.323	-0.123	-0.745	2.536	-0.054	1.009	0.465	1.205	1.522	-0.078	0.282	1.798

Entry pAB represents combined recordings. P_1, P_2, and P_3 define the 3D plane orientation, with root-mean-squared error (RMSE) measuring fit accuracy.
[1] and [2] denote RMSE values for personalized and generalized models, respectively.

TABLE III: RoM Normalized RMSE values

Partic.	f_{CPFDF} nRMSE (%)	f_{CPFDF} RoM (deg)	$f_{\alpha\text{INEV}}$ nRMSE (%)	$f_{\alpha\text{INEV}}$ RoM (deg)	$f_{\alpha\text{IRER}}$ nRMSE (%)	$f_{\alpha\text{IRER}}$ RoM (deg)
pA	4.84[1]	60.8	4.29[1]	33.4	3.88[1]	47.6
	4.86[2]	60.8	4.35[2]	33.4	3.97[2]	47.6
pB	3.39[1]	63.3	4.83[1]	20.3	3.52[1]	37.6
	3.46[2]	63.3	4.91[2]	20.3	3.64[2]	37.6
pAB	3.73	67.9	3.61	33.4	3.78	47.6

Entry pAB represents combined recordings. [1] and [2] denote RMSE values for personalized and generalized models, respectively. nRMSE (%) is normalized as RMSE/RoM × 100, using RoM from MOCAP angles and RMSE table III.

emerge as the dominant parameters. In contrast, for $f_{\alpha\text{IRER}}$, parameters P_1 and P_3 are identified as the most influential. In the $f_{\alpha\text{INEV}}$ plane, the parameter P_2 consistently hovers around 1.009 across participants, indicating a strong and stable contribution from a specific orientation in the plane fitting. Furthermore, the RMSE values for $f_{\alpha\text{INEV}}$ are relatively low, suggesting a good overall fit for this motion parameter. For $f_{\alpha\text{IRER}}$, slight variations in P_1 are observed across participants, particularly between the individual models. While the RMSE values for $f_{\alpha\text{IRER}}$ are higher than those for $f_{\alpha\text{INEV}}$, they remain moderate, reflecting a reasonable fit for this parameter.

Overall, participant pB's lower RMSE values across all parameters indicate more consistent and controlled movement patterns in relation to the exoskeleton encoders.

B. Range of Motion Analysis

For additional insights, Fig. 3 illustrates the distribution of measurement points across the RoM for the three ankle

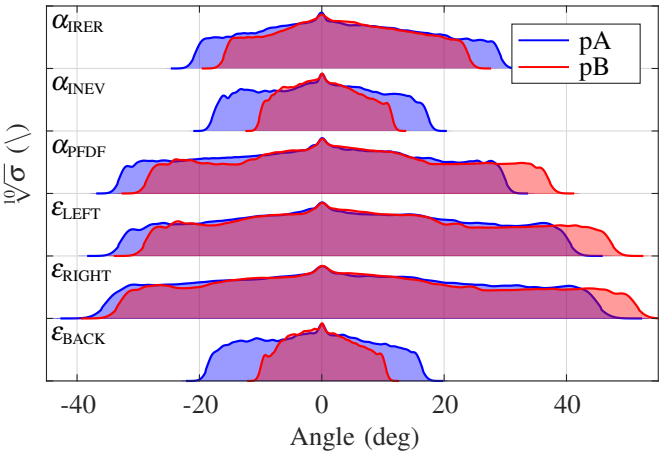


Fig. 3: Visualization of the distribution of ankle joint angles (α_{PFDF}, α_{INEV} and α_{IRER}) measured using MOCAP and exoskeleton encoder readings ($\varepsilon_{\text{LEFT}}$, $\varepsilon_{\text{RIGHT}}$ and $\varepsilon_{\text{BACK}}$) for two participants. The 10th root scaling of density values improves visualization of data distribution, especially in regions of high density.

angles (α_{PFDF}, α_{INEV} and α_{IRER}) alongside the three exoskeleton encoders ($\varepsilon_{\text{BACK}}$, $\varepsilon_{\text{LEFT}}$ and $\varepsilon_{\text{RIGHT}}$) for both participants. To improve visualization and address uneven data density, a 10th root scaling is applied to the density values. The intra-participant differences in the RoM for the α_{IRER} and α_{INEV} angles reach up to 10°. Notably, participant pB demonstrates a narrower RoM for both angles.

The RoM of α_{INEV} closely aligns with that of $\varepsilon_{\text{BACK}}$. Similarly, the RoM of the $\varepsilon_{\text{LEFT}}$ and $\varepsilon_{\text{RIGHT}}$ align with the α_{PFDF} for both participants. However, discrepancies are observed between the RoM of the $\varepsilon_{\text{LEFT}}$, $\varepsilon_{\text{RIGHT}}$, and α_{PFDF} angles.

Given the direct alignment of $\varepsilon_{\text{LEFT}}$ and $\varepsilon_{\text{RIGHT}}$ with the α_{PFDF} axis, these differences may indicate either a misalignment between the exoskeleton and the ankle joint or limitations in the MOCAP angle measurement principle described in [7] to fully capture the α_{PFDF} movement.

A notable observation in Fig. 3 and Table II is the inter-participant variation in both RoM and RMSE values. Table III addresses this by normalizing the RMSE values to RoM, aiming to reduce the impact of RoM variation. The table presents nRMSE values for the correction factor (f_{CPFDF}) and the two ankle angle estimates ($f_{\alpha\text{INEV}}$, and $f_{\alpha\text{IRER}}$) for two participants and two model types (personalized and generalized).

Participant pB demonstrates a smaller RoM for the $f_{\alpha\text{INEV}}$ and $f_{\alpha\text{IRER}}$ estimates compared to participant pA; however, the RoM for f_{CPFDF} is of similar magnitude between the two participants. Following normalization of the RMSE, participant pB exhibits lower nRMSE values for both f_{CPFDF} and $f_{\alpha\text{IRER}}$. In contrast, the nRMSE value for $f_{\alpha\text{INEV}}$ is higher in participant pB than in participant pA. The data indicate that the nRMSE values for $f_{\alpha\text{INEV}}$ and $f_{\alpha\text{IRER}}$ are much closer when accounting for the differences in RoM. Conversely, the nRMSE values for f_{CPFDF} remain distinct even after scaling by RoM, suggesting that the discrepancies in this parameter are more pronounced.

C. Ankle Rotation Estimate

This section examines the ankle joint motion of participant pA, who exhibited higher RMSE values compared to the other participant, necessitating closer analysis. Figure 4 compares MOCAP-derived measurements with encoder-based model predictions for three parameters: α_{PFDF}, α_{INEV}, and α_{IRER}. Both participant-specific (pA) and generalized (pAB) models are assessed for normal walking (left column) and stair ascending (right column).

The top row of Figure 4 shows the α_{PFDF} parameter, with three estimates compared against the MOCAP data. The first estimate is derived as a simple average of the left and right exoskeleton encoders ($\frac{\varepsilon_{\text{LEFT}}+\varepsilon_{\text{RIGHT}}}{2}$). The second incorporates a participant-specific correction factor ($f_{\text{CPFDF,pA}}$), while the third applies a generalized correction factor ($f_{\text{CPFDF,pAB}}$).

For the walking task, correction factors don't visibly improve the $\tilde{\alpha}_{\text{PFDF}}$ estimate, though slight improvements are seen during stair ascending. Discrepancies include overestimation of maximum dorsiflexion (DF) during heel touch in walking and pronounced deviation at maximum DF during

stair ascending. However, the model accurately captures minimum values in both tasks.

The $\tilde{\alpha}_{\text{INEV}}$ parameter exhibits closer alignment with the MOCAP measurements. Both walking and stair ascending tasks show well-captured trends, but also features small discrepancies. Interestingly, the results indicate no visible differences between the personalized and generalized models, suggesting comparable performance across both conditions.

For $\tilde{\alpha}_{\text{IRER}}$, the estimates demonstrate strong agreement with the MOCAP measurements during walking but show a poorer match during stair ascending. Larger deviations occur at extreme angles or during rapid transitions. Similar to $\tilde{\alpha}_{\text{INEV}}$, no visible differences are observed between the personalized and generalized models.

IV. DISCUSSION

The proposed approach successfully estimates ankle angles, with better performance for IN/EV and IR/ER compared to PF/DF, where maximum dorsiflexion was not well-captured. A major source of error presumably stems from the misalignment between the exoskeleton's axes and the user's biological joint axes. This misalignment is evidenced by the discrepancies observed between the RoM ankle PF/DF and the corresponding encoder ($\varepsilon_{\text{LEFT}}$ and $\varepsilon_{\text{RIGHT}}$) readings from the exoskeleton, as illustrated in Fig. 3. Based on the exoskeleton design, the PF/DF axis of the exoskeleton can be directly aligned with the PF/DF axis of the ankle joint. However, despite efforts to position the exoskeleton in relation to the outer malleolus of the ankle, challenges persist in achieving accurate alignment with the center of rotation of the ankle, particularly given the complexities associated with the 3 DoF design of the exoskeleton. This misalignment impacts the mapping of encoder readings to joint angles, especially for PF/DF, where precise alignment is evidently more critical than for the other two axes (IN/EV and IR/ER). Although users reported a high level of comfort while using the exoskeleton, any compliance in the shoe or attachment mechanism may have further contributed to discrepancies in alignment and motion, potentially affecting the overall effectiveness of the device.

The RMSE values reveal inter-participant variability, with participant pB demonstrating RMSE values nearly 30% lower than those of participant pA, as illustrated in Table II. Notably, RoM between the two participants exhibits visible differences, as depicted in Fig. 3. This variability suggests that individual factors, such as anthropometry and walking style, may play a large role in influencing estimation accuracy. These findings highlight the necessity for improved

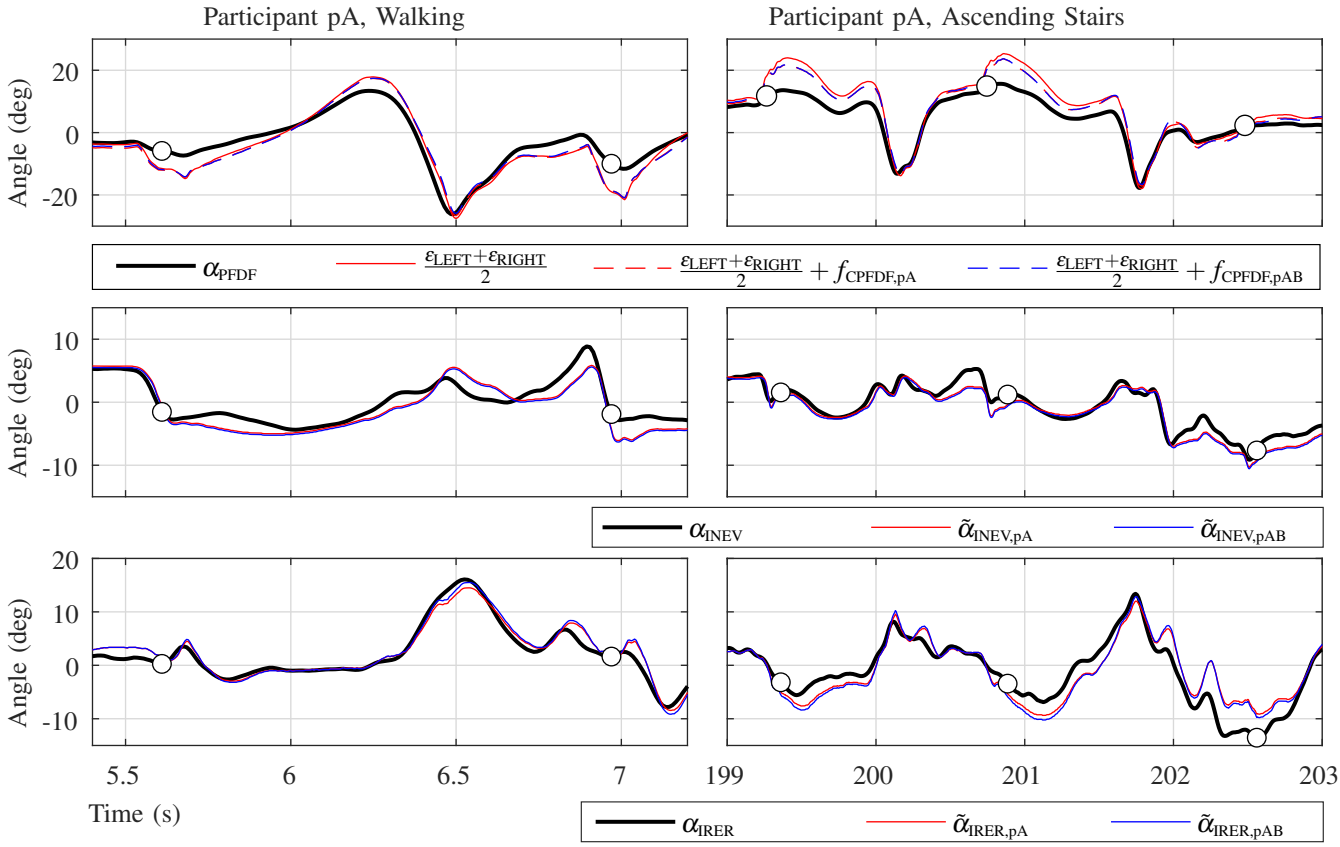


Fig. 4: Comparison of MOCAP-derived measurements (black lines) with encoder-based model predictions for f_{CPFDF}, α_{INEV}, and α_{IRER}. The participant-specific model (pA, red) and generalized model (pAB, blue) are evaluated. The top row shows the effect of correction factors on α_{PFDF}, improving alignment with MOCAP data. The middle and bottom rows illustrate the modeled values of α_{INEV} and α_{IRER}. The white point marks the stride

alignment protocols and the inclusion of larger sample sizes in future studies to enhance the generalizability of model performance. The RMSE values for PF/DF further emphasize the critical importance of achieving proper alignment along this axis to ensure accurate measurements. Consequently, future designs of exoskeletons should prioritize mechanical adjustments aimed at optimizing alignment, particularly for PF/DF, as well as implementing strategies to mitigate the effects of compliance and foot movement within the exoskeleton.

The current methodology, which evaluates each angle separately and relies on plane fitting, may limit the overall accuracy of the model. Personalizing the model yielded only marginal improvements compared to the generalized approach, showing potential for simplifications and generalization. The observed inter-participant variability underscores the necessity of a larger sample size for a robust evaluation of the model. Additionally, observed discrepancies at the peaks of motion indicate that factors such as velocity and dynamic effects, including tissue compliance, need to be integrated into future models. To address these limitations, a more unified approach that combines the assessment of multiple angles and incorporates additional parameters—potentially through machine learning techniques—could enhance both performance and generalizability.

V. CONCLUSION

This study demonstrates the potential of encoder-based models for estimating ankle angles in parallel exoskeletons, but challenges remain due to alignment issues, compliance effects, and inter-participant variability. While the current model is a step toward understanding the relationship between ankle motion and encoder readings, further research is needed to refine the approach. This includes incorporating additional parameters, testing with larger and more diverse participant pools, and exploring more advanced machine learning techniques. Ultimately, these efforts could improve the accuracy and generalizability of the model, paving the way for enhanced exoskeleton performance.

REFERENCES

[1] K. L. Poggensee and S. H. Collins, "How adaptation, training, and customization contribute to benefits from exoskeleton assistance," *Science Robotics*, vol. 6, no. 58, p. eabf1078, Sep. 2021.

[2] M. G. Alvarez-Perez, M. A. Garcia-Murillo, and J. J. Cervantes-Sánchez, "Robot-assisted ankle rehabilitation: A review," *Disability and Rehabilitation: Assistive Technology*, vol. 15, no. 4, pp. 394–408, May 2020.

[3] J. L. McGinley, R. Baker, R. Wolfe, and M. E. Morris, "The reliability of three-dimensional kinematic gait measurements: A systematic review," *Gait & Posture*, vol. 29, no. 3, pp. 360–369, 2009.

[4] G. Zhang, S. Cao, C. Wang, X. Ma, X. Wang, J. Huang, and C. Zhang, "Effect of a Semirigid Ankle Brace on the In Vivo Kinematics of Patients with Functional Ankle Instability during the Stance Phase of Walking," *BioMed Research International*, vol. 2019, pp. 1–10, 2019.

[5] J. Bessler-Etten, L. Schaake, G. B. Prange-Lasonder, and J. H. Buurke, "Assessing effects of exoskeleton misalignment on knee joint load during swing using an instrumented leg simulator," *Journal of NeuroEngineering and Rehabilitation*, vol. 19, no. 1, p. 13, 2022. [Online]. Available: https://jneuroengrehab.biomedcentral.com/articles/10.1186/s12984-022-00990-z

[6] T. Moeller, F. Moehler, J. Krell-Roesch, M. Dežman, C. Marquardt, T. Asfour, T. Stein, and A. Woll, "Use of lower limb exoskeletons as an assessment tool for human motor performance: A systematic review," *Sensors*, vol. 23, no. 6, 2023.

[7] M. Dežman, C. Marquardt, and T. Asfour, "Ankle exoskeleton with a symmetric 3 dof structure for plantarflexion assistance," in *IEEE International Conference on Robotics and Automation (ICRA)*, Yokohama, Japan, May 2024.

[8] K. A. Witte and S. H. Collins, "Design of Lower-Limb Exoskeletons and Emulator Systems," in *Wearable Robotics*, J. Rosen and P. W. Ferguson, Eds. Elsevier, 2020, pp. 251–274.

[9] A. Weerasingha, A. Pragnathilaka, W. Withanage, R. Ranaweera, and R. Gopura, "C-JAE: 3 DOF Robotic Ankle Exoskeleton with Compatible Joint Axes," in *2018 Moratuwa Engineering Research Conference (MERCon)*. Moratuwa: IEEE, May 2018, pp. 270–275.

[10] M. B. Hong, G. T. Kim, and Y. H. Yoon, "ACE-Ankle: A Novel Sensorized RCM (Remote-Center-of-Motion) Ankle Mechanism for Military Purpose Exoskeleton," *Robotica*, vol. 37, no. 12, pp. 2209–2228, 2019.

[11] L. M. Mooney and H. M. Herr, "Biomechanical walking mechanisms underlying the metabolic reduction caused by an autonomous exoskeleton," *Journal of NeuroEngineering and Rehabilitation*, vol. 13, no. 1, p. 4, Dec. 2016.

[12] Z. Que and K.-M. Lee, "Magnetic Pantographic Exoskeleton Illustrated With a Biomimetic Ankle-Foot Simulator for 3-DOF Noncontact Actuation/Measurements," *IEEE/ASME Transactions on Mechatronics*, vol. 29, no. 4, pp. 3028–3037, 2024. [Online]. Available: https://ieeexplore.ieee.org/document/10549930/

[13] S. Lee, J. Kim, L. Baker, A. Long, N. Karavas, N. Menard, I. Galiana, and C. J. Walsh, "Autonomous multi-joint soft exosuit with augmentation-power-based control parameter tuning reduces energy cost of loaded walking," *Journal of NeuroEngineering and Rehabilitation*, vol. 15, no. 1, p. 66, Dec. 2018.

[14] L. N. Awad, J. Bae, K. O'Donnell, S. M. M. De Rossi, K. Hendron, L. H. Sloot, P. Kudzia, S. Allen, K. G. Holt, T. D. Ellis, and C. J. Walsh, "A soft robotic exosuit improves walking in patients after stroke," *Science Translational Medicine*, vol. 9, no. 400, p. eaai9084, Jul. 2017.

[15] B. He, M. Li, R. Liang, Z. Liang, W. Yao, S. Sareh, J. Xie, G. Xu, and Y. Noh, "Optoelectronic-Based Pose Sensing for a Hand Rehabilitation Exoskeleton Continuous Structure," *IEEE Sensors Journal*, vol. 22, no. 6, pp. 5606–5615, 2022.

[16] Y. Mengüç, Y.-L. Park, H. Pei, D. Vogt, P. M. Aubin, E. Winchell, L. Fluke, L. Stirling, R. J. Wood, and C. J. Walsh, "Wearable soft sensing suit for human gait measurement," *The International Journal of Robotics Research*, vol. 33, no. 14, pp. 1748–1764, 2014.

[17] D. Goto, Y. Sakaue, T. Kobayashi, K. Kawamura, S. Okada, and N. Shiozawa, "Bending Angle Sensor Based on Double-Layer Capacitance Suitable for Human Joint," *IEEE Open Journal of Engineering in Medicine and Biology*, vol. 4, pp. 129–140, 2023.

[18] R. M. Chapman, M. T. Torchia, J.-E. Bell, and D. W. Van Citters, "Assessing Shoulder Biomechanics of Healthy Elderly Individuals During Activities of Daily Living Using Inertial Measurement Units: High Maximum Elevation Is Achievable but Rarely Used," *Journal of Biomechanical Engineering*, vol. 141, no. 4, p. 041001, 2019.

[19] B. H. Kim, S. H. Hong, I. W. Oh, Y. W. Lee, I. H. Kee, and S. Y. Lee, "Measurement of Ankle Joint Movements Using IMUs during Running," *Sensors*, vol. 21, no. 12, p. 4240, 2021.

[20] J. C. Arceo, L. Yu, and S. Bai, "Robust Sensor Fusion and Biomimetic Control of a Lower-Limb Exoskeleton With Multimodal Sensors," *IEEE Transactions on Automation Science and Engineering*, pp. 1–11, 2024.

[21] R. Kianifar, V. Joukov, A. Lee, S. Raina, and D. Kulić, "Inertial measurement unit-based pose estimation: Analyzing and reducing sensitivity to sensor placement and body measures," *Journal of Rehabilitation and Assistive Technologies Engineering*, vol. 6, p. 2055668318813455, 2019. [Online]. Available: https://journals.sagepub.com/doi/10.1177/2055668318813455

[22] K. Zhu, J. Li, D. Li, B. Fan, and P. B. Shull, "IMU Shoulder Angle Estimation: Effects of Sensor-to-Segment Misalignment and Sensor Orientation Error," *IEEE Transactions on Neural Systems and Rehabilitation Engineering*, vol. 31, pp. 4481–4491, 2023. [Online]. Available: https://ieeexplore.ieee.org/document/10312740/

Kinematics Estimation Using a Skin-Adhesive Strain Patch for Shoulder Rehabilitation: A Preliminary Study*

Chan Beom Park, Hyeok-Jun Kwon, Seongok Chae, Su Jae Lee, Seong Hyun Kim, and Hyung-Soon Park, *Member, IEEE*

***Abstract*— Shoulder kinematics has been required to be estimated using compact sensors to provide visual feedback on joint movements for patients undergoing home rehabilitation due to musculoskeletal diseases, such as stroke. Multiple strain patches have been used for shoulder kinematics estimation, either embedded in tight shirts or attached directly to the skin. However, it is desirable to eliminate the tight shirt while minimizing the number of strain patches for convenient use in home rehabilitation. This study presents a single all-in-one skin-adhesive strain patch that enables shoulder kinematics estimation through placement optimization. At the optimal on-skin position, strains caused by flexion-extension and abduction-adduction movements were generated significantly in different directions. The fabricated all-in-one strain patch measured these strains using embedded sensors oriented accordingly. Moreover, the patch was designed to be lightweight and ultra-thin, allowing for convenient attachment to the skin. Shoulder kinematics estimation using this strain patch was preliminarily evaluated with a subject, demonstrating that shoulder joint angles could be estimated with an average error of 15.8% of the range of motion for two degrees of freedom. The placement optimization reduced the total number of strain patches required for kinematics estimation, enhancing convenience for daily use.**

I. Introduction

Compact sensor-based shoulder kinematics estimation is necessary in home rehabilitation for motion-based visual feedback. Patients with musculoskeletal diseases, such as stroke, require adjustments in muscle activation coordination of the upper limb through rehabilitation [1-3] to improve functional outcomes, which can be facilitated by providing visual feedback based on shoulder movements [4-8]. Although various contactless sensors, such as camera, have been used to estimate joint movements [9-11], the bulky cameras required for such systems are less convenient for daily use. Therefore, compact sensors have been used for shoulder kinematics estimation

*This work was supported in part by the Institute for Information & Communications Technology Promotion (IITP) grant funded by the Korea government (MSIT, Grant No. 2022-0-00020, Imperceptible on-skin sensor devices for musculoskeletal monitoring and rehabilitation) and in part by the Technology Innovation Program(RS-2024-00443121) funded by the Ministry of Trade Industry & Energy(MOTIE, Korea). *(Corresponding authors: Seong Hyun Kim; Hyung-Soon Park.)*

C. B. Park, H.-J Kwon, S. Chae, and H.-S. Park are with the Department of Mechanical Engineering, Korea Advanced Institute of Science and Technology, Daejeon 34141, South Korea (e-mail: pcb3454@kaist.ac.kr; hj990713@kaist.ac.kr; polaris9327@kaist.ac.kr; hyungspark@kaist.ac.kr).

S. J. Lee and S. H. Kim are with the Flexible Electronics Research Section, Electronics and Telecommunications Research Institute , Daejeon 34129, South Korea (e-mail: leesujae@etri.re.kr; kimsh@etri.re.kr).

Tight shirts can estimate shoulder kinematics from measured skin strains using embedded strain patches [12-15]; however, their tightness, required to prevent slippage between the sensors and skin, causes inconvenience. The shirts should be designed to be tight, as measuring skin strain becomes challenging when slippage occurs between the skin and the strain sensors. However, it is desirable to design sensors that avoid applying strong pressure to the skin for convenient use. Moreover, these shirts pose challenges for use in harsh conditions, such as hot weather, due to sweating. Therefore, shoulder kinematics has been estimated using skin-adhesive strain patches.

Although shoulder kinematics can be estimated using multiple skin-adhesive strain patches [16-19], the number of patches should be minimized for convenient use. To estimate shoulder kinematics using conventional strain patches, multiple patches, each comprising a single strain sensor, should be attached distantly around the shoulder in different directions. However, considering the inconvenience caused by multiple patches, it is desirable to utilize a single strain patch for estimation.

The main objective of this paper is to present a skin-adhesive all-in-one strain patch capable of estimating shoulder kinematics by optimizing its placement based on strain distribution analysis during movements, which was preliminarily verified in an experimental setup. Three strain sensors, oriented in different directions, were embedded in the patch. Moreover, the patch was designed to be stretchable and ultra-thin, allowing it to be attached to the skin without causing discomfort. By optimizing the sensor placement, it was demonstrated that shoulder kinematics in two degrees of freedom (DOFs) could be predicted using the strain patch. This study includes the procedure for placement optimization, the evaluation method, and an assessment of its significance.

II. Materials and Methods

A. Overall Procedure for Shoulder Kinematics Estimation

Shoulder kinematics in two DOFs is preliminarily estimated using a single all-in-one strain patch, with its placement determined through optimization (Fig. 1). Placement optimization identifies the optimal on-skin position where the skin strains caused by horizontal flexion/extension (F/E) and abduction/adduction (A/A) movements are decoupled in different directions (i.e., principal strain) and show significant changes corresponding to its respective shoulder movements. The location of the optimal on-skin position is determined by measuring variations in the distance between reflective markers on a marker grid placed around the

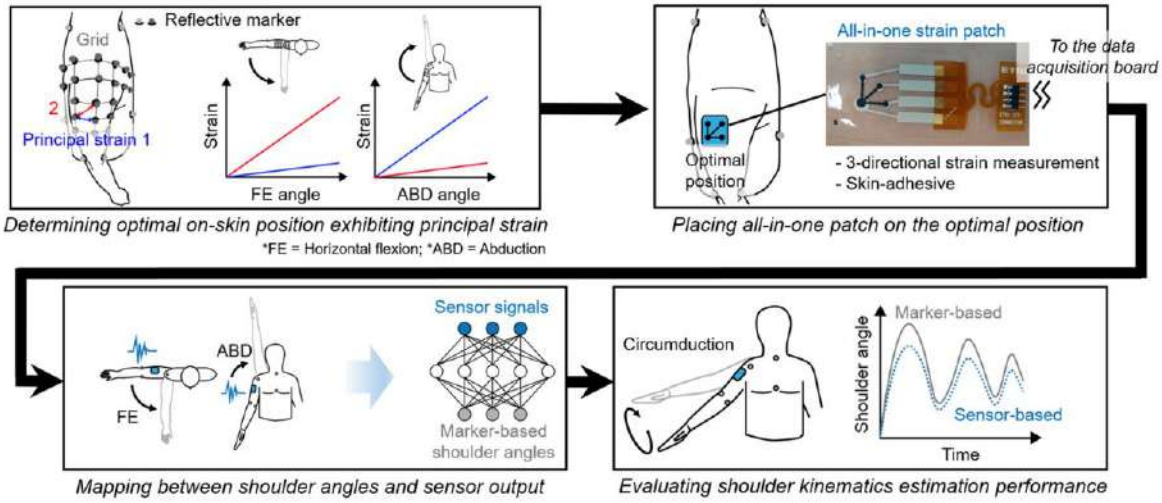


Fig. 1. Overall shoulder kinematics estimation procedure using the all-in-one strain patch through sensor placement optimization.

shoulder during F/E and A/A tasks. The all-in-one strain patch is then attached to the optimal on-skin position to measure the skin strains using embedded three strain sensors. The relationship between the sensor output and shoulder horizontal flexion (FE) and abduction (ABD) angles, measured by a marker-based setup during F/E and A/A tasks, is then established using machine learning. Using the established relationship, it is evaluated whether the single all-in-one strain patch, placed at the optimal position, can predict the targeted shoulder joint angles.

B. Subject Recruitment

A healthy 29-year-old male subject was recruited for evaluation of shoulder kinematics estimation. Exclusion criteria included subjects with limited shoulder joint range of motion (ROM) due to diseases, such as neurological impairments. This study was approved by the institutional review boards of the Korea Advanced Institute of Science and Technology (KH2022-048). The subject provided written consent before the study.

C. All-in-one Strain Patch Design

The all-in-one strain patch was designed to measure strains in different directions at the on-skin position (Fig. 2a). Graphite paste was applied to a polydimethylsiloxane (PDMS) substrate to sense strain changes in the 0°, 45°, and 90° directions. Voltage was applied to the graphite paste through silver (Ag) paste on the PDMS to measure the change in resistance (ΔR) relative to the initial resistance value (R_0), as shown in Fig. 2a. The total thickness of the all-in-one strain patch was less than 600 μm, allowing it to be easily attached to the skin. Note that a data acquisition board was used to acquire sensor resistance and transmit it to the PC via Bluetooth.

The resistance of the all-in-one strain patch showed linearity with respect to stretching (Fig. 2b). It was experimentally confirmed that the resistance linearly increases as the strain patch is stretched. Moreover, the sensitivity of the resistance variation to stretching converged to a consistent value with higher stretching cycles. However, the all-in-one strain patch exhibited non-linearity due to hysteresis (Fig. 2c) during cyclic stretching and velocity dependency.

D. Placement Optimization

The optimal on-skin position was identified based on the skin strains caused by F/E and A/A movements. All skin

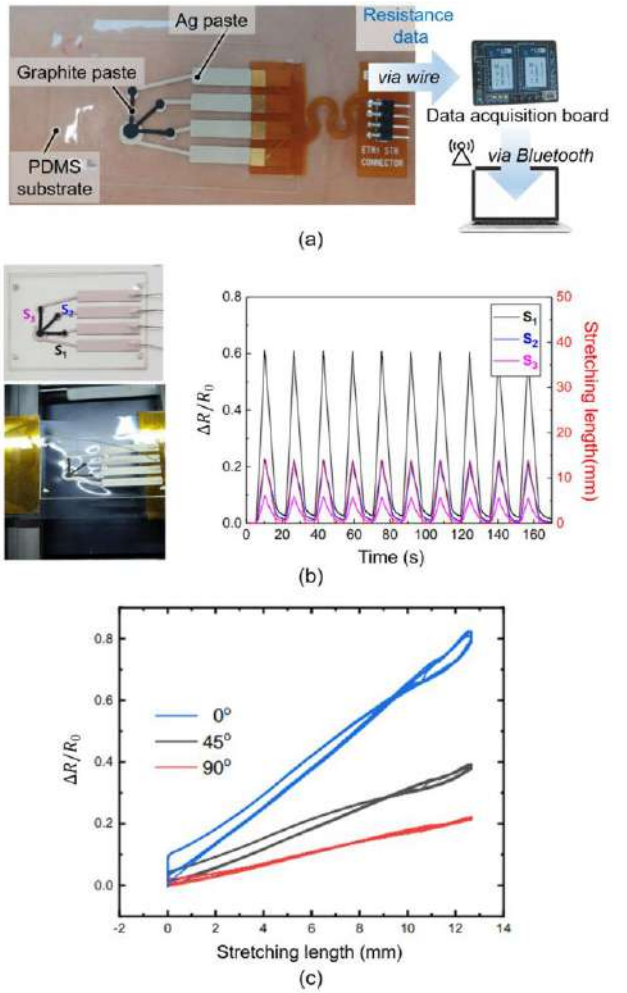


Fig. 2. Characteristics of the all-in-one strain patch. (a) Three strain sensors were embedded in the all-in-one strain patch to measure strain in different directions, (b) Resistance variation of the all-in-one strain patch by stretching, (c) Hysteresis observed in the all-in-one patch during stretching and releasing.

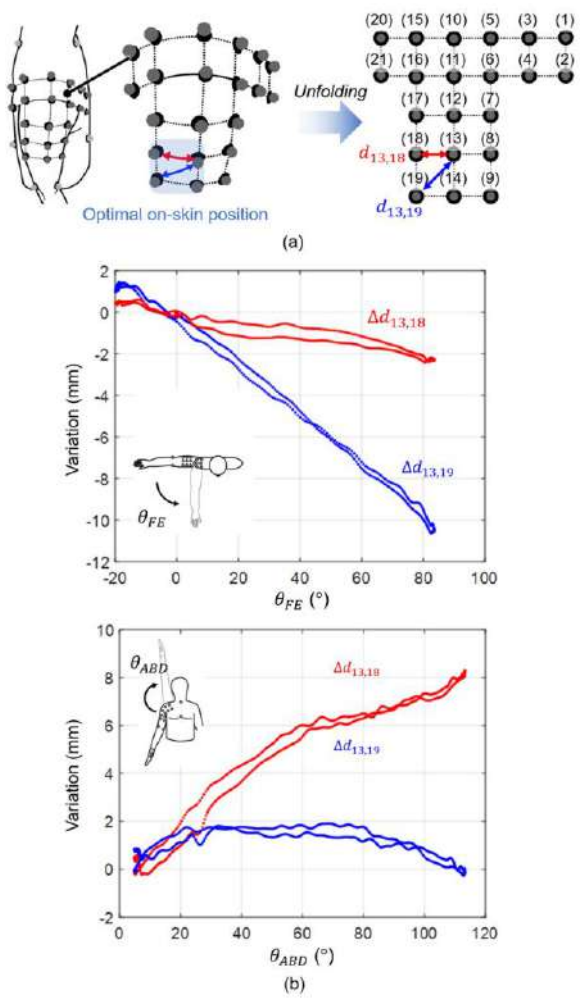


Fig. 3. Obtaining the optimal on-skin position by strain distribution analysis. (a) Identifying the optimal on-skin position where principal strains by shoulder joint movements are exhibited, (b) $d_{13,18}$ and $d_{13,19}$ were significantly changed by horizontal flexion/extension and abduction/adduction movements, respectively. Note that θ_{FE} and θ_{ABD} indicate horizontal flexion and abduction angles, respectively.

strains caused by these movements were measured using markers on a marker-grid placed around the shoulder (Fig. 3a). A marker grid was positioned around the shoulder, enabling the measurement of variations in distance between skin-to-skin positions using a motion capture system (VICON motion systems, Oxford, United Kingdom) at data acquisition frequency of 100 Hz. Note that this marker grid was designed to cover areas from the chest to the upper limb and the back. The distances between all adjacent markers within the grid were obtained during F/E and A/A tasks. Note that $d_{i,j}$ in Fig. 3a indicates the distance between the markers indexed by i and j. Thereafter, by using distance variations, the optimal on-skin position, where significant strains (i.e., principal strain) are generated by F/E and A/A movements in decoupled orientations, was determined. To find this position, two adjacent strains that significantly change due to only F/E and A/A movements, respectively, were identified among all strains by calculating their ratio during F/E and A/A movements, as follows:

$$\left\| \left(\left| \frac{\Delta d_{i,j,FE}}{\Delta d_{k,l,FE}} \right|, \left| \frac{\Delta d_{k,l,ABD}}{\Delta d_{i,j,ABD}} \right| \right) \right\|, where\ i = k\ or\ j = l \quad (1)$$

$\Delta d_{i,j,FE}$ and $\Delta d_{k,l,FE}$ indicate the distance variations between the markers indexed by i and j, and k and l, respectively, during the F/E movement. $\Delta d_{i,j,ABD}$ and $\Delta d_{k,l,ABD}$ indicate the distance variations between the markers indexed by i and j, and k and l, respectively, during the A/A movement. Note that (1) can be maximized at the optimal position due to the principal strains.

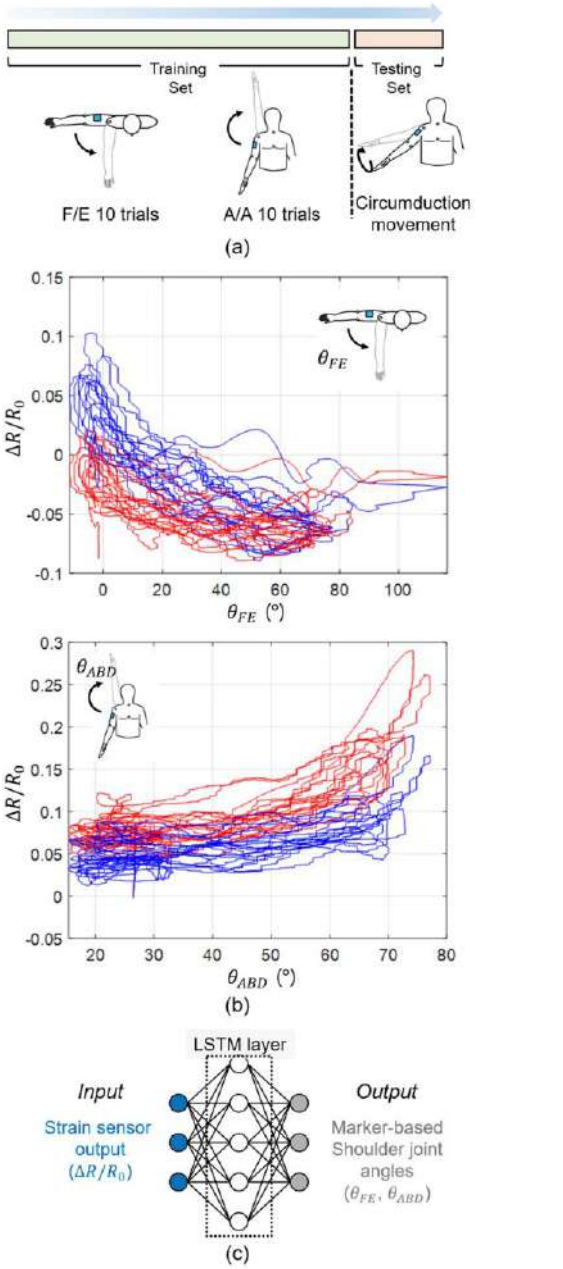


Fig. 4. Procedure to obtain relationship between sensor resistances and shoulder joint angles. (a) Sensor resistances and marker-based shoulder joint angles, measured during 10 repetitions of horizontal flexion-extension (F/E) and abduction-adduction (A/A) movements, were used for mapping. The all-in-one strain patch and reflective markers were attached for the measurement, (b) Recorded sensor resistances and shoulder joint angles. Note that θ_{FE} and θ_{ABD} indicate horizontal flexion and abduction angles, respectively, (c) Long-term short memory (LSTM) layer used to establish relationship between sensor resistances and shoulder joint angles.

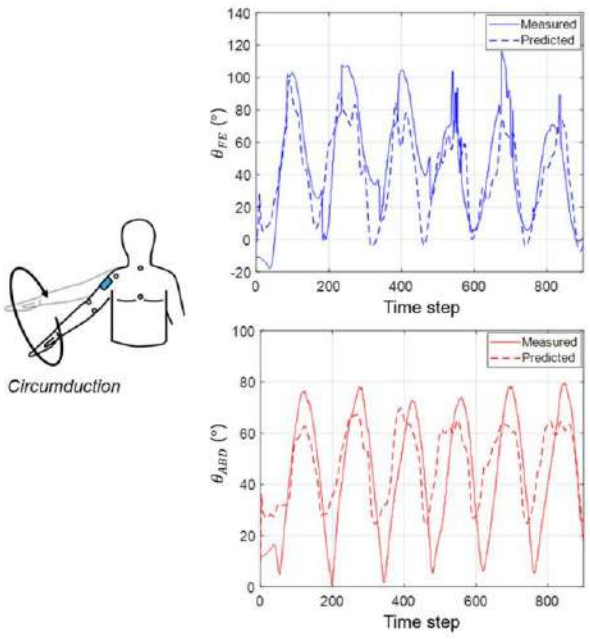


Fig. 5. Prediction results of θ_{FE} and θ_{ABD} using recorded resistance variations of the all-in-one strain patch. Note that θ_{FE} and θ_{ABD} indicate horizontal flexion and abduction angles, respectively.

The optimal skin position was found to be located at the marker indexed by 13 in Fig. 3a. Note that the principal strain (i.e., $d_{13,18}$ and $d_{13,19}$) on the optimal skin position and the corresponding shoulder joint angle exhibited a strong linear relationship (Fig. 3b).

E. Mapping between Shoulder Kinematics and Sensor Output

The relationship between the shoulder joint angle and the resistance variations of the all-in-one strain patch was established. To establish this relationship, the all-in-one patch was attached to the optimal on-skin position. Note that the reflective markers were simultaneously attached for shoulder joint angle measurement. The sensor resistances and marker trajectories were then recorded during 10 repetitions of F/E and A/A movements (Fig. 4a). Note that the sensor resistances were recorded at a frequency of 25 Hz. The subject was instructed to flex the shoulder horizontally and abduct it maximally for 2, 4, and 6 seconds, respectively. Using the recorded data (Fig. 4b), the relationship between the sensor resistances and marker-based shoulder joint angles was established using a machine learning (Fig. 4c). While the principal strain on the skin and the targeted shoulder joint angle exhibited a highly linear relationship, as shown in Fig. 3b, velocity dependency and hysteresis of the sensor led to non-linearity. Therefore, a single long short-term memory (LSTM) layer was used to establish the relationship using MATLAB software (MathWorks Inc. Natick, United States) with an Adam-based solver.

F. Evaluation Methods

1) Shoulder Kinematics Estimation: The estimation accuracy of shoulder kinematics using the all-in-one strain patch was evaluated. The subject was instructed to move the shoulder in circumduction (Fig. 4a), with the all-in-one strain patch attached to the determined optimal on-skin position. Note that reflective markers were also placed on the body to obtain marker-based shoulder joint angles (i.e., ground truth). Using the recorded sensor output, the FE and ABD angles were predicted and then compared with the ground truth.

2) Comfort: The subject was asked to mark a 10-cm-long line to indicate their satisfaction with the all-in-one strain patch in terms of comfort.

III. Results

A. Shoulder Kinematics Estimation

Shoulder kinematics could be estimated using the single all-in-one strain patch (Fig. 5). It was confirmed that the shoulder joint angle could be predicted with an error of 18.0° ± 11.7° for F/E and 14.9° ± 9.2° for A/A. These errors corresponded to 12.9% and 18.6% (15.8% on average) of their respective maximal ROM observed during the circumduction movement. The error was most significant when the shoulder joint was in a maximally flexed or abducted posture and was considered to be primarily attributed to the velocity-dependency and hysteresis of the sensor. Note that the trained LSTM layer could predict the training data set with a root mean square error (RMSE) less than 7.5°.

B. Comfort

The strain patch was rated 9.0 by the subject for comfort. The reduced score was attributed to the rigidity of the data acquisition board required to acquire the sensor output. Nonetheless, due to lightweight design of the patch (i.e., 2 g), the subject reported negligible inertia force from the sensor during shoulder movement. Additionally, no detachment of the patch from the skin was observed.

IV. Discussion

In this study, we present a skin-adhesive all-in-one strain patch capable of estimating shoulder kinematics through placement optimization based on the strain distribution analysis of skin during movements. The placement optimization enabled the single patch, where three strain sensors are embedded, to estimate shoulder kinematics by measuring skin strains generated during F/E and A/A movements. Specifically, the optimal skin position, where strains caused by F/E and A/A movements are decoupled, was identified, and the corresponding strains were measured by attaching the strain patch. Thus, by establishing the relationship between skin strains and shoulder joint angles, shoulder kinematics in two DOFs was predicted. For a single subject, it was preliminarily demonstrated that shoulder kinematics could be estimated using the single patch with optimized placement. Moreover, due to the lightweight (i.e., 2 g) and ultra-thin (i.e., < 600 μm) characteristics of the patch, the subject reported comfort while moving the shoulder with the patch attached.

The placement optimization can reduce the number of strain patches required for shoulder kinematics estimation. Shoulder kinematics have typically been estimated using a number of skin-adhesive strain patches equal to the targeted shoulder DOFs [16-18]. However, minimizing the number of

strain patches used for shoulder kinematics estimation is desirable for convenient use in daily life. Identifying the optimal on-skin position, where principal strains are generated, allows for the use of a single all-in-one strain patch to estimate shoulder joint angles. For the subject, this optimal on-skin position was found to be located on the upper limb, rather than near the shoulder. Note that the skin strains near the shoulder were influenced by both F/E and A/A movements. Additionally, the optimal on-skin position was easily accessible to the subject, allowing the all-in-one strain patch to be attached without assistance, demonstrating its potential for convenient use. This optimal on-skin position may vary between individuals due to differences in skin conditions, requiring placement optimization for each subject based on the strain distribution analysis of skin before use.

The principal strain and the corresponding shoulder joint angle show a strong linear relationship during movements, indicating the possibility of shoulder kinematics estimation without the use of machine learning. However, despite the linear relationship, machine learning was necessary due to the non-linearity between strain and sensor resistance, caused by velocity dependency and hysteresis, resulting in an error of 15.8% in kinematics estimation. This error was greater than the estimation accuracy reported with a tight shirt (i.e., 2.0% [12]) and comparable to that of multiple strain patches (i.e., 11.3% [16]). Although precise joint angle estimation using the strain patch was challenging, shoulder posture was considered sufficiently predictable, potentially allowing its application in rehabilitation games.

This study has limitations. Internal/external rotation was excluded from the kinematics estimation performed by the all-in-one strain patch. Moreover, the feasibility of using the all-in-one patch for shoulder kinematics estimation was preliminarily demonstrated only with a young subject. Further evaluation on elderly individuals is needed, as varying skin conditions may affect estimation accuracy. Additionally, the LSTM layer used in this study requires refinement to enhance shoulder kinematics estimation accuracy.

V. Conclusion

This study presents an all-in-one strain patch with optimized on-skin placement for shoulder kinematics estimation. To facilitate rehabilitation, minimizing the number of skin-adhesive strain patches required for motion feedback is essential. To achieve this, we propose a methodology to reduce the number of patches needed for the kinematics estimation. It was preliminarily demonstrated that shoulder kinematics could be predicted using the single patch at the optimal on-skin position.

In future studies, this placement optimization approach will be applied to the estimation of shoulder kinematics in 3 DOFs with more subjects. Additionally, to improve estimation accuracy, the LSTM layer will be refined by incorporating more layers and using additional sensor and shoulder joint angle data sets for training, while minimizing both the velocity dependency and hysteresis of the sensor patch through material optimization.

References

[1] J. -H. Park, J. -H. Shin, H. Lee, J. Roh and H. -S. Park, "Relevance of Upper Limb Muscle Synergies to Dynamic Force Generation: Perspectives on Rehabilitation of Impaired Intermuscular Coordination in Stroke," *IEEE Trans Neural Syst Rehabil Eng*, vol. 31, pp. 4851-4861, 2023.

[2] G. Seo, J.-H. Park, H.-S. Park, and J. Roh, "Developing new intermuscular coordination patterns through an electromyographic signal-guided training in the upper extremity," *J Neuroeng Rehabil*, vol. 20, no. 1, pp. 112, 2023.

[3] J.-H. Park, J.-H. Shin, H. Lee, J. Roh, and H.-S. Park, "Alterations in intermuscular coordination underlying isokinetic exercise after a stroke and their implications on neurorehabilitation," *J Neuroeng Rehabil*, vol. 18, pp. 1-17, 2021.

[4] K. Cha, J. Wang, Y. Li, L. Shen, Z. Chen, and J. Long, "A novel upper-limb tracking system in a virtual environment for stroke rehabilitation," *J Neuroeng Rehabil*, vol. 18, pp. 1-13, 2021.

[5] W.-S. Kim, S. Cho, J. Ku, Y. Kim, K. Lee, H.-J. Hwang, and N.-J. Paik, "Clinical application of virtual reality for upper limb motor rehabilitation in stroke: review of technologies and clinical evidence," *Journal of clinical medicine*, vol. 9, no. 10, pp. 3369, 2020.

[6] G. Alankus, and C. Kelleher, "Reducing compensatory motions in motion-based video games for stroke rehabilitation," *Human–Computer Interaction*, vol. 30, no. 3-4, pp. 232-262, 2015.

[7] O. Mubin, F. Alnajjar, A. Al Mahmud, N. Jishtu, and B. Alsinglawi, "Exploring serious games for stroke rehabilitation: a scoping review," *Disabil Rehabil Assist Technol*, vol. 17, no. 2, pp. 159-165, 2022.

[8] E. Ghorbel, R. Baptista, A. Shabayek, D. Aouada, M. G. Oramaeche, J. O. Lago, and L. O. Fernandez, "Home-based rehabilitation system for stroke survivors: a clinical evaluation," *Journal of medical systems*, vol. 44, pp. 1-11, 2020.

[9] I. Van Crombrugge, S. Sels, B. Ribbens, G. Steenackers, R. Penne, and S. Vanlanduit, "Accuracy assessment of joint angles estimated from 2D and 3D camera measurements," *Sensors*, vol. 22, no. 5, pp. 1729, 2022.

[10] A. Barzegar Khanghah, G. Fernie, and A. Roshan Fekr, "Joint angle estimation during shoulder abduction exercise using contactless technology," *BioMedical Engineering OnLine*, vol. 23, no. 1, pp. 11, 2024.

[11] G. Du, Z. Ding, H. Guo, M. Song, and F. Jiang, "Estimation of Lower Limb Joint Angles Using sEMG Signals and RGB-D Camera," *Bioengineering*, vol. 11, no. 10, pp. 1026, 2024.

[12] Y. Jin et al., "Soft Sensing Shirt for Shoulder Kinematics Estimation," *2020 IEEE Int Conf Robot Autom (ICRA)*, pp. 4863-4869.

[13] M. I. Mokhlespour Esfahani and M. A. Nussbaum, "A "Smart" Undershirt for Tracking Upper Body Motions: Task Classification and Angle Estimation," *IEEE Sensors Journal*, vol. 18, no. 18, pp. 7650-7658, 2018.

[14] K. Ogata and Y. Matsumoto, "Estimating Movements of Human Body for the Shirt-Type Wearable Device Mounted on the Strain Sensors Based on Convolutional Neural Networks," *2019 Annu Int Conf IEEE Eng Med Biol Soc (EMBC)*, pp. 5871-5876.

[15] A. Carnevale, U. Longo, E., Schena et al., "Wearable systems for shoulder kinematics assessment: a systematic review," *BMC Musculoskelet Disord*, vol.20, pp. 546, 2019.

[16] H. Lee, J. Cho and J. Kim, "Printable skin adhesive stretch sensor for measuring multi-axis human joint angles," *2016 IEEE Int Conf Robot Autom (ICRA)*, pp. 4975-4980.

[17] A. Dimo, U. G. Longo, E. Schena and D. L. Presti, "A 3-D-Printed Wearable Sensor Based on Fiber Bragg Gratings for Shoulder Motion Monitoring," *IEEE Sensors Journal*, vol. 24, no. 10, pp. 16145-16152, 2024.

[18] A. Carnevale et al., "Wearable stretchable sensor based on conductive textile fabric for shoulder motion monitoring," *IEEE International Workshop on Metrology for Industry 4.0*, vol.2020, pp. 106-110, 2020.

[19] R. Zhang, L. Chen, Y. Hu, Y. Zhang, J. Chen, T. Liang, X. Sun, and Q. Wang, "Textile-sensing wearable systems for continuous motion angle estimation: a systematic review," *International Journal of Human–Computer Interaction*, vol. 40, no. 23, pp. 7819-7839, 2024.

Comparative Analysis of Force Myography and Electromyography Signals in Isokinetic Ankle and Knee Joint Motion

Charlotte Marquardt*‡, Gunther Kurz†, Miha Dežman*, Thorsten Stein† and Tamim Asfour*‡

***Abstract*— Exoskeletons aim to enhance mobility by integrating muscle-level biomechanics and by addressing limitations like personalized control, with sensing methods such as electromyography (EMG) and force myography (FMG) to provide biofeedback. Previous comparative analyses of EMG and FMG were focused on specific classification and regression tasks without accounting for the full range of motion (RoM) of the human joints. This paper presents a descriptive analysis of both FMG and EMG signals of eight leg muscles obtained in a user study with ten participants, comparing both signals and their variations across the complete RoM of the ankle and knee joints during isokinetic motion at four different joint angular velocities. Results indicate that FMG signals exhibit higher repeatability in maximum amplitude and the corresponding joint angle, though they show higher variability in the signals' full width at half maximum. While EMG features are influenced by changes in angular velocities, FMG signals appeared to be more susceptible to cross-talk caused by opposing muscle activities. This analysis contributes to a better understanding of the relationship between FMG and EMG and their potential applications in the control of assistive wearable technologies.**

I. INTRODUCTION

Wearable robotic systems such as exoskeletons are created to aid or enhance mobility. While the primary focus of these devices has been on joint biomechanics, there is a growing interest in integrating muscle-level biomechanics for more effective interaction with the user's musculoskeletal system. Incorporating muscle-level biomechanics into the design and control of exoskeletons has the potential to address current limitations, such as the lack of personalized control. This includes the manual adjustment of control parameters for each user and monitoring user fatigue or energy expenditure [1]. Research on muscle biomechanics offers valuable data and insights for understanding human movements and joint function, thereby enhancing the effectiveness of exoskeleton control [2].

Muscle contraction is influenced by the frequency of electrical action potentials. The central nervous system activates slow muscle fibers at low frequencies and fast muscle fibers at high frequencies. Engaging more motor units, especially fast ones, during movement leads to greater force and more dynamic contractions [3]. Electromyography (EMG) gives the quantitative and objective recording of muscle function during a contraction and thus the recording of muscle activity [4]–[6]. Additionally, this facilitates the detection of changes in contraction patterns due to fatigue during prolonged exertion. Changes in EMG signals can generally be utilized to control the exoskeleton in various applications [7], [8]. Force myography (FMG) detects mechanical changes associated with muscle contraction rather than electrical effects. It measures the normal forces resulting from changes in muscle volume during contraction which is related to the muscle activity [9], [10].

To integrate muscle biomechanics into the control of exoskeletons, sensors and methods are required to acquire or approximate biosignals. Non-invasive technologies such as EMG or FMG offer the potential to measure muscle activity and integrate this information into control [1], [11]. The quality of the EMG signal is influenced by factors such as the positioning of the electrodes, tissue properties, physiological cross talk, and changes in the distance between the muscle and the electrodes due to muscle movement [12], [13]. Therefore, the recording of EMG signals involves precise preparation for data acquisition and extensive signal post-processing. On the other hand, FMG does not necessitate direct skin contact or as precise sensor placement and complex post-processing as EMG [9], [10].

Various research studies have been conducted on the performance of FMG and EMG in upper limb motion control applications. The findings suggest that FMG offers greater accuracy and repeatability compared to EMG, as well as higher stability over time, in both offline and online usability tests, particularly when there is a time gap between training and testing [9], [14]–[17]. This makes FMG more suitable

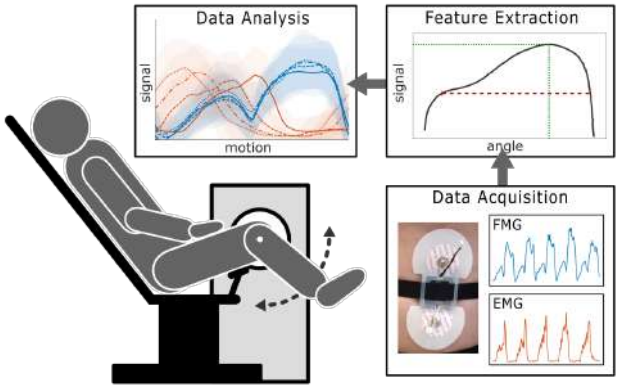


Fig. 1: Schematic demonstration of the experimental setup and process of data acquisition, feature extraction, and analysis.

This work has been supported by the Carl Zeiss Foundation through the JuBot project and the German Federal Ministry of Education and Research (BMBF) under the Robotics Institute Germany (RIG).

*High Performance Humanoid Technologies Lab, Institute for Anthropomatics and Robotics, Karlsruhe Institute of Technology (KIT), Germany
†BioMotion Center, Institute of Sports and Sports Sciences, Karlsruhe Institute of Technology (KIT), Germany
‡ Corresponding authors: {charlotte.marquardt,asfour}@kit.edu

for assistive exoskeleton applications for daily activities, as it does not require users to undergo retraining after frequent use. In contrast, EMG is better suited for rehabilitation applications where continuous monitoring of muscle activity is required [14]. And while an EMG signal can indicate the onset of contraction, an FMG signal is better suited for identifying the end of contraction [18]. Overall, FMG-based methods appear to be more effective for classification and regression control in daily exoskeleton use and are preferred by users [15]. This makes FMG a promising, yet less explored technology for the control of wearable systems.

Recent studies [16], [19]–[23] indicate that combining FMG and EMG sensing enhances muscle activity analysis. This integration can benefit from their complementary strengths for a more thorough assessment of muscle function. While most co-located, sensing devices are used in forearm or hand motion recognition, Wang et al. [23] introduced a dual-mode wearable system for monitoring lower-extremity muscular activity. It utilizes a multi-channel pressure sensing matrix to map FMG in a single muscle while simultaneously capturing electrophysiological signals with a custom EMG module. Experimental results indicate that this system effectively captures both the activation and structural changes in the tibialis anterior and gastrocnemius medialis muscle. Both sensor modalities demonstrate high stability and repeatability during walking, and the measured data of muscle activity complements each other during certain gait phases, enhancing gait phase recognition accuracy.

In our previous research, we investigated the application of FMG for exoskeletons, utilizing barometric pressure-based FMG units [10] and compared it to EMG regarding its positioning. Our current work diverges from previous studies by providing a comprehensive descriptive analysis of both FMG and EMG signals gathered concurrently and collocated. This study explores the similarities and variations in signal amplitude, occurrence of maximum amplitude, and variability between these two signal modalities throughout the full range of motion (RoM) of the ankle and knee joints in isokinetic sagittal motion. By examining these parameters, we aim to enhance our understanding of the relationships between FMG and EMG signals and their dependence on joint angle and joint velocity. The findings from this analysis not only contribute to the existing knowledge of FMG and EMG but pave the way for future research focused on optimizing exoskeleton performance through customized design options and control mechanisms.

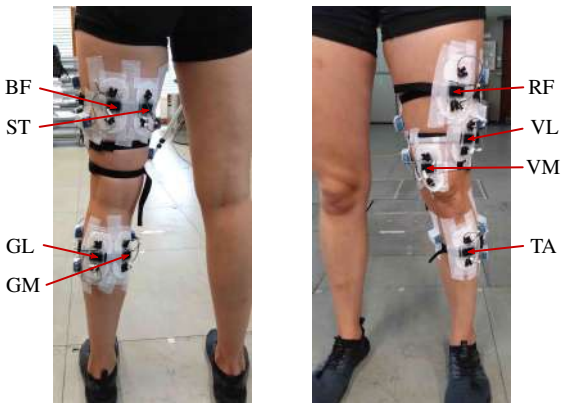
II. METHODS

This section outlines the sensor setup and the user study used for data acquisition, followed by the signal processing and feature extraction, and concluded by the analysis methods as indicated in Fig. 1.

A. Sensor Setup

The sensor unit for FMG, as explained in [10], detects the normal force resulting from alterations in the volume and stiffness of the human muscle beneath the cuff during leg movement. It contains five barometric pressure sensors on a single printed circuit board (PCB), all housed under a silicon dome. Changes in pressure identified by these sensors signify changes in the forces exerted on the silicon dome.

The muscle activity of *rectus femoris (RF)*, *biceps femoris (BF)*, *semitendinosus (ST)*, *vastus medialis (VM)*, *vastus lateralis (VL)*, *gastrocnemius medialis (GM)*, *gastrocnemius lateralis (GL)* and *tibialis anterior (TA)* was measured using eight FMG units and eight EMG electrode pairs placed at specific anatomical locations, as indicated in Fig. 2. The



(a) (b)

Fig. 2: EMG (white electrodes) and FMG (black straps) sensor positions on the back (a) and front (b) of the left leg.

placement of the sensors was determined based on recommendations from SENIAM [24] and real-time feedback from the EMG sensor. Each EMG electrode pair was positioned directly above and below the FMG sensor unit, leaving a distance of about 20 mm between the electrodes, along the muscle to ensure common measurement points. In addition, the respective angular position θ_J of the joints were recorded via the IsoMed 2000 device (Fig. 3).

B. User Study

The user study was conducted in a controlled laboratory setting using an IsoMed 2000 device. This device offers an integrated mode enabling isokinetic motion of one joint at a time in the sagittal plane (Fig. 3). In isokinetic motion, the velocity of limb movement remains constant even as muscle forces vary. Additionally, it provides a direct on-axis measurement of the true joint torque.

For this study, we analyzed ten healthy adults, their characteristics are detailed in Table I. The experimental protocol received approval from the Ethics Committee of the

TABLE I: Participant Information

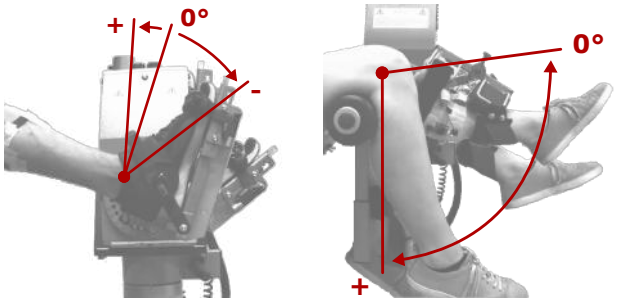
Age (y)	**Thigh length (cm)**	**Max. thigh circ. (cm)**
26.8 ± 3.2	44.0 ± 1.72	53.5 ± 4.28
Height (cm)	**Shank length (cm)**	**Max. shank circ. (cm)**
175.2 ± 6.78	42.0 ± 1.96	35.7 ± 1.44

Values represent the mean and standard deviations.

Karlsruhe Institute of Technology (KIT) as part of the JuBot project. All participants provided written informed consent before participating in the experiment, and all methods were conducted in accordance with the Declaration of Helsinki.

The experiment was conducted with participants seated on the IsoMed device, secured with their left leg on a foot or shank support. This enabled pure sagittal motion of the ankle or knee joint respectively (Fig. 3). Each participant had a familiarization period of up to 10 min with the IsoMed device. During this time, the alignment of the device's rotation axis with the sagittal joint axis of rotation was manually optimized using an integrated laser pointer. Additionally, the mechanical end stops of the device were adjusted to align with each user's maximum RoM within their anatomical limits. Following this, the participants performed two tasks in a random order:

- *Ankle*: The ankle joint was initially positioned at maximum dorsiflexion. The participant then performed five swing motions (Fig. 3a), including both dorsiflexion and plantarflexion, within their maximum active RoM. The five swing motions were repeated at four different angular velocities v_i: 30 °/s, 60 °/s, 90 °/s, and 120 °/s.
- *Knee*: The knee joint was first set to maximum extension for initialization. The participant then performed five swing motions (see Fig. 3b), including flexion and extension, within their maximum active RoM. These motions were executed at four different angular velocities v_i: 60 °/s, 90 °/s, 120 °/s, and 150 °/s.



(a) ankle (b) knee

Fig. 3: Participant set-up on the IsoMed 2000 device for ankle motion (a) and knee motion (b) and the corresponding definition of the joint angle θ_J.

The five swing motions of each joint were repeated three times for each velocity. For calibration, FMG was initialized before accessing the IsoMed device. This was done by standing upright and relaxing on both feet for approximately 10 seconds. Calibration measurements of the joint angle were conducted at each initial position $\theta_J = 0°$ as marked in Fig. 3.

C. Signal Processing

To process the EMG signals, a band-pass filter with a frequency range of 20 Hz to 500 Hz was applied, followed by rectification and a low-pass filter set at 6 Hz. All filters used were fourth-order zero-phase Butterworth filters. Outliers in the EMG signals were identified using a Hampel filter and replaced with linearly interpolated values derived from the neighboring non-outlier values. The baseline offset of the FMG was removed using the mean values obtained from the calibration measurements, no filter was applied to this signal.

The FMG sensor units have a maximum sampling rate of 200 Hz, while the EMG signals were sampled at 2000 Hz. To align and concatenate all the datasets, each dataset was linearly interpolated to achieve an equidistant number of data points. This process resulted in the down-sampling of the EMG data to match the FMG data. Both signals were normalized according to the minimum and maximum values measured for each participant and muscle after filtering.

The segmentation of each complete motion including flexion and extension of the knee joint and dorsi- and plantarflexion of the ankle joint was performed based on the joint angle and thus corresponding change in motion direction.

D. Analysis Methods

The analysis focused on the complete time-series signals during each swing motion, as well as specific features namely the peak amplitude and its corresponding joint angle, as well as the full width at half maximum (FWHM) (Fig. 4). The

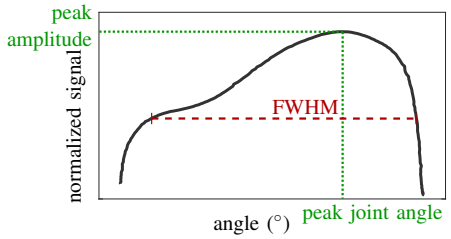
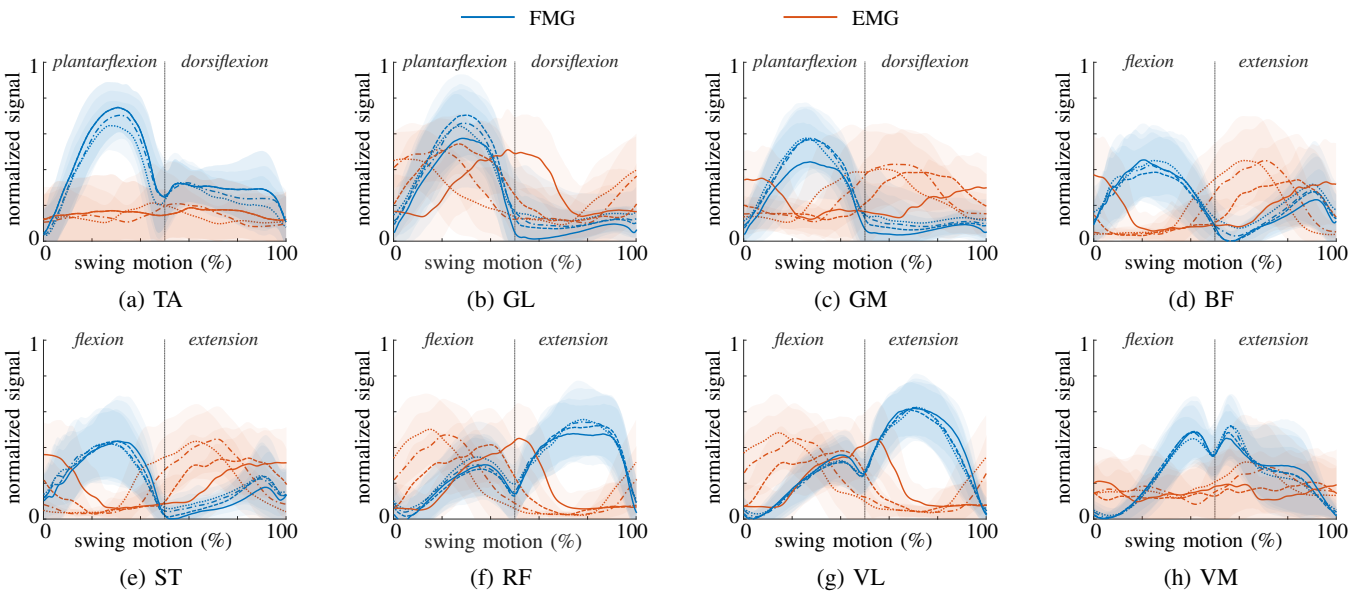


Fig. 4: Signal features analyzed in each complete swing motion over the full RoM.

peak amplitude is a distinct feature to evaluate the amount of muscular activity measured, the corresponding joint angle provides information on the amplitude distribution within the RoM and the FWHM indicates the the range of joint angles during which a muscle is active.

The variations of each feature were evaluated based on the coefficient of variation (CV), calculated for each feature over all swing motions of each participant and over all participants. The CV also known as relative or normalized standard deviation, is a standardized measure of signal variability. A lower CV corresponds to a lower variation and thus a higher repeatability of the signal. The variation analysis was conducted on the data of all four angular velocity recordings for each joint.

In a manner similar to the primary flexor and extensor muscles involved in the movement of each joint, the analysis of ankle joint motion focused on the TA (dorsiflexion), GM (plantarflexion), and GL (plantarflexion). For the knee joint motion analysis, the muscles examined included the RF (extension), VM (extension), VL (extension), BF (flexion), and ST (flexion). It's important to note that the effects of bi-articular muscles, which influence the movements of multiple joints simultaneously, were not considered in this analysis.



(a) TA (b) GL (c) GM (d) BF

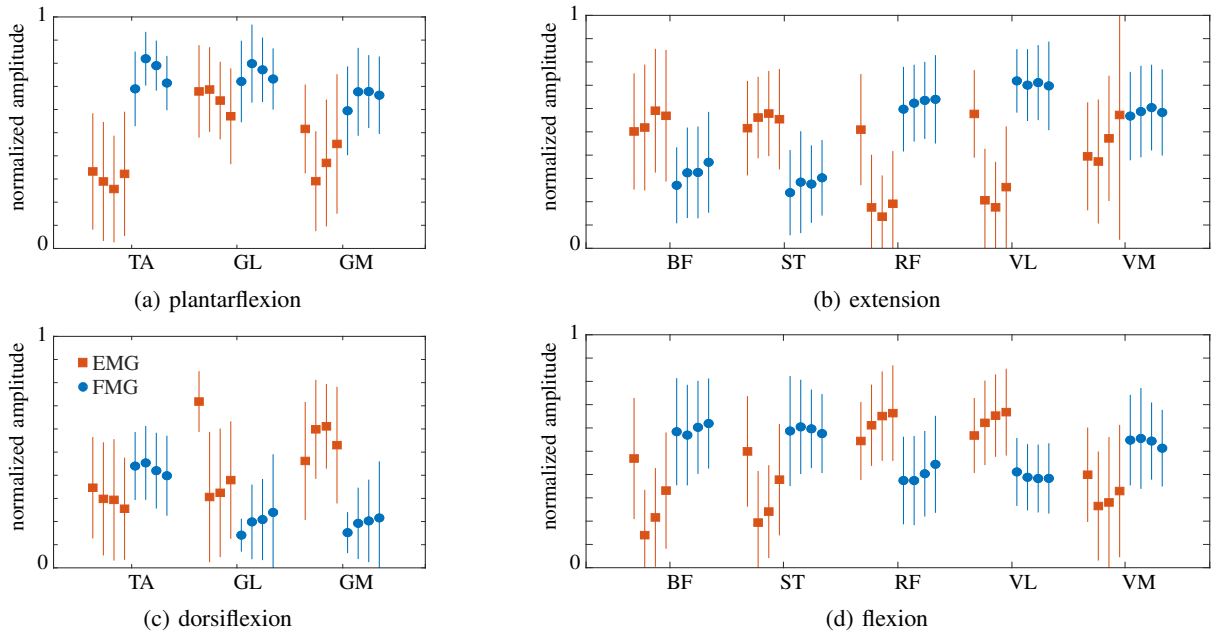
(e) ST (f) RF (g) VL (h) VM

Fig. 5: **Muscle signals**. Mean and standard deviation of the EMG and FMG signals over all participants. Each muscle is displayed separately for (a)-(c) ankle and (d)-(h) knee motion. Each graph includes all four velocities (v_1: solid, v_2: dashed, v_3: dash-dotted, v_4: dotted) of each EMG (orange) and FMG (blue) signal.

III. RESULTS

This chapter presents the results from the comparison between EMG and FMG signals after segmentation of all measurements to each complete swing motion, with a particular emphasis on three essential features: the maximum amplitude, the corresponding joint angle, and the FWHM, also considering each feature's variability.

Figure 5 displays the mean and standard deviation of the normalized EMG and FMG signals over one complete swing motion and across all participants. Each muscle is presented separately for both ankle and knee movements, and each graph includes data for all four angular velocities of the EMG and FMG signals. The transition between motion directions is emphasized in the middle of one swing motion by a



(a) plantarflexion (b) extension

(c) dorsiflexion (d) flexion

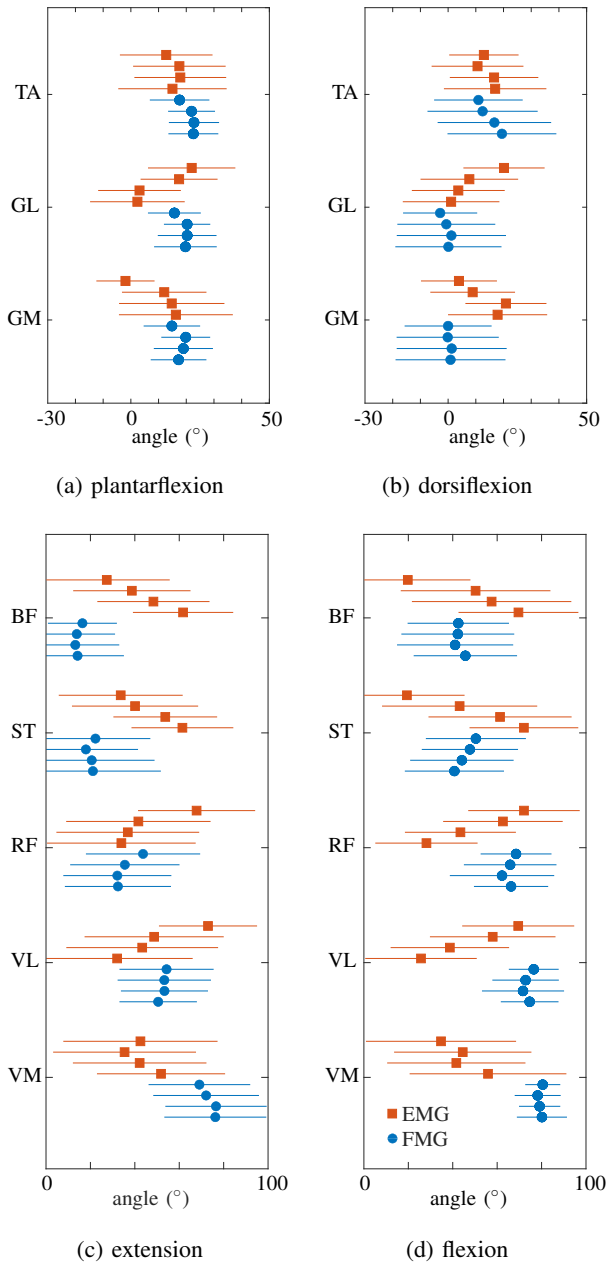
Fig. 6: **Peak signal amplitude**. Mean and standard deviation of the maximum signal amplitude for ankle (a) & (c) and knee (b) & (d) joint displayed for each motion direction. Muscle groups are categorized by the four velocities (from v_1 left to v_4 right) and by EMG (square) and FMG (circle).

vertical line. In most muscles, the EMG signal exhibits a single prominent peak, whereas the FMG signal tendentially shows two peaks, one peak per motion direction. Notably, one of these FMG peaks is generally more pronounced than the other. In the muscles contributing to knee motion, most dominantly in BF, ST, RF and VM, the muscles tend to show contrasting activity behavior between EMG and FMG. On the other hand, the TA and the VM muscle display no peak and thus consistent activation in EMG during the complete swing motion. Furthermore, the signal FMG shows a notable drop in its signal amplitude in the middle of the swing motion, coinciding with periods in which the angular velocity of the joint is zero and the direction of motion changes. This effect is not prominently observed in the EMG data. Furthermore, the EMG activation pattern appears to shift to the left with increasing velocity. In contrast, the FMG signal maintains a consistent activation pattern across all velocities.

The mean and standard deviation of the normalized maximum amplitude observed during flexion and extension in the knee joint and plantar- and dorsiflexion in the ankle joint is shown in Fig. 6. In both joints and both, EMG and FMG signals, it can be observed that the amplitude displays a contrasting behavior in its height between the flexor and extensor muscles in both motion directions. While the BF and ST muscle show a higher activity in the FMG signal during flexion of the knee joint, the opposite can be observed for the RF, VL and VM muscle. However, an opposing effect is displayed in the EMG signal. Generally, the effect is more prominent in the knee joint than in the ankle joint and the TA displays no such effect at all. Again, the FMG signal displays a higher consistency regarding the height of the maximum amplitude than the EMG signal throughout the four angular velocities.

Figure 7 shows the mean and standard deviation of the occurrence of the maximum amplitude during flexion and extension in the knee joint and plantar- and dorsiflexion in the ankle joint, dependent on the corresponding joint angle. The FMG signal demonstrates a higher consistency in the joint angle at which the maximum amplitude occurs, while the EMG has a higher dependency on the angular velocity at which the signal was obtained. It is especially notable in the EMG signal during knee joint motion that the flexor and extensor muscles (e.g. BF and ST compared with RF and VL) display a contrasting shift of the maximum amplitude within the RoM with increasing angular velocity. This shift is more pronounced in the flexion than in the extension of the knee joint. In the ankle joint this effect is less notable though still present.

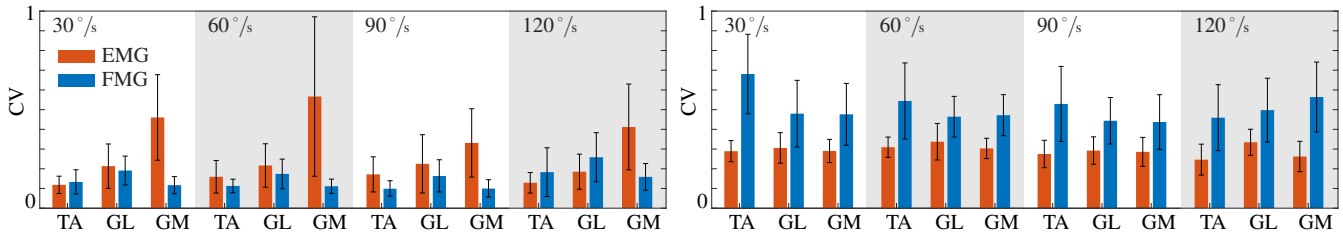
Variability was evaluated on the basis of the CV of the maximum signal amplitude and the FWHM (Figs. 8 and 9) in each muscle as the mean and standard deviation over all ten participants. The FMG generally demonstrates a lower CV for the peak signal amplitude compared to the EMG, both in terms of its mean and standard deviation. Only the TA and GL muscle demonstrate higher mean variation in FMG than in EMG at 120 °/s, RF muscle at both 120 °/s and 150 °/s. The highest variation can be observed in the EMG signal of the GM muscle in the ankle joint motion at 60 °/s and the BF muscle in the knee joint motion at 120 °/s. In contrast, the variation in the FWHM is higher for the FMG than for the EMG signal not only in its mean but also its standard deviation throughout all muscles and angular velocities. The greatest variation can be observed in the TA muscle for the FMG at 30 °/s during ankle joint motion and in the ST muscle at 120 °/s in the knee joint motion, whereas the EMG signal does not show one muscle standing out specifically.



(a) plantarflexion (b) dorsiflexion

(c) extension (d) flexion

Fig. 7: **Joint angle at peak amplitude**. Mean and standard deviation of the joint angles at the maximum signal amplitude for ankle (a)-(b) and knee (c)-(d) joint displayed for each motion direction. Muscle groups are categorized by the four velocities (from v_1 at the top to v_4 at the bottom) and by EMG (square) and FMG (circle).



(a) peak signal amplitude (b) FWHM

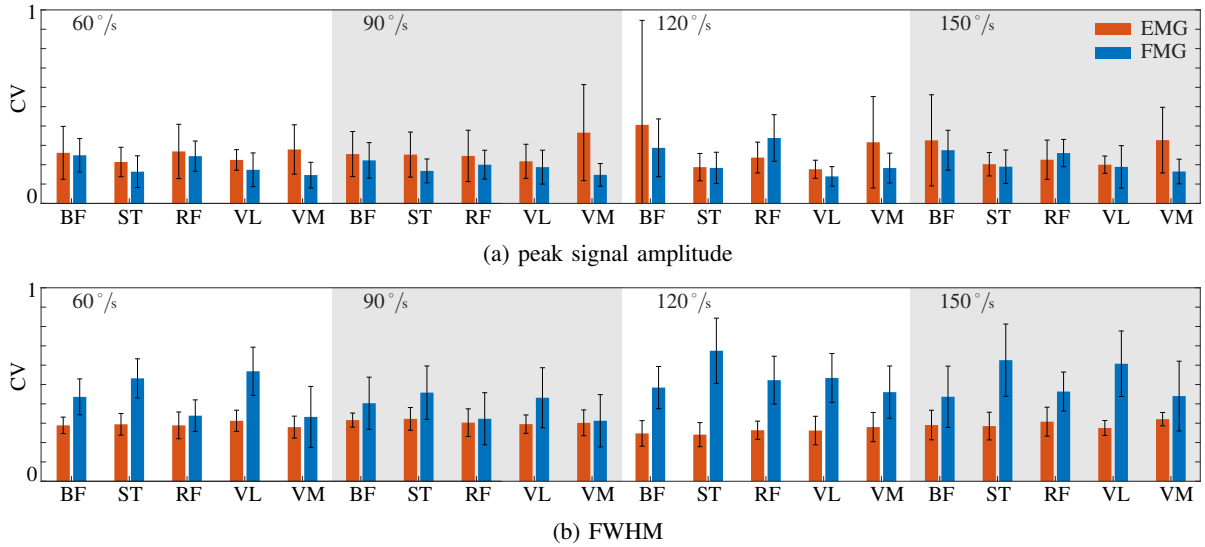
Fig. 8: **Coefficient of variation (ankle)**. Mean and standard deviation of the CV of (a) the maximum signal amplitude and (b) the FWHM of each EMG (orange, left) and FMG (blue, right) signal of each swing motion over all participants for the ankle joint.

IV. DISCUSSION

The evaluation of both FMG and EMG signals during isokinetic motion focused on maximum amplitude, the corresponding joint angle, and the FWHM. The first and last features were specifically examined for their variability. This evaluation explored the similarities and differences between these two signals throughout the RoM of the ankle and knee joints of ten participants.

Higher variations in the mean value of the maximum amplitude and the corresponding joint angle in the EMG signal (e.g. in the muscles BF and ST in Figs. 6d and 7d) suggest that EMG is more dependent on the angular velocity than FMG. The shift in the EMG signal amplitude with increasing angular velocity shown in Fig. 5 indicates a dependency on the joint angle. This observation supports the findings of Hahn et al. [25], who discovered that the excitation of all lower limb muscles measured by EMG changes based on knee flexion angles. This is also evident in the high mean values recorded for only the first angular velocity, as illustrated in Fig. 6. Notably, this includes the GL muscle during dorsiflexion, the RF and VL muscles during extension, and the BF and ST muscles during flexion, shifting them towards the opposing motion direction. On the other hand, the FMG signal exhibits a visible drop in amplitude during the transition between motion directions, as shown in Fig. 5. This occurs when the angular velocity is momentarily zero, indicating that the FMG signal is sensitive to sudden changes in angular velocity suggesting that joint acceleration has a larger influence on FMG. This supports the idea that a combination of both sensing methods could be beneficial not only in motion recognition but also in estimating kinematic and kinetic joint data.

The EMG signals show only one prominent peak during the swing motion, as displayed in Fig. 5. In contrast, the FMG signals exhibit two distinct peaks (e.g. RF, VL, and VM), corresponding to each direction of motion or a peak where no muscle activity was expected (e.g. TA) in Fig. 5. Whereas this effect is generally, more pronounced in the knee joint compared to the ankle joint, it is most drastic in the TA muscle. Since the TA muscle acts as a flexor of the ankle



(a) peak signal amplitude

(b) FWHM

Fig. 9: **Coefficient of variation (knee)**. Mean and standard deviation of the CV of (a) the maximum signal amplitude and (b) the FWHM of each EMG (orange, left) and FMG (blue, right) signal of each swing motion over all participants for the knee joint.

joint, its peak amplitude during plantarflexion should not be as prominent. A possible explanation for this is the cross-talk produced by the muscles that are covered by the strap attaching one or more FMG sensor units to the leg. Changes in shape and volume from the antagonistic muscle can affect the pressure signals measured from the agonistic muscle, either due to its muscle being activated in parallel or due to the passive motion of the leg. The soft tissue may function as a damper with its stiffness dependent on the subject or motion [26], affecting the transfer of forces between the agonistic and antagonistic muscles within the straps. Since the lower leg generally has less soft tissue than the upper leg, and the shinbone is situated close to the surface, the cross-talk observed in the TA muscle could be more pronounced. In the future, the effect based on passive motion could be studied and potentially excluded by measuring the FMG signal obtained by leg motion while the participant is in a relaxed state. Additionally, it is important for the design of an exoskeleton to consider the sensitivity of FMG sensors to cross-talk. When these FMG sensors are integrated into the cuffs of an exoskeleton, they should be designed to be as decoupled from one another as possible.

The analysis of the EMG signals from both the TA and VM muscles reveals a generally low signal amplitude, as depicted in Fig. 5, with a slightly lesser effect observed in the VM muscle. Enhanced noise can obscure significant maxima, leading to the filtering of insufficiently pronounced peaks and complicating data interpretation. The stochastic nature of EMG signals, characterized by rapid fluctuations, contributes to challenges in post-processing, potentially resulting in undetected outliers and reduced normalization quality. Furthermore, peaks in muscle activation may occur at varying stages of the swing motion for each participant, which could lead to cancellation when calculating the mean across participants. Addressing these limitations is essential for advancing our understanding of muscle activation patterns and improving the efficacy of wearable robotic systems in clinical and rehabilitative contexts.

The signals from EMG and FMG exhibit nearly opposite behaviors with respect to their signal amplitude. This phenomenon can be observed during a complete swing motion, where the normalized maximum amplitude occurs in contrasting phases/directions of the motion, which is especially prominent in the knee joint motion. This distinction may account for the improved performance of classification methods in [19]–[23] that combine both EMG and FMG signals, as their differing features and variability provide a complementary advantage for feature-based, data-driven machine learning approaches.

The EMG signals exhibit greater variability in the activation patterns between the participants compared to the FMG signals. Specifically, the FMG signals demonstrate enhanced repeatability in terms of maximum amplitude across multiple participants, aligning with the observations reported in previous studies [16], [17]. In contrast, the duration of muscle activity, as measured by FWHM, shows greater consistency in the EMG signals, as evidenced by their lower CV. This discrepancy suggests that while FMG signals may provide more reliable peak amplitude readings, the EMG signals offer a more stable representation of the duration of muscle activation. However, no general trend regarding variations within any angular velocity can be extracted from either EMG or FMG in the peak amplitude and the FWHM.

However, it is important to note that a limited number of participants exhibited a small subset of muscles with either a markedly elevated or non-existent CV. For instance, the VM muscle in two participants displayed such outlier behavior. In particular, these outliers did not correlate with any identifiable characteristics of the participants, suggesting that external factors may play a role in these variations. One plausible explanation for this phenomenon is sensor misalignment or interference caused by the attachment of participants to the IsoMed device. The necessity for precise positioning of the IsoMed actuation levers to avoid interference with the EMG and FMG electrode locations may have inadvertently introduced variability in the signal quality. This highlights the importance of ensuring optimal electrode placement and minimizing external influences to enhance the reliability of EMG and FMG readings.

The study's findings are based on a relatively small sample size of ten participants, which may limit the statistical power necessary for rigorous hypothesis-driven analysis. Consequently, we advise that these results be interpreted as preliminary indicators that warrant further investigation. It would be beneficial to explore these findings in subsequent research with a larger and more diverse participant group to enhance the validity and generalization of the conclusions drawn. Such efforts would contribute significantly to advancing our understanding of the topic.

Although the data presented in this paper provide valuable information on both EMG and FMG, the untapped potential remains to be explored. A more in-depth examination of each specific motion direction, focusing on both agonistic and antagonistic muscles, could yield additional information. Furthermore, a closer analysis of the FWHM alongside the corresponding joint angles may reveal relevant details about the range of motion detectable by the muscular signals of each sensing method and the extent to which they can be measured. The results of this paper offer strong potential for deeper exploration, especially in highlighting the benefits and limitations of FMG compared to EMG.

V. CONCLUSION

The evaluation of FMG and EMG signals during isokinetic motion reveals that FMG signals demonstrate higher repeatability in maximum amplitude and corresponding joint angle both within and across participants compared to EMG signals, which show more consistent muscle activity duration. Although high repeatability supports the generalization of control methods for different users of wearable robots, signals with higher variability can contribute to the personalization of control, allowing for the adaptation of the controller to satisfy the particular requirements of individual users. While EMG signals appear to be more affected by

angular velocity, FMG signals seem more sensitive to sudden changes in angular velocity. The contrasting and augmenting behavior of EMG and FMG signals, particularly in signal amplitude during motion phases, suggest that combining these signals enhances their performance in application due to their complementary features and indicates their potential for comprehensive motion recognition and joint data estimation. Future research could focus on exploring these complementary strengths to develop more effective control systems for wearable robotics, while also addressing FMG's sensitivity to cross-talk and EMG's normalization challenges. Furthermore, the results underscore FMG as a promising method for the integration of biofeedback in the control of wearable robotic technologies.

ACKNOWLEDGMENT

The authors would like to thank Melina Beyerlein, Michael Herzog, and Cagla Kettner from the BioMotion Center at the Institute of Sports and Sports Sciences (KIT) for their valuable input on the variability analysis and the corresponding features.

REFERENCES

[1] Z. S. Mahdian, H. Wang, M. I. M. Refai, G. Durandau, M. Sartori, and M. K. MacLean, "Tapping Into Skeletal Muscle Biomechanics for Design and Control of Lower Limb Exoskeletons: A Narrative Review," *Journal of Applied Biomechanics*, vol. 39, no. 5, pp. 318 – 333, 2023.

[2] J. Wang, D. Wu, Y. Gao, X. Wang, X. Li, G. Xu, and W. Dong, "Integral Real-time Locomotion Mode Recognition Based on GA-CNN for Lower Limb Exoskeleton," *Journal of Bionic Engineering*, Jul. 2022.

[3] E. Henneman, G. Somjen, and D. O. Carpenter, "Excitability and Inhibitibility of Motoneurons of Different Sizes," *Journal of Neurophysiology*, vol. 28, no. 3, pp. 599–620, May 1965.

[4] C. D. Joshi, U. Lahiri, and N. V. Thakor, "Classification of gait phases from lower limb EMG: Application to exoskeleton orthosis," in *2013 IEEE Point-of-Care Healthcare Technologies (PHT)*, Jan. 2013, pp. 228–231, iSSN: 2377-5270.

[5] J. Taborri, E. Palermo, S. Rossi, and P. Cappa, "Gait Partitioning Methods: A Systematic Review," *Sensors*, vol. 16, no. 1, 2016.

[6] S. Jiang, P. Kang, X. Song, B. Lo, and P. B. Shull, "Emerging Wearable Interfaces and Algorithms for Hand Gesture Recognition: A Survey," *IEEE Reviews in Biomedical Engineering*, pp. 1–1, 2021.

[7] P. Lukowicz, F. Hanser, C. Szubski, and W. Schobersberger, "Detecting and Interpreting Muscle Activity with Wearable Force Sensors," in *Pervasive Computing*. Berlin, Heidelberg: Springer Berlin Heidelberg, 2006, vol. 3968, pp. 101–116, series Title: Lecture Notes in Computer Science.

[8] L. A. Kallenberg, E. Schulte, C. Disselhorst-Klug, and H. J. Hermens, "Myoelectric manifestations of fatigue at low contraction levels in subjects with and without chronic pain," *Journal of Electromyography and Kinesiology*, vol. 17, no. 3, pp. 264–274, Jun. 2007.

[9] C. Castellini and V. Ravindra, "A wearable low-cost device based upon Force-Sensing Resistors to detect single-finger forces," in *5th IEEE RAS/EMBS International Conference on Biomedical Robotics and Biomechatronics*. Sao Paulo, Brazil: IEEE, Aug. 2014, pp. 199–203.

[10] C. Marquardt, P. Weiner, M. Dežman, and T. Asfour, "Embedded barometric pressure sensor unit for force myography in exoskeletons," in *IEEE/RAS International Conference on Humanoid Robots (Humanoids)*, Ginowan, Okinawa, Japan, 2022, pp. 67–73.

[11] Z. Zheng, Z. Wu, R. Zhao, Y. Ni, X. Jing, and S. Gao, "A Review of EMG-, FMG-, and EIT-Based Biosensors and Relevant Human–Machine Interactivities and Biomedical Applications," *Biosensors*, vol. 12, no. 7, p. 516, Jul. 2022, publisher: Multidisciplinary Digital Publishing Institute.

[12] D. G. E. Robertson, G. E. Caldwell, J. Hamill, G. Kamen, and S. N. Whittlesey, *Research Methods in Biomechanics*, 2nd ed. Human Kinetics, 2014.

[13] C. J. De Luca, "The Use of Surface Electromyography in Biomechanics," *Journal of Applied Biomechanics*, vol. 13, no. 2, pp. 135–163, May 1997.

[14] M. R. U. Islam, A. Waris, E. N. Kamavuako, and S. Bai, "A comparative study of motion detection with FMG and sEMG methods for assistive applications," *Journal of Rehabilitation and Assistive Technologies Engineering*, vol. 7, 2020, publisher: SAGE Publications Ltd STM.

[15] A. Belyea, K. Englehart, and E. Scheme, "FMG Versus EMG: A Comparison of Usability for Real-Time Pattern Recognition Based Control," *IEEE Transactions on Biomedical Engineering*, vol. 66, no. 11, pp. 3098–3104, Nov. 2019.

[16] M. Connan, E. Ruiz Ramírez, B. Vodermayer, and C. Castellini, "Assessment of a Wearable Force- and Electromyography Device and Comparison of the Related Signals for Myocontrol," *Frontiers in Neurorobotics*, vol. 10, 2016.

[17] D. A. Yungher, M. T. Wininger, J. B. Barr, W. Craelius, and A. J. Threlkeld, "Surface muscle pressure as a measure of active and passive behavior of muscles during gait," *Medical Engineering & Physics*, vol. 33, no. 4, pp. 464–471, May 2011.

[18] D. Esposito, G. D. Gargiulo, N. Parajuli, G. Cesarelli, E. Andreozzi, and P. Bifulco, "Measurement of muscle contraction timing for prosthesis control: a comparison between electromyography and force-myography," in *2020 IEEE International Symposium on Medical Measurements and Applications (MeMeA)*, Jun. 2020, pp. 1–6.

[19] A. Ke, J. Huang, L. Chen, Z. Gao, and J. He, "An Ultra-Sensitive Modular Hybrid EMG–FMG Sensor with Floating Electrodes," *Sensors*, vol. 20, no. 17, p. 4775, Jan. 2020, publisher: Multidisciplinary Digital Publishing Institute.

[20] A. Dwivedi, L. Gerez, W. Hasan, C. Yang, and M. Liarokapis, "A Soft Exoglove Equipped With a Wearable Muscle-Machine Interface Based on Forcemyography and Electromyography," *IEEE Robotics and Automation Letters*, vol. 4, no. 4, pp. 3240–3246, 2019.

[21] C. Liu, B. B. Atitallah, R. Ramalingame, R. Barioul, A. Djemal, H. Hellara, and O. Kanoun, "A Hybrid Measurement System for Hand Signs Recognition based on EMG-FMG Measurements," in *2022 IEEE 9th International Conference on Computational Intelligence and Virtual Environments for Measurement Systems and Applications (CIVEMSA)*. Chemnitz, Germany: IEEE, Jun. 2022, pp. 1–6.

[22] T. Wang, Y. Zhao, and Q. Wang, "A Wearable Co-Located Neural-Mechanical Signal Sensing Device for Simultaneous Bimodal Muscular Activity Detection," *IEEE Transactions on Biomedical Engineering*, vol. 70, no. 12, pp. 3401–3412, Dec. 2023.

[23] T. Wang, D. Jiang, Y. Lu, N. Xu, Z. Wang, E. Zheng, R. Wang, Y. Zhao, and Q. Wang, "A Dual-Mode, Scalable, Machine-Learning-Enhanced Wearable Sensing System for Synergetic Muscular Activity Monitoring," *Advanced Materials Technologies*, p. 2400857, Aug. 2024.

[24] H. J. Hermens, B. Freriks, R. Merletti, D. Stegeman, J. Blok, G. Rau, C. Disselhorst-Klug, and G. Hägg, "Seniam," 1999, publisher: Roessingh Research and Development. [Online]. Available: http://seniam.org/

[25] D. Hahn, "Lower Extremity Extension Force and Electromyography Properties as a Function of Knee Angle and Their Relation to Joint Torques: Implications for Strength Diagnostics," *Journal of Strength and Conditioning Research*, vol. 25, no. 6, pp. 1622–1631, Jun. 2011.

[26] S. Guitteny, Y. Lafon, V. Bonnet, R. Aissaoui, and R. Dumas, "Dynamic estimation of soft tissue stiffness for use in modeling socket, orthosis or exoskeleton interfaces with lower limb segments," *Journal of Biomechanics*, vol. 134, p. 110987, Mar. 2022.

System Performance Analysis of the Shoulder Elbow Perturbator

Jonathan C. van Zanten, Karien ter Welle, Claudia J.W. Haarman†, Alfred C. Schouten,
Mark van de Ruit, Winfred Mugge, and Arno H.A. Stienen∗
Biomechanical Engineering, Delft University of Technology, The Netherlands

***Abstract*—To increase the quality of life of stroke patients, better diagnostics with the ability to identify the cause of motor impairment are needed. Robotic diagnostics increases the resolution of measurements, allows for tracking progress over a longer period, and can be used to evaluate new treatments. The Shoulder Elbow Perturbator (SEP) was developed to improve the diagnostics of post-stroke motor impairment. The SEP has already been tested on patients, showing promising results in identifying the cause of motor impairment, but no SEP system performance analysis has been published. To identify the joint properties of the elbow accurately, the SEP should have a bandwidth of at least 12 Hz. Furthermore, admittance and velocity control are required for various possible experimental tasks. This paper shows that the SEP performs adequately for the desired perturbations and experimental conditions for system identification of the human elbow. The SEP's performance is analysed with multisine signals to determine the bandwidth and endpoint dynamics. The velocity controller bandwidth is 50 Hz, and the admittance controller bandwidth is 65 Hz. Furthermore, the controller is stable. Thus, the SEP meets all the requirements and should be able to provide the desired perturbations and experimental conditions needed for system identification of the human elbow.**

***Index Terms*—Shoulder Elbow Perturbator, spasticity, rehabilitation robotics, stroke, (Haptic) Manipulator**

I. Introduction

Stroke survival rate has increased drastically over the last decades. Due to the increased survival rate and an ageing society, the prevalence of disability due to stroke increases [1]. Post-stroke disability greatly impacts the patient's ability to perform activities of daily living (ADL). Improving therapeutic interventions will reduce the patient's physical and mental burden, the physician's workload, and healthcare costs [2]. Stroke can cause a wide variety of motor impairments. However, diagnosing whether the cause of motor impairment is neural or non-neural is difficult as they present similar symptoms, such as paresis, synergy, co-contraction, spasticity, or viscoelastic tissue property alterations [3]. A diagnosis capable of differentiation of the causes of impairment is desired. Clinically, impairment is quantified using ordinal scales based on a physicians assessments of a patient's voluntary joint movement and resistance to passive movement. Examples are the Modified Ashworth Scale, the Modified Tardieu Scale or the Fugl-Meyer assessment [4]. The manual assessment of motor impairment after a stroke makes quantification and distinguishing between various causes of motor impairments challenging. Therefore, there is a need for objective measurements of motor impairment, with a particular focus on differentiating between non-neural and neural components [5].

Objective measurement, with the use of robotic diagnostics, increases the resolution of measurements, allows for tracking progress over a longer period, and can be used to evaluate new treatments [5]. The system identification technique, which uses robotic diagnostics, aims to objectively identify the mechanical properties of human limbs to determine the severity and cause of the patient's motor impairment [6].

There are several joint manipulators for assessing motor function for research purposes [7, 8]. The Shoulder Elbow Perturbator (SEP) (Hankamp Rehab, Enschede), shown in Fig. 1, was developed to improve post-stroke motor impairment diagnostics. The SEP has already been tested on patients, showing promising results in identifying the cause of motor impairment [6, 9]. However, the performance of the SEP, along with its control, has not been analysed in detail.

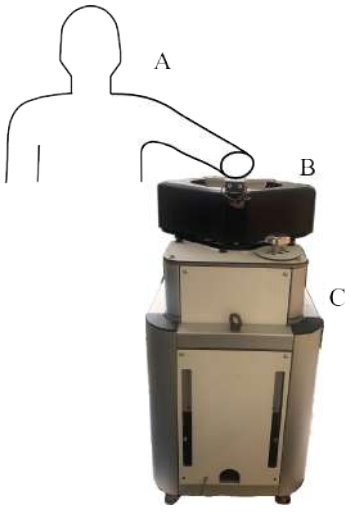


Fig. 1. The Shoulder Elbow Perturbator (SEP), with an illustration of a participant positioned in the device. The participant (A) is attached to the device with a clamp to the wrist on the ulnar and radial head. The table (B) can passively move in the vertical direction, allowing shoulder abduction and actively rotate the elbow in flexion and extension. The base (C) contains the motor and control detailed in Section II-B.

∗Jonathan C. van Zanten, Catherine S. ter Welle, Alfred C. Schouten, Mark van de Ruit, Winfred Mugge and Arno H.A. Stienen are with the Department of Biomechanical Engineering of Delft University of Technology (Netherlands). The email address for correspondence is J.C.vanZanten@tudelft.nl

†Claudia J.W. Haarman is with Hankamp Rehab, situated in Enschede.

TABLE I
HARDWARE SPECIFICATIONS OF THE SEP

Component	Hardware	Parameter	Specifications
Motor	Hiwin TMS3C	Encoder resolution	4,325,376 counts/revolution
Drive	Hiwin ED1-01	Device inertia	0.043 kg m^2
Transmission	Direct drive	Torque	60 Nm (180 Nm peak)
Force sensor & signal conditioner	Futek LCM200 AIAA100	Velocity	1,800 deg/s
		Acceleration	18,000 deg/s^2
Target PC	Lenovo Ideapad (Windows)	Range of motion (R1)	160 deg
Coupler & Terminals	Beckhoff EK1100 1x EL3102, 1x EL2002, 1x EL1202	Shoulder elevation range (D1)	20 cm

For this study, the controller performance of the SEP is optimized and the control is changed from only position control to admittance and velocity control. Admittance control is primarily used in combination with a position task. The advantage of using the position task with admittance control is that the control evokes consistent human motor control by interacting with adjustable virtual dynamics [10]. Velocity control is primarily used in combination with a force or relax task. Velocity control enables precise perturbation of the participant with the desired velocities, for example, to elicit stretch reflexes or quantify limb dynamics.

To be able to do experiments needed for system identification, the SEP should be able to perturb the arm with frequencies greater than or equal to three times the eigenfrequency of the elbow [7]. For the elbow joint, the eigenfrequency is approximately 3 Hz. For this paper, the requirement was set at four times the eigenfrequency, so the bandwidth of the SEP must be at least 12 Hz, with a stable controller. This paper shows the performance of the SEP for the desired perturbations and experimental conditions needed for system identification. The current paper shows the SEP's mechanical design, control scheme and analyses the overall system performance.

II. MECHANICAL DESIGN

A. Full Setup

A schematic representation of the mechanical setup of the SEP is shown in Fig. 2. The SEP can perturb the elbow in the horizontal plane with varying shoulder support. The elbow support is used to fixate the human elbow to the SEP by placing the elbow joint in line with the axis of rotation and clamping the wrist on the ulnar and radial head. The clamp's position can be adjusted to accommodate the patients' arm lengths. The sarrus linkage uses three parallel support beams to allow vertical movement of the elbow support while restricting horizontal movements. The linkage (3) connects the elbow support to the motor. This linkage is free to rotate whilst preserving vertical movement. The spring mechanism for the upward force provides an adjustable constant force over the range of motion. Table I presents the complete overview of the components used and their specifications [9]. Multiple safety layers, including mechanical end stops, electrical end stops, software end stops, and participant and operator emergency stops, ensure the safe operation of the SEP. The end stop location can be adjusted to ensure safety for participants with various passive ranges of motion.

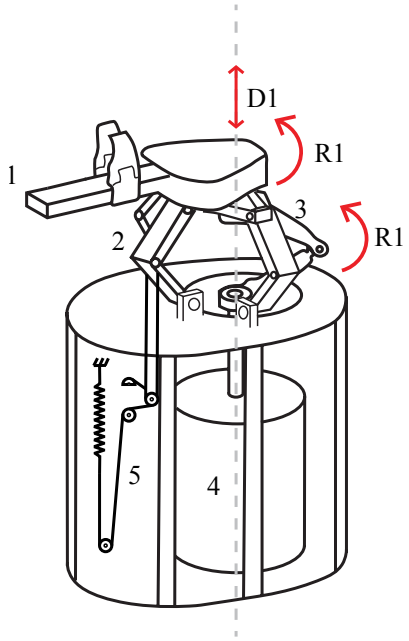


Fig. 2. Schematic representation of the SEP. The SEP contains the following parts: the elbow support (1), the Sarrus linkage, which houses the bearing for the rotation of parts 1 & 3, the linkage can not rotate or move horizontally (2), the motor-elbow support connection (3), the motor (4) and the spring mechanism exerting the constant upward force on the elbow support (5). R1 is the motor and elbow support rotation, of which the rotation axis is the grey dotted line. D1 is the possible passive vertical movement of the elbow support.

B. Hardware/Software architecture

The controller is implemented using Matlab Simulink 2024b. The Simulink model is converted to C-code and built onto the Beckhoff Twincat 3.1 software. Parameters can be controlled via Simulink in real-time. The motor driver is set to profile velocity mode. The motor driver is set to its tuneless function with the highest possible stiffness, so it follows the desired velocity to the tuneless function's maximum ability. The data used in the various control modes is transmitted back to the Simulink model from the motor and sensors. Fig. 3 shows the entire communication setup.

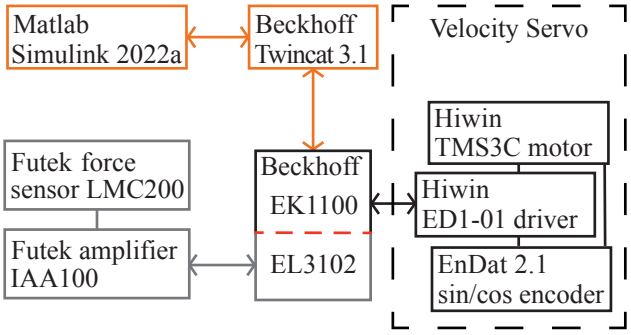


Fig. 3. Hardware/Software communication. The orange boxes represent the software running on a separate PC. The grey boxes are analogue sensors. The black boxes are digital hardware. The dotted red line represents the conversion of analogue to digital signals. The black dotted box shows the velocity servo hardware.

III. Control Scheme

The SEP has two modes of control: velocity control and admittance control. The following paragraphs explain both modes of control in detail.

A. Velocity control

In velocity control, the input is a velocity signal ($\dot{\theta}_d$) independent of the external loading in joint perturbations experiments caused by the arm and device dynamics. As mentioned in section II-B, the velocity servo is tuned to follow the input signal to its maximum ability. Thus, the motor produces the torque necessary to reach the desired velocity. The encoder measures the position (θ_m) and velocity ($\dot{\theta}_m$) of the motor used for analysis.

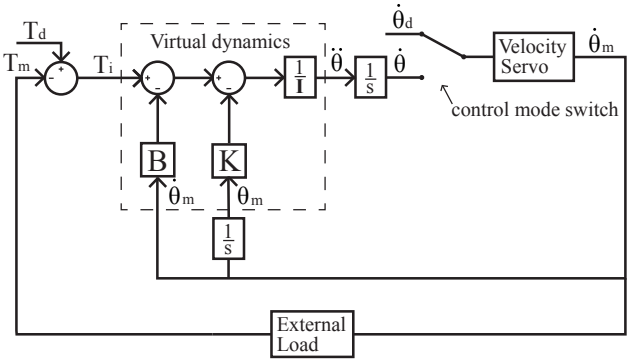


Fig. 4. Control diagram of the SEP for both modes of control. For admittance control, There is the measured torque (T_m), which is combined with a disturbance torque (T_d) to get the input for the virtual dynamics, referred to as the input torque (T_i). The virtual dynamics are the stiffness, damping and inertia, denoted with K, B and I, respectively. The output of the virtual dynamics is the desired acceleration, which is integrated to get the desired velocity. The desired velocity ($\dot{\theta}$) goes into the velocity servo, also shown in Fig. 3. The motor follows the desired velocity, resulting in a motor velocity ($\dot{\theta}_m$). The external load consists of the human and post-sensor device. The dynamics of the attached load (device + external load) on the motor create a resistance torque, the measured torque. For velocity control, there is a desired velocity ($\dot{\theta}_d$) as an input and a motor velocity ($\dot{\theta}_m$), which is the output of the driver.

B. Admittance control

In admittance control, the robotic controller's input is the external torque [11]. The controller has virtual dynamics that prescribe rotation, angular velocity, and angular acceleration in response to torque. Fig. 4 shows the admittance controller. The formula for the virtual dynamics is given in Equation 1

$$\ddot{\theta} I = T_d - T_m - B\dot{\theta}_m - K\theta_m \tag{1}$$

Where T_m is the measured torque. θ_m and $\dot{\theta}_m$ are measured the position and velocity, and T_d is the added disturbance torque for the performance analysis. Furthermore, the virtual dynamics are the stiffness, damping and inertia, denoted with K, B and I, respectively.

IV. Performance analysis

A. Perturbation signal for analysis

The perturbation signal is a multisine (i.e. a sum of sines) that excites the device over a wide frequency range of 0.1-100 Hz [12]. A wide range of perturbation frequencies helps to identify the frequency at which the servo velocity loop (H_{servo}) gain drops below -3 dB, indicating the controller bandwidth. The perturbation signal is scaled so the rotation remained within 6 degrees of the neutral position. For the experiments, the signal duration was 80 seconds. The signal was repeated four times in each trial, amounting to 320 s. Each trial was repeated five times to increase the accuracy of the performance analysis.

B. External load

The human arm introduces inertia, damping and stiffness as an external load. To ensure that the SEP functions with and without added external loads, external loading conditions were determined to mimic the extra load the human arm puts on the device. The human arm inertia was calculated by taking 2.5 kg as the weight of the arm [13], and 371 mm as the length of the forearm and hand [14] and the center of mass at 43% from its proximal end [13]. When calculating the inertia using these values, the arm inertia is 0.064 $\mathrm{kg\,m^2}$. The values are those of a large and heavy arm to get a high value for the inertia [13]. External damping is not introduced as elbow damping only makes a small contribution to the elbow joint impedance and is hard to realize. To mimic the added external stiffness of the human on the robot, two tension springs facing opposite directions are attached from the SEP to an external frame. Creating a bidirectional external stiffness of 0.84 $\mathrm{Nm/deg}$, which is in the order of magnitude of earlier identified elbow stiffness with the SEP [6]. The three external loading conditions are:

- No external load
- Added inertia (0.064 $\mathrm{kg\,m^2}$)
- Added inertia and rotational stiffness (0.064 $\mathrm{kg\,m^2}$ + 0.84 $\mathrm{Nm/deg}$)

C. Velocity control

The velocity servo's performance is tested in the velocity control mode, separately from the admittance control, to ensure that the admittance control's virtual dynamics do not suppress the high frequencies, which would create a less accurate estimate of the controllers' bandwidth.

D. Admittance control

The virtual dynamics were set to low impedance values that do not suppress too many high frequencies but maintain controller stability. The virtual dynamics were set to: $I = 0.01\ \mathrm{kg\,m^2}$, $B = 0.05\mathrm{Nm/s}$, $K = 0.5\ \mathrm{N/m}$.

E. Data processing

For the velocity control, the recorded signals during a trial were the numerically integrated input velocity (θ) and the motor position (θ_m). The frequency response function (FRF) ($\hat{H}_{velo}(f)$) is estimated in open-loop for the velocity control. For the estimation of FRFs, the power and cross-spectral densities were estimated using Welch averaging over four segments of 80 s. With these spectral densities ($\hat{S}_{output-input.}(f)$), the FRFs were estimated using the following equations:

$$\hat{H}_{velo}(f) = \frac{\hat{S}_{\theta_m\theta_d}(f)}{\hat{S}_{\theta_m\theta_m}(f)}. \tag{2}$$

Equation 3 calculates the coherence $\hat{\gamma}^2_{velo}(f)$ between the earlier defined variables (θ) and (θ_m). The coherence is a measure of the linearity and the signal-to-noise ratio. The coherence ranges from 0 to 1, with a value of 1 indicating the relationship between the input and output is linear and without noise. The coherence is estimated with the following equation:

$$\hat{\gamma}^2_{velo}(f) = \frac{|\hat{S}_{\theta_m\theta_d}(f)|^2}{\hat{S}_{\theta_m\theta_m}(f)\hat{S}_{\theta_d\theta_d}(f)}. \tag{3}$$

For the admittance control, the recorded signals during a trial were the disturbance torque (T_d), the measured torque (T_m), the input torque (T_i), the motor position (θ_m) and the numerically integrated input velocity (θ). Closed-loop estimators for the FRF were used to estimate the FRF for the virtual dynamics ($\hat{H}_{virt}(f)$), the velocity servo ($\hat{H}_{servo}(f)$), and the external load ($\hat{H}_{load}(f)$). These FRFs represent the virtual dynamics, velocity servo and external load block as defined in Fig. 4 respectively. For determining the controller stability, the open-loop FRF of the entire loop can be estimated ($\hat{H}_{loop}(f)$) with the earlier estimated FRFs. The FRFs were estimated using the following equations:

$$\hat{H}_{servo}(f) = \frac{\hat{S}_{\theta_m T_d}(f)}{\hat{S}_{\theta T_d}(f)}, \tag{4}$$

$$\hat{H}_{(f)} = \frac{\hat{S}_{\theta T_d}(f)}{\hat{S}_{T_i T_d}(f)}, \tag{5}$$

$$\hat{H}_{load}(f) = \frac{\hat{S}_{\theta_m T_d}(f)}{\hat{S}_{T_d T_m}(f)}, \tag{6}$$

$$\hat{H}_{loop}(f) = \hat{H}_{load}(f)\hat{H}_{servo}(f)\hat{H}_{virt}(f). \tag{7}$$

Finally, in addition to the FRF, the coherence $\hat{\gamma}^2_{adm}(f)$ between the disturbance torque and the output position was estimated.

$$\hat{\gamma}^2_{adm}(f) = \frac{|\hat{S}_{\theta T_d}(f)|^2}{\hat{S}_{\theta\theta}(f)\hat{S}_{T_d T_d}(f)}. \tag{8}$$

V. Results

A. Velocity control performance

Fig. 5 shows half a second of the desired- and output velocities for each loading condition, with the controller set to velocity control.

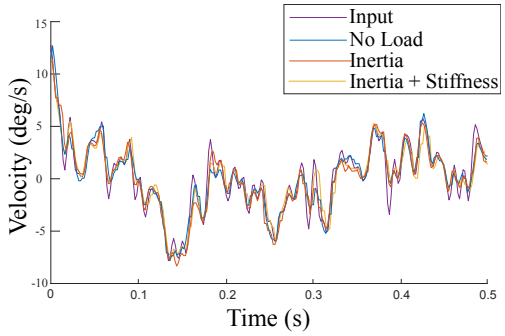


Fig. 5. Half a second of the desired- and motor velocity for each loading condition. The figure shows that the motor velocities of all external loading conditions approximate the desired velocity in this short time window.

The top two panels of Fig. 6 show the magnitude and phase of the velocity control FRF function ($\hat{H}_{velo}(f)$). The bandwidth of the velocity controller is 50 Hz. The bottom panel of Fig. 6 shows that the velocity controllers coherence $\hat{\gamma}^2_{velo}(f)$, which shows a linear behaviour throughout the required bandwidth.

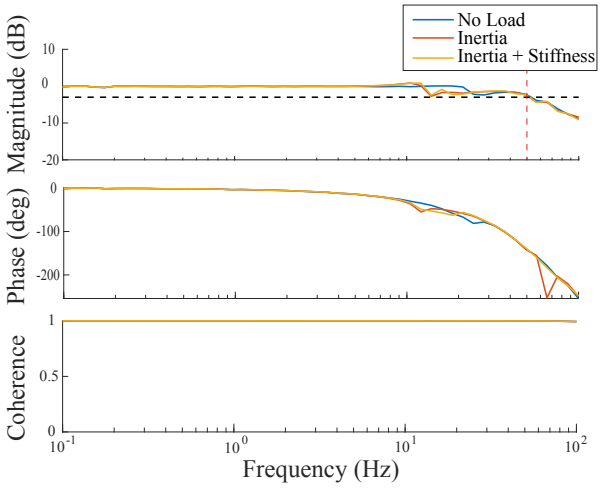


Fig. 6. The top two panels of the figure show the magnitude and phase of the FRF of the velocity controller ($\hat{H}_{velo}(f)$). The magnitude remains on the 0dB line up to 13 Hz and crosses the -3dB line at 50 Hz, shown with the red dotted line; the bottom panel shows the coherence between the actual and desired velocity $\hat{\gamma}^2_{velo}(f)$, which remains above 0.99 up to 100 Hz

B. Admittance control performance

Fig. 7 shows the FRF of the velocity servo of the admittance controller ($\hat{H}_{servo}(f)$) for the three loading conditions. The bandwidth of the ($\hat{H}_{servo}(f)$) of the admittance controller is 65 Hz when only external inertia is added and 76 Hz for the other external loading conditions.

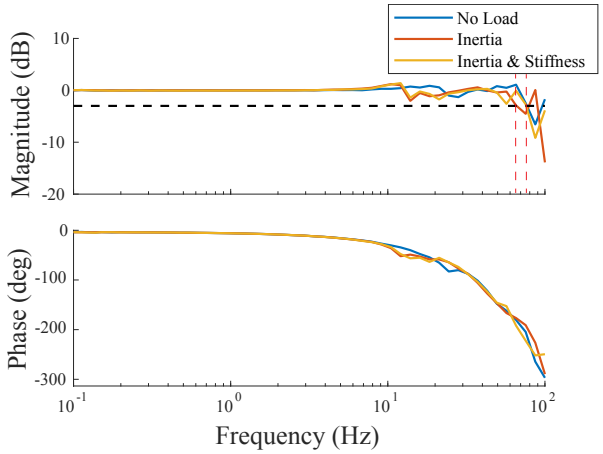


Fig. 7. Magnitude and phase plot of the FRF of the velocity servo of the admittance controller. The magnitude remains 0 dB for frequencies up to 24 Hz. The magnitude crosses the -3dB line at 65 Hz when only external inertia is added and at 76 Hz for the other external loading conditions. The magnitude crossing is shown with a red dotted line. The phase lag becomes noticeable beyond 10 Hz.

The top two panels of Fig. 8 show the magnitude and phase plots for $\hat{H}_{load}(f)$. For the frequencies between 0.3 Hz and 10 Hz the magnitude and phase plot clearly shows the dynamics of a system with only mass for the blue and orange lines and shows the dynamics of a system with mass and stiffness for the yellow line. The bottom panel of Fig. 8 shows the coherence $\hat{\gamma}^2_{adm}(f)$; the drop after 50 Hz indicates the noise becomes more prevalent than the signal.

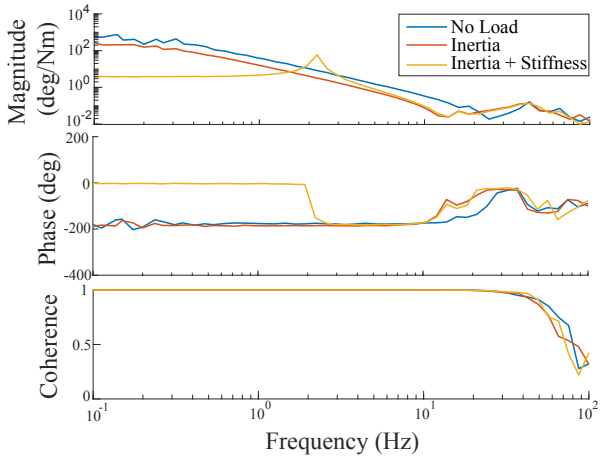


Fig. 8. The top two panels show the magnitude and phase plot of the external load $\hat{H}_{load}(f)$. The bottom panel shows the coherence $\hat{\gamma}^2_{adm}(f)$. The coherence drops below 0.9 at a frequency of 50 Hz.

From the Nyquist plot of the open-loop admittance control loop gain, the stability of a controller can be determined by checking if the (-1,0) point is encircled. The Nyquist plot of this controller showed no encirclement, so the control is stable.

VI. Discussion

This paper analysed whether the SEP performs adequately for the desired perturbations and experimental conditions needed for system identification with a stable controller. The bandwidth of the velocity servo in the admittance control mode is 65 Hz, while the same velocity servo in the velocity control mode has a bandwidth of 50 Hz. Both bandwidths are at least four times higher than the required bandwidth, so this requirement is met. The difference in bandwidth between the control modes could come from the fact that the virtual dynamics of the admittance controller suppress high frequencies, making the performance needed for the admittance controller to reach a specific bandwidth lower, explaining the higher bandwidth. For both controllers, the magnitude remains 0 up to at least 13 Hz, meaning the controller exactly follows the input. The phases of both controllers lag after a frequency of 10 Hz. Phase lag in the control system means a delay between the system's input and output, which can lead to instability. Yet, with the present phase lag, the controller is still stable. The phase lag can be reduced by increasing the sampling time of the controllers. The performance of the SEP can be compared to other robots used to identify human limb joint parameters. Schouten et al. [7] developed a robot to analyse the wrist joint. Here, the bandwidth needed for wrist parameter identification is 50Hz, which is also their controller's reached bandwidth. Another example of a robot identifying joint parameters is the ACT4D, which analyses the elbow joint. Stienen et al. [8] show a FRF that has a magnitude of 1(-) up to 40 Hz. However, their FRF does not go below 0.7 (being the -3dB line). Meaning the bandwidth of their controller is higher than 100 Hz. The performance of the shoulder elbow perturbator is somewhat lower but still meets the set requirements.

A. Limitations

One limitation is the low input velocity. A higher power of the desired velocity input asks more of the velocity servo and motor hardware, thus possibly decreasing bandwidth. This effect is also observed in the previously discussed difference between the bandwidth of the velocity and admittance control. As the current identified bandwidth is four times higher than the needed bandwidth, it is likely that the required 12 Hz bandwidth is still met with a higher input power. To ensure this is the case, further testing should be performed. A current limitation is that the data processing and collection are done at 500 Hz. A higher frequency may be needed for better performance and future controller extensions. A higher frequency will also reduce the phase lag observed in the results. Additionally, the experiment can be followed up by conducting tests on human subjects, providing us with further

insights into the SEP's comfort and usability, alongside the performance of the new controller of the SEP.

VII. Conclusion

This paper shows the performance of the SEP with velocity and admittance control. The bandwidth needed for system identification of the elbow must be higher than 12 Hz for both control modes. The bandwidth of the velocity servo of the admittance control mode is 65 Hz. The velocity controller has a bandwidth of 50 Hz. Both bandwidths are at least four times higher than the set requirement. Furthermore, the controller is stable. Lastly, the frequency response function of the external load clearly shows the dynamics introduced to the system, laying the foundation for further research. These results show that the SEP meets all the requirements, meaning it should be able to provide the desired perturbations and experimental conditions needed for system identification of the human elbow.

VIII. Acknowledgments

The authors wish to express their sincere gratitude for the invaluable support and collaboration of their partners: Hankamp Rehab, Amsterdam University Medical Center, Amsterdam Movement Sciences, Erasmus Medical Center, and Rijndam Revalidatie.

References

[1] C. O. Johnson, M. Nguyen, and G. A. et al. Roth. "Global, regional, and national burden of stroke, 1990–2016: A systematic analysis for the Global Burden of Disease Study 2016". In: *The Lancet Neurology* 18.5 (May 2019), pp. 439–458. ISSN: 1474-4422. DOI: 10.1016/S1474-4422(19)30034-1.

[2] H. P. Neil. "Stroke rehabilitation". In: *Critical Care Nursing Clinics of North America* 35.1 (Mar. 2023), pp. 95–99. ISSN: 0899-5885. DOI: 10.1016/j.cnc.2022.11.002.

[3] P. Raghavan. "Upper limb motor impairment after stroke". In: *Physical Medicine and Rehabilitation Clinics of North America* 26.4 (Nov. 2015), pp. 599–610. ISSN: 1047-9651. DOI: 10.1016/j.pmr.2015.06.008.

[4] A. D. Pandyan, G. R. Johnson, and C. I. M. et al. Price. "A review of the properties and limitations of the Ashworth and modified Ashworth scales as measures of spasticity". In: *Clinical Rehabilitation* 13.5 (Oct. 1999), pp. 373–383. ISSN: 0269-2155. DOI: 10.1191/026921599677595404.

[5] H. J. M. van der Krogt et al. "The gap between clinical gaze and systematic assessment of movement disorders after stroke". In: *Journal of NeuroEngineering and Rehabilitation* 9 (Aug. 2012), p. 61. ISSN: 1743-0003. DOI: 10.1186/1743-0003-9-61.

[6] M. van de Ruit et al. "System identification: A feasible, reliable, and valid way to quantify upper limb motor impairments". In: *Journal of NeuroEngineering and Rehabilitation* 20.1 (May 2023), p. 67. ISSN: 1743-0003. DOI: 10.1186/s12984-023-01192-x.

[7] A. C. Schouten et al. "Design of a torque-controlled manipulator to analyse the admittance of the wrist joint". In: *Journal of Neuroscience Methods* 154 (June 2006), pp. 134–141. ISSN: 0165-0270. DOI: 10.1016/j.jneumeth.2005.12.001.

[8] A. H. A. Stienen et al. "The ACT-4D: A novel rehabilitation robot for the quantification of upper limb motor impairments following brain injury". In: *2011 IEEE International Conference on Rehabilitation Robotics*. IEEE, June 2011, pp. 1–6. ISBN: 978-1-4244-9862-8. DOI: 10.1109/ICORR.2011.5975460.

[9] L. L. van der Velden et al. "Development of a single device to quantify motor impairments of the elbow: Proof of concept". In: *Journal of NeuroEngineering and Rehabilitation* 19.1 (Dec. 2022), p. 77. ISSN: 1743-0003. DOI: 10.1186/s12984-022-01050-2.

[10] W. Mugge et al. "A rigorous model of reflex function indicates that position and force feedback are flexibly tuned to position and force tasks". In: *Experimental Brain Research* 200 (Jan. 2010), pp. 325–340. ISSN: 0014-4819. DOI: 10.1007/s00221-009-1985-0.

[11] A. Q. L. Keemink, H. van der Kooij, and A. H. A. Stienen. "Admittance control for physical human–robot interaction". In: *The International Journal of Robotics Research* 37 (Sept. 2018), pp. 1421–1444. ISSN: 0278-3649. DOI: 10.1177/0278364918768950.

[12] R. Pintelon and J. Schoukens. *System Identification*. John Wiley & Sons, Mar. 2012.

[13] S. Plagenhoef, F. G. Evans, and T. Abdelnour. "Anatomical data for analyzing human motion". In: *Research Quarterly for Exercise and Sport* 54 (1983), pp. 169–178. URL: https://api.semanticscholar.org/CorpusID:143387656.

[14] *DINED*. 2004. URL: https://dined.nl/en/database/tool.

Feasibility and Acceptability of the Somnomat Casa Rocking Bed as a Stimulation Substitute for a Patient with Rhythmic Movement Disorder

Alexander Breuss
Sensory-Motor Systems Lab
ETH Zurich
Zurich, Switzerland
alexander.breuss@hest.ethz.ch

Stefania Oresta
SEMper Lab
IMT School for Advanced Studies
Lucca, Italy
stefania.oresta@imtlucca.it

Tim Vogel
Sensory-Motor Systems Lab
ETH Zurich
Zurich, Switzerland
vogeltim@ethz.ch

Manuel Fujs
Sensory-Motor Systems Lab
ETH Zurich
Zurich, Switzerland
manuel.fujs@hest.ethz.ch

Bigna K. Bölsterli
Division of Child Neurology
Children's Hospital of Eastern Switzerland
St. Gallen, Switzerland
bigna.boelsterliheinzle@kispisg.ch

Robert Riener
Sensory-Motor Systems Lab
ETH Zurich
Zurich, Switzerland
robert.riener@hest.ethz.ch

***Abstract*—Rhythmic Movement Disorder (RMD) is a parasomnia characterized by repetitive, rhythmic movements such as headbanging or body rocking. It typically occurs in infancy and early childhood, often disrupting sleep, and may occasionally persist into later childhood or, in rare cases, adulthood. Although its etiology remains poorly understood, RMD episodes may function as self-soothing behaviors to facilitate sleep. Current treatment options are limited, but vestibular stimulation, such as rocking, has shown potential to enhance sleep quality and reduce RMD symptoms. This study evaluated the feasibility, acceptability, and therapeutic potential of the Somnomat Casa, a robotic bed delivering vestibular stimulation, in a 14-year-old male with RMD. Over a 22-week protocol, including baseline, intervention, and washout phases, the bed applied varied frequencies (0.25 Hz and 0.30 Hz) and directions (lateral and longitudinal) of rocking. Data collection included camera recordings to quantify RMD episodes, a specific Somnomat questionnaire to assess intervention acceptability, as well as sleep quality questionnaires and polysomnographies to capture sleep quality. The intervention demonstrated high acceptability, with the participant reporting improved sleep quality and willingness to continue using the bed. Peak RMD frequency decreased by 17% during the final intervention compared to baseline, and temporal shifts in episode occurrence were observed during intervention phases. Polysomnography suggested potential changes in sleep architecture linked to vestibular stimulation. These findings support the Somnomat Casa as a promising non-pharmacological intervention for RMD, warranting further investigation in larger clinical trials.**

***Index Terms*—Integrated diagnostic and therapeutic systems; Robotic platforms in neuroscience; Technologies for neurodevelopmental disorders**

I. INTRODUCTION

Sleep is crucial for maintaining optimal brain function by managing changes in synaptic connection and homeostasis, enhancing brain plasticity, and regulating the encoding and storage of cognitive processes [1]–[5]. In children, sleep plays a vital role in development, as it supports the formation and consolidation of neural circuits during both critical and sensitive periods [6], [7]. Poor sleep quality in children is linked to reduced cognitive performance, negative effects on cardiometabolic health, and long-term lifestyle behaviors that may persist into adulthood [8]–[13].

Rhythmic Movement Disorder (RMD) is a type of parasomnia characterized by repetitive movements such as head banging or repeted body rocking, often accompanied by vocalizations. While RMD typically declines with age, with prevalences of around 66% for 9-month-old infants, 45% for 18-month-old toddlers and 6% for 5-year-old children [14], it can persist into adulthood in rare cases. However, these prevalence rates should be interpreted with caution as records are mainly based on parental reports [15].

Criteria to define an RMD episode were established by the American Psychiatric Association (APA) (2013) as movements occurring between $0.5\,\mathrm{Hz}$ to $2.0\,\mathrm{Hz}$ and lasting for at least four movements [16]. Polysomnography (PSG) studies have identified RMD episodes occurring before sleep onset, during transitions between sleep stages, or upon awakening [17]–[19]. However, current research fails to provide a comprehensive understanding of the sleep architecture in individuals with RMD. Furthermore, despite the prevalence of RMD being documented in infants and young children, the etiology of RMD remains poorly understood due to the absence of electrophysiological, neuroscientific, and genetic studies; a few hypotheses suggest that RMD episodes may serve as a form of self-soothing to facilitate sleep [15], [19].

Current treatments for RMD are limited and include psychological, behavioral, or pharmacological approaches. How-

*All authors contributed equally in this study.

ever, recent research highlights the potential of vestibular stimulation, such as rocking movements, to reduce RMD symptoms and improve sleep quality. Studies have shown that vestibular stimulation enhances sleep in various populations, and interventions such as hammocks have successfully reduced RMD episodes in children [20]–[24].

The Somnomat rocking beds previously developed at ETH Zurich, have demonstrated safety and efficacy across various populations in prior studies [25]–[28]. However, its specific long-term effects on RMD symptomatology and sleep architecture remain unexplored. This single-case study aims to evaluate whether long-term vestibular stimulation delivered through the Somnomat Casa (Figure 1) is an acceptable and feasible treatment option in an individual with RMD. Additionally, it presents a protocol for evaluating the therapeutic effects of these stimulations that can later be used in well-powered clinical trials to investigate the long-term effects of nocturnal vestibular stimulation in individuals with RMD. Finally, this study includes a preliminary attempt using PSG measurements to investigate sleep architecture in individuals with RMD and explore possible beneficial effects of overnight vestibular stimulation on sleep stages and, consequently, on sleep quality; if so, the exploratory protocol would reveal decreased sleep onset time and awekenings, and increased deep sleep..

II. METHODOLOGY



Fig. 1: Original version of the Somnomat Casa. It has dimensions $90\,\mathrm{cm} \times 200\,\mathrm{cm} \times 60\,\mathrm{cm}$ which are comparable to a standard-sized bed.

A. Study Participant

For this pilot study, a 14-year old male individual with a clinically confirmed diagnosis of RMD was recruited following a pre-screening and a review of his medical records. The participant and his guardian provided signed informed consent, in line with the principles outlined by the institutional ethics board. Furthermore, this study was exempted by the Cantonal Ethics Committee (BASEC Nr. Req-2023-00833) and approved by ETH Zurich's Ethics Board (EK-2023-N-329).

B. Intervention and Study Phases

The study was conducted over a 22-week period and was divided into four main phases: 1) a 3-week baseline period without intervention, 2) a 10-week intervention period where four 1-week period with varied vestibular stimulation parameters were alternated with three 2-weeks wash out periods, 3) a 2-month washout phase, and 4) 1-week period of follow-up acquisition without intervention. Depending on the intervention phase, the Somnomat Casa bed delivered two frequencies of vestibular stimulation: $0.25\,\mathrm{Hz}$ and $0.30\,\mathrm{Hz}$, once acting in longitudinal and once acting in lateral direction in comparison to the craniocaudal axis of the study participant (Table I). This would allow to study movements that are parallel and lateral to the vertical axis of the body, as suggested by previous literature [27]. Each frequency and motion configuration was planned for an equal number of nights and was separated by two-week washout phases (Figure 3), determined based on a previous study [26].

Movement Pattern	**Movement Direction**	**Frequency** (Hz)	**Acceleration** ($\mathrm{m\,s^{-2}}$)
P1	Lateral	0.25	0.25
P2	Lateral	0.30	0.35
P3	Longitudinal	0.25	0.25
P4	Longitudinal	0.30	0.35

TABLE I: Overview of the movement patterns applied in this study.

C. Required Modifications to the Somnomat Casa

As the Somnomat Casa in its original form (c.f. Figure 1) only allowed to stimulate in the longitudinal directions, hardware modifications were made. To keep the mechanical changes minimal, we added structural reinforcements to the top frame to increase stability. This allowed to widen the top frame from $90\,\mathrm{cm}$ to $180\,\mathrm{cm}$, allowing the participant to rotate 90 degrees in his bed. Furthermore, we padded the lateral extensions to cushion accidental contact with moving parts (Figure 2).

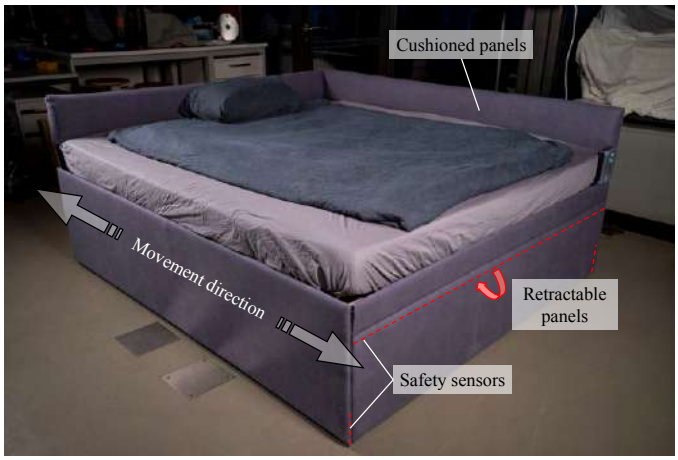


Fig. 2: Modifications performed to the Somnomat Casa. The top frame was widened, allowing the participant to rotate 90 degrees. Furthermore, cushioning was installed to reduce injury risk in case of headbanging.

D. Data Collection

Participant acceptability of the intervention was assessed through self-reported questionnaires. The participant was

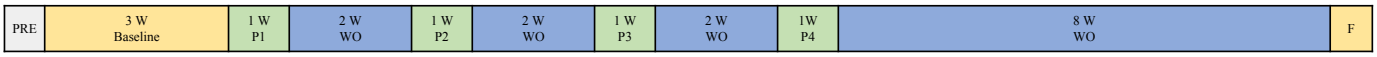


Fig. 3: Schedule of the study protocol. After a 3 weeks (W) baseline period without intervention, four 1 week intervention phases (P1...P4) followed, separated by 2 weeks wash out phases (P) without any intervention. A 1-week long follow up examination (F) was carried out two months after the end of the last intervention.

asked to complete the following subjective measures at predefined intervals to monitor domains of sleep quality, comfort, and any adverse experiences related to the intervention:

- Somnomat Casa Acceptability Questionnaire: A custom questionnaire designed to evaluate the participant's perceptions of the bed's comfort, intuitiveness, noise level, and movement smoothness.
- Karolinska Sleepiness Scale (KSS): Assessed each morning to record the subjective sleepiness and observe variations in sleep quality throughout the intervention.
- Pittsburgh Sleep Quality Index (PSQI): Conducted weekly to obtain a subjective measure of sleep quality by investiganting different domains of sleep such as sleep latency, sleep duration, and sleep disturbances.
- Mini Sleep Questionnaire (MSQ): Completed weekly to assess general symptoms of sleep and wakefulness, including disturbances in daytime and nighttime functioning.
- Checklist Individual Strength (CIS): A 20-item questionnaire conducted weekly to assess various aspects of fatigue, including subjective fatigue, motivation, concentration, and physical activity.
- Modified Epworth Sleepiness Scale (M-ESS): Administered weekly to evaluate fatigue and daytime sleepiness.
- Visual Analog Scale (VAS) for pain: Used weekly to monitor neck discomfort, as the participant had previously reported neck pain associated with his significant nightly movements.

Furthermore, data collected from a night vision camera (Reolink E1, Reolink, Hong Kong) were used to determine time spent in bed, as well as bed usage duration, providing a quantitative assessment of the overall acceptability. The camera footage also enabled unobtrusive monitoring of the participant's sleep position and movements. Using 5-minute epochs, the video data were scored by a single reviewer (to minimize inter-rater variability) to document and quantify RMD episodes based on the criteria from the APA [16].

Sleep architecture assessments were performed at baseline and after the completion of the intervention using a portable PSG device (Nox A1, NOX Medical), including electroencephalograophy (EEG) and electrooculography (EOG) recordings.

Finally, participant adherence to the protocol was recorded, including any deviations from the prescribed protocol, technical issues, or adverse events. This information provided insights into the feasibility of the protocol, highlighting potential challenges and indicating how realistically participants can follow the protocol. These findings will be valuable for refining the protocol in future studies.

III. RESULTS

A. Protocol Adherence

A total of 154 nights were planned for the study, with data collection scheduled for each of these nights. For the video recordings, a total of 107 nights were planned, but the actual number of nights varied across the phases, with a total of 85 recorded nights (69%). In the baseline phase, 12 video nights were completed, while intervention and washout phases saw varying levels of adherence.

Questionnaire adherence showed some variation, with the KSS, M-ESS, CIS, VAS, and MSQ being the most consistently completed assessments, with 134 out of 154 planned nights (87%). The Somnomat acceptability questionnaire was completed in 3 out of the 4 planned nights, and the MSQ was completed 13 times. The PSQI was planned for 14 nights, with 11 nights being fully completed without missing data. Global PSQI scores, reported in Table N, were assessed from the sel-reported answers to the questionnaire as a measure of percived sleep quality. The global scores didn't show a significant change during the overall protocol (Median= 6; IQR= 2) with a maximum of 9 points on 21 both at the beginning an at the end of the protocol.

B. Acceptability

The participant completed three out of four Somnomat acceptability questionnaires (during interventions 1, 2, and 4) assessing the intervention. Overall, the participant reported a positive experience, highlighting the perceived safety and the speed of the movements, particularly during the faster movement patterns (P2 and P4, c.f. Table I). The participant noted that the bed subjectively helped him fall asleep faster and did not cause awakenings during the night. However, the participant also reported that the bed occasionally struggled to counteract his strong, violent movements, resulting in some motion disturbances. Despite this, he expressed a desire to continue using the bed and reported a subjective improvement in his condition and sleep quality.

C. Therapeutic Effect

Throughout the entire study duration, the nocturnal rhythmic movements occurred consistently, visually identifiable by an initial peak followed by four additional peaks (c.f. Figure 4). Considering the movement patterns across the entire study phase, a temporal shift is prominent, with the first peak in Intervention 4 occurring approximately one hour later compared to the baseline phase. Furthermore, a general decrease in peak rhythmic movements is notable, from 12 episodes during the baseline down to 10 episodes per 30-minute window (80th percentile) during the intervention period.

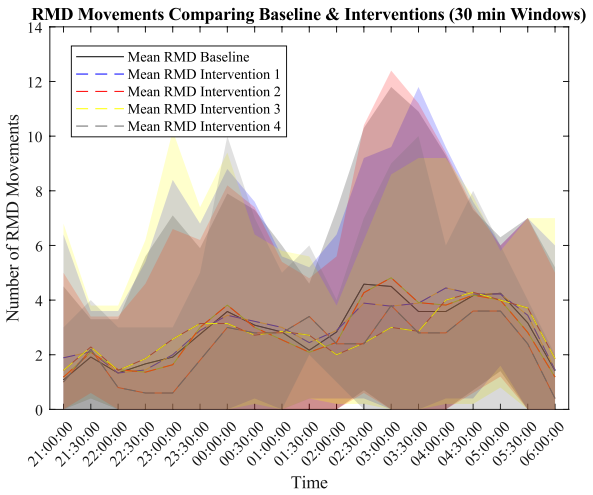


Fig. 4: Comparison of RMD episodes between baseline and intervention phases. In this figure, all nights of the respective phases are combined into a representative night defined through their mean and 80th percentile.

RMD episode percentages across phases indicate a decline in frequency during Washout 1, Intervention 2, and Washout 2 compared to Baseline. Washout 1 shows the most significant reduction, with RMD frequency less than half of Baseline levels. Figure 5 shows the normalized durations of rhythmic movements during the bed time for both Intervention Off and Intervention On periods.

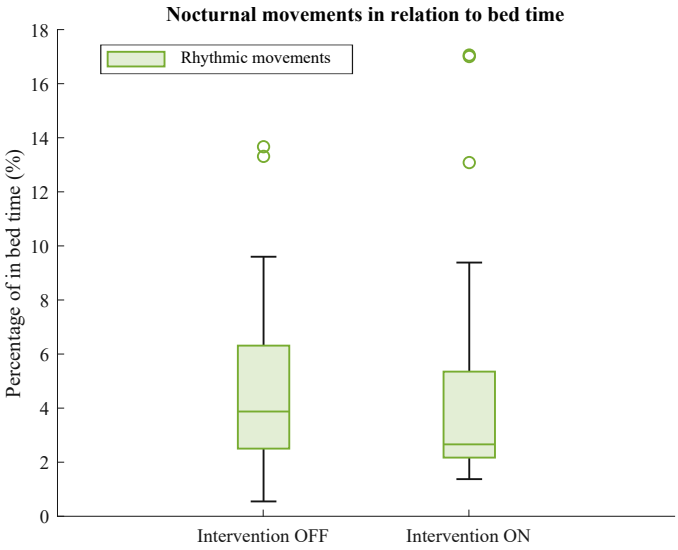


Fig. 5: Comparison of rhythmic movements between intervention-off and intervention-on periods.

Table II provides detailed data on RMD episodes and durations relative to in-bed time.

D. Sleep Architecture and Sleep Quality

Manual sleep scoring was assessed on PSG recordings by a certified sleep scorer classifying sleep stages in epoches of 30 seconds. The analysis of sleep architecture showed significant results comparing Baseline and Follow-Up, using Chi-Squared analysis of variance (Figure 6). In particular, results showed an increase of epochs spent in Non-REM Sleep 3 (NREM3) and Non-REM Sleep 2 (NREM2) ($p < 0.001$***), and a decrease of epochs classified as Wake ($p < 0.001$***). Moreover, despite an increase in sleep onset ($p < 0.001$***), the overall wake time decreased due to decreased awakenings ($p < 0.001$***). At last, it was possible to notice a significant reduction in epochs classified as movements and/or artifacts ($p < 0.001$***).

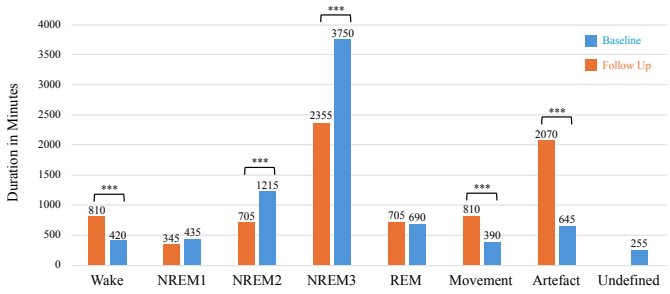


Fig. 6: Comparison on sleep stage, movement, and artifact durations between baseline and follow up. Statistical significance is indicated as *** for $p < 0.001$.

PSQI scores were explored for potential differences in sleep quality throughout the protocol but the analyses did not show a significant difference nor a trend in either a positive and negative direction (c.f. Table II).

IV. DISCUSSION

The intervention was well-tolerated, with the participant reporting improved sleep quality, reduced RMD symptoms, and willingness to continue using the bed. The participant highlighted the perceived safety, comfort, and therapeutic benefits of the bed's movements, although strong, violent movements occasionally disrupted the rocking mechanism as the output torque was limited to approximately $20\,\mathrm{N\,m}$ for safety concerns. These findings suggest that the Somnomat Casa could offer a non-invasive intervention for individuals with RMD but further adaptations to the Somnomat Casa have to be undertaken to counteract strong movements from the users.

Noticeble, the temporal shift of the first RMD episode when comparing baseline and last intervention week shows a delay in RMD symptomatology. This result might suggest that the experimental protocol might also have a positive influence on sleep patterns facilitating sleep onset and sleep quality in the first hours of bedtime.

Accordingly, the analyses of sleep architecture led to promising positive significant results with increased NREM3 and NREM2, and decreased wake time. However, these results might be biased by the number of movements and artifacts that, in turn, limit the possibility to perform a totally accurate sleep staging, which is inherent in the pathology.

Overall, the study demonstrated good adherence to the core components of the protocol, though some deviations were noted, particularly in the protocol adherence and usage of

Phase	Average Time in Bed (hh:mm)	Average RMD Episode Duration (mm:ss)	Standard deviation of RMD Episode Duration (mm:ss)	Mean PSQI Score
Baseline	8:49	00:28	00:13	6
Intervention 1	9:17	00:36	00:19	6
Washout 1	9:08	00:12	00:06	9
Intervention 2	9:38	00:26	00:11	7
Washout 2	8:58	00:28	00:19	8
Intervention 3	9:11	00:45	00:33	6
Washout 3	9:04	00:34	00:07	n/A
Intervention 4	9:25	00:50	00:30	8
Follow-Up	–	–	–	5

TABLE II: Progression of RMD metrics as well as PSQI scores throughout the study phases. The table summarizes average time spent in bed, as well as the average and standard deviation of RMD episode duration across baseline, intervention, washout, and follow-up periods, and the averaged PSQI scores.

the video camera and completion of the questionnaires. These deviations were primarily due to the complexity of the protocol and participant factors. The findings suggest that while the protocol was feasible, certain adjustments may be needed in future studies to further improve adherence, particularly for the more demanding components of the data collection process, as well as automated checks should be put into place that detect incomplete questionnaire data as early as possible.

Nonetheless, the primary limitation of this study was its single-case design, which limits the generalizability of the findings. In this regard, we also cannot draw conclusions on the effects of body-parallel versus body-orthogonal movements because the participant was free to change his lying position and frequently reoriented himself, regardless of the intended stimulation direction. Nonetheless, the individual's strong adherence to the protocol and his positive feedback indicate that the intervention is both feasible and well-tolerated, marking an important initial step toward studies with larger cohorts.

V. CONCLUSION

This pilot study demonstrates the feasibility and acceptability of using the Somnomat Casa as a therapeutic tool in a child with a diagnosis of RMD. This study also represents one of the first attempts to investigate sleep architecture using overnight PSG in a child diagnosed with RMD. The intervention showed potential in reducing peak RMD episode frequency and improving objective sleep architecture measures, particularly in enhancing deep sleep. While preliminary, these findings lay the groundwork for future research to explore the therapeutic effects of vestibular stimulation on RMD in larger cohorts. Ultimately, the Somnomat Casa may represent a novel, non-invasive, and accessible solution for managing sleep disorders, offering an alternative to pharmacological interventions.

ACKNOWLEDGMENT

The authors sincerely thank the patient and his family for their willingness to participate in this study and for their valuable contributions and feedback. The authors would like to extend their gratitude to Prof. Catherine Hill from the University of Southampton and Dr. Hasselman from the Ostschweizer Kinderspital in St. Gallen, Switzerland for their ideas and feedback in the design of this study. Deep appreciation goes to Michael Herold-Nadig and Marco Bader from ETH Zurich for their support in the development and fabrication of the Somnomat Casa. Alexander Breuss also gratefully acknowledges the financial support provided by the Promedica Foundation for supporting his research. Open access funding was provided by ETH Zurich.

REFERENCES

[1] P. Alhola and P. Polo-Kantola, "Sleep deprivation: Impact on cognitive performance," *Neuropsychiatr. Dis. Treat.*, vol. 3, no. 5, pp. 553–567, 2007.

[2] R. Stickgold, "Sleep-dependent memory consolidation," *Nature*, vol. 437, no. 7063, pp. 1272–1278, 2005.

[3] M. P. Walker and R. Stickgold, "Sleep, memory, and plasticity," *Annu. Rev. Psychol.*, vol. 57, no. 1, pp. 139–166, 2006.

[4] R. Huber, M. Felice Ghilardi, M. Massimini, and G. Tononi, "Local sleep and learning," *Nature*, vol. 430, no. 6995, pp. 78–81, 2004.

[5] G. Tononi and C. Cirelli, "Sleep and the price of plasticity: from synaptic and cellular homeostasis to memory consolidation and integration," *Neuron*, vol. 81, no. 1, pp. 12–34, 2014.

[6] J. T. Bruer, "A critical and sensitive period primer." 2001.

[7] E. I. Knudsen, "Sensitive periods in the development of the brain and behavior," *Journal of cognitive neuroscience*, vol. 16, no. 8, pp. 1412–1425, 2004.

[8] L. Matricciani, C. Paquet, B. Galland, M. Short, and T. Olds, "Children's sleep and health: a meta-review," *Sleep medicine reviews*, vol. 46, pp. 136–150, 2019.

[9] M. A. Short, S. Blunden, G. Rigney, L. Matricciani, S. Coussens, C. M. Reynolds, and B. Galland, "Cognition and objectively measured sleep duration in children: a systematic review and meta-analysis," *Sleep health*, vol. 4, no. 3, pp. 292–300, 2018.

[10] J. S. Quist, A. Sjödin, J.-P. Chaput, and M. F. Hjorth, "Sleep and cardiometabolic risk in children and adolescents," *Sleep medicine reviews*, vol. 29, pp. 76–100, 2016.

[11] S. P. Becker, C. A. Sidol, T. R. Van Dyk, J. N. Epstein, and D. W. Beebe, "Intraindividual variability of sleep/wake patterns in relation to child and adolescent functioning: A systematic review," *Sleep medicine reviews*, vol. 34, pp. 94–121, 2017.

[12] K. A. Matthews and E. J. Pantesco, "Sleep characteristics and cardiovascular risk in children and adolescents: an enumerative review," *Sleep medicine*, vol. 18, pp. 36–49, 2016.

[13] L. Matricciani, Y. S. Bin, T. Lallukka, E. Kronholm, D. Dumuid, C. Paquet, and T. Olds, "Past, present, and future: trends in sleep duration and implications for public health," *Sleep health*, vol. 3, no. 5, pp. 317–323, 2017.

[14] G. Klackenberg, "Rhythmic movements in infancy and early childhood," *Acta Paediatr Scand*, vol. 224, pp. 74–83, 1971.

[15] A. R. Gwyther, A. S. Walters, and C. M. Hill, "Rhythmic movement disorder in childhood: an integrative review," *Sleep medicine reviews*, vol. 35, pp. 62–75, 2017.

[16] M. Harm, M. Hope, and A. Household, "American psychiatric association, 2013, diagnostic and statistical manual of mental disorders, 5th edn, washington, dc: American psychiatric association anderson, j, sapey, b, spandler, h (eds), 2012, distress or disability?, lancaster: Centre for disability research, www. lancaster. ac. uk," *Arya*, vol. 347, p. 64.

[17] T. F. Hoban, "Sleep related rhythmic movement disorder," 2010.

[18] M. J. Sateia, "International classification of sleep disorders," *Chest*, vol. 146, no. 5, pp. 1387–1394, 2014.
[19] R. Manni and M. Terzaghi, "Rhythmic movements during sleep: a physiological and pathological profile," *Neurological Sciences*, vol. 26, pp. s181–s185, 2005.
[20] V. Hewertson and C. Hill, "Rhythmic movement disorder: a novel solution?# p58," *5th International Pediatric Sleep Association*, 2018.
[21] S. Besnard, B. Tighilet, C. Chabbert, M. Hitier, J. Toulouse, A. Le Gall, M.-L. Machado, and P. F. Smith, "The balance of sleep: role of the vestibular sensory system," *Sleep medicine reviews*, vol. 42, pp. 220–228, 2018.
[22] R. M. van Sluijs, Q. J. Rondei, D. Schluep, L. Jäger, R. Riener, P. Achermann, and E. Wilhelm, "Effect of rocking movements on afternoon sleep," *Frontiers in neuroscience*, vol. 13, p. 1446, 2020.
[23] R. M. van Sluijs, E. Wilhelm, Q. J. Rondei, L. Jäger, M. Gall, H. Garn, P. Achermann, O. G. Jenni, R. Riener, and C. M. Hill, "Sensory stimulation in the treatment of children with sleep-related rhythmic movement disorder: a feasibility and acceptability study," *Sleep Science and Practice*, vol. 4, pp. 1–9, 2020.
[24] R. van Sluijs, E. Wilhelm, Q. Rondei, X. Omlin, F. Crivelli, D. Straumann, L. Jäger, R. Riener, and P. Achermann, "Gentle rocking movements during sleep in the elderly," *Journal of sleep research*, vol. 29, no. 6, p. e12989, 2020.
[25] A. Breuss, M. Fujs, M. Müller, Z. Suter, N. Wyss, and R. Riener, "Design, development, and optimization of the somnomat casa: a rocking bed for sleep studies and nocturnal interventions in home settings," *at-Automatisierungstechnik*, vol. 72, no. 5, pp. 449–459, 2024.
[26] A. Breuss, M. Strasser, J.-M. Nuoffer, A. Klein, E. Perret-Hoigné, C. Felder, R. Stauffer, P. Wolf, R. Riener, and M. Gautschi, "Nocturnal vestibular stimulation using a rocking bed improves a severe sleep disorder in a patient with mitochondrial disease," *Journal of sleep research*, p. e14153, 2024.
[27] R. M. van Sluijs, E. Wilhelm, Q. J. Rondei, L. Jäger, M. Gall, H. Garn, P. Achermann, O. G. Jenni, R. Riener, and C. M. Hill, "Sensory stimulation in the treatment of children with sleep-related rhythmic movement disorder: a feasibility and acceptability study," *Sleep Science and Practice*, vol. 4, no. 1, p. 13, Jul 2020. [Online]. Available: https://doi.org/10.1186/s41606-020-00049-9
[28] F. Crivelli, X. Omlin, G. Rauter, J. Von Zitzewitz, P. Achermann, and R. Riener, "Somnomat: a novel actuated bed to investigate the effect of vestibular stimulation," *Medical & biological engineering & computing*, vol. 54, pp. 877–889, 2016.

Design of a Semi-Active Ankle Foot Prosthesis Using a Pneumatic and Hydraulic Hybrid for Stiffness and Energy Timing Control*

Sy Nguyen, Sepehr Ramezani, and Hwan Choi, *Member, IEEE*

***Abstract*—Lower-limb amputees require ankle-foot prostheses with adjustable stiffness and energy return timing to adapt to varying walking speeds, as well as adequate ankle push-off power to propel the body forward. Most passive prostheses utilize energy storage and return with carbon fiber blades (CFBs), but their single stiffness and early energy return timing limit their effectiveness for propulsion. Quasi-active or powered prostheses with CFBs also fail to fully utilize the energy storage and return capabilities of the CFB. As a result, many quasi-active prostheses lack precise energy return timing, while powered prostheses rely on large motors or bulky hydraulic cylinders. In this paper, we present the Pneumatic and Hydraulic Hybrid Prosthesis (PHHP), designed to adjust stiffness and energy return timing. The system leverages the compressible and incompressible properties of pneumatic and hydraulic systems to enable both stiffness adjustment and stored energy delivery timing. The PHHP includes three pneumatic chambers of varying sizes that adjust the resistance of a hydraulic cylinder by turning valves on and off, enabling variable stiffness. The hydraulic cylinder stores energy from the carbon fiber foot's deformation and releases it for push-off assistance via a hydraulic valve. Theoretical and experimental results show the PHHP's potential for push-off assistance and variable stiffness (24.3–54 N/mm), making it adaptable to different walking speeds for lower-limb amputees.**

I. Introduction

A lower limb amputation is often performed when a limb is irreparable or functionally compromised due to severe trauma, congenital deficiencies, infections, or tumors. Given the rising prevalence of diabetes, the number of lower limb amputations is expected to increase in the coming years [1]. Lower limb amputation frequently leads to biomechanical and neurological changes that reduce mobility, accelerate joint degeneration, and adversely impact quality of life. To restore essential functional movement for individuals with limb loss, numerous prosthetic feet have been developed [2-11]. Among these, the carbon fiber blade (CFB) prostheses are one of the most widely used due to its low cost, lightweight, and durability. It can return a portion of the energy stored during walking, delivering supportive and propulsive energy stored in the carbon fiber foot's deformation [2].

However, CFB prostheses provide a single level of stiffness and lack the ability to control the timing of energy release, which can lead to improper walking and increased muscular demands [3]. To enhance the efficiency of CFB prostheses, several studies have explored adjusting stiffness, commonly by using elastic beams [4,5] or spring-damper systems [6,7]. Recently, using a leaf spring with solenoid-driven linear actuators was proposed to adjust the level of stiffness [8]. Utilizing multiple linkage systems for ankle-foot prostheses represents a recent advancement in prosthetic design. For example, Gabert et al, developed a powered polycentric prosthesis using a four-bar mechanism, primary helical gear, and roller screw transmission [9]. Similarly, Rogers et al, designed a 2-DOF ankle with a U-joint and two linear actuators for a rock-climbing ankle-foot prosthesis [10]. Another approach by Lenzi et al, utilized a cam-driven ankle mechanism to design a variable stiffness prosthesis [11].

Although these prostheses can provide variable stiffness, the total amount of energy is used inefficiently to replicate the biological ankle, which generates more than 50% of the total limb power [12]. This inefficiency arises because these designs do not fully utilize the substantial amount of energy stored in the CFB, which could otherwise support push-off. Instead, the energy stored in the CFB is often released prematurely during midstance, requiring these devices to compensate with larger motors and batteries to deliver sufficient push-off power. Prior work has demonstrated that when prosthetic designs fail to control the timing of energy release effectively, they must rely on active power input to generate ankle work, leading to increased power consumption and larger motor requirements [13,14]. Semi-active prosthetic designs have been introduced to regulate the timing of energy release and improve efficiency [4,15]. Using a large motor and sophisticated mechanism fully leveraging the energy stored in the CFB remains an ongoing challenge in the field.

Using a hydraulic cylinder to capture force from a passive component, such as a CFB, is another method for adjusting stiffness. Commercially available ankle-foot prostheses, such as the OttoBock Triton Smart Ankle [16], Endolite Élan [17], and Freedom Innovations Kinnex [18], incorporate hydraulic components on the CFB to utilize the stored energy in the carbon fiber. However, the hydraulic cylinders of these prostheses are intended to absorb energy from heel strike in order to focus on delivering comfort to users. Thus, they do not contribute to energy support. Pneumatic actuators and cylinders, which behave similarly to mechanical springs, have the ability to provide adjustable stiffness in prosthesis. For example, pneumatic-driven, muscle-like actuators provide another method of control ankle prostheses [19]. Mooney et al., [20] developed the pneumatic transtibial ankle prosthesis that provides a wide range of motion for various activities. However, the size of the pneumatic chamber or hydraulic

*This work was supported by the National Science Foundation under FRR Program: Award # 2246671. (Corresponding Author: Hwan Choi)

S. Nguyen and H. Choi are with Mechanical and Aerospace Engineering Department, University of Central Florida, 4000 Central Florida Blvd., Fl 32816 USA (e-mail: sy.nguyen@ucf.edu, hwan.choi@ucf.edu)

S. Ramezani is with Optimus Tesla Bot, Tesla, Palo Alto, CA 94303 USA (e-mail: Ramezani.dan@gmail.com)

cylinder must be carefully considered to keep the system compact and energy efficient.

Despite notable advancements in prosthetic technology, significant technical challenges remain, such as single stiffness, high energy consumption, and inefficient use of the CFB's stored energy. With these findings, we present a pneumatic and hydraulic hybrid prosthesis (PHHP) that enables customized stiffness and effective push-off work while maintaining energy efficiency. The PHHP design leverages the compressibility of air to offer variable stiffness levels through adjustable pressures, while hydraulic components control the timing of energy release via the incompressible nature of fluid. First, numerical analyses were conducted to determine the physical parameters of the hydraulic-pneumatic system. Next, a prototype was fabricated. Finally, experiments were conducted to evaluate the stiffness variation and push-off functionality of the proposed device

II. PROSTHETIC DEVICE DEVELOPMENT

A. System overview

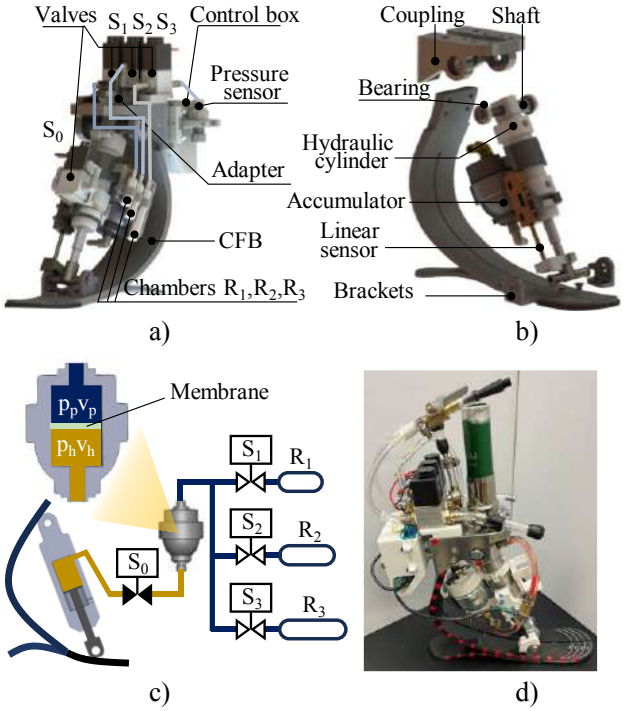


Fig. 1 The overall design of PHHP; (a) The overview of assembled prosthesis; (b) The exploded view of PHHP, (c) The pneumatic (chambers R_1, R_2, R_3 solenoids S_1, S_2, S_3) and hydraulic (solenoids S_1 and hydraulic cylinder) diagram; (d) The prototype of PHHP.

The overall design of the proposed prosthesis, incorporating a pneumatic and hydraulic hybrid system is illustrated in Fig. 1. The PHHP has a compact total dimension of L28 x H24 x W8 cm, (weight 2.7 kg) comparable to the size of a commercially available carbon fiber foot. The design comprises four main components:

1. **Carbon Fiber Blade:** Since our goal is to develop an affordable, lightweight prosthesis for commercialization, we employed a compliant CFB (Flex-Foot Cheetah, Össur, Reykjavík, Iceland) to provide the base stiffness. The CFB has been cut to create a low-profile structure, making the prosthesis compatible with various residual limb length of people with lower limb amputation. The upper part of CFB is fixed with a coupling, forming as single unit. This coupling connects to an adapter that links to the pylon, allowing anterior or posterior adjustments of CFB. It is mounted on the top of the device, enabling a custom fit for users.

2. **Hydraulic System**: Hydraulic system includes a hydraulic cylinder (DSNU-32-20-P, Festo, Esslingen, Germany), which is connected to the CFB via the coupling, an accumulator, and a hydraulic solenoid valve (12V Electric Solenoid Valve, Tailonz, China) (S_0). The S_0 valve connects to the hydraulic cylinder (HC) and the accumulator, allowing the PHHP to capture the stored energy on the deformed CFB by maintaining deformation using the incompressible of fluid. Then, S_0 valve also releases the stored energy on the CFB in an appropriate time to make efficient push-off and support during terminal stance. To achieve a low profile and a compact size, we placed the accumulator between HC and the CFB. Also, we set HC in a 65^0 of angle to effectively convey the pressurized force to the CFB and make the prosthesis fit into shoes. A pneumatic manifold is implemented directly onto the accumulator to avoid the need for piping, the design's complexity, and the risk of leakage. One end of HC can freely rotate around the shaft mounted by the coupling, while the opposite end (HC's rod) connects with a T-shape that is supported by fixed brackets on the CFB, as shown in Fig. 1b.

3. **Pneumatic System**: The pneumatic system comprises three pneumatic solenoid valves (12V Electric Solenoid Valve, Tailonz, China) (S1, S_2, and S_3) and three pneumatic chambers (R_1, R_2, and R_3) of different sizes. These components adjust the effective resistance of the HC by altering the states of S_1, S_2, and S_3, thus changing the stiffness of the entire prosthetic foot. Additionally, the system is equipped with a pressure sensor (150 Psi Pressure Sensor, AUTEX, Riverside, CA) to measure chamber pressure, a linear sensor (Sensors 9615R5, AUTEX, Riverside, CA) to monitor the displacement of the hydraulic cylinder's rod, and a control box to manage valve states during an operation.

4. **Accumulator:** An accumulator (AC 40-1/4, Hawe Hydraulic SE, Germany) is used to connects the pneumatic and hydraulic systems. As shown in Fig. 1c, the yellow line represents oil and blue line represents air. The accumulator features an elastic membrane which separates the hydraulic (yellow) and pneumatic (blue) chambers, enabling energy transfer between two sub-systems. The prototype of the proposed system is shown in Fig. 1d

B. Working principle of the PHHP

From heel strike to mid-terminal stance, the weight of the body deforms the CFB, and the total external force is distributed between the CFB and the HC. Because the level of CFB stiffness remains constant, we control the pneumatic system to provide additional stiffness on top of CFB. As shown in Fig. 1c, when the CFB is compressed by an external force (i.e., weight bearing of prosthetic user), it pushes the hydraulic piston, causing oil to flow into the accumulator. As oil flows into the accumulator, the membrane is displaced, reducing the volume of the pneumatic chamber while increasing its pressure. This process converts the energy of the external force into hydraulic energy and subsequently into

pneumatic energy, which is stored in the pneumatic chamber. Since each chamber is equipped with on/off valves, the total available volume of air can be adjusted by selecting different combinations of chambers via the three pneumatic valves. For instance, if all valves are closed, only the volume within the accumulator will be pressurized by movements in the hydraulic system and PHHP becomes stiffest. Conversely, when all valves are open, the maximum pneumatic volume is achieved, reducing the pressure to displacement changes in the hydraulic system. Additionally, once the stroke of HC reaches a maximum compressed displacement (the mid-terminal stance phase), the hydraulic valve closes, maintaining both CFB deformation and the HC position as oil is incompressible. Subsequently, the hydraulic valve opens, the stored energy of CFB and pneumatic chamber returns, and this generates a push-off force. This sequence repeats in each gait cycle.

C. *Modeling a static test*

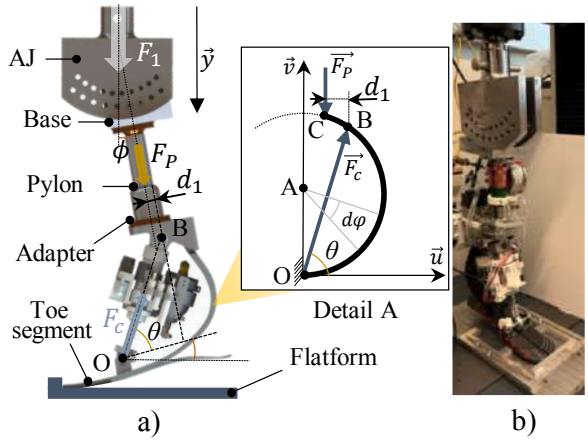


Fig. 2 Model for PHHP; (a) The 3D model of PHHP on the universal testing machine and modeling of PHHP (Detail A); (b) The experimental setup of the prototype on a universal test machine.

For the initial development of the prototype, the PHHP was installed on a universal testing machine (313 model, Test Resources, Shakopee, MN) to validate how the pneumatic system affects the overall stiffness of the prosthesis. We used an adjustable jig (AJ) and base with 5° rotational adjustment slots, allowing us to apply force in each dorsiflexion angle (Fig. 2a). We set the prosthesis in 0°, 5°, 10°, and 15° dorsiflexion and applied 950 N.

In the setup, a load representing the human weight bearing force (F_1) was applied vertically (y-direction), creating an angle ($\emptyset$) between the prosthetic pylon (or amputee's shank) and the y-axis. The load applied to the pylon is denoted as F_p, with the distance from F_p to the rotational point (B) designated as d_1, as amputee users may adjust the adapter position for comfort. L_1 represents the displacement of the HC from point B to point O when the prosthesis is under load, while F_c indicates the resistive force from the pneumatic system. Finally, θ represents the angle of the HC relative to the ground in the prosthesis's neutral position.

To determine the deformation at point B, a geometric model is derived using Castigliano's theorem [21]. In this model, point O is considered fixed, as the toe segment of the CFB contacts the ground, creating resistance in the hydraulic system through the force F_c, (Fig. 2a, detail A). We examined a curved beam fixed at one end (point O) and subjected to forces at the free end (point B). Given that the distance d_1 is small, we simplify the model by assuming the load F_p acts at a distance d_1 from the free end. Thus, the displacement of point B (γ) in the v-direction is represented in Eq. 1.

$$\gamma_{v_{F_i}} = \frac{\partial U}{\partial F_i} = U_1 + U_2 + U_3 \quad (1)$$

$$U_1 = \int_0^t \frac{1}{EI}\left(M\frac{\partial M}{\partial F_i}\right) Rd\varphi \quad (2)$$

$$U_2 = \frac{1}{EA}\int_0^t \left(N\frac{\partial N}{\partial F_i}\right) Rd\varphi \quad (3)$$

$$U_3 = \frac{2(1+\sigma)}{EA} K_x \int_0^t \left(V\frac{\partial V}{\partial F_i}\right) Rd\varphi \quad (4)$$

Where $\gamma_{v_{F_i}}$ represents the defection in direction v-direction at tip, caused by the input force F_i. U represents the deformation energy. M, N, and V refer to the normal moment, axial force (internal), and shear force (internal) contributions, respectively. R denote the radius of curvature, A is a cross-sectional area, K_x is a shear factor and σ represents is poisson's ratio. E and I refer to Young' modulus and the first moment of area, respectively. The φ represents the span angle of the beam, while t denotes angle of curvature ($\widehat{OAB}$).

Note that we primarily consider deflection in the v-direction, as deflection in the u-direction is neglected due to its minimal impact [21], which aligns with our testing conditions, where a vertical load will be applied to the prosthesis pylon on the testing machine. The input forces in our system consist of F_b and F_c; thus, the normal moment, axial force, and shear force are described in Eqs. 5, 6, and 7, respectively, while deflections in the u- and v-directions in Eqs. 8 and 9 can be achieved by substituting Eqs. 5, 6, and 7 into Eq. 1.

$$M(\varphi) = -F_P(Rs(\varphi) + d_1) + F_c s(\theta)Rs(\varphi) - F_c c(\theta)R(1 - c(\varphi)) \quad (5)$$

$$\mathrm{N}(\varphi) = -F_P s(\varphi) + F_c s(\theta)s(\varphi) - F_c c(\theta)\, c(\varphi)) \quad (6)$$

$$V(\varphi) = F_P c(\varphi) - F_c s(\theta)c(\varphi) - F_c c(\theta)\, s(\varphi)) \quad (7)$$

$$\gamma_v(\varphi) = \gamma_{v_{F_p}} + \gamma_{v_{F_c}} \quad (8)$$

$$\gamma_u(\varphi) = \gamma_{u_{F_p}} + \gamma_{u_{F_c}} \quad (9)$$

Here c and s refers to cosine and sine respectively. γ_v and γ_u represent the total deflection in v- and u-directions, while $\gamma_{v_{F_p}}$ and $\gamma_{v_{F_c}}$ are the single deflection caused by each input forces. F_c is force from hydraulic piston. Given the deflection and the angle of cylinder, we can determine the displacement of the HC stroke (L_1). Additionally, the relationship between the displacement of the cylinder rod and pressure of pneumatic system can be expressed as shown in Eq. 13.

$$F_c = P_{p1}A_c \quad (10)$$

$$P_{p1} = (P_h - \Delta P_1 - \Delta P_2)A_c \quad (11)$$

$$V_{p1} = V_{ac} + V_{cham1} + V_{cham2} + V_{cham3} \quad (12)$$

$$P_{p2} = P_{p1}\left(\frac{V_{p1}}{V_{p2}}\right)^n = P_{p1}\left(\frac{V_{p1}}{V_{p1} - \Delta V}\right)^n \quad (13)$$

Where P_{p1} and P_{p2} are the air pressure in the accumulator before and after loading. ΔP_1 and ΔP_2 denote pressure losses due to bends/turns, and different tube segments in the hydraulic system. V_{p1} and V_{p2} are the volumes of the pneumatic system before and after loading. V_{ac} and A_{cham1} , A_{cham2}, and A_{cham3} are the volumes of the accumulator and three chambers, respectively. $\Delta V = L_1 A_c$ volume change under loading, where A_c is a piston's area and n is a constant [22].

Note that the following assumptions are made for a rough estimation of the stiffness equation: (1) the stiffness of the accumulator membrane is negligible, (2) the volume change in the cylinder is equal to the volume change in the gas side of the accumulator, (3) friction within the HC is negligible, (4) the gas behaves ideally, and (5) pressure and temperature within the accumulator and chambers are homogeneous

D. Experimental setup

The first experiment aims to validate the hydraulic system's ability to provide push-off in desired time. The dorsiflexion angle at push-off is approximately 15° for unimpaired individuals. The dorsiflexion angle peaks during the late Terminal Stance phase of the gait cycle, also known as the energy storage phase, which typically occurs between 30 % and 50 % of the gait cycle. In our setup, the PHHP was tested at a dorsiflexion angle of 15°, closing the hydraulic valve at peak dorsiflexion to observe the response of the CFB's energy return timing.

The second experiment is to evaluate the variable stiffness system of the PHHP. The prototype was subjected to a static test using universal testing machine, as shown in Fig. 2a. The adjustable jig was connected to the head of the testing machine which has a load cell attached. The input is the applied load of 950 N was applied to the shank at a rate of 100 N/s, following the dorsiflexion test (ISO 10328 Standard Static Test) for a 100 kg human reference [23], and the output is the measured vertical displacement. In this experiment, shank angles (∅) of 0°, 5°, 10°, and 15° were tested under each valve condition.

For investigating the impact of varying pneumatic chamber configurations and accumulator pre-charge pressures on prosthesis stiffness, this study utilizes three pneumatic chambers with distinct volumes, labeled V_1, V_2, and V_3, alongside pre-charge pressures set at 100 kPa and 200 kPa. Initially, a pre-charge pressure of 100 kPa was applied to the pneumatic system with all pneumatic valves (S1, S2, and S3) in the open position. This configuration, termed "Open ALL," establishes a uniform system pressure of 100 kPa across the accumulator and all three pneumatic chambers. The experimental procedure then transitions to a second configuration, referred to as "Close 1," wherein valve 1 (S_1) is closed. Under this condition, the effective pneumatic volume is confined to the accumulator and pneumatic chambers 2 (V_2) and 3 (V_3). Subsequently, a third configuration, "Close 1,2," involves closing valves 1 (S_1) and 2 (S_2), effectively limiting the active pneumatic volume to the accumulator and pneumatic chamber 3 (V_3), while maintaining the initial pre-charge pressure of 100 kPa. Finally, in the fourth configuration, all three pneumatic valves are closed or "Close 1,2,3", resulting in an effective pneumatic volume that comprises only the accumulator, representing the system's minimum effective pneumatic volume. This sequence of configurations was replicated under the 200 kPa pre-charge condition to facilitate comparative analysis across different pressure levels. The symbols and its description/values of variables are summarized in Table 1.

TABLE 1. THE PARAMETERS OF PROPOSED PHHP

Symbol	Definition
θ = 65°	Initial angle of the HC relative to the ground
E = 63 Gpa	Young' Modulus [24]
I = 3.10^{-9} m^3	Moment of inertia
∅ = [0° ,5° ,10°, 15°]	Dorsiflexion angle
A_c = *8* 10^{-4} (m^2)	Piston head area
ΔP_1, ΔP_2 (Pa)	Hydraulic pressure losses
V_{ac} = *4* 10^{-7} (m^3)	Volume of accumulator
$[V_1, V_2, V_3]$ = *[4.5, 6.5, 9]*10^{-6} (m^3)	Volume of chamber 1, 2 and 3

III. RESULT AND DISCUSSION

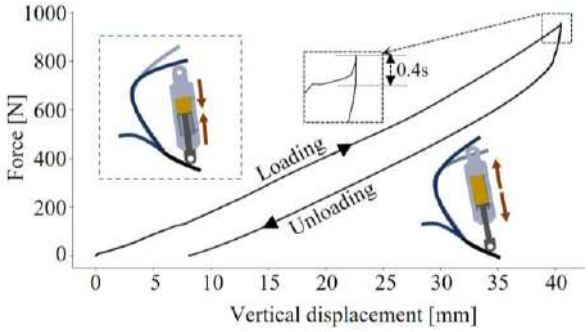


Fig. 3 CFB energy return time with hydraulic valve

In the first hydraulic valve and CFB experiment, we observed that the hydraulic valve can hold the CFB securely for approximately 0.4 seconds before losing holding force due to bubble formation and/or valve leakage, as shown in Fig. 3. The incompressible nature of oil enables PHHP to store energy and release just by turning on/off the valve. It is important to note that the holding force at peak dorsiflexion and the release of stored energy occur between 50 % and 60 % (preswing phase), which is approximately 1 millisecond for normal walking speed [25]. Based on these findings, the PHHP shows strong potential to store and deliver effective push-off work with given time during preswing phase.

In the second variable stiffness experiment, we found that the force-displacement curves follow a polynomial pattern. To simplify, a purely elastic model was used, and the linear stiffness was calculated [26]. For example, the stiffness of the prosthesis was experimentally determined to be 48.6 N/mm under the 100 kPa pre-charge condition with Open ALL, as shown in Fig. 4a. In addition, the percentage values next to the arrows in each bar indicate the discrepancy between theoretical and experimental results. An upward-pointing

arrow indicates that the theoretical result is higher than the experimental result by the specified percentage

In general, stiffness decreases as the dorsiflexion angle increases. At the neutral position, most of the load is applied to CFB, and the displacement direction of the HC aligns closely with the displacement of the CFB. Therefore, stiffness in this position primarily reflects the intrinsic stiffness of the CFB. However, as the dorsiflexion angle increases, the HC experiences more force, and the contribution of the compliant toe segment becomes more pronounced, thereby influencing the overall stiffness. The linear stiffness values increase with higher pre-charge pressure across all valve configurations and dorsiflexion angles. This effect is due to the high initial pressure in the accumulator, which enhances resistance to CFB's deformation under load (Figs. 4a, 4b). It is important to note that the pre-charge pressure can help establish a high baseline stiffness to meet the needs of individual amputees, and the variable stiffness can then be adjusted by modifying the effective pneumatic volume. We found that the linear stiffness of the proposed design is comparable to that of most commercial devices (25 N/mm to 54 N/mm) [27], indicating its potential adaptability for different users.

For 0° dorsiflexion, the discrepancy between theoretical and experimental stiffness is relatively small (approximately 4 % to 9 %), which aligns well with theoretical expectations. This is because, at neutral position, the toe segment does not significantly affect the overall stiffness. However, at higher dorsiflexion angles (5° and 10°), the toe segment of the CFB adds to stiffness, leading to a greater error. At the maximum dorsiflexion angle of 15 °, where the piston angle approaches nearly vertical alignment ($\varphi \cong 80°$), the pushing force is directed towards the HC, similar to the theoretical model. Although the toe segment still influences the initial phase of compression testing, the head of the toe segment is subjected to load rather than the body's toe segment. As a result, the toe segment experiences vertical loading instead of bending loads, such as at 5° or 10°. Consequently, the difference between theoretical and experimental results decreases as the dorsiflexion angle approaches 15°.

Although the proposed device exhibits minimal variation in total stiffness, Figs. 4a and 4b illustrate the combined stiffness of the passive CFB and the additional contribution from the pneumatic-hydraulic hybrid system, highlighting its promising performance relative to prior research. For example, the relative differences in stiffness between "Close 1", "Close 1,2", and "Close 1,2,3" configurations, compared to the baseline stiffness ("Open All") at 0° under a 200 kPa pre-charge condition, are 4.7%, 6.7%, and 7.9%, respectively. This is comparable to the increased average stiffness observed at walking speeds of 1 m/s (4.7%), 1.25 m/s (7.2%), and 1.5 m/s (13.7 %) compared to the stiffness at a 0.75 m/s speed [28]. In [29], the displacement measured during static testing was approximately 44 mm, 45.5 mm, and 48.5 mm for the compliant, stiff, and stiffest conditions, respectively, corresponding to stiffness variations of 3.4% and 10%. In [30], we observed that ankle torque during running at 2.6 m/s and 4.0 m/s differed by approximately 4%. Furthermore, from the force-displacement response, we calculated the elastic energy

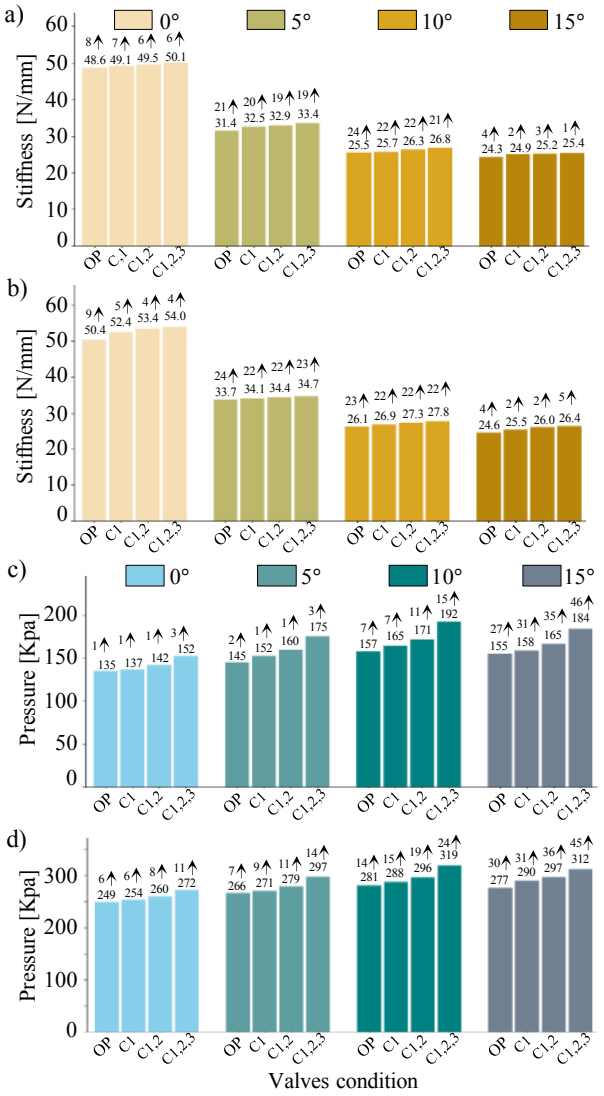


Fig. 4 Experimental and theoretical results; (a) The linear stiffness of PHHP under the 100 kPa pre-charge condition; (b) The linear stiffness of PHHP under the 200 kPa pre-charge condition; c) The pneumatic pressure under the 100 kPa pre-charge condition; (d) The pneumatic pressure under the 200 kPa pre-charge condition.

during loading and unloading. The PHHP demonstrated 72% to 84% energy return efficiency, indicating high energy effectiveness in the forefoot loading experiment [31].

Regarding pneumatic pressure, discrepancies may arise from factors such as membrane stiffness, cylinder friction, and air bubbles in the hydraulic system, as illustrated in Figs. 4c and 4d. Achieving complete oil saturation in the hydraulic tube of the prototype is challenging at this moment. Generally, we observed that the error increased with higher dorsiflexion angles. This discrepancy occurs because the model assumes that the displacement of the HC is directly proportional to changes in pneumatic volume. However, in practice, additional force is required to bend the toe segment, which reduces the HC's displacement compared to theoretical predictions. Additionally, we can see that the increased pressure provides a good amount of force for devices, leading to the big change in stiffness values. For example, as shown in Fig. 4a, the pressure reaches 135 kPa (equivalent to a force of 108.54 N acting on the piston). The additional pressure of 35

kPa (observed at OP in 0° under a 100 kPa pre-charge condition) corresponds to an extra force of 28 N on the piston, accounting for 26 % of the total force acting on the hydraulic piston compared to the pre-charge condition alone.

IV. CONCLUSION

In this study, we proposed a PHHP capable of not only providing variable stiffness but also storing energy, maintaining deformation to hold the stored energy, and releasing it at the desired time. The PHHP was modeled and validated by comparing theoretical model with experimental results. The energy transfer from the pneumatic system to the hydraulic system, facilitated by the membrane of the accumulator, enables the PHHP to generate various stiffness values, making it adaptable to different walking speeds for lower-limb amputees. Additionally, the proposed system provides push-off assistance with a simple on/off valve mechanism, resulting in a design that is both mechanically simple and energy-efficient.

For this initial investigation, we performed a feasibility analysis of the mechanism. As a next step, further refinement of the PHHP model is required, including optimization of the accumulator, tubing, and chamber dimensions to create a more compact system. The stiffness of the diaphragm in the accumulator, which affects the overall stiffness, should be considered. Finally, rather than employing three distinct sizes of pneumatic chambers, a single pneumatic cylinder and motor will be employed to alter the pneumatic volume to adjust stiffness and provide additional energy to users by actively compressing the air.

REFERENCES

[1] K. Ziegler-Graham et al., “Estimating the prevalence of limb loss in the United States: 2005 to 2050,” Arch. Phys. Med. Rehabil., vol. 89, no. 3, pp. 422–429, Mar. 2008

[2] N. P. Fey, G. K. Klute, and R. R. Neptune, “The influence of energy storage and return foot stiffness on walking mechanics and muscle activity in below-knee amputees,” Clin. Biomech., vol. 26, no. 10, pp. 1025–1032, 2011

[3] P. Cherelle et al., “Advances in propulsive bionic feet and their actuation principles,” Adv. Mech. Eng., vol. 6, 2014, Art. no. 984046

[4] E.M.GlanzerandP.G.Adamczyk,“Design and validation of a semi-active variable stiffness foot prosthesis,” IEEE Trans. Neural Syst. Rehabil. Eng., vol. 26, no. 12, pp. 2351–2359, Dec. 2018

[5] C. Lecomte, A. L. Ármannsdóttir, F. Starker, H. Tryggvason, K. Briem, and S. Brynjolfsson, ‘‘Variable stiffness foot design and valida tion,’’ J. Biomechanics, vol. 122, Jun. 2021, Art. no. 110440

[6] H. Tryggvason, F. Starker, C. Lecomte, and F. Jonsdottir, “Variable stiffnessprostheticfootbasedonrheologypropertiesofshearthickeningfluid,” Smart Mater. Structures, vol. 29, no. 9, 2020, Art. no. 095008

[7] H. Tryggvason, F. Starker, A. L. Armannsdottir, C. Lecomte, and F. Jonsdottir, ‘‘Speed adaptable prosthetic foot: Concept description, prototyping and initial user testing,’’ IEEE Trans. Neural Syst. Rehabil. Eng., vol. 28, no. 12, pp. 2978–2986, Dec. 2020

[8] E. Rogers-Bradley, S. H. Yeon, C. Landis, and H. M. Herr, “Design and evaluation of a quasi-passive variable stiffness prosthesis for walking speed adaptation in people with transtibial amputation,” IEEE/ASME Transactions on Mechatronics, vol. 29, no. 1, pp. 335–346, 2023

[9] E. A. Rogers, M. E. Carney, S. H. Yeon, T. R. Clites, D. Solav, and H. M. Herr, “An ankle-foot prosthesis for rock climbing augmentation,” IEEE Trans. Neural Syst. Rehabil. Eng., vol. 29, pp. 41–51, 2020.

[10] L. Gabert et al., “A compact, lightweight robotic ankle-foot prosthesis: Featuring a powered polycentric design,” IEEE Robot. Autom. Mag., vol. 27, no. 1, pp. 87–102,Mar.2020

[11] T. Lenzi, M. Cempini, J. Newkirk, L. J. Hargrove, and T. A. Kuiken, “Alightweight robotic ankle prosthesis with non-backdrivable cam-based transmission,” in Proc. IEEE 15th Int. Conf. Rehabil. Robot., Jul. 2017, pp. 1142–1147

[12] R. W. Nuckols, K. Z. Takahashi, D. J. Farris, S. Mizrachi, R. Riemer, and G. S. Sawicki, “Mechanics of walking and running up and downhill: A joint-level perspective to guide design of lower-limb exoskeletons,” PLoS One, vol. 15, no. 8, 2020

[13] S. K. Au, J. Weber, and H. Herr, “Powered ankle-foot prosthesis improves walking metabolic economy,” IEEE Trans. Robot., vol. 25, no. 1, pp. 51–66, Feb. 2009.

[14] H. She, J. Zhu, Y. Tian, Y. Wang, and Q. Huang, “Design of a powered ankle-foot prosthesis with an adjustable stiffness toe joint,” Adv. Robot., vol. 34, no. 10, pp. 689–697, May 2020.

[15] S. H. Collins and A. D. Kuo, “Recycling energy to restore impaired ankle function during human walking,” PLoS One, vol. 5, no. 2, pp. 1–6, Feb. 2010

[16] Ottobock, 2019, “ Triton Smart Ankle,” Ottobock, Duderstadt, Germany, accessed Dec. 20, 2019.

[17] Blatchford, Inc., 2019, “ Blatchford Elan Foot,” Blatchford, Miamisburg, OH, accessed Dec. 20, 2019, https://www.blatchfordus.com/products/elan/

[18] Freedom Innovations, 2019, “ Freedom Innovations Kinnex,” Freedom Innovations, Irvine, CA, accessed Dec. 20, 2019, https://www.freedom-innovations.com/kinnex/

[19] D. G. Caldwell, G. A. Medrano-Cerda, and M. Goodwin, “Control of pneumatic muscle actuators,” IEEE Control Syst., vol. 15, no. 1, pp. 40 48, Feb. 1995

[20] Mrazsko, H.X., Dekarske, J.T., Adamczyk, P.G., 2020. Design of a Variable Stiffness Pneumatic Ankle Prosthesis with Self-Recharging for weightlifting exercise. J. Med. Devices., vol 14, no 3, pp 034501, 2020

[21] H.Ahuett-Garza, O. Chaides, P. N. Garcia, and P. Urbina, Studies about the use of semicircular beams as hinges in large de ection planar com pliant mechanisms, Precis. Eng., vol. 38, no. 4, pp. 711727, Oct. 2014

[22] R. Dindorf, J. Takosoglu,and P. Wos "Challenges of robotic technology in sustainable construction practice." Sustainability," vol. 16, no. 13, pp. 5500., 2024

[23] J. Tabucol, T. M. Brugo, M. Povolo, M. Leopaldi, M. Oddsson, R. Carloni, and A. Zucchelli, ‘‘Structural FEA-based design and functionality verification methodology of energy-storing-and-releasing prosthetic feet,’’ Appl. Sci., vol. 12, no. 1, p. 97, Dec. 2021

[24] M. Omasta, D. Paloušek, T. Návrat, and J. Rosický, “Finite element analysis for the evaluation of the structural behaviour, of a prosthesis for trans-tibial amputees,” Med. Eng. Phys., vol. 34, no. 1, pp. 38–45, Jan. 2012

[25] B. R. Umberger and P. E. Martin, “Mechanical power and efficiency of level walking with different stride rates,” J. Exp. Biol., vol. 210, no. 18, pp. 3255–3265, 2007

[26] Doyen, Élodie, Fabien Szmytka, and Jean-François Semblat. "A novel characterisation protocol of mechanical interactions between the ground and a tibial prosthesis for long jump." Scientific Reports. vol.13,no. 1, pp 5226, 2023

[27] A. T. Turner, E. G. Halsne, J. M. Caputo, C. S. Curran, A. H. Hansen, B. J. Hafner, et al., "Prosthetic forefoot and heel stiffness across consecutive foot stiffness categories and sizes", Plos One., vol17., no 5., pp. e0268136, 2022.

[28] Rogers-Bradley, Emily, Seong Ho Yeon, Christian Landis, Duncan RC Lee, and Hugh M. Herr. "Variable-stiffness prosthesis improves biomechanics of walking across speeds compared to a passive device." Scientific Reports., vol 14, no. 1., pp. 16521., 2024

[29] Lecomte, et al., ”Variable stiffness foot design and validation,” Journal of Biomechanics, vol. 122, p.110440, 2021.

[30] M. Grimmer et al., “A powered prosthetic ankle joint for walking and running,” BioMed. Eng. Online, vol. 15, no. 3, pp. 37–52, 2016

[31] American Orthotic Prosthetic Association. "AOPA’S Prosthetic Foot Project: What It Is." What It Is Not, and What Patient Care Facility Providers/Practitioners Need to Know (2010)

A Control Method for Transtibial Prostheses with Bilateral Leg Data

Aniket Mazumder[1], Edsko E.G. Hekman[2], and Raffaella Carloni[1]

Abstract— **Micro-controlled lower limb prosthetic devices typically employ onboard sensors on the amputated side of the user's body to generate control patterns. However, balanced ambulation in a healthy subject requires synchronized neural control to facilitate appropriate positioning and orientation of both limbs. Building upon this idea, this study introduces a control architecture that utilizes information acquired from both limbs using only two inertial measurement units (one placed on the left shank, and one placed on the right thigh) to generate the control commands for a transtibial prosthesis prototype clamped to a table-top. Multiple trials were performed with a healthy subject walking on level ground at different speeds and undertaking an obstacle avoidance task. The results of the experiments suggest that incorporating data from each side provides comprehensive information about the limb's positions and orientations, thereby enabling a controller that can handle actuation timing and assist in precise prosthesis control through an understanding of the user's gait states.**

I. INTRODUCTION

Micro-controlled lower limb prostheses incorporate sensors that provide feedback to the prosthesis' controller to regulate its actuators and mechanical properties [1].

An approach to prosthesis control is the finite state-based impedance control. This method subdivides the entire gait cycle into multiple states along with the intermediate transition strategies for walking, standing, sitting [2], [3], [4], [5]. An intent recognizer, then, determines the gait state using sensor data, classified using probabilistic models, with the end-goal of matching the joint impedance and joint angles for the prosthetic system during ground contact.

Another prominent method solving the control problem involves use of a gait phase determination algorithm (volitional control) as demonstrated in [6], [7], [8], and [9]. Here, rotation rate measuring devices (e.g., gyroscopes, potentiometers) are placed on limb segment (tibia/shank), and the integration of rate of rotation yields the segment angles relative to the gravity vector [10], [11].

An initial attempt to control a prosthesis by using information from the sound limb is the echo control method [12], where the sound limb motion is used as a reference motion profile and played back for the prosthetic side. However, this control method is usually better suited for repetitive tasks, such as level ground walking. A second method that utilized data from the sound limb is the complementary limb motion estimation method, based on the principle that the limbs of a healthy human are inherently coupled through physiological couplings. While the method can successfully estimate the gait trajectories online, due to the nature of the coupling assumed in this method, it might not prove to be efficient during obstacle avoidance steps [13].

Since balanced ambulation necessitates optimal positioning of the entire body frame, accurate control ideally requires kinematic and dynamic information from all body segments. Based on this premise, the research presented in [14], [15], [16] and [17] demonstrated a system that employed a whole-body sensory array that uses a combination of seven inertial sensors placed on leg segments on both sides and the trunk, with force sensors placed in the insole of the shoe worn on the sound limb. The objective of this arrangement was to obtain as much sensory kinematic and dynamic information as possible from the subject and to perform level ground walking. The benefits of incorporating data from both sides become more apparent when undertaking complex tasks such as walking over obstacles [18], [19]. In such scenarios, the position information from the planted foot can be utilized to ensure the maintenance of a dorsiflexed toe of the moving foot while clearing the obstacle. Similar advantages can also be achieved when ascending/descending stairs, where power must be injected once sufficient loading of the amputated leg has occurred.

Inspired by [14], [15], [17], this study proposes an architecture to control the ankle joint angle of an active transtibial prosthesis that uses data collected from both legs to detect the states and phases of gait. For this, only two wireless inertial sensor units (IMUs) are used, which are strategically positioned on either side of the body, namely one on the shank of the leg wearing the transtibial prosthesis and one on the thigh of the contralateral healthy leg. Since the main focus of this study is the control method, it has been tested in a healthy participant, where data were taken from the shank and contralateral thigh, and the control system actuates a transtibial prosthesis on a fixed test bench. The ankle joint angle of the prosthesis is controlled by fusing information obtained from the two IMUs to achieve gait state and phase state estimation.

II. CONTROL SYSTEM

The controller design process begins with an analysis of Figure 1, which depicts the angular velocity of the shank and the angle of the thigh of the opposite sides of a healthy subject during ground level walking at a preferred speed [20].

This work was funded by the European Commission's Horizon 2020 Programme as part of the project MyLeg under grant no. 780871.

[1]Bernoulli Institute for Mathematics, Computer Science, and Artificial Intelligence, Faculty of Science and Engineering, University of Groningen, Nijenborgh 9, 9747 AG Groningen, The Netherlands. {a.mazumder, r.carloni}@rug.nl

[2]Department of Biomechanical Engineering, Faculty of Engineering Technology, University of Twente, Drienerlolaan 5, 7522 NB Enschede, The Netherlands. e.e.g.hekman@utwente.nl

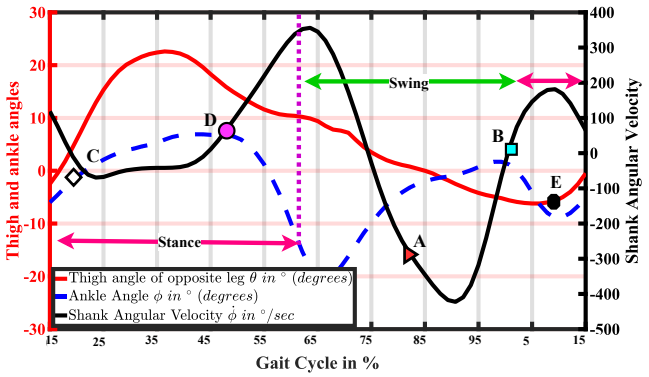


Fig. 1: Thigh angle and shank angular velocity from opposite limbs of a healthy subject during level-ground walking at a preferred speed as obtained from [20]. Point 'A', 'B','C', and 'D', are the reset step point, the step detection point, the stance rollover point and the power injection point, respectively. Point 'E' corresponds to the point where the thigh angle reaches its miniumum value. The plot has been shifted by 15% to demonstrate the linear nature of the thigh angle.

Previous research has demonstrated the existence of a relationship between the angle of the shank and shank angular velocity during walking [16], [21], [22], which allows for the generation of a gait phase variable relating both parameters that can act as an indicator for the overall progression of the gait. Conversely, the use of the angle of the thigh to derive a phase variable has been illustrated in [23], [24] and [25]. In these studies, phase relations from the same side were employed to control the prosthesis. With reference to Figure 1, several observations may be made regarding the *thigh angle* (red curve):

1) The thigh angle of the supporting leg (red curve) exhibits a linear nature with a negative slope from (35%) until (5%) into the next gait cycle.
2) A minimum in the curve, denoted by the black dot E, occurs at approximately the flat foot (7%) of the alternate leg. Then, beyond this point, the angle increases with a positive slope followed by a stance phase.
3) From rollover onward, the thigh angle continues to increase with a positive slope, and reaches its maximum value at approximately 40% of the next gait cycle.

Due to the presence of the linearity of the thigh angle along with a distinct minimum at approximately 7% of the gait cycle we argue that it is possible to utilize the thigh angle information from the contralateral side (lying at 180° out of phase) to provide an insight into the gait progression.

In contrast to the thigh angle, the *shank angular velocity* (black curve) exhibits a lesser degree of linearity. The shank angular velocity over a gait cycle can be subdivided into four sections around four control points (see Figure 1). The method for selecting these four points is as follows: i

1) A crossing of a threshold of approximately $-300^\circ/s$, corresponding to a gait progression of 80% in the plot is considered to be a 'Reset Step' point 'A'.
2) This is followed by a 'Step Detection' point 'B', corresponding to a value crossing $5^\circ/s$ around 100% of the gait cycle.
3) Subsequently, there is a 'Stance Rollover' point 'C', where the angular velocity falls below $5^\circ/s$ at approximately 20% of the gait cycle.
4) Finally, there is a 'Power Injection' point 'D', corresponding to a crossing of $70^\circ/s$ at approximately 50% of the gait cycle.

Based on these observations, we propose a controller that employs the *shank angular velocity data from the prosthetic-side* to regulate the prosthesis during level ground walking situations, while simultaneously utilizing the *thigh angle data from the contralateral side* as a supplementary tool for situations that require obstacle avoidance and for resetting the cycle and letting the controller know that a step detection point can be expected. A comprehensive description of the controller that has been designed based on the aforementioned points is presented in the following sections.

A. Controller Design

The design philosophy of the controller may be understood by considering a two part design as shown in Figure 2, with each part assigned the task of monitoring the motion of a dedicated (left/right) side of the subject. In the current application, the prosthetic side is monitored by the yellow portion in the figure, while the contralateral leg is monitored by the green portion in the figure. The combined monitoring, results in a fused signal that is used to control the overall motion of the prosthesis. The functioning of each side is explained further in the paragraphs below.

1) Monitor of the Prosthetic Side: The yellow portion of the controller in Figure 2 is always active and consists of the logic to detect the four points, namely the reset-step detection point, step detection point, stance rollover point, and the power injection points. This detection is performed by utilizing the shank angular velocity data as input and comparing it with the pre-determined thresholds (as described earlier). The thresholds in the current application were determined by taking and average of 15 trials performed overground by a test subject. The detection of each point is followed by an associated command such as 'Goto: Power Position', 'Goto: Reset Position' and 'Detect: New Step'.

To actuate the prosthesis, the actuation command accompanied by the updated desired velocity and acceleration are sent to the hardware controller. For every gait cycle, the actuation velocities and accelerations are calculated by comparing the last gait cycle time with the reference gait cycle time in [20], and are applied to the subsequent gait cycle. Thus, update to the actuation parameters happens every gait cycle. In this study, the gait cycle time is defined as the time taken between two consecutive steps, and a step is said to be detected when the condition 'B' (shown in the yellow portion of the figure) is satisfied. If no step is detected for a set period 'T', then the subject is said to be at rest, and consequently the prosthesis moves to the rest position where it only provides stationary support to the subject.

2) Monitor of the Contralateral Side: The green portion of the controller in Figure 2 is activated during instances of obstacle avoidance and uses the contralateral leg, which

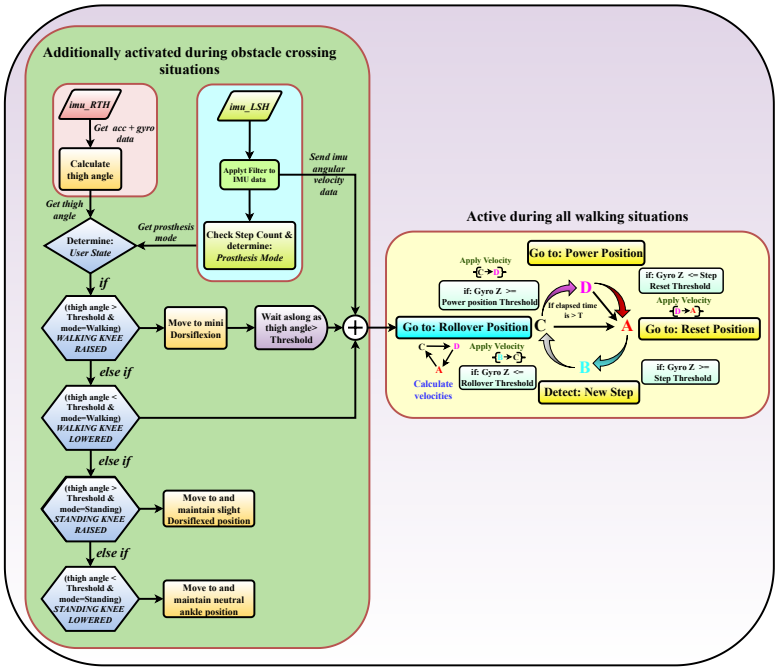


Fig. 2: Control architecture for a transtibial prosthesis, which uses data from two IMUs to generate position profiles and actuate the prosthesis. imu_RTH represents the IMU on the right thigh, whereas imu_LSH represents IMU on the left shank. The green block represents the logic where the data fusion from both IMUs occurs, whereas the yellow block shows the outcome of the decisions as applied to the prosthesis. The thigh angle threshold is set at 30°.

is continuously monitored. Data are obtained from two IMUs: imu_RTH (placed on the contralateral right thigh) and imu_LSH (placed on the amputated left shank). The acceleration and angular velocity data obtained from imu_RTH is first used to calculate the global thigh angle with respect to the direction of gravity (red box). This is accomplished by numerically integrating the gyroscope data over time using a complementary filter, as explained later. The information of the thigh angle is then utilized to determine the *'User State'*, which can either be *'Knee raised'* or *'Knee Lowered'* based on a thigh angle threshold determined to be 30° after multiple trials of raising a lowering the contralateral leg. On the other hand, the IMU data obtained from the imu_LSH is utilised to determine the number of steps taken by the prosthesis (cyan box). Based on the number of steps accumulated by the user, the *'Prosthesis Mode'*, is either set to *'Standing'* or *'Walking'*. Thus the two IMUs together consists of four possibilities viz. *'Walking knee raised'*, *'Walking knee lowered'*, *'Standing knee raised'* and *'Standing knee lowered'*. For the *'Walking knee raised'*, which happens primarily during walking over and obstacle, the prosthesis is moved to a mini dorsiflexion position and wait as long as the knee angle falls below a set threshold. This is done in order to assist the user in stepping over of the obstacle. When the knee is lowered sufficiently, normal roll-over, power pulse and reset phases follow (as explained in the yellow section). The same sequence happens for *'Walking knee lowered'*, without the intermediate waiting period. For the *'Standing knee raised'*, the prosthesis is instructed to move and maintain a dorsiflexed position, while for the *'Standing knee lowered'*, the prosthesis is instructed to move to and maintain a neutral ankle position. In both of these conditions, a supporting torque is provided to the ankle joint to aid standing.

By combining information from both sides, we are able to devise a controller that can respond to a user either undergoing level ground walking or walking over an obstacle.

B. Hardware and Control Software

The proposed control architecture has been implemented and tested on a transtibial prosthesis prototype, as shown in Figure 3 [26]. The design incorporates series-elastic springs for shock absorption, a ball screw-nut combination (Misumi BSSCK1204, Misumi Group, Europe, `de.misumi-ec.com`) for translation of rotation to linear motion, and a BLDC motor (Maxon EC-i 30, Maxon Group, Switzerland, `www.maxongroup.com`) as the prime mover. All three components are coupled using a timing belt and pulley system (Misumi S3M) around a hinge joint. This arrangement permits dorsiflexion and plantarflexion motion of the ankle around the hinge when power is applied to the motor. Clockwise rotation of the motor results in the rotation of the coupled ball screw. This rotation causes the ball-nut to slide upwards compressing the top spring (represented in green color) and pushes against the top fixture (represented in orange color), thereby moving the rear part of the mechanism upwards. This results in a plantar-flexion movement of the foot blade. A counterclockwise motor rotation unloads the springs, leading to the return of the foot to a neutral position. The details of the mechanical components used in this design are provided in [26].

The control hardware for the system comprises a Maxon EPOS4 motion controller, motor shaft encoders, and an ankle

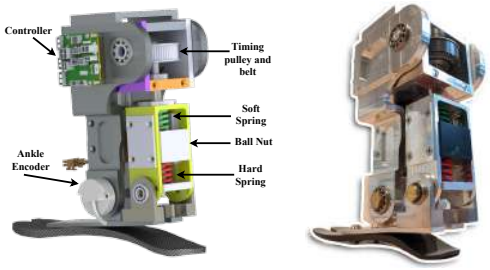


Fig. 3: Rendered image (left) of the transtibial prosthesis and the actual developed prototype (right).

joint for position feedback. Additionally, two MPU9250 IMUs capable of sensing rotation rates and accelerations are placed around the shank and thigh. These form the primary components of the control hardware. All software algorithms for the system are executed on a quad-core Raspberry Pi Zero 2W running Linux. Motion commands are transmitted to the controller from the Raspberry Pi via a USB connection. The system is powered by a 24V power supply.

III. Experiments

This section describes the experiments that have been performed on one healthy subject to validate the proposed control architecture. The subject's left leg simulated the prosthetic leg.

Multiple trials were conducted while allowing the user to self-select their gait progression speed as depicted in Figure 4[1]. Predetermined walking speeds were avoided to provide more generic values when choosing cut-off thresholds compared to when a specific speed or pattern is imposed on the subject. Initial experiments consisted of 10 calibration trials where a male subject (height 175 cm, weight 60 Kg) walked on level ground with the IMUs placed on his limbs. An average of these 10 trials were used to finalize the thresholds A, B, C, D, and E, as shown in Figure 1.

For the experiments, the IMUs were configured as shown in figure 4, with +X facing the direction of walking, +Y pointing downward towards gravity and the angular velocity of the shank about +Z (which points to the left) being used as the control signal for the prosthesis. Following this, 10 trials (divided into two parts) with the same sensor configuration and the thresholds programmed were conducted to assess the performance of the designed control algorithm. The prosthesis was secured to a table using a clamping mechanism that allowed it to perform its motion using wireless signals without being placed on the subject. The IMUs worn by the subject transmitted their data wirelessly in real-time to the prosthesis controller. The motion of the prosthesis and the shank/thigh angles were determined in real-time using an OptiTrack (Natural Point Inc,USA, `www.optitrack.com`) motion capture system.

The first part of the 15 trials consisted of the subject walking on level ground for multiple instances of gait initiation, speed maintenance, deceleration, and termination. Subsequently, obstacle avoidance tests were performed where a box-shaped obstacle measuring 10×15 cm which was placed in the subject's path. The subject was instructed to avoid the obstacle by first stepping over it with their right leg while placing their simulated prosthetic leg immediately in front of it, and then stepping over it with their other leg. The objective of this experiment was to evaluate the effectiveness of the controller in utilizing data from both limbs to set the response of the prosthesis as mentioned in Section II while the subject crossed the obstacle. The motion was executed smoothly and the response of the prosthesis along with angular calculations performed on IMU data were recorded.

We repeated this experimental procedure for multiple days over the course of a week. A video on the performed trials is provided as support material to this study.

[1]The study, under protocol number M22.298663, was evaluated and received a waiver by the Medical Ethics Review Committee of the University Medical Center Groningen (Groningen, The Netherlands) on June 9, 2022.

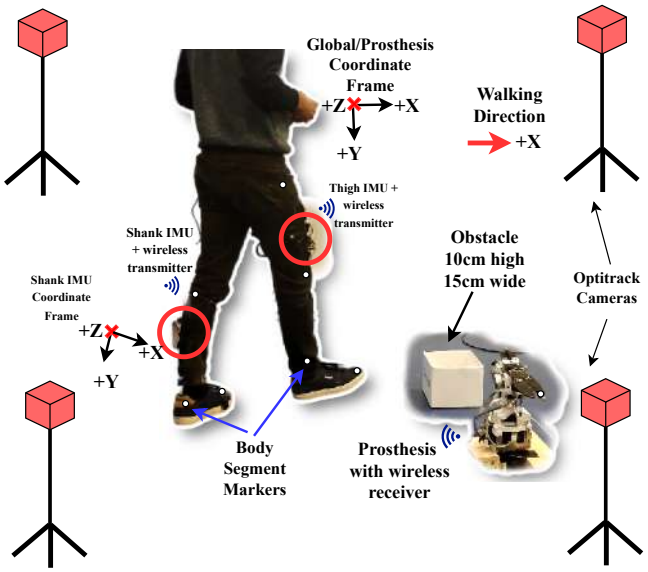


Fig. 4: The IMU on the left shank (imu_LSH) is analogous to the IMU present on the prosthesis; the imu_RTH is on the (contralateral) right thigh. The figure also shows the obstacle that the subject was asked to avoid by crossing over along with the prosthesis controlled by the algorithm. The body makers, co-ordinate systems and the optical cameras have also been shown.

IV. Results and Discussion

A. Results

Figure 5 displays the 15 gait cycle mean and standard deviation for thigh angle (in the global reference frame) during level-ground walking at preferred speed as calculated by fusing gyroscope and accelerometer data using the complementary filter described in Section II. This is compared to the angles of healthy subjects [20] and the angles measured by using the Optitrack system. One complete gait cycle in the figure lies between 0.2 s and 0.9 s of the experiment.

Figure 6 shows the prosthesis response while using the proposed control architecture that utilizes gyroscope data from the shank and the angle data from the contralateral thigh to step over an obstacle. The yellow areas represent instances where the subject is stepping over the obstacle,

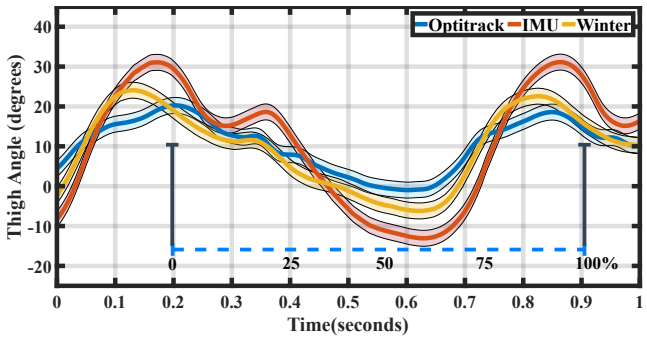


Fig. 5: Comparison between the angles(mean and standard deviation of 10 gait cycles) calculated by the control algorithm, the angles measured using the Optitrack motion capture system, and the reference angles from healthy subjects [20]. The figure shows data of more that one gait cycle. 0 to 100% grading of a single gait cycle is marked using the blue line.

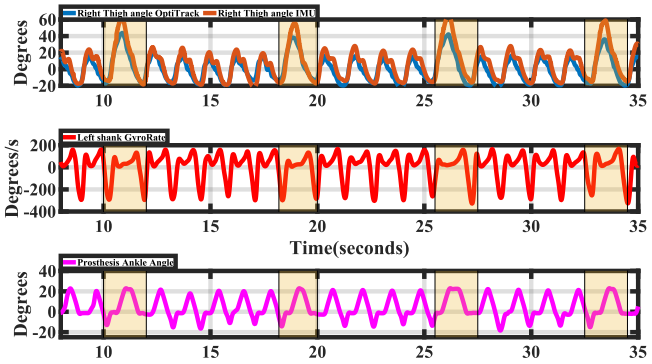


Fig. 6: Data collected during an experiment: the yellow areas represent instances where the subject is stepping over the 10×15 cm obstacle, while the white areas are when the subject walks on level ground.

while the white areas are when the subject walks on level ground. The variations in the thigh and shank as the subject moves overground, and their combined effect on the angles generated by the prosthesis can be noticed in the figure.

B. Discussion

Figure 5 shows a comparison between the thigh angle calculated with respect to vertical with the IMU, the measured angle using the Optitrack motion capture system, and the standard thigh angle as mentioned in [20]. The figure demonstrates that the thigh angle computation algorithm is able to generate angles comparable to those generated using standard optometry tools. In the figure, it is noticeable that there exits a correlation between the angle calculated using the complementary filter and the measured thigh angle. For the controller functionality, the thigh angle plot from the IMU and Optitrack shows the possibility of existence of a number of strategic control points which may be utilized as gait sub-dividing limits by the prosthesis controller. For example, the thigh angle curve has a minima at $\sim 60\%$ of the gait cycle, and a maximum at $\sim 85\%$ of gait cycle. For normal human gait, the minimum in the thigh angle signifies the end of the stance phase, whereas the maximum indicates the occurrence of a heel-contact [20].

Moreover, by tracking the thigh angle in real-time, it is also possible to indicate whether a leg has been raised beyond the normal limits for level ground walking. For example, angle values greater than the maximum for normal walking can indicate a raised leg. In the current application, we monitor the thigh angle for these abnormal values($>$30 degrees was considered as abnormal) and indicate the controller to suspend actuation and only to provide a supporting force while being fixated in a dorsiflexed position as long as the thigh angle remains higher than the threshold.

This concept has been demonstrated in Figure 6, where the yellow regions represent instances during which the contralateral knee has been raised to step over an obstacle while other regions represent normal walking on level ground. As the contralateral knee is raised, the prosthesis' response slows and a longer period is required for cycle completion. This is because, at this point, the thigh angle's threshold has been crossed and the controller then waits for the thigh to be lowered down before performing the power injection for the prosthesis plantarflexion. The left leg gait cycle also slows down but the rotation rate recorded by imu_LSH is maintained. The middle plot in Figure 6, shows the actual prosthetic angles generated on reception of the control signals. The angles generated by this method, are similar to that of a normal human ankle angle, however, for each gait cycle, the generated angles, shows a stagnation between 20% and 30% of the gait cycle. This is primarily due to the fact that a large temporal gap exists between the detection of points C and D, as shown in Figure 1. This delay in detection translates to a delay in sending motion commands to the actuator, resulting in the stagnation at $\sim 30\%$ of every gait cycle. In such a condition, a motor with higher speed than the one chosen here is required for the prosthesis to traverse the entire trajectory within a shorter time period and avoid angular deviation.

In this way, while during normal walking the angles are generated synchronously by being governed using the left shank angular velocity, during obstacle crossing with a raised leg, the angle generation deviates from the normal pattern and waits for the leg to be brought down so that the normal mode of the angle generation may resume.

C. Recommended Enhancements

Although the above results demonstrate that data from both legs can be utilized for the overall control of a transtibial prosthesis, there are areas of possible improvement.

1) 3D Orientation: In this study, we use an accelerometer and a gyroscope to get the absolute values of roll and pitch (2-DOF) of the subject. However, to accurately estimate orientation in 3D space, a magnetometer is necessary. With a complete 3D picture, it would be possible to design a more effective controller response that could account for controlling various activities of daily living. Implementations such as the Madgwick filter [27] or a Kalman filter [28] could also add to the existing capabilities of the controller.

2) Flexion/Extension of the Contralateral Leg: The controller presently employs information pertaining to the angle

of the thigh to ascertain whether the leg has been elevated to surmount an obstacle. Furthermore, this information may also be utilized to determine the degree of flexion and extension of the contralateral leg. When fused with information regarding angular velocity obtained from the prosthesis, this data may be employed to accurately establish the instant of power pulse during level ground walking. The integration of this logic into the controller could have the potential to enhance its response in cases of level ground walking.

V. Conclusions

This study presented a methodology for the control of transtibial prostheses, which utilizes wireless transmission of data from only two IMU sensors placed on both legs. The controller's performance was evaluated during level-ground walking and overstepping of an obstacle of fixed dimensions. The experiments demonstrate that the information obtained from both legs can be used by the controller to walk and to avoid obstacles, when the balancing ability of the prosthesis can be related to positioning the contralateral leg.

Augmenting the controller of a commercial prosthesis with that on a mobile phone, placed in the pocket of the contralateral side, could potentially offer a higher level of gait comprehension than what is possible using only the available onboard sensors on the prosthesis. A mobile application that can wirelessly communicate and exchange inertial information with the prosthesis in real-time could, thus, prove beneficial in providing orientation information of the contralateral leg. Such an arrangement may ultimately result in improved performance and satisfaction for transtibial prosthesis users. These tasks along with others shall be undertaken as future efforts.

References

[1] R. Gehlhar, M. Tucker, A. J. Young, and A. D. Ames, "A review of current state-of-the-art control methods for lower-limb powered prostheses," *Annual Reviews in Control*, 2023.

[2] B. E. Lawson, B. Ruhe, A. Shultz, and M. Goldfarb, "A Powered Prosthetic Intervention for Bilateral Transfemoral Amputees," *IEEE Transactions on Biomedical Engineering*, vol. 62, no. 4, pp. 1042–1050, 2015.

[3] S. K. Au, J. Weber, and H. Herr, "Powered ankle–foot prosthesis improves walking metabolic economy," *IEEE Transactions on Robotics*, vol. 25, no. 1, pp. 51–66, 2009.

[4] H. A. Varol, F. Sup, and M. Goldfarb, "Multiclass real-time intent recognition of a powered lower limb prosthesis," *IEEE Transactions on Biomedical Engineering*, vol. 57, no. 3, pp. 542–551, 2009.

[5] R. Unal, F. Klijnstra, S. Behrens, E. Hekman, S. Stramigioli, H. Koopman, and R. Carloni, "The control of recycling energy strorage capacity for WalkMECHadapt," in *IEEE International Symposium on Robot and Human Interactive Communication*, 2014, pp. 720–725.

[6] F. Zhang and H. Huang, "Source selection for real-time user intent recognition toward volitional control of artificial legs," *IEEE Journal of Biomedical and Health Informatics*, vol. 17, no. 5, pp. 907–914, 2012.

[7] F. Sup, H. Varol, J. Mitchell, T. Withrow, and M. Goldfarb, "Design and control of an active elctrical knee and ankle prosthesis," in *Proceedings of the IEEE RAS/EMBS International Conference on Biomedical Robotics and Biomechatronics*, 2008, pp. 523–528.

[8] A. Mazumder, E. E. Hekman, and R. Carloni, "An adaptive hybrid control architecture for an active transfemoral prosthesis," *IEEE Access*, vol. 10, pp. 52 008–52 019, 2022.

[9] S. Rezazadeh, D. Quintero, N. Divekar, E. Reznick, L. Gray, and R. D. Gregg, "A phase variable approach for improved rhythmic and non-rhythmic control of a powered knee-ankle prosthesis," *IEEE Access*, vol. 7, pp. 109 840–109 855, 2019.

[10] N. Thatte, T. Shah, and H. Geyer, "Robust and adaptive lower limb prosthesis stance control via extended kalman filter-based gait phase estimation," *IEEE Robotics and Automation Letters*, vol. 4, no. 4, pp. 3129–3136, 2019.

[11] D. Xu, S. Crea, N. Vitiello, and Q. Wang, "Online estimation of continuous gait phase for robotic transtibial prostheses based on adaptive oscillators," in *IEEE/ASME International Conference on Advanced Intelligent Mechatronics*, 2020, pp. 1890–1895.

[12] D. L. Grimes, "An active multi-mode above knee prosthesis controller," Ph.D. dissertation, Dept. of Mechanical Engineering, Massachusetts Institute of Technology, USA, 1979.

[13] H. Vallery, R. Ekkelenkamp, M. Buss, and H. van der Kooij, "Complementary limb motion estimation based on interjoint coordination: Experimental evaluation," in *2007 IEEE 10th International Conference on Rehabilitation Robotics*, 2007, pp. 798–803.

[14] L. Ambrožič, M. Goršič, J. Geeroms, L. Flynn, R. M. Lova, R. Kamnik, M. Munih, and N. Vitiello, "Cyberlegs: A user-oriented robotic transfemoral prosthesis with whole-body awareness control," *IEEE Robotics & Automation Magazine*, vol. 21, no. 4, pp. 82–93, 2014.

[15] M. Goršič, R. Kamnik, L. Ambrožič, N. Vitiello, D. Lefeber, G. Pasquini, and M. Munih, "Online phase detection using wearable sensors for walking with a robotic prosthesis," *Sensors*, vol. 14, no. 2, pp. 2776–2794, 2014.

[16] M. Grimmer, "Powered lower limb prostheses," Ph.D. dissertation, Dept. of Mechanical Engineering and Dept. of Human Movement Sciences, Technical University of Darmstadt, Germanny, 2015.

[17] L. Ambrožič, M. Gorišič, S. Šlajpah, R. Kamnik, and M. Munih, "Wearable sensory system for robotic prosthesis," *International Journal of Mechanics and Control*, vol. 15, pp. 53–59, 2014.

[18] M. Gordon, N. Thatte, and H. Geyer, "Online learning for proactive obstacle avoidance with powered transfemoral prostheses," in *2019 International Conference on Robotics and Automation (ICRA)*. IEEE, 2019, pp. 7920–7925.

[19] J. Mendez, S. Hood, A. Gunnel, and T. Lenzi, "Powered knee and ankle prosthesis with indirect volitional swing control enables level-ground walking and crossing over obstacles," *Science Robotics*, vol. 5, no. 44, p. eaba6635, 2020.

[20] D. A. Winter, *Biomechanics and Motor Control of Human Movement*. John Wiley & Sons, Inc., New Jersey, USA, 1990.

[21] D. J. Villarreal and R. D. Gregg, "A survey of phase variable candidates of human locomotion," *International Conference of the IEEE Engineering in Medicine and Biology Society*, pp. 4017–4021, 2014.

[22] R. D. Gregg, E. J. Rouse, L. J. Hargrove, and J. W. Sensinger, "Evidence for a time-invariant phase variable in human ankle control," *PloS One*, vol. 9, no. 2, p. e89163, 2014.

[23] M. Eslamy, F. Oswald, and A. Schilling, "Mapping thigh motion to knee motion: Implications for motion planning of active prosthetic knees," in *IEEE/RSJ International Conference on Intelligent Robots and Systems*, 2020, pp. 4120–4125.

[24] D. Quintero, D. J. Villarreal, D. J. Lambert, S. Kapp, and R. D. Gregg, "Continuous-phase control of a powered knee–ankle prosthesis: Amputee experiments across speeds and inclines," *IEEE Transactions on Robotics*, vol. 34, no. 3, pp. 686–701, 2018.

[25] T. K. Best, K. R. Embry, E. J. Rouse, and R. D. Gregg, "Phase-variable control of a powered knee-ankle prosthesis over continuously varying speeds and inclines," in *IEEE/RSJ International Conference on Intelligent Robots and Systems*, 2021, pp. 6182–6189.

[26] A. Mazumder, E. E. Hekman, and R. Carloni, "Towards controlling transtibial prostheses using a single degree of freedom inertial sensor system," *IEEE Access*, vol. 12, pp. 24 803–24 812, 2024.

[27] S. O. Madgwick, S. Wilson, R. Turk, J. Burridge, C. Kapatos, and R. Vaidyanathan, "An extended complementary filter for full-body MARG orientation estimation," *IEEE/ASME Transactions on Mechatronics*, vol. 25, no. 4, pp. 2054–2064, 2020.

[28] J.-O. Nilsson, I. Skog, P. Händel, and K. Hari, "Foot-mounted INS for everybody - An open-source embedded implementation," in *IEEE/ION Position, Location and Navigation Symposium*, 2012, pp. 140–145.

Differentiable Biomechanics for Markerless Motion Capture in Upper Limb Stroke Rehabilitation: Comparison with Optical Motion Capture

Tim Unger[*,1,2], Arash Sal Moslehian[*,3], J.D. Peiffer[*,4], Johann Ullrich[1,2], Roger Gassert[2], Olivier Lambercy[2], R. James Cotton[†,4,5], Chris Awai Easthope[†,1]

***Abstract*— Marker-based Optical Motion Capture (OMC) paired with biomechanical modeling is currently considered the most precise and accurate method for measuring human movement kinematics. However, combining differentiable biomechanical modeling with Markerless Motion Capture (MMC) offers a promising approach to motion capture in clinical settings, requiring only minimal equipment, such as webcams, and minimal effort for data collection.**

This study compares key kinematic outcomes from biomechanically modeled MMC and OMC data in 15 individuals with stroke performing the drinking task, a functional task recommended for assessing upper limb movement quality.

We observed a high level of agreement in kinematic trajectories between MMC and OMC, as indicated by high correlations (median $r > 0.95$ for the majority of kinematic trajectories) and median RMSE (root mean squared error) values ranging from $2°$–$5°$ for joint angles, 0.04 m/s for end-effector velocity, and 6 mm for trunk displacement. Trial-to-trial biases between OMC and MMC were consistent within participant sessions, with interquartile ranges of bias around $1-3°$ for joint angles, $0.01m/s$ in end-effector velocity, and approximately 3 mm for trunk displacement.

Our findings indicate that our MMC for arm tracking is approaching the accuracy of marker-based methods, supporting its potential for use in clinical settings. MMC could provide valuable insights into movement rehabilitation after stroke, potentially enhancing the effectiveness of rehabilitation strategies.

I. Introduction

The increasing number of individuals affected by stroke and related neurological conditions has created an urgent need to improve the effectiveness of rehabilitation strategies [1]. Over 70% of individuals with stroke suffer from acute upper limb impairment [2], necessitating accurate and frequent assessments of upper limb movement quality to customize interventions and monitor rehabilitation progress [3]. Ideally, recovery after a stroke involves neuroplasticity, where motor functions are restored by reorganizing neural pathways [4]. Compensatory strategies, such as relying on unaffected muscles or limbs, provide short-term functional benefits but can hinder neuroplastic recovery by reinforcing maladaptive patterns [5]. As a result, after controlling for altered movement due to pain, deviation in movement quality can serve as a biomarker for limited neuroplasticity and reduced genuine recovery [6], [7].

Consensus guidelines from European stroke experts recommend incorporating an instrumented drinking task to assess upper limb movement quality in individuals with stroke [3]. The drinking task comprises several relevant movement primitives, is easily standardized, is already learned, and the movement quality measures for this task were established using optical motion capture (OMC) in several studies [8]–[10]. While OMC does not directly measure bone movement, it is widely regarded as the gold standard for biomechanical assessment [11].

Traditional biomechanical modeling with markers follows a two-stage process: first, triangulated 3D markers are used to scale a biomechanical model to a specific individual (for example bone lengths, moments of inertia). Second, this scaled model is fit to follow marker trajectories during movements of interest [12]. This process assumes fixed marker placement on known landmarks, most of which are specific bony prominences. As marker placement is highly important for accurate biomechanical reconstruction [13], collecting OMC data requires a domain expert and significant setup time, limiting its accessibility in routine clinical practice.

Recent advances in human pose estimation with computer vision now enable Markerless Motion Capture (MMC) from RGB videos, providing a potentially viable alternative to OMC [14]. Critical to these approaches are keypoint detection algorithms which are trained on large datasets to detect "virtual" markers, termed keypoints, on raw RGB images [15]. These virtual markers can be internal locations inside joints, body landmarks or surface markers [16]. As these algorithms are increasingly robust and at minimum require a smartphone camera [17], there is great potential for MMC to be utilized in clinical settings. However, a critical limitation of keypoint detection algorithms is there are no biomechanical constraints to virtual marker locations.

To address this, Cotton et al. proposed an optimization approach allowing for simultaneous optimization of biomechanical model scaling parameters and movement trajectories [18], [19]. As this approach combines the scaling and trajectory fitting steps employed in traditional two-stage pipelines, we hereafter refer to this approach as "end-to-end" MMC. While this method has been validated for internal consistency and against instrumented walkways, [18], [20], it has not yet

part of this work is funded by Digitalisierungsinitiative der Zürcher Hochschulen (DIZH)

*co-first author, †co-senior author

[1] Data Analytics & Rehabilitation Technology (DART Lab), Lake Lucerne Institute (LLUI), Vitznau, Switzerland tim.unger@llui.org, chris.awai@llui.org

[2] Rehabilitation Engineering Laboratory (RELab), ETH Zurich, Switzerland

[3] Neuro-X Institute, EPFL Lausanne, Switzerland arash.salmoslehian@epfl.ch

[4] Dept of Biomedical Engineering, Northwestern University, Chicago, IL

[5] Shirley Ryan AbilityLab, Dept of PM&R, Northwestern University, Chicago, IL

been validated against OMC-based kinematic data.

In this study, we conduct the first comparative analysis between OMC and this novel end-to-end MMC approach. We evaluate the established drinking task movement quality measures in individuals with stroke and compare the underlying kinematic trajectories used to derive these measures. Our hypothesis is that the agreement between the two systems will be high across key kinematic trajectories, such as joint angles, end-effector velocities, and trunk displacement as well as in the established movement quality measures for the drinking task. We test this hypothesis using comparative plots for kinematic trajectories and movement quality measures as well as several comparative metrics such root mean squared error (RMSE), correlation (r), and bias to assess the agreement of movement quality measures and underlying kinematic trajectories produced by each system[1].

II. Methods

A. Participants

The study adhered to the ethical guidelines set forth by the local ethics committee (BASEC-No: 2022-00491). Individuals with stroke with mild and moderate upper limb impairment were recruited from the University Hospital Zurich Stroke Registry and the cereneo clinic. Eligible participants were invited for a single-session measurement. Inclusion criteria mandated that participants be at least 18 years old, capable of providing informed consent, and have a confirmed diagnosis of stroke. Additionally, participants were required to have at least partial ability to perform a reaching movement, and to grasp a cup unassisted using a cylindrical grip with the affected hand. Exclusion criteria consisted of pre-existing upper limb deficits, such as orthopedic impairments, and other neurological conditions. An ad-hoc sample of fifteen individuals with stroke (9 males, 6 females) was included in this study, with a mean age of 71 years (SD = 15) and an average time since stroke of 24 months. Participants had mild to moderate upper limb impairment, as indicated by a mean Fugl-Meyer Upper Limb Assessment (FMA-UE) score of 56.3 (SD = 8.4), with scores ranging from 39 to 66.

B. Data Acquisition and Preprocessing

Participants performed 40 repetitions of the standardized, seated drinking task as in [8] (standardized motor task with standardized start and end pose) with each the affected and unaffected arm while being recorded with OMC as well as five synchronized consumer-grade webcams for MMC. The OMC system operated at a sampling frequency of 100Hz, using technologies from Qualisys (8 cameras) and Optitrack (12 cameras) across different measurement setups. We applied the base marker set used by Alt Murphy et al. [8] for the drinking task and extended it with further markers for better representation of the movement (16 body markers - see Fig. 2, without finger markers). OMC data was manually gap-filled and labeled. Five synchronized consumer-grade webcams (Logitech Brio 4k) recorded the participants at 1080p and 60Hz. The five cameras were evenly distributed in a half circle around the participant with a spacing of roughly 45° (see Fig. 1). The videos were segmented into trials based on the OMC master trigger signal, resulting in a synchronized dataset composed of multiple trials, each representing a single repetition of the standardized drinking task.

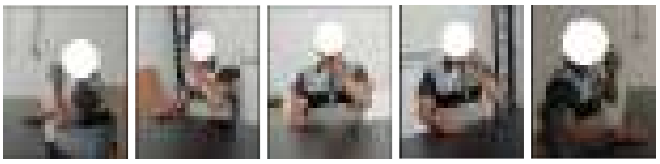


Fig. 1: Camera perspectives of the five webcams used for MMC.

C. Data Processing and Inverse Kinematics

1) Two-Stage OMC: The measured 3D markers from OMC during the initial static period of participants sitting at the table were used to scale a biomechancical model in OpenSim. The OpenSim model is based on the Rajagopal 2016 model [21], with modified ranges of motion for pronation and supination to better match the natural range of motion, as the original model constrained these motions. As the legs were stationary and occluded by the table during the drinking task, we removed all markers below the hip, effectively locking all leg degrees of freedom in the standard pose. Afterwards, inverse kinematics were calculated using the IK tool in OpenSim with the scaled model and the measured 3D marker trajectories from OMC. All calculations were performed using Python scripts, incorporating the OpenSim API to allow batch processing. Resulting kinematic trajectories of OMC were interpolated from 100Hz to 60Hz to compare directly with MMC.

2) End-to-End MMC: In contrast to two-stage approaches, previous work in MMC has simultaneously optimized body scale parameters and joint kinematic trajectories. This "end-to-end" optimization formulates model scaling, marker triangulation, and inverse kinematics as a single optimization problem [19]. Without requiring training data, this method has demonstrated improved internal consistency in biomechanical reconstructions of the lower limb [22] and upper limb [20], though it has not yet been validated against optical motion capture.

To apply this approach to the data collected here, we first used AniposeLib [23] to perform extrinsic and intrinsic calibration of cameras using a calibration recording with an A1-sized ChArUco board. Using PosePipe [24], we first extracted 87 2D keypoints from each webcam video using MeTrabs-ACAE [15] and then performed automatic person association using EasyMocap [25]. For videos where automatic person association failed, we manually performed person association.

[1]The code for the analysis is available at `https://github.com/DART-Lab-LLUI/diff-biomech-mmc-icorr-2025`

Finally, we reconstructed joint kinematics following [19]. In brief, this parameterizes the movement trajectory of a recording as an implicit function $f_\phi : t \rightarrow \theta$ mapping from time to joint angles where f_ϕ is implemented as a multi-layer perceptron. These parameters ϕ along with body scaling and marker offset parameters are jointly learned through optimization. At each optimization step, the joint angle output from the implicit function is passed through a biomechanical forward kinematic function in MuJoCo using the GPU accelerated Mjx version [26], [27] and 3D pose marker locations are projected into each camera frame using known camera extrinsics/intrinsics. This approach also employs a bilevel optimization which learns the body scale of a participant over multiple trials [28]. Since each of our participants presented here had approximately 80 trials, not all the trials could fit into our NVIDIA RTX 3080 GPU with 10GB of VRAM; thus, we performed bilevel optimization on a subset of each participant's trials, splitting them into eight batches. We used a modified version of the biomechanical model presented by Hamner et al. [29], [30] compatible with MuJoCo. We found no major differences in relevant model degrees of freedom between the models used for OMC (OpenSim) and MMC (MuJoCo).

D. System Comparison

1) Kinematic Trajectories: We exclusively included the essential kinematic trajectories (kinematic time series data, such as joint angles, displacements and velocity profiles) which are required for deriving the established movement quality measures in individuals with stroke performing the drinking task according to [8]. Specifically, these kinematic trajectories included: Shoulder Flexion, Shoulder Abduction, Elbow Flexion, Elbow Angular Velocity, Trunk Displacement, and End-Effector Velocity.

Joint angles were extracted from the inverse kinematic fits from OpenSim and MuJoCo for OMC and MMC, respectively. The end-effector velocity for OMC was computed by OpenSim based on the velocity of the center of geometry of the hand marker, while for MMC we differentiated the position of the hand keypoint. Trunk displacement was determined from the position of the trunk marker (sternum keypoint for MMC) after model fitting.

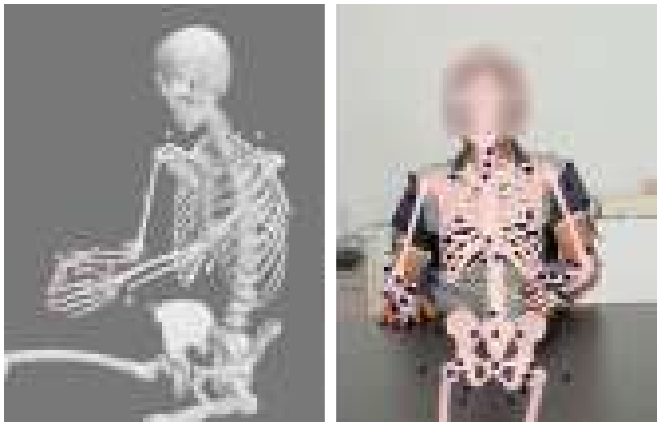


Fig. 2: Visualization of biomechnical modelling. left: OMC data with OpenSim; right: end-to-end MMC with MuJoCo.

For each trial and kinematic trajectory, we calculated the static offset between the two systems as the difference in the means of MMC and OMC trajectory. This bias (offset) was then added to the OMC signal. The static bias for each kinematic trajectory was recorded to evaluate the consistency of the offsets between the two methods across trials and participants. All further analyses of agreement were conducted with bias-removed kinematic trajectories.

To account for potential time offsets due to imperfect synchronization between the systems, we determined the optimal time lag between the two signals by shifting one kinematic trajectory over the other, up to 0.25 seconds. At each shift, we calculated the RMSE and identified the time lag that minimized this error. The resulting time lag was recorded as a measure of synchronization accuracy. Finally, we calculated the RMSE and Pearson correlation between the adjusted kinematic trajectories from OMC and MMC for each trial to assess the agreement between the two systems.

2) Movement Quality Measures: Movement quality measures for the drinking task, based on what was defined by Alt Murphy et al. [8], were derived from the kinematic trajectories of both MMC and OMC. These include: total movement time, number of movement units (smoothness), peak velocity (PV) in reaching, peak elbow angular velocity in reaching, time to peak velocity in reaching, time to first peak velocity in reaching, max elbow extension in reaching, max shoulder abduction angle in drinking / reaching, max trunk displacement during task, max shoulder flexion angle in reaching / drinking, interjoint coordination (Pearson correlation between elbow extension and shoulder flexion during reaching). Drinking task phase classification (Reaching, Forward, Drinking, Back, Returning, and Rest) for both systems was based on the end-effector velocity calculated from the OMC markers on the wrist and cup, following the approach in [8]. This eliminated any influence of difference in phase classification, thereby isolating the focus on kinematic data alone. Therefore, time to peak velocity and time to first peak velocity during reaching (in %) are not reported, as the phase duration is identical for MMC and OMC, making these measures redundant with those reported in seconds.

To evaluate alignment in the extraction of movement quality measures between the two systems, we visually assessed the measures from MMC and OMC using correlation plots. Additionally, Pearson correlations were calculated for each movement quality measure, both for individual trials (r_s) and for averaged movement measure (r_{av}) across all affected and unaffected trials per participant.

E. Data and Processing

In total 1160 trials of the drinking task of 15 participants were included with a median of 40 [39, 40] trials per affected arm and 39 [38, 41] trials per unaffected arm per participant. Trials were manually inspected, resulting in a 6% exclusion rate. Of the excluded trials, 51 were

due to incorrect movements, 13 due to end-to-end MMC reconstruction failures, and 5 due to synchronization issues between the two systems. Calculating inverse kinematics in OpenSim with cleaned OMC data required approximately 30 hours on a 13th Gen Intel® Core™ i9-13900H processor (2.60 GHz) with 32 GB of RAM. The entire end-to-end MMC process took around 12 days to complete all trials, leveraging an NVIDIA RTX 3080 GPU. The majority of this time was spent extracting 2D keypoints from a total of 5800 videos (comprising 5 cameras across 1160 trials).

III. Results

A. System comparison

1) Kinematic Trajectories: Visual inspection of the kinematic trajectories demonstrated a very high level of agreement between OMC and MMC across all kinematic trajectories (see Fig. 3).

Quantitative analysis further supported this (see Table I), with high correlation coefficients (r) observed between the two systems. Notably, shoulder flexion and elbow extension showed strong correlations ($r = 0.99$), indicating close alignment in these key movements. Among the kinematic trajectories, shoulder abduction on the unaffected side had the lowest correlation ($r = 0.88$ [0.78, 0.93]), though the RMSE remained low at $1.97°$ [$1.37°$, $2.71°$]. The lower correlation is due to the small range of motion in unaffected shoulder abduction, where slight trajectory discrepancies have a greater impact on correlation.

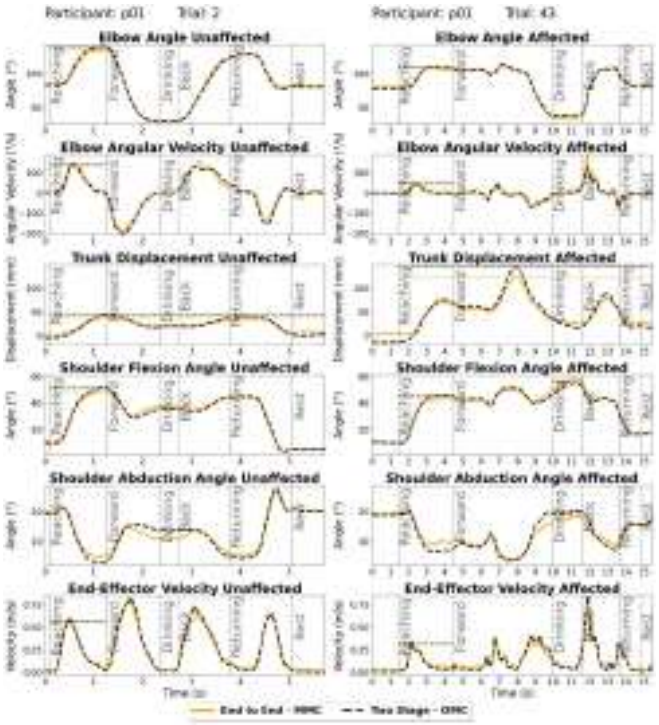


Fig. 3: Exemplary kinematic trajectories of participant p01, showing one trial each for the unaffected and affected arm (FMA-UE: 49). Horizontal lines outline the movement quality measures, and the x's on the end-effector velocity mark each movement unit.

TABLE I: Medians and [IQRs] for RMSE, r, bias, and time lag of kinematic trajectories, calculated across all patients and differentiating between the affected and unaffected arms.

Kinematic	Value	Unaffected arm	Affected arm
End-Effector Velocity	r	0.99 [0.97, 0.99]	0.99 [0.96, 0.99]
	RMSE (m/s)	0.04 [0.03, 0.07]	0.03 [0.03, 0.05]
	Bias (m/s)	0.00 [-0.01, 0.00]	0.00 [-0.01, 0.00]
	Time Lag (s)	0.00 [0.00, 0.02]	0.01 [0.00, 0.02]
Elbow Angular Velocity	r	0.96 [0.94, 0.97]	0.96 [0.93, 0.97]
	RMSE (°/s)	16.11 [12.13, 20.95]	13.12 [10.54, 17.54]
	Bias (°/s)	0.33 [-0.62, 1.22]	0.26 [-0.58, 1.05]
	Time Lag (s)	0.02 [0.00, 0.03]	0.02 [-0.02, 0.03]
Elbow Extension	r	0.99 [0.98, 0.99]	0.99 [0.98, 1.00]
	RMSE (°)	5.03 [3.83, 6.69]	4.18 [3.16, 5.58]
	Bias (°)	-7.52 [-13.84, -0.47]	-5.86 [-10.78, -2.45]
	Time Lag (s)	0.00 [-0.02, 0.03]	0.02 [-0.02, 0.03]
Shoulder Flexion	r	0.99 [0.99, 1.00]	0.99 [0.99, 1.00]
	RMSE (°)	2.39 [1.86, 3.03]	2.53 [1.73, 3.38]
	Bias (°)	-23.55 [-26.57, -20.40]	-23.57 [-26.17, -19.45]
	Time Lag (s)	-0.02 [-0.03, 0.02]	0.00 [-0.03, 0.02]
Shoulder Abduction	r	0.88 [0.78, 0.93]	0.89 [0.83, 0.94]
	RMSE (°)	1.97 [1.37, 2.71]	2.13 [1.50, 2.77]
	Bias (°)	7.42 [5.23, 11.11]	7.47 [3.52, 11.65]
	Time Lag (s)	0.03 [0.00, 0.05]	0.02 [-0.02, 0.03]
Trunk Displacement	r	0.95 [0.91, 0.98]	0.98 [0.91, 0.99]
	RMSE (mm)	5.41 [4.16, 7.00]	6.18 [4.30, 10.71]
	Bias (mm)	-4.62 [-8.10, -1.01]	-6.76 [-9.57, -3.39]
	Time Lag (s)	-0.02 [-0.07, 0.02]	-0.02 [-0.05, 0.02]

Overall, RMSE values were low, particularly for shoulder flexion and shoulder abduction (both approximately $2°$). Elbow extension showed the highest RMSE among joint angle trajectories, with a median RMSE around $4°$–$5°$.

The trial-to-trial variability of bias in kinematic trajectories between OMC and MMC was low for each participant, as shown in Table II, which presents the mean variability (IQR of bias per kinematic trajectory) across participants: $< 2°$ for shoulder, $< 4°$ for elbow extension, $< 2°/s$ for elbow angular velocity, and around 3 mm for trunk displacement. However, absolute bias varied between participants, as reflected in the higher bias IQR in Table I, which shows the mean bias and IQR across participants.

Temporal alignment between systems remained consistent across all kinematic trajectories, with small discrepancies ($<$ 0.03 s) primarily in shoulder and trunk metrics.

2) Movement quality measures: We observed high correlations between systems for trial-by-trial comparisons, with improved correlations when averaging over trials ($0.91 < r_{av} < 1$, except for interjoint coordination, see Table III). Joint angle measures showed high correlations overall, with shoulder flexion ($r_s = 0.97$, $r_{av} = 0.98$), elbow extension ($r_s = 0.98$, $r_{av} = 0.99$), and shoulder abduction ($r_s = 0.93$, $r_{av} = 0.94$). Interjoint coordination had the lowest

TABLE II: Mean IQR of bias across patients, representing the average variability of bias within a patient's trials.

Kinematic	bias	Unaffected arm	Affected arm
End-Effector Velocity	$\overline{IQR}$ (m/s)	0.01	0.01
Elbow Angular Velocity	$\overline{IQR}$ (°/s)	1.83	1.57
Elbow Extension	$\overline{IQR}$ (°)	3.69	3.88
Shoulder Flexion	$\overline{IQR}$ (°)	1.34	1.14
Shoulder Abduction	$\overline{IQR}$ (°)	1.20	0.91
Trunk Displacement	$\overline{IQR}$ (mm)	2.86	3.10

correlation ($r_s = r_{av} = 0.71$) with several outliers, while elbow angular PV showed lower correlation ($r_s = 0.87$, $r_{av} = 0.93$) and broader distribution of values (see Fig. 4). End-effector velocity measures exhibited high correlations ($0.90 < r_s < 0.98$, $0.96 < r_{av} < 1$), except for the number of movement units ($r_s = 0.77$, $r_{av} = 0.91$) which also showed a broader distribution of values (see Fig. 4). Trunk displacement showed high correlation ($r_s = 0.96$, $r_{av} = 0.97$), though MMC systematically underestimated values compared to OMC at higher magnitudes (see Fig. 4).

Following [31], we tested whether the MMC system could detect subtle movement differences in patients. Using the Mann–Whitney U test ($p << 0.05$), we found a significant difference in end-effector peak velocity between the affected and unaffected arms. This difference was observed in 14 out of 15 patients, consistently across both OMC and MMC data. These results further confirm that MMC kinematic assessments reliably approximate OMC values.

IV. Discussion

This is the first study comparing biomechanics-based kinematics from OMC with the end-to-end MMC approach proposed by Cotton et al. [19]. Only a few previous studies have compared biomechanically modeled upper limb kinematics from MMC to OMC such as using the commercial THEIA3D MMC (e.g., shadow boxing in able-bodied adults [32] (10 cameras), Box and Block in able-bodied children [33] (8 cameras)). To our best knowledge, this is also the first study to compare biomechanically modeled upper limb kinematics between OMC and MMC in neurological patients.

Overall, we find a high level of agreement between the systems for the kinematic trajectories of the drinking task in individuals with stroke and a strong correlation across the majority of movement quality measures.

The end-to-end MMC approach demonstrated high robustness, with failed reconstructions in only 1.6% of trials (13 out of 1160). For end-effector velocity, the small bias and low RMSE indicate precise wrist keypoint detection and consistent scaling across methods, likely supported by bilevel optimization, enabling direct comparability of end-effector velocity between systems.

Differences in elbow angle (median RMSE around $5°$), trunk displacement (median RMSE around 6mm), and shoulder angles (median RMSE around $2°$) are small and remaining differences between OMC and MMC may reflect

TABLE III: Movement quality measures comparing OMC and end-to-end MMC: r_s represents the correlation across all trials, while r_{av} denotes the correlation for averaged participant trials per arm between the two systems.

Movement Quality Measure	r_s	r_{av}
PV [m/s]	0.90	0.96
Elbow angular PV [°/s]	0.87	0.93
Time to PV [s]	0.98	1.00
Time to first PV [s]	0.94	0.99
Number of movement units [n]	0.77	0.91
Total movement time [s]	0.98	1.00
Interjoint coordination	0.71	0.71
Trunk displacement [mm]	0.96	0.97
Shoulder flexion [°]	0.97	0.98
Elbow extension [°]	0.98	0.99
Shoulder abduction [°]	0.93	0.94
Shoulder flexion D [°]	0.95	0.97

the influence of marker placement and model variations, which can cause slight discrepancies in trajectories. The differences in kinematic trajectories between OMC and MMC fall within the session-to-session variability observed with OMC alone [13], suggesting that the end-to-end MMC is nearing the accuracy and precision of OMC. Our results are consistent with, and slightly better than, prior MMC-OMC comparisons using the commercial THEIA3D system, which reported joint angle differences with RMSE $< 6°$ between systems [33]. Comparisons of MMC and OMC in upper limb kinematics remain limited, and no studies have yet evaluated non-commercial, biomechanics-based MMC kinematics against OMC. The end-to-end MMC approach presented here demonstrates an accuracy comparable to THEIA3D while outperforming earlier custom MMC systems tested for the drinking task [34].

A key advantage of the end-to-end approach over traditional MMC methods, such as based on DeepLabCut [35], is its optimal fitting of measured data to 3D keypoints within a biomechanical model, enhancing tracking stability.

MMC shows promise as a reliable alternative to OMC, offering significantly reduced setup and manual processing times.

Temporal discrepancies between the systems were negligible, with time lags ranging from 0 to $0.03\,\mathrm{s}$, supporting the reliability of the end-to-end MMC approach in capturing temporal aspects of movement with high accuracy.

Overall, the correlation between OMC and end-to-end MMC is high across most movement quality measures, with few outlier trials observed. Averaging trials generally improves correlation (e.g., $r_{av} = 1.00$ for time to peak velocity and total movement time), aligning with recommended clinical practice for performance stability [9]. While the number of trials needed to ensure performance stability is established for OMC [9], slight adjustments may be needed for MMC to account for measurement uncertainty. Averaging also aids in outlier detection, valuable for robustness in clinical applications.

Movement quality measures based on joint angles, such as shoulder flexion ($r_s = 0.97$, $r_{av} = 0.98$) and elbow

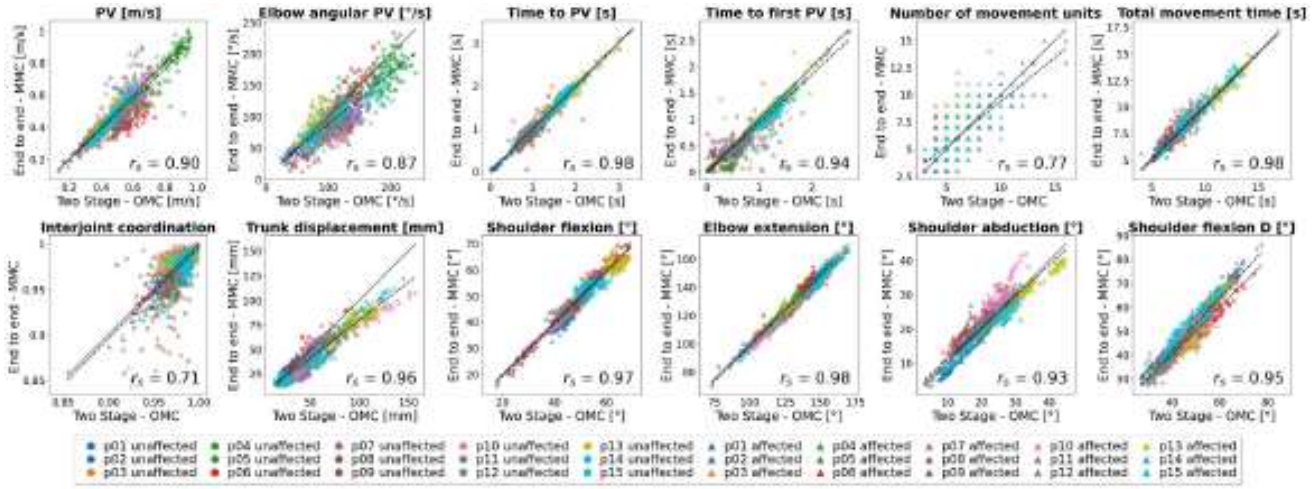


Fig. 4: Correlation plot for each measure, comparing two-stage OMC and end-to-end MMC. Each data point represents a single trial. Trials are color-coded per participant and shape-coded per arm. Solid black line: perfect correlation. Dashed grey line: observed correlation from data.

extension ($r_s = 0.98$, $r_{av} = 0.99$), as well as end-effector velocity measures like peak velocity and time to peak velocity, show strong agreement between systems, indicating high accuracy in detecting peak amplitudes in these key kinematic trajectories. Slight underestimation in trunk displacement (see Fig. 4) may result from model differences in chest marker placement, suggesting potential for model refinement.

Metrics like the number of movement units ($r_s = 0.77$, $r_{av} = 0.91$) and interjoint coordination ($r_s = r_{av} = 0.71$) show lower correlation, where small kinematic trajectory variations can produce larger discrepancies. Replacing the number of movement units with alternative smoothness metrics, such as Log Dimensionless Jerk (LDLJ) or Spectral Arc Length (SPARC) [36] , could improve the reliability of smoothness assessment.

Observed trial-to-trial biases in kinematic trajectories between OMC and MMC were consistent across trials within sessions, as evidenced by small IQR (approximately $1^\circ - 3^\circ$ for joint angles, 0.01 m/s for end-effector velocity and 3 mm for trunk displacement). This suggests a systematic bias per session, likely due to differences in marker/keypoint locations between systems (OMC anatomical landmarks vs. MMC-detected keypoints) or biomechanical model variations. The session-to-session (patient-to-patient) variation in bias may stem from variability in both OMC and MMC systems. In MMC, keypoint detection may slightly differ between individuals, while in OMC, minor differences in marker placement and registration can significantly impact inverse kinematics. Uchida and Seth [13] for example demonstrated that a 1–2 cm marker registration uncertainty can lead to a 5°–10° difference in knee flexion angles. Additionally, a prior study using the commercial THEIA3D MMC system demonstrated lower inter-session variability in MMC compared to OMC [37]. Thus, we assume that session-to-session bias variability is primarily due to OMC variability. However, definitive conclusions require further data, such as multi-session recordings of the same participants or true ground-truth bone movement data from dual-plane fluoroscopy.

Although the findings are promising, this study has several limitations. First, while OMC is generally considered the gold standard, it is not an absolute ground truth due to potential errors from marker misplacement and soft-tissue artifacts. Additionally, the used upper limb biomechanical models lack certain degrees of freedom (e.g., finger motion), which could provide a more complete assessment. For example, [20] extends the end-to-end MMC optimization approach to a full arm and hand model. The models in OpenSim for OMC and MuJoCo for end-to-end MMC are not identical, which may impact direct data comparability between the systems. Furthermore, while OMC uses a two-stage process, MMC employs an end-to-end approach; using OMC data in an end-to-end model could help better isolate the effects of marker-based versus markerless capture.

Phase classification was conducted exclusively with OMC data, meaning that MMC phase classification still requires validation for standalone application. Lastly, the study focuses on a specific patient population with mild to moderate impairment performing a single task. Results may vary with other tasks or populations, potentially introducing additional challenges and considerations for broader application.

The end-to-end MMC approach failed to reconstruct 13 trials, due to improper camera calibration, failed subject tracking, or poor initialization of the optimization. While this highlights a small limitation of the current MMC implementation, we note that OMC pipelines have undergone significantly more engineering refinement over time. As MMC methodologies continue to evolve and iterate, we expect improvements in robustness and reliability of the end-to-end approach.

Future research should focus on collecting datasets with simultaneous biplanar fluoroscopy, MMC, and OMC record-

ings to establish true ground truth for contextualizing clinical measurement uncertainty as in [38]. Additionally, research should investigate the impact of camera number and recording angles on MMC accuracy (including monocular setups [17]) and expand the analysis to encompass all upper body degrees of freedom, including fingers [20]. Additionally, studies should broaden the scope to include a more diverse neurological population. While this study focuses on measurement accuracy, future research should assess the system's usability in clinical settings, including acquisition time, the minimum required acquisitions, and reporting efficiency.

Integrating a fixed camera system into standard upper limb assessment setups in rehabilitation clinics could enable the routine collection of high-quality movement data while automating assessments, reducing therapist workload, and freeing up more time for therapy sessions. Enhanced outcome measures would not only support stroke research but also improve clinical workflows by optimizing interventions through more precise and sensitive assessments.

V. Conclusion

The end-to-end MMC accuracy and precision has improved with advanced keypoint detection and GPU-accelerated biomechanical modeling, now approaching OMC levels, as demonstrated in this study. By eliminating marker placement and reducing costs, this MMC offers a practical, low-complexity alternative using consumer-grade cameras. Our results highlight its potential to streamline clinical workflows by enabling precise movement data collection — beneficial for both clinicians and researchers — while potentially automating assessments, reducing therapists' workload, and allowing more time for therapy.

ACKNOWLEDGMENT

We sincerely thank the participants of this study.

References

[1] G. Kwakkel, N. A. Lannin, K. Borschmann, C. English, M. Ali, L. Churilov, G. Saposnik, C. Winstein, E. E. Van Wegen, S. L. Wolf, J. W. Krakauer, and J. Bernhardt, "Standardized measurement of sensorimotor recovery in stroke trials: Consensus-based core recommendations from the Stroke Recovery and Rehabilitation Roundtable," *International Journal of Stroke*, vol. 12, pp. 451–461, July 2017.

[2] E. S. Lawrence, C. Coshall, R. Dundas, J. Stewart, A. G. Rudd, R. Howard, . Charles, and D. A. Wolfe, "Estimates of the Prevalence of Acute Stroke Impairments and Disability in a Multiethnic Population," pp. 1279–1284, 2001.

[3] G. Kwakkel, E. E. H. V. Wegen, J. H. Burridge, C. J. Winstein, L. E. H. v. Dokkum, M. A. Murphy, M. F. Levin, and J. W. Krakauer, "Standardized measurement of quality of upper limb movement after stroke: Consensus-based core recommendations from the Second Stroke Recovery and Rehabilitation Roundtable," *International Journal of Stroke*, vol. 14, pp. 783–791, Oct. 2019. Publisher: SAGE Publications Inc.

[4] F. Su and W. Xu, "Enhancing Brain Plasticity to Promote Stroke Recovery," *Frontiers in Neurology*, vol. 11, p. 554089, Oct. 2020.

[5] C. Alia, C. Spalletti, S. Lai, A. Panarese, G. Lamola, F. Bertolucci, F. Vallone, A. Di Garbo, C. Chisari, S. Micera, and M. Caleo, "Neuroplastic Changes Following Brain Ischemia and their Contribution to Stroke Recovery: Novel Approaches in Neurorehabilitation," *Frontiers in Cellular Neuroscience*, vol. 11, Mar. 2017.

[6] S. Solnik, M. P. Furmanek, and D. Piscitelli, "Movement Quality: A Novel Biomarker Based on Principles of Neuroscience," *Neurorehabilitation and Neural Repair*, vol. 34, pp. 1067–1077, Dec. 2020.

[7] M. F. Levin, J. A. Kleim, and S. L. Wolf, "What do motor "recovery" and "compensationg" mean in patients following stroke?," *Neurorehabilitation and Neural Repair*, vol. 23, pp. 313–319, May 2009.

[8] M. A. Murphy, S. Murphy, H. C. Persson, U. B. Bergström, and K. S. Sunnerhagen, "Kinematic analysis using 3D motion capture of drinking task in people with and without upper-extremity impairments," *Journal of Visualized Experiments*, vol. 2018, Mar. 2018. Publisher: Journal of Visualized Experiments.

[9] G. E. Frykberg, H. Grip, and M. A. Murphy, "How many trials are needed in kinematic analysis of reach-to-grasp?—A study of the drinking task in persons with stroke and non-disabled controls," *Journal of NeuroEngineering and Rehabilitation*, vol. 18, pp. number–101, Dec. 2021. Publisher: BioMed Central Ltd.

[10] M. A. Murphy, C. Willén, and K. S. Sunnerhagen, "Movement kinematics during a drinking task are associated with the activity capacity level after stroke," *Neurorehabilitation and Neural Repair*, vol. 26, no. 9, pp. 1106–1115, 2012.

[11] Y. Liao, A. Vakanski, M. Xian, D. Paul, and R. Baker, "A review of computational approaches for evaluation of rehabilitation exercises," *Computers in Biology and Medicine*, vol. 119, p. 103687, Apr. 2020.

[12] M. Abdullah, A. A. Hulleck, R. Katmah, K. Khalaf, and M. El-Rich, "Multibody dynamics-based musculoskeletal modeling for gait analysis: a systematic review," *Journal of NeuroEngineering and Rehabilitation*, vol. 21, p. 178, Oct. 2024.

[13] T. K. Uchida and A. Seth, "Conclusion or Illusion: Quantifying Uncertainty in Inverse Analyses From Marker-Based Motion Capture due to Errors in Marker Registration and Model Scaling," *Frontiers in Bioengineering and Biotechnology*, vol. 10, May 2022. Publisher: Frontiers.

[14] W. W. T. Lam, Y. M. Tang, and K. N. K. Fong, "A systematic review of the applications of markerless motion capture (MMC) technology for clinical measurement in rehabilitation," Dec. 2023. ISSN: 17430003 Issue: 1 Publication Title: Journal of NeuroEngineering and Rehabilitation Volume: 20.

[15] I. Sárándi, A. Hermans, and B. Leibe, "Learning 3D Human Pose Estimation From Dozens of Datasets Using a Geometry-Aware Autoencoder To Bridge Between Skeleton Formats," pp. 2956–2966, 2023.

[16] S. Ghorbani, K. Mahdaviani, A. Thaler, K. Kording, D. J. Cook, G. Blohm, and N. F. Troje, "MoVi: A large multi-purpose human motion and video dataset," *PLOS ONE*, vol. 16, p. e0253157, June 2021. Publisher: Public Library of Science.

[17] J. Peiffer, K. Shah, S. Anarwala, K. Abdou, and R. J. Cotton, "Fusing Uncalibrated IMUs and Handheld Smartphone Video to Reconstruct Knee Kinematics," in *2024 10th IEEE RAS/EMBS International Conference for Biomedical Robotics and Biomechatronics (BioRob)*, pp. 1275–1282, Sept. 2024. ISSN: 2155-1782.

[18] R. J. Cotton, A. DeLillo, A. Cimorelli, K. Shah, J. Peiffer, S. Anarwala, K. Abdou, and T. Karakostas, "Optimizing Trajectories and Inverse Kinematics for Biomechanical Analysis of Markerless Motion Capture Data," in *2023 International Conference on Rehabilitation Robotics (ICORR)*, (Singapore, Singapore), pp. 1–6, IEEE, Sept. 2023.

[19] R. J. Cotton, "Differentiable Biomechanics Unlocks Opportunities for Markerless Motion Capture," Feb. 2024. arXiv:2402.17192 [cs].

[20] P. Firouzabadi, W. Murray, A. R. Sobinov, J. Peiffer, K. Shah, L. E. Miller, and R. J. Cotton, "Biomechanical Arm and Hand Tracking with Multiview Markerless Motion Capture," in *2024 10th IEEE RAS/EMBS International Conference for Biomedical Robotics and Biomechatronics (BioRob)*, (Heidelberg, Germany), pp. 1641–1648, IEEE, Sept. 2024.

[21] A. Rajagopal, C. L. Dembia, M. S. DeMers, D. D. Delp, J. L. Hicks, and S. L. Delp, "Full-Body Musculoskeletal Model for Muscle-Driven Simulation of Human Gait," *IEEE Transactions on Biomedical Engineering*, vol. 63, pp. 2068–2079, Oct. 2016.

[22] R. J. Cotton, A. Delillo, A. Cimorelli, K. Shah, J. D. Peiffer, S. Anarwala, K. Abdou, and T. Karakostas, "Optimizing Trajectories and Inverse Kinematics for Biomechanical Analysis of Markerless Motion Capture Data," in *IEEE International Conference on Rehabilitation Robotics*, IEEE Computer Society, 2023. ISSN: 19457901.

[23] L. Karashchuk, "AniposeLib," Nov. 2024.

[24] R. J. Cotton, "PosePipe: Open-Source Human Pose Estimation Pipeline for Rehabilitation Research," *Archives of Physical Medicine and Rehabilitation*, vol. 103, pp. e161–e162, Dec. 2022. Publisher: Elsevier.

[25] "EasyMoCap - Make human motion capture easier.," 2021.

[26] E. Todorov, T. Erez, and Y. Tassa, "MuJoCo: A physics engine for model-based control," in *2012 IEEE/RSJ International Conference on Intelligent Robots and Systems*, pp. 5026–5033, Oct. 2012. ISSN: 2153-0866.

[27] V. Caggiano, H. Wang, G. Durandau, M. Sartori, and V. Kumar, "MyoSuite: A Contact-rich Simulation Suite for Musculoskeletal Motor Control," in *Proceedings of The 4th Annual Learning for Dynamics and Control Conference*, pp. 492–507, PMLR, May 2022. ISSN: 2640-3498.

[28] K. Werling, M. Raitor, J. Stingel, J. L. Hicks, S. Collins, S. L. Delp, and C. K. Liu, "Rapid bilevel optimization to concurrently solve musculoskeletal scaling, marker registration, and inverse kinematic problems for human motion reconstruction," Aug. 2022.

[29] S. R. Hamner, A. Seth, and S. L. Delp, "Muscle contributions to propulsion and support during running," *Journal of Biomechanics*, vol. 43, pp. 2709–2716, Oct. 2010.

[30] F. Al-Hafez, G. Zhao, J. Peters, and D. Tateo, "LocoMuJoCo: A Comprehensive Imitation Learning Benchmark for Locomotion," 2023. Version Number: 2.

[31] A. Casile, G. Fregna, V. Boarini, C. Paoluzzi, F. Manfredini, N. Lamberti, A. Baroni, and S. Straudi, "Quantitative Comparison of Hand Kinematics Measured with a Markerless Commercial Head-Mounted Display and a Marker-Based Motion Capture System in Stroke Survivors," *Sensors*, vol. 23, p. 7906, Jan. 2023. Number: 18 Publisher: Multidisciplinary Digital Publishing Institute.

[32] B. K. Lahkar, A. Muller, R. Dumas, L. Reveret, and T. Robert, "Accuracy of a markerless motion capture system in estimating upper extremity kinematics during boxing," *Frontiers in Sports and Active Living*, vol. 4, p. 939980, July 2022.

[33] R. M. Hansen, S. L. Arena, and R. M. Queen, "Validation of upper extremity kinematics using Markerless motion capture," *Biomedical Engineering Advances*, vol. 7, p. 100128, June 2024.

[34] J. Huber, S. Slone, and J. Bae, "Computer vision for kinematic metrics of the drinking task in a pilot study of neurotypical participants," *Scientific Reports*, vol. 14, p. 20668, Sept. 2024. Publisher: Nature Publishing Group.

[35] A. Mathis, P. Mamidanna, K. M. Cury, T. Abe, V. N. Murthy, M. W. Mathis, and M. Bethge, "DeepLabCut: markerless pose estimation of user-defined body parts with deep learning," *Nature Neuroscience*, vol. 21, pp. 1281–1289, Sept. 2018. Publisher: Nature Publishing Group.

[36] M. I. Mohamed Refai, M. Saes, B. L. Scheltinga, J. van Kordelaar, J. B. J. Bussmann, P. H. Veltink, J. H. Buurke, C. G. M. Meskers, E. E. H. van Wegen, G. Kwakkel, and B.-J. F. van Beijnum, "Smoothness metrics for reaching performance after stroke. Part 1: which one to choose?," *Journal of NeuroEngineering and Rehabilitation*, vol. 18, p. 154, Oct. 2021.

[37] R. M. Kanko, E. Laende, W. S. Selbie, and K. J. Deluzio, "Inter-session repeatability of markerless motion capture gait kinematics," *Journal of Biomechanics*, vol. 121, p. 110422, May 2021.

[38] T. Unger, R. d. S. Ribeiro, M. Mokni, T. Weikert, J. Pohl, A. Schwarz, J. P. O. Held, L. Sauerzopf, B. Kühnis, E. Gavagnin, A. R. Luft, R. Gassert, O. Lambercy, C. A. Easthope, and J. G. Schönhammer, "Upper limb movement quality measures: comparing IMUs and optical motion capture in stroke patients performing a drinking task," *Frontiers in Digital Health*, vol. 6, 2024. Publisher: Frontiers Media SA.

Identifying gait patterns in sub-acute stroke patients based on open access gait kinematics

Celine Bouwmeester
Roessingh Research and Development & Department of Biomechanical Engineering, University of Twente
Enschede, Netherlands
c.bouwmeester@rrd.nl

Gerdienke B. Prange
Roessingh Research and Development & Department of Biomechanical Engineering, University of Twente
Enschede, Netherlands.
g.prange@rrd.nl

Leendert Schaake
Roessingh Research and Development
Enschede, Netherlands.
l.schaake@rrd.nl

Johan S. Rietman
Roessingh Research and Development & Department of Biomechanical Engineering, University of Twente
Enschede, Netherlands
j.s.rietman@rrd.nl

Erik C. Prinsen
Roessingh Research and Development & Department of Biomechanical Engineering, University of Twente
Enschede, Netherlands.
e.prinsen@rrd.nl

***Abstract*— Neurological disorders, such as stroke, can affect the ability to walk and balance. Robotic rehabilitation assists in training walking and balance capabilities of patients with neurological disorders. However, not all participants are good responders when using exoskeletons. This study aims to cluster gait patterns in stroke patients to provide insights into the pathology of stroke patients. Joint angles of the affected lower limb of 45 sub-acute stroke patients from an open access database were clustered based on a principal component analyses, followed by a k-means cluster analysis. A total of eight gait pattern clusters were retrieved and clinically rearranged into four categories. The results can be used in the field of robotic devices as well as a more clinical setting. Future research should focus on validating and using the retrieved clusters as clinical indicators for selecting suitable treatments, such as robotic devices or exoskeletons, to personalize rehabilitation.**

Keywords — Hemiplegia, technology, lower extremities, Cerebrovascular accident

I. Introduction

Neurological disorders, such as stroke, can affect the ability to walk and impair dynamic balance. Around 80% of stroke survivors reported difficulties with walking [1,2]. Consequently, stroke survivors have prioritized walking difficulties and balance as an area in which further research is needed, especially older stroke survivors [3]. Younger stroke survivors have prioritized post-stroke fatigue as the main research area [3]. The use of robotic devices, such as exoskeletons, in rehabilitation has the potential to address both aspects and could improve walking and balance with less exertion in patients with neurological disorders.

Robotic devices are seen as a valuable tool in improving walking abilities and reducing disabilities resulting in a better quality of life [4]. It enables controlled, intensive, repetitive, task-oriented motor training for the affected limb(s) and dynamic balance. The use of robot-assisted training devices has been proven to have a positive effect on balance [5,6] and the chance to walk independently [6,7] in the early rehabilitation phase. However, two systematic reviews explicitly stated that not all included studies contribute to this statement [5,7]. This is in line with other studies that found that not all participants are good responders when using an exoskeleton [8]. Identification of these 'good' and 'poor' responders to exoskeletons is of great importance in both the clinical and research settings. Identifying the so-called 'recovery phenotypes' can help in recommending specifications for inclusion of participants [9].

One way to understand the responsiveness of stroke patients to exoskeletons is with clinical outcomes and demographic features [8,10]. Five key features were derived as predictors for 'good' and 'poor' improvements (i.e. initial Berg Balance Scale score [8,10], final Berg Balance Scale score [8], final Modified Ashworth Scale score [8], initial Modified Barthel index score [8] and lower age [10]). However, some of these predictors are not available until after the intervention, hindering prediction of long-term outcomes after stroke aimed at treatment selection.

A first step towards the personalization of exoskeleton-based therapy is to identify differences between patients pre-intervention, ideally based on objective data, such as gait parameters. Previous research in classifying gait patterns of stroke patients has mainly focused on supervised learning (i.e. labeled data), trying to classify the patients into severity [11] or predefined gait patterns [12,13]. However, as seen in clinical settings, gait patterns differ greatly among stroke patients (e.g. drop foot, circumduction, hip hiking and stiff knee gait) and they are not always predefined, making it an unsupervised learning problem. In order to avoid neglecting subgroups and to make the data less dependent on subjectively scored clinical scales, this study provides a first attempt to use a clustering approach based on joint kinematic data during gait without predefined/labelled subgroups of stroke patients. Therefore, the aim of the current study is to assess whether gait patterns of stroke patients can be clustered based on objective gait parameters.

II. Methods

A. Study overview

This study used data from an open source dataset that contains kinematic data of 50 sub-acute stroke patients [14]. Stroke patients were included if they had a stroke onset within

This project has received funding from the European Union's Horizon Europe program under Grant Agreement No 101120408

five months and an age between 18 and 85 years. Participants were included if they had a stroke onset within five months and an age between 18 and 85 years. Participants were asked to walk across a 12 meter-pathway at a self-selected speed. Patients were excluded if they had ≥ 20 on the trunk impairment scale, functional ambulation score of ≤ 2 and if they were not able to sit independently. All in- and exclusion criteria are explained in more detail in [14]. The trial registration for the ethical approval of the study was validated. Three stroke patients were excluded from the current study as they used a walking aid during walking. No adaptations were made to the C3D data. Two patients were excluded based on missing variables in their C3D data.

The reference data of non-disabled subjects was retrieved from the reference dataset of our lab that was collected during previous published studies and all comply with ethical requirements. The subject characteristics are presented in Table I.

B. Data analysis

The gait events were visually checked using the provided software (VICON Motion System, Oxford, U.K.). The data analysis focused on nine metrics of the affected leg associated with regular gait analysis, i.e. foot progression, ankle dorsiflexion/plantarflexion, knee flexion/extension, hip flexion/extension, hip abduction/adduction, hip external rotation/internal rotation, pelvis anterior/posterior tilt, pelvic obliquity and pelvis external rotation/internal rotation. Four kinematic metrics, i.e. ankle eversion/inversion, ankle abduction/adduction, knee abduction/adduction and knee external/internal rotation, were excluded from the study as there were signs of knee varus/valgus crosstalk and marker wobble in the data.

C. Data preprocessing

Raw data were pre-processed and analyzed using an in-house developed python script (Python 3.12). Gait cycles (GC) were defined as the first initial contact from the affected lower limb till the next initial contact of the same lower limb. The nine parameters were resampled to 101 data points per GC, representing 0% (initial contact of affected leg) to 100% (subsequent initial contact of affected leg) of the GC.

D. Statistical analysis

Data were standardized (centered and scaled around 0) before starting the statistical analysis. The analysis consisted of two stages. First, a principal component analysis (PCA) from package *Scikit* was performed to reduce dimensions for all nine metrics separately (284 GC x 101) [15]. Principal components (PCs) that explained a cumulative variability of more than 80% were retained. PC scores were then calculated for each PC.

TABLE II. PC SCORES PER KINEMATIC PARAMETER

Principal components (PC)		
Kinematics	***# PCs***	***Total Explained variance (%)***
Pelvis tilt	1	88.9
Pelvis obliquity	2	90.1
Pelvis external/internal rotation	1	87.1
Hip flexion/extension	2	88.7
Hip abduction/adduction	1	85.3
Hip external/internal rotation	1	95.2
Knee flexion	2	81.1
Ankle dorsiflexion/plantairflexion	3	86.7
Foot progression	1	87.5

A k-means++ cluster analysis from package *Scikit* was then performed on the retained PC scores [15]. K-means++ was preferred to k-means as k-means++ could improve speed and accuracy of the algorithms [16]. The package *kneed* was used to provide the knee point (i.e. point of the line with maximum curvature) of the function and therefore the optimal number of clusters [17]. Ultimately, each GC was assigned to one of the clusters based on the Euclidean distance to the centroids.

III. RESULTS

Data from 45 stroke patients were included in the current analysis (Table I, including 14 non-disabled subjects as reference). A total of 284 GC were extracted from the kinematic data to retrieve the clusters. From the nine kinematic parameters, fourteen PCs were retrieved. Table II shows the extracted PCs per metric. The knee point of the function was eight and therefore the mathematically derived optimal number of clusters was set at eight. The sum of squares error (SSE) was 1209.

Table III presents the descriptives per cluster. The number of GC assigned to the 8 clusters ranged from 14 GC in cluster 5 to 82 GC in cluster 8. The number of participants assigned to the clusters ranged from only one participant in cluster 6 to fourteen participants to cluster 8. Eight of the 284 GC (2.8%) were assigned to a different cluster than the remaining GC of an individual. From this eight GC, three participants had one GC in both cluster 2 and 8, whereas two participants had one GC in both cluster 3 and 4. In addition, one participant had all GC equally distributed over clusters 2 and 5.

The mean and standard deviation of all nine kinematic parameters for the eight clusters are presented separately in Fig. 1, along with the reference data. Each cluster will be described in more detail below.

TABLE I. SUBJECT CHARACTERISTICS FROM NON-DISABLED DATASET AND STROKE PATIENTS [14]

	PP	**Affected side**	**Gender**	**Age**	**Weight**	**Height**	**Time post stroke**	**FAC**	**Gait speed**	**Step length**	**Step time**	**Stride length**	**Stride Time**
		Left/Right	***F/M***	***years***	***kg***	***cm***	***days***		***m/s***	***m***	***s***	***m***	***s***
Non-disabled	14	n.a.	4/10	50.20 (±16.80)	-	-	n.a.	n.a.	1.19 (±0.13)	0.64 (±0.08)	0.54 (±0.05)	1.30 (±0.15)	1.08 (±0.08)
Stroke	45	28/17	15/30	63.79 (±13.09)	71.04 (±13.08)	1700.74 (±80.21)	54.35 (±44.31)	2.79 (±0.84)	0.48 (±0.30)	0.34 (±0.16)	0.89 (±0.36)	0.68 (±0.16)	1.65 (± 0.50)

PP = participants, n.a. = not applicable, FAC = Functional Ambulation Category

A. Characteristics per cluster

The gait pattern represented by cluster 1 consists of a slightly less dynamic and decreased knee flexion at midstance and initial swing compared to the knee angles in the sagittal plane of non-disabled individuals. The internal rotation of the hip is increased during the whole GC. The decrease in knee flexion during the swing phase could be the result of the inadequate push-off and/or the internal rotation of the hip.

Cluster 2 is seen as representing 'good' walkers. The gait pattern of cluster 2 follows the gait pattern of non-disabled, but with a slightly reduced ankle plantar flexion during the push-off phase. There is a trend towards increased hip adduction and external rotation.

Cluster 3 shows a pattern with the knee in hyperextension during the stance phase. Also, the ankle in the sagittal plane remains rigid during the whole GC. This cluster seems to stabilizes the leg through the hyperextension. The affected leg does not seem to contribute towards an efficient walking gait. The cluster starts in (hyper)extension during the stance phase. At initial swing, the pelvis moves to posterior and, together with an increased hip hike, leads to a (small) increased hip flexion that eventually moves the affected leg forward.

Cluster 4 shows a decreased anterior tilt of the pelvis and decreased flexion of the knee and ankle over the whole gait cycle. The knee remains slightly in flexion during the stance phase. The knee and ankle do not contribute (much) to a gait pattern that is seen in non-disabled individuals.

The gait pattern of cluster 5 shows an increased dorsiflexion of the ankle. This results in an increased knee flexion and therefore an increase in hip flexion. It seems that the issues are mostly on the level of the ankle. The gait pattern of cluster 5 has similar features as cluster 4, especially regarding increased flexion of the knee and hip during stance, but with a less affected gait pattern.

Cluster 6 shows an increase in flexion in the knee and hip during midstance until the end of pre-swing. The cluster lands on the forefoot and has a reversed loading response. There seems to be a passive foot drop as there is no active push-off visible in the sagittal ankle kinematics. The knee is continuously in flexion and, together with the rigid hip flexion, the question arises if there is actual foot clearance.

Cluster 7 comprises increased hip abduction during the stance phase. In combination with increased hip drop and a slightly more posterior tilt of the pelvis, it forces the knee in a more rigid position during the stance phase. This shows a hip compensation strategy during stance that is different from the hip compensation strategy in cluster 4. During the swing phase, the hip returns to neutral.

The gait pattern of cluster 8 shows no clear push-off. The hip is in increased flexion whereas the ankle has an increase in plantarflexion. There is a decrease in active ankle control, which results in gait deviations similar to clusters 4 and 5, however these deviations are larger than seen in cluster 4 and smaller than cluster 5.

B. Kinematic differences between the clusters

From a clinical point of view, we can rearrange the eight clusters into four categories. In the first category, we can include cluster 1 and cluster 2. Both clusters showed similar gait patterns to that of non-disabled individuals. The main difference between clusters 1 and 2 is that cluster 1 is less dynamic in the knee and ankle compared to cluster 2, resulting in cluster 1 having a more affected gait pattern when compared to non-disabled walkers. This is reflected in the walking speed being the highest among all clusters, with cluster 2 showing the highest speed between the two clusters.

The second category comprises clusters 4, 5, 7 and 8. All four clusters show signs of a rigid knee as reflected in a limited range of motion across the GC. The four clusters also demonstrate a decrease in active ankle control. Clusters 4 and 7 show the most affected ankle control, and consequently most affected gait pattern, followed by cluster 8 and lastly cluster 5.

Cluster 7 shows similarities with cluster 4 regarding the ankle, knee, hip and pelvis patterns in the sagittal plane. However, this cluster seems to use another hip compensation strategy. Cluster 4 shows adduction of the hip during the stance phase, whereas cluster 7 shows abduction during stance. Furthermore, there is a simultaneous hip drop in cluster 7 whereas there is a hip hike in cluster 4. This suggests that clusters 4 and 7 are subclusters of the general pattern seen across clusters 5 and 8 in various degrees of deviation, with different hip compensation strategies to stabilize during the stance phase.

TABLE III. DESCRIPTIVES PER CLUSTER

Cluster	Counts	Affected Side[1]	Gender[1]	Age	Weight	Height	Time post stroke	FAC	Gait speed	Step length	Step time	Stride length	Stride Time
	# GC/#PP	*Left/Right*	*F/M*	*years*	*kg*	*cm*	*days*		*m/s*	*m*	*s*	*m*	*s*
1	40/8	30/10	9/31	69.43 (±15.50)	65.68 (±11.61)	1645.38 (±87.80)	63.45 (±42.02)	2.98 (±1.00)	0.60 (±0.11)	0.40 (±0.11)	0.75 (±0.16)	0.82 (±0.18)	1.41 (±0.24)
2	39/11	28/11	20/19	55.95 (±8.75)	70.82 (±7.86)	1708.21 (±68.78)	56.31 (±29.66)	3.33 (±1.22)	0.89 (±0.25)	0.55 (±0.12)	0.66 (±0.11)	1.08 (±0.22)	1.25 (±0.16)
3	25/4	20/5	3/22	68.36 (±6.96)	80.08 (±12.74)	1725.00 (±77.10)	69.72 (±16.31)	2.72 (±0.46)	0.19 (±0.08)	0.21 (±0.04)	1.21 (±0.18)	0.40 (±0.13)	2.24 (±0.34)
4	31/8	23/8	6/25	69.71 (±7.42)	77.42 (±15.55)	1760.00 (±44.94)	39.00 (±17.04)	2.16 (±0.37)	0.28 (±0.12)	0.23 (±0.10)	0.97 (±0.35)	0.47 (±0.17)	1.79 (±0.63)
5	14/2	11/3	14/0	45.21 (±12.35)	68.71 (±2.55)	1665.71 (±8.52)	60.21 (±0.43)	3.00 (±0)	0.24 (±0.03)	0.23 (±0.05)	0.83 (±0.08)	0.47 (±0.10)	1.92 (±0.22)
6	15/1	15/0	15/0	47.00 (± 0)	65.00 (±0)	1600.00 (±0)	104.00 (±0)	2.00 (±0)	0.11 (±0.01)	0.16 (± 0.02)	1.74 (±0.34)	0.28 (±0.02)	2.70 (±0.31)
7	38/6	33/5	1/37	68.58 (±6.38)	67.08 (±8.53)	1772.11 (±63.59)	56.13 (±12.11)	2.50 (±0.51)	0.35 (±0.21)	0.25 (±0.11)	1.00 (±0.49)	0.54 (±0.19)	1.76 (±0.47)
8	82/14	70/12	33/49	65.17 (±13.41)	71.94 (±16.14)	1685.73 (±66.36)	39.20 (±14.77)	2.95 (±0.74)	0.53 (±0.24)	0.37 (±0.13)	0.78 (±0.20)	0.72 (±0.22)	1.46 (±0.27)

[1] per gait cycle, GC = Gait Cycle, PP = Participants, FAC = Functional Ambulation Category

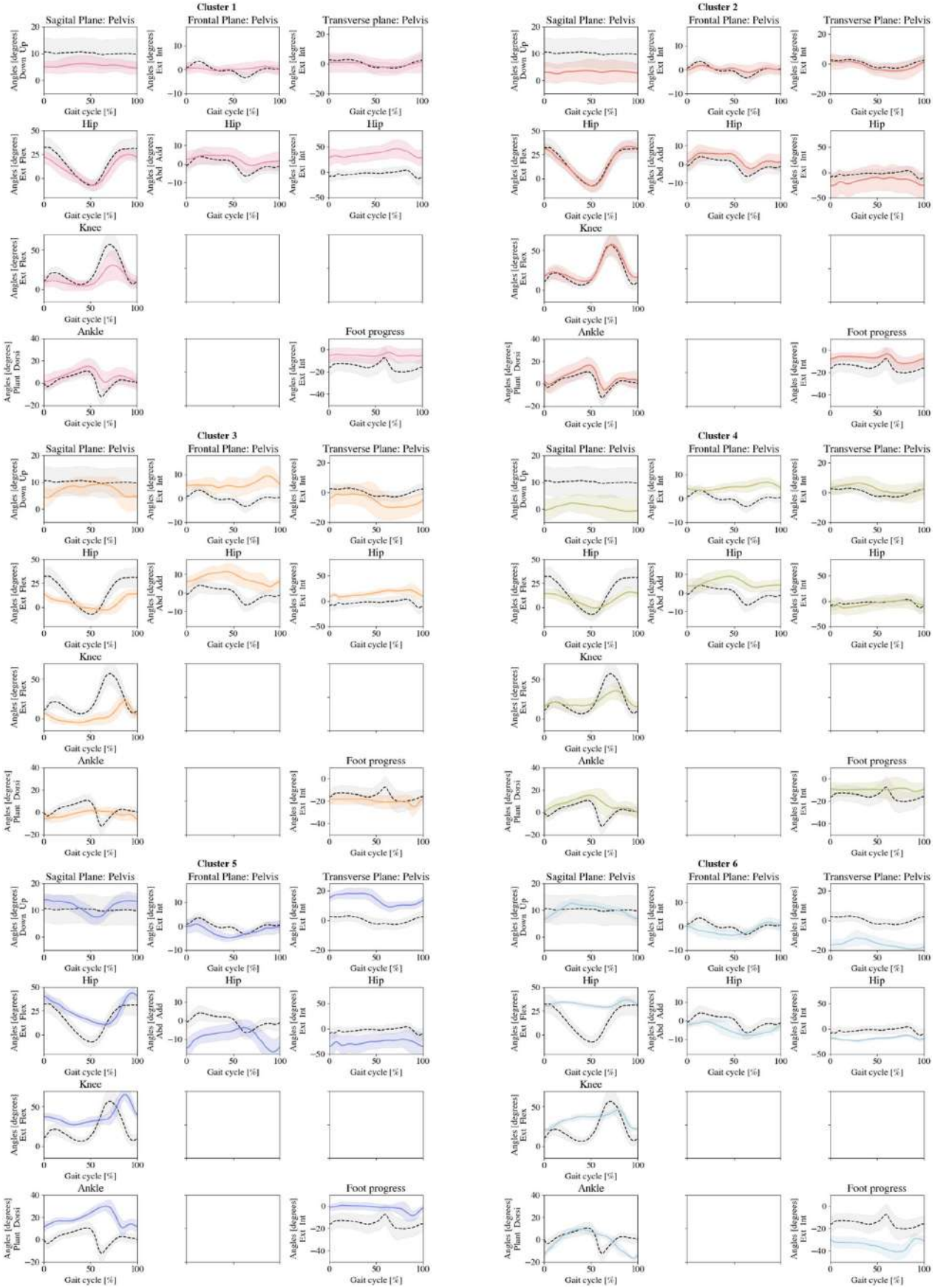


Fig. 1. Kinematic parameters for every cluster. Black dotted line represent the normal range of the angles.

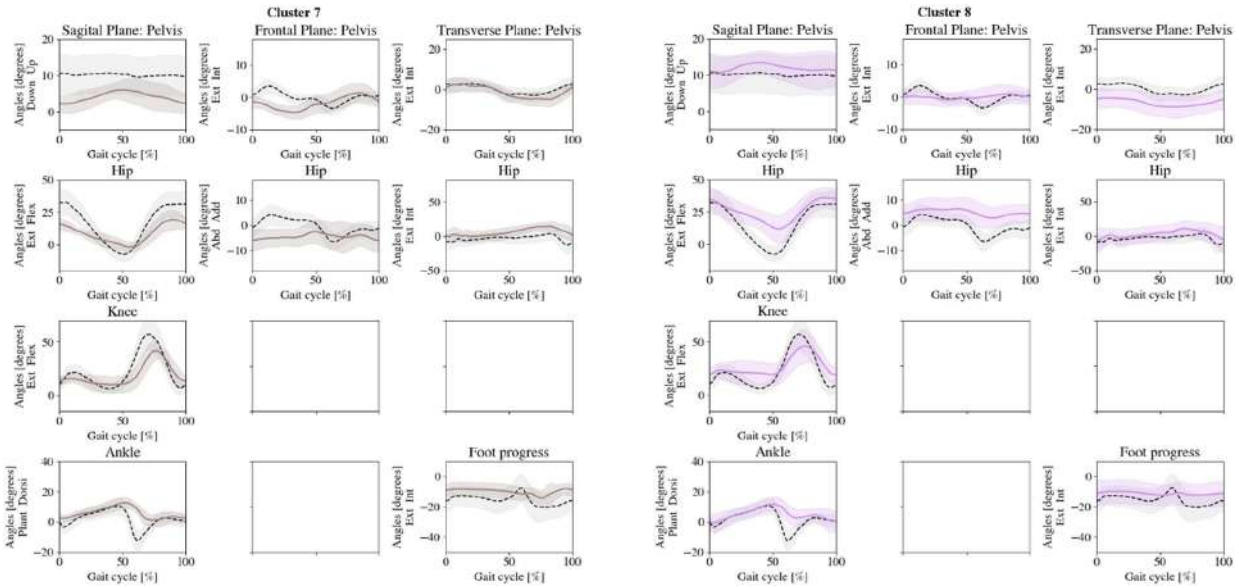


Fig. 1. Continued. Kinematic parameters in every retrieved cluster. Black dotted line represent the normal range of the angles.

The third category comprises cluster 3 and shows a knee (hyper)extension during the stance phase. The cluster also demonstrates a decrease in range of motion in the sagittal plane of the knee. This is reflected in a severely affected functional gait with very low walking speeds.

The last category consists of cluster 6 and is characterized by a (plantar) flexed position of the ankle, knee and hip. The knee is continuously in flexion and there is no variation in the hip angle. Due to the reversed loading response and no real change from dorsiflexion to plantarflexion during the pre-swing/initial swing phase, there could be a passive foot drop in this cluster. This prevents efficient walking, as reflected in the lowest walking speed among the eight clusters.

IV. Discussion

A total of eight clusters were retrieved based on nine kinematic parameters of the affected leg. These eight clusters provide insights into the various pathological gait patterns of stroke patients. These eight clusters can be rearranged into four categories from a clinical perspective.

This study used a methodology where pathological gait patterns were retrieved based on kinematic parameters and tried to translate the clusters into clinically meaningful categories as a first indication of the validity of the clustering. This is in line with the methodology of [18] in which they used almost the same approach to cluster gait patterns in growing children with Duchenne muscular dystrophy. Only one study has used the full kinematic GC to cluster and classify stroke patients simultaneously [19]. Previous research on clustering has been using spatial-temporal distance variables and discrete joint angles in stroke patients [19-21] with equinus deformity [22] and resulted in less clusters compared to the current study. The number of clusters ranged from three [20,22] to four [21] to six [19]. These clusters were mainly based on walking speed. Previous research has shown that individual's characteristic gait patterns were preserved across their range of walking speeds and were not grouped based on absolute walking speed [23]. Therefore, this study did not take walking speed into account, which might have contributed to the larger number of clusters found in the present study.

Two identified clusters should be considered with caution. Firstly, cluster 6, as all GC assigned to this cluster are from only one participant. In addition, only two participants are assigned to cluster 5 and the GC of one participant have been equally distributed over both cluster 5 and 2. Future research should investigate whether these trends are also found in other stroke patients or if these gait patterns are unique to this specific individual.

The majority of participants had all GC assigned to one cluster. Overall, only eight of 284 GC (2.8%) were assigned to a different cluster than the remaining GC of an individual. This indicates that the clustering was relatively consistent within subjects, especially in the case of stroke patients. This is in line with studies that demonstrated that there is less variation in GC within-subjects [23]. Although there are a few exceptions, the clustering consistency suggests that such unsupervised and unrestricted classification of gait patterns based on joint kinematics only is promising for further study.

Previous research on the comparison of non-disabled subjects and stroke survivors has highlighted the differences in ankle, knee and hip joints in the sagittal plane during the early stance phase and late stance to early swing phase [24]. The results of the current study demonstrated that not all clusters have deviations in the ankle (i.e. clusters 1, 7 and 8), knee (i.e. clusters 2 and 7) and hip (cluster 2) during the early stance phase and late stance to early swing phase. This indicates that research into the differences between stroke patients and non-disabled participants should be read with care as different types of gait patterns exist across stroke patients.

This study has several limitations. One of the limitations of the study is that only the affected leg is taken into account. Previous research has shown that the less-affected leg also demonstrated abnormal biomechanics variables compared to the control group [24]. This suggests

that the same approach of clustering can be executed with the less affected leg, retrieving clusters based on compensation strategies and/or a combination with the current approach. The second limitation is that the angles of the ankle and knee in frontal and transversal planes were excluded in the study as this did not comprise reliable information. Therefore, it might be that stroke patients have (additional) problems around the ankle and knee that are currently not accurately identified. Lastly, this study provides a first attempt to cluster gait patterns based on kinematic parameters. Future research is needed to validate the clusters with external databases and against clinical outcomes.

The results of this study provide insight into the gait pathology of stroke patients. The eight clusters demonstrate that there are variations among stroke patients in terms of gait kinematics of the affected leg. Ultimately, such clustering may be used by clinicians and physiotherapists to tailor rehabilitation programs based on the patients' assigned cluster. The identified clusters can also be relevant to the field of robot-assisted gait, by selecting the suitable type or amount of support. The clusters could be used as a tool to predict the outcome of specific robotic devices on the walking ability of stroke patients before the patient utilizes the device. Future research should therefore focus on the implementation of these clusters as clinical indicators for exoskeletons use, after the clustering has been validated.

V. Conclusion

This study provides a first attempt to cluster pathological gait patterns in stroke patients using principal component analysis and k-means clustering. A total of eight clusters were retrieved and rearranged into four clinically meaningful categories. The results show initial feasibility of clustering gait patterns in stroke patients. Future research should focus on validating the approach and using the clusters to identify the responsiveness of stroke patients to exoskeletons as a way to personalize rehabilitation programs.

Acknowledgment

We would like to thank the team of Van Criekinge [14] for making their dataset publicly available (used under CC-by 4.0 license). As the burden for stroke patients during activities of daily life, such as walking, is already high, the dataset is greatly appreciated.

References

[1] B. Algurén, A. Lundgren-Nilsson and K.S. Sunnerhagen. "Functioning of stroke survivors – a validation of the ICF core set for stroke in Sweden," *Disabil Rehabil*, 32, 2010, pp. 551-559

[2] P.W. Duncan, R. Zorowitz, B. Bates and et al., "Management of adult stroke rehabilitation care: a clinical practice guideline," *Stroke* vol. 36, no. 9, pp. e100-e143, 2005.

[3] A. S. Rudberg, E. Berge, A.C. Laska and et al., "Stroke survivors' priorities for research related to life after stroke," *Topics in Stroke Rehabilitation*, vol. 28, no. 2, pp. 153-158, 2020.

[4] M.F. Bruni, C. Melegari, M.C. De Cola, A. Bramanti and R.S. Calabrò, "What does best evidence tell us about robotic gait rehabilitation in stroke patients: a systematic review and meta-analysis," *Journal of Clinical Neuroscience,* vol. 48, no. 1, pp. 11-17, 2018.

[5] L. Wang, Y. Zheng and Y. Dang et al., "Effects of robot-assisted training on balance function in patients with stroke: a systematic review and metanalysis," *Journal of rehabilitation medicine,* vol. 53, no. 4, pp. 1-9, 2021.

[6] J.M. Veerbeek E. van Wegen, R. van Peppen and et al., "What is the evidence for physical therapy poststroke? A systematic review and meta-analysis," *PLoS One,* vol. 9, no. 2, pp.e87987, 2014

[7] J. Mehrholz, S. Thomas, J. Kugler, M. Pohl and B. Elsner, „Electromechanical-assisted training for walking after stroke (Review)," *Cochrane Database Syst Rev*, no. 10, pp. CD006185, 2020

[8] S. Park, J. Choi, Y. Kim and J.S.H. You, "Clinical machine learning prediction best stroke rehabilitation responders to exoskeletal robotic gait rehabilitation," *Neurorehabilitation,* vol. 54, no. 4, pp. 619-628, 2024.

[9] G. Kwakkel, N.A. Lannin, K. Borschmann and et al., "Standardized measurement of sensorimotor recovery in stroke trials: Consensus-based core recommendations from the Stroke Recovery and Rehabilitation Roundtable," *International Journal of Stroke*, vol. 12, no. 5, pp. 451-461, 2017

[10] B.H. Dobkin, S.E. Nadeau, A.L. Behrman and et al., "Prediction of responders for outcome measures of locomotor Experience Applied Post Stroke trial," *J Rehabil Res Dev*., vol. 51, no. 1, pp. 39-50, 2014

[11] J. Sung, S. Han, H. Park, S. Hwang, S.J. Lee and J.W. Park, "Classification of Stroke Severity Using Clinically Relevant Symmetric Gait Features Based on Recursive Feature Elimination With Cross-Validation," *IEEE Access*, vol. 10, pp. 119437-119447, 2022.

[12] F.-C Wang [2], S-F Chen, C-H Lin and et al., "Detection and classification of stroke gaits by deep neural networks employing inertial measurement units," *Sensors,* vol. 21, no. 5: 1864, 2021.

[13] K. Kaczmarczyk, A. Wit, M. Krawczyk and J. Zaborski, "Gait classification in post-stroke patients using artificial neural networks," *Gait & posture,* vol. 30, no. 2, pp. 207-210, 2009.

[14] T. van Criekinge, W. Saeys, S. Truijen et al., "A full-body motion capture gait dataset of 138 able-bodied adults across the life span and 50 stroke survivors," *Sci Data,* vol. 10, no. 1, pp. 852, 2023.

[15] F. Pedregosa, G. Varoquaux, A. Gramfort and et al., "Scikit-learn: machine learning in python," *The journal of machine learning research*, vol. 12, pp. 2825-2830, 2011.

[16] D. Arthur and S. Vassilvitskii, "K-means++: the advantages of careful seeding," *ACM-SIAM Symposium on Discrete Algorithms,* 2007.

[17] K. Arvai, "Kneed," *Zenodo,* 2023.

[18] I. Vandekerckhove, I. Papageorgiou, B. Hanssen et al., "Gait classification for growing children with duchenne muscular dystrophy," *Sci Rep,* vol. 14, pp. 10828, 2024.

[19] H. Kim, Y.-H Kim, S.-J. Kim and M.-T Choi, "Gait clustering analysis in patients after stroke using gait kinematics data," *21st International Conference on Control, Automation and Systems (ICCAS),* Jeju, Korea, Republic of, pp. 1405-1409, 2021.

[20] J. Pauk and K. Minta-Bielecka, "Gait patterns classification based on cluster and bicluster analysis," *Biocybernetics and Biomedical Engineering,* vol. 36, pp. 391-396, 2016.

[21] S. Mulroy, J. Gronley, W. Weiss, C. Newsam and J. Perry, "Use of cluster analysis for gait pattern classification of patients in early and late recovery phases following stroke," *Gait and Posture*, vol. 18, no. 1, pp. 114-125, 2003.

[22] S. Kinsella and K. Moran, "Gait pattern categorization of stroke participants with equinus deformity of the foot," *Gait & Posture,* vol. 27, pp. 144-151, 2008

[23] T.S. Winner, M.C. Rosenberg, K. Jain, T.M. Kesar, L.H. Ting and G.J. Berman, "Discovering individual-specific gait signatures from data-driven models of neuromechanical dynamics," PLoS Comput Biol 19(10): e1011556, 2023.

[24] J.W. Pan, A. Sidarta, T.L. Wu and et al., „Unraveling stroke gait deviations with movement analytics, more than meets the eye: a case control study," *Front Neurosci,* vol. 18, 2024.

Optimizing the Myokinetic Interface: A Finite Element Model to Predict Displacement in Amputated Muscles

Flavia Paggetti[1], Marta Gherardini[1], Alessandro Lucantonio[2], Christian Cipriani[1]

Abstract— **In recent years, a novel human-machine interface for prosthetic control has been developed: the myokinetic interface, which decodes the user intent by monitoring the displacement of implanted magnets in the muscles. Simulations and the first in-human demonstration of this interface indicate that the placement of the magnets is crucial for the range and stability of the control signals. Therefore, a preoperative estimation of individual muscle displacement is necessary to identify optimal implantation regions and generate synthetic datasets of magnet displacement. In this study, we developed a finite element model of pennate muscles, calibrated and validated using the geometries of healthy muscles and in vivo measurements from healthy subjects. The performance of the model was further assessed on three amputated muscles by comparing simulations with in vivo data from a limb-impaired individual. Overall, the simulation results aligned well with experimental data, with average errors below 0.7 mm for the healthy muscles and 1.7 mm for the amputated ones. These results suggest that this model could serve as a valuable tool for optimizing surgical procedures and control strategies prior to clinical implementation. This framework could be expanded to investigate muscle behavior in different amputee populations or individuals with neuromuscular diseases, to enhance understanding of muscle biomechanics and advance the design of personalized rehabilitation devices.**

I. Introduction

A limb amputation is a traumatic experience that profoundly impacts the quality of life of many individuals, significantly reducing their capability and independence in performing daily living activities. Despite the development of technologically advanced prostheses, the absence of human-machine interfaces capable of accurately and reliably monitor the user's intentions hinders the widespread adoption of these assistive devices. In the past years, multiple strategies to decode the user's intent have been developed. Most of these methods detect muscle activation by measuring the electromyographic signals generated during contraction [1], [2], using either surface electrodes or implantable sensors [3]. Recently, a new paradigm for decoding the user intent has emerged, based on the detection of muscle displacement. This approach can be implemented non-invasively by capturing muscle architectural changes using ultrasound probes (sonomyography) positioned on the stump [4], or by recording pressure changes on the skin surface (force myography) [5]. Another approach, the myokinetic interface [6], [7], involves tracking markers implanted within the muscle to monitor its contractile state. As multiple markers can be implanted in the muscles, the localization of their poses (position and orientation) allows to reconstruct the muscle deformation. Unlike sonomyography, this approach does not require continuous contact between the device and the skin, nor does it rely on the application of gels or moisture, which could cause skin problems with prolonged use. We developed this concept by implementing the myokinetic interface initially through laboratory studies, and eventually transitioning to clinical settings [8]. The concept has gained significant interest within the scientific community, resulting in numerous studies that underscore how muscle deformation, and consequently, the selection of implant sites, can profoundly influence the choice of control strategies, as well as the expected range of motion and signal resolution [9], [10]. This aspect was further validated during the first in-human trial involving a patient with transradial amputation: the positions of the magnets within the muscles proved to be crucial in determining the amplitude and consistency of the control signals [8]. These findings highlight the importance of preoperative planning and studying muscle deformation, focusing on the kinematics of amputated muscles.

Within this framework, preoperative estimation of muscle deformation and fiber rotation is crucial. Finite element (FE) models have the potential to provide such information, enabling to generate realistic dataset of muscle contractions. This capability can support the preoperative planning of surgical procedures, identifying the most suitable muscle regions for the magnet implantation, to maximize the range and consistency of control signals. Over the past decades numerous FE models of muscles have been developed, involving different constitutive laws to model both the passive and active components of the muscle tissue [11]. More recently, researchers have also included fiber direction in the model, demonstrating to be a key element in the muscle kinematics [12][13]. While most simulations have been applied to healthy muscles, only a limited number has focused on the behavior of amputated muscles. Among these, the majority focus on the lower limb, investigating limb-socket interactions to identify strategies for reducing discomfort and dermatological issues [14].

[1]BioRobotics Institute and the Department of Excellence in Robotics and AI, Scuola Superiore Sant'Anna, 56127 Pisa, Italy

[2] Department of Mechanical and Production Engineering, Aarhus University, Aarhus, Denmark

This work was supported by the Italian Ministry of Research, under the complementary actions to the PNRR "Fit4MedRob - Fit for Medical Robotics" Grant (number PNC0000007); INAIL, in the framework of the BioARMnext (grant number: PR23-RR-P3), NoProblem (grant number: PR23-CR-P3), and OsteoAMI (grant number: PR23-CR-P5) projects.

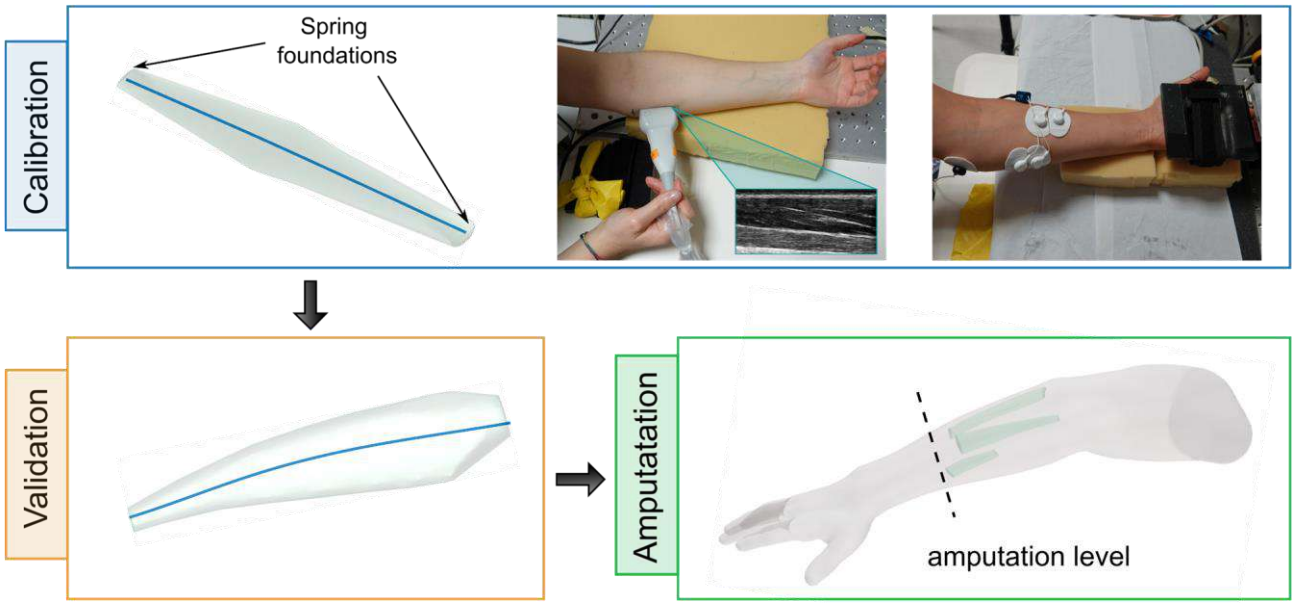


Fig 1 Block diagram showing all the steps of the experimental setup. *Calibration* was performed on the healthy geometry of the FCU muscle (on the left), with ultrasound images and EMG signals acquired to record the pennation angle and estimate force development (on the right). *Validation* was performed on the healthy geometry of the FCR muscle. Finally, *Amputation* was simulated on the geometries of three muscles (ED, FPL, FCU).

Within this framework, a finite element (FE) model of forearm amputated muscle becomes necessary to specifically address the displacement field generated during contraction. In this study, we calibrated and validated a model of muscle contraction [15] on the geometry of healthy forearm muscles, incorporating fiber direction and displacement specifically derived from in vivo measurements. Calibration was performed on a simplified geometry of the flexor carpi ulnaris (FCU) muscle to fine-tune material parameters. Subsequently, forces and displacements generated by a more realistic geometry of the flexor carpi radialis (FCR) were compared with those of healthy participants, validating the model performance. Finally, the model was applied to the geometry of three amputated muscles, and results were compared with muscle displacement data recorded from a limb-impaired participant. This work provides a preliminary development of an amputated forearm muscle model, that could potentially enable patient-specific preoperative planning and could be extended to any amputation level. This framework could be adapted to study muscle function in various groups of amputees or individuals with neuromuscular disorders, to improve understanding of muscle biomechanics and support the development of customized rehabilitation tools.

II. Materials and Methods

The FE model was implemented in Comsol Multiphysics 5.5 (COMSOL Inc. Stockholm, Sweden) and calibrated and validated through in vivo experimental measurements from 8 and 7 healthy participants, respectively (age range: 20-30 years old, two females, six males). The model was then applied to the geometry of three amputated muscles and the resulting displacement was compared with that recorded from one limb-impaired participant (Fig 1). Informed consent in accordance with the Declaration of Helsinki was obtained before conducting experiments from each participant. The studies were approved by the local ethical committee of the Scuola Superiore Sant'Anna, Pisa, Italy (Approval No. 10/2023). The methods were carried out in accordance with the approved guidelines.

A. Geometry, material and boundary conditions

The geometries of forearm muscles were extracted from a 3D model of healthy human forearm (Zygote, American Fork, US) already used in [9]. The model included muscle-tendon structures, bones, skin and vessels. Only the muscle-tendon units were retrieved and divided by transecting the distal and proximal tendons. Muscle bellies were modeled by implementing material-specific equations. As skeletal muscles are essentially incompressible and show a highly nonlinear stress-strain behavior, their passive properties can be described with hyperelastic models [16], as a combination of passive and active materials. In this work, muscle bellies were modeled according to the mixture active strain approach introduced by Riccobelli and Ambrosi [15]. The deformation gradient is multiplicatively split into an elastic (F_e) and an active (F_a) contribution. The choice of F_a is inspired by the microstructural architecture of the muscles

$$\mathbf{F} = \mathbf{F_e}\mathbf{F_a} \tag{1}$$

$$\mathbf{F_a} = (1-\gamma)\mathbf{M} + \frac{1}{\sqrt{(1-\gamma)}}(\mathbf{I}-\mathbf{M})$$

where $0 \leqslant \gamma < 1$ is a parameter that describes the microstructural degree of contraction of the muscle (0 corresponds to a relaxed state) and **M** the fiber direction. The mixture active strain approach considers the material as composed by an isotropic and an anisotropic phase. The former represents only passive constituents that do not contribute to muscle contraction, such as elastin and collagen,

whereas the latter describes the fiber contribution. The strain energy density function describing the material is the following:

$$\psi = \psi_{iso} + \psi_{ani} \tag{2}$$

$$\psi_{iso(F)} = -\mu \frac{I_{max}}{2} log\left(1 - \frac{I_1 - 3}{I_{max}}\right)$$

$$\psi_{\mathrm{ani}}(F) = \alpha\beta\left(\mathrm{I}_4^{\frac{1}{2\beta}} - 1\right)^2$$

A Gent material model has been adopted for the isotropic part, with μ being the shear modulus and I_{max} a constant setting the maximum value reachable by the first invariant I_1. The anisotropic part of the strain energy depends on the anisotropic parameter α (N/m^2), and a dimensionless constant β, which controls the stiffening behavior of the material.

The constitutive law presented in (2) was implemented in Comsol Multiphysics 5.5. The model requires as input the values of μ, I_{max}, α, β and the fiber orientation **M.** In all simulations, the shear modulus μ was set to a value comparable to human muscle shear stress (μ = 30 kPa [17]), and I_{max} to 0.41 as in Riccobelli's and Ambrosi's work. α and β were selected according to a calibration procedure described in *B*. The muscle fiber orientation was derived from ultrasound images of the muscle fibers (calibration phase) and from literature data for the validation and amputated muscle simulation. Muscles were modeled with a tetrahedral mesh (0.038 - 0.525 mm element size), while the proximal and distal tendons (when present) were represented by distributed springs (elastic modulus of 800 MPa [18]) with length equal to the tendon length.

Muscle simulations were performed by varying the degree of muscle contraction γ from 0 to 0.3 [19], with steps of 0.002. Variation in pennation angle, displacement field and force generated during different contraction intensities were monitored and compared with experimental data. Specifically, from the FE simulations, mean and standard deviation computed across the neighboring points of the muscle centerline were reported.

B. Calibration

A calibration procedure was performed to determine the optimal values of α and β. This calibration was carried out using a simplified 3D geometry of a healthy FCU muscle, selected due to its superficial location and large pennation values. Based on the 3D CAD model of the human forearm, a symmetric geometry for the FCU muscle belly was developed, preserving the original length and cross-sectional area (Fig 1). The material parameters α and β were optimized to match the measured muscle tensile force and pennation angle recorded during isometric contraction of eight healthy subjects. Specifically, the variations in pennation angle during isometric maximum voluntary contraction (MVC) were measured using B-mode ultrasound imaging. An 18 MHz linear transducer (Esaote Mylab, probe LA435) was used to capture images at the level of ~30%, ~50% and ~70% of the muscle length. The transducer was positioned in the coronal plane to detect the angle of fiber attachment relative to the tendon axis, in both relaxed and contracted states (Fig 1). The average fiber angles measured at rest were used to define the initial fiber orientation **M** in the FE model. The variation in fiber angle from resting state to maximum contraction was compared with results from the FE simulation.

The maximum force generated by the FCU was recorded by a load cell (Nano17 by ATI, SI 25-0.25), while participants were performing isometric wrist flexions to activate the FCU. Participants sat with their dominant forearm placed on the table, in a supine position and with the hand located right below the load cell. A rigid flat frame was tied on the palm of the hand, to provide a rigid interface with the measuring system, thus reducing eventual errors due to local skin deformation (Fig 1). Participants performed three maximum voluntary isometric contractions, isometrically flexing the wrist, with joint movement constrained by the load cell. Since the measured force reflected the combined contribution of both wrist flexor muscles (i.e., FCU and FCR), their electromyographic (EMG) activity was recorded to disentangle their individual contributions. Bipolar electrodes recorded activation from both muscles (Fig 1), and the signals were amplified, filtered (10–500 Hz), rectified, and low-pass filtered (15 Hz) to produce linear envelopes. Muscle contributions were estimated by comparing the amplitudes of these envelopes across trials and subjects, leveraging the established linear relationship between EMG and muscle force during isometric contractions [20] . Finally, using the known moment arms of both muscles [21] and the load, the balance of moments around the wrist joint was solved to estimate the actual contraction force developed by both muscles.

Multiple FE simulations were run by manually varying α (1 kPa -5 MPa) and β (0.8-2.5). Variation in pennation angle was evaluated as the average angle variation over a number of points along the centerline at the distal (30% muscle length), central (50%) and proximal (70%) muscle region. The force developed following maximum contraction was measured at the muscle-tendon interface of the distal extremity, by integrating the distributed spring force magnitude over the area of attachment. Finally, the values of α and β that produced FE results best matching the experimental data were identified and used in all the subsequent simulations.

C. Validation

A validation procedure assessed the generalization ability of the model towards different geometries and output variables, exploiting a realistic geometry of the healthy FCR muscle, obtained from the 3D model of human forearm (Fig 1). The muscle-tendon unit was transected distally and proximally to retain only the muscle belly, according to anthropometric data [22]. The initial pennation angle was set to 13°, in agreement with literature data [23]. The material parameters selected in the calibration phase were used to simulate contractions, again increasing γ up to 0.3.

The displacement and force developed by the FE model under different contraction intensities were compared with data from seven healthy subjects performing five isometric contractions at 20%, 50%, 70%, 90% of MVC. Ultrasound videos recorded the muscle contractions in the longitudinal plane, with the probe positioned at ~30% (proximal), ~50% and ~70% of muscle length. The displacement of visible

TABLE I. MEAN VALUES OF PENNATIN ANGLE FOR THE RELAXED AND CONTRACTED STATE, ALONG THE MUSCLE LENGTH

State	Mean pennation angle (deg)		
	20% muscle length	*50% muscle length*	*70% muscle length*
Relaxed in vivo	5.68 ± 2.04	4.56 ± 1.54	3.96 ± 0.89
Relaxed FEM	5.57	4.77	4.18
Active in vivo	8.13 ± 2.56	6.83 ± 1.80	5.47 ± 1.44
Active FEM	7.73	6.57	5.10

reference points (e.g. fiber attachment) was manually measured and compared to the FE displacement. Similarly, the force of FCR measured with the load cell during calibration was compared to the FE output.

D. Amputated muscle

The finite element model, developed through the calibration and validation phase, was used to simulate contractions in amputated muscles. Three forearm muscles have been considered, namely the extensor digitorum (ED), flexor pollicis longus (FPL) and FCU, with geometries obtained from the 3D CAD model of the human forearm (Fig 1). As in [9], the amputation was simulated by transecting the distal part of the muscle-tendon complex until the middle third. This resulted in the absence of tendon for the FPL and FCU muscle. The myodesis technique (anchoring of transected muscles directly to the bone) was simulated by applying a fixed constraint at the transected muscle end. For the ED muscle, a ~4 cm residual tendon was simulated through a spring foundation (elastic modulus of 800 MPa [18]). Finally, longitudinal ultrasound videos recorded muscle displacement at 25% and 50% of muscle length during 10 repetitions of 20%, 50%, 70% and 90% MVC. As for the validation process, the displacement of reference fibers was manually measured offline, and reported as mean and standard deviation computed over multiple contractions.

III. RESULTS

A. Calibration

The values of α and β that best matched the experimental measurements corresponded to α = 1.5 MPa and β = 1. Using these values, the simulation developed a force of 96.3 N during MVC of the FCU muscle. This result was comparable to the in vivo forces measured across subjects, which proved in the range 89.51 – 96.40 N, and was consistent with literature data [21]. Regarding the variation in pennation angle, results from the experimental session and the FE simulation are reported in Tab. I. A decreasing trend in fiber angles at rest was observed when moving distally along the muscle, consistent in both simulated and experimental data. The variation in fiber angle from relaxed to contracted state followed a similar pattern, showing a smaller increase in pennation angle distally (increment of ~2° proximally, ~1° distally), in both FE results and experimental observations. Notably, the results from the FE model consistently fell within the standard deviation of the experimental measurements, demonstrating its ability to replicate the overall trend of angle variation along the muscle (Fig 2). The maximum difference

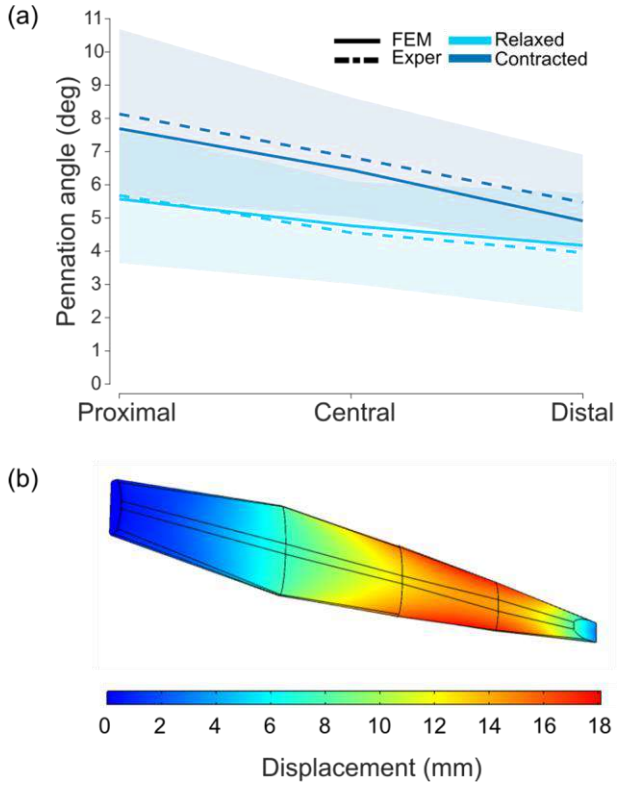


Fig 2 Calibration results. (a) Variation in pennation angle along the muscle: comparison between the FEM results (solid line) and the experimental results (dashed line) for the relaxed and contracted muscle state.

between experimental and simulated angles was always below 0.6°.

B. Validation

Overall, the displacement predicted by the FE model closely matched the experimental data across all contraction intensities (Fig 3). The discrepancy between the two profiles was consistently below 0.7 mm (17% of the maximum displacement), with the largest deviation observed at 50% of the muscle length, at 20% MVC. The maximum longitudinal displacement was observed at the highest contraction intensity and at 50% of the muscle length, with values ranging from 3.9 mm (in vivo measurements) to 4.1 mm (simulation). Both the proximal and distal regions exhibited similar displacement trends, while the central region consistently showed the largest displacement across all contraction intensities, except for the experimental data at 90% MVC (Fig 3). The force of the
FCR muscle estimated from the calibration process ranged from 91.73 N to 98.75 N during MVC. In contrast, the simulation predicted a force of 134.9N at the maximal contractile state.

C. Amputated muscle

All muscles and regions exhibited a displacement that increased with contraction intensity, though not always in a consistent manner for the in vivo measurements (Fig 4). The maximum in vivo displacement was found at 50% of the muscle length for all muscles, with values of 8.1 mm, 2.2 mm and 5.7 mm for ED, FPL and FCU, respectively. The

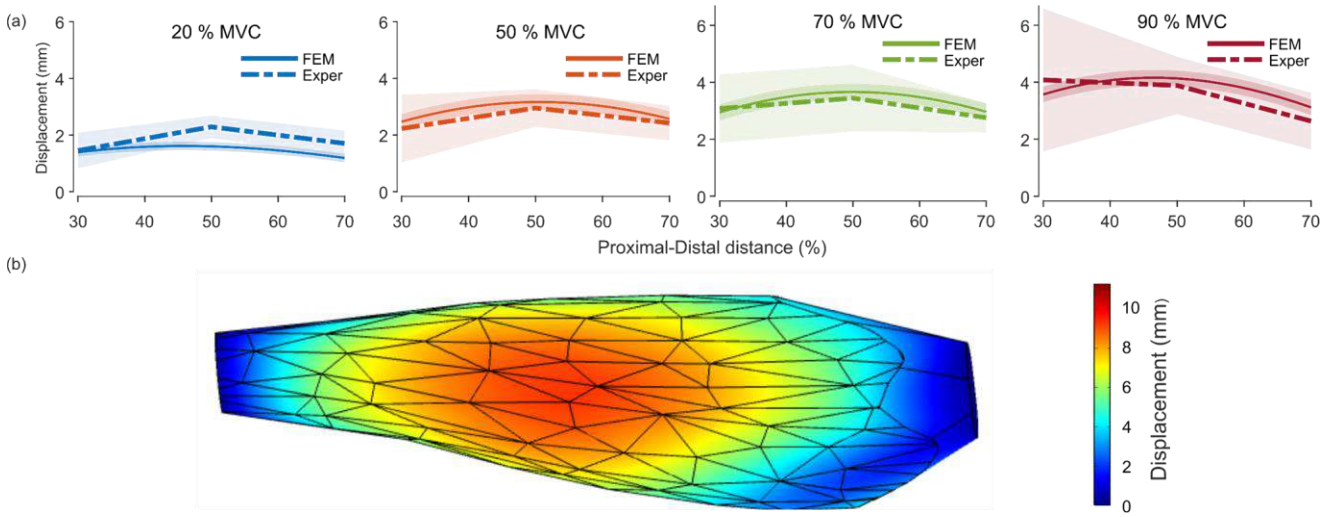


Fig 3 Validation results. (a) Displacement along the muscle for different contraction intensities: comparison between the FEM results (solid line) and the experimental results (dashed line). (b) Displacement field of FCR following maximum voluntary contraction.

discrepancy between measured and simulated displacement, averaged across contraction intensities, proved always below 1 mm for ED and FPL, and below 1.7 mm for FCU (12%, 45% and 30% of the muscle displacement, respectively). The maximum discrepancy was found in the central region of the FCU for 90% MVC, with an error of 3.5 mm (61%) with respect to the experimental data. Overall, except for the proximal region of the ED and FPL, the simulated displacement slightly underestimated the experimental one.

IV. Discussion and Conclusion

We developed a FE model of muscle, starting from a healthy configuration and then moving toward an amputated one. The model provided accurate estimates of force and displacement of healthy muscles, effectively capturing the overall dynamics and kinematics of pennate muscles. Preliminary assessments of amputated muscles demonstrated the model's capability to simulate realistic muscle contractions in amputated conditions, highlighting its potential applications for various limb amputations and related pathologies.

During the calibration phase, the distal region exhibited the largest pennation angle at rest and, unsurpisingly, showed the largest increase in pennation angle during contraction (Fig 2). These findings agree with previous studies indicating that the amount of fiber rotation highly correlates with the pennation angle at rest [24]. This aspect must be considered when planning magnet implantation, particularly if the variation in magnet orientation is a desired control signal. Indeed, a large change in pennation angle during contraction is expected to produce greater magnet rotation.

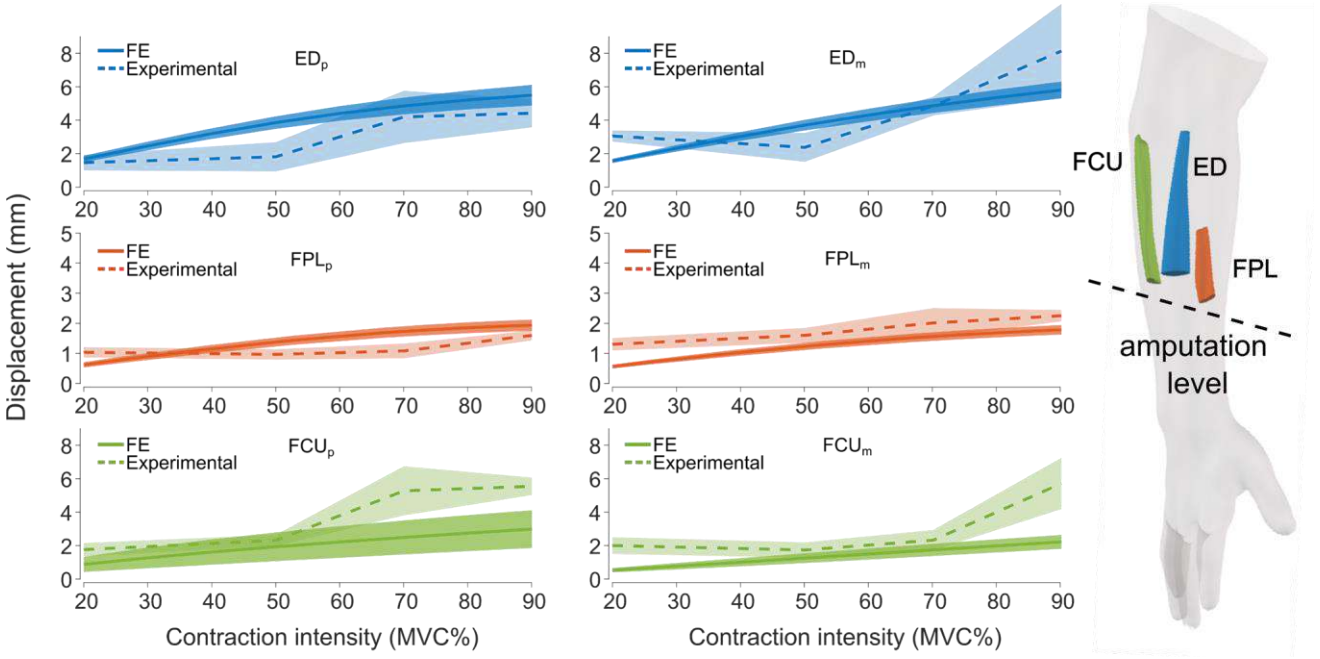


Fig 4 Amputated simulation results. Displacement as a function of contraction intensities for the three amputated muscles: comparison between the FEM results (solid line) and the experimental results (dashed line) for the proximal region (left column) and the central one (right column).

The discrepancy between the force generated by the FCR muscle in the FE model and the in vivo data is likely due to challenges in accurately visualizing the fiber angle in the ultrasound images. As a result, a literature-derived value was used instead of a subject-specific measurement. Incorporating more precise, subject-specific fiber orientation data could significantly improve force estimations, as fiber orientation is known to significantly affect force output [24].

Finally, the slightly higher discrepancy between the FE model and experimental data in the amputated configuration (Fig 4) could be attributed to several factors. First, the model parameter were calibrated and validated using a healthy muscle and were not specifically adapted for an amputated one. It is well-known that muscles in limb-impaired individuals may undergo atrophy and experience reduced volume due to decreased activity: future studies should take this into account. Additionally, the boundary conditions were modified to account for the shorter tendon length, assuming it was anchored via the myodesis technique. A different anchoring technique might explain the lower displacement estimated by the FE model compared to in vivo data. Therefore, future investigations should explore the influence of different suturing techniques on the muscle displacement, first in vivo and then by defining the appropriate boundary conditions in simulation.

Overall, these results demonstrate the feasibility of predicting the behavior of both healthy and amputated muscles, using fast in vivo measurements. Future studies should extend these findings to a larger population, by incorporating subject-specific geometries to refine the model parameters and enhance the overall accuracy. This work could be applied to estimate the muscle behavior in different amputee populations or individuals with neuromuscular diseases, paving the way for the development of novel and personalized rehabilitation strategies.

REFERENCES

[1] R. N. Scott and P. A. Parker, "Myoelectric prostheses: State of the art," *J Med Eng Technol*, vol. 12, no. 4, pp. 143–151, 1988, doi: 10.3109/03091908809030173/ASSET//CMS/ASSET/4AE5A330-1E93-470A-A757-93F2CD804BBE/03091908809030173.FP.PNG.

[2] K. Englehart and B. Hudgins, "A Robust, Real-Time Control Scheme for Multifunction Myoelectric Control," *IEEE Trans Biomed Eng*, vol. 50, no. 7, 2003, doi: 10.1109/TBME.2003.813539.

[3] R. F. F. Weir, P. R. Troyk, G. A. Demichele, D. A. Kerns, J. F. Schorsch, and H. Maas, "Implantable Myoelectric Sensors (IMESs) for Intramuscular Electromyogram Recording," 2009, doi: 10.1109/TBME.2008.2005942.

[4] V. Nazari and Y. P. Zheng, "Controlling Upper Limb Prostheses Using Sonomyography (SMG): A Review," *Sensors 2023, Vol. 23, Page 1885*, vol. 23, no. 4, p. 1885, Feb. 2023, doi: 10.3390/S23041885.

[5] S. L. Phillips and W. Craelius, "Residual kinetic imaging: A versatile interface for prosthetic control," *Robotica*, vol. 23, no. 3, pp. 277–282, May 2005, doi: 10.1017/S0263574704001298.

[6] S. Tarantino, F. Clemente, D. Barone, M. Controzzi, and C. Cipriani, "A myokinetic hmi for the control of hand prostheses: A feasibility study," *Biosystems and Biorobotics*, vol. 15, pp. 575–579, 2016, doi: 10.1007/978-3-319-46669-9_95/COVER.

[7] S. Tarantino, F. Clemente, D. Barone, M. Controzzi, and C. Cipriani, "The myokinetic control interface: Tracking implanted magnets as a means for prosthetic control," *Sci Rep*, vol. 7, no. 1, Dec. 2017, doi: 10.1038/s41598-017-17464-1.

[8] M. Gherardini *et al.*, "Restoration of grasping in an upper limb amputee using the myokinetic prosthesis with implanted magnets," *Sci. Robot*, vol. 9, p. 3260, 2024.

[9] F. Paggetti, M. Gherardini, A. Lucantonio, and C. Cipriani, "To what extent implanting single vs pairs of magnets per muscle affect the localization accuracy of the myokinetic control interface? Evidence from a simulated environment," *IEEE Trans Biomed Eng*, 2023, doi: 10.1109/TBME.2023.3272977.

[10] M. Daliri *et al.*, "The second clinical study investigating the surgical method for the kineticomyographic control implementation of the bionic hand," *Scientific Reports* |, vol. 13, p. 18387, 123AD, doi: 10.1038/s41598-023-45578-2.

[11] T. T. Dao and M. C. H. B. Tho, "A Systematic Review of Continuum Modeling of Skeletal Muscles: Current Trends, Limitations, and Recommendations," *Appl Bionics Biomech*, vol. 2018, no. 1, p. 7631818, Jan. 2018, doi: 10.1155/2018/7631818.

[12] S. S. Blemker, P. M. Pinsky, and S. L. Delp, "A 3D model of muscle reveals the causes of nonuniform strains in the biceps brachii," *J Biomech*, vol. 38, no. 4, pp. 657–665, 2005, doi: 10.1016/j.jbiomech.2004.04.009.

[13] J. D. Webb, S. S. Blemker, and S. L. Delp, "3D Finite Element Models of Shoulder Muscles for Computing Lines of Actions and Moment Arms," *Comput Methods Biomech Biomed Engin*, vol. 17, no. 8, p. 829, 2012, doi: 10.1080/10255842.2012.719605.

[14] A. S. Dickinson, J. W. Steer, and P. R. Worsley, "Finite element analysis of the amputated lower limb: A systematic review and recommendations," *Med Eng Phys*, vol. 43, pp. 1–18, May 2017, doi: 10.1016/J.MEDENGPHY.2017.02.008.

[15] D. Riccobelli and D. Ambrosi, "Activation of a muscle as a mapping of stress – strain curves," *Extreme Mech Lett*, vol. 28, pp. 37–42, 2019, doi: 10.1016/j.eml.2019.02.004.

[16] J. A. C. Martins, M. P. M. Pato, and E. B. Pires, "A finite element model of skeletal muscles," *Virtual Phys Prototyp*, vol. 1, no. 3, pp. 159–170, 2006, doi: 10.1080/17452750601040626.

[17] K. M. M. e Lima, J. F. S. Costa Júnior, W. C. de A. Pereira, and L. F. De Oliveira, "Assessment of the mechanical properties of the muscle-tendon unit by supersonic shear wave imaging elastography: a review," *Ultrasonography*, vol. 37, no. 1, pp. 3–15, Jan. 2018, doi: 10.14366/USG.17017.

[18] E. L. Bukowski, "Atlas of Amputations and Limb Deficiencies: Surgical, Prosthetic, and Rehabilitation Principles, ed 3," *Phys Ther*, vol. 86, no. 4, pp. 595–596, Apr. 2006, doi: 10.1093/PTJ/86.4.595.

[19] T. J. Burkholder and R. L. Lieber, "Sarcomere length operating range of vertebrate muscles during movement," *J Exp Biol*, vol. 204, no. Pt 9, pp. 1529–1536, 2001, doi: 10.1242/JEB.204.9.1529.

[20] A. L. Hof, "The relationship between electromyogram and muscle force," *Sportverletz Sportschaden*, vol. 11, no. 3, pp. 79–86, 1997, doi: 10.1055/S-2007-993372.

[21] K. R. S. Holzbaur, W. M. Murray, and S. L. Delp, "A model of the upper extremity for simulating musculoskeletal surgery and analyzing neuromuscular control," *Ann Biomed Eng*, vol. 33, no. 6, pp. 829–840, 2005, doi: 10.1007/s10439-005-3320-7.

[22] Hosapatna M, Souza A.D., Rao D., and Hari Ankolekar V, "Morphology and innervation of brachioradialis and flexor carpi radialis and their utility in tendon transfer surgeries: A Cadaveric Study," *Morphologie*, vol. 104, no. 345, 2020.

[23] A. T. Liu *et al.*, "Architectural properties of the neuromuscular compartments in selected forearm skeletal muscles," *J Anat*, vol. 225, no. 1, pp. 12–18, 2014, doi: 10.1111/JOA.12193.

[24] E. L. Brainerd and E. Azizi, "Muscle fiber angle, segment bulging and architectural gear ratio in segmented musculature," *Journal of Experimental Biology*, vol. 208, no. 17, pp. 3249–3261, 2005, doi: 10.1242/jeb.01770.

Head Tracking for Confirming User Selection for Human-Machine Interaction

Zeyad Ghulam[1,2], Greg French[1], Hussein A. Abdullah[1,3]
[1]*School of Engineering*, *University of Guelph*, Guelph, ON N1G 2W1, Canada
zghulam@uoguelph.ca, gfrench@uoguelph.ca, habdulla@uoguelph.ca
[2]*KITE Research Institute*, *Toronto Rehabilitation Institute*, *University Health Network*,
Toronto, ON M5G 2A2, Canada
[3]*Scientific Research Centre*, *Australian University*,
West Mishref Mubarak Al-Abdullah Al-Jaber Area, Kuwait City 13015, Kuwait

***Abstract*—This paper presents a human-machine interface designed to help individuals with upper-limb impairments select items on a screen using only head movements. The system allows users to make selections and confirm choices without requiring hand input. A study with 22 participants (11 male, 11 female, average age 23 years) evaluated its performance across three configurations. Results showed a clear learning curve, with participants achieving greater accuracy and consistency over time. Users adapted well to the system, maintaining stable mouth-opening and head-transition movements close to target values. Their range of motion in pitch and yaw also became more controlled, suggesting improved efficiency and ease of interaction. Survey responses reflected high confidence in system safety while highlighting areas for improving comfort and ease of use. These findings demonstrate the system's potential for accessible, intuitive interaction, with opportunities for further refinement to enhance user experience.**

***Index Terms*—Human-Machine Interface, Head Tracking System, Assistive Technology, Accessibility.**

I. Introduction

Over the last few decades, Human-Machine Interaction (HMI) has witnessed remarkable progress, this is primarily fueled by the integration of new technologies designed to enable users to communicate seamlessly with machines [1]. Researchers continue to push the boundaries of what these systems can accomplish. Despite significant advancements in assistive technologies, substantial gaps persist in meeting the diverse needs of individuals with physical impairments. The World Health Organization reports that over 2.5 billion people require one or more assistive products [2]. Upper limb impairments due to conditions such as degenerative diseases, strokes, or traumatic brain injury significantly impact an individual's ability to perform activities requiring selection and confirmation independently [3]. Furthermore, motor impairments caused by neuromuscular disorders, such as Amyotrophic Lateral Sclerosis (ALS) and cerebral palsy (CP), can severely limit fine motor control and the ability to interact with traditional HMI systems [4]. Additionally, impairments related to neurological disorders like multiple sclerosis, or Parkinson's disease can lead to tremors, muscle weakness, and involuntary movements, complicating the use of conventional devices [5]. For many individuals, these physical limitations pose great challenges in selecting and confirming choices, limiting their independence in essential tasks and daily activities [6], [7].

Traditional HMI systems are built upon various input methods, each with strengths and limitations. Joysticks have long been used for mobility aids, such as in powered wheelchairs, offering precise and proportional directional control. A proportional drive control allows the wheelchair's speed/direction to mirror the force/direction applied to the input device by the user [8]. Coltellaro emphasized that while joystick-controlled wheelchairs have evolved to become more adaptable, they still require a significant degree of upper limb coordination, presenting a barrier for those with severe motor function loss [6]. For users with neuromuscular disorders like ALS or CP, even slight upper limb movements may be difficult or impossible, further underscoring the need for more adaptable input methods [9].

Robotic assistive systems, such as feeding, use proportional (e.g., joysticks) and non-proportional (e.g., buttons, sip-and-puff) control options [8], [10]. While sip-and-puff systems allow users to control devices via breath, they may be unsuitable for those with respiratory issues or fatigue, particularly individuals with multiple sclerosis or traumatic brain injury [8], [9]. Recent innovations, including touchless sensors, still often rely on voice commands or auxiliary controls, which may not be feasible for non-verbal users or those with limited motor function [11].

Eye-tracking technology, such as Tobii Dynavox, offers an alternative for users unable to operate traditional controls [12], [13]. However, its effectiveness depends on precise calibration and controlled environments, limiting reliability in real-world settings [14]. Additionally, high costs and complexity hinder widespread adoption [15]. Voice-controlled systems, like Amazon Alexa and Google Assistant, provide hands-free interaction for individuals with upper limb impairments [16]. However, they exclude non-verbal users and those with speech disorders, such as dysarthria [17].

These limitations highlight the need for a more inclusive and intuitive control system, particularly for non-verbal individuals and those with severe upper limb impairments. While facial recognition and head tracking have been used in robotics and virtual reality, their potential as input methods in human-

machine interaction remains underexplored [18].

This work addresses the identified gaps by proposing a system that relies exclusively on head and mouth tracking to enable user selection and confirmation. The proposed system has the potential to simplify daily tasks for humans interacting with computing devices. Unlike traditional methods requiring significant hardware or extensive calibration, this approach is designed to be easily adaptable, minimizing the learning curve for users and caregivers. This ease of use is critical for individuals with upper limb impairments, as it reduces their reliance on external assistance, thereby improving independence. Jones et al. noted that user-friendly assistive technologies can substantially reduce the workload on caregivers and improve overall care efficiency [19].

Existing head-tracking systems, such as the HeadMouse Nano [20] and NuPoint [21], enable users to control on-screen cursors through head movements. These devices typically rely on dwell-based selection, requiring users to hold their head steady over a target area, which can increase fatigue and reduce efficiency over time. In contrast, our system introduces a **graph-based selection mechanism** that structures selectable items as interconnected nodes, allowing for more efficient navigation and reducing the physical demand on users. Additionally, while conventional systems rely solely on head movements for both navigation and selection, our approach leverages head movements for selection and mouth movements for confirmation, providing a more intuitive and less tiring user experience. The system can be scaled and adopted in a variety of HMI settings and applications, from home use to clinical environments. In conclusion, the development of these systems empowers individuals with disabilities to boost their engagement with assistive/computer devices, enhancing their independence while reducing the burden on caregiving resources [6], [7], [19]. To the best of the authors' knowledge, this is the first system that leverages head movements to select and mouth movements to confirm selections.

II. Method/Procedures

A. Hardware

The camera used for this research was an Intel RealSense D435i, and it was chosen due to its advanced depth-sensing capabilities and reliability in real-time 3D imaging. This camera was mounted on the wrist of the Fischer Scientific Fanuc F5 LR200ic 6DoF Robotic Arm and is used for both object detection task and facial tracking. This setup provides the flexibility needed for applications where accurate selection and confirmation are necessary, such as interacting with personal devices or assistive systems for daily activities.

The system was developed using a Linux operating system, specifically Ubuntu 22.04 LTS, and was equipped with ROS (Robot Operating System). This setup allowed for seamless integration and communication between the hardware components and the software system.

To create modular and adaptable layouts for different user interface configurations and system validation, 3D-printed boxes in sizes of 1x1 (7.6cm x 7.6cm x 4.7cm), 1x2 (15.8cm x 7.6cm x 4.7cm), and 2x2 (15.8cm x 15.8cm x 4.7cm) were assembled. These modular components allow for various selectable options, enabling the system to be used beyond food trays – for example, for interactive selection panels for communication aids, educational tools, or rehabilitation activities. Figures 1, 2 and 3 illustrate different tray compartments configurations, showing the potential variety in the layout of selectable items. The arrows signify the movement direction between containers, one sided arrows resemble movement in 1 direction (i.e from container 5 to 1) and two sided arrows resemble movement in 2 directions (from container 1 to 3 and from container 3 to 1). The blue dashed lines are decorative and resemble the midway point in 2x1 and 2x2 containers.

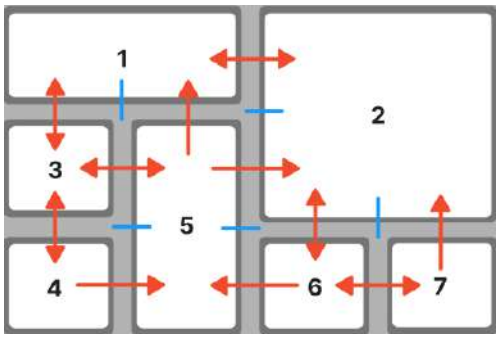


Fig. 1: Layout of Conf 1 which is comprised of four 1x1 boxes, two 2x1 boxes and one 2x2 box

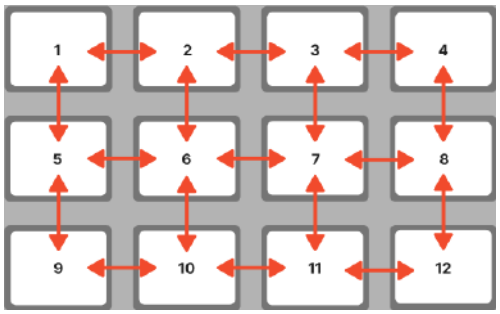


Fig. 2: Layout of Conf 2 which is comprised of twelve 1x1 boxes

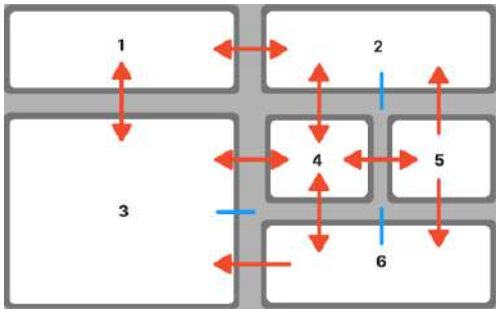


Fig. 3: Layout of Conf 3 which is comprised of two 1x1 boxes, three 2x1 boxes and one 2x2 box

B. Software

The software for this system, was developed in Python and was written as part of a bigger ROS (Robot Operating System) project. During the development process, a technique was needed that gave individuals using the system the ability to select which item/compartment they wanted to choose next from a tray of different items and configurations, without being able to use their arms. The idea was to have users choose items using only their head movements, leading to the work summarized in this paper. While the Python code developed for this system is tightly coupled with ROS's built-in publish/subscribe mechanism, the code can be generalized to be used outside of ROS for any head tracking and GUI selection system.

i. System flow

The process begins with the Intel RealSense camera, which captures an image of the arranged configured selection for the user interaction system. This image is then processed using a YOLOv9 machine-learning model that computes bounding boxes around each selectable tray box. The bounding box data is sent as a ROS message, formatted as an array of tuples containing the (x, y) coordinates of each of the four corners of each bounding box, starting with the top-left corner (x_1, y_1) and proceeding clockwise around the box (resulting in top-right (x_2, y_2), bottom-right (x_3, y_3), and bottom-left (x_4, y_4)). To determine the center point of each bounding box, the following formula is used, where x_1, y_1 represent the top-left corner and x_3, y_3 represent the bottom-right corner:

$$box_{\text{center}} = \left(\frac{x_1 + x_3}{2}, \frac{y_1 + y_3}{2} \right)$$

This center point and the bounding box coordinates are appended to the message. Once the data is received by the node responsible for handling user selection, it instantiates nodes representing each selectable box and arranges these nodes into a graph structure (refer to Figures 1, 2 and 3 for sample node configurations). The default starting node (the one initially selected for the user before any head tracking begins) is chosen randomly. Choosing a default node is application-specific and should be determined by the developers based on the intended use case. When collecting results used in this paper, the default node was always selected as the top-left node to maintain consistency between trials.

Once the graph is assembled, head tracking comes into play. A face detection node keeps track of head movement information. It computes the roll, pitch, and yaw of the user's head to determine directional intent (e.g., selecting items to the 'left', 'right', 'up', or 'down'). The system compares the current and previous directions to prevent unintended rapid movements between nodes. If the current direction matches the previous direction, no action is taken to ensure that selections occur one at a time. The system sends a message to update the active node if a new direction is detected. The system then moves the selection to the neighbouring node in the intended direction, visually highlighting the new active box/compartment to provide user feedback and confirm the successful transition.

ii. Graph Algorithm Development

The system models user navigation through selectable items using a graph structure. Nodes represent individual selectable boxes/items, while edges define allowed transitions between nodes based on spatial proximity. The algorithm constructs the graph as follows:

Algorithm 1 Graph Construction for Navigation

For each detected bounding box (node), extract corner coordinates: (x_1, y_1) (top-left), (x_2, y_2) (top-right), (x_3, y_3) (bottom-right), (x_4, y_4) (bottom-left)
for each node n_i **do**
  for each edge (left, right, top, bottom) **do**
    Generate three parallel test lines along the edge:
    - Midline: Centered on the edge
    - Offset$_+$: 50 pixels of box height above midline
    - Offset$_-$: 50 pixels of box height below midline
  end for
  for each other node n_j **do**
    if any test line from n_i intersects n_j's bounding box **then**
      Add bidirectional edge $n_i \leftrightarrow n_j$
    end if
  end for
end for

The resulting graph enables efficient traversal using head movements, with adjacency relationships corresponding to natural spatial relationships between items (as shown in Figures 1-3).

iii. Selecting choice

Selecting an option is facilitated using Python and the MediaPipe library [22]. The library tracks the head position in real-time to identify directional movements: right, left, up, and down. The system leverages facial landmark detection to compute head orientation changes and deduce the user's intended selection.

To provide immediate feedback to the user, the system includes a visual cue in the form of a green outline around the currently active node. This outline helps users understand which option is currently selected and enables them to confirm their selection with confidence.

Head pose estimation relies on algorithms such as the Rodrigues method and the Perspective-n-Point (PnP) algorithm to ensure accurate tracking of head movements [23]. The Rodrigues algorithm is used for converting rotation vectors into rotation matrices. It is known for its robust handling of facial landmark alignment, while the PnP algorithm is utilized to compute the pose of the head based on 2D-3D point correspondences. These algorithms work in tandem to translate subtle changes in roll, pitch, and yaw into corresponding movements across the graph of selectable nodes.

iv. Confirming choice

The process of confirming a selected option is based on tracking the user's mouth status (open vs. closed). This functionality is essential for ensuring that selections are deliberate and accurate. The face detection node monitors mouth movements and sends updates to the selection node whenever a change is detected.

When the system detects that the user's mouth is open, a circular status indicator begins to fill. If the mouth remains open for two continuous seconds, the indicator completes, and the selection is confirmed. During this period, the selection node halts the monitoring of head and mouth movements, effectively locking in the currently highlighted item. This step clearly indicates to the user that their choice has been successfully confirmed, represented by a green check mark appearing on the screen as shown in Figure 4.

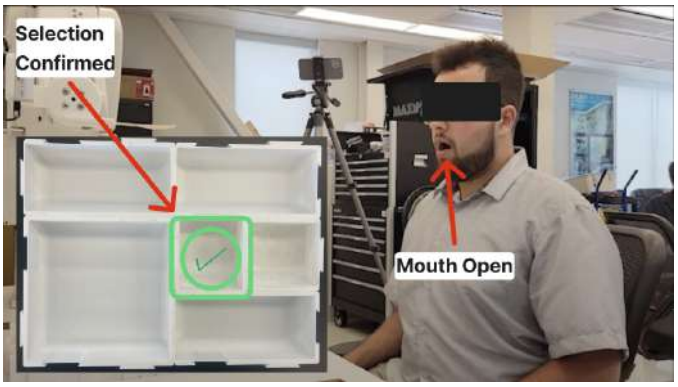


Fig. 4: Selecting and confirming user choice

The loading indicator decreases progressively if the user closes their mouth before the 2-second timer is complete. If the mouth is re-opened while the indicator is decreasing, the status resumes filling from the point where it last left off. This dynamic process ensures flexibility, allowing users to make adjustments without restarting the selection confirmation process entirely.

Visual feedback is critical for user interaction. Screenshots of the system show the status indicator in red when confirmation is not achieved, and green when the selection is successful. A red 'X' is displayed when the confirmation is interrupted, signaling that the user needs to restart the process if they wish to confirm the selection again.

This interactive mechanism ensures that selections are intentional and provides the user with a clear understanding of their interaction status. It facilitates a smooth user experience by eliminating accidental confirmations and giving users control over their choices.

C. Testing Study

To evaluate the effectiveness and user experience of the system, a testing study was conducted involving 22 healthy participants (11 males and 11 females) with an average age of approximately 23 years. Participants signed a consent form indicating that they have full control over their head and neck and they reported that they have no past medical conditions involving their upper extremities. Each participant tested the system for 30 to 45 minutes, spending approximately 12 minutes on each Config (configurations 1, 2, and 3, Figures 1, 2 and 3 respectively). The testing setup included a table with an Intel RealSense camera mounted on the Fanuc F5 Robotic Arm and a screen displaying a graphical user interface (GUI). The GUI showed a picture of the current Config and highlighted the currently selected option with a red bounding box.

Before beginning each Config, participants underwent a brief calibration step in which they were instructed to remain still for 3 seconds to establish their initial head position. During the study, participants followed pre-determined spoken commands given by the researcher. Each trial consisted of five commands involving randomized directional movements (Up, Down, Right, and Left). At the end of the fifth command in each trial, the word "Open" was spoken, prompting participants to open their mouths to confirm their selection. The commands set and order were consistent across all configurations to ensure uniform testing conditions.

Each Config involved 10 trials, with participants completing the same sequence of five commands per trial. Following each trial, participants filled out a post-trial questionnaire to rate on a Likert-scale (from 1 to 10), on how safe/comfortable/easy did the participant find using this system during the trial. This adapted instrument combined standardized Likert-scale principles [24] with context-specific modifications for HMI systems [25]. Participants were encouraged to provide their ratings immediately after the completion of the trial to capture their fresh impressions. Prior to recruiting participants and testing the system, the study was approved by the University of Guelph Research Ethics Board (protocol no. REB# 24- 07-017).

D. Performance Metrics

Four quantitative metrics were developed to evaluate system performance:

- **Head Tracking Accuracy (HTA)**: Percentage of correctly interpreted head movements relative to verbal commands. Calculated per Config as:

$$\text{HTA}_c = \left(\frac{\sum_{t=1}^{10} \text{CorrectMovements}_{t,c}}{\text{TotalCommands}_c} \right) \times 100\%$$

  Where c = Config (1-3), t = trial number, with 5 commands per trial. A movement was considered correct if the system detected user's head movement appropriately.
- **Graph Traversability Accuracy (GTA)**: Percentage of successful node transitions during command execution:

$$\text{GTA}_c = \left(\frac{\sum \text{ValidTransitions}_c}{\sum \text{AttemptedTransitions}_c} \right) \times 100\%$$

  A transition was valid only if the nodes traversed in accordance with the arrow directions outlined in Figures 1, 2 and 3.

- **Head Transition Movements (HTM)**: Average head movements per trial, normalized by:

$$\text{HTM}_c = \frac{1}{N} \sum_{t=1}^{10} \text{HeadMovementCount}_{t,c}$$

Where $N = 10$ trials per Config. The ideal HTM of 5 corresponds to the 5-command sequence per trial.

- **Mouth Opening Occurrences (MOO)**: Average count of mouth activations per trial required for confirmation:

$$\text{MOO}_c = \frac{1}{N} \sum_{t=1}^{10} \text{MouthOpenCount}_{t,c}$$

The ideal MOO = 1 reflects one intentional mouth opening for final selection confirmation per trial.

III. Results

The HTA and GTA accuracy plot in Figure 5 presents an evaluation of participant performance and system responsiveness across the configurations (Figure 1, 2, 3).

HTA results indicate a progression in accuracy across configurations. Config 1 recorded a mean HTA of 79.5% (range: 50–100%), Config 2 increased to 83.6% (range: 50–100%), and Config 3 further improved to 84.7% (range: 60–100%). GTA exhibited a similar pattern, with Config 1 achieving a mean of 85.9% (range: 40–100%), Config 2 increasing to 96.9%(range: 60–100%), and Config 3 at 92.6%(range: 70–100%). See Figure: 5, and Table: I).

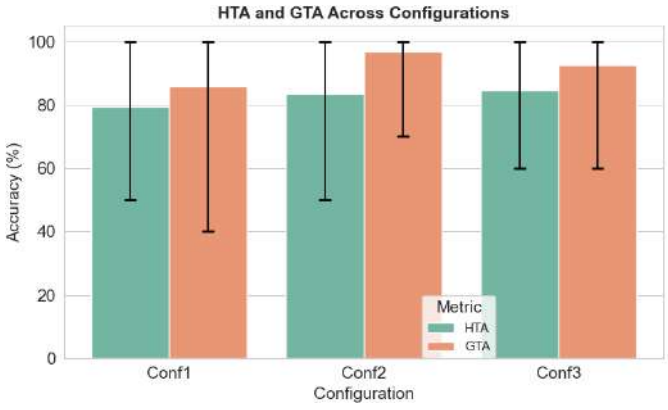


Fig. 5: Head tracking accuracy and graph tracking accuracy across three configurations

Mean MOO values remained close to the target of 1, which represents the ideal scenario where users confirm their selection with a single mouth opening per trial. Config 1 recorded **1.34** (range: 0.9–3.2), Config 2 had **1.38** (range: 1.0–2.9), and Config 3 achieved **1.23** (range: 1.0–8.5). Similarly, HTM values approached the target of 5, which corresponds to the expected number of head movements needed to traverse the interface effectively during a trial, as each trial is composed of 5 distinct head movements. Config 1 recorded a mean of **4.60** (range: 4.0–6.0), Config 2 averaged **4.39** (range: 4.0–4.7),

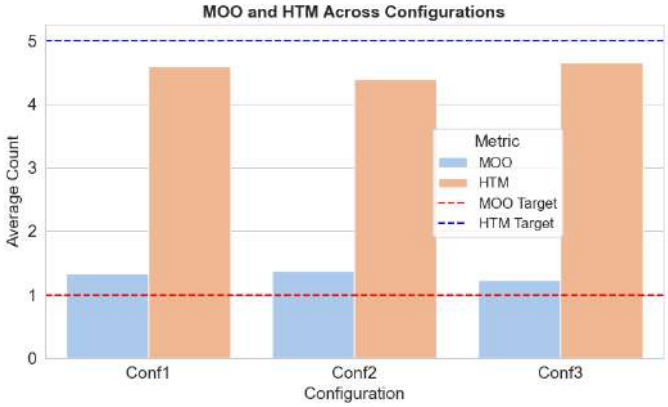


Fig. 6: MOO and HTM across three configurations. The red dashed line represents the MOO target of 1 occurrence per trial, while the blue dashed line represents the HTM target of 5 transitions per trial.

and Config 3 reached **4.65** (range: 3.4–5.0). See Figure: 6, and Table: I.

The range of motion (ROM) for pitch and yaw was computed by subtracting the minimum from the maximum ROM for each participant after normalizing to their neutral angle (calibration baseline). The system's movement thresholds were defined in absolute terms relative to this baseline, with pitch thresholds set at +2° for up and -2° for down, and yaw thresholds set at +2.5° for right and -2.5° for left. After calibration and normalization across all participants, the thresholds were computed as 19.23° (up) and 15.23° (down) for pitch (Figure 7), and 21.88° (right) and 16.88° (left) for yaw (Figure 8). These thresholds define the system's expected response limits for detecting up/down and left/right movements, serving as reference points that participants learned to align with over time.

For pitch (Figure 7), Config 1 exhibited a mean ROM of **15.8**° (range: 5.96°–42.2°), increasing slightly to **17.5**° in Config 2 (range: 9.47°–42.3°), before narrowing in Config 3 to **16.7**° (range: 13.4°–26.9°) (see Table: I).

Yaw (Figure 8) followed a similar trend, with Config 1 at **20.1**° (range: 11.6°–26.3°), decreasing to **18.9**° in Config 2 (range: 14.1°–23.6°), and further stabilizing at **19.3**° in Config 3 (range: 15.8°–22.2°) (see Table: I).

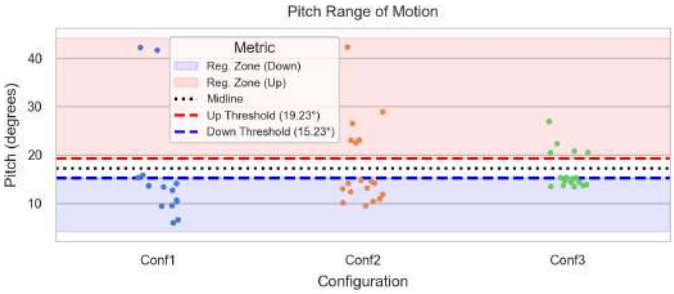


Fig. 7: Pitch range of motion across three configurations

TABLE I: Ranges and Mean Values for MOO, HTM, HTA, GTA, and Survey Responses Across Configurations

Metric	Conf1			Conf2			Conf3			Survey Ratings		
	Min	Mean	Max	Min	Mean	Max	Min	Mean	Max	Min	Mean	Max
MOO	0.9	1.34	3.2	1.0	1.38	2.9	1.0	1.23	1.85	-	-	-
HTM	4.3	4.60	6.0	4.0	4.39	4.7	3.4	4.65	5.0	-	-	-
HTA	50	79.5	100	40	83.6	100	60	84.7	100	-	-	-
GTA	40	85.9	100	60	96.9	100	70	92.6	100	-	-	-
Pitch	5.96	15.8	42.20	17.5	9.47	42.2	16.7	13.4	26.9	-	-	-
Yaw	11.59	20.1	26.25	14.14	18.9	23.6	15.8	19.3	22.2	-	-	-
Safety	-	9.69	-	-	-	-	-	-	-	7.0	9.69	10.0
Comfort	-	8.54	-	-	-	-	-	-	-	6.0	8.54	10.0
Ease of Use	-	8.59	-	-	-	-	-	-	-	5.0	8.59	10.0

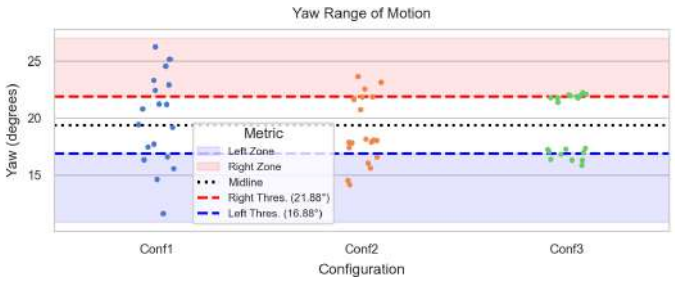


Fig. 8: Yaw range of motion across three configurations

Participants rated system safety at **9.69/10** (range: 8–10). Comfort received an average score of **8.54/10** (range: 6–10), while ease of use was rated at **8.59/10** (range: 7–10).

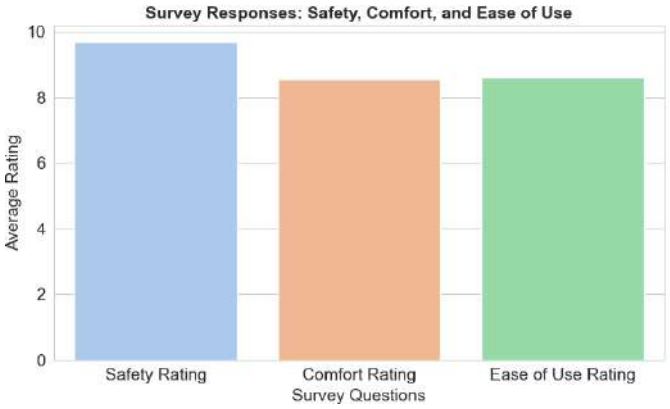


Fig. 9: Participant's survey results

IV. Discussion

HTA and GTA results suggest a learning effect, with accuracy improving progressively across configurations. The narrowing lower bounds in the latter configurations (raised from 50% in Config 1 to 60% in Config 3) indicate that participants became more consistent over time (see Figure 5, Table I). Config 1 exhibited greater variability, likely due to participants familiarizing themselves with the system's response mechanics. As they progressed to Config 2 and 3, accuracy improved, and variability decreased, implying that participants internalized movement thresholds and refined their selection strategies. The increase in mean GTA from **85.9%** in Config 1 to **96.9%** in Config 2, followed by slight stabilization in Config 3, suggests that the second Config facilitated rapid adaptation before plateauing. This aligns with motor learning principles, where repetition leads to increased precision and reduced effort [26], [27].

MOO and HTM remained stable across configurations. MOO values closely matched the target of **1** per trial, with minimal deviation. HTM values, while slightly below the target of **5** transitions per trial, showed refinement in movement execution over time. Config 1 exhibited greater variability, suggesting that participants initially explored different movement strategies. By Config 3, transitions became more consistent, indicating that participants had optimized their movements to minimize unnecessary shifts while maintaining effective interaction. These results indicate that the system facilitates intuitive adaptation, enabling participants to refine their control strategies efficiently.

ROM analysis further highlights participant adaptation. In Config 1, participants exhibited a broader ROM in both pitch and yaw, likely overcompensating to ensure input registration. The mean pitch ROM was **15.8**°, while yaw ROM averaged **20.1**°, with both showing wide variability across participants (see Figure 7, Figure 8, Table I).

As participants transitioned to Config 2, movement ranges narrowed, indicating greater control and confidence in system response. While the mean pitch ROM increased slightly to **17.5**°, the overall range decreased, suggesting improved consistency. Yaw ROM followed a different trend, with a reduced mean of **18.9**° and a tighter distribution, pointing to more refined lateral head movements.

By Config 3, ROM values closely aligned with the system's threshold lines. Pitch ROM decreased to **16.7**°, and yaw ROM stabilized at **19.3**°, with significantly reduced variability compared to earlier configurations. The tighter distribution suggests that participants had developed a precise understanding of movement registration, allowing them to execute more controlled and efficient interactions. This shift from exploratory to deliberate movement behavior is characteristic of motor learning, where repeated exposure leads to optimized motion patterns with minimal extraneous effort [28]. The continued reduction in ROM variability across configurations further

supports that participants adapted to the system's response mechanics over time, improving interaction efficiency.

Survey responses confirm strong participant confidence in system safety, with consistently high ratings. However, comfort and ease-of-use scores exhibited slightly broader variability. Most participants found the system intuitive, but some struggled with movement precision and input registration, highlighting individual differences in usability. Adjusting sensitivity and adding user-specific calibration could enhance comfort and ease of use.

Future work will evaluate the system with individuals with upper-limb impairments to assess real-world usability. Implementing user-specific calibration could enhance performance by adjusting tracking thresholds to suit different movement patterns. Additional interactive training mechanisms may further accelerate adaptation, helping new users quickly learn optimal movement strategies. Long-term studies will explore whether efficiency improvements persist over extended use and whether periodic recalibration enhances performance. These refinements aim to improve system adaptability, ensuring broader accessibility and an optimized user experience.

V. Conclusion

The analysis of participant performance and survey responses highlights the effectiveness and usability of the head-tracking system for HMI selection. Participants rated the system highly for safety (**9.69/10**), comfort (**8.54/10**), and ease of use (**8.59/10**). Performance metrics further reinforce the system's reliability, with a stable MOO value near the target of **1.0** and an HTM value approaching **4.6**/5, reinforcing that participants maintained high consistency in their interaction behavior.

A key finding is the progressive refinement in user interactions across configurations. HTA improved by **6.54%** from Config 1 to Config 3, while GTA increased by **7.80%**. Additionally, the reduction in variability of pitch and yaw movements suggests that participants adapted to the system's movement thresholds over time, this lowers the user's input effort thereby increasing comfort over time.

Lastly, the system was implemented as a modular ROS-based package, enabling seamless integration into various HMI applications. While the results demonstrate promising performance, further research is needed to evaluate its effectiveness across a more diverse user population. Expanding this evaluation will help refine movement thresholds through user-specific calibration, optimizing the system for different needs and interaction styles.

References

[1] B. Shneiderman, *Designing the User Interface: Strategies for Effective Human-Computer Interaction*, 6th ed. Pearson, 2020.

[2] World Health Organization, "Almost one billion children and adults with disabilities and older persons in need of assistive technology denied access, according to new report," 2022. [Online]. Available: https://www.who.int/news/item/16-05-2022-almost-one-billion-children-and-adults-with-disabilities-and-older-persons-in-need-of-assistive-technology-denied-access–according-to-new-report

[3] S. Sporn, M. Coll, S. Bestmann, and N. S. Ward, "Chronic stroke survivors underestimate their upper limb motor ability in a simple 2d motor task," *Journal of NeuroEngineering and Rehabilitation*, vol. 21, 2024.

[4] J. R. W. et al., "Brain–computer interface technology: A review of the first international meeting," *IEEE Transactions on Rehabilitation Engineering*, vol. 8, no. 2, pp. 164–173, 2000.

[5] World Health Organization, *Neurological Disorders: Public Health Challenges*. World Health Organization, 2006.

[6] J. Coltellaro, "Joystick control for powered mobility: Current state of technology and future directions," *Physical Medicine and Rehabilitation Clinics of North America*, vol. 21, no. 1, pp. 79–86, 2010.

[7] J. R. Pauszek, "An introduction to eye tracking in human factors healthcare research and medical device testing," *Human Factors in Healthcare*, vol. 3, 2023.

[8] K. Cezat, "Power wheelchair alternative drive controls in spinal cord injury," 2019. [Online]. Available: https://neuropt.org/docs/default-source/sci-sig/fact-sheets/scisig_factsheet_alternativedrivecontrols.pdf

[9] N. C. Joyce and C. Chatto, *Living with ALS: Functioning When Mobility is Affected by ALS*. Washington, DC: The ALS Association, 2017.

[10] L. N. et al., *Assistive Technologies for People with Disabilities: Part II - Current and Emerging Technologies*. Brussels: European Union, 2018.

[11] J. A. L. et al., "Development of a touchless control system for a clinical robot with multimodal user interface," *International Journal of Advanced Computer Science and Applications (IJACSA)*, vol. 14, no. 9, pp. 1068–1075, 2023.

[12] H. O. E. et al., "Eye-tracking assistive technologies for individuals with amyotrophic lateral sclerosis," *IEEE Access*, vol. 10, pp. 41 952–41 967, 2022.

[13] Tobii Dynavox, "Eye-tracking solutions for assistive technology." [Online]. Available: https://www.tobiidynavox.com

[14] A. T. Duchowski, *Eye Tracking Methodology: Theory and Practice*, 3rd ed. Springer, 2017.

[15] J. L. Rosch and J. J. Vogel-Walcutt, "A review of eye-tracking applications as tools for training," *Cognition, Technology & Work*, vol. 15, pp. 313–327, 2013.

[16] A. Pradhan, K. Mehta, and L. Findlater, ""accessibility came by accident": Use of voice-controlled intelligent personal assistants by people with disabilities," in *Proceedings of the 2018 CHI Conference on Human Factors in Computing Systems*, 2018.

[17] L. De Russis and F. Corno, "On the impact of dysarthric speech on contemporary asr cloud platforms," *Journal of Reliable Intelligent Environments*, vol. 5, pp. 163–172, 2019.

[18] A. e. a. Khalifa, "Face recognition and tracking framework for human–robot interaction," *Applied Sciences*, vol. 12, no. 11, p. 5568, 2022.

[19] K. M. Marasinghe, "Assistive technologies in reducing caregiver burden among informal caregivers of older adults: a systematic review," *Disability and Rehabilitation: Assistive Technology*, vol. 11, no. 5, pp. 353–360, 2016.

[20] B. A. Technology, "Headmouse nano," 2024, accessed: February 2025. [Online]. Available: https://www.boundlessat.com/Mobility/Head-Eye-Control/HeadMouse-Nano

[21] PRC-Saltillo, "Nupoint head tracking for accent 1400," 2024, accessed: February 2025. [Online]. Available: https://store.prc-saltillo.com/nupoint-head-tracking-for-accent-1400-17416-1

[22] C. L. et al., "Mediapipe: A framework for building perception pipelines," 2019.

[23] E. M. et al., "Pose estimation for augmented reality: A hands-on survey," *IEEE Transactions on Visualization and Computer Graphics*, vol. 22, no. 12, pp. 2633–2651, 2016.

[24] R. Likert, "A technique for the measurement of attitudes," *Archives of Psychology*, vol. 22, no. 140, pp. 1–55, 1932.

[25] J. R. Lewis, "Measuring usability with the use questionnaire," *Usability and user experience*, vol. 12, no. 1, pp. 3–6, 2015.

[26] R. A. Schmidt and T. D. Lee, *Motor Learning and Performance: From Principles to Application*, 6th ed. Human Kinetics, 2018.

[27] K. M. Newell, "Motor skill acquisition," *Annual Review of Psychology*, vol. 32, no. 1, pp. 89–113, 1981.

[28] J. D. Daniel M. Wolpert and J. R. Flanagan, "Principles of sensorimotor learning," *Nature Reviews Neuroscience*, vol. 12, pp. 739–751, 2011.

A simulation platform combining the myokinetic interface with the AMI surgery for prosthetic control

Marta Gherardini[1], Benedicta Akweley Barnor[1], Flavia Paggetti[1], and Christian Cipriani[1]

Abstract— **Amputations of the upper and lower limbs can significantly impact psychological well-being and functional independence, limiting a person's ability to perform daily tasks. Artificial limbs aim to restore lost functionality by replicating the natural limb as closely as possible. To this aim, the ideal human-machine interface (HMI) should provide seamless connection with the natural sources of control and sensory feedback. Recent advances in surgical techniques and prosthetic technologies have enhanced residual limb functionality and enabled direct connections with peripheral neural pathways. This study introduces a simulation platform integrating the agonist-antagonist myoneural interface (AMI) with a myokinetic interface based on implantable magnets, to generate synthetic data on muscle deformation and magnet displacement as potential control signals for an assistive device. A transtibial amputation was simulated, replicating the natural agonist-antagonist mechanical connection between paired muscles. The model simulated muscle contractions and magnet implantation, which displacement was tracked using a localization algorithm. Results demonstrated a combined contraction and stretching of the agonist and antagonist muscles and the feasibility of accurately tracking implanted magnets via external sensors. These findings suggest that combining the AMI with magnet implantation could contribute to more intuitive prosthetic control in the future. In this view, this simulation platform provides a valuable pre-operative planning tool to optimize magnet placement and enhance HMI performance for individual patients.**

Keywords— Agonist-antagonist myoneural interface (AMI), Myokinetic control Interface, lower-limb prosthesis, Magnetic sensors, Magnetic tracking.

I. INTRODUCTION

In Italy, around 1.2 million people have motor impairments, and among these approximately 200,000 individuals underwent lower limb amputation [1]. About 80% of these amputations affect older adults, primarily due to complications from diabetes or vascular issues, while 10% are in middle-aged adults, and another 10% in younger people, mostly due to road accidents, followed by traumatic injuries, congenital conditions, or tumors. The level of amputation often depends on the underlying cause, although the most common is below-the-knee (transtibial, 47%). To treat transtibial amputations, in recent years researchers have explored and enhanced the functionality of prosthetic ankles and feet, by imitating the natural biomechanics [2], [3]. Most are passive devices, offering simplicity, lightweight, and reduced costs, however they are unable to provide power as natural muscles do, thus limiting complex activities and augmenting the risk of compensatory movements [3]. Conversely, while limited by higher costs, weight and power consumption, powered prostheses provide net positive work, enabling the restoration of a more natural gait. Powered prostheses can be controlled using surface electromyographic (sEMG) signals, employed for over 50 years for the control of upper limb prostheses [4], but only recently applied to lower-limb prostheses for the volitional control of knee and ankle joints during non-weight-bearing conditions [5], [6]. Nevertheless, surface electrodes positioned on the skin suffer from intrinsic drawbacks including poor selectivity, filtering effects caused by subcutaneous tissues, and movement artifacts, which can compromise control reliability [7], [8]. Another aspect to consider is that amputation surgeries usually rearrange muscles cushion the bone, creating a suitable interface for a prosthetic socket, yet devoting little attention to preserving residual muscle contraction capabilities [9]. In addition, the amputation destroys the natural interplay between agonist and antagonist muscles, which activates receptors responsible for proprioceptive sensations during motion, essential to close the loop of motor control [10]. Enhancing collaboration between clinicians and engineers and developing tools to optimize surgery based on prosthetic requirements could greatly improve the usability of prosthetic devices.

This need is further emphasized by the emergence in the past decades of a new portfolio of possibilities combining surgery and technology [11]. Regarding surgical techniques, different solutions were proposed to improve the biomechanical integration of the prosthesis with the body [12], the quality of the control sources [13], as well as the sensory feedback restoration [9]. Among them, the agonist-antagonist myoneural interface (AMI) was introduced as a procedure in which a pair of muscles with antagonistic functions are mechanically coapted to restore natural dynamic muscle relationships, and allow proprioceptive signals from mechanoreceptors within both muscles to be sent to the brain [9]. The AMI procedure was successfully implemented in lower-leg amputees and demonstrated to improve control over prosthetic devices compared to traditional amputations [10], [14]. At the same time, different

[1]The BioRobotics Institute, Scuola Superiore Sant'Anna, 56127 Pisa, Italy, and the Department of Excellence in Robotics and AI, Scuola Superiore Sant'Anna, 56127 Pisa, Italy.

The development of the myokinetic interface is supported by: the Italian Ministry of Research, under the complementary actions to the PNRR "Fit4MedRob - Fit for Medical Robotics" Grant (number PNC0000007); INAIL, in the framework of the BioARMnext (grant number: PR23-RRP3), NoProblem (grant number: PR23-CR-P3), and OsteoAMI (grant number: PR23-CR-P5) projects.

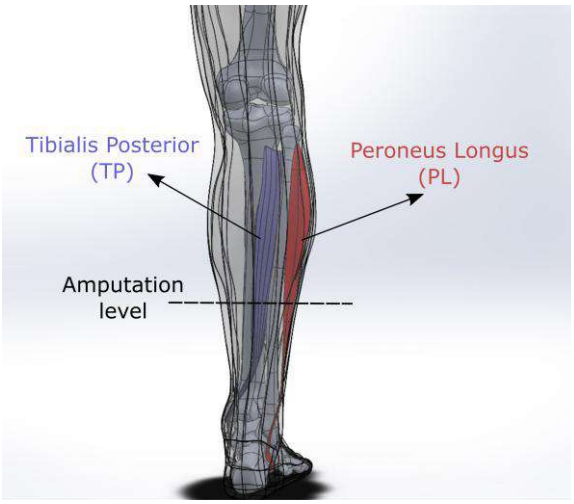


Fig. 1. 3D CAD model of the right lower-limb showing the two muscles selected for the AMI procedure (TP and PL). To simulate amputation, the two muscles were transected at the indicated level.

technologies were and are being developed to overcome the limitations of surface measurements, by recreating an intimate connection with the natural sources of control (muscles and nerves) [11]. For example invasive electromyography technology [15] demonstrated to provide better data quality than surface recordings [16]. Differently from traditional solutions measuring the electrical activity of the muscles, the myokinetic interface exploits implantable permanent magnets to monitor muscle contraction for control [17]. Specifically, small cylindrical magnets are inserted in target muscles through a minimally invasive surgical procedure, and external electronics is used to reconstruct the magnet displacement following muscle activation, with no need of percutaneous wires. The myokinetic interface was recently tested for the first time with an upper-limb amputee [18], yet its versatile architecture makes it readily transferable to other types of amputations, such as those at the lower limb.

We hypothesize that tracking magnets implanted within muscles could offer a more selective and granular measure of muscle activation compared to sEMG measurements. At the same time, control accuracy could be further enhanced by closing the feedback loop through the AMI procedure, enabling more realistic phantom motor imagery. In this study, we started to explore this possibility by developing a simulation platform that could be employed as a pre-surgical planning tool to optimize the integration of the AMI procedure with the myokinetic implant, to evaluate the potential effectiveness of such an interface. The simulated environment exploited a CAD model of lower limb muscles, and expanded a previously developed Finite Element Model (FEM) of muscle contraction [19] to simulate the AMI procedure by distally dissecting and coapting two muscles of the lower limb using a pulley-system simulating the biological tendon. Given as input the muscle degree of contraction, the model allowed to derive the corresponding deformation undergone by the muscles during contraction and elongation. FEM results were employed to simulate magnet implant and displacement according to muscle deformations, and such displacement was then reconstructed using a simulated array of magnetic field sensors and a localization algorithm.

Results showed that the FEM simulations reproduced the mechanical behavior described in the literature for muscles treated with the AMI, in which the contraction of the agonist results in a stretching of the antagonist [10]. Moreover, they showed that we could accurately track the displacement of magnets implanted in the muscles, both when the latter were contracting and being stretched. This work provides a viable tool to evaluate the usability of the myokinetic interface in combination with the AMI to control the movements of an ankle prosthesis. More in general, it introduces a versatile simulation framework that can be employed to reproduce different surgical and implant conditions and design patient-specific implantation and control strategies.

II. Materials and Methods

A. Finite Element Model of AMI and Muscle Contraction

A musculoskeletal model of the AMI was simulated using a Finite Element Model (FEM) of muscle contraction implemented in Comsol Multiphysics 5.5 (COMSOL Inc., Stockholm, Sweden), based on a mixture active strain approach proposed by Riccobelli and Ambrosi [20]. This model takes as input the muscle geometry, the fiber pennation angle and the microstructural degree of contraction γ, and outputs muscle deformation. The same model was already employed in [19], and has been experimentally validated for upper limb muscles in [21]. Muscle geometry was sourced from 3D CAD files of a healthy human lower limb comprising skin, muscles (including tendons), blood vessels and bones (Zygote, American Fork, US, Fig. 1). Only muscle-tendon units comprised between the fibula and tibial heads and the ankle joints of the right leg were considered to simulate transtibial amputation. Specifically, the muscle pair composed by the Tibialis Posterior (TP) and the Peroneus Longus (PL) was selected to simulate an AMI surgery aimed at achieving control over internal-external eversion of an ankle prosthesis. The tendons of the selected muscles were transected distally at the estimated boundary of the muscle-tendon unit [22], leaving only the muscle bellies of both muscles with an approximate length of 15 cm. Muscle distal ends were subsequently coapted to a geometry simulating a healthy tendon, which served as a biological pulley for the muscle pair as in traditional AMI. Both muscles and tendons were defined with materials that replicated biological tissue properties (see [19] for muscle parameters). Muscle fiber orientation (pennation angle, α) was defined for each muscle based on literature data, and was equal to 11° for the TP muscle and 12° for the PL muscle, respectively [22]. The distal tendon connecting the muscles was modeled as a material with a linear elastic behavior and an elastic modulus of 1 GPa [23]. A roller was applied to the central part of the tendon to simulate the synovial canal, used to provide a gliding mechanism in the AMI construction and avoid its displacement in the normal direction. At the proximal ends of the muscles, tendons were modeled as a spring (spring foundation in Comsol), considering the elastic modulus of human tendons [23]. Similarly, the muscle surfaces in contact

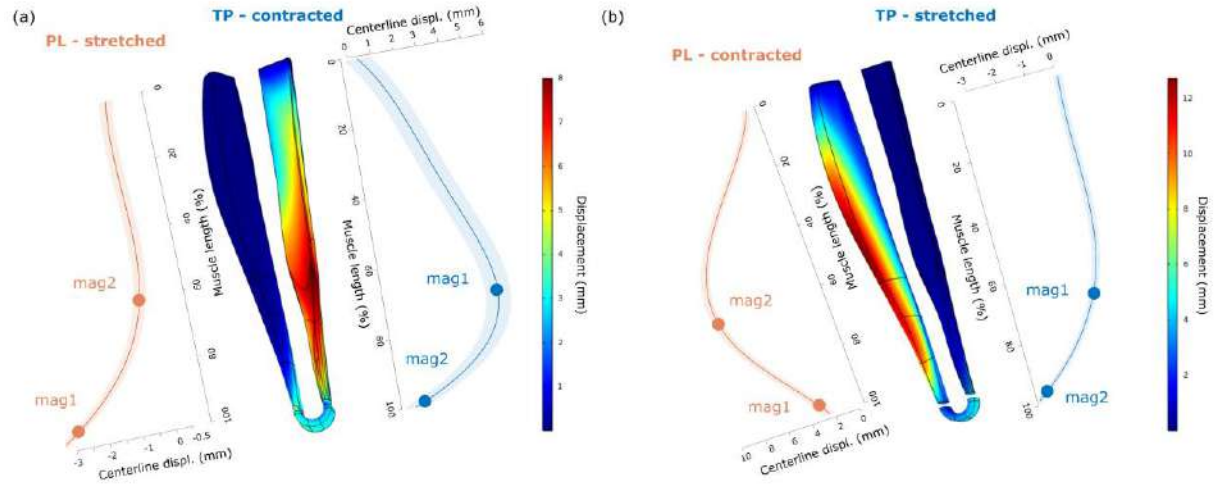


Fig. 2. FEM simulation results of muscle deformation. Color bars refer to the deformation obtained over the entire muscle volume. Specifically, mag1 was the magnet implanted in the point of maximum displacement, mag2 was implanted in the point of minimum displacement nearest to mag1. (a) The TP acted as the agonist and the PL as the antagonist muscle. Points along the TP centerline displaced along the muscle longitudinal axis according to a bell-shape curve. At the same time, the PL muscle was stretched in its distal section. Shaded areas represent the confidence interval of the muscle contraction model. (b) The PL acted as the agonist and the TP as the antagonist muscle. Points along the PL centerline displaced along the muscle longitudinal axis according to a bell-shape curve. At the same time, the TP muscle was stretched in its distal section.

with the bones were modeled through a spring foundation, considering the elastic modulus of skeletal muscles [24].

After modelling all elements, simulations were performed by alternatively contracting the agonist and antagonist muscle and deriving deformation data. Specifically, each muscle was incrementally activated by increasing the degree of contraction, γ, from 0 to 0.3 in steps of 0.005 (where 0.3 is approximately the maximum microstructural degree of contraction achieved in healthy muscles [25]). FEM simulation results were subsequently exported in Matlab (MathWorks, Natick, MA) to simulate magnet implantation and displacement. Specifically, the overall muscle deformation for different values of γ was obtained. In addition, each muscle centerline was derived from FEM simulation data by interpolating ~100 points in the center of the muscle belly. The displacement undergone by the points on the centerline along the longitudinal direction of the muscle was subsequently derived for both the agonist and antagonist muscle for $\gamma = 0.3$.

B. Magnet Implant Simulation

Two magnets were implanted in each muscle to simulate the application of the myokinetic interface exploiting differential measurements, which proved to be robust against external disturbances [19]. For both TP and PL, the longitudinal displacement of each point on the muscle centerline was used to determine potential magnet implantation sites for the magnet pairs. Specifically, the first magnet (mag1) was virtually implanted in the point undergoing maximum displacement, while the second magnet (mag2) was implanted in the nearest point to mag1 that showed almost null displacement, respecting the constraint of a minimum inter-magnet distance of 3cm [18]. This placement would allow to maximize the distance variation between the magnets, namely, the control signal of the assistive device. Candidate implantation sites were derived according to this procedure in correspondence of the maximum γ for the agonist muscle and the relative stretching for the antagonist one, and the procedure was repeated twice for the two agonist-antagonist configurations. As a results, two potential implant sites were derived for each magnet pair/each muscle. The final placement was empirically selected as the one that maximized the distance variation between the magnets both when the muscle acted as agonist and as antagonist.

Magnets were modeled as NdFeB axially magnetized cylindrical magnets (axial remanent magnetization Br = 1.27 T, radius = 2 mm, height = 2 mm). Contraction of the agonist and antagonist muscles were simulated in sequence. For each of them, magnet displacement was simulated by moving the magnets along 11-step trajectories, corresponding to equally spaced contraction degrees from 0% to 30%. A grid of 450 sensors was cylindrically arranged around the implantation site to sample the magnetic field produced by the magnets. The magnetic moment vectors of all magnets initially pointed radially (to maximize the magnetic field measured by the sensors), whereas during muscle contraction they rotated according to the fiber rotation predicted by the muscle model. The magnetic field was simulated by using an analytical model previously validated [26] and extensively employed in previous works [19]. A 4 mG white gaussian noise was added to the sensor recordings, to simulate the noise associated to actual 3-axis Hall-effect sensors in a real setup, akin to [19], [27]. Finally, sensor readings were fed to a localization algorithm which estimated the magnet poses (position and orientation) by exploiting numerical approximation methods. Extensive details on the localization algorithm can be found in previous works [17], [27]. Localization was repeated 10 times for each trajectory step by adding different random noises to the measurements, to account for variability in sensor recordings.

C. Performance Metrics

For each step of the trajectory and each repetition, the

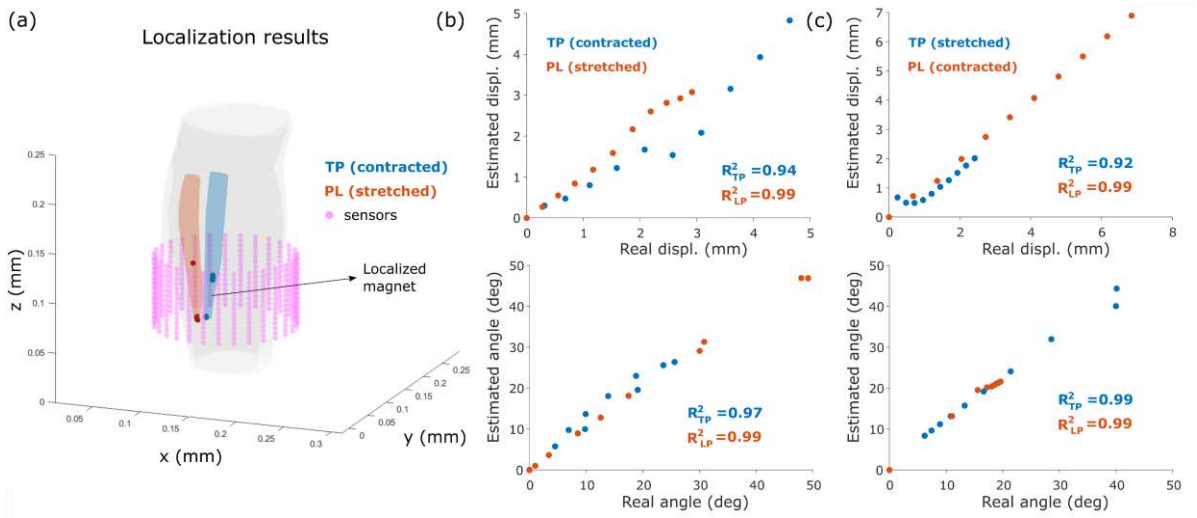


Fig. 3. Magnet localization results. (a) Results obtained when contracting the TP muscle. The figure shows the localized positions of the magnet pairs implanted in both TP and PL. An array of 450 sensors was positioned cylindrically around the implantation area to acquire the magnetic field generated by the magnets. (b) Real versus estimated displacement in terms of position (above) and orientation (below) when contracting the TP from 0 to 0.3 degree of contraction. The relationship between real and estimated displacement and angle proved linear for both magnet pairs ($R^2 \geq 0.94$, $p < 0.01$). (c) Real vs estimated displacement in terms of position (above) and orientation (below) when contracting the PL from 0 to 0.3 degree of contraction. The relationship between real and estimated displacement and angle proved linear for both magnet pairs ($R^2 \geq 0.92$, $p < 0.01$).

estimated (localized) displacement (Euclidean distance variation) and angle variation between the paired magnets with respect to their initial (rest) distance were derived. The median displacement and angle variation across repetitions were subsequently computed. The correlation between the estimated and the real value (i.e., the one set by the simulation) of the displacement/angle variation was then evaluated in terms of coefficient of determination (R^2) and associated *p* value. Finally, localization error was computed for both position and orientation. Specifically, considering the magnet pairs in TP and LG, position error was computed for each step and each repetition as the difference between the actual and estimated Euclidean distance between the magnets. Accordingly, the orientation error was derived as the difference between the actual and the estimated relative angle between the magnets.

III. Results

A. Finite Element Model of AMI and Muscle Contraction

For each agonist-antagonist muscle pair, the displacement of the points belonging to the muscle centerline along the muscle longitudinal axis for $\gamma = 0.3$ is first presented (Fig. 2a-b). Regarding the contracting (agonist) muscles, such displacement was described by a bell-shaped curve as a function of the distance from the muscle origin, with the maximum approximatively located in the middle of the muscle for PL (Fig. 2b), and more distally for TP (Fig. 2a). For the TP centerline, a maximum displacement of ~5.3 mm was derived, versus a maximum displacement of ~8.3 mm for PL. A different trend was observed for the antagonist behavior, as the displacement curves proved monotonically decreasing showing incrementally negative displacements towards the muscle distal end, corresponding to an increasing muscle stretching. Specifically, both antagonist muscles showed a maximum stretching of ~3.1 mm at the contact point with the connecting synovial canal. Such maximum stretching corresponded to a ~0.2 strain with respect to the overall muscle length. In all cases (agonist and antagonist behavior of both muscles), the displacement curves decreased towards the muscle origins, which were almost fixed.

B. Magnet Implant Simulation

Based on the derived displacement curves, mag1 was placed in TP and PL respectively in the points undergoing maximum positive and negative displacement when the TP was behaving as agonist and PL as antagonist muscle (Fig. 3a). This placement allowed to have both magnet pairs implanted towards the distal end of the muscles, with one magnet approximately in correspondence of the maximum longitudinal contraction/stretching in both the agonist and antagonist configuration (Fig. 3a-b). Specifically, mag1 was placed in TP in correspondence of 73% the total muscle length (where 0% indicates the proximal end), versus 98% for PL. Subsequently, mag2 was placed in the nearest point on the curve from the first magnet showing minimum (almost null) displacement. The latter resulted in the points corresponding to 99% the total muscle length for mag2 in TP, and 60% for mag2 in PL (Fig. 3a-b). Magnet pairs showed an initial Euclidean distance (relative angle) of 41 mm (128°) for TP, and of 58 mm (148°) for PL. Regarding magnet-to-sensor distance, mag1 and mag2 in PL showed a distance of 41.6 mm and 34.4 mm from the nearest sensor, respectively, against a distance of 55.9 mm and 51.2 mm derived for the corresponding magnets in TP.

Magnet trajectories were subsequently simulated and localization results derived for both configurations (TP contraction represented in Fig. 3a). Looking at localization results, when TP was contracting, a total displacement (angle variation) between magnet pairs of 4.8 mm (26.4°) was derived, against a real value of 4.6 mm (25.6°) (Fig. 3b). The magnets in PL showed a total displacement (angle variation)

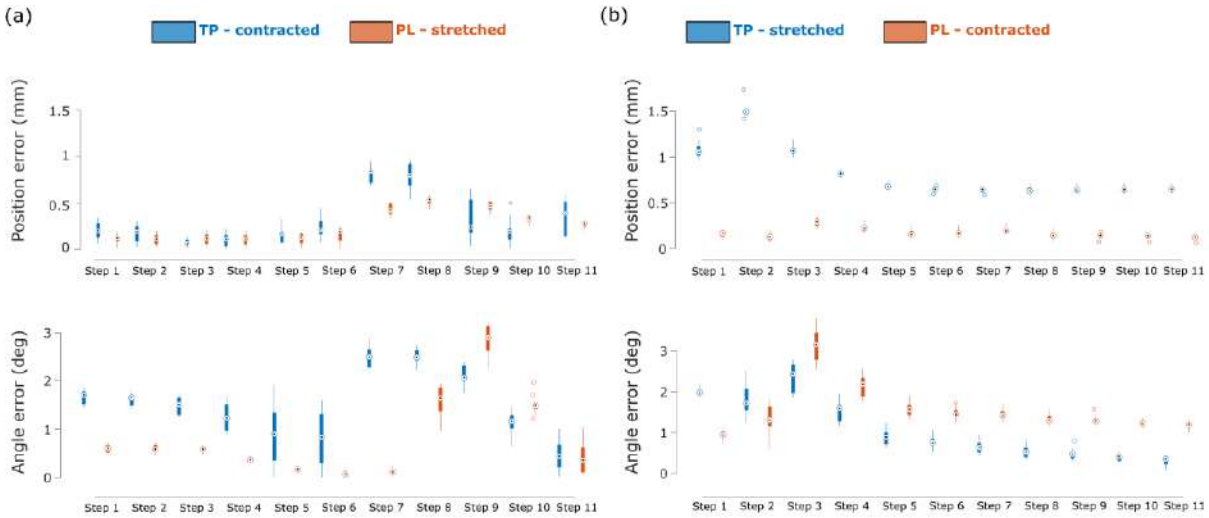


Fig. 4. Boxplots represent the localization error in terms of position (above) and orientation (below) obtained at each step (Step 1-11) of the magnet trajectory, considering all repetitions. Errors are reported both when (a) contracting the TP muscle (in blue). and stretching the PL muscle (in orange), and when (b) contracting the PL muscle (in blue). and stretching the PL muscle (in orange).

of 3.1 mm (46.9°), against a real value of 2.9 mm (49.2°). Differently, when PL was contracting, the magnets in TP showed a total displacement (angle variation) of 2 mm (44.5°), against a real value of 2.4 mm (40.0°) (Fig. 3c). The magnets in PL showed a total displacement (angle variation) of 6.9 mm (21.6°), against a real value of 6.8 mm (19.6°). In both agonist-antagonist configurations, the relationship between real and estimated displacement/relative angle proved always linear for both magnet pairs ($R^2 \geq 0.92$, $p < 0.01$) (Fig. 3b-c).

Regarding position errors along the 11-steps of the trajectories, when TP was contracting median errors proved always below 1 mm for both magnet pairs, with a maximum median error of 0.84 mm and 0.54 mm for the magnets in TP and PL, respectively. Similarly for orientation error, the magnets in TP generally showed higher error values, although a maximum median error of 2.9° was derived for magnets in PL against maximum median error of 2.5° for the magnets in TP (Fig. 4a). Similar error trends were found for position when the PL muscle was contracting (Fig. 4b). In this case, a maximum median position error of 1.49 mm and of 0.29 mm was found for the magnets in TP and PL, respectively. Conversely, regarding orientation, the magnets in PL generally showed higher errors, with a maximum median value of 3.1° versus 2.4° for the magnets in TP. Considering the agonist behavior of each muscle, the corresponding maximum median errors proved equal to 17% (9%) the total displacement (angle variation) travelled by the magnets in TP, and 4% (14%) that travelled by the magnets in PL. Overall, localization results demonstrated a good repeatability (precision) across different repetitions, with a maximum 25^{th}-75^{th} percentile range of 0.36 mm in terms of position, and of 1° in terms of orientation, both obtained during contraction of TP (Fig. 4a). These ranges respectively represented the 8% and 4% the total displacement and angle variation travelled by the corresponding magnet pair.

IV. Discussion and Conclusion

This work presented a simulation platform that allowed to reproduce the AMI surgical procedure applied to a pair of muscles, in this case muscles of the lower limb, and the subsequent implant of magnets in the muscle belly to implement a myokinetic control interface. Simulating agonist muscle contraction and combined antagonist stretching allowed to derive the amount of expected deformation in different areas of the muscles, and thus to identify potential optimal sites for magnet implantation. If combined with future work exploring a structured methodology for magnet placement, this platform could serve as a supporting tool for individualized pre-operative planning, as parameters such as muscle amputation level and contractility could be tuned to the patient's anatomy and pre-operative measurements (e.g., magnetic resonance imaging, EMG and ultrasound measurements). As a result, different magnet implantation sites and sensor arrangements could be virtually evaluated to maximize the interface efficiency for the control of an external assistive device, like an ankle prosthesis.

Results from the FEM simulations showed that, in line with literature results [10], the antagonist muscle was stretched in correspondence of a contraction of the agonist muscle (Fig. 2). A previous study evaluating two AMIs constructed between the Tibialis Anterior (TA) and the Lateral Gastrocnemius (LG) and the TP and PL of a transtibial amputee reported a fiber strain in the antagonist muscle of 0.16 (PL) and 0.8 (TA) when contracting the corresponding agonist muscles, respectively [10]. The FEM simulations implemented here resulted in a maximum strain of the antagonist muscles (both TP and PL) of 0.2 following contraction of the agonist one. Although fiber strain and muscle strain cannot be directly related, literature studies showed that length change of the muscle fibers tends to mirror that of the muscle-tendon unit if tendon compliance is poor [28], a condition that could apply to amputated muscles. Nevertheless, further clinical data are needed to comprehensively validate the developed model. Also, it

should be noted that current simulations did not consider contact in the synovial canal, thus friction was not taken into account. Future implementations should model the mechanics of tissue contact, for example by introducing a contact interface that interacts with the sliding tendon, to enhance the simulation reliability.

Localization errors generally proved higher for the magnets implanted in TP compared to those implanted in PL. These outcomes are in line with previous results from the literature which demonstrated that localization error positively correlates with magnet implantation depth [27]. Magnet-to-sensor distances obtained in the lower limb are generally larger than those obtained in the forearm, on which previous studies on the myokinetic interface were focused [17], [18]. Increasing magnet size for leg applications could be considered as an option to maximize the sensed magnetic field, thus potentially improving localization accuracy, especially for the antagonist muscles in which an overall smaller displacement is expected. Finally, in this work magnets were placed in the muscles following an empirical procedure aimed at maximizing displacement during both contraction and stretching. However, as anticipated above, we recommend investigating different placement strategies in future works to establish comprehensive guidelines based on patient-specific anatomy and placement rules, including those derived in previous works [27].

In conclusion, the simulation platform presented in this work, although open to future improvements and validations, could be effectively exploited as a testing platform to evaluate the functioning of the control interface prior to surgery, and help planning magnet implantation. Notably, it could also be readily translated to other applications, for example other level of lower-leg amputations or amputations at the upper limb.

REFERENCES

[1] P. K. Sadowski, S. Battista, G. Leuzzi, L. G. Sansone, and M. Testa, "Low Back Pain in People with Lower Limb Amputation: A Cross-Sectional Study," *Spine (Phila Pa 1976)*, vol. 47, no. 22, 2022, doi: 10.1097/BRS.0000000000004422.

[2] R. Gehlhar, M. Tucker, A. J. Young, and A. D. Ames, "A review of current state-of-the-art control methods for lower-limb powered prostheses," 2023. doi: 10.1016/j.arcontrol.2023.03.003.

[3] M. Asif *et al.*, "Advancements, Trends and Future Prospects of Lower Limb Prosthesis," *IEEE Access*, vol. 9, 2021, doi: 10.1109/ACCESS.2021.3086807.

[4] H. Schmidl, "The I.N.A.I.L. Myoelectric B/E Prosthesis," *Orthotics and Prosthetics*, vol. 19(4), pp. 298–303, 1965.

[5] L. J. Hargrove, A. M. Simon, R. Lipschutz, S. B. Finucane, and T. A. Kuiken, "Non-weight-bearing neural control of a powered transfemoral prosthesis," *J Neuroeng Rehabil*, vol. 10, no. 1, 2013, doi: 10.1186/1743-0003-10-62.

[6] A. Cimolato, J. J. M. Driessen, L. S. Mattos, E. De Momi, M. Laffranchi, and L. De Michieli, "EMG-driven control in lower limb prostheses: a topic-based systematic review," 2022. doi: 10.1186/s12984-022-01019-1.

[7] C. J. De Luca, L. Donald Gilmore, M. Kuznetsov, and S. H. Roy, "Filtering the surface EMG signal: Movement artifact and baseline noise contamination," *J Biomech*, vol. 43, no. 8, 2010, doi: 10.1016/j.jbiomech.2010.01.027.

[8] T. A. Kuiken, M. M. Lowery, and N. S. Stoykov, "The effect of subcutaneous fat on myoelectric signal amplitude and cross-talk," *Prosthet Orthot Int*, vol. 27, no. 1, 2003, doi: 10.3109/03093640309167976.

[9] S. Srinivasan *et al.*, "On prosthetic control: A regenerative agonist-antagonist myoneural interface," *Sci Robot*, vol. 2, no. 6, 2017, doi: 10.1126/scirobotics.aan2971.

[10] T. R. Clites *et al.*, "Proprioception from a neurally controlled lower-extremity prosthesis," *Sci Transl Med*, vol. 10, no. 443, 2018, doi: 10.1126/scitranslmed.aap8373.

[11] D. Farina *et al.*, "Toward higher-performance bionic limbs for wider clinical use," 2023. doi: 10.1038/s41551-021-00732-x.

[12] J. S. Hebert, M. Rehani, and R. Stiegelmar, "Osseointegration for lower-limb amputation: A systematic review of clinical outcomes," 2017. doi: 10.2106/JBJS.RVW.17.00037.

[13] T. A. Kuiken, A. K. Barlow, L. J. Hargrove, and G. A. Dumanian, "Targeted muscle reinnervation for the upper and lower extremity," *Techniques in Orthopaedics*, vol. 32, no. 2, 2017, doi: 10.1097/BTO.0000000000000194.

[14] H. Herr and M. J. Carty, "The Agonist-antagonist Myoneural Interface," *Techniques in Orthopaedics*, vol. 36, no. 4, 2021, doi: 10.1097/BTO.0000000000000552.

[15] R. F. Weir, P. R. Troyk, G. A. DeMichele, D. A. Kerns, J. F. Schorsch, and H. Maas, "Implantable myoelectric sensors (IMESs) for intramuscular electromyogram recording," *IEEE Trans Biomed Eng*, vol. 56, no. 1, 2009, doi: 10.1109/TBME.2008.2005942.

[16] M. Ortiz-Catalan, B. Håkansson, and R. Brånemark, "An osseointegrated human-machine gateway for long-term sensory feedback and motor control of artificial limbs," *Sci Transl Med*, vol. 6, no. 257, 2014, doi: 10.1126/scitranslmed.3008933.

[17] S. Tarantino, F. Clemente, D. Barone, M. Controzzi, and C. Cipriani, "The myokinetic control interface: Tracking implanted magnets as a means for prosthetic control," *Sci Rep*, vol. 7, no. 1, 2017, doi: 10.1038/s41598-017-17464-1.

[18] M. Gherardini *et al.*, "Restoration of grasping in an upper limb amputee using the myokinetic prosthesis with implanted magnets," *Science Robot*, vol. 9, p. 3260, 2024, [Online]. Available: https://www.science.org

[19] F. Paggetti, M. Gherardini, A. Lucantonio, and C. Cipriani, "To What Extent Implanting Single vs Pairs of Magnets per Muscle Affect the Localization Accuracy of the Myokinetic Control Interface? Evidence from a Simulated Environment," *IEEE Trans Biomed Eng*, vol. 70, no. 10, 2023, doi: 10.1109/TBME.2023.3272977.

[20] D. Riccobelli and D. Ambrosi, "Activation of a muscle as a mapping of stress–strain curves," *Extreme Mech Lett*, vol. 28, 2019, doi: 10.1016/j.eml.2019.02.004.

[21] F. Paggetti, M. Gherardini, A. Lucantonio, and C. Cipriani, "Optimizing the Myokinetic Interface: A Finite Element Model to Predict Displacement in Amputated Muscles," in *submitted to ICORR2025*,

[22] R. S. Sopher, A. A. Amis, D. C. Davies, and J. R. T. Jeffers, "The influence of muscle pennation angle and cross-sectional area on contact forces in the ankle joint," *Journal of Strain Analysis for Engineering Design*, vol. 52, no. 1, 2017, doi: 10.1177/0309324716669250.

[23] N. Maffulli, P. Renström, and W. B. Leadbetter, "Mechanical properties of tendons," in *Tendon Injuries: Basic Science and Clinical Medicine*, Springer, 2005, pp. 14–21. doi: 10.1007/b137778.

[24] Y. N. Feng, Y. P. Li, C. L. Liu, and Z. J. Zhang, "Assessing the elastic properties of skeletal muscle and tendon using shearwave ultrasound elastography and MyotonPRO," *Sci Rep*, vol. 8, no. 1, 2018, doi: 10.1038/s41598-018-34719-7.

[25] T. J. Burkholder and R. L. Lieber, "Sarcomere length operating range of vertebrate muscles during movement," 2001. doi: 10.1242/jeb.204.9.1529.

[26] N. Derby and S. Olbert, "Cylindrical magnets and ideal solenoids," *Am J Phys*, vol. 78, no. 3, 2010, doi: 10.1119/1.3256157.

[27] M. Gherardini, F. Clemente, S. Milici, and C. Cipriani, "Localization accuracy of multiple magnets in a myokinetic control interface," *Sci Rep*, vol. 11, no. 1, 2021, doi: 10.1038/s41598-021-84390-8.

[28] G. A. Lichtwark and C. J. Barclay, "The influence of tendon compliance on muscle power output and efficiency during cyclic contractions," *Journal of Experimental Biology*, vol. 213, no. 5, 2010, doi: 10.1242/jeb.038026.

FlexPAL (Flexible Pneumatic Actuated Linkage): The future of assistive robotics to improve quality of life

Yinan Meng
School of Engineering
The University of Manchester
United Kingdom
yinan.meng@manchester.ac.uk

Lutong Li
School of Engineering
The University of Manchester
United Kingdom
lutong.li@manchester.ac.uk

Helen Dawes
Medical School, NIHR Exeter BRC
University of Exeter
United Kingdom
h.dawes@exeter.ac.uk

Andrew Weightman
School of Engineering
The University of Manchester
United Kingdom
andrew.weightman@manchester.ac.uk

Charlie C.L. Wang
School of Engineering
The University of Manchester
United Kingdom
changling.wang@manchester.ac.uk

***Abstract*—Over 1.3 billion people, about 16% of the global population, suffer significant mobility impairments as of 2024. People with mobility impairments usually struggle with performing activities of daily living (ADLs), reducing their living quality. Assistive robots are a solution to support ADLs. However, the rigid structure of current assistive robots may cause secondary injuries due to safety, comfort, and suitability challenges for delicate health conditions. To overcome these challenges, this research introduces a novel soft wheelchair-mounted assistive robot named FlexPAL (Flexible Pneumatic Actuated Linkage) to provide safer, more comfortable and user-friendly daily assistance for people with mobility impairments. FlexPAL's lightweight (3.88kg) modular design allows size adjustments for diverse user needs. Its soft design ensures users' safety through controlled and gentle assistance. Its adaptable structure integrates seamlessly into daily scenarios within its 400x400x400mm workspace, delivering precise assistance (mean error=15.95mm) for payloads up to 1kg, suitable for most ADLs. The usability was evaluated based on the user case study with one healthy participant. The results of this research illustrate the high potential of soft wheelchair-mounted assistive robotics (FlexPAL) to address the limitations of rigid systems by offering higher adaptability, safety (i.e. assistance and human-robot interaction) and user comfort, making it more effective for assistance.**

Keywords—Assistive robotics, assistive technology, soft robotics, assistance, activities of daily living

I. INTRODUCTION

Mobility impairments are common among people with neurological or orthopedic disorders, significantly affecting their life quality. Several conditions can lead to individuals experiencing mobility disability, including high-level spinal cord injury (SCI), multiple sclerosis (MS), muscular dystrophy (MD), cerebral palsy (CP) and stroke. These conditions can cause both upper and lower limb disability, significantly reducing functional independence and preventing individuals from performing activities of daily living (ADLs) such as feeding, dressing, or reaching for objects, which are essential for maintaining independence and quality of life [1, 2]. More than 1.3 billion people are suffering significant mobility impairments all over the world, and around 16.1 million people in the UK are reported as having a disability, representing 24% of the total population [3].

Due to limited medical resources, many individuals with mobility impairments may not receive adequate assistance. [2]. A wheelchair-mounted assistive robot can address people's needs by providing extended reach, dexterity, and adaptability directly integrated into the user's mobility device. These robotic devices enable users to perform tasks that would otherwise require assistance from caregivers, improving autonomy and reducing dependence on others [4]. Additionally, wheelchair-mounted robots support users at home and work, enhancing satisfaction and social inclusion by enabling active engagement [5]. With their ability to provide safe, precise, and reliable support, wheelchair-mounted assistive robots (WMAR) are a valuable solution for improving the independence and quality of life of individuals with mobility impairments.

After the most well-known WMAR, MANUS, was introduced by a Dutch collaborative in 1984 [5], the development of WMAR accelerated, leading to the development of commercialized robots like KINOVA, which offers 6 or 7 degrees of freedom (DOF) for various applications, with the price up to £34,399 (Fig. 1) [6, 7].



Fig. 1. Current commercialised wheelchair assistive robot Kinova [7]

To the authors' knowledge, there are no applications of soft-WMAR. Most of the commercialized WMAR are rigid-structured systems, which have notable limitations. One significant drawback is their safety, as rigid robots can cause injuries even with limited force due to discomfort, collision or limited adaptability to human movements. As reported by Morris et al. in 2023, the safety concerns with the use of rigid assistive robotics include primary injuries, secondary injuries and infection control issues [4]. Rigid assistive robots lack natural compliance, which can lead to excessive force being applied to the user or objects, increasing the risk of bruises, pressure injuries, or joint stress. These systems may fail to adjust dynamically during physical interaction, increasing the risk of strain or collision injuries, especially in the case of mechanical failure [8]. Another major limitation of rigid robotics is their reliance on the rigid body structure, which often requires more space for movement [9]. Due to their limited flexibility, rigid robots may struggle to perform tasks within confined or cluttered environments, such as small homes or crowded public spaces, where space for movement is limited. In many cases of daily living, especially for people who live in small apartments, these rigid robots do not have enough space to operate effectively. For example, the Kinova Gen3 robotic arm and the FlexPAL system share a similar maximum reach of approximately 890 mm. However, the footprint requirements of these systems differ considerably. Articulated robotic arms, such as the Kinova Gen3, require additional clearance near the base due to joint movements. For example, if the end-effector must reach a target within 410 mm of the mounting position, the Kinova arm's closest joint needs at least 410 mm of operational space. The metal links of rigid robots can also appear intimidating, particularly to children and the elderly, making them hesitant to engage with new devices or technologies [10, 11]. Furthermore, the risk of collisions during close human-robot interactions adds to users' concerns, highlighting the need for more adaptive and user-friendly alternatives in assistive robotics [12]. These limitations emphasize the importance of exploring softer, more flexible robots for safe and effective assistive applications.

Soft assistive robots offer superior adaptability, comfort, and safety in human interactions, making them ideal for overcoming the limitations of rigid systems. Their high curvature flexibility enables effective operation in confined spaces [13], while compliant materials enhance safety and comfort [14, 15]. Their lightweight design further supports home use, particularly in portable or wearable applications, allowing seamless integration with assistive technologies [16]. Despite rapid advancements in soft assistive robotics, most research has focused on wearable devices [17, 18], with limited attention to wheelchair-mounted solutions.

Thus, this research aims to design and develop a soft-WMAR that allows people with mobility impairments to use it at home. The structure of this paper is as follows: the *Method section* introduces the design, development and control method of a novel soft assistive robotic named FlexPAL (Flexible Pneumatic Actuated Linkage). In the same section, the functionality and usability evaluation experimental set-up are described. The functionality and usability evaluation results of FlexPAL are demonstrated and discussed in *Result and Discussion sections*. *The conclusion section* summarizes the key contributions, addressing the limitations of this research and proposing the future research direction of assistive robotics.

II. METHOD

A. Design and development of FlexPAL

As the literature identified, assistive robotics should be safe, easy to use and can support users in performing ADLs [12]. According to the user's need, a soft assistive robotics named FlexPAL was developed that can be attached to a wheelchair to provide assistance for people with disability (Fig. 2). The main body of the FlexPAL was designed and assembled using three modular arm segments, allowing customization to meet the diverse needs and preferences of different users.

The FlexPAL consists of nine off-the-shelf bellows (V6-00325 from Freudenberg), each with three parallel chambers. To counteract shear forces, the bellows have a 2 mm wall thickness with a 59 mm outer diameter. The working length for each bellow ranges from 80 mm to 220 mm

Key features include a PLA-printed hard plate on the top and bottom of the bellows and a lightweight 0.45 kg gripper mounted on the lower segment, forming the base of the end-effector. The total mass of FlexPAL is 3.88 kg, with a load capacity of 1 kg (Table I). It achieves a maximum range of 420 mm between full extension and compression and a bending angle of up to 100 degrees.

Conductive springs are used to generate inductive signals for the proprioception of FlexPAL. The extension springs were made of piano steel wire (an outer diameter of 4.0 mm, and a wire diameter of 0.4 mm), resulting in the spring with a force rate of 0.054 N/mm. Their minimal force ensures no interference with joint movement. In each segment, three springs are fix*ed to* the outer chamber ridge using fixing rings, aligning their deformation with the air chamber's movement for accurate motion representation and preventing buckling during joint movement, which reduces error during proprioception network training.

The FlexPAL system utilizes a pneumatic actuation mechanism consisting of nine independently controlled pump units. Each chamber is regulated by a dedicated YOUCHEN VN-C1 brushless pump, integrated with two 3-way, 2-position valves to enable rapid switching between extension and compression. This configuration allows real-time pressure control at frequencies of up to 50 Hz, ensuring precise and responsive actuation. The operating pressure for each chamber ranges from -80 kPa to 40 kPa, providing a low-pressure actuation scheme designed to ensure user safety. Each pump operates at a noise level of 58 dB, ensuring quiet operation, and weighs 1100 g, contributing to a total pump system weight of approximately 12 kg. This weight allows for convenient installation of the pump system under a wheelchair, enhancing portability and usability for individuals requiring assistive support.

The FlexPAL system is mounted on a wheelchair using a custom-designed bracket, 3D-printed from PLA-CF (carbon fiber-reinforced polylactic acid) for a balance of strength and lightweight properties. This mounting structure allows for

secure attachment while minimizing additional weight. The design is adaptable, enabling customization based on different wheelchair models to ensure a stable and user-specific fit.

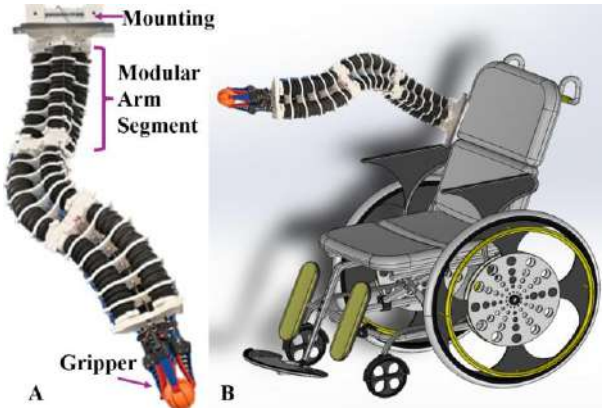


Fig. 2. Illustration of FlexPAL (A) and the assemble on a wheelchair (B) (Wheelchair copyright Mr Gean Hay)

TABLE I. SPECIFICATION OF THE FLEXPAL

Profile specification	Value
Profile size (mm)	180 x 180 x 940
Workspace (mm)	400 x 400 x 400
Elongation Range (mm/per module)	80-220
Max Bending Angle (Deg)	100
Pressure Range (Each Chamber) (kPa)	[-80, 40]
Self-Mass (kg)	3.88
Max Payload (kg)	1
Grasping Capability (Diameter-mm)	50
Manufacturing cost/per system (£)	9000

B. Perception and Control method of FlexPAL

To achieve proprioceptive feedback in FlexPAL, we adopted the method described in our previous work [19]. The proposed learning pipeline constructs the mapping function f_{smap} for proprioception through a two-stage process. First, a feedforward neural network (N_{smap}) is trained in simulation using a large dataset to capture the fundamental mapping function. Second, a lightweight network (N_{s2r}) is developed for sim-to-real transfer, trained with a smaller dataset collected from the physical environment. The datasets from the simulation and the real environment are utilized sequentially to train N_{smap} and N_{s2r}, ensuring accurate sim-to-real adaptation. This method provides precise proprioceptive feedback, facilitating robust and adaptive control of FlexPAL in dynamic and real-world conditions.

$$[T^{real}, R^{real}] = f_{smap}(s^{real}) \approx N_{s2r}\left(N_{smap}(s^{real})\right) \quad (1)$$

In this equation, s represents the spring signal with 9 dimensions. The real-world transformation (T^{real}) and rotation (R^{real}) are determined by the mapping function f_{smap}. This mapping function approximates the output of the feedforward neural network (N_{smap}), which takes as input the output of the lightweight sim-to-real transfer network (N_{s2r}) applied to the given real-world state signal (s^{real}).

During data acquisition for training, T^{real} and R^{real} are collected using a motion capture system. This system is utilized exclusively for the training phase to provide ground truth labels for real-world transformation and rotation. Once training is complete, the proprioception of the soft joints is derived solely from the spring sensor signals, utilizing the mapping function f_{smap}. This approach ensures the system remains independent of external motion capture during operation, relying entirely on the internal sensors of the FlexPAL.

The flowchart in Fig. 4 outlines the control method for FlexPAL, beginning with the desired target space, P^{ref}, which defines the desired transformation ($T^{desired}$) and rotation ($R^{desired}$) of the manipulator's end-effector (Fig. 3). The trained proprioception mapping function (f_{smap}) processes the sensor signals (s) from the geometry-based spring sensors to estimate the real-world transformation (T^{real}) and rotation (R^{real}) of the manipulator. These estimated values are compared with the desired target values to compute the errors in both transformation and rotation. The resulting error signals are then processed by a gradient control method that operates directly in the sensor space, effectively addressing discrepancies and generating sensor signals (s).

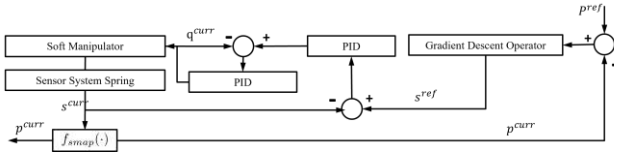


Fig. 3. Flowchart of sensor space gradient decent method for FlexPAL

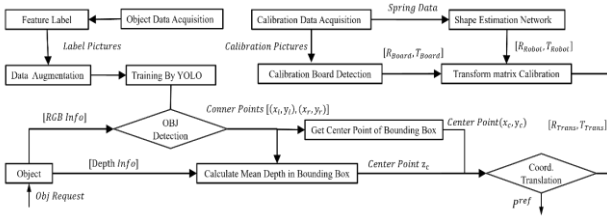


Fig. 4 Flowchart of pick and place control method for FlexPAL



Fig. 5 Data labeling and augmentation were performed using YOLO with data captured from an RGB-D camera.

The sensor signals are converted into actuation commands using a PID controller, which regulates the pressures in the soft chambers to achieve the required motion. This iterative process ensures the manipulator gradually aligns with the desired target state. The system operates within a continuous feedback loop, where updated sensor signals and error computations refine the manipulator's pose and orientation until the errors are minimized. This control strategy leverages the consistency and robustness of the sensor space for precise, adaptive manipulation.

To achieve assistance for ADLs (e.g. feeding or reaching objects), high-precision pick and place control is required. The pick and place control method for FlexPAL is illustrated in Fig. 4, comprising two key modules: ***Object Detection and Calibration.*** The Object Detection module employs a YOLO (You Only Look Once) model for real-time object detection. For example, in the experimental test for picking and placing a ball from a plate, the object detection model was trained using labelled data, as shown in Fig. 5. To enhance the model's robustness, we applied data augmentation techniques, which involve systematically altering the training images to improve the model's ability to generalize across different environments and lighting conditions. The Calibration module aligns sensor data with the robot's coordinate system through a shape estimation network and transformation matrix calculations. This process enables the conversion of object coordinates from the camera frame to the robot's coordinate system, ensuring accurate positioning for manipulation tasks

C. Evaluation experiment set up

Current assistive robots designed for individuals with mobility impairments must effectively support ADLs. Among these, feeding and dressing are the most common tasks, both of which demand high precision and safety in the robot's pick-and-place functionality. These tasks involve delicate interactions with objects and the human body, requiring the robot to adapt to various materials, positions, and user-specific needs [20]. For instance, a study on a dressing assistance robot highlights the importance of physical contact safety and the need for robots to adapt to dynamic contexts during dressing tasks [21]. Similarly, research on a robot-assisted feeding system emphasizes the necessity of comprehensive safety checks and adaptable control to cater to users with mobility impairments [22]. Ensuring safety and precision in these functions is critical to enhancing the usability and reliability of assistive robotics. In our research, functionality and usability evaluation of FlexPAL was conducted.

1) Functionality evaluation set-up

To evaluate the accuracy of FlexPAL, a two-stage experiment was conducted, encompassing random sampling and trajectory-following tests. In the first stage, random sampling was performed within the FlexPAL workspace, with over 500 random samples collected. This stage aimed to quantify the positional accuracy across the workspace. Non-parametric statistical analysis Kernel Density Estimation (KDE) was employed to analyze the system's error distribution. The KDE provided a robust visualization of the error data, facilitating an understanding of the overall consistency and precision of the FlexPAL's control system. In

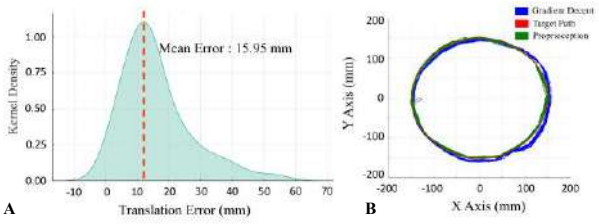


Fig. 6 Illustration of FlexPAL control accuracy through a Kernel Density Plot from a random sampling experiment (A) and trajectory tracking experiment of a circle with 150mm radius (B)

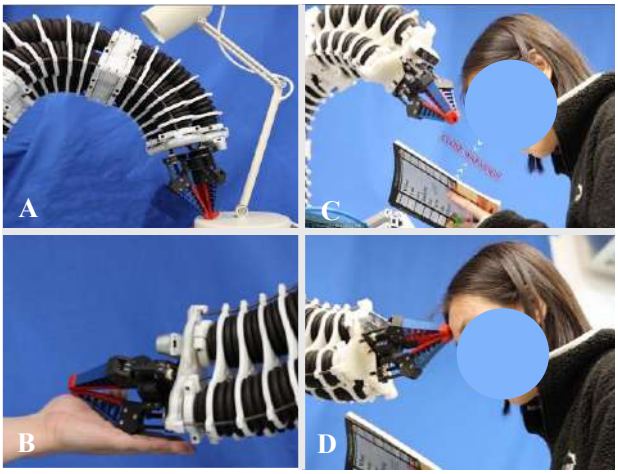


Fig. 7 Demonstration of daily assistance provided by FlexPAL (A: FlexPAL assisting a user in turning on a lamp; B : Physical interaction between FlexPAL and a human hand; C and D: FlexPAL monitoring and helping to maintain the distance between a book and the user's eyes during reading; more details can be seen in the showcase video https://www.youtube.com/watch?v=FcFkLvHGoXo)

the second stage, a trajectory-following test was conducted to evaluate its ability to perform continuous motion along a predefined path. The experiment involved following a circular trajectory with a radius of 150 mm. Target positions, current FlexPAL positions, and estimated positions were captured using a Vicon motion capture system and a proprioception network, respectively. For network training, the Adam optimizer was employed with a learning rate of 0.01 and a batch size of 128. The dataset, comprising 5000 samples from the simulator and 1000 samples from the physical setup, was divided into training, validation, and test sets.

2) Usability evaluation set-up

One healthy female from our research group participated in the usability evaluation for FlexPAL. Three user cases were conducted during this stage, including assisting users in turning on a lamp, monitoring the reading distance between the eyes and books, and evaluating physical contact between FlexPAL and the human hand to assess its ability to assist with ADLs and facilitate human-robot interaction. A focus group was conducted with one participant after identifying the user's satisfaction with FlexPAL.

According to the ethical requirement of the University of Manchester and NHS Health Research Authority, this research did not require ethical approval.

III. RESULTS

A. Functionality evaluation result: Control accuracy of FlexPAL

The KDE plot illustrates the distribution of errors observed during the random sampling experiment. The mean error was determined to be 15.59 mm, with the majority of errors tightly clustered around this value, as indicated by the sharp peak in the KDE plot (Fig. 6). This clustering highlights the consistency of the FlexPAL system, with minimal outliers, ensuring reliable positional accuracy throughout the workspace. The trajectory-following test confirmed FlexPAL's capability to handle complex motion tasks, validating its precision in real-time dynamic environments. The results demonstrated that FlexPAL maintained a smooth and continuous trajectory, closely adhering to the circular path. This capability is particularly important for tasks such as reaching, grasping, and interacting with objects in cluttered or unstructured settings, where accurate and responsive control is essential.

B. Usability evaluation results

The ability of FlexPAL to assist ADLs with safe and user-friendly human-robot interaction was demonstrated through a user case study, showcasing its practical application and effectiveness in real-world scenarios. The three different scenarios shown in Fig. 7 include assisting a user in turning on a lamp, monitoring and helping to maintain the distance between a book and the user's eyes during reading, and engaging in physical interaction between FlexPAL and a human.

IV. DISCUSSION

The results from both experiments collectively demonstrate that FlexPAL achieves a high level of positional precision, with errors well within acceptable thresholds for assistive tasks. The consistent performance across both random sampling and trajectory-following tasks highlights its suitability for assisting ADLs. These results affirm the potential of FlexPAL as a reliable and effective tool for applications requiring precision and adaptability in human-robot interaction.

Good usability is one of the most important requirements for both rehabilitation devices and assistive robotics, particularly those designed for home use [23, 24]. According to feedback from the focus group, the participants found FlexPAL to be comfortable and safe to use, attributing these qualities to its soft materials and user-friendly appearance. The modular design not only reduced physical discomfort during interaction but also minimized psychological barriers, especially for elderly users or those with limited mobility. Additionally, the participant expressed a strong willingness to use FlexPAL at home, emphasizing its lightweight design as a key factor in its integration into daily life. Furthermore, compared to currently commercialized WMAR (e.g. KINOVA up to £34,399 [7]), FlexPAL (£9,000) offers a more cost-effective solution, enhancing accessibility for people with mobility challenges and improving their quality of life.

Safety of physical human-robot interaction is one of the major requirements as well as the challenges of assistive robotics [8]. As emphasized by Bicchi et al. (2009), without proper safety measures, robots can pose significant risks during physical contact with humans [25]. This emphasizes that ensuring safety in physical human-robot interaction is paramount for the effective and responsible integration of assistive robots into environments where they interact closely with humans. Thus, assistive robotics must incorporate compliant mechanisms to ensure gentle and adaptive contact, minimizing the risk of injury during use. The common approaches to enhancing interaction safety include the use of compliant mechanisms, advanced control strategies, and biocompatible materials [26, 27]. For FlexPAL, soft biocompatible materials, specifically rubber, are used to construct the chambers, ensuring safety during physical contact with users.

In addition, unlike other WMAR, FlexPAL not only assists with ADLs but also actively monitors users' activities to help prevent the risk of injury. This dual functionality highlights FlexPAL's advanced design and adaptability. Its ability to assist with ADLs, such as reaching for objects or maintaining appropriate reading distances, ensures users can perform essential tasks independently. Meanwhile, its integrated monitoring system enhances user safety by detecting potential risks, such as improper posture or hazardous movements, and adapting its actions accordingly. This proactive approach to injury prevention sets FlexPAL apart from traditional assistive robots, emphasizing its role not only as a tool for physical assistance but also as a support for user well-being. These advantages make FlexPAL a comprehensive and user-centered solution for individuals with mobility impairments.

Additionally, customization is always the key desired feature for both rehabilitation and assistive robotics [28, 29]. Considering the varying levels of disability, the length of users' arms, and different home settings, the required size of a WMAR may vary. However, current commercialized assistive robots are designed in a generic size, making them unsuitable for diverse user needs. The participant also highlighted a preference for the modular design of FlexPAL, which enables customization to meet individual needs and enhances the accessibility of assistive devices to users.

Limitation

Despite its advantages, FlexPAL has certain limitations. The current design is not suitable for grasping objects weighing more than 1 kg, which restricts its ability to assist with a wider range of daily activities; increasing the payload capacity will be a focus for future development. Additionally, FlexPAL has yet to be evaluated by end-users, including therapists and individuals with mobility impairments. Future research will prioritize testing the system with individuals both with and without disabilities to gather feedback, refine its functionality, and ensure its effectiveness in real-world scenarios.

V. CONCLUSION

This research highlights the significant advantages of soft-WMAR, as exemplified by FlexPAL, in addressing the needs of individuals with mobility impairments. FlexPAL demonstrates its capability to provide sufficient assistance for various tasks, enhancing the independence and quality of life

for users. Its design prioritizes safety, reducing the risk of injury during human-robot interactions, particularly in scenarios where the robot works close to humans. The soft structure minimizes the risk of secondary injury, ensuring safe and gentle contact during assistance and physical contact. The high flexibility of its soft robotic structure allows it to adapt to diverse user needs and environments effectively. Additionally, the system offers superior user-friendliness, with a focus on appearance, texture, and comfort, ensuring a positive user experience. Furthermore, the modular and lightweight design of FlexPAL allows users to customize its size to accommodate different needs and adapt to various home environments. These combinations make FlexPAL a robust, adaptive, and user-centered solution in the field of WMAR.

ACKNOWLEDGMENT

This work was supported by the AMPI-The Advanced Machinery Productivity Institute [grant numbers 84646]. We sincerely thank AMPI for the essential funding and resources that facilitated the research and development in this work, as well as for their commitment to advancing scientific and industrial progress.

REFERENCES

[1] I. Rulik *et al.*, "Control of a Wheelchair-Mounted 6DOF Assistive Robot With Chin and Finger Joysticks," (in English), *Frontiers in Robotics and AI,* Original Research vol. 9, 2022-July-22 2022, doi: 10.3389/frobt.2022.885610.

[2] E. Warmerdam *et al.*, "Long-term unsupervised mobility assessment in movement disorders," *The Lancet Neurology,* vol. 19, no. 5, pp. 462-470, 2020, doi: 10.1016/S1474-4422(19)30397-7.

[3] E. Kirk-Wade, "UK disability statistics: Prevalence and life experiences," *House of Commons Library,* no. 09602, 2022.

[4] L. Morris, R. S. Diteesawat, N. Rahman, A. Turton, M. Cramp, and J. Rossiter, "The-state-of-the-art of soft robotics to assist mobility: a review of physiotherapist and patient identified limitations of current lower-limb exoskeletons and the potential soft-robotic solutions," *Journal of NeuroEngineering and Rehabilitation,* vol. 20, no. 1, p. 18, 2023/01/30 2023, doi: 10.1186/s12984-022-01122-3.

[5] B. J. F. Driessen, H. G. Evers, and J. A. v Woerden, "MANUS—a wheelchair-mounted rehabilitation robot," *Proceedings of the Institution of Mechanical Engineers, Part H: Journal of Engineering in Medicine,* vol. 215, no. 3, pp. 285-290, 2001, doi: 10.1243/0954411011535876.

[6] H. F. M. V. d. Loos, "VA/Stanford rehabilitation robotics research and development program: lessons learned in the application of robotics technology to the field of rehabilitation," *IEEE Trans Rehabil Eng,* vol. 3, no. 1, pp. 46-55, 1995, doi: 10.1109/86.372891.

[7] KINOVA. "KINOVA Assistive." https://assistive.kinovarobotics.com/ (accessed 22nd November, 2024).

[8] S. Haddadin, A. Albu-Schäffer, and G. Hirzinger, "Requirements for Safe Robots: Measurements, Analysis and New Insights," *The International Journal of Robotics Research,* vol. 28, no. 11-12, pp. 1507-1527, 2009, doi: 10.1177/0278364909343970.

[9] D. Trivedi, C. D. Rahn, W. M. Kier, and I. D. Walker, "Soft Robotics: Biological Inspiration, State of the Art, and Future Research," *Applied Bionics and Biomechanics,* vol. 5, no. 3, p. 520417, 2008, doi: https://doi.org/10.1080/11762320802557865.

[10] L. Li, S. Tyson, and A. Weightman, "Professionals' Views and Experiences of Using Rehabilitation Robotics With Stroke Survivors: A Mixed Methods Survey," (in English), *Frontiers in Medical Technology,* Original Research vol. 3, 2021-November-11 2021, doi: 10.3389/fmedt.2021.780090.

[11] L. Li, Q. Fu, S. Tyson, N. Preston, and A. Weightman, "A scoping review of design requirements for a home-based upper limb rehabilitation robot for stroke," *Topics in Stroke Rehabilitation,* pp. 1-15, 2021, doi: 10.1080/10749357.2021.1943797.

[12] P. Caleb-Solly, C. Harper, and S. Dogramadzi, "Standards and Regulations for Physically Assistive Robots," in *2021 IEEE International Conference on Intelligence and Safety for Robotics (ISR)*, 4-6 March 2021 2021, pp. 259-263, doi: 10.1109/ISR50024.2021.9419508.

[13] D. Rus and M. T. Tolley, "Design, fabrication and control of soft robots," *Nature,* vol. 521, no. 7553, pp. 467-475, 2015/05/01 2015, doi: 10.1038/nature14543.

[14] S. Coyle, C. Majidi, P. LeDuc, and K. J. Hsia, "Bio-inspired soft robotics: Material selection, actuation, and design," *Extreme Mechanics Letters,* vol. 22, pp. 51-59, 2018/07/01/ 2018, doi: https://doi.org/10.1016/j.eml.2018.05.003.

[15] S. Kim, C. Laschi, and B. Trimmer, "Soft robotics: a bioinspired evolution in robotics," *Trends in Biotechnology,* vol. 31, no. 5, pp. 287-294, 2013/05/01/ 2013, doi: https://doi.org/10.1016/j.tibtech.2013.03.002.

[16] Z. T. H. Tse *et al.*, "Soft Robotics in Medical Applications," *Journal of Medical Robotics Research,* vol. 03, no. 03n04, p. 1841006, 2018/09/01 2018, doi: 10.1142/S2424905X18410064.

[17] M. Pan *et al.*, "Soft Actuators and Robotic Devices for Rehabilitation and Assistance," *Advanced Intelligent Systems,* vol. 4, no. 4, p. 2100140, 2022, doi: https://doi.org/10.1002/aisy.202100140.

[18] E. Bardi, M. Gandolla, F. Braghin, F. Resta, A. L. G. Pedrocchi, and E. Ambrosini, "Upper limb soft robotic wearable devices: a systematic review," *Journal of NeuroEngineering and Rehabilitation,* vol. 19, no. 1, p. 87, 2022/08/10 2022, doi: 10.1186/s12984-022-01065-9.

[19] Y. Meng, G. Fang, J. Yang, Y. Guo, and C. C. L. Wang, "Spring-IMU Fusion-Based Proprioception for Feedback Control of Soft Manipulators," *IEEE/ASME Transactions on Mechatronics,* vol. 29, no. 2, pp. 832-842, 2024, doi: 10.1109/TMECH.2023.3320980.

[20] D. Feil-Seifer and M. J. Mataric, "Defining socially assistive robotics," in *9th International Conference on Rehabilitation Robotics, 2005. ICORR 2005.*, 28 June-1 July 2005 2005, pp. 465-468, doi: 10.1109/ICORR.2005.1501143.

[21] D. Delgado Bellamy, G. Chance, P. Caleb-Solly, and S. Dogramadzi, "Safety Assessment Review of a Dressing Assistance Robot," (in English), *Frontiers in Robotics and AI,* Original Research vol. 8, 2021-June-14 2021, doi: 10.3389/frobt.2021.667316.

[22] E. K. Gordon *et al.*, "An Adaptable, Safe, and Portable Robot-Assisted Feeding System," presented at the Companion of the 2024 ACM/IEEE International Conference on Human-Robot Interaction, Boulder, CO, USA, 2024. [Online]. Available: https://doi.org/10.1145/3610978.3641085.

[23] E. Q. Yumbla, Z. Qiao, W. Tao, and W. Zhang, "Human Assistance and Augmentation with Wearable Soft Robotics: a Literature Review and Perspectives," *Current Robotics Reports,* vol. 2, no. 4, pp. 399-413, 2021/12/01 2021, doi: 10.1007/s43154-021-00067-0.

[24] L. Fiorini *et al.*, "Assistive robots to improve the independent living of older persons: results from a needs study," *Disability and Rehabilitation: Assistive Technology,* vol. 16, no. 1, pp. 92-102, 2021/01/02 2021, doi: 10.1080/17483107.2019.1642392.

[25] A. Bicchi, M. A. Peshkin, and J. E. Colgate, "Safety for Physical Human–Robot Interaction," in *Springer Handbook of Robotics*, B. Siciliano and O. Khatib Eds. Berlin, Heidelberg: Springer Berlin Heidelberg, 2008, pp. 1335-1348.

[26] H. Modares, I. Ranatunga, F. L. Lewis, and D. O. Popa, "Optimized Assistive Human–Robot Interaction Using Reinforcement Learning," *IEEE Transactions on Cybernetics,* vol. 46, no. 3, pp. 655-667, 2016, doi: 10.1109/TCYB.2015.2412554.

[27] A. Mohebbi, "Human-Robot Interaction in Rehabilitation and Assistance: a Review," *Current Robotics Reports,* vol. 1, no. 3, pp. 131-144, 2020/09/01 2020, doi: 10.1007/s43154-020-00015-4.

[28] P. Bremner, U. Leonards, M. Giuliani, and M. S. Ahmed, "Customisation's impact on strengthening affective bonds and decision-making with socially assistive robots," (in English), *Frontiers in Robotics and AI,* Original Research vol. 11, 2024-October-14 2024, doi: 10.3389/frobt.2024.1384610.

[29] G. Yixing, C. Hyung Jin, and Y. Demiris, "User modelling for personalised dressing assistance by humanoid robots," in *2015 IEEE/RSJ International Conference on Intelligent Robots and Systems (IROS)*, 28 Sept.-2 Oct. 2015 2015, pp. 1840-1845, doi: 10.1109/IROS.2015.7353617.

Evaluation of a spring-loaded lumbar occupational exoskeleton with healthcare professionals

Sara Carmosino, Lorenzo Amati, Lorenzo Grazi, Nicola Vitiello, *Member, IEEE,* Francesco Giovacchini, Tommaso Bellandi, Emilio Trigili, *Member, IEEE,* Simona Crea

***Abstract*— Work-related musculoskeletal disorders significantly impact healthcare professionals during patient-handling tasks. This work presents the results of a study that evaluated a spring-loaded lumbar exoskeleton, called SAFE-T, in reducing the physical strain for caregivers. Fifteen healthcare professionals performed patient transfer and bed repositioning tasks in three conditions, without wearing the SATE-T and with SAFE-T using two different levels of assistance. A healthy volunteer simulated a partially collaborative patient. The effect of the exoskeleton was assessed through superficial electromyographic measurements, movement kinematics, and perceived exertion. Results showed that the exoskeleton significantly reduced muscle activation across back muscles, with both assistance levels demonstrating the effectiveness of this study. Specifically, muscle activity was significantly reduced in the right lumbar erector spinae (19-29%), thoracic erector spinae (10-21%), and left erector spinae iliocostal (23-29%) muscles. The global Rated Perceived Exertion scores decreased significantly in both tasks when using the SAFE-T ($p < 0.05$). These findings highlight the potential of this device to reduce physical strain and potentially mitigate the occurrence of work-related disorders in healthcare professionals.**

I. Introduction

Work-related musculoskeletal disorders (WRMSDs) represent one of the leading causes of occupational disability in Europe [1]. Prolonged maintenance of uncomfortable postures and execution of repetitive movements are considered the main risk factors for developing these disorders, due to the biomechanical overload of the human joints [1]. WRMSDs are particularly common among healthcare professionals [2]. Manual patient handling activities, such as lifting, holding, or moving patients, apply high loads on caregivers' lower back [3]. In 2017, the rate of overexertion injuries for hospital workers was 57 per 10.000, about twice the average across all industries (30 per 10.000) [4]. The implementation of preventive measures is crucial to improve workplace ergonomic conditions and reduce WMSDs and injury risk [5] [6].

In recent years, there has been growing interest in back-support exoskeletons for preventing lower back pain among healthcare professionals and caregivers [7]. Although research efforts on exoskeletons for healthcare professionals are still in the early stages, the first studies show promising results [4].

Hwang et al. [8] assessed the effect of three passive back-assist exoskeletons (FLx ErgoSkeleton, V22 ErgoSkeleton, and Laevo V2.5) on the lower back muscle activities during simulated wheelchair-to-bed patient transfers. Results showed a reduction in lower back muscle activation. Turja et al. [9] assessed the effect of the Laevo exoskeleton (Laevo, The Netherlands) in the geriatric care setting, with initial results showing reduced physical strain on nurses during wheelchair transfers, eating, and hygiene activities. Most nurses reported that the exoskeleton reduced lower back strain when assisting the patient. Schmidbauer et al. [10] tested the CareExo Lift exoskeleton (HUNIC GmbH, Germany) for hospital care activities, including lifting and repositioning people from bed and supporting personal hygiene tasks. The caregivers perceived the exoskeleton as comfortable on the back, especially in the lumbar spine region. Lastly, Miura et al. [11] tested a powered back assist exoskeleton aimed to show a reduction in lumbar load when transferring a 60-kg patient mannequin from a seated to a standing position, and simulated the tasks with non-professional volunteers.

In this context, the present study provides a comprehensive evaluation of the effects of a novel spring-loaded occupational lumbar exoskeleton on 15 healthcare professionals in caregiving activities in long-term care facilities. The exoskeleton generates the assistive torques through a spring-loaded mechanism that mechanically encodes two torque-vs-angle profiles, making it adaptable to the different work activities of caregivers. The evaluation included instrumental measurements, namely trunk muscle electromyography (EMG) indexes and kinematics, and rated perceived exertion (RPE). Healthcare caregivers were professionals of long-term care facilities where patients with limited personal autonomy are supported in daily activities.

The study presented in this paper was promoted by the Fondazione Cassa Risparmio di Lucca within the Proximity Care project (Project No. IPROX221SN Proximity Care – prossimità, innovazione tecnologica per la rete di protezione socio-sanitaria delle aree interne nella provincia di Lucca).

The SAFE-T technology has been developed within the EU Mari4_YARD project (H2020-MG-2020-SingleStage-INEA) under Grant Agreement: 101006798.

S. Carmosino, L. Amati, L. Grazi, E. Trigili, N. Vitiello and S. Crea are with The BioRobotics Institute, Scuola Superiore Sant'Anna, Pontedera 56025, Italy, and with the Department of Excellence in Robotics & AI, Scuola Superiore Sant'Anna, Pisa 56127, Italy.

T.Bellandi is with Patient safety unit, Tuscany NorthWest Trust, Lucca, Italy.

F.Giovacchini is with IUVO S.r.l, Via Puglie 9, 56025 Pontedera, Pisa, Italy.

F. Giovacchini, N. Vitiello, and S. Crea have interests in IUVO Srl, which developed the SAFE-T and owns the related IP.

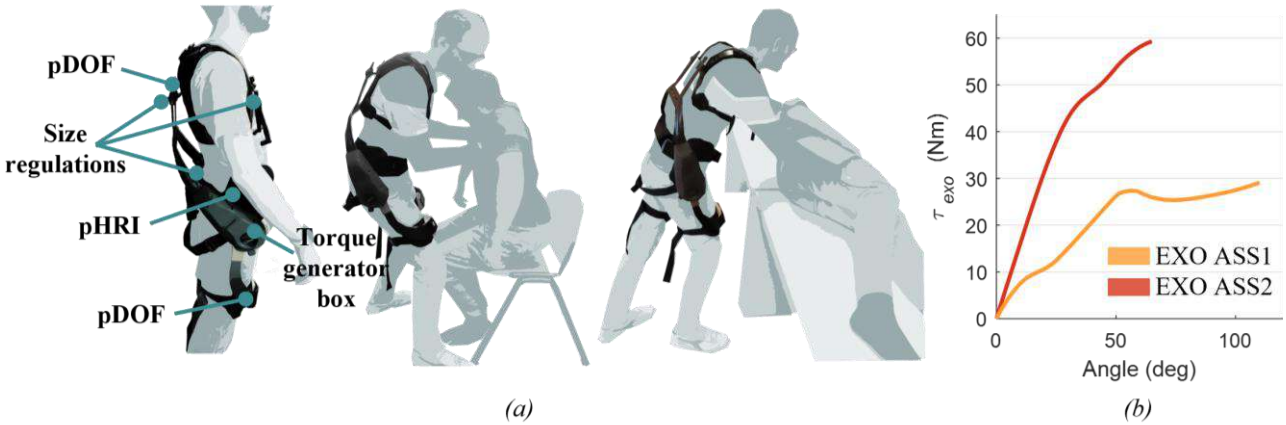


Fig. 1 Exoskeleton SAFE–T. (a) The main components of the exoskeleton are two torque generator boxes, the physical Human-Robot Interface (pHRI), passive degrees of freedom (pDOFs) and three size regulators. (b) Torque-Vs-Angle assistive profiles of the exoskeleton in the two modalities.

II. Materials and Methods

A. Spring-loaded lumbar occupational exoskeleton

The exoskeleton used in this study is called SAFE-T (System for Assisting the Flexion/Extension of the Trunk, Fig. 1). It is a spring-loaded lumbar occupational exoskeleton designed and developed by IUVO Srl (a spin-off company of Scuola Superiore Sant'Anna), within the European H2020 Mari4_YARD project. The exoskeleton is a modified version of the commercial lower-back exoskeleton MATE-XB (COMAU S.p.a., Italy), designed to reduce back strain during manual material handling activities, such as repetitive load lifting. The system weighs 3.5 kg and consists of four main components.

1. *Two torque generator boxes* (one for each side) are passive, spring-loaded actuation units that store and transform the elastic energy of parallel springs into assistive torque around the hip joint (τ_{exo}).
2. *A physical Human-Robot Interface (pHRI)* secures the device to the user's waist, trunk and legs, allowing the robot to transfer the assistive torque to the trunk and the legs.
3. A *passive degree of freedom (pDOFs)* are implemented to provide increased movement flexibility. The surface area has been expanded to improve pressure distribution and enhance overall user comfort during activities and a connector links the vest to the carbon fiber back frame (thoracic pDOF).
4. *Three size regulations* at the trunk, chest, and pelvis level allow the exoskeleton to be adapted to users with different anthropometries.

The peculiar characteristic of the present exoskeleton lies in the possibility for the user of selecting the most appropriate assistive profile for the specific task. A manual knob on each actuation unit allows the user to enable and disable the assistive torque or to choose between two different assistance profiles (ASS1 and ASS2). ASS1 can provide up to 30 Nm, while ASS2 up to 60 Nm, resulting in total peak torque at the lumbosacral joint of 60 Nm and 120 Nm, respectively. The two assistive profiles are designed to potentially support different job tasks, namely tasks involving relatively high trunk bending angle (such as transferring a patient from the bed to a chair or vice versa), or activities that require maintaining postures for extended periods with a relatively low trunk bending angle (such as caregiving tasks performed

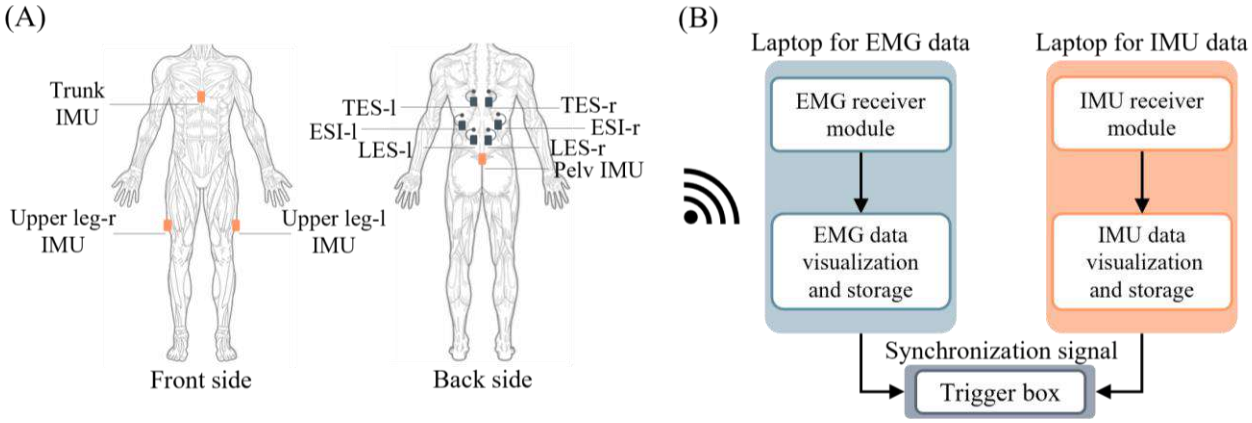


Fig. 2 Sensing system. (A) Schematic representation of the placement of EMG electrodes and IMUs sensors on the user's body. (B) Schematic representation in a block diagram of the measurement systems integration and communication.

on bedridden patients, including dressing or hygiene assistance).

B. Sensing system

A wireless EMG system (FREEEMG 1000, BT Bioengineering, Italy) was utilized to measure the activation of the participants' back muscles. Surface EMG probes were placed on the following muscles: left lumbar erector spinae (LES-l), right lumbar erector spinae (LES-r); left thoracic erector spinae (TES-l); right thoracic erector spinae (TES-r); left iliocostal erector spinae (ESI-l); right iliocostal erector spinae (ESI-r). The Xsens MTw motion capture system (XSens, The Netherlands) was utilized to measure the participant's movements (i.e., trunk flexion-extension and hip flexion-extension angles). Four inertial measurement units (IMUs) were placed on the following anatomical district: sternum; pelvis; upper left leg; and upper right leg. A FREEEMG Trigger Box (BTS Bioengineering, Italy) was used to synchronize the EMG and kinematic data offline. Fig. 2 shows the sEMG probes and IMUs placement and the network architecture of the acquisition system.

III. EXPERIMENTAL PROCEDURES

A. Participants and ethics approval

The project was supported by the management of the local health authority. Introductory meetings with caregivers and trial tests were conducted before the experimental sessions. These preliminary activities allowed for the organization of the experimental setup, following a participatory ergonomics approach, which was essential for the effectiveness of interventions aimed at improving workers' health [12]. The experiments took place at Hospice Villetta, RSA "Le Piane" (Castelnuovo in Garfagnana, Lucca, Italy) and at RSA "Paoli Puccetti" (Gallicano, Lucca, Italy). Fifteen caregivers were recruited to take part in the study (14 females, 1 male, age: 50.2 ± 12.1 years, height: 165.1 ± 6.2 cm, weight: 65.2 ± 14.1 kg). Participants did not report work limitations due to trunk or limbs musculoskeletal diseases. The study was approved by the Ethics Committee of Scuola Superiore Sant'Anna (approval n.24/2024) and followed the principles stated in the Declaration of Helsinki.

B. Experimental Protocol

Upon arrival, the participants received information about the study and the procedures and signed the written informed consent. With the help of the experimenters, the participants donned the exoskeleton and all size regulators were adjusted to ensure fit and comfort. The participants familiarized with the device for about 5 minutes, by performing free movements (such as trunk flexion and extension movements, with and without lifting objects), and simulating the subsequent experimental tasks. Before starting the experiments, commercial Ag/AgCl bipolar surface electrodes were placed on the muscles under their regular working clothes. Electrodes were placed following the SENIAM guidelines [13] and secured to the participant's skin using medical tape. The participants were asked to perform an isometric maximum voluntary contraction (MVCs) in three 5-second-long repetitions for each muscle, to be able to normalize EMG data and allow inter-condition and inter-subject comparison. The MVC was measured with the participants in a prone position following the procedures explained in [14]. IMU sensors were secured to the body segments of interest with the aid of elastic bands.

The experimental protocol (Fig. 3) consisted of a one-day testing session designed to simulate two fundamental caregiving tasks commonly performed in healthcare settings that do not require the use of mechanical lifts mandatorily. The first task, namely Patient Transfer Task (task #1), simulated a bed-to-chair transfer sequence and vice versa. The second task, namely Bed Repositioning Task (task #2), simulated patient repositioning procedures typically performed during daily hygiene care. In both tasks, a healthy volunteer acted as a patient with partial motor autonomy to ensure trial consistency. In particular, task #1 consisted of three distinct phases: (i) transfer from bed to chair, (ii) maintenance of a standing rest position, and (iii) transfer from chair back to bed. To maintain repetitive conditions, the bed height was adjusted to ensure maximum patient comfort and support during the task and remained constant among all participants. The chair was positioned at a 90° angle relative to the bed. Instead, task #2 involved simulating lateral patient movement, which required transferring the simulated patient

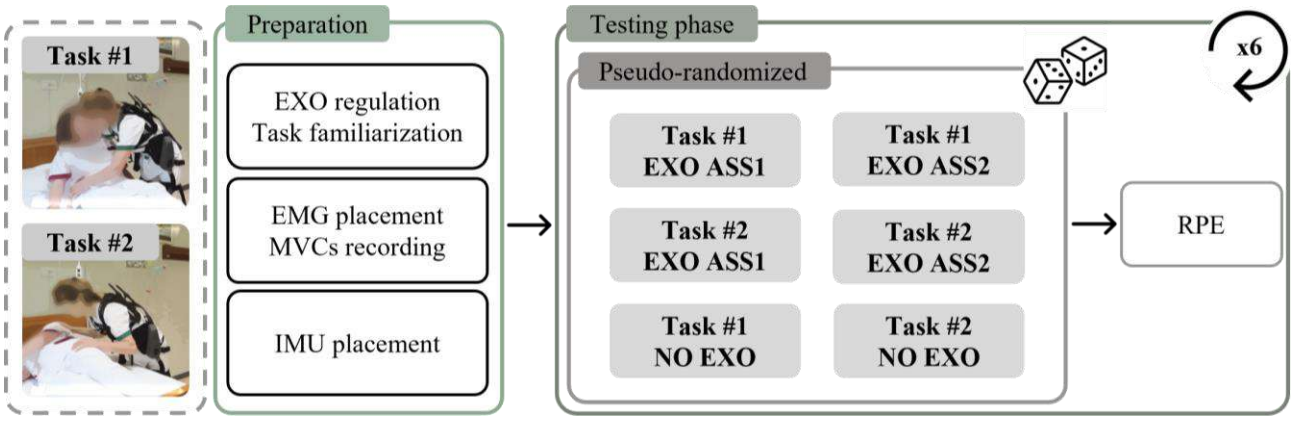


Fig. 3 Experimental protocol overview. The preparation phase includes exoskeleton regulation and familiarization, and placement of EMG and IMU sensors. During the testing phase, participants perform the task #1 and the task #2 in three different conditions (NOEXO, EXO ASS1, and EXO ASS2). At the end of each condition, participants complete questionnaires to assess effort (RPE).

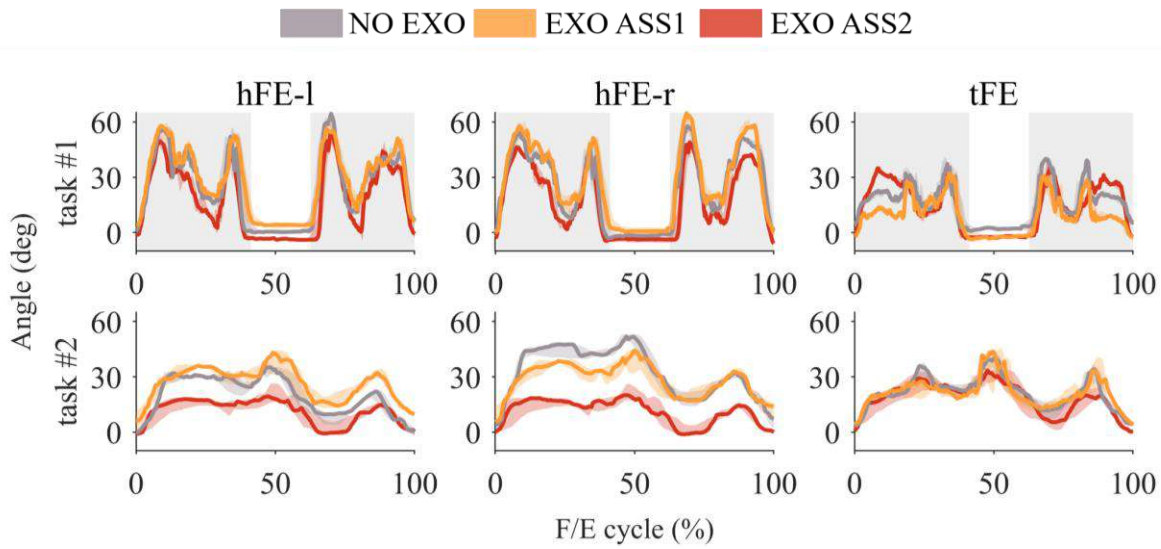


Fig. 4 Hip and trunk angles for task #1 and task #2. The two different phases of task #1 are indicated with a grey background: from left to right, the first phase is bed-to-chair, and the second phase is chair-to-bed.

across the bed surface, alternating between left and right positions. The bed was adjusted to its maximum height to optimize caregiver biomechanics during the task, consistently with ergonomic best practices in patient handling.

To assess the effect of the exoskeleton, each task was repeated five times in three different conditions: i) without wearing the exoskeleton (NO EXO), ii) wearing the exoskeleton with the assistance level set to EXO ASS1, and iii) wearing the exoskeleton with the assistance level set to EXO ASS2. The order of the three conditions was pseudo-randomized to avoid order bias: the NO EXO condition was always tested the first or last. At the end of each condition, the Rated Perceived Exertion (RPE) test [15] was used to assess the subjective perceptions. RPE scores were obtained using the Borg CR10 scale and evaluated the global and local effort perceived in four specific anatomical areas: upper back, middle back, lower back, and abdomen. The experimental session lasted about 90 minutes.

C. Data Analysis

Data analysis was performed offline using custom MATLAB R2022b (The MathWorks, Natick, MA, USA) routines. Raw EMG data were collected at 1 kHz. To obtain the linear envelope, the EMG data were processed with a band-pass filter (4th order Butterworth filter, filter range: 20–400 Hz) to remove high-frequency noise, and a notch filter (4th order Butterworth filter, cut-off frequencies 50 Hz and its harmonics) to remove AC interference. Then, the signal was rectified and low-pass filtered using a 100 ms moving average. The trunk flexion-extension (tFE) angles, the hip flexion-extension left (hFE-l) angles, and the hip flexion-extension right (hFE-r) angles were derived from IMU data, sampled at 100 Hz: from the rotation quaternions, the Euler angles of the trunk and the hip were derived, which represent the tFE and hFE angles respectively. For task#1, the EMG envelopes were manually segmented into two separate groups, according to the kinematics data, namely the bed-chair phase and the chair-bed phase. For task#2, the full cycle was considered. Representative profiles of hFE-l, hFE-r, and tFE angles are shown in Fig. 4. For each repetition of the tasks, the integrated EMG (*iEMG*) value was computed, following this equation:

$$iEMG = \int_{t1}^{t2} \frac{EMGenvelope(\tau)}{t2-t1} d\tau \qquad (1)$$

where *t1* and *t2* correspond to the beginning and the end of the considered time interval. Then, for each subject, muscle and condition, the *iEMG* values were normalized by the corresponding MVC value.

D. Statistical analysis

Statistical analysis was performed to evaluate differences in the three experimental conditions for two different tasks. All statistical analyses were conducted in MATLAB R2022b using a significance threshold $\alpha = 0.05$. Normality of the computed metrics' distributions was verified through the Shapiro-Wilk test and parametric or non-parametric statistical tests were applied accordingly. Since *iEMG* data was normally distributed, the effects of tasks and conditions on *iEMG* data were analyzed using a two-way repeated-measures ANOVA, and the assumption of sphericity was tested and verified using Mauchly's test. Separate analyses were conducted for each muscle. When the condition main effect was deemed to be significant, post-hoc pairwise comparisons were conducted to compare the EXO assistance conditions with the NO EXO condition, applying the Bonferroni correction to control for multiple comparisons. For the RPE score, the Friedman test was applied to compare with the NO EXO condition. Then, the Dunn-Sidak test was used for post-hoc comparison.

IV. RESULTS

Results on muscular and angular profiles and rated perceived exertion are reported in this section. During the experiments, two healthy volunteers alternated in simulating the patient (weight: 62 kg and 50 kg, respectively). They were experienced physical therapists who simulated the behavior of partially collaborative patients, ensuring that the testing

conditions reflected scenarios where the use of the automatic elevator was not mandatory.

A. *Muscular Activity Reduction*

The results related to the effects on back muscle activation are reported in Fig. 5. The analysis highlighted the observed differences in iEMG value as statistically significant for most of the muscles, for both the ANOVA main effects of task (all muscles $p < 0.001$) and condition (LES-r, TES-l and TES-r $p < 0.001$, ESI-l $p < 0.05$, LES-l $p < 0.01$), as well as for the ANOVA interaction effect (TES-l and TES-r $p < 0.001$, LES-r and ESI-l $p < 0.05$).

Post-hoc comparisons revealed statistically significant differences in *iEMGs* for both tasks. The median percentual variations in Fig. 5 are all reported in comparison to the NO EXO condition.

In task #1, the EXO ASS1 condition was found to reduce the muscle activity by 14%-23%, while the EXO ASS2 condition induced reductions ranging from 10% up to 29%. In task #2, the EXO ASS1 condition determined a reduction of 6%, while the EXO ASS2 condition showed significant reductions from 6% up to 15%.

B. *Reduced Perceived Effort*

Results of the RPE questionnaires are comprehensively reported in Fig. 6. The median RPE variations are all reported in comparison to the NO EXO condition. For task #1, the global RPE index and the local RPE indices for upper back and middle back were all reduced from 4 to 2 points by using the exoskeleton in EXO ASS1. For task #2, the global RPE scores were reduced from 3 to 2 points in EXO ASS1 condition and from 3 to 1 points in EXO ASS2 condition, while the local RPE scores were reduced in EXO ASS2 condition from 3 to 2 points for the upper back and middle back, and from 4 to 2 points for the lower back.

V. DISCUSSION

The results of this study suggest that the use of the lumbar exoskeleton with EXO ASS1 and EXO ASS2 can reduce physical strain during the Patient Transfer Task (task #1) and the Bed Repositioning Task (task #2). For task #1**,** both assistance levels of the exoskeleton demonstrated significant reductions in muscle activity. Specifically, the results revealed significant effects of the exoskeleton on the *iEMG* indexes within both phases of task #1. Reductions were more evident in the thoracic muscle (up to 24%) and in the lumbar muscle (up to 29%). These results suggest that the exoskeleton is effective in reducing lower back muscle activity in task #1, which requires substantial hip and trunk flexion effort. For task #2, EXO ASS2 demonstrated a more comprehensive and effective muscular activity reduction compared to EXO ASS1. The reduced muscle activations reported in this study are quantitatively in line with the results of other state-of-the-art studies during patient-handling tasks with professional caregivers ([8] [16]) and with university students [17] in laboratory settings. For example, in [8], the muscle activity of the erector spinae was significantly reduced by up to 11.2%, while in [16] it decreased by 7.78%–10.95%.

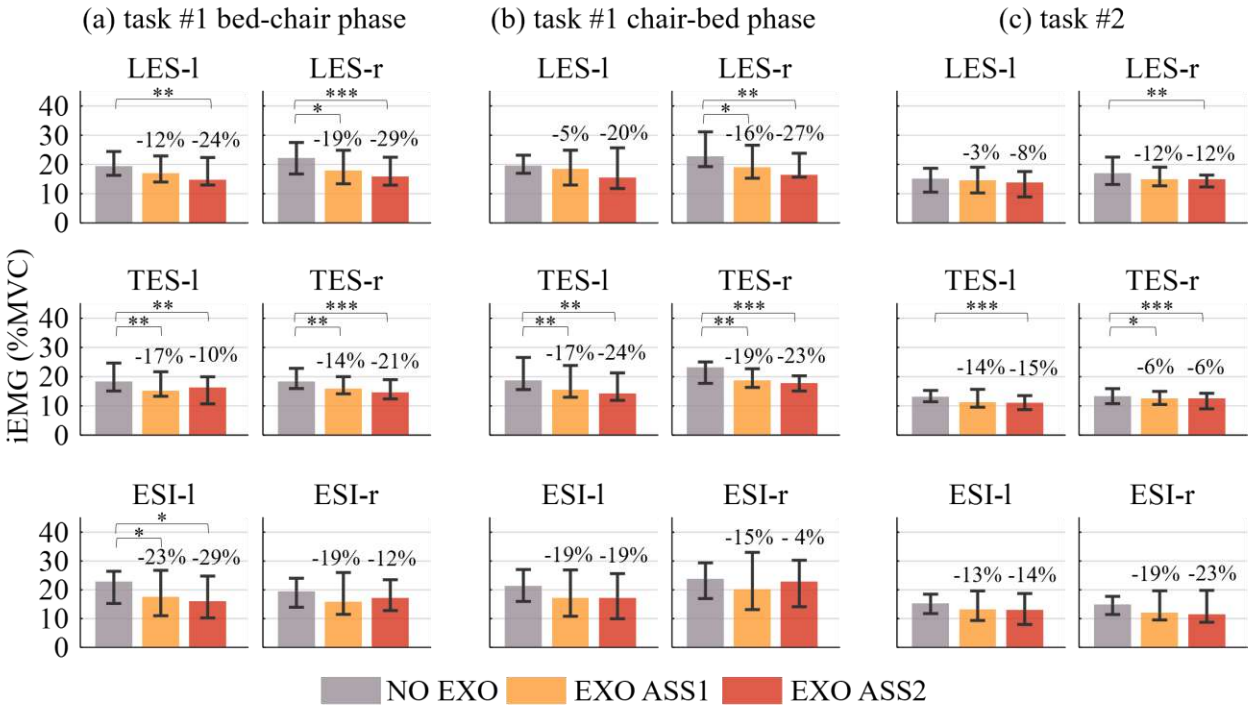


*Fig. 5 Average EMG results for the task #1 bed-chair phase, task #1 chair-bed phase and task #2. EMG results are shown for left lumbar erector spinae (LES-l), right lumbar erector spinae (LES-r), left thoracic erector spinae (TES-l), right thoracic erector spinae (TES-r), left iliocostal erector spinae (ESI-l), right iliocostal erector spinae (ESI-r). Bars represent median iEMG values expressed as percentage of the MVC, while the lower and upper end of the error bars represent the 25th and 75th percentile respectively. Median percentage variations with respect to the NO EXO condition are shown in correspondence of each bar. Asterisks indicated statistical significance due to the main effect of the intervention (*p<0.05, **p<0.01, ***p<0.001).*

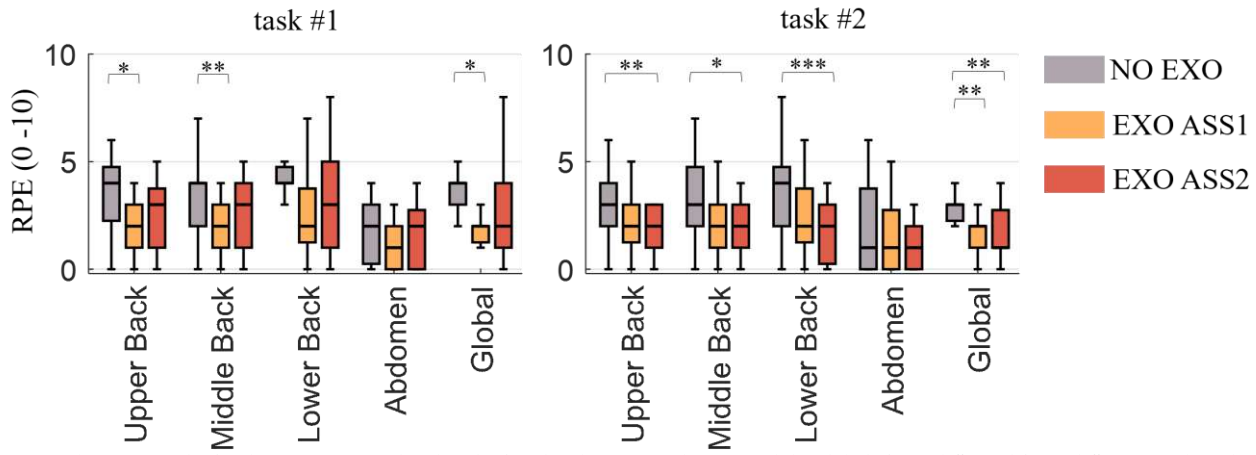


*Fig. 6 Subjective results for the RPE scores related to the four local anatomical areas and the global: for task #1 and for task #2. Asterisks indicated statistical significance due to the main effect of the intervention (*p<0.05, **p<0.01, ***p<0.001).*

Notably, the results of the present study may have reflected variability in the experimental conditions, which could have partially mitigated the observed effects. In particular, the use of a "simulated patient," who did not ensure consistent cooperation across repetitions and conditions, may have increased *iEMG* variability. Additionally, the reduction in iEMG activity of the LES muscles appears more pronounced on the right side. The higher LES muscle activity on the right side in the NOEXO condition, coupled with the greater reduction in the two assistive conditions, may be attributed to the sidedness of task #1, which required preferential turning from the right side of the bed thus likely influenced muscle activation patterns differently on the left and right sides. Finally, the slight differences in how the subjects performed the tasks may have contributed to the variability in the *iEMG* data.

Significant results were found regarding the effect of the exoskeleton on global RPE during task #1 using the EXO ASS1. Regarding the effect of the exoskeleton on global RPE during task #2, significant results were found using EXO ASS1 and EXO ASS2, with EXO ASS2 showing particular effectiveness in reducing lower back strain. These findings align with caregivers' subjective assessments, who preferred the use of the lower assistance during patient handling. This result may be due to the fact that with lower assistance, caregivers could perform movements while maintaining the same kinematics as when not wearing the exoskeleton. The higher assistance was perceived as more limiting for movement but was evaluated positively in task #2, which requires less mobility while benefiting from increased lumbar support.

Although no clear difference in effectiveness can be inferred between the EXO ASS1 and EXO ASS2 conditions, the presence of multiple assistance types seems justified by the results of subjective assessments. These evaluations highlight different user preferences, suggesting that offering both options could be an advantage to favor device subjective acceptance.

While field tests are inherently more challenging to control than laboratory studies, and the equipment available for monitoring and assessing exoskeleton efficacy in such settings is typically limited and less precise [18] [19] this study offered qualitative insights into the exoskeleton's efficacy under real-world conditions and was successful in capturing the operators' perceptions of use.

Finally, although evaluating the autonomous use of the exoskeleton was not an objective of this study, future research could adopt a more pragmatic approach to assess its usability, including autonomous use. Notably, an experienced user can don the exoskeleton in under 1 minute, suggesting that the device could be worn and removed multiple times throughout a shift, particularly during periods of more intense and repetitive tasks.

VI. CONCLUSIONS

This study examined the effect of SAFE-T on back muscles' activity and the subjective perception of effort. The results showed significant reductions in back muscles' activity. Additionally, the RPE scores were significantly reduced when using the exoskeleton. These preliminary findings highlight the potential benefits of using an exoskeleton for caregivers and further research is needed to fully assess its effectiveness and impact. Future studies will focus on investigating the long-term impact of the exoskeleton on caregivers during their daily patient-handling task.

ACKNOWLEDGMENT

The authors acknowledge the contribution of the research team from the Interdisciplinary Research Center for Health Science at the Sant'Anna School of Advanced Studies, as well as the professionals from the AUSL Toscana Nord Ovest Health Authority. The authors thank Valentina Grisanti and Maria Domenica Grandi from the Hospice "Le Piane" and Susanna Olivieri from RSA "Paoli Puccetti," along with all healthcare professionals, for their support and collaboration. The authors also thank the IUVO engineers who provided technical support during the study, namely Giulio Proface, Federica Aprigliano, Ilaria Pacifico and Andrea Parri.

REFERENCES

[1] European Foundation for the Improvement of Living and Working Conditions., 5th European working conditions survey :overview report. LU: Publications Office, 2012. Available: https://data.europa.eu/doi/10.2806/34660

[2] J. Jacquier-Bret and P. Gorce, "Prevalence of Body Area Work-Related Musculoskeletal Disorders among Healthcare Professionals: A Systematic Review," Int. J. Environ. Res. Public. Health, vol. 20, no. 1, Art. no. 1, Jan. 2023, doi: 10.3390/ijerph20010841.

[3] C. F. Böhlen, A. Brinkmann, C. Kowalski, O. Meyer, S. Hellmers, and A. Hein, "Reducing Caregiver's Physical Strain in Manual Patient Transfer with Robot Support," in 2020 5th International Conference on Automation, Control and Robotics Engineering (CACRE), Sep. 2020, pp. 189–194. doi: 10.1109/CACRE50138.2020.9230324.

[4] L. Zheng, A. L. Hawke, and K. Evans, "Critical review on applications and roles of exoskeletons in patient handling," Int. J. Ind. Ergon., vol. 89, p. 103290, May 2022, doi: 10.1016/j.ergon.2022.103290.

[5] F. Lanotte, L. Grazi, B. Chen, N. Vitiello, and S. Crea, "A Low-Back Exoskeleton can Reduce the Erector Spinae Muscles Activity During Freestyle Symmetrical Load Lifting Tasks," in 2018 7th IEEE International Conference on Biomedical Robotics and Biomechatronics (Biorob), Aug. 2018, pp. 701–706. doi: 10.1109/BIOROB.2018.8488094.

[6] G. Ramella, L. Grazi, F. Giovacchini, E. Trigili, N. Vitiello, and S. Crea, "Evaluation of antigravitational support levels provided by a passive upper-limb occupational exoskeleton in repetitive arm movements," Appl. Ergon., vol. 117, p. 104226, May 2024, doi: 10.1016/j.apergo.2024.104226.

[7] L. Farah, D. Roll, A. Sorais, and A. Vallée, "Assessment of Exoskeletons on Nurses' Quality of Work Life: A Pilot Study at Foch Hospital," Nurs. Rep., vol. 13, no. 2, Art. no. 2, Jun. 2023, doi: 10.3390/nursrep13020068.

[8] J. Hwang, V. N. Kumar Yerriboina, H. Ari, and J. H. Kim, "Effects of passive back-support exoskeletons on physical demands and usability during patient transfer tasks," Appl. Ergon., vol. 93, p. 103373, May 2021, doi: 10.1016/j.apergo.2021.103373.

[9] T. Turja, R. Saurio, J. Katila, L. Hennala, S. Pekkarinen, and H. Melkas, "Intention to Use Exoskeletons in Geriatric Care Work: Need for Ergonomic and Social Design," Ergon. Des., vol. 30, no. 2, pp. 13–16, Apr. 2022, doi: 10.1177/1064804620961577.

[10] Schmidbauer, Lukas. (2023). Inpatient Caregivers' Perceptions of the Use of Passive Exoskeletons in Daily Work -A Case Study. 549-558. 10.25929/7pmn-y556.

[11] K. Miura et al., "Successful Use of the Hybrid Assistive Limb for Care Support to Reduce Lumbar Load in a Simulated Patient Transfer," Asian Spine J., vol. 15, no. 1, pp. 40–45, Feb. 2021, doi: 10.31616/asj.2019.0111.

[12] I. Rivilis et al., "Effectiveness of participatory ergonomic interventions on health outcomes: A systematic review," Appl. Ergon., vol. 39, no. 3, pp. 342–358, May 2008, doi: 10.1016/j.apergo.2007.08.006.

[13] H. J. Hermens, B. Freriks, C. Disselhorst-Klug, and G. Rau, "Development of recommendations for SEMG sensors and sensor placement procedures," J. Electromyogr. Kinesiol., vol. 10, no. 5, pp. 361–374, Oct. 2000, doi: 10.1016/S1050-6411(00)00027-4.

[14] P. Konrad, "A Practical Introduction to Kinesiological Electromyography".

[15] N. Williams, "The Borg Rating of Perceived Exertion (RPE) scale," Occup. Med., vol. 67, no. 5, pp. 404–405, Jul. 2017, doi: 10.1093/occmed/kqx063.

[16] S. S. Man et al., "Effects of passive exoskeleton on trunk and gluteal muscle activity, spinal and hip kinematics and perceived exertion for physiotherapists in a simulated chair transfer task: A feasibility study," Int. J. Ind. Ergon., vol. 90, p. 103323, Jul. 2022, doi: 10.1016/j.ergon.2022.103323.

[17] Zheng L, Alluri CSV, Hawke AL, Hwang J. Evaluation of a passive back-support exoskeleton during in-bed patient handling tasks. Int J Occup Saf Ergon. 2024 Dec;30(4):1226-1233. doi: 10.1080/10803548.2024.2383077. Epub 2024 Aug 17.

[18] S. Crea et al., "Occupational exoskeletons: A roadmap toward large-scale adoption. Methodology and challenges of bringing exoskeletons to workplaces," Wearable Technol., vol. 2, p. e11, Jan. 2021, doi: 10.1017/wtc.2021.11.

[19] S. De Bock et al., "Benchmarking occupational exoskeletons: An evidence mapping systematic review," Appl. Ergon., vol. 98, p. 103582, Jan. 2022, doi: 10.1016/j.apergo.2021.103582.

Preliminary Results on the Integration of Muscle Oximetry Sensors for Exoskeleton Interfaces

Christopher van Vlerken[1,3], Stijn Hamelryckx[1,3], Kevin Langlois[1,2], Louis Flynn[1,3], Mengnan Wu[1], Eva Swinnen[4], David Beckwée[4], Bram Vanderborght[1,2] and Tom Verstraten[1,3]

***Abstract*— Providing assistance in wearable robots based on exertion levels enables targeted and energy-efficient support. Traditional fatigue estimators, such as surface electromyography (sEMG) are predominantly reactive, identifying fatigue only after it has occurred. Near-Infrared Spectroscopy (NIRS) offers a complementary approach by providing early insights into muscle oxygenation, with oxygen depletion strongly correlating with muscle fatigue, thereby enabling proactive monitoring.**

This study integrates chip-based NIRS sensors into a physical interface to monitor muscle oxygen saturation during both static and dynamic conditions. The experimental protocol included an occlusion test, a low-intensity walking trial, and a high-intensity cycling trial to evaluate the sensor's performance under varying levels of exhaustion. Preliminary results demonstrate the sensor's sensitivity to oxygenation changes, underscoring its potential for fatigue-adaptive assistance in wearable devices.

Index Terms — Fatigue, NIRS, Physical Interface, Wearable Robots.

I. INTRODUCTION

Real-time monitoring of muscle oxygenation offers a novel approach to enhancing wearable exoskeleton functionality by providing targeted assistance tailored to the user's physiological needs. Oxygenation data reflects trends in muscle fatigue and oxidative capacity, making it particularly valuable for applications like rehabilitation and elderly assistance [1]. Personalized support can adapt to a user's functional ability, such as providing less assistance when muscles are rested and more as fatigue sets in, encouraging activity and reducing risks of chronic conditions like hypertension, osteoarthritis, and sarcopenia [2].

Sensorized physical interfaces, which form the attachment points between the exoskeleton and the body, provide a promising solution for integrating oxygenation monitoring. Due to their close interaction with the user, these interfaces can incorporate sensors to meet various requirements. One critical requirement is developing more symbiotic interaction strategies that efficiently capture user intent, enabling more intuitive control. Current sensors for this purpose primarily rely on surface electromyography (sEMG) to measure muscle activation [3], [4] or inertial measurement units (IMUs) for kinematic estimation [5]. Another crucial requirement is ensuring comfort and safety, as uncontrolled or non-ergonomic force application can cause pain or injury [6]. To address this, force and pressure sensors are often integrated into physical interfaces to prevent excessive loading on the skin [7], [8]. Oxygenation monitoring complements these technologies by providing insights into oxidative capacity a critical marker of muscle performance and health that reflects the muscle's ability to extract and utilize oxygen. Unlike metrics that respond to immediate changes, oxidative capacity evolves over longer timescales, offering valuable information for understanding sustained muscle activity and recovery [9].

Near-Infrared Spectroscopy (NIRS) enables non-invasive, real-time monitoring of muscle oxygenation by measuring the balance of oxygenated and deoxygenated hemoglobin in tissue [10]. While NIRS is established in sports science and rehabilitation, its adoption in exoskeletons remains limited due to the size and complexity of existing devices, such as the Moxy Monitor and Portamon. Although some studies have explored NIRS for fatigue monitoring in exoskeletons [11], no work has integrated NIRS directly into physical interfaces for real-time control. Furthermore, many exoskeleton applications require multiple sensors to track oxygenation in several muscle groups or body segments, and the cost and proprietary algorithms or firmware of existing commercial devices such as Portamon and Moxy Monitor make them often impractical to deploy for muscle fatigue monitoring in exoskeletons.

This study addresses these gaps by integrating a chip-based NIRS sensor into a sensorized cuff for measuring oxygenation in the muscle belly of rectus femoris muscle. By using the chip-based NIRS sensor, we aim for complete control over optical geometry, data access, and integration with the mechanical design of a wearable robot. The paper reviews the theoretical background of NIRS, describes the sensor integration, and presents validation through occlusion and activity trials, including low-intensity walking and high-intensity cycling. Finally, the performance of the proposed sensor is compared to a commercially available muscle oximeter Moxy Monitor (see Figure 1).

*This work was partially supported by the FWO Strategic Basic Research project Revalexo (grant no. S001024N). Kevin Langlois is a postdoctoral fellow of the Research Foundation Flanders (FWO) with FWO grant 1258523N.

[1]Robotics & Multibody Mechanics (R&MM) Research Group, Vrije Universiteit Brussel, 1050 Brussels, Belgium, [christopher.konstantin.van.vlerken, stijn.hamelryckx, kevin.langlois, louis.flynn, mengnan.wu, bram.vanderborght, tom.verstraten]@vub.be

[2] IMEC, Kapeldreef 75, Leuven 3001, Belgium.

[3]Flanders Make, 1050, Brussels, Belgium.

[4]Rehabilitation Research, Department of Physiotherapy, Human Physiology and Anatomy, Vrije Universiteit Brussel, Laarbeeklaan 103, 1090 Jette, Belgium, [eva.swinnen, david.beckwee]@vub.be

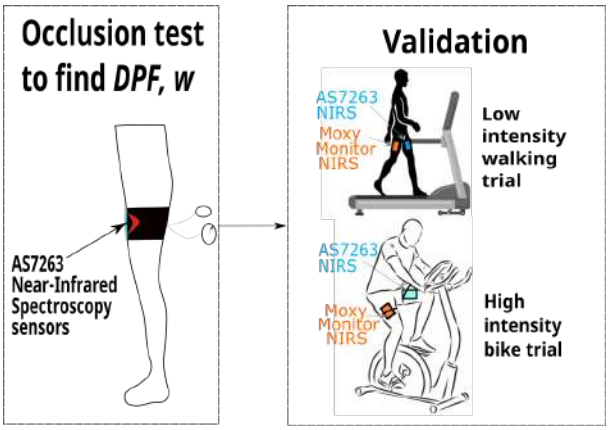


Fig. 1. Purpose of the study. The AS7263 NIRS sensors were integrated into a physical interface and subjected to an arterial occlusion test to derive the Differential Path Length Factor DPF and weighting parameter w, necessary for the Modified Beer-Lambert Law equation. The derived parameters were validated through a low intensity walking trial and a high intensity exercise trial, during which the proposed sensor's performance was compared to a gold-standard muscle oximeter.

II. Methods

A. Near-Infrared Spectroscopy: Working principle

Near-Infrared Spectroscopy (NIRS) non-invasively monitors the concentrations of oxyhemoglobin [HbO_2] and deoxyhemoglobin [Hb] in tissue, providing insights into oxygen supply and consumption [12]. In highly scattering media, the Beer-Lambert law must be modified by a differential pathlength factor (DPF) to account for the extended photon path, yielding the Modified Beer-Lambert Law:

$$\begin{cases} \Delta A_{770nm} = (\epsilon_{770nmHbO_2} * \Delta[HbO_2] + \\ \epsilon_{770nmHb} * \Delta[Hb]) * L * DPF \\ \Delta A_{850nm} = (\epsilon_{850nmHbO_2} * \Delta[HbO_2] + \\ \epsilon_{850nmHb} * \Delta[Hb]) * L * DPF \end{cases} \quad (1)$$

where ΔA_λ is the change in absorbance at wavelength λ, L is the emitter-detector distance, and ϵ_λ are the molar extinction coefficients.

Spatially Resolved Spectroscopy (SRS) reduces skin and adipose interference by placing multiple detectors at different distances (see Figure 2). The corrected absorbance ΔA_c is obtained by subtracting a weighted contribution (w) from the proximal detector (ΔA_p) from that of the distal detector (ΔA_d):

$$\begin{cases} \Delta A_{770nm,c} = \Delta A_{770nm,d} - w * \Delta A_{770nm,p} \\ \Delta A_{850nm,c} = \Delta A_{850nm,d} - w * \Delta A_{850nm,p} \end{cases} \quad (2)$$

From these corrected values, one can derive the muscle oxygen saturation S_{mO_2}, representing the fraction of oxygenated hemoglobin relative to total hemoglobin in the sampled muscle volume.

B. Experimental protocol

1) ***Materials****:* To assess accuracy relative to the Moxy Monitor, we employed 8-bit AS7263 NIRS sensors (SparkFun, USA, 3.3 V) covering wavelengths from 610–860 nm ($\pm$5 nm). Each sensor integrated a 3 mm through-hole LED emitting at 770 nm (MTE1077M3A-R, Marktech) for deoxyhemoglobin and 850 nm (SFH 4350, ams-OSRAM) for oxyhemoglobin. These were configured on two chip boards for Spatially Resolved Spectroscopy (SRS), spaced 35 mm apart along the muscle fibers to balance light penetration and minimize interference between LED sources. A custom thigh cuff (S-FIT-70-004-R3, Moovartes) with a 9 mm neoprene padding layer ensured comfort and alignment (see Figure 2). The AS7263-based cuff and the Moxy Monitor were placed on opposite legs to reduce motion artifacts, aligning with evidence that symmetrical tasks yield comparable relative bilateral oxygenation readings [13], [14].

Tests were performed on a single healthy male participant (26 years old, 1.68 m, 63 kg). The participant gave informed consent before starting the experiment and the protocol was approved by the institutional medical ethics committee of UZ Brussel and Vrije Universiteit Brussel (Belgium, B.U.N. 1432024000256).

2) ***Occlusion test****:* An occlusion test was conducted to evaluate the proposed spectrometer's sensitivity to oxygen deprivation in the muscle under static conditions. This arterial occlusion is a known method to temporarily restricts blood flow to a limb using a cuff, such as a sphygmomanometer, creating a controlled ischemic condition to monitor oxygen saturation changes and subsequent hyperemia upon release [15].

The primary objective was to identify time-sensitive events, such as oxygenation depletion and recovery, and estimate key parameters for the Modified Beer-Lambert Law, including the differential pathlength factor (DPF) and weighting factor (w), calculated using Equations 1 and 2. These parameters were optimized to improve correlation with the commercial oximeter.

For this test, an occlusion cuff was positioned proximally on the participant's thigh, with the Moxy Monitor and sensorized cuff placed just below it. The 4-minute test included a 2-minute occlusion period during which blood flow was restricted followed by the release of the occlusion. Three trials using AS7263 NIRS and Moxy monitor were performed with removal of the cuff between trials, which allows muscle reperfusion to baseline before the next measurement.

3) ***Validation****:* Following the occlusion test, two dynamic trials were conducted to evaluate oxygen saturation trends during low-intensity walking and high-intensity cycling. The walking trial, simulating an activity of daily living, lasted 20 minutes at 4 km/h on a standard treadmill. Four trials were performed using both the AS7263 and Moxy monitor, with removal of the cuff between trials. The bike trial, designed to induce muscle fatigue, lasted 7 minutes and included three phases: baseline at 60 W, 2 minutes of high resistance at 200 W, and 2 minutes of recovery at 60 W. The participant maintained a steady cadence of 75 rpm using a resistance-adjustable bike (Cyclus 2, Trek, Leipzig, Germany). The 200 W resistance level was chosen to ensure a challenging but feasible workload.

For both trials, the sensorized cuff and the Moxy Monitor



Fig. 2. Integration of Near-Infrared Sensors. The chip-based AS7263 NIRS sensor, integrated into the cuff, includes an embedded detector capable of detecting wavelengths between 610 nm and 860 nm and a custom through-hole near-infrared LED. The sensors are positioned to enable Spatially Resolved Spectroscopy (SRS) on the muscle belly of rectus femoris muscle (see right panel). In the diagram, I_0 represents the initial light source intensity, d_1 indicates the proximal detector, and d_2 represents the distal detector. This arrangement facilitates the subtraction of light absorption by skin and fat layers from the measured signal. Both the AS7263 sensor and the Moxy Monitor, used as the gold standard in this study, were placed on opposite legs to monitor oxygenation trends in the rectus femoris muscle.

were placed on opposite legs, just above the muscle belly of rectus femoris muscle, to monitor oxygenation levels.

C. Data processing

Data were collected via a Teensy 4.1 microcontroller (PJRC, USA) over I^2C and stored as .csv files. MATLAB R2021b (Mathworks, Natick, MA) handled processing, with oxygenation values normalized to $[0, 1]$ to mitigate hardware and optical-path discrepancies. Indeed, absolute oxygenation values can vary between devices due to differences in hardware design, optical paths, and signal processing algorithms. Normalization mitigates these discrepancies by focusing on relative trends in oxygenation changes rather than absolute values, ensuring that depletion and recovery dynamics remain comparable across sensors. Both the Moxy Monitor and AS7263 sampled at $0.5\,\text{Hz}$, and a $0.25\,\text{Hz}$ low-pass filter reduced high-frequency noise. Linear interpolation was applied to model key events (e.g., occlusion start/end, resistance phases). For multiple trials, mean and standard deviation of the AS7263 data were compared to normalized Moxy data, assessing consistency via coefficient of determination (R^2) and root-mean-square error (RMSE).

III. Results

A. Occlusion

As shown in Figure 3, muscle oxygen saturation declined after the occlusion onset (dashed line at 1 min), reflecting restricted blood flow and ischemia. Both the Moxy Monitor and AS7263 exhibited parallel downward trends, differing slightly in amplitude. In the first trial, the differential path-length factor (DPF) was 1.4 (proximal) and 5.59 (distal), and the weighting factor w was 0.2. Linear interpolations for both sensors illustrate the depletion phase, with slopes and R^2 values detailed in Table I.

Around 3 min, releasing the occlusion triggered post-occlusion hyperemia [15], a transient overshoot driven by vascular dilation. Both sensors showed steep recoveries, returning near baseline within similar timeframes (see Figure 3 and Table I). On average, depletion and recovery slopes across trials differed by 0.06 and 0.15 in normalized scale, respectively.

Figure 5 compares the mean AS7263 data to Moxy across all trials. Their correlation yielded $R^2 = 79\%$ and an RMSE of 11%, indicating strong agreement in oxygenation trends.

TABLE I

Depletion and recovery slopes of normalized oxygenation during the occlusion trial. Slopes and corresponding R^2 values are shown for both the Moxy Monitor and AS7263 trials, including individual trials and the mean of all AS7263 trials.

	Depletion[$\frac{1}{min}$]	Recovery [$\frac{1}{min}$]
Moxy Monitor	-0.32; R^2 = 99%	3.05; R^2 = 98%
AS7263 1st trial	-0.24; R^2 = 95%	2.49; R^2 = 95%
AS7263 2nd trial	-0.20; R^2 = 98%	3.19; R^2 = 90%
AS7263 3rd trial	-0.35; R^2 = 86%	2.95; R^2 = 85 %
AS7263 Mean trials	-0.26; R^2 = 96%	2.90; R^2 = 93 %

B. Low intensity walking trial

Figure 4 presents muscle oxygen saturation measurements from multiple trials using the AS7263 sensor and the Moxy Monitor during the walking trial. Both devices demonstrate a steadily increasing trend in oxygen saturation throughout the experiment, following a similar pattern. Unlike the occlusion test, the walking trial involved low-intensity activity, during which oxygen delivery exceeded consumption. This is because the muscles were not subjected to sustained high contractions that could compress blood vessels and restrict oxygen supply, as seen in ischemic conditions.

Figure 6 further illustrates the correlation between the normalized muscle oxygen saturation values obtained from the mean AS7263 sensor measurements and the Moxy Monitor. The linear interpolation, derived from the mean across all trials, highlights the agreement between the two devices. The coefficient of determination R-square between the devices was 89%, with a root mean square error (RMSE) of 9%, indicating the AS7263 sensor's reliability in tracking oxygenation dynamics during steady-state walking.

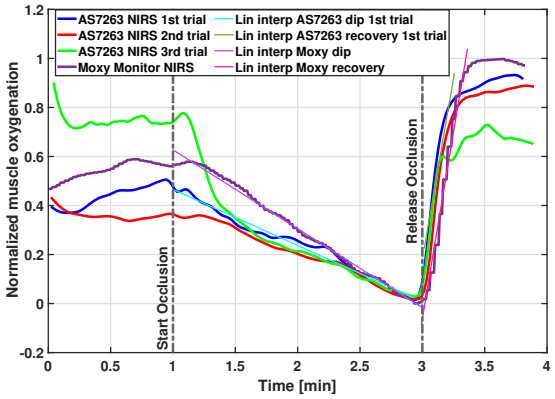


Fig. 3. **Occlusion Trial Over Time**. Muscle oxygen saturation measurements from both the AS7263 sensor and the Moxy Monitor during the occlusion trial. Dashed lines indicate the beginning and release of the occlusion. A gradual decline in oxygen saturation is observed during the occlusion phase due to restricted blood flow and ongoing oxygen consumption. Linear interpolations illustrate the depletion (dip) and recovery phases for both sensors. Upon release, a rapid increase in oxygen saturation reflects restored blood flow and oxygen supply, demonstrating the sensors' ability to capture real-time oxygen replenishment.

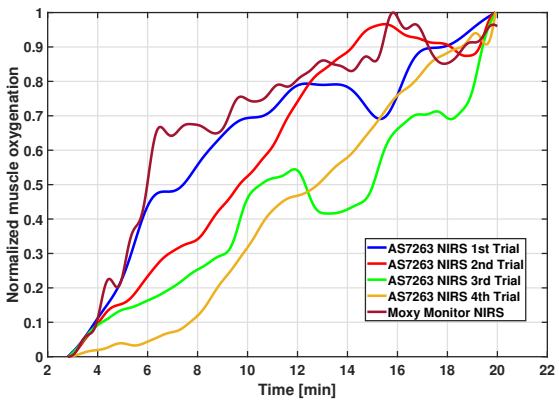


Fig. 4. **Low Intensity Walking Trial Over Time**. Normalized muscle oxygenation measured by the AS7263 sensor and the Moxy Monitor during a 20-minute walking trial. Both sensors show an increasing trend in oxygen saturation over time, indicating that the oxygen supply exceeds the demand during the activity. This occurs because the muscles did not experience prolonged intense contractions capable of compressing blood vessels and limiting oxygen flow, as observed in ischemic conditions.

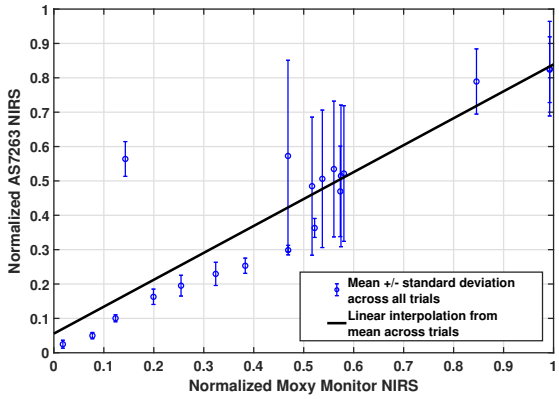


Fig. 5. **Normalized AS7263 NIRS against Normalized Moxy Monitor NIRS during Occlusion Test.** Normalized muscle oxygen saturation data from the AS7263 sensor (y-axis) and the Moxy Monitor (x-axis) are compared across three trials. The mean values are represented by blue dots with their corresponding standard deviations, while a black line depicts the linear interpolation of the mean. The coefficient of determination (R^2 = 79%) and root mean square error (RMSE = 11%) indicate strong agreement between the two sensors.

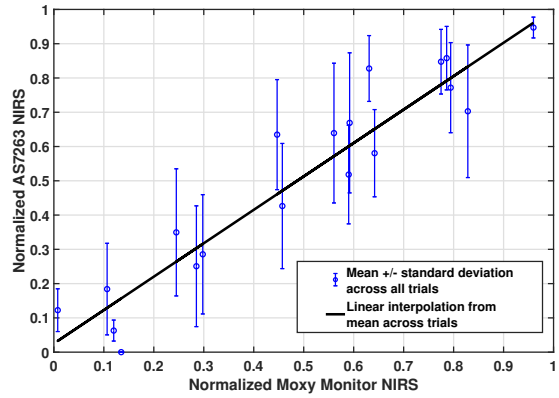


Fig. 6. **Normalized AS7263 NIRS against Normalized Moxy Monitor NIRS during Low-Intensity Walking.** Normalized muscle oxygen saturation from the AS7263 sensor (y-axis) is compared against the Moxy Monitor (x-axis) across four trials. Blue dots represent the mean values, and the black line shows the linear interpolation of the mean. The AS7263 sensor demonstrates trends comparable to the Moxy Monitor, with a coefficient of determination (R^2) of 89% and a root mean square error (RMSE) of 9%.

C. High intensity bike trial

Figure 7 shows the normalized muscle oxygen saturation from both the AS7263 sensor and the Moxy Monitor during baseline, a high-resistance phase at 200 W (starting at 3 min), and a recovery phase (beginning at 5 min). Both sensors recorded stable oxygenation at baseline, then a marked decrease under high load, reflecting increased metabolic demand. The Moxy Monitor and AS7263 showed depletion slopes of -0.47 [1/min] (R^2 = 93%) and -0.49 [1/min] (R^2 = 92%), respectively. When resistance returned to baseline at 5 min, both exhibited rapid recovery: 0.7 [1/min] (R^2 = 96%) for Moxy and 0.46 [1/min] (R^2 = 98%) for AS7263. This restoration of oxygenation arises from reduced oxygen consumption and lower intramuscular pressure, allowing blood flow to return to baseline levels.

Figure 8 compares the normalized data from both sensors, showing a lower R^2 of 32% than in other trials. The elliptical data distribution suggests a temporal misalignment, likely due to sensor response-time differences and possible motion artifacts affecting the AS7263.

IV. Discussion

The results from the AS7263-based NIRS sensor and the Moxy Monitor demonstrate comparable trends in muscle oxygen saturation during the depletion and recovery phases of the occlusion, low-intensity walking, and high-intensity bike trials. For the occlusion test, a coefficient of determination (R^2) of 79% and a root mean square error (RMSE) of

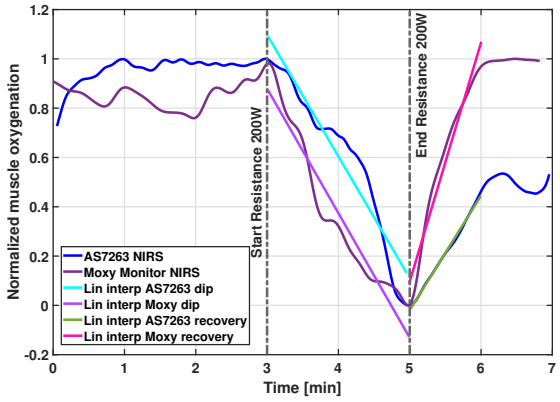


Fig. 7. **High Intensity Bike Trial Over Time.** Normalized muscle oxygen saturation data from the AS7263 sensor and the Moxy Monitor during a dynamic trial involving resistance changes on a bike. The dashed lines indicate the beginning and end of the high-resistance phase (200 W). Both sensors exhibit a decrease in oxygen saturation during the high-resistance phase, with similar slopes, reflecting the increased metabolic demand. When resistance is reduced to the baseline level, oxygenation increases as the oxygen supply surpasses the demand. Linear interpolations for both the depletion and recovery phases are shown, highlighting the sensors' ability to capture real-time oxygenation dynamics under varying resistance conditions.

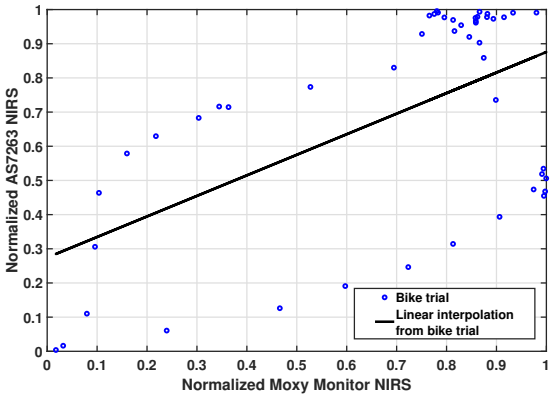


Fig. 8. **Normalized AS7263 NIRS against Normalized Moxy Monitor NIRS during High-Intensity Bike Trial.** Normalized muscle oxygen saturation from the AS7263 sensor (y-axis) is compared with the Moxy Monitor (x-axis), shown as blue dots. The linear interpolation yields a coefficient of determination(R^2) of 33% and an RMSE of 27%, highlighting challenges from motion artifacts and sensor differences during dynamic trials.

11% were observed, while the walking trial showed an R^2 of 89% with an RMSE of 9%. However, the bike trial exhibited a lower R^2 of 33% and an RMSE of 27%, indicating reduced agreement between the two sensors during high-intensity dynamic activity. The linear trendline was used as a simplified model to assess overall correlation, similar to the occlusion and walking trials, where both sensors showed strong agreement. The elliptical distribution of data points suggests that a temporal misalignment between the two sensors, possibly caused by response time differences, may have contributed to the reduced correlation. Future work will investigate temporal alignment and refine the AS7263's dynamic response for real-time monitoring.

Notably, the high variability across trials could also be attributed to differences in sensor placement. NIRS provides a localized assessment of oxygen saturation, and the heterogeneous activation of muscles can contribute to variability in the results [16]. This is particularly relevant for real-world applications, where relative motion and muscle heterogeneity can affect measurement reliability. Mitigating motion artifacts through secure, adjustable attachment mechanisms or motion compensation algorithms could enhance data stability. Despite variability, the bike trial demonstrated the AS7263 sensor's sensitivity to resistance changes, showing a 0.02 slope difference in oxygen depletion compared to the Moxy Monitor. This highlights the sensor's ability to capture real-time oxygenation changes under varying resistance conditions, reinforcing its potential for monitoring exhaustion in wearable robots using near-infrared spectroscopy.

Beyond validating the AS7263 sensor's ability to track muscle oxygenation, it remains unknown whether these measurements can inform exoskeleton control. Unlike biomechanical signals, which require high-frequency updates, muscle oxygenation changes occur over longer timescales and would be sampled less frequently (e.g., every 1 second) to track gradual trends rather than instantaneous fluctuations. In an exoskeleton framework, this data could modulate assistance dynamically, increasing support when sustained deoxygenation is detected and reducing it as oxygenation recovers to encourage active engagement. By combining oxygenation trends with faster biomechanical signals, a hybrid control strategy could use oxygenation as a longer-timescale fatigue indicator. Future work will focus on defining oxygenation thresholds for adaptive control and evaluating their impact on exoskeleton performance.

Differences in the attachment methods of the sensors could also influence measurements. The Moxy Monitor uses adhesive tape for direct skin application, whereas the AS7263 sensor is mounted within a cuff that encloses the thigh. Tightening the cuff excessively could create a pre-occlusion effect, altering blood flow dynamics and impacting oxygenation measurements. As a mitigation strategy, rather than maintaining perfectly constant pressure in future experiments, we plan to integrate secondary sensors such as pressure sensors that monitor cuff tension in real time. This will allow our algorithm to adjust for pressure variations and better isolate genuine physiological signals from artifacts. Moreover, the underlying algorithms play a significant role in the observed differences. The Moxy Monitor employs a Monte Carlo simulation-based algorithm, providing precise modeling of light scattering and absorption in complex tissue structures [17]. In contrast, the AS7263 sensor uses simpler model equations, which, while computationally efficient, lack the ability to account for intricate tissue-light interactions. Algorithmic enhancements, such as incorporating advanced tissue-light interaction modeling, could significantly improve the AS7263 sensor's performance under dynamic conditions. Additionally, the Moxy Monitor utilizes multiple wavelengths for oxygenation calculations, further enhancing its

accuracy compared to the AS7263 sensor, which relies on only two wavelengths.

Another important factor influencing muscle oxygenation measurements is the differential path length factor (DPF) and its associated weighting parameter. In this study, these parameters were fixed based on model assumptions, yet they are known to vary with changes in muscle contraction, relaxation, and adipose tissue thickness [18]. Variability in adipose tissue thickness, especially in populations such as the older or sarcopenic individuals, can affect light penetration depth and scattering properties, potentially reducing measurement accuracy. Integrating additional sensors, such as pressure sensors to detect muscle contraction, could allow real-time adjustments to DPF and weighting, compensating for tissue property variations and improving measurement precision.

Lastly, this study was conducted with a single healthy participant, and further validation across diverse populations is essential. Expanding to include more participants, particularly older and sarcopenic individuals, key candidates for exoskeletons, is crucial as their distinct physiological traits, such as increased adipose tissue thickness, reduced muscle mass, and peripheral vascular changes, may influence sensor performance. Testing these groups will enable further calibration and optimization of the sensor to address the specific needs of users reliant on exoskeletons. Additionally, systematic experimental protocols involving various activities of daily living could offer valuable insights into optimizing exoskeleton control strategies tailored to exhaustion and fatigue levels.

V. CONCLUSION

This study provides preliminary evidence that the AS7263-based NIRS sensor, integrated into a physical interface for exoskeletons, can monitor muscle oxygenation trends comparable to the Moxy Monitor. The occlusion test achieved a coefficient of determination of 79%, enabling the estimation of key parameters (DPF and w), while dynamic trials yielded 89% for low-intensity walking and 33% for high-intensity cycling, with comparable oxygen depletion and recovery trends observed. These results highlight the sensor's potential for monitoring oxygen depletion, a critical marker of muscle fatigue, and identify challenges like motion artifacts during high-intensity activities.

Based on findings from a single participant, further validation with diverse populations, including older and sarcopenic individuals, is essential. Future work should integrate advanced tissue-light interaction models and complementary sensors to improve robustness against motion artifacts and account for tissue variability. This study establishes a foundation for real-time muscle oxygenation monitoring, paving the way for fatigue-adaptive assistance in wearable assistive devices.

REFERENCES

[1] J. Wan, Z. Qin, P. Wang, Y. Sun, and X. Liu. Muscle fatigue: general understanding and treatment. *Experimental & Molecular Medicine*, 49(10):e384, October 2017.

[2] F. W. Booth, C. K. Roberts, and M. J. Laye. Lack of exercise is a major cause of chronic diseases. *Comprehensive Physiology*, 2(2):1143–1211, April 2012.

[3] Y. Sun, Y. Tang, J. Zheng, D. Dong, X. Chen, and L. Bai. From sensing to control of lower limb exoskeleton: a systematic review. *Annual Reviews in Control*, 53:83–96, January 2022.

[4] K. Langlois, J. Geeroms, G. Van De Velde, C. Rodriguez-Guerrero, T. Verstraten, B. Vanderborght, and D. Lefeber. Improved Motion Classification With an Integrated Multimodal Exoskeleton Interface. *Frontiers in Neurorobotics*, 15, 2021.

[5] F. Gao, G. Liu, F. Liang, and W. Liao. IMU-Based Locomotion Mode Identification for Transtibial Prostheses, Orthoses, and Exoskeletons. *IEEE Transactions on Neural Systems and Rehabilitation Engineering*, 28(6):1334–1343, June 2020. Conference Name: IEEE Transactions on Neural Systems and Rehabilitation Engineering.

[6] Y. He, D. Eguren, T. P. Luu, and J. L. Contreras-Vidal. Risk management and regulations for lower limb medical exoskeletons: a review. *Medical Devices (Auckland, N.Z.)*, 10:89–107, 2017.

[7] S. M. M. De Rossi, N. Vitiello, T. Lenzi, R. Ronsse, B. Koopman, A. Persichetti, F. Vecchi, A. J. Ijspeert, H. van der Kooij, and M. C. Carrozza. Sensing Pressure Distribution on a Lower-Limb Exoskeleton Physical Human-Machine Interface. *Sensors (Basel, Switzerland)*, 11(1):207–227, December 2010.

[8] K. Langlois, E. Roels, G. Van De Velde, C. Espadinha, C. Van Vlerken, T. Verstraten, B. Vanderborght, and D. Lefeber. Integration of 3D Printed Flexible Pressure Sensors into Physical Interfaces for Wearable Robots. *Sensors*, 21(6):2157, January 2021. Number: 6 Publisher: Multidisciplinary Digital Publishing Institute.

[9] M. Hargreaves and L. L. Spriet. Skeletal muscle energy metabolism during exercise. *Nature Metabolism*, 2(9):817–828, September 2020. Publisher: Nature Publishing Group.

[10] H. W. Siesler, Y. Ozaki, S. Kawata, and H. M. Heise. *Near-Infrared Spectroscopy: Principles, Instruments, Applications*. John Wiley & Sons, July 2008. Google-Books-ID: U7vqrf2YqmcC.

[11] E. B. Weston, M. Alizadeh, H. Hani, G. G. Knapik, R. A. Souchereau, and W. S. Marras. A physiological and biomechanical investigation of three passive upper-extremity exoskeletons during simulated overhead work. *Ergonomics*, 65(1):105–117, January 2022.

[12] M. Ferrari, M. Muthalib, and V. Quaresima. The use of near-infrared spectroscopy in understanding skeletal muscle physiology: recent developments. *Philosophical Transactions. Series A, Mathematical, Physical, and Engineering Sciences*, 369(1955):4577–4590, November 2011.

[13] P. Farzam, Z. Starkweather, and M. A. Franceschini. Validation of a novel wearable, wireless technology to estimate oxygen levels and lactate threshold power in the exercising muscle. *Physiological Reports*, 6(7):e13664, April 2018.

[14] C. Sendra-Pérez, J. I. Priego-Quesada, J. M. Murias, F. P. Carpes, R. Salvador-Palmer, and A. Encarnación-Martínez. Evaluation of leg symmetry in muscle oxygen saturation during submaximal to maximal cycling exercise. *European Journal of Sport Science*, 25(1):e12230, January 2025.

[15] V. Gerovasili, S. Dimopoulos, G. Tzanis, M. Anastasiou-Nana, and S. Nanas. Utilizing the vascular occlusion technique with NIRS technology. *International Journal of Industrial Ergonomics*, 40(2):218–222, March 2010.

[16] V. Quaresima, W. N. J. M. Colier, M. van der Sluijs, and M. Ferrari. Nonuniform Quadriceps O2 Consumption Revealed by Near Infrared Multipoint Measurements. *Biochemical and Biophysical Research Communications*, 285(4):1034–1039, July 2001.

[17] C. J. McManus, J. Collison, and C. E. Cooper. Performance comparison of the MOXY and PortaMon near-infrared spectroscopy muscle oximeters at rest and during exercise. *Journal of Biomedical Optics*, 23(1):015007, January 2018. Publisher: SPIE.

[18] T. Hamaoka. Muscle oxygenation monitoring using near-infrared spectroscopy. *The Journal of Physical Fitness and Sports Medicine*, 2(2):203–207, 2013.

Multi-Channel EMS-based Interface for Perceptual Sharing of Joint Stiffness in Telerehabilitation

Yoshiori Fujii[1], Yasuhiro Suzuki[2], Modar Hassan[2] and Kenji Suzuki[2]

***Abstract*— In recent years, the demand for telerehabilitation has been increasing, and its effectiveness has been verified for various diseases and injuries. However, especially in the field of physical rehabilitation, manual assessment is commonly used, and the therapist cannot touch the patient remotely. Therefore, we developed an interface using multi-channel electrical muscle stimulation (EMS) for the evaluation of joint stiffness, which is difficult to judge visually. The performance evaluation showed that the elbow joint drag force tended to increase as the stimulation intensity of the EMS increased. In the perceptual study, the proposed method significantly improved discrimination performance compared to the video meeting system for the individuals without disabilities (p=0.0051, the Wilcoxon signed-rank test). The results suggest that the proposed method can be applied to clinical practice by establishing a calibration method that is tailored to the individual characteristics of the users.**

I. Introduction

Telerehabilitation (TR) is a subgroup of telemedicine, which refers to the implementation of rehabilitation remotely via information and communication technology[1], [2]. TR is a generic term for medical rehabilitation services including "evaluation, assessment, monitoring, prevention, intervention, supervision, education, consultation, and coaching"[3]. TR has attracted attention as an effort to reduce barriers of travel distance, time, and cost, and also the need for TR has increased due to the COVID-19 pandemic[4], [5].

Especially in neurological diseases such as stroke, cerebral palsy, and spinal cord injury, the emphasis is on evaluation and treatment by physical therapists using manual methods. During rehabilitation, if joint stiffness, such as spasticity and contracture, is not properly assessed, it will not be possible to demonstrate therapeutic efficacy and can be a major limiting factor in a patient's daily life. However there are challenges in transitioning to TR since a therapist cannot touch a patient.

Computer vision and robotic systems have been studied to assist therapists in monitoring patient status and guiding exercise in a TR environment. Pathirana et al.[6] proposed a real-time bio-kinematics tracking system using Kinect. Their system can monitor kinematics, but evaluation of joint stiffness without displacement is not feasible. Lai et al.[7] developed a hand exoskeleton robot to assess muscle spasticity. Still, installing a robotic system for a specific body part in each patient's home is not cost-effective.

[1]Yoshiori Fujii is with the Doctoral Program in Empowerment Informatics, Graduate School of Science and Technology, University of Tsukuba, Japan yoshiori@ai.iit.tsukuba.ac.jp

[2]Yasuhiro Suzuki, Modar Hassan, and Kenji Suzuki are with the Institute of Systems and Information Engineering, University of Tsukuba, Japan yasuhiro@ai.iit.tsukuba.ac.jp, modar@iit.tsukuba.ac.jp, kenji@ieee.org

Therapists relying on manual methods are reluctant to implement complex systems such as those described above because they perform rehabilitation based on their own sensory perception[8]. Liu et al.[9] and Sommerhalder et al.[10] showed the effectiveness of a robotic interface focused on the remote interaction of the therapist with the patient. Although there have been many studies of remote interfaces using mechanical actuators, there have been few studies of simple, cost-effective devices that can be used in each patient's home.

The motivation of this study is to develop a cost-effective joint stiffness evaluation support system that is easy to implement in each patient's home and can be used sensibly by therapists. The realization of such a system would facilitate the transition to TR and reduce the geographic time and cost burden on both patients and therapists.

In this study, we propose a wearable patient-therapist sensory-sharing interface that does not require an mechanical actuator. Aiming at the application of joint stiffness evaluation we focused on communication by bio-signals. We developed an interface that enables the therapist to directly perceive changes in the joint stiffness of the patient by applying electrical muscle stimulation (EMS) to the therapist's muscles based on the electromyography (EMG) signals obtained from the patient's muscles. The purpose of this study is to verify the perceptual characteristics of joint stiffness changes induced by Multi-channel EMS and to explore the feasibility of adapting the interface to TR.

II. Related Works

A. Joint Stiffness Estimation by EMG

Many studies have been conducted to estimate joint stiffness based on multi-channel EMG. Wang et al.[11] shows a potential method for assessing elbow spasticity based on 2 channels EMG of the biceps and triceps brachii muscles. We attempted to measure EMG in 2 channels, biceps brachii and triceps brachii, which is the minimum number of channels, to obtain changes in elbow joint stiffness.

B. Perception Sharing Device

BioSync[12] is a perception-sharing device in which the timing of wrist muscle exertion can be synchronized between device users without using visual or acoustic information using EMS based on EMG measurement. It provides a shared sense of human motion. However, it targets only a single channel muscle, and it is unlikely to share changes in joint stiffness. We hypothesized that by extending this technology to multi-channel EMS, we could share the sensation of changes in human joint stiffness with others.

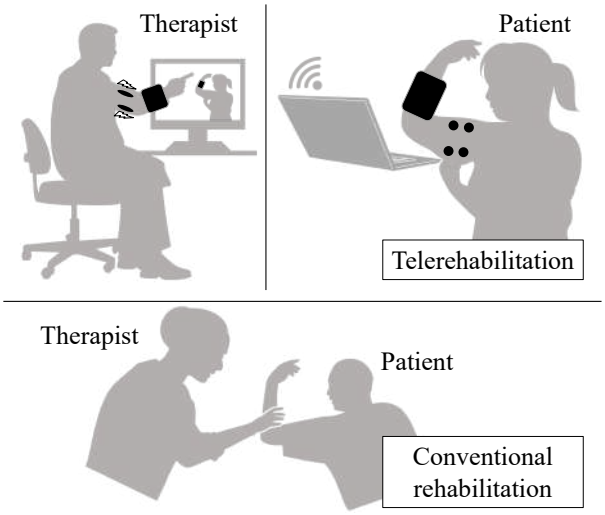


Fig. 1. The conceptional figure of an interface that can share elbow joint stiffness change using the proposal method in telerehabilitation

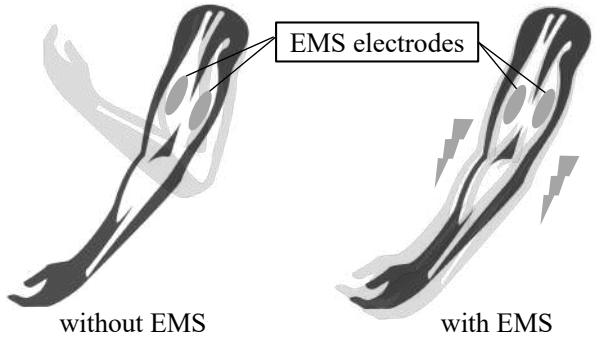


Fig. 2. Modulation of elbow joint stiffness by multi-channel EMS

III. Methodology

A. Proposed Approach

The proposed approach to improve the remote interaction of the therapist with the patient is a multi-channel EMS-based interface based on EMG inspired by BioSync[12]. Nishida et al.[13] evaluated shared wrist joint stiffness with multi-channel EMS based on EMG and showed a linear relationship between applied EMS intensity and joint stiffness with four levels of discrimination performance. In this study, we evaluate a more practical scenario in TR. Since the modified Ashworth scale (MAS) uses a 5-lebel discrimination method, we investigate the 5-level discrimination performance and compare it with the video meeting systems used in a conventional telerehabilitation setting. The elbow joint was chosen as the subject of this experiment because many stroke patients develop muscle spasticity and it is easy to perform in a chair in front of a desk for use in TR.

B. Concept for Perceptual Sharing of Joint Stiffness

Fig.1 shows the conceptional figure of an interface that can share elbow joint stiffness changes using the proposed method in TR. The therapist usually uses palpation to assess the patient's muscle condition, range of motion, and joint stiffness in conventional rehabilitation. In TR, patients and therapists are expected to communicate using a videophone

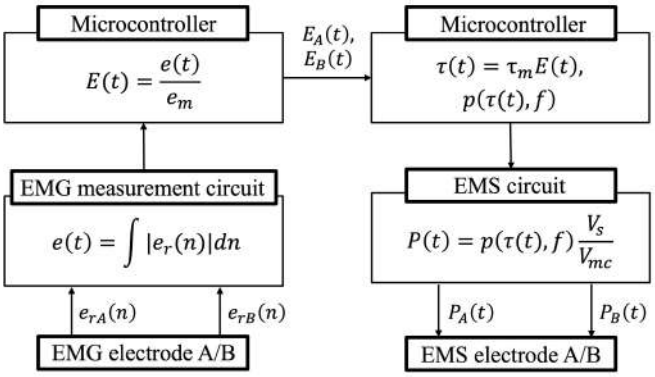


Fig. 3. The signal process from the EMG measurement device to the EMS device

or video meeting system on a PC or tablet device. We propose a wearable haptic interface that does not require mechanical actuators and can be easily integrated into conventional telecommunications equipment. The patient wears a device for measurement and the therapist wears a device for EMS. EMG signals measured from the patient are processed and sent to the therapist's device as bioelectrical signals. Based on the received signals at the therapist's side, multi-channel EMS is applied to the therapist to share the perception of joint stiffness changes. This does not replicate the conventional MAS, but allows the therapist to perceive the patient's joint condition as a force sensation.

C. Modulation of Joint Stiffness by Multi-Channel EMS

Fig.2 shows a conceptual diagram of the mechanism of elbow joint stiffness augmentation by multi-channel EMS. Functional electrical stimulation (FES) is one type of EMS technology that communicates control signals from an external device to the neuromuscular system for assisting or restoring motor functions[14]. When FES is applied to the biceps brachii, the elbow joint moves in the direction of flexion, and when FES is applied to the triceps brachii, the elbow joint moves in the direction of extension. Therefore, involuntary simultaneous contraction of the biceps and triceps muscles, which are the muscle antagonist pair to the elbow joint, makes it difficult to move the elbow joint. In this paper, joint stiffness is defined as the difficulty in moving the joint due to simultaneous contraction of the muscle antagonist pair, and changes in joint stiffness are promoted by changing the level of muscle contraction by EMS.

D. EMS Signal Model based on EMG

Fig. 3 shows the signal processing block diagram of the proposed method. A and B in the figure represent different muscle sites. $e_r(n)$ are the EMG signals amplified in the EMG measurement circuit based on the biopotential signals of muscles measured at discrete time n. The signals are absolutized and smoothed to express the magnitude of muscle contraction per constant time t. The smoothed signal $e(t)$ is expressed by the following equation (1).

$$e(t) = \int |e_r(n)|dn \tag{1}$$

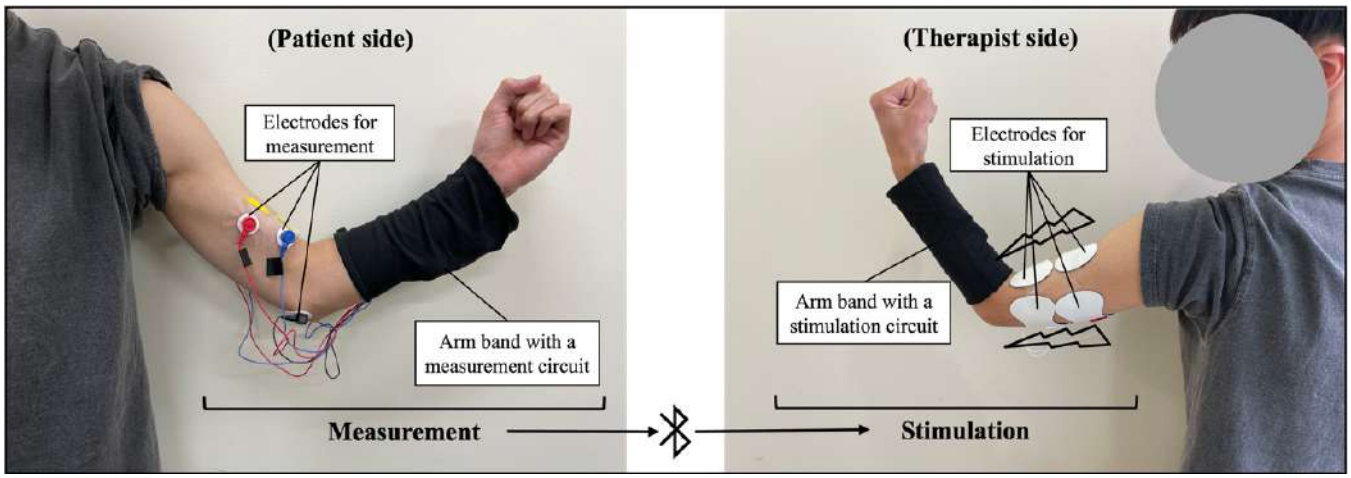


Fig. 4. System configuration

Each time the user wears the electrodes, the user voluntarily contracts the target muscle isometrically as much as possible, and the maximum value of the EMG signal e_m at that time is measured as the maximum voluntary contraction (MVC). The measured EMG signal $e(t)$ is normalized using e_m to obtain the voluntary contraction rate $E(t)$, which is expressed by the following equation (2).

$$E(t) = \frac{e(t)}{e_m} \tag{2}$$

In the device for EMS, the parameters of the square wave pulse signal for EMS are defined. When the frequency of the square wave pulse signal is f, the maximum pulse width is $\tau_m (0 \leq \tau_m < 1/f)$, and the pulse width $\tau(t)$ is expressed by the following equation (3).

$$\tau(t) = \tau_m E(t) \tag{3}$$

The square wave pulse signal function $p(\tau, f)$ is determined using the frequency f and $\tau(t)$ by the following equation (4).

$$p(\tau, f) = \begin{cases} V_{mc} & (0 \leq t < \tau) \\ 0 & (\tau \leq t < \frac{1}{f}) \end{cases} \tag{4}$$

Since the output voltage V_{mc} from the microcontroller is not sufficient for EMS, an external power supply is used in the EMS circuit to amplify V_{mc} to obtain the stimulation voltage V_s. The square wave pulse signals $P(t)$ are used as the output signal for EMS by the following equation (5).

$$P(t) = p(\tau, f)\frac{V_s}{V_{mc}} \tag{5}$$

IV. System configuration

A. EMG Measurement Unit

The EMG measurement unit is used for the patient's device. The microcontroller that controls the entire circuit is an ESP32-WROOM-32E, which sends signals from the EMG sensor to the EMS circuit. MyoWare is a module for EMG measurement and is equipped with a bandpass filter circuit, an amplification circuit, and an absolute value processing and smoothing circuit. A snap-button cable is used to connect the electrodes, allowing selective use of wet electrodes or conductive fabrics that conduct with the snap buttons.

B. EMS Unit

The EMS unit is used for the therapist's device. The microcontroller, ESP32-WROOM-32E, generates square pulse wave signals and receives data from the EMG measurement circuit. A photo coupler (PC817) is used as a relay element to electrically isolate the pulse wave control signal for EMS and the input potential to the stimulating electrode to prevent damage to the control circuit. A DC/DC converter (LM2733) is used to boost the voltage from a lithium-ion polymer battery rated at 3.7 V as an external power supply for muscle stimulation. A 10 mA constant current diode (S-103T) is inserted before the stimulating electrode connector to limit the current to avoid risk to the human body. An audio minijack is used as a connector for the stimulating electrode so that a conductive cable with an audio minijack can be easily connected and disconnected. The other end of the conductive cable can be connected to a snap button as with the EMG measurement circuit. The amplitude of the square-wave pulse signal for EMS is 10-40 V, the frequency is 1-200 Hz, and the maximum pulse width can be changed in the interval of 0-1000 µs. In this study, the maximum pulse width was set at 400 µs, which is less likely to cause pain or discomfort to the user due to EMS[15].

C. Attachment and Connection

Fig.4 shows how to wear the devices and connect each device to the other. The main body of the device can be worn to improve usability so that it does not interfere with the user's movement. The EMG measurement circuit or the EMS circuit is stored in the armband with a pocket, and only the snap-button cable is removed to connect to the electrodes. The microcontrollers can connected to other microcontrollers or PC via wired serial, Bluetooth, or Wi-Fi connection. In this study, we used Bluetooth connection, which is a wireless communication method and has stable communication. When introducing the system to TR, it is possible to switch to a Wi-Fi connection and realize communication via the Internet.

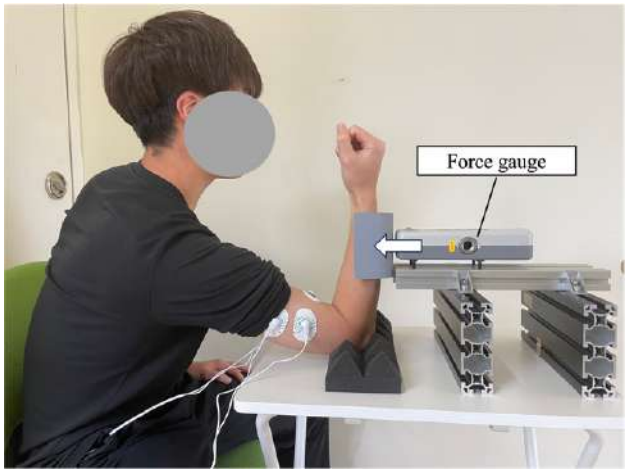


Fig. 5. The setup of the drag force measurement

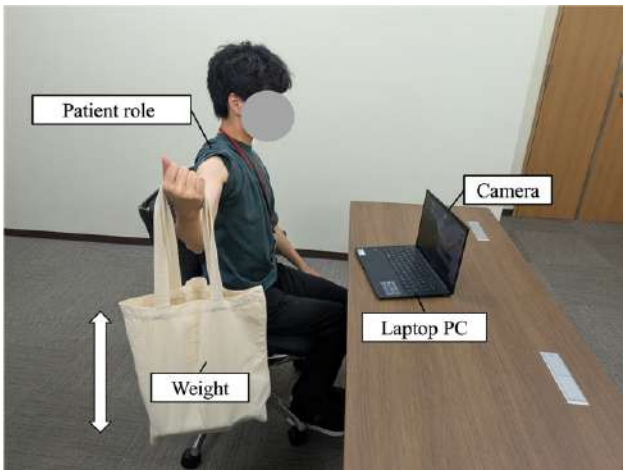


Fig. 6. The setup of the visual condition

V. Experiments

A. Performance Evaluation for EMS System

In this experiment, we aimed to validate joint stiffness modulation through the intensity of multi-channel EMS. We measured the drag force produced by displacement from the same joint angle and evaluated its characteristics. All participants in the experiment were tested at the same stimulus intensity to obtain individual characteristics.

The experiment setup is shown in Fig.5. The electrodes were attached to the biceps brachii and triceps brachii muscles, respectively, and the elbow was placed on a tabletop. A digital force gauge (ZTA-50N, Imada Corporation) was pressed horizontally against the forearm in a vertical position to move the joint, and the maximum drag force was measured at the right before the movement started. The participants were instructed to relax their arms and not to resist when the digital force gauge was pressed. The stimulation voltage was 30 V, the frequency of the stimulation signal was 40 Hz, and the pulse widths were 0, 100, 200, 300, and 400 µs and same values for both biceps brachii and triceps brachii muscles. A pulse width of 400 µs or less, which is less likely to cause pain or discomfort to the users due to EMS, was used to examine the characteristics in this experiment. The current was limited to 10 mA so as not to endanger the human body. The drag force was measured 3 times each and the average value was calculated.

4 male participants (Age: 23.25 $\pm$ 0.5) from our local organization with no history of neurological or musculoskeletal disorders participated in a total of 60 trials (4 participants $\times$ 5 stimulus strengths $\times$ 3 times).

B. Perceptual Study

The objective of this experiment was to evaluate the subjective discrimination performance of changes in elbow joint stiffness induced by multi-channel EMS under static conditions that do not cause angular displacement of the joint. No mapping to the true MAS score was performed, but we verified if there are 5 levels of discrimination performance.

The participant who is the patient role and the participant who is the therapist role were made visible to each other using a video meeting system (Zoom) in an online setting. The sound is muted to limit the transmission of information through the auditory sense. Fig.6 shows the setup of the visual condition in the experiment. In the visual condition, the patient maintains a 90-degree elbow joint angle and lifts a 0, 2, 4, 6, and 8 kg weight one time each. The weights are kept out of the camera's angle of view so that the therapist can only see the patient's upper arm muscles. The patient lifts the weights one time each in random order, and the therapist responds to the presented task by discriminating the relative stiffness of the joints in 5 levels. 2 different patient roles presented the visual conditions for participants P1-5 and P6-10. The therapist role is informed in advance that the mass of the weights are 0, 2, 4, 6, and 8 kg. In the haptic condition, the camera of the video meeting system is turned off so that the therapist role cannot see the patient role's upper arm muscles. The patient role then applies the stimuli one time each in random order at different intensities, and the therapist role then responds by discriminating the relative stiffness of the joints at each of the 5 levels. For the EMS to the therapist role, the stimulation voltage was 30 V, the frequency of the stimulation signal was 40 Hz, and the pulse widths were 0, 100, 200, 300, and 400 µs as 5 levels of joint stiffness and same values for both biceps brachii and triceps brachii muscles. Both conditions consisted of one familiarization session at each level, followed by 3 sets of recorded sessions.

The experiment was conducted on 10 non-expert male and female participants (Age: 22.9 $\pm$ 0.74) as the therapist role and two male participants (Age: 23.5 $\pm$ 0.71) as the patient role from our local organization. All participants in both roles had no upper limb motor impairment.

Both experiments were approved by the Research Ethics Committee of the Institute of Systems and Information Engineering, University of Tsukuba (No. 2024R874), and conducted with the informed consent of the participants.

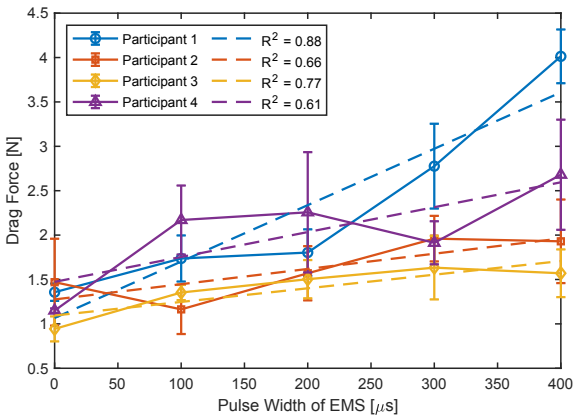


Fig. 7. The drag force measurement results

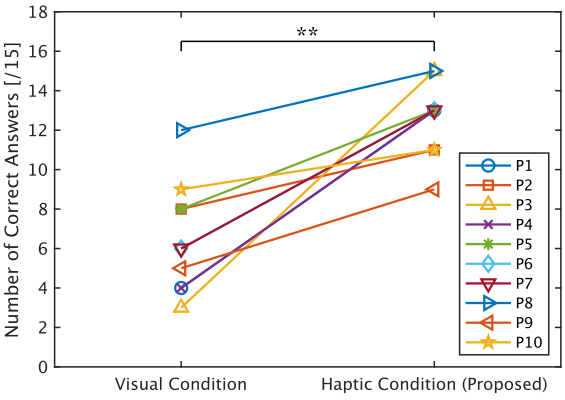


Fig. 8. Discrimination results of the perceptional study

VI. Experimental Results

A. Performance Evaluation for EMS System

Fig. 7 shows the average force obtained for each stimulus pulse width of each participant. The measured drag force tended to increase with increasing pulse width for each participant ($R^2 > 0.6$). However, the measured drag force decreased with increasing pulse width for pulse widths from 0 to 100 µs in participant 2 and from 200 to 300 µs in participant 4. It was also observed that the change in drag with increasing pulse width was not linear. These results suggest that differences in the physical characteristics of each participant can result in different thresholds of stimulus intensity at which a joint begins to move.

B. Perceptual Study

Fig. 8 and Table I show the discrimination results of the perception experiment of elbow joint stiffness change under static conditions. The numbers in the table indicate the percentage of correct responses for a total of 15 trials (5 levels, 3 sets). For all participants, the percentage of correct responses in the haptic condition was higher than in the visual condition, with an average of 6.1 points more correct responses. In the visual condition, the average correct response rate was 43.3%, whereas in the haptic condition, the average correct response rate was 84.0%. The Wilcoxon signed-rank test showed a significant difference in the number of correct responses between visual condition (Mdn = 6) and haptic condition (Mdn = 13), $W = 0$, $p = 0.0051 < 0.01$.

TABLE I
Discrimination results of the perceptional study

Participant	Visual condition	Haptic condition	Difference
P1	4/15	13/15	+9
P2	8/15	11/15	+3
P3	3/15	15/15	+12
P4	4/15	13/15	+9
P5	8/15	13/15	+5
P6	6/15	13/15	+7
P7	6/15	13/15	+7
P8	12/15	15/15	+3
P9	5/15	9/15	+4
P10	9/15	11/15	+2
Average[/15]	6.5 ± 2.76	12.6 ± 1.65	+6.1
Average[%]	43.3	84.0	+41.7

VII. Discussion

A. Performance Evaluation for EMS System

We measured and evaluated the elbow joint drag force during EMS to confirm that joint stiffness changes as the intensity of multi-channel EMS modulation. In all participants, the measured drag force tended to increase as the applied stimulus intensity increased. However, the regression analysis showed that the R^2 value was less than 0.9, indicating that the linear relationship between the measured drag force and pulse widths was lower than the results of Nishida et al.[13]. We applied the same stimulus intensity to all participants with EMS output pulse widths ranging from 0 to 400 µs to check for differences in individual characteristics. The stimulus intensity that Nishida et al.[13] used may be significantly higher than our maximum stimulus intensity because they determined the maximum stimulus intensity based on individual EMG measurements. The range of stimulus intensities that we applied was considered to have a threshold at which joint motion begins to be produced by EMS, thus more individualized features were obtained.

B. Perceptual Study

Since the TR systems currently in practical use are video meeting systems, we compared the discrimination performance between a video meeting system and the proposed method using multi-channel EMS for untrained participants. The discrimination performance of the proposed method was better than the visual condition for all participants, and the average number of correct answers was 6.1 points higher. It suggests the usefulness of the proposed method for TR by presenting force perception using multi-channel EMS.

The low average correct response rate of 43.3% in the visual condition was attributed to the difficulty of judging muscle contraction only visually within a limited angle of view when trying to discriminate joint stiffness. The fact that a certain number of correct responses were obtained even in the visual condition can indicate that the participants were able to visually confirm the muscle protuberance during muscle contraction. However, it is considered extremely

difficult to discriminate between the five levels of strength. In addition, the variability of correct responses across individuals in the visual condition (SD=2.76) was greater than that in the haptic condition (SD=1.65). It suggests that the visual condition is likely to depend on the perceptual ability of each individual. It should be noted that the results of the visual condition could be improved if experienced experts participated since this study was conducted with untrained participants.

On the other hand, the proposed method using multi-channel EMS can discriminate an average of 84.0%. It is considered superior in identifying different levels of muscle contraction, even during intense contractions near MVC. However, it is not always possible to obtain sufficient discrimination performance with EMG signals generated from the muscles of patients with different levels of paralysis, and this is an issue that should be considered in future studies.

The correct response rate for each participant in the EMS condition ranged from 60 to 100%. The results suggest that if changes in joint stiffness can be appropriately presented with the stimulus intensity calibrated for each person, the discrimination performance by force presentation is enough to be useful for understanding the modulation of joint stiffness of others.

C. Limitations and Future Works

The device we have developed treats human muscle activity as a relative value, which is highly dependent on individual characteristics, and it is impossible to obtain joint stiffness as an absolute value and simulate real spasticity. However, since spasticity is a state in which the antagonist muscles contract involuntarily[16], this method can be described as the presentation of a spastic state. We believe that this device can be used in clinical practice because relative evaluation based on MVC and manual evaluation based on the therapist's sensation are commonly used in the field of rehabilitation. We would like to establish a calibration method that is tailored to individual characteristics and improve performance.

In addition, since we have not been able to compare this experiment with the visual EMG feedback, we would like to clarify in future studies the effect of multi-channel EMS.

VIII. Conclusion

In this paper, we developed a remote interface between therapist and patient using multi-channel EMS for application to joint stiffness evaluation in TR. The device is wearable with adjustable settings and can be configured for wireless communication. In the performance evaluation, the measured elbow joint drag force tended to increase as the stimulation pulse width increased, and differences in characteristics between individuals in the low stimulation intensity range below 400 µs were confirmed. In the perceptual experiment, the haptic condition showed higher discrimination performance than the visual condition ($p = 0.0051$, the Wilcoxon signed-rank test), with an average discrimination performance of 84.0% for all participants. Although we could not obtain a five-step discrimination performance that could replace the MAS in clinical practice, we expect to improve the performance by calibrating the output signal parameters according to individual characteristics in the future. The method using multi-channel EMS has better discrimination performance than vision and is easier to implement than robotic systems. This suggests that it can be useful as part of a future TR system.

Acknowledgments

We sincerely thank Professor Dai Karasuno for his insightful recommendations on physical therapy practices and the experimental methods used in this research.

References

[1] M. Rogante, M. Grigioni, D. Cordella, and C. Giacomozzi, "Ten years of telerehabilitation: A literature overview of technologies and clinical applications," *NeuroRehabilitation*, vol. 27, no. 4, pp. 287–304, 2010.

[2] T. G. Russell, "Physical rehabilitation using telemedicine," *Journal of telemedicine and telecare*, vol. 13, no. 5, pp. 217–220, 2007.

[3] K. Shem, I. Irgens, and M. Alexander, "Getting started: mechanisms of telerehabilitation," in *Telerehabilitation*. Elsevier, 2022, pp. 5–20.

[4] M. McCue, A. Fairman, and M. Pramuka, "Enhancing quality of life through telerehabilitation," *Physical Medicine and Rehabilitation Clinics*, vol. 21, no. 1, pp. 195–205, 2010.

[5] A. Turolla, G. Rossettini, A. Viceconti, A. Palese, and T. Geri, "Musculoskeletal physical therapy during the covid-19 pandemic: is telerehabilitation the answer?" *Physical therapy*, vol. 100, no. 8, pp. 1260–1264, 2020.

[6] P. N. Pathirana, S. Li, H. M. Trinh, and A. Seneviratne, "Robust real-time bio-kinematic movement tracking using multiple kinects for tele-rehabilitation," *IEEE Transactions on Industrial Electronics*, vol. 63, no. 3, pp. 1822–1833, 2015.

[7] J. Lai and A. Song, "Design and characterization of a novel compact hand exoskeleton robot for telerehabilitation and muscle spasticity assessment," *IEEE/ASME Transactions on Mechatronics*, 2023.

[8] T. Geri, A. Viceconti, M. Minacci, M. Testa, and G. Rossettini, "Manual therapy: exploiting the role of human touch," *Musculoskeletal Science and Practice*, vol. 44, p. 102044, 2019.

[9] Y. Liu, S. Guo, Z. Yang, H. Hirata, and T. Tamiya, "A home-based tele-rehabilitation system with enhanced therapist-patient remote interaction: A feasibility study," *IEEE Journal of Biomedical and Health Informatics*, vol. 26, no. 8, pp. 4176–4186, 2022.

[10] M. Sommerhalder, N. Kurth, J. Song, and R. Riener, "Armstick-an intuitive therapist interface for upper-limb rehabilitation robots," in *2022 International Conference on Rehabilitation Robotics (ICORR)*. IEEE, 2022, pp. 1–6.

[11] L. Wang, X. Guo, P. Fang, Y. Wei, O. W. Samuel, P. Huang, Y. Geng, H. Wang, and G. Li, "A new emg-based index towards the assessment of elbow spasticity for post-stroke patients," in *2017 39th annual international conference of the IEEE engineering in medicine and biology society (EMBC)*. IEEE, 2017, pp. 3640–3643.

[12] J. Nishida and K. Suzuki, "Biosync: A paired wearable device for blending kinesthetic experience," in *Proceedings of the 2017 CHI conference on human factors in computing systems*, 2017, pp. 3316–3327.

[13] J. Nishida, K. Yagi, M. Hassan, and K. Suzuki, "Wearable kinesthetic i/o device for sharing wrist joint stiffness," in *2019 41st Annual International Conference of the IEEE Engineering in Medicine and Biology Society (EMBC)*. IEEE, 2019, pp. 3306–3310.

[14] V. C. Cheung, C. M. Niu, S. Li, Q. Xie, and N. Lan, "A novel fes strategy for poststroke rehabilitation based on the natural organization of neuromuscular control," *IEEE reviews in biomedical engineering*, vol. 12, pp. 154–167, 2018.

[15] N. A. Maffiuletti, J. Gondin, N. Place, J. Stevens-Lapsley, I. Vivodtzev, and M. A. Minetto, "Clinical use of neuromuscular electrical stimulation for neuromuscular rehabilitation: what are we overlooking?" *Archives of physical medicine and rehabilitation*, vol. 99, no. 4, pp. 806–812, 2018.

[16] G. Sheean, "The pathophysiology of spasticity," *European journal of neurology*, vol. 9, pp. 3–9, 2002.

Causal inference predicts that muscle excitation is both a contributor and response to frontal plane dynamic balance during gait of older individuals with and without transtibial amputation

Arianna S. Monteiro, Matthew J. Major, and Nicholas P. Fey, *Member, IEEE*

Abstract— **More than 50% of individuals with lower-limb amputations and ~40% of older individuals (over 65 years old) fall each year. To optimize prosthetic intervention for fall prevention, it is important to understand the neuromotor control of balance. We use a data-driven approach, Convergent Cross Mapping, to determine the relationships between lower-limb muscle excitation and whole-body and segmental angular momentum in the frontal plane. These relationships were determined for 10 able-bodied older individuals and 13 older individuals with transtibial amputations at normal and fast walking speeds. The results suggest that there were several group and group-speed interaction differences, especially in the medial hamstrings of the intact and amputated legs at normal speeds, which exhibited stronger relationships between muscle activity and momentum of the whole-body, trunk and arms relative to control subjects. Difference between the subject group interlimb coupling was also observed by the stronger contribution of the gastrocnemius in the intact limb to frontal-plane momentum of the contralateral arm for persons with limb loss. Nearly equal numbers of relationships at both speeds showed muscle activities of the lower extremity were most predictive of subsequent (i.e., future), current or previous states of angular momentum, suggesting that muscle activity is responsible for generation, regulation and likely a response of/to dynamic balance in the frontal plane, respectively. Finally, this approach analyzes the functional outcomes of prosthetic intervention and how amputation alters the neuromotor control of gait in older individuals. This analysis can be applied at the individual level to study effects of prosthesis selection.**

I. Introduction

Around 2.3 million people in the United States currently live with limb loss, where 91% of these cases result from lower-limb amputations (LLA) [1]. A major concern for individuals with LLA is the risk of falling, as around 52% of the population falls at least one time each year [2]. Falling not only compromises the quality of life but has also been associated with a decline in physical activity and social activities in older individuals as well as limb fracture and decreased prosthesis use in individuals with amputations [3], [4, 5]. Along with an increase in falls, individuals with LLA often develop secondary musculoskeletal conditions such as lower back pain and osteoarthritis, which may result from aberrant gait dynamics from compensatory mechanisms [6]. To better inform prosthetic designs that help reduce falls and secondary conditions from gait compensations, it is important to understand the neural control of balance and how it is regulated in individuals with and without LLA.

To quantify dynamic balance in older individuals with lower-limb amputations, the biomechanical measure of angular momentum (H), both whole-body and segmental, can be studied. H is a laboratory-based measure that is used to quantify rotations in three cardinal planes relative to the whole-body center-of-mass (COM) and has previously been associated with an increased risk of falling in individuals with LLA [7]. In this study, we are investigating H in the frontal plane, as older individuals have shown frontal plane instability after perturbations [8]. The consequences of falling laterally have also been associated with hip fractures and can severely impact the quality of life of older individuals with and without amputation [9]. However, the whole-body H alone does not provide a holistic view of the regulation of balance, especially in older individuals with lower-limb amputations. By studying the contribution of coordinated segments to the changes in the net whole-body H, researchers can gain insight into how balance strategies change in the absence of key lower-limb muscle groups. Previous literature has found that the trunk frontal-plane H increases during unanticipated transitions in able-bodied (AB) individuals [10]. These changes in trunk segmental H were also found in our previous study of older individuals with transtibial amputation (TTA); however, we found that these individuals also have an altered segmental H in the non-dominant leg/residual leg and in both arms during residual limb braking [11].

Although segmental H gives insight into differences in balance, it does not fully reveal the unique control mechanisms used by older individuals with lower-limb amputations to maintain dynamic balance. To gain insight into the control mechanisms used to generate H, muscle excitation can be studied through electromyography (EMG). Previous studies have found differences in muscle activation during braking of the residual leg bicep femoris, vastus lateralis, and rectus femoris of individuals with LLA compared to AB subjects [12]. We previously found similar results in the non-dominant/residual medial hamstrings during braking when comparing older individuals with and without TTA [11].

Since muscle forces create changes in H, simulations have been used to determine the relationship between muscle excitations and whole-body H in AB individuals. In the frontal plane, muscles like the vasti and adductor magnus contributed

* This work was partially supported by the U.S. Department of Veterans Affairs [#1IK2RX001322].

A. S. Monteiro is with the Department of Biomedical Engineering at the University of Texas at Austin, Austin, TX 78712 (arianna.s.monteiro@utexas.edu).

M. J. Major is with the Department of Physical Medicine & Rehabilitation at Northwestern University, Chicago, IL 60611 (matthew-major@northwestern.edu).

N. P. Fey is with the Walker Department of Mechanical Engineering at the University of Texas at Austin, Austin, TX 78712 (nfey@utexas.edu).

towards rotations during early stance, and the gluteus medius, soleus, and gastrocnemius contributed to rotations during late stance [13]. However, since it is difficult to model aging pathologies, to understand these relationships in older individuals with TTA, we previously correlated muscle excitations with whole-body and segmental *H* [11]. The main findings highlighted that generally muscle excitation was positively correlated with *H*; however, in older individuals with TTA, a higher residual medial hamstring excitation was negatively correlated with whole-body *H*.

Though previous results demonstrate trends of muscle excitation to changes in whole-body and segmental *H* over the entire gait cycle, they do not define causal predictive relationships. In this study, we utilize Convergent Cross Mapping (CCM), a novel data-driven approach that uncovers causal interactions of dynamical systems, in its first application to gait analysis [14]. The goal of this study was to determine how transtibial amputation and speed conditions change the causal relationships between muscle excitation and *H* in older individuals during over-ground walking. We hypothesized that these relationships would change between subject groups and would be speed-dependent.

II. Methods

A. Subjects and Protocol

We collected data from 10 AB older individuals (5 males, 5 females; 72±4 years; 168±6 cm; 77±8 kg) and 13 individuals with transtibial amputations (10 males, 3 females; 71±4 years; 176±9 cm; 86±14 kg), where the etiology of the amputations was due to trauma (n=10), infection (n=1), cancer (n=1), and vascular complications (n=1). All participants were instructed to walk back and forth along a 10-meter walkway at two self-selected speeds, comfortable normal and fast to capture a minimum of 11 gait cycles for analysis. For the individuals with and without TTAs, the normal speed corresponds to 1.07 (0.18) m/s and 1.14 (0.21) m/s, respectively. At the fast speed, the individuals with and without TTAs walked at speeds of 1.38 (0.19) m/s and 1.53 (0.24) m/s, respectively. The participants were instructed to "walk normally and comfortably as if walking in the community" and "at a brisk pace without breaking out into a jog" for the normal and fast speed conditions, respectively. Our previous study demonstrated that the walking speeds were not significantly different between subject groups, so we considered the speed-associated differences of each group the same [11]. During the trials, the group with TTAs wore their clinically prescribed prostheses. Ethical approval was granted by the Jesse Brown VA Medical Center IRB and participants provided written informed consent.

B. Data Collection and Processing

The whole-body kinematic data were recorded using a 12-camera Vicon motion capture system (120 Hz). The individuals were instrumented with a modified Helen Hayes marker set. The kinetic data were measured using ground reaction force plates (960 Hz) and were exported into Visual3D (C-Motion), where a 4th-order low-pass Butterworth filter with a 6 Hz cut-off frequency was applied. Then, a 12-segment model was applied to each participant, where the residual limb of the model applied to individuals with TTAs was adjusted according to mass and center of mass properties [15]. Then, laboratory-based measures of whole-body and segmental angular momentum (*H*) were calculated in the frontal plane. The *H* was calculated for each participant and speed condition, which was then normalized by body mass, height, and speed. In the analyses, the dominant leg in the AB group was compared to the intact leg of the group with TTAs. EMG data were recorded (960 Hz) using Delsys sensors on the tibialis anterior (TA), medial gastrocnemius (GAS), rectus femoris (RF), medial hamstring (HAM), and gluteus medius (GMED) on both legs, as appropriate and was synchronized with the *H* data. A band-pass filter (cut-off frequency 30-350 Hz) was applied to the EMG signals [16, 17]. After filtering, the signals were rectified, and a linear envelope was applied using a moving RMS (window size of 100 ms). The gait events labels which determined the start and end of a gait cycle were identified manually based on the motion of the heel and toe marker.

C. Data Analysis

Causal inference relationships were determined by the extended version of Convergent Cross-Mapping (CCM) [14, 18]. CCM is based on Takens' Theorem, which states the unobserved dynamics of a system can be reconstructed using time delays of a single observed variable in the system. Thus, if X causally influences Y, then X leaves information in Y [14]. Therefore, information about the hidden causal variable can be recovered given observations of the caused variable. This means that the response variable (Y) can be used to determine past values of the causal variable (X). Prior to performing CCM, the optimal embedding dimension, or the number of interacting variables, was determined to be 3 using Simplex projection [19]. Then, a 3-dimensional time delay embedding (τ=1) was computed for each EMG channel, whole-body *H*, and segmental *H* time series. These embeddings were then cross-mapped to the other variable. For example, if the whole-body *H* embedding (Y) can be used to predict the behavior of an EMG (X), then it is said that y cross-maps x (X causes Y). To determine the strength of the causal influence, this cross-mapped variable is Pearson correlated with the original signal (α=0.05). For example, the cross-mapped estimated whole-body *H* (using the EMG embedding) is Pearson correlated with the original whole-body *H* signal. If the correlation coefficient converges as the number of randomly sampled points increases, then it can be concluded that the two variables are causally related. The overall strength of the causal relationship is determined by the "skill" (ρ) value that it converges to. The ρ of the cross-map is computed as the average of the latest convergent correlation coefficients.

To understand if the causal variable acts on the response variable with a time delay, we used the extended CCM and performed cross-mapping with time lags (τ) -4 to 4, where each time lag is 1% of the stride [18]. This time lag range represents a temporally distributed sampling strategy where a window is repeatedly sampled across the entire gait cycle. A negative τ signifies a lag in the response to the causal variable and a positive τ means that the causal variable precedes changes in the response variable, indicating a lead. The more negative τ is, the larger the forward prediction. The ρ at each time lag was also computed for each participant and was

averaged across strides, then the average and standard deviation were computed for each subject group.

To fully capture the temporal behavior of physiological processes from the initial muscle excitation, muscle force production, and the subsequent change in velocity of body segments which contribute to changes in angular momentum, we conducted time lag analysis. These time lags account for 58 ms and 48 ms during comfortable normal and fast walking, respectively, which fully captures the natural occurrence of the activation and deactivation of muscles as well as electromechanical delay [20-22].

D. Statistical Analysis

Each participant's average ρ for each whole-body and segmental *H* v. EMG was used to compute group and group-speed interaction significances. To determine these significant differences, we used linear mixed modeling. We defined the subject groups (AB and individuals with TTAs) and the speed conditions (normal and fast walking) as the fixed effects and the participants as the random effect. We computed this statistical test in MATLAB for each time lag and highlighted significant group and group-speed interactions (α=0.05).

III. Results

The relationships between muscle activation and whole-body and segmental *H* were dependent on the group as well as the speed conditions (Fig. 1).

A. Subject Group Differences

There were significant subject group differences between the dominant TA and the whole-body *H* (τ: -4 to 4 as well as the trunk *H* (τ: 1 to 4), shown in Fig. 1 (blue or green) and Table I (in bold). The intact TA was more predictive of *H* for the group with TTAs compared to those without. These group differences were present in the dominant GAS and the non-dominant arm (τ: -4 to 4) where the group with TTAs had a higher prediction of *H*. The dominant RF had group differences in the dominant arm contributions to *H* (τ: -4 to 4) where the group with TTAs had better normal walking prediction of *H* compared to the AB group. In the non-dominant RF, there were significant group differences with the whole-body *H* (τ: -4 to 4) and the non-dominant leg *H* (τ: -3 to 4). In this comparison, the residual RF was more predictive of whole-body *H* but less predictive of non-dominant leg *H* for individuals with TTA compared to the AB individuals. Compared to the other EMG group differences, the dominant and non-dominant HAM had the most significant subject group differences with *H*. Specifically, the dominant HAM had significant group differences between the whole-body *H* (τ: -4 to 4), the trunk *H* (τ: -4 to 3), the non-dominant leg *H* (τ: -4 to 2), the dominant arm *H* (τ: -4 to 4), and the non-dominant arm *H* (τ: -3 to 2). In all of these relationships, the group with TTAs was better at predicting changes in *H*, except for the non-dominant leg *H*. Similarly, the non-dominant HAM had significant group differences with the whole-body *H* (τ: -4 to 4), the trunk *H* (τ: -4 to 0), and the dominant arm *H* (τ: -4 to 3). For this muscle, the group with TTAs was more predictive of *H* compared to the AB group. Lastly, only the dominant GMED had group differences with the trunk *H* (τ: -4 to 4), the dominant arm *H* (τ: -4 to 4), and the non-dominant arm *H* (τ: -4 to 4), where the group with TTAs had a stronger predictive relationship to *H*.

B. Subject Group-Speed Differences

Table I indicates that there is a significant group-speed difference in the relationship between the dominant TA and the whole-body *H* (COM) during fast walking. The strongest causal relationship (ρ) was found to be at τ=-1, therefore, according to CCM, the dominant TA is predictive of future changes in the whole-body *H*.

TABLE I. Maximum Rho and Lag

			Dom	Non-Dom	Intact	Residual
TA	WN	COM	**ρ=0.38, τ=1**	ρ=0.37, τ=-1	**ρ=0.51, τ=1**	
		Trunk	ρ=0.46, τ=-1	ρ=0.44, τ=-1	**ρ=0.54, τ=1**	
		Dom Leg	ρ=0.51, τ=1	ρ=0.45, τ=1	ρ=0.58, τ=1	
		Non-Dom Leg	ρ=0.52, τ=1	ρ=0.49, τ=2	ρ=0.47, τ=0	
		Dom Arm	ρ=0.44, τ=0	ρ=0.35, τ=0	ρ=0.51, τ=1	
		Non-Dom Arm	ρ=0.33, τ=-1	ρ=0.37, τ=-1	ρ=0.40, τ=-1	
	WF	COM	**ρ=0.55, τ=-1**	ρ=0.53, τ=-2	ρ=0.58, τ=1	
		Trunk	ρ=0.61, τ=-1	ρ=0.59, τ=-1	ρ=0.63, τ=0	
		Dom Leg	ρ=0.60, τ=1	ρ=0.46, τ=0	ρ=0.63, τ=1	
		Non-Dom Leg	ρ=0.44, τ=0	ρ=0.57, τ=2	**ρ=0.52, τ=1**	
		Dom Arm	ρ=0.52, τ=1	ρ=0.44, τ=0	ρ=0.60, τ=1	
		Non-Dom Arm	**ρ=0.38, τ=-2**	ρ=0.49, τ=0	**ρ=0.34, τ=0**	
GAS	WN	COM	ρ=0.60, τ=2	ρ=0.64, τ=1	ρ=0.65, τ=2	
		Trunk	ρ=0.55, τ=1	ρ=0.56, τ=2	ρ=0.58, τ=1	
		Dom Leg	ρ=0.68, τ=0	ρ=0.48, τ=1	ρ=0.64, τ=0	
		Non-Dom Leg	ρ=0.54, τ=2	ρ=0.75, τ=-1	ρ=0.51, τ=0	
		Dom Arm	ρ=0.38, τ=1	ρ=0.47, τ=1	ρ=0.50, τ=0	
		Non-Dom Arm	**ρ=0.42, τ=-1**	ρ=0.37, τ=-1	**ρ=0.59, τ=0**	
	WF	COM	ρ=0.58, τ=2	ρ=0.62, τ=2	ρ=0.59, τ=3	
		Trunk	ρ=0.59, τ=2	ρ=0.52, τ=2	ρ=0.57, τ=2	
		Dom Leg	ρ=0.67, τ=0	ρ=0.48, τ=1	ρ=0.68, τ=1	
		Non-Dom Leg	ρ=0.45, τ=1	ρ=0.67, τ=1	ρ=0.49, τ=0	
		Dom Arm	ρ=0.38, τ=1	ρ=0.34, τ=-1	ρ=0.46, τ=0	
		Non-Dom Arm	ρ=0.26, τ=-1	ρ=0.26, τ=0	ρ=0.53, τ=0	
RF	WN	COM	ρ=0.51, τ=0	**ρ=0.49, τ=0**	ρ=0.61, τ=-1	**ρ=0.64, τ=0**
		Trunk	ρ=0.55, τ=0	ρ=0.50, τ=1	ρ=0.68, τ=0	ρ=0.57, τ=-1
		Dom Leg	ρ=0.49, τ=1	ρ=0.49, τ=0	ρ=0.45, τ=0	ρ=0.49, τ=-1
		Non-Dom Leg	ρ=0.52, τ=1	**ρ=0.54, τ=0**	ρ=0.50, τ=0	**ρ=0.39, τ=0**
		Dom Arm	**ρ=0.43, τ=-1**	ρ=0.45, τ=0	**ρ=0.61, τ=-1**	ρ=0.41, τ=0
		Non-Dom Arm	ρ=0.50, τ=-1	ρ=0.47, τ=-1	ρ=0.51, τ=-1	ρ=0.55, τ=-1
	WF	COM	ρ=0.59, τ=1	**ρ=0.56, τ=0**	ρ=0.65, τ=0	**ρ=0.64, τ=0**
		Trunk	ρ=0.57, τ=1	ρ=0.55, τ=0	ρ=0.68, τ=1	ρ=0.60, τ=0
		Dom Leg	**ρ=0.49, τ=0**	ρ=0.53, τ=0	**ρ=0.50, τ=1**	ρ=0.53, τ=-1
		Non-Dom Leg	ρ=0.52, τ=-1	**ρ=0.50, τ=0**	ρ=0.48, τ=0	**ρ=0.54, τ=0**
		Dom Arm	**ρ=0.63, τ=0**	ρ=0.52, τ=1	**ρ=0.59, τ=-1**	ρ=0.52, τ=0
		Non-Dom Arm	ρ=0.50, τ=-1	ρ=0.43, τ=0	ρ=0.54, τ=-1	ρ=0.52, τ=-1
HAM	WN	COM	**ρ=0.30, τ=1**	**ρ=0.41, τ=1**	**ρ=0.50, τ=1**	**ρ=0.60, τ=0**
		Trunk	**ρ=0.35, τ=1**	ρ=0.46, τ=2	**ρ=0.49, τ=-1**	**ρ=0.58, τ=0**
		Dom Leg	ρ=0.40, τ=0	ρ=0.52, τ=0	ρ=0.42, τ=0	ρ=0.50, τ=-1
		Non-Dom Leg	**ρ=0.60, τ=1**	ρ=0.45, τ=2	**ρ=0.49, τ=1**	ρ=0.52, τ=1
		Dom Arm	**ρ=0.38, τ=-1**	**ρ=0.33, τ=1**	**ρ=0.57, τ=0**	**ρ=0.52, τ=0**
		Non-Dom Arm	**ρ=0.37, τ=1**	ρ=0.35, τ=0	**ρ=0.51, τ=0**	ρ=0.41, τ=0
	WF	COM	**ρ=0.38, τ=1**	ρ=0.42, τ=2	**ρ=0.47, τ=1**	ρ=0.60, τ=-1
		Trunk	ρ=0.44, τ=2	**ρ=0.51, τ=3**	ρ=0.46, τ=1	ρ=0.52, τ=0
		Dom Leg	ρ=0.47, τ=-1	ρ=0.56, τ=1	ρ=0.47, τ=0	ρ=0.51, τ=-1
		Non-Dom Leg	**ρ=0.51, τ=2**	ρ=0.39, τ=2	**ρ=0.52, τ=1**	ρ=0.52, τ=0
		Dom Arm	ρ=0.37, τ=-1	ρ=0.28, τ=2	ρ=0.51, τ=0	ρ=0.55, τ=0
		Non-Dom Arm	ρ=0.26, τ=1	ρ=0.22, τ=-1	ρ=0.39, τ=1	ρ=0.36, τ=0
GMED	WN	COM	ρ=0.60, τ=-1	ρ=0.57, τ=-2	ρ=0.69, τ=-1	ρ=0.64, τ=-2
		Trunk	**ρ=0.57, τ=0**	ρ=0.50, τ=-1	**ρ=0.72, τ=-1**	ρ=0.59, τ=-1
		Dom Leg	ρ=0.47, τ=0	ρ=0.41, τ=-1	ρ=0.44, τ=-1	ρ=0.41, τ=-4
		Non-Dom Leg	ρ=0.45, τ=0	ρ=0.41, τ=1	ρ=0.45, τ=-1	ρ=0.32, τ=1
		Dom Arm	**ρ=0.37, τ=0**	ρ=0.36, τ=0	**ρ=0.54, τ=-1**	ρ=0.35, τ=0
		Non-Dom Arm	**ρ=0.33, τ=-1**	ρ=0.41, τ=-2	**ρ=0.48, τ=-2**	ρ=0.47, τ=-2
	WF	COM	ρ=0.71, τ=-1	**ρ=0.65, τ=-1**	ρ=0.74, τ=-1	**ρ=0.61, τ=-1**
		Trunk	**ρ=0.66, τ=-1**	**ρ=0.69, τ=1**	**ρ=0.74, τ=-1**	**ρ=0.57, τ=-1**
		Dom Leg	ρ=0.51, τ=1	ρ=0.51, τ=-1	ρ=0.55, τ=1	ρ=0.49, τ=-1
		Non-Dom Leg	ρ=0.42, τ=-1	ρ=0.52, τ=1	ρ=0.49, τ=0	ρ=0.44, τ=0
		Dom Arm	ρ=0.37, τ=1	ρ=0.46, τ=0	ρ=0.52, τ=-1	ρ=0.49, τ=0
		Non-Dom Arm	**ρ=0.47, τ=-1**	ρ=0.34, τ=1	**ρ=0.52, τ=-2**	ρ=0.41, τ=-3

Table I. Maximum ρ values and time lags (% stride) for each causal relationship between an EMG and the whole-body or segmental *H*. The time lag at which the max ρ is found is the time of the strongest causal relationship where the muscle acts on the *H*. The more negative the τ is, the better the forward prediction. WN and WF denote normal and fast walking speeds, respectively and the COM denotes whole-body *H*. The values in bold in the WN and WF sections are significant group differences and significant group-speed differences, respectively.

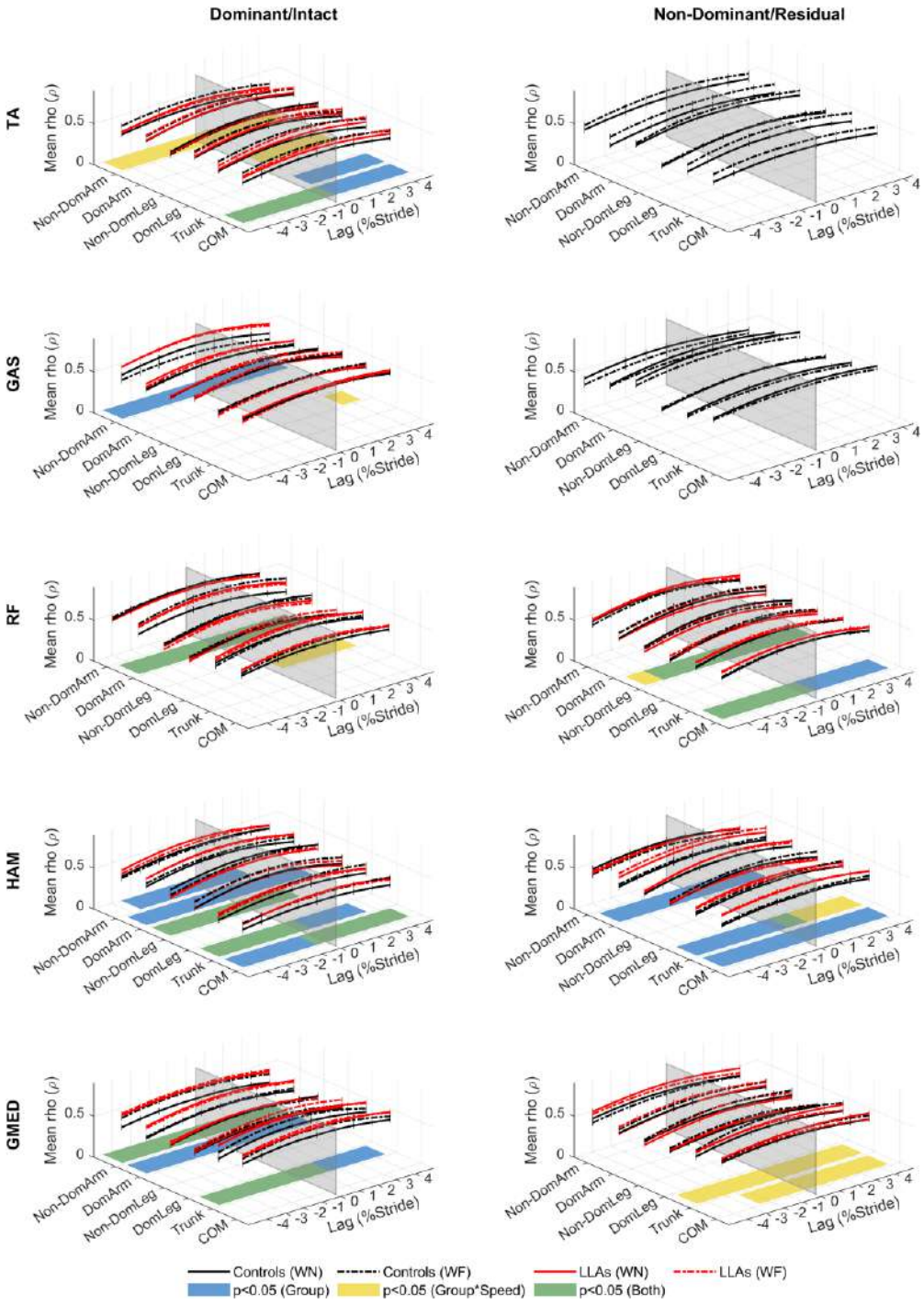


Figure 1. 3D plot of mean and 95% confidence intervals of the observed rho (ρ) vs. lag (% stride) vs. segmental *H*. WN and WF are normal and fast self-selected walking, respectively and COM is denoted as the whole-body *H*. The AB controls are labeled in black and the group with TTAs are in red. The ρ values signify the converged value of the correlation coefficient between the EMG cross-mapping the *H* and the true *H*-value. Higher red ρ values compared to black ρ values are interpreted as a stronger muscle to *H* causal inference relationship in older individuals with TTAs compared to those without. The shading underneath the curves signifies group and/or group*speed differences.

There were significant group-speed differences between the dominant TA and the whole-body *H* (τ: -4 to 0) and the non-dominant arm *H* (τ: -4 to 4). With the dominant TA, the prediction of whole-body *H* increased drastically at fast speeds in the AB group but remained similar in the group with TTAs. However, in the non-dominant arm *H,* the predictability decreased at fast speeds for the group with TTAs but increased in the AB group. The dominant GAS did not have any forward prediction causal relationships with *H*. The dominant RF had group-speed differences between the dominant leg *H* (τ: 1 to 4) and the dominant arm (τ: -4 to 4). The dominant RF predictability of the dominant leg *H* increased at fast speeds in the group with TTA; however, the opposite relationship occurred with the dominant arm *H*. The non-dominant RF had group-speed differences in the whole-body *H* (τ: -4 to 0) and the non-dominant leg *H* (τ: -3 to 4).

The predictability of the whole-body *H* and non-dominant leg *H* increased at higher speeds in the AB group and the group with TTAs, respectively. The dominant HAM had group-speed differences with the whole-body *H* (τ: 0 to 4), trunk *H* (τ: -4 to 0), and the non-dominant leg *H* (τ: -4 to 2). For this muscle, the predictability of the whole-body and trunk *H* increased at fast speeds in the AB group. There were group-speed differences in the dominant GMED and the trunk *H* (τ: -4 to 1) and the non-dominant arm *H* (τ: -4 to 4) as well as in the non-dominant GMED and the whole-body *H* (τ: -2 to 4) and trunk *H* (τ: -4 to 4), where the predictability increases at fast speeds in the AB group.

IV. Discussion

The goal of this study was to determine how TTAs and walking speed affects the forward prediction of causal relationships between muscle excitation and *H* in older individuals during over-ground walking. We accepted our hypothesis that these relationships would be subject group-dependent and would vary depending on walking speed.

We implemented a novel data-driven model to investigate the causal influence of muscle excitation on whole-body and segmental dynamic balance of the frontal plane. Interestingly, CCM has previously been used to determine the causal influence of the center of pressure on the center of mass in handstands [23]. However, previous analyses lacked information about the time-varying relationships between the two dynamical data. In this study, we apply time-dependent causal interaction analysis in its first application to gait to investigate how time changes the strength of these causal relationships. This method is beneficial in understanding the dynamic complexities of the relationships between lower-limb amputation and balance.

The most consistent findings in support of our hypothesis related to group differences were shown in the dominant and non-dominant HAM. The HAMs are often related to the generation of sagittal hip extensor moments during early stance to accelerate the leg as well as during braking in late swing [24]. However, these contributions to hip extension and the acceleration of the leg also demonstrate changes in the frontal plane. Previous studies have hypothesized that in individuals with TTAs, the residual leg HAM muscle activity increases to compensate for the lack of ankle plantar- and dorsi-flexors [12]. Fig. 1 shows that both the intact and residual HAM of the individuals with TTAs have a higher causal inference of whole-body and segmental contributions to *H* compared to the AB individuals. The only exception to this result is between the HAM and the contralateral leg *H*. In these cases, the HAM was a better causal predictor of the contralateral leg *H* in the AB group, which may be related to their more symmetrical gait pattern. Overall, the intact and residual HAM in the group with TTAs was a contributor to changes in *H* as there were more negative optimal time lags; however, in the AB group, the dominant and non-dominant HAM was a response, which was demonstrated by the positive optimal time lags.

Another significant finding that confirms previous literature is the group and group-speed differences seen between the residual RF and the whole-body *H*. The RF functions mostly to transfer energy from the leg to the torso during transition from load bearing to swing in the sagittal plane [25]. Our findings relate the non-dominant/residual leg RF activity to the frontal plane changes in *H*. Previous studies have described that the residual RF is more active during braking in individuals with TTAs and that the RF activity changed depending on speed [12]. We found that the residual RF in individuals with TTAs had a stronger predictive causal inference on whole-body *H* compared to AB individuals. This may suggest compensatory mechanisms used by these individuals to aid with braking and/or leg swing in the absence of the TA and GAS [7]. Both subject groups had more negative optimal time lags, suggesting that the RF is contributor to changes in *H*.

The TA and GMED demonstrate predictive causal differences between subject groups and group-speed interactions with the whole-body and trunk *H*. In all of these relationships, the group with TTAs demonstrated better causal relationships with *H*. The GMED's role in maintaining pelvic tilt is supported by the causal relationships in Fig. 1 [26]. Surprisingly, the group with TTAs had a stronger causal relationship between the GMED and the trunk, even though the residual GMED has been seen to have smaller abduction moment arms compared to AB group [27]. This may suggest the adoption of altered motor control strategies in individuals with TTAs in the absence of the TA and GAS, which is reflective of the distal to proximal redistribution of work.

Our findings also relate lower-limb muscle excitation to changes in upper-limb segmental *H*. These relationships indicate that the intact leg GAS was more predictive of the contralateral arm *H* in the group with TTAs. This may indicate that interlimb coupling changes in individuals with TTAs and suggests that a unique control mechanism may be used to compensate during the propulsion and braking of their residual limb [11]. One limitation of our study is that we also only investigate muscle activation causing changes in *H*. However, it is beneficial to study the opposite relationships to determine if there is an external driving factor that influences both muscle activation and *H*. In future applications, we also hope to analyze these causal predictive relationships in all three planes.

Our analyses could extend to applications in prosthesis selection. While the prosthesis across participants in the TTA group was not standardized and this may be considered a study limitation, our analysis characterized individual neuromotor signatures which accounted for the effects of each unique prosthesis and captured generalized differences between subject groups. Therefore, determining the causal prediction of muscle excitation to changes in *H* could help inform our understanding of how prostheses can be optimized to maximize dynamic balance for a person, which is particularly important for older individuals. These relationships could also guide prosthetic control systems. While current prosthetic technology frequently optimizes for factors like comfort or efficiency, many designs struggle to account for the detailed nature of how the user regulates their movement around the constraints of their prosthesis [28]. The data-driven modeling of muscle excitation can be used to inform intent recognition or the prediction of *H* that drives adaptive prostheses and exoskeletons. Recent studies show promising ubiquitous exoskeleton assistance through instantaneous estimates of lower-limb biological joint moments [29]. These

instantaneous estimates could be made for the relationships with an optimal time lag of 0, as shown in Table I. With these known muscle and *H* relationships, it could be possible to create balance-assistive devices for example. Previous studies also highlight the need for a fast reaction time of assistive devices to improve standing balance [30]. However, this need for the device reaction to precede physiological responses is even more important for dynamic balance during gait which relies on rapid responses to support postural control. By investigating optical time lags that occur at values less than 0, our applied method of CCM helps to inform the development of devices that forwardly react to postural disruptions to restore balance during gait and subsequently avoid a fall.

V. Conclusions

The results highlight that the causal predictive relationships between muscle excitation and dynamic balance are affected by the limb loss and walking speed. Between subject groups, the strength of relationships gives us insight into possible compensatory mechanisms used by individuals with lower-limb amputations and highlights how neuromuscular control changes at faster walking speeds. Also, the time-varying conditions demonstrate the role of muscles as a potential contributor, regulator and response to dynamic balance during gait. By determining the causal relationships and the time or phase-dependent delays at which they generate changes in angular momentum, we seek to utilize the user's control mechanisms to inform the development of prosthetic technology that can optimize behavior to maximize dynamic balance for preventing falls and secondary impairments.

Acknowledgment

The authors thank Rebecca Stine at the Northwestern University Prosthetics-Orthotics Center for help with participant recruitment and data collection.

References

[1] J. A. Rivera *et al.*, "Estimating Recent US Limb Loss Prevalence and Updating Future Projections," *Arch. Rehabil. Res. Clin. Transl.*, p. 100376, Oct. 2024.

[2] W. C. Miller, M. Speechley, and B. Deathe, "The prevalence and risk factors of falling and fear of falling among lower extremity amputees," *Arch. Phys. Med. Rehabil.*, vol. 82, no. 8, pp. 1031–1037, Aug. 2001.

[3] M. E. Tinetti and C. S. Williams, "The Effect of Falls and Fall Injuries on Functioning in Community-Dwelling Older Persons," *J. Gerontol. A. Biol. Sci. Med. Sci.*, vol. 53A, no. 2, pp. M112–M119, Mar. 1998.

[4] T. A. Behar, S. J. Burnham, and G. Johnson, "Major stump trauma following below-knee amputation. Outcome and recommendations for therapy," *J. Cardiovasc. Surg. (Torino)*, vol. 32, no. 6, pp. 753–756, 1991.

[5] C. Gauthier-Gagnon, M.-C. Grisé, and D. Potvin, "Enabling factors related to prosthetic use by people with transtibial and transfemoral amputation," *Arch. Phys. Med. Rehabil.*, vol. 80, no. 6, pp. 706–713, Jun. 1999.

[6] R. Gailey, "Review of secondary physical conditions associated with lower-limb amputation and long-term prosthesis use," *J. Rehabil. Res. Dev.*, vol. 45, no. 1, pp. 15–30, Dec. 2008.

[7] A. K. Silverman and R. R. Neptune, "Differences in whole-body angular momentum between below-knee amputees and non-amputees across walking speeds," *J. Biomech.*, vol. 44, no. 3, pp. 379–385, Feb. 2011.

[8] I. Kurz, E. Berezowski, and I. Melzer, "Frontal Plane Instability Following Rapid Voluntary Stepping: Effects of Age and a Concurrent Cognitive Task," *J. Gerontol. A. Biol. Sci. Med. Sci.*, vol. 68, no. 11, pp. 1402–1408, Nov. 2013.

[9] S. L. Greenspan *et al.*, "Fall Direction, Bone Mineral Density, and Function: Risk Factors for Hip Fracture in Frail Nursing Home Elderly," *Am. J. Med.*, vol. 104, no. 6, pp. 539–545, Jun. 1998.

[10] W. Li and N. P. Fey, "Neuromechanical Control Strategies of Frontal-Plane Angular Momentum of Human Upper Body During Locomotor Transitions," in *2018 7th IEEE International Conference on Biomedical Robotics and Biomechatronics (Biorob)*, Enschede: IEEE, Aug. 2018, pp. 984–989.

[11] A. S. Monteiro, M. J. Major, and N. Fey, "Transtibial Limb Loss Influences Muscle Excitation, 3d Dynamic Balance and Their Cross-Sectional Correlation in Older Individuals During Walking," 2025, *SSRN*. doi: 10.2139/ssrn.5070828.

[12] N. P. Fey, A. K. Silverman, and R. R. Neptune, "The influence of increasing steady-state walking speed on muscle activity in below-knee amputees," *J. Electromyogr. Kinesiol.*, vol. 20, no. 1, pp. 155–161, Feb. 2010.

[13] R. R. Neptune and C. P. McGowan, "Muscle contributions to frontal plane angular momentum during walking," *J. Biomech.*, vol. 49, no. 13, pp. 2975–2981, Sep. 2016.

[14] G. Sugihara *et al.*, "Detecting Causality in Complex Ecosystems," *Science*, vol. 338, no. 6106, pp. 496–500, Oct. 2012.

[15] J. D. Smith *et al.*, "Oscillation and Reaction Board Techniques for Estimating Inertial Properties of a Below-knee Prosthesis," *J. Vis. Exp.*, no. 87, p. 50977, May 2014.

[16] P. Konrad, *The ABC of EMG. A practical introduction to kinesiological electromyography.* Noraxon Inc. USA, 2005.

[17] C. J. De Luca, "The Use of Surface Electromyography in Biomechanics," *J. Appl. Biomech.*, vol. 13, no. 2, pp. 135–163, May 1997.

[18] H. Ye *et al.*, "Distinguishing time-delayed causal interactions using convergent cross mapping," *Sci. Rep.*, vol. 5, no. 1, p. 14750, Oct. 2015.

[19] G. Sugihara and R. M. May, "Nonlinear forecasting as a way of distinguishing chaos from measurement error in time series," *Nature*, vol. 344, no. 6268, pp. 734–741, Apr. 1990.

[20] S. A. Go *et al.*, "Evaluating skeletal muscle electromechanical delay with intramuscular pressure," *J. Biomech.*, vol. 76, pp. 181–188, Jul. 2018.

[21] H. Begovic *et al.*, "Detection of the electromechanical delay and its components during voluntary isometric contraction of the quadriceps femoris muscle," *Front. Physiol.*, vol. 5, Dec. 2014

[22] R. Hannah *et al.*, "Longer Electromechanical Delay Impairs Hamstrings Explosive Force versus Quadriceps," *Med. Sci. Sports Exerc.*, vol. 46, no. 5, pp. 963–972, May 2014.

[23] H. E. Wyatt *et al.*, "Bidirectional causal control in the dynamics of handstand balance," *Sci. Rep.*, vol. 11, no. 1, p. 405, Jan. 2021.

[24] M. G. Pandy, Y.-C. Lin, and H. J. Kim, "Muscle coordination of mediolateral balance in normal walking," *J. Biomech.*, vol. 43, no. 11, pp. 2055–2064, Aug. 2010.

[25] T. M. Annaswamy *et al.*, "Rectus femoris: Its role in normal gait," *Arch. Phys. Med. Rehabil.*, vol. 80, no. 8, pp. 930–934, Aug. 1999.

[26] R. R. Neptune and C. P. McGowan, "Muscle contributions to frontal plane angular momentum during walking," *J. Biomech.*, vol. 49, no. 13, pp. 2975–2981, Sep. 2016.

[27] G. F. Roda *et al.*, "The Amputated Limb Gluteus Medius is Biomechanically Disadvantaged in Patients with Unilateral Transfemoral Amputation," *Ann. Biomed. Eng.*, vol. 52, no. 3, pp. 565–574, Mar. 2024.

[28] J. Kim *et al.*, "The influence of powered prostheses on user perspectives, metabolics, and activity: a randomized crossover trial," *J. NeuroEngineering Rehabil.*, vol. 18, no. 1, p. 49, Dec. 2021.

[29] D. D. Molinaro *et al.*, "Task-agnostic exoskeleton control via biological joint moment estimation," *Nature*, vol. 635, no. 8038, pp. 337–344, Nov. 2024.

[30] O. N. Beck *et al.*, "Exoskeletons need to react faster than physiological responses to improve standing balance," *Sci. Robot.*, vol. 8, no. 75, p. eadf1080, Feb. 2023, doi: 10.1126/scirobotics.adf1080.

Muscle Network Analysis of a Dynamic Bilateral Task With an Upper Limb Exoskeleton

Vladimiro Suglia, Cristian Camardella, Gianluca Rinaldi, Domenico Chiaradia, Domenico Buongiorno, Hui Zhou, Antonio Frisoli, Daniele Leonardis, Vitoantonio Bevilacqua

***Abstract*—The coordination between muscles during the execution of a bilateral task can be analyzed by recurring to functional muscle networks, which indicates how human muscles are mutually synchronized - i.e., share an oscillatory common input - during the motor task. So far, no studies have studied the impact of an assistive exoskeleton on the neural substrates of human muscles. This work addresses this question by extracting functional muscle networks of healthy individuals during the execution of a bilateral dynamic task without and with the support of a shoulder exoskeleton. The outcomes have revealed a global stationarity of these networks, together with a slight change of synergies' shape, reflecting how the employed assistive device can change physiological patterns from both temporal and frequency domains. Despite the limited sample size, the authors claim the potential of functional connectivity analysis as an additional tool for the evaluation of inter-muscular coordination for such clinical purposes as rehabilitation robotics.**

***Index Terms*—Electromyography, Muscle Network, Muscle Synergies, Wearable Devices, Robotics, Exoskeleton, Rehabilitation, Assistance.**

I. Introduction

The shoulder joint plays an important role in various activities of daily living (ADLs), such as donning and doffing [1], drinking or eating [2]. However, the execution of such bilateral tasks involving shoulder flexion may be difficult to accomplish in case of impairments due to either a a neuromotor disorder [3] or the acute phase of post-surgery recovery [1]. Hence, shoulder movements should be assisted to prevent impaired people - e.g., post-stroke survivors in the acute phase [4] - from exploiting compensatory strategies to perform bilateral ADLs.

Robotic exoskeleton can be designed to support motor tasks entailing the shoulder joint for either healthy [5] and pathological subjects [3]. Nevertheless, such non-physiological patterns as the altered activity of non-assisted muscles are hypothesized to occur when performing motor tasks supported by an exoskeleton [6].

Functional muscle networks indicates how muscles are reciprocally synchronized [7] and allows to investigate inter-muscular coordination during the execution of a motor task by highlighting its neural substrates in the frequency domain [8]. Three frequency bands, which are the alpha, the beta, and the gamma (or Piper) bands, can be used to arrange muscle networks.

Functional muscle networks have been employed to analyze many bilateral tasks involving lower limbs, such as running [9] and walking [10], as well as postural control [8]. A few works employed functional connectivity analysis to study upper-limb motor tasks, which were mainly focused on the investigation of fatigue onset in healthy subjects [11] or isometric force generation in post-stroke patients [4]. Cancrini and colleagues used muscle synergy analysis to compare the execution of reaching tasks by both stroke and healthy participants in terms of inter-muscular coordination [12].

This work applies functional muscle networks to study the influence of an exoskeleton on the motor features exhibited by humans while performing a bilateral upper-limb task that mainly involve the shoulder flexion. The presented study contributes to the state-of-art through a functional connectivity analysis of the execution of a bilateral dynamic task by healthy people with and without an upper-limb shoulder exoskeleton [13]. Therefore, this work compares muscle networks and the corresponding metrics in the two conditions of free-execution and robot-assistance.

The article is structured as follows: Section II describes the exoskeleton, the experimental setup and protocol employed for data acquisition, and the methodology necessary to determine muscle networks; Section III reports and discusses the outcomes of the data analysis; ultimately, Section IV draws final remarks about the conducted study.

II. Methodology

A. Participants

Experiments have been performed on nine healthy subjects (27.64 ± 2.46 years old, all males, all right-handed except for one), who have neither a former familiarity with occupational exoskeletons nor any neuromotor disorders and gave informed consent before the experiments. The experimental sessions conformed to the standards of the Declaration of Helsinki and have been ethically approved by the Scuola Superiore Sant'Anna Ethical Review Board, ID 152021.

V. Suglia (ORCID: 0009-0002-5314-0093), D. Buongiorno (ORCID: 0000-0002-2024-5369) and V. Bevilacqua (0000-0002-3088-0788) are with the Department of Electrical and Information Engineering (DEI), Polytechnic University of Bari, 70126 Bari, Italy. (e-mail: vladimiro.suglia@poliba.it, domenico.buongiorno@poliba.it, and vitoantonio.bevilacqua@poliba.it).

C. Camardella (ORCID: 0000-0002-3856-5731), G. Rinaldi (0000-0003-4835-3406), D. Chiaradia (0000-0002-6183-0804), A. Frisoli (ORCID: 0000-0002-7126-4113), and D. Leonardis (0000-0001-8612-7085) are with the Institute of Mechanical Intelligence, Scuola Superiore Sant'Anna, 56010 Pisa, Italy (email: cristian.camardella@santannapisa.it, gianluca.rinaldi@santannapisa.it, domenico.chiaradia@santannapisa.it, antonio.frisoli@santannapisa.it, and daniele.leonardis@santannapisa.it).

H. Zhou (ORCID: 0000-0002-4900-4294) is with the Schoool of Automation, Nanjing University of Science and Technology, Nanjing, China. (email: zhouhui@njust.edu.cn).

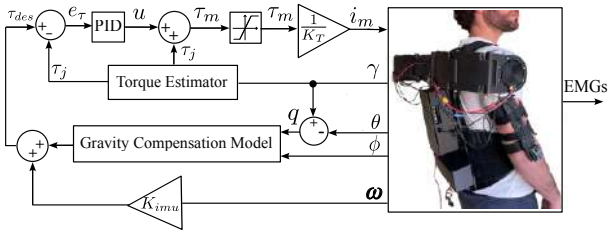


Fig. 1. Schematic diagram of the torque controller.

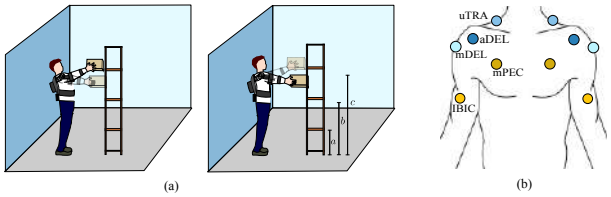


Fig. 2. Experimental setup. (a) The workspace used for the experiments encompasses a shelving unit with three heights (*a*, *b*, and *c*) from which the subject picks up a box and to which they shelve the object. (b) Placement of the EMG sensors on the human body.

B. Experimental Setup

1) Exoskeleton: Flexos is a light exoskeleton prototype that actively supports the shoulder flexion. The remaining passive shoulder degree of freedom is implemented by means of a kinematic structure; hence, torques can be transmitted from the active joint and the exoskeleton links can adapt to the body posture. The exoskeleton is made up of soft interfaces that are hand sewn to 3D-printed rigid parts. The subsystems of this robotic device are depicted in Fig. 1.

The exoskeleton is linked to the human body by a rigid interface positioned at the back, and by two links, fastened at the arms through Velcro straps. An underactuated kinematic chain, which is in parallel to the human arm, connects those two human-robot contact points: while one side of the chain is linked to the back interface, the other extremity is fixed to a series elastic actuator (SEA). This actuator is made up of a brushless DC motor (Motor AK80-9), which may transmit a maximum torque of torque of 9 Nm for assisting shoulder flexion.

Flexos is ensured to be portable thanks to a backpack, which embeds the communication and electronic control units, together with the energy storage, which is a LiFePO4 battery with a mass of 1 kg, a current of 10 Ah, and a voltage of 24 V.

The electronics communicates with three inertial measurement units (IMUs), which are placed on the two arm interfaces and at the back interface, and reads angular displacement from the SEA. It supports 500 Hz Ethernet communication with a 1 kHz control loop and an external PC. A previous work provides additional details about the electronics implementation [13].

A closed-loop torque control is integrated to partially compensate the gravity torque connected with a system to be lifted, which may be either integral to an additional object or the only arm.

The supporting torque comes from the combination between a gravity compensation control law u, which relies on a PID controller tuned according to the Ziegler-Nichols method, and a joint torque, which is used as a feedforward contribution and is estimated by the SEA according to Eq. 1:

$$\tau_j = k_j \sin\left(\frac{\gamma}{2}\right) \tag{1}$$

where k_j is the first-order joint stiffness, which was experimentally measured in [14], and γ is the angular displacement. This control law τ_m, which gives the motor torque command, is converted in a current value for the motors. The structural integrity of the exoskeleton is pursued by limiting the delivered torque to 5 Nm.

The reference torque τ_{des} is computed as follows:

$$\tau_{des} = \tau_{max} \sin(q - \phi) + K_{imu}\dot{q} \tag{2}$$

where $K_{imu}\dot{q}$ is a feedforward contribution depending on the velocity and allowing to consider the user's intentions, τ_{max} is the maximum output torque, and $\tau_{max} \sin(q-\phi)$ is the contribution related to the gravity compensation. Furthermore, the arm angle q is the difference between the series elastic joint angular displacement γ and the motor angular position θ.

This exoskeleton was originally designed for power-augmentation applications, but it is used to investigate the outcomes of muscle network analysis during a bilateral dynamic task, which recruits the shoulder motion in such ADLs as reaching overhead positions [15].

2) Motion tracking: Kinematic data are collected by means of a motion tracking system that entails three trackers (VIVE Tracker 3.0), which are placed at each subject's wrist and the target box, and four base stations (HTC SteamVR Base Station 2.0), which are located at the four sides of the experiments room. Kinematic measures (i.e., linear and angular positions and speeds) are transmitted at 250 Hz with the UDP protocol from each tracker to the PC. A SteamVR application is run on an external PC to manage trackers and base stations with a Python script.

3) Electromyography: A Trigno Wireless Biofeedback System (Delsys, Natick Massachusetts, USA) is used to measure the electromyography (EMG) activity of five upper-limb muscles that are biceps brachii (lBIC), anterior deltoid (aDEL), medial deltoid (mDEL), pectoralis major (mPEC), and upper trapezius (uTRA). For each body side, a Trigno Avanti and a Trigno Quattro EMG Sensor are comprised in the setup (Fig. 2c) and the SENIAM guidelines are followed to place each sensor uniton the human body [16]. The Delsys Trigger Module is utilized to synchronize the EMG recordings with those of the exoskeleton and the trackers.

4) Experimental Protocol: The experimental protocol comprises a dynamic task, in which the participant is asked to stay in front of the shelving unit with three shelves at a reference distance of 70 cm from the unit before starting the task execution. This shelving unit is the same for all subjects and has the characteristics reported in Table I; nonetheless,

TABLE I
DIMENSIONS CHARACTERIZING THE SHELVING UNIT.

Parameter		Value [m]
Shelving unit, *middle* shelf height	b	1.20
Shelving unit, *top* shelf height	c	1.59

it has not been modified since the height does not differ too much across subjects (183.4 ± 3.1) cm.

The dynamic task has a maximum duration of 2 minutes and is divided into the following motor actions:

1) *Upwards motion*: The participant bilaterally grabs an object placed at the *middle* shelf and move it onto the *top* shelf; then, both arms are brought back in the resting position - parallel to the trunk.
2) *Downwards motion*: The participant picks up the box with both hands from the *top* shelf and shelves it back onto the *middle* shelf: afterwards, both arms are brought back to the resting position.

Two subsequent beats of a metronome set at 20 bpm defines the pace at which subjects' are asked to perform each transition (i.e., up, down, rest). The dynamic task is executed in two conditions, which are without (w.o. Exo) and with the exoskeleton (w. Exo) with the torque controller activated, and only with a box of mass of 3 kg to prevent the individual from being affected by fatigue. Such conditions are presented in pseudo-randomized order such that a bias connected with possible learning effects is minimized. The participant are told to wait for ten minutes before the next task execution for the sake of muscle relaxation, thus preventing the subject from excessively accumulating fatigue [17].

C. Data processing

EMG signals are preprocessed in different ways depending on whether functional muscle networks or muscle synergies are computed.

1) Functional muscle network: Raw EMG data are first band-pass filtered (5-500 Hz) and then full-wave rectified by means of a Hilbert transform [18] to remove artifacts and preserve the neural oscillatory modulations in the frequencies of interest ($<$100Hz), [19]. Subsequently, EMG data are normalized by each subject's maximum voluntary contraction (MVC) and segmented by visually inspecting the object linear position.

The matching between muscle activations is quantified with the inter-muscular coherence (IMC), which is computed by extracting coherence matrices. These matrices are first averaged across trials and subjects and then decomposed with the non-negative matrix factorization (NNMF) [20], thus determining the matrix H of coherence patterns and the matrix W of edge weights according to the following formula:

$$IMC_{f*n} = (W_{f*r} \cdot H_{r*n}) + E_{f*n} \tag{3}$$

where f is the frequency, r is the number of frequency components (i.e., the rank of the matrix), n is the number of muscle pairs, and E is the residual error matrix of the NNMF. The variance accounted for (VAF), which is computed with the Frobenius norm of matrices E and IMC, is employed to minimize the coherence patterns explaining the total variance of the IMC with a threshold of 90%. As a result, this method optimized the number of muscle networks, namely frequency components (C1 and C2).

After normalizing the matrix W such that unit vectors are achieved for each component, adjacency matrices are computed by binarizing with a threshold-based method such that only the top 30% of the weights are included. Functional muscle networks are graphically depicted with a set of nodes (i.e., the muscles) and edges (i.e., inter-muscular connections) which are represented by a different thickness depending on whether the weight value lies in a range of 0%-33%, 34%-66%, or 67%-100% of the maximum of the adjacency matrix.

2) Muscle synergies: Raw EMG signals are first notch-filtered (50 Hz), band-pass filtered (5-500 Hz) and full-wave rectified, before being low-pass filtered (8 Hz) to determine the envelope [21], [22]. Afterwards, EMG data are normalized by each subject's MVC and segmented by using the object linear position as a visual reference.

Ultimately, each processed EMG matrix is decomposed with the NNMF, thus attaining two matrices of synergies and activation patterns [8]. Muscle synergies, whose number is determined with the VAF criterion to explain the 90% of the variance [23], are then reordered by similarity [8].

D. Metrics and statistics

The potential influence of the exoskeleton on motor patterns during the dynamic task is evaluated by comparing the w. Exo and w.o. Exo conditions through different metrics.

At first, the Pearson correlation coefficient is exploited to compute the similarity between the corresponding muscle synergies in w.o. Exo and w. Exo conditions [24]. Secondly, the activation intensity in the muscular coherence is quantified by computing the RMS of the activation matrix H - namely IMCfreq - for the three frequency bands of interest, which are the α-band (1Hz-10Hz), the β-band (10Hz-30Hz), and the γ-band (30Hz-60Hz).

Two network metrics derived from graph theory are extracted from the adjacency matrices: the clustering coefficient (CC) indicates how the neighbors of one node are neighbors among themselves as well, whilst the betweenness centrality (BC) quantifies the centrality of one node within the network [25]. These indexes are locally computed for each node and can be used to determine a global measure by averaging the values of BC and CC across nodes; in doing so, a scalar value is obtained for each subject, condition, and frequency component. The Brain Connectivity Toolbox is exploited to compute the above-mentioned network metrics [25].

The normality distribution of the metrics is verified with a Shapiro-Wilk test with a significance level of $\alpha = 0.05$. A statistical comparison between the index values in the w. Exo and w.o. Exo conditions is performed by means of a non-parametric Wilcoxon signed-rank test for non-normally distributed sets and with a paired t-test ($\alpha = 0.05$) for normally

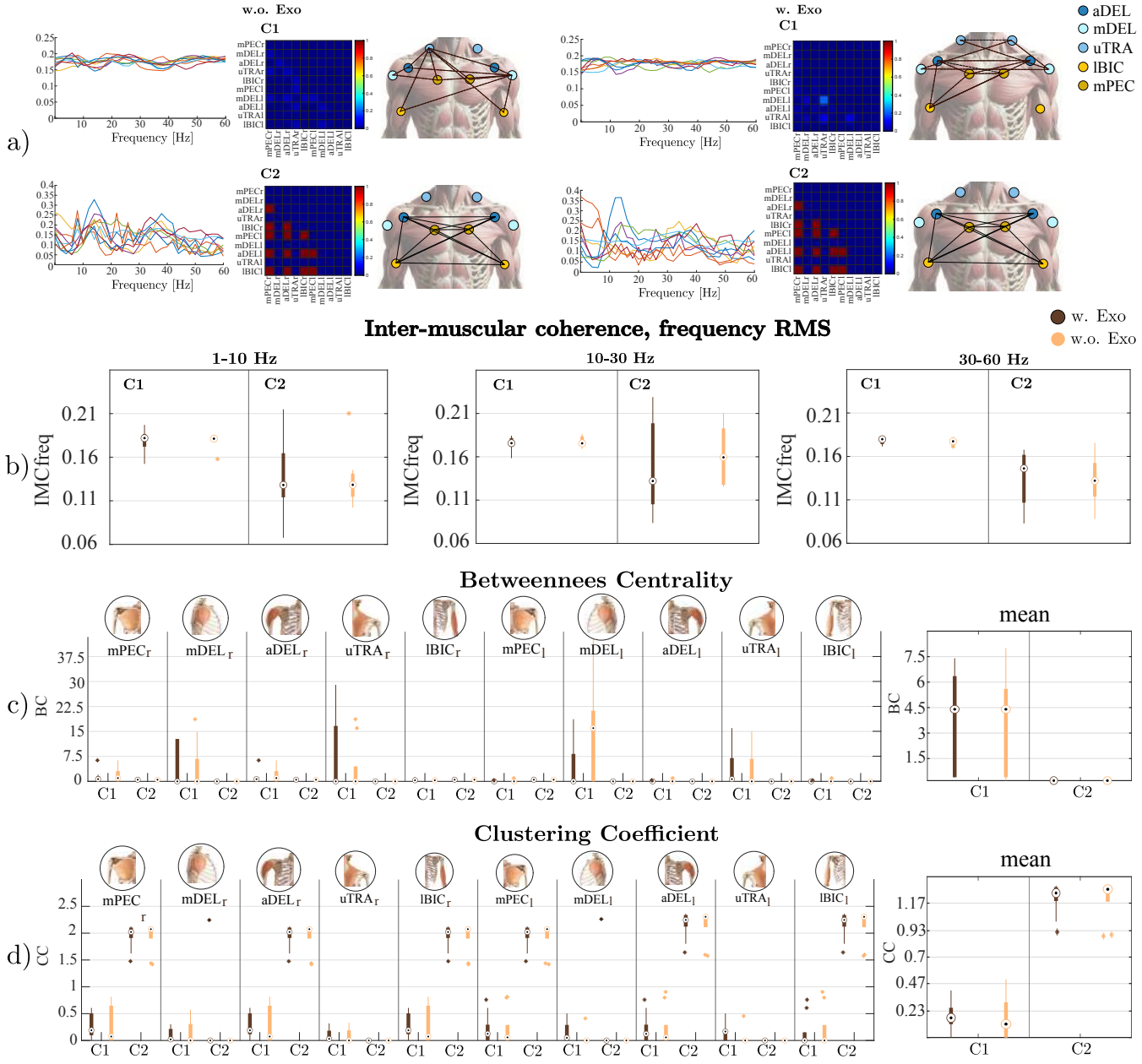


Fig. 3. Muscle network analysis outcomes of the dynamic task reported for both w.o. Exo and w. Exo conditions and both frequency components (C1 and C2). There can be found: a) the frequency components, the adjacency matrices, and the correspondent muscle networks; b) the RMS of the activation matrix H for the α-band (1Hz-10Hz), the β-band (10Hz-30Hz), and the γ-band (30Hz-60Hz); c) the betweenness centrality (BC) and d) clustering coefficient (CC), which are both computed for each muscle and averaged across muscles.

distributed ones. All the data analysis has been conducted using MATLAB 2022b and its toolboxes.

III. Results and Discussion

Functional connectivity analysis has allowed to determine muscle networks of the dynamic task, which are depicted in Figure 3 for both w.o. Exo and w. Exo conditions and both frequency components (C1 and C2) - see Subsection II-C.

As for Figure 3a, during a dynamic task the activation function oscillates in a limited range, which is larger in the second component than in the first one, and increases on average passing from the α-band (1Hz-10Hz) to the γ-band (30Hz-60Hz). However, for each component this frequency behavior is stable regardless of the condition - i.e., wearing the exoskeleton or not. The IMCfreq in the two conditions (Figure 3b) neither exhibits any statistically significant differences. For each condition, the network structure consists in bilateral connections that mainly involves shoulder flexors (e.g., aDEL, mPEC, lBIC) in the second component; on the other hand, the first component appears as a "support" for the lifting task, since such upper-limb muscles as uTRA and mDEL are more involved.

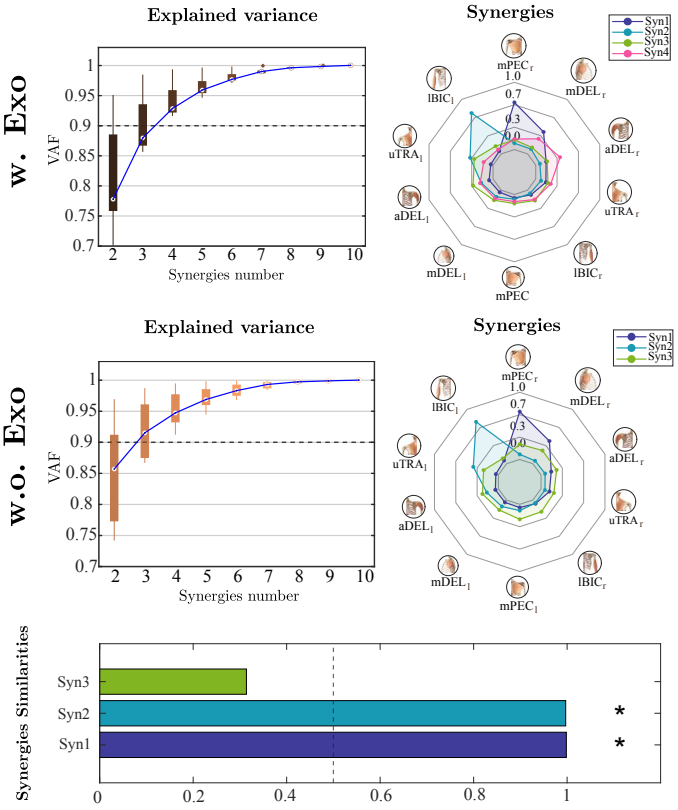


Fig. 4. Muscle synergies analysis outcomes of the dynamic task and for both w.o. Exo and w. Exo conditions. From the left side to the right side of the image there are: the cumulative of the variance explained for each number of synergies; the muscle synergies extracted with the NNMF algorithm; the similarity between the synergies related to the w.o. Exo and w. Exo conditions, where * represents a statistically significant correlation with $p < .05$.

The network topology, which is represented in Figure 3a, slightly changes between the two conditions in the first component. More in detail, the number of links between ipsilateral muscles is higher in the w.o. Exo condition than in the w. Exo condition, whereas the number of contralateral connections is lower in the former than in the latter condition; however, these inter-muscular connections are weak in both cases. In addition, the left uTRA and lBIC are isolated in the w.o. Exo and w. Exo conditions, respectively. On the other hand, the network structure is the same for the second component either wearing the exoskeleton or not. More specifically, in both conditions there are a few connections between muscles at the same side of the human body, whereas contralateral muscles are linked most of times. Furthermore, the trapezii and the medial deltoids are isolated, whilst the right mPEC, aDEL, and lBIC act as bridges allowing for direct connections between the two sides of the human body.

Accordingly, both network metrics BC and CC, which are respectively reported in Figure 3c and Figure 3d, change in the two components. Remarkably, considering the pectorales majores, the anterior deltoids and the biceps, the CC in the second component is higher (almost doubled) than the CC in the first component for each condition. Complementarily, the BC in the second component is lower than the one in the first component for the medial deltoids and the upper trapezii. Notwithstanding, no statistically significant differences can be found in terms of CC between the w.o. Exo and w. Exo conditions. The global measures of BC and CC follows the same pattern observed in the local counterpart.

The CC of one muscle reflects how the drives of its neighbors are synchronized among themselves as well, thus forming a cluster or not [25]. The complementary outcomes between the BC and CC, whether local or global, confirm that the network is more clustered in the second component than in the first one, in which case the segregated muscles are more central. Hence, a compensation strategy is arguably pursued to accomplish the dynamic task by recruiting the central nodes in the first component (upper trapezii and medial deltoids) to support the aggregated muscles in the second component (shoulder flexors).

The outcomes of muscle synergy analysis are depicted in Figure 4, which reports muscle synergies themselves and their number derived from the VAF-criterion, together with the similarity between the corresponding synergies in the w.o. Exo and w. Exo conditions. The minimum number of synergies describing the 90% of the variance differs with the condition, since it is 3 and 4 when wearing the exoskeleton or not, respectively. The first two synergies are almost the same and, accordingly, their similarity is statistically significant ($p < .05$). On the other hand, the third synergy exhibits the highest difference, as proved by the corresponding low similarity score. Wearing the exoskeleton led to the introduction of a fourth synergy that arguably contributes in a complementary way with respect to the third one: the synergy values are higher for the muscles at the right and left sides in the fourth and third synergies, respectively; nonetheless, they seem the decomposition of the third synergy extracted from the EMGs related to the w.o. Exo condition. Therefore, upper-limb muscles are mutually coordinated in a globally similar manner in terms of temporal motor pattern. The slight difference between the two conditions may be attributed to a higher difficulty of the task [26], which could have led to compensation strategies associated with the introduction of the exoskeleton acting as an external perturbation [15]. Such outcomes is analogous to other works in which either the patterns or the numbers of synergies are modified when an exoskeleton is worn [27]. It should be noted that an almost negligible alteration of muscle synergies should be pursued in the rehabilitative intervention aided by robotic devices, since motor performance should improve without altering natural muscular coordination patterns [15].

IV. Conclusion

In this work, functional connectivity between upper-limb muscles has been analyzed to investigate whether and how a shoulder exoskeleton influences the execution of a bilateral dynamic task in terms of muscular synchronization. The robotic support has kept muscle coherence globally unaltered,

while slightly but not excessively modifying the synergistic pattern, thus making functional connectivity and muscle synergy analyses two viewpoints on the overall investigation. In spite of the small sample size, the outcomes are in line with other studies evaluating robot-aided training oriented to rehabilitative purposes. Hence, the conducted method based on muscle network is claimed to be a valuable tool for assessing the motor recovery in clinical scenarios.

ACKNOWLEDGMENT

We acknowledge the support of the project 'BRIEF—Biorobotics Research and Innovation Engineering Facilities' (Mission 4, 'Istruzione e Ricerca'—Component 2, 'Dalla ricerca all'impresa'—Investment 3.1, 'Fondo per la realizzazione di un sistema integrato di infrastrutture di ricerca e innovazione', funded by European Union—NextGenerationEU, CUP: J13C22000400007).

REFERENCES

[1] A. B. Gurney, C. Mermier, M. LaPlante, A. Majumdar, K. O'Neill, T. Shewman, and J. G. Gurney, "Shoulder electromyography measurements during activities of daily living and routine rehabilitation exercises," *Journal of Orthopaedic & Sports Physical Therapy*, vol. 46, no. 5, pp. 375–383, 2016.

[2] C. v. d. S. A.M Oosterwijk, M.K Nieuwenhuis and L. Mouton, "Shoulder and elbow range of motion for the performance of activities of daily living: A systematic review," *Physiotherapy Theory and Practice*, vol. 34, no. 7, pp. 505–528, 2018. [Online]. Available: https://doi.org/10.1080/09593985.2017.1422206

[3] B. Noronha, C. Y. Ng, K. Little, M. Xiloyannis, C. W. K. Kuah, S. K. Wee, S. R. Kulkarni, L. Masia, K. S. G. Chua, and D. Accoto, "Soft, lightweight wearable robots to support the upper limb in activities of daily living: A feasibility study on chronic stroke patients," *IEEE Transactions on Neural Systems and Rehabilitation Engineering*, vol. 30, pp. 1401–1411, 2022.

[4] M. Houston, X. Li, P. Zhou, S. Li, J. Roh, and Y. Zhang, "Alterations in muscle networks in the upper extremity of chronic stroke survivors," *IEEE Transactions on Neural Systems and Rehabilitation Engineering*, vol. 29, pp. 1026–1034, 2021.

[5] Y. G. Kim, M. Xiloyannis, D. Accoto, and L. Masia, "Development of a soft exosuit for industrial applications," in *2018 7th IEEE International Conference on Biomedical Robotics and Biomechatronics (Biorob)*, 2018, pp. 324–329. [Online]. Available: https://doi.org/10.1109/BIOROB.2018.8487907

[6] E. Pirondini, M. Coscia, S. Marcheschi, G. Roas, F. Salsedo, A. Frisoli, M. Bergamasco, and S. Micera, "Evaluation of the effects of the arm light exoskeleton on movement execution and muscle activities: a pilot study on healthy subjects," *Journal of neuroengineering and rehabilitation*, vol. 13, pp. 1–21, 2016.

[7] R. O'Keeffe, S. Y. Shirazi, S. Mehrdad, T. Crosby, A. M. Johnson, and S. F. Atashzar, "Perilaryngeal functional muscle network in patients with vocal hyperfunction - a case study," in *2023 11th International IEEE/EMBS Conference on Neural Engineering (NER)*, 2023, pp. 1–5.

[8] T. W. Boonstra, A. Danna-Dos-Santos, H.-B. Xie, M. Roerdink, J. F. Stins, and M. Breakspear, "Muscle networks: Connectivity analysis of emg activity during postural control," *Scientific Reports*, vol. 5, no. 1, p. 17830, Dec 2015.

[9] Y. Luo, T. Guo, R. Wang, S. Mu, and K. Tao, "Decoding invariant spatiotemporal synergy patterns on muscle networks of lower-limb movements via surface electromyographic signals," *Biomedical Signal Processing and Control*, vol. 91, p. 106033, 2024. [Online]. Available: https://doi.org/10.1016/j.bspc.2024.106033

[10] T. Liang, H. Miao, H. Wang, X. Liu, and X. Liu, "Surface electromyography-based analysis of the lower limb muscle network and muscle synergies at various gait speeds," *IEEE Transactions on Neural Systems and Rehabilitation Engineering*, vol. 31, pp. 1230–1237, 2023.

[11] H. Guo, P. Gong, Y. Wang, F. Qi, C. Li, J. Li, and L. Sun, "Complex network properties analysis of muscle fatigue based on semg signals," *IEEE Sensors Journal*, vol. 23, no. 4, pp. 3859–3869, 2023.

[12] A. Scano, A. Chiavenna, M. Caimmi, M. Malosio, L. M. Tosatti, and F. Molteni, "Effect of human-robot interaction on muscular synergies on healthy people and post-stroke chronic patients," in *2017 International Conference on Rehabilitation Robotics (ICORR)*, 2017, pp. 527–532.

[13] G. Rinaldi, L. Tiseni, M. Xiloyannis, L. Masia, A. Frisoli, and D. Chiaradia, "Flexos: A portable, sea-based shoulder exoskeleton with hyper-redundant kinematics for weight lifting assistance," in *2023 IEEE World Haptics Conference (WHC)*. IEEE, 2023, pp. 252–258. [Online]. Available: https://www.doi.org/10.1109/WHC56415.2023.10224485

[14] L. Tiseni, G. Rinaldi, D. Chiaradia, and A. Frisoli, "Design and control of a linear springs-based rotary series elastic actuator for portable assistive exoskeletons," in *2021 30th IEEE International Conference on Robot & Human Interactive Communication (RO-MAN)*, 2021, pp. 434–439. [Online]. Available: https://doi.org/10.1109/RO-MAN50785.2021.9515444

[15] A. Cancrini, P. Baitelli, M. Lavit Nicora, M. Malosio, A. Pedrocchi, and A. Scano, "The effects of robotic assistance on upper limb spatial muscle synergies in healthy people during planar upper-limb training," *PLOS ONE*, vol. 17, no. 8, pp. 1–25, 08 2022. [Online]. Available: https://www.doi.org/10.1371/journal.pone.0272813

[16] "The seniam project (surface electromyography for the non- invasive assessment of muscles," http://www.seniam.org/, Last accessed on 2023-02-04.

[17] F. Missiroli, N. Lotti, E. Tricomi, C. Bokranz, R. Alicea, M. Xiloyannis, J. Krzywinski, S. Crea, N. Vitiello, and L. Masia, "Rigid, soft, passive, and active: A hybrid occupational exoskeleton for bimanual multijoint assistance," *IEEE Robotics and Automation Letters*, vol. 7, no. 2, pp. 2557–2564, 2022. [Online]. Available: https://doi.org/10.1109/LRA.2022.3142447

[18] J. N. Kerkman, A. Daffertshofer, L. L. Gollo, M. Breakspear, and T. W. Boonstra, "Network structure of the human musculoskeletal system shapes neural interactions on multiple time scales," *Science Advances*, vol. 4, no. 6, p. eaat0497, 2018.

[19] T. W. Boonstra and M. Breakspear, "Neural mechanisms of intermuscular coherence: implications for the rectification of surface electromyography," *Journal of Neurophysiology*, vol. 107, no. 3, pp. 796–807, 2012.

[20] D. D. Lee and H. S. Seung, "Learning the parts of objects by non-negative matrix factorization," *nature*, vol. 401, no. 6755, pp. 788–791, 1999.

[21] D. Buongiorno, M. Barsotti, E. Sotgiu, C. Loconsole, M. Solazzi, V. Bevilacqua, and A. Frisoli, "A neuromusculoskeletal model of the human upper limb for a myoelectric exoskeleton control using a reduced number of muscles," in *2015 IEEE World Haptics Conference (WHC)*, 2015, pp. 273–279. [Online]. Available: https://www.doi.org/10.1109/WHC.2015.7177725

[22] D. Buongiorno, F. Barone, M. Solazzi, V. Bevilacqua, and A. Frisoli, "A linear optimization procedure for an emg-driven neuromusculoskeletal model parameters adjusting: Validation through a myoelectric exoskeleton control," in *Haptics: Perception, Devices, Control, and Applications*, F. Bello, H. Kajimoto, and Y. Visell, Eds. Cham: Springer International Publishing, 2016, pp. 218–227.

[23] C. G. Mcdonald, B. J. Fregly, and M. K. O'Malley, "Effect of robotic exoskeleton motion constraints on upper limb muscle synergies: A case study," *IEEE Transactions on Neural Systems and Rehabilitation Engineering*, vol. 29, pp. 2086–2095, 2021.

[24] C. Camardella, K. C. Tse, A. Frisoli, and R. K.-Y. Tong, "Investigating muscle synergies changes after rehabilitation robotics training on stroke survivors: a pilot study," in *2020 42nd Annual International Conference of the IEEE Engineering in Medicine & Biology Society (EMBC)*, 2020, pp. 3731–3734.

[25] M. Rubinov and O. Sporns, "Complex network measures of brain connectivity: Uses and interpretations," *NeuroImage*, vol. 52, no. 3, pp. 1059–1069, 2010, computational Models of the Brain. [Online]. Available: https://www.sciencedirect.com/science/article/pii/S105381190901074X

[26] B. Pan, Z. Huang, J. Wu, and Y. Shen, "Primitive muscle synergies reflect different modes of coordination in upper limb motions," *Medical & Biological Engineering & Computing*, vol. 59, no. 10, pp. 2153–2163, Oct 2021. [Online]. Available: https://doi.org/10.1007/s11517-021-02429-4

[27] K. Zhao, Y. Feng, L. Li, Y. Zhou, Z. Zhang, and J. Li, "Muscle synergies and muscle networks in multiple frequency components in post-stroke patients," *Biomedical Signal Processing and Control*, vol. 95, p. 106417, 2024. [Online]. Available: https://doi.org/10.1016/j.bspc.2024.106417

Design and Application of Vibrotactile Feedback to Influence Gait Symmetry*

Aileen C. Naef[1,2,†], Mathilde L. Legrand[1,2,†], Zoé Jungi[1], Roger Gassert[2], Olivier Lambercy[2], and Chris Easthope Awai[1]

***Abstract*— Recovering gait is crucial for improving independence and quality of life after neurological injuries. While conventional gait therapies are beneficial, biofeedback is gaining interest for its potential to enhance motor learning and personalize training. It was established in previous work that visual feedback, which typically engages explicit motor learning mechanisms, was able to induce changes to stance time symmetry ratio and overall gait. Therefore, the goal of this study was to examine if vibrotactile feedback, which typically engages implicit motor learning techniques, can also induce such changes. To examine this, fifteen neurologically intact participants walked on a treadmill with vibrotactile feedback being provided at the level of the left ankle, knee, and hip, aimed at inducing a 20% gait asymmetry. Results revealed that participants could use biofeedback to adapt their gait, although several did not reach the target asymmetry. Additionally, there was an average Gait Deviation Index decrease of 12.8 points, representing just over one standard deviation away from the control mean, with fair correlations observed between stance time symmetry ratio and both push-off force (r = 0.45) and vertical ground reaction force (r = 0.40) symmetry ratios. These findings suggest that vibrotactile feedback can effectively help modify temporal gait parameters while also impacting kinematic and kinetic parameters.**

I. Introduction

Stroke and Parkinson's disease are among the most common causes of gait disorders worldwide [1]. Given that gait is essential for functional independence and quality of life, addressing these impairments is a central focus in neurorehabilitation settings [2], [3]. This is often done by means of repetitive practice, a fundamental principle of motor learning [4], [5]. In conventional therapies, this process is unfortunately often hindered, as feedback on performance, a fundamental component for motor learning, is only provided verbally by the therapist [6], [7]; as such, it lacks specificity in the timing, frequency, and content as it remains subjective in nature.

One possible solution to overcome this limitation is the use of biofeedback in the rehabilitation process [8], [9]. For this purpose, biofeedback is defined as the addition of an external stimulus (e.g., visual, auditory, haptic) delivered to an individual on the basis of physiological or motor performance data, acting as an information feedback system [10]. This process is thought to enhance motor learning in both healthy and post-stroke patients as the information gained from the biofeedback can be used to detect errors in performance by comparing executed actions to expected goals, and provide information so that subsequent attempts can be adapted [11]. Multiple studies in the field have already reported that visual, auditory, and haptic biofeedback can have beneficial effects on gait in post-stroke patients [12], [13], [14], [15], [16], [17]. However, while effective, all biofeedback modalities for gait training typically target a single parameter at a time, which fails to capture the interconnected nature of gait [18]. Consequently, it is still unclear how biofeedback targeting a single gait parameter might influence non-targeted parameters, as well as the overall gait quality. Moreover, identifying the optimal sensory modality remains a challenge.

To address these uncertainties, we conducted a feasibility study in previous work [19], investigating the influence of visual real-time biofeedback on stance time symmetry ratio and gait as a whole. It is well established in the field of motor learning that various techniques can be employed for this purpose [20], [21]. Visual feedback, for instance, provides learning with information about performance outcomes through visual cues. An example of this is an individual observing a bar approaching a target value as their stance time increases, indicating proximity to their goal [19]. This process is attributed to explicit learning as it requires conscious observation and interpretation to achieve the desired movement [22]. Explicit motor learning typically engages higher cognitive processes, supported by various brain regions [20], [21].

Conversely, implicit learning occurs without the need for explicit cognitive focus on external cues [22], [23]. Mechanisms for implicit learning might involve tactile or kinesthetic cues, such as vibrations, pressure, or force, which engage somatosensory pathways [22], [23]. Legrand et al., demonstrated that visual feedback could provide information that influenced changes in stance time symmetry ratio [19]. This finding raises the question of whether similar outcomes could be achieved using vibrotactile feedback, which is more commonly associated with implicit motor learning mechanisms [24].

Therefore, using similar methods as those explained by Legrand et al. [19], this study explored the evolution of the stance time symmetry ratio between natural walking and

*The authors would like to thank the medical research center "The LOOP Zurich", the Vontobel Foundation, and the P&K Foundation for supporting this work.

[1] Data Analytics & Rehabilitation Technology (DART), Lake Lucerne Institute, Switzerland (e-mail: chris.awai@llui.org).

[2] Rehabilitation Engineering Laboratory (RELab), ETH Zurich, Switzerland

[†] These authors contributed equally and share first authorship

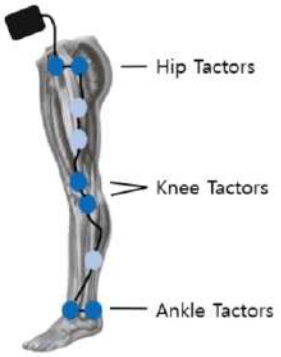


Fig. 1. Haptic tactor placement. Attachment sites were the ankle, knee, and hip of the left leg. Only six of nine available tactors were used for this study. Light blue circles represent the unused tactors.

walking with vibrotactile feedback. As neurologically intact individuals typically do not present gait asymmetries, the ability of the vibrotactile feedback to influence the stance time towards an asymmetric symmetry ratio was examined. This was done by examining the change in the Gait Deviation Index (GDI), a clinically meaningful metric of the overall gait pathology [25]. Additionally, the correlation between stance time symmetry ratio and the symmetry ratio of other spatiotemporal, kinetic, and kinematic gait parameters was examined. It is hypothesized that the neurologically intact participants of this study will be able to use the vibrotactile biofeedback in order to learn to walk with an asymmetric stance time. Moreover, it was expected that the change would not occur in isolation, thus decreasing the GDI while maintaining correlations with specific gait parameters such as the swing time symmetry ratio.

II. Methods

A. Participants

A total of 15 neurologically intact individuals (7 = female, 8 = male) participated in this study and ranged in age between 23 and 60 years of age (mean age = 35 ± 13.8 years). Participants provided their written informed consent after having the study information explained to them. The main inclusion criteria were a minimum age of 18 years, no identified sensory impairment (self-reported ability to feel the tactor vibration prior to study start), no acute or chronical musculoskeletal conditions or neurological disorders, and no reported gait impairments. Exclusion criteria included a history of neurological diseases, orthopedic diseases, rheumatologic diseases, epilepsy, or self-diagnosed acute or chronic psychiatric disorders. The study was approved by the ETH Zurich ethics committee (No. 2022-N-41) and carried out in accordance with the current version of the Declaration of Helsinki.

B. Study Design and Procedure

This study was conducted in a Computer Assisted Rehabilitation Environment (CAREN, Motek Medical), which includes a ten-camera motion capture system (Vicon Motion Systems Ltd), a split-belt treadmill with integrated force plates, and a handrail. Upon their arrival to the study room, participants were equipped with optical motion capture markers on 26 anatomical landmarks as defined by the Human Body Model 2 (HBM2) [26]. Using this system, gait parameters were computed in real-time and used as input for the vibrotactile biofeedback system. The setup used six of the nine available tactors of the commercially available Elitac Wearable Science Suit (Elitac B. V.) to provide the vibrotactile biofeedback. To simplify the vibration pattern and avoid restricting the walking movement due to the cabled connection of the tactors, two tactors were placed at each the ankle, knee, and hip joints on the left leg only; the control unit was worn at the hip (Fig. 1). While precise placement was not required, placing the tactors on tendons was avoided so as not to induce tendon vibration, which in turn could activate the muscle spindle afferents and initiate a muscle contraction as a result of the tonic vibration reflex [27]. Two tactors were placed as close together as possible at each location and used simultaneously to generate greater vibration intensity, with the activation of the two tactors being perceived as one due to their proximity.

For this study, the first step was to determine the preferred gait velocity for each participant. This was done using the self-pace mode of the treadmill meaning that the treadmill adapted to the users' walking speed following a one-minute period of walking at 1.3 m/s. The mean speed from two-minutes of self-paced walking was defined as the preferred gait velocity. Subsequently, participants completed a five-minute baseline measurement at their preferred gait velocity followed by a feedback phase of 11-minutes (Fig. 2). During the feedback phase participants walked at 80% of their preferred gait velocity to ensure they had enough time to react to the vibrotactile biofeedback and adapt their walking pattern. Data collected for minutes two, three, and four of the baseline walking were used to calculate the baseline symmetry ratio (see subsection II.C for more information).

During the feedback phase, participants were tasked with adapting their stance time. The feedback phase, which participants completed once, started with one-minute of natural walking, followed by three-minutes of feedback (FB) during which the participant was asked to react and modify



Fig. 2. Schematic outlining the experimental protocol. Abbreviations: FB, feedback; No FB, no feedback; Min, minutes; PGV, preferred gait velocity.

their gait according to the vibration of the tactors. Next, was a one-minute no feedback block (No FB), followed again by a three-minute FB block and a three-minute No FB block. The participants were instructed to try to retain the altered gait pattern also in the No FB blocks. This was done to prevent over-reliance on the feedback, which is important to ensure that the learned behavior can persist beyond the training period [11].

C. Symmetry Ratio for Biofeedback

As many post-stroke patients exhibit asymmetric gait, the aim of this feedback in the patient population would be to help train and induce gait symmetry [28]. However, this pilot study was conducted on neurologically intact individuals who did not suffer gait asymmetries. For this reason, the goal of the vibrotactile biofeedback was to induce gait asymmetry in the participants as a simple way to test the potential of our approach to influence gait symmetry. To achieve this, the vibration pattern of the feedback gave information about the current value of a left gait parameter with respect to a target value to be reached. The gait parameters computed included: stance time, swing time, step length, step width, angular plantarflexion at toe off, maximum knee flexion, mean vertical ground reaction force during stance phase, and push off force (antero-posterior ground reaction force at toe off). Per gait parameter, the target value was defined to achieve a specific asymmetry ratio defined as a measure of symmetry as in (1):

$$SR = (\text{left parameter value})/(\text{right parameter value}) \quad (1)$$

Therefore, the target value for the left leg could then be calculated as seen in (2), using data from the right leg as a reference. To reduce the variability over consecutive steps, the mean was taken over the last three gait cycles. Finally, the mean was multiplied by the target symmetry ratio (80% of the baseline walking symmetry ratio). The target was set to be in line with a pre-study conducted on the topic, and aligns with a change sufficient to represent pathological gait [29].

$$Target = 0.8 \times BSR \times \left(\frac{right_0 + right_{-1} + right_{-2}}{3}\right) \quad (2)$$

where Target represents the left target value, BSR corresponds to the baseline symmetry ratio of the gait parameter of interest, and $right_0$, $right_{-1}$, and $right_{-2}$ stand for the right parameter value in the current, last, and second last gait cycle, respectively.

The calculated symmetry ratio and target value was compared with the actual value of the current step. The feedback was subsequently given at the left toe off based on the deviation of the actual value achieved by the left leg (see subsection II.D). In other words, the target value for the left side was defined as being 80% of the symmetry ratio recorded during baseline walking.

Before beginning the feedback phase, participants were provided with the following information: i) that the side to be adapted based on the provided feedback was the left side; ii) the parameter targeted by the feedback was explained (i.e., what is stance time); and iii) how to interpret the vibration pattern (see subsection II.D). No information was provided to the participants about the gait pattern they should achieve (i.e., no information about symmetry being influenced). No other feedback (e.g., visual information about performance) was provided during the study.

D. Terminal Feedback Design

The vibration pattern used for this study was referred to as terminal feedback, meaning the feedback was provided directly after the motor task execution (i.e., after each step during the FB blocks) [8]. The terminal feedback was designed to vibrate for a fixed 0.4s starting at the toe off event of the left leg. Subsequently, based on the participant's performance with respect to the target value, a different tactor location vibrated (i.e., ankle, knee, or hip). When the targeted stance time was properly achieved (margin of ±5% based on a pre-study), the knee tactors vibrated, indicating to the participant that they did not need to adapt anything. If the vibrations were felt at the ankle or the hip it indicated that the stance time was too low or high, respectively, to correspond to the target value. The duration of the vibration felt at the hip or ankle also provided additional information, whereby the further away the current value was from the desired target value, the longer the vibration was. It was then up to the participant to interpret the meaning of the vibration and make real-time adaptations to their gait pattern. The intensity of the vibration was set to the highest possible setting for this device; this was deemed necessary in a pre-study assessment to ensure that the vibration of the treadmill did not interfere with the tactor vibration.

E. Data Analysis

Pre-processing of the motion data was performed using Vicon NexusTM (Vicon Motion Systems Ltd UK) and a python library, Gaitalytics, before being exported and analyzed using Python 3 (Python Software Foundation) [30]. Spatiotemporal and kinetic data were retrieved directly from Gaitalytics using the motion capture data, while kinematic parameters were retrieved from the D-Flow software (Motek Medical B. V.).

To evaluate the effectiveness of the vibrotactile biofeedback in modifying stance time, the symmetry ratio between the natural walking phase and the last minute of the second FB block was compared. A Linear Mixed Model was implemented in R (R Core Team) with the natural walking and the last minute of the second FB block as the fixed effects. The participant IDs were considered random effects. A significance level of 0.05 was defined. The scaled GDI, as defined in Schwartz et al. [25], was also computed for the natural walking and second FB block to assess the evolution of the overall gait pattern.

Additionally, Spearman's rank (ρ) coefficient was calculated to study the monotonic relationship between the stance time and the additional gait metrics [31]. For the computation of these coefficients, the symmetry ratio of the natural walking phase and the last minute of the second FB block were used. No statistical comparison was conducted due to the naturally high correlation between gait cycles.

III. Results

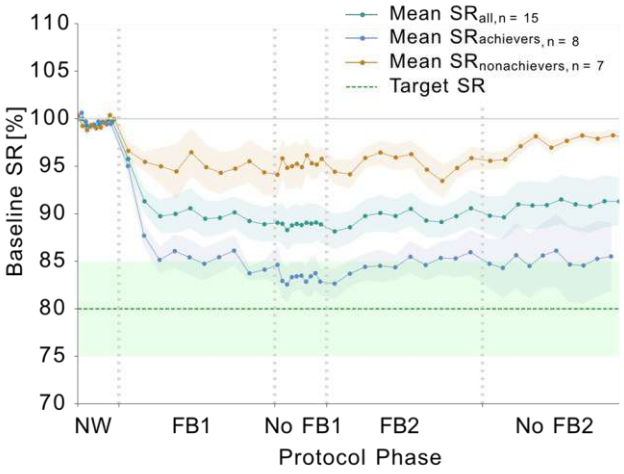


Fig. 3. Evolution of stance time symmetry ratio. Mean symmetry ratio of all participants and the split into *achievers* (blue) and *non-achievers* (orange). Abbreviations: FB, feedback; No FB, no feedback; NW, natural walking; SR, symmetry ratio.

A. Gait Symmetry

When examining the evolution of the stance time symmetry ratio over the course of the feedback phase, an ability to adapt the stance time towards the target could be seen (Fig. 3). Results from the Linear Mixed Effect model showed a statistically significant difference between the stance time at the end of the second FB block compared to during the natural walking ($p < 0.001$; CI = [-0.130, -0.057]). However, at the group level, while all participants responded to the feedback resulting in their stance time symmetry ratio becoming pathologic, the symmetry ratio did not decrease enough in all participants to reach the target value. Upon visual inspection, two separate groups could be distinguished based on their symmetry ratio during stance time; specifically, it was seen that only half the participants managed to adapt and maintain their stance time symmetry ratio to fall close to or within the target value margins (Fig. 3). Those that were able to reach the target margins were considered to be *achievers*, versus *non-achievers* who did not reach the target margins. It could also be seen visually that participants were able to maintain the altered symmetry ratio during the No FB blocks. Compared to the natural walking block, all changes were found to be significant in the second No FB block (all: $t = 3.66$, $p = .003$; *achievers*: $t = 3.99$, $p = .005$; *non-achievers*: $t = 6.06$, $p < .001$).

In addition to the stance time symmetry ratio, the symmetry ratios of the swing time ($t = 4.64$) and mean ground reaction force ($t = -5.32$) at the end of the second FB block were found to be significantly different from the symmetry ratios during natural walking ($p < 0.001$). The symmetry ratios of the push off force ($t = -1.19$, $p = 0.256$), step width ($t = 0.294$, $p = 0.773$), and step height ($t = 1.04$, $p = 0.315$) were not found to be statistically different at the end of the second FB block compared to natural walking .

B. Gait Deviation Index

The GDI is z-scaled, with a reference value of 100 set for the control group mean. The scaled GDI was calculated as the mean across all participants during natural walking and the last FB block. The stance time GDI during natural walking was found to be 100.4 and decreased to 87.6 (left leg = 84.2; right leg = 91.0) during the second FB block. These results were found to be statistically significant based on a paired t-test (combined: $t = 4.90$, $p < .001$; left: $t = 6.77$, $p < .001$; right: $t = 3.03$, $p = .009$). As explained in previous work, a GDI value of 100 indicates a gait that is absent of any pathology (i.e., there is no gait abnormality present) [25]. Every 10 points below 100 represents one standard deviation away from the control gait with no abnormality present. This indicates that the GDI achieved during the second FB block was approximately one standard deviation away from the control gait when both the left and right legs were averaged. However, when examining the legs separately it can be seen that there was a greater decrease in GDI on the left leg (i.e., the side the feedback was applied to) compared to the right.

C. Correlation Between Gait Parameters

The Spearman's rank correlation was computed to assess the monotonic relationship between the stance time symmetry ratio and the symmetry ratio of additional gait parameters (Table 1). The correlation found a negative relationship between the stance and swing time symmetry ratios. A positive correlation with the stance time could also be noted for both the push off force and mean ground reaction force. No other correlations of note were present.

IV. Discussion

The primary objective of this study was to assess whether vibrotactile biofeedback could be used to influence stance time symmetry ratio, specifically to enforce gait asymmetry in neurologically intact individuals. The results indicate that participants were able to quickly adapt their gait to achieve an altered, namely asymmetric, stance time. This shift occurred rapidly, within the first three-minute FB block, supporting the hypothesis that biofeedback can induce changes in gait. Additionally, this alteration in stance time symmetry ratio did not occur in isolation; it was accompanied by a reduction in the GDI and correlated with changes in the symmetry ratio of other gait parameters. These are important considerations for the potential use of biofeedback for the implementation of more personalized gait rehabilitation.

However, in line with the findings of Legrand et al. individual responses to the feedback varied, with only a subset of participants closely approaching target asymmetry [19]. A closer analysis of stance time evolution showed that

TABLE 1. SPEARMAN'S RANK CORRELATION COEFFICIENT BETWEEN THE SYMMETRY RATIOS OF STANCE TIME AND ADDITIONAL GAIT PARAMETERS.

	Swing Time	Push Off Force	Ankle Plantarflexion	Step Length	Step Width	Step Height	Mean GRFz[a]	Knee Flexion
Spearman (Rho)	-0.76	0.45	0.15	-0.12	-0.05	0.05	0.40	-0.02

[a]Vertical ground reaction force (z axis)

although a group of participants (*non-achievers*) did not reach the 20% target asymmetry shift, they did achieve an approximately 5% asymmetry shift. This amount of asymmetry could still be interpreted as a pathological gait pattern, in line with the study's aim [29]. Despite potential challenges in fully comprehending the feedback, non-*achievers* still adapted their gait towards asymmetry. It was noted that these participants adjusted both their left and right foot stance times almost equally, thus maintaining a balanced symmetry ratio despite altering their gait. Because the target symmetry ratio was calculated based on values from both feet (equation 1), these participants were unable to achieve the target asymmetry. This division into *achievers* and *non-achievers* suggests that identical feedback may not be intuitively interpreted by all individuals, hence indicating an individual variability. Providing participants with additional guidance on the symmetry ratio target, or providing the biofeedback on both legs, might have reduced the number of *non-achievers*. However, in this study, symmetry ratio information was intentionally withheld to allow participants to explore the feedback themselves. It is of course also possible that there are inherent limitations in the presentation of the biofeedback that made it less suitable for stance time feedback versus another potential target gait parameter.

When focusing on stance time symmetry ratio, noticeable alterations in gait patterns could be observed, as reflected by a decrease in the GDI during the feedback phase relative to natural walking. Since the GDI only incorporates spatial parameters (e.g., step length, step width) we know that these findings (i.e., decrease in GDI representing a global change in gait quality) come only from kinematic changes in the gait. This implies that even a targeted adjustment to stance time symmetry ratio can affect kinematic parameters (e.g., joint angles, velocities, accelerations) [25]. This result is promising, as it suggests that targeting a single gait parameter may influence overall gait, potentially benefiting rehabilitation. However, there is a caveat: this approach could also pose a risk, as it could lead to unintended maladaptive movements in patient populations. Since compensatory movements were not specifically examined, it is unclear whether they occurred. Changes in the GDI and correlations between the symmetry ratio of stance time and other gait parameters suggest a global shift in gait patterns. However, as healthy participants were deliberately pushed toward asymmetry, it is uncertain whether these changes reflect compensatory movements due to the lack of a reference point for distinguishing adaptive responses from maladaptive compensation. These observations should be kept in mind in view of implemented biofeedback on selected parameters for clinical applications.

Our correlation analysis sheds further light on the observed gait changes. As anticipated, a negative correlation was observed between the stance time symmetry ratio and the swing time symmetry ratio. This inverse relationship aligns with previous findings, reflecting the natural interaction between stance and swing time at a constant walking speed [19], [32]. Additionally, stance time symmetry ratio was positively correlated with push off force symmetry ratio and vertical ground reaction force symmetry ratio. These findings are consistent with the interconnectedness of stance time and these parameters, which may have an even more important role in post-stroke patients who often exhibit reduced stance time and force on the paretic side [33]. Legrand et al. found similar correlations in their study on visual biofeedback, specifically between stance time, swing time, push off force, and vertical ground reaction force [19]. Notably, while the knee flexion symmetry ratio correlated with the stance time symmetry ratio under visual feedback conditions, this association was absent with vibrotactile biofeedback. Neither this study, nor that of Legrand et al., found correlations between stance time (i.e., temporal parameter) and spatial parameters [19]. This suggests that alternative approaches may be necessary to explore how spatial symmetry can be influenced.

Moreover, while our findings apply only to neurotypical individuals, limiting their clinical interpretation, this limitation could be addressed by expanding the study to include neurologically impaired individuals. Together, our results and those of Legrand et al., reinforce the idea that modifications in a single gait parameter are rarely isolated [19], [34]. However, the broader implications of these changes, such as potential compensatory movements affecting other gait parameters, remains unclear. Another relevant limitation identified in this study would be the vibration intensity of the tactors. Some participants reported difficulty perceiving the feedback, with two participants only feeling the vibrations when actively pressing the tactor against their hip. This would be important to further examine to determine the optimal tactor attachment method, and what clothing should be worn during the measurements as these may both play a role in the vibration intensity felt by the participant. The ability to perceive the feedback may be particularly relevant for post-stroke patients, who often experience sensory deficits and may require a higher vibration intensity for effective feedback [35]. As the maximum vibration intensity of the Elitac Wearable Science Suit was already used for this study, this would need to be considered in future work.

While this study focused on the influence of vibrotactile biofeedback on stance time symmetry ratio, a spatiotemporal parameter, future research could explore the effects on kinetic and kinematic parameters. Additionally, comparing vibrotactile biofeedback with other biofeedback modalities, such as auditory or visual feedback, may provide insights into the most effective strategies for inducing gait changes as well as aspects such as the familiarization and adaptation time required for each.

V. Conclusion

This study found that terminal vibrotactile biofeedback was successfully able to influence gait symmetry in neurologically intact individuals. This change did not occur in isolation, with the change in stance time symmetry ratio generally influencing not only kinematic parameters, but also kinetic parameters as indicated by the decreased GDI and correlated gait parameters. These findings emphasize the importance of taking into consideration how using biofeedback to target a single gait parameter will most certainly also influence gait as a whole, and that care should be taken to not induce maladaptive movements.

REFERENCES

[1] S. McGee, "Chapter 7 - Stance and Gait," in *Evidence-Based Physical Diagnosis (Fourth Edition)*, S. McGee, Ed., Philadelphia: Elsevier, 2018, pp. 45-58.e2. doi: 10.1016/B978-0-323-39276-1.00007-X.

[2] A. Mirelman, S. Shema, I. Maidan, and J. M. Hausdorff, "Chapter 7 - Gait," in *Handbook of Clinical Neurology*, vol. 159, B. L. Day and S. R. Lord, Eds., in Balance, Gait, and Falls, vol. 159. , Elsevier, 2018, pp. 119–134. doi: 10.1016/B978-0-444-63916-5.00007-0.

[3] Md. Akhtaruzzaman, A. A. Shafie, and Md. R. Khan, "Gait analysis: systems, technologies, and importance," *J. Mech. Med. Biol.*, vol. 16, no. 07, p. 1630003, Nov. 2016, doi: 10.1142/S0219519416300039.

[4] J. Schröder, S. Truijen, T. V. Criekinge, and W. Saeys, "Feasibility and effectiveness of repetitive gait training early after stroke: a systematic review and meta-analysis," *Journal of Rehabilitation Medicine*, vol. 51, no. 2, Art. no. 2, 2019, doi: 10.2340/16501977-2505.

[5] D. M. Wolpert, J. Diedrichsen, and J. R. Flanagan, "Principles of sensorimotor learning," *Nat Rev Neurosci*, vol. 12, no. 12, pp. 739–751, Dec. 2011, doi: 10.1038/nrn3112.

[6] C. J. Winstein, "Knowledge of results and motor learning--implications for physical therapy," *Phys Ther*, vol. 71, no. 2, pp. 140–149, Feb. 1991, doi: 10.1093/ptj/71.2.140.

[7] R. A. Magill, *Motor learning and control : concepts and applications*. Boston : McGraw-Hill, 2004. Accessed: Nov. 20, 2024. [Online]. Available: http://archive.org/details/motorlearningcon00magi

[8] R. Sigrist, G. Rauter, R. Riener, and P. Wolf, "Augmented visual, auditory, haptic, and multimodal feedback in motor learning: a review," *Psychon Bull Rev*, vol. 20, no. 1, pp. 21–53, Feb. 2013, doi: 10.3758/s13423-012-0333-8.

[9] R. A. Schmidt, T. D. Lee, C. Winstein, G. Wulf, and H. N. Zelaznik, *Motor Control and Learning: A Behavioral Emphasis*. Human Kinetics, 2018.

[10] J. Spencer, S. L. Wolf, and T. M. Kesar, "Biofeedback for Post-stroke Gait Retraining: A Review of Current Evidence and Future Research Directions in the Context of Emerging Technologies," *Front. Neurol.*, vol. 12, Mar. 2021, doi: 10.3389/fneur.2021.637199.

[11] P. M. van Vliet and G. Wulf, "Extrinsic feedback for motor learning after stroke: what is the evidence?," *Disabil Rehabil*, vol. 28, no. 13–14, pp. 831–840, Jul. 2006, doi: 10.1080/09638280500534937.

[12] N. Hasegawa, K. Takeda, M. Mancini, L. A. King, F. B. Horak, and T. Asaka, "Differential effects of visual versus auditory biofeedback training for voluntary postural sway," *PLOS ONE*, vol. 15, no. 12, p. e0244583, Dec. 2020, doi: 10.1371/journal.pone.0244583.

[13] Y.-H. Choi, J.-D. Kim, J.-H. Lee, and Y.-J. Cha, "Walking and balance ability gain from two types of gait intervention in adult patients with chronic hemiplegic stroke: A pilot study," *Assistive Technology*, vol. 31, no. 2, pp. 112–115, Mar. 2019, doi: 10.1080/10400435.2017.1387616.

[14] M. D. Lewek, J. Feasel, E. Wentz, F. P. Brooks Jr, and M. C. Whitton, "Use of visual and proprioceptive feedback to Improve gait speed and spatiotemporal symmetry following chronic stroke: a case series," *Physical Therapy*, vol. 92, no. 5, pp. 748–756, May 2012, doi: 10.2522/ptj.20110206.

[15] R. Stanton, L. Ada, C. M. Dean, and E. Preston, "Biofeedback improves activities of the lower limb after stroke: a systematic review," *Journal of Physiotherapy*, vol. 57, no. 3, pp. 145–155, Jan. 2011, doi: 10.1016/S1836-9553(11)70035-2.

[16] K. A. Day, K. M. Cherry-Allen, and A. J. Bastian, "Individualized feedback to change multiple gait deficits in chronic stroke," *J Neuroeng Rehabil*, vol. 16, no. 1, p. 158, Dec. 2019, doi: 10.1186/s12984-019-0635-4.

[17] L. Y. Liu, S. Sangani, K. K. Patterson, J. Fung, and A. Lamontagne, "Real-time avatar-based feedback to enhance the symmetry of spatiotemporal parameters after stroke: instantaneous effects of different avatar views," *IEEE Transactions on Neural Systems and Rehabilitation Engineering*, vol. 28, no. 4, pp. 878–887, Apr. 2020, doi: 10.1109/TNSRE.2020.2979830.

[18] M. Drużbicki, A. Guzik, G. Przysada, A. Kwolek, A. Brzozowska-Magoń, and M. Sobolewski, "Changes in gait symmetry after training on a treadmill with biofeedback in chronic stroke patients: a 6-month follow-up from a randomized controlled trial," *Med Sci Monit*, vol. 22, pp. 4859–4868, Dec. 2016, doi: 10.12659/MSM.898420.

[19] M. L. Legrand *et al.*, "Augmented feedback to influence gait symmetry: a feasibility study to quantify effects on the global gait pattern," in *2024 10th IEEE RAS/EMBS International Conference for Biomedical Robotics and Biomechatronics (BioRob)*, Sep. 2024, pp. 1063–1068. doi: 10.1109/BioRob60516.2024.10719727.

[20] X. Deng, M. Liufu, J. Xu, C. Yang, Z. Li, and J. Chen, "Understanding implicit and explicit sensorimotor learning through neural dynamics," *Front. Comput. Neurosci.*, vol. 16, Aug. 2022, doi: 10.3389/fncom.2022.960569.

[21] R. D. Seidler and R. G. Carson, "Sensorimotor learning: neurocognitive mechanisms and individual differences," *Journal of NeuroEngineering and Rehabilitation*, vol. 14, no. 1, p. 74, Jul. 2017, doi: 10.1186/s12984-017-0279-1.

[22] M. Kleynen *et al.*, "Multidisciplinary views on applying explicit and implicit motor learning in practice: an international survey," *PLOS ONE*, vol. 10, no. 8, p. e0135522, Aug. 2015, doi: 10.1371/journal.pone.0135522.

[23] E. Kal, R. Prosée, M. Winters, and J. van der Kamp, "Does implicit motor learning lead to greater automatization of motor skills compared to explicit motor learning? A systematic review," *PLOS ONE*, vol. 13, no. 9, p. e0203591, Sep. 2018, doi: 10.1371/journal.pone.0203591.

[24] D. Kim, B. J. Johnson, R. B. Gillespie, and R. D. Seidler, "The effect of haptic cues on motor and perceptual based implicit sequence learning," *Front. Hum. Neurosci.*, vol. 8, Mar. 2014, doi: 10.3389/fnhum.2014.00130.

[25] M. H. Schwartz and A. Rozumalski, "The gait deviation index: a new comprehensive index of gait pathology," *Gait & Posture*, vol. 28, no. 3, pp. 351–357, Oct. 2008, doi: 10.1016/j.gaitpost.2008.05.001.

[26] A. J. van den Bogert, T. Geijtenbeek, O. Even-Zohar, F. Steenbrink, and E. C. Hardin, "A real-time system for biomechanical analysis of human movement and muscle function," *Med Biol Eng Comput*, vol. 51, no. 10, pp. 1069–1077, Oct. 2013, doi: 10.1007/s11517-013-1076-z.

[27] A. Aboutorabi, M. Arazpour, M. Bahramizadeh, F. Farahmand, and R. Fadayevatan, "Effect of vibration on postural control and gait of elderly subjects: a systematic review," *Aging Clin Exp Res*, vol. 30, no. 7, pp. 713–726, Jul. 2018, doi: 10.1007/s40520-017-0831-7.

[28] S. J. Olney and C. Richards, "Hemiparetic gait following stroke. Part I: Characteristics," *Gait & Posture*, vol. 4, no. 2, pp. 136–148, Apr. 1996, doi: 10.1016/0966-6362(96)01063-6.

[29] K. K. Patterson, W. H. Gage, D. Brooks, S. E. Black, and W. E. McIlroy, "Evaluation of gait symmetry after stroke: a comparison of current methods and recommendations for standardization," *Gait & Posture*, vol. 31, no. 2, pp. 241–246, Feb. 2010, doi: 10.1016/j.gaitpost.2009.10.014.

[30] "gaitalytics on Pypi," Libraries.io. Accessed: Nov. 10, 2024. [Online]. Available: https://libraries.io/pypi/gaitalytics

[31] A. Rovetta, "Raiders of the lost correlation: a guide on using pearson and spearman coefficients to detect hidden correlations in medical sciences," *Cureus*, vol. 12, no. 11, p. e11794, Nov. 2020, doi: 10.7759/cureus.11794.

[32] A. Leal-Junior and A. Frizera-Neto, "Gait analysis: overview, trends, and challenges," in *Optical Fiber Sensors for the Next Generation of Rehabilitation Robotics*, A. Leal-Junior and A. Frizera-Neto, Eds., Academic Press, 2022, pp. 53–64. doi: 10.1016/B978-0-32-385952-3.00011-1.

[33] B. Balaban and F. Tok, "Gait disturbances in patients with stroke," *PM&R*, vol. 6, no. 7, pp. 635–642, 2014, doi: 10.1016/j.pmrj.2013.12.017.

[34] F. Doerks, L. Riedel, A.-K. Einfeldt, H. Windhagen, C. Hurschler, and E. Jakubowitz, "Contribution of various forefoot areas to push-off peak at different speeds and slopes during walking," *Gait & Posture*, vol. 108, pp. 264–269, Feb. 2024, doi: 10.1016/j.gaitpost.2023.12.016.

[35] S. S. Kessner, U. Bingel, and G. Thomalla, "Somatosensory deficits after stroke: a scoping review," *Topics in Stroke Rehabilitation*, vol. 23, no. 2, pp. 136–146, Feb. 2016, doi: 10.1080/10749357.2015.1116822.

Hybrid Brain Computer Interface-based rehabilitation addressing post-stroke maladaptive movement patterns

J. Toppi, *Member, IEEE*, G. Savina, E. Colamarino, V. de Seta, F. Patarini, F. Cincotti, F. Pichiorri, and D. Mattia

***Abstract*— Hybrid Brain-Computer Interfaces (hBCI) integrate brain and muscle signals to enhance motor rehabilitation of stroke survivors, by closing the loop between the lesioned brain and the paretic limb. To date, little attention has been devoted to their potential efficacy in managing the maladaptive movement patterns that afflict post-stroke motor outcome (unwanted abnormal co-contrations, spasticity). This study proposes a comparison of Cortico-Muscular Coherence (CMC) patterns assessed in stroke patients before and after a 1-month rehabilitation intervention based on a hBCI-controlled Functional Electrical Stimulation (FES) treatment, which included a module to monitor non-physiological movement patterns. Results demonstrated the efficacy of this type of assistive technology for post-stroke rehabilitation, addressing patient-tailored interventions able to reduce the maladaptive mechanisms.**

I. Introduction

Stroke is a major cause of adult disability. Upper limb motor impairment is often persistent after the acute event and is a crucial limiting factor that determines the patient's capability to regain social and work position [1]. Stroke modifies the connectivity between brain and periphery, resulting in impaired motor function with respect to physiological conditions [2] and is characterized by features related to maladaptive plasticity in terms of both compensatory and mirror movements, which should be monitored and discouraged during rehabilitation [3]. Several technological aids have been proposed to address upper limb motor recovery, and among those Electroencephalography (EEG)-based Brain-Computer Interface (BCI) systems [4]. BCIs rely on the reinforcement of motor related brain activity to boost post stroke plasticity underlying favorable motor outcome [5], [6]. Such reinforcement is provided within the closed-loop paradigm that is peculiar to the BCI approach, in which the patient receives instant feedback based on their own mental activity; such feedback can be visual or enriched with sensorimotor content as if provided by a Functional Electrical Stimulator (FES). The FES has been applied in stroke rehabilitation with beneficial effects on motor outcome in terms reducing spasticity and improving motor function and even muscle strengthening [4], [7]. Worth of note that electrical stimulation of muscle contraction needs to be synchronized with intended movement to restore motor function in paralysis condition. Hybrid BCIs (hBCI) are defined as systems that employ signals other than those derived from the brain, such as the muscular activity recorded via surface Electromyography (EMG).

Recently, Cortico-Muscular Coherence (CMC), an intrinsically hybrid feature encoding EEG-EMG coupling during voluntary motor actions [8], has been employed in BCIs for the real-time detection of different hand movements with high classification performances [9], [10] and proved to be a valid objective measure for the upper limb motor deficit assessment in stroke survivors [11]. Providing more complete and synergistic information could actually confirm the CMC as a valid measure to better identify and even monitor maladaptive plasticity effects than using same nature biosignals, e.g. EEG or EMG alone [12]. Specifically, in [11] we have identified CMC features related to unwanted co-contractions in a population of stroke patients and implemented their detection within a novel hBCI system in order to discourage them during hBCI-based FES training of upper limb.

The aim of this study is to evaluate the restoration of aphysiological brain-muscle communication in a convenience sample of post-stroke patients who underwent a rehabilitation training with such novel system, that is able to efficiently trigger the FES intervention and at the same time discourage dysfunctional movements.

II. Material and Methods

A. Participants

Five stroke participants recruited within the inpatients and outpatients services of Fondazione Santa Lucia, IRCCS, Rome, Italy, participated in the study. Demographic and clinical details were reported in Table I. The inclusion criteria consisted in i) first-ever unilateral, cortical, subcortical, or mixed stroke, caused by ischemia or hemorrhage, ii) upper limb hemiparesis that was caused by the stroke; and iii) age between 18 and 80 years. The exclusion criteria were the presence of (i) neuropsychological deficits preventing the ability to understand the instructions related to the experiment; (ii) concomitant diseases affecting the upper limb

*Research partially supported by the Italian Ministry of Health (GR-201812365874), by Sapienza University of Rome - Progetti di Ateneo (LEAF, RM123188F229EC72 and RP123188F7621611) and by the Italian Ministry of University and Research (PRIN MUR 20207S3NB8).

J. Toppi (corresponding author to provide e-mail: jlenia.toppi@uniroma1.it), G. Savina, E. Colamarino, F. Patarini and F. Cincotti are with the Department of Computer, Control, and Management Engineering, Sapienza University of Rome, Italy and with IRCCS Fondazione Santa Lucia, Rome, Italy (e-mail: giulia.savina@uniroma1.it, emma.colamarino@uniroma1.it, francesca.patarini@uniroma1.it and febo.cincotti@uniroma1.it).

V. de Seta is with the Defitech Center for Interventional Neurotherapies, CHUV, Lausanne, Switzerland and with the Neuro-X Institute Swiss Federal Institute of Technology (EPFL), Lausanne, Switzerland (e-mail: valeria.deseta@epfl.ch).

F. Pichiorri and D. Mattia are with IRCCS Fondazione Santa Lucia, Rome, Italy (e-mail: f.pichiorri@hsantalucia.it and d.mattia@hsantalucia.it).

TABLE I. PATIENTS OVERVIEW[A]

ID	Gender	Age (y)	Lesion Side	Time from event (m)	FMA pre	FMA post
P01	M	63	L	5	18	Drop out
P02	M	67	L	3	26	41
P03	M	52	R	11	30	34
P04	M	62	R	19	30	34
P05	M	64	L	9	30	33
	5M	62±6	3L/2R	9.4±6.2	27±6	35±4

List of acronyms: FMA: Fugl-Meyer Assessment, L: left, M: male, m: month, R: right, y: year

motor function (i.e., orthopedic injuries or other neurologic diseases affecting reaching or grasping); (iii) spasticity of each segment of the upper limb scored higher than 4 on the Modified Ashworth Scale (MAS [13]); (iv) presence of any contraindication to FES (such as pregnancy, proneness to faint, epilepsy, compromised integrity of the stimulated limb, compromised sensation). The study was approved by the local ethics board at Fondazione Santa Lucia, IRCCS, Rome, Italy (CE PROG.752/2019) and all the participants signed an informed consent.

B. Study Design

All the patients underwent a 1-month rehabilitation intervention (three days per week for four weeks - 12 sessions) based on the hBCI-controlled Functional Electrical Stimulation (FES) treatment (described in section II.E) in addition to the standard rehabilitation program (usual care). At study entry (PRE) and at the end of the entire rehabilitation program (POST) all patients underwent a clinical/functional (section II.C) and neurophysiological (section II.D) screening to assess the effect of hBCI-FES-based rehabilitation training. Data collected in PRE session were also used to identify control features for the hBCI-FES system (section II.F).

C. PRE/POST Clinical/Functional evaluation

In PRE and POST sessions all patients were screened by means of the following clinical scales: i) the upper extremity section of the Fugl-Meyer Assessment scale (FMA), comprising the four sub-scales "Upper Limb", "Wrist", "Hand", "Coordination and Velocity" to describe the paretic upper limb residual function [14], ii) the Manual Muscle Test (MMT) to assess strength in the paretic upper limb testing shoulder abduction, elbow flexion/ extension and wrist flexion/extension [15] and iii) the MAS scale to assess spasticity of shoulder, elbow and wrist muscles [13]. For the purpose of this study, we considered only the FMA scale since it provides an overall measure of the motor function that we managed to restore.

D. PRE/POST Neurophysiological evaluation

The neurophysiological assessment consisted in the simultaneous collection of high-density EEG (61 electrodes at 1 kHz) and EMG (16 upper limbs muscles - 8 per side - at 2 kHz) signals during hand extension collected separately with the unaffected and affected hand (UH and AH, respectively) according to a block design approach. Each of the 2 per hand administered blocks consisted of 40 trials: 20 task trials of 8s each during which patients were asked to perform/attempt the extension (EXT) of UH/AH (4s of preparation and 4s of execution/attempt) and 20 rest trials of 4s each. The order of presentation for both i) trials within blocks and ii) blocks was randomly assigned and different for all the patients included in order to ensure as uniform as possible experimental conditions by preventing any learning, fatigue or expectancy effects which could influence the results beyond our aim.

EEG was recorded from the scalp by means of active electrodes (Brain Products GmbH, Germany) arranged according to an extension of 10–20 International System (reference on left mastoid and ground on right mastoid). Surface bipolar EMG signals were recorded by means of Pico EMG sensors (Cometa S.r.l., Italy) from the following 16 muscles: extensor digitorum (ED), flexor digitorum superficialis (FD), lateral head of the triceps muscle (TRI), long head of the biceps brachii muscle (BIC), pectoralis major (PEC), lateral deltoid (Lat_DELT), anterior deltoid (Ant_DELT) and upper trapezius (TRAP) of both sides (AH: and UH). EEG signals were band-pass filtered [3-60]Hz and Independent Component Analysis was used to remove ocular artifacts. EMG signals were downsampled to 1000Hz, band-pass filtered [3-500]Hz and the electrocardiographic component was rejected through template matching. A notch filter at 50Hz was applied to remove power-line artifacts on both signals and data were segmented according to the different experimental conditions. The EEG edge electrodes (Fpz, Fp2, AF8, F8, FT8, T8, TP8, P8, PO8, O2, Oz, O1, PO7, P7, TP7, T7, FT7, F7, AF7, Fp1) were excluded from the analysis to avoid synchronization between the EEG and EMG signal due to residual muscular component in the first one.

CMC was estimated as in [11] for each movement (EXT_AH, EXT_UH) and frequency band (Alpha [8-12] Hz, Beta [13-30] Hz) in both PRE and POST assessment sessions for each patient. We computed statistical CMC patterns at single-subject level by comparing (independent samples t-test, alpha=0.05) CMC values obtained for each band and EEG-EMG pair between task and rest conditions. In order to quantify the CMC patterns properties in each condition and describe their changes induced by the intervention we extracted objective indices measuring specific properties useful for describing the effect of hBCI-FES training over the patients' brain-muscles communication. In particular we computed the following indices for each patient and frequency band in PRE and POST sessions, which have already been proved to be valid CMC metrics for our purpose in a previous study [11]: i) CMC weight defined as the average strength of the connections linking the target muscle (ED in affected limb) and all the EEG electrodes considered in the study; ii) two indices related to network density describing in terms of total number of existing connections the dysfunctional involvement of proximal muscles (BIC, TRI, Lat_DELT, Ant_DELT) in affected limb or mirror movements (ED or FD) in unaffected limb.

E. Description of the hybrid Brain-Computer Interface system used in the study

The hBCI-FES device is a hBCI system that controls FES of upper limb muscles: the patient is asked to attempt simple upper limb movements (e.g., extension of fingers); the device recognizes (in correct trials) close-to-normal EEG-EMG co-

activation (see section II.G for details) and initiates FES of extensor muscles in the forearm. The hBCI-FES includes the following hardware components: i) an EEG and an EMG acquisition system used to record simultaneously brain and muscular activity; ii) a laptop where the hBCI software runs; iii) a FES stimulator (RehaMOVE2 system - Hasomed GmbH, Germany) used to deliver the stimulation to the patient. FIAB4 fully gelled electrodes are used for neurostimulation.

F. Experimental protocol used during the hBCI-FES-based rehabilitation session

The hBCI-assisted paradigm was designed as driven by the therapist and consists in several trials/repetitions of the rehabilitative exercise: at the beginning of each trial a beep sound is delivered informing the patient to get ready to attempt the movement, after 3s an acoustic cue "GO" invites the patient to start the task. The stimulation is delivered to the patient when a physiological movement is detected, without the need to continue attempting it. The target muscle is stimulated for 4s, after which the therapist's interface makes the therapist wait at least 8s before the next trial (duty cycle: 1:2 to preserve muscle fatigue development). After 4s from the acoustic cue, if no physiological movement is detected the trial ends with a "time out".

G. Extraction of control features for hBCI-FES system

EEG and EMG data acquired during the PRE neurophysiological assessment were used to select 2 hBCI-FES control features (CMC values obtained for two EEG-EMG pairs where the EMG channel is the target muscle - ED) [10] and, if present, 2 different features identifying the undesired involvement of muscles not directly related to the requested movement and that should be discouraged. FES is activated only when the BCI correctly classifies the movement attempt by means of the two control features, but at the same time, the CMC values obtained for the two discouraged features remained below a null-case statistical threshold of activation tailored for each patient. During the online BCI sessions, the EEG and EMG signals of the electrodes chosen during the feature selection were acquired, the attempted motor task was predicted and the EEG-EMG pairs to discourage were monitored along the rehabilitative exercise. FES parameters were set specifically for each patient at every session according to standard guidelines [16] to achieve full movement to avoid any kind of discomfort for them. Such parameters were identified stimulating in an open-loop modality the target muscle.

III. RESULTS

A. Clinical outcome evaluation

In Table I we reported for each patient the FMA scores collected at the enrollment and at the end of the rehabilitation programme. Worth of note is that all patients showed a trend of improvement, more evident in 3 out of them.

B. hBCI-FES system control features

A list of all the control and discouraged features selected for each patient is reported in Table II. In particular, the control features involving EEG channels contralateral to the hand involved in the movement in all the 5 patients were included. As for the discouraged features, in 3 out of the 5 patients we set a control for mirror movements (P02, P03, P04), while in P05 we control only for the involvement of proximal muscles of the affected limb. Only in P01 we discouraged movements involving both distal muscles of unaffected limb and proximal muscles of affected limb.

TABLE II. FEATURES SET IN THE HBCI-FES SYSTEM FOR EACH PATIENT

ID	Control Features	Discouraged Features
P01	FC5-EDR C1-EDR	P5-Lat_DELTR P6-FDL
P02	C1-EDR CP1-EDR	FC3-EDL
P03	C6-EDL P6-EDL	C3-EDR
P04	CP2-EDL C2-EDL	C3-EDR
P05	P5-EDR CP3-EDR	C3-BICR

C. Reinforcement of CMC patterns induced by hBCI-FES training

In Fig. 1 we compared the values obtained for CMC weight index extracted from CMC patterns in alpha and beta bands related to the extension of affected (panel a) and unaffected (panel b) hand in PRE and POST sessions. It is interesting to notice how, when patients attempted to execute the extension of their affected hand, the CMC value of the connections involving target muscle (ED of affected limb) increased after the hBCI-FES training in both frequency bands. Instead, during the execution of the extension of the unaffected hand the weights of CMC connections involving the ED of unaffected limb remained almost comparable between PRE and POST sessions. Together with an increase of this index involving particularly the target muscle (i.e., ED

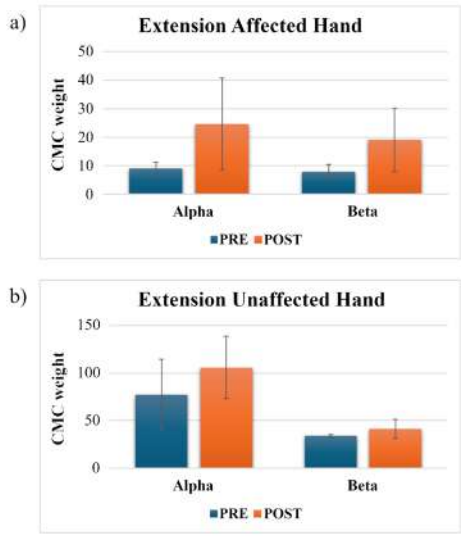


Figure 1. Barplot comparing grand average CMC weight index (average N=5 ± standard deviation) extracted from CMC patterns obtained in alpha and beta bands during the extension of affected (panel a) and unaffected (panel b) hand in PRE and POST sessions.

of affected limb), we obtained an evident increase even in variability characterizing the post-timepoints.

D. Reduction of maladaptive CMC patterns according to patients' specific features

In Fig. 2 and 3 we reported instead the PRE vs POST results for two representative patients who received a hBCI-FES training where specific dysfunctional movements were discouraged. In particular, Fig. 2 showed data related to patient P02 who was discouraged in executing mirror movements when attempting to extend the affected hand. By qualitatively comparing PRE and POST CMC patterns in both alpha and beta bands (panel a), we noticed how before starting the hBCI-FES treatment the patient showed CMC patterns strongly influencing the target muscle (ED in right limb) but also the ED in unaffected limb. Such behavior strongly reduces in the POST session. The reduction of mirror movements was confirmed by an evident reduction after the hBCI-FES training of the number of connections involving distal muscles of unaffected limb in both alpha and beta bands (panel b).

Fig. 3 showed the results related to the representative patient P04 who executed a hBCI-FES training which blocked FES activation everytime the patient engaged proximal

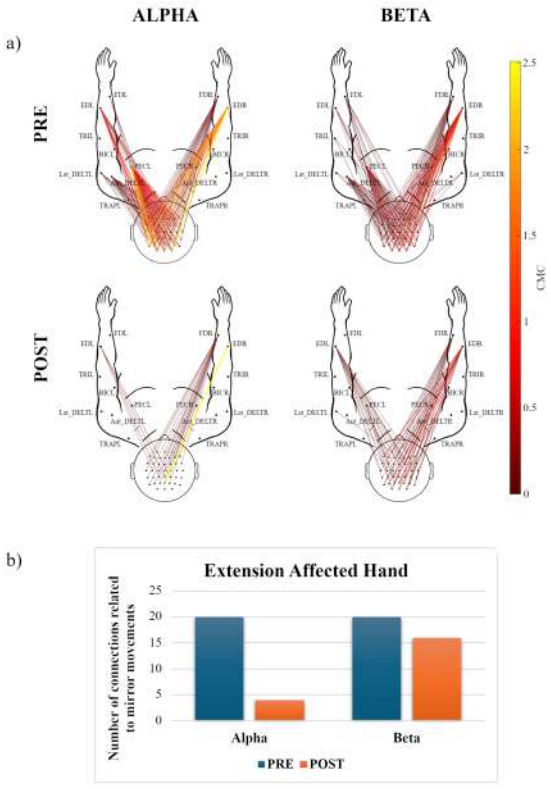


Figure 2. Results obtained for a representative patient (P02) in alpha and beta bands for PRE and POST training sessions in terms of a) CMC patterns during the extension of their affected hand (right) and b) number of connections related to mirror movements computed from CMC patterns.

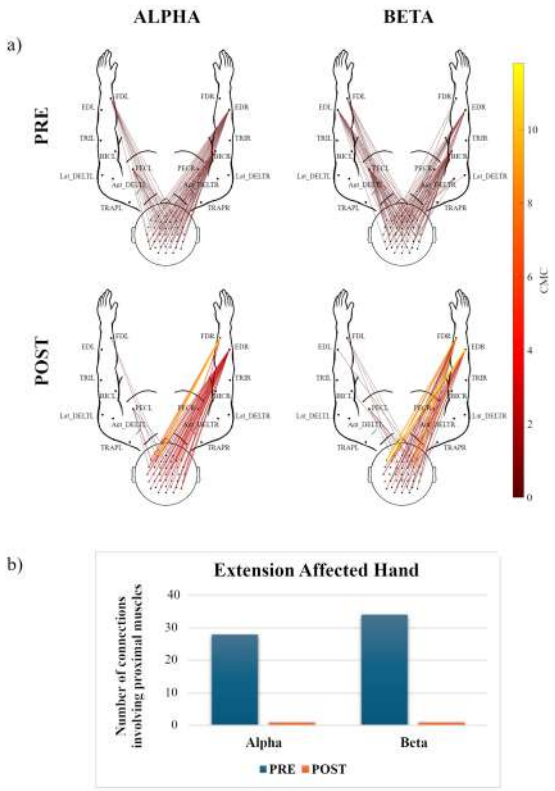


Figure 3. Results obtained for a representative patient (P04) in alpha and beta bands for PRE and POST training sessions in terms of a) CMC patterns during the extension of their affected hand (right) and b) number of connections involving proximal muscles of the affected limb computed from CMC patterns.

muscles of the affected limb when attempting to execute the AH extension. CMC patterns in PRE session showed the involvement of right BIC in both alpha and beta bands that was clearly reduced after the 1-month hBCI-FES training period (panel a). This is confirmed by a PRE vs POST reduction of the number of connections involving the proximal muscles of affected limb in both alpha and beta bands (panel b).

IV. Discussion

Our results confirm that hBCI-based FES training is able to reinforce CMC patterns involving scalp electrodes on the stroke affected hemisphere and target muscles on the paretic upper limb, thus efficiently closing the loop between the damaged brain and the periphery [9], [10]. CMC plays a critical role in motor control by reflecting the functional coupling between cortical and spinal motor networks, which is essential for voluntary movement execution and motor learning [8].

A reduction in CMC is observed after a stroke lesion and the magnitude of such reduction has been correlated with the severity of motor impairment [17], [18], [19]. This decline is thought to result from disrupted corticospinal connectivity and impaired sensorimotor integration, both of which are key targets for neurorehabilitation interventions [20], [21].

The restoration of CMC strength observed at the end of our intervention is particularly relevant, as it is specific to the trained upper limb and thus likely related to the training itself, suggesting that the improvement is directly related to the training itself rather than to generalized neuroplastic changes. Previous studies have shown that rehabilitative interventions that enhance CMC, such as neurofeedback training and brain-computer interface (BCI)-mediated therapies, are associated with improved motor function and neural reorganization in stroke patients [10]. However, while our data support the feasibility and neurophysiological impact of this intervention, its direct influence on clinical and functional upper limb motor outcomes requires further investigation. Larger-scale clinical studies with extended follow-ups are needed to establish whether CMC restoration translates into tangible improvements in motor performance and daily-life functionality.

The most innovative aspect of our hBCI-FES system is the ability to automatically detect and discourage specific CMC features related to maladaptive movement patterns. These patterns are often present in patients with stroke, and despite the efforts of specialized therapists, they remain a significant challenge in post-stroke rehabilitation. Traditional rehabilitation methods, while effective in promoting motor recovery, may not always be able to specifically target these dysfunctional motor synergies. The proposed system, by contrast, offers the advantage of real-time, objective assessment and intervention, allowing for continuous monitoring and immediate correction of unwanted motor patterns. The system automatically selects the most relevant CMC features based on the unique motor characteristics of the patient, ensuring that the intervention is personalized. This tailored approach contrasts with more generalized rehabilitation strategies, which may not always address the specific needs of each patient. While a specialized therapist is invaluable for guiding rehabilitation and providing personalized care, the hBCI-FES system provides a complementary role by offering an objective, automated mechanism that operates continuously. This has the potential to prevent the persistence of maladaptive motor synergies by providing real-time feedback that may be difficult to achieve during traditional therapy sessions, which are limited by time and the subjective nature of human observation.

Our results indicate both an increase of brain-muscles synchrony in the affected hand (targeted by the hBCI-FES intervention) and a reduction of the mirror and compensatory movements, as effect of the hBCI based training we proposed. We investigated it in both alpha and beta frequency bands since they are simultaneously active in motor planning and execution [22]. These results actually demonstrate the clinical significance of our work, specifically how the intervention we proposed well fit the recently born field of restoring physiological brain-muscle connections in post-stroke impaired upper limb [23], [24]. Specifically, alpha band seems to better encode this restoration than beta band in terms of grand average CMC weight increase and single-subject mirror movements reduction. This is probably due to the fact that alpha rhythm is primarily engaged for the local processing of information, whereas beta rhythm coordinates neurophysiological processes on a wider scale in sensorimotor tasks [25]. Moreover, the higher variability shown in post-timepoints could reveal a correlation between each patient's response to the hBCI system and the time since the event, that should be better investigated in future works even enlarging the sample's breadth.

One of the limitations of our work is the fact that patient's ability to perform the task was assessed only in a qualitative way. Future works may provide also kinematic measures. Despite the preliminary nature of this study, the results are promising for an application of CMC not only as a rehabilitation outcome metric but also as an online control feature for a rehabilitative hBCI, which to our knowledge is the first able to monitor and reduce post-stroke motor abnormalities.

ACKNOWLEDGMENT

We thank Giorgio Tartaglia (neurophysiology technician) for the support in data recording.

REFERENCES

[1] C. E. Lang, M. D. Bland, R. R. Bailey, S. Y. Schaefer, and R. L. Birkenmeier, "Assessment of upper extremity impairment, function, and activity after stroke: foundations for clinical decision making," *J. Hand Ther.*, vol. 26, pp. 104–115, April 2013.

[2] A. G. Guggisberg, P. J. Koch, F. C. Hummel, and C. M. Buetefisch, "Brain networks and their relevance for stroke rehabilitation," *Clin. Neurophysiol.*, vol. 130, pp. 1098–1124, July 2019.

[3] N. Takeuchi and S.-I. Izumi, "Maladaptive plasticity for motor recovery after stroke: mechanisms and approaches," *Neural Plast.*, vol. 2012, p. 359728, 2012.

[4] F. Pichiorri and D. Mattia, "Brain-computer interfaces in neurologic rehabilitation practice," *Handb. Clin. Neurol.*, vol. 168, pp. 101–116, 2020.

[5] S. Mansour, K. K. Ang, K. P. S. Nair, K. S. Phua, and M. Arvaneh, "Efficacy of brain-computer interface and the impact of its design characteristics on poststroke upper-limb rehabilitation: a systematic review and meta-analysis of randomized controlled trials," *Clin. EEG Neurosci.*, vol. 53, pp. 79–90, January 2022.

[6] F. Pichiorri et al., "Brain–computer interface boosts motor imagery practice during stroke recovery," *Ann. Neurol.*, vol. 77, pp. 851–865, 2015.

[7] K. Takeda, G. Tanino, and H. Miyasaka, "Review of devices used in neuromuscular electrical stimulation for stroke rehabilitation," *Med. Devices: Evid. Res.*, vol. 10, pp. 207–213, August 2017.

[8] T. Mima and M. Hallett, "Corticomuscular coherence: a review," *J. Clin. Neurophysiol.*, vol. 16, pp. 501–511, November 1999.

[9] A. Chowdhury, H. Raza, Y. K. Meena, A. Dutta, and G. Prasad, "An EEG-EMG correlation-based brain-computer interface for hand orthosis supported neuro-rehabilitation," *J. Neurosci. Methods*, vol. 312, pp. 1–11, January 2019.

[10] V. de Seta et al., "Cortico-muscular coupling to control a hybrid brain-computer interface for upper limb motor rehabilitation: A pseudo-online study on stroke patients," *Front. Hum. Neurosci.*, vol. 16, November 2022.

[11] F. Pichiorri et al., "Exploring high-density corticomuscular networks after stroke to enable a hybrid brain-computer interface for hand motor rehabilitation," *J. NeuroEng. Rehabil.*, vol. 20, p. 5, January 2023.

[12] E. Colamarino et al., "Inter-limb muscle synergy similarity as marker of post-stroke impairment in Box & Block Test," *Gait Posture*, vol. 105, pp. S16–S17, October 2023.

[13] A.-B. Meseguer-Henarejos, J. Sánchez-Meca, J.-A. López-Pina, and R. Carles-Hernández, "Inter- and intra-rater reliability of the Modified Ashworth Scale: a systematic review and meta-analysis," *Eur. J. Phys. Rehabil. Med.*, vol. 54, pp. 576–590, August 2018.

[14] A. R. Fugl-Meyer, L. Jääskö, I. Leyman, S. Olsson, and S. Steglind, "The post-stroke hemiplegic patient. 1. a method for evaluation of physical performance," *Scand. J. Rehabil. Med.*, vol. 7, pp. 13–31, 1975.

[15] E. Fan, N. D. Ciesla, A. D. Truong, V. Bhoopathi, S. L. Zeger, and D. M. Needham, "Inter-rater reliability of manual muscle strength testing in ICU survivors and simulated patients," *Intensive Care Med.*, vol. 36, p. 1038, March 2010.

[16] "Overview | Stroke rehabilitation in adults | Guidance | NICE," October 2023.

[17] R. Krauth et al., "Cortico-muscular coherence is reduced acutely post-stroke and increases bilaterally during motor recovery: a pilot study," *Front. Neurol.*, vol. 10, 2019.

[18] T. Mima, K. Toma, B. Koshy, and M. Hallett, "Coherence between cortical and muscular activities after subcortical stroke," *Stroke*, vol. 32, pp. 2597–2601, November 2001.

[19] Z. Guo et al., "Altered corticomuscular coherence (CMCoh) pattern in the upper limb during finger movements after stroke," *Front. Neurol.*, vol. 11, 2020.

[20] Z. Gao et al., "Influencing factors of corticomuscular coherence in stroke patients," *Front. Hum. Neurosci.*, vol. 18, March 2024.

[21] J. Liu, Y. Sheng, and H. Liu, "Corticomuscular coherence and its applications: a review," *Front. Hum. Neurosci.*, vol. 13, March 2019.

[22] F. Klostermann et al., "Task-related differential dynamics of EEG alpha- and beta-band synchronization in cortico-basal motor structures," *Eur. J. Neurosci.*, vol. 25, pp. 1604–1615, 2007.

[23] A. Sarasola-Sanz et al., "A hybrid brain-muscle-machine interface for stroke rehabilitation: usability and functionality validation in a 2-week intensive intervention," *Front. Bioeng. Biotechnol.*, vol. 12, April 2024.

[24] E. Colamarino et al., "Corticomuscular and intermuscular coupling in simple hand movements to enable a hybrid brain-computer interface," *Int. J. Neural Syst.*, vol. 31, p. 2150052, November 2021.

[25] A. Athanasiou et al., "Investigating the role of alpha and beta rhythms in functional motor networks," *Neuroscience*, vol. 378, pp. 54–70, May 2018.

MyoAssist 0.1: MyoSuite for Dexterity and Agility in Bionic Humans

Chun Kwang Tan[1], Cheryl Wang[2,3], Shirui Lyu[4], Balint K. Hodossy[5], Pierre Schumacher[6], Elizabeth B. Wilson[7], Vittorio Caggiano[4,8,9], Vikash Kumar[8,10], Dario Farina[5], Letizia Gionfrida[4], Elliott J. Rouse[7], Guillaume Durandau[2,3], Seungmoon Song[1*]

***Abstract*— Accurate and reliable digital twins of humans and wearable robots can revolutionize rehabilitation robotics. Here, we introduce MyoAssist 0.1, a sub-suite of MyoSuite focused on musculoskeletal simulation environments with assistive devices such as prosthetics and exoskeletons. This open-source platform enables the study and development of human-device interactions, control strategies, and assistive robotics. We present two new simulation environments: myoMPL featuring an arm amputee model with a robotic prosthetic arm, and myoOSL featuring a leg amputee model with a robotic prosthetic leg. The myoMPL environment features a bimanual manipulation task for a shoulder disarticulation amputee using a Modular Prosthetic Limb (MPL), where the task is to pick up an object with the biological hand, pass it to the prosthetic hand, and place it at a target location. The myoOSL environment simulates an above-knee amputee using the Open-Source Leg (OSL) to traverse challenging terrains such as rough surfaces, hills, and stairs. Despite some simplifications in modeling the nuanced constraints of human and prosthetic systems under real-world conditions, these environments provide a foundational simulation framework that supports interdisciplinary research on the interplay between musculoskeletal dynamics and assistive devices. Both myoMPL and myoOSL are featured in MyoChallenge, an annual competition at the NeurIPS conference. All code is accessible through the MyoSuite GitHub repository.**

I. Introduction

Simulation frameworks with accurate and reliable computational models of humans, rehabilitation robots, and their interactions have the potential to transform the field of rehabilitation robotics. These digital twins could enable researchers and clinicians to develop new rehabilitation treatments, refine assistive devices, study patient-specific responses, and optimize therapeutic protocols [1]–[5]. Despite substantial progress, the integration of human-prosthetic interfaces in real-world environments remains a challenge, necessitating the creation of computational models that represent the diverse and dynamic conditions encountered in daily life. Furthermore, learning motor behaviors in simulated musculoskeletal systems with robotic limbs remains an open challenge that requires collaboration across multiple disciplines to achieve successful outcomes [5], [6].

To collectively address these challenges, we are introducing MyoAssist, a sub-suite of MyoSuite focused on musculoskeletal simulation environments that integrate assistive devices such as prosthetics and exoskeletons [7]. MyoSuite is a collection of musculoskeletal environments and tasks in MuJoCo physics simulator [8] in the OpenAI Gym format [9]. Our vision is to create a unified framework where researchers can collaboratively develop and investigate assistive devices, advance sim-to-real transfer, and explore physical human-robot interactions in various settings. MyoAssist aims to foster a shared collection of models and task environments that facilitate the development and refinement of assistive technologies through an accessible and versatile simulation environment. The initial collection will primarily focus on wearable robots, such as exoskeletons and prostheses, with the intention to gradually extend to include other types of assistive devices. The long-term vision is that as MyoSuite advances to include musculoskeletal and control models of people with motor impairments, these models will be seamlessly integrated with MyoAssist.

In this paper, we present MyoAssist 0.1, which introduces two novel models and their respective environments: myoMPL, a model of a shoulder disarticulation amputee using the Modular Prosthetic Limb (MPL) in a manipulation environment, and myoOSL, a model of a transfemoral amputee using the Open-Source Leg (OSL) in a locomotion environment. The two environments are also featured in the most recent series of the MyoChallenge annual competition at the NeurIPS conferences [10], MyoChallenge'24 - Physiological Dexterity and Agility in Bionic Humans. The myoMPL environment focuses on bimanual manipulation in a scenario involving a shoulder amputee wearing an MPL [11], a robotic prosthetic arm starting from a shoulder joint, including the elbow and wrist joints, down to an articulated hand. The MPL is integrated with myoArm, representing a fully articulated intact arm with 63 muscles. The task is to use the intact arm to pick up an object, hand it over to the MPL, and place it at a target location. The myoOSL environment presents a robust locomotion task for an above-knee transfemoral amputee wearing an OSL [12], a robotic knee-ankle prosthetic. The OSL is integrated with myoLeg, a full-body model featuring an articulated leg with 54 muscles (40 in the intact leg and 14 in the hip joint of the amputated leg) to traverse various

*Correspondence: s.song@northeastern.edu

[1]Department of Mechanical and Industrial Engineering, Northeastern University, Boston, MA, USA

[2]Department of Mechanical Engineering, McGill University, Montreal, QC, Canada

[3]Jewish Rehabilitation Hospital, Montreal, QC, Canada

[4]Department of Informatics, King's College London, London, UK

[5]Department of Bioengineering, Imperial College London, London, UK

[6]Max Planck Institute for Intelligent Systems, Tübingen, Germany

[7]Department of Mechanical Engineering and Department of Robotics, University of Michigan, Ann Arbor, MI, USA

[8] MyoLab, New York, NY, USA

[9] Harvard Medical School and Spaulding Rehabilitation Hospital, Boston, USA

[10] Robotics Institute, Carnegie Mellon University, Pittsburgh, PA, USA

terrains.

This paper will first review the current status of MyoSuite and MyoChallenge (Section II). It will then present the details of the myoMPL (Section III) and myoOSL (Section IV) environments, including descriptions of the musculoskeletal and prosthetic models, task setups, reward structures, and baseline controllers. Lastly, we discuss the implications of these environments and outline our future plans to extend MyoAssist with more assistive devices and scenarios (Section V).

II. MyoSuite and MyoChallenge

MyoSuite [13] is an open-source collection of environments and tasks consisting of musculoskeletal models that run in the MuJoCo physics simulator [8], wrapped in a reinforcement learning-friendly interface, OpenAI Gym API [9]. By November 2024, MyoSuite consisted of 7 models and 300 environments/tasks and had been downloaded over 70K times on PyPI alone. All the MyoSuite software including the new environments presented in this paper, myoMPL and myoOSL, are accessible through the MyoSuite GitHub repository [14].

The MyoSuite team has been hosting the MyoChallenge as an official annual competition at the NeurIPS conference, since 2022. The themes include "Learning Physiological Dexterity" (2022) [10], "Towards Human-Level Dexterity and Agility" (2023) [15], and "Physiological Dexterity and Agility in Bionic Humans" (2024) [16]. The myoMPL and myoOSL environments were featured in the MyoChallenge'24, and are released as part of the collection of task environments in Myosuite [7]. The MyoAssist 0.1 initiative was introduced to organize and expand musculoskeletal simulation environments that integrate assistive devices, such as prosthetics and exoskeletons, under a unified framework within MyoSuite.

III. myoMPL Environment

The myoMPL environment simulates a shoulder disarticulation amputee using the Modular Prosthetic Limb (MPL) [11] for a bimanual manipulation task (Fig. 1). The goal is to train a policy to hand an object over from the biological arm to the prosthetic arm and then maneuver the object to a specific target location. The control space includes both muscle activations of the biological arm and motor actuators for the MPL. In the current version, users have the flexibility to either focus on exploring the complexities of controlling a bimanual system with a single policy (without explicitly modeling the limited access to the state and action of human-prosthetic controls in real-world scenarios) or to implement their own policy constraints that better reflect the specific conditions of their system of interest.

A. myoArm and Modular Prosthetic Limb

The right arm of myoArm model is adopted, which comprises 27 degrees of freedom (DOFs) and 63 muscle-tendon units. The model was converted from OpenSim MoBL arm model [17], [18] via MyoConverter [19], [20] and has been used in previous MyoChallenges for manipulation tasks [10], [15]. The entire left arm is replaced with MPL.

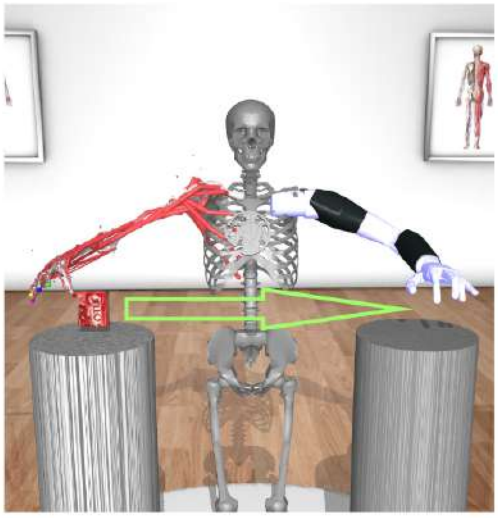


Fig. 1: The myoMPL environment. The task involves moving an object from the pillar on the left side (from the reader's perspective) to the pillar on the right, using both the biological arm and the MPL.

The MPL system has 17 controllable actuators that drive 26 DOFs [11]. Each finger has 3 coupled DOF for flexion. Additional DOFs are provided for abduction in the index, ring, and little fingers, where the latter two are coupled. The thumb has 4 DOFs: three flexions and one abduction. The wrist has 3 DOFs, and the elbow and the humeral rotator each have 1 DOF. The shoulder complex consists of two serial hinge joints for flexion-extension and abduction-adduction, enabling broad upper-arm movements. This model has a near-human level of strength and speed and closely resembles the kinematics of a human arm.

B. Bimanual Manipulation Task

The torso and lower limbs are fixed at the center of a round stage and two pillars are placed at a distance to ensure that both arms can only reach the pillar closer to them. The start and goal positions are defined as the centers of the top surfaces of the left and right pillars. The default object to manipulate is a box weighing 97 g, with dimensions of $72 \times 88 \times 28$ mm, following the YCB benchmark object set [21]. The object's start position and goal position are randomly initialized in each episode (i.e., simulation trial). Additionally, the physical attributes of the object are varied, including its dimensions ($\pm$0–5% for width, $\pm$0–10% for depth, and $\pm$0–5% for height), mass ($\pm$50 grams), and friction (default friction coefficients: 1.0, 0.005, and 0.0001 for sliding, torsional, and rolling friction respectively; variations: $\pm$0.1, $\pm$0.001, and $\pm$0.00002, respectively).

A simulation trial is completed when the object is placed on the goal pillar within 0.1 m along each axis. Each trial lasts up to 10 seconds and terminates early if the object falls below 0.3 m. To ensure bimanual manipulation, each limb must maintain contact with the object for at least 1 second.

C. Action and Observation Spaces

The action space consists of an 80-dimensional continuous vector in the range [-1, 1], comprising 63 muscle actions and 17 MPL position actions. In the simulation, muscle actions are normalized to the range [0, 1] using:

$$s_m = 1/(1 + \exp(-5 * (u_m - 0.5))), \quad (1)$$

where u_m is the muscle action and s_m represents the muscle stimulation, with 0 and 1 indicating no stimulation and full stimulation, respectively. The 17 MPL position actions are mapped to their corresponding joint range of motion for target angle-based control.

A policy/controller has access to a 222-dimensional observation space, extensively describing the body, object, and environment state at each time step (Table I). This observation space includes joint positions and velocities of both myoArm and the MPL, the 6-DOF position and velocity of the object, as well as the muscle stimulations of the arm. Additionally, the contact status of the object is provided, with five labels indicating whether it is touching the biological hand, MPL, start pillar, goal pillar, or any other part of the environment. A full description of the observations is available on the MyoChallenge'24 documentation page [22].

D. Reward and Evaluation

The environment does not provide a predefined reward for completing the task, as we did not want to prescribe a specific approach to solving the task. Instead, users are encouraged to design their own reward structures that are suitable for their chosen methods, whether it be curriculum learning, imitation learning, heuristic control, or any other approach. See an example of the reward for the baseline controller in the following subsection. Another reference for evaluation is the primary criterion in MyoChallenge'24: the success rate of completion across 100 evaluation trials.

E. Baseline Controllers

We provide a baseline solution for the proposed task (Fig. 2). This baseline policy combines a simple position control for the MPL with a deep neural network, trained through reinforcement learning, to manage the grasping behavior of the myoArm. The baseline demonstrates a success rate of approximately 25% in the default simulation setting, which drops to around 3% when full object and environment variations are introduced.

MyoArm Control: The myoArm policy was trained using a heuristically designed curriculum learning setup [23]. The training process was divided into three consecutive curricula: (1) positioning the palm near the object, (2) wrapping the fingers around the object, and (3) bringing the object close to the MPL hand. Across all stages, the policy was trained with the following reward function, which is based on the Euclidean distance between the target and current positions, with the weights σ_{i} varying across the curricula:

$$r_{\mathrm{d}} = \exp(-\sum_i \sigma_{\mathrm{i}} ||q_t^i - q_o^i||^2), \quad (2)$$

where q_o^i and q_t^i are the three-dimensional Cartesian coordinates of the object and body segment i, respectively, and i represents the palm, fingers, and MPL segments. Training begins with the first stage, during which σ_{i} for the palm is set to a high value. As the policy succeeds in stage one and the training progresses through the second and then the third stages, σ_{i} for the fingers and MPL segments are set to be higher, respectively. Once the biological hand reaches within 0.1 m of the MPL arm (indicating completion of stage three), the hand muscles are relaxed, allowing the object to fall freely.

Our algorithm utilizes a symmetric multi-layer perceptron (MLP) architecture for both the policy and value function networks. Each network comprises two hidden layers with 256 units each, employing the ReLU activation function. We trained these networks using Proximal Policy Optimization (PPO) [24], leveraging the stable-baselines3 package [25]. We used an entropy coefficient of 0.001 and a learning rate of 0.0003 for training.

Observation	Dimension
Elapsed time	1
Joint positions of myoArm	38
Joint velocities of myoArm	38
Joint positions of MPL	26
Joint velocities of MPL	26
Position and orientation of object	7
Velocities of object	6
Start position	3
Goal position	3
Object contact information	5
Muscle activations	63
Hand reaching error	3
Hand passing error	3
Total	222

TABLE I: Observation space of myoMPL manipulation task

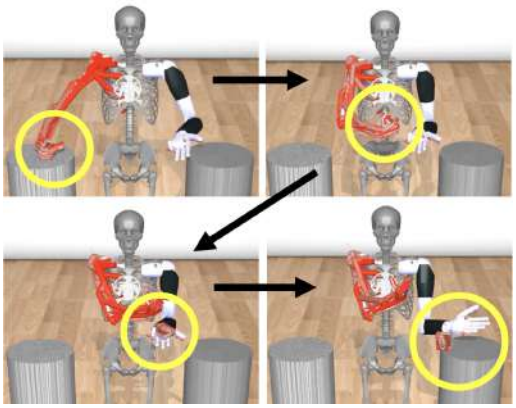


Fig. 2: Snapshots of a baseline solution for the bimanual manipulation task. The biological arm picks up an object from the left pillar, hands it over to the prosthetic arm, and finally, the prosthetic arm places it on the right pillar. The yellow circle highlights the trajectory of the object.

MPL Control: The MPL control was designed to coordinate with the trained myoArm movements. It operates as a position controller that sequentially reaches three target poses, each defined by 17 target joint angles, which switch based on predetermined time intervals. The three target poses are illustrated in Figure 2, with transitions occurring at 2.5 and 3.5 seconds, respectively.

IV. MYOOSL ENVIRONMENT

The myoOSL environment simulates an above-knee amputee using an Open-Source Leg v2 (OSL) system [12], [26] to traverse a straight path over various terrain types (Fig.3). OSL is an open-source platform that provides both hardware designs and a range of control algorithms. The goal is to train a controller for the musculoskeletal model and OSL to effectively traverse challenging terrains, with the OSL behavior modulated by switching between five user-defined control parameter sets. This setup reflects a condition where the user could manually select the control mode using a handheld controller, adjusting to varying terrain conditions.

A. MyoLeg and the Open-Source Leg

The myoLeg model was adapted to represent a person with a right-leg, transfemoral amputation. The original myoLeg contains 28 DOFs and 80 muscle-tendon units. It was converted from the OpenSim full body model [27] via MyoConverter [20] and has been used previously been used in a previous MyoChallenge [16]. The myoLeg was modified to represent a transfemoral amputation at a 50% level. These modifications involved removing muscles that articulate the knee and ankle joints on the amputated side [28], as well as readjusting the femoral inertial properties to reflect the altered geometry and mass distribution of the residual limb.

The myoOSL model integrates the amputated myoLeg with an OSL model. The OSL model is implemented with torque actuators that match its real mass (5.377 kg), peak torques (knee: 142.2 Nm; ankle: 168.2 Nm), and ranges of motion (knee: 0–120 deg; ankle: -30–30 deg) [26], [29]. The myoOSL model features 23 internal DOFs: 19 are actuated by 54 muscles and two OSL actuators, while the remaining 4 DOFs between the residual limb and the OSL represent socket movement and are passively constrained [30].

OSL Control: The OSL model is controlled using a finite-state machine with four states, each implementing impedance control (Fig. 3-(b)). This controller is the default controller provided in the OSL project [31], which we have reimplemented for myoOSL. The four states are early stance, late stance, early swing, and late swing. Each state is defined by eight parameters, where three (stiffness, damping, and target/equilibrium angle) are used for impedance control, and the other five (load, knee angle, knee velocity, ankle angle, and ankle velocity) determine the state transition conditions. Thus, there are 32 parameters (8 parameters per state $\times$ 4 states) for full OSL control. In the myoOSL environment, the user can predefine five sets of these control parameters, which can then be selected by the policy at any moment during a simulation trial. This setup represents a scenario where the prosthesis user, for instance, uses a handheld device to select the appropriate control mode.

B. Robust Locomotion Task

The task is to develop a controller/policy for the amputee musculoskeletal model, as well as to determine OSL control selections, to maximize walking distance across various terrains. The environment includes five types of terrains, each 3 m wide and 100 m long: 1) flat ground, 2) rough terrain, 3) hills, 4) stairs with 3 ascending and 3 descending steps, and 5) a mixture of all terrain types (Fig. 4). The difficulty of the terrain increases progressively with the distance traveled;

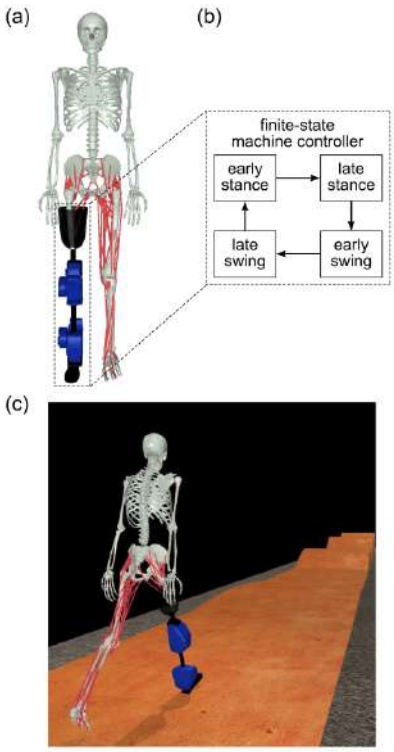


Fig. 3: The myoOSL environment. (a) An amputee model using the OSL v2, which is controlled by (b) the OSL's finite-state machine controller. (c) A myoOSL task environment.

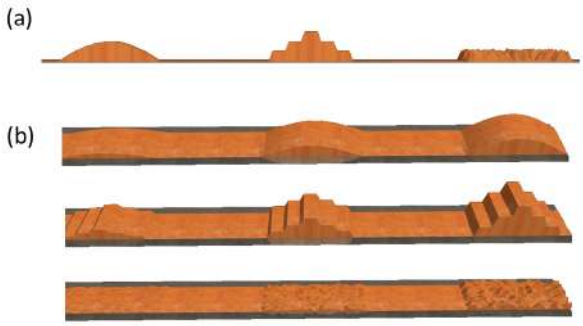


Fig. 4: Terrains in myoOSL. (a) Side view of a mixed terrain sample. (b) Different terrain types with progressively increasing difficulty over the traveled distance.

at 100 m, the roughness reaches 60 cm, the hills become approximately 50 degrees steep and 1.5 m high, and each step on the stairs is 50 cm high.

A simulation trial is considered completed if the amputee model traverses the entire 100 m path without falling. A trial is terminated early if the model falls (head height $<$ 1.5 m) or deviates from the 3 m wide path.

C. Action and Observation Spaces

The action and observation spaces are designed to represent the motor control system of an amputee wearing the OSL. The action space consists of 54 muscle actions (that are converted to muscle stimulations; Eq. 1) and an additional output, [0, 1, 2, 3, 4], that selects between the five control parameter sets that are predefined by the user. A policy/controller has access to proprioception (e.g., joint angles and velocities, and muscle states) and 10 $\times$ 10 height map of the 2 $\times$ 2 m terrain around the amputee, at each time step (Table II). A full description of the actions and observations is available on the MyoChallenge'24 documentation page [20].

D. Reward and Evaluation

The myoOSL environment provides a straightforward reward based on the distance traveled. In MyoChallenge'24, solutions are evaluated over 100 simulation trials on randomly generated terrains.

E. Baseline Controllers

We do not currently provide a baseline controller for the myoOSL environment. However, baseline controllers for the original myoLeg model (featuring two intact biological legs) that produce stable walking are available in MyoSuite [14]. These include the DEP-RL controller [32] and a reflex-based controller [33].

V. Discussion

In this paper, we introduce MyoAssist 0.1, a sub-suite of MyoSuite that includes the myoMPL and myoOSL environments, focusing on musculoskeletal simulations with assistive devices. These environments are part of NeurIPS 2024: MyoChallenge, with respective tracks on manipulation and locomotion. The myoMPL environment simulates a shoulder disarticulation amputee using an MPL to move an object from a pillar on the biological arm's side to a pillar on the MPL arm's side, using both arms. The myoOSL environment presents an above-knee amputee walking across challenging terrains with an OSL v2 prosthesis.

Observation	Dimension
Elapsed time	1
Terrain type	1
Joint positions of myoLeg	17
Joint velocities of myoLeg	17
Ground Reaction forces of myoLeg	2
Socket forces	3
Pelvis angle (in world frame)	4
Muscle activations	54
Muscle lengths	54
Muscle velocities	54
Muscle forces	54
Planar Pelvis position (in world frame)	2
Planar Pelvis velocity (in world frame)	2
Terrain height map	100
Total	365

TABLE II: Observation space of myoOSL locomotion task

The environments have certain limitations in reflecting their real-world scenarios. In MyoMPL, a user can develop a policy that has full access to the observations and actions of both the musculoskeletal and MPL systems, which is not possible in the real world with current techniques. While this approach does not fully replicate the limitations of independent user control of the human arm and prosthetic limb, it aims to investigate the complexities of a bimanual arm paired with a prosthetic arm. Moreover, one can implement realistic policy constraints that better reflect their system of interest.

The myoOSL environment presents a more realistic scenario where the amputee can select between predefined control modes of the prosthetic leg, for instance, using a handheld controller. In myoOSL, the policy mostly represents the neural control of the musculoskeletal system that produces muscle stimulations based on proprioceptive feedback and environmental cues. Additionally, the policy can select from five predefined control parameter sets for the OSL. In the current setting, the OSL control switch can occur at every time step, which is not realistic. Users can easily implement constraints (e.g., a minimum time interval between OSL control switches or limiting control changes to once per footstep) to better reflect realistic scenarios.

Despite some simplifications, these environments serve as a first step toward developing more comprehensive and sophisticated control systems for prosthetics. The myoMPL and myoOSL environments offer a foundation for studying the interplay between musculoskeletal dynamics and assistive devices, as well as understanding physical human-robot interactions. Future iterations will aim to introduce greater realism in modeling physical human-device interactions [34], expand to more complex tasks such as opening jars (manipulation) and avoiding obstacles (locomotion), and improve the robustness of baseline controllers.

Our goal is to advance MyoAssist into an open-source collaborative platform that fosters innovation in assistive technology and neurorehabilitation. In the future MyoAssist 1.0 release, we plan to incorporate a broader range of assistive devices, with a particular focus on various types of hip and ankle exoskeletons [35]. We invite researchers, particularly those specializing in assistive devices that involve physical interactions with humans while needing a means of investigating the devices in simulation, to contribute and collaborate in MyoAssist. By bringing together expertise from biomechanics, robotics, machine learning, and clinical applications, we can push the boundaries of simulation-based assistive technology research, ultimately improving the effectiveness of rehabilitation and the quality of life for individuals with motor impairments.

REFERENCES

[1] David J Reinkensmeyer, Etienne Burdet, Maura Casadio, John W Krakauer, Gert Kwakkel, Catherine E Lang, Stephan P Swinnen, Nick S Ward, and Nicolas Schweighofer. Computational neurorehabilitation: modeling plasticity and learning to predict recovery. *Journal of NeuroEngineering and Rehabilitation*, 13(1):42, April 2016.

[2] Bryce A Killen, Antoine Falisse, Friedl De Groote, and Ilse Jonkers. In silico-enhanced treatment and rehabilitation planning for patients with musculoskeletal disorders: Can musculoskeletal modelling and dynamic simulations really impact current clinical practice? *Applied Sciences*, 10(20), 2020.

[3] Vahid Firouzi, Andre Seyfarth, Seungmoon Song, Oskar von Stryk, and Maziar Sharbafi. Biomechanical models in the lower-limb exoskeletons development: A review. *Authorea Preprints*, 2023.

[4] Vincent Ton, Dana Solav, and Seungmoon Song. Impact of sole designs of offloading afo on gait dynamics: A predictive neuromechanical simulation study. In *2024 10th IEEE RAS/EMBS International Conference for Biomedical Robotics and Biomechatronics (BioRob)*, pages 1709–1714. IEEE, 2024.

[5] Joshua GA Cashaback, Jessica L Allen, Amber Hsiao-Yang Chou, David J Lin, Mark A Price, Natalija K Secerovic, Seungmoon Song, Haohan Zhang, and Haylie L Miller. Nsf dare—transforming modeling in neurorehabilitation: a patient-in-the-loop framework. *Journal of NeuroEngineering and Rehabilitation*, 21(1):23, 2024.

[6] Cheng Fang, Luka Peternel, Ajay Seth, Massimo Sartori, Katja Mombaur, and Eiichi Yoshida. Human modeling in physical human-robot interaction: A brief survey. *IEEE Robotics and Automation Letters*, 8(9):5799–5806, 2023.

[7] Vittorio Caggiano, Huawei Wang, Guillaume Durandau, Kumar Sartori, Massimo, and Vikash. Myosuite: A contact-rich simulation suite for musculoskeletal motor control. In *4th Annual Conference on Learning for Dynamics and Control (L4DC)*. Proceedings of Machine Learning Research, 2022.

[8] Emanuel Todorov, Tom Erez, and Yuval Tassa. Mujoco: A physics engine for model-based control. In *2012 IEEE/RSJ International Conference on Intelligent Robots and Systems*, pages 5026–5033. IEEE, 2012.

[9] Greg Brockman, Vicki Cheung, Ludwig Pettersson, Jonas Schneider, John Schulman, Jie Tang, and Wojciech Zaremba. Openai gym. *arXiv preprint arXiv:1606.01540*, 2016.

[10] Vittorio Caggiano, Huawei Wang, Guillaume Durandau, Seungmoon Song, Yuval Tassa, Massimo Sartori, and Vikash Kumar. Myochallenge: Learning contact-rich manipulation using a musculoskeletal hand. `https://sites.google.com/view/myochallenge`, 2022.

[11] Matthew S. Johannes, Eric L. Faulring, Kapil D. Katyal, Matthew P. Para, John B. Helder, Alexander Makhlin, Tom Moyer, Daniel Wahl, James Solberg, Steve Clark, Robert S. Armiger, Travis Lontz, Kathryn Geberth, Courtney W. Moran, Brock A. Wester, Thomas Van Doren, and Julio J. Santos-Munne. *The Modular Prosthetic Limb*, page 393–444. Elsevier, 2020.

[12] A. F. Azocar, L. M. Mooney, J. F. Duval, A. M. Simon, L. J. Hargrove, and E. J. Rouse. Design and clinical implementation of an open-source bionic leg. *Nature Biomedical Engineering*, 4, 2020.

[13] Vittorio Caggiano, Huawei Wang, Guillaume Durandau, Massimo Sartori, and Vikash Kumar. Myosuite – a contact-rich simulation suite for musculoskeletal motor control, 2022.

[14] MyoHub. Github - myosuite. `https://github.com/MyoHub/myosuite`.

[15] Vittorio Caggiano, Huawei Wang, Guillaume Durandau, Seungmoon Song, Tan Chun Kwang, Berg Cameron, Schumacher Pierre, Massimo Sartori, and Vikash Kumar. Myochallenge 2023: Towards human-level dexterity and agility. `https://sites.google.com/view/myosuite/myochallenge/myochallenge-2023`, 2023.

[16] Vittorio Caggiano, Guillaume Durandau, Seungmoon Song, Chun Kwang Tan, Huiyi Wang, Balint Hodossy, Pierre Schumacher, Letizia Gionfrida, Massimo Sartori, and Vikash Kumar. Myochallenge 2024: Physiological dexterity and agility in bionic humans. In *NeurIPS 2024 Competition Track*, 2024.

[17] Katherine R Saul, Xiao Hu, Craig M Goehler, Meghan E Vidt, Melissa Daly, Anca Velisar, and Wendy M Murray. Benchmarking of dynamic simulation predictions in two software platforms using an upper limb musculoskeletal model. *Computer methods in biomechanics and biomedical engineering*, 18(13):1445–1458, 2015.

[18] SimTK. Upper extremity dynamic model. `https://simtk.org/projects/upexdyn`.

[19] Aleksi Ikkala and Perttu Hämäläinen. Converting biomechanical models from opensim to mujoco. In *Converging Clinical and Engineering Research on Neurorehabilitation IV: Proceedings of the 5th International Conference on Neurorehabilitation (ICNR2020), October 13–16, 2020*, pages 277–281. Springer, 2022.

[20] Huawei Wang, Vittorio Caggiano, Guillaume Durandau, Massimo Sartori, and Vikash Kumar. Myosim: Fast and physiologically realistic mujoco models for musculoskeletal and exoskeletal studies. In *2022 International Conference on Robotics and Automation (ICRA)*, pages 8104–8111. IEEE, 2022.

[21] Berk Calli, Arjun Singh, Aaron Walsman, Siddhartha Srinivasa, Pieter Abbeel, and Aaron M Dollar. The ycb object and model set: Towards common benchmarks for manipulation research. In *2015 international conference on advanced robotics (ICAR)*, pages 510–517. IEEE, 2015.

[22] MyoSuite. MyoChallenge-2024 Documentations `https://myosuite.readthedocs.io/en/latest/challenge-doc.html`, 2024.

[23] Yoshua Bengio, Jérôme Louradour, Ronan Collobert, and Jason Weston. Curriculum learning. In *Proceedings of the 26th Annual International Conference on Machine Learning*, ICML '09. ACM, June 2009.

[24] John Schulman, Filip Wolski, Prafulla Dhariwal, Alec Radford, and Oleg Klimov. Proximal policy optimization algorithms. *arXiv preprint arXiv:1707.06347*, 2017.

[25] Antonin Raffin, Ashley Hill, Adam Gleave, Anssi Kanervisto, Maximilian Ernestus, and Noah Dormann. Stable-baselines3: Reliable reinforcement learning implementations. *Journal of Machine Learning Research*, 22(268):1–8, 2021.

[26] T Kevin Best, Gray C Thomas, Senthur R Ayyappan, Robert D Gregg, and Elliott J Rouse. A compensated open-loop impedance controller evaluated on the second-generation open-source leg prosthesis. *IEEE/ASME Transactions on Mechatronics*, 2024.

[27] Apoorva Rajagopal, Christopher L. Dembia, Matthew S. DeMers, Denny D. Delp, Jennifer L. Hicks, and Scott L. Delp. Full-body musculoskeletal model for muscle-driven simulation of human gait. *IEEE Transactions on Biomedical Engineering*, 63(10):2068–2079, 2016.

[28] Vishal Raveendranathan, Vera G. M. Kooiman, and Raffaella Carloni. Musculoskeletal model of osseointegrated transfemoral amputees in OpenSim. *PLOS ONE*, 18(9):e0288864, September 2023.

[29] Alejandro F. Azocar, Luke M. Mooney, Levi J. Hargrove, and Elliott J. Rouse. Design and characterization of an open-source robotic leg prosthesis. In *2018 7th IEEE International Conference on Biomedical Robotics and Biomechatronics (Biorob)*, pages 111–118, 2018.

[30] A.K. LaPrè, M.A. Price, R.D. Wedge, B.R. Umberger, and Frank C. Sup. Approach for gait analysis in persons with limb loss including residuum and prosthesis socket dynamics. *International Journal for Numerical Methods in Biomedical Engineering*, 34(4):e2936, April 2018.

[31] OpenSourceLeg. OSL Finite State Machine Controller `https://opensourceleg.readthedocs.io/en/latest/examples/finite_state_machine.html`, 2022.

[32] Pierre Schumacher, Daniel F.B. Haeufle, Dieter Büchler, Syn Schmitt, and Georg Martius. Dep-rl: Embodied exploration for reinforcement learning in overactuated and musculoskeletal systems. In *Proceedings of the Eleventh International Conference on Learning Representations (ICLR)*, May 2023.

[33] Seungmoon Song and Hartmut Geyer. A neural circuitry that emphasizes spinal feedback generates diverse behaviours of human locomotion. *The Journal of physiology*, 593(16):3493–3511, 2015.

[34] Cheng Fang, Luka Peternel, Ajay Seth, Massimo Sartori, Katja Mombaur, and Eiichi Yoshida. Human modeling in physical human-robot interaction: A brief survey. *IEEE Robotics and Automation Letters*, 2023.

[35] Gregory S Sawicki, Owen N Beck, Inseung Kang, and Aaron J Young. The exoskeleton expansion: improving walking and running economy. *Journal of neuroengineering and rehabilitation*, 17:1–9, 2020.

iAssistADL: Intelligent assistive device for patients with neuro-degenerative movement disorder: Concepts and first implementations

Winfried Ilg[1], Isabell Wochner[2], Jhon P.F. Charaja[1], Veronika Hofmann[4,5], Ole Strenge[4,5], Melanie Adam[1], Regine Lendway[1], Jan Kerner[1], Bhavya Deep Vashisht[2], Marko Ackermann[2,9], Friedemann Bunjes[1], Urs Schneider[4,5], Martin Giese[1], Andreas Bulling[6], Syn Schmitt[7], Christophe Maufroy[4,5] and Daniel Haeufle[1]

***Abstract*— Upper-limb activities of daily living like eating and drinking are crucial for self-determination and autonomy and, thus, quality of life. Patients with neurodegenerative diseases such as Parkinson's disease, multiple sclerosis or cerebellar ataxia are often severely impaired in performing these activities of daily living. While these patients are still able to plan motor actions, and their muscle strength is rarely impaired, tremor or overshooting movements disturb the intended movements. This occurs progressively in the course of disease in a way that independent eating and drinking becomes increasingly difficult. The goal of this research project is to develop a non-invasive assistive device suppressing pathological movement components while allowing intended movement. The newly designed hardware will be controlled by a combination of computational methods to detect user intention, detect pathological movement components within intended movements, and predict the required correction forces for several upper-limb activities of daily living. In this manuscript, we will describe concepts of control hard- and software as well as first implementation and experiments with the individual components we plan to integrate in the future.**

I. Introduction

Cutting food or filling a glass from a bottle while dining is crucial for self-determination and autonomy and, thus, quality of life. Patients suffering from neurodegenerative diseases, such as Parkinson's disease, multiple sclerosis or cerebellar ataxia might not be able to perform such activities of daily living (ADL) all the time.

Although these patients are able to plan motor actions, and their muscle strength is rarely impaired, different types of tremor [1] [2] or dysmetric movements (over- and undershooting of goal-directed movements in cerebellar ataxia) [3] [4] [5] disturb the intended movements.

This occurs progressively in the course of disease such that independent eating and drinking becomes increasingly difficult. Assistive devices, which pro-actively suppress pathological movement components and restore the intended movement could dramatically improve patients' motor abilities, as has been shown in approaches to wearable systems for tremor suppression [6].

We here address the field of ADL with the focus on situations like a regular meal where food has to be cut, forked, brought to the mouth and a glass of water has to be filled from a bottle and brought to the mouth. These activities are characterized by a finite number of objects and tasks, a meaningful order of some tasks, but generally open in the location of objects and user and situation-specific in their execution order.

The goal of this research project is to develop a non-invasive assistive device with the capability to suppress pathological movement components while allowing intended movement in patient-relevant ADLs.

A. Methodological Approach

We address the following challenges in the development of such assistive devices:

1) Predicting planned movements during ADL and detecting pathological movement components within executed movements in real-time.
2) Designing a lightweight and mobile assistive device with minimal mechanical complexity and sufficient transparency (to not hinder the movement of the user) and, at the same time, the capacity to apply in real-time the amount of corrective forces sufficient to suppress pathological movement components.

To this end, we combine computational methods to detect (a) the user intention, predict the human arm movement corresponding to the intention, (b) differentiate between desired movement and pathological movement components and (c) develop a neuromechanical model to predict the required correction forces and (d) apply them with an adequately designed assistive device (Figure 1).

The presented concepts differ significantly from concepts for stroke patients, where paralysis of the limbs or spasticity is the main issue (e.g. [7],[8]. Devices for stroke need to exert forces large enough to generate the entire movement and—typically slowly—follow given trajectories, thus, they typically place fewer demands on the real-time constraints in intention detection [9] and movement correction [6].

This paper reports about the overall concept and our first implementations and test of the sub-components. At this

*corresponding author: daniel.haeufle@uni-tuebingen.de, [1]Hertie Institute for Clinical Brain Research, and Centre for Integrative Neuroscience, University of Tübingen, Germany. [2]Institute of Computer Engineering (ZITI), Heidelberg University, Germany. [3]Max Planck Institute for Intelligent Systems, Tübingen, Germany. [4]Institut for Industrial Manufacturing and Management (IFF), University of Stuttgart, Germany. [5]Fraunhofer Institute for Manufacturing Engineering and Automation (IPA), Stuttgart, Germany.[6]Institute for Visualization and Interactive Systems, University of Stuttgart, Germany. [7]Institute for Modelling and Simulation of Biomechanical Systems, University of Stuttgart, Germany. [8]Department of Computer Science, University of Tübingen, Germany. [9]Institute for Anthropomatics and Robotics, Karlsruhe Institute of Technology, Germany.

This work was financed by the Baden-Württemberg Stiftung in the scope of the AUTONOMOUS ROBOTICS project *iAssistADL* granted to WI, MG, SS, and DH.

point, these components are not integrated yet leaving the validation of the concept as future work.

II. Methods

A. Multi-modal sensor setup

Multiple sensor modalities were captured synchronously to assess the subject's motion behaviour and infer the intention (Figure 2). To determine gaze direction in real-life scenarios, we used the eye tracking glasses Neon by PupilLabs (Pupil Labs GmbH, Berlin, Germany) [10], which additionally record a video from the egocentric perspective and give information about head movements via an inertial sensor. Multiple IMUs from Xsens Technologies (Movella DOT, Xsens Technologies B.V., Enschede, Netherlands) were placed on both arms and the sternum to track and quantify arm and trunk movements. The stereo depth camera ZED 2i from Stereolabs (Stereolabs Inc., San Francisco, USA) were placed across the table of the subjects and captures the depth and RGB information of the experimental setup. Based on this depth and RGB information, object recognition and skeleton tracking routines were implemented using the camera-related APIs. Fusion of the IMU and depth-camera sensor signals allows for combining the benefits of both sensors: high time-resolution and local accuracy of IMU's and global position accuracy of the depth-image to compensate for drift in the IMU signals. Details of the sensor fusion concept are provided in the next section.

A software architecture based on the ROS2 (Robot Operating System) middleware was implemented to acquire all sensors synchronously with the sensor-specific real-time constraints. ROS2 provides the ability to reliably exchange and store large amounts of data at high frequency and is widely used in medical and industrial applications [11] [12] [13].

B. Development of a Kalman filter-based sensor fusion algorithm for motion tracking

Intention detection, tremor recognition, and prediction of movements require sensor-fusion approaches to combine different sensor modalities. To perform robust motion tracking, we developed and evaluated a Kalman filter-based algorithm for motion tracking and state estimation. The primary aim was to integrate data from multiple sensors to achieve accurate tracking of upper limb motion, particularly the hand and wrist. For this, we combined the complementary strengths of two sensors: the Xsens Movella DOT IMU system, which provides fast precise acceleration and angular velocity data but shows a drift when estimating global positions, and the Stereolabs ZED 2i stereo camera with skeleton fitting, which delivers global 3D position data, but at a lower frequency.

The Kalman filter was selected for its ability to perform real-time state estimation in dynamic systems. Specifically, we employed a discrete-time linear Kalman filter to estimate the states of position, velocity, and acceleration. The filter's structure consists of a prediction step, which uses a kinematic motion model to estimate the next state based on the current state, and an update step, which refines this estimate using sensor measurements. In the filter, weights were assigned to each sensor based on their noise characteristics, ensuring robust performance even under noisy conditions.

The state transition model for the Kalman filter estimates the position $\mathbf{x}$, velocity $\mathbf{v}$, and acceleration $\mathbf{a}$ of the wrist. The discrete state-space model can be expressed as:

$$\mathbf{s}_{k+1} = \mathbf{F}\mathbf{s}_k + \mathbf{w}_k, \quad \mathbf{z}_k = \mathbf{H}\mathbf{s}_k + \mathbf{v}_k$$

where

$$\mathbf{s}_k = \begin{bmatrix} \mathbf{x}_k \\ \mathbf{v}_k \\ \mathbf{a}_k \end{bmatrix}, \quad \mathbf{F} = \begin{bmatrix} \mathbf{I} & \Delta t\mathbf{I} & \frac{\Delta t^2}{2}\mathbf{I} \\ \mathbf{0} & \mathbf{I} & \Delta t\mathbf{I} \\ \mathbf{0} & \mathbf{0} & \mathbf{I} \end{bmatrix}, \quad \mathbf{H} = \begin{bmatrix} \mathbf{I} & \mathbf{0} & \mathbf{0} \\ \mathbf{0} & \mathbf{0} & \mathbf{I} \end{bmatrix},$$

where $\mathbf{F}$ is the state transition matrix, $\mathbf{H}$ is the measurement matrix, $\mathbf{w}_k$ and $\mathbf{v}_k$ are the process and measurement noise, respectively, and Δt is the sampling time.

To evaluate the filter's performance, we first designed a testing framework using an ideal trajectory overlaid with experimentally derived noise. Noise profiles for the IMU and stereo camera were characterized through calibration experiments, where the sensors were subjected to static placement evaluation to get their base noise readings. The accelerometer's and stereo camera signal variances were used to estimate the measurement noise covariance matrix.

The primary metric for evaluating performance was the Root Mean Square Error (RMSE) of the reconstructed trajectory compared to the ground truth. Ground truth data was generated using (a) mathematical simulation and (b) a high-accuracy optical motion capture system, which provided precise positional and velocity measurements for the ideal trajectory. By calculating the RMSE, we assessed the algorithm's accuracy in estimating states under various noise levels.

Finally, the sensor fusion approach was validated using real experimental data. This included datasets captured with both the IMU and stereo camera in scenarios simulating upper-limb motion. The fusion algorithm was tested in realistic conditions, accounting for sensor noise, data loss, and calibration challenges.

C. Online detection of pathological movement components

For the detection of pathological movement components, we concentrated on tremors and dysmetric movements (over- and undershooting). In the case of tremors, we have to take into account that the frequency of the tremor may change within the movement in the action and intention tremors. Therefore, we used a Bandlimited Multiple Fourier Linear Combiner improved with a Kalman Filter [14] to estimate thesinusoidal movements with changing frequencies to identify the tremor component of the voluntary motion in real-time. See subsection III-B for preliminary results.

D. Neuromechanical modeling of healthy and impaired movement

Using neuromusculoskeletal arm simulations, we can predict both healthy and impaired movements and estimate the necessary assistive forces for correction [15]. These

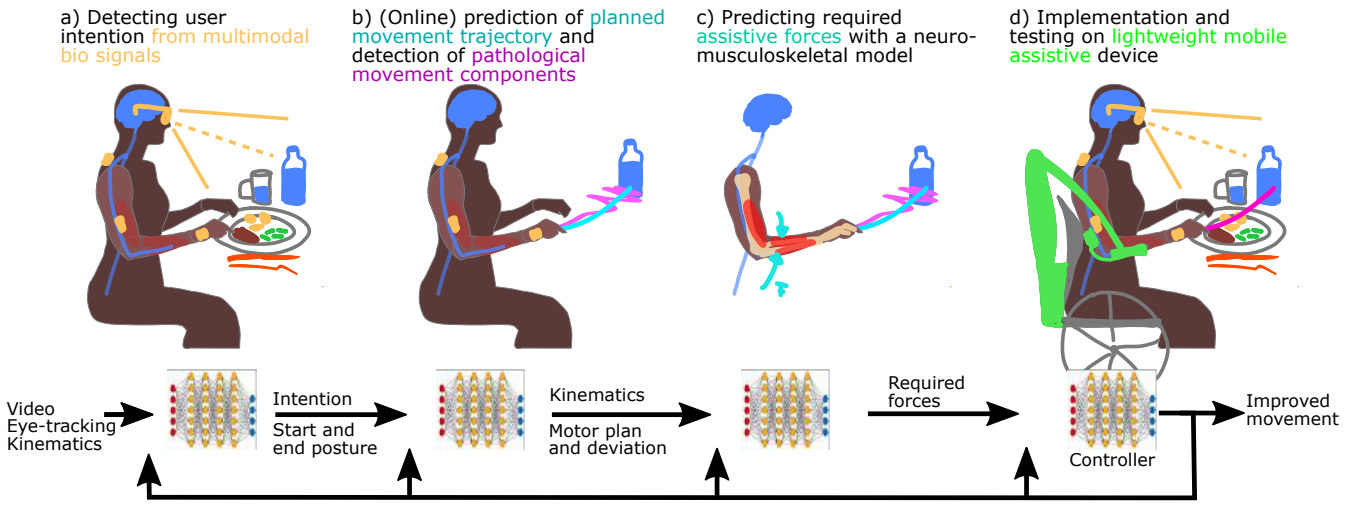


Fig. 1: Overview of the overall control architecture and its individual components.

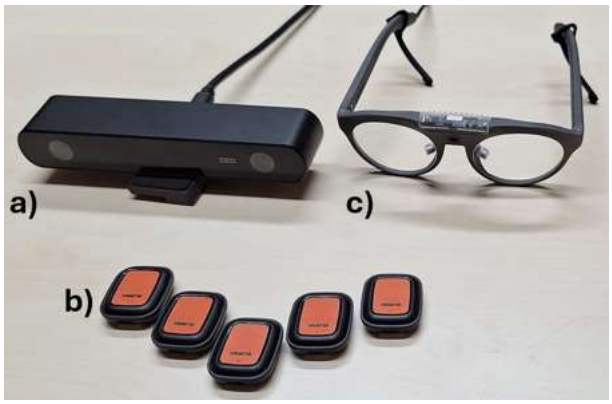


Fig. 2: The used sensor modalities to collect various data. a) ZED2i stereo camera b) Movella DOT IMUs c) Eye tracking system Pupil Labs Neon.

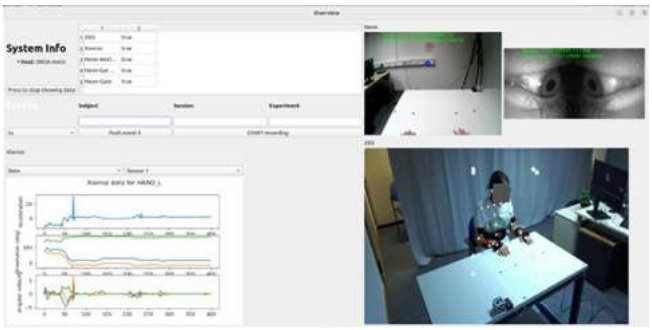


Fig. 3: Screenshot of the Graphical User Interface. System information is shown on the top left, including possible runtime errors such as data loss due to restricted data buffer size. It also features the recording control and a button for event generation. Live data of the motion sensor is shown below. The two top right shows the eye-tracking system with an overlay of gaze data and timestamps. Bottom right shows the RGB image of the ZED2i, overlayed with skeleton data.

predictions helpt to determine the corrective forces required as control inputs to the assistive device, which, in turn, will in the future apply forces to the human arm to correct dysfunctional movements (see Figure 1 c)).

To predict healthy movements, we developed a simulation approach for 3D arm movements that integrates three key factors: optimality principles, task requirements, and stochastic noise. Muscle and multibody dynamics were simulated using the MuJoCo physics engine [16] due to its computational speed and applied reinforcment learning (DEP-MPO) [17] to synthesize the control policy. We build on our previous work with a simplified, two degree-of-freedom arm model with six muscles-tendon units [18]. In this work, we achieved highly realistic arm trajectories (realism index > 0.9), comparable to those of healthy individuals.

Expanding this framework, we tested a more complex model with seven degrees of freedom and 27 muscle-tendon units (see Fig. 4). Our pior work showed that this 3D arm model predicts stiffness characteristics that closely match experimental data recorded from data while still being computationally efficient [19]. This model therefore allows us to predict the effect of corrective forces for our assistive device when attempting to mitigate the effects of motor control impairments.

As a first attempt to simulate pathological movement components, we added a sinusoidal signal to the elbow flexor muscle with frequencies occurring in the targeted diseases and varying amplitudes, generating stereotypic tremor movements (Fig. 4). Albeit its simplicity, this isolated approach is beneficial to determine (joint-)specific correction forces. However, we aim at simulating more naturalistic tremors in the future, by transferring our own and previous experimental data onto the model [20], [15] and by considering neurological origins of dysmetria and tremor [21], [22], [23].

E. Design requirements and hardware development

A lightweight assistive device, schematically represented in Fig. 5, was devised to apply corrective forces. It includes a prismatic joint along the z-axis, enabling force application in the vertical direction (blue), along with two revolute joints arranged in series (both axes parallel to the z-axis) in red and green, which mimic the human shoulder and elbow joints. This coordinated arrangement allows for the application of forces in any direction within the horizontal

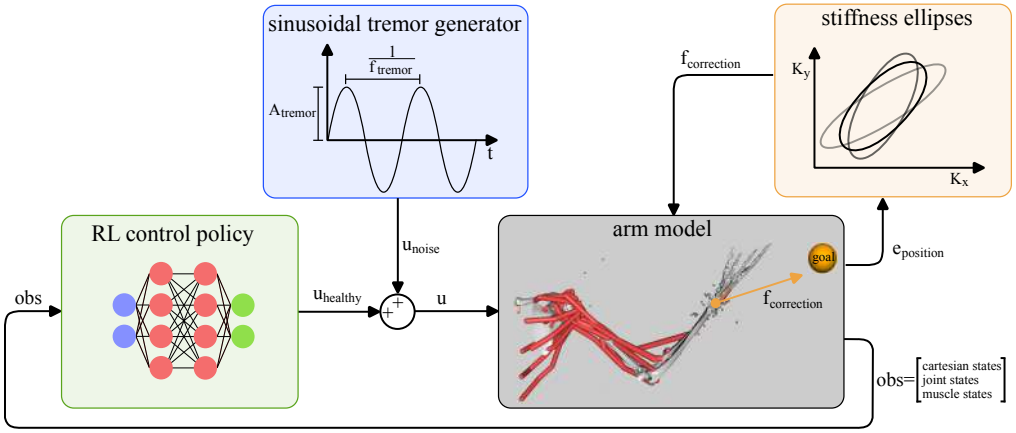


Fig. 4: Simulation of pathological arm movement: RL control policy computes the muscle control command (u_{healthy}) to generate healthy arm movements, while a sinusoidal tremor generator produces a perturbation signal (u_{noise}) with characteristic amplitude ($a_{\mathrm{tremor}} = 0.25$) and frequency ($f_{\mathrm{tremor}} = 4\,Hz$). This perturbation is added to the muscle control command to simulate hand tremors. Finally, corrective forces ($f_{\mathrm{correction}}$) are computed based on stiffness ellipses and position deviation to attenuate hand oscillations.

plane. Although preliminary investigations in simulation suggested that a force of 5 N applied to the hand can already effectively reduce or prevent the aforementioned movement disorders, the device was designed to provide a force of 10 N to account for the more proximal point of application of the corrective forces (forearm) and potential intersubject variability. We chose a bi-articular actuation scheme for the elbow joint actuation, spanning both the shoulder and elbow joints, as simulations indicated that this approach reduces the maximum torque required by the shoulder actuator compared to a mono-articular elbow actuation scheme. Two mechanisms were used to relocate both shoulder and elbow actuators proximally with respect to the vertical prismatic joint: a ball spline mechanism was utilized to transmit the shoulder actuator moment through the linear bearing of the prismatic joint, while a cable transmission was integrated into the scissor mechanism that connects the prismatic joint output to its driving actuator. The integration of the scissor mechanism also facilitated the compact incorporation of a spring mechanism for passive weight balancing of the robotic arm (see Fig. 5(a)(1)). As all three actuators were attached to the base of the device, the moving part of the designed robotic arm is lightweight and exhibits low apparent inertia, which positively contributes to reducing resistance to user movement when no correction is needed.

A mechanical interface (see Fig. 5 (b)) fixed at the tip of the robotic arm facilitates the application of corrective forces to a point approximately located at the midpoint of the user's forearm, thus enabling the generation of corrective moments at both the elbow and shoulder. This interface employs a mechanism similar to a gimbal, ensuring that the applied force is centered relative to the forearm, thereby preventing the generation of parasitic moments. The interface was constructed with two passive revolute joints, with the freedom of rotation along the forearm's longitudinal axis provided by the relative motion of soft tissues with respect to the user's skeleton. The mechanical interface also extends to the wrist, allowing for the application of forces along the longitudinal axis of the forearm with minimal slippage.

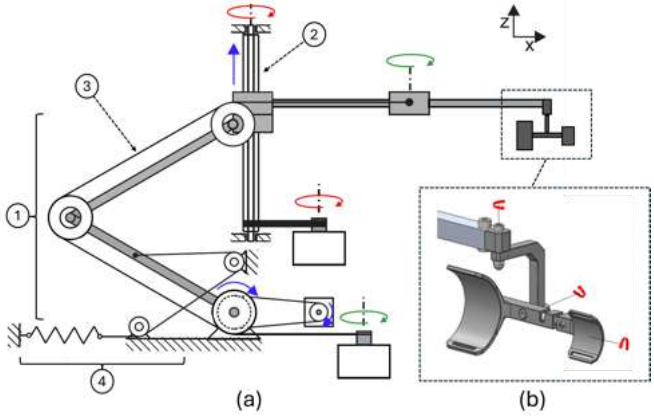


Fig. 5: (a) Schematic of the assistive device with three active DoF. From proximal to distal: a prismatic joint along the z-axis (blue) actuated via a scissor mechanism (1) which motion is constrained by the ball spline mechanism (2), a first rotational joint along the ball spline axis (red) and a second rotational joint bilaterally actuated using cables (3) routed through the scissor mechanism (green). All actuators are fixed to the base of the device, which significantly lowers the mass of the mobile part (arm) of the device. A passive spring mechanism (4) is used to balance the weight of the arm. (b) Close-up of the user interface with 3 passive DoF.

A preliminary evaluation study was performed with the unactuated device. First, we measured the resistive torques or forces experienced when moving each robotic arm DoF with joint velocities typical for the envisioned ADL. Second, we carried out a study with 5 healthy individuals to evaluate the device transparency (Task 1) and range of motion (Task 2). In Task 1, the subjects performed the ADL "Drinking" (fill a glass with the bottle using their right hand and then drink the water from the glass) with the device and were asked to rate from 0 to 10 how much the device was disturbing them (<3: not disturbing; 4-6: little disturbing; >7: very disturbing). In Task 2 the participants were instructed to sequentially place the bottle as close as possible to the four corners of a rectangular workspace drawn on the table in front of them, while avoiding to lean forward.

F. Experimental data acquisition

To achieve the project goal, a novel dataset will be recorded that includes kinematic data, gaze data, and scene

video including depth information (approved by the local ethics committee in Tübingen 474/2023B02). The developed ROS2 software architecture will be used to record a patient group (n = 20) and a group of age-matched healthy controls (n=20).

TABLE I: Planned experimental tasks.

Complex ADLs	Clinical test
Holding an object	Pointing on the table
Peeling, cutting and eating a banana	Moving objects
Drinking from a glass	Drawing the Archimedian spiral
Meal preparation	

The patient group comprises subjects suffering from neurodegenerative diseases such as Parkinson's disease, multiple sclerosis, or cerebellar ataxia exhibiting ataxic dysmetric movements (over- and undershooting of goal-directed movements in cerebellar ataxia) or tremors such as action and intention tremors.

The participants will be recorded performing different tasks that involve the upper extremities, e.g., meal preparation, while sitting at a table. A standardized data acquisition and experimental protocol was developed. The choice of tasks matches the future application scenario of the assistive device, but also fundamental knowledge is gained about the pathological movements (see Table I). This includes tasks with a high level of standardization and tasks with a higher amount of flexibility.

In the eating task, participants will be instructed to peel a banana, to cut the banana with a knife into smaller pieces, and to eat the pieces with a fork. The drinking task includes opening a bottle and pouring water into a glass. In the context of meal preparation, a Tupperware container is to be opened and the noodles inside emptied into a bowl. The Tupperware box should then be closed. In a follow-up task the noodles should be scooped out from the bowl into a cup using a laddle. The "clinical test" includes pointing movements at different locations on the table with the index finger, moving wooden bricks from one place to another predefined location, and drawing the Archimedian spiral in the clockwise and anti-clockwise direction.

The experimental protocol will also include a questionnaire to obtain further information that is relevant for analyzing the recorded data and developing the assistive device. The questionnaire covers socio-demographic and anthropometric data on each subject; pathology and associated symptoms; and expectations, doubts and requirements of such a non-invasive assistive device.

III. Preliminary Results

A. Preliminary Results of Kalman Filter

After preliminary data collection, raw data from the IMU and stereoscopic camera were synchronized and preprocessed before being put into the Kalman filter. Preprocessing included removal of gravity component from raw acceleration data, shifting of coordinate systems of the Xsens IMU and the ZED 2i camera, and upscaling data of the stereo camera to match IMU sampling frequency to enable sensor fusion. The coordinate systems of the stereo camera and the IMU at the wrist were aligned by first translating the origins to the same point and applying a rotation matrix computed using the the Kabsch algorithm [24]. The stereo camera data, although accurate, occasionally suffered from tracking loss, particularly during rapid movements. These limitations were mitigated through the sensor fusion.

In the testing framework using an ideal trajectory as ground truth, the filter achieved low RMSE values of 7.8, 7.8 and 7.4 m^{-4}, in the X, Y, Z directions, respectively. The tests with realistic experimental data demonstrated that the Kalman filter effectively fuses data from the IMU and stereo camera, producing smooth wrist trajectories under varying conditions. The filter successfully estimates motion trajectories while filtering out high-frequency noise.

B. Online detection of pathological movement components



Fig. 6: Snapshot of the recording of the drinking scenario for a tremor patient. Green dots represent the subject's workspace as identified by the stereo camera. Purple dots show the key points of the skeleton tracking. The left part of the image shows the online tracking of the inertial sensors, showing specific accelerations on the wrist sensor for different subphases of movement.

Results on the data collected so far show varying tremor frequencies not only for different patients but also for the same patient in different phases of movement (Fig. 6 + 7). This reflects the clinical impression of action and intention tremors. Such changing frequencies could be tracked with Bandlimited Multiple Fourier Linear Combiner, improved with a Kalman Filter, to estimate the changing frequencies. It allowed to separate the tremor offline (Fig. 7) and in real-time (Fig. 6). Further approaches will aim to incorporate prior knowledge about patient-specific tremor frequencies in order to optimize fast online detection.

C. Simulation of healthy and impaired arm movement

The synthesized control policy can generate both healthy and impaired point-to-point 3D reaching movements (Fig. 8). On the one hand, the direct application of the muscle control command u_{healthy} resulted in arm reaching movements with healthy kinematics characteristics: (i) roughly straight hand trajectories and (ii) bell-shaped velocity profiles (see early

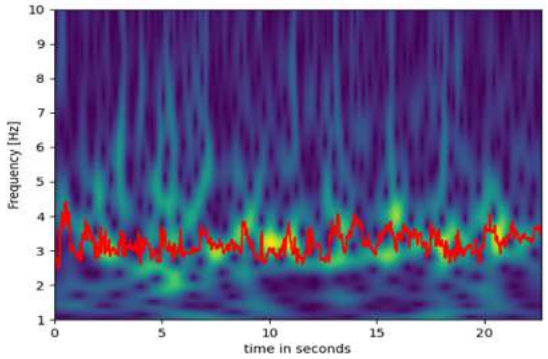


Fig. 7: The bandlimited multiple-fourier linear combiner with Kalman filter adapts to the frequencies of the pathological movement component (red).

reaching phase in Fig. 8, both in healthy and pathological movement). The addition of a sinusoidal signal to the muscle control command of the elbow flexor resulted in periodic positional oscillations around the target position, which is an approximation of tremors.

D. Hardware: Preliminary evaluation of device prototype

The evaluation study (see Fig. 9) revealed that the workspace reachable by the test subjects and available for executing the ADLs was only very marginally (2,2% in average) reduced by the device usage. The test subjects also evaluated positively the mechanical transparency of the device (average rating of 2,2: not disturbing), especially for motions in the horizontal plane but reported a noticeable resistance to vertical motions. This subjective evaluation was confirmed by the quantitative tests: low resistive torques (mean value $<= 0.1$ Nm) were measured for the rotational joints, while a mean resistive force of about 3 N (primarily dry friction) was measured for motions along the z-axis, attributed to internal friction in the ball spline mechanism. In summary, the selected transmission mechanisms, characterized by low internal friction, were shown to enable efficient torque transmission. This design allows using reasonably lightweight motors (approximately 1 kg per actuator) in a quasi-direct drive mode (reduction ratio < 3) to generate the necessary corrective forces. Based on the performance of the direct drive actuation, it is anticipated that interaction forces can be accurately estimated using motor current measurements in the horizontal plane, whereas active force control may be necessary to compensate for friction in the vertical direction. To address this, a single uniaxial force sensor will be integrated in the next iteration between the arm's tip and the mechanical interface with the user.

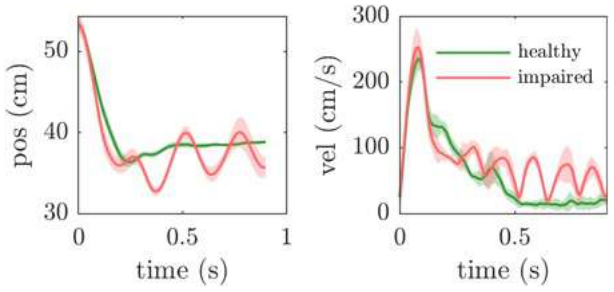


Fig. 8: Neuromechanical simulation of healthy (green) and impaired (red) arm movements. The impaired movement was simulated by adding a sinusoidal signals with frequencies occurring in the related diseases and different amplitudes added to the simulated muscle control signal. Here we show exemplarily 4 Hz and an amplitude of 0.5 (50% maximum muscle stimulation)

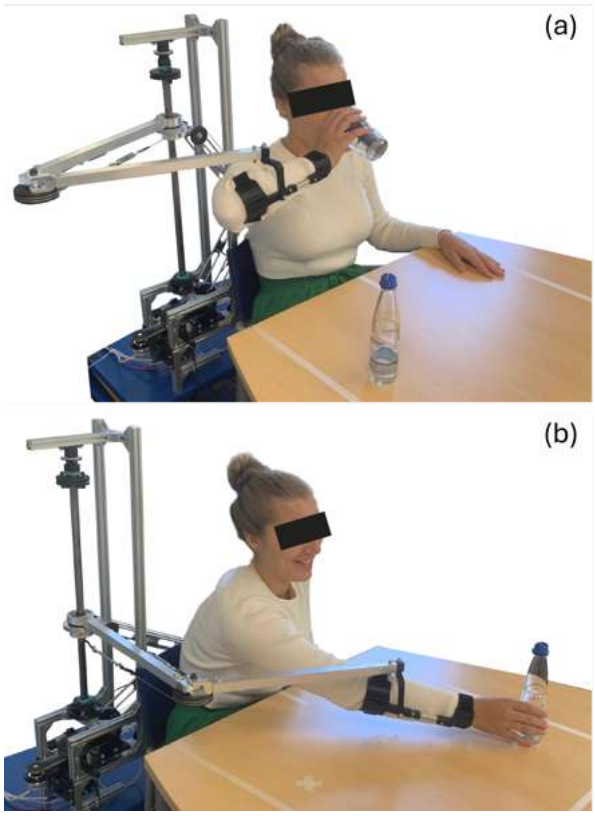


Fig. 9: (a) Subject performing ADL "Drinking", (b) ROM tests.

IV. Discussion

In this manuscript, we presented the concepts and first implementations of the individual components of our hardware and software architecture for an assistive device for patients with neurodegenerative movement disorders like cerebellar ataxia, multiple sclerosis or Parkinson's disease. These specific movement impairments result in pathological movement components overlaying the intended movements. This leads to specific requirements in the hardware and software concepts [15],[6] which differ significantly from concepts for stroke patients, where paralysis of the limbs or spasticity is the main issue (e.g. [7],[8]. Devices for stroke need to exert forces large enough to generate the entire movement and—typically slowly—follow given trajectories or predefined tasks and, thus, they typically place fewer demands on the real-time constraints in intention detection [9] and movement correction [6]. Thus, the two specific aspects of (a) rapid correction of complex everyday movements with (b) a lightweight and low-cost assistive device are the focus of our developments. With the developments and results so far, we have already been able to take some substantial steps in this direction. However, we still develop the individual components. Next steps will include ML methods for intention detection by combining the gaze estimation

of the eye-tracker with the current state of the movement tracking [25]; more naturalistic modeling of dysfunctional movements [23], [22], [15]; prediction of corrective forces with the neuromechanical model [22], [23], [15]; the real-time integration of all components; first user test.

REFERENCES

[1] M. Sun, W. Jung, K. Koltermann, G. Zhou, A. Watson, G. Blackwell, N. Helm, L. Cloud, and I. Pretzer-Aboff, "Parkinson's disease action tremor detection with supervised-leaning models," in *Proceedings of the 8th ACM/IEEE International Conference on Connected Health: Applications, Systems and Engineering Technologies*, 2023, pp. 1–10.

[2] D. Paredes-Acuna, N.and Utpadel-Fischler and K. e. a. Ding, "Upper limb intention tremor assessment: opportunities and challenges in wearable technology." *J NeuroEngineering Rehabil*, vol. 21, no. 8, 05 2024.

[3] N. H. Bhanpuri, A. M. Okamura, and A. J. Bastian, "Predicting and correcting ataxia using a model of cerebellar function," *Brain*, vol. 137, no. 7, pp. 1931–1944, 05 2014.

[4] K. Oh, D. Cao, N. Cowan, and A. J. Bastian, "Sensitivity of cerebellar reaching ataxia to kinematic and dynamic demands," *bioRxiv*, pp. 2024–10, 2024. [Online]. Available: https://doi.org/10.1101/2024.10.28.620711

[5] D. Hermle, R. Schubert, P. Barallon, W. Ilg, R. Schüle, R. Reilmann, M. Synofzik, and A. Traschütz, "Multifeature quantitative motor assessment of upper limb ataxia including drawing and reaching," *Annals of Clinical and Translational Neurology*, vol. 11, no. 5, pp. 1097–1109, 2024.

[6] J. S. Lora-Millan, G. Delgado-Oleas, J. Benito-León, and E. Rocon, "A review on wearable technologies for tremor suppression," *Frontiers in Neurology*, vol. 12, 2021.

[7] R. Hennig, J. Gantenbein, J. Dittli, H. Chen, S. P. Lacour, O. Lambercy, and R. Gassert, "Development and evaluation of a sensor glove to detect grasp intention for a wearable robotic hand exoskeleton," in *2020 8th IEEE RAS/EMBS International Conference for Biomedical Robotics and Biomechatronics (BioRob)*. IEEE, 2020, pp. 19–24.

[8] M. Gardner, C. S. Mancero Castillo, S. Wilson, D. Farina, E. Burdet, B. C. Khoo, S. F. Atashzar, and R. Vaidyanathan, "A multimodal intention detection sensor suite for shared autonomy of upper-limb robotic prostheses," *Sensors*, vol. 20, no. 21, p. 6097, 2020.

[9] J. Gantenbein, J. Dittli, J. Meyer, R. Gassert, and O. Lambercy, "Intention detection strategies for robotic upper-limb orthoses: A scoping review considering usability, daily life application, and user evaluation." *Frontiers in Neurorobotics*, vol. 16, 2022.

[10] C. Baumann and K. Dierkes, "Neon accuracy test report," 2023. [Online]. Available: https://zenodo.org/doi/10.5281/zenodo.10420388

[11] M. Hutter, C. Gehring, D. Jud, A. Lauber, C. D. Bellicoso, V. Tsounis, J. Hwangbo, K. Bodie, P. Fankhauser, M. Bloesch, R. Diethelm, S. Bachmann, A. Melzer, and M. Hoepflinger, "Anymal - a highly mobile and dynamic quadrupedal robot," in *2016 IEEE/RSJ International Conference on Intelligent Robots and Systems (IROS)*, 2016, pp. 38–44.

[12] W. Chambers, A. Oyake, M. Deans, K. Hambuchen, and B. Roberts, "Space robot operating system (space ros)," in *ROS Conference (ROSCon) 2021*, 2021.

[13] H. Saeidi, J. D. Opfermann, M. Kam, S. Raghunathan, S. Leonard, and A. Krieger, "A confidence-based shared control strategy for the smart tissue autonomous robot (star)," in *2018 IEEE/RSJ International Conference on Intelligent Robots and Systems (IROS)*, 2018, pp. 1268–1275.

[14] K. C. Veluvolu and W. T. Ang, "Estimation of physiological tremor from accelerometers for real-time applications," *Sensors*, vol. 11, no. 3, pp. 3020–3036, 2011.

[15] Z. Habibollahi, Y. Zhou, M. E. Jenkins, S. J. Garland, M. D. Naish, and A. L. Trejos, "Multimodal tremor suppression of the wrist using fes and electric motors–a simulation study," *IEEE Robotics and Automation Letters*, vol. 8, no. 11, pp. 7543–7550, Nov. 2023.

[16] E. Todorov, T. Erez, and Y. Tassa, "MuJoCo: A physics engine for model-based control," in *2012 IEEE/RSJ International Conference on Intelligent Robots and Systems*. IEEE, 10 2012.

[17] P. Schumacher, D. Häufle, D. Büchler, S. Schmitt, and G. Martius, "DEP-RL: Embodied exploration for reinforcement learning in over-actuated and musculoskeletal systems," in *The Eleventh International Conference on Learning Representations*, 2023.

[18] J. Charaja, I. Wochner, P. Schumacher, W. Ilg, M. Giese, C. Maufroy, A. Bulling, S. Schmitt, and D. F. Haeufle, "Generating realistic arm movements in reinforcement learning: A quantitative comparison of reward terms and task requirements," in *2024 IEEE RAS/EMBS International Conference for Biomedical Robotics and Biomechatronics(BioRob)*. IEEE, 2024.

[19] M. Sapounaki, P. Schumacher, W. Ilg, M. Giese, C. Maufroy, A. Bulling, S. Schmitt, D. F. Haeufle, and I. Wochner, "Quantifying human upper limb stiffness responses based on a computationally efficient neuromusculoskeletal arm model," in *2024 IEEE RAS/EMBS International Conference for Biomedical Robotics and Biomechatronics(BioRob)*. IEEE, 2024.

[20] A. C. Pigg, J. Thompson-Westra, K. Mente, C. W. Maurer, D. Haubenberger, M. Hallett, and S. K. Charles, "Distribution of tremor among the major degrees of freedom of the upper limb in subjects with essential tremor," *Clinical Neurophysiology*, vol. 131, no. 11, pp. 2700–2712, nov 2020.

[21] N. H. Bhanpuri, A. M. Okamura, and . Bastian, Amy J., "Predicting and correcting ataxia using a model of cerebellar function," *Brain*, vol. 137, no. 7, pp. 1931–1944, 2014.

[22] K. Stollenmaier, I. Rist, F. Izzi, and D. F. Haeufle, "Simulating the response of a neuro-musculoskeletal model to assistive forces: implications for the design of wearables compensating for motor control deficits," in *2020 8th IEEE RAS/EMBS International Conference for Biomedical Robotics and Biomechatronics (BioRob 2020)*. Piscataway, NJ: IEEE, Oct. 2020, pp. 779–784.

[23] W. C. Pinheiro, H. B. Ferraz, M. C. F. Castro, and L. L. Menegaldo, "An opensim-based closed-loop biomechanical wrist model for subject-specific pathological tremor simulation," *IEEE Transactions on Neural Systems and Rehabilitation Engineering*, vol. 32, pp. 1100–1108, 2024.

[24] T. Novacek, C. Marty, and M. Jirina, "Project multileap: Fusing data from multiple leap motion sensors," in *2021 IEEE 7th International Conference on Virtual Reality (ICVR)*, 2021, pp. 19–25.

[25] Z. Hu, S. Schmitt, D. Haeufle, and A. Bulling, "Gazemotion: Gaze-guided human motion forecasting," in *Proceedings of the 2024 IEEE/RSJ International Conference on Intelligent Robots and Systems*, 2024.

Development and Evaluation of a Device to Assess Finger Individuation in Neurorehabilitation

Anna Sophie Knill[1,2], Shuyang Shi[1], Chris Awai Easthope[2], Meret Branscheidt[2,3,4], and Olivier Lambercy[1,5]

***Abstract*— Finger individuation, the ability to independently control fingers, is a critical component of hand function that is often impaired in people with neurological conditions. To address the need for sensitive tools to measure finger individuation in clinical and research settings, an assessment device was developed and tested. Equipped with force sensors under each finger, an individuation index (IndX) in both flexion and extension was calculated. Feasibility of the device was assessed by measuring able-bodied participants and neurological patients. The reliability of the finger individuation assessments was evaluated in a test-retest setting, showing high consistency, with Intraclass Correlation Coefficients (ICC) and Spearman correlation classified as moderate to excellent (ICC for flexion of thumb: 0.73, p <0.001; index: 0.68, p <0.001; middle: 0.48, p =0.003; ring: 0.72, p <0.001; little: 0.80, p <0.001). Validity was further examined by comparing the IndX across fingers and between groups, utilizing t-tests and the Area Under the Curve (AUC) from Receiver Operating Characteristic analysis. Although AUC values indicated a mixed discriminative ability, the device successfully captured differences in finger control between able-bodied individuals and patients. These results indicate that the device offers a reliable and effective means of quantifying finger individuation, opening the door to advanced fine hand motor control research and through that, personalized rehabilitation.**

I. INTRODUCTION

The ability to selectively activate fingers in an independent manner, defined as finger individuation, is crucial for fine motor control and hand functionality in everyday life. Finger individuation can be severely affected in patients with neurological impairments, such as stroke or Parkinson's [1], [2], [3], leading to limitations in hand dexterity and overall quality of life. While the clinical significance of impaired finger individuation, which is referred to as higher finger enslaving, is well-recognized [4], the assessment of this specific function is not yet systematically integrated into routine clinical evaluations, primarily due to the scarcity of clinically usable tools to finely measure finger individuation.

Technology-based assessments offer promising solutions for evaluating finger individuation in a sensitive manner. Various devices have been employed in previous studies, including setups that utilize force sensors under the fingertips [5], [6], dual-sensor configurations [7], [8], [9], and robotic devices with cables [10], [11] or rods [12] for force transduction. Others have used instrumented gloves to track individual finger movements and forces [4], [13], [14].

However, existing measurement systems present several limitations. Some do not measure all fingers [5], [10], [15], [8], require two devices for bilateral assessments [6], [16], [17], or are restricted to finger flexion only [18]. The latter is particularly problematic, as it has long been established that enslaving effects also occur during extension movements [19]. Additionally, some devices rely on dynamic tasks [4], [13], which typically require complex and bulky mechanisms to directly move the fingers [4], [9], thereby limiting their clinical applicability. Furthermore, some systems require specific hand positioning, such as pronation on a flat surface [6], restrict the hand to a cylindrical grip [12], or rely on metal ring finger attachments [15], which can compromise comfort and usability.

Thus, there is a need for a measurement device that answers the limitations of existing technologies by providing a more ergonomic, adaptable, and compact system capable of easily assessing both hands, offering accurate and sensitive measurements for each independent finger in both flexion and extension.

In this paper, we present the development and evaluation of a novel device designed to measure finger individuation that builds on the assessments proposed by Xu and colleagues [6]. The key aspects tested is the feasibility of the device and assessment procedures, along with the reliability of its outcome measures (primarily the individuation index, IndX, adapted from Xu and colleagues [6] for both flexion and extension), ensuring accurate and consistent measurements across repeated tests. We hypothesized that i) it would be feasible for neurologically impaired patients to use the device for assessing finger individuation, and that ii) the extracted outcome measures would show high reliability in able-bodied subjects, as well as discriminative ability.

II. METHODS

A. Finger individuation device

The device implemented in this study expands on a previously built prototype designed for assessing finger motor control that was used in prior studies [6]. Its development followed a user-centered design approach, to improve its feasibility for clinical and research applications. The technical requirements were based on literature and clinicians' inputs and an iterative development approach was followed

[1]Rehabilitation Engineering Laboratory (RELab), ETH Zurich, Switzerland (e-mail: anna.knill@hest.ethz.ch)

[2]Lake Lucerne Institute (LLUI), Switzerland

[3]cereneo, center for neurology and rehabilitation, Switzerland

[4]Department of Health Sciences and Technology, ETH Zurich, Switzerland

[5]Future Health Technologies program, Singapore - ETH Centre, Campus for Research Excellence and Technological Enterprise (CREATE), Singapore

with end-user testing throughout. This included three design circles (involving five neurological patients) focusing on the software (e.g., comprehensive interface) and hardware (e.g., hand positioning) components. As a result, the novel version of the device consists of six bi-directional load cells (DYLY-109, DAYSEN-SOR, China, -98 to 98N), one for measuring the thumb on each side and four for the remaining fingers, that can be positioned under each fingertip, thanks to linear sliders, to measure the forces exerted by each digit (see Fig. 1A). The force sensors are linked to an amplifier (HX711 analog-to-digital converter) and the signals are then processed by a microcontroller (Arduino Mega 2560, Arduino, Italy), that is connected to a laptop with a custom designed assessment software developed using the MATLAB Designer App (MathWorks, USA) to record, visualize, and analyze the collected force data. The software offers a user-friendly interface, enabling clinicians and researchers to monitor the force applied by each finger individually in real-time during the assessment (Fig. 1B).

The hand is securely positioned on the device with adjustable Velcro straps around each fingertip ensuring proper force transmission in flexion and extension and accommodating for different finger sizes. Additional Velcro straps stabilize the proximal phalanges to prevent unintended bending of the hand. A larger forearm strap secures the arm for proper alignment and a relaxed hand position. This fixation system ensures stability, ergonomic positioning, and accurate force measurements by maintaining a consistent hand position across sizes. Additionally, the device features a rotational axis to switch sides, allowing for measurements of the left and right side in an ergonomical forearm supination with the same apparatus.

B. Finger individuation assessment procedure

Once the hand is secured in the apparatus, the experimenter can choose between the assessment of isometric flexion or extension. The individuation assessment is based on previous studies [6] and starts with a baseline measurement. The subject is asked to relax the hand and fingers and a mean resting force over five seconds is calculated for each finger, which is later subtracted from all force measurements to only measure actively produced forces. Following this, the Maximum Voluntary Force (MVF) is measured. Subjects are asked to flex or extend one finger for five seconds as hard as possible while solely seeing a visual representation of the produced force of the instructed finger on the screen. For each measurement, the maximum is defined as the 95th percentile value of the maximum recorded force data. The MVF is calculated as the mean of three attempts with any measurements falling below 60% of the other values being discarded.

To assess finger individuation subjects are then asked to produce flexion or extension force respectively, with one instructed finger at a time until they reach a desired target range (± 10% of the target force) visualized on the screen (see Fig. 1B). The target force is based on the MVF and is evaluated on four Force Levels (FL): 20, 40, 60, and 80% of the MVF. Each level is repeated four times per block with a trial (i.e., applying the specific force level) being considered successful if the force of the instructed finger remains within the target range for about 0.5 seconds within the 10 seconds trial duration. The force applied by each finger is visualized during the individuation trial, providing feedback on the finger enslaving, and a change in color of the instructed finger indicates that the target range is reached. To ensure true flexion and extension, trials with a MVF smaller (or bigger for extension) than $(FL - 100)/FL$ times the baseline force were discarded.

C. Outcome measure of finger individuation

During the finger individuation assessment, raw force data over time for all fingers is recorded. Based on this, the individuation index (IndX) is calculated to quantify finger individuation which reflects the ability of each finger to produce isolated force as introduced by Xu and colleagues [6]. In our implementation of the IndX, it is calculated by evaluating the force of all uninstructed fingers during all cumulative time points (N) where the instructed finger is within the target range (see blue shaded area in Fig. 2A,B), hence allowing for an analysis of partially completed trials

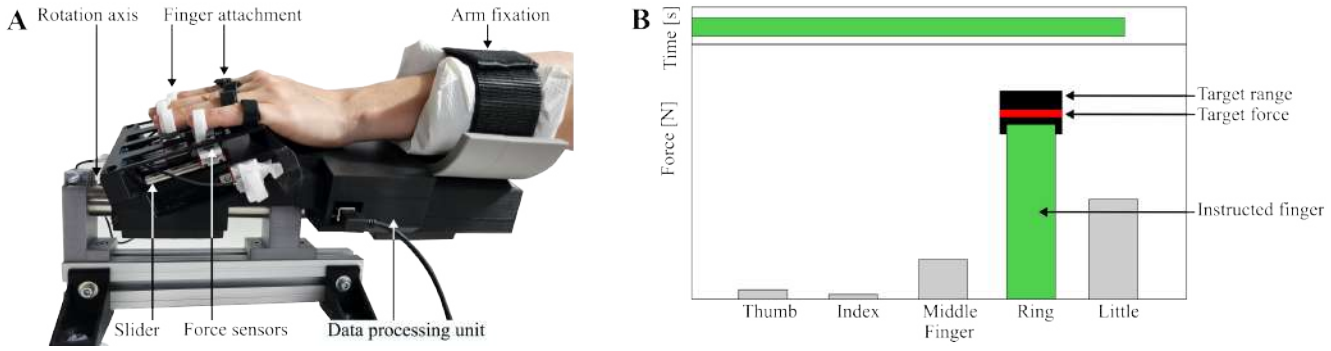


Fig. 1. A: Adjustable finger individuation device with force sensors located under each fingertip to measure isometric flexion and extension forces. B: Visual representation of a finger individuation assessment trial. Participants receive feedback on the force produced by each finger (gray bars) while trying to produce and maintain for 0.5 seconds a target force with the instructed finger (here ring finger). Once within the target range (black box), the bar representing the produced force changes color from blue to green. The target range is defined as 20% of the target force (red) that corresponds to 20, 40, 60, or 80% of the Maximum Voluntary Force (MVF).

as well. With a sampling rate of 80 Hz, the minimum N was set to be 40, reflecting around 0.5 seconds. Afterwards, the Root Mean Square (RMS) of the difference between the baseline force (BF_i) and the force executed by the uninstructed fingers ($F_{n,i}$) for all uninstructed fingers (i) is taken, as can be seen in the equation (1) below:

$$RMS = \frac{1}{N}\sum_{n=0}^{N} \sqrt{\sum_{i=uninstructed} (F_{n,i} - BF_i)^2} \quad (1)$$

Higher deviations from the baseline force in the uninstructed fingers correspond to more enslaving and hence poorer independent control of the fingers. To then calculate the IndX, the mean RMS per block is plotted against the force of the instructed finger for all four force levels, FL (see example in Fig. 2C). Performing a linear regression without intercept gives a slope for every finger, which represents the IndX. A smaller slope (IndX closer to zero), due to less co-activation in the uninstructed fingers, corresponds to better individuation of the instructed finger.

D. Evaluation study

To test the reliability and validity of the individuation device, young able-bodied subjects as well as neurological inpatients from the cereneo, center for neurology and rehabilitation (Vitznau and Hertenstein, Switzerland) were recruited. The study was approved by the local ethics committee (Ethikkommission Nordwest- und Zentralschweiz, 2023-00731). To participate in the study, able-bodied subjects had to be between 18 and 40 years old, show no cognitive impairment, no history of neurological diseases, and no pathologies of the upper extremities. Inclusion criteria for patients were a previously diagnosed neurological disease, subjective impairment of hand dexterity, between 18 and 100 years old, and able to understand task instructions and give consent. Patients with severe visual impairments, pain in the upper extremities, major psychiatric illness, previous experience with the device, or severe hand spasticity or tremor were excluded.

After providing informed consent all participants underwent the baseline and MVF measurement followed by a familiarization trial of the individuation assessment. The testing then included extension and flexion measurements with the force levels and instructed fingers appearing in random order. For the able-bodied participants a second round of testing was performed after a ten minute break, where the hand was removed from the device. This re-test included the measurements of two fingers (thumb and ring) for extension and all fingers for flexion. As a secondary analysis and to validate the strength measurements, the MVF was compared to grip strength (assessed with a Jamar dynamometer) in able-bodied subjects.

E. Statistical analysis

Descriptive statistics, including mean values and standard deviation, were calculated to compare the two groups. Feasibility of the device as an assessment of finger individuation was assessed by observing whether patients could be measured with the device and the corresponding set-up time, while the number of successful trials and the total assessment time was used to determine its clinical applicability. The IndX was computed for each finger to assess finger individuation. Reliability of the MVF and IndX was evaluated in able-bodied subjects using Intraclass Correlation Coefficients (ICC) and Spearman correlation (ρ) to confirm the consistency of measurements across repeated trials. Reliability was classified as follows: ICC values $<$0.5 indicated poor, 0.5–0.75 moderate, 0.75–0.9 good, and $>$0.9 excellent reliability [20]. Spearman correlation coefficients were categorized as $|\rho|$ $<$0.39 for weak, 0.4–0.69 for moderate, 0.7-0.89 strong, 0.9–1 for very strong correlation [21] and statistical significance was always set at a p-value of $\alpha \leq$0.05. For the MVF, concurrent validity was analyzed through a Spearman's rank correlations with respect to clinical assessments of grip strength. Differences in IndX between fingers were tested using t-tests (with a Bonferroni Correction) to compare mean values. Additionally, the Area Under the Curve (AUC) from Receiver Operating Char-

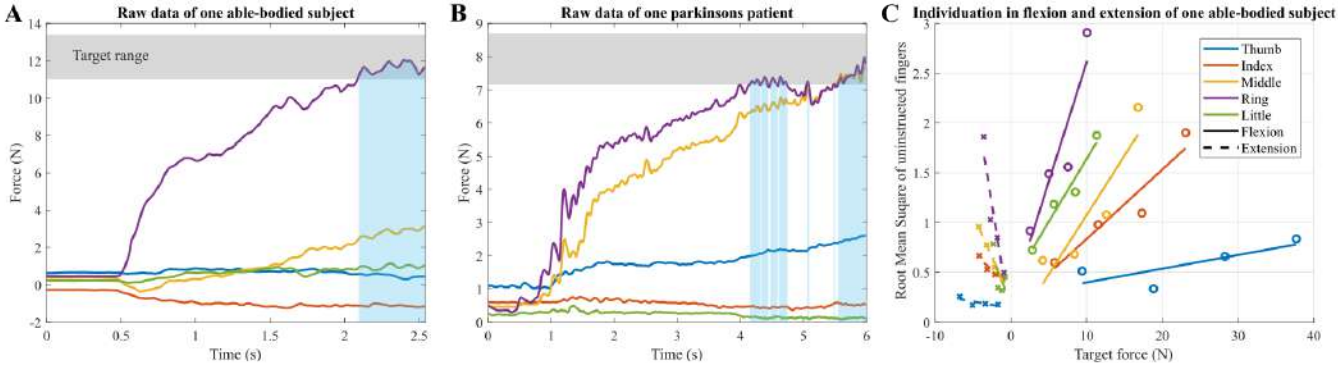


Fig. 2. Raw data of finger individuation assessment of a ring finger flexion trial to reach 80% Maximum Voluntary Force (MVF) for an able-bodied subject (A) and Parkinson's patient (B). Blue shaded areas indicate timepoints where the instructed finger remains within the target range (gray area), which are considered for the calculation of the individuation index (IndX). C: Example of the IndX for flexion (continuous line) and extension (dashed line) in one able-bodied subject. The index is calculated as the slope of the regression line formed by points representing the four levels of MVF versus the Root Mean Square force of the uninstructed fingers. Flatter slopes indicate better individuation.

acteristic (ROC) analysis was calculated to evaluate the discriminative ability of the IndX, determining whether the device could successfully differentiate between patients and able-bodied subjects. AUC values for ROC were classified as 0.90–1.00 for outstanding, 0.80–0.89 for excellent, 0.70–0.79 for acceptable, 0.50–0.69 for poor discrimination, and 0.50 for no discrimination [22].

III. RESULTS

A. Feasibility of the individuation device

Thirty able-bodied subjects and four patients with different neurological conditions and levels of upper limb performance (assessed by Action Research Arm Test, ARAT, with corresponding scores of 53, 44, 56, and 38 points) were assessed to evaluate feasibility (for details see Table 1). This cohort allowed for an analysis of the device's applicability in a real-world clinical setting. Mounting to the device was done in less than five minutes with no report of discomfort at any time and no difficulties understanding the task.

The average total time required to complete a single modality assessment (e.g., flexion) was 19 minutes in able-bodied subjects (with constantly reduced measurement durations in the following sessions) and 23 minutes in patients. Out of the 606 completed trials for the patients 516 were successful (85.15%), demonstrating effectiveness. It has to be noted, that 64 of 90 failed trials can be associated to one subject (patient 4) who suffered from tremor and that solely 5 trials in total could not be analyzed as the total time spent within the target range for those was below 0.5 seconds. For comparison, the 30 able-bodied subjects assessed had a 99.98% success rate (8159 out of 8160 trials).

B. Finger individuation

To quantify finger enslaving, the IndX was derived from the force data collected during the assessment, providing a clear metric for evaluating isolated finger force in flexion and extension (Fig. 2C). Higher levels of enslaving in the uninstructed fingers could be observed with higher force levels, which is represented in the positive IndX (and slopes in Fig. 2C) for flexion and negative IndX for extension respectively (Table 2).

TABLE I

PARTICIPANT DEMOGRAPHICS AND CHARACTERISTICS

Characteristic	**Able-bodied**	**Patients**
Number of participants	30	4
Age (mean ± SD)	24.3 (±2.8)	69.5 (±2.7)
Sex (m, f)	13, 17	3, 1
Handedness (l, r)	5, 25	0, 4
Impaired side (l, r)	NA	1, 3
Condition	NA	Stroke = 1 Parkinson's = 2 Brain tumor = 1
Grip strength (mean ± SD) Dynamometer [N]	(n = 26) 36.68 (±9.35)	(n = 3) 23.43 (±5.50)

C. Reliability

Details of the test-retest reliability analysis in able-bodied subjects is reported in Table 2. For the MVF, ICC indicates good to excellent reliability and strong to very strong correlations between the two measurements for all fingers. Moderate to good reliability (except for the middle finger flexion and thumb extension), as indicated by the ICC, can be seen for the IndX and the results from the Spearman correlation show moderate to strong correlations (except for the thumb in extension) respectively.

D. Validity

For the MVF measurements, all fingers showed significant moderate correlations (thumb: ρ = 0.64, p $<$ 0.001; index: ρ = 0.63, p $<$ 0.001; middle: ρ = 0.63, p $<$ 0.001; ring: ρ = 0.64, p $<$ 0.001; little: ρ = 0.67, p $<$ 0.001) indicating that the strength measurements align well with the established gold standard.

The ability of the IndX to differentiate between able-bodied subjects and patients is visualized in Fig. 3. Extension of the little finger for patient 1 is missing, as the relationship between maximum strength and baseline did not allow for a pure extension assessment. This was also the case for three other 20% MVF blocks in patients, which nevertheless allowed for a calculation of the IndX.

The AUC indicates outstanding discriminant validity for the flexion of the thumb (AUC = 0.99) and excellent for the little finger (AUC = 0.88). Acceptable discrimination was achieved for the flexion of the ring (AUC = 0.71) and poor for the index and middle in flexion (AUC = 0.60 and 0.59)

TABLE II

MVF AND INDX VALUES WITH TEST-RETEST RELIABILITY IN FLEXION AND EXTENSION FOR ABLE-BODIED SUBJECTS

Finger	Thumb		Index		Middle		Ring		Little	
Mean ±SD	Test	Retest	Test	Retest	Test	Retest	Test	Retest	Test	Retest
MVF flex	44.7 ±17.3	47.0 ±19.1	28.9 ±9.6	28.8 ±9.8	26.5 ±9.6	25.7 ±8.7	18.1 ±6.7	17.5 ±5.9	15.9 ±5.6	15.7 ±5.5
MVF ext	-11.0 ±3.4	10.5 ±3.3	-8.2 ±2.4	NA	-6.9 ±1.8	NA	-5.2 ±1.8	-5.4 ±1.9	-4.0 ±1.1	NA
IndX flex	0.03 ±0.02	0.03 ±0.04	0.16 ±0.13	0.13 ±0.10	0.16 ±0.09	0.14 ±0.10	0.29 ±0.15	0.26 ±0.16	0.29 ± 0.29	0.33 ±0.27
IndX ext	-0.09 ±0.09	-0.11 ±0.11	-0.12 ±0.15	NA	-0.29 ±0.20	NA	-0.46 ±0.26	-0.54 ±0.31	-0.34 ±0.30	NA
Stats	ICC (p)	ρ (p)	ICC (p)	ρ (p)	ICC (p)	ρ (p)	ICC (p)	ρ (p)	ICC (p)	ρ (p)
MVF flex	0.91* (0.00)	0.90* (0.00)	0.88* (0.00)	0.89* (0.00)	0.90* (0.00)	0.92* (0.00)	0.77* (0.00)	0.79* (0.00)	0.91* (0.00)	0.94* (0.00)
MVF ext	0.81* (0.00)	0.81* (0.00)	NA	NA	NA	NA	0.91* (0.00)	0.92* (0.00)	NA	NA
IndX flex	0.73* (0.00)	0.64* (0.00)	0.68* (0.00)	0.62* (0.00)	0.48* (0.00)	0.51* (0.00)	0.72* (0.00)	0.72* (0.00)	0.80* (0.00)	0.70* (0.00)
IndX ext	0.22 (0.12)	0.08 (0.66)	NA	NA	NA	NA	0.59* (0.00)	0.65* (0.00)	NA	NA

MVF = Maximum Voluntary Force; IndX = Individuation index; SD = Standard Deviation; ICC = Intraclass Correlation Coefficient; ρ = Spearman correlation; p = significance (* p $\leq$ 0.05)

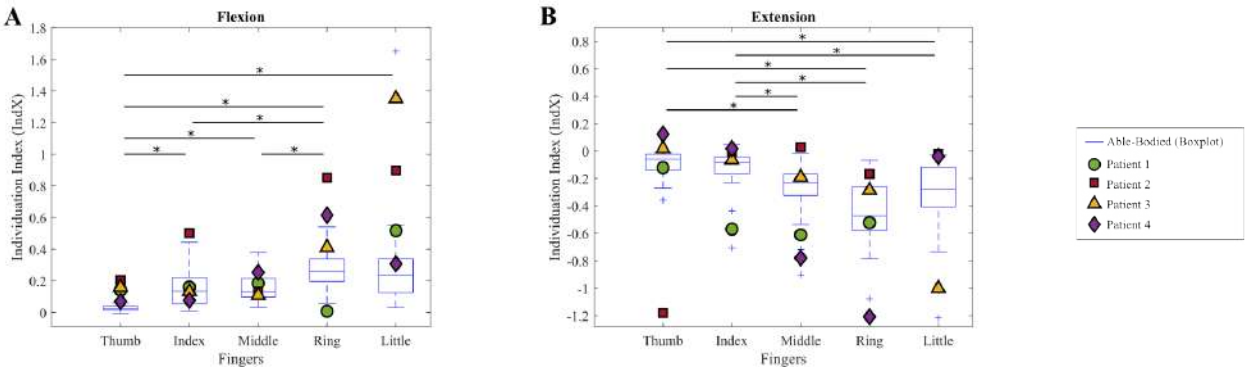


Fig. 3. Individuation index (IndX) for able-bodied participants (blue) and patients (green, red, yellow, purple) in flexion (A) and extension (B) showing medians and interquartile ranges. IndX values closer to zero indicate better individuation. Statistically significant differences between the fingers of the able-bodied subjects are marked with an asterisk.

as well as little, index, and thumb in extension (AUC = 0.67, 0.59, 0.58) while the other fingers indicate no differentiation ability with an AUC of 0.43 and 0.48 and for middle, and ring finger extension respectively.

IV. Discussion

This study presents the development and evaluation of a device for assessing finger individuation, designed to be both user-friendly and reliable. The device allowed for successful measurements of able-bodied subjects and neurological patients, confirming its feasibility and clinical applicability. Across both user groups, adjustable hand and finger fixations via Velcro straps and sliders ensured proper ergonomic positioning and stability for both hands. These findings confirm that the device is well-suited for integration into clinical settings, potentially easing the accessibility of finger individuation measures which could allow for a better identification of the deficit and hence support the development of personalized therapy.

To objectively quantify isometric finger independence, the individuation index (IndX) was developed based on previously established methodologies [6]. Overall, the results obtained align well with findings from similar studies, that demonstrate higher enslaving with higher forces of the instructed finger (Fig. 2C) [5], [15]. In addition, the IndX reveals a distinct pattern of enslaving, with the ring and little finger exhibiting the highest enslaving, followed by the index and middle showing similar levels of enslaving, and the thumb showing the best individuation (Fig. 3 and Table II). This pattern slightly differs from earlier findings [19], [23], where the index was found to show less enslaving than the middle finger. These differences likely stem from differences in calculation of the IndX. Unlike previous studies that could only measure unidirectional forces [6], [5], our approach considers both flexion and extension forces produced by the uninstructed fingers during the individuation task, providing a more comprehensive analysis, but possibly contributed to higher enslaving values. This is partly confirmed by our results better aligning with the individuation pattern found by Xu et al. [24], where all dimensions of the finger (flexion, extension, adduction, and abduction) were measured. Notably, enslaving was generally more pronounced in extension than in flexion, aligning with results from Sanei and Yu [15], [12], with a slight exception for the index finger. Finally, when taking the average IndX of all fingers, it tends to be higher than the slope recorded in previous research (0.087 ±0.046) [6]. This could possibly be explained by the fact that our implementation of the IndX solely considers forces applied while the instructed finger is within the target force, rather than during the entire task duration, as in previous research [6]. While our implementation should better capture enslaving at the defined force levels, it underlines the need for consensus on the calculation of the individuation index to further enhance comparability across studies.

The high test-retest reliability, as reflected in the ICC and Spearman correlation values, indicates the device's consistency in delivering reproducible measurements for MVF and individuation of most fingers. Reliable data collection is essential for both clinical and research applications, as it enables clinicians to track a patient's progress over time and researchers to compare data across studies. Low levels of reliability have only been observed for the thumb during extension. An explanation for this might be the challenge in consistent fixation of that specific finger over different trials, which might be the reason why previous researchers have not considered the thumb in their individuation device [5], [10], [15].

Strong correlations were found between grip strength and MVF assessed with the individuation device, indicating the device's potential to provide an objective strength measurement that corresponds to established clinical evaluations. However, the variable AUC values indicate mixed abilities to distinguish between able-bodied participants and patients in terms of individuation, which might be influenced by the limited number of patients measured and the fact that the patients included in the study did not necessarily exhibit specific impairments in finger individuation. Previous research by Xu et al. [25] summarized that in stroke patients' individuation is decreased, especially in extension. Relatively preserved individuation abilities may be the reason why this pattern is not evident in our study and thereby reducing

the observable differences in enslaving between flexion and extension.

Future studies should investigate the relationship of individuation to other factors influencing dexterity and expand this research to include larger and more varied populations which would provide a clearer picture of the device's applicability across different groups.

V. CONCLUSIONS

This study presents an improved device for the assessment of finger individuation, demonstrating good reliability and moderate validity. The device has potential for clinical applications to more sensitively quantify hand function and provide valuable insights into patient's rehabilitation progress, enabling clinicians to tailor interventions based on individual needs. The practical design of the assessment tool also facilitates its use in research, allowing for standardized measurements in studies investigating hand fine motor control and hence advancing the understanding of finger individuation.

ACKNOWLEDGMENT

The authors would like to thank all the participants that took part in this study. Additional thanks go to Lukas Gerber and Jay Song for their work in the development of the device.

REFERENCES

[1] C. E. Lang and M. H. Schieber, "Reduced Muscle Selectivity During Individuated Finger Movements in Humans After Damage to the Motor Cortex or Corticospinal Tract," *Journal of Neurophysiology*, vol. 91, no. 4, pp. 1722–1733, Apr. 2004, publisher: American Physiological Society.

[2] M. Térémetz, F. Colle, S. Hamdoun, M. A. Maier, and P. G. Lindberg, "A novel method for the quantification of key components of manual dexterity after stroke," *Journal of NeuroEngineering and Rehabilitation*, vol. 12, no. 1, p. 64, Aug. 2015.

[3] J. Park, Y.-H. Wu, M. M. Lewis, X. Huang, and M. L. Latash, "Changes in multifinger interaction and coordination in Parkinson's disease," *Journal of Neurophysiology*, vol. 108, no. 3, pp. 915–924, Aug. 2012, publisher: American Physiological Society.

[4] P. Raghavan, E. Petra, J. W. Krakauer, and A. M. Gordon, "Patterns of Impairment in Digit Independence After Subcortical Stroke," *Journal of Neurophysiology*, vol. 95, no. 1, pp. 369–378, Jan. 2006, publisher: American Physiological Society.

[5] V. M. Zatsiorsky, Z.-M. Li, and M. L. Latash, "Coordinated force production in multi-finger tasks: finger interaction and neural network modeling," *Biological Cybernetics*, vol. 79, no. 2, pp. 139–150, Aug. 1998.

[6] J. Xu, N. Ejaz, B. Hertler, M. Branscheidt, M. Widmer, A. V. Faria, M. D. Harran, J. C. Cortes, N. Kim, P. A. Celnik, T. Kitago, A. R. Luft, J. W. Krakauer, and J. Diedrichsen, "Separable systems for recovery of finger strength and control after stroke," *Journal of Neurophysiology*, vol. 118, no. 2, pp. 1151–1163, Aug. 2017.

[7] E. T. Wolbrecht, J. B. Rowe, V. Chan, M. L. Ingemanson, S. C. Cramer, and D. J. Reinkensmeyer, "Finger strength, individuation, and their interaction: Relationship to hand function and corticospinal tract injury after stroke," *Clinical Neurophysiology*, vol. 129, no. 4, pp. 797–808, Apr. 2018.

[8] H. Taheri, J. B. Rowe, D. Gardner, V. Chan, D. J. Reinkensmeyer, and E. T. Wolbrecht, "Robot-assisted Guitar Hero for finger rehabilitation after stroke," in *2012 Annual International Conference of the IEEE Engineering in Medicine and Biology Society*, Aug. 2012, pp. 3911–3917, iSSN: 1558-4615.

[9] H. Taheri, J. B. Rowe, D. Gardner, V. Chan, K. Gray, C. Bower, D. J. Reinkensmeyer, and E. T. Wolbrecht, "Design and preliminary evaluation of the FINGER rehabilitation robot: controlling challenge and quantifying finger individuation during musical computer game play," *Journal of NeuroEngineering and Rehabilitation*, vol. 11, p. 10, Feb. 2014.

[10] V. M. Zatsiorsky, Z.-M. Li, and M. L. Latash, "Enslaving effects in multi-finger force production," *Experimental Brain Research*, vol. 131, no. 2, pp. 187–195, Mar. 2000.

[11] L. Dovat, O. Lambercy, B. Salman, V. Johnson, T. Milner, R. Gassert, E. Burdet, and T. C. Leong, "A technique to train finger coordination and independence after stroke," *Disability and Rehabilitation. Assistive Technology*, vol. 5, no. 4, pp. 279–287, Jul. 2010.

[12] W. S. Yu, H. van Duinen, and S. C. Gandevia, "Limits to the Control of the Human Thumb and Fingers in Flexion and Extension," *Journal of Neurophysiology*, vol. 103, no. 1, pp. 278–289, Jan. 2010, publisher: American Physiological Society.

[13] K. O. Thielbar, T. J. Lord, H. C. Fischer, E. C. Lazzaro, K. C. Barth, M. E. Stoykov, K. M. Triandafilou, and D. G. Kamper, "Training finger individuation with a mechatronic-virtual reality system leads to improved fine motor control post-stroke," *Journal of NeuroEngineering and Rehabilitation*, vol. 11, p. 171, Dec. 2014.

[14] C. E. Lang and M. H. Schieber, "Differential impairment of individuated finger movements in humans after damage to the motor cortex or the corticospinal tract," *Journal of Neurophysiology*, vol. 90, no. 2, pp. 1160–1170, Aug. 2003.

[15] K. Sanei and P. J. Keir, "Independence and control of the fingers depend on direction and contraction mode," *Human Movement Science*, vol. 32, no. 3, pp. 457–471, Jun. 2013.

[16] N. Ejaz, J. Xu, M. Branscheidt, B. Hertler, H. Schambra, M. Widmer, A. V. Faria, M. Harran, J. C. Cortes, N. Kim, T. Kitago, P. A. Celnik, A. Luft, J. W. Krakauer, and J. Diedrichsen, "Finger recruitment patterns during mirror movements suggest two systems for hand recovery after stroke," Apr. 2017, pages: 129510 Section: New Results.

[17] F. Mawase, K. Cherry-Allen, J. Xu, M. Anaya, S. Uehara, and P. Celnik, "Pushing the Rehabilitation Boundaries: Hand Motor Impairment Can Be Reduced in Chronic Stroke," *Neurorehabilitation and Neural Repair*, vol. 34, no. 8, pp. 733–745, Aug. 2020, publisher: SAGE Publications Inc STM.

[18] J. Kilmarx, E. Oblak, J. Sulzer, and J. Lewis-Peacock, "Towards a common template for neural reinforcement of finger individuation," *Scientific Reports*, vol. 11, no. 1, p. 1065, Jan. 2021, number: 1 Publisher: Nature Publishing Group.

[19] K. T. Reilly and G. R. Hammond, "Independence of force production by digits of the human hand," *Neuroscience Letters*, vol. 290, no. 1, pp. 53–56, Aug. 2000.

[20] T. K. Koo and M. Y. Li, "A Guideline of Selecting and Reporting Intraclass Correlation Coefficients for Reliability Research," *Journal of Chiropractic Medicine*, vol. 15, no. 2, pp. 155–163, Jun. 2016.

[21] P. Schober, C. Boer, and L. A. Schwarte, "Correlation Coefficients: Appropriate Use and Interpretation," *Anesthesia & Analgesia*, vol. 126, no. 5, p. 1763, May 2018.

[22] D. W. J. Hosmer, S. Lemeshow, and R. X. Sturdivant, "Assessing the Fit of the Model," in *Applied Logistic Regression*. John Wiley & Sons, Ltd, 2013, pp. 153–225, section: 5.

[23] G. Kamara, O. Rajchert, D. Solomonow-Avnon, and F. Mawase, "Generalization indicates asymmetric and interactive control networks for multi-finger dexterous movements," *Cell Reports*, vol. 42, no. 3, Mar. 2023, publisher: Elsevier.

[24] J. Xu, T. Ma, S. Kumar, K. Olds, J. Brown, J. Carducci, A. Forrence, and J. Krakauer, "Loss of finger control complexity and intrusion of flexor biases are dissociable in finger individuation impairment after stroke," *bioRxiv*, p. 2023.08.29.555444, Aug. 2023.

[25] J. Xu, F. Mawase, and M. H. Schieber, "Evolution, biomechanics, and neurobiology converge to explain selective finger motor control," *Physiological Reviews*, vol. 104, no. 3, pp. 983–1020, Jul. 2024, publisher: American Physiological Society.

The Impact of Phase Variable Accuracy on Continuous Controller Performance for Knee-ankle Prostheses: A Case Study

David J. Kelly and Patrick M. Wensing

***Abstract*— Robust and effective control algorithms are essential for advancing powered lower-limb prostheses from laboratory settings to broader commercial use. Continuous controllers, which estimate an individual's gait progression to determine desired joint actuator outputs, have recently shown great promise. However, their success relies on accurately estimating the individual's progression through the gait cycle to ensure proper actuator behavior. This study introduces an improved method for computing gait cycle progression using only the global sagittal thigh angle for a knee-ankle prosthesis user, and explores how the accuracy of gait progression estimation impacts controller performance. Two controllers were tested with the original and improved gait cycle estimation algorithm: a joint-level impedance controller and a task-level center of mass controller, extended to the knee-ankle configuration herein. Experiments were conducted with an individual without amputation walking on a knee-ankle prosthesis. Higher linearity in gait estimation (R^2=0.984 vs. R^2=0.980) using the improved method resulted in lower shank velocity (>25%), better symmetry of shank velocity (∼75%), and lower impact into the mechanical hardstop during knee extension in swing for the impedance controller.**

I. Introduction

Over the past decades, there has been an increased effort on the design [1] and control [2] of powered lower-limb prostheses in the research community. This effort has focused on the common goal of improving the performance and capabilities of these powered devices such that they may be made available for commercial use for individuals with lower-limb amputation (LLA).

While there have been recent improvements in design [1] and performance capabilities [3] of powered prostheses, powered knee-ankle prostheses are not yet commercially available. Appropriate control of these devices remains an open research topic to demonstrate clinically significant outcomes to push these devices beyond the laboratory [4]. However, several control methodologies have shown promising outcomes for further progress towards daily use.

A control methodology that has been successfully implemented pairs finite state machines with impedance control [5]. The gait cycle is segmented into discrete phases (e.g., early stance, late stance, early swing, late swing), each with their own set of control parameters for actuator output, and switching conditions handled by sensor data. A downside of finite state machines, however, is the parameter explosion dilemma [6]. For each activity mode, each discrete phase uses its own control parameters and switching conditions, which take time and expertise to tune to the user [5], [7].

This work was funded through the NSF CAREER Grant, award ID CMMI-1943703.

Authors are with the Department of Aerospace and Mechanical Engineering, University of Notre Dame

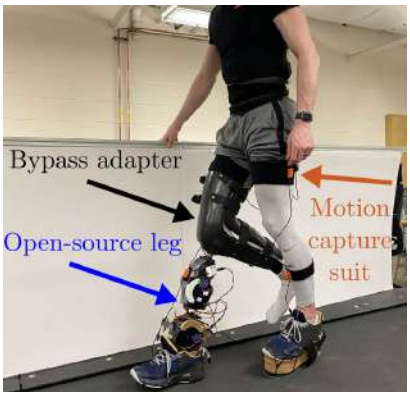


Fig. 1. Visualization of the hardware setup used for the case study. The individual donned a bypass adapter to walk on the Open Source knee-ankle prosthesis, while wearing an Xsens motion capture suit.

Beyond discrete parameter sets and switching conditions, many continuous controllers have also shown promising outcomes. Complementary limb motion estimation combined joint kinematics of the sound limb with a model of inter-leg coordination to continuously determine prosthetic-side actuation [8]. Impedance controllers have defined parameters (joint equilibrium angle, stiffness, and damping) as continuous trajectories [9], which aligns with experimental observations of joints behaving like variable impedance systems [2]. Data-driven approaches to explicitly mimic normative joint kinematics [10], kinetics [9], or both [11], have been used to generate these reference trajectories, either through hand-tuning [10] or optimization methods [11]. A recent task-space control (TSC) framework from the authors demonstrated that reference trajectories for desired center of mass (CoM) kinematics and ground reaction forces (GRFs) could be used to calculate desired joint torques continuously throughout the stance phase for ankle prostheses [12].

The reference trajectories for these controllers are typically defined with respect to the gait cycle, which is estimated using phase variables [2], [13]. The measurable characteristics used for phase variables must result in monotonic progression. For ankle prostheses, the phase portrait of the global sagittal shank angle and shank angular velocity [14] provided robust tracking for level-ground walking [9], [12]. Shank-based methods are less suitable for knee-ankle control however, since the user no longer directly controls the shank.

For knee-ankle control, thigh-based methods have been implemented with varying success [11], [15], [16]. Similar phase portraits have been attempted using the global sagittal thigh angle in combination with either thigh angular velocity [17] or the integral of the thigh angle [18]. However the velocity-based portrait is not monotonic without appropriate

filtering, and the integral-based method drifts without very accurate integration. To remove reliance on temporal factors, phase has been estimated directly from the global sagittal thigh angle using piecewise equations based on different sections of the thigh angle profile [11], [15]. The first implementation of this method (see Sec. II-A.1 for more details) did not account for the fact that the thigh angle retracts prior to heel strike, which led to early saturation of phase estimation [15]. A more recent implementation of this method addressed these issues by introducing a more granular subsectioning of the thigh angle profile, along with a feedforward phase progression when thigh angular velocity was low [11].

This work is inspired by the improvements for thigh-based phase estimation in [11], and looks to investigate extending the methodology used in [15] to avoid incorporating reliance on temporal sensitivities. More specifically, the main contribution of this work is a phase variable for level-ground walking based purely on global sagittal thigh angle progression. The phase variable from [15] is extended to consider maximum thigh flexion near the end of the gait cycle to mitigate early phase saturation without introducing reliance on feedforward or temporal parameters. A secondary contribution is the extension of the TSC framework in [12] for knee-ankle control. The rest of this paper is organized as follows. The phase variable from [15], and the proposed phase variable in this work are defined. The two continuous controllers of interest, an impedance controller and the TSC controller extended to knee-ankle control, are briefly outlined. Results from testing with an individual without amputation (Fig. 1) are presented, followed by discussion.

II. Methods

In this section, two thigh-based phase variables of interest are first defined in Sec. II-A. The two continuous controllers that test the effectiveness of the phase variables are briefly outlined in Sec. II-B. For this work, the global sagittal thigh angle is measured with respect to the vertical, with flexion representing the positive direction.

A. Phase Variable Design

As previously noted, this work draws inspiration from the thigh-based phase variables used in [11] and [15]. To build the piecewise-continuous phase variables, it is important to understand the general thigh angle profile during level ground walking. As illustrated in Fig. 2, the thigh initially starts in a flexed (positive angle) position in front of the individual at heel strike, denoted by θ_{HS}. The individual then vaults over their leg as the thigh progresses towards maximum extension, θ_{ME}. The thigh then moves towards maximum flexion, θ_{MF}, during swing, before retracting back slightly right before the next contact event.

1) Two-piece Phase Variable: The work in [15] assumed that the thigh angle profile was composed of two monotonic sections, separated based on θ_{HS} and θ_{ME}. The phase variable ϕ_{orig} for estimating gait progression was then defined using the following piecewise-continuous equation

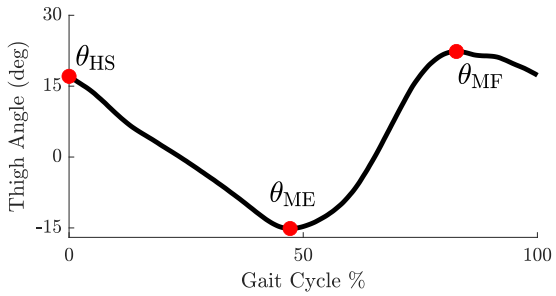


Fig. 2. Global sagittal thigh angle profile over the gait cycle for level-ground walking. Points denoted θ_{HS} (heel strike), θ_{ME} (max extension), and θ_{MF} (max flexion) are key parameters used for phase estimation.

$$\phi_{\mathrm{orig}} = \begin{cases} \frac{\theta_{\mathrm{HS}}-\theta}{\theta_{\mathrm{HS}}-\theta_{\mathrm{ME}}}\phi_{\mathrm{ME}} & \theta_{\mathrm{HS}} \rightarrow \theta_{\mathrm{ME}} \\ 1+(1-\phi_{\mathrm{ME}})\frac{\theta-\theta_{\mathrm{HS}}}{\theta_{\mathrm{HS}}-\theta_{\mathrm{ME}}} & \theta_{\mathrm{ME}} \rightarrow {\theta_{\mathrm{HS}}}^{+} \end{cases}, \quad (1)$$

where θ is the current thigh angle, ϕ_{ME} is the expected progression at θ_{ME} ($\sim$55% [19]), and ${\theta_{\mathrm{HS}}}^{+}$ denotes heel strike of the next gait cycle. Note that a slight change in this work is the use of ϕ_{ME} in the first part of the equation, while [15] used a tunable parameter based on toe-off.

Since initial values for θ_{HS} and θ_{ME} may not align with real-time measurements, these values are updated online at the end of each gait cycle. For each gait cycle, θ_{HS} is determined at ground contact, while θ_{ME} is found when a minimum thigh value is detected. Using the past three gait cycles, the value for θ_{HS} used in (1) is the average value of θ_{HS} for the past three gait cycles, while θ_{ME} is the maximum value (smallest thigh extension) to avoid divergent behaviors that would cause the user to take longer and longer strides.

2) Three-piece Phase Variable: The formulation for calculating ϕ_{orig} above ignores the fact that the thigh flexes beyond θ_{HS}, and retracts back towards θ_{HS} prior to heel strike. The proposed phase variable ϕ_{ours} extends the methodology described above to include considerations of this retraction period by segmenting the thigh angle profile into three monotonic sections. The first section is still defined between θ_{HS} and θ_{ME}. The second section for ϕ_{ours} progresses from θ_{ME} to θ_{MF}, while the third section accounts for θ_{MF} to ${\theta_{\mathrm{HS}}}^{+}$. The phase variable ϕ_{ours} for estimating gait progression was then defined by the piecewise-continuous equation

$$\phi_{\mathrm{ours}} = \begin{cases} \frac{\theta_{\mathrm{HS}}-\theta}{\theta_{\mathrm{HS}}-\theta_{\mathrm{ME}}}\phi_{\mathrm{ME}} & \theta_{\mathrm{HS}} \rightarrow \theta_{\mathrm{ME}} \\ \phi_{\mathrm{ME}}+(\phi_{\mathrm{MF}}-\phi_{\mathrm{ME}})\frac{\theta-\theta_{\mathrm{ME}}}{\theta_{\mathrm{MF}}-\theta_{\mathrm{ME}}} & \theta_{\mathrm{ME}} \rightarrow \theta_{\mathrm{MF}} \\ 1+(1-\phi_{\mathrm{MF}})\frac{\theta_{\mathrm{HS}}-\theta_{\mathrm{MF}}}{\theta-\theta_{\mathrm{HS}}} & \theta_{\mathrm{MF}} \rightarrow {\theta_{\mathrm{HS}}}^{+} \end{cases}, \quad (2)$$

where ϕ_{MF} is the expected progression at maximum flexion ($\sim$80% [19]). In this formulation, the parameters θ_{HS}, θ_{ME}, and θ_{MF} were updated following the same methodology used in [11]. The values for these parameters were recorded from the previous five gait cycles, with θ_{HS} calculated as the average of the median three values, and θ_{ME} and θ_{MF} determined as the average of the maximum and minimum three values, respectively. Offline analysis confirmed that the

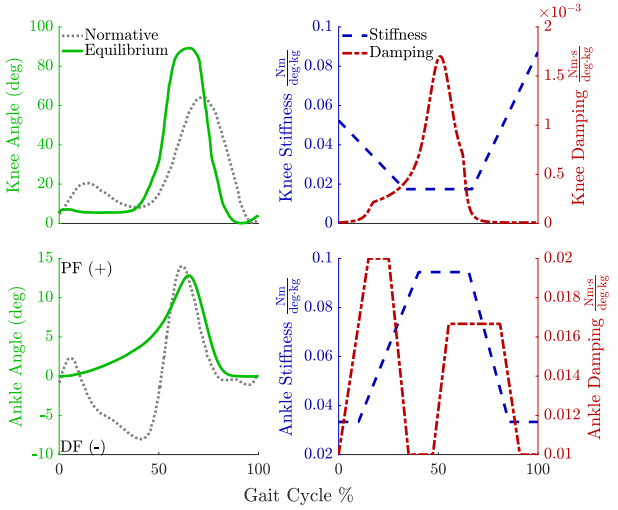


Fig. 3. Impedance parameter trajectories for the impedance controller (top: knee, bottom: ankle). PF denotes plantar flexion, DF denots dorsiflexion.

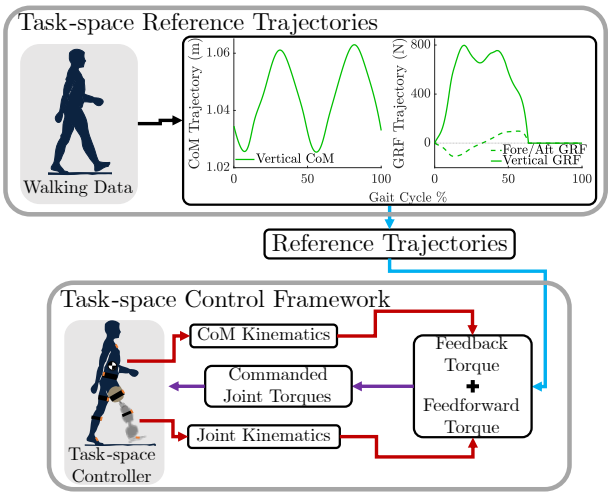


Fig. 4. High-level overview of the TSC framework. Reference trajectories for the CoM kinematics and GRFs are generated offline. Online, the reference trajectories are used in conjunction with real-time motion capture data to determine desired feedforward and feedback joint torques.

different methods for averaging θ_{HS} and θ_{ME} between ϕ_{orig} and ϕ_{ours} did not significantly change phase estimation.

B. Continuous Controllers

To test the efficacy of the two phase variables previously defined, two continuous frameworks were built for control of a knee-ankle prosthesis. The first controller uses an impedance framework to control the prosthesis, while the second controller extends the task-level framework implemented in [12] from ankle-only to knee-ankle control. Note that since the prosthesis used in this work can only be controlled in the sagittal plane, all joint angles are with respect to the sagittal plane. Likewise, all TSC references are defined in the fore/aft and vertical directions.

1) Phase-based Impedance Controller: As previously noted, continuous impedance controllers require reference trajectories to command the appropriate joint torque. For the ankle joint, these reference trajectories are the same as used in [9], [12]. The equilibrium angle, stiffness, and damping trajectories are illustrated in Fig. 3, and manually tuned to replicate a normative ankle torque profile [20]. Note that the equilibrium references do not directly match the normative trajectories in order to properly generate torque.

For the knee joint, the stiffness and damping trajectories are based on [11] for level-ground walking (Fig. 3). Note that the impedance parameters in [11] are only defined for the stance phase since a position controller is used during swing. Therefore, the stiffness and damping trajectories during swing are manually tuned to ensure proper knee flexion for ground clearance, as well as proper knee extension to prepare for weight acceptance at the end of swing. Similarly, the equilibrium angle is designed to ensure weight support during stance and proper knee flexion during swing.

The commanded joint torques $\boldsymbol{\tau}_{\text{I}}$ are then calculated by $\boldsymbol{\tau}_{\text{I}} = \mathbf{K}_{\text{I}}(\boldsymbol{\theta}_{\text{I}} - \boldsymbol{\theta}_{\text{J}}) - \mathbf{B}_{\text{I}}\dot{\boldsymbol{\theta}}_{\text{J}}$, where $\boldsymbol{\theta}_{\text{I}}$, $\mathbf{K}_{\text{I}}$, and $\mathbf{B}_{\text{I}}$ are the joint equilibrium angles, joint stiffnesses, and joint damping matrices, and $\boldsymbol{\theta}_{\text{J}}$ and $\dot{\boldsymbol{\theta}}_{\text{J}}$ are the measured joint kinematics.

2) Task-space Controller: For sake of brevity, a high-level description of TSC is provided here, along with a visual in Fig. 4. The reader is referred to [12] for full details on TSC.

While the impedance controller uses reference joint impedance trajectories to calculate desired joint torques, TSC uses reference system-level trajectories, in this case CoM kinematics and GRF profiles. This methodology aligns with previous research that suggests system-level characteristics may govern observed joint-level responses to balance recovery [21] and natural stride-to-stride variations [22].

These reference trajectories are generated by normalizing able-bodied CoM kinematics [23] by easily measurable parameters (e.g., height and stride duration). For a particular user, these kinematics are then rescaled by that individual's values for those measurable parameters. A custom-built optimization framework then fits the dynamics of human walking template models to the rescaled CoM kinematics, which yields the desired CoM and GRF profiles [24]. This trajectory generation is illustrated at the top of Fig. 4.

The reference trajectories are used in tandem with an Xsens motion capture suit [25] online to determine desired joint torques. The leg on the amputation side is modeled as a three-link system (thigh, shank, foot) with a fixed base at the pelvis, assuming negligible effect from external forces. The reference GRFs $\mathbf{F}$ are converted into feedforward joint torques $\boldsymbol{\tau}_{\text{FF}}$ via the Jacobian $\mathbf{J}$ of the three-link model

$$\boldsymbol{\tau}_{\text{FF}} = \mathbf{S}_{\text{FF}}\mathbf{J}^{\top}\mathbf{F} \tag{3}$$

Note that this formulation calculates torques for the hip, knee, and ankle, though only the knee and ankle components are used via the selector $\mathbf{S}_{\text{FF}} = [0\ \ 1\ \ 0; 0\ \ 0\ \ 1]^{\top}$.

The residual between the reference and real-time CoM kinematics (reference minus real-time), $\boldsymbol{\Delta}_{\text{com}}$, is used for a feedback force correction term. The resulting feedback joint torques on each joint are determined using

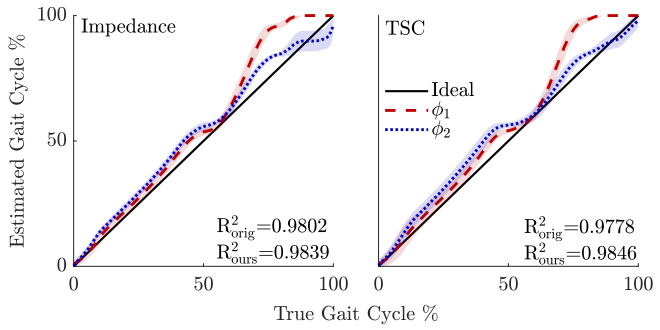


Fig. 5. Average phase estimation throughout the gait cycle for each controller (left: impedance, right: TSC) based on estimation method. An 'ideal' estimation line is included, along with the R^2 linearity values.

$$\begin{aligned} \tau_{\mathrm{FB},i} &= \mathbf{S}_{\mathrm{FB},i}\mathbf{J}^\top(\mathbf{K}_i\boldsymbol{\Delta}_{\mathrm{com}}) - D\dot{\theta}_{\mathrm{J},i} \\ \mathbf{K}_i &= \frac{mg}{H}\boldsymbol{\alpha}_i \end{aligned} \tag{4}$$

where $\mathbf{K}_i$ converts $\boldsymbol{\Delta}_{\mathrm{com}}$ into a force correction term, $D = 8.0\,\mathrm{Nm}\cdot\mathrm{deg/s}$ is a heuristically tuned joint velocity feedback gain, m and H are the mass (kg) and height (m) of the user, g is gravitational acceleration (m/s^2), and $i \in \{\mathrm{knee}, \mathrm{ank}\}$. The matrices $\boldsymbol{\alpha}_{\mathrm{knee}} = \mathrm{diag}([0.1\ \ 13])$ and $\boldsymbol{\alpha}_{\mathrm{ank}} = \mathrm{diag}([0.1\ \ 50])$ each tune the CoM gains for the knee and ankle, respectively. The gains D and $\boldsymbol{\alpha}_i$ do not change across users. The selectors $\mathbf{S}_{\mathrm{FB,knee}} = [0\ 1\ 0]^\top$ and $\mathbf{S}_{\mathrm{FB,ank}} = [0\ 0\ 1]^\top$ choose the appropriate joint torque based off corresponding feedback gains. The feedback joint torques are then $\boldsymbol{\tau}_{\mathrm{FB}} = [\tau_{\mathrm{FB,knee}}\ \ \tau_{\mathrm{FB,ank}}]^\top$.

The feedforward and feedback joint torques are additively combined such that the overall desired joint torques $\boldsymbol{\tau}_{\mathrm{T}} = \boldsymbol{\tau}_{\mathrm{FF}} + \boldsymbol{\tau}_{\mathrm{FB}}$. Since $\boldsymbol{\tau}_{\mathrm{FF}}$ requires GRFs, $\boldsymbol{\tau}_{\mathrm{T}}$ is only active during the stance phase, while $\boldsymbol{\tau}_{\mathrm{I}}$ is active during swing. To ensure continuity between $\boldsymbol{\tau}_{\mathrm{T}}$ and $\boldsymbol{\tau}_{\mathrm{I}}$, a transition torque $\boldsymbol{\tau}^*$ is calculated during the last 7.5% of stance,

$$\begin{aligned} \boldsymbol{\tau}^* &= C_1\boldsymbol{\tau}_{\mathrm{I}} + (1 - C_1)\boldsymbol{\tau}_{\mathrm{T}} \\ C_1 &= \max\left(\min\left(\frac{\phi_i - \phi_{\mathrm{TO}} + 7.5\%}{7.5\%}, 1\right), 0\right) \end{aligned} \tag{5}$$

where C_1 is the weight factor, ϕ_i is the estimated phase variable using either of the methods previously defined, and ϕ_{TO} is the expected phase value at toe-off based on the optimized reference trajectories (typically ∼63%).

C. Hardware

Trials were conducted on the Open Source Leg (OSL) V1 [1] actuated by a Dephy ActPack motor V0.2B [26]. An Xsens MVN Link inertial motion capture suit streamed real-time CoM and lower-limb kinematics at 240Hz using the lower-body plus sternum configuration [25], while two pressure sensors (SEN-08685; SparkFun Electronics) at the heel and toe of the prosthetic foot provided contact estimation. A Raspberry Pi 4 microcomputer handled data reception and code execution. The pressure sensors and motor were wired directly to the Pi, while Xsens data was wirelessly streamed over IP and UDP protocol on a private network using the Xsens Analyze software. Real-time kinematics experimentally ran at ∼210Hz, while data for post-trial analysis was collected at ∼105Hz using the Lightweight Communications and Marshalling library [27]. The individual donned a bypass adapter for the knee-ankle configuration of the OSL, visualized in Fig. 1.

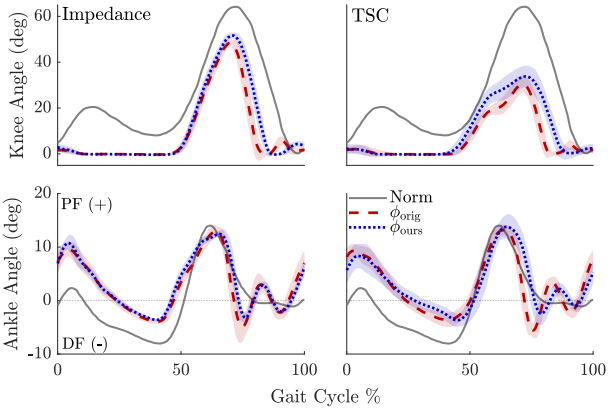


Fig. 6. Average joint progression (top: knee, bottom: ankle) for each controller (left: impedance, right: TSC) based on phase estimation method. Normative kinematics are included for reference [20].

Trials were conducted with an individual without amputation (Male, 28 yrs, 75 kg). Before testing, the Xsens suit IMUs were attached according to the Xsens Link manual, and IMU calibration was conducted as outlined in the Xsens Analyze software protocol [25]. After calibration, the individual acclimated to each continuous controller and phase variable. The individual then walked on the impedance controller with ϕ_{orig} then ϕ_{ours}, then walked using TSC mode with ϕ_{orig} and ϕ_{ours} for a total of four trials. Each trial consisted of walking on a treadmill at 0.7 m/s for 60 seconds, resulting in at least 32 continuous walking strides.

III. Results

A. Phase Estimation

The average phase estimation for each trial is visualized in Fig. 5. For both controllers, ϕ_{orig} saturated to 100% gait cycle early (∼80%) as expected. The first half of the gait cycle was very similar between ϕ_{orig} and ϕ_{ours}, since both methods used the same piecewise function during that time. However, ϕ_{ours} did not saturate early due to the additional piecewise function for thigh retraction. For each gait cycle within a trial (32-35 cycles), the linearity of the phase estimation was calculated. For each controller type, a two-sample t-test was conducted to compare the linearity of the phase estimations. Higher linearity ($p<0.001$) was achieved when using ϕ_{ours} compared to ϕ_{orig} for both controller types.

B. Lower-limb Kinematics

The average sagittal knee and ankle progression for all tested configurations is provided in Fig. 6. The knee kinematics generated using the TSC framework qualitatively match trends for the impedance controller during level-ground walking, however the peak flexion is ∼20° less

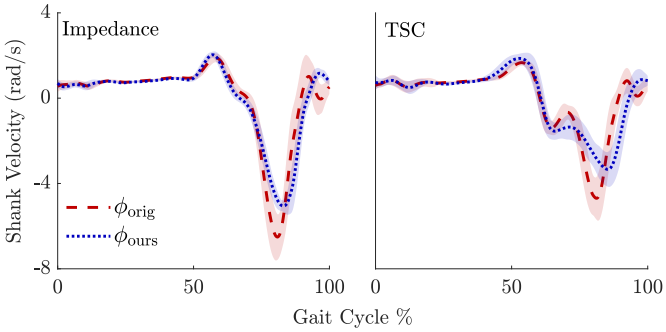


Fig. 7. Average shank angular velocity of the prosthesis for each controller and phase estimation method. Gait cycle starts at heel strike.

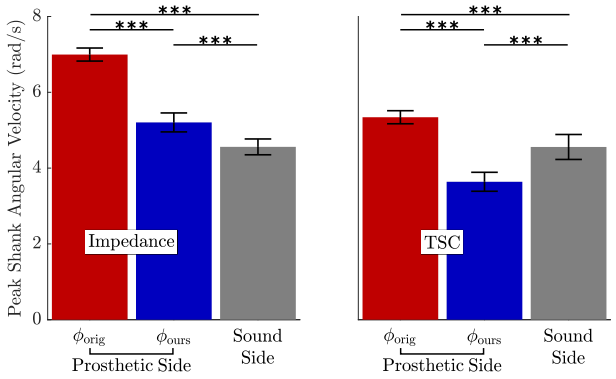


Fig. 8. Average peak shank angular velocity for contralateral shank and each controller (left: impedance, right: TSC) based on phase-estimation method. Asterisks denote statistical significance (***p<0.0005).

than the impedance controller. For each gait cycle, peak knee flexion was recorded for TSC mode using both phase estimation methods. A two-sample t-test showed that using ϕ_{ours} achieved larger flexion compared to ϕ_{orig} (p<0.001).

The angular velocity of the shank was analyzed to investigate why the knee joint hit its mechanical hardstop with higher velocity during the swing phase with ϕ_{orig}, causing some discomfort for the individual. The differences in angular velocity of the shank are shown in Fig. 7, where the peak (minimum) velocity of the shank is on average larger (more negative) when using ϕ_{orig} (7.00 rad/s and 5.34 rad/s for impedance and TSC respectively compared to ϕ_{ours} (5.21 rad/s and 3.64 rad/s for impedance and TSC respectively). For each trial, the peak angular velocity of the shank was recorded for each gait cycle. For each controller type, a two-sample t-test showed statistically significant differences between each phase estimation method (p<0.001).

Fig. 8 compares the average peak shank angular velocity for each trial. While neither estimation method led to strong agreement with the peak shank velocity between prosthetic and contralateral side for either controller (two-sample t-test p<0.0001), the peaks were lower and better aligned for ϕ_{ours} compared to ϕ_{orig}.

IV. Discussion

A. Phase Estimation

Both phase estimation methods used the same calculation through the first $\sim 55\%$ of the gait cycle, which resulted in very similar behavior (Fig. 5). However, accounting for θ_{MF} in ϕ_{ours} eliminated the early saturation seen using ϕ_{orig}, resulting in closer matching to the ideal case of a perfect linear progression using ϕ_{ours}. While ϕ_{ours} saw larger variation during the thigh retraction period, this did not translate to larger variation in joint kinematics during that portion of the gait cycle. This larger variation is because ϕ_{orig} is consistently at 100% during this time.

An interesting consequence of accounting for θ_{MF} in gait estimation is the reliance on thigh retraction prior to ground contact. While θ_{MF} does exist across multiple locomotion modes (e.g., stair ascent/descent, ramp ascent/descent) [19], the timing within the gait cycle does significantly change, such that future work will need to consider updating ϕ_{ME} and ϕ_{MF} based on activity mode or walking speed [19].

B. Lower-limb Kinematics

Extending the TSC framework to knee-ankle control showed promising results. Without any explicit joint characteristics defined in the framework, knee and ankle kinematics were qualitatively similar to those generated by the impedance controller. Compared to normative characteristics [20], early stance lacks knee flexion for both controllers, which may be due to the moment applied to the knee joint locking the joint to its hardstop. The lower knee flexion for TSC may be due to the transition torque between the stance and swing control modes. Increasing flexion is important for future trials to avoid fall risk from foot scuffing.

It is important to note that for each controller, only the phase estimation method changed between trials. The reference trajectories remained the exact same to isolate the impact that phase estimation accuracy has on overall controller performance. Some changes in joint progression did occur when phase estimation diverged. Most notably, for both controllers, the ϕ_{orig} method resulted in earlier knee extension, moreso with TSC than the impedance controller (Fig. 6). However, viewing these joint trajectories without context, there are no discernible characteristics that would suggest one phase method was more favorable than another.

Both visually and in terms of the sound of the prosthesis, the accompanying video highlights the performance impact of the slightly early knee extension in Fig. 6. When using ϕ_{orig} for phase estimation, the early saturation leads to the wrong impedance or task-space parameters being commanded to the motor at the wrong time in the gait cycle, which causes aggressive knee rotation into the mechanical hardstop and oscillations in the prosthetic side limb, which do not occur when using ϕ_{ours}. Removing the saturation with ϕ_{ours} resulted in lower peak shank velocity (Fig. 7 and Fig. 8), leading to improved shank velocity symmetry between the prosthetic side and the contralateral side compared to the controllers using ϕ_{orig}.

C. Limitations

The statistical strength of the results is limited by the lack of subject diversity. Individuals with amputation can experience muscle atrophy and adapt compensatory movements

[28], which impact overall biomechanics such as the presence and magnitude of θ_{MF}. If θ_{MF} is not present, then ϕ_{ours} may not achieve adequate gait progression, which can cause the controller to not achieve appropriate knee extension for the next heel strike. Future work is focused on individuals with amputation across level-ground walking and stair navigation to investigate the efficacy of the ϕ_{ours} and to improve the statistical significance of the outcomes.

The current implementation of the TSC framework uses a motion capture suit to estimate CoM and lower-limb kinematics. Future implementations of this framework may consider simplifying the sensor suite to IMUs attached to the prosthesis, and a single IMU attached to the pelvis.

V. Conclusion

In conclusion, we presented a new proposed phase variable based on the global sagittal thigh angle profile during level-ground walking, which extended a previously existing phase estimation method to account for thigh retraction. It was demonstrated that accounting for thigh retraction improved the linearity of the phase variable and mitigated early saturation. This phase variable was tested on a knee-ankle prosthesis using a continuous impedance controller and a task-space control framework. The improvements in phase estimation significantly impacted controller performance, including less aggressive shank velocity during the knee extension phase of swing. This work also demonstrated that the TSC framework can be extended to knee-ankle control, which will focus future subject trials for level-ground and stair navigation.

References

[1] A. F. Azocar, L. M. Mooney, J.-F. Duval, A. M. Simon, L. J. Hargrove, and E. J. Rouse, "Design and clinical implementation of an open-source bionic leg," *Nature biomedical engineering*, vol. 4, no. 10, pp. 941–953, 2020.

[2] R. Gehlhar, M. Tucker, A. J. Young, and A. D. Ames, "A review of current state-of-the-art control methods for lower-limb powered prostheses," *Annual reviews in control*, vol. 55, pp. 142–164, 2023.

[3] K. Yang, M. Dickens, J. Schmiedeler, and E. Bolívar-Nieto, "Extending the benefits of parallel elasticity across multiple actuation tasks: A geometric and optimization-based approach," *arXiv preprint arXiv:2409.08889*, 2024.

[4] V. G. Kooiman, E. S. van Staveren, R. A. Leijendekkers, J. H. Buurke, N. Verdonschot, E. C. Prinsen, and V. Weerdesteyn, "Testing and evaluation of lower limb prosthesis prototypes in people with a transfemoral amputation: a scoping review on research protocols," *Journal of neuroengineering and rehabilitation*, vol. 20, no. 1, p. 1, 2023.

[5] R. R. Posh, J. P. Schmiedeler, and P. M. Wensing, "Finite-state impedance and direct myoelectric control for robotic ankle prostheses: Comparing their performance and exploring their combination," *IEEE Transactions on Neural Systems and Rehabilitation Engineering*, vol. 31, pp. 2778–2788, 2023.

[6] F. Sup, H. A. Varol, and M. Goldfarb, "Upslope walking with a powered knee and ankle prosthesis: initial results with an amputee subject," *IEEE transactions on neural systems and rehabilitation engineering*, vol. 19, no. 1, pp. 71–78, 2010.

[7] A. M. Simon, K. A. Ingraham, N. P. Fey, S. B. Finucane, R. D. Lipschutz, A. J. Young, and L. J. Hargrove, "Configuring a powered knee and ankle prosthesis for transfemoral amputees within five specific ambulation modes," *PloS one*, vol. 9, no. 6, p. e99387, 2014.

[8] H. Vallery, R. Burgkart, C. Hartmann, J. Mitternacht, R. Riener, and M. Buss, "Complementary limb motion estimation for the control of active knee prostheses," 2011.

[9] R. R. Posh, J. A. Tittle, D. J. Kelly, J. P. Schmiedeler, and P. M. Wensing, "Hybrid volitional control of a robotic transtibial prosthesis using a phase variable impedance controller," in *IEEE International Conference on Robotics and Automation (to appear)*, 2024.

[10] W. Hong, V. Paredes, K. Chao, S. Patrick, and P. Hur, "Consolidated control framework to control a powered transfemoral prosthesis over inclined terrain conditions," in *2019 International Conference on Robotics and Automation (ICRA)*. IEEE, 2019, pp. 2838–2844.

[11] T. K. Best, C. G. Welker, E. J. Rouse, and R. D. Gregg, "Data-driven variable impedance control of a powered knee–ankle prosthesis for adaptive speed and incline walking," *IEEE Transactions on Robotics*, 2023.

[12] D. J. Kelly, R. R. Posh, and P. M. Wensing, "Task-space control of a powered ankle prosthesis," in *2024 IEEE International Conference on Robotics and Automation (ICRA)*. IEEE, 2024, pp. 3262–3268.

[13] D. J. Villarreal and R. D. Gregg, "A survey of phase variable candidates of human locomotion," in *2014 36th Annual international conference of the ieee engineering in medicine and biology society*. IEEE, 2014, pp. 4017–4021.

[14] M. A. Holgate, A. W. Bohler, and T. G. Suga, "Control algorithms for ankle robots: A reflection on the state-of-the-art and presentation of two novel algorithms," in *2008 2nd IEEE RAS & EMBS international conference on biomedical robotics and biomechatronics*. IEEE, 2008, pp. 97–102.

[15] S. Rezazadeh, D. Quintero, N. Divekar, E. Reznick, L. Gray, and R. D. Gregg, "A phase variable approach for improved rhythmic and non-rhythmic control of a powered knee-ankle prosthesis," *IEEE Access*, vol. 7, pp. 109 840–109 855, 2019.

[16] W. Hong, N. A. Kumar, and P. Hur, "A phase-shifting based human gait phase estimation for powered transfemoral prostheses," *IEEE Robotics and Automation Letters*, vol. 6, no. 3, pp. 5113–5120, 2021.

[17] D. Quintero, D. J. Lambert, D. J. Villarreal, and R. D. Gregg, "Real-time continuous gait phase and speed estimation from a single sensor," in *2017 IEEE Conference on Control Technology and Applications (CCTA)*. IEEE, 2017, pp. 847–852.

[18] X. Tan, B. Zhang, G. Liu, X. Zhao, and Y. Zhao, "Phase variable based recognition of human locomotor activities across diverse gait patterns," *IEEE Transactions on Human-Machine Systems*, vol. 51, no. 6, pp. 684–695, 2021.

[19] S. Cheng, E. Bolívar-Nieto, and R. D. Gregg, "Real-time activity recognition with instantaneous characteristic features of thigh kinematics," *IEEE Transactions on Neural Systems and Rehabilitation Engineering*, vol. 29, pp. 1827–1837, 2021.

[20] D. A. Winter, *Biomechanics and motor control of human movement*. John Wiley & Sons, 2009.

[21] S. A. Safavynia and L. H. Ting, "Long-latency muscle activity reflects continuous, delayed sensorimotor feedback of task-level and not joint-level error," *Journal of neurophysiology*, vol. 110, no. 6, pp. 1278–1290, 2013.

[22] M. E. Toney and Y.-H. Chang, "Humans robustly adhere to dynamic walking principles by harnessing motor abundance to control forces," *Experimental brain research*, vol. 231, pp. 433–443, 2013.

[23] C. A. Fukuchi, R. K. Fukuchi, and M. Duarte, "A public dataset of overground and treadmill walking kinematics and kinetics in healthy individuals," *PeerJ*, vol. 6, p. e4640, 2018.

[24] D. J. Kelly and P. M. Wensing, "Center of mass kinematic reconstruction during steady-state walking using optimized template models," *PloS one*, (to appear).

[25] D. Roetenberg, H. Luinge, P. Slycke *et al.*, "Xsens mvn: Full 6dof human motion tracking using miniature inertial sensors," *Xsens Motion Technologies BV, Tech. Rep*, vol. 1, pp. 1–7, 2009.

[26] J.-F. Duval and H. M. Herr, "Flexsea: flexible, scalable electronics architecture for wearable robotic applications," in *2016 6th IEEE International Conference on Biomedical Robotics and Biomechatronics (BioRob)*. IEEE, 2016, pp. 1236–1241.

[27] A. S. Huang, E. Olson, and D. C. Moore, "Lcm: Lightweight communications and marshalling," in *2010 IEEE/RSJ International Conference on Intelligent Robots and Systems*. IEEE, 2010, pp. 4057–4062.

[28] M. Finco, S. Kim, W. Ngo, and R. A. Menegaz, "A review of musculoskeletal adaptations in individuals following major lower-limb amputation," *Journal of Musculoskeletal & Neuronal Interactions*, vol. 22, no. 2, p. 269, 2022.

Closed-Loop Control of Large Assistive Torques to Unknown External Loads via a Back Support Exoskeleton

Lorenzo Sterzi[1,2], Mohamed Irfan Refai[1,†*], and Massimo Sartori[1*]

***Abstract*— Most control strategies for active back-support exoskeletons (BSEs) do not target users' internal forces while providing assistance, limiting synergy with the user. In our previous study, we proposed a neuromechanical model-based controller (NMBC) that directly targeted lumbosacral (L5/S1) active moments. Despite promising results, the use of a soft exosuit limited the maximum assistance possible, leaving unclear whether increased assistance would have more benefits for the user. Therefore, in this study, we adapted the NMBC to provide assistance via an active rigid BSE and were able to provide higher assistive torques, up to 114.5Nm. We tested three support levels (20%, 50%, 80% of estimated active L5 / S1 moments) provided to three participants lifting two loads (5kg, 15kg) and two lifting techniques (stoop, squat) and compared it with transparent mode (MINIMP) and without exoskeleton (NOEXO). All assisted conditions significantly reduced L5/S1 moments compared to NOEXO, despite the BSE being heavy. A general trend towards reduced effort was observed with higher gains, although, not statistically significant. However, large assistive torques also caused deteriorated torque tracking and instabilities. The system adapted to unknown loads for both techniques. This study demonstrated for the first time the feasibility of using NMBC with larger support gains, highlighting both its potential benefits and challenges.**

***Index Terms*— adaptive support, EMG-driven musculoskeletal model, large assistance, rigid back exoskeletons.**

I. Introduction

Low back pain (LBP) is a prevalent occupational health issue, with an incidence 45% higher in jobs involving manual handling of heavy loads compared to other occupations [1]. The compression forces experienced by the back spine during repetitive lifting cycles can achieve considerable values, increasing injury risk or accelerating degeneration of spinal elements [2]. This process plays a key role in the onset of chronic LBP [3].

In the last few decades, back support exoskeletons (BSEs) have been developed for occupational use to reduce strain on back muscles during manual handling tasks. Passive BSEs utilize elastic components to support the user. Research has demonstrated the significant potential of these devices to reduce back muscle activation during lifting cycles [4], [5]. Furthermore, reductions in mean lumbosacral (L5/S1) joint moments and spinal compression forces have been reported, ranging from 6% to 12% and 5% to 14% respectively[6], [7]. However, their inability to adapt to variations in task dynamics and external loads limit their effectiveness in real-world scenarios.

Active BSEs provide greater control over assistance profiles throughout the lifting cycle and generate larger assistive torques by integrating actuators with advanced controllers. They typically consist of a pelvis module with hip rotational actuators, thigh cuffs, and, in most cases, a thoracic harness [4], [7]. Some designs, however, utilize pneumatic actuators [8]. The median maximal assistance for active BSEs reported in the literature is approximately 72 Nm, compared to 20 Nm for passive ones[4], [5], [7]. Thanks to their higher assistance, active BSEs have a greater impact on user biomechanics than passive ones, achieving greater reductions in muscle activity [4]. Significant reductions in peak compression forces (17.7% on average) and L5/S1 joint moments (11.9% on average) were also reported compared to a no-exoskeleton condition [9]. A key factor in active BSEs effectiveness is selecting a control strategy that ensures synergy with the user's movements. Most control strategies rely on motion-based information, typically using predefined torque profiles [8], [10]. However, these systems often lack adaptability, providing the same assistance regardless of the weight being lifted. To address this limitation, some studies have proposed incorporating electromyographic (EMG) measurements into the control loop to detect movement onset and adapt assistance to different lifting conditions [8]. In these systems, the assistance is directly proportional to the muscle activity. However, since muscle forces depend on the dynamics of muscular contraction, EMG signals or joint angles alone are insufficient to tailor assistance to the user's needs, limiting the synergy with the user [11].

Moya-Esteban et al. (2023) [12] proposed a neuromechanical model-based controller (NMBC) for an active soft exosuit. This controller aimed to exploit model-estimated back muscle moments for support, accounting for the non-linear relationship between EMG signals and biological forces. It used a real-time EMG-driven musculoskeletal model to estimate the active component of L5/S1 joint moments (M_a^{L5S1}). The estimated M_a^{L5S1} was then scaled by a support gain and used to compute the desired assistive force, which was delivered by two linear actuators via force transmission cables. The NMBC significantly reduced mean EMG activity (5kg: 14.4%, 15kg: 25.2%), L5/S1 joint moments (5kg: 18.3%, 15kg: 23.9%), and compressive forces (5kg: 12.1%, 15kg: 16.8%) compared to not wearing the exosuit during stoop lifting. The exosuit design also prevented the use of squat as a lifting technique. The support gain was limited to

(*) equal contribution

This work was supported by Horizon Europe RIA (Grant No. 101120408; S.W.A.G.) and by the ERC Consolidator Grant ROBOREACTOR (Grant No. 101123866)

[1]Department of Biomechanical Engineering, University of Twente, The Netherlands, [2]Department of Information Engineering, Università degli Studi di Padova, Padova, Italy, †Correspondence: m.i.mohamedrefai@utwente.nl

20% due to mechanical constraints, restricting the maximum support provided. Higher assistance is expected to induce greater biomechanical reductions, but EMG fluctuations may be amplified causing large, unwanted torque fluctuations.

The main goal of this work was to evaluate whether increasing the support gain could enhance the biomechanical load reduction observed in our previous work [12]. To achieve this, we used a rigid active BSE, as soft exosuits are unable to provide large assistances. The study included both squat and stoop lifting techniques to investigate the NMBC's adaptability to different external loads. This research aims to identify the potential benefits of higher assistive torques on user biomechanics while exploring the associated challenges.

II. Methods

A. Exoskeleton used

A rigid active BSE (weight: 16.5kg) was used in this study. The BSE was developed by the University of Twente (UT) and Delft University of Technology and consisted of a C-shaped rigid frame with 4 series elastic actuators (Bacchus V3, TU Delft), one aligned with the L2-L3 joint and one with the hip on each side. The BSE was attached to the user using an adjustable thorax vest (Laevo FLEX, Laevo, the Netherlands) and two bilateral thigh rigid cuffs. The lumbar actuators were mechanically fixed at an angle of -13° relative to the vertical human axis. The maximum torque of the hip actuators was limited to 60 Nm each for safety. The actuators included torque sensors and encoders to measure joint angles, communicating with a basestation at 1 kHz over EtherCAT, interfacing through TwinCAT 3 (Beckhoff Automation, Verl, Germany). The basestation consisted of a Beckhoff C6025-0000 Industrial PC (Core i5-8365UE 1.6GHz CPU, 8GB of RMA, Windows 10).

B. User instrumentation

EMG signals from back and abdominal muscles were recorded at 1 kHz using 8 Ottobock 13E400 bipolar surface EMG electrodes (Ottobock SE&Co. KGaA, Duderstadt, Germany) following the indications reported in [6]. Raw EMG signals were bandpass filtered (30–300 Hz), rectified and low-pass filtered (3Hz) with 2nd order Butterworth online filters to obtain EMG linear envelopes. Joint angles were recorded at 60Hz using MVN Link inertial motion capture system (Movella, Enschede, The Netherlands). The sensors were placed and calibrated following the manufacturer's guidelines for "Upper Body No Hands" configuration. Both joint angles and EMG linear envelopes were transmitted over Automation Device Specification (ADS) communication protocol to Calibrated EMG-informed neuromusculoskeletal real-time (CEINMS-RT) modeling toolbox [13], where the neuromechanical model was implemented (see section II-C). Within CEINMS-RT, EMG were normalized on maximum voluntary contraction (MVC) values, recorded with isometric contraction tasks for each participant. Before using the system, the model was scaled and calibrated to user-specific biomechanics (see section II-C). To scale the model and compute inverse dynamics (ID) reference moments, the positions of 36 reflective markers on participants' bony landmarks and one on the box's upper edge were recorded. A 12-camera Qualisys motion capture system (Qualisys Medical AB, Sweden) captured the data at 100Hz.

C. Real-time EMG-driven musculoskeletal modeling

A simplified version of the OpenSim lifting full-body model [6] was scaled on each participant geometry using 3D marker data from a static recording (see section II-B) and OpenSim 4.1. The scaled models were then used to build real-time EMG-driven musculoskeletal models, using CEINMS-RT [13] toolbox as described in [12], to estimate user-specific M_a^{L5S1}. Aiming at supporting active muscles' effort, only the active components – i.e., contribution of muscles' contractile element – of the MTU forces were estimated during the model execution. The tendon in the Hill-type MTU model was represented as an infinitely stiff element with a length equal to the slack length. To reduce noise amplification introduced by the derivation of inertial measurement unit (IMU)-recorded joint angles, the force-velocity relationship was neglected. Estimation accuracy was reduced in favor of smoother torque profiles for control purposes. In view of the aforementioned changes, M_a^{L5S1} during model execution was computed as follows:

$$M_a^{L5S1}(t) = \sum_{k=1}^{164} r_k F_k^{mt}(t) \tag{1}$$

where the summation over k spans the 164 MTUs included in the model, r_k is the MTU moment arm over L5/S1 joint, $F_k^{mt}(t)$ the MTU force computed with the following formula:

$$F_k^{mt}(t) = F_{o,k}^m f_a(\bar{l}_k^m(t)) a_k(t) \cos(\phi_k(t)) \tag{2}$$

where $F_{o,k}^m$ is the maximum isometric force, $\bar{l}_k^m$ is the muscle fiber length normalized on the optimal fiber length, a_k is the muscle activation, $f_a(\bar{l}_k^m)$ is the active length-force relationship and ϕ_k is the pennation angle.

For each participant, to obtain a user-specific EMG-driven model F_o^m, tendon slack length coefficient, optimal fiber length and activation dynamic shape factor were calibrated for each MTU. Simulated annealing [14] was used as optimization algorithm, minimizing the summed squared error between reference ID L5/S1 moments and model estimated ones, comprehensive of both active and passive components. The calibration algorithm used EMG signals, L5/S1 joint angles and ID L5/S1 moments of one repetition for each lifting task (see section II-E). ID was performed using OpenSim 4.1 based on IMU-recorded joint angles. The L5/S1 flexion-extension range of motion (ROM) in MVN software differed significantly from OpenSim model. MVN modeled the lumbar spine with 2 segments and 3 joints, while OpenSim accounted for all lumbar vertebrae, making intermediate lumbar joint angles linearly dependent on L5/S1. Therefore, L5/S1 flexion-extension angles were renormalized

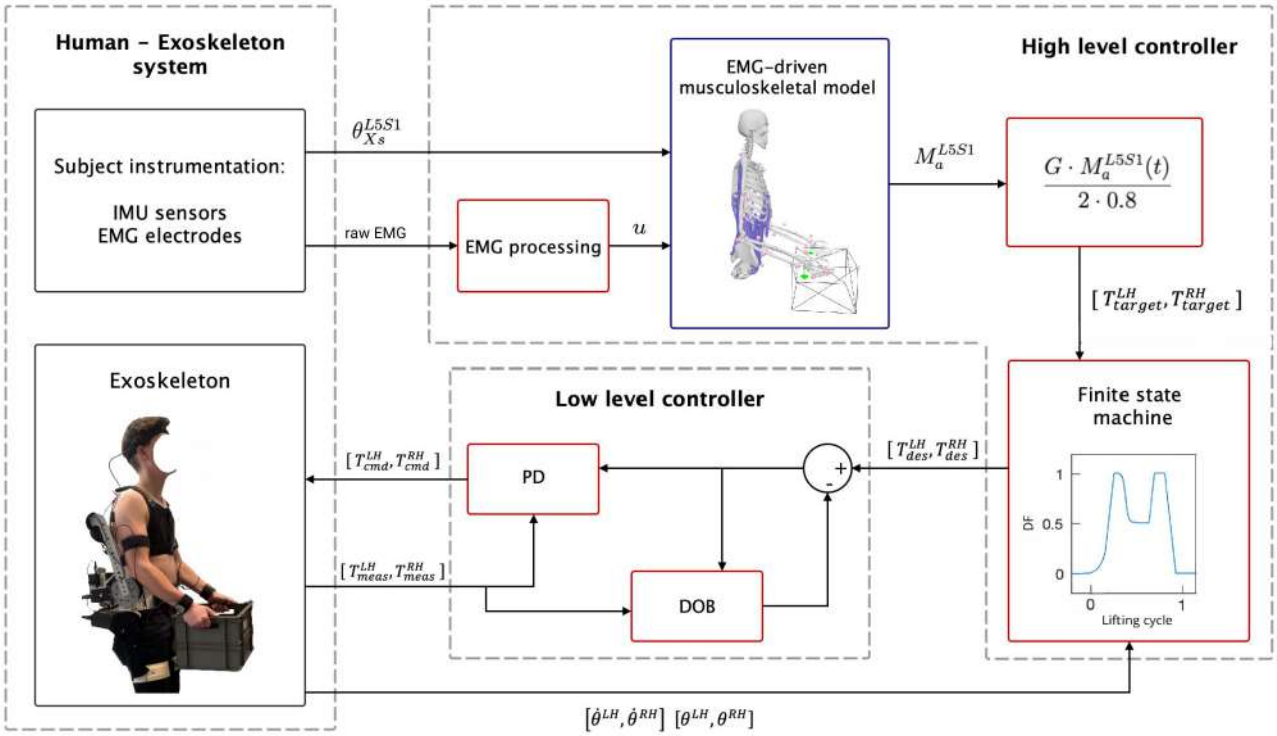


Fig. 1. Schematic diagram of the low-level and high-level controllers used to control the BSE. Blue blocks are executed in CEINMS-RT [13], red blocks are executed in TwinCAT 3. Target torque (T_{target}), desired torque (T_{des}) and command torque (T_{cmd}) are computed for both actuators (left hip (LH), right hip (RH)) in parallel. T_{meas} is the torque measured by the actuators' spring encoders. θ and $\dot{\theta}$ are the actuator's joint angle and velocity respectively.

to match the OpenSim ROM. Gravitational forces acting on participants' hands were added manually to compute ID by calculating the magnitude based on the known load. By tracking the box marker's acceleration, we determined when participants lifted it and the timing of force application. Once optimal internal parameters values were identified, the EMG-driven models were used in open-loop to predict M_a^{L5S1} as a function of measured EMG and IMU data.

D. Neuromechanical model based controller (NMBC)

The control scheme included high-level and low-level controllers (Fig. 1). The low-level controller [15], consisted of an inner loop proportional-derivative (PD) controller and an outer loop disturbance observer (DOB). It regulated torque output at each actuator, tracking a reference torque (T_{des}) set by the high-level controller. Measured torque (T_{meas}) at each actuator was fed back to close the control loop.

The high-level controller, i.e., the NMBC, can be divided into three main stages (Fig. 1). In the first stage, the real-time EMG-driven model estimated M_a^{L5S1}. In the second stage, M_a^{L5S1} was multiplied by a support gain (G), manually set to tune the level of assistance, and divided by a lumbar/hip support ratio fixed to 80%. This value aligned with the physiological ratio of muscle moments at the lumbar and hip levels during lifting tasks [16]. The resulting torque was then equally split between the left and the right hip actuators obtaining a target torque for each one (T_{target}). In the third stage, T_{target} is multiplied by a dynamic factor (DF) tuned by a finite state machine (FSM) to modulate T_{des} at each actuator. The FSM was implemented to minimize interference with the user's movements, particularly during bending, when the assistive torques - always acting against gravity - could otherwise prevent the user from reaching the box to be lifted.

The FSM states were defined as follows:

1) Upright static posture with no weight: DF $= 0$ (no support), ensuring unrestricted movement before lifting;
2) Flexion and static flexed posture without weight: DF exponentially increasing, capped at 1, allowing smooth engagement of assistance;
3) Extension: DF $= 1$ (maximum support), providing full assistance when the user lifts the load;
4) Static weight holding: DF is dynamically modulated, decreasing according to a sigmoid to $0.1/G$, preventing excessive assistance when simply holding the weight;
5) Flexion with weight: DF $= 0.1/G$, ensuring minimal resistance during bending with the load;
6) Static flexed posture while releasing weight: DF exponentially increasing, capped at 1, ensuring a gradual transition back to full support after the weight is released.

The NMBC was implemented in Simulink (MathWorks) and executed in real-time on the basestation in TwinCAT 3 at 1 kHz. CEINMS-RT [13] transmitted the estimated M_a^{L5S1} to TwinCAT 3 via ADS communication protocol.

E. Experimental protocol

The study involved three participants with no history of LBP, aged 23.3 ± 0.6 years, with a body weight of 66.3 ± 8.4 kg, and a height of 1.72 ± 0.05 m. All participants provided their explicit written consent to participate in the study and the experimental protocol was approved by the ethical committee of UT (reference: 240059). The experiment design included 4 lifting tasks of a box (width x depth x height: 40 x 30 x 22 cm) from a 52.2cm high table, given by the combination of two loading conditions (5kg, 15kg) and two lifting techniques (squat and stoop). Each participant was asked to join both a model calibration session and a measurement session. In the former, EMG signals, joint angles and markers' trajectories were measured in one static trial and one dynamic trial for each lifting task to perform model calibration. In the latter, participants performed the four lifting tasks without the exoskeleton (NOEXO), wearing the exoskeleton in transparent mode (MINIMP) and with three increasing support gains – 20% (S20), 50% (S50) and 80% (S80) - for a total of 20 trials, 5 repetitions each. Before the measurement trials, the participants familiarized with the exoskeleton for 15 minutes. All conditions were randomized. To control the speed at which the movement was performed and the timing of each repetition, a metronome at 35 beats-per-minute indicated the start of each stage of the lifting cycle. Participants rested for 2 minutes between trials to minimize fatigue.

F. Data analysis

We assessed NMBC's ability to reduce user effort with large assistive torques by computing mean M_a^{L5S1} normalized to the participant's body weight across the box-lifting stages (mean L5/S1 AM_Ext) for all support conditions, participants and lifting tasks. Each repetition was divided into 12 time-segments (8.33% of the lifting cycle each), with three segments corresponding to a complete movement, from upright to fully flexed posture and back with and without load (similar to [6]). Mean L5/S1 AM_Ext was computed on segments 4 and 5, excluding segment 6, corresponding to near-upright standing. This phase is of high interest as the peak of assistance is expected; the muscles must develop high forces to counteract the effect of gravity [6]. Mean L5/S1 AM_Ext was averaged across the five repetitions of each trial. To evaluate the controller's ability to provide large assistive torques while increasing the support gain and adapt to unknown external loads, maximum sum of the actuators' T_{meas} across the whole lifting cycle (max assistance) was analyzed by plotting its distribution across repetitions of each trial. To assess NMBC's performance in controlling large assistive torques, we computed the root mean square error (RMSE) between T_{des} and T_{meas} across the whole lifting cycle, normalized by T_{des} peak value (TTR RMSE).

G. Statistical analysis

To statistically assess variations in mean L5/S1 AM_Ext and max assistance, a mixed effect model was created with "subject" as random factor, and "lifting task" and "support condition" as fixed factors. Residuals' normality and homoscedasticity were then assessed via Shapiro-Wilk and Breusch-Pagan tests, respectively. Model assumptions were not met for max assistance; therefore, a two-way ANOVA was applied only to mean L5/S1 AM_Ext. Since no significant interaction effect was found, Tukey's multiple comparisons test was used on each fixed factor to identify differences between support conditions and between lifting tasks.

III. Results

A. Torque tracking and controller performance

Considering all lifting tasks and participants, our controller exhibited a TTR RMSE ranging from 14.4 ± 3.3% (subject 2, squat, 15kg) to 39.3 ± 1.5% (subject 2, stoop, 5kg, S80). The average TTR RMSE across all trials associated with the same assisted condition increased with higher support gains (S20: 23.4 ± 6.7%, S50: 26.7 ± 5.7%, S80: 32.1 ± 5.8%). No evident differences were observed in torque tracking between participants that could be attributed to user-specific characteristics or the lifting task. The real-time EMG-driven musculoskeletal model introduced an average time delay of 45.5 ± 38.8 ms across participants, while T_{target} and T_{des} computations added a delay of 76.8 ± 24.7 ms.

B. Maximum assistance provided

Fig. 2 shows the distribution of the maximum assistive torque provided to the user by the exoskeleton actuators throughout the entire lifting cycle (max assistance) for each assisted condition, participant, and lifting task. The mean max assistance across repetitions increased while increasing the support gain for all participants and lifting tasks. The mean percentage variation (MPV) across participants was more pronounced between S20 and S50 (stoop 5kg: 65.5 ± 39.6%, squat 5kg: 67.2 ± 23.1%, stoop 15kg: 65.2 ± 37.4%, squat 15kg: 67.6 ± 40.6%) compared to S50 and S80 conditions (stoop 5kg: 15.1 ± 4.4%, squat 5kg: 19.3 ± 5.3%, stoop 15kg: 14.8 ± 14.7%, squat 15kg: 10.9 ± 3.2%). The max assistance distribution shifted upward for 15 kg tasks compared to 5 kg tasks across all assisted conditions and participants, with an average increase in the distribution mean of 30.1 ± 17.3%. Shapiro-Wilk and Breusch-Pagan tests showed non-normality ($p < 0.01$) and heteroscedasticity ($p < 0.01$) of the mixed model residuals, precluding the use of a two-way ANOVA. The highest max assistance value was recorded in subject 1 during the S80 stoop 15kg trial (114.5Nm).

C. Reduction in L5/S1 moments while wearing the exoskeleton

Fig. 3 reports differences in model-estimated M_a^{L5S1} profiles under the 5 support conditions for a representative participant. Data were averaged across the 5 repetitions of each trial and refer to a squat lifting task with a 5 kg load. During the 4th and 5th time segments (see section II-F), a reduction in M_a^{L5S1} was observed in the assisted conditions (S20, S50, S80) compared to both MINIMP and NOEXO

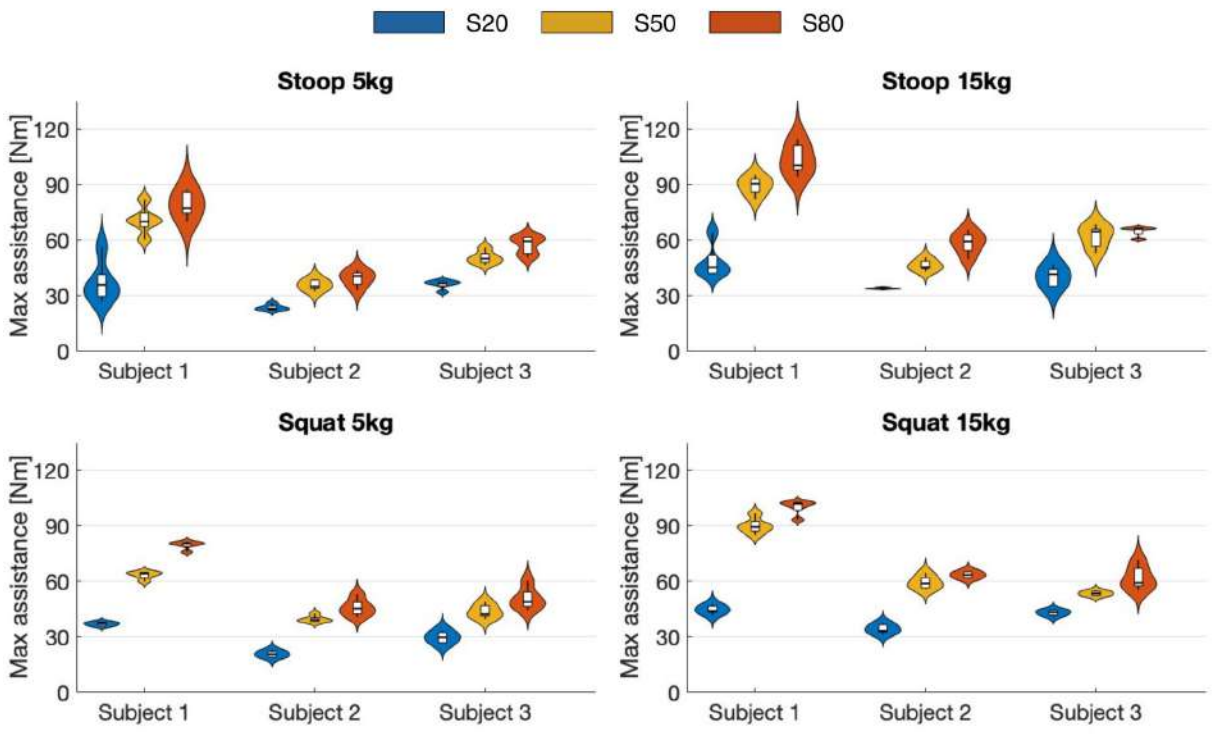


Fig. 2. Violin and box plot distributions across the 5 repetitions of each trial of the measured peak assistive torque (Nm) throughout the lifting cycle (max assistance). Each panel shows data for one lifting task, grouped by subject. The distributions for the 20% support gain condition are shown in blue, those for the 50% condition in yellow, and those for the 80% condition in red.

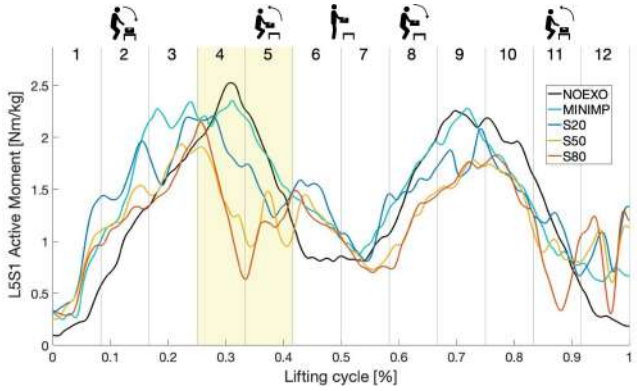


Fig. 3. Real-time model-estimated L5/S1 active moment normalized to participant's body weight (Nm/kg) across the lifting cycle. Data are referred to subject 1 squat 5kg trials: NOEXO (black), MINIMP (light blue), S20 (dark blue), S50 (yellow), S80 (red) conditions. Vertical lines divide the lifting cycle into 12 time segments. Highlighted segments show the instants across which mean L5/S1 AM_Ext was computed (time segments 4 and 5).

conditions based on visual inspection. 2-way ANOVA on mean L5/S1 AM_Ext showed a significant effect for both fixed factors, "support condition" ($F(4,280) = 9.16$, $p < 0.001$) and "lifting task" ($F(3,280) = 32.76$, $p < 0.001$), while their interaction was not significant ($F(12,280) = 1.58$, $p = 0.097$). Tukey's multiple comparisons test on the "support condition" factor revealed a significantly reduced mean L5/S1 AM_Ext in all assisted conditions (S20, S50, S80) compared to NOEXO condition. Similarly, S50 and S80 conditions showed a significantly reduced mean L5/S1 AM_Ext compared to MINIMP condition, while the difference between MINIMP and S20 conditions was not significant. Table I reports the absolute mean difference between the two groups being compared (MeanDiff) and its statistical significance (p-value). The honest significant difference (HSD) was 0.3115. Fig. 4 illustrates the exoskeleton-induced reduction of mean L5/S1 AM_Ext across most lifting tasks, both within participants and as a mean across participants. The MPV across participants for the MINIMP condition compared to the NOEXO condition showed a general decrease in the mean L5/S1 AM_Ext across all lifting tasks: stoop 5 kg (-13.9% ± 21.8%), squat 5 kg (-2.5% ± 21.8%), stoop 15 kg (-3.6% ± 24.7%), and squat 15 kg (-6.5% ± 15.9%). However, the large SD indicated substantial variability among participants. By visually inspecting Fig. 4, no consistent behavior was observed between participants and tasks for the MINIMP and NOEXO conditions. Table II shows Tukey's multiple comparisons test results for the "lifting task" predictor similarly to table I, with an HSD of 0.2318. Mean L5/S1 AM_Ext significantly increased in all lifting tasks with a 15kg load compared to those with a 5kg load. A significant difference between tasks using different techniques but the same load was found only between stoop lifting with 5kg and squat lifting with 5kg.

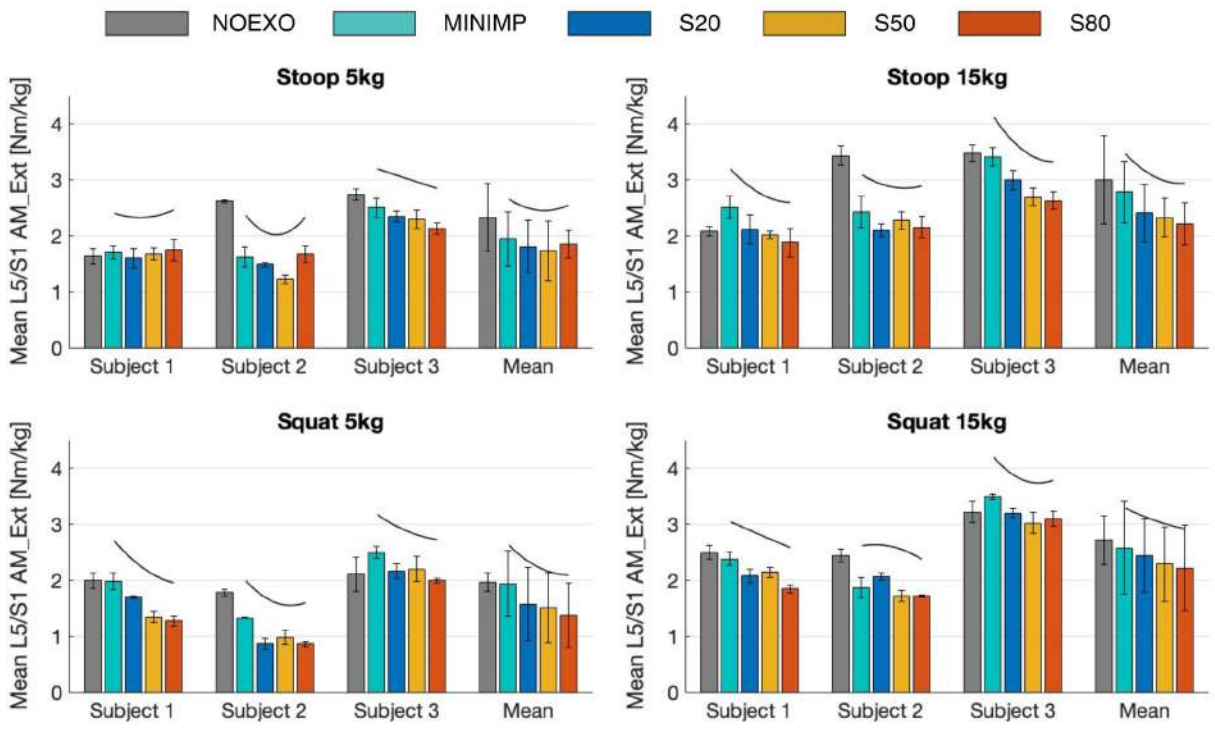


Fig. 4. Mean L5/S1 AM_Ext normalized to participants' body weight (Nm/kg). In each panel, bars are divided into four groups. The first three groups refer to each participant while the bars report the mean of mean L5/S1 AM_Ext across the 5 repetitions of each trial with the relative standard deviation (SD). The last group shows the mean values across participants with the relative error bars (SD). Second-degree polynomial fit of the MINIMP, S20, S50, S80 conditions are reported above each group (curves were shifted along the y-axis for visual purposes).

TABLE I
TUKEY'S MULTIPLE COMPARISONS TEST ON SUPPORT CONDITIONS

Group1	Group2	MeanDiff	pValue
NOEXO	MINIMP	0.1947	0.0159
NOEXO	S20	0.4460	<**0.001**
NOEXO	S50	0.5159	<**0.001**
NOEXO	S80	0.5586	<**0.001**
MINIMP	S20	0.2513	0.0019
MINIMP	S50	0.3212	<**0.001**
MINIMP	S80	0.3640	<**0.001**
S20	S50	0.0699	0.3848
S20	S80	0.1126	0.1617
S50	S80	0.0428	0.5948

TABLE II
TUKEY'S MULTIPLE COMPARISONS TEST ON LIFTING TASKS

Group1	Group2	MeanDiff	pValue
Stoop 5kg	Squat 5kg	0.2510	<**0.001**
Stoop 5kg	Stoop 15kg	0.6138	<**0.001**
Stoop 5kg	Squat 15kg	0.5103	<**0.001**
Squat 5kg	Stoop 15kg	0.8647	<**0.001**
Squat 5kg	Squat 15kg	0.7613	<**0.001**
Stoop 15kg	Squat 15kg	0.1035	0.1042

D. Effect of large support gains on L5/S1 moments

No significant differences across the different assisted conditions were found in mean L5/S1 AM_Ext (Table I). To better illustrate the general trend, a second-degree polynomial was used to fit the mean L5/S1 AM_Ext values across MINIMP and assisted conditions for each participant as well as for the mean across participants (Fig. 4). A decreasing trend in mean L5/S1 AM_Ext as the support gain increased was observed in most participants. MPV in L5/S1 AM_Ext relative to the MINIMP condition was also found to decrease while increasing the support gain in 3 lifting tasks out of 4. For the stoop 5 kg task, the mean variations were as follows: S20: -7.0 ± 1.2%, S50: -11.6 ± 11.5%, S80: -3.1 ± 10.0%. For the stoop 15 kg task, reductions were S20: -13.8 ± 1.6%, S50: -15.6 ± 8.05%, S80: -19.8 ± 7.3%. In the squat 5 kg task, the decreases were more pronounced: S20: -20.8 ± 12.0%, S50: -23.6 ± 10.6%, S80: -30.3 ± 8.9%. Finally, for the squat 15 kg task, the reductions were: S20: -3.6 ± 12.1%, S50: -10.6 ± 2.6%, and S80: -13.9 ± 7.5%. Same trend of the MPV was found in comparison with the NOEXO condition but with much higher variations. It ranged from -10.9 ± 9.1% (squat 15 kg, S20) to -31.0 ± 23.4% (squat 5 kg, S80), with an average value of -20.3 ± 19.7%. In some assisted trials, fluctuations up to 1 Nm/kg were observed during the second half of the trunk extension movement, both with and without

the lifted box, corresponding to time segments 5, 6, 11, and 12 (Fig. 3). This behavior occurred more frequently in trials involving the S50 and S80 conditions and was present across all repetitions of those trials.

IV. Discussion

In this study, we demonstrate the use of an NMBC to apply large assistance proportional to the changes in muscle forces via an active rigid BSE. We successfully increased the support gain up to 80% compared to the previous maximum of only 20% using the same methodology. All assisted conditions reduced muscle effort compared to the NOEXO condition, achieving a net reduction even with an heavy exoskeleton. This reduction was statistically significant, demonstrating for the first time that NMBC can be used with large gains. Furthermore, a decreasing trend in muscle effort with increasing support gain suggests a positive effect of higher assistive torques. However, torque tracking issues and user-exoskeleton interactions likely underestimated results, while the lack of statistical significance prevents drawing definitive conclusions on increasing assistance.

For the first time, we used an NMBC to control an active rigid BSE, adapting a previously proposed controller [12]. To achieve smooth torque profiles, the EMG-driven model was simplified by neglecting the MTU force-velocity relationship and assuming the tendon to be infinitely stiff. To ensure model accuracy, the calibration procedure was refined by using IMUs-based joint angles for computing IK and ID, consistent with the model execution. Additionally, a six-states FSM was integrated in the control loop to prevent the assistive torques from hindering the user's movements when bending. The tracking performance of the system was low, showing an average TTR RMSE of 23.4% even at the lowest support gain. The average TTR RMSE across all trials increased with higher gains, suggesting that the controller's torque tracking ability deteriorates as assistance increases. This likely contributed to the underestimation of the impact of large assistive torques on M_a^{L5S1}. The high-level controller introduced a delay of 122.3 ± 45.98 ms from EMG detection to torque generation, comparable to the physiological electromechanical delay (EMD) (80 ms) [17]. Faster contraction velocities, likely induced by large assistive torques, may have desynchronized assistive and biological moments, compromising user-exoskeleton synergy and causing the fluctuations in Fig. 3.

Despite unfavorable torque tracking performance, we were able to provide large assistive torques, as high as 114.5 Nm. We observed a clear trend of increasing maximum assistive torque as the support gain was raised, confirming the effectiveness of the system in scaling assistance accordingly. Max assistance distributions were distinctly different in most participants and lifting tasks, with no overlap between S20 and S80 in multiple cases, indicating a clear separation (Fig. 2). The larger assistance during 15kg lifting tasks compared to 5kg tasks aligns with the expected outcome. This finding demonstrates the ability of the NMBC to adapt to different external loads with no *apriori* information both for stoop and squat lifting techniques, addressing a gap in prior research [12]. Max assistance differences, observable in Fig. 2, differ across participants since the NMBC is estimated from user specific biological moments. Notably, the maximum torque limit set for the actuators (120 Nm) did not impact the results, as it was never reached during any of the trials.

For three participants, the mean L5/S1 AM_Ext was significantly reduced during the assisted conditions (S20, S50, S80) compared to the NOEXO condition, with an average decrease of 20.3% (Fig. 4). This result highlights the potential of the NMBC applied to an active rigid BSE to reduce biomechanical load during lifting tasks, despite the exoskeleton's considerable weight (16.5 kg). Mean L5/S1 AM_Ext generally decreased in MINIMP compared to NOEXO condition. This effect could be attributed to a shift of load from active to passive tissues, influenced by changes in movement kinematics. However, the difference between MINIMP and NOEXO was not statistically significant. Additionally, no consistent behavior was observed between participants and tasks strengthening the need for a user-specific approach. Lack of significant differences between the S20 and MINIMP conditions suggests that lower support gains may provide insufficient assistance to achieve a substantial reduction in biomechanical load (Table I). Higher support gains (S50, S80) reduced the MPV of mean L5/S1 AM_Ext between assisted and MINIMP conditions, with the exception of stoop 5kg S80 trials. A decreasing trend while increasing assistance, fitted by a 2nd-degree polynomial, was observed for most participants and tasks, as well as in the case of the mean across participants (Fig. 4). However, a two-way mixed-effects ANOVA followed by Tukey's post-hoc test found no significant effects of different support gains on mean L5/S1 AM_Ext, likely due to the high variability in the data. The effect of the "lifting task" predictor was significant, with heavier loads resulting in higher mean L5/S1 AM_Ext, as expected (Table II). The support conditions did not significantly interact with lifting tasks, suggesting that the exoskeleton adaptively modulated support across tasks to match biomechanical demands.

There are a few limitations to the study. The study was conducted on a small number of participants. Moreover, the duration of the experiments and weight of the exoskeleton could have introduced fatigue, which was not quantified. High TTR RMSE values, even at low support gains, suggest that the system struggled to properly track the desired torque, delivering assistive torques lower than intended. This effect may have contributed to an underestimation of the system's beneficial effects on mean L5/S1 AM_Ext. Furthermore, we used a FSM to ensure that the support was provided only during desired instances, which requires inclination information during lifting.

This study must be followed up with experiments from larger and more heterogeneous group of participants. Moreover, the potential impact of the exoskeleton support on other body parts, such as lower limbs and shoulders, should be investigated to fully assess the broader biomechanical impact of assistance. Finally, utilizing garments with embedded

sensors can help reduce the ease of use and applicability of the NMBC in real-world situations [18].

V. Conclusion

This study demonstrates the novel application of an NMBC for providing large assistive torques with an active rigid BSE. Net L5/S1 joint moment reductions were observed for three participants under assisted conditions compared to not wearing the exoskeleton, despite the heavy BSE used. Although not significant, increasing support gains (up to 80%) showed a trend toward reducing muscle effort. Additionally, the results demonstrated the system's adaptability to unknown external loads and user-specific biomechanics. However, challenges in torque tracking and user-exoskeleton interaction must be addressed to improve performance. This study highlights the feasibility of applying large assistive torques with an NMBC, providing evidence of its potential to reduce lumbar effort. These findings support the translation of BSEs into real-life occupational environments, where reducing spinal load is critical for preventing LBP.

References

[1] A. Petit and Y. Roquelaure, "Low back pain, intervertebral disc and occupational diseases," *International Journal of Occupational Safety and Ergonomics*, vol. 21, no. 1, pp. 15–19, Jan. 2, 2015.

[2] I. Kingma, G. S. Faber, and J. H. Van Dieën, "How to lift a box that is too large to fit between the knees," *Ergonomics*, vol. 53, no. 10, pp. 1228–1238, Oct. 2010.

[3] E. Johanning, "Evaluation and management of occupational low back disorders," *American Journal of Industrial Medicine*, vol. 37, no. 1, pp. 94–111, Jan. 2000.

[4] M. Schwartz, K. Desbrosses, J. Theurel, and G. Mornieux, "Biomechanical consequences of using passive and active back-support exoskeletons during different manual handling tasks," *International Journal of Environmental Research and Public Health*, vol. 20, no. 15, p. 6468, Jul. 28, 2023.

[5] M. I. Mohamed Refai, A. Moya-Esteban, L. Van Zijl, H. Van Der Kooij, and M. Sartori, "Benchmarking commercially available soft and rigid passive back exoskeletons for an industrial workplace," *Wearable Technologies*, vol. 5, e6, 2024.

[6] A. Moya-Esteban, G. Durandau, H. Van Der Kooij, and M. Sartori, "Real-time lumbosacral joint loading estimation in exoskeleton-assisted lifting conditions via electromyography-driven musculoskeletal models," *Journal of Biomechanics*, vol. 157, p. 111 727, Aug. 2023.

[7] M. Pesenti, A. Antonietti, M. Gandolla, and A. Pedrocchi, "Towards a functional performance validation standard for industrial low-back exoskeletons: State of the art review," *Sensors*, vol. 21, no. 3, p. 808, Jan. 26, 2021.

[8] S. Toxiri, M. B. Näf, M. Lazzaroni, *et al.*, "Back-support exoskeletons for occupational use: An overview of technological advances and trends," *IISE Transactions on Occupational Ergonomics and Human Factors*, vol. 7, no. 3, pp. 237–249, Oct. 2, 2019.

[9] A. S. Koopman, S. Toxiri, V. Power, *et al.*, "The effect of control strategies for an active back-support exoskeleton on spine loading and kinematics during lifting," *Journal of Biomechanics*, vol. 91, pp. 14–22, Jun. 2019.

[10] R. Govaerts, S. De Bock, S. Provyn, *et al.*, "The impact of an active and passive industrial back exoskeleton on functional performance," *Ergonomics*, vol. 67, no. 5, pp. 597–618, May 3, 2024.

[11] S. Heitmann, N. Ferns, and M. Breakspear, "Muscle co-contraction modulates damping and joint stability in a three-link biomechanical limb," *Frontiers in Neurorobotics*, vol. 5, 2012.

[12] A. Moya-Esteban, S. Sridar, M. I. M. Refai, H. van der Kooij, and M. Sartori, *Adaptive assistance with an active and soft back-support exosuit to unknown external loads via model-based estimates of internal lumbosacral moments*, 2023. arXiv: 2311.01843 [cs.RO]. [Online]. Available: https://arxiv.org/abs/2311.01843.

[13] M. Sartori, M. I. Refai, L. A. Gaudio, *et al.*, "Ceinms-rt: An open-source framework for the continuous neuro-mechanical model-based control of wearable robots," *TechRxiv*, Jan. 2025. [Online]. Available: https://doi.org/10.36227/techrxiv.173397962.28177284/v1.

[14] W. L. Goffe, G. D. Ferrier, and J. Rogers, "Global optimization of statistical functions with simulated annealing," *Journal of Econometrics*, vol. 60, no. 1, pp. 65–99, Jan. 1994.

[15] W. F. Rampeltshammer, A. Q. L. Keemink, and H. Van Der Kooij, "An improved force controller with low and passive apparent impedance for series elastic actuators," *IEEE/ASME Transactions on Mechatronics*, vol. 25, no. 3, pp. 1220–1230, Jun. 2020.

[16] S. Hwang, Y. Kim, and Y. Kim, "Lower extremity joint kinetics and lumbar curvature during squat and stoop lifting," *BMC Musculoskeletal Disorders*, vol. 10, no. 1, p. 15, Dec. 2009.

[17] A. Del Vecchio, A. Úbeda, M. Sartori, J. M. Azorín, F. Felici, and D. Farina, "Central nervous system modulates the neuromechanical delay in a broad range for the control of muscle force," *Journal of Applied Physiology*, vol. 125, no. 5, pp. 1404–1410, Nov. 1, 2018.

[18] D. Simonetti, M. Hendriks, J. Herijgers, *et al.*, "Automated spatial localization of ankle muscle sites and model-based estimation of joint torque post-stroke via a wearable sensorised leg garment," *Journal of Electromyography and Kinesiology*, vol. 72, p. 102 808, 2023, ISSN: 1050-6411.

Mitigating Compensatory Movements in Prosthesis Users via Adaptive Collaborative Robotics

Marta Lagomarsino[1], Robin Arbaud[1,2], Francesco Tassi[1], and Arash Ajoudani[1]

***Abstract*— Prosthesis users can regain partial limb functionality, however, full natural limb mobility is rarely restored, often resulting in compensatory movements that lead to discomfort, inefficiency, and long-term physical strain. To address this issue, we propose a novel human-robot collaboration framework to mitigate compensatory mechanisms in prosthesis users by exploiting their residual motion capabilities while respecting task requirements. Our approach introduces a personalised mobility model that quantifies joint-specific functional limitations and the cost of compensatory movements. This model is integrated into a constrained optimisation framework that computes optimal user postures for task performance, balancing functionality and comfort. The solution guides a collaborative robot to reconfigure the task environment, promoting effective interaction. We validated the framework using a new body-powered prosthetic device for single-finger amputation, which enhances grasping capabilities through synergistic closure with the hand but imposes wrist constraints. Initial experiments with healthy subjects wearing the prosthesis as a supernumerary finger demonstrated that a robotic assistant embedding the user-specific mobility model outperformed human partners in handover tasks, improving both the efficiency of the prosthesis user's grasp and reducing compensatory movements in functioning joints. These results highlight the potential of collaborative robots as effective workplace and caregiving assistants, promoting inclusion and better integration of prosthetic devices into daily tasks.**

***Index Terms*— Robot-aided mobility; Human-machine interfaces and robotic applications**

I. Introduction

The loss of a body limb or digit profoundly impacts an individual's physical capabilities and mental well-being. Prosthetic devices aim to mitigate these issues by restoring functionality and enabling users to regain independence in daily living and work-related activities. Prostheses can be classified into three categories: passive, body-powered, and externally powered [1]. Passive devices primarily focus on restoring appearance rather than mechanical functionality [2], however, they can still help to restore opposing grasp capabilities [3]. Body-powered devices, in contrast, utilise the motion of another muscle or limb to control the prosthesis, offering a mechanical and functional simple solution [4], [1]. Externally powered devices rely on actuators, often electric or pneumatic, to restore finer control and dexterity, albeit at the cost of increased complexity, reliance on a power source, and higher expense [5], [6]. By comparison, body-powered devices strike a balance between functionality and usability due to their simplicity and straightforward use.

Despite their benefits, prostheses remain far from replicating the full functionality of natural limbs [7]. They often impose constraints on the user's body mobility, leading to compensatory mechanisms that may involve uncomfortable non-ergonomic postures or inefficient movement patterns [8], [9]. This is especially true for body-powered systems, which by design require some muscles to control the prosthesis in addition to their normal purposes [10], [11]. Over time, these compensations can result in strain, discomfort, and even long-term physical issues. Unfortunately, such challenges are frequently overlooked in the design and assessment of prosthetic devices. To address this gap, studying how human kinematics can effectively adapt to residual impairments and prosthetic limitations provides an opportunity to enhance user comfort, efficiency, and overall experience.

Beyond individual adaptations, the environments where prosthesis users operate (such as workplaces, care facilities, and homes) can be modified to support more ergonomic and functional interactions. In this context, collaborative robots (CoBots) constitute a promising solution [12]. CoBots have demonstrated their ability to improve physical ergonomics by online adapting interaction poses [13] or optimising shared kino-dynamics in co-carrying and co-manipulation tasks [14], [15]. They have also been shown to promote cognitive ergonomics by adapting the proximity and reactivity of the CoBot to balance safety, user stress, and productivity [16]. While some initial attempts aimed at facilitating tasks for users with impairments, these approaches often focused on completely substituting the impaired limb functionality with a robotic system [17], [18] or limiting the movement of the impaired arm in Cartesian space [19]. However, such strategies overlook the nuanced needs of prosthetic users who experience joint-level and task-specific constraints. Additionally, these methods fail to exploit the residual functionality of restricted-mobility users, potentially reinforcing a sense of inability and frustration.

This work takes a novel step toward addressing these challenges by introducing a human-robot collaboration framework that supports prosthesis users in overcoming joint-level limitations and exploiting their residual motion but avoiding harmful compensatory mechanisms. We propose a model of joint-specific functional limitations of prosthesis users and quantify the cost of compensatory mechanisms in functioning joints. This model informs an optimisation problem that computes the optimal user posture for performing

This work was supported by PR FESR 2021–2027: Incentivi alle imprese per attività collaborativa di ricerca industriale e sviluppo sperimentale. Bando DGR 2026/2021. Progetto RE-FINGER: Prat. n. 2022/38.

[1]Human-Robot Interfaces and Interaction, Istituto Italiano di Tecnologia, Genoa, Italy. [2] Dept. of Informatics, Bioengineering, Robotics and System Engineering, University of Genoa, Genoa, Italy.

Corresponding author's email: marta.lagomarsino@iit.it

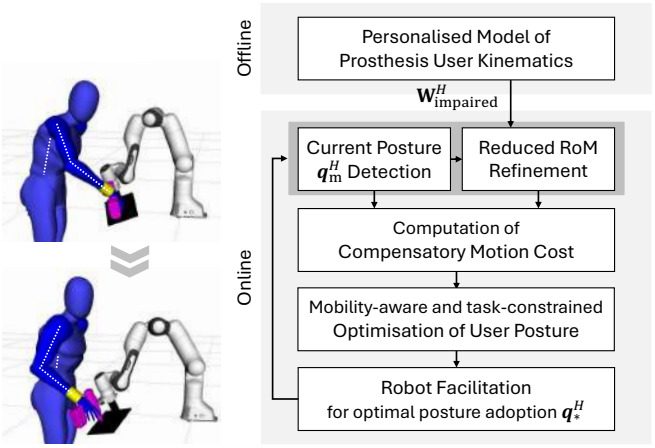


Fig. 1. Overview of the procedure to assess the mobility diversity of prosthesis users and mitigate compensatory movements while adhering to task constraints.

a collaborative task in a functional and comfortable manner, considering task constraints. The solution guides the robot to reconfigure the task environment thus promoting the adoption of the recommended posture. Finally, we present a novel body-powered prosthetic device for single-finger amputees, designed to enhance grasping capabilities through synergistic hand closure but posing constraints in wrist motion. The device serves as a testbed to validate the proposed method.

The remainder of the paper is organised as follows: Section II describes the modelling of impairments and the formulation of the optimisation problem for robot-assisted facilitation to minimise the use of joints with restricted mobility and mitigate the cost associated with compensatory mechanisms. Section III presents the experimental campaign to validate the proposed approach in handover tasks. Section IV discusses the results and outlines potential directions for future work.

II. Methods

The proposed procedure to mitigate compensatory movements in prosthesis users is outlined in Fig. 1. In the offline phase, we first model the user mobility diversity and scale a digital model to automatically match their specific body measurements. During the interaction phase, we continuously monitor the prosthesis user's posture and eventually refine the Range of Motion (RoM) based on modelled residual mobility and prosthetic limitations. Consequently, we calculate the current cost of compensatory motions, defined as the deviation of the functioning joints from a natural, comfortable posture. A constrained optimisation technique is then solved to determine a more comfortable and functional posture that still respects the user's mobility constraints and task requirements. Finally, a robot-assisted motion is planned to facilitate the adoption of such posture.

A. Prosthesis User Kinematics Model

This study models the kinematics of a prosthesis user by assigning a local coordinate frame to each joint, where the x-, y-, and z-axes define the rotation axes for abduction/adduction, flexion/extension, and internal/external rotation, respectively, as outlined in [20]. To account for arm kinematic redundancy, the arm is represented as a seven Degrees-of-Freedom (DoF) system, denoted by $\boldsymbol{q}^H \in \mathbb{R}^7$ and consists of two rigid links: the upper arm ($\boldsymbol{l}_{\text{humerus}}$) and the forearm ($\boldsymbol{l}_{\text{radius}}$) [21].

A coordinate frame is also assigned to the L5 lumbar spine vertebra to represent spine flexion through the first joint angle, q_1^H, and the link, $\boldsymbol{l}_{\text{spine}}$. This inclusion reflects the well-documented role of increased trunk motion as a compensatory mechanism in the literature [11]. The resulting model presents $M = 8$ DoFs, where size-related parameters can be adjusted to fit different arm and trunk sizes.

The shoulder is modelled as a spherical joint, providing abduction/adduction (q_2^H), flexion/extension (q_3^H), and internal/external rotation (q_4^H). The elbow consists of both a hinge and a pivot joint that allows for forearm flexion/extension (q_5^H) and pronation/supination (q_6^H). Finally, the wrist joint is represented as a condyloid joint, enabling flexion/extension (q_7^H) and ulnar/radial deviation (q_8^H) of the hand. Table I provides the Denavit-Hartenberg (DH) parameters used for this kinematic model.

TABLE I
Denavit-Hartenberg parameters of the adopted human kinematic model.

axis, i	$\boldsymbol{\theta}_i$	a_i	α_i	d_i
1	q_1^H	l^z_{spine}	$-\frac{\pi}{2}$	$-l^y_{\text{spine}}$
2	q_2^H	0	$\frac{\pi}{2}$	$-l^x_{\text{spine}}$
3	$q_3^H+\frac{\pi}{2}$	0	$\frac{\pi}{2}$	0
4	$q_4^H-\frac{\pi}{2}$	$-l^x_{\text{humerus}}$	$\frac{\pi}{2}$	$-l^z_{\text{humerus}}$
5	$q_5^H+\pi$	0	$\frac{\pi}{2}$	$-l^y_{\text{humerus}}$
6	$q_6^H+\frac{\pi}{2}$	$-l^y_{\text{radius}}$	$\frac{\pi}{2}$	$-l^z_{\text{radius}}$
7	$q_7^H+\frac{\pi}{2}$	0	$\frac{\pi}{2}$	$-l^x_{\text{radius}}$
hand	q_8^H	0	0	0

Prostheses assist users by restoring some functionality, though they may not fully replicate natural limb mobility, and can impose limitations on surrounding joints. For instance, wearing a partial hand prosthesis may pose limitations in wrist movement, which can lead to compensatory movements in the elbow and/or shoulder. To capture these constraints in the model, we define a diagonal matrix, $\mathbf{W}^H_{\text{impaired}} \in \mathbb{R}^{M\times M}$. This matrix modifies the kinematic model by prioritising movement in healthy or prosthesis-supported joints and reducing or entirely limiting mobility in impaired or blocked joints. This allows for flexibility in modelling partial or complete impairments across joints. For joints with complete functional loss, we set $\mathbf{W}^H_{\text{impaired}}(i,i) = 1$, whereas partially impaired joints are defined proportionally to reflect a preference for minimal use unless essential. In clinical practice, standardised impairment indices are used to assess joint functionality in patients with conditions such as arthritis, injuries, or neurological damage [22]. These indices can be applied to define specific joint limitations within $\mathbf{W}^H_{\text{impaired}}$, helping to personalise the kinematic model to the particular needs and abilities of each prosthesis user.

The cost $\Psi(k) \in \mathbb{R}$, quantifying the impact of compensatory mechanisms at the time instant k, is calculated as:

$$\Psi(k) = \left\| \left(\mathbf{I} - \mathbf{W}^H_{\text{impaired}}\right) \left(\boldsymbol{q}^H(k) - \boldsymbol{q}^H_{\text{n}}\right) \right\|^2, \quad (1)$$

where $\boldsymbol{q}^H_{\text{n}}$ denotes the natural posture, representing a neutral and comfortable arm configuration for the user. This cost measures the deviation of functioning joints from this natural posture. It aligns with established metrics in the literature, such as "instantaneous joints usage" or "ergonomic cost" [23], [13], but is refined here by including weights that account for the desired mobility of each joint, as defined by the matrix $\left(\mathbf{I} - \mathbf{W}^H_{\text{impaired}}\right)$. This modification provides a more precise and personalised assessment of alignment with a comfortable and functional posture, tailored to the user's specific impairments and requirements.

B. Robot Reactive Facilitation for Prosthesis Users

The objective of the robot reactive facilitation is to guide prosthesis users in performing the interactive task in a more effective way, avoiding unnatural postures adopted to compensate for constraints imposed or not fully addressed by the prosthesis. To achieve this, the robot generates movements designed to facilitate human adoption of this recommended configuration. The optimal posture minimises the usage of partially impaired joints, completely restricts motion in blocked joints, and promotes alignment of healthy null-space joints with a comfortable and functional posture throughout the interaction.

The robot reactive behaviour is formulated as an online optimisation problem that considers the user's impaired mobility, kinematic constraints, task requirements, and safety distance thresholds. The optimisation is defined by the following cost function and constraints:

$$\begin{aligned} \min_{\boldsymbol{q}^H} \; & \left\| \mathbf{W}^H_{\text{impaired}} \left(\boldsymbol{q}^H - \boldsymbol{q}^H_{\text{m}}\right) \right\|^2 + \alpha \left\| \left(\mathbf{I} - \mathbf{W}^H_{\text{impaired}}\right) \left(\boldsymbol{q}^H - \boldsymbol{q}^H_{\text{n}}\right) \right\|^2 \\ \text{s.t.} \quad & \boldsymbol{q}^H \in \left[\boldsymbol{q}^H_{\text{min,impaired}}, \boldsymbol{q}^H_{\text{max,impaired}}\right], \\ & \boldsymbol{x}_{\text{obj}}(\boldsymbol{q}^H) \in \boldsymbol{\chi}^R_{\text{task}}, \\ & p_{\text{obj}}(\boldsymbol{q}^H) = p_{\text{task}}, \\ & d^H_{\text{obj}} \geq d_{\text{safe th}}, \\ & d^H_{\text{elbow}} \geq d_{\text{elbow th}}, \end{aligned} \quad (2)$$

where $\boldsymbol{q}^H_{\text{m}}$ is the current measured human posture and $\boldsymbol{q}^H_{\text{n}}$ denotes the natural and comfortable posture for a healthy individual. In the cost function, the first term aims to minimise the deviation of fully or partially impaired joints from their current configuration. This is implemented through the matrix $\mathbf{W}^H_{\text{impaired}}$, which weights the squared distance based on the severity of each joint functional limitation, effectively prioritising the minimisation of displacement for more severely impaired joints. The second term instead minimises the cost Ψ of the compensatory mechanism, namely the squared distance of the functioning joints from the nominal most comfortable arm configuration, weighted by their desired mobility. The parameter $\alpha \in \mathbb{R}$ is a scaling factor that gives less importance to the second term. This reflects the prioritisation of maintaining the current position of impaired joints while subtly promoting the comfortable positioning of the healthy, unconstrained joints.

The optimisation constraints ensure that the joint angles $\boldsymbol{q}^H$ remain in the feasible impaired range, which is derived by reducing the standard RoM to account for user-specific impairments. For prosthesis users, this reduction is modelled by modifying the healthy joint boundaries $\boldsymbol{q}^H_{\text{min}}$ and $\boldsymbol{q}^H_{\text{max}}$ using the matrix $\mathbf{W}^H_{\text{impaired}}$, as follows:

$$\begin{aligned} \boldsymbol{q}^H_{\text{min,impaired}} &= \boldsymbol{q}^H_{\text{min}} + \mathbf{W}^H_{\text{impaired}}\big((\boldsymbol{q}^H_{\text{m}} - \zeta) - \boldsymbol{q}^H_{\text{min}}\big), \\ \boldsymbol{q}^H_{\text{max,impaired}} &= \boldsymbol{q}^H_{\text{max}} - \mathbf{W}^H_{\text{impaired}}\big(\boldsymbol{q}^H_{\text{max}} - (\boldsymbol{q}^H_{\text{m}} + \zeta)\big), \end{aligned} \quad (3)$$

where the parameter $\zeta \in \mathbb{R}$ allows small adjustments in the joint angles, even in severely impaired joints. Task-specific constraints ensure that the position $\boldsymbol{x}_{\text{obj}}$ of the object or tool, which will be in the human's hand during the interaction with the environment ($\boldsymbol{x}_{\text{obj}} = \boldsymbol{x}_{\text{obj}}(\boldsymbol{q}^H)$), is located within the task space of the robot $\boldsymbol{\chi}^R_{\text{task}}$ and satisfies task objectives. In particular, we consider the possibility of imposing an equality constraint on a specific Cartesian coordinate $p_{\text{obj}} = \{x_{\text{obj}}; y_{\text{obj}}; z_{\text{obj}}\} \in \mathbb{R}$ to match the task requirement p_{task}. Finally, the horizontal distance $d^H_{\text{obj}} \in \mathbb{R}$ between the object and the user's body must exceed a safety threshold $d_{\text{safe th}}$ and the horizontal distance d^H_{elbow} between the user's elbow and pelvis is required to exceed $d_{\text{elbow th}}$ to ensure a proper elbow pose.

C. Finger Prosthesis System

In this work, we introduce a novel body-powered finger prosthetic device specifically designed to enhance grasping for individuals with single-finger amputations, featuring a mechanical coupling mechanism that enables synergistic closure with the hand. The prosthesis features an underactuated 3-joint finger, whose motion is controlled by a single tendon. Elastic elements bring the finger back into an open position when the tendon is not actively pulled. As illustrated in Fig. 2, we built a wearable prototype around a wrist brace with a 3D-printed part attached to it. The latter holds a pulley, through which the tendon is rerouted. The other end of the tendon is attached to a ring, which the user has to wear on the finger controlling the prosthetic. Bending that finger will then pull on the tendon and bend the prosthetic. Additionally, a lead screw mechanism can be used to adjust the pretension of the tendon by changing the position of the pulley. For testing purposes, we mounted the designed prosthesis as a supernumerary finger placed near the index. This configuration allows non-impaired individuals to simulate the experience of the prosthesis users.

It is important to note that while the prosthesis enhances grasping functionality, it also imposes constraints on the wrist flexion/extension and ulnar/radial deviation. These limitations can be encoded in the $\mathbf{W}^H_{\text{impaired}}$ by setting the last two diagonal elements to 1, informing the optimisation process of the immobilised wrist.

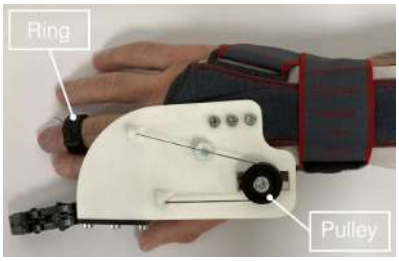


Fig. 2. Picture of the wearable prototype for testing the proposed body-powered prosthesis as a supernumerary finger.

III. Experiments

A. Experimental Setup and Protocol

Experiments were conducted with two healthy human subjects to assess the effectiveness of the proposed method in facilitating functional and comfortable interaction with a prosthetic device[1]. The participants included Subject 1, a 29-year-old male with a height of 1.83 m, and Subject 2, a 28-year-old female with a height of 1.58 m. Diverse physical profiles were deliberately chosen to validate the method ability to adapt to diverse anthropometric characteristics.

The experimental task required subjects to grasp a hotmelt glue pistol positioned at varying lateral distances from their pelvis, i.e. $y_{\text{task}} = \{0.05\text{m}; -0.20\text{m}; -0.45\text{m}\}$. To simulate a quite realistic prosthesis-user scenario, participants performed the task while wearing the proposed prosthetic device configured as a supernumerary finger (see Fig. 2). Before the task, participants underwent a familiarisation phase with the prosthesis. The setup included a table in front of the prosthesis user, marked with three tape lines indicating the potential lateral directions from which the object could be delivered. The healthy RoM was derived from the literature [24] and the nominal prosthesis user posture, $\boldsymbol{q}_{\text{n}}^{H}$, was defined as the most ergonomic posture based on the Rapid Upper Limb Assessment (RULA) Tool [25], with the elbow flexed at $90°$ and all other joint angles set to $0°$. The parameters were set as follows: $\alpha = 0.10$, $\zeta = 5°$, $d_{\text{safe th}} = 0.20\text{m}$ from the human pelvis, and $d_{\text{elbow th}} = 0.25\text{m}$.

The experiment involved two sessions: human passing (*HP*) and robot passing (*RP*). In the *HP* session, a human participant passed the object to the prosthesis user once for each lateral distance y_{task}, simulating traditional handover scenarios involving a human co-worker in industrial settings or a caregiver in assistive contexts. Five healthy participants (four males and a female, 28.2 ± 2.4 years old) were recruited to serve as object passers in this condition. In the *RP* session, the task was executed in collaboration with a Franka Emika Panda manipulator, controlled at 1 kHz, equipped with the Robotiq 2-Finger Gripper 2F-85. The robot optimised the object transfer pose online by solving the constrained optimisation problem defined in Eq. (2), implemented through the Augmented Lagrangian method of the ALGLIB library[2] in a C++ environment. To ensure smooth execution, a B-spline trajectory was generated to achieve the optimised handover pose, which was tracked by the robot Cartesian impedance controller, as in [16]. The robot repeated the object passing at different y_{task} five times to ensure a consistent comparison with the *HP* condition.

We used a wearable MVN Biomech suit (Xsens Tech.BV) equipped with inertial measurement unit sensors to measure body segment lengths and automatically personalise the kinematic model and digital mannequin meshes for the subject. The motion capture system continuously tracked the prosthesis user's movements throughout the experiment. The post-hoc statistical analysis compared the effectiveness of the robot-assisted (*RP*) condition to the baseline human passing (*HP*) condition, with a focus on the impact of embedding a user impairment model in the robot behaviour. Initially, the gathered data were tested for normality using the Anderson-Darling test. If normality was confirmed, repeated measures ANOVA was conducted. In cases where normality was not confirmed, the non-parametric Friedman test was employed to evaluate significant differences. Three performance metrics on the prosthesis user's motion were computed:

- *Task duration* (T_f): the time taken by the prosthesis user to complete the approach and grasping phases, measured from the first movement of the grasping subject, until he/she had full control of the object;
- *Functioning joints usage* ($\bar{\Psi}$): calculated during the duration T_f (with time samples $k = 1, \ldots, K_f$) as:

$$\bar{\Psi} = \frac{1}{K_f} \sum_{k=1}^{K_f} \Psi[k], \tag{4}$$

  where $\Psi[k]$ is the cost associated with compensatory mechanisms performed by the functioning joints, as defined in Eq. (1);
- *Smoothness of joint motion* (J): defined as:

$$J = \Delta t \sum_{k=1}^{K_f} \| \dddot{\boldsymbol{q}}_{\text{m}}^{H}[k] \|^2, \tag{5}$$

  where Δt is the data sampling rate of the Xsens system and $\dddot{\boldsymbol{q}}_{\text{m}}^{H} \in \mathbb{R}^M$ is the joint jerk vector derived numerically from joint velocity measurements.

B. Experimental Results

Figure 3 shows the sequential frames of the middle finger and the supernumerary prosthetic finger in motion to illustrate the progressive flexion movements enabled by the coupling mechanism.

The results of mobility-aware optimisation tailored to specific prosthesis users are reported in Fig. 4, revealing its ability to effectively configure human-robot interaction under varying physical profiles and task constraints. The digital model was automatically scaled to match the anthropometric characteristics of both users based on motion-tracking data. The robot complied with task requirements, namely maintaining different lateral distances from the user's pelvis and adhering to task-specific object positioning areas (indicated by green planes in the figure). More importantly,

[1]The experiments were carried out at the HRII Laboratory of the Istituto Italiano di Tecnologia in accordance with the Helsinki Declaration, and the protocol was approved by the ethics committee Azienda Sanitaria Locale Genovese N.3 (Protocol IIT_HRII_ERGOLEAN 156/2020).

[2]https://www.alglib.net/



Fig. 3. Illustration of the coordinated flexion movement of the user's finger and the prosthetic one.

the robot adapted the position and orientation of the handover object to eliminate wrist movement entirely and mitigate compensatory movements. Each subfigure also reports the cost associated with compensatory mechanisms, Ψ_*, for the ideal case where the human assumed the optimal posture derived from the optimisation.

Figure 5 compares the handover scenarios between human-to-prosthesis user interaction conducted by Participant 3 (*HP*) and the optimised robotic handover (*RP*). Despite the human passer's aim to facilitate the prosthesis user's grasp, the resulting object transfer pose necessitated pronounced compensatory movements from the user due to wrist blockage. Specifically, as shown in the bottom-left plot of Fig. 5, the prosthesis user exhibited greater elbow flexion (purple line), substantial shoulder flexion (orange line), and an elevated elbow posture, which induced larger shoulder external rotation (yellow line) and forearm pronation (green line). Further, the prosthesis user required approximately a second to stabilise the prosthetic grasp in this configuration. Additionally, a hesitation at the beginning of the movement suggested a slightly increased demand on the neural mechanisms for motion planning, as also reported by the prosthesis user. In contrast, the optimised robotic handover, tailored to accommodate the prosthesis user's mobility limitations, enabled a more accessible and efficient grasp. The robot facilitation induces the user to adopt a posture closely aligned with the optimised configuration $\boldsymbol{q}_*^H$ obtained by the mobility-aware optimisation problem (depicted with dashed lines in the bottom-right plot of Fig. 5). While the optimised posture recommended greater reliance on elbow flexion and reduced shoulder flexion, the user adopted a configuration with more balanced flexion between the elbow and shoulder. Despite these minor deviations due to the user's slightly different resolution of the redundancy, the optimised robotic

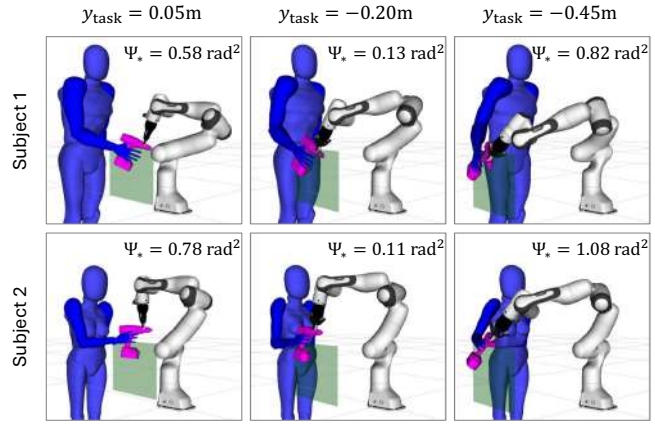


Fig. 4. Optimised robot-to-prosthesis user handover configurations at different lateral distances from the human pelvis on the table, tailored to diverse human body measurements.

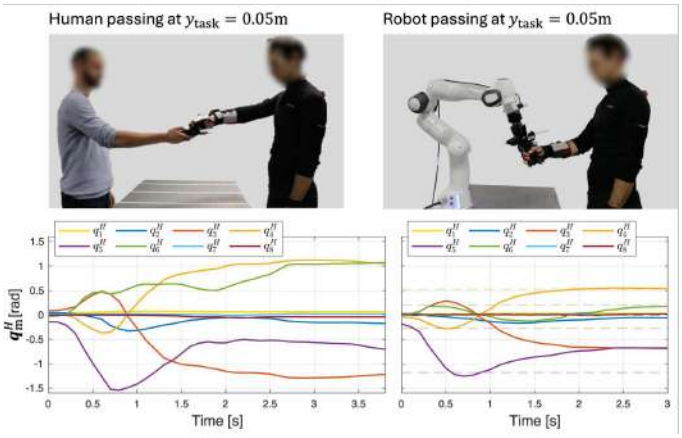


Fig. 5. Comparison between human-to-prosthesis user handover performed by a participant (*HP*) and optimised robotic handover adapted to the prosthesis user's mobility limitations (*RP*).

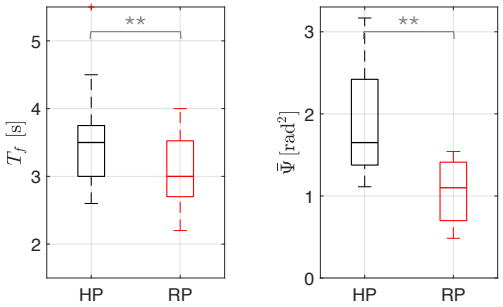


Fig. 6. Statistical comparison between human passing (*HP*) and robotic passing (*RP*) conditions: (left) duration of the approach phase, indicating improved efficiency in robotic handover; (right) mean cost of compensatory movements $\bar{\Psi}$ over the approach phase, highlighting reductions in functioning joints usage. Significance levels are indicated at $^{**}p < 0.01$.

facilitation notably reduced the compensatory movements cost Ψ both at the interaction pose and throughout the approach phase compared to the *HP* condition.

The statistical analysis comparing *HP* and *RP* conditions across all tested y_{task} values demonstrated that the robot handover significantly improved both the efficiency and comfort of the prosthesis user's grasp. Indeed, a significant reduction in the duration of the approach phase was observed, as shown in the left box plot of Fig. 6. Additionally, the measured cost associated with compensatory movements, $\Psi(t_{\text{interaction}})$, at the interaction pose, and the mean cost representing the functioning joints usage, $\bar{\Psi}$, exhibited significant decreases, as depicted in the right box plot of Fig. 6. The norm of joint displacements at the wrist remained consistently close to zero in both handover conditions, as expected. However, in the *HP* condition, wrist displacements occasionally reached up to $6°$, indicating instances where the prosthesis user was forced to violate the wrist constraint to enable the grasp. Regarding joint motion smoothness, the integral of the squared joint jerk during the approach phase (J) was not presented as a box plot due to value variations introduced by the monitoring system and numerical derivation, but comparisons between the two conditions (*HP* and *RP*) provided consistent and meaningful insights. A significant 52.7% reduction in J ($p < 0.01$) in the robotic handover condition revealed smoother

and more seamless grasping approaches.

IV. Discussion and Conclusions

In this work, we presented a novel online method for mitigating compensatory movements in prosthesis users with restricted mobility, an often overlooked issue that can lead to long-term harm. Our approach involves creating a personalised mobility model for the prosthesis user and integrating it into a constrained optimisation framework. This framework computes the optimal user posture for task performance in a functional and comfortable manner, considering task requirements, and informs the robot, which reconfigures the task accordingly to promote the adoption of such a posture. Initial results with healthy subjects using a proposed body-powered finger prosthesis as a supernumerary finger demonstrated that a robotic assistant embedding the user-specific mobility model outperformed human partners. Improvements were observed in both the reduction of compensatory movements in functioning joints and the efficiency of the prosthesis user's grasp during handover tasks. These findings are promising for introducing collaborative robots as workplace and caregiving assistants, promoting inclusion, and facilitating the seamless integration of prosthetic devices into users' daily lives. Despite these encouraging results, we observed some deviations in how users resolved redundancy in joint usage, leading to slight differences in performance. Future works will focus on providing guidance to users on configuring their functioning joints, potentially through visual feedback interfaces developed in our simulations or vibrotactile feedback systems [26]. Additionally, we plan to test the framework with prosthetic devices handling more complex amputations, such as those involving the elbow, and consider partial impairments. Finally, we aim to extend our framework to more complex interactive tasks, further evaluating its potential for enhancing prosthetic device usability in diverse real-world scenarios.

References

[1] I. Imbinto, C. Peccia, M. Controzzi, A. G. Cutti, A. Davalli, R. Sacchetti, and C. Cipriani, "Treatment of the partial hand amputation: an engineering perspective," *IEEE reviews in biomedical engineering*, vol. 9, pp. 32–48, 2016.

[2] M. C. Goiato, D. N. Mancuso, P. M. Ferreira, and D. M. Dos Santos, "Finger prosthesis: the art of reconstruction," *J Coll Physicians Surg Pak*, vol. 19, no. 10, pp. 670–671, 2009.

[3] C. M. Fraser, "An evaluation of the use made of cosmetic and functional prostheses by unilateral upper limb amputees," *Prosthetics and Orthotics International*, vol. 22, no. 3, pp. 216–223, 1998.

[4] S. L. Carey, D. J. Lura, and M. J. Highsmith, "Differences in myoelectric and body-powered upper-limb prostheses: Systematic literature review." *Journal of Rehabilitation Research & Development*, vol. 52, no. 3, 2015.

[5] G. Milazzo, S. Lemerle, G. Grioli, A. Bicchi, and M. G. Catalano, "Design, characterization, and validation of a variable stiffness prosthetic elbow," *IEEE Transactions on Robotics*, 2024.

[6] A. Marinelli, N. Boccardo, F. Tessari, D. Di Domenico, G. Caserta, M. Canepa, G. Gini, G. Barresi, M. Laffranchi, and L. De Michieli, "Active upper limb prostheses: A review on current state and upcoming breakthroughs," *Progress in Biomedical Engineering*, vol. 5, no. 1, p. 012001, 2023.

[7] M. Bumbaširević, A. Lesic, T. Palibrk, D. Milovanovic, M. Zoka, T. Kravić-Stevović, and S. Raspopovic, "The current state of bionic limbs from the surgeon's viewpoint," *EFORT open reviews*, vol. 5, no. 2, pp. 65–72, 2020.

[8] S. L. Carey, M. J. Highsmith, M. E. Maitland, and R. V. Dubey, "Compensatory movements of transradial prosthesis users during common tasks," *Clinical Biomechanics*, vol. 23, no. 9, pp. 1128–1135, 2008.

[9] A. J. Metzger, A. W. Dromerick, R. J. Holley, and P. S. Lum, "Characterization of compensatory trunk movements during prosthetic upper limb reaching tasks," *Archives of physical medicine and rehabilitation*, vol. 93, no. 11, pp. 2029–2034, 2012.

[10] S. M. Engdahl, C. Lee, and D. H. Gates, "A comparison of compensatory movements between body-powered and myoelectric prosthesis users during activities of daily living," *Clinical Biomechanics*, vol. 97, p. 105713, 2022.

[11] A. M. Valevicius, Q. A. Boser, C. S. Chapman, P. M. Pilarski, A. H. Vette, and J. S. Hebert, "Compensatory strategies of body-powered prosthesis users reveal primary reliance on trunk motion and relation to skill level," *Clinical Biomechanics*, vol. 72, pp. 122–129, 2020.

[12] A. Nanavati, V. Ranganeni, and M. Cakmak, "Physically assistive robots: A systematic review of mobile and manipulator robots that physically assist people with disabilities," *Annual Review of Control, Robotics, and Autonomous Systems*, vol. 7, pp. 123–147, 2024.

[13] A. Bestick, R. Pandya, R. Bajcsy, and A. Dragan, "Learning human ergonomic preferences for handovers," in *Proceedings of International Conference on Robotics and Automation (ICRA)*, 2018, pp. 3257–64.

[14] W. Kim, M. Lorenzini, P. Balatti, P. Nguyen, U. Pattacini, V. Tikhanoff, L. Peternel, C. Fantacci, L. Natale, G. Metta, and A. Ajoudani, "Adaptable workstations for human-robot collaboration: A reconfigurable framework for improving worker ergonomics and productivity," *IEEE Robotics & Automation Magazine*, pp. 14–26, 2019.

[15] F. Ferraguti, R. Villa, C. T. Landi, A. M. Zanchettin, P. Rocco, and C. Secchi, "A unified architecture for physical and ergonomic human–robot collaboration," *Robotica*, vol. 38, no. 4, pp. 669–683, 2020.

[16] M. Lagomarsino, M. Lorenzini, E. De Momi, and A. Ajoudani, "Promind: Proximity and reactivity optimisation of robot motion to tune safety limits, human stress, and productivity in industrial settings," *arXiv preprint arXiv:2409.06864*, 2024.

[17] D. Torielli, L. Bertoni, L. Muratore, and N. Tsagarakis, "A laser-guided interaction interface for providing effective robot assistance to people with upper limbs impairments," *IEEE Robotics and Automation Letters*, 2024.

[18] S. Poirier, F. Routhier, and A. Campeau-Lecours, "Voice control interface prototype for assistive robots for people living with upper limb disabilities," in *Proceedings of International Conference on Rehabilitation Robotics (ICORR)*. IEEE, 2019, pp. 46–52.

[19] P. Ardon, M. E. Cabrera, E. Pairet, R. P. A. Petrick, S. Ramamoorthy, K. S. Lohan, and M. Cakmak, "Affordance-aware handovers with human arm mobility constraints," *IEEE Robotics and Automation Letters*, pp. 3136–3143, 2021.

[20] M. Leonori, M. Lorenzini, L. Fortini, J. M. Gandarias, and A. Ajoudani, "The bridge between xsens motion-capture and robot operating system (ros): Enabling robots with online 3d human motion tracking," *arXiv preprint arXiv:2306.17738*, 2023.

[21] A. Bertomeu-Motos, A. Blanco, F. J. Badesa, J. A. Barios, L. Zollo, and N. Garcia-Aracil, "Human arm joints reconstruction algorithm in rehabilitation therapies assisted by end-effector robotic devices," *Journal of NeuroEngineering and Rehabilitation*, pp. 1–11, 2018.

[22] R. D. Rondinelli, E. Genovese, R. T. Katz, T. G. Mayer, K. L. Mueller, M. I. Ranavaya, and C. R. Brigham, "Ama guides® to the evaluation of permanent impairment, 2023," in *AMA Guides® to the Evaluation of Permanent Impairment*. American Medical Association, 2023.

[23] S. Gholami, M. Lorenzini, E. De Momi, and A. Ajoudani, "Quantitative physical ergonomics assessment of teleoperation interfaces," *IEEE Transactions on Human-Machine Systems*, pp. 169–180, 2022.

[24] M. Whitmore, J. Boyer, and K. Holubec, "Nasa-std-3001, space flight human-system standard and the human integration design handbook," in *Industrial and systems engineering research conference*, 2012.

[25] L. McAtamney and N. Corlett, "Rapid upper limb assessment (rula)," in *Handbook of human factors and ergonomics methods*. CRC Press, 2004, pp. 86–96.

[26] M. Lorenzini, S. Ciotti, J. M. Gandarias, S. Fani, M. Bianchi, and A. Ajoudani, "Performance analysis of vibrotactile and slide-and-squeeze haptic feedback devices for limbs postural adjustment," in *Proceedings of International Symposium on Robot and Human Interactive Communication (RO-MAN)*. IEEE, 2022, pp. 707–713.

Exploring Usability Standards in Robotic Rehabilitation: A meta-analysis of System Usability Scale scores

Giovanna Nicora[1], Gabriele Santangelo[1], Giacomo Marzero[1], Arianna Dagliati[1], Irene Aprile[2], Silvana Quaglini[1]

[1] *Department of Electrical, Computer and Biomedical Engineering, University of Pavia*
Via Ferrata n. 5, Pavia 27100, Italy

[2] *IRCCS Fondazione Don Carlo Gnocchi*
Via di Scandicci n. 269, 50143 Firenze, Italy

giovanna.nicora@unipv.it

***Abstract*— Increasing integration of robotic devices in rehabilitation necessitates robust usability assessments to ensure effective human-robot interaction. This study presents a meta-analysis of System Usability Scale (SUS) scores reported in robotics-assisted rehabilitation, to evaluate whether the usability of these devices meets the standard SUS benchmark (mean = 68, SD = 12.5) and to identify any factors influencing usability across different users and device types. Following a systematic literature search, we analyzed 67 studies evaluating usability of robotic devices. Devices were categorized into 8 types, including upper- and lower-limb exoskeletons, end effectors and sensor-based systems. From each study, we extracted SUS means, user information (healthy individuals, healthcare practitioners or patients), and scoring origin (developer vs. external investigator). Our results indicate that robotic devices in rehabilitation generally achieve good usability (74 on average), but current studies have a limited sample size (13 on average). Comparisons with the standard SUS benchmark showed a statistically significant deviation in most device categories, thus underscoring the importance of tailored usability standards in robotics-assisted rehabilitation. Future research should focus on larger, more diverse sample sizes and explore usability challenges specific to certain devices and user roles to enhance the development of accessible, user-friendly rehabilitation robots.**

Keywords—Benchmarking, SUS for robotic rehabilitative devices, assistive device usability

I. Introduction

Technological advancement in the field of robotics and Artificial Intelligence (AI) over the last 30 years has led to the development of a wide range of heterogeneous devices, from end effectors to exoskeletons, potentially able to increase efficiency and accessibility to therapy [1]. In 2022, the global rehabilitation robot market was valued at USD 239.1 million, and it is expected to reach USD 1026.2 million by 2030 [2]. As robotics-assisted rehabilitation is spreading, evaluating the usability of such devices in clinical practice can identify potential gaps and drive the development of easy-to-use robots. In fact, the integration of user needs is essential to develop a satisfactory human-robot interaction [3]. According to ISO 9241-11, an important international standard related to usability, usability is defined as "*the extent to which a product can be used by specified users to achieve specified goals with effectiveness, efficiency and satisfaction in a specified context of use*" [4]. To measure usability, one of the most popular tools is the System Usability Scale (SUS), a questionnaire of 10 questions to be answered on a 5-point Likert scale (from "Strongly disagree" to "Strongly agree"). Half of the questions refer to "positive statements", asking, for instance, whether the respondent would like to use the device frequently, or if the device is easy to use, while the remaining 5 questions are "negative statements", covering aspects such as the perceived complexity of the device and its inconsistency [5]. A final score from 0 to 100 can be calculated from the 10 questions, with 100 indicating the maximum level of usability. Various studies have investigated whether the SUS scores can be translated into categories to quantify user experience. For example, [6] gathered 1,000 SUS compiled for various types of technologies, such as cell phones and TVs. By adding an additional adjective question to measure the overall usability (from "Worst imaginable" to "Best Imaginable" in a 7-point Likert scale), the authors found that the SUS threshold to consider a device to have sufficient usability is 50.9. Another study analyzed more than 5000 individual SUS responses for various devices, and reported a mean SUS score of 68, with a standard deviation of 12,5 [7]. Following [7], [8], the acceptable SUS threshold for usability is usually considered to be 68. Recently, a review investigated the usability of robots and virtual reality devices in rehabilitation, finding that the SUS was the most utilized scale [9]. However, the study did not examine whether the mean SUS across robotics devices was in line with the aforementioned thresholds for benchmarking [7]. Nonetheless, comparing SUS results obtained from robotics-devices users in rehabilitation with those reported by large-scale studies on heterogeneous, non-robotics devices, such as mobile apps, might be unreliable. Another essential factor in assessing usability in rehabilitation is that there are two primary user groups—therapists and patients—each with distinct characteristics and needs.

Here, our goal is to quantify the reported usability of various types of robotic devices for rehabilitation in terms of SUS scores and to examine whether the benchmark SUS distribution of 68 (SD 12,5) [7] can be reliably used for evaluating the usability in the field of robotics-assisted rehabilitation. In particular, the research questions addressed in this paper are the following:

RQ1: What are the distributions of reported SUS scores across various types of robotics devices?

RQ2: Is there a statistically significant difference between the distribution of SUS scores in robotics-assisted rehabilitation and the benchmark distribution [7]?

RQ3: Are there any differences in usability between patients and therapists?

RQ4: Is there a difference in reported SUS scores when the usability study is conducted directly by robot developers?

To answer the research questions, we have performed an extensive literature search in Scopus, IEEEXplore and Google Scholar to gather studies performing SUS usability assessment on robotics devices in rehabilitation. For each retrieved paper, we extracted the category of device(s) investigated, the reported statistics on the SUS score (mean, standard deviation, median, minimum and maximum, when available), the number and the category of participants (patients, therapists, and healthy volunteers). The device categories, described in the next section, have been previously identified based on the basis of the function (rehabilitative or assistive device); the rehabilitative devices were classified based on their type (robot, advanced technological systems, sensor-based device); the robots were then classified into end-effectors and exoskeletons, and also depending on the body area treated (upper limb, lower limb); the advanced technological systems included devices for the treatment of walking (advanced treadmill) and balance (proprioceptive platform). Sensor-based devices include those using virtual reality, and those for cognitive training.

II. Materials and Methods

A. Literature search and device organization

We first retrieved the literature studies investigating real-world usability in robotics-assisted rehabilitation following the PRISMA guidelines for systematic reviews: we queried the Scopus and IEEEXplore database on October 9th, 2024 using the following query on the Title, Abstract and Keywords: (System Usability Scale) AND Robot AND (Rehabilitation OR Cognitive). We excluded studies that did not report at least the median SUS of the participants. We also queried Google Scholar for specific categories of devices (reported below) to augment the number of retrieved studies.

For each study, we categorized the evaluated technologies into the following eight categories of robotic rehabilitative devices:

(i) assistive and mobile servants, such as eye tracking communicator and market-available robots such as Pepper, developed by SoftBank Robotics

(ii) advanced treadmill, such as the Walker View developed by Technobody

(iii) upper limb (UL) exoskeleton, such as Gloreha Sinfonia

(iv) lower limb (LL) end effector, for example Erigo

(v) LL exoskeleton, such as Lokomat

(vi) assistive UL or UL end effector, for example Amadeo

(vii) Proprioceptive, stabilometric and balanced platform,

(viii) sensor-based, virtual reality and cognitive robots, such as Pablo.

We then extracted the number of participants, the reported mean SUS score, the standard deviation of the median SUS score, the Interquartile range, and the minimum and maximum SUS score (if reported). Additionally, we report whether the study was conducted by robot developers as part of an evaluation of their system or by external investigators (i.e. non-developers), for instance, to evaluate a device before introducing it into clinical practice. The studies were also stratified according to the targeted users, namely the therapists, the patients, or even healthy subjects

B. Statistical analysis

Following [8], we performed a meta-analysis by computing the mean of the retrieved mean SUS scores over the collected papers, but also stratifying for devices categories and target users as described before. The retrieved dataset was analysed with Matlab and Python. To test for normality, we used the Shapiro test. To test the equality distribution of the robotics-related SUS and the benchmark, we used the Kolmogorov-Smirnov and the Mann Whitney test.

III. Results

A. General statistical analysis

A unique number of 67 papers were retrieved (43 from retrieved thanks to the systematic query, the remaining from Google Scholar search). These studies have been conducted in the last 10 years, as the oldest study retrieved was published in 2014 [10]. Among these, one study collected SUS answers from both healthcare practitioners (HPCs) and healthy subjects [11], 7 studies engaged both HPCs and patients[12], [13], [14], [15], [16], [17], [18], and 1 collected results from healthy participants and patients [19]. The majority of the studies focused on usability on patients (86%), involving a total of 816 individuals. Over the 67 papers, the average number of subjects that compiled the SUS among patients was 14, while among HPCs and healthy subjects was 9 and 15,6 respectively. The mean of the reported SUS scores mean across all devices categories is 74,4 with a standard deviation of 11,28. 58% of the studies were conducted by robot developers, showing a mean SUS score of 76, while the mean SUS score for studies conducted by non-developers is 72,5. Figure 1 shows the boxplot of mean SUS scores in studies, stratified by the relevant groups that promoted the study, i.e., robot developers or non-developers. While the distribution of SUS scores seems to be lower in the case of studies promoted by researchers not involved in the development of the robot, we cannot conclude that they come from different populations (Kolmogorov-Smirnov test p-value >0.05).

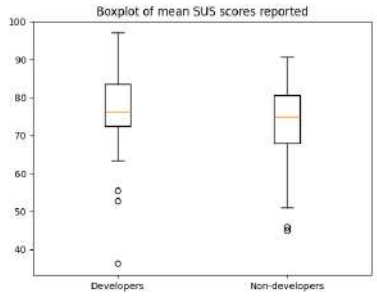


Figure 1: Boxplot of the mean SUS scores, stratified by the relevant groups that promoted the study, i.e. robot developers or non-developers [7]

When analysed according to the respondents types (HCPs, patients, or healthy subjects), we observed that healthy participants usually exhibit higher SUS scores (Figure 2), but their difference is not statistically significant according to the Mann Whitney test.

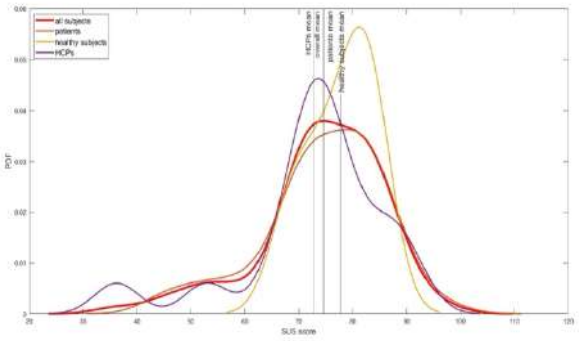


Figure 2: Density plot of mean SUS scores across all studies (red line), or stratified by types of respondents (patients, healthy subjects and healthcare practitioners – HCPs).

We then compared the distribution of SUS scores in robotics-assisted rehabilitation with the benchmark (normal distribution with a mean equal to 68 and a standard deviation of 12,5 [7] (Figure 3). We performed the Kolmogorov-Smirnov test and found a low p-value (<5e-8), indicating a significant difference between the SUS scores reported in rehabilitation and the benchmark, in favor of the former.

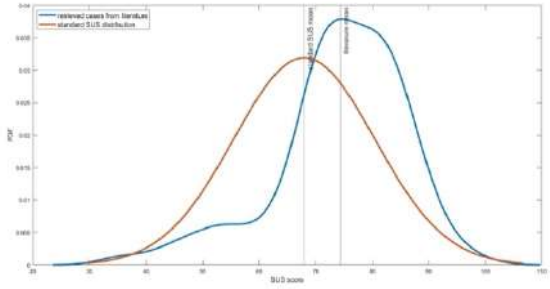


Figure 3: Density plot of the mean SUS scores of robotics devices for rehabilitation (blue) and density plot of the normal benchmark SUS scores distribution [7].

B. Statistical analysis across devices categories

Most studies (15) dealt with assistive (generic) and mobile servants [10], [14], [17], [20], [21], [22], [23], [24], [25], [26], [27], [28], [29], [30], [31]. Thirteen studies evaluated the usability of UL end effector [32], [33], [34], [35], [36], [37], [38], [13], [39], [40], [41], [42], [43]. Twelve studies focused on UL exoskeleton[44], [45], [46], [12], [19], [47], [48], [49], [50], [51], [52], [53]. Eleven studies dealt with Sensor based/Virtual Reality/Cognitive robots [54], [11], [55], [56], [57], [58], [15], [59], [60], [18], [61]. Six studies evaluated usability of LL exoskeleton [62], [63], [64], [65], [66], [67] and LL end effector [68], [69], [70], [16], [71], [72]. Only three studies dealt with Proprioceptive/stabilometric/balance platform [73], [74], [75]. We were able to retrieve only one study evaluating the SUS for advanced treadmill [76]. The boxplot of the reported mean across device categories is reported in Figure 4. Lower limb end effector exhibits the highest median of SUS scores, but also greater variability. For advanced treadmills, the unique study evaluating the SUS on the 6 patients reported a mean SUS score of 68, with a standard deviation of 13 [76], very similar to the current benchmark. When compared to the benchmark, we found a statistically significant difference in the SUS scores for Sensor based/VR/cognitive devices (p-value 0.005), assistive UL or UL end effector (p-value 0.003), UL exoskeleton (p-value 0.002), LL end effector (p-value 0.015).

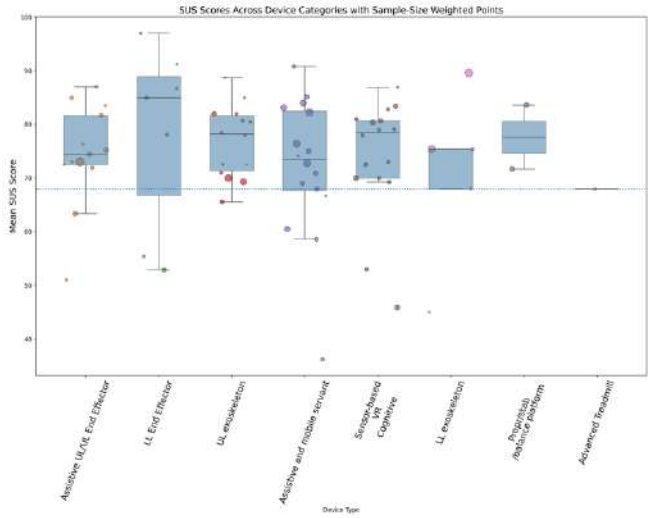


Figure 4: Boxplot of the mean SUS scores across categories. The horizontal blue dotted line represents the commonly used threshold for usability [7]. Each SUS data point is also reported. Each data point has a size proportional to the sample size of the study. The minimum sample size is 4 [15], while the maximum is 47 [33].

Table I reports, across all types of devices and users, the mean and standard deviation of SUS scores. Notably, for the device category "Assistive and mobile servant", patients and healthy participants indicated good usability (above 74), while the SUS mean for HPCs is 62,6, below the 68 thresholds, and with high variability (standard deviation of 17,6). On the contrary, LL end effector exhibits a higher mean SUS on HPCs rather than on patients.

IV. Discussion

In this meta-analysis, we examine the reported usability of robotic devices used in rehabilitation. Given the heterogeneity of these technologies, ranging from exoskeletons to virtual reality systems, meaningful comparisons of SUS scores within the same type of device required a standardized categorization. This classification was established through consensus among researchers and clinicians in the rehabilitation field, resulting in eight distinct categories. However, we recognize that as the field evolves, additional categories may emerge, and certain devices may fit into multiple groups. Nonetheless, for the purpose of this analysis, a single categorization was necessary. The results of our meta-analysis provide important insights into the usability of robotic devices in rehabilitation, as measured by the System Usability Scale (SUS). Below, we discuss these findings in relation to our research questions, highlighting key observations and implications for future development in this field.

Regarding general usability trends and variability across different types of devices (RQ1), Overall, the SUS scores of robotic devices in rehabilitation indicate good usability, with mean scores generally above the widely accepted threshold of 68 (Figure 4). This trend reflects a positive user experience across diverse devices, affirming the progress in designing robots that meet the usability expectations of end-users in clinical settings. However, notable variability exists across device types and user groups. In particular, the mean SUS score for assistive and mobile servant devices, when evaluated by therapists, falls below the 68 benchmark, with a mean of 62 and a high standard deviation (17.6). This lower score may reflect specific usability challenges encountered by therapists, such as operational complexities or inconsistencies in device performance, which could impede effective use in clinical practice. Among the device types, upper-limb (UL) end effectors exhibited the highest SUS scores, highlighting their generally favorable reception by users.

The comparison with the standard SUS benchmark distribution (RQ2) reveals a significant difference in the SUS score distribution for robotics-assisted rehabilitation compared to the standard SUS benchmark (mean = 68, SD = 12.5). This difference was statistically significant across most device categories, reinforcing the notion that robotics devices in rehabilitation generally offer a distinct usability profile compared to other technologies. However, this variance was not significant for certain devices, including lower-limb (LL) exoskeletons, proprioceptive platforms, and assistive and mobile servant devices. For these categories, usability scores aligned more closely with the established benchmark, suggesting that these devices may share usability characteristics with other types of technology or face similar limitations. Based on this finding, we propose establishing a new benchmark specifically for robotic devices. However, given the relatively small sample sizes in previous studies (with a mean of 13 participants), larger-scale studies should be encouraged to ensure more robust and reliable benchmarks. Since the SUS is a general usability assessment tool, the field could benefit from the development of new questionnaires specifically designed for robotic devices in rehabilitation, considering their unique characteristics and requirements. A more tailored approach could not only enhance usability evaluations but also help identify specific needs that should be addressed in the development of future robotic systems. Additionally, future research should explore whether—and to what extent—high usability translates into widespread clinical adoption.

Regarding relevant user group differences (RQ3), we observed no statistically significant differences in SUS scores between therapists and patients, suggesting a generally consistent usability experience across these user groups. This consistency may indicate that the usability design of rehabilitation robots has effectively addressed the requirements of both types of end-users, despite their different roles and interaction needs with the devices.

We also investigated the potential influence of developer involvement on usability score (RQ4). Our analysis indicated that studies conducted by developers tended to report slightly higher SUS scores compared to those conducted by external investigators. However, this difference was not statistically significant, suggesting that while there may be some degree of positive bias when developers assess their own devices, the impact on SUS scores is relatively minor. Additionally, studies involving healthy participants, which were mostly conducted by developers, tended to have a higher recruitment rate (mean of 15.6 participants). This outcome underscores the challenge of recruiting clinical participants, particularly for studies led by external researchers who may not have direct access to patient populations. The results of this meta-analysis underscore the overall positive usability of robotic devices in rehabilitation, yet highlight specific areas for improvement, especially for assistive and mobile servant robots when used by therapists. As the field advances, targeted enhancements in the user interface and operational ease of use for this subgroup could help bridge this usability gap. Furthermore, future usability studies would benefit from expanding beyond developer-led investigations and increasing sample sizes, especially for clinical populations. More diverse and larger samples would help validate findings across broader contexts and contribute to robust usability benchmarks tailored specifically for rehabilitation technologies.

In conclusion, the SUS remains a valuable and adaptable tool for assessing usability in rehabilitation robotics. By continuously benchmarking against a standardized usability distribution and incorporating feedback from varied user groups, developers can refine robotic technologies to better serve the needs of both patients and therapists, ultimately enhancing the integration and impact of these devices in therapeutic settings.

Acknowledgment

This work was supported by the Italian Ministry of Research, under the complementary actions to the NRRP "Fit4MedRob - Fit for Medical Robotics" Grant (#PNC0000007)"

References

[1] J. Laut, M. Porfiri, and P. Raghavan, 'The Present and Future of Robotic Technology in Rehabilitation', *Curr Phys Med Rehabil Rep*, vol. 4, no. 4, pp. 312–319, Dec. 2016, doi: 10.1007/s40141-016-0139-0.
[2] pxdraft, 'Rehabilitation Robots Market Size & Share | Report, 2030'. Accessed: Nov. 11, 2024. [Online]. Available: https://www.kingsresearch.com/rehabilitation-robots-market-319
[3] J. T. Meyer, R. Gassert, and O. Lambercy, 'An analysis of usability evaluation practices and contexts of use in wearable robotics', *Journal of NeuroEngineering and Rehabilitation*, vol. 18, no. 1, p. 170, Dec. 2021, doi: 10.1186/s12984-021-00963-8.
[4] 'ISO 9241-11:2018', ISO. Accessed: Nov. 11, 2024. [Online]. Available: https://www.iso.org/standard/63500.html
[5] john Brooke, 'SUS: A "Quick and Dirty" Usability Scale', in *Usability Evaluation In Industry*, CRC Press, 1996.
[6] 'Determining What Individual SUS Scores Mean: Adding an Adjective Rating Scale - JUX', JUX - The Journal of User Experience. Accessed: Oct. 30, 2024. [Online]. Available: https://uxpajournal.org/determining-what-individual-sus-scores-mean-adding-an-adjective-rating-scale/
[7] J. Sauro and J. R. Lewis, *Quantifying the User Experience: Practical Statistics for User Research*. Elsevier Science, 2016. [Online]. Available: https://books.google.it/books?id=USPfCQAAQBAJ
[8] M. Hyzy *et al.*, 'System Usability Scale Benchmarking for Digital Health Apps: Meta-analysis', *JMIR Mhealth Uhealth*, vol. 10, no. 8, p. e37290, Aug. 2022, doi: 10.2196/37290.
[9] F. Zanatta, A. Giardini, A. Pierobon, M. D'Addario, and P. Steca, 'A systematic review on the usability of robotic and virtual reality devices in neuromotor rehabilitation: patients' and healthcare professionals' perspective', *BMC Health Services Research*, vol. 22, no. 1, p. 523, Apr. 2022, doi: 10.1186/s12913-022-07821-w.
[10] A. L. Threatt, J. Merino, K. E. Green, I. Walker, J. O. Brooks, and S. Healy, 'An assistive robotic table for older and post-stroke adults: results from participatory design and evaluation activities with clinical staff', in *Proceedings of the SIGCHI Conference on Human Factors in Computing Systems*, in CHI '14. New York, NY, USA: Association for Computing Machinery, Apr. 2014, pp. 673–682. doi: 10.1145/2556288.2557333.
[11] M. Kennard, M. Hassan, Y. Shimizu, and K. Suzuki, 'Max Well-Being: a modular platform for the gamification of rehabilitation', *Front. Robot. AI*, vol. 11, May 2024, doi: 10.3389/frobt.2024.1382157.
[12] A. Yurkewich, S. Ortega, J. Sanchez, R. H. Wang, and E. Burdet, 'Integrating hand exoskeletons into goal-oriented clinic and home stroke and spinal cord injury rehabilitation', *Journal of Rehabilitation and Assistive Technologies Engineering*, vol. 9, p. 20556683221130970, Jun. 2022, doi: 10.1177/20556683221130970.
[13] A. Nehrujee *et al.*, 'Plug-and-Train Robot (PLUTO) for Hand Rehabilitation: Design and Preliminary Evaluation', *IEEE Access*, vol. 9, pp. 134957–134971, 2021, doi: 10.1109/ACCESS.2021.3115580.
[14] A. Bouzida, A. Kubota, D. Cruz-Sandoval, E. W. Twamley, and L. D. Riek, 'CARMEN: A Cognitively Assistive Robot for Personalized Neurorehabilitation at Home', in *2024 19th ACM/IEEE International Conference on Human-Robot Interaction (HRI)*, Mar. 2024, pp. 55–64. Accessed: Nov. 18, 2024. [Online]. Available: https://ieeexplore.ieee.org/document/10660884
[15] C. Goumopoulos, E. Drakakis, and D. Gklavakis, 'Augmented and Virtual Reality Based Exergames in GAME2AWE for Elderly Fall Prevention', in *2022 18th International Conference on Wireless and Mobile Computing, Networking and Communications (WiMob)*, Oct. 2022, pp. 100–105. doi: 10.1109/WiMob55322.2022.9941651.
[16] R. Formicola, C. Amici, M. Mor, L. Bissolotti, and A. Borboni, 'Design of Medical Devices with Usability in Mind: A Theoretical Proposal and Experimental Case Study Using the LEPRE Device', *Designs*, vol. 7, no. 1, Art. no. 1, Feb. 2023, doi: 10.3390/designs7010009.
[17] M. E. Taylor *et al.*, 'Pilot feasibility study of a home-based fall prevention exercise program (StandingTall) delivered through a tablet computer (iPad) in older people with dementia', *Australas J Ageing*, vol. 39, no. 3, pp. e278–e287, Sep. 2020, doi: 10.1111/ajag.12717.
[18] R. van Lieshout, M. F. Pisters, B. Vanwanseele, R. A. de Bie, E. J. Wouters, and M. J. Stukstette, 'Biofeedback in Partial Weight Bearing: Usability of Two Different Devices from a Patient's and Physical Therapist's Perspective', *PLoS One*, vol. 11, no. 10, p. e0165199, 2016, doi: 10.1371/journal.pone.0165199.
[19] C. Lambelet *et al.*, 'Characterization and wearability evaluation of a fully portable wrist exoskeleton for unsupervised training after stroke', *J NeuroEngineering Rehabil*, vol. 17, no. 1, p. 132, Oct. 2020, doi: 10.1186/s12984-020-00749-4.
[20] M. A. Miskam, S. Shamsuddin, H. Yussof, I. M. Ariffin, and A. R. Omar, 'A questionnaire-based survey: Therapist's response on emotions gestures using humanoid robot for autism', in *2015 International Symposium on Micro-NanoMechatronics and Human Science (MHS)*, Nov. 2015, pp. 1–7. doi: 10.1109/MHS.2015.7438298.
[21] D. Hoevenaars *et al.*, 'Mobile App (WHEELS) to Promote a Healthy Lifestyle in Wheelchair Users With Spinal Cord Injury or Lower Limb Amputation: Usability and Feasibility Study', *JMIR Formative Research*, vol. 5, no. 8, p. e24909, Aug. 2021, doi: 10.2196/24909.
[22] R. A. C. M. Olde Keizer *et al.*, 'Using socially assistive robots for monitoring and preventing frailty among older adults: a study on usability and user experience challenges', *Health Technol.*, vol. 9, no. 4, pp. 595–605, Aug. 2019, doi: 10.1007/s12553-019-00320-9.
[23] J. J. Chen, D. M. Cooper, F. Haddad, A. Sladkey, E. Nussbaum, and S. Radom-Aizik, 'Tele-Exercise as a Promising Tool to Promote Exercise in Children With Cystic Fibrosis', *Frontiers in Public Health*, vol. 6, p. 269, Sep. 2018, doi: 10.3389/fpubh.2018.00269.
[24] A. Di Nuovo *et al.*, 'Usability Evaluation of a Robotic System for Cognitive Testing', in *2019 14th ACM/IEEE International Conference on Human-Robot Interaction (HRI)*, Mar. 2019, pp. 588–589. doi: 10.1109/HRI.2019.8673187.
[25] A. Blanchard, S. M. Nguyen, M. Devanne, M. Simonnet, M. Le Goff-Pronost, and O. Rémy-Néris, 'Technical Feasibility of Supervision of Stretching Exercises by a Humanoid Robot Coach for Chronic Low Back Pain: The R-COOL Randomized Trial', *BioMed Research International*, vol. 2022, no. 1, p. 5667223, 2022, doi: 10.1155/2022/5667223.
[26] P. Jansons, J. Dalla Via, R. M. Daly, J. J. Fyfe, E. Gvozdenko, and D. Scott, 'Delivery of Home-Based Exercise Interventions in Older Adults Facilitated by Amazon Alexa: A 12-week Feasibility Trial', *The Journal of nutrition, health and aging*, vol. 26, no. 1, pp. 96–102, Jan. 2022, doi: 10.1007/s12603-021-1717-0.
[27] J. Carmichael, S. Flynn, T. Struessel, S. Bini, M. Bade, and J. Stevens-Lapsley, 'Assessment of a Downloadable Application with Avatar Guidance for PT-Prescribed Home Exercise after Total Knee Arthroplasty: A 30-Day Usability and Feasibility Study', *Advances in Aging Research*, vol. 11, no. 4, Art. no. 4, Jun. 2022, doi: 10.4236/aar.2022.114008.
[28] S. Macis *et al.*, 'Design and Usability Assessment of a Multi-Device SOA-Based Telecare Framework for the Elderly', *IEEE Journal of Biomedical and Health Informatics*, vol. 24, no. 1, pp. 268–279, Jan. 2020, doi: 10.1109/JBHI.2019.2894552.
[29] S. Pareek, 'iART: An intelligent assistive robotic therapy system for home-based stroke rehabilitation', Thesis, University of Illinois at Urbana-Champaign, 2020. Accessed: Nov. 19, 2024. [Online]. Available: https://hdl.handle.net/2142/107933
[30] A. Seregni *et al.*, 'Virtual Coaching for Rehabilitation: The Participatory Design Experience of the vCare Project', *Front. Public Health*, vol. 9, Dec. 2021, doi: 10.3389/fpubh.2021.748307.
[31] S. Mohanraj, H.-J. Young, M. Thirumalai, and L. Malone, 'The Spinal Cord Injury Program in Exercise (SCIPE) Study: Usability and Acceptability of the Teleexercise Platform', *Archives of Physical Medicine and Rehabilitation*, vol. 105, no. 4, p. e61, Apr. 2024, doi: 10.1016/j.apmr.2024.02.171.
[32] B. Radder *et al.*, 'A wearable soft-robotic glove enables hand support in ADL and rehabilitation: A feasibility study on the assistive functionality', *Journal of Rehabilitation and Assistive Technologies Engineering*, vol. 3, p. 2055668316670553, Jan. 2016, doi: 10.1177/2055668316670553.
[33] B. Radder *et al.*, 'Home rehabilitation supported by a wearable soft-robotic device for improving hand function in older adults: A pilot randomized controlled trial', *PLOS ONE*, vol. 14, no. 8, p. e0220544, Aug. 2019, doi: 10.1371/journal.pone.0220544.
[34] R. Ranzani *et al.*, 'Feasibility of Adjunct Therapy with a Robotic Hand Orthosis after Botulinum Toxin Injections in Persons with Spasticity: A Pilot Study', *Toxins*, vol. 16, no. 8, 2024, doi: 10.3390/toxins16080346.
[35] Y.-C. Pei, J.-L. Chen, A. M. K. Wong, and K. C. Tseng, 'An Evaluation of the Design and Usability of a Novel Robotic Bilateral Arm Rehabilitation Device for Patients with Stroke', *Front. Neurorobot.*, vol. 11, Jul. 2017, doi: 10.3389/fnbot.2017.00036.

[36] M. Gandolla *et al.*, 'An assistive upper-limb exoskeleton controlled by multi-modal interfaces for severely impaired patients: development and experimental assessment', *Robotics and Autonomous Systems*, vol. 143, p. 103822, Sep. 2021, doi: 10.1016/j.robot.2021.103822.
[37] B. Radder, G. Prange-Lasonder, A. I. R. Kottink, A. Melendez-Calderon, J. H. Buurke, and J. S. Rietman, 'Feasibility of a wearable soft-robotic glove to support impaired hand function in stroke patients', *J Rehabil Med*, vol. 50, no. 7, pp. 598–606, Jul. 2018, doi: 10.2340/16501977-2357.
[38] 'Preliminary Results from Functional and Usability Assessment of the WiGlove - a Home-based Robotic Orthosis for Hand and Wrist Therapy after stroke'. Accessed: Nov. 19, 2024. [Online]. Available: https://personales.upv.es/thinkmind/dl/conferences/achi/achi_2024/achi_2024_3_170_20075.pdf
[39] M. Zbytniewska-Mégret *et al.*, 'Design and Preliminary Evaluation of a Robot-assisted Assessment-driven Finger Proprioception Therapy', in *2022 International Conference on Rehabilitation Robotics (ICORR)*, Jul. 2022, pp. 1–6. doi: 10.1109/ICORR55369.2022.9896602.
[40] G. Devittori *et al.*, 'Unsupervised robot-assisted rehabilitation after stroke: feasibility, effect on therapy dose, and user experience', *J NeuroEngineering Rehabil*, vol. 21, no. 1, p. 52, Apr. 2024, doi: 10.1186/s12984-024-01347-4.
[41] M. Gandolla, C. Mariani, L. Pozzi, M. Mancini, G. M. Foglia, and A. Pedrocchi, 'Hand grip support for rehabilitation and assistance: from patent to TRL5', *IEEE Int Conf Rehabil Robot*, vol. 2022, pp. 1–6, Jul. 2022, doi: 10.1109/ICORR55369.2022.9896562.
[42] R. Ranzani *et al.*, 'Design, characterization and preliminary usability testing of a portable robot for unsupervised therapy of hand function', *Front. Mech. Eng.*, vol. 8, Jan. 2023, doi: 10.3389/fmech.2022.1075795.
[43] S. Guillén-Climent *et al.*, 'A usability study in patients with stroke using MERLIN, a robotic system based on serious games for upper limb rehabilitation in the home setting', *J NeuroEngineering Rehabil*, vol. 18, no. 1, p. 41, Feb. 2021, doi: 10.1186/s12984-021-00837-z.
[44] G. Salvietti *et al.*, 'Integration of a Passive Exoskeleton and a Robotic Supernumerary Finger for Grasping Compensation in Chronic Stroke Patients: The SoftPro Wearable System', *Front. Robot. AI*, vol. 8, Jun. 2021, doi: 10.3389/frobt.2021.661354.
[45] P. Sale, G. Stellin, S. Masiero, F. Becchi, and W. Sieklicki, 'FEX a Fingers Extending eXoskeleton for Rehabilitation and Regaining Mobility', in *Advances in Service and Industrial Robotics*, C. Ferraresi and G. Quaglia, Eds., Cham: Springer International Publishing, 2018, pp. 813–824. doi: 10.1007/978-3-319-61276-8_86.
[46] B. Aruanno and M. Covarrubias Rodriguez, 'Handy: Novel hand exoskeleton for personalized rehabilitation', 2021, doi: 10.14733/CADAPS.2022.405-425.
[47] C. E. Proulx, J. Higgins, and D. H. Gagnon, 'Occupational therapists' evaluation of the perceived usability and utility of wearable soft robotic exoskeleton gloves for hand function rehabilitation following a stroke', *Disabil Rehabil Assist Technol*, vol. 18, no. 6, pp. 953–962, Aug. 2023, doi: 10.1080/17483107.2021.1938710.
[48] S. Dalla Gasperina *et al.*, 'Upper-limb actuated exoskeleton for muscular dystrophy patients: preliminary results', in *2019 41st Annual International Conference of the IEEE Engineering in Medicine and Biology Society (EMBC)*, Jul. 2019, pp. 4431–4435. doi: 10.1109/EMBC.2019.8857725.
[49] J. Alvarez-Pastor *et al.*, 'Development of a single actuator exoskeleton for wrist and forearm rehabilitation', *Annu Int Conf IEEE Eng Med Biol Soc*, vol. 2021, pp. 6247–6250, Nov. 2021, doi: 10.1109/EMBC46164.2021.9630636.
[50] S. D. Gasperina *et al.*, 'AGREE: an upper-limb robotic platform for personalized rehabilitation, concept and clinical study design', *IEEE Int Conf Rehabil Robot*, vol. 2022, pp. 1–6, Jul. 2022, doi: 10.1109/ICORR55369.2022.9896569.
[51] F. Amirabdollahian *et al.*, 'Design, development and deployment of a hand/wrist exoskeleton for home-based rehabilitation after stroke - SCRIPT project', *Robotica*, vol. 32, no. 8, pp. 1331–1346, Dec. 2014, doi: 10.1017/S0263574714002288.
[52] V. Longatelli *et al.*, 'User-centred assistive SystEm for arm Functions in neUromuscuLar subjects (USEFUL): a randomized controlled study', *J NeuroEngineering Rehabil*, vol. 18, no. 1, p. 4, Jan. 2021, doi: 10.1186/s12984-020-00794-z.
[53] I.-M. Alguacil-Diego *et al.*, 'Validation of a Hybrid Exoskeleton for Upper Limb Rehabilitation. A Preliminary Study', *Sensors*, vol. 21, no. 21, Art. no. 21, Jan. 2021, doi: 10.3390/s21217342.
[54] T. Vanbellingen, S. J. Filius, T. Nyffeler, and E. E. H. van Wegen, 'Usability of Videogame-Based Dexterity Training in the Early Rehabilitation Phase of Stroke Patients: A Pilot Study', *Front. Neurol.*, vol. 8, Dec. 2017, doi: 10.3389/fneur.2017.00654.
[55] M. G. Maggio, A. Luca, C. D'Agate, M. Italia, R. S. Calabrò, and A. Nicoletti, 'Feasibility and usability of a non-immersive virtual reality tele-cognitive app in cognitive rehabilitation of patients affected by Parkinson's disease', *Psychogeriatrics*, vol. 22, no. 6, pp. 775–779, 2022, doi: 10.1111/psyg.12880.
[56] S. Marcos-Antón, A. Jardón-Huete, E. D. Oña-Simbaña, A. Blázquez-Fernández, L. Martínez-Rolando, and R. Cano-de-la-Cuerda, 'sEMG-controlled forearm bracelet and serious game-based rehabilitation for training manual dexterity in people with multiple sclerosis: a randomised controlled trial', *J NeuroEngineering Rehabil*, vol. 20, no. 1, p. 110, Aug. 2023, doi: 10.1186/s12984-023-01233-5.
[57] P. Antoniotti, V. Biscaro, F. Mancini, M. Caprino, P. Tropea, and M. Corbo, 'Rehabilitation activities with tablet (REACT) in Parkinson's disease', *Neurol Sci*, vol. 45, no. 7, pp. 3173–3181, Jul. 2024, doi: 10.1007/s10072-024-07414-x.
[58] F. Escalona, E. Martinez-Martin, E. Cruz, M. Cazorla, and F. Gomez-Donoso, 'EVA: EVAluating at-home rehabilitation exercises using augmented reality and low-cost sensors', *Virtual Reality*, vol. 24, no. 4, pp. 567–581, Dec. 2020, doi: 10.1007/s10055-019-00419-4.
[59] A. Rojo *et al.*, 'PedaleoVR: Usability study of a virtual reality application for cycling exercise in patients with lower limb disorders and elderly people', *PLoS One*, vol. 18, no. 2, p. e0280743, 2023, doi: 10.1371/journal.pone.0280743.
[60] R. Bertoni *et al.*, 'Effects of immersive virtual reality on upper limb function in subjects with multiple sclerosis: A cross-over study', *Mult Scler Relat Disord*, vol. 65, p. 104004, Sep. 2022, doi: 10.1016/j.msard.2022.104004.
[61] Department of Biomedical Engineering, Mahidol University, Nakhon Pathom, Thailand, T. Ruangrong, and P. Ritthipravat, 'EMG Analysis on Gyro-Roller Rehabilitation Device for Stroke Patients', *IJBBB*, vol. 7, no. 3, pp. 153–161, 2017, doi: 10.17706/ijbbb.2017.7.3.153-161.
[62] R. B. van Dijsseldonk, I. J. W. van Nes, A. C. H. Geurts, and N. L. W. Keijsers, 'Exoskeleton home and community use in people with complete spinal cord injury', *Sci Rep*, vol. 10, no. 1, p. 15600, Sep. 2020, doi: 10.1038/s41598-020-72397-6.
[63] J. C. L. Lau and K. Mombaur, 'Preliminary Study on a Novel Protocol for Improving Familiarity with a Lower-Limb Robotic Exoskeleton in Able-Bodied, First-Time Users', *Front. Robot. AI*, vol. 8, Jan. 2022, doi: 10.3389/frobt.2021.785251.
[64] M. Semprini *et al.*, 'User-centered design and development of TWIN-Acta: A novel control suite of the TWIN lower limb exoskeleton for the rehabilitation of persons post-stroke', *Front. Neurosci.*, vol. 16, Nov. 2022, doi: 10.3389/fnins.2022.915707.
[65] C. Basla, I. Hungerbühler, J. T. Meyer, P. Wolf, R. Riener, and M. Xiloyannis, 'Usability of an exosuit in domestic and community environments', *J NeuroEngineering Rehabil*, vol. 19, no. 1, p. 131, Dec. 2022, doi: 10.1186/s12984-022-01103-6.
[66] T. Luger, M. Bär, R. Seibt, M. A. Rieger, and B. Steinhilber, 'Using a Back Exoskeleton During Industrial and Functional Tasks—Effects on Muscle Activity, Posture, Performance, Usability, and Wearer Discomfort in a Laboratory Trial', *Hum Factors*, vol. 65, no. 1, pp. 5–21, Feb. 2023, doi: 10.1177/00187208211007267.
[67] A. Manuli *et al.*, 'Is intensive gait training feasible and effective at old age? A retrospective case-control study on the use of Lokomat Free-D in patients with chronic stroke', *Journal of Clinical Neuroscience*, vol. 92, pp. 159–164, Oct. 2021, doi: 10.1016/j.jocn.2021.08.013.
[68] A. Smiley, T. Y. Tsai, and J. Finkelstein, 'Wireless Real-Time Exercise System for Physical Telerehabilation', in *2022 IEEE Long Island Systems, Applications and Technology Conference (LISAT)*, May 2022, pp. 1–6. doi: 10.1109/LISAT50122.2022.9923944.
[69] H. J. A. van Hedel, I. Rosselli, and S. Baumgartner-Ricklin, 'Clinical utility of the over-ground bodyweight-supporting walking system Andago in children and youths with gait impairments', *J NeuroEngineering Rehabil*, vol. 18, no. 1, p. 29, Feb. 2021, doi: 10.1186/s12984-021-00827-1.

[70] V. Costa *et al.*, 'Development and Clinical Validation of a Rehabilitation Platform for Hip Fracture in Elderly Population', *IEEE Trans Neural Syst Rehabil Eng*, vol. 30, pp. 1340–1349, 2022, doi: 10.1109/TNSRE.2022.3175688.
[71] O. Kuzmicheva *et al.*, 'Overground robot based gait rehabilitation system MOPASS - overview and first results from usability testing', *2016 IEEE International Conference on Robotics and Automation (ICRA)*, pp. 3756–3763, May 2016, doi: 10.1109/ICRA.2016.7487563.
[72] R. Pérez-Rodríguez *et al.*, 'FriWalk robotic walker: usability, acceptance and UX evaluation after a pilot study in a real environment', *Disabil Rehabil Assist Technol*, vol. 15, no. 6, pp. 718–727, Aug. 2020, doi: 10.1080/17483107.2019.1617795.
[73] P. Altorfer, M. Adcock, E. D. de Bruin, F. Graf, and E. Giannouli, 'Feasibility of Cognitive-Motor Exergames in Geriatric Inpatient Rehabilitation: A Pilot Randomized Controlled Study', *Front. Aging Neurosci.*, vol. 13, Nov. 2021, doi: 10.3389/fnagi.2021.739948.
[74] A. Schättin *et al.*, 'Design and Evaluation of User-Centered Exergames for Patients With Multiple Sclerosis: Multilevel Usability and Feasibility Studies', *JMIR Serious Games*, vol. 9, no. 2, p. e22826, May 2021, doi: 10.2196/22826.
[75] P. Manser, H. Poikonen, and E. D. de Bruin, 'Feasibility, usability, and acceptance of "Brain-IT"—A newly developed exergame-based training concept for the secondary prevention of mild neurocognitive disorder: a pilot randomized controlled trial', *Front. Aging Neurosci.*, vol. 15, Sep. 2023, doi: 10.3389/fnagi.2023.1163388.
[76] A. T. C. Booth, M. M. van der Krogt, A. I. Buizer, F. Steenbrink, and J. Harlaar, 'The validity and usability of an eight marker model for avatar-based biofeedback gait training', *Clinical Biomechanics*, vol. 70, pp. 146–152, Dec. 2019, doi: 10.1016/j.clinbiomech.2019.08.013.

TABLE I

Robotics device	**Healthcare practitioners**			**Patients**			**Healthy participants**		
	# of studies	***Mean # of participants***	***Mean SUS (std)***	***# of studies***	***Mean # of participants***	***Mean SUS (std)***	***# of studies***	***Mean # of participants***	***Mean SUS (std)***
Assistive and mobile servant	4	11,25	62,6 (17,6)	12	18,8	75 (10,7)	1	36	74
Advanced treadmill	-	-	-	1	6	68	-	-	-
UL exoskeleton	3	7	72 (6,2)	10	10,6	78 (6,7)	1	15	72
LL end effector	3	5,3	85,4 (6,6)	4	9,5	72,5 (22)	-	-	-
LL exoskeleton	-	-	-	6	17,3	70,7 (16,3)	-	-	-
Assistive UL or LL end effector	1	15	75,2	12	11,6	73,6 (10)	1	5	83,5
Proprioceptive/ Stabilometric/Balance platform	-	-	-	2	20	77,65 (8,4)	-	-	-
Sensor-based/Virtual Reality/Cognitive	5	8,4	73,28 (12,8)	10	13,5	75 (11)	1	10	69,25

Imitation Learning for Adaptive Control of a Virtual Soft Exoglove

Shirui Lyu[1], Vittorio Caggiano[2], Matteo Leonetti[1], Dario Farina[3], and Letizia Gionfrida[1,4]

***Abstract*— The use of wearable robots has been widely adopted in rehabilitation training for patients with hand motor impairments. However, the uniqueness of patients' muscle loss is often overlooked. Leveraging reinforcement learning and a biologically accurate musculoskeletal model in simulation, we propose a customized wearable robotic controller that is able to address specific muscle deficits and to provide compensation for hand-object manipulation tasks. Video data of a same subject performing human grasping tasks is used to train a manipulation model through learning from demonstration. This manipulation model is subsequently fine-tuned to perform object-specific interaction tasks. The muscle forces in the musculoskeletal manipulation model are then weakened to simulate neurological motor impairments, which are later compensated by the actuation of a virtual wearable robotics glove. Results shows that integrating the virtual wearable robotic glove provides shared assistance to support the hand manipulator with weakened muscle forces. The learned exoglove controller achieved an average of 90.5% of the original manipulation proficiency.**

I. INTRODUCTION

The use of wearable robots has shown promising potential both in neurological rehabilitation protocols [1] and in passive supports to boost neural motor performance [2]. Patients with upper limb neurological dysfunctions or impairments often experience varying degrees of dexterity loss [3]. A personalized rehabilitation strategy is essential to enhance their independence, thereby improving their quality of life [4]. However, designing a tailored rehabilitative intervention that accounts for rapidly changing, patient-specific clinical indicators [5], particularly through wearable robotic devices, remains a significant challenge.

One of the challenges in realizing an intelligent controller for assistive wearable robots is the translation of the unique medical conditions of individual patient into adaptable controllers. For example, patients recovering from ischemic or hemorrhagic strokes, often experience significant limitations in their range of motion, characterized by symptoms such as reduced muscle strength or limitation of range of motion [6]. In clinical settings, such diverse medical conditions are typically managed through ad-hoc manual rehabilitation programs administered under the supervision of trained professionals [4]. However, in the context of wearable robotic rehabilitation, the device controller needs to be timely adjusted to provide clinical support [7], [8]. The development of automated methods for adapting wearable device control to individual patient needs is crucial for enabling personalized and accessible rehabilitation interventions.

Data-driven control approaches for wearable robotics have become widely adopted, enabling more general and accessible solutions for wearable robotic control [9]–[14]. These approaches learn biological features of the user such as kinematics, and muscle dynamics, from sufficient data to control the assistive devices. However, they focus on general rather than specific user behaviours, thus leaving a gap in addressing practical individual-based rehabilitation needs.

The development of personalized control strategies for wearable robots has been employing musculoskeletal models to facilitate adaptable controller training through Reinforcement Learning (RL) [15], [16]. Despite their utility, these approaches often yield non-intuitive behaviours [17] attributable to the absence of reliable human-reference data. To address these limitations, the integration of vision and imitation learning within RL training frameworks offers a promising solution. These methods enhance the fidelity of natural human behaviour modelling by providing enhanced biomechanical insights.

In this work, we propose a framework that uses imitation learning to derive user-specific reference trajectories from a healthy subject's video dataset [18]. These trajectories are used to reconstruct kinematics and muscle dynamics in silico, where hand impairments are simulated. Finally, a tendon-driven exoskeleton glove (exoglove) control strategy that adapts to the simulated impairments is tested using the healthy reference as a basis for optimization reference.

The proposed approach consists of three stages (Fig.1). First, reference trajectories are extracted from video data and learned by imitating the behaviour of a healthy subject through *MyoHand* [19], a biologically accurate musculoskeletal hand model, to replicate the user's natural behaviour. Second, RL-driven manipulation is applied to simulate hand-object manipulation tasks within the musculoskeletal model, and then a simulated impairment is incorporated to reflect reduced functionality in the hand. Finally, a virtual exoglove, modeled after a real device [20], is implemented in simulation, where an adaptive control strategy is developed to compensate for the impaired hand, optimizing hand-object manipulation and improving functionality for the impaired hand.

*This work was supported by The Royal Academy of Engineering Research Fellowship (RF2324-23-229).

[1]S. Lyu, M.Leonetti and L. Gionfrida are with the Department of Informatics, King's College London, London, WC2R 2LS, UK. (shirui.lyu, matteo.leonetti, letizia.gionfrida)@kcl.ac.uk

[2]V. Caggiano is with MyoLab, New York, USA and Harvard Medical School and Spaulding Rehabilitation Hospital, Boston, USA caggiano@gmail.com

[3]D. Farina is with the Department of Bioengineering, Faculty of Engineering, Imperial College London, London, SW7 2AZ, UK d.farina@imperial.ac.uk

[4]L. Gionfrida is also with John A. Paulson School of Engineering and Applied Sciences, Harvard University, Cambridge, MA, USA.

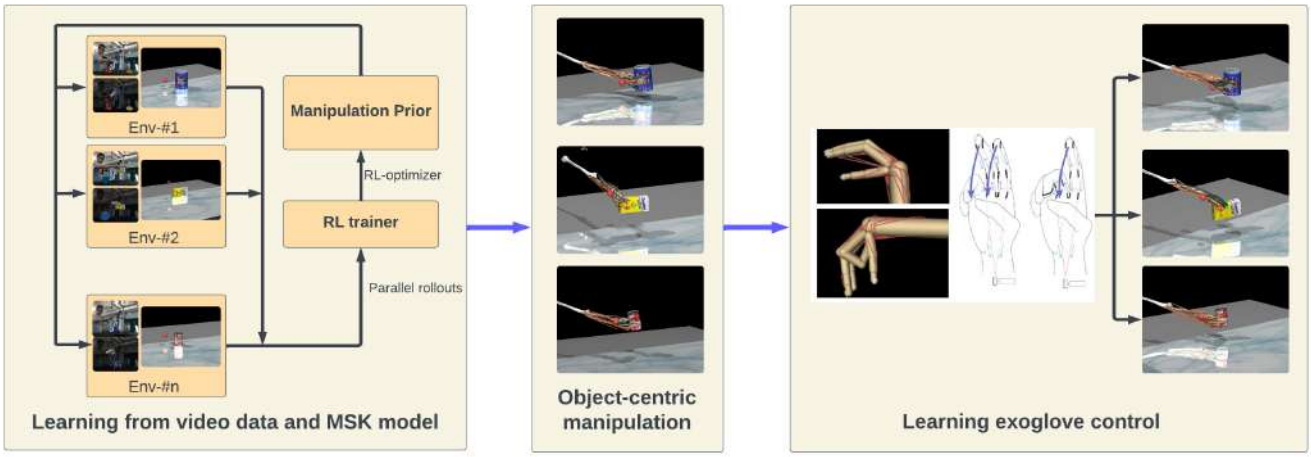


Fig. 1. Pipeline overview illustrating the three main stages: (1) extraction of user behavior via imitation learning from healthy subject video data, (2) training a biologically accurate musculoskeletal hand model for object-centric manipulation and simulating muscle impairments, and (3) development and testing of a tendon-driven exo-glove controller to compensate for impaired hand functionality.

II. Related Work

A. Learning manipulations from human videos and RL

As human video inherently captures the intricate kinematics of hand-object interactions, including the complexity and precision required for dexterous manipulation, extensive research has focused on understanding and modeling these interactions [18], [21]–[23]. Those recorded interactions provide sufficient context for the understanding of dexterous manipulation and facilitate other robotics applications such as handling previously unseen manipulation tasks [24]. Nevertheless, the learned model, referring to computational models trained on human video data to predict or replicate manipulation strategies, depends heavily on human video data and is less robust in handling unseen objects.

RL-based manipulation, on the other hand, is often data-inefficient and explores solutions with computational resources over data. Such an approach gives rise to manipulation understanding that is less relevant to human demonstrations. Object-centric approaches [25], [26], for example, mainly match the object in hand with a reference trajectory, and learn a manipulation strategy even with a high Degree of Freedom (DoF) musculoskeletal hand model.

Recent work [27]–[29] has attempted to combine the advantage from both sides: by using human demonstration video to facilitate RL training, and by using RL to train robust grasping behaviours. In addition, Wan et al. [30] leveraged RL and computer vision to first generate multiple grasping gestures before applying conditioned policy training to achieve generalized grasping behaviour. Chen et al. [17] proposed to use of human demonstration video to guide the RL training while leaving space for RL exploration to handle robot-object interactions. However, most previous works generalize the grasping behaviour and few of the studies were conducted on model-based RL for rehabilitative robotics applications.

B. Model-based wearable robotics control

Recent studies [10], [12], [14], [31], on wearable robotics systems, have focused on integrating high-level task control with low-level hardware control to enhance system performance. This combined approach allows wearable robots to execute tasks more effectively while adapting to the mechanical and dynamic constraints of the hardware. Introducing high-level perceptual information such as egocentric views [32], [33], or user-intent [15], into the control architecture usually improves the system's responsiveness and adaptability. However, deriving accurate and reliable perceptual information requires meticulous modelling of biological states. These models must be biologically accurate to ensure that the system's responses align appropriately with the user's physiological and cognitive conditions, thereby enhancing the overall efficacy and safety of the wearable robot. Hodossy and Farina [15] proposed to use a humanoid model and motion tracking to learn a robust locomotion model to inform the training of an intention-aware prosthesis. Luo et al. [16] leveraged a human musculoskeletal model to train an exoskeleton to provide locomotion support based on the user states. However, few studies have focused on upper-limb wearable robotics aimed at providing shared assistance through musculoskeletal hand models.

III. Methodology

Our approach consists of three main stages. First, we learn the user's behavior context by extracting joint kinematics from a video dataset [18] of a healthy subject. Second, a biologically accurate musculoskeletal hand model is trained for object-centric manipulation tasks, enabling the simulation of hand-object interactions that reflect the user's behaviour. In this stage, the model is also adapted to simulate a designated muscle-weakened hand impairments. Lastly, a tendon-driven soft exoglove is applied to the musculoskeletal hand, with an RL-based glove controller, to support dexterous manipulation

of the impaired hand model. The trained controller is then tested on a muscle-weakened hand model to evaluate its effectiveness in assisting with grasping actions, compensating for the impaired hand's functionality. The pipeline overview is illustrated in Fig.1 .

A. Learning behaviour context from video data

Leveraging video data of a subject grasping daily objects [18], we first learn the subject's behaviour context by distilling them into a musculoskeletal hand model controller via RL-based imitation learning. Three objects of varying size, including a master-chef can, a tomato can and a sugar box from the YCB [34] dataset are used to evaluate the learned hand-object manipulation. The reference grasping type on those objects resembles two commonly used grasp taxonomy types [35], power-grasp and precision-grasp, with variations in object sizes. The hand model observes the reference joint positions and learns a mapping to control the hand's muscle activation signals to follow the reference trajectory. Similar to a previous study [26], a prior model is first trained to capture the essence of the subject's general behaviour context by extracting a joint experience from a number of reference trajectories but from the same subject for training efficiency. The behaviour prior is later fine-tuned to individual hand-object interaction tasks for accuracy. We have observed that learning such behaviour prior can contribute to faster training convergence on previously unseen trajectories and objects. The reward function of such prior model training only comprises the degree of matching of the reference trajectory with the rough gesture shape, similar to the approach by Chen et al. [17]. Nevertheless, we increased the weighting of the thumb tip, to balance it with the other 4 fingertips to follow the reference gesture.

B. Musculoskeletal object manipulator

Imitation learning from video references effectively models user behaviours by capturing hand joint kinematics. However, it does not account for critical hand-object interaction details, such as the contact information for stable grasping and manipulation. To model the contact between hand and object, an RL-based manipulator is employed on the Mujoco [36] physics simulator together with a existing musculoskeletal hand model from Myosuite [19].

In addition, clinical tests such as the Box and Block Test [37] and the Action Research Arm Test [38] are common evaluations of dexterous proficiency of patients with upper-limb motor impairment. Such tests involve moving objects along a required trajectory as in most routine tasks. Thus, we define our exoglove controller training via an object-centric [25] RL approach, namely manipulating an object following a predefined trajectory to align with clinical rehabilitative requirements.

Problem definition

Similar to a previous work [25] on RL-based object-centric manipulation, the problem is defined as a Markov Decision Process (MDP) and solved via reinforcement learning. The Markov decision process is defined as a tuple $M = (S, A, T, R, \rho, \gamma)$, where $S \subseteq \mathbb{R}^n$ and $A \subseteq \mathbb{R}^m$ represent the continuous state space of observations and the action space respectively. The unknown transition dynamics are described by $s' \sim T(\cdot|s, a)$. In addition, $R : S \to [0, R_{\max}]$, denotes the reward function, $\gamma \in [0, 1)$ denotes the discount factor, and ρ the initial state distribution. In RL, a policy is a mapping from states to a probability distribution over actions, i.e. $\pi : S \to P(A)$, which is parameterized by θ. The goal of the agent is to learn a policy $\pi_\theta(a|s) = \arg\max_\theta[J(\pi, M)]$, where $J = \max_\theta \mathbb{E}_{s_0 \sim \rho(s), a \sim \pi_\theta(a_t|s_t)} [\sum_t R(s_t, a_t)]$.

State space

The state space for the musculoskeletal hand model and the exoglove consists of $\{\phi, \psi, \tau, \hat{\theta}\}$. ϕ a 58-dimensional vector of 23 hand and 6 arm joints positions and velocity of the musculoskeletal model. ψ is the object pose (3-dimensional), orientation (3-dimensional) and velocity (3-dimensional). τ is a positional encoding used to represent time steps in the tasks to handle possible repetitions [39]. In addition, the reference motion $\hat{\theta}$ is incorporated as a 63-dimensional vector to indicate the joint position of the wrist, and the four finger joints, including the metacarpophalangeal (MCP), the distal interphalangeal (DIP), proximal interphalangeal (PIP) joints and the fingertip from the human demonstrations.

Action space

The action space for the manipulation baseline is a 45-dimensional vector that consists of continuous activations for 39 muscles of the upper right arm, together with 3D translation and rotation of the shoulder, as in MyoDex [26].

The action space for the exoglove controller is a 3-dimensional vector representing finger contraction and extensions applied on the index and middle finger, with one extra dimension for thumb support.

Reward function

Similar to a previous work by Chen et al. [17], we define two reward functions to support the training. The first function is defined on the object center of mass matching with the one from the reference trajectory, and a second function is defined as matching the musculoskeletal hand joint positions with those from the human demonstration.

For object position $x_t^{(p)}$ and orientation $x_t^{(o)}$ at time step t, the reward function for matching the object position and orientation to the reference trajectory is defined by:

$$\mathbf{R}_{obj} := \lambda_1 exp\{-\alpha_1 ||x_t^{(p)} - \hat{x}_t^{(p)}||_2 - \beta|\angle x_t^{(o)} - \angle \hat{x}_t^{(o)}|\}$$

The reward function for matching the joints' position with those from the human demonstration is:

$$\mathbf{R}_{demo} := -\lambda_2\{\alpha_2 ||x_t^{(p)} - q(t)||_2\}$$

where $(\hat{x}_t^{(p)}, \hat{x}_t^{(o)})$ are the object's reference trajectory's position and orientation at time t, and $q(t)$ denotes the reference joints position from human demonstration data at time t. Here we selected the fingertips of all five fingers and the wrist to accommodate the musculoskeletal hand model. In addition, we increased the weighting of the thumb tip to balance the gesture with reference tracking accuracies. The

constants α, β and λs are part of training hyper-parameters, following the same set-up as in MyoDex [26].

In terms of RL training, both the behaviour prior model that tracks human demonstration and the object-oriented manipulator are equipped with the same state space and action space. Yet the reward function applied to train the two models is slightly different. The prior model is trained by collecting parallel roll-out from a number of manipulation tasks with human demonstrations, each of which contains a different human demonstration, and the reward used is purely $\mathbf{R}_{demo}$ to maximize the following of trajectory. On the other hand, the manipulation model is trained on a reward function defined by $\mathbf{R} = \mathbf{R}_{demo} + \mathbf{R}_{obj}$, to take account of the influence from both the video demonstration and object manipulation for each time step in the training environment and are subject to the specific manipulation tasks.

Object centered interaction

To achieve a realistic interaction modelling with the musculoskeletal model, the hand-object interaction is then trained by fine-tuning the prior model from human demonstrations on individual manipulation tasks. In each of the simulation environments, the controller is required to move the object to follow a predefined reference trajectory, extracted from the human demonstration dataset, and learns a successful manipulation strategy for each object and reference trajectory. To reduce the complexity of the tasks, the controller is trained on top of the human demonstration prior, which was capable of following the human references to facilitate training. In the interaction tasks, the musculoskeletal controller's objective is to find a balance between following the reference and the object manipulation proficiency.

C. Development of the exoglove controller

On top of the manipulation baseline, a tendon-driven exoglove based on a real prototype [20] was implemented in the simulation. Yet the simulated exoglove has an extended degree of freedom (DoF) with a total of 3 controlling dimensions: finger contraction, extension and passive thumb support. To align with the design of the physical prototype, the glove actuation is only applied to the index and middle fingers. The following (Fig. 2) shows the actuation mechanism of the glove in simulation. The thumb support dimension simulates passive support to the palm and only provides internal rotation.

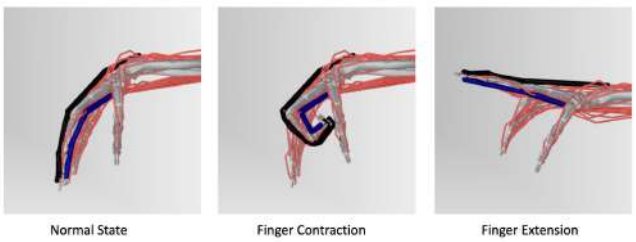


Fig. 2. Visualization of the tendon-driven exoglove actuation in simulation, based on a real prototype [20]. This figure visualizes the exoglove actuation mechanism, from left to right are the hand in normal state, finger contraction, and extension.

Learning compensatory movements

Deriving a suitable, personalized exoglove controlling strategy based on the user behaviour context is challenging. To train such a shared assistive exoglove controller, we adopt the same object-centric approach to support the manipulation behaviour. The objective of such an approach is to match the interacted object coordinates and orientation with a reference trajectory in simulation, which aligns with the needs of motor-impaired users.

Similar to recent work on RL-based prosthesis control [15], the glove controller is equipped with the same set of training hyper-parameters, reward and observation space as for the musculoskeletal hand-on-object manipulation. The aim of such a design is to align the glove controller and musculoskeletal hand model with the same objective of learning how to maximize shared assistance. This design also ensures the information observed by the glove controller is suitable for practical applications, as those features can be extracted via well-researched computer vision algorithms.

IV. Experiments

A. Learning behaviour context from video data

The human behaviour reference data used in this experiment is derived from a video-based dataset DexYCB [18]. The dataset includes a subject manipulating different YCB objects [34], providing the hand joint positions as extracted via computer vision. In our case, the reference trajectories are defined by the extracted joint kinematics, and the data to learn such behaviour all come from the same subject (with ref code: 20200709-subject-01 [18]). Then the training environment for the musculoskeletal model is recreated from the reference dataset using the Myosuite [19] simulator for efficient contact-rich computations.

To extract the behavioral context from the video data, a control agent is initially trained as a motion prior to establish general trajectory tracking capabilities with the musculoskeletal hand model. This agent is then fine-tuned to accurately replicate the specific trajectories of the individual user. A total of 16 environments of extracted reference joint kinematics are incorporated in simulation, including the interaction with 6 objects: chef can, tomato can, tuna can, mustard bottle, pudding box and sugar box. The RL agent learns from the joint experience of the 16 environments by collecting their parallel rollout to control the musculoskeletal hand model. The policy is trained until convergence as a motion prior and is then fine-tuned on individual downstream tasks. Fig. 3 shows the learned prior policy interacting with a chef can and a sugar box. Regarding model robustness, a random Gaussian noise with zero mean and 3% standard deviation is included in the observation space on hand joints and object kinematics in the prior training. We also test the model performance with random initialization (Fig. 4).

The learning of a prior model is a common approach for tasks with high DoF [26]. In this case, we show that this prior model improves the time to convergence for previously unseen reference trajectories from the same subject's data (Fig. 5). The trajectory following error is defined as the

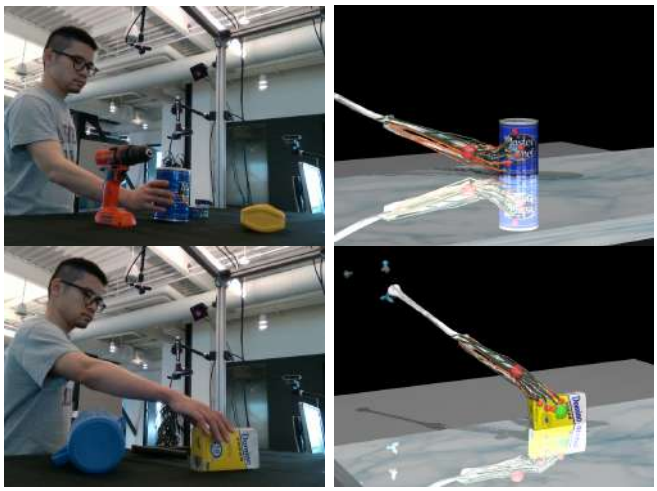


Fig. 3. Visualization of the learned musculoskeletal model policy. The policy is initially trained as a motion prior, capturing general trajectory tracking capabilities, and is subsequently fine-tuned for specific downstream tasks. The figure illustrates the learned prior policy applied to manipulating a chef can (top row) and a sugar box (bottom row).

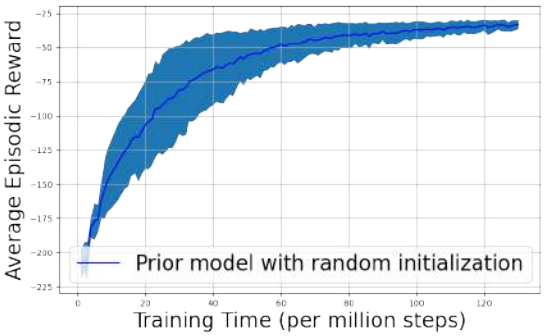


Fig. 4. Prior model training with random initialization

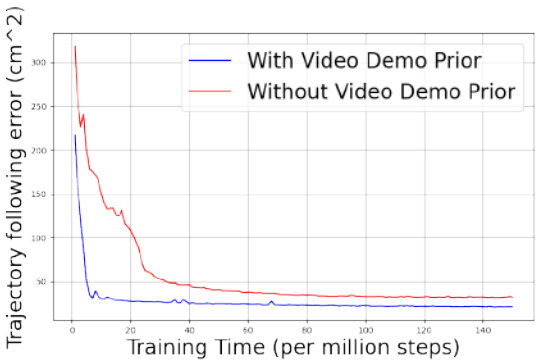


Fig. 5. Comparison of model training **WITH** (blue) and **WITHOUT** (red) the learned behaviour prior on previously unseen object and trajectory pair.

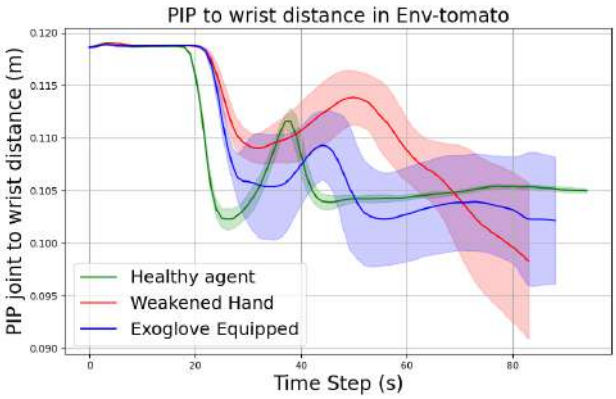


Fig. 6. Comparison of hand actuation behaviours for the tomato can, illustrating the reduction in distance from the proximal interphalangeal (PIP) joint to the wrist during the contraction phase for the healthy baseline (green), weakened hand without assistance (red), and weakened hand with exoglove compensation (blue). The mean and the standardization of the middle finger PIP joint to the wrist are recorded from a total of 30 trials. The figure depicts the exoglove's functionality in compensating for the weakened hand's reduced performance .

absolute value of the average $\mathbf{R}_{demo}$ reward over a training episode. The value serves as an indicator of the spatial difference between the position from human reference and the observed position of the musculoskeletal model. This shows that learning from a collection and diverse range of manipulation video data helps better understand the user's behaviour context.

B. Training of hand-object manipulation tasks

Leverage demonstration prior, a musculoskeletal hand controller is fine-tuned to learn the interaction with specific object and trajectory pairs. For each object-trajectory pair, a single control policy is learned on top of the prior model and the same set of hyper-parameters from MyoDex [26] is given to the RL algorithm. However, the reward function used for object manipulation is the sum of $\mathbf{R}_{demo}$ and $\mathbf{R}_{obj}$. The manipulation model is then trained for 26 million environment steps until fully converge. For each step during evaluation, the object's centre of mass has to be within a 2.5-cm range from the reference position to be considered a success step. The success rate is computed by dividing successful steps over the total steps. Previous literature [25] has noted that human perceives a task as successful if the success rate exceeds 80%. The outcome of the policy training (Fig. 4) and the average success rate over 30 trials on individual objects are recorded in Tab. I.

TABLE I

SUCCESS RATES UNDER 26 MILLION STEPS

Objects	Chef can	Sugar box	Tomato can
Performances	89%	97.6%	93.8%

C. Learning of exoglove control

To simulate neurological muscle weakness, the sarcopenia model from Myosuite [19] is introduced to reduce the maximum muscle strength of the musculoskeletal hand. Then, on top of the weakened hand model, the exoglove controller is trained to compensate for the impaired hand's movements via shared assistance. With the weakened musculoskeletal hand model frozen, the exoglove controller is trained to

learn a compensatory movement based on the hand joint kinematics to provide shared assistance. The exoglove controller is equipped with the same observation space and reward function as the musculoskeletal hand, an approach to ensure alignment in the RL agents' objectives [15]. The exoglove controller is trained until converge, and experiments are conducted to validate the learned exoglove behavior in terms of finger biomechanics and succssess rate, defined in Sec. IV-B.

D. Validation of exoglove biomechanics in simulation

The actuation of the exoskeleton glove exerts a force on the index and middle fingers to support the contraction and extension of the finger during grasping. Given the actuation mechanism, the distance between the PIP joint and the wrist is measured as an indicator of glove support.

Fig. 6 shows the biomechanical assistance provided by the exoskeleton glove. In the healthy case, the distance from the PIP joint to the wrist is first reduced during the closure of the palm, and then increased to hold the grasp gesture. Whereas in the case with simulated muscle weakness, the hand fails to achieve the same contraction due to the lack of muscle strength, causing the hand to drop the object. In contrast, the learned exoglove controller is able to restore an actuation pattern that matches to that of the healthy case, in terms of joint angle changes.

Fig. 7 shows the effect of the exoglove controller to support object-centric manipulations, and measured by an error matrix. The error measures the distance between the object's observed position and the reference position. When the deviation is large, defined by an error of 20 cm away from the reference position, a punishment value is added. The rapid rising of accumulated error, thus, indicates that the simulated motor impairments result in a lack of grasping force, rendering the musculoskeletal hand to drop the object after certain time steps, which aligns to the observed joint angle change as in Fig. 6. Meanwhile, the learned glove controller was able to capture the hand's behaviour and learned a control strategy to provide suitable assistance for enhanced graspin. These results prove that the learned exoglove controller can capture the subject's joint kinematics and provide suitable support.

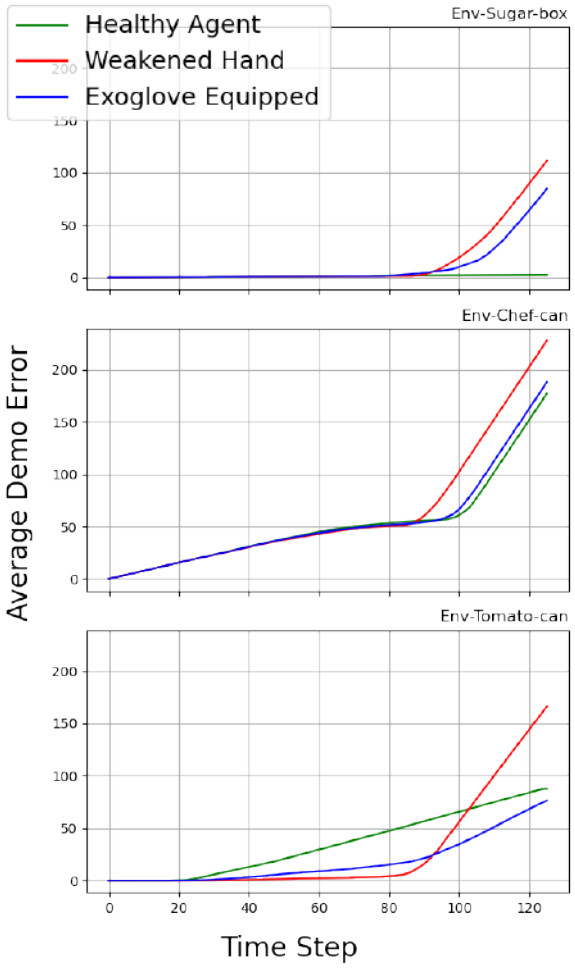


Fig. 7. Accumulated error in object manipulation tasks with the exoglove controller's compensation showing healthy (green) and motor impaired (red) hands, and motor impaired hand with exoglove support (blue). Objects from left to right: chef can, sugar box and tomato can from the YCB objects [34]. The accumulated error illustrates the effectiveness of the exoglove in supporting grasping. The glove controller restores an average of 90.5% of the original success rate.

V. Discussion and Conclusion

In this work, we presented a framework for deriving user-specific reference trajectories using imitation learning, focusing on hand joint kinematics extracted from video data of a healthy subject. These trajectories served as a foundation for reconstructing kinematics and muscle dynamics in silico, where a hand impairment was simulated. We introduced a tendon-driven soft exoglove control strategy designed to compensate for impaired hand functionality. This approach leveraged the healthy reference as a baseline for optimizing the exoglove's control, enabling personalized assistance.

The current approach is not without its limitations. A primary challenge involves translating the simulated outcomes into real-world applications, which remains inherently difficult for most RL-based models. While the state space in simulation can be accurately observed through vision-based extraction algorithms, real-world scenarios introduce complexities such as visual occlusions and partially observable inputs, posing challenges to the exoglove controller's adaptability. Although prior research has explored distilling simulation-trained policies into vision-based policies, the unpredictable nature of real-world environments, particularly in the case of impairments, continues to present a challenge for translating robust and reliable control strategies.

Future work will focus on addressing the deployment of this framework in real-world scenarios, validating the controller with muscle-weakened hands. Additional efforts will also be directed towards bridging the gap between simulation and real-world implementation, increasing generalizability and ensuring the adaptive controller's robustness in dynamic environments across multiple users, objects and tasks.

REFERENCES

[1] S. M. Hatem, G. Saussez, M. Della Faille, V. Prist, X. Zhang, D. Dispa, and Y. Bleyenheuft, "Rehabilitation of motor function after stroke: a multiple systematic review focused on techniques to stimulate upper extremity recovery," *Frontiers in human neuroscience*, vol. 10, p. 442, 2016.

[2] R. W. Nuckols, S. Lee, K. Swaminathan, D. Orzel, R. D. Howe, and C. J. Walsh, "Individualization of exosuit assistance based on measured muscle dynamics during versatile walking," *Science robotics*, vol. 6, no. 60, p. eabj1362, 2021.

[3] R. Gassert and V. Dietz, "Rehabilitation robots for the treatment of sensorimotor deficits: a neurophysiological perspective," *Journal of neuroengineering and rehabilitation*, vol. 15, pp. 1–15, 2018.

[4] H. Rodgers and C. Price, "Stroke unit care, inpatient rehabilitation and early supported discharge," *Clinical Medicine*, vol. 17, no. 2, pp. 173–177, 2017.

[5] C. L. Richards, F. Malouin, and S. Nadeau, "Stroke rehabilitation: clinical picture, assessment, and therapeutic challenge," *Progress in brain research*, vol. 218, pp. 253–280, 2015.

[6] V. Azzollini, S. Dalise, and C. Chisari, "How does stroke affect skeletal muscle? state of the art and rehabilitation perspective," *Frontiers in Neurology*, vol. 12, p. 797559, 2021.

[7] G. Kwakkel, B. J. Kollen, J. van der Grond, and A. J. Prevo, "Probability of regaining dexterity in the flaccid upper limb: impact of severity of paresis and time since onset in acute stroke," *Stroke*, vol. 34, no. 9, pp. 2181–2186, 2003.

[8] Y. Nishimura, H. Onoe, Y. Morichika, S. Perfiliev, H. Tsukada, and T. Isa, "Time-dependent central compensatory mechanisms of finger dexterity after spinal cord injury," *Science*, vol. 318, no. 5853, pp. 1150–1155, 2007.

[9] N. Lotti, M. Xiloyannis, G. Durandau, E. Galofaro, V. Sanguineti, L. Masia, and M. Sartori, "Adaptive model-based myoelectric control for a soft wearable arm exosuit: A new generation of wearable robot control," *IEEE Robotics & Automation Magazine*, vol. 27, no. 1, pp. 43–53, 2020.

[10] X. Zhang, E. Tricomi, F. Missiroli, N. Lotti, and L. Masia, "Real-time assistive control via imu locomotion mode detection in a soft exosuit: An effective approach to enhance walking metabolic efficiency," *IEEE/ASME Transactions on Mechatronics*, 2023.

[11] K. Li, J. Kim, X. Xiong, K. A. Hamed, Y. Yue, and A. D. Ames, "Data-driven predictive control for robust exoskeleton locomotion," *arXiv preprint arXiv:2403.15658*, 2024.

[12] D. Simonetti, M. Hendriks, B. Koopman, N. Keijsers, and M. Sartori, "A wearable gait lab powered by sensor-driven digital twins for quantitative biomechanical analysis post-stroke," *Wearable Technologies*, vol. 5, p. e13, 2024.

[13] D. D. Molinaro, K. L. Scherpereel, E. B. Schonhaut, G. Evangelopoulos, M. K. Shepherd, and A. J. Young, "Task-agnostic exoskeleton control via biological joint moment estimation," *Nature*, vol. 635, no. 8038, pp. 337–344, 2024.

[14] E. Tricomi, F. Missiroli, M. Xiloyannis, N. Lotti, X. Zhang, M. Stefanakis, M. Theisen, J. Bauer, C. Becker, and L. Masia, "Soft robotic shorts improve outdoor walking efficiency in older adults," *Nature Machine Intelligence*, pp. 1–11, 2024.

[15] B. K. Hodossy and D. Farina, "Shared autonomy locomotion synthesis with a virtual powered prosthetic ankle," *IEEE Transactions on Neural Systems and Rehabilitation Engineering*, vol. 31, pp. 4738–4748, 2023.

[16] S. Luo, M. Jiang, S. Zhang, J. Zhu, S. Yu, I. Dominguez Silva, T. Wang, E. Rouse, B. Zhou, H. Yuk, *et al.*, "Experiment-free exoskeleton assistance via learning in simulation," *Nature*, vol. 630, no. 8016, pp. 353–359, 2024.

[17] Z. Chen, S. Chen, C. Schmid, and I. Laptev, "ViViDex: Learning vision-based dexterous manipulation from human videos," in *arXiv:2404.15709*, 2024.

[18] Y.-W. Chao, W. Yang, Y. Xiang, P. Molchanov, A. Handa, J. Tremblay, Y. S. Narang, K. Van Wyk, U. Iqbal, S. Birchfield, J. Kautz, and D. Fox, "DexYCB: A benchmark for capturing hand grasping of objects," in *IEEE/CVF Conference on Computer Vision and Pattern Recognition (CVPR)*, 2021.

[19] V. Caggiano, H. Wang, G. Durandau, M. Sartori, and V. Kumar, "Myosuite: A contact-rich simulation suite for musculoskeletal motor control," in *Proceedings of The 4th Annual Learning for Dynamics and Control Conference* (R. Firoozi, N. Mehr, E. Yel, R. Antonova, J. Bohg, M. Schwager, and M. Kochenderfer, eds.), vol. 168 of *Proceedings of Machine Learning Research*, pp. 492–507, PMLR, 23–24 Jun 2022.

[20] E. Rho, D. Kim, H. Lee, and S. Jo, "Learning fingertip force to grasp deformable objects for soft wearable robotic glove with tsm," *IEEE Robotics and Automation Letters*, vol. 6, no. 4, pp. 8126–8133, 2021.

[21] O. Taheri, N. Ghorbani, M. J. Black, and D. Tzionas, "GRAB: A dataset of whole-body human grasping of objects," in *European Conference on Computer Vision (ECCV)*, 2020.

[22] Y. Liu, Y. Liu, C. Jiang, K. Lyu, W. Wan, H. Shen, B. Liang, Z. Fu, H. Wang, and L. Yi, "Hoi4d: A 4d egocentric dataset for category-level human-object interaction," in *Proceedings of the IEEE/CVF Conference on Computer Vision and Pattern Recognition (CVPR)*, pp. 21013–21022, June 2022.

[23] Y. Hasson, G. Varol, D. Tzionas, I. Kalevatykh, M. J. Black, I. Laptev, and C. Schmid, "Learning joint reconstruction of hands and manipulated objects," in *Proceedings of the IEEE/CVF conference on computer vision and pattern recognition*, pp. 11807–11816, 2019.

[24] E. Chane-Sane, C. Schmid, and I. Laptev, "Learning video-conditioned policies for unseen manipulation tasks," in *2023 IEEE International Conference on Robotics and Automation (ICRA)*, pp. 909–916, IEEE, 2023.

[25] S. Dasari, A. Gupta, and V. Kumar, "Learning dexterous manipulation from exemplar object trajectories and pre-grasps," in *2023 IEEE International Conference on Robotics and Automation (ICRA)*, pp. 3889–3896, 2023.

[26] V. Caggiano, S. Dasari, and V. Kumar, "Myodex: a generalizable prior for dexterous manipulation," in *International Conference on Machine Learning*, pp. 3327–3346, PMLR, 2023.

[27] Y. Qin, Y.-H. Wu, S. Liu, H. Jiang, R. Yang, Y. Fu, and X. Wang, "Dexmv: Imitation learning for dexterous manipulation from human videos," in *European Conference on Computer Vision*, pp. 570–587, Springer, 2022.

[28] P. Mandikal and K. Grauman, "Dexvip: Learning dexterous grasping with human hand pose priors from video," in *Conference on Robot Learning*, pp. 651–661, PMLR, 2022.

[29] K. Shaw, S. Bahl, and D. Pathak, "Videodex: Learning dexterity from internet videos," in *Conference on Robot Learning*, pp. 654–665, PMLR, 2023.

[30] W. Wan, H. Geng, Y. Liu, Z. Shan, Y. Yang, L. Yi, and H. Wang, "Unidexgrasp++: Improving dexterous grasping policy learning via geometry-aware curriculum and iterative generalist-specialist learning," in *Proceedings of the IEEE/CVF International Conference on Computer Vision*, pp. 3891–3902, 2023.

[31] Z. Li, X. Li, Q. Li, H. Su, Z. Kan, and W. He, "Human-in-the-loop control of soft exosuits using impedance learning on different terrains," *IEEE Transactions on Robotics*, vol. 38, no. 5, pp. 2979–2993, 2022.

[32] L. Gionfrida, D. Kim, D. Scaramuzza, D. Farina, and R. D. Howe, "Wearable robots for the real world need vision," *Science Robotics*, vol. 9, no. 90, p. eadj8812, 2024.

[33] D. Kim, B. B. Kang, K. B. Kim, H. Choi, J. Ha, K.-J. Cho, and S. Jo, "Eyes are faster than hands: A soft wearable robot learns user intention from the egocentric view," *Science Robotics*, vol. 4, no. 26, p. eaav2949, 2019.

[34] B. Calli, A. Singh, A. Walsman, S. Srinivasa, P. Abbeel, and A. M. Dollar, "The ycb object and model set: Towards common benchmarks for manipulation research," in *2015 international conference on advanced robotics (ICAR)*, pp. 510–517, IEEE, 2015.

[35] T. Feix, J. Romero, H.-B. Schmiedmayer, A. M. Dollar, and D. Kragic, "The grasp taxonomy of human grasp types," *IEEE Transactions on human-machine systems*, vol. 46, no. 1, pp. 66–77, 2015.

[36] E. Todorov, T. Erez, and Y. Tassa, "Mujoco: A physics engine for model-based control," in *2012 IEEE/RSJ International Conference on Intelligent Robots and Systems*, pp. 5026–5033, 2012.

[37] V. Mathiowetz, G. Volland, N. Kashman, and K. Weber, "Adult norms for the box and block test of manual dexterity," *The American journal of occupational therapy*, vol. 39, no. 6, pp. 386–391, 1985.

[38] N. Yozbatiran, L. Der-Yeghiaian, and S. C. Cramer, "A standardized approach to performing the action research arm test," *Neurorehabilitation and neural repair*, vol. 22, no. 1, pp. 78–90, 2008.

[39] A. Vaswani, "Attention is all you need," *Advances in Neural Information Processing Systems*, 2017.

Impedance Control for Ankle Preparation Phase in BALANSens Platform

Hafiz Muhammad Bilal
Living Robotics Laboratory
Electrical and Electronics Engineering
Istanbul Medipol University
Istanbul, Türkiye

Mahmut Beyaz
Living Robotics Laboratory
Electrical and Electronics Engineering
Istanbul Medipol University
Istanbul, Türkiye

Ramazan Unal
Human-Centred Design Laboratory
Mechanical Engineering
Ozyegin University
Istanbul, Türkiye

Elif Hocaoglu*
Living Robotics Laboratory
Electrical and Electronics Engineering
Research Institute for Health Sciences and Technologies (SABITA)
Istanbul Medipol University
Istanbul, Türkiye

***Abstract*—Ankle injuries and musculoskeletal disorders often necessitate long-term rehabilitation to restore mobility and balance. The BALANSens robotic platform, designed within the Integrated Balance Rehabilitation (I-BAR) framework, combines ankle, balance, and stepping therapies into a cohesive rehabilitation process. This paper focuses on implementing impedance control on the BALANSens platform, which regulates the dynamic interaction between human limbs and the robotic system, making it suitable for active rehabilitation exercises. Traditional impedance control methods rely on costly six-axis force sensors to measure applied torques. However, this work proposes an affordable alternative using multiple load cells placed under the foot sole. These load cells not only measure ankle joint torques but also capture foot pressure distribution data, a key factor in the later stages of rehabilitation. The paper presents the derivation of joint space impedance control for the platform, with force measurements using load cells, and evaluates the system in a real hardware environment. The results underscore the promise of this approach for active rehabilitation, offering a cost-effective solution that simultaneously enriches the scope of patient assessment data.**

I. Introduction

Ankle injuries and musculoskeletal disorders significantly affect mobility and balance [1], often requiring long-term rehabilitation to restore function. Robotic systems have emerged as valuable tools in rehabilitation, offering precise control over joint movements and allowing for personalized therapy programs. The BALANSens robotic platform [2], [3] was recently developed to implement the Integrated Balance Rehabilitation (I-BAR) framework [4], [5]. This framework provides a continuous rehabilitation process by integrating ankle, balance, and stepping therapies into a structured, sequential program.
There are various control strategies [6]–[8] that can be utilized for rehabilitation robots. Position control is suitable for passive therapeutic movement of the limb along the desired trajectory when no human force is applied [9], [10]. The dynamic control strategy is required for active rehabilitation when both human and robot apply force [11]. Impedance control stands out as one of the effective methods for regulating the dynamic interaction between human limbs and robotic devices [12], [13]. It offers the ability to regulate the dynamic relation between the human applied force and position response of the system, making it particularly suitable for active rehabilitation exercises [14], [15].
Impedance control can be implemented without force sensing [16], [17]. However, for active rehabilitation training, force measurement plays a pivotal role in impedance control, as it enables the robot to adjust its behavior based on the user's applied forces. Traditionally, six-axis force sensors have been employed for this purpose, providing comprehensive data on force and torque in multiple directions. However, these sensors are costly, and usually applied torque measurement is needed only in the direction of ankle movements i.e. dorsiflexion-plantarflexion (DP) or inversion-eversion (IE) directions. Therefore, we propose the use of multiple load cells under the foot sole as an affordable alternative for force measurement [18]. Load cells offer the dual advantage of measuring both ankle joint torque and foot pressure distribution. Knowledge of foot pressure distribution is also important in later phases of I-BAR rehabilitation framework i.e. balance and stepping rehabilitation. By incorporating load cells, we not only reduce system cost but also expand the range of data available for rehabilitation analysis, paving the way for more efficient and cost-effective rehabilitation protocols.
The contribution of this paper includes the derivation of impedance control law and its implementation on the BALANSens robotic platform using the foot pressure distribution as a force measurement for potential active rehabilitation therapy. The outline of the paper is as follows. Firstly, the kinematics and dynamics of the BALANSens robotic platform are discussed briefly and then joint space impedance control

This study was supported by the Scientific and Technological Research Council of Türkiye (TUBITAK) under Grant Number 122E246.
*Corresponding author (e-mail: ehocaoglu@medipol.edu.tr)

derivation is presented and force measurement using the load cells is discussed. Then impedance control verification is done in the simulation environment and implementation on actual hardware is presented and results are shown. Finally, the conclusion is drawn.

II. Methodology

BALANSens robotic platform has a 3-DOF parallel robot with the revolute-prismatic-spherical (RPS) configuration specifically designed for ankle, balance and stepping rehabilitation considering the I-BAR framework. The lower platform and upper platform are connected with prismatic joints through revolute and spherical joints, respectively. The prismatic joints are actuated whereas spherical and revolute joints are passive joints. The BALANSens robot has been developed and shown in the Fig. 1.

A. Kinematics and Dynamics

Kinematics plays a crucial role in the implementation of impedance control for robotic systems like the 3-RPS parallel robot. To achieve this, an accurate model of the robot's motion in Cartesian space, particularly the position, velocity, and acceleration of the end-effector, is essential. The cartesian position in terms of the joint positions and vice versa can be obtained through forward kinematics and inverse kinematics, respectively, and can be represented as

$$X = f(q) \tag{1}$$

$$q = g(X) \tag{2}$$

where, $X = [x \quad y \quad z \quad \alpha \quad \beta \quad \gamma]^T$ and $q = [l_1 \quad l_2 \quad l_3]^T$. The velocity level kinematics of the 3-RPS parallel robot involves calculating the linear and angular velocities of the moving platform based on the joint velocities of the robot and vice versa and can be represented as

$$\dot{X} = J_{a(6\times3)}\dot{q} \tag{3}$$

$$\dot{q} = J_{k(3\times6)}\dot{X} \tag{4}$$

where, $\dot{X} = [\dot{x} \quad \dot{y} \quad \dot{z} \quad \dot{\alpha} \quad \dot{\beta} \quad \dot{\gamma}]^T$, $\dot{q} = [\dot{l_1} \quad \dot{l_2} \quad \dot{l_3}]^T$ and J_k and J_a, are the kinematic and analytic jacobian matrices of 3-RPS parallel robot respectively. Acceleration of moving platform in terms of the joint variables i.e. link lengths and vice versa can be computed by taking the derivative of the equations (3) and (4).

$$\ddot{X} = \dot{J}_a\dot{q} + J_a\ddot{q} \tag{5}$$

$$\ddot{q} = \dot{J}_k\dot{X} + J_k\ddot{X} \tag{6}$$

The Lagrangian representation of the dynamic model of the 3-RPS parallel can be written as

$$M(X)\ddot{X} + C(X,\dot{X}) + G(X) = F \tag{7}$$

where,

$$\begin{cases} M(X) \in R^{6\times6} & \text{Mass Matrix,} \\ C(X,\dot{X}) \in R^{6\times1} & \text{Coriolis's Vector,} \\ G \in R^{6\times1} & \text{Gravity Vector,} \\ F \in R^{6\times1} & \text{Generalized forces/moments Vector.} \end{cases}$$

Substituting the value of $\ddot{X}$ from equation (5) to equation (7)

$$M(J_a\ddot{q} + \dot{J}_a\dot{q}) + C + G = F$$

Now multiplying J_a^T on both sides and simplifying we get,

$$J_a^T M J_a\ddot{q} + J_a^T M\dot{J}_a\dot{q} + J_a^T C + J_a^T G = J_a^T F \tag{8}$$

The right-hand side of the above equation (8) can be simplified by utilizing the fact that the work done represented in generalized coordinates is equal to the work done represented in joint coordinates, i.e.,

$$\delta q^T.\tau = \delta X^T.F \tag{9}$$

where, $\tau \in R^3$ is the linear actuator force vector and $F \in R^6$ are generalized coordinates forces and moments. Putting $\delta X = J_a\delta q$ from equation (3) to equation (9),

$$\delta q^T.\tau = \delta q^T.J_a^T F$$

$$\tau = J_a^T.F \tag{10}$$

Utilizing the equation (10), we can write the the equation (8) in simplified form as

$$\tilde{M}\ddot{q} + \tilde{C}(q,\dot{q}) + \tilde{G} = \tau \tag{11}$$

where,

$$\begin{cases} \tilde{M} & = J_a^T M J_a \quad \text{is a } 3\times3 \text{ matrix} \\ \tilde{C} & = J_a^T M\dot{J}_a\dot{q} + J_a^T C \quad \text{is a } 3\times1 \text{ matrix} \\ \tilde{G} & = J_a^T G \quad \text{is } 3\times1 \text{ matrix} \\ \tau & = [\tau_1 \quad \tau_2 \quad \tau_3] \quad \text{is linear actuators force vector} \end{cases}$$

B. Impedance Control

Impedance control regulates the interaction between the robot and the external environment by defining a desired dynamic relationship between the forces exerted by the robot and the resulting motion. Impedance control can be implemented in either joint space or cartesian space coordinates. Here, we considered the joint space impedance control.

1) Mathematical derivation: In interaction with its environment, the dynamic model of the robot as presented in equation (9) can be written as

$$\tilde{M}\ddot{q} + \tilde{C}(q,\dot{q}) + \tilde{G} = \tau - \tau_e \tag{12}$$

where, τ_e is the external torque from the environment, τ is the control torque, M, C and G are the Mass, Coriolis and gravity matrices. To generate the desired dynamic interaction behavior of the robot in response to the applied external torque, the impedance model can be defined as

$$M_d(\ddot{q_d} - \ddot{q}) + B_d(\dot{q_d} - \dot{q}) + K_d(q_d - q) = \tau_e \tag{13}$$

where:

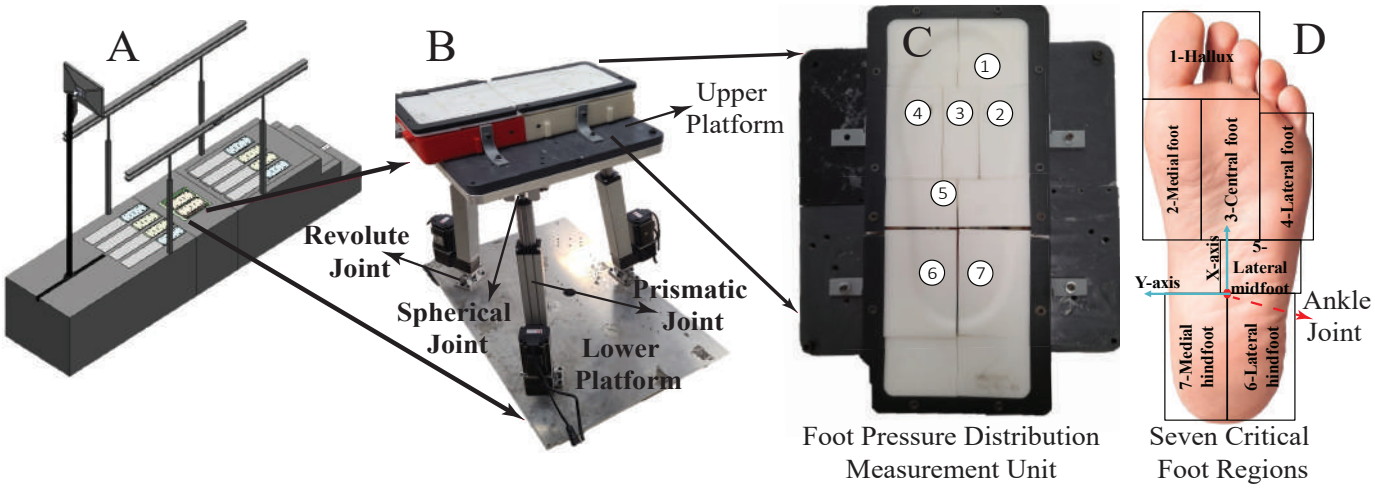


Fig. 1. Representation of the System Details (A) BALANSens platform, (B) 3-RPS parallel robotic manipulator (C) Foot pressure distribution measurement unit (D) Critical foot regions and estimated location of ankle joint

- τ_e is the applied external torque vector.
- M_d, B_d and K_d are the desired mass, damping and stiffness matrices for desired impedance relation.
- q, $\dot{q}$ and $\ddot{q}$ are the actual joints position, velocity and acceleration.
- q_d, $\dot{q}_d$ and $\ddot{q}_d$ are the desired joints position, velocity and acceleration.

we can re-write the equation (13) as

$$\ddot{q} = \ddot{q}_d + M_d^{-1}[B_d(\dot{e}) + K_d(e) - \tau_e] \tag{14}$$

where, $\dot{e} = \dot{q}_d - \dot{q}$ and $e = q_d - q$ are the position and velocity errors. Putting the value of $\ddot{q}$ from equation (14) to equation (13).

$$\tau - \tau_e = \tilde{M}[\ddot{q}_d + M_d^{-1}[B_d(\dot{e}) + K_d(e) - \tau_e]] + \tilde{C}(q, \dot{q})\dot{q} + \tilde{G}$$

by simplification, the following control equation is obtained

$$\tau = \tilde{M}_c M_d^{-1}[M_d\ddot{q}_d + B_d(\dot{e}) + K_d(e) - \tau_e] + \tilde{C}(q, \dot{q}) + \tilde{G} + \tau_e \tag{15}$$

where, τ is the impedance control input torque that ensures the desired impedance behavior between the applied external torque and the robot.

2) Parameters selection: To achieve the desired dynamic response, the matrices M_d, B_d and K_d must be carefully selected. The mass matrix M_d should be selected based on the inertia properties of the robot to avoid oscillations or instability. The damping matrix B_d should be set to provide critical damping or slight over-damping to ensure stability without overshooting. The stiffness matrix K_d should be chosen based on the desired accuracy in positioning, where higher stiffness values correspond to greater resistance to deviations from the reference trajectory. By adjusting these parameters, precise control over the motion while responding appropriately to external forces or disturbances can be achieved. To achieve the desired dynamic response of each linearly actuated joint, the characteristic equation of second order mass, spring and damper system is utilized to select the appropriate M_d, B_d and K_d matrices as follows.

$$s^2 + 2\zeta\omega_n s + \omega_n^2 = 0, \quad s^2 + \frac{B}{M}s + \frac{K}{M} = 0 \tag{16}$$

$$\omega_n = \sqrt{\frac{K_d}{M_d}}, \quad \zeta = \frac{B_d}{2\sqrt{M_d K_d}} \tag{17}$$

whereas, M_d, B_d and K_d are $3X3$ matrices having the mass, damping and stiffness values of three linearly actuated joints.

C. Foot-Ankle torque measurement using load cells

A foot pressure distribution measurement assembly containing the load cells is placed on the upper platform of the BALANSens robot as shown in Fig. 1-B, C. While previous studies (e.g., [19]) have divided the foot into multiple regions, space constraints and physiotherapist consultation led to the selection of seven key regions for load cell placement. The 7 key regions are of hallux, medial foot, central foot, lateral foot, lateral mid-foot, medial hind-foot and lateral hind-foot for the load cells placements as shown in the Fig. 1-D. To ensure accurate measurements, the load cells were calibrated using known weights, and linear fitting was applied to compensate for non-linearity. Additionally, baseline offsets were corrected to eliminate measurement bias. Ankle torque is estimated by leveraging the vertical forces applied by the foot in these regions. A coordinate system is defined with an approximated ankle joint as an origin. The x-axis is defined in the anterior-posterior direction (heel-to-toe), the y-axis is defined in the Medial-lateral direction (side-to-side) and the z-axis is defined in the vertical direction. The ankle joint origin is estimated to be approximately 7-8 cm forward from the back of the heel along the x-axis and 2-3 cm from the medial side (inside) of the foot along the y-axis, based on an average foot size. The subject's foot is positioned so that the actual ankle joint aligns

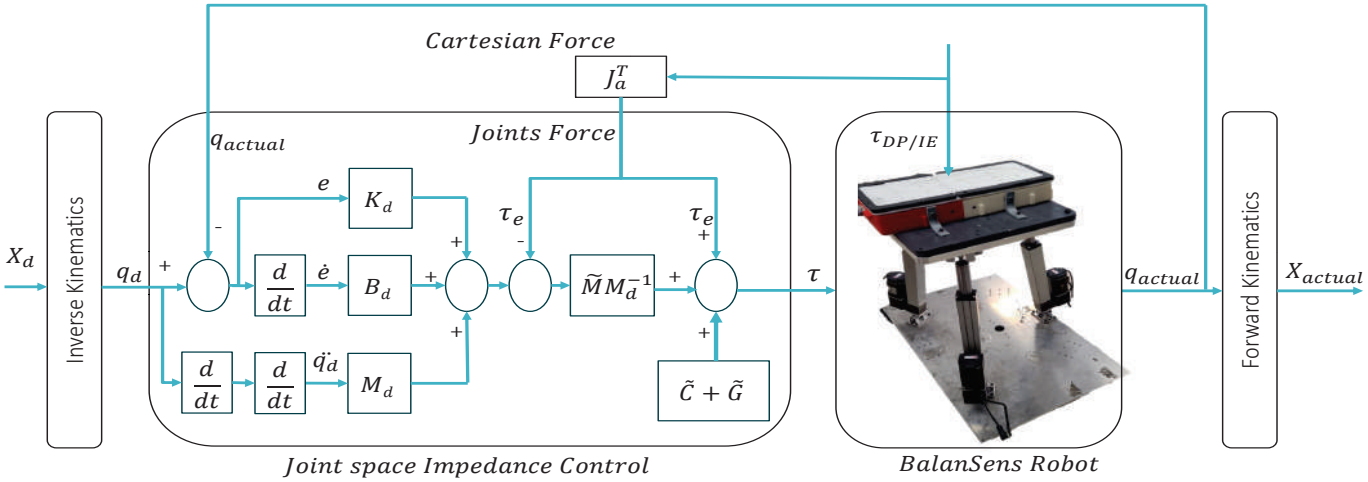


Fig. 2. Block diagram of impedance control implementation on BALANSens Robotic Platform

with this estimated origin. The ankle torque is calculated as the sum of individual torques due to the vertical force of each region about the origin. The torque calculation in DP direction τ_{DP} and IE direction τ_{IE} are represented in equation (18).

$$\tau_{DP} = \sum_{i=1}^{7} x_i F_{zi}, \quad \tau_{IE} = \sum_{i=1}^{7} y_i F_{zi} \tag{18}$$

where x_i, and y_i are the distances between the center of the ith region and the origin along the x and y axis, respectively and F_{zi} is the vertical force measured by the ith load cell. This calculated torque τ_{DP} and τ_{IE} are the applied torque in cartesian coordinates representing the torque in α and β rotations. These are converted to the corresponding torque exerted on the linear actuators by multiplying the cartesian torque with the transpose of jacobian matrix J_a^T using the equation (10) and used in the control loop.

III. Implementation and Results

The mathematical models derived in previous sections were implemented in the MATLAB Simulink environment to validate their accuracy. For real-time application on the actual robotic hardware, these models were programmed in structured text language on an industrial PC. A reference trajectory was generated and fed as an input to the inverse kinematics block, which then computed the necessary link lengths, velocities, and accelerations. These joint space variables, together with external torques acting on the joints, were provided to the impedance control block. This block calculated the torque input required for the servo drives to achieve the desired impedance behaviour. The servo drives used this torque as a reference, with their inner control loops driving the motors to move the robot accordingly. Feedback from encoders measuring the actual link lengths was used in the forward kinematics block to determine the real-time position and orientation of the robot's moving platform. This allowed for a direct comparison between the desired and actual Cartesian space trajectories. A block diagram illustrating the implementation of impedance control on the BALANSens robot is shown in Fig. 2. The parameters K_d, B_d and M_d were selected using equations (16) and (17), ensuring that the system exhibited a second-order dynamic response characterized by a natural frequency of ω_n= 6 and a damping ratio of ζ = 0.5. To test and verify the robot's impedance behavior, an experiment involving a human subject was designed, focusing on three specific test cases for DP and IE movements, as shown by the vertical dashed lines in Figs. 3 and 4. The studies involving human participants are reviewed and approved by the University Research Ethics Council of Istanbul Medipol University under the E-66291034-772.02-4494 number. The participant provided his written informed consent to participate and data sharing in this study. The design testing is performed on one of the authors without a formal recruitment process, i.e., the recruitment period is not used in this paper. In the first test case, the subject applied torque via their ankle while the robot remained in its neutral, zero-reference position. The second test case introduced a sinusoidal reference trajectory without any external torque from the subject, to assess the accuracy of reference tracking during free motion. In the third case, while the robot tracked a sinusoidal reference, the subject applied force with their ankle, allowing observation of the robot's dynamic response to the applied torque.

Figure 3 illustrates the results of the robot's DP motion. In Fig. 3-A, the torque applied by the human subject in the end effector frame (Cartesian space) during the DP motion is shown, while Fig. 3-B displays the corresponding change in the β angle (DP angle of the ankle) of the robotic platform in response to the applied torque. The graphs reveal that the subject applied torque between 4 and 14 seconds, with the β angle showing a standard, slightly over-damped response. Between 22 and 34 seconds, the robot followed a sinusoidal reference trajectory with no torque applied by the subject. After 35 seconds, the subject applied torque multiple times while the robot continued to track the sinusoidal reference. The changes in the β angle in response to the applied torques

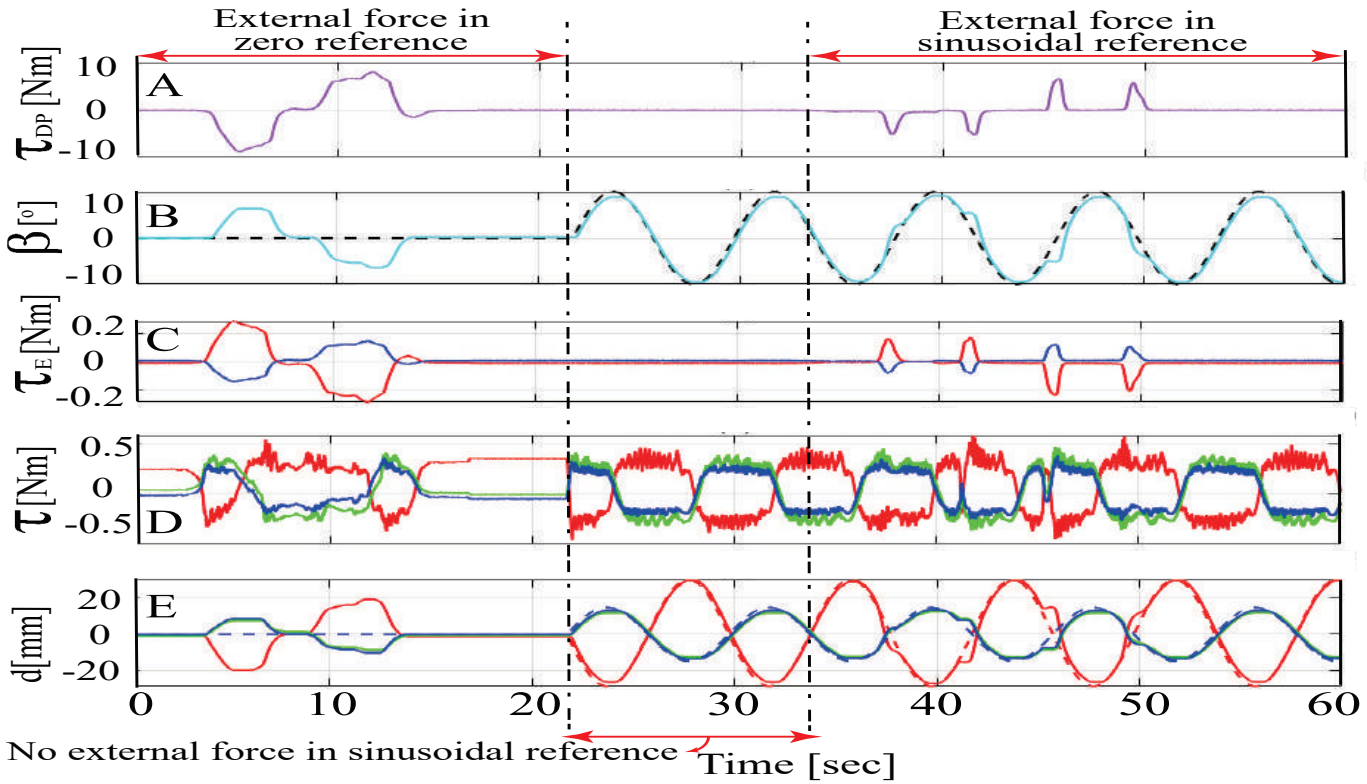


Fig. 3. Dorsiflexion-Plantarflexion (DP) movement: (A) Applied external torque by a human during DP movement (B) DP Angle(β): (Reference:dashed-line, Actual:solid-line) (C) Equivalent external torque on linear joints (Joint1:Red, Joint2:green and Joint3:blue), (green and blue overlapping) (D) Joint Torques: (Joint1:Red, Joint2:green and Joint3:blue), (Reference torque: dashed-line, Actual torque:solid-line) (E) Joint Positions: (Joint1:Red, Joint2:green and Joint3:blue), (Reference position: dashed-line, Actual position:solid-line)

demonstrate the second-order dynamic interaction between the torque and the motion. Figures 3-C and 3-D show the corresponding human torque applied to the linear joints and the reference torque given to the servo drives (calculated from impedance control block) versus actual torques of these joints, respectively, while Fig. 3-E compares the reference and actual positions of the linear joints. The corresponding human applied torque on the second (green-line) and third actuators (blue-line) in Fig. 3-C overlap, while the torque and position tracking of these joints in Fig. 3-D and 3-E show slight deviations due to differences in the dynamic characteristics of each linear actuator. Similarly, Fig. 4 presents the results for the robot's IE motion, considering the same three test cases. These include the response of the robot (Fig. 4-B) when subjected to the torque applied by the subject (Fig. 4-A) while in a zero reference position, the robot's performance during sinusoidal reference tracking without external force, and its response when an external torque is applied while tracking a sinusoidal reference. Figures 4-C, 4-D, and 4-E shows the corresponding human applied torque on the linear joints, torques generated by impedance control and the corresponding change in the linear joint positions, respectively.

The results demonstrate that the BALANSens robotic platform can achieve the desired second-order dynamic relationship between user-applied torque and the angular displacement of the platform using impedance control. Conceptually, the moving platform behaves as if connected to the fixed lower platform by three adjustable leg structures, each modeled with mass, spring, and damper elements. By modifying the values of K_d, B_d and M_d matrices, the system's compliance to the user-applied torque can be adjusted to be more or less responsive. This adaptability makes the approach suitable for customizing compliance levels to match the varying abilities of different users. The limitations of this study include the lack of subject-specific calibration methods to account for variations in foot size and alignment issues, as well as the need for more refined impedance tuning strategies to adapt to individual rehabilitation responses. A video demonstration of the BALANSens platform with impedance control to further illustrate the implementation and functionality is available at https://youtu.be/seuiG2Nziho.

IV. Conclusion

This study successfully demonstrates the implementation of the impedance control method for the BALANSens robotic platform, emphasizing affordability and feasibility for active ankle rehabilitation. By utilizing load cells placed under the foot sole instead of costly six-axis force sensors, the platform effectively measures ankle torques, addressing both cost constraints and data richness. The derived impedance control architecture has been validated experimentally through the

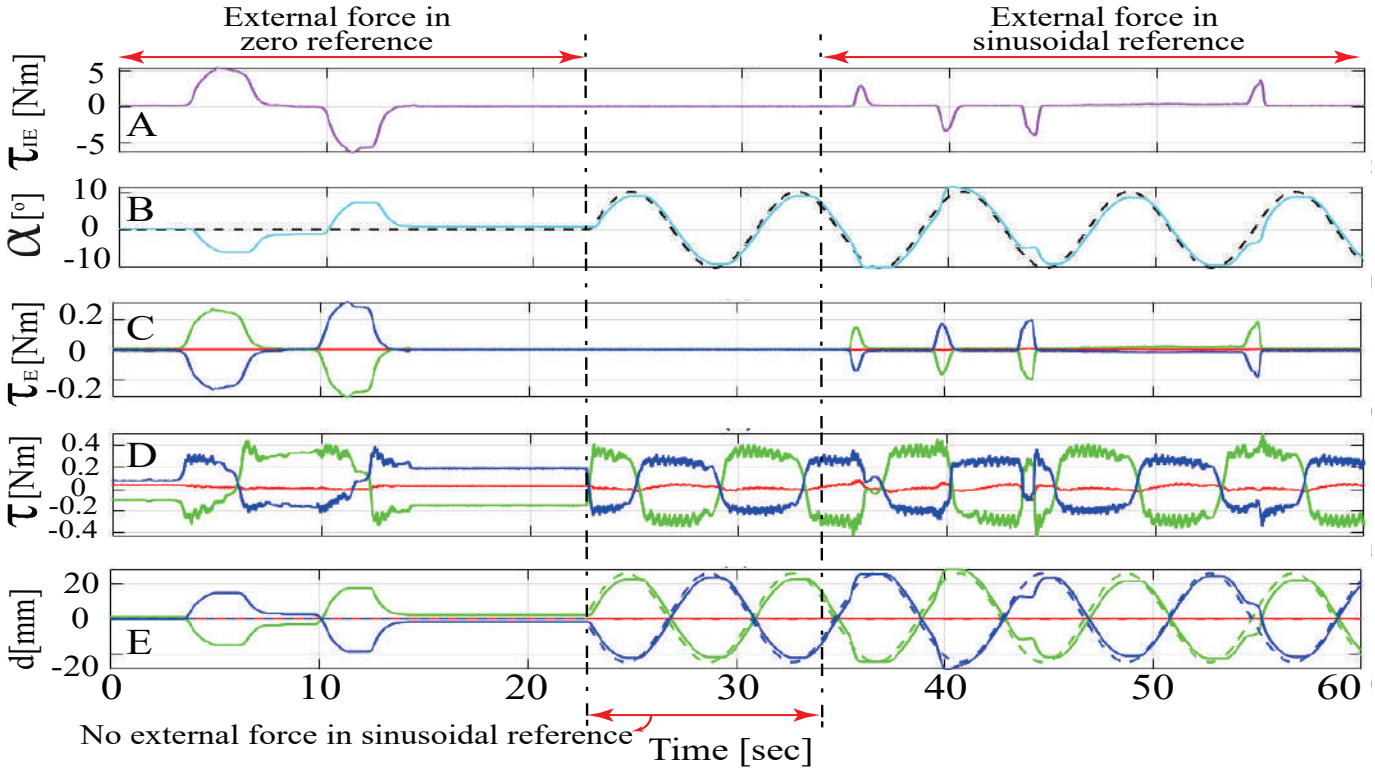


Fig. 4. Inversion-Eversion (IE) movement:(A) Applied external torque by human during IE movement (B) IE Angle(α): (Reference:dashed-line, Actual:solid-line) (C) Equivalent external torque on linear joints (Joint1:Red, Joint2:green and Joint3:blue) (D) Joint Torques: (Joint1:Red, Joint2:green and Joint3:blue), (Reference torque: dashed-line, Actual torque:solid-line) (E) Joint Positions:(Joint1:Red, Joint2:green and Joint3:blue), (Reference position: dashed-line, Actual position: solid-line)

prototype with a human subject, confirming the feasibility of this approach in realistic rehabilitation scenarios. Future work will focus on real-time regulation of compliance levels to accommodate varying ankle strength abilities. Additionally, it includes developing a foot pressure measurement assembly for both feet and extending the platform's application to balance rehabilitation exercises.

References

[1] D. Günther *et al.*, "The burden of neurological diseases in europe: An analysis for the global burden of disease study 2017," *The Lancet Public Health*, vol. 5, no. 10, pp. e551–e567, 2020.

[2] T. Ersoy and E. Hocaoglu, "A 3-DoF robotic platform for the rehabilitation and assessment of reaction time and balance skills of ms patients," *PLoS ONE*, vol. 18, p. 0280505, 2023.

[3] T. Ersoy, P. Kaya, E. Hocaoglu, and R. Unal, "Design of BalanSENS: Functional evaluation in ankle preparation phase," *Journal of Bionic Engineering*, vol. 21, 2024.

[4] ——, "I-BaR: integrated balance rehabilitation framework," *Frontiers in Neurorobotics*, vol. 18, p. 1401931, 2024.

[5] H. Bilal, E. Hocaoglu, R. Unal, and P. Kaya, "An overview of integrated balance rehabilitation (I-BaR) framework," in *International Conference on NeuroRehabilitation (ICNR)*, 2024.

[6] J. He, H. Jiang, D. Cong, Z. M. Ye, and J. W. Han, "A survey on control of parallel manipulator," *Key Engineering Materials*, vol. 339, pp. 307–313, 2007.

[7] H. Z. Arabshahi and A. B. Novinzadeh, "Comparison of motion control techniques for a 3rps parallel manipulator," in *International Conference on Robotics and Mechatronics (ICROM)*. IEEE, 2015, pp. 302–307.

[8] H. Zhang *et al.*, "Dynamic modeling and adaptive robust synchronous control of parallel robotic manipulator for industrial application," *Complexity*, vol. 2020, no. 1, p. 5640246, 2020.

[9] G. Zhang, J. Wu, P. Liu, and H. Ding, "Dynamic analysis and model-based feedforward control of a 2-dof translational parallel manipulator driven by linear motors," *Industrial Robot: An International Journal*, vol. 40, no. 6, pp. 597–609, 2013.

[10] S.-H. Lee, J.-B. Song, W.-C. Choi, and D. Hong, "Position control of a stewart platform using inverse dynamics control with approximate dynamics," *Mechatronics*, vol. 13, no. 6, pp. 605–619, 2003.

[11] S. Chiaverini, B. Siciliano, and L. Villani, "A survey of robot interaction control schemes with experimental comparison," *IEEE/ASME Transactions on mechatronics*, vol. 4, no. 3, pp. 273–285, 1999.

[12] N. Hogan, "Impedance control: An approach to manipulation," in *1984 American control conference*. IEEE, 1984, pp. 304–313.

[13] N. Hogan and S. P. Buerger, "Impedance and interaction control," in *Robotics and automation handbook*. CRC press, 2018, pp. 375–398.

[14] H. Sadjadian and H. D. Taghirad, "Impedance control of the hydraulic shoulder a 3-dof parallel manipulator," in *2006 IEEE International Conference on Robotics and Biomimetics*. IEEE, 2006, pp. 526–531.

[15] H. Z. Arabshahi and A. B. Novinzadeh, "Impedance control of the 3rps parallel manipulator," in *2014 Second RSI/ISM International Conference on Robotics and Mechatronics (ICRoM)*. IEEE, 2014, pp. 486–492.

[16] J. Fabian *et al.*, "Sensorless impedance control for the ur5 robot," in *International Conference on Control, Automation and Diagnosis (ICCAD)*. IEEE, 2020, pp. 1–6.

[17] Y. Wang, "Impedance control without force sensors with application in homecare robotics," Ph.D. dissertation, Univ. of British Columbia, 2014.

[18] T. M. Vieira *et al.*, "How much does the human medial gastrocnemius muscle contribute to ankle torques outside the sagittal plane?" *Human movement science*, vol. 32, no. 4, pp. 753–767, 2013.

[19] C. K. Ang, M. I. Solihin, W. J. Chan, and Y. Y. Ong, "Study of plantar pressure distribution," in *MATEC Web of Conferences*, vol. 237. EDP Sciences, 2018, p. 01016.

Ambulation with a transfemoral bone-anchored powered knee-ankle prosthesis: A case study

Ann M. Simon
Center for Bionic Medicine, Shirley Ryan AbilityLab
Dept of PhysicalMed and Rehab, Northwestern University
Chicago, IL, USA
asimon@sralab.org

Andrea J. Ikeda
Center for Bionic Medicine, Shirley Ryan AbilityLab
Chicago, IL, USA
aikeda@sralab.org

Suzanne B. Finucane
Center for Bionic Medicine, Shirley Ryan AbilityLab
Chicago, IL, USA
sfinucane@sralab.org

Shawana Anarwala
Center for Bionic Medicine, Shirley Ryan AbilityLab
Chicago, IL, USA
sanarwala@sralab.org

Kayan Abdou
Center for Bionic Medicine, Shirley Ryan AbilityLab
Chicago, USA
kabdou@sralab.org

Levi J. Hargrove
Center for Bionic Medicine, Shirley Ryan AbilityLab
Dept of PhysicalMed and Rehab and Dept of Biomedical Engineering, Northwestern University
Chicago, IL, USA
lhargrove@sralab.org

***Abstract*— Recent advancements in powered prosthetic leg devices offer enhanced potential for mobility for individuals with lower limb amputations; however, challenges persist, particularly for those with transfemoral amputations and short residual limbs. This study investigates the combination of a bone-anchored prosthetic interface via osseointegration and a powered knee-ankle prosthesis, aiming to assess initial feasibility, functionality, and user experience. A 39-year-old female with a very short residual limb participated, using the Hybrid Knee and Polycentric Ankle powered leg connected to an osseointegrated implant. Training involved level-ground and incline walking, stair climbing, and sit-to-stand weight transfers. Results indicated successful ambulation across all activities, with the participant demonstrating ease in reciprocal stair climbing and improved ease of sit-to-stand movements compared to her prescribed, passive prosthesis. User feedback highlighted the benefits of level-walking knee swing assist and powered ankle plantarflexion, and stair ascent and sit-to-stand knee extension power, though cosmesis and weight remained areas of preference for her prescribed device. This case underscores the potential of combining osseointegration and powered prostheses to enhance functionality and mobility, paving the way for further research on this promising technology.**

Keywords—above-knee amputation, artificial limb, bone-anchored implant, rehabilitation

I. Introduction

Recent advances in prosthetic technology have impacted individuals with lower limb amputations. Despite improvements in prosthetic devices, this population faces substantial challenges in daily mobility, such as high energy expenditure during walking, difficulty with stair climbing, and limitations in other essential activities [1], [2], [3], [4]. Functional mobility often becomes increasingly difficult for individuals with transfemoral amputations when they have a shorter residual limb [5]. Traditional socket-based prostheses, while functional, come with significant drawbacks related to comfort, fit, and mobility for these individuals.

Bone-anchored interfaces offer a promising alternative by allowing direct attachment of the prosthesis to the residual bone, thus eliminating the need for a socket. Osseointegration creates a structural connection between the bone and a biocompatible implant, facilitating natural load transfer and providing a stable attachment point for the prosthesis. Originally developed for dental implants, osseointegration has now been adapted for limb prosthetics and has shown improvements in quality of life when compared to a conventional socket [6], [7]. Various osseointegration systems are actively in use or in clinical trials around the world [8]. To the authors knowledge, use of these lower limb systems with powered prosthetic knees and ankles has not been investigated.

Powered prostheses incorporate motors and sensors that actively assist users in performing activities of daily living. For individuals with a transfemoral amputation, coordinated control of powered knee and ankle joints may allow for improved function and mobility [9]. Studies using powered leg prostheses have reported that users can ambulate on level-ground and inclines, climb stairs with reciprocal gait, and stand up from a seated position with more normative kinematics and kinetics [10], [11], [12], [13], [14].

The increased weight of these powered prosthetic devices can exacerbate socket instability, especially for those with shorter residual limbs who are known to exhibit greater gait deviations [5]. Directly anchoring the prosthesis to the

This work is supported by the Congressionally Directed Medical Research Program (CDMRP) Peer Reviewed Orthopedic Research Program award W81XWH-22-1-0850.

skeletal system via a bone-anchored interface could provide a stable and secure attachment point for powered prostheses. With osseointegration, the load from the powered prosthesis would be transmitted directly to the bone rather than through soft tissue. This secure attachment could make powered prostheses more feasible for everyday use, enhancing the user's ability to perform high-impact or repetitive activities that demand greater strength and stability.

Despite the promising potential of combining osseointegration with powered prostheses, there has been limited research exploring this combination. Recent studies by Frossard et al. [15], [16] have demonstrated that ambulation with a powered knee prosthesis (OSSUR Power Knee™, OSSUR, Reykjavík, Iceland) paired with the Australian Press-Fit bone-anchored system, was safe from a loading perspective. That is, the forces and moments generated by the powered knee prosthesis during walking, as well as ascending and descending ramp and stairs, maintained a safety margin greater than three when compared to published maximum femoral loads observed in able bodied running [15]. To date, there are no published studies discussing the quality of ambulation pairing a bone-anchored interface with a powered knee and powered ankle prosthesis.

This study aims to investigate the feasibility and benefits of combining lower limb osseointegration with powered prosthetics, assessing user control and comfort. In this case study, a 39 year old female was trained to use a powered knee and ankle prosthesis for multiple ambulation modes including reciprocal stair climbing. We include prosthesis sensor data during ambulation as well as the participant's subjective feedback.

II. Methods

A. Participant

A 39 year old female with a right transfemoral amputation (very short residual limb) due to trauma nine years prior participated in this study. She was two years post-completion of osseointegration Stage 2 surgery with the OPRA™ Implant System (Integrum, Mölndal, Sweden). She was 1.75 m tall and weighed 47.6 kg when not wearing her prosthesis. Her clinically prescribed prosthesis, which she used for two years, included an Ottobock C-Leg® knee, Ottobock Trias foot (Ottobock, Duderstadt, Germany), OPRA Axor™ II (Integrum, Mölndal, Sweden), and Ottobock torsion adapter. The prosthesis weighed 3.6 kg. She was an active individual and reported using her prosthesis regularly for recreation and activities including yoga and pilates. She reported no problems using her prosthesis. With her prescribed prosthesis, she ascended stairs using a step-to gait and descended stairs using a reciprocal gait. This study was approved by Northwestern University Institutional Review Board and the individual provided written informed consent to participate.

B. Powered Knee-Ankle Prosthesis

Prior to fitting the powered prosthesis, a 1.5kg weight was added distally to the participant's prescribed prosthesis (i.e., on the distal pylon, just proximal to the prosthetic foot) to simulate the added weight of the powered prosthesis. She was then asked to walk over level ground, ascend and descend a 10 degree ramp, and climb stairs (ascend with a step-to gait, and descend with a reciprocal gait). The participant reported no discomfort or interference with her mobility and thus was fit with the powered device.



Figure 1. Participant with osseointegration using the powered leg prosthesis (Hybrid Knee and Polycentric Ankle).

A certified prosthetist fit the powered knee-ankle prosthesis. The powered prosthesis included the Hybrid Knee [17] and Polycentric Ankle [18], OPRA Axor™ II (Integrum Mölndal, Sweden), and Ottobock torsion adapter (Figure 1). The prosthesis weighed 5.2 kg.. Embedded sensors in each joint measured knee and ankle joint position, velocity and motor currents. Additional sensors included a six degree-of-freedom load cell and an inertial measurement unit (IMU) both mounted in the shank. Shank inclination angle was calculated using the IMU and thigh angle was calculated using the IMU and knee encoder.

The powered knee-ankle prosthesis was controlled in active mode using an impedance-based model according to (1):

$$\tau = -k(\theta - \theta_d) - b\dot{\theta} \quad (1)$$

where τ was the commanded joint torque, θ was the joint angle, and $\dot{\theta}$ was the joint angular velocity. The three impedance parameters were stiffness, k, equilibrium angle, θ_d, and damping coefficient, b.

A finite state machine originally developed by Sup et al. [19] and further developed across various activities with a wide range of individuals [10], [14], [20], [21], [22], [23]. Similar to this previous work, stance and swing phases of each activity and transitions between activities including standing, walking, sit-to-stand and stand-to-sit weight transfers were controlled via mechanical sensor thresholding (e.g., axial load or inclination angle thresholding for state transitions). Transitions between stairs, ramps, and level-ground walking were controlled via a key fob.

Therapist-led functional mobility training was provided according to [24], including starting with educating the participant on the ability of the prosthesis to provide power in knee flexion and extension and the ankle to provide powered plantarflexion and dorsiflexion across multiple activities. Powered prosthesis parameters were only modified if necessary based on user and therapist feedback (i.e., empirical tuning similar to [22]). The participant began in the parallel bars and practiced transitioning between standing and walking. At heel strike, the knee is active and extended to provide a stable knee during weight acceptance. As the user

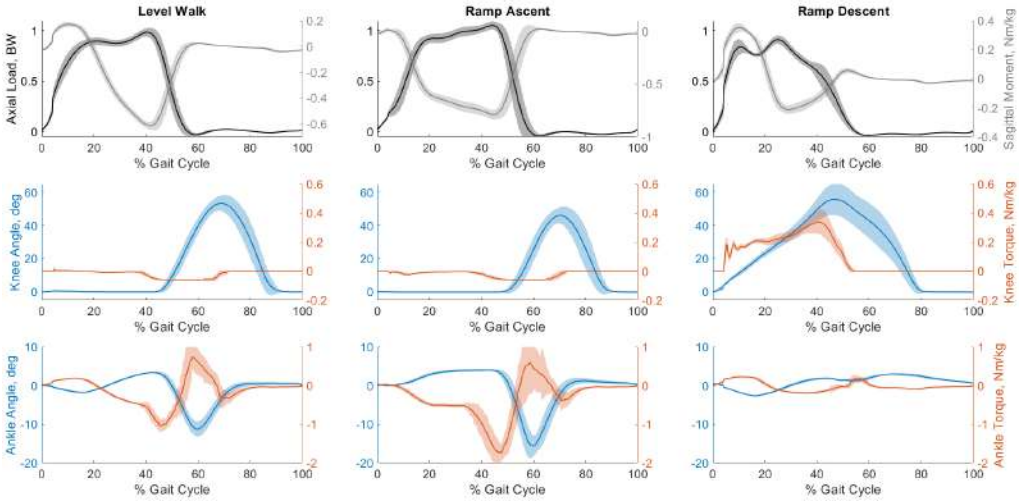


Figure 2. Signals from the powered prosthesis averaged across the gait cycle during level walking (*left*), ramp ascent (*middle*), and ramp descent (*right*) including axial load and sagittal moment both measured in the shank (*top*), knee angle and torque (*middle*), and ankle angle and torque (*bottom*). Positive knee torque indicates knee extension torque and negative values represent knee flexion torque. Positive ankle torque indicates ankle dorsiflexion torque and negative values indicate ankle plantarflexion torque.

progresses over the foot into terminal stance, the prosthesis begins to provide powered ankle plantarflexion and a small amount of powered knee flexion to assist with the transition to swing phase. At the transition of toe-off the knee actively flexes and the ankle actively dorsiflexes for swing clearance and then the leg extends to prepare the prosthesis for heel strike. The participant's training quickly moved from walking within parallel bars to walking around the laboratory.

Training progressed to powered weight transfers. For sit-to-stand, the participant was instructed on proper foot placement, forward trunk lean, and increased hip flexion to aid standing, enabling a smoother transfer of weight through the powered prosthesis. During the stand-up movement, the knee actively extends and the ankle actively moves to a neutral position. For stand-to-sit movements, she was instructed to distribute her weight equally and attempt to sit with forward trunk lean and active hip flexion. During the sit down movement, the knee and ankle provide supportive resistance for sitting. She was instructed to utilize the armrests for balance if needed and trained to sit/stand from various height chairs.

Training for stair climbing began with a shorter curb-like stair step to confirm her residual limb hip flexion strength to raise the prosthesis to the height of the step and confirm her comfort with the knee extension lifting her up. When the prosthetic foot was placed fully onto the step, she was instructed to push down into the prosthesis. This transfer of weight activated knee extension power to assist in stepping up. Training then progressed to a six-step staircase (6" rise) where the user was instructed on reciprocal stair ascent gait. Since the participant was already familiar with reciprocal stair descent with her prescribed prosthesis, minimal training for this activity was necessary, although slight variations in foot placement were explored.

Training was also provided for ascending and descending an 10-degree ramp. For ramp ascent, the prosthesis provided similar stance support, late-stance powered ankle plantarflexion, and active knee flexion and ankle dorsiflexion for swing clearance. For ramp descent, the knee provided stance resistance to "ride" the knee down for controlled descent into knee flexion. The participant was familiar with riding the knee down in a similar way with her prescribed prosthesis.

After comfortable across all trained activities, the research participant completed a custom user feedback questionnaire on her comfort, preference, and ability to perform the activities with the powered prosthesis compared to her prescribed prosthesis.

Sensor data, including joint angles, joint torques, axial load, and sagittal moment, were segmented into strides from heel contact to heel contact based on axial load. The signals were then averaged across multiple strides for each activity and plotted along with their standard deviation.

III. Results

The participant was successful in safely and comfortably ambulating with the powered knee and ankle prosthesis across level-ground, inclines, and staircases. Initial training across all activities took approximately one hour and then additional practice was provided. Though the prosthesis was heavier than her prescribed device, the participant reported that during this training session the additional weight did not cause discomfort at the osseointegrated implant.

Figure 2 shows powered prosthesis signals averaged across the gait cycle for level-ground walking (*left*), ramp ascent (*middle*), and ramp descent (*right*). During level-ground walking and ramp ascent, these graphs show in late stance a burst of ankle torque for propulsion, and in late stance and early swing a small amount of knee torque to aid knee swing flexion. The participant reported increased ease of walking on level ground and inclines with powered plantarflexion and swing assist. During ramp descent, the knee provides extension power to provide stance support as the user rides the knee into stance flexion and (for this session) the ankle provided static ankle support.

The participant was successful in ascending stairs with a reciprocal gait (Figure 3), noting that she could feel the extension assistance of the powered device. Additionally, without a socket to limit hip range of motion, she was able to ascend a staircase with higher-rise steps with ease. For stair

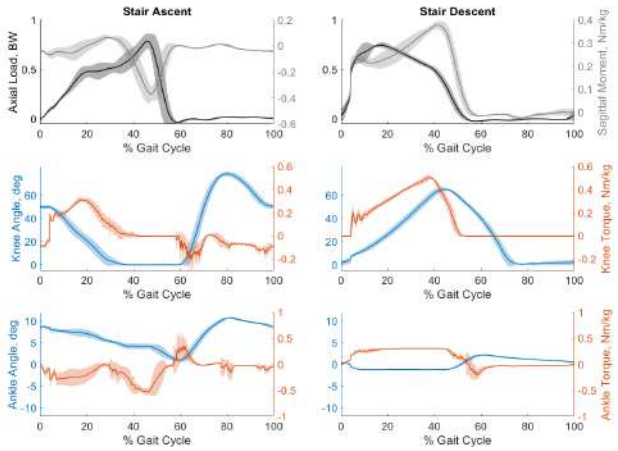


Figure 3. Signals from the powered prosthesis averaged across the gait cycle during stair ascent (*left*) and stair descent (*right*) including axial load and sagittal moment both measured in the shank (*top*), knee angle and torque (*middle*), and ankle angle and torque (*bottom*). Positive knee torque indicates knee extension torque and negative values represent knee flexion torque. Positive ankle torque indicates ankle dorsiflexion torque and negative values indicate ankle plantarflexion torque.

descent, she preferred foot placement similar to her prescribed prosthesis: half off the stair to ride the knee down but not utilize the ankle range of motion.

She was also able to perform sit-to-stand and stand-to-sit movements with ease including successfully transitioning from chairs of various heights. Unfortunately, not all necessary signals were recorded for the sit-to-stand activities to fully reconstruct plots for these weight transfers. Additionally, the participant demonstrated improved ability to reach for low objects and pick items up from the floor, aided by forward trunk bending and hip flexion to lower herself. The subject also utilized the sit-down feature of the prosthesis for squatting tasks.

The participant provided feedback that she preferred the powered knee and ankle prosthesis for level-ground walking, ascending and descending stairs and sit-to-stand and stand-to-sit movements. She preferred her prescribed prosthesis for incline walking and found it more favorable in terms of weight.

IV. Discussion

To the authors knowledge, this study represents the first instance of a participant with a transfemoral amputation and osseointegration walking on a powered knee-ankle prosthesis, highlighting both the potential benefits and unique considerations of combining a bone-anchored interface with advanced prosthetic technology. During training, care was taken to ensure that the powered prosthetic joint torques did not cause discomfort in the participant's residual limb near the implant. While she described some movements as feeling "different" or "odd," she confirmed that they were not painful.

Individuals with transfemoral amputations using traditional socket-based systems face challenges with fit, suspension and stability; those individuals with very short residual limbs inherently have reduced surface area in which to distribute loads [25]. In our decade of experience testing various powered leg prototypes [24], this participant had a shorter residual limb than anyone who used the device with socket suspension. In contrast to these other users, this participant's bone-anchored prosthesis offered quicker fit, improved suspension, and likely enhanced perception of the prosthetic limb compared to a socket. In this case study, these benefits of osseointegration were maintained while using the powered knee and ankle prosthesis. The improved suspension and the potential for osseoperception (e.g., foot placement awareness) suggest that osseointegration could enhance use of powered devices.

Although the participant noted the increased weight of the powered prosthesis, she still preferred it over her prescribed, passive prosthesis for certain activities including level-ground walking, stair climbing and sit-to-stand and stand-to-sit movements. In level-ground walking, she noted being able to feel the powered plantarflexion and swing assist. In stair climbing, she appreciated the knee extension power and enjoyed the ability to climb stairs with a reciprocal gait, noting she had not done this since her injury. She also appreciated the knee extension power during sit-to-stand movements. Although the participant preferred and appreciated the powered assistance, the knee and ankle torques provided were considerably lower than those observed in able-bodied gait and below the device's full capabilities [17], [26]. The session intentionally started with reduced torque levels to ensure comfort at the bone-anchored interface, with plans to gradually increase joint torque to improve movement quality based on her preference, task performance, and therapist feedback. However, during this initial training session, the participant successfully completed each task and found the initial torque levels sufficient. Further testing is needed to determine the optimal joint torques and to assess functionality and comfort over an extended duration.

In this case study, the participant received limited functional mobility training to use the powered prosthesis. This initial training was mostly focused on ensuring comfort through the bone-anchored interface and minor empirical tuning of prosthesis based on user and therapist feedback. Configuration time was similar to other participants who have walked on powered devices with socket suspension. Fortunately, the powered leg control did not need any modifications beyond what was typically configured. Research with more participants with bone-anchored prostheses is necessary to see if similar results extend to a larger population.

There are several limitations of this study including that training and use occurred over a short period of time and were with a highly functional participant. While this study demonstrated effective use of the powered prosthesis, there was no formal biomechanical analysis or comparison with her prescribed, passive prosthesis. Additional studies should include these comparisons including the use of clinical outcomes to quantify differences between devices for individuals with bone-anchored interfaces.

V. Conclusion

This trial demonstrated that an individual with a very short residual limb and a bone-anchored interface could

effectively use a fully powered knee and ankle prosthesis across multiple ambulation modes. Future studies involving a larger sample of participants are needed to explore the broader implications of this approach, including comparing clinical outcomes to passive devices.

ACKNOWLEDGMENT

The authors thank the members of the Center for Bionic Medicine mechatronics team for all hardware and software development and support.

REFERENCES

[1] H. Burger, C. Marincek, and E. Isakov, "Mobility of persons after traumatic lower limb amputation," *Disabil. Rehabil.*, vol. 19, no. 7, pp. 272–277, 1997.

[2] B. J. Hafner, L. L. Willingham, N. C. Buell, K. J. Allyn, and D. G. Smith, "Evaluation of function, performance, and preference as transfemoral amputees transition from mechanical to microprocessor control of the prosthetic knee," *Arch. Phys. Med. Rehabil.*, vol. 88, no. 2, pp. 207–217, Feb. 2007, doi: 10.1016/j.apmr.2006.10.030.

[3] E. G. Halsne, M. G. Waddingham, and B. J. Hafner, "Long-term activity in and among persons with transfemoral amputation," *J. Rehabil. Res. Dev.*, vol. 50, no. 4, p. 515, 2013, doi: 10.1682/JRRD.2012.04.0066.

[4] S. Ettema, E. Kal, and H. Houdijk, "General estimates of the energy cost of walking in people with different levels and causes of lower-limb amputation: A systematic review and meta-analysis," *Prosthet. Orthot. Int.*, vol. 45, no. 5, pp. 417–427, 2021, doi: 10.1097/PXR.0000000000000035.

[5] J. C. Bell, E. J. Wolf, B. L. Schnall, J. E. Tis, L. L. Tis, and B. K. Potter, "Transfemoral amputations: The effect of residual limb length and orientation on gait analysis outcome measures," *J. Bone Jt. Surg.*, vol. 95, no. 5, pp. 408–414, 2013, doi: 10.2106/JBJS.K.01446.

[6] R. Brånemark, P. I. Brånemark, B. Rydevik, and R. R. Myers, "Osseointegration in skeletal reconstruction and rehabilitation: a review," *J. Rehabil. Res. Dev.*, vol. 38, no. 2, pp. 175–181, 2001.

[7] J. S. Hoellwarth, K. Tetsworth, A. Rozbruch, S. Robert Handal, M. Brianne Coughlan, and M. Al Muderis, "Osseointegration for amputees current implants, techniques, and future directions," *JBJS Rev.*, vol. 8, no. 3, p. e0043, 2020, doi: 10.2106/JBJS.RVW.19.00043.

[8] A. Thesleff, R. Brånemark, B. Håkansson, and M. Ortiz-Catalan, "Biomechanical characterisation of bone-anchored implant systems for amputation limb prostheses: A systematic review," *Ann. Biomed. Eng.*, vol. 46, no. 3, pp. 377–391, 2018, doi: 10.1007/s10439-017-1976-4.

[9] R. Gehlhar, M. Tucker, A. J. Young, and A. D. Ames, "A review of current state-of-the-art control methods for lower-limb powered prostheses," *Annu. Rev. Control*, vol. 55, pp. 142–164, 2023, doi: 10.1016/j.arcontrol.2023.03.003.

[10] F. Sup, H. A. Varol, and M. Goldfarb, "Upslope walking with a powered knee and ankle prosthesis: Initial results with an amputee subject," *IEEE Trans. Neural Syst. Rehabil. Eng.*, vol. 19, no. 1, pp. 71–78, Feb. 2011, doi: 10.1109/TNSRE.2010.2087360.

[11] E. D. Ledoux, M. Goldfarb, T. J. Withrow, and K. E. Zelik, "Control and evaluation of stair ascent with a powered transfemoral prosthesis," *IEEE Trans Neural Syst Rehabil Eng*, vol. 25, no. 7, pp. 917–924, 2017, doi: 10.1109/TNSRE.2017.2656467.

[12] G. Hunt, S. Hood, and T. Lenzi, "Stand-up, squat, lunge, and walk with a robotic knee and ankle prosthesis under shared neural control," *IEEE Open J. Eng. Med. Biol.*, vol. 2, no. July, pp. 267–277, 2021, doi: 10.1109/ojemb.2021.3104261.

[13] H. L. Bartlett, S. T. King, M. Goldfarb, and B. E. Lawson, "A semi-powered ankle prosthesis and unified controller for level and sloped walking," *IEEE Trans. Neural Syst. Rehabil. Eng.*, vol. 29, pp. 320–329, 2021, doi: 10.1109/TNSRE.2021.3049194.

[14] A. M. Simon, N. P. Fey, K. A. Ingraham, S. B. Finucane, E. G. Halsne, and L. J. Hargrove, "Improved weight-bearing symmetry for transfemoral amputees during standing up and sitting down with a powered knee-ankle prosthesis," *Arch. Phys. Med. Rehabil.*, vol. 97, no. 7, pp. 1100–1106, Jul. 2016, doi: 10.1016/j.apmr.2015.11.006.

[15] L. Frossard, S. Laux, M. Geada, V. Valgeirsdóttir, S. Jónsdóttir, and K. Lechler, "Margin of safety of load applied by transfemoral bone-anchored prostheses fitted with state-of-the-art components," in *ISPO 19th World Congress*, Guadalajara, Mexico, 2023, p. 235.

[16] L. Frossard, S. Laux, M. Geada, V. V Valgeirsdóttir, S. Jónsdóttir, and K. Lechler, "Osseointegration gait and biomechanics," in *ISPO 19th World Congress*, Guadalajara, Mexico, 2023, p. 234.

[17] T. Lenzi, M. Cempini, L. Hargrove, and T. Kuiken, "Design, development, and testing of a lightweight hybrid robotic knee prosthesis," *Int. J. Rob. Res.*, vol. 37, no. 8, pp. 953–976, 2018, doi: 10.1177/0278364918785993.

[18] M. Cempini, L. J. Hargrove, and T. Lenzi, "Design, development, and bench-top testing of a powered polycentric ankle prosthesis," *IEEE Int. Conf. Intell. Robot. Syst.*, pp. 1064–1069, 2017, doi: 10.1109/IROS.2017.8202276.

[19] F. Sup, H. A. Varol, J. Mitchell, T. J. Withrow, and M. Goldfarb, "Preliminary evaluations of a self-contained anthropomorphic transfemoral prosthesis," *IEEE ASME Trans Mechatron*, vol. 14, no. 6, pp. 667–676, Dec. 2009, doi: 10.1109/TMECH.2009.2032688.

[20] B. Lawson, A. Varol, A. Huff, E. Erdemir, and M. Goldfarb, "Control of stair ascent and descent with a powered transfemoral prosthesis," *IEEE Trans. Neural Syst. Rehabil. Eng.*, vol. 21, no. 3, pp. 466–473, 2013, doi: 10.1109/TNSRE.2012.2225640.

[21] H. A. Varol, F. Sup, and M. Goldfarb, "Powered sit-to-stand and assistive stand-to-sit framework for a powered transfemoral prosthesis," *IEEE Int. Conf. Rehabil. Robot.*, vol. 5209582, pp. 645–651, 2009, doi: 10.1109/ICORR.2009.5209582.

[22] A. M. Simon *et al.*, "Configuring a powered knee and ankle prosthesis for transfemoral amputees within five specific ambulation modes," *PLoS One*, vol. 9, no. 6, p. e99387, Jun. 2014, doi: 10.1371/journal.pone.0099387.

[23] A. M. Simon, S. B. Finucane, A. J. Ikeda, R. J. Cotton, and L. J. Hargrove, "Powered knee and ankle prosthesis use with a K2 level ambulator: a case report," *Front. Rehabil. Sci.*, vol. 4, no. June, pp. 1–8, 2023, doi: 10.3389/fresc.2023.1203545.

[24] S. B. Finucane, L. J. Hargrove, and A. M. Simon, "Functional mobility training with a powered knee and ankle prosthesis," *Front. Rehabil. Sci.*, vol. 3, p. 790538, 2002, doi: doi:10.3389/fresc.2022.790538.

[25] C. M. Schuch, "Transfemoral Amputation: Prosthetic Management," in *Atlas of Limb Prosthetics: Surgical, Prosthetic, and Rehabilitation Principles*, 2nd ed., J. H. Bowker and J. W. Michael, Eds., Rosemont, IL: American Academy of Orthopaedic Surgeons, 1992, ch. 20B. [Online]. Available: http://www.oandplibrary.org/alp/

[26] R. Reiner, M. Rabuffetti, and C. Frigo, "Joint powers in stair climbing at different slopes," *Proc. IEEE Int. Conf. Eng. Med. Biol.*, vol. 1, p. 530, 1999.

Towards the development of dynamic hand orthosis without conventional joints

Leon Schaeffer[1], Felix Rambach[1], Theresa Schmaußer[1], David Herrmann[1], Lukas Lehmann[1] and Valter Boehm[1]

***Abstract*— The human hand is an exceptionally complex anatomical structure with 31 degrees of freedom. In the development of dynamic wrist-hand orthoses, the wrist's multiaxial mobility is of particular interest. To accurately replicate these natural movements, a promising approach is the use of compliant tensegrity structures. Tensegrity structures allow pivot points and axes of rotation to align with anatomical positions, enabling unrestricted mobility in all directions without conventional joints. Additionally, they permit customized movement restrictions based on therapeutic needs. The orthosis's minimalist, lightweight design ensures both effective joint stabilization and free access to key injured regions. Customizing each orthosis to the patient's unique anatomy and functional needs is crucial to prevent unnecessary strain from improper positioning. The positioning of the orthosis is directly linked to the forces applied to the wrist while using. A precise understanding of the behavior of the orthosis and its influence on the wrist forces present is therefore essential. This work explores key aspects of tensegrity-based orthosis development, emphasizing accurate 3D scanning of hand anatomy, initial experimental measurements, and simulated calculations. The proposed methodology provides a solid foundation for the design of initial prototypes of tensegrity-based hand orthoses.**

I. Introduction

The human hand is a complex body region, consisting of 27 bones, 36 joints and 39 active muscles and having three main sections: carpus, metacarpus, and digiti manus. Hand movements are affected by 33 muscles, which are divided into flexors and extensors [1]. Treatment of hand injuries often requires the use of both static and dynamic hand orthoses, with early motion therapy being crucial for effective healing. However, many of the currently available dynamic orthoses are limited by their degree of freedom (DOF), as they typically only allow for uni-axial motion, limiting their functionality during everyday activities. Orthoses with two or more DOF can be bulky or require motors for actuation [2]–[8]. This highlights the need for orthoses that provide multiple DOF, replicating the multiaxial hand movement, without relying on external actuators. Recent research has highlighted the potential of mechanically prestressed compliant structures [9]. In previous studies [15], [16], a possible concept of a dynamic prestressed compliant hand orthosis has been introduced. The orthosis is designed to be based solely on the user's hand movements, providing natural hand movement with adjustable resistance and immobilization for therapeutic purposes. The adjustment of the range of motion (ROM) is possible by carefully selecting parameters such as the stiffness and initial length of the tensioned members, typically made of elastomeric materials [10], [11], to meet specific therapeutic requirements. Current research is primarily focused on the general feasibility of these structures, without restriction to specific diseases or injuries. In comparison to these earlier works, the objective of this study is to present the general development process and additional development steps required for the development of a prestressed compliant dynamic hand orthosis. These steps include, among others, the individual adaptation of the hand geometry to the orthosis. While the functional components of the orthosis rely on standardized parts and regions, the anatomy of each patient is unique, necessitating a method to effectively combine these aspects. Compared to traditional treatment methods such as a plaster cast, it has been shown that customized Orthoses reduce the time of use during treatment and accelerate functionality [12]. The use of customized orthoses compared to conventional, standard-sized orthoses is also evident in an improvement in grasp force and return to activity [13], [14]. As the wrist is a complex joint in which mechanical loads that occur during therapy can influence local muscle activity and joint forces, potentially spreading compensatory forces throughout the body not only 3D adaptation is needed. In order to ensure that dynamic hand orthoses in particular

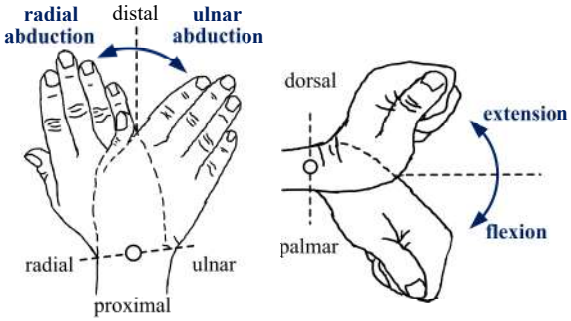


Fig. 1: Range of Motion (ROM) of the human hand with respect to the two main rotational movement possibilities.

This work was supported by Deutsche Forschungsgemeinschaft DFG (Project No. BO 4114/3-2), and by the Regensburg Center of Biomedical Engineering.

[1] Faculty of Mechanical Engineering, OTH Regensburg, 93053 Regensburg, Germany
leon.schaeffer@oth-regensburg.de
felix.rambach@st.oth-regensburg.de
theresa.schmausser@st.oth-regensburg.de
david.herrmann@st.oth-regensburg.de
lukas.lehmann@st.oth-regensburg.de
valter.boehm@oth-regensburg.de

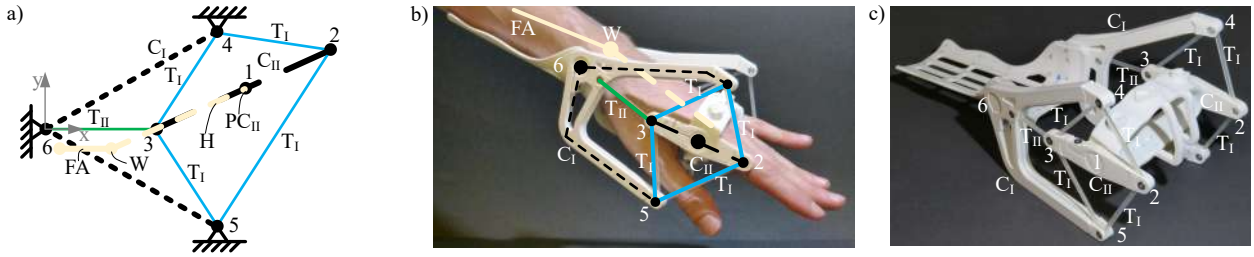


Fig. 2: Hand orthosis, a) 2D tensegrity structure with the applied boundary conditions used for form-finding; PC_{II}: center point of C_{II}, b) Human hand with the first demonstrator of the orthosis based on the described concept and c) Isometric view of the first demonstrator based on the described concept.

can be used effectively as part of therapy, a deeper, more complete understanding of the reaction forces in the hand is essential. For this, this study introduces a first prototype of an experimental test stand for measuring wrist forces. The concept and methodology will be explained, and initial tests will be presented to demonstrate the general functionality of the orthosis as a proof of concept. The test stand is designed to experimentally measure wrist forces as well as basic muscle forces. Furthermore, the maximum deflection and stiffness of the orthosis will be recorded. The work is organized as follows: Section II briefly discusses the anatomy of the human hand, followed by an overview of the hand orthosis in Section III. Section IV explores various methods for studying the body's response to the orthosis. Section V outlines an approach for capturing, digitizing, and processing the human anatomy as these are crucial steps in developing such orthoses with proper placement. Section VI introduces a first prototype test rig for experimental characterization of the hand orthosis.

II. Hand Orthosis

A. Human Hand

The wrist is composed of two joints: the proximal and distal wrist. The proximal wrist is an ellipsoidal joint that allows movement along two axes, while the distal joint acts as a hinge, contributing to stability and enabling grasping and manipulation. The wrist moves along two axes, the transverse axis for flexion and extension and the sagittal axis for radial and ulnar abduction, a third DOF is achieved through forearm rotation, enabling pronation and supination (Fig. 1) [19]. The ROM of the wrist varies depending on the direction and individual flexibility. In the neutral-0-position (0° of deflection in each direction), the hand rests along its axes, stabilized only by a tendon prestress of 8 to 9 N according to [20] independent of resting orientation. From the neutral-0-position, the wrist typically allows an angular deflection range of 50° to 90° for extension and 35° to 95° for flexion. Radial abduction permits an angular deflection of 30° to 60°, while ulnar abduction allows 15° to 35°. Pronation and supination can each achieve a maximum angular deflection of 80° to 90° [21].

B. Compliant Tensegrity Structures

A promising solution which considers the complexity and multi-axis movement of the human hand is the use of orthoses based on prestressed, compliant structures that are inspired by the tensegrity principle. Tensegrity structures consist of a series of compressed members connected by a continuous network of elastic, compliant, tensioned members. In conventional tensegrity structures, only two types of members are used: compressed and tensioned members, which are loaded in uniaxial compression and uniaxial tension. The connection between the members and the properties of the members (such as stiffness and initial length) define the prestress of these structures, their shape and the overall mechanical stiffness. The concept of using mechanically prestressed compliant tensegrity structures to develop dynamic orthoses is interesting for several reasons: With clever design, these structures can accommodate several joint axes with pivot points and axes of rotation outside the structure itself. By choosing the right structural parameters, a single structure can replicate several conventional joints. Appropriate design ensures that the pivot points and axes of rotation of the joints correspond to the anatomical positions, allowing unrestricted mobility in all directions of rotation and permitting individual restrictions of hand movement. By adjusting the prestress through selection of proper mechanical properties, including the initial free length and stiffness of the tensioned members, the overall stiffness can be customized to specific individual requirements. The minimalist composition of the structures through the use of only a few essential members ensures that the affected joint remains freely accessible, while the right design protects it from external loads.

C. Prestressed Compliant Dynamic Hand Orthosis

In previous work [15], [16] such an dynamic orthosis concept based on a compliant tensegrity joint was developed. The joint described has a V-shaped compressed member C_I with a connection to the forearm (FA) and a compressed member C_{II} with a connection point PC_{II} to the hand (H) (Fig. 2a). The compressed members C_I and C_{II} are connected to each other by five compliant tensioned members T_I and T_{II}. Due to the elasticity of the tensioned members, this structure allows movement between the compressed members in the x-y plane (x- and y-axis translation and z-axis rotation) without the use of conventional joints. By extending this tensegrity joint principle into 3D space, dynamic hand orthoses can be realized that allow a wide range of hand movements, including flexion, extension, radial and ulnar abduction. The ROM of the joint depends on the applied

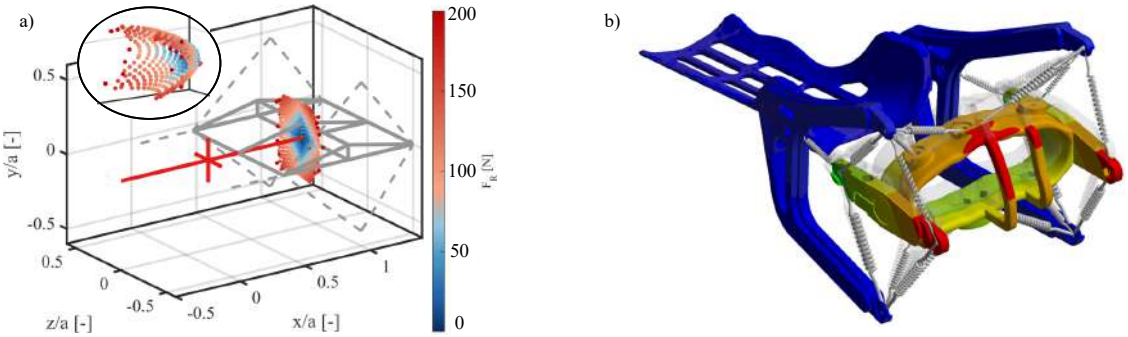


Fig. 3: a) 3D flexibility plots of the orthosis for k = 0.1 N/mm, L = 35 mm ("symmetric orthosis"), standardized muscle force F_S = 100 N, blue (minimum) to red (maximum): resulting joint force F_R; b) equilibrium configuration of the 3D model in the prestressed case with k = 1 N/mm and L_0 = 30 mm for all tensioned members; the two members C_I and the forearm element are fixed (blue; no displacement), the palm element and the two members C_{II} are colored based on the displacement of the equilibrium position (red = maximum displacement) to the initial position (transparent).

forces and is directly related to the stiffness of the structure, ensuring adaptability to different users. Fig. 2b, 2c show a first demonstrator of such an orthosis based on the proposed principle of operation. In the first demonstrator, the individual compressed members of the orthosis are designed to connect form-fittingly to the hand and forearm. The equilibrium arrangement of the structure is determined by the properties of the orthosis members (initial length and stiffness) and the position of the human wrist. By suitably selecting the properties of the tensioned members (initial length and stiffness) and the lengths of the compressed members, the relative position between the two compressed members can be set precisely. The structure is in a prestressed state because the lengths of the tensioned members in equilibrium are greater than in their unloaded initial state.

III. Mechanical Model and Simulations

The design of the dynamic orthosis with regard to their overall stiffness based on the properties of the orthosis members has a significant influence on the resulting body reactions. A profound understanding of the behavior of the orthosis when varying these parameters or when used on different hands is therefore essential in the development process. In the first step in orthosis-characterization the so called form-finding process is applied [22]. In this step the equilibrium position of the orthosis without external forces is determined. This orthosis configuration, which is initially unknown, is given by the parameters of the tensioned members and the shapes of the compressed members. Various methods can be used for form-finding, such as force imbalance [25], consideration of the potential energy of the structure, which is minimal in the stable equilibrium position [15], or with the help of the geometrically nonlinear static FEA [16]. The FEA approach can be realized in MATLAB® using [23], [24] or in commercial tools like Ansys®. Based on the form-finding, the actual characterization of the orthosis itself or in conjunction with the hand can then be carried out. The aim of this analysis is to examine the behavior of the structure under the influence of external forces or the movement of the hand. In this analysis, the overall directional stiffness (force-deflection characteristics) of the orthosis can be determined as a function of the parameters of the tensioned members (stiffness and initial length). In conjunction with the human hand, not only the orthosis' behavior but also the wrist loads can be analyzed. This systematic approach provides a substantiated evaluation of the mechanical behavior of the orthosis and the load on the wrist-joint, and builds the basis for optimization of the orthosis. Fig. 3a illustrates a 3D model of the orthosis, showing the deflection of its center when forces are applied to the cross-shaped segment, referred to as flexibility plots. The tensioned members (dashed lines) have a stiffness of k = 0.1 N/mm and an initial length of L_0 = 35 mm. The results represents one specific case based on the chosen parameters and corresponding orthosis dimensions. The underlying model is generic, while the final orthosis is individually adapted to the patient, directly influencing the final parameter values. Red members represent the human hand, with the red cross marking ideal muscle attachment points, mimicking real hand anatomy. A standardized muscle force (F_S = 100 N) is applied simultaneously to all four endpoints, causing deflection of the orthosis and hand. The force magnitude depends on muscle activity, with 100% activity corresponding to 100 N and 0% activity to 0 N. Varying activity levels at each endpoint produce angular deflections of the hand in one or two directions. The resulting joint force ($F_R = F_x^2 + F_y^2 + F_z^2)^{0.5}$ is shown at the respective deflection positions (blue to red). The shown flexibility plot is symmetric due to the symmetric tensioned members parameters. Fig. 3b shows an example of the equilibrium position determined after form-finding using geometrically non-linear static FEA in Ansys®. The tensioned members, shown here as longitudinal springs, have a stiffness of k = 1 N/mm and an initial length of L_0 = 30 mm. The initial position here is chosen to be in the center of the orthosis, but is chosen random in general.

IV. Digitization of human hand anatomy

Orthoses are typically manufactured in standard sizes, but these may not always meet the individual anatomical needs of patients. This lack of customization can limit therapeutic effectiveness due to poor fit. In the following, a potential methodology for 3D scanning and manufacturing is

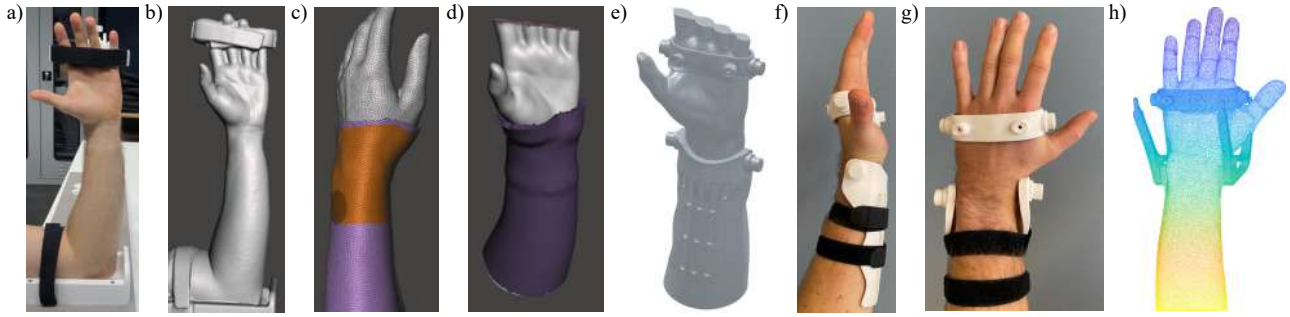


Fig. 4: Process of digitization of the human hand anatomy using 3D scans and the transfer of these scans into patient-specific orthosis using a own custom-developed CAD sequence; a) Human Hand, prepared for 3D scan; b) 3D scan of the human hand, including fixation (Artec® Spider); c-d) shell definition based on the 3D scans using Offset feature (Meshmixer®); e) 3D-adapted, patient-specific orthosis (Solid Edge); f-g) Test subject with 3D-adapted, patient-specific orthosis; h) patient-specific movement model of the hand volume (MATLAB®).

described (Fig. 4), focusing on its application rather than the specific software used, as the methodology itself is software-independent. The cross-software .stl file format can be used throughout the entire methodology. The method is developed using the patient's real arm and hand as demonstrated in Fig. 4a. For obtaining 3D scanned body region data, the Artec® Spider 3D scanner, a portable structured light scanner, was used here to capture the human hand. It has a working distance of 17 to 35 cm and a capture speed of 7.5 FPS. Using Artec Studio software, the individual scans of the hand are merged into a single 3D scan (Fig. 4b). In order to precisely adapt the forearm and palm elements to the patient's individual anatomy the 3D scan must now be included in a CAD design software. However, preparatory steps are necessary beforehand. The first step here is the definition of 3D shells based on the scans, here Meshmixer® was used, which serve as the basis for standardized CAD geometries that are applied to these in order to obtain patient-specific forearm and palm elements (Fig. 4c). Corresponding areas in the 3D mesh of the scan are selected where the orthosis is in contact with the body. An offset is used to create a thickening in these areas, which form the base for the shells (Fig. 4d). The 2D mesh of the scan becomes a 3D solid. The finer the 3D scan and therefore the mesh, the more accurate the fitting of the shells. The shells can be further optimized in terms of local thickness, mesh geometry and smoothness. For example, areas that are subject to higher loads can be reinforced. Optionally, to avoid processing errors and long processing times the shells can be subjected to surface reconstruction. Here NX® CAD software was used. The 3D shells created in this way can now be converted into final forearm and palm elements using a CAD Software (Fig. 4e). Here Solid Edge® was used. The final design is carried out using a custom-developed sequence of operations, which is independent of any specific software and can be applied across different platforms, on the basis of which the 3D bodies can be adapted to the previously developed basic design using your own predefined commands and sketches. This enables standardized and precise placement of component geometries. For this purpose, a temporary wrist point, which is only required for the creation of the CAD models, is defined in the area of the real wrist joint. At a later stage, the joint point will be defined exactly at the previously calculated point using determination methods yet to be developed. However, this current definition is sufficient for the general development of the methodology. The shells are modified in a structured manner, with each functional area of the final hand orthosis being modeled step by step. Once the fitting process is complete, patient-specific orthotic forearm and palm elements are created on the basis of 3D Scans, but with predefined, uniform functional areas (Fig. 4e). In Fig. 4f and Fig. 4g forearm and palm elements manufactured on the basis of this methodology are shown on a test subject. For the development of the orthosis, it is also important to know how far the patient can currently move their hand and to what maximum range it should be deflected as part of the therapy. This helps to further individualize the orthosis for everyday use without the need for a physical model. One method of measuring, recording and visualizing the ROM of the hand, i.e. the volume of hand movement, is described below. The movement of the individual hand segments is measured using "outside-in" motion capturing systems. The software Captury-Live® is used here for this purpose. The motion capture data is imported into MATLAB® with the MoCap toolbox [26] and processed using a custom-developed sequence. The recorded movement data represent coordinates of the individual segments over the recorded time. For the graphical visualization of the captured volume, the previously recorded 3D scans of the respective patients are divided into the same, individual hand segments, which were measured using Captury®. The movement data of the individual segments (forearm, metacarpus, phalanges) are assigned to the corresponding 3D segments. This creates a movable 3D model of the patient's hand, which can be animated using the recorded movement data (Fig. 4e). The resulting ROM or volume can then be used to refine the orthosis design, for example to define areas that must not be overlapped by the orthosis structure.

V. Experimental Setup

A test rig (Fig. 5) was set up to experimentally characterize the mechanical behavior of the orthosis and to determine the joint forces during hand movement. It measures wrist joint forces and primitive muscle forces using an movable artificial hand with a cable-guided actuator system, including tendon pretension, in combination with the dynamic hand orthosis.

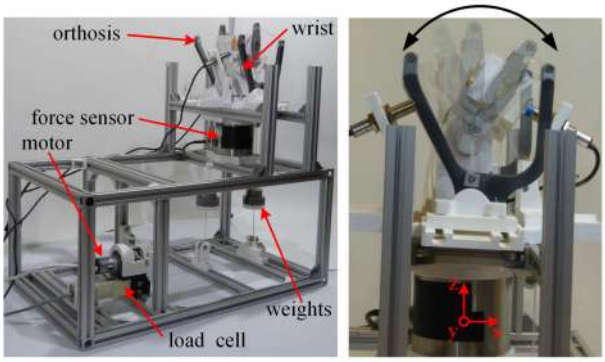


Fig. 5: Test rig for the experimental determination of wrist forces and moments of an artificial hand in combination with a prestressed, compliant dynamic orthosis using cable-based actuation; left: isometric view, right: side view with wrist and orthosis during movement.

The cable pull mechanism mimics the actuation of the hand by muscles. The test rig can be divided into two sections, a lower section with the electronics and the control system and an upper section with the artificial hand, the orthosis and the measuring components. The hand is approximated by a hinge joint with one DOF, which is mounted on a force sensor (ME-Systems, K6D68) that measures the forces in three perpendicular directions in the joint. The outer orthosis members and other test rig components are mounted on a plate that is decoupled from the sensor. This ensures that only joint-related forces are measured and external influences are excluded. By rotating this plate, measurements in different directions (flexion and extension or radial and ulnar abduction) are possible without costly modification of the experimental setup. A motor (33G-312 DC gear motor) with an idle speed of 18 rpm and a peak torque of 0.9 Nm is used for angular deflection of the joint. The movement is controlled quasi-statically by an L298N H-bridge. The cable pull is a closed circuit with one side of the cable pull under tension while the other side is relaxed. The pretension of the cables/muscles, 8 to 9 N according to [20], is simulated by added weights on the cable. A load cell (HBM PW6DC3MR) measures the tensile force exerted by the motor, which can be interpreted as “muscle force”. An inertial measurement unit (IMU; GY-521-MPU6050) is used to measure the position and orientation of the artificial hand. The H-bridge receives, independent of the IMU, a signal from an inductive proximity sensor (LJ12A3-4-Z/BX-5V) when the artificial hand has reached the desired maximum deflection and automatically reverses the rotation direction of the motor. An Arduino Uno R3 is used to control the entire test rig. The start and end of a measurement is indexed by the software Catman® EasyScript in order to activate all sensors and load cells simultaneously. The measurement signals are amplified by an HBM amplifier (1615B) before being processed by Catman®. The position and deflection data determined by the IMU are transmitted via two Bluetooth modules (ESP32C3). The first module (ESP1) is directly connected to the IMU inside the artificial hand and is powered by a 3.7 V battery for cable free operation. The second module (ESP2) receives the data and transmits it serially to the Arduino. The described testing rig can be used to measure the joint forces acting on the wrist for various prestressed, compliant dynamic hand orthoses. In addition, the position, orientation and deflection of the hand as well as the necessary “muscle force” can be determined. To ensure the functionality of the test rig, a first proof of concept measurement was carried out using an orthosis with soft (0.087 N/mm; red) and stiff (0.125 N/mm; blue) tensioned members (Fig. 6). The angular deflection of the artificial hand and the corresponding cable-force (”muscle-force”) and wrist-joint force in x-direction (main direction) in the case flexion and extension were examined. The results show that the movement of the hand and the resulting behavior of the orthosis correspond to the expected behavior. However, there are short plateau phases between the deflection of the neutral 0 positions in the area of the bounce. The maximum deflection of the hand also increases with increasing duration. This effect can only be attributed to a limited extent to the material properties of the tensioned members, as this should only occur with a significant time delay. Overall, however, the proof of concept can be confirmed for the test stand.

VI. Conclusion

In this paper, a prestressed, compliant dynamic hand orthosis enabling hand movements without relying on conventional joints was presented. It can be adapted to the complex multiaxial movements of the hand and thus enables the hand to move over the entire ROM without physical restrictions, although the movement can be limited in certain directions according to the desired therapy. Furthermore, important steps in the development process of the considered orthosis were presented. Selected simulation methods for the theoretical description of the behavior of the orthosis and the wrist loads were discussed. A precise fit between the orthosis elements and the hand, which is crucial for the functionality of the orthosis, is important. For this a possible methodology for digitizing the hand anatomy and designing patient-specific orthoses using 3D scanning was presented. The results show that detailed 3D data of hands can be created with simple 3D scanners and little to no effort. Based on this, the methodology can be used to establish a reproducible, software-independent process for the rapid ($<$ 2 h) production of customized orthoses. In future work regarding the methodology, the current time-precise definition of the reference joint point should be improved. The current self-developed flow chart should also be further developed so that it automatically processes the fabrication. Initial exemplary measurement results confirm the applicability of the measurement principle of the test rig. However, the plateau phases around the neutral-0-positions should be examined to determine their underlying causes. Additionally, the relationship between maximum deflection and the stiffness of the artificial wrist requires further investigation. Future studies with the test rig will focus on comparing the impact of different hand sizes in comparison with the simulation models. A detailed analysis of mate-

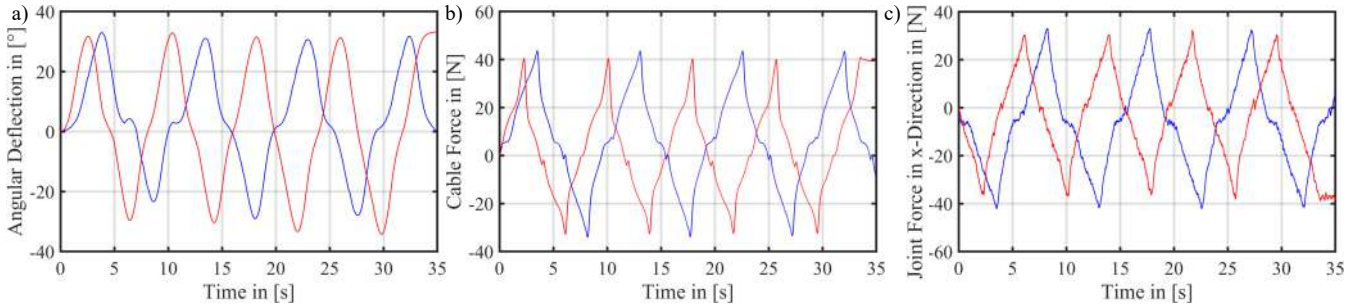


Fig. 6: Evaluation of the test stand for an orthosis with soft (0.087 N/mm; red) and stiff (0.125 N/mm; blue) tensioned members for 4 cycles, 1 cycle corresponds to an angular deflection from neutral-0-position to both maximums in each direction and the return to the neutral-0-position: a) angular deflection, b) cable force and c) joint force in x-direction (main).

rial fatigue in the tensioned members is also of interest. Overall, the results pave the way for future research that could investigate the behavior of the orthosis under external influences such as vibrations, harmonic or transient dynamics or even more realistic simulations of hand movements and muscle activity. Additionally, the developed 3D adjustment methodology allows for consideration of each patient's individual circumstances, proving useful even during the initial practical testing of the orthosis in near future.These findings will improve both the simulated and experimental models, which would further support the practical application of the orthosis in real-life scenarios.

REFERENCES

[1] Hirt, B., Seyhan, H., Wagner, M. & Zumhasch, R. Hand and Wrist Anatomy and Biomechanics: A comprehensive Guide. Thieme (2017)

[2] Meng, W., Sheng, B., Klinger, M., Liu, Q., Zhou, Z. & Xie, S. Design and Control of a Robotic Wrist Orthosis for Joint Rehabilitation. *2015 IEEE International Conference On Advanced Intelligent Mechatronics (AIM)*. pp. 1235-1240 (2015)

[3] Bartlett, N., Lyau, V., Raiford, W., Holland, D., Gafford, J., Ellis, T. & Walsh, C. A Soft Robotic Orthosis for Wrist Rehabilitation. *ASME Design Of Medical Devices Conference*. (4,2015)

[4] Hope, J. & Mcdaid, A. Development of Wearable Wrist and Forearm Exoskeleton with Shape Memory Alloy Actuators. *Journal Of Intelligent & Robotic Systems*. 86 (2017,6)

[5] Tsabedze, T., Hartman, E., Brennan, C. & Zhang, J. A Compliant Robotic Wrist Orthosis Driven by Twisted String Actuators. *2021 International Symposium On Medical Robotics (ISMR)*. pp. 1-7 (2021)

[6] Tsabedze, T., Hartman, E., Abrego, E., Brennan, C. & Zhang, J. TSA-BRAG: A Twisted String Actuator-powered Biomimetic Robotic Assistive Glove. *2020 International Symposium On Medical Robotics (ISMR)*. pp. 159-165 (2020)

[7] Higuma, T., Kiguchi, K. & Arata, J. Low-Profile Two-Degree-of-Freedom Wrist Exoskeleton Device Using Multiple Spring Blades. *IEEE Robotics And Automation Letters*. 3, 305-311 (2018)

[8] Dittli, J., Vasileiou, C., Asanovski, H., Lieber, J., Lin, J., Meyer-Heim, A., Van Hedel, H., Gassert, R. & Lambercy, O. Design of a Compliant, Stabilizing Wrist Mechanism for a Pediatric Hand Exoskeleton. *2022 International Conference On Rehabilitation Robotics (ICORR)*. pp. 1-6 (2022)

[9] Lee, G., Hong, G. & Choi, Y. Tendon-Driven Compliant Prosthetic Wrist Consisting of Three Rows Based on the Concept of Tensegrity Structure. *IEEE Robotics And Automation Letters*. 6, 3956-3963 (2021)

[10] Schorr, P., Schale, F., Otterbach, J. M., Zentner, L., Zimmermann, K. & Böhm, V. Investigation of a Multistable Tensegrity Robot applied as Tilting Locomotion System. *2020 IEEE International Conference On Robotics And Automation (ICRA)*. pp. 2932-2938 (2020)

[11] Zappetti, D., Jeong, S., Shintake, J. & Floreano, D. Phase Changing Materials-Based Variable-Stiffness Tensegrity Structures. *Soft Robotics*. 7, 362-369 (2020)

[12] Hecker, A., Tax, L., Giese, B., Schellnegger, M., Pignet, A., Reinbacher, P., Watzinger, N., Kamolz, L. & Lumenta, D. Clinical Applications of Three-Dimensional Printing in Upper Extremity Surgery: A Systematic Review. *J Pers Med*. 13 (2023,2)

[13] Chen, Y., Lin, H., Yu, Q., Zhang, X., Wang, D., Shi, L., Huang, W. & Zhong, S. Application of 3D-Printed Orthopedic Cast for the Treatment of Forearm Fractures: Finite Element Analysis and Comparative Clinical Assessment. *Biomed Res Int*. 2020 pp. 9569530 (2020,7)

[14] Zheng, Y., Liu, G., Yu, L., Wang, Y., Fang, Y., Shen, Y., Huang, X., Qiao, L., Yang, J., Zhang, Y. & Hua, Z. Effects of a 3D-printed Orthosis Compared to a Low-temperature Thermoplastic Plate Orthosis on Wrist Flexor Spasticity in Chronic Hemiparetic Stroke Patients: A Randomized Controlled Trial. *Clin Rehabil*. 34, 194-204 (2019,11)

[15] Schaeffer, L., Herrmann, D., Schratzenstaller, T., Dendorfer, S. & Böhm, V. Preliminary Theoretical Considerations on the Stiffness Characteristics of a Tensegrity Joint for the Use in Dynamic Orthoses. *Journal Of Medical Robotics Research*. 8(03n04), 2340008 (2023)

[16] Schaeffer, L., Herrmann, D. & Böhm, V. Theoretical Investigations on a Dynamic Hand Orthosis Based on a Prestressed Compliant Structure with Respect to Stiffness and Wrist-Forces. *2024 International Symposium On Medical Robotics (ISMR)*. pp. 1-7 (2024)

[17] Arias, D. & Varacallo, M. StatPearls: Anatomy, Shoulder and Upper Limb, Hand Bones. (2022)

[18] Heo, P., Gu, G., Lee, S., Rhee, K. & Kim, J. Current Hand Exoskeleton Technologies for Rehabilitation and Assistive Engineering. *International Journal Of Precision Engineering And Manufacturing*. 13 (2012,5)

[19] Eschweiler, J., Li, J., Quack, V., Rath, B., Baroncini, A., Hildebrand, F. & Migliorini, F. Anatomy, Biomechanics, and Loads of the Wrist Joint. *Life (Basel)*. 12 (2022,1)

[20] Weaver, L., Tencer, A. & Trumble, T. Tensions in the Palmar Ligaments of the Wrist. I. The Normal Wrist. *Journal Of Hand Surgery*. 19, 464-474 (1994,5)

[21] Ombregt, L. Applied Anatomy of the Wrist, Thumb and Hand. *A System Of Orthopaedic Medicine (Third Edition)*. pp. e102-e111 (2013)

[22] Juan, S. & Mirats Tur, J. Tensegrity Frameworks: Static Analysis Review. *Mechanism And Machine Theory*. 43, 859-881 (2008)

[23] Böhm, V., Sumi, S., Kaufhold, T. & Zimmermann, K. Compliant Multistable Tensegrity Structures. *Mechanism And Machine Theory*. 115, 130-148 (2017)

[24] Zhang, L., Li, Y., Cao, Y. & Feng, X. Stiffness Matrix based Form-finding Method of Tensegrity Structures. *Engineering Structures*. 8, 36-48 (2014)

[25] Schaeffer, L., Herrmann, D. & Böhm, V. Preliminary Theoretical Considerations of a Hand Orthosis Based on a Prestressed, Compliant Structure. *2023 International Symposium On Medical Robotics (ISMR)*. pp. 1-7 (2023)

[26] Burger, B. & Toiviainen, P. MoCap Toolbox - A Matlab Toolbox for Computational Analysis of Movement Data. *Proceedings Of The 10th Sound And Music Computing Conference, Stockholm, Sweden*. (2013,8)

Mechanical Development and Preliminary Control Results of a Cable-Driven Robotic Platform for Whole-Body Rehabilitation*

Juan Fang[1], Michael Haldimann[1] and Niklaus Stocker[2]

Abstract— **To promote whole-body rehabilitation in the early post-injury phase, a system is desirable to provide user transfer, automatic posture change and therapy for various arm-leg movements. This work aimed to present a cable-driven robotic platform that can provide whole-body rehabilitation for the user in a lying position and to demonstrate preliminary results for generation of 3D leg movements. Seventeen compact cable-driven actuators (CDAs) were designed and mounted on a robotic frame. One CDA is the drive for a lift mechanism, while the other 16 CDAs work jointly to change the user's posture and to produce arm-leg movement therapy. The kinematics for production of two representative leg movements were analysed. Using PID and impedance algorithms, a CDA alone provided user-defined resistive training with position guidance (force error: 3.5 N and position error: 21.4 mm). Preliminary control of six CDAs demonstrated the system's ability to produce a 3D leg movement in a back-lying position (mean force error: 12.8 N, mean position error: 52.1 mm) and a walking-like leg movement in a side-lying position (mean force error: 13.7 N, mean position error: 57.0 mm). Through concept description, prototype development, and preliminary control testing, the study showed that the proposed cable-driven robotic platform could potentially offer convenient user transfer, automatic posture change and synchronised 3D arm-leg movement therapy. Future work will present kinetic analysis and control strategies for automatic posture change and arm movement assistance.**

Keywords— cable-driven actuators, whole-body rehabilitation, impedance control, force control, 3D movement control

I. Introduction

Many lower-limb rehabilitation robotic systems focus on producing two-dimensional (2D) movements, despite the fact that 3D body movements are often performed in daily life. The exoskeleton-based robotic systems primarily produce the movement in the sagittal plane. Due to mechanical constraints, the movements in the frontal plane, such as hip abduction/adduction, are not possible [1]. Very few robotic systems modify the structures to allow passive medial-lateral movement [2, 3]. However, hip abductors/adductors should be actively trained to learn walking patterns properly, as they enhance mediolateral balance during walking [4]. During heel strike, the hip adductors contribute to the medial-lateral components of hip loading [5]. To promote walking rehabilitation, patients should practise 3D natural movements.

Cable-driven robotic systems are often employed to provide natural movement guidance. One advantage of these systems over the traditional exoskeleton-based systems is that the cable-driven actuators (CDAs) work analogically to our biological limb in generating dynamic body movements. Our body has muscles which act as actuators for production of daily movement. To achieve accurate movement control, our body relies on a sophisticated sensory system where muscle spindles measure the length and velocity of muscle bundles, while Golgi tendon organs detect the tension [6]. A standard CDA consists of a motor with an encoder, a drum with a wound cable, and a force sensor. The motor provides the power for the required movement, the encoder measures the rotation angle of the drum, from which the length and velocity of the cable can be estimated, and the force sensor measures the tension of the cable. As the configuration of sensors and actuators in CDAs is similar to the sensory-muscular interaction in the human body, cable-driven systems are considered capable of generating natural body movements [7]. Similar to the neuromuscular system where each segment has multiple muscle fascicles for generation of agile movement, cable-driven robotic systems employ multiple CDAs to produce a 3D movement of a segment.

Literature on cable-driven robotic systems shows that four to six CDAs are used to generate a 3D movement of one segment. A minimum of four CDAs are required to produce a 3D movement [7]. In a study on assisted walking on a treadmill [7], four CDAs were used for each leg to produce one degree of freedom (DOF) for rotation and two degrees of freedom for translation. Riener et al. developed the Reactive Rope Robot (r^3) to produce versatile dynamic movement [8]. It consisted of a large-scale cave environment and CDAs. Five CDAs were employed to produce 3D force on one arm for rowing simulation [9]. Due to the versatile structure, r^3 was easily reconfigured to include six CDAs in total for simulation of tennis playing [10]. Similarly, six CDAs were used in the CUBE system [11] to produce a 3D movement for the rehabilitation of a wrist or foot.

Current research on cable-driven rehabilitation robots has led us to envisage a rehabilitation platform for 3D whole-body rehabilitation. Interlimb neural coupling during walking [12] implies that patients should practise synchronised arm-leg training to promote walking rehabilitation. To assist patients in whole-body training during the early rehabilitation phase, especially those confined to a bed or wheelchair, a multifunctional rehabilitation platform has been proposed [13]. The functional requirements include (i) convenient user transfer: to transfer the user between the medical bed/wheelchair and the rehabilitation platform; (ii) automatic

* Research supported by Innosuisse - Swiss Innovation Agency (Grant No. 46786.1 IP-LS).

1. rehaLab – The Laboratory for Rehabilitation Engineering, HuCE – Institute for Human Centred Engineering, Department of Mechatronics and Systems Engineering, School of Engineering and Computer Science, Bern University of Applied Sciences, Quellgasse 21, Postfach 2501 Biel, Switzerland.

2. Liberty MedTech Sagl, C/O Open Lab Group SA, Ticino, Switzerland.

Niklaus Stocker ist he CEO of the Liberty MedTech Sagl. Juan Fang is a professor at rehaLab of BUAS. Michael Haldimann is a research assistant at rehaLab of BUAS. Juan Fang is the corresponding author (phone: +41 34 426 42 74; e-mail: juan.fang@bfh.ch).

posture change: to transition between sitting and back/side-lying postures; and (iii) 2D/3D arm-leg synchronised movement therapy: to provide ipsilateral/bilateral whole-body training, such as shoulder/hip abduction/adduction and arm-leg synchronised walking-like movement patterns in a lying position.

As the preliminary investigation of the proposed platform, we previously developed two belt-driven robotic systems to produce various leg movements on a bed [13, 14]. However, both systems exhibited swaying problems during the production of walking-like stepping in a side-lying position. The initial system actuated the leg using only one active belt [13]. Leg swaying was expected, because one belt cannot constrain the leg to move solely in the sagittal plane. In the improved system [14], four passive belts meeting at one point were used, but the leg still swayed slightly. Pertinent to these studies, we developed a robotic gait system that demonstrated a well-controlled leg movement using four active CDAs [15]. It was envisaged that a system with active CDAs could provide a solution to the swaying problem.

The aim of this work was to present a cable-driven robotic platform that can provide whole-body rehabilitation for users in a lying position and to demonstrate the preliminary results for generation of 3D leg movements. Future work will include kinetic analysis of various arm-leg movements and generation of automatic posture change and arm movements.

II. Methods

The overall structure of the robotic platform was developed using SolidWorks (Version 2018, Solid Solutions AG, Zurich, Switzerland). The control system comprises an industrial PC and five motion controllers for 17 motors. The movement control algorithms were developed in TwinCAT 3 software (Beckhoff Automation GmbH & Co., Germany).

A. Mechanical Design

The platform included a therapy bed, and a robotic frame made of Bosch profile (Figs 1-2). One CDA (Fig. 3a) is used in a lift mechanism for user transfer, while 16 CDAs (Fig. 3b) are employed for posture change and arm-leg movement production. Each CDA has a compact design, consisting of a motor-controlled drum and a force sensor. The lift system is mounted on the top of the robotic frame. By controlling the length and the tension of the belt, the user is transferred between the wheelchair and the therapy bed (Figs. 1(a-b)). To facilitate posture change and generate various arm-leg movements, 16 CDAs (Fig. 2) are fixed on the top and side of the robotic frame. During training in a back-lying position, the user is in a stable situation without requirement of trunk support from any CDAs. Sixteen CDAs are employed to produce bilateral 3D arm and leg movements (Fig. 2a), with four CDAs jointly actuating one segment (wrist or ankle joint). To enable training in a side-lying position, four CDAs fixed on the top frame are firstly utilised to change the user's posture (Fig. 1c): two CDAs are connected to the harness to stabilise the shoulder, while the other two CDAs, via deflection units, pull the pelvic in the anterior/posterior direction. These four CDAs work in tandem to transition the user between back-lying and side-lying positions. During training in a side-lying position, these four CDAs stabilise the

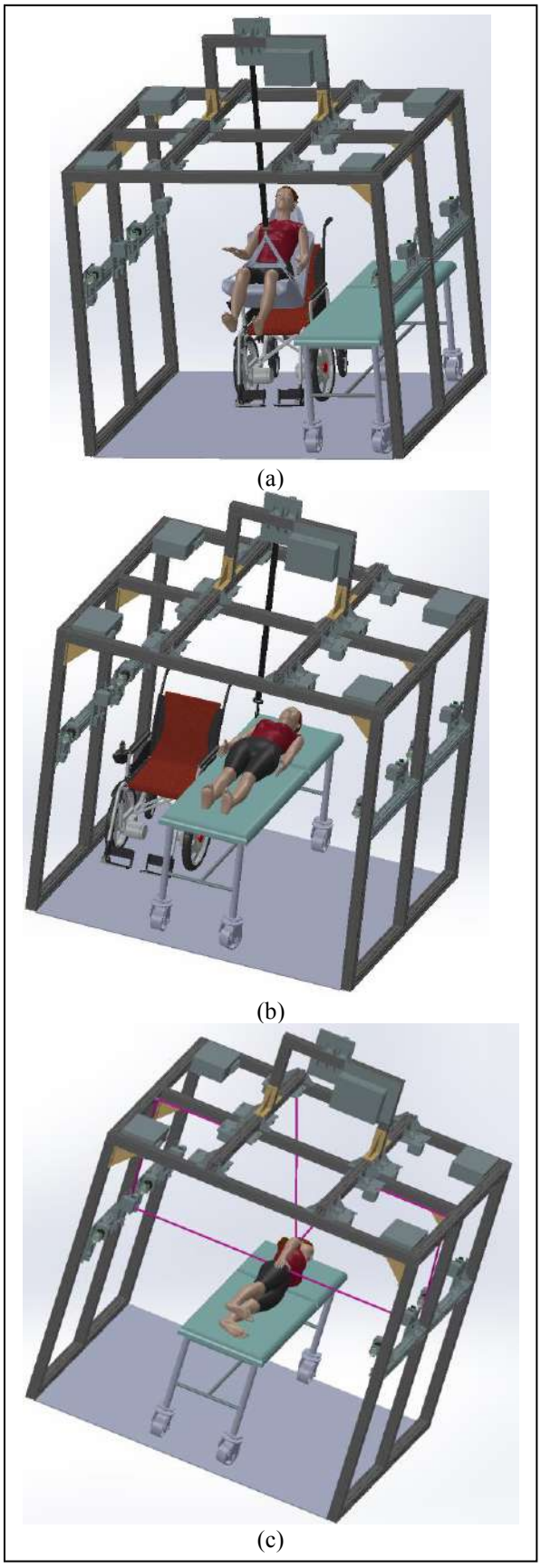


Fig. 1. The concept of the robotic platform: user transfer from sitting on the wheelchair (a) to lying on the therapy bed (b) via one CDA, and posture stabilisation (c) using four CDAs.

trunk of the user. Six CDAs jointly actuate the wrist, while the remaining six CDAs move the ipsilateral ankle joint (Fig. 2b).

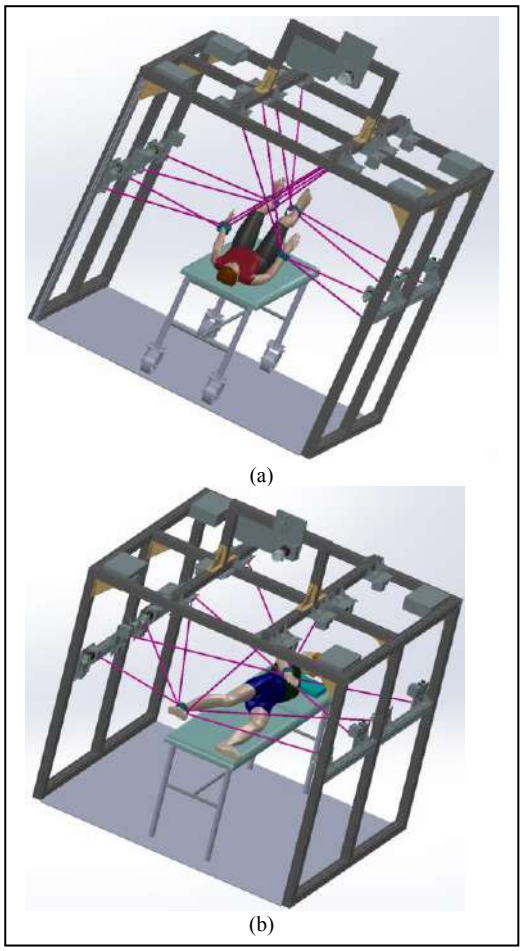


Fig. 2. Cable fixation for production of synchronised arm-leg movement. (a) Bilateral 3D arm-leg movement in a back-lying position; and (b) unilateral arm-leg walking-like pattern in a side-lying position.

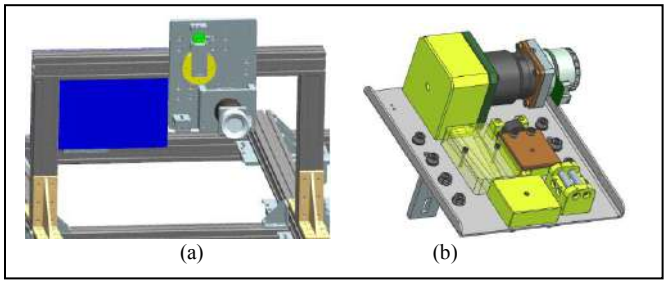


Fig. 3. (a) Lift mechanism with one CDA and its control case; and (b) one of the 16 CDAs for posture change & arm-leg movement generation.

In the prototype (Fig. 4), the commercial aluminium Bosch profile (80 mm × 80 mm) was used to build the robotic frame (size: 2.40 m ×2.16 m ×2.56 m). The lift mechanism (Fig. 5a) on the top of the frame used the CDA assembly (EC motor model EC90, gearhead with a ratio of 100, Encoder MILE 1024 CPT; maxon motor, Switzerland). Sixteen CDA assemblies (EC motor model EC60, gearhead with a ratio of 12, Encoder MILE 1024 CPT; maxon motor, Switzerland), shown in Fig. 5b, are the drives for posture change and arm-leg movement therapy.

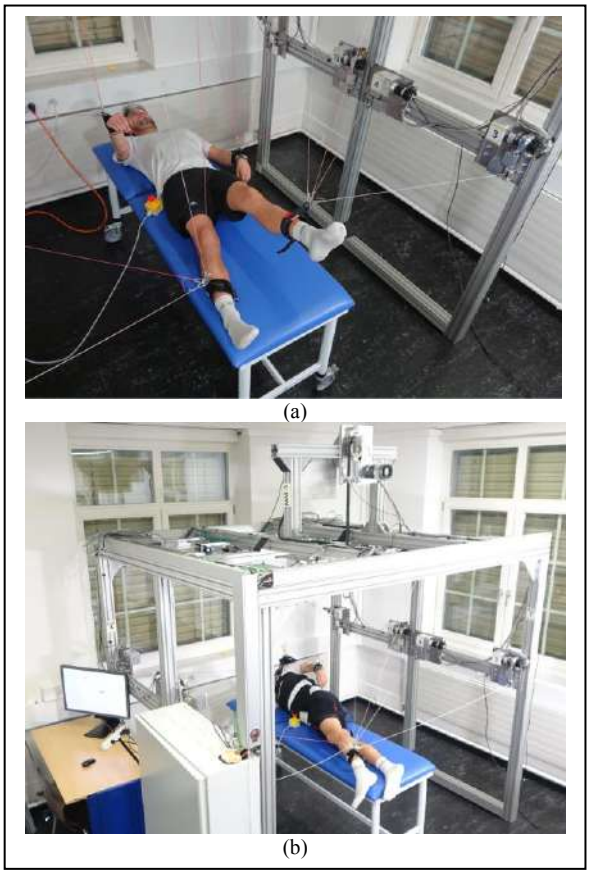


Fig. 4. The prototype of the platform and two examples of cable fixation. (a) Bilateral 3D arm-leg movement in a back-lying position; and (b) unilateral arm-leg walking-like pattern in a side-lying position.

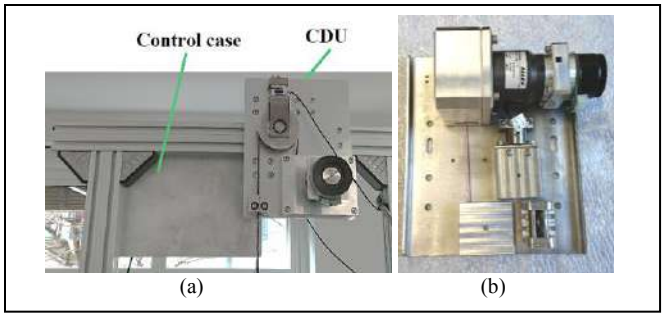


Fig. 5. The prototypes of the lift mechanism (a) and one CDA (b) which is used for posture change & arm-leg movement.

B. Kinematic Analysis

In preparation for movement control (Section II.C), kinematic analysis was conducted to calculate the target cable length of each CDA based on the target segment trajectory. This section focuses on the kinematic analysis of leg movements, although similar algorithms can be applied for production of various arm movements. As shown in Section II.A, the robotic platform can produce various leg movements. However, this section only analyses the kinematics for producing two representative ankle trajectories: a 3D leg movement in a back-lying position (Fig. 6a), and a walking-like ankle trajectory in a side-lying position (Fig. 6b). These movements are produced through simultaneous actuation of the same six CDAs, which are CDA 0, 1, 3, 4, 6 and 7.

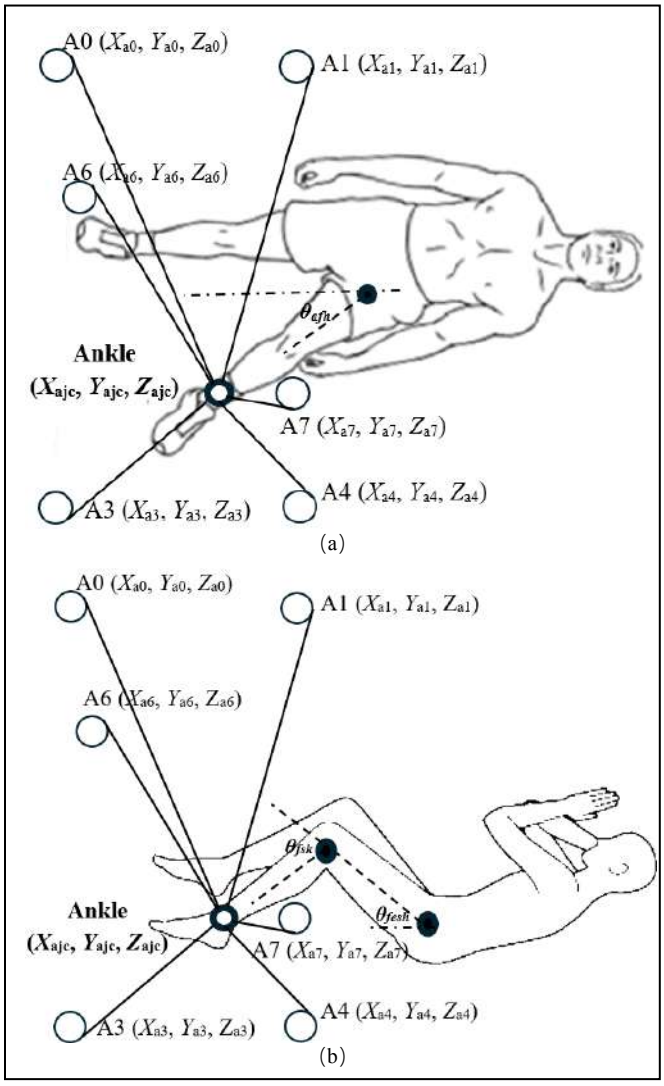


Fig. 6. Top-view of the configuration of six actuators for production of two representative leg movements. (a): 3D leg movement in a back-lying position. (b) Walking-like leg movement in a side-lying position.

Cables 0, 1, 3, and 4, connected to the right-distal-middle (A0), right-proximal-middle (A1), left-distal-middle (A3) and left-proximal-middle (A4) actuators, respectively, were attached to the ankle. To compensate for the weight of the leg, two additional cables, 6 and 7, connected to the right-distal-top (A6) and left-proximal-top (A7) actuators, were also attached to the ankle joint. The centre of the frame is defined as the reference centre (0, 0, 0). The user is positioned in the system by aligning the centre of the two hip joints with the reference centre (0, 0, 0). Using the geometric configuration of the mechanical system, the positions (*X*, *Y* and *Z* coordinates) of the six actuators were determined, and the cable contacting points on the actuators—A0, A1, A3, A4, A6 and A7—were determined (Fig. 6).

The representative 3D leg movement in the back-lying position was defined as a combination of a sinusoidal abduction- adduction in the hip joint angle θ_{afh} in the frontal plane and a sinusoidal flexion of the hip joint angle θ_{fsh} in the sagittal plane. The two angles were defined as:

$$\theta_{afh} = A_{afh} \sin(\frac{2\pi}{T_{afh}} t), \quad (1)$$

$$\theta_{fsh} = A_{fsh} \sin(\frac{2\pi}{T_{fsh}} t + \frac{\pi}{2}), \quad (2)$$

where the amplitudes A_{afh}, A_{fsh} are defined to be π/6, while the cycle time T_{afh}, T_{fsh} are defined to be 4π s. The position of the ankle joint centre in a back-lying position (Fig 6a) was calculated as:

$$X_{ajc} = (L_t + L_s) \sin\theta_{afh} + \frac{1}{2} D_{lrhjc}, \quad (3)$$

$$Y_{ajc} = -(L_t + L_s) \cos\theta_{afh}, \quad (4)$$

$$Z_{ajc} = (L_t + L_s) \sin\theta_{fsh}, \quad (5)$$

where L_t and L_s are the length of the thigh and shank, and D_{lrhjc} is the distance between the left and right hip joint centre.

To produce the walking-like movement, the representative hip and knee joint trajectories in the sagittal plane, θ_{fesh} and θ_{fsk}, recorded in our previous gait analysis experiment [16], were used in this study as the target ankle trajectory:

$$X_{ajc} = L_t \sin\theta_{fesh} - L_s \sin(\theta_{fsk} - \theta_{fesh}), \quad (6)$$

$$Y_{ajc} = -L_t \cos\theta_{fesh} - L_s \cos(\theta_{fsk} - \theta_{fesh}), \quad (7)$$

$$Z_{ajc} = \frac{1}{2} D_{lrhjc}. \quad (8)$$

With the trajectory of the ankle joint centre, the reference length of the cables, L_{ri}, is therefore determined using:

$$L_{ri} = \sqrt{(X_{Ai} - X_{ajc})^2 + (Y_{Ai} - Y_{ajc})^2 + (Z_{Ai} - Z_{ajc})^2}, \quad (9)$$

where *i* means the cable number, which equals respectively 0, 1, 3, 4, 6 and 7. The cable length is used as the reference length L_r for each cable in Section II.C.

C. Movement Control of CDAs

The control system included a power unit, which was fixed on the side of the robotic frame, and five control cases. The programmable motion controllers (MiniMACS6 EtherCAT; maxon motor, Switzerland) were used to regulate the output force from the CDAs. Each motion controller can control 4 EC motors. The 16 CDAs required four motion controllers, which were placed in four control cases at the four corners of the top frame (see the video: https://youtu.be/gLlQfQfEBsY). Each CDA used a force sensor (Bengbu Sensor Company, China; resolution 0.012 N) to measure the actual cable force. The amplifiers of the four force sensors were fixed in one control case. The force measurement was recorded using the analogue input port of the motion controllers. The fifth control case, which was to control the CDA assembly of the lift mechanism, was fixed on the frame of the lift mechanism (Fig. 5a).

As a preliminary production of synchronised movement, this work presents only one control strategy (Fig. 7), which includes a force controller and an impedance controller. Similar control algorithms were implemented in our previous work [17].

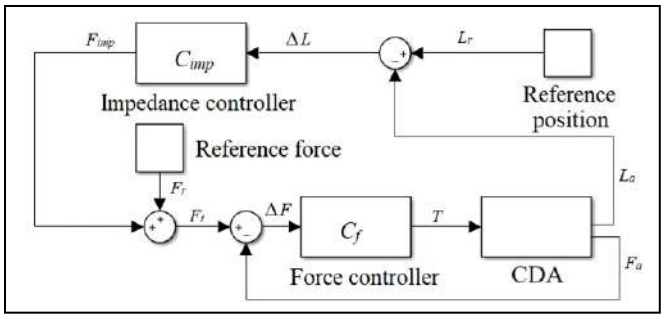


Fig. 7. Impedance control plus force control strategy.

In order to provide force training with a user-defined profile, a PID force controller C_f was implemented in each CDA. The input to and output from C_f are respectively ΔF (the difference between the target and actual force F_t and F_a) and target torque T to CDA. The transfer function of C_f is:

$$\Delta F \rightarrow T\text{: } C_f = K_{pf} + \frac{K_{if}}{s} + \frac{K_{df} s}{\frac{1}{\omega_{lpf}} s + 1}, \tag{10}$$

where K_{pf}, K_{if}, K_{df} and ω_{lpf} are the proportional, integral, derivative gains and the cut-off frequency of the low pass filter, respectively. The reference force F_r for Cables 0, 1, 3 and 4 was set to a constant 10 N. The reference force for Cables 6 and 7 was defined as 20 N, where the joint upward force corresponds to the pull force for a leg of a person of 50 kg, based on the anthropometric data [18].

To provide movement trajectory guidance, a high-level impedance controller was implemented:

$$\Delta L \rightarrow F_{imp}\text{: } C_{imp} = K_{pimp} + \frac{K_{vimp} s}{\frac{1}{\omega_{lpimp}} s + 1}, \tag{11}$$

where ΔL is the difference between the reference and actual cable position L_r and L_a, F_{imp} is the output from the impedance controller. The target force F_t is the sum of the reference force F_r and F_{imp}. The impedance parameters K_{pimp}, K_{vimp} and ω_{lpimp}, which are the stiffness, damping ratio and the cut-off frequency of the low pass filter, respectively.

The force control accuracy was calculated using the root-mean-square error (RMSE) between the target force F_t and the actual force F_a:

$$\mathrm{RMSE}_F = \sqrt{\frac{1}{N}\sum_{t=t_0}^{t_1}(F_a(t) - F_t(t))^2}, \tag{12}$$

where N is the number of data points in the interval t_o and t_1. Replacing the force variables F_t and F_a in Eq. (12) with the cable length variables L_r and L_a, the position control accuracy RMSE_L was calculated.

Test of the controller was performed with informed consent on a healthy person (age of 40 yrs, height of 1.61 m, body mass of 50 kg). An emergency stop was held by the test person (see the attached video). If the system did not move well, then the test person could immediately press the button to stop the system. Since the data are not generalisable, it does not fall under the Swiss Federal Act on Research Involving Human Beings. No ethical approval was needed.

III. Results

This section presents the preliminary test results of movement control using six CDAs. Kinematic analysis yielded the reference lengths of the 6 CDAs (Fig. 8). Cables 0, 1, 3 and 4 have similar ranges of movement, while the movement of Cables 6 and 7 depends on the required movement in Z axis.

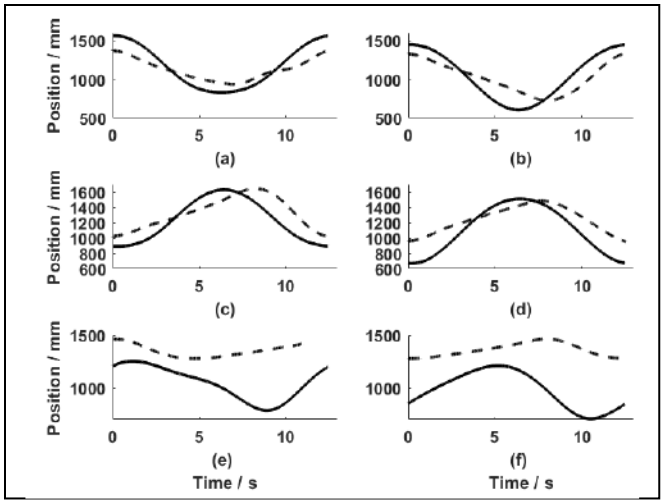


Fig. 8. The reference cable length trajectory of the six CDAs to produce the 3D leg movement in a back-lying (solid lines) and walking-like leg movement in a side-lying position (dashed lines). (a)-(f): CDAs 0, 1, 3, 4, 6 and 7.

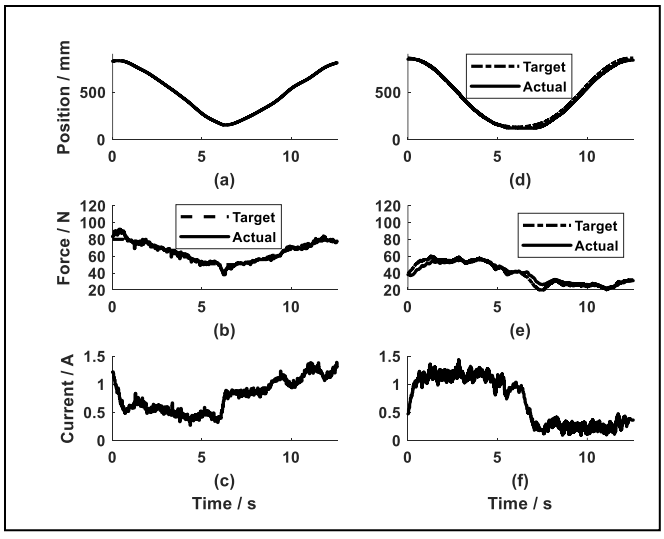


Fig. 9. Control results from one representative CDA 0 alone. (a)-(c): force control alone while (d-f): impedance control plus force control.

During development of the control strategy, an initial test was performed on each CDA alone to tune the parameters of the force and impedance controllers. Using the PID algorithms k_{pf}= 70, k_{if}= 1, k_{df}= 0.01, and a filter with a cut-off frequency of 10 rad/s), each CDA independently produced good dynamic force control (Fig. 9a). For position control with a target profile of a sinusoidal curve, the impedance algorithms

(stiffness of 0.8 N/mm, damping ratio of 0.001 Ns/mm, and a filter with a cut-off frequency of 10 rad/s) worked well. The representative results of CDA 0 were shown in Fig. 9 (d-f). The error in force and position control was 3.5 N and 21.4 mm, respectively.

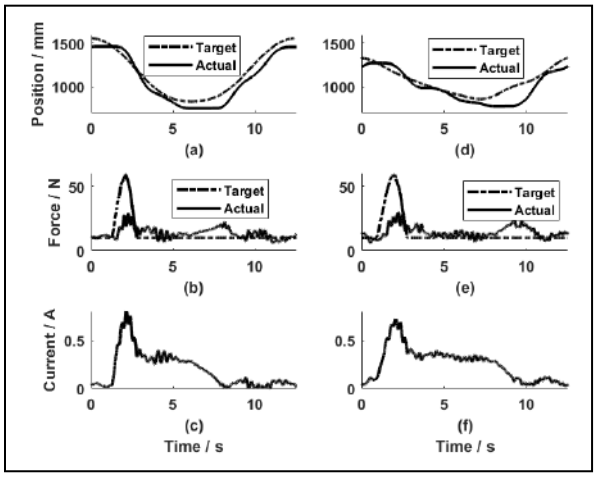


Fig. 10. Movement control results from a representative CDA 0 for production of 3D leg movement in the back-lying position (a-c) and walking-like movement in a side-lying position (d-f).

TABLE I. MOVEMENT CONTROL ACCURACY OF THE SIX CDAS. STD: STANDARD DEVIATION.

CDAs	Back-lying position		Side-lying position	
	RMSE$_F$ (N)	**RMSE$_L$ (mm)**	**RMSE$_F$ (N)**	**RMSE$_L$ (mm)**
Cable 0	9.3	87.0	10.4	97.9
Cable 1	19.7	54.5	21.3	58.8
Cable 3	14.2	45.0	18.3	48.8
Cable 4	18.0	54.6	21.1	67.2
Cable 6	6.7	39.6	6.1	38.5
Cable 7	8.7	32.0	4.8	30.8
Mean±STD	12.8±5.3	52.1±19.2	13.7±7.5	57.0±24.0

The six CDAs (0, 1, 3, 4, 6 and 7) were attached to the ankle joint of the test person so as to produce the two required leg movements. To prevent vibration, the force and position control parameters were reduced to k_{pimp} =10, k_{pimp}=0.3 N/mm for all CDAs. The movement control results of the representative CDA 0 for the back-lying position (Figs. 10 (a-c)) showed a force control error of 9.3 N, and a position control error of 87.0 mm (Table 1). Production of walking-like movement in the side-lying position was also achieved ($RMSE_F$=10.4 N, $RMSE_L$=97.9 mm in Figs. 10 (d-f) and Table 1). The mean force and position errors of the six CDAs were 13.25 N and 54.55 mm, respectively (Table 1).

The prototype of the robotic platform and test results were also presented by a video (https://youtu.be/gLlQfQfEBsY). After the introduction of the main components of the system (Part 1), the video demonstrates the production of the two representative leg movements (Part 2). The control algorithms were first tested on objects, before being implemented on the test person. It was demonstrated that the robotic platform produced 3D leg movement in the back-lying position and walking-like movement in the side-lying position.

IV. DISCUSSION

With the aim of promoting whole-body rehabilitation in the early post-injury phase, we proposed a cable-driven robotic platform to provide convenient user transfer, automatic posture change and various arm-leg movement therapy for users in a lying position. The robotic platform was manufactured with 17 CDAs. The movement control algorithms of PID force controller and impedance controller were implemented in six CDUs. The preliminary results showed that simultaneous actuation of six CDAs produced hip abduction/adduction and hip flexion in the back-lying position, and walking-like movement in the side-lying position. With the potential implementation of a similar strategy to all CDAs, the platform demonstrated the capability to provide automatic patient transfer, enable posture change and produce various 3D arm-leg synchronised movement when the user is in a lying position.

This work presented a multifunctional robotic platform with well-configured CDAs. Our previous research on producing various leg movements [13, 14] revealed the limitations of passive belt actuation. Based on the literature on robotics for 3D movement control [7, 9, 11], we designed the system with a parallel cable-driven robotic structure. A key factor in the design was determination of the suitable number of CDAs. For convenient user transfer, the lift mechanism requires at least one CDA. The generation of bilateral 3D arm-leg movement required 16 CDAs. Using the same configuration of CDAs, the cable fixation for producing unilateral walking with arm swing in a side-lying position was determined: four CDAs would be used to change the patient between back-lying and side-lying positions, while 12 CDAs would be applied for arm-leg movement. Compared to our previous design of CDAs [15], the CDAs developed in the current work had a compact structure, because a drum without threads was used, and the force sensor was fixed next to the drum. Using 16 compact CDAs with a unified structure reduced the manufacturing costs. Similar to [10, 11], the CDAs could easily be reconfigured on the platform, showing potential to generate various 3D arm-leg movements required for general daily activities. An inverse kinematic analysis will be performed in the future to see the overall movement potential of the developed robotic platform.

The control system and movement regulation strategy produced 3D leg movements. Unlike our previous studies [1, 15] which used single-axis servo controllers, we employed multi-axis motion controllers in the current study. The force control algorithms of CDAs were implemented in the motion controllers. The PID algorithms tracked the target cable force (mean force control error of 3.5 N). Based on the movement position trajectory error, the impedance algorithms calculated the new target force, thereby providing position guidance (average position control error of 21.4 mm). The active movement control algorithms were implemented on six CDAs simultaneously to produce 3D leg movements. Compared to our previous systems [13, 14], the current cable-driven robotic platform resolved the leg swaying problem. However, vibration was observed when all six cables were connected to actuate the ankle joint movement. Preliminary investigation

showed that the vibration amplitude was related to the weight of the actuated body and the control parameters. The current study reduced the vibration by lowering down the control parameters. Therefore the control accuracy during production of leg movements was reduced, but still acceptable, which can be seen from Table 1 and the attached video. A detailed investigation into the vibrations will be conducted soon.

The novelties of this study are the concept development and prototype validation of the cable-driven robotic platform for whole-body rehabilitation. Compared to studies [7, 15, 19] which produced walking-like leg movement using CDAs, we introduced additionally two CDAs to produce 3D leg movements. Arm movement has also been produced by cables in studies [20, 21]. Our robotic platform reconfigured multi-CDAs to enable whole-body rehabilitation. Furthermore, production of walking-like movement in a side-lying position was an innovative approach. Compared to studies [22, 23] which produced walking-like movement but in a back-lying position, the platform developed in the current study can prevent high pressure on the pelvic during training. For the safety issue, the test person could press the emergency button in the current study. for the final system which produces the arm-leg movement, then a hand-held emergency button will be implemented, as in our previous study [1]. Furthermore, clinical feasibility, safety and functionality will be investigated in the future.

The current study has several limitations. The 16 CDAs were fixed without performing an inverse kinematic analysis. Force control of the CDAs showed large influence of friction. To improve the control accuracy, new strategies, such as a lead controller [15] or a friction compensator [19], might be required. To ensure an accurate position control, the kinetics of 3D segment movement should be analysed, which will be described in future work. The test of automatic posture change and actuation of 3D arm movement will be performed soon.

V. Conclusion

A robotic platform with 17 CDAs was designed and manufactured. Implementing automatic movement control strategies on six CDAs demonstrated that the system produced a 3D leg movement in a back-lying position and walking-like leg movement in a side-lying position. Using similar control strategies, the innovative cable-driven platform can potentially provide convenient user transfer, automatic posture change and 3D arm-leg synchronised movement required in daily life.

References

[1] J. Fang and K. J. Hunt, "Mechanical design and control system development of a rehabilitation robotic system for walking with arm swing," *Frontiers in Rehabilitation Sciences,* vol. 2, 2021.

[2] Y. Long, Z.-j. Du, W. Wang, and W. Dong, "Development of a wearable exoskeleton rehabilitation system based on hybrid control mode," *International Journal of Advanced Robotic Systems,* vol. 13, p. 1-10, 2016.

[3] S. H. Hyon, J. Morimoto, T. Matsubara, T. Noda, and M. Kawato, "XoR: Hybrid drive exoskeleton robot that can balance," in *2011 IEEE/RSJ International Conference on Intelligent Robots and Systems*, 2011, pp. 3975-3981.

[4] A. Alili, A. Fleming, V. Nalam, M. Liu, J. Dean, and H. Huang, "Abduction/adduction assistance from powered hip exoskeleton enables modulation of user step width during walking," *IEEE Transactions on Biomedical Engineering,* vol. 71, pp. 334-342, 2024.

[5] T. A. Correa, K. M. Crossley, H. J. Kim, and M. G. Pandy, "Contributions of individual muscles to hip joint contact force in normal walking," *Journal of Biomechanics,* vol. 43, pp. 1618-1622, 2010.

[6] D. A. Hagen, A. Marjaninejad, G. E. Loeb, and F. J. Valero-Cuevas, "insideOut: A bio-inspired machine learning approach to estimating posture in robots driven by compliant tendons," *Frontiers in Neurorobotics,* vol. 15, 2021

[7] Y. Zou, N. Wang, X. Wang, H. Ma, and K. Liu, "Design and experimental research of movable cable-driven lower limb rehabilitation robot," *IEEE Access,* vol. 7, pp. 2315-2326, 2019.

[8] J. v. Zitzewitz, G. Rauter, R. Steiner, A. Brunschweiler, and R. Riener, "A versatile wire robot concept as a haptic interface for sport simulation," in *IEEE International Conference on Robotics and Automation*, 2009, pp. 313-318.

[9] G. Rauter, J. v. Zitzewitz, A. Duschau-Wicke, H. Vallery, and R. Riener, "A tendon-based parallel robot applied to motor learning in sports," in *IEEE RAS & EMBS International Conference on Biomedical Robotics and Biomechatronics*, 2010, pp. 82-87.

[10] J. Von Zitzewitz, A. Morger, G. Rauter, L. Marchal-Crespo, F. Crivelli, D. Wyss, T. Bruckmann, and R. Riener, "A reconfigurable, tendon-based haptic interface for research into human-environment interactions," *Robotica,* vol. 31, pp. 441-453, 2013.

[11] D. Cafolla, M. Russo, and G. Carbone, "CUBE, a cable-driven device for limb rehabilitation," *Journal of Bionic Engineering,* vol. 16, pp. 492-502, 2019.

[12] D. P. Ferris, H. J. Huang, and P.-C. Kao, "Moving the arms to activate the legs," *Exercise and Sport Sciences Reviews,* vol. 34, pp. 113-120, 2006.

[13] J. Fang, A. Schuwey, N. Stocker, B. Pedrini, A. Sampaio, and K. J. Hunt, "Preliminary development and technical evaluation of a belt-actuated robotic rehabilitation platform," *Technology and Health Care,* vol. 29, pp. 595-607, 2021.

[14] J. Fang, M. Haldimann, N. Stocker, B. Pedrini, A. Sampaio, and K. J. Hunt, "Development of a belt-actuated robotic platform for early rehabilitation," in *International Conference on Rehabilitation Robotics (ICORR)*, Rotterdam, the Netherlands, 2022, pp. 1-6.

[15] J. Fang, M. Haldimann, L. Marchal-Crespo, and K. J. Hunt, "Development of an active cable-driven, force-controlled robotic system for walking rehabilitation," *Frontiers in Neurorobotics,* vol. 15, 2021.

[16] J. Fang and K. J. Hunt, "Development of a cable-driven device for neuromuscular rehabilitation," *6th International Conference on NeuroRehabilitation (ICNR),* La Granja, Spain, 2024.

[17] J. Fang, Z. Mu, Z. Xu, L. Xie, G.-Y. Yang, and Q. Zhang, "Models for temporal-spatial parameters in walking with cadence ratio as the independent variable," *Medical & Biological Engineering & Computing,* vol. 57, pp. 877–886, 2019.

[18] D. A. Winter, *Biomechanics and Motor Control of Human Movement*, Fourth ed.: John Wiley & Sons, Inc., 2009.

[19] X. Jin, X. Cui, and S. K. Agrawal, "Design of a cable-driven active leg exoskeleton (C-ALEX) and gait training experiments with human subjects," in *IEEE International Conference on Robotics and Automation (ICRA)*, 2015, pp. 5578-5583.

[20] Y. Mao and S. K. Agrawal, "Design of a cable-driven arm exoskeleton (CAREX) for neural rehabilitation," *IEEE Transactions on Robotics,* vol. 28, pp. 922-931, 2012.

[21] Y. Zou, X. Wu, B. Zhang, Q. Zhang, A. Zhang, and T. Qin, "Stiffness analysis of parallel cable-driven upper limb rehabilitation robot," *Micromachines,* vol. 13, 2022.

[22] V. Monaco, G. Galardi, M. Coscia, D. Martelli, and S. Micera, "Design and evaluation of NEUROBike: a neurorehabilitative platform for bedridden post-stroke patients," *IEEE Transactions on Neural Systems and Rehabilitation Engineering,* vol. 20, pp. 845-852, Nov 2012.

[23] J. Fang, G.-Y. Yang, and L. Xie, "Development of an automatic rotational orthosis for walking with arm swing," in *15th IEEE International Conference on Rehabilitation Robotics (ICORR)*, London, UK, 2017, pp. 264-269.

Development of an End-Effector-Based System for Arm Support and Swing during Rehabilitation of Walking*

Juan Fang[1], Michael Haldimann[1,2] and Robert Riener[2,3]

Abstract— **The theory of interlimb neural coupling suggests that arm swing should be integrated into gait training to promote neural control of walking. We previously developed a mobile gait trainer which followed the user during free overground walking. However, it did not provide assistance in the synchronised arm and leg movements. This work aimed to develop a robotic arm module for the mobile gait trainer which offers stiff vertical arm support for balance, provides adaptable arm movement guidance during assisted walking, and allows free arm swing as experienced in daily walking. Based on an analysis of the wrist movement from normal gait, an end-effector-based system was developed, which used a screw drive to produce the vertical wrist movement and a timing belt drive with a force sensor to control the anterior-posterior wrist movement. Position controllers were employed to generate arm swing in passive training. Admittance algorithms were developed for the timing belt drive to generate adaptable horizontal movement. Free movement was produced by simplifying the admittance algorithms to include only a damping term. Preliminary tests showed that the position control algorithms produced arm swing in passive training with an accuracy of 1.78 mm vertically and 3.17 mm horizontally. The admittance controller produced adaptable anterior-posterior movement, where the active force modified the range of swing amplitude. The simplified admittance controller enabled the user to move freely with negligible interference from the robotic arm module. The system managed to offer rigid support for balance, to provide assisted arm swing for gait training with adaptable anterior-posterior movement, and to allow free arm swing. Integration of the arm movement with the mobile gait trainer and mechanism for leg movement will be investigated in future work.**

Keywords—arm swing, adaptable assistance, arm support, admittance control, rehabilitation of walking

I. Introduction

Walking involves not only rhythmic leg movements, but also synchronised arm swing [1]. Coordinated arm and leg movements are demonstrated in newborn infants and are maintained throughout their development [2]. Arm swing stabilises gait stability and optimises energy efficiency [3]. Reflex studies have implied that arm swing during gait is a neural-coordinated motor output [4]. Arm swing modulated the neural activity of the legs during rhythmic locomotion-like tasks [5]. Studies of interlimb neural coupling during walking have suggested a new paradigm for gait rehabilitation: moving the arms to activate the legs [6-8]. Arm swing is an integral component of the afferent input, which is required to facilitate lower limb motor output during walking.

Gait restoration is a process of motor relearning through repetitive training with appropriate guidance. The guidance should be tailored to individual needs. It has been hypothesised that patients should actively learn how to perform tasks through guidance, but should not become dependent on the guidance to perform the tasks [9]. This guidance hypothesis has been validated in many clinical studies [10, 11], where training with assistance-as-needed produced better results compared to the rigid training in passive mode. Physical guidance should be adjusted according to varying needs with the training progress.

In order to accelerate gait restoration process, a platform for overground rehabilitation of walking was envisaged by the coauthors, which inlcudes: (i) arm swing to activate and maximally exploit the neural control of walking for neurological recovery; and (ii) adaptable guidance so that the user can actively relearn walking according to the severity of their impairment. A mobile gait trainer was developed in our previous work [12]. Using computer-vision-based pose estimation, the mobile trainer followed the user during free overground walking. For patients with motor pathologies, assistance in the arm swing and leg movement is desirable. The task of this study was to develop an arm mechanism for the mobile gait trainer, so that patients get their arms actively involved in gait training. The system for assisted leg movement will be investigated soon.

As preparation for robotic development, clinical interviews with physiotherapists and patients were conducted to determine the required functionalities of the arm support mechanism. It was found that the patients after spinal cord injury rely on their upper limbs for balance and stability while standing and walking [13, 14]. Therefore, some SCI patients, such as those who have certain spared arm functions, may prefer to use their arms to maintain balance during training. In this case, stiff vertical support for the arm is required. Hemiplegic stroke patients often have reduced arm swing on the affected side [15, 16]. Assisted arm swing is required to increase gait symmetry [17]. Patients with some arm functions are often instructed to use their arms to propel their legs [18]. Therefore, an adaptable arm swing is desirable. According to research on ballistic walking, arm swing is a natural movement resulting from the energetic optimisation of the

*Research supported by the Swiss National Science Foundation (Grant No. 32HW-0_220453).

1. rehaLab – The Laboratory for Rehabilitation Engineering, Institute for Human Centred Engineering HuCE, Department of Mechatronics and Systems Engineering, School of Engineering and Computer Science, Bern University of Applied Sciences (BUAS), Quellgasse 21, Postfach 2501 Biel, Switzerland.

2. Sensory-Motor Systems (SMS) Lab, Institute of Robotics and Intelligent Systems, Department of Health Sciences and Technology, ETH Zurich, 8092 Zurich, Switzerland.

3. SCI Center, University Hospital Balgrist, Medical Faculty, University of Zurich, 8092 Zurich, Switzerland.

Robert Riener is the head of SMS Lab. Juan Fang is a professor at rehaLab of BUAS. Juan Fang is the corresponding author (phone: +41 34 426 42 74; e-mail: juan.fang@bfh.ch). Michael Haldimann is a research assistant at rehaLab of BUAS, and a PhD student at the SMS Lab.

walking pattern. Therefore, patients with relatively good arm function may not need assistance for their upper limbs. Instead, they may prefer to swing naturally without any interference from the robot. In summary, the designed arm mechanism should be able to offer stiff vertical support, produce adaptable guidance of arm swing, and also allow natural, free arm movement as experienced in daily walking.

There are many robotic systems for arm movement, but none of them has produced the functions described above. The systems for rehabilitation of upper limbs range from rigid systems [19, 20] to dedicated cable-driven robots [21]. Detailed information has been summarised in the reviews [22, 23]. Most systems have focused on production of daily arm movement, such as lifting or eating. For generation of arm swing, rigid systems such as a single-link pendular bar [24] or a soft system like a pulley [18] have been developed. However, none of these systems provide stiff support and adaptable arm movement as required in the current study.

As an advancement to walking rehabilitation for individuals with mobility impairments, this work aimed to develop a robotic arm module for the mobile gait trainer which offers stiff vertical arm support for balance, provides adaptable arm movement guidance during assisted walking, and allows free arm swing as experienced in daily walking.

II. Methods

The movement analysis (MATLAB, version 2024, The MathWorks GmbH, Bern, Switzerland) was conducted using a dataset from overground walking. Based on the results of the analysis and conception phase, a robotic arm mechanism with two motors was designed in NX (Version 2019, Siemens AG, Zürich, Switzerland). The system program for movement control was developed in TwinCAT 3 software (Beckhoff Automation GmbH & Co., Lyssach, Switzerland).

A. Target Movement Analysis

The wrist movement during overground walking from our previous study [25] was used as the target trajectory for the wrist. To ensure accurate position control, the target trajectory should be smooth. Therefore, the vertical and horizontal trajectories of the target wrist movement were calculated using functions consisting of lengths of upper and lower arms and angles of shoulder and elbow joints. The Curve Fitting Toolbox in MATLAB was used. The functions were further implemented as trajectory generators in TwinCAT 3 to produce the reference trajectories for motion control (*Section C*). The target wrist position yielded smooth speed and acceleration of the required movement, which are about a maximal speed of 1.5 m/s, acceleration of 11 m/s^2 for the horizontal movement, and about a maximal speed of 0.4 m/s, acceleration of 5 m/s^2 for the vertical movement.

B. Description of the Robotic Arm Mechanism

Based on the required movement analysis, a drive (torque:1.21 Nm, speed: 1500 rpm) with a pulley-belt (diameter: 24.24 mm) was required to produce the horizontal movement. A drive (torque: 0.96 Nm, speed: 3000 rpm) with a trapezoidal thread (pitch: 8 mm, diameter: 10.5 mm) was required to produce the vertical movement. Therefore, two electric motor assemblies (EC90, 400W, with an encoder 6400 CPT, maxon motor AG, Sachseln, Switzerland) were used. The system included a U-shaped frame (Fig. 1a), on which the pulley-belt drive was mounted to produce the horizontal movement of the wrist. The U-shaped frame and the rigid support bar were mounted on the lead screw drive so as to move vertically.

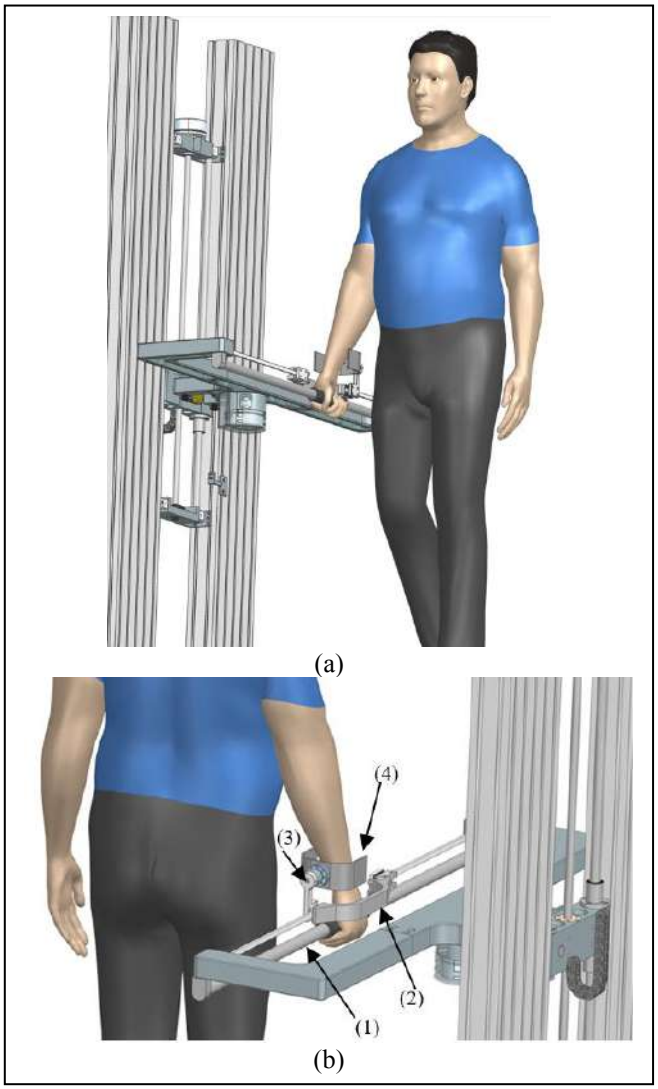


Fig. 1. The CAD concept of the robotic arm mechanism. (a) The U-shaped frame with two drives is mounted on the mobile trainer frame and (b) arm fixation. (1) The rigid bar for stiff arm support, (2) the metal connector for the timing belt, (3) the force sensor and (4) the wrist cuff.

The U-shaped frame was manufactured with aluminum. It was 1.5 m wide to accommodate users with a height between 1.50 m and 2.00 m (Fig. 2). The robotic mechanism was attached to the static frame of the mobile gait trainer. As this work focused on the development of the arm mechanism, the integration of the arm swing and the gait trainer movement was not investigated. Therefore, the trainer was static in this study. A treadmill was used to test the generated arm movement while walking.

As shown in Figs. 1(b) and 2(b), the wrist was fixed in a metal cuff with a soft pad. The two ends of the timing belt were fixed on a metal connector. A force sensor (500 N, Bengbu Sensor Company, China) was fixed on the connector, and a single-channel amplifier (EP3356-0022, EtherCAT

Box, Beckhoff) was fixed on the U-shaped frame. The metal cuff was fixed on the other end of the force sensor. The interaction force between the user and the robotic arm mechanism was measured by the force sensor.

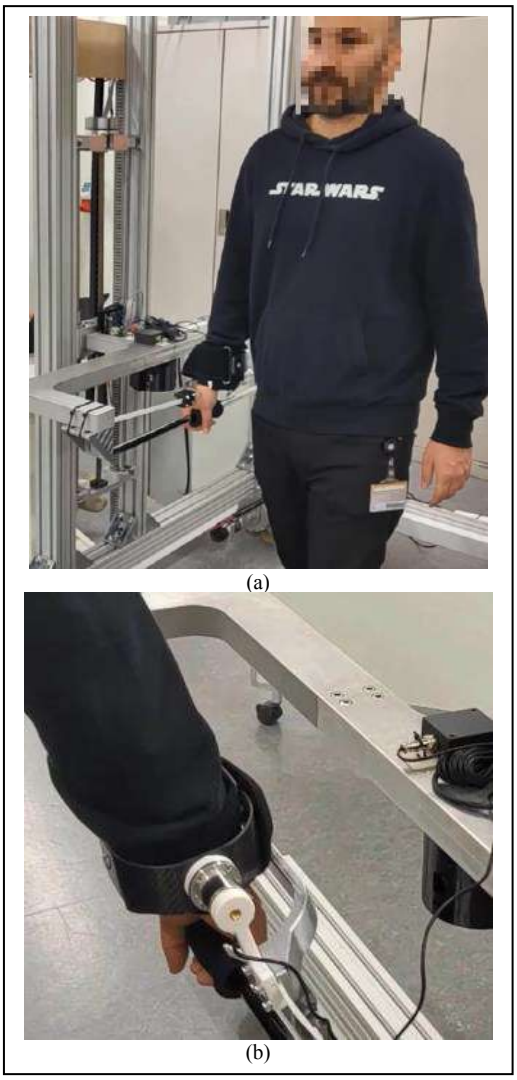


Fig. 2. Prototype of the robotic arm mechanism that is fixed on the mobile trainer. (a) A person walks on the treadmill with the robotic arm mechanism and (b) the fixation of the wrist to the mechanism.

The control system included an industrial PC (IPC, C6032-0070, Beckhoff Automation GmbH & Co., Lyssach, Switzerland) and two positioning controllers (EPOS4 Compact 50/15, maxon motor AG, Sachseln, Switzerland). The positioning controllers were connected in series to the IPC with EtherCAT communication protocol.

C. Movement Control Strategies

The positioning controller has embedded algorithms to get the motor running in torque, velocity and position modes, where the control parameters can be determined using the auto-tuning function in EPOS Studio (maxon motor AG, Sachseln, Switzerland). In this study, the position mode was used. The auto-tuning procedure of the screw drive yielded the PID algorithms (k_p = 21008 mA/rad, k_i = 27392 mA/rads, and k_d = 493 mAs/rad) combined with the feedward velocity (a gain of 45 mAs/rad) and feedward acceleration (a gain of 4.6 mAs^2/rad) to produce the vertical movement. Similarly, the well-tuned PID position algorithms for the belt drive (k_p = 30000 mA/rad, k_i = 480000 mA/(rad.s), and k_d = 580 mA.s/rad) combined with the feedward velocity gain of 55 mA.s/rad and acceleration gain of 4.4 mA.s^2/rad were used to produce the horizontal movement. The passive mode was always implemented in the vertical axis, while three modes were implemented in the horizontal axis: passive, adaptable and free-movement training. During passive training, a rigid position trajectory was provided, where the user followed the movement passively. During adaptable training, the horizontal range of movement was adjusted by the user, while in free-movement training, the user could freely control the anterior-posterior arm movement.

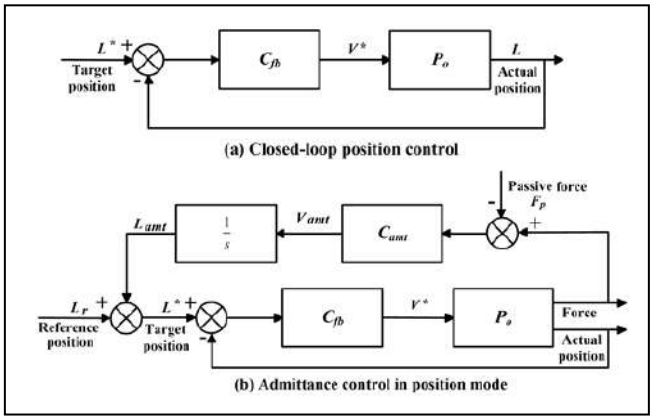


Fig. 3. Movement control strategies.

During passive training, position control algorithms (Fig. 3a) were implemented on the motors for the screw drive and the belt drive. The force sensor on the belt measured the interaction force during passive training F_p.

In order to produce adaptable movement, an admittance controller C_{amt} (Fig. 3b) was implemented on the belt drive. The input to and output from C_{amt} are ΔF (the difference between the actual force and the force during passive training F_p, which is the active force from the user) and the new velocity V_{amt} of the belt drive, respectively. The transfer function of C_{amt} is:

$$\Delta F \rightarrow V_{amt}: C_{amt} = \frac{1}{ms + d + \frac{k}{s}}, \quad (1)$$

where the parameters m, d and k are the mass, damping ratio and stiffness of the system, respectively. An integrator was implemented to get the position L_{amt}. Based on the active force, the target position was adjusted. When the mass and stiffness were set as zero, the system ran in free-movement mode, where the input force was linearly scaled to be the speed of the drive V_{amt}. In this case, no reference position was defined, i.e., L_r=0.

The control algorithms were tested on a healthy person (age of 27 years, height of 1.74 m and body mass of 85 kg). Since the data are not generalisable, it does not fall under the Swiss Federal Act on Research Involving Human Beings. No ethical approval was needed. During the test, he fixed his right wrist on the robotic arm mechanism, held on the palm holder which allows free sliding on the support bar, and then

walked on the treadmill at 2.0 km/h and 120 steps per minute. In passive training, he followed the movement produced by the robotic arm mechanism, while in the adaptable training, he actively swung his arm. In the free-movement training, he tried to swing his arm naturally. Detailed information of the test can be found in the attached video.

The control programme was developed in TwinCAT 3 and downloaded to the IPC. The IPC implemented the programme in real time at a sample rate of 1000 Hz. A Visulisation Manager page was developed to operate the robotic arm mechanism. The position of the U-shaped frame and the offset of the wrist cuff could be adjusted according to the height of the user. The walking speed could be defined. The data were saved using the measurement toolbox in TwinCAT 3.

III. Results

With the aid of MATLAB, the reference wrist position in the vertical and horizontal axes were determined (dashed lines in Figs. 4(a) and 5(a)). The zero position of the horizontal axis is when the wrist is in a neutral, straight alignment with the arm in the upright standing still position. The ground is defined as the zero position of the vertical axis. Implementing the trajectories in TwinCAT 3, the reference trajectories for the screw drive and the timing belt drive were defined.

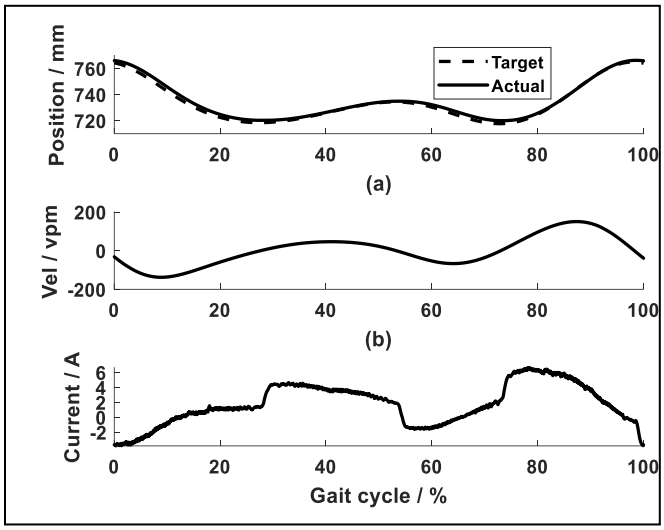


Fig. 4. Vertical movement control in passive training.

The position controller (Fig. 3(a)) produced the actual vertical movement (the solid line in Fig. 4(a)) with a high accuracy. The root-mean-square error (RMSE) between the target position L^* and the actual position L was 1.78 mm. In subsequent tests of the robotic arm mechanism, the same controller was always employed for the vertical movement. By monitoring the motor current of the screw drive (Fig. 4(c)), it was possible to detect whether the user pressed the horizontal bar or not. If yes, the bar could provide stiff support by setting the target vertical velocity of the screw drive to 0.

In order to produce the three types of anterior-posterior movement, admittance controllers in position mode (Fig. 3) were used in the timing belt drive. The position controller (Fig. 3(a)) produced the actual movement (the solid line in Fig. 5(a)) with a high accuracy (RMSE of 3.17 mm). Such a small position difference is barely observable in Fig. 5(a). The average force between the test person and the wrist cuff (Fig. 5(c)) in passive training was 2.17 N forward and 1.15 N backward.

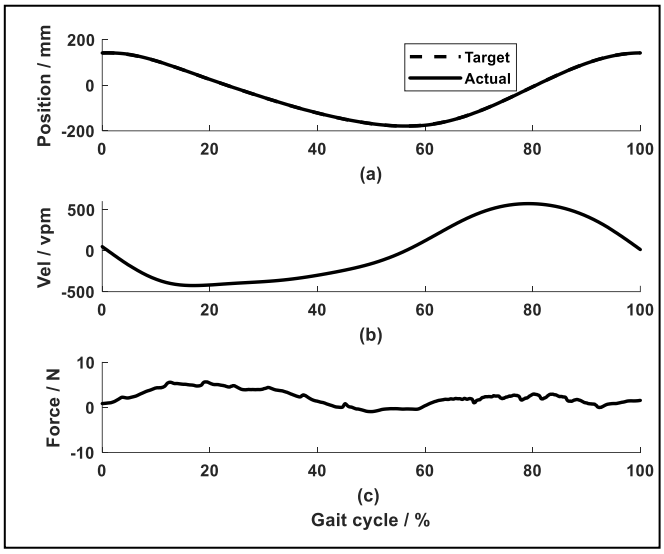


Fig. 5. Anterior-posterior movement control in passive training.

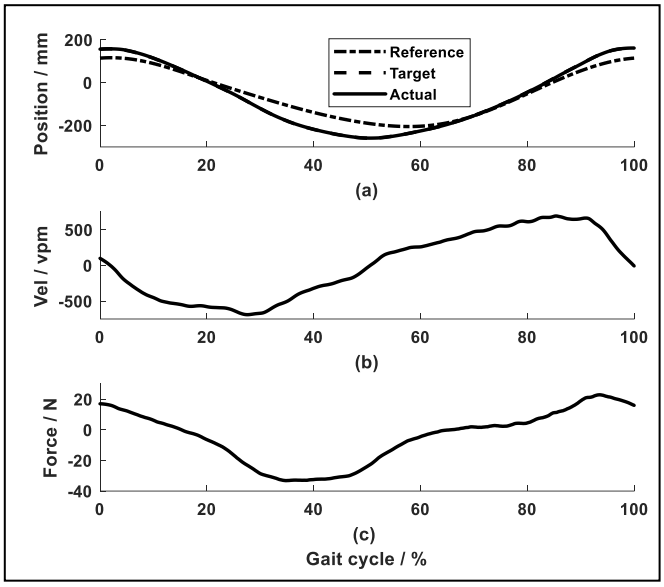


Fig. 6. A representative adaptable movement from the admittance controller.

To test the feasibility of the admittance controller in producing adaptable movements, a controller with parameters (Mass m = 1.0 kg, damping ratio d = 1.0 Ns/m and stiffness k = 1117 N/m) was used. An active forward force of 16.7 N (Fig. 6c) produced an additional forward position of 42 mm (Fig. 6a). The position controller yielded a high accuracy (RMSE = 2.70 mm). The parameters of the admittance controller could be tuned to get movement with different adaptabilities. A lower stiffness or lower damping ratio enabled the user to change the range of movement more easily.

When the admittance controller only included the damping item, the arm mechanism produced free arm movement. A low damping ratio means a larger velocity from the same active force input. To improve system sensibility, a damping ratio d = 0.2 Ns/m was used in the test. The motor moved at a velocity

of about 500 rpm in response to a small active force of 6 N (Fig. 7). Behaving similarly in the transparent mode, the mechanism allowed free natural arm swing.

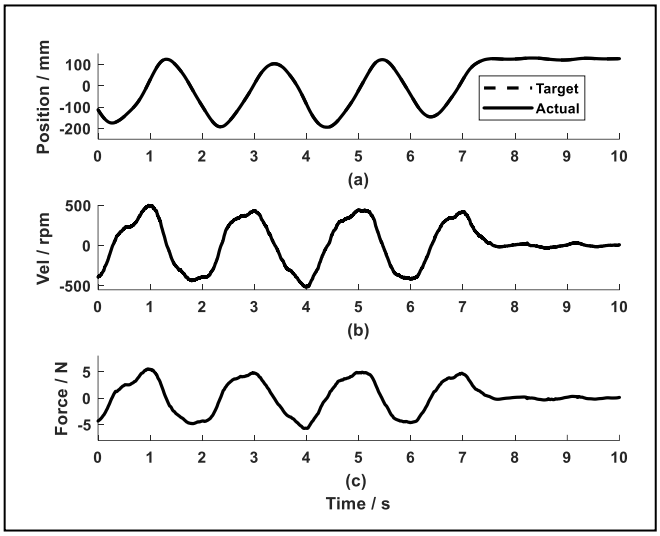


Fig. 7. Free-movement training.

IV. Discussion

This work aimed to develop a robotic arm module for the mobile gait trainer which offers stiff vertical arm support for balance, provides adaptable arm movement guidance during assisted walking, and allows free arm swing as experienced in daily walking. Mounted on the mobile gait trainer, the robotic arm module included a screw drive and a timing belt drive with a force sensor. Implementing admittance control algorithms when the motors ran in position mode, the system produced the required wrist movement. With easy operation, stable communication and adaptable movement algorithms, the developed robotic system was proven to be technically feasible to support arm movement during walking rehabilitation.

The robotic arm module included rigid and soft mechanical components, which made it mechanically possible to provide stiff support, adaptable guidance and free movement. As the clinical test [26] showed that end-effector systems produced significant improvements in the upper limbs compared to exoskeletons, we designed the robotic arm with the end-effector approach. To ensure a stiff vertical support, a trapezoid lead screw drive was used. The user held the rigid bar with a slidable palm holder, so that she/he could keep balance using the arm if necessary. The wrist cuff was driven by a timing belt to produce the anterior-posterior movement during arm swing. The tension of the belt could be adjusted to be softer or stiffer, depending on the user's training requirements. The belt provided anterior-posterior movement without medial-lateral constraints, which allowed natural arm swing in the free-movement training. Compared to the cable-driven devices, which are often over-actuated [27], the timing-belt drive also produces flexible movement but with fewer motors. From a mechanical point of view, the system offered several possibilities, which served as the mechanical base for generation of the required functionality.

In addition to the innovative mechanical structures, the position control strategies were crucial for achieving the required functions. The position strategy embedded in the advanced positioning controller offered convenient parameter-tuning package and provided easy programming environment for movement control. The robotic arm module produced the target wrist movement with high accuracies in passive training. The admittance controller produced adaptable anterior-posterior movement during assisted walking. Compared to our previous study [28] where similar admittance strategies were used, the current study used the robust position control algorithms, which enabled accurate tracking of the target movement. In the free-movement mode, the robotic system produced movement which is similar to that in the transparent mode. The traditional method of generating a transparent mode, as shown in [29], needs to remove the influences from the friction and segment mass. Friction compensation requires repetitive tests to find the friction-speed relationship. By regulating the motor velocity based on the active force input from the user, the current study enabled free movement with relatively good results. Preliminary control tests demonstrated that the system was sensitive to the active force and moved in a manner similar to the natural arm swing. Using the embedded position controller and self-developed admittance algorithms, the arm mechanism not only provided stiff vertical support and adaptable horizontal movement, but also allowed the arm to swing freely.

The functionalities of the robotic arm module were technically evaluated, but more investigation is required prior to clinical application of the system. The robotic arm module belongs in a greater pipeline to a novel neurorehabilitation gait trainer [12]. Representative robotic systems for walking, such as Lokomat and Andago, have rigid bars for balance support. It was found that even a light touch of the fingertip on the bar is useful to reduce postural sway in stroke patients [30]. Clinical study on SCI patients [13] revealed their arm muscles were often involved in the adapted postural control strategies. Therefore, a rigid bar was included in the arm mechanism to contribute to postural stabilisation of the stroke and SCI patients. Furthermore, arm movement has been clinically included to enhance leg activity [18, 31]. It should be noted that the developed arm module can only work in situations where the patients are able to perform assisted arm movement without pain. Formal analysis will be performed to investigate the clinical feasibility of the robotic arm module.

This study has some limitations and requires further work. The timing belt was used to produce flexible horizontal movement. However, belt deformation was observed because the relatively heavy components, such as the metal connector, force sensor and metal wrist cuff, were attached on it. As only a small force was interacted between the user and the cuff, the connector and wrist cuff can be replaced with plastic components. The adaptable movement and free arm swing can be improved by implementing admittance controllers in the vertical axis as well. In order to achieve this, a force sensor can be additionally attached on the palm holder to detect the active vertical press or lift from the user. To enable walking training overground, arm movement should be synchronised with the mobile gait trainer, which will be investigated in future work.

V. Conclusion

An end-effector-based system was developed for arm support and arm swing, as a module to the mobile gait trainer. The innovative mechanical structure with rigid and soft mechanical components enabled the robotic arm module to provide stiff vertical support without medial-lateral constraints of the wrist. Using admittance algorithms, the arm mechanism technically provided adaptable guidance in anterior-posterior movement for arm swing, and allowed free, natural arm movement as experienced in daily walking. The robotic arm mechanism can be integrated into the mobile trainer to assist the required arm movement during rehabilitation of walking. Synchronisation of the arm movement with the mobile gait trainer and the assistance of leg movement will be investigated in future work.

References

[1] R. Zhou, L. Alvarado, R. Ogilvie, S. L. Chong, O. Shaw, and V. K. Mushahwar, "Non-gait-specific intervention for the rehabilitation of walking after SCI: role of the arms," *Journal of Neurophysiology,* vol. 119, pp. 2194-2211, 2018.

[2] N. Dominici, Y. P. Ivanenko, G. Cappellini, A. d'Avella, V. Mondì, M. Cicchese*, et al.*, "Locomotor primitives in newborn babies and their development," *Science,* vol. 334, pp. 997-9, Nov 18 2011.

[3] J. D. Ortega, L. A. Fehlman, and C. T. Farley, "Effects of aging and arm swing on the metabolic cost of stability in human walking," *Journal of biomechanics,* vol. 41, pp. 3303-3308, Dec 5 2008.

[4] E. P. Zehr and J. Duysens, "Regulation of arm and leg movement during human locomotion," *The Neuroscientist,* vol. 10, pp. 347-361, 2004.

[5] F. Massaad, O. Levin, P. Meyns, D. Drijkoningen, S. P. Swinnen, and J. Duysens, "Arm sway holds sway: Locomotor-like modulation of leg reflexes when arms swing in alternation," *Neuroscience,* vol. 258, pp. 34-46, 2014.

[6] D. P. Ferris, H. J. Huang, and P.-C. Kao, "Moving the arms to activate the legs," *Exercise and Sport Sciences Reviews,* vol. 34, pp. 113-120, 2006.

[7] C. Kaupp, G. E. Pearcey, T. Klarner, Y. Sun, T. S. Barss, H. Cullen*, et al.*, "Rhythmic arm cycling training improves walking and neurophysiological integrity in chronic stroke: the arms can give legs a helping hand in rehabilitation," *Journal of Neurophysiology,* vol. 119, pp. 1095-1112, 2018.

[8] D. de Kam, J. Duysens, and V. Dietz, "Do we need allowing arm movements for rehabilitation of gait?," in *Converging Clinical and Engineering Research on Neurorehabilitation*, Berlin, Heidelberg, 2013, pp. 957-961.

[9] R. A. Schmidt, D. E. Young, S. Swinnen, and D. C. Shapiro, "Summary knowledge of results for skill acquisition: Support for the guidance hypothesis," *Journal of Experimental Psychology: Learning, Memory, and Cognition,* vol. 15, pp. 352-359, 1989.

[10] J. Hidler, D. Nichols, M. Pelliccio, K. Brady, D. D. Campbell, J. H. Kahn*, et al.*, "Multicenter randomized clinical trial evaluating the effectiveness of the lokomat in subacute stroke," *Neurorehabilitation and Neural Repair,* vol. 23, pp. 5-13, Jan 2009.

[11] T. G. Hornby, D. D. Campbell, J. H. Kahn, T. Demott, J. L. Moore, and H. R. Roth, "Enhanced gait-related improvements after therapist- versus robotic-assisted locomotor training in subjects with chronic stroke," *Stroke,* vol. 39, pp. 1786-1792, 2008.

[12] J. Fang, M. Haldimann, B. Amiryavari, E. A. Aksöz, and R. Riener, "Development of a mobile gait trainer using pose estimation," in *International Conference on Neurorehabilitation (ICNR)*, La Granja, Spain, 2024.

[13] M. Moynahan, "Postural responses during standing in subjects with spinal-cord injury," *Gait & Posture,* vol. 3, pp. 156-165, 1995/09/01/ 1995.

[14] K. A. Bernhardt, L. A. Beck, J. L. Lamb, K. R. Kaufman, S. Amin, and L. A. Wuermser, "Weight bearing through lower limbs in a standing frame with and without arm support and low-magnitude whole-body vibration in men and women with complete motor paraplegia," *Am J Phys Med Rehabil,* vol. 91, pp. 300-8, Apr 2012.

[15] J. K. Ma, T. A. Floegel, L. C. Li, J. Leese, M. A. De Vera, M. R. Beauchamp*, et al.*, "Tailored physical activity behavior change interventions: challenges and opportunities," *Transl Behav Med,* vol. 11, pp. 2174-2181, Dec 14 2021.

[16] M. P. Ford, R. C. Wagenaar, and K. M. Newell, "Phase manipulation and walking in stroke," *Journal of Neurologic Physical Therapy* vol. 31, pp. 85-91, 2007-Jun 2007.

[17] Y. I. Hwang and D. H. An, "Immediate effects of an elastic arm sling on walking patterns of chronic stroke patients," *J Phys Ther Sci,* vol. 27, pp. 35-7, Jan 2015.

[18] D. Vega and C. J. Arellano, "Using a simple rope-pulley system that mechanically couples the arms, legs, and treadmill reduces the metabolic cost of walking," *Journal of NeuroEngineering and Rehabilitation,* vol. 18, p. 96, 2021/06/07 2021.

[19] R. Loureiro, F. Amirabdollahian, M. Topping, B. Driessen, and W. Harwin, "Upper limb robot mediated stroke therapy-GENTLE/s approach," *Autonomous Robots,* vol. 15, pp. 35-51, 2003.

[20] B. Kim, K.-H. Ahn, S. Nam, and D. J. Hyun, "Upper extremity exoskeleton system to generate customized therapy motions for stroke survivors," *Robotics and Autonomous Systems,* vol. 154, p. 104128, 2022/08/01/ 2022.

[21] J. D. Sanjuan, A. D. Castillo, M. A. Padilla, M. C. Quintero, E. E. Gutierrez, I. P. Sampayo*, et al.*, "Cable driven exoskeleton for upper-limb rehabilitation: A design review," *Robotics and Autonomous Systems,* vol. 126, p. 103445, 2020/04/01/ 2020.

[22] R. Gassert and V. Dietz, "Rehabilitation robots for the treatment of sensorimotor deficits: a neurophysiological perspective," *Journal of neuroengineering and rehabilitation,* vol. 15, pp. 46-46, 2018.

[23] R. C. Loureiro, W. S. Harwin, K. Nagai, and M. Johnson, "Advances in upper limb stroke rehabilitation: a technology push," *Med Biol Eng Comput,* vol. 49, pp. 1103-18, Oct 2011.

[24] J. Yoon, B. Novandy, C. Yoon, and K. Park, "A 6-DOF gait rehabilitation robot with upper and lower limb connections that allows walking velocity updates on various terrains," *IEEE/ASME Transactions on Mechatronics,* vol. 15, pp. 201-215, 2010.

[25] J. Fang, K. J. Hunt, L. Xie, and G.-Y. Yang, "Modelling of the toe trajectory during normal gait using circle-fit approximation," *Medical & Biological Engineering & Computing,* vol. 54, pp. 1481-1489, 2016.

[26] S. H. Lee, G. Park, D. Y. Cho, H. Y. Kim, J. Y. Lee, S. Kim*, et al.*, "Comparisons between end-effector and exoskeleton rehabilitation robots regarding upper extremity function among chronic stroke patients with moderate-to-severe upper limb impairment," *Sci Rep,* vol. 10, p. 1806, Feb 4 2020.

[27] J. Fang, M. Haldimann, L. Marchal-Crespo, and K. J. Hunt, "Development of an active cable-driven, force-controlled robotic system for walking rehabilitation," *Frontiers in Neurorobotics,* vol. 15, 2021.

[28] Z. Mu, Q. Zhang, G.-Y. Yang, L. Xie, and J. Fang, "Development of an improved rotational orthosis for walking with arm swing and active ankle control," *Frontiers in Neurorobotics,* vol. 14, 2020.

[29] J. Fang, B. Tan, W. Zhang, L. Xie, and G.-Y. Yang, "Impedance control and test of an automatic rotational orthosis for walking with arm swing," *Brain Network and Modulation,* vol. 2, 2023.

[30] B.P. Cunha, S.R. Alouche, I.M.G. Araujo, S. Freitas, " Individuals with post-stroke hemiparesis are able to use additional sensory information to reduce postural sway," *Neuroscience Letters,* vol. 513, pp. 6-11, 2012.

[31] R. Zhou, L. Alvarado, R. Ogilvie, S. L. Chong, O. Shaw, and V. K. Mushahwar, "Non-gait-specific intervention for the rehabilitation of walking after SCI: role of the arms," *Journal of Neurophysiology,* vol. 119, pp. 2194-2211, 2018.

A Task-Agnostic Approach to Unified Multi-Activity Gait Phase Estimation via Bilateral Sensing

Ryan R. Posh and Robert D. Gregg

***Abstract*— Estimating the gait phase is a key aspect for controlling many lower-limb rehabilitation robots, including transfemoral prostheses. Current control approaches often rely on high-level activity classification to then employ a task-specific phase algorithm, which can limit adaptability across tasks and introduce risks associated with misclassification. This study proposes a novel unified phase variable framework with two approaches, one using activity classification and one being entirely task-agnostic. The framework uses predicted gait event information to continuously define a unified phase variable across level walking, ramp ascent/descent, and stair ascent/descent at various inclines and speeds. The classification approach senses the unilateral thigh angle, whereas the task-agnostic approach expands sensing to include the contralateral thigh angle. Simulated evaluations using an able-bodied dataset demonstrate average phase root-mean-square error of 6.8% with classification and 6.3% in the task-agnostic mode. The bilateral task-agnostic approach notably performed the same or better than the unilateral classification-based approach, showing improved consistency across subjects and tasks, particularly during stair ascent. These results highlight the feasibility of task-agnostic gait phase estimation for prosthesis control, demonstrating performance comparable to task-specific models while removing reliance on activity classification.**

I. Introduction

Robotic lower-limb prostheses offer great potential to improve the mobility and quality of life for individuals with lower-limb amputation, but reaching this potential could be largely dependent on the selected control approach. Several prosthetic controllers have been developed for effective level-ground walking [1], [2], demonstrating more normative joint biomechanics [3], less energy expenditure [4], and potentially more endurance [5] when compared to passive prostheses. While these benefits highlight the potential of these devices, it is critically important to develop control algorithms that are also effective across a wide range of activities of daily living (ADLs).

Research focus has shifted to controlling activities beyond level walking, including ramp walking [6]–[8], stair climbing [9], [10], sit/stand activities [11], [12], and even non-standard activities [13]–[15]. The prevailing approach to enabling multi-activity prosthesis control is to employ a high-level task classifier to determine the user's desired activity, and then discretely switch between mid-level controllers with task-specific properties [16], [17]. Several classification approaches in lab settings have achieved accuracy rates greater than 99% [18]–[22], which could enable users to receive the benefits from powered prostheses during several ADLs. However, even infrequent misclassifications leading to the deployment of the wrong mid-level controller could cause negative consequences such as falls. Furthermore, classification approaches require a limited, predefined set of activities, usually leaving many possible tasks (e.g., continuous variations of a predefined task) unaccounted for.

More recently, there has been increasing interest in task-agnostic control approaches that do not require any knowledge of the intended activity. Broadly speaking, there are two primary perspectives for pursuing task-agnostic control: Machine Learning (ML)-based and biomechanical model-based frameworks. ML-based control approaches that account for multiple ADLs without classification often use neural networks (NNs) to map directly from kinematic inputs to joint level outputs such as torque [23]–[26]. These approaches offer high theoretical promise but have demonstrated several associated limitations, including sensitivity to the training data such as bias towards level walking, the potential for unexpected behavior when encountering out-of-distribution inputs, and reduced interpretability, all potentially limiting clinical and commercial acceptance.

The second approach to task-agnostic prosthetic control is to impose some level of structure based on typical human locomotion biomechanics. Incorporating these principals into the model structure could make this framework more robust and interpretable when continuously spanning multiple locomotion tasks. These model-based, multi-activity control methods include heuristic control laws [27] or continuous phase variables that monitor the progression of gait [8], [28]. The ability to continuously monitor gait progression (gait phase) is a key element to many model-based approaches, and has also been used for bipedal robot control [29], exoskeleton control [30], and clinical gait analysis [31].

A phase variable can be defined as a biomechanical parameter that indicates the phase progression from the beginning to end of a locomotion activity, which is typically cyclic in nature. Candidate phase variables have included the center of pressure (for stance progression only) [2], tibia kinematics (typically for prosthetic ankle control) [32], [33], and various hip/thigh kinematics (common for knee-ankle control) [34]. These phase variables support different control architectures including position control [2], [6], [28] and impedance control [7], [8], [33], and they have been used in both model-based and ML-based approaches [35], [36]. In [36], an ML-based, multi-activity phase estimation approach is presented

This work was supported by the National Institute of Child Health & Human Development of the NIH under Award R01HD094772. The content is solely the responsibility of the authors and does not necessarily represent the official views of the NIH. (Corresponding author: Ryan R. Posh)

The authors are with the Department of Robotics, University of Michigan, Ann Arbor, MI 48109. {poshr, rdgregg}@umich.edu

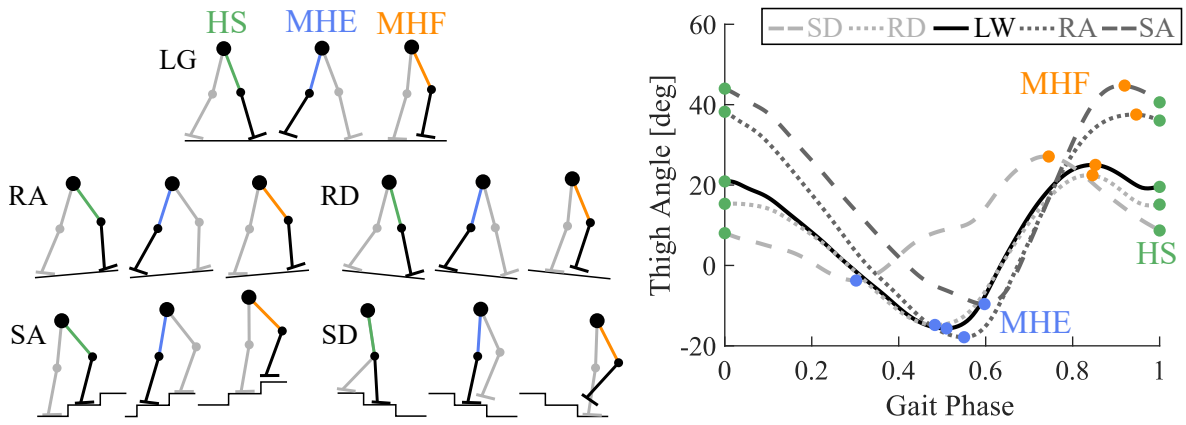


Fig. 1. Left: Gait events of heel strike (HS), maximum hip extension (MHE), and maximum hip flexion (MHF) are each observed in locomotion tasks of level walking (LW), ramp ascent (RA) and descent (RD), and stair ascent (SA) and descent (SD). Right: The corresponding gait phase and thigh angle magnitude of these gait events changes based on locomotion task.

for exoskeletons, but is not shown to generalize to varying speeds, ramp inclines, or stair heights. Model-based phase variables typically have task-specific definitions (e.g., differing definitions for walking and stair climbing tasks [9]) and thus rely on accurate task classification. There is currently no model-based phase variable definition that is unified across the primary ADLs, which limits the development of more robust and interpretable task-agnostic control approaches.

Therefore, in this work, we present a novel piecewise-monotonic phase variable framework that maintains a unified definition across level walking, ramp ascent/descent, and stair ascent/descent at several different inclines and speeds. The contribution herein includes two novel phase model definitions: 1) a unified phase variable based on unilateral thigh sensing that maintains the state-of-the-art task classification structure, and 2) one based on bilateral thigh sensing that is entirely task-agnostic. Both of these definitions represent the first model-based phase variable that is structurally unified across these primary ADLs. By simulating with an able-bodied dataset [37], the effectiveness and potential of these approaches are demonstrated with an overall phase RMSE error of 6.8% with classification and 6.3% when task agnostic. These results suggest that this unified phase variable could be a promising component of seamless prosthesis controllers across locomotion tasks that can be incorporated in a variety of control frameworks.

II. Unified Gait Phase Estimation

A. Piecewise Phase Variable Definition

As in or previous work [8], [9], [38], the phase variable is estimated from the global thigh orientation in the sagittal plane, which can be measured by an inertial measurement unit (IMU) onboard the thigh segment of the prosthesis. The piecewise phase variable, as first proposed in [39], structures the phase estimation with a finite-state machine (FSM), consisting of generally monotonic thigh trajectory regions. A key observation when adjusting for task unification is that the primary tasks of level walking (LW), ramp ascent (RA) and descent (RD), and stair ascent (SA) and descent (SD) all share an initial descending thigh orientation section, followed by an ascending thigh orientation section, and ending again with a descending section (Fig. 1). These three sections define the three states of the FSM (S1, S2, and S3).

Forward progression through this state machine can be defined by key gait events: 1) heel strike (HS), defined as initial foot contact with the ground, triggers the transition to S1; 2) maximum hip extension (MHE), defined as the minimum detected thigh angle for a given stride that occurs after HS, triggers the transition to S2; and 3) maximum hip flexion (MHF), defined as the maximum detected thigh angle for a given stride that occurs after MHE, triggers the transition to S3. These three gait events (HS, MHE, and MHF) are shared events across these primary locomotion tasks, but the corresponding gait phase and thigh angle at which these events occur changes based on the task (Fig. 1). Backwards progression through the state machine can also be considered when implementing in real-time, as in [38], but is not implemented in this work.

To be considered a phase variable that is unified across locomotion tasks, it is critical to ensure that the definition and structure of the phase variable ϕ remain the same for all tasks. Toward this, we define the unified piecewise phase variable to be

$$\phi = \begin{cases} \frac{\theta_{\text{th}}^{\text{HS}}}{\hat{\theta}_{\text{th}}^{\text{MHE}}} \frac{\theta_{\text{th}}}{\hat{\theta}_{\text{th}}^{\text{MHE}}} \hat{\phi}^{\text{MHE}} & \text{if S1,} \\ \phi^{\text{MHE}} + \frac{\theta_{\text{th}}}{\hat{\theta}_{\text{th}}^{\text{MHF}}} \frac{\theta_{\text{th}}^{\text{MHE}}}{\theta_{\text{th}}^{\text{MHE}}} (\hat{\phi}^{\text{MHF}} - \phi^{\text{MHE}}) & \text{if S2,} \\ \phi^{\text{MHF}} + \frac{\theta_{\text{th}}^{\text{MHF}}}{\theta_{\text{th}}^{\text{MHF}}} \frac{\theta_{\text{th}}}{\hat{\theta}_{\text{th}}^{\text{HS}}} (1 - \phi^{\text{MHF}}) & \text{if S3,} \end{cases} \quad (1)$$

where $\theta_{\text{th}}^{\text{HS}}$, $\theta_{\text{th}}^{\text{MHE}}$, and $\theta_{\text{th}}^{\text{MHF}}$ are the measured thigh angle at the detected HS, MHE, and MHF, respectively, and ϕ^{MHE} and ϕ^{MHF} are the most recent estimated gait phase when MHE and MHF are detected (black in (1)). The model parameters $\hat{\theta}_{\text{th}}^{\text{MHE}}$ (blue), $\hat{\theta}_{\text{th}}^{\text{MHF}}$ (orange), and $\hat{\theta}_{\text{th}}^{\text{HS}}$ (green) are the predicted thigh angle for the upcoming MHE, MHF, and HS, respectively, and $\hat{\phi}^{\text{MHE}}$ (blue) and $\hat{\phi}^{\text{MHF}}$ (orange) are the predicted corresponding gait phases for the upcoming MHE and MHF. By definition, the predicted gait phase

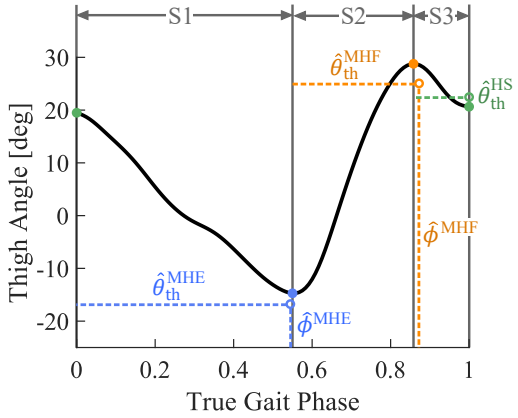


Fig. 2. The phase variable (ϕ) is based on the sagittal plane thigh orientation (θ_{th}). Three key gait events, MHE, MHF, and HS generally subdivide the gait cycle into an initial descending thigh angle state (S1), an ascending thigh angle state (S2), and a final descending state (S3). The unified piecewise phase variable transitions through these finite states by detecting HS, MHE, and MHF and seeks to accurately predict the thigh angle ($\hat{\theta}_{\text{th}}$) and the gait phase ($\hat{\phi}$) of the upcoming gait event (MHE is shown in blue, MHF in orange, and HS in green).

corresponding to the upcoming HS is a value of 1. An additional constraint exists on (1) such that if the phase variable ϕ is estimated to be greater than one or less than zero, it is saturated to stay within these bounds.

These 5 parameters ($\hat{\theta}_{\text{th}}^{\text{MHE}}$, $\hat{\theta}_{\text{th}}^{\text{MHF}}$, $\hat{\theta}_{\text{th}}^{\text{HS}}$, $\hat{\phi}^{\text{MHE}}$, and $\hat{\phi}^{\text{MHF}}$), representing predictions or initial guesses for the thigh angle and gait phase of the upcoming gait events (Fig. 2), collectively define the phase variable. Finding ways to accurately predict these upcoming gait features (referred to as the model parameters hereafter) is critical to ensuring a smooth, accurate, and monotonic phase variable progression. Two approaches for determining these model parameters are described below, first with task classification (Section II-B) and second without any knowledge of the locomotion task, but with contralateral-side sensor measurements (Section II-C).

B. Phase Variable Unification With Classification

If we assume accurate and robust classification among a predefined set of locomotion tasks (an area that has received extensive research focus over the past decade [16], [17]), we may use the classified task to determine the appropriate model parameters to employ. Fig. 3 shows that a relationship exists between the ground inclination (spanning stairs, ramps, and level ground) and the five model parameters. By classifying the locomotion task, these relationships can be used as a lookup table to generate the predictions for the upcoming gait features. In this work, the models for $\hat{\theta}_{\text{th}}^{\text{MHE}}$, $\hat{\theta}_{\text{th}}^{\text{MHF}}$, $\hat{\phi}^{\text{MHE}}$, and $\hat{\phi}^{\text{MHF}}$ are given in Figs. 3a, 3b, 3d, and 3e, respectively and are used directly for the tasks represented in the dataset. Unlike the other parameters, the final predicted parameter $\hat{\theta}_{\text{th}}^{\text{HS}}$ (Fig. 3c) is based on the most recently measured thigh angle at MHF ($\theta_{\text{th}}^{\text{MHF}}$) and the expected change in thigh angle between MHF and HS. This was also explored for other parameters, but only offered benefit when predicting $\hat{\theta}_{\text{th}}^{\text{HS}}$ due to the relatively small change in thigh angle between MHF and HS. Training for these parameter models is described further in Section II-D.

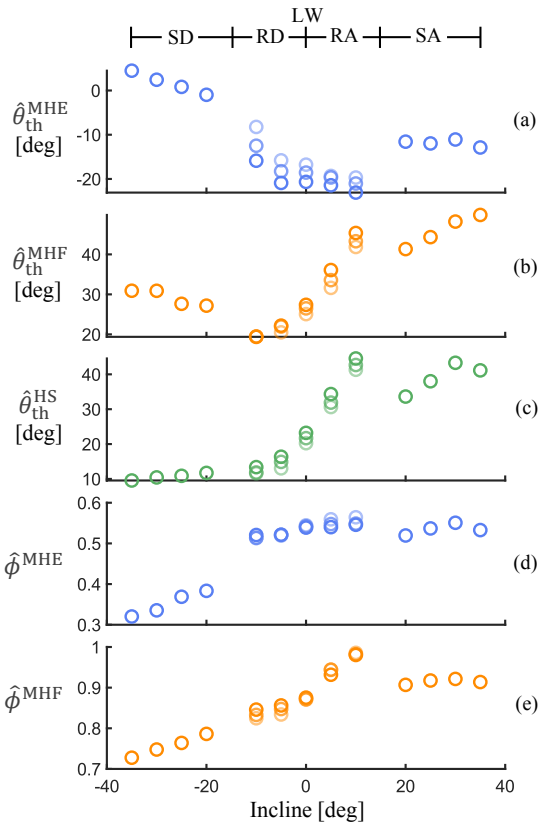


Fig. 3. Using classification, predictions for the expected thigh angle ($\hat{\theta}_{th}$) and gait phase ($\hat{\phi}$) at MHE, MHF, and HS can be generated based on the classified locomotion task. For walking tasks, speeds include 0.8 (more transparent), 1.0 (less transparent), and 1.2 m/s (no color transparency).

While this model is well suited for control frameworks that have high-fidelity task classification, this dependence could potentially be limiting. Using more continuous estimates of speed or ground slope could reduce the classification demands and improve the overall performance [19], but the dependence on classification for this phase variable approach may still be undesirable. Therefore, we also propose a second approach for a unified phase variable definition that is completely task-agnostic in Section II-C.

C. Task-Agnostic Phase Variable Unification

An alternative way to generate predictions for the upcoming gait event parameters is to use bilateral sensing. Figure 3 from the previous model shows that, without classification, the model parameters based only on the prosthesis-side thigh orientation would be redundant across some tasks. For example, there is not enough information contained in the unilateral thigh orientation to distinguish between stair-ascent and −10-degree ramp descent when predicting $\hat{\theta}_{\text{th}}^{\text{MHE}}$ (Fig. 3a) or $\hat{\phi}^{\text{MHE}}$ (Fig. 3d). By measuring the global thigh orientation in the sagittal plane from *both* the prosthesis-side and intact-side legs, sufficient information can be obtained to predict the thigh orientation and timing of the next gait event. In particular, the bilateral thigh orientations of the

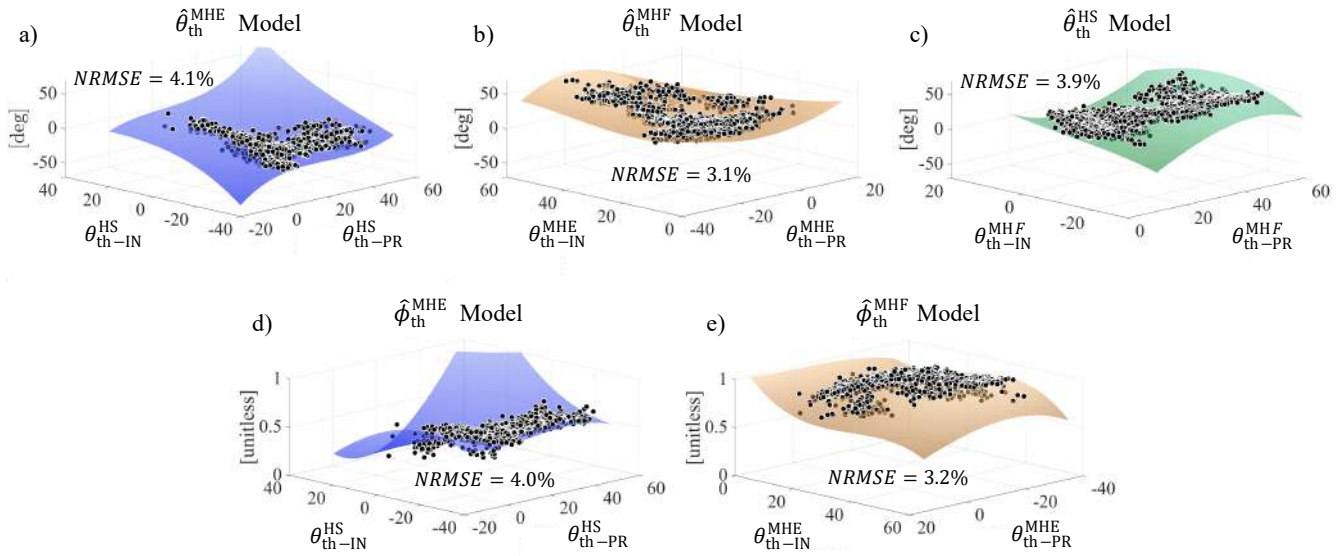


Fig. 4. Without any knowledge of the locomotion task, models spanning several activities can be generated to predict the upcoming gait event information based on bilateral thigh angle information at the time of the previous gait event. The measured thigh angle on the prosthesis-side leg at the moment of prosthesis-side HS ($\theta_{\text{th}}^{\text{HS}}{}_{\text{PR}}$) and the measured thigh angle on the intact-side leg at the moment of prosthesis-side HS ($\theta_{\text{th}}^{\text{HS}}{}_{\text{IN}}$) can be used to predict a) the upcoming prosthesis-side thigh angle at the upcoming MHE ($\hat{\theta}_{\text{th}}^{\text{MHE}}$) and d) the corresponding gait phase ($\hat{\phi}^{\text{MHE}}$). Likewise, measured bilateral thigh angles at the moment of prosthesis-side MHE can be used to predict prosthesis-side MHF thigh angle (b) and gait phase (e). Measured thigh angles at prosthesis-side MHF can predict $\hat{\theta}_{\text{th}}^{\text{HS}}{}_{\text{PR}}$, and the gait phase of the upcoming HS is always 1. All horizontal axes are in units of degrees.

current gait event can be used to define a continuous model for the upcoming gait event, as shown in Fig. 4.

For example, Fig. 4a uses the measured thigh orientation from both legs at the moment of prosthesis-side HS to predict the orientation of the prosthesis-side thigh at MHE. Each parameter is modeled as a cubic surface, taking the form

$$\begin{aligned}\hat{X} = p_{00} + p_{10}x + p_{01}y + p_{20}x^2 + p_{11}xy \\ +p_{02}y^2 + p_{30}x^3 + p_{21}x^2y + p_{12}xy^2 + p_{03}y^3,\end{aligned} \tag{2}$$

where $\hat{X}$ is the model parameter corresponding to the predicted upcoming gait feature, x is the prosthesis-side thigh angle measured at the most recent prosthesis-side gait event, and y is the intact-side thigh angle measured at the same instant. In Fig. 4d, for example, $x = \theta_{\text{th}}^{\text{HS}}{}_{\text{PR}}$ and $y = \theta_{\text{th}}^{\text{HS}}{}_{\text{IN}}$ are used as inputs to predict $\hat{X} = \hat{\phi}^{\text{MHE}}$, the predicted gait phase at the upcoming prosthesis-side MHE. The polynomial coefficients are fit by minimizing the L2-norm of the difference between the predicted and actual signals (e.g., $\hat{\phi}^{\text{MHE}}$ and ϕ^{MHE}) from the training data (details in Section II-D). The normalized root-mean-squared error (NRMSE) performance for each model is given in Fig. 4 as a percentage of the signal range (100 deg for thigh angle parameters and 1 for phase parameters), showing good predictive performance for each model.

D. Data Processing

Both the classification-dependent model (Section II-B) and the task-agnostic model (Section II-C) were assessed using an able-bodied open access dataset consisting of 10 able-bodied individuals completing several tasks [37]. To train both the classification-dependent and task-agnostic models, the data from five of the subjects in [37] were used, and the remaining five subjects were used for validation. Tasks of LW at 0.8, 1.0, and 1.2 m/s speeds, RA and RD at 5 and 10 degrees using the same 3 speeds, and SA and SD at inclines of 20, 25, 30, and 35 degrees at a self-selected pace were used for training and validation. Walking was more represented in the training data than stair climbing, so relative weights were added to the optimization cost to balance the contribution from each task equally. Thigh angles were calculated as the sum of the negative global pelvis angle from vertical and the positive hip angle, both in the sagittal plane, such that a positive/negative thigh orientation corresponds to hip flexion/extension. Heel strike was provided by the dataset and the ground-truth gait phase was defined as the normalized time between consecutive heel strikes. MHE was determined for all strides as the moment between HS events at which thigh angle was minimized, and MHF was determined as the first maximum peak in thigh angle that occurred between MHE and the upcoming HS (a single peak existed in 88.4% of strides in all activities, with 6.8% having no peaks and 4.8% having 2 peaks).

Only steady-state strides were used for all activities. For walking tasks, the right leg was treated as the prosthesis-side, but for stair trials the prosthesis-side was selected as the leading foot to ensure that there were two HS events in steady state on the 4-step staircase [37]. For the task-agnostic model that uses bilateral thigh information, the intact-side thigh information was taken from the continuous streaming dataset, which contained bilateral sensing. Strides exhibiting erroneous discrete jumping behavior in the dataset were removed (6 total out of 4,215), but no outliers were removed otherwise. The classification-dependent gait event prediction models (Fig. 3) were generated by taking the average thigh angle and gait phase for each gait event of HS, MHE, and MHF. For validation, phase prediction error

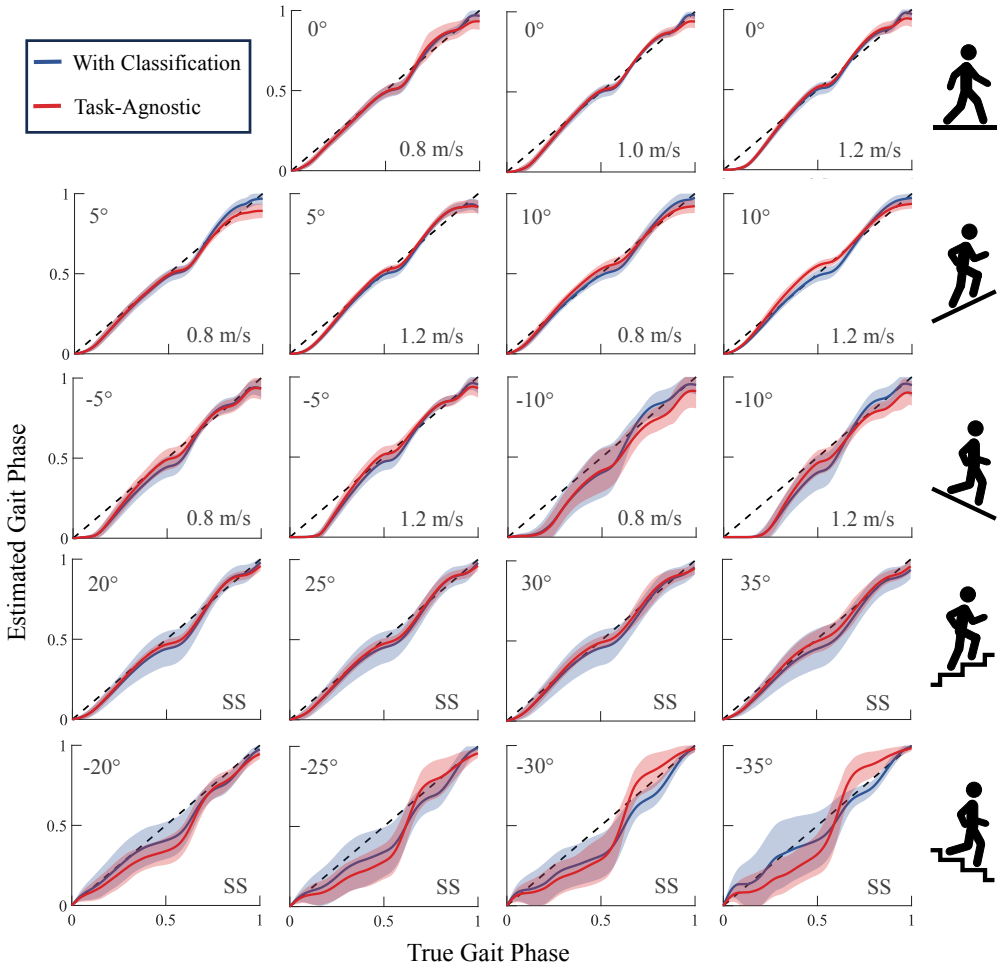


Fig. 5. The average gait phase estimation ± one standard deviation is compared to the true time-normalized gait phase (dashed grey). For each locomotion activity, the task incline is displayed in the top left corner, and the task speed in the bottom right corner (SS indicating self-selected). Averaged across subjects, the unified phase model with classification (blue) and without knowledge of the task (red) exhibit comparable prediction performance across tasks, with the task-agnostic approach having less subject-to-subject variability.

was quantified for each stride by taking the root-mean-squared error (RMSE) between the ground-truth gait phase and the model predicted gait phase. Differences between the classification-dependent and task-agnostic phase models were compared using a two-tailed paired t-test.

III. Results and Discussion

A. Simulation Results

The overall phase estimation performance across multiple ADLs and speeds is shown in Fig. 5 both with classification and without classification (task-agnostic). Across all tasks, subjects, and strides, the overall average RMS phase error for this unified phase approach was 6.8% with classification and 6.3% when task-agnostic. The corresponding average RMS phase error is summarized for individual tasks in Fig. 6. For level walking (LW), the phase estimation is very consistent both with and without the use of classification, with an average phase RMSE between 4-5% for both conditions at all three speeds. This consistency is maintained for ramp ascent tasks, where both models have RMS error less than 5% on average for all speeds and ramp inclinations.

For stair ascent (SA), the task-agnostic approach demonstrated higher accuracy (phase RMSE of 4.9% across stair heights) than the classification-dependent model (phase RMSE of 8.1%) with statistical significance ($p = 4.0 \times 10^{-17}$). The SA phase estimation with classification exhibited higher subject variability, performing better for some subjects (such as AB05: average phase RMSE 5.8% for 35 deg SA) than for others (AB09: 8.6%). SA phase estimation was more consistent across subjects using the task-agnostic model (AB05: 4.4%, AB09: 4.8%, for the same trials). The task-agnostic phase model's better accommodation of subject variability over the approach with classification is also observed in the reduced standard deviation throughout Fig. 5. This is likely due to the incorporation of more recent gait event information in the task-agnostic predictions.

During 5-degree ramp descent, the unified phase approaches maintained repeatability across strides and subjects (low standard deviation in Fig. 5) and an average phase RMSE less than 7.2% with classification and 6.6% with the task-agnostic framework. Phase estimation error increased for the steeper ramp descent of 10 degrees, with an average

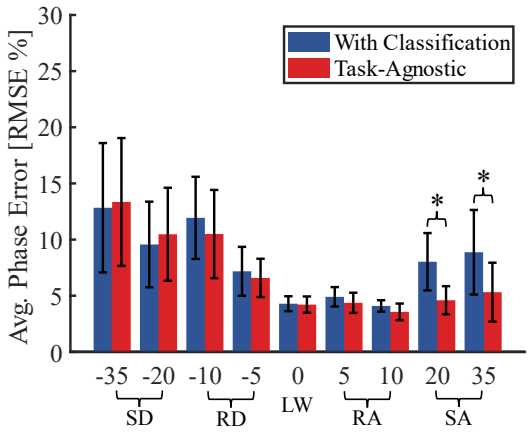


Fig. 6. The average phase root-mean-squared error (RMSE) ± one standard deviation for each locomotion task is measured as a percentage. The task-agnostic approach (red) performed consistently during level walking and all ascent tasks, with increased error for descent tasks. The classification-dependent approach (blue) behaved similarly, but with significantly larger error during stair ascent (SA) across stair heights ($p = 4.0 \times 10^{-17}$).

phase RMSE less than 12% with classification and less than 11% with task agnosticism. Fig. 5 reveals that a significant error exists in the early stance phase (weight acceptance) for ramp descent and generally becomes larger with increased speed and more significant ground inclination. In this region, the phase tends to saturate at zero, meaning that the thigh angle begins to flex after heel strike rather than to approach the predicted MHE value for these tasks. This behavior is consistent with early stance weight acceptance, which is generally increased with higher walking speeds and steeper declines. This early stance error (exhibited in [8] and [9] as well) can also be observed to a lesser degree for LW, with the largest early stance errors presented at 1.2 m/s. Future work could consider an additional optional state to the FSM that could accommodate this early hip flexion for some tasks, although this would introduce increased sensing and modeling demands that could be difficult in practice.

Among all locomotion tasks, stair descent (SD) consistently showed the poorest model performance, with mean phase RMSEs of 12.1% (with classification) and 12.7% (without), particularly at larger stair heights (Fig. 6). The causes of reduced accuracy, however, seemed to differ between the two approaches. In this framework, poor phase estimation generally reflects discrepancies between predicted parameters $\hat{\theta}_{\text{th}}^{\text{MHE}}$, $\hat{\theta}_{\text{th}}^{\text{MHF}}$, $\hat{\theta}_{\text{th}}^{\text{HS}}$, $\hat{\phi}^{\text{MHE}}$, and $\hat{\phi}^{\text{MHF}}$ and their ground-truth values. Figure 7 shows that with classification, SD phase predictions varied across subjects, with better accuracy for some (e.g., AB09) and worse for others (e.g., AB07), occasionally resulting in phase over- or underestimates. The task-agnostic approach, however, consistently underestimated gait phase at MHE and thigh angle at MHF, creating an S-shaped phase curve across subjects. While the task-agnostic model was generally more consistent, its large phase RMS errors for SD reflect optimization trade-offs that prioritize balanced performance across all activities over individual task accuracy.

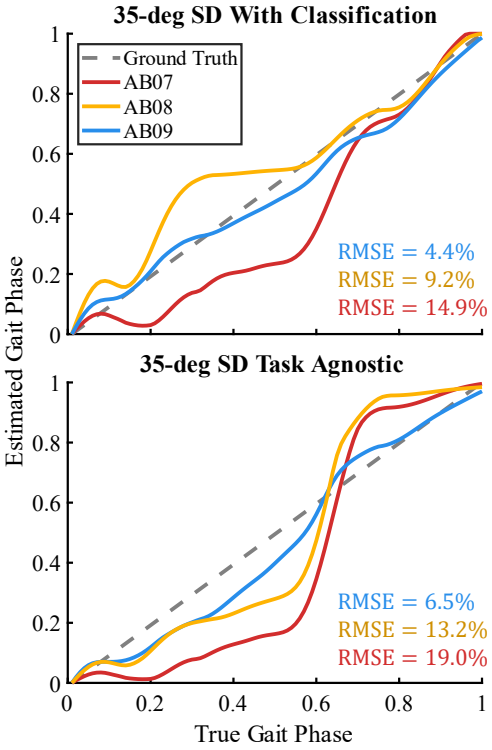


Fig. 7. Both the classification-dependent (top) and task-agnostic (bottom) approaches had the highest phase prediction error during 35-degree stair descent (SD). These models performed better for some subjects (e.g., AB09, blue) and worse for others (e.g., AB07, red).

B. Comparison with Other Multi-Activity Phase Estimators

This work is inspired by the phase definitions in [8], [9], [38] that accommodate variable slope/speed walking, variable-height stair climbing, and obstacle avoidance, respectively; however, the unified phase definition presented herein is the first to unify these definitions into a single framework. Continuous gait phase monitoring across multiple ADLs without classification dependence has also been explored in [18] for prostheses and [30], [36], [40] for exoskeletons. For example, [18] used bilateral sensing to simultaneously predict gait phase and task for a robotic ankle prosthesis, achieving average phase errors under 2% for walking and under 4% for stairs. Similarly, [30] used bilateral sensing and a random forest regression algorithm to estimate gait phase and classify tasks for a soft exosuit, showing effective phase prediction for walking and stairs, with a nearly three-fold error increase during SD compared to LW. Using bilateral sensing and deep neural networks, [36] achieved an overall phase RMSE of 5.04% for exoskeleton control across ten subjects, with errors increasing by 50% during RD compared to LW. RMSE errors reached nearly 10% during SD, similar to the trends observed in this study. With very steep slope walking, [40] also used bilateral sensing to achieve an average phase RMSE of 4.8%, and exhibited large subject dependence in performance.

Each of these approaches used bilateral sensing to obtain a task-agnostic phase estimate, and the present work is the first to do so towards transfemoral prostheses. The related

work and our approaches herein saw a notable decrease in performance during stair descent, which could be due to the relatively small range of motion of the hip that causes sensitivity between the angle of the user's thigh and the gait phase, as proposed in [9]. Unlike [30], [36], this unified phase definition is a model-based approach that does not incorporate ML. The imposed model structure based on common kinematics observed across tasks (Fig. 1) could also be used to enhance ML approaches that could learn the structured model parameters, rather than to learn the full mapping from lower-limb kinematics to gait phase. This could aid in prediction robustness when encountering out-of-training inputs, such as new speeds and inclines. Our approach to unified phase also depends only on bilateral thigh sensing (omitting any trunk, shank, or foot sensors as found in [18], [30], [36], [40]), which holds significant promise for the control of transfemoral prostheses.

C. Challenges for Real-Time Implementation

The analysis presented in this work detected HS, MHE, and MHF offline. In practice, heel strike (or foot strike) information is relatively simple to obtain in real-time, but it can be more difficult to accurately detect MHE and MHF without delay. Fast real-time detection algorithms have been developed to detect peaks in the thigh angle associated with MHE and MHF from a single thigh IMU based on thresholding [38] and multiple moving average algorithms [9]. Appropriate performance of this unified phase definition depends on this real-time detection.

Furthermore, the use of bilateral sensing (as in this work and [18], [30], [36], [40]) increases donning requirements, especially for the use of unilateral prosthetic control, which is undesirable from the perspective of clinical and commercial adoption. If it can be shown, however, that performance or robustness to latent variability could be dramatically increased with the incorporation of additional sensors (such as a single additional IMU on the contralateral limb in this case), the benefits may justify the perceived drawbacks. In this work, we preliminarily suggest that a task-agnostic framework for continuously estimating phase across locomotion tasks may not be feasible with a single thigh IMU, but that it can be done with a pair of bilateral thigh IMUs. While both approaches showed similarly good performance, breaking the dependence on classification is a significant advantage as classification between many activities is challenging and fundamentally unscalable.

D. Limitations and Future Work

While the unified and task-agnostic approach presented has shown promise when simulated offline, future work will seek to validate these results in real-time hardware experimentation. It will be important to ensure the robustness of this approach when transitioning to real environments, accounting for the sensor challenges as discussed, and implementing this with the target population of individuals with unilateral transfemoral amputation.

The primary performance limitation presented for both the classification and task-agnostic approaches is that subject variability was high, leading to good performance for some subjects and worse for others. Personalization of these phase prediction models could lead to significant improvement in performance. While it is undesirable to increase tuning demands, which would require extensive clinician time and training, this approach is an ideal candidate for personalizing to a specific user over time, with techniques such as the Kalman filter (as in [40]). After the gait event information for MHE, MHF, and HS is predicted by the model, the corresponding ground-truth information is then measured for each stride. Comparing the predicted and ground-truth values could be used to improve the model for an individual user over time, which could also reduce the effects of latent variability. Future work will pursue such personalization techniques that do not increase tuning demands.

IV. Conclusion

In this study, we presented a novel unified phase variable framework for robotic lower-limb prostheses, enabling both classification-based and task-agnostic control across a diverse range of locomotion tasks. By unifying phase definitions across level walking, ramp ascent/descent, and stair ascent/descent with several speeds and inclines, this approach addresses limitations of existing methods that are classification-reliant and employ activity-specific phase definitions. Simulation results demonstrated that both classification-based and task-agnostic implementations achieve low phase RMSE, with the task-agnostic approach exhibiting reduced subject-specific variability. The task-agnostic model also outperformed the classification-based model during stair ascent, which highlights its robustness across diverse activities and may justify the use of bilateral sensing. These findings highlight the feasibility of using task-agnostic frameworks in the development of robust and versatile prosthetic control systems that can accommodate a wide range of locomotion tasks.

Acknowledgment

The authors would like to thank Kevin Best, Ross Cortino, and Shihao Cheng for their support of this project.

References

[1] B. E. Lawson, J. Mitchell, D. Truex, A. Shultz, E. Ledoux, and M. Goldfarb, "A robotic leg prosthesis: Design, control, and implementation," *IEEE Robot Autom Mag*, vol. 21, no. 4, pp. 70–81, 2014.

[2] R. D. Gregg, T. Lenzi, L. J. Hargrove, and J. W. Sensinger, "Virtual constraint control of a powered prosthetic leg: From simulation to experiments with transfemoral amputees," *IEEE T Robot*, vol. 30, no. 6, pp. 1455–1471, 2014.

[3] M. Tran, L. Gabert, S. Hood, and T. Lenzi, "A lightweight robotic leg prosthesis replicating the biomechanics of the knee, ankle, and toe joint," *Sci Robot*, vol. 7, no. 72, p. eabo3996, 2022.

[4] S. K. Au, J. Weber, and H. Herr, "Powered ankle–foot prosthesis improves walking metabolic economy," *IEEE T Robot*, vol. 25, no. 1, pp. 51–66, 2009.

[5] T. K. Best, C. A. Laubscher, R. J. Cortino, S. Cheng, and R. D. Gregg, "Improving amputee endurance over activities of daily living with a robotic knee-ankle prosthesis: A case study," in *IEEE Int Conf Intell Robots Syst (IROS)*, 2023, pp. 2101–2107.

[6] D. Quintero, D. J. Villarreal, D. J. Lambert, S. Kapp, and R. D. Gregg, "Continuous-phase control of a powered knee–ankle prosthesis: Amputee experiments across speeds and inclines," *IEEE T Robot*, vol. 34, no. 3, pp. 686–701, 2018.

[7] N. Anil Kumar, S. Patrick, W. Hong, and P. Hur, "Control framework for sloped walking with a powered transfemoral prosthesis," *Frontiers in Neurorobotics*, vol. 15, p. 790060, 2022.

[8] T. K. Best, C. G. Welker, E. J. Rouse, and R. D. Gregg, "Data-driven variable impedance control of a powered knee–ankle prosthesis for adaptive speed and incline walking," *IEEE T Robot*, vol. 39, no. 3, pp. 2151–2169, 2023.

[9] R. J. Cortino, T. K. Best, and R. D. Gregg, "Data-driven phase-based control of a powered knee-ankle prosthesis for variable-incline stair ascent and descent," *IEEE T Med Robot Bionics*, vol. 6, no. 1, pp. 175–188, 2023.

[10] S. Culver, H. Bartlett, A. Shultz, and M. Goldfarb, "A stair ascent and descent controller for a powered ankle prosthesis," *IEEE T Neur Sys Reh*, vol. 26, no. 5, pp. 993–1002, 2018.

[11] C. G. Welker, T. K. Best, and R. D. Gregg, "Improving sit/stand loading symmetry and timing through unified variable impedance control of a powered knee-ankle prosthesis," *IEEE T Neur Sys Reh*, 2023.

[12] A. M. Simon, N. P. Fey, K. A. Ingraham, S. B. Finucane, E. G. Halsne, and L. J. Hargrove, "Improved weight-bearing symmetry for transfemoral amputees during standing up and sitting down with a powered knee-ankle prosthesis," *Arch Phys Med Rehab*, vol. 97, no. 7, pp. 1100–1106, 2016.

[13] R. R. Posh, J. P. Schmiedeler, and P. M. Wensing, "Finite-state impedance and direct myoelectric control for robotic ankle prostheses: Comparing their performance and exploring their combination," *IEEE T Neur Sys Reh*, vol. 31, pp. 2778–2788, 2023.

[14] G. R. Hunt, S. Hood, and T. Lenzi, "Stand-up, squat, lunge, and walk with a robotic knee and ankle prosthesis under shared neural control," *IEEE Open J Eng Med Biol*, vol. 2, pp. 267–277, 2021.

[15] V. Rai and E. Rombokas, "A framework for mode-free prosthetic control for unstructured terrains," in *IEEE Int Conf Rehabil Robot (ICORR)*, 2019, pp. 796–802.

[16] A. Fleming, N. Stafford, S. Huang, X. Hu, D. P. Ferris, and H. H. Huang, "Myoelectric control of robotic lower limb prostheses: a review of electromyography interfaces, control paradigms, challenges and future directions," *J Neur Eng*, vol. 18, no. 4, p. 041004, 2021.

[17] R. Gehlhar, M. Tucker, A. J. Young, and A. D. Ames, "A review of current state-of-the-art control methods for lower-limb powered prostheses," *Ann Rev Control*, 2023.

[18] R. Posh, S. Li, and P. Wensing, "Simultaneous locomotion mode classification and continuous gait phase estimation for transtibial prostheses," *arXiv preprint: 2411.08136*, 2024.

[19] S. Cheng, C. A. Laubscher, T. K. Best, and R. D. Gregg, "Ambilateral activity recognition and continuous adaptation with a powered knee-ankle prosthesis," *IEEE T Robot*, 2025.

[20] H. A. Varol, F. Sup, and M. Goldfarb, "Multiclass real-time intent recognition of a powered lower limb prosthesis," *IEEE T Biomed Eng*, vol. 57, no. 3, pp. 542–551, 2009.

[21] B. Chen, E. Zheng, and Q. Wang, "A locomotion intent prediction system based on multi-sensor fusion," *Sensors*, vol. 14, no. 7, pp. 12 349–12 369, 2014.

[22] A. M. Simon, K. A. Ingraham, J. A. Spanias, A. J. Young, S. B. Finucane, E. G. Halsne, and L. J. Hargrove, "Delaying ambulation mode transition decisions improves accuracy of a flexible control system for powered knee-ankle prosthesis," *IEEE T Neur Sys Reh*, vol. 25, no. 8, pp. 1164–1171, 2016.

[23] V. Rai, A. Sharma, D. Boe, P. Preechayasomboon, and E. Rombokas, "Continuous and unified modeling of joint kinematics for multiple activities," *IEEE Access*, vol. 10, pp. 47 509–47 523, 2022.

[24] M. Eslamy, F. Oswald, and A. F. Schilling, "Estimation of knee angles based on thigh motion: A functional approach and implications for high-level controlling of active prosthetic knees," *IEEE Cont Syst Mag*, vol. 40, no. 3, pp. 49–61, 2020.

[25] M. Kim, A. M. Simon, and L. J. Hargrove, "Seamless and intuitive control of a powered prosthetic leg using deep neural network for transfemoral amputees," *Wear Tech*, vol. 3, p. e24, 2022.

[26] C. P. Nuesslein and A. J. Young, "A deep learning framework for end-to-end control of powered prostheses," *IEEE Robot Autom Lett*, 2024.

[27] S. Hood, L. Gabert, and T. Lenzi, "Powered knee and ankle prosthesis with adaptive control enables climbing stairs with different stair heights, cadences, and gait patterns," *IEEE T Robot*, vol. 38, no. 3, pp. 1430–1441, 2022.

[28] S. Cheng, C. A. Laubscher, and R. D. Gregg, "Controlling powered prosthesis kinematics over continuous inter-leg transitions between walking and stair ascent/descent," *IEEE T Neur Sys Reh*, 2024.

[29] E. R. Westervelt, J. W. Grizzle, C. Chevallereau, J. H. Choi, and B. Morris, *Feedback Control of Dynamic Bipedal Robot Locomotion*. CRC Press, 2018.

[30] X. Zhang, E. Tricomi, F. Missiroli, N. Lotti, and L. Masia, "Real-time assistive control via imu locomotion mode detection in a soft exosuit: An effective approach to enhance walking metabolic efficiency," *IEEE T Mechatron*, 2023.

[31] L. Filli, T. Sutter, C. S. Easthope, T. Killeen, C. Meyer, K. Reuter, L. Lörincz, M. Bolliger, M. Weller, A. Curt *et al.*, "Profiling walking dysfunction in multiple sclerosis: characterisation, classification and progression over time," *Sci Rep*, vol. 8, no. 1, p. 4984, 2018.

[32] M. A. Holgate, T. G. Sugar, and A. W. Bohler, "A novel control algorithm for wearable robotics using phase plane invariants," in *IEEE Int Conf Robot Autom (ICRA)*, 2009, pp. 3845–3850.

[33] R. R. Posh, J. A. Tittle, D. J. Kelly, J. P. Schmiedeler, and P. M. Wensing, "Hybrid volitional control of a robotic transtibial prosthesis using a phase variable impedance controller," in *IEEE Int Conf Robot Autom (ICRA)*, 2024, pp. 4555–4561.

[34] D. J. Villarreal and R. D. Gregg, "A survey of phase variable candidates of human locomotion," *IEEE Int Conf Eng Med Biol Soc (EMBC)*, pp. 4017–4021, 2014.

[35] N. Thatte, T. Shah, and H. Geyer, "Robust and adaptive lower limb prosthesis stance control via extended kalman filter-based gait phase estimation," *IEEE Robot Autom Lett*, vol. 4, no. 4, pp. 3129–3136, 2019.

[36] I. Kang, D. D. Molinaro, S. Duggal, Y. Chen, P. Kunapuli, and A. J. Young, "Real-time gait phase estimation for robotic hip exoskeleton control during multimodal locomotion," *IEEE Robot Autom Lett*, vol. 6, no. 2, pp. 3491–3497, 2021.

[37] E. Reznick, K. R. Embry, R. Neuman, E. Bolívar-Nieto, N. P. Fey, and R. D. Gregg, "Lower-limb kinematics and kinetics during continuously varying human locomotion," *Sci Data*, vol. 8, no. 1, p. 282, 2021.

[38] S. Cheng, C. A. Laubscher, and R. D. Gregg, "Automatic stub avoidance for a powered prosthetic leg over stairs and obstacles," *IEEE T Biomed Eng*, 2023.

[39] D. J. Villarreal, D. Quintero, and R. D. Gregg, "Piecewise and unified phase variables in the control of a powered prosthetic leg," in *IEEE Int Conf Rehabil Robot (ICORR)*, 2017, pp. 1425–1430.

[40] R. L. Medrano, G. C. Thomas, C. G. Keais, E. J. Rouse, and R. D. Gregg, "Real-time gait phase and task estimation for controlling a powered ankle exoskeleton on extremely uneven terrain," *IEEE T Robot*, vol. 39, no. 3, pp. 2170–2182, 2023.

Pattern Recognition Control of a 2 Degree-of-Freedom Prosthetic Device

Laura A Miller
Center for Bionic Medicine
Shirley Ryan AbilityLab
Chicago, IL, USA
ORCID: 0000-0002-7271-6214

Courtney Smyth
Prosthetics and Orthotics
Shirley Ryan AbilityLab
Chicago, IL, USA
ORCID: 0009-0005-5839-6540

Kristi L Turner
Center for Bionic Medicine
Shirley Ryan AbilityLab
Chicago, IL, USA
ORCID: 0009-0003-5163-0539

Levi J Hargrove
Center for Bionic Medicine
Shirley Ryan AbilityLab
Chicago, IL, USA
ORCID: 0000-0002-1705-0050

Abstract— **For individuals with transradial limb loss or difference, myoelectric prostheses providing advanced functionality are often controlled through two control strategies: Amplitude and Threshold Control (ATC) and Pattern Recognition (PR). While ATC, a conventional method which is sometimes called direct control, is commonly used, it can be less intuitive for multi-degree-of-freedom tasks. PR, leveraging machine learning to classify muscle activation patterns, accesses movements using physiologically appropriate contractions. This study evaluates a Reduced-Contact PR (RC-PR) system, against ATC with rate-sensitive switching. Four individuals with transradial limb loss participated in a randomized crossover trial using a two-degree-of-freedom prosthesis. Functional outcomes, manual dexterity, and user perception were assessed using the Box & Blocks Test, Clothespin Relocation Test, AM-ULA, ACMC, and a User-Perceived Control Questionnaire. RC-PR demonstrated superior performance across all metrics and was preferred by participants for its intuitive operation. These findings suggest that RC-PR offers significant advantages in functional outcomes and user satisfaction, presenting a promising alternative to traditional ATC systems.**

Keywords—prosthesis, control, EMG, pattern recognition

I. INTRODUCTION

It is estimated that 541,000 individuals in the United States have upper limb loss, with 41,000 being major loss (wrist disarticulation or higher)[1, 2]. Loss of the hand and wrist can profoundly impact overall function and how an individual is able to complete activities of daily living. Though it is possible to build very complex powered prosthetic devices, one of the greatest challenges is how an individual can control the prosthesis.

The contents of this manuscript were developed under grants from the Department of Defense (DoD) W81XWH2210431, Discretionary laboratory funding, and the National Institute on Disability, Independent Living, and Rehabilitation Research (NIDILRR) 90REGE0003. NIDILRR is a Center within the Administration for Community Living (ACL), Department of Health and Human Services (HHS). The contents of this report do not necessarily represent the policy of NIDILRR, ACL, or HHS, and you should not assume endorsement by the Federal Government.

Historically, individuals with upper limb loss or difference (eg. amputation or congenital absence) would use electromyographic (EMG) signals from agonist/antagonist muscle pairs to control the two directions of movement associated with a degree-of-freedom. This style of control is typically achieved by adjusting the EMG signal amplitude using gains and thresholds [3]. We will refer to this as amplitude and threshold control (ATC) although this is sometimes called direct control. Specifically, a configured gain and threshold allows the processed wrist extensor EMG signal to open the hand, while a similar process using wrist flexor EMG signals enables hand closure. To control a second degree-of-freedom (eg. wrist rotation), a user would use the ATC system with a trigger (ATC-T), such as co-contraction to switch the control of the 2 EMG signals to the second movement [4].

An alternative method to select which degree-of-freedom is operated is to combine ATC with the rate of change (ATC-R) of the EMG signal amplitude to select which motor would be activated. This is achieved by setting a second, higher threshold for each EMG signal in the agonist/antagonist pair [4]. For example, with ATC-R, a quick and strong wrist extension contraction above the second higher threshold within the defined time limit would result in wrist supination and a quick and strong signal of the wrist flexors creates a signal to pronation the wrist. If the user makes a slower contraction, or a contraction that does not surpass the second threshold within the set time, then the respective hand movements would be operated. Using ATC-R allows users to directly access each degree-of-freedom without using a trigger toggle between degree-of-freedom.

For individuals with acquired upper-limb loss, many of the muscles that control hand and wrist functions are maintained in the upper forearm. By recording EMG signals around the forearm from these muscles, pattern recognition (PR) algorithms can be trained to identify these movements allowing for an alternative control that uses more physiologically appropriate contractions and does not rely on unnatural triggers. PR systems are now commercially available [5], with three companies (Coapt, Otto Bock, and Infinite Biomedical Technologies) selling Class II medical devices cleared by the US Food and Drug Administration.

Early research on PR control evaluated various factors of the algorithms to try to identify the optimal values for

clinical applications [6]. One of the factors that was investigated was the number of EMG channels required to identify various patterns of hand and wrist function. From an analysis of offline classification accuracy of 10 movements, it was found that 6-8 optimally placed EMG channels would be required for approximately 93% percent accuracy [7]. Based on plateau in classification accuracy beyond 4-6 channels for six movements, it was estimated that eight channels placed around the EMG of interest would be sufficient and would help to limit the computational requirements of an embedded controller.

More recently, the controllability of two degrees-of-freedom, one at the hand and one at the wrist, in individuals with transradial upper-limb loss or difference using 4, 8 and 16 channels to control a virtual prosthesis and a physical prosthetic device showed 16 channels outperformed conditions with 4 and 8 channels [8]. Additionally, users rated the condition with 16 channels as easier to control when blinded to the condition. This work has shown that additional channels may be useful to control multiple degrees-of-freedom, however it is unclear if these additional channels are necessary for control of simpler system with a wrist rotator and single degree-of-freedom hand. Furthermore, while use of 16 channels of EMG provided improved control, it does provide clinical challenges in placing the electrode contacts within the socket. This can be mitigated by having EMG signals share electrode contacts (Fig. 1), resulting in a reduced electrode contact set. Prior work has shown that sharing electrode contacts provides additional discriminatory information

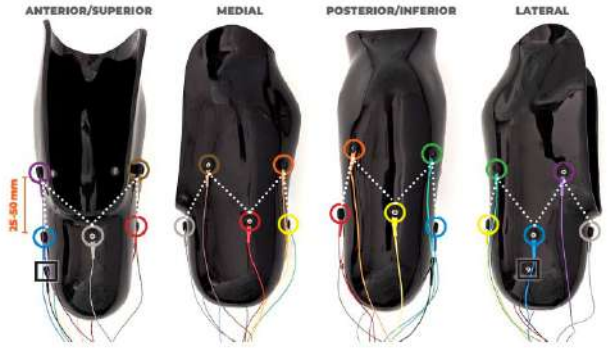


Fig. 1. EMG contact configuration for RC-PR. Image courtesy of Coapt Engineering

that can be useful for classification[9].

PR control systems have proven the ability to control powered upper limb prostheses with three or more degrees-of-freedom more efficiently than ATC systems [10]. While these studies have demonstrated important benefits of myoelectric PR control, there is a lack of evidence comparing PR and ATC when fewer degrees-of-freedom are used. A case study by Resnik et al. attempted to fill this gap by evaluating control with both PR and conventional ATC control for a 2 degree-of-freedom prosthesis [11]. They found similar results in 74% of the metrics examined and improvements in the remaining 26% with ATC-T. However, these findings include those of only one participant who used a ATC device as their home system.

The goal of this project was to evaluate differences in control of a prosthetic system including a powered wrist rotator and a single degree-of-freedom hand. The first control evaluated included a PR system with eight EMG channels configured in a connected zig-zag pattern to reduce the number of EMG contacts from 17 (2 per bipolar channel plus a ground) to 9 (Fig. 1). It was hypothesized that functional outcome performance would be higher with this reduced contact PR control (RC-PR) compared to a two EMG channel ATC-R system.

II. Methods

A. Study Design and Participants

Four participants with unilateral, transradial limb loss secondary to trauma were recruited to participate in a randomized crossover study to compare the two control systems.. Three were male and one was female with ages ranging from 40 to 60 (average age 52). None of the individuals reported having undergone targeted muscle reinnervation (TMR), and all participants had at least minimal prior experience with myoelectric prostheses, whether in their home prosthesis or through participation in research. Of the four, one had experience with only ATC-R (S4), one had experience with only PR (S2), and two were experienced in both ATC-R and PR control (S1, S3). Additional demographic data can be found in Table 1, including age, time since amputation, experience with the various control systems either from previous research experience or past home fittings, and recent home prosthesis useThe study was approved by the Northwestern University IRB and all participants provided written informed consent.

TABLE I. Participant Demographics

ID	*Age*	*Years since injury*	*PR/ATC/ ATC-R experience*	*Recent Home Prostheses*
S1	60	45	Y/Y/N	2-site myo w/ manual wrist rotator
S2	53	1	Y/N/N	Body-powered
S3	40	1	Y/Y/N	2-site myo w/ manual wrist rotator (device 1) & Body-powered (device 2)
S4	55	37	N/Y/Y	2-site myo w/ electric wrist rotator

B. Device

Participants were fit with a prosthetic socket under the supervision of a certified prosthetist. If necessary, a second socket was fabricated if the EMG electrode positions of the two systems did not allow for placement in the same socket. All sockets were designed to be self-suspending and fit over the epicondyles to reduce the amount of intact pronation and supination available and encourage use of the powered wrist rotator. An auxiliary suspension sleeve was utilized when needed.

The prosthetic components included an Ottobock powered wrist rotator and VariPlus Speed Hand (Fig. 2). The two control systems used were the Ottobock Healthcare Myorotronic (ATC-R) and prototype PR system provided by Coapt that came pre-configured such that only 9 electrode contacts created 8 unique EMG channels (RC-

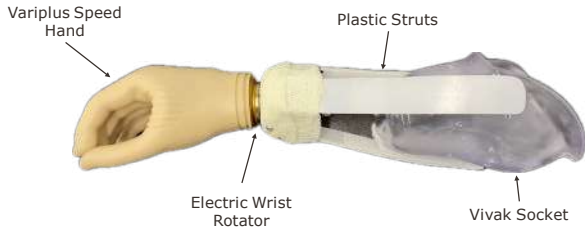


Fig. 2. Prosthetic componentry used for both conditions.



Fig. 3. Myotesting procedure using the Ottobock MyoBoy for configuration of EMG placement for ATC-R

PR). The order of testing with the two conditions was randomized.

For the ATC-R system, myotesting was performed to identify the two best locations for isolated agonist-antagonist control using Ottobock Myobock 13E200 electrodes (Fig. 3). Openings were made for the electrodes in the socket and the participant was trained using the Ottobock PAULA software. The Ottobock Myoselect was used to configure the Myorotronic to "Myobock Program 1" which allows for rate sensitive access of the wrist rotator.

For the RC-PR system, 9 electrode domes were placed around the residual limb over the forearm musculature (proximal third of the residual limb) in a zig-zag pattern, creating 8 EMG channels plus a ground contact following the recommendations provided by Coapt (Fig. 1). EMG signals were digitally filtered between 70-300 Hz, and 3rd order notch filters were used to filter power-line frequencies. Time-domain features [12] and coefficients from a 6-order autoregressive model were used to extract information from 200 ms of data from each signal using a sliding window approach with 50 ms window increments [13]. Features were classified using a linear discriminant analysis classifier. Finally, the speed of each movement was estimated using a previously developed proportional control algorithm [14]. Calibration for the RC-PR system was completed prior to and throughout testing, as necessary.

Participants worked with an occupational therapist in all sessions for each control and practiced with the device for one to two sessions prior to progressing to outcomes testing. Participants began training with basic activities, such as opening and closing the prosthetic hand in various planes without errors (e.g., unintended hand opening). As proficiency improved, they progressed from one-handed to two-handed functional tasks. Training duration and progression to outcomes were tailored to each participant's ability and comfort with functional tasks.

C. Outcomes

For each control condition, after a brief warm-up (10-15 minutes) participants completed the Box and Blocks Test (BBT, number of blocks moved in 1 minute, 3 trials) [15], the Clothespin Relocation Test (CRT, time to move 3 clothespin from a horizontal to a vertical bar, 3 trials) [16], the Activities Measure for Upper Limb amputees (AM-ULA, a scored measure of pre-defined simulated ADL-like activities, 1 trial)[17], and the Assessment of Capacity for Myoelectric Control (ACMC, a Clinician-scored assessment of myoelectric control capacity when performing a bimanual functional task, 1 trial) [18]. Outcomes were typically completed in 1-2 hours, allowing for rest breaks. Outcome testing for each control condition was completed on separate days. After each test session, participants were asked to draw a line on a visual analog scale (horizontal line) to indicate how easy or hard it was to control the prosthesis, overall. A new line was provided for each condition, so marks for the second control configuration were independent from the first. At the conclusion of the study, they were asked which configuration they preferred and why.

Data from all participants who completed the study were used to compare outcomes of the two control schemes. BBT, CRT, AM-ULA, ACMC, and User Perceived Control results were averaged across participants by each of the two conditions and standard error was then calculated.

III. Results

Results of the BBT (Fig. 4) found all four participants performed better with the RC-PR over the ATC-R and a greater than Minimal Detectible Change based on a 90 percent confidence interval (MDC_{90}) improvement (MDC_{90} = 6.49)[19] in performance for RC-PR over ATC-R was noted for two participants. The average blocks moved per minute was 12.83±1.76 (mean ± standard error) with RC-PR as compared to 7.75±1.60 with ATC-R.

RC-PR was also found to outperform ATC-R in the CRT by 31.19 seconds. Group results for the RC-PR and four-channel ATC-R were 17.93±3.10 and 49.12±6.45, respectively (Fig. 4). All four participants had improved performance with the RC-PR configuration, as indicated by the reduced time to complete the task.

Results of the AM-ULA (possible range 0-40, MDC_{90} = 3.70) [17] showed improvement in performance with the RC-PR configuration over ATC-R (Fig. 4). All 4 participants had individual scores higher for RC-PR. Group means were 12.36±0.47 with ATC-R and 16.25±0.83 with RC-PR, with the group difference of 3.89 exceeding the MDC_{90}.

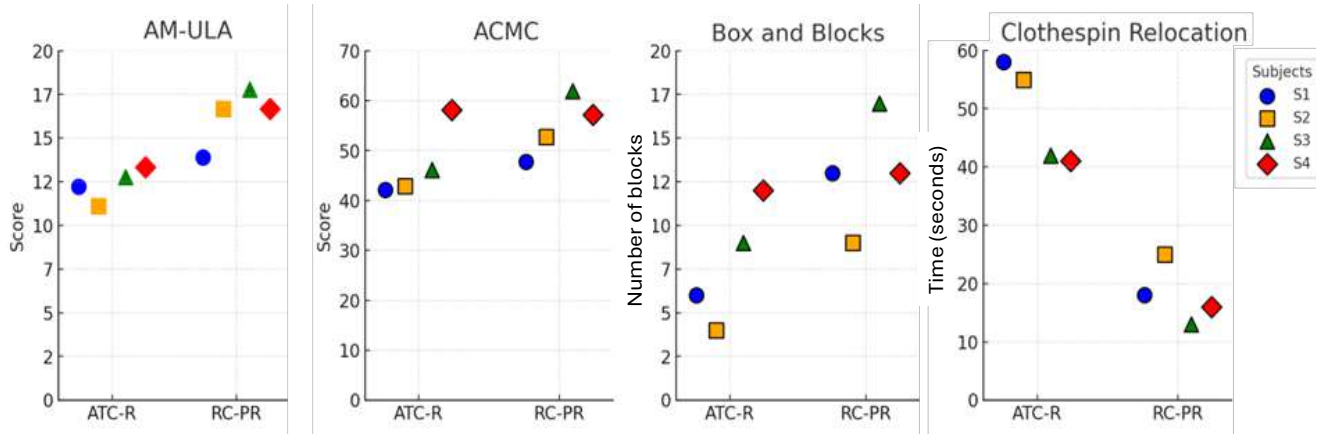


Fig. 4. Outcome results for the four participants. From left to right: AM-ULA (total score), ACMC (total score), Box and Blocks (number of blocks moved in 1 minute), Clothespin Relocation Task (time to move three clothespins). Improved performance is indicated by a higher score for the AM-ULA, ACMC, and Box and Blocks and a lower score for the Clothespin Relocation Task.

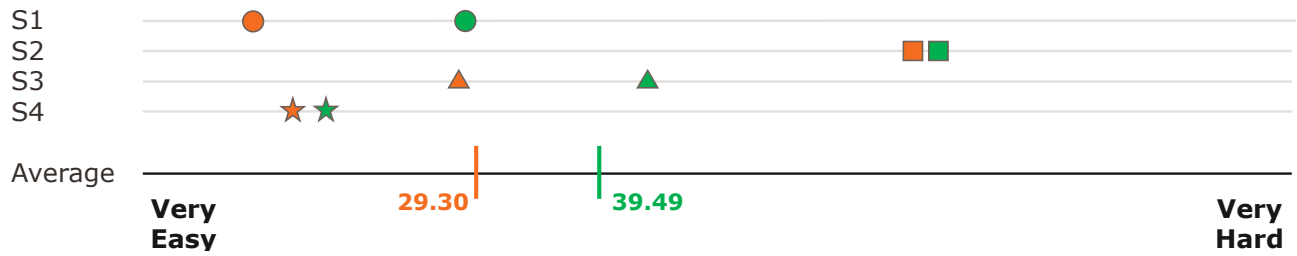


Fig. 5. Overall perceived control. Participants were asked to mark their overall perceived control of the prosthesis on a visual analog scale labeled as "Very Easy" on the left and "Very Hard" on the right. The location of each mark on the line was converted to a percentage of the entire line length. Green symbols correspond to ATC-R ratings and orange symbols to RC-PR.

For the ACMC (possible range 0-100, MDC_{95} = 2.5) [20, 21] the group average score increased from 47.35±3.72 with ATC-R to 54.95±3.03 with RC-PR (Fig. 4). This difference of 7.6 is greater than the MDC_{95} of 2.5 (single rater). Of the four participants who completed the measure, three (S1-S3) achieved higher scores with RC-PR as compared to ATC-R. S4 scored one point higher with the ATC-R configuration.

Following completion of the outcome measures for each control system, participants were asked to mark their overall perceived control of the prosthesis on a visual analog scale labeled as "Very Easy" on the left and "Very Hard" on the right (Fig. 5). The location of each mark on the line was converted to a percentage of the entire line length. Once data collection of both conditions was complete, participants were asked which control scheme they preferred and to provide an explanation as to why. Average overall control difficulty was reported as 39.49±11.36 with ATC-R and 29.30±13.11 with RC-PR. All four participants indicated that the prosthesis was easier to control with the RC-PR configuration and they reported they preferred RC-PR to ATC-R.

IV. Discussion

Amplitude and threshold control and PR are among the most widely used methods for operating myoelectric upper limb prostheses. While there are an increasing number of studies that have found improved prosthetic control and functionality with PR as compared to ATC, there are few studies comparing performance when controlling lower degree-of-freedom devices. This study served to fill this gap by comparing functional outcome measures and user-perceived control of a 2 degree-of-freedom prosthesis using both ATC-R and RC-PR control methods. Though a statistical analysis was not appropriate for only four participants, differences were found in quantitative outcome measures, with RC-PR outperforming ATC-R, as well as in user perceived control difficulty score. Even the participant who utilized ATC-R performed better or similar for the RC-PR condition and was the only participant whose ACMC score was higher (by 1 point) for ATC-R. For the three functional measures with an identified MDC (BBT, AM-ULA and ACMC), 58% of the within participant comparisons (7 of the 12) were higher for pattern recognition. None exceeded the MDC in favor of ATC-R.

These results are different than those reported by Resnik, who found fewer differences between the conditions [11]. A possible explanation is that the prior study used an ATC-T strategy whereas an ATC-R strategy was used in this study. We chose to implement the ATC-R strategy for two reasons. Firstly, with co-contraction switching, a user is much less likely to have inadvertent wrist rotation, unless they accidentally trigger this switching action. However, if this trigger is difficult to perform, this may discourage a user from accessing the wrist movements. With rate control, a user is able to more easily access the wrist movements by changing the magnitude and speed of the signal; but this can result in

more inadvertent movement, specifically when they try to use the hand in a very rapid manner. This may explain the reduction in the number of blocks moved during the BBT compared to the PR condition. The second reason was more practical—the ATC-R was the clinically configured control approach for one of the participants identified for the study and it was decided to keep this condition consistent throughout the trial.

In the current study, RC-PR not only outperformed ATC-R, but participants expressed a strong preference for RC-PR. This is clinically significant as we look to provide transradial prosthesis users with functional devices to optimize their performance in their daily activities. The participants reported RC-PR offered a more intuitive control experience for their prosthesis, as noted by their preferred condition. When selecting the best prosthesis design for users, clinicians must consider ease of control as a crucial factor that can enhance functional potential and reduce the risk of abandonment.

TABLE II. SUBJECT FEEDBACK (PARAPHRASED FROM NOTES)

ID	***Preferred Control***	***Reason***
S1	PR	-ATC-R was too complicated -ATC-R needed more time and practice -PR takes less "brain power"
S2	PR	-PR is easier to maneuver -PR responded more to my intended motions
S3	PR	-PR is easier to control and requires less focus -I have to stop more with ATC-R -With ATC-R, I have to think how hard and fast, where PR it just follows what I do
S4	PR	-PR movements are more natural, but I had to practice to retrain my brain away from ATR-R -PR is easier, especially could see for someone who is a new amputee

Another indicator of ease of control was the estimated training time needed for participants to achieve proficiency. Although training time was not initially recorded, it became apparent during data analysis that this may be a notable factor. Based on visit documentation, the average estimated time to achieve proficiency with the RC-PR and ATC-R systems, excluding socket fitting time, was 1.6 hours and 2.3 hours, respectively. While training time for the study was abbreviated as compared to clinical training, this suggests that RC-PR may require less time to learn, highlighting its more intuitive operation. A reduction in training time is clinically significant, as it helps to promote quicker integration of the prosthesis into users' daily lives.

While the general set-up of the RC-PR system was easier, it required more attention to the overall socket fit. To ensure consistent prosthetic control, full contact of all nine dome locations with the user's limb is necessary. This is crucial when performing tasks in different positions or while carrying a load, as such activities can often lead to loss of contact, particularly anteriorly and posteriorly in the socket. In contrast, a typical ATC system has fewer contact points, with electrodes positioned more medially and laterally, making them less affected by elbow position and load.

Future research is needed to investigate the control of 2 degree-of-freedom transradial prostheses using RC-PR and ATC within a larger population. Additionally, incorporating both rate control and co-contraction switching methods for all participants in the ATC condition would enable a more comprehensive comparison with RC-PR. Examining the degree to which users employ the wrist and any resulting compensatory movements when it is not utilized effectively could reveal the clinical impacts of choosing one system over the other in the daily lives of users. Future studies should also more precisely evaluate differences in set-up and training times for the various control configurations. Including home trials and implementing washout periods would address existing limitations and provide a clearer understanding of how long-term learning influences user control and function.

V. CONCLUSION

This study suggests that RC-PR outperforms ATC-R for a two degree-of-freedom transradial prosthesis across functional outcome measures and user-perceived control difficulty. RC-PR provided improved performance, reduced training times, and stronger user preference, highlighting its potential for more intuitive and effective control. These findings emphasize the importance of developing control systems that enhance ease of use and functionality, thereby reducing the risk of prosthesis abandonment. Future research with larger populations and extended home trials is needed to validate these results and further explore the clinical benefits of RC-PR.

REFERENCES

[1] K. Ziegler-Graham, E. J. MacKenzie, P. L. Ephraim, T. G. Travison, and R. Brookmeyer, "Estimating the prevalence of limb loss in the United States: 2005 to 2050," *Archives of Physical Medicine and Rehabilitation,* vol. 89, no. 3, pp. 422-429, Mar 2008. [Online]. Available: <Go to ISI>://000253958100006

[2] J. Rivera, K. Churovich, A. Anderson, and B. Potter, "Estimating Recent US Limb Loss Prevalence and Updating Future Projections," *Archives of Rehabilitation Research and Clinical Translation* vol. in Press, 2024, doi: doi.org/10.1016/j.arrct.2024.100376.

[3] D. Childress and R. F. f. Weir, "Control of Limb Prostheses," in *Atlas of Amputations and Limb Deficiencies*, D. G. Smith, J. W. Michael, and J. H. Bowker Eds., 3 ed. Rosemont, IL: American Academy of Orthopaedic Surgeons, 2004.

[4] T. W. Williams, "Control of Powered Upper Extremity Prostheses," in *Functional Restoration of Adults and Children with Upper Extremity Amputation*, R. H. Meier and D. J. Atkins Eds. New York, NY: Demos Medical Publishing, 2004, pp. 207-224.

[5] H. Huang, L. Hargrove, M. Ortiz-Catalan, and J. Sensinger, "Integrating Upper-Limb Prostheses with the Human Body: Technology Advances, Readiness, and Roles in Human–Prosthesis Interaction," *Annual Review of Biomedical Engineering,* vol. 26, 2024, doi: https://doi.org/10.1146/annurev-bioeng-110222-095816.

[6] E. Scheme and K. Englehart, "Electromyogram pattern recognition for control of powered upper-limb prostheses: State of the art and challenges for clinical use," (in eng), *J Rehabil Res Dev,* vol. 48, no. 6, pp. 643-60, 2011. [Online]. Available: http://www.ncbi.nlm.nih.gov/pubmed/21938652.

[7] G. Li, A. E. Schultz, and T. A. Kuiken, "Quantifying pattern recognition-based myoelectric control of multifunctional transradial prostheses," *IEEE Transactions on Neural Systems and Rehabilitation Engineering,* vol. 18, no. 2, pp. 185-92, April 2010 2010.

[8] A. Simon *et al.*, "Implications of EMG channel count: enhancing pattern recognition online prosthetic testing," *Front. Rehabil. Sci.,* vol. 5, 2024, doi: https://doi.org/10.3389/fresc.2024.1345364.

[9] A. J. Young, L. J. Hargrove, and T. A. Kuiken, "The Effects of Electrode Size and Orientation on the Sensitivity of Myoelectric Pattern Recognition Systems to Electrode Shift," *IEEE Transactions on Biomedical Engineering,* vol. 58, no. 9, pp. 2537-2544, Sep 2011, doi: 10.1109/tbme.2011.2159216.

[10] A. M. Simon *et al.*, "User Performance With a Transradial Multi-Articulating Hand Prosthesis During Pattern Recognition and Direct Control Home Use," *IEEE Transactions on Neural Systems and Rehabilitation Engineering,* vol. 31, pp. 271-281, 2023, doi: 10.1109/TNSRE.2022.3221558.

[11] L. Resnik, H. Huang, A. Winslow, D. Crouch, F. Zhang, and N. Wolk, "Evaluation of EMG pattern recognition for upper limb prosthesis control: a case study in comparison with direct myoelectric control," *Journal of Neuroengineering and Rehabilitation,* vol. 15, p. 23, 2018, doi: https://doi.org/10.1186/s12984-018-0361-3.

[12] B. Hudgins, P. Parker, and R. N. Scott, "A new strategy for multifunction myoelectric control," (in eng), *IEEE Trans Biomed Eng,* vol. 40, no. 1, pp. 82-94, Jan 1993, doi: 10.1109/10.204774.

[13] H. Yonghong, K. B. Englehart, B. Hudgins, and A. D. C. Chan, "A Gaussian mixture model based classification scheme for myoelectric control of powered upper limb prostheses," *IEEE Transactions on Biomedical Engineering,* vol. 52, no. 11, pp. 1801-1811, 2005, doi: 10.1109/TBME.2005.856295.

[14] E. Scheme, B. Lock, L. Hargrove, W. Hill, U. Kuruganti, and K. Englehart, "Motion Normalized Proportional Control for Improved Pattern Recognition-Based Myoelectric Control," (in eng), *IEEE Trans Neural Syst Rehabil Eng,* vol. 22, no. 1, pp. 149-57, Jan 2014, doi: 10.1109/tnsre.2013.2247421.

[15] V. Mathiowetz, G. Volland, N. Kashman, and K. Weber, "Adult norms for the box and blocks test of manual dexterity," *American Journal of Occupational Therapy* vol. 39, no. 6, pp. 386-391, 1985.

[16] L. A. Miller, K. A. Stubblefield, R. D. Lipschutz, B. A. Lock, and T. A. Kuiken, "Improved Myoelectric Prosthesis Control Using Targeted Reinnervation Surgery: A Case Series," *Neural Systems and Rehabilitation Engineering, IEEE Transactions on [see also IEEE Trans. on Rehabilitation Engineering],* vol. 16, no. 1, pp. 46-50, 2008.

[17] L. Resnik *et al.*, "Development and evaluation of the activities measure for upper limb amputees," *Arch Phys Med Rehabil,* vol. 94, no. 3, pp. 488-494, 2013, doi: 10.1016/j.apmr.2012.10.004.

[18] L. M. Hermansson, A. G. Fisher, B. Bernspang, and A. C. Eliasson, "Assessment of capacity for myoelectric control: a new Rasch-built measure of prosthetic hand control," (in eng), *J Rehabil Med,* vol. 37, no. 3, pp. 166-71, May 2005, doi: 10.1080/16501970410024280.

[19] L. Resnik and M. Borgia, "Reliability and validity of outcome measures for upper limb amputation," *Journal of Prosthetics and Orthotics,* vol. 24, pp. 192-201, 2012.

[20] L. N. Hermansson, H. Y. Lindner, and W. Hill, "Assessment of Capacity for Myoelectric Control v3.0 Manual," 2015.

[21] H. Y. Lindner, A. Langius-Eklof, and L. N. Hermansson, "Test-retest reliability and rater agreements of assessment of capacity for myoelectric control version 2.0," *J Rehabil Res Dev,* vol. 51, no. 4, pp. 635-644, 2014.

Personalization of Wearable Sensor-Based Joint Kinematics Estimation Using Computer Vision for Hip Exoskeleton Applications

Changseob Song[1]*, Bogdan Ivanyuk-Skulskyi[2]*, Adrian Krieger[1], Kaitao Luo[1], and Inseung Kang[1]

***Abstract*— Accurate lower-limb joint kinematics estimation is critical for patient monitoring, rehabilitation, and exoskeleton control. While previous studies have employed wearable sensor-based deep learning (DL) models for estimating joint kinematics, these methods often require extensive new datasets to adapt to unseen gait patterns. Meanwhile, researchers in computer vision have advanced human pose estimation models, which are easy to deploy and capable of real-time inference. However, such models are infeasible in scenarios where cameras cannot be used. To address these limitations, we propose a computer vision-based DL adaptation framework for real-time joint kinematics estimation. This framework requires only a small dataset (i.e., 1–2 gait cycles) and does not rely on professional motion capture setups. Using transfer learning, we adapted our temporal convolutional network (TCN) to stiff knee gait data, allowing the model to reduce root mean square error by 9.7% and 19.9% compared to a TCN trained on only able-bodied and stiff knee dataset, respectively. Our framework demonstrated a potential for smartphone camera-trained DL model to estimate real-time joint kinematics across novel users in clinical populations with applications in wearable robots.**

***Index Terms*— Joint kinematics estimation, Human pose estimation, Computer vision, Deep learning, Transfer learning**

I. Introduction

Estimating lower-limb joint kinematics has been an important agenda in patient monitoring, rehabilitation, and exoskeleton control [1], [2]. Accurate and rapid estimation of joint kinematics allows biomechanics and exoskeleton researchers to better understand gait patterns and assist users more effectively. This is important for quantifying irregular and pathological gait patterns, which helps identify gait characteristics and find out appropriate treatment or assistance strategies [3], [4]. Hip exoskeletons are particularly important because they support the hip joint, which plays a major role in locomotion energetics. [5], [6]. Precise joint kinematics data is essential for controlling hip exoskeletons: it allows real-time synchronization with the user's natural gait and facilitates personalized assistance [7], [8].

Recent biomechanics and exoskeleton studies have utilized deep learning (DL) models to estimate biomechanical parameters from wearable sensor data without professional motion capture setups [9], [10]. Among wearable sensors, inertial measurement units (IMUs) are particularly popular, as they capture kinematics of limb segments, such as acceleration and angular velocity [9], [10]. Deep learning models leverage this data to accurately predict users' joint kinematics in real time. However, training these models still requires motion capture systems to provide ground-truth labels.

Although many studies have used motion capture systems to extract body kinematics, those systems are expensive, hard to setup, and cannot be easily moved to different places [11]. Particularly, marker-based motion capture is cumbersome, requiring over 10 minutes to attach the markers, and it is accessible only to skilled operators who can accurately locate anatomical key points. Additionally, marker-based methods yield less repeatable results because different experimenters may attach markers in different positions [12].

Marker-less motion capture systems alleviate the burdens of marker-based systems owing to the rapid advances of human pose estimation (HPE) by artificial intelligence (AI) [13], [14]. They detect skeletal joints from raw image frames, estimate the human poses, and reconstruct three-dimensional (3D) skeletal models. However, commercial motion capture systems are proprietary and demand significant computing resources, limiting the accessibility of both marker-based and markerless systems to professional biomechanical facilities. As a result, they are challenging to implement in home settings or remote clinics in smaller hospitals. At the same time, open-source-based HPE algorithms enables the use of a single monocular camera, such as a personal smartphone, to estimate human poses and build kinematic models [13]. Joint kinematics can be easily extracted without incurring additional costs or requiring labor-intensive preparation. These tools can efficiently capture gait information from untrained users, providing valuable biomechanical data.

Recent studies have explored deploying vision models to estimate joint kinematics. For example, OpenCap, a portable biomechanics system, utilizes minimal smartphone cameras to monitor gait patterns [11]. Cotton et al. developed a framework to generate a smooth trajectory of joint positions [15] and fused IMU data with vision-based motion data to enhance knee joint angle estimation [16]. Similarly, Shin et al. established a joint kinematics estimation pipeline using synthetic IMU and video data from extensive datasets [17]. While these studies deployed HPE models to reconstruct 3D joint kinematics, these technologies cannot run in real time for practical uses, especially during outdoor locomotion. Compact vision models capable of real-time operation have been proposed [18], [19], but their accuracy is limited, and they are unsuitable for daily outdoor ambulation due to the requirement for third-person scene capture. Access to a re-

This work was supported in part by the Kwanjeong Educational Foundation. Changseob Song and Bogdan Ivanyuk-Skulskiy contributed equally to this work. Corresponding author: Changseob Song, changseob@cmu.edu.

[1]C. Song, A. Krieger, K. Luo, and I. Kang are with the Department of Mechanical Engineering, Carnegie Mellon University, Pittsburgh, PA 15213, USA.

[2]B. Ivanyuk-Skulskyi is with the CRIStAL, University of Lille, Lille, 59000, France and Cyclope.ai, Nanterre, 92000, France.

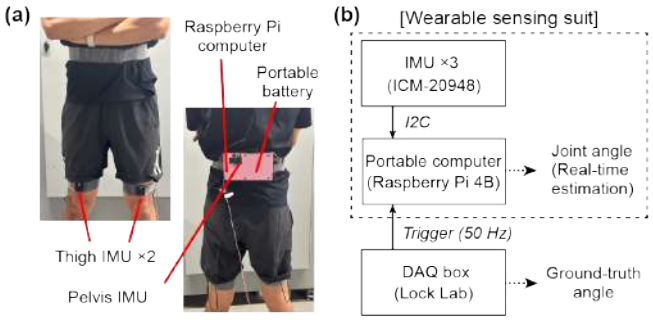


Fig. 1. Wearable sensing suit for joint angle estimation. (a) Components of the sensing suit hardware. (b) Data flow within the sensing suit for sensor data logging and real-time inference of joint kinematics.

liable, real-time joint kinematics estimation mechanism that can adapt effectively across diverse users would significantly enhance applications requiring real-time functionality, such as robotic exoskeleton control [7], [20].

Here, we propose an adaptive joint kinematics estimation framework that leverages computer vision and DL models to accommodate users with irregular gait patterns. We hypothesize that computer vision-based HPE models can serve as a new ground truth for training DL models to estimate irregular gait patterns with minimal settings. This can be achieved by using an open-source HPE pipeline with a monocular video input. By capturing irregular gait patterns and utilizing this information to train the wearable sensor-based DL models, we expect improvements in model performance. This approach will enable biomechanics researchers to have valuable insights to monitor each patient's gait patterns. Additionally, our framework can enhance existing exoskeleton control systems by rapidly personalizing the estimation model to accommodate individuals with irregular gait patterns.

II. Methods

A. Wearable Sensing Suit

We built a wearable sensing suit that can collect IMU data and estimate joint kinematics in real time. The sensing suit consists of 3 IMUs (ICM-20948, TDK InvenSense, Japan) positioned at the pelvis, left thigh, and right thigh, which are fastened by a Velcro strap and a compression band as shown in Fig. 1a. We used a portable computer (Model 4B, Raspberry Pi, UK) to collect IMU data, with a range of ± 1000 deg/s for gyroscope and ± 8g for acceleration, via I2C communication protocol and perform real-time inference in 50 Hz, as illustrated in Fig. 1b. The portable computer was powered by a portable battery inside of a 3D-printed control box. To synchronize ground-truth labels with timestamps logged by a data acquisition box (Lock Lab, Vicon, UK), the potable computer's software architecture was programmed to receive a 50 Hz trigger. Each iteration took less than 20 ms to log the sensor data and perform real-time inference.

B. Computer Vision-Based Kinematics Estimation Pipeline

We used computer vision models to extract the user's body kinematics. We utilized the MMpose [21] library to build

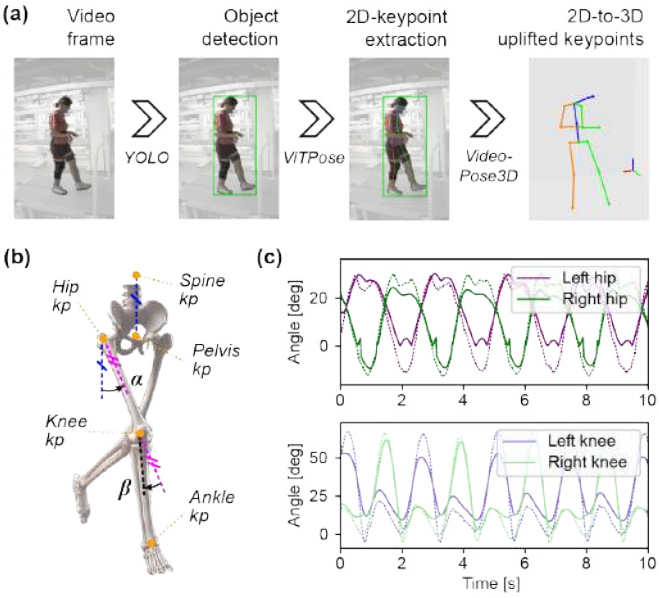


Fig. 2. Pose estimation pipeline using a human vision model. (a) Overall pipeline for extracting 3D joint keypoints from video frames. (b) Visual diagram depicting how joint angles are measured from the 3D keypoints. (c) Plot of estimated joint angles (solid lines) for an able-bodied subject walking at 1.0 m/s, generated using the pose estimation pipeline, compared to the ground-truth joint angles (dotted lines).

the pipeline presented in Fig. 2a that includes: (i) object detection; (ii) two-dimensional (2D) keypoint estimation; (iii) 2D-to-3D keypoint uplifting.

Using 3D keypoints, we calculated the hip joint angle α by measuring the angle between the vector connecting the pelvis and the spine keypoints, and the vector connecting the hip and the knee keypoints. For the knee joint angle, we calculated the angle β between the vector connecting the hip and the knee keypoints, and the vector connecting the knee and the ankle keypoints. We used six RGB cameras (BFS-U3-23S3C-C, Teledyne Vision Solutions, USA; resolution: 1920 × 1200, sampling rate: 100 Hz) to measure ground-truth joint angles with a commercial marker-less motion capture system (Theia3D, Theia Markerless Inc., CA) [12], [22], as depicted in Fig. 3. We selected one of the six cameras as the input of our vision model-based pipeline.

We used the ViTPose [23] human body keypoint estimation model that was pre-trained on the COCO dataset [24], due to its state-of-the-art performance, wide adoption in the field, and robust keypoint predictions. ViTPose utilizes plain, non-hierarchical vision transformers as backbones to extract features from a given person instance, followed by a lightweight decoder for pose estimation. The decoder comprises two deconvolution blocks that upsample the feature maps, followed by a convolution layer that generates localization heatmaps for keypoints. Furthermore, we examined the estimation performance of different ViTPose models across six different camera views depicted in Fig. 3 by averaging root mean square errors (RMSE) between estimated and ground-truth angles for both hip and knee

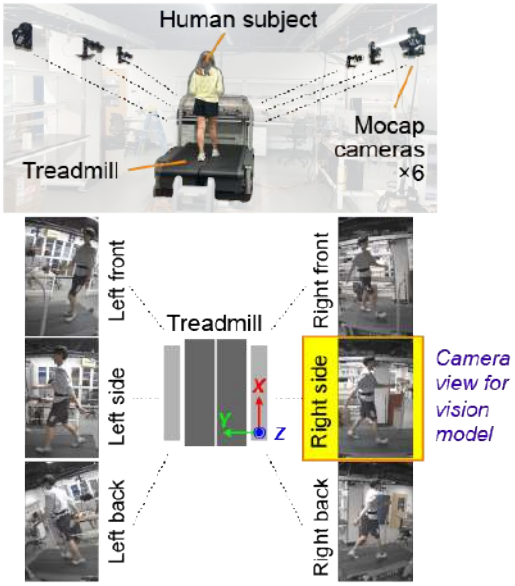


Fig. 3. Motion capture setup for measuring ground-truth joint angles and vision model-calculated joint angles.

joints. As shown in Table I, we obtained the best joint angle detection results from ViTPose-base in the right-side camera view (Fig. 2c) because the side camera views are aligned with the sagittal motion plane, and the right-side view is positioned further away than the left, providing a more direct perspective. After selecting the vision model and camera view, we applied a Savitzky–Golay filter with a window size of 50 and a fourth-order polynomial to reduce jittery noise from the vision pipeline. Overall, for further validation experiments, we used YOLOv8 [25] to detect the human subject, ViTPose-base to detect 2D biological keypoints within the image frames, and Video-Pose3D [26] to reconstruct 3D keypoints from the detected 2D coordinates.

TABLE I
JOINT KINEMATICS ESTIMATION ERRORS OF VITPOSE MODELS ACROSS DIFFERENT CAMERA VIEWS

RMSE [deg] ↓	**Camera view**					
Vision model	**Left front**	**Left side**	**Left back**	**Right front**	**Right side**	**Right back**
ViTPose-small	16.30	10.01	10.88	12.75	9.66	10.82
ViTPose-base	16.50	10.03	10.74	13.04	**9.60**	10.53
ViTPose-large	16.46	10.07	10.90	13.64	9.79	10.41
ViTPose-huge	16.40	10.89	10.81	13.89	9.94	10.50

C. Temporal Convolutional Network

For DL models that are used to infer biomechanical information from wearable sensor data, it is essential for DL models to capture temporal features from the input data. While long short-term memory (LSTM) networks [27] have been used for processing sequential data, they are slow to train and have substantial memory requirements. Other popular models like recurrent neural networks (RNNs) face a vanishing gradient problem [28].

Conversely, a temporal convolutional network (TCN) is better suited to handle time-series data because TCNs have dilated convolutional layers, which allows the model to parallelize multiple convolutions and learn long-term dependencies [29]. Therefore, TCNs are faster to train and more memory-efficient than LSTMs or RNNs [30] and have been deployed by many previous studies [29], [31]–[34].

In our TCN implementation (Fig. 4), we built five temporal blocks to extract relevant features from the time-sequential 18-channel data of three IMUs. Each temporal block included two convolutional layers and dilation factor. After passing through the temporal blocks, a fully connected layer mapped four joint angle values. We trained the TCN model using an Adam optimizer with a learning rate of 0.001 and a batch size of 32, for 50 epochs with early stopping. Each convolutional layer had 32 channels with a kernel size of 7, followed by ReLU activation function and a dropout rate of 0.1, which was optimized by a hyperparameter sweep. Once trained, we converted it to an open neural network exchange (ONNX) format to minimize inference latency.

D. Experimental Protocol

We recruited three able-bodied (AB) subjects, one female and two males, mean ± SD: age 25.3 ± 2.1 years, height 174.7 ± 6.5 cm, and weight 67.3 ± 9.0 kg. Within each subject, we collected a training dataset in four constant speed conditions (i.e., 0.4, 0.7, 1.0, 1.3 m/s), 1 minute per trial. Along with collecting IMU data with sensing suit, we obtained the ground-truth kinematic data using the camera setup shown in Fig. 3. Afterwards, to emulate an irregular and asymmetric gait pattern, each AB subject was equipped with a knee brace (Fig. 5a) to constrain their right knee joint motion, which served as a stiff knee (SK) gait pattern as plotted in Fig. 5b. This device not only restricted the right knee motion, but also induced asymmetry between hip joints and lengthened each subject's gait stride. We collected the SK dataset using the same protocol as the AB dataset.

After training the TCN model on the AB dataset (AB model), we adapted the baseline model to an AB+SK model via transfer learning using kinematic data extracted from the HPE pipeline. As shown in Fig. 5c, we analyzed how SK-to-AB dataset ratio affected estimation error on the SK test dataset. To evaluate model performance, we used the RMSE metric, which is particularly advantageous for highlighting outliers by heavily penalizing larger errors. When the SK portion reached 6% (equivalent to approximately 1 to 2 gait cycles for each speed condition) the AB+SK model's test error (on 10% of the total dataset) converged to 4.7 ± 0.4 deg RMSE, while the SK model's error remained at 5.9 ± 0.5 deg RMSE. For real-time validation experiments, we utilized the AB+SK model trained with a 6% SK-to-AB ratio. Similarly, the SK model was trained using the same SK-to-AB ratio, but without leveraging any pre-trained model.

To validate the DL model's estimation performance under various walking speeds and transient conditions with

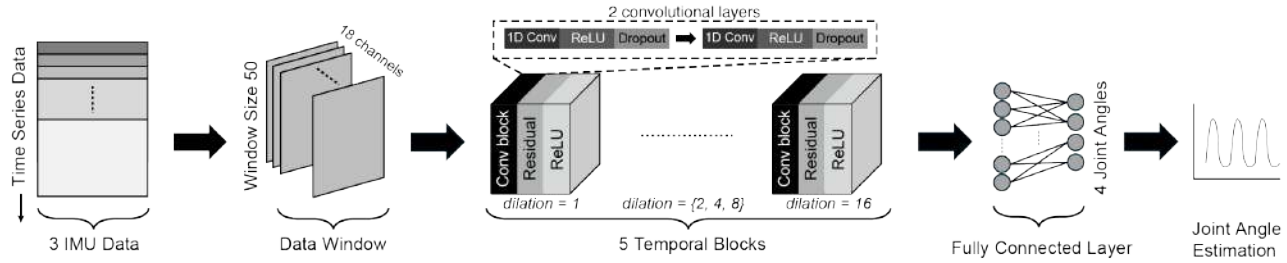


Fig. 4. Structure of the Temporal Convolutional Network (TCN) for training the kinematics estimation model. The dashed line represents a single convolutional block that comprises of two convolutional layers.

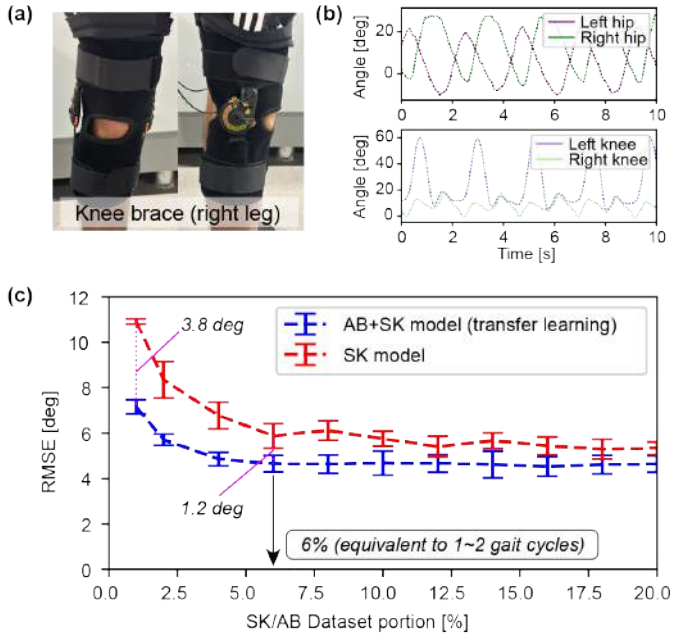


Fig. 5. Experimental setup for evaluating stiff-knee (SK) behavior and the estimation error of a transfer-learned, adapted machine learning model. (a) Knee brace used to replicate the SK gait pattern. (b) Ground-truth joint angle trajectories during SK gait for a single subject walking at 1 m/s. (c) Comparison of estimation errors between the SK model and the adapted AB+SK model across varying SK-to-AB dataset ratios (mean ± SD, three SK subjects).

changing speeds, we conducted experiments using a treadmill (FIT5, Bertec, USA) with the speed profile shown in Fig. 6a. Starting from a stationary position, each subject experienced four speeds (1.1, 0.5, 1.2, and 0.6 m/s, sequentially), which were different from the speeds used during TCN model training. The subject also experienced transient intervals with an acceleration or deceleration of 0.5 m/s². The speed profile lasted 185 seconds in total.

III. Results

To validate real-time estimation performance of the trained TCN model on various subjects, we began by evaluating the AB model's performance on AB subjects as demonstrated in Fig. 6b. For AB model-to-AB subject validation, the hip joint RMSE (3.7 deg) was lower than the knee joint RMSE (7.0 deg). When the AB model was used to estimate the SK subjects' joint kinematics, the hip joint RMSE increased to 5.8 deg, while the knee joint RMSE increased to 10.6 deg. This increase was accompanied by an asymmetry in RMSE values between the right and left legs due to the asymmetric gait patterns, with the right knee joint (stiff knee) exhibiting the highest estimation error among all joints.

For SK model-to-SK subject validation, the average estimation error across all four joints was the highest among all experiments (RMSE of 9.3 deg). Specifically, the hip joint angle estimation RMSE was 6.7 deg, while the knee joint angle estimation RMSE was 11.8 deg. In contrast, using the adapted AB+SK model for SK subjects reduced the hip joint angle RMSE to 4.8 deg and the knee angle estimation RMSE to 10.1 deg, resulting in an average joint angle estimation RMSE of 7.4 deg. This represents an improvement of 9.7% compared to the AB model-to-SK subject case and 19.9% compared to the SK model-to-SK subject case. For estimation performances across different speed conditions, estimation performance during high speed intervals (i.e., 1.1 m/s and 1.2 m/s) was the lowest compared to the low speed and transient speed intervals as shown in Fig. 6c.

IV. Discussion

In this work, we proposed the adaptable joint kinematics estimation framework for irregular gait patterns, particularly using a combination of the computer vision-based HPE algorithm and a TCN model. The vision-trained, adapted AB+SK model exhibited a decreased hip joint angle estimation RMSE of 4.8 deg and the knee joint angle estimation RMSE of 10.1 deg, outperforming the AB model-to-SK subject case by 9.7% and the SK model-to-SK subject case by 19.9%. This result corroborates our hypothesis that computer vision models can facilitate wearable sensor-based DL models to adapt to new gait patterns, which could not be learned by a pre-existing DL model that was trained solely for AB gait patterns. This framework has the potential to function as an effective tool for monitoring joint kinematics in real time, especially in scenarios where only limited datasets are available for model training and professional motion capture systems are inaccessible. Furthermore, we anticipate that our system can be deployed to a hip exoskeleton system where DL models can be generalizable to both AB and SK users.

An unexpected outcome was the higher estimation error of the SK model on SK subjects compared to the estimation

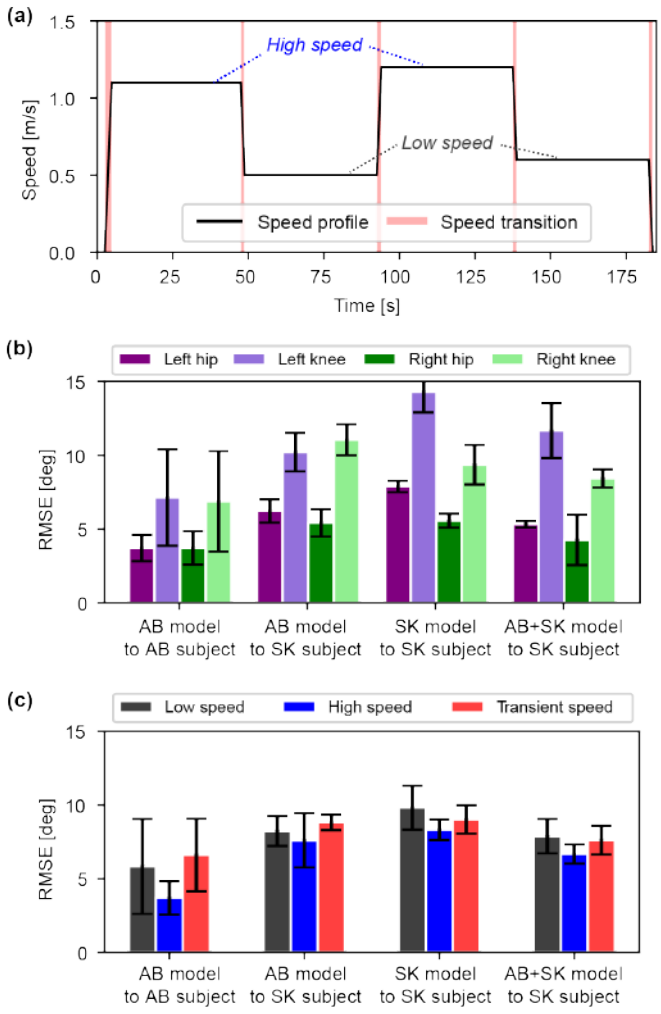


Fig. 6. Results of the Validation Experiments on Real-Time Kinematics Estimation. (a) Speed profile of the treadmill used during the validation experiments. (b) Estimation RMSE for each model across four lower-limb joints (mean ± SD, based on three SK subjects). The trial names indicate the specific TCN models (e.g., AB model, SK model, and AB+SK model) used to estimate data from specific subjects (e.g., AB subjects and SK subjects). (c) Estimation RMSE for each model under varying treadmill speed conditions (mean ± SD, based on three SK subjects).

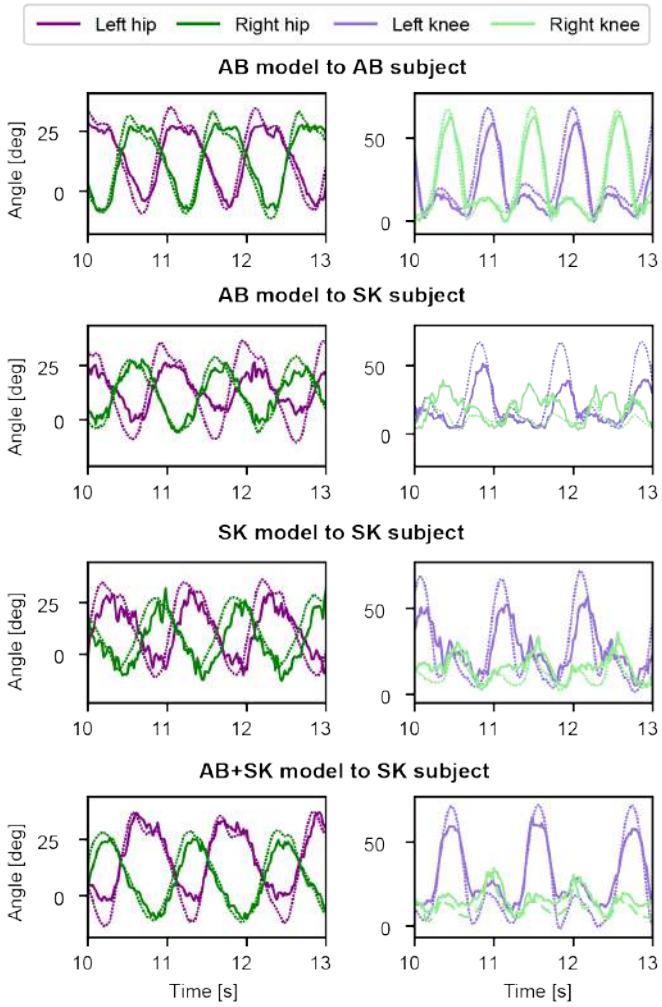


Fig. 7. Exemplary plots of real-time kinematics estimations for each joint across experimental trials. The data corresponds to Subject 1 during a high-speed interval at 1.1 m/s. Solid lines represent the estimated joint angle values, while dotted lines indicate the ground-truth joint angle values.

error of the AB model on the same group, even though the SK gait pattern was different from the AB gait patterns. This could be attributed to our study having a much smaller SK dataset size compared to the AB dataset, which was equivalent to only 1 to 2 gait cycles. Nevertheless, this small dataset portion effectively fine tuned the adapted AB+SK model, resulting in the lowest overall estimation error for SK subjects across all experiments. In addition, knee joint angle estimation errors were consistently higher than the hip joint angle estimation errors. This discrepancy in estimation performance was potentially stemmed from the sensing modality of our suit, which only included pelvis and thigh IMUs. For more precise knee joint estimation (or ankle joints), future work will involve reinforcing our sensing suite with additional IMUs being located at distal lower-limb segments.

The SK model and the AB+SK model also exhibited higher estimation error for the left leg than the right leg in both hip and knee joints. These errors were due to the model failing to track the hip joint angle around its minimum peak as illustrated in Fig. 7. Considering that we selected the right side view camera among six cameras, occlusion effects likely contributed to these left-side errors, as the vision-extracted kinematic data was used for training both SK and AB+SK models. Considering that we utilized only the right side view camera, the observed errors are likely caused by occlusion effects as outlined in [35], hindering accuratadrie detection and introducing noise into the joint kinematics data.

In future work, we aim to replace our monocular camera setup with a multiple camera system to implement a triangulation method, mitigating the occlusion effect from single-side views. We will also examine the estimation accuracy across different vertical camera positions, as well as horizontal camera positions we already tested in (Table I). This analysis will incorporate newly released HPE models, such as Sapiens [36]. Although one of the reasons we used one

of motion capture cameras was to easily synchronize with the ground-truth data, we also plan to build a smartphone camera-based framework for general use. Furthermore, we will expand the size of our AB dataset to enhance the pre-trained model's ability to generalize across diverse gait patterns from different subjects, creating a more robust baseline model that can be further adapted to irregular gait patterns. Since real pathological gaits exhibit additional unique characteristics, we plan to investigate their applicability to real gait impairments. Lastly, we will implement our wearable sensor-based joint kinematics estimation framework for enhancing robotic hip exoskeleton control in real time.

V. Conclusion

We developed a lower-limb joint kinematics estimation framework using a wearable IMU sensor-based TCN model. We adapted this model using computer vision-based HPE. With transfer learning, using a dataset of only 1–2 gait cycles of a new gait pattern, the adapted estimation model achieved improvements of 9.7% and 19.9% in RMSE compared to the models trained solely on the AB dataset and the SK dataset, respectively. This pipeline holds promise as a real-time joint kinematics estimation tool that can be quickly adapted to new gait patterns without requiring a specialized setup.

References

[1] P. B. Shull, W. Jirattigalachote, M. A. Hunt, M. R. Cutkosky, and S. L. Delp, "Quantified self and human movement: A review on the clinical impact of wearable sensing and feedback for gait analysis and intervention," *Gait & Posture*, vol. 40, no. 1, pp. 11–19, 2014.

[2] L. C. Benson, C. A. Clermont, E. Bošnjak, and R. Ferber, "The use of wearable devices for walking and running gait analysis outside of the lab: A systematic review," *Gait & Posture*, vol. 63, pp. 124–138, 2018.

[3] R. Spain *et al.*, "Body-worn motion sensors detect balance and gait deficits in people with multiple sclerosis who have normal walking speed," *Gait & Posture*, vol. 35, no. 4, pp. 573–578, 2012.

[4] A. Adkin, B. Bloem, and J. Allum, "Trunk sway measurements during stance and gait tasks in parkinson's disease," *Gait & Posture*, vol. 22, no. 3, pp. 240–249, 2005.

[5] G. S. Sawicki, C. L. Lewis, and D. P. Ferris, "It pays to have a spring in your step," *Exerc. Sport Sci. Rev.*, vol. 37, pp. 130–138, July 2009.

[6] G. S. Sawicki, O. N. Beck, I. Kang, and A. J. Young, "The exoskeleton expansion: improving walking and running economy," *J. Neuroeng. Rehabil.*, vol. 17, p. 25, Feb. 2020.

[7] A. Foroutannia, M.-R. Akbarzadeh-T, and A. Akbarzadeh, "A deep learning strategy for emg-based joint position prediction in hip exoskeleton assistive robots," *Biomedical Signal Processing and Control*, vol. 75, p. 103557, 2022.

[8] J. Kim *et al.*, "Reducing the metabolic rate of walking and running with a versatile, portable exosuit," *Science*, vol. 365, no. 6454, pp. 668–672, 2019.

[9] E. Rapp, S. Shin, W. Thomsen, R. Ferber, and E. Halilaj, "Estimation of kinematics from inertial measurement units using a combined deep learning and optimization framework," *Journal of Biomechanics*, vol. 116, p. 110229, 2021.

[10] V. Hernandez, D. Dadkhah, V. Babakeshizadeh, and D. Kulić, "Lower body kinematics estimation from wearable sensors for walking and running: A deep learning approach," *Gait & Posture*, vol. 83, pp. 185–193, 2021.

[11] S. D. Uhlrich *et al.*, "Opencap: Human movement dynamics from smartphone videos," *PLOS Computational Biology*, vol. 19, pp. 1–26, 10 2023.

[12] R. M. Kanko, E. Laende, W. S. Selbie, and K. J. Deluzio, "Inter-session repeatability of markerless motion capture gait kinematics," *Journal of Biomechanics*, vol. 121, p. 110422, 2021.

[13] C. Zheng *et al.*, "Deep learning-based human pose estimation: A survey," *ACM Comput. Surv.*, vol. 56, Aug. 2023.

[14] J. Wang *et al.*, "Deep 3d human pose estimation: A review," *Computer Vision and Image Understanding*, vol. 210, p. 103225, 2021.

[15] R. J. Cotton *et al.*, "Markerless motion capture and biomechanical analysis pipeline," *arXiv preprint arXiv:2303.10654*, 2023.

[16] J. Peiffer, K. Shah, S. Anarwala, K. Abdou, and R. J. Cotton, "Fusing uncalibrated imus and handheld smartphone video to reconstruct knee kinematics," in *2024 10th IEEE RAS/EMBS International Conference for Biomedical Robotics and Biomechatronics (BioRob)*, pp. 1275–1282, 2024.

[17] S. Shin, Z. Li, and E. Halilaj, "Markerless motion tracking with noisy video and imu data," *IEEE Transactions on Biomedical Engineering*, vol. 70, no. 11, pp. 3082–3092, 2023.

[18] S. Choi, S. Choi, and C. Kim, "Mobilehumanpose: Toward real-time 3d human pose estimation in mobile devices," in *Proceedings of the IEEE/CVF Conference on Computer Vision and Pattern Recognition (CVPR) Workshops*, pp. 2328–2338, June 2021.

[19] D. Mehta *et al.*, "Vnect: real-time 3d human pose estimation with a single rgb camera," *ACM Trans. Graph.*, vol. 36, July 2017.

[20] I. Kang *et al.*, "Real-time gait phase estimation for robotic hip exoskeleton control during multimodal locomotion," *IEEE Robotics and Automation Letters*, vol. 6, no. 2, pp. 3491–3497, 2021.

[21] MMPose Contributors, "Openmmlab pose estimation toolbox and benchmark." https://github.com/open-mmlab/mmpose, 2020.

[22] S. D'Souza, T. Siebert, and V. Fohanno, "A comparison of lower body gait kinematics and kinetics between Theia3D markerless and marker-based models in healthy subjects and clinical patients," *Sci. Rep.*, vol. 14, p. 29154, Nov. 2024.

[23] Y. Xu, J. Zhang, Q. Zhang, and D. Tao, "Vitpose: Simple vision transformer baselines for human pose estimation," *arXiv preprint arXiv:2204.12484*, 2022.

[24] T.-Y. Lin *et al.*, "Microsoft coco: Common objects in context," *arXiv preprint arXiv:1405.0312*, 2015.

[25] Ultralytics, "Ultralytics yolov8." https://docs.ultralytics.com/models/yolov8/, 2023. Accessed: Feb. 9, 2025.

[26] D. Pavllo, C. Feichtenhofer, D. Grangier, and M. Auli, "3d human pose estimation in video with temporal convolutions and semi-supervised training," in *2019 IEEE/CVF Conference on Computer Vision and Pattern Recognition (CVPR)*, pp. 7745–7754, 2019.

[27] S. Hochreiter and J. Schmidhuber, "Long short-term memory," *Neural Computation*, vol. 9, no. 8, pp. 1735–1780, 1997.

[28] Y. Bengio, P. Simard, and P. Frasconi, "Learning long-term dependencies with gradient descent is difficult," *IEEE Transactions on Neural Networks*, vol. 5, no. 2, pp. 157–166, 1994.

[29] D. D. Molinaro, I. Kang, J. Camargo, M. C. Gombolay, and A. J. Young, "Subject-independent, biological hip moment estimation during multimodal overground ambulation using deep learning," *IEEE Transactions on Medical Robotics and Bionics*, vol. 4, no. 1, pp. 219–229, 2022.

[30] S. Bai, J. Kolter, and V. Koltun, "An empirical evaluation of generic convolutional and recurrent networks for sequence modeling," *arXiv preprint arXiv:1803.01271*, 2018.

[31] D. D. Molinaro, I. Kang, and A. J. Young, "Estimating human joint moments unifies exoskeleton control, reducing user effort," *Science Robotics*, vol. 9, no. 88, p. eadi8852, 2024.

[32] Y. K. Kim *et al.*, "Leveraging deep learning and wearables for automatically identifying gait event: Effects of age and location of sensors on the assessment of gait events," *IEEE Sensors Journal*, vol. 25, no. 1, pp. 792–802, 2025.

[33] A. Guez, B. Hodossy, D. Farina, and R. Vaidyanathan, "Transferring gait predictors across emg acquisition systems with domain adaptation," in *2023 International Conference on Rehabilitation Robotics (ICORR)*, pp. 1–6, 2023.

[34] C. P. O. Nuesslein and A. J. Young, "A deep learning framework for end-to-end control of powered prostheses," *IEEE Robotics and Automation Letters*, vol. 9, no. 5, pp. 3988–3994, 2024.

[35] R. Gu, G. Wang, and J.-N. Hwang, "Exploring severe occlusion: Multi-person 3d pose estimation with gated convolution," in *2020 25th International Conference on Pattern Recognition (ICPR)*, pp. 8243–8250, 2021.

[36] R. Khirodkar *et al.*, "Sapiens: Foundation for human vision models," *arXiv preprint arXiv:2408.12569*, 2024.

People with Chronic Stroke Adopt Gait Patterns that Enhance Control of Center-of-Mass Dynamics in Response to Movement Amplification

1st Anna Shafer
Research Services
Edward Hines, Jr. VA Hospital
Hines, USA
anna.shafer@northwestern.edu

2nd Shamali Dusane
Feinberg School of Medicine
Northwestern University
Chicago, USA
0000-0002-7220-2491

3rd Jane Gyarmaty
Feinberg School of Medicine
Northwestern University
Chicago, USA
0009-0002-5257-5976

4th Katherine Martinez
Feinberg School of Medicine
Northwestern University
Chicago, USA
0000-0003-0444-9262

5th Mia Costa
Feinberg School of Medicine
Northwestern University
Chicago, USA
0000-0003-0444-9262

6th Keith E. Gordon
Feinberg School of Medicine
Northwestern University
Chicago, USA
0000-0001-6057-7651

***Abstract*—There is a need to develop effective physical therapy interventions to enhance walking balance in ambulatory people with chronic stroke (PwCS). Interventions that amplify self-generated movements may accelerate motor learning by enhancing sensorimotor feedback. Here, we applied this concept to walking balance. Specifically, during treadmill walking we used a cable-driven robot to apply lateral forces to the pelvis of 19 PwCS that were proportional in magnitude to real-time lateral center of mass (COM) velocity. The resulting movement amplification (MA) field increased the challenge to control lateral motion of the COM. We found that following 10-min of walking in the MA field, PwCS responded by adopting gait patterns that significantly increased control of COM dynamics (reduced lateral excursion and peak lateral velocity) and resulted in moderate but non-significant improvements in symmetry when compared to walking in a Null (no applied forces) field. These findings motivate further investigation to explore if extended walking practice performed in an MA field can improve walking balance in PwCS.**

***Index Terms*—stroke, biomechanics, walking balance, robotics, force-field**

I. Introduction

Most people with chronic stroke (PwCS) exhibit significant balance deficits that contribute to a multitude of gait impairments [1], [2] and alarmingly low levels of physical activity, including walking [3], [4]. Given the strong association between balance and functional independence [5], there is broad recognition that rehabilitation interventions should directly target walking balance [3], [6]. Thus, there is a compelling need to develop effective interventions to enhance walking balance in ambulatory PwCS.

Current clinical practice guidelines for PwCS recommend practicing walking tasks at moderate to high cardiovascular intensity to improve walking speed and distance [7]. However, interventions engaging in only forward walking have not been found to improve walking balance [8]. Indeed, among twelve gait and balance interventions (e.g., dual-task balance and gait training, treadmill training with external stimulation, etc.) a recent meta-analysis found that simple treadmill training was the least effective modality for improving functional balance in people with stroke [9]. We believe that improvements in walking balance during treadmill training can be substantially enhanced with the addition of external forces applied to the body that directly challenge walking balance, augment balance-related feedback, and encourage practice of movement strategies that control whole body center-of-mass (COM) dynamics. To address this urgent need to design effective strategies for improving walking balance in PwCS, we have developed a simple robotic tool to create and incorporate these balance-challenging training elements into treadmill based gait-training interventions.

Specifically, we use the Agility Trainer, a custom-built, cable-driven robot, to amplify a participant's movement by applying lateral forces to the pelvis proportional in magnitude and in the same direction as the participant's real-time lateral velocity [10]–[12]. The resulting Movement Amplification (MA) field increases the difficulty to maintain lateral balance during a straight walking trajectory. The effect is that when a person moves to the right, the robot simultaneously pulls them to the right, amplifying their motion by the velocity field gain. This setup has several important components for improving walking balance. First, the MA field is designed to challenge medio-lateral motion because the requirements of the nervous system to control lateral balance during walking are considerable in comparison to sagittal plane balance, which benefit from stabilizing body segment mechanics [13]. This is

This study was funded by the Eunice Kennedy Shriver National Institute of Child Health and Human Development (#1 R21HD112813), and the American Heart Association (#24POST1195671).

highly relevant for PwCS where the challenges of controlling lateral walking balance are well established [14]. Second, because the ability to control COM dynamics (i.e., position and velocity) is critical for maintaining walking balance [15]–[17], the MA field is designed to increase these demands by applying forces that directly amplify lateral COM velocity. Finally, our motivation for creating the MA field is based on research suggesting that interventions that amplify self-generated movements (e.g., error augmentation or movement amplification) will enhance sensorimotor feedback [18]. Thus, amplification may heighten perception and enable PwCS to detect even small movement errors that may otherwise be neglected due to sensory impairments. While movement amplification approaches have shown promise for retraining reaching movements in PwCS [18], [19], this approach has not yet been used to improve walking balance in PwCS.

The purpose of the current experiment was twofold. First, we sought to confirm that in PwCS the MA field would reduce dynamic stability during walking as previously observed in other populations [11], [20]. As the MA field specifically challenges control of lateral COM velocity, we estimated gait stability based on the maximum Lyapunov exponent of lateral COM velocity, a measure that has been suggested to estimate probability of falling [21]. Second, we sought to quantify if and how PwCS change their gait dynamics (COM position and velocity, stepping characteristics, and the relationship between the two) in response to walking in the MA field. If PwCS do not modify their gait when placed in the MA field, the effect would be greater lateral COM peak-to-peak excursions and peak lateral velocity. However, based on our observations in neurologically-intact adults [11], we hypothesized that, with practice in the MA, PwCS would adapt their gait patterns (shorter and wider steps) that in turn would reduce the magnitude of their lateral COM dynamics (excursion and peak lateral speed) when compared to walking in a Null field. If this hypothesis is supported, it would suggest that exposure to a challenging MA field can encourage PwCS to adopt locomotor patterns that, with sufficient practice, could be beneficial for improving the ability to control COM dynamics, a critical component of walking balance.

II. Methods

The Northwestern University Institutional Review Board approved the study protocol. All participants provided informed written consent. Twenty ambulatory individuals (5 females, age: 63 ± 8 years) with stroke related hemiparesis enrolled in the study (9 with right-sided hemiparesis, Stroke chronicity: 9 ± 7 years). Participants had Chedoke-McMaster Stroke Assessment (1-7 scale for the level of stroke-related motor impairment, with 7 indicating performance at the level of a neurologically-intact adult) scores of 4 ± 0.6 and 3 ± 0.9 for the leg and foot, respectively. Inclusion criteria included the ability to walk 10 meters without manual assistance or an assistive device other than a passive ankle-foot orthosis (AFO). Exclusion criteria included cognitive impairment (score $\leq 22/30$ on the Montreal Cognitive Assessment scale) and/or presence of aphasia (score $\leq 71/100$ on the Mississippi Aphasia Screening Test).

A. Experimental Setup

Kinematic data was recorded as participants walked on an oversized treadmill (TuffTread, Willis, TX) in either a Null (no forces applied to the waist) or MA field. A 12-camera motion capture system was used, operating at 100 Hz (Qualisys, Gothenburg Sweden), to record 3D kinematic data from 19 reflective markers placed on the pelvis and feet.

For safety, participants wore a trunk harness attached to a passive overhead support (ZeroG, Aretech, USA). Additionally, a physical therapist and a study team member positioned on either side of the participant provided non-contact guard (or manual assistance in the event of a loss of balance) during treadmill walking.

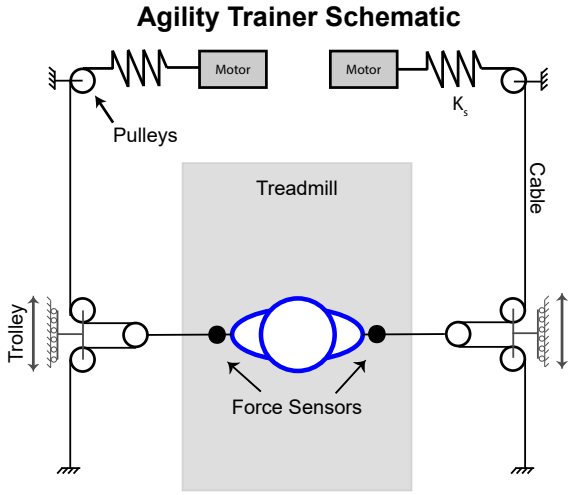


Fig. 1. The Agility Trainer is a cable-driven robotic device used to apply lateral forces to a participant's pelvis [10]. The device consists of two independent series elastic actuators (a linear motor coupled with a spring, $K_s = 0.32N/m$) and a cable transmission system which connects each actuator to either side of a pelvic harness inline with a force sensor to complete the feedback loop. A trolley system allows free fore-aft motion and minimal restriction of normal lateral motion.

The Agility Trainer was used to generate the MA field by applying lateral forces to the pelvis during treadmill walking [10], [11]. The Agility Trainer can generate forces large enough to substantially accelerate the COM of a person (up to 15% bodyweight), minimally restrict normal walking movements, precisely control an unstable field (MA) and operate at bandwidths greater than the frequency of lateral COM movements during walking [10] (Fig. 1). Here, we set the MA field gain to -45 $N\frac{s}{m}$. This field gain was used in a prior study with neurologically-intact adults [11]. A constant field gain was used for all participants to minimize variables. Prior to this study, each participant completed a feasibility session that included a brief exposure (12 min) to the MA field to confirm that they could successfully walk in and tolerate the field gain. The selected field gain was found to be challenging but tolerable for all PwCS enrolled in the current

study. Applied forces from each cable were capped at 100 N for safety.

B. Experimental Protocol

During two walking sessions, spaced a week apart to limit possible carryover effect, participants walked either in the Null or MA field. The order of these conditions (**Null** or **MA**) was randomized across participants. Within each session, participants performed five 2-min bouts of treadmill walking at their preferred speed. The walking bouts were separated by rest breaks and included a mandatory sitting break after the second and fourth bout to reduce potential fatigue. During treadmill walking, participants did not use assistive devices (canes, walkers, handrails) except for any habitually worn passive AFO. Participants were instructed to walk in the manner they felt most comfortable. During MA field sessions, participants were informed that the field would amplify their side-to-side movements and were allowed to interact with the field while standing before the treadmill was started for data collection.

C. Data Analysis

We analyzed the first (**Early**) and last **(Late**) 2-min walking bout of each session. We processed kinematic data in Qualisys Track Manager to label markers, then used Visual3D (HAS-Motion, Kingston, Ontario) to identify gait events, gap-fill and low-pass filter (Butterworth, 6 Hz cut-off frequency) marker data, and generate the COM trajectory from a pelvic model [22]. We found the velocity of the COM (VCOM) by taking the derivative of filtered COM position (same filter as marker data). We used MATLAB (Mathworks, Natick, MA) to compute all metrics.

1) Stability: As an estimate of local, dynamic stability, we calculated the short-term maximum Lyapunov exponent (λ_s) of the lateral VCOM over the last 100 steps of the Early and Late walking bout in the respective field. This measure quantifies the average logarithmic rate of divergence of a system and has shown predictive validity in walking when divergence is considered with respect to the gait cycle [21]. The slope of the mean log of the divergence curves in state space for strides 0-0.5 is reported here as detailed in our prior work [11]. Higher λ_s values correlate with faster divergence from a steady state trajectory and therefore lower local stability.

2) COM Dynamics & Step Characteristics: Parameters occurring every gait cycle including lateral COM excursion the peak-to-peak displacement of COM trajectory per stride (COMexc), step width and length, and the absolute value of VCOM peaks in both directions to yield peak COM speed were calculated. We report the average of peak COM speeds as this is informative of the velocity-field interactions experienced per person, given the set field gain. The mean and standard deviation was found for each parameter during the Early and Late walking bouts.

The spatial, medio-lateral margin of stability (MOS) was evaluated as a metric of coordination between the base of support (BOS), defined as the 5th metatarsal marker on each foot during stance phase, and the COM state (1).

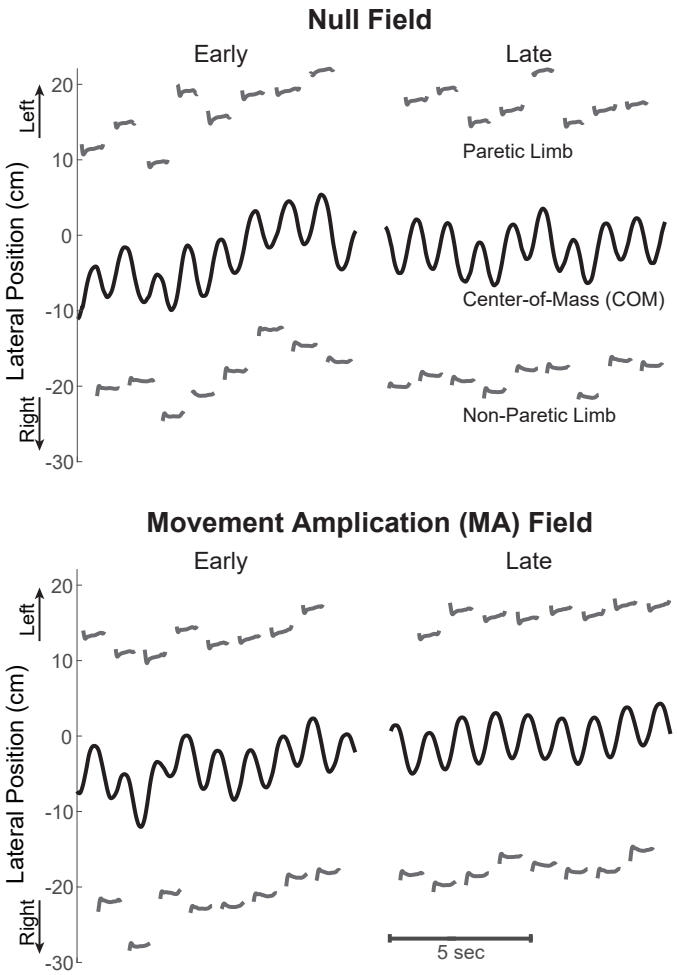


Fig. 2. The COM trajectory and marker data from the 5th metatarsal of each foot (base-of-support (BOS)) during foot contact (heel strike to toe off) for a representative participant with left sided weakness during the first 10-sec of walking in each condition.

$$MOS = BOS - XCOM \tag{1}$$

Where XCOM is the extrapolated COM derived from the COM position and the VCOM divided by the pendulum eigenfrequency [15]. The minimum MOS per step was found to identify the most unstable point within that step. We then found the mean (μ) and the standard deviation (σ) of these values across the Early and Late walking bouts for each condition to evaluate the overall effect of field on instantaneous stability and how consistent this effect was, respectively.

The average MOS across a walking session may have limited value when asymmetric gait is present [23]; therefore, we also investigate the asymmetry of MOS between the paretic and non-paretic limbs. As a measure of balance asymmetry, the MOS per side was evaluated to quantify which side was dominant [24].

$$Asym.MOS = \frac{(MOS_p - MOS_{np})}{(MOS_p + MOS_{np})} \tag{2}$$

Where MOS_p is the $\mu(MOS)$ on the paretic side and MOS_{np} is the $\mu(MOS)$ on the non-paretic side, yielding a value on a scale from -1 to 1 assuming there are no negative $\mu(MOS)$. A positive result indicates greater MOS on the paretic side, negative indicates greater MOS on the non-paretic side, and 0 represents equal MOS on both limbs.

D. Statistics

Paired t-tests were used to check for differences between conditions during the Early walking bout to see if there was an initial effect of field. Then the delta (Δ) of the above mentioned biomechanical measures from Early to Late field was calculated to identify any adaptation from 10-min of walking in the respective field, while accounting for the effect of fatigue. A mixed ANOVA was used with a between-subjects factor of Sequence (order of field exposure), a within-subjects factor of Field (MA or Null), and an Interaction factor between Sequence and Field to compare the effect of each field and test for any bias of exposure order. Significance was set at $p < 0.05$ for all tests and comparisons and python was used to perform them.

III. Results

Nineteen participants completed both sessions without requiring handheld assistance and are reported here. Mean preferred walking speed during the 2-min bouts was $0.45 \pm 0.2(m/s)$. Each participant used the same speed for both sessions. Fig. 2 illustrates the effect of walking in each field for a representative participant.

A significant difference was found during Early walking between field conditions for the λ_s of VCOM, with a higher exponent in the MA field (Table I). No significant differences in Δ λ_s were found between field conditions (Fig. 3).

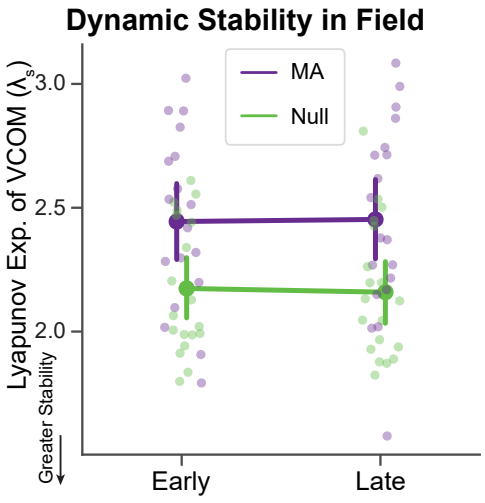


Fig. 3. The rate of divergence of the lateral component of the VCOM as an estimate of local, dynamic stability shows that the MA field was significantly challenging dynamic stability. Note that lower values correspond to a greater metric of stability.

A significant difference was found during Early walking between field conditions for COMexc, with a smaller COMexc in the MA field (Table I). The lateral COMexc increased Early to Late in both fields and no significant differences in Δ COMexc were found between field conditions (Fig. 4).

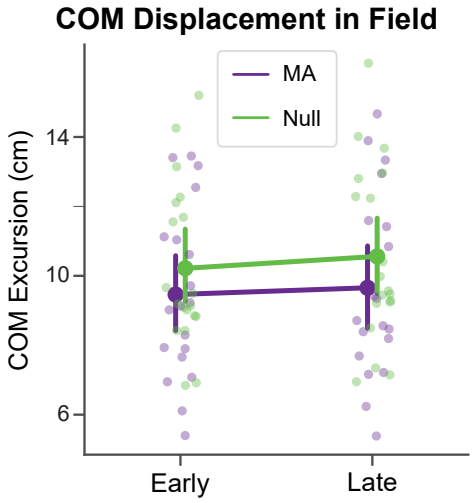


Fig. 4. The lateral displacement of the COM was evaluated per stride and the total excursion averaged across the Early and Late 2-min bouts.

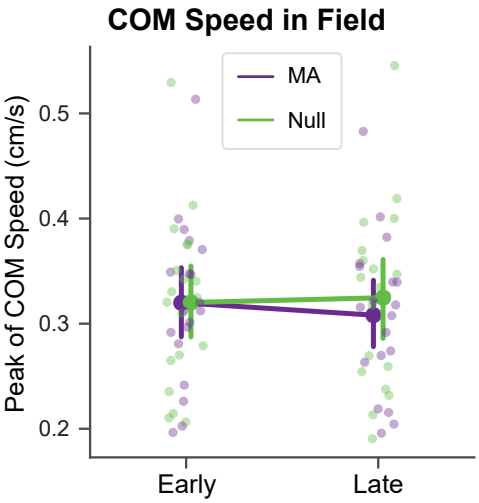


Fig. 5. Peak lateral speed of COM evaluated per stride and averaged across the Early and Late 2-min bout.

No significant differences were found during Early walking between field conditions for the peak of the lateral COM speed (Table I). The peak COM speed decreased after walking in the MA field, and the Δ was significantly different between the field conditions (Fig. 5).

A significant difference was found during Early walking between field conditions for the step length, with shorter steps taken in the MA field. Step width was also slightly wider in the MA field but not significantly (Table I). The Δ step length and step width were not significantly different between field conditions. There was an effect of Sequence for step length but when post-hoc t-tests were performed between the field subgroups by order of exposure, no differences were found.

A significant difference was found during Early walking

TABLE I
SUMMARY AND STATISTICS

Variable	Field	Early Field Mean (Std Dev)	t-test t	t-test p-value	Δ in Field Mean (Std Dev)	Mixed ANOVA for Δ in Field	F(1,17)	p-value
λ_s of VCOM	MA	2.44 (0.34)	-5.33	**<0.001**	0.008 (0.19)	Sequence	0.22	0.64
	Null	2.17 (0.26)			-0.02 (0.17)	Field	0.15	0.70
						Interaction	0.32	0.58
COMexc (cm)	MA	9.46 (2.48)	3.3	**0.004**	0.19 (0.60)	Sequence	0.42	0.52
	Null	10.2 (2.35)			0.34 (0.71)	Field	0.94	0.35
						Interaction	3.12	0.10
Peak COM Speed (cm/s)	MA	0.32 (0.08)	0.04	0.97	-0.01 (0.02)	Sequence	1.10	0.31
	Null	0.32 (0.08)			0.004 (0.02)	Field	12.0	**0.003**
						Interaction	2.59	0.13
Step Width (cm)	MA	31.3 (5.82)	-2.04	0.06	0.03 (0.85)	Sequence	4.08	0.06
	Null	30.1 (5.08)			0.22 (0.66)	Field	1.3	0.27
						Interaction	0.15	0.70
Step Length (cm)	MA	30.6 (12.4)	2.34	**0.03**	0.57 (1.10)	Sequence	4.77	**0.04**
	Null	31.6 (12.6)			0.15 (1.13)	Field	1.66	0.21
						Interaction	1.31	0.27
μ(MOS) (cm)	MA	6.83 (2.93)	-2.6	**0.02**	-0.14 (0.47)	Sequence	0.39	0.54
	Null	5.97 (2.23)			0.06 (0.51)	Field	0.02	0.9
						Interaction	2.43	0.14
σ(MOS) (cm)	MA	2.10 (0.93)	0.08	0.93	-0.13 (0.33)	Sequence	2.20	0.16
	Null	2.12 (1.33)			-0.10 (0.36)	Field	0.003	0.96
						Interaction	1.77	0.20
Asym. MOS	MA	0.21 (0.24)	1.68	0.11	-0.025 (0.05)	Sequence	2.14	0.16
	Null	0.27 (0.27)			-0.007 (0.12)	Field	0.44	0.52
						Interaction	0.11	0.75

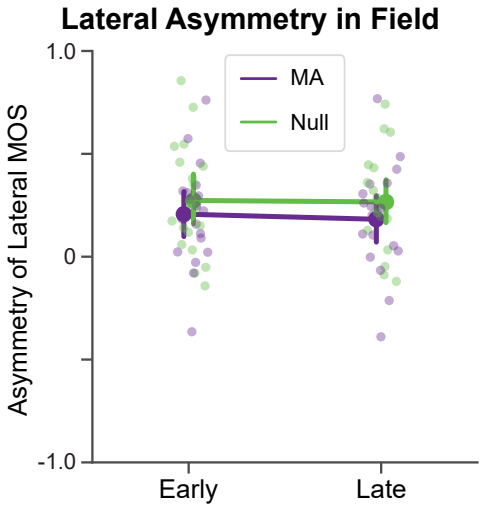


Fig. 6. The lateral margin of stability (MOS) was evaluated per side for symmetry. The Asymmetry of MOS was defined on a scale from 1 to -1 with 0 being equal contributions and a positive value indicating greater magnitude of MOS on the paretic side.

between field conditions for the μ(MOS), with a higher MOS in the MA field (Table I). No significant differences in $\Delta\mu$(MOS) were found between field conditions. No significant differences were found during Early walking between field conditions for the σ(MOS) or the Δ between field conditions (Table I).

No significant differences were found during Early walking between field conditions for the Asymmetry of MOS (Table I). Both groups tended to be more symmetric Late with a greater but not statistically significant improvement in the MA field (Fig. 6). There were no negative $\mu(MOS)$s in the dataset, so the assumptions for the Asym. MOS in (2) held.

IV. DISCUSSION

Our first hypothesis was supported—PwCS did show reduced dynamic stability in the MA field, as evidenced by the greater λ_s of medio-lateral VCOM during walking. This is a positive indication that the MA field can successfully challenge lateral walking balance for PwCS and warrants further exploration of MA as a gait training tool to specifically and continuously challenge lateral balance during walking.

Our secondary goal, to quantify if and how PwCS change their gait dynamics when presented with the challenge of walking in a MA field, also yielded interesting results. A smaller COMexc and greater μ(MOS)observed Early in the MA field indicates that participants immediately responded by adopting walking patterns that could improve stability. The decrease in peak COM speed in the MA field from Early to Late shows that participants further adapted their gait patterns with practice. This is an interesting change since the COMexc actually increased from Early to Late for both fields, and suggests that the VCOM is being modulated directly. This change in VCOM may be due to the sensorimotor feedback experienced in the MA field.

The initial changes in step characteristics—shorter, slightly wider steps—did not last by the end of the 10-min, which implies that in response to the MA field participants initially modulated their stepping characteristics to counteract the effects of the external forces on their COM dynamics. However, by the Late trials, the stepping characteristics in the MA field returned to those similar to the Null condition, while the COM dynamics did not. This suggests that the primary gait adaptation occurred in the COM velocity alone and that participants were capable of decoupling control of the COM velocity and excursion from stepping characteristics when provided with the sensorimotor feedback in the MA

field. This is a positive indication that PwCS can adapt to the specific balance challenges imposed by the MA field and that the MA field may be helpful for facilitating practice of gait patterns that actively control COM velocity in PwCS.

Finally, though not significant, the improvement of symmetry while in the MA field was seen immediately in the first 2-min of walking and was sustained throughout the whole 10-min, even with possible fatigue. Although there was not a significant change in the symmetry over time, it is possible that extended training in the MA field may result in more symmetrical gait patterns. The greater symmetry may have resulted from attempts to control the VCOM or through the increased sensorimotor feedback provided by the MA field.

V. Conclusions

We found that participants, despite being observably challenged to control their walking balance in the MA field, decreased their COMexc immediately and peak COM speed over time in response to the stimulus of the velocity-driven force field. The changes in the COM dynamics were independent of stepping characteristics and led to modest improvements in symmetry as seen in the Asym MOS. This rapid adaptation indicates that PwCS changed their COM dynamics in response to the MA field in a manner that improved control of lateral COM motion. We postulate that the enhanced sensorimotor feedback created by walking in the balance-challenging MA field may help PwCS to identify small movement errors and adopt anticipatory balance control strategies that improve walking balance and symmetry. Potentially exciting is the decoupling of the COM dynamics from stepping characteristics which allowed participants to minimize interactions with the destabilizing effect of the MA field without adopting inefficient general protective strategies (e.g., wider steps).

Our preliminary data finds that in response to walking in a MA field, PwCS adapt their gait in a manner that improved control of their lateral COM motion. While this study was limited to looking at short-term adaptations within the MA field, the observed enhanced control of COM dynamics motivates future research on the efficacy of extended walking practice in the MA field to improve walking balance in PwCS. Training walking balance of PwCS by amplifying self-generated movements is a departure from current practice and could create effective new clinical interventions.

References

[1] S. F. Tyson, M. Hanley, J. Chillala, A. Selley, and R. C. Tallis, "Balance disability after stroke," *Physical Therapy*, vol. 86, no. 1, pp. 30–38, 01 2006.

[2] P. W. Duncan, R. Zorowitz, B. Bates, J. Y. Choi, J. J. Glasberg, G. D. Graham, R. C. Katz, K. Lamberty, and D. Reker, "Management of adult stroke rehabilitation care," *Stroke*, vol. 36, no. 9, pp. e100–e143, 2005.

[3] K. M. Michael, J. K. Allen, and R. F. Macko, "Reduced ambulatory activity after stroke: The role of balance, gait, and cardiovascular fitness," *Archives of Physical Medicine and Rehabilitation*, vol. 86, no. 8, pp. 1552–1556, 2005.

[4] N. A. Fini, A. E. Holland, J. Keating, J. Simek, and J. Bernhardt, "How physically active are people following stroke? systematic review and quantitative synthesis," *Physical therapy*, vol. 97, pp. 707–717, 7 2017.

[5] G. Vincent-Onabajo, E. Joseph, and H. Y. Musa, "Impact of balance on functional independence after stroke: A cross-sectional study at rehabilitation settings in nigeria." *NeuroRehabilitation*, vol. 42 4, pp. 499–504, 2018.

[6] C. Pollock, J. Eng, and S. Garland, "Clinical measurement of walking balance in people post stroke: a systematic review," *Clinical Rehabilitation*, vol. 25, no. 8, pp. 693–708, 2011, pMID: 21613511.

[7] T. G. Hornby, D. S. Reisman, I. G. Ward, P. L. Scheets, A. Miller, D. Haddad, E. J. Fox, N. E. Fritz, K. Hawkins, C. E. Henderson, K. L. Hendron, C. L. Holleran, J. E. Lynskey, and A. Walter, "Clinical practice guideline to improve locomotor function following chronic stroke, incomplete spinal cord injury, and brain injury," *Journal of Neurologic Physical Therapy*, vol. 44, pp. 49–100, 1 2020.

[8] T. G. Hornby, C. E. Henderson, A. Plawecki, E. Lucas, J. Lotter, M. Holthus, G. Brazg, M. Fahey, J. Woodward, M. Ardestani, and E. J. Roth, "Contributions of stepping intensity and variability to mobility in individuals poststroke," *Stroke*, vol. 50, no. 9, pp. 2492–2499, 2019.

[9] M. Zhang, Z. Liang, Y. Li, J. Meng, X. Jiang, B. Xu, H. Li, and T. Liu, "The effect of balance and gait training on specific balance abilities of survivors with stroke: a systematic review and network meta-analysis," *Frontiers in Neurology*, vol. 14, 2023.

[10] G. Brown, M. M. Wu, F. C. Huang, and K. E. Gordon, "Movement augmentation to evaluate human control of locomotor stability," *Annual International Conference of the IEEE Engineering in Medicine and Biology Society. IEEE Engineering in Medicine and Biology Society. Annual International Conference*, vol. 2017, pp. 66–69, 9 2017.

[11] M. M. Wu, G. L. Brown, J. L. Woodward, S. M. Bruijn, and K. E. Gordon, "A novel movement amplification environment reveals effects of controlling lateral centre of mass motion on gait stability and metabolic cost," *Royal Society open science*, vol. 7, 1 2020.

[12] K. E. Gordon, S. Dusane, J. H. Kahn, A. Shafer, G. Brazg, H. Henderson, and K. Y. A. Kim, "Amplify gait to improve locomotor engagement in spinal cord injury (AGILE SCI) trial: study protocol for an assessor blinded randomized controlled trial," *BMC Neurology*, vol. 24, pp. 1–15, 12 2024.

[13] A. D. Kuo, "Stabilization of lateral motion in passive dynamic walking," *The International Journal of Robotics Research*, vol. 18, no. 9, pp. 917–930, 1999.

[14] V. Weerdesteyn, M. Niet, H. Duijnhoven, and A. Geurts, "Falls in individuals with stroke," *Journal of rehabilitation research and development*, vol. 45, pp. 1195–213, 02 2008.

[15] A. L. Hof, M. G. J. Gazendam, and W. E. Sinke, "The condition for dynamic stability," *Journal of Biomechanics*, vol. 38, no. 1, pp. 1–8, 2005.

[16] L. Hof, "The 'extrapolated center of mass' concept suggests a simple control of balance in walking," *Human Movement Science*, vol. 27, no. 1, pp. 112–125, 2008.

[17] S. Dusane, A. Shafer, W. L. Ochs, T. Cornwell, H. Henderson, K.-Y. A. Kim, and K. E. Gordon, "Control of center of mass motion during walking correlates with gait and balance in people with incomplete spinal cord injury," *Frontiers in Neurology*, vol. 14, 2023.

[18] F. Huang, J. Patton, and F. Mussa-Ivaldi, "Manual skill generalization enhanced by negative viscosity," *Journal of neurophysiology*, vol. 104, pp. 2008–19, 10 2010.

[19] J. L. Patton, M. E. Stoykov, M. Kovic, and F. A. Mussa-Ivaldi, "Evaluation of robotic training forces that either enhance or reduce error in chronic hemiparetic stroke survivors," *Experimental brain research*, vol. 168, pp. 368–383, 1 2006.

[20] T. Cornwell, J. Woodward, W. Ochs, and K. E. Gordon, "Stabilization strategies for fast walking in challenging environments with incomplete spinal cord injury," *Frontiers in Rehabilitation Sciences*, vol. 2, 2021.

[21] S. M. Bruijn, O. Meijer, P. Beek, and J. H. van Dieen, "Assessing the stability of human locomotion: a review of current measures," *Journal of the Royal Society Interface*, vol. 10, no. 83, p. 20120999, 2013.

[22] K. L. Havens, T. Mukherjee, and J. M. Finley, "Analysis of biases in dynamic margins of stability introduced by the use of simplified center of mass estimates during walking and turning," *Gait & Posture*, vol. 59, pp. 162–167, 2018.

[23] A. Hof, "Afterthoughts.pdf," 03 2021.

[24] F. B. van Meulen, D. Weenk, E. H. F. van Asseldonk, H. M. Schepers, P. H. Veltink, and J. H. Buurke, "Analysis of balance during functional walking in stroke survivors," *PLOS ONE*, vol. 11, pp. 1–20, 11 2016.

Exploring Cortical Responses to Blood Flow Restriction through Deep Learning

1st Jonas Koellner
Institute of Signal Processing and System Theory
University of Stuttgart
Stuttgart, Germany
jonas.koellner@iss.uni-stuttgart.de

2nd Martin Wimpff
Institute of Signal Processing and System Theory
University of Stuttgart
Stuttgart, Germany
martin.wimpff@iss.uni-stuttgart.de

3rd Dr. Leonardo Gizzi
Institute for Manufacturing Engineering and Automation
Fraunhofer
Stuttgart, Germany

4th Dr. Ivan Vujaklija
Department of Electrical Engineering and Automation
Aalto University
Aalto, Finland

5th Dr. Bin Yang
Institute of Signal Processing and System Theory
University of Stuttgart
Stuttgart, Germany

Abstract—Blood flow restriction (BFR) training, which combines low-intensity resistance exercises with restricted blood flow, is effective in promoting muscle hypertrophy and strength. However, its impact on cortical activity remains largely unexplored, presenting an opportunity to investigate neural mechanisms using brain-computer interfaces (BCIs). Deep learning (DL)-based BCIs, with their large capacity for decoding complex brain signals, offer a promising avenue for such exploration.
This study utilized magnetoencephalography (MEG) to analyze cortical responses in six subjects across three conditions—before, during, and after BFR. After preprocessing steps, such as data standardization and Euclidean-space alignment to optimize performance, the BaseNet architecture was utilized to classify the data. The models were tested using within-subject, cross-subject, and cross-time data splits.
The results revealed classification accuracy well above 90% for individual subjects, indicating that cortical responses to BFR are detectable on a personal level. However, cross-subject models achieved only chance-level accuracy (33%), highlighting significant variability between individuals. Cross-time models showed better performance, with accuracy exceeding 50%. These findings suggest that while BFR elicits distinct cortical activity patterns, these responses are highly individualized, presenting challenges for generalization.

Index Terms—blood flow restriction, brain computer interface, neural variability.

I. Introduction

Blood flow restriction (BFR) training, a technique that combines low-intensity resistance exercises with restricted blood flow, has emerged as a promising method for promoting muscle strength and hypertrophy [1]. Its effects on muscle growth are comparable to those of high-intensity resistance training [2], achieved by partial restriction of arterial inflow and full restriction of venous outflow, which create a hypoxic and acidic environment within the targeted muscles [3]. While substantial research has explored the peripheral adaptations induced by BFR [4], investigations into its neuromuscular effects are more recent [5], and its central mechanisms within the brain remain largely unexplored.
Current understanding suggests that BFR alters sensory input by inhibiting type I and II fibers, which are responsible for transmitting sensory feedback from muscle spindles and Golgi tendon organs. This inhibition leads to a reduction in proprioceptive awareness of the cuffed limb. At the same time, BFR leads to increased activation of type III and IV fibers [6]. As a result, BFR alters the overall sensory information relayed to the central nervous system (CNS). In response, the CNS compensates by enhancing the neural drive along efferent pathways [7] and recruiting higher threshold motor units [5], [6]. However, the precise nature of these alterations in afferent and efferent pathways, particularly whether afferent signals are blocked or negatively modulated, remains uncertain.
This study seeks to address these gaps by investigating the changes in central neural drive during BFR. To achieve this, we employ a deep learning (DL)-based brain-computer interface (BCI). Recent advancements in BCIs and DL offer unique opportunities for such explorations [8], as neural networks excel at uncovering patterns in large and complex datasets that traditional analytical methods may overlook [9]. However, the high amount of noise and information present in MEG and electroencophalography (EEG) can lead to overfitting to the time or subject domain of the training data. To mitigate this limitation, BCI models are typically shallow, encouraging them to capture more generalized

features and avoid domain-specific memorization [10]. This can be in part achieved by integrating convolutional layers within the architecture, as they are able to capture spatial as well as temporal patterns in M/EEG data [11]. Using deep learning, we aim to classify and characterize cortical responses related to BFR training, offering new insights into neural processes that may inform novel rehabilitation strategies and enhance the study of sensorimotor degradation.

II. Methods

The dataset used in this study comprised MEG recordings of six subjects while their left index finger was stimulated under BFR conditions. In this chapter, we describe the MEG recordings and stimulation protocols, followed by the preprocessing pipeline. Additionally we introduce the various train-test splits performed in this study to evaluate the model's generalizability across subjects and recording conditions. Finally, we outline the deep learning model and training procedure used to classify MEG trials based on experimental conditions.

A. Data

Before the measurements, the subjects were informed about the contents and procedures of the experiment by the experimenters, and by reading the information sheet and the privacy notice. The procedures of the study complied with the Declaration of Helsinki and were authorized by the local Ethical Committee of Aalto University, Espoo.

The dataset was acquired at the Aalto Neuroimaging (ANI) Infrastructure (Aalto University, Espoo, Finland) in a 3-layer magnetically shielded room (Imedco AG, Switzerland). They were measured using a 306-channel MEG system (TRIUX neo, Megin Oy, Finland), consisting of 102 magnetometers and 204 gradiometers, recorded at 1000 Hz.

The subjects were stimulated in two distinct forms: electrical (ES) and mechanical (MS). To determine the intensity of the ES the mechanical threshold (MT) and sensory threshold (ST) for the stimulation were measured before MEG acquisition. MT marked muscle contraction onset, while ST identified the point of sensory detection of an electrical impulse. Different types of stimulation were then defined for ES and MS: ES amplitudes were set at 120%, 140%, and 160% of the MT and ST. MS involved motor-driven passive flexion and extension of the index finger in 6s cycles (3s per movement). Each stimulation was performed 50 times in succession.

For evaluation of the cortical response to BFR, the data was acquired before (AP01), during (HP01), and after (AP02) BFR. AP01 is designated as the baseline measurement against which HP01 will be evaluated, while AP02 has been differentiated to ascertain whether the neural drive returns to the baseline or is altered on a short term basis.

With a a single measurement comprisng 50 stimulations, each ES block featuring three (120%, 140%, 160% of MT or ST), and MS block involving two types of stimulation (extension and flexion), the resulting number of trials per condition was 250. Repeating this process across three conditions (AP01, HP01, AP02) under the same threshold produced 750 trials per MT or ST block and 1500 trials per subject. Across six subjects, 9000 trials were available.

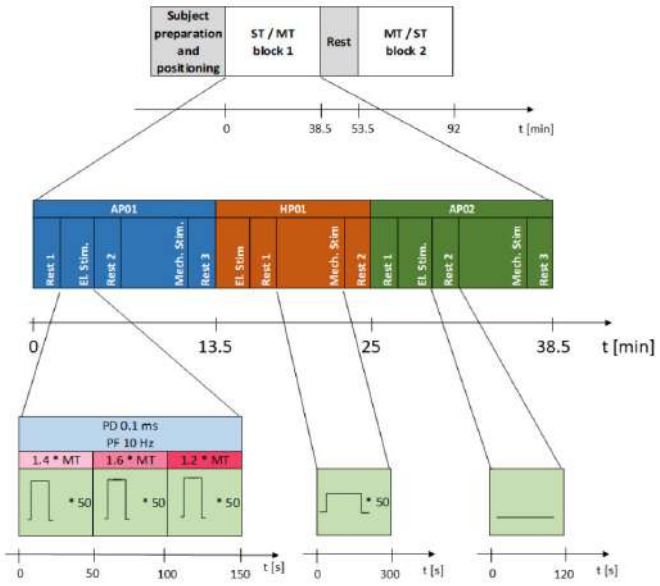


Fig. 1. The experimental protocol, with the lowest level outlining the nature of the different types of stimulation, the middle level detailing how these stimulations are categorized, and the uppermost level presenting the overall protocol framework.. Taken from [12].

1) Preprocessing: In this study, standard MEG preprocessing was employed, starting with a visual inspection for bad channels. During this procedure, peaks in the left hemisphere of the brain were observed, occurring simultaneously with the ES stimulus. Since the right hemisphere innervates the left half of the body, the spatial and temporal attributes of those peaks suggest that they are artifacts of the ES. Therefore those channels were discarded, reducing the number of channels to 288.

This was followed by spatiotemporal signal-space-separation (tSSS). Signal-space separation (SSS) is a method that decomposes the magnetic field measurements into two independent subspaces: one for sources inside the sensor helmet (such as brain signals) and another for external interference. This is accomplished by modeling the magnetic fields with spherical harmonics, allowing the method to mathematically separate the contributions based on their spatial characteristics without relying on previously recorded data. Spatiotemporal SSS (tSSS) extends this approach by identifying and removing temporal components that are common to both the internal

and external subspaces—particularly those arising from sources close to the sensors—thereby preserving the uncorrelated brain signals while further reducing artifacts and interference [13], [14].
Following this step, is the bandpass filtering of 1 to 40Hz. The lower cut-off frequency is used to prevent low-frequency drifts, whereas the higher frequency is chosen as the signals of interest lie within the theta (4 to 8Hz), alpha (8 to 12Hz), and beta (12 to 30Hz) frequency bands, rendering 40Hz cut-off sufficient.
Prior to preparing the data for interpretation by the model, Independent Component Analysis (ICA), in particular the FastICA algorithm, is employed. The goal is to remove artifacts not adressed by previous filtering methods. Once the MEG signal is decomposed, each component is compared against sumultaneaously recorded electrooculography (EOG) and electrocardiography (ECG) signals (eye blinking and heartbeat). Components exhibiting a correlation above a certain threshold are omitted during the reconstruction of the MEG signal [15].
Following the preprocessing steps, the data was scaled. Two distinct approaches were employed for this: standardization, as has been done with similar data for DL-models [16], and Euclidean-space alignment [17].
Standardizing (STA) the data effectively centers the mean at zero with a standard deviation of one, which improves both the convergence and training speed of the training process [18]. This process ensures that all input features are on a similar scale, which prevents features with larger magnitudes (such as gradiometer readings) from dominating the optimization process. In the case of MEG data, this is applied to each channel individually, normalizing the variability across sensors.
The objective of Euclidean-space (EA) alignment is to enhance the similarity between the data distributions of subjects from disparate cohorts, thereby augmenting the model's capacity to generalize to novel subjects. This is achieved through the initial estimation of a reference matrix $\bar{R}$,

$$\bar{R} = \frac{1}{n}\sum_{i=1}^{n} X_i X_i^T, \tag{1}$$

where $X_i \in \mathbb{R}^{C\times T}$ denotes the i^{th} trial of a subject. This is, in effect, an estimation of the covariance matrices for each trial, which are then averaged for each subject. Thereafter, the alignment of all trials of that subject can be performed:

$$\tilde{X}_i = \bar{R}^{\propto 1/2} X_i. \tag{2}$$

The statistics for both methods—namely, the mean, standard deviation, and reference matrix—were calculated separately for each subject. For the within-subject and cross-recording splits, where a subject's data appears in both training and test sets of a model, statistics must be computed exclusively from the training set of the subject to prevent data leakage. These calculated statistics are then applied to all of the subject's data. In the cross-subject split, each subject's data is entirely in either the training or test set, i.e., no information of the test-subject's data is known to the models during training. Consequently, all of a subject's trials can be used for computing their statistics and standardizing or aligning their data.

2) Data Splits: The following section will provide a detailed explanation of the data splits conducted in this study.

a) Within-Subject: In order to assess the models' general ability to learn and classify the conditions for each subject, several models were trained on the data of one subject each. The data was divided into two distinct sets: a training set and a test set. Randomly selected trials from all measurements were allocated to either the training set or the test set, with a distribution of 80% and 20%, respectively. To quantify the effect of temporal autocorrelation, i.e., the similarity of proximal M/EEG trials independent of stimulation type [19], a non-random split was tested as well. This yielded no difference in accuracy.
Overall, six models were trained on within-subject data split, each of which was trained on 1200 trials and tested on the remaining 300 trials of that subject. This process was repeated for both STA and EA data, with each model trained and tested once. In subsequent chapters, these models will be referenced as WS-EA/STA.

b) Cross Subject Models: In evaluating the model's capacity to generalise the learned features for the classification of AP01, HP01, and AP02, and to apply those to an unseen subject, six models were trained. In this instance, each model was trained on five subjects and tested on the remaining one. The data pertaining to the training subjects was divided into three distinct sets: training, validation, and early stopping validation. The validation set was employed to supervise the models' performance on the known subjects using trials not available during training. The training set constituted 75% of the total number of trials in the training data, the validation set constituted 15%, and the early stopping validation set constituted 10%. The early stopping technique was employed to prevent the model from exhibiting overfitting tendencies with respect to the training data. The data were distributed once more randomly across the sets in accordance with the aforementioned method. This resulted in the formation of sets comprising 5625, 1125, and 750 trials, respectively, with the test set containing the 1500 trials of the subject that was excluded from the training process. The models were trained on EA and STA data and henceforth will be referred to as CS-EA/STA. ´

c) Cross Recording Models: In order to assess the model's capacity to generalise across temporal domains, namely the same subject at a subsequent point in time, a training and test split by recording was conducted. This entailed training the models on all subjects' MT data and testing them on all ST data, and vice versa. This process was repeated for both EA and STA data, resulting in the creation of four models in total. The training data was once more divided at random into a training set comprising 80% of the data and a validation set comprising the remaining 20%. This resulted in a total of 3600, 900, and 4500 trials for the training, validation, and test sets, respectively. The cross-recording models will be designated as CR-MT/ST-EA/STA, with the threshold in question representing the training data of the model.

B. Deep Learning Model

For the task at hand, the BaseNet model [10] was employed, a neural network specifically developed for motor imagery (MI) tasks using EEG data. The model features a typical DL-BCI stem block, which includes a temporal and spatial filter implemented through convolutional layers [20]. Additionally, BaseNet incorporates batch normalization within its architecture, ensuring consistent learning and training across different batches and subjects [21]. The model also uses average pooling and 1×1 convolutional layers, which help reduce the number of features and learnable parameters, allowing the network to either perform feature reduction or enable learnable transformations in a more flexible way. Since BaseNet is a shallow neural network, with this input it comprised less than 10 000 learnable parameters.

C. Training

The classification task in this study was to discriminate between the BFR conditions for a MEG trial, defining the labels as AP01, HP01, and AP02. Subsequently, the input of the models was one preprocessed, and either standardized or euclidean-space aligned, MEG trial $X_i \in \mathbb{R}^{C \times T}$. Here C denotes the the number of channels (288) and T the number of samples per trial. Since the data was sampled at 1000Hz and epoched with -0.2 and 0.8s from the point of stimulation t_0, T was equal to 801.

III. Results

The within-subject mean accuracies and their standard deviation is shown in Table I. Whilst STA-trained models achieve a high accuracy, it is surpassed by EA-trained models reaching 99.9% accuracy. The discrepancy between the accuracies of both data types can be attributed to the methodology employed. As discussed earlier, standardization ensures consistent and efficient backpropagation during training. In contrast, EA enhances this process by aligning individual trials to a subject's reference state, further optimizing the learning process. Although such remarkably high accuracy, especially with a limited amount of training data, may suggest potential overfitting [22], this risk is mitigated by the reduced complexity of the shallow deep learning model and the incorporation of regularization techniques, such as dropout [23]. To evaluate whether the models are learning recording-specific features or are capable of generalizing across different sessions for the same subject, further testing is required using data from separate recordings of the same individual.

TABLE I
Mean and Standard Deviation of Singular Subject Models' Accuracies

Model		Test
Within-Subject	EA	99.9 ± 0.1
	STA	85.2 ± 13.1

The validation accuracies of the cross-subject- and cross-recording-models facilitate a similar accuracy as the singular subject models, as can be seen in Table II, exceeding 90%. However, the test accuracy drops significantly when the model is evaluated on domains, time frames or subjects, that were excluded during training. Notably, models tested on unseen subjects do not surpass 40%, staying near the guessing accuracy of 33%. In contrast, the CR accuracy reaches approximately 50%.

TABLE II
Mean and Standard Deviation of Cross Domain Models' Accuracies

Model		Validation	Test
Cross Subject	EA	99.8 ± 0.2	35.9 ± 8.0
	STA	88.6 ± 2.4	39.7 ± 10.6
Cross Recording	EA	99.9 ± 0.0	45.9 ± 20.9
	STA	91.8 ± 1.8	51.3 ± 16.9

The difference in the model's performance between an unseen subject and a different recording of the same subject suggests that the model is learning subject-specific features rather than features relevant to BFR conditions that are consistent across subjects.
This line of reasoning is further supported by recent research highlighting the general flaw in BCI-NNs to learn domain specific patterns [24]. However, visualizing the features learned by the models—exemplified in Fig. 2 for the CS-STA/EA-4 models—provides an additional perspective. These features, extracted as the 96-dimensional output from the second-to-last layer of the BaseNet, were analyzed using t-SNE dimensionality reduction [25], where each dot represents a trial. The visualization reveals clear subject-specific clustering within the broader clusters of BFR conditions. Notably, the extent of subject clustering varies across subjects and conditions, but certain subjects, such as subject 6, consistently occupy specific regions within the clusters.

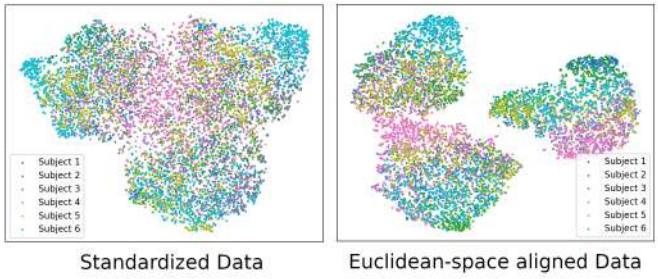


Fig. 2. Feature space of a Cross-Subject model trained on standardized and Euclidean-space aligned data, where subject 4 was left out. The 96 dimensional features were reduced to two dimensions using t-SNE, with every point representing a trial.

While EA-trained models tend to perform worse than STA models on the test data, they demonstrate a clearer distinction between conditions on the known domains. One possible explanation for their poorer performance is the pronounced separation of test trials based on features learned during training. The difference in clustering can be seen in Fig. 3, where all trials are visualized, but the clusters of the conditions are separated more clearly. This pronounced separation of features learned during training likely contributes to the poorer test performance of the EA models, as these features may not generalize well to unseen data. In contrast, STA models show greater overlap in the clustering of label features, which can increase the likelihood of "lucky guesses" by relying on less distinct but more generalized feature representations. While Euclidean-space alignment does not enhance overall performance on unseen domains, its ability to highlight clearer feature separation provides valuable insights into the characteristics the models rely on for classification tasks.

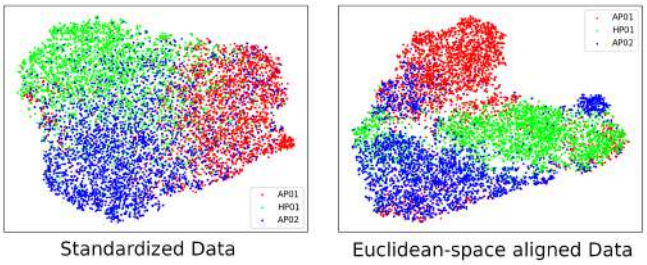


Fig. 3. The feature space of the CR-ST-EA/STA models for all available data, which the models were trained and tested on. The 96 dimensional features were reduced to two dimensions using t-SNE, with every point representing a trial.

Since the CS-models only achieve the guessing accuracy of 33%, a deeper investigation of the confusion for the test data will likely not yield concise insight and will therefore not be discussed further. But the CR models, with their accuracies around 50% may yield information on the nature of the cortical responses. For this purpose, the confusion matrices of the CR-MT/ST-EA models are displayed in Fig. 4. For both, the classification of HP01 seemed to be the most difficult, with a high confusion for AP02. Additionally, for CRT-MT-EA AP01 gets confused with AP02 to a similar extent, same for the AP02 condition with HP01. CR-ST-EA model on the other hand achieves less confusion for both those cases and the wrong classification for AP01 and AP02 are roughly equally distributed between the remaining conditions.

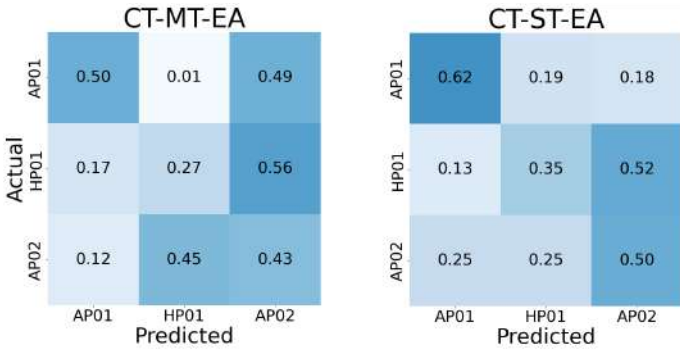


Fig. 4. The confusion matrices of the CS-MT/ST-EA models on their respective test sets. I.e., for the CT-MT-EA model its confusion of the conditions of the ST-data is displayed and vice versa.

IV. Discussion

The models exhibited high classification accuracy when evaluated on within-subject data. Preprocessing with the EA method significantly enhanced model performance, consistently achieving well above 95% accuracy. This preprocessing approach facilitated faster training convergence, effectively highlighted peaks in cortical responses, and improved the model's ability to distinguish between experimental conditions.

However, cross-domain testing, particularly across subjects, revealed significant limitations. Models frequently seemed to prioritize time-specific or subject-specific features rather than cortical responses that differentiated across domains.

The average test accuracy for CS models was below 40%, with substantial variability across subjects in cortical responses. This inconsistency highlights the difficulty of generalizing features across individuals.

The generalization across thresholds yielded more consistent results, with models demonstrating moderate capability to classify conditions across varying stimulation intensities. Nonetheless, performance remained inferior to within-subject classification.

These findings underscore the challenges of extracting generalized cortical features from MEG data, paralleling difficulties observed in similar BCI tasks. Comparable challenges have been reported with EEG data, where achieving high cross-subject generalization accuracy has been notoriously difficult to achieve or replicate [19], [24].

The higher accuracy for the CR-ST-EA model compared to CR-MT-EA can be explained with the increased stimulation intensity of MT, likely yielding more pronounced cortical responses. When training a model on the ST set, i.e., with weaker responses, it likely becomes more sensitive to the data of the MT and is able to better classify the BFR trials.

These findings not only highlight the nuanced effects of stimulation intensity on model performance but also verify the change in cortical responses to stimulations during the BFR conditions. This is further emphasized by the confusion matrices, which reveal a clear separation in cortical responses to BFR. This distinction between conditions supports the supposition of the WS models not overfitting and the possibility of individual models correctly classifying the cortical responses to BFR. The cortical responses do not revert to the baseline of AP01, as the primary confusion is between the conditions HP01 and AP02. This supports the hypothesis [7] of an alteration in the cortical response to BFR within the 40-minute timeframe of the recording. The effect of the alterations of the prior to the subsequent recording block (MT/ST) could not be evaluated in this study, due to the varying stimulation intensities.

The cortical response to BFR shows a high degree of variability across subjects. This variability, both between subjects and within the same subject, has been well-documented in previous research [26], [27]. Therefore the findings discussed above, for BFR to elicit highly individual responses, support this theory. Additionally, the low test accuracies of the cross-domain models can be explained with the "strategic variability", which postulates that the human brain operates in a time-dependent and subject-specific manner [28]. The low test accuracy of the CR models, which perform relatively poorly, although all subjects are known to the model, is a likely result of the time-dependant strategic variability.

The observed limitations in model generalization and the pronounced variability in cortical responses emphasize the need for methodological advancements. A key limitation of this study is the small sample size, which may restrict the model's ability to capture broader neural patterns across subject domains. Expanding datasets to include a larger number of subjects and recordings across multiple sessions could improve model generalizability across domains. Additionally, randomizing stimulation protocols could help reduce temporal autocorrelation [19], encouraging models to prioritize condition-specific features rather than time- or subject-specific patterns.

Overall, this study successfully verified the presence of a cortical response to BFR, along with its highly individualized nature. However, the specific nature of the changes occurring in the afferent pathways could not be clearly identified. Future studies integrating MEG recordings with high-density surface electromyography could offer a more comprehensive understanding of these mechanisms.

V. Conclusion

This study confirms that BFR training elicits measurable cortical responses, which vary significantly between and within subjects. Using MEG data and DL-models, we achieved high accuracy for within-subject classifications but encountered challenges in generalizing across subjects. These findings reflect the individualized nature of neural adaptations to BFR and emphasize the limitations of current deep learning approaches in capturing generalized patterns in brain activity. The achievements made in this study bring us closer to developing tools to better understand the neural processes occuring during BFR training, which may eventually lead to novel rehabilitation strategies and more informed observation of sensorimotor degradation. Future work should focus on expanding datasets, refining preprocessing methods, and diversifying experimental protocols to enhance model generalizability and further explore the neural mechanisms of BFR.

Acknowledgment

We would like to thank Mansour Taleshi and Pascal Brunner for their support in the development and implementation of the experimental methodology.

This study was supported by the Academy of Finland projects SomSPer (#11350419–494 T41019) and Hi-Fi BiNDIng (#333149), Deutsche Forschungsgemeinschaft (DFG) under the German Excellence Strategy (EXC 2075 390740016, PN2, Project PN2-3A), and Programm des projektbezogenen Personenaustauschs Finnland (#57609899).

References

[1] J. P. Loenneke, J. M. Wilson, P. J. Marín, M. C. Zourdos, and M. G. Bemben, "Low intensity blood flow restriction training: a meta-analysis," European journal of applied physiology, vol. 112, pp. 1849–1859, 2012.

[2] L. Hughes, B. Paton, B. Rosenblatt, C. Gissane, and S. D. Patterson, "Blood flow restriction training in clinical musculoskeletal rehabilitation: a systematic review and meta-analysis," British Journal of Sports Medicine, vol. 51, no. 13, pp. 1003–1011, Mar. 2017.

[3] P. M. Martin, R. M. Bart, R. L. Ashley, T. Velasco, and S. R. Wise, "An overview of blood flow restriction physiology and clinical considerations," Current Sports Medicine Reports, vol. 21, no. 4, pp. 123–128, 2022.

[4] S. J. Pearson and S. R. Hussain, "A review on the mechanisms of blood-flow restriction resistance training-induced muscle hypertrophy," Sports Medicine, vol. 45, no. 2, pp. 187–200, Sep. 2014.

[5] T. R. Montgomery, A. Olmos, K. N. Sears, P. J. Succi, S. M. Hammer, H. C. Bergstrom, E. C. Hill, M. A. Trevino, and T. K. Dinyer-McNeely, "Influence of blood flow restriction on neuromuscular function and fatigue during forearm flexion in men," Journal of Strength and Conditioning Research, vol. 38, no. 7, pp. e349–e358, Jul. 2024.

[6] L. Gizzi, U. c. Yavuz, D. Hillerkuss, T. Geri, E. Gneiting, F. Domeier, S. Schmitt, and O. Röhrle, "Variations in muscle activity and exerted torque during temporary blood flow restriction in healthy individuals," Frontiers in Bioengineering and Biotechnology, vol. 9, Mar. 2021.

[7] F. Bubeck, A. Tomalka, T. Siebert, O. Röhrle, and L. Gizzi, "Altered muscle fibre activation in an antagonistic muscle pair due to perturbed afferent feedback caused by blood flow restriction," Journal of Electromyography and Kinesiology, vol. 79, p. 102922, 2024.
[8] B. J. Edelman, S. Zhang, G. Schalk, P. Brunner, G. Müller-Putz, C. Guan, and B. He, "Non-invasive brain-computer interfaces: State of the art and trends," IEEE Reviews in Biomedical Engineering, pp. 1–25, 2024.
[9] X. Zhang, L. Yao, X. Wang, J. Monaghan, D. McAlpine, and Y. Zhang, "A survey on deep learning-based non-invasive brain signals: recent advances and new frontiers," Journal of Neural Engineering, vol. 18, no. 3, p. 031002, Mar. 2021.
[10] M. Wimpff, L. Gizzi, J. Zerfowski, and B. Yang, "Eeg motor imagery decoding: a framework for comparative analysis with channel attention mechanisms," Journal of Neural Engineering, vol. 21, no. 3, p. 036020, May 2024.
[11] Z. Khademi, F. Ebrahimi, and H. M. Kordy, "A review of critical challenges in mi-bci: From conventional to deep learning methods," Journal of Neuroscience Methods, vol. 383, p. 109736, 2023. [Online]. Available: https://www.sciencedirect.com/science/article/pii/S016502702200262X
[12] P. Brunner, "Investigating cortical representation of sensory information by means of somatosensory perturbations and magnetoencephalography," Master's thesis, University of Stuttgart, 2023.
[13] S. Taulu and M. Kajola, "Presentation of electromagnetic multichannel data: The signal space separation method," Journal of Applied Physics, vol. 97, no. 12, Jun. 2005.
[14] S. Taulu and J. Simola, "Spatiotemporal signal space separation method for rejecting nearby interference in meg measurements," Physics in Medicine and Biology, vol. 51, no. 7, pp. 1759–1768, Mar. 2006.
[15] J. Dammers, M. Schiek, F. Boers, C. Silex, M. Zvyagintsev, U. Pietrzyk, and K. Mathiak, "Integration of amplitude and phase statistics for complete artifact removal in independent components of neuromagnetic recordings," IEEE Transactions on Biomedical Engineering, vol. 55, no. 10, pp. 2353–2362, Oct. 2008.
[16] I. Zubarev, R. Zetter, H.-L. Halme, and L. Parkkonen, "Adaptive neural network classifier for decoding meg signals," NeuroImage, vol. 197, pp. 425–434, Aug. 2019.
[17] H. He and D. Wu, "Transfer learning for brain–computer interfaces: A euclidean space data alignment approach," IEEE Transactions on Biomedical Engineering, vol. 67, no. 2, pp. 399–410, Feb. 2020.
[18] Y. Lecun, L. Bottou, Y. Bengio, and P. Haffner, "Gradient-based learning applied to document recognition," Proceedings of the IEEE, vol. 86, no. 11, pp. 2278–2324, 1998.
[19] R. Li, J. S. Johansen, H. Ahmed, T. V. Ilyevsky, R. B. Wilbur, H. M. Bharadwaj, and J. M. Siskind, "The perils and pitfalls of block design for eeg classification experiments," IEEE Transactions on Pattern Analysis and Machine Intelligence, vol. 43, no. 1, pp. 316–333, 2021.
[20] J. Peksa and D. Mamchur, "State-of-the-art on brain-computer interface technology," Sensors, vol. 23, no. 13, p. 6001, Jun. 2023.
[21] S. Ioffe and C. Szegedy, "Batch normalization: Accelerating deep network training by reducing internal covariate shift," 2015.
[22] B. O. Ayinde, T. Inanc, and J. M. Zurada, "Regularizing deep neural networks by enhancing diversity in feature extraction," IEEE transactions on neural networks and learning systems, vol. 30, no. 9, pp. 2650–2661, 2019.
[23] M. M. Bejani and M. Ghatee, "A systematic review on overfitting control in shallow and deep neural networks," Artificial Intelligence Review, vol. 54, no. 8, pp. 6391–6438, 2021.
[24] X. Xu, B. Wang, B. Xiao, Y. Niu, Y. Wang, X. Wu, and J. Chen, "Beware of overestimated decoding performance arising from temporal autocorrelations in electroencephalogram signals," 2024.
[25] L. Van der Maaten and G. Hinton, "Visualizing data using t-sne." Journal of machine learning research, vol. 9, no. 11, 2008.
[26] M. B. Miller, C.-L. Donovan, C. M. Bennett, E. M. Aminoff, and R. E. Mayer, "Individual differences in cognitive style and strategy predict similarities in the patterns of brain activity between individuals," NeuroImage, vol. 59, no. 1, pp. 83–93, Jan. 2012.
[27] S. Saha and M. Baumert, "Intra- and inter-subject variability in eeg-based sensorimotor brain computer interface: A review," Frontiers in Computational Neuroscience, vol. 13, Jan. 2020.
[28] M. L. Seghier and C. J. Price, "Interpreting and utilising intersubject variability in brain function," Trends in Cognitive Sciences, vol. 22, no. 6, pp. 517–530, Jun. 2018.

Modeling Personalized Difficulty of Rehabilitation Exercises Using Causal Trees

Nathaniel Dennler[1], Zhonghao Shi[1], Uksang Yoo[2], Stefanos Nikolaidis[1], Maja Matarić[1]

***Abstract*—Rehabilitation robots are often used in game-like interactions for rehabilitation to increase a person's motivation to complete rehabilitation exercises. By adjusting exercise difficulty for a specific user throughout the exercise interaction, robots can maximize both the user's rehabilitation outcomes and the their motivation throughout the exercise. Previous approaches have assumed exercises have generic difficulty values that apply to all users equally, however, we identified that stroke survivors have varied and unique perceptions of exercise difficulty. For example, some stroke survivors found reaching vertically more difficult than reaching farther but lower while others found reaching farther more challenging than reaching vertically. In this paper, we formulate a causal tree-based method to calculate exercise difficulty based on the user's performance. We find that this approach accurately models exercise difficulty and provides a readily interpretable model of why that exercise is difficult for both users and caretakers.**

I. Introduction

Stroke is a leading cause of serious long-term disability in the United States [1]. In order to restore mobility, people affected by stroke must engage in long-term neurorehabilitation exercises. Through sustained practice of such exercises, stroke survivors can more easily complete activities of daily living (ADLs), leading to increased quality of life [2]. However, motivation is a major barrier to successfully completing rehabilitation exercises. Rehabilitation robots can increase motivation to perform neurorehabilitation exercises by physically interacting with users and adapting the difficulty of an exercise throughout the exercise session [3]. Adapting exercise difficulty provides an appropriate challenge for the user without making the exercise too difficult to complete.

Previous algorithms that adapted difficulty throughout the exercise have assumed there is only one controllable variable that changes the difficulty of the exercise, such as the distance to reach [4], speed of a virtual competitor [5], or the stiffness of a robot resisting motion [6]. In exercises that reflect daily activities, however, there are many variables that may affect difficulty for a specific user and those variables may vary greatly among people. For example, one stroke survivor may find elbow flexion easier than shoulder flexion, but another may have the opposite experience. To adjust for such differences, clinicians often manually determine exercise difficulty through careful observation of patients [7].

* This work was supported by a National Science Foundation Graduate Research Fellowship #DGE-1842487.

[1]Thomas Lord Department of Computer Science, University of Southern California, Los Angeles, CA, USA. Contact: dennler@usc.edu.

[2]Robotics Institute, Carnegie Mellon University, Pittsburgh, PA, USA.

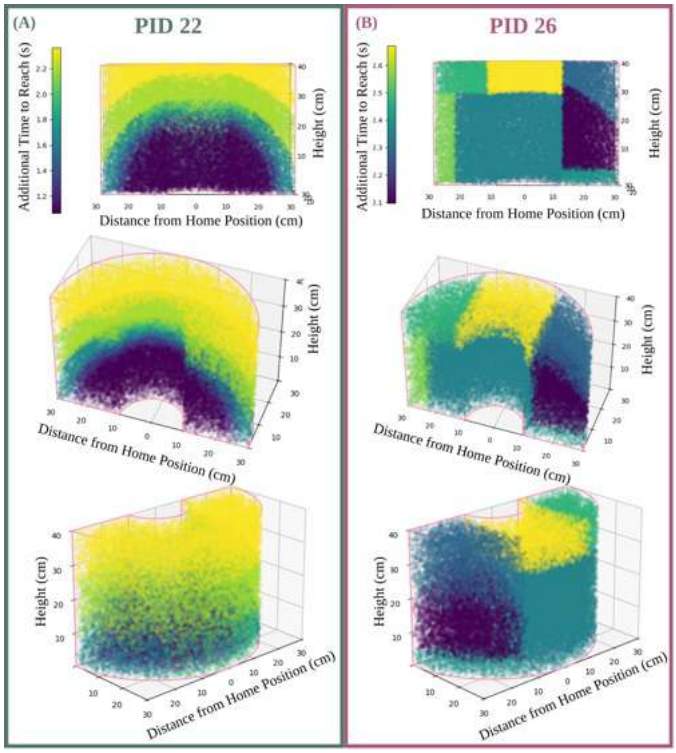


Fig. 1: Multiple views of two users' personalized difficulty scores. Lighter colors indicate regions of higher difficulty, determined by statistically significant increases in individual reach times from baseline values.

Rehabilitation robots have the potential to computationally determine exercise difficulty and subsequently perform these physical exercises. Robots can store these exercise completion data and allow both clinicians and users with limited mobility to track rehabilitation progress. This data collection process provides three key benefits that can aid in rehabilitation. First, robots can provide objective metrics that are difficult for people to accurately measure, and can communicate those objective metrics to support clinicians and stroke survivors in setting personalized goals [8]. Second, robots can encourage exercise by providing instruction and social support while reducing social pressure during the exercise [9]. Finally, robots in homes can provide flexible and consistent access to exercise support for users.

In this work, we present a general algorithm for learning personalized difficulty metrics for rehabilitation exercises from

user data. We designed this algorithm to provide explainable reports for both users and clinicians to understand personal difficulty levels, as shown in Fig. 1. We evaluate the proposed algorithm using data collected from 15 stroke survivors performing a reaching task with a physically assistive robot arm and a socially assistive robot companion.

II. Related Work

Previous work on quantifying exercise difficulty has generally taken one of two approaches. One approach has been to assess the difficulty associated with several specific motor movements in isolation [6], [10], while the other approach has used concepts from control theory to assist people throughout entire tasks as needed [11], [12].

Assessing task difficulty through specific movements in isolation can create a very detailed understanding of personal differences when performing movements such as pinching, elbow flexion, and arm supination [10]. Past work used these assessments to initialize difficulty levels for a variety of rehabilitation games [6]. Assessing individual movements in isolation, however, may not directly transfer to tasks that holistically evaluate combinations of those movements. This is important because activities of daily living involve combinations of many motor functions working together rather than individual motor functions.

In control theory-based approaches, robots adapt in real time to a user to account for the user's level of mobility and other aspects that affect performance, such as fatigue [12]. Often, those approaches rely on exo-skeleton-type assistance to obtain a continuous control signal such as torque exerted by the user [11]. In end-effector rehabilitation robots, however, the control signal is typically more sparse. The decision to increase or decrease difficulty can be made after the task is achieved; for example, after an opponent scores in a game [3] or after the user performs a reaching task [4]. In such approaches, parameters of the exercise are increased by a fixed amount, but that approach does not always correspond to a fixed increase in exercise difficulty.

In this work we aim to augment existing approaches by developing an algorithm that estimates how difficult a task is based on features of that task. Consequently, adaptive rehabilitation exercises can make meaningful difficulty adjustments that correspond to individualized difficulty measurements.

III. Modeling Personalized Difficulty

The Challenge Point Framework (CPF) [13] is a motor learning framework that identifies that there is an optimal level of task difficulty to best acheive task improvement. CPF describes two kinds of task difficulties: *nominal task difficulty* and *functional task difficulty*. *Nominal difficulty* refers to the intrinsic difficulty of a task, regardless of the person performing it. *Functional difficulty* refers to difficulty of a task relative to the skill of the person performing the task.

Quantitatively estimating the difference between nominal difficulty and functional difficulty can be challenging due to the high variance in performance measurements for the same task. To address this measurement variance, we leverage advances from works that estimate heterogeneous treatment effects from patient covariates [14]. Algorithms that estimate treatment effects identify factors that significantly impact outcome measurements, which is highly related to the problem of quantifying task difficulty. At a high level, we learn nominal difficulty by leveraging data collected from neurotypical users completing rehabilitation tasks, and we learn functional difficulty by leveraging the data collected from a specific post-stroke user engaged in the same rehabilitation task.

In order to apply this approach to difficulty estimation, we must make two assumptions. First, we assume that exercises have at least one continuous and measurable outcome, for example the time to complete the exercise, that we will denote as Y. Second, we assume that there are d numerical exercise characteristics that can be modified, e.g., the (x, y, z) location that a user should reach to, that we denote as $X \subset \mathbb{R}^d$. We can use the potential outcomes framework [15] to formalize individual exercise difficulty for task $\vec{x} \in X$ as:

$$\tau(\vec{x}) = \mathbb{E}\left[Y^{(1)} - Y^{(0)} | X = \vec{x}\right] \tag{1}$$

Where $Y^{(1)}$ denotes the outcome measure of a post-stroke user performing the exercise $\vec{x}$ and $Y^{(0)}$ denotes the outcome measure of a neurotypical user performing exercise $\vec{x}$, i.e., the nominal task difficulty. The quantity $\tau(\vec{x})$ denotes the functional difficulty of exercise $\vec{x}$.

Estimating $\tau(\vec{x})$ directly is challenging because Y_i can be noisy due to unmodeled aspects of the task. For example, if the outcome measure is time to completion and a participant is distracted and misses the cue to begin the exercise, they will take longer than usual to reach to the specified (x, y, z) location. Averaging outcome measures of nearby exercises that the user has performed reduces such noise.

Thus, previous works have found that creating a causal decision tree is a robust technique to determine the nearby points in X that should be included when calculating $\tau(\vec{x})$ [14]. Decision trees iteratively partition X by calculating a splitting rule that separates X into two regions, X_{left} and X_{right}. An example splitting rule may be $\vec{x}_z < 0.4m$, where X_{left} consists of all reaching tasks lower than 0.4 meters and X_{right} consists of all reaching tasks higher than 0.4 meters. The specific rule is selected by finding the exercise characteristic that results in the greatest difference in functional difficulty between X_{left} and X_{right}. Formally, the causal tree learns a function $L(\vec{x})$ that assigns each exercise $\vec{x} \in X$ to a unique set L, called a leaf. The estimated functional difficulty for each leaf L is expressed as a difference of averages:

$$\hat{\tau}(\vec{x}) = \frac{1}{|L|} \sum_{\vec{x} \in L} Y^{(1)} - \frac{1}{|L|} \sum_{\vec{x} \in L} Y^{(0)} \tag{2}$$

For more details on the algorithm we used to create the tree, refer to Wagner and Athey [14]. In summary, the causal tree is created using labeled examples from a neurotypical population, $(\vec{x}, Y^{(0)})$ and a single post-stroke participant $(\vec{x}, Y^{(1)})$.



Fig. 2: A post-stroke participant performing a reaching exercise. The Socially Assistive Robot (left) provided instructions and feedback. The robot arm (right) moved the reaching target in front of the user. The user reached to the button 100 times using their more affected side.

The tree can then be used to predict the functional difficulty $Y^{(1)}$ for a given task $\vec{x}$ for the single post-stroke participant.

IV. User Study

To evaluate our technique for estimating individualized user difficulty for a reaching exercise. We collected data from 10 neurotypical participants to use as a baseline value, and we collected data from 15 post-stroke participants to asses how well our approach models individual differences in difficulty. The full user study procedure is detailed by Dennler et al. [9] and only briefly summarized here for context.

A. System Description

Our robotic system that encouraged users to perform reaching exercises, pictured in Fig. 2, consisted of a robot arm and a socially assistive robot (SAR). The robot arm was the Kinova JACO2 assistive arm selected because it is lightweight and has the similar affordances as end-effector robots typically used for other rehabilitative interactions that have been shown to be effective for neurorehabilitation [16]. The SAR was the Lux AI QTRobot that consisted of a screen face running PyLips [17], a 2 degree-of-freedom head, and two 3 degree-of-freedom arms. This SAR platform had previously been validated in motivational rehabilitation games with children with cerebral palsy [18]. The purpose of the SAR was to communicate instructions to the participant, provide positive social reinforcement, and initiate each exercise. This function is similar to previous SAR use in other rehabilitation contexts [18], [19].

We additionally created two low-cost devices to facilitate the reaching exercise. Both were 3D printed and communicated with the robot system via WiFi using an Adafruit Feather M0 development board. One of the devices was a target object that the Kinova arm held in its end-effector for the users to reach for. The target object consisted of a plastic button with an LED light that turned on to indicate the user should press it. The other device was a home position block for the participant to return to after each reaching exercise. The block consisted of two contact sensors that were 2cm in diameter for participants to rest their left and right pointer fingers. The home position block was placed in front of the midline of the participant and the participant's chair was adjusted so that the participant's elbows formed a right angle when resting their hands on the home position block. The chair also used a harness to minimize compensatory trunk movement during the reaching task.

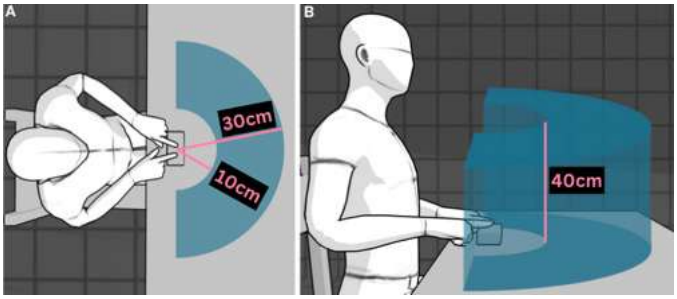


Fig. 3: Participants' workspace. The arm moved the target to different points within the blue-shaded region to estimate difficulty.

B. Procedure

All procedures were approved by the University of Southern California institutional review board under #UP-22-00461. Before beginning the exercise session, the experimenter generated a set of 100 evenly-spaced points in a workspace in front of the home position block, visualized in Fig. 3. This workspace was defined as a region that extends radially from the home position from 10cm to 30cm in a 180 degree arc. The region extended from 0–40cm above the table. The order of these 100 points was then randomized.

Before the participants began the experiment, they signed the consent form. A board-certified physical therapist specializing in neurorehabilitation with more than two years of experience performed the Fugl-Meyer Upper Extremity Motor assessment [20] and the experimenter performed the Mini Mental State Exam [21] to determine eligibility. Participants were eligible to participate if they scored higher than 25 out of 66 on the Fugl-Meyer assessment and scored higher than 25 of 30 on the Mini Mental State Exam.

When the participant began the experiment, the SAR provided instructions about the reaching task to inform the participant what would happen. The robot arm then moved to the first randomized point. The light on the target button turned on, and the SAR cued the person to reach to the button by saying "move", "ok", "reach", or "now". The participant reached to the button with their more affected side. When they pressed the button, the light turned off and the time to reach the button was logged to a file. The SAR periodically provided feedback at random intervals to encourage the participant such as "Awesome job! That was great.", "I'm glad to see that you're working hard.", and "Well done, <Participant's Name>". The participant returned to the home position and

TABLE I: Demographic information of the neurotypical group

	Median	Minimum	Maximum
Age (years)	69.5	45	82
Gender	5 Men, 5 Women		
Ethnicity	2 Asian, 2 Black, 6 White		

TABLE II: Demographic information of the post-stroke group

	Median	Minimum	Maximum
FM-UE Motor Score (66 maximum)	59	27	64
Age (years)	55	32	85
Time between sessions (days)	6.5	4	19
Gender	9 Men, 6 Women		
Affected Side	6 Left, 9 Right		
Ethnicity	4 Asian, 3 Black, 4 Hispanic, 3 White, 1 Mixed-race		

Abbreviations: FM-UE, Fugl-Meyer Upper Extremity;

the robot moved to the next randomized point. This was repeated for all 100 points. The SAR updated the participant on their progress at the 25%, 50%, and 75% completion points by saying statements such as "Three-quarters done! Almost there!".

Each Neurotypical participant completed the procedure once. Each post-stroke participant repeated this procedure up to three times, with at least four days between each consecutive visit. This allowed us to assess the transferability of our approach across sessions.

C. Participants

We first recruited neurotypical participants to model nominal task difficulty and to adjust any system errors before evaluating on our target population of stroke survivors. This practice helps to minimize the chance of any unforeseen risk to marginalized populations, such as post-stroke participants. All neurotypical participants were right-hand dominant; their demographic information is summarized in Table I. The average age of neurotypical participants was 67 $\pm$ 10 years.

We found no major issues with the setup after neurotypical participants completed their exercises. We then recruited post-stroke participants to collect data to model functional task difficulty. All post-stroke participants were premorbidly right-hand dominant. Two participants did not meet the study criteria after screening. Thirteen of the remaining fifteen participants completed all three sessions, and two participants completed two sessions due to scheduling constraints. The average age of post-stroke participants was 57 $\pm$ 11 years; demographic information is summarized in Table II.

V. Results

A. Dataset Overview

We collected two datasets: the neurotypical dataset and the post-stroke dataset. Both datasets used time to reach as the outcome measure, Y, and the following numerical exercise characteristics that define each exercise in X: (1) x-position, (2) y-position, (3) z-position, (4) x-position squared—to reflect distance from the participant's midline, (5) distance from home position, and (6) the cue the robot gave to the participant to begin the reaching trial—measured as a categorical variable with four levels.

TABLE III: Hyperparameters used for our experiments.

Model	Hyperparameters
Causal Forest (Ours)	*n_estimators=100, min_samples=5*
XGBoost	n_estimators = 200, learning_rate=0.2, max_depth=7
Random Forest	n_estimators=100, max_depth=100
Neural Network	hidden_sizes=(50, 50), learning_rate=1e-3, max_iter=500
SVM	C=10, gamma=0.0001, kernel='rbf'
k-Nearest Neighbors	n_neighbors=15, weights ='distance', metric='manhattan'
Decision Tree	max_depth=10, min_samples_split=10, min_samples=4

B. Evaluation Procedure

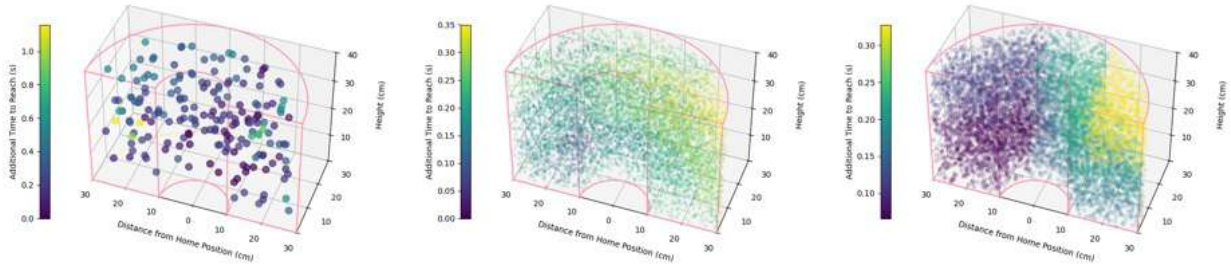
Our Method. We evaluated our method as described in Sec. III. First, we concatenated the training datasets of the participant and the neurotypical population. We created a group-level variable called "condition" and marked entries from the participant as "1" and entries from the neurotypical group as "0". We trained the tree using the econML package [22] with the column "condition" as the treatment variable.

Baselines. The key advantage of using causal trees is that they reduce variance in each leaf by jointly reasoning about the neurotypical and post-stroke exercise variance, i.e., learning both nominal and functional difficulty *simultaneously*. Thus, we evaluate our approach using baselines that attempt to estimate the outcome for each group *separately* and subtract the two estimates, i.e., the baselines were of the form $f_s(\vec{x}) - f_n(\vec{x})$, where f_s is a machine learning model that directly estimates the time to reach for the post-stroke participant ($Y^{(1)}$) and f_n is a machine learning model that estimates the time to reach for all neurotypical participants ($Y^{(0)}$). We evaluated with the following machine learning models as baselines: Decision Tree, Random Forest, Neural Network, Support Vector Machine, k-Nearest Neighbors.

Ground Truth. We are interested in modeling the functional difficulty of the participant, as this difficulty indicates what exercises should be assigned under the Challenge Point Framework. We define the ground truth functional difficulty for a given participant for the exercise $\vec{x}$ in the workspace as the average time of a single post-stroke participant reaches within a ball with a radius of 5cm centered at $\vec{x}$ minus the average time of all neurotypical participant reaches within the same 5cm ball. Because this value includes data from all of the participant reaches, this serves as an accurate measure of the actual time difference between the participant and the neurotypical group.

C. Training Details

We are interested in estimating the personal functional difficulty of a participant. To evaluate this, we aggregated each user's data across visits, so each participant corresponded to a dataset of up to 300 reaches. We split each dataset into 80% training and 20% testing. We used the same neurotypical dataset as the baseline for all participants, reflective of a real-world use case where baseline data are collected prior to system deployment.



(a) PID 33 ground truth. (b) PID 33 XGBoost map of difficulties. (c) PID 33 causal map of difficulties

Fig. 4: Visual comparison of methods. We show the user's ground truth difference from the neurotypical population (a). Independently estimating the stroke survivor and neurotypical data leads to homogenous difficulty estimates over the workspace (b). Using causal trees instead provides distinctive regions of differences in difficulty that are robust to outliers (c).

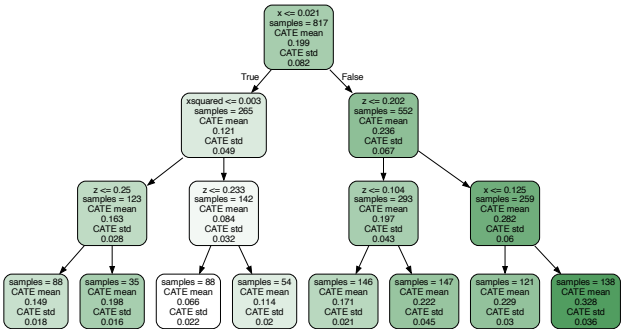


Fig. 5: Tree interpretation of the difficulty map for PID 33.

We randomly selected five participants to tune hyperparameters for all of the algorithms, and used the other participants to evaluate the algorithms. This ensures we do not leak any information from the training set into the testing set. We present the hyperparameters we used for each of the algorithms we tested in Table III. We evaluated across 20 random seeds.

D. Personalized Functional Difficulty Estimation

To evaluate each model, we perform a *within-subject evaluation* and a *aggregated evaluation*. We present our results in Table IV. The *within-subject evaluation* used the mean-squared error (MSE) metric to assess the average difference between predicted and actual functional difficulty, expressed in seconds squared for each participant, we then averaged each participant's MSE to report the final value. We found that causal trees have the lowest MSE of all baseline methods, achieving an MSE of .3 s^2. Our *aggregated evaluation* calculated the r^2 value across all participants' predicted and actual functional difficulty, expressed as a proportion of explained variance to total variance. Causal trees also perform the better than all the baselines we tested, with an r^2 that indicates that 82.6% of the variance in times are explained with this approach. These results indicate that causal trees result in better user models compared to non-causal approaches because they can better reason about uncertainty. We qualitatively compare the causal tree approach and the best performing baseline for PID 33 in Fig. 4, showing that causal trees lead to clearer regions of varied difficulties.

TABLE IV: Personalized functional difficulty results. Arrows indicate the direction of better performance for each metric.

Model	MSE ↓ ($\pm SE$)	agg. r^2 ↑ ($\pm SE$)
Causal Forest (Ours)	**.300 ± .019**	**.826 ± .006**
XGBoost	.324 ± .021	.812 ± .006
Random Forest	.337 ± .021	.805 ± .006
Neural Network	.345 ± .022	.800 ± .006
Support Vector Machine	.488 ± .020	.718 ± .008
k-Nearest Neighbors	.380 ± .024	.780 ± .006
Decision Tree	.745 ± .045	.571 ± .011

E. Visualization of Difficulty

Fig. 4 and Fig. 5 illustrates two techniques to visualize our approach for estimating individual difficulty metrics. In the workspace view (Fig. 4), we show the regions of similar exercise difficulty spatially. These areas are distinctive, which allows clinicians or rehabilitation robots to sample from a particular region in the space to manage difficulty while providing slightly different exercises.

The tree view (Fig. 5) is an explainable diagram that shows how the causal tree splits regions of the workspace based on the user's performance. Each node is colored with the difficulty level; darker colors indicate more difficult exercise regions. Each level of the tree shows different granularities of exercise difficulty. For example, if a rehabilitation specialist only cares about two levels of difficulty, they can examine the second level of the tree, but if they want to reason about eight levels of difficulty, they can examine the fourth level of the tree.

VI. Discussion

This work presented an algorithm that estimates nominal and functional exercise difficulty given a set of exercise parameters and outcome measures. We evaluated this technique on a reaching task performed by both neurotypical participants and post-stroke participants. We found that our method results in more accurate estimations of personalized functional difficulty.

A key benefit of this approach is that it can be applied to other kinds of exercises and outcome measures to estimate difficulty and facilitate adaptation. For example, previous work that adapts tasks based on physiological features [23] or

game performance [3] could leverage this approach to select specific exercises with target difficulty levels. This additionally provides a principled technique for determining difficulty for a variety of tasks, which can encourage the development of new exercises that have various adaptable characteristics, such as in serious games [3].

Limitations. We evaluated our algorithm on a difficulty value based on time to reach. However, there are many metrics that are important for assessing difficulty. For example, movement quality is typically a metric of interest for clinicians and users with limited mobility [2]. Future work may leverage computer vision techniques to predict movement quality as a separate metric and frame personalized functional difficulty modeling as a multi-outcome causal inference problem. Other future work may design metrics that factor both time and quality into a single value to use as an outcome metric.

We additionally only evaluated our difficulty estimation technique on a reaching task. Other tasks may involve other numerical exercise characteristics, such as stiffness for an arm that users push against, which may be more difficult to visualize for users. Future work may evaluate personalized functional difficulty modeling on different tasks, as well as iterate over data visualizations to understand how to effectively communicate these difficulty models to users and clinicians.

Conclusion. We presented a technique for learning individualized models of user difficulty based on causal trees. We found that jointly modeling neurotypical and stroke survivor performance better estimates exercise difficulty compared to separately estimating these quantities, which we evaluated across several stroke survivors. Causal trees provide readily interpretable visualizations that can aid in communication between clinicians and stroke survivors. We hope that this technique opens new directions for adaptable and personalized rehabilitation practices.

APPENDIX

We provide the code used in this experiment at `https://github.com/interaction-lab/stroke-exercise-difficulty-estimation`.

REFERENCES

[1] C. W. Tsao, A. W. Aday, Z. I. Almarzooq, A. Alonso, A. Z. Beaton, M. S. Bittencourt, A. K. Boehme, A. E. Buxton, A. P. Carson, Y. Commodore-Mensah *et al.*, "Heart disease and stroke statistics—2022 update: a report from the american heart association," *Circulation*, vol. 145, no. 8, pp. e153–e639, 2022.

[2] C. Winstein, B. Kim, S. Kim, C. Martinez, and N. Schweighofer, "Dosage matters: a phase iib randomized controlled trial of motor therapy in the chronic phase after stroke," *Stroke*, vol. 50, no. 7, pp. 1831–1837, 2019.

[3] M. Goršič, A. Darzi, and D. Novak, "Comparison of two difficulty adaptation strategies for competitive arm rehabilitation exercises," in *2017 international conference on rehabilitation robotics (ICORR)*. IEEE, 2017, pp. 640–645.

[4] R. Colombo, F. Pisano, A. Mazzone, C. Delconte, S. Micera, M. C. Carrozza, P. Dario, and G. Minuco, "Design strategies to improve patient motivation during robot-aided rehabilitation," *Journal of neuroengineering and rehabilitation*, vol. 4, pp. 1–12, 2007.

[5] L. Zimmerli, M. Jacky, L. Lünenburger, R. Riener, and M. Bolliger, "Increasing patient engagement during virtual reality-based motor rehabilitation," *Archives of physical medicine and rehabilitation*, vol. 94, no. 9, pp. 1737–1746, 2013.

[6] J.-C. Metzger, O. Lambercy, A. Califfi, D. Dinacci, C. Petrillo, P. Rossi, F. M. Conti, and R. Gassert, "Assessment-driven selection and adaptation of exercise difficulty in robot-assisted therapy: a pilot study with a hand rehabilitation robot," *Journal of neuroengineering and rehabilitation*, vol. 11, no. 1, pp. 1–14, 2014.

[7] M. Sommerhalder, N. Kurth, J. Song, and R. Riener, "Armstick-an intuitive therapist interface for upper-limb rehabilitation robots," in *2022 International Conference on Rehabilitation Robotics (ICORR)*. IEEE, 2022, pp. 1–6.

[8] M. Demers, A. Cain, L. Bishop, T. Gunby, J. B. Rowe, D. K. Zondervan, and C. J. Winstein, "Understanding stroke survivors' preferences regarding wearable sensor feedback on functional movement: a mixed-methods study," *Journal of NeuroEngineering and Rehabilitation*, vol. 20, no. 1, p. 146, 2023.

[9] N. Dennler, A. Cain, E. De Guzman, C. Chiu, C. J. Winstein, S. Nikolaidis, and M. J. Matarić, "A metric for characterizing the arm nonuse workspace in poststroke individuals using a robot arm," *Science Robotics*, vol. 8, no. 84, p. eadf7723, 2023.

[10] M. L. Woodbury, K. Anderson, C. Finetto, A. Fortune, B. Dellenbach, E. Grattan, and S. Hutchison, "Matching task difficulty to patient ability during task practice improves upper extremity motor skill after stroke: a proof-of-concept study," *Archives of physical medicine and rehabilitation*, vol. 97, no. 11, pp. 1863–1871, 2016.

[11] H. J. Asl, T. Narikiyo, and M. Kawanishi, "An assist-as-needed control scheme for robot-assisted rehabilitation," in *2017 American control conference (ACC)*. IEEE, 2017, pp. 198–203.

[12] A. Basteris and F. Amirabdollahian, "Adaptive human-robot interaction based on lag-lead modelling for home-based stroke rehabilitation: Novel mechanisms for assessment and performance based adaptation of task difficulty," in *2013 IEEE International Conference on Systems, Man, and Cybernetics*. IEEE, 2013, pp. 3414–3419.

[13] M. A. Guadagnoli and T. D. Lee, "Challenge point: a framework for conceptualizing the effects of various practice conditions in motor learning," *Journal of motor behavior*, vol. 36, no. 2, pp. 212–224, 2004.

[14] S. Wager and S. Athey, "Estimation and inference of heterogeneous treatment effects using random forests," *Journal of the American Statistical Association*, vol. 113, no. 523, pp. 1228–1242, 2018.

[15] D. B. Rubin, "Estimating causal effects of treatments in randomized and nonrandomized studies." *Journal of educational Psychology*, vol. 66, no. 5, p. 688, 1974.

[16] S. H. Lee, G. Park, D. Y. Cho, H. Y. Kim, J.-Y. Lee, S. Kim, S.-B. Park, and J.-H. Shin, "Comparisons between end-effector and exoskeleton rehabilitation robots regarding upper extremity function among chronic stroke patients with moderate-to-severe upper limb impairment," *Scientific Reports*, vol. 10, no. 1, pp. 1–8, 2020.

[17] N. S. Dennler, E. Torrence, U. Yoo, S. Nikolaidis, and M. Mataric, "Pylips: an open-source python package to expand participation in embodied interaction," in *Adjunct Proceedings of the 37th Annual ACM Symposium on User Interface Software and Technology*, 2024, pp. 1–4.

[18] N. Dennler, C. Yunis, J. Realmuto, T. Sanger, S. Nikolaidis, and M. Matarić, "Personalizing user engagement dynamics in a non-verbal communication game for cerebral palsy," in *2021 30th IEEE International Conference on Robot & Human Interactive Communication (RO-MAN)*. IEEE, 2021, pp. 873–879.

[19] R. Feingold-Polak, O. Barzel, and S. Levy-Tzedek, "A robot goes to rehab: a novel gamified system for long-term stroke rehabilitation using a socially assistive robot—methodology and usability testing," *Journal of NeuroEngineering and Rehabilitation*, vol. 18, no. 1, pp. 1–18, 2021.

[20] A. R. Fugl-Meyer, L. Jääskö, I. Leyman, S. Olsson, and S. Steglind, "A method for evaluation of physical performance," *Scand. J. Rehabil. Med*, vol. 7, no. 1, pp. 13–31, 1975.

[21] M. F. Folstein, S. E. Folstein, and P. R. McHugh, ""mini-mental state": a practical method for grading the cognitive state of patients for the clinician," *Journal of Psychiatric Research*, vol. 12, no. 3, pp. 189–198, 1975.

[22] M. EconML, "Econml: A python package for ml-based heterogeneous treatment effects estimation," 2019.

[23] N. Shirzad and H. M. Van der Loos, "Adaptation of task difficulty in rehabilitation exercises based on the user's motor performance and physiological responses," in *2013 IEEE 13th international conference on rehabilitation robotics (ICORR)*. IEEE, 2013, pp. 1–6.

Optimizing Cross-Modal Matching for Multimodal Motor Rehabilitation

Anway S. Pimpalkar
Dept. of Biomedical Engineering
Johns Hopkins University
Baltimore, MD, USA
apimpal1@jhu.edu

A. Michael West Jr.
Dept. of Mechanical Engineering
Johns Hopkins University
Baltimore, MD, USA
awest36@jhu.edu

Jing Xu
Dept. of Kinesiology
University of Georgia
Athens, GA, USA
jing.xu@uga.edu

Jeremy D. Brown
Dept. of Mechanical Engineering
Johns Hopkins University
Baltimore, MD, USA
jdelainebrown@jhu.edu

***Abstract*—Stroke often causes sensorimotor deficits, impairing hand dexterity and disrupting independence for millions worldwide. While rehabilitation devices leveraging visual and haptic feedback show promise, their effectiveness is limited by a lack of perceptual equity, which is necessary to ensure fair comparisons between sensory modalities. This study refines cross-modal matching protocols to address this gap, enabling unbiased evaluation of multimodal feedback. Using the Hand Articulation and Neurotraining Device (HAND), 12 healthy participants matched visual and haptic stimuli in a structured task. A streamlined protocol, requiring just 2–3 blocks and 3 reference intensities, reduced experimental time fivefold while preserving data integrity. Data were analyzed using linear and exponential models applied to both full and reduced datasets. The results demonstrated consistent participant performance across trials, with higher matching errors at greater stimulus intensities, likely attributable to sensory saturation effects. Furthermore, the study offered practical methodological insights, including the use of reduced data sampling paradigms to enhance experimental efficiency significantly while preserving data integrity. This work advances perceptual equity in multisensory feedback systems, addressing sensory encoding variability to support scalable, personalized therapeutic strategies for stroke recovery.**

***Index Terms*—Cross-modal Matching, Perception, Haptic Feedback, Vibrotactile Feedback, Dexterity, Rehabilitation**

I. Introduction

The human hand is fundamental to performing essential activities of daily living, such as grasping, manipulating objects, and executing precise movements. However, hand dexterity is often compromised by neurological conditions like stroke, which impacts over 12.2 million individuals globally each year [1]. The loss of hand functionality not only reduces independence and quality of life but also places significant physical, emotional, and economic burdens on individuals [2].

Efforts to address this challenge have driven the development of innovative strategies to restore hand dexterity post-stroke. Among these approaches, hand rehabilitation devices have shown significant promise by leveraging advancements in robotics, neurorehabilitation, and haptic feedback to promote motor recovery and neural plasticity [3], [4]. Despite these advances, challenges remain in ensuring the accessibility, personalization, and effectiveness of these devices to meet the diverse needs of stroke patients [5].

The Hand Articulation and Neurotraining Device (HAND) was co-developed by Carducci, Xu, and their collaborators [6], [7] to explore individuated finger control and multidimensional co-activation patterns following stroke. Here, we focus on adapting the HAND to study the pinch grasp, a critical fine motor skill required for handling delicate or brittle objects. Pinch grip deficits, often observed in stroke patients, are linked to impairments in sensorimotor processing pathways. These deficits result in diminished tactile and proprioceptive feedback, reducing the ability to accurately modulate grip forces and perform everyday tasks independently [8].

While many existing rehabilitation devices rely heavily on visual feedback for training and recovery [9], evidence suggests that visual feedback alone is insufficient to optimize motor recovery outcomes [10]. Recent studies highlight the potential of integrating multisensory feedback, particularly haptic cues, to promote neural plasticity and enhance functional motor rehabilitation [11]. In this work, we aim to understand how multisensory feedback should best be provided in the HAND by utilizing visual and haptic cues to augment somatosensory pathways. By addressing these gaps, this study contributes to advancing therapeutic strategies and optimizing neurorehabilitation outcomes for stroke patients.

Sensory and motor deficits arising from stroke manifest in diverse and highly individualized ways, resulting in variations in how stimuli are perceived across individuals [10]. To effectively leverage multisensory feedback in rehabilitation, it is crucial for sensorimotor tasks to account for such variability and ensure fairness across modalities. Establishing *perceptual equity* – ensuring that any observed differences in performance between visual and haptic feedback reflect true differences in sensory encoding rather than biases introduced by the experimental setup — is essential for accurately comparing the efficacy of these modalities in healthy participants. This process, known as cross-modal matching, involves calibrating sensory intensities to establish a balance between modalities, enabling fair and unbiased comparisons [12], [13].

Cross-modal matching provides a standardized framework to evaluate the encoding and integration of sensory information across modalities, ensuring perceptual equity by aligning stim-

This work was supported by the National Institute of Neurological Disorders and Stroke (NINDS) of the NIH under Award Number R01NS130210 and by the Johns Hopkins University Provost's Postdoctoral Fellowship.

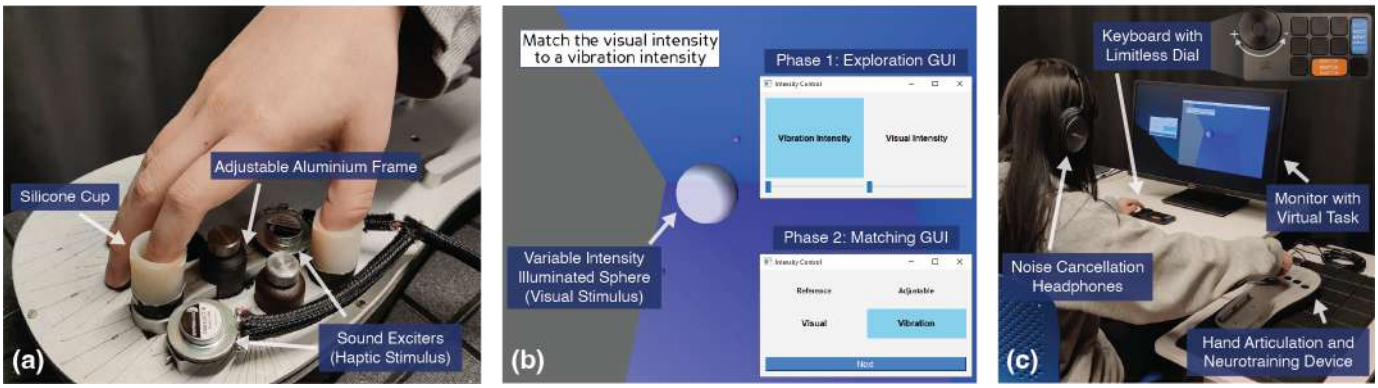


Fig. 1. A modified Hand Articulation and Neurotraining Device (HAND) [6], [7] setup used in this study. (a) Participants interact with the device by placing their fingers in silicone cups mounted on an aluminum frame, with vibrating voice coils providing mechanical haptic stimuli. (b) The virtual task includes a variable-brightness sphere for visual feedback and two user interfaces: the exploration phase, where reference sliders are present, and the matching phase, where no reference sliders are displayed. (c) Wearing noise-canceling headphones, participants use a limitless keyboard dial to adjust the intensity of the presented feedback. Feedback is either haptic – delivered through the HAND or visual – rendered within a virtual task.

ulus intensities. This process is crucial for isolating genuine differences in sensory encoding from biases introduced by experimental setups. However, it can be time-consuming and variable across individuals, which poses a significant challenge, particularly for stroke patients who often experience fatigue during extended tasks [14]. To address these issues, one of the critical aims of this study is to develop pre-experiment cross-modal matching protocols that streamline the process, minimize fatigue, and maintain accuracy. We believe the guidelines derived from this study with healthy individuals will provide a foundational framework for developing efficient, reliable methods in neurorehabilitation research with stroke patients, seamlessly integrating with existing clinical techniques.

II. Methods and Implementation

A. Participants

We evaluated the ability of N=12 individuals with no history of stroke or upper-extremity disabilities (5 males and 7 females; mean age: 25.2±6.1 years; 9 right-handed, 1 left-handed, and 2 ambidextrous) to match the intensity of one feedback modality to an equivalent intensity of another using a custom rehabilitation interface under two distinct feedback conditions. Each participant's handedness was assessed using the Laterality Quotient derived from the administered Edinburgh Handedness Inventory after obtaining their consent [15]. The experiment lasted approximately 60 minutes, and participants were compensated at a rate of $10 per hour. All participants provided informed consent in accordance with a protocol approved by the Johns Hopkins School of Medicine Institutional Review Board (Study #IRB00209185).

B. Experimental Setup

The study utilized a modified Hand Articulation and Neurotraining Device (HAND) built and validated in prior studies [6], [7]. The HAND includes two silicone cups mounted on an aluminum frame, precisely positioned to naturally align with each participant's index finger and thumb, allowing for a customized and comfortable fit as shown in Fig. 1(a). The device is set up for the participants' right hand, and all participants, regardless of handedness, use the same configuration. Each cup is mechanically coupled with a Dayton Audio DAEX13CT-8 Sound Voice Coil, which provides the vibrotactile haptic feedback necessary for the tasks.

The voice coils are driven through a custom amplifier board controlled by a 600 MHz Teensy 4.0 microcontroller. This microcontroller communicates with the primary control software, a Python script running on the computer via a serial interface. The virtual task program transmits 9-bit values to the Teensy, which adjusts the intensity of the voice coil output. Upon receiving these values, the microcontroller employs a MAX521BCPP digital-to-analog converter (Maxim Integrated) and a TPA3122D2 Class-D audio power amplifier (Texas Instruments) to generate 250 Hz sine waves with a variable peak-to-peak voltage range of 0 to 7 V. These signals drive the voice coils, delivering haptic stimuli to participants.

The virtual task consists of a 3D environment featuring a centrally positioned, fixed-size gray sphere illuminated by a distant light source, as shown in Fig. 1(b). The sphere's brightness is adjusted to provide visual stimuli, matching the 9-bit resolution used for the haptic stimuli generated by the voice coils. The virtual environment is created in Python 3.6 and rendered using Panda3D Open Source Framework.

C. Cross-modal Matching Implementation

To ensure fairness and perceptual equity in neurorehabilitation experiments, cross-modal matching is essential for calibrating stimulus intensities across modalities, ensuring that observed differences reflect genuine sensory encoding rather than experimental bias. Building on this principle, we implemented a cross-modal matching task based on the paradigm developed by Pitts et al. [12], [13], constructing participant-specific psychometric curves to align haptic and visual stimulus intensities. The participants were instructed to sit in front of a monitor running the virtual task and rest their

right hand comfortably on the HAND as shown in Fig.1(c). Participants wore noise-canceling headphones that played 60 Hz white noise at a comfortable volume to eliminate potential auditory interference from the voice coils. The experiment was broken into two phases.

1) Intensity Exploration: In the first phase, participants used a graphical user interface (GUI) to explore the full range of vibrotactile and visual stimulus intensities for two minutes. The stimuli were presented continuously, with their intensities adjustable via a limitless dial on an XPPen ACK05 wireless shortcut keyboard (XPPen, China) as shown in Fig. 1(c). Two sliders on the screen indicated stimulus intensity being presented in real time. A clockwise click on the dial increased the intensity, while a counterclockwise click decreased it by 1 unit within a range of 0 to 255. A designated button on the keyboard allowed participants to toggle between the two modalities during the exploration phase, enabling them to choose which modality to adjust. Participants were instructed to familiarize themselves with the full ranges of the haptic and visual stimuli and their correlation, using the sliders as a reference. They were informed that the sliders would not be available in the subsequent phase.

2) Intensity Matching: In the intensity matching phase, participants were tasked with aligning the intensity of one sensory modality (haptic or visual) to a reference intensity provided in the other modality. This involved two distinct conditions: a haptic reference modality, where participants matched the visual stimulus to a given haptic intensity, and a visual reference modality, where they matched the haptic stimulus to a given visual intensity.

Following this setup, participants completed two experimental blocks in each condition. Specifically, participants used the same limitless dial configuration as in the intensity exploration phase to adjust the intensity of one stimulus to match a given reference stimulus. However, in this phase, the sliders were no longer displayed. Participants were allotted 90 seconds to submit their matched intensity for each trial, after which the current value was automatically recorded if the time limit was exceeded. Eight reference intensities, normalized and evenly distributed within the range of 0 to 1 (excluding endpoints), were used. The 8 reference intensities were shown 4 times in a block randomized order for a total of 32 trials. The sequence of reference intensities was maintained across both blocks. The order in which haptic and visual reference stimuli were presented, whether the haptic or visual modality served as the reference first, was counterbalanced across participants.

Upon completing each block, participants completed the NASA Task Load Index (NASA-TLX) questionnaire to evaluate cognitive workload [16]. At the conclusion of the session, participants were asked for a description of their strategies.

D. Data Analysis

We obtained two datasets for each participant: (1) the visual reference experiment and (2) the haptic reference experiment. Before analysis, the matched intensity was normalized such that values ranged from 0 to 1. This enabled a one-to-one relationship between the two modalities. The following analyses of these datasets will aim to (1) compare participants' performance across the two experimental conditions and (2) develop a protocol to help future researchers find participant-specific models that ensure perceptual equity in multimodal motor control experiments.

1) Comparing Dataset and Fit: We compared two different modeling approaches for deriving participant-specific models: a linear model and an exponential model. The linear model was selected because the experimental protocol inherently established a linear relationship between the haptic and visual modalities. Additionally, we included the exponential model because it has been employed in prior research [13], [17]. Thus, for each participant and experiment, the observed data were fit to both linear and exponential models using MATLAB 2024 b's *fitlm* and *fitnlm* functions, respectively.

Prior to model fitting, we applied two distinct data sampling paradigms. In the first paradigm, referred to as "All Data," we used all 32 data points collected across the four blocks, each consisting of eight reference intensities. In the second paradigm, referred to as "Average + Origin," we averaged the data across blocks at the eight reference intensities and added a ninth data point at the origin, as it is assumed that participants can identify when no reference intensity is provided. This second approach aligns with the methodology used in [17].

In summary, for each participant and each experiment, we generated a total of four models, combining two datasets ("All Data" and "Average + Origin") with two fits (linear and exponential). For each model, we report the coefficient of determination, R^2, as a measure of the goodness of fit. To compare each model's ability to sufficiently describe the data, we run a 2×2 (2 datasets × 2 fits) ANOVA on R^2.

2) Finding the Optimal Reduced Fit: To optimize the cross-modal matching procedure for efficiency, we aimed to determine the minimum number of blocks and reference intensities needed to achieve a model fit comparable to that obtained with the full experimental dataset. To this end, we conducted a Monte Carlo simulation for each participant, experiment, and fit. This simulation fit the data under 657 different conditions, derived as follows: we considered three block configurations (2, 3, or 4 blocks, preserving their sequential order to simulate truncated experiments) and all possible subsets of 3 to 8 reference intensities for each stimulus. The subsets of reference intensities were determined using the binomial coefficient $\left]\binom{n}{k}\right)$, where $n = 8$ and k ranged from 3 to 8. Note that a minimum of three reference points was required for fitting a linear model. This resulted in $\sum_{k=3}^{8} \left]\binom{8}{k}\right) = 219$ combinations of reference intensities. Multiplying these 219 combinations by the three block configurations yielded 657 total conditions. By systematically varying these parameters, we aimed to identify an experimental design that balances efficiency and accuracy by minimizing the cost function:

$$cost = \frac{blocks}{4} \cdot \frac{intensities}{8} \cdot 10 \cdot (x_1\ error + x_2\ error) \quad (1)$$

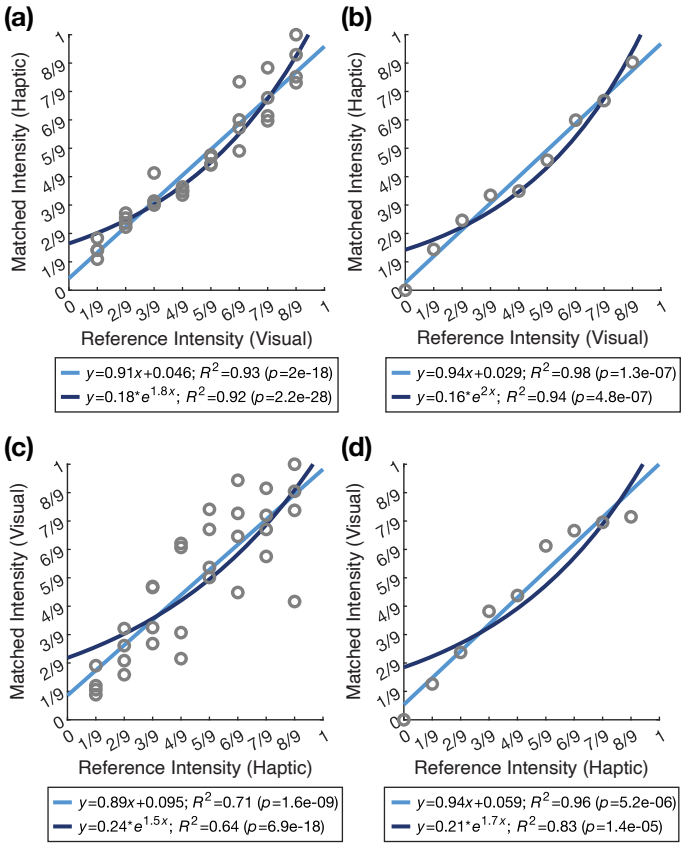


Fig. 2. Linear and exponential fits for a representative participant (Participant 10) in the cross-modal matching experiment. Subplots include: (a) visual modality as the reference (All Data), (b) visual modality as the reference (Average + Origin), (c) haptic modality as the reference (All Data), and (d) haptic modality as the reference (Average + Origin).

where $blocks$ is the number of blocks used, $intensities$ is the number of intensities used. x_1 $error$ and x_2 $error$ represent the deviation between the model's coefficients fitted to the subset of data and the model's coefficients fitted to the full dataset. A weighting factor of 10 was applied to the error term to heavily penalize deviations from the original fit heavily, ensuring the reduced dataset is consistent with the full dataset's fit.

After running the simulation, we identified the best fit for each case as the one that minimized the cost function defined in Eq. 1. This process yielded 24 optimal fits (12 participants $\times$ 2 experiments) for each dataset. To compare the characteristics of these optimally reduced fits, we conducted a paired Student's t-test to evaluate differences in the number of intensities, number of blocks, x_1 error, x_2 error, cost, and R^2 across the datasets.

3) Task Performance: We sought to understand how participants' performance varied between the two experiments. To quantify performance, we calculated error as the absolute difference between the normalized matched intensity and the normalized reference intensity $error = |matched - reference|$. Recall that in Section II-C, the relationship between the two

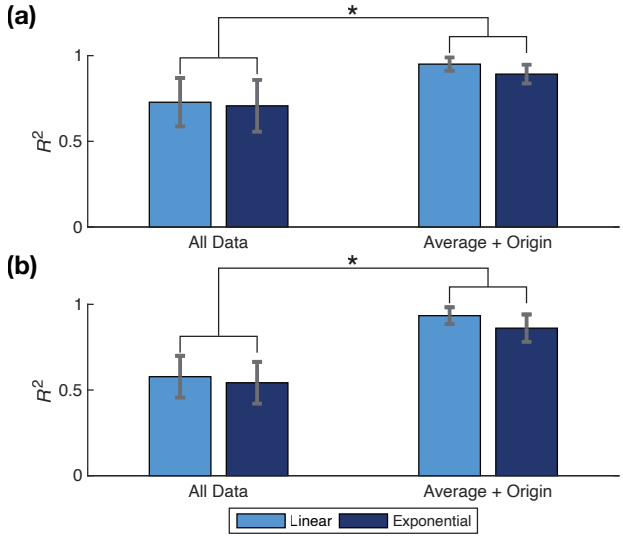


Fig. 3. Average coefficient of determination, $R^2, \pm$ 1 standard deviation for each dataset and fit across participants, with (a) visual modality as the reference and (b) haptic modality as the reference.

modalities was inherently linear; after normalization, it became one-to-one. If participants understood the underlying relationship perfectly, their normalized matched intensity would equal the normalized reference intensity.

To compare performance across experiments, we conducted a paired Student's t-test on the average error for each participant (averaged across all trials within each experiment). Additionally, we tested whether reference intensity or fatigue influenced performance. For reference intensity, we averaged each participant's error across trials at each intensity level and fit a linear model to error as a function of reference intensity. A significant slope would indicate that reference intensity affects performance. For fatigue, we averaged each participant's error across trials within each block and fit a linear model to error as a function of the block. A significant positive slope would indicate a decline in performance over time.

We analyzed NASA-TLX data using a two-way ANOVA to evaluate the effects of reference modality and category (mental demand, physical demand, temporal demand, effort, frustration, and perceived performance) on subjective workload ratings. If a significant effect was found, post-hoc paired Students' t-test was used to identify any significant differences between subcategories.

All data processing and statistical analyses were performed using custom scripts in MATLAB 2024. The significance level for statistical tests was $\alpha = 0.05$.

III. Results

A. Comparing Dataset and Fit

Fig. 2 illustrates the linear and exponential fits for a representative participant, providing a visual comparison of model performance. The models were assessed using the coefficient of determination, R^2, as a measure of goodness of fit.

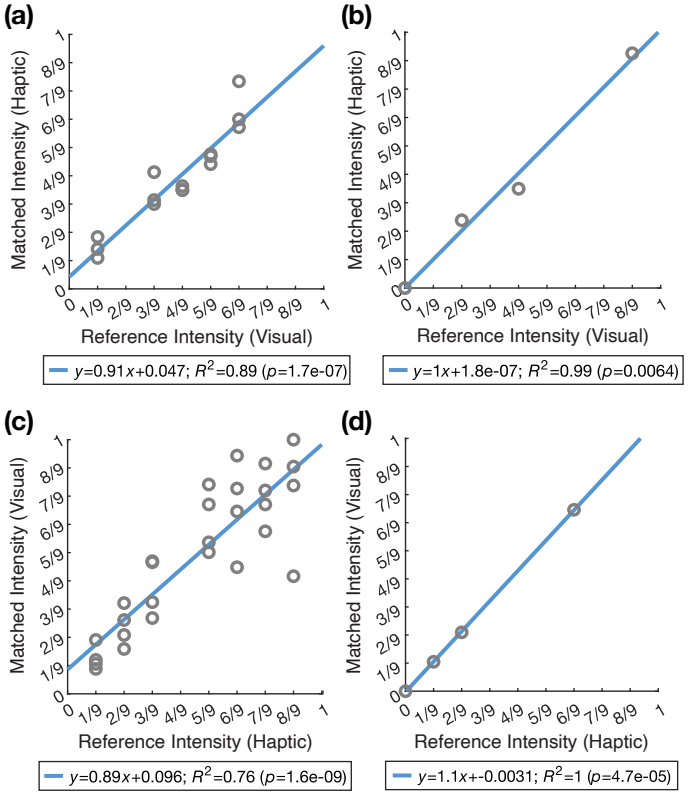


Fig. 4. Optimal reduced fit example for a representative participant (Participant 10), highlighting the reduced blocks and reference intensities. Subplots include: (a) visual modality as the reference (All Data), (b) visual modality as the reference (Average + Origin), (c) haptic modality as the reference (All Data), and (d) haptic modality as the reference (Average + Origin).

Fig. 3 shows the average R^2 across participants separated by experiment, dataset, and fit. Table I shows how each of the 4 models performed, in describing a participant's experimental data. Of note, all models were statistically significant. A 2×2 (2 datasets × 2 fits) ANOVA revealed a significant effect of dataset ($F_{1,95} = 6.458, p = 0.0127$); there was not a significant effect of fit ($p > 0.05$) nor a significant interaction ($p > 0.05$). However, the linear fit generally outperformed the exponential fit.

B. Finding the Optimal Reduced Fit

While the previous analysis included two datasets and two fits, we focused here on the linear fit for succinctness, as it generally performed better than the exponential fit and aligned with the underlying linear relationship in the task. An example for participant 10 is shown in Fig. 4.

Across the 24 optimal reduced fits produced for each of the Linear "All Data" and linear "Average + Origin" data we compared the number of intensities, number of blocks, x_1 error, x_2 error, cost and R^2 across the datasets. A paired Student's t-test revealed a significant effect of dataset on number of blocks ("All": M=3.54, SD=0.88; "Average + Origin": M=2.38, SD=1.06; p<0.001), number of intensities ("All": M=5.42, SD=1.44; "Average + Origin": M=3, SD=0; p<0.001), x_1 error ("All": M=1.4e-03, SD=1.6e-03; "Average + Origin": M=5.2e-03, SD=5.1e-03; p=1.19e-03), x_2 error ("All": M=1.2e-03, SD=1.7e-03; "Average + Origin": M=4.8e-03, SD=7.3e-03; p=2.19e-02), and R^2 ("All": M=0.66, SD=0.17; "Average + Origin": M=0.97, SD=0.022; p<0.001). However, there was not a significant effect on cost ("All": M=0.10, SD=8.9e-02; "Average + Origin": M=0.15, SD=0.11; p=0.10).

TABLE I

THE COEFFICIENT OF DETERMINATION, R^2, OF EACH MODEL FIT TO EACH PARTICIPANT'S DATA SEPARATED BY EXPERIMENT, DATASET, AND FIT. THE ABBREVIATIONS 'ALL,' AND 'AVG + O,' DENOTE THE ALL DATA AND AVERAGE + ORIGIN DATASETS, RESPECTIVELY. THE ABBREVIATIONS 'LIN,' AND 'EXP,' DENOTE THE LINEAR AND EXPONENTIAL FITS, RESPECTIVELY. AVG AND SD DENOTE THE AVERAGE AND STANDARD DEVIATIONS ACROSS PARTICIPANTS.

	Visual Reference				Haptic Reference			
Data Type	**All**		**Avg + O**		**All**		**Avg + O**	
Fit Type	**Lin**	**Exp**	**Lin**	**Exp**	**Lin**	**Exp**	**Lin**	**Exp**
P 1	0.51	0.47	0.93	0.82	0.56	0.54	0.97	0.95
P 2	0.78	0.81	0.96	0.97	0.57	0.58	0.97	0.95
P 3	0.74	0.69	0.94	0.88	0.52	0.44	0.80	0.68
P 4	0.89	0.87	0.99	0.92	0.53	0.51	0.92	0.89
P 5	0.89	0.87	0.99	0.94	0.69	0.65	0.98	0.93
P 6	0.82	0.76	0.98	0.90	0.45	0.39	0.94	0.82
P 7	0.62	0.57	0.95	0.86	0.30	0.29	0.91	0.84
P 8	0.65	0.65	0.98	0.93	0.55	0.49	0.90	0.78
P 9	0.52	0.50	0.87	0.78	0.71	0.70	0.94	0.93
P 10	0.93	0.92	0.98	0.94	0.71	0.64	0.96	0.83
P 11	0.76	0.79	0.90	0.92	0.64	0.63	0.97	0.91
P 12	0.63	0.60	0.92	0.85	0.70	0.63	0.94	0.83
Avg	0.73	0.71	0.95	0.89	0.58	0.54	0.93	0.86
SD	0.14	0.14	0.04	0.05	0.12	0.12	0.05	0.08

TABLE II

PERCENTAGE OF TIMES EACH REFERENCE INTENSITY APPEARED IN THE 24 OPTIMAL REDUCED FITS. 'ALL,' AND 'AVG + O,' DENOTE THE ALL DATA AND AVERAGE + ORIGIN DATASETS.

	Reference Intensity							
	1/9	**2/9**	**3/9**	**4/9**	**5/9**	**6/9**	**7/9**	**8/9**
All	0.71	0.58	0.63	0.58	0.75	0.67	0.75	0.75
Avg + O	0.58	0.29	0.33	0.42	0.42	0.38	0.25	0.33

Table II shows the percentage of times each reference intensity appeared in the 24 optimal reduced fits. In the "All Data" dataset, edge reference intensities (e.g., 1/9 and 8/9) were the most frequently used, but overall, the dataset exhibited some uniformity by often including more than five intensities. In contrast, the "Average + Origin" dataset used an average of approximately 3.54 reference intensities, and mostly included the intensities 1/9, 4/9, 5/9, and 6/9, in that order. This dataset generally excluded higher reference intensities.

C. Performance

Participants' performance was quantified by calculating the error as the absolute difference between the normalized matched intensity and the normalized reference intensity. Then, a paired Student's t-test was conducted to compare average errors across the two experiments for each participant. The test revealed no significant effect of the experiment on performance ($p > 0.05$). However, participants performed better in the visual reference experiment, as seen in Fig. 5.

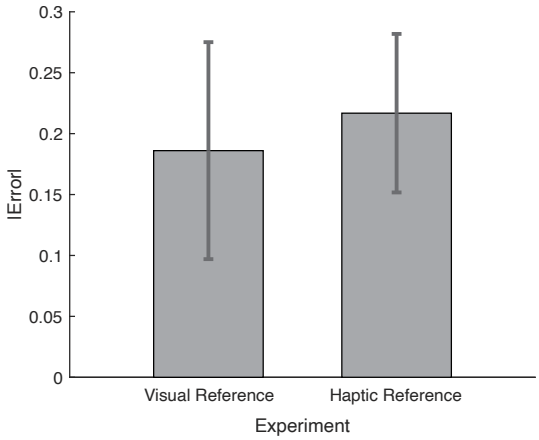


Fig. 5. Absolute error comparison between visual and haptic reference conditions.

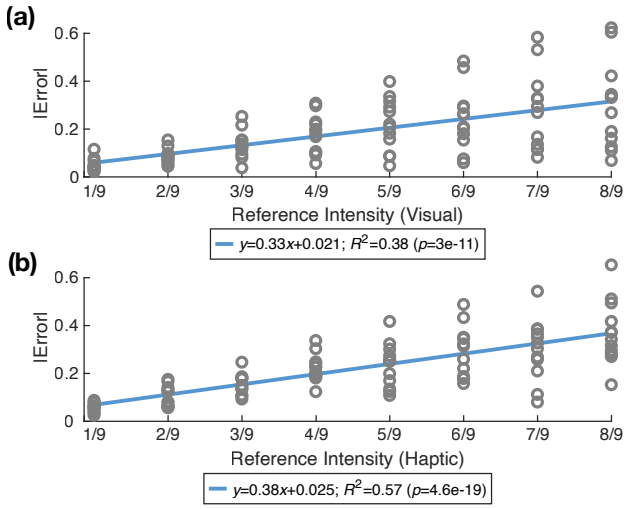


Fig. 6. Participant error as a function of reference intensity, demonstrating increased error at higher intensities. Subplots include: (a) visual modality as the reference and (b) haptic modality as the reference.

To examine the impact of reference intensity on performance, a linear model was fit to the error as a function of reference intensity. In both experiments, the model returned a significant positive slope (visual reference: M=0.33, p<0.001 and haptic reference: M=0.38, p=<0.001) indicating that participants performed worse at higher reference intensities, as shown in Fig. 6.

Similarly, to evaluate the impact of fatigue, a linear model was fit to the error as a function of block. In both experiments, the model did not yield a significant slope (visual reference: M=5.7e-04, p>0.05 and haptic reference: M=1.4e-06, p>0.05), indicating that participants' performance neither decreased nor increased as the experiment progressed, as shown in Fig. 7. This suggests that participants did not suffer from fatigue over the course of the study.

Finally, the two-way ANOVA on workload ratings revealed no statistically significant differences in NASA-TLX scores

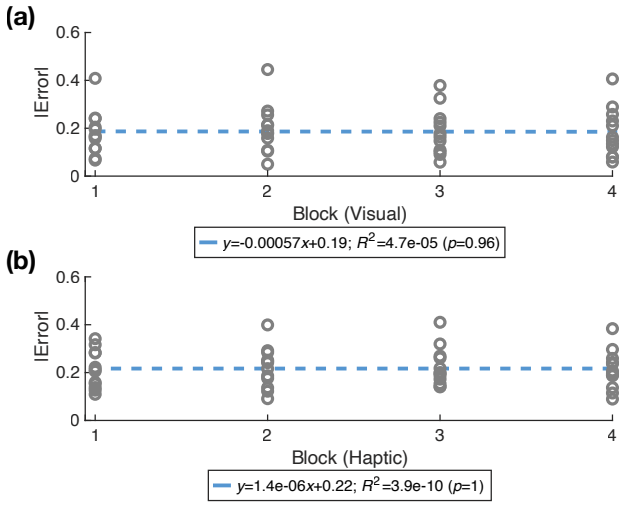


Fig. 7. Participant error as a function of block, showing stable performance throughout the experiment. Subplots include: (a) visual modality as the reference and (b) haptic modality as the reference.

TABLE III
NASA TLX SCORES FOR EACH WORKLOAD DIMENSION ACROSS THE VISUAL AND HAPTIC REFERENCE CONDITIONS. AVG AND SD DENOTE THE AVERAGE AND STANDARD DEVIATIONS ACROSS PARTICIPANTS.

	Visual Reference	Haptic Reference
Mental Demand	-1.25±3.72	0.75±4.77
Physical Demand	-3.33±3.72	-2.58±5.37
Temporal Demand	-5.75±4.18	-6.00±4.35
Effort	0.17±4.06	2.83±3.66
Frustration	-4.50±5.16	-3.08±3.66
Perceived Performance	11.58±5.16	9.58±2.94

across task categories or reference modalities. Additionally, there was no significant interaction. The survey data is summarized in Table III.

IV. Discussion

This study refined cross-modal matching procedures to enhance perceptual equity in multimodal psychophysics and non-psychophysics experiments by systematically evaluating and optimizing experimental parameters. Twelve participants completed two matching experiments using the HAND [6], [7], aligning visual and haptic stimuli according to a visual or haptic reference (Fig. 1). Data were analyzed using two datasets (All Data" and Average + Origin") and two fits (linear and exponential). The linear fit consistently outperformed the exponential fit, aligning with the task's inherent linear relationship. Simulations identified the minimum number of blocks and reference intensities needed to achieve comparable model fits to the full dataset. The All Data" approach utilized a broader range of intensities, while Average + Origin" favored low-to-mid-range intensities, excluding higher ones. Participants showed greater error at higher intensities but exhibited no signs of fatigue throughout the experiment. These findings provide actionable guidelines for streamlining cross-modal matching protocols while maintaining accuracy and efficiency, contributing to developing effective rehabilitation protocols.

When comparing goodness of fit (R^2), we found that the 'Average + Origin' dataset statistically outperformed the 'All Data' dataset (Table I). This result is supported by mathematical reasoning. The 'Average + Origin' dataset uses fewer data points and averages across blocks, resulting in one matched (output) point for each reference (input) point (Fig 2). This reduction in variance around the fit line increases R^2, producing an artificial advantage. It underscores a trade-off: improved model performance comes at the cost of ignoring trial-level variability. Importantly, the 'Average + Origin' dataset captures the overall trend between modalities, the primary goal of cross-modal matching. By prioritizing the overarching relationship, this approach ensures perceptual equity without being hindered by trial-level noise.

While the 'Average + Origin' method modeled the data well for healthy participants, it assumes no perceptual bias at zero intensity. This assumption may not hold in clinical populations, such as stroke survivors, who often experience sensory deficits or altered perceptual baselines. Testing this paradigm with individuals exhibiting perceptual biases could reveal whether the 'All Data' method provides better fits. Such findings could refine the protocol and offer deeper insights into how sensory encoding variability impacts calibration methods across populations. These considerations will guide future studies to improve the adaptability and robustness of cross-modal matching protocols for motor rehabilitation.

The optimal reduced order fits generated through the Monte Carlo simulation revealed an important observation: while the "Average + Origin" dataset achieved a significantly worse x_1 and x_2 error compared to the "All Data" dataset, the overall cost was not significantly different between the two datasets (refer to Section III-B. Upon closer inspection, the errors in both datasets were quite small (x_1 error: $\sim 1.4 \times 10^{\infty 3}$ and $\sim 5.2 \times 10^{\infty 3}$ for "All Data" and "Average + Origin," respectively; x_2 error: $\sim 1.2 \times 10^{\infty 3}$ and $\sim 4.8 \times 10^{\infty 3}$, respectively). This indicates that the 'Average + Origin' dataset, while slightly sacrificing fit accuracy compared to the non-reduced dataset, achieved this with fewer blocks and reference intensities. The reduced order fit suggested 2-3 blocks and 3 reference intensities. While participants were allotted 1 minute per trial, they completed each trial in an average of 12 seconds. Based on this performance, a full experiment following the reduced order fit, including both reference modalities, would take less than 5 minutes. Even if participants used the full allotted time, the reduced protocol would take only 12 to 18 minutes, significantly shorter than the original maximum length of 64 minutes (4 blocks × 8 reference intensities × 2 experiments). The result is a more efficient protocol that still captures the cross-modal relationship between modalities. This trade-off highlights the utility of the 'Average + Origin' approach for balancing efficiency with maintaining critical insights into sensory integration.

The performance of participants, measured by absolute error, did not differ significantly between the two tasks (Fig. 5). This result is further confirmed by the NASA-TLX results, which showed no significant differences in workload across the tasks. This consistency across tasks highlights the robustness of this cross-modal matching experiment and its potential applicability beyond the visual and haptic modalities explored here. Such an approach could be useful for studying other sensorimotor modalities where perceptual equity is critical, such as auditory-haptic or proprioceptive-visual interactions. Future work should build on this foundation by conducting similar experiments to explore these modalities, further broadening the scope and impact of cross-modal matching techniques in sensorimotor research.

Participant performance, measured by absolute error, was unaffected by the number of blocks in the experiment (Fig. 7). Performance remained consistent across blocks, indicating no significant changes due to fatigue or learning effects as the experiment progressed. This stability suggests that reducing the number of blocks, as proposed by the reduced order fit, would not negatively impact results. By maintaining consistent performance throughout the task, the reduced order approach ensures overall trends are captured accurately without compromising data integrity or missing potential learning effects. This finding further supports the feasibility of streamlining cross-modal matching experiments for improved efficiency.

In contrast, there was a clear effect of reference intensity on participants' error; participants exhibited greater errors at higher intensities, possibly due to sensory saturation (Fig. 6). This trend explains why the optimal reduced fits in the 'Average + Origin' dataset tended to exclude data points at higher intensities. This observation is a critical consideration for future experimenters. It suggests that certain ranges within a modality, in this case, higher intensities, may lead to diminished performance and weaker correlations between modalities. To address this, experiments should avoid operating within these problematic ranges and exclude them from cross-modal matching tasks to ensure robust results. Our formulation of reduced order fits offers a distinct advantage here: it programmatically identified these problematic intensity ranges and excluded them. Moreover, in stroke survivors, altered sensory processing may exacerbate sensory saturation, impacting clinical applicability. Future work should explore adaptive scaling corrections to optimize feedback precision.

A. Limitations

In this study, we initially compared linear and exponential fits to the data and found no statistical difference between the two fits. Based on this result and the predetermined understanding that the relationship between visual and haptic modalities in this task is inherently linear, we focused our analysis on linear fits. This approach was justified for this specific task, as the experimental design deliberately established a one-to-one relationship between modalities after normalization. However, other experiments may not have such a predetermined understanding of the underlying relationship between modalities. In these cases, it may be necessary to explore a wider range of models, including nonlinear fits, to accurately capture the relationship in the data. However, that is beyond the scope of this study.

Another limitation of this study is that it was conducted exclusively with healthy participants, which may limit generalizability to clinical populations, such as stroke survivors. However, our results showed that performance remained stable across blocks in healthy participants, with no evidence of fatigue affecting performance. This finding justifies the use of a reduced protocol, as reducing the number of blocks does not compromise data quality. Such a streamlined protocol is particularly valuable for patient populations, where fatigue and task duration are critical concerns. Additionally, stroke survivors' perceptual deficits may introduce non-linearity in matching tasks; here, we included exponential fits to account for such variations. Nonetheless, future research should validate these reduced protocols with clinical populations to ensure they retain effectiveness while accommodating the unique challenges posed by sensory and motor impairments.

B. Impact

This work advances cross-modal matching experiments by identifying reduced experimental designs that maintain accuracy while minimizing participant fatigue and time requirements. Here, we reduced the duration of the study by a factor of 5. These streamlined protocols are particularly beneficial in neurorehabilitation, where patients often face physical and cognitive limitations. By reducing the number of trials and reference intensities, this approach simplifies the experimental process while preserving data quality, paving the way for broader adoption in clinical and research settings.

The study also emphasizes the importance of perceptual equity in multimodal experiments by providing a framework for fair comparisons across sensory modalities. By aligning stimuli to achieve comparable intensities, it addresses a key challenge in sensory integration research [5]. These principles extend beyond visual and haptic modalities, offering a methodological foundation for investigating other sensory interactions and their roles in motor control and neurorehabilitation. For example, strategies such as limiting the upper stimulus range or implementing real-time adaptive algorithms could help mitigate errors in individuals with sensory deficits [18] and enhance clinical utility.

The methodological framework introduced in this study extends beyond just visual and haptic matching. This approach could complement protocols like those of Xu et al. [7] and Seim et al. [19], enabling perceptual equity calibration during individuated finger training. Integrating cross-modal matching into functional grasping or co-activation tasks could better tune sensory feedback across modalities, optimizing patient outcomes. By programmatically optimizing experimental parameters, this method scales to other sensorimotor modalities, such as auditory-haptic or proprioceptive-visual interactions. This scalability broadens its relevance to fields like prosthetics, virtual reality, and human-computer interaction, where multimodal integration is critical. Efficiently determining perceptual equity across modalities provides researchers with a versatile tool for advancing both experimental research and practical applications. Establishing perceptual equity through cross-modal matching is not just a refinement – it is a necessary evolution for multimodal research, rehabilitation, and beyond.

REFERENCES

[1] V. L. Feigin, M. Brainin, B. Norrving, S. Martins, R. L. Sacco, W. Hacke, M. Fisher, J. Pandian, and P. Lindsay, "World stroke organization (wso): Global stroke fact sheet 2022," *International Journal of Stroke*, vol. 17, no. 1, p. 18–29, Jan. 2022.

[2] R. B. King, "Quality of life after stroke," *Stroke*, vol. 27, no. 9, p. 1467–1472, Sep. 1996.

[3] B. Lee, I. D. Saragih, and S. O. Batubara, "Robotic arm use for upper limb rehabilitation after stroke: A systematic review and meta-analysis," *The Kaohsiung Journal of Medical Sciences*, vol. 39, no. 5, p. 435–445, Mar. 2023.

[4] J. M. Veerbeek, A. C. Langbroek-Amersfoort, E. E. H. van Wegen, C. G. M. Meskers, and G. Kwakkel, "Effects of robot-assisted therapy for the upper limb after stroke: A systematic review and meta-analysis," *Neurorehabilitation and Neural Repair*, vol. 31, no. 2, p. 107–121, Sep. 2016.

[5] C. M. Stinear, C. E. Lang, S. Zeiler, and W. D. Byblow, "Advances and challenges in stroke rehabilitation," *The Lancet Neurology*, vol. 19, no. 4, p. 348–360, Apr. 2020.

[6] J. Carducci, K. Olds, J. W. Krakauer, J. Xu, and J. D. Brown, "Novel planar strain sensor design for capturing 3-dimensional fingertip forces from patients affected by hand paralysis," *Sensors*, vol. 22, no. 19, p. 7441, Sep. 2022.

[7] J. Xu, T. Ma, S. Kumar, K. Olds, J. Brown, J. Carducci, A. Forrence, and J. Krakauer, "Loss of finger control complexity and intrusion of flexor biases are dissociable in finger individuation impairment after stroke," *eLife*, Nov. 2023.

[8] G. V. Pennati, J. Plantin, L. Carment, P. Roca, J.-C. Baron, E. Pavlova, J. Borg, and P. G. Lindberg, "Recovery and prediction of dynamic precision grip force control after stroke," *Stroke*, vol. 51, no. 3, p. 944–951, Mar. 2020.

[9] F. Abdollahi, E. D. Case Lazarro, M. Listenberger, R. V. Kenyon, M. Kovic, R. A. Bogey, D. Hedeker, B. D. Jovanovic, and J. L. Patton, "Error augmentation enhancing arm recovery in individuals with chronic stroke: A randomized crossover design," *Neurorehabilitation and Neural Repair*, vol. 28, no. 2, p. 120–128, Aug. 2013.

[10] J. A. Semrau, T. M. Herter, S. H. Scott, and S. P. Dukelow, "Vision of the upper limb fails to compensate for kinesthetic impairments in subacute stroke," *Cortex*, vol. 109, p. 245–259, Dec. 2018.

[11] A. Ahmed, B. Hugo, S. Lucas, R. Diana, O. Etienne, and G. Pascal, "Distinct and additive effects of visual and vibratory feedback for motor rehabilitation: an eeg study in healthy subjects," *Journal of NeuroEngineering and Rehabilitation*, vol. 21, no. 1, Sep. 2024.

[12] B. J. Pitts, S. A. Lu, and N. B. Sarter, "Cross-modal matching: The development and evaluation of a new technique," *Proceedings of the Human Factors and Ergonomics Society Annual Meeting*, vol. 57, no. 1, p. 1760–1764, Sep. 2013.

[13] B. J. Pitts and N. B. Sarter, "Crossmodal matching: Validation of a more reliable technique," *Proceedings of the Human Factors and Ergonomics Society Annual Meeting*, vol. 58, no. 1, p. 1751–1755, Sep. 2014.

[14] M. Paciaroni and M. Acciarresi, "Poststroke fatigue," *Stroke*, vol. 50, no. 7, p. 1927–1933, Jul. 2019.

[15] R. Oldfield, "The assessment and analysis of handedness: The edinburgh inventory," *Neuropsychologia*, vol. 9, no. 1, p. 97–113, Mar. 1971.

[16] S. G. Hart and L. E. Staveland, *Development of NASA-TLX (Task Load Index): Results of Empirical and Theoretical Research*. Elsevier, 1988, p. 139–183.

[17] N. Thomas, G. Ung, C. McGarvey, and J. D. Brown, "Comparison of vibrotactile and joint-torque feedback in a myoelectric upper-limb prosthesis," *Journal of NeuroEngineering and Rehabilitation*, vol. 16, no. 1, p. 70, jun 2019.

[18] C. Hazelton, K. McGill, P. Campbell, A. Todhunter-Brown, K. Thomson, D. J. Nicolson, J. D. Cheyne, C. Chung, L. Dorris, D. C. Gillespie, S. M. Hunter, and M. C. Brady, "Perceptual disorders after stroke: A scoping review of interventions," *Stroke*, vol. 53, no. 5, p. 1772–1787, May 2022.

[19] C. Seim, B. Chen, C. Han, D. Vacek, L. S. Wu, M. Lansberg, and A. Okamura, "Relief of post-stroke spasticity with acute vibrotactile stimulation: controlled crossover study of muscle and skin stimulus methods," *Frontiers in Human Neuroscience*, vol. 17, Aug. 2023.

Challenge-Based Adaptation of Exoskeleton Assistance and Gamified Biofeedback Enables Automated Gait Rehabilitation

Siddharth R. Nathella[1], Keya Ghonasgi[1], Taryn A. Harvey[1], Lena H. Ting[1,2], Kinsey R. Herrin[1,3], and Aaron J. Young[1,3] *Senior Member, IEEE*

***Abstract*— Robotic and biofeedback-assisted interventions are promising alternatives to surgical intervention and supplements for traditional physical therapy for children with gait impairments. This work utilizes a human-in-the-loop optimization strategy to adaptively modulate parameters for a lightweight robotic knee exoskeleton and biofeedback video game to maximize learning potential following the challenge point framework. We tested our approach on three able-bodied participants and one pediatric patient with genu recurvatum, a common walking pattern in children with neurological injuries. We implement a Covariance Matrix Adaptation-Evolutionary Strategy (CMA-ES) optimizer to enforce a target success rate of 70% by continuously adjusting visual biofeedback and exoskeleton assistance parameters. Our experimental results demonstrate the system's ability to maintain the target challenge level for the pediatric participant. Stance hyperextension decreased significantly from pre- to post-training trials on day 2 (9.2°) and 3 (3.2°) of the case study. Swing flexion approached the clinical target of 65° by the end of the third day. The promising optimizer performance and changes in gait kinematics validate the feasibility of autonomous parameter tuning to maximize learning potential in pediatric gait rehabilitation.**

I. INTRODUCTION

Children with neurological injuries often have walking movement disorders that impact the knee joint, with a common presentation being genu recurvatum. Genu recurvatum is characterized by knee hyperextension during the stance phase of gait and limited knee range of motion during swing phase. Typically patients with genu recurvatum hyperextend between 0° and -15° [1]. Genu recurvatum limits functional mobility and can lead to long-term joint and ligament pain [2]. Treatments include strength training of the calf and quadriceps muscles and motor control exercises [2]. In many cases, invasive treatments like surgical alterations of the bony and soft tissue elements is required [3]. Physical rehabilitation is another effective tool for treatment of genu recurvatum and similar walking impairments, but it is time-intensive, requires clinician expertise, and is physically demanding for the therapist.

This work was supported by Shriners Hospitals for Children and NIH Grant No. 1DP2HD111709-01.

[1]Siddharth R. Nathella, Keya Ghonasgi, Taryn A. Harvey, Lena H. Ting, Kinsey R. Herrin, & Aaron J. Young are with the George W. Woodruff School of Mechanical Engineering, Georgia Institute of Technology, Atlanta, GA, USA snathella@gatech.edu

[2]Lena H. Ting is also with the Wallace H. Coulter Department of Biomedical Engineering, Georgia Insitute of Technology & Emory University, Atlanta, GA, USA

[3]Kinsey R. Herrin & Aaron J. Young are with the Institute for Robotics and Intelligent Machines, Georgia Insitute of Technology, Atlanta, GA, USA

Recent research on autonomous robotic exoskeletons has shown potential for assisting gait rehabilitation by offloading the clinician's physical effort to a robotic system [4]. The addition of biofeedback has further been demonstrated to help improve outcomes and engage the participant more actively in therapy [5]. Conner & Lerner [6] showed that children using visual biofeedback with a robotic exoskeleton had higher levels of plantar flexor muscle activity compared to using the exoskeleton alone. Importantly, effective rehabilitation can only occur when the patient is learning from the interaction. Research suggests that to encourage volitional learning, the training environment should engage the participant and provide sufficient challenge to promote learning without discouraging participation [7], [8].

The challenge point framework [8] suggests that the optimal challenge level for learning a given task varies as the individual's skill increases. The nominal difficulty of the task should increase alongside skill so as to track the optimal success rate to facilitate the fastest transition from "novice" to "expert". Prior work explored this approach for stroke rehabilitation, with a video game as the task, where users self-selected a challenge level [9]. The authors found that participants settled at a 74% success rate. In a similar study, players with an approximate 70% success rate showed the most learning in a "Pong" style video game. This evidence suggests that physical rehabilitation may be encouraged and more effective if an ideal success rate is enforced (where the task is not too hard or too easy) [10]. However, the modulation of challenge may be patient-specific, task-specific, etc., and manual tuning of multi-parameter systems is infeasible [11]. Thus, automated approaches for personalizing rehabilitation systems to specified challenge levels are necessary to deploy these devices in practice.

Human-in-the-loop optimization (HILO) has been used to individually customize exoskeleton parameters, resulting in superior performance over using generic device settings [12]. Exoskeleton control policies, even with few parameters, can result in different behaviors across individuals and finding ideal parameter combinations is non-trivial. In HILO, a formal numerical optimizer looks for the control policy that best fits a particular individual by testing and evaluating different parameter combinations. Covariance Matrix Adaptation-Evolutionary Strategy (CMA-ES) [13] is a common HILO optimization framework, particularly suitable when an individual's response to the same set of parameters is expected to vary with time, such as due to motor adaptation or learning [12]. Few studies have extended HILO

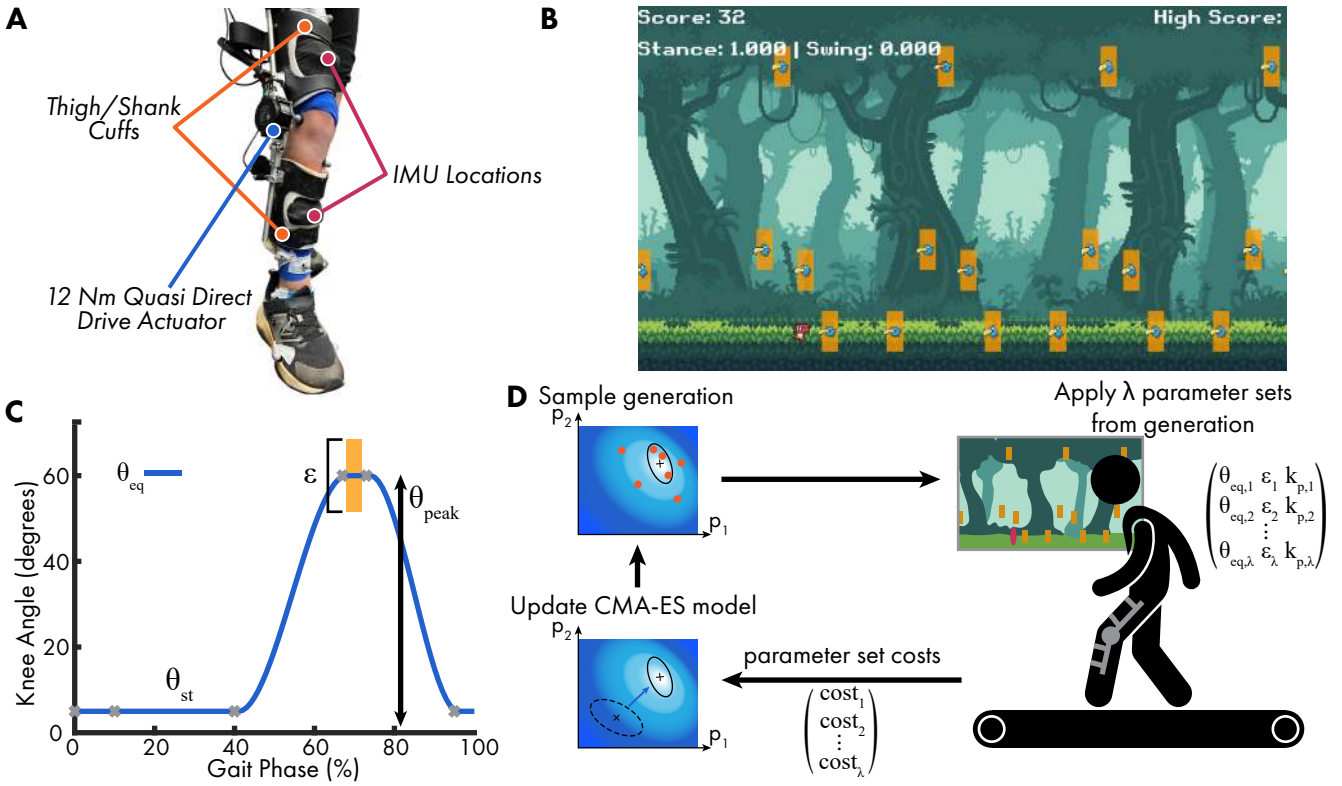


Fig. 1. (A) Knee exoskeleton designed to provide unilateral torque assistance. (B) The biofeedback video game. The red dinosaur avatar displays the user's knee angle, and the yellow boxes/birds represent the target kinematic profile for θ_{eq}, an example of which is shown in (C). The yellow box shows the tolerance factor ϵ. While the current knee angle is inside the tolerance, the assistance is set to $0\,\mathrm{Nm}$. (D) The algorithm loop to personalize gait parameters. Each CMA-ES generation applies λ parameter sets, the cost for each set is computed and used to update its estimate of the optimal region.

to rehabilitation or to motor adaptation and learning contexts. Li et al. [14] implemented HILO to encourage active voluntary participation in an upper limb movement task in stroke patients. Wang et al. [15] targeted engagement in a virtual cycling task by optimizing parameters to maximize neural engagement. This prior research and the relatively small number of studies exploring HILO for motor learning applications form the motivation for adaptively modulating challenge level, or task difficulty, to maximize the learning potential during gait training with an exoskeleton augmented by gamified biofeedback.

In this work, we formulated a knee exoskeleton and visual biofeedback system as a HILO problem to maximize learning in a walking task. We collected experimental data from three able-bodied (AB) participants challenged to walk in a crouch gait pattern, and one pediatric clinical participant with genu recurvatum (GR) prescribed to walk with a normative knee angle profile. The visual biofeedback system showed the user a goal kinematic profile in the form of a video game, while the exoskeleton applied assistive torque as needed to correct deviations from that profile. Independent stance and swing CMA-ES optimizers modified various system parameters to maintain the targeted 70% challenge level.

II. METHODS

A. Knee Exoskeleton Hardware

A lightweight ($\sim$1 kg) powered knee exoskeleton was developed to provide torque assistance to the wearer (Fig. 1A). The device assisted unilaterally, actuated by a quasi-direct drive motor (CyberGear Micromotor, Xiaomi Corp., CN), capable of $12\,\mathrm{Nm}$ of peak torque and a continuous torque of $4\,\mathrm{Nm}$. The device is an adapted version of the system in [16]. The knee joint featured a frontal plane passive degree of freedom, allowing the device to fit on individuals with deviation in frontal plane knee angles (i.e. valgus/varus). The device was secured to the participant with thermoplastic cuffs at the thigh and shank, both of which could be rotated to accommodate varying tibiofemoral transverse alignment. The device was powered by a $20\,\mathrm{V}$ off-the-shelf lithium polymer power tool battery (Dewalt, MD). A waist belt held the battery and mircrocontroller and acted to suspend the device to prevent movement during long walking sessions.

B. Knee Exoskeleton Control

The device was controlled with a Nvidia Jetson Orin Nano (Nvidia, CA) and programmed in Python 3.11. Assistance was applied using an impedance control law (Eq. 1), where the torque was defined by a stiffness parameter k_p, the measured knee angle θ_k, and an error from an equilibrium angle θ_{eq}, and an additional velocity damping term k_d, set to a constant value of $0.002\,\frac{\mathrm{Nm}}{\mathrm{deg{\cdot}s}}$. A tolerance, ϵ, was defined to set zero assistance if the error was less than ϵ, which created an assist-as-needed effect.

$$\tau = \begin{cases} 0 & |\theta_k - \theta_{eq}| \leq \epsilon \\ k_p(\theta_k - \theta_{eq}) - k_d\dot{\theta}_k & \text{else} \end{cases} \quad (1)$$

TABLE I
PARTICIPANT DEMOGRAPHIC DATA

Participant	Age	Weight (kg)	Height (cm)	Gender	Gait Pathology
AB1	28 yr	64.9	170	Male	N/A
AB2	22 yr	63.6	175	Female	N/A
AB3	24 yr	78.0	180	Male	N/A
GR1	12 yr	37.0	155	Male	*genu recurvatum*

Stance and swing optimizers use independent variables.

Knee angle was computed using two 9-axis inertial measurement units (IMU) (Microstrain by HBK, VT), placed on the thigh and shank. The difference in the roll orientation between the two sensors defined the knee angle, zeroed to a static measurement taken during quiet standing. The orientations were computed using the built-in sensor fusion algorithm. Gait phase was estimated in real-time using ground reaction forces from the treadmill, with a foot-contact threshold of $40\,\mathrm{N}$, and communicated to the controller over UDP. The estimated gait time averaged the previous two gait cycles. The controller was transitioned from stance phase into swing phase at toe-off and back to stance phase at heel contact. All control and sensing was executed at $200\,\mathrm{Hz}$.

C. Visual Biofeedback Game

The biofeedback game displayed an avatar representing the IMU measured knee angle of the participant, with targets placed along a goal kinematic trajectory (Fig. 1B). The trajectory was defined by a Piecewise Cubic Hermite Interpolating Polynomial (`pchip`), with prescriptions for stance knee angle (θ_{st}) and peak knee flexion (θ_{peak}), and all other points being interpolated. The θ_{eq} profile definition (Fig. 1C) used control points at 0, 10, 40, 67, 73, and 95% gait cycle. The game targets were displayed at 10, 40, 60, 70, and 85% gait cycle, and the target movement across the screen was aligned with the real-time estimated gait phase. The user controlled the avatar vertically on the screen, by flexing or extending their knee joint. The player received points for each target they hit and were instructed to score as many points as possible. The game was written in the Godot Game Engine (Godot Foundation) using free online assets [17], [18], [19]. The game communicated with the controller over UDP to receive real-time knee angle estimates.

D. Difficulty Adaptation Optimizer

The system was optimized using CMA-ES, a method designed to optimize black box systems by sampling and producing generations of parameter sets, ranking them by cost, and adapting its estimate of the search space. A "generation" consists of parameter sets sampled from the same search space. We selected CMA-ES based on its previous use in rehabilitation context and its suitability to time-varying spaces, but to our knowledge, this algorithm has yet to be applied in gait rehabilitation with the explicit goal of maximizing learning potential. Stance and swing phases were simultaneously optimized by independent optimizers, with the stance parameters being θ_{st}, ϵ_{st}, and $k_{p,st}$, and swing being θ_{peak}, ϵ_{sw}, and $k_{p,sw}$. Each parameter set's cost was the absolute difference between the target, 70%, and actual success rate, defined as the ratio of points scored to the total possible points over the last 10 strides of a parameter set.

$$\text{cost} = |\text{success rate} - 0.7| \tag{2}$$

For the AB participants, the bounds on θ_{st} and θ_{peak} were set to $[25, 45]^\circ$ and $[60, 85]^\circ$ respectively to challenge them to walk in a crouched posture. The bounds for the GR participant were set to $[0, 15]^\circ$ and $[45, 65]^\circ$ to encourage a normative gait profile [20], [21]. Both stance and swing bounds on ϵ were set at $\pm[1, 10]^\circ$. For the stiffness parameters, we set the maximum allowable torque to 20% of the expected peak knee moment, when the error between the current knee angle and equilibrium angle was 20°. Expected peak knee moment was taken from average kinetic profiles from literature [20], to be $0.5\,\frac{\mathrm{Nm}}{\mathrm{kg}}$ and $0.25\,\frac{\mathrm{Nm}}{\mathrm{kg}}$ for stance and swing respectively. Thus, bounds for $k_{p,st}$ and $k_{p,sw}$ were set at $[0, 0.005]\,\frac{\mathrm{Nm}}{\mathrm{deg}\cdot\mathrm{kg}}$ and $[0, 0.0025]\,\frac{\mathrm{Nm}}{\mathrm{deg}\cdot\mathrm{kg}}$. The optimizer was implemented using the `cmaes` package in Python 3.11 [22]. For the AB participants, the optimizer was configured with default recommended parameters and parameters were normalized to the recommended scaling [23]. For the GR participant, population size (λ, number of parameter sets per generation) was set to 5 instead of the default of 7. This change was made to increase the adaptation rate of the optimizer, slightly sacrificing global search performance for faster convergence, so the participant would spend more of the experiment close to the target learning rate. The effect of this change was tested using an offline bootstrapped simulation with a population size of 5. An analysis of experimental results from AB participants showed that using $\lambda = 5$ causes a shift in the next generation's estimate of each parameter by less than 10% compared to $\lambda = 7$. Given the high time cost of collecting experimental data with a pediatric subject, the smaller λ was used for this case study.

E. Experimental Protocol

We recruited N=3 able-bodied (AB) pilot subjects and N=1 pediatric genu recurvatum (GR) participant. Each visit consisted of a one-minute pre-training baseline walking trial, followed by the training session, and a one-minute post-training baseline. The primary outcome for the AB participants was optimizer performance and so they were only evaluated over one visit. The GR participant completed three visits on subsequent days to additionally evaluate knee kinematic changes. During training, the participant wore the exoskeleton and played the biofeedback game simultaneously. Every 30 seconds, a new parameter set was sampled from the CMA-ES optimizer. Once all parameter sets from a generation were trialed, the optimizer was updated (Fig. 1B). AB1 and AB3 completed 8 generations, while AB2 only completed 7 due to time restrictions. For the GR participant, 10 generations were collected each day, and the optimizer retained its state from the previous day. Kinematic data were collected using motion capture (Vicon, UK), and inverse kinematics was performed to compute joint angles (OpenSim, CA). Participants walked on a force-plate instrumented treadmill (Bertec, OH) at 80%

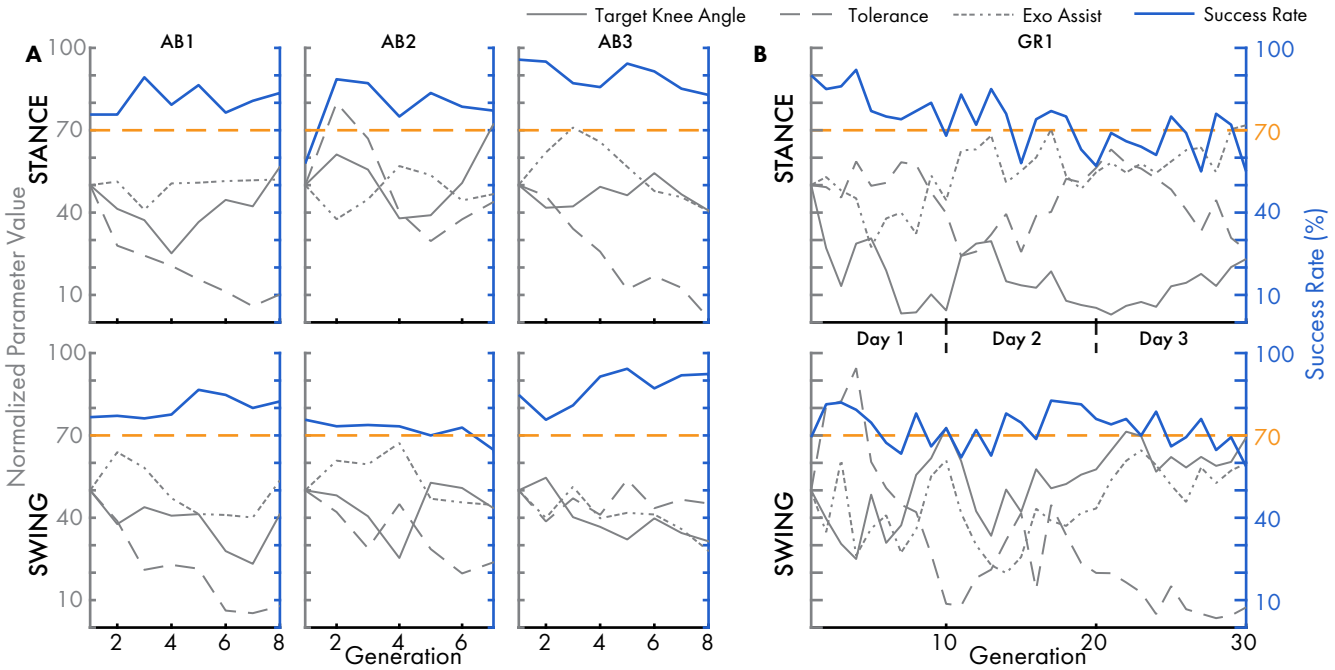


Fig. 2. Success rate and optimizer estimates over each generation for (A) AB subjects and (B) GR subjects. Blue lines denote the average success rate of each generation and grey lines denote each parameters normalized mean. Yellow dashed line marks 70% target success rate.

self-selected speed, determined through the 10-meter walk test across an instrumented gait mat (Protokinetics, PA). The AB participants took breaks as needed and breaks were enforced every 3 generations for the GR participant to minimize fatigue. The experimental protocols H19167 and H19006 were approved by the Georgia Institute of Technology Institutional Review Board.

F. Data Analysis Approach

The CMA-ES optimizer's performance was evaluated by its ability to maintain the participant's success rate at 70%. We estimated the relevance of each parameter to the optimizer by computing the variance of the optimal estimate for AB participants. High variance indicates the high relevance to maintaining the success rate. To better quantify the GR participant's responses to changes in parameters, we fit a linear model (`fitlm`, MATLAB, Mathworks, MA) comparing the inter-iteration change in parameter values (Δparam) to the change in success rate (Δsuccess rate) for each parameter. The 149 parameter set differences across three days allowed for significant correlations to be determined for this single participant. Next, we computed a personalized challenge level for each phase using a 2-norm of the set of parameters at a single iteration, where each parameter was weighted by its coefficient in the linear model, and normalized to the maximum possible challenge. Knee kinematic results were evaluated within the GR participant using one-way ANOVA with a Tukey post-hoc test to determine significant changes between conditions (`multcompare`).

III. RESULTS

A. Optimizer Performance

1) Able-Bodied Subjects: AB1 and AB3 showed a relatively high performance in the task both during stance and swing, with the optimizer being unable to pull either subject to 70% success rate by the end of the session. The optimizer was more successful with AB2, with stance phase ending within 10% of the target success rate, and achieving the target success rate during swing within 5 generations (Fig. 2A). During stance phase, for all AB participants, the target tolerance parameter selected by the optimizer consistently varied the most. For swing phase, we saw similar results for AB1 and AB2, with tolerance being the most varied parameter. In AB3, the peak knee flexion angle and exoskeleton assistance were varied more by the optimizer.

2) Pediatric Genu Recurvatum Subject: The CMA-ES optimizer was able to maintain the targeted score rate for the GR participant (Fig. 2B). During stance we saw a decreasing trend towards the 70% target, coming to within 10% of the target by the end of day 1. This target was maintained on subsequent days with mean success rates of 72% and 66.2% on days 2 & 3 respectively. The swing phase score rate started and remained close to the target across all days, with mean success rates of 73.4%, 74%, and 70.27% on days 1, 2, and 3 respectively. The stance optimizer varied all three parameters to a similar extent across the three days, whereas the swing optimizer primarily varied the tolerance parameter.

B. Score Rate Changes and Challenge for GR Participant

The swing phase score rate model identified tolerance as the only significant parameter ($p \ll 0.001$) and the others are excluded from the challenge level estimation. The knee angle and tolerance parameters were significant factors ($p \ll 0.001$) affecting stance phase score rate (Table II). The challenge level estimated from these parameters (Fig. 3) shows a strong increasing trend in swing and a soft increasing trend in stance ($p \ll 0.001$).

TABLE II

PARAMETER IMPORTANCE: (*:$p < 0.05$)

Δsuccess rate $= \beta_0 + \beta_1 \Delta\theta_{st/peak} + \beta_2 \Delta\epsilon_{st/sw} + \beta_3 \Delta k_{p,st/sw}$		
	Δstance success rate	Δswing success rate
β_0	0.0384	0.1119
β_1	3.3265*	-1.6403
β_2	4.8127*	5.0875*
β_3	1.6784	0.1668
stance challenge$_i$ $= \left\| \begin{bmatrix} \beta_1 \theta_{st,i} \\ \beta_2 \epsilon_{st,i} \end{bmatrix} \right\|_2$		swing challenge$_i$ $= \epsilon_{st,i}$

C. Kinematic Outcomes for GR Participant

Knee kinematic results were compared during the pre-training and post-training baseline conditions, as well as the last generation (5 parameter sets) on each visit for the GR participant (Fig. 4A, Section II-F). For knee hyperextension (stance phase), significant improvements between pre-training and the last generation of training were seen on all visits (4.3°, 7.3°, 7.5° on days 1, 2, and 3 respectively, $p < 0.05$). Significant improvement between the pre- and post-training was seen on days 2 (9.2°) & 3 (3.2°) (Fig. 4B). During swing flexion, we set 65° as a reference, because that was the maximum target the system could show the participant. The day 1 pre-training baseline had the lowest peak knee flexion and in each subsequent condition, peak knee flexion exceeded the 65° reference. We saw significant changes in peak knee flexion (Fig. 4C) and, at the end of the last day, the participant was closest to the 65° reference.

IV. DISCUSSION

In this work, we demonstrate a HILO approach to customize exoskeleton and biofeedback parameters to maintain a specified level of success during a task. Through an experimental study, we 1) establish the efficacy of an adaptive algorithm for challenge modulation, 2) quantify parameter importance identified from the algorithm's estimations, and 3) evaluate the effects of the exoskeleton-biofeedback framework on joint kinematics. Our results from a pilot experiment with three AB participants and a clinical case study with a pediatric participant with GR provide promising evidence for simultaneous exoskeleton and biofeedback modulation to target kinematic adaptation for gait rehabilitation.

The CMA-ES algorithm showed limited ability to match the desired score rate in AB participants, despite increasing task difficulty. They could easily achieve the crouch gait with a high success rate, rendering parameters needed for a 70% success rate outside the set parameter bounds. The algorithm was more successful for the pediatric participant, as walking with a normative gait was more challenging due to their GR. The parameters required to keep the GR participant at the 70% success rate changed over time suggesting the participant was improving. An optimization strategy that cannot account for a dynamic environment (such as human adaptation) like Bayesian Optimization or Gradient Descent would not track changes in optimal parameters. Our results indicate a need for a time-varying algorithm like CMA-ES. A potential limitation of CMA-ES is the time of convergence. Some approaches to address this limitation include shrinking search spaces and faster adaptation rates.

The parameter importance computed from the sampled parameter sets suggests that target tolerance was the most important parameter for both stance and swing optimizers. A decrease in tolerance requires more precise knee motion to hit the kinematic targets, thus requiring increased volitional control over the knee joint. For the GR participant, a higher knee flexion target was associated with lower success rates in swing phase, but an increase in stance flexion target lowered the challenge of the task. This likely stems from compensatory crouch gait behavior that individuals with GR often use to avoid hyper-extension. A target stance angle close to 0° could not be met using crouch gait resulting in lower score rate due to lack of precise volitional control. Thus, the stance knee angle target had a similar effect as tolerance, forcing the participant toward precise knee joint control to prevent hyperextension. In stance, the exoskeleton assistance parameter was near-significance ($p = 0.0519$) and further experimental analysis is necessary to verify whether this parameter is important in participants with more severe impairment or different impairments, such as crouch gait.

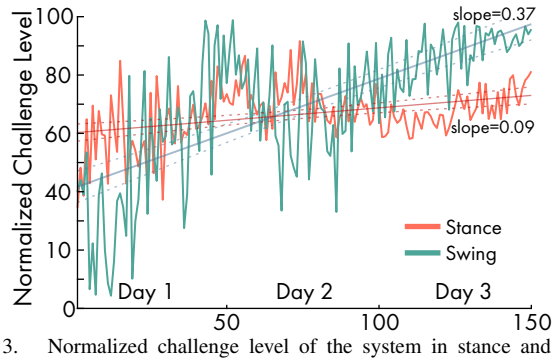


Fig. 3. Normalized challenge level of the system in stance and swing phase over each iteration for the GR subject. Both conditions trend towards higher challenge levels by the end of the experiment.

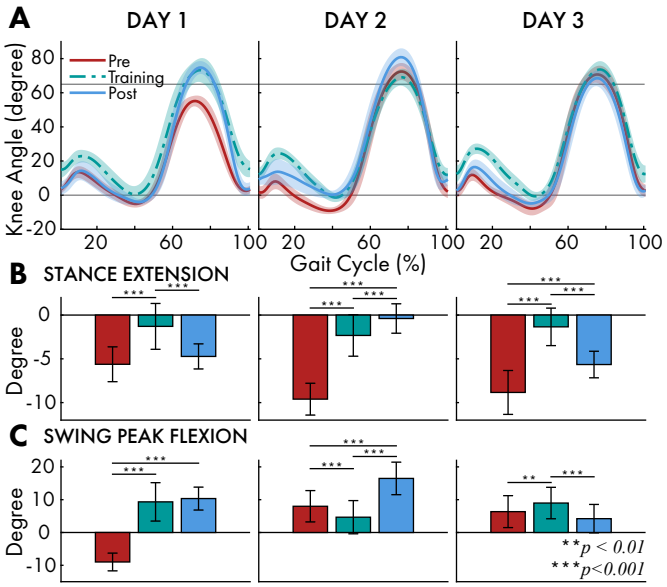


Fig. 4. (A) Knee profiles for the GR subject from (red) pre-, (teal) last generation, and (blue) post-training. (B) Minimum stance extension. (C) Peak swing flexion difference from 65°. Error bars and shaded areas: ±1 standard deviation.

In swing, the changes in exoskeleton assistance did not significantly change the success rate. However, there was a significant positive correlation ($R^2 = 0.44$) between the optimal peak knee flexion angle and exoskeleton assistance that the optimizer estimated (Fig. 2B). This correlation suggests that for the optimizer to maintain the intended success rate, increases in the peak knee flexion parameter must be accompanied by increases in exoskeleton assistance. In other words, the participant may have relied on the device to achieve more challenging knee flexion targets consistently. Future versions of the optimizer could be tuned to limit over-utilization of the device over the course of rehabilitation to ensure users receive maximal carryover benefit.

The exoskeleton and biofeedback system affected immediate changes in gait kinematics toward the target behaviors, with some evidence for retention across days. Although the pediatric participant exhibited exaggerated peak swing flexion (i.e. steppage gait) on the first and second days going beyond the target of 65°, on day 3, this exaggeration was less severe. This trend suggests the participant adapted to the desired behaviors over time despite initial overcompensation. In stance phase, hyperextension improved during training on all visits, with carryover from pre- to post-training on days 2 and 3. Both these kinematic outcomes could be negatively affected by a limitation of the visual biofeedback game which only rewards meeting the knee angle targets. As the game does not explicitly penalize hyperextension during stance or exaggerated flexion during swing it may inadvertently reinforce compensatory behaviors. Future versions of the game will incorporate such penalties alongside positive rewards.

The long-term goal of this research is to encourage gait rehabilitation in pediatric patients with gait impairments such as genu recurvatum and crouch gait. The able-bodied pilot and pediatric clinical case study presented in this paper are a first step toward this goal. Future work in this direction should aim to further evaluate different adaptation algorithms, their effect on a larger population and more diverse set of impairments, and the efficacy of adaptive training for long-term rehabilitation. The current study and ongoing improvements in the design and control of exoskeletons and serious games highlight the promising potential of adaptive training protocols for gait retraining through autonomous modulation of task difficulty to encourage learning.

ACKNOWLEDGMENT

We thank our participants for their time. We also thank Emily Rice, Dennis Green, Arina Kucinskaja, and Antonio Garcia Jimenez for their help during data collections.

REFERENCES

[1] D. A. Yngve, "Recurvatum of the Knee in Cerebral Palsy: A Review," *Cureus*, vol. 13, p. e14408, Apr. 2021.

[2] J. K. Loudon, H. L. Goist, and K. L. Loudon, "Genu Recurvatum Syndrome," *Journal of Orthopaedic & Sports Physical Therapy*, vol. 27, pp. 361–367, May 1998. Publisher: Journal of Orthopaedic & Sports Physical Therapy.

[3] R. S. Dean, N. R. Graden, D. H. Kahat, N. N. DePhillipo, and R. F. LaPrade, "Treatment for Symptomatic Genu Recurvatum: A Systematic Review," *Orthopaedic Journal of Sports Medicine*, vol. 8, p. 2325967120944113, Aug. 2020. Publisher: SAGE Publications Inc.

[4] D. Lee, M. K. Shepherd, S. C. Mulrine, J. D. Schneider, K. F. Moore, E. M. Eggebrecht, B. M. Rogozinski, K. R. Herrin, and A. J. Young, "Reducing Knee Hyperextension With an Exoskeleton in Children and Adolescents With Genu Recurvatum: A Feasibility Study," *IEEE Transactions on Biomedical Engineering*, vol. 70, pp. 3312–3320, Dec. 2023.

[5] T. C. Bulea, Z. F. Lerner, A. J. Gravunder, and D. L. Damiano, "Exergaming with a pediatric exoskeleton: Facilitating rehabilitation and research in children with cerebral palsy," in *2017 International Conference on Rehabilitation Robotics (ICORR)*, pp. 1087–1093, July 2017. ISSN: 1945-7901.

[6] B. C. Conner and Z. F. Lerner, "Improving Ankle Muscle Recruitment via Plantar Pressure Biofeedback during Robot Resisted Gait Training in Cerebral Palsy," in *2022 International Conference on Rehabilitation Robotics (ICORR)*, pp. 1–6, July 2022. ISSN: 1945-7901.

[7] J. A. Kleim and T. A. Jones, "Principles of experience-dependent neural plasticity: implications for rehabilitation after brain damage," *Journal of speech, language, and hearing research: JSLHR*, vol. 51, pp. S225–239, Feb. 2008.

[8] M. A. Guadagnoli and T. D. Lee, "Challenge point: a framework for conceptualizing the effects of various practice conditions in motor learning," *Journal of Motor Behavior*, vol. 36, pp. 212–224, June 2004.

[9] Q. Sanders, V. Chan, R. Augsburger, S. C. Cramer, D. J. Reinkensmeyer, and A. H. Do, "Feasibility of Wearable Sensing for In-Home Finger Rehabilitation Early After Stroke," *IEEE Transactions on Neural Systems and Rehabilitation Engineering*, vol. 28, pp. 1363–1372, June 2020.

[10] N. Al-Fawakhiri, S. Kayani, and S. D. McDougle, "Evidence of an optimal error rate for motor skill learning," July 2023. Pages: 2023.07.19.549705 Section: New Results.

[11] K. Ghonasgi, R. Mirsky, S. Narvekar, B. Masetty, A. M. Haith, P. Stone, and A. D. Deshpande, "Capturing Skill State in Curriculum Learning for Human Skill Acquisition," in *2021 IEEE/RSJ International Conference on Intelligent Robots and Systems (IROS)*, pp. 771–776, Sept. 2021. ISSN: 2153-0866.

[12] P. Slade, C. Atkeson, J. M. Donelan, H. Houdijk, K. A. Ingraham, M. Kim, K. Kong, K. L. Poggensee, R. Riener, M. Steinert, J. Zhang, and S. H. Collins, "On human-in-the-loop optimization of human–robot interaction," *Nature*, vol. 633, pp. 779–788, Sept. 2024. Publisher: Nature Publishing Group.

[13] N. Hansen, "The CMA Evolution Strategy: A Comparing Review," in *Towards a New Evolutionary Computation: Advances in the Estimation of Distribution Algorithms* (J. A. Lozano, P. Larrañaga, I. Inza, and E. Bengoetxea, eds.), pp. 75–102, Berlin, Heidelberg: Springer, 2006.

[14] N. Li, Y. Yang, T. Yang, W. Chen, Y. Wang, P. Yu, W. Wang, N. Xi, and L. Liu, "Human-in-the-loop Optimization for Adaptive Assist-as-Needed Rehabilitation," in *2022 12th International Conference on CYBER Technology in Automation, Control, and Intelligent Systems (CYBER)*, pp. 1050–1054, July 2022. ISSN: 2642-6633.

[15] J. Wang, W. Wang, S. Ren, W. Shi, and Z.-G. Hou, "Engagement Enhancement Based on Human-in-the-Loop Optimization for Neural Rehabilitation," *Frontiers in Neurorobotics*, vol. 14, Nov. 2020. Publisher: Frontiers.

[16] D. Lee, S. Lee, and A. J. Young, "AI-driven universal lower-limb exoskeleton system for community ambulation," *Science Advances*, vol. 10, p. eadq0288, Dec. 2024.

[17] "Dino Character Sprites by Arks." https://arks.itch.io/dino-characters.

[18] "Pixel Adventure 2 by Pixel Frog." https://pixelfrog-assets.itch.io/pixel-adventure-2.

[19] "Jungle Asset Pack by Jesse Munguia." https://jesse-m.itch.io/jungle-pack.

[20] M. H. Schwartz, A. Rozumalski, and J. P. Trost, "The effect of walking speed on the gait of typically developing children," *Journal of Biomechanics*, vol. 41, pp. 1639–1650, Jan. 2008.

[21] J. Camargo, A. Ramanathan, W. Flanagan, and A. Young, "A comprehensive, open-source dataset of lower limb biomechanics in multiple conditions of stairs, ramps, and level-ground ambulation and transitions," *Journal of Biomechanics*, vol. 119, p. 110320, Apr. 2021.

[22] M. Nomura and M. Shibata, "cmaes : A Simple yet Practical Python Library for CMA-ES," Oct. 2024. arXiv:2402.01373.

[23] N. Hansen, "The CMA Evolution Strategy: A Tutorial," 2016. Publisher: arXiv.

Improving Wrist Tremor Suppression via Targeted Application of Afferent and Interferential Stimulation Techniques*

Vidisha Ganesh
Joint Dept. of Biomedical Engineering
North Carolina State University
University of North Carolina-Chapel Hill
Raleigh, USA
vganesh3@ncsu.edu

Xiangming Xue
Joint Dept. of Biomedical Engineering
North Carolina State University
University of North Carolina-Chapel Hill
Raleigh, USA
xxue5@ncsu.edu

Dr. Daniel Roque
Department of Neurology
University of North Carolina-Chapel Hill
Durham, USA
droque@neurology.unc.edu

Dr. Nitin Sharma
Joint Dept. of Biomedical Engineering
North Carolina State University
University of North Carolina-Chapel Hill
Raleigh, USA
nsharm23@ncsu.edu

***Abstract*—Upper limb tremors from Parkinson's Disease (PD) and Essential Tremor (ET) disease affect an estimated 6% of the global population. Patients face difficulties performing activities of daily living, leading to a reduced quality of life. Though treatments such as medication and deep brain stimulation exist, their limited applicability and potential risk leaves a large patient subset untreated. In contrast, non-invasive peripheral electrical stimulation (ES) therapies can be tailored to the user to optimally mitigate the symptoms of tremor. Fatigue-inducing functional electrical stimulation (FES) protocols have the highest efficacy of ES methods, with suppression ratios in the 50%s. In this work, we aimed to suppress tremors at the same level using sensory electrical stimulation (SES), which currently has efficacy levels in the 30-45 percent range. In addition to specially targeting the forearm pronator and supinator for stimulation, we introduce the use of deep interferential current (DIC) as a method to suppress postural wrist tremors in PD and ET populations. 1 ET and 1 PD subject completed a cup lift-and-hold task to elicit tremor as we applied and evaluated SES and DIC techniques. We found significant variability in performance between our PD and ET subjects, with the highest suppression (>60%) observed during SES for the PD subject. However, suppression was observed in all subjects for both SES and DIC, demonstrating the viability of our DIC approach while indicating the need for significant protocol optimization and individualization.**

***Index Terms*—tremor suppression, interferential current, sensory electrical stimulation**

I. Introduction

Approximately 7 million people in the United States and as much as 6% of the world population experiences upper-limb tremors that lead to difficulties in performing activities of daily living (ADL) such as buttoning a shirt, holding a cup, etc. Parkinson's Disease (PD) is a prevalent condition that leads to tremors in about a third of the affected population. Essential tremor disease (ET), which affects an even larger population, is an idiopathic condition from which patients experience mostly upper-limb tremors. There are no known biomarkers and the neural pathways or localized biomechanisms by which the tremors propagate are unclear, making personalized symptom-mitigation the focus of treatments rather than addressing the root cause. [1]- [3]

Current treatments for tremors include pharmacological supplements, surgical intervention, and assistive devices. Pharmacological solutions have limited efficacy while expensive surgical interventions are only prescribed for unmanageable symptoms and carry high associated risk [4]. Recently, non-invasive electrical stimulation (ES) techniques, which apply low-level current to motor or sensory neurons, have shown efficacy in suppressing tremors with no side effects. ES approaches address the limitations of other orthotic devices by being lightweight and highly wearable, as adhesive transcutaneous electrodes are easy to apply and remove [2]. Peripheral nerves are targeted at stimulation (current) amplitudes above or below the motor threshold (around 4-8 mA) depending on the protocol. Functional electrical stimulation (FES) methods stimulate above motor threshold and are effective in tremor suppression with about a 50% reduction in intensity [2]. However, the associated muscle fatigue due to unnatural muscle recruitment patterns limits the duration it can be used [5]. In contrast, sensory electrical stimulation (SES) methods stimulate sensory neurons below the motor threshold, which does not result in any muscle fatigue. When used to mitigate tremors, SES methods are currently less effective than FES methods, with suppression ratios in the 30%s and 40%s [13].

Both SES and FES are traditionally implemented using

This work was partially supported by NIH grant #1R21EB032059.

two stimulation sites in a given pair of agonist/antagonist muscles, with the most popular being the flexor carpi radialis (FCR) and the extensor carpi radialis (ECR). This type of method mainly addresses one axis of tremor: the flexion and extension component. However, most tremors manifest in multiple degrees of freedom (DOF). In particular, the rotational component of tremor has not been significantly explored, and with evidence suggesting that wrist pronation-supination is a significant contributor to PD tremor [10], the need for more rotation-targeted tremor suppression becomes apparent.

To address suppression in multiple DOF, FES or SES must be capable of stimulating multiple muscle groups, some of which are deeply located and are inaccessible through non-invasive means.

In this work, we introduce the pronator and supinator muscles as stimulation targets as well as the use of deep interferential current (DIC) to suppress wrist tremors. DIC is conventionally used in pain reduction [7] [8], but the potential to stimulate the deeper forearm pronator [6] and supinator muscles encourages its use in tremor suppression. DIC stimulation amplitudes remain below motor threshold so electrical stimulation-induced fatigue is minimal or nonexistent, making it more comfortable for the user [8].

The primary benefit of DIC over other stimulation methods is the administration of current via high frequency carrier waveforms that maintain an outer frequency equivalent to conventional SES methods. An example of DIC and SES 10 Hz outer frequency waveforms are shown in Fig. 1. This carrier frequency allows the current to better penetrate through tissue and reach the target muscle. The mechanism by which it works is fully described in [9].

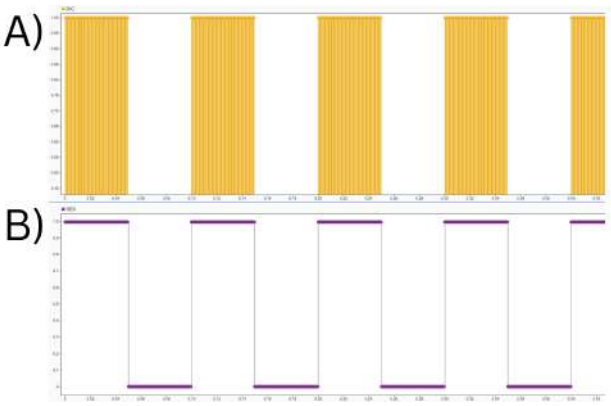


Fig. 1. DIC (A) vs SES (B) Stimulation Waveform Visual Example

II. Methods

1 PD and 1 ET subject were recruited for this study. Informed consent was collected prior to any experimentation, with methods approved by the Institutional Review Board of North Carolina State University.

We compared the tremor suppression efficacy of our DIC approach against an SES-based technique during active tremoring. For both techniques, we stimulated the four major forearm muscle groups: FCR, ECR, pronator, and supinator. Our subjects were asked to perform a cup lift-and-hold task for a period of one minute. This task is typically used by clinicians to elicit and observe tremor. As shown in Fig. 2 (muscle diagrams reproduced and edited from [11] with same-colored icons corresponding to antagonist-pair stimulation targets), electrodes were placed on each subject's FCR, ECR, pronator, and supinator, and an inertial measurement unit (IMU, Yost Labs) was securely attached to the back of their hand to collect data on tremor kinematics. Electrode and IMU positioning remained constant throughout all trials. The cup lift-and-hold task has the subject, when prompted, grabbing the handle of a standard mug (<450 g) and lifting it off a table in front of them for the trial's duration. The goal of the lift is to ensure there is no support to the subject's elbow, and they are holding their arm in free space. No stimulation was applied for the first fifteen seconds to allow for tremor to occur and to measure the trial's tremor amplitude baseline. Stimulation was turned on at fifteen seconds and applied continuously for the remainder of the trial (45 s). During a given trial, only one of a SES (II-A) or DIC (II-B) approach was used. A no-stimulation trial was also collected separately for further baseline use. Five DIC and three SES trials were conducted, with at least a minute of rest given between trials to remove any residual effects of stimulation. For consistency, SES trials were performed first, and a ten-minute break given before starting DIC trials.

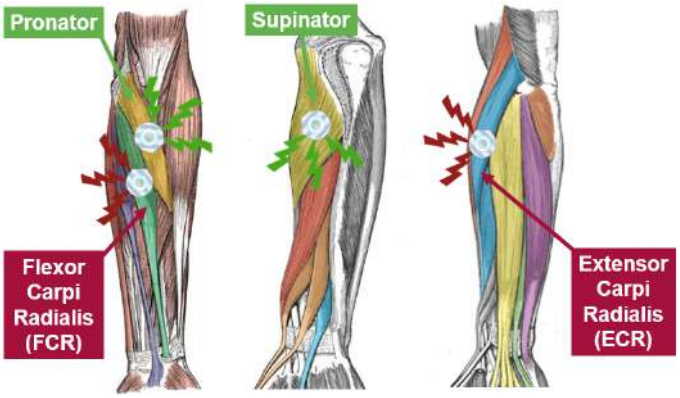


Fig. 2. Forearm Electrode Placements

A. SES Protocol

For the SES-based tremor suppression protocols, we stimulated all four electrode pairs using a Rehastim device (Rehastim, HASOMED GmbH, Magdeburg, Germany). This differentiation allowed us to determine the impact of introducing the pronator and supinator as stimulation sites. Before experimentation, the optimal stimulation inner wave frequency for each subject was determined using a process described by us in [12]. The same frequency was used throughout all SES trials. Each subject's SES parameters are listed in Table I. As we stimulated at 10 Hz, the outer frequency, or pulse-width, was 0.1 seconds.

TABLE I
SES STIMULATION PARAMETERS

Subject ID	Inner Pulse Frequency (Hz)	Amplitude (mA)
S1	150	4
S2	200	4

B. DIC Protocol

In the DIC protocol, we connected the electrodes on each subject's pronator and supinator to a Digitimer device (Digitimer DS8R, Digitimer Ltd., United Kingdom), which allowed us to apply DIC to only these muscles while SES was applied to the FCR and ECR. The rationale is that since the FCR and ECR are relatively superficial, SES is sufficient for activation and DIC is reserved for the deeper muscles.

For consistency, we applied the same DIC stimulation parameters across all subjects. The carrier frequency was 2 kHz and the burst (outer) frequency was 10 Hz (outer pulse width 0.1 seconds). The carrier frequency was chosen by the capabilities of the stimulating device, and the burst frequency selected from a range of 2-12 Hz, which are considered the lower and upper limits of tremor muscle activation frequency. For comparison with SES, 10 Hz was selected for both stimulation methods.

C. Data Analysis

Tremor suppression ratios, expressed as a percentage, were calculated for each DOF (see Fig. 3) within each trial to ensure comparability between trials. The formula is given in (1).

$$R_{suppression} = (1 - \frac{T_{stim}}{T_{base}}) \times 100 \quad (1)$$

where T_{base} is average tremor amplitude during the baseline period of no stimulation and T_{stim} is average tremor amplitude during stimulation. The amplitudes are derived from the angular velocity data given by the IMU. The tremor suppression rate for each trial is calculated separately to isolate the effects of stimulation on the tremor that occurred during a given trial.

III. RESULTS

The average suppression ratios for each subject are shown in Fig. 4. Positive suppression ratios indicate that stimulation has mitigated tremor for a given DOF. On average, we observed tremor suppression in all DOF for both SES and DIC protocols. However, the scale of suppression was different between subjects. Our PD subject (S1) experienced notable suppression (>60%) in all DOF with SES, whereas the largest suppression ratio for DIC trials was 47.9% in the z-axis. In contrast, our ET subject (S2) had suppression ratios ranging from 14.1-37.6% for SES trials and 9.5-29.5% for DIC trials. Notably, S2's highest suppression was from SES in the z-axis.

IV. DISCUSSION

Our results indicate that there are benefits to our targeted stimulation approach as an extension of current 2-stimulation-site SES methods. With the complexity with which tremors

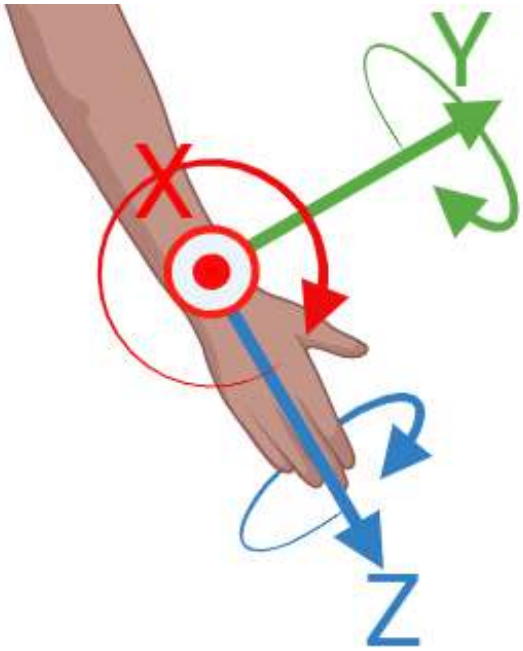


Fig. 3. DOF Axes for Tremor Suppression Calculations

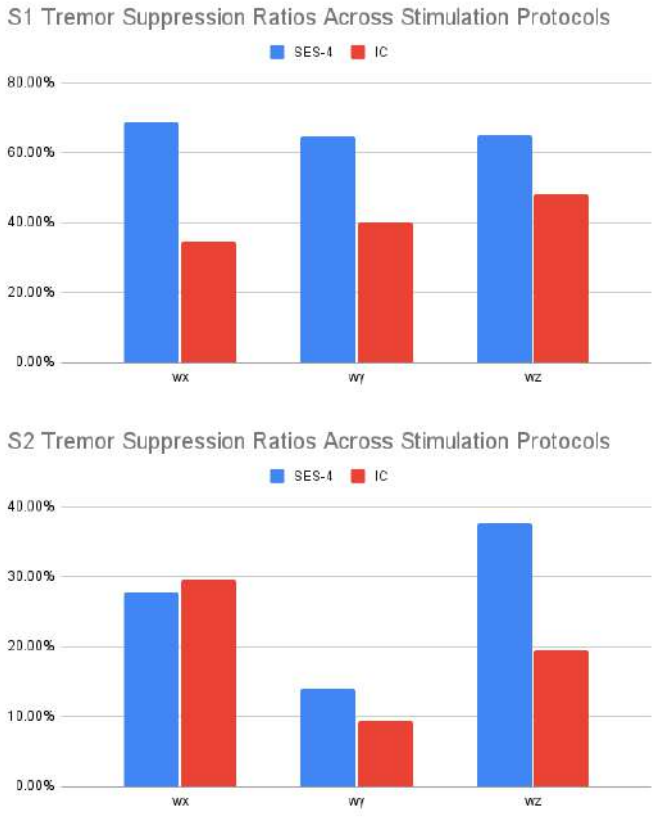


Fig. 4. Avg. Tremor Suppression Ratios in each DOF for SES and DIC Protocols

manifest in each individual, it stands that expanding the stimulation targets from two to four muscle groups may improve tremor suppression in individuals that experience tremor in all 3 DOF. However, the variability in our results underline the importance of tailoring stimulation protocols to the individual.

For our PD subject to experience average tremor suppression ratios in the 60's from SES demonstrates that for this individual, SES has approximately the same level of efficacy as FES protocols tend to have for the PD population. In order to strengthen our findings, we will compare tremor suppression with our 4-stimulation-site SES and DIC methods against the traditional 2-stimulation-site SES and FES methods.

We used the same DIC protocols for both subjects, but personalizing these protocols may improve tremor suppression. Even with basic stimulation of only the ECR and FCR, simply altering the inner stimulation frequency results in visible differences in how tremors are mitigated [12]. These optimal values can vary greatly per person, and depend on when stimulation is applied (e.x. right when the tremor begins/is detected, after a brief delay, or in pulses at a given outer frequency with or without a starting delay). Similar parameters can be adjusted for DIC, including the carrier frequency (going anywhere from 2-12 kHz) and burst frequency (2-12 Hz). This work is meant to demonstrate the feasibility of using DIC in tremor suppression, so even though we observed higher suppression ratios with SES compared to DIC, we find promise in the significant room for optimization of stimulation protocols. We plan to expand on our results in this work by trying a variety of carrier and burst combinations and introducing a variable time delay at the start of stimulation to determine each subject's optimal DIC protocols. Particularly, higher carrier frequencies are known to better penetrate into muscles, so we will focus on the higher end of the spectrum (10-12 kHz). In theory, this should improve activation of the appropriate neural pathways that lead to tremor suppression and lead to functional benefits in individuals that experience tremors.

We also collected qualitative data on user experience for each protocol. All subjects reported feeling no discomfort during any of the protocols. There was also no noticeable difference in feeling between the DIC and SES protocols, which is to be expected with the low current amplitude - differences would be difficult to observe so close to the sensory threshold. Our PD subject noted prior to experimentation that they felt their tremor had a significant rotational component (corresponding to the z-axis), and they felt and saw it almost disappear during the DIC trials. Since this is not supported by the observed findings - DIC resulted in smaller suppression ratios than SES - we are very interested in exploring subject perception in relation to stimulation approaches. The same subject also self-reported a potential carry-over effect of DIC stimulation, with their tremor appearing to be slightly mitigated in the period directly following experimentation. We are interested in quantifying these findings in the future using clinical scales.

V. Conclusion

Previous studies have shown that SES is a viable method of wrist tremor suppression for people who have PD or ET. However, the limited stimulation sites and activation from SES limited its efficacy, especially compared to fatigue-inducing FES protocols. In this work, we introduced the use of deep interferential current as a method to activate the forearm pronator and supinator during wrist tremors, thereby providing suppression with the absence of FES-induced muscle fatigue that SES methods have. Our DIC approach has significant room to improve by individualizing stimulation protocols and experimenting with different application timings, with the results of this work supporting continued research in this area.

References

[1] H. S. Nguyen and T. P. Luu, "Tremor-Suppression Orthoses for the Upper Limb: Current Developments and Future Challenges," Frontiers in Human Neuroscience, vol. 15, Apr. 2021, doi: https://doi.org/10.3389/fnhum.2021.622535.

[2] J. Mo and R. Priefer, "Medical Devices for Tremor Suppression: Current Status and Future Directions," Biosensors, vol. 11, no. 4, p. 99, Mar. 2021, doi: https://doi.org/10.3390/bios11040099.

[3] J. Kim, T. Wichmann, O. T. Inan, and S. P. Deweerth, "A Wearable System for Attenuating Essential Tremor Based on Peripheral Nerve Stimulation," IEEE Journal of Translational Engineering in Health and Medicine, vol. 8, pp. 1–11, 2020, doi: https://doi.org/10.1109/JTEHM.2020.2985058.

[4] P. Song et al., "The global prevalence of essential tremor, with emphasis on age and sex: A meta-analysis," Journal of Global Health, vol. 11, 2021, doi: https://doi.org/10.7189/jogh.11.04028.

[5] G. Grimaldi, S. Camut, and M. Manto, "Functional electrical stimulation effect on upper limb tremor," International Journal of Biomagnetism, vol. 13, no. 3, pp. 123–124, 2011.

[6] H. Ohara and S. Hasegawa, "An Electrical Stimulation Method to Control Deep Muscle Contraction using Surface Electrodes," Jan. 2022, doi: https://doi.org/10.21203/rs.3.rs-1201798/v1.

[7] S. Kitchen, Electrotherapy E-Book: evidence-based practice, [Review of Electrotherapy E-Book: evidence-based practice]. Elsevier Health Services. ed. 11, 2001

[8] M. I. Johnson and G. Tabasam, "An investigation into the analgesic effects of interferential currents and transcutaneous electrical nerve stimulation on experimentally induced ischemic pain in otherwise pain-free volunteers," Physical therapy, vol. 83 no. 3, pp. 208–223, 2003.

[9] A. R. Ward and N. Shkuratova, "Russian Electrical Stimulation: The Early Experiments," Physical Therapy, vol. 82, no. 10, pp. 1019–1030, Oct. 2002, doi: https://doi.org/10.1093/ptj/82.10.1019.

[10] M. A. Thenganatt and E. D. Louis, "Distinguishing essential tremor from Parkinson's disease: bedside tests and laboratory evaluations," Expert Review of Neurotherapeutics, vol. 12, no. 6, pp. 687–696, Jun. 2012, doi: https://doi.org/10.1586/ern.12.49.

[11] R. Howden and H. Gray, Anatomy, descriptive and applied. London: Longmans, Green And Co, 1918.

[12] A. Iyer et al., "Ultrasound Imaging Triggered Tremor Suppression with Personalized Afferent Stimulation Frequency," in IEEE Transactions on Biomedical Engineering, doi: 10.1109/TBME.2024.3519628.

[13] J. L. Dideriksen et al., "Electrical stimulation of afferent pathways for the suppression of pathological tremor," in Front. Neurosci., 2017, doi: 10.3389/fnins.2017.00178

Towards Safer Rehabilitation: Improving Gait Trajectory Tracking for Lower Limb Exoskeletons Using Offline Reinforcement Learning

Matthew Wong Sang[1], Jyotindra Narayan[3], Bukeikhan Omarali[2], A. Aldo Faisal[1,2,3]

***Abstract*— The application of online reinforcement learning (RL) in lower limb exoskeleton control has the potential to improve gait rehabilitation for individuals with impaired mobility. However, online RL approaches require real-time exploration and pose safety risks during training as suboptimal policies can lead to unstable or unsafe actions being executed by the exoskeleton. This study explores the application of offline RL methods, including Implicit Q-Learning (IQL), Twin Delayed Deep Deterministic Policy Gradient with Behavior Cloning (TD3+BC), and Revisited Behavior Regularized Actor-Critic (ReBRAC), for trajectory control of lower limb exoskeletons using a pre-collected dataset. The transition involved generating a diverse and representative dataset using online RL methods like Proximal Policy Optimization (PPO), which was then utilized to optimize offline RL models with advanced hyperparameter tuning via Optuna. Our results demonstrate improved gait trajectory tracking over a PPO baseline, with our TD3+BC model achieving the best performance. These findings highlight the potential of offline RL to enhance exoskeleton trajectory control while minimizing safety risks inherent in online approaches.**

I. Introduction

Gait impairment, commonly caused by neurological disorders such as spinal cord injury and stroke [1], affects millions worldwide, severely impacting their mobility and quality of life [2]. Conventional gait rehabilitation methods, while effective, often require intensive manual therapy, limiting scalability and accessibility [3]. Lower limb exoskeletons have emerged as a promising solution for providing repetitive, task-oriented training, which is essential for motor recovery [4]. However, controlling these devices effectively is complex due to the variability in human-exoskeleton interactions [5]. This complexity has driven interest in advanced control strategies such as reinforcement learning (RL), which can adaptively address these challenges.

RL allows controllers to learn directly from interaction data while bypassing the need for predefined dynamics models. Initial RL applications used algorithms like State-Action-Reward-State-Action (SARSA) [11] and Q-learning [12] to tune control parameters dynamically. More recent approaches leverage Deep Reinforcement Learning (DRL) to handle the high-dimensional nature of multi-joint human-exoskeleton systems. For instance, DRL-based controllers, using algorithms like Proximal Policy Optimization (PPO) [13], have been developed to adapt assistive torque profiles in real-time [14], while others use DRL methods completely end-to-end to directly map sensor data to control actions [15]. Additionally, DRL has shown promise in rehabilitation settings beyond exoskeletons, such as functional electrical stimulation cycling, where DRL controllers outperform traditional methods in providing adaptive neurostimulation for cycling movements in paralysed patients [16], [17], [18]. While these online RL approaches have demonstrated success in adaptive control, such methods require extensive interaction data and policy exploration, which can be potentially unsafe in real-world clinical environments [19]. This is because real-time training with online RL can result in suboptimal policies being deployed during learning, potentially leading

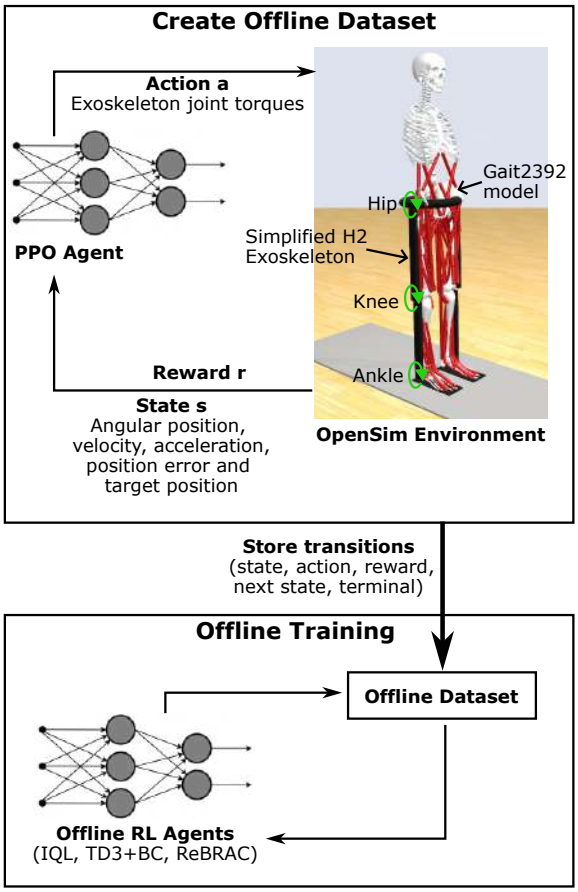


Fig. 1. Overview of proposed methodology. Online training is conducted using the Stable Baselines 3 library [6], in a custom RL environment based on OpenAI's Gymnasium library [7], which leverages biomechanical simulations in OpenSim [8]. These online interactions are stored in an offline dataset which is used for offline training using the d3rlpy [9] library. Models are optimized using Optuna [10] and their performance is evaluated and compared.

[1]Brain and Behaviour Lab, Department of Bioengineering, Imperial College London, UK. [2]Brain and Behaviour Lab, Department of Computing, Imperial College London, UK. [3]Chair in Digital Health, Universität Bayreuth, Germany
{aldo.faisal}@imperial.ac.uk

to unstable or unsafe actions by the exoskeleton, which risks causing discomfort or harm to the user.

Offline RL addresses these challenges by enabling models to learn from pre-collected, fixed datasets, eliminating the need for real-time exploration and reducing risks associated with direct patient interactions [20]. Designed to handle distributional shifts and prevent unsafe actions [19], offline RL is particularly well-suited for clinical settings where safety is critical. However, unlike online RL, offline RL lacks the ability to adapt dynamically to new patient-specific variations, as it does not continuously interact with the environment. This trade-off prioritizes safety but limits immediate adaptability. Additionally, offline RL's reliance on a fixed dataset may exclude certain types of gait impairment if unrepresented, potentially limiting its effectiveness. Nevertheless, the dataset can be incrementally expanded with new observations, improving generalization to evolving patient conditions over time. In rehabilitation robotics, offline RL has been primarily applied to robotic knee prostheses, where a policy iteration-based approach was used to optimize impedance parameters from pre-collected data [21].

In this work, we focus on applying offline RL to lower-limb exoskeleton control. We first trained an online model using PPO to generate an offline dataset instead of using an existing one to ensure consistency between the simulation environment and the collected data. This approach allowed us to construct a dataset with well-defined state transitions, control inputs, and reward functions tailored to the specific exoskeleton control task. This was then leveraged to train and evaluate our offline models based on IQL[22], TD3+BC[23], and ReBRAC[24]. Our goal is to enhance gait rehabilitation outcomes by developing control systems that can safely improve trajectory tracking and accommodate individual variability over time. This paper explores the potential of offline RL in overcoming the limitations of online methods, contributing to the advancement of data-driven exoskeleton-based rehabilitation.

II. Methods

Our proposed methodology (see Fig.1) begins with the description of the simulated human-exoskeleton system, including the creation of a custom *gym* environment. Next, the generation of the offline dataset using the PPO algorithm is described. This dataset is used to train offline RL models using the IQL, TD3+BC, and ReBRAC algorithms. Finally, the evaluation metrics used to assess the performance of our models are detailed.

A. Human-Exoskeleton System

OpenSim was chosen as the multi-body dynamics simulator due to its open-source availability and widespread use in biomechanical research [8]. The Gait2392 musculoskeletal model [25], commonly used in gait simulation and analysis research, was employed to develop the human-exoskeleton system. This model was scaled to represent a subject with a height of 1.8 meters and a mass of 82 kg, ensuring consistency with the selected subject from a publicly available dataset containing gait patterns from 138 able-bodied individuals and 50 post-stroke individuals [26].

TABLE I

Adapted H2 Exoskeleton Model Parameters [27], [28]

Body	**Thigh**	**Shank**	**Foot**	**Hip Support**
Mass[kg]	1.5	1.5	0.5	5
Length[m]	0.47	0.42	0.26	-
I_{xx} [kg m^2] *	0.015	0.059	0.337	0.003
I_{yy} [kg m^2] *	0.005	0.003	0.009	0.051
I_{zz} [kg m^2] *	0.014	0.057	0.338	0.063
Joint limits **	**Hip**	**Knee**	**Ankle**	**Pelvis**
Minimum (°)	-20	-3	-20	N/A
Maximum (°)	100	100	20	N/A

* The I_{xx}, I_{yy}, and I_{zz} are the moments of inertia.
** Negative joint angles indicate extension/plantarflexion while positive ones indicate flexion/dorsiflexion

To define the desired gait trajectory, a pair of individuals—one post-stroke patient and one able-bodied individual—were selected based on their similar physical characteristics, including sex, height, and weight. This approach ensures that the desired gait pattern assigned to the hypothetical gait-impaired patient is realistically achievable. The desired trajectory used in the simulation corresponds to the gait pattern of the able-bodied individual walking on level ground.

The Gait2392 model components were modified to include an adaptation of the H2 ambulatory lower limb exoskeleton [27], consisting of thigh, shank, and foot bodies, along with a hip support (see Fig. 1). To achieve the desired simulation, torque actuators were added at the hip, knee, and ankle joints to represent the assistance provided by the exoskeleton controller. The exoskeleton operates in *passive-assist mode*, meaning that the simulated subject is assumed to be lower-limb paralyzed, and the exoskeleton provides the necessary torque to track the desired gait trajectory. The exoskeleton actuators, originally rated at 220 Nm on the H2, were increased to 400 Nm. This adjustment allows our approach to be applicable to heavier individuals and exoskeletons with higher torque capacities. All exoskeleton parameters discussed in this section are summarized in Table I.

B. The Reinforcement Learning Environment

To develop and evaluate our models, a custom RL gym environment was created. This environment, was built using OpenAI's Gymnasium library [7] and integrated with OpenSim. The primary objective of the RL agent in this environment is to learn the assistive torques required to minimize the deviation of the observed joint angles of the simulated human from the desired gait trajectory while adhering to joint limits - ensuring patient safety.

1) Action Space: The environment's action space is defined as a continuous three-dimensional space, with each dimension corresponding to the control input for the exoskeleton actuators at the hip, knee, and ankle joints. The control signals are in [-1, 1] range, representing the proportion of the maximum actuator torque applied at each joint.

2) Observation Space: The observation space provides a comprehensive state representation of the human-exoskeleton system. Specifically, the observation vector includes 15 features: the current joint angle, angular velocity, angular acceleration and position error, and the target angle, for each joint. The observation space is bounded to reflect the physical limits of the exoskeleton's joints, ensuring that the RL agent operates within a realistic and safe range.

3) Reward Function Design: A critical component of the environment is the reward function, which is designed to encourage the agent to achieve the desired gait pattern while adhering to joint limits. The reward, r is composed of three main components and is bounded in [-1, 1] range:

$$r = w_{tr} r_{tr} + w_{acc} r_{acc} + w_{lim} r_{lim} \quad , \quad r \in [-1, 1] \quad (1)$$

Here, r_{tr} is the trajectory tracking reward with weight w_{tr}, r_{acc} provides an additional reward for maintaining errors within an acceptable margin with weight w_{acc}, and r_{lim} is the joint limit reward with weight w_{lim}. These weights were assigned values of 1. Importantly, the agent starts in a state where r_{acc} and r_{lim} are received by default, effectively incentivizing the agent to take safe steps in the environment from the outset. These rewards are then reduced based on the agent's deviation from the desired trajectory, as measured by r_{tr}.

This reward structure is designed to balance exploration and safety, ensuring that the agent learns to prioritize both trajectory tracking accuracy and adherence to joint constraints. By providing a baseline reward for acceptable behavior and penalizing deviations from the desired trajectory, this approach helps to stabilize the training process and aligns with the safety-critical nature of exoskeleton control for gait rehabilitation.

a) Trajectory tracking reward: This component encourages the agent to minimize the absolute error between the observed angles q and desired angles q_{des} at each joint. The reward is structured to provide no penalty when the trajectory error is zero, and a linearly increasing penalty as the error grows:

$$r_{tr} = w_h A_h(q) + w_k A_k(q) + w_a A_a(q) \quad (2)$$

where w_h, w_k and w_a are weights for the hip, knee and ankle respectively. We opted for values of one third for these weights.

$$A_i(q) = -\frac{|q - q_{des}|}{q_{\max} - q_{\min}} \quad (3)$$

where i represents the hip h, knee k and ankle a. The error is normalized by dividing by the maximum deviation possible at each joint, i.e. the difference between the upper $q_{\max}$ and lower $q_{\min}$ exoskeleton joint limits.

b) Acceptable Margin Reward: A scalar reward is given to the agent if the absolute hip, knee and ankle joint errors are less than a specified threshold m. We chose m=2° to balance tracking precision with minor gait variations.

$$r_{acc} = B_h(q) + B_k(q) + B_a(q) \quad (4)$$

TABLE II
PPO HYPERPARAMETERS USED TO CREATE THE OFFLINE DATASET.

PPO Hyperparameter	Value
Learning Rate (α)	1e-4 - 7e-4
Number of Steps	1024
Number of Epochs	10
Batch Size	64
Discount Factor (γ)	0.99
GAE Lambda (λ)	0.95
Clip Range (ϵ)	0.2
Entropy Coefficient	5e-4 - 5e-2
Value Function Coefficient	0.5
Maximum Value for Gradient Clipping	0.5

$$B_i(q) = \begin{cases} 0.3 & \text{if } |q - q_{des}| \leq m \\ 0 & \text{otherwise} \end{cases} \quad (5)$$

c) Joint Limit Reward: To encourage safe and realistic joint angles, a reward is given if all joint angles stay within their expected ranges $[q_{\min}, q_{\max}]$ across the gait cycle.

$$r_{lim}(q_i) = \begin{cases} 0.1 & \text{if } q_{i,\min} \leq q_i \leq q_{i,\max} \\ 0 & \text{otherwise} \end{cases} \quad (6)$$

The weights and scalars were chosen to maintain a bounded reward function and ensure smooth gradients, facilitating stable and effective learning.

4) Episode Description: Each episode begins by resetting the OpenSim model to its initial state—the first state of the desired gait pattern. The RL agent must control the exoskeleton throughout the simulated gait cycle, applying appropriate torques to guide the limb along the desired trajectory. An episode is terminated when any joint angle goes beyond its limits defined in Table I, or when the end of the trajectory is reached. In our simulation environment, unintended randomness, likely stemming from numerical solvers and simulation time-stepping, introduced variations across episodes. Rather than removing this randomness, we retained it to inject noise into the system and evaluate the robustness of our models.

C. Dataset Generation Using Proximal Policy Optimization

To enable the use of Offline RL, we required a pre-collected dataset of transitions $\mathcal{D}$ generated by a behavior policy π_β. We trained an online agent for this purpose using the Proximal Policy Optimization (PPO) algorithm [13]. In our study, we utilized the open-source implementation of PPO provided by Stable-Baselines3 (SB3) [6]. This implementation integrated seamlessly with our OpenSim simulation environment, facilitating the training process. The key hyperparameters used in training are presented in Table II. Parameters not mentioned were held at their SB3 defaults to aid rapid development and progression to the offline training phase.

The dataset $\mathcal{D}$ was generated by storing transitions in the form of (s, a, r, s', d) tuples during the later stages of training, where s denotes the current state, a the action taken, r the reward received, s' the next state, and d a boolean value indicating episode termination. The dataset

consists of 207 episodes and approximately 200,000 transitions. The maximum undiscounted return observed in the dataset, representing the highest performance achieved by the PPO behavior policy π_β, was 813.2 (see Fig. 2 for the corresponding trajectory tracking sample). This policy serves as the baseline for evaluating our Offline RL models.

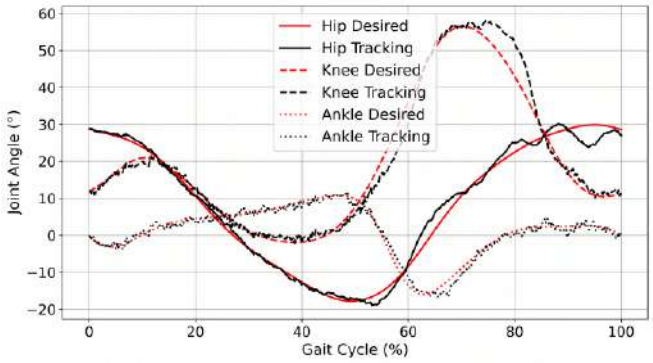


Fig. 2. Best trajectory tracking performance from the PPO dataset based on the undiscounted return

D. Offline Training

With the dataset created, we applied a set of offline RL algorithms: IQL, TD3+BC and ReBRAC. These algorithms were chosen due to their established effectiveness on continuous control tasks within the Datasets for Deep Data-Driven RL (D4RL) benchmark, with each offering distinct advantages for tackling challenges typically encountered in offline RL scenarios.

1) Implicit Q-Learning: The core of IQL involves alternating between fitting a value function through expectile regression and performing Bellman updates on the Q-function [22]. After the Q-function has successfully converged, the corresponding policy is derived using advantage-weighted behavioral cloning. By leveraging this technique, the method avoids explicitly querying out-of-distribution actions, which could lead to suboptimal or unstable learning behavior. Instead, it focuses on dataset-supported generalization, ensuring that the extracted policy remains well-grounded within the training data distribution and effectively captures high-value decision-making strategies [22].

2) Twin-Delayed Deep Deterministic Policy Gradient + Behavior Cloning: The TD3 algorithm, when combined with Behavior Cloning (BC), provides a balanced approach to policy improvement in offline RL [23]. By modifying the policy update to include a behavior cloning term, TD3+BC encourages the learned policy to stay close to the behavior policy present in the dataset, while still permitting generalization and exploration.

3) Revisited Behavior Regularized Actor-Critic: ReBRAC[24] builds upon TD3+BC, incorporating several key modifications aimed at enhancing performance in offline RL settings. By leveraging these enhancements, ReBRAC demonstrates state-of-the-art performance among competing offline RL methods [24], providing robust solutions to diverse continuous control tasks.

TABLE III
TUNED HYPERPARAMETERS FOR IQL, TD3+BC, AND REBRAC

Tuned Hyperparameter	IQL	TD3+BC	ReBRAC
Actor Learning Rate (α_{actor})	8.5e-04	4.1e-04	3.0e-04
Critic Learning Rate (α_{critic})	2.3e-03	7.4e-03	3.0e-03
Batch Size	128	512	512
Discount Factor (γ)	0.990	0.993	0.999
Soft Update Rate (τ)	0.004	0.007	0.005
Expectile (τ_{exp})	0.785	N/A	N/A
Alpha (α)	N/A	0.136	N/A

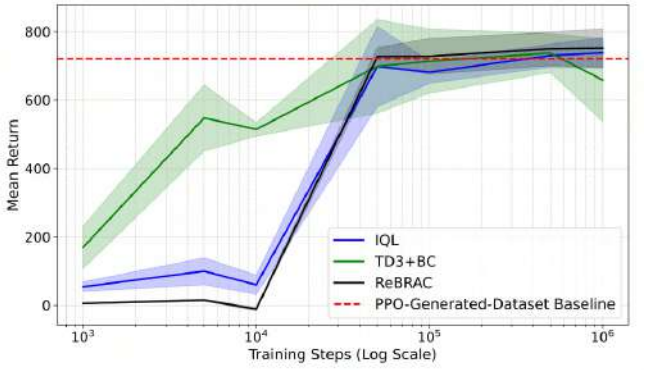


Fig. 3. Learning curves for IQL, TD3+BC and ReBRAC. Models checkpoints during training were saved and evaluated for 10 episodes. The mean is indicated by the solid line and the shaded regions represent the standard deviation. The mean return of the PPO dataset is illustrated by the red line. Note that the standard deviation for ReBRAC was very small and is barely visible until after 10^5 steps.

4) Implementation and Training: These offline RL algorithms were implemented using d3rlpy [9], an open-source offline RL library. In addition, Optuna [10] was used to perform automatic hyperparameter tuning. The best parameters from each optimization session are shown in Table III, while parameters not explicitly mentioned were maintained at their default values. Using these optimized parameters, we retrained our models for 1 million training steps to ensure convergence. We saved the models at various intervals and evaluated them over 10 episodes, to monitor mean returns during the training, see Fig. 3. All models demonstrated convergence after the 50k training step checkpoint.

E. Model Evaluation

The evaluation of our offline RL models against π_β was carried out using the Mean Absolute Error (MAE), Root Mean Squared Error (RMSE) and undiscounted return. The MAE indicates how closely the exoskeleton follows the desired trajectory, the RMSE offers additional insight by penalizing larger errors more heavily and identifying significant deviations from the desired trajectory, and the undiscounted return reflects the cumulative success of the policy in achieving the desired behavior during the gait cycle. We conducted our evaluation over 100 episodes for each offline model and analyzed the resulting distributions. We performed the Shapiro-Wilk test and the Mann-Whitney U

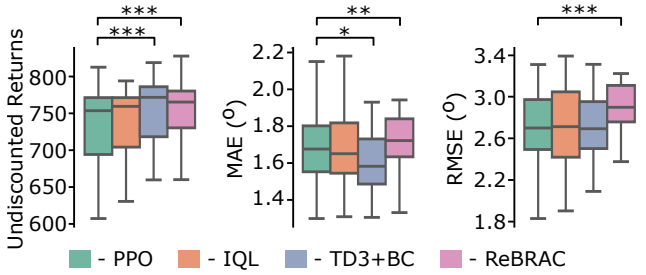


Fig. 4. Comparison of Return, MAE and RMSE Distributions across models. *p<0.05, **p<0.01, ***p<0.001 Mann-Whitney U test.

test using the SciPy python package, employing a significance level of 0.05.

III. Results

After computing the metrics for each model, we assessed normality using the Shapiro-Wilk test and determined that all metrics for all models were not normally distributed. Consequently, in Table IV, we present the median and interquartile range (IQR) of the MAE and RMSE across the hip, knee, and ankle joints. The overall distributions of these metrics are visually inspected in Fig. 4 and statistically analyzed using the Mann-Whitney U test to determine the significance of observed differences between models.

The results indicate that the TD3+BC and ReBRAC models achieved statistically significant improvements in returns compared to the baseline, while no significant improvement was observed for IQL. For MAE and RMSE, TD3+BC demonstrated improvements in both metrics, with the reduction in MAE being statistically significant. In contrast, IQL showed no statistically significant changes. Interestingly, while ReBRAC achieved higher returns, it exhibited a statistically significant decline in MAE and RMSE performance, suggesting a potential trade-off between maximizing returns and maintaining precise trajectory tracking.

Despite overall improvements in gait tracking, all models exhibited biomechanical anomalies at specific gait cycle points, likely inherited from the offline dataset. These include a pronounced hip oscillation near the end of the gait cycle, a prolonged knee flexion phase at 70–80% of the cycle, and high-frequency noise throughout ankle control.

Fig. 5 presents the trajectory tracking of each model, illustrating their ability to follow the desired gait pattern. OpenSim snapshots of TD3+BC's tracking throughout the gait cycle are visualized in Fig. 6, demonstrating its response to multi-joint control challenges. While TD3+BC achieved the best balance across joints, the observed anomalies highlight the influence of dataset artifacts on offline RL models, underscoring the importance of dataset quality in the future.

IV. Discussion

This study applied offline RL algorithms—namely IQL, TD3+BC, and ReBRAC—to train safe and effective control policies for lower-limb exoskeletons using a pre-collected PPO dataset. Our results demonstrate the feasibility of offline

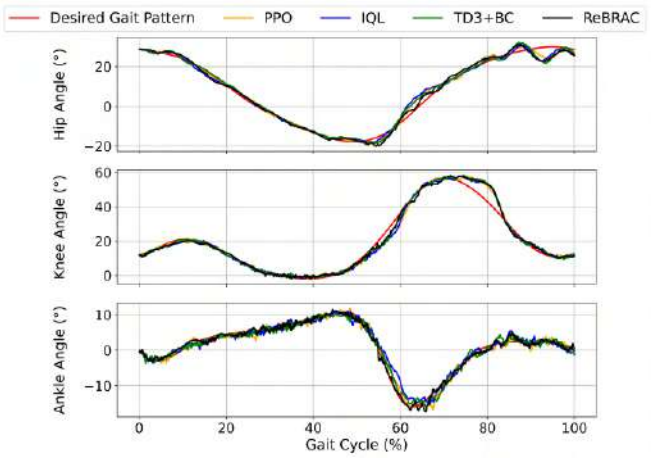


Fig. 5. Comparison of PPO (orange), IQL (blue), TD3+BC(green) and ReBRAC (black) in tracking the desired trajectory (red) for the hip, knee and ankle joints across a full gait cycle.

RL for exoskeleton trajectory control, with TD3+BC emerging as the best-performing model. This is consistent with the work of Li et al. [21], which optimized knee prosthesis impedance parameters via offline policy iteration. Our study extends offline RL to multi-joint gait trajectory tracking, relevant to rehabilitation for stroke and spinal cord injury patients [14].

A key advantage of offline RL is its *improved safety* over online RL, as training occurs without real-time exploration risks. This is particularly valuable in clinical applications, where direct policy learning poses significant safety and feasibility challenges. However, our findings also highlight a fundamental limitation: policies are constrained by dataset quality. The observed gait anomalies—hip oscillations, prolonged knee flexion, and ankle noise—suggest that our offline models inherited imperfections from the PPO dataset. Improving dataset diversity and quality is crucial to enhancing offline RL performance.

To address these limitations, future work should incorporate multiple subjects with varied impairments and walking speeds, introduce gait perturbations to assess adaptability, and explore transitioning from passive-assist to active-assist control for a more comprehensive rehabilitation scenario. Additionally, recent sim-to-real advancements [29] demonstrate that exoskeleton controllers trained entirely in simulation can successfully transfer to real-world devices, achieving significant reductions in metabolic costs across multiple locomotion tasks. Future work will involve real-world data collection to validate our approach outside simulation.

V. Conclusion

This study demonstrates the feasibility of offline RL for lower-limb exoskeleton trajectory control, offering a safer alternative to online RL. While TD3+BC showed the best performance, model effectiveness remained constrained by dataset quality. Future work will focus on improving data diversity, testing adaptability via gait perturbations, and validating models on real exoskeletons to bridge the gap between

TABLE IV

PERFORMANCE METRICS (MAE AND RMSE) ACROSS MODELS IN CONTROLLING HIP, KNEE, AND ANKLE JOINTS, MEDIAN±INTERQUARTILE

	Hip		Knee		Ankle	
Model	**MAE** (°)	**RMSE** (°)	**MAE** (°)	**RMSE** (°)	**MAE** (°)	**RMSE** (°)
PPO	1.76 ± 0.23	2.63± 0.39	2.05± 0.19	3.31± 0.35	1.22± 0.10	1.97± 0.30
IQL	1.64 ± 0.13	2.37± 0.22	2.13± 0.30	3.55± 0.58	1.24± 0.13	2.05± 0.35
TD3+BC	1.59 ± 0.16	2.38± 0.23	2.13± 0.18	3.64± 0.31	1.06± 0.12	1.79± 0.31
ReBRAC	1.69 ± 0.20	2.54± 0.25	2.25± 0.17	3.78± 0.33	1.23± 0.07	2.13± 0.22

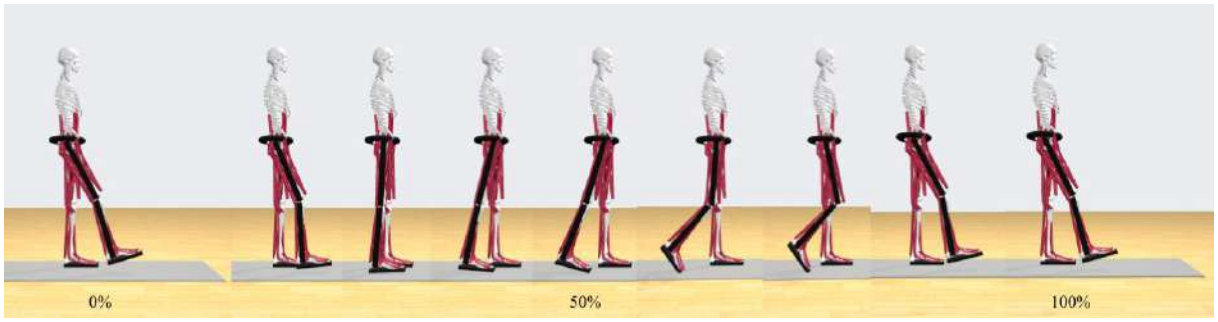


Fig. 6. OpenSim simulation of human-exoskeleton walking under the control of the TD3+BC model from 0 to 100% of the gait cycle.

simulation and clinical deployment.

REFERENCES

[1] W. Pirker and R. Katzenschlager, "Gait disorders in adults and the elderly: A clinical guide," *Wiener Klinische Wochenschrift*, vol. 129, no. 3-4, pp. 81–95, 2017.

[2] P. Mahlknecht, S. Kiechl, B. R. Bloem, J. Willeit, C. Scherfler, A. Gasperi, G. Rungger, W. Poewe, and K. Seppi, "Prevalence and burden of gait disorders in elderly men and women aged 60–97 years: a population-based study," *PloS One*, vol. 8, no. 7, 2013.

[3] T. K. Uchida and S. L. Delp, *Biomechanics of movement: the science of sports, robotics, and rehabilitation*. Mit Press, 2021.

[4] J. Teodoro, S. Fernandes, C. Castro, and J. B. Fernandes, "Current trends in gait rehabilitation for stroke survivors: A scoping review of randomized controlled trials," *J. Clin. Med.*, vol. 13, no. 5, 2024.

[5] B. Kalita, J. Narayan, and S. K. Dwivedy, "Development of active lower limb robotic-based orthosis and exoskeleton devices: a systematic review," *Int. J. Soc. Rob.*, vol. 13, pp. 775–793, 2021.

[6] A. Raffin, A. Hill, A. Gleave, A. Kanervisto, M. Ernestus, and N. Dormann, "Stable-baselines3: Reliable reinforcement learning implementations," *J. Machine Learn. R.*, vol. 22, no. 268, pp. 1–8, 2021.

[7] G. Brockman, V. Cheung, L. Pettersson, J. Schneider, J. Schulman, J. Tang, and W. Zaremba, "Openai gym," *arXiv:1606.01540*, 2016.

[8] A. Seth, J. L. Hicks, T. K. Uchida, A. Habib, C. L. Dembia, J. J. Dunne, C. F. Ong, M. S. DeMers, A. Rajagopal, M. Millard, *et al.*, "Opensim: Simulating musculoskeletal dynamics and neuromuscular control to study human and animal movement," *PLoS Comp. Bio.*, vol. 14, no. 7, 2018.

[9] T. Seno and M. Imai, "d3rlpy: An offline deep reinforcement learning library," *J. Machine Learn. R.*, vol. 23, no. 315, pp. 1–20, 2022.

[10] T. Akiba, S. Sano, T. Yanase, T. Ohta, and M. Koyama, "Optuna: A next-generation hyperparameter optimization framework," in *ACM SIGKDD*, 2019, pp. 2623–2631.

[11] G. Bingjing, H. Jianhai, L. Xiangpan, and Y. Lin, "Human–robot interactive control based on reinforcement learning for gait rehabilitation training robot," *Int. J. Advanced Robotic Systems*, vol. 16, no. 2, 2019.

[12] S. G. Khan, M. Tufail, S. H. Shah, and I. Ullah, "Reinforcement learning based compliance control of a robotic walk assist device," *Advanced Robotics*, vol. 33, no. 24, pp. 1281–1292, 2019.

[13] J. Schulman, F. Wolski, P. Dhariwal, A. Radford, and O. Klimov, "Proximal policy optimization algorithms," *arXiv:1707.06347*, 2017.

[14] S. Luo, G. Androwis, S. Adamovich, E. Nunez, H. Su, and X. Zhou, "Robust walking control of a lower limb rehabilitation exoskeleton coupled with a musculoskeletal model via deep reinforcement learning," *J. Neuroeng. and Rehab.*, vol. 20, no. 1, p. 34, 2023.

[15] L. Rose, M. C. Bazzocchi, and G. Nejat, "End-to-end deep reinforcement learning for exoskeleton control," in *SMC*. IEEE, 2020, pp. 4294–4301.

[16] N. Wannawas, M. Subramanian, and A. A. Faisal, "Neuromechanics-based deep reinforcement learning of neurostimulation control in fes cycling," in *NER*. IEEE/EMBS, 2021, pp. 381–384.

[17] N. Wannawas and A. A. Faisal, "Towards ai-controlled movement restoration: Learning fes-cycling stimulation with reinforcement learning," in *ICORR*, 2023, pp. 1–6.

[18] N. Wannawas, C. Diaz-Pintado, J. Narayan, and A. A. Faisal, "Controlling fes of arm movements using physics-informed reinforcement learning via co-kriging adjustment," in *ICRA*, 2024, pp. 5555–5560.

[19] S. Levine, A. Kumar, G. Tucker, and J. Fu, "Offline reinforcement learning: Tutorial, review, and perspectives on open problems," *arXiv:2005.01643*, 2020.

[20] R. Agarwal, D. Schuurmans, and M. Norouzi, "An optimistic perspective on offline reinforcement learning," in *ICLR*. PMLR, 2020, pp. 104–114.

[21] M. Li, X. Gao, Y. Wen, J. Si, and H. H. Huang, "Offline policy iteration based reinforcement learning controller for online robotic knee prosthesis parameter tuning," in *ICRA*. IEEE, 2019, pp. 2831–2837.

[22] I. Kostrikov, A. Nair, and S. Levine, "Offline reinforcement learning with implicit q-learning," in *ICLR*. PMLR, 2022.

[23] S. Fujimoto and S. S. Gu, "A minimalist approach to offline reinforcement learning," *Adv. in Neur. Info. Processing Sys.*, vol. 34, pp. 20 132–20 145, 2021.

[24] D. Tarasov, V. Kurenkov, A. Nikulin, and S. Kolesnikov, "Revisiting the minimalist approach to offline reinforcement learning," *Adv. in Neur. Info. Processing Sys.*, vol. 36, 2024.

[25] D. Thelen, A. Seth, F. C. Anderson, and S. L. Delp, "Gait 2392 and 2354 models," 2024.

[26] T. Van Criekinge, W. Saeys, S. Truijen, L. Vereeck, L. H. Sloot, and A. Hallemans, "A full-body motion capture gait dataset of 138 able-bodied adults across the life span and 50 stroke survivors," *Scientific data*, vol. 10, no. 1, p. 852, 2023.

[27] M. Bortole, A. Venkatakrishnan, F. Zhu, J. C. Moreno, G. E. Francisco, J. L. Pons, and J. L. Contreras-Vidal, "The h2 robotic exoskeleton for gait rehabilitation after stroke: early findings from a clinical study," *J. Neuroeng. and Rehab.*, vol. 12, pp. 1–14, 2015.

[28] L. Rose, M. C. Bazzocchi, and G. Nejat, "A model-free deep reinforcement learning approach for control of exoskeleton gait patterns," *Robotica*, vol. 40, no. 7, pp. 2189–2214, 2022.

[29] S. Luo, M. Jiang, S. Zhang, J. Zhu, S. Yu, I. Dominguez Silva, T. Wang, E. Rouse, B. Zhou, H. Yuk, *et al.*, "Experiment-free exoskeleton assistance via learning in simulation," *Nature*, vol. 630, no. 8016, pp. 353–359, 2024.

Robotic-Assisted Leg Stretching Techniques Facilitated by a Powered Exercise Machine and Functional Electrical Stimulation

Steven Evangelos[1], Nicholas Rubino[1], Steven W. Brose[2], Victor H. Duenas[1]

***Abstract*— Flexibility training involving stretching aims to increase the range of motion (ROM) about a joint and mitigate factors that limit mobility. Stretching has been used for improving human performance and preventing injuries. Further, stretching can be used as spasticity treatment in people with spinal cord injury to provide relief from muscle spasms and improve passive ROM. Therapists apply manual stretching to participants; however, providing personalized and repeatable stretching forces is caregiver intensive. This paper describes the methods to apply three stretching techniques and determines the feasibility of implementing their protocols using a powered device and open-loop Functional Electrical Stimulation (FES) patterns. This paper develops a robust kinematic closed-loop controller to emulate the static, active-isolated (AIS), and proprioceptive neuromuscular facilitation (PNF) stretching techniques targeting the hamstring complex in which the human lies in a supine position. The robust electric motor controller rotates the leg from its initial position through a desired ROM using a rigid pivot arm actuated by a Bowden cable. When the leg reaches the target end ROM, FES inputs are applied for AIS and PNF stretching. Experiments were safely conducted in two able-bodied individuals to demonstrate the device's feasibility of implementing each stretching technique on the hamstring complex. A Lyapunov stability analysis ensures exponential tracking of the motor controller.**

***Index Terms*— Active-Isolated Stretching; Functional Electrical Stimulation (FES); Human-Robot Interaction; Proprioceptive Neuromuscular Facilitation (PNF); Static Stretching.**

I. INTRODUCTION

Flexibility describes the neuromuscular system allowing for muscular and connective tissue extensibility that enables a joint to safely achieve its full range of motion (ROM) [1]. Flexibility training involving stretching aims to increase the ROM about a joint and mitigate factors that limit mobility. In athletic applications, stretching exercises have been included in warm-up routines to improve human performance and prevent injuries [2]. In rehabilitative applications, stretching remains a primary treatment for spasticity in patients with spinal cord injury (SCI) and is a widely accepted standard-of-care therapy [3], [4]. Spasticity degrades the ability to functionally use voluntary muscle contraction for leg control, which impairs balance, body transfers, exercise, and ambulation [5], [6]. Leg stretching can enhance maximal performance in able-bodied individuals and improve quality of life for people with spasticity after SCI. Whether intended for athletic or rehabilitative benefits, a systematic framework of flexibility is needed to customize the implementation of different stretching techniques for people with varying movement and sensory capacities.

In this paper, the muscle to be stretched is the hamstring complex (i.e., the agonist). The three stretching techniques implemented in this paper and described in Section II include: static, active-isolated (AIS), and proprioceptive neuromuscular facilitation (PNF). Static stretching exploits the principle of autogenic inhibition to increase ROM [7]. AIS takes advantage of the principle of reciprocal inhibition by concentrically contracting the antagonist (i.e., quadriceps complex) for timed repetitions to produce a reciprocally inhibiting (i.e., lengthening) response in the agonist [1], [8]. PNF stretching uses the principle of Golgi Tendon Organ (GTO) activation of an agonist in a long position, followed by an immediate, slow, and passive increase in ROM [9].

Typically, stretching techniques are administered manually (i.e., hands-on) by a healthcare practitioner or trainer. Physical therapists and caregivers routinely perform manual stretching to provide relief from muscle spasms, maintain soft tissue extensibility, and improve flexibility. However, the demand for incorporating flexibility-based treatment protocols for patients in rehabilitative settings has been steadily increasing faster than the number of therapists that can be trained and made available to provide these treatments (e.g., due to staffing shortages). Further, challenges related to repeatability, consistency, and personalization have motivated the rehabilitation robotics community to generate novel, innovative solutions to facilitate on-demand stretching.

The technical challenges associated with developing a device and closed-loop controllers to implement the static, AIS, and PNF stretching techniques through human-robot interaction in a rehabilitative setting are safety and customization. Save the structural specifications in the physical design, the true measure of any device's feasibility for integration into a rehabilitative setting rests on the accuracy and precision with which the machine follows industry-accepted protocols/guidelines for how to effectively emulate the process of receiving manual therapy. Therefore, closed-loop feedback control methods are critical to ensure the safe, correct implementation of the stretching techniques and thus, ensure optimal performance and recovery.

People with SCI rely heavily on static stretching as a treatment for spasticity [4]. Instead of applying manual

*Research reported in this publication was supported in part by the National Science Foundation under Grant No. 2023354340 and by the award 1I21RX004652-01A1 from the VA R&D. The contents are solely the responsibility of the authors and do not necessarily represent the official views of the NSF or VA R&D.

[1]Department of Mechanical and Aerospace Engineering, Syracuse University, Syracuse NY 13244, USA. Email: {sevang01,narubino,vhduenas}@syr.edu

[2]Department of Physical Medicine and Rehabilitation, SUNY Upstate Medical University and Syracuse VA Medical Center, Syracuse NY 13210, USA. Email: {Steven.Brose}@va.gov

forces, a powered machine can customize the rotation of the leg through a desired ROM. Further, these individuals are typically unable to voluntarily contract and relax agonists and antagonists, which inherently contraindicates manual AIS or PNF stretching techniques. In this paper, open-loop functional electrical stimulation (FES) inputs are applied to the antagonist (i.e., quadriceps complex) for AIS and to the agonist (i.e., hamstring complex) for PNF stretching, which could broaden and automate the scope of available treatments for people with SCI, without compromising safety. FES has been applied to characterize muscle fatigue during leg extension [10], combined with an electric motor for FES-cycling [11], and integrated with an exoskeleton for walking [12]. Traditional FES control facilitates concentric muscle contraction, and along with a robotic machine can produce torque about a joint for leg movement. Differently, this paper integrates FES with a powered machine to implement the stretching techniques in a supine position.

The main contribution of this paper is the design and implementation of a closed-loop kinematic motor controller and open-loop FES patterns for automated leg stretching of the hamstring complex using the static, AIS, and PNF techniques. Starting from a supine position, the electric motor rotates the leg through a desired ROM by exploiting the hip joint kinematics in the sagittal plane. Once the leg has reached the desired ROM, the motor maintains the leg in a static position. Then, a high amplitude FES pattern can be applied to the quadriceps complex (antagonist) for AIS, or a low amplitude FES pattern can be applied to the hamstring complex (agonist) for PNF stretching. Preliminary experiments in two able-bodied individuals were conducted to demonstrate feasibility of the proposed methods. A Lyapunov-based stability analysis is developed to ensure exponential kinematic tracking of the motor controller.

II. Stretching Techniques

The protocols governing the three stretching techniques implemented in this paper using the powered machine and FES are informed by the following standardized guidelines for manual treatment [1], [9], [13]:

Static Stretching. Once the hip joint arrives at the degree of hip flexion in the sagittal plane to elicit a muscle spindle response in the agonist, the joint is passively held in position, giving the body time to carry out the process of inhibiting the agonist so it can lengthen. One set involves a 60-second hold at the muscle spindle response angle of hip flexion in the sagittal plane.

Active-Isolated Stretching (AIS). Once the hip joint arrives at the degree of hip flexion in the sagittal plane to elicit a muscle spindle response in the agonist, the joint is passively held in position for 60-seconds. Different from static stretching, during the 60-seconds, active contraction of the (short) antagonist will be used to inhibit the agonist. Each repetition has a duty cycle of: 3-seconds of relaxed antagonist followed by 3-seconds of concentric contraction of the antagonist. Thus, one repetition is a 6-second process. One set involves 10 repetitions over 60-seconds.

Proprioceptive Neuromuscular Facilitation (PNF). Once the hip joint arrives at the degree of hip flexion in the sagittal plane to elicit a muscle spindle response in the agonist, the joint is passively held in position for 60-seconds. Different from static and AIS, during the 60-seconds, active contraction of the (long) agonist will be used to excite the GTO and create an inhibitory response. Each repetition has a duty cycle of: 10-seconds of relaxed agonist, 6-seconds of concentric contraction of the agonist, 20-seconds of increasing ROM to a new final position (where the final ROM is equal to the muscle spindle response ROM plus 10%), and 24-seconds of passive hold at the new final position. One set involves one repetition over 60-seconds.

III. Dynamics and Control Development

A. Dynamic Model

A leg rotating about the hip joint in the sagittal plane with the knee fixed in the extended position can be modeled as a single degree-of-freedom inverted pendulum as

$$J\ddot{q}+P(q,\dot{q})+G(q)+d(t)=\tau_{motor}(t)+\tau_{FES}(q,\dot{q},t), \quad (1)$$

where $J \in \mathbb{R}_{>0}$ denotes the uncertain positive constant corresponding to the lumped inertia of the leg and device, $q:\mathbb{R}_{\geq t_0}\to\mathcal{Q}$ denotes the measurable hip angular position, $\dot{q},\ddot{q}:\mathbb{R}_{\geq t_0}\to\mathbb{R}$ denote the measurable angular velocity and unmeasurable angular acceleration of the hip, respectively, $\mathcal{Q}$ is the set of hip angles, $t_0 \in \mathbb{R}$ is the initial time; $P:\mathcal{Q}\times\mathbb{R}\to\mathbb{R}$ denotes the effects of elasticity due to joint stiffness and the viscous damping effects in the musculotendon complex defined in [14]–[16]; $G:\mathcal{Q}\to\mathbb{R}$ denotes the effects of gravity; $d:\mathbb{R}_{\geq t_0}\to\mathbb{R}$ denotes unmodeled effects and external disturbances; $\tau_{FES}:\mathcal{Q}\times\mathbb{R}\times\mathbb{R}_{\geq t_0}\to\mathbb{R}$ denotes the torque evoked due to the applied open-loop FES input; and $\tau_{motor}:\mathbb{R}_{\geq t_0}\to\mathbb{R}$ denotes the torque applied by the motor about the hip joint, which is defined as

$$\tau_{motor}=B_e u_{motor}(t), \quad (2)$$

where $B_e \in \mathbb{R}_{>0}$ is a known motor torque constant and $u_{motor}:\mathbb{R}_{\geq t_0}\to\mathbb{R}$ denotes the motor current input designed in the subsequent subsection. The dynamic model in (1) satisfies the following assumption and properties that are exploited in the control design and stability analysis.

Assumption 1. *The additive disturbance d is bounded as $|d|\leq\zeta_d$, where $\zeta_d\in\mathbb{R}_{>0}$ is a known positive constant.*

Property 1. $|P(q,\dot{q})|\leq c_{p1}+c_{p2}|\dot{q}|$, *where $c_{p1},c_{p2}\in\mathbb{R}_{>0}$ are known constants [11].*

Property 2. $|G(q)|\leq\overline{g}$, *where $\overline{g}\in\mathbb{R}_{>0}$ is a known constant [17, Ch. 3].*

B. Kinematic Motor Tracking Controller

The kinematic motor tracking controller is designed to move the leg through the desired ROM for the three stretching techniques by following a desired hip joint trajectory in the sagittal plane denoted as $q_d:\mathbb{R}_{\geq t_0}\to\mathbb{R}$. To quantify the kinematic tracking objective, a measurable joint angular

position error $e : \mathbb{R}_{\geq t_0} \to \mathbb{R}$ and auxiliary filtered tracking error $r : \mathbb{R}_{\geq t_0} \to \mathbb{R}$ are defined as

$$e(t) = q_d(t) - q(t), \tag{3}$$

$$r(t) = \dot{e}(t) + \alpha e(t), \tag{4}$$

where $\alpha \in \mathbb{R}_{>0}$ is a selectable constant control gain. The desired trajectory q_d is bounded and continuously differentiable with bounded derivatives, such that $|q_d(t)| \leq \xi_{d_1}$, $|\dot{q}_d(t)| \leq \xi_{d_2}$, and $|\ddot{q}_d(t)| \leq \xi_{d_3}$, where $\xi_{d_1}, \xi_{d_2}, \xi_{d_3} \in \mathbb{R}_{>0}$ are known positive constants. Taking the time derivative of (4) and premultiplying by J, substituting for (1), (3) and (4) yields

$$J\dot{r} = J\ddot{q}_d + P(q, \dot{q}) + G(q) + d(t) - \tau_{motor} - \tau_{FES} + J\alpha(r - \alpha e). \tag{5}$$

Performing algebraic manipulation to (5) and combining terms that can be upper bounded by functions of the errors or by constants yields

$$J\dot{r} = \tilde{W} + N_d - \tau_{motor} - \tau_{FES} - e, \tag{6}$$

where the auxiliary signals $\tilde{W} \in \mathbb{R}$ and $N_d \in \mathbb{R}$ are defined as

$$\tilde{W} \triangleq P(q, \dot{q}) + J\alpha(r - \alpha e) - c_{p1} - c_{p2}\dot{q}_d + e, \tag{7}$$

$$N_d \triangleq G(q) + d(t) + J\ddot{q}_d(t) + c_{p1} + c_{p2}\dot{q}_d. \tag{8}$$

The auxiliary signal in (8) can be upper bounded using Property 2 and Assumption 1 as

$$|N_d| \leq \xi_d, \tag{9}$$

where $\xi_d \in \mathbb{R}_{>0}$ is a known positive constant. By using Property 1, (3) and (4), an upper bound can be obtained for (7) as

$$|\tilde{W}| \leq c_1 \|z(t)\|, \tag{10}$$

where $c_1 \in \mathbb{R}_{>0}$ is a known positive constant and $z : \mathbb{R}_{\geq t_0} \to \mathbb{R}^2$ is a composite vector of error signals defined as $z(t) \triangleq \begin{bmatrix} e(t) & r(t) \end{bmatrix}^T$. Given the open-loop error system in (6), the control input u_{motor} in (2) is designed as

$$u_{motor}(t) = k_1 r + k_2 \text{sgn}(r) + k_3 \|z\| \text{sgn}(r), \tag{11}$$

where $k_1, k_2, k_3 \in \mathbb{R}_{>0}$ are selectable constant gains and $\text{sgn}(\cdot)$ is the signum function. The closed-loop error system is obtained by substituting (11) into (6) as follows

$$J\dot{r} = \tilde{W} + N_d - \tau_{FES} - B_e(k_1 r + (k_2 + k_3\|z\|)\text{sgn}(r)) - e. \tag{12}$$

IV. STABILITY ANALYSIS

Theorem 1. *Given the closed-loop error dynamics in (12), the control input in (11) achieves global exponential tracking when $\tau_{FES} = 0$ in the sense that*

$$\|z(t)\| \leq \sqrt{\frac{\lambda_2}{\lambda_1}} \|z(t_0)\| exp^{-\frac{\beta}{2\lambda_2}(t - t_0)}, \tag{13}$$

provided the following gain conditions are satisfied

$$k_2 \geq \frac{\xi_d}{c_e} \text{ and } k_3 \geq \frac{c_1}{c_e}. \tag{14}$$

Proof. Let $V_1 : \mathbb{R}^2 \to \mathbb{R}$ be a positive definite, continuously differentiable Lyapunov function candidate defined as

$$V_1(e, r) = \frac{1}{2}e^2 + \frac{1}{2}Jr^2, \tag{15}$$

which satisfies the following inequalities $\lambda_1\|z\|^2 \leq V_1(z,t) \leq \lambda_2\|z\|^2$, where $\lambda_1 \triangleq \min(\frac{1}{2}, \frac{J}{2})$, $\lambda_2 \triangleq \max(\frac{1}{2}, \frac{\bar{J}}{2})$, and $\underline{J} \leq J \leq \bar{J}$, where $\underline{J}, \bar{J} \in \mathbb{R}_{>0}$. Let $z(t)$ be a Filippov solution to the differential inclusion $\dot{z} \in K[h](z)$, where $K[\cdot]$ is defined as [18], [19] and h is defined using (4) and (12) as $h \triangleq \begin{bmatrix} h_1 & h_2 \end{bmatrix}$, where $h_1 = r - \alpha e$ and $h_2 = J^{-1}\{\tilde{W} + N_d - \tau_{FES} - B_e(k_1 r + k_2 \text{sgn}(r) + k_3 \text{sgn}(r)\|z\|) - e\}$. The control input in (11) contains the signum function; hence, the time derivative of (15) exists almost everywhere (a.e.), i.e., for almost all t. Based on [20, Lemma 1], $\dot{V}_1(z,t) \overset{a.e.}{\in} \dot{\tilde{V}}_1(z,t)$, where $\dot{\tilde{V}}_1$ is the generalized derivative of (15) along the Filippov trajectories of $\dot{z} = h(z)$ defined as in [20] as $\dot{\tilde{V}}_1 \triangleq \bigcap_{\xi \in \partial V_1} \xi^T K \begin{bmatrix} \dot{e} & \dot{r} & 1 \end{bmatrix}^T (e,\, r,\, t)$, where $\partial V_1(z,t)$ is the generalized gradient of V_1 at (z,t), since $V_1(z,t)$ is continuously differentiable in z, $\partial V_1 = \{\nabla V_1\}$, $\dot{\tilde{V}}_1 \overset{a.e.}{\subset} [e,\, Jr] K \begin{bmatrix} \dot{e} & \dot{r} \end{bmatrix}^T$. Therefore, after substituting for (12), setting $\tau_{FES} = 0$ (i.e., FES input is not applied while the leg is rotated through the ROM), and canceling common terms, the time derivative of (15) can be expressed as follows

$$\dot{\tilde{V}}_1 \overset{a.e.}{\subset} -\alpha e^2 + \tilde{W}r + N_d r - c_e(k_1 r^2 + k_2|r| + k_3|r|\|z\|), \tag{16}$$

where $c_e \leq B_e \leq c_E$ and $c_e, c_E \in \mathbb{R}_{>0}$. By substituting (9) and (10) into the previous expression, cancelling common terms, and provided the sufficient gain conditions in (14) are satisfied, the following upper bound can be obtained

$$\dot{\tilde{V}}_1 \overset{a.e.}{\leq} -\alpha e^2 - k_1 c_e r^2 \overset{a.e.}{\leq} -\beta\|z\|^2, \tag{17}$$

where $\beta \triangleq \min\{\alpha, k_1 c_e\}$. Since $V_1 > 0$ and $\dot{V}_1 \overset{a.e.}{\leq} 0$, $V_1 \in \mathcal{L}_\infty$. Therefore, $e, r \in \mathcal{L}_\infty$ and thus, $z \in \mathcal{L}_\infty$, and $\dot{e}, \dot{q}, q \in \mathcal{L}_\infty$. Since $z \in \mathcal{L}_\infty$, then $u_{motor} \in \mathcal{L}_\infty$ in (11). Using (15) and (17), the exponential upper bound in (13) is obtained.

To account for the open-loop FES input in the stability of the motor controller when holding the leg in a static position at the end of the ROM, the subsequent analysis is provided. The closed-loop error system in (12) is output strictly passive (OSP) when $\tau_{FES} \neq 0$, i.e., when FES is applied, provided the sufficient gain conditions in (14) are satisfied. Using (17), the generalized time derivative of (15) can be further upper bounded as $\dot{\tilde{V}}_1 \overset{a.e.}{\leq} -\alpha|e|^2 - k_1 c_e |r|^2 + \tau_{FES}|r|$ and its integration yields $\int_{t_1}^{t} \tau_{FES}(\,)|r(\,)|d \overset{a.e.}{\geq} \tilde{V}_1(t) - \tilde{V}_1(t_1) + \alpha \int_{t_1}^{t} |e(\,)|^2 d + k_1 c_e \int_{t_1}^{t} |r(\,)|^2 d$, where $t_1 \in \mathbb{R} > t_0$, which can be used to prove that the closed-loop error system in (12) is OSP from input τ_{FES} to output r [21] since τ_{FES} is bounded due to the bounded open-loop FES input. ∎

V. EXPERIMENTS

This section presents the apparatus, FES patterns, experimental protocols, and results obtained with the custom powered machine depicted in Fig. 1. The experiments are

motivated to demonstrate the ability of the machine and FES to safely provide a user experience that is consistent with the protocols outlined for manual stretching of the hamstring complex using the static, AIS, and PNF techniques (as introduced in Section II). Three experiments (one for each flexibility technique) were conducted in two able-bodied participants (male, age 40 and male, age 24). The first experiment is a single static set. The second experiment is a single set of 10 AIS repetitions. The third experiment is a single set of one PNF repetition. Prior to the experiments, the participants provided written, informed consent consistent with IRB protocol at Syracuse University (IRB #: 22-404). The hypothesis is that the combination of a closed-loop robust kinematic motor controller and open-loop FES inputs can accurately follow industry protocols for static, AIS, and PNF stretching of the hamstring complex.

A. Apparatus

The apparatus depicted in Fig. 1 consists of a rigid pivot arm that supports the participant's leg and rotates in the sagittal plane about a pin aligned with the participant's hip joint (Fig. 1A). An optical encoder (US Digital) is affixed to the pin and is used to measure the hip angular position and compute the angular velocity (Fig. 1B). An offboard 24 VDC brushless electric motor (Maxon) using a Bowden cable and pulley system (Fig. 1C) applies torque about the hip by raising the rigid pivot arm that supports the participant's leg. A load cell (OMEGA LC201-300) is placed in series to measure the tension in the cable (Fig. 1D).

The motor controller designed in (11) is implemented using a desktop computer (Windows 10 OS, Microsoft) running a real-time target (QUARC 2.6, Quanser) using MATLAB/Simulink 2018a (Mathworks), and operating with a sampling frequency of 1 kHz. Data acquisition devices (Quanser QPIDe, Q8-USB) command motor inputs computed by (11) and collect data from the sensors. Software stop conditions limit the angular position and velocity of the pivot arm and an emergency stop button is available to the participant.

B. FES for AIS and PNF Stretching

Transcutaneous electrical stimulation was applied to the quadriceps and hamstring complexes for AIS and PNF stretching, respectively. Pulse width (70 μs) and stimulation frequency (60 Hz) were fixed while the pulse amplitude was varied using open-loop control (i.e., the stimulation pattern was predetermined). Current amplitude is controlled in a bipolar configuration to facilitate concentric contraction cycles of the antagonist and agonist for AIS and PNF stretching, respectively. Biphasic symmetric electrical stimulation was delivered from a current-controlled stimulator (Fig. 1E) (Hasomed GmbH, RehaStim).

For AIS, two 3" $\times$ 5" adhesive electrode pads (ValuTrode) are placed on the skin inferior to the proximal origin and superior to the distal insertion (above the knee) of the participant's quadriceps complex (Fig. 1F).

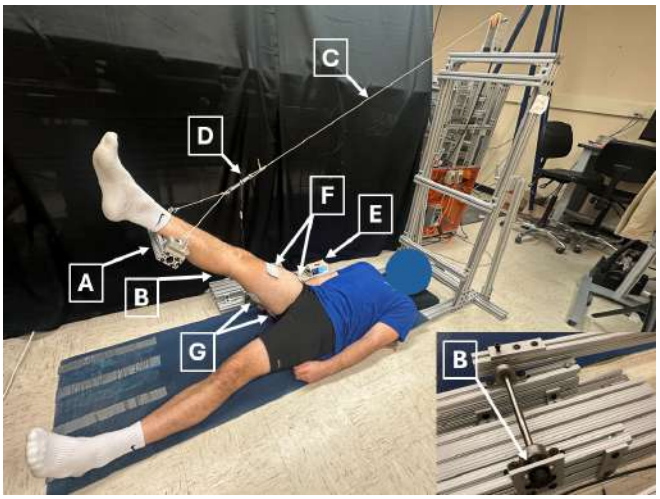


Fig. 1. A participant laying supine with the right hip being moved into hip flexion by the robust kinematic controller. A denotes the pivot arm. B denotes the optical encoder. C denotes the Bowden cable system. D denotes the load cell. E denotes the RehaStim FES module. F & G denote the FES electrode pad placement for AIS and PNF stretching, respectively. The sub-image shows the optical encoder from the participant's right side

For PNF stretching, two 3" $\times$ 5" adhesive electrode pads (ValuTrode) are placed on the skin inferior to the proximal origin and superior to the distal insertion (above the knee) of the participant's hamstring complex (Fig. 1G).

C. Protocol

Each experiment began with the participant laying supine on a thin, padded mat with the hip joint aligned to the rotational axis of the pivot arm. Using the kinematic motor controller defined in (11), the leg was rotated in tandem (slowly, as per industry standard guidelines) with the pivot arm about the hip joint in the sagittal plane from the horizontal (i.e., 0°) position to the desired end ROM and then held at that position until the end of the experiment (except in the case of PNF, where the kinematic controller increases the hip flexion angle by an additional 10% following FES-induced activation). The desired hip angular position, velocity, and acceleration, $q_d, \dot{q}_d, \ddot{q}_d$, are computed using hyperbolic tangent functions (two in the case of PNF) and their analytical derivatives.

For static stretching, five seconds after the robust kinematic controller is activated, the device begins to increase the angle of hip flexion in the sagittal plane to the target end ROM over 40 seconds – this rate of change in muscle lengthening of the agonist satisfies protocol guidelines to lift the leg slowly/passively. Once the leg reaches the target end ROM position, the device holds the leg static for 60 seconds.

For AIS, the leg is lifted similarly to the static case. However, once the leg is at the target end ROM position, FES is applied to the antagonist (i.e., quadriceps complex) with an open-loop high pulse amplitude with fixed pulse width and pulse frequency. The FES duty cycle for one set is consistent with the guidelines in Section II (see *Active-Isolated Stretching*).

For PNF stretching, the leg is lifted similarly to the static case. However, once the leg is at the target end ROM position for ten seconds, FES is applied to the agonist (i.e., hamstring complex) with an open-loop low pulse amplitude using fixed pulse width and pulse frequency. The FES duty cycle for one set is consistent with the guidelines in Section II (see *PNF Stretching*).

D. Results

For both participants, across all experiments, the kinematic controller gains were selected as $[\alpha,\ k_1,\ k_2,\ k_3] \triangleq [10,\ 0.0825,\ 0.015,\ 0.015]$. Fig. 2 shows the position tracking error e for each stretching experiment. Fig. 3 shows the desired q_d and actual q kinematic trajectories of each participant for each stretching experiment. Fig. 4 shows the open-loop FES patterns for the AIS and PNF stretching experiments.

As illustrated in Figs. 2-3, it can observed for all experiments that the kinematic controller was able to accurately follow the desired trajectory q_d.

For AIS, FES is applied for 10 antagonist contractions with minimal disturbance of the kinematic tracking. After the 10 FES-induced contractions, the experiment is concluded.

For PNF stretching, after the single set contraction of the agonist, the FES input is turned off and the kinematic controller tracks an increased target ROM over 20-seconds. Once the new position is held for an additional 24-seconds, the experiment is concluded. As depicted in Figs. 2-3, following the application of FES input, from 65-85 seconds, the kinematic controller was able to accurately increase the ROM by a factor of 10% over 20-seconds.

Fig. 5 shows the load cell tension and open-loop FES inputs of the AIS and PNF stretching experiments for Participant 1. The results in Fig. 5 illustrate an inversely proportional relationship between antagonist activation and load cell tension when using AIS and a proportional relationship between agonist activation and load cell tension when using PNF stretching. It can also be observed that following the (post-FES) PNF increase in ROM, the load cell tension remained at a magnitude consistent with the magnitude measured at the initial target ROM.

E. Discussion

The experimental results in the two able-bodied individuals present limitations to the statistical significance of the data: (i) the desired stretching trajectories q_d can be optimized to personalize the stretching techniques across participants, (ii) the sample size in this paper is small to achieve statistically significant results, which motivates future testing including people with SCI, and (iii) the design of a closed-loop FES controller is needed to customize the applied intensities across the participants (e.g., based on a percentage of a given participant's maximum voluntary contraction).

VI. CONCLUSION

In this paper, a closed-loop kinematic controller was combined with open-loop FES inputs to safely and consistently implement industry-standard guidelines for static, AIS, and PNF stretching of the hamstring complex using a custom powered machine. The closed-loop motor controller was developed to track a desired hip joint kinematic trajectory to reach a target end ROM and hold the leg at that position. Once the leg had reached the target end ROM, open-loop FES was applied in the AIS and PNF stretching experiments to the quadriceps and hamstring complexes, respectively. During the static stretching case, no FES was applied. The combination of the motor controller that rotates the hip to a desired ROM and maintains the leg in a fixed position (for static, AIS, and PNF) while FES is applied on the antagonist

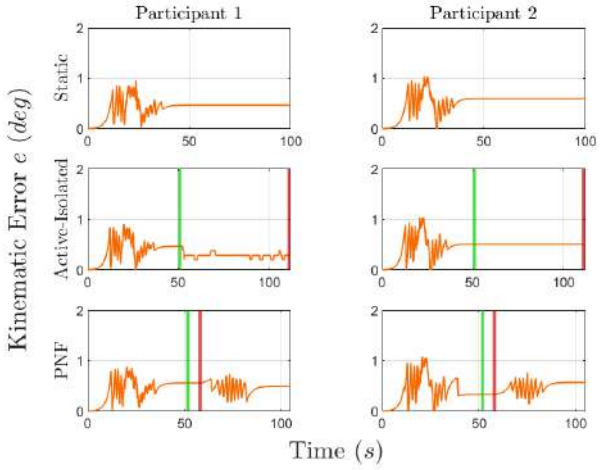


Fig. 2. The position tracking errors, e, for each experiment reported in degrees. The green and red vertical lines denote when the open-loop FES inputs were activated and stopped, respectively. Small perturbations in the kinematic error during the second half of PNF stretching were expected due to the applied FES on the hamstring complex and its interaction with the motor cable controller.

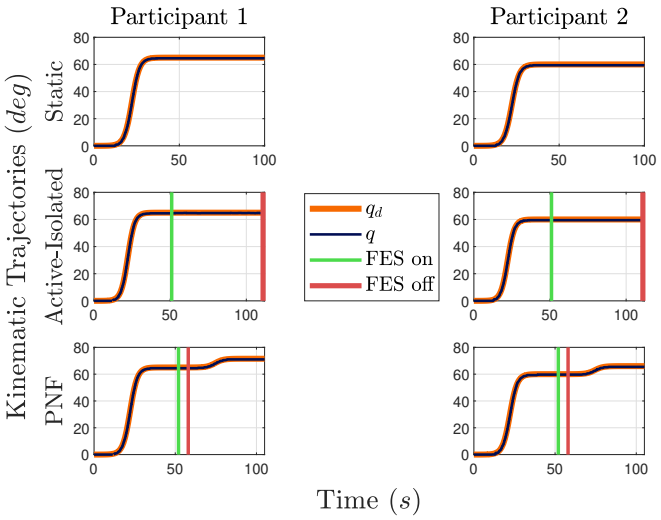


Fig. 3. The desired, q_d, and actual, q, kinematic trajectories from each experiment reported in degrees. The desired trajectory q_d was set to reach 65° and 60° for Participants 1 and 2, respectively. The trajectories q_d were determined for each participant in prior manual assessments using a goniometer. The green and red vertical lines denote when the open-loop FES patterns were started and stopped, respectively.

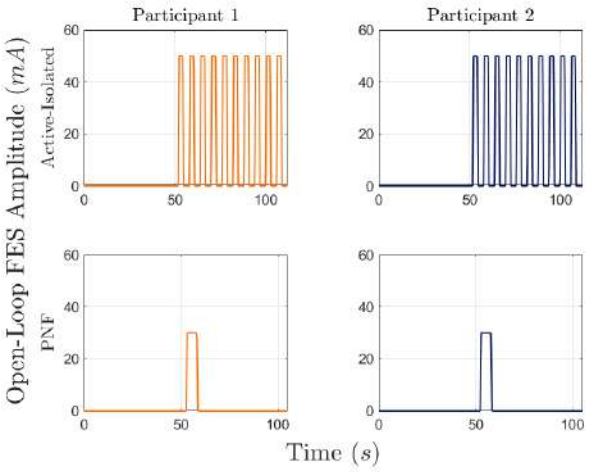


Fig. 4. The open-loop FES patterns for active-isolated stretching (AIS) and PNF stretching reported in milliamps (mA) for Participant 1 in orange and for Participant 2 in blue.

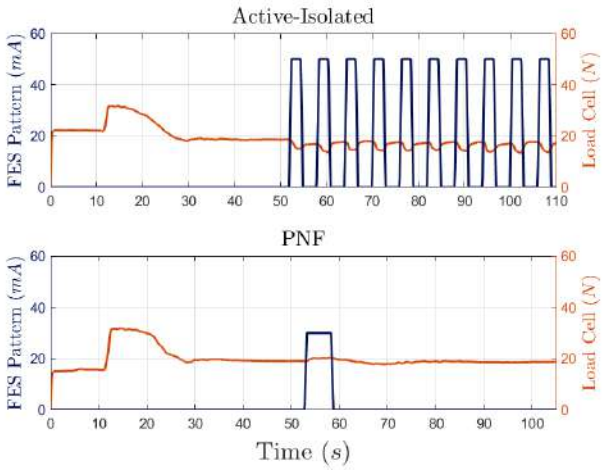


Fig. 5. The load cell measurements and FES patterns from Participant 1 during the active-isolated stretching (AIS) and PNF stretching experiments.

or agonist (for AIS and PNF, respectively) could reduce the labor-intensive burden of manual therapies and mitigate challenges related to staffing shortages in clinical settings. Preliminary experiments in two able-bodied individuals were conducted to show feasibility of the controller using each stretching technique. A Lyapunov-based stability analysis was developed to show that the electric motor controller achieves global exponential tracking.

References

[1] R. J. C. Michael A. Clark Scott Lucett, *NASM Essentials of Personal Fitness Training (3rd Edition)*. Lippincott, Williams, and Wilkins, 2008.

[2] R. M. Enoka, *Neuromechanics of Human Movement*, 6th. Human Kinetics, 2024.

[3] L. A. Harvey, R. D. Herbert, J. Glinsky, *et al.*, "Effects of 6 months of regular passive movements on ankle joint mobility in people with spinal cord injury: A randomized controlled trial," *Spinal Cord*, vol. 47, no. 1, pp. 62–66, 2009.

[4] S. Kirshblum and V. W. Lin, *Spinal Cord Medicine*, 3rd. Demos Medical, 2018.

[5] M. Adams and A. Hicks, "Spasticity after spinal cord injury," *Spinal Cord*, vol. 43, pp. 577–586, 2005.

[6] J. S. Walter, J. Sacks, R. Othman, *et al.*, "A database of self-reported secondary medical problems among VA spinal cord injury individuals: Its role in clinical care and management," *J. Rehabil. Res. Dev.*, vol. 39, no. 1, pp. 53–61, 2002.

[7] U. H. Mitchell, J. W. Myrer, J. T. Hopkins, *et al.*, "Neurophysiological reflex mechanisms' lack of contribution to the success of pnf stretches," *J. Sport Rehabil.*, vol. 18, 3 2009.

[8] P. T. Kukkonen, "Scientific basis of active isolated stretching: A review," *J. Exerc. Physiol. Online*, vol. 22, no. 2, pp. 58–70, 2019.

[9] A. K. Nagarwall, K. Zutshi, C. Ram, *et al.*, "Improvement of Hamstring Flexibility: A Comparison between Two PNF Stretching Techniques," *Int. J. Sports Sci. Eng.*, vol. 4, 1 2009.

[10] R. J. Downey, M. J. Bellman, H. Kawai, *et al.*, "Comparing the induced muscle fatigue between asynchronous and synchronous electrical stimulation in able-bodied and spinal cord injured populations," *IEEE Trans. Neural Syst. Rehabil. Eng.*, vol. 23, no. 6, pp. 964–972, 2015.

[11] M. J. Bellman, R. J. Downey, A. Parikh, *et al.*, "Automatic control of cycling induced by functional electrical stimulation with electric motor assistance," *IEEE Trans. Autom. Science Eng.*, vol. 14, no. 2, pp. 1225–1234, Apr. 2017.

[12] N. A. Alibeji, V. Molazadeh, F. Moore-Clingenpeel, *et al.*, "A muscle synergy-inspired control design to coordinate functional electrical stimulation and a powered exoskeleton: Artificial generation of synergies to reduce input dimensionality," *IEEE Control Syst. Mag.*, vol. 38, no. 6, pp. 35–60, 2018.

[13] L. Lempke, R. Wilkinson, C. Murray, *et al.*, "The Effectiveness of PNF Versus Static Stretching on Increasing Hip-Flexion Range of Motion," *Hum. Kinet. J.*, vol. 27, 3 2018.

[14] R. J. Downey, T.-H. Cheng, M. J. Bellman, *et al.*, "Switched tracking control of the lower limb during asynchronous neuromuscular electrical stimulation: Theory and experiments," *IEEE Trans. Cybern.*, vol. 47, no. 5, pp. 1251–1262, May 2017.

[15] T. Schauer, N. O. Negård, F. Previdi, *et al.*, "Online identification and nonlinear control of the electrically stimulated quadriceps muscle," *Control Eng. Pract.*, vol. 13, no. 9, pp. 1207–1219, Sep. 2005.

[16] R. Riener, F. Ferrarin, E. E. Pavan, *et al.*, "Patient-driven control of FES-supported standing up and sitting down: Experimental results," *IEEE Trans. Rehabil. Eng.*, vol. 8, no. 4, pp. 523–529, 2000.

[17] F. L. Lewis, D. M. Dawson, and C. T. Abdallah, *Robot Manipulator Control*. 2003, p. 638.

[18] A. F. Filippov, "Differential equations with discontinuous right-hand side," in *Fifteen papers on differential equations*, ser. American Mathematical Society Translations - Series 2, vol. 42, American Mathematical Society, 1964, pp. 199–231.

[19] B. E. Paden and S. S. Sastry, "A Calculus for Computing Filippov's Differential Inclusion with Application to the Variable Structure Control of Robot Manipulators," *IEEE Trans. Circuits Syst.*, vol. 34, no. 1, pp. 73–82, 1987.

[20] N. Fischer, R. Kamalapurkar, and W. E. Dixon, "LaSalle-Yoshizawa corollaries for nonsmooth systems," *IEEE Trans. Autom. Control*, vol. 58, no. 9, pp. 2333–2338, Sep. 2013.

[21] H. K. Khalil, *Nonlinear Systems*, 3rd ed. Upper Saddle River, NJ: Prentice Hall, 2002.

A Novel Patient-Centered Robotic Rehabilitation Approach for Retraining Reaching and Grasping Functions for Individuals with Stroke

Aisha Raji, Cesar Marquez-Chin, Urvashy Gopaul, and Milos R. Popovic

Abstract— **This study introduces a novel robotic rehabilitation system for improving upper extremity function by retraining reaching and grasping in individuals with stroke. The system integrates a collaborative robotic arm equipped with a force sensor and gripper with functional objects to create a patient-centred approach that simulates real-world activities and stimulates sensorimotor activity during training sessions. The system constantly assesses the user's extent of reach and presents the individual objects as reaching and grasping targets at different positions within and slightly beyond the user's reach.**

Preliminary testing involved one participant without stroke and one individual with hemiplegia reaching and grasping 19 objects of various weights and textures. The results indicate that the participant without stroke reached objects in an average of 3.47 seconds with a mean grasping force of 3.28 ± 0.05 N, while the participant with stroke took 5.66 seconds, with a mean of 1.04 ± 0.02 N exerted to grasp objects.

Our findings suggest that the proposed robotic rehabilitation system may be suitable for improving reaching and grasping after stroke.

Keywords— Collaborative robot (cobot), upper extremity, reaching, grasping, stroke, robotic rehabilitation, Toronto Rehabilitation Institute – Hand Function Test (TRI-HFT), Range of movement.

I. Introduction

Stroke is a leading cause of long-term disability globally that severely impairs motor and sensory functions and reduces independence [1], [2]. Annually, over 15 million people experience a stroke, resulting an economic burden that exceeds $721 billion worldwide [3], [4]. Approximately 70% of stroke survivors experience upper extremity impairment [5], [6], [7]. Upper extremity function is vital for performing activities of daily living (ADLs) and enhancing quality of life. Rehabilitation plays a crucial role in restoring voluntary motor function, with several systematic reviews highlighting the importance of meaningful, mass-practiced, intensive (amount of time spent in therapy), and task-specific activities for improving motor function during rehabilitation [8], [9], [10].

Robot-assisted rehabilitation is a promising intervention that can provide consistent, repeatable, and intensive training opportunities while also reducing the physical burden on therapists [11]. Robotic systems offer precise control and adaptability, enabling therapy tailored to an individual's needs and progress. Furthermore, integrating motor, tactile, and proprioceptive training through interactive and functional tasks enhances neuroplasticity and promotes motor recovery [12].

Despite important advancements, there remains a need for robotic rehabilitation systems to focus on addressing both motor and functional recovery to facilitate the seamless translation of improvements into real-world ADLs [13], [14]. Some existing robotic devices incorporate game-based elements to engage patients; however, they lack the capability to imitate everyday activities, which is crucial for ensuring that improvements in reaching and grasping directly enhance functional independence [15]. Several studies have demonstrated the potential of robotic rehabilitation to improve upper extremity movement, especially among individuals with chronic stroke [16], [17]. However, current evidence suggests that the efficacy of robot-assisted rehabilitation is often similar to other upper extremity interventions [18], [19], [20], with improvements being either marginal or not clinically meaningful [19].

This work presents a novel approach to robotic rehabilitation that redefines the role of robots in delivering therapy. The system retrains reaching and grasping functions in individuals with upper extremity impairments by allowing users to explore three-dimensional space without restraints. It integrates a collaborative robotic (cobot) arm with force-sensing capabilities, a gripper, and functional objects from the Toronto Rehabilitation Institute – Hand Function (TRI-HFT) [21]. This integration facilitates a patient-centered approach by using real objects to assess each user's unique reach and strategically presenting them as targets within and slightly beyond this reach. By incorporating real-world tasks, the system provides meaningful sensorimotor inputs during training and encourages progressive motor engagement and sensorimotor adaptation by dynamically assessing the user's reach in three-dimensional space and presenting individual TRI-HFT objects as targets positioned on or just outside the user's reach. We tested the proposed protocol on neurologically intact individuals before testing on a person with a stroke that affects their upper extremity. This work presents preliminary data from two individuals – one without and one with a stroke - as part of a study to provide insights into how this system may support the transition of motor and sensation gains into functional everyday activities.

All Authors are with KITE – Toronto Rehabilitation Institute – University Health Network, Toronto, Toronto, M5G 2A2, Canada (corresponding author to provide phone: 416 597 3422 x 7661; e-mail: aisha.raji@mail.utoronto.ca).

A. Raji, C. Marquez-Chin, M.R. Popovic are also with the Institute of Biomedical Engineering, University of Toronto, Toronto, M5S 3G9, Canada.

II. METHODS

A. System Specification and Setup

In this study, we used a UR5e cobot arm (Universal Robots, Denmark), which has six degrees of freedom, allowing each joint to move independently within a ±360° range and extend up to 85 cm from its base. The UR5e, with a payload capacity of 5 kg, was mounted on a table measuring 150 cm by 75 cm. We equipped the robotic arm with a 2F-85 gripper (Robotiq Inc., Canada) for object gripping and manipulation. This gripper has an adjustable grip force ranging from 20 to 235 N and can open up to 85 mm. For enhanced safety, we covered the arm with AIRSKIN module pads (Blue Danube Robotics GmbH, Austria). These pressure-sensitive pads require a minimum force of 5 N to stop the robot's movement.

We used 3D-printed objects of the TRI-HFT, including a mug, a sheet of paper, a book, a reusable plastic bag filled with golf balls, a soda can, a die, a sponge, a credit card, a wireless home telephone, a pencil, and nine rectangular blocks. The blocks were categorized into sets of three based on weight (100 g, 200 g, and 300 g) and surface friction (smooth, medium, and rough) [21].

Using SolidWorks (Dassault Systèmes, USA), we modified these objects to enhance the robot's picking and manipulation capabilities during rehabilitation exercises. The redesign involved creating external, internal, or handleless configurations to ensure compatibility with the gripper and facilitate smooth interactions between the objects, the robot, and the participants, as illustrated in Fig. 1. These modified objects were 3D-printed and stored on a custom-designed shelf mounted on the robot's table (Fig. 2), enabling the cobot to access them.

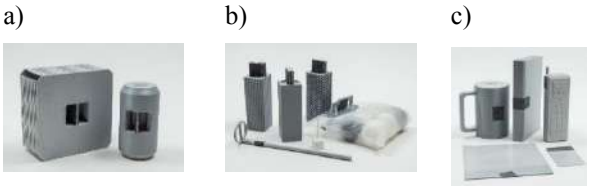


Figure 1: The modified 3D TRI-HFT items with a) Internal handles, b) External handles, and c) Handleless design



Figure 2: The UR5e robotic arm holding a soda can with the shelf mounted on the table

A. Rehabilitation Exercise Procedure

Participants sat on a chair facing the robot at a safe and comfortable distance from the table's edge. We provided participants with clear instructions and expectations, including a video demonstration to familiarize them with the procedure. We then configured the robot by selecting the affected upper extremity to be used throughout the session. An experimental session consisted of two phases (described next), in which the participant performed a series of tasks following visual cues. Ethics approval for this study was obtained from the Research Ethics Board (REB) at the University Health Network, Toronto, Canada. Participants provided written and informed consent for participation.

Phase 1: 3D Assessment of the Extent of *Reach*

In the first phase of the rehabilitation session, we conducted a one-time extent-of-reach assessment to evaluate each participant's three-dimensional workspace (range of movement (ROM)) – specifically focusing on the affected extremity in the individual with stroke. This assessment identified the maximum and comfortable reach limits across various axes, which were used to guide the subsequent phase of the session. The robot presented a rectangular block at the center of the table's edge without releasing it. When the "start exploration" visual indicator illuminated, we asked if the participants were comfortable with the block's position and adjusted it if necessary.

Participants then freely used their affected upper extremity to move the block vertically as high as possible on the z-axis and gradually draw the largest spiral possible while gradually moving the block towards the table surface. This movement captured their maximum reach in the x-, y-, and z-axes (lateral, anterior, and vertical). Figure 3 illustrates the setup and data recorded during this process. After the exploration, the "start exploration" indicator illuminated again, and the robot waited 10 seconds to ensure that the user had released their grasp before returning the block to the shelf.

Phase 2: Object Reaching and Grasping Task

In the second phase, the system randomly selected and adaptively presented objects for a reach-and-grasp task at two random positions within each participant's unique movement range, identified in the first phase. The sponge was the only exception, and it was used for a high-five-reaching task to increase the participant's motivation. When the "grasp object" indicator illuminated, the participant reached, grasped, and pulled the object until the indicator deactivated. The indicator turned off either after a force threshold of 5N has been exceeded or one minute (if the participant was not able to reach the target position).

We implemented a challenge mode to encourage participants to extend their reach beyond the measured range of movement. After the "grasp object" indicator deactivated at the second target position, the "challenge mode" indicator illuminated, prompting the participant to accept the challenge. If the participant accepted, the robot moved the object 5 cm outside the previously determined workspace. By reaching beyond arm's reach, the participants need to flex the trunk to reach the target. The "grasp object" indicator illuminated again at the challenge position, prompting the participant to grasp

and pull the object. Once the indicator deactivated, the robot dropped off the object and returned to its default home position. We use the 3D-printed sponge (Square 142 × 142 mm) to replicate a high-five gesture by providing a compliant surface for participants to tap, as illustrated in Figure 3b.

B. Data Analysis

We collected the data with a frequency of 500 samples per second and applied a low-pass filter to them with a cutoff frequency of 1 Hz to align with the frequency range of human motion [22], [23]. To evaluate the ROM, we rescaled the data using equation (1) and evaluated both the range of reach and force exerted on the object on each axis.

$$x_{normalized} = \frac{x - \sigma}{\sqrt{n}} \quad \dots (1)$$

where n is the number of data points recorded and σ is the standard deviation of the data.

In the second phase, the robot used the data from the first phase to calculate the maximal reaching workspace by selecting the outer edge of the path and the area of the workspace. We evaluated the mean grasp time as the interval between the object grasp cue and the participant's actual grasp, and we assessed the mean force exerted on each object as the force measured between the object grasp and release along each axis.

The standard error of the mean (SEM) was calculated using equation (2).

$$SEM = \frac{\sigma}{\sqrt{n}} \dots (2)$$

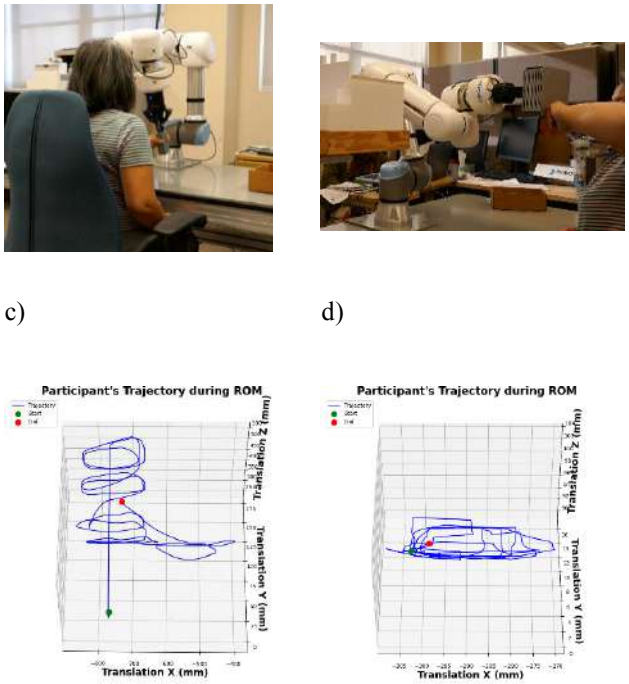
III. Results

The study involved two participants: one without stroke and one with left upper extremity impairment due to a stroke sustained seven years prior to participating in this study. Neither participant had previous experience with robotic rehabilitation, and both engaged in a single three-hour exercise session to evaluate the preliminary results of the system. The results presented here focus on their performance during the ROM exploration and object-reaching and grasping tasks.

A. ROM Exploration

Figure 3 illustrates the participant performing the tasks and the trajectory and performance data recorded during the extent-of-reach assessment, highlighting the three-dimensional spatial pathway with the start and end points. The results show that the participant without stroke covered a wider area and produced more defined, symmetrical spirals compared to the participant with stroke, who had a limited reach. This pattern may indicate that motor performance in the affected arm was constrained. These findings are supported by the data in Figure 4 and Table 1.

a) b)



c) d)

Fig. 3: a) Participant with stroke moving object with the affected hand during extent-of-reach assessment; (b) Participant with stroke performing high-five with the sponge; (c) and (d) show 3D visualizations of the recorded trajectories during the assessment for the participant —(c) without stroke (d) with stroke.

The table (150 x 75 cm) provides the spatial context for our analysis. Figure 4 and Table 1 show that the participant without stroke achieved a maximum range of 86.86 cm along the x-axis, with the smallest range of 32.15 cm recorded on the y-axis, which is consistent with normative data for horizontal reaches (80–100 cm) [24], [25], [26]. The individual with stroke reached a maximum of 30.93 cm along the x-axis and a minimum of 10.47 cm along the z-axis. This suggests that there is more restriction in the vertical movement and reduced variation in the area reached. Table 1 further presents the translation values captured during ROM assessment, with the mean and standard deviation values highlighting variability across all axes.

TABLE 1: POSITION RECORDED IN VARIOUS AXES DURING EXTENT-OF-REACH ASSESSMENT

Position	Range (cm) (without stroke)	Mean ± SD (cm) (without stroke)	Range (cm) (with stroke)	Mean ± SD (cm) (with stroke)
Translation X	86.86	54.03 ± 0.00	30.93	19.97 ± 0.00
Translation Y	32.15	16.88 ± 0.00	15.14	5.95 ± 0.00
Translation Z	54.75	25.85 ± 0.00	10.47	6.59 ± 0.00

a)

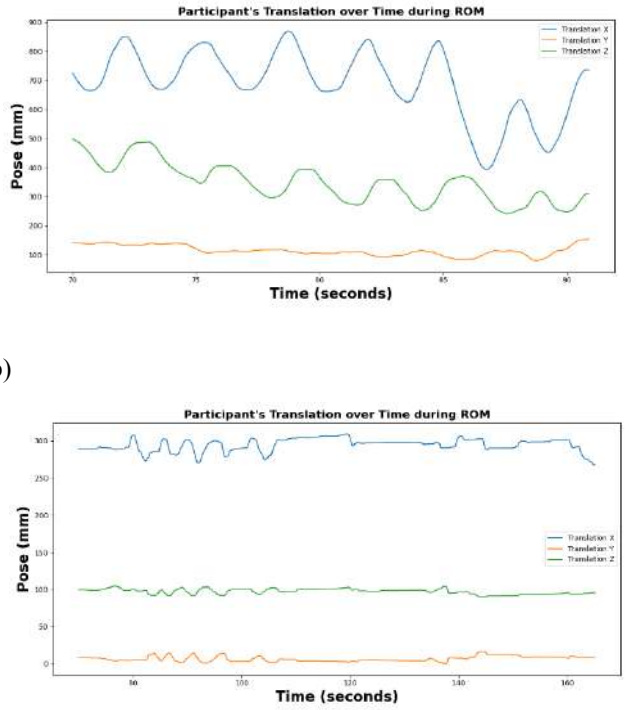


Fig. 4: 2D representation of reach in various axes during extent-of-reach assessment for the participant a) without stroke (b) with stroke.

The recorded force during ROM assessment is presented in Figure 5 and detailed in Table 2. The participant without stroke generated a total force of 6.47 N, with mean forces of 0.62 N, 2.28 N, and 0.381 N on the x-, y-, and z-axes, respectively, while the participant with stroke generated a total force of 1.38 N, with mean forces of 0.59 N, 0.39 N, and 0.06 N along the x-, y-, and z-axes, respectively. The relatively higher force exerted along the x-axis for the individual with stroke may reflect an increased effort to overcome the robot's internal resistance or muscle stiffness in the lateral direction.

TABLE 2: FORCES RECORDED IN VARIOUS AXES DURING EXTENT-OF-REACH ASSESSMENT

Force Axis	Range (N) (without stroke)	Mean ± SD (N) (without stroke)	Range (N) (with stroke)	Mean ± SD (N) (with stroke)
X	1.78	0.62 ± 0.01	0.76	0.59 ± 0.01
Y	4.11	2.28 ± 0.04	0.54	0.39 ± 0.01
Z	0.58	0.38 ± 0.01	0.08	0.06 ± 0.00
Total	**6.47**	**3.28 ± 0.05**	**1.38**	**1.04 ± 0.02**

B. Reaching and Grasping Task

The data recorded in this phase revealed notable differences between the participant without stroke and the participant with stroke. The participant without stroke spent an average of 2.47 seconds reaching objects, with a mean grasp time ranging between 1.31 to 3.32 seconds, as displayed on Table 3. Objects like the sponge, most blocks, and pencil required shorter grasp times, while the phone and credit card

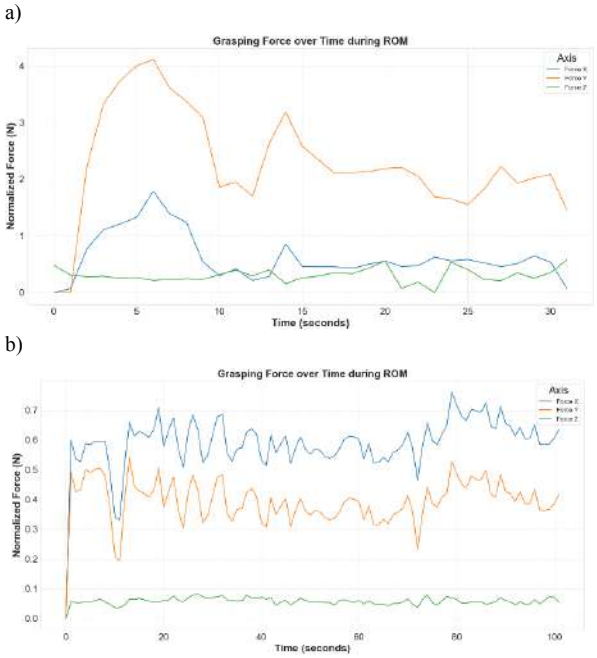


Figure 5: The grasping force exerted in various axes during extent-of-reach assessment for the participant a) without stroke (b) with stroke.

took slightly longer, their overall times remained within a manageable range, as shown in Figure 6a.

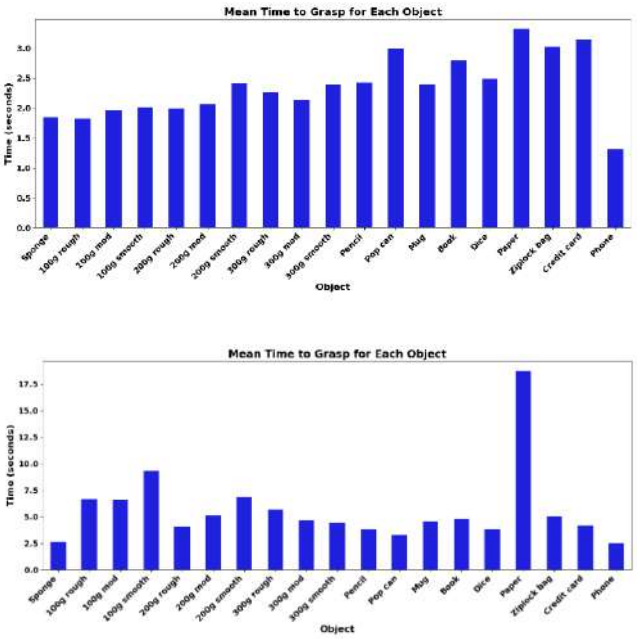


Fig. 6: Mean time to grasp each object for the participant a) without stroke b) with stroke

The participant with stroke had a longer mean time to grasp of 5.66 seconds, with a mean grasp time ranging between 2.65 to 19.59 seconds, as shown in Figure 6b. The characteristics of each object had a significant impact on performance. For example, the paper presented a considerable challenge due to its smooth texture and lack of rigidity, resulting in a grasp time of 45.31 seconds during the initial target presentation.

TABLE 3: MEAN TIME TO GRASP OBJECT AT VARIOUS TARGET POSITIONS (PARTICIPANT WITHOUT STROKE)

S/N	Object	Weight (gm)	Time to grasp (seconds)			
			Target 1	Target 2	Target 3 (challenge mode)	Mean
1	Sponge	178	2.01	1.43	2.10	1.85
2	100g rough block	100	2.08	1.38	1.99	1.82
3	100g moderate block	100	2.04	1.69	2.18	1.97
4	100g smooth block	100	2.12	1.74	2.19	2.02
5	200g rough block	200	2.01	1.89	2.06	1.99
6	200g moderate block	200	2.49	1.48	2.25	2.07
7	200g smooth block	200	3.51	2.10	1.63	2.41
8	300g rough block	300	2.29	2.39	2.14	2.27
9	300g moderate block	300	3.05	1.69	1.69	2.14
10	300g smooth block	300	3.24	1.83	2.10	2.39
11	Pencil	7	2.18	2.73	2.38	2.43
12	Pop can	360	3.37	3.28	2.35	3.00
13	Mug	545	3.22	1.77	2.22	2.40
14	Book	316	2.92	2.47	3.01	2.80
15	Dice	5	3.21	1.97	2.3	2.49
16	Paper	14	5.06	3.08	1.83	3.32
17	Ziplock bag with golf balls	228	3.84	2.38	2.84	3.02
18	Credit card	3	4.07	2.46	2.88	3.14
19	Phone	215	2.62	1.31	1.88	1.31
	Mean		**2.91**	**2.17**	**2.33**	**2.47**

TABLE 4: MEAN TIME TO GRASP OBJECT AT VARIOUS TARGET POSITIONS (PARTICIPANT WITH STROKE)

S/N	Object	Weight (gm)	Time to grasp (seconds)			
			Target 1	Target 2	Target 3 (challenge mode)	Mean
1	Sponge	178	4.04	1.96	1.96	2.65
2	100g rough block	100	5.64	8.31	6.08	6.68
3	100g moderate block	100	5.59	10.39	3.89	7.50
4	100g smooth block	100	9.44	14.70	3.91	9.35
5	200g rough block	200	4.63	4.50	3.03	4.05
6	200g moderate block	200	5.48	6.70	3.12	5.10
7	200g smooth block	200	6.08	3.09	11.35	6.84
8	300g rough block	300	4.41	5.38	7.22	5.67
9	300g moderate block	300	5.04	4.48	4.27	4.60
10	300g smooth block	300	5.15	4.19	4.01	4.45
11	Pencil	7	5.07	3.48	2.74	3.76
12	Pop can	360	5.16	2.81	1.84	3.27
13	Mug	545	5.27	6.02	2.26	4.52
14	Book	316	8.96	2.04	3.32	4.77
15	Dice	5	5.58	2.59	3.22	3.80
16	Paper	14	45.31	10.21	3.26	19.59
17	Ziplock bag with golf balls	228	6.87	4.87	3.46	5.07
18	Credit card	3	5.77	2.60	4.14	4.17
19	Phone	215	5.01	2.64	Skipped	3.83
	Mean		**4.04**	**1.96**	**1.96**	**2.65**

However, by target 3, the grasp time reduced significantly to 3.26 seconds, suggesting the participant's adaptability and improved efficiency through learning and practice, as displayed on Table 4. The book and 100g smooth block also had a longer reach time (8.96 and 9.44 seconds) at the first target. This may be due to the initial unfamiliarity with the objects and their presentation distance and orientation. Notably, the participant without stroke mostly demonstrated a longer reach time during the challenging task, which may reflect that the participant was able to fully extend their arm during the ROM assessment, resulting in a target position that was more demanding to achieve.

Furthermore, the participant with stroke demonstrated decreasing time to grasp objects from Target 1 to Target 3 across multiple objects, indicating learning and adaptation. For example, smoother items, such as blocks, paper, and smooth blocks, exhibited a longer mean time to grasp, suggesting difficulty due to reduced friction. Nevertheless, the participant adapted their grasping approach to compensate for these challenges.

Figure 7 shows the translation and force changes for the sponge, which had the lowest mean reach time of 1.85 and 2.65 seconds, for the individual without and with stroke, respectively, and a high mean force of 0.93 N and 2.32 N. This

outcome may result from the absence of a grasping component in the sponge task, and the participant reported finding the task motivating.

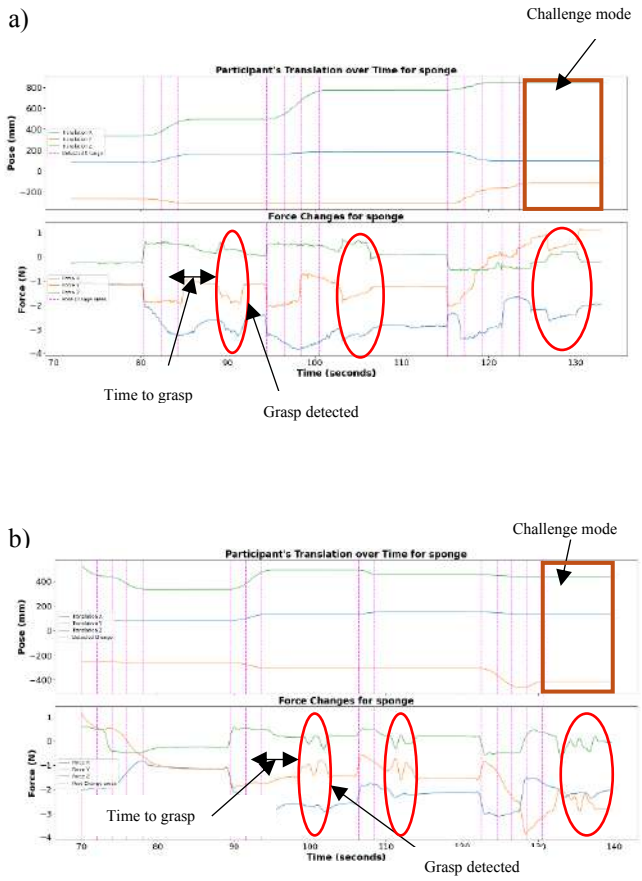


Figure 7: Target position and force changes during the task with the sponge for the participant a) without stroke (b) with stroke.

Figure 8 and Table 5 show the mean resultant force exerted on each object by the participant without stroke, indicating variations depending on object weight and texture. The highest force was 3.80 N, recorded for the 200g moderate block, while the lowest was 0.76 N for the pencil (7g). Force exertion also varied across different object textures, with higher forces mostly applied to rough and moderate-textured objects.

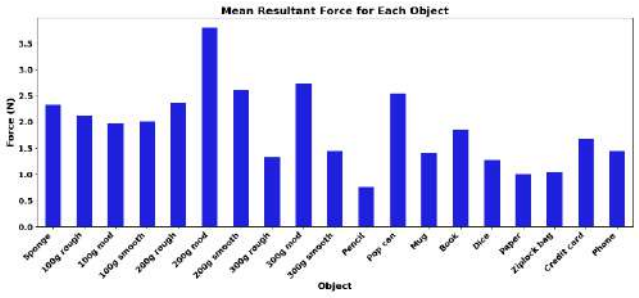


Figure 8: Mean Resultant Force Exerted on each Object (participant without stroke)

The participant applied higher forces during the challenge mode (target 3) for most objects. This may likely be due to the increased difficulty and the extended task duration (5 seconds), encouraging the participant to apply more force to maintain a secure grip and complete the task.

TABLE 5: RESULTANT FORCE EXERTED ON OBJECTS DURING EXERCISE (PARTICIPANT WITHOUT STROKE)

S/N	Object	Weight (gm)	Resultant force exerted (N)			
			Target 1	Target 2	Target 3 (challenge mode)	Mean
1	Sponge	178	2.10	2.01	2.87	2.33
2	100g rough block	100	1.47	1.99	2.90	2.12
3	100g moderate block	100	1.70	1.94	2.25	1.98
4	100g smooth block	100	1.43	1.69	2.95	2.02
5	200g rough block	200	1.82	2.31	2.99	2.37
6	200g moderate block	200	4.87	2.86	3.68	3.80
7	200g smooth block	200	2.08	2.63	3.12	2.61
8	300g rough block	300	1.13	1.69	1.19	1.34
9	300g moderate block	300	2.19	2.90	3.14	2.74
10	300g smooth block	300	1.51	0.94	1.89	1.45
11	Pencil	7	0.58	0.84	0.85	0.76
12	Pop can	360	2.69	2.20	2.76	2.55
13	Mug	545	2.16	0.56	1.52	1.41
14	Book	316	1.2	0.97	3.40	1.86
15	Dice	5	1.44	1.24	1.12	1.27
16	Paper	14	0.85	1.04	1.12	1.00
17	Ziplock bag with golf balls	228	1.13	1.44	0.58	1.05
18	Credit card	3	1.14	1.05	2.84	1.68
19	Phone	215	2.38	1.97	2.45	1.45
	Mean		**1.78**	**1.79**	**2.42**	**2.00**

Figure 9 and Table 6 illustrate the mean resultant force on each object by the participant with stroke, indicating lower force values and less variability compared to the participant without stroke. The highest force of 1.17 N was recorded for the mug, the heaviest object (545g), while the lowest force was 0.34 N on the paper (14g). Although heavier objects typically require greater force exertion, the participant did not exhibit a

clear increase in the force exerted across different objects, suggesting difficulty in adjusting grip strength.

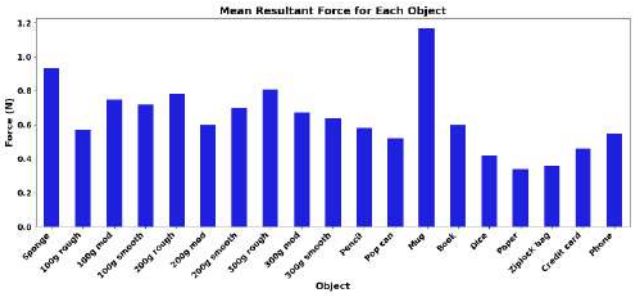


Figure 9: Mean Resultant Force Exerted on each Object (participant with stroke)

Force application was relatively low across all objects, with minimal adjustments based on weight and texture. Unlike the participant without stroke, who applied greater force to objects, the participant with stroke maintained a more uniform force. This may indicate reduced grip strength and a limitation in the participant's ability to adjust force based on object characteristics. Smooth objects like paper (0.34 N) and ziplock bag (0.36 N), posed challenges, likely due to the reduced friction and difficulty securing a stable grasp.

Additionally, the participant with stroke did not consistently increase the force exerted in the challenge mode**,** as observed in the participant without a stroke. This result may suggest difficulty in generating additional force, potentially due to muscle weakness. However, in the sponge task**,** which did not require grasping, the participant applied a higher force (0.93 N), indicating that challenges in generating force were more evident in grip-dependent tasks.

IV. Conclusion

This study introduces a new paradigm for robotic rehabilitation that redefines the role of robots in retraining reaching and grasping functions after a stroke. Unlike existing wearable exoskeleton robots such as the AGREE [27] and ARMin III [28] systems that attach directly to users and offer training modalities (passive, active assistive, assist-as-needed, or resistive) through predefined trajectories, activities displayed on screens, and counterweights for gravitational support, our approach minimizes joint misalignment by avoiding direct attachment to the user and simulates real-life scenarios without gravity assistance. Consequently, participants can engage in reaching tasks using diverse hand configurations that closely reflect natural movement, and our design facilitates finger movement practice to replicate everyday tasks more accurately.

We integrated functional objects into the training to imitate daily tasks and provide users with real sensorimotor inputs, including proprioceptive and tactile feedback. The system dynamically assesses each user's extent of reach and adaptively presents targets within and slightly beyond the measured ROM. This patient-driven strategy may enhance the relevance of training and help identify specific challenges that may be addressed in subsequent interventions.

TABLE 6: RESULTANT FORCE EXERTED ON OBJECTS DURING EXERCISE (PARTICIPANT WITH STROKE)

S/N	Object	Weight (gm)	Resultant force exerted (N)			
			Target 1	Target 2	Target 3 (challenge mode)	Mean
1	Sponge	178	0.79	0.94	1.06	0.93
2	100g rough block	100	0.82	0.45	0.44	0.57
3	100g moderate block	100	1.03	0.50	0.72	0.75
4	100g smooth block	100	0.83	0.59	0.74	0.72
5	200g rough block	200	0.71	0.91	0.73	0.78
6	200g moderate block	200	0.60	0.56	0.65	0.60
7	200g smooth block	200	0.85	0.75	0.49	0.70
8	300g rough block	300	0.75	0.85	0.84	0.81
9	300g moderate block	300	0.72	0.45	0.84	0.67
10	300g smooth block	300	0.65	0.64	0.62	0.64
11	Pencil	7	0.35	0.66	0.72	0.58
12	Pop can	360	0.57	0.44	0.54	0.52
13	Mug	545	1.00	1.10	1.40	1.17
14	Book	316	0.84	0.31	0.65	0.60
15	Dice	5	0.38	0.35	0.53	0.42
16	Paper	14	0.25	0.51	0.26	0.34
17	Ziplock bag with golf balls	228	0.41	0.38	0.30	0.36
18	Credit card	3	0.36	0.44	0.57	0.46
19	Phone	215	0.69	0.97	Skipped	0.55
	Mean		**0.66**	**0.62**	**0.64**	**0.64**

Preliminary results from two participants - one with stroke and one without - demonstrate the potential of this approach for upper extremity rehabilitation. For the participant without stroke, the system showed the capability of providing challenging tasks, as evidenced by the time taken to grasp objects during the challenge phase of the session. Additionally, the participant with stroke showed significant improvements in reaching time across all tasks, suggesting adaptability and motor learning. The decreased grasp times, particularly with initially challenging objects like the paper, may suggest

increased familiarity and skill development, which may be transferred into ADLs. Furthermore, the use of real objects provides the advantage of identifying specific areas where participants encounter difficulties, which could become targets for subsequent rehabilitation sessions.

However, challenges remain with smooth and lightweight objects, as exhibited by the extended grasp times for paper and smooth blocks, likely due to reduced friction. In addition, target placement and fatigue may have also influenced performance, particularly in the skipped trial with the phone. Further research will focus on evaluating the usability of this approach with a larger group of individuals with stroke, refining training protocols by gradually increasing task difficulty and reducing exercise duration, and implementing targeted interventions to address muscle stiffness in axes with limited ROM. Providing additional training with difficult objects may enhance dexterity and outcomes.

Although not all individuals with stroke may benefit from this system, our approach offers notable advantages compared to existing systems that rely on multiple layers of control and gravity compensation. By allowing participants to practice reaching and grasping tasks without restrictive attachments, our system promotes the performance of functional tasks with real objects in a more natural way. Furthermore, this paradigm may enhance neuroplasticity by increasing cortical activity in the motor and somatosensory cortices, thereby contributing to improved functional recovery. Additionally, our system creates opportunities to integrate complementary technologies for neurorehabilitation, such as functional electrical stimulation (FES), brain-computer interface (BCI), and other robotic devices. Combining our system with these modalities may enhance rehabilitation outcomes by leveraging the unique strengths of each system to improve recovery of individuals with stroke.

REFERENCES

[1] P. Raghavan, "Upper limb motor impairment after stroke," Phys. Med. Rehabil. Clin., vol. 26, no. 4, pp. 599–610, 2015.

[2] S. F. Tyson, M. Hanley, J. Chillala, A. B. Selley, and R. C. Tallis, "Sensory loss in hospital-admitted people with stroke: characteristics, associated factors, and relationship with function," Neurorehabil. Neural Repair, vol. 22, no. 2, pp. 166–172, 2008.

[3] V. L. Feigin et al., "World Stroke Organization (WSO): Global Stroke Fact Sheet 2022," Int. J. Stroke Off. J. Int. Stroke Soc., vol. 17, no. 1, pp. 18–29, Jan. 2022.

[4] S. Strilciuc et al., "The economic burden of stroke: a systematic review of cost of illness studies," J. Med. Life, vol. 14, no. 5, pp. 606–619, 2021.

[5] M. Boakye, B. C. Leigh, and A. C. Skelly, "Quality of life in persons with spinal cord injury: comparisons with other populations," J. Neurosurg. Spine, vol. 17, no. Suppl1, pp. 29–37, 2012.

[6] D. Dutta, S. Sen, S. Aruchamy, and S. Mandal, "Prevalence of post-stroke upper extremity paresis in developing countries and significance of m-Health for rehabilitation after stroke - A review," Smart Health, vol. 23, p. 100264, Mar. 2022.

[7] J. A. Binks, J. R. Emerson, M. W. Scott, C. Wilson, P. van Schaik, and D. L. Eaves, "Enhancing upper-limb neurorehabilitation in chronic stroke survivors using combined action observation and motor imagery therapy," Front. Neurol., vol. 14, 2023, Accessed: Jun. 07, 2023.

[8] B. French et al., "Repetitive task training for improving functional ability after stroke," Cochrane Database Syst. Rev., vol. 2016, no. 11, p. CD006073, Nov. 2016.

[9] N. Takeuchi and S.-I. Izumi, "Rehabilitation with Poststroke Motor Recovery: A Review with a Focus on Neural Plasticity," Stroke Res. Treat., vol. 2013, p. 128641, 2013.

[10] J. M. Veerbeek et al., "What is the evidence for physical therapy poststroke? A systematic review and meta-analysis," PloS One, vol. 9, no. 2, p. e87987, 2014.

[11] N. Norouzi-Gheidari, P. S. Archambault, and J. Fung, "Effects of robot-assisted therapy on stroke rehabilitation in upper limbs: systematic review and meta-analysis of the literature," 2012.

[12] H. Rodgers et al., "Robot assisted training for the upper limb after stroke (RATULS): a multicentre randomised controlled trial," The Lancet, vol. 394, no. 10192, pp. 51–62, Jul. 2019.

[13] P. Poli, G. Morone, G. Rosati, and S. Masiero, "Robotic technologies and rehabilitation: new tools for stroke patients' therapy," BioMed Res. Int., vol. 2013, no. 1, p. 153872, 2013.

[14] E. Oña, R. Cano-de La Cuerda, P. Sánchez-Herrera, C. Balaguer, and A. Jardón, "A review of robotics in neurorehabilitation: towards an automated process for upper limb," J. Healthc. Eng., vol. 2018, no. 1, p. 9758939, 2018.

[15] L. Piron et al., "Assessment and treatment of the upper limb by means of virtual reality in post-stroke patients," in Advanced Technologies in Rehabilitation, IOS Press, 2009, pp. 55–62.

[16] N. Nordin, S. Q. Xie, and B. Wünsche, "Assessment of movement quality in robot-assisted upper limb rehabilitation after stroke: a review," J. Neuroengineering Rehabil., vol. 11, pp. 1–23, 2014.

[17] R. Bertani, C. Melegari, M. C. De Cola, A. Bramanti, P. Bramanti, and R. S. Calabrò, "Effects of robot-assisted upper limb rehabilitation in stroke patients: a systematic review with meta-analysis," Neurol. Sci., vol. 38, pp. 1561–1569, 2017.

[18] W. Chien, Y. Chong, M. Tse, C. Chien, and H. Cheng, "Robot-assisted therapy for upper-limb rehabilitation in subacute stroke patients: A systematic review and meta-analysis," Brain Behav., vol. 10, no. 8, p. e01742, 2020.

[19] A. C. Lo et al., "Robot-Assisted Therapy for Long-Term Upper-Limb Impairment after Stroke," N. Engl. J. Med., vol. 362, no. 19, pp. 1772–1783, May 2010.

[20] G. Kwakkel, B. J. Kollen, and H. I. Krebs, "Effects of robot-assisted therapy on upper limb recovery after stroke: a systematic review," Neurorehabil. Neural Repair, vol. 22, no. 2, pp. 111–121, 2008.

[21] N. Kapadia, V. Zivanovic, M. Verrier, and M. R. Popovic, "Toronto Rehabilitation Institute–Hand Function Test: Assessment of Gross Motor Function in Individuals With Spinal Cord Injury," Top. Spinal Cord Inj. Rehabil., vol. 18, no. 2, pp. 167–186, 2012.

[22] K. A. Mann, F. W. Wernere, and A. K. Palmer, "Frequency spectrum analysis of wrist motion for activities of daily living," J. Orthop. Res., vol. 7, no. 2, pp. 304–306, 1989.

[23] Y. Xiong and F. Quek, "Hand Motion Gesture Frequency Properties and Multimodal Discourse Analysis," Int. J. Comput. Vis., vol. 69, no. 3, pp. 353–371, Sep. 2006.

[24] D. A. Winter, Biomechanics and motor control of human movement. John wiley & sons, 2009.

[25] C. E. Lang, J. M. Wagner, A. W. Dromerick, and D. F. Edwards, "Measurement of upper-extremity function early after stroke: properties of the action research arm test," Arch. Phys. Med. Rehabil., vol. 87, no. 12, pp. 1605–1610, 2006.

[26] A. Shumway-Cook, "Motor control: Translating research into clinical practice," Lippincoot Williams Wilkins, 2007.

[27] S. Dalla Gasperina et al., "AGREE: A compliant-controlled upper-limb exoskeleton for physical rehabilitation of neurological patients," IEEE Trans. Med. Robot. Bionics, vol. 5, no. 1, pp. 143–154, 2023.

[28] T. Nef, M. Guidali, and R. Riener, "ARMin III–arm therapy exoskeleton with an ergonomic shoulder actuation," Appl. Bionics Biomech., vol. 6, no. 2, pp. 127–142, 2009.

Design and Evaluation of a Single-Sided Mobility Assistive Exoskeleton (SMAEXO) for Hemiplegia

Xiaoyue Yan[1, 2], Wei Yun Yau[3], Isaac Okumura Tan[2], Longbin Zhang[2, 4], Youlong Wang[1, 2], Oliver Roberts[2], Seng Kwee Wee[5], Wei Tech Ang[1, 2]

***Abstract*— This study presents the Single-Sided Mobility Assistive Exoskeleton (SMAEXO), a novel, single-sided, multi-joint device designed to enhance mobility and rehabilitation for individuals with hemiplegia. SMAEXO provides active assistance at the hip and knee, combined with a passive, flexible ankle joint to prevent foot drop, ensuring comprehensive support throughout the gait cycle. Its innovative design optimizes reaction force support and weight distribution, promoting balance and reducing strain on the affected side. Additionally, its modular, customizable design accommodates diverse body dimensions and biomechanical needs, while safety features such as self-locking mechanisms, cushions, bumpers, and elastic components enhance user safety and comfort. The SMAEXO's usability, comfort, safety, and assistance were assessed through trials with eight able-bodied participants, including physiotherapists simulating stroke gait patterns. Participants reported the device as comfortable, safe, and effective, highlighting its benefits during level and slope walking and obstacle negotiation. Notable feedback included the need for enhanced ventilation, reduced device weight, and improved ease of donning and doffing. The results demonstrate SMAEXO's potential to deliver comprehensive multi-joint assistance for individuals with hemiplegia. This work contributes to advancing rehabilitation and assistive technologies for post-stroke individuals, enabling more effective and personalized mobility support.**

I. Introduction

Stroke, a leading cause of disability, often results in hemiparesis, affecting 65% of survivors with impairing gait [1]. Common issues include asymmetry, poor balance, and foot drop [2], requiring intensive rehabilitation to restore mobility. Traditional therapy is labor-intensive, requiring two physiotherapists per session, limiting scalability [3]. Exoskeletons offer a more efficient solution, providing consistent, automated support to enhance rehabilitation while reducing therapist workload [4].

Most lower-limb exoskeletons are bilateral, providing full mobility support by targeting the hip, knee, and ankle. Devices like Ekso Indego [5], ReWalk [6], and Rex [7] assist users with severe motor loss, such as spinal cord injury patients. However, their bulky design, high cost, and reliance on position control make them unsuitable for stroke survivors, who need responsive, tailored support [8].

For hemiplegic patients, unilateral exoskeletons offer a simpler, lighter alternative. Unlike bilateral devices, which restrict natural movement and disrupt gait symmetry [9], unilateral exoskeletons assist only the affected limb, enhancing mobility with less burden on the wearer.

However, the unilateral approach introduces its own challenges. The asymmetric structure of these devices can make it difficult to maintain balance, and the limited reaction force support hampers the generation of sufficient torque to adequately stabilize and propel the affected limb.

Furthermore, many unilateral exoskeletons assist only one joint, limiting their effectiveness for stroke-related multi-joint impairments. Knee devices like the University of Michigan's passive exoskeleton [10], the University of New York's active exoskeleton [11], and the REFLEX system [12] aid the knee for stance support and swing clearance. Similarly, ankle exoskeletons such as the ReStore Exo-Suit [13] and Northern Arizona University's device [14] improve plantarflexion and dorsiflexion but provide only partial support, neglecting impairments in other joints. Multi-joint unilateral devices such as HAL [15], AGoRA [16] and LitteStepper [17] attempt to assist multiple joints simultaneously but tend to be heavier, less user-friendly, and more challenging to integrate seamlessly with the user's intent.

In practice, existing unilateral exoskeletons still fall short of delivering seamless, multi-joint assistance while maintaining usability, comfort, and safety. These limitations underscore the need for a new generation of unilateral exoskeletons that can provide comprehensive, user-centered support for hemiparetic individuals.

To address these gaps, this work introduces the Single-Sided Mobility Assistive Exoskeleton (SMAEXO), a novel multi-joint device specifically engineered for individuals with hemiparesis. SMAEXO incorporates innovative features designed to optimize reaction force management and weight distribution, while ensuring that assistance at the hip, knee, and ankle joints is both effective and intuitive. The key contributions of this work include:

1) Development of the SMAEXO enables integrated assistance across the hip, knee, and ankle joints, providing comprehensive support to the affected limb. Optimized weight distribution and reaction force management strategies ensure that the device can effectively stabilize and support the user without compromising comfort, safety or ease of movement.

2) The performance of SMAEXO is validated through

This research is supported by ASTAR under the National Robotics Programme (NRP) BAU grant, Project - Assistive Robotics Programme (Award No: M22NBK0074).

[1]School of Mechanical and Aerospace Engineering, Nanyang Technological University, Singapore.

[2]Rehabilitation Research Institute of Singapore, Nanyang Technological University, Singapore.

[3]Institute for Infocomm Research, A*STAR, Singapore.

[4]School of Robotics, Hunan University, Changsha, China.

[5]Tan Tock Seng Hospital, Singapore.

Corresponding authors' e-mails: {xiaoyue.yan, wtang}@ntu.edu.sg

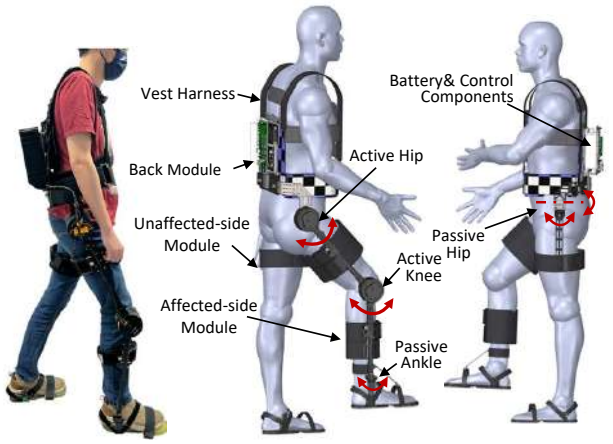


Fig. 1. Architecture of the single-sided mobility assistive exoskeleton (SMAEXO). The red arrows indicate joint movements.

a user study involving eight participants. This evaluation focuses on usability, comfort, safety, and effectiveness, offering valuable insights into SMAEXO's practicality and its potential to enhance the rehabilitation process for stroke survivors.

By offering a thoughtfully engineered solution that meets the unique needs of hemiparetic individuals, the SMAEXO has the potential to transform stroke rehabilitation.

II. System Overview

A. Architecture of SMAEXO

SMAEXO was developed through close collaboration with physiotherapists specializing in stroke rehabilitation and lower-limb exoskeletons. This consultative process ensured that the system aligns with the unique needs of individuals with hemiplegia, emphasizing usability, safety, comfort and comprehensive assistance. The device features a modular design comprising four primary components (Fig. 1):

- **Affected-side module:** Incorporates active hip and knee joints powered by quasi-direct drive (QDD) motors, which combine high-torque motors with a low gear ratio transmission (1:6) to deliver high bandwidth and backdrivability. Additionally, a passive ankle joint paired with a footplate is involved to prevent foot drop.
- **Unaffected-side module:** Features a passive hip joint that facilitates hip flexion/extension and abduction/adduction, ensuring natural movement on the unaffected side.
- **Back module:** Connects all modules and houses the control components and battery, strategically placing the battery on the unaffected side to optimize weight distribution and balance.
- **Vest harness:** Distributes device weight and reaction force evenly across the user's core, enhancing comfort and stability.

For safety and comfort, all joints incorporate both hard and soft limiters to restrict the range of motion (ROM) within the user's biomechanical capabilities. The soft limiters, implemented as joint buffers, absorb impacts when the joint approaches the hard limiters (Fig. 2 (b)). The joint buffers can be easily replaced to accommodate users with limited ROM. Additionally, all the leg bars are equipped with cuffs and cushions, as shown in Fig. 2 (d), these cuffs can be easily opened for quick donning and doffing and the major semi-axis, minor semi-axis of the cuffs can be easily adjusted to accommodate users with varying leg circumferences.

To further enhance adaptability and alignment, the SMAEXO features the corresponding adjustable mechanisms to allow tool-free adjustments for waist width, upper and lower leg bar lengths, and foot size, accommodating users of various body dimensions (Fig. 2 and Fig. 3 (a)). All adjustable mechanisms are equipped with reset springs to ensure the locked status for safety.

The main specifications of the SMAEXO system are summarized in Table I.

TABLE I
SPECIFICATIONS OF THE SMAEXO.

Items	Specifications
Motion Range (°)	Hip: (-20, 125); Knee: (0, 135); Ankle: (-40, 24)
Length Range (mm)	Upper Limb: 400–500 (Long), 300–400 (Short); Lower Limb: 380–480 (Long), 280–380 (Short); Hip Width: 335–435; Feet: 250–305
Hip and Knee Motors	Rated Torque: 12Nm; Max Torque: 37Nm; Ratio: 1:6; Weight: 0.759kg
Battery	Lithium Battery Pack, 24V 6Ah, Weight: 0.82kg
Weight (kg)	Total: 7.5; Affected-side Module: 3.3; Unaffected-side Module: 0.3 Back Module: 2.1 Vest Harness: 1.8

B. Efficient Reaction Force Management and Weight Distribution

Effective reaction force management is key to minimizing discomfort and enhancing usability. Double-sided exoskeletons like Ekso Indego [5], ReWalk [6], and Rex [7] achieve this through heavier self-weight and extensive user contact, enabling higher assistive torque but increasing bulk and reducing mobility. In contrast, lightweight exoskeletons face torque limitations due to weaker reaction force support. For example, Honda's SMA device provides 4 Nm of hip torque [18], while Samsung's GEMS, with a hip brace for additional support, reaches 12 Nm [19]. Unilateral devices like AGoRA improve torque and balance with bilateral configurations but increase mass to 17 kg [16].

The SMAEXO addresses these challenges by integrating innovative features for efficient reaction force management and weight distribution. Through a combination of an ergonomic vest harness and a flexible ankle joint coupled with a footplate, SMAEXO ensures effective stabilization and comprehensive assistance while maintaining a lightweight and user-friendly profile.

- **Ergonomic Vest Harness**

As depicted in Fig. 3 (a), the SMAEXO vest harness is designed to conform closely to the wearer's body. It consists

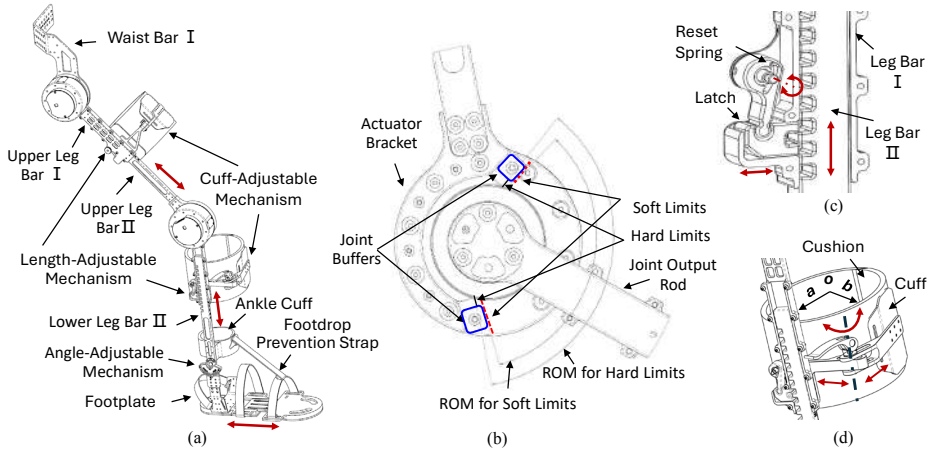


Fig. 2. The affected-side module of the SMAEXO. (a) Module with length adjustments (red arrows). (b) Joint with limited ROM, featuring replaceable buffers to absorb impact. (c) Length-adjustable mechanism with a reset spring for secure locking. (d) Cuff-adjustable mechanism with linear (a, b) and rotational adjustments for leg circumference and easy donning (red arrows).

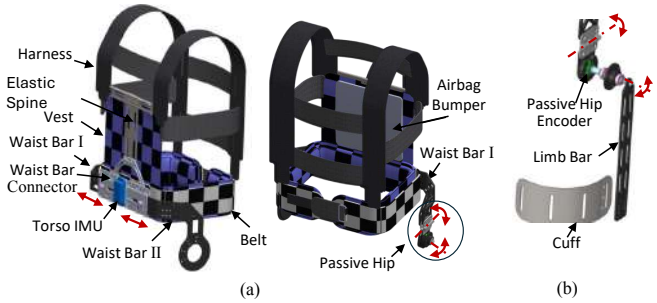


Fig. 3. The SMAEXO vest harness, back, and unaffected-side modules. (a) The back module, paired with the vest harness, includes an IMU for torso angle monitoring. (b) The unaffected-side module features a passive hip with an encoder to measure sagittal hip angles. Red arrows indicate linear adjustments for waist width and hip movement.

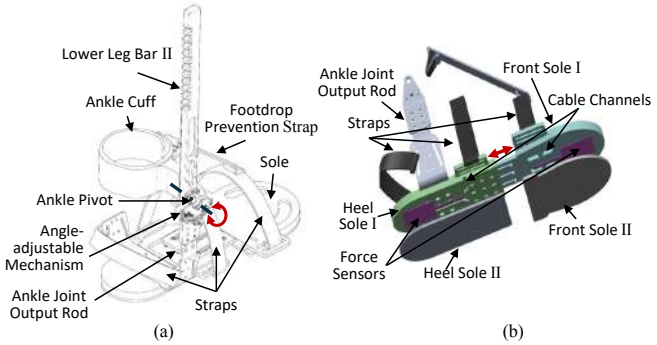


Fig. 4. The ankle joint and footplate of the SMAEXO. (a) The ankle joint connects to the footplate via an output rod and an elastic foot-drop prevention strap, which acts like a spring with adjustable tension for user adaptability. (b) The footplate features adjustable length via a sliding front sole I over heel sole I, accommodating various foot sizes. Embedded force sensors in front sole I and heel sole I are protected by an additional layer (front sole II and heel sole II). Integrated cable channels facilitate wiring.

of a vest integrated with a harness and belt, featuring an elastic spine made from flexible materials such as spring steel, which naturally adapts to the wearer's spinal curvature. To enhance fit and contact, an adjustable airbag bump is included, allowing compatibility with diverse body shapes and improving overall user comfort. This configuration efficiently utilizes the wearer's waist, chest, abdominal, and back muscles to stabilize reaction forces, reducing discomfort and enhancing mobility.

- **Flexible Ankle Joint**

Unlike most exoskeletons, such as Knee-Ankle-Foot Orthoses, ReWalk™ [6], and HAL [15], which use fixed ankle joints and rigid footplates to prevent foot drop and transfer weight to the ground, SMAEXO features a versatile ankle joint design that prioritizes both comfort and a natural gait. This innovative design adapts to individual user needs, facilitating improved mobility.

As depicted in Fig. 4 and Fig. 5, the SMAEXO ankle joint incorporates the following features: (1) An angle-adjustable mechanism, which can either be allowed to rotate within a controlled range or fixed at a specific angle. (2) A flexible footplate with force sensors at the heel and forefoot to detect gait events. (3) Effective weight transfer to the ground during stance without impeding force sensor functionality. (4) Integration with an elastic strap and ankle cuff to prevent foot drop during swing. (5) Adjustable footplate length to accommodate various foot sizes. (6) Construction using elastic and durable materials such as polyurethane (PU), rubber, and ethylene-vinyl acetate (EVA) for natural ground contact and durability. This configuration facilitates a natural gait while offering personalized adjustments to align with individual walking patterns and assistance needs, enhancing both comfort and mobility.

With its advancements in reaction force management and weight support, the SMAEXO achieves a maximum assistive torque of 25 Nm. This capability addresses the high torque demands of hemiplegia rehabilitation while ensuring user

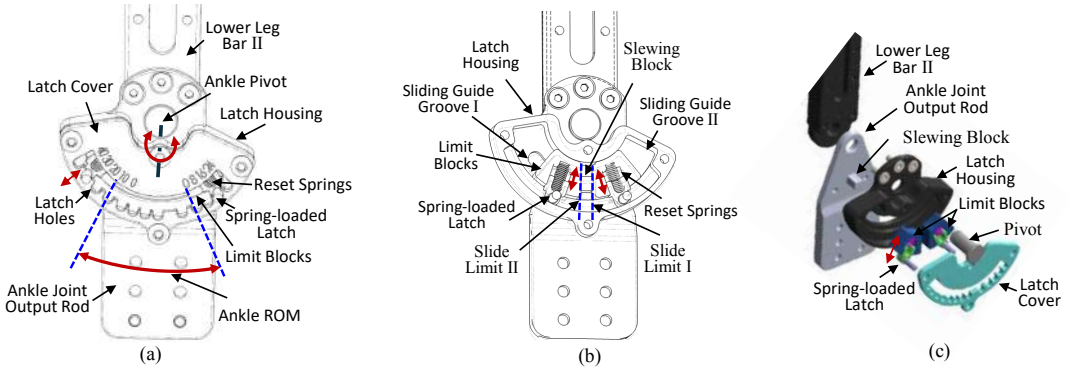


Fig. 5. The angle-adjustable mechanism of ankle joint. (a) Locked with limited movement. (b) Fixed at a specific angle. (c) Exploded view. The mechanism enables controlled ankle rotation or fixed positioning using a latch housing, sliding guide grooves, a slewing block, spring-loaded limit blocks, a pivot, and a latch cover. The limit blocks rotate along guide groove II and lock when the spring-loaded latch engages a latch hole. Unlocking releases the latch, restoring movement. The slewing block rotates within guide groove I and locks the ankle at a set angle when contacting both limit blocks.

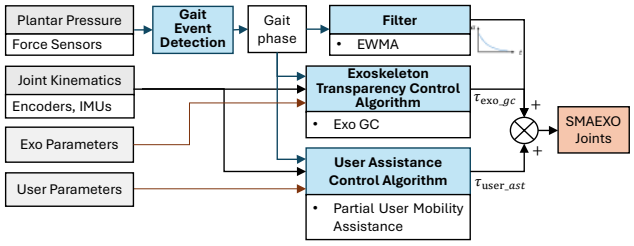


Fig. 6. Control block diagram of the SMAEXO.

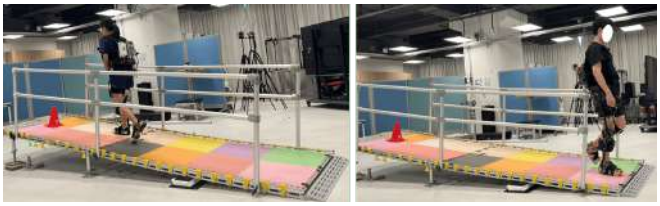


Fig. 7. Experiment setup.

comfort, providing an effective and user-friendly solution for mobility assistance.

C. Control Scheme

The SMAEXO utilizes a multi-level control strategy with a reliable and cost-effective sensor system to enhance its functionality. This system incorporates a torso IMU and encoders embedded in the hip and knee joints to provide accurate joint kinematic measurements. Foot pressure measurements from force sensors, combined with kinematic data, are employed to identify gait phases during various daily activities, including sit-to-stand transitions and walking on flat surfaces, ramps, or stairs. The control system leverages this gait phase information to implement exoskeleton transparency(e.g., Gravity Compensation) and partial user mobility assistance for optimized support and a better user experience. Additionally, exoskeleton and user parameters are tailored to meet individual assistance needs, while filters like the Exponentially Weighted Moving Average (EWMA) ensure a smooth torque profile throughout the entire gait cycle (Fig. 6).

III. Experiments

To evaluate the usability, comfort, safety, and assistance provided by the SMAEXO, eight able-bodied participants were recruited, including two physiotherapists specializing in lower-limb rehabilitation. During testing, physiotherapists simulated stroke gait patterns—including foot drop, stiff knee, circumduction, and weak knee—based on their experience to evaluate the exoskeleton's effectiveness from a patient's perspective. Demographic and anthropometric details of the participants are provided in Table II. All participants gave written informed consent after being briefed on the study's objectives and potential risks. The study protocol received approval and oversight from the Nanyang Technological University Institutional Review Board.

During the experiment, participants could take rest breaks, stop, or withdraw from testing at any time. The assessment consisted of two sessions (with and without the exoskeleton), each comprising three tasks. Participants repeated each task at least three times:

- 10-meter level walking;
- 4-meter slope with 8 degrees inclination up and down;
- Stepping over a 10 cm high, 12.5 cm wide obstacle.

In the second session, participants were familiarized with the exoskeleton for 30 minutes before testing. Investigators guided them on exoskeleton use and ensured acclimatization. Participants were instructed to report any discomfort or pain, which was documented and addressed.

At the study's conclusion, participants completed a questionnaire assessing the exoskeleton's usability, comfort, safety and assistance. All questions are rated 1 to 5, with 1 as "strongly disagree" and 5 as "strongly agree".

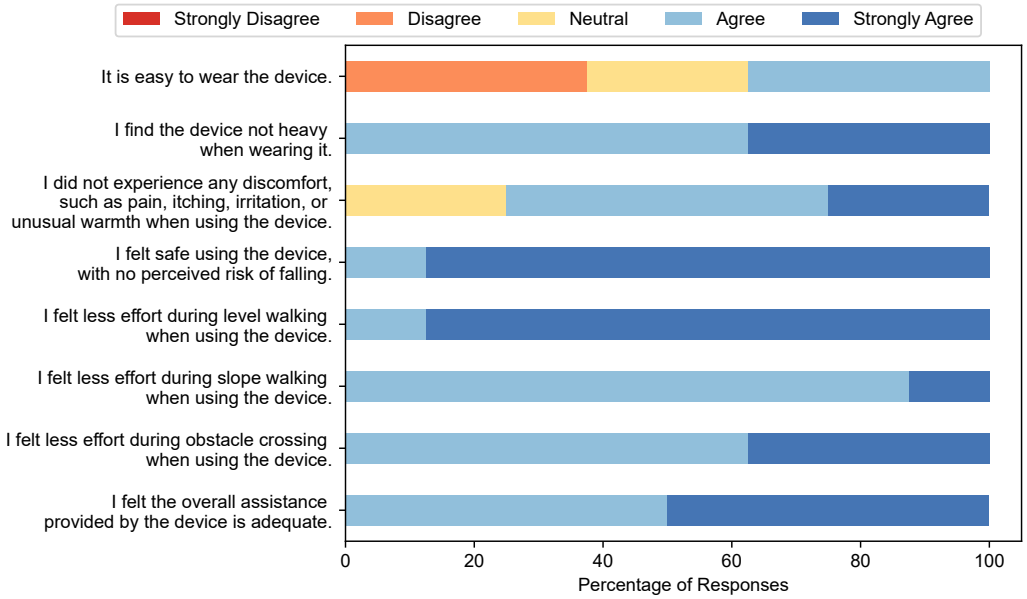


Fig. 8. User questionnaire responses to the SMAEXO during level and slope walking, as well as obstacle crossing tasks.

TABLE II

DEMOGRAPHIC AND ANTHROPOMETRIC DETAILS OF PARTICIPANTS.

Participants	Age	Sex	Height (cm)	Mass (kg)
P1	31-40	F	155	54.5
P2	21-30	M	171	70
P3	31-40	F	163	55
P4	31-40	M	183	76
P5	21-30	M	183	73
P6	21-30	M	181	85
P7	21-30	M	176	85
P8	41-50	M	169	71

TABLE III

SPECIFICATIONS OF THE SMAEXO.

Devices	HAL (Cyberdyne)	LiteStepper (Angelexo)	SMAEXO
Control Strategy	Model-based control (amplify muscle activities) or Predefined gait trajectory	Replicate gait trajectory of intact limb & Crutch handle to initiate walk	Hybrid Model-based control
Actuators	2 Brushless DC motors	2 Brushless DC motors	2 QDD motors
Sensors Used	Kinematic Sensors Sole Pressure Sensors EMGs	Kinematic Sensors Sole Pressure Sensors Cane Pressure Sensor	Kinematic Sensors (4) Sole Pressure Sensors
Footplates Type	Customized shoes with rigid shoes insole	Mechanical footplates	Flexible footplates
Weight Support	Rigid insole(ground)	Vest (core) Footplates (ground)	Vest Harness (core) Footplates (ground)
Weight	9 kg	16.9 kg	7.5 kg

IV. RESULTS AND DISCUSSION

As shown in Fig. 8, participants appreciated SMAEXO's modular design and tool-free adjustments for easy donning and doffing. However, its unbalanced structure made maintaining a neutral position challenging, especially when seated. Physiotherapists noted that post-stroke users often require two assistants for stabilization. Incorporating a support frame could address this issue by providing stability during the donning process.

Participants considered the device's weight acceptable. During the stance phase, the SMAEXO effectively transferred weight to the ground, reducing the burden on the knee joint. However, physiotherapists raised concerns regarding hemiplegic users, as the unaffected leg bears the device's weight during the swing phase. This could potentially increase stress on the unaffected knee, particularly concerning for elderly post-stroke individuals who are more susceptible to knee issues, such as osteoarthritis. Further reducing the exoskeleton's weight is recommended to alleviate this strain.

The device was reported to be comfortable, with no instances of pain, itching, or irritation. The adjustable mechanisms enabled proper adaptation to various body dimensions, ensuring a snug fit that effectively engaged the user's core muscles for optimal reaction force management and weight distribution. However, two participants experienced slight perspiration on their backs after wearing the device for more than an hour, likely due to the vest and airbag bump. Incorporating breathable materials into these components could enhance comfort during prolonged use.

Regarding safety, participants indicated no concerns about falling or other safety issues during the trials, indicating that the SMAEXO's design effectively solved the weight distribution and balance challenges. However, one participant highlighted the potential risk of the footplate contacting obstacles or stairs if the straps were not tightly secured. This emphasizes the importance of ensuring that all straps are properly adjusted and secured to maintain safety during use.

Participants reported the SMAEXO provided adequate assistance during level and slope walking, as well as obstacle negotiation, reducing their effort. This shows the SMAEXO offered comprehensive joint support throughout the gait cycle by combining active hip and knee assistance with a passive, flexible ankle joint.

Compared to double-sided exoskeletons, the SMAEXO

demonstrated advantages in weight reduction and freedom of movement, while offering more comprehensive support than single-joint devices. Table III compares the main features of our device with commercial unilateral exoskeletons, HAL and LiteStepper. SMAEXO offers advantages in compact design, lighter weight, an intuitive and cost-effective sensor system, improved force management, and more flexible footplates for natural gait. However, challenges remain in minimizing the overall weight and improving the ease of donning and doffing, particularly due to the lack of a stable sitting pose without external support. Future iterations should focus on incorporating a dedicated support mechanism to address this limitation and further enhance usability.

Compared to double-sided exoskeletons, SMAEXO offers reduced weight and greater freedom of movement while providing more comprehensive support than single-joint devices. Table III compares its key features with commercial unilateral exoskeletons, HAL [20] and LiteStepper [17]. SMAEXO excels in compact design, lighter weight, an intuitive and cost-effective sensor system, improved force management, and flexible footplates for natural gait. However, challenges remain in further reducing weight and improving donning and doffing, particularly due to the lack of stable sitting posture without external support. Future iterations should integrate a dedicated support mechanism to enhance usability.

V. Conclusion

In this study, we developed the Single-Sided Mobility Assistive Exoskeleton (SMAEXO), a single-sided, multi-joint lower limb exoskeleton designed to enhance mobility in individuals with hemiplegia. SMAEXO actively supports the hip and knee while incorporating a passive, flexible ankle joint to prevent foot drop, ensuring dynamic assistance throughout the gait cycle. Its tool-free adjustments, optimized weight distribution, and reaction force management enhance usability, balance, comfort, and safety while minimizing strain on the affected side.

We evaluated usability, safety, comfort, and assistance with eight able-bodied participants during level walking, slope walking, and obstacle crossing. Participants reported the device as safe, comfortable, and effective, with no adverse effects such as itching or irritation, and found the assistance beneficial. However, areas for improvement were noted, including better cooling, reduced weight, and simplified donning.

This study is limited by a small and unbalanced participant sample, which may impact the generalizability of the findings. Future work will address this by conducting extensive testing with a larger, more diverse participant pool for robust validation.

Building on the these findings, we will advance to clinical trials to evaluate SMAEXO's effectiveness in post-stroke individuals. Comprehensive data analysis will inform design refinements to enhance functionality, comfort, and user experience. With continued development, SMAEXO holds the potential to significantly improve mobility and quality of life for individuals with hemiplegia.

References

[1] V. L. Feigin, M. Brainin, B. Norrving, S. Martins, R. L. Sacco, W. Hacke, M. Fisher, J. Pandian, and P. Lindsay, "World stroke organization (wso): global stroke fact sheet 2022," *International Journal of Stroke*, vol. 17, no. 1, pp. 18–29, 2022.

[2] Y. Li, T. Fan, Q. Qi, J. Wang, H. Qiu, L. Zhang, X. Wu, J. Ye, G. Chen, J. Long *et al.*, "Efficacy of a novel exoskeletal robot for locomotor rehabilitation in stroke patients: A multi-center, non-inferiority, randomized controlled trial," *Frontiers in aging neuroscience*, vol. 13, p. 706569, 2021.

[3] G. Chen, C. K. Chan, Z. Guo, and H. Yu, "A review of lower extremity assistive robotic exoskeletons in rehabilitation therapy," *Critical Reviews™ in Biomedical Engineering*, vol. 41, no. 4-5, 2013.

[4] E. Read, C. Woolsey, C. A. McGibbon, and C. O'Connell, "Physiotherapists' experiences using the ekso bionic exoskeleton with patients in a neurological rehabilitation hospital: A qualitative study," *Rehabilitation research and practice*, vol. 2020, no. 1, p. 2939573, 2020.

[5] "Ekso indego," Ekso Bionics. [Online]. Available: https://eksobionics.com/ekso-indego-therapy/

[6] "Rewalk personal exoskeleton," Lifeward. [Online]. Available: https://golifeward.com/products/rewalkpersonal-exoskeleton/

[7] "Rex," Rex Bionics. [Online]. Available: https://www.rexbionics.com/product-information/

[8] J. S. Lora-Millan, J. C. Moreno, and E. Rocon, "Coordination between partial robotic exoskeletons and human gait: A comprehensive review on control strategies," *Frontiers in Bioengineering and Biotechnology*, vol. 10, p. 842294, 2022.

[9] J. M. Hidler and A. E. Wall, "Alterations in muscle activation patterns during robotic-assisted walking," *Clinical Biomechanics*, vol. 20, no. 2, pp. 184–193, 2005.

[10] E. P. Washabaugh, T. E. Augenstein, A. M. Ebenhoeh, J. Qiu, K. A. Ford, and C. Krishnan, "Design and preliminary assessment of a passive elastic leg exoskeleton for resistive gait rehabilitation," *IEEE Transactions on Biomedical Engineering*, vol. 68, no. 6, pp. 1941–1950, 2020.

[11] J. Wang, X. Li, T.-H. Huang, S. Yu, Y. Li, T. Chen, A. Carriero, M. Oh-Park, and H. Su, "Comfort-centered design of a lightweight and backdrivable knee exoskeleton," *IEEE Robotics and Automation Letters*, vol. 3, no. 4, pp. 4265–4272, 2018.

[12] J. S. Lora-Millan, F. J. Sanchez-Cuesta, J. P. Romero, J. C. Moreno, and E. Rocon, "A unilateral robotic knee exoskeleton to assess the role of natural gait assistance in hemiparetic patients," *Journal of NeuroEngineering and Rehabilitation*, vol. 19, no. 1, p. 109, 2022.

[13] "Restore exo-suit," Lifeward. [Online]. Available: https://golifeward.com/products/restore-exo-suit/

[14] G. Orekhov, Y. Fang, C. F. Cuddeback, and Z. F. Lerner, "Usability and performance validation of an ultra-lightweight and versatile untethered robotic ankle exoskeleton," *Journal of neuroengineering and rehabilitation*, vol. 18, pp. 1–16, 2021.

[15] H. Kawamoto, T. Hayashi, T. Sakurai, K. Eguchi, and Y. Sankai, "Development of single leg version of hal for hemiplegia," in *2009 Annual international conference of the IEEE engineering in medicine and biology society*. IEEE, 2009, pp. 5038–5043.

[16] L. J. A. Mayag, M. Múnera, and C. A. Cifuentes, "Human-in-the-loop control for agora unilateral lower-limb exoskeleton," *Journal of Intelligent & Robotic Systems*, vol. 104, no. 1, p. 3, 2022.

[17] Y. Jin, B. Xiong, L. Chen, W. Zhao, Z. Li, C. Zhang, and X. Xu, "Efficacy and safety of using a unilateral lower limb exoskeleton combined with conventional treatment in post-stroke rehabilitation: a randomized controlled trial," *Frontiers in Bioengineering and Biotechnology*, vol. 12, p. 1441986, 2024.

[18] R. Kitatani, K. Ohata, H. Takahashi, S. Shibuta, Y. Hashiguchi, and N. Yamakami, "Reduction in energy expenditure during walking using an automated stride assistance device in healthy young adults," *Archives of physical medicine and rehabilitation*, vol. 95, no. 11, pp. 2128–2133, 2014.

[19] K. Seo, J. Lee, Y. Lee, T. Ha, and Y. Shim, "Fully autonomous hip exoskeleton saves metabolic cost of walking," in *2016 IEEE International Conference on Robotics and Automation (ICRA)*. IEEE, 2016, pp. 4628–4635.

[20] "Hal for well-being (lower limb type)," Cyborg. [Online]. Available: https://www.cyberdyne.jp/english/products/fl05.html

Preference Augmented Q-Learning for Patient Exercise Scheduling in a Robotic Rehabilitation Gym

Varun R. Bharadwaj*, Benjamin A. Miller*, Vesna D. Novak and Chao Jiang

***Abstract*— Robotic rehabilitation gyms enable groups of patients to perform motor rehabilitation under the guidance of a single therapist. While software can help process and present patient exercise information in an easy-to-understand manner, certain characteristics like motivation and fatigue are harder to quantify using sensors. Human therapists are able to observe these characteristics without precise sensor measurements and use them to make intelligent patient-robot assignment decisions. However, actively observing every patient in the group and changing which robot they exercise with would distract the therapist from delivering effective therapy. To help with this, we propose a Preference Augmented Q-Learning assignment scheduler that learns to create patient-robot assignment schedules for group rehabilitation. The scheduler is trained to leverage expert assignment preferences and implicitly incorporate motivation and fatigue through expert guidance. The assignment scheduler was tested using 1000 simulated patient groups with its results compared against several baselines. Our assignment scheduler outperformed all tested baselines, except for schedules created by a simulated expert who had access to all the patients' characteristics and could predict future exercise outcomes. In simulation, the results show the effectiveness of incorporating expert preferences into reinforcement learning models to improve assignment scheduling without directly measuring hard-to-quantify factors.**

I. Introduction

Rehabilitation robots are designed to assist patients during motor rehabilitation, with results roughly as good as traditional aid delivered by a human therapist [1], [2]. More recently, the effectiveness of rehabilitation robots has sparked interest in robotic rehabilitation gyms: rehabilitation venues with multiple rehabilitation robots that enable multiple patients to exercise at the same time [3]. These robotic gyms enable a single physical or occupational therapist to oversee the exercise of multiple patients at once. Analysis software, such as HocoNet [4], can further aid therapists by keeping track of and consolidating the performance of every patient in the group. This consolidated data provide a clearer picture of individual progress and group dynamics. However, even with this information, therapists may face challenges in creating optimal group adjustments in real time due to the complexity and volume of data. By further analyzing trends in patient performance, the software could potentially suggest reassigning patients to different robots or exercises that are better aligned with their current skill level and needs. If implemented, such adjustments could help ensure that each patient focuses on exercises most beneficial to their rehabilitation goals.

A. Previous Work

Recent simulation research suggests that it is possible to train an automatic robotic rehabilitation gym scheduler to create group rehabilitation exercise schedules based on measured patient performance metrics, though the simulated environments were rather simplistic [5]–[9]. Initial simulations consisted of groups of patients performing exercises using different rehabilitation robots in fully observable, deterministic environments where results could be predicted before patients performed an exercise [7]. In this simplified environment, patient exercise scheduling was framed as a mixed-integer nonlinear programming problem and solved using optimization software to create exercise schedules.

More recent studies included stochastic environments where patients' skill levels were not measurable during a session (mirroring the impracticality of measuring a patient's true motor skill during a session) [5], [6], [10]. Instead, the patients' success rates (a measure of how well the patients performed their exercise) and their effort were measured. In such simplified environments, it was shown that a machine learning model could be trained to mimic a therapist's assignment decisions and produce schedules that outperform several baselines [5], [6].

However, these schedulers prioritized short-term over long-term skill improvement [5], [6]. Additionally, the simplified environment meant that all relevant variables were directly measurable. In real-life scenarios, certain characteristics like motivation and fatigue that influence skill improvement are hard to measure [11]–[13]. Without knowledge of these hidden characteristics, the schedulers would not be able to create optimal schedules in more complex environments. Our work aims to address this issue by developing a Preference Augmented Q-Learning algorithm that trains the scheduler via a combination of Reinforcement Learning (RL) [14] and direct therapist feedback.

II. Methodology

A. Simulated Robotic Gym Environment

Similar to previous studies [5]–[9], the robotic rehabilitation gym consists of J different robots and K exercises, where each of the J robots can be used to perform one of the K exercises. Each exercise additionally has three

*Both authors contributed equally to the work. This work was supported by the National Science Foundation under grant no. 2024813.

Varun R. Bharadwaj and Chao Jiang are with the Department of Electrical Engineering and Computer Science, University of Wyoming, Laramie, WY 82071 USA. {vbharadw, cjiang1}@uwyo.edu

Benjamin A. Miller and Vesna D. Novak are with the Department of Electrical and Computer Engineering, University of Cincinnati, Cincinnati, OH 45221 USA. mille7ba@mail.uc.edu and novakdn@ucmail.uc.edu

difficulty levels, where patient performance changes based on the difficulty of the exercise relative to the patient's skill level. The three difficulty levels serve to better model reality where rehabilitation robots can offer differing amounts of support or resistance [15]. Similar to a previous study [6], the difficulty for each exercise is always set by the expert so that each patient exercises at the difficulty best suited for their current skill level. Each robot can only be used by one patient at a time and a patient may only exercise with one robot at any given moment. Only one patient group at a time can use the gym, with a patient group consisting of *I* simulated patients. All patients in the group stay in the gym for an entire exercise session and each exercise session is divided into *T* equal blocks of time, called timesteps. Each patient in the patient group is assigned to exercise with a robot at the beginning of each timestep and cannot switch to a new robot until the start of the next timestep.

Ideally, real patient motor rehabilitation data would be used in this study. However, due to a lack of preexisting data and the difficulty of collecting the necessary amount, this was not feasible. Instead, we updated a patient motor rehabilitation data generator from our previous work [5], [6], [8]. The previous data generator modeled patient success rate, effort, and skill level, with these measurements being analogous to real performance metrics and patient characteristics (e.g., percentage of completed motion, amount of force/torque applied during the exercise, range of motion, etc.) that can be measured using sensors [5], [6], [8], [16], [17]. A patient's success rate and effort were generated based on their current skill level, while their skill improvement after a timestep of exercise was determined by their resulting success rate and effort. In our current work, the simulator was updated to better model a real rehabilitation gym where exercises can have different levels of difficulty and where patient motivation and fatigue can affect their performance.

B. Patient Characteristics and Performance Metrics

Each patient has a corresponding skill level for each of the *K* different exercises. This value is hidden during an exercise session, simulating real-life scenarios where it is difficult to directly measure a patient's skill level without a time-consuming series of tests (such as the Fugl-Meyer Assessment [10]). Skill level improves whenever they exercise with the corresponding robot. The amount of improvement is determined by how successfully the patient performed the exercise (their success rate) and how much work they put in (their effort). Exercising also affects a patient's motivation and fatigue, with their motivation changing based on how successful they were and their fatigue changing based on how long they have performed each exercise [11], [13], [18]. Motivation reflects a person's enthusiasm to engage in a task, whereas fatigue indicates their level of physical exhaustion.

1) Motivation: A patient's current level of motivation is determined by the patient's motivation in the previous timestep and change in motivation (denoted as Δ*motivation*). Δ*motivation* is proportional to the patient's exercise performance as shown in Fig. 1 (right) [11], [18]. We model

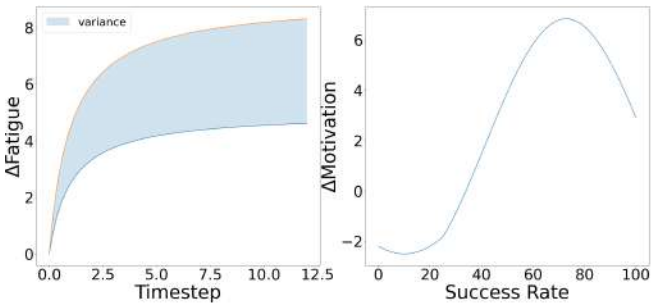


Fig. 1: Δfatigue vs number of timesteps a patient has performed an exercise (left) and Δmotivation vs success rate (right). The shaded region in the left plot represents the range of possible random values for the change in fatigue (Δfatigue) based on the time spent performing an exercise

motivation using the following equations:

$$motivation(t+1) \;=\; motivation(t) + \Delta motivation \quad (1)$$

with its values capped between 0 and 100.

2) Fatigue: Patients have separate levels of fatigue for each exercise. Performing an exercise increases the corresponding level of fatigue while decreasing the level of fatigue for all other exercises (as the patient is not exercising that specific muscle group) [12], [13]. Additionally, if a patient does not perform an exercise, the corresponding fatigue for all exercises decreases as well. A patient's overall level of fatigue is the sum of all of their exercise fatigues and a patient will refuse to exercise while their overall level of fatigue is greater than 100. A patient's change in fatigue is denoted as $\Delta fatigue_k$ where k denotes the corresponding exercise. $\Delta fatigue_k$ when a patient performs exercise k is shown in Fig. 1 (left). $\Delta fatigue_k$ when a patient does not perform exercise k is -0.05 $fatigue_k(t)$. Patient fatigue is modeled using the following equations:

$$fatigue_k(t+1) = fatigue_k(t) + \Delta fatigue_k \quad (2)$$

with a minimum value of 0.

3) Effect of Motivation and Fatigue: High fatigue and low motivation reduce patient performance [11]–[13], [19]. The overall effect that motivation and fatigue have on patient performance is modeled as a factor, α, representing the average of the fatigue and motivation, where motivation and fatigue are scaled such that alpha is between 0 and 1.

$$\alpha = \frac{(motivation/100) + (1 - fatigue_k/100)}{2} \quad (3)$$

This allows both fatigue and motivation to have an equal effect on patient performance.

4) Skill Improvement, Success Rate, and Effort: Patient skill improvement, success rate and effort are all modeled using stochastic equations, mimicking the uncertainty of patient exercise. These values (base performance metrics) are first calculated without factoring in the effect of fatigue and motivation. After all three are calculated, the effects of motivation and fatigue are accounted for by scaling the base performance metrics with the factor α. All three values are

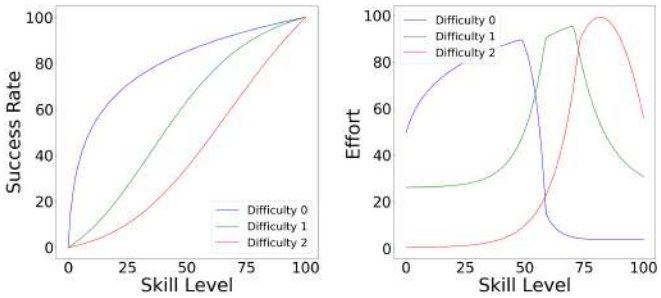


Fig. 2: Success rate (left) and effort (right) across different difficulty levels

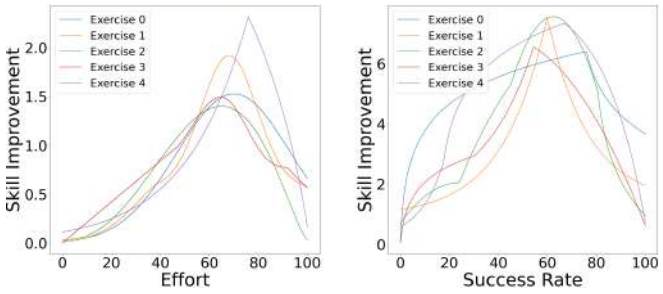


Fig. 3: Skill improvement from success rate and effort

capped between 0 and 100. Patient success rate increases with skill if difficulty level is kept unchanged (Fig. 2 (left)) [19], [20]. Similar to previous studies [6], [9], the skill level to success rate curve for the medium difficulty (difficulty 1) was roughly linear, but with a slightly higher growth in success rate at lower skill levels. The skill level to success rate curve for the low difficulty (difficulty 0) used a logarithmic curve such that patients always had a higher success rate compared to higher difficulties, with success rate increasing more rapidly at earlier skill levels before becoming roughly linear. The skill level to success rate curve for the high difficulty (difficulty 2) resembled an exponential function, such that patient skill level was always lowest at this difficulty. It then became roughly linear at medium to higher skill levels.

Similarly, a patient's effort varies according to their skill level in an exercise relative to the difficulty level of the exercise, where a patient exerts less effort if a task is too easy or too hard to perform for their current skill level (Fig. 2 (right)) [6]. Effort is lower when a patient's skill level is too low for the current exercise difficulty, modeling how patients cannot properly engage with an exercise if it is too difficult for them (e.g., patients with a lower skill level cannot move if a robot applies too much resistance) [6], [21]. Effort increases as the patient's skill level becomes more appropriate for the current difficulty, modeling how the patient becomes skilled enough to perform the exercise and thus works harder. Effort then starts decreasing as the patient becomes too skilled for the current difficulty, modeling how patients do not need to try as hard to complete the exercise.

Patient skill improvement before factoring fatigue and motivation directly depends on their success rate, effort, and exercise difficulty, with optimal improvement occurring when the exercise is moderately challenging (Fig. 3). The curves are based on the challenge point framework (a mathematical model describing the relationship between skill level, performance, and skill improvement), but modified to allow for different exercises to have different skill improvement curves [19], [20]. A patient's total skill improvement is modeled as the sum of improvements due to success and effort. Fig. 2 and 3 show the deterministic versions of patient-exercise characteristics and performance metrics. When simulating our gym, we add stochasticity to the patient-exercise characteristics and performance metrics. For success rate and effort, we first calculate their deterministic value and then add a random value sampled from a uniform distribution ranging from -2 to 2. For skill improvement, the stochastic values were chosen from a range from 0 to 20 percent of the maximum possible deterministic skill improvement for the exercise.

C. Assignment Scheduler

Our Preference Augmented Q-Learning algorithm is a two-stage assignment scheduler. The first stage uses a neural network to generate scores for patient-robot assignments and the second stage performs conflict resolution based on the scores from the previous stage. The scheduler aims to assign patients to robots at each time step, in such a way that the expected skill improvement of the group is maximized. Exact measurements of patient skill level, motivation, and fatigue are difficult to measure during an exercise session and thus cannot be used by the assignment scheduler, aligning with characteristics of Partially Observable Systems [10]–[13]. However, motivation and fatigue still affect the patient's exercise outcomes, and thus the assignment scheduler must learn how to account for them. To do this, we leverage expert knowledge and patient exercise history to infer about these factors while training the scheduler. The second stage, a binary constraint search tree [22], then finds the schedule that is expected to give the largest long-term skill improvement.

1) The Neural Network: The long-term benefit of each patient-robot assignment is estimated by a Deep Q-Network (DQN) trained using RL [14], [23]. The sparse nature of our environment (i.e., the lack of skill measurements) means that our neural network cannot be trained using a patient's true immediate skill improvement as the immediate reward. Additionally, the assignment scheduler must be designed and trained to account for the hard-to-quantify factors (fatigue and motivation). Hence, we leverage the expertise of a domain expert (such as a therapist) to guide the training of our model, and utilize the patient exercise history to infer about motivation and fatigue. While this work involves simulation, the data generation was designed to emulate how the data could be collected in the real world.

The inputs to the network are as follows:

- All of each patient's previously recorded success rates denoted by $Gh_{pi,rj} = \{g_{pi,rj}(1), g_{pi,rj}(2), ..., g_{pi,rj}(t)\}$

- All of each patient's previously recorded effort denoted by $Eh_{pi,rj} = \{e_{pi,rj}(1), e_{pi,rj}(2), ..., e_{pi,rj}(t)\}$
- The current timestep in the session, denoted by T_t
- The number of timesteps remaining in the session denoted by $T_r = T - T_t$.

$Gh_{pi,rj}$ and $Eh_{pi,rj}$ are the same size as the total number of timesteps in one session and are initialized to zeros. The current timestep in the session is used as an input, as motivation and fatigue directly affect patient performance and are affected by how long the patients have been exercising. On the other hand, using the remaining number of timesteps as an input helps the network know how far into the future it should plan for when assigning patients to robots.

2) Network Architecture: Our DQN's input layer has the same dimension as the feature vector $(Gh_{pi,rj}, Eh_{pi,rj}, T_t, T_r)$. We have two hidden layers with 128 and 256 neurons respectively. We have dropout layers in between all the hidden layers with a dropout probability of 0.27. All hidden layers use L2 regularization with λ = 10^{-5}. The L2 regularizer shrinks the weights to be small but nonzero coefficients, preventing one feature from dominating the model's predictions and improves generalization.

3) Training Data Generation: To generate training data, 10000 simulated patients each exercise in the gym alone for one exercise session, where a session lasts for 12 timesteps. During this training process, there are 5 robots in the gym and each robot is used to perform a different exercise. At the beginning of each timestep, two actions are selected: one by a simulated expert and one by our algorithm. The simulated expert provides the robot assignment they prefer based on the current patient performance metrics. Our simulated expert's scheduling policy is intended to be optimal: they always make the assignment that is expected to produce the largest skill improvement for the current timestep. To do this, the expert is given total knowledge of the patient's characteristics and performance metrics, including their current motivation, fatigue levels, and expected skill improvement if they perform each exercise. Importantly, this means that the expert has significantly more information than what our model will ever have. Our model either selects a random robot with probability ε or the robot it thinks is best. Allowing our model to pick a random robot ε percent of the time during training helps ensure that we have a wide variety of data to train our model and that our model explores actions it would otherwise not. ε starts at 100 percent and decays based on how much data has been generated. The simulated patient then performs the exercise selected by the algorithm. This causes the patient's success rate, effort values, fatigue, motivation and skill values all to change based on the previously described relationships.

4) Reward Design: During training, our model is given rewards based on the quality of its assignments. The network receives a reward based on three things: whether its selected assignment matches the expert's (the preference reward), the rate of change of patient success rate between consecutive timesteps, i.e., $g_{pi,rj}(t+1) - g_{pi,rj}(t) > g_{pi,rj}(t) - g_{pi,rj}(t-1)$ (success rate reward), and if the patient starts exercising at a higher difficulty level (difficulty reward). The total reward is the sum of all three and is denoted by L_{total}. If the assignment suggested by the model is the same as the expert's, we assign a reward $L_{\text{pref_r}}$ (preference reward) of 10, but if they are different we give the model a reward based on the equations shown below:

$$R_e = Q(s, a_e) + \sqrt{(Q(s, a_e) - Q(s, a_m))^2} \quad (4)$$

$$R_m = Q(s, a_m) - \sqrt{(Q(s, a_e) - Q(s, a_m))^2} \quad (5)$$

$$L_{\text{pref_r}} = \left[\left(\frac{e^{R_n}}{e^{R_e} + e^{R_m}} \right) * 40 \right] - 20 \quad (6)$$

Here, a_e represents the expert's preferred action, and a_m the action chosen the model. $Q(s, a_e)$ measures how good the model currently thinks the expert's action is, and $Q(s, a_m)$ measures the model's own action. Intermediate values R_e and R_m are used to calculate the preference reward, which is inversely proportional to the difference in Q-values between the two assignments. This encourages the model to align with the expert's preferences by rewarding similar assignments and penalizing dissimilar ones.

Along with human guidance, we also consider rate of change in success rate as well as their difficulty level in shaping our reward. If the change in a patient's success rate when they perform an exercise is larger than the previous time they performed the exercise, or if the expert assigns the patient to a higher difficulty, the model earns an additional reward of 5. This promotes actions that drive rapid skill improvement. After computing rewards, the success rate, effort, reward and selected action for the current timestep are stored. At the end of the session, the model is updated using the deep Q-learning algorithm [23] with the following loss function, where γ is the discount factor.

$$L(\theta) = \mathbb{E}_{s,a,s'} \left[(L_{\text{total}} + \gamma Q_{\theta'}(s', \arg\max_{a'} Q_\theta(s', a')) - Q_\theta(s, a))^2 \right] \quad (7)$$

D. Evaluation

1) Baselines: We additionally simulated six other scheduling philosophies to compare and evaluate the effectiveness of our assignment scheduler.

a) Simulated Expert: The simulated expert has access to all patient characteristics and performance metrics including motivation and fatigue, and can predict the expected immediate skill improvement for all patient-robot combinations at each timestep. The expert uses this knowledge to make assignments that are expected to be optimal at each timestep.

b) Immediate Best: Each patient is assigned to a single robot for the entire session. Each patient's robot is selected such that the expected skill improvement of the group after the first timestep is maximized based on each patient-robot combination's expected skill improvement. This is done by simulating a single exercise timestep for each patient-robot combination where all stochastic values are set to their expected (mean) result. This mimics a realistic scenario where a therapist may be able to predict which robots would be most immediately beneficial for each patient [1].

c) Two Immediate Best: Identical to "Immediate Best", but patients switch to their second-best robot halfway through the session. As skill improvement tends to slow down at higher skill levels, having patients change robots mid-session can encourage greater overall skill improvement.

d) One Best: Identical to "Immediate Best", but the entire session is simulated for each patient-robot combination instead of only a single timestep. As this baseline simulates the entire session to determine every patient's optimal robot, this baseline has knowledge of the expected future result of patient exercise (including motivation, fatigue and all skill improvements) and relies on post-hoc optimization. Hence it is not practical in a real-world setting.

e) Two Best: Identical to "Two Immediate Best", but the entire session is simulated for each patient-robot combination when deciding which robots are optimal. Again, this baseline has future knowledge and relies on post-hoc optimization, making it impractical. It serves as a theoretical best schedule under the condition that patients must switch robots once halfway through the session.

f) Random: This method assigns each patient to a random robot at each timestep as a sanity check to confirm that our approach is effectively learning and not performing randomly.

2) Patient Groups: 1000 simulated patient groups were created to test the effectiveness of our scheduler in creating group assignment schedules that maximize group skill improvement. Each group consisted of 5 patients and 5 robots (i.e., $I = 5$ and $J = 5$), where each robot could be used to perform a different exercise (i.e., $K = 5$). Each patient's initial skill levels were generated randomly between 0 and 100 and their initial success rate and effort were then generated based on these initial skill values. This is done before the simulated session officially "begins" and is analogous to an initial pre-session assessments of patient abilities. Each patient's motivation was randomized between 0 and 100. As patients have yet to perform any exercise, their initial fatigue values for each exercise were randomized between 0 and 20.

Each patient group exercised for one 12-timestep session for each different scheduler. During each session, patients performed scheduled exercises, and their characteristics were updated in the same manner as in training data generation.

III. Results and Discussion

Fig. 4 shows the performance of the different schedulers for 1000 patient groups. One-way repeated-measures Analysis of Variance on Ranks with post-hoc Tukey tests was conducted and showed that all schedulers are significantly different from each other at $p < 0.05$. The scheduler type had a large impact on patient group skill improvement, with the "Expert" performing the best, followed by our model and then "Two Best" (Fig. 4). This highlights the importance of intelligent, dynamic patient-robot assignment based on patient performance. This is further supported by the "Random" scheduler outperforming "Immediate Best" and "One Best" schedulers, which did not allow patients to change exercises.

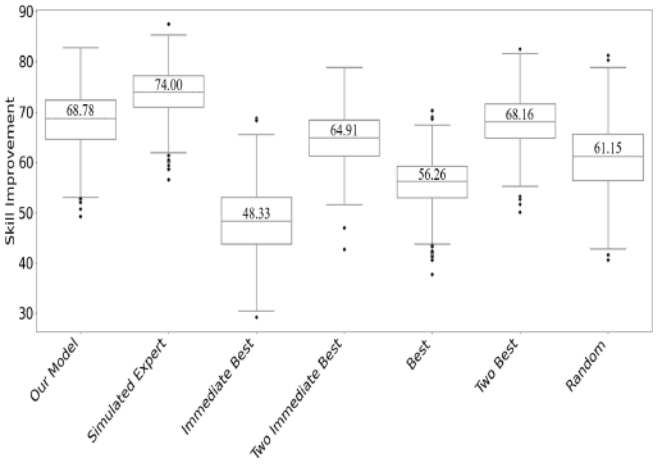


Fig. 4: Boxplot of the skill improvement for 1000 patient groups with different assignment methods. Top and bottom box edges represent 25th and 75th percentiles, whiskers extend to the most extreme observation within 1.5 times interquartile range from the nearest quartile, and circles represent individual outliers. Median values are labeled.

Importantly, our model produced the second largest median skill improvement even without access to patient motivation and fatigue values. This shows the benefit of human-in-the-loop feedback during data generation and model training. Without input from the expert, our model would lack any means to learn how harder-to-quantify characteristics like motivation and fatigue influence the choice of robots that a patient should exercise with. By leveraging expert knowledge, our model learned to make intelligent decisions without needing motivation or fatigue values. Additionally, our model performed better than baselines that could accurately predict the future ("One Best" and "Two Best"). This demonstrates that our model can effectively learn from the expert and optimize for long-term rewards.

A. Expanding the Scenario Simplifications

1) Therapist Feedback: Future work will address the simplifications in our simulated gym scenario. Specifically, reducing the therapist's involvement in data generation could be achieved by storing expert feedback and corresponding patient metrics. Once sufficient data are generated, new feedback could be auto-generated based on similarities in patient performance. Additionally, our current methodology depends on the expert to assign the correct difficulty level. This could be improved by adapting our network to output difficulty levels along with robot assignments.

2) Different Sizes of Rehabilitation Gyms: Only scenarios involving 5 patients, 5 robots, and 12 timesteps were tested in this study. However, real rehabilitation centers could have variable sizes. While our scheduler was designed to work for any number of patients, a new network would need to be trained each time a new robot is added or removed from the gym. Additionally, due to optimizing for a specific number of timesteps, the performance of the scheduler would likely suffer if it is used in other scenarios.

3) Number of Patients Needed for Training and Testing: The number of patients used to train and test our scheduler is likely impractical in the real world. However, only a small number of patient groups are needed to test the quality of the scheduler, and the current 1000 groups were used to reduce the effects of randomness in the gym model. Future work will focus on reducing the number of patients required to train our scheduler to better align with practical limitations.

4) Additional Stochasticity: Several other factors that were not modeled in this study likely affect patient performance and skill acquisition. While modeling these additional factors would be challenging, a preliminary analysis of their effects could be performed by increasing the amount of stochasticity in the simulation model. The increased stochasticity would roughly reflect the increased uncertainty due to additional unknown environmental factors.

B. Real-World Robot Gym Evaluations

While this study uses a simulated environment, the goal of the research is to eventually create an assignment scheduler usable in the real world. Indeed, a simplified version of the assignment scheduler could already be evaluated in a simplified robotic gym. For example, fifty healthy participants could be used to collect data by performing three simple exercises. Afterwards, groups of healthy participants could be brought into the simplified robot gym and exercise using schedules produced by the assignment scheduler.

While our model accounts for motivation, fatigue, and difficulty through expert-guided RL, it was not based on empirical data. The relationships between these hidden states and observable metrics rely on theoretical frameworks and prior studies rather than real-world validation. Additionally, motivation and fatigue were modeled such that they changed similarly for all patients. In reality, motivation and fatigue can vary between patients. Future work will better account for interpersonal differences and will evaluate the effectiveness of our scheduler in the real world. While real-world data is expected to have more stochasticity because of additional unmodeled factors, our machine learning algorithm should still be effective as it aims to capture the underlying logic of patient development based on expert feedback.

IV. Conclusion

Our work addresses the challenge of optimizing patient-robot assignments in a robotic rehabilitation gym where hard-to-measure patient characteristics, such as fatigue and motivation, have a large impact on patient performance. Unlike prior works [5]–[9] that ignore these hidden characteristics, our method factors in the hidden characteristics in exercise scheduling by leveraging a combination of RL and expert input. This allows us to optimize patient skill improvement and create more effective rehabilitation schedules compared to several baselines that had access to the hard-to-quantify characteristics. Practically, while this work was performed in simulation, it is a step towards developing a patient-robot assignment scheduler for real-world applications.

References

[1] Aprile *et al.*, "Upper limb robotic rehabilitation after stroke: a multicenter, randomized clinical trial," *J. Neurol. Phys. Ther.*, vol. 44, no. 1, pp. 3–14, 2020.

[2] A. C. Lo *et al.*, "Robot-assisted therapy for long-term upper-limb impairment after stroke," *N. Engl. J. Med*, vol. 362, no. 19, pp. 1772–1783, 2010.

[3] K. Bustamante Valles, S. Montes, M. d. J. Madrigal, A. Burciaga, M. E. Martínez, and M. J. Johnson, "Technology-assisted stroke rehabilitation in mexico: a pilot randomized trial comparing traditional therapy to circuit training in a robot/technology-assisted therapy gym," *J. Neuroeng. Rehabil*, vol. 13, pp. 1–15, 2016.

[4] Hocoma, "Hoconet." https://www.hocoma.com/us/solutions/hoconet-connected-care/, 2024. Accessed on August 30, 2024.

[5] B. A. Miller, B. Adhikari, C. Jiang, and V. D. Novak, "Automated patient-robot task assignment in a simulated stochastic rehabilitation gym," in *Int. Conf. Rehabil. Rob*, pp. 1–6, IEEE, 2023.

[6] B. Adhikari, V. R. Bharadwaj, B. A. Miller, V. D. Novak, and C. Jiang, "Learning skill training schedules from domain experts for a multi-patient multi-robot rehabilitation gym," *IEEE Trans. Neu. Sys. Rehabil. Eng*, vol. 31, pp. 4256–4265, 2023.

[7] B. A. Miller, B. Adhikari, C. Jiang, and V. D. Novak, "Automated patient-robot assignment for a robotic rehabilitation gym: a simplified simulation model," *J. NeuroEng. Rehabil*, vol. 19, no. 1, p. 126, 2022.

[8] V. R. Bharadwaj, B. A. Miller, V. D. Novak, and C. Jiang, "Learning skill training schedules from domain experts in a rehabilitation gym using inverse reinforcement learning," in *Int. Conf. for Biomed. Rob. Biomech.*, pp. 1815–1821, IEEE, 2024.

[9] B. Adhikari, S. Ranashing, B. A. Miller, V. D. Novak, and C. Jiang, "Learning dynamic patient-robot task assignment and scheduling for a robotic rehabilitation gym," in *2022 Int. Conf. Rehabil. Rob.*, pp. 1–6, IEEE, 2022.

[10] A. R. Fugl-Meyer, L. Jääskö, I. Leyman, S. Olsson, and S. Steglind, "A method for evaluation of physical performance," *Scand. J. Rehabil. Med*, vol. 7, no. 1, pp. 13–31, 1975.

[11] G. Verrienti, C. Raccagni, G. Lombardozzi, D. De Bartolo, and M. Iosa, "Motivation as a measurable outcome in stroke rehabilitation: a systematic review of the literature," *Int. J. Env. Res. Pub. Health*, vol. 20, no. 5, p. 4187, 2023.

[12] J. Finsterer and S. Z. Mahjoub, "Fatigue in healthy and diseased individuals," *Amer. J. Hos. Palliat. Med*, vol. 31, no. 5, pp. 562–575, 2014.

[13] S. V. As, D. G. J. Beckers, H. P. Veling, S. A. E. Geurts, and M. Husain, "The impact of cognitive fatigue on motivation to exert physical effort," *J. Sport. Exer. Psy*, vol. 42, no. 1, 2020.

[14] R. S. Sutton and A. G. Barto, *Reinforcement learning: An introduction 1st edition*, vol. 30. MIT Press, 1998.

[15] K. d. O. Andrade, T. B. Pasqual, G. A. Caurin, and M. K. Crocomo, "Dynamic difficulty adjustment with evolutionary algorithm in games for rehabilitation robotics," in *2016 IEEE Int. Conf. Ser. Games App. Health.*, pp. 1–8, IEEE, 2016.

[16] S. Balasubramanian, R. Colombo, I. Sterpi, V. Sanguineti, and E. Burdet, "Robotic assessment of upper limb motor function after stroke," *Amer. J. Phys. Med. Rehabil*, vol. 91, no. 11, pp. S255–S269, 2012.

[17] N. Nordin, S. Q. Xie, and B. Wünsche, "Assessment of movement quality in robot-assisted upper limb rehabilitation after stroke: a review," *J. Neuroeng. Rehabil*, vol. 11, pp. 1–23, 2014.

[18] E. L. Deci, A. H. Olafsen, and R. M. Ryan, "Self-determination theory in work organizations: The state of a science," *Annual. Review. Org. Psy. Org. Behaviour*, vol. 4, no. 1, pp. 19–43, 2017.

[19] N. J. Hodges and K. R. Lohse, "An extended challenge-based framework for practice design in sports coaching," *J. Sports. Sci*, vol. 40, no. 7, pp. 754–768, 2022.

[20] M. A. Guadagnoli and T. D. Lee, "Challenge point: a framework for conceptualizing the effects of various practice conditions in motor learning," *J. Motor. Behavior*, vol. 36, no. 2, pp. 212–224, 2004.

[21] R. Gassert and V. Dietz, "Rehabilitation robots for the treatment of sensorimotor deficits: a neurophysiological perspective," *J. Neuroeng. Rehabil.*, vol. 15, pp. 1–15, 2018.

[22] S. Choudhury, J. K. Gupta, M. J. Kochenderfer, D. Sadigh, and J. Bohg, "Dynamic multi-robot task allocation under uncertainty and temporal constraints," *Auto. Rob*, vol. 46, no. 1, pp. 231–247, 2022.

[23] V. Mnih *et al.*, "Human-level control through deep reinforcement learning," *Nature*, vol. 518, no. 7540, pp. 529–533, 2015.

Cardiovascular Assessment of Manual Wheelchair Users With 6-Minute Push Test: VO_2 Formula

Madisyn R. Adelman
Department of Biomedical Engineering
University of Wisconsin-Milwaukee
Milwaukee, WI, USA
adelman3@uwm.edu

Maja Goršič
Department of Biomedical Engineering
University of Wisconsin-Milwaukee
Marquette University
Milwaukee, WI, USA
gorsic@uwm.edu

Grace McClatchey
Department of Biomedical Engineering
University of Wisconsin-Milwaukee
Milwaukee, WI, USA
gofasipe@uwm.edu

Jacob R. Rammer
Department of Biomedical Engineering
University of Wisconsin-Milwaukee
Milwaukee, WI, USA
jrrammer@uwm.edu

***Abstract*—Manual wheelchair users are prone to a more sedentary lifestyle due to their limited mobility and, therefore, decreased cardiovascular health. Regular assessment of their cardiovascular fitness can help with appropriate interventions and overall improvement in their quality of life. One way of assessing cardiovascular health of manual wheelchair users is the 6-minute push test (6MPT), adapted from the 6-minute walk test. In this study, 5 novice and 5 expert wheelchair users performed the 6MPT while wearing a heart rate monitor and VO_2 mask. Significant correlation (r=0.685, p=0.029) was found between the distance completed and the max value of the VO_2 recorded during the 6MPT. Additionally, a linear regression model was constructed and found statistically significant (F(1,8)=22.3, p=0.0015). The model can serve clinicians as a convenient and direct indicator of cardiovascular fitness for manual wheelchair users without the need of additional heartrate sensors or VO_2 mask.**

Keywords—cardiovascular health, 6-minute push test, VO_2, physical exertion, manual wheelchair users, oxygen consumption, heart rate.

I. Introduction

Cardiovascular fitness plays an essential role in the overall health and quality of life for manual wheelchair users [1], [2]. Poor cardiovascular health can hinder their mobility and functional independence [1], [3]. Regular movement and physical activity are important in limiting secondary health issues like pressure sores, musculoskeletal problems, and cardiovascular disease [2], [3], [4], [5], [6]. Understanding the maximal oxygen uptake (VO_{2max}), a key indicator of aerobic capacity and overall cardiovascular health, can provide insights into the physical demands and health conditions of those with mobility impairments [7], [8], [9], [10].

Traditional testing methods for VO_2 involve maximal exercise protocols, such as treadmill or cycle ergometer tests [11], which can be challenging for manual wheelchair users and may require specialized laboratory equipment and trained personnel. While accurate and reliable [11], [12], [13], these approaches are often expensive, require an extensive setup, add complexity to the testing process, and can be impractical for regular testing in a community setting [14]. These considerations can limit their usefulness in monitoring cardiovascular health over time for people with mobility impairments. This underscores the need for a simpler and easier field-based method to estimate VO_{2max}, specifically tailored to the functional abilities of manual wheelchair users.

One key way of measuring cardiovascular health in manual wheelchair users is the 6-Minute Push Test (6MPT), adapted from the 6-Minute Walk Test [15]. The 6MPT involves the manual wheelchair user propelling themselves as far as they can in 6 minutes [16]. The test provides insights into cardiovascular health and overall fitness levels [3], [7], [13], [17], [18], [19], which are essential for daily functioning and mobility. Literature has demonstrated that specific physiological responses, such as heart rate, speed, and distance covered during the test, correlate with VO_2 consumption [9], [10], [20], [21], [22], [23], [24]; however, to our knowledge, no formula has been derived for predicting VO_{2max} from the 6MPT. Predictive models of VO_2 could offer an accessible alternative to direct VO_2 testing, thus providing a valuable tool for ongoing cardiovascular fitness assessment.

In this study, we aim to develop a simplified equation to predict VO_2 based on the recorded parameters of the 6MPT. By establishing a predictive equation, this work aims to create a feasible, repeatable, and cost-effective method for healthcare practitioners to monitor aerobic capacity outside the laboratory, enhancing the monitoring and rehabilitation of wheelchair users.

II. Methods

This study was approved by the University of Wisconsin – Milwaukee Institutional Review Board (IRB#23.347).

A. Participants

The participants for this study were recruited under the following inclusion criteria; at least 18 years of age, physically able to propel themselves in a manual wheelchair, no record of epilepsy, claustrophobia or increased sensitivity to light and free from any upper extremity injury or surgery within the past year. Moreover, participants with health issues or medications relating to blood pressure, heart or

cardiovascular conditions were encouraged to consult their doctor before participating.

Ten participants were recruited for this study: 5 long-term wheelchair users that use a manual wheelchair for at least 70 percent of their daily mobility and 5 able-bodied controls, who never used a wheelchair before the study. At the start of each lab appointment, informed consent was obtained and the participant completed a demographics questionnaire. The demographics questionnaire reported; gender, age, height, weight, injury level (if applicable) and estimated weekly activity level. The participants weekly activity level was categorized as high (more than 3h/week), moderate (2-3h/week) or low (under 2h/week) based on weekly hours of activity. Participants demographics are presented in Table I.

B. *Experiemental Setup and Sensors*

- **Six Minute Push Test Setup:** The set up for the 6MPT was identical to the protocol described in our previous study [25]. In a long hallway, with a smooth floor, two cones were set up 30 meters away from each other in a straight line, see Fig. 1. Before beginning the 6MPT, participants were given the opportunity to practice propelling themselves in the testing location. The control group used the laboratory wheelchair (see Fig. 2) while expert wheelchair users participated with their own daily wheelchair.
- **VO_2 Tracking:** This study utilized the VO2 Master Analyzer (VO2 Master Health Sensors Inc., Vernon, BC, Canada) to record VO_2 output. The portable analyzer is secured to the participant with a Hans Roudolph facemask and adjustable headgear following the instructions provided, see Fig 2. Oxygen consumption is recorded by electro-galvanic oxygen and differential flow sensors throughout the duration of the 6MPT. VO_2 output data is used to analyze and compare the user's aerobic exertion throughout the test.

TABLE I. PARTICIPANT DEMOGRAPHICS: 5 NOVICE AND 5 EXPERT WHEELHCAIR USERS; SCI – SPINAL CORD INJURY, BMI – BODY MASS INDEX

#ID	Gender	Age	BMI	Injury Type	Weekly Activity
1	F	37	28.1	N/A	High
2	M	33	25.8	N/A	Moderate
3	M	41	31.2	N/A	Low
4	F	22	28.3	N/A	Low
5	M	18	21.5	N/A	High
6	M	27	31.9	T10 incomplete SCI	Moderate
7	F	23	22.5	Neuromuscular autoimmune	High
8	F	30	24.9	T3 Incomplete SCI	High
9	M	33	39.1	Spina bifida	High
10	F	31	39.5	Cerebral palsy	High

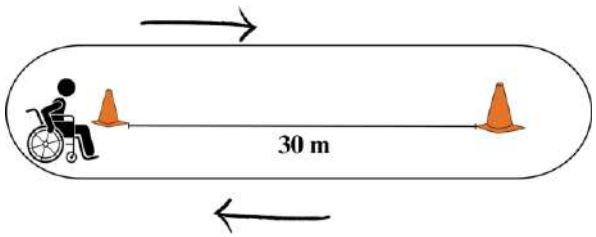


Fig 1. 6-Minute Push Test Setup: 30 meters long hallways marked with 2 cones. Wheelchair user starts on one end and pushes themselves around the cones as many times as possible in 6 minutes.

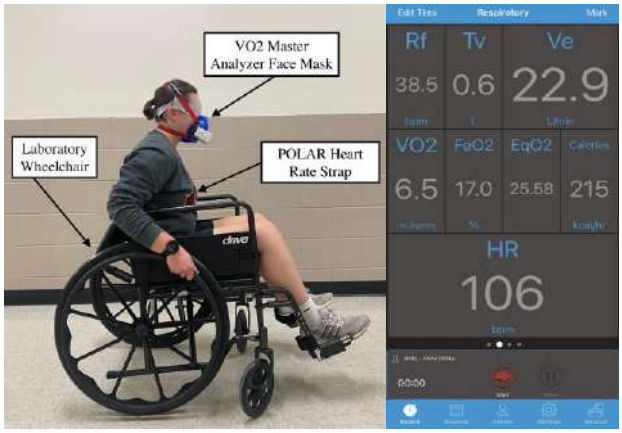


Fig 2. On the left, a picture displaying a novice wheelchair user set-up with the VO2 Master Analyzer, POLAR heart rate strap and laboratory wheelchair. On the right is a screenshot of the VO2 Master Manager Application (VO2 Master Health Sensors Inc., Vernon, BC, Canada) dashboard during a test recording.

- **Heartrate Monitoring:** A Polar H10 heartrate strap (Polar Electro Oy, Kempele, Finland) was provided with the VO2 Master Analyzer to record heartrate, see Fig 2. The Polar strap uses surface electrodes to measure the electrical signals from the heart during cardiovascular expenditure. The resulting electrocardiogram was used to evaluate physiological exertion throughout the test.

C. *Study Protocol*

Each participant was given a complete description of the study protocol. After informed consent was obtained and the demographics questionnaire was completed, the participant was equipped with a Polar heartrate strap, secured horizontally across the torso, just below the sternum. The participant was instructed to sit in an upright position, with their eyes open and no talking, while an observer recorded resting heartrate data for two minutes. Once completed, the VO_2 mask was secured on the participants' head before the start of the 6MPT. For each participant without a manual wheelchair, a lab wheelchair was provided to them.

The participant was positioned adjacent to the first cone, facing the second cone down the hallway and asked to propel themselves as fast as possible down the hallway, turning around the second cone and returning to the starting cone, repeating this until the end of the six-minute timer. Throughout the 6 minutes, the observer counted all

complete laps and provided verbal cues at the beginning, middle and end of the test.

At the end of the 6 minutes, the participant was instructed to safely come to a complete stop before the VO_2 mask and heart rate strap were removed. The participant was then asked to report their perceived level of effort during the 6MPT using the modified Borg Rated Perceived Exertion (RPE) scale [26], [27].

All participants received $25 compensation for their participation and signed a reimbursement form at the end of the study.

D. Data Processing

All heart rate and VO_2 data were recorded and processed into summarized reports for each participant by the VO2 Master Manager (VO2 Master Health Sensors Inc., Vernon, BC, Canada, 2024) application. Each report included the Max, Min and Average of the participant's heart rate, frequency of breath per minute, tidal volume, ventilation of oxygen, and fraction of expired oxygen recorded during the 6MPT.

Statistical analysis was performed to find any correlations between the collected variables. First, a Shapiro-Wilk test was conducted to assess the normality of the data for each variable, including age, gender, resting heart rate, max heart rate, distance, and max 6MPT VO2 max. The results indicated that the assumption of normality was violated ($p < 0.05$) for multiple variables. Consequently, a Spearman's rank-order correlation was used to assess the relationships between the collected variables and max VO_2, as it is a non-parametric test that does not require normality. All correlations were conducted using SPSS (version 29.0.1.0, SPSS Inc., Chicago, IL, USA), and statistical significance was set at $p < 0.05$.

Next, a linear regression analysis was conducted to further examine the relationship between the distance completed (m) and max VO_2 values (mL/kg/min) for the 6MPT for each participant. The regression model was fit using MATLAB (version R2023a, The MathWorks, Inc., Natick, MA, USA) with the following formula:

$$y = \beta 0 + \beta 1 * dist$$

where y represents the predicted max 6MPT VO_2 value and dist represents the distance completed during the 6MPT in meters. The model's fit was assessed using the Root Mean Squared Error (RMSE), R-squared, and Adjusted R-squared values. Statistical significance was evaluated with a significance threshold set at $p<0.05$.

III. Results

Descriptive statistics observed and calculated from the 6MPT data for all participants are presented in Table II. The first 5 rows present novice data while the second 5 rows consist of expert wheelchair user data. Fig. 3 shows an example of a VO_2 and heart rate data for participant 5 collected by the VO_2 mask and heart rate sensor, respectively.

TABLE II. Parameters Collected from the 6-Minute Push Test Data: 5 Novice and 5 Experienced Wheelchair Users; HR – Heart Rate, 6MPT – 6 Minute Push Test, RPE – Rate of Perceived Exertion

ID	Distance completed (m)	Resting HR (bpm)	Max 6MPT HR (bmp)	Max 6MPT VO_2 (mL/kg/min)	RPE [1-10]
1	420	44	93	18.7	3
2	405	85	158	18.8	8
3	360	89	175	9.7	3
4	480	74	198	21.4	7
5	435	59	130	16.9	3
6	1125	97	180	40.9	8
7	765	98	168	33.2	7
8	345	76	186	18.3	7
9	910	70	155	25.1	6
10	559	97	143	13.2	7
$\bar{X}$ (σ)	581 (265)	79 (18)	159 (31)	22 (10)	6 (2)

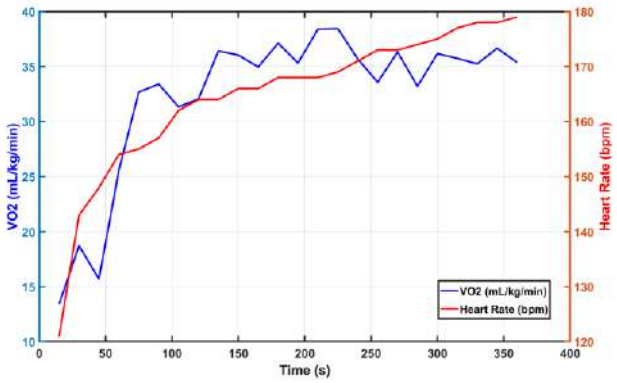


Fig 3. Example of a VO_2 and heart rate data for Participant 5.

Spearman's rank-order correlation found a strong positive correlation ($r=0.685$, $p=0.029$) for the distance completed during the 6MPT and the recorded max 6MPT VO_2 values. No other variables showed significant correlations with max 6MPT VO_2 in this analysis.

Further, a linear regression model was constructed to predict max 6MPT VO_2 based on the distance completed during the 6MPT. The intercept of the model ($\beta 0$) was 4.115 (SE = 4.042, $t=1.02$, $p=0.34$), and the slope coefficient for laps ($\beta 1$) was 0.030 (SE = 0.006, $t=4.72$, $p=0.0015$).

The model explained 73.6% of the variance in max 6MPT VO_2 ($R^2 = 0.736$), with an adjusted R^2 of 0.703. The RMSE was 5.08, indicating that, on average, the predictions deviated from the observed max 6MPT VO_2 by approximately 5.08 mL/kg/min. The overall model was statistically significant, $F(1,8)=22.3$, $p=0.0015$.

IV. Discussion

It can be observed from the recorded data (Table II) that 4 out of 5 experienced wheelchair users completed over

500m distance while all 5 novice users completed under 500m distance during the 6MPT. This outcome could be affected by the participants' everyday activity levels: 4 out of 5 expert wheelchair users reported high weekly activity compared to only 2 out of 5 in the novice group (see Table I). This difference can also be observed by the lower max VO_2 levels recorded during the 6MPT (Table II).

Additionally, 3 out of 5 novice users reported an RPE value of 3 – which is a fairly low perceived level of exertion despite being asked to use as much effort as possible. When asked about this, some novice users mentioned that their skill level limited their ability to achieve their maximum cardiovascular capacity. This is likely another reason for the occurrence of lower max VO_2 levels among novice users recorded during the 6MPT.

Statistical analysis found a strong positive Spearman's correlation between the distance completed and the recorded max 6MPT VO_2 levels ($r=0.685$, $p=0.029$). This relationship held for both novice and experienced wheelchair users. This suggests that the further the distance travelled during the 6MPT the higher the max 6MPT VO_2 value, which indicates a better cardiovascular health of the participant.

The following equation constructed from the overall model was statistically significant, $F(1,8)=22.3$, $p=0.0015$, indicating that the distance (m) completed during the 6MPT is a significant predictor of max 6MPT VO_2 (mL/kg/min):

$$\text{max 6MPT } VO_2 = 4.115 + 0.030 * \text{6MPT distance}$$

The predictive model was created to provide a foundation for an easily accessible and cheap means of monitoring VO_2 outside of traditional measurement methods. Since VO_2 has been recognized as the single best measure of aerobic fitness, estimating VO_2 throughout the 6MPT serves as a more direct assessment of cardiovascular health compared to measuring heart rate alone [8], [9], [11], [21], [22].

One of the limitations for the developed equation and observed relationship is the sample size and diversity of participant activity levels. Future studies can include a larger population with more diverse activity levels of the participants to ensure the robustness of the current model.

V. Conclusion

Our study demonstrates the foundation for estimating the VO_2 of manual wheelchair users from the results of the 6MPT. This has the potential to provide rehabilitation specialists and healthcare workers with a simpler means of assessing their patients' cardiovascular fitness without the need for specialized equipment and extensive procedures. Furthermore, by utilizing our equation, the cardiovascular health of manual wheelchair users can be more easily monitored on a regular basis and inspire prompt interventions to improve their quality of life.

References

[1] D. W. Dunstan, S. Dogra, S. E. Carter, and N. Owen, "Sit less and move more for cardiovascular health: emerging insights and opportunities," *Nat. Rev. Cardiol.*, vol. 18, no. 9, pp. 637-648, May 2021, doi: https://doi.org/10.1038/s41569-021-00547-y.

[2] G. Fasipe, M. Goršič, M. H. Rahman, and J. Rammer, "Community mobility and participation assessment of manual wheelchair users: a review of current techniques and challenges," *Front. Hum. Neurosci.*, vol. 17, p. 1331395, Jan. 2024, doi: 10.3389/fnhum.2023.1331395.

[3] T. D. Lavis, W. M. Scelza, and W. L. Bockenek, "Cardiovascular Health and Fitness in Persons with Spinal Cord Injury," *Phys. Med. Rehabil. Clin. N. Am.*, vol. 18, no. 2, pp. 317–331, May 2007, doi: 10.1016/j.pmr.2007.03.003.

[4] D. E. Warburton, C. W. Nicol, and S. S. Bredin, "Health benefits of physical activity: the evidence," *CMAJ Can. Med. Assoc. J.*, vol. 174, no. 6, p. 801, Mar. 2006, doi: 10.1503/cmaj.051351.

[5] K. A. Martin Ginis, S. Jörgensen, and J. Stapleton, "Exercise and Sport for Persons With Spinal Cord Injury," *PM&R*, vol. 4, no. 11, pp. 894–900, 2012, doi: 10.1016/j.pmrj.2012.08.006.

[6] L. Van der Westhuizen, D. J. Mothabeng, and T. M. Nkwenika, "The relationship between physical fitness and community participation in people with spinal cord injury," *South Afr. J. Physiother.*, vol. 73, no. 1, p. 354, 2017, doi: 10.4102/sajp.v73i1.354.

[7] K. M. S. Damen *et al.*, "6-Minute Push Test in Youth Who Have Spina Bifida and Who Self-Propel a Wheelchair: Reliability and Physiologic Response.," *Phys. Ther.*, vol. 100, no. 10, pp. 1852–1861, 2020, doi: 10.1093/ptj/pzaa121.

[8] T. Nabi, N. Rafiq, and O. Qayoom, "Assessment of cardiovascular fitness [VO2 max] among medical students by Queens College step test," *Int J Biomed Adv Res*, vol. 6, no. 5, pp. 418–21, 2015.

[9] C. C. Grant, C. Murray, D. C. Janse Van Rensburg, and L. Fletcher, "A comparison between heart rate and heart rate variability as indicators of cardiac health and fitness," *Front. Physiol.*, vol. 4, Nov. 2013, doi: 10.3389/fphys.2013.00337.

[10] T. A. Astorino, R. P. Allen, D. W. Roberson, and M. Jurancich, "Effect of High-Intensity Interval Training on Cardiovascular Function, V̇o2max, and Muscular Force," *J. Strength Cond. Res.*, vol. 26, no. 1, p. 138, Jan. 2012, doi: 10.1519/JSC.0b013e318218dd77.

[11] K. Buttar, N. Saboo, and S. Kacker, "A review: Maximal oxygen uptake (VO2 max) and its estimation methods," *Int. J. Phys. Educ. Sports Health*, Nov. 2019, Accessed: Nov. 17, 2024. [Online]. Available: https://www.semanticscholar.org/paper/A-review%3A-Maximal-oxygen-uptake-(VO2-max)-and-its-Buttar-Saboo/eec05d83a23b3cfe65a3f9aafa6c064b8fd12196

[12] M. J. Peterson, C. F. Pieper, and M. C. Morey, "Accuracy of VO2(max) prediction equations in older adults," *Med. Sci. Sports Exerc.*, vol. 35, no. 1, pp. 145–149, Jan. 2003, doi: 10.1097/00005768-200301000-00022.

[13] B. A. Baattaiah *et al.*, "Association of Six Minute Push Test Distance and Measures of Cardiorespiratory Fitness in Spinal Cord Injury: 1472 Board #147 June 1 9: 00 AM - 10: 30 AM," *Med. Sci. Sports Exerc.*, vol. 49, no. 5S, p. 409, May 2017, doi: 10.1249/01.mss.0000518002.99303.73.

[14] A. W. Midgley, K. Earle, L. R. McNaughton, J. C. Siegler, P. Clough, and F. Earle, "Exercise tolerance during VO2max testing is a multifactorial psychobiological phenomenon," *Res. Sports Med.*, vol. 25, no. 4, pp. 480–494, Oct. 2017, doi: 10.1080/15438627.2017.1365294.

[15] J. Beaverson, L. Beaudreau, J. Filkowski, C. A. Robinson, P. N. Matsuda, and A. Shumway-Cook, "ASSESSING FACTORS IMPACTING COMMUNITY MOBILITY AFTER STROKE," *J. Neurol. Phys. Ther.*, vol. 29, no. 4, p. 203, Dec. 2005, doi: 10.1097/01.NPT.0000282359.32537.bf.

[16] "6 Minute Push Test | RehabMeasures Database." Accessed: Nov. 17, 2024. [Online]. Available: https://www.sralab.org/rehabilitation-measures/6-minute-push-test

[17] R. E. COWAN, M. K. CALLAHAN, and M. S. NASH, "The 6-min Push Test Is Reliable and Predicts Low Fitness in Spinal Cord Injury," *Med. Sci. Sports Exerc.*, vol. 44, no. 10, pp. 1993-2000, Oct. 2012, doi: https://doi.org/10.1249/mss.0b013e31825cb3b6.

[18] R. Solanki, P. Chaudhari, and A. Bhise, "Cardio Respiratory Fitness Testing in Spinal Cord Injury Patients Using 6 Minute Push Test," *Heal. J.*, vol. 7, no. 1, pp. 60-63, Jan. 2017.

[19] O. Verschuren, M. Ketelaar, J. De Groot, Fá. Vila Nova, and T. Takken, "Reproducibility of two functional field exercise tests for children with cerebral palsy who self-propel a manual wheelchair,"

Dev. Med. Child Neurol., vol. 55, no. 2, pp. 185–190, 2013, doi: 10.1111/dmcn.12052.

[20] J. Lee and X. L. Zhang, "Physiological determinants of VO2max and the methods to evaluate it: A critical review," *Sci. Sports*, vol. 36, no. 4, pp. 259–271, Sep. 2021, doi: 10.1016/j.scispo.2020.11.006.

[21] J. S. Skinner *et al.*, "Heart rate versus %VO2max: age, sex, race, initial fitness, and training response--HERITAGE," *Med. Sci. Sports Exerc.*, vol. 35, no. 11, pp. 1908–1913, Nov. 2003, doi: 10.1249/01.MSS.0000093607.57995.E3.

[22] M. Matabuena, J. C. Vidal, P. R. Hayes, and F. Huelin Trillo, "A 6-minute sub-maximal run test to predict VO2 max," *J. Sports Sci.*, vol. 36, no. 22, pp. 2531–2536, Nov. 2018, doi: 10.1080/02640414.2018.1468149.

[23] T. Eaton, P. Young, D. Milne, and A. U. Wells, "Six-Minute Walk, Maximal Exercise Tests," *Am. J. Respir. Crit. Care Med.*, vol. 171, no. 10, pp. 1150–1157, May 2005, doi: 10.1164/rccm.200405-578OC.

[24] M. Jalili, F. Nazem, A. Sazvar, and K. Ranjbar, "Prediction of Maximal Oxygen Uptake by Six-Minute Walk Test and Body Mass Index in Healthy Boys," *J. Pediatr.*, vol. 200, pp. 155–159, Sep. 2018, doi: 10.1016/j.jpeds.2018.04.026.

[25] G. Fasipe, M. Goršič, E. V. Zabre, and J. R. Rammer, "Inertial Measurement Unit and Heart Rate Monitoring to Assess Cardiovascular Fitness of Manual Wheelchair Users during the Six-Minute Push Test," Sensors, vol. 24, no. 13, Art. no. 13, Jan. 2024, doi: 10.3390/s24134172.

[26] K. L. Lamb, R. G. Eston, and D. Corns, "Reliability of ratings of perceived exertion during progressive treadmill exercise," Br. J. Sports Med., vol. 33, no. 5, pp. 336–339, Oct. 1999, doi: 10.1136/bjsm.33.5.336.

[27] J. S. Skinner, R. Hutsler, V. Bergsteinová, and E. R. Buskirk, "The validity and reliability of a rating scale of perceived exertion," Med. Sci. Sports, vol. 5, no. 2, pp. 94–96, 1973.

HERO Glove Insight: Utilizing Computer Vision and Force Sensors for Object-Specific Force Control

Daimen Landori-Hoffmann, Jordan Mihalache, Osatohamen Aziegbe, Mitchell Vella, Meaghan Charest-Finn, Member, *IEEE*, Aaron Yurkewich, Member, *IEEEAutomotive & Mechatronics Engineering, Ontario Tech University, Oshawa, Canada*

daimen.landorihoffmann@ontariotechu.net

***Abstract*— This research developed and integrated new mechatronic features to the Hand Extension Robot Orthosis (HERO) Glove soft exoskeleton to improve the assistive abilities of the device. The added features include low weight actuators, anchoring structures, force sensors, a camera and a cascaded computer vision driven Proportional Integral Derivative (PID) algorithm. Supporting electronics were developed to ensure that the integrated system can provide accurate grip force control based on situational awareness. The upgraded version of the HERO glove was evaluated and showed a 55% increase in grip strength, improved durability, and new force sensing and control capabilities as accurate as 0.1 Newtons. The algorithm uses computer vision software to recognize the object that the user intends to grip and then adjusts the target grip force commanded during autonomous gripping. This enhanced system, HERO Glove Insight is designed to overcome usability challenges in grasp stability and grip force modulation faced by stroke and spinal cord injury survivors when utilizing soft hand exoskeletons to enable their independence in home and community settings.**

Keywords*— *Stroke, Rehabilitation, Assistive Devices, Hand Exoskeleton, Design, Control, Computer Vision, Soft Robotics

I. INTRODUCTION

Chronic stroke survivors that receive three or more hours of high intensity upper limb therapy per day show substantial, clinically meaningful, gains in motor recovery [1], [2]. However, stroke survivors typically receive an average of just one hour of therapy per week after discharge [3]. Exoskeleton robots provide forces on the human's limbs to assist motion and provide haptic feedback, enabling people with impaired motor function to practice more engaging therapeutic tasks and accelerate their motor recovery [4]. Soft exoskeleton robots have potential to enhance the comfort, portability and inconspicuousness of their heavy, bulky, and difficult to maneuver exoskeleton predecessors, enabling extended use of exoskeletons in the clinic, home and community to deliver accessible high intensity rehabilitation and provide immediate benefits through assistance in everyday life [5], [6].

When portability is considered, the resulting soft exoskeletons utilize a small number of compact actuators and provide just enough assistive force to perform basic activities of daily living (ADLs), resulting in performance gains that are near the lower bound of being clinically meaningful [5], [7]. This has resulted in low usability ratings and technology abandonment and a need for enhanced mechanics that improve their assistive capabilities to enable greater independence.

Soft hand exoskeletons commonly utilize buttons, inertial measurement units (IMU) or pressure sensors to trigger grip assistance during unsupervised tasks at home, due to their intuitiveness, cost-effectiveness and predictable control operation [5], [7], [8] . However, button control requires use of the second hand and IMU and pressure sensor control require that the user has residual arm and hand motion. Further, these on-off control strategies do not modulate the grip force, resulting in large forces on fragile objects and suboptimal grasp postures for tool use. Myoelectric controllers utilize the user's electromyography (EMG) amplitudes to modulate the exoskeleton's velocity and assistive forces; however, these controllers are difficult to integrate into unsupervised home use cases as they require comprehensive electronics and extensive calibration and can cause unstable object interactions for users with motor control impairments [9], [10], [11].

There is a trend of integrating machine learning and artificial intelligence tools such as computer vision and smart sensing into real-world systems. This has allowed technology to surpass traditional barriers and offer new functionality in the next generation of automated systems, such as soft exoskeletons [12], [13]. More recently, the development of semi-autonomous control methodologies has opened opportunities for the development of human assistive technologies as well as human augmentation, with exoskeletons taking center stage in these [14]. Key challenges involved in developing these systems are the problems of perceiving the operating environment and capturing the dynamics of the human-in-the-loop system to achieve good control. Common strategies for overcoming these include using computer vision to describe the exoskeleton operating environment [15], [16] and control methodologies for force and position feedback systems [17], [18]. This enables independence by estimating the appropriate grasp posture and force regardless of muscle activation and ensure a reliable grasp through closed-loop control [19], [20]. Future works combining environmental awareness with assist-as-needed and myoelectric controllers could then be utilized to enable soft exoskeletons to enable independence in everyday life without sacrificing the user's rehabilitation goals.

This work was supported in part by NSERC CGS-M and AGE-WELL NCE Inc..

The study presented here focuses on integrating added systems to a Hand Extension Robot Orthosis (HERO) Glove to extend the functionality of the glove for safe and convenient at home use during rehabilitation. The paper is organized as follows, the design and integration of the added value feature for the glove are presented, a cascaded computer vision driven PID control algorithm is designed and tested on the upgraded HERO Glove, the results of the closed-loop gripping force control with situational awareness are shown and discussed and, future directions of development are recommended before concluding the paper.

II. Methodology

The HERO Grip Glove, an open-source portable wearable soft-exoskeleton was used as the base platform for this research due to its portability and customizability and to enhance its usability based on clinical trial feedback [21]. HERO Glove Insight incorporates mechanical, electrical and software modifications to the original device that were required to enhance the maximum grip force and allow for object-specific grip force control that are shown in Fig. 1.

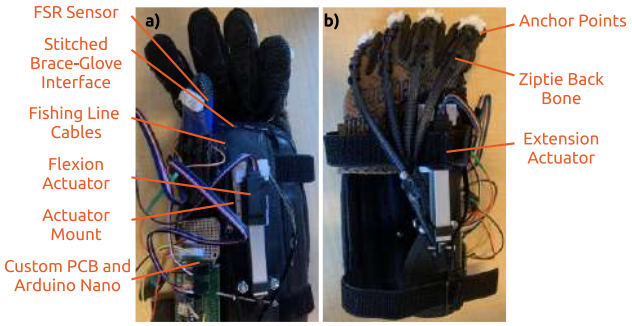


Fig. 1. HERO Glove Insight a) proximal and b) dorsal side views highlighting the modifications made to the original HERO Grip Glove.

A. Design

Mechanically, the HERO Grip Glove required improvements in its serviceability and robustness. To accomplish this, a mixture of custom and standard mounting brackets were designed to fix the linear actuators in place. Custom brackets were designed, and 3D printed using polylactic acid, then mounted to the wrist brace using threaded heat inserts and screws. This allowed the actuators and mounting brackets to be replaced with ease, while providing sufficient support. The end of the actuators are held in place using the mounting brackets and fixtures provided with the actuators. To improve the system's grip force, fishing line was routed from the front of the fingers and through custom designed and 3D printed anchors on the dorsal side of the fingertips. This modification redirects the pull force, so it is applied directly to the dorsal side of the fingertips and also keeps the proximal side of the fingertip more exposed for tactile sensation.

B. Sensing

The electrical and software components of the HERO Glove were updated to provide grip force control. The electrical subsystem was updated, and the microcontroller was changed from an Intel Curie board to an Arduino Nano BLE 33 Sense Rev 2. The microcontroller's onboard inertial measurement unit (IMU) provided the necessary sensor information for the HERO Glove's original control system as well as an RGB LED for providing the user with operation mode feedback. Additionally, a custom PCB was developed for sensor customizability and ease of assembly. A force sensing resistor (FSR Tekscan A101) and voltage divider circuit were added to provide grip force information. The location of the FSR was carefully selected after experimenting with different locations. The ideal position of the FSR was determined to be on the side of the interphalangeal joint of the thumb as it was observed that the research team would grasp objects at this location rather than the pad of their thumbs.

The added software features include the development of a library of functions to support object-oriented code and ease of development for future work. This library handles all the filtering, timing, control system and error handling functions. This is especially important as the HERO Glove is an open-source project and the development of the library which is self-contained allows for other developers to iterate on previous work.

A computer-vision system using the well-established open model You Only Look Once V3 (YOLO V3) [22] and Python open CV Library object identification routine was integrated into the control system. This is used to assign the correct setpoint for HERO Glove Insight's grip force controller, based on pre-defined object-specific grip force targets. The overall automation procedure begins by classifying the object that is in the field of view of a webcam (Logitech C920) and sending this information to the microcontroller's serial monitor, where the controller's setpoint is updated. In this article a stationary webcam was used. An important area of future development will be determining the ideal placement of the camera as well as determining the optimal number of cameras to use, as multiple cameras could provide depth perception and circumvent occlusions.

C. Calibration

Once the FSR sensor was installed and the mechanical changes were implemented, it was necessary to reduce the noise from the FSR sensors when the actuators were moving. To do this, a Kalman filter was designed with the noise covariance, measurement map scalar, process noise covariance, and error covariance values 1, 1, 0.1, and 1, respectively.

Calibration of the HERO Glove Insight was completed by commanding system to close fully around a Vernier Go Direct® isometric hand dynamometer used to measure grip force. Linear regression was used to model the relationship between the FSR sensor and dynamometer grip force readings. The results from the average of five trials of the filtered FSR sensor and hand dynamometer test are presented in Fig. 2.

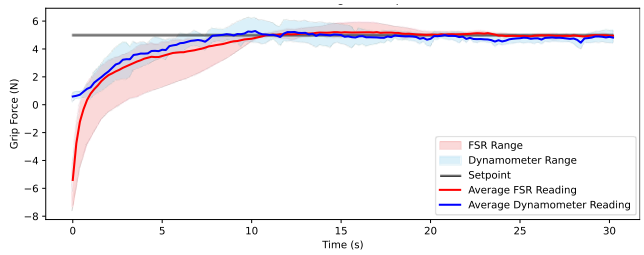


Fig. 2. FSR sensor comparison to hand dynamometer ground truth.

D. Control

To develop the transfer function for the HERO Glove Insight system, an open loop response was obtained by giving the flexion actuator a signal to provide maximum grip strength around the hand dynamometer. The filtered FSR readings were recorded and plotted using MATLAB to obtain the open loop response observed in Fig. 3.

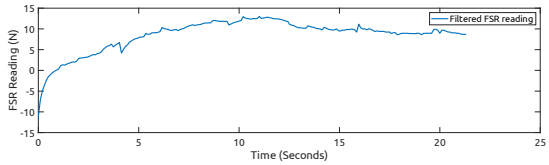


Fig. 3. Open Loop response of HERO Glove Insight at maximum grip force.

The transfer function was obtained using the general form of a first order system and the method described in [23] to obtain the transfer function of the open loop response.

$$G(s) = 1 / ((100)(4s+1)) \quad (1)$$

Using (1), a Simulink model was created and a PID controller was tuned using the PID tuning app. The PID controller was tuned to minimize overshoot and rise time.

The developed control system architecture is shown in Fig. 4., beginning by selecting the mode of operation. The IMU amplitude trigger is used to bring the system into the controlled state where the computer vision system identifies the object in front of the webcam. By identifying the object, the grip force setpoint is selected and HERO Glove Insight begins to grasp the object. The controller provides position commands to the linear actuator and the linear actuator has an in-built position controller, resulting in a nested feedback loop. The force control system operates at 5Hz and the computer vision system sends a new setpoint if the object changes.

E. Experimental Setup

To test the system's capabilities, the experimental setup shown in Fig. 5 and Fig. 6 was created. First, the user dons the HERO Glove, and the webcam is presented with the desired object. The HERO Glove system then begins to grasp the object. During this time, the FSR readings are saved in a CSV file using a Python script. This is repeated 7 times for each object.

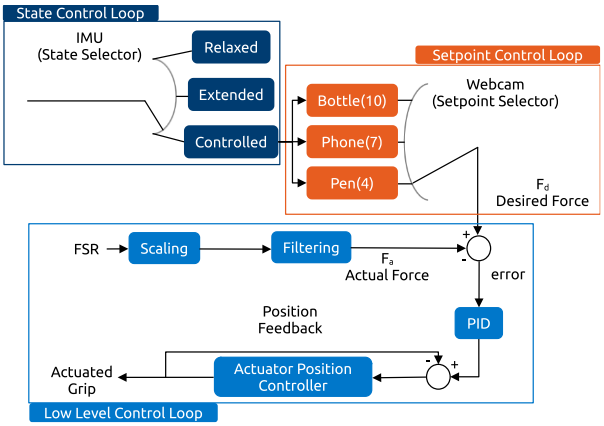


Fig. 4. HERO Glove Insight Control System Architecture.



Fig. 5. HERO Glove Insight experimental setup.

A water bottle, phone, and pen with pre-defined grip force targets of 10N, 7N and 4N, respectively, were selected as the objects for the experiments as they are common objects that people interact with every day and provide a benchmark that covers different sizes, geometries and grip force needs. These objects are easily recognizable in the pretrained YOLOV3 model. The subject in this experiment was familiar with HERO Glove Insight and kept their hand in a relaxed state to provide negligible additional input to the system during experimentation. In future works, many healthy subjects should be recruited that are unfamiliar with HERO Glove Insight to collect data and verify the system's performance.

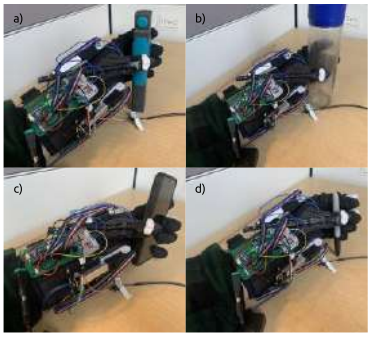


Fig. 6. Gripping orientation of selected objects for grasping tasks. a) Vernier isometric hand dynamometer. b) Glass water bottle. b) An iPhone 13. d) A sharpie marker. The orientations depecited in this image were the same orientations used to perform the grasping tasks for data collection.

III. Results

The computer vision classification system performed well. The accuracy of the class identification was approximately 98% and required less than 50ms to identify the objects. During the tasks, it was found that if no other objects were in frame of the webcam, YOLOV3 was very capable of identifying the object. The computer-vision system would classify the table causing an error during the experiment. To combat this, specific classes could be removed from the model or limits could be placed on the size of classifiable objects.

The water bottle gripping task yielded a 15% overshoot (4.27% standard deviation) with an average settling time of 27.4s (6.46s standard deviation). The results exhibited a negative force at the start of each trial due to the interaction between the sensor's tare function and the Kalman filter. The Kalman filter requires settling time prior to the collection of the data, but the data collection occurred as soon as the controlled state was entered. During each of the trials, when the system settled, the actuator would oscillate close to the setpoint generating a high pitch noise.

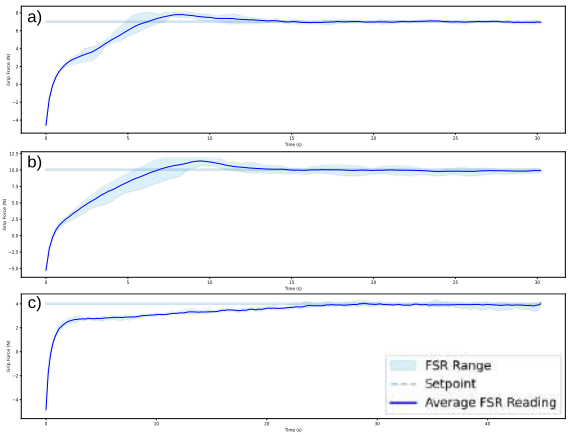


Fig. 7. Closed loop system responses of HERO Glove system grasping A) a rigid water bottle. B) a phone. C) a pen. Legend colours applies to each plot.

The phone gripping task yielded similar results with a 13.22% overshoot (2.85% standard deviation) and a settling time of 29.91s (0.7s standard deviation). While conducting these trials, the steady state oscillations caused an audible actuator response indicating the system was attempting to adjust to small changes in grip force. The negative force at the beginning of the data collection was also present.

The pen gripping task was strikingly different from the other two experiments, yielding a 4.29% overshoot (2.85% standard deviation) with a settling time of 42.8s (3.89s standard deviation). During these trials, the high-pitched noise from the actuator oscillation at the setpoint was minimal compared to the other experiments. A summary of the key characteristics of the grasping tasks are presented in Table 1.

TABLE I. Key Characteristics of Gripping Tasks

Metric	Average Reading		
	Bottle	***Phone***	***Pen***
Rise Time(s)	5.06 (1.09)	4.66 (0.62)	24.04 (8.24)
Settling Time(s)	27.40 (6.46)	29.91 (0.70)	42.80 (3.89)
Percent Overshoot(%)	15.00 (4.27)	13.22 (2.85)	4.28 (2.85)

IV. Discussion

Soft hand exoskeletons conform to the hand's anatomical structures and assist users in grasping a variety of objects. This article contributes anchoring techniques, sensing systems and an autonomous control architecture for soft hand exoskeletons. These features are integrated into the HERO Glove to evaluate their utility in increasing grip force output and applying object-specific grip forces without additional cognitive or physical load. HERO Glove Insight elevates the capabilities of soft hand exoskeletons and could be used as a rehabilitation tool that enables people to live independently and use their affected upper limb during everyday tasks in clinic, home, and community settings.

A. Enhancing Assistive Capabilities

Soft hand exoskeletons provide a range of grip forces, with fully portable systems providing under 20N and tethered systems reaching above 80N [24], [25], [26], [27]. Portable hand exoskeletons typically target assistance in activities of daily living; however, when integrating HERO Glove Insight into unsupervised home trials the users desired to perform a wider range of activities including instrumental activities of daily living, occupational and leisure activities [5]. The upgraded HERO Glove Insight provides 55% more grip force, increasing the force from 8.9N to 13.2N without modifying the power requirements or number of actuators. This increase allows us to fully assist 32% more activities of daily living and instrumental activities of living [28]. In addition to grip force, the grasping postures contribute significantly to the user's ability to complete a task [28]. The version of the HERO Glove Insight presented here does not control the grip type. To compensate for this limitation some fingers must apply larger forces to create a stable grasp. Further innovations could include increasing the number of actuators to command finger-specific loading profiles [7], [26], clutch mechanisms to command various grasp postures with a reduced number of actuators and differential mechanisms to evenly distribute the force across the fingertips without increasing the actuator count [29]. Integrating passive components, such as thumb support and support throughout the upper limb, could enable reach-to-grasp activities without considerable additions to device weight and control complexity [30], [31]. Further investigation of exoskeleton mechanics is needed to enhance device usability and acceptance in unsupervised home and community settings and restore pre-injury grasping behaviors and levels of upper limb activity.

The audible noise present during grasping is disruptive for the user and reduces the system's longevity. Constraining the change in grasp force will prevent the actuators from

adjusting aggressively to slight changes in sensor feedback. Additionally, the worm gear friction contributes heavily to the audible and signal noise generated by the actuator. This can be reduced by changing the material or gearing configuration. The noise from these actuators is 55dB. Numerous application studies [32] have reported audible noise as a problem, particularly in pneumatic systems but these studies do not include noise measurements. As a result, it is difficult to set a benchmark for the audible noise of soft exoskeletons. Future improvements to the HERO Glove Insight include a more fine-tuned control system to eliminate oscillations and subsequent audible noise as the user grasps the object.

B. Enabling Independence to Users Without Hand Function

In the development of HERO Glove Insight, a webcam camera was selected for its low cost, weight, and computational power. This contribution explores capturing situational awareness to provide force setpoints for the gloves control system. The next developmental step for this computer vision system is to mount the webcam to the user's shoulder or chest or Glove to track what the user is looking at and grasping and use the BLE capabilities of the microcontroller to communicate wirelessly with a device capable of running the object recognition model and use a model which recognizes more objects. This will enhance the portability of HERO Glove Insight for use in home and community settings and allow for the HERO Glove Insight to be usable in a larger range of scenarios. With improved situational awareness HERO Glove Insight will be able to interpret the user's intended grasp type by identifying the object and providing the correct output [15], [33].

The goal of the PID controller was to minimize the grip force overshoot and rise time relative to the object-specific grip force target. Observing the results presented in Table 1, the two larger objects, water bottle and phone, followed a much closer relationship to each other than the pen. For the pen task, the proportional gain was insufficient, resulting in a 24s rise time in comparison to less than 5s for the rise time in the other tasks. While the overshoot observed in each of the trials is not worrisome for rigid objects, more delicate objects could be broken if the overshoot is too high. The PID controller was a suitable proof-of-concept controller to evaluate the performance of the system, though future iterations should explore adaptive control schemes utilized in previous exoskeletons to provide more desirable transient responses [34], [35]. For instance, gain scheduling could be used to adjust the PID gains to create object-specific transient responses and model-predictive control could be used to personalize the model and controller to user's biomechanics and grasp orientation and reduce the oscillations of the gripping motion and thus the noise generated. As a higher voltage for this actuator model is not possible, a lower gear reduction could be used to increase the speed at the cost of the force provided.

C. Considering Users' Goals for Independence and Motor Recovery

Future works will explore the development of a model which includes the user in the loop. This will lay the foundation for developing a cooperative therapy mode which considers the user's goals, abilities and fatigue, such as in [34], where the assistance is only offered upon reaching the boundary of the user's working envelope and sensing a decrease in velocity. Using computer vision, the system could also monitor the progress of the user's grasping task to provide assistance only when needed. Other methods of optimizing grip on objects will also be explored, such as measuring slippage of the object, which could be accomplished by adding piezoresistive tactile sensors to the fingers [36].

D. Limitations

Current limitations of the research presented include reduced portability and small sample sizes. The current computer vision system is hosted on a computer and validated in uncluttered environments. The current iteration of the HERO Glove Insight is not optimized for weight. It currently weighs approximately 360 grams which is an increase of 210 grams from the previous version. To make the HERO Glove Insight more portable, the weight will need to be optimized, and the computer vision system added to the glove. This can be accomplished by using plastic fixtures for mounting the components instead of steel and by adding a harness for users to wear with the webcam. Healthy subject studies are required to validate the system's specifications ahead of portability refinements and clinical trials. Clinical trials then need to be conducted with a diverse group of participants with motor impairments after stroke and spinal cord injury to evaluate the safety, comfort and usability and effectiveness of HERO Glove Insight.

V. Conclusion

This research develops HERO Glove Insight, which integrates added value features to a HERO Glove. Improvements to the design have increased the maximum grip force and the system's robustness. Models of the sensor and transmission dynamics were derived and integrated with a computer vision-PID control system to provide automated object-specific grip force control. This system demonstrates opportunities that sensing and computer vision can provide to increase the functionality and ease of use of soft exoskeletons and identifies areas where future development and clinical trials are required to support safe and functional grasps for assistive and rehabilitation contexts.

Acknowledgment

Special thanks to the members of the OntarioTech MAMLab and WearLab for their support and inspiration.

References

[1] N. S. Ward, F. Brander, and K. Kelly, "Intensive upper limb neurorehabilitation in chronic stroke: outcomes from the Queen Square programme," *J. Neurol. Neurosurg. Psychiatry*, vol. 90, no. 5, pp. 498–506, May 2019.

[2] G. Uswatte *et al.*, "Rehabilitation of stroke patients with plegic hands: Randomized controlled trial of expanded Constraint-Induced

Movement therapy," *Restor. Neurol. Neurosci.*, vol. 36, no. 2, pp. 225–244, Mar. 2018.

[3] C. E. Lang *et al.*, "Observation of Amounts of Movement Practice Provided During Stroke Rehabilitation," *Arch. Phys. Med. Rehabil.*, vol. 90, no. 10, pp. 1692–1698, Oct. 2009.

[4] J. Mehrholz, M. Pohl, T. Platz, J. Kugler, and B. Elsner, "Electromechanical and robot-assisted arm training for improving activities of daily living, arm function, and arm muscle strength after stroke," *Cochrane Database Syst. Rev.*, vol. 2018, no. 9, Sep. 2018. Accessed: Nov. 20, 2024. [Online]. Available: https://doi.wiley.com/10.1002/14651858.CD006876.pub5

[5] A. Yurkewich, S. Ortega, J. Sanchez, R. H. Wang, and E. Burdet, "Integrating hand exoskeletons into goal-oriented clinic and home stroke and spinal cord injury rehabilitation," *J. Rehabil. Assist. Technol. Eng.*, vol. 9, p. 20556683221130970, Jun. 2022.

[6] L. N. Awad, A. Esquenazi, G. E. Francisco, K. J. Nolan, and A. Jayaraman, "The ReWalk ReStore™ soft robotic exosuit: a multi-site clinical trial of the safety, reliability, and feasibility of exosuit-augmented post-stroke gait rehabilitation," *J. NeuroEngineering Rehabil.*, vol. 17, no. 1, p. 80, Dec. 2020.

[7] J. Dittli *et al.*, "Mixed methods usability evaluation of an assistive wearable robotic hand orthosis for people with spinal cord injury," *J. NeuroEngineering Rehabil.*, vol. 20, no. 1, p. 162, Dec. 2023.

[8] A. I. R. Kottink *et al.*, "Therapy effect on hand function after home use of a wearable assistive soft-robotic glove supporting grip strength," *PLOS ONE*, vol. 19, no. 7, p. e0306713, Jul. 2024.

[9] S. R. Chang *et al.*, "Myoelectric Arm Orthosis Assists Functional Activities: A 3-Month Home Use Outcome Report," *Arch. Rehabil. Res. Clin. Transl.*, vol. 5, no. 3, p. 100279, Sep. 2023.

[10] X. L. Hu, K. Y. Tong, X. J. Wei, W. Rong, E. A. Susanto, and S. K. Ho, "The effects of post-stroke upper-limb training with an electromyography (EMG)-driven hand robot," *J. Electromyogr. Kinesiol.*, vol. 23, no. 5, pp. 1065–1074, Oct. 2013.

[11] A. Yurkewich *et al.*, "Myoelectric untethered robotic glove enhances hand function and performance on daily living tasks after stroke," *J. Rehabil. Assist. Technol. Eng.*, vol. 7, p. 2055668320964050, Jan. 2020.

[12] X. Chen *et al.*, "A Wearable Hand Rehabilitation System With Soft Gloves," *IEEE Trans. Ind. Inform.*, vol. 17, no. 2, pp. 943–952, Feb. 2021.

[13] J. Guggenheim, R. Hoffman, H. Song, and H. H. Asada, "Leveraging the Human Operator in the Design and Control of Supernumerary Robotic Limbs," *IEEE Robot. Autom. Lett.*, vol. 5, no. 2, pp. 2177–2184, Apr. 2020.

[14] E. Q. Yumbla, Z. Qiao, W. Tao, and W. Zhang, "Human Assistance and Augmentation with Wearable Soft Robotics: a Literature Review and Perspectives," *Curr. Robot. Rep.*, vol. 2, no. 4, pp. 399–413, Dec. 2021.

[15] S. H. Bengtson *et al.*, "Computer Vision-Based Adaptive Semi-Autonomous Control of an Upper Limb Exoskeleton for Individuals with Tetraplegia," *Appl. Sci.*, vol. 12, no. 9, Art. no. 9, Jan. 2022.

[16] M. Khalili and S. Ozgoli, "Environment Recognition for Controlling Lower-Limb Exoskeletons, by Computer Vision and Deep Learning Algorithm," in *2022 8th International Conference on Control, Instrumentation and Automation (ICCIA)*, Mar. 2022, pp. 1–5. Accessed: Nov. 18, 2024. [Online]. Available: https://ieeexplore.ieee.org/document/9737195/?arnumber=9737195

[17] H. J. Lee, K.-S. Kim, and S. Kim, "Generalized Control Framework for Exoskeleton Robots by Interaction Force Feedback Control," *Int. J. Control Autom. Syst.*, vol. 19, no. 10, pp. 3419–3427, Oct. 2021.

[18] Y. Guo, H. Wang, Y. Tian, and J. Xu, "Position/force evaluation-based assist-as-needed control strategy design for upper limb rehabilitation exoskeleton," *Neural Comput. Appl.*, vol. 34, no. 15, pp. 13075–13090, Aug. 2022.

[19] J. Likitlersuang *et al.*, "EEG-Controlled Functional Electrical Stimulation Therapy With Automated Grasp Selection: A Proof-of-Concept Study," *Top. Spinal Cord Inj. Rehabil.*, vol. 24, no. 3, pp. 265–274, Jun. 2018.

[20] Y. Gao, S. Matsuoka, W. Wan, T. Kiyokawa, K. Koyama, and K. Harada, "In-Hand Pose Estimation Using Hand-Mounted RGB Cameras and Visuotactile Sensors," *IEEE Access*, vol. 11, pp. 17218–17232, 2023.

[21] A. Yurkewich, I. J. Kozak, D. Hebert, R. H. Wang, and A. Mihailidis, "Hand Extension Robot Orthosis (HERO) Grip Glove: enabling independence amongst persons with severe hand impairments after stroke," *J. NeuroEngineering Rehabil.*, vol. 17, no. 1, p. 33, Feb. 2020.

[22] J. Redmon and A. Farhadi, "YOLOv3: An Incremental Improvement," Apr. 08, 2018, *arXiv*: arXiv:1804.02767. Accessed: Nov. 20, 2024. [Online]. Available: http://arxiv.org/abs/1804.02767

[23] E. Peperoni *et al.*, "Self-Aligning Finger Exoskeleton for the Mobilization of the Metacarpophalangeal Joint," *IEEE Trans. Neural Syst. Rehabil. Eng.*, vol. 31, pp. 884–894, 2023.

[24] D. Popov, I. Gaponov, and J.-H. Ryu, "Portable Exoskeleton Glove With Soft Structure for Hand Assistance in Activities of Daily Living," *IEEEASME Trans. Mechatron.*, vol. 22, no. 2, pp. 865–875, Apr. 2017.

[25] C. J. Nycz, M. A. Delph, and G. S. Fischer, "Modeling and design of a tendon actuated soft robotic exoskeleton for hemiparetic upper limb rehabilitation," in *2015 37th Annual International Conference of the IEEE Engineering in Medicine and Biology Society (EMBC)*, Milan: IEEE, Aug. 2015, pp. 3889–3892. Accessed: Nov. 20, 2024. [Online]. Available: http://ieeexplore.ieee.org/document/7319243/

[26] C. G. Rose and M. K. O'Malley, "Hybrid Rigid-Soft Hand Exoskeleton to Assist Functional Dexterity," *IEEE Robot. Autom. Lett.*, vol. 4, no. 1, pp. 73–80, Jan. 2019.

[27] H. In, B. B. Kang, M. Sin, and K.-J. Cho, "Exo-Glove: A Wearable Robot for the Hand with a Soft Tendon Routing System," *IEEE Robot. Autom. Mag.*, vol. 22, no. 1, pp. 97–105, Mar. 2015.

[28] M. M. Keller, R. Y. Barnes, and C. Brandt, "Activities of daily living with grasp types and force measurements during object manipulation," *South Afr. J. Occup. Ther.*, vol. 54, no. 1, pp. 15–21, Apr. 2024.

[29] P. Capsi-Morales, C. Piazza, G. Grioli, A. Bicchi, and M. G. Catalano, "The SoftHand Pro platform: a flexible prosthesis with a user-centered approach," *J. NeuroEngineering Rehabil.*, vol. 20, no. 1, p. 20, Feb. 2023.

[30] T. Bützer, O. Lambercy, J. Arata, and R. Gassert, "Fully Wearable Actuated Soft Exoskeleton for Grasping Assistance in Everyday Activities," *Soft Robot.*, vol. 8, no. 2, pp. 128–143, Apr. 2021.

[31] F. Missiroli *et al.*, "Rigid, Soft, Passive, and Active: A Hybrid Occupational Exoskeleton for Bimanual Multijoint Assistance," *IEEE Robot. Autom. Lett.*, vol. 7, no. 2, pp. 2557–2564, Apr. 2022.

[32] L. Cappello *et al.*, "Assisting hand function after spinal cord injury with a fabric-based soft robotic glove," *J. NeuroEngineering Rehabil.*, vol. 15, no. 1, p. 59, Dec. 2018.

[33] D. Kim *et al.*, "Eyes are faster than hands: A soft wearable robot learns user intention from the egocentric view," *Sci. Robot.*, vol. 4, no. 26, p. eaav2949, Jan. 2019.

[34] T. G. Sugar *et al.*, "Design and Control of RUPERT: A Device for Robotic Upper Extremity Repetitive Therapy," *IEEE Trans. Neural Syst. Rehabil. Eng.*, vol. 15, no. 3, pp. 336–346, Sep. 2007.

[35] W. He, Z. Li, Y. Dong, and T. Zhao, "Design and Adaptive Control for an Upper Limb Robotic Exoskeleton in Presence of Input Saturation," *IEEE Trans. Neural Netw. Learn. Syst.*, vol. 30, no. 1, pp. 97–108, Jan. 2019.

[36] B. J. Lee, "Development of Intelligent Exoskeleton Grasping Through Sensor Fusion and Slip Detection," 2018. [Online]. Available: http://hdl.handle.net/10919/83924

Evaluating Feedback Modality Preferences of Power Wheelchair Users During Manual Robotic Arm Control

Breelyn Kane Styler[1] Lesong Jia[2] Henny Admoni[3] Reid Simmons[3] Rory Cooper[1,4] Na Du[2] and Dan Ding[1,4]

***Abstract*— Assistive robotic arms can extend a user's capabilities, but they can be hard to control because users do not always have good situational awareness at the robot's end effector. This study investigates whether explicit feedback about the robot's distance to task-relevant objects can help users manually control such robots more easily. Specifically, we investigate light and sound as feedback modalities. In a within-subjects study, users controlled a robot arm in a kitchen task. We compared a no-feedback condition with four feedback types: discrete light, discrete sound, continuous light, and continuous sound. We assess usability, performance outcomes, mental workload and user preferences. Our findings indicate that adding feedback improved task success; however, user preferences did not consistently align with performance metrics like task efficiency or success. Instead, preferences varied, revealing insights into user perspectives on each feedback modality.**

I. INTRODUCTION

Assistive technologies that enhance user functionality can provide non-verbal feedback for increasing task understanding and operation [1]. Specifically, manual operation of robotic arms is complicated by challenges such as depth perception, object alignment, and obstructed line of sight [2], [3], [4]. Line of sight is a further challenge for power wheelchair users, whose limited trunk control prevents them from repositioning their bodies to gain better visibility of objects during pick and place tasks. To address these difficulties, our work focuses on providing intuitive operation through unobtrusive light and sound feedback that enhances an operator's ability to perceive distance to objects. By improving control, we promote user independence which increases a user's engagement in everyday activities.

Recent research emphasizes the desire for better situational awareness and the importance of users feeling in control during arm operation [2]. However, for users with disabilities, who experience additional cognitive, visual, or hearing impairments, delivering situational feedback while maintaining the user's sense of control and minimizing distractions remains unclear. Auditory-visual interactions improve perception [5], and facilitate skill learning [6]. These modalities not only improve perception accuracy compared to others, such as haptic or temperature feedback [7], but offer familiar and intuitive communication channels.



Fig. 1: User manually operating robotic arm through a Keurig task.

Building on these insights, we investigated light and sound feedback in two forms: discrete and continuous representations. These modalities were used to convey proximity while maintaining manual robot arm control. We conducted five trials with power wheelchair users, testing no feedback and four distinct feedback methods. During these trials, we collected usability, performance, and workload metrics. Additionally, we gathered qualitative preference feedback throughout and between each condition to address the following four research questions:

1. **Usability:** *Do users find feedback-enhanced methods more usable?* Usability was assessed by comparing user rankings with System Usability Scale (SUS) scores, [8], gathered after each of the five conditions.

2. **Performance:** *Does the addition of feedback methods increase task efficiency and success?* To explore this, we measured task times and success rates across feedback conditions.

3. **Workload:** *Does feedback improve ease and intuitive use of the system by decreasing mental workload?* We evaluated this using NASA Task Load Index (NASA-TLX) workload assessments following each condition [9] .

4. **Preference:** *Do users prefer light or sound feedback more when grasping and placing objects?* User rankings and qualitative feedback during tasks provided insights into preferences for light versus sound feedback, as well as

[1]Human Engineering Research Laboratories, VA Pittsburgh Healthcare System, Pittsburgh, PA, USA
[2]School of Computing and Information Science, University of Pittsburgh, Pittsburgh, PA, USA
[3]Robotics Institute, Carnegie Mellon University, Pittsburgh, PA, USA
[4]Department of Rehabilitation Science and Technology, University of Pittsburgh, Pittsburgh, PA, USA

discrete versus continuous feedback.

II. RELATED WORK

Situational awareness is an important aspect of user-centered design, particularly for assistive technologies supporting users with disabilities. In user interfaces, providing increased situational awareness enables operators to focus on task-relevant information, filter out distractions, and integrate current information to anticipate future states. In related work, this has been described as the operator's ability to understand the current state and project their understanding into future states [10].

Despite teleoperation being one of the oldest applications in human-assistive interaction, recent research highlights the lack of user-centered approaches, with teleoperation interfaces often restricted to expert use cases [11]. This further emphasizes the need to investigate interfaces that provide intuitive feedback for untrained users and improve understandability which is a key design guideline for human-robot interaction systems [12]. These systems should also convey their current state while minimizing cognitive demands, such as context switching between the environment and the interface [12].

Motivated by these previous studies, our work investigates the use of light and sound feedback. Visual and auditory modalities were chosen because they enhance perception [5], improve perceptual accuracy for users [7], aid in learning new skills [6], and serve as a preferred familiar communication method [13].

Auditory signals are commonly used to provide spatial awareness, as humans naturally rely on hearing for internal positioning [14]. Many assistive systems leveraging auditory cues focus on aiding users with visual impairments, such as providing spatial knowledge or localizing objects in space [15]. Examples include smart wheelchairs that use auditory cues to convey obstacle proximity, system status, or direction changes [16]. Additionally, non-verbal auditory signals, such as tones or broadband sounds, have been researched for their effectiveness in localization and communication tasks [17].

In contrast, there is a notable lack of research focusing on light-based feedback to convey object distance during robotic arm manipulation. Much of the existing work combines multiple modalities or explores haptic feedback [18]. While multimodal feedback methods can improve performance, this creates a gap in understanding individual user preferences and the effectiveness of individual feedback modalities, which is what our study aims to address.

Existing work on multimodal feedback often combines modalities, such as in powered wheelchairs, where sensors provide combined visual and auditory cues for navigation and obstacle avoidance [19]. Additionally, most research on robotic arm operation focuses on remote teleoperation interfaces, where the user is not physically co-located with the robot. These interfaces often aim to simplify free-positioning with techniques like point-and-click interfaces or constrained positioning for users with disabilities [20]. There is comparatively little focus on systems where the robotic arm is co-located with the user.

For systems that are in the same physical space as the user, research has focused on shared-control visualizations, emphasizing the importance of designing interfaces that improve predictability and legibility for the user [21]. Other studies examine multimodal feedback for co-located systems, such as tactile, visual, and auditory combinations [22]. However, there is still a lack of research isolating individual feedback modalities in these settings.

Our study provides a focused investigation where this contribution not only addresses gaps in user-centered feedback design but also offers insights into how specific modalities support operators with disabilities in direct-control assistive tasks.

III. SYSTEM DESIGN AND FEEDBACK CONDITIONS

A. System Setup

Users tele-operated a Kinova Gen3 robotic arm mounted on a table at the height of their power wheelchair positioned on the side opposite their dominant hand. An overhead camera was used to identify objects within the scene and was calibrated at the start of the trials relative to the robotic arm's base frame. To minimize movement, foam padding was placed beneath the pod holder and Keurig machine. Any residual movement was managed by the overhead camera, which continuously updated object positions using fiducial tags affixed to the pod holder and Keurig. Light feedback was provided through an LED ring on the robotic arm's wrist, and sound feedback through an external speaker. The task setup is illustrated in Figure 2.

The position of the end effector was translated into the overhead camera's frame by capturing four distinct poses of the end effector and applying the Umeyama Algorithm. This



Fig. 2: Overhead view of the task setup with overhead camera, pod holder, and Keurig. Fiducial tags mark objects in the scene, and the end effector tag is used at task start to calibrate the overhead frame into the robot arm's base frame.

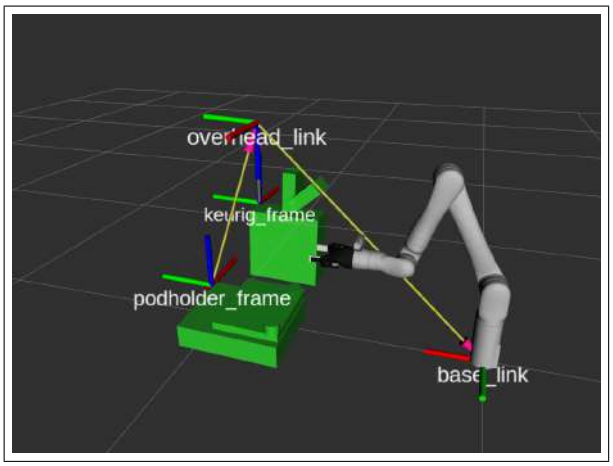


Fig. 3: Reference frames for the task.

calibration allowed the system to determine the position of all scene objects relative to the arm's base frame. A depiction of the reference frames is shown in Figure 3.

For providing light feedback, as shown in Figure 4, we wrapped the wrist of the robotic arm with a WS2812 LEDs light strip wrapped in silicone. This strip was wired to a ESP-WROOM-32 Arduino board with the wire cased and affixed to the arm's base via velcro wire wraps. An NVIDIA Jetson AGX Orin was used to communicate via Bluetooth (Tiny Bluetooth Library) to the Arduino (ESP32 BLE library) which sent signals using FastLED to control the lights. Light control was sent to the wrist LEDs via a function parametrized by color, brightness, and blink frequency.

For sound feedback, a sine wave function generator was used to generate a 300Hz wave file, a frequency chosen for its familiarity and relatively low pitch. This frequency is close to middle C (approximately 256 Hz) and falls within a range that is commonly encountered in everyday sounds. The file could then be played from the Jetson to a bluetooth speaker with a pitch factor setting from 0 to 1. For example, a pitch factor of 0.8 would be a frequency of 240 Hz. Audio control was sent to the speaker via a function parameterized by beep frequency, and pitch factor.

B. State Transitions

We provided users with five feedback conditions: no feedback, two light feedback options, and two sound feedback options. Each feedback modality (light and sound) included a discrete and a continuous condition. All feedback methods operated across four internal task states, *far from target*, *midway to target*, *near target*, and *action executable*, with feedback parameters varying according to both the task state (pod or keurig) and the feedback condition. These states and transitions are depicted in Figure 5.

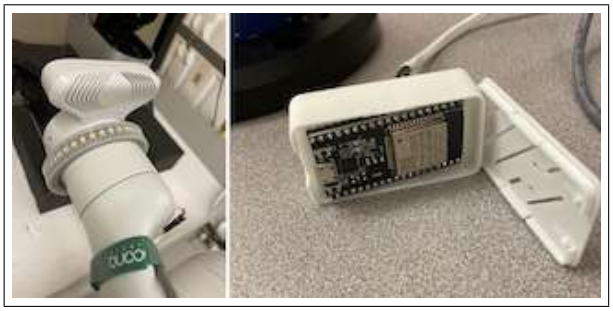


Fig. 4: Wrist light and arduino wired board.

In the pod-grasping phase, all four states were included. Transitions between states occurred based on the spatial relationship between the robotic end-effector links and predefined boundaries within the scene. These boundaries were established relative to the object's frame. Specifically, *far from target* encompassed the area outside the *midway to target* goal box. The *midway to target* area referred to the region within the first goal box. The *near target* state was defined as the region where the end-effector links intersected the inner goal box but the pod's line segment did not intersect the plane defined by the open gripper of the end-effector. Finally, the action executable state was achieved when the plane defined by the open gripper intersected the pod's line segment within the innermost goal box, Figure 5.

The line segment used to define the pod's position dynamically adjusted based on the gripper's orientation. For side and front grasps, the segment aligned vertically. For overhead grasps, the segment rotated to a horizontal orientation whenever the end-effector pitch in the base frame exceeded a specific threshold. This was determined by the roll angle in the end-effector frame, where the y-axis points out of the side: a roll of 90 degrees indicated a flat front or side grasp, while a roll exceeding 114 degrees positioned the end-effector overhead. Overlapping goal boxes were created for all pods in the holder; however, for consistent experiment starts, only two pods were available for retrieval, positioned at opposite ends of the bottom row.

In the Keurig pod-placing phase, only three states were used: *far from target*, *midway to target*, and *action executable*. Here, the definitions for far and midway remained the same as in the grasping phase. The *action executable* state was achieved when the end-effector links entered the innermost goal box.

C. Feedback Conditions

For the continuous feedback shown in the top graph, Figure 5, only the frequency of blinking (light) or beeping (sound) was adjusted. The light remained white with consistent brightness, while the sound retained the same tone. The frequency of blinking or beeping in the *far from target* and *midway to target* state increased linearly as the end-effector approached the target, normalized across a parameterized range. If the *action executable* area was triggered, the light or tone would go solid.

For discrete feedback, thresholds changed with each state, as shown in the bottom step graph of Figure 5. For sound, tones increased by a musical fourth, starting at 180 Hz (*far from target*), progressing to 240 Hz (*midway*), 300 Hz (*near*), and culminating in a distinct dinging sound for the final *action executable* state. For light, states transitioned

TABLE I: Demographic Information. Abbreviations include Spinal Cord Injury (SCI), Multiple Sclerosis (MS), Traumatic Brain Injury (TBI).

Diagnosis	Age	Cognitive Impairment	Hearing Loss	Vision Loss
SCI/TBI	74	Yes	No	mono vision
SCI	28	No	Left	No
SCI	67	No	No	No
Stroke	63	Yes	Both	No
MS	58	Yes	Left	No
MS	64	Yes	No	No
SCI	52	No	No	No
SCI/Stroke	75	Yes	Both	forgot glasses
SCI	64	No	Both	No
MS	60	Yes	No	No
SCI	64	No	Both	No
SCI/TBI	62	Yes	Right	double vision
SCI	64	No	No	forgot glasses

between white (*far from target*), yellow (*midway*), red (*near*), and green (*action executable*).

IV. METHODS

The study was completed in no more than two hours and approved as a minimal risk study under the Institutional Review Board of the VA Pittsburgh Healthcare System, protocol number IRBNet 1720292.

A. Participant Recruitment and Demographics

A total of 15 participants were recruited from the National Veteran Wheelchair Games, with two having scheduling conflicts, resulting in 13 participants for the study. Inclusion criteria was: 1) individuals over 18 years of age, 2) power wheelchair users, and 3) individuals with upper limb impairments that hinder daily manipulation tasks. Table I shows demographic characteristics of the thirteen Veteran participants. Seven were African American and six Caucasian with eleven identifying as male and two as female. Seven of the participants described having a cognitive impairment, two from a traumatic brain injury, two from stroke, and three from multiple sclerosis. Seven participants also described having a hearing impairment with the side indicated, three said this was from tinnitus. Despite these hearing impairments all participants indicated they could hear the sound feedback, we believe this was due to using a low pitch. Additionally, while many had glasses four participants indicated vision impairments with two forgetting to bring their glasses, one describing double vision, and the fourth describing mono-vision. Lastly, nine of the thirteen participants indicated some loss of sensation describing numbness in all or parts of fingers on their hands.

B. Study Design

The study followed a within-subjects, repeated-measures design in which each participant experienced five conditions. To control for order effects, the conditions were counterbalanced using a Latin Square design. The conditions included: no feedback, continuous light feedback (a blinking white light with a blink rate that varied with proximity to the goal), discrete light feedback (a light that changed color based on proximity to the goal), continuous sound feedback (a steady tone where the beeping rate increased as proximity to the goal decreased), and discrete sound feedback (a tone that changed pitch based on proximity to the goal).

C. Experiment Procedure

Participants began the study by providing informed consent and completing a demographic survey. The demographic survey collected details about participants' age, gender, diagnosis, and technology viewpoints. After completing the survey, participants underwent a 30-40 minute robotic arm training session. During this session, they were introduced to the joystick's four control modes: lateral end-effector movement, wrist roll and height changes, wrist orientation changes, and gripper opening and closing. To reinforce these controls, participants practiced moving the robotic arm to touch the investigator's hand at different spatial positions. They also completed three grasping tasks, which included a front grasp of a water bottle, an over-the-top grasp of a small cereal bowl, and a side grasp of a raised thin notebook.

Before each trial, the experimenter configured the feedback system via a setup file, explained the feedback modality to the participant, and ensured the participant could see the lights or hear the sounds. Once participants confirmed their understanding and readiness, they began the task. The primary coffee-making task required participants to retrieve a Keurig pod from the holder and place it in the top of the Keurig machine, as illustrated in Figure 6.

For consistency, participants were instructed to pick either of the two pods from the holder. If one pod was dropped, they were to proceed with the remaining pod. If both pods fell, the experimenter replaced them to ensure consistent start locations for the overhead system. Task success was defined as successfully grasping the pod without dropping it and placing it into the Keurig without it falling out.

D. Data Collection and Analysis

During each trial, task performance metrics, including task completion time and success rates, were recorded. To evaluate usability, participants completed the System Usability Scale (SUS) [8] after each trial. The SUS consists of 10 items rated on a Likert scale ranging from 'Strongly disagree' to 'Strongly agree,' with a total score ranging from 0 to 100, where higher scores indicate greater perceived usability. Participants also completed the NASA Task Load Index (NASA-TLX) [9] to assess workload across six dimensions: Mental Demand, Physical Demand, Temporal Demand, Performance, Effort, and Frustration. Therefore, each participant completed five SUS and five NASA-TLX questionnaires.

In addition to quantitative data, qualitative data was collected through video recordings and participant feedback. Audio recordings of participant comments were transcribed and analyzed to identify categories which included preferences, likes, and dislikes for each feedback modality. Participant rankings of the feedback conditions were also recorded at the completion of all trials.

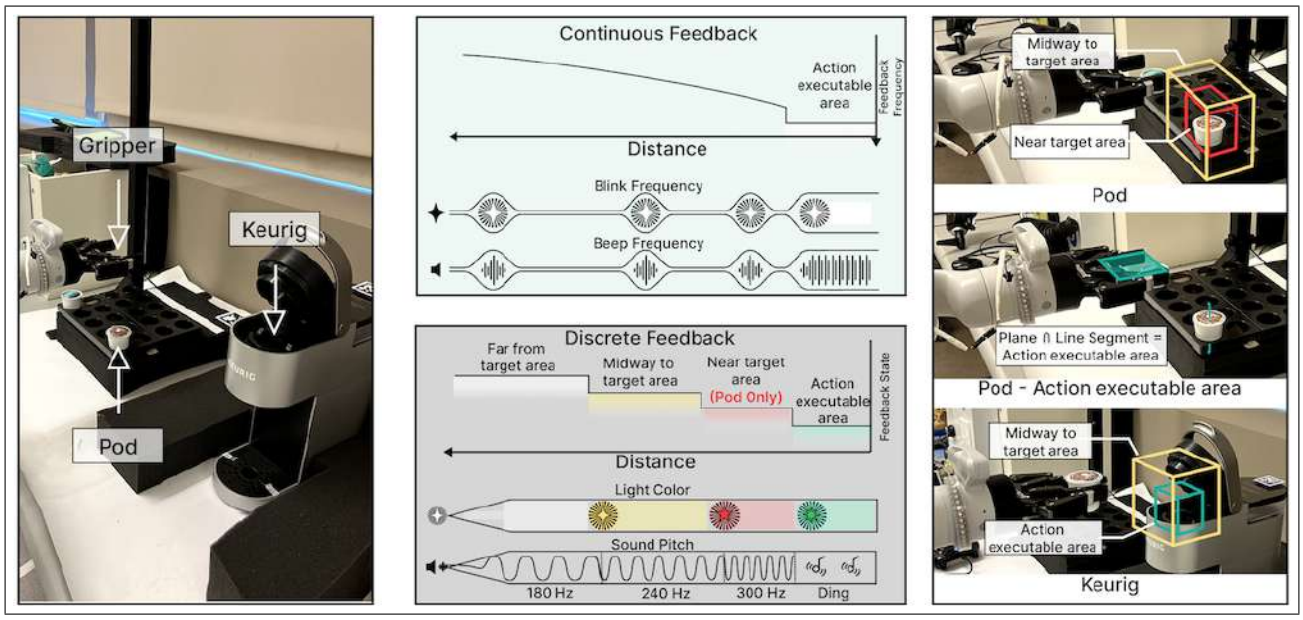


Fig. 5: States for continuous and discrete light and sound feedback.

Quantitative data was analyzed using IBM SPSS Statistics 29.0.2.0. Performance metrics, including task completion times and success rates, were first summarized using descriptive statistics. Pearson correlation coefficients were also calculated to explore relationships between success rates and other variables. To compare success rates across feedback conditions, Cochran's Q test was performed, as this test is suitable for binary data, such as success or failure outcomes. Task completion times were analyzed using a repeated measures ANOVA, which is appropriate for continuous, normally distributed data collected under multiple conditions within subjects.

For usability, differences in SUS scores across feedback conditions were analyzed using the Friedman Two-Way ANOVA by Ranks, a non-parametric test ideal for ordinal data in repeated-measures designs. The same test was applied to analyze the six workload dimensions of the NASA-TLX, as these measures are also ordinal and do not assume normality. Participant preference rankings of feedback modalities were analyzed using the Independent-Samples Kruskal-Wallis test, which is appropriate for comparing ordinal data across multiple groups.



Fig. 6: Two subtasks: grasping pod and placing pod in Kuerig.

V. RESULTS

A. Usability

No statistically significant differences or trends were found between usability scores and the feedback method, the user's ranked feedback preference, or the order in which the task was presented. Overall, usability scores grouped by feedback method had mean values greater than 68, as shown in Table II.

TABLE II: System Usability Scale Average per Feedback Condition.

	Mean SUS
No Feedback	80.2 ± 19.8
Continuous Light	78.8 ± 20.6
Discrete Light	82.1 ± 18.3
Continuous Sound	75.0 ± 22.0
Discrete Sound	79.2 ± 21.1

B. Performance

There was no statistical significant difference between the user's task success rate and ranked preference (favorite feedback method was not the most successful), and users did not succeed more with more practice (no order effect found for success), but there was a statistically significant difference among the success rates of individual feedback methods. In order of least successful to most successful, no feedback was least successful with four failures. Three of these failures occurred during pod grasping and one having to retrieve a second pod after dropping during Keurig placement. Discrete sound had three pod grasping failures, and continuous light with one grasping failure. A Cochran Q non-parametric test for binary results was performed with a calculated Q statistic

of 10.154(d=4) and a p-value of 0.038 indicating significant heterogeneity. Therefore, the addition of feedback methods did increase task success but this success rate did not seem to impact the users preference ranking. Success rates and task times were grouped by feedback method, as shown in Table III.

There was no statistically significant difference or trend among the feedback methods for overall task times. Nor were any trends found when grouping overall task times by user's feedback rank or the order tasks were presented. Therefore, the addition of feedback methods did not show evidence of increasing task efficiency. The task times grouped by feedback method are displayed in Table III. We did find a moderate negative linear relationship (pearson correlation $r(65) = -0.529, p < .001$) between total task time, and success rate (success rate increases as total time decreases).

C. Mental Workload

The NASA TLX workload evaluation included six workload dimensions. Results were analyzed based on the feedback method presented, the user's preferred feedback ranking, and task order. Of these dimensions, only the mental demand dimension showed a significant result, attributed to the order in which tasks were presented. Using Friedman's Two Way Analysis of Variance the results indicated a significant difference between task orders, $X^2(4) = 9.59, p = 0.048$.

The remaining five dimensions (performance, effort, temporal demand, physical demand, and frustration) did not show statistically significant differences when grouped by feedback method, users' preferred feedback rankings, or task order.

D. Feedback Preferences

Participants provided varied preferences for the five feedback methods, with no overarching trend favoring light over sound or discrete over continuous feedback. However, discrete color feedback emerged as the most preferred overall, while continuous beeping was the most preferred sound-based method.

Although statistical significance was not observed, a general trend toward color feedback as the most favored method was evident (Figure 7). After ranking all feedback methods, six out of thirteen participants listed color as their top choice. Of the remaining seven, three ranked color second, resulting in nine of thirteen participants placing color feedback in their top two preferences. This trend aligns with qualitative data, as several participants cited the intuitive nature of color changes which effectively signaled task progress. For example, one user noted, "I backed off, and it was yellow one time. Then once I backed off, the colors changed, and when it turned green, I knew I was right on point."

TABLE III: Performance Metrics per Feedback Condition.

	Success Rate	Mean Task Time (s)
No Feedback	0.69 ± 0.48	232.8 ± 114.5
Continuous Light	0.92 ± 0.28	257.8 ± 150.4
Discrete Light	1.00 ± 0.00	248.5 ± 104.6
Continuous Sound	1.00 ± 0.00	191.9 ± 090.5
Discrete Sound	0.77 ± 0.44	255.9 ± 145.1

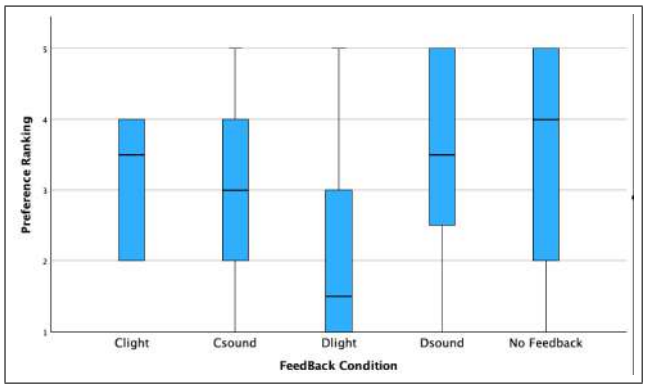


Fig. 7: Boxplots showing ranked feedback preferences grouped by feedback method.

When analyzing participants' top two feedback preferences, we found varied combinations. Four participants preferred visual feedback exclusively, ranking both color and blinking light in their top two. Two participants preferred sound feedback, selecting both beeping and tone. Four included no feedback among their top two preferences, while the remaining three participants had mixed preferences combining light and sound feedback. This variability suggests individual differences in processing visual and auditory signals during task execution.

In terms of light feedback, color changes were favored over blinking light by the majority of participants. Eight participants explicitly stated that they did not notice the blinking light, which limited its effectiveness. One participant explained, "The colors got my attention more than the blinking. I could kind of forget about [the blinking], ... but when the colors were changing I could really see that." This suggests that while blinking lights provided continuous feedback it may have been hard for the user to distinguish the range of information given, discrete color zones made feedback more salient and easier to interpret.

Sound feedback garnered mixed reactions. Six participants remarked sound feedback got their attention most. However, three participants described aspects of the sound, whether tone or beeping, as annoying, two of the six actually preferred sound because it captured their attention. One participant stated, "I liked the beeping the best because I'm used to it. I was a truck driver, and that 'beep, beep' gets my attention." Another participant also preferred the continuous sound due to familiarity: "I think because I got used to the car, I liked the going faster sound better." These quotes show users connect familiarity to preferences and feedback preferences are influenced by individual experiences.

When comparing discrete feedback methods, participants found color changes more intuitive and less intrusive than tone. While the tone conveyed proximity, three participants found it annoying, noting that the constant background sound was hard to ignore. One participant said,"Why do I like the color best? Because it's passive. The tone kind of got on my

nerves after a while ... a subtle hint versus like a dial tone." Although, one participant liked the tone during object pickup, with two others saying they prefer feedback more for pick rather than place tasks. This leads to further research with manipulation actions matching feedback needs for specific subtasks.

Several participants shared insights into broader feedback preferences and potential improvements. Six participants expressed a desire for feedback tied to the amount of pressure applied with the grippers which could enhance control. Additionally, three participants mentioned the importance of customization, with one explaining, "I think some people would like to customize the colors or sounds ... that would be up to the individual their likes and dislikes, man voice or woman voice, or for something more critical you might have a harsh voice."

Interestingly, three participants preferred no feedback because they felt it allowed them to focus better on the task. One participant noted, "I could concentrate better without the lights or sound by looking at the cup." However, the same participant acknowledged the benefits of feedback, adding, "I trust it more with the sound and lights." Another user that preferred the no feedback over other methods mentioned, "I definitely felt a lot more comfortable, but now I almost miss something telling me, 'hey', I did find that I was looking around a lot more, ... having something [feedback] is nice." This suggests a need to toggle feedback on or off.

Finally, there was no statistical significance between participants' feedback preferences and the task order in which feedback methods were presented. For example, the first task or last task's feedback method was not the method preferred most.

VI. DISCUSSION

A. **Usability** *Do users find feedback-enhanced methods more usable?* Usability, as measured by the SUS, did not vary significantly across feedback conditions or align with users' preference rankings. This result shows participants' preferences and their reported usability experiences did not always correlate.

B. **Performance** *Does the addition of feedback methods increase task efficiency and success?* The addition of feedback methods improved task success rates; however, this did not appear to influence users' preference rankings. Conversely, feedback methods did not show evidence of improving task efficiency, as task times remained statistically unchanged across conditions. This aligns with findings from related studies on auditory feedback, which reported no significant improvement in task completion time but noted a reduction in perceived subjective difficulty when auditory feedback was present [23]. Some participants in our study echoed this sentiment, stating they felt they had to "pay more attention" when feedback methods were absent.

C. **Workload** *Does feedback improve ease and intuitive use of the system by decreasing mental workload?* No specific feedback method demonstrated a significant reduction in overall workload as measured by the NASA-TLX. However, an order effect was observed within the mental demand dimension, suggesting that as participants became more familiar with the task, their workload decreased, independent of feedback modality. Participant comments about increased attention demands in the absence of feedback suggest that feedback may play a role in mitigating perceived workload, even if objective measures were not captured.

D. **Preference** *Do users prefer light or sound feedback more when grasping and placing objects?* User preferences were mixed, with an overall trend favoring discrete color feedback. Sound feedback was generally more effective for capturing attention, but gave diverse reactions: some participants valued it for its alerting nature, while others found it annoying. These findings are consistent with multimodal feedback in wheelchair navigation, which noted that "auditory feedback may be best for capturing attention," [24]. These auditory preferences aligned with work which found that broadband sounds (with varying frequencies) were preferred over constant, alarm-like tones due to reduced user annoyance [25]. In contrast, light feedback was favored for its subtlety, with discrete color changes being intuitive for understanding state transitions. However, blinking light feedback was often difficult to notice, likely due to challenges in distinguishing subtle changes in blink patterns for conveying distance. Participants typically preferred discrete light feedback over continuous blinking light, citing its clarity. Conversely, continuous sound feedback was favored over discrete sound for its familiarity. Some participants compared it to the beeping of a car in reverse. Even so, discrete sound was mentioned to be more effective for specific actions, such as object pickup.

E. *Limitations*

This study was limited to recruiting participants from a single venue, specifically Veterans, which may not be a full representation of the population. Additionally, the participant group was predominantly male, highlighting the need for greater female representation to ensure a more balanced perspective.

Another limitation is that the study setup required an overhead camera, which does not fully reflect a real-world deployment. However, our focus was on understanding user preferences for light and sound feedback, not system implementation. In practice, alternative camera placements such as a fixed home setup, a wrist-mounted pre-scan, or integration with a moving device localized within a fixed base frame could provide the necessary ground truth information.

VII. CONCLUSION

This study explored user preferences and the effectiveness of light and sound feedback modalities for enhancing usability, task performance, and intuitiveness while power wheelchair users manually moved a robotic arm through a coffee making grasping and placement task. While no single feedback method was universally preferred, discrete color feedback was the most favorable for many participants. User

preferences for feedback were not only varied but also task-dependent. Some participants emphasized the importance of context, favoring certain feedback methods for specific actions, such as object pickup over placement, while others gravitated toward feedback modalities that felt more familiar or aligned with their prior experiences.

Interestingly, the addition of feedback did not statistically improve task efficiency, but it did appear to enhance perceived situational awareness and task performance. This suggests that feedback's value lies more in supporting user experience and decision-making rather than directly accelerating task completion. Additionally, participants expressed a desire for customizable feedback, such as the ability to select specific colors or tones, to better suit their personal preferences. These findings show the potential advantages of multimodal feedback systems that can adapt to the user's preferences and the specific demands of the task.

ACKNOWLEDGMENT

This work was supported by Career Development Award 1IK1RX004259 from the United States (U.S.) Department of Veterans Affairs; Rehabilitation Research and Development Service. The contents do not represent the views of the U.S. Department of Veterans Affairs or the United States Government. We would also like to thank the voluntary participants of the 2024 NVWG.

REFERENCES

[1] Z. Han, J. Allspaw, A. Norton, and H. A. Yanco, "Towards a robot explanation system: a survey and our approach to state summarization, storage and querying, and human interface," *arXiv preprint arXiv:1909.06418*, 2019.

[2] B. K. Styler, W. Deng, R. Simmons, H. Admoni, R. Cooper, and D. Ding, "Exploring control authority preferences in robotic arm assistance for power wheelchair users," in *Actuators*, vol. 13, no. 3. MDPI, 2024, p. 104.

[3] S. Arévalo Arboleda, T. Dierks, F. Rücker, and J. Gerken, "Exploring the visual space to improve depth perception in robot teleoperation using augmented reality: The role of distance and target's pose in time, success, and certainty," in *Human-Computer Interaction–INTERACT 2021: 18th IFIP TC 13 International Conference, Bari, Italy, August 30–September 3, 2021, Proceedings, Part I 18*. Springer, 2021, pp. 522–543.

[4] A. Padmanabha, J. Gupta, C. Chen, J. Yang, V. Nguyen, D. J. Weber, C. Majidi, and Z. Erickson, "Independence in the home: A wearable interface for a person with quadriplegia to teleoperate a mobile manipulator," in *Proceedings of the 2024 ACM/IEEE International Conference on Human-Robot Interaction*, 2024, pp. 542–551.

[5] D. A. Bulkin and J. M. Groh, "Seeing sounds: visual and auditory interactions in the brain," *Current opinion in neurobiology*, vol. 16, no. 4, pp. 415–419, 2006.

[6] A. R. Seitz, R. Kim, and L. Shams, "Sound facilitates visual learning," *Current biology*, vol. 16, no. 14, pp. 1422–1427, 2006.

[7] M. S. Marambe, B. S. Duerstock, and J. P. Wachs, "Optimization approach for multisensory feedback in robot-assisted pouring task," in *Actuators*, vol. 13, no. 4. MDPI, 2024, p. 152.

[8] J. Brooke, "Sus: A quick and dirty usability scale," *Usability Evaluation in Industry*, 1996.

[9] S. G. Hart, "Nasa-task load index (nasa-tlx); 20 years later," in *Proceedings of the human factors and ergonomics society annual meeting*, vol. 50, no. 9. Sage publications Sage CA: Los Angeles, CA, 2006, pp. 904–908.

[10] J. D. Oury, F. E. Ritter, J. D. Oury, and F. E. Ritter, "How user-centered design supports situation awareness for complex interfaces," *Building Better Interfaces for Remote Autonomous Systems: An Introduction for Systems Engineers*, pp. 21–35, 2021.

[11] D. J. Rea and S. H. Seo, "Still not solved: A call for renewed focus on user-centered teleoperation interfaces," *Frontiers in Robotics and AI*, vol. 9, p. 704225, 2022.

[12] A. Wilkinson, M. Gonzales, P. Hoey, D. Kontak, D. Wang, N. Torname, A. Sinclaire, Z. Han, J. Allspaw, R. Platt, *et al.*, "Design guidelines for human–robot interaction with assistive robot manipulation systems," *Paladyn*, vol. 12, no. 1, pp. 392–401, 2021.

[13] J. Ward, *The student's guide to cognitive neuroscience*. Routledge, 2019.

[14] J. X. Maier and J. M. Groh, "Multisensory guidance of orienting behavior," *Hearing research*, vol. 258, no. 1-2, pp. 106–112, 2009.

[15] K. Papadopoulos, K. Papadimitriou, and A. Koutsoklenis, "The role of auditory cues in the spatial knowledge of blind individuals." *International journal of special education*, vol. 27, no. 2, pp. 169–180, 2012.

[16] A. Pellichero, K. L. Best, F. Routhier, P. Viswanathan, R. H. Wang, and W. C. Miller, "Blind spot sensor systems for power wheelchairs: Obstacle detection accuracy, cognitive task load, and perceived usefulness among older adults," *Disability and Rehabilitation: Assistive Technology*, vol. 18, no. 7, pp. 1084–1092, 2023.

[17] B. J. Zhang and N. T. Fitter, "Nonverbal sound in human-robot interaction: a systematic review," *ACM Transactions on Human-Robot Interaction*, vol. 12, no. 4, pp. 1–46, 2023.

[18] F. Sorgini, R. Caliò, M. C. Carrozza, and C. M. Oddo, "Haptic-assistive technologies for audition and vision sensory disabilities," *Disability and Rehabilitation: Assistive Technology*, vol. 13, no. 4, pp. 394–421, 2018.

[19] R. H. Wang, S. M. Gorski, P. J. Holliday, and G. R. Fernie, "Evaluation of a contact sensor skirt for an anti-collision power wheelchair for older adult nursing home residents with dementia: Safety and mobility," *Assistive Technology*, vol. 23, no. 3, pp. 117–134, 2011.

[20] D. Kent, C. Saldanha, and S. Chernova, "A comparison of remote robot teleoperation interfaces for general object manipulation," in *Proceedings of the 2017 ACM/IEEE international conference on human-robot interaction*, 2017, pp. 371–379.

[21] C. Brooks and D. Szafir, "Visualization of intended assistance for acceptance of shared control," in *2020 IEEE/RSJ International Conference on Intelligent Robots and Systems (IROS)*. IEEE, 2020, pp. 11 425–11 430.

[22] T. Uthayakumar, M. R. A. M. Rifa, and J. G. Samarawickrama, "Teleoperation of a robotic arm through tactile sensing, visual and haptic feedback," in *2020 5th International Conference on Control and Robotics Engineering (ICCRE)*. IEEE, 2020, pp. 63–67.

[23] N. Mavridis, G. Pierris, P. Gallina, Z. Papamitsiou, and U. Saad, "On the subjective difficulty of joystick-based robot arm teleoperation with auditory feedback," in *2015 IEEE 8th GCC Conference & Exhibition*. IEEE, 2015, pp. 1–6.

[24] R. H. Wang, A. Mihailidis, T. Dutta, and G. R. Fernie, "Usability testing of multimodal feedback interface and simulated collision-avoidance power wheelchair for long-term-care home residents with cognitive impairments." *Journal of Rehabilitation Research & Development*, vol. 48, no. 7, 2011.

[25] E. Cha, N. T. Fitter, Y. Kim, T. Fong, and M. J. Matarić, "Effects of robot sound on auditory localization in human-robot collaboration," in *Proceedings of the 2018 ACM/IEEE international conference on human-robot interaction*, 2018, pp. 434–442.

Simulating Safe Bite Transfer in Robot-Assisted Feeding with a Soft Head and Articulated Jaw

Yi Heng San[1,*], Vasanthamaran Ravichandram[1,*], J-Anne Yow[1,2,*], Sherwin Stephen Chan[1,*], Yifan Wang[1], Wei Tech Ang[1,2]
[*]These authors contributed equally

***Abstract*—Ensuring safe and comfortable bite transfer during robot-assisted feeding is challenging due to the close physical human-robot interaction required. This paper presents a novel approach to modeling physical human-robot interaction in a physics-based simulator (MuJoCo) using soft-body dynamics. We integrate a flexible head model with a rigid skeleton while accounting for internal dynamics, enabling the flexible model to be actuated by the skeleton. Incorporating realistic soft-skin contact dynamics in simulation allows for systematically evaluating bite transfer parameters, such as insertion depth and entry angle, and their impact on user safety and comfort. Our findings suggest that a straight-in-straight-out strategy minimizes forces and enhances user comfort in robot-assisted feeding, assuming a static head. This simulation-based approach offers a safer and more controlled alternative to real-world experimentation. Supplementary videos can be found at: https://tinyurl.com/224yh2kx.**

***Index Terms*—Robot-Assisted Feeding, Physical Human-Robot Interaction, Physically Assistive Devices, Human Factors and Human-in-the-loop, Simulation and Animation,**

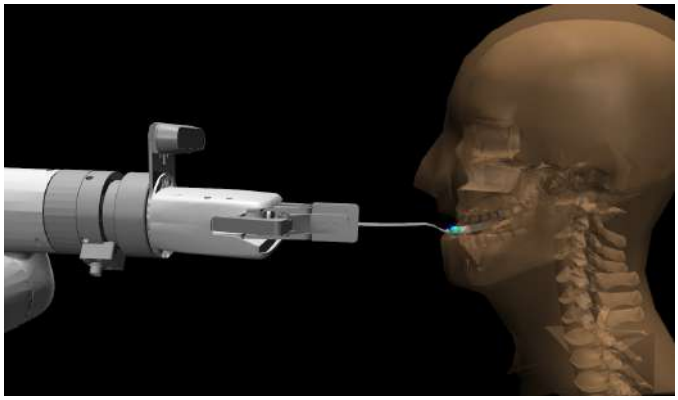


Fig. 1: Physical human-robot interaction simulation of bite transfer with contact forces between the spoon and the soft-body mouth shown by the blue and green spheres. The opacity of the head and skull is decreased to show the contact points.

I. Introduction

Robot-assisted feeding systems offer a promising solution for improving the quality of life of individuals requiring feeding assistance while also alleviating caregiver burden. However, implementing safe and effective bite transfer – the process of delivering food from a utensil into a user's mouth – presents unique challenges due to the close, physically interactive nature of the task.

Autonomous bite transfer has been proposed, with earlier works detecting the user's mouth pose and positioning the food in front of a care recipient's mouth [1], [2]. However, leaning forward for an outside-mouth bite transfer can be impossible or tiring for those with more severe upper body and neck mobility limitations, prompting recent works to study in-mouth bite transfer. To further enhance user comfort and safety, compliant controllers based on force feedback have been implemented, adjusting compliance during entry and exit phases [3] or classifying physical interactions using visual and haptic feedback to select a suitable controller [4]. Despite these advancements, current methods generally assume a fixed, pre-planned path and rely solely on force feedback to adapt to contact forces without adjusting bite transfer parameters such as insertion depth, exit angle, or exit depth.

Ensuring user safety is paramount in developing robot-assisted feeding systems, as direct physical contact risks excessive force, resulting in discomfort or even injury to sensitive areas like the mouth. Exploring different ways to perform bite transfer with real users is challenging due to ethical and safety concerns.

Human-in-the-Loop (HITL) simulation has been applied to assistive tasks that demand a high level of safety, such as assisted dressing [5] and exoskeleton control [6]. These simulations have proven valuable in enabling the development and evaluation of robotic controllers that involve physical Human-Robot Interaction (pHRI) and in some cases, facilitated the sim-to-real transfer of robotic controllers, particularly for complex pHRI tasks, such as learning and optimizing exoskeleton control [7]. However, most existing approaches rely on rigid-body skeletal [8], musculoskeletal [7], or primitive-shaped human models [9], which lack the ability to accurately model detailed physical interactions, particularly at the contact level. This limitation poses a significant challenge for tasks requiring precise contact modelling, such as robot-assisted feeding.

In robot-assisted feeding, particularly the bite transfer process, research in pHRI simulation remains sparse [10], [11].

The research was conducted at the Future Health Technologies at the Singapore-ETH Centre, which was established collaboratively between ETH Zurich and the National Research Foundation Singapore. This research is supported by the National Research Foundation Singapore (NRF) under its Campus for Research Excellence and Technological Enterprise (CREATE) programme.

[1]School of Mechanical and Aerospace Engineering, Nanyang Technological University Singapore
[2]Singapore-ETH Centre, Future Health Technologies Programme
Corresponding authors' e-mails: {sherwins001, janne001}@e.ntu.edu.sg

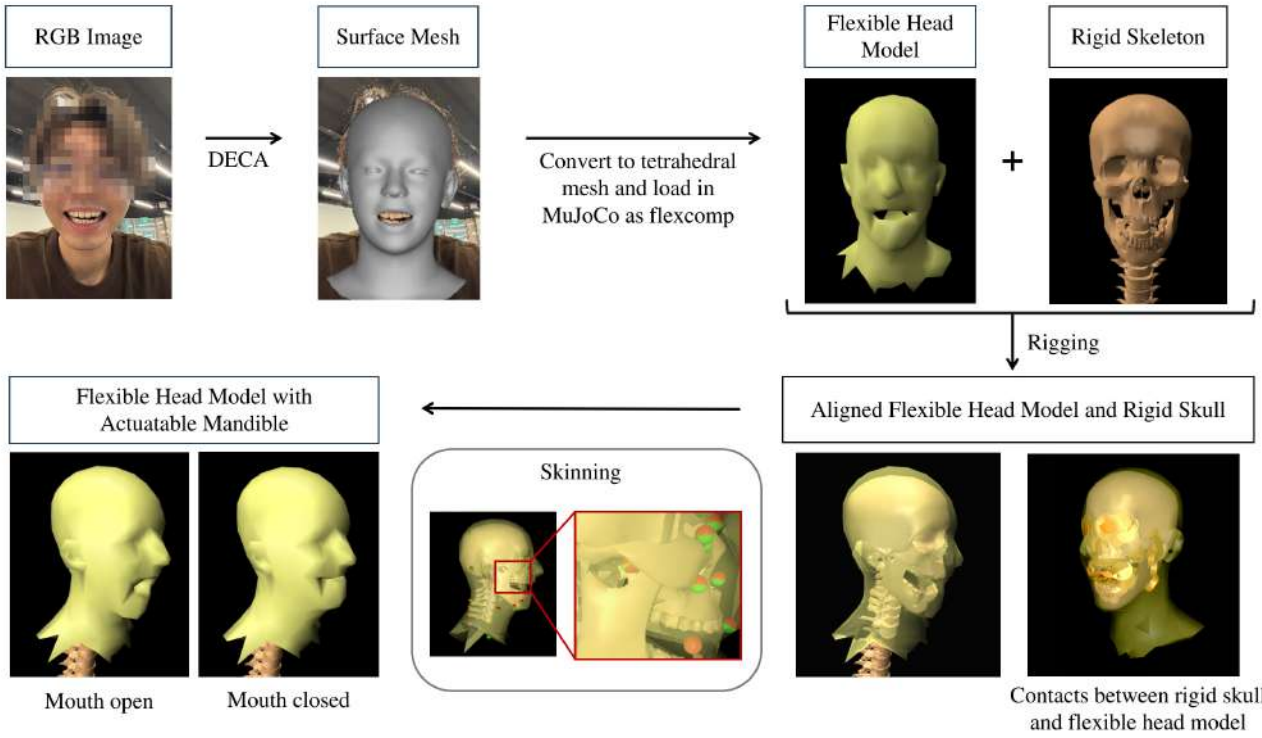


Fig. 2: Overview of our approach to model a head with soft-body dynamics. (Top) A flexible head model is generated from an RGB image through surface mesh reconstruction, tetrahedral meshing, and loading into MuJoCo as a flexible element. (Bottom) The flexible head model is combined with a rigid skeleton through rigging, and skinning is applied to bind the two. Contacts are detected and marked with yellow cylinders (bottom right), after which sites are created at the detected points, visualized using red and green balls (bottom center). Tendon elements then connect the sites to form a fully rigged and actuated head model. This setup enables realistic deformation, mandible actuation, and mouth movement simulations.

This gap is largely attributed to the absence of a high-quality face and mouth model capable of accurately representing the shape and motions involved in chewing and biting. To date, the only physics-based simulator attempting to integrate soft-body human modelling for assistive robotics is RCareWorld [11]. However, its human models are constrained to predefined configurations with fixed shape and mobility parameters, limiting personalization to individual users. While skinned biomechanical human models, such as those described in [12], have introduced deformable skin, they have largely overlooked the internal dynamics between the skin and the underlying skeleton in a physics-based simulation. Similarly, our previous approach [13], which manually rigged the skin and skeleton as a unified whole-body model using rigid `pin` elements, further highlighted these limitations. Although functional, this method introduced redundant contact forces during interactions, underscoring the need for a more sophisticated approach to model soft-tissue dynamics and natural interactions. These limitations highlight the need for a high-fidelity simulation framework capable of accurately modelling soft-body dynamics and human features, particularly the face and mouth, to enable detailed investigation of contact forces and motion dynamics in tasks such as robot-assisted feeding.

To address these gaps, we present a novel framework for simulating bite transfer using a soft-body human head model with an articulated mandible developed in MuJoCo [14]. This model enables the analysis of how variations in bite transfer parameters impact force distribution on the user, facilitating systematic experimentation without safety risks. By simulating these interactions, we aim to identify optimal bite transfer strategies that maximize user comfort by minimizing contact forces. Key contributions of this work include:

1) A method for creating a realistic, flexible human head model with a movable mandible from an RGB image, enabling the simulation of mouth opening and closing by controlling the joint of the rigid mandible.
2) Novel evaluation and analysis of bite transfer parameters to minimize contact forces and enhance user comfort.

These contributions provide a foundation for improving safety in robot-assisted feeding systems and modelling physical human-robot interactions more accurately.

II. Approach

To facilitate bite transfer parameter analysis in simulation, we developed a human head model in MuJoCo featuring soft-body contact dynamics. Using the `flexcomp` body element in MuJoCo, we constructed a volumetric, deformable head model that mimics the mechanical properties of human skin

and tissue. The head model was rigged with a rigid skull structure, enabling mandible actuation to simulate realistic mouth opening and closing motions. This section provides a detailed explanation of the human head model creation process.

A. Generation of Flexible Head Model

We take an RGB image of a human head and process it using DECA [15] to reconstruct a facial model, generating a rigid surface mesh of the head (Fig. 2). This surface mesh is then converted into a high-quality tetrahedral mesh using the method described in [16], which incrementally inserts triangles to create a volumetric mesh. The conversion to a tetrahedral mesh is necessary for compatibility with MuJoCo, which requires a volumetric representation of the mesh to create the necessary relationships across all vertices for soft-body dynamics. To improve computational efficiency, the mesh is simplified to produce a final model with 342 vertices.

To define the soft body properties in simulation, the `flexcomp` elasticity attributes in MuJoCo were utilized to represent the mechanical behaviour of deformable materials accurately. The parameters used – Young's modulus and Poisson's ratio – were selected based on a combination of literature review of human soft tissue material [17], [18] (Table I) and the empirical testing of the functional requirements of the model. We used a Young's Modulus of 5×10^4 and a Poisson Ratio of 0.4. To ensure realistic mass distribution, we assigned a total mass of 5 kg to the flexible head model, consistent with the plausible range of human head mass reported in the literature [19]. This mass was evenly distributed across all vertices of the flexible head, while the mass of the rigid skull was set to near zero to avoid redundancy and ensure that the flexible head accurately represents the primary source of soft tissue mass.

TABLE I: Material Properties of Human Soft Tissues

Tissue Type	Poisson Ratio	Young's Modulus/kPa
Connective Tissue	0.3	2.25×10^5 - 1.5×10^6
Muscle	0.3 - 0.493	39 - 164
Fat	0.13 - 0.5	18 - 24

1) Rigging the Head Model: To enable mouth opening and closing movements, we utilized a rigid-body head and neck model from OpenSim [20] and converted it to a MuJoCo model [21]. The rigid skull consists of two components – the upper skull and the mandible. We created a six-degree-of-freedom (DoF) joint between these two bodies to simulate realistic mandible movement. We manually align the position of the skull inside the flexible head model due to the differences in the initial orientation.

2) Skinning: Skinning refers to the process of binding the flexible head model to the rigid skull by associating regions of the head's surface with specific parts of the skull, ensuring that movements of the skull result in corresponding deformations of the skin, as seen in the mouth opening and closing in Fig. 2. To model the internal dynamics between the soft skin and the skull, we mimicked the natural anatomical attachment of soft tissues to the underlying skeletal structure. Ideally, the flexible head would be attached to underlying muscles; however, in the absence of detailed muscle models for the skull, the flexible head was directly attached to the skeleton. In this context, the `tendon` element in MuJoCo was employed to represent fascia and connective tissues, which exhibit viscoelastic properties. These properties facilitate the independent yet cohesive motion of the skin in response to movements of the mandible. The `tendon` was created according to assigned pairs of `site` attributes on both the skin and the skull. All interaction forces between the skin and the skull were transmitted exclusively through the defined `tendon` elements.

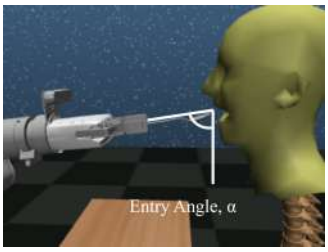
To determine the appropriate locations for the `tendon` elements, we analyzed the natural contact points between a rigid skull and a volumetric flexible head. After rigging the rigid skull and volumetric flexible head in MuJoCo, contact interactions between the surface of the skull and internal volume of the flexible head were identified. These contact points served as the primary indicators of potential locations where structural interactions between the skin and the skull should occur, ensuring stability during simulation runtime. Based on these contact points, the tendon elements were positioned by identifying the closest vertices of the soft head model to the contact points, effectively aligning the tendons with areas of natural contact.

With the detected set of contact points $C = \{c_1, c_2, \ldots, c_n\} \subset \mathbb{R}^3$ and the vertex set of soft body head model $V = \{v_1, v_2, \ldots, v_n\} \subset \mathbb{R}^3$, a linear search algorithm was applied to identify the subset of vertices $V_{closest} \subseteq V$ nearest to each contact point. To ensure the uniqueness of `tendon` element in each interaction area, the algorithm built an injective mapping $M : C \to V_{closest}$ by iterating through each contact point and calculating the Euclidean distance between that point and each vertex, represented as following:

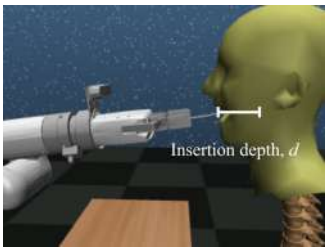
$$M(c_i) = \arg \min_{v_j \in V \setminus V_{\text{closest}}} \|c_i - v_j\|_2, \quad \text{where } c_i \in C \qquad (1)$$

For each $v_k \in V_{closest}$, a pair of `site` attributes were created at the coordinates of v_k and assigned to both the rigid skull and flexible head. The `tendon` elements were used to link each pair of corresponding `site` attributes. These `tendon` elements were configured with adjustable viscoelastic properties and allowable stretching ranges, which were empirically determined through testing and refinement to ensure realistic behavior. Once the `tendon` elements were activated, default contact interactions between the rigid skull and flexible head were disabled. This ensured that the motion of the flexible head was driven exclusively by the `tendon` connections, with all interaction forces transmitted solely through these elements. By relying on tendon-driven dynamics, the head model exhibited predictable and controlled movements, entirely driven by the motion of the mandible.

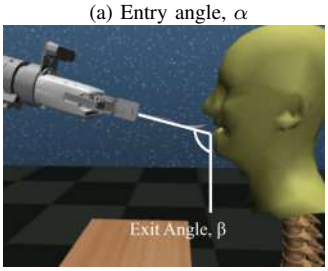
The developed skinning method is novel in that it addresses the internal dynamics between the flexible head and skull, enabling realistic motion actuation and force transmission. In



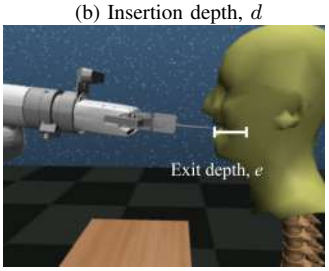
(a) Entry angle, α



(b) Insertion depth, d



(c) Exit angle, β



(d) Exit depth, e

Fig. 3: Bite transfer parameters modified in our experiments

our application, this integration enables precise control of the head model, facilitating detailed simulations of bite transfer in robot-assisted feeding systems. We believe that this method has the potential to be extended to other body parts in future work, enabling applications beyond head modeling, such as full-body modeling and biomechanical interaction studies, to support a broader range of research and simulation contexts.

B. Modifying In-Mouth Bite Transfer Trajectories

To analyse the physical human-robot interaction forces exerted on the user by a spoon during bite transfer, we defined bite transfer as a parameterized trajectory, as shown in Fig. 3. In general, bite transfer can be divided into 2 phases, the entry phase and exit phase [3]. We assume that bite transfer starts at a fixed initial pose p, defined by a fixed distance of $50mm$ away from the mouth pose. The spoon enters the user's mouth with an insertion depth d (Fig. 3b) and entry angle α (Fig. 3a) during the entry phase. After the user closes the mouth and a bite is detected, the spoon exits the user's mouth with an exit depth e (Fig. 3d) and exit angle β (Fig. 3c).

These parameters are then systematically adjusted within our simulation environment to observe their effects on contact forces exerted during bite transfer.

III. Experiments and Results

We conducted experiments in simulation to identify the optimal set of bite transfer parameters that maximise user comfort during bite transfer, defined here as minimising contact forces applied during the interaction.

A. Experiment Setup

We set up a simulated environment in MuJoCo [14] with the xArm-6 robotic arm (UFactory) grasping a spoon and the head model (Fig 1). We selected this robotic arm as we have access to the physical device for future experimental validation. However, our approach is not limited to this specific robot and can be adapted to other robotic arms. The starting pose of the robot arm is fixed throughout the experiment for consistency. After the spoon is inserted into the user's mouth in the entry phase, we actuated the mandible joint of the head model to simulate mouth closing. We assume the rest of the human body remains static, reflecting scenarios where patients have limited head mobility. This assumption simplifies the analysis and allows us to focus on the influence of bite transfer parameters on bite transfer interaction forces.

TABLE II: Bite Transfer Parameter Ranges and Increments

Phase	Parameter	Range	Increment
Entry	Entry Angle (α)	80° to 110°	10°
	Insertion Depth (d)	50 mm to 100 mm	10 mm
Exit	Exit Angle (β)	80° to 120°	10°
	Exit Depth (e)	0 mm to 40 mm	10 mm

To evaluate the impact of different bite transfer parameters, we measured the contact forces applied during the bite transfer phase. As multiple contact points could exist per time step, we compute the average force exerted per time step, denoted as f_t. The key metrics considered were:

- **Peak contact force**: the maximum average force f_t^{max} recorded during the interaction
- **Total contact force**: the summation of the average forces $\sum f_t$ applied throughout the bite transfer

The best parameters should minimize both peak and total contact forces. Peak force affects instantaneous user comfort, as high forces in a short duration can cause discomfort or injury. Total force, the cumulative force over time, impacts overall comfort as prolonged low-level forces that can still cause discomfort if sustained for extended periods.

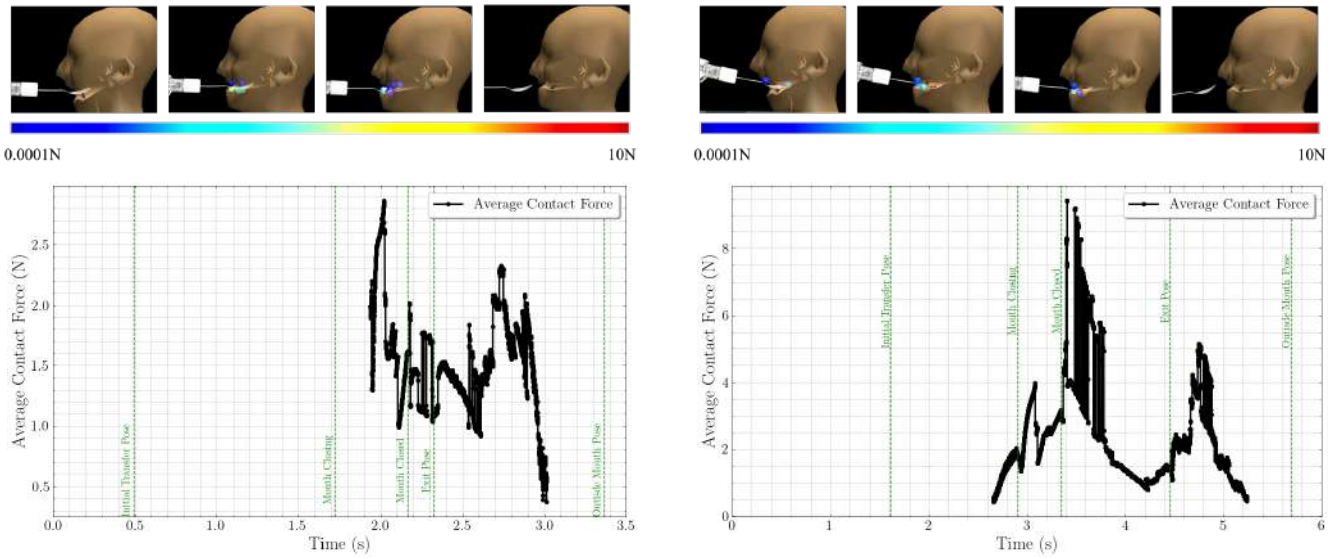
We performed a series of trials to analyze bite transfer parameters, as detailed in Fig. 3. The parameters were first varied during the entry phase to identify the optimal settings, followed by similar trials for the exit phase. Table II summarises the specific parameter ranges and increments. These ranges were set based on human eating behaviour and the geometry of the spoon, where the spoon bowl length was 60mm.

B. Results and Analysis

The results of our experiments are shown in Figures 5 and 6.

1) Entry Phase: The simulation results show that both total and peak contact forces generally increase with greater insertion depths at entry angles of 100° and 110°. This is due to the larger contact surface between the spoon and the inside of the mouth as depth increases. The entry angle of 80° exhibits higher total and peak contact forces, especially at deeper depths, due to the tip of the spoon contacting the mouth more.

The lowest total contact force of 993.99N occurs at $\alpha = 90°$ and $d = 70$mm. Although the lowest peak contact force of 2.08N occurs at $\alpha = 110°$ and $d = 50$mm, the peak force of $\alpha = 90°$ and $d = 70$mm is only slightly higher at 2.89N.



(a) Bite transfer with optimal parameters ($\alpha = 90°$, $d = 70$mm, $\beta = 90°$, $e = 10$ mm)

(b) Bite transfer with suboptimal parameters ($\alpha = 100°$, $d = 80$mm, $\beta = 80°$, $e = 40$mm)

Fig. 4: Bite transfer in simulation: The top row shows screen captures of the bite transfer process, with contact forces visualized as coloured spheres, showing increased contacts in (b). The bottom row shows the corresponding contact forces over time. Note that the y-axis scales are different for clarity.

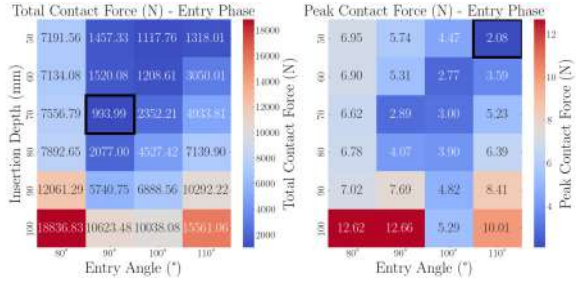


Fig. 5: Force Analysis Results – Entry Phase

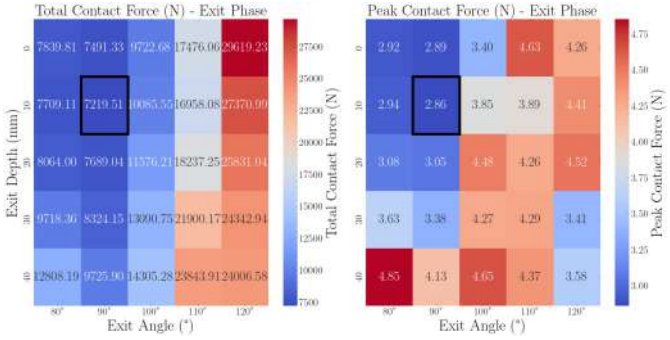


Fig. 6: Force Analysis Results – Exit Phase

This marginal increase in peak contact force of less than 1N is unlikely to be perceptible to a human. This minimal difference in peak contact force, combined with the substantially lower total contact force, makes $\alpha = 90°$ and $d = 70$mm the more optimal parameter set. The optimal entry angle suggests the spoon should be perpendicular to the mouth, while the optimal insertion depth should be slightly longer than the spoon bowl to minimize contact forces.

As shown in Fig. 4, the peak contact force for the entry phase occurs when the mouth is closing, which aligns with the expected increase in forces when the mouth interacts with the spoon.

2) Exit Phase: For the exit phase, the results indicate a general trend where the peak contact force increases as the exit depth e increases. Additionally, exit angles closer to 90° show lower total and peak contact forces. As the exit angle deviates further from 90°, the transition from the exit depth pose to the exit angle pose results in more rotation within the mouth, leading to increased forces.

Based on the results, the parameter combination that minimizes the total contact force with the mouth and maximises the comfort of the user is an entry angle $\alpha = 90°$, an insertion depth $d = 70$mm, an exit angle $\beta = 90°$ and an exit depth $e = 10$mm. Screen captures of the bite transfer process for both the optimal set of parameters ($\alpha = 90°$, $d = 70$mm, $\beta = 90°$, $e = 10$ mm) and a random set of suboptimal parameters ($\alpha = 100°$, $d = 80$mm, $\beta = 80°$, $e = 40$mm) are shown in Fig. 4 to better visualise the difference in contact forces for each stage of the bite transfer process. For the optimal set of bite transfer parameters, the peak contact force occurs during the entry phase when the mouth is closing, while the peak contact force occurs during the exit phase for suboptimal parameters.

Thus, from our experiments, we observe that having a simple bite transfer process of "straight-in, straight-out" given the same entry α and exit angle β of 90° minimises both the total and peak contact forces, and is most comfortable for the

user, with the assumption that the head remains stationary.

IV. Conclusion and Future Work

This paper presents a novel approach for modeling physical human-robot interaction in simulation, addressing a gap in assistive robotics. By leveraging MuJoCo's accurate contact dynamics, we developed a soft-body human head model with an articulated mandible. Our integration of the flexible head model with a rigid skull captures the internal dynamics between the skin and the underlying skeleton, enabling realistic motion actuation and force transmission.

Using this head model that accounts for soft-body contacts, we could capture detailed contact interactions between a spoon and the mouth during bite transfer. This capability enables systematic evaluation of bite transfer parameters, offering valuable insights into how variations in bite transfer parameters like insertion depth, entry angle, exit depth, and exit angle influence contact forces. These insights are important in improving user safety and comfort in robot-assisted feeding.

Nevertheless, the current approach assumes a static head during bite transfer, which overlooks the natural movements of the head in response to the spoon. Furthermore, the current model lacks a detailed oral cavity, tongue and lip actuation, which limits the realism of the simulated interactions. Future work will incorporate dynamic head and neck movements, and validate the simulation forces with real-world data.

References

[1] D. Park, Y. K. Kim, Z. M. Erickson, and C. C. Kemp, "Towards assistive feeding with a general-purpose mobile manipulator," *arXiv preprint arXiv:1605.07996*, 2016.

[2] D. Gallenberger, T. Bhattacharjee, Y. Kim, and S. S. Srinivasa, "Transfer depends on acquisition: Analyzing manipulation strategies for robotic feeding," in *2019 14th ACM/IEEE International Conference on Human-Robot Interaction (HRI)*. IEEE, 2019, pp. 267–276.

[3] L. Shaikewitz, Y. Wu, S. Belkhale, J. Grannen, P. Sundaresan, and D. Sadigh, "In-mouth robotic bite transfer with visual and haptic sensing," in *2023 IEEE International Conference on Robotics and Automation (ICRA)*. IEEE, 2023, pp. 9885–9895.

[4] R. K. Jenamani, D. Stabile, Z. Liu, A. Anwar, K. Dimitropoulou, and T. Bhattacharjee, "Feel the bite: Robot-assisted inside-mouth bite transfer using robust mouth perception and physical interaction-aware control," in *Proceedings of the 2024 ACM/IEEE International Conference on Human-Robot Interaction*, 2024, pp. 313–322.

[5] A. Kapusta, Z. Erickson, H. M. Clever, W. Yu, C. K. Liu, G. Turk, and C. C. Kemp, "Personalized collaborative plans for robot-assisted dressing via optimization and simulation," *Autonomous Robots*, vol. 43, pp. 2183–2207, 2019.

[6] V. C. Kumar, S. Ha, G. Sawicki, and C. K. Liu, "Learning a control policy for fall prevention on an assistive walking device," in *2020 IEEE International Conference on Robotics and Automation (ICRA)*. IEEE, 2020, pp. 4833–4840.

[7] S. Luo, M. Jiang, S. Zhang, J. Zhu, S. Yu, I. Dominguez Silva, T. Wang, E. Rouse, B. Zhou, H. Yuk *et al.*, "Experiment-free exoskeleton assistance via learning in simulation," *Nature*, vol. 630, no. 8016, pp. 353–359, 2024.

[8] S. S. Chan, M. Lei, H. Johan, and W. T. Ang, "Creation and evaluation of human models with varied walking ability from motion capture for assistive device development," in *2023 International Conference on Rehabilitation Robotics (ICORR)*. IEEE, 2023, pp. 1–6.

[9] A. Clegg, Z. Erickson, P. Grady, G. Turk, C. C. Kemp, and C. K. Liu, "Learning to collaborate from simulation for robot-assisted dressing," *IEEE Robotics and Automation Letters*, vol. 5, no. 2, pp. 2746–2753, 2020.

[10] Z. Erickson, V. Gangaram, A. Kapusta, C. K. Liu, and C. C. Kemp, "Assistive gym: A physics simulation framework for assistive robotics," in *2020 IEEE International Conference on Robotics and Automation (ICRA)*. IEEE, 2020, pp. 10 169–10 176.

[11] R. Ye, W. Xu, H. Fu, R. K. Jenamani, V. Nguyen, C. Lu, K. Dimitropoulou, and T. Bhattacharjee, "Rcare world: A human-centric simulation world for caregiving robots," in *2022 IEEE/RSJ International Conference on Intelligent Robots and Systems (IROS)*. IEEE, 2022, pp. 33–40.

[12] M. Keller, K. Werling, S. Shin, S. Delp, S. Pujades, C. K. Liu, and M. J. Black, "From skin to skeleton: Towards biomechanically accurate 3d digital humans," *ACM Transactions on Graphics (TOG)*, vol. 42, no. 6, pp. 1–12, 2023.

[13] K. Y. Loke, S. S. Chan, M. Lei, H. Johan, B. Zuo, and W. T. Ang, "Personalised 3d human digital twin with soft-body feet for walking simulation," in *2024 International Conference on Social Robotics (ICSR)*. IEEE, 2024.

[14] E. Todorov, T. Erez, and Y. Tassa, "Mujoco: A physics engine for model-based control," in *2012 IEEE/RSJ international conference on intelligent robots and systems*. IEEE, 2012, pp. 5026–5033.

[15] Y. Feng, H. Feng, M. J. Black, and T. Bolkart, "Learning an animatable detailed 3D face model from in-the-wild images," vol. 40, no. 8, 2021. [Online]. Available: https://doi.org/10.1145/3450626.3459936

[16] Y. Hu, T. Schneider, B. Wang, D. Zorin, and D. Panozzo, "Fast tetrahedral meshing in the wild," 2020.

[17] G. Singh and A. Chanda, "Mechanical properties of whole-body soft human tissues: a review," *Biomedical Materials*, vol. 16, no. 6, p. 062004, oct 2021. [Online]. Available: https://dx.doi.org/10.1088/1748-605X/ac2b7a

[18] N. Arnold, J. Scott, and T. R. Bush, "A review of the characterizations of soft tissues used in human body modeling: Scope, limitations, and the path forward," *Journal of Tissue Viability*, vol. 32, no. 2, pp. 286–304, 2023. [Online]. Available: https://www.sciencedirect.com/science/article/pii/S0965206X23000141

[19] N. Yoganandan, F. A. Pintar, J. Zhang, and J. L. Baisden, "Physical properties of the human head: mass, center of gravity and moment of inertia," *Journal of biomechanics*, vol. 42, no. 9, pp. 1177–1192, 2009.

[20] J. D. Mortensen, A. N. Vasavada, and A. S. Merryweather, "The inclusion of hyoid muscles improve moment generating capacity and dynamic simulations in musculoskeletal models of the head and neck," *PloS one*, vol. 13, no. 6, p. e0199912, 2018.

[21] A. Ikkala and P. Hämäläinen, "Converting biomechanical models from opensim to mujoco," in *Converging Clinical and Engineering Research on Neurorehabilitation IV: Proceedings of the 5th International Conference on Neurorehabilitation (ICNR2020), October 13–16, 2020*. Springer, 2022, pp. 277–281.

Spatial Robust Whole-Body Dynamic Trajectory Optimization of a Lower-Limb Exoskeleton

Shahriar Sheikh Aboumasoudi[1,2], Ander Vallinas[1], Sjors de Bruin[1], Hakan Köroğlu[2], Herman van der Kooij[1] and Arvid Keemink[1]

***Abstract*—The goal of this paper is to design spatial (3D) robust reference trajectories for lower limb exoskeletons through optimization. Robustness is defined as the magnitude of the smallest force applied at the Center of Mass that cannot be rejected without violating joint torque or ground reaction force bounds. A larger robustness margin in the reference trajectory increases the capability of the controller to reject perturbations. A trajectory optimization problem was augmented by adding the maximization of this robustness metric to it. The augmented trajectory optimization is then employed to design dynamic trajectories for three different tasks. We demonstrated that our method increases the robustness metric value by comparing the results from the proposed method with a nominal trajectory optimization that does not take robustness into account. Moreover, the designed trajectories were implemented on a lower limb exoskeleton with a paraplegic user to show the feasibility of the proposed method. The user managed successfully to walk on level ground, perform side-stepping, and ascend stairs.**

***Index Terms*—Robust trajectory optimization, direct collocation, whole-body dynamics, lower-limb exoskeleton**

I. Introduction

According to the World Health Organization (WHO), in the year 2021, there were more than 15.4 million individuals with Spinal Cord Injury (SCI), afflicted with partial or complete loss of motor functions [1]. Lower limb exoskeletons (LLEs) have emerged as a technological solution to help these individuals regain their ability to walk. Furthermore, it has been shown [2] that the repeated use of LLEs can mitigate secondary health complications related to SCI.

In the past few years, several commercial LLEs [3], [4], [5] and research prototypes [6], [7] have been developed. All these devices need reference trajectories to drive the individuals wearing them. In general, the methods employed to design the reference trajectories belong to one of the following design strategies, namely manual design, kinematic and reduced dynamic model optimization, Central Pattern Generator-based (CPG) method, and Hybrid Zero Dynamics (HZD), which will be explained below.

Manual design of reference trajectories involves adapting the joint angles of healthy humans to an exoskeleton. An example of this strategy is [8] where the authors used multiple prerecorded healthy gaits in the sagittal plane and a look-up table to transition between different trajectories. This strategy's inflexibility to changes in motion parameters such as speed, step length, etc. limits its widespread adoption.

With the advent of highly efficient and fast solvers, kinematic optimization strategy has gained popularity among the robotics community. Giannattasio et al. [9] considered four n-degree polynomials, each corresponding to one phase of gait for the joints in the sagittal plane, and solved a minimum-jerk optimization to find the polynomials of the swing phase. Other polynomials were designed to enforce a smooth transition between gait phases and kinematic constraints, such as maintaining contact during the double support phase. Mohammad et al. [10] proposed a three-stage gait generator that designs reference trajectories for the Center of Mass (CoM), the support leg, and the swing leg in the sagittal plane. Their goal is to minimize the CoM acceleration, keeping the Center of Pressure (CoP) close to the support ankle and minimizing the joint torque of the swing leg. Griffin et al. [11] designed the 2D swing foot trajectory of their exoskeleton in the cartesian space with the goal of minimizing jerk and then solved an inverse kinematic problem to obtain the reference trajectories for the hip and knee joint. However, they designed the reference trajectories in joint space for the support leg by keeping the knee straight. Zhang et al. [12] designed reference trajectories in the task space for an exoskeleton to ascend stairs and proposed a method to avoid singular configurations when solving the inverse kinematic problem.

The major shortcoming of the kinematic and simple dynamic model optimization is that it does not consider the full dynamics of the human-robot system, which could result in reference trajectories that are not dynamically feasible. An example of this is a reference trajectory that is kinematically compatible with the robot's mechanical structure but requires joint torques that are beyond the capacity of the actuators. Also, the designed trajectories in most cases are restricted to the sagittal plane.

A CPG is a biologically-inspired dynamic network that can generate patterns of rhythmic activity from non-oscillatory inputs. Sharifi et al. [13] took the Fourier transform of healthy gait and fed it to a system of adaptive CPGs that would generate the desired joint position trajectories. Additionally, they designed an observer to estimate the human-robot interaction torque that influences the desired trajectories further. Schrade

This work was financed by the Dutch Ministry of Education, Culture, and Science as part of the "Sectorplan Techniek" program.

[1]Department of Biomechanical Engineering, University of Twente, Enschede, The Netherlands

[2]Department of Mechanics of Solids, Surfaces & Systems, University of Twente, Enschede, The Netherlands

Corresponding author: Shahriar Sheikh Aboumasoudi
(e-mail:s.s.sheikhaboumasoudi@utwente.nl)

et al. [14] employed CPGs to design joint torque references for the sagittal model of an exoskeleton and to modulate its knee stiffness. Fang et al. [15] developed a lower limb exoskeleton with four Degrees of Freedom (DoFs), namely two hip and two knee joints, controlled by CPGs. They found the optimal parameters of the CPG by using a genetic algorithm and setting the fitness function as the error between the raw gait data and the output of the CPG. Despite the success in generating periodic motion using CPGs, none of the studies mentioned, conducted experiments with paraplegic patients.

Another powerful tool for trajectory generation in bipedal robots is HZD [16]. The key idea of this method is to introduce some virtual constraints that encode the desired behavior of the dynamical system and perform a feedback linearization to find the control law that ensures the satisfaction of the constraints. Furthermore, through an optimization routine, the system becomes invariant to impacts, meaning that the virtual constraints will be satisfied even when the bipedal robot makes and breaks contact with the environment. This method was used to enable a paraplegic user to walk in an Atalante X exoskeleton (Wandercraft, France) without using crutches, which is a remarkable achievement [17]. However, the feasibility of this method for lighter and simpler exoskeletons has not been explored.

Trajectory Optimization (TO) is a widely adopted method to generate trajectories in humanoids and quadrupeds [18], [19], [20]. TO is an optimization framework that can automate the process of trajectory generation while taking into account the dynamics of the system, as well as its kinematic and mechanical constraints.

Even though TO is an extremely potent trajectory design strategy, nominal TO does not address robustness, meaning that external perturbation forces on the system are not explicitly addressed. By increasing the robustness of the designed reference trajectories, the robot can recover from greater external perturbations forces. In this work, after defining robustness based on the work of Ferrolho et al. [21], we will incorporate it into TO. We will then utilize the resultant robust TO to design 3D reference trajectories for an LLE and verify the feasibility of the designed trajectories by conducting an experiment with a paraplegic user.

In short, the contributions of this work are twofold.

- Introducing a robustness condition into TO similar to [21] but in a less restrictive fashion and with the goal of improving balance robustness and using the augmented TO to design spatial (3D) trajectories to perform different tasks with an LLE.
- Implementing the designed spatial trajectories on an LLE with a paraplegic user to show their feasibility.

The paper is structured as follows. The theoretical background is explained in Sec. II, while Sec. III details the definition of robustness and how it can be incorporated into TO. In Sec. IV the implementation of the method is described. The results of the experiment are presented in Sec. V and a discussion of the results is given in Sec. VI.

II. Background

This section summarizes the dynamical model of a legged robot and TO as a method to plan its motion.

A. Dynamical Model

The dynamical equation that governs the behavior of a legged robot is

$$M(q)\dot{v} + h(q,v) = Su + J_\lambda^T(q)\lambda, \tag{1}$$

where $q \in \mathbb{R}^{n_q} \times SE(3)$ denotes the generalized position coordinates with n_q being the number of joints, v, $\dot{v} \in \mathbb{R}^{n_v}$ denote the generalized velocity and acceleration respectively, with n_v being the dimension of the generalized velocity. Matrix $M(q) \in \mathbb{R}^{n_v \times n_v}$ represents inertia, $h(q,v) \in \mathbb{R}^{n_v}$ shows the effect of Coriolis, centrifugal, and gravitational forces. Vector $u \in \mathbb{R}^{n_a}$ is the stack of joint torques with n_a being the number of actuated joints, $S \in \mathbb{R}^{n_v \times n_a}$ is the actuation matrix, $\lambda \in \mathbb{R}^{3n_c}$ is the vector of Ground Reaction Forces (GRFs) at n_c contact points and $J_\lambda(q) \in \mathbb{R}^{3n_c \times n_v}$ is the aggregated analytic Jacobian of the contact points.

B. Trajectory Optimization

TO is a framework for designing trajectories for a dynamic system to reach a desired final state from an initial state in a way that optimizes a certain objective while respecting a set of constraints. In this work, the continuous nonlinear TO problem is transcribed using the direct collocation method, where a series of time instants, called collocation points, are defined, and a set of optimization variables is assigned to each collocation point. Furthermore, the constraints and the objective function are discretized as well and are only evaluated at the collocation points. This way, the original time-continuous TO can be transformed into a nonlinear optimization problem, whose formulation is as follows:

$$\min_{Q,V,U,\Lambda} \sum_{k=0}^{N-1} \mathcal{L}_{n,k}\Delta t, \tag{2a}$$

$$\text{where } \mathcal{L}_{n,k} = \|u_k\|^2_{W_u} + \|\lambda_k\|^2_{W_\lambda} + \|u_{k+1} - u_k\|^2_{W_{\dot{u}}} + \|v_{k+1} - v_k\|^2_{W_{\dot{v}}} + \|\lambda_{k+1} - \lambda_k\|^2_{W_{\dot{\lambda}}}, \tag{2b}$$

such that

$$\begin{bmatrix} q_0^T & v_0^T & q_N^T & v_N^T \end{bmatrix}^T = \begin{bmatrix} q_{\text{ini}}^T & v_{\text{ini}}^T & q_{\text{fin}}^T & v_{\text{fin}}^T \end{bmatrix}^T, \tag{2c}$$

and for $i = 0, \ldots, N-1$:

$$M(q_i)\frac{(v_{i+1} - v_i)}{\Delta t} = -h(q_i, v_i) + Su_i + J_\lambda^T(q_i)\lambda_i, \tag{2d}$$

$$q_{i+1} - q_i - \Delta t B_{i+1} v_{i+1} = 0, \tag{2e}$$

and for $i = 0, \ldots, N$:

$$A_u u_i \leq b_u, \tag{2f}$$

$$A_\lambda D_j \lambda_i \leq b_\lambda \qquad \text{if } i \in \mathcal{C}_j, j = 1, \ldots, n_c, \tag{2g}$$

$$E_j J_\lambda(q_i) v_i = 0 \qquad \text{if } i \in \mathcal{C}_j, j = 1, \ldots, n_c, \tag{2h}$$

$$D_j \lambda_i = 0 \qquad \text{if } i \notin \mathcal{C}_j, j = 1, \ldots, n_c. \tag{2i}$$

In the above formulation, $\|.\|^2_{W_\star} = (\cdot)^T W (\cdot)$ and N is the total number of collocation points. Vectors q_i, v_i, u_i, and

λ_i represent the joint position, joint velocity, control input, and GRF respectively at time instant i, with Q, V, U, and Λ being the stacked vectors of these variables. Constraint (2c) enforces the initial and final desired configuration where q_{ini} and v_{ini} denote the initial generalized position and velocity respectively and q_{fin} and v_{fin} represent the desired final position and velocity respectively. Equations (2d) and (2e) show semi-implicit Euler integration of the dynamics, where Δt is the time step. We use quaternions to represent the spatial rotation of the floating base. Matrix $B_{i+1} \in \mathbb{R}^{(n_q+7)\times n_v}$ maps the generalized velocity to the rate of change of the generalized position that allows us to relate the rotational velocity to the rate of change of quaternions. Matrix A_λ and vector b_λ encode the constraints on the GRFs including the friction pyramid, which is an inner approximation of the Coulomb friction cone. Matrix $D_j \in \mathbb{R}^{3n_c\times 3n_c}$ selects the GRF components associated with the contact point j. Matrix A_u and vector b_u describe the bounds on the control input. Set $\mathcal{C}_j$ contains all the time steps that contact point j is in contact with the environment and n_c is the total number of contact points. When the contact point j is in contact, its velocity is set to zero through enforcing (2h). Matrix $E_j \in \mathbb{R}^{3\times 3n_c}$ is another selection matrix that selects those rows in the analytical Jacobian J_λ that are associated with the contact point j.

III. Proposed Method

Although TO is a powerful tool for motion planning of a dynamic system given its capability to take account of the system's dynamic and kinematic constraints, there is always this possibility that the designed trajectories only satisfy the constraints marginally. This means that a slight change in the environment or a mismatch between the robot and the model could make tracking the designed trajectory infeasible since one or more of the constraints might need to be violated to that end. To prevent such a violation and increase the margin of robustness against the model mismatch, some additional conditions can be incorporated in the TO formulation that will keep the designed trajectories as far away from the bounds as possible, especially the control input and GRF bounds.

Dai et al. [22] improved the robustness of reference trajectories against ground height uncertainty by minimizing the cost-to-go associated with the states in case of an untimely impact. Tucker et al. [23] designed robust reference trajectories for an exoskeleton utilizing discrete-time barrier functions to find the largest forward invariant set associated with a nominal limit cycle. In the present work, we will explicitly improve the robustness of the designed trajectories with respect to perturbation forces.

The definition of robustness employed in this work is a modified version of what is used in [21] and the notion of Smallest Unrejectable Force (SUF). In short, the idea is to find a solution (a control input sequence along with the associated state trajectories and GRFs) in the feasible domain of the variable space, that has the longest distance (in the Euclidean sense) from all the control input and GRF bounds. The equivalent mathematical representation of this idea is finding the largest inscribed Chebyshev ball within the feasible region by maximizing its radius. For further details, the reader is referred to [21].

By maximizing the SUF, the robot can withstand stronger perturbation forces without experiencing any change in its DoF's accelerations. We further developed this idea by restricting this requirement only to the robot's center of mass (CoM) and not all of its DoFs. This allows for a change in other joints' accelerations as long as the CoM's acceleration remains unchanged, which is less restrictive than the original method and still prevents movements of the CoM that would bring it to the edge of the base of support.

Consider the whole-body dynamics in (1) and the centroidal dynamics

$$A_G(q)\dot{v} + \dot{A}_G(q,v)v = w_g + J_{G,\lambda}^T(q)\lambda, \tag{3}$$

where $A_G(q) \in \mathbb{R}^{6\times n_v}$ represents the Centroidal Momentum Matrix (CMM) [24], $w_g \in \mathbb{R}^6$ is the gravitational wrench and $J_{G,\lambda}^T(q) \in \mathbb{R}^{6\times 3n_c}$ is the Jacobian transpose that maps the contact forces to the net force and moment on/around the CoM. If a perturbation force f_c at the CoM is applied to the system, a change in the accelerations, GRFs, and actuation appears in (1) and (3) with respect to no force being applied, giving

$$M(\dot{v}+\delta\dot{v}) + h = S(u+\delta u) + J_\lambda^T(\lambda+\delta\lambda) + J_c^T f_c, \tag{4}$$

$$A_G(\dot{v}+\delta\dot{v}) + \dot{A}_G v = w_g + J_{G,\lambda}^T(\lambda+\delta\lambda) + Rf_c, \tag{5}$$

where dependencies on q and v have been dropped for readability. In (4) and (5), terms with δ represent a change in the relevant quantity, f_c is the 3D perturbation force applied at the CoM, the matrix $R = \begin{bmatrix}0_{3\times 3} & I_3\end{bmatrix}^T$, and $J_c \in \mathbb{R}^{3\times n_v}$ is the Jacobian that maps differential CoM motion to differential generalized coordinate motions. It should be noted that the perturbed dynamics in (4) and (5) describe the dynamics of the system at the time instant the perturbation force is applied at the CoM. So there is a variation on the acceleration level but not on the velocity or position level. We desire no variation in the centroidal acceleration, which translates to having $A_G\delta\dot{v}$ equal to zero. By enforcing this requirement and subtracting (4) and (5) from (3) and (1) respectively, we arrive at the following system of equations:

$$\begin{bmatrix} A_G & 0 & 0 \\ M & -S & -J_\lambda^T \end{bmatrix} \begin{bmatrix} \delta\dot{v} \\ \delta u \\ \delta\lambda \end{bmatrix} = \begin{bmatrix} 0_{6\times 3} \\ J_c^T \end{bmatrix} f_c. \tag{6}$$

The underlying assumption implied by setting the change in the centroidal acceleration to zero is that there is an ideal controller that can react instantaneously to the perturbation; hence, we do not see the effect of disturbance on the velocity and position level. Even though such a controller might not be realizable perfectly in practice, reference trajectories generated in a way to respect (6) would possess an inherent robustness property. Designing a controller whose output resembles that of the ideal controller as closely as possible is outside the scope of this work.

To relate the change in the variables to the perturbation, we can write the perturbation force as $f_c = \xi\rho$ where the unit-length vector $\xi = f_c/\|f_c\|$ represents the direction and the scalar $\rho = \|f_c\|$ denotes the magnitude. Furthermore, we introduce gain matrices $K_a \in \mathbb{R}^{n_v\times 3}$, $K_\lambda \in \mathbb{R}^{3n_c\times 3}$, and $K_u \in \mathbb{R}^{n_a\times 3}$ that map the normalized perturbation force to acceleration, GRF, and control torque spaces respectively as follows:

$$\delta\dot{v} = K_a\xi, \tag{7a}$$
$$\delta u = K_u\xi. \tag{7b}$$
$$\delta\lambda = K_\lambda\xi, \tag{7c}$$

Substituting (7a)-(7c) in (6) results in the following equations:

$$A_G K_a = 0, \tag{8a}$$
$$SK_u + J_\lambda^T K_\lambda + J_c^T\rho - MK_a = 0. \tag{8b}$$

To add the robustness condition to TO, the formulation introduced in (2) needs to be augmented in the following way:

$$\min_Z \sum_{k=0}^{N-1} (\mathcal{L}_{n,k} - W_\rho\rho_k)\Delta t, \tag{9a}$$
such that for $i = 0,\dots,N-1$:
Initial and final configuration (2c), (9b)
Integration of the dynamics (2d), (2e), (9c)
and for $i = 0,\dots,N$:
$$A_{G,i}K_{a,i} = 0, \tag{9d}$$
$$SK_{u,i} + J_{\lambda,i}^T K_{\lambda,i} + J_{c,i}^T\rho_i - M_i K_{a,i} = 0, \tag{9e}$$
$$A_u u_i + \|A_u K_{u,i}\| \le b_u, \tag{9f}$$
$$A_\lambda D_j\lambda_i + \|A_\lambda D_j K_{\lambda,i}\| \le b_\lambda, \text{ if } i\in\mathcal{C}_j, j=1,\dots,n_c, \tag{9g}$$
Stationary contact point (2h), (9h)
Zero GRF for swinging contact point (2i), (9i)

where $Z = Z_n \cup \{K_{a,0}, K_{\lambda,0}, \rho_0, \dots, K_{a,N}, K_{\lambda,N}, \rho_N\}$ is the vector containing all the unwrapped optimization variables with Z_n being that of the nominal trajectory optimization (2), and i denotes times instants. The objective function (2a) needs to change to (9a), which contains $\mathcal{L}_{n,k}$ from (2b), the nominal cost, and an extra term that concerns robustness, where W_ρ is the weight assigned to this new objective. Constraints (9d) and (9e) need to be added to the nominal TO, while (2f) and (2g) have to be replaced by (9f) and (9g) respectively. These two inequality constraints ensure that the bounds on the control input and GRF still hold even in case of a perturbation. We follow [21] in solving K_u from (9e) in terms of K_a and K_λ, and replacing it in (9f), to reduce the number of variables in the optimization.

It is desired to maximize ρ without violating any of the optimization constraints, which translates to the robot being able to withstand greater perturbation forces without its CoM experiencing an acceleration change, feet slipping, or requiring joint torques that its actuators cannot deliver. The main difference between what we propose in this work and [21] is the addition of (9d) and the extra term in (9e) to the constraints. As mentioned, this stems from the fact that we no longer require zero variation in acceleration in all DoFs but the CoM. Our version is less restrictive and more practical since, the motion of CoM is more important for a balanced gait than that of individual joints as long as their motion respects the bounds.

IV. Experiments

To show that the trajectories designed using the proposed method are feasible and executable on an actual exoskeleton, we conducted experiments with a paraplegic user and showed that this method could be used to perform different locomotion tasks. In the following, we first briefly introduce the exoskeleton used in the experiments, then the locomotion modes are mentioned, and finally, the designed control pipeline to replay the trajectory on the robot is explained.

A. Exoskeleton and Software

We used the Symbitron exoskeleton [25] for the experiments in this work. This full lower-body exoskeleton features five DoF in each leg: hip ab-/adduction, hip flexion/extension, knee flexion/extension, ankle plantar-/dorsiflexion, and ankle in-/eversion with the first 4 DoFs being actuated and the last one being passive. The active DoFs are actuated with Series Elastic Actuators (SEA) allowing accurate torque tracking [26]. The robot's computer runs TwinCAT3, which provides real-time communication between the sensors and actuators based on the EtherCAT protocol. Furthermore, we designed a graphical user interface with Matlab R2022b (The MathWorks, Inc., Natick, MA, USA.) which allowed us to communicate with TwinCAT to send commands and receive sensor and actuator data.

B. Locomotion Modes

Three different tasks or locomotion modes were performed during the experiments, namely, level ground walking (LGW), stair ascending (SA), and side-stepping (SS). The step length during LGW was 25 cm and the step height (the minimum distance of the toe and the heel from the floor) was 10 cm. The staircase used for the SA task has exactly the same dimensions as that of the stair ascending task in the Cybathlon 2024 [27] competition with a stair depth and stair height of 27 cm and 17 cm respectively. During SS, the step width was 15 cm with a step height of 8 cm.

C. Control Pipeline

To enable the robot and the paraplegic user to perform these tasks, the following procedure must be performed. First, we use the formulation in (9) to design spatial robust trajectories for each task. The nonlinear optimization problem is constructed in Matlab R2022b using CasADi v3.6.6 [28] for finding gradients and Jacobians analytically and is solved by Ipopt [29].

The trajectories for LGW and SA contain three distinct steps: the opening, the intermediate, and the closing step. The opening is the first step that the robot takes from the initial (home) configuration, which takes it from a parallel to a staggered stance. The intermediate step is the next one

where the foot in the front and the foot in the back swap being the leading and the trailing foot. The closing step is the one that follows afterward and takes the robot from a staggered to a parallel stance, at the end of which the robot assumes the same pose as the home configuration. The intermediate step is designed such that the robot's configuration at the end of it is the mirror image of the robot's configuration at the beginning of the step. This scheme allows us to generate trajectories for any desired number of steps by simply mirroring the intermediate step and appending it to the trajectory as many times as needed to generate the reference for the robot, without solving a high-dimensional optimization problem. To endow this symmetry to the portion of the trajectory associated with the intermediate step, the following constraint needs to be added to the TO:

$$x_{l,T} = x_{r,2T}, \tag{10a}$$

$$x_{r,T} = x_{l,2T}. \tag{10b}$$

In (10a) and (10b), x_r and x_l denote the position and velocity states of the right and the left leg joints respectively and T is the duration of each step.

After obtaining the solution, the position and velocity trajectories are interpolated linearly since the low-level controller of the robot runs at 1 kHz and expects a torque reference each millisecond, whereas the continuous TO was discretized at 20 Hz (collocation points are 50 ms apart temporally).

The high-level controller comprises a state machine (SM) and a PD feedback control. Based on the user input, the SM decides which task should be executed and which reference trajectory must be tracked. The PD controller generates the desired torques to track the position and velocity references and sends them to the low-level controller of the robot, which ensures that the desired torques are generated by the actuators and delivered at the joints. The implementation is based on the feedback control that enables the robot to counteract against possible disturbances, thereby leading to a feasibility check of the reference trajectories. Besides positions and velocity trajectories, TO gives the feedforward torques as well. However, in this work, we did not use the feedforward torques and only utilized the state trajectories and had the robot track those trajectories by employing a feedback PD controller. The P and D gains for all joints are 800 Nm/rad and 5 Nms/rad respectively.

D. Experiment Protocol

We tested our proposed method by asking an individual with complete SCI (from now on referred to as the pilot) to wear the Symbitron exoskeleton and had them perform the tasks mentioned in Sec IV.B. The experimental protocol and the tasks to be performed were explained to the pilot and he gave informed written consent to participate in this study. All the procedures were approved by the Natural Sciences and Engineering Sciences Ethics Committee of the University of Twente, nr. 240878.

During the experiment, two spotters accompanied the pilot for safety, who were instructed not to interfere unless the pilot lost balance. Furthermore, we attached the robot to the ZeroG (Aretech L.L.C, Sterling, Virginia, USA), a body-weight support system that would catch the pilot and the robot in the case of loss of balance. The ZeroG was set to follow the pilot and exert a pulling force that compensates for 5 kg of weight, which is the lowest pulling force that needs to be maintained for the ZeroG to follow the pilot.

For each task, the pilot did a few trials to get familiar with the robot's motion. The best trial for each task was recorded and reported in this manuscript. The video recordings of the experiment are available online[1].

TABLE I
MEAN SUF (N) AND RMS OF CONTROL INPUT (NM) FOR ROBUST AND NOMINAL METHODS

Method	LGW		SA		SS	
	Cont.	SUF	Cont.	SUF	Cont.	SUF
Robust	**47.3**	**97.4**	**43.4**	**79.9**	**39.9**	**114.5**
Nominal	30.4	82.0	41.1	60.0	32.0	93.6

V. RESULTS

The pilot performed all 3 required tasks successfully after a few trials as seen in Fig. 1.

The weights used in the nominal TO (2) are as follows: we set W_u to $20\mathbf{I}_8$, W_λ to $0.05\mathbf{I}_{24}$, $W_{\dot{u}}$ to $\mathbf{I}_8$, $W_{\dot{v}}$ to $\mathbf{I}_{16}$, and $W_{\dot{\lambda}}$ to $0.1\mathbf{I}_{24}$. For robust TO (9) we set all the weights to zero except for $W_{\dot{v}}$ and W_ρ that are set to $0.05\mathbf{I}_{16}$ and 1 respectively. By setting all other weights to zero in (9), we are asking the optimization to emphasize increasing the robustness and smoothness of velocity reference trajectories. The latter is important for practical reasons as it would regulate the acceleration of the joints and make the motion of the robot more comfortable for the pilot.

The magnitude of the SUF corresponding to each task's reference trajectory is shown in Fig. 2. The magnitude of the SUF for both methods is similar during the swing phase but bigger for the robust trajectories during the Double Support (DS) phase. However, this greater robustness margin comes at the cost of higher joint torques.

Fig. 3 shows joint torques and positions associated with the robust and nominal methods. Table I summarizes the comparison between the two methods. The mean SUF and the RMS of joint torques are larger for the robust trajectories in all tasks. Furthermore, Table I shows that the side-stepping task has the highest mean robustness and stair ascending has the lowest.

On average, the optimization process to design reference trajectories for LGW, SS, and SA took approximately 9, 6, and 15 minutes respectively on a PC with an Intel i7-12700H, 2.3 GHz CPU, and 32 GB memory.

VI. DISCUSSION

In this work, we introduced a robust trajectory optimization method that can be used to design spatial (3D) dynamically

[1]https://www.youtube.com/channel/UCXIrttu3bMumesUIDPXPH_w

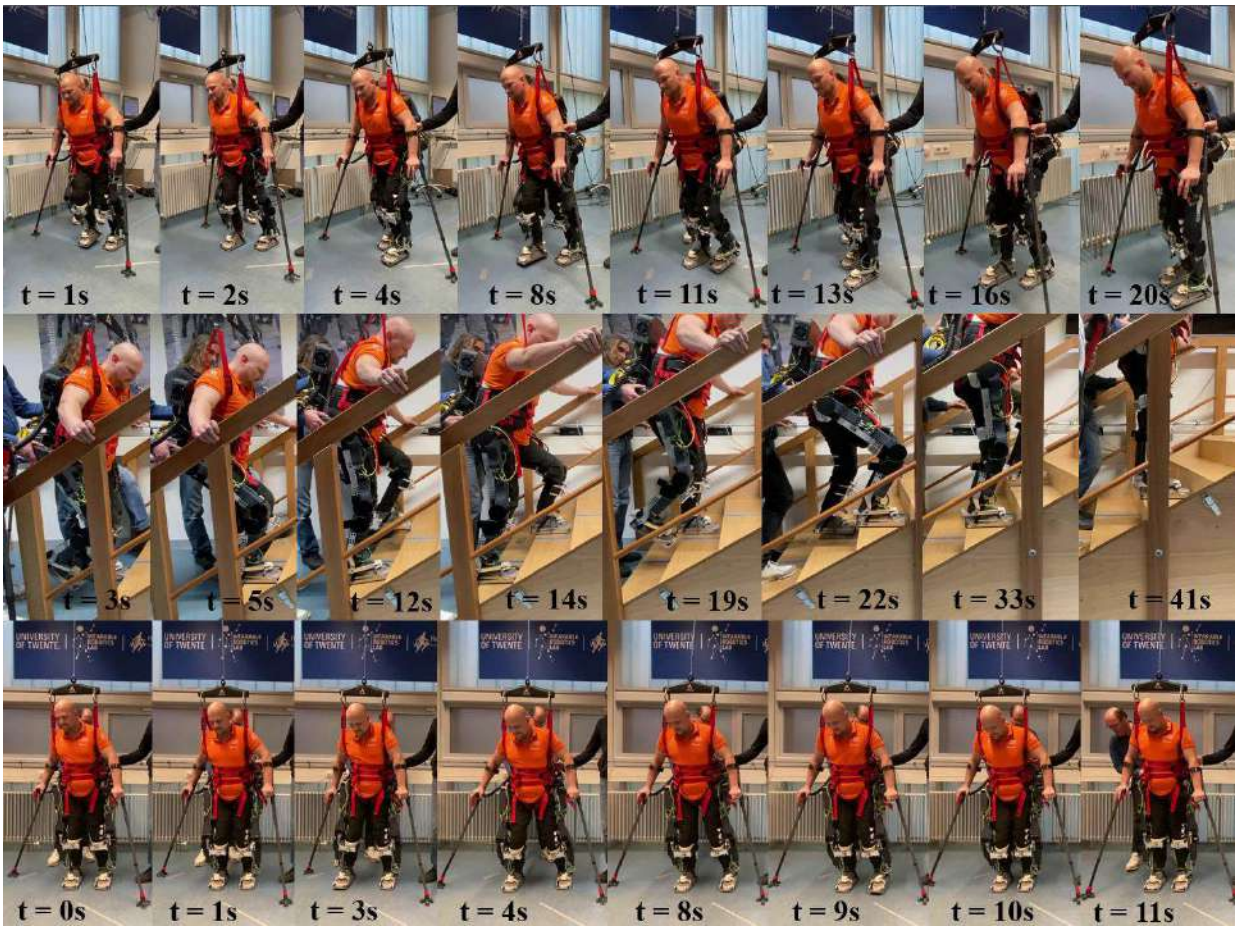


Fig. 1. The pilot performing the given tasks (LGW, SA, and SS from top to bottom) with the Symbitron exoskeleton. Everyone in the pictures consented to their face being visible.

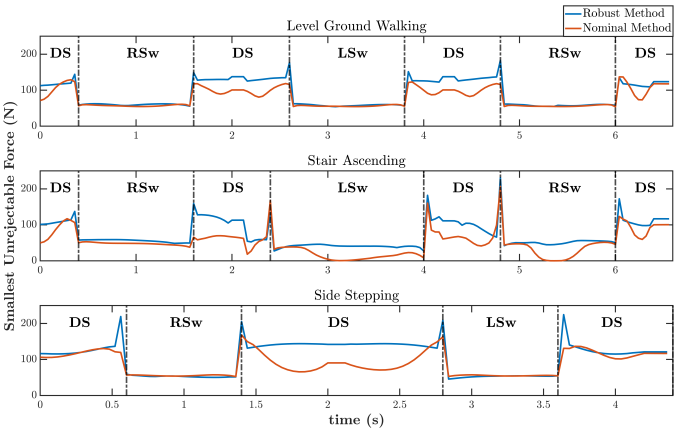


Fig. 2. A comparison between the magnitude of the SUF associated with the robust and nominal trajectories across different tasks. For each locomotion mode, various phases of gait are separated by dashed lines and labeled by DS, RSw, and LSw, which stand for Double Support, Right Swing, and Left Swing respectively.

feasible trajectories for an exoskeleton with a greater margin of robustness, i.e. an increased ability to withstand perturbations without undergoing any change in the acceleration at the CoM level. The difference between the robust and nominal trajectory optimization methods is evident from Fig. 3. The motion profile and the required control input are quite different between the two methods. Even though the robust trajectories would require higher joint torques, the increase in the balance robustness is far more valuable to an SCI patient as long as the joint torques remain within the bounds and the designed trajectories are non-aggressive, which is indeed the case here. Moreover, we showed the practicality and feasibility of the proposed method by implementing the designed trajectories on an LLE with a paraplegic user and having him perform different tasks including level-ground walking, side stepping, and stair ascending.

The robust optimization finds a trajectory with a higher mean SUF by modulating the GRF (while meeting the bounds on GRF and joint torques) since this is the force used to steer the robot's CoM motion. By exerting a higher vertical force on the ground, the maximum tangential force required to make

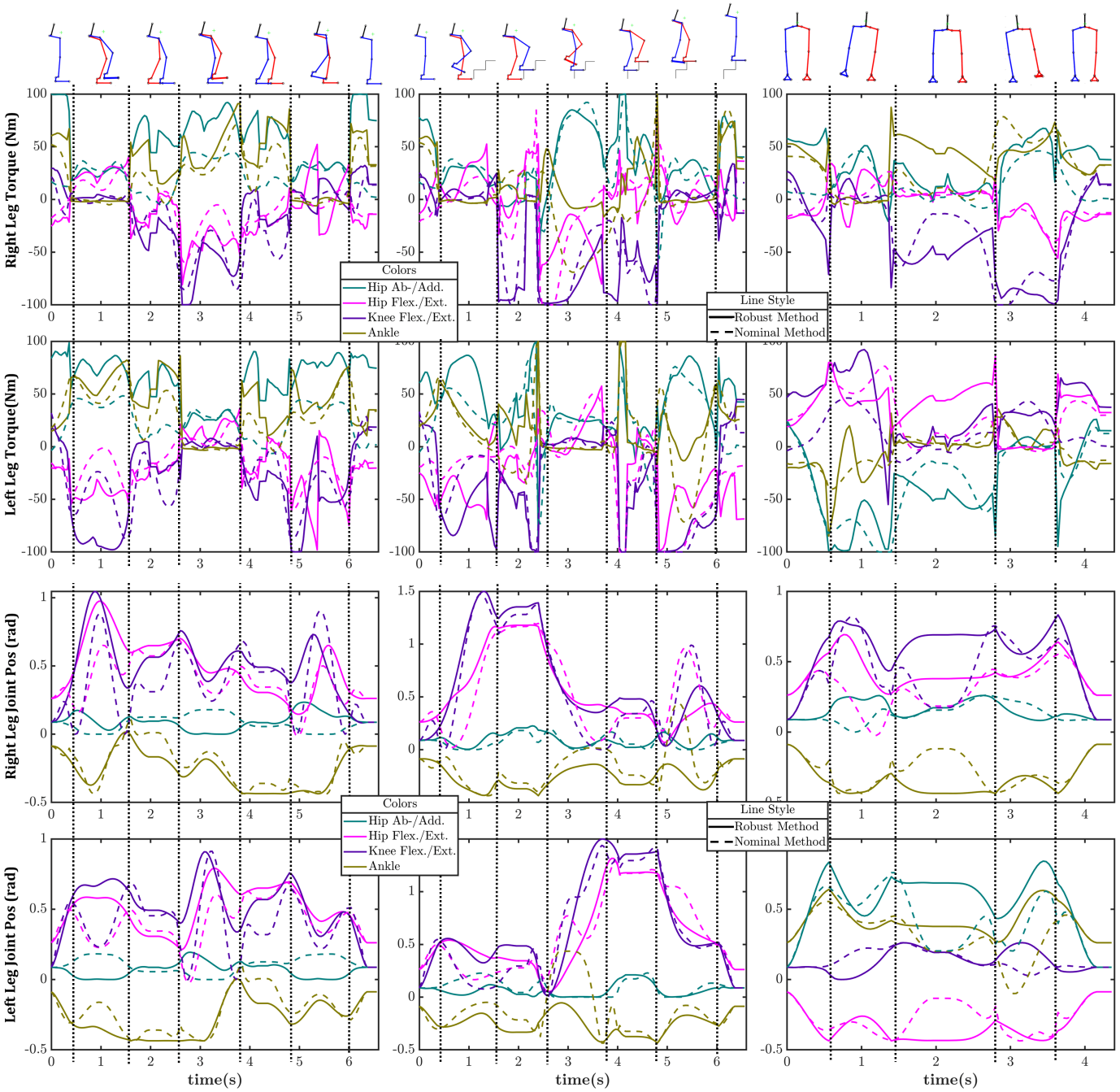


Fig. 3. A comparison of joint torque and position between the robust and nominal methods for different locomotion modes. The right leg is in blue and the left is in red. The stick figures above the plots show different phases of gait separated by the dashed vertical lines.

the contact point slip becomes higher. Therefore the robot can withstand perturbation forces with larger tangential components before the friction polynomial constraint is violated. We observed this behavior at the beginning of the DS phase. With the robust trajectory, the robot tends to stomp its foot on the ground to generate higher vertical GRFs, hence the higher peaks at the start of the DS phase for the robust method in Fig. 2. In the DS phase, the optimization has more freedom in manipulating the GRFs to increase robustness and that is why the difference in SUF between the robust and nominal methods is more noticeable in the DS phase than the other two gait phases.

The increased robustness margin becomes specifically important in scenarios where TO gives marginally feasible solutions and the margin of robustness is close to zero, such as in the case of stair ascending. By looking at Fig. 2, it can be seen that for the stair ascending task, the nominal SUF is very close to zero at some time instants, which means that a

small perturbation force applied at the CoM could result in a violation of either control input or GRF related constraints but the robust method increases the margin of robustness and yields trajectories that are further away from the bounds. However, the increased robustness comes with an increase in joint torques and behaviors such as foot stomping, which is not present in the nominal method. It must be noted that these behaviors can be mitigated by increasing the weight of the joint torque minimization objective and ground reaction force regulation with respect to the robustness weight.

Although the robust TO introduced in this work is a powerful method for generating trajectories for an LLE, the full potential of this method will be unlocked once it runs in an online fashion, which allows online modification of reference trajectories. A real-time implementation of this method or a simplified version of it along with a thorough analysis of balance and stability will be the focus of future work.

REFERENCES

[1] World Health Organization, "Spinal cord injury," 2024, accessed: 2024-11-19. [Online]. Available: https://www.who.int/news-room/fact-sheets/detail/spinal-cord-injury

[2] Y. He, Y. Xu, M. Hai, Y. Feng, P. Liu, Z. Chen, and W. Duan, "Exoskeleton-assisted rehabilitation and neuroplasticity in spinal cord injury," *World Neurosurgery*, vol. 185, pp. 45–54, 2024.

[3] C. Tefertiller, K. Hays, J. Jones, A. Jayaraman, C. Hartigan, T. Bushnik, and G. F. Forrest, "Initial outcomes from a multicenter study utilizing the indego powered exoskeleton in spinal cord injury," *Topics in Spinal Cord Injury Rehabilitation*, vol. 24, no. 1, pp. 78–85, 11 2017.

[4] A. Esquenazi, M. Talaty, A. Packel, and M. Saulino, "The rewalk powered exoskeleton to restore ambulatory function to individuals with thoracic-level motor-complete spinal cord injury," *American journal of physical medicine & rehabilitation*, vol. 91, no. 11, pp. 911–921, 2012.

[5] M. Sczesny-Kaiser, R. Trost, M. Aach, T. A. Schildhauer, P. Schwenkreis, and M. Tegenthoff, "A randomized and controlled crossover study investigating the improvement of walking and posture functions in chronic stroke patients using hal exoskeleton–the halestro study (hal-exoskeleton stroke study)," *Frontiers in neuroscience*, vol. 13, p. 259, 2019.

[6] T. Vouga, R. Baud, J. Fasola, M. Bouri, and H. Bleuler, "Twiice—a lightweight lower-limb exoskeleton for complete paraplegics," in *2017 International Conference on Rehabilitation Robotics (ICORR)*. IEEE, 2017, pp. 1639–1645.

[7] J. Choi, B. Na, P.-G. Jung, D.-w. Rha, and K. Kong, "Walkon suit: A medalist in the powered exoskeleton race of cybathlon 2016," *IEEE Robotics & Automation Magazine*, vol. 24, no. 4, pp. 75–86, 2017.

[8] K. A. Strausser, T. A. Swift, A. B. Zoss, H. Kazerooni, and B. C. Bennett, "Mobile exoskeleton for spinal cord injury: Development and testing," in *Dynamic Systems and Control Conference*, vol. 54761, 2011, pp. 419–425.

[9] R. Giannattasio, S. Maludrottu, G. Zinni, E. De Momi, M. Laffranchi, and L. De Michieli, "An adaptable ankle trajectory generation method for lower-limb exoskeletons by means of safety constraints computation and minimum jerk planning," in *2024 IEEE International Conference on Robotics and Automation (ICRA)*. IEEE, 2024, pp. 5548–5554.

[10] H. Mohamad and S. Ozgoli, "Online gait generator for lower limb exoskeleton robots: Suitable for level ground, slopes, stairs, and obstacle avoidance," *Robotics and Autonomous Systems*, vol. 160, p. 104319, 2023.

[11] R. Griffin, T. Cobb, T. Craig, M. Daniel, N. van Dijk, J. Gines, K. Kramer, S. Shah, O. Siebinga, J. Smith, and P. Neuhaus, "Stepping forward with exoskeletons: Team ihmc's design and approach in the 2016 cybathlon," *IEEE Robotics and Automation Magazine*, vol. 24, no. 4, pp. 66–74, 2017.

[12] F. Zhang, L. Shi, and S. Li, "Online trajectory generation with variable geometry stair ascent for powered exoskeleton," *IEEE Robotics and Automation Letters*, 2024.

[13] M. Sharifi, J. K. Mehr, V. K. Mushahwar, and M. Tavakoli, "Autonomous locomotion trajectory shaping and nonlinear control for lower limb exoskeletons," *IEEE/ASME Transactions on Mechatronics*, vol. 27, no. 2, pp. 645–655, 2022.

[14] S. O. Schrade, Y. Nager, A. R. Wu, R. Gassert, and A. Ijspeert, "Bio-inspired control of joint torque and knee stiffness in a robotic lower limb exoskeleton using a central pattern generator," in *2017 International Conference on Rehabilitation Robotics (ICORR)*. IEEE, 2017, pp. 1387–1394.

[15] J. Fang, Y. Ren, and D. Zhang, "A robotic exoskeleton for lower limb rehabilitation controlled by central pattern generator," in *2014 IEEE International Conference on Robotics and Biomimetics (ROBIO 2014)*. IEEE, 2014, pp. 814–818.

[16] E. R. Westervelt, J. W. Grizzle, and D. E. Koditschek, "Hybrid zero dynamics of planar biped walkers," *IEEE transactions on automatic control*, vol. 48, no. 1, pp. 42–56, 2003.

[17] T. Gurriet, S. Finet, G. Boeris, A. Duburcq, A. Hereid, O. Harib, M. Masselin, J. Grizzle, and A. D. Ames, "Towards restoring locomotion for paraplegics: Realizing dynamically stable walking on exoskeletons," in *2018 IEEE international conference on robotics and automation (ICRA)*. IEEE, 2018, pp. 2804–2811.

[18] H. Dai, A. Valenzuela, and R. Tedrake, "Whole-body motion planning with centroidal dynamics and full kinematics," in *2014 IEEE-RAS International Conference on Humanoid Robots*. IEEE, 2014, pp. 295–302.

[19] R. Budhiraja, J. Carpentier, and N. Mansard, "Dynamics consensus between centroidal and whole-body models for locomotion of legged robots," in *2019 International Conference on Robotics and Automation (ICRA)*. IEEE, 2019, pp. 6727–6733.

[20] A. W. Winkler, C. D. Bellicoso, M. Hutter, and J. Buchli, "Gait and trajectory optimization for legged systems through phase-based end-effector parameterization," *IEEE Robotics and Automation Letters*, vol. 3, no. 3, pp. 1560–1567, 2018.

[21] H. Ferrolho, V. Ivan, W. Merkt, I. Havoutis, and S. Vijayakumar, "Roloma: Robust loco-manipulation for quadruped robots with arms," *Autonomous Robots*, vol. 47, no. 8, pp. 1463–1481, 2023.

[22] H. Dai and R. Tedrake, "Optimizing robust limit cycles for legged locomotion on unknown terrain," in *2012 IEEE 51st IEEE Conference on Decision and Control (CDC)*. IEEE, 2012, pp. 1207–1213.

[23] M. Tucker, K. Li, and A. D. Ames, "Synthesizing robust walking gaits via discrete-time barrier functions with application to multi-contact exoskeleton locomotion," in *2024 IEEE International Conference on Robotics and Automation (ICRA)*. IEEE, 2024, pp. 1136–1142.

[24] P. M. Wensing and D. E. Orin, "Improved computation of the humanoid centroidal dynamics and application for whole-body control," *International Journal of Humanoid Robotics*, vol. 13, no. 01, 2016.

[25] C. Meijneke, G. van Oort, V. Sluiter, E. van Asseldonk, N. Tagliamonte, F. Tamburella, I. Pisotta, M. Masciullo, M. Arquilla, M. Molinari *et al.*, "Symbitron exoskeleton: Design, control, and evaluation of a modular exoskeleton for incomplete and complete spinal cord injured individuals," *IEEE Transactions on Neural Systems and Rehabilitation Engineering*, vol. 29, pp. 330–339, 2021.

[26] W. F. Rampeltshammer, A. Q. L. Keemink, and H. van der Kooij, "An improved force controller with low and passive apparent impedance for series elastic actuators," *IEEE/ASME transactions on mechatronics*, vol. 25, no. 3, pp. 1220–1230, 2020.

[27] ETH Zürich, "Exoskeleton discipline - cybathlon 2024," 2024, accessed: 2024-11-21. [Online]. Available: https://cybathlon.ethz.ch/en/event/disciplines/exo

[28] J. A. E. Andersson, J. Gillis, G. Horn, J. B. Rawlings, and M. Diehl, "CasADi – A software framework for nonlinear optimization and optimal control," *Mathematical Programming Computation*, vol. 11, no. 1, pp. 1–36, 2019.

[29] A. Wächter and L. T. Biegler, "On the implementation of an interior-point filter line-search algorithm for large-scale nonlinear programming," *Mathematical programming*, vol. 106, pp. 25–57, 2006.

Force myography shows higher correlation to force output compared to ARV EMG features

Marek Sierotowicz[1], Claudio Castellini[1], and Khairul Anam[2]

***Abstract*— Force myography, or FMG, is an emerging technology which, despite not quite yet achieving the same maturity as surface electromyography, still shows much promise for the purposes of muscle activity-based human-machine interfaces. Compared to surface electromyography, FMG setups can be very cost-effective and robust, and they offer the fundamental advantage of not requiring direct contact between sensor and skin. These factors make FMG sensors an attractive option for the purpose of controlling assistive wearable robotics or prostheses, for instance. Electromyographic features have been demonstrated to lead the force output by a sizable margin, which can be taken advantage of in various applications. However, FMG as a modality is inherently correlated with muscular force, we hypothesize that it should also exhibit a higher correlation with measurable force output of the extremities in healthy subjects compared to commonly used electromyographic features. In this study, we set out to prove this hypothesis by performing a regression analysis evaluating how well isometric pressure exerted by fingers can be predicted based on FMG signals as opposed to electromyographic signals. Additionally, we demonstrated the effectiveness of a system that is particularly low-cost, which in conjunction with the robustness of FMG sensors, would make them an attractive solution to be used in resource-constrained settings.**

I. INTRODUCTION

In the field of Human-Machine Interfaces (HMIs), measuring muscular activity is an attractive solution for the purpose of inferring movement intention in the case of, e.g., prosthesis control, or current force output and direction in the case of wearable robotics. Force MyoGraphy (FMG) is a muscle activity measurement technique based on the monitoring of pressure exerted by bulging muscles during contraction [1]. Although FMG has been successfully used to control assistive robotic appliances in the past [2][3], it is still an emerging technology in the field of biosignal-based controls, and especially in prosthetic control. Possible reasons for this comparatively scarce adoption are vulnerability to artifacts due to external pressure being applied to the FMG sensors, or the lack of an anticipatory edge like that of certain features of electromyographic signals, as shown for example in [4].

As a sensor modality, FMG can provide measurements that are directly correlated with output force [5]. For comparison, surface electromyography (sEMG) measures neural activity which is mediated by electrochemical dynamics before causing muscle contraction and force output, thus leading to potentially lower correlation between commonly used sEMG features and force output, depending on the examined task [6] [7] [8] [9]. Furthermore, FMG sensor technology can be implemented at very low costs, compared to most sEMG sensors available commercially [6] [8] [10]. Various studies demonstrated how deep learning-based prediction algorithms can predict hand gestures even if relying on low-cost sEMG sensors [11] or few channels [12]. Nevertheless, Phillips and colleagues identify the necessity of sEMG for direct contact with clean skin surface as one of the obstacles to the wider adoption of myoelectric prostheses in low- and middle-income countries, where the majority of the amputee population needs to rely for their income on manual labor in environments where cleanliness might not be ensured [13]. Even though Phillips and colleagues do acknowledge that the complexity of electronic prostheses is in it of itself a limitation, since it leads to higher costs and complexities, they do specifically identify sEMG sensors as a limitation. Since FMG does not require direct contact to the skin, and because of the cost effectiveness and robustness of the sensors, force myography could be a factor contributing towards a wider adoption of electronic prostheses in low- and middle-income countries [3].

In this paper we present the results of a study implementing a comparison between a commercially available, low-cost sEMG sensorized armband with 8 channels, and a self-produced FMG sensor array. The signals from these sensors were used to predict individual finger pressures. We adopted a regression analysis between FMG sensor signals and the fingertip force output, and demonstrated how FMG signals show better correlation with the same output forces. The study is similar in methodology to those presented in [5] and [8]. The main difference with respect to those studies relies in the focus on low cost devices, with the intent of proving their potential usability in a constrained resource setting for applications such as prosthesis control. Additionally, we investigated the influence of fatigue on both sEMG and FMG.

II. METHODS

A. Setup

The setup consisted of a board featuring an array of Force-Sensitive Resistor (FSR)-based pressure sensors, a bracelet-mounted array of FMG sensors, and an EMG bracelet, as shown in Fig. 1. The FSR sensors allow to measure pressure from all fingers, as well as thumb flexion and rotation. The measurements are converted to a voltage ranging from $0\,\mathrm{V}$

[1]Marek Sierotowicz and Claudio Castellini are with the Institute of Assistive Intelligent Robotics, Friedrich-Alexander Universität Erlangen-Nürnberg, 91052 Erlangen, Germany marek.sierotowicz@fau.de Marek Sierotowicz and Claudio Castellini are also affiliated with the Institute of Robotics and Mechatronics, German Aerospace Center, 82234 Wessling, Germany.

[2] Khairul Anam is with the Department of Electrical Engineering, Universitas Jember, Jl. Kalimantan 37 Jember, Indonesia

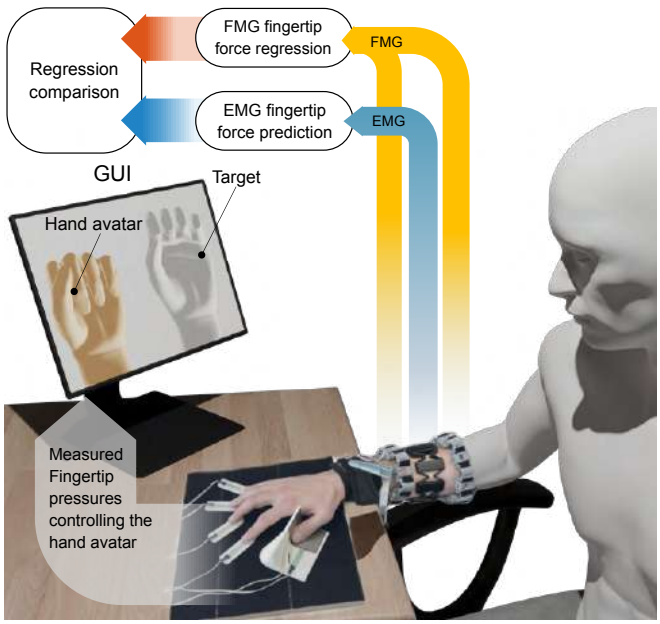


Fig. 1. Illustrative picture of the experimental setup. The hand was locked by means of a spanner, and the elbow was lying on an armrest. The participants were shown a target gesture which they had to match by controlling an avatar hand by pressing on FSR pads at their fingertips.

to 3.5 V by means of an amplification circuit. The same type of sensor is used to measure FMG signals on 13 channels. The FMG and fingertip force measurement setups both use the same data acquisition board, which samples at 400 Hz. For more details about the sensor technology used here, we recommend the sources [2], [5] and [6]. The sEMG was measured by means of a Myo armband (Thalmic Labs), which provides band-pass filtered EMG on 8 channels at a rate of 200 Hz.

B. Participants

A total of 13 able-bodied individuals participated in the study (8 males, 5 females, $1.77\,\mathrm{m}\pm0.11\,\mathrm{m}$, $76.92\,\mathrm{kg}\pm13.45\,\mathrm{kg}$, 27.92 ± 4.92 years old, 2 left-handed, 11 right-handed). The experiment was conducted with the permission of the ethical committee of the Friedrich-Alexander Universität Erlangen-Nürnberg (ID 22-278-S) and in conformity with the declaration of Helsinki in its latest revision of 2013. Each participant signed an informed consent form, and was extensively briefed by the experimenters about the study itself.

C. Experimental protocol

The participants were directed to control an avatar hand, shown in Fig. 1 in the GUI on the left, by pressing on the FSRs under their fingertips to follow a target. The target consisted of holding a given force output at the fingertips, consistent across all participants, for 7 s, which was displayed as a gesture of a target hand, shown in Fig. 1 in the GUI on the right. The participants had to match the gesture displayed by the target hand by pressing on the corresponding FSRs, which controlled the avatar hand. The total number of commanded force output configurations is 14, not counting the resting position, in a non-randomized order. Each participant performed 6 repetitions of the experiment. The fingertip pressure targets are shown in Fig. 2. The participants were instructed to never lift their fingers from the pads. The main reason for avoiding the extension of fingers as much as possible is that the pads would not have been able to measure that a force is being exerted. There was no attempt to avoid the co-activation of flexor and extensor muscles, on the other hand, as both sensor modalities were assumed capable of measuring both agonistic and antagonistic muscle activity.

D. Analysis

Prior to the analysis, all relevant signals, namely the 13 channels of the FMG, the 6 channels of the fingertip force measurement setup, and the 8 channels of the sEMG, were synchronized and brought to the same rate by means of a linear interpolation, using the timestamps of the sEMG as reference. The signals were additionally filtered (for the FMG and the fingertip force measurement, a sliding window filter of 50 samples width was used) and, in the case of the EMG, the Average Rectified Value (ARV) features were extracted using a sliding window of width 300. In order to eliminate the influence of transients, the signals were only considered starting 1 s after the commanded onset of contraction. Furthermore, for each finger, the measured fingertip force was only considered if the finger itself was required to exert pressure in a given time window. The reason for this decision is that the fingertip force pads can only measure downward pressures, and cannot monitor forces pointing upwards. Although the participants were instructed to never raise their fingers from the sensor pads, only when a pressure was actually required the downward force measurement can be considered reliable.

The prediction based on sEMG and FMG are compared based on Root Mean Square Error (RMSE) and Pearson's R^2 coefficient. Initial Kolmogorov-Smirnov normality tests indicated that neither the RMSE nor Pearson's R^2 are normally distributed. For this reason, Student's t-test was foregone in favor of a Wilcoxon signed-rank test in order to ascertain any statistical difference between the sEMG and FMG-based prediction of the fingertip pressure. The model's performance over repetition number was also monitored, as was done in [8]. Furthermore, any identifiable trends in the signals was gauged by fitting a linear regression model of the form $y = b + g \cdot t$ using time $t \in \mathbb{R}$ as independent variable, where $b, g \in \mathbb{R}$ are the model parameters, and y is the model estimate of EMG ARV features, FMG and fingertip pressure, depending on the case. For the fitting step, the model was fed the signals offset by their mean and normalized by their standard deviation, in order to allow for comparison of the proportional weight g between the models fitted on EMG ARV, FMG and FSR. Since the Kolmogorov-Smirnov test for normality showed that the distribution of the fitted parameter

g across all subjects and repetition is normally distributed, the appropriate form of t-test was used in this case.

For the purposes of analyzing fatigue, the progression of all signals was monitored over time. As a proxy for fatigue measurement, we considered the mean frequency of the raw sEMG. The mean frequency was calculated using a rectangular window. We elected to focus on the instances were the highest overall muscular contraction could be expected. Therefore, the mean frequency was calculated on the time windows where pressure was being exerted on all FSRs for each of the six repetitions. This is the case for target force output number 7, as shown in Fig. 2. Shifts in mean frequency over the course of the experiment were assessed on individual channels over all participants by means of a Wilcoxon signed-rank test between first and last repetition.

III. RESULTS

The signed-rank test shows significant differences between FMG and sEMG both in RMSE and R^2, with $p < 0.001$ in both cases in favor of the FMG-based prediction. Linear regression from FMG to fingertip pressure achieves RMSE of $0.221\,\mathrm{V} \pm 0.126\,\mathrm{V}$ and R^2 of 0.661 ± 0.170. Linear regression from sEMG to fingertip pressure achieves RMSE $0.253\,\mathrm{V} \pm 0.133\,\mathrm{V}$ and R^2 of 0.558 ± 0.189. Fig. 3 shows the distribution of RMSE and R^2 for EMG and FMG-based fingertip pressure prediction in the form of violin plots, with the corresponding box plots shown as well. Fig. 4 shows a representative plot of the used signals.

No significant effect of time on model performance could be detected. However, some significant changes over repetition number could be detected for the mean frequency on one of the sEMG channels, namely on channel 5, lying on the ventral side of the arm, across all participants. The mean frequency shows a decrease of $1.5\,\mathrm{Hz}$ in median between the first and last repetition (signed rank test on $n = 13$ shows $p = 0.0171$). No effects could be detected for any features in the time domain.

Looking at the progression over time of the various signals, the ARV features show the lowest slope over time. The FMG signal, on the other hand, shows a distribution of proportionality coefficients g with respect to time that significantly deviates from 0 (ttest, $n = 12$, $p = 0.03$). The same cannot be said for ARV features and the fingertip forces. However, both the fingertip force and the FMG show significantly higher correlation with time compared to EMG ARV features (right-tailed t-test, $p < 0.05$). Fig. 6 shows the boxplots of the gains g for FMG, ARV and fingertip forces, respectively, while Fig. 5 shows a representative case for the progression over time of all signals of interest during the instances where pressure is applied on all fingers.

Looking at the average levels calculated over the instances of pressure being exerted on all fingers, FMG exhibits highly significant correlation with the exerted forces over time ($R = 0.54$, $p < 0.0001$ without offsetting for individual means, $R = 0.53$, $p < 0.0001$ otherwise). In contrast, average ARV features show lower correlation with the average force output ($R = 0.16$, $p = 0.16$ without offsetting individual means, $R = 0.38$, $p < 0.001$ otherwise). Fig. 7 shows the average muscular activity signals over average force output across all participants and repetitions for the instances where all fingers were exerting pressure.

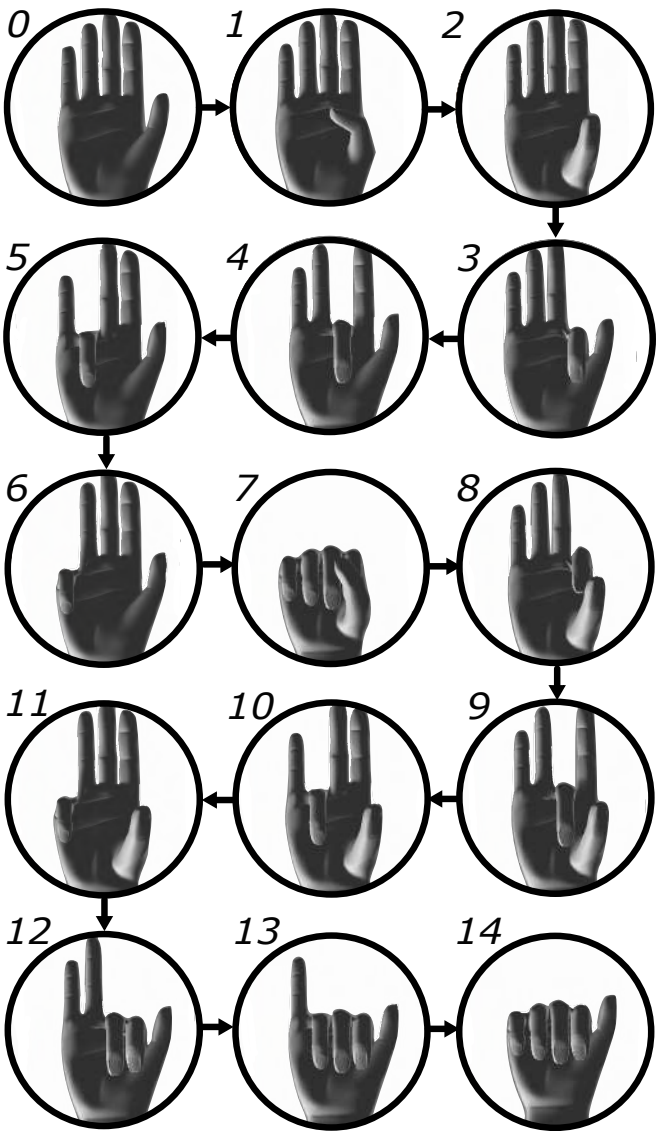


Fig. 2. Prompts shown to the participants. The flexion of the fingers symbolizes the required exertion of finger pressure. The fingertip pressure measured through the FSR pads underneath the participant's fingertips controls the avatar hand. The participants were prompted to have the avatar hand perform the same gesture as the target hand.

IV. DISCUSSION

The results indicate that FMG measurements are inherently better correlated with the force output achieved by the extremities moved by the monitored muscles, as compared to sEMG ARV features. The study specifically focused on low-cost equipment, in the hope of identifying a sensor solution

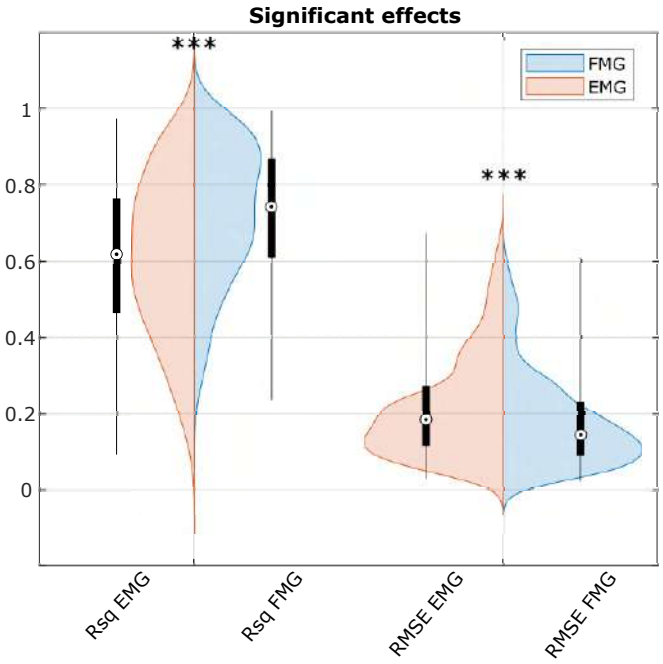


Fig. 3. Violin- and boxplots of R^2 and RMSE for FMG-based and EMG-based prediction. The significant effects are shown as well ($p < 0.001$ based on signed-rank test, $n = 468$ for both R^2 and RMSE).

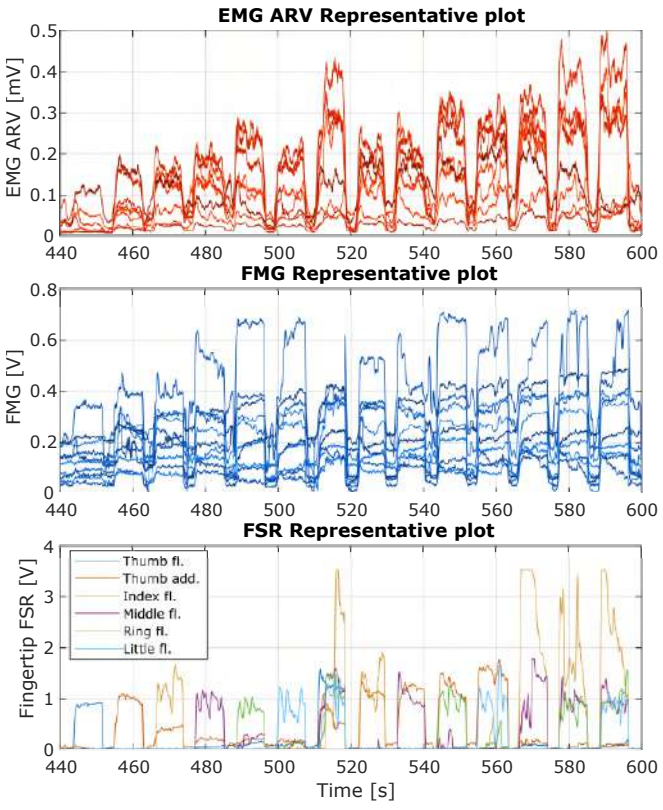


Fig. 4. Representative plot of the EMG ARV features, FMG voltages and FSR voltages correlating with fingertip pressure.

more suitable for resource-constrained settings. Previous studies were mainly concerned with comparing accuracy of hand gesture classification based on FMG and sEMG, or metrics related to classification such as Fisher's separateness index [6] [7]. Other studies [8] have focused on regression metrics, but found no significant difference between FMG and sEMG-based prediction. It is however true that some previous studies did confirm better real-time performance of FMG-based human machine interfaces in terms of task outcome metrics and path efficiency in target reaching tasks [14].

The more significant dependency on time of the FMG signals is worth further discussion. The main factors influencing measurable muscular activity during contractions are force output and fatigue, if absolutely no change in hand pose is assumed. The lowering in mean frequency would indicate that, overall, an increasing trend on fatigue can be inferred across all participants, especially considering that the ARV features do not seem to vary significantly over time [15]. Fingertip force is also not showing clear progression over time, and this is likely due to the fact that the fingertip forces were guided throughout the experiment. It is however possible that some effect is present, but the sample in this study makes the analysis statistically under-powered. An indicator in this sense is the fact that, while the dependency between force output and time is not significant, certain metrics are at the edge of significance, and furthermore the Pearson score for the linear regression model over time is significantly higher for the best-fit line of the FSR signals. This causes uncertainty as for whether the observed changes in average FMG signal is due to subtle changes in force output or due to other processes such as fatigue. While the progression of FMG over time seems to show an increasing trend overall, since only one model could be fit for participant, with the exclusion of one participant for which the measurement setup

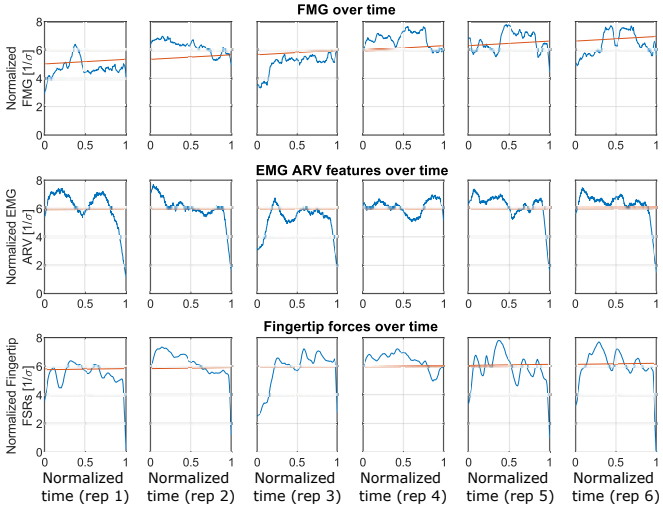


Fig. 5. Representative plot of the EMG ARV features, FMG voltages and FSR voltages over time (all in blue), as well as the best fit line (orange). The signals are shown over repetitions with time being normalized by the length of the repetition itself.

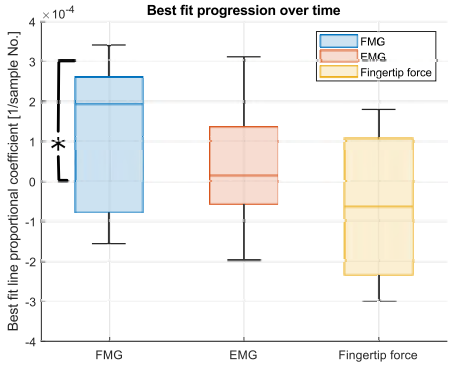


Fig. 6. Box plots of the gains g of the fitted linear regression models for FMG, ARV features from sEMG, and fingertip forces (n = 12), respectively. In this case, one participant was not considered, as the measurement setup was switched to a higher gain in the middle of the experiment, which would lead to an unreliable estimate of the g parameter.

was changed in the middle of the session, only $n = 12$ data points are available for this metric. The progression of FMG over time could be due to multiple causes. Nevertheless, since FMG shows high correlation with output force, it could reveal fatigue by, e.g., monitoring the decrease of force output over time under maximum voluntary contraction or under electrical stimulation [16]. This approach would likely be more reliable than time-domain EMG features, which show high variance across individuals as a response to fatigue [16], since the mechanisms coupling measurable electrical activation and force generation are more numerous than those connecting force output and muscle bulging. This would make it an interesting sensor modality to be adopted in, e.g., FES applications to monitor the progression of fatigue. Studies are in progress to assess this perspective application.

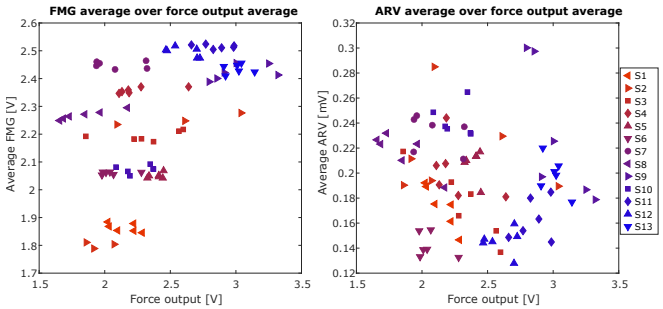


Fig. 7. Average muscular activity signals over average force output measurements across all participants and repetitions. Each color represents six repetitions of an individual participant. All 13 participants are represented in this plot.

A. Limitations

This study presents some principal limitations. As previously stated, the use of a mono-directional force measurement setup limits the reliability of our regression analysis to the instances where pressure is being detected. On the other hand, when the sensor is not being pressed, there is no guarantee that the participant is not actively exerting force upwards. Future studies should make use of a setup able to measure both downwards and upward forces, such as the FFLS [17]. Some adjustments in the posture of the hand throughout the experiment could not be avoided, and this could affect the regression from muscular activity to force output. FMG would be particularly affected by changes in posture, since the resting pressure could change across different hand poses. Furthermore, the experimental protocol was not aiming at causing fatigue, and therefore the only proxy for its observation is the progression of force output over time, the spectral features of the sEMG, which are limited by the relatively low sampling rate of the myo armband, and the reports of the participants. As for the comparison between the two muscular activity sensing modalities, the FMG sensor arrangement has more channels compared to the EMG bracelet used in this study, and furthermore the measurement sites for each modality differ. It is however worth mentioning that the sensor density was similar between the two sensor modalities (with an inter-sensor distance of circa $2\,\mathrm{cm}$). The sensor density would arguably have been a more determining factor given the density of the forearm's muscles. Both the FMG and the EMG bracelets had the same amount of sensors along the arm's circumference. An ideal solution would be one like that proposed in [18], but the mounting of the FMG sensors is of great importance, and potential trade-offs in designing such concurrent sEMG-FMG sensor mountings might be harder to navigate. The higher number of channels was also implemented as a precaution, since the adopted FMG amplifier design is prone to saturation, and needs careful mounting to ensure that the circuit is operating in its linear point. This can be achieved by carefully increasing or decreasing the resting tension of the bracelet. An alternate solution, which is currently being evaluated, is to shift the amplifier's operating point electronically using variable resistors. While the overall complexity of the sensor is increased, this solution can result in much broader usability, and because bracelet tension is not as crucial, it could also result in higher sensor spatial density being possible. Finally, the comparison between force output predictions performed here is limited to ARV features and linear regression, and it could be argued that a better choice in EMG features or the use of non-linear regression models could alter the results. ARV features are singled out in multiple studies, together with root mean square, as having particularly high correlation with both static and dynamic force output [19] [20] [21]. The choice of ARV features was furthermore motivated by the

intent of mimicking a real-time capable setup as commonly used in commercial prosthetic applications. While in most commercially available prosthetic applications single digit control is not available, the higher correlation of FMG to force output could still lead to benefits.

V. CONCLUSIONS

In this study, we provided evidence that FMG measurements show higher correlation with fingertip force output compared to ARV features obtained from a low-cost sEMG sensor. This, in addition to the greater robustness of the FMG sensors, on account of them not needing direct contact with the skin, could make them a conduit towards wider adoption of electronic, muscle activity-controlled prostheses in resource-constrained settings [13]. This statement is corroborated by the interest of various research groups in developing countries in FMG as a prosthesis control solution [3]. FMG sensors are indeed extremely cost effective and robust compared to most sEMG sensors, but it is also worth mentioning that FMG sensors are prone to artifacts due to external pressure being applied to the sensor. sEMG, on the other hand, is not as influenced by external forces. The fact that the present experiment is limited to an isometric exercise with the hand held in a constant position makes it hard to evaluate the influence of movement or external loads on the FMG-based force output calculation. Previous studies [2] have tested control loops based on such predictions in non-isometric scenarios, but did not compare it to the same computation obtained based on EMG measurements. The present study did not validate the quality of the prediction in real time, as was done, e.g., in [14] and [22], but is limited to a multivariate linear regression analysis. Future work should focus on the direct integration of FMG sensors in the robotic appliance they are supposed to drive, which is itself a non-trivial task, as force interactions between the robot, the sensor and the user could well lead to artifacts. The inclusion of the target population of patients will certainly be necessary.

ACKNOWLEDGMENT

This work was partially supported by the German Federal Ministry of Education and Research (BMBF) under the Robotics Institute Germany (RIG).

REFERENCES

[1] Z. G. Xiao and C. Menon, "A review of force myography research and development," *Sensors*, vol. 19, no. 20, p. 4557, 2019.

[2] M. Sierotowicz, D. Brusamento, B. Schirrmeister, M. Connan, J. Bornmann, J. Gonzalez-Vargas, and C. Castellini, "Unobtrusive, natural support control of an adaptive industrial exoskeleton using force myography," *Frontiers in Robotics and AI*, vol. 9, p. 919370, 2022.

[3] A. Prakash, A. K. Sahi, N. Sharma, and S. Sharma, "Force myography controlled multifunctional hand prosthesis for upper-limb amputees," *Biomedical Signal Processing and Control*, vol. 62, p. 102122, 2020.

[4] M. Sierotowicz, M.-A. Scheidl, and C. Castellini, "Adaptive filter for biosignal-driven force controls preserves predictive powers of semg," in *2023 International Conference on Rehabilitation Robotics (ICORR)*. IEEE, 2023, pp. 1–6.

[5] C. Castellini and V. Ravindra, "A wearable low-cost device based upon force-sensing resistors to detect single-finger forces," in *5th IEEE RAS/EMBS International Conference on Biomedical Robotics and Biomechatronics*. IEEE, 2014, pp. 199–203.

[6] M. Connan, E. Ruiz Ramírez, B. Vodermayer, and C. Castellini, "Assessment of a wearable force-and electromyography device and comparison of the related signals for myocontrol," *Frontiers in neurorobotics*, vol. 10, p. 17, 2016.

[7] X. Jiang, L.-K. Merhi, Z. G. Xiao, and C. Menon, "Exploration of force myography and surface electromyography in hand gesture classification," *Medical engineering & physics*, vol. 41, pp. 63–73, 2017.

[8] V. Ravindra and C. Castellini, "A comparative analysis of three non-invasive human-machine interfaces for the disabled," *Frontiers in neurorobotics*, vol. 8, p. 24, 2014.

[9] Z. Zheng, Z. Wu, R. Zhao, Y. Ni, X. Jing, and S. Gao, "A review of emg-, fmg-, and eit-based biosensors and relevant human–machine interactivities and biomedical applications," *Biosensors*, vol. 12, no. 7, p. 516, 2022.

[10] O. Sherif, M. M. Bassuoni, and O. Mehrez, "A survey on the state of the art of force myography technique (fmg): analysis and assessment," *Medical & Biological Engineering & Computing*, vol. 62, no. 5, pp. 1313–1332, 2024.

[11] Z. Ilyas, K. Anam, Widjonarko, C. Avian, A. Z. Muttaqin, and M. E. Ramadhan, "Evaluation of gated-recurrent unit for estimating finger-joint angle using surface electromyography signal," in *2022 9th International Conference on Electrical Engineering, Computer Science and Informatics (EECSI)*, 2022, pp. 25–28.

[12] K. Anam and A. Al-Jumaily, "Performance evaluation of srelm on bio-signal pattern recognition using two electromyography channels," 2020.

[13] B. Phillips, G. Zingalis, S. Ritter, and K. Mehta, "A review of current upper-limb prostheses for resource constrained settings," in *2015 IEEE global humanitarian technology conference (GHTC)*. IEEE, 2015, pp. 52–58.

[14] A. Belyea, K. Englehart, and E. Scheme, "Fmg versus emg: A comparison of usability for real-time pattern recognition based control," *IEEE Transactions on Biomedical Engineering*, vol. 66, no. 11, pp. 3098–3104, 2019.

[15] M. Cifrek, V. Medved, S. Tonković, and S. Ostojić, "Surface emg based muscle fatigue evaluation in biomechanics," *Clinical biomechanics*, vol. 24, no. 4, pp. 327–340, 2009.

[16] N. K. Vøllestad, "Measurement of human muscle fatigue," *Journal of neuroscience methods*, vol. 74, no. 2, pp. 219–227, 1997.

[17] R. Koiva, B. Hilsenbeck, and C. Castellini, "Ffls: An accurate linear device for measuring synergistic finger contractions," in *2012 Annual International Conference of the IEEE Engineering in Medicine and Biology Society*. IEEE, 2012, pp. 531–534.

[18] J. Sanford, R. Patterson, and D. O. Popa, "Concurrent surface electromyography and force myography classification during times of prosthetic socket shift and user fatigue," *Journal of Rehabilitation and Assistive Technologies Engineering*, vol. 4, p. 2055668317708731, 2017.

[19] A. O. Andrade and C. I. Andrade, "On the relationship between features extracted from emg and force for constant and dynamic protocols," in *2012 Annual international conference of the IEEE engineering in Medicine and Biology Society*. IEEE, 2012, pp. 3392–3395.

[20] H. U. Kuriki, E. M. Mello, F. M. De Azevedo, L. S. O. Takahashi, N. Alves, and R. de Faria Negrão Filho, *The relationship between electromyography and muscle force*. Citeseer, 2012.

[21] H. Milner-Brown and R. Stein, "The relation between the surface electromyogram and muscular force." *The Journal of physiology*, vol. 246, no. 3, pp. 549–569, 1975.

[22] U. Zakia and C. Menon, "Estimating exerted hand force via force myography to interact with a biaxial stage in real-time by learning human intentions: A preliminary investigation," *Sensors*, vol. 20, no. 7, p. 2104, 2020.

Human-Interface Dynamics of Knee Exoskeletons with Lateral and Anteroposterior Attachment

Yichen Wang, José A. Montes Pérez, Robert D. Gregg, and Gray C. Thomas

***Abstract*— Assistive lower-body exoskeletons aim to improve quality of life for broad populations including older adults and people in physically exhausting manual jobs. By applying torque to augment human motion with backdrivable actuators, these devices can reduce human joint effort without restricting volitional motion. However, these backdrivable actuators are coupled by mechanical interfaces to soft tissues of the human body that together introduce resonator dynamics that can delay or diminish the torque assistance. Low interface stiffness and uncompensated dynamics can cause inefficient power delivery to the user, alter their perceived assistance and comfort, and destabilize feedback controllers. We hypothesize that the low stiffness in lateral strap interfaces, like those in the open-source M-BLUE exoskeleton, can be improved by mechanical redesign. Building on the open-source M-BLUE exoskeleton, this paper introduces an alternative interface design that loads the leg through anterior and posterior pads (normal loading) and straps, in which the pads provide extension assistance and the straps provide flexion assistance. We compare the interface dynamics of lateral and normal loading interfaces on N=10 human subjects using both quasi-static spring measurements and frequency response methods, finding the new design to be 85.7% stiffer ($p < 0.01$) for a range of leg poses and in both flexion and extension loading.**

I. Introduction

Lightweight, backdrivable lower-body exoskeletons that provide assistive torques have the potential to greatly improve quality of life for a large number of people struggling with physical disabilities, aging, or physical overexertion at work. Partial assistance exoskeletons can aid in many activities of daily living, for people who struggle with walking, using stairs, or lifting and lowering heavy objects [1]–[3]. For able-bodied people, exoskeletons can aid with material handling, repetitive movements, or awkward body positions at physically taxing jobs [4], [5]. Usage of exoskeletons can prevent injuries and fatigue, and increase worker comfort.

However, A core contributor to this efficacy is the manner by which the exoskeleton attaches to the human body. Soft tissue between rigid exoskeletons and our human endoskeleton system allows for relative motion and dynamic behavior. These dynamics are viscoelastic, and unfortunately time varying, nonlinear, and hard to predict for an individual [6], [7]. Thus they are typically left out of models [2] and lumped among the neglected factors that limit the performance of feedback controllers. In some cases, these dynamics can be quantified as a low-pass filter with respect to the actuator torque [8]. Generally speaking, the stiffer an interface the more closely it will resemble the rigid assumption and the less likely it will cause instabilities and time delays [9]. However, there is a lack of studies that quantify typical interface stiffness and dynamics for common exoskeleton configurations, or the extent to which it can be ameliorated through mechanical design.

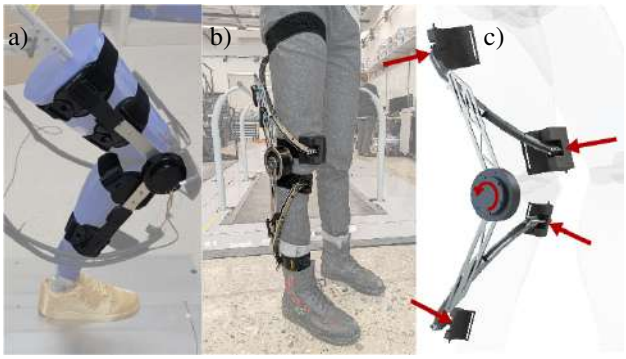


Fig. 1. **Exoskeleton attachments**—a) original attachment via lateral straps, b) new attachment in this paper, c) loading in the new system is via forces on the body (red arrows) that are normal to the surface of the leg.

The exoskeleton's attachment also impacts the efficiency of energy transfer from the exoskeleton to the user. Estimates suggest that in some cases, up to 50% of energy expended by the exoskeleton is used to compress soft tissue instead of doing work on the skeleton structure [10]. This inefficient energy transfer results in less effective assistance for the user, requiring larger torques powered by larger batteries to achieve the desired effect. However, there are limits to the amount of force the human body can tolerate [11].

While the rigidity of the exoskeleton interface is important, so are user comfort, generalizability, and ease of adjustment. Exoskeletons are commonly attached to the human with fabric straps [3], [12]–[14], which must be tightened to apply high pressure for increased rigidity [15]. However, this method becomes painful and uncomfortable for the user if the straps are over-tightened. Additionally, human soft tissue changes shape throughout the range of motion, causing an exoskeleton fitted at one particular body position to be uncomfortably tight or overly loose at others [16], which cannot be remedied by tightening straps. Instead of using straps, another attachment style molds rigid shapes to prominences on each user [17]. Human extremities have high local variations in stiffness that can be used to our advantage by carefully selecting the points of attachments [18]. Both

This work was supported by the National Institute of Biomedical Imaging and Bioengineering of the NIH under Award Number R01EB031166. The content is solely the responsibility of the authors and does not necessarily represent the official views of the NIH.

Y. Wang, J. Montes Pérez, and R. Gregg are with the Department of Robotics, University of Michigan, Ann Arbor, MI 48109, USA. G. Thomas is with the J. Mike Walker '66 Department of Mechanical Engineering, Texas A&M University, College Station, TX 77840, USA.

of these methods come at the cost of user generalizability, as an exoskeleton molded to one user may not fit another.

Exoskeletons that attach laterally to the joint and limb, such as the M-BLUE platform [5], [12] or clothing-integrated exoskeleton [13] developed under Skip and Arc'teryx have a simple design concept that is well-suited to a lightweight construction. Having attachments in the same plane as the joint movement dramatically eases re-fitting, and this low complexity enables a cheap, low-barrier-to-entry solution for research exoskeletons [12]. However, the lateral attachments convert applied flexion-extension force into a twisting moment around the femur and tibia-fibula (Figure 2), resulting in a significant mechanical deflection relative to compressive loading [19].

With attachment locations anterior-posterior to the limb (Figure 2, left), many exoskeletons have achieved more direct torque transmission at a weight penalty due to the heavier structures necessary to wrap around the leg and transmit force above and below the limb [14], [20], [21]. However, targeted research in human-exoskeleton interface dynamics is uncommon, and stops far short of quantifying the advantage in dynamic performance [22]. Research has analyzed skin compliance as a material property [18], but would require a complex simulation to relate to interface design. Exoskeleton-focused research offers some stiffness estimates for exoskeletons in special purpose tests (and have typically not measured the nonlinearity in the stiffness parameters) [8], [19], [20], [23]. A direct comparison of lateral and normal attachment strategies using a common exoskeleton platform and analyzing the dynamics of the mechanical interface would therefore aid mechanical designers in choosing an appropriate exoskeleton attachment style for their purposes.

This study investigates the interface dynamics of two versions of the M-BLUE exoskeleton platform, configured for lateral-strap and normal (anteroposterior) loading of the knee joint. In particular, we contribute: A) a sheet-metal and 3D printed plastic attachment design for normal loading attachment (Figure 1); B) quasi-static nonlinear spring measurements of both exoskeletons on $N = 10$ participants in three knee angle postures; C) frequency-response identification of the motor torque to exoskeleton deflection transfer function across subjects, exoskeletons, and extension vs. flexion loading, D) analysis of regressed nonlinear model coefficients for the quasi-static spring rate; and E) analysis of the dynamic stiffness differences arising due to the loading condition, knee angle, and exoskeleton design. We found the normal loading configuration to be consistently stiffer for all three tested leg poses and both loading directions ($p < 0.01$). In particular, we found an 85.5% increase in the quasi-static linear stiffness, 91.9% increase in the quasi-static progressive stiffness, and 85.7% increase in the average dynamic stiffness between 3 and 15 Hz.

II. Exoskeleton Interfaces

A. Interface Descriptions

Knee exoskeletons usually consist of an actuator connected to the person through attachments in the thigh link and shank link. Among many attachment methods, two main paradigms stand out.

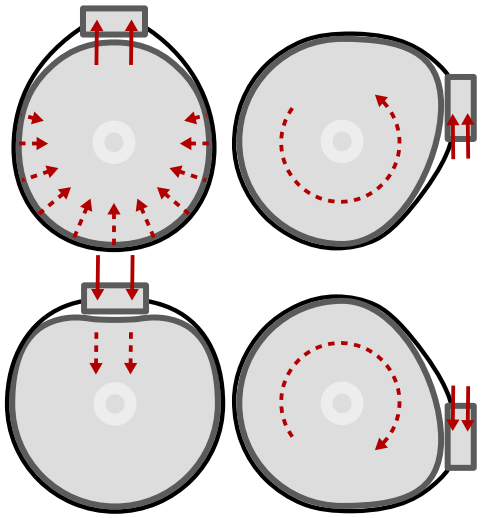


Fig. 2. **Normal loading (left) compared to lateral loading (right)** when applying knee flexion (top) and knee extension (bottom) on a cross-section of the leg. Deformation and deflections are exaggerated for illustrative purposes.

Lateral-strap loading exoskeletons (Figure 2, right) interface with the human through straps that surround the shank and thigh. The straps are then rigidly connected to the actuator through structures lateral to the limb. As the exoskeleton applies assistive torques, lateral forces applied to soft tissue causes twisting relative to the underlying bone. As the deflection becomes greater, the straps begin to compress the anterior or posterior of the limb, stiffening the connection. This interaction can be modeled as a nonlinear stiffness that grows as the deflection loads the straps and compresses the soft tissue against the skeleton. This series-spring and rotational effect results in an dynamic error between the desired and applied torque similar to a delay. Because humans are very sensitive to the timing of torques from exoskeletons [24], any disruption in torque application can be detrimental to the performance of the exoskeleton.

In contrast, normal-loading exoskeletons (Figure 2, left) transfer torques to the limb via pads placed anterior and posterior to the shank and thigh and straps around their circumference. The exoskeleton loads the limb by pressing into the soft tissue with pads or pulling on the limb with straps, depending on the torque direction. Relative to the lateral-strap configuration, this avoids the deflection due to torsion about the bone, instead compressing soft tissue immediately upon loading. Since it does not rotate soft tissue, we expect normal-loading exoskeletons to have a higher interface stiffness as well as a faster increase in stiffness.

B. Exoskeleton Mechanical Design

For the lateral strap exoskeleton, we used a modified version of the existing M-BLUE [12] exoskeleton. M-BLUE uses pads and straps from a T-Scope knee brace (Breg, Carlsbad, CA, USA) with sheet metal plates attaching to a

ActPack actuator (Dephy, Inc., Boxborough, MA, USA). In contrast from the original design of M-BLUE, we removed the aluminum uprights from the medial position. The configuration used in the experiments can be seen in Figure 4. This provides more comfort to the user in a bilateral configuration since the medial straps would often collide with one another when walking. Therefore, this is more representative of a deployed bilateral exoskeleton, and more similar to other exoskeletons of its class [13], [25].

We designed our normal-loading attachment system (Figure 1) with the goals of high interface stiffness, high structural stiffness, and high adjustability to a wide variety of body types. We chose to optimize the exoskeleton for applying extension knee torque, due to the fact that the knee joint applies a much higher peak torque in the extension direction than the flexion direction, especially in torque-demanding tasks such as stair ascent-descent [26]. Secondary goals that were important to the experiment were comfort while sitting down, and ease of donning and doffing. Some additional goals that we had which were less relevant to the experimental design but still important for a general use exoskeleton were reducing the weight of the exoskeleton, simple manufacturing by using common materials and accessible manufacturing techniques such as laser-cut sheet metal and 3D printing.

To ensure high interface stiffness, we placed two vertically offset pads for the shank and the thigh to effectively transmit a sagittal plane extension torque via pad compression alone (Figure 1). Because we chose to optimize the force application in the extension direction, we placed the proximal thigh pad posterior to the leg and the distal thigh pad anterior to the leg. Conversely, the proximal shank pad is anterior to and the distal pad posterior to the shank. Each pad is held in place by a inelastic strap that attaches it to limb, fixing it and the exoskeleton in place. The straps are chosen to have comparable materials to those used on the lateral-loading exoskeleton. When the exoskeleton applies a force in the extension direction, the pads compressed directly into the soft tissue, while in the flexion direction, straps surround and pull on the limb without rotation of the soft tissue. At design time, it was unclear if the two loading methods would result in different stiffness characteristics, and we hypothesized that a difference would be more pronounced than for the lateral straps of M-BLUE.

To be fit to a wide range of leg shapes, spacing between the pads needs to be adjusted. Our design achieved this through the integration of a C-shaped structural member that wraps around the leg and connects the pads. The angle of the C-shaped beam relative to the leg controls the sagittal spacing between the pads. As accurate relative vertical positioning of the pads is not necessary for a snug fitment, rotating the beam alone provides ample freedom of adjustment for user comfort. Cam handles placed on the joint between beams and the actuation arms enables fast loosening of the exoskeleton during fitment, and can be easily tightened once the pads and straps are applied and taut. Because the C shape is a key structural member of the exoskeleton, it is constructed of an aluminum and 3D printed plastic laminate for high bending stiffness and a low weight.

III. Experimental Methods

A. System Identification of Interface Dynamics

Exoskeleton tests are comprised of two two parts: a quasi-static loading test analyzes the soft tissue compliance at the exoskeleton attachments as a nonlinear spring, and a frequency response test analyzes it as a transfer function. Quasi-static loading represents the compliance of the attachment areas for torques that are applied at a low rate and represent steady-state stiffness. Dynamic loading represents interface dynamics when torques are applied at a high rate, and include factors of time-dependent effects and inertial recruitment. The exoskeleton might have different stiffness properties depending the type of loading (dynamic vs. quasi-static), the direction the torque is applied (extension vs. flexion), and the knee angle. Therefore, we designed an experiment that accounts for these variations by testing each separately (Figure 3).

In the quasi-static case, the soft tissue interface can be considered as a nonlinear spring attaching the exoskeleton to the underlying bone structure. To quantify the spring rate, we apply a low-frequency of 0.1 to 1 Hz and relatively higher amplitude of 10 Nm peak-to-peak signal to measure the nonlinear spring part of the system. We then use this data to calculate the deflection of the exoskeleton compared to the human. As the the human base of the system is fixed, any change in the encoder position of the motor represents a deflection of soft-tissue. The low frequency enables the motor to come to a complete equilibrium before the torque changes direction, and eliminates higher order inertial and damping effects from the measurement.

To quantify the stiffness during quasi-static loading we perform a least-squares regression that analyzes both the linear and nonlinear components of the spring behavior. In order to capture differences in dynamics resulting from loading directions, we regress separate flexion and extension models. The equations for the regression are then

$$\tau = \begin{cases} \begin{bmatrix} \theta & -\theta^2 \end{bmatrix} \begin{bmatrix} \alpha_1 \\ \beta_1 \end{bmatrix}, & \theta < 0, \\ \begin{bmatrix} \theta & \theta^2 \end{bmatrix} \begin{bmatrix} \alpha_2 \\ \beta_2 \end{bmatrix}, & \theta > 0, \end{cases} \tag{1}$$

where τ is the calculated torque of the motor, θ is the measured deflection of the exoskeleton with respect to the person, $\alpha_{1,2}$, represents the linear stiffness, and $\beta_{1,2}$ represent progressive stiffness. Because of soft tissue dynamics, the quasi-static tests observed a large amount of hysteresis. To accommodate for this hysteresis, which are not modeled in the regression model below, we binned the data into 100 equally distributed buckets according to the applied torque, and took the average of all data points within each bucket. The resulting 100 binned averages are then used as inputs for a least squares fit to the piecewise quadratic polynomial model mentioned above in (1). Piecewise models

are chosen to capture potential differences in stiffness in different loading directions as a result of asymmetry in loading through pads versus straps. A quadratic polynomial is an established modeling method for joint stiffnesses [27].

For the dynamical stiffness parameters, we consider the interface as a mass-spring-damper system. This means that there is a virtual mass that represents the exoskeleton which is attached to the human's bones via a parallel spring-damper. Since we are mainly interested in the spring component, we only quantify that aspect of the system. We do this by performing a system identification using a frequency sweep. Namely, we define the interface as a single input single output (SISO) system, with the input as the torque of the motor, and the output as the deflection of the motor encoder. A transfer function is defined with the gain being the output divided by the input, in this case, motor position over applied torque. Applied torque is calculated naively using the motor current, torque constant, and transmission ratio:

$$\tau = nK_m i, \tag{2}$$

where τ is the applied torque, i is the measured torque, $K_m = 0.105$ is the motor torque constant, and $n = 9$ is the transmission ratio. In order to account for possible differences in motor friction, inertia, and torque constant, the same motor is used for all experiments.

The dynamical loading test is broken down into an extension experiment and flexion experiment. Both tests use a smaller amplitude of 4 Nm peak-to-peak torque with a 2 Nm torque offset for flexion and a -2 Nm torque offset for extension. This torque range is lower than those typically applied during exoskeleton use, however we found larger amplitudes uncomfortable in the context of a frequency sweep test. The frequency for the dynamic test varies from 1 Hz to 50 Hz using a exponential interpolation following Equation 3 to measure the inertial and damping parts of the system. The exponential interpolation is defined as

$$\omega = \omega_0 \left(\frac{\omega_f}{\omega_0}\right)^{t/T}, \tag{3}$$

where ω_0 and ω_f are start and end frequencies, t is current time, and T is the end time. Each test lasts 60 seconds.

We used a closed-chain test posture (Figure 4) to isolate interface dynamics without allowing leg motion, similar to tests conducted by Shepherd et al. [8]. The subject is placed in a seated position, where the position of the hip is constrained by the body weight of the subject, and the position of the foot is constrained using a spring loaded device. The spring loaded device also functions as a cue for the subject to apply a force roughly equal to one quarter that of an average adult body weight, in order to stimulate a consistent level of muscle co-contraction during activities. Because the hip joint and the ankle joint are both constrained, the position and motion of the knee joint is also considered to be fixed.

For the dynamical system test, we process the resultant frequency domain information to estimate dynamic stiffness. Given that the data under 3 Hz are very noisy and data above 15 Hz are dominated by inertial behavior, we decided to limit our usable observations from 3 Hz to 15 Hz. We then define the effective stiffness that we use to compare the two exoskeletons as the average magnitude of the transfer function over this range.

We calculate percentage improvement in stiffness parameters (α, β, and the effective dynamic stiffness) from lateral strap to normal loading attachments as the average percent difference over all conditions. For two stiffnesses, s_1 and s_2, we define the percent difference as $2(s_1 - s_2)/(s_1 + s_2)$. To validate that our results are statistically significant we perform a one tailed T-test between the normal loading and lateral loading stiffness.

B. Experiment Protocol

People trace through a large range of knee angles throughout the range of motion of walking and daily tasks. During walking, the knee remains fairly extended, while in stair climbing is is more flexed, and in a sit-to-stand motion it is almost flexed to 90 degrees. To capture the dynamics at a range of knee angles, we conducted experiments for three knee angles within the range of motion represented in daily tasks [28]: 90 degrees, 135 degrees, and 180 degrees.

At the start of the experiment, the first tested exoskeleton is decided using a coin flip. Once the exoskeleton is fastened, we place the subject's leg between 90 degrees, 135 degrees and 180 degrees, the order of which is chosen using a random number generator. Once the leg is held at a particular angle, we run the quasi-static test, the dynamic flexion test, and the dynamic extension test in series. The quasi-static test is always conducted first to allow for lateral comparisons, while the two dynamic loading tests are randomized via a random number generator. Optional rest periods are provided between each leg angle, and a longer rest period is provided in the middle of the experiment to dismount and fit the remaining exoskeleton. After testing on the first exoskeleton, the motor is swapped to the remaining exoskeleton and aforementioned process repeated. We do not further randomize the two exoskeletons, since swapping the motor from one exoskeletons to another accelerates wear and tear.

Muscle stiffness changes when under co-contraction or applying force [29]. During most motion tasks, leg muscles are applying force, often to support the body against gravity or achieve a desired movement. In order to partially simulate this co-contraction while maintaining a safe experimental environment, we designed a spring loaded pedal device, on which we instruct the subject to step. The pedal applies a force of around 200N at max compression, roughly simulating half of the force applied through one foot when standing, based on the average body mass of American adults [30]. The subject is instructed to keep the pedal fully depressed against the hard stop, ensuring a minimum level of muscle force. The pedal also ensures the position of the foot remains constant and fixed throughout the experiments.

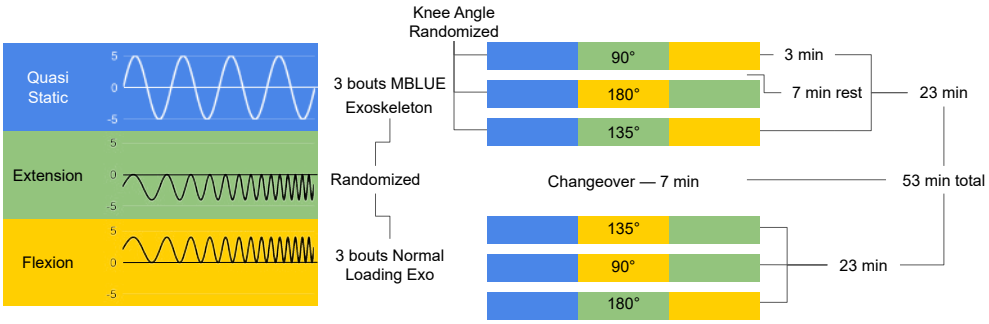


Fig. 3. **Experimental procedure**. Three tests are done per randomized leg position across both exoskeletons. Quasi-static test (blue) are done first for every trial and range from -5 Nm to 5 Nm of torque. Extension and flexion trials are then performed in random order and range from -4 Nm to 0 Nm and, from 0 Nm to 4 Nm respectively.

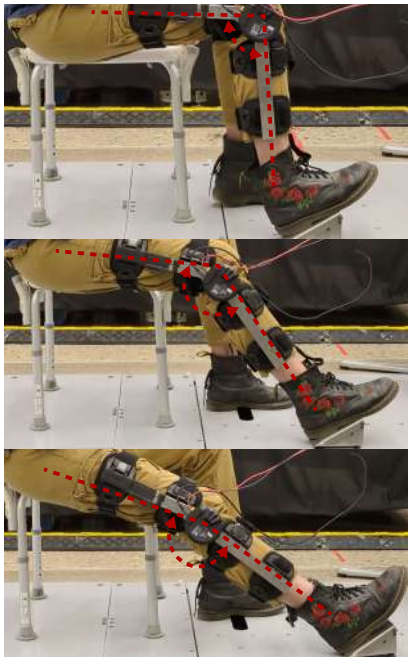


Fig. 4. **Experimental setup** illustrating three tested poses (90°, 135°, 180°), exoskeleton mounting, torque directions, and the spring-loaded pedal.

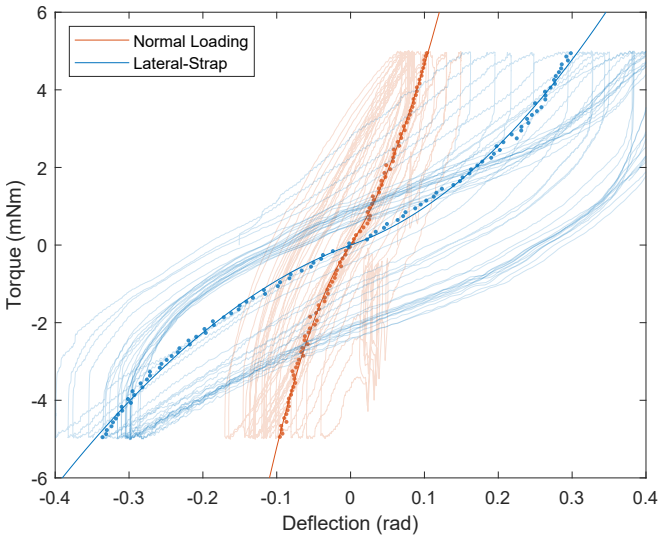


Fig. 5. **Quasi-static experiment results** of both the Lateral-Strap and Normal Loading attachments for one subject, showing the raw data (faint lines), binned averages (scatter plot in the middle), and piecewise quadratic regression (distinct line in the middle) used to approximate the data.

IV. RESULTS

A. *Quasi-Static Stiffness*

Pairwise t-tests show both linear and progressive components of stiffness are significantly higher for the normal loading configuration than the lateral-strap configuration for all loading directions and poses ($p < 0.01$). On average, the linear stiffness parameter α is 85.5% higher for the normal loading attachment, and the progressive stiffness parameter β is 91.9% higher. To visualize the goodness-of-fit we plot raw torque vs. deflection data for one subject at the 180 degree leg configuration in Figure 5. The regressed model (solid line) closely matches the binned data (scatter plot) for the 180 degree trial (Averaged R^2 value across all trials is is 0.982). While the rest of the data is obviated for clarity, the total fits for every subject across both exoskeletons and the different leg conditions (less opaque lines) and the average fit (solid lines) can be observed in Figure 6. We observe a higher slope in the normal loading case indicating higher stiffness. The increase in stiffness can be better understood by looking at the distribution of linear stiffness parameters $\alpha_{1,2}$ and progressive stiffness parameters $\beta_{1,2}$ in Figure 7. Despite the apparent discrepancies in distributions, we failed to find a significant difference in the coefficient of variation using an F-test in either the linear or quadratic parameters.

Surprisingly, we found that there was no significant difference between extension and flexion for the linear and progressive stiffness for either normal loading or lateral strap attachments. For the different knee angle conditions, we found that the linear quasi-static stiffness at a knee angle of 90 deg is higher than the stiffness at knee angles of 135 degrees and 180 degrees for both exoskeleton configurations ($p< 0.01$). A similar trend is yielded by a comparison of the quadratic terms of quasi-static stiffness. Quadratic coefficients at a knee angle of 90 degrees is higher than stiffnesses at both 135 and 180 degrees for both exoskeletons

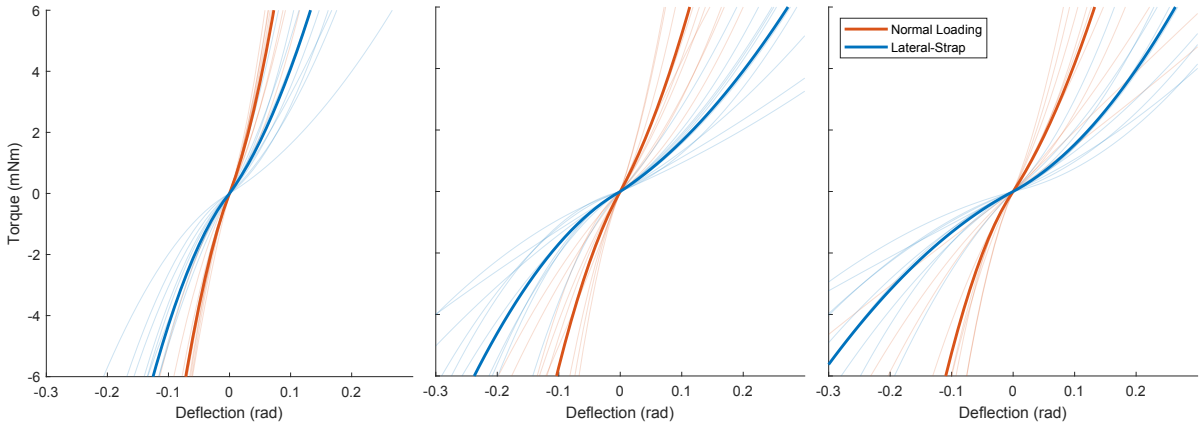


Fig. 6. **Comparison of output deflection vs. input torque** for 3 different knee angles: 90, 135, and 180 degrees. Lines shows piecewise quadratic regressions for each subject, and thick lines show the average of all subjects.

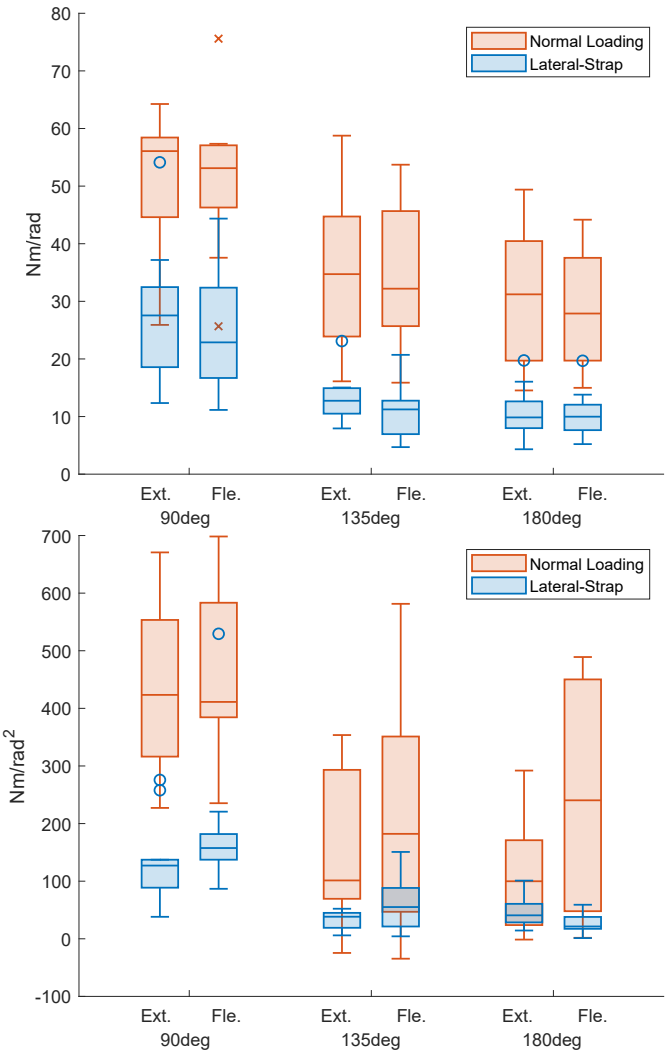


Fig. 7. **Quasi-static interface stiffness distribution** of the regression coefficients for extension α_1, β_1 (Ext.) and flexion α_2, β_2 (Fle.) of regressions (1) of Lateral-Strap vs. Normal Loading attachments in three different poses and two loading directions.

($p< 0.01$), and no significant difference is found between stiffnesses at 135 and 180 degrees.

B. Dynamic Stiffness

In line with the results for the quasi-static case, the normal loading exoskeleton design improved the dynamic interfacial stiffness compared to the lateral straps design ($p< 0.01$). We calculated the average percent difference of dynamic stiffness between the normal loading attachment and the lateral-strap attachment to be 85.7%. Representative Bode plots of the dynamic loading tests are shown in Figure 8, which also highlights the 3-15 Hz frequency window used to find the effective dynamic stiffness (average stiffness over the valid range) presented by the dotted straight line. We included two comparisons to illustrate a range of possible effective stiffnesses of the dynamic loading tests. A box and whiskers plot illustrates the consistency of the improvement from lateral strap to normal loading across the three poses and extension/flexion loading conditions (Figure 9).

There was no significant difference between the flexion and extension loading directions. We found that dynamic stiffness at 90 deg is significantly higher than stiffness at both knee angles of 135 degrees and 180 degrees for both exoskeleton configurations and both loading directions ($p< 0.01$), while there is no significant difference between stiffnesses at knee angles of 135 and 180 degrees. Dynamic stiffness for the Normal Loading attachment is consistently higher in extension than flexion ($p< 0.01$), while no difference is shown for the lateral-strap attachment. Similar to the quasi-static case, we found no significant difference in the coefficient of variance between normal loading and lateral-strap attachments.

V. Discussion and Conclusion

The normal loading exoskeleton resulted in stiffer interface stiffness across the quasi-static test and the dynamic test for all loading directions and knee angles ($p< 0.01$). In particular, we found an 85.5% increase in the quasi-static linear stiffness, 91.9% increase in the quasi-static progressive stiffness, and 85.7% in the dynamic effective stiffness.

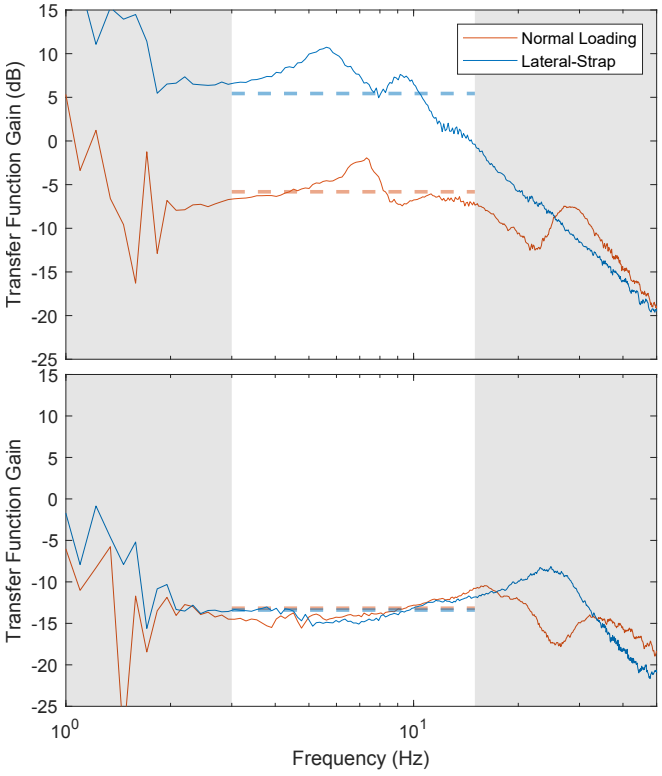


Fig. 8. **Dynamic compliance bode plots** showing extremes of gap between Normal Loading and Lateral-Strap stiffness for all experiments. An arithmetic average of the transfer function gain from 3Hz to 15Hz (highlighted area) is taken to represent the dynamic stiffness of the exoskeleton (dashed line). (Magnitude is in low-level device units of encoder tics per mNm.) Top graph is results from subject 10 at a knee angle of 90 degrees and in the extension direction. Bottom graph is from subject 6 at a knee angle of 180 degrees in the extension direction.

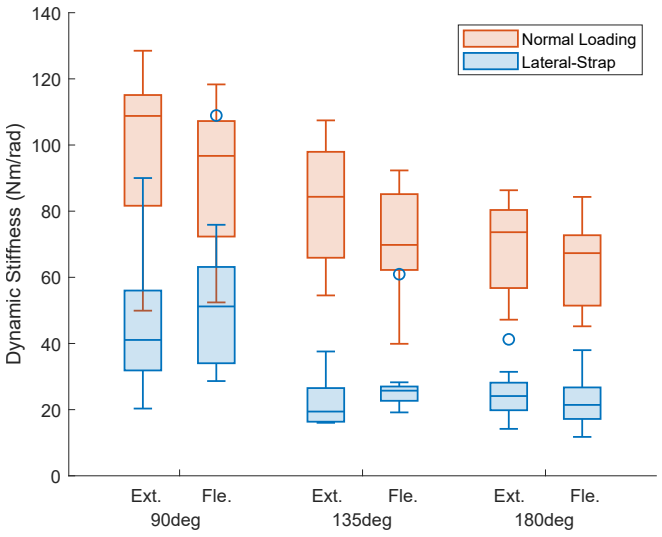


Fig. 9. **Dynamic interface stiffness distribution** between the two exoskeletons across three kinematic positions and across flexion and extension loading conditions. All 10 subjects represented in Box-Whisker plots. Ext. denotes loading in the extension direction, and Fle. denotes loading in the flexion direction.

Even though the normal loading attachment transfers force through straps in the flexion direction, the result was still significantly stiffer than for a comparable loading condition using the laterally attached exoskeleton. Moreover, we failed to find a statistically significant difference in the normal loading exoskeleton when loading in the flexion and extension direction. This reinforces our notion that a normal loading exoskeleton is stiffer due to more direct force transfer that avoids rotating tissue around an underlying bone.

Across knee angles, exoskeleton attachments, and loading directions, nonlinear stiffness terms represent a large amount of the total stiffness of both exoskeletons. At the end of the range of deflection, quadratic stiffness terms account for roughly half of all of the applied torque. The presence of progressive stiffness implies that tasks that have low deflection will result in less overall stiffness. For example, low-torque activities like level walking will be less stiff than high torques activities like sit-to-stand.

When comparing the linear stiffness in the quasi-static case to the dynamic stiffness we observe that the dynamic stiffness is generally larger. This is due to the fact that our analysis of the dynamic response assumes the system is linear, in which case the overall stiffness takes into account both the linear and quadratic term. Due to the large effect of the quadratic stiffness mentioned above, the linear term only represents a fraction of the overall stiffness represented in the dynamic test. Therefore, a one-to-one comparison between those values is not meaningful. However, we do note that they are in the same order of magnitude.

When comparing our results to the field, we see that at a knee angle of 90 degrees, the dynamic stiffness estimator had an average stiffness of 108.8Nm/rad in extension of 96.7Nm/rad in flexion. This is significantly lower compared to Shepherd et al.'s measurement of 327Nm/rad [8]. A few design differences in the tested exoskeletons may have resulted in this discrepancy: the Normal Loading attachment attaches to the shank directly, while Shepherd et al. attaches through both the shank and a foot plate; the Normal Loading attachment has a much lower system weight; and the Normal Loading attachment interfaces with the human body with a smaller area and thinner straps.

Despite the design of the experimental protocol, there are some variables that may not be well controlled and may skew the result of the experiment. For example, strap tightness was based on user comfort and not measured across different leg positions. Therefore there could be inter and intra-subject variations for each testing condition. The subjects are also not perfectly statically fixed during the experiment which can add noise to the measured deflection. The human subject may also move volitionally in response to slow loading, which is why we have excluded frequencies below 3 Hz from analysis in the dynamic test. The poses subjects are placed in may not be identical between experiments due to high variances in goniometer measurements of the knee angle [31].

Our modeling of the exoskeleton-human system might also have limited our explainability of the results. Inspection of bode plots reveal that most tests present with two dis-

tinct resonance peaks. Each peak corresponds to a specific resonance behavior, and we hypothesize that this is due to the two coupled mass-spring-damping systems that the exoskeleton-human interface can be abstracted into. As the exoskeleton is suspended by the thigh and shank attachments, oscillating forces resonate with the respective inertias, and result in the shape of the bode plot. Furthermore, quasi-static testing revealed a large amount of hysteresis in the interface behavior of the exoskeleton. Our analysis method obscures hysteretic parameters, but it may be useful to examine. We also do not analyze the phase model in the frequency domain, which may reveal dynamic hysteretic terms. Further research may be conducted to extract each parameter of the system and compensate for tissue dynamics in the controller.

Considered together, our experiments highlight the benefits of anteroposterior versus lateral human-exoskeleton interface attachments, as well as demonstrating an anteroposterior attachment design that is lightweight and relatively inexpensive to fabricate. Ideally, these results would inform design choices, especially for assistive exoskeletons that could benefit from feedback control and desire improved dynamic performance.

REFERENCES

[1] M. Grimmer, R. Riener, C. J. Walsh, and A. Seyfarth, "Mobility related physical and functional losses due to aging and disease-a motivation for lower limb exoskeletons," *J. Neuroeng. Rehabil.*, vol. 16, pp. 1–21, 2019.

[2] G. Lv, H. Zhu, and R. D. Gregg, "On the design and control of highly backdrivable lower-limb exoskeletons: A discussion of past and ongoing work," *IEEE Control Syst.*, vol. 38, no. 6, pp. 88–113, 2018.

[3] H. Zhu, C. Nesler, N. Divekar, V. Peddinti, and R. D. Gregg, "Design principles for compact, backdrivable actuation in partial-assist powered knee orthoses," *IEEE/ASME Trans. Mechatron,*, vol. 26, no. 6, pp. 3104–3115, 2021.

[4] M. P. De Looze, T. Bosch, F. Krause, K. S. Stadler, and L. W. O'sullivan, "Exoskeletons for industrial application and their potential effects on physical work load," *Ergonomics*, vol. 59, no. 5, pp. 671–681, 2016.

[5] N. V. Divekar, G. C. Thomas, A. R. Yerva, H. B. Frame, and R. D. Gregg, "A versatile knee exoskeleton mitigates quadriceps fatigue in lifting, lowering, and carrying tasks," *Science Robotics*, vol. 9, no. 94, p. eadr8282, 2024.

[6] M. B. Yandell, B. T. Quinlivan, D. Popov, C. Walsh, and K. E. Zelik, "Physical interface dynamics alter how robotic exosuits augment human movement: implications for optimizing wearable assistive devices," *J. Neuroeng. Rehabil.*, vol. 14, pp. 1–11, 2017.

[7] M. S. Cherry, S. Kota, A. Young, and D. P. Ferris, "Running with an elastic lower limb exoskeleton," *J. Appl. Biomech.*, vol. 32, no. 3, pp. 269–277, 2016.

[8] M. K. Shepherd and E. J. Rouse, "Design and validation of a torque-controllable knee exoskeleton for sit-to-stand assistance," *IEEE/ASME Trans.Mechatronics*, vol. 22, no. 4, pp. 1695–1704, 2017.

[9] M. B. Yandell, B. T. Quinlivan, D. Popov, C. Walsh, and K. E. Zelik, "Physical interface dynamics alter how robotic exosuits augment human movement: implications for optimizing wearable assistive devices," *J. Neuroeng. Rehabil.*, vol. 14, pp. 1–11, 2017.

[10] A. J. Young and D. P. Ferris, "State of the art and future directions for lower limb robotic exoskeletons," *IEEE Trans. Neural Syst. and Rehabil. Engineering*, vol. 25, no. 2, pp. 171–182, 2016.

[11] M. B. Yandell, D. M. Ziemnicki, K. A. McDonald, and K. E. Zelik, "Characterizing the comfort limits of forces applied to the shoulders, thigh and shank to inform exosuit design," *PloS one*, vol. 15, no. 2, p. e0228536, 2020.

[12] C. Nesler, G. Thomas, N. Divekar, E. J. Rouse, and R. D. Gregg, "Enhancing voluntary motion with modular, backdrivable, powered hip and knee orthoses," *IEEE Robotics and Automation Letters*, vol. 7, no. 3, pp. 6155–6162, 2022.

[13] D. D. Molinaro, K. L. Scherpereel, E. B. Schonhaut, G. Evangelopoulos, M. K. Shepherd, and A. J. Young, "Task-agnostic exoskeleton control via biological joint moment estimation," *Nature*, vol. 635, no. 8038, pp. 337–344, 2024.

[14] J. S. Lora-Millan, F. J. Sanchez-Cuesta, J. P. Romero, J. C. Moreno, and E. Rocon, "A unilateral robotic knee exoskeleton to assess the role of natural gait assistance in hemiparetic patients," *J. Neuroeng. Rehabil.*, vol. 19, no. 1, p. 109, 2022.

[15] K. Langlois, D. Rodriguez-Cianca, B. Serrien, J. De Winter, T. Verstraten, C. Rodriguez-Guerrero, B. Vanderborght, and D. Lefeber, "Investigating the effects of strapping pressure on human-robot interface dynamics using a soft robotic cuff," *IEEE Trans. Medical Robotics and Bionics*, vol. 3, no. 1, pp. 146–155, 2020.

[16] M. Sposito, S. Toxiri, D. Caldwell, J. Ortiz, and E. De Momi, "Towards design guidelines for physical interfaces on industrial exoskeletons: overview on evaluation metrics," in *Wearable Robotics*. Springer, 2019, pp. 170–174.

[17] K. Langlois, M. Moltedo, T. Bacek, C. Rodriguez-Guerrero, B. Vanderborght, and D. Lefeber, "Design and development of customized physical interfaces to reduce relative motion between the user and a powered ankle foot exoskeleton," in *IEEE Int. Conf. Biomedical Robotics and Biomechatronics*. IEEE, 2018, pp. 1083–1088.

[18] E. E. Neumann, T. M. Owings, and A. Erdemir, "Regional variations of in vivo surface stiffness of soft tissue layers of musculoskeletal extremities," *J. Biomech.*, vol. 95, p. 109307, 2019.

[19] M. Shafiei and S. Behzadipour, "The effects of the connection stiffness of robotic exoskeletons on the gait quality and comfort," *J. Mechanisms and Robotics*, vol. 12, no. 1, p. 011007, 2020.

[20] D. S. Chander, M. Böhme, M. S. Andersen, J. Rasmussen, J. Zentner, and M. P. Cavatorta, "A comparison of different methods for modelling the physical human-exoskeleton interface," *Int. J. Human factors modelling and simulation*, vol. 7, no. 3-4, pp. 204–230, 2022.

[21] B. J. McLain, D. Lee, S. C. Mulrine, and A. J. Young, "Effect of assistance using a bilateral robotic knee exoskeleton on tibiofemoral force using a neuromuscular model," *Ann. Biomed. Eng.*, vol. 50, no. 6, pp. 716–727, 2022.

[22] M. d. C. Sanchez-Villamañan, J. Gonzalez-Vargas, D. Torricelli, J. C. Moreno, and J. L. Pons, "Compliant lower limb exoskeletons: a comprehensive review on mechanical design principles," *J. Neuroeng. Rehabil.*, vol. 16, pp. 1–16, 2019.

[23] S. Guitteny, Y. Lafon, V. Bonnet, R. Aissaoui, and R. Dumas, "Dynamic estimation of soft tissue stiffness for use in modeling socket, orthosis or exoskeleton interfaces with lower limb segments," *J. Biomech.*, vol. 134, p. 110987, 2022.

[24] A. J. Young, J. Foss, H. Gannon, and D. P. Ferris, "Influence of power delivery timing on the energetics and biomechanics of humans wearing a hip exoskeleton," *Front. Bioeng. Biotechnol.*, vol. 5, p. 4, 2017.

[25] Skip Innovations, "Skip - move more with powered movewear technology," https://www.skipwithjoy.com/.

[26] R. J. Farris, H. A. Quintero, and M. Goldfarb, "Performance evaluation of a lower limb exoskeleton for stair ascent and descent with paraplegia," in *IEEE nt. Conf. Eng. Med. Biol. Soc.* IEEE, 2012, pp. 1908–1911.

[27] Y. Chun, C. P. McGowan, J. Kim, and J. P. Bailey, "Application of polynomial regression model for joint stiffness," *Int. J. of Exercise Science*, vol. 15, no. 1, p. 1236, 2022.

[28] M. A. Wimmer, W. Nechtow, T. Schwenke, and K. C. Moisio, "Knee flexion and daily activities in patients following total knee replacement: a comparison with iso standard 14243," *BioMed Research Int.*, vol. 2015, no. 1, p. 157541, 2015.

[29] Y. Lee, M. Kim, and H. Lee, "The measurement of stiffness for major muscles with shear wave elastography and myoton: a quantitative analysis study," *Diagnostics*, vol. 11, no. 3, p. 524, 2021.

[30] C. D. Fryar, M. D. Carroll, Q. Gu, J. Afful, and C. L. Ogden, "Anthropometric reference data for children and adults: United states, 2015-2018," *Vital and Health Statistics*, no. 46, 2021.

[31] D. C. Boone, S. P. Azen, C.-M. Lin, C. Spence, C. Baron, and L. Lee, "Reliability of goniometric measurements," *Phys. Ther.*, vol. 58, no. 11, pp. 1355–1360, 1978.

Green Means Go(Bot): Using an Assistive Robot to Encourage Independent Walking Practice by a Child with Motor Disabilities

Ameer Helmi[1], Tze-Hsuan Wang[2], Samuel W. Logan[2], and Naomi T. Fitter[1]

***Abstract*— For children with motor disabilities, a wide range of assistive technologies (such as exoskeletons, treadmill trainers, and body-weight support harnesses) exist to support learning to walk. However, after the onset of independent walking, few technologies are geared toward helping children with motor disabilities to practice walking and improve walking control. In this paper, we assess the ability of GoBot, a custom assistive robot with multiple game modes, to encourage one child with a motor disability to improve their amount, speed, and control of independent walking. We conducted a 12-session single-subject study and found that the child walked more and faster while engaging in lightly competitive races against a directly teleoperated GoBot, compared to during experiences in a standard of care condition. As a second and more exploratory element of our work, we equipped GoBot to autonomously play the common children's game red light, green light (RLGL) with the user as an entertaining way to motivate balance practice. Anecdotally, this RLGL activity led to some of the highest levels of child engagement. The preliminary findings of our single-subject study can benefit researchers working with assistive robots and physical therapists working with children with independent walking practice goals.**

I. Introduction

Children with motor disabilities typically experience delays in major motor milestones such as walking [1]. Research into improving children's ability to walk has primarily focused on helping children develop the skill of walking through physical therapy interventions with devices such as a treadmill trainer [2]. However, outside of adaptive physical education programs [3], few works have evaluated assistive-technology-mediated methods to support the continual improvement of children's amount and speed of overground walking after they develop the ability to independently walk. This gap is important; children with enhanced walking stamina and control are able to better participate in activities of daily living [4] and accomplish higher levels of physical activity [5]. In this work, we designed a proof-of-concept intervention with a custom assistive robot to help augment the methods available for encouraging a child with a motor disability to walk more, faster, and with more control.

Our custom assistive robot, GoBot, uses gamification in the presented interactions with the end user. Gamification of physical therapy interventions (e.g., with virtual reality [6]) is a common strategy for improving child engagement, but gamified motor interventions for children have primarily centered on treadmill training for children who are still learning to walk. One novel emergent method to motivate the practice of walking is the use of assistive robots; a robot's embodiment allows it to facilitate compelling gamified interactions in the physical world to keep children engaged during interventions. Two past efforts have shown the benefits of using peer-like assistive robots to improve motor practice by children with motor disabilities who are still using mobility aids [7], [8]. This promising initial work motivated us to research a robot-mediated intervention for a child who was beginning to walk independently, but required motivation to continue practicing aspects of walking such as stamina, speed, and control.

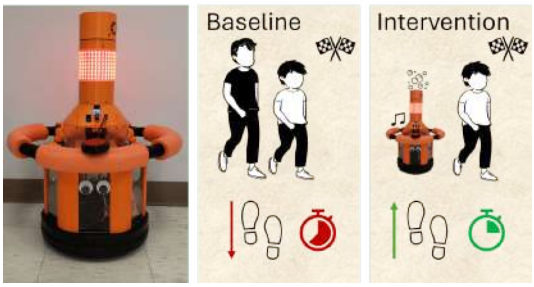


Fig. 1: *Left*: GoBot, our custom assistive robot with light, sound, and bubble rewards. *Center and Right*: Depiction of the key methods and results for our study phases.

Our main research goal in the presented work was to *evaluate if an assistive robot could motivate a child with a motor disability to improve their amount and speed of independent walking*. We used a GoBot robot [9], as shown in Fig. 1, that was equipped with racing and red light, green light (RLGL) game modes to conduct a 12-session single-subject study with a child who was focused on improving their independent walking. In this paper, Section II covers related work on the improvement of children's walking skills, gamification, and assistive robotics. Then, we elaborate on the robot design and the methods of the multi-month single-subject study in Section III. As conveyed in Section IV, our study results showed that the child tended to improve their amount and speed of walking while racing against the robot when compared with the baseline (i.e., standard of care) condition. Additionally, the child was able to successfully understand and play the RLGL game independently. Finally, we discuss the implications, strengths, and limitations of this work in Section VI. The main contribution of this work is early evidence that an assistive robot could help improve a child's amount, speed, and control of independent walking.

II. Related Work

Related work on improving children's walking skills, gamification strategies in pediatric interventions, and assistive robot design helped to inform the presented work.

[1]Collaborative Robotics and Intelligent Systems (CoRIS) Institute, Oregon State University, Corvallis, Oregon, USA. [helmia, fittern]@oregonstate.edu

[2]Disability and Mobility Do-It-Yourself Cooperative, Oregon State University, Corvallis, Oregon, USA.

When forming the presented work, we learned from our clinical collaborators that for some children with disabilities who are beginning to walk independently, physical therapy goals range from increasing the amount of walking to increasing speed and balance. Increasing levels of physical activity for young children is vital for health and carries benefits such as improving bone density and cardiometabolic health [10], [11]. Children typically perform the most physical activity in physical education (PE) programs at school, but adaptive physical education programs for children with disabilities continue to lag behind PE programs for children without motor disabilities [3], [12]. Outside of school programs, children with motor disabilities will engage in physical therapy interventions using rehabilitation technologies such as the previously mentioned treadmill trainer to improve motor skills [2]. Exoskeletons are another technology that could help young children (before and after the onset of walking) via different levels of support for walking more and faster, but these devices are cost-prohibitive and primarily tailored towards children still learning to walk [13], [14]. This leaves a gap for children with motor disabilities who need to improve their walking functions; they still need engaging interventions designed to help encourage the further improvement of walking. In our study design, we focused on improving our child end user's amount and speed of walking through lightly competitive races with a robot and enhancing their walking control via playing RLGL with the robot.

Keeping children engaged in any pediatric intervention is a key component of further enhancing motor gains. Researchers have focused on using gamification strategies with technologies such as virtual reality (VR) or biofeedback to encourage social and cognitive interaction during an intervention, but have primarily incorporated these technologies into assistive devices such as treadmill trainers. One team designed a VR soccer game to allow children on a treadmill trainer to walk and kick a virtual soccer ball [6] while another team designed a VR world for a child to experience while walking on a treadmill trainer [15]. Researchers have also developed biofeedback tools as another method for increasing engagement during treadmill training interventions. While the child is walking on the treadmill, changes in heart rate or breathing rate prompts visual or audio cues on a tablet or larger screen that are designed to celebrate walking more or faster and continue to encourage movement [16], [17]. While these tools could be used for a child walking with or without assistance on a treadmill, there are benefits to children walking overground, such as social and cognitive benefits that complement the motor gains [8]. This idea encouraged us to use assistive robots, a newer tool in pediatric interventions, as the external motivating factor to encourage child motor practice during overground walking.

Assistive robots can offer more motivation than similar types of technologies which are not embodied in the physical world [18], and have achieved preliminary success in child mobility encouragement. Assistive robots encouraging physical activity are often studied with older adult populations [19], but fewer works have investigated using robots to encourage physical activity for young children without motor disabilities [9], [20]. For children with motor disabilities, robotic treadmill trainers such as the Lokomat have shown success in providing direct support to a child's gait during treadmill training interventions [21], but these tools are focused on children still learning to walk. In our own related work, we found preliminary evidence that GoBot could encourage a child with a motor disability using a body-weight support harness (BWSH) to take more supported steps in the environment [7], while a different research team using a BWSH found promising results using NAO and Dash robots [8]. These benefits of using robots for motivation during physical activity interventions encouraged us to develop multiple game modes for GoBot and conduct a multi-month single-subject intervention designed to encourage a child with a motor disability to independently walk more and faster.

III. Single-Subject Study Methods

We conducted a single-subject study to evaluate if the presence of an assistive robot could motivate a child to independently walk more and faster during physical therapy, compared to in standard-of-care experiences. Our university ethics board approved the study (protocol #IRB-2020-0723).

A. Study Design

The study lasted for 12 sessions using a single-case ABAB withdrawal study design [22]. With this design, the study was divided into 4 phases: two 3-session baseline phases (labeled as "A1 and A2") in which the assistive robot was not present and two 3-session intervention phases (labeled as "B1 and B2") in which the assistive robot encouraged the child to walk. We alternated the baseline and intervention phases in an AAA-BBB-AAA-BBB pattern as further described below:

- *First Baseline - A1* (3 sessions): The child independently walked during races with a clinician or research staff, but no assistive robot.
- *First Intervention - B1* (3 sessions): The child independently walking during races with a teleoperated GoBot, which used its reward features (as further explained in Section III-B) to encourage the child.
- *Second Baseline - A2* (3 sessions): As in the first baseline phase, the child walked with a clinician/researcher.
- *Second Intervention - B2* (3 sessions): As in the first intervention phase, the child walked with the robot.

In alignment with the single-subject style of this work, the participant served as their own baseline, allowing us to observe the impact of introducing the assistive robot on the child's amount and speed of walking.

Each session lasted up to 30 minutes and occurred approximately every two weeks over a six-month period. These sessions took place between the participant's usual every other week physical therapy sessions.

B. Robotic System

We used a teleoperated GoBot (see Fig. 2) with flashing lights, bubble-blowing, and a library of sounds as motivating stimuli to encourage the child to walk during the robot races. Further detail on the early design of GoBot and its reward

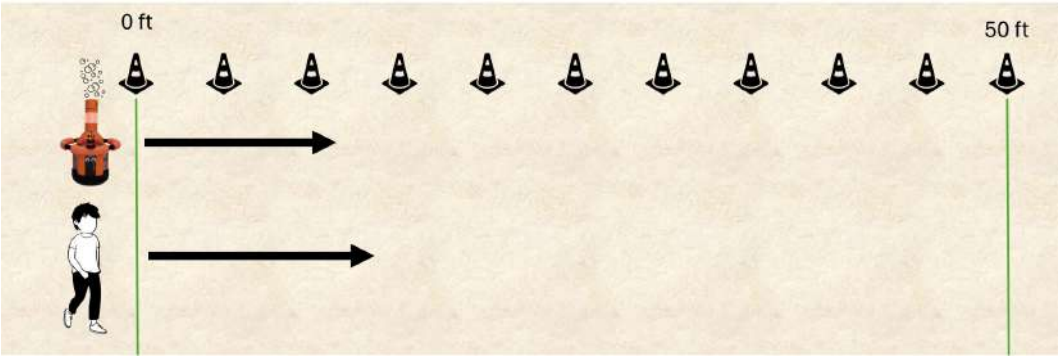


Fig. 2: Schematic of the robot races setup, including the child participant, robot, and cones for easily tracking distance walked. A complete "lap" was marked each time the child reached one extreme end of the cones.

features is available in our past work, e.g., [23]. Briefly, this robot has a custom reward hardware stack on top of a TurtleBot2 robot. It is capable of two-dimensional overground motion as well as the aforementioned reward features. The robot is orange to match the Oregon State University colors while also providing high-contrast and easy visibility.

C. Participant

Our participant was male and 7.1 years old. The participant has a diagnosis of multiple malformation syndromes with global developmental delay. At the start of the study, the participant primarily used wall walking and bottom scooting at home and was able to walk independently, but frequently required assistance. He communicated with single words, as well as through signs and gestures. The clinicians' goal was to improve his walking balance, endurance, and speed.

D. Procedure

Each study session was administered by one clinician and two research assistants. At the start of the study, the parents reviewed and signed an informed consent form and completed a demographics survey and a pre-study survey, as further explained in Section III-E. Before the start of a session, cones were laid out in a straight line at 5ft (1.5m) intervals to the side of the participant's walking course, ending at 50ft (15.2m) away. During intervention phases (B1 and B2), GoBot was placed alongside the child prior to beginning the session. A Canon camera recorded a front view while a GoPro Hero Black 7 recorded a side view. Four ActiGraph GT9X Link sensors were placed on the right and left ankle, right wrist, and hip of the child.

During the session, the child was tasked to race alongside either a clinician or research assistant (in baseline sessions) or GoBot (in intervention sessions) to the end of the cones. Each time the child reached the end of the cones, we noted a completed lap. At the end of each lap, we asked the child if they wanted to immediately turn around and start a new lap or take a break. During each lap, the child could request direct physical assistance from the clinician or parent in the form of holding one hand. A researcher noted the duration of each lap using a stopwatch. The researcher also recorded if the lap was completed independently or was assisted at any point by a clinician/parent. During the intervention phases, a researcher teleoperated GoBot to race alongside the child and used its features to encourage them to walk faster than the robot. Figure 2 shows a schematic of the study setup. Each session lasted 30 minutes.

At the end of a session, the sensors were removed from the child. Parents completed the post-session survey and were compensated $15 for each session. At the end of the study, parents completed the post-study survey. (These surveys are further explained in Section III-E.)

E. Measurements and Analysis

Measurements collected included *movement* data and *self-report* data. For each movement-based measurement, the data was analyzed for trends between baseline and intervention phases and the log response ratio (LRR) was calculated to compare each baseline and intervention phase. The LRR compares the intervention phase mean (M_t) to its preceding baseline phase mean (M_b) using the following equation:

$$LRR = ln(\frac{M_t}{M_b}) \quad (1)$$

LRR is commonly used in single-case work across domains such as ecology [24], special education [25], and behavioral psychology [26] to show changes in a measurement between the baseline and intervention. A positive LRR value indicates an upward trend for the measurement, an LRR value of zero marks no change, and a negative LRR value indicates a decline in the trend for the measurement. Larger LRR values represents a larger change between phases. For each of the movement-based measurements, we calculated the LRR value for the first intervention phase against the first baseline phase (i.e., B1 to A1; identified as LRR_1) and the second intervention phase against the second baseline phase (i.e., B2 to A2; LRR_2). We report each individual LRR value, as well as the overall mean LRR (LRR_M).

1) Movement-Based Measurements: This data included a count of ankle movements (calculated from the ActiGraph data recordings), the total distance of independent walking (transcribed during study sessions and later checked), the number of completed independent laps (live transcribed and checked), and the average duration of independent laps from each session (live transcribed and checked), as further elaborated below.

Ankle Movement Counts came from ActiGraph sensor data that was processed through an algorithm in related work [27] to compute a count of events that were likely

be *ankle movements*. We first used ActiLife v6.13.4 software to extract the recorded accelerometer and gyroscope data from the ActiGraph sensors. In this work, we focused on analyzing only the ankle sensor recordings since we were most interested in walking movement. The algorithm operates by first calculating the root mean square (RMS) acceleration and angular velocity from the raw ankle sensor recordings and then filtering the output by rejection ranges clarified in the related work [27]. After incorporating a 0.5-second window moving average filter, the algorithm identified an ankle movement starting when both the acceleration and gyroscope thresholds were exceeded and ending when the gyroscope data dropped below the associated threshold. We used the algorithm to calculate the total count of ankle movements for each session, including movement during both independent and assisted laps.

Independent Walking Metrics (i.e., total amount of independent walking, number of completed independent laps, and average duration of independent laps) came from live transcription during the study sessions by a researcher who actively monitored each lap. This live transcription data was then reviewed post hoc using video recordings; a video coder work with the original note-taker to ensure a 100% match rate in the coding. For both coding rounds, each lap was marked as completed fully independently (i.e., no physical assistance while walking) or assisted (i.e., holding one or both of the clinician's hands while walking). We only considered laps that were completed fully independently by the participant in the coding, as the the child's goals centered on amount and speed of independent walking specifically. We calculated the total amount of independent walking (in ft) by multiplying the number of laps completed fully independently by the length of the walking course (50ft). We also tallied the total number of fully completed independent laps for each session and calculated the mean duration of the fully independent laps during each session (in seconds).

2) Self-Reports: These inventories included demographic questions, pre-/post-study surveys, and a post-session survey.

Demographic questions collected child age, gender, diagnoses, and if the child was able to walk or crawl.

The pre-study survey included the following:

- All three components of the Negative Attitudes towards Robots Scale (NARS) [28], which the parents responded to using Likert-type scales from Strongly Disagree (1) to Strongly Agree (7).
- Trust Perception Scale-HRI (TPS-HRI) subscale items [29] rated as a percentage from 0 to 100. We used the 14-item abridged version.
- Free-response questions asking about the parents' prior experiences with robots.

At the end of each session, parents completed a survey which included Likert-type questions relating to the child's experience during each session. Specifically, parents answered the following custom Likert-type questions after every session:

- "How excited was your child today?" from Very Calm (1) to Very Excited (7)
- "What was the enjoyment level for your child?" from Very Unhappy (1) to Very Happy (7)
- "How well do you think your child interacted with others?" from Very Poor (1) to Very Well (7)

For intervention sessions with the robot, parents also answered the following Likert-type and free response post-session questions about their perception of the robot:

- "Do you think your child was engaged with the robot throughout the session?" from Strongly Disagree (1) to Strongly Agree (7)
- "Do you think robots can be useful to improve the well-being of children?" from Strongly Disagree (1) to Strongly Agree (7)
- "How do you think robots can be used to improve the well-being of children?"
- "In general, how did your child interact with the robot throughout the session?"
- "In general, what was your perception of the robot used in this session?"

At the end of the study, parents completed the same NARS and TPS-HRI survey items with additional questions asking about their final perceptions of the assistive robot.

IV. Single-Subject Study Results

The participant completed all 12 sessions and the assistive robot was fully functional for every intervention session. In this section, movement-based results are presented first, followed by self-report results. ActiGraph sensor results for session 8 were lost due to a recording error.

A. Movement-Based Results

The results of the study show that the child tended to increase their amount of independent walking throughout the study. Figure 3 shows the results for each measurement while Table I shows the LRR outcomes for each baseline and intervention phase combination. The participant completed at least one independent lap in every session. Although ankle count (including independent and assisted steps) results showed a decrease during the first intervention phase with the robot, independent walking distance generally increased during the first intervention phase's sessions. Step counts were generally high during the second half of the study, and LRR results showed a repeated increase in independent walking distance for the second intervention phase (when compared with the second baseline phase), although the second LRR value was not as high. The independent lap results closely mirrored the independent walking distance results. The highest number of completed laps occured during session 10 (a robot intervention session). Results also elucidated that the participant sped up their average duration of independent laps in the second half of the study. The child's fastest independent laps occurred during session 10, with the robot.

B. Self-Report Results

Self-report results for the per-session surveys are shown in Fig. 4. The parents tended to rate the child's excitement, enjoyment, and interaction level as above average for most

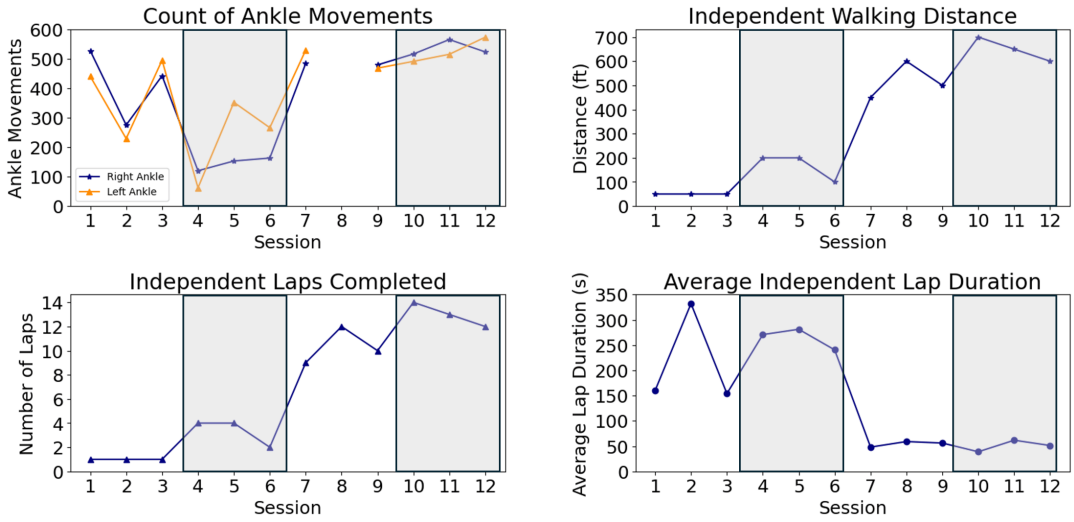


Fig. 3: Movement results by session, including the count of ankle movements, distance of independent walking, completed independent laps, and average duration of completed independent laps. The participant completed at least one independent lap in every session. The shaded area denotes the intervention phases.

TABLE I: Log response ratio (LRR) results, where a positive value indicates a higher intervention value (compared to the preceding baseline). Shaded values specify large increases in child movement (i.e., LRR > 1).

Measurement	LRR_1	LRR_2	LRR_M
Ankle Movements	-0.77	0.08	-0.20
Independent Walking	1.20	0.23	0.36
Independent Laps	1.20	0.23	0.36
Fastest Lap	0.2	-0.07	0.15

sessions, with the exception of session 3. Overall, the parents rated the child as being very engaged during intervention sessions with the robot ($M = 6.7$, $SD = 0.5$). For the NARS questionnaire, there was no change in the average ratings between the start and end of the study for the interaction component ($M = 3.6$, $SD = 0.9$ before; $M = 3.6$, $SD = 1.1$ after). There tended to be a decrease in ratings for the social component ($M = 3.3$, $SD = 1.1$ before; $M = 3$, $SD = 0$ after) and an increase in the emotional component ($M = 2.3$, $SD = 0.8$ before; $M = 3.3$, $SD = 0.8$ after). A decrease in ratings for each component of the NARS would indicate that the parent tended towards a more positive attitude towards robots for that component. Trust ratings tended to stay the same between the start and end of the study ($M = 78.0$, $SD = 11.4$ before; $M = 77.0$, $SD = 9.5$ after). Free-text responses from the parents offer insights into interactions with the robot. The parents noted that "[he] seemed more interactive with [GoBot] and I understand why because of mobility" and "[GoBot's] movement, lights, and bubbles kept him more engaged." For the final session, the parents responded that "he appeared to be competitive during racing and attentive during interactions."

V. Exploratory RLGL Interaction

Although we were able to evaluate walking amount and speed using the single-subject-style study, this interaction did not provide much of an ability to study motion control, another important part of motor development and practice.

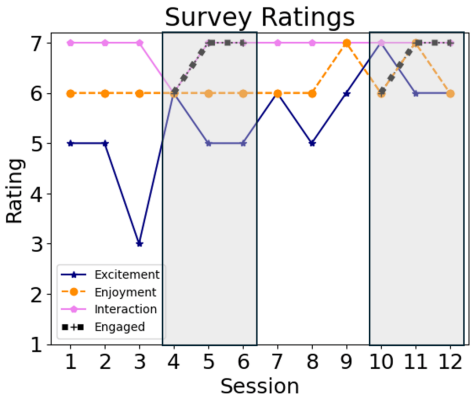


Fig. 4: Self-report results by session. Results include parent ratings of excitement, enjoyment, interaction, and engagement with the robot. Engagement questions were only distributed during intervention sessions.

Accordingly, we added a brief (exploratory) RLGL interaction to the close of intervention sessions as a way to begin to assess this interaction's viability for motor control practice. We chose to use RLGL for this child based on a collaborative discussion between the researchers, clinicians, parents, and child. The game includes a high stimulus-response agreement between green means "go" and red means "stop" while also encouraging starting and stopping movement control.

A. RLGL Interaction Methods

At the close of the intervention sessions, we presented the participant with the opportunity to play RLGL with the robot.

Gameplay Procedure: The participant could play RLGL with GoBot for up to five minutes (i.e., one or two games' duration). We placed GoBot 20ft (6.1m) from the starting mark and a researcher started the autonomous game mode, as further described in the next paragraph. Figure 5 demonstrates the setup for the game.

GoBot's RLGL game mode involved three states: *green light*, *red light*, and *game win*. Typically, the green light

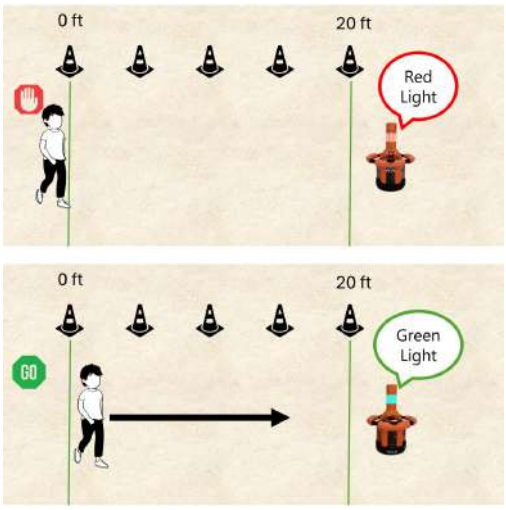


Fig. 5: Schematic of the exploratory RLGL setup.

and red light states alternated until the child reached the robot and pressed the robot's big red button, which activated the game win state. The green light state involved the robot turning away from the participant (i.e., the googly eyes looked away) while flashing the green lights, and saying "green light" out loud. In the red light state, the robot turned to face the participant, flashed the red lights, and said "red light" out loud. Based on the typical rules of the game, the child needed to move toward the robot during the green light state and to stop moving during the red light state. Both states alternated with a random duration in the range of 3-5 seconds. The game ended when the child pressed the robot's onboard button during a green light state. At that point, the robot indicated that the game was complete by flashing the green lights, blowing bubbles, and playing a cheering sound. The leftmost panel of Fig. 1 shows the robot in the red light state.

Measurement: During the RLGL game, a researcher took field notes which included observations, the number of times the game was played, and the percentage of games in which the child walked independently.

B. RLGL Interaction Results

Results from playing RLGL are shown in Table II. The child completed the game at least once every intervention session and displayed an understanding of the game by stopping and starting during the correct game states. In session 10, the child asked to play the game a second time before the session ended and walked independently during all time spent playing the game. The parents noted "his best interaction was during red light/green light" in session 10. Anecdotally, we also observed that the child would make a "stop" gesture with his hand during the red light phase and would point forward during the green light phase while making a train engine sound.

VI. Discussion

In this work, we evaluated how GoBot could motivate a child with a motor disability to independently walk more and faster by engaging in lightly competitive races. We found that the robot tended to encourage the child to independently walk more and faster, especially during the second half of the study. The largest change in independent movement was between sessions 6 and 7, perhaps due to an additional family member being present at session 7. However, the child continued to improve their levels of independent movement for the rest of the study, and the highest amount of independent movement/fastest independent lap overall occurred during session 10 with GoBot. The parents observed that their child was more engaged during intervention sessions and seemed motivated by the robot's reward features and mobility.

TABLE II: RLGL results from intervention sessions. The RLGL game was played at least once during each intervention session. For each session, the number of games played and the percentage of independent walking during the game was noted. Shaded cells denote sessions where the child played RLGL independently at least once.

Session	Games Played	% Independent
4	1	0
5	1	0
6	1	0
10	2	100
11	2	50
12	1	0

The RLGL game offered a different interaction premise to continue encouraging independent walking and balance. The child demonstrated an understanding of the game and asked to play a second time in sessions 10-11. The nature of RLGL encourages stopping and starting, which helped the child to practice balancing and starting to walk again. The presence of the button on the robot provided a clear goal for the child and facilitated celebration through bubbles and lights once the game was won. The majority of games played involved assisted movement, which may have been a result of the child being tired at the end of a session. There was no baseline comparison made against RLGL so further study is warranted to understand how the robot-mediated RLGL experience compares to other analogous experiences. The flexibility of GoBot to incorporate novel reward modules and different types of gameplay enables a plethora of interaction paradigms for children with unique needs.

A key *strength* of this work is its multi-month duration and preliminary demonstration that an assistive robot could motivate a child with a motor disability to independently walk more and faster. The robot races seemed to offer light competitiveness and encourage the child to move faster through the robot's mobility and rewards. A second strength is that the RLGL mode demonstrated that different robot paradigms can potentially motivate a child to work towards different goals, such as improving balance. A *limitation* of this study was the small sample size. The single-case design provided unique insights into this specific child's progress throughout the study, but further study with larger samples is needed to generalize the results. A second limitation is that we did not use any assessments such as the GMFCS [30] or collect self-reports from the child directly. Future work with this robot may include a focus on children with cerebral palsy, a more common developmental disability, and in gameplay

sessions with multiple children (i.e., group play).

We set out to understand whether an autonomous assistive robot could promote more independent walking for a child with a motor disability who was already walking. We conducted a longer-term successful single-case study and showed that the robot tended to motivate more and faster movement during robot races. Additionally, we found that the child understood and enjoyed playing the RLGL game with the robot during exploratory interactions, demonstrating potential for a future study focused on improving the child's balance, cognitive, and social abilities with RLGL. We encourage others in the assistive robotics space to consider ways that robots can help children to "start their engines" and play.

ACKNOWLEDGMENTS

We thank Dr. Dianne Hrubec, April X. Murray, Sydney Fujimoto, and Rafael Morales Mayoral for data collection support. NSF award CMMI-2024950 supported this work.

REFERENCES

[1] A. Ghassabian, R. Sundaram, E. Bell, S. C. Bello, C. Kus, and E. Yeung, "Gross motor milestones and subsequent development," *Pediatrics*, vol. 138, no. 1, 2016.

[2] K. L. Willoughby, K. J. Dodd, and N. Shields, "A systematic review of the effectiveness of treadmill training for children with cerebral palsy," *Disability and Rehab*, vol. 31, no. 24, pp. 1971–1979, 2009.

[3] J. P. Winnick and D. L. Porretta, *Adapted Physical Education and Sport*. Human Kinetics, 2016.

[4] M. Wouters, H. M. Evenhuis, and T. I. Hilgenkamp, "Physical activity levels of children and adolescents with moderate-to-severe intellectual disability," *Jrnl of Applied Research in Intellectual Disabilities*, vol. 32, no. 1, pp. 131–142, 2019.

[5] P. C. Hallal, L. B. Andersen, F. C. Bull, R. Guthold, W. Haskell, U. Ekelund, L. P. A. S. W. Group *et al.*, "Global physical activity levels: Surveillance progress, pitfalls, and prospects," *The Lancet*, vol. 380, no. 9838, pp. 247–257, 2012.

[6] K. Brütsch, T. Schuler, A. Koenig, L. Zimmerli, L. Lünenburger, R. Riener, L. Jäncke, A. Meyer-Heim *et al.*, "Influence of virtual reality soccer game on walking performance in robotic assisted gait training for children," *Jrnl of Neuroeng and Rehab*, vol. 7, no. 1, pp. 1–9, 2010.

[7] A. Helmi, T.-H. Wang, S. W. Logan, and N. T. Fitter, "Harnessing the power of movement: A body-weight support system & assistive robot case study," in *Proc of the Int Conf on Rehab Robotics (ICORR)*. Singapore: IEEE, 2023, pp. 1–6.

[8] E. Kokkoni, E. Mavroudi, A. Zehfroosh, J. C. Galloway, R. Vidal, J. Heinz, and H. G. Tanner, "GEARing smart environments for pediatric motor rehabilitation," *Jrnl of Neuroeng and Rehab*, vol. 17, no. 1, pp. 1–15, 2020.

[9] R. M. Mayoral, A. Helmi, S. W. Logan, and N. T. Fitter, "Gobot go! using a custom assistive robot to promote physical activity in children," *Jrnl of TranslEng in Health and Med*, 2024.

[10] B. W. Timmons, A. G. LeBlanc, V. Carson, S. Connor Gorber, C. Dillman, I. Janssen, M. E. Kho, J. C. Spence, J. A. Stearns, and M. S. Tremblay, "Systematic review of physical activity and health in the early years (aged 0–4 years)," *Applied Physiol, Nutrition, and Metabolism*, vol. 37, no. 4, pp. 773–792, 2012.

[11] T. J. Saunders, C. E. Gray, V. J. Poitras, J.-P. Chaput, I. Janssen, P. T. Katzmarzyk, T. Olds, S. Connor Gorber, M. E. Kho, M. Sampson *et al.*, "Combinations of physical activity, sedentary behaviour and sleep: relationships with health indicators in school-aged children and youth," *Applied Physiol, Nutrition, and Metabolism*, vol. 41, no. 6, pp. S283–S293, 2016.

[12] N. Shields and A. Synnot, "Perceived barriers and facilitators to participation in physical activity for children with disability: a qualitative study," *BMC Pediatrics*, vol. 16, pp. 1–10, 2016.

[13] E. Garces, G. Puyuelo, I. Sánchez-Iglesias, J. C. F. Del Rey, C. Cumplido, M. Destarac, A. Plaza, M. Hernández, E. Delgado, and E. Garcia, "Using a robotic exoskeleton at home: An activity tolerance case study of a child with spinal muscular atrophy," *Jrnl of Pediatric Nursing*, vol. 67, pp. e71–e78, 2022.

[14] Y. Zhang, M. Bressel, S. De Groof, F. Dominé, L. Labey, and L. Peyrodie, "Design and control of a size-adjustable pediatric lower-limb exoskeleton based on weight shift," *IEEE Access*, vol. 11, pp. 6372–6384, 2023.

[15] C. Cho, W. Hwang, S. Hwang, and Y. Chung, "Treadmill training with virtual reality improves gait, balance, and muscle strength in children with cerebral palsy," *The Tohoku Jrnl of Experimental Med*, vol. 238, no. 3, pp. 213–218, 2016.

[16] G. R. Colborne, F. V. Wright, and S. Naumann, "Feedback of triceps surae emg in gait of children with cerebral palsy: a controlled study," *Archives of Phys Med and Rehab*, vol. 75, no. 1, pp. 40–45, 1994.

[17] A. T. Booth, A. I. Buizer, J. Harlaar, F. Steenbrink, and M. M. van der Krogt, "Immediate effects of immersive biofeedback on gait in children with cerebral palsy," *Archives of Phys Med and Rehab*, vol. 100, no. 4, pp. 598–605, 2019.

[18] W. A. Bainbridge, J. W. Hart, E. S. Kim, and B. Scassellati, "The benefits of interactions with physically present robots over video-displayed agents," *Int Jrnl of Social Robotics*, vol. 3, pp. 41–52, 2011.

[19] B. Görer, A. A. Salah, and H. L. Akın, "An autonomous robotic exercise tutor for elderly people," *Autonomous Robots*, vol. 41, no. 3, pp. 657–678, 2017.

[20] J. Raja Vora, A. Helmi, C. Zhan, E. Olivares, T. Vu, M. Wilkey, S. Noregaard, N. T. Fitter, and S. W. Logan, "Influence of a socially assistive robot on physical activity, social play behavior, and toy-use behaviors of children in a free play environment: A within-subjects study," *Frontiers in Robotics and AI*, p. 368, 2021.

[21] A. R. Alashram, G. Annino, and E. Padua, "Robot-assisted gait training in individuals with spinal cord injury: A systematic review for the clinical effectiveness of lokomat," *Jrnl of Clinical Neuroscience*, vol. 91, pp. 260–269, 2021.

[22] R. H. Horner, E. G. Carr, J. Halle, G. McGee, S. Odom, and M. Wolery, "The use of single-subject research to identify evidence-based practice in special education," *Excep Child*, vol. 71, no. 2, pp. 165–179, 2005.

[23] A. Helmi, S. Noregaard, N. Giulietti, S. W. Logan, and N. T. Fitter, "Let them have bubbles! Filling gaps in toy-like behaviors for child-robot interaction," in *Proc of the IEEE Int Conf on Robotics and Automation (ICRA)*, 2022, pp. 7417–7422.

[24] L. V. Hedges, J. Gurevitch, and P. S. Curtis, "The meta-analysis of response ratios in experimental ecology," *Ecology*, vol. 80, no. 4, pp. 1150–1156, 1999.

[25] E. A. Common, K. L. Lane, J. E. Pustejovsky, A. H. Johnson, and L. E. Johl, "Functional assessment–based interventions for students with or at-risk for high-incidence disabilities: Field testing single-case synthesis methods," *Remedial and Special Education*, vol. 38, no. 6, pp. 331–352, 2017.

[26] C. Wong, S. L. Odom, K. A. Hume, A. W. Cox, A. Fettig, S. Kucharczyk, M. E. Brock, J. B. Plavnick, V. P. Fleury, and T. R. Schultz, "Evidence-based practices for children, youth, and young adults with autism spectrum disorder: A comprehensive review," *Jrnl of Autism and Dev Disorders*, vol. 45, pp. 1951–1966, 2015.

[27] I. A. Trujillo-Priego, C. J. Lane, D. L. Vanderbilt, W. Deng, G. E. Loeb, J. Shida, and B. A. Smith, "Development of a wearable sensor algorithm to detect the quantity and kinematic characteristics of infant arm movement bouts produced across a full day in the natural environment," *Technologies*, vol. 5, no. 3, p. 39, 2017.

[28] D. S. Syrdal, K. Dautenhahn, K. L. Koay, and M. L. Walters, "The Negative Attitudes towards Robots Scale and Reactions to Robot Behaviour in a Live Human-Robot Interaction Study," in *Proc Convention of the Society for the Study of Artificial Intelligence and Simulation of Behaviour (AISB)*, 2009, pp. 109–115.

[29] K. E. Schaefer, "Measuring trust in human robot interactions: Development of the 'Trust Perception Scale-HRI'," in *Robust Intelligence and Trust in Autonomous Sys*. Springer US, 2016, pp. 191–218.

[30] R. Palisano, P. Rosenbaum, S. Walter, D. Russell, E. Wood, and B. Galuppi, "Gross motor function classification system for cerebral palsy," *Dev Med Child Neurol*, vol. 39, no. 4, pp. 214–23, 1997.

Novel method for setting population-specific joint torque assistance requirements with applications to exoskeleton design

Stijn Hamelryckx [1,3], Christopher van Vlerken[1,3], Louis Flynn[1,3], Mengnan Wu[1], Bram Vanderborght[1,2] and Tom Verstraten[1,3]

***Abstract*— This paper presents a novel methodology to calculate assistance requirements for wearable robotic devices (e.g., exoskeletons) using Maximum Voluntary Contraction (MVC) measurements. While other methods for determining assistance requirements focus on the kinematics and kinetics of specific tasks to be performed, our method determines the assistance needed for a population to reach the overall physical capabilities of another reference population. While applicable to any joint and population, we demonstrate its effectiveness on the lower limb joints of older adults. Unlike conventional methods that assume the need to provide 100% of the peak torque during the assisted task, our approach calculates the required assistance and identifies a 20–25% torque deficit for setting assistive torque requirements. This discrepancy underscores the importance of addressing the physical deficits of its users when designing assistive devices. As our method provides torque deficit as a function of joint velocity, the characteristics of the actuator can be chosen to match these deficits. Additionally, as the torque deficit is described as a function of joint angle, non-linear transmissions can be designed in future actuation systems of assistive wearable devices.**

Index Terms - Exoskeletons, Assistance Requirements, Elderly

I. Introduction

Exoskeletons can provide assistance or resistance to a specific human joint by applying an external torque. By doing so, exoskeletons can either assist, train, or augment a specific part of the wearer's body [1]. For the elderly, exoskeletons can allow the patient to maintain a high quality of life no matter the stage of muscle deterioration and can also be used for resistive training to slow down the rate of muscle mass loss.

The design of wearable robotic devices (e.g. exoskeletons) should consider both the intended use cases as well as the capabilities of the user [2]. For users with strength or mobility impairments, exoskeletons can provide assistive torque to a user's joints to help them accomplish various tasks. To maintain a high quality of life, the exoskeleton should support all important activities of daily life (ADLs), which are usually considered to be (slope)walking, stair ascent and descent, and sit-to-stand transitions [3]. Many diverse populations can benefit from wearable assistive devices, including persons who have had spinal cord injuries or strokes. As these populations have very different physical capabilities and assistance requirements [1], exoskeleton designers should more thoroughly understand the physical capabilities of the wearer in order to correctly dimension the actuator system and minimize the overall weight and size of the exoskeleton.

However, no systematic method exists to determine joint torque assistance level, which is important for actuator selection. Common practice [4][5][6] for calculating torque assistance levels is to take an arbitrary percentage of peak torques extracted from kinematic and kinetic datasets for specific populations and activities (e.g. [7] and [8]). Limitations of this method are that it assumes the same percentage deficit to all joints and does not consider the effect of joint angle and joint velocity on the torque generating capacity of the joint [7]. An alternative method [9] selects the actuator based on task requirements, but it does not consider the wearer's abilities. Another alternative method [10] proposes using simulations to determine assistance requirements, where muscle deficit is simulated by reducing the maximal isometric strength by an arbitrary percentage. However, since these deficits are simulated, it is uncertain if they represent actual populations. Furthermore, the muscle deficit is assumed to be the same for each muscle and exertion direction.

To address gaps in current methods for determining assistance levels, [5] proposes a methodology that takes into account both the wearer and task. They collect kinematic and kinetic data and calculate inverse dynamics to determine the joint torque during a specific task. This task-specific joint torque is compared with existing data on the maximum voluntary contraction (MVC) - a measure of the maximum force a muscle can generate during a voluntary contraction [11] - to understand how close to their physical limit the user is during the task. While this approach is promising, [12] showed that the MVC depends on joint angle and joint speed, which are not considered in [5]. Comparing task joint torques to MVCs without considering joint angle and speed can result in a significant overestimation of the person's physical "reserve." Furthermore, the torque-generating capacities of flexor and extensor muscles are asymmetric, highlighting the importance of understanding the biomechanical characteristics of the studied population [13].

In this paper, we propose a novel method to calculate joint assistance torque requirements for a wearable robotic device based on user capabilities that can be applied to any set of activities/tasks. We propose using MVCs measured at

[1]Robotics & Multibody Mechanics (R&MM) Research Group, Vrije Universiteit Brussel, 1050 Brussels, Belgium, [stijn.hamelryckx, christopher.konstantin.van.vlerken, louis.flynn, mengnan.wu, bram.vanderborght, tom.verstraten]@vub.be

[2] IMEC, Kapeldreef 75, Leuven 3001, Belgium.

[3]Flanders Make, 1050, Brussels, Belgium.

multiple joint angles and velocities and extrapolating them for the entire range of motion of interest based on the model developed in [12]. This model provides the peak joint torque as a function of joint angle and velocity. Our method differs from the one described in [5] as we do not use kinematic or kinetic data from a specific task. To demonstrate our method, we determine assistance requirements for a target population of unimpaired older adults with unimpaired young adults as the reference population.

II. Methods

Our method calculates joint torque assistance requirements to aid in actuator selection for a wearable assistive device. Torque deficits are calculated as differences in peak torques between a target and reference population across a range of joint angles and velocities. For this study, unimpaired younger adults were selected as the reference group and unimpaired older adults as the target group, but our methods can be used to compare any two populations. Unimpaired young adults were chosen as a reference group since this population has peak muscle mass and the highest level of locomotion capabilities [14].

We chose the range of joint angles and velocities based on common activities of daily living (ADLs) (I). Two sets of ADLs were considered for two cases of wearable assistive devices that support different levels of quality of life. The first case includes all movements for a high quality of life [3]: (slope)walking, stair ascent/descent, and sit-to-stand transitions. The second case includes only stair ascent/descent to allow comparison of our results to that of [5], which only examined these two tasks in unimpaired elderly adults.

TABLE I

Joint velocity and joint angle ranges for activities of daily living/stair ascent and descent used in the model based on kinematic data [8][7].

	Min velocity (°/s)	**Max velocity (°/s)**	**Min angle (°)**	**Max angle (°)**
Ankle	-225/-225	350/175	-30/-30	40/30
Knee	-500/-450	500/450	0/10	110/110
Hip	-250/-125	250/225	-20/-10	80/65

We obtained MVC measurements for our chosen populations from the dataset in [12]. The dataset was collected from 14 unimpaired younger adults (mean +/- SD ages: 19.6 +/- 1.2 years, weight: 67.5 +/- 8.6 kg, height: 167.7 +/- 8.7 cm) and 6 unimpaired elderly adults (mean +/- SD ages: 70 +/- 2.9 years, weight: 75.4 +/- 13.6 kg, height: 168 +/- 9 cm) with equal gender distributions for both populations. MVCs were measured using a Biodex System 3 dynamometer (Biodex Medical Systems , Inc. Shirley, New York, USA). Isometric and isokinetic measurements were performed on the hip, knee, and ankle. Isometric measurements were performed at six joint angles in both exertion directions (e.g. flexion and extension), with two repetitions per angle and direction. Concentric isokinetic measurements were performed at three velocities (60, 120, and 500 deg/s for the hip and ankle; 75, 150, and 500 deg/s for the knee). Eccentric isokinetic measurements were performed at one velocity (60 deg/s for the hip and ankle; 75 deg/s for the knee). Four repetitions were performed for each velocity and joint.

We input the MVC measurements to the model developed by [12] to obtain peak torques for each population across a range of joint angles and velocities. The torque model splits total torque into passive and active components [12]. The passive torque is based on exponential equations [15], while the active torque is based on the Hill model [16]. The model [12] uses MVC measurements as inputs and outputs peak torques (Equation 1 and 2). The active torque is found by: For $\dot{\theta} \geq 0$:

$$T_{Active}(\theta, \dot{\theta}) = C_1 \cos(C_2(\theta - C_3))\zeta(\dot{\theta}) \tag{1}$$

For $\dot{\theta} < 0$:

$$T_{Active}(\theta, \dot{\theta}) = C_1 \cos(C_2(\theta - C_3))\zeta(\dot{\theta})(1 - C_6\dot{\theta}) \tag{2}$$

With:

$$\zeta(\dot{\theta}) = \frac{2C_4C_5 + |\dot{\theta}|(C_5 - 3C_4)}{2C_4C_5 + |\dot{\theta}|(2C_5 - 4C_4)} \tag{3}$$

The model has six parameters, each of which has a physical interpretation. C_1 is the isometric peak torque (Nm/kg). C_2 is equal to $\frac{\pi}{\theta_{active}}$, where θ_{active} is the range of motion where active muscle force generation occurs. C_3 is the joint angle (radians) at which the peak torque occurs. C_4 and C_5 are the velocities (rad/s) at which the torque is 75% and 50% of the isometric peak torque, respectively; these parameters influence the velocity behavior of the model. Finally, C_6 is the ratio of eccentric to concentric torque, where a positive value indicates that the eccentric torque is higher than the concentric torque. We used mean C_i parameters from [12].

We calculated torque deficits of our target population - unimpaired elderly adults - by subtracting their peak torques from that of the unimpaired young adults. We also calculated power deficits as a function of joint angle, since power requirements are important for dimensioning the actuator of the wearable assistive device and its potential battery pack. To find the maximum power deficits for each joint angle, the following formula was used:

$$\delta P(\theta) = max(\delta T(\theta, \dot{\theta}_i)\dot{\theta}_i) \tag{4}$$

Power deficit ($\delta P(\theta)$) was found by multiplying the torque deficit ($\delta T(\theta, \dot{\theta}_i)$) by its corresponding joint velocity at each joint angle.

Torque and power deficits were calculated for males and females separately in case of gender effects. To compare our results to the common method of choosing an arbitrary percent torque deficit, the average torque and power deficits were divided by the peak torque of young adults, to find the percentage of deficit that occurs in unimpaired older adults.

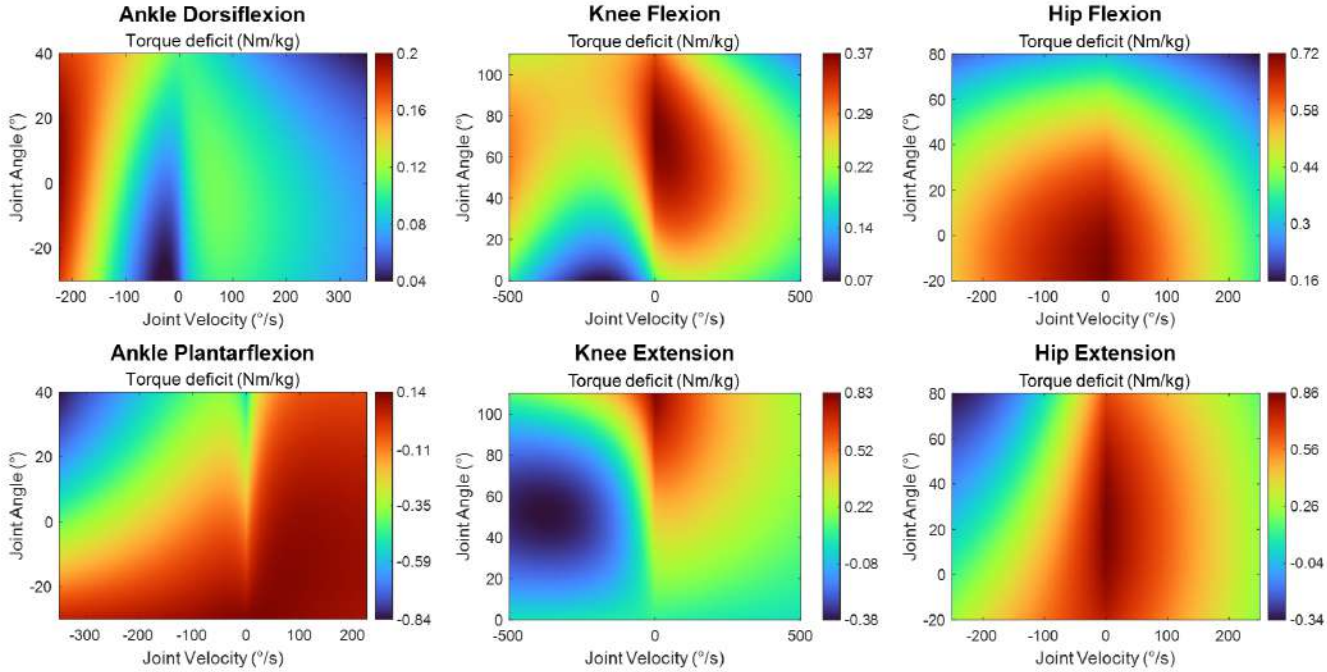


Fig. 1. The average torque deficits (normalized by body weight) as a function of joint angle and joint velocity for female unimpaired older adults across different exertion directions. The peak torque occurs at different joint angle and joint velocities for different exertion directions.

III. Results

A. Assistance requirements for older adults across activities of daily living

Our method yields different torque deficits for older adults depending on exertion directions (Fig 1). The largest deficit for dorsiflexion occurs at eccentric joint velocities at a joint angle of 5°. The largest torque deficit in plantarflexion is during concentric joint velocities and remains constant across joint angles. For both flexion and extension of both the knee and hip, the main deficit occurs at lower joint velocities, near the isometric condition. Peak deficits appear at joint angles of 70° and 100° for knee flexion and extension, respectively, and at -15° and 20° for hip flexion and extension, respectively. Although some values are different from previous work [17], our torque deficits are generally similar to previously reported ranges. We show torque deficits of 0.14 Nm/kg for ankle dorsiflexion whereas [17] found a deficit of 0.11 Nm/kg (torque normalized reported mass) for isokinetic MVC measurements. Ankle plantarflexion has a torque deficit of 0.23 Nm/kg while [17] reported 0.67 Nm/kg. Hip extension and flexion show torque deficits of 0.66 Nm/kg and 0.48 Nm/kg, respectively, compared to a reported deficit of 0.96 Nm/kg and 0.56 Nm/kg in [17]. Finally, the torque deficit in knee extension and flexion is 0.69 Nm/kg and 0.35 Nm/kg, respectively, compared to 0.93 Nm/kg and 0.51 Nm/kg from [17].

Older adults exhibit a reduction in torque capacity (positive torque deficit) across most joint angles and velocities compared to younger adults. However, a negative torque deficit—indicating greater torque capacity in older adults than in younger adults—is observed for eccentric torques in ankle plantarflexion, knee extension, and hip extension.

TABLE II

Power and torque deficits averaged across genders (n=6), considering all activities of daily living. Deficit values are normalized by peak values for young adults.

	Relative power deficit (%)	Relative torque deficit (%)
Ankle dorsiflexion	19.4	21.6
Ankle plantarflexion	11.3	12.9
Knee flexion	22.0	21.6
Knee extension	17.1	25.8
Hip flexion	20.8	23.4
Hip extension	13.5	22.9

Our trends for power deficits are sometimes different from those for torque deficits, especially for the hip and knee joints. For the ankle, both the highest torque and power deficits occur in the same exertion direction. However, for the hip and knee, the greatest torque deficit occurs in extension while the highest power deficit occurs in flexion; this is due to the fact that, at higher velocities, changes in velocity contribute more to power than changes in torque. Overall, maximum joint power deficits (Fig. 2) and joint torque deficits (Fig. 1) generally occur at similar joint angles. However, for the hip and knee, the highest maximum power deficits occur in flexion (60°) while the maximum torque deficits are observed in extension (100°). Similarly, the peak hip power deficit occurs at -15°, whereas the peak torque deficit occurs at 20° (Fig. 1). Average peak joint power

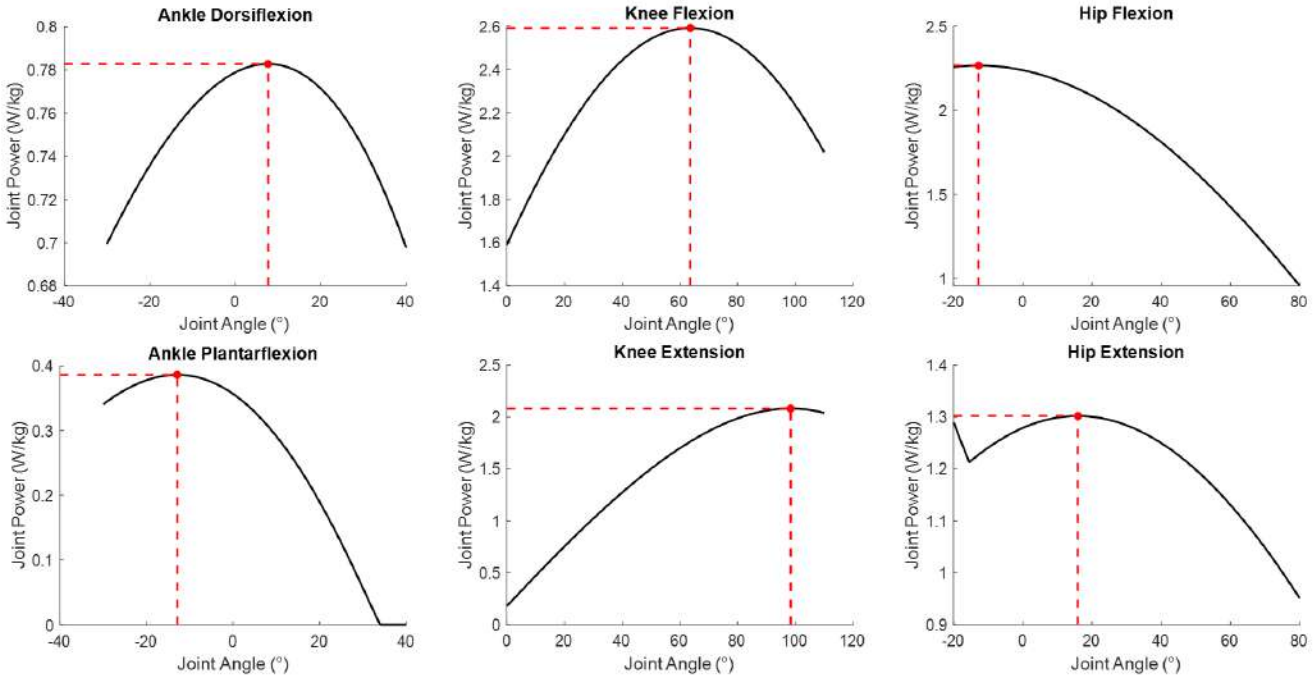


Fig. 2. Average joint power deficits (normalized by body weight) as a function of joint angle and joint velocity for female unimpaired older adults (n = 3) for different exertion directions. The red dot indicates the peak joint power deficit.

deficits are 1.2 W/kg for the ankle (which occurs during plantarflexion), 1.6 W/kg for the hip (during flexion), and 2.6 W/kg for the knee (during flexion).

Our results for power deficits also suggest potential sex-based differences (Table III), with females tending to exhibit higher deficits than males in both hip extension and flexion, consistent with the findings of [18]. Conversely, males tend to have a higher power deficit in ankle plantarflexion. Overall, for most joints and exertion directions a torque deficit of 20-25% was found (Table II). However, the deficit in plantarflexion was significantly lower at around 12%.

B. Assistance requirements for stair ascent and descent

TABLE III

AVERAGE MAXIMUM POWER DEFICITS FOR UNIMPAIRED OLDER ADULTS FOR EACH EXERTION DIRECTION FOR STAIR ASCENT AND DESCENT.

Joint Power (W/kg)	Female	Male	Average
Ankle Plantarflexion	0.39	0.91	0.65
Ankle Dorsiflexion	0.78	0.17	0.48
Hip Extension	1.3	0.76	1.0
Hip Flexion	2.2	0.71	1.5
Knee Extension	2.1	1.8	1.9
Knee Flexion	1.9	2.0	1.9

Power deficits for stair ascent and descent (Table III) are lower compared to those for all tasks required for a high quality of life, while torque deficits were similar for both cases. Our torque deficits are similar to values from [5]:we found a deficit 0.22 Nm/kg while they they found peak deficits of 0.2 Nm/kg in plantar flexion. While we found a deficit of 0.68 Nm/kg, they found a deficit of 1 Nm/kg in knee extension. For joint power deficits, we found a maximum deficit of 0.65 W/kg where they found 1 W/kg for ankle plantar flexion. Lastly, we found a power deficit of 1.9 W/kg for knee extension which they also found.For the hip, our results suggest that assistive power of 1.5 W/kg could be beneficial for older adults while results from [5] suggest that no assistance is needed. During stair ascent and descent, peak hip extension torque (0.8 Nm/kg) occurs at a joint velocity of 125 °/s and joint angle of 35°. The peak torque that an older adult can supply at this joint velocity and joint angle is 1.2 Nm/kg while young adults have a peak torque capability of 1.5 Nm/kg. Thus, older adults have less torque ”reserve” than younger adults at the point where peak hip extension torque is required.

IV. DISCUSSION

The validity of our method is supported by the agreement of our results with previous work [17][5]. Our torque deficits are similar to previously reported ranges, except for the ankle. A large plantarflexion deficit of 39% was reported in [19], but the older adults in the dataset we used [12] participated in a high level of physical activity (2-4 times per week) and were 5 years younger, on average, than the ones in [19]. As expected, older adults exhibit a reduction in torque capacity (positive torque deficit) across most joint angles and velocities compared to younger adults. The negative torque deficits we found may be due to the combination of relatively high eccentric torque capabilities in the elderly with substantial variability in MVC measurements and warrants further investigation. Our results show a lower magnitude

of torque deficits in eccentric contractions, aligning with the result that eccentric torque capacity is better preserved than concentric torque capacity in older adults found in [20].

Our results suggest that traditional approaches for estimating assistance requirements may lead to an overdimensioned actuation system, particularly for certain populations. While it is common practice to determine assistive torque requirements based on the kinetic demands of specific tasks, our approach quantifies the torque deficit of the user for each joint across any chosen tasks. Conventional methods typically result in torque requirements equivalent to 100% of the peak torque observed in the most demanding task [4]. In contrast, our findings indicate much smaller torque deficits of 20-25%.

Although they considered a different population, our results suggest that the assumption of equal deficits for all muscles in [10] is not valid. While most joints and exertion directions have similar deficits, ankle plantar flexion has a much lower deficit. This finding would heavily influence the exoskeleton design described in [10] and shows the importance of detailed knowledge of the effects of the impairment on joint deficits.

While the state-of-the-art method [5] determines assistance requirements based on torque required to perform a specific task in the same *manner* as a reference population, our more general method determines the assistance required for a reference population to reach the maximum physical *capabilities* of a reference population. The previous study [5] calculated assistance required for older adults to perform specific activities (with set combinations of joint angles and velocities) similar to young adults, while our method calculates the assistance required for any target population to reach the same physical capabilities as a reference population across joint angle and velocity combinations that can be chosen based on any activities. For stair ascent and descent, our results are generally similar to those of [5], except for the hip joint, where our results reveal potential benefits of assistance while the task-specific method does not show any assistance required. Furthermore, while their method requires time-series kinematics and kinetics measurements for each activity considered, our method requires only MVC measurements and allows the designer to select the range of joint angles and velocities based on any set of activities.

Another major advantage of providing torque deficit as a function of joint angle and joint velocity is that it allows the design of actuator systems for an assistive device to be matched to the specific characteristics of the user's deficit. By doing so, the actuator size can be reduced by allowing the actuator system to have a higher peak torque for a specific joint angle where it is needed and a lower peak torque but higher velocity for a different region of the ROM [21]. This type of design has already been used in prostheses, where the stiffness of the knee changes for different joint angles [22]. Our results may help optimize non-linear transmission systems, similar to what was observed in simulations from [23]. Non-linear transmission mimics human biological muscles, where the torque output of the muscle depends on the joint angle [24].

Demonstrating how our method can be used to set assistance requirements for an example population, our results show that a wearable lower limb assistive device for unimpaired older adults should be able to provide a peak ankle joint power of 1.2 W/kg, knee joint power of 2.6 W/kg, and hip joint power of 1.6 W/kg. Additionally, we found that the peak power and torque deficits for the hip and knee occur at different joint angles, which suggests the benefits of non-linear transmissions at these joints.

The choice of a reference group depends on the design intentions of the wearable robotic device. The designer can always opt for young adults as a reference population, envisioning an exoskeleton that would give the wearer ideal locomotion capabilities. Alternatively, for an example target group of sarcopenia patients, a reference group could be non-sarcopenic older adults to match the capabilities of a similar age group. An example of a slightly different approach to selecting "groups" in stroke patients could be to choose the target and reference "groups" as datasets from the paretic and non-paretic legs, respectively, of the same individuals. This would result in an exoskeleton that creates symmetric capabilities for both legs.

Two limitations of our method are that it cannot be used to control the assistive devices without additional information, and that MVC measurements are known to be variable due to factors such as encouragement [25]. Developing a controller based on our method requires additional kinematic and kinetic information on the wearer's task. One way to incorporate our method into a controller is by determining the assistance level based on the 'relative torque deficit.' This relative torque deficit is the torque deficit calculated by our method divided by the maximum torque capability of the reference population for a given joint angle and joint velocity. The relative torque deficit needs to be combined with kinetic data of the task to create a controller where the assistance level varies based on the amount of deficit a person has for a specific joint angle and joint velocity. MVC measurements are known to be variable, depending, for example, on encouragement to the person measured and variations between days. Best practices for collecting MVC measurements should be followed according to [25].

Finally, our results suggest potential differences in power deficits between males and females. However, as the dataset of unimpaired older adults utilized in this study includes only six participants (three per gender), this trend should be validated in a larger sample population.

V. Conclusion

In this study, we developed a novel methodology to set assistance requirements for exoskeletons based on physical capabilities. This method uses MVC measurements and was demonstrated on unimpaired older adults. We found that our results match previously found deficits from [17] and [5]. From our method, the torque deficit of healthy elderly

was found to be around 20-25%, contrary to traditional methods taking 100% of the peak torque of the task requiring assistance. This difference highlights the importance of understanding the underlying deficit of the user of the assistive device for the dimensioning of its actuator system. As our method provides torque deficit as a function of joint velocity, the characteristics of the actuator can be closely matched with those of the measured deficit. Additionally, as our method provides information on the deficit as a function of joint angle, non-linear transmission systems can be exploited to further reduce the size and weight of the actuation system. Our method found that the main power deficit at the ankle is in plantarflexion and is 1.2 W/kg and a peak torque deficit 0.23 Nm/kg. For the knee, flexion needs most assistance and has a power deficit of 2.6 W/kg and a torque deficit in extension of 0.69 Nm/kg. Finally, the hip has a main power deficit in flexion with 1.6 W/kg while the main torque deficit is in extension with a deficit of 0.66 Nm/kg. Due to the small sample size, the found results cannot be generalized over the entire healthy elderly population. However, the method shows promising trends that warrant further investigation in future research. This methodology can be used for any population and any joint.

ACKNOWLEDGMENT

This project was partially supported by the FWO Strategic Basic Research project Revalexo (grant no. S001024N).

REFERENCES

[1] Norazam Aliman, Rizauddin Ramli, and Sallehuddin Mohamed Haris. Design and development of lower limb exoskeletons: A survey. *Robotics and Autonomous Systems*, 95:102–116, September 2017.

[2] Felipe Ballen-Moreno, Daniel Gomez-Vargas, Kevin Langlois, Jan Veneman, Carlos A. Cifuentes, and Marcela Múnera. Fundamentals for the Design of Lower-Limb Exoskeletons. In Carlos A. Cifuentes and Marcela Múnera, editors, *Interfacing Humans and Robots for Gait Assistance and Rehabilitation*, pages 93–120. Springer International Publishing, Cham, 2022.

[3] M. Grimmer, R. Riener, C. J. Walsh, and A. Seyfarth. Mobility related physical and functional losses due to aging and disease - a motivation for lower limb exoskeletons. *Journal of NeuroEngineering and Rehabilitation*, 16(1), 2019.

[4] Massimo Cenciarini and Aaron M. Dollar. Biomechanical considerations in the design of lower limb exoskeletons. In *2011 IEEE International Conference on Rehabilitation Robotics*, pages 1–6, June 2011. ISSN: 1945-7901.

[5] Max Böhme, Felix Weiske, Jens Jäkel, Johannes Zentner, and Maren Witt. Evaluation of the power deficit of elderly people during stair negotiation: Which joints should be assisted at least by an exoskeleton and with what amount? *Wearable Technologies*, 3:e4, January 2022.

[6] Ümit Önen, Fatih M. Botsalı, Mete Kalyoncu, Mustafa Tınkır, Nihat Yılmaz, and Yusuf Şahin. Design and Actuator Selection of a Lower Extremity Exoskeleton. *IEEE/ASME Transactions on Mechatronics*, 19(2):623–632, April 2014. Conference Name: IEEE/ASME Transactions on Mechatronics.

[7] Jonathan Camargo, Aditya Ramanathan, Will Flanagan, and Aaron Young. A comprehensive, open-source dataset of lower limb biomechanics in multiple conditions of stairs, ramps, and level-ground ambulation and transitions. *Journal of Biomechanics*, 119:110320, April 2021.

[8] Emma Reznick, Kyle R. Embry, Ross Neuman, Edgar Bolívar-Nieto, Nicholas P. Fey, and Robert D. Gregg. Lower-limb kinematics and kinetics during continuously varying human locomotion. *Scientific Data*, 8(1):282, October 2021. Number: 1 Publisher: Nature Publishing Group.

[9] Andrea Calanca, Stefano Toxiri, Davide Costanzi, Enrico Sartori, Rudy Vicario, Tommaso Poliero, Christian Di Natali, Darwin G. Caldwell, Paolo Fiorini, and Jesús Ortiz. Actuation Selection for Assistive Exoskeletons: Matching Capabilities to Task Requirements. *IEEE Transactions on Neural Systems and Rehabilitation Engineering*, 28(9):2053–2062, September 2020. Conference Name: IEEE Transactions on Neural Systems and Rehabilitation Engineering.

[10] Maarten Afschrift, Friedl De Groote, Joris De Schutter, and Ilse Jonkers. The effect of muscle weakness on the capability gap during gross motor function: a simulation study supporting design criteria for exoskeletons of the lower limb. *BioMedical Engineering OnLine*, 13(1):111, August 2014.

[11] Malgorzata Klass, Stéphane Baudry, and Jacques Duchateau. Voluntary activation during maximal contraction with advancing age: a brief review. *European Journal of Applied Physiology*, 100(5):543–551, July 2007.

[12] Dennis E. Anderson, Michael L. Madigan, and Maury A. Nussbaum. Maximum voluntary joint torque as a function of joint angle and angular velocity: Model development and application to the lower limb. *Journal of Biomechanics*, 40(14):3105–3113, January 2007.

[13] Simon Barrué-Belou, Marc-Antoine Démaret, Alexis Wurtz, Alicia Ducloux, François Fourchet, and Hugo Bothorel. Absolute and Normalized Normative Torque Values of Knee Extensors and Flexors in Healthy Trained Subjects: Asymmetry Questions the Classical Use of Uninjured Limb as Reference. *Arthroscopy, Sports Medicine, and Rehabilitation*, 6(1):100861, February 2024.

[14] I. Janssen, S. B. Heymsfield, Z. M. Wang, and R. Ross. Skeletal muscle mass and distribution in 468 men and women aged 18-88 yr. *Journal of Applied Physiology (Bethesda, Md.: 1985)*, 89(1):81–88, July 2000.

[15] Y. S. Yoon and J. M. Mansour. The passive elastic moment at the hip. *Journal of Biomechanics*, 15(12):905–910, January 1982.

[16] E. E. Zajac. A Geometric Treatment of Averch-Johnson's Behavior of the Firm Model. *The American Economic Review*, 60(1):117–125, 1970. Publisher: American Economic Association.

[17] Thomas Harbo, John Brincks, and Henning Andersen. Maximal isokinetic and isometric muscle strength of major muscle groups related to age, body mass, height, and sex in 178 healthy subjects. *European Journal of Applied Physiology*, 112(1):267–275, January 2012.

[18] Katherine A. Boyer, Gary S. Beaupre, and Thomas P. Andriacchi. Gender differences exist in the hip joint moments of healthy older walkers. *Journal of Biomechanics*, 41(16):3360–3365, December 2008.

[19] Atsuki Kanayama, Saki Yamamoto, Ryoga Ueba, Mio Kobayashi, Toshimitsu Ohmine, and Akira Iwata. Age-related changes and sex differences in ankle plantarflexion velocity. *Scientific Reports*, 13(1):22943, December 2023. Publisher: Nature Publishing Group.

[20] Geoffrey A. Power, Nordan Flaaten, Brian H. Dalton, and Walter Herzog. Age-related maintenance of eccentric strength: a study of temperature dependence. *Age*, 38(2):43, March 2016.

[21] Jan Babič, Matteo Laffranchi, Federico Tessari, Tom Verstraten, Domen Novak, Nejc Šarabon, Barkan Ugurlu, Luka Peternel, Diego Torricelli, and Jan F. Veneman. Challenges and solutions for application and wider adoption of wearable robots. *Wearable Technologies*, 2:e14, January 2021.

[22] Serge Pfeifer, Anna Pagel, Robert Riener, and Heike Vallery. Actuator With Angle-Dependent Elasticity for Biomimetic Transfemoral Prostheses. *IEEE/ASME Transactions on Mechatronics*, 20(3):1384–1394, June 2015. Conference Name: IEEE/ASME Transactions on Mechatronics.

[23] Henning Koch and Katja Mombaur. ExoOpt - A framework for patient centered design optimization of lower limb exoskeletons. In *2015 IEEE International Conference on Rehabilitation Robotics (ICORR)*, pages 113–118, August 2015. ISSN: 1945-7901.

[24] Josh R. Baxter and Stephen J. Piazza. Plantar flexor moment arm and muscle volume predict torque-generating capacity in young men. *Journal of Applied Physiology*, 116(5):538–544, March 2014. Publisher: American Physiological Society.

[25] B. Peacock, T. Westers, S. Walsh, and K. Nicholson. Feedback and maximum voluntary contraction. *Ergonomics*, 24(3):223–228, March 1981. Publisher: Taylor & Francis.

A powerful customized fabric-based soft robotic glove for assistance and rehabilitation

Rui Chen[1*], Daniele Leonardis[1], Antonio Frisoli[1], and Domenico Chiaradia[1]

***Abstract*—Soft robotic gloves assist stroke patients in restoring hand function, and improve their ability to perform activities of daily living (ADLs). This study introduces a powerful, customized, fabric-based soft robotic glove designed for assistance and rehabilitation. The pneumatic fabric actuators were customized to achieve a configuration that aligns with the natural curvature of the flexed fingers when inflated. This ergonomic design ensures that the actuators provide precise and efficient torque assistance to the finger joints. Experimental results demonstrate that the glove actuator produces a block tip force of 19.1 N at 100 kPa. Moreover, at 97 kPa, the 73 g glove can grip an object weighing 3126 g, highlighting its robust assistive capabilities. Finally, preliminary tests conducted with healthy subjects performing grasping tasks showed that the soft glove effectively supports users in their daily activities.**

***Index Terms*—soft robotic glove; pneumatic actuator; hand assistance, exoskeleton.**

I. Introduction

Neurological disorders, such as stroke [1], incomplete spinal cord injuries [2], and muscular dystrophy, significantly impair hand functionality, often leading to the partial or complete loss of the ability to perform essential activities of daily living (ADLs) [3]. These conditions not only affect an individual's independence but also have a profound impact on their overall quality of life [4]. Consequently, effective rehabilitation strategies aimed at restoring hand function are critically needed. In this context, robotics has emerged as a promising field, offering innovative solutions that facilitate rehabilitation and provide controlled assistance to help patients regain functional capabilities [5].

Among various robotic aids, soft robotic gloves have gained attention as an innovative approach for hand rehabilitation and functional assistance. By utilizing soft materials and advanced actuation mechanisms, these gloves are designed to replicate the natural movements of the hand, thereby reducing the discomfort and physical constraints commonly associated with rigid exoskeletons [6], [7]. Recent advancements in material science have enabled the integration of diverse materials, including polymers [8], elastomers [9]–[13], and fabrics [14]–[18]. The use of these soft materials and actuation allows for natural joint movements, which are essential for effective rehabilitation.

Despite notable advancements in the development of soft robotic gloves, several challenges persist, particularly in the areas of customization, ergonomic fit, and user comfort [9]. Many current designs employing single-chamber pneumatic actuators face difficulties in achieving precise alignment with the user's finger joints [12], [19]. Such misalignment may lead to unintended torque distribution across different joint positions, potentially diminishing the efficiency and comfort of force transmission to the anatomical structures of the user's hands [20]. Although modular approaches incorporating rigid components have been developed to enhance customization, these designs often increase the overall weight and complexity of the system, potentially compromising its comfort and simplicity [21], [22].

To address these challenges, this study presents a novel powerful, customized, fabric-based soft robotic glove. At 100 kPa, the actuator generates a maximum block tip force of 19.1 N. The glove, weighing only 73 g, successfully grips objects up to 3126 g at the pressure of 97 kPa, demonstrating its powerful assistive capabilities. The customized fabric-based pneumatic actuators are engineered to conform to the unique dimensions of an individual's hand and finger joints. By aligning actuator segments precisely with the finger joints, the glove not only offers an ergonomic fit but also enhances comfort and effectiveness during hand flexion.

This innovative approach improves the precision of assistive forces applied to each finger while preserving the lightweight and flexible characteristics essential for creating a natural-feeling assistive device. The development of this customized fabric-based soft robotic glove presents a way for personalized and effective rehabilitation solutions that can adapt to the specific needs of each user.

II. The Customized Glove

A. Glove Design

As highlighted in the literature, finger sizes vary significantly among individuals, and gloves tailored to the user's specific finger dimensions are more ergonomic, minimizing misalignment. Assuming that the glove's actuator is customized according to the finger's flexion state after inflation, such tailored actuators can deliver a safer and more accurate assistive torque to the joints. Therefore, we propose a customized, soft robotic glove, as illustrated in Fig. 1.

The glove consists primarily of five custom-fabricated pneumatic actuators and a fabric glove that interfaces with the user. Each actuator corresponds to one of the five fingers of the hand. Each finger actuator is equipped with an independent air supply line, enabling theoretical individual control of finger flexion. This design allows for task-specific assistance and

[1] All the authors are with the Institute of Mechanical Intelligence, Scuola Superiore Sant'Anna, Pisa, Italy.

[*] corresponding author: rui.chen@santannapisa.it

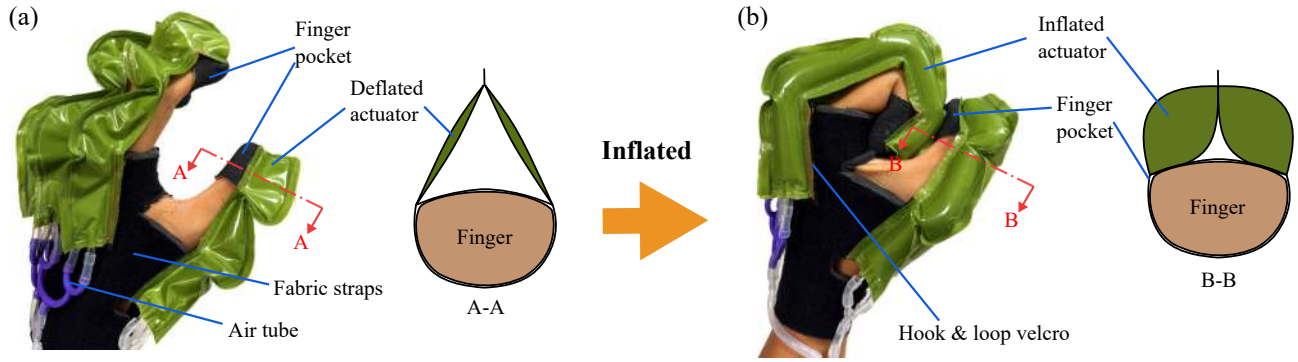


Fig. 1. Illustration of the customized soft robotic glove prototype. (a) Deflated customized soft robotic glove. (b) Inflated customized soft robotic glove.

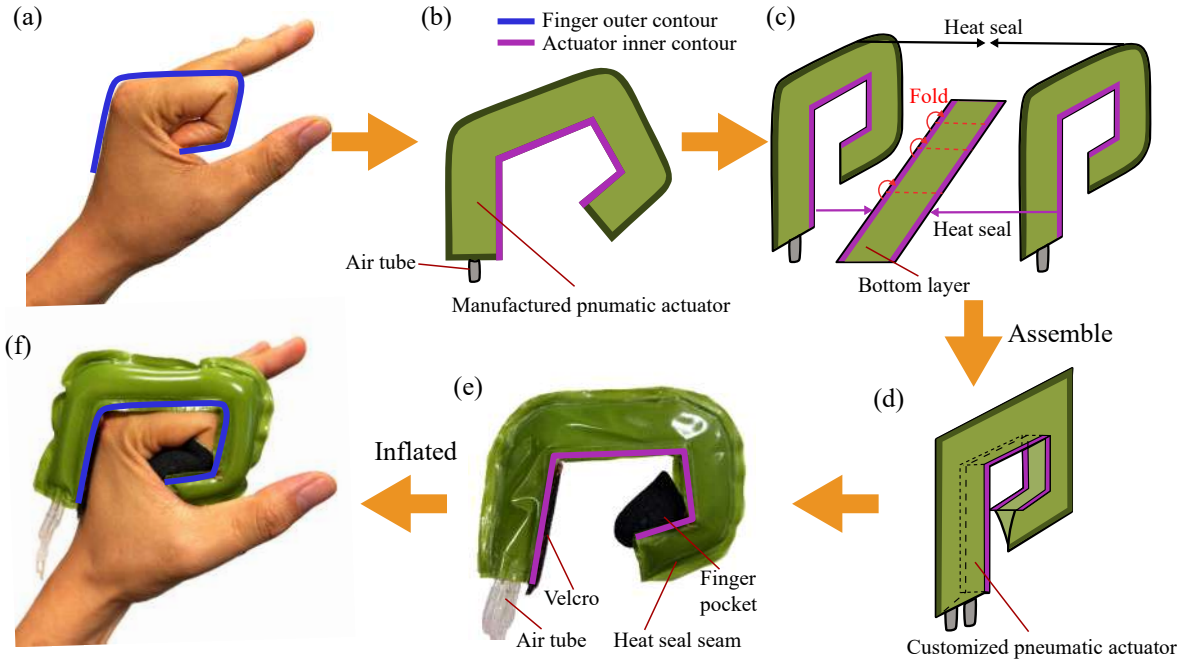


Fig. 2. Process of customization for one finger. (a) Measure the finger's outer contour in its flexed position. (b) Manufacture the fabric pneumatic actuator based on the contour. (c) Heat seal two actuators to a bottom layer. (d) Assemble the customized actuator for the finger. (e) Completed actuator for the finger. (f) Pair the inflated actuator with the finger.

rehabilitation, providing tailored support to meet the requirements of specific activities or therapeutic goals. The tip of each actuator features a finger sleeve, which aids in determining the finger's position, while the opposite end of the actuator is secured to the fabric glove using Velcro straps. The glove itself is fastened to the user's hand with additional straps and Velcro. Notably, this glove is extremely lightweight, weighing only 73 g, making it lighter than other existing fabric soft robotic gloves [14] (99 g), [16] (128 g), [18] (107 g).

B. Customization Process

Customization is achieved by tailoring the fabric-based pneumatic actuator according to the finger's flexion contour, and the process of customizing one finger is shown in Fig. 2. The process begins with measuring the outer contour of the finger in its flexed position (Fig. 2(a)). Next, the two thermoplastic polyurethane (TPU)-coated fabric layers (40D double-sided TPU-coated ripstop fabric, Adventure Expert) are laser cut (VLS350, Universal Laser Systems) and heat-sealed to create the pneumatic actuator based on the measured contour (Fig. 2(b)). Two pneumatic actuators are then thermally sealed with a bottom layer to create a customized, symmetrical fabric-based actuator (Fig. 2(c) and (d)). A finger pocket and Velcro are sewn onto the customized pneumatic actuators in preparation for integration with the fabric glove (Fig. 2(e)). When inflated, the customized fabric pneumatic actuators should align well with the finger's flexion configuration (Fig. 2(f)).

The process is repeated for each finger, ensuring the actuators match the specific dimensions of all five fingers. Afterward, the actuators are positioned onto the fabric glove, where they are securely attached to provide uniform flexion support across the hand. The customization process is now

complete.

The elastic strap and Velcro-based open design of the soft robotic glove significantly simplify the donning and doffing process, offering exceptional user-friendliness, particularly for individuals with impaired hand muscle control. The pneumatic actuators are attached to the fabric glove via Velcro, allowing for positional adjustments that improve the glove's adaptability to varying hand sizes. While the glove is tailored to a specific hand size, it accommodates a range of hand dimensions effectively. Specifically, the recommended hand length—measured from the tip of the longest finger to the crease beneath the palm—should deviate no more than ±5 mm from the designed size.

Importantly, the flexible design of the customized fabric-based pneumatic actuators allows for tailoring based on various degrees of finger flexion or even extension. This adaptability makes it possible to design the glove to support different hand postures and functionalities.

III. Experimental Evaluation

A. Block Tip Force

The block tip force is a widely used parameter for soft gloves, as it quantifies the assistance force provided during grasping [17], [18], [23]. Similar methodology for measuring block tip was used to evaluate the block tip force in this work, and a test platform for the customized pneumatic actuator was set up, as shown in Fig. 3(a). The actuator is placed laterally on the actuator support, with one end fixed to the support and the other end in contact with a force sensor (LSB205, Futek). The actuator's flexion acts against the sensor when it is inflated, generating reaction force. The actuator's curvature is constrained by a top surface, and its height is controlled by a height block, based on design. The nonlinear effects caused by the curvature are minimized by constraining the top surface of the actuator [20]. The experimental test platform has actual dimensions of 220 mm in length, 40 mm in width, and 96 mm in height, including the height of fix platform.

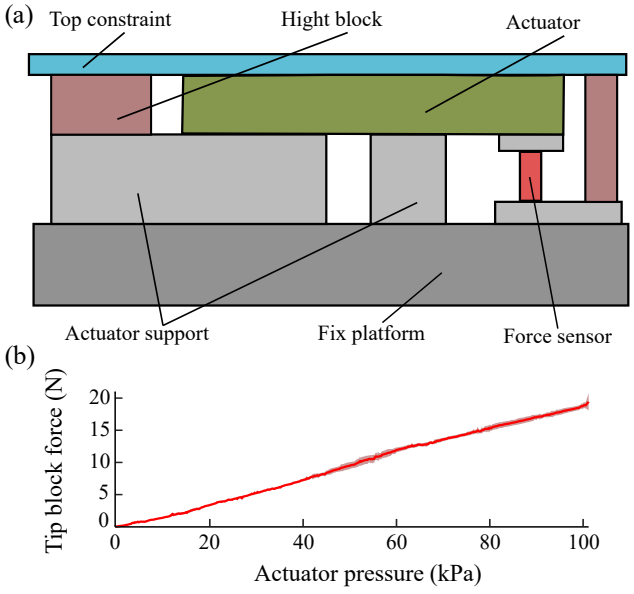


Fig. 3. Measurement of block tip force. (a) Experimental setup for block tip force. (b) Experimental results of block tip force.

The block tip force of the thumb actuator was measured at actuator pressures ranging from 0 to 100 kPa at a frequency of 50 Hz, with data smoothed using a moving window of size 10. The final result was obtained as the average of three repetitions. The actuation pressure was provided by a commercial air compressor (F6000/50, FIAC) and regulated using a pneumatic regulator (IR1000A, SMC).

The experimental results of the block tip force are shown in Fig. 3(b). The block tip force increases proportionally with increasing actuator pressure. The thumb actuator generated a maximum block tip force of 19.1 N at an actuator pressure of 100 kPa. The actuator is capable of generating a higher maximum block tip force compared to existing work at the same actuation pressure [17] (14 N), [18] (10 N), estimating from the picture).

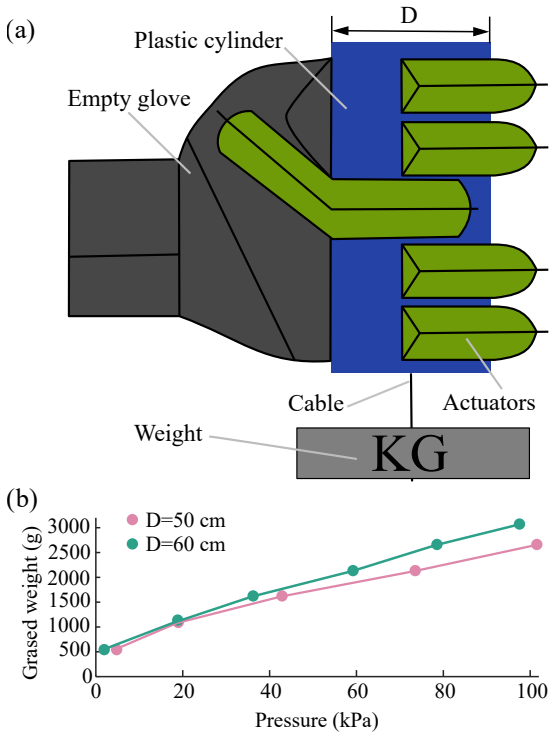


Fig. 4. Evaluation of grasp strength. (a) Experimental setup for grasp strength. (b) Experimental result of grasp strength.

B. Grasp Strength Evaluation

Experiments were conducted to evaluate the grasping strength of the soft glove (Fig. 4(a)). In this setup, a plastic cylinder with a diameter (either 50 mm or 60 mm) is placed inside the fixed empty soft glove. The lower end of the cylinder is connected to a weight via a cable. During the experiment, the pressure is first applied at its maximum level and then gradually reduced until slippage occurs between the glove and the cylinder. The pressure at the point of slippage is recorded.

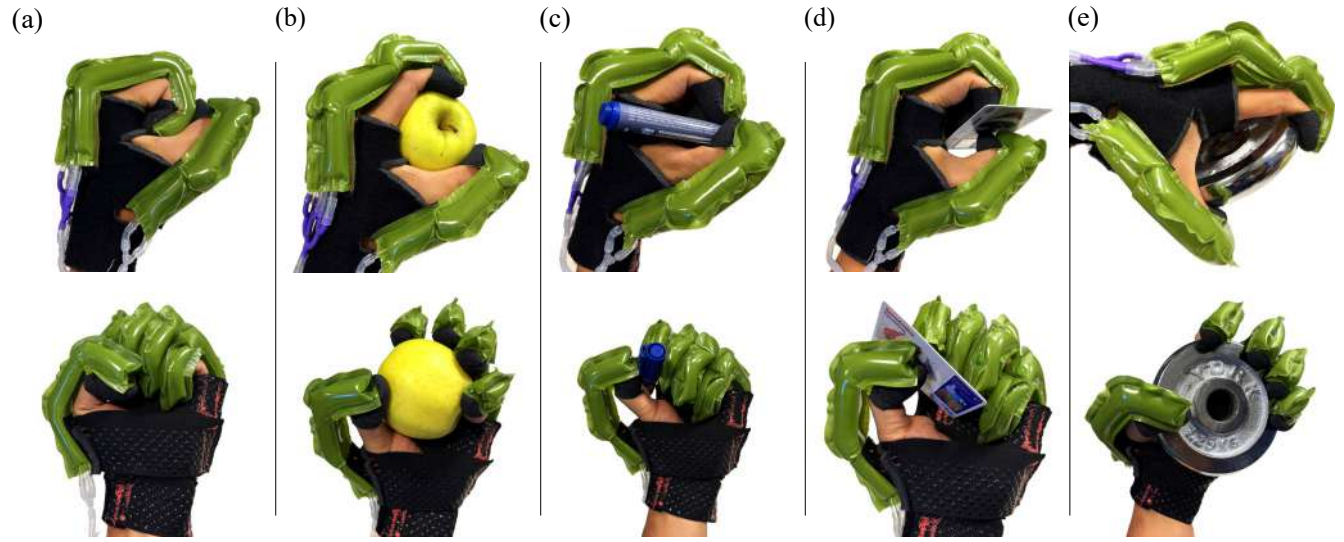


Fig. 5. Grasping various objects in daily life. (a) Grasping nothing. (b) Grasping an apple. (c) Grasping a marker pen. (d) Grasping an ISO card. (e) Grasping a weight.

This procedure is repeated three times for each weight, and the average pressure is used as the final data point.

The experimental results are shown in Fig. 4(b), where the grasped weight is plotted as a function of pneumatic pressure for two cylinder diameters (50 mm and 60 mm). The data reveal a nearly linear relationship between the weight being grasped and the pressure required, indicating that the glove can generate progressively greater grasping forces as pressure increases. Notably, the glove's ability to maintain a grip on a 60 mm cylinder exceeds that of the 50 mm cylinder at equivalent pressures. For instance, at 97 kPa, the glove can hold a load of 3126 g with the 60 mm cylinder, whereas it requires 101.3 kPa to hold 2706 g with the 50 mm cylinder. The output force is sufficient for a wide range of daily tasks (usually not more than 1000 g), demonstrating the glove's potential as an assistive device for individuals requiring enhanced hand strength [24].

Interestingly, even at very low pressures (approaching 0 kPa), the glove can still maintain a grasp on approximately 5 N. This residual force may be attributed to the glove's customized shape according to flexed finger, which provides minimal initial gripping force due to its structural bias toward flexion.

C. Grasping Various Objects in Daily Life

Experiments were conducted on a healthy subject to evaluate the performance of the soft glove in grasping various objects. Four daily objects were tested: an apple (188 g), a marker pen (16 g), an ISO card (85.6 mm x 53.98 mm x 0.76 mm), and a 1132 g weight, representing a ball-type object, a small cylinder, a daily card, and a heavy object (Fig. 5(b)-(e)). The healthy participant was first asked to open their hand with the deflated glove, palms facing up. The objects were then properly placed in the hand, and the soft glove was pressurized to 50 kPa. The subject was instructed to relax all hand muscles during pressurization to eliminate any intentional contributions from the user. Finally, the participant was asked to turn their hands over with palms facing down to test their ability to grasp the object.

Upon pressurization, the glove successfully grasped all the test objects. The smaller (thinner) the object, the better the fit between the glove and the subject's hand. The experiments demonstrated that the glove is capable of effectively assisting with gripping a wide range of objects commonly encountered in daily life.

D. Preliminary User Study

Preliminary tests were conducted on healthy subjects to evaluate the assistance effects of the soft glove by comparing muscle activation patterns during object grasping tasks with and without glove assistance.

Four male subjects (aged 28 to 34) participated in the evaluation. The glove, designed for a hand length of 200 mm, was matched to participants with a hand length of $200 \pm 5\,\mathrm{mm}$. At the start of each session, participants were briefed on the procedure and provided written informed consent.

The test simulated a common daily-life grasping task. Participants lifted an object (50 mm diameter, 1001 g weight) from a starting position, moved it to a target location (300 mm distance), returned it to the starting position, and placed it down (Fig. 6(a)). This task was repeated 10 times under two conditions: with and without glove assistance at a pressure of 60 kPa. A 5-second rest period was given between repetitions. Participants wore the glove on their left hand and controlled its activation manually with their right hand. Task order was randomized to minimize bias.

Muscle activity was recorded at 2222 Hz using surface electromyography (sEMG) sensors (Trigno Quattro Sensor, Delsys Incorporated) placed on six forearm muscles: extensor digitorum (ED), extensor carpi radialis longus (ECRL), abduc-

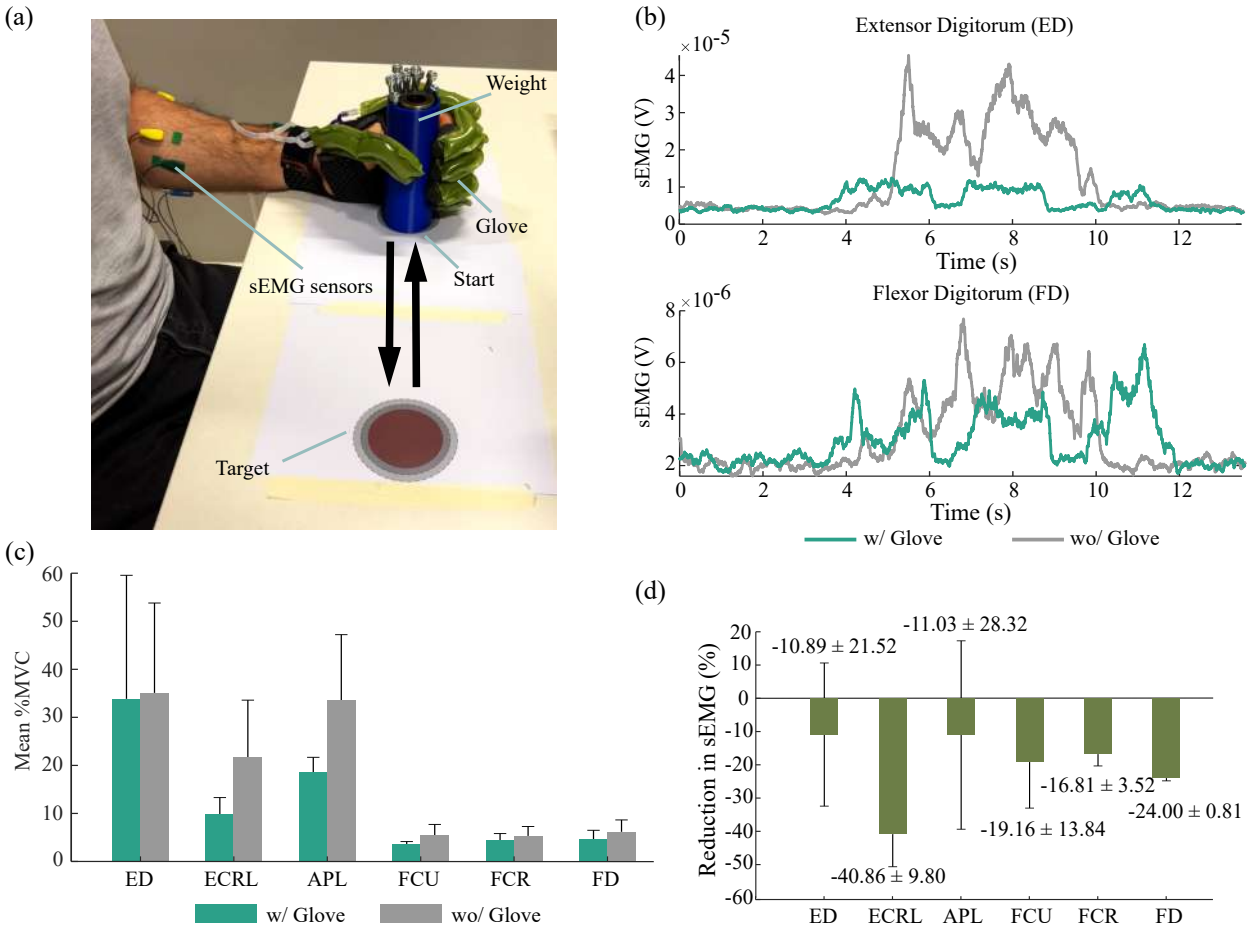


Fig. 6. Preliminary tests on healthy subjects. (a) Experimental setup. (b) sEMG data plot of ED and FD. (c) RMS of sEMG signals for all evaluated muscles. (d) Percentage reduction of muscle activity in compared conditions.

tor pollicis longus (APL), flexor carpi ulnaris (FCU), flexor carpi radialis (FCR), and flexor digitorum (FD). A maximum voluntary contraction (MVC) test was conducted at the start of each session to normalize muscle activity for cross-subject comparison.

The sEMG signals were processed using a band-pass Butterworth filter (20–450 Hz), followed by noise reduction, rectification, and smoothing with a moving average filter (0.2-second window). Signals were normalized to MVC, and the root mean square (RMS) values were calculated to quantify muscle activation [25].

For illustrative purposes, the SEMG signals of the FD and ED muscles from one representative participant are presented in Fig. 6 (b). The results consistently demonstrate reduced muscle activity with glove assistance compared to the unassisted condition, highlighting the glove's ability to mitigate muscular effort required during grasping tasks.

Aggregate results for all participants (Fig. 6(c)) revealed reduced muscle activity across all evaluated muscles when using the glove. Notably, the ECRL and APL muscles showed the largest reductions in average activity. Although slightly higher extensor activity was required to open the deflated glove during grasping and releasing, this was outweighed by the glove's ability to provide significant assistance during the grasping phase. Reduced flexor muscle activity during object-holding also indirectly decreased opposing extensor activity, confirming the glove's overall effectiveness in minimizing muscular exertion.

The percentage of the averaged reduction in muscle activity is detailed in Fig. 6(d). The ECRL exhibited the greatest reduction ($40.86 \pm 9.80\%$), followed by FD ($24.00 \pm 0.81\%$), FCU ($19.16 \pm 13.84\%$), and FCR ($16.81 \pm 3.52\%$). Reductions for ED ($10.89 \pm 21.52\%$) and APL ($11.03 \pm 13.84\%$) were more variable, likely due to muscle distribution complexity and task-specific variations.

Overall, these findings demonstrate that the glove effectively provides assistive forces, reducing the muscle activity required for grasping tasks and enhancing ergonomic support.

IV. Conclusion

In this study, we present a lightweight, fabric-based soft robotic glove designed for assistance and rehabilitation. By customizing pneumatic fabric actuators, the shape of the inflated actuators conforms to the natural flexion of the fingers. This ensures that the torque applied to the wearer's finger

joints is ergonomically precise. The customization and personalization of the glove enhance its safety, comfort, and overall effectiveness in providing assistance.

Experimental testing of the actuators and the glove demonstrated the impressive gripping capabilities of the customized design. Preliminary trials conducted on healthy participants further validated that the glove effectively aids wearers in performing gripping tasks.

While preliminary experiments were conducted solely on healthy subjects in this study, future research will focus on evaluating the glove's performance in diverse patients (different ages and degrees of hand function impairment), assessing its therapeutic effectiveness and suitability for clinical use. Additionally, future efforts will aim to optimize both the functionality and the structure of the glove, with plans to add a finger extension function and potentially incorporate abduction assistance for the thumb, as well as to achieve a more precise pinch.

ACKNOWLEDGMENT

The work was supported by the European Union. Domenico Chiaradia was supported by the Next Generation EU project ECS00000017 'Ecosistema dell'Innovazione' Tuscany Health Ecosystem (THE, PNRR, Spoke 4: Spoke 9: Robotics and Automation for Health), and Rui Chen was supported by MSCA-DN / Project 101073374 - ReWire. Views and opinions expressed are however those of the author(s) only and do not necessarily reflect those of the European Union or the European Research Executive Agency (REA). Neither the European Union nor the granting authority can be held responsible for them.

We thank KhalilianMotamed Bonab, Ali for providing help in the glove experiments.

REFERENCES

[1] V. L. Feigin, M. Brainin, B. Norrving, S. Martins, R. L. Sacco, W. Hacke, M. Fisher, J. Pandian, and P. Lindsay, "World stroke organization (wso): global stroke fact sheet 2022," *International Journal of Stroke*, vol. 17, no. 1, pp. 18–29, 2022.

[2] A. Anjum, M. D. Yazid, M. Fauzi Daud, J. Idris, A. M. H. Ng, A. Selvi Naicker, O. H. R. Ismail, R. K. Athi Kumar, and Y. Lokanathan, "Spinal cord injury: pathophysiology, multimolecular interactions, and underlying recovery mechanisms," *International journal of molecular sciences*, vol. 21, no. 20, p. 7533, 2020.

[3] S. S. Martin, A. W. Aday, Z. I. Almarzooq *et al.*, "2024 heart disease and stroke statistics: a report of us and global data from the american heart association," *Circulation*, vol. 149, no. 8, pp. e347–e913, 2024.

[4] S. M. Michaelsen, R. Dannenbaum, and M. F. Levin, "Task-specific training with trunk restraint on arm recovery in stroke," *Stroke*, vol. 37, no. 1, pp. 186–192, 2006. [Online]. Available: https://www.ahajournals.org/doi/abs/10.1161/01.STR.0000196940.20446.c9

[5] R. Gassert and V. Dietz, "Rehabilitation robots for the treatment of sensorimotor deficits: a neurophysiological perspective," *Journal of neuroengineering and rehabilitation*, vol. 15, pp. 1–15, 2018.

[6] P. Maceira-Elvira, T. Popa, A.-C. Schmid, and F. C. Hummel, "Wearable technology in stroke rehabilitation: towards improved diagnosis and treatment of upper-limb motor impairment," *Journal of neuroengineering and rehabilitation*, vol. 16, pp. 1–18, 2019.

[7] C. Correia, K. Nuckols, D. Wagner, Y. M. Zhou, M. Clarke, D. Orzel, R. Solinsky, S. Paganoni, and C. J. Walsh, "Improving grasp function after spinal cord injury with a soft robotic glove," *IEEE Transactions on Neural Systems and Rehabilitation Engineering*, vol. 28, no. 6, pp. 1407–1415, 2020.

[8] B. B. Kang, H. Lee, H. In, U. Jeong, J. Chung, and K.-J. Cho, "Development of a polymer-based tendon-driven wearable robotic hand," in *2016 IEEE International Conference on Robotics and Automation (ICRA)*, 2016, pp. 3750–3755.

[9] J.-H. Low, M. H. Ang, and C.-H. Yeow, "Customizable soft pneumatic finger actuators for hand orthotic and prosthetic applications," in *2015 IEEE International Conference on Rehabilitation Robotics (ICORR)*, 2015, pp. 380–385.

[10] P. Polygerinos, K. C. Galloway, S. Sanan, M. Herman, and C. J. Walsh, "Emg controlled soft robotic glove for assistance during activities of daily living," in *2015 IEEE International Conference on Rehabilitation Robotics (ICORR)*, 2015, pp. 55–60.

[11] T. Bagneschi, D. Chiaradia, G. Righi, G. D. Popolo, A. Frisoli, and D. Leonardis, "A soft hand exoskeleton with a novel tendon layout to improve stable wearing in grasping assistance," *IEEE Transactions on Haptics*, vol. 16, no. 2, pp. 311–321, 2023.

[12] Hong Kai Yap, Jeong Hoon Lim, Fatima Nasrallah, James Cho Hong Goh, and Chen-Hua Yeow, "Characterisation and evaluation of soft elastomeric actuators for hand assistive and rehabilitation applications," *Journal of Medical Engineering & Technology*, vol. 40, no. 4, pp. 199–209, 2016, pMID: 27007297. [Online]. Available: https://doi.org/10.3109/03091902.2016.1161853

[13] P. Polygerinos, Z. Wang, K. C. Galloway, R. J. Wood, and C. J. Walsh, "Soft robotic glove for combined assistance and at-home rehabilitation," *Robotics and Autonomous Systems*, vol. 73, pp. 135–143, 2015, wearable Robotics. [Online]. Available: https://www.sciencedirect.com/science/article/pii/S0921889014001729

[14] H. K. Yap, P. M. Khin, T. H. Koh, Y. Sun, X. Liang, J. H. Lim, and C.-H. Yeow, "A fully fabric-based bidirectional soft robotic glove for assistance and rehabilitation of hand impaired patients," *IEEE Robotics and Automation Letters*, vol. 2, no. 3, pp. 1383–1390, 2017.

[15] R. Alicea, M. Xiloyannis, D. Chiaradia, M. Barsotti, A. Frisoli, and L. Masia, "A soft, synergy-based robotic glove for grasping assistance," *Wearable Technologies*, vol. 2, p. e4, 2021.

[16] L. Ge, F. Chen, D. Wang, Y. Zhang, D. Han, T. Wang, and G. Gu, "Design, modeling, and evaluation of fabric-based pneumatic actuators for soft wearable assistive gloves," *Soft Robotics*, vol. 7, no. 5, pp. 583–596, 2020, pMID: 31995436. [Online]. Available: https://doi.org/10.1089/soro.2019.0105

[17] D. Y.-L. Lim, H.-S. Lai, and R. C.-H. Yeow, "A bidirectional fabric-based soft robotic glove for hand function assistance in patients with chronic stroke," *Journal of NeuroEngineering and Rehabilitation*, vol. 20, no. 1, p. 120, 2023.

[18] J. Lai, A. Song, J. Wang, Y. Lu, T. Wu, H. Li, B. Xu, and X. Wei, "A novel soft glove utilizing honeycomb pneumatic actuators (hpas) for assisting activities of daily living," *IEEE Transactions on Neural Systems and Rehabilitation Engineering*, vol. 31, pp. 3223–3233, 2023.

[19] L. Cappello, J. T. Meyer, K. C. Galloway, J. D. Peisner, R. Granberry, D. A. Wagner, S. Engelhardt, S. Paganoni, and C. J. Walsh, "Assisting hand function after spinal cord injury with a fabric-based soft robotic glove," *Journal of neuroengineering and rehabilitation*, vol. 15, pp. 1–10, 2018.

[20] P. Polygerinos, Z. Wang, J. T. B. Overvelde, K. C. Galloway, R. J. Wood, K. Bertoldi, and C. J. Walsh, "Modeling of soft fiber-reinforced bending actuators," *IEEE Transactions on Robotics*, vol. 31, no. 3, pp. 778–789, 2015.

[21] S.-S. Yun, B. B. Kang, and K.-J. Cho, "Exo-glove pm: An easily customizable modularized pneumatic assistive glove," *IEEE Robotics and Automation Letters*, vol. 2, no. 3, pp. 1725–1732, 2017.

[22] S. Kokubu, R. Nishimura, and W. Yu, "Deriving design rules for personalization of soft rehabilitation gloves," *IEEE Access*, vol. 12, pp. 14 474–14 486, 2024.

[23] M. Feng, D. Yang, and G. Gu, "High-force fabric-based pneumatic actuators with asymmetric chambers and interference-reinforced structure for soft wearable assistive gloves," *IEEE Robotics and Automation Letters*, vol. 6, no. 2, pp. 3105–3111, 2021.

[24] K. Matheus and A. M. Dollar, "Benchmarking grasping and manipulation: Properties of the objects of daily living," in *2010 IEEE/RSJ International Conference on Intelligent Robots and Systems*, 2010, pp. 5020–5027.

[25] M. Xiloyannis, D. Chiaradia, A. Frisoli, and L. Masia, "Physiological and kinematic effects of a soft exosuit on arm movements," *Journal of neuroengineering and rehabilitation*, vol. 16, pp. 1–15, 2019.

Assessment Scores for Patients with Central Neurological Conditions in Rehabilitation: a Systematic Review

Silvia Campagnini, Kaan Borekci, Kyle Embry, Arun Jayaraman

***Abstract*— In rehabilitation, evidence-based practice relies on evaluating patients' standardized outcomes to manage care plans and resources; however, the selection of tools to use is globally inconsistent. Alternatively, emerging technologies can measure high-resolution biomarkers, but their implementation remains a challenge. Given the amount of measures, interest in new scoring systems of patient health synthesizing multi-source data is rising. Emerging research in rehabilitation lacks standardized guidelines and psychometric validation of these scores. Hence, this review systematically examines the methods used for developing and validating patient assessment scores in rehabilitation. A systematic search included studies on the development and validation of scores to assess adult patients with central neurological disorders in rehabilitation. Nineteen studies were synthesized. In the score development, simpler methods and input data were more common (11 studies used statistics, 12 clinical data). In the validation, the heterogeneity in reference standards and tests in scores' psychometric analysis highlights the need for evidence and standardized processes in this field. Clinically relevant information is crucial for implementable scores able to guide clinical decision-making and care strategies. Future studies should adopt exploratory approaches, analyzing various input data, methods, and psychometric properties' impact on the score capability to assess patient health.**

***Index Terms*— Central Nervous Disorder, Outcome Assessment, Psychometrics, Rehabilitation, Score, Systematic Review.**

I. Introduction

Evidence-based practice is a fundamental concept in rehabilitation, where a patient's care is guided by complex decision-making based on their individual characteristics and institutional guidelines [1]. A necessary part of this process is assessing the patient's health status and tracking it over time. These patient assessments are used to design treatments, measure the impact of treatments, and manage care resources including long-term services and reimbursement [2].

Currently, patients are assessed using a broad set of standardized outcome measures in clinical rehabilitation [3]. These measures can be classified under the International Classification of Functioning, Disability and Health (ICF, [4]) and represent a common clinical language for communication across different institutions and healthcare professionals to understand and treat their patients. However, there are broad institutional inconsistencies about which measures are collected, and given concerns about high clinician workloads and the time and costs of frequent assessments [5], it is impractical to collect them all [3]. As a result, there is a continued desire to evaluate existing and new assessments for their ability to capture comprehensive patient outcomes.

A wave of research is exploring alternative patient assessments derived from technological devices (e.g., wearable sensors), neuroimaging, and biological/genetic analyses. These methods have demonstrated promise for providing complementary biomarkers correlated with patients' diagnosis, disease severity, and prognosis [6]. Such assessments could provide objective and high-resolution data about mechanistic and physiological changes, offering a potential solution for easier implementation across different settings/institutions [7].

Given the diversity and volume of data now available from these different sources, there is increased interest in developing and validating new types of assessment scores to easily and reliably evaluate patients. Big data analytics are becoming more common to synthesize and extract clinically meaningful information from these massive, multi-source data volumes and generate new assessment scores [8]. A primary goal is to simplify the process of obtaining comprehensive and accurate information about a patient's health or disease state, which can be used to design effective, individualized rehabilitation interventions and support efficient management of healthcare resources [9]. To date, this work has been primarily focused on acute medicine (i.e., emergency departments, intensive care units, and imaging) [10], [11], [12], while the rehabilitation field is beginning to see the emergence of the first examples [13], [14], [15], [16].

Among the few studies available, the methodologies used to develop a scoring systems are very heterogeneous (e.g., statistical transformation of input data [15], machine learning -ML- [16], or item response theory -IRT- [13], [14]) and there are no clinically accepted guidelines to support the process. Additionally, the validation of these scoring systems (i.e., analyzing their psychometric properties to examine their ability to capture a desired characteristic) is often overlooked. A study examining the 2017 measures list from the Center for Medicare and Medicaid Services (CMS) Quality Payment Program reported that only 37% of 271 measures were deemed valid [17]. Additionally, developing a patient assessment score without validating its psychometric properties potentially endangers its usability in clinical practice, creating frustration in healthcare professionals toward a non-trustworthy tool, increasing assessment time and costs, and

This work was funded by Shirley Ryan AbilityLab. S.C. and A.J. are with the Max Nader Lab for Rehabilitation Technologies & Outcomes Research and K.E. is the with Center for Bionic Medicine, Shirley Ryan AbilityLab, Chicago, USA. They are also with the Dept. of PM&R, Northwestern University, Chicago, USA. A.J. is also with the Dept. of Physical Therapy and Human Movement Science, Northwestern University, Chicago, USA (corresponding author: ajayaraman@sralab.org). K.B. is with the Dept. of Biomedical Engineering, Northwestern University, Chicago, USA.

ultimately compromising patient recovery [17].

Thus, the objective of this work is to systematically review available methodologies employed in developing and validating patient scoring systems during rehabilitation, with a specific focus on patients with central neurological injuries/disorders. The review examines the methods utilized for the development of scores, the type of input data used, and their validation based on psychometric properties, in order to examine eventual gaps and properly direct future research.

II. Methods

This systematic review was performed following the Preferred Reporting Items for Systematic Reviews and Meta-Analyses (PRISMA) guidelines [18]. The protocol was registered on PROSPERO (ID CRD42024506880).

A. Selection criteria

To favor systematic search and transparency and reproducibility of the results, the selection criteria for the records in this review were designed following the Population, Intervention, Comparison and Outcome (PICO) framework, suitable for quantitative clinical studies.

The population included adults (age$\geq$18 years) affected by a central neurological injury or disorder. Only records in the rehabilitation field were retained; when the study setting was unclear, records that included patients onset$\geq$30 days after injury/diagnosis (targeting post-acute care) were retained.

The intervention was the development and validation of a new score for patient assessment. A score was defined as a univariate and objective measure obtained by condensing data related to patient health, impairment, or function through a numerical and synthetic value. No constraint was posed on the type and amount of input data. Records were excluded if they only presented the development of a score, without validating it through analysis of at least one psychometric property.

Studies with any type of comparison (or no comparison) and any type of outcome were included. Study protocols, conference abstracts and proceedings, reviews, and overviews were excluded. Additionally, records not in English or whose full text could not be retrieved were excluded.

B. Search

A systematic search of papers, by means of a search string, was conducted on the 9th of May 2024 in the following databases: PubMed, Web of Science, Scopus, and CENTRAL. The search string was designed on six concepts, two of which derived from the population criterion (central neurological disorder and rehabilitation setting) and four by the intervention type (score, new development, validation, and patient assessment) (**Figure 1**). A parallel search was also conducted in the Public Reporting section of the CMS website [19]. The search was manually conducted by a CMS expert (A.D.), utilizing the above-mentioned criteria.

All studies were screened first by title or abstract, then by full text; the screening phases involved initial semi-automatic procedures (The MathWorks, Inc. 2021, MATLAB version: 9.10.0 R2021a), followed by manual screening (Rayyan [20] and ASReview version 1.6.3 [21]).

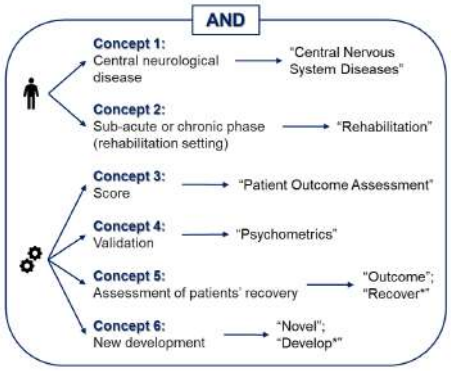


Fig. 1. String search concepts.

C. Risk of bias assessment

The Quality Assessment of Diagnostic Accuracy Studies-2 (QUADAS-2) [22] tool was used to assess the risk of bias in the included studies. Since no optimal tool exists for evaluating both the development and validation of scores, QUADAS-2—typically used for assessing diagnostic test studies—was chosen to emphasize the validation aspect and, consequently, the clinical applicability of the scores. This tool evaluates the risk of bias across four key domains: patient selection, index test, reference standard, and flow and timing.

D. Data collection and synthesis

In accordance with the PICO framework, the following were extracted from each study: *study characteristics*, *score development*, and *score validation*. A narrative description of the results was synthesized.

III. Results

A. Search results

A total of 8087 papers were retrieved from databases and 28 technical reports from CMS website (**Figure 2**). Overall, 19 studies were analyzed in the systematic review, including 18 papers and one technical report.

The most common reason for excluding papers was a non-rehabilitation setting (52.8%), followed by an intervention (30.4%) or diagnosis (11.2%) outside the scope of this review. Most technical reports were also excluded due to an intervention outside of scope (81.8%).

B. Risk of bias

The risk of bias analysis reported "Some concerns" for all the 19 studies, except for the study by Magliacano et al. [16], which reported an overall "Low" risk of bias. The domains most often reporting "Some concerns" across studies were the *Reference standard*, followed by *Flow and timing*.

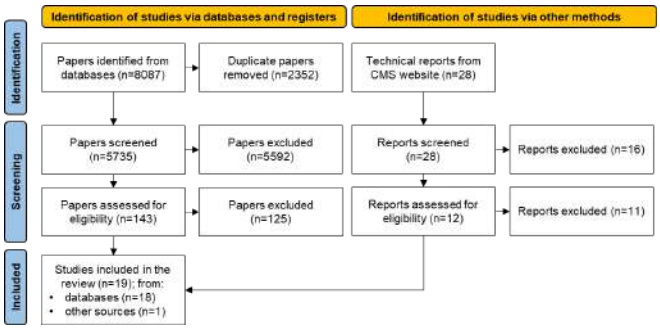


Fig. 2. PRISMA chart.

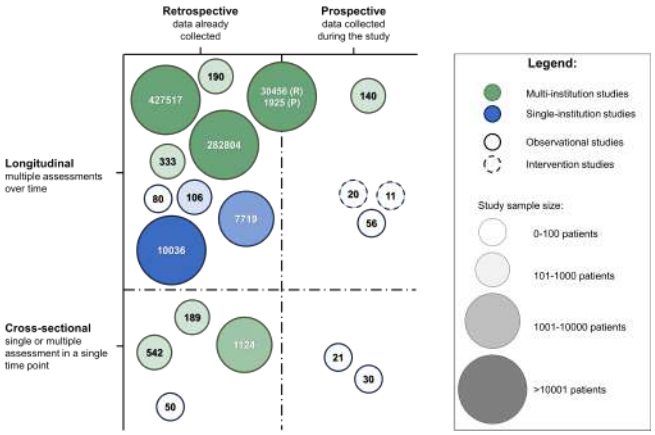


Fig. 3. Characteristics of the 19 included studies. Study design can be either retrospective or prospective, and either cross-sectional or longitudinal. One study used both retrospective and prospective data for the score training and validation, respectively. Dimensions/shades, colors, and line styles represent the sample size, the presence of one or more centers, and the presence of intervention of the included studies, respectively.

C. Study characteristics

Most studies were published between 2013 and 2023, with one record focused on the development of a score for co-morbidities on individuals with stroke published in 1997 [23]. **Figure 3** summarizes the study design and sample size of each included study. There were a similar number of single- and multi-institution studies (9 and 10, respectively), and most studies (12) were retrospective by design. One study [23] proposed the development of a score for the assessment of co-morbidities on a retrospective sample and externally validated it on a prospective one. Retrospective longitudinal studies were characterized by higher sample sizes with one study using a sample of below 100 participants (80 [24]), three studies having more between 100 and 500 participants (106 [23], 190 [25], and 333 [16]), and four over 5000 participants (7719 [13], 10036 [14], 282804 [26], and 427956 [27]).

Two studies with the highest sample sizes performed development and validation of mobility and self-care scores [27] and discharge function score [26] by aggregating average data across patients (i.e., institution-level analysis). Conversely, all the other studies used the data from each individual patient to develop and validate their scores (i.e., patient-level analysis). Lastly, while the majority of the studies utilized data collected during traditional rehabilitation and therapeutic care, two studies utilized data collected during experimental therapy, including upper-limb bilateral tasks in virtual reality [28] and walking tasks with functional electrical stimulation [29].

Concerning the patient populations, four studies included participants with multiple diagnoses, five with stroke, five with disorder of consciousness from traumatic and non-traumatic brain injury (TBI), two with TBI, one with multiple sclerosis, one with dementia, and one with traumatic spinal cord injury.

D. Score development

A total of 30 different scores were developed in the 19 studies, with 13 studies developing one score, three studies developing two scores [27], [30], [23], two studies developing three scores [29], [24], and one study developing five scores [31] to assess functional ability levels on individuals with spinal cord injury. Following their review, the scores were classified using the ICF model [4] (**Figure 4, Panel A**). Specifically, a first and second-level classification were provided, i.e., specifying the health-related domain and its sub-components.

In 14 studies, the methodological steps included pre-processing the input data before computing the score, whereas no pre-processing was applied in the remaining five studies. Pre-processing included feature extraction (5 [28], [29], [32], [33], [34]), feature weighting (1, through principal component analysis [24]), missing data imputation (2, through fixed value [26], [27]), and feature selection (7).

Methods used to develop the scores were categorized as ML, IRT, or statistics. Statistics was further categorized into either cut-off calculation, statistical regressions, or statistical manipulation such as data transformations or scaling. ML was further classified into supervised or unsupervised ML (**Figure 4, Panel B**). A total of 10 studies utilized one methodology only, six [31], [34], [30], [27], [28], [26] and three [35], [33], [24] used a combination of two and three methodologies, respectively. A total of 11 studies utilized only statistics.

The source of input data used for score development was initially classified as instrumental, biological, or clinical (**Figure 4, Panel C**). Most studies utilized one data source (12 clinical, 2 instrumental data), two had a combination of clinical and instrumental data (from markerless motion capture [28], surface electromyography, and stereophotogrammetry-based gait analysis [29]), and one included clinical, instrumental, and biological data (from electroencephalography and somatosensory evoked potential, as well as neuron-specific enolase [33]). Clinical data was further categorized into personal information, pathology description, standardized outcome measures, Patient-Reported Outcome Measures (PROMs), and other clinical descriptions such as co-morbidities.

Among the 14 studies considering scales or questionnaires, i.e., standardized outcome measures or PROMs, 10 studies developed scores from these data at an item-specific level, while the remaining four used the total scale scores. Lastly, none of the included studies considered dynamic information

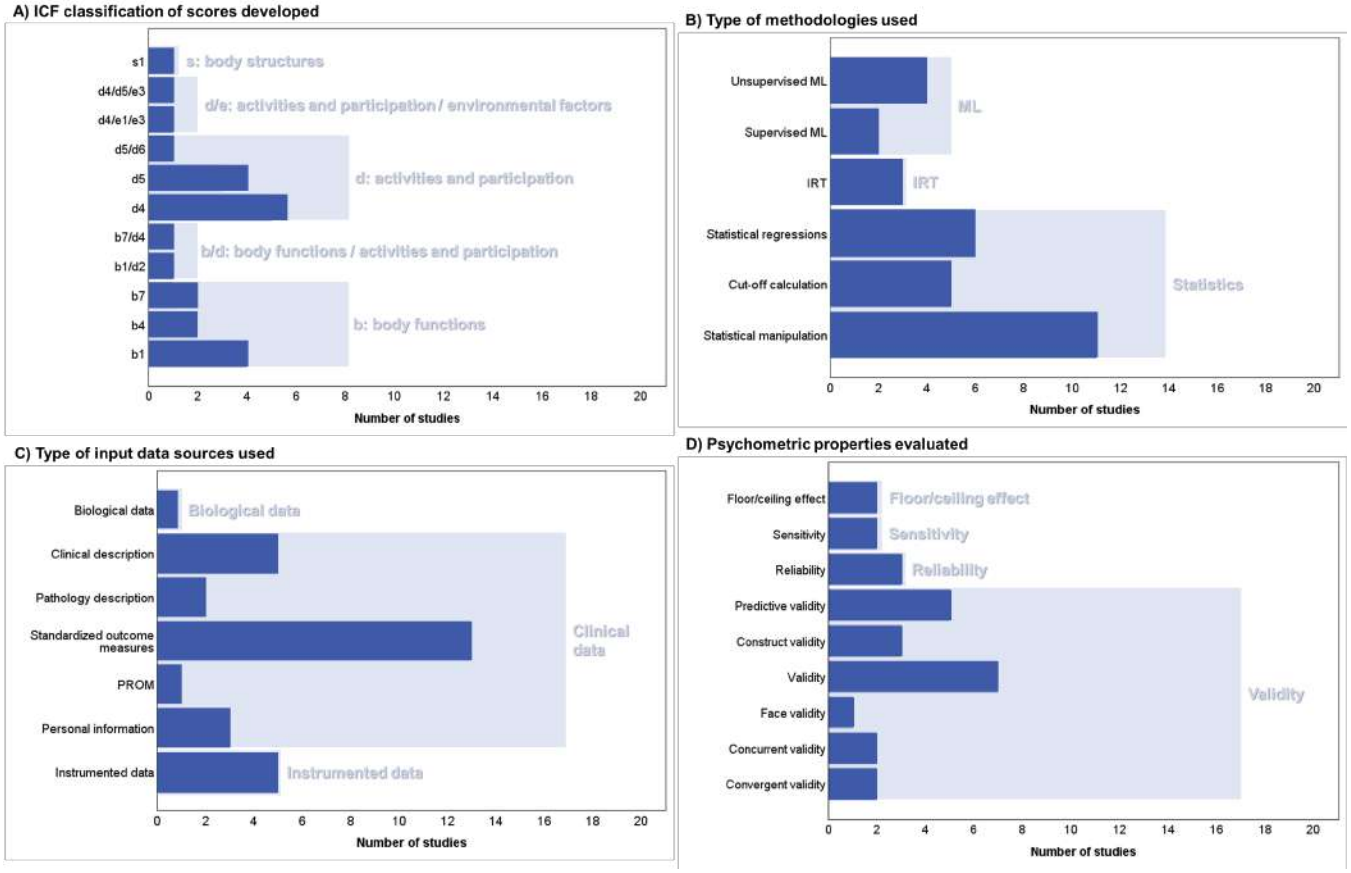


Fig. 4. Bar charts related to the ICF classification of the developed scores (Panel A), methodologies (Panel B) for the development of scores, data sources (Panel C), and psychometric properties evaluated (Panel D). Light-blue bars represent macro-categorization of these domains, dark blue bars refer to sub-categorizations.

over time, but instead relied on a unique assessment over time, even in the cases of instrumental data sources.

E. Score validation

The following psychometric properties were analyzed: validity, reliability, sensitivity, and floor and ceiling effect; the first was further categorized into concurrent validity, convergent validity, face validity, construct validity, and predictive validity (**Figure 4, Panel D**). Additionally, in a few studies (7), the type of validity tested was not reported. Most studies (13) evaluated only one psychometric property, four studies analyzed two properties (2 sensitivity and floor/ceiling effects [13], [14], one construct and convergent validity [36], one reliability and construct validity [27]), and two studies validated the score on three psychometric properties (one face validity, reliability, and convergent validity [26] and one concurrent validity, predictive validity, reliability [23]).

A total of 60 different reference standards were used across all studies as a benchmark for comparing the scores during their validation. The number of reference standards used for each score validation ranged from a minimum of 0 to a maximum of 8. The majority of reference standards spanned multiple ICF domains, specifically 9 in body functions, activities and participation, and environmental factors (b-d-e) and 20 in body functions and activities and participation (b-d). Five reference standards were in the domain of body functions only (b) and five in the domain of activities and participation only (d). The remaining 18 reference standards did not enter the ICF classification, as demographic or administrative factors such as age, sex, length of stay, etc., were selected. In three studies, at least one analysis did not use a reference standard due to the nature of the psychometric property assessed (reliability, construct validity, and face validity [26], [27], [23], which do not require one). The analysis of the psychometric properties on each score-reference standard pair led to a total of 94 validation analyses across all studies.

IV. Discussion

The aim of this systematic review was to examine recent advancements in the development and validation of patient assessment scores in the rehabilitation field. The ultimate goal of this work was to understand current practices, identify gaps, and guide future work to ensure patient assessments are clinically meaningful (**Figure 5**).

There has been arguably more success in introducing new scoring systems based on synthesized data in acute care settings [10], such as when characterizing critical conditions [11] and reporting results from complex imaging [12]. On the contrary, in rehabilitation, this is still an emerging field, with no cohesive processes for bringing together data from new sources to assess patient health or recovery. The presence of

limited research in rehabilitation was confirmed during this systematic work by the great heterogeneity of terminology used across studies (with the terms "score", "index", and "scale" often intertwined). Additionally, there was no single risk of bias tool that could appropriately evaluate potential sources of bias both in the development and validation of these scores. In this work, we selected the QUADAS-2 tool, which mainly analyzing the risk of bias arising in the validation process. Having a unified framework introducing definition of terms and appropriate tools for the analyses of the scoring system would be beneficial for the analytical rigor and consistency in both the development and validation phases of scoring systems. Such a framework would not only standardize the evaluation process but also improve the reliability and comparability of results across studies.

The characteristics of the included studies showed that retrospective designs are more common and often connected to larger data volumes (**Figure 3**). Furthermore, the presence of dedicated digital infrastructures and strong inter-institutional collaboration emerge as critical factors for the development of scalable and generalizable scoring systems. Scores derived from extensive data availability have the potential to deliver valuable insights at both the patient and institutional levels (e.g., Deutsch et al. [27] and Acumen-Technical Report [26]). Hence, patient-specific scores can aid in the local optimization of rehabilitation plans, while institution-level scores can support global resource management strategies.

Most studies used one source of input data only, with clinical data being the most common (**Figure 4, Panel C**). These numbers could be the result of the retrospective nature of the included studies, and the reduced costs and complexity represented by the utilization of data already in use in the clinical practice. In fact, even across clinical data, standardized clinical outcome measures were the most common data source, given their widespread use in current practice. Conversely, PROMs were incorporated less frequently, perhaps due to their subjective nature and variability in their design and administration [37], [38], [39], or the challenge of acquiring these patient-reported measures for some individuals with neurological injuries, since since their cognition, communication, sensation, and other relevant factors might be affected.

Most studies employed simpler, statistical methods (**Figure 4, Panel B**) during score development. Contrary to expectations, with the exception of Chung et al. [28], these methodologies were generally used when multiple input data sources were combined. On the other hand, ML approaches were more frequently chosen when a larger number of input features or bigger sample sizes were available. Importantly, none of the studies in this review examined or compared the performance of multiple methodologies, nor did they assess how the choice of method influenced the outcome of the score. This is a critical point, as the resolution and final characteristics of a score are fundamental for a reliable and precise assessment of patients and they largely depend on the methodology used in the score development. Therefore, for future research, we encourage the use of multiple methods,

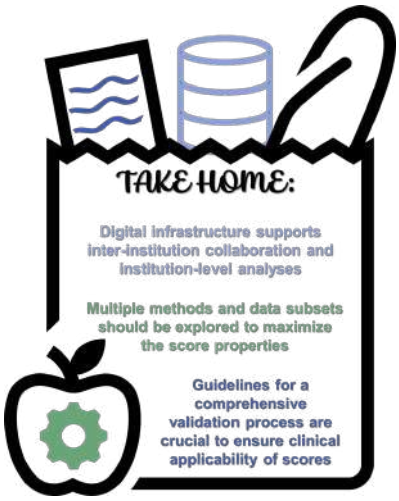


Fig. 5. Take home messages of the study.

starting with simpler approaches to maintain control and interpretability of the results (e.g., with simple statistical methods or manipulations). Then, depending on the characteristics of the input data, IRT and/or ML could be applied. It is essential to consider the advantages of each method: statistical methods offer simplicity and interpretability and allow for more elaborated modeling of the relationship among input features (e.g., mediation, moderation, etc...), while ML excels in managing large volumes of data and multisource information. IRT, on the other hand, is particularly suited for exploring the relationship between input features and latent traits, including non-linear ones, providing valuable insights into the underlying structure of the data.

Similar considerations should be made regarding the selection of psychometric properties and reference standards during the validation process. The goal of validation is to assess how well the score reflects the patient's health or recovery and to determine whether external factors influence this assessment. This process is crucial for the successful implementation of the score in clinical practice, where it can play a key role in decision-making and the selection of appropriate care strategies. However, in this review, the majority of studies (14 out of 19) only evaluated validity, often without specifying the type of validity used (**Figure 4, Panel D**). Moreover, a broad range of methods and reference standards were employed to validate the scores. Future research should focus on validating a comprehensive set of psychometric properties and selecting sets of multiple reference standards across different ICF domains and sub-categories. This is particularly important for scores that assess more complex, higher-level ICF domains (e.g., activities and participation), where the influence of external factors is likely to be more impactful.

V. Conclusions

This work summarized the current state of the art concerning the development and validation of patient assessment scores during rehabilitation from central neurological disorders/injuries. This review highlighted how this field is still in preliminary stages and deeply intertwined with a process of

digitalization and data-driven reorganization of healthcare facilities. Standardized processes for both the development and validation of scores are lacking. Hence, it is recommended for future studies to adopt an explorative approach, evaluating how different input data subsets, methodologies, and reference standards impact on the psychometric properties of the scores.

REFERENCES

[1] K. A. McKibbon, "Evidence-based practice.," *Bulletin of the Medical Library Association*, vol. 86, pp. 396–401, July 1998.

[2] M. e. a. Rashid, "Comprehensive rehabilitation outcome measurement scale (CROMS): development and preliminary validation of an interdisciplinary measure for rehabilitation outcomes," *Health and Quality of Life Outcomes*, vol. 20, p. 160, Dec. 2022.

[3] Z. Liao and Y. Quintana, "Challenges to Global Standardization of Outcome Measures," *AMIA Summits on Translational Science Proceedings*, vol. 2021, pp. 404–409, May 2021.

[4] "International Classification of Functioning, Disability and Health (ICF)."

[5] J. e. a. Lorkowski, "Overload of Medical Documentation: A Disincentive for Healthcare Professionals," in *Medical Research and Innovation* (M. Pokorski, ed.), pp. 1–10, Cham: Springer International Publishing, 2021.

[6] W. e. a. Cao, "Rehabilomics: A state-of-the-art review of framework, application, and future considerations," *Frontiers in Neurology*, vol. 14, p. 1103349, Mar. 2023.

[7] I. e. a. Clay, "Sensor Data Integration: A New Cross-Industry Collaboration to Articulate Value, Define Needs, and Advance a Framework for Best Practices," *Journal of Medical Internet Research*, vol. 23, p. e34493, Nov. 2021.

[8] D. Cirillo and A. Valencia, "Big data analytics for personalized medicine," *Current Opinion in Biotechnology*, vol. 58, pp. 161–167, Aug. 2019.

[9] K. e. a. Kawamoto, "Improving clinical practice using clinical decision support systems: a systematic review of trials to identify features critical to success," *BMJ : British Medical Journal*, vol. 330, p. 765, Apr. 2005.

[10] A. G. Rapsang and D. C. Shyam, "Scoring systems in the intensive care unit: A compendium," *Indian Journal of Critical Care Medicine : Peer-reviewed, Official Publication of Indian Society of Critical Care Medicine*, vol. 18, pp. 220–228, Apr. 2014.

[11] J.-L. Vincent and R. Moreno, "Clinical review: Scoring systems in the critically ill," *Critical Care*, vol. 14, p. 207, Mar. 2010.

[12] U. e. a. Mothiram, "Digital radiography exposure indices: A review," *Journal of Medical Radiation Sciences*, vol. 61, pp. 112–118, June 2014.

[13] A. J. e. a. Bodine, "Development of a Multidimensional, Multigroup Measure of Self-Care for Inpatient Rehabilitation," *Archives of Physical Medicine and Rehabilitation*, vol. 102, pp. 97–105, Jan. 2021.

[14] C. E. e. a. Deom, "A Mobility Measure for Inpatient Rehabilitation Using Multigroup, Multidimensional Methods," *Journal of Neurologic Physical Therapy*, vol. 45, pp. 101–111, Apr. 2021.

[15] D. e. a. Sattin, "The Coma Recovery Scale Modified Score: a new scoring system for the Coma Recovery Scale-revised for assessment of patients with disorders of consciousness," *International Journal of Rehabilitation Research. Internationale Zeitschrift Fur Rehabilitationsforschung. Revue Internationale De Recherches De Readaptation*, vol. 38, pp. 350–356, Dec. 2015.

[16] A. e. a. Magliacano, "Predicting Long-Term Recovery of Consciousness in Prolonged Disorders of Consciousness Based on Coma Recovery Scale-Revised Subscores: Validation of a Machine Learning-Based Prognostic Index," *Brain Sciences*, vol. 13, p. 51, Dec. 2022.

[17] C. H. e. a. MacLean, "Time Out — Charting a Path for Improving Performance Measurement," *New England Journal of Medicine*, vol. 378, pp. 1757–1761, May 2018. Publisher: Massachusetts Medical Society _eprint: https://www.nejm.org/doi/pdf/10.1056/NEJMp1802595.

[18] D. e. a. Moher, "Preferred reporting items for systematic reviews and meta-analyses: the PRISMA statement," *PLoS medicine*, vol. 6, p. e1000097, July 2009.

[19] "Public Reporting: Provider Preview Report and Requests for CMS Review of Data | CMS."

[20] M. e. a. Ouzzani, "Rayyan—a web and mobile app for systematic reviews," *Systematic Reviews*, vol. 5, p. 210, Dec. 2016.

[21] R. e. a. van de Schoot, "An open source machine learning framework for efficient and transparent systematic reviews," *Nature Machine Intelligence*, vol. 3, pp. 125–133, Feb. 2021. Publisher: Nature Publishing Group.

[22] P. F. e. a. Whiting, "QUADAS-2: a revised tool for the quality assessment of diagnostic accuracy studies," *Annals of Internal Medicine*, vol. 155, pp. 529–536, Oct. 2011.

[23] M. e. a. Liu, "Comorbidity measures for stroke outcome research: A preliminary study," *Archives of Physical Medicine and Rehabilitation*, vol. 78, pp. 166–172, Feb. 1997.

[24] Y. e. a. Hirano, "Development of a prognostic scale for severely hemiplegic stroke patients in a rehabilitation hospital," *Clinical Neurology and Neurosurgery*, vol. 158, pp. 108–113, July 2017.

[25] P. Liuzzi, F. De Bellis, A. Magliacano, A. Estraneo, and A. Mannini, "Consciousness-Domain Index: a data-driven clustering-based consciousness labeling," in *2022 44th Annual International Conference of the IEEE Engineering in Medicine & Biology Society (EMBC)*, (Glasgow, Scotland, United Kingdom), pp. 1062–1065, IEEE, July 2022.

[26] "Acumen, llc 500 airport blvd., suite 365 burlingame, ca 94010, discharge function score for inpatient rehabilitation facilities (irfs) technical report, 2023."

[27] A. e. a. Deutsch, "Inpatient Rehabilitation Facility Change in Self-Care and Change in Mobility Quality Measures: Development and Reliability and Validity Testing," *Archives of Physical Medicine and Rehabilitation*, vol. 103, pp. 1105–1112, June 2022.

[28] C.-R. e. a. Chung, "An Intelligent Motor Assessment Method Utilizing a Bi-Lateral Virtual-Reality Task for Stroke Rehabilitation on Upper Extremity," *IEEE Journal of Translational Engineering in Health and Medicine*, vol. 10, pp. 1–11, 2022.

[29] M. e. a. Gandolla, "Validation of a Quantitative Single-Subject Based Evaluation for Rehabilitation-Induced Improvement Assessment," *Annals of Biomedical Engineering*, vol. 43, pp. 2686–2698, Nov. 2015.

[30] R. G. e. a. Kumar, "Development and Validation of a Functionally Relevant Comorbid Health Index in Adults Admitted to Inpatient Rehabilitation for Traumatic Brain Injury," *Journal of Neurotrauma*, vol. 39, pp. 67–75, Jan. 2022.

[31] R. e. a. Sinha, "Functional Ability Level Development and Validation: Providing Clinical Meaning for Spinal Cord Injury Functional Index Scores," *Archives of Physical Medicine and Rehabilitation*, vol. 96, pp. 1448–1457, Aug. 2015.

[32] Z. e. a. Zhang, "Objective Assessment of Upper Limb Mobility for Post-stroke Rehabilitation," *IEEE Transactions on Biomedical Engineering*, pp. 1–1, 2015.

[33] X.-g. e. a. Kang, "Development of a simple score to predict outcome for unresponsive wakefulness syndrome," *Critical Care*, vol. 18, no. 1, p. R37, 2014.

[34] S. e. a. Morozova, "Conventional Structural Magnetic Resonance Imaging in Differentiating Chronic Disorders of Consciousness," *Brain Sciences*, vol. 8, p. 144, Aug. 2018.

[35] D. e. a. McKechnie, "Development of the Sydney Falls Risk Screening Tool in brain injury rehabilitation: A multisite prospective cohort study," *Journal of Clinical Nursing*, vol. 27, pp. 958–968, Mar. 2018.

[36] A. e. a. Kuspinar, "Using existing data to identify candidate items for a health state classification system in multiple sclerosis," *Quality of Life Research: An International Journal of Quality of Life Aspects of Treatment, Care and Rehabilitation*, vol. 23, pp. 1445–1457, June 2014.

[37] M. J. e. a. Calvert, "Patient reported outcome assessment must be inclusive and equitable," *Nature Medicine*, vol. 28, pp. 1120–1124, June 2022. Publisher: Nature Publishing Group.

[38] C. H. Fung and R. D. Hays, "Prospects and challenges in using patient-reported outcomes in clinical practice," *Quality of life research : an international journal of quality of life aspects of treatment, care and rehabilitation*, vol. 17, pp. 1297–1302, Dec. 2008.

[39] T. Weldring and S. M. Smith, "Patient-Reported Outcomes (PROs) and Patient-Reported Outcome Measures (PROMs)," *Health Services Insights*, vol. 6, pp. 61–68, Aug. 2013.

Actuator- and Control-less Ankle Exoskeleton for Push-off Assistance During Treadmill Walking: A Proof-of-Concept Study

1st Matej Tomc
University Rehabilitation Institute Republic of Slovenia, and Faculty of Electrical Engineering, University of Ljubljana
Ljubljana, Slovenia
https://orcid.org/0009-0007-8366-3115

2nd Matjaž Zadravec
University Rehabilitation Institute Republic of Slovenia
Ljubljana, Slovenia
matjaz.zadravec@ir-rs.si

3rd Andrej Olenšek
University Rehabilitation Institute Republic of Slovenia
Ljubljana, Slovenia
andrej.olensek@ir-rs.si

4th Zlatko Matjačić
University Rehabilitation Institute Republic of Slovenia and Faculty of Electrical Engineering, University of Ljubljana
Ljubljana, Slovenia
zlatko.matjacic@ir-rs.si

***Abstract*—We have previously proposed a novel tethered ankle exoskeleton AN-EXTRA-Push. It operated by exploiting the posterior movement of the leg on the treadmill to stretch an elastic tendon. The exoskeleton was controlled using an electromechanical brake.**

The objective of this case study with one healthy and one hemiparetic subjects was to test the feasibility of AN-EXTRA-PUSH, modified in such a way that one end of the elastic tendon is permanently attached to a fixed point, eliminating any control.

Subjects walked on a split-belt treadmill under 4 experimental conditions: one unassisted and at three different assistance levels. The healthy subject repeated the experimental procedure at three different walking speeds. The hemiparetic subject walked at a constant self-selected speed.

In healthy subject, AN-EXTRA-PUSH assistance caused a decrease in peak biological torque accompanied with an increase in exoskeleton torque in the ankle joint. Biological power remained similar across conditions with the additional exoskeleton power contributing to increased total power generation. Exoskeleton torque and power increased with higher walking speeds.

In hemiparetic subject, AN-EXTRA-PUSH did not affect biological torque and power, however, it added torque and power to reach higher totals.

These preliminary results show that the proposed actuator- and control-less version of AN-EXTRA-Push is feasible and warrants further research.

***Index Terms*—ankle, exoskeleton, walking assistance, rehabilitation, control**

I. Introduction

The muscule-tendon complex of the ankle joint plays a vital role in generating mechanical power for propulsion during healthy human walking. The majority of this power is spent in a short sub-phase of a gait cycle named push-off. The key elements of the ankle muscle-tendon complex in this process are *m. triceps surae* and Achilles tendon, that work in series and both contribute to ankle platarflexion torque generation. During the stance phase, muscle fascicles of *m. triceps surae* remain relatively isometric, while the Achilles tendon stretches and stores elastic energy [1]. The tendon then supplements the force created by the contracting muscles during push-off, which results in efficient production of a high burst of positive power. In terms of power, both the tendon and muscles contribute in roughly equal parts [2].

Part of the need for power generation at the ankle can be offloaded onto ankle exoskeletons. These robotic devices have shown the potential to improve human walking economy and endurance, but their effectiveness is significantly dependent on the timing and power of the delivered assistance [3], with needs varying from person to person. An important aspect of ankle exoskeleton development is therefore the search for optimal control. Currently, the leading approach towards individualized assistance relies on human-in-the-loop optimization (HILO) [4].

Modern control methods in general require dedicated, high-performance hardware with high-computational power and ample time to arrive at optimal settings for a single optimization parameter, most notably metabolic cost. However, various other factors such as users' comfort and, in case of neurologically-impaired subjects, also high variability in walking patterns may further complicate the optimization process. Further development of HILO-based control approaches foresees utilization of high-scale personalized musculoskeletal modelling that would allow for off-line training of HILO controllers through simulations using the real-time walking data, thus even further increasing demands on technology, which in turn may drive modern exoskeletons further away from practical use. Even if we assume that the described approach may in the future become feasible for individualized use in able-bodied subjects, it seems that great variability

This research was supported by the Slovenian Research and Innovation Agency under research program number P2-0228.

surrounding gait of various neurologically-impaired populations would preclude successful implementation in clinical applications.

On the other hand, there have been successful implementations of entirely passive ankle exoskeletons that were able to reduce metabolic cost of walking in healthy individuals at certain speeds while requiring no control (e.g. [5]), however with an important limitation that they could not inject additional energy during the push-off, which greatly limits their practical potential, especially in rehabilitation. Considering the ability of active ankle exoskeletons to inject substantial amounts of energy and the ability of passive ankle exoskeletons to recoil timely during the push-off there is a question whether would it be possible to conceive an ankle exoskeleton that could deliver desired amount of additional energy into the biological push-off, similarly to active exoskeletons in a semi-active way and at the same time that would, similarly to entirely passive exoskeletons, not require any control.

Inspired by the elastic nature of ankle plantarflexor muscle-tendon complex, we have previously proposed a novel device: ANkle EXoskeleton using TReadmill Actuation for Push-off assistance (AN-EXTRA-Push) [6]. AN-EXTRA-Push is an ankle exoskeleton that combines features of active and passive exoskeletons. It is a tethered device, which allows for lightweight design, similar to passive exoskeletons, while offering additional power for generating torque, which it harnesses from a moving treadmill. The only actively controlled part of the device is a brake that, while disengaged, allows for free movement of the tether that is tensioned only by a soft constant force spring, and while engaged, fixes one end of the tether in place. Posterior movement of the foot on the treadmill throughout stance phase then stretches the elastic tendon of AN-EXTRA-Push, loading it with energy. Using a combination of coaxial spools of different radii, the force is transferred to a rigid tendon at the back of the device, where it pulls on the foot and the shank, creating plantarflexion torque. In our previous studies, we have observed that omitting a brake might be a feasible modification to the device, which would even further simplify AN-EXTRA-PUSH, rendering it completely actuator- and control-less.

The objective of this study was to test the feasibility of AN-EXTRA-PUSH, modified in such a way that the elastic tendon is permanently attached to a fixed point. In a case study with a healthy human volunteer and with a subject with hemiparesis we provide first preliminary results showing that the proposed ankle exoskeleton exhibits performance that is comparable to SoA HILO controlled powered ankle exoskeletons.

II. Methods

A. AN-EXTRA-Push

The device used in this study is a modified version of AN-EXTRA-Push, roughly described in the introduction and previously presented in [7] and [8]. Schematic representation of its operation is shown in Fig. 1. One end of the elastic tendon is fixed on a point in front of the treadmill. The other end is split in two and wound around a structure of coaxial spools attached to the shoe at the back of the orthosis. A rigid cable is wound around a spool of a smaller radius on one end and attached to a cuff on the shank on the other end (see Fig. 1 A). In stance phase, the leg is moved posteriorly by the treadmill and the ankle is dorsiflexed. This stretches the elastic tendon, generating force. The force is transferred to the rigid cable at the back of the device, amplified to five times its magnitude due to the structure of coaxial spools, where it pulls on the foot and the shank, creating plantarflexion torque (see Fig. 1 B). After push-off initiation, the ankle plantarflexes rapidly, releasing the majority of the energy stored in the elastic tendon. Any remaining energy pulls the leg in the anterior direction in swing phase. At the start of the next gait cycle, the device is essentially reset and ready to assist in the next step. Fig. 2 shows the current version of AN-EXTRA-Push prototype that was used in this study.

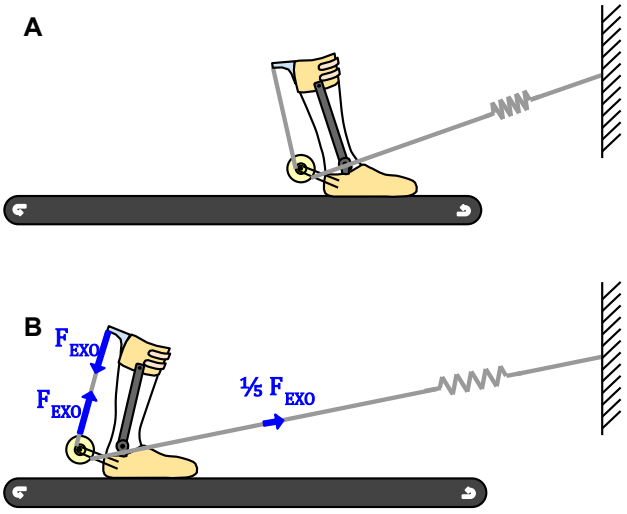


Fig. 1. Schematic representation of AN-EXTRA-Push and exoskeleton forces during its operation. A) No forces are present at heel strike. B) The leg was pulled posteriorly by the treadmill, stretching the elastic tendon. Forces in the rigid cable at the back of the device are 5 times the force in the elastic tendon due to being transferred over the spools of different radii.

B. Study participants

One healthy adult male and one adult male suffering from left-side hemiparesis participated in this study (healthy subject – age: 27 years, height: 179 cm, weight: 89 kg and post-stroke subject – age: 53 years, height: 179 cm, weight: 99 kg). The study was approved by National Medical Ethics Committee of the Republic of Slovenia.

At the time of study, subject with hemiparesis was receiving treatment at University Rehabilitation Institute Republic of Slovenia, following a stroke 8 weeks prior. He was an independent ambulator (FAC score 4) who exhibited limited push-off generation capabilities.

C. Instrumentation and data acquisition

Participants walked on a custom-built split-belt treadmill. They wore AN-EXTRA-Push on their left leg. The left part

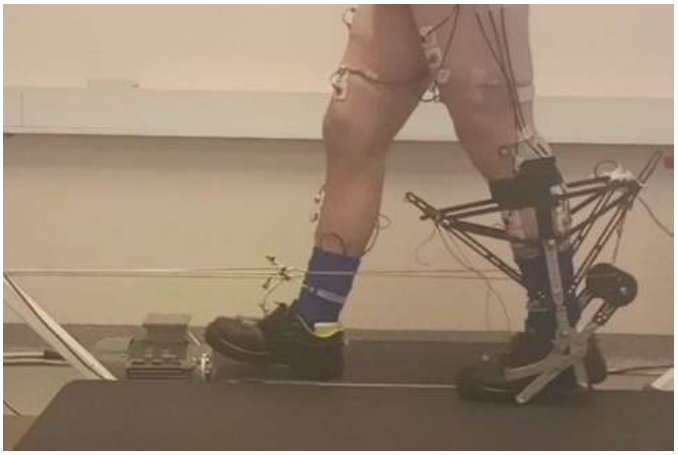


Fig. 2. A photograph of the prototype, taken during one of the experiments.

of the treadmill stood on four force transducers (K3D120, ME Systeme GmbH, GER) that measure ground reaction forces (GRF) with a frequency of 250 Hz.

Gait kinematics were measured using motion capture cameras (Optitrack, NaturalPoint, Inc., USA). 18 reflective markers were placed on the body of the participant, 16 of them following the Plug-In Gait lower-body marker set. Kinematic measurements were sampled at a frequency of 120 Hz. AN-EXTRA-Push was equipped with a force sensor (U9C, HBM, GER) that measured the force in the rigid cable at the back of the device. A Beckhoff CX5020 embedded PC was used to record the force sensor data.

For the healthy subject, surface electromyography was measured for six muscle groups: *m. soleus, m. gastrocnemius lateralis, m. tibialis anterior, m. vastus medialis, m. biceps femoris, and m. rectus femoris*. Pairs of 3.5x4 mm electrodes (3M, Maplewood, USA) with inter electrode distance of 4mm were placed atop appropriately prepared skin surface above muscle bellies. Data was sampled using TelemyoMini 16 (Neurodata, Vienna, AUT) at 1 kHz.

D. Experimental procedure

Both subjects had no previous experience with walking with AN-EXTRA-Push. In this experiment, they walked under 4 different experimental conditions: while wearing AN-EXTRA-Push, but without the tendons being connected (Unassisted) and in three different active assistance conditions (Weakest –elastic tendon implemented with one elastic rope, Medium – two elastic ropes in parallel and Strongest – three elastic ropes in parallel). Each elastic rope had a stiffness of 35 N/m.

The healthy subject repeated the experimental procedure at three different walking speeds: 0.4 m/s, 0.8 m/s and 1.2 m/s. The subject suffering from hemiparesis walked at a constant self-selected speed of 0.5 m/s.

Each measurement consisted of about 2 minutes of walking which amounted to at least 44 completed strides (more at higher speeds). Measurements were done in the following order: Unassisted, Weakest, Medium, Strongest. They were recorded one after another with a minute long break in between them.

E. Data processing

Raw marker data were processed in Motive 2.2.0 software (NaturalPoint, Inc., USA). Marker trajectories were smoothed using the built-in filtering algorithm. Joint angles were calculated using the Plug-in Gait kinematic model. Ground reaction forces, center of pressure positions, and exoskeleton force values were filtered using a Butterworth filter (4th order, 7 Hz). Using a Newton-Euler inverse dynamics algorithm, joint torques and powers were calculated, taking into account the additional weight and inertia of the exoskeleton attached to the left leg.

EMG signals were first filtered using a 20-140 Hz band-pass and 49-51 Hz notch filter, then rectified and filtered using a 150 ms moving average filter. Each subject's EMG signals were normalized relative to the peak muscle activity during the unassisted condition at the highest recorded walking speed to compare muscle activation across conditions.

Data were segmented into gait cycles. Left heel strike was chosen as the beginning of a stride. A heel strike event was marked when the vertical ground reaction force exceeded 30 N. The last 30 strides during each experimental condition were used for the analysis.

III. Results

A. Healthy subject

Figures 3-5 show kinematics, kinetics and EMGs around the ankle joint for all experimental conditions at three gait speeds. In comparison to unassisted walking, AN-EXTRA-PUSH causes a decrease in peak biological torque accompanied with an increase in exoskeleton torque in the ankle joint. Overall, the sum of biological and exoskeleton ankle torque remains comparable to Unassisted experimental condition, indicating that volitional human effort decreased with increased assistance. This is reflected in a decrease of peak soleus and gastrocnemius muscle activation throughout the stance phase.

This is followed by an increase in the activation of tibialis anterior in the initial swing phase, which is probably a consequence of residual energy stored in the elastic tendon that drives foot towards plantarflexion during the initial swing. The residual tension in the elastic tendon dissipates throughout swing phase as the foot once again approaches the front of the treadmill.

At walking speeds that are low (0.8 m/s, Fig. 4) and very low (0.4 m/s, Fig. 5) for a healthy human, the subject did not retain the same joint kinematics across conditions as well compared to while walking at a more comfortable speed of 1.2 m/s (Fig. 3). At the slower two speeds, the biological power remained similar across conditions with the additional exoskeleton power contributing to increased total power generation at the ankle despite minimal changes in total ankle torque.

Exoskeleton torque and power increased with higher walking speed, although not linearly. The relative contributions of

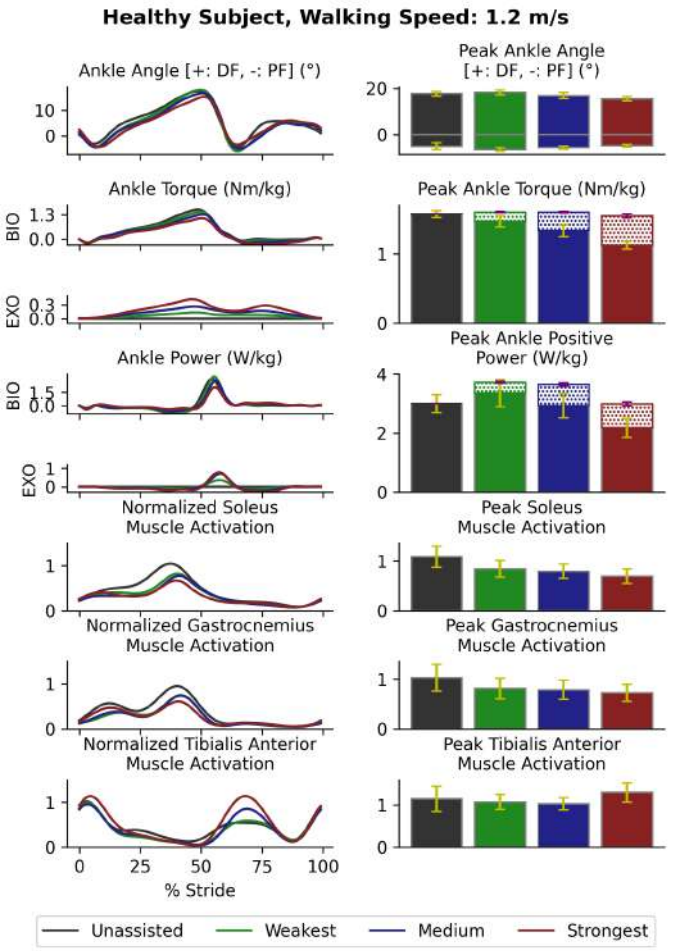


Fig. 3. Results for the healthy subject walking at 1.2 m/s. Trajectories for an average stride are shown on the left. On the right, bar charts depict peak values of the measured quantities. For peak ankle torque and positive power charts, the base section represents biological contributions (solid color), while exoskeleton contributions (hatched region) are stacked on top. Yellow and purple error bars indicate the variability of biological and exoskeleton contributions respectively.

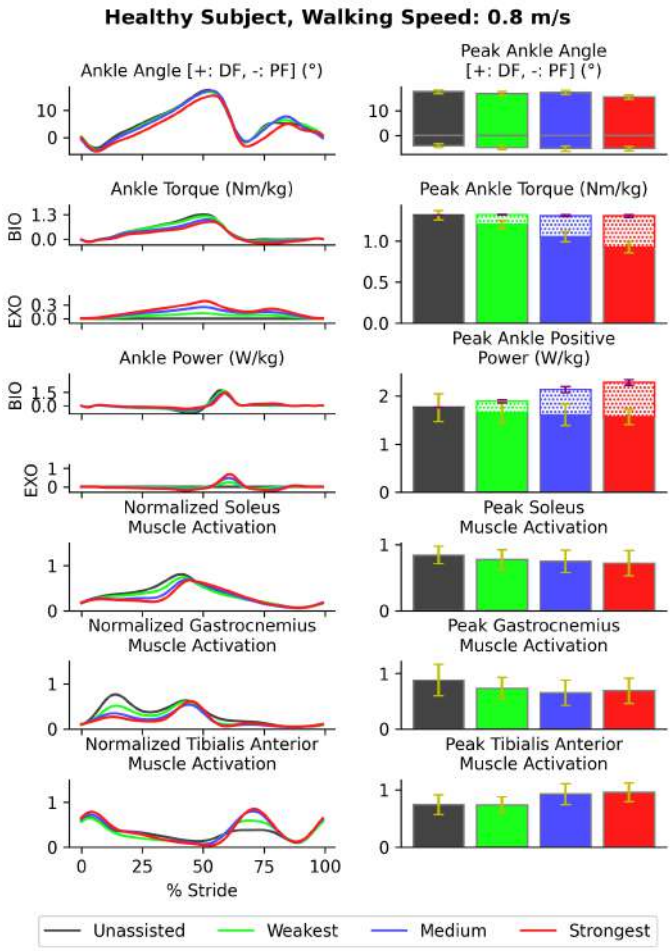


Fig. 4. Results for the healthy subject walking at 0.8 m/s. Trajectories for an average stride are shown on the left. On the right, bar charts depict peak values of the measured quantities. For peak ankle torque and positive power charts, the base section represents biological contributions (solid color), while exoskeleton contributions (hatched region) are stacked on top. Yellow and purple error bars indicate the variability of biological and exoskeleton contributions respectively.

the exoskeleton assistance to torque and power generation at the ankle was larger at lower speeds.

Inter-stride variability is only indicated by the error bars on the bar charts on the right side of the figures 3-5 to preserve the readability of the average trajectories on the left. Exoskeleton torque and power were applied consistently, their relative variability (coefficient of variation) being about the same compared to relative variability of biological torque and power.

B. Subject with hemiparesis

Figure 6 shows kinematics and kinetics for all experimental conditions. AN-EXTRA-PUSH largely did not affect biological torque and power, however, it progressively added torque and power, resulting in an increase in peak effective ankle torque of approximately 20 % and around 50 % increase in peak effective positive ankle power at the highest level of assistance compared to the Unassisted condition.

IV. Discussion and Conclusions

The effects of providing push-off assistance during gait with this actuator- and control-less version of AN-EXTRA-Push match how an assistive ankle exoskeleton should function based on the literature and our pre-experiment expectations. The healthy subject had an intact neuro-muscolo-skeletal system and was thus capable of exploiting the additional ankle plantarflexion torque and power. He was able to maintain a substantially similar walking pattern while offloading some of the volitional effort onto the device, which manifested in lower biological torque generation and plantar flexor muscles activation. The effect is most clearly visible in the reduced *m. soleus* activation, which is to be expected, since AN-EXTRA-Push functions directly in parallel to *m. soleus*.

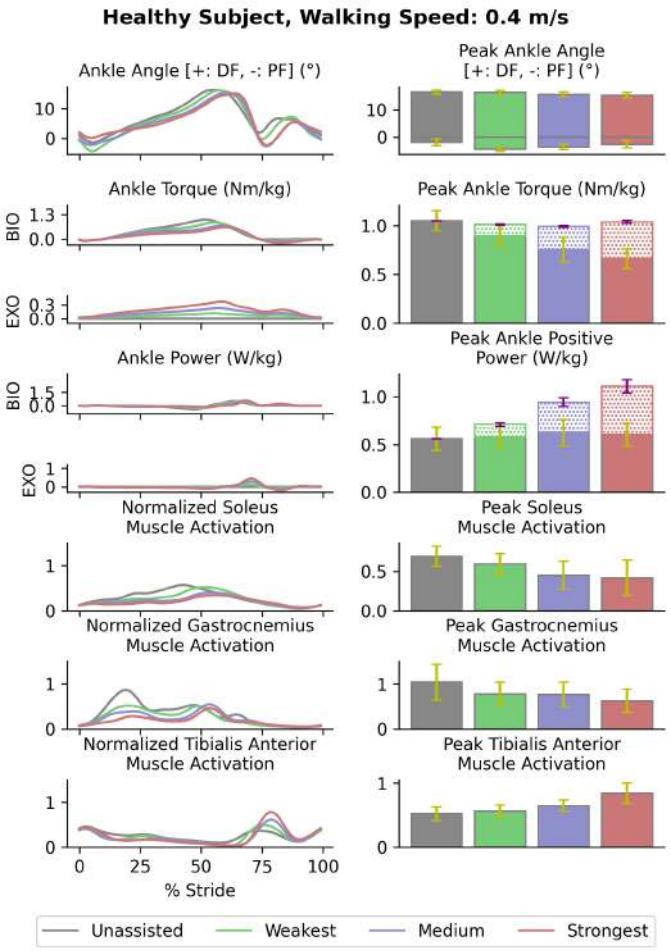


Fig. 5. Results for the healthy subject walking at 0.4 m/s. Trajectories for an average stride are shown on the left. On the right, bar charts depict peak values of the measured quantities. For peak ankle torque and positive power charts, the base section represents biological contributions (solid color), while exoskeleton contributions (hatched region) are stacked on top. Yellow and purple error bars indicate the variability of biological and exoskeleton contributions respectively.

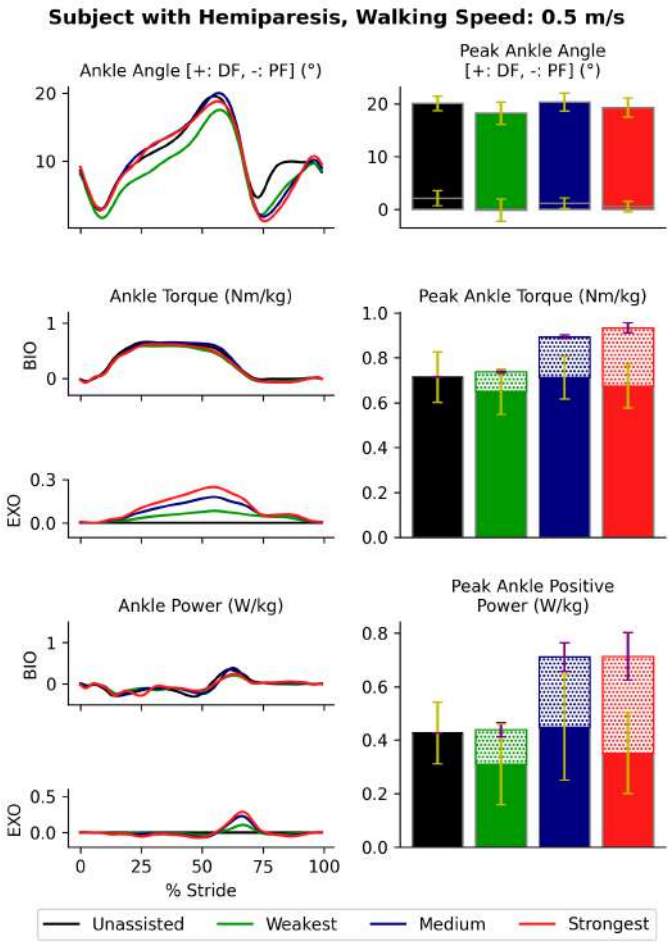


Fig. 6. Results for the post-stroke subject walking at 0.5 m/s. Trajectories for an average stride are shown on the left. On the right, bar charts depict peak values of the measured quantities. For peak ankle torque and positive power charts, the base section represents biological contributions (solid color), while exoskeleton contributions (hatched region) are stacked on top. Yellow and purple error bars indicate the variability of biological and exoskeleton contributions respectively.

Previously to the study, the subject suffering from hemiparesis had by himself been unable to generate the plantar flexion torque necessary for healthy-like push-off during walking. The subject continued to exert near-full volitional effort into walking (the biological torque and power were largely unchanged throughout the experiments). The device appears to have helped supplement their torque generating capabilities and approach healthy-like kinetics.

In both healthy and post-stroke subject experiments, the assistance was delivered during the appropriate time window. For healthy subject, this is reflected in the peak reduction of biological ankle torque and power which coincides with the peak torque and power in the unassisted condition. These peaks don't coincide as well for the post-stroke subject since his torque trajectory is abnormal and fails to reach the peak value in late stance, when plantarflexion torque is most needed to push off.

Inter-stride assistance variability is proportional to inter-stride variability of biological quantities. Since the assistance could partially adapt to large changes in walking speeds across the experimental protocol, it appears that AN-EXTRA-Push was able to adapt its assistance to the small changes in walking pattern in real-time. Put another way, a unusually longer stride is immediately supported by more exoskeleton assistance, which is to be expected based on the mechanical design of AN-EXTRA-Push. This means that AN-EXTRA-Push is likely to provide appropriate assistance even to users with highly variable gait patterns that typically occur with neuro-muscular impairments. This stands in opposition to exoskeletons that optimize their assistance pattern to a steady state gait.

After pushing off and transitioning to swing phase, the force exerted by the still partially stretched elastic tendon necessitates some active dorsiflexion torque by the user. Both the healthy and post-stroke subject were able to actively

compensate for that.

The two case studies were intended to demonstrate proof-of-concept and check that the simplified AN-EXTRA-Push design performs to expectations. Specific results showing how the two subjects responded to assistance with AN-EXTRA-Push should not be generalized, especially to patient populations. Inherent adaptation of AN-EXTRA-Push observed across different speeds and stride to stride differences, however, is an encouraging sign that increases our confidence that such approach is feasible and warrants further research.

By harvesting the energy from the moving treadmill, AN-EXTRA-Push is not limited to low power assistance like contemporary passive devices. While powerful, timely assistance does not require precise control of an actuator as with state of the art active ankle exoskeletons. Instead, it is achieved passively due to its biomimetic design.

In rehabilitation, time to find appropriate control parameters is a commodity that we cannot afford. Training sessions are typically limited to at most half of an hour; additionally, complex systems that need substantial knowledge to be operated are not desirable in clinical settings. Technical solutions that are simple, easy to don/doff and intuitive for use are likely to be accepted by primary users and therapists.

As such the proposed ankle exoskeleton may be perfectly suited for use in a treadmill-based training of walking in various neurological populations as it is easy to use and delivers extra push-off power in synchrony with volitional human efforts in every step without a need for time-consuming optimization of control parameters. Unlike the HILO controlled ankle exoskeletons that, once properly trained, require stationary gait in order to be successful our approach delivers timely assistance in each step regardless of the inherent step-to-step variability of the push-off initiation of a human, which is of paramount relevance in neurological populations.

REFERENCES

[1] A. Lai, G. A. Lichtwark, A. G. Schache, Y.-C. Lin, N. A. T. Brown, and M. G. Pandy, "In vivo behavior of the human soleus muscle with increasing walking and running speeds," Journal of Applied Physiology, vol. 118, no. 10, pp. 1266–1275, May 2015, doi: 10.1152/japplphysiol.00128.2015.

[2] D. J. Farris and G. S. Sawicki, "The mechanics and energetics of human walking and running: a joint level perspective," J R Soc Interface, vol. 9, no. 66, pp. 110–118, Jan. 2012, doi: 10.1098/rsif.2011.0182.

[3] G. S. Sawicki, O. N. Beck, I. Kang, and A. J. Young, "The exoskeleton expansion: improving walking and running economy," Journal of NeuroEngineering and Rehabilitation, vol. 17, no. 1, p. 25, Feb. 2020, doi: 10.1186/s12984-020-00663-9.

[4] J. Zhang et al., "Human-in-the-loop optimization of exoskeleton assistance during walking," Science, vol. 356, no. 6344, Art. no. 6344, Jun. 2017, doi: 10.1126/science.aal5054.

[5] S. H. Collins, M. B. Wiggin, and G. S. Sawicki, "Reducing the energy cost of human walking using an unpowered exoskeleton," Nature, vol. 522, no. 7555, Art. no. 7555, 2015.

[6] M. Tomc and Z. Matjačić, "Harnessing Energy of a Treadmill for Push-Off Assistance During Walking: In-Silico Feasibility Study," Frontiers in Bioengineering and Biotechnology, vol. 10, 2022, [Online]. Available: https://www.frontiersin.org/article/10.3389/fbioe.2022.832087.

[7] M. Tomc, M. Zadravec, A. Olenšek, and Z. Matjačić, "Harnessing Energy of a Treadmill for Push-Off Assistance During Walking: a Proof of Concept study," in 2022 International Conference on Rehabilitation Robotics (ICORR), Rotterdam, Netherlands, Jul. 2022, pp. 1–6, doi: 10.1109/ICORR55369.2022.9896554.

[8] M. Tomc, A. Olenšek, M. Zadravec, and Z. Matjačić, "Inherent Synchrony Between an Ankle Exoskeleton and its Wearer Achieved Through Mechanical Design," in 2024 10th IEEE RAS/EMBS International Conference for Biomedical Robotics and Biomechatronics (BioRob), Sep. 2024, pp. 858–863. doi: 10.1109/BioRob60516.2024.10719696.

Tailoring ankle-foot orthoses stiffness to end-users' needs: which performance variables matter?

Sejin Yi Yoo[1,†], Emma A. Gille[2,†], Jorge Gómez[1], Eduardo Rocon[1], Ignacio Martínez-Caballero[3], Edwin van Asseldonk[2], and Cristina Bayón[1,*]

***Abstract*— Ankle Foot Orthoses (AFOs) are devices designed to assist or rehabilitate gait. The stiffness of the AFO is an important parameter that needs to be tailored to the end-user's characteristics. However, the lack of clinical guidelines for optimizing AFO stiffness has led to inconsistent outcomes and low user satisfaction in existing experimental approaches. This inconsistency may stem from two reasons: (1) the limited number of variables considered by these methods, which may fail to capture the full complexity of gait; and (2) the variability in the relationship between stiffness and gait variables among users. To address these challenges, we propose a user-tailored optimization framework that identifies and incorporates relevant gait variables based on individual needs and preferences. In this pilot study, we explore key performance variables in two participants with cerebral palsy (CP), analyzing the results using XGBoost and SHAP values. Our findings highlight the importance of multiple performance variables in capturing gait complexity and reveal that the most relevant variables differ between participants. This study underscores the potential of personalized approaches to improve AFO optimization and user outcomes.**

I. INTRODUCTION

Ankle foot orthoses (AFOs) are devices frequently used to assist or rehabilitate gait in people with motor or neurological disorders [1]. These devices provide support to the ankle joint, correct gait deviations, and effectively reduce energy cost when walking. To maximize the benefit of an AFO, it is important to tailor its stiffness to the end-user's needs, as the stiffness highly influences the final user's performance [1], [2], [3], [4].

Optimal stiffness varies depending on the user's capacity [5], [3], the task [6] and the terrain type [7], among other factors. Therefore, objective data on user performance under all these different conditions would be useful to inform clinical-decision making in prescribing new AFOs [8]. However, clear clinical guidelines to determine a personalized value of the AFO's stiffness are lacking [8], and available experimental methods still face challenges like long measuring times and lack of inclusion of user preferences [1].

Human in the loop optimization (HILO) is a method aiming to optimize AFO stiffness based on an objective function that most often targets metabolic cost [9]. This target variable is computed indirectly from breath by breath measurements of carbon dioxide and oxygen. Nevertheless, metabolic cost requires a long measuring time, and even when a reduction in metabolic cost is achieved via HILO, this improvement is not reliably perceived by the user [10]. This can be explained by the fact that users prioritize several aspects of gait simultaneously, with metabolic cost not being the highest priority. Therefore, trying to optimize a single physiological measurement (i.e., metabolic cost) without considering other variables and user preferences, may not yield the desired results in terms of user satisfaction and acceptance [10].

Gait domains, aside from effort, that may also be relevant for optimization include kinematics, spatio-temporal parameters, balance, and muscular control. Variables related to these domains are typically not used in combination, limiting the understanding of gait performance [9]. When considered together, the combination is often partial, constrained by the use of predefined decision schemes [11]. These decision methods assess the performance of each target variable at different stiffness levels and rank optimal stiffness based on the first target variable. In case of a tie, they use subsequent variables one by one to make a decision. The hierarchy of target variables in these decision schemes is manually selected by researchers, potentially leading to high variability in the results between participants [11].

Tankink et al. [12] highlighted the importance of selecting the appropriate cost function (including the objective and variables), as different choices can highly influence the results and, in turn, affect the ability to design personalized features that suit the individual. This emphasizes that a "one-size-fits-all" approach may be suboptimal. Therefore, optimization of AFO stiffness should be improved by incorporating a tailored multi-variable hierarchy that aligns with user's priorities.

To propose an alternative approach that better captures the complexity of gait, it is necessary first to analyze how different gait variables are influenced by stiffness on an individual basis and how these results differ between users. Variables with weaker correlations to stiffness may be less effective for optimization and could therefore be excluded, reducing the number of sensors required and potentially increasing user comfort. Optimization can then focus on the most relevant variables while incorporating user preferences. This study introduces a method for identifying key variables using an explainability technique based on Shapley Additive

[1]Sejin Yi Yoo, Jorge Gómez, Eduardo Rocon and Cristina Bayón are with BioRobotics group, Centro de Automática y Robótica CAR-CSIC-UPM, Madrid, Spain, *Correspondence: c.bayon@csic.es

[2]Emma A. Gille and Edwin van Asseldonk are with the Department of Biomechanical Engineering, University of Twente, Enschede, The Netherlands

[3]Ignacio Martínez-Caballero is with the Hospital Niño Jesús, Madrid, Spain

[†]These authors have contributed equally to this work.

Explanations (SHAP) values, integrated with an artificial intelligence model utilizing Extreme Gradient Boosting (XGBoost). We tested this method in two pediatric participants with cerebral palsy (CP) using the inGAIT-VSO device [13].

II. METHODS

This section first details the methods employed for feature (or variable) selection, which form the core of our proposed approach. Subsequently, we describe the methods used to pilot this approach with two participants diagnosed with CP.

A. Feature selection

1) Performance variables: To take into account different aspects of gait, we defined five domains: 1. Kinematic Properties, 2. Spatio-Temporal Characteristics, 3. Balance and Stability, 4. User Perception and Physiological Demand, and 5. Muscular Control (Table I). Within each domain, specific performance variables were selected to comprehensively assess both functional and physiological aspects of user performance, with a particular focus on the ankle joint. We based our selection on previous literature [14] and prioritized variables that could be measured using wearable and onboard lab equipment, aiming to minimize duplication and redundancy within and between domains.

For the Kinematics domain, we computed the angle between foot and shank at heel strike, and the peak ankle dorsiflexion (DF) observed during the stance phase for every gait cycle (Table I). Within the Spatio-Temporal domain, walking speed, the percentage of the stance phase duration, and the walk ratio (understood as the ratio between step length and cadence) were computed every gait cycle as variables representative of pace, rhythm and coordination respectively. Additionally, the stance duration variability was determined every 20-meter walking segment by looking at the standard deviation of the percentage of stance phase durations computed along that segment. For the Balance and Stability domain, we computed the trunk lateral motion as a form of compensation mechanism every gait cycle, and the step time asymmetry (STA) every 20-meter segment. Trunk lateral motion was derived from the root mean square of the lateral acceleration as done in [15]. The STA was computed using the formula presented in [16]:

$$\text{STA} = \frac{\sum_{i=2}^{n}(ST_i - ST_{i-1})}{2n} \tag{1}$$

where ST_i is the step time of the step i in milliseconds, and n is the total number of steps on the corresponding walking segment. For the domain User Perception and Physiological Demand, we computed the Physiological Cost Index (PCI) [17] every walking segment as:

$$\text{PCI} = \frac{\text{HR}_{\text{walk}} - \text{HR}_{\text{rest}}}{\text{walking speed}} \tag{2}$$

where HR_{rest} and HR_{walk} are the heart rate measurements at resting and during walking, respectively. Moreover, the Borg's scale [18] was used to report user's perceived effort. Finally, for the Muscular Control domain, we computed the co-contraction index (CCI) during stance phase as presented in [19]:

$$\text{CCI} = \sum_{i=1}^{101} \frac{\text{EMG}_L(i)}{\text{EMG}_M(i)}(\text{EMG}_L(i) + \text{EMG}_M(i)) \tag{3}$$

where i represents the individual time points of stance phase (0–100%, or 101 data points), and $\text{EMG}_L(i)$ and $\text{EMG}_M(i)$ are the normalized activations of the less and more active muscles at point i, respectively. This was computed using the antagonist muscles, tibialis anterior (TA) and gastrocnemius medialis (GM).

2) Classification model for feature importance: A classification model was developed to predict the stiffness level based on the values of the different performance variables, with an XGBoost algorithm selected for its implementation. This model enhances the basic gradient boosting method by passing residuals from each decision tree to the next, hierarchically (Fig. 1). It offers the benefit of being well-suited for high-dimensional datasets and includes inherent regularization to prevent overfitting [20]. The purpose of training this model and employing an explainability framework was to identify the variables that were significantly affected by stiffness. To train the XGBoost model, observations of each performance variable were obtained across a range of stiffness levels (see section II-B). The values of the variables, estimated each trial or walking segment, were repeated according to the number of gait cycles within each respective trial or walking segment.

To quantify the contribution of each variable to the predictions, SHAP was employed [21]. SHAP values explain the contribution of each individual variable to the overall prediction. The SHAP value of a variable is calculated by assessing the effect of excluding that variable from the prediction process. If removing the variable has no effect on the result, its SHAP value will be 0, indicating the variable's irrelevance to the prediction. Different combinations of variables were tested to account for interactions between features, ensuring accurate calculation of SHAP values. The XGBoost model for classification and SHAP for result explanation were performed individually for each participant in the following pilot study.

B. Pilot study

1) Variable stiffness orthosis: The inGAIT-VSO is a pediatric-focused Variable Stiffness Orthosis (VSO) designed for children with CP [13], [6]. It features a non-actuated mechanism that provides a non-linear ankle angle-torque curve, active during both the stance and swing phases. The stiffness curve can be manually adjusted according to user/clinician preferences to impact the user's gait. The inGAIT-VSO is sensorized and allows for data capturing without needing sophisticated lab equipment. For a detailed description of the inGAIT-VSO, refer to [13].

2) Participants: Two participants with CP participated in a pilot-study to test the optimization model (weight 31 $\pm$ 7 kg, height 1.365 $\pm$ 0.025 m, age 9 $\pm$ 0.5 years old) (Table II). Participants met the following inclusion criteria:

TABLE I

SUMMARY OF PERFORMANCE VARIABLES AND THEIR CORRESPONDING DOMAIN, GAIT ASPECTS AND COMPUTATION INTERVAL

Domain	Gait Aspect	Performance Variables	Computation Interval
Kinematics	Amplitude	Strike angle dorsiflexion (deg)	Gait cycle
		Peak ankle dorsiflexion (deg)	Gait cycle
Spatio-Temporal	Pace	Walking speed (m/s)	Gait cycle
	Rhythm	Stance duration (%)	Gait cycle
	Variability	Stance duration variability (%)	Walking segment
	Coordination	Walk ratio (cm·min/step)	Gait cycle
Balance	Body compensation	Trunk lateral motion (m/s^2)	Gait cycle
	Asymmetry	Step time asymmetry (ms)	Walking segment
User Perception	Effort	Physiological cost index (beats/m)	Walking segment
		Perceived effort (Borg's scale)	Walking trial
Muscular Control	Smoothness	Co-contraction index (–)	Gait cycle

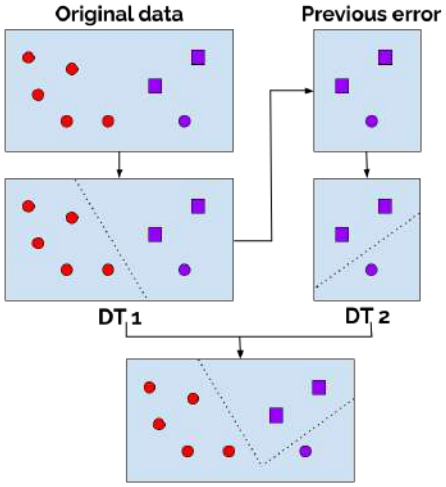


Fig. 1. Schematic illustration of functioning of XGBoost models. Original data has two classes circles and squares. The first decision tree (DT1) gives an imperfect classification. The errors or residuals from DT1 are fed as input to the next decision tree (DT2). DT1 and DT2 are combined to give the final prediction

aged 5–17 years, predominantly spastic uni- or bilateral CP, Gross Motor Function Classification System (GMFCS) [22] levels I–III, sufficient cognitive ability, and the capacity to complete the walking protocol. Flexible equinus deformities or drop-foot were preferred, with Ashworth scale scores ranging from 1 to 3. Exclusion criteria included leg surgery in the previous 6 months or botulinum toxin A injections in the previous 3 months, significant musculoskeletal deformities, unhealed skin lesions, gastrocnemius shortening $>10°$, or visual impairments or behavioral issues that could hinder protocol performance. The Local Ethics Committee at Hospital Infantil Universitario Niño Jesús (HNJ) gave the approval (R-0064/23) and ensured the study was conducted in alignment with the Declaration of Helsinki. Participants and their families were informed accordingly, and parental consent was obtained before participation.

The pilot involved a single session per participant of about 2h. Initially, participants were assisted in putting on

TABLE II

PARTICIPANTS CHARACTERISTICS.

Participant ID	CP01	CP02
Age (years-old)	9	10
Weight (kg)	38	24
Height (m)	1.39	1.34
Shoe size (EU)	36	33
Pathology	Hemiparesia (left)	Spastic diplegia
GMFCS	I	III
Sex	Male	Female
Daily-use orthosis	Articulated AFO	-

the inGAIT-VSO, and were given the opportunity to walk with the equipment and report any discomfort. After a brief familiarization with the device, they performed five trials of two-minute walking tests (2mwt) [23], walking back and forth along a 20-meter straight corridor, while they were instructed to walk as fast as possible without running. For each trial, the inGAIT-VSO was set to a different stiffness level: (1) no stiffness (spring disconnected), (2) low stiffness (0.2 Nm/kg as peak restoring torque at 12 deg of DF), (3) medium stiffness (0.4 Nm/kg at 12 deg of DF), (4) high stiffness (0.6 Nm/kg at 12 deg of DF), and (5) very high stiffness (0.8 Nm/kg at 12 deg of DF). The value of 12 degrees of DF was chosen in accordance with previous literature [13], [24] as it is the approximate maximum value reached during stance in healthy gait.

To minimize fatigue-related bias, the order of trials (i.e., stiffness levels) was randomized for each participant. Participants were allowed to rest as needed between trials.

C. Data acquisition

During the 2mwt trials, a combination of sensors was used to compute the required performance variables exposed in Table I. Magnetic encoders (AS5048b, AMS-OSRAM AG, Premstaetten, Austria) integrated in the inGAIT-VSO recorded the ankle angle in the sagittal plane at 100 Hz. Force-sensitive resistors (FSRs, FlexiForce A502, Tekscan Inc, MA, USA) embedded within the insoles were used to detect heel strike and toe-off events also at 100 Hz [13]. Two GaitUp sensors (Physilog, Lausanne, Switzerland) were

attached to the shoes to monitor foot movements sampled at 128 Hz. Surface electromyography (EMG) electrodes (Trigno Delsys, Natick, MA, USA) were bilaterally placed on the TA, GM, soleus (SOL), and gastrocnemius lateralis (GL) muscles to register muscle activity with a sampling rate of 1926 Hz. An inertial measurement unit (IMU) was attached to the trunk of the participants at the sternum height, and recorded torso motion at 100 Hz. Finally, a smartwatch (Versa 3, Fitbit, San Francisco, USA) was used to measure heart rate at 1 Hz. Participants also reported their perceived effort after each trial using the Borg's scale [18].

D. Data processing

Data from the sensors of the inGAIT-VSO, EMG sensors, IMU sensor, and smartwatch were processed using MATLAB 2021b (MathWorks, Natick, MA, USA). Data from the GaitUp sensors were processed using GaitUp Lab (Physilog, Lausanne, Switzerland).

EMG data were pre-processed to remove noise and artifacts. This involved band-pass filtering (30-300 Hz), full-wave rectification, and low-pass filtering (3 Hz). The resulting linear envelopes were normalized to the maximum activation observed in the no stiffness walking trial. After pre-processing, all data were resampled to the same frequency and synchronized. The data were then segmented into gait cycles using heel strike events detected by the FSRs. Each gait cycle was linearly interpolated, resulting in 300 data points per cycle. Variables were calculated as described in Section II-A.1 with a computation interval specified in Table I.

III. RESULTS

Data acquisition during the pilot sessions proceeded smoothly for both participants, enabling computation of performance variables for each trial (Fig. 2). Visual inspection revealed that some variables exhibited greater response with respect to stiffness levels (Fig. 2). The increase in stiffness corresponded to the decrease in the maximum ankle DF values in both participants. Perceived effort showed a slight increasing trend in CP02, while no clear pattern emerged for CP01. For CCI, both participants showed higher values for the left side compared to the right.

Upon training an XGBoost model for each participant, SHAP values representing the contribution of each variable to stiffness prediction were computed (Fig. 3). SHAP values were calculated for data at each stiffness level, and values were stacked to observe the overall contribution of each variable.

Variables did not consistently hold the same level of influence across participants and stiffness levels. For CP01, the SHAP values revealed that peak ankle DF had a dominant influence on the model's predictions, with the remaining variables contributing substantially less. In contrast, for CP02, the PCI was the most impactful variable, though the influence on the prediction was evenly distributed among other variables, each belonging to a different gait domain. Regarding differences between stiffness levels, SHAP values

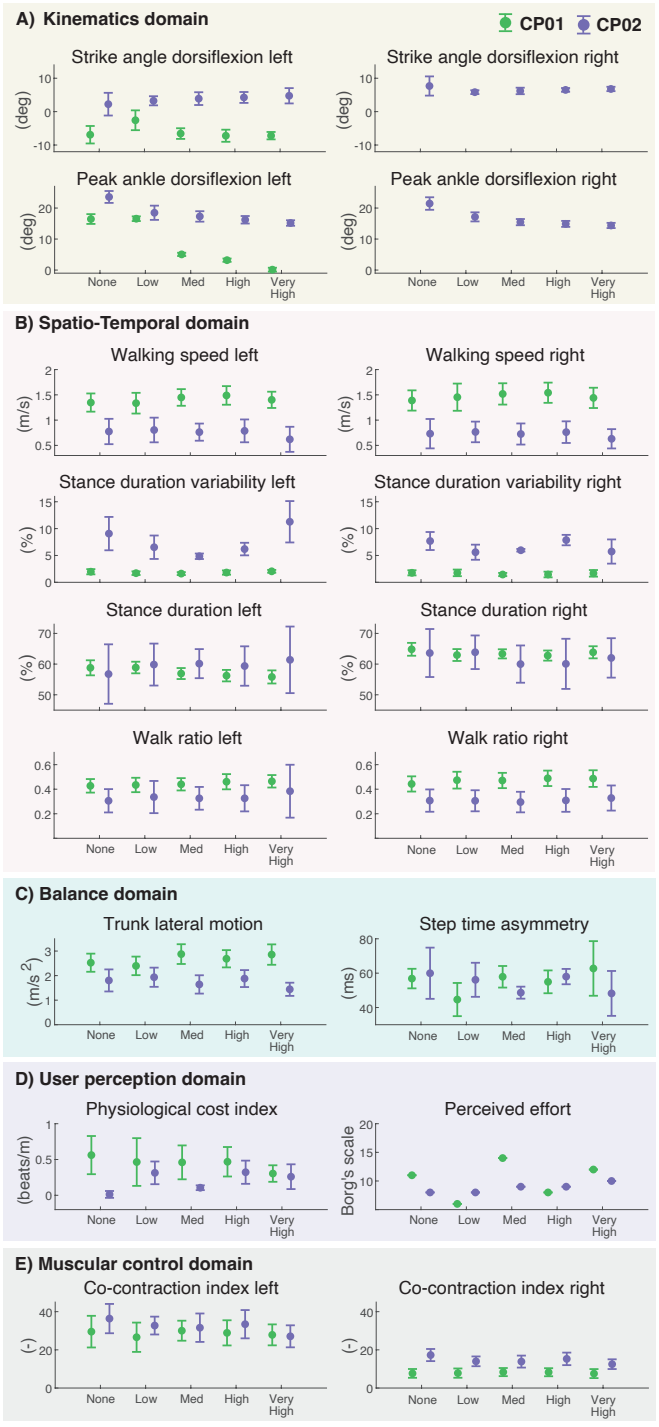


Fig. 2. Means and standard deviations for the different performance variables calculated for CP01 (green) and CP02 (purple). Variables for the Kinematics domain on the right side were not computed for CP01, as the participant was hemiparetic and only wore the AFO on the left side.

for PCI in CP02 were lower at very high stiffness compared to lower stiffness levels. Lastly, some variables were not relevant for any participant. For example, the SHAP values for the walk ratio (both on the left and right sides) were close to 0 for both participants. Walking speed, CCI and trunk lateral motion also had a minimal contribution.

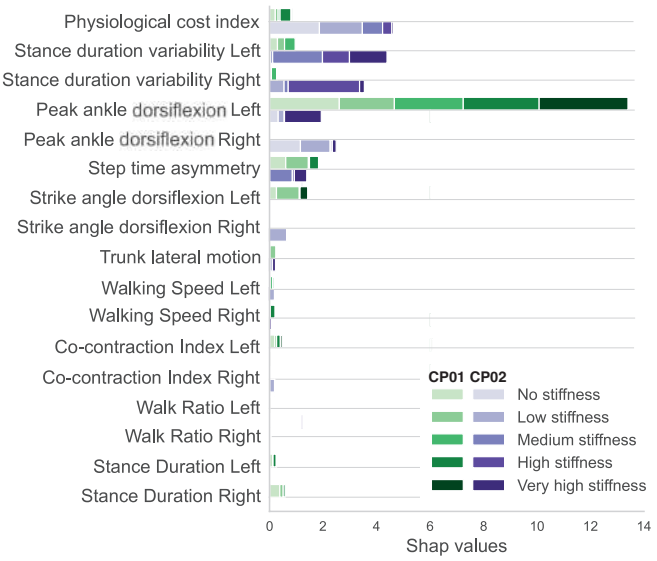


Fig. 3. SHAP values for CP01 (green) and CP02 (purple). The bars are formed by stacked SHAP values obtained for each stiffness level, and represent the impact on stiffness prediction, with larger bars indicating greater influence.

IV. DISCUSSION

In this work, we proposed a series of performance variables reflecting different aspects of gait and explored their relevance for stiffness in a pilot study with two participants with CP using the inGAIT-VSO. Key findings showed a different distribution of the influence of performance variables on stiffness predictions between participants. This could explain why optimization effectiveness varied across participants in previous studies that relied solely on a limited set of predefined variables [11], [9]. These findings highlight the importance of having customized cost functions that move away from "one-size-fits-all" approaches.

Looking just to the variables with the largest contributions in both participants, we observed that they differed, as for example, the PCI had the largest contribution for stiffness prediction in CP02, but the same variable had a low impact in CP01. This variability also extended to other variables in our study, with the top-ranking SHAP values for CP01 not being as relevant for CP02 and vice-versa.

For CP01, there was a clear dominant variable: the peak ankle DF left, side in which this hemiparetic participant worn the inGAIT-VSO. However, for participant CP02, there was a more uniform distribution across six variables (i.e., PCI, stance duration for the left and right sides, peak ankle DF for the left and right sides, and STA), being these the primary drivers for prediction. Excluding any of these variables, which belonged to different gait domains, would result in the loss of valuable information regarding gait characterization in this participant. These results in CP02 highlight the potential pitfall of relying on a reduced number of variables or domains that might not be enough to capture the complexity of gait.

Our findings using SHAPP values indicate that the stiffness optimization problem should: 1) account for multiple variables to capture the diverse domains of gait, and 2) be customized for each user, as the impact of individual variables can vary significantly between users. However, while this pilot study identified performance variables most sensitive to changes in stiffness, optimizing stiffness solely based on these variables –which primarily reflect the user's physical characteristics– may not be sufficient, as it does not guarantee that the resulting stiffness configuration aligns with the user's personal preferences. To address this limitation, future research should also incorporate user preferences into the optimization process. This would allow the optimal stiffness value to reflect the best solution, considering both the user's physical state and personal preferences. However, aligning user preferences with clinical goals can be challenging. Previous studies have highlighted divergences between the priorities of healthcare professionals and those of patients [8], [25], [4]. Therefore, future research should aim to strike a balance between these two aspects to ensure both clinical efficacy and user satisfaction.

Lastly, the current study protocol requires individual testing for each stiffness level, which may be impractical in a real-world clinical setting. However, with a larger dataset, it may be possible to infer the effects of each stiffness configuration without directly measuring each one. This approach could simplify the testing protocol, making it more practical for clinical use.

A. Study limitations

The first acknowledged limitation is the involvement of only two participants, limiting the generalization of the findings. However, even with two participants we proved the need for an individualized stiffness optimization. Future work will include a larger sample size to strengthen conclusions and potentially simplify the protocol.

A second limitation was the variation in the computation intervals for the different variables. Three of the 11 variables were extracted per walking segment, while one was calculated only once per trial, leading to repeated values across observations (i.e., gait cycles). This might have introduced some bias.

The Borg's scale to estimate perceived effort was excluded from predictions due to bias in registering this variable. Specially for CP01, ratings consistently increased with the (randomized) trial order, suggesting that this participant compared the new rating with the one of the previous trial.

Lastly, the study focused on kinematic and temporal domains but excluded kinetics, as measuring them requires assessment of forces along the 20-meter corridor. The ankle torque measured with inGAIT-VSO was also excluded to avoid bias in SHAP values, as it directly relates to the AFO stiffness. The inclusion of kinetics and other joints' kinematics in the future could provide deeper insights.

V. CONCLUSION

This study aimed to identify relevant optimization variables and observe how they varied between users. Our

findings show that multiple variables were classified as important, supporting the hypothesis that relying on a single variable is insufficient to capture the complexity of gait. Additionally, the variability in relevant variables between participants highlights the need for individualized optimization. Taking this research a step further, future studies aim to incorporate user and clinician preferences to achieve a more personalized optimization. This would yield higher levels of user satisfaction and acceptance.

ACKNOWLEDGMENT

This work has been carried out with the financial support from the Dutch Research Council NWO (Veni-TTW-2020, 18079). Authors would like to acknowledge all participants of the study.

REFERENCES

[1] D. Totah, M. Menon, C. Jones-Hershinow, K. Barton, and D. H. Gates, "The impact of ankle-foot orthosis stiffness on gait: a systematic literature review," *Gait & posture*, vol. 69, pp. 101–111, 2019.

[2] J. S. Lora-Millan, M. Nabipour, E. H. F. van Asseldonk, and C. Bayón, "Advances on mechanical designs for ankle-foot orthoses," *submitted to Frontiers in Bioengineering and Biotechnology*, 2023.

[3] P. Meyns, Y. L. Kerkum, M. A. Brehm, J. G. Becher, A. I. Buizer, and J. Harlaar, "Ankle foot orthoses in cerebral palsy: Effects of ankle stiffness on trunk kinematics, gait stability and energy cost of walking," *European Journal of Paediatric Neurology*, vol. 26, pp. 68–74, 2020. [Online]. Available: https://doi.org/10.1016/j.ejpn.2020.02.009

[4] C. Bayón, "Moving forward: The importance of tailored orthotic management in children with cerebral palsy," *Developmental Medicine & Child Neurology*, vol. 00, jun 2023. [Online]. Available: https://onlinelibrary.wiley.com/doi/10.1111/dmcn.15684

[5] N. F. Waterval, F. Nollet, J. Harlaar, and M.-A. Brehm, "Modifying ankle foot orthosis stiffness in patients with calf muscle weakness: gait responses on group and individual level," *Journal of NeuroEngineering and Rehabilitation*, vol. 16, pp. 1–9, 2019.

[6] N. V. Crey, D. J. Lam, E. A. Bywater, M. Shepherd, and E. J. Rouse, "The Variable Stiffness Orthosis: Customizable Mechanics for Assistance and Rehabilitation," *TechRxiv*, vol. 27-11, nov 2024.

[7] M. K. Shepherd and E. J. Rouse, "The vspa foot: A quasi-passive ankle-foot prosthesis with continuously variable stiffness," *IEEE Transactions on Neural Systems and Rehabilitation Engineering*, vol. 25, no. 12, pp. 2375–2386, 2017.

[8] C. Bayón, M. v. Hoorn, A. Barrientos, E. Rocon, J. P. Trost, and E. H. v. Asseldonk, "Perspectives on ankle-foot technology for improving gait performance of children with cerebral palsy in daily-life: requirements, needs and wishes," *Journal of neuroengineering and rehabilitation*, vol. 20, no. 1, p. 44, 2023.

[9] M. A. Diaz, M. Voss, A. Dillen, B. Tassignon, L. Flynn, J. Geeroms, R. Meeusen, T. Verstraten, J. Babič, P. Beckerle *et al.*, "Human-in-the-loop optimization of wearable robotic devices to improve human–robot interaction: A systematic review," *IEEE Transactions on Cybernetics*, vol. 53, no. 12, pp. 7483–7496, 2022.

[10] R. L. Medrano, G. C. Thomas, and E. J. Rouse, "Can humans perceive the metabolic benefit provided by augmentative exoskeletons?" *Journal of neuroengineering and rehabilitation*, vol. 19, no. 1, p. 26, 2022.

[11] N. F. Waterval, M.-A. Brehm, J. Harlaar, and F. Nollet, "Individual stiffness optimization of dorsal leaf spring ankle–foot orthoses in people with calf muscle weakness is superior to standard bodyweight-based recommendations," *Journal of neuroengineering and rehabilitation*, vol. 18, no. 1, p. 97, 2021.

[12] T. Tankink, J. M. Hijmans, R. Carloni, and H. Houdijk, "Human-in-the-loop optimization of rocker shoes via different cost functions during walking," *Journal of biomechanics*, vol. 166, p. 112028, 2024.

[13] L. van Noort, N. V. Crey, E. J. Rouse, I. Martínez-Caballero, E. H. van Asseldonk, and C. Bayón, "A usability study on the ingait-vso: effects of a variable-stiffness ankle-foot orthosis on the walking performance of children with cerebral palsy," *Journal of neuroengineering and rehabilitation*, vol. 21, 12 2024. [Online]. Available: https://pubmed.ncbi.nlm.nih.gov/39090725/

[14] L. Carcreff, C. N. Gerber, A. Paraschiv-Ionescu, G. De Coulon, C. J. Newman, K. Aminian, and S. Armand, "Comparison of gait characteristics between clinical and daily life settings in children with cerebral palsy," *Scientific Reports*, vol. 10, no. 1, pp. 1–11, 2020.

[15] M. B. Speedtsberg, S. B. Christensen, J. Stenum, T. Kallemose, J. Bencke, D. J. Curtis, and B. R. Jensen, "Local dynamic stability during treadmill walking can detect children with developmental coordination disorder," *Gait and Posture*, vol. 59, 2018.

[16] P. Natarajan, R. D. Fonseka, L. Sy, R. J. Mobbs, and M. Maharaj, "Proposed objective scoring algorithm for clinical evaluation of walking asymmetry in lumbar disc herniation, based on relevant gait metrics from wearable devices: The gait symmetry index (gsitm) – observational study," *Brain and Spine*, vol. 2, 2022.

[17] P. Butler, M. Engelbrecht, R. E. Major, J. H. Tait, J. Stallard, and J. H. Patrick, "Physiological Cost Index of Walking for Normal Children and Its Use As an Indicator of Physical Handicap," *Developmental Medicine & Child Neurology*, vol. 26, no. 5, pp. 607–612, 1984. [Online]. Available: http://doi.wiley.com/10.1111/j.1469-8749.1984.tb04499.x

[18] G. Borg, "Psychophysical scaling with applications in physical work and the perception of exertion," *Scandinavian Journal of Work, Environment and Health*, vol. 16, pp. 55–58, 1990.

[19] B. A. Knarr, J. A. Zeni Jr, and J. S. Higginson, "Comparison of electromyography and joint moment as indicators of co-contraction," *Journal of Electromyography and Kinesiology*, vol. 22, no. 4, pp. 607–611, 2012.

[20] T. Chen and C. Guestrin, "Xgboost: A scalable tree boosting system," in *Proceedings of the 22nd acm sigkdd international conference on knowledge discovery and data mining*, 2016, pp. 785–794.

[21] S. M. Lundberg, G. G. Erion, and S.-I. Lee, "Consistent individualized feature attribution for tree ensembles," *arXiv preprint arXiv:1802.03888*, 2018.

[22] R. Palisano, P. Rosenbaum, S. Walter, D. Russell, E. Wood, and B. Galuppi, "Development and reliability of a system to classify gross motor function in children with cerebral palsy," *Developmental medicine & child neurology*, vol. 39, no. 4, pp. 214–223, 1997.

[23] T. W. Pin and H. L. Choi, "Reliability, validity, and norms of the 2-min walk test in children with and without neuromuscular disorders aged 6-12," *Disability and rehabilitation*, vol. 40, pp. 1266–1272, 5 2018. [Online]. Available: https://pubmed.ncbi.nlm.nih.gov/28637155/

[24] E. Owen, "The importance of being earnest about shank and thigh kinematics especially when using ankle-foot orthoses," *Prosthetics and orthotics international*, vol. 34, no. 3, pp. 254–269, 2010.

[25] N. L. Zaino, M. Yamagami, D. J. Gaebler-Spira, K. M. Steele, K. F. Bjornson, and H. A. Feldner, ""That's frustrating": Perceptions of ankle foot orthosis provision, use, and needs among people with cerebral palsy and caregivers," *Prosthetics & Orthotics International*, vol. 00, no. 00, pp. 1–8, jul 2022. [Online]. Available: https://journals.lww.com/10.1097/PXR.0000000000000165

Encoding Desired Postural Synergies in a Single-Actuator Soft Robotic Prosthetic Hand Through Finger Joint Stiffness Modulation

Alireza Mohammadi, Ki Hoon Han, Monireh Ahmadi Bani, Jaimie , Silvia Ursula Raschke, Ying Tan, Peter Choong, and Denny Oetomo

***Abstract*— This paper presents the design and analysis of a single-actuator robotic prosthetic hand based on soft flexure joints, enabling the encoding of desired postural synergies of fingers through their joint stiffness modulation. Finger movements are coordinated using a simple whiffletree mechanism, which simultaneously pulls all tendons, with the synergy determined by the varying stiffness of the flexure joints. A forward quasi-static model is developed to predict joint angles based on tendon displacement driven by the actuator, assuming known joint stiffness values. Then, an inverse model is introduced to compute the required stiffness of finger joints for achieving a desired postural synergy. The proposed design is validated through simulations and real-world experiments on a 3D-printed soft robotic prosthetic hand. The hand successfully demonstrates a postural synergy that produces both pinch and power grasp types. This approach provides a lightweight and mechanically simple solution for robotic prosthetic hands with single actuator, enabling desired postural synergy while maintaining functionality and adaptability for grasping tasks.**

I. INTRODUCTION

Soft robotic hands have received significant attention in recent years due to their inherent safety, lightweight design, and cost-effective fabrication enabled by 3D printing [1]. These characteristics are particularly beneficial in the field of prosthetics, where safety, comfort, affordability are essential to meet the needs of users [2].

Various actuation systems and force transmission methods have been employed in the design of soft robotic prosthetic (bionic) hands. Actuation approaches include pneumatic systems [3], shape memory alloys [4], and DC motors [5], while transmission mechanisms often rely on tendons, gears, or pulleys [6]. Among these, tendon-driven mechanisms actuated by DC motors are the most prevalent due to their high power-to-weight ratio and lightweight design [7].

In tendon-driven bionic hands, achieving a variety of grasp types typically requires multiple actuators, with each actuator responsible for controlling an individual finger or joint [3]. While this approach enables precise and independent movements, it often results in prosthetic hands that are bulky, heavy, and complex to manufacture and maintain. Such characteristics can significantly reduce the appeal of these hands, especially for users who prioritise lightweight and compact designs such as paediatric users [2].

To address the challenges associated with multi-actuator prosthetic hands, several studies have explored highly underactuated designs that use a single actuator to drive multiple fingers. These designs rely on carefully engineered transmission mechanisms and underactuated finger design with spring or flexure joints [8] to return the finger to the original position after flexion. In [9], [10], a direct actuation system was utilised to move all the fingers simultaneously, enabling basic grasping functionality. While this approach simplifies the mechanical design, the mechanism provides only a single grasp type and lacks adaptability.

In [11], a continuum differential mechanism combined with passive thumb movement was employed to enable a grasp adaptable to objects of varying shapes and sizes. In [12], a combination of coalesced whiffletree differential mechanism, a locking mechanism that switches between power and tripod grasps, and manual repositioning of the thumb enables three distinct and adaptive grasp types. However, this will require intervention from other intact hand to switch between different grasp types.

The SoftHand Pro [13] employs a single actuator to control 19 joints, utilising the concept of postural synergies to coordinate finger movements. Elastic tendons and a differential transmission mechanism enable the hand to adapt to various object shapes. The finger synergies, derived from experimental studies on grasping objects of different shapes and sizes [14], provide the hand with multi-grasp capabilities, such as power and precision grips. However, reliance of the design on multiple tendons in the finger joints and elastic components introduces mechanical complexity, requiring precise calibration to ensure consistent performance.

In this paper, we present a single-actuator robotic prosthetic hand with soft flexure joints in the fingers. The design achieves the desired finger synergy by modulating stiffness of the flexure joints, enabling the hand to produce desired coordination of the fingers. The stiffness modulation is achieved by altering the geometrical parameters of the flexure joints in the fingers. While previous studies, such as [15], have explored stiffness modulation to achieve a desired trajectory for a single finger, our work extends this concept by investigating how joint stiffness can be optimised to achieve the desired synergy among multiple fingers. A whiffletree

This project is funded by the Valma Angliss Foundation and The War Amps. Alireza Mohammadi, Ki Hoon Han, Ying Tan, and Denny Oetomo are with the Department of Mechanical Engineering, The University of Melbourne, Parkville, VIC 3010, Australia. (email: kihoonh@student.unimelb.edu.au; {alireza.mohammadi, yingt, doetomo}@unimelb.edu.au). Peter Choong is with the Department of Surgery, St. Vincent's Hospital Melbourne, The University of Melbourne, Fitzroy, VIC 3065, Australia. (email: pchoong@unimelb.edu.au). Monireh Ahmadi Bani and Jaimie Borisoff are with the Department of Rehabilitation, British Columbia Institute of Technology, 3700 Willingdon Avenue, Burnaby, Canada. (email: Jaimie_Borisoff@bcit.ca). Silvia Ursula Raschke is with the MAKE+, BCIT Applied Research, 3700 Willingdon Avenue, Burnaby, BC, Canada. (email: silvia_raschke@bcit.ca).

transmission mechanism drives all tendons simultaneously, with finger coordination dictated by the varying stiffness of the flexure joints.

We first develop a forward quasi-static model to predict the joint angles of the fingers as a function of the tendon cable length pulled by the actuator, assuming predefined joint stiffness values. Using this model, we then introduce an inverse model to calculate the required joint stiffness values necessary to achieve a desired finger synergy. Through simulations, we validate that for a desired synergy providing two grasp types of pinch and power, the required stiffness values for each joint can be determined to achieve the intended functionality. This is further demonstrated through real-world experiments using a 3D-printed hand fabricated with flexible materials and integrated with a whiffletree mechanism, driven by a single servo motor. The proposed approach simplifies the design while enabling the encoding of desired synergies to perform a wide range of grasping tasks.

II. Forward Quasi-static Modeling

This section provides a detailed kinematic analysis of the tendon-driven soft bionic hand, actuated by a single motor in combination with a whiffletree mechanism, as illustrated in Fig. 1. The mechanism consists of four links, each arranged in parallel to distribute forces evenly across the fingers.

The proposed design incorporates two flexure joints per finger: the metacarpophalangeal (MCP) joint and the proximal interphalangeal (PIP) joint. To simplify the design without compromising the generality of the proposed control method, the distal interphalangeal (DIP) joint is assumed to be fixed. We also assumed that the friction between the tendon cable and the elastic finger is negligible. Each flexure joint is modeled as a torsional spring with a fixed axis of rotation, as depicted in Fig. 2.

A. Quasi-static modeling of the fingers

Modelling the flexure joints as torsion springs, Hooke's law expresses the force applied by the tendon and the angular displacement, θ_{ij}, of the *ij*-th joint as:

$$\begin{aligned} \tau_1 &= k_{ij}\theta_{ij}, \\ F_i * r_{ij} &= k_{ij}\theta_{ij}, \\ F_i &= \frac{k_{ij}\theta_{ij}}{a_{ij}\sin(\angle J_{ij}B_{ij}A_{ij})}, \end{aligned} \tag{Eq.1}$$

where F_i is the actuation force acting on the *i*-th finger and r_{ij} is the perpendicular distance from the *ij*-th joint rotation axis, J_{ij}, to the tendon, $\overrightarrow{A_{ij}B_{ij}}$.

The torsional stiffness, k_{ij}, is dictated by the geometrical parameters of the flexure joint including a_{ij}, b_{ij}, and ϕ^0_{ij} as well as the Shore hardness of the material (more details in [5]). Additionally, a_{ij} and b_{ij} denotes the magnitude of $\overrightarrow{J_{ij}A_{ij}}$ and $\overrightarrow{J_{ij}B_{ij}}$, which remain constant during bending. Note that the angular displacement is constrained to $0^\circ \leq \theta_{ij} \leq \phi^0_{ij}$ due to the joint itself resisting further bending once it reaches ϕ^0_{ij} (angle ϕ_{ij} at relaxed state). Thus, applying

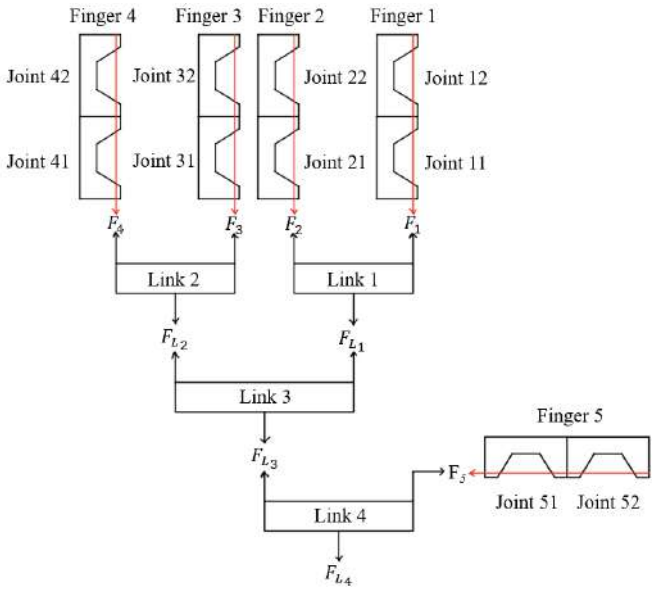


Fig. 1: Schematic diagram of simplified two-joint single-actuator driven soft bionic hand. The red lines illustrate the tendons used to transfer the actuation force to each joint.

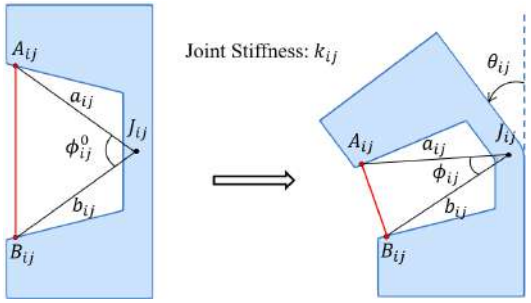


Fig. 2: Schematic diagram of a single *ij*-th joint with geometrical parameters a_{ij}, b_{ij}, and ϕ^0_{ij} for stiffness modulation

the laws of sines and cosines to Eq.1 gives the generalised equation that relates the actuation force and the joint angle displacements for any *i*-th finger:

$$\begin{aligned} F_i &= f(k_{ij}, \theta_{ij}, a_{ij}, b_{ij}, \phi^0_{ij}) \\ &= \frac{k_{ij}\theta_{ij}\sqrt{a_{ij}^2 + b_{ij}^2 - 2a_{ij}b_{ij}\cos(\phi^0_{ij} - \theta_{ij})}}{a_{ij}b_{ij}\sin(\phi^0_{ij} - \theta_{ij})} \end{aligned} \tag{Eq.2}$$

for $i = 1, 2, 3, 4, 5$ and $j = 1, 2$.

Moreover, the relationship between the total length of the tendon corresponding to the *i*-th finger and the angular displacements of its constituent joints, θ_{ij}, can be described using the law of cosines for the triangle $\Delta A_{ij}J_{ij}B_{ij}$, as follows:

$$l_i = \sum_{j=1}^{2} |\overrightarrow{A_{ij}B_{ij}}| = \sum_{j=1}^{2} \sqrt{a_{ij}^2 + b_{ij}^2 - 2a_{ij}b_{ij}\cos(\phi^0_{ij} - \theta_{ij})}.$$

Consequently, the change in length of the tendon associated with the *i*-th finger, as induced by the actuator, can be

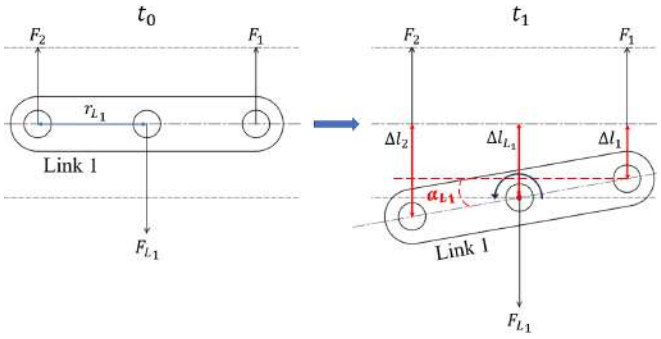


Fig. 3: Schematic diagram of the simplified primary linkage system.

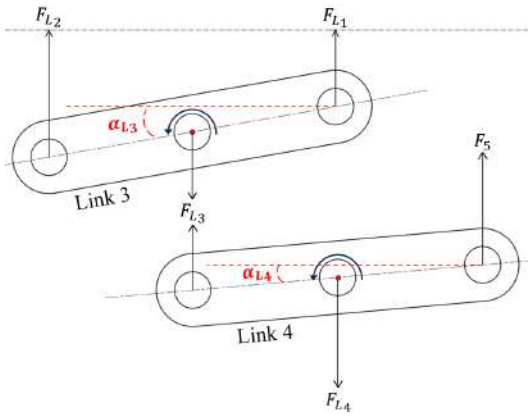


Fig. 4: Schematic diagram of the simplified secondary linkage system

expressed as:

$$\Delta l_i = l_i^0 - l_i, \tag{Eq.3}$$

where l_i^0 denotes the length of the wire of *i*-th finger at its relaxed position with θ_{ij}^0 being the initial offset of joint angular displacements. Δl_i is the length of tendon pulled for a given *i*-th finger. Thus, Eq.3 represents the relationship between the joint angular displacements and the length of tendon cable displaced for each finger.

B. Quasi-static modeling of the linkage system

1) Primary linkage system modeling: Primary linkage system refers to the links that are only connected to the fingers, i.e., Link 1 and Link 2 (refer to Fig. 1). A pair of fingers are actuated through tendons attached to a shared link, represented using a simplified two-dimensional geometry, as illustrated in Fig. 3. Focusing on Link 1, and assuming that Finger 1 has higher stiffness than Finger 2, the entire link will rotate about its central pivot point when the tendon located at the centre is pulled. Due to its lower stiffness, Finger 2 will experience displacement first, causing Link 1 to rotate by an angle α_{L_1} from its equilibrium position. It is important to note that the deviation angle α_{L_k} for any arbitrary link is expected to be small, as the tendon displacement for each link is constrained by the size of the palm. This assumption allows all tendons to be considered as remaining vertical throughout the travel of the links.

Assuming the link is symmetrical about its centre lines, the centre-to-centre distance between the outer holes and the centre hole will be equal, i.e., $r_{L_1} = r_{L_2}$. Subsequently, the quasi-static forward modeling of Link 1 can be described as:

$$+\uparrow \sum F_{vertical} = 0 : F_1 + F_2 = F_{L_1},$$

$$\circlearrowleft + \sum M_{pivot} = 0 : F_1 = F_2 = \frac{F_{L_1}}{2}.$$

Hence, referring to Eq.2, the following relationship must hold true:

$$f_{ij} = f(k_{ij}, \theta_{ij}, a_{ij}, b_{ij}, \phi_{ij}^0) = \text{Constant}, \tag{Eq.4}$$

for $i = 1, 2$ and $j = 1, 2$.

Furthermore, the relationship between the displacement of the bottom tendon, Δl_{L_k}, and the top tendons, Δl_1 and Δl_2, can be described as:

$$\begin{aligned} \Delta l_{L_1} &= \Delta l_1 + r_{L_1} \sin \alpha_{L_1} \\ &= \Delta l_2 - r_{L_1} \sin \alpha_{L_1}, \end{aligned} \tag{Eq.5}$$

where:

$$\alpha_{L_1} = \arcsin\left(\frac{|\Delta l_2 - \Delta l_1|}{2 r_{L_1}}\right). \tag{Eq.6}$$

The maximum theoretical angle of α_{L_1} is when the link has rotated fully vertically. This remains true irrespective of which finger has greater stiffness. Using the properties of inverse trigonometric functions, where $\sin(\arcsin x) = x$, for $x \in [-1, 1]$, Eq.5 can be simplified as:

$$\begin{aligned} \Delta l_{L_1} &= \min(\Delta l_1, \Delta l_2) + \frac{|\Delta l_2 - \Delta l_1|}{2} \\ &= \max(\Delta l_1, \Delta l_2) - \frac{|\Delta l_2 - \Delta l_1|}{2}. \end{aligned} \tag{Eq.7}$$

Therefore, Eq.4 and Eq.7 form a system of equations that obtains the constituent joint angles θ_{ij} for Fingers 1 and 2 for a known length of the wire displacement of Link 1. The same analysis approach can be applied to Link 2.

2) Secondary linkage system modeling: The secondary linkage system refers to the links that are situated within the palm that are only or partially connected to other links, i.e., Link 3 and Link 4. This section addresses the modeling of these links and hence completes the forward quasi-static modeling of the entire underactuated bionic hand. The configuration of the secondary linkage system, Fig. 4, is similar to that of the primary linkage system (Fig. 3).

Similar to the analysis of a link shown in the previous subsection, the quasi-static forward modeling of Link 3 can be described as:

$$+\uparrow \sum F_{vertical} = 0 : F_{L_1} + F_{L_2} = F_{L_3},$$

$$\circlearrowleft + \sum M_{pivot} = 0 : F_{L_1} = F_{L_2} = \frac{F_{L_3}}{2}.$$

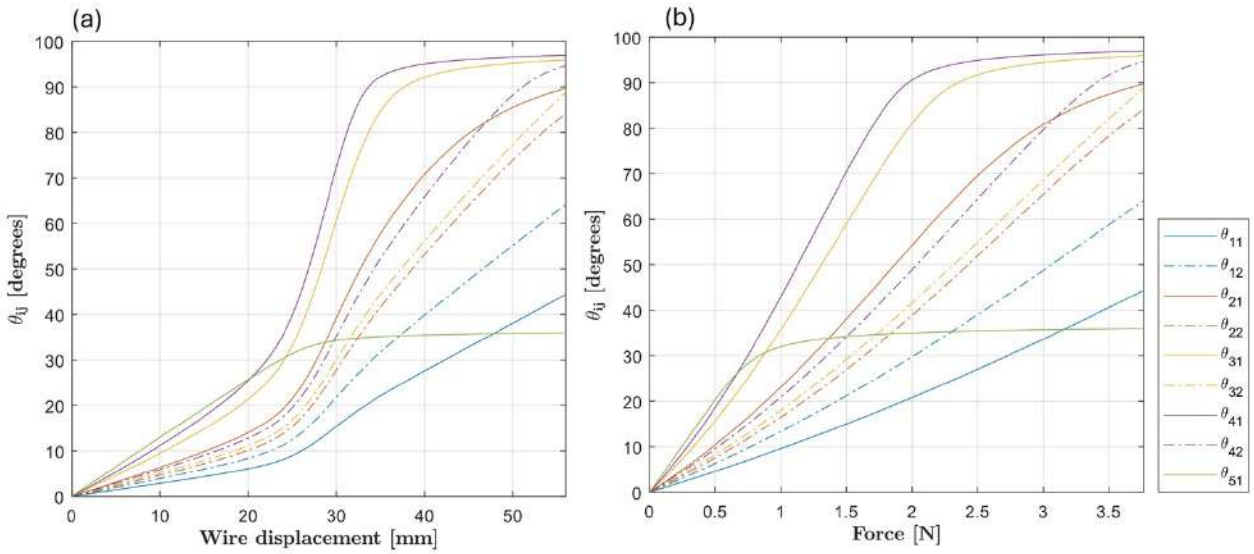


Fig. 5: The variation of the joint angles based on: (a) length of wire pulled by the actuator, and (b) force applied by the actuator

Recall that:

$$F_1 = F_2 = \frac{F_{L_1}}{2} \quad \text{and} \quad F_3 = F_4 = \frac{F_{L_2}}{2}.$$

Hence, F_{L_3} can be expressed as:

$$F_{L_3} = 4F_1 = 4F_2 = 4F_3 = 4F_4.$$

Following a similar analysis for Link 4:

$$F_{L_4} = 2F_5 = 8F_i, \quad \text{for } i = 1, 2, 3, 4. \tag{Eq.8}$$

where F_{L_4} is the magnitude of actuation force produced by the single servo motor. Eq.8 also describes the relationship between the force applied to the thumb (Finger 5) relative to the rest of the fingers. With this, we can create a system of equations that relate the forces applied to each joint, as follows:

$$f_{ij} = \begin{cases} f_{ij}, & \text{if } i = 1, 2, 3, 4 \text{ and } j = 1, 2 \\ \frac{1}{4} f_{ij}, & \text{if } i = 5 \text{ and } j = 1, 2 \end{cases} \tag{Eq.9}$$

where:

$$f_{ij} = \frac{k_{ij}\theta_{ij}\sqrt{a_{ij}^2 + b_{ij}^2 - 2a_{ij}b_{ij}\cos(\phi_{ij}^0 - \theta_{ij})}}{a_{ij}b_{ij}\sin(\phi_{ij}^0 - \theta_{ij})}.$$

Moreover, the relationship between the tendon displacement at the actuator, Δl, and at the fingers, Δl_i, can be expressed using a similar method of analysis used to derive Eq.7 as:

$$\Delta l = \min(\Delta l_5, \Delta l_{L_3}) + \frac{|\Delta l_{L_3} - \Delta l_5|}{2}, \tag{Eq.10}$$

where:

$$\Delta l_{L_3} = \min(\Delta l_{L_1}, \Delta l_{L_2}) + \frac{|\Delta l_{L_2} - \Delta l_{L_1}|}{2}.$$

Thus, Eq.9 and Eq.10 form a system of ten equations that make it possible to obtain all the joint angles θ_{ij} for $i = 1, 2, 3, 4, 5$ and $j = 1, 2$ for a given length for wire displacement at the actuator Δl.

III. Inverse Design for Encoding Desired Synergy of Fingers

The objective of the inverse design is to produce the required joint stiffness values, k_{ij}, for all joints for a given desired synergy of the fingers and the tendon displacement at the actuator, Δl. This inverse design aims to obtain the stiffness values that minimise the constituent joint angular discrepancy between the finger synergy produced and the desired synergy. A finger synergy refers to the coordinated set of joint angles that achieves a desired hand motion trajectory. However, this preliminary study will solely focus on a single desired pose. In future works, the inverse design is to be implemented such that it finds the most suitable stiffness values for each joint that yield the closest joint motion to the desired finger synergy. Thus, the inverse design becomes an optimisation problem, which is defined as:

$$\min_{k_{ij}} \sum_{i=1}^{5}\sum_{j=1}^{2} || \ \theta_{ij} - \theta_{ij}^* \ ||^2,$$
$$\text{s.t.} \quad \text{Eq.9}$$

where θ_{ij}^* denotes the target joint angles required to produce the desired finger synergy. If we are interested in implementing specific constraints on the joints, they can be included in the optimisation formulation above.

IV. Simulation Results

In this section, we analyse an example finger synergy to determine the required stiffness of each finger joint to achieve the intended coordination. Since the goal is to design a robotic hand with multi-articulation capabilities that can perform more than one grasp type for manipulating a variety of objects, we focus on a synergy that enables both power and pinch grasps. Together, these two grasp types account for over 70% of the grasping actions required for activities of

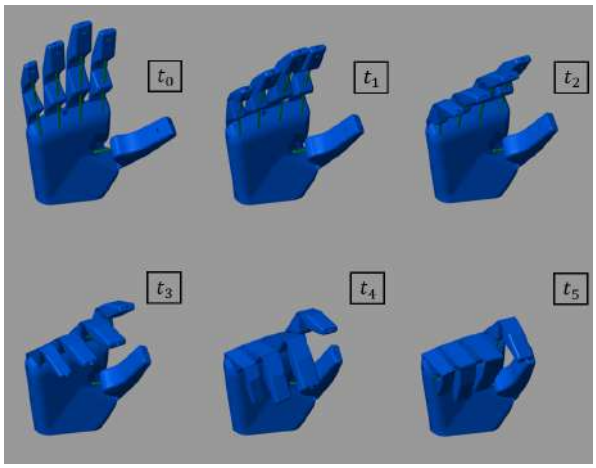


Fig. 6: Visual illustration of the obtained finger synergy.

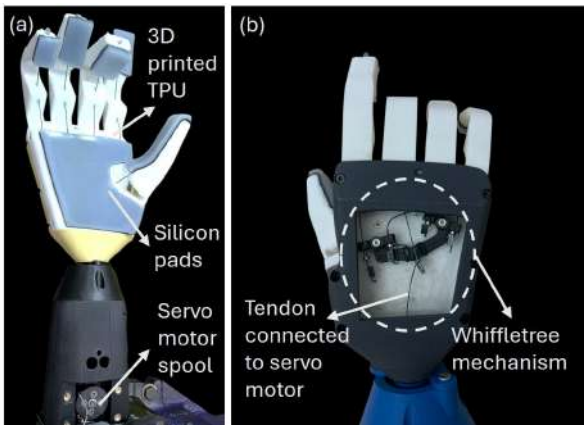


Fig. 7: Overall design of the single-actuator, tendon-driven soft robotic prosthetic hand with flexure joints: (a) front view; (b) back view with force transmission mechanism

daily living by prosthetic hand users [16]. Achieving multiple grasp types with a single actuator ensures that the prosthetic hand remains lightweight and compact while providing the functionality needed for a wide range of applications.

The described finger synergy enables both types of grasp by allowing the user to perform a power grasp initially, followed by a pinch grasp as the angular displacement of the joints increases. To approximate this finger synergy as closely as possible, the final joint angles listed in Table I are used as input parameters for the inverse analysis. While the general analysis was conducted for ten joints (two per digit), the simulation was simplified to nine joints: two per finger and one for the thumb, the latter ensuring a stable pinch grip as it will limit further movement of the thumb after a certain stage of tendon actuation, so the user can focus on controlling the index finger.

For this demonstration, the joints' geometrical parameters are provided in Table II. The tendon displacement is assumed to be $\Delta l = 57$ mm. The joint stiffness values, k_{ij}, generated by the inverse design are shown in Table III.

Using the calculated joint stiffness values, Fig. 5 illustrates

TABLE I: Desired joint angles to produce two grasp type finger synergy

Desired Joint Angles (degrees)								
θ^*_{11}	θ^*_{12}	θ^*_{21}	θ^*_{22}	θ^*_{31}	θ^*_{32}	θ^*_{41}	θ^*_{42}	θ^*_{51}
45	65	90	85	96	90	97	95	36

TABLE II: Geometrical parameters of the finger joints

	Joint								
	J_{11}	J_{12}	J_{21}	J_{22}	J_{31}	J_{32}	J_{41}	J_{42}	J_{51}
a_{ij} (mm)	15.5	16.1	18.7	17.4	16.3	16.5	16.3	17.1	25
b_{ij} (mm)	15.5	16.1	15.2	19.6	15.2	16.5	15.4	16.5	27
ϕ^0_{ij} (deg)	95	95	104.5	108	99	99	99	100	37
θ^0_{ij} (deg)	0 (all zeros)								

the variation in joint angles for each finger as a function of the displacement of the tendon cable driven by the actuator, as well as the force exerted on the tendon by the actuator.

Fig. 6 visualises the finger synergy from t_0 to t_5, corresponding to different stages of tendon cable displacement. The results demonstrate that the encoded finger synergy in the robotic hand enables both power and pinch grasps. From t_0 to t_3, the hand performs a power grasp suitable for holding larger objects. Subsequently, from t_3 to t_5, the hand transitions to performing a pinch grasp or a power grasp for objects with smaller diameters.

V. Experimental Demonstration

To demonstrate the applicability of the proposed method in a real-world soft bionic arm, we developed a flexure joint-based soft robotic prosthetic hand, using the designs proposed in [5] and [17]. Fig. 7 illustrates the overall design of the bionic hand. The hand was 3D-printed in a single process using a benchtop 3D printer (Bambu P1S) with Thermoplastic Polyurethane (TPU) of Shore hardness 85A.

The fingers are actuated via a fishing line connected to a whiffletree mechanism, which is driven by a digital servo

TABLE III: Result of inverse analysis of feasible joint stiffness values.

Feasible Joint Stiffness (Nm/rad)								
k_{11}	k_{12}	k_{21}	k_{22}	k_{31}	k_{32}	k_{41}	k_{42}	k_{51}
0.43	0.33	0.20	0.28	0.14	0.25	0.12	0.22	0.88

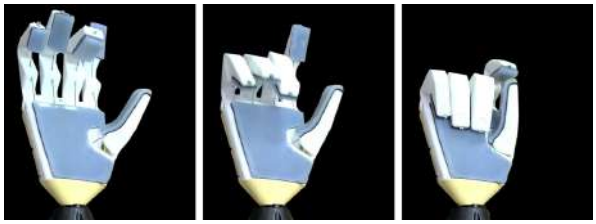


Fig. 8: Postural synergy of the 3D printed soft bionic hand



Fig. 9: Performance of the bionic hand in using pinch and power grips for grasping objects with various shapes and weights

motor with a spool to pull the tendon cable attached to the final link of the mechanism. The servo motor is included in the forearm of the bionic arm close to the wrist. The postural synergies of the fingers are depicted in Fig. 8.

To validate the functionality of the hand in grasping objects of various shapes, sizes, and weights, we conducted experiments involving ten objects that required power and pinch grasps. The grasping results are shown in Fig. 9. A supplementary video (Video-S1.mp4) demonstrating these experiments is included with the paper.

VI. Conclusion and Future Work

This paper presented the design, modeling, and experimental validation of a single-actuator soft robotic prosthetic hand that encodes desired postural synergies through the use of flexure joints with varying geometrical parameters. The results demonstrated that a simple tendon-driven mechanism, combined with tailored stiffness in the flexure joints, can effectively produce postural synergies, enabling multiple grip types for grasping a wide range of objects with different shapes and sizes. Future work will focus on conducting clinical trials to assess the practical utility, adaptability, and user experience of the proposed prosthetic hand design.

References

[1] D. Rus and M. T. Tolley, "Design, fabrication and control of soft robots," *Nature*, vol. 521, no. 7553, pp. 467–475, 2015.

[2] F. Cordella, A. L. Ciancio, R. Sacchetti, A. Davalli, A. G. Cutti, E. Guglielmelli, and L. Zollo, "Literature review on needs of upper limb prosthesis users," *Frontiers in neuroscience*, vol. 10, p. 209, 2016.

[3] G. Gu, N. Zhang, H. Xu, S. Lin, Y. Yu, G. Chai, L. Ge, H. Yang, Q. Shao, X. Sheng *et al.*, "A soft neuroprosthetic hand providing simultaneous myoelectric control and tactile feedback," *Nature biomedical engineering*, vol. 7, no. 4, pp. 589–598, 2023.

[4] H.-I. Kim, M.-W. Han, W. Wang, S.-H. Song, H. Rodrigue, and S.-H. Ahn, "Design and development of bio-mimetic soft robotic hand with shape memory alloy," in *2015 IEEE International Conference on Robotics and Biomimetics (ROBIO)*, 2015, pp. 2330–2334.

[5] A. Mohammadi, J. Lavranos, H. Zhou, R. Mutlu, G. Alici, Y. Tan, P. Choong, and D. Oetomo, "A practical 3d-printed soft robotic prosthetic hand with multi-articulating capabilities," *PloS one*, vol. 15, no. 5, p. e0232766, 2020.

[6] S. R. Kashef, S. Amini, and A. Akbarzadeh, "Robotic hand: A review on linkage-driven finger mechanisms of prosthetic hands and evaluation of the performance criteria," *Mechanism and Machine Theory*, vol. 145, p. 103677, 2020.

[7] S. Shirafuji, S. Ikemoto, and K. Hosoda, "Development of a tendon-driven robotic finger for an anthropomorphic robotic hand," *The International Journal of Robotics Research*, vol. 33, no. 5, pp. 677–693, 2014.

[8] A. Mohammadi, E. Hajizadeh, Y. Tan, P. Choong, and D. Oetomo, "A bioinspired 3d-printable flexure joint with cellular mechanical metamaterial architecture for soft robotic hands," *International Journal of Bioprinting*, vol. 9, no. 3, 2023.

[9] L. Ccorimanya, M. Hassan, R. Watanabe, T. Ueno, Y. Hada, and K. Suzuki, "A personalized 3d-printed hand prosthesis for early intervention in children with congenital below-elbow deficiency: User-centered design case study," *IEEE Access*, vol. 11, pp. 50 235–50 251, 2023.

[10] D. De Barrie, R. Margetts, and K. Goher, "Simpa: Soft-grasp infant myoelectric prosthetic arm," *IEEE Robotics and Automation Letters*, vol. 5, no. 2, pp. 699–704, 2020.

[11] K. Xu, H. Liu, Z. Liu, Y. Du, and X. Zhu, "A single-actuator prosthetic hand using a continuum differential mechanism," in *2015 IEEE International Conference on Robotics and Automation (ICRA)*, 2015, pp. 6457–6462.

[12] M. T. Leddy and A. M. Dollar, "The yale myoadapt hand: A highly functional and adaptive single actuator prosthesis," *IEEE Transactions on Medical Robotics and Bionics*, vol. 4, no. 3, pp. 807–820, 2022.

[13] C. Della Santina, C. Piazza, G. Grioli, M. G. Catalano, and A. Bicchi, "Toward dexterous manipulation with augmented adaptive synergies: The pisa/iit softhand 2," *IEEE Transactions on Robotics*, vol. 34, no. 5, pp. 1141–1156, 2018.

[14] M. Santello, M. Flanders, and J. F. Soechting, "Postural hand synergies for tool use," *Journal of neuroscience*, vol. 18, no. 23, pp. 10 105–10 115, 1998.

[15] I. Hussain, G. Salvietti, M. Malvezzi, and D. Prattichizzo, "On the role of stiffness design for fingertip trajectories of underactuated modular soft hands," in *2017 IEEE International Conference on Robotics and Automation (ICRA)*, 2017, pp. 3096–3101.

[16] A. Mohammadi, J. Lavranos, R. Howe, P. Choong, and D. Oetomo, "Grasp specific and user friendly interface design for myoelectric hand prostheses," in *2017 International Conference on Rehabilitation Robotics (ICORR)*, 2017, pp. 1621–1626.

[17] A. Mohammadi, J. Lavranos, Y. Tan, P. Choong, and D. Oetomo, "A paediatric 3d-printed soft robotic hand prosthesis for children with upper limb loss," in *2020 42nd Annual International Conference of the IEEE Engineering in Medicine & Biology Society (EMBC)*, 2020, pp. 3310–3313.

A Novel Approach to Trunk Rehabilitation: Designing an Upper Body Robotic Mobilizer for Neurological Disorders

Giulia Bodo[1,2], Gianluca Capitta[2], Mattia Modenese[1,2], Luca De Guglielmo[2], Eleonora Guanziroli[3] and Matteo Laffranchi[2]

***Abstract*— After a neurological adverse event, restoring trunk functionality is essential for regaining balance, proprioception, and strength, all of which are critical for performing activities of daily living and enabling rehabilitation for impaired upper and lower limbs. Traditional therapy focuses on enhancing core strength, stability, and proprioceptive capabilities. Recent advancements in the field propose robotic solutions that utilize platforms to induce specific movements, stimulating muscular activation and prompting patients to respond to guided motions. These solutions often employ robotic seats that mimic traditional clinical tools, such as cushions or physiotherapy balls, to assist in mobilizing patients.**

In this work, we introduce a novel approach to trunk rehabilitation through a robotic system: a Series Elastic Actuator (SEA)-based trunk robotic mobilizer. This device is paired with a suite of control strategies designed to address various neurological conditions, including spinal cord injury, post-stroke impairments, and pusher syndrome.

I. INTRODUCTION

In the last decades, a growing demand for advanced technologies that facilitate neuromotor and functional rehabilitation of the upper body has emerged. The complexity of the rehabilitation scenario increases when neurological disorders cause the disability: in such cases, impairments such as spasticity, synkinesias, and cognitive or sensory deficits compound the existing limitations [1], making the treatment even more challenging. Effective and lasting rehabilitation in these cases requires active patient involvement [2]. Patients must be encouraged to voluntarily perform movements to stimulate natural processes of neural reorganization and regeneration [3]. Robotic-mediated rehabilitation is emerging as a promising solution to address the challenges faced in traditional therapy. This approach caters to neurological rehabilitation needs, offering the potential for more effective and efficient treatment outcomes. These technologies aim to provide repetitive, precise, and intensive training [4] across different stages of rehabilitation, transitioning from fully supported modes to scenarios where the patient is increasingly active and engaged. After a neurological event, the trunk often remains an impaired area, significantly impacting both balance and activities of daily living (ADLs) [5].

The trunk is essential for stabilizing the upper body, and when its function is compromised, it can lead to challenges in maintaining balance and performing routine tasks. In stroke patients, trunk muscle contractions, both isometric and isokinetic, are typically weaker than those in healthy individuals [6], several studies have demonstrated strong correlations between trunk impairment, functional performance, and muscle activity [7]. Similarly, individuals with Spinal Cord Injury (SCI) who experience paralysis of the trunk muscles [8] often have diminished control over trunk movements and struggle to maintain a stable posture [9]. Another clinical condition that significantly disrupts trunk motor activity is Pusher Syndrome (or lateropulsion) [10], a specific variation of stroke characterized by a loss of proprioception related to one's posture. Individuals with this syndrome tend to apply a strong, constant push toward their hemiplegic side, regardless of their position [11]. This behaviour actively resists any attempts to correct their posture passively, such as shifting their weight toward the body's midline or, through it, to the unaffected side. Pusher Syndrome presents various neuropsychological symptoms that affect motor function in distinct ways. Specifically, individuals often struggle in antigravity situations, showing an inability to recognize and process proprioceptive feedback. This leads to unbalanced postures misaligned with the body's midline [12]. Patients with pusher syndrome and those in the post-acute phase are typically treated in a seated position to regain control of imbalance-related falls [13] [10].

The authors explored a different concept of upper body robotic mediated rehabilitation, going outside the state-of-the-art concept that mostly proposes the adoption of motorized seats and platforms. Instead, a robotic mobilizer meant to provide robust and stable rehabilitation of the core muscles is directly interfaced with the trunk of the subject, aiming at improving its mobility and stability. This work will present the developed prototype and the different control strategies that have been implemented and tested using a real-time Rapid Control Prototyping (RCP) approach.

II. DEVICE DESIGN

The ideation of the proposed design stemmed from close collaboration between researchers, engineers, and clinicians, following a user-centered design approach. The mechanical and control design requirements were gathered from feedback during interactions with clinicians. The primary goal was to enable patient rehabilitation using a robotic device from the early acute phases, when trunk proprioception and balance have yet to be restored, providing clinicians with a

[1]Politecnico di Torino, Torino, Corso Duca degli Abruzzi 24, 10129, Italy.

[2]Rehab Technologies Laboratory at Istituto Italiano di Tecnologia, Genova, Via Morego 30, 16163, Italy.

[3]Villa Beretta Rehabilitation Center, Costa Masnaga, Via N. Sauro 17, 23845, Italy.

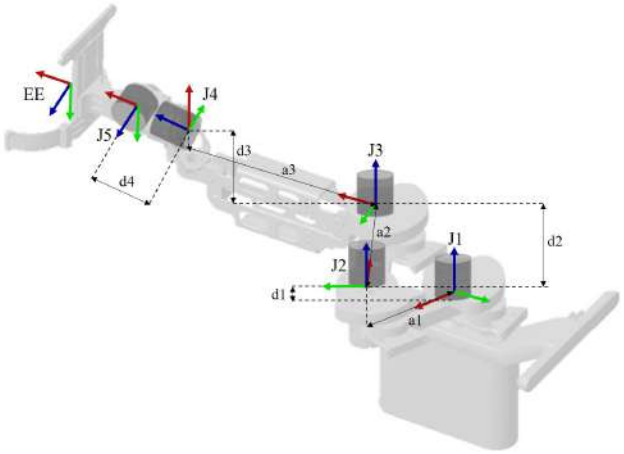


Fig. 1: Graphical representation of the Denavit-Hartenberg convention parameters, as defined in Table I. The parameters *a* and *d* correspond to translations along the x and z-axes of the current frame, respectively. The depicted configuration represents the zero-rotation reference for each joint. Consequently, the range of motion (ROM) values in Table II should be considered relative to this reference.

valuable tool to mobilize the trunk and stimulate the recovery of upper body control.

A. Kinematics

The device is inspired by the passive multi-jointed arm supporting the Float exoskeleton [14]. Compared to the Float multi-jointed arm, the new design incorporates actuation via Series Elastic Actuators (SEAs) for the planar kinematics. Additionally, two more SEA joints are added at the end of the kinematic chain to enable frontal and lateral trunk flexion, and a corset has been designed to support and interface with the patient's trunk. Unlike in the Float system, where the central part of the arm (regarding Figure 1, the link connecting J3 to J4) was adjustable in height, it is now a fixed connection link. The proposed system is designed with five actuated degrees of freedom, as shown in Figure 1. Joints J1, J2, and J3 enable planar movement, which is particularly active during trunk rotation. These joints also work in synergy with J4, primarily involved in lateral flexion, and J5, responsible for trunk flexion in the frontal plane.

The kinematic of the system follows the Denavit-Hartenberg convention and can be described as reported in Table I; the parameters have been identified as shown in Figure 1. The joints' ranges of motion are reported in Table II; those are defined with respect to the zero-configuration shown in Figure 1.

TABLE I: Trunk robotic device Denavit-Hartenberg kinematic parameters.

$Link_{id}$	a $[m]$	α $[rad]$	d $[m]$	θ_i
l_1	0.240	0	0.075	θ_1
l_2	0.240	0	0.033	θ_2
l_3	0.533	$\pi/2$	0.082	θ_3
l_4	0	$\pi/2$	0.101	θ_4

TABLE II: Ranges of motion for each joint, constrained by its mechanical end of travel. These angles are measured relative to the robot's zero-configuration, shown in Figure 1.

$Joint_{id}$	θ_{min} $[deg]$	θ_{max} $[deg]$
$J1$	-67	30
$J2$	-20	65
$J3$	-82	41
$J4$	-20	20
$J5$	-10	30

Following clinicians' requests, the links connecting the different joints and the actuation system have been dimensioned to guarantee the frontal and lateral flexion ranges of motion reported in Table II (J4, J5). Specifically, the system allows for ± 20 deg of lateral flexion in the frontal plane, -10 deg of extension and 30 deg of flexion in the sagittal plane.

B. Actuation

All the joints are equipped with torque sensors. Series Elastic Actuators (SEAs) have been adopted in the design to implement control strategies that account for human interaction in the loop.

The joints are actuated using EC45 Maxon brushless motor for J1-J2-J3 and EC60 for J4-J5. They are combined with a Harmonic drive with a reduction ratio of 1:100 and 1:120, respectively. The SEAs' characteristic element is a custom torsional spring; two different spring designs have been incorporated into the joints: a titanium spiral spring (SPTF1P) for J1-J2-J3 and a steel spiral (SPS1P) spring for J4-J5. They have been characterized and presented in a previous work by Bodo et al. in [15]. The torque estimation can be obtained by exploiting Hooke's law (Equation 6). The values of the spring stiffness k and the linear model intercept $\Delta_{\tau_{lm}}$ obtained from bench characterization of the joints are reported in Table III. Aksim-2 absolute position encoders are adopted to measure the spring displacement and translate it into a torque measurement. Since 19-bit encoders are adopted, the sensor torque resolution ranges from 0.011 Nm to 0.018 Nm, depending on the stiffness of the compliant element.

TABLE III: SEAs spring linear model: stiffness k and linear intercept $\Delta_{\tau_{lm}}$.

	J1	J2	J3	J4	J5
Spring type	SPTF1P	SPTF1P	SPTF1P	SPS1P	SPS1P
k $[Nm/rad]$	878	1017	920	1528	1517
$\Delta\tau_{lm}$ [Nm]	0.056	0.451	0.047	0.306	2.594

C. Design Specifications

Aligning with traditional therapeutic approaches, the device has been designed to mobilize a seated patient. The system has been dimensioned to accommodate a 95th-percentile male to guarantee upper body weight support.

The device configurations corresponding to the maximum joint loads were analyzed using the Mechanism tool provided by CREO PTC CAD software. These configurations

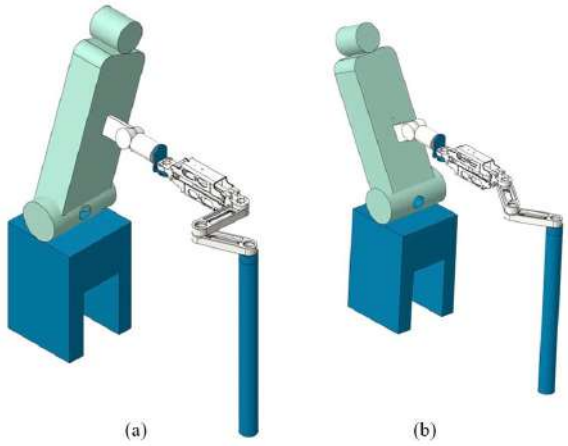


Fig. 2: Device configurations adopted for the load static analysis performed in the CREO PTC CAD software. The manikin represents the 95th percentile in 20 deg lateral flexion and 30 deg frontal flexion positions.

maximize leverage relative to the joints' rotational axes, specifically during full frontal flexion (30 deg) and full lateral flexion (20 deg), as shown in Figure 2.

The load analysis was conducted using the following settings: the simulation was performed for a 95th percentile male (body weight: 96.78 kg, upper body weight: 48.39 kg). All joint rotations were restricted, and only the effects of gravitational force were considered. The obtained system specifications, including the maximum torques required to be supported by the joints, are summarized in Table IV.

TABLE IV: Torque values, simulated in CREO PTC Mechanism analysis, for maximum lateral and frontal flexion across joints.

	τ_{J1}	τ_{J2}	τ_{J3}	τ_{J4}	τ_{J5}
τ Lateral Flex. [Nm]	-15.56	15.93	**-18.25**	0.00	0.00
τ Frontal Flex. [Nm]	-8.82	**25.25**	8.06	-0.08	0.00

To achieve these maximum target torques, specifically with the joints of the planar complex actuated with EC45 motors, an additional reduction stage with a ratio of 1:2.88 was implemented for the joints composing the planar complex. This design choice was guided by the following considerations: movement simulations were performed in CREO PTC in agreement with clinicians' suggestions, and the maximum desired speed for exercise performance was set to 6.66 rad/s (40 deg/s). The SEAs used in the joints embed a harmonic drive with a 1:100 reduction ratio, resulting in a fast shaft speed of:

$$\omega_{\text{fast}} = rr \cdot \omega_{\text{slow}} = 100 \cdot 6.66 = 666 \text{ rpm} \quad (1)$$

From the harmonic drive data sheet, the maximum average input speed is given as $\omega_{HD_{\text{avgMax}}} = 3500$ rpm. To meet this limitation, the maximum allowable second-stage reduction ratio can be computed as follows:

$$rr_{\text{secondStage}} = \frac{\omega_{HD_{\text{avgMax}}}}{\omega_{\text{fast}}} = \frac{3500}{666} = 5.25 \quad (2)$$

The maximum slow shaft torque deliverable by the SEA is the product of the motor's nominal torque and the harmonic drive reduction ratio:

$$\tau_{SEA_{\text{max}}} = \tau_{nomEC45} \cdot rr = 0.167 \cdot 100 = 16.7 \text{ Nm} \quad (3)$$

This respects the datasheet limit of 27 Nm for the harmonic drive output torque. Finally, considering space constraints and assembly requirements, a new reduction stage was implemented using a geared mechanism with two gears (18 and 52 teeth, respectively), resulting in:

$$rr_{\text{secondStage}} = \frac{52}{18} = 2.88 \quad (4)$$

This design allows for the delivery of a maximum output torque of:

$$\tau_{\text{max}} = \tau_{SEA_{\text{max}}} \cdot rr_{\text{secondStage}} = 16.7 \cdot 2.88 = 48.09 \text{ Nm} \quad (5)$$

which is sufficient to support the computed maximum loads presented in Table IV, also ensuring a safety coefficient of 1.9.

D. Electronic setup

The prototype has been connected to a Speedgoat baseline real-time target machine [16]. Five EPOS boards were programmed to control the motors, and custom logic boards were used for each motor to read data from the Aksim-2 encoders on both sides of the SEA torsional spring. Both the boards communicated with the target machine via CAN. A 36 V line supplied EPOS and logic boards, while a 12 V line powered the CAN.

E. Human-Robotic device interface

An orthopaedic corset was incorporated to maintain the patient in the correct position and to support their weight. A custom interface was designed to secure the corset and attach it to the device's end effector (Figure 3, Figure 4). This interface is adjustable in width and height to accommodate different body sizes. It offers a height adjustment range from 20 mm to 100 mm, measured from the centre of the corset, and a side width adjustment range from 285 mm to 375 mm, ensuring compatibility with various body percentiles.

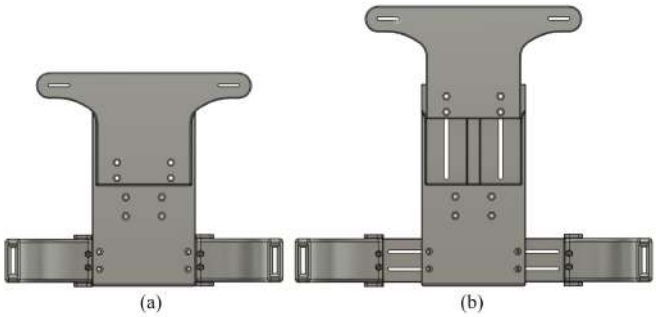


Fig. 3: Custom adaptable interface: (a) completely closed configuration to accommodate lower anthropometric percentiles, (b) fully extended corset configuration.

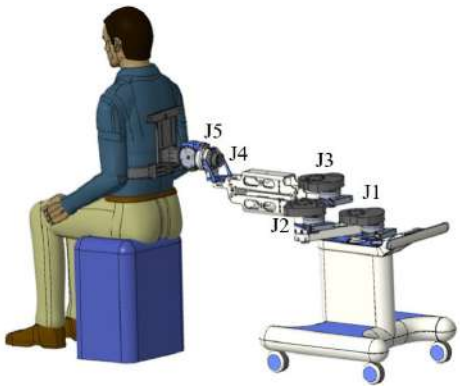


Fig. 4: Example of user positioning during device usage. The user is seated in front of the robotic device and secured to it using a custom corset.

III. CONTROL DESIGN

The control system adopts the RCP model proposed in [17], which architecture has been modified and adapted for the trunk device by developing control strategies for the following use cases: (i) Post-Stroke use case: retraining of elementary movements. (ii) Pusher Syndrome use case: fixed target impedance control to restore posture proprioception. (iii) Spinal Cord Injury use case: resistive control to train muscle strength.

The control model was developed in the MATLAB 2022b Simulink environment. A state-machine logic was implemented to manage the various tasks involved in device control, including receiving signals from sensors and from a graphical user interface (designed using MATLAB App Designer), processing these signals, and computing the target control signals (position or torque targets).

The processing unit is responsible for computing the torques sensed by the series elastic actuators (SEAs) and estimating gravity torques (τ_{g_i}) using MATLAB's *gravityTorque* function from the Robotics Toolbox. This function calculates the gravity torques that must be compensated at each joint based on the robot's dynamic and kinematic parameters. Additionally, a state-machine logic for friction compensation (τ_{f_i}) has been implemented as described in [17].

The model also includes a trajectory generation module, enabling the selection of different exercises with adjustable parameters such as the number of repetitions, amplitude, and duration. The model and a custom Graphic User Interface (GUI) operate in real-time at a frequency of 500 Hz. The architecture allows users to select exercise types (movement type, number of repetitions, amplitude, and duration) and control modes (kinematic, assistive, posture-holding, or resistive) directly from the GUI.

A. SEA torque estimation

Thanks to incorporating SEAs, designing closed-loop control systems that account for human-robot interaction becomes feasible. Specifically, the torque sensed by the SEAs can be computed as:

$$\tau_{SEA} = ((\theta_{AkOut} - \theta_{AkIn}) - \Delta\theta_{AkOffset}) \cdot k + \Delta\tau_{lm} \quad (6)$$

Here, θ_{AkOut}, θ_{AkIn}, and $\Delta\theta_{AkOffset}$ represent, respectively, the angular displacement measured after the spring, the angular displacement measured before the spring, and the encoder offset of the assembly. Additionally, $\Delta\tau_{lm}$ denotes the intercept of the linear model, while k corresponds to the stiffness of the spring (see Table III).

B. Control Modes

The following control modes have been implemented:

a) Passive kinematic exercises: In position control mode, the device rigidly mobilizes the user, guiding them through standard rehabilitative movements, such as frontal and lateral flexions. For this control mode, a trajectory generation algorithm has been implemented for the real-time generation of target positions. The exercise trajectories have been designed by simulating the movements in the CAD software, constraining the end effector position on the desired planes. These trajectories, which could be modelled as straight lines or cosine functions, were then implemented in the Simulink model. To allow customization of the movement range (q_{rng}) and duration (Δt), the trajectories were integrated into the control framework using the following general formula:

$$q_{t_i} = \frac{q_{rng_i}}{\Delta t} \cdot (\Delta t_{el}) + q_{start_i} \quad (7)$$

where Δt_{el} is the elapsed time from the beginning of the movement, and q_{start} is the joint exercise starting position.

b) Assistive Control and Posture-Holding mode: In torque control mode, the same movements proposed in the passive kinematic mode can be performed gradually, actively involving the user in the movement. Three levels of assistance have been empirically tuned by modulating the impedance control's virtual stiffness and damping coefficients (parameters are reported in Table V).

TABLE V: Virtual impedance stiffness (k_v) and damper (β_v) parameters set for the different assistance levels.

	High	Medium	Low
$k_v[Nm/rad]$	250	125	31
$\beta_v[Nm \cdot s/rad]$	35	25	15

The lower the level of assistance, the greater the involvement required from the user. The impedance contribution can be computed as:

$$\tau_{i_i} = (q_{t_i} - q_i) \cdot k_v + \dot{q_i} \cdot \beta_v, \quad i = 1 \dots N \quad (8)$$

The resulting torque control signal for each joint can be written as:

$$\tau_{ctrl_i} = \tau_{g_i} + \tau_{f_i} + \tau_{i_i}, \quad i = 1 \dots N \quad (9)$$

Suppose the *Posture-Holding* mode is selected from the GUI. In that case, impedance control is applied with the springs' equilibrium points centred on the resting position (Figure

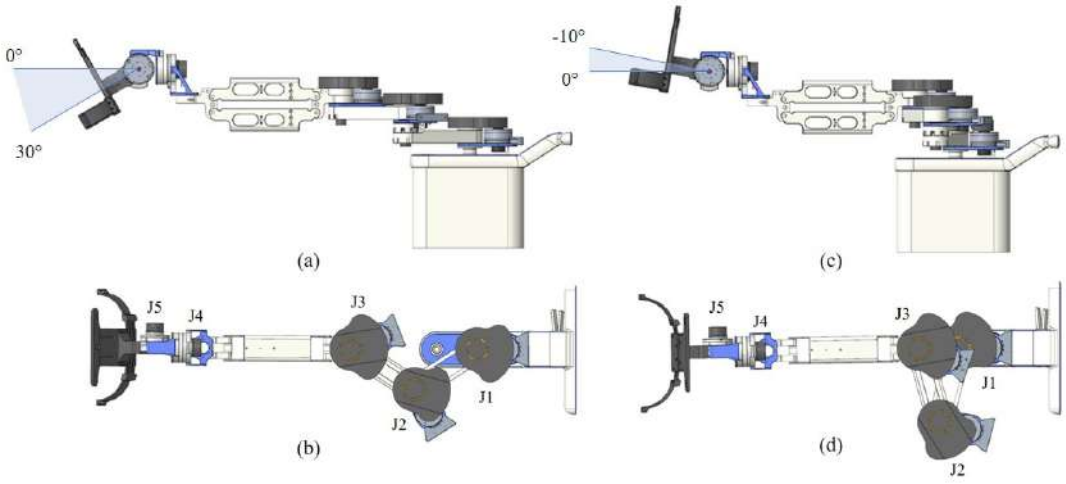


Fig. 5: Trunk device kinematic configurations at the frontal flexion maximum range of motion: (a, b) 30 deg flexion and (c, d) -10 deg extension

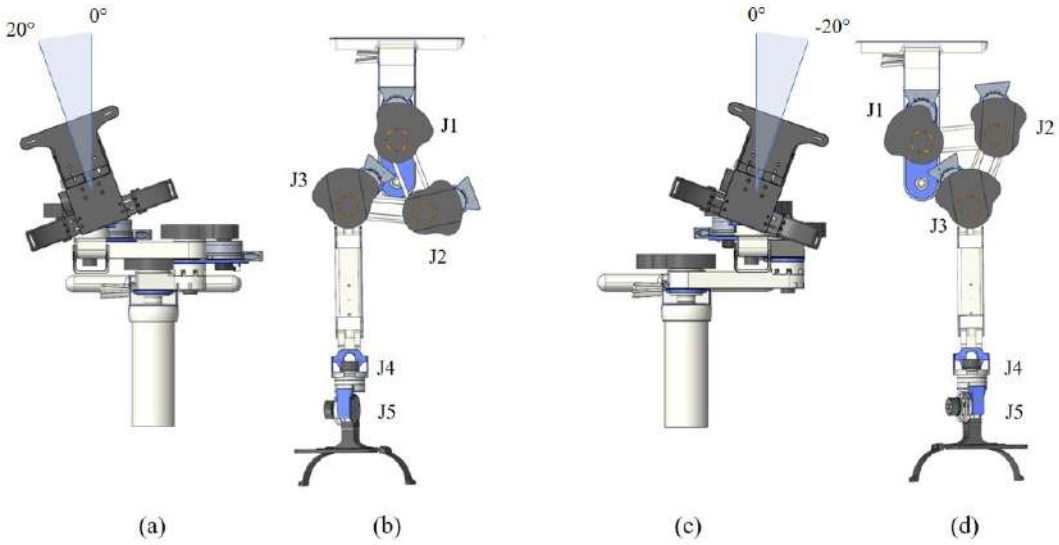


Fig. 6: Trunk device kinematic configurations at the lateral flexion maximum range of motion: (a, b) 20 deg lateral flexion and (c, d) -20 deg lateral flexion.

1 configuration), thus the target positions $q_{t_i} = const$. This control strategy uses a virtual spring-damper effect to correct deviations from the correct posture, guiding the subject back to the proper position through the resulting virtual forces (Figure 7). The levels of assistance featuring the parameters described in Table V are also available for this control mode.

c) Resistive Control Mode: In this mode, a constant resistive contribution is provided along with an impedance contribution (τ_{i_i}) exploited to guarantee a compliant and safe interaction with the machine. The resistance opposing the user's motion can be selected from the GUI for each SEA joint ranging from 1 Nm to 15 Nm ($\tau_{res} = const$), allowing to customize the training, targeting a specific movement and selecting the exercise intensity.

d) Against Interaction Mode: Exploiting the SEA reading, it is possible to compute the interaction torque as:

$$\tau_{int_i} = \tau_{SEA_i} - \tau_{g_i} \tag{10}$$

Interaction-based resistive contributions can be implemented as:

$$\tau_{res_i} = \%_{res_i} \cdot \tau_{int_i} \tag{11}$$

The resistance is expressed as a percentage ($\%_{res}$) of the user's driving force. The gain factor can be selected for each joint, allowing customization of the delivered resistive therapy. For example, if 50% resistance is selected, the system opposes half of the force transmitted via human-machine interaction. If 100% resistance is selected, the user should not be able to move the system. To avoid excessively rigid behaviour, also, in this case, a low impedance term (τ_i) is applied to the joints so that the device remains partially

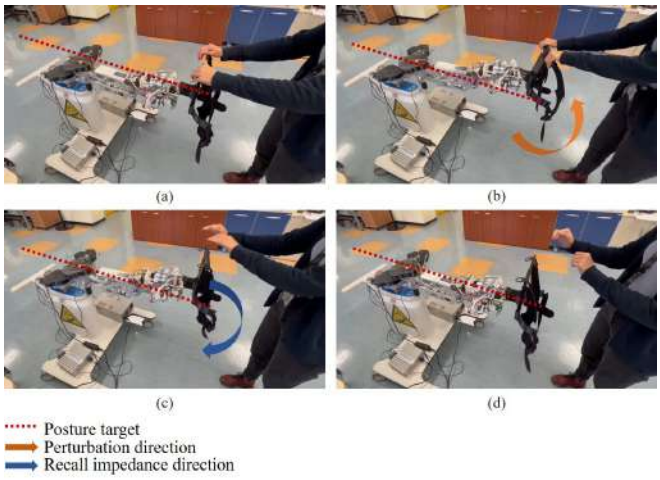


Fig. 7: Experimental testing of Posture-Holding mode: (a) the device operates in torque control, maintaining a fixed target position. (b) An operator manually perturbs the device to simulate posture deviations. (c) In response, the device applies a recall force until (d) it returns to the target position.

compliant with human interaction even when an opposing force is generated.

The torque control signals for the aforementioned resistive control strategies can be computed as:

$$\tau_{ctrl_i} = \tau_{g_i} + \tau_{f_i} + \tau_{i_i} + \tau_{res_i}, \quad i = 1 \dots N \tag{12}$$

In torque control modes, the computed control signal is processed through a PI closed-loop torque controller, where τ_{ctrl} is compared with the SEA torque estimation (τ_{SEA}). This signal is then converted into a current signal using the motor's torque-to-current constant and regulated by the PID controller of the EPOS driver boards. In contrast, the position targets generated by the kinematic mode are directly handled by the EPOS position controller.

IV. DISCUSSION AND CONCLUSION

In this work, we proposed a novel approach meant specifically to target trunk core rehabilitation, showcasing the mechanics and control design of an upper body robotic mobilizer. The device was developed with input and suggestions from clinical partners, ensuring its suitability for addressing various neurological pathologies. The control strategies were implemented using a Rapid Control Prototyping approach and validated through bench testing, confirming the functionality of different control modes. Future work will focus on obtaining hardware and software certification to enable testing on healthy subjects, followed by trials with patients. Additionally, the integration of EMG signal acquisition is planned to fine-tune the assistive and resistive controllers. This will enhance the machine's support capabilities (assistive mode) and optimize muscle activation to promote strengthening and recovery (resistive mode).

ACKNOWLEDGMENT

This work was funded by the Istituto Nazionale per l'Assicurazione contro gli Infortuni sul Lavoro (INAIL) under grant agreements "PR19-RR-P2 - RoboGYM and "PR23-RR-P2 - ClinicEXO".

REFERENCES

[1] M. E. Khallaf. Effect of task-specific training on trunk control and balance in patients with subacute stroke. *Neurology Research International*, 2020:5090193, 2020.

[2] M. Maier, B. R. Ballester, and P. F. M. J. Verschure. Principles of neurorehabilitation after stroke based on motor learning and brain plasticity mechanisms. *Frontiers in Systems Neuroscience*, 13:74, 2019.

[3] J. A. Kleim and T. A. Jones. Principles of experience-dependent neural plasticity: Implications for rehabilitation after brain damage. *Journal of Speech, Language, and Hearing Research*, 51(1):S225–S239, 2008.

[4] A. Pollock, S.E. Farmer, M.C. Brady, P. Langhorne, G.E. Mead, J. Mehrholz, and F. van Wijck. Interventions for improving upper limb function after stroke. *Cochrane Database of Systematic Reviews*, 11, 2014.

[5] N. Moreno-Segura, R. Martín-San Agustín, S. García-Bafalluy, and A. Escriche-Escuder. Effects of core training on trunk function, balance, and gait in stroke patients: A systematic review and meta-analysis of randomised controlled trials. *Clinical Rehabilitation*, 36:1635–1654, 2022.

[6] R. Pilkar, A. Veerubhotla, O. Ibironke, and N. Ehrenberg. A novel core strengthening intervention for improving trunk function, balance, and mobility after stroke. *Brain Sciences*, 12(5):668, 2022.

[7] J. H. Kim, S. M. Lee, and S. H. Jeon. Correlations among trunk impairment, functional performance, and muscle activity during forward reaching tasks in patients with chronic stroke. *Journal of Physical Therapy Science*, 27(9):2955–2958, 2015.

[8] B. Xuefeng and F. Aidan et Al. An integrated control system for optimal human trunk motion. In *2020 8th IEEE RAS/EMBS International Conference for Biomedical Robotics and Biomechatronics (BioRob)*, pages 1055–1060, 2020.

[9] N.S. Tharu, A.Y.L. Wong, and Y.P. Zheng. Neuromodulation for recovery of trunk and sitting functions following spinal cord injury: a comprehensive review of the literature. *Bioelectronic Medicine*, 9(1):11, May 29 2023. Erratum in: Bioelectron Med. 2023 Jun 29;9(1):14. doi: 10.1186/s42234-023-00116-3.

[10] H.O. Karnath and D. Broetz. Understanding and treating "pusher syndrome". *Physical therapy*, 83 12:1119–25, 2003.

[11] J. Nolan, A. Jacques, E. Godecke, et al. Clinical practice recommendations for management of lateropulsion after stroke determined by a delphi expert panel. *Clinical Rehabilitation*, 37(11):1559–1574, 2023.

[12] F. Gigli and G. Leanza. La riabilitazione nella pusher syndrome: una particolare manifestazione clinica dello stroke, January 2009. Accessed: 2024-10-01.

[13] R. Cabanas-Valdés, L. Boix-Sala, M. Grau-Pellicer, J. Guzmán-Bernal, F.M Caballero-Gómez, and G. Urrútia. The effectiveness of additional core stability exercises in improving dynamic sitting balance, gait and functional rehabilitation for subacute stroke patients (core-trial): Study protocol for a randomized controlled trial. *International Journal of Environmental Research and Public Health*, 18(12), 2021.

[14] S. Buccelli, F. Tessari, F. Fausto, L. De Guglielmo, and G. Capitta et Al. A gravity-compensated upper-limb exoskeleton for functional rehabilitation of the shoulder complex. *Applied Sciences*, 12(7), 2022.

[15] G. Bodo, F. Tessari, S. Buccelli, L. De Guglielmo, G. Capitta, M. Laffranchi, and L. De Michieli. Customized series elastic actuator for a safe and compliant human-robot interaction: Design and characterization. *IEEE Int Conf Rehabil Robot. 2023.*, sep 2023.

[16] Speedgoat website. `https://www.speedgoat.com/products-services/real-time-target-machines/baseline-real-time-target-machine`.

[17] G. Bodo, F. Tessari, S. Buccelli, and M. Laffranchi. A rapid control prototyping and hardware-in-the loop approach for upper limb robotic exoskeletons control. *Applied Sciences*, 14(5), 2024.

Adaptive Torque Control of Exoskeletons under Spasticity Conditions via Reinforcement Learning

1st Andrés Chavarrías
Neuro AI and Robotics Group
Cajal International Neuroscience Center
Spanish National Research Council
Rey Juan Carlos University (URJC)
Madrid, Spain
0000-0001-7861-5951

2nd David Rodriguez-Cianca
Neuro AI and Robotics Group
Cajal International Neuroscience Center
Spanish National Research Council
Madrid, Spain
0000-0002-9503-8508

Pablo Lanillos
Neuro AI and Robotics Group
Cajal International Neuroscience Center
Spanish National Research Council
Madrid, Spain
0000-0001-9154-0798

***Abstract*—Spasticity is a common movement disorder symptom in individuals with cerebral palsy, hereditary spastic paraplegia, spinal cord injury and stroke, being one of the most disabling features in the progression of these diseases. Despite the potential benefit of using wearable robots to treat spasticity, their use is not currently recommended to subjects with a level of spasticity above 1^+ in the Modified Ashworth Scale. The varying dynamics of this velocity-dependent tonic stretch reflexes makes difficult to deploy safe personalized controllers. Here, we describe a novel adaptive torque controller via deep reinforcement learning (RL) for a knee exoskeleton under joint spasticity conditions, which accounts for task performance and interaction forces reduction. To train the RL agent, we developed a digital twin, including a musculoskeletal-exoskeleton system with joint misalignment and a differentiable spastic reflexes model for the muscles activation. Results for a simulated knee extension movement showed that the agent learns to control the exoskeleton for individuals with different levels of spasticity. The proposed controller was able to reduce maximum torques applied to the human joint under spastic conditions by an average of 10.6% and decreases the root mean square until the settling time by 8.9% compared to a conventional compliant controller.**

***Index Terms*—Wearable Robotics, Spasticity, Movement disorders, Reinforcement Learning, Musculoskeletal systems.**

I. Introduction

Spasticity is a neurological impairment consequence of an upper motor neuron syndrome commonly seen in neurodegenerative movement disorders associated with damage to the brain, spinal cord and motor nerves. It often manifests as one of the initial motor symptons in conditions such as cerebral palsy, hereditary spastic paraplegia, spinal cord injury or stroke, and is one of the most disabling features as these diseases progress [1]–[3]. This phenomenon was defined by James Lance in 1980 as "a motor disorder characterized by a velocity-dependent increase in tonic stretch reflexes with exaggerated tendon jerks, resulting from hyperexcitability of the stretch reflex" [4]. Users with joint spasticity often experience posture and movement abnormalities due to increased muscle tone and persistent primitive reflexes, leading to limitations in walking speed, balance, and specific movements. Within these mobility restrictions, the knee joint presents particular complications due to its crucial role in gait mechanics and weight-bearing [5].

Wearable robots (WRs), such as robotic exoskeletons, have proven to be valuable tools for therapists in rehabilitation and assistive applications. Under spasticity conditions, the use of WRs has shown that intensive early rehabilitation can potentially prevent the later onset of spasticity, revealing intra-session changes in muscle resistance to passive extension in elbows [6] and limb joint [7]. In addition, it has been shown that the use of exoskeletons in spastic patients during gait has an important influence on the distribution of plantar pressure [8]. Despite the potential benefit on using WRs to treat spasticity, their use is not currently recommended to subjects with a level of spasticity above 1^+ in the Modified Ashworth Scale (MAS) [9], from a maximum level of four, due to safety restrictions. Indeed, the use of WRs under spastic conditions presents several challenges. Conversely to assistance in healthy subjects [10], the primary goal of WRs in movement disorders is not performance (e.g., to speed-up the movement) but to ensure safety (e.g., reducing undesired interaction forces) during the recovery or assistance period. Hence, adaptive control of WRs is an essential feature to ensure safety under different users and scenarios.

A. Related works in WRs control

While there is wide research in WR control, most current market-available solutions are primarily open-loop driven by PID low-level controllers. In essence, these approaches force the leg to follow a specific trajectory without adapting to user or pathology-specific needs. Thus, these usually need to be calibrated for each subject, implying the need for technicians and experts during rehabilitation, and do not adhere to any complex safety restrictions and physical interactions between the robot, the human musculo-skeletal (MS) system and the environment [11]. Model-based controllers are also investigated [12], e.g., model predictive control for prosthetics [13], but require complex dynamic models that are prone to changes due to user-dependent characteristics and errors due to unknown and changing environmental conditions.

A.C.S. and D.R.C. are funded by the RL-EXO project and 2nd Body project, MOMENTUM program, Spanish National Research Council.

B. Learning to control exoskeletons under movement disorders

Particularly in the WRs field, where the exoskeleton needs to adapt to both human interactions and the environment, the use of learning-based control algorithms could be greatly beneficial. Among these, RL [14]—learning to interact with the environment by maximizing the expected future reward—appears as one of the most promising approaches given the recent results in assisting healthy users to reduce energy consumption during walking [10]. Still, the use of RL in WRs, particularly in neurorehabilitation is currently in an early research stay—see [15] for a review. Few works focused on enhancing gait rehabilitation but oversimplified the MS-exo system (e.g., joint misalignments) and only addressed muscles weakness pathologies. Besides, RL has been also used for optimizing the parameters of compliant controllers [16]. RL control under movement disorders, such as spasticity, has not been properly investigated, while being a potential solution due to the challenging nature of the MS changing dynamics, its heterogeneity and safety requirements.

C. Contribution

This work presents a novel adaptive torque controller via Reinforcement Learning (RL) for a knee exoskeleton (Exo) under joint spasticity conditions. This is, learning to control exoskeletons when the dynamics of the human MS system change depending on its velocity and position, while reducing undesired interaction forces to promote user's safety. This is challenging as the controller should be adjusted for each spasticity level and subject. This work contributes with: i) a digital twin of the Human-Exo system that accounts for joint misalignments and relative human-exoskeleton displacements due to soft tissues; ii) A differentiable model of different levels of spasticity; iii) an adaptive WR torque controller, providing improved compliant control for different levels of spasticity compared to a standard PID torque controller.

II. Methods

We developed musculoskeletal spasticity models within a digital human-exoskeleton environment and implemented a Deep RL architecture for training and testing an end-to-end torque controller for a knee exoskeleton in the presence of different levels of knee spasticity—Fig. 1. The digital twin includes: the human MS coupled with a knee exoskeleton, incorporating realistic MS-Exo coupling able to account for the presence of joint misalignments (Sec. II-A), and spastic reflexes model, with a characterization of several pathological spasticity levels (Sec. II-B). We also describe the Deep RL architecture, explaining the reward function design and the implemented policy improvement algorithm (Sec. II-C). Finally, we introduce the experimental setup and the simulation framework (Sec. II-D).

A. Human MS system with Exo coupling

We modeled an adult of 1,75 m and 70 Kg with a leg exoskeleton (Fig. 2), using the Myosuite conversion of Rajagopal's gait model [17] as a close reference. The model

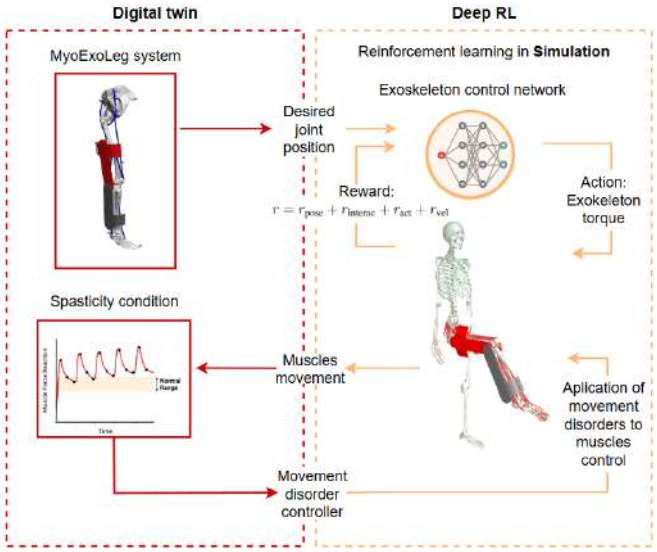


Fig. 1. RL Exo Pipeline. Digital twin development with MyoexoLeg system and spastic model in a red box at left. Deep RL architecture in simulation with RL algorithm and environment in orange box at rigth. The interactions between the digital twin and Deep RL architecture are presented at the middle.

is a unique stand up body with a fixed 90º right hip flexion, allowing freedom of the knee and ankle joints that includes 40 Hill-based muscles with tendon compliance [18]. Human knee joint has a special feature, it rotation axis varying under the sagittal plane during the flexo-extension movement, which implies significant challenges in achieving effective coupling with the Exo. To solve these delineations, this MS-Exo union was designed with 4 DOF, 1 DOF for Exo knee joint and 3 DOF simulating a soft coupling with straps.

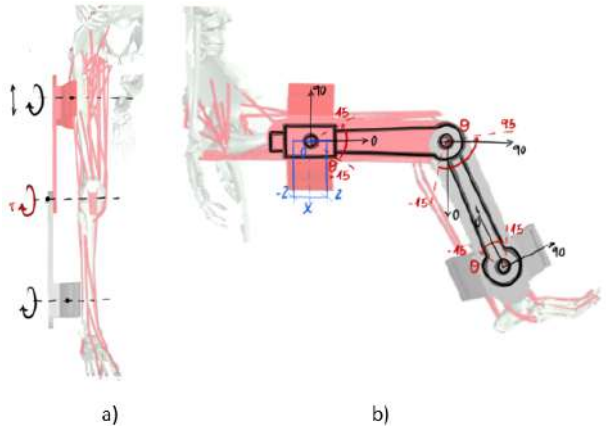


Fig. 2. Knee-Exo coupling model with the upper Exo in red and lower Exo in grey. a) Front view of the Human-Exo attachment, including passive joints in black and actuated joints in red. b) Lateral view of the Slider-Crank mechanism designed to simulate a soft knee-Exo coupling, with angular joints ranges for thigh's and shank's cranks in red and thigh's slider range in blue.

The MS-Exo coupling (Fig. 2) was modeled by means of a slider-crank mechanism with two attachment points; i) the first, on the upper part of the thigh, with two joints, a linear joint with a slide range of $x_{\text{slider}} \in [-0.02m, 0.02m]$ and a

linear friction coefficient of $\eta = 0.97$, and a pin joint with a rotation range of $\theta = \pm 15°$, and ii) the second, on the lower limit of the shank with a pin joint and a rotation range of $\theta = \pm 15°$, in order to simulate the relative movement of the exoskeleton due to human soft tissue compliance. The Exo included one active pin joint at the union of the upper Exo (attached on thigh) and the lower Exo (on the shank) to drive the knee joint that included an actuator with a maximum torque of 100 Nm and a joint range of $\theta_{\text{Torque}} \in [-15°, 95°]$.

B. Spastic reflex model

Joint spasticity is defined as a velocity-dependent muscle tone increase and a muscular activation according to the level of intensity of the muscular reflex and the joint range in the MAS. Here, we provide a spasticity model for muscular activation with a angular velocity parameter [19] and a joint range dependency. The parameter of the four spasticity levels are described in Table: I following the sign convention presented in Fig. 2. We merged level 1 with level 1+ due to their close similarities [20] and left out the most severe level (level 4) due to the inability of these subjects to perform any movement without a potentially harmful increase in muscle tone.

TABLE I
SPASTICITY LEVELS AND CORRESPONDING PARAMETERS

Lv	Muscular activation range limits	Activation coefficient
0	Knee joint range (θ): [-45, 95]° Velocity limit (v): [-10, 10] rad/s	Angular Spasticity s_θ: 0 Velocity Spasticity s_v: 0
1	Knee joint range: (θ): [-35, 80]° Velocity limit (v): [-1, 1] rad/s	Angular Spasticity s_θ: 0.2 Velocity Spasticity s_v: 0.2
2	Knee joint range (θ): [-30, 75]° Velocity limit (v): [-0.5, 0.5] rad/s	Angular Spasticity s_θ: 0.3 Velocity Spasticity s_v: 0.3
3	Knee joint range (θ): [-15, 60]° Velocity limit (v): [-0.25, 0.25] rad/s	Angular Spasticity s_θ: 0.3 Velocity Spasticity s_v: 0.5
4	Not Implemented	

1) Spasticity coefficient to model muscle activation: Muscular activation was implemented as a spasticity coefficient (SC), adjusting muscular tone based on angular and velocity readings at the knee joint following Eq. 1. The SC is composed by an angular and velocity coefficient as follows:

$$SC_{\text{total}} = sc_{\text{angular}}(\theta) + sc_{\text{velocity}}(v) \quad (1)$$

Both coefficient functions are defined using sigmoid equations across thresholds (differentiable model) to avoid non-linear transitions and creating spastic reflexes that increase or decrease around specified angle and velocity limits (See table. I and Fig. 3). The appearance and the intensity of spasticity for each individual was modeled by a transition slope k [0, 0.5, 0.2, 0.1] depending on the spasticity level. This slope allows modelling the appearance of spasticity by a muscular activation value in the last part of the joint range for the level 1 and the progressive and maintained behaviour of the upper levels 2 and 3 (Fig. 3). The SC equation given the sigmoid adjustable slope k and β, β_0 the joint position and velocity range limits results in:

$$\phi(k, \beta, \beta_0) = \frac{1}{1 + e^{k(\beta - \beta_0)}} \quad (2)$$

We define:

a) Angle-based spasticity coefficient: To account for the angle-dependent nature of spasticity, we added a term that considers both flexion and extension limits for the appearance of spasticity depending on the severity level sc_{a}:

$$sc_{\text{a}}(\theta) = s_{\theta\text{Max}} \left[1 - (\phi(k_{\text{ang}}, \theta, \theta_{\text{flex}}) - \phi(k_{\text{ang}}, \theta, \theta_{\text{ext}}))\right] \quad (3)$$

where $s_{\theta\text{Max}}$ is the maximum SC, k_{ang} the slope of the sigmoid transition depending spasticity level muscular activation, θ_{flex} and θ_{ext} the angle threshold for flexion and extension respectively.

b) Velocity-based spasticity: Analogously, lower v_{lower} and upper v_{upper} velocity limits are used in sc_{v} as a function of the velocity v:

$$sc_{\text{v}}(v) = s_{\text{vMax}} \left[1 - (\phi(k_{\text{vel}}, v, v_{\text{lower}}) - \phi(k_{\text{vel}}, v, v_{\text{upper}}))\right] \quad (4)$$

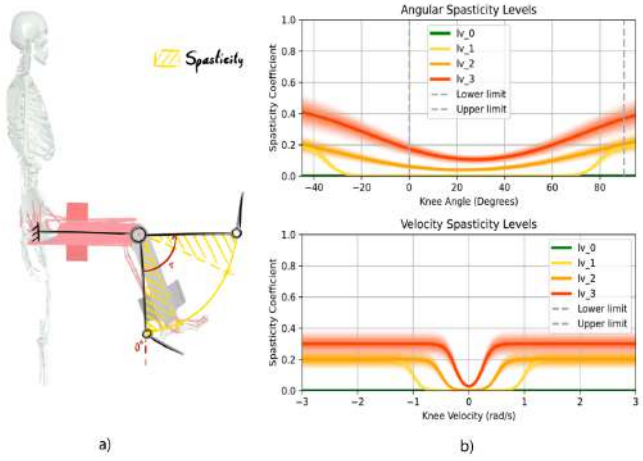


Fig. 3. Knee flexion-extension and spasticity model. (a) Spastic regions (yellow), knee joint extension movement (red). (b) Spasticity coefficients as a function of the knee angle (top) and velocity (bottom) for each spasticity level including individual variance to account for inter-subject variability. Level 0 (green), level 1 (yellow), level 2 (orange) and level 3 (red).

2) Using the spasticity coefficient in the MS model: SC_{total} represents a normalized measure of the percentage of maximum isometric force generated by each muscle. Consequently, when spastic reflexes are incorporated into the simulation, each muscle produces a spastic force proportional to its maximum isometric capacity. Spastic reflexes were implemented in 11 muscles involved in knee joint flexion-extension movement grouped into two categories, based on the literature [21]: i) Flexion-related muscles, including Gastrocnemius Lateral and Gastrocnemius Medial on the Calf, and Semimembranosus, Semitendinosus, Biceps Sural Long and Biceps Sural Short on the Hamstrings; and ii) Extension-related muscles, comprising Gracillis on rectus, and Vastus Medialis, Vastus Lateralis, Vastus Intermedius, and Rectus Femoris on the cuadriceps.

3) Generating individual subjects: To account for inter-subject variability and ensure the robustness of the model, the parameters for the different levels of table I, necessary for eq.3 and eq.4, were generated by introducing Gaussian noise η with a standard deviation of 10% of the absolute parameter value. This approach enables the simulation to capture natural variations observed across individuals, providing a more realistic representation of subject-specific dynamics.

C. Deep Reinforcement Learning Architecture

To address the challenges of adaptive exoskeleton control in the presence of spasticity, we designed and trained a deep reinforcement learning architecture able to provide torque control commands to the exoskeleton that fulfill the following objectives:

- Learning to reach a specific angular joint position.
- Reducing undesired Human-Exo interaction forces.
- Minimizing joint velocity.
- Ensuring smooth Exo actuation to guarantee user comfort.

These control objectives were translated into a reward function with four main terms:

$$r = r_{\text{pose}} + r_{\text{interac}} + r_{\text{vel}} + r_{\text{act}} \tag{5}$$

Pose reward (r_{pose}) is based on the position error (e_{pose}), using a exponential equation with σ^2 as a growth factor and penalized by a linear term.

$$r_{\text{pose}} = \exp\left(-\frac{e_{\text{pose}}}{2 \cdot \sigma^2}\right) - \|e_{\text{pose}}\| \tag{6}$$

Additionally, a cumulative reward of 0.01 is added to r_{pose} when these 2 conditions are satisfied: i) $r_{\text{pose}} < 0.05$ rads and ii) $knee_{\text{vel}} < 0.05$ rads/s.

$\tau_{\text{exo_torque}}$ represent the sum of torques applied (exo and spastic reflexes) on the MS knee joint obtained as an output from Myosuite physics simulator. r_{interact} modulates the maximum torque applied to the human knee joint with a linear normalization penalty of $\nabla_{\text{exo_torque}}$ and a quadratic penalty based on $\tau_{\text{threshold}}$ of 75Nm.

$$r_{\text{inter}} = \begin{cases} \|\nabla_{\text{exo_torque}}\|^2, & \text{if } \tau_{\text{exo_torque}} \leq \tau_{\text{threshold}}, \\ \|\nabla_{\text{exo_torque}}\|^2 + \tau^2_{\text{exo_torque}}, & \text{if } \tau_{\text{exo_torque}} > \tau_{\text{threshold}}. \end{cases} \tag{7}$$

r_{act} and r_{vel} use a linear normalization penalty of the gradients $[\nabla_{\text{exo_control}}, \nabla_{\text{knee_vel}}]$ to reduce undesired motor current spikes and promote a smooth control signal:

$$r_{\text{act}} = \|\nabla_{\text{exo_control}}\|^2 \quad ; \quad r_{\text{vel}} = \|\nabla_{\text{knee_vel}}\| \tag{8}$$

Solving the current continuous control problem using RL requires finding the policy that optimizes the maximum expected reward. From the policy optimizers already tested in WRs [15] we selected the Soft Actor Critic Algorithm (SAC) [22] due to the changing dynamics of the environment and its exploratory properties. SAC is a policy improvement method with an additional policy entropy parameter for data-expensive and complex environments where the agent has to interact and explore a real-world. The SAC model implemented is summarized in table II

TABLE II
NEURAL NETWORK ARCHITECTURE FOR SAC

Component	**Layer Type**	**Input Dim**	**Output Dim**
Actor Network (Policy)			
Input	Observation (state)	93	93
Layer 1	Fully Connected (Dense)	93	64
Layer 2	Fully Connected (Dense)	64	64
Output Layer	Fully Connected (Dense)	64	1
Activation	GELU	-	Tanh
Critic Networks (Q1 and Q2)			
Input	Obs(state) + Action	93 + 1	94
Layer 1	Fully Connected (Dense)	94	64
Layer 2	Fully Connected (Dense)	64	64
Output Layer	Fully Connected (Dense)	64	1
Activation	GELU	-	Linear
Parameters	**Value**	**Parameters**	**Value**
Memory buffer	$5e^6$	Steps	$5e^7$
Adam lr	10^{-4}	Tau	0.05
Batch size	4096	Gamma	0.99

D. Simulation setup and training

The experiment was designed for a point to point trajectory, simulating an almost complete extension of the knee joint (Fig. 3.a). The movement begins at a 90º knee flexion position up until a total knee extension rotation of 83º to avoid the risk of knee hyperextension. The policy was derived from the best-performing model after training for 50 million steps, corresponding to approximately 10,000 full knee joint extension cycles. Spasticity levels were uniformly randomized to ensure a balanced number of interactions across all four implemented levels. Additionally, at the start of each iteration, spastic reflex parameters were generated according to the level of spasticity using the methodology described earlier, simulating individual-specific conditions. The results from the SAC controller were compared to those of a baseline PID-based compliant torque controller to assess its improvement over a classical control method. It produced torque control commands based on angular position deviations from the target position using a PID controller tunned to a spasticity level of 1 following the Ziegler-Nichols method with $K_{\text{p}} = 7$, $K_{\text{i}} = 40$ and $K_{\text{d}} = 0.05$. This comparison aims to demonstrate the adaptive capability of the SAC controller, which employs a single agent, compared to a classical control method optimized for a single spasticity level.

III. RESULTS

The dynamic behavior of control strategies is crucial in managing spasticity during motor tasks, particularly as spasticity severity increases. Hence, we evaluated our developed RL-based controller with respect to the PID-based torque controller over 1000 trials in generated subjects with and without spasticity. We studied the evolution of the following metrics: i) leg extension performance, using the angular position error; ii) smooth behavior, using the control input signal and iii) interaction torques, expressed as the sum of the total torque applied at the knee joint, including the Exo actuation and the spastic reflexes.

A. SAC learned behaviours over spasticity levels

Figure 4 shows the behavior of the SAC controller for different levels of spasticity, grouped by color. In the upper graph, the angular position error during knee extension, where differences are observed in terms of the evolution and settling time within 2% of the final value corresponding to 0.26 s, 0.78 s, 3.77 s, 7.94 s for levels 0, 1, 2, and 3, respectively.

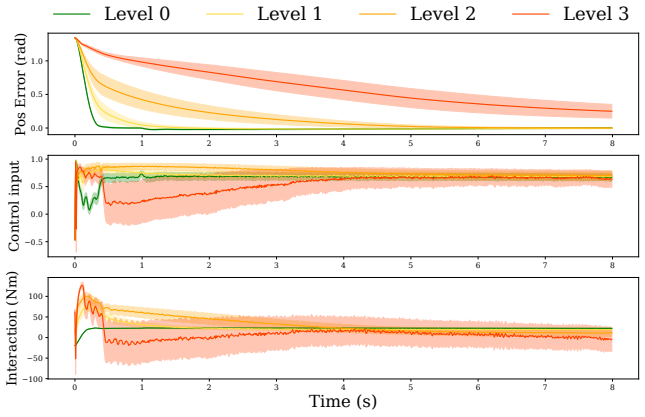


Fig. 4. Simulation results of the SAC algorithm for the implemented spasticity levels. In green, yellow, orange and red for level 0 to 3. The upper graph shows the joint position error, the middle graph, the control signal and the lower graphs shows the interaction torques, during 8s of simulation.

As observed, at level 3 the controller is unable to achieve full knee extension, reaching a steady-state angular error of 11.45º. The middle graph corresponds to the exoskeleton control signal, normalized within a control range of [-1, 1] corresponding to [-100, 100] Nm. Its behavior has a closely relation with the observed in the depicting graph, the summary of torques exerted on the knee joint. The results reveals an increase in the exerted torque proportionally to the severity of the spasticity for levels 0, 1 and 2.

B. Comparison with a PID torque controller baseline

Figure 5 presents a graphical comparison of the RL trained single agent SAC controller over a classical PID torque controller, optimized for a single spasticity level (level 1), for the three metrics discussed earlier (angular position error, control input, and interaction torques), organizing the data by columns corresponding to the four implemented levels of spasticity, with level 0 comparison being the first column. Analysis of these data for the angular position error reveals an overshoot in the PID controller's performance at levels 0 and 1. At levels 2 and 3, where spastic reflexes are more pronounced, the PID controller achieves full extension with a final error of 6.3º at level 2 and 9.3º at level 3. In contrast, the SAC controller achieves position errors of less than 1º for levels below and equal to level 2 but encounters a superior error of 11.45º at level 3.

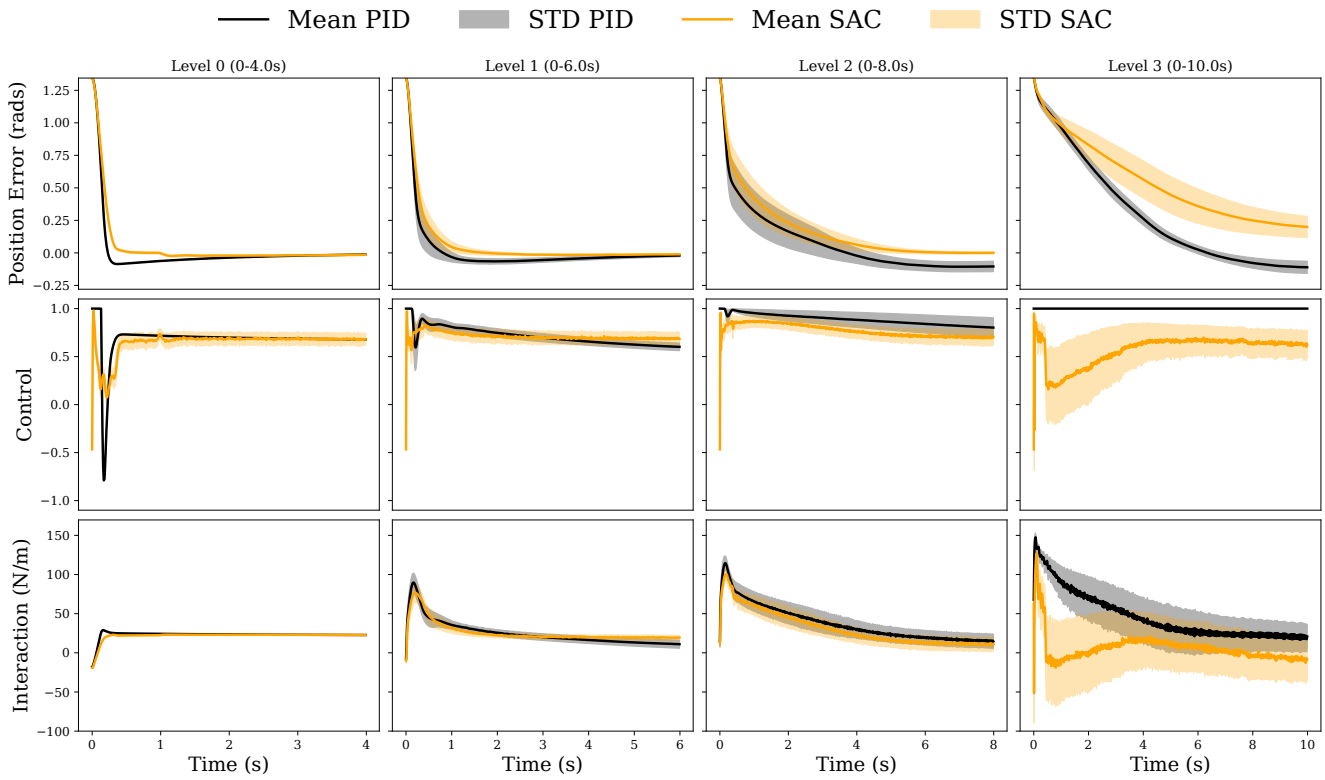


Fig. 5. Comparison of PID and SAC algorithms for different levels of spasticity, grouped in columns. In black, PID; in yellow, SAC, representing their mean and standard deviation values. From left to right in columns, the levels of spasticity implemented from a) Level 0 b) Level 1 c) Level 2 d) Level 3. From top to bottom the comparison of a) Position error b) Control signal c) Interaction torque summary exerted by the exoskeleton and spastic reflexes.

The final row of graphs compares the interaction torques between the exoskeleton and the knee joint. A trend similar to the control signal (middle row graphs) is observed, with lower interaction torques values achieved by the SAC controller throughout the simulation period. The difference is more pronounced at spasticity level 3 compared to the other levels. The subsequent results section delves deeper into these interaction torques, analyzing the most representative parameters.

C. Interaction torques analysis

The aim of the present work was to reduce the MS-Exo interaction forces, thus increasing the safety of the system in spastic conditions.

1) Reduction of undesired interaction torques during the settling interval: The evolution of the torque exerted by the exoskeleton is analyzed through the Root Mean Square (RMS) value of the interaction torques over the settling time obtained at each level within 2% of the final value (Fig. 6) for 1000 simulations . The graph demonstrates an increase in settling time corresponding to the severity of spasticity, as well as higher RMS values. However, the SAC controller achieves lower RMS values across all four levels, reducing RMS by 35.3%, 9.7%, and 8.1% in levels 0, 1, and 2, respectively, where full knee extension is achieved.

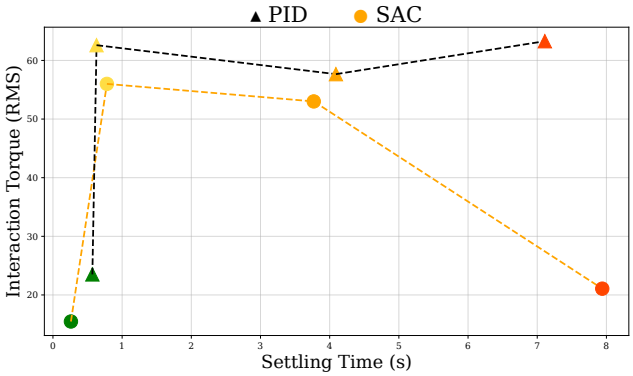


Fig. 6. Mean RMS of interaction torques up to the settling time for the implemented spasticity levels. Spasticity levels are color-coded as follows: Level 0 (green), Level 1 (yellow), Level 2 (orange), and Level 3 (red). The control strategies are represented by distinct markers, with circles for the SAC controller and triangles for the PID controller.

2) Reduction of the maximum torque applied at the knee joint: Figure 7 compares the maximum torques achieved by the SAC and PID controller for different spasticity levels. The SAC controller demonstrates a mean peak torque reduction of 10.8±3.4 Nm, corresponding to decreases of 23.6% at level 0, 12.5% at level 1, 8.8% at level 2, and 11.3% at level 3.

Level 1 exhibits the highest variability in both controllers, with fluctuations in maximum torque reaching a mean of 48 Nm within the Interquartile Range (IQR). Variations of 27.5 Nm and 13 Nm are observed for levels 2 and 3, respectively.

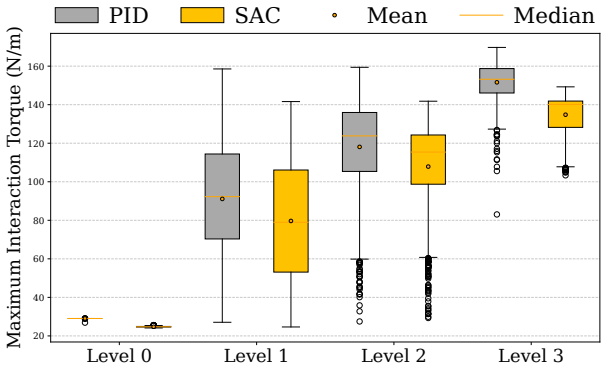


Fig. 7. Peak interaction torque for the SAC and PID controllers across the implemented spasticity levels. The results are presented for spasticity levels 0, 1, 2, and 3, with SAC represented in orange and PID in grey. The box plots show the mean (dot), median (line), interquartile range (IQR) (box), and data spread (outliers).

IV. Discussion and Conclusions

This paper presented an adaptive torque controller for a knee exoskeleton under joint spasticity conditions using RL, offering a suitable approach for wearable robotics for subjects with motor disorders that present muscle position-velocity changing dynamics. The main goal of the approach was to ensure safety (e.g., reducing the amount of undesired interaction forces to complete the task) and provide individualized behavior.

The results of the proposed method demonstrated the effectiveness of the SAC controller to perform the task and reduce maximum torques applied to the human knee joint under spastic conditions by an average of 10.6% (Fig. 7) and decreasing the root mean square (RMS) of the torque until the settling time by 8.9% (Fig. 6) compared to a conventional PID torque controller. Most importantly, the settling time in these cases shows improved results, with reductions at levels 0 and 2 and similar values at level 1. This indicates that the SAC controller is capable of performing knee extension in less time and with reduced effort. These improvements could translate into enhanced safety during repetitive exercises aimed at spasticity treatment.

The reduced steady-state interaction torque at the final joint position in high levels of spasticity for the SAC controller avoids the application of high torques over prolonged periods, highlighting the controller priority of user safety (reduced interaction forces) over task performance. This was particularly noticeable at level 3 (Fig. 5), where the SAC controller prioritized not achieving the target position when the torque required was excessive. Regarding the control input graphs a difference in signal smoothness between the PID and SAC controllers is observed. The SAC controller, driven by the RL algorithm, demonstrates more reactive behavior with a less stable control signal. However, this instability does not propagate to the position response, as the system filters the over-adjustments effectively. Notably, the SAC controller, despite achieving better final position results, maintains a lower control signal than the optimal PID control method

across all cases, maintaining a maximum standard deviation below 5% across randomized spasticity parameters for levels 1 and 2.

Although the evaluation was conducted in a simulated environment, the digital twin model incorporated critical biomechanical characteristics, including joint misalignments and relative displacements of the human exoskeleton due to soft tissue interactions. These considerations enhance the potential for future deployment in physical exoskeleton systems and eventual application in human trials. This physical implementation falls within the scope of the research framework, encompassing the methodologies employed such as domain randomization and physical or non-physical retraining, as well future work aims to extend this approach to address a broader spectrum of motor disorders, such as ataxia and tremor, with the ultimate goal of developing a reinforcement learning-based controller capable of ensuring comprehensive safety and efficacy for individuals with neurodegenerative conditions involving complex and multifaceted movement impairments.

Environment code availability

The Myosuite environment used in this study is available at a repository of NAIR Group Github page: https://github.com/neuro-ai-robotics/RL_Exo.

Acknowledgment

We thank Abián Torres, member of NAIR Group, for his insightful help at the algorithmic and data implementation and Pierre Schumacher for technical details with the Myosuite environment.

References

[1] B. Hanssen, N. Peeters, I. Vandekerckhove, N. De Beukelaer, L. Bar-On, G. Molenaers, A. Van Campenhout, M. Degelaen, C. Van Den Broeck, P. Calders, and K. Desloovere, "The Contribution of Decreased Muscle Size to Muscle Weakness in Children With Spastic Cerebral Palsy," *Frontiers in Neurology*, vol. 12, p. 692582, Jul. 2021.

[2] Z. J. Billington, A. M. Henke, and D. R. Gater, "Spasticity Management after Spinal Cord Injury: The Here and Now," *Journal of Personalized Medicine*, vol. 12, no. 5, p. 808, May 2022.

[3] H. Lackritz, Y. Parmet, S. Frenkel-Toledo, M. C. Baniña, N. Soroker, J. M. Solomon, D. G. Liebermann, M. F. Levin, and S. Berman, "Effect of post-stroke spasticity on voluntary movement of the upper limb," *Journal of NeuroEngineering and Rehabilitation*, vol. 18, no. 1, p. 81, Dec. 2021.

[4] J. Lance, "Pathophysiology of spasticity and clinical experience with baclofen. spasticity: disordered motor control," *Edited by*, 1980.

[5] M. Abid, N. Mezghani, and A. Mitiche, "Knee Joint Biomechanical Gait Data Classification for Knee Pathology Assessment: A Literature Review," *Applied Bionics and Biomechanics*, vol. 2019, pp. 1–14, May 2019.

[6] S. Crea, M. Cempini, S. Mazzoleni, M. C. Carrozza, F. Posteraro, and N. Vitiello, "Phase-II Clinical Validation of a Powered Exoskeleton for the Treatment of Elbow Spasticity," *Frontiers in Neuroscience*, vol. 11, p. 261, May 2017.

[7] Z. Hui, W. Qi, Y. Zhang, M. Wang, J. Zhang, D. Li, and D. Zhu, "Efficacy of a Soft Robotic Exoskeleton to Improve Lower Limb Motor Function in Children with Spastic Cerebral Palsy: A Single-Blinded Randomized Controlled Trial," *Brain Sciences*, vol. 14, no. 5, p. 425, Apr. 2024.

[8] C. Cumplido-Trasmonte, E. Barquín-Santos, M. D. Gor-García-Fogeda, A. Plaza-Flores, D. García-Varela, L. Ibáñez-Herrán, C. Alted-González, P. Díaz-Valles, C. López-Pascua, A. Castrillo-Calvillo, F. Molina-Rueda, R. Fernández, and E. García-Armada, "Modularity Implications of an Overground Exoskeleton on Plantar Pressures, Strength, and Spasticity in Persons with Acquired Brain Injury," *Sensors*, vol. 24, no. 5, p. 1435, Feb. 2024.

[9] R. W. Bohannon and M. B. Smith, "Interrater Reliability of a Modified Ashworth Scale of Muscle Spasticity."

[10] S. Luo, M. Jiang, S. Zhang, J. Zhu, S. Yu, I. Dominguez Silva, T. Wang, E. Rouse, B. Zhou, H. Yuk, X. Zhou, and H. Su, "Experiment-free exoskeleton assistance via learning in simulation," *Nature*, vol. 630, no. 8016, pp. 353–359, Jun. 2024.

[11] J. Bessler, G. B. Prange-Lasonder, L. Schaake, J. F. Saenz, C. Bidard, I. Fassi, M. Valori, A. B. Lassen, and J. H. Buurke, "Safety Assessment of Rehabilitation Robots: A Review Identifying Safety Skills and Current Knowledge Gaps," *Front. Robot. AI*, vol. 8, p. 602878, Mar. 2021.

[12] A. Rodríguez-Fernández, J. Lobo-Prat, and J. M. Font-Llagunes, "Systematic review on wearable lower-limb exoskeletons for gait training in neuromuscular impairments," *Journal of NeuroEngineering and Rehabilitation*, vol. 18, no. 1, p. 22, Dec. 2021.

[13] M. Sartori, G. Durandau, S. Došen, and D. Farina, "Robust simultaneous myoelectric control of multiple degrees of freedom in wrist-hand prostheses by real-time neuromusculoskeletal modeling," *Journal of Neural Engineering*, vol. 15, no. 6, p. 066026, Dec. 2018.

[14] R. S. Sutton and A. G. Barto, *Reinforcement learning: an introduction*, second edition ed., ser. Adaptive computation and machine learning series. Cambridge, Massachusetts: The MIT Press, 2018.

[15] A. C. Sánchez, D. R. Cianca, and P. Lanillos, "Rl-based control methodologies for exoskeletons: a summary," in *Actas del Simposio de Robótica, Bioingeniería y Visión por Computador: Badajoz, 29 a 31 de mayo de 2024*. Servicio de Publicaciones, 2024, pp. 156–162.

[16] S. G. Khan, M. Tufail, S. H. Shah, and I. Ullah, "Reinforcement learning based compliance control of a robotic walk assist device," *Advanced Robotics*, vol. 33, no. 24, pp. 1281–1292, Dec. 2019.

[17] A. Rajagopal, C. L. Dembia, M. S. DeMers, D. D. Delp, J. L. Hicks, and S. L. Delp, "Full-Body Musculoskeletal Model for Muscle-Driven Simulation of Human Gait," *IEEE Transactions on Biomedical Engineering*, vol. 63, no. 10, pp. 2068–2079, Oct. 2016.

[18] M. Millard, T. Uchida, A. Seth, and S. L. Delp, "Flexing Computational Muscle: Modeling and Simulation of Musculotendon Dynamics," *J. Biomech. Eng.*, vol. 135, no. 2, p. 021005, Feb. 2013.

[19] H.-M. Lee, J.-J. J. Chen, M.-S. Ju, C.-C. K. Lin, and P. P. Poon, "Validation of portable muscle tone measurement device for quantifying velocity-dependent properties in elbow spasticity," *Journal of Electromyography and Kinesiology*, vol. 14, no. 5, pp. 577–589, Oct. 2004.

[20] A. Pandyan, M. Gregoric, M. Barnes, D. Wood, F. V. Wijck, J. Burridge, H. Hermens, and G. Johnson, "Spasticity: Clinical perceptions, neurological realities and meaningful measurement," *Disability and Rehabilitation*, vol. 27, no. 1-2, pp. 2–6, Jan. 2005.

[21] K. J. Deluzio, U. P. Wyss, B. Zee, P. A. Costigan, and C. Serbie, "Principal component models of knee kinematics and kinetics: Normal vs. pathological gait patterns," *Human Movement Science*, vol. 16, no. 2-3, pp. 201–217, Apr. 1997.

[22] T. Haarnoja, A. Zhou, P. Abbeel, and S. Levine, "Soft Actor-Critic: Off-Policy Maximum Entropy Deep Reinforcement Learning with a Stochastic Actor," Aug. 2018, arXiv:1801.01290 [cs, stat].

HADAR Hand : 13-DoF Hybrid Actuation-based Dextrous Anthropomorphic Robotic Hand

Prashanth Jonna, Madhav Rao
IIIT Bangalore, prashanth.jonna@iiitb.ac.in, mr@iiitb.ac.in

***Abstract*— Dextrous robotic hand designs are pivotal in advancing the field of hand prosthetics, enabling users to perform robust grasping tasks essential for daily activities and improved quality of life. However, the widespread adoption of such dextrous hand prosthetics remains hindered by prohibitive costs that arise from the high number of actuators used to replicate natural human hand movements. This research seeks to address this challenge by critically evaluating the necessity of replicating many human hand DoFs and instead proposing a design that achieves 95% of human grasp configurations with a significantly reduced actuator count compared to conventional biomimetic robotic hands. We present the Hybrid-Actuated dextrous Anthropomorphic Robotic (HADAR) Hand, a novel 13-DoF robotic hand optimised for dextrous object grasping with a high degree of visual anthropomorphism. The HADAR Hand employs a hybrid actuation strategy, combining linkage-driven mechanisms for robust proximal joint control and tendon-based actuation for compliant distal joint movement, which is essential for delicate object handling. Utilizing insights from long-term occupational studies and Functional Range of Motion (FROM) data, rigid and elastomeric couplings were developed to bring down the actuator count to less than half the number of major tendons present in the human hand without compromising on the ability to perform human-like grasp configurations. Comprehensive performance evaluations validate the HADAR Hand's capabilities, with results demonstrating success in replicating hand grasps as per Cutkosky's taxonomy (14/15), Feix's GRASP taxonomy (31/33), and the Kapandji thumb opposability test (6/10). To promote accessibility and reproducibility, the HADAR Hand leverages cost-effective, widely available actuators, additive manufacturing techniques, and a compact, two-layer PCB capable of concurrently driving all 13 N20 DC motors that drive the HADAR Hand. This work represents a significant step in developing affordable, high-performance prosthetics and robotic hands.**

I. Introduction

Upper-limb prosthetics have evolved dramatically over the centuries, transitioning from rudimentary wooden limbs to sophisticated robotic systems designed to mimic human hand functionality [1]. Although a huge step forward, modern hand prosthetics still deal with the lack of dexterity [2]. As physical interfaces in human environments are inherently designed for the human hands, anthropomorphic robotic hands have emerged as a promising solution for achieving greater closure, dexterity, and manipulability [3]. But the complexity of the human hand, with over 100 tendons (27 of which are essential for motor functions), presents significant hurdles in replicating its structure and functionality within a compact form factor. Since the field of hand prosthetics significantly overlaps with that of robotic hands, we shall also look at robotic hand research to understand the design optimizations made to enhance dexterity with low actuator count. Biomimetic robotic hands like the Shadow Hand [4] that intend to closely replicate human dexterity typically rely on a high number of actuators, which dramatically increases the system's weight, footprint, and cost, limiting their widespread adoption. Conversely, simpler double four-bar linkage based designs commonly utilized in many prosthetic hands [5], [6] are relatively cost-effective but lack the fine-grained control necessary for precise manipulation tasks. This highlights a pressing need for a cost-effective yet dextrous robotic hand prosthetic.

The field of robotic hands was earlier dominated by high-DoF designs like the Shadow Hand, UB Hand IV, MPL v2 [4], [7]. These high-end robotic hands achieved exceptional dexterity using custom actuation mechanisms but are constrained by their high cost, weight, and reliance on custom components. On the other hand, there has also been the rise of simpler low-DoF robotic hands like InMoov [8], HRI Hand [9], and underactuated prosthetic hand designs like the Bebionic Hands [5], and Hannes [6], which prioritize affordability and durability but trade off dexterity and joint independence, limiting their application for high-dexterity demanding tasks. Direct drive-style robotic hands like ALLEGRO Hand [10] and LEAP Hand [11], although relatively cost-effective, are 30% larger than typical human hands, have higher inertia at joints due to the mass of embedded motors, and either lack critical movements like abduction/adduction or rely heavily on expensive actuators. Their lack of visual anthropomorphism also prevents them from being used as hand prosthetics.

Visual anthropomorphism has long been a priority in prosthetic design, but with the rise of humanoid robotics in the service and entertainment sectors, its importance has grown even further. The primary objective of this research with the development of the HADAR hand is to design a cost-effective, dextrous robotic hand that can achieve 95% human grasp configurations as defined by widely recognized grasp taxonomies while utilising a minimal number of actuators. Maintaining visual anthropomorphism and robust grasping capabilities were also priorities. By reducing actuator count and leveraging additive manufacturing, we aim to enhance functionality and minimize production costs and system weight. Recent advancements in additive manufacturing have led to more durable and affordable prosthetic solutions, as seen in designs like OpenBionics and the PSYONIC Ability Hand [12]. These developments highlight the growing potential of high-performance, low-cost 3D-printed prosthetics, reinforcing our decision to use 3D-printed components in the

HADAR Hand's fabrication. Moreover, because the HADAR Hand closely matches the size and proportions of a human hand and its digits, data from real-world human-hand object interactions can be used for imitation learning without any additional post-processing for prosthetic hand control at a later stage.

II. Design Considerations

Before we design the robotic hand, it is crucial to evaluate the functionality provided by the many degrees of freedom in human hands and their role in hand object interactions. There are many studies in literature that go in depth quantifying the utility of each DoF using measures like active range of motion (AROM), functional range of motion (FROM) and also look at the frequency of different hand grasps used by workers in real-world settings. Many robotic hand designs have also intelligently utilized such statistics to optimize for the number of DoFs in their design; therefore, we shall also look at the many robotic hand designs of the past to gain better insights on how we could reduce the number of actuators for the HADAR Hand.

A. AROM, FROM studies and Couplings

The active range of motion (AROM) that results from the constraints placed by ligaments on hand joints is a crucial metric to keep in mind while designing a robotic hand. However, it has also been noticed that the full active range of motion provided by our joints is not utilized during our day-to-day tasks and grasping activities. Hence, many scientific reviews focused on the topic of functional range of motion (FROM) have been published. This paper [13] notes that the FROM of MCP joints and palmar arch is highly dependent on hand size and gender since having a bigger hand would require one to flex more of his fingers and palm to grasp the same object. Although many robotic hands implement full-range MCP joints, palmer arch is often ignored, but is crucial in providing good closure while grasping objects. Abduction between fingers is found to have a high difference between AROM and FROM measures, with the abduction of the middle finger being quite low compared to other joint movements. Another study by Bain et al. [14], used electrical goniometry and made participants perform tasks as per the Sollerman test for hand grip function. They found out that 90% of the tasks could be completed with the utilization of only 48% of AROM at MCP, 59% at PIP, and 60% at DIP joints. To perform all the tasks as per the Sollerman test, a significant amount of extra movement at the MCP was required with not much difference in movement at the PIP and DIP joints. From this, we get to know that the movement at MCP is much more crucial than the ones at the PIP and DIP joints in the case of pre-grasp postures while performing precise manipulation tasks as stated in [5]. The work stated in [15] deals with reducing the number of DOFs in the hand by observing certain constraints present in our hands. It defines 1^{st}-degree constraints which are typical range of motion limits at each joint, and defines 2^{nd}-degree constraints as dynamic constraints like the PIP DIP motion constraint. Other dynamic constraints include how the range of abduction/adduction at an MCP joint of a digit is also limited by the flexion/extension at the MCP joint of the same digit. Certain observations have also mentioned that the abduction/adduction of the middle finger is close to zero.

B. DoF Design Strategies in Robotic Hands

Certain commonly used intra-finger couplings in many robotic designs are between the PIP and the DIP joints. The angle at the DIP is approximately $\frac{2}{3}^{rd}$ the angle at the PIP joint [15]. After observing the grasps present in most taxonomies, it is stated that the little finger plays a non-critical role in most grasps and hence is one of the less required DOFs. This is probably the reason behind assigning a minimal number of DOFs in the second version of Robonaut hand by NASA and the RoboRay hand by Samsung. In some cases, the little finger is completely removed, as seen in the ALLEGRO, LEAP hands. Another paper [15] focused on the hand joint couplings mentions the minimal movement of the middle finger in grasping different object geometries. Reduction of DoFs by eliminating the middle finger's abduction/adduction can be seen in the Schunk SVH 5-fingered robotic hand [16], which provides abduction/adduction movement for all digits except the middle finger. The CMC joint of the thumb is generally fixed in many prosthetics but has shown considerable movement in FROM studies, hence we will include all the major 4 DOFs of the thumb as seen in human hands. The 5^{th} DOF of the thumb involves changing the orientation of the thumb in order to provide appropriate opposition with other digits. This is generally fixed in most robotic hands at a particular orientation. We will adopt a similar architecture to the RoboRay Hand in terms of hybrid actuation to ensure that our robotic hand can be precisely manipulated, and also be compliant enough to handle delicate objects.

III. HADAR Hand system design

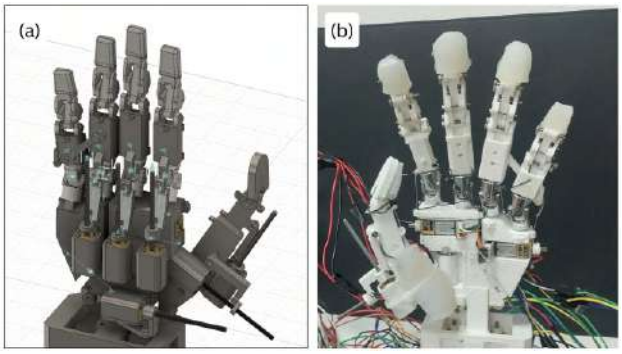


Fig. 1: (a) CAD model of the HADAR Hand in Fusion 360 (b) the fabricated HADAR Hand.

From the observations made in the previous section, we deduced certain design guidelines for the HADAR hand design. The PIP and DIP joints are coupled using four-bar linkages similar to the designs like the HRI hand [9]. Due to the comparatively lower involvement of the little finger in hand-object interactions, we constrain the MCP

joint of the little finger to the MCP joint of the ring finger. Although this decision can lead to a lack of imitation of certain possible human hand configurations, the effect of such a modification is minimal from a grasp point of view. One particular DOF typically overlooked by many robotic hand designs and crucial for better grasping is the mobility provided by the CMC joint below the ring and the little finger that provides palmar arching. We have modeled this DoF as a passive mechanism using elastomers. Abduction and adduction are some of the least utilized DOFs, but from a functional point of view, the abduction/adduction motion is crucial to performing power grasp, which is the most utilized grasp by household workers [17]. But the middle finger's MCP joint does not participate in the power grasp, and hence we eliminated it for the HADAR hand design. We use a set of tendon-driven actuation systems for the PIP-DIP-coupled movement for inherent compliance and use linkage-driven transmission for MCP joint movement to enhance precise control. The thumb plays the most important role in dextrous object grasping and in most cases acts as a single virtual finger by itself, therefore, we decided to use linkage-driven control at the CMC, MCP joints and tendon-driven control at the DIP joint. With the couplings decided and abstract actuation system design in place, our robotic hand will have 3 DOFs for the index finger (abd/add at MCP + flex/ext at MCP + flex/ext at PIP/DIP), 2 for the middle finger (flex/ext at MCP + flex/ext at PIP/DIP), 3 for the ring finger (abd/add at MCP + flex/ext at MCP + flex/ext at PIP/DIP) and 1 for the little finger (abd/add and flex/ext at MCP is coupled, only flex/ext at PIP/DIP is controllable). Here the notation abd stands for abduction, add represents adduction, $flex$ refers to flexion, and ext represents extension.

A. Components of the HADAR Hand

The HADAR Hand was designed in Fusion 360 as seen in Figure 1, with all the parts and linkages printed using a 0.1 mm layer height setting with an Ultimaker Cura S3 3D printer with PLA Pro material at 90% infill density. The MCP joints use a commonly available Stanley STMT86011-8B Chrome Vanadium Steel Universal Joint (1/4-inch), and the N20 motors used to drive the MCP flexion and extension are fitted with an M3 threaded rods and encoders. The N20 motors used for actuating the M3 leadscrew are the 6V 2000 rpm variant. The abduction of the index finger and the coupled ring-little finger is performed by 60 rpm 6V variant N20 motors embedded into the palm of the robotic hand. This is done instead of placing them in the forearm, as positioning them farther away increases tendon path, and concedes frictional losses, with degrading fine control of movement. The mobile CMC joint of the hand is introduced similar to the version 1 of InMoov Hand [8]; there are mechanical limits to ensure that the palmar arch does not cross 30°of inward rotation. Silicone finger pads and thumb tissue were designed to assist in the gripping of objects. All the fingertips were designed to replicate human fingertip's softness and elasticity. LSR-110 grade liquid silicone rubber was chosen for making fingertips as it is specifically rated to be used for mimicking the softness and elasticity of human upper limb parts and is generally used in prosthetic designs.

B. Kinematic Analysis of HADAR Hand



Fig. 2: Gradual flexion of index finger PIP-DIP joints.

1) Four-bar linkage kinematics for pip-dip coupling: The implemented four-bar linkage design follows exactly the same kinematics as described in the HRI hand paper [9] shown in Figure 2, since it mimics the natural human finger flexion and extension action. The mathematical equations that relates to the input and output angles are derived using loop closure and utilizes trigonometric identities, θ_b is the input at the PIP-DIP coupling, and θ_c is the output. Four bar linkages are quite popularly used and hence the widely available models are omitted in this paper for the sake of brevity. Figure 2 shows the four bar linkage in action.

2) Ring-little fingers abduction/adduction coupling: In Figure 3, we can see a barebones structural view of the proposed linkage mechanism in which a denotes the little finger, b denotes the ring finger, d represents the linkage and c is the grounded fixed distance between the MCP joints of the ring and little fingers. Using cosine and sine rules, we can easily compute the value of beta given the values of a, b, d and α.

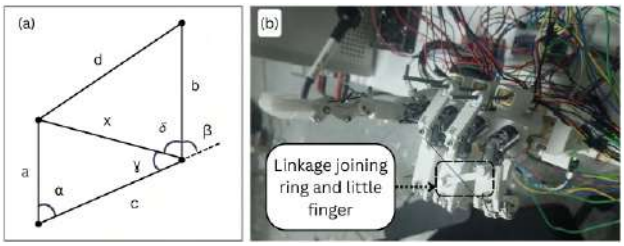


Fig. 3: (a) Mathematical representation of ring-little finger linkage (b) little-ring finger linkage of the HADAR Hand.

$$\alpha = \cos^{\propto 1}\left(\frac{a^2 + c^2 - x^2}{2ac}\right) \tag{1}$$

$$x = \sqrt{a^2 + c^2 - 2ac\cos(\alpha)} \tag{2}$$

$$\gamma = \sin^{\propto 1}\left(\frac{a\sin\alpha}{x}\right) \tag{3}$$

$$\delta = \cos^{\propto 1}\left(\frac{x^2 + b^2 - d^2}{2xb}\right) \tag{4}$$

$$\beta = 180 - \gamma - \delta \tag{5}$$

To optimize for the best coupling output, we set two conditions, when α is 68°, β should be in the range of $68° \pm m$, and when α is 118°, β should be in the range

of 88°± m, m refers to the margin. Setting up a python program configured to execute the mathematical model described above. The optimal a, b, and d parameters with least m was established. The optimal solution with m of β of 63.33°, α of 92.76 °, a of 14.0 mm, b of 27.2 mm, d of 29.8 mm for a given c of 20.6 mm was found.

3) MCP joint flexion/extension actuation mechanism: The Figure 4 is representative of the MCP flexion-extension movement produced using the lead screw mechanism actuated by N20 DC motors. The 'l2' side is the changing linear length actuated by the N20 lead screw mechanism, the 'l1' length is fixed and represents the parallel distance between the lead-screw attached to the N20 motor shaft and the vertical upward direction at the MCP joint. 'c' represents the length of the linkage used and 'r' represents the distance along the lower phalange from the MCP joint where the linkage is attached to the finger. Using trigonometric identities, one can easily derive the relation between the vertical actuation of the lead screw and the angle bent at the MCP joint, also expressed in the Equations 6, 7, and 8. By simulating the linkage mechanism, the effect of lengths 'r', 'c', 'l1' in the Figure 4 on 'l2' and θ was analyzed. Post optimization, we arrived at a solution for which around 25 mm actuation ('l2') would lead to a 0 to 90-°shift in θ. The range of motion at the MCP joint is 90 °and the linkage actuated motion derived from 'r', 'c', 'l1' parameters is demonstrated in Figure 4.

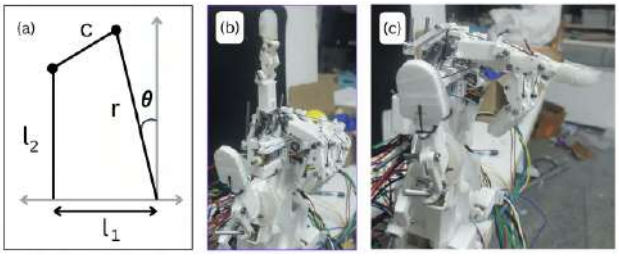


Fig. 4: (a) Mathematical diagram illustrating MCP flexion/extension model, (b) Snapshot of Index MCP joint fully extended, and (c) Snippet of Index MCP joint fully flexed.

$$(l_2 - r\cos\ \theta)^2 + (l_1 - r\ \sin\ \theta)^2 = c^2 \tag{6}$$

$$l_1 \sin\theta + l_2 \cos\ \theta = \frac{l_1^2 + l_2^2 + r^2 - c^2}{2r} \tag{7}$$

$$\sin\theta + \frac{l_2}{l_1}\cos\theta = \frac{l_1^2 + l_2^2 + r^2 - c^2}{2rl_1} \tag{8}$$

We take m = l_2/l_1 and the RHS of the above equation as k, shift the sin term to RHS and square the equation,

$$m^2 \cos^2\theta = k^2 + \sin^2\theta - 2k\sin\theta \tag{9}$$

$$(m^2+1)\sin^2\theta - 2k\sin\theta + (k^2 - m^2) = 0 \tag{10}$$

We now solve this quadratic equation by substituting a = m^2 + 1, b = -2k and c = k^2 - m^2 in the below standard quadratic equation solution to obtain the possible sin(θ) values and take inverse of sine to get the required θ values.

C. Electrical schematic

We use Teensy 4.0 as the main microcontroller for controlling the robotic hand. This choice has been influenced primarily by the 600 MHz clock speed of the ARM Cortex-M7 processor, which helps in managing sensor data in addition to high-density tactile sensor information. Controlling 13 N20 motors is a tedious task for any microcontroller, hence we designed a PCB that utilizes external IO pin extenders and PWM signal generators that continuously provide the required control signals to drive the N20 motors, significantly offloading processing from the microcontroller board. PCA9685 12-bit 16-channel PWM generator and PCF8575 16-bit digital IO expander were used for this purpose. This PCB is entirely controlled using an I2C bus, hence any microcontroller with an I2C bus can effectively control the speed and direction of 13 actuators concurrently. The encoder pins from the N20 motors are attached to Teensy directly and are programmed to trigger interrupts on the rising edge of the encoder signal. Due to the high clock speed of Teensy 4.0, multiple interrupts are generally triggered for one rising edge event, hence software debounce timers were implemented to resolve this issue.

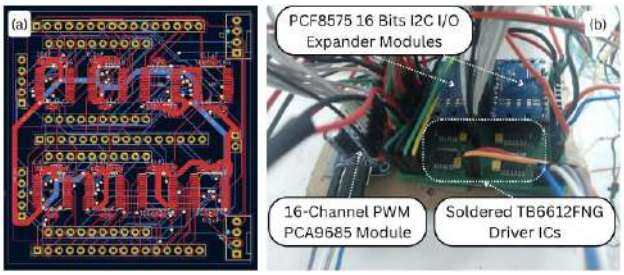


Fig. 5: (a) Designed PCB in KiCAD tool, (b) Manufactured and assembled PCB board that controls the HADAR Hand.

The PCB design for the 16-channel motor driver was done in KiCAD v7 as shown in Figure 5. A two-layer PCB was designed and SMD versions of TB6612FNG, tantalum capacitors and 0603 package resistors were used. Decoupling capacitors were placed near the motor driver ICs and the PCB by itself only contained 8 TB6612FNG and 2 PCF9685 digital IO extender modules that were used to stack on top of the TB6612FNG SMD components. This was established to make the design as compact as possible. The PCA9685 PWM module is connected to the PCB board externally and is wired again into the PCB's middle section using jumper wires to enable efficient track routing as in Figure 5. The routing was completed using auto-routing plugin in KiCAD. The track widths were chosen as per the total usual operation current load estimated to be drawn by 16 N20 motors concurrently when in operation. We did not include current during stall torque condition in our estimation as that would result in 16 A in the worst-case scenario, resulting in designing a very high track width that cannot be allowed in our 2-layered compact PCB due to routing issues caused by such high track width. The manufacturing cost of the developed HADAR hand system was under 300 USD.

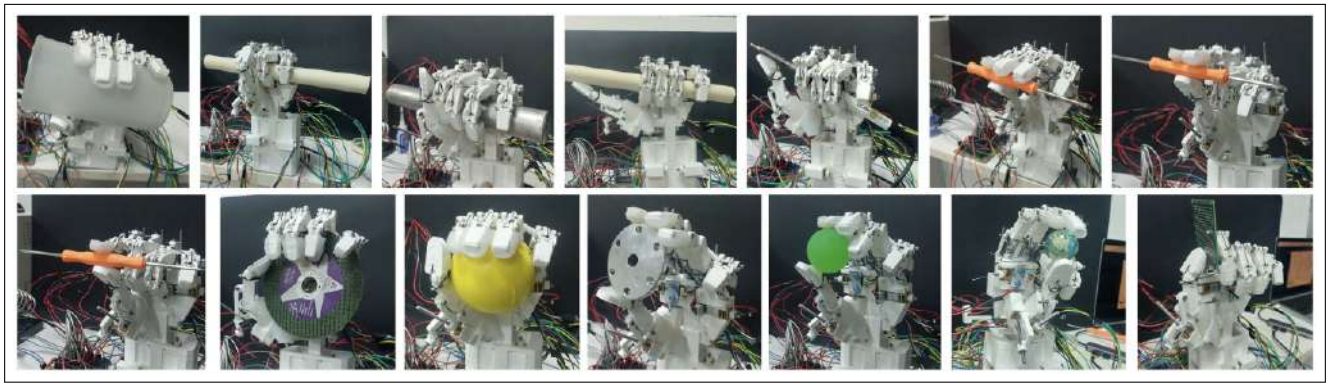


Fig. 6: The grasps imitated by the proposed HADAR hand as per the Cutkosky Taxonomy. The mentioned grasps are depicted in the order of left to right, top to bottom. The numbers assigned for each of the grasp motion matches the original Taxonomy: (1) Large Diameter, (2) Small Diameter, (3) Medium Wrap, (4) Abducted thumb, (5) Light tool, (6) Thumb 4 finger, (7) Thumb 3 finger, (8) Thumb 2 finger, (9) Thumb index finger, (10) Disk (Power), (11) Sphere (Power), (12) Disk (Precision), (13) Sphere (Precision), (14) Tripod, (16) Lateral Pinch. Score achieved: 14 out of 15, Prismatic 4-finger grasp was not robust enough.

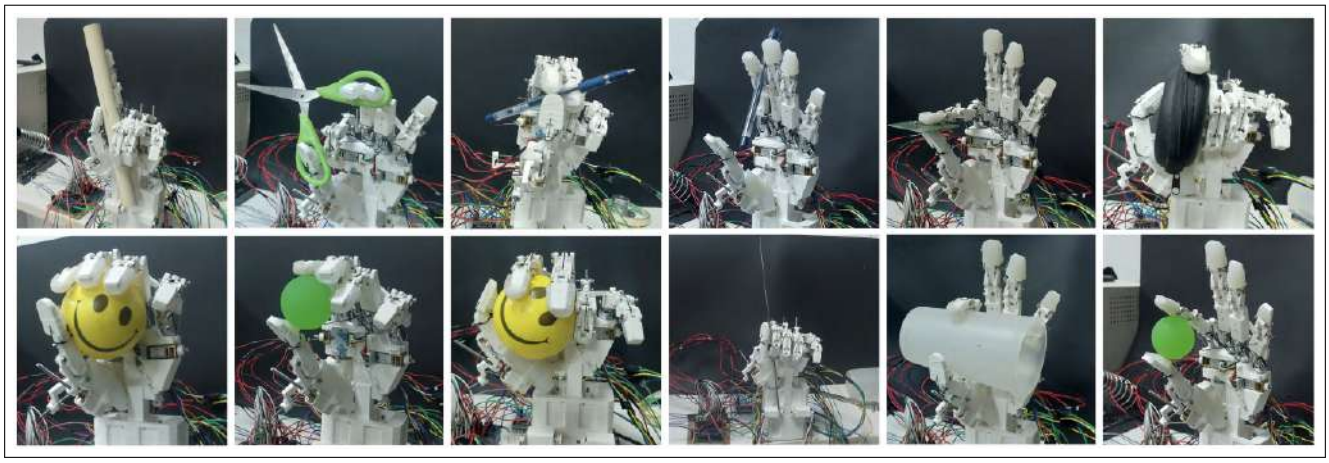


Fig. 7: Imitation of unique grasps from Feix's GRASP Taxonomy in the order of left to right, top to bottom (the numbers here are as per the number assigned to hand grasps in the original Feix taxonomy) : (17) Index finger extension, (19) Distal type, (20) Writing Tripod, (23) Adduction Grip, (24) Tip Pinch, (25) Lateral Tripod, (27) Quadpod, (28) Sphere - 3 finger, (29) Stick, (31) Ring, (33) Inferior Pincer. Score achieved: 31 out of 33, Prismatic 4 finger and Tripod variation grasps was not robust enough.

IV. Experiments and Results

Structuring and organizing hand grasps into a hierarchical taxonomy is useful to better understand the interaction of the hands with different objects as well as to advance and evaluate the graspability of prosthetics and biomimetic robotic hands that try to imitate human hands. Hand taxonomies are such systems used to classify and categorize various hand gestures, movements, and configurations. Hence we will look at the most popular hand taxonomies used in literature and evaluate our developed HADAR hand using them. The significant ones that are highly cited in this domain and well-accepted are Cutkosky's taxonomy [18], the grasp taxonomy [19], and kapandji's thumb opposibility test [20]. Cutkosky's Taxonomy is one of the first widely used taxonomies that aid the design of rehabilitation devices, prosthetics and robotic hands to this day. The cutkosky taxonomy is a rather highly discretized taxonomy and the author of this taxonomy admits that the taxonomy proposed is not complete and that many grasps are not covered individually in this categorization. The author calls them "children" of a particular described grasp type as these are typically slight modifications to one of the grasp types proposed in the taxonomy. Since many robotic hands have benchmarked using this taxonomy in literature, and hence for the sake of completeness, the same was used to benchmark our proposed HADAR hand. As can be seen in Figure 6, our designed HADAR Hand is able to perform 14 out of the 15 grasps present in Cutkosky taxonomy, unable to reproduce the prismatic 4 finger due to the little-ring coupling we introduced. We shall also evaluate our HADAR hand against Feix's grasp taxonomy, which is known to be the most extensive taxonomy incorporating all the grasps possible by human hand. The authors of this taxonomy state that the GRASP taxonomy is the product of a comparison of 22 wide-hand grasp taxonomies proposed

in the literature. The authors make a bold claim by stating that the proposed taxonomy is the most complete to date and they have never encountered a hand grasp that cannot fit into the taxonomy. As we can see in Figure 7, the HADAR hand is able to robustly mimic 31 of the 33 grasps. Hand grasps (18), (22), (30), and (31) from the Felix GRASP taxonomy are not displayed here as they are basic grasps performable by most under-actuated robotic hands and do not require even a mediocre amount of dexterity to imitate. (21) The Tripod variation was not replicated by the HADAR hand as it required precise force controls and hence was omitted. (29) Stick and (32) Ventral had very minimal difference and hence (32) was omitted for the sake of conciseness. The developed robotic hand was manually controlled to grasp different objects presented in Figures 6 and 7. A kapandji thumb opposibility score of 6 is attainable by the HADAR Hand as can be seen in Figure 8.



Fig. 8: Robotic hand grasp configurations that lead to Kapandji score of 6/10.

V. Conclusion and Future Work

This paper introduced the HADAR Hand, designed to achieve near human-like dexterity with a minimal number of actuators. We deeply questioned the necessity of replicating every joint of the human hand and employed couplings by analyzing the functional range of motion (FROM) statistics in literature to bring down the number of actuators required to drive the HADAR Hand. The system was rigorously assessed against established grasp taxonomies, such as those of Cutkosky and Feix, to quantitatively evaluate its versatility. Future work will focus on enhancing and quantitatively measuring grasp robustness and exploring synergy-based control strategies. Additionally, to advance its application as a prosthetic, we aim to integrate EMG signals with egocentric vision, high-density tactile sensing, and proprioceptive feedback for autonomous object grasping.

References

[1] K. J. Zuo and J. L. Olson, "The evolution of functional hand replacement: From iron prostheses to hand transplantation," *Plastic Surgery*, vol. 22, no. 1, pp. 44–51, 2014.

[2] F. Cordella, A. L. Ciancio, R. Sacchetti, A. Davalli, A. G. Cutti, E. Guglielmelli, and L. Zollo, "Literature review on needs of upper limb prosthesis users," *Frontiers in neuroscience*, vol. 10, p. 209, 2016.

[3] P. Varaganti and S. Seo, "Recent advances in biomimetics for the development of bio-inspired prosthetic limbs," *Biomimetics*, vol. 9, no. 5, p. 273, 2024.

[4] S. R. Company, "Shadow dexterous hand series," https://www.shadowrobot.com/dexterous-hand-series/, date Accessed : [February 16, 2024].

[5] C. Medynski and B. Rattray, "Bebionic prosthetic design." Myoelectric Symposium, 2011, https://hdl.handle.net/10161/4733. Date Accessed : [March 21, 2024].

[6] M. Laffranchi, N. Boccardo, S. Traverso, L. Lombardi, M. Canepa, A. Lince, M. Semprini, J. A. Saglia, A. Naceri, R. Sacchetti *et al.*, "The hannes hand prosthesis replicates the key biological properties of the human hand," *Science robotics*, vol. 5, no. 46, p. eabb0467, 2020.

[7] M. S. Johannes, J. D. Bigelow, J. M. Burck, S. D. Harshbarger, M. V. Kozlowski, and T. Van Doren, "An overview of the developmental process for the modular prosthetic limb," *Johns Hopkins APL Technical Digest*, vol. 30, no. 3, pp. 207–216, 2011.

[8] G. Langevin, "Inmoov: Hand and forearm," https://inmoov.fr/hand-and-forarm/, date Accessed : [February 16, 2024].

[9] H. Park and D. Kim, "An open-source anthropomorphic robot hand system: Hri hand." *HardwareX*, vol. 7, p. e00100, 2020. doi: https://doi.org/10.1016/j.ohx.2020.e00100.

[10] A. Hand, "Tech info," https://www.allegrohand.com/tech-info, date Accessed : [February 26, 2024].

[11] K. Shaw, A. Agarwal, and D. Pathak, "Leap hand: Low-cost, efficient, and anthropomorphic hand for robot learning." *arXiv preprint arXiv:2309.06440*, 2023. doi: https://doi.org/10.48550/arXiv.2309.06440.

[12] A. Akhtar, "3d-printing hands that feel," *GetMobile: Mobile Computing and Communications*, vol. 24, no. 4, pp. 10–16, 2021.

[13] V. Gracia-Ibáñez, M. Vergara, J. L. Sancho-Bru, M. C. Mora, and C. Piqueras, "Functional range of motion of the hand joints in activities of the international classification of functioning, disability and health." *Journal of Hand Therapy*, vol. 30, no. 3, pp. 337–347, 2017. doi: https://doi.org/10.1016/j.jht.2016.08.001.

[14] G. I. Bain, N. Polites, B. Higgs, R. Heptinstall, and A. McGrath, "The functional range of motion of the finger joints." *Journal of Hand Surgery (European Volume)*, vol. 40, no. 4, pp. 406–411, 2015. doi: https://doi.org/10.1177/1753193414533754.

[15] J. Lin, Y. Wu, and T. S. Huang, "Modeling the constraints of human hand motion." in *Proceedings workshop on human motion*. IEEE, 2000. doi: https://doi.org/10.1109/HUMO.2000.897381, pp. 121–126.

[16] S. W. Ruehl, C. Parlitz, G. Heppner, A. Hermann, A. Roennau, and R. Dillmann, "Experimental evaluation of the schunk 5-finger gripping hand for grasping tasks." in *2014 IEEE International Conference on Robotics and Biomimetics (ROBIO 2014)*. IEEE, 2014. doi: https://doi.org/10.1109/ROBIO.2014.7090710, pp. 2465–2470.

[17] I. M. Bullock, J. Z. Zheng, S. De La Rosa, C. Guertler, and A. M. Dollar, "Grasp frequency and usage in daily household and machine shop tasks." *IEEE transactions on haptics*, vol. 6, no. 3, pp. 296–308, 2013. doi: https://doi.org/10.1109/TOH.2013.6.

[18] M. R. Cutkosky *et al.*, "On grasp choice, grasp models, and the design of hands for manufacturing tasks." *IEEE Transactions on robotics and automation*, vol. 5, no. 3, pp. 269–279, 1989. doi: https://doi.org/10.1109/70.34763.

[19] T. Feix, J. Romero, H.-B. Schmiedmayer, A. M. Dollar, and D. Kragic, "The grasp taxonomy of human grasp types." *IEEE Transactions on human-machine systems*, vol. 46, no. 1, pp. 66–77, 2015. doi: https://doi.org/10.1109/THMS.2015.2470657.

[20] A. I. Kapandji, "Clinical evaluation of the thumb's opposition," *Journal of Hand Therapy*, vol. 5, no. 2, pp. 102–106, 1992. [Online]. Available: https://www.sciencedirect.com/science/article/pii/S0894113012802651

Muscle Synergy Analysis of Healthy Subjects Using a Soft Elbow Exosuit During Load-Carrying Tasks

Ali KhalilianMotamed Bonab[1*], Cristian Camardella[1], Antonio Frisoli[1], and Domenico Chiaradia[1]

***Abstract*—Soft assistive wearable robotics, or soft exosuits, have shown great potential in enhancing human motor function while preserving the user's natural movement. They are increasingly used to reduce fatigue and the risk of injury during physically demanding tasks and everyday activities. A deeper understanding of how assistive forces from soft exoskeletons influence muscle coordination during various tasks is crucial for developing optimized control and rehabilitation strategies for these devices. This study investigates muscle synergies in healthy participants carrying loads, as often performed in daily activities, over an extended period, both with and without the assistance of a soft elbow exosuit. Synergies similarity was analyzed by comparing the extracted patterns in both conditions, as well as their composition in terms of muscle contributions. The results show that, on average, in the with-exosuit condition fewer synergies are required to explain the performed movements. This suggests the idea that the assistive device "aggregates" motor primitives while reducing muscle activation. Furthermore, we found that synergies dominated by the wrist flexor, biceps, and infraspinatus were not altered by the exosuit assistance. However, the deltoid-dominated synergy observed during load carrying without the exosuit was altered by the exosuit assistance, shifting to a triceps-dominated synergy.**

I. Introduction

Soft assistive wearable robotics, or soft exosuits, have shown great potential in enhancing human motor function and are increasingly used to reduce fatigue [1], [2] and the risk of injury during physically demanding tasks [2], [3], as well as in everyday activities [4]. These devices provide mechanical assistance while preserving the natural movement patterns of the user. Understanding how humans adapt during assisted movements along with analyzing the individual muscle recruitment patterns is crucial for comprehensively assessing the impact of these devices on user performance and for optimizing their assistance strategies to develop more effective and generic support, and rehabilitation control strategies.

Muscle synergy analysis is a computational approach used to understand how the central nervous system (CNS) simplifies the control of muscles during complex movements [5]. According to the theory, rather than managing individual muscles, the CNS coordinates groups of functionally related muscles called muscle synergies, which act as motor primitives to perform tasks. This reduces the dimensionality of motor control, allowing for more efficient movement coordination despite the large number of muscles involved [5], [6].

Muscle synergies are typically extracted from electromyography (EMG) data by decomposing the muscle activation patterns into synergy vectors, representing the contribution of each muscle, and time-varying activation patterns, which reflect how these synergies are activated over time [7]. Methods such as non-negative matrix factorization (NNMF) [8] are commonly used for this decomposition [7]. The combination of these components helps reconstruct the original EMG signals, providing insights into the neuromuscular strategies used for movement.

Recent studies have emphasized the importance of muscle synergy analysis in developing effective control strategies, like myoelectric control [9], and gaining deeper insights into the performance of assistive robotics, particularly in the context of neurological impairments. In healthy individuals, research has shown that the constrained limb movements imposed by robotic rigid exoskeletons do not significantly alter muscle synergies, indicating that muscle coordination patterns remain stable under robotic assistance [10]. Similarly, studies have found that muscle synergies during lifting tasks remain consistent with and without the use of passive exoskeletons, suggesting that natural muscle recruitment strategies are preserved in non-pathological conditions [11]. However, during fatiguing stoop-lifting tasks with lumbar support exoskeletons, changes in muscle coordination were observed, particularly in the timing coefficients of synergy activation, highlighting how exoskeletons can influence the dynamics of muscle recruitment under more strenuous conditions [12]. Additionally, the use of ankle exoskeletons has been shown to modulate muscle recruitment patterns in healthy individuals, suggesting potential applications for rehabilitation by adapting muscle coordination strategies [13].

From a rehabilitation perspective, abnormal synergy patterns have been observed in patients with multiple sclerosis and stroke, revealing disrupted motor control that can be targeted for therapeutic interventions [14]. In stroke patients, robotic rehabilitation interventions have been shown either to modify muscle synergies to more closely resemble those of healthy individuals [14], improving motor control and upper limb function during activities of daily living (ADL) [15], or, mainly on chronic stroke patients, not to alter pre-existing compensation strategies, with muscle synergies resembling a new motor control [16]. In multiple sclerosis patients, exoskeleton-

[1] All the authors are with the Institute of Mechanical Intelligence, Scuola Superiore Sant'Anna, Pisa, Italy.

[*] corresponding author: Ali.KhalilianMotamedBonab@santannapisa.it

The work of A.K.B and C.C. was funded by the Horizon Europe Research & Innovation Programme under Grant agreement N. 101092612 (Social and hUman ceNtered XR - SUN project), and by Tuscany Region, Italy, project TELOS (CUP J52F20001040002). The work of D.C. and A.F. was supported by the Next Generation EU project ECS00000017 'Ecosistema dell'Innovazione' Tuscany Health Ecosystem (THE, PNRR, Spoke 4: Spoke 9: Robotics and Automation for Health). Views and opinions expressed are however those of the author(s) only and do not necessarily reflect those of the European Union or the European Research Executive Agency (REA). Neither the European Union nor the granting authority can be held responsible.

assisted walking influenced muscle activation patterns without altering the existing synergy modules [17].

Despite extensive research on muscle synergies in various exoskeleton applications, no studies have specifically investigated how soft exosuits affect muscle synergy patterns in healthy individuals during load-carrying tasks. Understanding how assistive forces from soft exoskeletons influence muscle coordination in different tasks is crucial for developing optimized control and rehabilitation strategies [18] for soft wearable robotics. To bridge this gap, this study investigates muscle synergies in healthy participants while carrying loads within the range of daily activities over an extended period, both with and without the assistance of a soft elbow exosuit. By analyzing changes in muscle activation patterns, we aim to reveal how soft exosuit assistance modifies muscle coordination in isometric, load-bearing tasks. The insights gained will contribute to the design of more effective assistive strategies for wearable soft robotics, with applications in both everyday and occupational settings.

II. Methodology

A. Elbow Exosuit

The elbow exosuit, shown in Figure 1, used in this study is designed to support the extension and flexion movements of the elbow joint as a tendon-driven exosuit that delivers the assistive force to the elbow joint by pulling tendons wrapped around the joint. The actuation unit incorporates a brushless DC motor (Cubemars AK80-9) with an integrated 9:1 planetary gearbox, capable of producing a rated torque of 9 N·m. This motor is connected to a pulley that manages four stainless steel cables (AISI 316, 6 x 19 - WSC, PA -12 Coated, Carl Stahl) arranged in an antagonistic configuration—two cables facilitate elbow flexion while the other two assist with extension. These cables pass through Bowden sheaths (Jagwire, LEX-SL, ⌀4 mm) to connect to the proximal anchor points.

The exosuit body includes a back attachment, shoulder harness, upper-arm cuff, forearm cuff, and hand brace. The back attachment houses the actuation unit, electronics, and battery. The shoulder harness (Master-03, Reh4mat) secures the upper-arm cuff, which acts as the proximal anchor point and transfers reaction forces to the wearer's body. The upper-arm cuff contains four proximal anchor points that transmit force from the actuation unit to the elbow joint, along with a custom-designed board equipped with an inertial measurement unit (IMU, BNO 055) for data acquisition from load cells and the distal IMU (BNO 055), and transmitting them to the main control board. The forearm cuff secures the four distal anchor points, with two of the anchor points having loadcells (LSB201, Futek) linked to one flexion and one extension cable to measure tendon tension, complemented by another IMU (BNO 055) that works in conjunction with the upper-arm cuff's IMU to calculate elbow kinematics. The total weight of the exosuit is 4085 grams, including a 1400-gram battery.

The control system, adapted from Xiloyannis et al. [4], is designed to provide assistance by partially compensating for the gravitational load on the wearer's arm while minimizing interference with natural arm kinematics, thereby reducing interaction forces between the user and the exosuit. The control architecture employs a collocated admittance controller [19], featuring an outer-loop admittance control along with gravitational assistance and an inner-loop velocity controller. The main control board connects to an external laptop via Ethernet for command input and data transfer. Both the main control board and the upper-arm cuff board execute high-level control and communication at a frequency of 500 Hz.

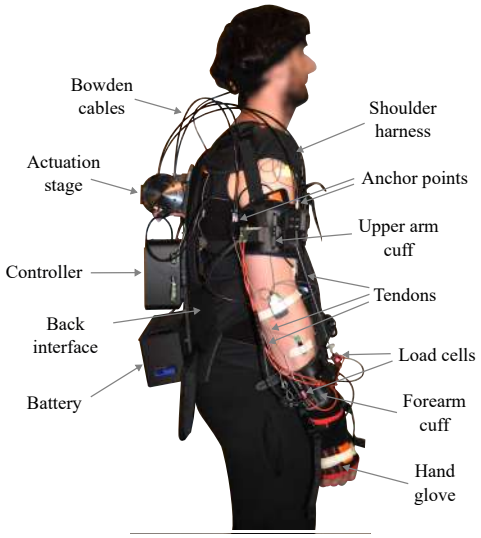


Fig. 1. Components of the soft elbow exosuit, with mechanical components, electronics, and sensing units.

B. Experimental Procedure

This study is aimed at characterizing the upper-limb muscle synergies in healthy participants while carrying a load with and without receiving assistance from an elbow soft exosuit. The experiments were conducted with 10 healthy participants (9 male and 1 female, age: 29.7 $\pm$ 2.75 years, height: 178 $\pm$ 6.32 cm, weight: 77.3 $\pm$ 10.01 kg, mean $\pm$ std). All subjects were right-handed and had no impairments that could affect them in performing the task. They were instructed to avoid fatiguing themselves prior to the experiments. Participants were briefed on the experimental procedures and provided informed consent. The experimental protocol and procedures were approved by the Scuola Superiore Sant'Anna Review Board.

To evaluate muscle coordination, participants walked on a treadmill while carrying a 3.5 kg weight, maintaining their elbow at a 90-degree angle. The experiment duration varied between 4 to 6 minutes, with all participants completing at least 4 minutes. If a participant was able to continue, the trial was extended up to a maximum of 6 minutes. This approach ensured that each participant could perform the task without excessive fatigue while maintaining a comparable effort level across subjects. The arm orientation was continuously monitored throughout the experiment. At the beginning of

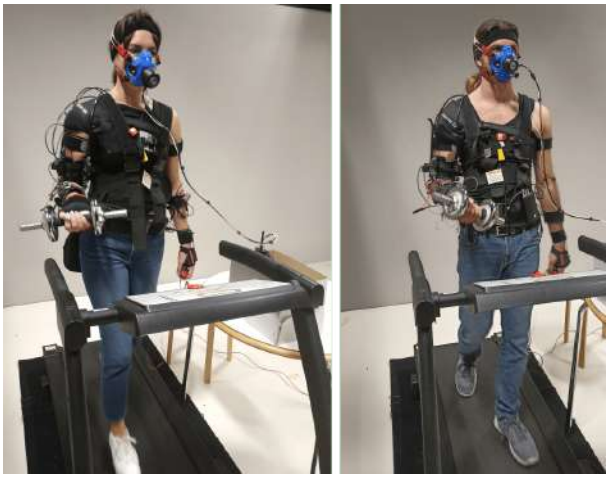


Fig. 2. The setup of the load-carrying experiment. The subjects in the figure wear the soft elbow exoskeleton while carrying a load on the right limb, also walking at a self-selected comfortable speed. Upper body kinematic, EMG, and calorimetry data were collected. Calorimetry data has not been used in this study.

the session, participants were familiarized with the task and determined their preferred walking speed.

Participants were then asked to walk under two conditions: (a) carrying the weight without wearing the exosuit, and (b) carrying the weight while receiving assistance from the elbow exosuit. The conditions were presented in a randomized order to minimize any learning effects, and participants were given at least 5 minutes of rest between the conditions to prevent fatigue effect on the experimental results. A sample experimental session is shown in Figure 2.

At the start of each experimental session, nine electromyography (EMG) sensors (Delsys, Trigno Quattro, and Trigno Avanti) were applied to the primary muscles involved in shoulder, elbow, and wrist movements, including the Deltoid (Anterior, Posterior, Middle), Infraspinatus, Triceps Long Head, Biceps Short Head, Brachioradialis, Extensor Carpi Ulnaris, and Flexor Carpi Radialis. EMG signals were captured with a sampling rate of 2148.1 Hz and the electrode placement was performed according to the guidelines in [20]. The acquired raw EMG data underwent post-processing, i.e. band-pass filtering (30–450 Hz), full-wave rectification, and low-pass filtering at 6 Hz using a zero-phase second-order Butterworth filter. For comparability across conditions and participants, the processed EMG envelopes were normalized to maximum voluntary contractions (MVC), which were measured at both the beginning and end of the session and then averaged to mitigate potential fatigue effects on the measurements. Finally, abnormal peaks and artifacts were manually removed to prevent distortions in metric calculations and statistical analyses.

C. Synergy Extraction

For each participant and condition, muscle synergies were derived from the normalized EMG envelopes of nine muscles using the non-negative matrix factorization (NNMF) algorithm [8], [21]. This algorithm decomposes the EMG envelope into a specified number of positive components, referred to as muscle synergies, as shown in Equation 1. The structure of each synergy is defined by the contribution (weight coefficient) of each muscle, represented in the weight matrix W, while the activation profile is given by the activation coefficients in matrix H. The residual error is represented by matrix E.

$$\mathrm{EMG}_{n\times m}(t) = W_{n\times r}H_{r\times m}(t) + E_{n\times m}(t) \tag{1}$$

To account for the potential of the iterative algorithm to converge on a local rather than a global minimum, the extraction process was repeated fifty times, and the solution with the highest overall explained variance was selected. The NNMF algorithm requires specifying the number of muscle synergies to extract; here, synergy extraction was performed with values ranging from two to seven, resulting in six sets of muscle synergies for each subject under each condition.

To assess the quality of synergy reconstruction, we employed the Variance Accounted For (VAF) metric [22], as defined in Equation 2. This metric quantifies the proportion of variance captured by comparing the sum of squared errors to the total squared sum of the EMG data. VAF values were calculated for each subject under each experimental condition.

$$\mathrm{VAF} \ = 1 - \frac{\mathrm{EMG}_{n\times m}\,(t) - W_{n\times r}H_{r\times m}\,(t)}{\mathrm{EMG}_{n\times m}\,(t) - \overline{\mathrm{EMG}}_{n\times 1}} \tag{2}$$

Here, EMG represents the recorded EMG signals, and $\overline{\mathrm{EMG}}$ denotes their mean values, while W and H correspond to the synergy weights and activation matrices, respectively. By comparing the sum of squared errors to the total squared sum of the EMG data, this method evaluates the quality of synergy reconstruction for each subject and condition. To determine the optimal number of muscle synergies, we applied two established criteria based on the Variance Accounted For (VAF) values across different synergy counts. The first criterion involves assessing the slope of the VAF curve: when the mean squared error of a linear fit to the remaining portion of the curve falls below a predefined threshold, indicating that adding more synergies results in negligible improvement, the current count is selected. The second criterion is based on a target VAF threshold; the smallest number of synergies whose median distribution exceeds this threshold is identified. The final choice of the optimal synergy count is the maximum between the two criteria, ensuring both adequate data representation and minimized redundancy.

In order to reorder the synergies of subjects and maximize the match between them, a random subject was selected as a reference. The similarity between the synergies of other subjects and those of the reference subject was calculated using cosine similarity, as expressed in Equation 3.

$$S = \frac{\mathbf{A}\cdot\mathbf{B}}{|\mathbf{A}|\,|\mathbf{B}|} \tag{3}$$

Here, $\mathbf{A}$ and $\mathbf{B}$ represent the synergy vectors for two different subjects, with $\mathbf{A}$ corresponding to the reference subject and $\mathbf{B}$ to another subject. The computed similarity

matrix was then used to reorder the synergies for each subject across both conditions.

D. Statistics

The Pearson correlation coefficient was used to compute the similarity between synergy in two different conditions. The Pearson correlation coefficient is defined as Equation 4.

$$R = \frac{1}{N-1} \sum_{i=1}^{N} \left(\frac{A_i - \mu_A}{\sigma_A} \right) \left(\frac{B_i - \mu_B}{\sigma_B} \right) \tag{4}$$

Here, $\mathbf{A}$ and $\mathbf{B}$ represent the two synergy vectors, N is the number of scalar observations, μ_A and σ_A are the mean and standard deviation of $\mathbf{A}$, respectively, and μ_B and σ_B are the mean and standard deviation of $\mathbf{B}$.

The computed R value for the correlation of synergies was then compared against the critical value from the Pearson correlation lookup table [23]. If the R value exceeded the threshold corresponding to $p = 0.05$, the null hypothesis was rejected, indicating that the two synergies were significantly correlated.

III. Results and Discussion

In this study, a VAF threshold of 90 % [22] and a slope threshold of 0.001 were applied to determine the optimal number of synergies. These criteria identified three synergies as optimal for the without-exosuit condition and four for the with-exosuit condition. However, four synergies were selected for both conditions, given both the wide distribution of values in the with-exosuit condition and to facilitate better matching and to enable a proper comparison. The VAF values across different synergy numbers are shown in Figure 3. As shown in this figure, the exosuit created an "aggregation" effect on synergies: given a certain number of synergies, the variability of the signal explained by them, i.e. the VAF distribution, is always higher than the without-exosuit counterpart, meaning that, for some of the involved subjects, less synergies are required to explain the performed movements and muscles are "aggregated" in fewer motor primitives. This behavior is comparable to other studies in literature: Tan et al. [12] showed that in stoop lifting task, under fatigue conditions, the VAF was higher in the with-exoskeleton (i.e. the HAL lower limb exoskeleton) condition. The same effect has been found by Ding et al. [11] in load lifting tasks with and without an upper limb exoskeleton.

The mean optimal muscle synergies for the with and without exosuit conditions, along with the Pearson correlation coefficient is presented in Figure 4. The analyses of similarities show that there are significant correlations between the first, second, and fourth synergies indicating that the assistance provided by the exosuit does not alter these synergies while carrying a load. Analyzing the shape of extracted common synergies, it is easy to find dominant muscles in each of them. The first synergy is easily explained by the particular hand pose subjects had to perform while holding the weight: having the up-oriented hand palm put the wrist flexor under the influence of gravity, thus, requiring it to be over-activated in a specific functional motor action. Looking at figure 5, it can be clearly visualized the influence of the FCU in driving the first synergy: the synergetic activation (Synergetic Activations, left) in the case of the with-exosuit condition progressively increases as the muscle activity increases (EMG activations, right) while it stays constant in the without-exosuit condition, reflecting the related FCU muscle activity. Other increasing muscle activity over time, like in the case of BRACH or ECU are distributed among multiple synergies, thus not constituting the main contribution of independent motor primitives. The second and fourth synergies are dominated respectively by the biceps and the infraspinatus, revealing typical lifting and arm supporting motor actions [24]. These synergies stay constantly activated in the case of the with-exosuit condition with a lower activation value compared to the without-exosuit revealing the contribution of the assistive device in the motor actions (see figure 5). The fourth synergy in particular, in the case of the without-exosuit condition, in its increasing behavior, reflects the increasing support of the infraspinatus in the load-carrying motion, given the absence of additional supports. A specific discussion is deserved for the third synergy which is a deltoid-dominated synergy during carrying the load without an exosuit was altered by the exosuit assistance shifting it to a triceps-dominated synergy.

This shift could be explained by considering the primary functions of the anterior deltoid and triceps muscles. The anterior deltoid plays a key role in shoulder flexion and stabilization during forward-reaching and load-carrying tasks, and it has been shown that external support, such as assistance to the forearm, can reduce the activity of this muscle [25]. With the exosuit providing active assistance during load carriage, the workload on the anterior deltoid, which helps stabilize the shoulder complex, may decrease. As a result, muscle activation may shift towards the triceps, which could become more involved in stabilizing the elbow joint, particularly during tasks that require both elbow flexion and extension.

The findings of this study are consistent with those reported in a simulation of an elbow-wrist exosuit used for lifting a similar load [26]. Both this study and similar simulation-based study [27] indicate that the human body optimizes muscle coordination across the entire muscle group, implying that

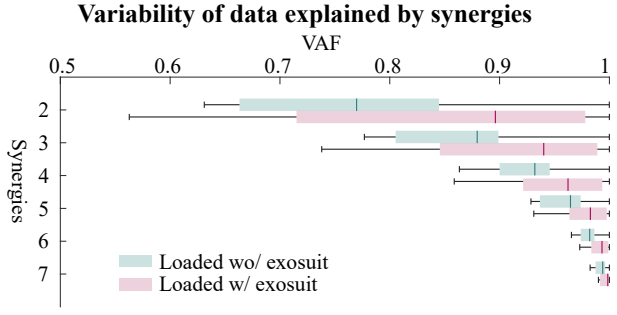


Fig. 3. The variability of data explained by synergies (i.e. VAF) in both experimental conditions, for an increasing number of synergies.

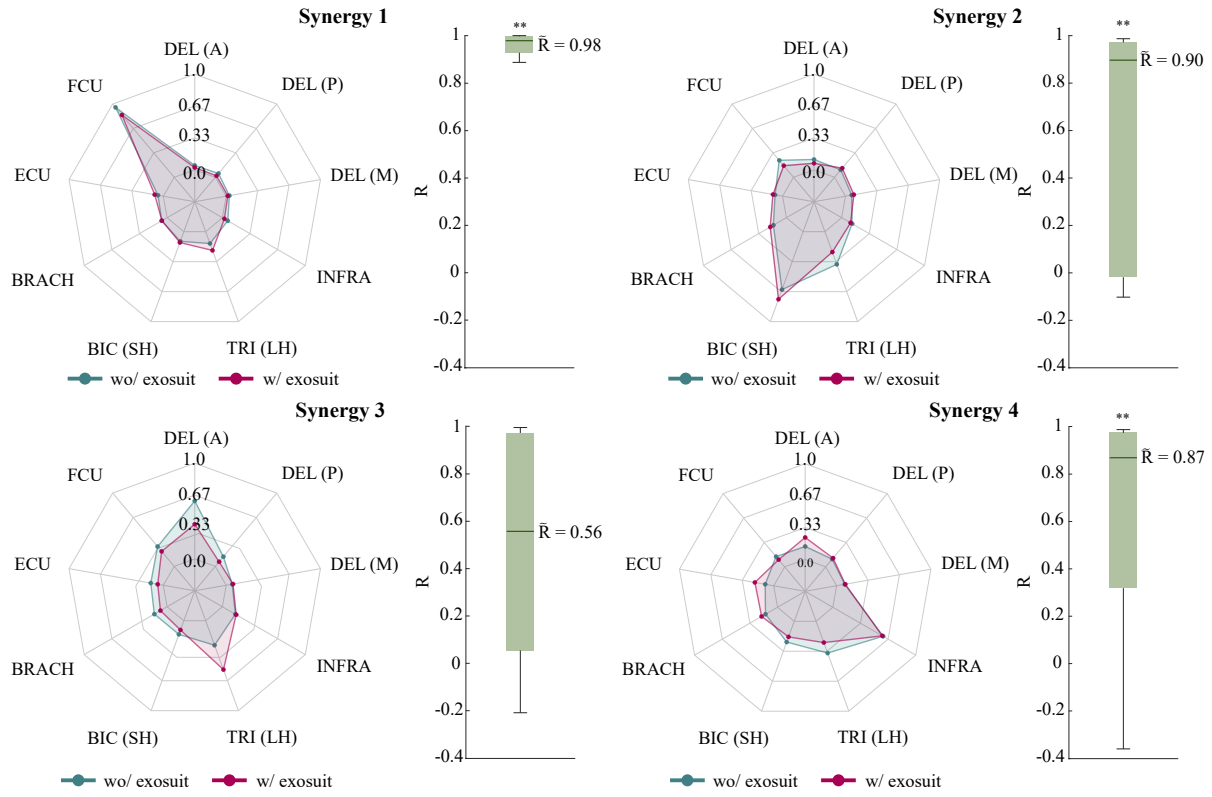


Fig. 4. The mean muscle synergies across two experimental conditions and their Pearson correlation. Radar plots show the synergy weights (W matrix in Equation 1) muscle by muscles, where the vertexes of the polygon represent a value equal to 1. The Pearson coefficient is computed through the comparison between synergy patterns (i.e. arrays) in without exosuit condition and with exosuit condition.

assistance at one joint can influence the activity of muscles that do not directly span that joint. Specifically, this study experimentally demonstrates that providing assistance at the elbow joint during a prolonged load-bearing task can decrease the involvement of the anterior deltoid, leading to a shift towards a triceps-dominant synergy.

IV. Conclusion

In this study, a muscle synergy analysis was performed on an elbow soft exosuit demonstrating that it allows for physiological load-carrying movements under an assistive control strategy, with the possibility to catch even little variations on physiological patterns and to reveal important improvements that can be applied to the device. This outcome supports the idea of using soft exoskeletons, such as the ones with cable actuation, both in clinical environments to perform upper limb rehabilitation sessions and to support activities of daily living. It also confirms the usefulness of muscle synergies as an assessment tool for detecting both patterns in motor coordination and potential alterations of these while wearing assistive devices.

It is important to note that the task analyzed in this study involved an isometric contraction of the elbow, thus these findings should not be directly generalized to other movement conditions. To address this limitation, future work will focus on gaining deeper insights into the effects of soft exosuits on muscle synergies by assessing functional movements. Such studies would provide a more comprehensive understanding of how exosuits influence arm motor function. This knowledge could guide the design of more effective soft exosuit-based therapy sessions, maximizing their therapeutic impact and improving outcomes for patients undergoing rehabilitation.

References

[1] H. Jeong, P. Haghighat, P. Kantharaju, M. Jacobson, H. Jeong, and M. Kim, "Muscle coordination and recruitment during squat assistance using a robotic ankle–foot exoskeleton," *Scientific Reports*, vol. 13, no. 1, p. 1363, 2023.

[2] A. Hess, J. V. Jacobs, S. Sullivan, D. O. R. Williams, L. N. Awad, D. Dalton, C. J. Walsh, and D. A. Quirk, "Active back exosuits demonstrate positive usability perceptions that drive intention-to-use in the field among logistic warehouse workers," *Applied Ergonomics*, vol. 122, p. 104400, 2025.

[3] Y. M. Zhou, C. J. Hohimer, H. T. Young, C. M. McCann, D. Pont-Esteban, U. S. Civici, Y. Jin, P. Murphy, D. Wagner, T. Cole *et al.*, "A portable inflatable soft wearable robot to assist the shoulder during industrial work," *Science Robotics*, vol. 9, no. 91, p. eadi2377, 2024.

[4] M. Xiloyannis, D. Chiaradia, A. Frisoli, and L. Masia, "Physiological and kinematic effects of a soft exosuit on arm movements," *Journal of neuroengineering and rehabilitation*, vol. 16, pp. 1–15, 2019.

[5] A. d'Avella, P. Saltiel, and E. Bizzi, "Combinations of muscle synergies in the construction of a natural motor behavior," *Nature neuroscience*, vol. 6, no. 3, pp. 300–308, 2003.

[6] E. Bizzi and V. C. Cheung, "The neural origin of muscle synergies," *Frontiers in computational neuroscience*, vol. 7, p. 51, 2013.

[7] J. Taborri, V. Agostini, P. K. Artemiadis, M. Ghislieri, D. A. Jacobs, J. Roh, and S. Rossi, "Feasibility of muscle synergy outcomes in clinics, robotics, and sports: a systematic review," *Applied bionics and biomechanics*, vol. 2018, no. 1, p. 3934698, 2018.

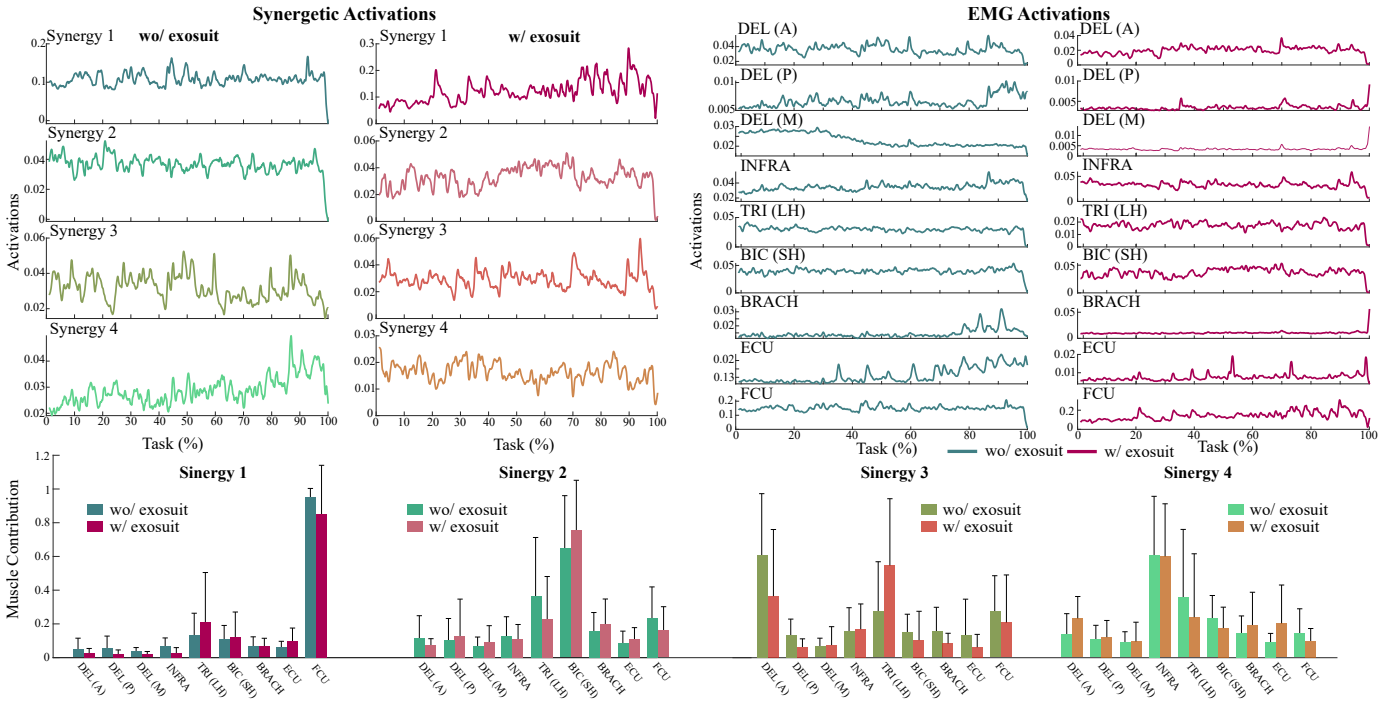


Fig. 5. Overview of EMG signals (on the right), extracted synergies (bottom), and activation signals of synergies (left) in both conditions (without exosuit and with exosuit). Synergistic activations show the content of the H matrix (see Equation 1 after the synergy decomposition, while the synergy weights show the content of the W matrix. Abbreviations for muscles: DEL (A) – Anterior Deltoid, DEL (M) – Middle Deltoid, DEL (P) – Posterior Deltoid, INFRA – Infraspinatus, TRI – Triceps Brachii, BIC – Biceps Brachii, BRACH – Brachioradialis, ECU – Extensor Carpi Ulnaris, FCU – Flexor Carpi Ulnaris.

[8] D. D. Lee and H. S. Seung, "Learning the parts of objects by non-negative matrix factorization," *nature*, vol. 401, no. 6755, pp. 788–791, 1999.

[9] C. Camardella, M. Barsotti, L. P. Murciego, D. Buongiorno, V. Bevilacqua, and A. Frisoli, "Evaluating generalization capability of bio-inspired models for a myoelectric control: A pilot study," in *International Conference on Intelligent Computing*. Springer, 2019, pp. 739–750.

[10] C. G. Mcdonald, B. J. Fregly, and M. K. O'Malley, "Effect of robotic exoskeleton motion constraints on upper limb muscle synergies: A case study," *IEEE Transactions on Neural Systems and Rehabilitation Engineering*, vol. 29, pp. 2086–2095, 2021.

[11] Y. Ding, B. Tang, K. Xiang, J. Luo, M. Pang, and Z. Lu, "Muscle synergy structure consistency during lifting motion with exoskeleton," in *2023 9th International Conference on Electrical Engineering, Control and Robotics (EECR)*. IEEE, 2023, pp. 46–49.

[12] C. K. Tan, H. Kadone, K. Miura, T. Abe, M. Koda, M. Yamazaki, Y. Sankai, and K. Suzuki, "Muscle synergies during repetitive stoop lifting with a bioelectrically-controlled lumbar support exoskeleton," *Frontiers in Human Neuroscience*, vol. 13, p. 142, 2019.

[13] K. M. Steele, R. W. Jackson, B. R. Shuman, and S. H. Collins, "Muscle recruitment and coordination with an ankle exoskeleton," *Journal of biomechanics*, vol. 59, pp. 50–58, 2017.

[14] T. Lencioni, L. Fornia, T. Bowman, A. Marzegan, A. Caronni, A. Turolla, J. Jonsdottir, I. Carpinella, and M. Ferrarin, "A randomized controlled trial on the effects induced by robot-assisted and usual-care rehabilitation on upper limb muscle synergies in post-stroke subjects," *Scientific reports*, vol. 11, no. 1, p. 5323, 2021.

[15] C. He, C.-H. Xiong, Z.-J. Chen, W. Fan, X.-L. Huang, and C. Fu, "Preliminary assessment of a postural synergy-based exoskeleton for post-stroke upper limb rehabilitation," *IEEE Transactions on Neural Systems and Rehabilitation Engineering*, vol. 29, pp. 1795–1805, 2021.

[16] C. Camardella, K. C. Tse, A. Frisoli, and R. K.-Y. Tong, "Investigating muscle synergies changes after rehabilitation robotics training on stroke survivors: a pilot study," in *2020 42nd Annual International Conference of the IEEE Engineering in Medicine & Biology Society (EMBC)*. IEEE, 2020, pp. 3731–3734.

[17] T. Afzal, F. Zhu, S.-C. Tseng, J. A. Lincoln, G. E. Francisco, H. Su, and S.-H. Chang, "Evaluation of muscle synergy during exoskeleton-assisted walking in persons with multiple sclerosis," *IEEE Transactions on Biomedical Engineering*, vol. 69, no. 10, pp. 3265–3274, 2022.

[18] S. Safavynia, G. Torres-Oviedo, and L. Ting, "Muscle synergies: implications for clinical evaluation and rehabilitation of movement," *Topics in spinal cord injury rehabilitation*, vol. 17, no. 1, pp. 16–24, 2011.

[19] A. Calanca, R. Muradore, and P. Fiorini, "A review of algorithms for compliant control of stiff and fixed-compliance robots," *IEEE/ASME transactions on mechatronics*, vol. 21, no. 2, pp. 613–624, 2015.

[20] E. Criswell, "Cram's introduction to surface electromyography," *Jones &Bartlett Learning*, 2010.

[21] D. Lee and H. S. Seung, "Algorithms for non-negative matrix factorization," *Advances in neural information processing systems*, vol. 13, 2000.

[22] G. Torres-Oviedo, J. M. Macpherson, and L. H. Ting, "Muscle synergy organization is robust across a variety of postural perturbations," *Journal of neurophysiology*, vol. 96, no. 3, pp. 1530–1546, 2006.

[23] R. A. Fisher, "Statistical methods for research workers," in *Breakthroughs in statistics: Methodology and distribution*. Springer, 1970, pp. 66–70.

[24] A. Song, N. Kuznetsov, S. Winges, and M. MacLellan, "Muscle synergy for upper limb damping behavior during object transport while walking in healthy young individuals," *Experimental Brain Research*, vol. 238, pp. 1203–1218, 2020.

[25] J. S. Gonçalves, C. S. Moriguchi, K. S. Takekawa, H. J. C. G. Coury, and T. de Oliveira Sato, "The effects of forearm support and shoulder posture on upper trapezius and anterior deltoid activity," *Journal of physical therapy science*, vol. 29, no. 5, pp. 793–798, 2017.

[26] A. KhalilianMotamed Bonab, D. Chiaradia, A. Frisoli, and D. Leonardis, "A framework for modeling, optimization, and musculoskeletal simulation of an elbow–wrist exosuit," *Robotics*, vol. 13, no. 4, p. 60, 2024.

[27] C. L. Dembia, A. Silder, T. K. Uchida, J. L. Hicks, and S. L. Delp, "Simulating ideal assistive devices to reduce the metabolic cost of walking with heavy loads," *PloS one*, vol. 12, no. 7, p. e0180320, 2017.

Running with an exotendon can reduce metabolic rate across a range of speeds

Olivia Felton
University of Colorado Boulder
Boulder, Colorado
olivia.felton@colorado.edu

Chadwick Healy
University of Colorado Boulder
Boulder, Colorado
chadwick.healy@colorado.edu

David Phair
University of Colorado Boulder
Boulder, Colorado
david.phair@colorado.edu

Alaa Ahmed
University of Colorado Boulder
Boulder, Colorado
alaa@colorado.edu

Cara Gonzalez Welker
University of Colorado Boulder
Boulder, Colorado
cara.welker@colorado.edu

***Abstract*—Metabolic rate, the amount of energy expended over time, can be influenced by passive assistive devices like specialized footwear and exoskeletons. While most assistive device research has focused on elite athletes or recreational runners at a single speed, few studies have explored how these devices might affect metabolic rate across a range of running speeds. This study investigates the effect of a passive assistive device (exotendon), which connects a runner's legs, on metabolic rate in recreational runners across multiple speeds. In contrast to previous work, only 9 of 16 participants reduced metabolic rate with the device at 2.67 m/s, by an average of 7.6%. While all participants significantly increased stride frequency - a key factor identified in previous work for its influence on metabolic rate - the group that did not reduce metabolic rate exhibited greater variability in average stride frequency for both conditions. For those who reduced metabolic rate with the exotendon at 2.67 m/s, similar improvements extended across speeds from 1.68 to 4.36 m/s. These results indicate that the exotendon's effect on metabolic rate varies across individuals but can extend beyond a single running speed in those who respond to the device. This suggests that passive assistive devices may benefit some runners across a range of speeds, with potential applications for training and performance as well as rehabilitation, where reducing energy demand could aid recovery and mobility.**

***Index Terms*—metabolic rate, human running, assistive device**

I. Introduction

Techniques to reduce and understand metabolic rate (MR) have garnered the attention of numerous researchers, engineers, and athletes alike. If a product or technique could reduce the energy demand of running, would athletes use it? Here, we explore the use of an exotendon to influence MR and investigate its effects across a range of running speeds.

MR reflects the rate of energy expenditure during running and is assessed by analyzing oxygen consumption and carbon dioxide production [1]. MR demonstrates how energy is used at various speeds, with recreational runners showing a linear increase in MR as running speed increases from ∼2-4 m/s [2]–[4]. Comparing MR across populations or conditions can provide insight into the energy demands of running.

Various biomechanical factors, including gait patterns, kinematics, and kinetics, influence MR [5]–[7]. By optimizing these factors, runners can reduce their energy expenditure at various speeds [8]–[11]. As speed increases, the relative contribution of these factors shifts; for example, increasing stride length initially drives performance improvements, but eventually plateaus, necessitating further speed increases to come primarily from stride frequency [12]. This shift reflects the body's adaptation to maintain efficiency, conserving energy even as speed increases. Reducing MR is beneficial not only for improving running economy performance [13], [14] but also potentially for rehabilitation. Passive assistive devices, such as the exotendon, may facilitate recovery by minimizing MR, enabling injured runners to maintain activity and gradually reintegrate into training [15].

Specialized footwear is another factor that has been shown to reduce MR; however, most research has focused on elite athletes [16], [17], with only a few studies exploring benefits in recreational runners [14]. One notable example is the Nike Vaporfly 4% (VP4), which has demonstrated an average MR reduction of 3-4% compared to mass-normalized shoes, based on studies involving highly trained athletes at speeds of ∼4-5 m/s [18], [19]. Although research on recreational runners is limited, one study showed that at speeds of ∼3-4 m/s, recreational runners wearing the VP4 had a 4.3% reduction in MR compared to running in their habitual shoes [14]. Collectively, these findings highlight the ability of specialized footwear to reduce MR at varying speeds and levels of athletes.

Efforts to reduce MR have expanded beyond footwear to include passive assistive devices, such as lower-limb exoskeletons, which are designed to provide mechanical assistance at the hip, knee, and/or ankle joints [20]–[22]. These devices have demonstrated MR reductions in recreational runners when tested at fixed speeds of 2.5 and 2.67 m/s. For example, two recently developed devices focused on hip augmentation have shown MR reductions of 8-9% when running on a treadmill at 2.5 m/s [20], [21]. Another device, the exotendon, is a spring connecting a runner's legs that targets the metabolic energy

expended for leg swing. Their study demonstrated a 6.4% reduction in MR at 2.67 m/s, with the exotendon reducing MR by increasing the energy-optimal stride frequency [22]. While these advancements in assistive devices are notable, the focus on a single speed limits our understanding of their impact on MR across a broader range of speeds.

In this study, we first replicated the work of Simpson et al. [22] to determine whether running with the exotendon reduced MR at a fixed speed of 2.67 m/s. Expanding on this, we tested the hypothesis that MR would decrease across a range of speeds (between $\sim$2 and 4 m/s) when running with the exotendon, compared to without, for those who responded positively to the device at 2.67 m/s.

II. Methods

A. Participants

A total of 18 healthy young adults (9 female) with no known musculoskeletal or cardiopulmonary impairments participated in the first phase of this study. All participants were self-classified as recreational runners, with typical running speeds ranging from 2.67 to 3.35 m/s [23]. Two participants were excluded from data analysis due to missing data or discomfort interacting with the device. Additionally, seven participants were excluded from the primary analysis because they did not demonstrate a reduction in MR when running with the exotendon at 2.67 m/s (see details in section IIE). Therefore, nine participants are included in the primary analyses focused on MR outcomes across a range of speeds (5 female; age=28 ± 4.2 yrs.; mass=64.6 ± 8.6 kg; height=170.7 ± 9.9 cm; mean ± s.d.). The study protocol was approved by the University of Colorado Boulder's Institutional Review Board (Protocol #23-0292) and all participants provided written consent prior to participation in the study.

B. Experimental Protocol

Participants completed a three-day experimental protocol (Fig. 1A) involving running on a force-instrumented treadmill (Bertec, OH, USA) at both fixed and self-paced speeds. To allow participants to recover from fatigue while maintaining their familiarity with both the self-pacing treadmill and the exotendon, each experimental session was spaced 16-72 hours apart. During each session, participants ran one mile either with the exotendon ('exotendon running') or without ('natural running') in a randomized order, with at least a 5-minute rest between trials.

Consistent with the original work by Simpson et al., the exotendon was constructed from hollow cylindrical natural latex rubber surgical tubing (0.95 cm outer diameter, 0.64 cm inner diameter, 120 N/m stiffness). For each participant, the tubing was cut to 25% of their leg length (determined as the length between the lateral malleolus and anterior superior iliac crest) and attached to their shoelaces with two carabiners [22] (Fig. 1C). Participants were told that the exotendon was designed to improve running efficiency and were instructed to 'relax into running with the device' and to try to 'think about something else while running'.

C. Self-pacing Algorithm

During self-paced trials, participants were free to vary their speed naturally on the treadmill. We developed a self-paced controller based on previous work [24], [25]. Unlike previous control algorithms, our algorithm control is based on footstrike position rather than an estimated center of mass during double-stance. Importantly, this enables us to test self-paced running, which does not have a double-stance phase.

The controller is a linear-proportional controller using force plate data to estimate subject footstrike position on the treadmill, updating each time a footstrike is detected. If the subject speeds up, resulting in a footstrike further forward on the treadmill, the treadmill speeds up proportionally to the distance they moved forward, ultimately moving the subject back to the desired position. If the subject slows down, the opposite occurs. This approach allowed participants to self-select a comfortable pace during both exotendon and natural running.

D. Session 1 – Exotendon and self-paced treadmill training

The objective of session 1 was to expose participants to the exotendon and self-paced treadmill, allowing them to gain familiarity with both before the main experimental trials. Participants first completed three 1-mile exotendon runs at a fixed speed of 2.67 m/s, with rest periods in between. This pace is consistent with the preferred running speed of healthy recreational runners in previous treadmill studies [23], [26], as well as with the previous study by Simpson et al. [22]. The number of training runs was chosen based on prior work, where participants demonstrated reduced MR by the end of the fourth 1-mile exotendon run at 2.67 m/s [22]. However, in our study, we note that all three training runs occurred during a single session and did not alternate with natural runs in order to minimize the total miles run and to distribute the running distance more evenly across the three sessions.

Following the fixed speed runs, participants completed two 0.5-mile self-paced natural runs on the force-instrumented treadmill with the self-pacing algorithm. During the first trial, participants received real-time visual feedback of their relative speed in the form of a 2D speed versus time plot on a screen in front of them (Fig. 1B). This visual feedback helped participants quickly understand and adapt to the self-pacing algorithm. After a brief rest, participants completed a second 0.5-mile self-paced run without visual feedback to assess how well they could maintain their speed independently using the self-pacing treadmill. For the final 0.25 miles of this trial, participants were instructed to maintain a consistent speed, and speed variability was analyzed. Participants were required to keep speed variability within 5.5% of the standard deviation of their average speed, a threshold chosen to mimic variability during natural running [27], and were excluded from further participation in the study if they exceeded this variability.

E. Session 2 – MR qualification and self-paced testing

The goal of session 2 was to assess whether participants reduced MR when running with the exotendon at 2.67 m/s and to determine their self-paced running speeds in both natural

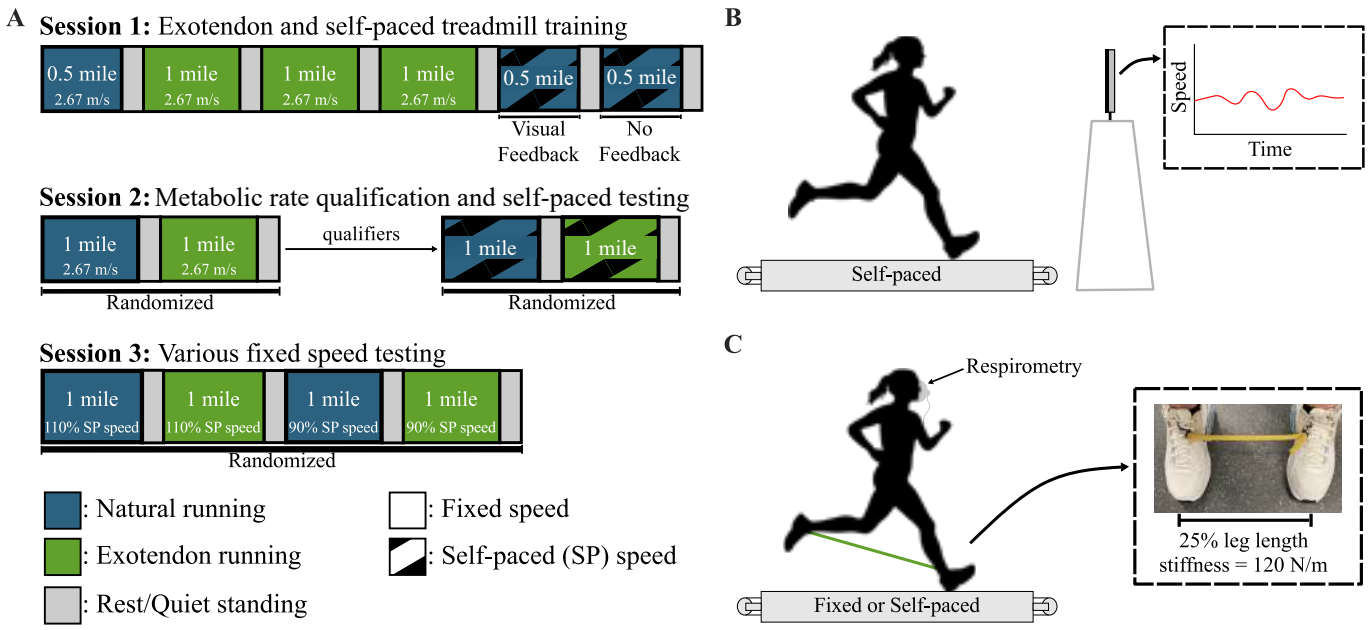


Fig. 1. **(A) Overall Protocol.** During session 1, participants trained with the exotendon at a fixed speed of 2.67 m/s and learned to use the self-pacing algorithm. Metabolic data were collected during all runs in sessions 2 and 3. Participants who showed a reduction in MR when running with the exotendon during the first two runs of session 2 ("qualifiers") proceeded with the remainder of the study. Self-paced runs in session 2 determined the participants' preferred speeds with and without the exotendon. During session 3, participants ran at fixed speeds based on the average of their session 2 self-paced speeds. The order of runs in sessions 2 and 3 was randomized, with at least 5 minutes of rest between trials. **(B) Self-paced Treadmill Acclimation.** During the first self-paced run of session 1, participants received visual feedback in the form of a relative speed versus time plot on a monitor placed in front of the treadmill. **(C) Exotendon Running Setup.** Participants completed both fixed and self-paced running trials with the exotendon, alternating with natural running trials.

and exotendon conditions. Participants were first instrumented with indirect calorimetry equipment (K5, COSMED, Rome, Italy) and completed a 5-minute quiet standing trial to measure baseline metabolic energy expenditure. Participants then completed two 1-mile runs at 2.67 m/s, one exotendon and one natural, with rest between. Net MR was compared between the natural and exotendon runs to determine whether participants reduced MR when running with the exotendon, compared to natural running. Participants who did not demonstrate a reduction in MR with the exotendon were excluded from further participation in the study.

Qualified participants then completed two 1-mile self-paced runs, one with the exotendon and one natural. Average speed was calculated over the whole trial for both runs to determine each participant's natural and exotendon self-paced running speeds. These values were then used to establish a comfortable range of running speeds for each participant.

F. Session 3 – Various fixed speed testing

The objective of session 3 was to assess the effect of the exotendon on MR across a range of running speeds, relative to each participants' self-selected speeds from session 2. Participants were again instrumented with indirect calorimetry equipment and completed a 5-minute quiet standing trial. Following that, participants completed four 1-mile fixed speed runs, two at 90% and two at 110% of their average self-paced speeds from session 2, with and without the exotendon. These speeds were chosen to evaluate the exotendon's performance across a wide range of fixed running speeds while ensuring participants ran at comfortable paces. Net MR was compared between the natural and exotendon running trials at the two tested speeds.

G. Data Analysis

1) Running speeds: For all trials, speed data were collected from the treadmill at a sampling frequency of 10 Hz. In session 1, treadmill speed was averaged over the final 0.25 miles of the second self-paced run, and variability was measured using the standard deviation of treadmill speed. In the second session, average running speed was calculated over the entire duration of each self-paced trial to determine natural and exotendon self-paced running speeds.

2) Stride Frequency: Ground reaction force (GRF) data were collected at a sampling frequency of 1000 Hz (Nexus 2.15.0) for the entirety of each running trial. Vertical GRF data were low-pass filtered using a 2nd order Butterworth filter with a cut-off frequency of 15 Hz. Foot contacts were identified using a threshold of 200 Newtons to determine the start of each stride. Stride frequency was calculated using the total number of strides recorded during the last minute of each trial, as in Simpson et al. [22].

3) Metabolics: For all fixed speed trials, gross MR was calculated from indirect calorimetry by averaging the time-normalized data from the last 2 minutes of each run [28]. Baseline MR, determined from the last two minutes of the quiet standing trial, was subtracted from the gross MR to

yield net MR for each run. The percentage change in net MR from natural running to exotendon running was calculated to determine participant qualification and results.

We analyzed net MR at both the previously studied speed (2.67 m/s) and across a range of speeds. First, we compared net MR between natural and exotendon running at all grouped speeds (2.67 m/s, 90% self-paced speed, and 110% self-paced speed). A Kolmogorov-Smirnov test indicated that the data were not normally distributed for all speeds (h=1, $p<0.001$), so we used a Wilcoxon signed-rank test for comparison. Next, we used two linear mixed effects models (LMMs) to evaluate net MR across speeds. In the first model, we incorporated fixed effects for speed and condition (natural versus exotendon) while accounting for individual subject variability as a random effect. This allowed us to isolate the effects of speed and running condition on net MR while controlling for individual differences. In a second model, we used speed as a fixed effect to analyze its influence on the percent different in net MR between conditions. We assessed the residuals of both models for normality using the Shapiro-Wilk test, which confirmed they were normally distributed (P=0.23).

III. Results

During the self-paced treadmill familiarization in session 1, all participants were able to mimic natural running variability with a standard deviation of 3.47 ± 1.25% of their average speed, below the designated threshold of 5.5% [27]. We found that running with the exotendon at 2.67 m/s led to a small reduction in MR of 2.44 ± 7.05% across all participants, but this was not significant (P=0.23, Wilcoxon signed-rank test; Fig.2A). Of the 16 participants, nine reduced MR when running with the exotendon at 2.67 m/s (”qualifiers”) and seven did not (”non-qualifiers”). All participants significantly increased stride frequency when running with the exotendon at 2.67 m/s. Non-qualifiers showed a larger range of average stride frequency values compared to qualifiers, despite having a smaller average percent change in stride frequency (5.94 ± 2.64%) compared to the qualifiers (4.73 ± 2.07% increase) (Fig. 2B).

The qualifiers had an average net MR reduction of 7.60 ± 4.36% when running with the exotendon at 2.67 m/s (P=0.004, Wilcoxon signed-rank test; Fig. 2C). For the qualifiers, we classified speeds as ”slow” (90% of each participants’ self-paced speed) and ”fast” (110% of each participants’ self-paced running speed). We found that participants significantly reduced their MR at both their slow speed (P=0.011, Wilcoxon signed-rank test) and their fast speed (P=0.004, Wilcoxon signed-rank test) when running with the exotendon. (Fig. 2C).

When compared across all speeds for the qualifiers, MR was significantly reduced by an average of 6.7% when running with the exotendon at speeds between 1.68 and 4.36 m/s ($P=1.03x10^{\propto 6}$, LMM; Fig. 3A). The percent change in MR was consistent across all speeds, as the slope of the line modeling this relationship was not statistically significant (slope=0.12, 95% CI=[-2.94, 3.18], P=0.94, LMM; Fig. 3B). Despite variability in individual speeds and MRs, nearly all participants reduced their MR when running with the exotendon at each tested speed (2.67 m/s, slow, and fast) (Fig. 4).

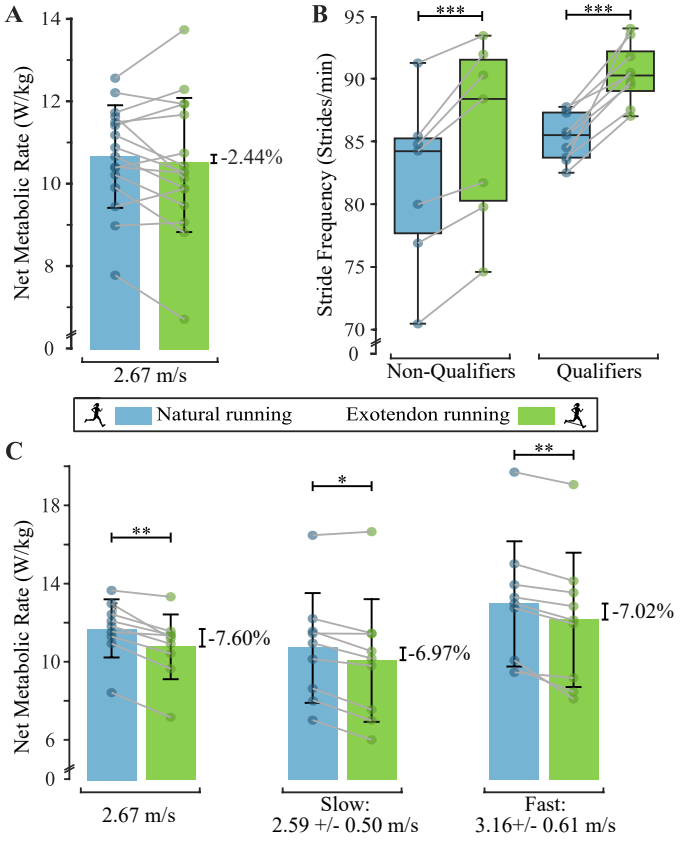


Fig. 2. **(A)** There was no significant change in net MR for all participants (P=0.23, Wilcoxon signed-rank test). **(B)** Both qualifiers and non-qualifiers significantly increased stride frequency when exotendon running, compared to natural running. **(C)** The qualifiers significantly reduced MR at 2.67 m/s (P=0.004, Wilcoxon signed-rank test). Additionally, they significantly reduced MR when running with the exotendon at speeds 10% above (“fast”) (P=0.011, Wilcoxon signed-rank test) and 10% below (“slow”) (P=0.004, Wilcoxon signed-rank test) their average self-paced speed. Error bars represent 1 standard deviation. Asterisks indicate statistical significance with confidence levels $p<0.05$ (*), $p<0.01$ (**), and $p<0.001$ (***).

IV. Discussion

This study examined whether running with an exotendon could reduce MR across a range of speeds. Across participants, we observed a smaller average reduction of 2.4% in MR when running with the exotendon at 2.67 m/s compared to that reported by Simpson et al. [22]. However, for those that did reduce MR, the average reduction was within one standard deviation of their reported value, suggesting that the exotendon has similar effects on MR in certain individuals [22]. Extending the analysis to a wider range of speeds (1.68 to 4.36 m/s), we found an average MR reduction of 6.7% at all speeds, which supports our hypothesis that the exotendon reduces MR beyond a single, fixed speed for those who responded positively to the device at 2.67 m/s.

Our findings contribute to a growing body of research suggesting that passive assistive devices can reduce MR [20]–

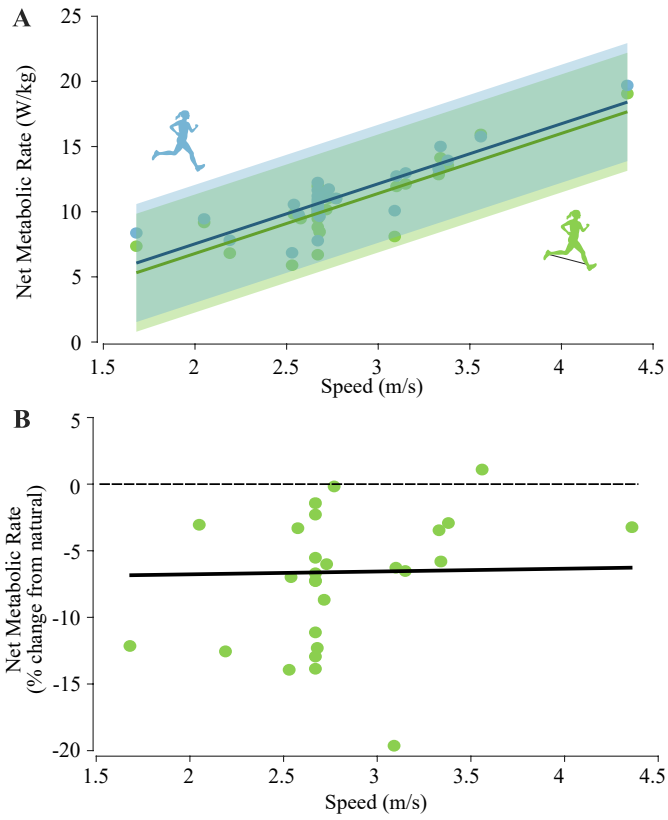


Fig. 3. **(A)** Net MR across speeds was significantly lower during exotendon running, compared to natural running (P=1.03x10^{-6}, LMM). There was a significant linear relationship between speed and MR (P=2.92x10^{-30}, LMM). Shaded regions show the 95% confidence interval of curve fits. **(B)** MR reductions were consistent across speeds, as the slope of the line modeling this relationship was not statistically significant (slope=0.12, 95% CI=[-2.94, 3.18], P=0.94, LMM).

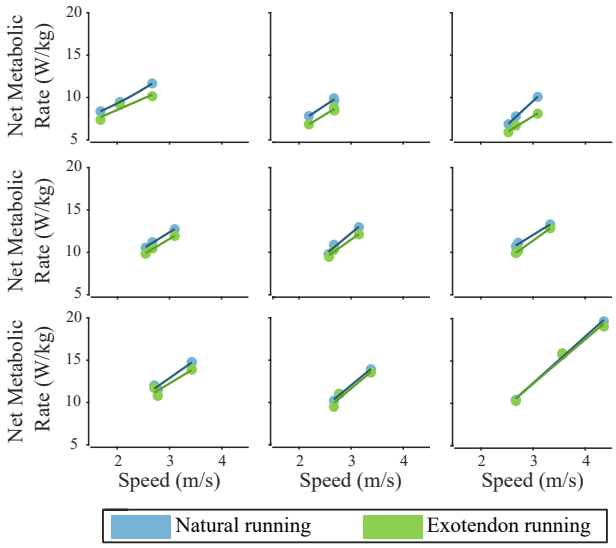


Fig. 4. There was considerable variation in net MR among subjects. Each subplot represents the net MR for an individual participant at 2.67 m/s, as well as at speeds 10% above and 10% below each of their average self-paced speeds. Based on previous findings of a linear relationship between MR and speed in both exotendon and natural conditions (Fig. 3), we enforced linearity for individual subject plots.

[22]. Unlike previous work with assistive devices, which often focus on singular speeds [20]–[22] or elite athletes [16], [17], our results show that the exotendon can benefit recreational runners across multiple running speeds. This broader applicability demonstrates the ability of the exotendon and other assistive devices to benefit a diverse range of athletes as well as individuals in rehabilitation, helping reduce MR across varying levels of performance.

In agreement with the literature regarding the relationship between speed and MR, our results displayed a linear relationship across all speeds for both exotendon and natural running [2]–[4]. However, our results differed slightly from those of Simpson et al., as only 9 of 16 participants achieved MR reductions at 2.67 m/s, compared to 100% in their study [22]. This discrepancy may be attributed to differences in training protocols. In our study, exotendon training sessions were held back-to-back during the first session, whereas Simpson et al. spaced their training across two sessions, alternating between natural and exotendon runs [22]. Prior work suggests that distributing training across multiple days can enhance retention of adaptations [29]. Thus, the timing and structure of training sessions may play a more critical role in maximizing the exotendon's effectiveness than anticipated.

The difference in subject populations may also contribute to the smaller MR reductions at 2.67 m/s found in our study, as compared to Simpson et al. [22]. Although all participants in our study met the pacing criteria for recreational runners (2.67 to 3.35 m/s), all but one were already running more than three hours per week. This amount of training time could contribute to biomechanical adaptations, such as improved movement efficiency or resistance to adaptations, that are often associated with higher running volumes [30]. As previous research suggests [31], assistive devices may be less effective for experienced runners due to their already optimized biomechanics, which may explain why our participants experienced smaller reductions in MR compared to those in Simpson et al.'s study [22].

Simpson et al. demonstrated that the exotendon reduced MR by increasing the energetically optimal stride frequency by approximately 8%, resulting in energy savings during both the swing and stance phases of running [22]. In our study, both the non-qualifiers and qualifiers significantly increased stride frequency when running with the exotendon, by 4.73% and 5.94%, respectively. We found that the non-qualifiers had greater variability in their average stride frequency, compared to the qualifiers. These differences may suggest that the non-qualifiers were unable to align their stride frequency with the energetically optimal frequency facilitated by the exotendon, which could explain why these individuals did not experience reductions in MR at 2.67 m/s. Preliminary analyses suggest that no single factor can fully predict whether a participant will reduce MR when running with the exotendon. Rather, a combination of factors likely influences its effectiveness, and

exploring this will be important for future research.

For the qualifier group, we expanded testing to both slower and faster speeds. The results confirmed that the MR reductions observed at 2.67 m/s extended to other paces. While the percent change in MR between natural and exotendon runs was consistent across speeds, additional data are necessary to confirm this trend.

Future work is necessary to better understand how individual factors influence MR. Investigating the differences between qualifiers and non-qualifiers could provide insights into the mechanisms underlying MR reductions when running with the exotendon. Additionally, studies examining how MR reductions influence self-paced running speeds could offer a deeper understanding of how these devices might affect performance.

V. Conclusion

Although not all runners reduced MR when running with the exotendon, those who did experienced reductions across multiple speeds. The exotendon's simplicity and versatility make it a promising tool for both training and performance, as well as a valuable option in rehabilitation settings, where aiding movement efficiency and reducing metabolic demand could be beneficial in return to sport post-injury. Further research is necessary to explore individual factors influencing the device's effectiveness and to determine the conditions under which it optimally enhances performance and rehabilitation outcomes.

References

[1] E. Ferrannini, "The theoretical bases of indirect calorimetry: A review," *Metabolism*, vol. 37, pp. 287–301, 1988.

[2] J. Helgerud, Støren, and J. Hoff, "Are there differences in running economy at different velocities for well-trained distance runners?" *European Journal of Applied Physiology*, vol. 108, no. 6, pp. 1099–1105, 2010.

[3] R. Margaria, P. Cerretelli, P. Aghemo, and G. Sassi, "Energy cost of running," *Journal of Applied Physiology*, 1963.

[4] D. R. Menier and L. G. C. E. Pugh, "The relation of oxygen intake and velocity of walking and running, in competition walkers," *The Journal of Physiology*, vol. 197, no. 3, 1968.

[5] P. R. Cavanagh and K. R. Williams, "The effect of stride length variation on oxygen uptake during distance running," *Medicine & Science in Sports & Exercise*, vol. 14, no. 1, p. 30, 1982.

[6] M. P. Tartaruga, J. Brisswalter, L. A. Peyré-Tartaruga, A. O. V. Ávila, C. L. Alberton, M. Coertjens, E. L. Cadore, C. L. Tiggemann, E. M. Silva, and L. F. M. Kruel, "The Relationship Between Running Economy and Biomechanical Variables in Distance Runners," *Research Quarterly for Exercise and Sport*, vol. 83, no. 3, pp. 367–375, 2012.

[7] R. Kram and C. R. Taylor, "Energetics of running: a new perspective," *Nature*, vol. 346, no. 6281, pp. 265–267, 1990.

[8] K. R. Williams and P. R. Cavanagh, "Relationship between distance running mechanics, running economy, and performance," *Journal of Applied Physiology*, vol. 63, no. 3.

[9] J. K. Rathkey and C. M. Wall-Scheffler, "People choose to run at their optimal speed," *American Journal of Physical Anthropology*, vol. 163, no. 1, pp. 85–93, 2017.

[10] K. R. Barnes and A. E. Kilding, "Running economy: measurement, norms, and determining factors," *Sports Medicine - Open*, vol. 1, no. 1, p. 8, 2015.

[11] I. S. Moore, "Is There an Economical Running Technique? A Review of Modifiable Biomechanical Factors Affecting Running Economy," *Sports Medicine*, vol. 46, no. 6, pp. 793–807, 2016.

[12] J. P. Bailey, T. Mata, and J. Mercer, "Is the relationship between stride length, frequency, and velocity influenced by running on a treadmill or overground?" *International Journal of Exercise Science*, vol. 10, no. 7, pp. 1067–1075, 2017.

[13] W. Hoogkamer, S. Kipp, B. A. Spiering, and R. Kram, "Altered Running Economy Directly Translates to Altered Distance-Running Performance," *Medicine and Science in Sports and Exercise*, vol. 48, no. 11, 2016.

[14] K. Hébert-Losier, S. J. Finlayson, M. W. Driller, B. Dubois, J.-F. Esculier, and C. M. Beaven, "Metabolic and performance responses of male runners wearing 3 types of footwear: Nike Vaporfly 4%, Saucony Endorphin racing flats, and their own shoes," *Journal of Sport and Health Science*, vol. 11, no. 3, pp. 275–284, 2022.

[15] H. K. Vincent, A. Madsen, and K. R. Vincent, "Role of antigravity training in rehabilitation and return to sport after running injuries," *Arthroscopy, Sports Medicine, and Rehabilitation*, vol. 4, pp. 141–149, 2022.

[16] R. G. Cochrum, R. T. Connors, J. M. Coons, D. K. Fuller, D. W. Morgan, and J. L. Caputo, "Comparison of Running Economy Values While Wearing No Shoes, Minimal Shoes, and Normal Running Shoes," *The Journal of Strength & Conditioning Research*, vol. 31, no. 3, 2017.

[17] S. A. Ruiz-Alias, A. Molina-Molina, V. M. Soto-Hermoso, and F. García-Pinillos, "A systematic review of the effect of running shoes on running economy, performance and biomechanics: analysis by brand and model," *Sports Biomechanics*, vol. 22, no. 3, pp. 388–409, 2023.

[18] W. Hoogkamer, S. Kipp, J. H. Frank, E. M. Farina, G. Luo, and R. Kram, "A Comparison of the Energetic Cost of Running in Marathon Racing Shoes," *Sports Medicine*, vol. 48, no. 4, pp. 1009–1019, 2018.

[19] I. Hunter, A. McLeod, D. Valentine, T. Low, J. Ward, and R. Hager, "Running economy, mechanics, and marathon racing shoes," *Journal of Sports Sciences*, vol. 37, no. 20, pp. 2367–2373, 2019.

[20] T. Zhou, C. Xiong, J. Zhang, D. Hu, W. Chen, and X. Huang, "Reducing the metabolic energy of walking and running using an unpowered hip exoskeleton," *Journal of NeuroEngineering and Rehabilitation*, vol. 18, no. 1, 2021.

[21] R. Nasiri, A. Ahmadi, and M. N. Ahmadabadi, "Reducing the Energy Cost of Human Running Using an Unpowered Exoskeleton," *IEEE Transactions on Neural Systems and Rehabilitation Engineering*, vol. 26, no. 10, pp. 2026–2032, 2018.

[22] C. S. Simpson, C. G. Welker, S. D. Uhlrich, S. M. Sketch, R. W. Jackson, S. L. Delp, S. H. Collins, J. C. Selinger, and E. W. Hawkes, "Connecting the legs with a spring improves human running economy," *Journal of Experimental Biology*, vol. 222, no. 17, 2019.

[23] A. E. Minetti, L. Boldrini, L. Brusamolin, P. Zamparo, and T. McKee, "A feedback-controlled treadmill (treadmill-on-demand) and the spontaneous speed of walking and running in humans," *Journal of Applied Physiology*, vol. 95, no. 2, pp. 838–843, 2003.

[24] R. E. Pimentel, J. N. Feldman, M. D. Lewek, and J. R. Franz, "Quantifying mechanical and metabolic interdependence between speed and propulsive force during walking," *Frontiers in Sports and Active Living*, vol. 4, 2022.

[25] S. Song, H. Choi, and S. H. Collins, "Using force data to self-pace an instrumented treadmill and measure self-selected walking speed," *Journal of NeuroEngineering and Rehabilitation*, vol. 17, no. 1, 2020.

[26] P. W. Kong, T. M. C. Koh, W. C. R. Tan, and Y. S. Wang, "Unmatched perception of speed when running overground and on a treadmill," *Gait & Posture*, vol. 36, no. 1, pp. 46–48, 2012.

[27] J. C. Selinger, J. L. Hicks, R. W. Jackson, C. M. Wall-Scheffler, D. Chang, and S. L. Delp, "Running in the wild: Energetics explain ecological running speeds," *Current Biology*, vol. 32, no. 10, pp. 2309–2315, 2022.

[28] J. M. Brockway, "Derivation of formulae used to calculate energy expenditure in man," *Human Nutrition. Clinical Nutrition*, vol. 41, no. 6, pp. 463–471, 1987.

[29] L. A. Malone, E. V. L. Vasudevan, and A. J. Bastian, "Motor Adaptation Training for Faster Relearning," *The Journal of Neuroscience*, vol. 31, no. 42, pp. 15 136–15 143, 2011.

[30] V. R. e. a. Dos Anjos Souza, "Running economy in long-distance runners is positively affected by running experience and negatively by aging," *Physiology Behavior*, vol. 258, 2023.

[31] P. Witte, Kirby A. Fiers, A. L. Sheets-singer, and S. H. Collins, "Improving the energy economy of human running with powered and unpowered ankle exoskeleton assistance," *Science Robotics*, vol. 5, no. 3, 2020.

Design and Control of an Actuated Prosthetic Elbow to Restore Arm Swing for Persons with Upper Limb Absence

Michael Jenz
Dept. of Mechanical Engineering
Northwestern University
Evanston, United States
michaeljenz2026@u.northwestern.edu

Allan Garcia-Casal
Dept. of Mechanical Engineering
Northwestern University
Evanston, United States
AllanGarcia-casal2023@u.northwestern.edu

Yael Ben Shalom
Dept. of Mechanical Engineering
Northwestern University
Evanston, United States
yael.bshalom@gmail.com

Matthew L. Elwin
Dept. of Mechanical Engineering
Northwestern University
Evanston, United States
elwin@northwestern.edu

Matthew J. Major
Dept. of Physical Medicine and Rehabilitation
Northwestern University
Chicago, United States
matthew-major@northwestern.edu

***Abstract*—Dynamic balance in human locomotion relies on the regulation of whole-body angular momentum. Asymmetry in upper extremity body mass and motion that occurs from upper limb absence disrupts this regulation. Conventional transhumeral prostheses do not restore controlled arm swing, leaving this asymmetry unresolved. This project aimed to develop an actuated prosthetic elbow that mimics natural elbow rotations to restore arm swing during walking. Two prototypes with contrasting designs were fabricated and tested. Prototype 1, featuring a direct drive motor, tracked arm swing trajectories based on able-bodied data with less than 5% position error. It enabled evaluation of predicted elbow torque requirements, showing that a double-pendulum dynamic model overestimates torque needs. This finding supports using smaller, lighter direct drive motors for natural arm swing. While Prototype 1 performed well, its motor was too large for practical integration. Prototype 2 successfully fit the drive and control system into a standard prosthetic envelope for enhanced applicability. Testing revealed that gearbox friction hindered control, and successful operation required synchronizing elbow movement with natural arm swing frequency. Despite using the same control system, both prototypes produced notably different outcomes. These results highlight potential for future designs incorporating a small direct drive motor to match Prototype 1's performance while maintaining Prototype 2's compact form.**

***Index Terms*—Robotic prostheses, Amputation, Prosthesis, Upper extremity, Mechatronics, Gait, Arm swing, Balance**

I. Introduction

Reciprocal arm motion is essential for balancing leg momenta to minimize whole-body angular momentum that facilitates locomotor balance in bipedal human gait [1]. Recent evidence has revealed that individuals with unilateral upper limb absence experience bilateral asymmetry in both upper extremity body mass and motion [2]–[4], which affects the tight regulation of whole-body angular momentum during walking [5], [6]. This asymmetry and impact on dynamic balance may contribute to the high prevalence of falls in persons with upper limb absence, in which 67% of reported falls occur during walking [7]. While persons with unilateral transhumeral-level limb absence exhibit a small amount of affected limb arm swing during walking (nearly a third of the intact limb) [2]–[4] that gives rise to this asymmetry, conventional transhumeral prostheses are not designed to restore controlled arm swing and facilitate the inter-limb segment momenta cancellation required to minimize whole-body angular momentum [3], [6]. In fact, the limited arm swing of the affected side during walking remains the same whether or not a conventional arm prosthesis is being worn [2], [3].

Therefore, interventions are needed to restore the biomechanical symmetry of angular momentum and aid dynamic balance in persons with unilateral upper limb absence. This project aimed to develop a mechatronic prosthetic elbow that generates stereotypical elbow rotations to restore affected limb arm swing of persons with transhumeral-level limb absence during walking [8]. This paper describes steps for the design, development, and preliminary testing of two mechatronic systems that showcase contrasting design methods.

II. Methods

Two mechatronic designs of a robotic elbow were implemented to accommodate different motors for actuation. Prototype 1 is powered by a larger, brushless, direct-drive motor. Prototype 2 is powered by a small brushed motor with a high gear ratio, extracted from a servo motor, developed in response to the high cost and complexity required to use a brushless motor. Prototype 2 aimed to replicate Prototype 1 function with reduced complexity. Since Prototype 2 was developed after Prototype 1, it features a more compact design and prosthetic arm attached to the elbow, rather than a mock prosthesis that is weighted to mimic anatomical inertia (as seen in Prototype 1). These prototypes were developed

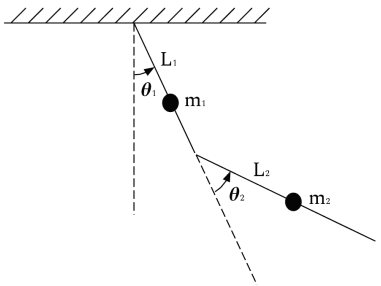


Fig. 1. Model representation of arm-body dynamics during walking as a double pendulum. System configuration is defined by shoulder angle θ_1 and elbow angle θ_2. The model predicts the required torque output at the elbow joint to generate desired swing trajectories.

only to assess the control and actuation platforms. This section contrasts the prototypes designs.

A. Prototype 1

1) Arm-Body Dynamics Simulation: The arm-body dynamics for arm swing during walking can be modeled as a double pendulum system as seen in Fig. 1. The system can be fully defined using the configuration $q = [\theta_1, \theta_2]$, the angles of shoulder and elbow flexion.

In this model, the arm is treated as a separate entity from the body, with energy input at the shoulder joint to simulate body-generated movement. The model calculates the torque required at the elbow joint to generate desired arm swing trajectories.

The Euler-Lagrange equations relate the system configuration q and its first and second derivative to the external forces acting on the system at a given time. This relationship can be used to forward integrate the behavior of the system and simulate its dynamics.. In this case, user data with trajectories (that is position, velocity, and accelerations) of the elbow are substituted into the Euler-Lagrange equations for a double pendulum to derive the required torque:

$$\frac{d}{dt}\frac{\partial L}{\partial \dot{q}} - \frac{\partial L}{\partial q} = \tau \tag{1}$$

Here, τ is the joint torque vector and L is the Lagrangian defined as the difference between the kinetic and potential energy of the system.

2) Motor Selection: The power specifications for the motor can be estimated by the results from the Euler-Lagrange back-calculated torque. The motor specifications will be defined by the maximum output from the model. The arm swing trajectory that produces these maximum values is the most energetic arm swing. After examination of arm swing trajectory data collected from an able-bodied person, it was determined that the maximum speed at which data was collected, $1.4\frac{m}{s}$, was when the person produced the most energetic arm swing trajectory. Therefore, the largest torque output required from a motor was calculated from these configuration data. Fig. 2 displays the torque vs angular velocity profile, where the torque is the output from the Euler-Lagrange equations and the velocity is the time derivative of the angular position.

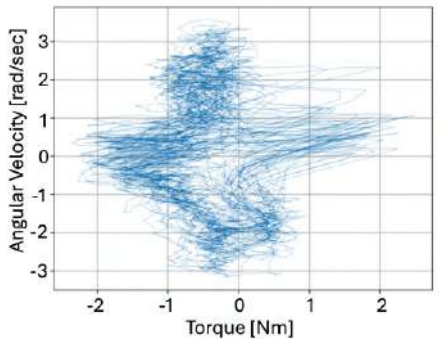


Fig. 2. Angular velocity versus torque landscape for an example user trajectory collected at walking speed $1.4\frac{m}{s}$ for 40s. The area of this curve represents the required power at the elbow. The maximum motor torque required nears $2.9\mathrm{Nm}$ and maximum velocity nears $3\frac{rad}{s}$.

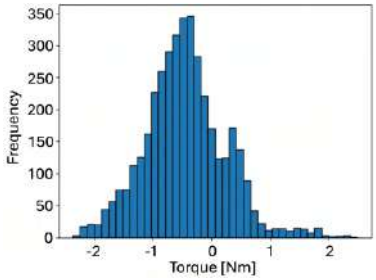


Fig. 3. Histogram of motor output torque over 40s trial collected at 100Hz with bucket size of $0.125\mathrm{Nm}$. Much less time was spent on torques outside $\pm 1\mathrm{Nm}$. This challenges the torque specifications required from the motor.

The motor power envelope should encompass the entire angular velocity-torque landscape such that it encompasses the largest entries of elbow torque and angular velocity. Approximately, the largest angular velocity required is $3\frac{\mathrm{rad}}{\mathrm{s}}$ while the peak torque required is $2.9\mathrm{Nm}$.

To enable the arm to swing according to the natural arm-swing trajectory while minimizing energy use, the elbow joint should have minimal friction. A direct drive brushless DC motor is relatively low friction because there is no transmission: the only friction involved is that in the bearings.

The size of the motor was constrained by its mechanical design and prosthesis design concerns. Excessive weight of an upper limb prosthesis is often cited as a comfort-related reason for device abandonment [9], so a design goal was to select a motor that minimized mass of the system.

To discover the true motor torque requirement, the calculated torque trajectory was decomposed into time spent at various torque output levels. This leads to Fig. 3 which shows the frequency at torque buckets of size $0.125\mathrm{Nm}$.

3) Control System: The most direct way to generate human arm swing during walking is to command the motor along predefined swing trajectories. However, motors take in current as their input. So, to use the desired positions as a set point for the motor we added a second layer to control the actual input into the motor. Each controller takes in an error determined by the difference between the desired and actual value. Then, the controller transforms the error and outputs it to the next step in the controller (Fig. 4). This describes a closed loop feedback system that drives the motor based on

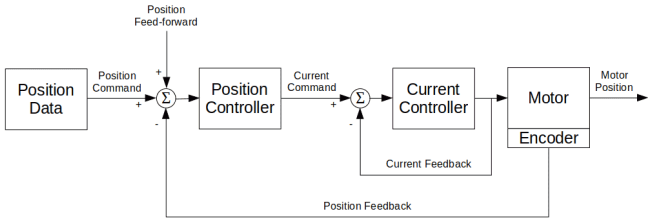


Fig. 4. Double nested closed loop feedback system. The Σ junctions represent the controllers.

the error generated. With control loops running fast enough and arm swing trajectories to follow this system will output arm swing trajectories.

4) Evaluation: Prototypes were tested to assess functionality as the device was carried on a person's arm while walking on a treadmill (qualified as development activity and *not human subjects research*). Prototype 1 was designed to validate arm swing trajectories at several fixed walking speeds that affected cadence: 0.7, 0.8, 1.0, 1.1, and $1.4\frac{m}{s}$. Torque trajectories for each speed were predefined from unpublished inertial measurement data walking at each of these speeds. Performance of the elbow was evaluated by the expected versus actual angle output, and current data was collected to analyze the actual output torque.

B. Prototype 2

1) Motor Selection: Prototype 2 uses a motor with internal gearing, enabling use of a smaller motor that can still produce sufficient torque to enable arm swing. Although a motor with power capable of reproducing a natural swing trajectory could be selected, there was concern that a motor would exhibit excess speed but insufficient torque to complete the swing task. This disparity means that a motor with minimal power, geared down significantly, can satisfy the torque and angular velocity requirements at a considerably lower weight than a motor with sufficient torque but no gearing.

2) Controller: Prototype 2 uses the same control system as Prototype 1. Although performance disadvantages are anticipated with a geared motor, some of these may be alleviated by the controller. The position controller should track arm trajectories regardless of the gearing of the motor because any response that is slowed by the transmission characteristics will generate more error that the controller will account for in its response.

3) Step Detection and Adaptive Control: People do not walk at a fixed cadence during community ambulation. Therefore, a usable prosthetic arm should be able to track the wearer's cadence and match arm swing trajectory to that cadence such that it is synchronized with contralateral leg swing. Cadence was estimated through registration of foot initial contact (i.e., collision) with the ground. This real-time registration was performed through data collected from an accelerometer attached to the prosthetic elbow and a peak signal detection algorithm, meaning that the control system should be able to adapt to a change of cadence and update its dynamics accordingly (with some reasonable lag).

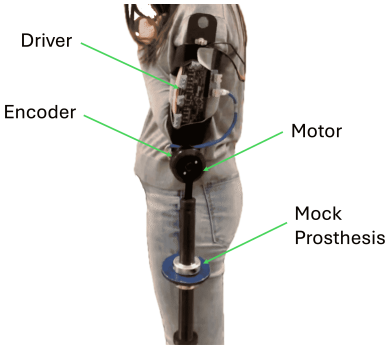


Fig. 5. The final Prototype 1 design features the motor and mock forearm that mimics the mass and inertia of a conventional prosthesis. The prototype is suitable for simulation based controller testing.

4) Evaluation: As with Prototype 1, Prototype 2 was tested as a person carried the prosthesis on their arm and walked on a treadmill. Arm swing trajectories of the wearer were collected at walking speeds of 0.7, 0.9, 1.1, and $1.3\frac{m}{s}$ to be used in the controller and tested during trials at the same speeds. Tests were conducted both at individual speeds to test the performance of the controller as well as at variable speed to test the step detection and adaptive control. The prototype was also tested on the bench without the prosthetic forearm and with the axis aligned with gravity, thus removing any external force on the motor.

III. Results

A. Prototype 1

1) Final Design Overview: The final design of Prototype 1 as seen in [10, Fig. 5] is composed of a driver, encoder, motor, and mock prosthesis. The motor selected is a direct drive system (R60, CubeMars, Jiangxi, China) with a peak torque of $2.3\mathrm{Nm}$, making it capable of outputting almost any torque required based on the Euler-Lagrange estimation. The mock prosthesis consisted of a plastic tube and disc weights that were positioned to simulate the length, mass, and center-of-mass position of a conventional prosthetics forearm/terminal device, which matched the forearm component in the arm-body dynamics model.

The prosthesis was controlled using a PIDF (proportional, integral, derivative, feed forward) controller to correct for error in position and current. The gains were tuned by hand during bench testing. The PIDF controller is simple and widely used, making it the first choice for this system. In addition to error generated response, the feed forward term generates output based on the desired value, resulting in a faster response.

2) Evaluation Results: The results from testing show that Prototype 1 performed well in tracking the desired trajectories. As seen in Fig. 6 the output position matches closely with the desired, and hovers between $\pm 5\%$ absolute position error.

When comparing the actual and theoretical torques as calculated previously, we discovered that the prosthesis does not require as much torque as was predicted to accurately track the trajectory. Fig. 7 shows that the actual torque output

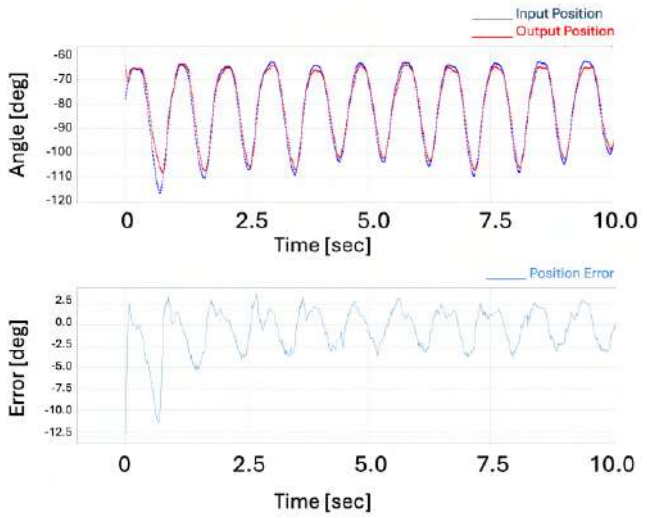


Fig. 6. Actual and desired position for Prototype 1 during testing (top), and error (bottom). The desired position was tracked with less than 5% error.

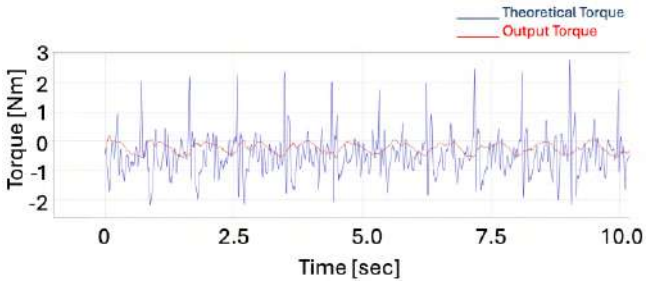


Fig. 7. Actual torque output superimposed on theoretical torque. The red signal displays the actual torque required to follow trajectories during testing, from its smallest to largest torques it ranges a total of 1Nm. This result suggests use smaller motors to achieve the same results achieved before.

varies at most 1Nm from the smallest to the largest actual torque outputs (compared to the simulations predicted range of 4.6Nm from smallest output torque to largest).

B. Prototype 2

1) Final Design Overview: Prototype 2 in Fig. 8 takes on a form similar to typical prosthetic arms, featuring an elbow that interfaces with a prosthetic socket, a prosthetic forearm with terminal device, and an external electronics center. The elbow joint motor interface and housing were designed around a commercial elbow joint (E400, Fillauer, Chattanooga, TN). Future iterations will condense the electronics such that it can be discretely fit inside a hollow forearm segment.

The motor selected for this iteration was a Coreless Servo (HiWonder, Shenzhen, China) with peak torque output of 3.4Nm. This high output torque from a smaller motor is achieved via its gearbox with a gear ratio of 1:342. Servo motors are typically controlled by a PWM signal that corresponds to a position. Instead of using this capability, which is sometimes inaccurate, the servo potentiometer was used as an encoder and the motor was controlled directly via its positive and negative terminals. Modifying the servo motor

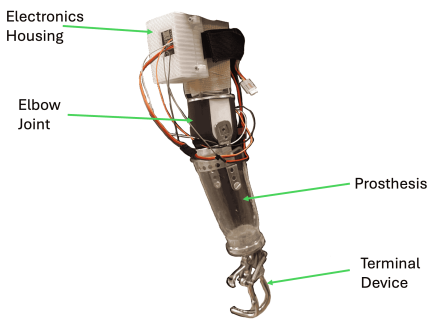


Fig. 8. Prototype 2 features an industry standard elbow envelope, conventional prosthetic socket and forearm/terminal device for universal application, as well as housed mechanical and electrical components.

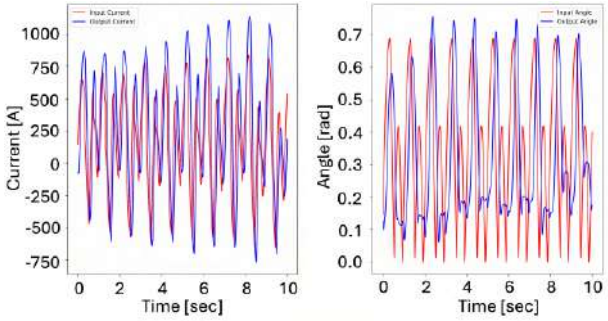


Fig. 9. Prototype 2 testing results with position control collected at $1.3\frac{m}{s}$ walking speed, displaying current (left) and position (right) output. There is deadband between the desired and actual output position. The controller tracks the desired trajectory with both overshoot and undershoot depending on the flexion or extension phase.

and incorporating current sensing allows for the same double nested control system as in Prototype 1 to be used for this motor (although the high gear ratio makes current sensing and torque control relatively inaccurate).

The controller for Prototype 2 uses a PIDF controller with a modified version of feed forward control to help overcome gearbox friction. Regular feed forward control is proportional to the desired output. However, the desired output is always nonnegative (since the elbow is restricted from hyperextension), so, it generates positive torque output from this term. Therefore, the feed forward coefficient was modified to be positive when the desired position was increasing (elbow flexion) and negative when the desired position was decreasing (elbow extension). This adjustment helps the motor overcome static gearbox friction when changing direction and kinetic gearbox friction during dynamic operations.

2) Evaluation Results: Exemplary results from testing with Prototype 2, displayed in Fig. 9, demonstrate success in tracking the shape of the arm swing trajectory. However, there is pronounced deadband between the desired and the actual trajectory, and the output does not track smaller arm swings presented in the desired trajectory.

Other results from Prototype 2 testing displayed less desirable behavior from the controller. In Fig. 10 the output position is overshooting and undershooting as it comes in and out of phase with the target arm swing frequency. The

phase difference was mitigated if the wearer aligned their cadence with the prosthesis output. However, if there was any discrepancy between the controller and the target arm swing trajectory, results like Fig. 10 were produced.

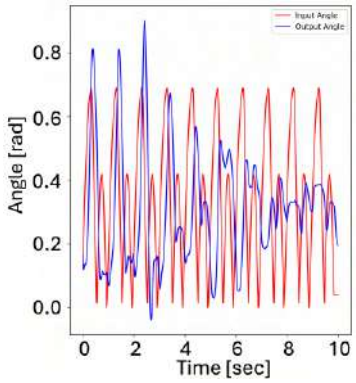


Fig. 10. Prototype 2 testing results with position control collected at $1.3\frac{m}{s}$ walking speed. The controller was unable to track the desired trajectory as it comes in and out of phase with the target arm swing.

The results in Fig. 11 are from testing with external forces removed from the motor to reveal the pure behavior of the motor within the control system.

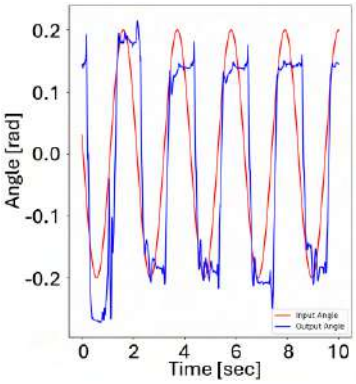


Fig. 11. Bench testing results on elbow joint tracking a sinusoidal trajectory with prosthesis and external forces due to gravity removed. The fast acceleration plateaus magnify the problems presented by gearbox friction that prevents the motor from moving at slow speeds from rest.

3) Adaptive Control and Step Detection: Initial results from testing of the step detection and adaptive control were promising. The step detection algorithm was able to accurately identify cadence when the wearer walked on solid ground, however, during treadmill walking the impact of footfalls was diminished and not registered by the automatic algorithm, thereby reducing its efficacy and challenging adaptive control. Future work will continue to refine this algorithm to enhance accuracy across different terrain.

IV. Discussion and Conclusion

1) Controller: The results of Prototypes 1 and 2 indicate that the same controller can have vastly different results depending on the prosthesis design. The promising results from Prototype 1 indicate that a double-nested position and current controller can work. The difficulties manifested in Prototype 2 are therefore likely resulting from the motor and transmission selection.

For Prototype 2, desynchronization with the wearer's cadence was likely due to the absence of control on the timing of the response. The desired arm swing trajectory was not aligned with any biomechanical marker such that the output phase is correctly timed. Issues with phase synchronization should be addressed in future iterations such that the arm auto-aligns its swing frequency with that of the user. This improvement would solve problems with undershooting the desired arm swing trajectory: phase alignment would prevent destructive interference between the elbow output torque and natural arm swing.

The overshoot of the desired arm swing trajectory during testing of Prototype 2 in Fig. 9 and Fig. 10 may be caused by the control system itself. The position control system should, in theory, be able to compensate for the additional energy added to the system by shoulder extension during walking as it monitors the position output in real time. However, the trajectory overshoot may be explained by the controller not anticipating extra energy added to the system by shoulder flexion/extension. When the torque output and arm momentum combine it generates a trajectory that overshoots the desired position. This interpretation is supported by the current output in Fig. 9. The motor current suddenly jumps during exaggerated arm swing, indicating that external forces drove the motor farther and required the controller to send more current through the motor to maintain the trajectory.

2) Motors: Prototype 2 testing demonstrated that use of a direct drive motor as in Prototype 1 has advantages. The sudden accelerations observed in Fig. 11 during bench testing likely resulted from internal gearbox friction. The controller is sending current to the motor proportional to the desired output, but the motor does not move until the torque output can overcome static friction. These jumps are then a manifestation of the limits of the motors operating torque from rest. If the motor was moving in one direction continuously, this characteristic would not be problematic. In this case the motor could not reflect the periodic flexion/extension of natural arm swing.

Sudden accelerations after plateaus did not appear during walking tests, likely due to the comparatively higher arm swing trajectory frequency. There was a deadband which manifested in the output difference between the desired and actual position. As observed in bench test results (Fig. 11) the motor is unable to track a sinusoidal trajectory without external forces. Since testing did not reveal firmware issues, we theorize that gearbox friction is the source of this deadband.

A. Future Work

1) Motor Selection: A direct-drive brushless motor has proven essential, offering significant advantages over geared motors. While direct-drive motors tend to be larger, Prototype 1 results suggest that a smaller, lighter brushless motor

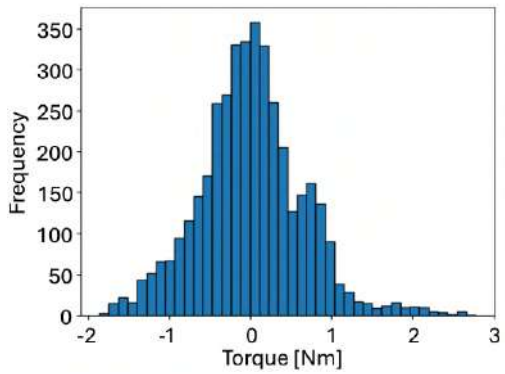


Fig. 12. Histogram of motor output torque over a 40s trial collected at 100Hz with a bucket size of $0.125\mathrm{Nm}$. These results incorporate a torsional spring with stiffness $k = 0.5\frac{\mathrm{Nm}}{\mathrm{rad}}$, which shifts the distribution's center toward zero, moving much of the torque output into the $\pm 1\mathrm{Nm}$ range. This design would allow use of a smaller motor.

could achieve similar torque output without compromising performance and still reduce device weight.

As seen in Fig. 3, the torque output was not centered at zero and the range is negative biased. Hence, a motor tasked with tracking the torque trajectory must output higher magnitudes than if the distribution was zero-centered. A design solution would be to add a torsional spring that reduces the maximum torque output required from the motor and allows a smaller motor to be used. The simulated histogram results from adding a spring with stiffness $k = 0.5\frac{\mathrm{Nm}}{\mathrm{rad}}$ to the arm-body model can be seen in Fig. 12, which is now shifted towards zero.

2) Control System: As for controlling the arm, there was success in using the existing control system. However, it has been shown that the controller output needs to be aligned with some wearer input such that its frequency matches the wearer's dynamics. Foot initial contact as estimated through data collected by the embedded accelerometer is a simple biomechanical marker to record and would correlate to desired time signatures in an arm swing trajectory.

3) Adaptive Response: Adapting the trajectory of the prosthetic arm to the user's walking cadence is a critical step to improve gait symmetry and natural movement. This adaptation can be achieved by reliably estimating the walking cadence through real-time measurement of the initial contact of the foot in different terrains and walking speeds. Consequently, the arm can dynamically adjust its trajectory to match the user's cadence, ensuring a smoother and more synchronized motion.

One possible approach to implementing this adaptive response is to use large datasets of arm swing trajectories collected from wearers at various walking speeds. The data would serve as a lookup table, such that the prosthesis would select the trajectory at a speed most similar to the user's walking speed. However, a library of generalized behavior would have to be generated that may not always map well to wearer dynamics, potentially requiring interpolation.

An alternative approach involves training a predictive model to generate arm swing trajectories based on the wearer's anthropometry (e.g. height, leg length, arm length). This model would generalize arm swing trajectories across users, and require easily measurable parameters to prepare (i.e., calibrate) the prosthesis for use. This solution reduces the need for extra data collection and enhances applicability of the prosthesis. Future work will implement these design approaches and conduct human subject trials to assess functionality of the prosthesis and its affect on user gait dynamics.

B. Conclusion

We have designed two embodiments of a mechatronic prosthetic elbow that has demonstrated the potential to restore symmetry in arm swing during walking for persons with transhumeral-level limb absence. The success of Prototype 1 demonstrated the viability of using a position-based controller with a brushless motor. Prototype 2 demonstrated the ability to integrate the elbow with a conventional prosthetic system and highlighted the potential for deeper user integration, paving the way for more intuitive and self-sufficient control systems. By combining insights from both prototypes, future iterations will focus on refining these features and conducting human subject trials to assess the impact of a motorized prosthetic arm on improving dynamic balance during walking and potentially reducing the risk of falls for upper limb prosthesis users.

ACKNOWLEDGMENT

We thank Zachary Hoegberg and Lily Centra for assistance with testing, and support from the NU Departments of Physical Medicine & Rehabilitation and Mechanical Engineering.

REFERENCES

[1] H. Herr and M. Popovic, "Angular momentum in human walking," *Journal of Experimental Biology*, vol. 211, pp. 467–81, Feb 2008.

[2] M. J. Major, S. M. McConn, J. L. Zavaleta, R. Stine, and S. A. Gard, "Effects of upper limb loss and prosthesis use on proactive mechanisms of locomotor stability," *Journal of Electromyography and Kinesiology*, vol. 48, pp. 145–51, Oct 2019.

[3] J. A. Dunn, N. G. Gomez, B. Wong, S. K. Sinclair, H. B. Henninger, K. B. Foreman, and K. N. Bachus, "Transhumeral prosthesis use affects upper body kinematics and kinetics," *Gait & Posture*, vol. 112, pp. 59–66, Jul 2024.

[4] S. Topuz, E. Kirdi, A. I. Yalcin, O. Ulger, H. Keklicek, and G. Sener, "Effects of arm swing on spatiotemporal characteristics of gait in unilateral transhumeral amputees," *Gait & Posture*, vol. 68, pp. 95–100, Feb 2019.

[5] J. A. Kent and M. J. Major, "Asymmetry of mass and motion affects the regulation of whole-body angular momentum in individuals with upper limb absence," *Clinical biomechanics*, vol. 76, p. 105015, Jun 2020.

[6] J. A. Dunn, N. G. Gomez, B. Wong, S. K. Sinclair, K. B. Foreman, K. N. Bachus, and H. B. Henninger, "Transhumeral prosthesis use and disuse affects whole-body angular momentum," *Clinical Biomechanics*, vol. 120, p. 106365, Dec 2024.

[7] M. Major, "Fall prevalence and contributors to the likelihood of falling in persons with upper limb loss," *Physical therapy*, vol. 99, pp. 377–87, Apr 2019.

[8] M. Major, R. Knox, Y. Ben Shalom, and M. Elwin, "Method and system to activate limb movement in amputees," U.S. Patent 2021-035-02 17/705,665, May 3, 2021.

[9] L. Smail, C. Neal, C. Wilkins, and T. Packham, "Comfort and function remain key factors in upper limb prosthetic abandonment: findings of a scoping review." *Disability and rehabilitation. Assistive technology*, vol. 16, pp. 821–30, Nov 2021.

[10] M. Major, Y. Ben Shalom, and M. Elwin, "A motorized prosthetic elbow for restoring arm swing," *49th American Academy of Orthotists & Prosthetists Annual Meeting & Scientific Symposium*, Mar 2023.

An AI-Driven Telemonitoring System Exploiting Sensorized Glasses and Insoles to Correlate Cognitive Load and Mobility During ADLs

Giulia Bodo[*,1,4], Giulio Sciortino[*,2], Ludovico Pedullà[3], Erica Grange[3], Sara Giordanino[1,4], Gian Luca Bailo[2], Andrea Tacchino[3], Jessica Podda[3], Giampaolo Brichetto[3], Alexey Petrushin[1], Carlos Beltrán-González[2], Alessio Del Bue[+,2] and Matteo Laffranchi[+,1]

***Abstract*— Smart environments can play a crucial role in providing personalized assessment protocols for individuals. This study proposes a wearable telemonitoring system for non-invasively collecting and tracking mobility and mental effort parameters. The system consists of sensorized glasses, insoles, and AI algorithms for evaluating key metrics. To extract data, the activity "preparing coffee for two people" was performed by healthy participants. Preliminary results indicate that, on average, participants completed the task in 8 minutes. Mental workload, assessed through pupil diameter, showed a mean pupil diameter of $\mu = 5.19\ mm$ with a standard deviation of $\sigma = 0.99\ mm$. On average, participants took 340 steps during the task. Questionnaire responses demonstrated good system usability. The findings provide insights into user perceptions of the monitoring approach and highlight the system's potential for clinical adoption.**

I. Introduction

In clinical practice, independence in and performance of activities of daily living (ADLs) are usually assessed by occupational therapists using observation-based instruments that include actual performance analysis and take into account the complexity of daily activities [1], [2]. However, these methods have several limitations, including low sensitivity to mild impairments, difficulty detecting smaller and more specific changes over time, and potential influence from raters' sensitivity [3]. Limited attention has been dedicated to the quantitative assessment of ADLs through technological solutions, such as non-intrusive environmental or wearable sensors, home-testing biomarker-sensing devices, immersive virtual reality devices, and assistive robots that can operate in everyday life situations [4]. Recently, the use of technology and IoT device-based smart diagnosing assistance systems has been integrated into clinical research and practice to monitor and recognize specific ADLs performed by older adults in their home setting [5], [6]. However, no literature is currently available regarding the use of technological devices and wearables to assess the quality and independence of ADLs performance for people with neurological conditions. Moreover, despite the growing number of assessment and rehabilitation tools, greater efforts must be dedicated to personalizing these strategies, taking into account the complexity of each individual [7].

Telemonitoring is showing great promise as a non-invasive method for tracking health-related parameters [8], particularly through the use of wearable devices that do not interfere with ADLs [9], ensuring the ability to perform tasks while maintaining an ecological setting for the test environment [10]. Thus, smart environments equipped with advanced sensors and artificial intelligence algorithms offer the possibility to quantify motor and cognitive performances through continuous measurements [11]. Several studies highlight the use of sensorized insoles for monitoring and evaluating gait, enabling the recognition and identification of different walking phases [12]. Additionally, research demonstrates the potential of using gaze characteristics, such as pupil diameter variation, to study and understand the cognitive load associated with tasks requiring varying mental effort [13],[14], as well as to assess participant engagement [15].

This work presents the results of a collaboration between our research institute and clinical partners specialized in Multiple Sclerosis (MS), a chronic degenerative condition characterized by inflammation and damage to the central nervous system. MS leads to symptoms such as impaired mobility and cognitive decline [16]. The objective of this study is to design and evaluate a telemonitoring system for continuously assessing MS patients' performance. By leveraging collected data, the system aims to promptly detect changes in participants' abilities [17]. This paper describes the experimental setup of a smart monitoring system, which integrates wearable sensors, including sensor-equipped glasses (Tobii) and sensorized insoles, with AI-based algorithms. This combination enables the aggregation of data from multiple sources and the extraction of multidimensional metrics essential for assessing individuals' health status and activities. The study includes a pilot experiment involving six healthy participants performing a specific ADL, preparing coffee for two people, while wearing the wearable devices. This preliminary study is essential for evaluating the system's usability and functionality before introducing it to more vulnerable populations. It allows researchers to identify and address technical issues, design flaws, and user interface

[*]Co-First authors, equal contribution

[+]Co-Last authors, equal contribution

[1]Rehab Technologies Laboratory at Istituto Italiano di Tecnologia, Genova, Via Morego 30, 16163, Italy.

[2]Pattern Analysis and Computer Vision at Istituto Italiano di Tecnologia, Genova, Via Enrico Melen 83, 16152, Italy.

[3]Scientific Research Area, Italian Multiple Sclerosis Foundation, Genova, Via Operai 40, 16149, Italy.

[4]Politecnico di Torino, Torino, Corso Duca degli Abruzzi 24, 10129, Italy.

challenges without the added complexity of managing health-related risks. Additionally, it facilitates the collection of an initial dataset of normative values for motor and cognitive metrics. These baseline values will later be compared with data from individuals with MS in a follow-up study planned for the next phase of the project.

II. Methods

A. Experimental protocol

As a daily living task, Preparing a coffee with a coffee maker and serving it for two people was chosen, based on the Assessment of Motor and Process Skills (AMPS) assessment tool [18]. This task requires the participant to focus on both motor and cognitive skills, allowing for a comprehensive evaluation of the participants' performance. The participants were asked to prepare the coffee for two people and serve it on a table. Before starting the task execution, a familiarization with the set-up of the environment, including the location of all needed tools and materials is provided. Participants were also asked to restore and return unneeded items to their original storage place, place dirty utensils in or besides the sink, wipe up any crumbs or spills. There were no specific rules regarding the coffee preparation process. The participants should proceed as they would at home. Ideally, the participant should not interact with the examiner, as they have all the information needed to complete the task independently. However, questions may be asked if necessary. The examiner will take notes as the participant performs the task. Before to start the task, sensorised glasses and insoles were worn by the participant as shown in Figure 1.



Fig. 1: Experimental Setup: (a) The wearable sensors are worn by the participant, with the insoles placed directly into their shoes. (b) Illustrates the glasses auto-calibration procedure, where the participant focuses on a fixed target to calibrate the gaze analysis. (c) Represents one participant wearing the devices during the test. (d) Shows the two devices adopted.

B. Sensorized glasses

The Tobii glasses are wearable devices equipped with a front-facing camera that records the surrounding environment and internal cameras that track the participant's eyes to analyze gaze and pupil behavior. Thanks to this device, it is possible to gather data on the cognitive load of the participant. Extensive literature highlights how pupillometry, particularly the assessment of variations in pupil diameter, is closely correlated with mental effort, as explained in [19], [13].

C. Sensorized insoles

The Sensing Tex sensorized insoles, fitted with 16 resistive pressure sensors, capture data on plantar pressure distribution through a 4×3 matrix of acquisition points located in the forefoot area and a 2×2 matrix in the rearfoot region. These flexible insoles are designed to fit comfortably inside regular shoes.

Both sensors communicate wireless with a central acquisition system, which manages the start and stop of data collection and gathers the recorded information at the end of each trial session.

III. Algorithms Design

The proposed analysis aims to collect a comprehensive dataset from wearable sensors to describe user activity at both cognitive and mobility levels. The algorithms are specifically designed to track: the participant's time spent in specific zones of the testing environment, the interactions with objects used during task preparation and mobility-related data (e.g., number of steps and average step cadence). Through the adoption of an analysis pipeline and evaluation of the results, the authors propose a correlation between cognitive load (assessed via pupillometric analysis) and the zones or phases of the test performed.

A. Object and QR code detection algorithm

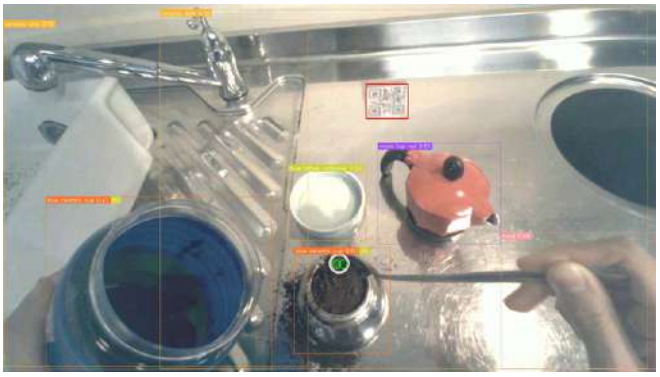


Fig. 2: Processing of a single frame from an experimental session. Bounding labeled boxes identify the recognized QR code zones and the detected objects.

The proposed system consists in a cascade of algorithms designed to perform object detection, QR code reading, and

hand-object interactions. For object detection, we employed YOLO World [20] a specialized version of YOLO v8 [21] fine-tuned on real-time open-vocabulary object detection, which demonstrated robust performance. YOLO World offers an easy way to detect a vast number of common-use objects without collecting and labeling an extensive dataset, resulting in a meaningful reduction of resources. Additionally, avoiding a manual fine-tuning process allowed us to quickly change setup during the first experimental phases and would not require any additional effort if the setting will change in the future. The ontology of the detected object is: coffee maker top red, coffee maker metallic bottom, hand, cup, coffee jar, spoon. As for the hand-object interaction, we selected frames in which the center of the bounding box of a detected object falls within that of a detected hand. When such situation occurs, it is interpreted as the hand holding the object.

The QR codes, stuck in the environment in their corresponding zone, were used to perform the detection of the zones involved in the scene during the execution of the task (an example of QR code and object detection is shown in Figure 2). The read QR codes correspond to shelf, stove area (coffee preparation area), living room and stock. The total time presence of these QR codes determines the presence of the user in the areas. The chosen python library was qreader.

B. Gait analysis pattern recognition: YOLO Model

The extraction of the useful metrics from the gait data was performed by first predicting the foot state in each time frame, then using a Python script we computed the total number of steps, where a step is a succession of detected $foot \rightarrow forefoot \rightarrow foot$ classes. Then a time frame of 250 to 2000 milliseconds was empirically chosen to exclude unrealistic data from the sample, for example, when the sensor or the model missed a foot or a forefoot. Regarding cadence calculations, only effective steps were considered during actual walking periods. The analysis of kinematic parameters includes step duration, step count, and cadence. For each participant, the evaluated metrics comprised:

- Number of steps (N_{steps}).
- Step duration: determined by taking the difference between the current contact time of one foot and the previous foot contact time of the same foot, whenever the pattern $foot \rightarrow forefoot \rightarrow foot$ occurs.
- Step cadence: it is calculated as the number of steps taken divided by the acquisition duration (in seconds), starting from the first step. The result is then converted to steps per minute.

$$Step_{cadence} = \left(\frac{N_{steps}}{\Delta T_{acquisition}(s)} \right) \cdot 60 \qquad (1)$$

Due to the variability of participants' foot size and body weight, interpreting the step phase numerically via pressure data is unfeasible. Therefore, we adopted YOLOv8m for detecting the step phase based on the shape of the pressure distribution on the sole. We chose version 8 due to our experience with it and compatibility with our environment,

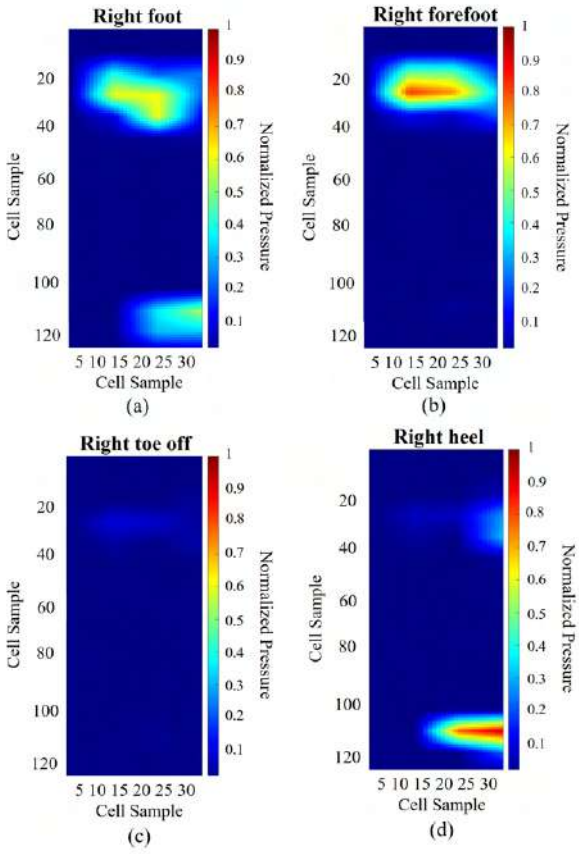


Fig. 3: Example of pressure maps captured from sensorized insoles for the right foot, illustrating different phases of gait: (a) stance, (b) push-off, (c) swing, and (d) heel strike.

specifically the medium model which offers a good balance between resources and precision. Object detection models offer an effective solution by assigning labels to pressure map configurations, and automatically recognize gait phases. This approach avoids manual analysis of individual sensor activations and uses labels to distinguish gait phases. Among the models considered for this purpose, YOLO was identified. The walking data over a distance of 6 meters were previously collected from 8 healthy participants and used to train the employed YOLO model. A MATLAB code was developed to convert the pressure maps, provided by the insoles, into jpeg images, by doing so we gathered a dataset of 2194 pressure map images for both feet (an example of the obtained pressure maps are shown in Figure 3). The dataset has been manually annotated. The following labels were used for the gait analysis:

- right_heel, left_heel: to identify heel strike
- right_foot, left_foot: to identify stance phase
- right_forefoot, left_forefoot: to identify the push-off
- right_toe_off, left_toe_off: to identify the swing phase

A total of 1123 samples were labeled for the left foot and 1071 for the right foot. The samples were then split into a training set and a validation set to train and validate the AI model. The split was randomized, assigning 20% of the

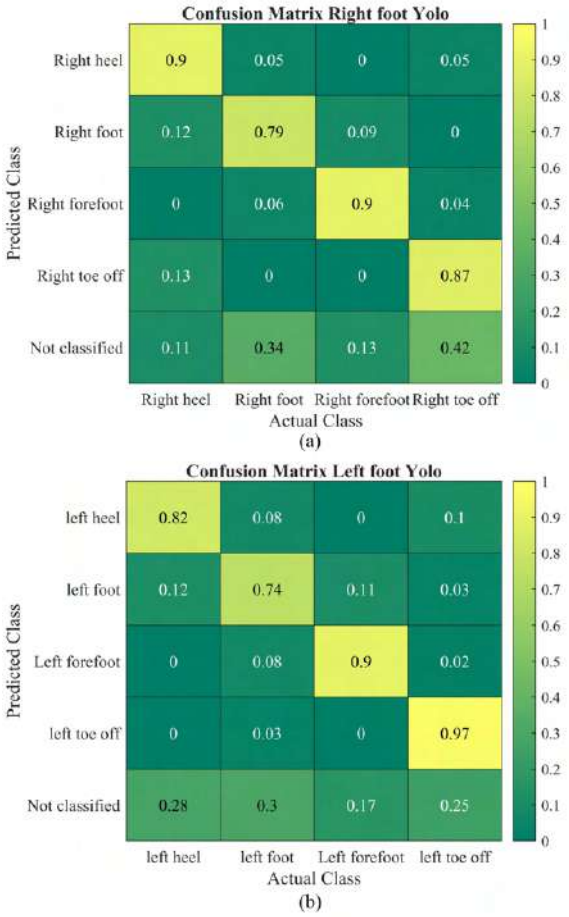


Fig. 4: Confusion matrices, related to the YOLO models for the right and left foot, evaluated on the validation set.

samples to the validation set: the training set contained 894 samples for the left foot and 854 for the right foot, while the validation set included 229 samples for the left foot and 217 for the right. Two distinct models were then trained, one for the right foot and one for the left foot. Each model was trained for 200 epochs and $lr0 = 0.1$, with results from the training process saved for further analysis. To evaluate the performance of the models, the confusion matrices for both left and right foot models are provided in Figure 4, and common metrics, as precision and recall are adopted to evaluate object detection models. Results as shown in Table I.

TABLE I: Precision and Recall for all classes in left and right foot YOLO model.

Class	**Left foot**		**Right foot**	
	p	***r***	***p***	***r***
Heel	67%	82%	71%	90%
Foot	60%	74%	64%	79%
Forefoot	76%	90%	80%	90%
Toe off	71%	97%	63%	87%

IV. Results

This section presents the results of monitoring the activities performed by the participants, reporting metrics related to both mobility and cognitive load. Due to hardware issues, the connection was lost with the sensors for two participants. As a result, sensor data are only available for four participants. The questionnaire responses were completed by all six participants.

A. Mobility and Cognitive metrics

1) Zone permanence timing: The different room areas were tagged with QR codes to track the participants' movements within the environment, without relying on additional external sensors (such as floor sensors or cameras to capture the participant's movements). The objective was to analyze the time participants spent in each of the four identified areas. The results show that, on average, the percentage of the total task duration spent in each area is as follows: 4.75% in the shelf area (where the coffee maker and cups are stored), 66% in the coffee area (where the coffee maker is prepared), 2% in the stock area (where coffee and spoons are kept), and 27% in the living room (where the coffee is consumed). The proportion of time each participant spent in each area, relative to the overall task duration, is represented in the bar charts in Figure 5.

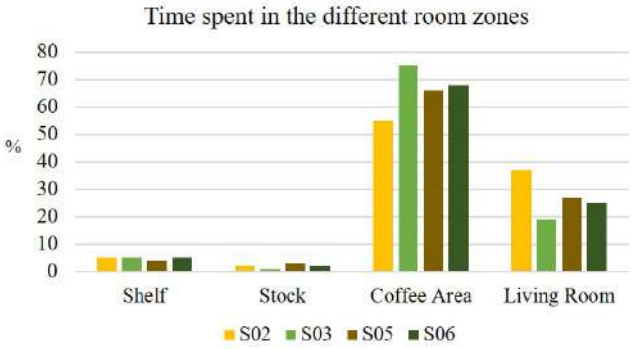


Fig. 5: The bar chart shows the proportion of total time each participant spent in four zones of the test area to complete the task. The zones are: the coffee preparation area (coffee area), the storage area for ingredients and spoons (stock), the coffee serving area (living room), and the shelf where the coffee maker and cups are stored (shelf). Results are provided for four participants.

2) Gait analysis: Insoles data were analyzed to compute the step numbers, cadence and mean duration as reported in Table II. Some anomalies were detected in participant S06's data, which can be attributed to manufacturing defects in the sensorized insole, whereas participants S03 and S02 exhibited a notably low cadence, attributed to frequent interruptions in their walking patterns.

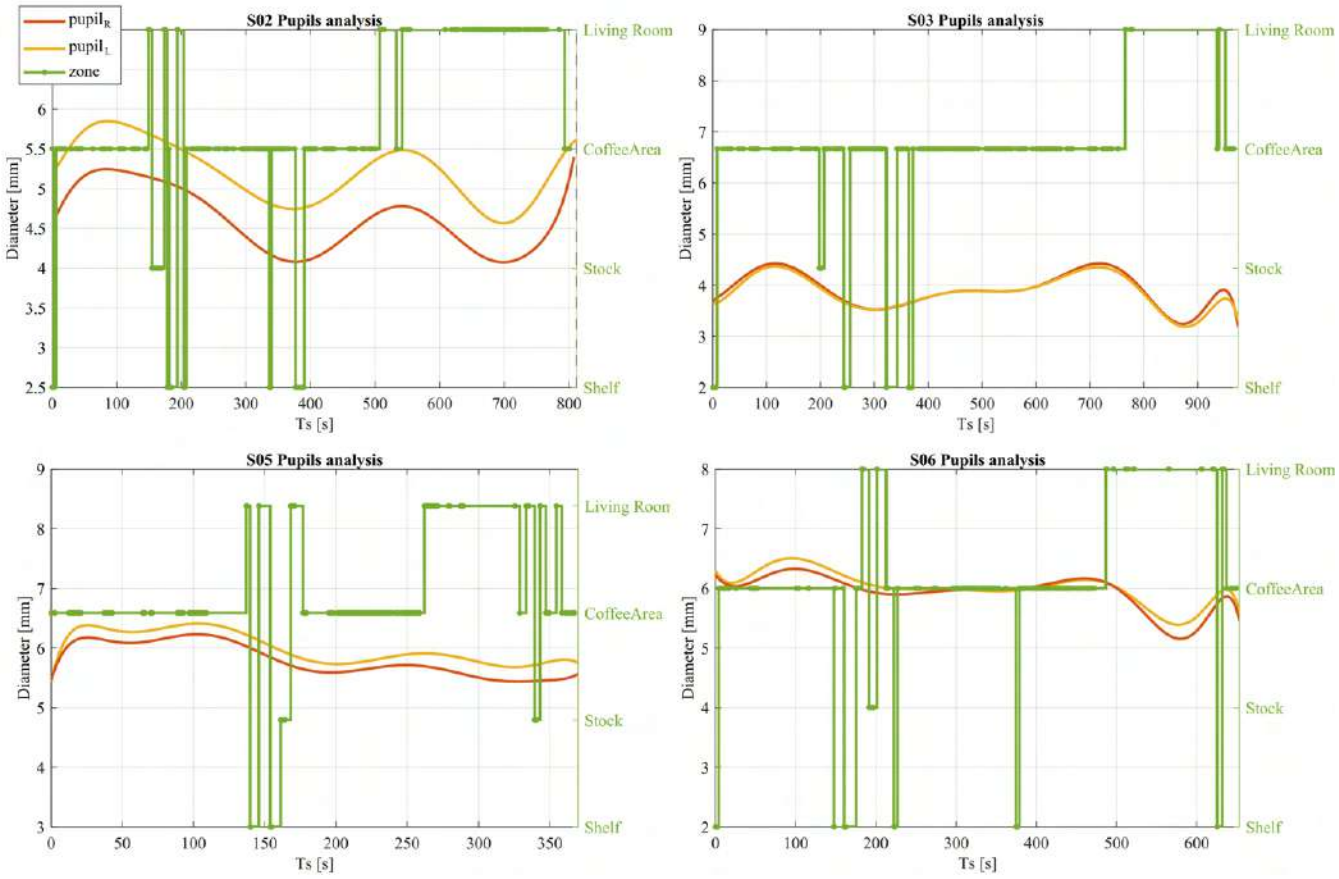


Fig. 6: The graphs show task duration, participant permanence in the different room zones (based on QR code data) and pupil diameter changes (left and right eyes). This allows for assessing mental effort during different task phases, with larger pupil dilation indicating greater mental effort.

TABLE II: Measured gait metrics.

id	N_{steps}	*Step Cadence* $[\frac{steps}{min}]$	Δt_{mean} $[ms]$
S02	529	54.7	448.5
S03	406	27.7	371.3
S05	343	85.1	320.7
S06	83	9.7	295.2

3) Pupillometry analysis: Table III lists, for each participant, the minimum and maximum pupil dilation values, along with the corresponding room zones where these measurements were taken and the pupil's coefficients of variation, computed as:

$$CV = \frac{\sigma}{\mu} \tag{2}$$

where μ is the signal mean and σ is the standard deviation. Statistical considerations can be done on the recorded pupils analysis, by aggregating both right and left pupils signals recorded it is possible to compute the overall weighted mean μ_{tot} of the n signals and the overall standard deviation σ_{tot}.

$$\mu_{\text{tot}} = \frac{1}{n}\sum_{i=1}^{n}\mu_i \tag{3}$$

$$\sigma^2_{\text{tot}} = \frac{\sum(\sigma_i^2 + \mu_i^2)}{n} - \mu^2_{\text{tot}},\ \sigma_{\text{tot}} = \sqrt{\sigma^2_{\text{tot}}} \tag{4}$$

Results indicate $\mu_{\text{tot}} = 5.187\ [mm]$ and $\sigma_{\text{tot}} = 0.992\ [mm]$. Figure 6 presents a correlation graph showing the relationship between cognitive load, as measured by pupil dilation, and the room zones where the participant was performing the task. With reference to Figure 6, in the case of S02, we can observe an increase in mental effort during the first part of the task, when the objects are retrieved and the coffee maker is prepared (from 0 to 200 seconds). Following this, as the participant waits for the coffee maker to be ready, pupil diameter decreases (from 200 to 450 seconds). The mental effort then increases again when the participant pours the coffee into the cups and brings them to the table (from 450 to 600 seconds). Finally, during the time spent in the living room, mental effort decreases once more. This analysis and interpretation are made easier by the availability of the video recorded with the Tobii system. Similar patterns can be observed in other participants, though the analysis is customizable for each participant.

4) Object interaction timing: The time participants spent interacting with key objects relevant to task completion was evaluated. The total interaction time with the coffee maker pot, cups, coffee jar, and spoon is summarized in Table IV. For all participants, the longest interaction time was with the coffee maker. This evaluation offers a useful

TABLE III: Pupillometry analysis includes maximum and minimum pupil dilation (right and left) associated with high and low cognitive effort zones, as well as the coefficients of variation for recorded pupil signals. The total task duration Δt is also reported, measured from the end of the experiment explanation to the completion of table tidying.

id	$\phi_{R_{min}}$ $[mm]$	$\phi_{L_{min}}$ $[mm]$	*Min. Eff. Zone*	$\phi_{R_{max}}$ $[mm]$	$\phi_{L_{max}}$ $[mm]$	*Max. Eff. Zone*	Δt *[min]*	CV_R	CV_L
S02	2.98	3.18	Coffee Area	6.59	6.88	Stock	13.36	0.115	0.104
S03	2.4	2.11	Living Room	6.43	6.08	Coffee Area	16.18	0.124	0.122
S05	4.28	3.83	Living Room	7.51	7.34	Coffee Area	6.23	0.086	0.0762
S06	3.42	3.38	Living Room	7.02	6.92	Living Room	10.96	0.063	0.062

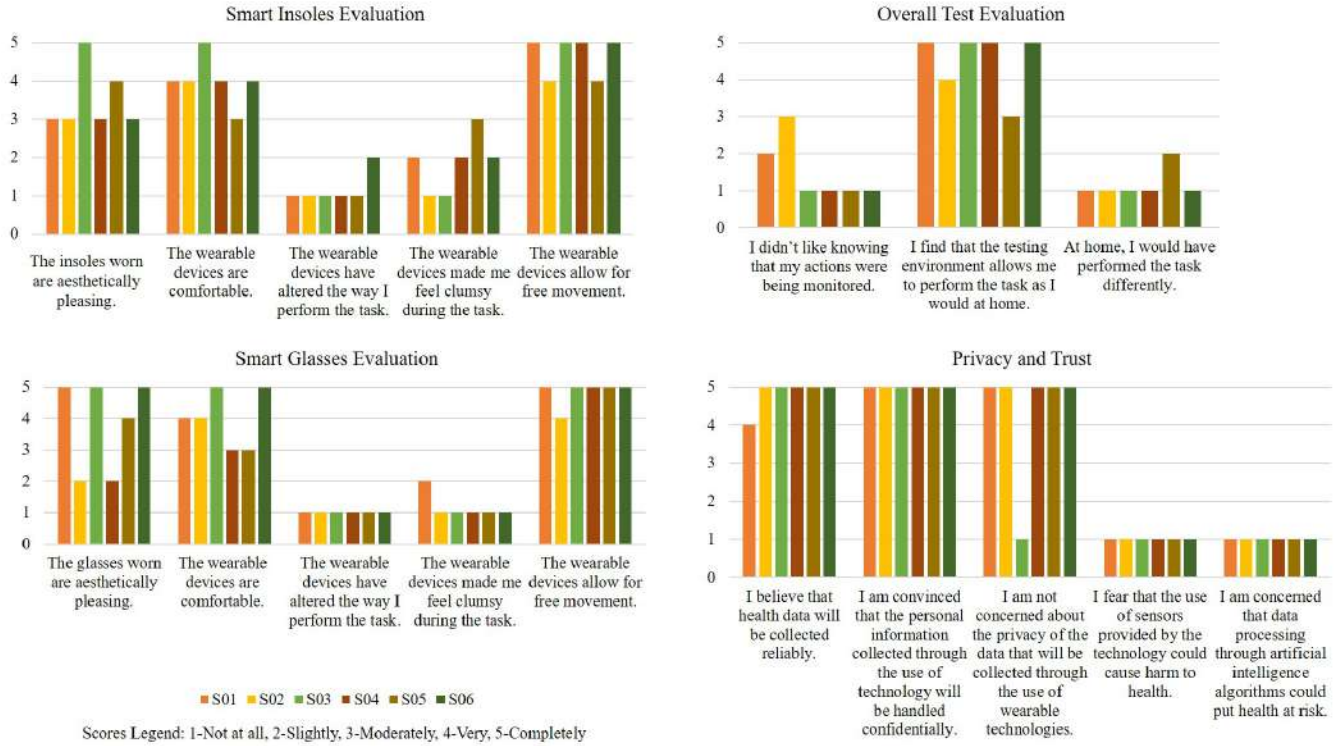


Fig. 7: The results of the questionnaires administered to participants at the end of the activities are presented. Participants were asked to evaluate various statements on a 1-5 scale (ranging from 'completely disagree' to 'strongly agree'). The investigation focused on both the usability and perception of the two wearables (insoles and glasses), as well as the overall impression of a telemonitoring AI-driven approach, including privacy-related concerns.

insight into the average coffee maker preparation time for a healthy participant that from this initial dataset, was found to be 7.93 minutes. Notably, participant S05 was particularly efficient, completing the task in a shorter time than the other participants (see Table III). The interaction time with the cups is also significant, especially in understanding the time required to "take the object and transport it" from the coffee preparation area to the living room and back. The average time for this action was about 48 seconds, consistent with the proximity of the two areas.

TABLE IV: Interaction time with various objects held by participants: the interaction duration is automatically computed using data derived from the YOLO processing algorithms for object detection. Four objects were considered for this analysis: a coffee maker pot, a cup, a coffee jar, and a spoon.

id	*Coffee maker* Δt $[min]$	*Cup* Δt $[min]$	*Coffee Jar* Δt $[min]$	*Spoon* Δt $[min]$
S02	8.22	1.13	3.00	0.77
S03	10.62	1.18	2.08	2.08
S05	4.17	0.57	1.25	0.14
S06	8.72	0.31	0.89	1.02

B. Questionnaires

The questionnaires results, shown in Figure 7, indicate that the proposed solution is user-friendly and highly acceptable to healthy participants. Both the insoles and the glasses were rated as aesthetically pleasing and comfortable, with minimal impact on task performance. Participants were able to move freely during the experiment, and notably, they reported that they would have performed the task in the same way at home. This suggests that the assessment provides a reliable reflection of daily-life performance. Additionally, no concerns regarding privacy or data collection were raised, indicating trust in the process.

V. Discussion and Conclusion

The results of this preliminary study offer valuable insights for future clinical applications. The extended interaction time with the coffee maker suggests that the chosen task is an effective proxy for assessing daily-life performance, reflecting challenges that may arise from cognitive or motor impairments (particularly manual dexterity), or a combination of both. Additionally, participants in this pilot study exhibited varying distributions of interaction times with objects and movement patterns across different areas of the room, indicating reliance on individualized strategies. This confirms that the task allows for personal planning, enabling participants to schedule activities freely while providing a quantitative and technologically robust assessment in a realistic, ecological environment. Pupil dilation data further highlight critical points in the task that may indicate increased effort, offering valuable insights into participants' specific challenges. Finally, gait analysis revealed that the participant who completed the task most quickly maintained the highest cadence, suggesting a correlation between lower-limb mobility, gait, balance and the achieved performance in completing the task. In future studies, it will be necessary to increase the sample size to 10–20 participants, as recommended for usability testing of eHealth devices [22]. Future acquisitions will be used to validate estimated interaction times and gait parameters, leveraging manual annotations of task phases and additional sensors such as a step counter. Additionally, correlations with individual characteristics, such as standard cognitive and motor assessments, will be examined. These analyses could help identify specific challenges faced by individuals with MS during this task and guide the development of personalized rehabilitative interventions. In conclusion, this study underscores the potential of task-based assessments in realistic settings to provide meaningful insights into the daily-life challenges. By integrating quantitative metrics, such as pupil dilation and gait parameters, with task performance analysis, authors believe that individual strategies and difficulties can be better understood. This approach lays the foundation for developing personalized, evidence-based interventions aimed at enhancing functional independence and quality of life for people with MS. The proposed solution holds also significant potential for extension to other conditions characterized by mobility impairments, fatigue, or cognitive challenges. By adapting the system's features to address condition-specific symptoms, it can be tailored to support elderly individuals or people with neurological disorders such as Parkinson's disease, stroke, or cerebral palsy, as well as other chronic conditions affecting functional independence.

ACKNOWLEDGMENT

Funded by the European Union - NextGenerationEU and by the Ministry of University and Research (MUR), National Recovery and Resilience Plan (NRRP), Mission 4, Component 2, Investment 1.5, project "RAISE - Robotics and AI for Socio-economic Empowerment" (ECS00000035).

References

[1] A Buzaid, MP Dodge, L Handmacher, and PJ Kiltz. Activities of daily living: evaluation and treatment in persons with multiple sclerosis. *Physical Medicine and Rehabilitation Clinics of North America*, 24(4):629–638, Nov 2013.

[2] J Jansa, S Ferdinand, M Milo, IG Løyning, T Huilla, L Kallmayer, S Ilsbroukx, N Filló, J Raats, J Jakobson, and D Kos. Performance of activities of daily living in people with multiple sclerosis. *Multiple Sclerosis and Related Disorders*, 57:103342, Jan 2022.

[3] N Mohammed Alotaibi, K Reed, and M Shaban Nadar. Assessments used in occupational therapy practice: an exploratory study. *Occupational Therapy in Health Care*, 23(4):302–318, Oct 2009.

[4] Tanuja Chitnis et al. Quantifying neurologic disease using biosensor measurements in-clinic and in free-living settings in multiple sclerosis. *NPJ Digital Medicine*, 2:123, Dec 11 2019.

[5] N Camp, M Lewis, K Hunter, J Johnston, M Zecca, A Di Nuovo, and D Magistro. Technology used to recognize activities of daily living in community-dwelling older adults. *International Journal of Environmental Research and Public Health*, 18(1):163, Dec 28 2020.

[6] YJ Park, SY Jung, TY Son, and SJ Kang. Self-organizing iot device-based smart diagnosing assistance system for activities of daily living. *Sensors (Basel)*, 21(3):785, Jan 25 2021.

[7] SD Stowe and S Harding. Telecare, telehealth and telemedicine. *European Geriatric Medicine*, 1:193–197, 2010.

[8] A Petrushin, M Freddolini, G Barresi, and et Al. Iot-powered monitoring systems for geriatric healthcare: overview. *Internet of Things for Human-Centered Design: Application to Elderly Healthcare*, pages 99–122, 2022.

[9] VJ Block, R Bove, C Zhao, and et Al. Association of continuous assessment of step count by remote monitoring with disability progression among adults with multiple sclerosis. *JAMA network open*, 2(3):e190570–e190570, 2019.

[10] C Reinier and GP Hancke. Development of a robust active infrared-based eye tracker. *IET Computer Vision*, 8(6):523–534, 2014.

[11] JO Taylor, JD Chulay, CF Landers, WB Hood Jr, and WH Abelmann. Monitoring high-risk cardiac patients during transportation in hospital. *The Lancet*, 296(7685):1205–1208, 1970.

[12] C Baoliang, M Xiaofan, X Feiyun, C Pin, and W Yong. Arch index measurement method based on plantar distributed force. *Journal of Biomechanics*, 144:111326, 2022.

[13] R Bauer, L Jost, B Günther, and P Jansen. Pupillometry as a measure of cognitive load in mental rotation tasks with abstract and embodied figures. *Psychological Research*, 86(5):1382–1396, 2022.

[14] S Mathôt. Pupillometry: Psychology, physiology, and function. *Journal of cognition*, 1(1), 2018.

[15] J Causer, SA McCormick, and PS Holmes. Congruency of gaze metrics in action, imagery and action observation. *Frontiers in human neuroscience*, 7:604, 2013.

[16] ND Chiaravalloti and J DeLuca. Cognitive impairment in multiple sclerosis. *The Lancet Neurology*, 7(12):1139–1151, 2008.

[17] SC Peirce, AR Hardisty, AD Preece, and G Elwyn. Designing and implementing telemonitoring for early detection of deterioration in chronic disease: defining the requirements. *Health Informatics J.*, 17(3):173–190, 2011.

[18] AG Fisher. *Assessment of Motor and Process Skills. Vol. 1: Development, Standardization, and Administration Manual*. Three Star, Fort Collins, CO, 6th edition, 2006.

[19] H Mitre-Hernandez, R Covarrubias Carrillo, and C Lara-Alvarez. Pupillary responses for cognitive load measurement to classify difficulty levels in an educational video game: Empirical study. *JMIR Serious Games*, 9(1):e21620, 2021.

[20] T Cheng, L Song, Y Ge, W Liu, X Wang, and Y Shan. Yolo-world: Real-time open-vocabulary object detection, 2024.

[21] G Jocher, A Chaurasia, and J Qiu. Ultralytics yolov8. `https://github.com/ultralytics/ultralytics`, 2023.

[22] SJ Coons, CJ Gwaltney, RD Hays, et al. Recommendations on evidence needed to support measurement equivalence between electronic and paper-based patient-reported outcome (pro) measures: Ispor epro good research practices task force report. *Value in Health*, 12:419–429, 2009.

Investigating Osseoperception in Distal Regions of the Upper Limb for Augmented Sensory Feedback

Cristian Felipe Blanco-Diaz, *Graduate Student Member, IEEE*, Mariateressa Pedone, Sophie Skach, Camilla Baselli, Leonardo Cappello, *Senior Member, IEEE*

***Abstract*— The somatosensory function is crucial for motor control, but is often deemed secondary in the design of assistive technologies for individuals with neuromotor impairments. This study investigates osseoperception—auditory and vibrotactile sensations evoked through bone stimulation—at the wrist pisiform bone (PB) and metacarpal head (MCH) of the index finger in 12 participants. Vibratory stimuli (100–6000 Hz) were applied during four psychophysical experiments: sensation discrimination, perception thresholds, sensory mapping, and loudness evaluation. Tactile sensations occurred below 940 Hz at the PB and 1000 Hz at the MCH, while auditory sensations predominated above these thresholds. Stimulation at 400 Hz expanded tactile zones, with PB sensations extending to the forearm and MCH sensations to carpal and interphalangeal joints. MCH stimulation had lower perception thresholds (0.14 N), while PB stimulation exhibited frequency-dependent loudness variations. These findings suggest the MCH and wrist as promising sites to elicit osseoperception, paving the way for the development of sensory feedback strategies to complement the effect of assistive technologies, especially those interfaced through osseointegration.**

I. Introduction

The loss of sensory feedback, resulting from neurological disorders, peripheral nerve damage, amputation, trauma, and degenerative diseases, may significantly impair the ability to perform fundamental movements for the activities of daily living (ADLs), such as grasping [1]. This because sensory information plays a crucial role in motor control, enabling precise adjustments through feedback and feedforward mechanisms [2]. The central nervous system (CNS) achieves this through internal models in the cerebellum: the inverse model predicts movements, while the forward model anticipates their sensory outcomes based on an efferent copy of the motor command [3]. Discrepancies between predicted and actual sensory feedback, known as sensory prediction errors, initiate corrective actions to reduce the error during motor performance, closing the control loop [4], [5].

Sensory information originates from mechanoreceptors embedded in the skin of the hand. These specialized sensory neurons detect and process tactile stimuli and are characterized by different properties such as spatial and temporal resolutions, and adaptability [5]. Superficial receptors, i.e., Merkel cells and Meissner corpuscles, enable fine-texture and shape detection, while deeper receptors, such as Pacinian corpuscles and Ruffini endings, detect vibrations and stretch. Loss of tactile, visual, or proprioceptive sensitivity disrupts fine motor control, grasp force, and prehension patterns, leading to significant functional impairments [6].

Sensory feedback can be intrinsic - arising naturally from sensory receptors in skin, muscles, tendons, and joints —, or extrinsic, artificially provided through external devices [6]. Extrinsic feedback, also referred as augmented feedback, is generally provided in the form of visual (through display monitors), auditory (through speakers, headphones), haptic cues (through robots, vibrotactile actuators), or a combination of them [7], [8]. Despite its importance, many assistive and rehabilitation technologies, such as robotic exoskeletons, focus primarily on motor assistance and overlook sensory feedback, possibly hindering their potential to restore natural and intuitive movements [9]. A reason could be the lack of optimal sensory modalities for providing effective augmented feedback, particularly with lightweight, fast-response, noninvasive devices.

Bone conduction has emerged as a promising approach for delivering augmented sensory feedback [10], [11]. By applying vibrational cues to the bones, it is possible to selectively elicit local vibrotactile sensations, stimulating the mechanoreceptors in the periosteum, or auditory sensations, when the vibrations reach the skull and stimulate the cochlea, i.e., osseoperception. This offers the advantage of conveying rich sensory information, using a single, lightweight, low-power transducer [10]. Previous studies have explored invasive applications, where bone transducers were attached to osseointegrated abutments in transhumeral amputees [10], and non-invasive applications, where the transducers were applied on the bone prominence of the elbow in healthy and amputee participants [11]. However, osseoperception in more distal upper-limb segments, such as the wrist or metacarpal bones, remains unexplored. Our preliminary explorations have focused on estimating the minimum perceivable stimulus on the wrist, limited to small sample sizes [12].

In this study, we investigated osseoperception by applying vibratory stimuli to the pisiform bone (PB) of the wrist and the Metacarpal Head (MCH) bone of the index finger. We conducted four psychometric tests to assess tactile, auditory, and combined sensory responses across different stimulation frequencies and forces. We used sensory mapping techniques

* This work was co-funded by INAIL (the italian National Workers' Compensation Authority) under the HANDeVAL project (G.A. PR23-SV-P1). The work of L.C. was co-funded by the European Union (ERC, MUSE, G.A. 101116249). Views and opinions expressed are however those of the author(s) only and do not necessarily reflect those of the European Union or the European Research Council. Neither the European Union nor the granting authority can be held responsible for them.

C.F. Blanco-Diaz, M. Pedonne, S. Skach, C. Baselli, and L. Cappello are with the Department of Excellence in Robotics and AI, The BioRobotics Institute, Scuola Superiore San' Anna, 56127 Pisa, Italy. (e-mail: cristianfelipe.blancodiaz@santannapisa.it, l.cappello@santannapisa.it).

to delineate the vibration perception zones across the upper-limb and quantified auditory sensation loudness using a categorical scaling procedure. To the best of our knowledge, this approach has not been previously applied to the distal regions of the upper limb. By exploring osseoperception at these underexplored sites, our study contributes new insights into its potential application for restoring sensory feedback in individuals with neuromotor impairments. Furthermore, we believe that osseoperception as supplementary sensory feedback modality could be leveraged to facilitate controlling assistive technologies, such as osseointegrated prostheses (e.g., prosthetic hands or fingers), offering a promising avenue for enhancing prosthetic functionality.

II. Material and Methods

A. Participants

Twelve healthy participants (age between 24 and 35 yrs, equal number of male and female volunteers) were recruited for this study. Experiments were conducted under the Declaration of Helsinki and the guidelines of the Ethics Committee of the Scuola Superiore Sant'Anna (Approval No.10/2023). Participants were seated in front of a computer and given detailed instructions before the beginning of each experiment. Subsequently, they wore earplugs (35.5 dB, Tokelu, GE) and noise-canceling headphones (Peltor X5A, 3M, US), as recommended in prior studies [10], [11], [13]. These measures minimized external auditory interference, creating an isolated environment for our sensory assessments.

B. Experimental setup

The experimental setup, shown in Fig.1, included a Personal Computer (PC), a function generator, an audio amplifier, and a bone conduction transducer, detailed hereinafter. This design was inspired by previous studies in the literature [10], [11], [13]. A Graphical User Interface (GUI) was developed in MATLAB® (2021b, Mathworks, US) to adaptively set stimulation amplitudes and frequencies and record user responses. A multifunction DAQ module (PCI 6259, National Instruments, US) served as the function generator for sinusoidal signals with a 44.1 kHz sampling frequency. These signals were subsequently amplified and filtered (AK-170 Audio Amplifier, Hi-fi, CN) before being delivered to the bone transducer (B-81, Radioear, US). The bone transducer was positioned on the PB of the participant's wrist using a 3D-printed support, secured with adjustable elastic bands and Velcro straps to ensure stability [12]. The flat surface of the bone transducer was placed in direct contact with the target boney prominence, ensuring minimized contact with adjacent bones and hence unwanted vibrational effects, and a static force of 3-5 N was applied. This force range, determined based on prior studies, was sufficient to elicit bone conduction [10], [14]. The same experimental procedure was repeated with the transducer positioned on the metacarpal head (MCH) of the index finger (Fig. 1A). Prior to testing, the bone transducer was calibrated to ensure correct amplitude and frequency vibration using an artificial mastoid (4930, Bruel &Kjaer, DK).

C. Psycophysical experiments

1) Sensation Discrimination

This experiment aimed to evaluate what sensation was elicited by varying the parameters of the stimuli, i.e., frequency and amplitude. A single stimulus (1 s) was delivered to the participant, who was asked to report the elicited sensation among four options: tactile (T), auditory (A), both at the same time (T+A), or no perceived stimulus, by clicking on the corresponding button on the GUI (Fig. 1B). The stimulation frequency was randomly picked among seven values: 100, 200, 400, 750, 1500, 3000, 6000 Hz, based on values used in previous studies [10], [13]. Nine values of stimulation amplitude were randomly presented across the whole output range of the transducer (0-1 N of vibrational force). Each pair of parameters was presented to the participant twice, giving a total of 126 stimulations.

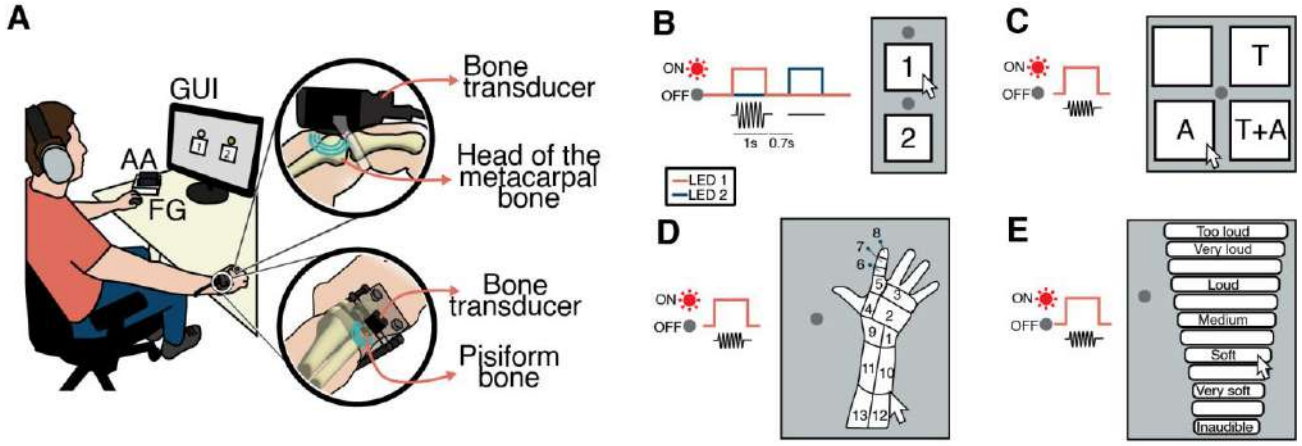


Fig. 1. (A) Experimental setup showing the PC running the GUI, connected to a Function Generator (FG), an Audio Amplifier (AA), and a bone transducer. The bone transducer was placed onto either the Pisiform Bone (PB) or the Metacarpal Head (MCH) of the index finger using two custom 3D-printed supports. A static force of 3–5 N was applied to ensure stable contact and effective vibration transmission. Timing of stimulation and user interface (gray background) for the four psychological experiments performed by the individuals: (B) Sensation discrimination, where the participants were asked to report which sensation (not perceived, tactile – T, auditory – A, or both – T+A); (C) Perception threshold, where the participants were asked to detect when a stimulus was delivered, discriminating against the null stimulus; (D) sensation zone, where the participants were asked to indicate the approximate zone were a tactile stimulus was elicited among 13 zones; (E) loudness evaluation, where the participants were asked to rate the auditory stimulus among 11 levels of loudness scaling.

For each participant, data were grouped by frequency. A logistic psychometric function was then fitted to each group of sensory responses, allowing to estimate the amplitude value corresponding to a 50% detection threshold (D50) for each sensation type. The D50 value indicates the sensitivity threshold for detecting each sensation, with lower D50 values signifying a higher sensitivity. The sensation with the lowest D50 at each frequency was classified as the predominant sensation. This methodology was based on the experimental procedures described in [10].

2) Perception threshold

The amplitude perception threshold (i.e., the minimum perceivable amplitude stimulus each participant could detect) was assessed upon stimulation at various frequencies. A single trial was administered, composed of a standard two-interval forced choice threshold procedure, in which participants discriminated between a target and a null stimulus (both 1 s in duration) in random order, separated by a retention interval of 0.7 s (Fig. 1C). The amplitude of the target stimulus was adjusted using a stochastic approximation staircase (SAS) method. If the participant's response to the previous trial was incorrect, the amplitude was increased; if correct, it was decreased. The step size of the SAS was calculated according to previous studies [10], [12]. Each SAS was stopped after 50 trials per frequency, and the value of the stimulus that would have been presented as the 51st trial was considered as the perception threshold. We selected 100, 400, and 750 Hz, since previous studies identified them to predominantly evoke tactile, combined tactile-auditory, and auditory responses, respectively [10], [11]. This methodology was based on the experimental procedures described in [10].

3) Sensory map

To assess the spatial distribution of tactile sensation, we conducted a test where a single vibrational stimulus (1 s) was delivered to the participant, who was asked to identify the approximate region where the tactile sensation was perceived. Then, the participant was asked to select one or more of 13 predefined regions displayed in the GUI (Fig. 1D). Since no prior studies have mapped the regions of tactile sensations elicited by bone-conducted vibrations on the upper-limb, we based the region layout on previous studies examining haptic points distribution [15], [16]. Stimulation frequencies were randomly selected between 100 and 400 Hz, known to elicit tactile sensations [10]. Nine stimulation amplitude levels were randomly presented across the whole output range of the transducer (0-1 N of vibrational force). Each frequency-amplitude combination was presented to the participant twice, for a total of 36 stimulations.

For each participant, responses were grouped by frequency and amplitude. The probability of stimulus perception in each zone was calculated as follows: 100% for consistent reports across the two stimuli, 50% for one report, and 0% for no reports.

4) Loudness evaluation

This experiment aimed to evaluate the loudness of sounds perceived by the participants, conveyed through bone conduction when their upper limb was stimulated. To achieve this, we used the categorical loudness scaling method following the recommendations of ISO:16832, similarly to [17]. The scaling procedure was presented through the GUI with 11 response options (Fig. 1E), each representing a 5-unit categorical increase in loudness, from 0-50 categorical units (cu).

The procedure consisted of delivering a single vibrational stimulus (1 s) to each participant at two frequencies, 1500 and 3000 Hz, chosen because they are known to convey auditory sensations only [9], [10]. The amplitude levels were calibrated using categorical loudness scaling with “Inaudible” (0 cu) and “Too loud” (50 cu) as reference points. We determined these levels with a staircase method, initially setting the bone transducer’s vibrational force to 0.6 N and incrementally increasing it by 0.05 N until the sound was rated as “Too loud”. Then, the amplitude was reduced by 0.10 N until the sound was rated “Inaudible”. If participants did not select the “Too loud” or “Inaudible” options, the vibrational force was limited between 0.2- 1 N to operate within the optimal range of the bone transducer (Fig. 1E). To obtain the loudness function for each participant, the following iterative procedure was employed.

i) **Initial Function Generation:** Using the stimulation forces at 0 and 50 cu, a linear interpolation function $F(L)$ was created to associate vibrational force L with the categorical loudness levels: “Very soft” (5 cu), “Soft” (15 cu), “Medium” (25 cu), “Loud” (35 cu), and “Very loud” (45 cu) (Fig. 1E). Variables k_{lo}, k_{hi}, and L_{cut} were initialized, with k_{lo} and k_{hi} representing the gradients of the interpolation (in cu/N), and L_{cut} representing the force associated with F(L)= 25.

ii) **Participant Ratings:** Five stimulation levels, corresponding to each loudness category (Fig.1E), were presented, and participants rated their perceived loudness using the GUI.

iii) **Updating the Function:** For each stimulation level, the perceived loudness c might differ from the function $F(L)$ prediction. Thus, the actual function $F_p(L)$ was computed using a piecewise approach:

   a) $Fp(L)=k_{lo}(L-L_{cut})+25$ for $c\leq 15$ cu
   b) $Fp(L)=k_{hi}(L-L_{cut})+25$ for $c\geq 35$ cu
   c) $Fp(L)=bezier(L,k_{lo},k_{hi},L_{cut})$ for 15 cu < c <35 cu

iv) **Function Refinement:** The variables k_{lo}, k_{hi}, and L_{cut} were iteratively updated by minimizing the mean squared error between the initial function F(L) and the estimated function Fp(L).

v) **Recalculation of Forces:** New stimulation forces L were calculated using the inverse function $F^{-1}(L)$ and the updated parameters, corresponding to the five intermediate loudness levels: 5, 15, 25, 35, and 45 cu.

vi) **Iteration:** Steps **ii** through **v** were repeated three times

The final function F(L), derived after three iterations, provided the best-fit loudness function for each participant. This methodology was based on the experimental procedures described in [17].

D. Statistical Analysis

For the sensation discrimination test, D50 values were grouped by sensation type and frequency across all participants. The normality and homogeneity of variances were assessed using the Kolmogorov-Smirnov and Levene tests, respectively. A one-way ANOVA was conducted to evaluate whether the D50 for one sensation was significantly lower than for the other two sensations at each frequency (α=0.05). Subsequently, post hoc comparisons were applied using the Tukey-Kramer method. The null hypothesis posited no significant differences among the sensations, while the alternative hypothesis suggested that one sensation was better perceived (lower D50) than the others [10].

For threshold perception, data from all participants were grouped by frequency (100, 400 and 750 Hz) and stimulation zone (i.e., PB and MCH). Normality and variance uniformity were confirmed using the same methodology as in the sensation discrimination test. A paired t-test was then employed to compare the minimum thresholds between the PB and MCH zones for each frequency. The null hypothesis stated no significant differences between zones, while the alternative hypothesis suggested statistically different thresholds (α=0.05).

For the loudness experiment, data were grouped by frequency (1500 Hz and 3000 Hz) and stimulation zone (PB and MCH). Normality and homogeneity of variances were assessed as before, and a paired t-test was applied to determine whether perceived loudness significantly differed by frequency or stimulation zone. The null hypothesis suggested no significant differences, while the alternative hypothesis posited that perceived loudness varied significantly. Results are presented as [mean ± standard deviation].

III. Results

A. Sensation Discrimination

Tactile D50 values were significantly lower than auditory D50 values at 100 Hz ($p<0.05$), 200 Hz ($p<0.05$), and 400 Hz for both wrist and MCH stimulation (Fig. 2). In contrast, auditory D50 values were significantly lower than tactile D50 values at 750 Hz and above, including 1500 Hz ($p<0.05$), 3000 Hz ($p<0.05$), and 6000 Hz ($p<0.05$). However, participants P01 and P12 did not perceive stimuli at 6000 Hz during wrist stimulation, and participants P02 and P12 failed to perceive stimuli at this frequency during MCH stimulation.

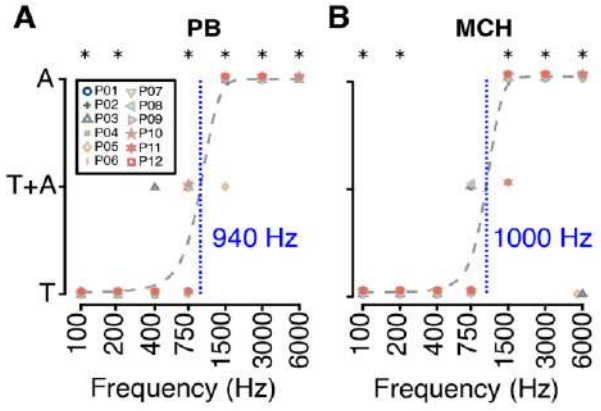


Fig. 2. Comparison of 50% of detection level (D50) for tactile (T), auditory (A), and combined tactile-auditory (T+A) sensations, measured across all participants. A) D50 values during stimulation of the PB of the wrist and (B) D50 values during stimulation of the MCH bone of the index finger. (*) Indicates statistically significant difference ($p<0.05$)

Some participants experienced combined tactile and auditory sensations. For instance, at 400 Hz, participant P03 reported both sensations during wrist stimulation, while at 750 Hz, this combined sensation was reported by participants P01, P02, P01, P02, P03, P05, P08, and P10. During MCH stimulation, combined sensations were reported by participants P01, P03, P04, and P08 at 750 Hz, and by participant P11 at 1500 Hz. Psychometric logistic functions revealed that the frequency threshold separating tactile and auditory sensations was approximately 940 Hz for wrist stimulation and 1000 Hz for MCH stimulation.

B. Perception threshold

On average, across all evaluated frequencies, the perception threshold was lower during MCH stimulation compared to wrist stimulation, although the difference is not statistically significant ($p>0.05$). The lowest average threshold was observed at 400 Hz during MCH stimulation (0.14±0.15 N), while the highest average threshold was recorded at 100 Hz during wrist stimulation (0.35±0.08 N) (see Fig. 3). At 400 Hz, the lowest perception thresholds were observed for the wrist (0.06 N, participant P08) and MCH (0.06 N, participant P06). In contrast, the highest perception thresholds were observed during wrist stimulation at 750 Hz (0.50 N, participant P05) and MCH stimulation at 100 Hz (0.51 N, participant P01).

C. Sensory map

Across all participants, the probability of detecting tactile sensations was higher during MCH stimulation than wrist stimulation (Fig. 4). At 100 Hz, the highest detection probabilities for wrist stimulation were in zones 1 (62% at 0.8 N) and 2 (38% at 0.9 N), while for MCH stimulation, zones 5 (77% at 0.4 N) and 6 (54% at 0.6 N) showed the highest probabilities (Figs. 4B, 4D). At 400 Hz, tactile sensations were perceived across additional zones compared to 100 Hz. For wrist stimulation, these included zones 3, 9, and 10, while for MCH stimulation, they expanded to zones 3, 4, 7, and 8. Furthermore, the probability of detecting tactile stimuli at lower vibration force amplitudes increased with frequency (e.g., from 100 Hz to 400 Hz), aligning with the trends observed in perception thresholds (Figs. 4C, 4E).

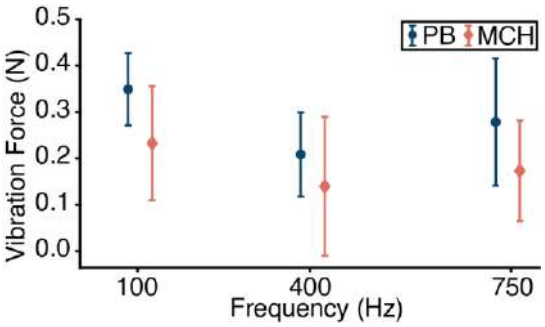


Fig. 3. Averaged perception thresholds across all participants per frequency using SAS technique. Error bars represent standard deviations.

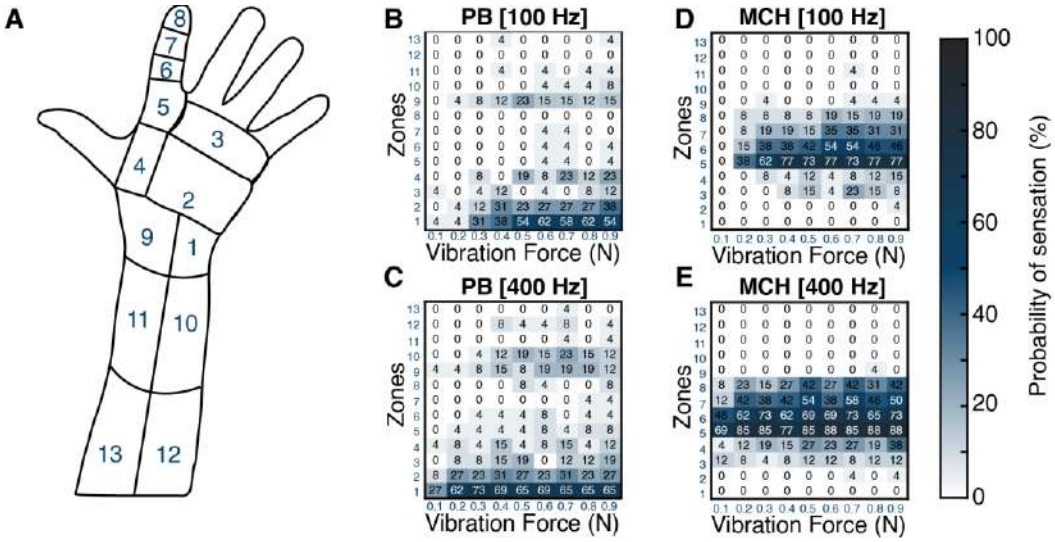


Fig. 4. (A) Reference image displayed in the GUI, showing the 13 perceptual zones that can be selected after stimulation. (B, C) Average probability of tactile perception across all participants in each zone during PB of the wrist (B) and MCH bone of the index finger (C) stimulation at 100 Hz. (D, E) Average probability of tactile perception during PB of the wrist (D) and MCH bone of the index finger (E) stimulation at 400 Hz. Results are shown for all vibration force amplitudes.

D. Loudness evaluation

The estimated loudness functions for 3000 Hz and 6000 Hz showed an approximately linear relationship between perceived loudness and stimulation force (Fig. 5). In general, higher vibration forces were required to achieve the same loudness perception at the wrist compared to the MCH. Additionally, a significant variation in vibration force (Δ) was observed between the two frequencies (3000 Hz and 6000 Hz) during wrist stimulation, indicating a frequency-dependent effect on loudness perception ($p<0.05$). However, this variation was almost null during MCH stimulation.

IV. Discussion and Conclusion

This study investigated evoking osseoperception in humans by stimulating with vibrotactile transducers two anatomical sites, i.e., the PB of the wrist and the MCH of the index finger. Four psychophysical experiments were carried out with healthy participants to assess their sensations.

All participants perceived vibrotactile sensations between 100 and 750 Hz and auditory sensations between 1500 and 3000 Hz for both PB and MCH stimulation, which is consistent with prior findings [10], [13]. However, the stimulation site influenced the threshold frequency distinguishing tactile and auditory sensations. Psychometric analysis suggested that this threshold frequency was approximately 940 Hz for PB stimulation and 1000 Hz for MCH stimulation. Previous studies reported different thresholds depending on the stimulation site: Clemente *et al.*[10] found a threshold near 309 Hz using an invasive interface on transhumeral amputees, while Mayer *et al.* reported thresholds between 400 and 750 Hz when stimulating the elbow of healthy participants [13]. These results suggest that the frequency required to evoke tactile, auditory, or combined sensations depends on the stimulation site. Furthermore, there may be a proportional relationship between the distance of the stimulation site from the mastoid bone and the required frequency, indicating that more distal sites require higher frequencies to convey auditory sensations [10]. However, further investigation is required to confirm this trend and identify its underlying mechanisms.

Our study found that the minimum perception thresholds occur during the stimulation of MCH at 400 Hz with a force of approximately 0.14 N. While Clemente *et al.* [10] reported the lowest thresholds at 100 Hz, our findings align more closely with Mayer *et al.*[13], who observed no consistent pattern in thresholds at frequencies above 200 Hz. This variability may be influenced by factors such as population sensitivity or the invasiveness of stimulation. Furthermore, the difference between the minimum thresholds during MCH and PB stimulation was not significant. This can be associated with the limited statistical power due to the sample size in this study.

Vibration strength and frequency significantly influenced the zones where tactile sensations are perceived. For instance, stimulating the pisiform bone elicited sensations around the wrist and forearm, particularly towards the ulnar side. In contrast, stimulation of the MCH produced sensations

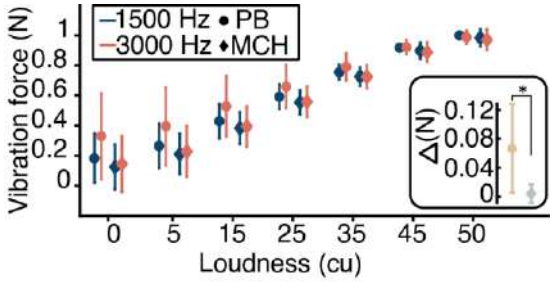


Fig. 5. Averaged loudness functions derived from the categorical loudness scaling procedure across all participants, plotted against varying vibration force and frequency for PB of the wrist and MCH bone of the index finger. (Δ) represents the difference in vibration force between frequencies, highlighting variations in categorical loudness scaling at each stimulation site. (*) indicates statistically significant differences ($p<0.05$). Error bars represent standard deviations.

extending to the carpal bones and the interphalangeal joints. These effects were intensified when the stimulation frequency was 400 Hz. Due to the rigid nature of the bone, mechanical waves, i.e., vibrations, can travel across it [18]. Consequently, these waves can stimulate the mechanoreceptors in the periosteum [9] and, possibly, the nearby innervated areas, potentially leading to sensations perceived in different regions in proximity of the bone [2], [10], [14].

The iterative scaling procedure provided accurate measures of loudness perception for each frequency. Our results suggest that higher loudness is perceived when vibration force increases, consistent with findings by Stenfelt *et al.* [17]. They found a proportional relationship between loudness and vibration force using bone transducers placed on the mastoid. However, the loudness ranges found when the transducer was placed on the mastoid were higher than those observed in this study. This can be associated with the attenuation of mechanical waves caused by the distance between the transducer and the cochlea [9]. Additionally, we observed that when the stimulation point was the PB, perceived loudness varied significantly with frequency (e.g., between 1500 Hz and 3000 Hz), which was not observed when stimulating the MCH.

To conclude, this study investigated psychophysical responses to vibrational stimuli applied to distal upper-limb bones for the first time [10], [11], [13], expanding the current understanding of osseoperception. However, it is important to note that our knowledge of osseoperception is still limited and further research is required before its clinical application. A potential limitation may be the perceivable sound generated by the mechanical waves applied by the transducers during auditory tests, particularly pronounced at high stimulation forces. Although measures were taken to minimize this effect—such as verifying the transducer's range and equipping participants with earplugs and noise-canceling headphones—sounds exceeding 35 dB are sometimes generated, possibly influencing psychophysical responses [10], [11], [13]. Future studies should implement stricter noise isolation measures or alternative calibration methods to enhance reliability of auditory perception data. Additionally, the relatively small sample size and the limited age range of participants may restrict the generalizability of our findings. Future approaches should include a more diverse sample to better understand individual differences and their impact on osseoperception.

The findings of this work indicate that the MCH region is more effective for eliciting tactile sensations, as evidenced by lower perception thresholds and more distinct sensory maps. In contrast, the wrist showed greater efficacy for auditory sensations, as shown by results from the sensation discrimination experiment and loudness scaling. These differences may be attributed to anatomical and physiological factors: the high density of mechanoreceptors in the hand likely contributes to the superior tactile sensitivity in the MCH [2], [10], [14], while the wrist's proximity to the cochlea may justify enhanced auditory perception [10], [18]. These findings emphasize the importance of both the stimulation site and frequency on the phenomenon of osseoperception. We aim at conducting other studies involving both healthy individuals and people with neuromotor impairments, focusing on functional tasks and possibly exploring its application to deliver augmented sensory feedback in assistive devices. This will allow us to explore the potential of osseoperception for enhancing tactile and auditory perception, and eventually extending the reach of assistive technologies.

REFERENCES

[1] N. Lan *et al.*, "Achieving Neural Compatibility With Human Sensorimotor Control in Prosthetic and Therapeutic Devices," *IEEE Trans Med Robot Bionics*, vol. 1, no. 3, pp. 122–134, Aug. 2019, doi: 10.1109/TMRB.2019.2930356.

[2] R. S. Johansson and J. R. Flanagan, "Coding and use of tactile signals from the fingertips in object manipulation tasks," *Nat Rev Neurosci*, vol. 10, no. 5, pp. 345–359, May 2009, doi: 10.1038/nrn2621.

[3] M. Kawato *et al.*, "Internal forward models in the cerebellum: fMRI study on grip force and load force coupling," *Prog Brain Res*, pp. 171–188, 2003, doi: 10.1016/S0079-6123(03)42013-X.

[4] D. M. Wolpert, J. Diedrichsen, and J. R. Flanagan, "Principles of sensorimotor learning," *Nat Rev Neurosci*, vol. 12, no. 12, pp. 739–751, Dec. 2011, doi: 10.1038/nrn3112.

[5] R. S. Johansson and J. R. Flanagan, "Tactile Sensory Control of Object Manipulation in Humans," in *The Senses: A Comprehensive Reference*, Elsevier, 2008, pp. 67–86. doi: 10.1016/B978-012370880-9.00346-7.

[6] L. Cappello *et al.*, "Noninvasive augmented sensory feedback in poststroke hand rehabilitation approaches," in *Somatosensory Feedback for Neuroprosthetics*, Elsevier, 2021, pp. 207–244. doi: 10.1016/B978-0-12-822828-9.00006-X.

[7] R. Sigrist *et al.*, "Augmented visual, auditory, haptic, and multimodal feedback in motor learning: A review," *Psychon Bull Rev*, vol. 20, no. 1, pp. 21–53, Feb. 2013, doi: 10.3758/s13423-012-0333-8.

[8] C. Demolder *et al.*, "Recent advances in wearable biosensing gloves and sensory feedback biosystems for enhancing rehabilitation, prostheses, healthcare, and virtual reality," *Biosens Bioelectron*, vol. 190, Oct. 2021, doi: 10.1016/j.bios.2021.113443.

[9] N. Bolognini, C. Russo, and D. J. Edwards, "The sensory side of post-stroke motor rehabilitation," *Restor Neurol Neurosci*, vol. 34, no. 4, pp. 571–586, Aug. 2016, doi: 10.3233/RNN-150606.

[10] F. Clemente *et al.*, "Touch and Hearing Mediate Osseoperception," *Sci Rep*, vol. 7, Mar. 2017, doi: 10.1038/srep45363.

[11] R. M. Mayer *et al.*, "Tactile Feedback in Closed-Loop Control of Myoelectric Hand Grasping: Conveying Information of Multiple Sensors Simultaneously via a Single Feedback Channel," *Front Neurosci*, vol. 14, Apr. 2020, doi: 10.3389/fnins.2020.00348.

[12] C. F. Blanco-Diaz *et al.*, "Exploring Osseoperception at the Wrist: Towards an Augmented Sensory Feedback Interface," in *6th International Conference on NeuroRehabilitation (ICNR2020) [in press]*, 2024.

[13] R. M. Mayer *et al.*, "Bone Conduction as Sensory Feedback Interface: A Preliminary Study," in *2019 41st Annual International Conference of the IEEE Engineering in Medicine and Biology Society (EMBC)*, 2019, pp. 5322–5325. doi: 10.1109/EMBC.2019.8856424.

[14] I. Klineberg *et al.*, "A consensus statement on osseoperception," *Clin Exp Pharmacol Physiol*, vol. 32, no. 1–2, pp. 145–146, Jan. 2005, doi: 10.1111/j.1440-1681.2005.04144.x.

[15] J. Leo, "The Upper Limb," in *Clinical Anatomy and Embryology*, Cham: Springer International Publishing, 2023, pp. 241–292. doi: 10.1007/978-3-031-41119-9_6.

[16] C. C. J. Alleblas, M. P. H. Vleugels, and T. E. Nieboer, "Ergonomics of laparoscopic graspers and the importance of haptic feedback: the surgeons' perspective," *Gynecol Surg*, vol. 13, no. 4, pp. 379–384, Nov. 2016, doi: 10.1007/s10397-016-0959-z.

[17] S. Stenfelt and M. Zeitooni, "Loudness functions with air and bone conduction stimulation in normal-hearing subjects using a categorical loudness scaling procedure," *Hear Res*, vol. 301, pp. 85–92, Jul. 2013, doi: 10.1016/j.heares.2013.03.010.

[18] I. Pyykkö *et al.* , "Transmission of vibration in the hand-arm system with special reference to changes in compression force and acceleration.," *Scand J Work Environ Health*, vol. 2, no. 2, pp. 87–95, Jun. 1976, doi: 10.5271/sjweh.2820.

A Flexible Clinician-Friendly Interface for Upper Limb Rehabilitation with Industrial Robots

Chiara Alessi
Department of Electrical, Computer, and Biomedical Engineering
University of Pavia
Pavia, Italy
chiara.alessi02@universitadipavia.it

Nikolas Sacchi
Department of Electrical, Computer, and Biomedical Engineering
University of Pavia
Pavia, Italy
nikolas.sacchi01@universitadipavia.it

Antonella Ferrara
Department of Electrical, Computer, and Biomedical Engineering
University of Pavia
Pavia, Italy
antonella.ferrara@unipv.it

***Abstract*—This paper presents a flexible software with a Graphical User Interface (GUI) designed to assist clinicians in upper limb robotic rehabilitation sessions. The flexibility comes from the fact that, since it relies on the Robot Operating System 2 (ROS2) framework, it is potentially compatible with any collaborative industrial robot, with relatively low integration effort. The software collects and analyzes data related to each session to identify critical movement directions for each patient, detecting improvements or regressions through statistical tests, thus reducing subjectivity. Moreover, it suggests personalized physical and cognitive rehabilitation exercises focusing on the most critical movement directions. Results are visualized through intuitive graphs, allowing clinicians to design custom trajectories tailored to each patient's needs. The software has been tested in combination with a Franka Emika Panda robot proving its seamless integration and ability to process data in real time.**

***Index Terms*—robotic rehabilitation, evaluation methods, interfaces for rehabilitation**

I. Introduction

Each year, millions of people are affected by chronic neurological diseases [1]–[3]. A prompt intervention with motor and cognitive rehabilitation therapies is crucial to mitigate the disease effects in chronic cases or to help recover lost functions in acute cases [4]. The variability in a patient's abilities from session to session creates the need for personalized therapies [5]. Robotics has proven to be an effective tool in rehabilitation, helping the therapists in performing repetitive movements with the patient. Moreover, it allows objective assessments of patient abilities using sensor-based evaluations.

The Center Out Point To Point (CO-PTP) exercise, commonly used in upper limb rehabilitation robotics, involves moving the robot end-effector from a central point to targets around a circle [6]. In the meantime, kinematic and dynamic data are collected and employed in the computation of Quality Metrics (QMs) such as the smoothness, the precision error, the mean velocity, and the duration. Such QMs have been proven to correlate with established clinical scales (e.g., Medical Research Council Muscle Power Scale and Fugl Meyer Assessment Scale [7]), commonly used for the assessment of the upper-limb function in post-stroke patients [8], [9]. A peculiarity of CO-PTP is that it can identify movements that require more effort by the patient [6], being an ideal exercise in the treatment of neurological patients.

An ideal automated system should interpret data and adjust rehabilitation exercises to maximize their benefit on the patient. However, learning the relationship between a patient's condition and optimal actions is challenging due to limited data, patient variability, complex setups, and legal and safety constraints [10]. While relying on therapists circumvents data issues, it introduces inefficiencies, interrupting sessions and reducing therapy time. To address this, therapists must quickly interpret data and intuitively adjust robotic settings [11]. Graphical data visualization enhances data accessibility, while a safe, user-friendly interface facilitates interaction. In particular, a recent study demonstrated that the teaching by demonstration of a trajectory is a very appreciated functionality in the physiotherapy realm [11]. Such a tool allows to manually move the robot, record the trajectory, and enable the robot to automatically replay it to guide the patient's hand in tracking the end-effector path accomplishing the Trajectory Tracking (TT) exercise.

Various technologies have been developed to achieve these goals, using mechanical devices specifically designed for medical purposes and user-friendly GUIs [12]–[15]. However, while these devices offer tailored solutions, they often come with high development and manufacturing costs and limited scalability making them less accessible and adaptable. A recent and cost-effective solution proposed is the use of industrial collaborative robots for rehabilitation purposes (e.g. [16]–[18]). The adoption of industrial robots in the recovery realm offers advantages such as lower cost due to mass production, versatility and scalability, as well as established maintenance and technical support. However, they are still rarely used in rehabilitation practice [17]. Moreover, only a few of this kind of systems feature software with GUIs that allow for intuitive reading, processing, and visualization of results and, to our knowledge, no system offers a software that can be used with different robotic models. Recently, however, a dashboard has been developed to process and visualize dynamic data from multiple robotic rehabilitation sessions, conducted with any rehabilitation system capable of collecting such data [19].

The work has been supported by the Italian Ministry for University and Research in the framework of the Fit4MedRob project - PNC0000007.

However, this software only allows for result visualization and does not enable the programming of new exercises.

In this article, we propose a new software designed for clinicians who are responsible for managing multiple patients during various rehabilitation sessions based on the use of a generic industrial collaborative manipulator. The software is equipped with an intuitive GUI and is capable of exchanging information with the robot by means of the Robot Operating System 2 (ROS2) communication framework, collecting data while the patient is performing the rehabilitation exercises. Such data are employed to identify the movement directions that are most critical for the patient and, through statistical tests, detect improvements or regressions. This allows the software to tailor the rehabilitation sessions, customizing standard rehabilitation exercises such as the CO-PTP, to promote movements in the most critical directions. In addition, by visualizing the data using intuitive graphs, clinicians can design custom trajectories for the TT exercise that best suit the needs of each patient, relying on objective information. The compatibility of the proposed software with collaborative industrial manipulators was assessed by testing it in combination with the Franka Emika Panda robot.

The rest of the paper is organized as follows. Section II describes the complete flexible rehabilitation framework, Section III presents the modes of operation of the robotic system, Section IV describes in details the proposed intuitive GUI. Finally, in Section V the experimental test is described, while some conclusions are drawn in Section VI.

II. Flexible Rehabilitation Framework

This section presents the proposed flexible robotic rehabilitation framework, depicted in Fig. 1, and its components.

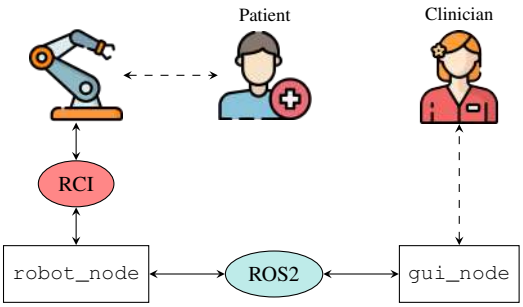


Fig. 1: Graphical representation of the flexible rehabilitation framework. The red ellipse represents the communication via the robot robot control interface (RCI), while the blue one the communication via ROS2. The dashed lines represent physical access.

To be compatible with the interface presented in this work, the robot must be a torque-controlled collaborative robot manipulator compliant with the safety requirements specified in the ISO/TS 15066:2016, and should allow the installation of a custom end-effector that facilitates the interaction with the patient.

In general, manipulators are characterized by $n \in \mathbb{N}_{>0}$ revolute joints, whose positions, expressed in radians, are collected in the joint variable vector $q \in \mathbb{R}^n$ [20]. The dynamics of the robot is modeled according the Euler-Lagrange formulation as

$$M(q)\ddot{q} + C(q,\dot{q})\dot{q} + g(q) + F(q,\dot{q}) = \tau + J \quad (q) f_h, \quad (1)$$

where $M : \mathbb{R}^n \to \mathbb{R}^{n\times n}$ is the inertia matrix, $C : \mathbb{R}^n \times \mathbb{R}^n \to \mathbb{R}^{n\times n}$ is the matrix of Coriolis and centripetal effects, $g : \mathbb{R}^n \to \mathbb{R}^n$ is the gravitational torque, $F : \mathbb{R}^n \times \mathbb{R}^n \to \mathbb{R}^n$ is the vector of frictions, $\tau \in \mathbb{R}^n$ is the control input torque, $J : \mathbb{R}^n \to \mathbb{R}^{6\times n}$ is the geometric Jacobian, while $f_h \in \mathbb{R}^6$ is the force applied by the patient or the clinician to the end-effector of the robot through the handle.

In general, the control of the robot is carried out by means of a software that interacts with the low level controllers via an application program interface provided by the robot manufacturer. In the rest of the paper, this last one will be referred to as robot control interface (RCI). In the majority of cases, RCIs are interfaced with external software components by means of network communication protocols such as TCP/IP or UDP. Despite the effectiveness of this approach, it lacks of flexibility since it requires significant integration work in order to synchronize the transmission of information.

In the proposed rehabilitation framework, the robot should communicate with a rehabilitation interface, which is a GUI that allows to program, monitor, and analyze rehabilitation sessions. Due to the articulated nature of this last one (more details in Section IV), implementing a robust communication with the robot may require significant integration effort. Hence, both the control software and the rehabilitation interface are programmed as ROS2 nodes, denoted respectively as `robot_node` and `gui_node`, which share information about the robot state an the control actions by means of the ROS2 topics in Table I. The objective of the `robot_node`, which embeds the RCI, is to broadcast information about the state of the robot and, at the same time, receive a new control torque reference τ by the `gui_node` and send it to the low-level controllers through the RCI. It is important to note that while the `gui_node` is already implemented in Python programming language and requires no modifications (making the system "flexible"), the `robot_node` varies depending on the robot and must be implemented by the user to integrate the GUI with a new robot. However, this node is designed to be simple to develop and should be implemented following the flowchart shown in Fig. 2. More details are provided later in Section III.

TABLE I: ROS2 topics used to exchange information between the robot control software and the rehabilitation interface.

Topic name	Description
`/r/state/joints/pos`	Joints position vector
`/r/state/joints/vel`	Joints velocity vector
`/r/state/ee/pose`	End-effector pose
`/r/state/ee/vel`	End-effector velocity
`/r/ctrl/torques`	Input torque
`/r/ctrl/hg/start`	Start the robot handguide mode
`/r/ctrl/tc/start`	Start the robot torque control mode
`/r/ctrl/stop`	Stops the control of the robot

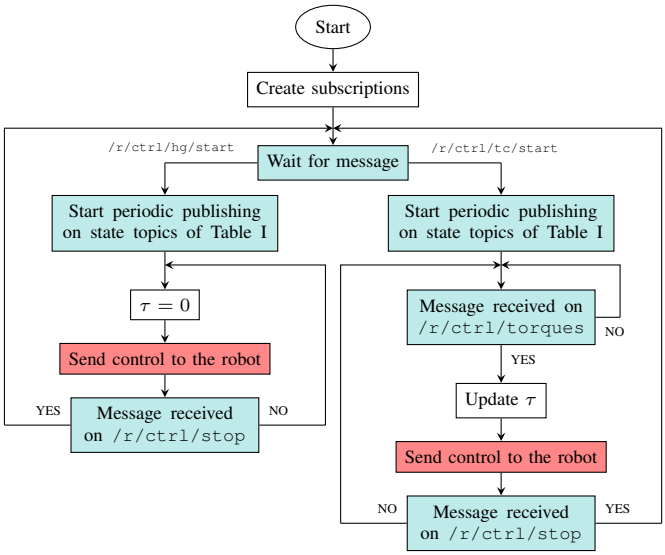


Fig. 2: Flowchart of the `robot_node` structure: red blocks indicate RCI communication, blue blocks indicate ROS2 communication.

III. Modes of Operation

The aim of this section is to provide a brief description of the modes of operation of the proposed robotics rehabilitation system, i.e., CO-PTP, trajectory recording, and TT, and how the robot is controlled in each of these modes.

A. Center Out Point To Point

In this mode of operation, the patient performs the CO-PTP exercise. In particular, the patient is asked to grasp the robot end-effector using the handle and move it from a starting point, toward one of the targets placed along a circle whose center coincides with the starting point, as depicted in Fig. 3, and reach back the center. The exercise can be performed in Traditional Mode (TM) and Cognitive Exercise Mode (CEM) that requires a mnemonic effort and consequently serves as both a physical and neurological training.

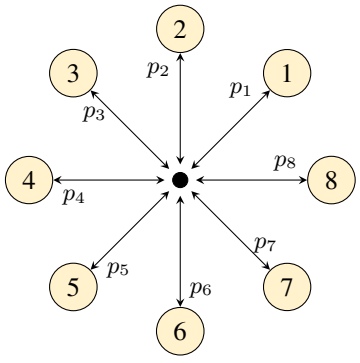


Fig. 3: Targets in the CO-PTP exercise with the associated ideal movement directions and selection probabilities.

In TM, the patient is simply instructed to perform a Reaching Movement (RM) on a specific target $i \in \{1, 2, \ldots, 8\}$. A RM is defined as the composition of two movements, the Center To Point (CTP) movement which starts from the center and ends in the target, and, vice versa, the Point To Center (PTC) movement which starts from the target and ends in the center. The system automatically detects when a RM is completed and the patient is instructed to perform another RM on target $i+1$. In particular, the RM is considered completed when both the velocity of the end effector and its distance from the central point are lower than 0.0005 m/s and 0.03 m, respectively. Once the operation is repeated for all the targets, the exercise is completed.

On the other hand, when the exercise is executed in CEM, the patient is asked to perform RMs on a sequence of the targets, in an order that is shown before the beginning of the exercise. The length of the sequence depends on the results of previous exercise iterations, while the speed with which the sequence is displayed depends on a parameter chosen by the clinician, and described in Section IV. The sequence depends on the past results and this is required since some patients, especially those affected by stroke, may have difficulties moving in specific directions. Therefore, the choice of targets in the sequence is not random but is designed to prioritize directions that require more effort from the patient, as described in the following.

Let $n_i \in \mathbb{N}_{>0}$ be the number of RMs carried out in the last rehabilitation session toward the i-th target, with $i \in \{1, 2, \ldots, 8\}$. Then, let $S_i \in \mathbb{R}_{>0}$ be a penalty score related to the i-th target defined as

$$S_i = \frac{\bar{s}_i + \bar{v}_i}{\bar{d}_i + \bar{e}_i} \tag{2}$$

where $\bar{d}_i, \bar{e}_i, \bar{s}_i, \bar{v}_i \in \mathbb{R}_{>0}$ are the sum of the normalized QMs described in Table II. In particular, let $x_i \in \{e_i, s_i, v_i, d_i\}$, then

$$\bar{x}_i = \sum_{j=1}^{n_i} \frac{x_{i,j} - \min_j x_{i,j}}{\max_j x_{i,j} - \min_j x_{i,j}}, \tag{3}$$

where $x_{i,j}$ is the QM associated with the j-th RM toward the i-th target.

TABLE II: Quality Metrics associated with the i-th target.

QM	Name	Description
e_i	Precision error	Distance between the endpoint of the CTP movement and the target
s_i	Smoothness	Ratio between the average speed and the maximum speed of the end-effector in a RM
v_i	Mean speed	Average speed of the end-effector in a RM
d_i	Duration	Time taken to complete a RM

Finally, the probability of the i-th target of being selected during the computation of the sequence can be defined as

$$p_i(\alpha_{\text{IOP}}) = \gamma(\alpha_{\text{IOP}}) + \sigma_i(\alpha_{\text{IOP}}), \tag{4}$$

with $p_i \in [0, 1]$ and $\sum_{i=1}^{8} p_i = 1$, and where $\alpha_{\text{IOP}} \in [0, 0.8]$ is a constant related to the Impact Of the Performance (IOP) of the previous sessions, and it is chosen by the clinician via the GUI, as detailed in Section IV. The first term of (4) is the same for all targets and it is defined as

$$\gamma = \frac{(1 - \alpha_{\text{IOP}})}{8}, \tag{5}$$

while the second one depends on the previous performance obtained by the patient moving toward the i-th target and is defined as

$$\sigma_i = \alpha_{\text{IOP}} \frac{S_i}{\sum_{i=1}^{n} S_i}. \tag{6}$$

To perform the CO-PTP exercise, the robot should be put in handguide mode. This can be done by the clinician which, by simply pressing a button of the GUI, publishes a message on the associated topic (see Table I). Since the patient, which, as detailed in (1), exerts a force f_h on the robot, should be able to move the end-effector effortlessly, the robot must be controlled so that it compensates the gravitational torque g. Since in the majority of the industrial robots gravity is compensated directly by internal controllers, it is sufficient that `robot_node` controls the manipulator setting $\tau = 0$.

B. Trajectory Recording

In this mode of operation, the clinician defines a three dimensional trajectory which is recorded and stored, along with the associated trajectory in the joint space.

During the recording phase, the robot is set into the handguide mode as described at the end of Section III-A, and the clinician is supposed to instruct the robot using a teaching by demonstration approach. In particular they need to grasp the end-effector and move it in the three dimensional space along a trajectory that the patient should follow with their hand afterwards in the TT mode. The value of the joint positions is stored locally to construct a trajectory $q^\star(t) \in \mathbb{R}^n$.

C. Trajectory Tracking

In this mode of use, the patient is required to grip the handle placed on the end effector and allow themselves to be guided by the robot, as it follows a prerecorded trajectory. The start of this exercise, and thus the beginning of the robot movement, is triggered by the clinician through the GUI, and involves the activation of torque control on the robot by means of the publication of a message on the associated topic (see Table I). Then, the `gui_node` computes the control signal as

$$\tau = K_P \Big] q - q^\star \big) + K_I \int_0^t \Big] q - q^\star \big) dy + \tau_r, \tag{7}$$

where $K_P, K_I \in \mathbb{R}^{n \times n}$ are diagonal gain matrices, while τ_r is a robust control component which aims to compensate the force f_h that the patient exerts on the robot while being carried by this last one. In particular, since f_h acts as a bounded matched disturbance, τ_r can be designed according to the *Sliding Mode Control* [21], widely adopted in the domain of robot control [22], [23], having

$$\tau_r = -\rho \frac{C_1(q - q^\star) + C_2(\dot{q} - \dot{q}^\star)}{||C_1(q - q^\star) + C_2(\dot{q} - \dot{q}^\star) + \varepsilon||}, \tag{8}$$

where $\rho \in \mathbb{R}_{>0}$ is a control gain, $C_1, C_2 \in \mathbb{R}^{n \times n}$ are diagonal design matrices with positive entries, while $\varepsilon \in \mathbb{R}_{>0}$ is a small design constant.

IV. The Proposed Graphical User Interface

The GUI, programmed in the `gui_node` and designed through Qt Designer, is structured as in Fig. 4, identifying three sections: the Trajectory Recording Section (TRS), the Patients Management Section (PMS), and the Individual Monitoring and Therapy Section (IMTS).

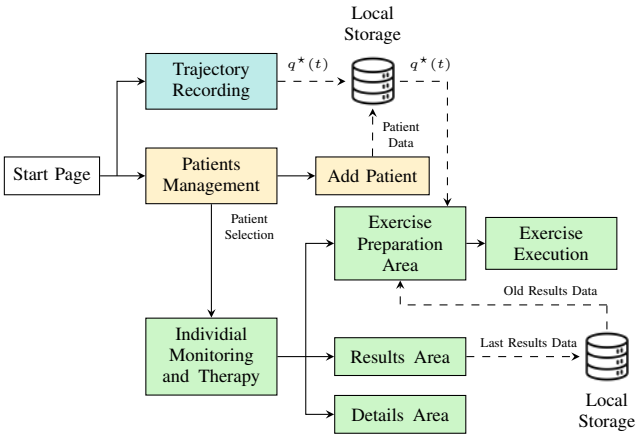


Fig. 4: Diagram of the GUI structure. The dashed lines represent interactions with the local storage.

The TRS is composed by a page from which the clinician can start the recording, then move the robot, defining a three dimensional trajectory for the end-effector from which the associated joints position trajectory $q^\star(t)$ is computed. Once the recording is completed, the user can choose to save both the end-effector and the joint position trajectory. In particular, this last one will be employed in the TT exercise, as detailed in Section III-C.

In the PMS, which can always be accessed by the user from a navigation bar placed on the top of the GUI, the clinician has access to information about patients that have been already registered in the system. From the same page, it is possible to register a new patient entering details that include first name, last name, the neurological condition and, optionally, a note with relevant information about the therapy. From the PMS page the clinician can enter the IMTS page for a patient.

In the IMTS, the clinician can monitor the patient's status by observing the results achieved in completed rehabilitation sessions and prepare and start exercises for the patient in a new rehabilitation session. The section is further divided into three areas, accessible through a sidebar: the Details Area (DA), the Exercise Preparation Area (EPA), and the Results Area (RA). In the DA the clinician can view and edit all the patient's details entered during the registration procedure. In the EPA, depicted in Fig. 5 the clinician can select the exercise for the patient and, if needed, adjust parameters governing how the exercise is conducted. Specifically, the user can choose between TT and CO-PTP as exercises to administer to the patient. The TT exercise, described in Section III-C, has only one mode of execution. Hence, the clinician is only required to select from a drop-down menu a trajectory among the ones that have been already recorded and ask the patient to grasp

the robot end-effector. Then, by pressing a button, the robot starts reproducing the trajectory. As for the CO-PTP exercise, described in Section III-A, it can be performed in TM or CEM. Hence, the clinician is asked to choose between the TM and CEM modes. If CEM is selected, the clinician is prompted to adjust the velocity and the parameter α_{IOP} in (4), by means of two sliders.

Independently from the mode, during the CO-PTP exercise the patient is provided with visual feedback on a screen, by means of a real-time plot that shows the actual path the patient is following, overlapped to the desired straight line trajectories connecting the center and the targets in Fig. 3.

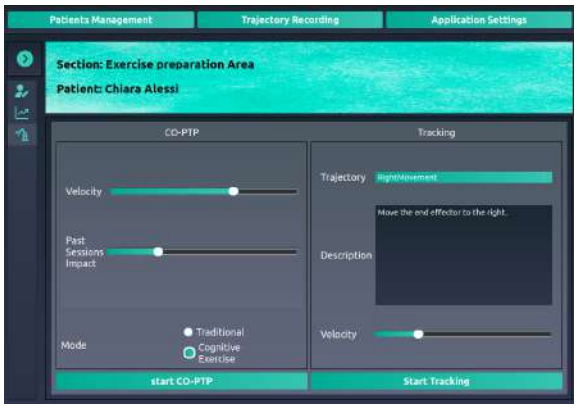


Fig. 5: Screenshot of the EPA, in which the clinician can setup the parameters of the exercises.

In the RA, the clinician can review the results obtained by the patient during the CO-PTP exercise. These results, based on the QMs in Table II, are presented in three different formats, *single session*, *statistical comparison*, and *progress*.

As for the results of a single session associated with a specific QM, they are displayed using a radar plot, in which each vertex is related to one of the CO-PTP targets. Given a specific movement direction, the distance between the center and the associated vertex depends on the value of the selected QM achieved by the patient while moving the end-effector during the session. An example is presented in Fig. 6.

As for the progress format, it allows the clinician to select a QM and a target index $i \in \{1, 2, \ldots, 8\}$, identified by an angle. Then, it generates a plot depicting the trend over time of the mean value of the QM computed during the movement accomplished toward the selected target.

Finally, it is possible to see the results associated with a specific QM in the statistical comparison format. In particular, the QM scores obtained during all the RMs that have been carried out by the patient, are divided by session and by target, and stored in a dataset. The two ways Friedman test is then used to check whether there exists at least one session in which the selected QMs scores are statistically different from the ones of the other sessions. In case there is no significant difference, the clinician is informed via text message; otherwise, a heat map like the one in Fig. 7 is presented. This heatmap, which represents the results of a Nemenyi post hoc test for multiple

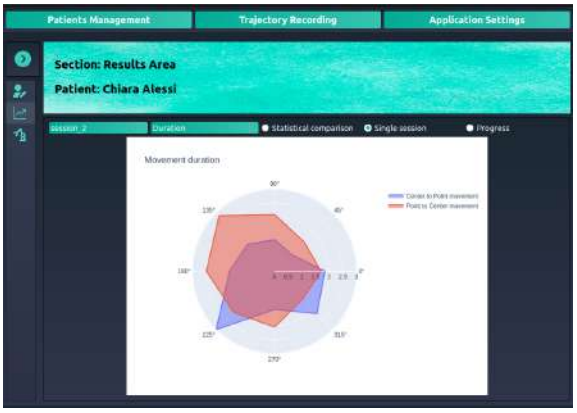


Fig. 6: Example of a radar plot to show the results of a single session related to CO-PTP duration d_i, including the results obtained in the CTP motion (blue) and the PTC motion (red)

comparisons, consists of a matrix in which each element is associated with a couple of sessions. If the difference between such sessions is significant, the color of that element of the heatmap is darker and the p-value of the post hoc test for multiple comparison, written in the center of the element, is lower than 0.05.



Fig. 7: Example of heatmap showing presence of statistical differences between sessions.

V. Case Study

In order to assess the effectiveness of the software and its compatibility with industrial robots, it was tested in combination with Franka Emika Panda, a collaborative robot characterized by 7 degrees of freedom. A customized 3D-printed handle was attached to the end effector, to allow the user to move it. The software was installed on a workstation running Ubuntu 22.04 with ROS2 Foxy. Communication with the Franka Emika Panda was managed through the dedicated `robot_node`, implemented in C++ following the workflow illustrated in Figure 2. The Robot Control Interface (RCI) was based on the *libfranka* library, which provides low-level access to the robot's control and state information. Several key functionalities were tested, including the recording of a new trajectory for TT exercises as described in Section III-B, the

configuration and execution of rehabilitation exercises and the visualization of results data provided by the GUI. The robot demonstrated full compatibility with the software, successfully enabling real-time data visualization and collection during the CO-PTP exercise and the trajectory recording.

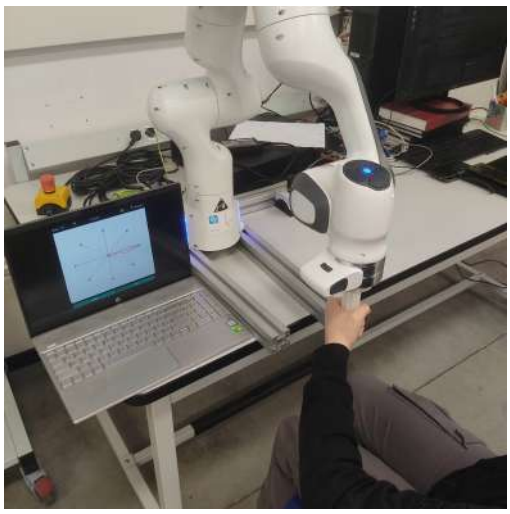


Fig. 8: Experimental testing of the compatibility of the software with the Franka Emika Panda robot: real-time feedback visualization during CO-PTP exercise

VI. Conclusions

In this paper, a software equipped with GUI for a flexible upper limb robotic rehabilitation via industrial manipulator has been proposed. The main purpose of such a software is to help the clinician in the evaluation phase, allowing them to monitor the condition of the patient through sessions via intuitive graphs, and design new exercises via simple interaction with the robot. Unlike other GUI-based software, the proposed one can be interfaced seamlessly with any industrial collaborative manipulator, making it an easily adaptable solution which allows for robotics rehabilitation sessions which do not require any customized technology. The software has been assessed in combination with the Franka Emika Panda robot, demonstrating its full compatibility and real-time data processing capabilities. In future studies, we aim to evaluate the system's usability and effectiveness in a clinical environment. Additionally, we plan to expand the graphical interface by integrating exergames to enhance patient engagement.

References

[1] J. Dumurgier and C. Tzourio, "Epidemiology of neurological diseases in older adults," *Revue neurologique*, vol. 176, no. 9, pp. 642–648, 2020.

[2] E. R. Dorsey, A. Elbaz, E. Nichols, N. Abbasi, F. Abd-Allah, A. Abdelalim, J. C. Adsuar, M. G. Ansha, C. Brayne, J.-Y. J. Choi *et al.*, "Global, regional, and national burden of parkinson's disease, 1990–2016: a systematic analysis for the global burden of disease study 2016," *The Lancet Neurology*, vol. 17, no. 11, pp. 939–953, 2018.

[3] G. Collaborators, V. L. Feigin, B. A. Stark, C. O. Johnson, G. A. Roth, C. Bisignano, G. G. Abady, M. Abbasifard, M. Abbasi-Kangevari, F. Abd-Allah *et al.*, "Global, regional, and national burden of stroke and its risk factors, 1990–2019: a systematic analysis for the global burden of disease study 2019," *The Lancet Neurology*, vol. 20, no. 10, pp. 795–820, 2021.

[4] C. Nicholson-Smith, V. Mehrabi, S. F. Atashzar, and R. V. Patel, "A multi-functional lower-and upper-limb stroke rehabilitation robot," *IEEE Transactions on Medical Robotics and Bionics*, vol. 2, no. 4, pp. 549–552, 2020.

[5] J. B. Fernandes, C. Godinho, T. F. Outeiro, and C. L. Baixinho, "Personalized care in neurological diseases," p. 1216902, 2023.

[6] N. Nordin, S. Q. Xie, and B. Wünsche, "Assessment of movement quality in robot-assisted upper limb rehabilitation after stroke: a review," *Journal of neuroengineering and rehabilitation*, vol. 11, no. 1, pp. 1–23, 2014.

[7] D. J. Gladstone, C. J. Danells, and S. E. Black, "The fugl-meyer assessment of motor recovery after stroke: a critical review of its measurement properties," *Neurorehabilitation and neural repair*, vol. 16, no. 3, pp. 232–240, 2002.

[8] V. Do Tran, P. Dario, and S. Mazzoleni, "Kinematic measures for upper limb robot-assisted therapy following stroke and correlations with clinical outcome measures: A review," *Medical engineering & physics*, vol. 53, pp. 13–31, 2018.

[9] L. Zollo, E. Gallotta, E. Guglielmelli, and S. Sterzi, "Robotic technologies and rehabilitation: new tools for upper-limb therapy and assessment in chronic stroke." *European journal of physical and rehabilitation medicine*, vol. 47, no. 2, pp. 223–236, 2011.

[10] L. Savaré, F. Ieva, G. Corrao, and A. Lora, "Mining and evaluation of patients' diagnostic therapeutic paths through state sequences analysis," *arXiv preprint arXiv:2209.04384*, 2022.

[11] M. Sommerhalder, N. Kurth, J. Song, and R. Riener, "Armstick-an intuitive therapist interface for upper-limb rehabilitation robots," in *2022 International Conference on Rehabilitation Robotics (ICORR)*. IEEE, 2022, pp. 1–6.

[12] M. Ríos-Hernández, J. M. Jacinto-Villegas, O. Portillo-Rodríguez, and A. H. Vilchis-González, "User-centered design and evaluation of an upper limb rehabilitation system with a virtual environment," *Applied Sciences*, vol. 11, no. 20, p. 9500, 2021.

[13] Y. Zimmermann, A. Forino, R. Riener, and M. Hutter, "Anyexo: A versatile and dynamic upper-limb rehabilitation robot," *IEEE Robotics and Automation Letters*, vol. 4, no. 4, pp. 3649–3656, 2019.

[14] H. Ren, T. Liu, and J. Wang, "Design and analysis of an upper limb rehabilitation robot based on multimodal control," *Sensors*, vol. 23, no. 21, p. 8801, 2023.

[15] P. Maciejasz, J. Eschweiler, K. Gerlach-Hahn, A. Jansen-Troy, and S. Leonhardt, "A survey on robotic devices for upper limb rehabilitation," *Journal of neuroengineering and rehabilitation*, vol. 11, pp. 1–29, 2014.

[16] E. Kyrkjebø, M. J. Laastad, and Ø. Stavdahl, "Feasibility of the ur5 industrial robot for robotic rehabilitation of the upper limbs after stroke," in *2018 IEEE/RSJ international conference on intelligent robots and systems (IROS)*. IEEE, 2018, pp. 1–6.

[17] B. Sheng, S. Xie, L. Tang, C. Deng, and Y. Zhang, "An industrial robot-based rehabilitation system for bilateral exercises," *IEEE Access*, vol. 7, pp. 151 282–151 294, 2019.

[18] M. Caimmi, N. Pedrocchi, A. Scano, M. Malosio, F. Vicentini, L. M. Tosatti, and F. Molteni, "Proprioceptivity and upper-extremity dynamics in robot-assisted reaching movement," in *2012 4th IEEE RAS & EMBS International Conference on Biomedical Robotics and Biomechatronics (BioRob)*. IEEE, 2012, pp. 1316–1322.

[19] C. Liakopoulou, M. Mansourvar, A. Bøglid, A. Naemi, and A. Stengaard Sørensen, "Data vizualization dashboards in robotic rehabilitation," in *Public Health and Informatics*. IOS Press, 2021, pp. 278–282.

[20] B. Siciliano, L. Sciavicco, L. Villani, and G. Oriolo, *Robotics: Modelling, Planning and Control*. Springer London, 2008.

[21] V. Utkin, J. Guldner, and X. Shi, *Sliding Modes in Elctromechanical Systems*. Taylor & Francis, 1999.

[22] A. Ferrara and G. P. Incremona, "Design of an integral suboptimal second-order sliding mode controller for the robust motion control of robot manipulators," *IEEE Transactions on Control Systems Technology*, vol. 23, no. 6, pp. 2316–2325, 2015.

[23] N. Sacchi, E. Vacchini, and A. Ferrara, "Human-robot ergonomic handover via deep neural network based adaptive integral sliding mode control," in *2024 European Control Conference (ECC)*. IEEE, 2024, pp. 585–590.

Adaptive Motor Unit Decomposition During Walking: Towards Systematic Validation

Antonio Gogeascoechea*, Nathan van Dieren*, Utku S. Yavuz, and Massimo Sartori

***Abstract*— Understanding motor unit (MU) behavior during locomotion is essential for uncovering the neural control of human movement and advancing the development of assistive technologies. Although high-density electromyography (HD-EMG) allows for the extraction of individual MU firing activity, conventional methods are typically restricted to isometric or slow dynamic contractions. Additionally, accurate characterization of MU twitch responses is essential for decoding the mechanical output of muscle contractions. In this study, we present an adaptive online-capable methodology for decoding soleus' MU firing events and MU-specific activation dynamics along with a conservative validation during locomotion. Our proposed framework incorporates advanced blind source separation techniques, adapted for the detection of low-threshold MUs and capable of addressing non-stationary MU action potential variations. The framework is built on three main components: (1) an offline process to derive decomposition parameters and optimal twitch characteristics from isometric and walking trials, (2) an online approach that includes both static and adaptive decomposition strategies to refine MU firing event estimation and apply derived twitch properties for real-time MU-specific activation, and (3) a validation of the decoded MU spike trains against those derived from intramuscular EMG, as well as a comparison of MU-specific activation against ankle joint moments. Experimental results demonstrated that the adaptive approach improved the agreement with intramuscular EMG-derived spike trains and provided strong correlations between MU-specific activation and ankle joint moments.**

This work holds significant promise for future real-time applications in assistive devices that can more effectively adapt to individual patient needs and track their progress over time.

I. Introduction

Interfacing with motor units (MUs) *in vivo* provides a unique window into the neural commands that drive human movement. Each MU, comprising an α-motor neuron and the muscle fibers it innervates, represents the smallest functional unit of force generation, making it essential for understanding both healthy and impaired motor function (*e.g.* [1]–[3]). Decoding MU activity can therefore play a pivotal role in advancing mobility restoration and enhancing rehabilitation outcomes for individuals with motor impairments.

High-density electromyography (HD-EMG) combined with blind source separation (BSS) has become a promising approach for decoding MU behavior, with significant potential for advancing rehabilitation technologies. BSS techniques allow for the identification of MU discharge patterns without *a priori* knowledge of MU action potential (MUAP) shapes, relying solely on the statistical properties of MU discharges [4]. This approach has enabled the non-invasive characterization of α-motor neuron discharge patterns in both healthy and neurologically impaired individuals [1]–[3].

Despite their promise, BSS techniques face two significant limitations. First, they typically assume stationary conditions [4], [5], restricting their application to isometric or slow dynamic contractions. This assumption poses challenges for more complex, real-world scenarios such as walking, where MUAPs vary continuously and muscle activations are rapid and high in amplitude. Second, BSS is susceptible to MU amplitude cancellation [6], a phenomenon that complicates the accurate decomposition of low-threshold MUs during high-force activities. Overcoming these challenges is essential for reliable MU analysis during locomotion. Additionally, decoding actual joint moments requires more than just MU firing patterns; it needs linking these patterns to their corresponding twitch contractile responses to translate neural commands into force production effectively.

In this context, our previous work [7] laid the foundation for real-time decoding of both MU firing events and their corresponding twitch responses during locomotion. Specifically, our proposed MU-specific formulations [7], [8] provided activation patterns that better described ankle joint moments compared to conventional EMG envelopes. To achieve this, we integrated state-of-the-art methodologies aimed at reducing amplitude cancellation effects, including peel-off approaches [9], [10], and decomposing MUs online using offline-estimated separation vectors (MU Filters) [11]–[13]. Additionally, we focused on the soleus muscle, which experiences minimal fiber length variation during the push-off phase of the gait cycle [14], [15], making it well-suited for decoding MUs during walking. However, the non-stationary nature of MUAPs remained a challenge, as MUAPs can vary even in isometric conditions (*e.g.* contraction intensity [16])). Furthermore, validation at the MU firing level is still required. While our findings indicated that the decoded MUs produced activation profiles closely correlated with joint moments, we lacked ground truth data to confirm the accuracy of the decoded firings.

In this study, we focus on extending our methodology to address variations in MUAP shapes during locomotion and validating its accuracy using intramuscular EMG (iEMG) as a benchmark for MU decomposition. These enhancements improve the robustness of our framework and allow for more precise muscle activation estimates. Our validated method-

*Both authors contributed equally to this work.

Research supported by the European Research Council (ERC) Consolidator Grant ROBOREACTOR (grant no. 101123866) and ERC Proof of Concept Grant SMARTSENS (grant no. 101113279).

A. Gogeascoechea and M. Sartori are with the Department of Biomechanical Engineering, University of Twente, The Netherlands. (email: a.d.j.gogeascoecheahernandez@utwente.nl). N. van Dieren and U.S. Yavuz are with the Biomedical Signals and Systems Group, University of Twente.

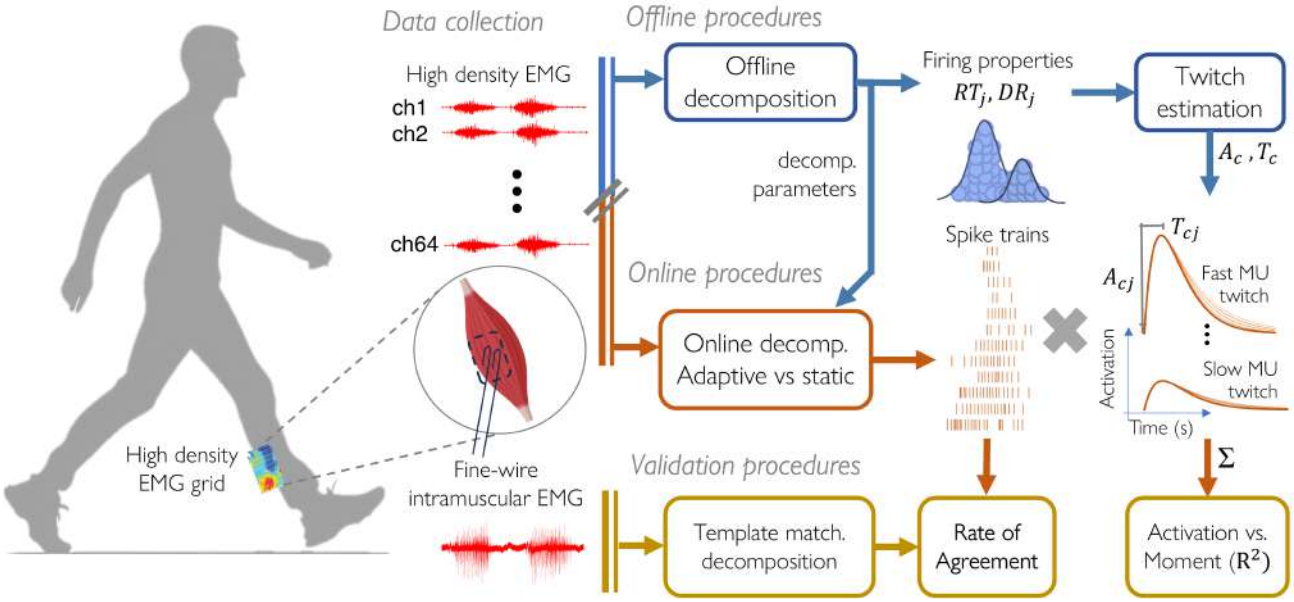


Fig. 1. Study overview. HD-EMG and iEMG are recorded from the soleus muscle during walking and low-force isometric trials. The HD-EMG data are split for offline and (pseudo-)online decomposition of motor unit (MU) firing events. The offline processes provide decomposition parameters and MU twitch properties. These are then used online for decoding MU spike train and activation using adaptive and static approaches. HD-EMG-derived MU spike trains are validated against spike trains obtained from iEMG (via template-matching). Muscle activations are assessed against ankle joint moments derived from inverse dynamics. RT, DR, A_c, and T_c represent recruitment threshold, discharge rate, twitch amplitude, and contraction time, respectively.

ology has the potential to transform the control of assistive devices, allowing real-time adaptability and feedback that seamlessly integrate with the user's neuro-musculoskeletal system, ultimately promoting a more natural and effective rehabilitation experience.

II. Methods

Overview of our framework

Our framework comprises three main components (Fig. 1). First, an offline procedure for extracting decomposition parameters and optimal twitch characteristics from a training dataset including isometric and walking trials (Section II-B). Second, two online decomposition approaches: a static approach that reuses the pre-determined decomposition parameters and an adaptive approach that updates them to improve the estimation of MU firing events. Both approaches use the derived twitch characteristics to produce MU-specific activation dynamics (Section II-C). Third, a validation step involving the comparison of HD-EMG-decoded firing events with those obtained from iEMG, as well as an assessment of the activation profiles against ankle moments (Section II-D). All procedures were approved by the ethical committee CMO region Arnhem-Nijmegen (protocol ID: NL73230.091.20).

A. Data Collection

Kinematic, kinetic, iEMG, and HD-EMG data were collected from a healthy participant during isometric and walking trials. The experimental protocol included walking for a minute at three different speeds (preferred, slow, and fast), along with a sustained push-off trial at a sub-maximal force levels (∼30% MVC).

Motion capture data and ground reaction forces (GRFs) were synchronously recorded using a motion tracking system (Qualisys, Goteborg, Sweden, 100 Hz) and a force plate (Bertec Co., Columbus, OH, USA, 2000 Hz). Reference ankle angles and moments were derived from marker trajectories and GRFs via inverse kinematics and inverse dynamics.

EMG recordings were performed using TMSi amplifiers (TMS International B.V., Oldenzaal, The Netherlands). IEMG signals were recorded with a 16-channel EMG amplifier at 17295 Hz (TMSi Refa). A bipolar fine-wire electrode was inserted diagonally at a shallow depth (∼1 cm) into the medial part of the soleus to record from superficial fibers. For HD-EMG recordings, an 8x8 electrode grid (4.5mm of inter-electrode distance) was placed over the intramuscular electrode. HD-EMG data were collected using a 64-channel EMG amplifier at a sampling rate of 4000 Hz (TMSi SAGA).

The HD-EMG data were split into sets for estimating and refining MU filters (offline procedures), and for (pseudo) online decomposition. For the offline decomposition, we employed the low-force push-off trial and half of the walking cycles. For the pseudo-online decomposition, we used the remaining walking data. HD-EMGs were band-pass filtered between 10-500 Hz with a fourth-order Butterworth filter, and poor-quality channels (low signal-to-noise) were excluded. IEMGs were high-pass filtered at 1000 Hz with a first-order Butterworth filter [17].

B. Offline procedures

1) Decomposition parameter estimation: To estimate decomposition parameters offline, which are subsequently utilized for online procedures (Section II-C), we employed a de-convolutive blind source separation (BSS) approach [4], [5] as follows (1):

$$s_j = c_{s_j z}^T C_{zz}^{-1} z, \tag{1}$$

where $w_j = c_{s_j z}^T C_{zz}^{-1}$ is the separation vector of the j_{th} MU, $c_{s_j z}$ is the cross-correlation vector between the source s_j and

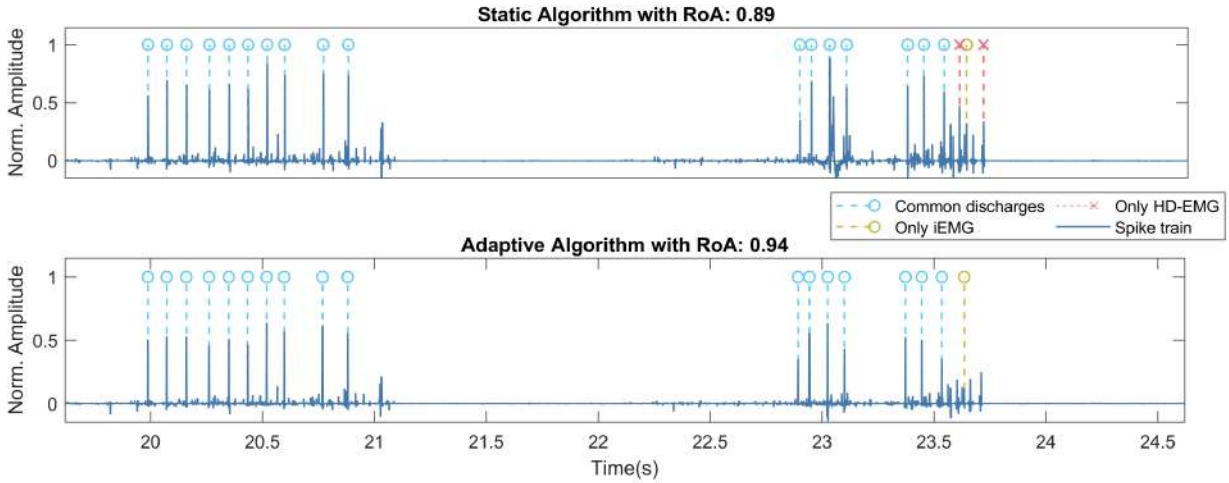


Fig. 2. Validation of HD-EMG-decoded spike trains against reference derived from iEMG (representative example, walking speed: 0.4 m/s)

the whitened extended signals z, and C_{zz} is the covariance matrix of the whitened extended signals.

The extension of the signals was computed by incorporating their delayed versions by a factor of 16. The extended signals were subsequently whitened using singular value decomposition. A fixed-point algorithm [5] was then applied to increase the sparsity of each source (s_j). For each iteration, the separation vector (w_j) was initialized as the vector with the maximum squared summation of the extended signals (z) across all time points, which indicates the instance with the highest signal activity potentially representing one or more MU discharges [4]. We then maximized the level of the sparsity of each source (contrast function: log cosh) until convergence (tolerance: 10^{-4}). For obtaining MU spike trains, the resulting source was squared to identify peaks with a minimum separation of 20 ms. The peaks were classified as spikes or noise using K-means classification [5], [18].

A refinement algorithm was then employed to enhance the estimation of MU spike trains by iteratively recalculating the separation vector (w_j) and updating the source estimation process (squaring, peak detection, and classification) until the maximum silhouette value was achieved [7], [19]. Separation vectors were selected and considered MU filters if their corresponding MU spike train estimation yielded silhouette values exceeding 0.87 (indicating high-quality separability).

To decode low-threshold MUs in walking data, the MU filters derived from isometric trials were further refined. The refinement algorithm was initialized with MU filters obtained from the sub-maximal isometric contraction trial [7], and these were adjusted using walking data. The resulting spike trains from the refined MU filters were compared against those detected in the walking trials, and duplicates were removed (common discharges $> 30\%$).

This step yielded MU filters, classification centroids, covariance matrix, extension factor, EMG mask (with good-quality channels), and normalization factors.

2) MU twitch properties estimation: Each MU twitch response (a) was modeled as the impulse response of a second-order system [20] defined by two twitch properties: peak amplitude and contraction time. In prior work, we characterized these properties by identifying a wide range of MU types [8], [21] and assigning specific twitch responses to individual MU spike trains based on this characterization. In this work, we applied the firing-to-twitch property transformations established in [8] to generate initial estimates for MU twitch properties and activation dynamics.

These initial estimates were further optimized through an iterative calibration process to minimize the delay and enhance the correlation between the resulting MU-specific activation profiles and the ankle moment [7]. Specifically, contraction times and peak amplitudes were iteratively adjusted provided that the delay decreased and the correlation improved. This approach was chosen to enhance the responsiveness of the activation model [20] while preserving its congruence with the resulting force.

C. Online procedures

We simulated an online setting by segmenting the EMGs of the test cycles in batches of several sizes.

1) Adaptive decomposition: To adapt to the non-stationarities in the signals, we propose an adaptive algorithm that only updates the separation vectors every time new spikes are detected. It uses the non-whitened equivalent of the CKC algorithm:

$$s_j = c_{s_j x}^T C_{xx}^{-1} x. \tag{2}$$

In every batch, the covariance matrix was updated with [19] (3):

$$C_{\bar{x}\bar{x}} = (1-\lambda) \cdot C_{\bar{x}\bar{x}} + \lambda \cdot C_{\Delta\Delta x}. \tag{3}$$

in which λ is the learning rate and $\Delta\bar{x}$ the extended EMG signals in the new batch. A new source estimation was made Eq. 2 and if any spikes (Ψ_i) were found, the filter was updated with (4):

$$c_{s_j x} = (1-\lambda) \cdot c_{s_j,x} + \lambda \cdot \frac{1}{\text{card}(\Psi_i)} \sum_{n_k \in \Psi_i} \bar{x}(n_k). \tag{4}$$

Unlike Chen et al. [10], we used a weighted average to update the $c_{s_j x}$ with the newfound spikes. The centroids

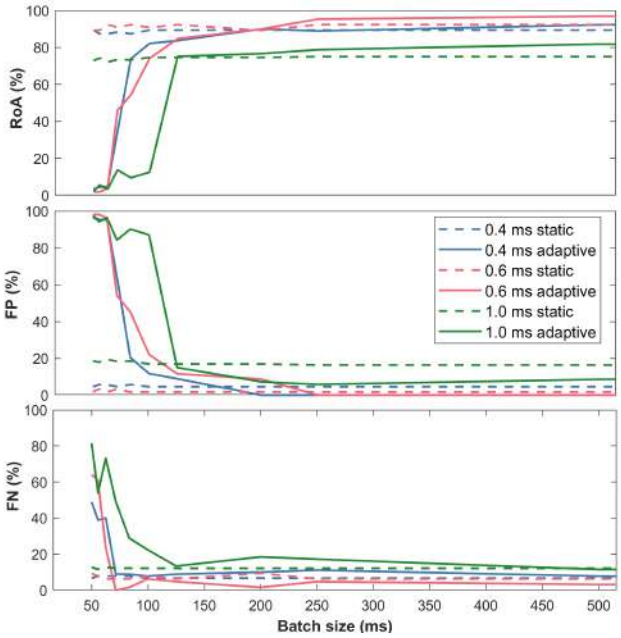


Fig. 3. Accuracy (RoA, FP, FN) across batch sizes

were updated with the following weighted average calculation [10](5):

$$T_{ij} = \frac{w_1 T_{ij} + w_2 T_{ij}^{'}}{w_1 + w_2}, \quad i = 1, 2, \tag{5}$$

where T_{ij} is the previous centroid of spikes (i = 1) and noise (i = 2) for the j_{th} spike train, T'_{ij} is the mean of the newfound spikes. $w1$ and $w2$ are the weighting factor of the centroids. $w1$ was set to 5 empirically, $w2$ was determined as the number of newfound spikes in a batch. λ was set at 0.05 empirically.

2) Static decomposition: To compare the adaptive method with traditional static approaches (*e.g.*, [18]), we re-used the offline identified MU filters to estimate the sources using Eq. (1). Similarly, spike classification was performed by re-applying the derived centroids and normalization factors.

3) MU-specific activation dynamics: To compute MU activation profiles online, the activation was discretized [22] to filter each spike train with its offline-estimated twitch model. The combined contributions of all MUs were summed to define the overall muscle activation.

D. Validation procedures

1) iEMG template matching: A reference decomposition was performed through template matching of iEMG [17]. All identified spikes and templates were thoroughly inspected and validated by an expert to ensure accuracy.

2) MU firing validation: Both decompositions (iEMG and HD-EMG) were compared by calculating the rate of agreement (RoA) for the static and adaptive algorithm (6):

$$RoA = \frac{C}{C + I + O} \cdot 100\%, \tag{6}$$

where C is the number of common discharges between iEMG and HD-EMG decomposition (tolerance window $\pm$ 0.5 ms),

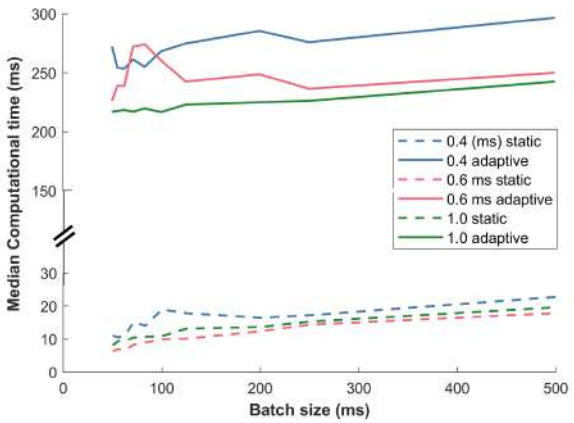


Fig. 4. Computational time (ms) across batch sizes

I the number of spikes only identified in iEMG, and O the number of spikes only identified in HD-EMG decomposition. Two spike trains were classified as originating from the same MU if the common discharges (C) were larger than 30% [4], [5]. Also, both false positive and false negative rates were calculated as (7,8):

$$FN = \frac{I}{I + C} \cdot 100\%, \tag{7}$$

$$FP = \frac{O}{O + C} \cdot 100\%, \tag{8}$$

3) MU-specific activation assessment: The coefficients of determination (R^2) between the estimates of muscle activation (static and dynamic approaches, and EMG envelopes) and moments were computed per gait cycle as the square of the maximum normalized correlation. Statistical significant differences were tested using the Wilcoxon signed-rank test.

4) Real-time assessment: To test the real-time capabilities of our methodology, the median values of the computational times were calculated for the pseudo-online algorithms. All the procedures were executed on a computer with an Intel Core i7-9750H CPU (2.60 GHz) with 16 GB RAM.

III. Results

In offline decomposition, 9, 10, and 9 MUs were identified in 0.4, 0.6, and 1.0 m/s walking trials, respectively, with 4, 1, and 2 extra MUs refined from low-force isometric MUs. One common MU was found between decompositions at each speed. Figure 2 presents a representative example (slow walking speed), comparing spike trains derived from HD-EMG using both adaptive and static approaches against the ground truth spike trains obtained from iEMG. Figure 3 summarizes the overall results of these comparisons across batch sizes, highlighting the RoA, FN, and FP. The validation of our framework at the MU firing level demonstrated superior performance of the adaptive approach compared to the static approach, particularly for windows larger than 200 ms. For slow speeds ($\leq$ 0.6 m/s), RoAs $>$ 90% were found for both static and adaptive algorithms. Fig. 4 shows the median computational times for the online procedures across batch sizes. Figure 5 illustrates a comparison between the

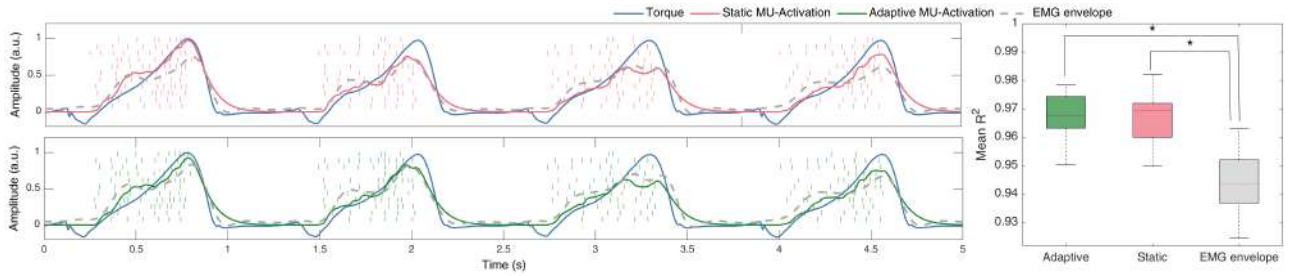


Fig. 5. Comparison between normalized activation estimates and ankle moments. Left panel: Calculated activation versus joint moment for 1.0 ms speed. Right panel: Coefficients of determination between activation estimates and ankle moments per gait cycle. * indicates significant differences (P<0.001).

MU activation estimates and the joint ankle moment, along with the R^2 values for the test trial (1.0 m/s speed). The R^2 values of the adaptive and static algorithms were higher than those of the EMG envelope ($P < 0.001$).

IV. Discussion

We proposed and validated an online-capable adaptive methodology for decoding MU firing events and their associated MU-specific activation dynamics during locomotion, yielding preliminary results in a healthy participant. Our approach offered three key contributions: first, we adapted advanced decomposition algorithms [5], [18] to facilitate the identification of low-threshold MUs [7] and to account for variations in MUAPs [10], [19] during locomotion. Second, we incorporated our established methodology [7], [8] for decoding MU twitch responses and deriving muscle activation. Third, we validated our methodology at both the MU firing level, using iEMG, and the activation level, through comparison with joint moments.

The validation of our framework at the MU firing level demonstrated superior performance of the adaptive approach compared to the static approach, particularly over longer observation windows (Fig. 3). Although the static approach is computationally faster and could be advantageous for real-time applications, its reliance on pre-defined MU filters limits its adaptability. A potential strategy could combine the strengths of both approaches, using the static method to deliver rapid estimates while the adaptive algorithm runs in parallel to refine the MU filters approximately every 200 ms (Figure 4). This integrated approach balances real-time performance with enhanced accuracy, offering a practical solution for continuous decoding during locomotion.

The assessment of our framework against joint moment predictions revealed comparable results for both the adaptive and static approaches (Fig. 5). This similarity may arise from several factors. One potential explanation is that the twitch models act as low-pass filters, which may reduce resolution and mask differences between the methods. Another contributing factor might be the fact of comparing activation profiles with joint torque, which does not capture nonlinearities in resulting musculoskeletal function. To enhance joint-level assessments, future work should integrate our framework with personalized neuro-musculoskeletal (NMS) models [8], [23], [24] to generate muscle force and joint moment predictions. These models can generate detailed predictions of muscle force and joint moments, allowing for a more precise and direct comparison of predicted joint moments with actual measurements. Such integration would not only enhance the validation but also establish a robust NMS tool, serving as a digital twin to simultaneously decode MU, muscle-tendon unit, and joint-level functions.

Moreover, to further improve the accuracy of the twitch models, future work should consider incorporating an adaptive approach that accounts for time-dependent properties of MU twitches, such as potentiation and fatigue [25], [26]. These features are crucial for capturing the full range of MU behavior during sustained and repetitive movements, and could potentially improve the activation accuracy. Furthermore, a significant challenge remains in validating twitch models in vivo due to the complexities of capturing real-time muscle responses. In this regard, recent advancements in imaging techniques, such as ultra-fast ultrasound imaging [27] and microendoscopy [28], present promising alternatives for in vivo validation. These emerging technologies have the potential to offer the resolution and temporal accuracy required to assess twitch dynamics and validate their integration into our adaptive framework, ultimately improving the realism and applicability of MU-driven models in clinical and rehabilitation contexts.

Once coupled with personalized NMS models, our framework could serve as a tool for driving neuro-robotic devices, enabling MU-driven control strategies for rehabilitation applications. Specifically, it was designed to assist with push-off during the gait cycle in individuals with neurological impairments. This methodology could facilitate real-time parameter adjustments, dynamically adapting to the patients immediate needs. Beyond in-session adjustments, our framework may offer clinicians valuable insights into longer-term rehabilitation progress, such as changes in MU behavior and remodeling [29], [30]. This information could be used to fine-tune rehabilitation strategies across multi-week sessions, ensuring personalized and progressive adaptation to the patients evolving motor function.

A key limitation of this study is its validation on a single able-bodied participant. Before translating our methodology into practical MU-driven control of neuro-modulatory devices, future research should prioritize evaluating its robustness across a broader and more diverse cohort, particularly individuals with neurological impairments. Pathological conditions often involve altered MU behavior, such as increased persistent inward currents (PICs) and abnormal synergies [31], [32]. Differentiating between healthy and pathological

MU behavior is crucial for ensuring that the framework can accurately identify desired MU activity and provide clinically relevant insights, such as tracking MU remodeling over time. Expanding the participant pool will not only help validate the frameworks adaptability to diverse clinical scenarios but also ensure its potential for tailoring interventions to address individual variations in MU behavior.

In conclusion, we presented a validated, online-capable framework for decoding MU firing events and their corresponding activation dynamics during locomotion. Our methodology demonstrated the potential to provide insights into MU-specific contributions to joint moments and to inform the design of neuro-rehabilitation devices. With further validation in a broader and more diverse population, this framework could enable real-time adjustments to device parameters while providing clinicians with detailed information on long-term adaptations at the MU, muscle, and joint levels, ultimately supporting more personalized and effective neuro-rehabilitation strategies.

REFERENCES

[1] E. Martinez-Valdes, F. Negro, A. Botter, P. A. Pincheira, G. L. Cerone, D. Falla, G. A. Lichtwark, and A. G. Cresswell, "Modulations in motor unit discharge are related to changes in fascicle length during isometric contractions," *Journal of Applied Physiology*, vol. 133, pp. 1136–1148, 11 2022.

[2] A. Holobar, V. Glaser, J. A. Gallego, J. L. Dideriksen, and D. Farina, "Non-invasive characterization of motor unit behaviour in pathological tremor," *Journal of Neural Engineering*, vol. 9, no. 5, 2012.

[3] A. Gogeascoechea, A. Kuck, E. van Asseldonk, F. Negro, J. R. Buitenweg, U. S. Yavuz, and M. Sartori, "Interfacing With Alpha Motor Neurons in Spinal Cord Injury Patients Receiving Trans-spinal Electrical Stimulation," *Frontiers in Neurology*, vol. 11, p. 493, 6 2020.

[4] A. Holobar and D. Zazula, "Multichannel blind source separation using convolution Kernel compensation," *IEEE Transactions on Signal Processing*, vol. 55, pp. 4487–4496, 9 2007.

[5] F. Negro, S. Muceli, A. M. Castronovo, A. Holobar, and D. Farina, "Multi-channel intramuscular and surface EMG decomposition by convolutive blind source separation," *Journal of Neural Engineering*, vol. 13, no. 2, 2016.

[6] K. G. Keenan, D. Farina, R. Merletti, and R. M. Enoka, "Amplitude cancellation reduces the size of motor unit potentials averaged from the surface EMG," *Journal of Applied Physiology*, vol. 100, pp. 1928–1937, 6 2006.

[7] A. Gogeascoechea, M. I. Mohamed Refai, U. S. Yavuz, and M. Sartori, "Towards Real-Time Decoding of Motor Unit Firing Events and Resulting Muscle Activation During Human Locomotion and High-Force Contractions," *Proceedings of the IEEE RAS and EMBS International Conference on Biomedical Robotics and Biomechatronics*, pp. 1434–1439, 2024.

[8] A. Gogeascoechea, R. Ornelas-Kobayashi, U. S. Yavuz, and M. Sartori, "Characterization of Motor Unit Firing and Twitch Properties for Decoding Musculoskeletal Force in the Human Ankle Joint In Vivo," *IEEE Transactions on Neural Systems and Rehabilitation Engineering*, vol. 31, pp. 4040–4050, 2023.

[9] M. Chen and P. Zhou, "A novel framework based on FastICA for high density surface EMG decomposition," *IEEE Transactions on Neural Systems and Rehabilitation Engineering*, vol. 24, pp. 117–127, 1 2016.

[10] C. Chen, S. Ma, X. Sheng, D. Farina, and X. Zhu, "Adaptive Real-Time Identification of Motor Unit Discharges from Non-Stationary High-Density Surface Electromyographic Signals," *IEEE Transactions on Biomedical Engineering*, vol. 67, pp. 3501–3509, 12 2020.

[11] H. Zhao, X. Zhang, M. Chen, and P. Zhou, "Online Decomposition of Surface Electromyogram into Individual Motor Unit Activities Using Progressive FastICA Peel-off," *IEEE Transactions on Biomedical Engineering*, 1 2023.

[12] H. Zhao, X. Zhang, M. Chen, and P. Zhou, "Adaptive Online Decomposition of Surface EMG Using Progressive FastICA Peel-off," *IEEE Transactions on Biomedical Engineering*, pp. 1–11, 2024.

[13] V. Glaser, A. Holobar, and D. Zazula, "Real-time motor unit identification from high-density surface EMG," *IEEE Transactions on Neural Systems and Rehabilitation Engineering*, vol. 21, no. 6, pp. 949–958, 2013.

[14] J. Rubenson, N. J. Pires, H. O. Loi, G. J. Pinniger, and D. G. Shannon, "On the ascent: The soleus operating length is conserved to the ascending limb of the force-length curve across gait mechanics in humans," *Journal of Experimental Biology*, vol. 215, no. 20, pp. 3539–3551, 2012.

[15] E. M. Arnold and S. L. Delp, "Fibre operating lengths of human lower limb muscles during walking," *Philosophical Transactions of the Royal Society B: Biological Sciences*, vol. 366, p. 1530, 5 2011.

[16] D. Farina, M. Gazzoni, and F. Camelia, "Low-threshold motor unit membrane properties vary with contraction intensity during sustained activation with surface EMG visual feedback," *Journal of Applied Physiology*, vol. 96, pp. 1505–1515, 4 2004.

[17] K. C. McGill, Z. C. Lateva, and H. R. Marateb, "Emglab: An interactive emg decomposition program," *Journal of Neuroscience Methods*, vol. 149, p. 121133, Dec. 2005.

[18] J. Rossato, F. Hug, K. Tucker, L. Lacourpaille, D. Farina, S. Avrillon, and M. U. Hub, "I-Spin live: An open-source software based on blind-source separation for decoding the activity of spinal alpha motor neurons in real-time," *bioRxiv*, vol. 12, p. 2023.04.14.536933, 2023.

[19] D. Yeung, F. Negro, and I. Vujaklija, "Adaptive HD-sEMG decomposition: Towards robust real-time decoding of neural drive," *bioRxiv*, p. 2023.09.18.558259, 9 2023.

[20] A. J. Fuglevand, D. A. Winter, and A. E. Patla, "Models of recruitment and rate coding organization in motor-unit pools," *Journal of Neurophysiology*, vol. 70, no. 6, pp. 2470–2488, 1993.

[21] A. Gogeascoechea, R. O. Kobayashi, U. S. Yavuz, and M. Sartori, "Identification of Motor Unit Twitch Properties in the Intact Human in Vivo," *Proceedings of the Annual International Conference of the IEEE Engineering in Medicine and Biology Society, EMBS*, pp. 6310–6313, 2021.

[22] R. R. Cisi and A. F. Kohn, "Simulation system of spinal cord motor nuclei and associated nerves and muscles, in a Web-based architecture," *Journal of Computational Neuroscience*, vol. 25, pp. 520–542, 12 2008.

[23] C. Pizzolato, D. G. Lloyd, M. Sartori, E. Ceseracciu, T. F. Besier, B. J. Fregly, and M. Reggiani, "CEINMS: A toolbox to investigate the influence of different neural control solutions on the prediction of muscle excitation and joint moments during dynamic motor tasks," *Journal of Biomechanics*, vol. 48, pp. 3929–3936, 11 2015.

[24] G. Durandau, D. Farina, and M. Sartori, "Robust Real-Time Musculoskeletal Modeling Driven by Electromyograms," *IEEE Transactions on Biomedical Engineering*, vol. 65, no. 3, pp. 556–564, 2018.

[25] A. Del Vecchio, F. Negro, F. Felici, and D. Farina, "Associations between motor unit action potential parameters and surface EMG features," *Journal of Applied Physiology*, vol. 123, pp. 835–843, 10 2017.

[26] J. R. Potvin and A. J. Fuglevand, "A motor unit-based model of muscle fatigue," *PLOS Computational Biology*, vol. 13, p. e1005581, 6 2017.

[27] R. Rohlén, R. Raikova, E. Stålberg, and C. Grönlund, "Estimation of contractile parameters of successive twitches in unfused tetanic contractions of single motor units A proof-of-concept study using ultrafast ultrasound imaging in vivo," *Journal of Electromyography and Kinesiology*, vol. 67, p. 102705, 12 2022.

[28] G. N. Sanchez, S. Sinha, H. Liske, X. Chen, V. Nguyen, S. L. Delp, and M. J. Schnitzer, "In Vivo Imaging of Human Sarcomere Twitch Dynamics in Individual Motor Units," *Neuron*, vol. 88, p. 1109, 12 2015.

[29] N. A. Kelly, K. G. Hammond, C. S. Bickel, S. T. Windham, S. C. Tuggle, and M. M. Bamman, "Effects of aging and Parkinson's disease on motor unit remodeling: Influence of resistance exercise training," *Journal of Applied Physiology*, vol. 124, pp. 888–898, 4 2018.

[30] E. J. Jones, S. Y. Chiou, P. J. Atherton, B. E. Phillips, and M. Piasecki, "Ageing and exercise-induced motor unit remodelling," *Journal of Physiology*, vol. 600, pp. 1839–1849, 4 2022.

[31] M. A. Gorassini, M. E. Knash, P. J. Harvey, D. J. Bennett, and J. F. Yang, "Role of motoneurons in the generation of muscle spasms after spinal cord injury," *Brain*, vol. 127, no. 10, pp. 2247–2258, 2004.

[32] L. M. McPherson and J. P. Dewald, "Abnormal synergies and associated reactions post-hemiparetic stroke reflect muscle activation patterns of brainstem motor pathways," *Frontiers in Neurology*, vol. 13, p. 934670, 10 2022.

A Novel Robotic Technique for Evaluating Thumb Proprioception Predicts Hand Function after Stroke

Luis Garcia-Fernandez
Dept Mech and Aero Eng
University of California
Irvine, USA
garciaf7@uci.edu

Andria Farrens
Dept Mech and Aero Eng
University of California
Irvine, USA
farrensa@uci.edu

Raymond Rojas
Dept Mech and Aero Eng
University of California,
Irvine, USA
rdrojas1@uci.edu

Vicky Chan
Dept Mech and Aero Eng
University of California
Irvine, USA
vchan2@uci.edu

Eric Wolbrecht
Dept Mech Eng
University of Idaho
Moscow, USA
ewolbrec@uidaho.edu

Joel C. Perry
Dept Mech Eng
University of Idaho
Moscow, USA
jperry@uidaho.edu

David J. Reinkensmeyer
Dept Mech and Aero Eng
University of California
Irvine, USA
dreinken@uci.edu

***Abstract*— The thumb has been called a "hallmark of humanity", and yet, in stroke rehabilitation, there are few studies that have examined thumb function and even fewer that have focused specifically on thumb sensory function. Here we describe a novel robotic technique to assess thumb proprioception and apply it to quantify the relationship between thumb proprioception and hand function after stroke. Based on a video game, "SomatoCircleJump" challenges participants to "jump" to radial targets presented on a screen as their thumb rotates around a circle, driven by a robot. Proprioceptive ability is quantified by radial jump error. We evaluated 35 individuals in the chronic phase post-stroke as part of a randomized controlled trial of robotic finger training. Compared to an age-matched control group, people with stroke had significantly increased jump error ($p < 0.001$). Thumb proprioception ability predicted hand function, as measured by the Box and Block Test score ($\rho = -0.44$, $p = 0.01$) and the Nine-Hole Peg Test time ($\rho = 0.49$, $p = 0.006$). Jump error was also correlated with an independent robotic measure of finger proprioception ($\rho = 0.54$, $p = 0.003$). These results validate a novel robotic method to quantify thumb proprioception and indicate thumb proprioception deficits are common after stroke, co-occur with finger proprioception deficits, and relate to functional hand ability.**

Keywords—neurorehabilitation, proprioception, serious games, stroke, thumb

I. Introduction

Despite extensive therapeutic efforts during rehabilitation, the chances of regaining full use of the affected hand after a stroke are low. Three months after a stroke, only 12% of survivors experience no issues with hand function, whereas 38% report substantial difficulties in hand use [1]. Given the importance of the hand for activities of daily living, it is surprising that relatively little emphasis is placed on a critical aspect of hand function after stroke: proprioception. Proprioceptive impairments greatly affect an individual's capacity to sense and control limb position, leading to challenges in motor coordination and performing functional tasks [2]. Proprioceptive impairments are common in the fingers after stroke [3], [4], [5] and predict potential for recovery [6]. Yet only 1% of therapists assess proprioception after stroke [7]. Recent research studies have highlighted the importance of objective and reliable methods for assessing hand proprioception, particularly in clinical populations with neurological impairments. Robotic assessments have been increasingly used to quantify proprioceptive deficits in the index finger [8], [9], but they have not yet been widely adopted in clinical settings.

This gap in proprioceptive assessment is particularly severe for the thumb. Evolution of the opposable thumb conveyed key survival advantages to humans, making it a "hallmark of humanity" because of its association with increased tool use [10], [11], [12]. The importance of thumb sensation for hand function is evidenced by the large somatosensory cortex representation of the thumb [13]. Despite the critical role of thumb sensation, traditional assessments of thumb proprioception focus on coarse indicators such as identifying the direction of a movement that is externally imposed on the thumb by a clinician [14]. To our knowledge, beyond these coarse clinical methods, no other clinical assessment methods specifically focused on thumb proprioception have been developed. This limits our understanding of the role thumb proprioception impairment plays in hand function recovery after stroke.

To tackle this challenge, we developed a novel robotic assessment of thumb proprioception called SomatoCircleJump. The assessment quantifies a person's ability to estimate the location of their thumb as a robot moves it in a circle. We embedded the assessment in a computer game that requires participants to indicate when they feel their moving thumb align with a target shown on a visual display, in order to "jump" to the target. We hypothesized that proprioceptive deficits quantified by jump error would predict hand function after stroke, as quantified by standard clinical assessments.

This work was supported in part by the NIH under Grant R01HD062744.
This work was supported in part by the NIDILRR under Grant 90REGE0010.

II. Methodology

A. Design of the thumb proprioception assessment task

We established four design criteria for the novel thumb proprioception assessment. First, we desired a high resolution measure of thumb localization ability. The test we settled on provides a continuous measure of error. Second, we desired that the task be engaging so as to maintain attention. Thus, we embedded the task in a popular phone game, Super Circle Jump [15]. Third, we desired that people with severe thumb motor impairment could still participate in the test. The resulting test does not require active thumb movement ability. Lastly, we desired that the test be safe and simple to implement. The movement we selected is a circle, which is a comfortable movement for the thumb and can be implemented with a single motor.

Super Circle Jump involves the player triggering a jump when a ball, rotating around a centralized circle, aligns with a visual target, represented by another circle (Fig. 1 Right). This game can also be viewed as shooting an orbiting ball at a target. For SomatoCircleJump, we modified the game so that a robot moves the player's visually hidden thumb in a circular motion in a vertical plane parallel to the screen to represent the ball's rotation around the circle. The player must press a button with their other hand to make the ball jump to the target, relying on sensing their thumb location to determine when to press the button. This strategy is an example of a "Propriopixels" gaming strategy, in which a game element is presented proprioceptively rather than visually [16], [17]. In this case, the location of the orbiting ball is presented by moving the thumb in a circle.

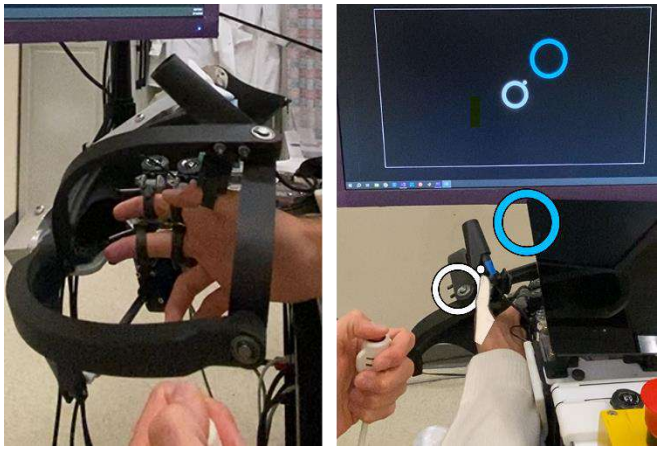


Fig. 1. Left: Side view of thumb exoskeleton of the FINGER robot used for the proprioception assessment. A spherical mechanism controls the thumb in 2 DOFs. Right: Participant's view of the SomatoCircleJump game with graphics overlaid in hand space (drawn thumb, white ball, and center and target circles) to illustrate game play. The robot guides the thumb in a circular path (orbiting a ~5 cm diameter circle in thumb space, shown by the overlaid white circle) following the position of the white ball, and the participant must press a button with their other hand when the thumb is closest to the blue target circle. After each press, the blue circle shifts to a new position. During task familiarization, a white cursor (ball) represents the thumb's position, but this visual aid is removed for the proprioceptive assessment and vision of the hand is blocked with a movable screen.

Thumb movement was applied using the thumb module of the Finger INdividuation Grasp Exercise Robot (FINGER), which uses a 2-degree-of-freedom (2-DOF) spherical 5-bar thumb exoskeleton (Fig. 1 Left) actuated by two high bandwidth, low-friction, linear, electric actuators [18], [19].

We quantified thumb localization ability using the "jump error" between the angle of the ball when the button is pressed and the optimal jump angle, defined by the line connecting the centers of the white orbit and the colored target circles (**Error! Reference source not found.** 1 Right). Following the button press, the SomatoCircleJump game instantaneously displays a small ball that jumps from the current thumb location along a path radially outward toward the target. The ball turns green if it collides with the target circle, denoting a successful shot, and red otherwise. The test also provides numerical feedback going from 0 to 10 depending on how close they were to a perfect jump, with 10 being a perfect jump. Total score is shown at the top of the screen.

B. Experimental design

We conducted an experiment to assess thumb proprioception ability after stroke using SomatoCircleJump as part of a randomized controlled trial (RCT) of robotic finger training. The Institutional Review Board of UC Irvine approved the protocol and participants provided informed consent.

Subjects: Thirty-five individuals with single or multiple ischemic or hemorrhagic stroke, confirmed through radiological imaging, showing residual weakness in one hand, and being at least 6 months post-stroke, were recruited for the study. Additional inclusion criteria required participants to score at least 3 blocks on the Box and Block Test (BBT), with their score on the affected arm being at least 20% lower than that of the unaffected arm. Exclusion criteria included severe muscle tone in the upper extremity (score > 3 on the Modified Ashworth Spasticity Scale), severe aphasia (score of 3 on the NIH Stroke Scale, question 9), concurrent participation in another study related to stroke recovery, and evidence of major depression, as defined by DSM V criteria or a score on the Geriatric Depression Scale > 10.

SomatoCircleJump protocol: We assessed the participants' thumb proprioception using the SomatoCircleJump game in a single visit at the beginning of the RCT. During the session, participants played four games, all of them at a speed of ~60 deg/s, a workspace of 5 cm in diameter, and in the clockwise direction of rotation. The first game was played with vision of the white ball and their thumb. For the second game, the graphical image of the ball was removed from the game so the participants could not see the ball but still had vision of their thumb. The last two games were without vision of either the ball or their thumb. The first two games were used to teach them how to play the game, while the last two games were the assessments that we analyzed to quantify proprioception. Training games were played with 10 jumps, although some participants were allowed more practice if needed. Assessment games were comprised of 20 jumps.

Control group: Additionally, a group of 24 age-matched, unimpaired older adults (50+ years old, mean = 63.8 ± 10.1 years old, 14 females, 4 left-hand dominant) performed one SomatoCircleJump game with 20 jumps under the same

conditions as the post-stroke group as a control for quantifying intact thumb proprioception ability.

Clinically accepted hand dexterity tests: Besides the thumb proprioception assessment, we measured upper extremity impairment with the Fugl-Meyer Assessment for Upper Extremity (FMA-UE) [20], hand/arm function with the Box and Block Test (BBT) [21], and fine dexterity with the Nine-Hole Peg Test (NHPT) [22]. BBT performance was quantified as the total number of blocks transferred in one minute by the affected limb. NHPT performance was scored as the total time required to place and remove 9 pegs with the affected hand, with an upper limit of 1 minute. On the FMA-UE, items are scored on a 3-point ordinal scale (0 = cannot perform, 1 = performs partially, 2 = performs fully). Out of the 4 motor function sections of the assessment (Upper Extremity, Wrist, Hand, and Coordination/Speed), the most relevant to this study is the third one, related to the function of the hand. Inside the hand section, there are four tasks that involve the active use of the thumb:

1. Thumb adduction: grasp a sheet of paper with pure thumb adduction.
2. Pincer grasp, opposition: oppose thumb pad against pad of index finger with a pencil interposed.
3. Cylinder grasp: grasp cylinder-shaped object, e.g. small can, with volar surface of thumb and index finger wrapped around object.
4. Spherical grasp: grasp a tennis ball with all 5 fingers.

For these four tasks, a score was given based on the established criteria: 0 points if the participant could not perform the action, 1 point if they could keep the object in place but not against a tug, and 2 points if the object held well against a tug. Participants scored from 0 to 8 in total for this selection of the FMA-UE.

Independent robotic test of finger proprioception: Finally, we conducted a finger proprioception test called Crisscross for all stroke participants using the FINGER robot. The goal was to assess the correlation between the finger proprioception errors obtained in this validated research test and the thumb proprioception errors obtained in SomatoCircleJump. In the Crisscross test [23], the FINGER robot moves the participant's affected index and middle fingers in a crossing pattern, with the hand occluded from view. They are instructed to press a button with their non-affected hand when they perceive their fingers are aligned, without visual feedback. Proprioceptive error is measured as the mean absolute crossing error. Previous studies have shown that Crisscross is sensitive to aging [23], detects the presence of stroke [4], and can predict the functional benefit of robotic hand movement training after a stroke [24].

C. Data analysis

We performed correlation analyses between thumb proprioception error and all the different clinical and robotic assessments previously mentioned. We checked the normality of the data by visually inspecting all variables using a histogram and a Q-Q plot, and then performed the Shapiro-Wilk test [25]. Since all the data was assumed to be monotonic but was non-normally distributed, we used Spearman's rank correlation.

III. Results

We measured thumb proprioceptive ability of people in the chronic phase post-stroke (mean days post-stroke = 1645 ± 1354) using a novel technique called SomatoCircleJump (SCJ). Their mean age was 56 ± 15 years old, and there were 25 males and 10 females, 9 right-side impaired and 26 left-side impaired. Their mean Box and Block score was 23.3 ± 15.7. We instructed participants to indicate by pushing a button with their unaffected hand when their affected thumb was pointing at a target located radially around a central circle as a robotic device moved their thumb in a circular motion. We quantified proprioceptive ability by "jump error", i.e., the difference between thumb and target angular location at button press.

A. Jump error was increased after stroke

The mean of the absolute value of jump error was 52.3º ± 24.5º, indicating substantial levels of error at the task. The older unimpaired group had a mean absolute error of 26.8º ± 10.6º, which was significantly lower than that obtained for the individuals post-stroke (unpaired t-test, $p < 0.001$).

B. Jump error predicted clinical scores of UE function

The Spearman's rank correlation between thumb proprioception error and the total FMA-UE score approached significance (Fig. 2, $\rho = -0.33$, $p = 0.07$). The correlation between thumb proprioception error and the sum of the scores of the four selected FMA-UE tasks related to thumb function also approached significance (Fig. 3, $\rho = -0.33$, $p = 0.07$). Although the correlations did not reach statistical significance at the 0.05 level, they suggested a weak-to-moderate negative association that may warrant further investigation.

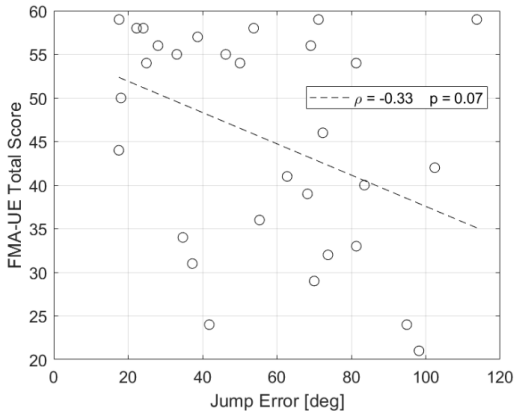


Fig. 2. Relationship between the total score of the FMA-UE and the thumb jump error obtained in SomatoCircleJump. Dashed line shows robust fit, and statistics show result of correlation using Spearman's Rank correlation.

We conducted a Spearman's rank correlation analysis on the non-normally distributed BBT data. Thumb proprioception error and BBT score were significantly correlated (Fig. 4, $\rho = -0.44$, $p = 0.01$).

We conducted a Spearman's rank correlation analysis on the non-normally distributed NHPT data. Thumb proprioception error was significantly correlated to NHPT score (Fig. 5, $\rho = 0.49$, $p = 0.006$).

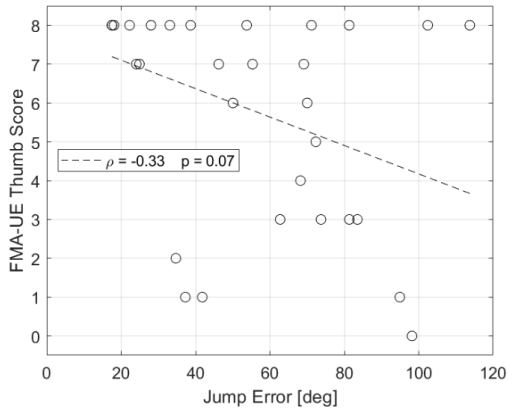


Fig. 3. Relationship between the sum of the scores obtained on four FMA-UE tasks related to the thumb total score of the FMA-UE and the thumb jump error obtained in SomatoCircleJump. Dashed line shows robust fit, and statistics show result of correlation using Spearman's Rank correlation.

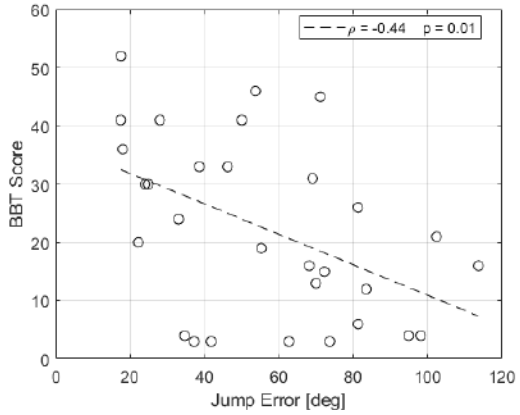


Fig. 4. Relationship between BBT score and thumb proprioception ability measured by jump error during game play of SomatoCircleJump. Dashed line shows robust fit, and statistics show result of correlation using Spearman's Rank correlation.

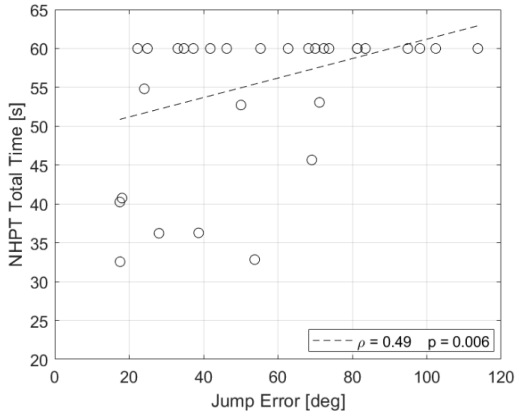


Fig. 5. Relationship between the time taken to perform the NHPT compared to the jump error for SomatoCircleJump. Dashed line shows robust fit, and statistics show result of correlation using Spearman's Rank correlation.

C. *Thumb localization error was related to finger proprioception ability*

We compared thumb jump error with finger proprioception error measured with the Crisscross test. Thumb and finger errors were significantly correlated (Fig. 6, $\rho = 0.54$, $p = 0.003$).

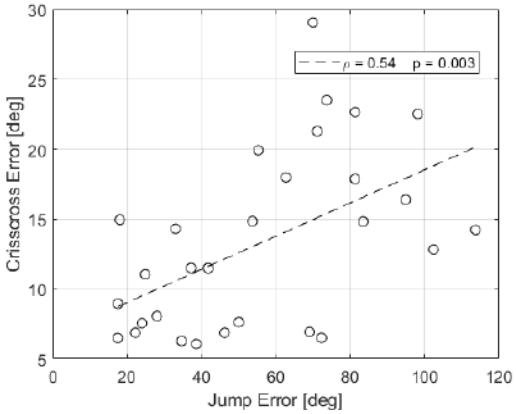


Fig. 6. Relationship between finger proprioception crossing errors obtained using the Crisscross assessment and thumb jump errors in SomatoCircleJump. Dashed line shows robust fit, and statistics show result of correlation using Spearman's Rank correlation.

IV. Discussion

In this study we developed a novel robotic thumb proprioception test in which participants had to sense the position of their thumb in order to "shoot" (or "jump") an orbiting ball at different targets. We used it to measure thumb proprioception ability, quantified as jump error, in persons with chronic stroke and found that: 1) thumb proprioceptive error was, on average, significantly increased after stroke and approximately double that of age-matched controls; 2) hand function on two clinical tests was significantly correlated with thumb proprioception error; and 3) finger and thumb proprioception errors were correlated. These results are further discussed below, followed by limitations and future directions.

A. *Development of a novel thumb proprioception test*

Despite the importance of the thumb for human hand function, there is a lack of rehabilitation technology for assessing a key aspect of the thumb – its proprioceptive ability. Clinical assessments of thumb proprioception, such as the *joint movement and movement direction discrimination* test, part of the Rivermead Assessment of Somatosensory Performance [26], [27], are simple and quick to apply, but provide only a coarse indication, focusing on the ability of the patient to gauge the direction of a movement that is externally imposed on the thumb by a clinician [14]. And, even with its simplicity, this assessment is rarely applied in stroke rehabilitation [7]. Few other methods have been developed to quantify thumb proprioception. One study positioned the fingers and thumb of one hand and asked unimpaired people to indicate their locations with a mouse pointer [28]. They found that finger and thumb

proprioception were surprisingly inaccurate, with average errors up to several centimeters. A limitation of this test is that it only measured static proprioception. We are not aware of previous studies that have measured dynamic thumb proprioception, or thumb proprioception after stroke.

Accurate performance on the test described here requires a complex set of proprio-visual-motor processes to occur. SomatoCircleJump is a dynamic test, so the brain must proprioceptively sense not only the position but also the speed of the thumb in order to anticipate the correct moment to push the button (this could be considered "internal model #1" for this task). The brain must also build into its estimate of the button press moment the fact that it must initiate the motor command to push the button sufficiently in advance of the thumb/target crossing moment so that the command has time to descend, activate hand muscles, and cause the force of the button press at the right time (call this internal model #2). Finally, a visual-proprio mapping is required (internal model #3), as SomatoCircleJump presents the target visually on a screen, and the brain must map the thumb location into screen coordinates (or vice versa). So, a seemingly simple proprioceptive test is probing at least three types of internal models, as well as the ability to sense thumb location and speed as inputs to those models. The finger proprioception test that we used as a basis for comparison, Crisscross, also relies on two similar internal models: #1 for predicting the position and speed of both the index and middle finger, and #2 to send the command for the non-assessed hand to press the button [23]. This reliance on similar types of internal models may help explain why SomatoCircleJump error was correlated with Crisscross error.

B. Stroke impairs thumb proprioception ability

We found that stroke increased thumb proprioception error. Several studies of the fingers [4], [6], [24], as well as studies of the arm [29], have found that proprioceptive error is increased in the upper extremity after stroke. It would be odd if stroke did not also affect the thumb, given the thumb's large cortical representation that is integrated with the representations of the fingers [30], [31]. Indeed, we found that if people tended to have more severe finger proprioception impairment, they also tended to have more severe thumb proprioception error, consistent with the overlap of thumb and finger proprioception representations in somatosensory cortex [13].

A recent systematic review of over 1,350 proprioception assessment methods found that results of different proprioceptive tests are mostly uncorrelated in unimpaired individuals, demonstrating no associations between joints, highlighting the site- and method-specific nature of proprioceptive ability [27]. In the present study, thumb proprioception error assessed in stroke participants using SomatoCircleJump showed a moderately strong correlation with the finger proprioception crossing error measured by Crisscross, an independent technique performed with the same robot (FINGER) [19], [24]. This suggests site specificity within the hand breaks down when there are lesions due to stroke.

C. Thumb proprioceptive deficits predicted hand dexterity

Our motivation for this study was the idea that quantifying thumb proprioception would be valuable for stroke rehabilitation because of the importance of the thumb for hand function. As we hypothesized, we found that proprioceptive errors quantified by SomatoCircleJump were moderately correlated with two common clinical measures of hand function: BBT and NHPT. This is consistent with the idea that the thumb and its sensory feedback are important in performing fine motor tasks. The correlation with the total FMA-UE score only approached significance, likely due to the broad nature of the FMA-UE that is aimed at coarse characterization of upper limb movement impairment. Another explanation could be that the hand-related components of the FMA-UE mainly assess motor execution and grip strength rather than proprioceptive function.

D. Future directions

The mean thumb proprioception errors were large after stroke: participants misestimated their thumb location by over 50 degrees. An interesting question for future research is how to partition this error into impairments in the various proprioceptive sensing and neural modeling processes outlined in subsection IV.A. Another interesting question is whether some of the error is due to disuse of the hand after stroke, as it is well established that proprioceptive ability is modifiable with activity, as well as training and exercise [32], [33]. A questionnaire like the Motor Activity Log could be used to categorize individuals with varying levels of hand use post-stroke and SomatoCircleJump could be used to compare their proprioception accuracy.

We would like to make SomatoCircleJump clinically practical to use as a thumb proprioception assessment. Although we used a sophisticated thumb robot to implement SomatoCircleJump in this study, the circular thumb movement could be implemented by a low-cost rotary motor in a hand-held device. The test itself only takes 2-3 minutes to implement with 20 jumps. The SomatoCircleJump paradigm is also potentially translatable to other joints (e.g. finger, wrist, elbow, shoulder, hip, ankle), as all of these joints can move in circles. An interesting question is whether proprioceptive ability varies at these different joints.

We would also like to explore use of SomatoCircleJump as a proprioceptive training tool, capitalizing on its engaging and entertaining video game structure. There are currently only a few gamified proprioception training techniques [16], [34].

Interesting rehabilitation science questions that SomatoCircleJump could help answer are: "Does thumb proprioception ability predict the ability to respond to hand rehabilitation therapies?"; "To what extent is thumb proprioception ability modifiable after stroke with training?"; and "Does improving thumb proprioception improve functional hand outcomes?"

REFERENCES

[1] P. S. Lum, S. B. Godfrey, E. B. Brokaw, R. J. Holley, and D. Nichols, "Robotic Approaches for Rehabilitation of Hand Function After Stroke," *American Journal of Physical Medicine &*

Rehabilitation, vol. 91, no. 11, p. S242, Nov. 2012, doi: 10.1097/PHM.0b013e31826bcedb.

[2] Y. Yu, Y. Chen, T. Lou, and X. Shen, "Correlation Between Proprioceptive Impairment and Motor Deficits After Stroke: A Meta-Analysis Review," *Frontiers in Neurology*, vol. 12, 2022.

[3] S. S. Kessner, U. Bingel, and G. Thomalla, "Somatosensory deficits after stroke: a scoping review," *Topics in Stroke Rehabilitation*, vol. 23, no. 2, pp. 136–146, Feb. 2016, doi: 10.1080/10749357.2015.1116822.

[4] M. L. Ingemanson *et al.*, "Neural Correlates of Passive Position Finger Sense After Stroke," *Neurorehabilitation and Neural Repair*, vol. 33, no. 9, pp. 740–750, Sep. 2019, doi: 10.1177/1545968319862556.

[5] D. Rand, "Proprioception deficits in chronic stroke—Upper extremity function and daily living," *PLOS ONE*, vol. 13, no. 3, p. e0195043, Mar. 2018, doi: 10.1371/journal.pone.0195043.

[6] M. L. Ingemanson, J. R. Rowe, V. Chan, E. T. Wolbrecht, D. J. Reinkensmeyer, and S. C. Cramer, "Somatosensory system integrity explains differences in treatment response after stroke," *Neurology*, vol. 92, no. 10, pp. e1098–e1108, Mar. 2019, doi: 10.1212/WNL.0000000000007041.

[7] J. E. Hoh, M. R. Borich, T. M. Kesar, D. S. Reisman, and J. A. Semrau, "Limitations in utilization and prioritization of standardized somatosensory assessments after stroke: A cross-sectional survey of neurorehabilitation clinicians," *Topics in Stroke Rehabilitation*, vol. 31, no. 1, pp. 29–43, Jan. 2024, doi: 10.1080/10749357.2023.2200304.

[8] M. Zbytniewska-Mégret *et al.*, "Reliability, validity and clinical usability of a robotic assessment of finger proprioception in persons with multiple sclerosis," *Multiple Sclerosis and Related Disorders*, vol. 70, p. 104521, Feb. 2023, doi: 10.1016/j.msard.2023.104521.

[9] M. Zbytniewska-Mégret *et al.*, "The Evolution of Hand Proprioceptive and Motor Impairments in the Sub-Acute Phase After Stroke," *Neurorehabilitation and Neural Repair*, vol. 37, no. 11–12, pp. 823–836, Dec. 2023, doi: 10.1177/15459683231207355.

[10] M. Harris, "Culture, People, Nature: An Introduction to General Anthropology," *Harper Collins College Publishers*, 1993.

[11] T. Tyler, "The Rule of Thumb," *Journal of Advanced Composition*, vol. 30, no. 3/4, pp. 435–456, 2010.

[12] F. A. Karakostis *et al.*, "Biomechanics of the human thumb and the evolution of dexterity," *Current Biology*, vol. 31, no. 6, pp. 1317-1325.e8, Mar. 2021, doi: 10.1016/j.cub.2020.12.041.

[13] D. Janko, K. Thoenes, D. Park, W. R. Willoughby, M. Horton, and M. Bolding, "Somatotopic Mapping of the Fingers in the Somatosensory Cortex Using Functional Magnetic Resonance Imaging: A Review of Literature," *Frontiers in Neuroanatomy*, vol. 16, Jun. 2022.

[14] R. Cantero-Téllez and I. Medina Porqueres, "Practical exercises for thumb proprioception," *Journal of Hand Therapy*, vol. 34, no. 3, pp. 488–492, Jul. 2021, doi: 10.1016/j.jht.2020.03.005.

[15] "Super Circle Jump - Mobile Game for iOS and Android." Accessed: Nov. 19, 2024. [Online]. Available: https://www.pixelclash.com/supercirclejump/

[16] D. S. Reinsdorf, E. E. Mahan, and D. J. Reinkensmeyer, "Proprioceptive Gaming: Making Finger Sensation Training Intense and Engaging with the P-Pong Game and PINKIE Robot," in *2021 43rd Annual International Conference of the IEEE Engineering in Medicine & Biology Society (EMBC)*, Mexico: IEEE, Nov. 2021, pp. 6715–6720. doi: 10.1109/EMBC46164.2021.9631041.

[17] D. S. Reinsdorf, "Engineering for Arm Use After Stroke: A Precision Rehabilitation Model, Minimalistic Robot Design Pattern, and Proprioception-Targeting Gaming Paradigm," Ph.D. dissertation, MAE Dept., Univ. of California Irvine, Irvine, CA, USA, 2022.

[18] V. D. Ketkar, E. T. Wolbrecht, J. C. Perry, and A. Farrens, "Design and Development of a Spherical 5-Bar Thumb Exoskeleton Mechanism for Poststroke Rehabilitation," *Journal of Medical Devices*, vol. 17, no. 2, p. 021002, Jun. 2023, doi: 10.1115/1.4056864.

[19] H. Taheri *et al.*, "Design and preliminary evaluation of the FINGER rehabilitation robot: controlling challenge and quantifying finger individuation during musical computer game play," *Journal of NeuroEngineering and Rehabilitation*, vol. 11, no. 1, p. 10, Feb. 2014, doi: 10.1186/1743-0003-11-10.

[20] M. L. Woodbury, C. A. Velozo, L. G. Richards, P. W. Duncan, S. Studenski, and S.-M. Lai, "Dimensionality and Construct Validity of the Fugl-Meyer Assessment of the Upper Extremity," *Archives of Physical Medicine and Rehabilitation*, vol. 88, no. 6, pp. 715–723, Jun. 2007, doi: 10.1016/j.apmr.2007.02.036.

[21] V. Mathiowetz, G. Volland, N. Kashman, and K. Weber, "Adult norms for the Box and Block Test of manual dexterity," *American Journal of Occuppational Therapy*, vol. 39, no. 6, pp. 386–391, Jun. 1985, doi: 10.5014/ajot.39.6.386.

[22] V. Mathiowetz, K. Weber, N. Kashman, and G. Volland, "Adult Norms for the Nine Hole Peg Test of Finger Dexterity," *The Occupational Therapy Journal of Research*, vol. 5, no. 1, pp. 24–38, Jan. 1985, doi: 10.1177/153944928500500102.

[23] M. L. Ingemanson, J. B. Rowe, V. Chan, E. T. Wolbrecht, S. C. Cramer, and D. J. Reinkensmeyer, "Use of a robotic device to measure age-related decline in finger proprioception," *Experimental Brain Research*, vol. 234, no. 1, pp. 83–93, Jan. 2016, doi: 10.1007/s00221-015-4440-4.

[24] J. B. Rowe, V. Chan, M. L. Ingemanson, S. C. Cramer, E. T. Wolbrecht, and D. J. Reinkensmeyer, "Robotic Assistance for Training Finger Movement Using a Hebbian Model: A Randomized Controlled Trial," *Neurorehabilitation and Neural Repair*, vol. 31, no. 8, pp. 769–780, Aug. 2017, doi: 10.1177/1545968317721975.

[25] N. M. Razali and Y. B. Wah, "Power comparisons of Shapiro-Wilk, Kolmogorov-Smirnov, Lilliefors and Anderson-Darling tests," *Journal of Statistical Modeling and Analytics*, vol. 2, no. 1, pp. 21–33, Jan. 2011.

[26] C. E. Winward, P. W. Halligan, and D. T. Wade, "The Rivermead Assessment of Somatosensory Performance (RASP): standardization and reliability data," *Clinical Rehabilitation*, Aug. 2002, doi: 10.1191/0269215502cr522oa.

[27] S. Hillier, M. Immink, and D. Thewlis, "Assessing Proprioception: A Systematic Review of Possibilities," *Neurorehabilitation and Neural Repair*, vol. 29, no. 10, pp. 933–949, Nov. 2015, doi: 10.1177/1545968315573055.

[28] B. Dandu, I. A. Kuling, and Y. Visell, "Proprioceptive Localization of the Fingers: Coarse, Biased, and Context-Sensitive," *IEEE Transactions on Haptics*, vol. 13, no. 2, pp. 259–269, Apr. 2020, doi: 10.1109/TOH.2019.2899302.

[29] S. E. Findlater and S. P. Dukelow, "Upper Extremity Proprioception After Stroke: Bridging the Gap Between Neuroscience and Rehabilitation," *Journal of Motor Behavior*, vol. 49, no. 1, pp. 27–34, Jan. 2017, doi: 10.1080/00222895.2016.1219303.

[30] W. Penfield and T. Rasmussen, *The cerebral cortex of man; a clinical study of localization of function*. in The cerebral cortex of man; a clinical study of localization of function. Oxford, England: Macmillan, 1950, pp. xv, 248.

[31] K. Nakamura, K. Sakai, and O. Hikosaka, "Neuronal Activity in Medial Frontal Cortex During Learning of Sequential Procedures," *Journal of Neurophysiology*, vol. 80, no. 5, pp. 2671–2687, Nov. 1998, doi: 10.1152/jn.1998.80.5.2671.

[32] J. Han, J. Anson, G. Waddington, and R. Adams, "Proprioceptive performance of bilateral upper and lower limb joints: side-general and site-specific effects," *Experimental Brain Researh*, vol. 226, no. 3, pp. 313–323, May 2013, doi: 10.1007/s00221-013-3437-0.

[33] H. G. Seo, S. J. Yun, A. J. Farrens, C. A. Johnson, and D. J. Reinkensmeyer, "A Systematic Review of the Learning Dynamics of Proprioception Training: Specificity, Acquisition, Retention, and Transfer," *Neurorehabilitation and Neural Repair*, p. 15459683231207354, Oct. 2023, doi: 10.1177/15459683231207354.

[34] C. Curry, N. Elangovan, R. G. Reid, J. Xu, and J. Konczak, "Gamification in a Physical Rehabilitation Setting: Developing a Proprioceptive Training Exercise for a Wrist Robot," in *SIGGRAPH Asia 2019 Posters*, in SA '19. New York, NY, USA: Association for Computing Machinery, Nov. 2019, pp. 1–2. doi: 10.1145/3355056.3364572.

Miniaturized Wearable Ultrasound System for Simultaneous Prediction of Wrist Angle and Grip Force During Dynamic Reaching

Afsana Hossain Rima
Dept. of Electrical & Computer Engineering
George Mason University
Fairfax, VA, USA
arima@gmu.edu

Zahra Taghizadeh
Dept. of Bioengineering
George Mason University
Fairfax, VA, USA
ztaghiza@gmu.edu

Ahmed Bashatah
Dept. of Bioengineering
George Mason University
Fairfax, VA, USA
abashat2@gmu.edu

Abhishek Aher
Dept. of Bioengineering
George Mason University
Fairfax, VA, USA
aaher@gmu.edu

Siddhartha Sikdar
Dept. of Bioengineering
Center for Advancing Systems Science and Bioengineering Innovation
George Mason University
Fairfax, VA, USA
ssikdar@gmu.edu

***Abstract*—Predicting grip force and wrist angle during dynamic hand movements is crucial for advancing upper-limb prosthetic systems, enabling simultaneous and proportional control of multiple degrees of freedom (DOFs). This study introduces a novel wearable ultrasound-based system that leverages M-mode data from four single-element transducers placed on the forearm to capture muscle activity for the concurrent prediction of grip force and wrist angle. A multi-layer perceptron (MLP) regressor was utilized for the simultaneous prediction of both parameters, and a comparative analysis was conducted using a Gaussian process regressor (GPR), which is commonly adopted previously in similar studies. The system was validated on unseen data from five participants without limb loss. The MLP demonstrated superior performance compared to GPR, achieving R^2 values of 0.85±0.06 for wrist angle prediction and 0.74±0.07 for grip force. These findings underscore the challenges of predicting simultaneous grip force and wrist angle during dynamic hand movements and highlight the need to address these issues for intuitive and practical prosthetic control in real-world scenarios.**

***Index Terms*—simultaneous and proportional control, wearable ultrasound, dynamic movements, multi-layer perceptron regressor, gaussian process regressor.**

I. Introduction

The ability to predict grip force and wrist angle during dynamic hand movements is critical for advancing the control of upper-limb prosthetics. These systems are essential for rehabilitation, providing individuals with limb loss the ability to regain functional independence and perform everyday tasks with greater efficiency [1], [2]. Simultaneous and proportional control (SPC) of grip force and wrist angle is especially important for tasks requiring seamless coordination, such as manipulating objects in a reachable workspace. Despite its importance, current prosthetic systems often fall short of offering intuitive and natural control during dynamic and combined motions, limiting their effectiveness in real-world applications [3].

While significant progress has been made in prosthetic control, most prior studies have relied on surface electromyography (sEMG) signals to achieve SPC across multiple degrees of freedom (DoFs) [4]–[7]. Data-driven methods, including non-negative matrix factorization (NMF) [8], linear regression (LR) [9], support vector regression (SVR) [10], and neural network-based approaches, have been employed to map sEMG signals to joint kinematics. However, these methods are often limited by the stochastic and nonstationary nature of sEMG, low spatial resolution, and susceptibility to crosstalk effects. Advanced machine learning techniques [11]–[13], such as bidirectional long short-term memory (Bi-LSTM) networks [14], recurrent neural networks (RNNs), and transformer architectures, have demonstrated improved performance [11], [15], [16] yet these methods require extensive calibration and lack transferability across tasks, which limits their practicality in real-world scenarios.

Sonomyography (SMG) has emerged as a promising alternative to sEMG, offering higher spatial and temporal resolution and robustness by capturing muscle morphology and tissue deformation using ultrasound [3], [17]. SMG has been shown to outperform sEMG in gesture classification and joint kinematics prediction, particularly when employing B-mode ultrasound imaging systems [18]. However, such methods have primarily focused on static or isolated motions [5], [6], [19]–[22], and these systems have large footprint making them unsuitable for incorporating inside a prosthetic socket. Recent advancements, including the use of single-element transducers [21], have enabled SMG-based systems to classify hand gestures and estimate finger movements with reduced complexity, making them suitable for wearable applications. Despite these

advances, a critical gap persists in extending SMG-based systems to achieve seamless, simultaneous control of wrist and grip motions during dynamic reaching, and miniaturizing the systems for further translation towards incorporation inside a socket. Addressing this limitation is essential to fully realize the potential of SMG-based systems and make them truly wearable for real-life, dynamic applications.

Time Delay Spectrometry (TDS), an ultrasound imaging technique, offers a promising solution to this challenge. TDS uses continuous, frequency-modulated signals to capture tissue properties with high spatial and temporal resolution [23]. Unlike traditional pulse-echo ultrasound methods, which rely on high excitation voltages and complex hardware, TDS operates at low excitation voltages and requires significantly simplified instrumentation. These features make it particularly well-suited for wearable applications. In our previous work, we introduced a wearable ultrasound system developed based on TDS, incorporating only four small single-element ultrasound transducers and front end electronics that is no more complicated than a frequency-modulated radio, and demonstrated its capability for dynamic imaging of muscle activity [24].

The aim of this study is to leverage a compact wearable system with four ultrasound sensors to evaluate SPC predictions for natural, reachable workspace movements. Our approach overcomes the limitations of static-position studies, advancing toward real-world prosthetic applications. Additionally, we highlight the impact of muscle fatigue, a critical factor that affects the accuracy of grip force predictions over time.

II. Problem Formulation

In this study, we aim to establish a mapping between M-mode ultrasound data collected over a time period T and the biomechanical outputs of grip force (f) and wrist angle (ω). Our dataset consists of m trials from N participants, totaling mN observations. For each trial i (where $i = 1, 2, \ldots, mN$), the ultrasound data is captured as depth-wise measurements over time. By discretizing the time period T into K time points $\{t_1, t_2, \ldots, t_K\}$, we represent the ultrasound data for trial i as a matrix:

$$\mathbf{X}_i = \begin{bmatrix} \mathbf{x}_i(t_1) \\ \mathbf{x}_i(t_2) \\ \vdots \\ \mathbf{x}_i(t_K) \end{bmatrix} \in \mathbb{R}^{K \times D},$$

where $\mathbf{x}_i(t_k) \in \mathbb{R}^D$ is the ultrasound measurement at time t_k, and D is the depth dimension.

The corresponding biomechanical outputs for trial i are represented as a vector:

$$\mathbf{y}_i = \begin{bmatrix} \omega_i \\ f_i \end{bmatrix} \in \mathbb{R}^2,$$

where ω_i is the wrist angle and f_i is the grip force. Our objective is to learn a function $h_{\text{MLP}} : \mathbb{R}^{K \times D} \to \mathbb{R}^2$ using a Multi-Layer Perceptron (MLP) that maps the ultrasound data $\mathbf{X}_i$ to the biomechanical outputs $\mathbf{y}_i$:

$$\mathbf{y}_i = h_{\text{MLP}}(\mathbf{X}_i) + \boldsymbol{\varepsilon}_i,$$

TABLE I
Demographics of the Study Participants

Participant ID	Age	Gender	Dominant Arm
AB01	33	Female	Right
AB02	34	Female	Left
AB03	29	Female	Left
AB04	30	Male	Right
AB05	27	Male	Right

where $\boldsymbol{\varepsilon}_i \in \mathbb{R}^2$ represents the residual error vector for trial i. By formulating the problem as a regression task that maps high-dimensional temporal data $\mathbf{X}_i$ to low-dimensional outputs $\mathbf{y}_i$, we aim to predict simultaneous grip force and wrist angle from M-mode ultrasound data, advancing towards real-world prosthetic applications by focusing on natural, dynamic movements within a reachable workspace.

III. Materials and Methods

A. Participants

Five participants without limb loss (mean age: 30 ± 5 years) were recruited for this study. The demographic details of the participants are presented in Table I. Written informed consent was obtained from all participants prior to their involvement in the research. Ethical approval for the study was granted by the Institutional Review Board (IRB) at George Mason University.

B. Experimental Procedure

For the experimental setup, the sensors were placed on the marked forearm location after palpation and volitional movement assessment. An IMU was positioned on the wrist, and participants held a hand dynamometer. Participants performed dynamic hand movements within a reachable workspace while seated comfortably. Their dominant arm was positioned to allow natural wrist and hand motions throughout the experiment. Participants were instructed to perform dynamic hand movements across three positions: a neutral position, a shoulder-level position, and a position crossing the midline of the body illustrated in Fig. 1 . These positions were chosen to simulate real-world hand and arm movements while maintaining consistency in the experimental setup. During the tasks, participants

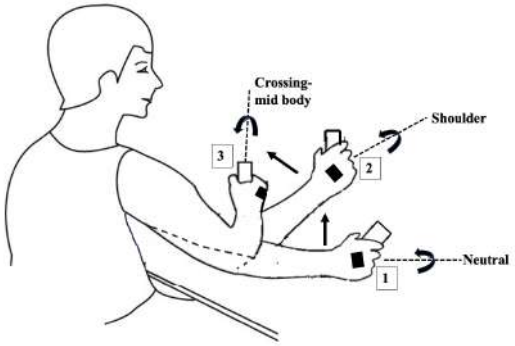


Fig. 1. Different arm positions with dynamic movements.

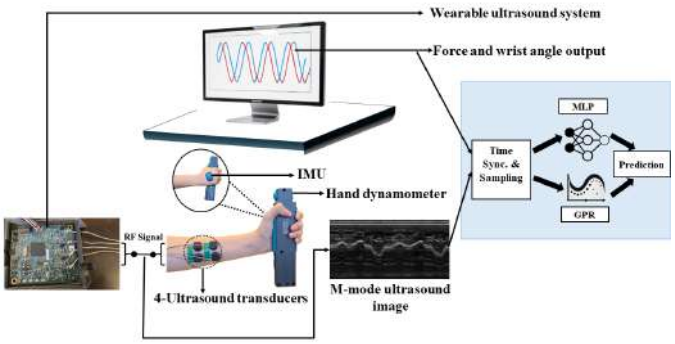


Fig. 2. Experimental setup illustrating the wearable ultrasound system attached to the participant's forearm, the hand dynamometer used to measure grip forces, and the IMU sensor used to measure wrist angles. The monitor displays the force and wrist angle trajectories, while M-mode ultrasound data is collected for simultaneous grip force and wrist angle prediction.

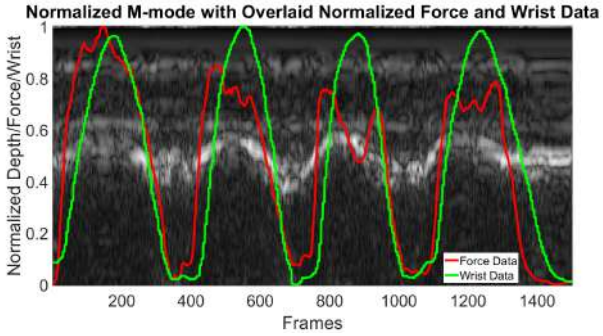


Fig. 3. Normalized m-mode with overlaid normalized force and wrist data from one of the participants.

were instructed to increase their grip force progressively to their maximum capacity while simultaneously rotating their wrist. Once the maximum grip force was achieved, they were guided to release their grip force back to zero while returning their wrist to a neutral angle. A wearable ultrasound system, developed for sonomyography (SMG) analysis, was secured on the forearm using a custom-designed holder. The system utilized four ultrasound transducers in 3D printed housing (each measuring 15×15×6 cm) driven by a 12-bit frequency sweeper (AD5930, Analog Devices, Burlington, USA) to generate linearly swept sinusoidal chirps between 3 MHz and 5 MHz with a sweep time of 10 ms and a peak-to-peak amplitude of 5 V. The echoes from the muscle tissues were processed by a specially constructed analog front-end, where the signals were amplified and digitized using independent 16-bit analog-to-digital converters (TMS320F28379D, Texas Instruments, Dallas, USA), sampled simultaneously at 40 kSa/s. To reduce the computational load, the M-mode ultrasound signals were processed using a 1024-point fast Fourier transform (FFT), and the relevant depth of 4 cm was retained for analysis [24]. This design ensured reliable and efficient collection of SMG data for simultaneous grip force and wrist angle prediction.

Ground truth data included synchronized grip force and wrist angle measurements. Grip force was recorded using a hand dynamometer (Vernier, Beaverton, OR, USA), and wrist angle trajectories were captured using an IMU sensor (WitMotion, Shenzhen, China) attached to the wrist. Participants were tasked with gripping and rotating their wrist while dynamically transitioning through the specified arm positions (neutral, shoulder-level, and midline-crossing). The tasks required participants to modulate their grip force—progressively increasing to their maximum force while rotating their wrist to its extreme position, and then decreasing the force to zero while rotating the wrist back to a neutral angle. A screen placed in front of the participants displayed real-time feedback on their grip force and wrist angle trajectories, aiding in maintaining consistency and accuracy during the experiment.

Fig. 2 depicts the experimental setup, showcasing the wearable ultrasound system positioned on the participant's forearm, the dynamometer used for grip force measurement, and the IMU sensor for wrist angle tracking.

Three trials of data were collected from each participant, with each trial lasting 30 seconds. During each trial, participants performed grip force tasks and wrist rotations while dynamically transitioning between the neutral, shoulder-level, and midline-crossing positions. SMG signals from the wearable ultrasound system, grip force from the dynamometer, and wrist angle from the IMU sensor were recorded via a Python interface for visualization and analysis, enabling the evaluation of the system's ability to predict grip force and wrist angle during dynamic movements across varied arm positions.

C. Data Processing and Model Optimization

Data processing was conducted using three trials collected during each data collection paradigm. To ensure unbiased evaluation, a leave-one-trial-out validation strategy was employed. In this approach, one trial was reserved for validation, while the remaining two were used for training the model. This process was repeated for all three trials, ensuring that each trial served as the validation set once. By rotating the validation trial in this manner, any potential bias caused by good or poor data quality in a particular trial was minimized. The average validation performance across the three iterations was calculated, providing a reliable and robust measure of the model's generalization capability.

All data, including ultrasound signals, grip force, and wrist angle measurements, were synchronized and sampled at 50 Hz to ensure temporal alignment for predicting grip force and wrist angle. Fig. 3 illustrates a representative example of one of the four M-mode ultrasound channels (each channel having a Y-axis size of 130), overlaid with normalized force and wrist angle data obtained from the dynamometer and IMU, respectively. Each 30-second trial generates 520 spatial samples across four channels, with all data time synchronized and min-max normalized to maintain consistency and support robust model training.

We employed both Multi-Layer Perceptron (MLP) and Gaussian Process Regressor (GPR) for estimating wrist angle

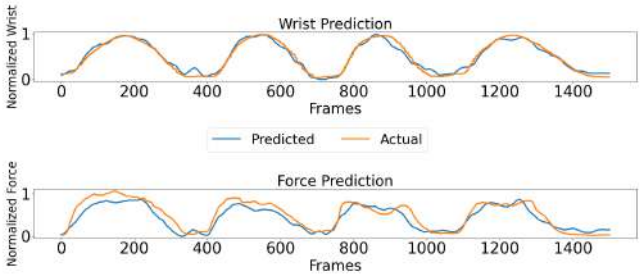


Fig. 4. Validation data wrist angle and grip force prediction from one of the participants.

and grip force, allowing for a comprehensive comparative analysis of their performance on both biomechanical outputs. For the MLP model [25], we utilized a neural network architecture with two hidden layers, each incorporating rectified linear unit (ReLU) activation functions [26]. The ReLU activation introduced non-linearity while mitigating the vanishing gradient problem, enhancing the model's ability to learn complex relationships within the data. Training was conducted over 500 iterations to balance computational efficiency with predictive accuracy. The MLP effectively captured non-linear dependencies in the M-mode ultrasound signals, providing robust predictions for both wrist angle and grip force.

For the GPR model [27], we applied principal component analysis (PCA) [28] to the M-mode ultrasound data to reduce dimensionality. PCA retained the most significant features, eliminating redundant or noisy information, which improved computational efficiency and focused the model on meaningful patterns within the data. The GPR model employed a combination of a radial basis function (RBF) kernel and a white noise kernel [27]. The RBF kernel captured smooth, continuous variations, while the white noise kernel accounted for residual variability and noise, ensuring robust predictions for both grip force and wrist angle despite potential inconsistencies in the input data.

The integration of data synchronization, feature normalization, and advanced modeling techniques enabled reliable training and validation for simultaneous grip force and wrist angle prediction.

D. Evaluation Metric

The performance of the proposed system was assessed using two evaluation metrics: mean squared error (MSE) and the coefficient of determination (R^2), to evaluate both wrist angle and grip force predictions.

a) Mean Squared Error (MSE): The MSE quantified the average squared difference between the predicted values and the ground truth, measuring prediction accuracy:

$$\text{MSE} = \frac{1}{N}\sum_{i=1}^{N}(y_i - \hat{y}_i)^2 \tag{1}$$

where y_i represents the true value, $\hat{y}_i$ is the predicted value, and N is the number of data points.

b) Coefficient of Determination (R^2): The R^2 value measured the proportion of variance in the ground truth that was captured by the model's predictions:

$$R^2 = 1 - \frac{\sum_{i=1}^{N}(y_i - \hat{y}_i)^2}{\sum_{i=1}^{N}(y_i - \bar{y})^2} \tag{2}$$

where $\bar{y}$ is the mean of the true values. An R^2 value closer to 1 indicates a better fit between the predicted and true values.

By leveraging these metrics, the effectiveness of the proposed method was validated across dynamic hand movements and varied arm positions.

IV. Result

The wearable ultrasound-based system was evaluated for its ability to simultaneously predict grip force and wrist angle during dynamic hand movements across three arm positions: neutral, shoulder-level, and midline-crossing. Fig. 4 shows the predicted wrist angle and grip force for validation data from one participant. The Multi-Layer Perceptron (MLP) model consistently outperformed the Gaussian Process Regressor (GPR) in predicting both biomechanical outputs. For wrist angle prediction, the MLP achieved an average R^2 of 0.85 ± 0.06 and a mean squared error (MSE) of 0.018 ± 0.006, reflecting strong predictive accuracy and consistent performance across participants. Similarly, for grip force prediction, the MLP attained an average R^2 of 0.74 ± 0.07 and an MSE of 0.026 ± 0.005, outperforming the GPR model, which achieved an average R^2 of 0.70 ± 0.05 and an MSE of 0.030 ± 0.005.

Performance metrics for individual participants, as summarized in Table II and showed across the the trials in Fig. 5, reveal that wrist angle predictions using the MLP were highly consistent, with all participants achieving R^2 values above 0.80. For grip force predictions, the MLP also outperformed the GPR but exhibited greater variability among participants, with R^2 values ranging from 0.65 (AB03) to 0.77 (AB01). The higher variability in grip force prediction can be attributed to differences in individual muscle behavior and fatigue effects during extended trials. Despite the observed variability in grip force predictions, the system effectively captured simultaneous wrist angle and grip force during dynamic, multi-positional tasks, highlighting the potential of the wearable ultrasound-based system for real-world upper-limb prosthetic applications.

V. Discussion

This study demonstrates the feasibility of a wearable ultrasound-based system for the simultaneous prediction of grip force and wrist angle during dynamic hand movements across varied arm positions. Unlike previous work, which evaluated SPC with the arm static in neutral positions, this study focused on dynamic, reaching movements likely encountered in daily living.

The current dataset, consisting of gradual, simultaneous increases and decreases in wrist angle and grip force, proved effective for initial evaluation but limited the model's generalizability to more complex tasks. This limitation likely

TABLE II
PERFORMANCE METRICS ACROSS ALL PARTICIPANTS

Participant ID	MLP Results				GPR Results			
	Wrist (R^2)	Wrist (MSE)	Force (R^2)	Force (MSE)	Wrist (R^2)	Wrist (MSE)	Force (R^2)	Force (MSE)
AB01	0.904	0.011	0.823	0.016	0.873	0.015	0.770	0.022
AB02	0.810	0.023	0.710	0.029	0.637	0.045	0.667	0.033
AB03	0.770	0.027	0.653	0.032	0.697	0.036	0.637	0.034
AB04	0.873	0.014	0.780	0.023	0.763	0.025	0.687	0.033
AB05	0.897	0.014	0.753	0.030	0.790	0.021	0.730	0.027
Average	**0.851**	**0.018**	**0.744**	**0.026**	**0.752**	**0.028**	**0.698**	**0.030**

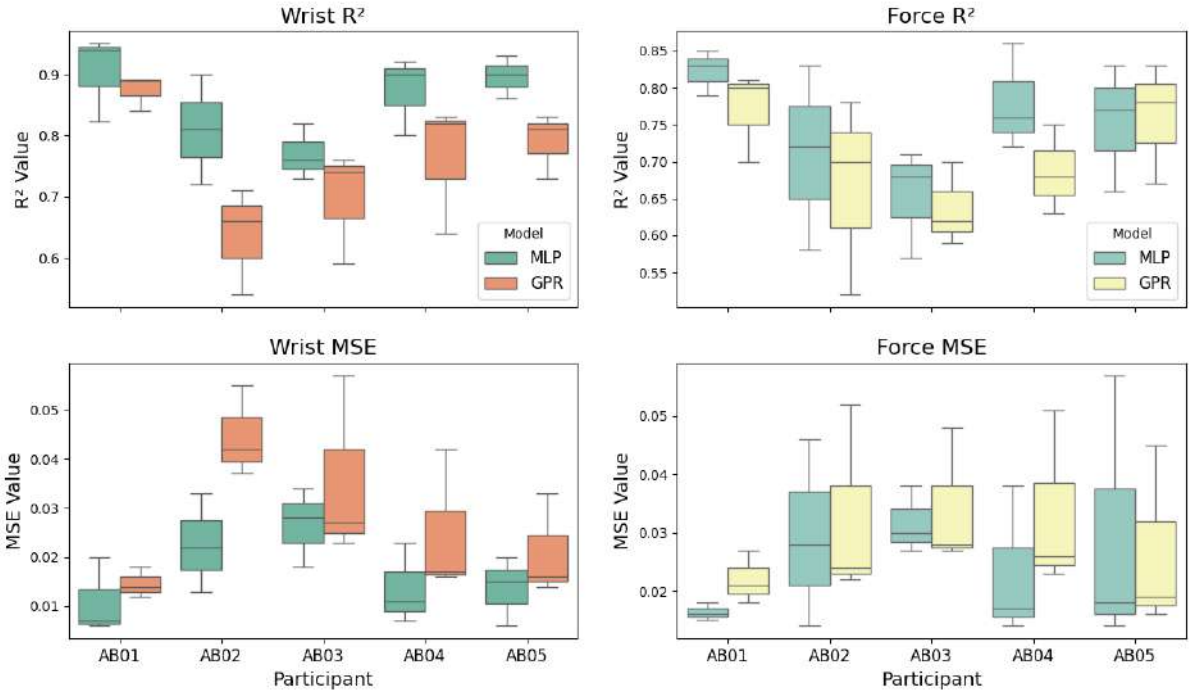


Fig. 5. Comparison of MLP and GPR models for R^2 and MSE across participants for Wrist and Force metrics. The top row shows R^2 values, and the bottom row shows MSE values.

contributed to PCA's inability to effectively separate wrist angle and grip force, as observed in prior studies [19], [21]. Expanding the dataset to include diverse dynamic movement patterns, such as non-linear or abrupt transitions, remains a priority for future work to enhance dimensional separation and robustness. Prediction models based on raw ultrasound echo envelopes were employed in this study, with the Gaussian Process Regressor (GPR) using RBF and white noise kernels outperforming default configurations, but proving computationally intensive. The Multi-Layer Perceptron (MLP) model demonstrated superior accuracy and computational efficiency, making it better suited for real-time implementation.

The MLP consistently outperformed the GPR, achieving higher R^2 values and lower MSE across participants, as shown in Table II and Fig. 5. For wrist angle, the MLP achieved R^2 values above 0.80, demonstrating its ability to model complex relationships. For grip force, the MLP also outperformed the GPR, though greater variability was observed due to differences in muscle activation patterns across participants. While the MLP effectively captured non-linear dependencies, future research will explore recurrent networks (RNNs or LSTMs) to better leverage the sequential nature of M-mode ultrasound data.

The system's computational efficiency makes the MLP suitable for real-time applications, unlike the computationally intensive GPR. Ongoing work is focused on validating the system in individuals with limb differences and integrating the MLP into a real-time prosthetic control system. To train models without direct ground truth data for individuals with limb difference, a cursor control task or a mirrored movement

approach using the intact limb will be utilized to generate training data for the affected limb.

VI. Conclusion

This study introduces a wearable ultrasound system for the simultaneous prediction of grip force and wrist angle during dynamic hand movements, effectively addressing challenges in proportional control for real-world applications. By using M-mode ultrasound data and the MLP model, which outperformed GPR in both accuracy and computational efficiency, this work establishes a foundation for dynamic prosthetic control. However, the dataset's limited movement diversity may restrict generalizability. Expanding the dataset with diverse dynamic movements and exploring recurrent models (RNNs/LSTMs) will be key to enhancing the system's robustness. These advancements will further enable the development of intuitive, real-time prosthetic control systems for individuals with limb differences.

References

[1] A. Mongardi *et al.*, "Hand Gestures Recognition for Human-Machine Interfaces: A Low-Power Bio-Inspired Armband," *IEEE Transactions on Biomedical Circuits and Systems*, vol. 16, no. 6, pp. 1348–1365, Dec. 2022. [Online]. Available: https://ieeexplore.ieee.org/document/9907861/

[2] B. G. Sgambato *et al.*, "High Performance Wearable Ultrasound as a Human-Machine Interface for Wrist and Hand Kinematic Tracking," *IEEE Transactions on Biomedical Engineering*, vol. 71, no. 2, pp. 484–493, Feb. 2024. [Online]. Available: https://ieeexplore.ieee.org/document/10227550/

[3] S. M. Engdahl, S. A. Acuña, R. R. Kaliki, and S. Sikdar, "Sonomyography for Control of Upper-Limb Prostheses: Current State and Future Directions," *JPO Journal of Prosthetics and Orthotics*, vol. 36, no. 3, pp. 174–184, Jul. 2024. [Online]. Available: https://journals.lww.com/10.1097/JPO.0000000000000482

[4] S. N. Sidek and A. J. Haja Mohideen, "Mapping of EMG signal to hand grip force at varying wrist angles," in *2012 IEEE-EMBS Conference on Biomedical Engineering and Sciences*. Langkawi, Malaysia: IEEE, Dec. 2012, pp. 648–653. [Online]. Available: http://ieeexplore.ieee.org/document/6498069/

[5] Y. Wang, L. Zheng, J. Yang, and S. Wang, "A Grip Strength Estimation Method Using a Novel Flexible Sensor under Different Wrist Angles," *Sensors*, vol. 22, no. 5, p. 2002, Mar. 2022. [Online]. Available: https://www.mdpi.com/1424-8220/22/5/2002

[6] Q. Zhang, L. Fang, Q. Zhang, and C. Xiong, "Simultaneous estimation of joint angle and interaction force towards sEMG-driven human-robot interaction during constrained tasks," *Neurocomputing*, vol. 484, pp. 38–45, May 2022. [Online]. Available: https://linkinghub.elsevier.com/retrieve/pii/S0925231221015757

[7] H. Mao *et al.*, "Simultaneous estimation of grip force and wrist angles by surface electromyography and acceleration signals," *Biomedical Signal Processing and Control*, vol. 79, p. 104088, Jan. 2023. [Online]. Available: https://linkinghub.elsevier.com/retrieve/pii/S1746809422005511

[8] Ning Jiang, K. Englehart, and P. Parker, "Extracting Simultaneous and Proportional Neural Control Information for Multiple-DOF Prostheses From the Surface Electromyographic Signal," *IEEE Transactions on Biomedical Engineering*, vol. 56, no. 4, pp. 1070–1080, Apr. 2009. [Online]. Available: http://ieeexplore.ieee.org/document/4663628/

[9] L. H. Smith, T. A. Kuiken, and L. J. Hargrove, "Evaluation of Linear Regression Simultaneous Myoelectric Control Using Intramuscular EMG," *IEEE Transactions on Biomedical Engineering*, vol. 63, no. 4, pp. 737–746, Apr. 2016. [Online]. Available: http://ieeexplore.ieee.org/document/7214240/

[10] R. Roy, F. Xu, D. G. Kamper, and X. Hu, "A generic neural network model to estimate populational neural activity for robust neural decoding," *Computers in Biology and Medicine*, vol. 144, p. 105359, May 2022. [Online]. Available: https://linkinghub.elsevier.com/retrieve/pii/S0010482522001512

[11] D. Li, P. Kang, Y. Yu, and P. B. Shull, "Graph-Driven Simultaneous and Proportional Estimation of Wrist Angle and Grasp Force via High-Density EMG," *IEEE Journal of Biomedical and Health Informatics*, vol. 28, no. 5, pp. 2723–2732, May 2024. [Online]. Available: https://ieeexplore.ieee.org/document/10460104/

[12] Z. He, Z. Qin, and Y. Koike, "Continuous Estimation of Finger and Wrist Joint Angles Using a Muscle Synergy Based Musculoskeletal Model," *Applied Sciences*, vol. 12, no. 8, p. 3772, Apr. 2022. [Online]. Available: https://www.mdpi.com/2076-3417/12/8/3772

[13] J. Li, S. Yue, and L. Pan, "Simultaneous and Proportional Control of Wrist and Hand Movements Based on a Neural-Driven Musculoskeletal Model," *IEEE Transactions on Neural Systems and Rehabilitation Engineering*, vol. 31, pp. 3999–4007, 2023. [Online]. Available: https://ieeexplore.ieee.org/document/10274877/

[14] C. Ma *et al.*, "A Bi-Directional LSTM Network for Estimating Continuous Upper Limb Movement From Surface Electromyography," *IEEE Robotics and Automation Letters*, vol. 6, no. 4, pp. 7217–7224, Oct. 2021. [Online]. Available: https://ieeexplore.ieee.org/document/9484719/

[15] H. Su *et al.*, "Deep Neural Network Approach in EMG-Based Force Estimation for Human–Robot Interaction," *IEEE Transactions on Artificial Intelligence*, vol. 2, no. 5, pp. 404–412, Oct. 2021. [Online]. Available: https://ieeexplore.ieee.org/document/9380441/

[16] G. Hajian and E. Morin, "Deep Multi-Scale Fusion of Convolutional Neural Networks for EMG-Based Movement Estimation," *IEEE Transactions on Neural Systems and Rehabilitation Engineering*, vol. 30, pp. 486–495, 2022. [Online]. Available: https://ieeexplore.ieee.org/document/9718209/

[17] X. Yang, C. Castellini, D. Farina, and H. Liu, "Ultrasound as a Neurorobotic Interface: A Review," *IEEE Transactions on Systems, Man, and Cybernetics: Systems*, vol. 54, no. 6, pp. 3534–3546, Jun. 2024. [Online]. Available: https://ieeexplore.ieee.org/document/10436655/

[18] S. M. Engdahl, S. A. Acuña, E. L. King *et al.*, "First-in-human demonstration of functional task performance using a sonomyographic prosthesis," *PREPRINT (Version 1) available at Research Square*, February 2022. [Online]. Available: https://doi.org/10.21203/rs.3.rs-1370686/v1

[19] X. Yang *et al.*, "Simultaneous Prediction of Wrist/Hand Motion via Wearable Ultrasound Sensing," *IEEE Transactions on Neural Systems and Rehabilitation Engineering*, vol. 28, no. 4, pp. 970–977, Apr. 2020. [Online]. Available: https://ieeexplore.ieee.org/document/9020139/

[20] A. T. Kamatham *et al.*, "Sparse Sonomyography-Based Estimation of Isometric Force: A Comparison of Methods and Features," *IEEE Transactions on Medical Robotics and Bionics*, vol. 4, no. 3, pp. 821–829, Aug. 2022. [Online]. Available: https://ieeexplore.ieee.org/document/9769757/

[21] X. Yang *et al.*, "Self-supervised learning for intuitive control of prosthetic hand movements via sonomyography," *IEEE Transactions on Cybernetics*, pp. 1–12, 2024.

[22] A. T. Kamatham *et al.*, "SonoMyoNet: A Convolutional Neural Network for Predicting Isometric Force From Highly Sparse Ultrasound Images," *IEEE Transactions on Human-Machine Systems*, vol. 54, no. 3, pp. 317–324, Jun. 2024. [Online]. Available: https://ieeexplore.ieee.org/document/10529644/

[23] R. C. Heyser, "Acoustical measurements by time delay spectrometry," *Journal of the Audio Engineering Society*, vol. 15, no. 4, pp. 370–382, 1967.

[24] A. Bashatah *et al.*, "Wearable Ultrasound System Using Low-Voltage Time Delay Spectrometry for Dynamic Tissue Imaging," *IEEE Transactions on Biomedical Engineering*, vol. 71, no. 11, pp. 3232–3243, Nov. 2024. [Online]. Available: https://ieeexplore.ieee.org/document/10557691/

[25] L. B. Almeida, "Multilayer perceptrons," in *Handbook of Neural Computation*, 1st ed. CRC Press, 1996.

[26] V. Nair and G. E. Hinton, "Rectified linear units improve restricted boltzmann machines," in *Proceedings of the 27th International Conference on Machine Learning (ICML)*, 2010, pp. 807–814.

[27] C. E. Rasmussen and C. K. I. Williams, *Gaussian Processes for Machine Learning*. MIT Press, 2006. [Online]. Available: http://www.gaussianprocess.org/gpml/

[28] I. T. Jolliffe, *Principal Component Analysis*, 2nd ed., ser. Springer Series in Statistics. Springer, 2002. [Online]. Available: https://doi.org/10.1007/b98835

Accuracy of IMUs and monocular human pose estimation at measuring elbow flexion

David Rode[1,*], Alessandro Ceccarelli[2], Adrian Esser[1], Peter Wolf[1], Robert Riener[1,3]

***Abstract*—Markerless human pose estimation and inertial measurement units are two common methods for human movement analysis. They are cost-effective and easy to use, but their accuracy compared to established optical motion capture methods is yet to be determined for some movements. This study compared the accuracy of IMUs and BlazePose, a markerless monocular 3D human pose estimator, against a marker-based optical system for measuring elbow flexion angles. After performing a static offset calibration to account for differences in anatomical coordinate systems, these were reduced to a mean absolute error of 4.2° and a root mean square error of 6.0°. The accuracy of markerless pose estimation was significantly influenced by the orientation of the participants to the camera. The optimal camera orientation was achieved when participants performed the movement fully within the image plane, with a mean absolute error of 10.5° and a root mean square error of 14.7° after performing a static offset calibration. Bland-Altman analysis indicated mostly constant deviations for the IMUs but non-constant deviations for HPE, which underestimated large elbow flexion angles. The findings of this study underscore the importance of camera orientation for monocular HPE accuracy. IMUs display much higher accuracy at measuring elbow flexion than monocular HPE. Further improvements in the accuracy of HPE independent of orientation might broaden its applications in motion analysis.**

***Index Terms*—Inertial measurement units, markerless pose estimation, optical motion capturing, elbow flexion, joint angles**

I. Introduction

Measurement of joint angles is of significant interest in a multitude of fields, including clinical diagnoses, movement science, and home-based applications, such as gamified home therapy [1]. Optical motion capturing (OMC) with passive reflective markers is considered a state-of-the-art method among non-invasive measurement techniques. This method requires the attachment of markers that reflect infrared light to specific anatomical landmarks on the human body. Infrared cameras are capable of detecting the reflections off these markers with a high degree of accuracy. The orientations of body segments and joint angles can be reconstructed from the marker positions by means of kinematic models. However, the use of OMC in clinical or home settings is limited by several factors. These include the time-consuming setup and calibration processes, the high hardware requirements, the substantial financial investments, and the expertise required for marker attachment and system operation.

Recent technological advances have led to the emergence of novel, user-friendly, and cost-effective measurement techniques capable of tracking joint motion. Two notable examples of this include the analysis of human motion by inertial measurement units (IMUs) [2], and markerless human pose estimation (HPE) [3]. These methods can track human motion with significantly lower hardware requirements, faster setup and calibration times, and higher ease of use than with OMC. Furthermore, because they do not require expert knowledge to prepare and operate, they could be used in home applications, such as remote clinical assessments, gamified therapy, and the control of rehabilitation devices.

IMUs are wearable sensors that utilize gyroscopes and accelerometers to quantify the angular velocity and specific force experienced by the sensor. Additionally, some IMUs include magnetometers to measure the magnetic field of the Earth, but these sensors are often sensitive to external electromagnetic noise and can cause significant drift over time [4], [5].

Markerless human pose estimation aims to detect human joints and poses from images or videos. Most current HPE methods rely on learning-based methods to identify humans within image frames and determine the location of anatomical landmarks within these frames. Monocular pose estimators require only one camera, which makes them particularly appealing for applications with strict time requirements, such as home applications. The straightforward setup and calibration process reduces the overall time required for data acquisition. The absence of markers or sensors which have to be attached to anatomical landmarks makes them suitable for use by non-expert users.

It is evident that both IMUs and HPE-based methods are user-friendly, require minimal setup time, and have low hardware requirements. However, the accuracy of these methods must be evaluated in comparison with established techniques to determine their suitability for specific applications. This study evaluated the accuracy and precision of IMUs and HPE in determining the flexion angle of the elbow joint by comparing them with marker-based OMC on a dataset of five participants performing five repetitions of isolated elbow flexion and extension.

[1] Sensory-Motor Systems (SMS) Lab, Institute of Robotics and Intelligent Systems (IRIS), Department of Health Sciences and Technology (D-HEST), ETH Zurich, Switzerland

[2] CREO Lab, Faculty of Engineering, Università Campus Bio-Medico di Roma, Italy

[3] Reharobotics Group, Spinal Cord Injury Center, Balgrist University Hospital, Medical Faculty, University of Zurich, Switzerland

[*] Corresponding author: david.rode@hest.ethz.ch

II. Methods

A. Participants and Tasks

A total of five participants were recruited for this study and each provided their written informed consent. The study was reviewed and approved by the ETH Zurich Ethics Committee, with the approval number 24 ETHICS-294.

TABLE I
Overview over the participants included in this study. The values represent the mean and values within square brackets indicate the range of values.

Gender	Age (years)	Height (cm)	Weight (kg)
Female (n = 4)	27 [24 - 30]	166 [158 - 180]	53 [43 - 64]
Male (n = 1)	29	173	67
Overall (n = 5)	28 [24 - 30]	167 [158 - 180]	56 [43 - 67]

Participants were instructed to maintain a fixed standing position during each test and only move their dominant forearm, which was the right side for all participants. They performed a flexion movement of the elbow from a fully extended starting configuration with their arms at their side and their palms facing forward. They were instructed to flex their elbow to approximately 90° and fully extend it again afterwards for a total of five repetitions for each condition. This movement was repeated for three conditions with different orientations of the participants towards a RGB camera. One condition of this movement was performed fully within the image plane at an angle of 0°, one was performed facing the camera at an angle of 45°, and one was performed fully facing the camera at an angle of 90°.

B. Optical Motion Capturing

A passive marker OMC system was employed as a ground truth reference method. The OMC system consisted of eight infrared motion capturing cameras (Miqus M3, Qualisys, Sweden). An RGB camera (Miqus Video Plus, Qualisys, Sweden) was connected to the OMC measurement system, thereby ensuring simultaneous measurements and identical start and stop times. The RGB camera was placed 3 m from the participants at a height of 1.12 m. The OMC cameras ran at a sampling frequency of 100 frames per second (FPS).

The videos recorded by the RGB camera were used as visual inputs for the subsequent markerless pose estimation process. The OMC measurements and RGB video recordings were conducted within the same software program (Qualisys Track Manager, Qualisys, Sweden). A commonly used kinematic model (Upper Limb Model, Vicon, United Kingdom) was selected and processed in another processing software program (Nexus 2.15, Vicon, United Kingdom). This kinematic model requires a set of 15 markers attached to defined anatomical landmarks of the upper body (see Fig. 1). Throughout all trials, the markers and IMUs were placed by the same expert.

The kinematic model outputs the joint center locations and joint angles for the dominant side of the upper body. Capturing a static calibration is necessary for this model to return accurate joint angles. During this static calibration trial, participants stood in a stationary position with their hands on their sides and their palms pointing anterior. After this calibration, the participants performed the three conditions in succession. The selected kinematic model treated the elbow joint as a universal joint with two degrees of freedom: flexion and pronation-supination. As this study compared the accuracy of different methods at measuring elbow flexion, the pronation-supination angle was not considered after processing the kinematic model.

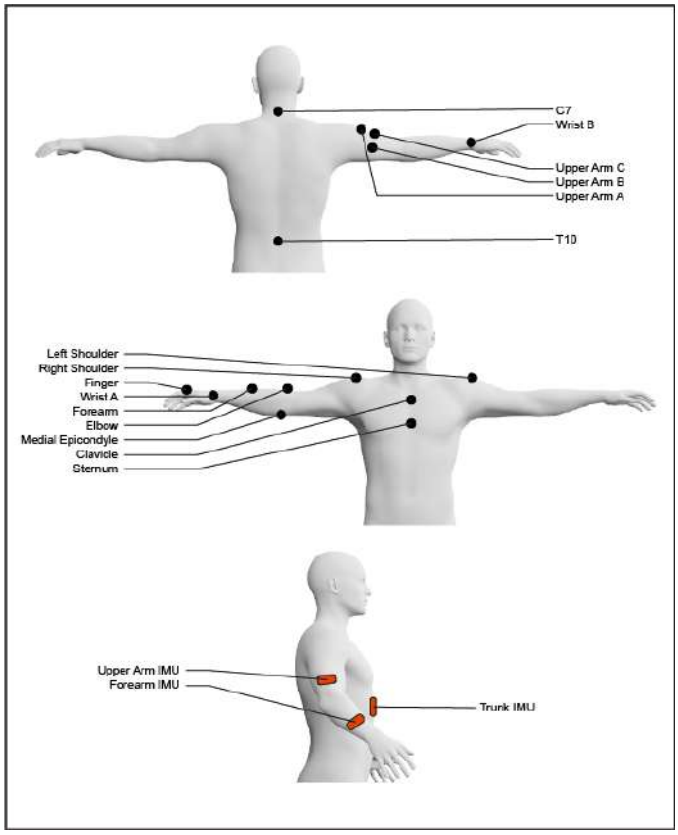


Fig. 1. Overview over the placement of markers and IMUs on the participants. The Upper Limb Model (Vicon, United Kingdom) marker set required attaching 15 reflective markers (black). Three IMUs were attached to the torso, upper arm and forearm (red). The IMUs and markers were placed by the same trained expert during the entire study and were worn simultaneously throughout all measurements.

C. Markerless Pose Estimation

Due to its accuracy, user-friendliness and high processing speed, BlazePose (Mediapipe Version 1.09, Google, USA) was selected for this study [6]. BlazePose is a markerless monocular human pose estimator that is capable of direct three-dimensional pose estimation [7]. We used the "Global" operating mode of BlazePose which returned coordinates in metric units with the "Heavy" model, which is the most accurate among the available models.

As the RGB camera was connected to the OMC system, their signals were already synchronized. The RGB camera captured frames at a sampling frequency of 50 FPS. BlazePose returned a set of 33 three-dimensional landmark locations of the human body for each frame in which a pose was detected. Some of these landmarks represent joint center locations, whereas others represent characteristic features of the face,

hands, and feet. The elbow flexion angle was computed by the scalar product formula, using a three-dimensional vector constructed from the shoulder joint to the elbow joint and a three-dimensional vector pointing from the elbow joint to the wrist joint.

D. Inertial Measurement Units

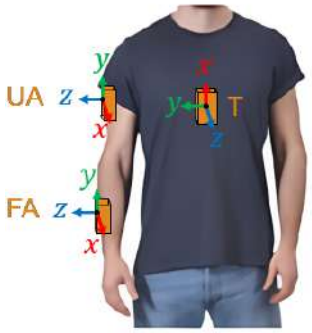


Fig. 2. The locations and orientations of the trunk (T), upper arm (UA), and forearm (FA) IMUs during the static calibration pose.

Three IMUs (NGIMU, x-io Technologies, United Kingdom) were attached to the participants (see Fig. 2). To determine the angles of the upper body joint in the dominant arm for subsequent comparison, an IMU was placed on the trunk, another on the dominant upper arm, and a third on the dominant lower arm [8]. All were worn simultaneously with the marker set. The recording of the three IMUS occurred synchronously in the same software program (Synchronized Network Manager version 1.18, x-io Technologies, United Kingdom) at a sampling frequency of 50 Hz. As IMU recordings were started from a different program than OMC and HPE measurements, the raw IMU signals were not synchronized with OMC and HPE. The IMUs ran an onboard Attitude and Heading Reference System (AHRS) fusion algorithm, fusing the accelerometer and gyroscope data to provide an estimate of the global orientation of each IMU relative to the world frame. The magnetometers were disabled, and prior to the trial of each subject, the three IMUs were aligned and reset to calibrate their headings.

The following reference frames were considered:

- The World reference frame (W)
- The IMU reference frames ($\mathrm{I_i}$, $i \in \{T, UA, FA\}$)
- The Body reference frames ($\mathrm{B_i}$, $i \in \{T, UA, FA\}$)

The attached IMUs did not directly measure the orientations of the segment frames. Therefore, a calibration procedure was used to calibrate the measured IMU orientations [9]. Before each trial, participants stood upright for five seconds, with their palms facing their hips and elbows fully extended (see Fig. 2). The elbow flexion angle was assumed to be zero during this calibration procedure.

The calibration procedure resulted in a rotation that defines the orientation change from the world frame to the IMU frame while in the calibration pose: ${}_{W}\mathbf{R}_{I,i,0}$ This matrix was assumed to be time-invariant. If the IMU sensors are moved relative to the body of the wearer, this calibration procedure should be repeated.

The time-varying rotations between the world frame and the IMU frames (during motion) were defined as ${}_{W}\mathbf{R}_{I,i}(t)$

Thus, the rotation from the IMU orientation at static calibration towards the IMU orientation in any posture was given by:

$$ {}_{I,i,0}\mathbf{R}_{I,i}(t) = ({}_{W}\mathbf{R}_{I,i,0})^{-1} \cdot {}_{W}\mathbf{R}_{I,i}(t) \tag{1}$$

We assumed that the IMUs and the body frames moved together rigidly, thus:

$$ {}_{B,i,0}\mathbf{R}_{B,i}(t) = {}_{I,i,0}\mathbf{R}_{I,i}(t) \tag{2}$$

Finally, the orientation of the body frames relative to the world frame was found from the following:

$$ {}_{W}\mathbf{R}_{B,i}(t) = {}_{W}\mathbf{R}_{B,i,0} \cdot {}_{B,i,0}\mathbf{R}_{B,i}(t) \tag{3}$$

$$ = {}_{W}\mathbf{R}_{B,i,0} \cdot ({}_{W}\mathbf{R}_{I,i,0})^{-1} \cdot {}_{W}\mathbf{R}_{I,i}(t) \tag{4}$$

The rotation matrix ${}_{W}\mathbf{R}_{B,i,0}$ represents the rotation from the world frame to the body frame during the calibration pose. These rotations are time-invariant and depend on the orientation by which the IMUs were attached to the participant. These rotations are defined intrinsically as:

$$ {}_{W}\mathbf{R}_{B,T,0} = \mathbf{R}_x(\pi) \cdot \mathbf{R}_y(\frac{\pi}{2}) \tag{5}$$

and

$$ {}_{W}\mathbf{R}_{B,UA,0} = {}_{W}\mathbf{R}_{B,FA,0} = \mathbf{R}_x(\frac{\pi}{2}) \tag{6}$$

where $\mathbf{R}_x(\cdot)$ and $\mathbf{R}_y(\cdot)$ represent principle rotations about the x and y axes, respectively.

With ${}_{W}\mathbf{R}_{B,UA}(t)$ and ${}_{W}\mathbf{R}_{B,FA}(t)$, the elbow angle is the angle between the y-axes of these two frames in the world frame. Defining:

$$ \overrightarrow{y}_{UA} = {}_{W}\mathbf{R}_{B,UA}(t) \cdot \begin{bmatrix} 0 \\ 1 \\ 0 \end{bmatrix} \tag{7}$$

$$ \overrightarrow{y}_{FA} = {}_{W}\mathbf{R}_{B,FA}(t) \cdot \begin{bmatrix} 0 \\ 1 \\ 0 \end{bmatrix} \tag{8}$$

We defined the elbow flexion angle at time t as α_t^{IMU}, which is given by:

$$ \alpha_t^{IMU} = \arccos\left(\frac{\overrightarrow{y}_{UA,\ t} \cdot \overrightarrow{y}_{FA,\ t}^{T}}{\| \overrightarrow{y}_{UA,\ t} \| \cdot \| \overrightarrow{y}_{FA,\ t} \|} \right) \tag{9}$$

This elbow flexion angle corresponds to the first angle in the ISB joint coordinate system, which prescribes a Z-X-Y order of rotations, with the first angle being elbow flexion-extension, the second angle being elbow pronation-supination, and the third angle being the passive carrying angle, which is often not reported [10].

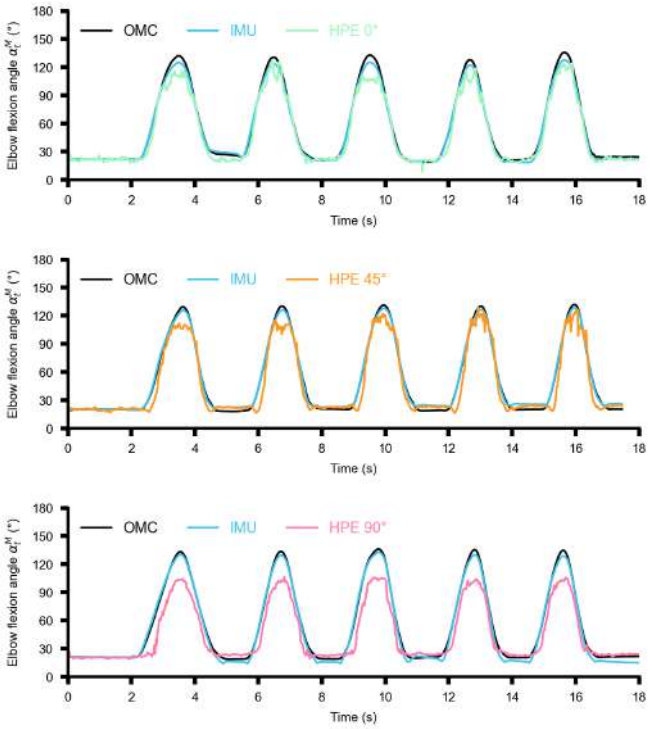


Fig. 3. The elbow flexion angle as captured by passive marker optical motion capturing, inertial measurement units, and markerless human pose estimation with different camera orientations for one exemplary participant. Note that a static offset calibration has been performed on these IMU and HPE flexion angles to account for differences in anatomical coordinate systems. At an orientation of 0°, participants performed elbow flexion within the image plane, while at an orientation of 90°, they faced the camera frontally.

E. Metrics

To compute the differences between the measured angles, we first synchronized all signals from the different measurement methods and transformed them to a common sampling frequency. First, the OMC measurements were downsampled to 50 FPS by dropping every second frame to have the same frequency as the HPE and IMU measurements. As the OMC measurements and the RGB videos for HPE were recorded from the same system, they were already synchronized. The IMU measurements were synchronized with the OMC measurements by maximizing the cross-correlation of the flexion angles for each trial. Then we applied a static offset calibration to the HPE and IMU flexion angles to account for different definitions of the anatomical coordinate systems between the different measurement methods (see Fig. 3). The constant offset factor was determined by comparing the average OMC flexion angle to the average of each measurement method during the first second of each test for each participant and condition. We then applied this constant offset factor to the entire trial.

The mean absolute error (MAE) and the root mean square error ($RMSE$) were the primary metrics investigated for the accuracy. Defining the elbow flexion angle at time t measured by method M as α_t^M, these are:

$$MAE^M = \frac{1}{N_{timestamps}} \cdot \sum_{t=1}^{N_{timestamps}} |\alpha_t^M - \alpha_t^{OMC}| \quad (10)$$

$$RMSE^M = \sqrt{\frac{1}{N_{timestamps}} \cdot \sum_{t=1}^{N_{timestamps}} (\alpha_t^M - \alpha_t^{OMC})^2} \quad (11)$$

These values were computed by averaging over all timestamps in the dataset, including all participants and repetitions.

III. Results

A. Accuracy of IMUs and HPE

Before performing a static offset calibration, the elbow flexion angles were measured by IMU with a MAE of 13.8 ° and a RMSE of 15.2 ° when averaged over all participants and conditions (see Fig. 4). The same elbow flexion angles were measured by HPE with a MAE of 18.7° and RMSE of 23.8° when averaged over all participants and all orientations.

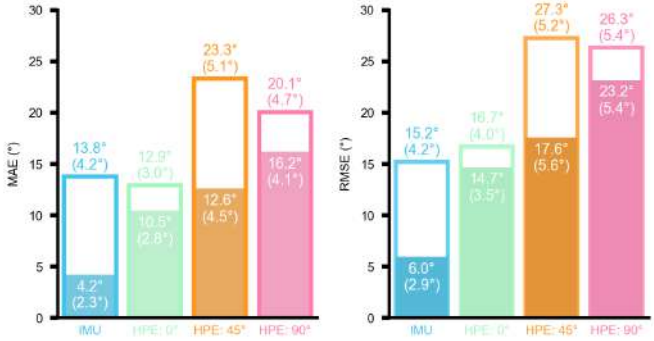


Fig. 4. Overview of root mean square errors and mean absolute errors before and after performing static offset calibration. The hollow bars and colored values represent the accuracy before calibration, whereas the filled bars and white values indicate the accuracy after calibration. The values in brackets represent the inter-participant variability as standard deviation. Static offset calibration accounted for the differences in anatomical coordinate systems and led to a great increase of accuracy for the IMUs. Notice the higher overall accuracy demonstrated by the IMUs and the large effect of participant orientation on HPE accuracy. Movements performed fully within the image plane at an orientation angle of 0° led to the highest accuracy for HPE.

The static offset calibration reduced the MAE of the IMUs to 4.2° and the RMSE to 6.0°.

Overall, markerless HPE using BlazePose "Global" with the "Heavy" model showed a MAE of 13.05° and a $RMSE$ of 18.75° after performing static offset calibration and when averaging over all participants and all orientations. When participants performed the elbow flexion movement fully within the image plane at an orientation of 0°, the MAE was 10.5° and $RMSE$ was 14.7° over all participants. When participants faced the camera at an angle of 45°, the MAE was 12.6° and the $RMSE$ was 17.6° over all participants. Lastly, when the participants were facing the camera frontally at an angle of 90° with respect to the image plane, the MAE was 16.2° and the $RMSE$ was 23.2° over all participants.

B. Bland-Altman analysis of HPE

When comparing the different conditions in a Bland-Altman plot, non-constant deviations are observable for all three orientation angles (see Fig. 5). The mean differences and limits of agreement increased with an increasing angle of the participants towards the image plane.

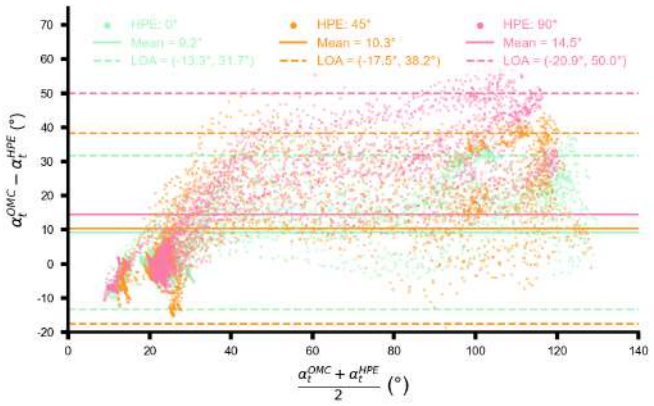


Fig. 5. Bland-Altman plot of markerless pose estimation for all camera orientation angles after performing static offset calibration. The mean deviations to optical motion capturing and the limits of agreement are indicated for each orientation. Observe the non-constant behavior of the deviations for all orientation angles. Performing the movement fully within the image plane at an angle of 0° resulted in the tightest LOAs, whereas facing the camera frontally at 90° led to the largest LOAs. HPE tends to underestimate large elbow flexion angles irrespective of the orientation towards the camera.

C. Bland-Altman analysis of IMUs

The Bland-Altman plot of the IMU measurements shows mainly constant deviations (see Fig. 6). The three conditions of participant six are highlighted to exemplify this behavior. These constant deviations varied by participant and, at times, even showed considerable changes between conditions.

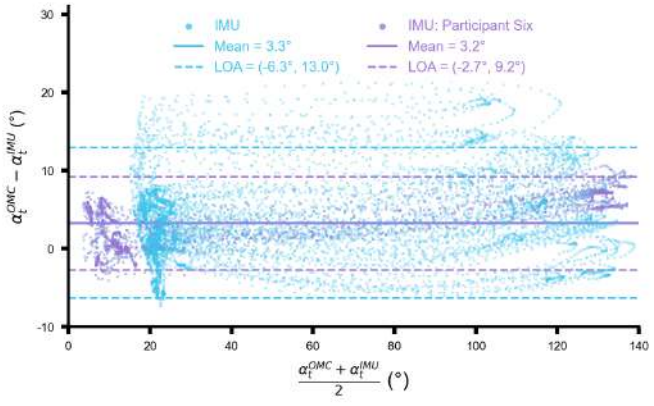


Fig. 6. Bland-Altman plot of all IMU measurements after performing static offset calibration. The mean deviation to optical motion capturing and the limits of agreement are indicated. The IMU measurements of participant six are highlighted to emphasize the behavior of the IMU deviations. Observe the more constant behavior of the deviations when compared to HPE.

IV. Discussion

The Bland-Altman analysis of the calibrated flexion angles reveal that the IMUs showed more constant deviations than BlazePose for all orientations (see Figs. 5 and 6). BlazePose showed non-constant behavior of the deviations for all orientations, as it underestimated large flexion angles when compared to OMC (see Fig. 5). This non-constant behavior did not allow for a simple static offset calibration to greatly reduce the deviations (see Fig. 4).

In contrast, the Bland-Altman plot of the IMU measurements shows more constant deviations throughout the measured range of elbow flexion angles (see Fig. 6). The constant deviations are likely caused by different definitions of the anatomical coordinate systems and can be accounted for by applying a static offset calibration, which greatly reduced the errors for IMUs. After static offset calibration was performed, the IMUs clearly demonstrated higher accuracy than BlazePose for any orientation (see Fig. 4).

When comparing the accuracy of the calibrated HPE data, a clear dependence of the measurement accuracy on the orientation of the participant is visible (see Fig. 4). The most accurate measurements were achieved when participants performed the flexion movement fully within the image plane. The accuracy decreased greatly when increasing the angle towards the image plane and was lowest when participants stood perpendicular to the image plane and faced the camera frontally at an angle of 90° towards the image plane. This is likely due to the greater errors in depth estimation than within the image plane for monocular HPE methods. Therefore, when using these methods, great attention should be paid to the orientation of participants towards the camera and the plane in which movement occurs. HPE could be an alternative to IMUs and OMC for non-critical applications like home therapy or remote assessments when the measured movement is fully within the image plane. If the movement is three-dimensional or cannot be captured purely within the image plane, IMUs will display much greater accuracy than HPE and are preferable if the application allows them.

The accuracy values after performing a static offset calibration align with reported values. An assessment of IMU accuracy at measuring elbow flexion with anthropomorphic robotic arms found an RMSE of up to 5.7° [11]. Another study compared the elbow flexion angle during swimming motions measured by IMUs to an OMC system and found a RMSE between 2.23 and 5.84° [12].

Currently, there is a lack of information on the accuracy of markerless HPE methods at measuring upper body joint kinematics [13]. A study comparing the accuracy of markerless multi-view HPE found an RMSE of up to 7.4° in elbow flexion compared to OMC [13]. Another multi-view HPE method showed an MAE of 6.8 ° in elbow flexion compared to OMC [14]. Therefore, the errors found in this study for a monocular 3D HPE method are reasonable, as the lacking multi-view information results in lower accuracies.

This study solely investigated BlazePose, so these insights may

not extend to other pose estimators due to different training data and model architectures. Furthermore, the IMUs in this study were calibrated before each measurement condition to correct for drift and integration errors, so the reported accuracy may not be achievable in practical applications. Lastly, the choice of reference measurement system and kinematic model affect the resulting accuracy of the tested methods. In this study, we chose passive marker OMC as a reference, which is known to suffer from marker displacements due to soft tissue deformations [15]. Furthermore, upper body kinematic models lack the amount of validation that gait models have had [16]. Nevertheless, we chose passive marker OMC as reference due to its wide-place adoption in research and very high accuracy compared with other non-intrusive methods.

Future studies in this domain might determine the accuracy of HPE methods for other joint angles of the upper body. Increasing the accuracy of monocular HPE methods irrespective of the orientation of users towards the capturing camera could increase their usability and allow for more use cases. This could be accomplished by using different model architectures and collecting training data with diverse poses using established systems to obtain accurate joint locations.

V. Conclusion

This study compared the accuracy of IMUs and BlazePose, a monocular markerless human pose estimator, to passive marker optical motion capturing at measuring elbow flexion angles. IMUs consistently outperformed BlazePose in accuracy across all orientations, with lower errors and tighter limits of agreement. The accuracy of BlazePose varied strongly with the orientation of the participants to the camera, achieving the best results when elbow flexion was completely within the image plane. It underestimated the larger elbow flexion angles for all investigated orientations of the participants. Whereas a static offset calibration showed great results on the accuracy of the IMUs, this could not be achieved for BlazePose. Selecting the optimal camera orientation is crucial for accurate motion analysis when using HPE methods. Future research might investigate the accuracy of both methods for other joint angles of the upper body. Enhancing the accuracy of monocular HPE methods across all orientations could lead to a broader range of use cases.

Acknowledgments

The authors thank Michael Herold-Nadig, Marco Bader, and Juri Nowak for their contributions to this study.

References

[1] G. Amos, D. Rode, N. A. Maffiuletti, M. Bizzini, M. Mauch, C. A. Easthope, F. Haufe, M. Xiloyannis, P. Wolf, and R. Riener, "Gamification of physical therapy exercises using commercial entertainment content: A safety and feasibility study," in *IEEE International Conference on Rehabilitation Robotics*. IEEE Computer Society, 2023.

[2] R. Islam, M. Bennasar, M. Al-Amri, S. Holland, P. Mulholland, and B. Price, "Democratizing Clinical Movement Analysis: Assessing the Versatility of MoJoXlab with Open-protocol Inertial Sensors," *Procedia Computer Science*, vol. 246, pp. 2360–2369, 2024. [Online]. Available: https://linkinghub.elsevier.com/retrieve/pii/S187705092402581X

[3] E. Souza Dos Reis, L. A. Seewald, R. S. Antunes, V. F. Rodrigues, R. Da Rosa Righi, C. A. Da Costa, L. G. Da Silveira Jr., B. Eskofier, A. Maier, T. Horz, and R. Fahrig, "Monocular multi-person pose estimation: A survey," *Pattern Recognition*, vol. 118, p. 108046, Oct. 2021. [Online]. Available: https://linkinghub.elsevier.com/retrieve/pii/S0031320321002338

[4] N. F. Ribeiro and C. P. Santos, "Inertial measurement units: A brief state of the art on gait analysis," in *ENBENG 2017 - 5th Portuguese Meeting on Bioengineering, Proceedings*. Institute of Electrical and Electronics Engineers Inc., 3 2017.

[5] N. Ahmad, R. A. R. Ghazilla, N. M. Khairi, and V. Kasi, "Reviews on various inertial measurement unit (imu) sensor applications," *International Journal of Signal Processing Systems*, pp. 256–262, 2013.

[6] A. A. Hulleck, M. Mohseni, M. K. A. Hantash, R. Katmah, M. Almadani, N. Arjmand, K. Khalaf, and M. E. Rich, "Accuracy of computer vision-based pose estimation algorithms in predicting joint kinematics during gait," 8 2023. [Online]. Available: https://www.researchsquare.com/article/rs-3239200/v1

[7] I. Grishchenko, V. Bazarevsky, A. Zanfir, E. G. Bazavan, M. Zanfir, R. Yee, K. Raveendran, M. Zhdanovich, M. Grundmann, and C. Sminchisescu, "Blazepose ghum holistic: Real-time 3d human landmarks and pose estimation," 2022. [Online]. Available: https://arxiv.org/abs/2206.11678

[8] Z. Fang, S. Woodford, D. Senanayake, and D. Ackland, "Conversion of upper-limb inertial measurement unit data to joint angles: A systematic review," *Sensors*, vol. 23, no. 14, 2023. [Online]. Available: https://www.mdpi.com/1424-8220/23/14/6535

[9] A. Cereatti, R. Gurchiek, A. Mündermann, S. Fantozzi, F. Horak, S. Delp, and K. Aminian, "ISB recommendations on the definition, estimation, and reporting of joint kinematics in human motion analysis applications using wearable inertial measurement technology," *Journal of Biomechanics*, vol. 173, p. 112225, Aug. 2024. [Online]. Available: https://linkinghub.elsevier.com/retrieve/pii/S0021929024003038

[10] G. Wu, F. C. Van Der Helm, H. (DirkJan) Veeger, M. Makhsous, P. Van Roy, C. Anglin, J. Nagels, A. R. Karduna, K. McQuade, X. Wang, F. W. Werner, and B. Buchholz, "ISB recommendation on definitions of joint coordinate systems of various joints for the reporting of human joint motion—Part II: shoulder, elbow, wrist and hand," *Journal of Biomechanics*, vol. 38, no. 5, pp. 981–992, May 2005. [Online]. Available: https://linkinghub.elsevier.com/retrieve/pii/S002192900400301X

[11] M. Lapresa, C. Tamantini, F. Scotto di Luzio, M. Ferlazzo, G. Sorrenti, F. Corpina, and L. Zollo, "Validation of magneto-inertial measurement units for upper-limb motion analysis through an anthropomorphic robot," *IEEE Sensors Journal*, vol. 22, no. 17, pp. 16 920–16 928, 2022.

[12] B. Guignard, O. Ayad, H. Baillet, F. Mell, D. Simbaña Escobar, J. Boulanger, and L. Seifert, "Validity, reliability and accuracy of inertial measurement units (IMUs) to measure angles: application in swimming," *Sports Biomechanics*, vol. 23, no. 10, pp. 1471–1503, Oct. 2024. [Online]. Available: https://www.tandfonline.com/doi/full/10.1080/14763141.2021.1945136

[13] B. K. Lahkar, A. Muller, R. Dumas, L. Reveret, and T. Robert, "Accuracy of a markerless motion capture system in estimating upper extremity kinematics during boxing," *Frontiers in Sports and Active Living*, vol. 4, p. 939980, Jul. 2022. [Online]. Available: https://www.frontiersin.org/articles/10.3389/fspor.2022.939980/full

[14] S. Auer, F. Süß, and S. Dendorfer, "Using markerless motion capture and musculoskeletal models: An evaluation of joint kinematics," *Technology and Health Care*, vol. 32, no. 5, pp. 3433–3442, Sep. 2024. [Online]. Available: https://journals.sagepub.com/doi/full/10.3233/THC-240202

[15] A. G. Cutti, G. Paolini, M. Troncossi, A. Cappello, and A. Davalli, "Soft tissue artefact assessment in humeral axial rotation," *Gait and Posture*, vol. 21, pp. 341–349, 2005.

[16] R. Baker, F. Leboeuf, J. Reay, and M. Sangeux, *The Conventional Gait Model - Success and Limitations*. Springer International Publishing, 2018, pp. 489–508.

A wearable pneumatic platform to automatically assess tactile sensitivity

Giulia Castiglioni[†] *, Jacopo Quaglierini[†] *, Cristian Felipe Blanco-Diaz[†] , Simone Rossi[†] , Camilla Baselli[†] , Sophie Skach[†] , Leonardo Cappello[†]
[†]*The Biorobotics Institute, Scuola Superiore Sant'Anna*, Pisa, Italy
Department of Excellence in Robotics and AI, Scuola Superiore Sant'Anna, Pisa, Italy
*These authors equally contributed to this work.

***Abstract*—Sensory deficits caused by neurological disorders, *i.e.*, loss of tactile sensitivity and/or limb proprioception, hinder object manipulation and precise movements, and ultimately lead to a significant slow-down in motor rehabilitation. Although sensory rehabilitation has been catching on more and more, current procedures for evaluating tactile sensitivity are still inefficient in terms of equipment portability, test execution time, and specific training required for healthcare personnel. While some automated tactile stimulation platforms have been developed for other applications, robotic systems designed to evaluate residual tactile sensitivity are still largely under-explored. Here we propose a hand-wearable, pneumatically-driven device, which exploits an air chamber to transmit contact forces to the user's fingertip by means of sliding pin, which can then be used to assess tactile sensitivity in a quantitative and reproducible manner. We tested the proposed platform on five healthy participants, and obtained pressure perception thresholds in the order of 0.01 bar, with a median of ~ 0.03 bar, which showed a good correlation ($\rho = 0.8441$) with the Semmes-Weinstein test. Although these results are preliminary, they suggest the potential of the proposed device as a complementary assessment tool of tactile sensitivity.**

***Index Terms*—Design and development in rehabilitation robotics, Wearable robotic systems, Integrated diagnostic and therapeutic systems**

I. Introduction

Neurological disorders, such as stroke, spinal cord injury, multiple sclerosis, and other neurodegenerative diseases, lead to motor impairments: reduction in voluntary motor control, anomalous muscular contractions, worsening of motor coordination, muscle weakness, and longer reaction times, among the others [1]. However, sensory deficits, *i.e.*, loss of tactile sensitivity and/or limb proprioception, may also arise. For instance, 85% of post-stroke patients suffer from some form of reduced tactile or proprioceptive sensitivity [2].

In turn, a chronic loss of sensitivity hinders the execution of fine and complex movements [3], such as object manipulation and precision movements [1, 2, 3], thus significantly hampering the overall progress in motor rehabilitation [4]. While restoration of muscle strength and motor coordination is paramount, rehabilitation strategies should then also focus on somatosensory recovery. In this regard, next to motor rehabilitation therapy, also sensory rehabilitation – where patient's discrimination of tactile stimulations is evaluated and trained – has been catching on more and more in recent years [3]. However, following clinical focus groups, we believe that current procedures for evaluating tactile function – Semmes-Weinstein monofilament test, two-points acuity, JVP domes – are not optimized. Although they are virtually widespread, limited equipment portability, long test execution time, and specific training required for healthcare personnel hamper their efficiency and thus their application. While some automated tactile stimulation platforms have been developed for other applications (such as tactile stimulation during MRI studies [5, 6] and augmented feedback in virtual reality [7, 8]), robotic systems designed to evaluate residual tactile sensitivity after a brain lesion still lay uncharted.

In this study, we report on the development of a hand-wearable, pneumatically-driven device (shown in Fig. 1a), designed to evaluate residual tactile sensitivity in a streamlined fashion. The system is made of a fabric glove endowed with a fingertip stimulation module, which hosts a pneumatic



Fig. 1. a) The developed fingertip module, mounted on a fabric glove and worn by a user. b) Upper view of the fingertip module: a custom support hosts an air chamber, which is attached to a sliding pin.

This work was co-funded by INAIL (the Italian National Workers' Compensation Authority) under the HANDeVAL project (G.A. PR23-SV-P1). The work of L.C. was co-funded by the European Union (ERC, MUSE, G.A. 101116249). Views and opinions expressed are however those of the author(s) only and do not necessarily reflect those of the European Union or the European Research Council. Neither the European Union nor the granting authority can be held responsible for them.

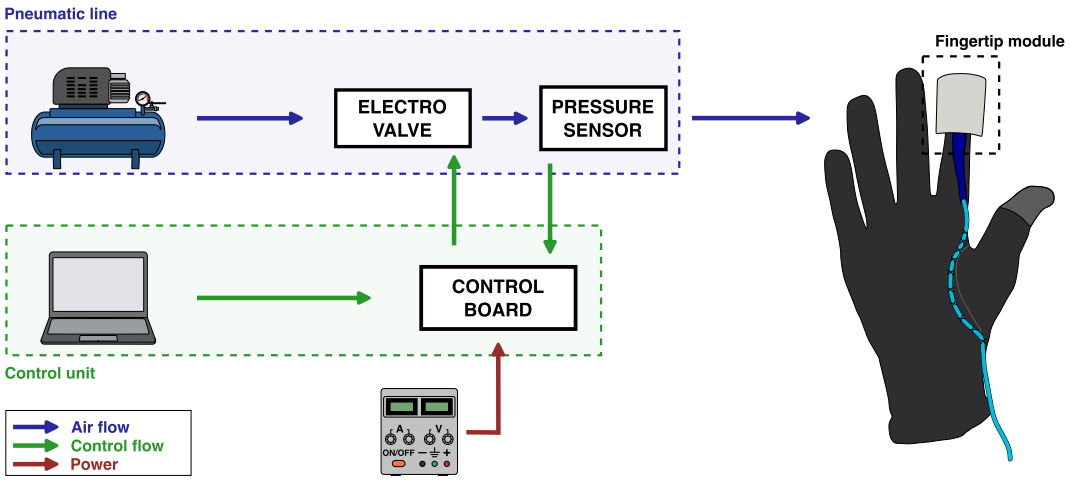


Fig. 2. Schematic of the proposed platform. A PC sends control inputs to a control board, powered by an external supply, which operates the inlet electrovalve connected to an external air compressor. According to the set target, the control board regulates the pressure of the fingertip module by controlling in closed loop the air flow from the inlet electrovalve.

chamber that, upon pressurization, transmits a contact force to the user by means of a sliding pin (Fig. 1b), which can be used to assess their tactile sensitivity in a quantitative and reproducible manner. After a characterization of the relationship between chamber's pressure and exerted force, we tested the proposed platform on five healthy participants to compare its performances against the Semmes-Weinstein monofilament test, which is regarded as the gold standard in assessing tactile sensitivity [9, 10].

The remainder of this paper is organized as follows. In Section 2, we outline the architecture of the device and report its manufacturing steps. In Section 3, we describe the workbench characterization procedure of the device as well as the experimental protocol for tests on healthy participants. In Section 4, we report the device characterization curve and discuss the results of tactile sensitivity tests, comparing them with the Semmes-Weinstein test. Finally, in Section 5 we draw our conclusions, highlighting some limitations of the proposed device and outlining possible future directions.

II. Device Architecture

Our device consists of a wearable fabric glove endowed with a fingertip stimulation module, which is composed of an inflatable air chamber, a retractable sliding pin placed on top of it, and a 3D-printed custom support to house them (see Fig. 1b). Upon pressurization, the air chamber inflates and pushes the pin in contact with the user's fingertip, thus transmitting a contact force that can be controlled by modulating the pressure of the system. In this way, it is possible to administer a reproducible stimulation to infer the tactile sensitivity of the user.

The full system is composed of a pneumatic line (from an air source to the chamber), the fingertip stimulation module (support, chamber and sliding pin), and a control unit (a microcontroller and a PC) connected to an external power supply (see Fig. 2). A detailed description is given in the remaining part of this section.

A. Pneumatic Line

The pneumatic line comprises a commercial air compressor integrated with a pressurized air reservoir, two solenoidal electrovalves to regulate inlet and outlet flows, a custom air chamber and a pressure sensor. We used a proportional valve (PVQ13-5L-08-M5-A, SMC, Japan), controlled in pulse-width modulation (PWM), to regulate the inlet air flow and in turn the inner pressure in a continuous way, while we adopted an ON/OFF valve (VZ110-5MOZ-M5-Q, SMC, Japan) for the exhaust line.

B. Fingertip Stimulation Module

The air chamber was designed with an oval shape, to better adapt to a fingertip, and realized using a commercial polyester fabric coated in thermoplastic polyurethane (TPU), to have an airtight yet flexible material that allows quick inflation-deflation, while minimizing distal encumbrance and weight. Two layers of the TPU-coated fabric, spaced by an insulation layer cut in the desired chamber profile, were heat-sealed using a heat-press (TC7 SMART, Secabo, Germany), running at 140 °C for 20 seconds, in order to form an airtight bladder (see Fig. 3a). The excess material was then cut out, and a plastic tube of 2 mm in diameter was inserted in the chamber and fixed using superglue and sodium bicarbonate.

The chamber was then embedded in a commercial fabric glove at the level of the right index fingertip, by means of a custom 3D-printed support fastened with an elastic band: the air chamber is housed inside the support, and a custom-made pin is placed on top of it (see Fig. 3b). The side of the support in contact with the skin presents a central through-hole, which allows sliding motion of the pin: upon actuation of the chamber, the pin slides through the hole and comes into contact with the user's skin. Finally, to avoid pre-stressing the target skin area with a continuous contact pressure, the surface of the support was grooved around the through-hole and, to allow a direct contact between the skin and the pin, a portion of the glove fabric was cut out.

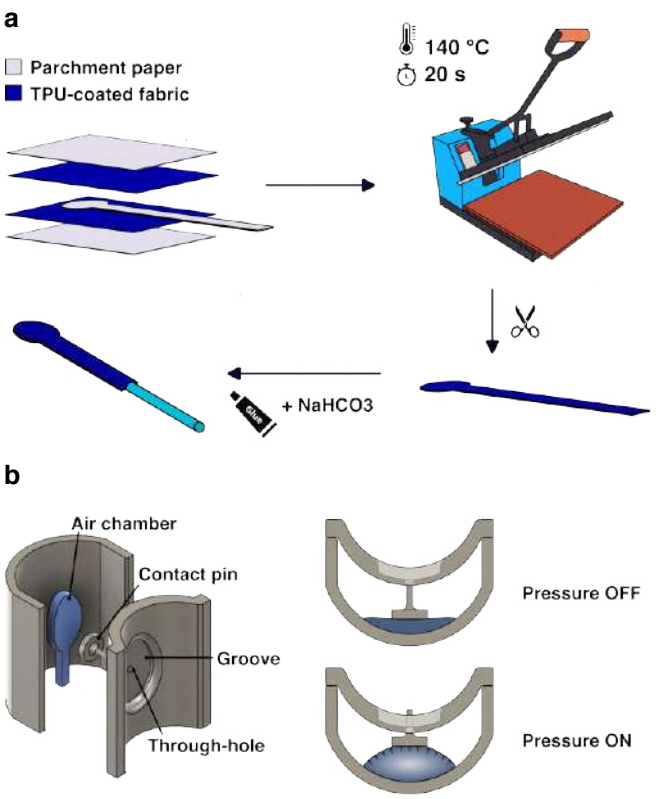


Fig. 3. a) Schematic of the fabrication process of the air chamber. Layers in the heat-press were arranged as follows: parchment paper as an insulation layer, first TPU-coated fabric layer, a piece of parchment paper shaped like the chamber profile, second TPU-coated fabric layer, and a last layer of parchment paper. After the heat treatment, the desired profile was cut from the bonded layers. Finally, a plastic tube was inserted and glued into the elongated portion of the chamber. b) CAD of the custom support, printed in a photoresistive resin. Upon pressurization, the air chamber pushes the pin that slides through the support and comes into contact with the skin.

C. Control Unit

A commercial board (UNO R3, Arduino, Italy) was used to monitor and control the inner pressure of the air chamber in closed-loop, implementing a PID controller. The chamber pressure is read with an absolute pressure sensor (ELVH-150A-HAND, Amphenol All Sensors, US) and the difference between the read value and a target one, set via software, is fed to a PID function; finally, the output of the PID is used as the duty cycle value of the PWM voltage signal that drives the inlet proportional valve, thus closing the control loop.

Based on the literature [11], we modeled the air chamber with a third-order transfer function and fitted its parameters according to the system's response to a chirp signal. Specifically, the proportional inlet valve received as input a PWM signal with duty cycle D given by

$$D(t) = 0.5 + 0.5 \sin\left(2\pi\left(f_0 + \frac{f_1 - f_0}{T}t\right)t\right), \quad (1)$$

that is, an up-chirp where $f_0 = 0.001\,\text{Hz}$ is the initial frequency, $f_1 = 50\,\text{Hz}$ is the final one, and $T = 30\,\text{s}$ is the duration of the signal. The pressure output corresponding to the chirp input was then imported in MATLAB 2023a (The MathWorks, US), and the System Identification Toolbox was used to determine a third-order transfer function. Finally, using the obtained model for the air chamber, PID parameters were tuned by means of the PID Tuner app in MATLAB ($P = 149.28$, $I = 300$, $D = 9.17$).

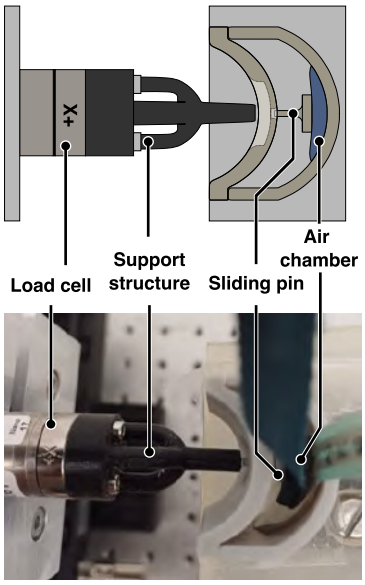


Fig. 4. Experimental setup for the pressure-force characterization of the system. A 3D-printed support was mounted on a load cell and interfaced with the sliding pin in order to measure the force exerted upon pressurization.

III. Experimental Validation

A. Device Characterization

We characterized the relationship between the air chamber's inner pressure and the contact force exerted by the pin using a load cell (Nano17, ATI Industrial Automation, US). The fingertip module was positioned in front of the load cell, so that the through-hole was centered with it. Upon pressurization of the air chamber, the pin slid and came into contact with a custom 3D support mounted on the load cell, which read the exerted force (see Fig. 4). We measured this force 5 times for each of 20 inner pressures, ranging from 0.1 to 1.3 bar.

B. Tests on Healthy Participants

To have a preliminary validation of our device, we recruited five healthy participants (24-29 yrs, 4 males and 1 female). Experiments were conducted under the Declaration of Helsinki and the guidelines of the Ethics Committee of the Scuola Superiore Sant'Anna (Approval No. 10/2023).

At the beginning of the experimental session, we assessed the participant's tactile sensitivity at the right index fingertip by administering the Semmes-Weinstein monofilament test, expressed in gram-force (gf) [9, 10]. We then used our platform to measure their tactile sensitivity in terms of amplitude perception threshold, that is, the minimum perceivable stimulus upon indentation of their fingertip, according to the following experimental protocol.

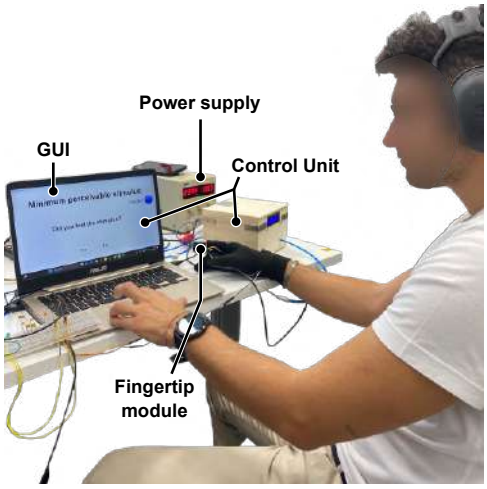


Fig. 5. Example of an experimental session with the proposed device.

Experimental Protocol: Participants were asked to wear the device on their right hand, and the fingertip module was mounted on their index. Additionally, participants were asked to wear a noise-canceling headset during the experiments, to avoid biases due to the noise produced by electrovalves. Tests followed a Two-Interval Forced Choice (2-IFC) procedure. Each trial was made of three phases: a first stimulation window, a short interval, and a second stimulation window. Participants received an actual tactile stimulus in one of the two windows, randomly chosen, and no stimulation (null stimulus) in the other one; they were then asked to indicate in which of the two windows they had perceived a tactile event (see Fig. 5), by means of a custom MATLAB GUI adapted from [12]. The amplitude of the following stimulation was then adaptively modified by means of a Stochastic Approximation Staircase (SAS) algorithm. After 50 trials, the perception threshold was selected as the stimulus amplitude adjusted for the hypothetical 51^{st} trial [13].

IV. Results and Discussion

A. Force-Pressure Calibration Curve

The force-pressure curve obtained from the load cell characterization (see Fig. 6) was highly linear ($\rho = 0.9986$) and had low variability (average IQR $= 0.0116$). This result suggests that the device is capable of exerting a normal contact force in a reliable manner without noticeable non-linearities, despite the presence of the soft air chamber, a characteristic that is particularly desirable for the automatic control of the system.

B. Comparison of Sensitivity Thresholds

Sensitivities measured with the monofilament test ranged from 0.02 to 0.07 gf, with a median of 0.04 gf (IQR 0.04-0.04); pressure perception thresholds obtained with our device were in the order of 0.01 bar, with a median of 0.034 bar (IQR 0.031-0.068) (see Table I and Fig. 7 for complete results). Although not statistically significant ($p > 0.07$), results of the two tests showed a high correlation

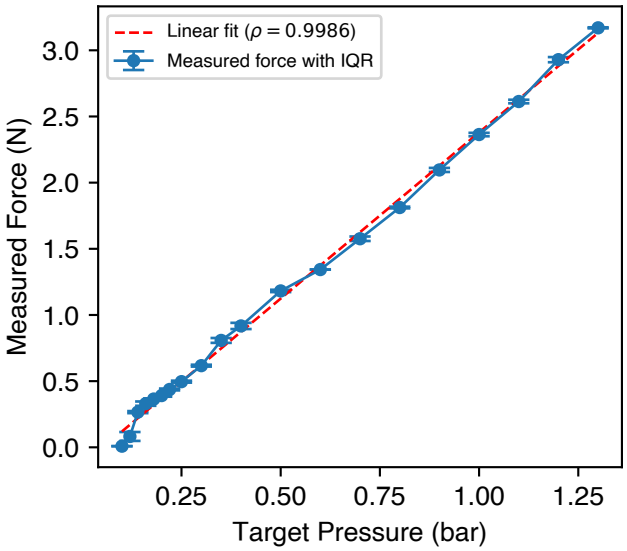


Fig. 6. Pressure-force characterization curve (median with interquartile range, IQR, blue curve) with its linear fitting ($\rho = 0.9986$, red dashed curve).

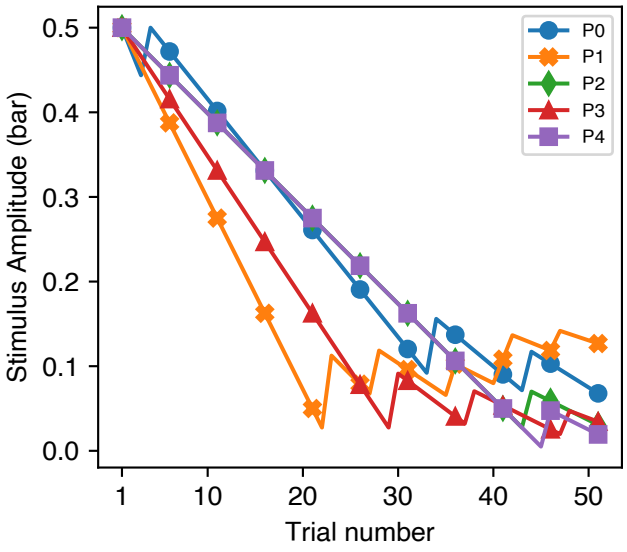


Fig. 7. Staircase stimulation curves of the five participants, where the amplitude adjusted for the hypothetical 51^{st} stimulus is selected as the threshold.

TABLE I
Sensitivity Thresholds Comparison

Participant	Semmes-Weinstein (gf)	Device (bar)
P0	0.04	0.07
P1	0.07	0.13
P2	0.02	0.03
P3	0.04	0.03
P4	0.04	0.02
Median	**0.04**	**0.03**

($\rho = 0.8441$); the unexplained variance could be due to the intrinsic differences in their psychophysics. Specifically, the monofilament test involves a single ascending method of limits where, for the lowest-force filaments ($< 1.4\,\mathrm{gf}$), it is possible to perform up to three stimulations before proceeding to the next filament. Therefore, it is sufficient to perceive only one out of three consecutive stimulations to declare the investigated force as the sensitivity threshold. On the other hand, we implemented an adaptive staircase method to estimate the threshold above which the user has a probability to correctly identify the stimulus ≥ 0.85 [13].

Additionally, the monofilament test has an intrinsic subjective component: to leverage the buckling of the filament, the examiner should approach its critical load in a quasi-static fashion. Since it is not possible to accurately control the speed of indentation, the level of exerted force could cross the critical load, effectively exerting a force higher than intended. Moreover, a higher stimulation rate could elicit different recruitments of mechanoreceptors: the Semmes-Weinstein test, which consists in tapping the participant's fingertip, could excite mainly "fast-adapting" mechanoreceptors, while our device, based on a pneumatic actuation system that exhibits a slower dynamics, could recruit mainly "slow-adapting" ones, characterized by a lower sensitivity [14].

Finally, the prototype nature of the device plays a role, too: at low inner pressures, friction could hamper sliding motion of the pin, making it fail to properly contact the user's skin.

V. Conclusions and Outlook

We developed a wearable pneumatically-driven device for the assessment of tactile sensitivity, which exploits a small air chamber to transmit a indentation force to the user's fingertip. The proposed platform can be used to assess the tactile perception threshold of the user in an automated and repeatable fashion, at a controllable rate and intensity.

Experimental results on five healthy participants showed an overall satisfying performance and suggested the potential of the device as a complementary clinical assessment tool. However, this preliminary investigation also highlighted some limitations to be addressed in future work: increasing the portability of the system, optimizing the fingertip module, and using a direct force measurement as a feedback signal.

In future studies, we aim to increase the number of participants, the number of stimulation modules to target other areas of the hand that can be addressed with the monofilament test, as well as to adapt the device to assess tactile acuity, possibly increasing the number of pins on the same location.

References

[1] N. Byl, J. Roderick, O. Mohamed, M. Hanny, J. Kotler, A. Smith, M. Tang, and G. Abrams, "Effectiveness of sensory and motor rehabilitation of the upper limb following the principles of neuroplasticity: Patients stable poststroke," *Neurorehabilitation and Neural Repair*, vol. 17, no. 3, pp. 176–191, Sep. 2003.

[2] M. Suda, M. Kawakami, K. Okuyama, R. Ishii, O. Oshima, N. Hijikata, T. Nakamura, A. Oka, K. Kondo, and M. Liu, "Validity and reliability of the Semmes-Weinstein monofilament test and the thumb localizing test in patients with stroke," *Frontiers in Neurology*, vol. 11, Jan. 2021.

[3] N. Bolognini, C. Russo, and D. J. Edwards, "The sensory side of post-stroke motor rehabilitation," *Restorative Neurology and Neuroscience*, vol. 34, no. 4, pp. 571–586, Aug. 2016.

[4] L. Cappello, R. Baldi, L. Frederik, and C. Cipriani, *Noninvasive augmented sensory feedback in poststroke hand rehabilitation approaches*. Elsevier, 2021, pp. 207–244.

[5] S. Jia, L. Wang, H. Wang, X. Lv, J. Wu, T. Yan, C. Li, and B. Hu, "Pneumatical-mechanical tactile stimulation device for somatotopic mapping of body surface during fmri," *Journal of Magnetic Resonance Imaging*, vol. 52, no. 4, pp. 1093–1101, May 2020.

[6] J. Wu, C. Wang, L. Wang, Y. Wang, J. Yang, T. Yan, D. Suo, L. Wang, X. Liu, and J. Zhang, "Development of a piezoelectric actuated tactile stimulation device for population receptive field mapping in human somatosensory cortex with fMRI," *Journal of Magnetic Resonance Imaging*, vol. 56, no. 4, pp. 1055–1065, Mar. 2022.

[7] Y. Shi, F. Wang, J. Tian, S. Li, E. Fu, J. Nie, R. Lei, Y. Ding, X. Chen, and Z. L. Wang, "Self-powered electro-tactile system for virtual tactile experiences," *Science Advances*, vol. 7, no. 6, Feb. 2021.

[8] F. Carpi, M. C. Valles, G. Frediani, T. Toci, and A. Grippo, "EEG investigation on the tactile perceptual performance of a pneumatic wearable display of softness," *Actuators*, vol. 12, no. 12, p. 431, Nov. 2023.

[9] S. Weinstein, "Fifty years of somatosensory research," *Journal of Hand Therapy*, vol. 6, no. 1, pp. 11–22, Jan. 1993.

[10] J. A. Bell-Krotoski, E. E. Fess, J. H. Figarola, and D. Hiltz, "Threshold detection and Semmes-Weinstein monofilaments," *Journal of Hand Therapy*, vol. 8, no. 2, pp. 155–162, Apr. 1995.

[11] O. F. A. Aal, M. A. Aal, and M. R. Al-Masaed, "Robust control of a proportional solenoid valve," in *2021 9th International Conference on Control, Mechatronics and Automation (ICCMA)*. IEEE, Nov. 2021, pp. 72–77.

[12] C. F. Blanco-Diaz, S. Rossi, J. Quaglierini, and L. Cappello, "Exploring osseoperception at the wrist: Towards an augmented sensory feedback interface," in *2024 6th International Conference on NeuroRehabilitation (ICNR2024), in press*.

[13] L. Faes, G. Nollo, F. Ravelli, L. Ricci, M. Vescovi, M. Turatto, F. Pavani, and R. Antolini, "Small-sample characterization of stochastic approximation staircases in forced-choice adaptive threshold estimation," *Perception & Psychophysics*, vol. 69, no. 2, pp. 254–262, Feb. 2007.

[14] R. S. Johansson and A. B. Vallbo, "Tactile sensory coding in the glabrous skin of the human hand," *Trends in neurosciences*, vol. 6, pp. 27–32, 1983.

Evaluating Differences in Smart Walker-assisted Locomotion in Augmented and Virtual Reality Environment

Matheus Loureiro
Graduate Program in Electrical Eng.
Federal University of Espirito Santo
Vitória, Espirito Santo
matheus.loureiro@edu.ufes.br

Weslley Oliveira
Graduate Program in Electrical Eng.
Federal University of Espirito Santo
Vitória, Espirito Santo
weslley.oliveira@edu.ufes.br

Fabiana Machado
Graduate Program in Informatics
Federal University of Espirito Santo
Vitória, Espirito Santo
fabiana.machado@ufes.br

Igor Vieira
Graduate Program in Electrical Eng.
Federal University of Espirito Santo
Vitória, Espirito Santo
igor.vieira@edu.ufes.br

Ricardo Mello
Graduate Program in Electrical Eng.
Federal University of Espirito Santo
Vitória, Espirito Santo
ricardo.c.mello@ufes.br

Anselmo Frizera, *Senior Member IEEE*
Graduate Program in Electrical Eng.
Federal University of Espirito Santo
Vitória, Espirito Santo
anselmo.frizera-neto@ufes.br

***Abstract*—The global trend of population aging has increased demand for healthcare professionals, particularly those assisting individuals with mobility impairments. To aid these people, rehabilitation robotics, such as smart walkers (SW), can be used to enhance motor capabilities. However, repetitive and painful tasks in rehabilitation can reduce patient engagement and motivation. To help enhance motivation during rehabilitation, tools such as augmented reality (AR) and virtual reality (VR) can be used. In this way, this paper presents a study aimed at evaluating the differences between using AR and VR in locomotion assisted by a SW. Fourteen healthy volunteers were recruited to perform a 3-minute walk, collecting items while assisted by an SW in both AR and VR environments. The results showed a slight increase of 6.2% more items collected in the AR environment. In terms of enjoyment, volunteers reported greater enjoyment using AR, with Physical Activity Enjoyment Scale (PACES) questionnaire scores increasing by 5.6% points in AR compared to VR, with a statistically significant difference (p-value = 0.03). These findings suggest that while both AR and VR provide enjoyment during the task, AR may offer a more enjoyable experience and promote greater confidence using the SW. This paper highlights the potential of AR as a valuable tool to improve user engagement in robotic rehabilitation, suggesting that integrating AR with robotic systems could enhance rehabilitation outcomes.**

***Index Terms*—Augmented Reality, Rehabilitation Robotics, Smart Walker, Virtual Reality.**

I. Introduction

Population aging, once a common process observed only in high-income countries, is now becoming a global trend across others nations [1]. This demographic shift has significantly increased the demand on healthcare professionals, particularly for those caring for individuals with mobility impairments, whose quality of life is deeply impacted by the decline in motor abilities [2], [3].

To mitigate the effects of motor ability decline, rehabilitation robotics devices, such as exoskeleton, instrumented treadmill and smart walkers (SW), are becoming increasingly prominent in clinics and hospitals [4]. SW provide physical support during overground locomotion, aiding in the recovery of muscle strength, balance, and coordination throughout the rehabilitation process, while also offering sensory and cognitive assistance [5].

Nevertheless, a common challenge in rehabilitation is the frustration among patients to perform repetitive and often painful tasks, which demands significant attention from healthcare professionals to maintain patient motivation and prevent dropouts [6]. To address this challenge, augmented reality (AR) and virtual reality (VR) are technologies that can be used to enhance patient engagement, transforming rehabilitation into a more interactive and enjoyable experience [7].

AR overlays virtual elements onto the real world, offering guidance and visual feedback that simplify and enhance the interactivity of real-world tasks [8]. Meanwhile, VR creates a virtual environment that offers a similar set of guidance and feedback as AR, but in a complete virtual world, where users interact with virtual environments and elements [8].

Both technologies have limitations that can impact user experience. For instance, they can induce motion sickness symptoms, such as nausea and headaches, particularly during extended use [9], [10]. AR may also contribute to cognitive overload due to the constant flow of information presented to the user [11]. On the other hand, VR, being fully immersive, lacks real-time tracking of the user's body in the physical environment, which can lead to a disconnect from the user's surroundings and potentially diminish situational awareness

Financial support received from FAPES (PROAPEX, 2023-XDHHW, 2022-D48XB, 2022-C5K3H, 2022-NGKM5, 2021-GL6OJ, 2021-07KJ2), CNPq (308155/2023-8, 403753/2021-0), FINEP (0036/21, 2784/20) and CAPES (Funding Code 001).

[10]. For example, in the study performed by [12], nearly 90% of volunteers assessed the use of VR as having good potential in walking settings. However, they experienced some side effects during VR walking, including a 7.3% reduction in walking speed in the VR condition.

Despite these limitations, AR and VR remain promising tools for gait rehabilitation [13], [14], especially when integrated with overground walking robots, such exoskeletons and SWs. These robotic devices enable users to move freely on a mobile base, supporting the practice of a more natural gait without restrictions, which can enhance the outcomes of rehabilitation programs [15], [16]. Therefore, understanding the differences between AR and VR in similar rehabilitation tasks is important to identify their respective benefits and challenges. This insight can guide the optimization of rehabilitation programs, maximizing their effectiveness while minimizing potential drawbacks.

To assess the efficacy of AR and VR tools in gait rehabilitation, an approach combining both quantitative and qualitative methods should be employed. This evaluation should include metrics such as walking speed, physical activity enjoyment, incidence of motion sickness, heart rate, and cognitive load, among others [15], [17]. These diverse measures will provide a thorough understanding of the pros and cons of these technologies and how they impact rehabilitation outcomes.

Our research group has been working with SW over the last decade, developing strategies for autonomous navigation, human-robot interaction, and cloud-based data processing systems [18]. More recent works have focused on integrating SW with VR to combine overground walking robots with interactive rehabilitation scenarios. In general, the results show good acceptance of the SW combined with VR by the elderly population, promoting engagement without compromising other aspects, such as kinematic parameters and the presence of motion sickness [15], [19]. Furthermore, advancements in Head-Mounted Display (HMD) technology have enabled the development of these same scenarios for AR.

In this context, this paper presents a study aimed at evaluating the differences between the use of AR and VR in smart walker-assisted locomotion. The objective is to compare user performance and experience when performing the same task in different reality-based environments. The paper is structured as follows. Section 2 present the methodology employed for the system's development, Section 3 shows the results and discussion, and Section 4 concludes with the findings and future researches.

II. Methodology

A. Materials

The materials used in this study were the UFES WalkerXR, a robotic assistive device developed at the Human Centered Systems (HCS) research group, and a HMD, the Meta Quest 3 (Meta, USA). This robotic device is an enhanced version of the UFES vWalker [20], which initially featured VR feedback interfaces to aid user navigation. Building on this, the UFES WalkerXR incorporates AR capabilities, enabling the creation of extended reality (XR) environments. This integration combines real-world and virtual elements to provide interactive feedback, enhancing both user safety and navigation support.

As shown in Fig. 1a, the UFES WalkerXR is equipped with two DC motors (Imobras, Brazil), two encoders (Autonics, South Korea), an IMU (Movella, Netherlands), a LiDAR (SLAMTEC, China), two biaxial force sensors (ProCal, Brazil), and a mini PC (DELL, USA). The IMU and encoders work together for odometry and localization, while the motorized and castor wheels assist with propulsion and stability. The LiDAR is responsible not only for obstacle detection and environmental mapping, but it also monitors the distance between the user's legs and the WalkerXR, ensuring safe interaction during movement. The biaxial force sensors capture the user's motion intentions, converting them into linear and angular reference velocities via an admittance controller [21].

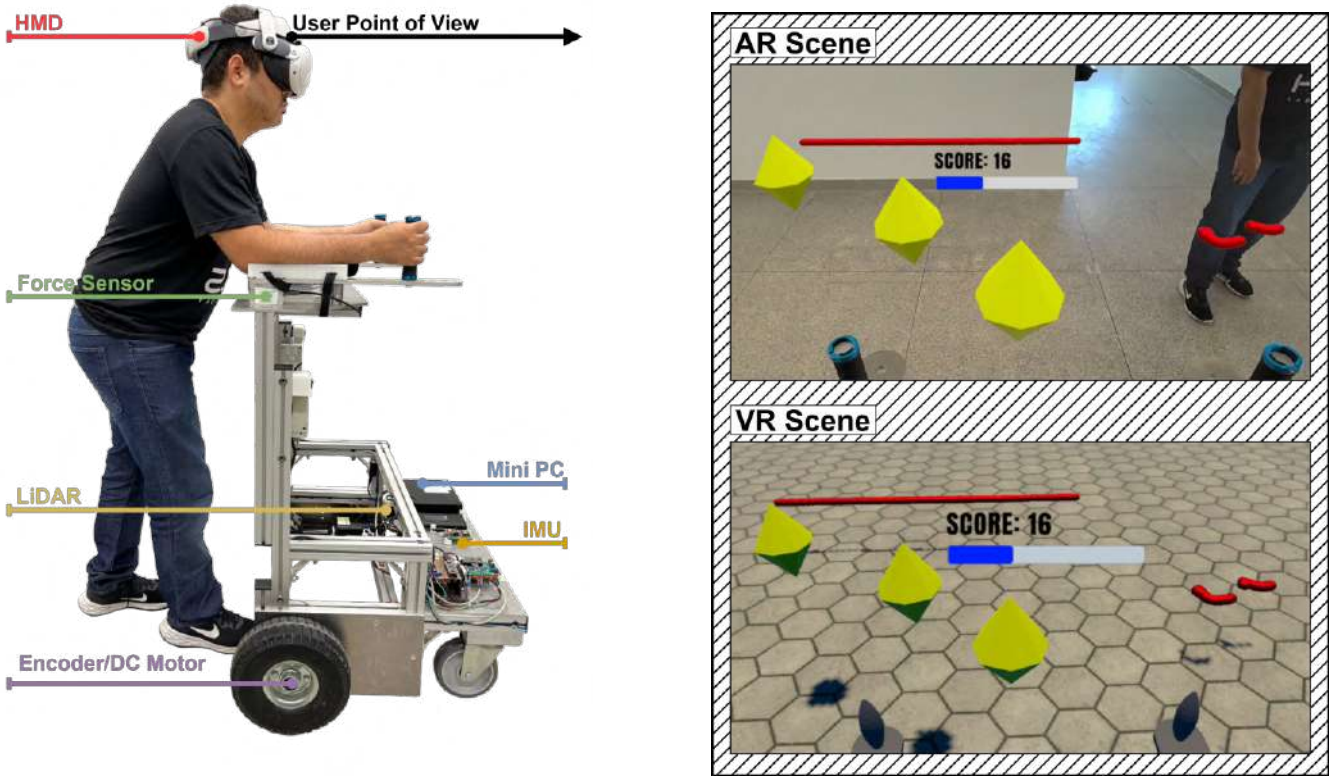
Sensor data from these components are processed by a microcontroller (STM32), which handles low-level control functions. The data is then transmitted to the mini PC, running the Robot Operating System middleware (ROS, Version: Humble), to control the UFES WalkerXR's behavior. These components are depicted in Fig. 1a.

B. Augmented and Virtual Reality Environments

The AR and VR environments were developed using Unity, a powerful engine designed for creating games and other applications. Two plugins were utilized within Unity: the Meta XR All-in-One SDK, which offers essential tools for developing immersive experiences in both AR and VR, and the Rosbridge package alongside the ROS# plugin, which enables communication between Unity and the robot's sensor data. The interaction between the UFES WalkerXR and Unity is bidirectional, facilitated by WebSocket protocols from the Rosbridge package. These protocols convert JSON strings to ROS calls and vice versa. Messages received in Unity are converted from JSON format into Unity-readable data, while messages sent from Unity to the UFES WalkerXR are converted back into JSON format before transmission. This setup enables real-time data exchange, enhancing interaction and ensuring enhanced integration between the virtual and physical environments.

By utilizing ROS#, the displacement and sensor readings from the UFES WalkerXR are replicated in Unity through a digital twin, allowing users wearing an HMD to immerse themselves in both AR and VR environments. Fig. 1b presents a comparison of the user's point of view at corresponding moments, recreated across both realities, highlighting the transition between the two experiences.

The UFES WalkerXR displacement occurs by combining its odometry data with a pre-mapped environment created before the experiments. Probabilistic localization is then applied using the Monte Carlo localization approach, implemented via the ROS2 navigation stack [22]. The experiments were also conducted in a well-lit environment to ensure good tracking performance of the HMD, in line with the manufacturer's



(a) (b)

Fig. 1: The UFES WalkerXR and his sensor in (a) and the point of view of the user in the AR and VR environments in (b).

recommendations. These configurations were implemented to avoid tracking issues during the experiments.

The AR environment in Fig. 1b depicts the user collecting yellow virtual items to increase their score, which is represented by the blue bar and the text in the center of the screen. Physical obstacles within a 2-meter radius, such as walls, chairs and people, detected by the LiDAR sensor, are highlighted by red spheres, alerting the user to nearby surroundings. On the other hand, in the VR environment, the environment is completely virtual. The physical device is replaced by its digital twin, while physical obstacles continue to be indicated by red spheres to maintain the user's awareness of the physical world. The virtual items and scoring system remain the same.

The yellow virtual items were evenly distributed in both environments to define a Bernoulli lemniscate path with a α = 2.0, determining the size of the lemniscate. This path is divided into two phases: the first phase consists of a leftward circle, and the second phase is a full circle to the right.

C. Experimental Protocol

To assess the differences between the AR and VR environments using the UFES WalkerXR, fourteen healthy volunteers (20.8 ± 2.6 years) were recruited for the experiment. The volunteers were university students with no prior experience using AR, VR, or the robotic device, and they were unaware of the experiment's objectives. The experiment was approved by the Research Ethics Committee of the Federal University of Espírito Santo under registration number 6.294.101 and all participants provided written informed consent.

Prior to the experiment, all volunteers underwent a familiarization session to learn how to operate the UFES WalkerXR before perform the AR and VR tasks. The volunteers were then randomly assigned to two groups. In the first group (AR-VR), volunteers began by walking for 3 minutes in the AR environment, collecting as many yellow items as possible while following a lemniscate path. After a 15-minute rest, they repeated the task in the VR environment. In the second group (VR-AR), volunteers performed the same tasks but in the reverse order, starting with the VR environment and then the AR environment.

Before and after completing the tasks in both the AR and VR environments, volunteers completed the Virtual Reality Sickness Questionnaire (VRSQ) [23] to assess any symptoms of motion sickness. Also, at the end of each task, the volunteers had to fill out the Physical Activity Enjoyment Scale (PACES), an 18-item questionnaire designed to measure the level of enjoyment during the activity, with scores ranging from 0 to 126 [24]. When the experiment was concluded, the volunteers answered an open-ended question regarding which environment (AR or VR) they preferred and to provide an explanation for their choice.

The focus of this paper was to evaluate the differences between AR and VR across different variables during similar tasks: the presence of motion sickness symptoms (measured by the VRSQ), enjoyment of the activity (measured by PACES), volunteers' self-perception of the preferred environment (through an open-ended question), and distance traveled during the 3-minute session (indicated by the number of yellow items collected).

D. Statistical Analysis

A statistical analysis was conducted to assess whether significant differences existed in the PACES questionnaire scores and in the number of items collected for four categories of comparison. The first and second comparisons were between the AR-VR group and the VR-AR group. The third comparison was between the AR and VR environments (AR vs. VR), regardless of which task was performed first. Lastly, the fourth comparison was between the first and second tasks (T1 vs. T2), independent of whether AR or VR was performed first.

The data from the seven volunteers in both the AR-VR and VR-AR groups were analyzed to determine if transitioning between environments (AR to VR or VR to AR) influenced participant performance or enjoyment. The results from all 14 volunteers were compared in the AR vs. VR analysis to assess overall differences between the two environments. Additionally, the T1 vs. T2 comparison was used to explore potential learning effects and examine how task order might have influenced participant outcomes.

For the statistical analysis, the Shapiro-Wilk test was first applied to assess the normality of the data, and Levene's test was used to verify the homogeneity of variances. Based on these results, a paired t-test was used to compare the means between conditions when the assumptions of normality and homogeneity were met. In cases where the data did not meet the assumptions for parametric tests, the Wilcoxon signed-rank test was used as a non-parametric alternative.

III. Results and Discussions

Analyzing the results in the VRSQ questionnaire, no motion sickness symptoms were detected either before or after the experiment in both AR and VR environments. The reason that may have prevented the presence of these symptoms is the support provided by the UFES WalkerXR during the tasks, which offered increased stability and safety for the volunteers during use. Additionally, the displacement of the volunteers, the UFES WalkerXR, and its digital twin in a synchronized manner within the VR/AR environments, may contribute to the absence of symptoms.

Regarding the number of items collected, only slight variations in the means were observed across the AR-VR, VR-AR, AR vs. VR, and T1 vs. T2 comparisons, as indicated in Fig. 2. Despite these differences, no statistically significant results were found, as shown in Table I.

In the AR-VR group, volunteers collected an average of 69.14 items in the AR task, which decreased by 1.7 items in the VR task. In the VR-AR group, the average number of items collected increased by 6 items when volunteers performed the task in the AR environment. Overall, in the AR vs. VR comparison, volunteers collected an average of 3.9 more items in the AR environment than in the VR environment, though this difference was not statistically significant.

One potential factor contributing to the absence of a statistically significant difference in the increased number of items collected is the limited speed of the UFES WalkerXR. This limitation was intentional, as the device - and smart walkers in general - is specifically designed for individuals with mobility impairments [15]. The restricted speed may have prevented participants from walking faster, which could explain the slight but non-significant increase in items collected in the AR environment compared to the VR environment.

A similar explanation may account for the lack of a statistically significant difference when comparing task order, regardless of the reality environment (T1 vs. T2). Participants collected only 2.1 more items in the second trial (T2), suggesting minimal evidence of a learning effect during the experiment.

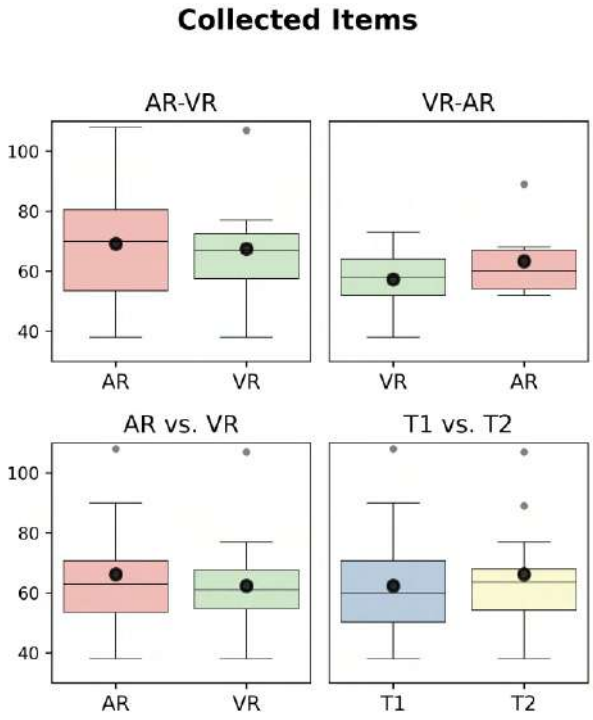


Fig. 2: Boxplots of items collected in the four comparisons. The first and second boxplots represent the AR-VR and VR-AR groups, respectively. The third boxplot shows data from AR and VR, regardless of task order. The fourth boxplot compares the first and second tasks. The red, green, blue, and yellow boxes represent AR, VR, first task, and second task, respectively. The black circle in the middle indicates the mean value.

In the PACES questionnaire scores, larger variations in the

TABLE I: Descriptive statistics for the number of items collected in both AR and VR environments, including the mean, minimum (min), and maximum (max) values, and the p-value from the paired t-test in the four comparisons.

Collected Items					
		Mean	**Min**	**Max**	**p-value (t-test)**
AR-VR	AR	69.14	38	108	0.69
	VR	67.42	38	107	
VR-AR	VR	57.28	38	73	0.24
	AR	63.28	52	89	
AR vs. VR	AR	66.21	38	108	0.22
	VR	62.35	38	107	
T1 vs. T2	T1	63.21	38	108	0.51
	T2	65.35	38	107	

means were observed across the AR-VR, VR-AR, AR vs. VR, and T1 vs. T2 comparisons, as indicated in Fig. 3. Statistically significant differences were found in the VR-AR and AR vs. VR comparisons, as shown in Table II.

In the VR-AR group, volunteers reported an average score of 91.14 in the VR task, which increased by 9.57 points in the AR task, a statistically significant difference. When comparing AR vs. VR, the AR environment received an average score of 99.14, significantly higher than the VR environment's score of 93.85 ($p = 0.03$). These results suggest that volunteers experienced greater enjoyment not only when transitioning from VR to AR but also in the AR environment in general.

The AR-VR group reported an average score of 97.57 for the AR task, which slightly decreased by 1.0 point to 96.57 in the VR task. Although the AR environment received a higher score in this comparison, the difference was not statistically significant. A similar result was observed in the T1 vs. T2 comparison, where the score increased by 3.5 points in T2, but no significant difference was found. This suggests that task order did not significantly affect volunteers' overall enjoyment, measured by the PACES questionnaire.

The results of this experiment suggest that both tasks (AR and VR) provided a high level of enjoyment, as reflected in the PACES scores (mean 99.14 out of 126 for AR and mean 93.85 out of 126 for VR). However, the paired t-test indicate that volunteers had a more favorable experience in AR compared to VR, especially when the AR task followed the VR task.

From the open-ended question, 10 volunteers preferred the AR environment over the VR environment (5 from the AR-VR group and 5 from the VR-AR group). These results align with the higher PACES scores for the AR environment. Participants explained their preferences, with many highlighting that the visibility of the real world in the AR environment offered increased confidence and a stronger sense of safety while operating the UFES WalkerXR. This perception may also account for the slightly higher number of items collected in the AR environment, as participants felt more at ease while walking. On the other hand, those who favored the VR environment often cited the immersive experience of being transported to an entirely different world, which they found particularly enjoyable.

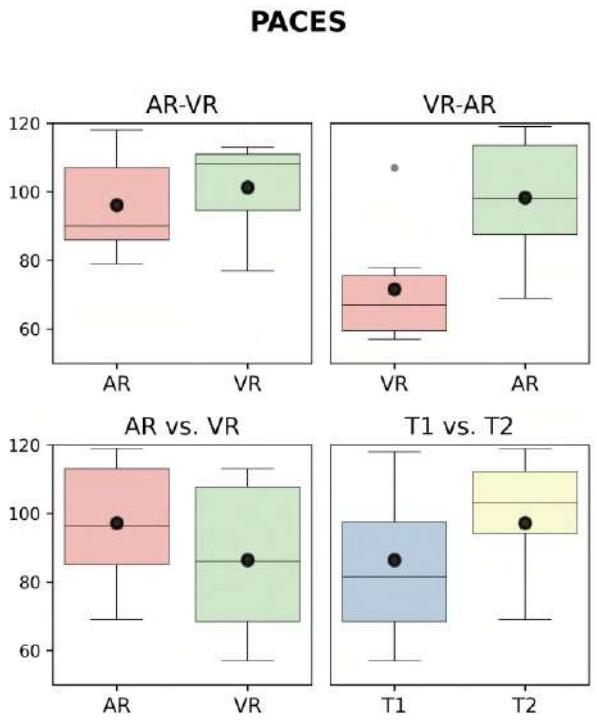


Fig. 3: Boxplots of score in PACES in the four comparisons. The first and second boxplots represent the AR-VR and VR-AR groups, respectively. The third boxplot shows data from AR and VR, regardless of task order. The fourth boxplot compares the first and second tasks. The red, green, blue, and yellow boxes represent AR, VR, first task, and second task, respectively. The black circle in the middle indicates the mean value.

IV. Conclusions and Future Work

This paper evaluated differences in walking assisted by a smart walker (SW) in augmented reality (AR) and virtual reality (VR) environments. Fourteen volunteers, with no prior experience with AR, VR, or the robotic device, were divided into two groups: AR-VR and VR-AR. Both groups performed a task of collecting virtual items while walking with the UFES WalkerXR in both AR and VR environments.

The results showed a slight increase of 6.2% more items collected in the AR environment, although no significant difference was found when analyzing this variable. In terms of enjoyment, volunteers reported greater enjoyment using AR, with a difference that was statistically significant, as measured by PACES questionnaire scores (mean 99.14 out of 126 for AR and mean 93.85 out of 126 for VR). These findings are supported by the responses to the open-ended question, where 10 out of 14 volunteers expressed a preference for AR, citing increased confidence and a sense of safety due to the ability to see the real world.

The main contribution of this paper lies in its exploration of how AR and VR environments affect the walking experience when using a SW. The study demonstrates that while

TABLE II: Descriptive statistics for PACES questionnaire in both AR and VR environments, including the mean, minimum (min), and maximum (max) values, and the p-value from the paired t-test in the four comparisons.

PACES					
		Mean	**Min**	**Max**	**p-value (t-test)**
AR-VR	AR	97.57	84	118	0.76
	VR	96.57	77	109	
VR-AR	VR	91.14	69	107	**0.005**
	AR	100.71	74	119	
AR vs. VR	AR	99.14	74	119	**0.03**
	VR	93.85	69	109	
T1 vs. T2	T1	94.71	74	118	0.17
	T2	98.28	69	119	

both AR and VR offer enjoyable experiences, AR may offer greater enjoyment and confidence. The integration of virtual elements into the real world appears to enhance participants' sense of safety and control during assisted walking. These findings provide promising evidence of AR's applicability in rehabilitation contexts, encouraging future studies to explore its potential benefits for individuals with mobility impairments.

Despite these insights, a limitation of the study is that all participants were a small sample size of young healthy adults, while the UFES WalkerXR is intended for individuals with cognitive and gait impairments, typically older adults. Future research will address this limitation by testing the device with the appropriate target population in real rehabilitation scenarios.

Therefore, these findings will inform future investigations, with plans to evaluate the UFES WalkerXR among volunteers with cognitive and gait impairments. Additionally, further research could explore the long-term benefits of AR and VR technologies in enhancing functional outcomes, quality of life, and motivation in rehabilitation settings.

REFERENCES

[1] W. H. Organization, "Ageing and health," https://www.who.int/news-room/fact-sheets/detail/ageing-and-health, 2024.

[2] P. Maresova, O. Krejcar, R. Maskuriy, N. A. A. Bakar, A. Selamat, Z. Truhlarova, J. Horak, M. Joukl, and L. Vítkova, "Challenges and opportunity in mobility among older adults–key determinant identification," *BMC geriatrics*, vol. 23, no. 1, p. 447, 2023.

[3] A. A. Ravankar, S. A. Tafrishi, J. V. S. Luces, F. Seto, and Y. Hirata, "Care: Cooperation of ai robot enablers to create a vibrant society," *IEEE Robotics & Automation Magazine*, vol. 30, no. 1, pp. 8–23, 2022.

[4] R. S. Calabrò, A. Cassio, D. Mazzoli, E. Andrenelli, E. Bizzarini, I. Campanini, S. M. Carmignano, S. Cerulli, C. Chisari, V. Colombo *et al.*, "What does evidence tell us about the use of gait robotic devices in patients with multiple sclerosis? a comprehensive systematic review on functional outcomes and clinical recommendations." *European journal of physical and rehabilitation medicine*, vol. 57, no. 5, pp. 841–849, 2021.

[5] G. Verdezoto, J. Ballesteros, and C. Urdiales, "Smart rollators aid devices: Current trends and challenges," *IEEE Transactions on Human-Machine Systems*, vol. 52, no. 6, pp. 1103–1110, 2022.

[6] D. Vancampfort, T. Van Damme, R. L. McGrath, L. Hemmings, V. Gillis, K. Bernar, E. Bitencourt, and F. Schuch, "Dropout from exercise interventions in adults with knee or hip osteoarthritis: a systematic review and meta-analysis," *Archives of Physical Medicine and Rehabilitation*, 2024.

[7] V. Patil, J. Narayan, K. Sandhu, and S. K. Dwivedy, "Integration of virtual reality and augmented reality in physical rehabilitation: a state-of-the-art review," *Revolutions in Product Design for Healthcare: Advances in Product Design and Design Methods for Healthcare*, pp. 177–205, 2022.

[8] P. Milgram and F. Kishino, "A taxonomy of mixed reality visual displays," *IEICE TRANSACTIONS on Information and Systems*, vol. 77, no. 12, pp. 1321–1329, 1994.

[9] M. E. McCauley and T. J. Sharkey, "Cybersickness: Perception of self-motion in virtual environments," *Presence: Teleoperators & Virtual Environments*, vol. 1, no. 3, pp. 311–318, 1992.

[10] A. Hamad and B. Jia, "How virtual reality technology has changed our lives: an overview of the current and potential applications and limitations," *International journal of environmental research and public health*, vol. 19, no. 18, p. 11278, 2022.

[11] M. Akçayır and G. Akçayır, "Advantages and challenges associated with augmented reality for education: A systematic review of the literature," *Educational research review*, vol. 20, pp. 1–11, 2017.

[12] B. Horsak, M. Simonlehner, L. Schöffer, B. Dumphart, A. Jalaeefar, and M. Husinsky, "Overground walking in a fully immersive virtual reality: A comprehensive study on the effects on full-body walking biomechanics," *Frontiers in bioengineering and biotechnology*, vol. 9, p. 780314, 2021.

[13] M. J. V. Gil, G. Gonzalez-Medina, D. Lucena-Anton, V. Perez-Cabezas, M. D. C. Ruiz-Molinero, and R. Martín-Valero, "Augmented reality in physical therapy: systematic review and meta-analysis," *JMIR Serious Games*, vol. 9, no. 4, p. e30985, 2021.

[14] M. J. Casuso-Holgado, R. Martín-Valero, A. F. Carazo, E. M. Medrano-Sánchez, M. D. Cortés-Vega, and F. J. Montero-Bancalero, "Effectiveness of virtual reality training for balance and gait rehabilitation in people with multiple sclerosis: a systematic review and meta-analysis," *Clinical rehabilitation*, vol. 32, no. 9, pp. 1220–1234, 2018.

[15] M. Loureiro, A. Elias, F. Machado, M. Bezerra, C. Zimerer, R. Mello, and A. Frizera, "Analysis of gait kinematics in smart walker-assisted locomotion in immersive virtual reality scenario," *Sensors*, vol. 24, no. 17, p. 5534, 2024.

[16] R. S. Calabrò, A. Cacciola, F. Bertè, A. Manuli, A. Leo, A. Bramanti, A. Naro, D. Milardi, and P. Bramanti, "Robotic gait rehabilitation and substitution devices in neurological disorders: where are we now?" *Neurological Sciences*, vol. 37, pp. 503–514, 2016.

[17] E. Evans, K. E. Naugle, A. S. Kaleth, B. Arnold, and K. M. Naugle, "Physical activity intensity, perceived exertion, and enjoyment during head-mounted display virtual reality games," *Games for Health Journal*, vol. 10, no. 5, pp. 314–320, 2021.

[18] R. C. Mello, M. R. Ribeiro, and A. Frizera-Neto, "Introduction to cloud robotics," in *Implementing Cloud Robotics for Practical Applications: From Human-Robot Interaction to Autonomous Navigation*. Springer, 2022, pp. 1–11.

[19] F. Machado, M. Loureiro, M. Bezerra, C. Zimerer, R. Mello, and A. Frizera, "Virtual obstacle avoidance strategy: Navigating through a complex environment while interacting with virtual and physical elements," *Sensors (Basel, Switzerland)*, vol. 24, no. 19, p. 6212, 2024.

[20] F. Machado, M. Loureiro, R. C. Mello, C. A. Diaz, and A. Frizera, "A novel mixed reality assistive system to aid the visually and mobility impaired using a multimodal feedback system," *Displays*, vol. 79, p. 102480, 2023.

[21] M. F. Jiménez, M. Monllor, A. Frizera, T. Bastos, F. Roberti, and R. Carelli, "Admittance controller with spatial modulation for assisted locomotion using a smart walker," *Journal of Intelligent & Robotic Systems*, vol. 94, pp. 621–637, 2019.

[22] S. Macenski, T. Moore, D. V. Lu, A. Merzlyakov, and M. Ferguson, "From the desks of ros maintainers: A survey of modern & capable mobile robotics algorithms in the robot operating system 2," *Robotics and Autonomous Systems*, vol. 168, p. 104493, 2023.

[23] H. K. Kim, J. Park, Y. Choi, and M. Choe, "Virtual reality sickness questionnaire (vrsq): Motion sickness measurement index in a virtual reality environment," *Applied ergonomics*, vol. 69, pp. 66–73, 2018.

[24] S. P. Mullen, E. A. Olson, S. M. Phillips, A. N. Szabo, T. R. Wójcicki, E. L. Mailey, N. P. Gothe, J. T. Fanning, A. F. Kramer, and E. McAuley, "Measuring enjoyment of physical activity in older adults: invariance of the physical activity enjoyment scale (paces) across groups and time," *International Journal of Behavioral Nutrition and Physical Activity*, vol. 8, pp. 1–9, 2011.

Enhancing Seated Lower Limb Training: Evaluating an Exergame-Integrated Stepper for Weight-Shift and Muscle Activation

Beycan EMRE *Student Member ICORR*, Ofori SEYRAM, L.W.R. JOSHUA, Ashwin Narayan *Associate Member IEE*, Haoyong YU *Senior Member, IEEE*

***Abstract*— Incorporating technology into exercise-based treatments is a prominent and promising strategy in rehabilitation. This study compares the biomechanics of the seated ankle dorsi-plantar flexion (ADPF) exercises performed without a stepper (WoS) to seated stepping-in-place exercises performed with an exergame-integrated stepper (WS). Does an exergame-integrated stepper device enhance seated lower limb training by providing the weight-shift and muscle activation compared to conventional ankle dorsi-plantar flexion exercises without a stepper? Ten healthy participants completed exercises at 0° and 45° tilted sitting conditions. Weight-shift, and electromyographic (EMG) activity of gait muscles were measured bilaterally during exercises. In the WS condition, weight-shift significantly increased by 72% during 0° sitting and increased by 22% during 45° sitting conditions ($p < 0.05$). EMG activation significantly decreased for all muscles in the WS condition ($p < 0.05$) except in the Rectus Femoris activation (Left RF: $p = 0.646$, Right RF: $p = 0.445$). This initial study combines bilateral training with the exergame-integrated stepper device, demonstrating its potential to provide weight-shift and muscle training for the lower limb. Seated stepping exercises can be implemented on current rehabilitation protocols and developed device can be an alternative to conventional ADPF exercise in stroke rehabilitation.**

I. Introduction

Stroke causes motor impairment, particularly affecting the lower limb, which hinders the mobility and functional independence of individuals [1]. Loss of weight-shifting ability [2] and muscle weakness [3] result in prolonged sitting, either in a standard chair or wheelchair during the early stages of rehabilitation. Seated exercises such as ankle dorsi-plantar flexion (ADPF) are safe and frequently utilized in conventional rehabilitation for early-stage stroke patients due to their accessibility and low risk of falls [4]. However, the ADPF exercise, applied unilaterally, represents a limited approach to addressing comprehensive lower limb rehabilitation. Integrating exergaming technologies with seated stepping exercises that target bilateral lower limb exercises into rehabilitation interventions holds promise for enhanced treatment.

Corresponding author: B. Emre, E-mail: emre.beycan@u.nus.edu.

H. Yu is with the Biomedical Engineering Department, National University of Singapore, 9 Engineering Drive 1, Singapore 117575, Singapore.

E. Beycan (e0669568@u.nus.edu), O. Seyram, L.W.R Joshua, Narayan Ashwin, and W. Zhao are with the Biomedical Engineering Department, National University of Singapore, 15 Kent Ridge Cres, Singapore 119276, Singapore.

Seated exercises play a pivotal role in stroke rehabilitation [5], particularly for older and/or severely affected patients [6]. During the initial stages of recovery, 41% of post-stroke patients relied on wheelchairs, highlighting the considerable demand for seated rehabilitation interventions [7]. A randomized controlled trial, which implemented seated stepping as an exercise, demonstrated significant improvement in gait performance among stroke patients [8]. Although seated stepping is a safe and promising exercise, its biomechanical effects, such as weight-shift and muscle activation, need further study to support its implementation in seated rehabilitation.

Rehabilitation techniques, including unilateral and bilateral methods, are essential for addressing post-stroke lower limb impairments [9]. Bilateral training demonstrated superior effectiveness compared to unilateral alone in the lower limb [10]. Training on the inactive side proved equally vital in improving stability and walking ability. Moreover, bilateral coordination is crucial for various activities of daily living (ADL), including walking, running, and jumping [11]. Engaging in bilateral exercises activates both the unimpaired and impaired hemispheres, promoting neuroplasticity in the brain [12].

Active patient involvement is essential during the early stages of intensive stroke rehabilitation [13]. Muscle weakness, induces muscle fatigue, thereby constraining the patient's participation in treatment [3] and diminishing the repetitions in exercises [14]. A parallel relationship was observed between fatigue and activation of muscle, indicating that reduced muscle activation could facilitate intensive therapy [15]. Therefore, we aim to compare ADPF and stepping exercises based on muscle activation, as this aspect still needs to be more adequately understood.

Weight-shift, the ability to distribute body weight efficiently and effectively, is fundamental to maintaining balance and postural stability during various ADLs [16]. However, post-stroke individuals commonly exhibit deficits in weight-shift capacity, which can further compromise their balance and mobility [17]. Weight-shift training approaches, including both static and dynamic exercises, have occurred as potential strategies to enhance postural control [18], weight-bearing symmetry [19], balance [20], and functional mobility [21] in individuals

recovering from stroke. The existing literature lacks comprehensive investigations of alternative methods for seated weight-shift training.

Clinical trials have demonstrated the safety and efficacy of ADPF and stepping exercises in stroke and elderly individuals. However, a comprehensive analysis and comparison of their biomechanical properties currently need to be included in the academic literature. Our study evaluated and compared the biomechanics of ADPF and stepping exercises based on weight-shift and muscle activity under sitting at 0°and 45° tilted conditions. We hypothesized that an exergame-integrated stepper during seated stepping exercise would offer lower muscle activation and facilitate wider weight-shift in the lower limb compared to ADPF exercise.

II. Materials and Methods

A. Development of the Exergame-Integrated Stepper

The stepper device utilized in this investigation (see Fig. 1) has been adapted from the commercially available MS100 stepper (Decathlon, Singapore). Two sandals are attached to footplates that move reciprocally through a mechanical connection. This device facilitates stepping training, engaging the left and right lower limbs. For improved portability, the electronic components have been positioned at the front. The device's left joint has been adjusted with a stabilizer to integrate a magnetic rotary encoder for measuring movement angles. The data from the sensor were read using a custom-made STM32F446 microcontroller and transmitted to the PC over a serial port.

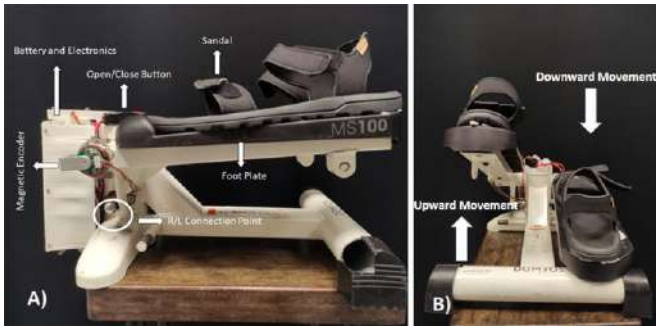


Figure 1. Stepper Components (A) and Movements of the Stepper (B)

The 3D farmer exergame was created utilizing Unity-3D and integrated with the device to provide feedback. The main objective of the exergame is to guide participants in performing bilateral stepping exercises by synchronizing their movements with on-screen targets. During each cycle, participants must time their stepping movements to 'catch' virtual animals appearing alternately on the leftmost and rightmost sides of the screen, each lasting for 2 seconds. The angular data acquired from the magnetic encoder served as the basis for controlling the avatar. Specifically, the angle data were mapped to control the left (Figure 2A) and right (Figure 2B) movements of the avatar. The game's design ensures that players must utilize the entire motion of the device to successfully catch the appearing animals, as shown in Figure 2.

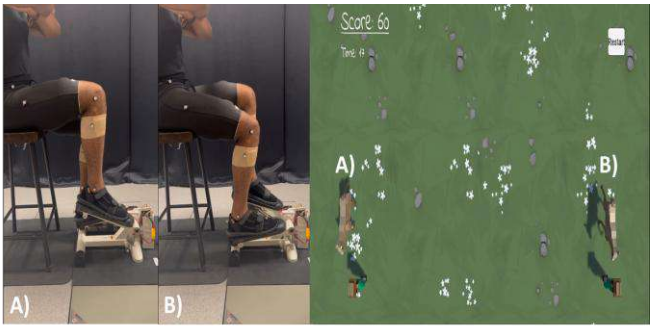


Figure 2. Exergame and stepping exercise interaction seated position. A) Avatar moves left when left foot goes down, B) Avatar moves right when right foot goes down.

B. Participants

Ten healthy volunteers (5F, 5M, mean ± SD, age: 24.8 ± 2.8 years, height: 167.5 ± 8.7 cm, weight: 70.2 ± 16.8 kg, BMI: 24.5 ± 3.9 kg/m2) were enlisted to confirm the viability and effectiveness of the bilateral stepping exercise for rehabilitation. Inclusion criteria were (a) aged 21-40, (b) no disability or chronic lower limb disease, (c) completion of the PAR-Q questionnaire that shows no restrictions or contraindications for physical activity [22], and (d) refrained from engaging in intense physical activity before the study. The recruitment of subjects, information sheet, permission form, data form, and experimental questionnaire received approval from the National University of Singapore Institutional Review Board (NUS-IRB-2022-9) on November 24, 2022.

C. Data Collection

During the experiment, two types of data were gathered. First, the vertical component of the ground reaction force (GRF) from both the left and right sides represents the vertically applied force (Fz). Second, electromyographic activity (EMG) depicts muscle status through electrical signals in the lower limb.

The GRF data were captured using two adjacent AMTI force plates (Advanced Mechanical Technology Inc., MA, USA) embedded parallel in the floor. In the WoS condition, each foot was placed directly on an individual force plate, allowing direct measurement of the vertical GRF applied by each side. In the WS condition, the stepper device was positioned on top of both force plates, meaning that force applied by one foot to the stepper could be partially transmitted to the opposite side. This setup was taken into account during the analysis of weight-shift measurements.

Maximum voluntary contraction (MVC) and EMG activation of lower limb muscles: Rectus Femoris (RF), Tibialis Anterior (TA), Biceps Femoris (BF), Gastrocnemius Medialis (GM), and Soleus was recorded using ten Trigno™ Sensor (SC-F03) wireless EMG sensors (Delsys, USA) bilaterally. The skilled

physical therapist placed EMG sensors to ensure correct positioning based on the SENIAM guide [23].

D. Experimental Protocol

The selected exercises for this study were bilateral ADPF (Fig. 3A, 3C) and stepping performed by an exergame-integrated stepper (Fig. 3B, 3D). Participants performed exercises seated at two different tilt angles (0° and 45°). To ensure a consistent initial knee angle across participants, seat height was adjusted based on individual leg lengths. This helped maintain a standardized starting posture despite differences in lower limb dimensions. Participants completed the exercises seated with their feet positioned on either the force plates or the stepper. To minimize compensatory upper body movements, they were instructed to keep their arms crossed over their chest during trials. Figure 3 images are posed to illustrate the experimental setup.

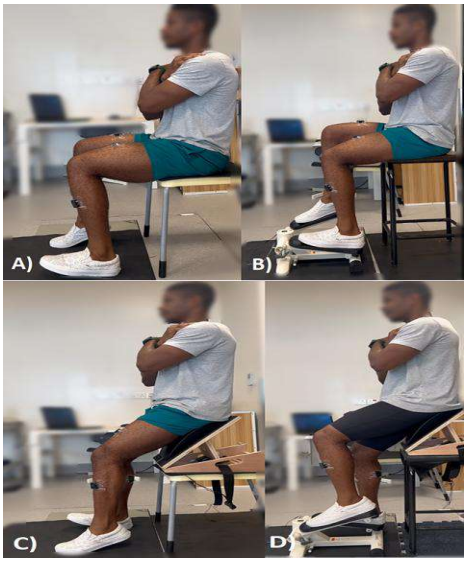


Figure 3. Exercise with stepper and without sitting at 0° ((A), ((B)) and 45° ((C), ((D)) tilted positions.

The first trial involved a bilateral ADPF exercise called without stepper (WoS). Participants performed bilateral ADPF exercises at 30 beats per minute (bpm). They were instructed to achieve maximum dorsiflexion and plantarflexion during each repetition while synchronizing their movements with the metronome beat. The exercise comprised two sets of 10 repetitions. Overall, each trial lasted 30 seconds, including 5 seconds waiting at the start, 20 seconds doing exercise, and 5 seconds waiting at the end.

In the subsequent second trial, participants adhered to the same sets and repetitions as in the first trial, but with an exergame-integrated stepper device. In the exergame, participants were requested to catch animals that appeared on both sides of the screen alternatingly at two-second intervals using the stepping exercise. The two-second interval of the exergame matched the 30 beats per minute (bpm) to ensure comparability with WoS exercise.

E. Data Analysis

The collected Fz data were filtered with a third-order low-pass Butterworth filter at 100 Hz. The filtered Fz data of each subject were normalized based on their total body weight. Afterward, MATLAB (R2023a) was utilized to apply a Butterworth (low-pass sixth order) filter with a cutoff frequency of 1 Hz to extract the envelope of the normalized force data. This process was iterated for each subject's force data, then averaging the first and second sets.

Weight-shift analysis was performed by calculating the differences between the peak Fz values of the right and left sides, as shown in Fig. 4 (A). For each of the ten repetitions, the peak Fz value of the right side during its downward phase was labeled as R1, and the lowest Fz value of the left side during its upward phase was denoted as L1. We employed a modified version of Sato and Heise's method to calculate weight-shift, tailoring it to our specific experimental conditions and objectives [24]:

$$WS = \frac{1}{N}\sum_{k=1}^{N}|(R_k - L_k)|$$

where WS is the average weight shift, R_k and L_k represent the peak vertical GRF values for the right and left sides in each repetition, and N is the total number of repetitions per trial. By subtracting the corresponding Fz values and averaging them across the repetitions, an overall measure of weight shift bilaterally during the stepping exercise was obtained. Then, weight-shift analysis was conducted by first computing the peak weight shift values for each trial separately and then averaging these discrete values across the two sets. This approach ensured that variations in timing did not artificially influence the results.

The raw MVC and EMG data underwent band-pass filtering with Butterworth (second order, 10-450 Hz) [25]. Subsequently, the filtered EMG data were normalized based on their corresponding peak MVC values. A low-pass Butterworth filter (fourth-order, 3 Hz) was then employed to generate the envelope. Then, the first and second sets were averaged.

Statistical analysis was conducted using MATLAB (R2023a). The Shapiro-Wilk test was utilized to assess normal distribution of the data, revealing a lack of normal distribution. Wilcoxon signed-rank test was employed to compare the mean values using the α-level of 0.05.

III. Results

The study involved ten (5M, 5F) healthy participants engaging in ADPF and stepping exercises. The ADPF referred to as the 'Without stepper' condition, was compared with the stepping exercise performed with an exergame-integrated stepper device. The analysis focused on weight shift and muscle activation under both 0° and 45° tilt conditions in the lower limb.

A. Weight-shift

Figure 4B illustrates a bar graph representing the average weight-shift without and with stepper conditions under 0° and 45° tilt. Our results demonstrate a significant increase of 72% at 0° tilt and an increase of 22% at 45° tilt in the WS compared to WoS condition ($p < 0.05$). This substantial shift was apparent in the transition from 0° to 45° tilted sitting positions, exhibiting a significant increase of 188% ($p < 0.01$) in the WoS and a significant increase of 93% ($p < 0.01$) in the WS conditions.

B. Muscle Activity

Figure 5 displays electromyographic (EMG) recordings of lower limb muscles, specifically RF, TA, BF, GM, and Soleus, under both 0° and 45° tilt conditions.

All muscles engaged in bilateral exercises exhibited decreased muscle activation in the WS compared to WoS conditions. The reduction in muscle activation for all muscles was statistically significant ($p < 0.05$), except for rectus femoris (Left RF: $p = 0.646$, Right RF: $p = 0.445$) at 0° and 45° tilt positions. The results demonstrate a direct influence of the exergame-integrated stepper in reducing muscle activity, especially on the main ADPF muscles, TA, GM, and Soleus. Detailed results and p-values for each muscle are shown in Table 1.

Table 1. With-without stepping EMG differences and p-values of lower limb muscles. Percentage differences indicate changes in EMG amplitude normalized by maximum voluntary contraction (MVC).

Muscles	0° Seated % Difference (p-value)	45° Tilted % Difference (p-value)
Left RF	7% (p = 0.646)	%4% (p = 0.646)
Right RF	13% (p = 0.445)	4% (p = 0.445)
Left TA	75% (p<0.01) **	71% (p<0.01) **
Right TA	80% (p<0.01) **	78% (p<0.01) **
Left BF	17% (p = 0.05) *	26% (p = 0.05) *
Right BF	22% (p = 0.05) *	40% (p = 0.05) *
Left GM	48% (p<0.01) **	48% (p<0.01) **
Right GM	58% (p<0.01) **	50% (p<0.01) **
Left Soleus	%56 (p<0.01) **	%32 (p<0.01) **
Right Soleus	%65 (p<0.01) **	%26 (p<0.01) **

'*' denotes ($p < 0.05$), while '**' denotes statistical significance ($p < 0.01$).

IV. Discussion

We assessed the biomechanics of ADPF and stepping, performed with a developed exergame-integrated stepper device, exercises, and compared weight-shift and muscle activity variables.

Rhythmic bilateral training of the lower limb has emerged as a promising approach to stroke rehabilitation [26]. Studies have shown the benefits of synchronizing exercises with visual and auditory cues, such as metronome beats and exergames [27, 28]. Moreover, the majority of ADLs necessitate the bilateral use of the lower extremities, Jeon and Hwang (2018) [10] demonstrated the superiority of the bilateral approach over unilateral methods in post-stroke lower limb rehabilitation. Our results show that a developed exergame-integrated stepper can provide rhythmic and bilateral lower-limb stepping exercises. Thus, exergame-integrated stepper training can be a promising approach to address deficits in motor coordination, enhancing functional mobility, and ADL training for stroke survivors.

After a stroke, individuals commonly encounter challenges in bearing weight on their affected limb [29-31]. Mizrahi et al. indicate that a significant majority (79% to 87%) of stroke survivors bear less weight on their affected limbs during static and dynamic activities [32]. Furthermore, Goldie et. all, reported that healthy individuals exhibit a mediolateral weight-bearing ability of 95%, whereas stroke patients demonstrate 65% [33]. In our study, we observed that the weight-shift was greater in the condition involving the stepper compared to the condition WoS, indicating that the integration of the stepper device promotes a greater weight-shift. Cheng, et. all, have proposed that the uneven distribution of body weight during rising from a chair may contribute to falls in stroke survivors [34]. Aruin et. all, showed that creating a height difference between the right and left sides facilitates weight shift in the lower limb [19]. Our results were parallel with this and suggest that bilateral ADPF exercise induces weight shift, however, the developed exergame-integrated stepper, which has a 10 cm height difference between the right and left sides, provides more weight shift.

Muscle weakness is commonly observed during acute-stage post-neurological diseases, leading to neuromuscular fatigue, limiting patient attendance, and exercise repetitions [3, 35]. Ducrocq and Blain, observed a connection between escalating neuromuscular fatigue and heightened exercise intensity, as evidenced by EMG amplitude during exercise [15]. In parallel with this, reducing muscle activation plays an important role in facilitating intensive treatment in rehabilitation [36]. Our findings indicated that the stepper device could provide lower EMG activation than the WoS condition. Specifically, during the stepping exercise with the exergame-integrated stepper, significantly lower EMG activation

was observed in the TA, GM, and Soleus muscles except RF, which was lower but not significant. The stepper's capability to synchronize the movement of both sides, enabling bilateral assistance, may primarily contribute to the observed reduction in muscle activation. Thus, this synchronization mechanism of the stepper can alleviate the challenge of exercising against gravity, resulting in lower EMG activation.

There are several limitations to this study. Firstly, the sample size was small, consisting of only ten healthy participants, which could potentially restrict the generalizability of the findings. Secondly, due to the limited time frame, each condition involved completing 2 sets of 10 repetitions, which may restrict the depth of analysis and the ability to capture the nuanced effects of the measurement. Nevertheless, our results can be transferred to stroke rehabilitation, as seated stepping exercises can be utilized at 0° seated for early-stage rehabilitation and at 45° seated for stroke patients who are capable of sitting in a tilted position. Future studies should evaluate seated stepping's impact on functional outcomes in stroke patients or the elderly over extended exercise durations.

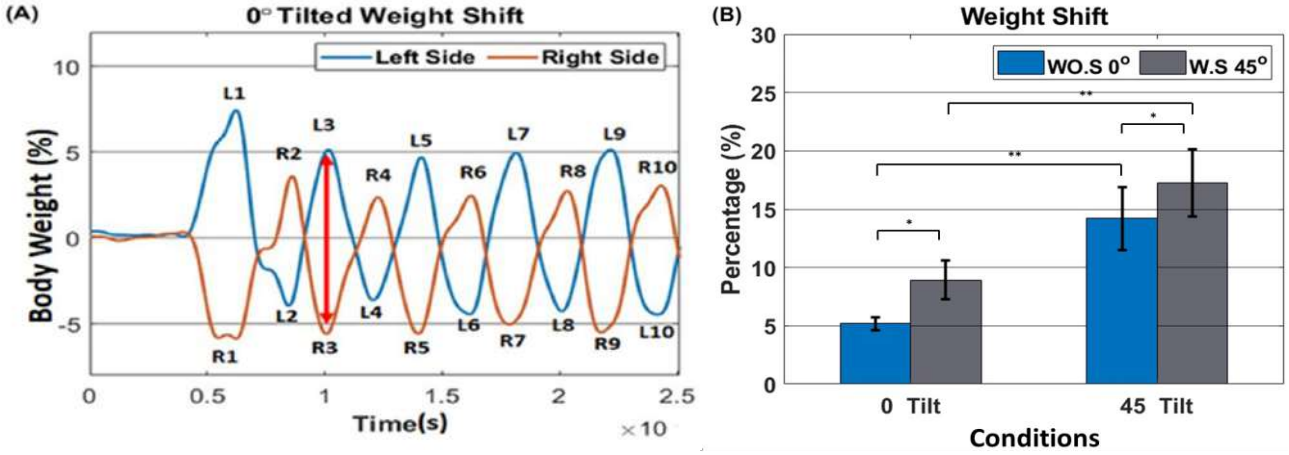


Figure 4. Sample of subject 7's weight-shift data on 0° Tilted Stepper condition (A), Average weight-shift of all subjects under conditions; 0° and 45° Tilted. (B). '*' denotes ($p < 0.05$), while '**' denotes statistical significance ($p < 0.01$).

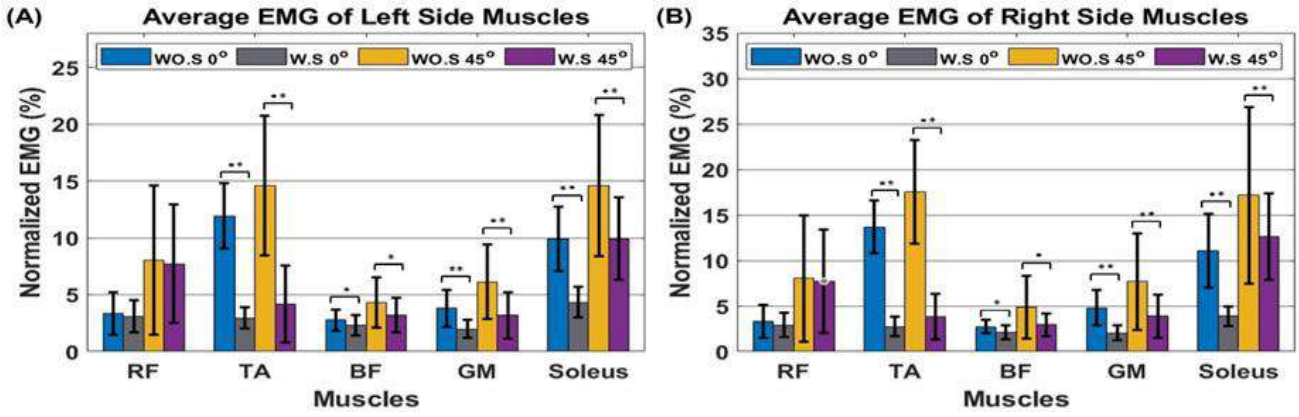


Figure 5. Average EMG graphs for the right (R) and left (L) sides under two conditions (WO. S: without stepper, W.S: with stepper) at 0° and 45° tilts. '*' denotes ($p < 0.05$), while '**' denotes statistical significance ($p < 0.01$).

V. Conclusion

This study is the first to explore the biomechanics of seated ankle dorsi-plantar flexion (ADPF) and exergame-integrated stepping exercises based on weight shift and muscle activation in the lower limb. Our study clearly contributes to rehabilitation literature by highlighting the potential advantages of incorporating bilateral seated stepping exercises, demonstrating their positive impact on lower limb weight shift and muscle training. We recommend implementing stepping exercises in future clinical trials to thoroughly investigate their impact on functional outcomes, including walking speed, balance, and activities of daily living (ADL) capacities.

VI. Acknowledgments

This work was partially supported by a Promotion of Doctoral Studies scholarship from the Singapore International Graduate Awards (SINGA). The study sponsor had no involvement in the study design, data collection, analysis, interpretation, manuscript writing, or the decision to submit the manuscript for publication. The authors express their gratitude to Ayşegül Asalıoğlu Beycan for her valuable contributions.

REFERENCES

[1] S. Frenkel-Toledo, S. Ofir-Geva, L. Mansano, O. Granot, N. Soroker, Stroke Lesion Impact on Lower Limb Function, Front Hum Neurosci 15 (2021) 592975.

[2] P.V. Tsaklis, W.J. Grooten, E. Franzen, Effects of weight-shift training on balance control and weight distribution in chronic stroke: a pilot study, Top Stroke Rehabil 19(1) (2012) 23-31.

[3] V. Gray, C.L. Rice, S.J. Garland, Factors that influence muscle weakness following stroke and their clinical implications: a critical review, Physiother Can 64(4) (2012) 415-26.

[4] N. Klempel, N.E. Blackburn, I.L. McMullan, J.J. Wilson, L. Smith, C. Cunningham, R. O'Sullivan, P. Caserotti, M.A. Tully, The Effect of Chair-Based Exercise on Physical Function in Older Adults: A Systematic Review and Meta-Analysis, Int J Environ Res Public Health 18(4) (2021).

[5] P. Mackie, J.J. Eng, The influence of seated exercises on balance, mobility, and cardiometabolic health outcomes in individuals living with a stroke: A systematic review and meta-analysis, Clin Rehabil 37(7) (2023) 927-941.

[6] B.P. Sexton, N.F. Taylor, To sit or not to sit? A systematic review and meta-analysis of seated exercise for older adults, Australas J Ageing 38(1) (2019) 15-27.

[7] A.D. Mountain, R.L. Kirby, D.A. MacLeod, K. Thompson, Rates and predictors of manual and powered wheelchair use for persons with stroke: a retrospective study in a Canadian rehabilitation center, Arch Phys Med Rehabil 91(4) (2010) 639-43.

[8] M. Yamada, T. Aoyama, B. Tanaka, K. Nagai, N. Ichihashi, Seated stepping exercise in a dual-task condition improves ambulatory function with a secondary task: a randomized controlled trial, Aging Clin Exp Res 23(5-6) (2011) 386-92.

[9] P. Harjpal, M.I. Qureshi, R.K. Kovela, M. Jain, Efficacy of Bilateral Lower-Limb Training Over Unilateral Lower-Limb Training To Reeducate Balance and Walking in Post-Stroke Survivors: A Randomized Clinical Trial, Cureus 14(10) (2022) e30748.

[10] H.J. Jeon, B.Y. Hwang, Effect of bilateral lower limb strengthening exercise on balance and walking in hemiparetic patients after stroke: a randomized controlled trial, J Phys Ther Sci 30(2) (2018) 277-281.

[11] R. Sleimen-Malkoun, J.J. Temprado, L. Thefenne, E. Berton, Bimanual training in stroke: How do coupling and symmetry-breaking matter?, BMC Neurol 11 (2011) 11.

[12] J.H. Cauraugh, J.J. Summers, Neural plasticity and bilateral movements: A rehabilitation approach for chronic stroke, Prog Neurobiol 75(5) (2005) 309-20.

[13] H.K. Kristensen, M. Tistad, L. Koch, C. Ytterberg, The Importance of Patient Involvement in Stroke Rehabilitation, PLoS One 11(6) (2016) e0157149.

[14] H.M. Abd-Elfattah, F.H. Abdelazeim, S. Elshennawy, Physical and cognitive consequences of fatigue: A review, J Adv Res 6(3) (2015) 351-8.

[15] G.P. Ducrocq, G.M. Blain, Relationship between neuromuscular fatigue, muscle activation and the work done above the critical power during severe-intensity exercise, Exp Physiol 107(4) (2022) 312-325.

[16] J.J. Eng, K.S. Chu, Reliability and comparison of weight-bearing ability during standing tasks for individuals with chronic stroke, Arch Phys Med Rehabil 83(8) (2002) 1138-44.

[17] V.S. Mercer, J.K. Freburger, S.H. Chang, J.L. Purser, Measurement of paretic-lower-extremity loading and weight transfer after stroke, Phys Ther 89(7) (2009) 653-64.

[18] A.A. Lobo, A.M. Joshua, A. Nayak, P.P. Mithra, Z. Misri, S. Pai, Effect of Compelled Body Weight Shift (CBWS) Therapy in Comparison to ProprioceptiveTraining on Functional Balance, Gait, andMuscle Strength Among Acute Stroke Subjects, Ann Neurosci 28(3-4) (2021) 162-169.

[19] A.S. Aruin, N. Rao, A. Sharma, G. Chaudhuri, Compelled body weight shift approach in rehabilitation of individuals with chronic stroke, Top Stroke Rehabil 19(6) (2012) 556-63.

[20] J.W. Hung, C.X. Chou, Y.W. Hsieh, W.C. Wu, M.Y. Yu, P.C. Chen, H.F. Chang, S.E. Ding, Randomized comparison trial of balance training by using exergaming and conventional weight-shift therapy in patients with chronic stroke, Arch Phys Med Rehabil 95(9) (2014) 1629-37.

[21] P.T. Cheng, C.M. Wang, C.Y. Chung, C.L. Chen, Effects of visual feedback rhythmic weight-shift training on hemiplegic stroke patients, Clin Rehabil 18(7) (2004) 747-53.

[22] R. Adams, Revised Physical Activity Readiness Questionnaire, Can Fam Physician 45 (1999) 992, 995, 1004-5.

[23] D.S.a.H. Hermens, Standards for surface electromyography: The European project Surface EMG for non-invasive assessment of muscles (SENIAM), Enschede: Roessingh Research and Development 10 (2007) 8-12.

[24] K. Sato, G.D. Heise, Influence of weight distribution asymmetry on the biomechanics of a barbell back squat, J Strength Cond Res 26(2) (2012) 342-9.

[25] L. Moreira, J. Figueiredo, P. Fonseca, J.P. Vilas-Boas, C.P. Santos, Lower limb kinematic, kinetic, and EMG data from young healthy humans during walking at controlled speeds, Sci Data 8(1) (2021) 103.

[26] H.Y. Chen, A.M. Wing, D. Pratt, The synchronisation of lower limb responses with a variable metronome: the effect of biomechanical constraints on timing, Gait Posture 23(3) (2006) 307-14.

[27] K.G.F. Chan, Y. Jiang, W.T. Choo, H.J. Ramachandran, Y. Lin, W. Wang, Effects of exergaming on functional outcomes in people with chronic stroke: A systematic review and meta-analysis, J Adv Nurs 78(4) (2022) 929-946.

[28] B. Emre, O. Seyram, L.W.R. Joshua, W. Zhao, H. Yu, Investigating the Effect of Novel Gamified Stepper on Lower Limb Biomechanics in Seated Healthy Subjects, IEEE Int Conf Rehabil Robot 2023 (2023) 1-6.

[29] B.O. Adegoke, O. Olaniyi, C.O. Akosile, Weight bearing asymmetry and functional ambulation performance in stroke survivors, Glob J Health Sci 4(2) (2012) 87-94.

[30] R. Dickstein, M. Nissan, T. Pillar, D. Scheer, Foot-ground pressure pattern of standing hemiplegic patients. Major characteristics and patterns of improvement, Phys Ther 64(1) (1984) 19-23.

[31] A. Shumway-Cook, D. Anson, S. Haller, Postural sway biofeedback: its effect on reestablishing stance stability in hemiplegic patients, Arch Phys Med Rehabil 69(6) (1988) 395-400.

[32] J. Mizrahi, P. Solzi, H. Ring, R. Nisell, Postural stability in stroke patients: vectorial expression of asymmetry, sway activity and relative sequence of reactive forces, Med Biol Eng Comput 27(2) (1989) 181-90.

[33] P.A. Goldie, T.A. Matyas, O.M. Evans, M. Galea, T.M. Bach, Maximum voluntary weight-bearing by the affected and unaffected legs in standing following stroke, Clin Biomech (Bristol, Avon) 11(6) (1996) 333-342.

[34] P.T. Cheng, M.Y. Liaw, M.K. Wong, F.T. Tang, M.Y. Lee, P.S. Lin, The sit-to-stand movement in stroke patients and its correlation with falling, Arch Phys Med Rehabil 79(9) (1998) 1043-6.

[35] S.M. Mah, A.M. Goodwill, H.C. Seow, W.P. Teo, Evidence of High-Intensity Exercise on Lower Limb Functional Outcomes and Safety in Acute and Subacute Stroke Population: A Systematic Review, Int J Environ Res Public Health 20(1) (2022).

[36] G.P. Ducrocq, T.J. Hureau, T. Bogseth, O. Meste, G.M. Blain, Recovery from Fatigue after Cycling Time Trials in Elite Endurance Athletes, Med Sci Sports Exerc 53(5) (2021) 904-917.

Effect of Robotic Assistance on the Synergistic Organization of Reaching Movements

Indya Ceroni[1,2], Florencia Garro [1] and Marianna Semprini[1]

***Abstract*— Wearable robotic devices for rehabilitation have gained particular interest as they can improve the intensity and repeatability of rehabilitative treatments, leading to better rehabilitation outcomes. However, objective characterization of the effects of robotic interventions is still missing. Here we leverage on muscle synergies theory to provide a quantitative assessment of the effects of an upper limb exoskeleton on the organization of reaching movements in healthy individuals. For this, we computed muscle synergies from 20 subjects performing a standardized reaching task. We found that the robotic assistance does not disrupt the physiological structure of reaching movement but modulates it: a higher number of motor modules are necessary to explain the structure of reaching when using the exoskeleton. We derived an objective analysis of the implications of the more complex and fragmented movement strategy, which can potentially inform the design and testing of robotic prototypes, with the ultimate aim of improving technology-supported rehabilitation interventions.**

I. INTRODUCTION

Motor impairments induced by neurological disorders have a severe impact on the independence and quality of life of affected subjects [1]. In this context, numerous technological solutions have been introduced, including robot-assisted rehabilitation systems designed to aid recovery [2]. These devices operate either by driving an end effector or by being wearable, allowing movement within them [3]. However, despite advancements in mechatronic design and control, these devices can influence how motor actions are performed, making it crucial to monitor differences with unassisted movements. To accurately evaluate how assistive devices influence motor control, we need objective and reliable measurements of motor performance, along with standardized tasks enabling comparisons of motor output across different contexts [4].

Muscle synergies are defined as coordinated patterns of muscle activation, which the central nervous system uses to simplify motor control [5]. They have been employed to investigate the neural basis of motor control [6] and quantify the effect of neurological diseases on motor production [7].

Here, muscle synergies are used to assess whether and how the assistance provided by the Float upper limb exoskeleton [8] affects the modular organization of physiological reaching movement. This investigation is done by exploiting a standardized benchmarking platform, named *NeBULA* (i.e., Neuromechanical Biomarkers for Upper Limb Assessment), specifically designed to evaluate and compare the effects of different robotic technologies for upper limb rehabilitation [9]. NeBULA implements a standardized reaching task framework to extract neuromechanical biomarkers derived from electromyography (EMG) and electroencephalography (EEG), allowing a reliable and repeatable quantification of the effects of different types of robotic assistance on motor control during functional tasks [9].

This study aims to: (i) characterize the synergistic organization of reaching in unassisted and in exoskeleton-assisted movements; (ii) investigate modulation of level of assistance on synergy recruitment. From these findings, we will derive implications for further iterations of exoskeleton design.

II. MATERIALS AND METHODS

A. Participants

20 healthy right-handed subjects were enrolled in the study (10 male, 10 female, age 31.6+/-6.2 years old). Subjects with any chronic inflammatory diseases, orthopedic conditions or neuro-muscular disorders were excluded from the study. All participants signed an informed consent and the experimental procedures were approved by the local ethical committee (CER Liguria: 784/2022 - DB id 12044).

B. The Float upper limb exoskeleton

Float has been developed at the Rehab Technologies Lab of IIT to support the rehabilitation of the shoulder complex in orthopaedic and neurological subjects [8]. It consists of five rotational joints, with each degree of freedom representing a movement of the shoulder complex. Float features a model-based feed-forward compensation of friction at each joint. This 'transparency mode' also provides active assistance at the level of joint 4, which helps the user to flex the shoulder and perform upward vertical motion of the arm. The assistance can be set at two different levels: low and high. The gains for these assistance levels are fixed and were calibrated empirically based on the average weight of a human arm as described in [8].

This work was supported by the Italian Ministry of Research, under the complementary actions to the NRRP "Fit4MedRob - Fit for Medical Robotics" Grant (PNC0000007). It is also funded by the European Union - NextGenerationEU and by the Ministry of University and Research (MUR), National Recovery and Resilience Plan (NRRP), Mission 4, Component 2, Investment 1.5, project "RAISE - Robotics and AI for Socio-economic Empowerment" (ECS00000035) and by the Istituto Nazionale Assicurazione Infortuni sul Lavoro (INAIL) (Project grant number PR19-RR-P2 - ROBO-GYM).

[1]I. Ceroni, F. Garro and M. Semprini are with Rehab Technologies, Istituto Italiano di Tecnologia, Genoa, Italy. indya.ceroni@iit.itflorencia.garro@iit.it, marianna.semprini@iit.it, corresponding author indya.ceroni@iit.it

[2]I. Ceroni is also with the Department of Informatics, Bioengineering, Robotics and Systems Engineering, University of Genoa, Genoa, Italy

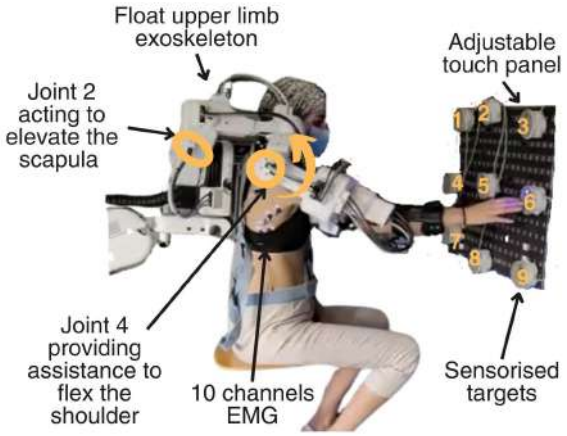


Fig. 1. Setup of the experiment, featuring the Float upper limb exoskeleton providing two different levels of assistance for shoulder flexion and an ad-hoc adjustable touch panel endowed with nine sensorized targets. 10 channels of surface EMG are synchronized with the touch panel.

C. Experimental design

The experimental procedure followed the standardized framework NeBULA [9]. During the experiment, participants were seated in an adjustable chair in front of a touch panel with nine targets arranged to allow full arm extension (Fig. 1). The targets were positioned to adapt to the user's anthropometric measures. Each target has a light indicator that cued the participant to reach that specific target. The time instant in which the participant reached the target was recorded thanks to the capacitive layer.

The experimental task involved 10 repetitions of reaching towards each of the 9 targets in a pseudorandomized order (Fig. 2 A). Each participant repeated the task three times: without wearing Float (free condition), wearing Float providing low assistance (low condition), and wearing Float providing high assistance (high condition). The order of assistance levels was randomized across participants.

Surface EMG signals were recorded from 10 muscle groups of the right upper limb: 1) biceps brachii (long head), 2) anterior deltoid, 3) middle deltoid, 4) posterior deltoid, 5) triceps brachii (long head), 6) upper trapezius, 7) medial trapezius, 8) lower trapezius, 9) pectoralis major, and 10) brachioradialis. EMG was acquired at 1 KHz, using the Cometa Waveplus System, synchronized with the panel.

D. EMG preprocessing

EMG was first segmented in the reaching phase. For each epoch, we applied a band-pass filter between 20 and 350 Hz (4th order Butterworth with zero-phase distortion) and rectified. Then, we applied an ad-hoc median filter, and values over 600 μV were substituted with the median in a 50-sample sliding window. In addition, we applied a 4th order Butterworth low-pass filter at 5 Hz with zero-phase distortion to obtain the envelope of the signal. We normalized the EMG envelopes taking the maximum value achieved for each muscle in the complete dataset [10], [11]. Since the task was self-paced, we time-scaled all epochs to the same duration of 500 samples (0.5 s) [12].

E. Synergies extraction

First, we concatenated the EMG data from all muscles. Then, we used the non-negative matrix factorization algorithm (NNMF) [13] to factorize the concatenated EMG matrix into N vectors of 10 constant weights w_i and N time-varying coefficients $c_i(t)$

$$EMG(t) = \sum_{i=1}^{N} c_i(t) w_i \tag{1}$$

Each spatial synergy w_i is a set of 10 weights describing how muscles synergistically couple to each other to produce movements. The coefficients of activation $c_i(t)$ describe how much each synergy is active during movement.

To investigate how the exoskeleton modulates reaching movements, we extracted muscle synergies for each subject using two different datasets. First, we applied NNMF in the free condition to identify the muscle synergies that characterize the physiological reaching movement performed without any external assistance ("free dataset synergies"). Then, we considered all conditions together to characterize the modularity of the entire experimental paradigm ("whole dataset synergies"). During every synergy extraction procedure, we implemented NNMF with alternating least squares and repeated it 100 times starting from new random values to avoid local minima [11].

To select the appropriate number (N) of free and whole dataset synergies for each subject, we repeated the NNMF extracting a number of synergies ranging from 1 to the number of EMG channels. For each factorization, we computed the percentage of variance of the original EMG data that was reconstructed by the extracted synergies, as $R^2 = 1 - SSE/SST$, where SSE is the sum of squared residuals and SST is the sum of the squared differences with the mean EMG vector [10].

For each subject, we selected the smallest number of synergies for which the variance accounted for (R^2 or VAF) was equal to or greater than 0.9 (i.e., 90% of data variability is explained by the combination of extracted muscle synergies and coefficients of activation).

We then averaged the obtained number of synergies across subjects to compute an average number of free (N_{free}) and whole dataset synergies (N_{whole}). Finally, NNMF was applied for each subject, imposing the extraction of N_{free} free dataset synergies from the free condition and N_{whole} whole dataset synergies from the entire experiment.

F. Synergies averaging

To represent the modularity shared by the 20 participants, we averaged spatial synergies across subjects. A preliminary clustering procedure was needed as not all subjects shared the same synergies, and also the shared synergies could be extracted in different order across different subjects due to the random initialization of the NNMF algorithm. The

clustering procedure implemented was inspired by [12] and was built on the identification of the synergies shared among at least half of the participants. Synergies were grouped using a measure of similarity based on the cosine of the angle between the vectors representing the spatial synergies, as in [10]. Such similarity measures range from 1 (identical synergies) to 0. Briefly, we divided free and whole dataset synergies into 10 clusters based on the most expressed EMG channel in each synergy. We explicitly excluded synergies of the same subject in the same cluster. Then, we selected clusters containing at least 10 synergies. We averaged the selected clusters to obtain a set of "reference synergies".
We then regrouped single subjects' synergies based on their cosine similarity with the reference synergies, excluding single subjects' synergies with less than 0.5 similarity with one of the reference synergies.
Synergies were finally averaged to obtain a set of averaged free and whole dataset synergies. The first represented the modularity of the physiological anterior reaching movement, and the second the modularity of the entire experimental protocol, characterizing the effect of robotic assistance.

G. Computation of activation coefficients

Activation coefficients c_i describe how each of the averaged free and whole dataset synergies is enrolled during each repetition of reaching of the entire experiment. We computed the activation coefficients of the averaged free and whole dataset synergies at the subject level for movements performed in all the conditions (free, low, and high). For this, we calculated the Moore-Penrose pseudoinverse [14] of the averaged synergies and computed the dot product of the pseudoinverse with the matrix of concatenated EMG of each subject, as in [12]. We averaged across repetitions to obtain the activation coefficients for each subject, which ranged from 0 to 1 and were distributed over 500 temporal samples.

III. Results

A. Characterization of spatial muscle synergies

During the first computation of free and whole dataset synergies, we respectively extracted an average of 4 free dataset synergies (3.75 ± 0.97) and 5 whole dataset synergies (4.5 ± 0.83) per subject, with an average VAF of 0.93.

The free and whole dataset synergies extracted from each subject were grouped based on the most expressed muscle within each synergy (Fig. 3). For free dataset synergies, 3 clusters contained more than 10 synergies and thus were selected to compute the reference synergies, while for whole dataset synergies we selected 6 (Sec. II-F).

The free dataset synergies of single subjects (80 in total) were then grouped in 3 clusters, based on their similarity with the three reference synergies (Fig. 3). During this procedure, 2 synergies out of 80 (2.5 %) were excluded as their cosine similarity with the reference synergies was below 0.5. Similarly, the whole dataset of synergies of single subjects (100 in total) was grouped in 6 clusters based on their similarity with the 6 reference synergies, and 13 synergies (13 %) were excluded.

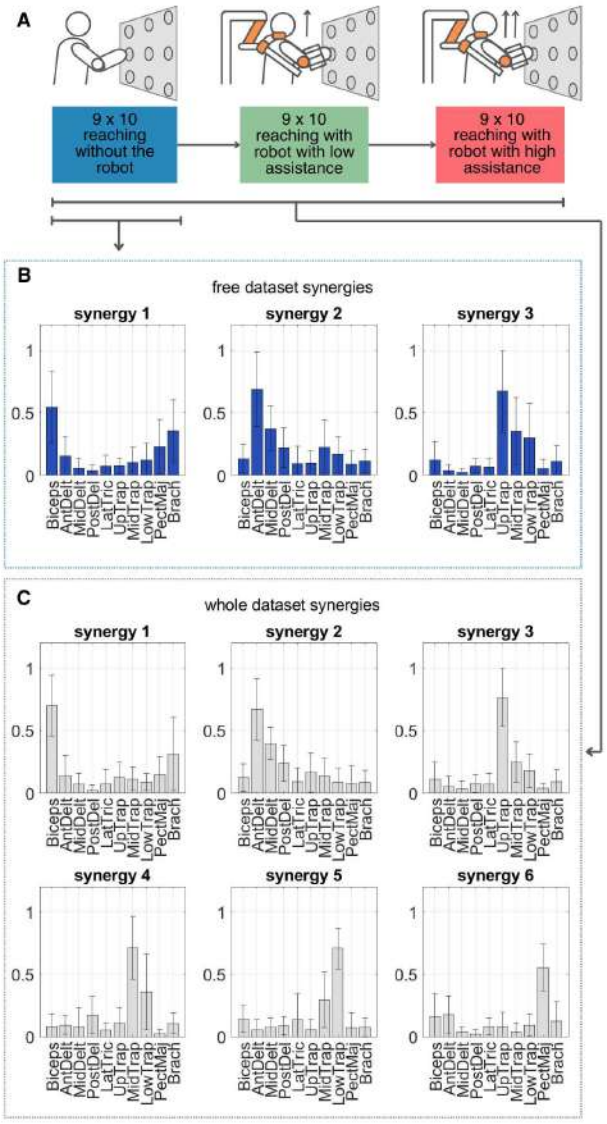


Fig. 2. A) Experimental paradigm involving 10 repetitions of reaching movement towards each of the 9 targets in a pseudorandomized order. The task is repeated without the robot and with the robot with low and high assistance. B) Free dataset synergies obtained considering only repetitions executed without the robot. C) Whole dataset synergies obtained considering all reaching movements of the entire experimental paradigm.

Free and whole dataset synergies were averaged within each group to obtain 3 free and 6 whole dataset synergies representative of the modularity shared by the 20 healthy subjects that participated in the study. The three averaged free dataset synergies (Fig. 2 B) are extremely similar to the first three whole dataset synergies (Fig. 2 C). The values of cosine similarity between the two sets of synergies are shown in Fig. 4, which exhibits high similarity between synergy 1 of free (s1_free) and whole (s1_whole) dataset (0.975) as well as between synergy 2 of free (s2_free) and whole (s2_whole) dataset (0.9861) and synergy 3 of free (s3_free) and whole (s3_whole) dataset synergies (0.9751). For synergies 4 of the whole dataset (s4_whole) high similarity values are obtained

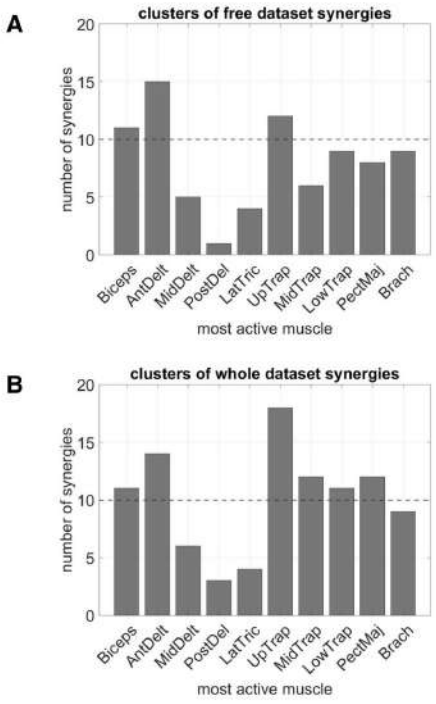


Fig. 3. Clusters of synergies based on the most active EMG channel inside the synergy. A) Clusters of free dataset synergies. B) Clusters of whole dataset synergies.

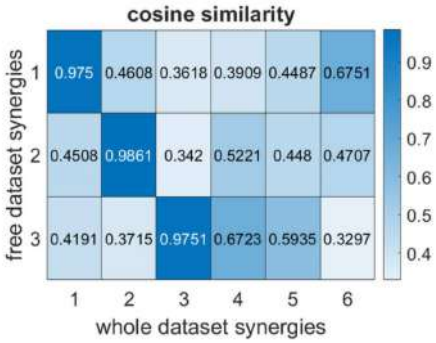


Fig. 4. Cosine similarity between the averaged free and whole dataset synergies. Cosine similarity is computed as the dot product of the synergies vectors divided by the product of their magnitude.

with synergies s3_free (0.6723) as well as for synergy 5 of the whole dataset (s5_whole, 0.5935). Synergy 6 of whole dataset (s6_whole) had highest similarity with s1_free (0.6751).

For both s1_free and s1_whole the two most expressed muscles are biceps and brachioradialis. These two muscles work synergistically to produce the flexion of the elbow; thus, we can consider these synergies as representative of elbow flexion. In s1_free also the pectoralis shows some activation, while in s1_whole the weight of the pectoralis is much lower. This can be due to the fact that for the whole dataset, the pectoralis is mostly expressed in s6_whole, which indeed shows good similarity (0.6751) with s1_free. s2_free and s2_whole mainly express the anterior and middle deltoids that are responsible for shoulder flexion and shoulder abduction, respectively. s3_free and s3_whole express a significant activation of the trapezius muscle with the predominance of the upper trapezius, which elevates the scapula to ensure a full range of motion for arm elevation. The less significant contribution of middle and lower trapezius in s3_whole with respect to s3_free can be the results of the presence of two additional synergies: s4_whole and s5_whole. s4_whole mainly expresses the middle trapezius that retracts the scapula, while s5_whole shows greater contribution of lower trapezius, which medially rotates the scapula.

B. Characterization of activation coefficients

Coefficients of activation for each averaged free and whole dataset synergy are depicted in Fig. 5 for two representative movements, i.e., towards target 1 and towards target 5.
We divided the time span of 500 samples into 3 equal segments, and we computed the integral of the activation coefficients over each segment. Wilcoxon signed rank test was performed on the estimated integrals to test for any statistical difference between the activation coefficients of each synergy in the free, low, and high assistance conditions. The results were corrected for multiple comparisons following the Bonferroni criterion. Horizontal blue/gray brackets above the temporal coefficients in Fig. 5 indicate the presence of a statistically significant difference across conditions in that specific time interval.
The activation coefficient of s3_free in the initial phase of movement towards target 1 is statistically higher during the high condition with respect to the free condition (Fig. 5 A). The same was found for movements towards target 2. A similar statistical difference between free and high condition was found for s3_free in the final phase of movement towards target 9.
In the last phase of movement towards target 5, the activation coefficient of s3_whole is significantly higher when wearing Float with high assistance with respect to the free movement (Fig. 5 B).
Table I reports the statistically significant differences found for the free vs. high condition, while no differences were found neither for the free vs. low condition nor for the low vs. high condition.

TABLE I
COMPARISON OF ACTIVATION COEFFICIENTS

Synergy	Target	Phase of movement	Conditions	p-value
s3_free	1	initial	free vs high	0.00039
s3_free	2	initial	free vs high	0.00052
s3_free	9	final	free vs high	0.00045
s3_whole	5	final	free vs high	0.00039

IV. DISCUSSION

With this analysis, we obtained two sets of spatial synergies that represent the common modularity among all subjects. We found that: (i) the synergistic structure of reaching is preserved during exoskeleton-assisted movement;

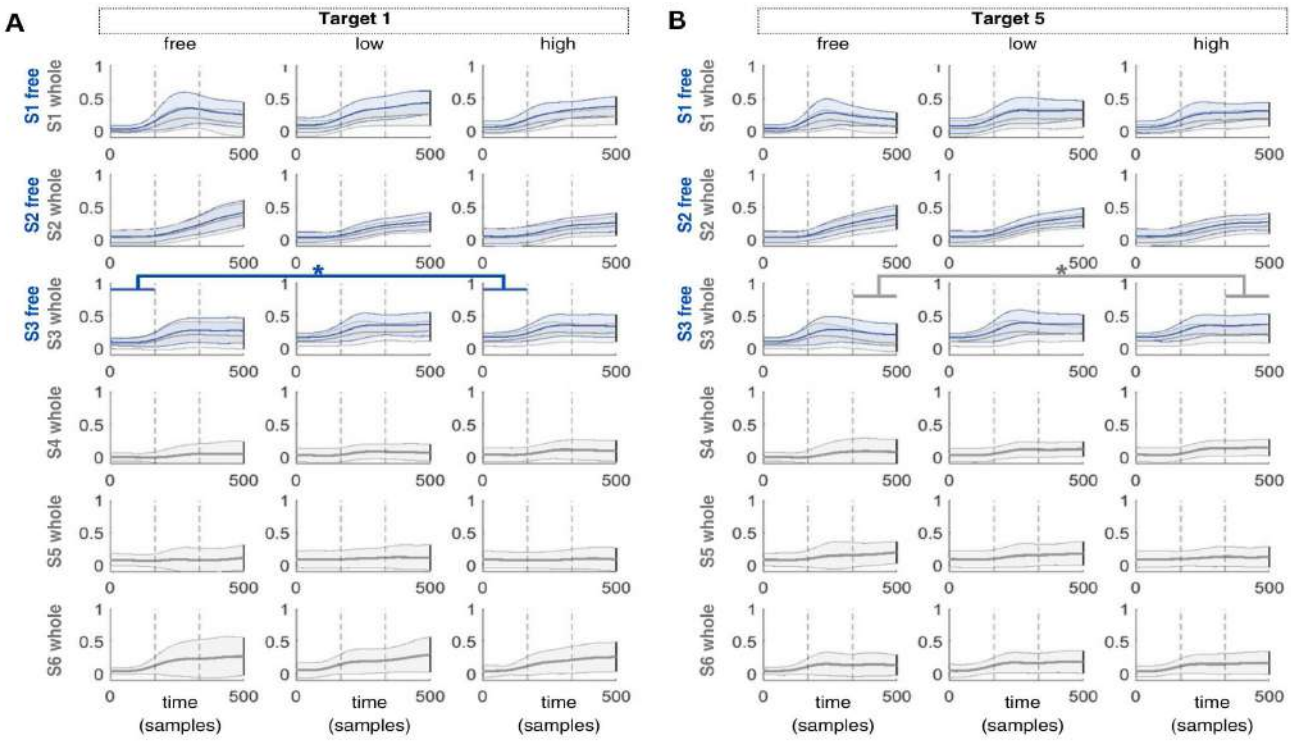


Fig. 5. Activation coefficients for movements towards target 1 (A) and target 5 (B). The solid lines represent the mean and the shaded areas the standard deviation over subjects. In blue are reported the coefficients of the free dataset synergies and in gray the ones of whole dataset synergies. Horizontal blue/gray brackets over the temporal coefficients indicate a statistical difference between the coefficients of free and of the whole dataset synergies for that time interval.

(ii) the use of the exoskeleton enforces increased activation of the upper trapezius.

A. Synergistic structure of reaching

The 3 free dataset synergies (Fig. 2 B) are coherent with previous literature investigating frontal reaching [15]. s1_free mainly expresses biceps and brachioradialis and enforces elbow flexion; s2_free mainly expresses the deltoids with a prevalence of the anterior deltoid and enforces shoulder flexion and abduction, while s3_free mainly expresses the trapezius muscle with a prevalence of upper trapezius, stabilizing and rotating the scapula upwards. The high similarity between these synergies and the first three synergies of the whole dataset suggests that the fundamental synergistic structure of reaching is preserved when movement is assisted by Float.

Moreover, 3 additional synergies emerge in the whole dataset (s4_whole, s5_whole, s6_whole, Fig. 2 C), which express mainly the middle trapezius, lower trapezius, and pectoralis. These muscle groups are present with a significant activation also in the free dataset synergies (Fig. 2 B): middle and lower trapezius are active in s3_free and pectoralis in s1_free. This suggests that a simplified yet efficient actuation of the shoulder and elbow joints is obtained in the free condition, while the control of joint movements appears fragmented into the activation of single muscles or couples of muscles when including the movement with the robotic assistance.

B. Modulation of synergy recruitment

We found significantly higher activation coefficients of high vs free conditions for s3_free and s3_whole (Table I). This occurred in the initial phase of movement towards targets 1 and 2 and in the final phase of movement towards target 9 for s3_free as well as in the final phase of movement towards target 5 in s3_whole. Both s3_free and s3_whole represent trapezius activation, making the increased activity of this muscle during assisted movement appear counterintuitive. However this could be attributed to the presence of the corset that constitutes the interface between Float and the user, as it forces the user to maintain a posture more rigid and straighter with respect to the natural sitting position. Moreover, we observed that in the initial phase of movement, s3_free presents a significantly higher tonic activity in high with respect to the free condition, probably generated to counterbalance the exoskeleton's weight (Fig. 5 A). We thus hypothesize that a high assistance during shoulder flexion increases the weight perceived by the user on the shoulder complex. To reduce this effect, joint 2 of Float (Fig. 1) should cooperate with the upper trapezius muscle in supporting scapula elevation.

Future work foresees examination on the effect of assistance on the phasic and tonic component of muscle activity [10].

C. Implications for exoskeleton design

Our data suggest that joint 2 acts in resistance to the action of upper trapezius, in particular in the initial phase

of movement. This could be due to the model-based friction compensation of the exoskeleton. This model compensates friction by providing a low-frequency sinusoidal voltage to the motors if the velocity is null. Otherwise, for non-null velocities, it models friction torque as a function of angular velocity. Such model, although sub-optimal, has proven to be effective when movements are performed slowly and continuously as it occurs during rehabilitation sessions. In our case study, the limitations of this model-based friction compensation were more evident, since we tested self-paced functional movements in healthy subjects. Especially in movements towards higher targets (i.e., 1 and 2) performed with high assistance, the friction compensation resulted ineffective. This lead to a greater tonic activation of the trapezius muscle (in particular the upper portion) to elevate the scapula and counterbalance the inertia perceived.

Currently, Float provides assistance exclusively on joint 4 (Fig. 1, Sec. II-B), which actuates purely shoulder flexion. This assistance reduces the synergies' activation for shoulder flexion (Fig. 5 A-B). We thus propose that implementing a feed forward assistance at joint 2 could be an effective strategy to reduce the described tonic activation of upper trapezius.

Moreover, Float reduces the activation coefficients of synergy 2 of free/whole dataset without altering the synergy pattern, similar to what happens when applying arm weight support [16]. This is highly promising as interventions with arm weight support have demonstrated to improve the reaching function both in healthy subjects and in stroke patients [17] [18]. Reducing the activation of anterior and middle deltoid could be beneficial for stroke patients, as it may counteract the abnormal coupling between shoulder abductors and elbow flexors that often affects stroke survivors [19]. Future works will extend this analysis to post-stroke subjects, to verify this hypothesis and whether model-based compensation of friction could affect already altered patterns of motor production.

V. Conclusion

This work exploits the NeBULA framework to compute standardized metrics, allowing objective characterization of movement's performance. We applied muscle synergy analysis to quantitatively describe the effects of the assistance of Float on the structural organization of reaching movements and found that synergistic organization of reaching is mainly preserved during assisted movements. Moreover, this study characterized the potential benefits and limitations of Float for shoulder rehabilitation interventions, by studying its impact on the patterns of muscle activity of healthy individuals. These findings have direct implications on Float control strategies and therapeutic interventions, aiming at enhancing its design to maximize its beneficial impact.

ACKNOWLEDGMENT

We special thank members of Rehab Technologies Lab for continuous support during the project. We also thank L. De Michieli, M. Laffranchi and A. Turolla for useful discussion.

References

[1] J. M. Veerbeek *et al.*, "What is the evidence for physical therapy poststroke? A systematic review and meta-analysis," PLoS One, vol. 9, no. 2, p. e87987, 2014, doi: 10.1371/journal.pone.0087987.

[2] M. Semprini *et al.*, "Technological Approaches for Neurorehabilitation: From Robotic Devices to Brain Stimulation and Beyond," Front Neurol, vol. 9, p. 212, Apr. 2018, doi: 10.3389/fneur.2018.00212.

[3] R. Iandolo *et al.*, "Perspectives and Challenges in Robotic Neurorehabilitation," Applied Sciences, vol. 9, no. 15, Art. no. 15, Jan. 2019, doi: 10.3390/app9153183.

[4] F. Garro, M. Chiappalone, S. Buccelli, L. De Michieli, and M. Semprini, "Neuromechanical Biomarkers for Robotic Neurorehabilitation," Front. Neurorobot., vol. 15, Oct. 2021, doi: 10.3389/fnbot.2021.742163.

[5] E. Bizzi, V. C. K. Cheung, A. d'Avella, P. Saltiel, and M. Tresch, "Combining modules for movement," Brain Research Reviews, vol. 57, no. 1, pp. 125–133, Jan. 2008. DOI: 10.1016/j.brainresrev.2007.08.004.

[6] A. d'Avella, P. Saltiel, and E. Bizzi, "Combinations of muscle synergies in the construction of a natural motor behavior," Nat Neurosci, vol. 6, no. 3, pp. 300–308, Mar. 2003, doi: 10.1038/nn1010.

[7] V. C. K. Cheung *et al.*, "Muscle synergy patterns as physiological markers of motor cortical damage," Proc Natl Acad Sci U S A, vol. 109, no. 36, pp. 14652–14656, Sep. 2012, doi: 10.1073/pnas.1212056109.

[8] S. Buccelli *et al.*, "A gravity-compensated upper-limb exoskeleton for functional rehabilitation of the shoulder complex," Applied Sciences, vol. 12, no. 7, p. 3364, Jan. 2022. DOI: 10.3390/app12073364.

[9] F. Garro *et al.*, "NeBULA: A standardized protocol for the benchmarking of robotic-based upper limb neurorehabilitation," in 2023 45th Annual International Conference of the IEEE Engineering in Medicine & Biology Society (EMBC), Sydney, Australia, Jul. 2023, pp. 1–4. DOI: 10.1109/EMBC40787.2023.10340242.

[10] A. d'Avella, A. Portone, L. Fernandez, and F. Lacquaniti, "Control of fast-reaching movements by muscle synergy combinations," The Journal of Neuroscience, vol. 26, no. 30, pp. 7791–7810, Jul. 2006. DOI: 10.1523/JNEUROSCI.0830-06.2006.

[11] A. Cancrini, P. Baitelli, M. L. Nicora, M. Malosio, A. Pedrocchi, and A. Scano, "The effects of robotic assistance on upper limb spatial muscle synergies in healthy people during planar upper-limb training," PLOS ONE, vol. 17, no. 8, p. e0272813, Aug. 2022. DOI: 10.1371/journal.pone.0272813.

[12] M. Semprini, A. V. Cuppone, I. Delis, V. Squeri, S. Panzeri, and J. Konczak, "Biofeedback signals for robotic rehabilitation: Assessment of wrist muscle activation patterns in healthy humans," IEEE Transactions on Neural Systems and Rehabilitation Engineering, vol. 25, no. 7, pp. 883–892, Jul. 2017. DOI: 10.1109/TNSRE.2016.2636122.

[13] D. D. Lee and H. S. Seung, "Learning the parts of objects by non-negative matrix factorization," Nature, vol. 401, no. 6755, pp. 788–791, Oct. 1999, doi: 10.1038/44565.

[14] R. Penrose, "A generalized inverse for matrices," Mathematical Proceedings of the Cambridge Philosophical Society, vol. 51, no. 3, pp. 406–413, Jul. 1955, doi: 10.1017/S0305004100030401.

[15] A. Scano, L. Dardari, F. Molteni, H. Giberti, L. M. Tosatti, and A. d'Avella, "A Comprehensive Spatial Mapping of Muscle Synergies in Highly Variable Upper-Limb Movements of Healthy Subjects," Front. Physiol., vol. 10, Sep. 2019, doi: 10.3389/fphys.2019.01231.

[16] M. Coscia *et al.*, "The effect of arm weight support on upper limb muscle synergies during reaching movements," Journal of NeuroEngineering and Rehabilitation, vol. 11, no. 1, p. 22, Mar. 2014, doi: 10.1186/1743-0003-11-22.

[17] G. B. Prange *et al.*, "Influence of gravity compensation on muscle activity during reach and retrieval in healthy elderly," J Electromyogr Kinesiol, vol. 19, no. 2, pp. e40-49, Apr. 2009, doi: 10.1016/j.jelekin.2007.08.001.

[18] G. B. Prange, M. J. A. Jannink, A. H. A. Stienen, H. van der Kooij, M. J. Ijzerman, and H. J. Hermens, "Influence of gravity compensation on muscle activation patterns during different temporal phases of arm movements of stroke patients," Neurorehabil Neural Repair, vol. 23, no. 5, pp. 478–485, Jun. 2009, doi: 10.1177/1545968308328720.

[19] [1] T. M. Sukal, M. D. Ellis, and J. P. A. Dewald, "Shoulder abduction-induced reductions in reaching work area following hemiparetic stroke: neuroscientific implications," Exp Brain Res, vol. 183, no. 2, pp. 215–223, Nov. 2007, doi: 10.1007/s00221-007-1029-6.

Concurrent Learning Augmented DNN-based and Admittance Control of a Hybrid Exoskeleton

Sujata Basyal*, Kislaya Mishra*, Jonathan Ting*, Brendon Allen*

***Abstract*—People suffering from neurological conditions (NCs) can benefit from motorized functional electrical stimulation (FES)-based rehabilitation equipment, called hybrid exoskeletons. These hybrid exoskeletons incorporate muscle-motor interaction that requires both the control of human muscles (i.e., FES) and robot motors to obtain a desirable performance. Two types of controllers (deep neural networks (DNN)-based and Admittance-based) were developed in this paper for a hybrid exoskeleton to control both human muscles and the exoskeleton's motors. The uncertain dynamics of the hybrid exoskeleton are approximated by DNN to enable efficient FES control. The approximated DNN weights and biases were implemented in a control law where they were updated in multiple timescales. Specifically, the inner-layer DNN weights were updated iteratively offline while the outer-layer weights were updated online in real-time. The update law for the output-layer DNN weights was augmented with a concurrent learning (CL) inspired term to improve the learning performance of the DNN and, consequently, the overall system performance. The admittance-based motor controller uses torque feedback and desired torque contribution from the participant to modify the motor's desired trajectory without forcing the participant to follow along predetermined trajectories and to promote the overall safety of the system. A Lyapunov-based stability analysis was completed for both control systems to ensure overall system performance.**

I. Introduction

In America, neurological conditions (NCs) such as cerebral palsy, spinal cord injury, neuromuscular disorders, and Parkinson's disease, affect millions of people and account for billions of annual medical expenses each year [1]–[5] which negatively affects the quality of life of the individuals. The majority of patients with NCs have restricted muscular movement, which may contribute to further secondary health issues like diabetes, obesity, etc [6]–[10]. To address the variety of health issues brought by muscle inactivity, different rehabilitation exercises have been introduced that increase muscle mobility and ultimately improve an individual's health condition. Unfortunately, individuals with NCs might not have the strength or motor control necessary for rehabilitative exercises using traditional machines, which makes it challenging to reach the exercise intensities necessary to reap the advantages of training.

*Department of Mechanical Engineering, Auburn University, Auburn AL 36849-0001, USA Email: {szb0233, kzm0074, jat0076, bca0027}@auburn.edu

This research is supported in part by NSF award number 2230971. Any opinions, findings and conclusions, or recommendations expressed in this material are those of the author(s) and do not necessarily reflect the views of the sponsoring agency.

In order to compensate for the limitations of traditional rehabilitation tools and techniques, functional electrical stimulation (FES) was introduced for rehabilitation training. FES aids the individual in attaining the adequate threshold for exercise intensity, improving neuromuscular conditions. FES sends electrical pulses to the neuromuscular complex, which induces artificial, involuntary contractions in particular muscles, resulting in the functional movement of a body part [11], [12]. However, FES-based control involves a combination of continuous and discrete dynamics which consequently results in a jump discontinuity in the dynamics. Careful control of FES-based systems is necessary to facilitate the intended neuromuscular restoration. Hybrid exoskeletons that integrate FES control with rehabilitation machines have proven to improve musculoskeletal and cardiorespiratory fitness as well as other neurological, physiological, and psychological measures [13].

The majority of prior control strategies for hybrid exoskeletons focus on tracking desired position or force trajectories (cf. [14]–[16]). However, these trajectory-based control schemes are unable to provide customized control for each person because they are designed to follow the same basic trajectory and torque objective. The admittance control approach developed by [17] is a suitable addition since it strikes a balance between force and position control [18]–[24]. Implementing admittance control to the control structure enables the indirect tracking of desired torques, thereby augmenting the human-robot interaction experience. Admittance-based control is more concerned with a system's dynamic performance than its explicit position and torque tracking. It offers a clever approach for robots to engage with humans in a safe manner by resolving conflicts in motion between the humans and robots. The admittance parameter can be modified [25], [26] based on individual need for support or to oppose torque required during rehabilitation exercise [27]. Although admittance control is considered to be safer than a general force tracking controller, improper selection of a control parameter might result in the instability of the overall system. Therefore, a stability analysis of the developed controller is required to guarantee a stable response of the system.

The primary objective of this paper is to develop a safe and stable control law for a hybrid exoskeleton that is used in rehabilitation. Therefore in this paper, a DNN- and admittance-based control framework for a hybrid exoskeleton is developed. Specifically, DNNs were used to approximate the complex dynamics of a hybrid exoskeleton and were inte-

grated into the FES controller. Admittance is integrated into the motor controller of the hybrid exoskeleton to indirectly track a desired torque trajectory. An advantage of DNN-based FES control is that it is an adaptive control approach and can be adjusted according to user dynamics. High FES inputs can be uncomfortable and result in a rapid onset of fatigue, which could impede rehabilitation. In this work, the inner-layer weight and biases of the DNNs are updated offline; whereas, the output-layer weights are updated online using a Lyapunov-based adaptive update law. In an effort to improve the DNN performance, this work builds upon the authors' preliminary works in [28], [29] to augment the real-time output-layer DNN update law with concurrent learning (CL) inspired terms for the first time in a hybrid exoskeleton (i.e, dynamic model with two inputs). CL is a data-based approach that uses both current and past data concurrently to enable the output-layer DNN weights to converge to a small neighborhood around their ideal values. This work represents the first to develop a closed-loop admittance and DNN-based control scheme, the first to develop a DNN-based controller for a multi-joint hybrid exoskeleton, and the first to augment the DNN with CL for a hybrid exoskeleton system. The FES system presented unique challenges due to its switched nature that were solved in this work. Lyapunov-based stability and passivity analyses were performed to ensure semi-global uniformly ultimately bounded position tracking of FES controller and passivity of the admittance controllers in addition to global tracking of the admittance errors. Finally, a preliminary simulation was done to evaluate the performance of the proposed control approach.

II. Dynamics

The switched, nonlinear dynamic model for an FES-based n-joint rehabilitation robotic system can be modeled as[1]

$$M(q)\ddot{q} + C(q,\dot{q})\dot{q} + G(q) + P(q,\dot{q}) + F\dot{q} + d(t) = \underbrace{B_F(q,\dot{q},t)u_f(t)}_{\tau_{FES}(q,\dot{q},t)} + \underbrace{B_{mor}u_{mor}(t)}_{\tau_{motor}(t)}, \tag{1}$$

where $q : \mathbb{R}_{\geq 0} \to \mathcal{Q}^n$ denotes measurable joint angles, $Q^n \subseteq R^n$ denotes the set of all possible joint angles for the rehabilitation robot, and $\dot{q} : \mathbb{R}_{\geq 0} \to \mathbb{R}^n$ and $\ddot{q} : \mathbb{R}_{\geq 0} \to \mathbb{R}^n$ denote the measurable joint angular velocities and unmeasurable joint angular accelerations, respectively. The dynamic functions $M : \mathcal{Q}^n \to \mathbb{R}^{n\times n}$, $C : \mathcal{Q}^n \times \mathbb{R}^n \to \mathbb{R}^{n\times n}$, $G : \mathcal{Q}^n \to \mathbb{R}^n$, $P : \mathcal{Q}^n \times \mathbb{R}^n \to \mathbb{R}^n$, $F \in \mathbb{R}^{n\times n}$, and $d : \mathbb{R}_{\geq 0} \to \mathbb{R}^n$ denote the inertia matrix, centripetal-Coriolis matrix, gravitational effects, viscoelastic tissue effects, viscous coefficient matrix, and unknown disturbances, respectively. The torques applied to each joint by the exoskeleton's electric motors are denoted by $\tau_{motor} : \mathbb{R}_{\geq 0} \to \mathbb{R}^n$ and are defined as $\tau_{motor} = B_{mor}u_{mor}(t)$, where $B_{mor} \in \mathbb{R}^{n\times n}$ denotes the known current to torque scaling factor for the motor and $u_{mor} : \mathbb{R}_{\geq 0} \to \mathbb{R}^n$ denotes the motor input. The torque generated from FES is defined as $\tau_{FES} = B_F(q,\dot{q},t)u_f(t)$, where $u_f : \mathbb{R}_{\geq 0} \to \mathbb{R}^n$ denotes the FES control input and $B_F : \mathcal{Q}^n \times \mathbb{R}^n \times \mathbb{R}_{\geq 0} \to \mathbb{R}^{n\times n}$ denotes the diagonal and unknown lumped FES control effectiveness matrix and is defined as

$$B_{F,i}(q,\dot{q},t) \triangleq \sum_{m\in\mathcal{M}_i} B_m(q_i,\dot{q}_i,t)\,k_m\sigma_m(u_{f,i}(t)), \forall i \in \mathcal{N} \tag{2}$$

where, $\mathcal{N} \triangleq \{1, 2, \ldots, n\}$, $B_{F,i}$ denotes the i^{th} diagonal element of B_F (i.e., $B_{F,i}$ is the lumped FES effectiveness about the i^{th} joint of the exoskeleton), q_i and $\dot{q}_i$ are the i^{th} joint's angular position and velocity, respectively, $\mathcal{M}_i$ is the set of muscles that produce forces about the i^{th} joint and is defined as $\mathcal{M}_i \triangleq \{Ag_i, An_i\}$, Ag_i and An_i denote the agonist and antagonist muscle groups acting about the i^{th} joint, and u_i is the FES input associated with the i^{th} joint. Furthermore, for each muscle $m \in \mathcal{M}_i$ and $\forall i \in \mathcal{N}$, $k_m \in \mathbb{R}_{>0}$ denotes a selectable constant, $B_m : \mathcal{Q}\times\mathbb{R}\times\mathbb{R}_{\geq 0} \to \mathbb{R}$ denotes the muscle's unknown stimulation-to-torque scaling factor, and $\sigma_m : \mathbb{R} \to \{0, 1, -1\}$ denotes a piecewise constant FES switching signal. The stimulation input into the m^{th} muscle is denoted by $u_m : \mathbb{R}_{\geq 0} \to \mathbb{R}$ and is defined as $u_m(t) \triangleq k_m\sigma_m(u_{f,i}(t))u_{f,i}(t)$. The FES switching signal $\sigma_m, \forall m \in \mathcal{M}$, must be designed in such a way that B_F defined in (2) remains invertible to facilitate the subsequent analysis. The switching signal σ_m can be defined $\forall m \in \mathcal{M}_i$ and $\forall i \in \mathcal{N}$ as

$$\sigma_{Ag_i}(u_{f,i}) \triangleq \begin{cases} 1, & u_{f,i} \geq 0 \\ 0, & u_{f,i} < 0 \end{cases}$$
$$\sigma_{An_i}(u_{f,i}) \triangleq \begin{cases} -1, & u_{f,i} < 0 \\ 0, & u_{f,i} \geq 0 \end{cases}. \tag{3}$$

The switching signal in (3) allows for an agonist-antagonist muscle pair to be effectively treated as a single actuator with a lumped FES control effectiveness $B_{F,i}$ and FES input $u_{f,i}$, where positive $u_{f,i}$ is applied across an electrode on the agonist muscle and negative $u_{f,i}$ is applied across an electrode on the antagonist muscle. It should be noted that the stimulation input into a muscle must be positive. This factor motivated the use of a -1 in the antagonist switching signal in (3). Furthermore, it should be noted that $B_m > 0$ for agonist muscles and $B_m < 0$ for antagonist muscles. Consequently, the design of (3) ensures that $B_{F,i}$ is continuous and that $B_{F,i} > 0$ always holds, and thus B_f^{-1} always exists. The dynamics in (1) have the following common properties:

Property 1. The inertial matrix M can be upper and lower bounded as $c_m \leq \|M(q)\| \leq c_M$, where $c_m, c_M \in \mathbb{R}_{>0}$ are known constants and $\|\cdot\|$ is the standard Euclidean norm.

Property 2. The centripetal-Coriolis matrix satisfies $C(q,x)v = C(q,v)x, \quad \forall x, v \in \mathbb{R}^n$ and can be upper bounded such that $\|C(q,\dot{q})\| \leq c_C\|\dot{q}\|$, where $c_C \in \mathbb{R}_{>0}$ is a known constant.

[1]For the notational brevity, all explicit dependence on time, t, within the terms $q(t)$, $\dot{q}(t)$, and $\ddot{q}(t)$ is suppressed.

Property 3. The gravitational constant, viscoelastic tissue effects, viscous coefficient, and unknown disturbances can be upper bounded as $\|G(q)\| \leq c_G$, $\|P(q,\dot{q})\| \leq c_{P1} + c_{P2}\|\dot{q}\|$, $\|F\| \leq c_F$, and $\|d(t)\| \leq c_D, \forall t \geq t_0$, where c_G, c_{P1}, c_{P2}, c_F, and $c_D \in \mathbb{R}_{>0}$ are the known constants and $t_0 \in \mathbb{R}_{\geq 0}$ is the initial time.

Property 4. The system follows the skew-symmetric property such that the centripetal-Coriolis effects and the time derivative of the inertial effects satisfy $x^T\left(\frac{1}{2}\dot{M}(q) - C(q,\dot{q})\right)x = 0,\ \forall x \in \mathbb{R}^n$.

Property 5. The torque generated by FES, $B_F(q,\dot{q},t)\,u_f(t)$, can be linearly parameterized as

$$B_F(q,\dot{q},t)\,u_f(t) = Y(q,\dot{q},t,u_f(t))\,\theta, \tag{4}$$

where $Y(q,\dot{q},t,u_f(t)) \in \mathbb{R}^{n\times g}$ is a measurable regression matrix, $g \in \mathbb{N}$ is the number of unknown parameters in the unknown lumped FES control effectiveness matrix, and $\theta \in \mathbb{R}^g$ is a constant vector with unknown terms. The i^{th} component of the unknown vector θ, θ_i, can be bounded as $\underline{\theta}_i \leq \theta_i \leq \overline{\theta}_i$ where $\underline{\theta}_i$ and $\overline{\theta}_i \in \mathbb{R}_{>0}$ are lower and upper bounds of θ_i for all i, respectively. Since B_F is unknown, an approximation is necessary to facilitate the control development which can be done by an estimation of the FES torque, denoted as $\hat{\tau}_{FES}$, and defined as $\hat{\tau}_{FES} \triangleq \hat{B}_F u_f$, where $\hat{B}_F(q,\dot{q},t) : \mathcal{Q}^n \times \mathbb{R}^n \times \mathbb{R}_{\geq 0} \to \mathbb{R}^{n\times n}$ is an estimate of $B_F(q,\dot{q},t)$. Note that the estimate of the FES torque can expressed as

$$\hat{B}_F(q,\dot{q},t)\,u_f(t) = Y(q,\dot{q},t,u_f(t))\,\hat{\theta}, \tag{5}$$

where $\hat{\theta} \in \mathbb{R}^q$ is an estimate of θ.

Property 6. The difference between the unknown vector θ and its estimate $\hat{\theta}$ can be quantified as a parameter estimation error $\tilde{\theta} \in \mathbb{R}^g$, which is defined as $\tilde{\theta} \triangleq \theta - \hat{\theta}$.

III. Controller Development

In the subsequent sections, an admittance control system is developed for the system's motors to ensure safety and a DNN-based FES control system is developed to track a desired trajectory within FES regions. The admittance controller is developed to be passive with respect to the FES torque and is designed to help the individual indirectly track a desired torque. The DNN-based controller is augmented with a Lyapunov-based CL update law which guarantees convergence of the output-layer DNN weights towards a neighborhood of their ideal values.

A. Admittance Controller

The admittance-based motor controller uses force feedback to modify the motors desired trajectory, allowing the exoskeleton to safely interact with the participant without forcing them to adhere to predefined trajectories. Admittance control is commonly used for tracking torque indirectly by employing an interaction torque error, denoted as $e_\tau : \mathbb{R}^n \times \mathbb{R}_{\geq 0} \to \mathbb{R}^n$, which is defined as $e_\tau \triangleq \tau - \tau_d$, where $\tau, \tau_d : \mathbb{R}_{\geq 0} \to \mathbb{R}^n$ denote the actual and desired interaction torques between the exoskeleton and the participant. As is typically the case, the interaction torque is assumed to be measurable and bounded (i.e., $\tau \in \mathcal{L}_\infty$). A feature of admittance control is that it will enable the motors to assist or resist the participant as is required. The trajectory for the admittance control law can be obtained by implementing an admittance filter defined as[2]

$$e_\tau \triangleq M_d\ddot{q}_a + B_d\dot{q}_a + K_d q_a, \tag{6}$$

where $q_a,\ \dot{q}_a,\ \ddot{q}_a : \mathbb{R}_{\geq 0} \to \mathbb{R}^n$ denote the admitted trajectory, and $M_d, B_d, K_d \in \mathbb{R}^{n\times n}$ represent the desired inertia, damping, and stiffness, respectively, selected to ensure that $q_a,\ \dot{q}_a,\ \ddot{q}_a \in \mathcal{L}_\infty$ (i.e., the transfer function of the filter is passive [30, Lemma 6.4]). The tracking performance of the admittance controller can be quantified using an admittance error system defined as

$$\xi(t) \triangleq q_a(t) + q_d(t) - q(t), \tag{7}$$

where $q_d : \mathbb{R}_{\geq 0} \to \mathbb{R}^n$ denotes the desired angular joint positions. The desired angular position, its derivative, and its double derivative are designed to be bounded such that $q_d,\ \dot{q}_d,$ and $\ddot{q}_d \in L_\infty$. The auxiliary admittance error denoted as $\Psi : \mathbb{R}_{\geq 0} \to \mathbb{R}^n$ can be defined as

$$\Psi(t) \triangleq \dot{\xi}(t) + \beta\xi(t), \tag{8}$$

where $\beta \in \mathbb{R}_{>0}$ is a known constant. Notice that if the participant is generating the desired torque that the admitted trajectory generated from (6) will be approximately zero, which will cause the admittance controller to drive the exoskeleton towards q_d. The open-loop error dynamics for the admittance-based system can be obtained by taking the time derivative of (8), multiplying it by M, and substituting in (1), (7), and (8), and is represented as

$$M\dot{\Psi} = -C\Psi - B_F u_f - B_{mor}u_{mor} + \chi_1, \tag{9}$$

where χ_1 represents an auxiliary signal that is defined as $\chi_1 \triangleq M\ddot{q}_a + M\beta\dot{\xi} + M\ddot{q}_d + C(\dot{q}_a + \dot{q}_d + \beta\xi) + G + P + F\dot{q} + d$ and can be upper bounded using Properties 1-3 such that $\|\chi_1\| \leq c_t + c_u\|\phi\| + c_v\|\phi\|^2$, where $c_t,\ c_u,$ and $c_v \in \mathbb{R}_{\geq 0}$ are known constants, and the error vector $\phi \in R^{5n}$ is defined as $\phi \triangleq \left[\xi^T,\ \Psi^T,\ q_a^T,\ \dot{q}_a^T,\ \ddot{q}_a^T\right]^T$. Based on the admittance open-loop error system in (9), an admittance controller is developed as

$$u_{mor} \triangleq B_{mor}^{-1}\left(k_1\Psi + (k_2 + k_3\|\phi\| + k_4\|\phi\|^2)\,\mathrm{sgn}(\Psi) + \xi\right), \tag{10}$$

where $k_1,\ k_2,\ k_3,$ and k_4 are user-selected constants and sgn$(\cdot)$ denotes the signum function. Substituting the controller in (10) into the open-loop error dynamics in (9) yields the closed-loop error dynamics as

$$\begin{aligned} M\dot{\Psi} = \ & -C\Psi - B_F u_f - k_1\Psi - \xi + \chi_1 \\ & - \left(k_2 + k_3\|\phi\| + k_4\|\phi\|^2\right)\mathrm{sgn}(\Psi). \end{aligned} \tag{11}$$

[2]For notational brevity, all functional dependencies are hereafter suppressed unless required for clarity of exposition.

B. DNN-based FES Controller

The tracking objective for the FES controller can be quantified using an angular position error denoted as $e : \mathbb{R}_{\geq 0} \to \mathbb{R}^n$ and is defined as

$$e \triangleq q_d - q. \tag{12}$$

The auxiliary position error for the dynamics (1) is denoted as $r : \mathbb{R}_{\geq 0} \to \mathbb{R}^n$ and can be defined as

$$r \triangleq \dot{e} + \alpha e, \tag{13}$$

where $\alpha \in \mathbb{R}_{>0}$ is a user-selectable constant. Using the position error in (12) and the auxiliary error in (13), the composite error vector $z : \mathbb{R}_{\geq 0} \to \mathbb{R}^{2n}$ is defined as $z \triangleq \left[r^T,\ e^T\right]^T$. Taking the time derivative of (13), multiplying it by M, and substituting in (1) and (12) yields the open-loop error system as

$$\begin{aligned} M\dot{r} &= M\ddot{q}_d + C\dot{q} + G + P + F\dot{q} + \chi_2 \\ &\quad -B_F u_f - B_{mor} u_{mor}, \end{aligned} \tag{14}$$

where the auxiliary term χ_2 is equal to $\chi_2 \triangleq M\alpha\dot{e} + d$. Using Properties 1 and 3, the auxiliary term can be upper bounded as $\|\chi_2\| \leq c_a + c_b \|z\|$, where c_a and c_b are known constants.

Property 7. Using the definition of z, Property 2, and the error definitions in (12) and (13), $C(q, \dot{q})$ can be upper bounded as $C \leq (c_d + c_e \|z\|)$, where c_d and c_e are known constants.

1) DNN Approximation: The uncertain dynamics in (1) are approximated using a DNN that is augmented with CL-inspired terms. To facilitate the CL development, the dynamics being approximated by a DNN are represented by a function, denoted as $f_1(x_1) : \mathbb{R}^{3n} \to \mathbb{R}^n$, and defined as

$$f_1(x_1) \triangleq M\ddot{q} + C\dot{q} + G + P + F\dot{q}, \tag{15}$$

where $x_1 \triangleq \left[q^T,\ \dot{q}^T,\ \ddot{q}^T\right]$. Substituting (15) into the dynamic model in (1) yields

$$f_1(x_1) + d = B_F u_f + B_{mor} u_{mor}. \tag{16}$$

However, $\ddot{q}$ is unknown in real-time and thus cannot be implemented in the control system. Consequently, the function f_1 can be rewritten as $f_2(x_2) : \mathbb{R}^{3n} \to \mathbb{R}^n$, which is defined as

$$f_2(x_2) \triangleq M\ddot{q}_d + C\dot{q} + G + P + F\dot{q}, \tag{17}$$

where $x_2 \triangleq \left[q^T,\ \dot{q}^T,\ \ddot{q}_d^T\right]$. Functions in (15) and (17) have similar form, however angular the acceleration $\ddot{q}$ in (15) has been replaced by desired acceleration $\ddot{q}_d$ in (17). A DNN will be developed to approximate f_2, called DNN2, and will be included in the FES control system since x_2 is known. However, the update laws for the DNN will include CL terms, which motivates the use of a DNN to approximate f_1, called DNN1 (otherwise bounds for $\ddot{q}$ would need to be determined a priori). Since the CL terms use previously recorded data, $\ddot{q}$ can be numerically determined and filtered prior to use in the CL framework. A multiple timescale approach is used to update both DNNs. Specifically, a gradient descent algorithm is used to retrain the inner-layers of the DNNs offline using data collected concurrent to real-time execution and the retrained DNNs can then be updated in batch updates. Furthermore, a Lyapunov-based adaptive law is used to update the output-layer DNN weights in real-time. Another challenge is that DNNs can only estimate functions that lie on a compact set, which requires x_1 and x_2 to be bounded. Let $\Omega \subset \mathbb{R}^{3n}$ be a simply connected compact set, then if $x_1, x_2 \in \Omega$, the functions (15) and (17) can be represented using the universal function of approximation theorem of neural networks.

For the function $f_1(x_1)$, there exists a DNN (named DNN1) with ideal biases, weights, and activation functions as per the universal function approximation theorem for neural networks such that it can be represented as

$$f_1(x_1) = W^T \varrho(\Phi_1(x_1)) + \epsilon_1(x_1), \tag{18}$$

where $W : \mathbb{R}_{\geq 0} \to \mathbb{R}^{u \times n}$ represents the ideal DNN output-layer weight matrix, $\varrho : \mathbb{R}^p \to \mathbb{R}^u$ represents the unknown vector of activation functions, $\Phi_1 : \mathbb{R}^n \to \mathbb{R}^p$ represents the unknown inner-layer weights and activation functions for DNN1, and $\epsilon_1 : \mathbb{R}^n \to \mathbb{R}^n$ represents the unknown reconstruction errors. The unknown inner-layers of DNN1 with unknown weights and activation functions can be represented as $\Phi_1 = V_{L_1}^T \phi_{L_1}(V_{L_1-1}^T \phi_{L_1-1}(V_{L_1-2}^T \phi_{L_1-2}(\ldots V_1^T \phi_1(x_1))$, where V_j represents the weights of the j^{th} inner-layer $\forall j \in [1, L_1]$, ϕ_j represents activation functions for the j^{th} inner-layer $\forall j \in [1, L_1]$, and $L_1 \in \mathbb{N}$ represents DNN1's number of inner-layers. The function $f_1(x_1)$'s DNN estimation can be denoted as $\hat{f}_{1,k} : \Omega \to \mathbb{R}^n$ and can be expressed as

$$\hat{f}_{1,k} = \widehat{W}^T \hat{\varrho}_{1,k}(\Phi_{1,k}(x_1)), \tag{19}$$

where $\widehat{W} : \mathbb{R}_{\geq 0} \to \mathbb{R}^{u \times n}$ represents the estimate of the output-layer weight matrix for DNN1, $\hat{\varrho}_{1,k} : \mathbb{R}^p \to \mathbb{R}^u$ represents the k^{th} estimate of the activation functions for DNN1's output-layer, and $\hat{\Phi}_{1,k} : \mathbb{R}^n \to \mathbb{R}^p$ represents the k^{th} estimate of the inner-layers of DNN1, and $k \in \mathbb{N}$ indexes the training iteration for DNN1.

Similarly, for the function $f_2(x_2)$, there exists a DNN (named DNN2) with ideal biases, weights, and activation functions as per the universal function approximation theorem for neural networks such that it can be expressed as

$$f_2(x_2) = W^T \varrho(\Phi_2(x_2)) + \epsilon_2(x_2), \tag{20}$$

where the terms in DNN2 are defined similarly to those in DNN1. The function $f_2(x_2)$'s DNN estimate can be denoted as $\hat{f}_{2,i} : \Omega \to \mathbb{R}^n$, and can be expressed as

$$\hat{f}_{2,i} = \widehat{W}^T \hat{\varrho}_{2,i}(\Phi_{2,i}(x_2)), \tag{21}$$

where $i \in \mathbb{N}$ indexes the training iteration for DNN2, $\hat{\varrho}_{2,i} : \mathbb{R}^p \to \mathbb{R}^u$ represents the i^{th} estimate of the activation functions for DNN2's output-layer, and $\hat{\Phi}_{1,i} : \mathbb{R}^n \to \mathbb{R}^p$ represents the i^{th} estimate of the inner-layers of DNN2. The

difference between the output-layer weight matrix and its estimate can be quantified by the weight estimation error $\widetilde{W}(t) : \mathbb{R}_{\geq 0} \to \mathbb{R}^{u \times n}$, which is defined as

$$\widetilde{W}(t) = W - \widehat{W}(t). \tag{22}$$

Property 8. The ideal output-layer DNN weights, W, the activation functions, ϱ, the function estimation errors of DNN1, ϵ_1, and DNN2, ϵ_2, and the estimate of the ideal activation functions for DNN1, $\hat{\varrho}_{1,k}$, and DNN2, $\hat{\varrho}_{2,i}$, can be upper bounded by $\overline{W}$, $\overline{\varrho}$, $\overline{\epsilon}_1$, $\overline{\epsilon}_2$, $\overline{\hat{\varrho}}_1$, $\overline{\hat{\varrho}}_2 \in \mathbb{R}_{>0}$, respectively, such that $\|W\| \leq \overline{W}$, $\|\varrho\| \leq \overline{\varrho}$, $\sup_{x_1(t)\in\Omega} \|\epsilon_1(x_1)\| \leq \overline{\epsilon}_1$, $\sup_{x_2(t)\in\Omega} \|\epsilon_2(x_2)\| \leq \overline{\epsilon}_2$, $\|\hat{\varrho}_{1,k}\| \leq \overline{\hat{\varrho}}_1, \forall k \in \mathbb{N}$, and $\|\hat{\varrho}_{2,i}\| \leq \overline{\hat{\varrho}}_2, \forall i \in \mathbb{N}$.[3] Additionally, the estimate of DNN1 is selected such that $\sup_{x_1(t)\in\Omega} \|\varrho(\cdot) - \hat{\varrho}_{1,k}(\cdot)\| \leq \overline{\tilde{\varrho}}, \forall k \in \mathbb{N}$, where $\overline{\tilde{\varrho}} : \mathbb{R}_{\geq 0}$ denotes a known constant.

2) Control Development: Substituting (17) into the open-loop error law in (14), adding and subtracting $Y\hat{\theta}$, and using Properties 5 and 6 yields

$$M\dot{r} = \chi_2 + f_2(x_2) - Y\widetilde{\theta} - B_{mor}u_{mor} - \hat{B}_F u_f. \tag{23}$$

A modified open-loop error system is developed by substituting (20) into (23), which can be expressed as

$$\begin{aligned} M\dot{r} = \; & \chi_2 + W^T\varrho(\Phi_2(x_2)) + \epsilon_2(x_2) - Y\widetilde{\theta} \\ & - B_{mor}u_{mor} - \hat{B}_F u_f. \end{aligned} \tag{24}$$

Based on (24), the controller for the FES input can be developed as

$$\begin{aligned} u_f \triangleq \; & \hat{B}_F^{-1}\sigma_s(q)\Big(k_5 r + e + \hat{f}_{2,i} + \\ & \left(k_6 + k_7\|z\| + k_8\|z\|^2 + k_u\|u_{mor}\|\right)\operatorname{sgn}(r)\Big), \end{aligned} \tag{25}$$

where k_5, k_6, k_7, k_8, and $k_u \in \mathbb{R}_{\geq 0}$ are user-defined constants and $\sigma_s(q)$ is a switching signal, defined as

$$\sigma_s(q) \triangleq \begin{cases} 1, & q \in \mathcal{Q}_{FES} \\ 0, & \text{otherwise} \end{cases}, \tag{26}$$

where $\mathcal{Q}_{FES} \subseteq \mathcal{Q}$ is a set of joint angles where the lumped FES control effectiveness is above a user-selected threshold (i.e., joint angles that correspond to effective FES-based torque production). Substituting (25) and (21) into (24) yields the closed-loop error system as

$$\begin{aligned} M\dot{r} = \; & \chi_2 + W^T\varrho(\Phi_2(x_2)) + \epsilon_2(x_2) - Y\tilde{\theta} \\ & - \sigma_s k_5 r - \sigma_s e - \sigma_s\widehat{W}^T\hat{\varrho}_{2,i}\left(\hat{\Phi}_{2,i}(x_2)\right) \\ & - \sigma_s\Big(k_6 + k_7\|z\| + k_8\|z\|^2 \\ & + k_u\|u_{mor}\|\Big)\operatorname{sgn}(r) - B_{mor}u_{mor}. \end{aligned} \tag{27}$$

Based on the subsequent stability analysis, the adaptive laws to estimate the unknown vector, θ, and the output-layer weight matrix, W, are denoted as $\dot{\hat{\theta}} \in \mathbb{R}^g$ and $\dot{\widehat{W}}(t) : \mathbb{R}_{\geq 0} \to \mathbb{R}^{u\times n}$ and are designed as[4]

$$\dot{\hat{\theta}} = -\text{proj}\left(\Gamma_2 Y^T(q, \dot{q}, t, u_f(t))\, r(t)\right), \tag{28}$$

$$\begin{aligned} \dot{\widehat{W}} = \; & \text{proj}\left(\Gamma_1\hat{\varrho}_{2,i}\left(\hat{\Phi}_{2,i}(x_2)\right) r^T\right. \\ & + k_{cl}\Gamma_1 \sum_{j=1}^{h} \hat{\varrho}_{1,k}\left(\hat{\Phi}_{1,k}(x_{1,j})\right) \\ & \left.\left(\tau_{total,j} - \widehat{W}^T\hat{\varrho}_{1,k}\left(\hat{\Phi}_{1,k}(x_{1,j})\right)\right)^T\right), \end{aligned} \tag{29}$$

where $\Gamma_1 \in \mathbb{R}^{u\times u}$ and $\Gamma_2 \in \mathbb{R}^{g\times g}$ are positive definite user-defined gains for the output-layer weights and the unknown constant parameter vector, respectively, proj$(\cdot)$ is the smooth projection function used in [31] and it is used to ensure that the unknown parameter estimates in $\hat{\theta}$ and the output-layer weight estimates in $\hat{W}$ stay within user-defined bounds, $k_{cl} \in \mathbb{R}_{\geq 0}$ is a user-selected control gain, $\tau_{total,j} \in \mathbb{R}^n$ is the total applied torque defined as $\tau_{total,j} \triangleq \hat{\tau}_{FES,j} + \tau_{motor,j}$, $\{x_{1,j}, \tau_{total,j}\}_{j=1}^{h}$ denotes the recorded history stack of previous states and total torque for the times corresponding to $t_j \leq t, \forall j$, and $h \in \mathbb{N}$ denotes the history stack size.

Property 9. Using Property 8 and the update laws presented in (29) the weight estimation error $\widetilde{W}$ defined in (22) can be upper bounded, by a known constant $\overline{\widetilde{W}} \in \mathbb{R}_{>0}$, such that $\left\|\text{vec}\left(\widetilde{W}\right)\right\| \leq \overline{\widetilde{W}}$. Furthermore, using Properties 5 and the update law in (28), the parameter estimation error $\widetilde{\theta}$ defined in Property 6 can be upper bounded as $\left\|\widetilde{\theta}\right\| \leq \overline{\widetilde{\theta}}$, where $\overline{\widetilde{\theta}} \in \mathbb{R}_{>0}$.

Assumption 1. There is sufficient excitation of the system over a finite duration of time such that $\lambda_{\min}(A_{el}) > \lambda_{ss} > 0, \forall t \geq T$, where $\lambda_{ss} \in \mathbb{R}_{>0}$ is a user-defined constant, $\lambda_{\min}$ is the minimum eigenvalue of $(\cdot)$, $T \in \mathbb{R}_{\geq 0}$ is finite time, and

$$A_{el} = \sum_{j=1}^{h} \hat{\varrho}_{1,k}\left(\hat{\Phi}_{1,k}(x_{1,j})\right)\hat{\varrho}_{1,k}\left(\hat{\Phi}_{1,k}(x_{1,j})\right)^T. \tag{30}$$

Data collected from previous experiments can be used to pre-train the estimation of the DNNs in (19) and (21). The initial estimates of inner-layers of the DNNs, $\hat{\Phi}_{1,1}(\cdot)$ and $\hat{\Phi}_{2,1}(\cdot)$, and the output-layer weights of both DNNs, $\widehat{W}$, can be determined by the pre-training of DNN1 and DNN2. The inner-layer weights of the DNNs are updated iteratively using traditional DNN training methods while the output-layer weight are updated in real-time using an update law comprised of CL terms. The states and inputs are collected in real-time and are used to train the inner-layer weights of the DNNs offline. Likewise, the states and input data

[3] DNN activation functions for both DNNs, $\hat{\varrho}_{1,k}\left(\hat{\Phi}_{1,k}(x_1)\right)$ and $\hat{\varrho}_{2,i}(\Phi_{2,i}(x_2))$, can be represented as $\hat{\varrho}_{1,k}$ as $\hat{\varrho}_{2,i}$, respectively, for notational brevity.

[4] The update law for the output-layer weights of the DNNs consists of two parts; an adaptation part, based on more traditional Lyapunov-based methods, and an innovative CL part. It should be noted that the adaptation part of the law comprises DNN2 terms and the CL part comprises DNN1 terms. Having two DNNs facilitates the numerical analysis, especially the analysis of the CL developments.

are collected in real-time and stored in the history stack for the CL law. Once the inner-layers of DNN1 and DNN2 are trained with sufficient data, these inner-layers are updated to develop the next iteration of the inner-layer DNN estimates, $\hat{\Phi}_{1,k+1}(\cdot)$ and $\hat{\Phi}_{2,i+1}(\cdot)$.

IV. Stability Analysis

To facilitate the following analysis, switching times are represented as $\left\{t_n^i\right\}, i \in \{s, e\}, n \in \{0, 1, 2, ...\}$, which represent the instants in time when σ_s becomes one ($i = s$) or zero ($i = e$). For the subsequent analysis, a positive definite storage function denoted as $V_1 : \mathbb{R}^{2n} \times \mathbb{R}_{\geq 0} \to \mathbb{R}_{\geq 0}$ is defined as

$$V_1 \triangleq \frac{1}{2}\Psi^T M \Psi + \frac{1}{2}\xi^T \xi, \tag{31}$$

where $\varsigma \in \mathbb{R}^{2n}$ is the concatenated error vector defined as $\varsigma \triangleq \left[\Psi^T,\ \xi^T\right]^T$. The storage function in (31) can be bounded using Property 1 such that $\rho_1 \|\varsigma\|^2 \leq V_1 \leq \rho_2 \|\varsigma\|^2$, where $\rho_1,\ \rho_2 \in \mathbb{R}_{\geq 0}$ are known constants and are defined as $\rho_1 \triangleq \min\left(\frac{1}{2}c_m, \frac{1}{2}\right)$ and $\rho_2 \triangleq \max\left(\frac{1}{2}c_M, \frac{1}{2}\right)$. For the stability analysis of a position tracking DNN-based controller, a common Lyapunov function candidate is denoted as $V_2 : \mathbb{R}^{n(2+u)+g} \times \mathbb{R}_{\geq 0} \to \mathbb{R}_{\geq 0}$ and is defined as

$$\begin{aligned} V_2(y,t) \triangleq\ & \tfrac{1}{2} r^T M r + \tfrac{1}{2} e^T e + \tfrac{1}{2}\text{trace}\left(\widetilde{W}^T \Gamma_1^{-1} \widetilde{W}\right) \\ & + \tfrac{1}{2}\widetilde{\theta}^T \Gamma_2^{-1} \widetilde{\theta}, \end{aligned} \tag{32}$$

where $y \in \mathbb{R}^{n(2+u)+g}$ is the concatenated state vector defined as $y \triangleq \left[r^T,\ e^T,\ \text{vec}\left(\widetilde{W}\right)^T,\ \widetilde{\theta}^T\right]^T$ and $\text{vec}(\cdot)$ is the vectorization of $(\cdot)$. The Lyapunov function candidate in (32) can be bounded using Properties 1 and 9 such that

$$\begin{aligned} \eta_1 \|z\|^2 &\leq V_2 \leq \eta_2 \|z\|^2 + w_1, \\ \eta_3 \|x\|^2 &\leq V_2 \leq \eta_4 \|x\|^2 + w_2, \\ \beta_1 \|y\|^2 &\leq V_2 \leq \beta_2 \|y\|^2, \end{aligned} \tag{33}$$

where $\eta_1 \triangleq \frac{1}{2}\min(c_m, 1)$, $\eta_2 \triangleq \frac{1}{2}\max(c_M, 1)$, $\eta_3 \triangleq \frac{1}{2}\min\left(\eta_1, \lambda_{\min}\left(\Gamma_1^{-1}\right)\right)$, $\eta_4 \triangleq \frac{1}{2}\max\left(\eta_2, \lambda_{\max}\left(\Gamma_1^{-1}\right)\right)$, $\beta_1 \triangleq \frac{1}{2}\min\left(\eta_3, \lambda_{\min}\left\{\Gamma_2^{-1}\right\}\right)$, $\beta_2 \triangleq \frac{1}{2}\max\left(\eta_4, \lambda_{\max}\left\{\Gamma_2^{-1}\right\}\right)$, $x \triangleq \left[r^T,\ e^T,\ \text{vec}\left(\widetilde{W}\right)^T\right]^T$, $w_1 \triangleq \frac{1}{2}\lambda_{\max}\left(\Gamma_1^{-1}\right)\overline{\widetilde{W}}^2 + \frac{1}{2}\lambda_{\max}\left(\Gamma_2^{-1}\right)\overline{\widetilde{\theta}}^2$, and $w_2 \triangleq \frac{1}{2}\lambda_{\max}\left(\Gamma_2^{-1}\right)\overline{\widetilde{\theta}}^2$.

Theorem 1. *For the admittance error dynamic model in (6) and the closed-loop admittance error law in (11), the admittance-based control input in (10) is passive from input $\|\tau_{FES}\|$ to output $\|\Psi\|$ provided that the gain conditions in (34) are satisfied.*

$$k_2 \geq c_t,\ k_3 \geq c_u,\ k_4 \geq c_v\ . \tag{34}$$

Additionally, when FES is not applied to the system (i.e. $\|\tau_{FES}\| = 0$), the admittance controller yields global exponential tracking such that

$$\|\varsigma(t)\| \leq \sqrt{\frac{\rho_2}{\rho_1}}\|\varsigma(t_0)\| \, exp\left(-\frac{\delta}{2\rho_2}(t - t_0)\right), \tag{35}$$

where $\delta \triangleq min(k_1, \beta), \forall t \in [t_0, \infty)$.

Proof: Let $\varsigma(t)$ be a Filippov solution for $t \in [t_0, \infty)$ to the differential inclusion $\dot{\varsigma} \in K[h_1](\varsigma)$, where $h_1 : \mathbb{R}^{2n} \to \mathbb{R}^{2n}$ is defined as $h_1 \triangleq \left[\dot{\xi}^T, \dot{\Psi}^T\right]^T$ and $K[\cdot]$ is the differential inclusion operator defined in [32]. Due to the discontinuity occurring in the admittance-based controller in (10), the derivative of V_1 exists almost everywhere (a.e.) for almost all $t \in [t_0, \infty)$ such that $\dot{V}_1(\varsigma) \overset{a.e.}{\in} \dot{\widetilde{V}}_1(\varsigma)$, where $\dot{\widetilde{V}}_1$ is the generalized derivative of (31). Taking the generalized derivative of (31), using the calculus of $K[\cdot]$ from [32] and Property 4, substituting in the closed-loop error dynamics in (11) and the auxiliary error in (8), and canceling common terms yields

$$\begin{aligned} \dot{\widetilde{V}}_1 \subseteq\ & -k_1 \Psi^T \Psi - \beta \xi^T \xi + \Psi^T \chi_1 - \Psi^T K[B_F u_f] \\ & - \left(k_2 + k_3\|\phi\| + k_4\|\phi\|^2\right)\Psi^T K[\text{sgn}(\Psi)]. \end{aligned} \tag{36}$$

Notice that the design of the switching signals in (3) ensure that B_F is always continuous. Consequently, $K[B_F u_f] = B_F u_f = \tau_{FES}$ when $q \in \mathcal{Q}_{FES}$ (i.e., when $\sigma_s = 1$) and $K[B_F u_f] = 0$ when $q \notin \mathcal{Q}_{FES}$. Considering the case when $q \in \mathcal{Q}_{FES}$ (i.e., $t \in [t_n^s, t_n^e), \forall n$), noting that $-\Psi^T K[\text{sgn}(\Psi)] \leq -\|\Psi\|$, using the upper bound of χ_1 from under (9) and the gain conditions in (34) yields an upper bound for (36) as

$$\dot{V}_1 \overset{\text{a.e.}}{\leq} -k_1\|\Psi\|^2 - \beta\|\xi\|^2 + \|\Psi\|\|\tau_{FES}\|, \tag{37}$$

$\forall t \in \left[t_n^e, t_{n+1}^s\right), \forall n$. As per definition 6.3 in [30], the exoskeleton system dynamics are strictly passive with $\|\tau_{FES}\|$ as the input, $\|\Psi\|$ as the output, and V_1 as the storage function. Considering times when $q \notin \mathcal{Q}_{FES}$ (i.e., $t \in \left[t_n^e, t_{n+1}^s\right), \forall n$) results in no FES forces being present (i.e., $\|\tau_{FES}\| = 0$). Consequently, the derivative in (37) can be further bounded by using the V_1 bound defined after (31) and the definitions of ς and δ as

$$\dot{V}_1 \overset{\text{a.e.}}{\leq} -\frac{\delta}{\rho_2}V_1,\ \forall t \in \left[t_n^e, t_{n+1}^s\right), \forall n. \tag{38}$$

Therefore, the storage function V_1, as per the zero-state observability condition defined in [30, Definition 6.5], can be considered as a positive definite (PD) Lyapunov function and results in global exponential admittance trajectory tracking when $\tau_{FES} = 0$. The result in (35) considers a scenario where FES is never applied (i.e., $\tau_{FES} = 0, \forall t$) and is obtained by solving (38) and using the bounds under (31). Recall that it was previously assumed that the participant's interaction torque is bounded, which requires that the FES-induced forces are likewise bounded. This is a reasonable assumption since human strength is finite and since all implemented FES systems saturate the FES input (often in an ad-hoc manner) to ensure participant comfort and safety.

Consequently, the passivity result in (37) and the result in (38) imply that $V_1 \in \mathcal{L}_\infty$, which implies that $\varsigma \in \mathcal{L}_\infty$ and thus that $\Psi\,, \xi \in \mathcal{L}_\infty$. Furthermore, recall that (6) is designed such that $q_a,\ \dot{q}_a,\ \ddot{q}_a \in \mathcal{L}_\infty$. Therefore, it can be proven that the motor controller in (10) is bounded. ■

Theorem 2. *For the closed-loop error law in (27) and for $q \in \mathcal{Q}_{FES}$, the DNN-based control input in (25) yields a bounded result prior to sufficient learning in the sense that*

$$\|y(t)\| \leq max\left(\sqrt{\frac{\beta_2}{\beta_1}}\|y(t_0)\|, \sqrt{\frac{v_1}{\delta_1\beta_1}}\right), \tag{39}$$

$\forall t \in [t_0, T) \cap [t_n^s, t_n^e)$, *where* $\delta_1 \triangleq \frac{min(\alpha, k_5)}{\eta_2}$ *and* $v_1 \triangleq \frac{min(\alpha, k_5)}{\eta_2} w_1 + C_1\widetilde{\overline{W}}$, *and semi-global exponential convergence toward an ultimate bound after learning has been completed in the sense that*

$$\begin{aligned}\|y(t)\|^2 \quad \leq \quad & \tfrac{\beta_2}{\beta_1}\|y(t_n^s)\|^2 \exp\left(-\delta_2(t-t_n^s)\right) \\ & + \tfrac{v_2}{\delta_2\beta_1}\left[1-\exp\left(-\delta_2(t-t_n^s)\right)\right],\end{aligned} \tag{40}$$

$\forall t \in [T, \infty) \cap [t_n^s, t_n^e)$, *where* $\delta_2 \triangleq \frac{min\left(k_z, \frac{1}{2}k_{cl}\lambda_{ss}\right)}{\eta_4}$ *and* $v_2 \triangleq \frac{min\left(k_z, \frac{1}{2}k_{cl}\lambda_{ss}\right)}{\eta_4} w_2 + \frac{C_1^2}{2k_{cl}\lambda_{ss}}$, *provided that the subsequent gain conditions are satisfied:*

$$\begin{aligned} k_6 &\geq c_a + \overline{W}\left(\overline{\varrho} + \overline{\hat{\varrho}}_2\right) + \overline{\epsilon}_2 \\ k_7 &\geq c_b + c_d,\ k_8 \geq c_e,\ k_u \geq c_{b_m}. \end{aligned} \tag{41}$$

Proof: Taking a generalized derivative of (32) using a procedure similar to Theorem 1, substituting in the closed-loop error dynamics in (27), the adaptive laws in (28) and (29), the auxiliary error law in (13), and the estimation errors in (22) and Property 6, using Property 4 and the properties of the trace and vectorization operators, considering the case when FES forces are present (i.e., $[t_n^s, t_n^e), \forall n$ such that $K[\sigma_s] = 1$) and an arbitrary $k \in \mathbb{N}$ and $i \in \mathbb{N}$ such that terms with subscript i and k are continuous, using the gain conditions in (41), the fact that $\|r\| \leq \|z\|$ and $-r^T K[\text{sgn}(r)] \leq -\|r\|$, adding and subtracting terms, noting that $\|B_{mor}\| \leq c_{b_m}$, and using Properties 7 and 8, and the upper bound of χ_2 yields

$$\begin{aligned}\dot{V}_2 \overset{\text{a.e.}}{\leq} \quad & -\alpha\|e\|^2 - k_5\|r\|^2 \\ & -\text{trace}\left(k_{cl}\widetilde{W}^T \sum_{j=1}^{h} K\left[\hat{\varrho}_{1,k}\left(\hat{\Phi}_{1,k}(x_{1,j})\right)\right] \times \right. \\ & \left.\left(\tau_{total,j} - \widehat{W}^T K\left[\hat{\varrho}_{1,k}\left(\hat{\Phi}_{1,k}(x_{1,j})\right)\right]\right)^T\right).\end{aligned} \tag{42}$$

Now using (16), (18), (22), (30), and Properties 3 and 8 yield

$$\begin{aligned}\dot{V}_2 \overset{\text{a.e.}}{\leq} \quad & -k_z\|z\|^2 - \text{trace}\left(k_{cl}\widetilde{W}^T A_{el}\widetilde{W}\right) \\ & + \left\|\text{vec}\left(\widetilde{W}\right)\right\| C_1,\end{aligned} \tag{43}$$

where $k_z \triangleq \min(\alpha, k_5)$ and $C_1 \in \mathbb{R}_{\geq 0}$ is a known constant. The inequality in (43) holds true for all $t \in [t_n^s, t_n^e), \forall n$ because it holds true for any arbitrary i or k. If sufficient excitation has not been reached, A_{el} will be positive semidefinite, as stated in Assumption 1; whereas A_{el} will be PD after learning has been completed. Using Property 9 and Assumption 1 for both the cases prior (i.e., $t \in [t_0, T)$) and after sufficient learning (i.e., $t \in [T, \infty)$, in addition to completing the squares yields

$$\begin{aligned}\dot{V}_2 &\overset{\text{a.e.}}{\leq} -k_z\|z\|^2 + C_1\widetilde{\overline{W}}, \forall t \in [t_0, T) \cap [t_n^s, t_n^e) \\ \dot{V}_2 &\overset{\text{a.e.}}{\leq} -k_x\|x\|^2 + \tfrac{C_1^2}{2k_{cl}\lambda_{ss}}, \forall t \in [T, \infty) \cap [t_n^s, t_n^e),\end{aligned} \tag{44}$$

where $k_x \triangleq \min\left(k_z, \frac{1}{2}k_{cl}\lambda_{ss}\right)$. Using (33) with (44) yields the results in (39) and (40). From (39) and (40) and the results in Theorem 1, the DNN-based FES controller in (25) is bounded. ■

V. Simulation

A preliminary simulation using the Euler-Lagrange dynamics in (1) was performed for a knee extension exercise (note that the system model is omitted due to space constraints). Both of the DNNs (i.e., DNN1 and DNN2) used in the control law had five layers and a similar architecture. The output-layer had a linear activation function while the other four layers had a tangent sigmoid function as their activation functions. The number of neurons in the input-layer, and the first, second, and third hidden-layers were 15, 10, 7, and 7, respectively. To collect the data for pre-training the DNN, a simulation of the actual dynamics was performed using the desired trajectory and its derivative as the input. The input and output data from the simulation were collected and used to pre-train the DNN. After pre-training, the DNN- and admittance-based controllers were implemented for the Euler-Lagrange dynamics. The re-trainings of the DNN were performed while running the simulation. The input and output data obtained during the simulation were used to retrain the DNN. The simulation ran for 150s at in which two re-trainings were done and error graphs were developed to analyze the performance of developed controllers.

VI. Results

The tracking of the developed controllers is depicted in Figure 1. The first solid vertical line Figure 1 indicates that the DNN re-training had been started for the first time and the second solid vertical line indicates the time when the second re-training started. The dashed vertical lines indicate the times when the newly trained weights and biases were implemented. Row 1 of Figure 1 shows the difference between the desired angle and the actual angle, and Row 2 of Figure 1 depicts the auxiliary position error. It can be seen that the angular position error is gradually improving with time and with each retraining, demonstrating the effectiveness of the proposed controllers.

VII. Conclusion

Hybrid exoskeletons require the control of both humans and robots for optimal rehabilitation. In this project, two controllers were proposed to obtain proper rehabilitation for

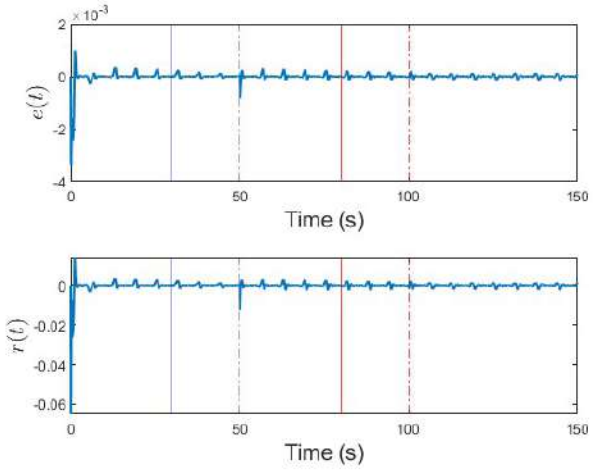


Figure 1. The tracking error and auxiliary error for the knee extension dynamics are depicted. The solid lines indicate the times when the DNN re-training started and dashed lines indicate when the retrained weights and biases were implemented.

individuals with NCs. The FES controller utilized DNN-based control approaches to track a desired trajectory. Furthermore, the DNN update law for the output-layer weights was augmented with CL to improve the DNN learning performance. Conversely, admittance was implemented to the robot controller to enhance robot-human interaction and augment rehabilitation. A rigorous Lyapunov-like stability analysis was performed for both of the controllers to ensure stability. Finally, the simulation result demonstrates the potential of the proposed control framework.

REFERENCES

[1] Andrew W. Selassie, Eduard Zaloshnja, Jean A. Langlois, Ted Miller, Paul Jones, and Claudia Steiner. Incidence of long-term disability following traumatic brain injury hospitalization, United States, 2003. *J. Head Trauma Rehabil.*, 23(2):123–131, 2008.

[2] Donna L. Hoyert and Jiaquan Xu. Deaths: Preliminary data for 2011. *National vital statistics reports*, 61(6), 2012.

[3] Tarun Dua and Paul Romani. Atlas: Multiple sclerosis resources in the world 2008. *World Health Organization*, 2008.

[4] G. Adelman, S. G. Rane, and K. F. Villa. The cost burden of multiple sclerosis in the United States: a systematic review of the literature. *J. Med. Econ.*, 16(5):639–647, 2013.

[5] Spinal cord injury facts and figures at a glance. *J. Spinal Cord Med.*, 2017.

[6] Judith Mackay. *The atlas of heart disease and stroke*, volume 5. World Health Organization, 2004.

[7] M. J. Bellman, T.-H. Cheng, R. J. Downey, and W. E. Dixon. Stationary cycling induced by switched functional electrical stimulation control. In *Proc. Am. Control Conf.*, pages 4802–4809, 2014.

[8] DJ Newham and N de N Donaldson. FES cycling. *Op. Neuromod.*, pages 395–402, 2007.

[9] James H. Rimmer. Physical fitness levels of persons with cerebral palsy. *Dev. Med. Child Neurol.*, 43(3):208–212, 2001.

[10] James H. Rimmer and Jennifer L. Rowland. Health promotion for people with disabilities: implications for empowering the person and promoting disability-friendly environments. *Am. J. Lifestyle Med.*, 2(5):409–420, 2008.

[11] T. Mohr, J. Pødenphant, F. Biering-Sørensen, H. Galbo, G. Thamsborg, and M. Kjær. Increased bone mineral density after prolonged electrically induced cycle training of paralyzed limbs in spinal cord injured man. *Calcif. Tissue Int.*, 61(1):22–25, 1997.

[12] Marc Bélanger, Richard B Stein, Garry D Wheeler, Tessa Gordon, and Bernard Leduc. Electrical stimulation: can it increase muscle strength and reverse osteopenia in spinal cord injured individuals? *Arch. Phys. Med. Rehabil.*, 81(8):1090–1098, 2000.

[13] Steven P Hooker, Stephen F Figoni, Mary M Rodgers, Roger M Glaser, Thomas Mathews, Agaram G Suryaprasad, and Satyendra C Gupta. Physiologic effects of electrical stimulation leg cycle exercise training in spinal cord injured persons. *Arch. Phys. Med. Rehabil.*, 73(5):470–476, 1992.

[14] A. J. Del-Ama, A. D. Koutsou, J. C. Moreno, A. De-Los-Reyes, Á. Gil-Agudo, and J. L. Pons. Review of hybrid exoskeletons to restore gait following spinal cord injury. *J. Rehabil. Res. Dev.*, 49(4):497–514, 2012.

[15] F. Anaya, P. Thangavel, and H. Yu. Hybrid FES–robotic gait rehabilitation technologies: a review on mechanical design, actuation, and control strategies. *Int. J. Intell. Robot. Appl.*, pages 1–28, 2018.

[16] J. Ting, S. Basyal, and B. C. Allen. Deep neural network based saturated adaptive control of muscles in a lower-limb hybrid exoskeleton. In *ASME Int. Mech. Eng. Congr. Expo. (IMECE)*, 2023.

[17] N. Hogan. Impedance control: An approach to manipulation: Parts I, II, III. *J. Dyn. Syst. Meas. Control*, 107:1–24, 1985.

[18] C. Cousin, V. H. Duenas, C. Rouse, and W. E. Dixon. Stable cadence tracking of admitting functional electrical stimulation cycle. In *Proc. ASME Dyn. Syst. Control Conf.*, 2018.

[19] C. A. Cousin, V. Duenas, C. Rouse, and W. E. Dixon. Admittance control of motorized functional electrical stimulation cycle. In *Proc. IFAC Conf. Cyber. Phys. Hum. Syst.*, pages 328–333, 2018.

[20] C. Cousin, V. H Duenas, C. Rouse, and W. E. Dixon. Cadence and admittance control of a motorized functional electrical stimulation cycle. In *Proc. IEEE Conf. Decis. Control*, pages 6470–6475, December 2018.

[21] C. A. Cousin, C. A. Rouse, V. H. Duenas, and W. E. Dixon. Controlling the cadence and admittance of a functional electrical stimulation cycle. *IEEE Trans. Neural Syst. Rehabil. Eng.*, 27(6):1181–1192, June 2019.

[22] C. Cousin, V. H. Duenas, C. Rouse, and W. E. Dixon. Admittance trajectory tracking using a challenge-based rehabilitation robot with functional electrical stimulation. In *Proc. Am. Control Conf.*, pages 3732–3737, 2018.

[23] C. A. Cousin, C. A. Rouse, and W. E. Dixon. Split-crank functional electrical stimulation cycling: An adapting admitting rehabilitation robot. *IEEE Trans. Control Syst. Tech.*, 29(5):2153–2165, 2021.

[24] C. Cousin, P. Deptula, C. Rouse, and W. E. Dixon. Cycling with functional electrical stimulation and adaptive neural network admittance control. In *Proc. Am. Control Conf.*, pages 1742–1747, 2019.

[25] Yanan Li, Shuzhi Sam Ge, and Chenguang Yang. Learning impedance control for physical robot–environment interaction. *Int. J. Control*, 85(2):182–193, 2012.

[26] Yanan Li and Shuzhi Sam Ge. Impedance learning for robots interacting with unknown environments. *IEEE Trans. Control Sys. Tech.*, 22(4):1422–1432, 2014.

[27] Isura Ranatunga, Frank L Lewis, Dan O Popa, and Shaikh M Tousif. Adaptive admittance control for human–robot interaction using model reference design and adaptive inverse filtering. *IEEE Trans. Control Sys. Tech.*, 25(1):278–285, 2017.

[28] S. Basyal, J. Ting, K. Mishra, and B. C. Allen. Concurrent learning and Lyapunov-based updates of deep neural networks for Euler-Lagrange dynamic systems. In *Proc. Am. Control Conf.*, 2024.

[29] S. Basyal, J. Ting, K. Mishra, and B. C. Allen. Augmentation of a Lyapunov-based deep neural network controller with concurrent learning for control-affine nonlinear systems. In *Proc. Am. Control Conf.*, 2024.

[30] H. K. Khalil. *Nonlinear Systems*. Prentice Hall, Upper Saddle River, NJ, 3 edition, 2002.

[31] Z. Cai, M. S. de Queiroz, and D. M. Dawson. A sufficiently smooth projection operator. *IEEE Trans. Autom. Control*, 51(1):135–139, January 2006.

[32] A. F. Filippov. Differential equations with discontinuous right-hand side. In *Fifteen papers on differential equations*, volume 42 of *American Mathematical Society Translations - Series 2*, pages 199–231. American Mathematical Society, 1964.

Dynamic Adaptation of Robotic Ankle-Foot Prostheses to Compliant Terrain: Reacting to Surface Stiffness Changes in Real-Time

Charikleia Angelidou, Benjamin Chen and Panagiotis Artemiadis*, *IEEE Senior Member*

***Abstract*— Real-time adaptability to varying terrain stiffness is a critical factor in enhancing the functionality of robotic ankle-foot prostheses. This paper introduces a novel reactive control framework that classifies surface stiffness and adjusts the prosthesis' behavior in real-time on compliant terrain, utilizing kinematic data from the prosthesis. The framework is tested with three able-bodied participants who completed treadmill walking trials on simulated rigid and compliant surfaces, replicating typical real-life scenarios. The proposed framework employs a Support Vector Machine (SVM) classifier that leverages data such as ankle angle, ankle moment, and Inertial Measurement Unit (IMU) measurements from a powered prosthesis to differentiate between terrains of different stiffness. Results show a classification accuracy of up to 88%, while the classification process is streamlined for rapid decision-making, enabling surface adaptation within milliseconds of initial foot-ground contact. This approach represents a significant step toward creating responsive, user-centric assistive technologies for individuals with lower-limb amputation.**

I. Introduction

Navigating dynamic terrains, including compliant surfaces and non-level ground, remains a significant challenge for individuals relying on robotic lower-limb prostheses [1,2]. Specifically for individuals with lower-limb amputation (LLA), transitions between surfaces of varying stiffness, such as transitioning from a paved sidewalk to grass or sand, can destabilize gait and compromise user safety [3]. While modern prostheses excel in replicating steady-state walking patterns on rigid terrain [4] and enable safe transitions between different locomotion modes [5, 6], their limited ability to adapt dynamically to surface changes highlights a critical need for improved control frameworks that integrate both environmental sensing and human feedback.

A growing body of research highlights the importance of considering human-robot interaction as a holistic system, where both human and robotic feedback play a critical role in optimizing performance. In this context, effective physical human-robot interaction requires bidirectional communication, encompassing not only the robotic system's ability to adapt to environmental cues but also its capacity to interpret and respond to signals from the human user [7]. Specifically in the context of compliant terrains, recent works have delved deeper into the latter, closely studying the mechanisms of human locomotion over surfaces of varying stiffness and utilizing biomechanical inputs from the human user to predict the upcoming surface stiffness [8, 9].

These works specifically elaborate on a high-level control framework for lower-limb prosthesis, which based on the predicted surface compliance, adjusts the prosthetic limb's behavior before foot contact with the ground, making real-time modifications to match the terrain. The prosthetic limb then moves according to these adjustments and interacts with the environment, a mechanism illustrated in Fig. 1. Feedback from interacting with the compliant environment shows potential for developing reactive control frameworks that refine prosthesis control in real-time, especially during unexpected terrain stiffness changes that could result from sensory occlusion (i.e. not visually perceiving an upcoming compliance change) or distracted walking (i.e. reduced anticipation). Although leveraging the generated prosthesis feedback can enhance both prosthetic functionality and user experience, it remains unexploited in the field of powered prostheses and their adaptation to compliant terrains.

As a preliminary effort to address this gap and improve mobility for individuals with LLA, this paper presents a novel reactive control framework designed to respond to surface stiffness changes in real time, utilizing direct feedback from the user's wearable device or powered prostheses. The goal of this research is to develop a compensatory control mechanism that will identify surface stiffness promptly after the initial contact of the prosthesis with the new surface to improve overall stability and robustness of the prosthesis. By classifying terrain characteristics within a few milliseconds after initial contact with the ground, the goal is to facilitate rapid prosthesis adjustments, mimicking the natural reflexive responses of the human nervous system. The overarching objective of this work is to provide a personalized and intuitive experience for individuals with LLA, ultimately improving the quality of life for users relying on assistive and prosthetic devices.

II. Methods

The proposed control framework was designed, developed, and tested using experiments with able-bodied participants wearing a robotic ankle-foot prosthesis using a bypass adapter. The methodology encompassed data acquisition, data preprocessing, and segmentation, supervised machine learning model training, as well as real-time simulation testing. The following sections present each of the distinct study components in more detail.

*This material is based upon work supported by the National Science Foundation under Grants No. 2020009, 2015786, 2025797, and 2018905.

Charikleia Angelidou and Panagiotis Artemiadis are with the Mechanical Engineering Department, at the University of Delaware, Newark, DE 19716, USA. cangelid@udel.edu, partem@udel.edu.

Benjamin Chen is with the Department of Mechanical Engineering at the Carnegie Mellon University, Pittsburgh, PA 15213, USA. bc2@andrew.cmu.edu.

*Corrresponding author

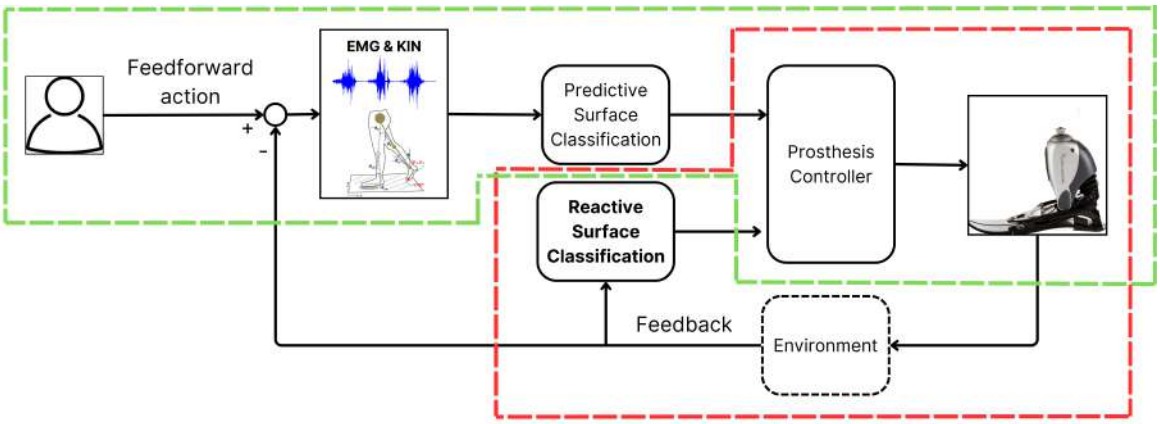


Fig. 1: Overview of the proposed research framework and its application on a robotic ankle-foot prosthesis that interacts with the human user and the environment. The green dashed line represents the anticipatory module of the proposed framework [8, 9]. The red dashed line represents the compensatory module discussed in detail in this work.

A. Experiment Protocol

1) Ruggedized Odyssey Ankle Prosthesis: For this study, the powered Ruggedized Odyssey Ankle (ROA) prosthesis (SpringActive, Inc) was used (see Fig. 2) [10, 11]. The ankle features a 250 W brushless DC motor connected in series with a 377 kN/m elastic spring, which transitions to a rigid carbon fiber foot. This design allows the spring to store and release elastic energy during the gait cycle, while the motor supplements any additional energy required. A motor encoder tracks the motor position, and an ankle encoder monitors the ankle angle. Additionally, an inertial measurement unit (IMU) is integrated within the casing above the ankle joint. The spring-generated ankle moment is estimated using a lookup table, developed by SpringActive, Inc., based on the motor position and ankle angle.

By default, the ROA prosthesis is controlled using a continuous phase-variable controller called the tibia controller (TC) [12]. The TC utilizes tibia kinematics to produce a reference motor trajectory that replicates the ankle angle patterns typically observed in the gait of healthy individuals without gait impairments. The TC has successfully been tested with individuals with transtibial (TT) LLA in walking and running activities on rigid terrain [12, 13]. However, the TC performance on bilaterally compliant terrain remains inferior to a recently proposed admittance controller (AC) [14], tailored for compliant surface walking.

2) Variable Stiffness Treadmill 2: The walking assessment of the recruited participants was performed using a specialized robotic platform developed by our lab, known as the Variable Stiffness Treadmill 2 (VST 2) [15] (see Fig. 2). The VST 2 can independently adjust the stiffness of both belts to simulate walking on compliant terrain. This experimental platform allows for the simulation of everyday walking conditions by recreating compliant surfaces and mimicking real-world stiffness scenarios in the lab.

3) Participant Data: Three healthy participants (two females, one male; age: 22 $\pm$ 1.73 years; height: 1.66 $\pm$ 0.03 m; weight: 58.98 $\pm$ 2.27 kg) completed walking trials on the VST 2 [15] wearing the ROA prosthesis. The prosthesis was attached via a carbon fiber bypass adapter on the left leg of the participants, preserving knee movement, while an adjustable shoe-lift (Evenup Corp., Buford, GA) was used on the right leg to compensate for height differences.



Fig. 2: Front and side view of a subject standing on the VST 2, while wearing the powered ankle-foot prosthesis Ruggedized Odyssey Ankle (ROA) attached to an ankle bypass adapter.

The study involved two sessions for training and data collection, respectively. During the training session, participants acclimated to the treadmill's stiffness levels without the prosthesis. They were then asked to identify a comfortable walking speed while using the prosthesis under rigid stiffness conditions. The independently selected comfortable walking speed was 0.65 m/s for all three study participants, which also reflects the preferred treadmill speeds previously reported by individuals with gait impairments (e.g., individuals with LLA or stroke survivors) [16]. Subsequently, participants performed short trials at that speed across rigid and compliant terrains, using the default controller (TC) of the ROA.

4) Data Acquisition: During the data collection session, participants completed walking trials at their self-selected comfortable speed. The first trial included walking for 200 gait cycles on a rigid surface using the TC. Subsequent trials included walking on bilaterally compliant terrain with stiffness levels mimicking rubber-on-foam (63 kN/m) and foam pads (25 kN/m), using the TC. Five-minute rest periods

between trials were imposed to minimize participant fatigue. All participants provided written consent, and the presented experimental protocol was approved by the University of Delaware Institutional Review Board (IRB ID#: 1520622-8).

A motion capture system equipped with 8 cameras was used to collect kinematic data at 100 Hz (Vicon Motion Systems Ltd.). Additionally, the vertical Ground Reaction Force (GRF) response and the center of pressure (CoP) under each leg of the subjects was recorded at 65 Hz using a force sensor mat (Medical Sensor 3140TM, Tekscan, Inc., South Boston, MA) placed underneath both belts of the treadmill. Data from the prosthesis, such as ankle angle and moment, were recorded at a rate of 100 Hz.

B. Data Analysis

Based on previous works, it is safe to assume that the TC is the optimal controller for walking over rigid surfaces [12], while the AC performs better for walking tasks on compliant terrain [14]. This work aims to address the switch between the two controllers during transitions from rigid to compliant surfaces, aiding the rapid, real-time adaptation of the ROA to the new terrain. Considering that a natural human reflexive response takes place after a sensory stimulus (i.e. contact of the foot with a surface of different compliance), there is a reaction delay in the resulting compensatory response (i.e. adapting ankle stiffness to the new terrain). This reaction delay can be analogously compared to the time required to classify terrain stiffness upon contact with the ground and switch from a rigid ground controller (TC) to a compliant terrain controller (AC). During this time delay, the prosthesis controller remains set to its default setting for rigid surface walking. For this reason, this work will only focus on using trial data recorded using the default (TC) controller of the ROA. Additionally, it should be noted that since the focus of this study is concentrated on utilizing direct feedback from the ROA, the motion capture and force data will not be further analyzed within the scope of this work. From hereon, all data analysis will refer solely to the kinematic data captured by the ROA. Finally, analysis will be centered around classifying between the rigid (1000 kN/m) and the most compliant (25 kN/m) surface cases.

Data collected from the prosthesis included 22 quantifiable variables related to the prosthetic kinematics, including but not limited to ankle angle, ankle moment, IMU measurements, and gait parameters, such as gait progression and stride length among others. Kinematic data were sampled at 100Hz. Utilizing the prosthesis parameters, the ankle angular velocities were also derived as the time derivatives of the ankle angles. All kinematic data was then filtered via a 2nd order, low-pass Butterworth filter with a cut-off frequency of 5 Hz. Following the visual inspection of all prosthesis variables and comparing the average gait cycle data across the stiffness conditions of interest (1000 kN/m and 25 kN/m), we identified significant differences in the average values of several variables during the stance phase of gait. Statistical significance was calculated using an independent 2-sample t-test at the 95% confidence level and the selected variables included the ankle angle, ankle moment, IMU gyroscopic data (x-axis), and ankle angle velocity. Distinguishing between surface types during the first half of the gait cycle (i.e., the stance phase) was particularly critical, as surface identification in the latter half has minimal impact on user stability. This highlights the importance of focusing on early gait phases for effective terrain classification and stability enhancement.

Data were subsequently segmented into individual gait cycles and labeled according to terrain stiffness. These labeled data were then split into training (70%) and testing (30%) sets, with the training set used to develop machine learning classifiers capable of differentiating between rigid and compliant terrains and the testing set for real-time evaluation of the classification framework.

C. Classification Framework

1) Windowing Segmentation: A windowing segmentation analysis with non-overlapping windows was employed to preprocess the data for use as inputs to our classifier. Segmenting data into windows is a well-established practice in time-series analysis, as it enables the extraction of localized patterns and trends within specific intervals of the data [17]. Non-overlapping windows simplify computation by avoiding redundancy and ensuring that each segment contributes unique information to the model. This approach is particularly advantageous in gait analysis, where biomechanical variables such as ankle angle or moment evolve systematically over the gait cycle. By isolating discrete segments of the data, the classifier can more effectively learn distinct signals associated with different surface stiffness levels. Additionally, the segmentation process aligns with the natural periodicity of human locomotion, ensuring that inputs represent physiologically meaningful intervals.

For this reason, we utilized a windowing segmentation of 5 and 10 samples per window - corresponding to a window duration of 50 ms and 100 ms, respectively- to compare the effect of the window length in our classification strategy. The segmentation started at the beginning of the gait cycle – defined at heel-strike – and extended up to sample 60 ($\approx 50\%$ of the gait cycle), resulting in a total of 12 or 6 windows, respectively, for the 50 and 100 ms windows. The windowing process was capped at 50% of the gait cycle, which corresponds to the late stance phase of gait, as decisions made after this point offer limited practical value for identifying transitions to compliant surfaces.

2) Support Vector Machine (SVM) Classifier: Our goal is to classify gait cycles into two class labels according to whether the transition happens on a (1) rigid or (2) compliant surface. We therefore analyzed the efficiency of different classification methods in identifying and classifying walking patterns related to compensatory reactions during early transitions between surfaces of variable stiffness.

Using MATLAB's Classification Learner, we evaluated various classifier types, including k-Nearest Neighbors (kNN), Linear Discriminant Analysis (LDA), Neural Networks (NN), and Support Vector Machines (SVM). While

the results across kNN, Neural Networks, and SVM were similar, SVM generally outperformed the other models in terms of both accuracy and computational efficiency. For our SVM model, we utilized MATLAB's $fitcsvm$ function to train the SVM models on the provided dataset for each segmented window. To further enhance performance, we ran hyperparameter optimization for each window to determine the best parameters tailored to the specific characteristics of the data within that window.

3) Final Classification Decision: In this preliminary study, a total of 6 (or 12) decisions were made during the SVM classification phase, corresponding to the 100 ms (or 50 ms) segmented windows within the gait cycle. To derive a reliable classification outcome, a consensus-based approach was employed to consolidate these individual predictions into a single, final decision.

Specifically, the classifier confirmed its prediction if at least four (out of 6) or seven (out of 12) consecutive windows agreed on the outcome, prioritizing consistency in predictions over a simple majority vote. This method was chosen to leverage the temporal coherence of gait data, ensuring that decisions are based on stable trends rather than isolated predictions.

If consecutive agreement was not feasible, the final decision defaulted to the prediction of the last segmented window. This assumption rests on the premise that the later in the gait cycle a prediction is made, the more informative the classification inputs are likely to be.

4) Real-Time Testing and Framework Evaluation: A real-time simulation framework was designed to emulate the process of continuous data streaming from the ROA. The experimental data, gathered in the previously described controlled trials, were used offline to train the different classifiers. The partitioned test set data were then processed as if they were being streamed live from the prosthesis, simulating the conditions of real-time operation without the need to conduct new walking trials.

Specifically, data were simulated to arrive at a frequency of 100 Hz, replicating the actual sampling rate of the prosthesis sensors. The gait progression variable, a key output of the ROA, was used to detect heel-strike events, which served as markers to initiate the windowing segmentation outlined in earlier sections of this paper. To maintain robustness, a sliding buffer aggregated incoming data in chunks corresponding to the size of each window that was defined as 5 or 10 samples, equivalently 50 or 100 ms, per window. The segmented data windows were then filtered using a 2nd order, low-pass Butterworth filter (cut-off frequency of 5 Hz) to prepare them for classification, following the same processing pipelines as the training set data. Each window was passed sequentially to its respective trained classifier for real-time prediction. The distinct classifiers each provided a classification output that was then used to derive a conclusion about the stiffness of the terrain. A consensus-based decision-making process was used, in which a decision was finalized after achieving consistency across several consecutive outputs. This approach was aimed at mitigating the impact of transient noise or errors in individual predictions.

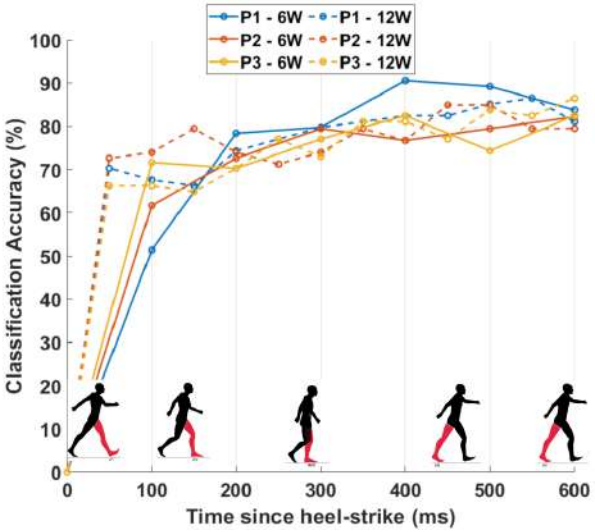


Fig. 3: Accuracy metric across participants (P1, P2, P3) using SVM window-classifiers within 600 ms of heel-strike. The solid lines represent the accuracy progression for the case of the 100 ms windows, corresponding to a segmentation of 6 Windows (6W). The dashed lines represent the accuracy progression for the case of the 50 ms windows, corresponding to a segmentation of 12 Windows (12W).

The performance of the framework was assessed by comparing predicted classifications with ground truth labels and the results were visualized using confusion charts. The framework was evaluated on a series of metrics based on the structure of a binary classification confusion matrix [18]. The metrics that were chosen to evaluate our model are briefly presented below.

- Accuracy: Proportion of true results (both Rigid and Compliant) in the data.
- Precision: A metric representing how many observations predicted as Compliant were in fact Compliant.
- Recall: A metric representing how many observations out of all Compliant observations have been classified as Compliant.
- F1-score: Harmonic mean between precision and recall. It ranges between 0 and 1, with 1 indicating perfect precision and recall.

Finally, the framework was evaluated not only on its accuracy, but also on how quickly decisions could be made following the detection of a heel-strike event, ensuring that the system's response time met the requirements for real-time prosthesis control. This simulation approach allowed for rigorous testing of the classifiers under conditions that closely mimic real-world prosthesis operation.

III. Results

A. Performance Comparison using 50 ms versus 100 ms Windows

In our comparison of the SVM classifier's performance with 50 ms and 100 ms window sizes, we found that a finer segmentation (50 ms) did not yield significant improvements

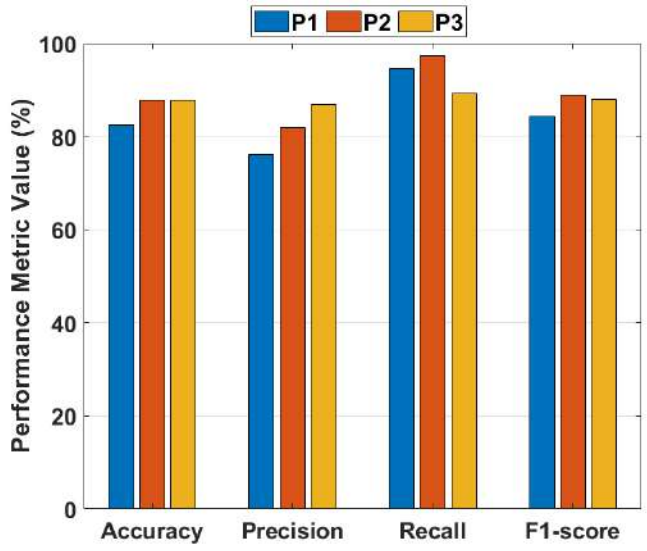


Fig. 4: Performance evaluation metrics across participants (P1, P2, P3) using SVM window-classifiers. The classification results depict the final decision metrics for the case of the 600 ms classification (decision taken at late stance phase) using a consensus-based decision process.

in classification metrics when compared to the 100 ms windows (see Fig. 3).

This can be attributed to the bandwidth limitations of the prosthesis, which constrain its ability to detect or respond to rapid changes within a 50 ms window. As a result, the signals extracted over shorter windows may not exhibit significant variability, leading to comparable classification outcomes between the 50 ms and 100 ms windows. Interestingly, classification accuracy was also observed to spike between 150 ms and 400 ms, highlighting the classifier's ability to make prompt and reliable decisions during the early and mid-stance phases of gait. This performance suggests that the 100 ms window allows enough time for the system to effectively adjust prosthesis parameters during these critical phases of walking.

B. SVM Classifier Performance

The performance of the proposed SVM-based binary classification framework demonstrates its ability to reliably distinguish between rigid and compliant surfaces with high accuracy and responsiveness within a short period of time after heel contact of the prosthesis with the ground. The detailed performance metrics for each participant are summarized in Fig. 4 for the full 600 ms. Across all participants, the SVM classifier consistently achieved high accuracy (82.4%–87.8%) along with strong precision, recall, and F1 scores. These results indicate that the classifier not only predicted surface compliance correctly in most cases but also maintained a balanced performance across true positives and false negatives, ensuring reliability in its decision-making. The high recall values should be noted, as they reflect the classifier's capacity to minimize misclassifications while ensuring accurate predictions of rigid and compliant surfaces.

Interestingly, looking at the precision scores of all participants, analysis of misclassified instances reveals a bias toward predicting rigid surfaces as compliant rather than the reverse. This behavior is advantageous in practical applications, as it prioritizes safety by ensuring that the prosthesis errs on the side of caution. Misclassifying a compliant surface as rigid could result in insufficient adjustments, potentially leading to instability or falls. In contrast, treating a rigid surface as compliant poses a lower risk, as the prosthesis would still be able to provide the required support to walk on a rigid terrain, ensuring a sub-optimal, yet stable gait [14].

By reliably distinguishing between rigid and compliant surfaces and prioritizing safety in its classification biases, the framework offers a reactive approach to terrain adaptation.

C. Classification Timing and Implications for Real-Time Prosthetic Control

The consensus-based approach demonstrated the ability to provide reliable predictions for the majority of gait cycles by the time we reached window 4, eliminating the need to wait through all 6 windows. This early decision-making process highlights the potential of leveraging such techniques to enhance the robustness of the final prediction. As shown in Fig. 5, which illustrates the number of correctly classified gait cycles versus misclassifications across all participants, the majority of gait cycles were accurately predicted by the time window 4 (W4) was reached (i.e., when 4 consecutive identical predictions occurred). Misclassifications were minimal, especially for participants P1 and P2. For participant P3, predictions were more evenly distributed across windows 4 (W4), 5 (W5), and 6 (W6), with a comparable number of misclassifications occurring in W4 and W6. These findings demonstrate the promising potential of using data from the early stance phase of gait for accurate terrain classification, thus underscoring the ability of our system to make reliable decisions early in the gait cycle. However, the consensus-based approach introduces some practical limitations, as alternative methods — such as probabilistic models or confidence-weighted voting — could potentially provide more robust and nuanced final decisions. Future work will explore these possibilities to improve the reliability, adaptability, and speed of the classification process.

IV. Discussion

The proposed reactive control framework demonstrates promise in adapting robotic prostheses to varying terrain conditions. However, some limitations need to be addressed. Specifically, this study was conducted at a fixed walking speed, so future work will investigate how the framework performs across different speeds to improve its adaptability. While the classification response time closely aligns with the average human reaction times reported previously in the literature [19], further optimization is needed to enhance real-time performance. Adaptive control strategies could refine reaction times, making prosthetic adjustments even more seamless. Additionally, the current approach differentiates only between rigid and one level of compliant surfaces.

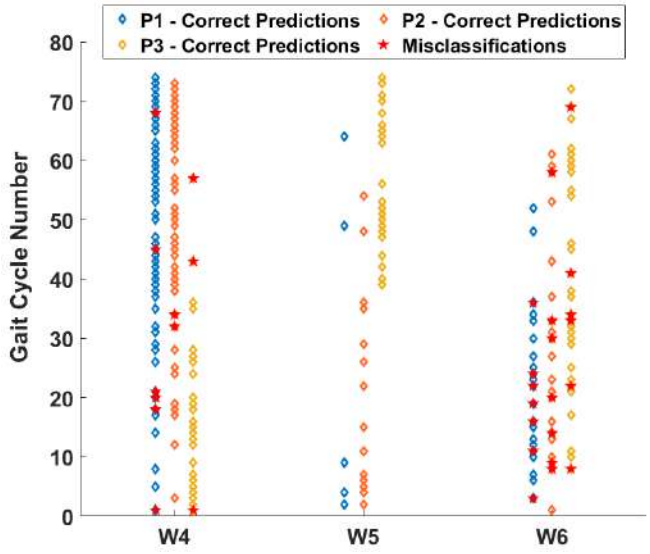


Fig. 5: Final classification prediction across participants (P1, P2, P3) per tested gait cycle following a consensus-based decision process for the case of the 600 ms classification. W4, W5, and W6 correspond to the segmented windows 4,5, and 6.

Expanding classification to intermediate stiffness levels will improve real-world applicability, while integration into a closed-loop prosthetic system and validation through testing on individuals with TT LLA remain crucial next steps. These efforts will refine the framework, making it more robust for everyday prosthetic use.

V. Conclusion

This paper introduces the first reactive controller framework using SVM-based classification to adaptively adjust robotic prosthesis ankle stiffness in response to surface compliance changes. The proposed framework incorporates kinematic data from a robotic ankle-foot prosthesis, enabling real-time classification of surface stiffness upon 400 ms after initial foot-ground contact. The SVM-based classifier demonstrated reliable performance in distinguishing between rigid and compliant surfaces, achieving an accuracy of up to 88%. This ability to classify surface compliance in real-time utilizing direct feedback from the prosthesis allows for adaptive control strategies that dynamically tune the prosthesis's parameters during locomotion. The integration of this reactive control mechanism into a high-level prosthetic system could enable reactive adjustments, enhancing both the stability and adaptability of prosthetics and wearables during transitions from rigid to compliant surfaces.

The results of this study are particularly significant as they underline the feasibility of using machine learning-driven classification to inform real-time control in lower-limb prosthetics. This approach paves the way for advanced prosthetic and wearable devices that consider human-robot interaction as a holistic system, where both human and robotic feedback play a critical role in optimizing performance.

VI. Acknowledgments

We sincerely thank Dr. Chrysostomos Karakasis for generously providing the experimental data used in this study.

References

[1] B. J. Hafner, S. J. Morgan, D. C. Abrahamson, and D. Amtmann, "Characterizing mobility from the prosthetic limb user's perspective: Use of focus groups to guide development of the prosthetic limb users survey of mobility," *Prosthetics and Orthotics International*, vol. 40, pp. 582–590, 10 2016.

[2] M. E. V. D. Berg, C. J. Barr, S. Cavenett, and M. Crotty, "Gait analysis in individuals with transtibial amputation walking on sand: Comparing everyday prosthesis with a water-activity prosthesis," *Prosthetics and Orthotics International*, vol. 32, pp. 107–115, 4 2020.

[3] J. Kim, M. J. Major, B. Hafner, and A. Sawers, "Frequency and circumstances of falls reported by ambulatory unilateral lower limb prosthesis users: A secondary analysis," *Physical Medicine and Rehabilitation*, vol. 11, pp. 344–353, 4 2019.

[4] D. Quintero, A. E. Martin, and R. D. Gregg, "Toward unified control of a powered prosthetic leg: A simulation study," *IEEE transactions on control systems technology : a publication of the IEEE Control Systems Society*, vol. 26, pp. 305–312, 1 2018.

[5] S. Cheng, C. A. Laubscher, and R. D. Gregg, "Controlling powered prosthesis kinematics over continuous transitions between walk and stair ascent," pp. 2108–2115, 12 2023.

[6] J. Mendez, S. Hood, A. Gunnel, and T. Lenzi, "Indirect volitional swing control allows for level-ground walking and crossing over obstacles with a powered knee and ankle prosthesis," *Science robotics*, vol. 5, p. eaba6635, 7 2020.

[7] K. Ghonasgi, T. Higgins, M. E. Huber, and M. K. O'Malley, "Crucial hurdles to achieving human-robot harmony," *Science Robotics*, vol. 9, 11 2024.

[8] C. Angelidou and P. Artemiadis, "On predicting transitions to compliant surfaces in human gait via neural and kinematic signals," *IEEE Transactions on Neural Systems and Rehabilitation Engineering*, vol. 31, pp. 2214–2223, 2023.

[9] C. Angelidou and P. Artemiadis, "On intuitive control of ankle-foot prostheses: A sensor fusion-based algorithm for real-time prediction of transitions to compliant surfaces," *IEEE International Conference on Intelligent Robots and Systems*, pp. 2122–2127, 2023.

[10] M. Grimmer, M. Holgate, J. Ward, A. Boehler, and A. Seyfarth, "Feasibility study of transtibial amputee walking using a powered prosthetic foot," *International Conference on Rehabilitation Robotics*, pp. 1118–1123, 8 2017.

[11] J. Ward, K. Schroeder, D. Vehon, R. Holgate, A. Boehler, and M. Grimmer, "A rugged microprocessor controlled ankle-foot prosthesis for running," in *in 39th annual meeting of the american society of biomechanics (ASB)*, 08 2015.

[12] M. A. Holgate, T. G. Sugar, and A. W. Bohler, "A novel control algorithm for wearable robotics using phase plane invariants," *Proceedings - IEEE International Conference on Robotics and Automation*, pp. 3845–3850, 11 2009.

[13] J. Ward, K. Schroeder, D. Vehon, R. Holgate, A. Boehler, and M. Grimmer, "A rugged microprocessor controlled ankle-foot prosthesis for running," 08 2015.

[14] C. Karakasis, R. Salati, and P. Artemiadis, "Adjusting the quasi-stiffness of an ankle-foot prosthesis improves walking stability during locomotion over compliant terrain," *IEEE International Conference on Intelligent Robots and Systems*, pp. 2140–2145, 2023.

[15] V. Chambers, B. Hobbs, W. Gaither, Z. Thé, A. Zhou, C. Karakasis, and P. Artemiadis, "The variable stiffness treadmill 2: Development and validation of a unique tool to investigate locomotion on compliant terrains," *Journal of Mechanisms and Robotics*, vol. 17, 3 2025.

[16] C. E. Capó-Lugo, C. H. Mullens, and D. A. Brown, "Maximum walking speeds obtained using treadmill and overground robot system in persons with post-stroke hemiplegia," *Journal of NeuroEngineering and Rehabilitation*, vol. 9, pp. 1–14, 10 2012.

[17] G. Wang, Q. Li, L. Wang, W. Wang, M. Wu, and T. Liu, "Impact of sliding window length in indoor human motion modes and pose pattern recognition based on smartphone sensors," *Sensors 2018, Vol. 18, Page 1965*, vol. 18, p. 1965, 6 2018.

[18] M. Shirdel, M. D. Mauro, and A. Liotta, "Worthiness benchmark: A novel concept for analyzing binary classification evaluation metrics," *Information Sciences*, vol. 678, p. 120882, 9 2024.

[19] A. Jain, R. Bansal, A. Kumar, and K. Singh, "A comparative study of visual and auditory reaction times on the basis of gender and physical activity levels of medical first year students," *International Journal of Applied and Basic Medical Research*, vol. 5, p. 124, 2015.

Stimulation in Training Data to Improve Proportional Motor Control in a Dexterous Sensorimotor Task

Caroline H. Casumpang, Nathan Griffin, and Mark Brinton, *Member, IEEE*

***Abstract*—While electrocutaneous stimulation provides a low-cost approach to sensory feedback, it produces signal artifact which corrupts sEMG and can create errors in sEMG motor control. Eight volunteers with intact limbs controlled a 5-degree-of-freedom virtual hand using surface electromyography. The hand was trained by mimicking flexion and extension of each degree-of-freedom five times, holding each position for three seconds. Participants received sensory feedback in the form of electrocutaneous stimulation: 100 microsecond pulses at 100 Hz with amplitude linearly proportional to the force experienced by the index finger while pressing a virtual block. We compared ability to discriminate between block compliance when using training data with and without stimulation artifact. Though not statistically significant, randomly occurring stimulation during training improved ability to discriminate more compliant objects from 76 to 82% and 72 to 85% correct for two proportional control algorithms—a modified Kalman filter and a convolutional neural network. This approach requires no extra computational resources while providing improved motor control for bidirectional prostheses.**

I. Introduction

Between 30-50% of upper-limb amputees do not regularly use their prosthesis, in part because the prosthesis does not provide a sense of touch [1], [2]. Electrocutaneous stimulation is a low-cost approach to sensory feedback that has a slim form factor that could be easily integrated with clinically available prostheses. Different than transcutaneous electrical stimulation (which targets underlying nerve bundles to induce referred sensations in the distal limb), electrocutaneous stimulation aims to activate the underlying mechanoreceptors in the skin. This requires a small active electrode (about 1 cm2, or smaller), placed close to one or more larger return electrodes, to create a localized region of high current density near the active electrode. The localized, tactile sensations generated provide similar sensitivity to changes in stimulus intensity as those produced with intraneural stimulation [3]. Constant current stimulation is preferred to ensure changes in impedance at the electrode skin interface (which can vary widely from tens to hundreds of kilo-ohms with skin dryness, sweating, or other environmental conditions) have little impact on the cutaneous current density [4]. Stimulation paradigms often mimic invasive neurostimulation with cathodic-first, biphasic, constant-current pulses delivered at frequencies of 0 to over 150 Hz [3], [5] (even up to 2kHz [6]). Current amplitude is often in the range of a few milliamps, but depends on both the electrode size and the pulse-width (which can range between tens of μs to about 1 millisecond) [3], [7], [8]. The biggest difference in stimulation parameters for electrocutaneous stimulation is the need for high-voltage (often over a hundred volts) to drive pulses of current through the high-impedance electrode-skin interface [7]. As with other types of invasive and noninvasive neurostimulation, these high-voltage, pulses of current generate artifacts that can corrupt the recorded surface electromyography (sEMG) used to decode arm movements [9], [10]. These artifacts can be particularly disruptive for proportional control algorithms—a class of movement decoders which predict arm positions in real-time and provide the user with the fine motor control necessary to perform delicate sensory tasks [11], [12].

Only a few studies have explored removing stimulation artifacts in sEMG controlled upper-limb prostheses, and most of these were focused on classification algorithms. Early work demonstrated that separating the recording and stimulating electrodes several centimeters apart enabled interference-free traditional myoelectric control; however, separation of stimulation and recording electrodes is not always possible, particularly for individuals with short residual limbs [13]. More recently in participants with upper-limb amputations, various signal blanking procedures improved classification of arm position during electrocutaneous stimulation to the performance level of classifiers using data without any artifact [9]. They also demonstrated that blanking worked for pulse widths up to 400 μs and frequencies of 150 Hz. While blanking may be useful with classification algorithms, they are more likely to interfere with real-time proportional control algorithms that constantly rely on up-to-date data to predict new arm positions at regular intervals (e.g., 30 Hz) [12]. More advanced algorithms have relied on template subtraction (e.g., mathematically subtracting artifacts identified during stimulation from newly collected, artifact-corrupted data) and algorithms that predict the artifact waveform and subtract it from recorded EMG in real-time using an adaptive least-mean-squares algorithm. This study used invasive nerve stimulation in two transhumeral amputees (i.e., implanted nerve cuff electrode)—noninvasive stimulation would likely produce different outcomes [14].

We expanded on these studies with upper-limb, myoelectric prostheses, by exploring the effect of stimulation artifacts in training data for two proportional control algorithms: a modified Kalman filter (KF) [12] and a convolutional neural network (CNN) [11]. We explore whether the addition of electrocutaneous stimulation in the training data improves ability to distinguish between two-

*Student research supported by Elizabethtown College Summer Scholarship and Creative Arts Program.

C. C. is with the Engineering Department at Elizabethtown College, Elizabethtown, PA, USA.

N. N. was with Engineering Department at Elizabethtown College, Elizabethtown, PA, USA.

M. B. is with Engineering Department at Elizabethtown College, Elizabethtown, PA, USA (phone: 717-361-1563; e-mail: brintonm@etown.edu).

levels of force applied to the index finger of a virtual hand during a sensorimotor block-push task.

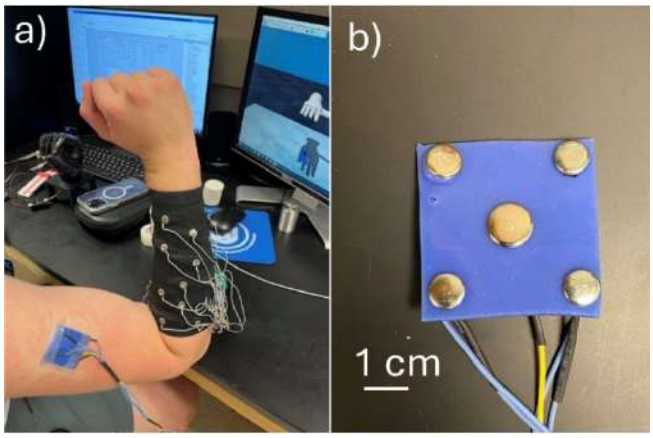


Figure 1. (a) The surface electromyography (sEMG) sleeve was placed on the participant forearm for signal recording and the electrocutaneous (EC) stim pad was placed on the lateral upper-arm. (b) The stim pad had a 1-cm diameter active electrode with 0.75-cm return electrodes at each corner of a 9-cm2 quincunx pattern.

II. Methods

A. Participants

Eight participants (5 male, 3 female) with intact limbs were recruited for the study (ages 18-45). All participants provided informed consent prior to the experiment. All procedures were approved by the Elizabethtown College Institutional Review Board.

B. Experiment Preparation

For sEMG collection, a 32-electrode sleeve was placed on the forearm (Fig. 1a), lining up the signal-recording ground and reference electrodes along the ulna. The electrodes and associated wires were securely wrapped to the forearm, reducing the likelihood of movement artifacts and ensuring stable contact throughout the experiment. Participants were instructed to rest their elbow on the table and to maintain a similar position throughout the experiment.

Participants dampened their skin using a wet paper towel on their upper arm to enhance the skin conductivity prior to taping the stimulation pad (Fig. 1b) on the lateral side of the upper arm, about 1/3 of the way between the shoulder and elbow (Fig. 1a). We found the minimum amplitude threshold of detection using the method of descending limits—reducing the amplitude until they could not feel the stimulation anymore.

Prior to the main experiment, participants underwent a practice session to familiarize themselves with how to train the arm by mimicking predefined hand movements. The training guided participants through 5 degrees-of-freedom (DOFs), including thumb flexion/extension, thumb adduction/abduction, index finger flexion/extension, middle finger flexion/extension, and wrist flexion/extension. Each DOF was repeated for five trials, with each position held for 3 seconds before returning to the natural resting position. Coaching was provided to ensure participants understood the movement patterns and when to flex and relax their muscles.

C. Motor Decoders and Control

To decode motor intent, we employed a KF and a CNNF [11]. During training participants mimicked movements of a 5-DOF virtual arm (MuJoCo, DeepMind) [15], [16]. sEMG signals were sampled at 2 kHz, filtered (15 to 375Hz bandpass; 60/120/180Hz notch), digitized and recorded using the Explorer Quest and front-end amplifiers (Ripple Neuromed; Salt Lake City, Utah). These recording parameters were chosen to capture the full range of muscle activity while minimizing noise and interference from other biological signals.

A total of 496 mean-absolute-value (MAV) features were extracted from the sEMG data using a 300-ms buffer and all possible differential pairs of the 32-electrode array. Of these features, the 48 most relevant were selected using Gram-Schmidt forward selection [17], [18] for use in the KF model based on correlation with the intended movements. This feature selection process ensured that only the most informative signals were used, improving the efficiency and accuracy of the decoding algorithm. The KF and CNN algorithms allowed for precise and adaptive decoding of motor intent based on the participants' sEMG data. After training, all DOFs were fixed in position except the index finger, which had a latching filter applied to further smooth movements [17]. By fixing the thumb, middle, ring and little fingers in position, unwanted movements during index control were ignored—allowing researchers to more easily visualize each block-push and preventing the middle finger from inadvertently moving the block from its rest position (occasional possibility for first time myoelectric users like our participants). Because we were focused primarily on object discrimination and participants were blind to all movements of the virtual hand, this simplification allowed them to focus on moving the index finger and interpreting the sensory response. By training on 5 DOFs, even though they were not used in the experimental setup, we ensured that algorithm training and data collected describe the more general scenario of 5-DOF control. Custom Matlab® software with a user interface was developed to manage the training process and decode movements in real time.

D. Electrocutaneous Stimulation

Stimulation was provided by an Arduino-based custom high-voltage constant current stimulator [7]. For the block-push experiment, participants completed the 5-DOF training (10 trials per DOF) twice: once with stimulation (S) and once without stimulation (NS). Half of the participants trained first with stimulation, and the other half with no stimulation first. Stimulation consisted of 100-µs biphasic, cathodic-first, pulses delivered at 100-Hz to the upper arm through a 0.8-cm² electrode. Pulse frequency at 100-Hz was selected because higher frequencies feel more natural and more like pressure than stimulation at lower frequencies which feels like tapping rather than continuous touch [19][20]. The selection of pulse-width is not as important; however, using a short pulse width (e.g., 100 µs) allows a wider range of pulse-amplitude before the sensations become intense or uncomfortable. During experimentation, stimulation amplitude varied with the applied force. During motor control training, bursts of 100-Hz, 100-µs pulses occurred randomly with each DOF movement

and with one of three randomly selected durations (3.8, 1.9, or 0.95 sec) and amplitudes (2, 4, or 6 mA).

E. Block-Push Experiment

During the main experiment, participants interacted with the virtual environment by pressing blocks and receiving sensory feedback (Fig. 2). After pushing a block, participants were prompted to provide their perception of the block's hardness—whether they pushed against a "soft" or "hard" block. The 2x1.7x1.7-cm block could slide along a frictionless virtual table, recoiling back to its initial location after release (i.e., stiffness set to 100 N/m and the damping set to 500 N-sec/m; the mass of the block was 50kg). The stimulation for sensory feedback was proportional to the normal force experienced by the virtual fingertip touch sensor (normalized to the range 0-1 for sensory encoding). For the "hard" block, the force was scaled by 1.5, and for a "soft" block, by 0.75 prior to encoding the stimulation amplitude (because the object shape was not compressible, we opted to scale the force directly rather than adjust the block stiffness and/or damping). Scale factors were set based on pilot data so that performance without stimulation in training data would be near 75% correct in the box-push task (e.g., half-way between chance, 50%, and perfection, 100%). Stimulation amplitudes ranged linearly between the minimum amplitude threshold of detection to 3-mA above the threshold.

To avoid order effect in the collected data, participants completed the block-push experiment 4 times, in a pseudorandom order: KF trained on data with stimulation, KF trained on data without stimulation, CNN trained on data with stimulation, CNN trained on data without stimulation. For each training condition, 32 blocks were presented (of which 16-17 were "soft", and 15-16 were "hard"). Participants were blind to the virtual environment and focused solely on the sensory feedback provided. The collected data was analyzed to determine the participants' ability to distinguish between different levels of stimulation and block hardness.

F. Data Analysis

The percentage of correctly identified "soft" and "hard" blocks were calculated for each participant. Tests for normality indicated that the data were non-parametric (Kolmogorov-Smirnov; $p < 0.01$). The resulting non-parametric tests for an effect due to stimulation in the training data indicated a non-significant result (Friedman's test: $p = 0.13$; $df = 1$; $\chi 2 = 2.26$). However, this may be a result of the limited power of non-parametric tests with very small sample sizes ($n = 8$).

III. Results

The percent correctly judged "soft" and "hard" were calculated for each participant and are presented in Fig. 3. With stimulation included in the training data, both the KF and the CNN led to more correctly identified "soft" blocks: 75.9% to 81.8% and 71.8% to 84.9%, respectively. Although the increases were not significant, performance trends toward improvement with stimulation artifact in the training data in all cases. Identifying the "hard" blocks appears to be more difficult under all scenarios. For the CNN there seemed to be

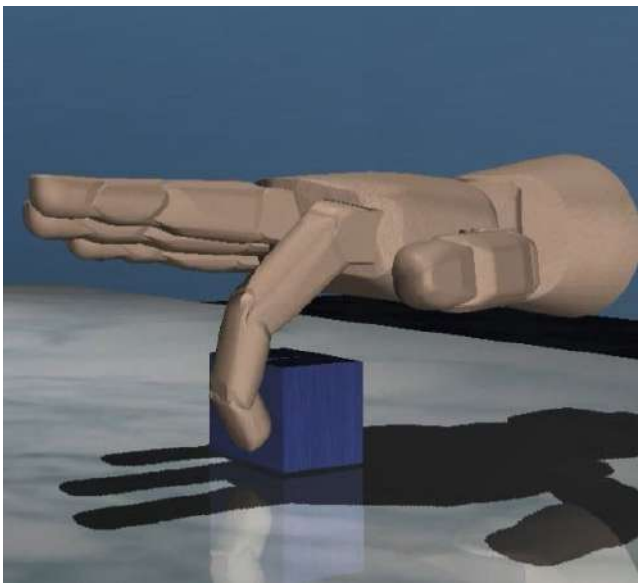


Figure 2. Participants controlled an arm in the virtual (MuJoco software). During the experiment, the user pushed a block while feeling electrocutaneous stimulation proportional to the force experienced by the virtual finger. Based on the sensory feedback, the user identified the blocks' hardness (i.e., "hard" or "soft").

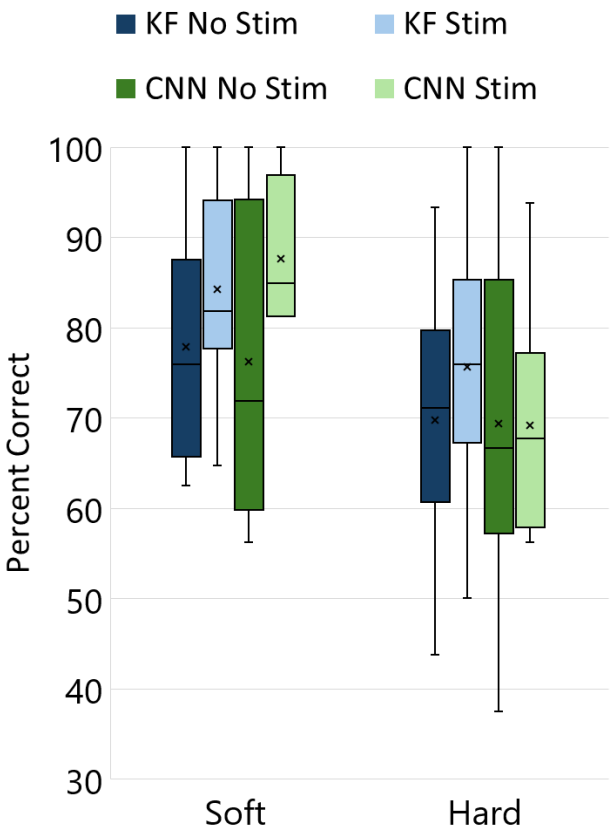


Figure 3. The percentage of trials that participants correctly identified as either "soft" or "hard" for the Kalman filter (KF) and the convolutional neural network (CNN), with and without stimulation in the training data. The box represents the interquartile range (IQR; 25th and 75th percentiles) and the line inside the box represents the median (x = mean).

little benefit from stimulation in the training data when identifying "hard" blocks. There is large variability in most conditions, where some participants performed perfectly and others much worse.

IV. Discussion and Conclusions

Our data suggests that training with stimulation may improve discrimination of "soft"-blocks from the "hard". It appears that both proportional control algorithms could reduce the effect of stimulation artifact on hand control in sensorimotor tasks—though the results need to be confirmed with larger sample sizes and stimulation electrodes located closely to the sEMG recording sites.

This is the first exploration of sEMG artifact removal during proportional motor control, as well as the first to explore how the artifacts in training data affect algorithm performance in sensorimotor tasks. We have shown previously that for these two decoding algorithms, decoder performance depends on the training data and training paradigms used [11]. Here, we also observed that both algorithms seemed to exhibit improved motor control when trained on data that included stimulation artifact in the sEMG. Because many sensorimotor tasks require proportional control to adapt in real-time to sensory feedback, it is paramount to develop methods that ignore or are unaffected by stimulation artifact.

Improvement in object detection likely occurs from improved motor control. Occasionally, we observed that algorithms trained without artifact would jump, either flexing or extending, on contact with the object and at the onset of stimulation. This uncontrolled behavior would immediately disrupt the typical movement of the block, the force applied to the index finger, and the resulting sensory feedback. Because participants were blind to the movement of the index finger, inconsistent feedback signals would easily lead to confusion and a guess at whether the block was soft or hard to push.

The benefits of this approach, in comparison to others who implemented specific algorithms to filter artifact [14], is that it requires no extra computation during real-time predictions. It may also work for various algorithms with high- (CNN) and low- (KF) computational demands; and perhaps even more so for our low-computationally demanding algorithm, making it an attractive approach for deployment in clinical systems. Our approach differs from the signal blanking during stimulation method [9] because it avoids removal of potentially useful data near or during stimulation. Dexterous proportional control relies on continuous sEMG inputs so that blanking data could substantially degrade control during the types of object manipulation where dexterous control is most useful. Furthermore, because natural feeling feedback occurs with higher frequency stimulation, this effect could be exacerbated with stimulation designed for natural feeling sensory percepts [20]; however future work should confirm these hypotheses.

The limitations of this approach include that the algorithms train on the artifacts available during training alone, which are likely to present differently throughout the day as the user moves and moisture accumulates at electrodes' interfaces (a common problem for any myoelectric system with or without sensory feedback). Second, while we did not observe a movement delay, increased variation in the sEMG features could produce movement delay for the KF which relies on the variance of its feature distributions to decide how much weight to place on a new prediction. Third, stimulation artifacts may be larger and more difficult to address in individuals with limb amputation where the recording and stimulating electrodes are more closely located. Out of convenience in experimental setup, we placed stimulation electrodes several centimeters away from recording electrodes. It is likely that relocating stimulation closer to recording electrodes could increase the benefit of including artifact in the training data because artifact could be larger and more likely to interfere with motor control. In any event, in a clinical setting, recording and stimulating electrodes are likely to be placed near each other in a prosthetic socket, so future studies should explore this configuration and its effects on motor control.

References

[1] E. A. Biddiss and T. T. Chau, "Upper limb prosthesis use and abandonment: A survey of the last 25 years," Prosthet. Orthot. Int., vol. 31, no. 3, pp. 236–257, 2007, doi: 10.1080/03093640600994581.

[2] D. J. Tyler, "Neural interfaces for somatosensory feedback: bringing life to a prosthesis," Curr. Opin. Neurol., vol. 28, no. 6, pp. 574–581, 2015, doi: 10.1097/WCO.0000000000000266.

[3] J. A. George, M. R. Brinton, P. C. Colgan, G. K. Colvin, S. J. Bensmaia, and G. A. Clark, "Intensity Discriminability of Electrocutaneous and Intraneural Stimulation Pulse Frequency in Intact Individuals and Amputees," in Proceedings of the Annual International Conference of the IEEE Engineering in Medicine and Biology Society, EMBS, Jan. 2020, vol. 2020-July, pp. 3893–3896, doi: 10.1109/EMBC44109.2020.9176720.

[4] J. L. Vargas Luna, M. Krenn, J. A. Cortés Ramírez, and W. Mayr, "Dynamic impedance model of the skin-electrode interface for transcutaneous electrical stimulation," PLoS One, vol. 10, no. 5, 2015, doi: 10.1371/journal.pone.0125609.

[5] D. R. Merrill, M. Bikson, and J. G. Jefferys, "Electrical stimulation of excitable tissue: design of efficacious and safe protocols," J. Neurosci. Methods, vol. 141, no. 2, pp. 171–198, 2005, doi: 10.1016/j.jneumeth.2004.10.020.

[6] E. Imatz-Ojanguren and T. Keller, "Evoked sensations with transcutaneous electrical stimulation with different frequencies, waveforms, and electrode configurations," Artif. Organs, vol. 47, no. 1, pp. 117–128, Sep. 2023, doi: 10.1111/aor.14400.

[7] M. A. Trout, A. T. Harrison, M. R. Brinton, and J. A. George, "A portable, programmable, multichannel stimulator with high compliance voltage for noninvasive neural stimulation of motor and sensory nerves in humans," Sci. Rep., vol. 13, no. 1, p. 3469, Mar. 2023, doi: 10.1038/s41598-023-30545-8.

[8] R. Midura and M. Brinton, "Effect of Biomimicry on Perceived Intensity, Naturalness, and Pleasantness Using Non-Invasive Electrical Stimulation," Myoelectric Control. Symp., 2024, doi: https://doi.org/10.57922/mec.2502.

[9] C. Hartmann, S. Došen, S. Amsuess, and D. Farina, "Closed-loop control of myoelectric prostheses with electrotactile feedback: Influence of stimulation artifact and blanking," IEEE Trans. Neural Syst. Rehabil. Eng., vol. 23, no. 5, pp. 807–816, Sep. 2015, doi: 10.1109/TNSRE.2014.2357175.

[10] A. H. Arieta, H. Yokoi, T. Arai, and W. Yu, "Study on the effects of electrical stimulation on the pattern recognition for an EMG prosthetic application," in Annual International Conference of the IEEE Engineering in Medicine and Biology - Proceedings, 2005, vol. 7, pp. 6919–6922, doi: 10.1109/iembs.2005.1616097.

[11] J. A. George, M. R. Brinton, C. C. Duncan, D. T. Hutchinson, and G. A. Clark, "Improved Training Paradigms and Motor-Decode Algorithms: Results from Intact Individuals and a Recent Transradial Amputee with Prior Complex Regional Pain Syndrome," in Proceedings of the Annual International Conference of the IEEE Engineering in Medicine and Biology Society, 2018, vol. 2018-July, pp. 3782–3787, doi: 10.1109/EMBC.2018.8513342.

[12] J. A. George, T. S. Davis, M. R. Brinton, and G. A. Clark, “Intuitive neuromyoelectric control of a dexterous bionic arm using a modified Kalman filter,” J. Neurosci. Methods, vol. 330, p. 108462, Aug. 2019, doi: 10.1016/j.jneumeth.2019.108462.

[13] C. Almström, A. Anani, P. Herberts, and L. Körner, “Electrical stimulation and myoelectric control. A theoretical and applied study relevant to prosthesis sensory feedback,” Med. Biol. Eng. Comput., vol. 19, no. 5, pp. 645–653, Sep. 1981, doi: 10.1007/BF02442780.

[14] E. J. Earley, A. Berneving, J. Zbinden, and M. Ortiz-Catalan, “Neurostimulation artifact removal for implantable sensors improves signal clarity and decoding of motor volition,” Front. Hum. Neurosci., vol. 16, no. October, pp. 1–12, 2022, doi: 10.3389/fnhum.2022.1030207.

[15] “MuJoCo: Advanced physics simulation.” https://mujoco.org/ (accessed Feb. 20, 2025).

[16] E. Todorov, T. Erez, and Y. Tassa, “MuJoCo: A physics engine for model-based control,” IEEE Int. Conf. Intell. Robot. Syst., pp. 5026–5033, 2012, doi: 10.1109/IROS.2012.6386109.

[17] J. Nieveen, M. Brinton, D. J. Warren, and V. J. Mathews, “A Nonlinear Latching Filter to Remove Jitter from Movement Estimates for Prostheses,” IEEE Trans. Neural Syst. Rehabil. Eng., vol. 28, no. 12, pp. 2849–2858, Dec. 2020, doi: 10.1109/TNSRE.2020.3038706.

[18] K. Z. Mao, “Orthogonal Forward Selection and Backward Elimination Algorithms for Feature Subset Selection,” IEEE Trans. Syst. Man, Cybern. Part B Cybern., vol. 34, no. 1, pp. 629–634, Feb. 2004, doi: 10.1109/TSMCB.2002.804363.

[19] S. J. Bensmaia, D. J. Tyler, and S. Micera, “Restoration of sensory information via bionic hands,” Nat. Biomed. Eng., pp. 1–13, Nov. 2020, doi: 10.1038/s41551-020-00630-8.

[20] E. L. Graczyk, B. P. Christie, Q. He, D. J. Tyler, and S. J. Bensmaia, “Frequency Shapes the Quality of Tactile Percepts Evoked through Electrical Stimulation of the Nerves,” J. Neurosci., vol. 42, no. 10, pp. 2052–2064, Mar. 2022, doi: 10.1523/JNEUROSCI.1494-21.2021.

User Testing for Performance and Brain Engagement with the HOPE Hand Exoskeleton for Individuals with Spasticity due to Brain Injury

1st Tess B. Meier
Robotics Engineering
Worcester Polytechnic Institute
Worcester, MA, USA
tbmeier@wpi.edu

2nd Kehan Yang
Robotics Engineering
Worcester Polytechnic Institute
Worcester, MA, USA

3nd Andrew Daudelin
Physics
Worcester Polytechnic Institute
Worcester, MA, USA

4rd Gregory S. Fischer
Robotics Engineering
Worcester Polytechnic Institute
Worcester, MA, USA

5th Gretchen R. Meier
Physical Therapist
Pine Bush Physical Therapy
Pine Bush, NY, USA

6th Benjamin Nephew
Biology & Biotechnology
Worcester Polytechnic Institute
Worcester, MA, USA

7th Erin T. Solovey
Computer Science
Worcester Polytechnic Institute
Worcester, MA, USA

8th Christopher J. Nycz
Robotics Engineering
Worcester Polytechnic Institute
Worcester, MA, USA

***Abstract*—Hand spasticity and hypertonia are common in individuals who have sustained an upper motor neuron (UMN) injuries due to stroke and traumatic brain injury. While rehabilitation robots and hand exoskeleton-based therapy treatments have shown great promise of improving motor function, the frequency of use and the nature of the repetitive therapeutic tasks can limit the promotion of neuroplasticity. The use of an assistive hand exoskeleton, meant to help the user perform activities of daily living (ADL), leverages the principals of neuroplasticity regarding increased frequency of use and increased specificity in doing functional tasks, to further improve neuroplasticity. Therefore, the use of an assistive hand exoskeleton may have neurorehabilitative benefits. The HOPE Hand — hand orthosis with powered finger extension — was designed to provide active finger flexion and extension of the fingers in the presence of increased muscle tone to assist individuals to perform ADLs. User testing was conducted with 3 control subjects and 2 subjects with hand spasticity and hypertonia due to a traumatic brain injury (TBI) and a stroke, respectively. This user test evaluated the user's ability to perform a functional task with the hand exoskeleton as well as their brain's engagement in the task using functional near-infrared spectroscopy (fNIRS) towards understanding neurorehabilitation benefits of assistive exoskeleton use. Results show the impaired subjects performed the functional water bottle task in significantly less time with the exoskeleton than without it. The fNIRS data showed that their motor cortex and speech centers of the brain were activating despite sustaining damage. By combining performance metrics and neuroimaging, we can further evaluate the HOPE Hand and other assistive exoskeletons to study their potential for promoting neurorehabilitation.**

***Index Terms*—Assistive device, hand exoskeleton, wearable robotics, hemiparesis, hand spasticity, neurorehabilitation**

This material is based on work partially supported by the National Science Foundation (NSF) under Grant No DGE-1922761, 1927275. Any opinions, findings, and conclusions or recommendations expressed in this material are those of the authors and do not necessarily reflect the views of the NSF

I. Introduction

Stroke and traumatic brain injury (TBI) can result in upper motor neuron injuries, leaving 55-75% of survivors with hemiparesis and subsequent upper limb motor impairment, including hand impairment [1]. Hand impairment can physically manifest as both positive and negative symptoms in the upper limb. Negative symptoms like weakness and loss of dexterity manifest as a flaccid hand. Positive symptoms like spasticity—a velocity dependent increase in muscle tone—and hypertonia—an increased resting muscle tone—result in the individual exhibiting a closed fist posture. In addition to increased finger flexion, this flexor synergy pattern also includes reflexive wrist flexion, elbow flexion, and internal rotation of the shoulder [2]. Individuals with this condition can have some to no volitional ability to extend their fingers, wrist, or elbow. Stimuli such as physical tasks or cognitive tasks may trigger the reflexive synergy, increasing the muscle tone of the hand, and leading to stronger flexion forces.

Robotic motor rehabilitation has been shown to improve rehabilitation outcomes, comparable to or beyond conventional therapy [3]. Upper limb and hand exoskeletons are used to engage the impaired limb in movement routines, promoting neuroplasticity and use of the limb [4]. Some have employed rehabilitation games with robotic exoskeletons [5]. While these devices show great promise for motor rehabilitation, there are some inherent limitations. Rehabilitative hand exoskeletons, such as those previously mentioned, are typically used for short sessions a few times a week, limiting the user to the clinical environment and repetitive motor activities, as opposed to engaging in activities of daily living (ADLs).

In regards to daily life, these individuals have learned to compensate by performing single-handed and bimanual tasks with their able hand. Excluding the impaired hand and limb

from ADLs can lead to learned non-use; the brain reallocates resources, leading to poor functional improvement or rehabilitation of the limb. This a principal of neuroplasticity, "use it or lose it" [6]. Non-robotic therapy methods have shown that maximizing the use of the impaired limb can prevent or reverse learned non-use [7]. Assistive devices like hand exoskeletons can also be used to re-engage the impaired hand enabling individuals to complete ADLs, especially bimanual tasks [8]. According to additional principals of neuroplasticity, the more frequent, specific, and salient the use of the impaired limb is, the better the neurorehabilitative outcomes [6]. As an individual uses an assistive hand exoskeleton to perform necessary tasks for daily independent living with increased frequency and purpose, we can hypothesize that they will experience increased neurorehabilitative outcomes. Neuroimaging can be used to measure this brain engagement during exoskeleton use. Portable neuroimaging techniques such as functional near-infrared spectroscopy allow for the brain data to be collected in a real-world environment to monitor the brain's engagement with assistive technology [9].

Assistive exoskeleton user studies allow us to evaluate user performance with the device and monitor the brain's response to the technology with neuroimaging. Spasticity has precluded some individuals from participating in user studies. One large user study was conducted with an upper limb exoskeleton and 60% of the candidates were excluded from the study because they had moderate to severe spasticity [10]. We want to study exoskeleton use for people with hand spasticity.

The goal of our user study is to evaluate individuals' ability to perform a functional task with an exoskeleton designed to accommodate spasticity and to record their the neurological response during use. Neuroimaging data can provide insights into brain activation and engagement in tasks, with implications for neurorehabilitation. To conduct this study, an exoskeleton capable of extending the fingers of individuals with spasticity was needed. The exoskeleton must apply adequate torque at the finger joints, not obstruct the palmar surface of the hand, and minimize weight where possible.

Of the existing hand exoskeletons designed to accommodate spasticity, some only allow for passive finger extension, such as the saeboFlex glove by Saebo (Saebo, North Carolina, USA). This device works well for individuals who have decent motor control of hand flexion. However, the passive finger extension is applying constant forces, without an active way to release those forces. Gasser et al. presented an upper limb exoskeleton that can accomplish hand opening and closing (the power grasp) in the presence of muscle tone and spasticity [11]. The fingers are designed to move together which limits the amount of functional grasps that can be performance by the device. Individuated finger motion can be beneficial in power grasps because it allows for conformal grasping, meaning the fingers can flex to the contours of the object for a more stable grasp. Gasser et al. conducted user testing with their exoskeleton using a water bottle opening and closing task. This task requires the use of both hands, is a functional task, and can be timed to assess performance as speed [11]. This functional task was incorporated into the user study presented in this work. Yurkewich et al. presented the HERO Grip Glove which provides individuated finger extension, however their testing was limited to subjects with mild to moderate spasticity with Modified Ashworth Scale (MAS) scores ≤ 2 [12].

In this paper we present the Hand Orthosis with Powered Extension (the HOPE Hand), designed for individuals with hand spasticity and hypertonia, to assist them in completing ADLs. We present the design requirements, mechanical design, actuation design, and simulated, or "Wizard-of-Oz", voice control. In addition to providing assistance, the daily use of hand exoskeletons may also have neurorehabilitative benefits. To evaluate the performance and neural engagement with the hand exoskeleton, a user study was conducted with three control subjects and two subjects with hand impairment due to TBI and stroke, respectively. Time for task completion was used as a performance metric, and functional near-infrared spectroscopy was used to measure changes in brain activation towards demonstrating brain engagement during exoskeleton use.

II. Hand Exoskeleton Design

A. Design Requirements

The HOPE Hand was designed with the following requirements:

- Apply greater than 0.5 Nm of torque at the interphalangeal joints and 0.75 Nm of torque at the metacarpophalangeal (MCP) joint to extend the fingers [13]
- Provide individuated finger flexion to allow the user's hand to conform to the object being grasped
- Avoid components on the palmer surface of the hand which would interfere with grasping
- Allow for portable use with greater than two hours of battery life
- Minimize weight
- Employ a user interface that is compatible with individuals with spasticity due to upper motor neuron injuries

B. Design and Construction

The HOPE Hand consists of a semi-rigid hand orthosis worn on the dorsal surface of the hand, and an actuation unit to provide the pushing and pulling forces which is worn on the upper arm (Figure 2).

1) Hand Orthosis: Each finger was designed based on the kinematic concepts shown in Figure 1. Cable guides attached to the dorsal surface of the hand create an offset d to the joint centers of the MCP and proximal interphalangeal (PIP) joints, reducing the cable tension needed to oppose the resisting torque at each of these joints. The distal interphalangeal (DIP) joint was splinted in a straight position as coordination of the PIP and DIP in the presence of spasticity is difficult with non-rigid mechanisms. The exoskeleton provides two degrees of motion for the thumb. A channel across the back of the hand guides a cable to the thumb's metacarpal where it is fixed. Rotation and abduction of the thumb into opposition is accomplished by manually pushing the cable across the

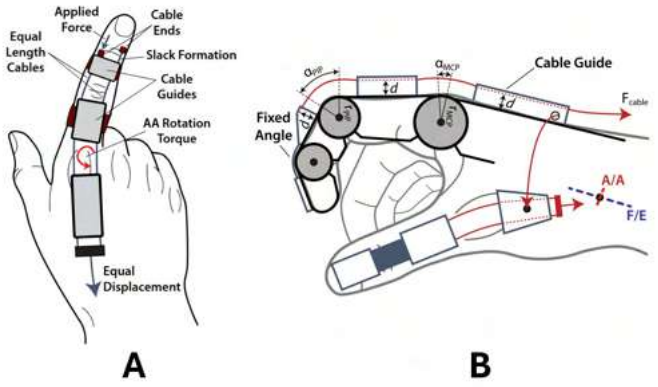


Fig. 1. A) Self regulating abduction/adduction rotation using two cables for finger extension. Due to a constant path length for both cables and an equal displacement imposed by the actuation unit, slack forms between the cable guide on the inside radius and the terminal cable guide. This causes an imbalance in tension between the two cables which creates a moment that seeks to re-center the abduction/adduction axis of the MCP joint [14] B) Flexion/Extension (FE) of the fingers and the thumb provided by pushing and pulling cables running along their dorsal surface. Abduction/adduction/opposition (AA) of the thumb's carpalmetacarpal joint was provided by manually pushing and pulling a cable across the dorsal surface of the hand terminating at the first metacarpal [15].

hand as in the kinematic drawing in Figure 1 B, and in the Figure 2. To maintain thumb opposition, a screw is used to lock the cable position. Flexion/extension of the thumb's MCP can be achieved actively by pushing or pulling a second cable running along the dorsal surface, in a similar direction to the FE force for the fingers. The exoskeleton is 3D printed from a photopolymer material (Durable Resin, Formlabs) and weighs 240g with Bowden cables, not including actuation unit [15].

2) Actuation Unit: Force is applied to the finger extension/flexion cables using DC motor driven linear actuators. Based on the peak torque measured in [13], a desired 1 second response from full flexion to full extension, and an assumed quintic joint velocity profile, a peak power of 3-5W delivered to each finger was determined necessary to extend the joints against chronic spasticity. A ballscrew with 90% efficiency (MTF-0601, THK) was used to generate the cable pull through a 60-70% efficient Bowden cable (Figure 3). Based on these parameters, a 3W continuous power (DCX14L EB SL 6V, Maxon, inc.) brushed DC motor was chosen under the provision that over-driving by 2-3 times the continuous power rating is permissible for several seconds as per manufacturer guidelines. Four of these motor and ballscrew actuators were integrated into a remote actuation unit mounted to the upper arm as seen in Figure 4. A SAM3X8E ARM Microcontroller (ATMEL, USA), on the remote actuation unit, can connect to a host controller via wired USB or XBee wireless communication (S2C DigiMesh Mesh 2.4, Digi International). The microcontroller runs position control loops for each of the linear actuators with the orthosis's compliance regulating the force applied to the user. The actuation unit weighs 768g with battery capacity of 12.2Wh [15].

3) Summary of Significant Characteristics: The HOPE Hand weighs approximately 1 kg including the actuation unit and the hand orthosis. It can provide individuated finger motion with up to 0.75 Nm of torque at the finger joints for finger extension. It can perform active finger flexion to accomplish conformable power grasps with an unobstructed palmar hand surface. Finger flexion is accomplished using a combination of the cable stiffness pushing the fingers into flexion, the relieving of extension forces, and the user's spasticity to close the hand.

III. Experimental Assessment

A. Subjects

This study was approved by the Worcester Polytechnic Institute's institutional review board (HHS 00007374). Three control subjects (2 male, 1 female; 22 ± 0.5 y.o.) and two impaired subjects (1 male, 32 y.o.; 1 female, 28 y.o.) were recruited for this study. The control subjects were recruited from the population of graduate students at Worcester Polytechnic Institute (Massachusetts, USA). Control subjects had no neurological or muscular injuries or conditions, were right handed, and were native English speakers. The impaired subjects were recruited from the patient population at Pine Bush Physical Therapy (New York, USA) through recommendation by their physical therapist. Inclusion criteria for impaired subjects was as follows: (a) individual has a neurological condition affecting the motor system, (b) individual displays spasticity in their hand with MAS $\geq$ 2 (c) individual exhibits mild to moderate Broca's aphasia (d) individual is deemed to be a candidate for an upper limb assistive device by the collaborating physical therapist. All subjects were able to provide informed consent.

Both impaired subjects had hand impairment due to an upper motor neuron injury: one had a stroke, and the other had a TBI. Both impaired subjects exhibited mild to moderate Broca's aphasia. Impaired subjects completed the disabilities of arm, shoulder, and hand (DASH) questionnaire to quantify their level of upper limb disability. Our collaborating physical therapist evaluated the subjects' level of hand spasticity using the Modified Ashworth Scale on the finger flexor muscle group; both impaired subjects had a MAS = 3, no volitional ability to extend their fingers, and some ability to volitionally flex their fingers. Subject information is shown in Table I.

B. User Interface and Control

When designing a user interface, it is important to consider not only the symptoms of hand impairment but also the comorbidities often associated with hemiparesis, such as speech aphasia. 80% of individuals with Broca's aphasia also have hemiplegia, and these conditions "do not just coexist, they interact" . This comorbidity presents an opportunity to implement a user interface that engages multiple areas of the damaged brain, as motor and speech rehabilitation have synergistic positive effects [16]. Therefore, voice control is a promising user interface for the HOPE hand as it could lead to improvements in both speech and motor rehabilitation.

All subjects wearing the HOPE Hand used verbal commands of "open" and "close," to control the opening and

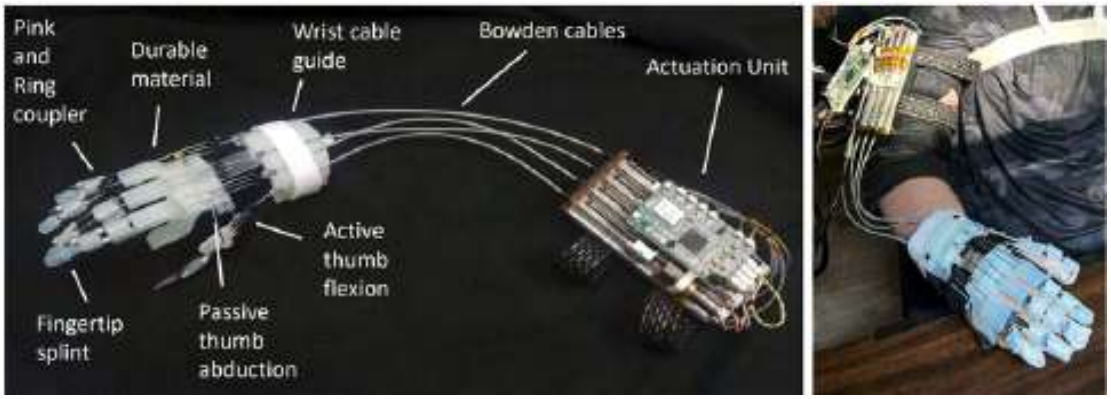


Fig. 2. *On the left:*Annotated image of the Hand Orthosis with Powered Extension (HOPE) Hand. *On the right:* Impaired subject wearing the HOPE Hand.

TABLE I
SUBJECT DEMOGRAPHICS

Subject	Age(Yrs)	Height (cm)	Weight (kg)	Gender	Mod. Ash.	DASH	Condition	Years since Injury
1	28	165	58.5	F	3	57	TBI	9
2	32	178	127	M	3	44	Stroke	3
Controls (3)	22 ± 0.5	176 ± 9	75.6 ± 2.8	4F/4M	-	-	-	-

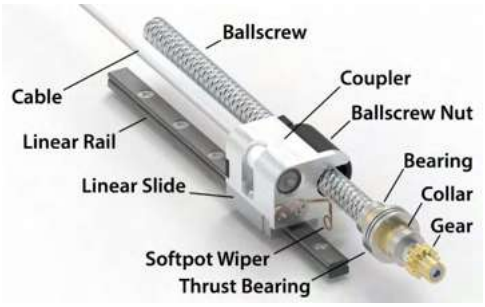


Fig. 3. Ballscrew-based linear actuator designed for providing cable tension toan orthosis for extension against moderate to severe increases in muscle tone [14].

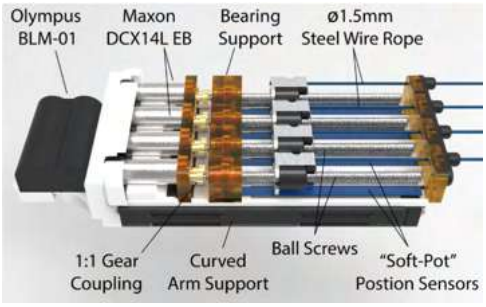


Fig. 4. Annotated render of the actuation unit [14].

closing of the exoskeleton, respectively, through a "Wizard-of-Oz" interface. This means that the users perceived the voice control as autonomous while, a researcher manually interoperated the open and close input using a graphical user interface (GUI) in response to their interpretation of subjects' verbal commands. Individuals with Broca's aphasia, including the two impaired subjects recruited for this study, have discontinuous, non-fluent speech. This makes it challenging for speech recognition algorithms and devices to interpret their speech [17], even when their speech is interpretable by other humans (as was the case for the two impaired subjects in this study). In order to simulate a "perfectly accurate" speech recognition algorithm for a hand exoskeleton user interface, this "Wizard-of-Oz" approach was implemented in HOPE Hand testing. This idealized user interface removed potential confounding factors of frustration resulting from any command recognition errors. In future versions of the HOPE Hand, a robust automated voice control algorithm will be implemented so the device can be used independently.

Upon the HOPE hand receiving an "open" command from the GUI, the DC motors turn the ballscrew, moving the coupler further from the exoskeleton, pulling the cable to extend the finger, while monitoring the position of the finger using the position sensors connected to the coupler. When the set point is reached the exoskeleton remains stationary. Similarly, receiving a "close" command from the GUI moves the coupler closer to the exoskeleton, pushing the cables and flexing the fingers until the desired set point is reached. The extension and flexion set points are entered into the GUI during the exoskeleton fitting stage, to ensure the subject's finger length and the stroke length of the cable movement will be sufficiently matched.

C. Neuroimaging

A NIRScout functional near-infrared spectroscopy (fNIRS) Neuroimaging System (NIRx, Orlando, Florida, USA) was used to measure changes in the concentration of oxygenated hemoglobin (HbO) and de-oxygenated hemoglobin (HbR) in the brain as a proxy for brain activation during all tasks. Measuring blood oxygenation level dependent (BOLD) signal changes in the brain allows us to explore the neurological

effects of exoskeleton use by looking at which areas of the cortex are activating during which tasks. The hemodynamic response function describes how the changes in brain activation result in changes of measured BOLD signal; this response is typically delayed 2-5 seconds following a stimulus.

A montage consisting of eight sources (red dots) and eight detectors (yellow dots) using the 10-20 system was created to capture activation in the motor cortex and Broca's area of the brain (Figure 8 top). During active hand motor tasks, it is expected that the medial motor cortex will be activated. During the water bottle task with the verbal "open" and "close" commands the lateral motor cortex and Broca's area will be activated. Passive hand movement tasks may or may not show activation in the motor cortex. The regions mentioned can be seen in Figure 8. The homunculus shows the location on the motor cortex in which the hands and mouth are controlled.

D. Experimental Protocol

Subjects were seated at a table throughout the study session. Research assistants put the fNIRS cap on the subject's head to ensure proper placement. Subjects performed two motor tasks prior to putting the exoskeleton on to collect brain data and performance metrics on tasks with no exoskeleton assistance. The HOPE Hand was then put on the subject, starting with a soft commercial splinting elbow brace (TISMOD, China) to immobilize the elbow joint approximately 135-100°to prevent reflexive elbow flexion, keeping the forearm and hand in a usable workspace to manipulate objects on the table from a seated position. A soft wrist brace was used to immobilize the user's wrist in a neutral position. The actuation unit was strapped to the upper arm, and the hand orthosis was attached to the dorsal surface of the hand using a velcro palm strap. The length of the exoskeletal fingers were adjusted on the HOPE Hand to account for subjects' various finger lengths, and the rigid finger segments were attached the subjects' fingers using medical tape. Subjects were given a short demonstration of the task and were allowed one practice trial. Subjects then performed the motor tasks with exoskeleton assistance. The tasks are listed below in the order in which they were completed by all subjects.



Fig. 5. Experimental set-up: subject shown with HOPE Hand on his right arm and hand. Subject shown performing the task of grasping a water bottle with the exoskeleton.

To collect the neuroimaging data in a block paradigm, each task was broken into Active blocks [A], during which the subject was doing a task for a set or variable amount of time, and Rest blocks [R] during which the subject was asked to stare at a fixation cross. As to not rush the subjects, some active blocks were initiated by the researchers and concluded when the subject completed the task, represented by time "X," which is how long it took the subject to complete each active block, respectively [XA]. Each Rest block (R) was 60 seconds represented as [60R].

- **Hand Open and Close - No Assist.** Subject was instructed to move their right hand opened and closed through the range of motion repeatedly during active blocks. Task paradigm was the following [60R - 30A - 60R - 30A - 60R].
- **Water Bottle Task - No Assist.** Subjects were instructed to grasp a water bottle with their impaired/right hand, unscrew the cap with their able/left hand, screw it back on, and remove the hand from the water bottle. Impaired subjects were given guidance from the physical therapist on the best approach for getting their impaired hand around the water bottle. The time it took to complete each water bottle open and close was recorded as a performance metric [11]. Task paradigm was the following [60R - XA - 60R].
- **Hand Open and Close - Exo Assist.** Subject was instructed to relax their hand (be passive) as the hand exoskeleton moves the right hand through the range of motion repeatedly. This task represents a potential rehabilitation routine, moving the user's hand through the range of motion to maintain flexibility and prevent contractures. Task paradigm was the following [60R - XA - 60R - XA - 60R].
- **Water Bottle Task - Exo Assist.** Subjects were instructed to used voice commands "open" and "close" to use the hand exoskeleton to grasp a water bottle with their impaired/right hand, unscrew the cap with their able/left hand, screw it back on, and remove the hand (with the exo) from the water bottle. Impaired subjects were given guidance from the physical therapist on the best approach for getting their impaired hand around the water bottle. The time it took to complete each water bottle open and close was recorded as a performance metric [11]. Task paradigm was the following [60R - XA - 60R].

1) Data Analysis: A performance metric was collected during the water bottle tasks, both with and without the use of the HOPE Hand. Control subjects were asked to open and close the water bottle five times without the HOPE Hand and five times with the HOPE Hand. The water bottle task consisted of a sequence of subtasks: grasping the bottle, unscrewing the cap, screwing it back on, and removing their hand. This was considered one trial. The time it took to complete each trial was recorded to the nearest second. The individuals with TBI and stroke were only asked to complete the water bottle task without the HOPE Hand three times because their hand spasticity made the task challenging. These individuals completed the water bottle task with the HOPE

hand six times each, as it was a unique opportunity for them to use the exoskeleton. The water bottle task was recorded during TBI and stroke subject sessions to extract the completion time for each subtask.

In addition to this functional performance time-completion measurement, brain activation data was collected using fNIRS. This data was first pre-processed using nirsLab (NIRx, Florida, USA). Pre-processing steps included removing spike artifacts due to motion, checking the signal quality (channels with a coefficient of variation below 20% were used in further analysis), and band pass filtering with a high pass frequency cutoff of 0.17Hz, and a low pass frequency cutoff of 0.005Hz. Then a Generalized Linear Model (GLM) was used to calculate the activation of each channel during active blocks convolved with the hemodynamic response function. Statistical parametric mapping was used to spatially display statistically significant activation ($p < 0.05$) as changes in HbR across the measured brain region.

IV. Results

A. Task Performance

The time it took the subjects to complete each water bottle trial is shown in Figure 6; trials with no exoskeleton assistance are shown on the left, and trials with exoskeleton assistance on the right. The median time it took control subjects to complete water bottle trials with no exoskeleton assistance was $10seconds$, and the range was from $8seconds$ to $14seconds$. For the TBI and stroke subjects, trials ranged from $61seconds$ to $94seconds$, approximately 6-9 times higher than the control subjects. Figure 7 shows the average time it took for the TBI and stroke subjects to complete each subtask, which demonstrates that the increased time is largely due to the challenge of getting their hand around the water bottle.

In comparison, the time it took for control subjects to complete the water bottle trials with the exoskeleton was higher than without, with a median of $30seconds$ and a range from $25seconds$ to $34seconds$. The time it took for the TBI and stroke subjects to complete the trials decreased to $34seconds$ to $46seconds$, which overlaps with the upper range of the control trials. There is also a decrease in variability between the time metric of the TBI trials with no exo assistance ($54 - 94seconds$) and with exo assistance ($34 - 46seconds$). Figure 7 shows the same subtask breakdown for both impaired subjects using the exoskeleton to complete the tasks, and the grasping subtask decreased by approximately $49.7seconds$ for the TBI subject and approximately $12.1seconds$ for the stroke subject. The stroke subject also showed an $11.8second$ decrease in the unscrewing the cap and an $8.3seconds$ decrease in screwing-on the cap.

B. Neuroimaging Results

The SPM results can be seen in Figure 10, with the columns representing the tasks, and the rows representing the subjects. The colored locations on each head represent significant brain activation measured as changes in de-oxygenated hemoglobin during the task.

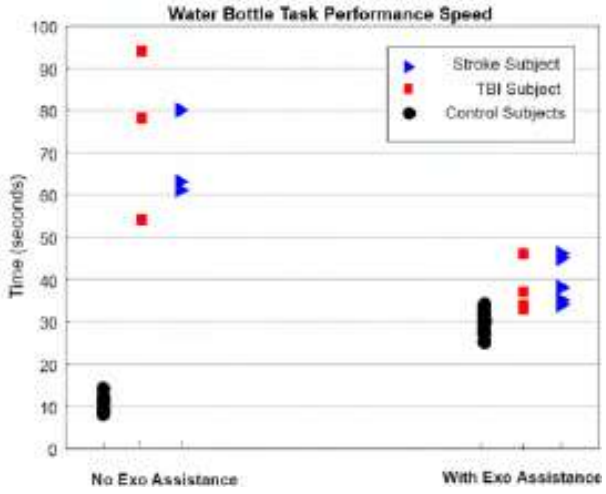


Fig. 6. 15 trials from 3 control subjects (5 each) shown as black circles for trials with no exo assistance, and with exo assistance, respectively. Individual trials from TBI and Stroke subjects shown as a red square and blue triangle, respectively.

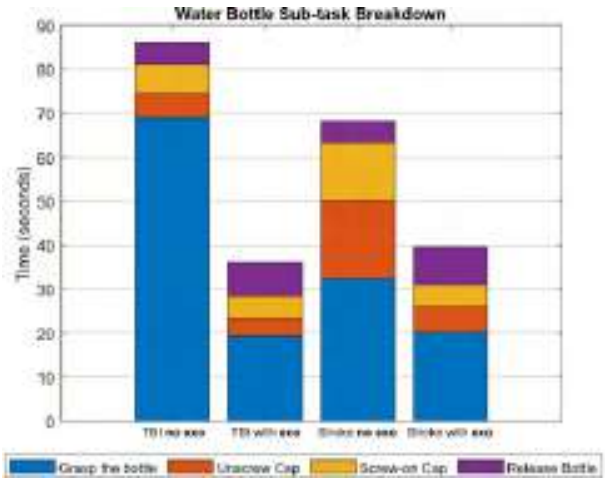


Fig. 7. Average breakdown for TBI subject without exo (n=2) and with exo assistance(n=6), and stroke subject without exo (n=3) and with exo assistance (n=5)

More activation can be seen in the medial motor cortex (cortex for hand motor control) in the tasks with no assistance, especially the water bottle task because it requires the use of both hands. When participants are actively participating in a task, there is more activation, as opposed to the exoskeleton assisted tasks in which the users are instructed to remain passive. For the water bottle with exoskeleton assistance task, there is activation in the lateral motor cortex (cortex for mouth motor control and Broca's region) which reflects the subject using verbal commands to open and close the exoskeleton.

Both the TBI and stroke subjects sustained their brain injuries on the left side of their brain, resulting in hemiparesis of the right side of their body. It is encouraging to see brain activation in the left side hand motor cortex for both impaired subjects (D.i., D.ii., D.iii., E.i., E.ii., E.iv.) because it shows

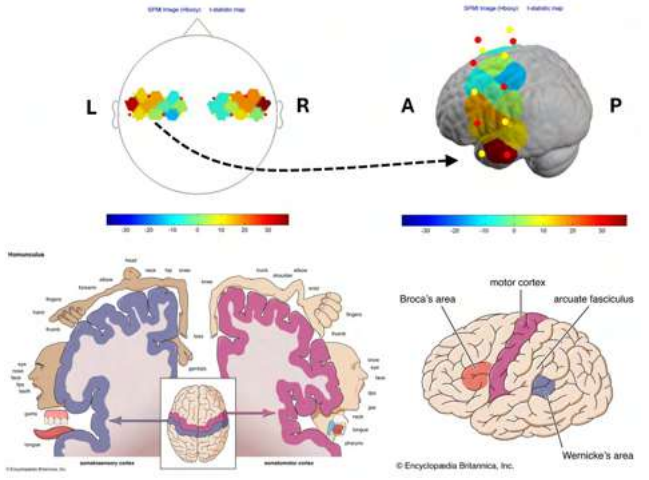


Fig. 8. The fNIRS montage shown in the top two images was designed to capture brain activation in the motor cortex, and the broca's area of the brain [18]. The homunculus and the image of the brain in the bottom right contextualize the locations of the brain to their functional purpose [19]. We expect to see activation in the Broca's area during the use of voice commands, and we expect to see activation in the medial left motor cortex, which control the right hand.

there may have been engagement with the damaged areas of the brain. There is also activation in the speech areas of the brain (D.iv.,E.iv.) during the water bottle with exoskeleton assisted tasks, which is also encouraging as they both have Broca's aphasia.



Fig. 9. Stroke subject performing the water bottle task without exoskeleton assistance. Subject's impaired hand (right hand) is shown tightly around the top of the water bottle, partially obstructing the cap.

V. Discussion

The HOPE Hand exoskeleton can successfully open and close the hand in the presence of increased muscle tone (MAS $\geq$2). It can assist the user in accomplishing functional bimanual tasks such as opening a water bottle. The "Wizard-of-Oz" voice control demonstrated that an accurate, robust, voice recognition algorithm and control would be a feasible user interface for individuals who have speech aphasia in addition to hand spasticity, and it also elicited brain activation in the speech production centers of the brain which could have rehabilitative benefits.

The results of the water bottle task show that the use of the HOPE Hand decreases the time it takes to complete the task for

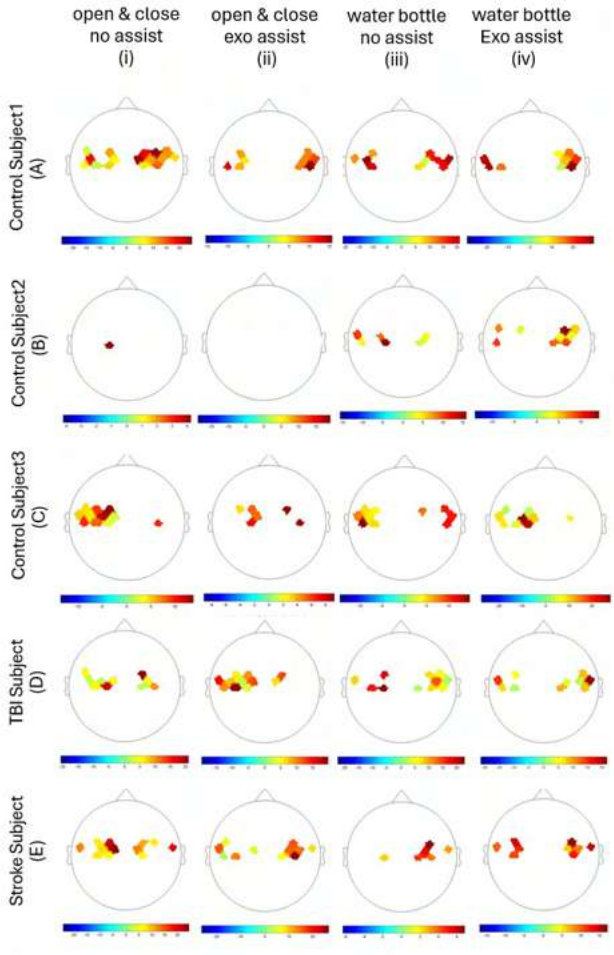


Fig. 10. Statistical Parametric Mapping (SPM) results for two impaired subjects and 3 control subjects. The colored bar along the bottom of each head figure is the intensity of the hemodynamic response. Only channels with significant activation ($p<0.05$) are shown.

impaired subjects, being the most helpful for the grasping and unscrewing subtasks. The decrease in variability also suggests the consistency provided by the exoskeleton. While the able-handed individuals are able to perform the task faster on their own than using the exoskeleton, the impaired subjects are able to achieve close to the same performance with the exoskeleton as the controls with the exoskeleton. The TBI subject was relatively consistent in the unscrew cap, screw-on cap, and remove hand subtasks in both no exo and with exo trials, while the stroke subject took longer to unscrew the cap and screw-on the cap. This was due to the physical limitation of getting his hand low enough on the bottle to have clear space around the cap making it challenging for his able hand to then unscrew and screw-on the cap (shown in Figure 9). With the exoskeleton, his hand was able to open wider, allowing him to position his hand lower on the bottle and giving him space to access the cap.

The SPM results from the impaired subjects show that the damaged areas of the brain may still be active during motor

and speech tasks. This interpretation assumes that the montage provides adequate coverage and that activation would occur in the expected areas according to a standard brain atlas. While this assumption may be inaccurate due to functional reorganization of the brain, anatomical references and assumptions must be made with the limited spatial coverage.

More brain engagement seen with tasks when the subject is actively moving their own hand. This means that a hand exoskeleton user may see more of a rehabilitative benefit by trying to use their hand even in exoskeleton assisted tasks. Because actively engaging their impaired hand often leads to increase muscle tone, it is increasingly important that hand exoskeletons are designed to resist their muscle forces. The combination of the neuroimaging data and the performance data illuminate important questions at the intersection of assistance and rehabilitation.

While fNIRS is commonly used to study brain activation, there is speculation on whether a single subject's fNIRS data can be interpreted individually, although the field is trying to move in this direction. For example, Control Subject 2 showed no significant activation in the Hand Open & Close - Exo Assist Task (Figure 10). Assumptions are made that the optodes are placed in the desired anatomical locations to collect brain activation from specific cortical areas, but heads can be a variety of shapes and sizes that make the cap fit differently for each person. Controlling these variables for able-bodied subjects is challenging, and these assumptions are more tenuous when working with injured brains. Brain activity does guarantee that learning or adaptive neuroplasticity occurred, especially over one session, however changes in brain engagement over time could indicate learning, which is a topic of interest for future work. Despite the challenges, fNIRS is a promising neuroimaging technique for capturing brain activation in real-world settings, and the results shown in this study have implications for future hand exoskeleton development, control, and rehabilitation techniques.

Small sample size is another limitation of this study as it prevents statistical significance calculations on the group level. In future work, we will conduct a longitudinal study with a larger number of impaired subjects, in which they use the voice-controlled exoskeleton daily at home to assist with ADLs. Their rehabilitative progress would be monitored over time using intermittent neuroimaging and clinical evaluations.

VI. Conclusion

The HOPE Hand was presented as an assistive hand exoskeleton design for individuals with spasticity and Broca's aphasia following a brain injury. A user study was conducted on 3 control subjects and 2 subjects with hand impairment and Broca's aphasia due to UMN injuries. We evaluated the ability of the exoskeleton to assist the user in functional tasks, and measured subjects' brain response to exoskeleton use. Using a combination of performance metrics and neuroimaging we can gain insights into how assistive exoskeletons may be used to increase neuroplasticity through increased purposeful hand engagement.

References

[1] C. O. Wodu, G. Sweeney, M. Slachetka, and A. Kerr, "Stroke survivors' interaction with hand rehabilitation devices: Observational study," *JMIR Biomedical Engineering*, vol. 9, no. 1, p. e54159, 2024.

[2] R. T. Katz and W. Z. Rymer, "Spastic hypertonia: mechanisms and measurement," *Archives of physical medicine and rehabilitation*, vol. 70, no. 2, pp. 144–155, 1989.

[3] N. Singh, M. Saini, N. Kumar, M. P. Srivastava, and A. Mehndiratta, "Evidence of neuroplasticity with robotic hand exoskeleton for post-stroke rehabilitation: a randomized controlled trial," *Journal of neuroengineering and rehabilitation*, vol. 18, no. 1, p. 76, 2021.

[4] L. Bonanno, A. Cannuli, L. Pignolo, S. Marino, A. Quartarone, R. S. Calabrò, and A. Cerasa, "Neural plasticity changes induced by motor robotic rehabilitation in stroke patients: the contribution of functional neuroimaging," *Bioengineering*, vol. 10, no. 8, p. 990, 2023.

[5] O. Mubin, F. Alnajjar, N. Jishtu, B. Alsinglawi, and A. Al Mahmud, "Exoskeletons with virtual reality, augmented reality, and gamification for stroke patients' rehabilitation: systematic review," *JMIR rehabilitation and assistive technologies*, vol. 6, no. 2, p. e12010, 2019.

[6] J. A. Kleim and T. A. Jones, "Principles of experience-dependent neural plasticity: implications for rehabilitation after brain damage," 2008.

[7] B. R. Ballester, M. Maier, R. M. San Segundo Mozo, V. Castañeda, A. Duff, and P. F. MJ Verschure, "Counteracting learned non-use in chronic stroke patients with reinforcement-induced movement therapy," *Journal of neuroengineering and rehabilitation*, vol. 13, pp. 1–15, 2016.

[8] P. Tran, S. Jeong, K. R. Herrin, and J. P. Desai, "Hand exoskeleton systems, clinical rehabilitation practices, and future prospects," *IEEE Transactions on Medical Robotics and Bionics*, vol. 3, no. 3, pp. 606–622, 2021.

[9] P. Liu, X. Yang, F. Han, G. Peng, Q. Li, L. Huang, L. Wang, and Y. Fan, "Brain activation pattern caused by soft rehabilitation glove and virtual reality scenes: A pilot fnirs study," *IEEE Transactions on Neural Systems and Rehabilitation Engineering*, 2024.

[10] H. T. Peters, S. J. Page, and A. Persch, "Giving them a hand: wearing a myoelectric elbow-wrist-hand orthosis reduces upper extremity impairment in chronic stroke," *Archives of physical medicine and rehabilitation*, vol. 98, no. 9, pp. 1821–1827, 2017.

[11] B. W. Gasser, A. Martínez, E. Sasso-Lance, C. Kandilakis, C. M. Durrough, and M. Goldfarb, "Preliminary assessment of a hand and arm exoskeleton for enabling bimanual tasks for individuals with hemiparesis," *IEEE Transactions on Neural Systems and Rehabilitation Engineering*, vol. 28, no. 10, pp. 2214–2223, 2020.

[12] A. Yurkewich, I. J. Kozak, D. Hebert, R. H. Wang, and A. Mihailidis, "Hand extension robot orthosis (hero) grip glove: enabling independence amongst persons with severe hand impairments after stroke," *Journal of neuroengineering and rehabilitation*, vol. 17, pp. 1–17, 2020.

[13] C. J. Nycz, T. B. Meier, P. Carvalho, G. Meier, and G. S. Fischer, "Design criteria for hand exoskeletons: Measurement of forces needed to assist finger extension in traumatic brain injury patients," *IEEE Robotics and Automation Letters*, vol. 3, no. 4, pp. 3285–3292, 2018.

[14] C. J. Nycz, "Modeling analysis of design parameters for portable hand orthoses to assist upper motor neuron syndrome impairments and prototype design," Ph.D. dissertation, Ph.D. Dissertation, Dept. Robotics Eng., Worcester Polytechnic Institute, Worcester, Massachusetts, 2018. [Online]. Available: https://digital.wpi.edu/concern/etds/1r66j131z?locale=en.

[15] T. B. Meier, P. A. Carvalho, K. Y. Gandomi, G. S. Fischer, and C. J. Nycz, "Assisting hand movement of tbi patients through robotic orthoses," *In Hamlyn Symposium on Medical Robotics*, pp. 85–86, 2019.

[16] D. Anderlini, G. Wallis, and W. Marinovic, "Language as a predictor of motor recovery: the case for a more global approach to stroke rehabilitation," *Neurorehabilitation and neural repair*, vol. 33, no. 3, pp. 167–178, 2019.

[17] V. Young and A. Mihailidis, "Difficulties in automatic speech recognition of dysarthric speakers and implications for speech-based applications used by the elderly: A literature review," *Assistive Technology*, vol. 22, no. 2, pp. 99–112, 2010.

[18] *left hemisphere of the brain*. Encyclopædia Britannica, Inc. [Online]. Available: https://www.britannica.com/science/Broca-area/media/1/135877/3601

[19] S. N. Kapusta, *homunculus*. Encyclopædia Britannica. [Online]. Available: https://www.britannica.com/science/homunculus-biology/media/1/270724/277135

Design of a Breakaway Utensil Attachment for Enhanced Safety in Robot-Assisted Feeding

Hau Wen Chang[1], J-Anne Yow[1,2], Lek Syn Lim[1] Wei Tech Ang[1,2]

***Abstract*—Robot-assisted feeding systems enhance the independence of individuals with motor impairments and alleviate caregiver burden. While existing systems predominantly rely on software-based safety features to mitigate risks during unforeseen collisions, this study explores the use of a mechanical fail-safe to improve safety. We designed a breakaway utensil attachment that decouples forces exerted by the robot on the user when excessive forces occur. Finite element analysis (FEA) simulations were performed to predict failure points under various loading conditions, followed by experimental validation using 3D-printed attachments with variations in slot depth and wall loops. To facilitate testing, a drop test rig was developed and validated. Our results demonstrated a consistent failure point at the slot of the attachment, with a slot depth of 1 mm and three wall loops achieving failure at the target force of 65 N. Additionally, the parameters can be tailored to customize the breakaway force based on user-specific factors, such as comfort and pain tolerance. CAD files and utensil assembly instructions can be found here: https://tinyurl.com/rfa-utensil-attachment**

***Index Terms*—Robot-Assisted Feeding, Assistive Robotics, Mechanical Fail-Safe**

I. Introduction

Robot-assisted feeding systems offer a promising solution for improving the quality of life of those requiring feeding assistance and alleviating the burden on caregivers. Despite significant advancements in developing robust, intelligent, and personalized robot-assisted feeding systems [1], [2], a notable gap exists in designing mechanical fail-safes to ensure user safety. One of the critical safety concerns is the excessive force that can be applied during feeding due to the close physical human-robot interaction required for the task, which poses risks such as discomfort, injury, or damage to the user's oral cavity.

To address this, designing robot systems that limit the force applied during interaction is paramount. Current research systems often focus on sophisticated control algorithms and sensor feedback mechanisms to reduce force [3], [4]; however, mechanical fail-safes provide an additional layer of protection, particularly in unforeseen scenarios where software-controlled mechanisms may not respond. A mechanical solution offers a passive, reliable response to excessive force without relying on the system's active feedback loops.

This work presents a breakaway utensil attachment designed for robot-assisted feeding. The mechanism ensures that when the robotic arm applies excessive force on the user, the spoon automatically detaches, effectively preventing further force transmission to the user. By incorporating this passive fail-safe, we aim to enhance user safety and provide a safeguard against potential harm in unpredictable scenarios.

II. Related Work

A. Utensil Attachments for Robot-Assisted Feeding

Grasping a utensil directly using a two-finger gripper, commonly found on robot manipulators, is challenging. To address this, utensil attachments are typically employed to enable secure grasping by connecting utensils, such as spoons or forks, to structures that are easier for the robot to handle [1]–[5]. Additionally, force-torque (FT) sensors are often integrated into these attachments to provide haptic feedback, enabling more precise control during feeding tasks.

Recently, more innovative utensil designs have been proposed that do not take the form of a traditional spoon or fork – Kiri-spoon [6] uses a soft kirigami structure, allowing it to encapsulate and release food easily during bite acquisition. Separately, Gordon *et. al.* [2] presented their robot-assisted feeding system, which features a utensil attachment with a mechanically engineered weak point. This weak point is designed to break when excessive force is applied, eliminating any physical interaction between the robot and the user. However, the design specifics of this mechanism are not detailed, and there remains limited research exploring the integration of mechanical fail-safes in robot-assisted feeding systems.

B. Safety in Assistive Robotics

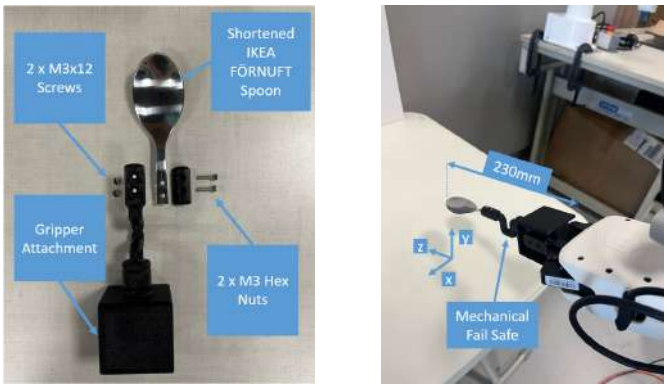
Safety in human-robot interaction is paramount, especially in assistive robotics, where physical human-robot interaction is common, and robots operate in close proximity to vulnerable users. Existing research on safety can be categorized into three main categories – control methods, motion planning, and behavior prediction. Approaches relying on control methods typically use force-torque sensors, impedance control, or compliance-based control to detect and mitigate excessive forces during interaction [3], [4]. Motion planning approaches aim to preemptively avoid collisions by generating safe trajectories based on real-time sensing and constraints [7]. However, contact is unavoidable in physically assistive tasks such as feeding. For behavior prediction, the focus is on

The research was conducted at the Future Health Technologies at the Singapore-ETH Centre, which was established collaboratively between ETH Zurich and the National Research Foundation Singapore. This research is supported by the National Research Foundation Singapore (NRF) under its Campus for Research Excellence and Technological Enterprise (CREATE) program.

[1]School of Mechanical and Aerospace Engineering, Nanyang Technological University Singapore

[2]Singapore-ETH Centre, Future Health Technologies Programme

Corresponding author's email: janne.yow@ntu.edu.sg



(a) (b)

Fig. 1: Utensil attachment with a mechanical failsafe (a) Components of our proposed utensil attachment (b) Utensil attachment grasped by a two-finger gripper

predicting human intent and motion [8], [9], enabling the robot to adapt its actions proactively to prevent potentially unsafe interactions.

While these methods effectively reduce safety risks, they primarily rely on software-based solutions and AI-driven models, which can be limited by sensor inaccuracies, computational latency, and unanticipated failure modes. Furthermore, these approaches often depend on complex system integrations [10] that may not respond adequately in every scenario. In contrast, our work introduces a safety feature based on mechanical principles, providing an additional safety layer in assistive robotic systems.

III. Approach

A. Design Considerations and Constraints

We designed a utensil attachment for the IKEA Förnuft spoon, ensuring compatibility with any robot manipulator with a two-finger gripper. To secure the spoon, its handle was shortened and attached to the utensil holder using two M3 screws and nuts, as shown in Fig. 1a. The utensil and attachment's total length was limited to a maximum of 230mm to maintain the robot's range of motion during feeding and prevent interference with its movements of the surrounding environment (Fig. 1b).

In assistive feeding, excessive force can occur in two scenarios: (1) sudden impact collisions and (2) slow compressive forces. Sudden impact collisions, such as an unintended rapid movement of the arm striking the user, pose a greater hazard as they can deliver high, localized forces in a very short time frame, increasing the risk of injury. Thus, this work focuses on addressing sudden impact collisions. The mechanical fail-safe was optimized to break at an impact force of $F_{\text{impact}} = 65N$, based on the maximum permissible force that collaborative robots can safely exert on a human face, as defined by ISO 15066 [11], which details safety requirements for collaborative robots.

Additionally, the utensil attachment must be robust enough to withstand forces encountered during normal feeding operations, such as acquiring food and transferring it to the user's mouth. To determine the minimum force threshold, we recorded force-torque data while scooping uncooked black beans, representing a high-force food scenario. To account for variability in food textures, we applied a safety factor of 2.5, resulting in a minimum force threshold of $F = 25N$. This balance between breakaway safety and functional durability is critical to the attachment's performance in real-world use.

B. Breakaway Mechanism Design

Standard breakaway mechanisms like shear pins, slip clutches, and magnetic couplings were initially considered but introduced bulk, complexity, and higher costs. Instead, we integrated the failure point directly into the 3D-printed shaft, eliminating additional components while maintaining a compact design. We achieved controlled failure by leveraging force moments and reducing the cross-sectional diameter, amplifying stress within the part. Localized stress concentration features, such as notches and slots, were introduced to create predictable failure points, ensuring a consistent breakaway force while maintaining a compact and lightweight design.

The reduced diameter d in these regions increases both torsional stress τ and bending stress σ, as described by:

$$\tau = \frac{16T}{\pi d^3}, \sigma = \frac{32M}{\pi d^3} \tag{1}$$

where T is the applied torque, M is the bending moment, and d is the diameter of the shaft. These stresses combine to produce higher equivalent (Von-Mises) stresses σ_e, which predict failure under complex loading conditions. Von-Mises stress is calculated as:

$$\sigma_e = \sqrt{\sigma_x^2 + \sigma_y^2 + \sigma_x^2\sigma_y^2 - 3\tau_{xy}^2} \tag{2}$$

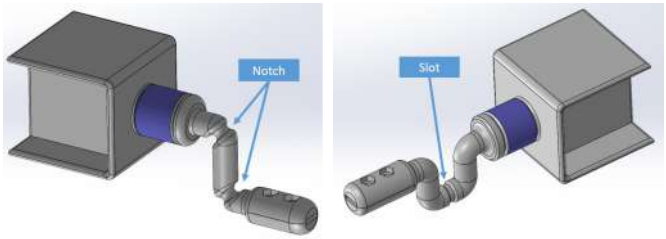
where σ_x and σ_y are the normal stresses in the x and y directions, and τ_{xy} is the shear stress in the x-y plane. Von-Mises stress is used in Section III-C to analyze how the stress is distributed under different loading conditions (Fig. 3).

Guided by these principles, two breakaway mechanism designs were developed: (1) an L-shaped design with notches at the corners and (2) a U-shaped design with a slot in the horizontal section (Fig. 2). These features ensure failure occurs predictably at the intended points under applied forces.

C. Finite Element Analysis (FEA)

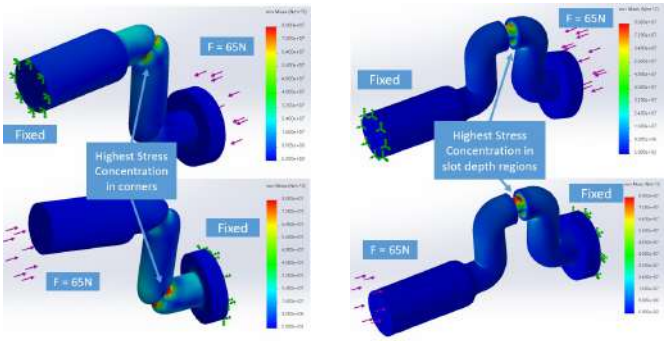
Finite Element Analysis (FEA) was conducted using SolidWorks to evaluate the stress distribution and predict the failure points for each design under a compressive force of $F_{\text{compressive}} = 65N$, corresponding to the ISO 15066 [11] threshold. Regions with high-stress concentrations were identified as likely failure points under accidental impacts.

To simulate real-world conditions, FEA was performed with different ends of the part fixed, accounting for variations in how the utensil attachment might interact with the robot's end-effector or contact the user. This provided a comprehensive



(a) (b)

Fig. 2: Utensil attachment designs – (a) L-shaped design with notches at both corners (b) U-shaped design with a slot in the horizontal section



(a) (b)

Fig. 3: Finite element analysis (FEA) on the L-shaped (left)o and U-shaped (right) design. (Top) FEA where the spoon end is fixed and (bottom) FEA where the opposite end is fixed.

evaluation of stress behavior. We focused on front-facing impacts, as they are the most common during feeding, with the robot and spoon approaching the user from the front.

As the parts were designed for 3D printing, anisotropic strength properties resulting from the layer-by-layer construction process introduced challenges in accurately simulating their performance [12], [13]. Factors such as print orientation, infill pattern, and wall thickness influence strength, making it difficult for FEA to provide exact predictions [14]. Therefore, the FEA results were treated as qualitative guides for identifying potential failure points rather than definitive performance metrics.

FEA results on the L-shaped design revealed that stress concentrations were highest at the corners of the bend (Fig. 3a). However, the specific failure location varied based on which end of the part was fixed. This made predicting the exact failure location challenging, complicating systematic testing and parameter adjustments.

In contrast, the U-shaped design demonstrated consistent stress concentrations at the slot, resulting in a single predictable failure point (Fig. 3b). Given its predictability, the U-shaped design was ultimately selected. The slot depth d was identified as a key variable for systematically evaluating breakage forces.

D. Fabrication via 3D printing

To facilitate rapid prototyping and iterative testing, the utensil attachments were 3D printed. Beyond varying the slot depth d, 3D printing parameters such as wall thickness w and print orientation (Fig. 4a) were adjusted to control the strength and performance of each part. A 15%-density grid pattern was used as the infill for all printed parts. All parts were printed using the Bambu Lab X1C 3D printer (China) and the eSun PLA+ 1.75mm filament (China) to ensure uniformity across iterations and eliminate variability from printer inconsistencies.

Print orientation was critical due to the anisotropic strength of 3D-printed parts. Initially, parts were oriented with layer lines perpendicular to the intended breaking line to maximize strength [15], [16]. However, this configuration resulted in inconsistent and unclean breaks (Fig. 4b), making it more challenging to predict the failure behavior.

To address this, the layer lines were aligned parallel to the breaking line (Fig. 4c). This orientation leveraged the inherent layer-to-layer weakness of 3D printing, ensuring predictable failure at the desired location. The mechanical failure point resulting from a collision produces a clean break with smooth edges, minimizing the risk of injury to the patient. Wall thickness w was also varied to fine-tune the breakaway force, with thicker walls increasing strength and thinner walls reducing the force.

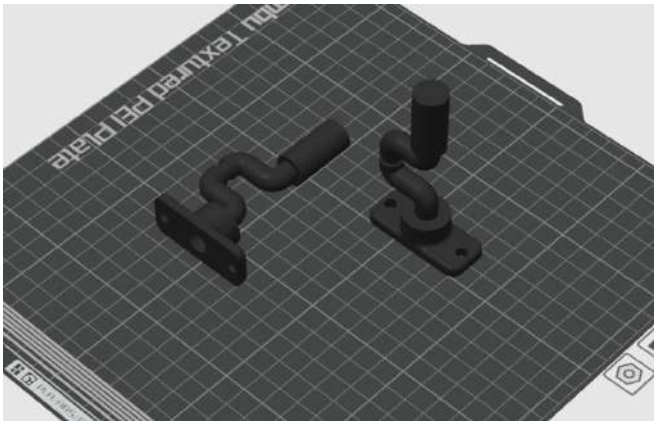
IV. Experiments

A. Experimental Setup and Design

A drop test rig was developed to evaluate the impact strength of the utensil attachments (Fig. 5). The rig included a 20kg single-point load cell with an intrinsic resolution of 1/3000 of its full-scale range (SIWAREX WL260 SP-S SA, Siemens, Germany) to measure the impact forces. Data acquisition (DAQ) was facilitated using a 24-bit amplifier (DAT 1400, Pavone Systems, Italy), which amplified and conditioned the signals from the load cell. The system was calibrated using the Optimation software (Pavone Systems, Italy) with a scaling factor of 1V = 20N for voltage-to-force conversion. The amplifier's display resolution was set to $\pm 0.01N$.

A motion capture system (Qualisys AB, Sweden) was employed to record the load cell readings and the kinematics of each drop, including position, velocity, and acceleration. Retro-reflective optical markers were placed on the basket of the test rig for precise motion tracking. The Qualisys Track Manager (QTM) v2019 was used as an integrated software interface for seamless and easy-to-use data recording, which we used to synchronize the cameras with the load cell. The trajectories of the markers and the load cell readings were captured synchronously at 200Hz and 2000Hz, respectively.

To ensure consistent alignment during testing, a 500mm linear guide rail with two linear guide blocks stabilized the weight basket. Grease was applied to the rail interface to reduce friction and ensure smooth motion. The weight basket was designed to hold varying masses, and the test parts were attached to it for drop testing.



(a)



(b)



(c)

Fig. 4: 3D printing orientations – (a) Visualization of two 3D printing orientations in the Bambu slicer: the left corresponds to (b), and the right corresponds to (c). (b) Print orientation with layer lines perpendicular to the breaking line for strength, resulting in an unclean break (c) Print orientation with layer lines parallel to the breaking line, producing a clean break

The drop height was controlled using a 3D-printed slot and a brass rod mechanism. The slot, mounted on the central aluminum profile, held the brass rod in place until manually released. This setup ensured consistent and reliable impact force readings at each height.

The rig's framework was constructed using 40 x 40mm aluminum profiles and secured with L-brackets to minimize structural damping during collisions. Additionally, two 10kg weights were placed on the rig to enhance stability and further reduce damping effects.

B. Validation of Test Rig

Before conducting our experiments, we conducted some validation checks. Static validation was performed by loading calibrated weights onto the load cell and verifying that the readings matched the known weights. The measured readings were consistent with the known weights, confirming the static accuracy of the load cell.

The actual impact force F_{actual} was determined using the peak voltage V_{peak} from the voltage-time graph recorded by the load cell. With a scaling factor of 1V/20N, the impact force was calculated as:

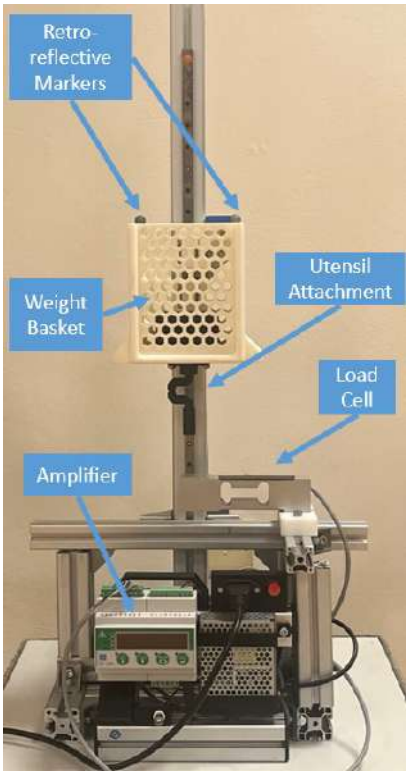


Fig. 5: Drop test rig

$$F_{\text{impact}} = (\frac{20N}{V})V_{\text{peak}} \tag{3}$$

The theoretical impact force $F_{theoretical}$ was calculated based on the principle of energy conservation, assuming no energy losses during impact. The kinetic energy of the weight basket and utensil attachment before impact KE was equated to the work done WD on the load cell:

$$KE = \frac{1}{2}mv^2, WD = Fd_{\text{stop}}, KE = WD$$

From these equations, the impact force was derived as:

$$F_{theoretical} = \frac{mv^2}{2d_{\text{stop}}} \tag{4}$$

where m is the total mass of the weight basket and attachment, v is max velocity before impact, and d_{stop} is the stopping distance, approximated as the difference between the resting position p_{rest} and the lowest position p_{lowest}, i.e. $d_{\text{stop}} = p_{\text{rest}} - p_{\text{lowest}}$. The lowest position is determined by identifying the lowest point on the displacement vs. time graph, while the resting position is obtained from the initial state when the weight basket rests on the load cell.

The sample values used in the validation are summarized in Table I. As expected, the theoretical impact force was greater than the experimental value due to the assumption of no energy losses in the theoretical calculation. In real-life experiments,

TABLE I: Sample Values for Impact Force Validation

Variable	Value
Mass, m	0.735 kg
Resting Position, p_{rest}	690.489 mm
Lowest Position, p_{lowest}	687.429 mm
Max Velocity, v	860.634 mm/s
Theoretical Impact Force, $F_{\text{theoretical}}$	89.0 N
Peak Voltage, V_{peak}	3.78 V
Actual Impact Force, F_{actual}	75.6 N
Percentage Error, e	17.7%

energy losses occur due to factors such as sound generation and damping in the rig structure. The difference between the theoretical and actual impact forces of $13.4N$ corresponds to an error of 17.7%, which is within the acceptable range, validating the rig for further testing.

C. Experiment Procedure

In our experiments, we evaluated the strength of the utensil attachment by varying two parameters: the slot depth d and the number of wall loops w used during 3D printing. To determine the minimum force required to break the attachment, we conducted drop tests by varying the height at which the weight basket and attachment were released onto the load cell. If the attachment did not break, we recorded the peak forces and incrementally increased the drop height by $1.0cm$ until the attachment broke.

Once the approximate range of heights where the part transitioned between breaking and not breaking, we refined our testing by reducing the height increments to $0.2cm$. Height increments were limited to $0.2cm$ during this stage, as smaller increments of $0.1cm$ were impractical to achieve consistently. For instance, if the part broke at $h = 5.0cm$ but did not break at $h = 4.0cm$, we tested intermediate heights such as $h = 4.8cm$ and $h = 4.6cm$. Starting from the highest height within the identified range, we conducted three trials at each height to ensure consistency and reliability of the results.

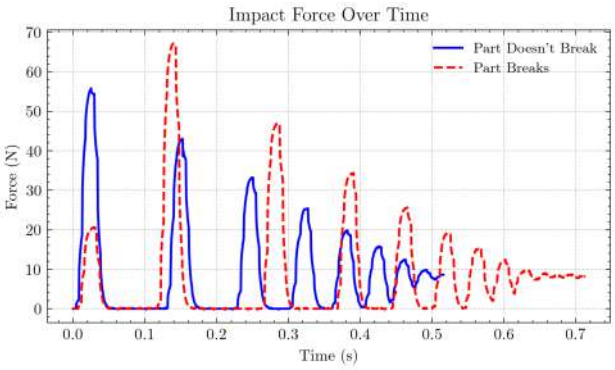
If the part consistently broke at a specific height, we decreased the height incrementally and repeated the trials until the parts stopped breaking. The impact force was the primary peak force in the force-time graph for parts that did not break (Fig. 6a). However, for parts that broke, the impact force could not be derived from the graph due to the smaller first peak, as energy is dissipated through the breaking process rather than being fully transferred to the load cell (Fig. **??**). Thus, the breaking height was the highest height where the part did not consistently break across trials. For example, if the part consistently broke at $h = 4.6cm$ but started not breaking at $h = 4.4cm$, we considered $h = 4.4cm$ as the breaking height as shown in Table II.

Once the breaking height was determined, we calculated the average peak force recorded during the trials at that height, where some or all parts did not break, to estimate the breaking force. This approach provided a conservative estimate of the breaking force, reflecting the force just below the threshold of consistent failure. Hence, the actual impact force required to break the attachment is slightly higher than the average impact force recorded.

TABLE II: Peak Impact Forces for $d = 1.0mm$ and $w = 3$

Height (cm)	t_1 (N)	t_2 (N)	t_3 (N)	Average (N)
4.2	62.8	63.4	63.4	63.2
4.4	N/A	65.0	N/A	65.0
4.6	N/A	N/A	N/A	N/A
4.8	N/A	N/A	N/A	N/A
5.0	N/A	N/A	N/A	N/A

N/A indicates that part broke during testing



(a)

Fig. 6: Force-time graph for a part that does not break (blue solid line) and a part that breaks (red dashed line). The impact force is determined from the primary peak in the blue solid line, representing the maximum impact force experienced by the part. In contrast, for the red dashed line, the impact force cannot be derived due to the smaller first peak, which occurs as the part breaks upon impact.



Fig. 7: Consistent failure point at the slot of the breakaway mechanism

V. Results

The results from the experiments are summarized in Table III. Based on the data, we observe that the impact force

TABLE III: Effect of Slot Depth d and Wall Loop w on Impact Force

Slot Depth d (mm)	Wall Loops w	Average Peak Force F_{avg} (N)
1.0	6	75.6
1.0	3	65.0
2.0	6	53.1
2.0	3	45.0

required to break the attachment increases with the slot depth d and decreases with the number of wall loops w.

The configuration that produces an impact force closest to the maximum permissible force $F_{\text{max}} = 65N$ is achieved when the attachment has a slot depth of $d = 1mm$ and is printed with $w = 3$ wall loops, which yielded an average impact force of $F_{\text{impact}} = 65.0N$. This configuration is selected as the optimal design for the breakaway mechanism.

In scenarios where the maximum permissible force needs to be reduced – for example, to accommodate lower pain thresholds or to prioritize enhanced safety – the parameters can be refined to achieve the desired reduction. For instance, if a maximum permissible force of $F_{\text{max}} = 50N$ is desired, the configuration with $d = 2.0mm$ and $w = 6$ wall loops, which produces an average impact force of $F_{impact} = 53.1N$, could be adjusted by reducing the number of wall loops to lower the breaking force further.

These results demonstrate the utility of systematically varying slot depth and wall loop parameters to design a breakaway mechanism that can be tailored to meet specific force requirements. Furthermore, our experiments revealed that our design resulted in a consistent failure point, which is at the slot of the utensil attachment (Fig. 7).

VI. Conclusion and Future Work

In conclusion, we designed a utensil attachment with a mechanical fail-safe that breaks around the maximum permissible force exerted on a human face by robots $F_{\text{max}} = 65N$. To ensure the part breaks at a consistent breaking point, the parts were printed with the layer lines parallel to the intended breaking line, allowing for controlled and predictable failure behavior. To evaluate the performance of the mechanism, we developed a drop test rig, simulating collisions between the robot arm and the user and conducted systematic experimental testing. Through our experiments, we established how design parameters such as slot depth d and wall loops w affect the impact force required to break the attachment.

While the results offer valuable insights into designing effective mechanical fail-safes, the study has some limitations. For instance, the testing procedure did not account for impacts at angles, which could affect the breaking behavior. The experiments were also conducted in a controlled setting using a drop test rig, which does not fully replicate real-world interactions between the utensil and user.

Future work should address these limitations by testing angled impacts and testing with the actual robotic arm and utensil to evaluate performance under real-world conditions. Additionally, other design and 3D printing parameters, such as infill density and infill pattern, could also be investigated to optimize the attachment further. Furthermore, determining the maximum permissible force based on user-specific factors, such as pain tolerance and comfort levels [17], could further enhance the safety and customization of these attachments.

References

[1] D. Park, Y. Hoshi, H. P. Mahajan, H. K. Kim, Z. Erickson, W. A. Rogers, and C. C. Kemp, "Active robot-assisted feeding with a general-purpose mobile manipulator: Design, evaluation, and lessons learned," *Robotics and Autonomous Systems*, vol. 124, p. 103344, 2020.

[2] E. K. Gordon, R. K. Jenamani, A. Nanavati, Z. Liu, D. Stabile, X. Dai, T. Bhattacharjee, T. Schrenk, J. Ko, H. Bolotski *et al.*, "An adaptable, safe, and portable robot-assisted feeding system," in *Companion of the 2024 ACM/IEEE International Conference on Human-Robot Interaction*, 2024, pp. 74–76.

[3] L. Shaikewitz, Y. Wu, S. Belkhale, J. Grannen, P. Sundaresan, and D. Sadigh, "In-mouth robotic bite transfer with visual and haptic sensing," in *2023 IEEE International Conference on Robotics and Automation (ICRA)*. IEEE, 2023, pp. 9885–9895.

[4] R. K. Jenamani, D. Stabile, Z. Liu, A. Anwar, K. Dimitropoulou, and T. Bhattacharjee, "Feel the bite: Robot-assisted inside-mouth bite transfer using robust mouth perception and physical interaction-aware control," in *Proceedings of the 2024 ACM/IEEE International Conference on Human-Robot Interaction*, 2024, pp. 313–322.

[5] S. Belkhale, E. K. Gordon, Y. Chen, S. Srinivasa, T. Bhattacharjee, and D. Sadigh, "Balancing efficiency and comfort in robot-assisted bite transfer," in *2022 International Conference on Robotics and Automation (ICRA)*. IEEE, 2022, pp. 4757–4763.

[6] M. N. Keely, H. Nemlekar, and D. P. Losey, "Kiri-spoon: A soft shape-changing utensil for robot-assisted feeding," *arXiv preprint arXiv:2403.05784*, 2024.

[7] P. A. Lasota, G. F. Rossano, and J. A. Shah, "Toward safe close-proximity human-robot interaction with standard industrial robots," in *2014 IEEE international conference on Automation science and engineering (CASE)*. IEEE, 2014, pp. 339–344.

[8] P. A. Lasota and J. A. Shah, "Analyzing the effects of human-aware motion planning on close-proximity human–robot collaboration," *Human factors*, vol. 57, no. 1, pp. 21–33, 2015.

[9] D. Zhao, J. Yang, M. O. Okoye, and S. Wang, "Walking assist robot: A novel non-contact abnormal gait recognition approach based on extended set membership filter," *IEEE Access*, vol. 7, pp. 76 741–76 753, 2019.

[10] M. Hamad, S. Nertinger, R. J. Kirschner, L. Figueredo, A. Naceri, and S. Haddadin, "A concise overview of safety aspects in human-robot interaction," in *International Workshop on Human-Friendly Robotics*. Springer, 2023, pp. 1–18.

[11] *ISO 15066 Robots and robotic devices—Collaborative robots*, International Organization for Standardization, 2016.

[12] I. Gibson, D. W. Rosen, B. Stucker, M. Khorasani, D. Rosen, B. Stucker, and M. Khorasani, *Additive manufacturing technologies*. Springer, 2021, vol. 17.

[13] A. M. Forster and A. M. Forster, "Materials testing standards for additive manufacturing of polymer materials: state of the art and standards applicability," 2015.

[14] D. Abbot, D. Kallon, C. Anghel, and P. Dube, "Finite element analysis of 3d printed model via compression tests," *Procedia Manufacturing*, vol. 35, pp. 164–173, 2019.

[15] Ö. Keleş, C. W. Blevins, and K. J. Bowman, "Effect of build orientation on the mechanical reliability of 3d printed abs," *Rapid Prototyping Journal*, vol. 23, no. 2, pp. 320–328, 2017.

[16] V. Kovan, G. Altan, and E. S. Topal, "Effect of layer thickness and print orientation on strength of 3d printed and adhesively bonded single lap joints," *Journal of Mechanical Science and Technology*, vol. 31, pp. 2197–2201, 2017.

[17] D. Han, M. Park, J. Choi, H. Shin, D. Kim, and S. Rhim, "Assessment of pain onset and maximum bearable pain thresholds in physical contact situations," *Sensors*, vol. 22, no. 8, p. 2996, 2022.

Learning Speed-Adaptive Walking Agent Using Imitation Learning With Physics-Informed Simulation

Yi-Hung Chiu*[1], Ung Hee Lee*[2], Changseob Song[1], Manaen Hu[1], and Inseung Kang[1] *Member, IEEE*

***Abstract*— Virtual models of human gait, or digital twins, offer a promising solution for studying mobility without the need for labor-intensive data collection. However, challenges such as the sim-to-real gap and limited adaptability to diverse walking conditions persist. To address these, we developed and validated a framework to create a skeletal humanoid agent capable of adapting to varying walking speeds while maintaining biomechanically realistic motions. The framework combines a synthetic data generator, which produces biomechanically plausible gait kinematics from open-source biomechanics data, and a training system that uses adversarial imitation learning to train the agent's walking policy. We conducted comprehensive analyses comparing the agent's kinematics, synthetic data, and the original biomechanics dataset. The agent achieved a root mean square error of 5.24±0.09 degrees at varying speeds compared to ground-truth kinematics data, demonstrating its adaptability. This work represents a significant step toward developing a digital twin of human locomotion, with potential applications in biomechanics research, exoskeleton design, and rehabilitation.**

***Index Terms*— Speed-Adaptive Walking Agent, Imitation Learning, Physics-Informed Simulation, Human Locomotion**

I. Introduction

Human mobility is a fundamental aspect of daily life, as it allows essential activities, promotes health through physical exercise, and contributes to psychological well-being [1], [2]. However, millions of people in the United States alone face mobility challenges due to conditions such as loss of limbs, paraplegia, and obesity, which decrease quality of life by affecting daily tasks, limiting exercise, and often leading to mental health issues such as depression and anxiety [3], [4]. Restoring gait functionality is crucial to improving the quality of life of people with mobility impairments, necessitating a deep understanding of gait mechanics. Although traditional methods such as motion capture systems and force plates have been used for gait analysis [2], [5], these approaches are costly, time-consuming, and labor intensive, highlighting the need for more efficient and accessible alternatives to support rehabilitation and improve mobility outcomes.

Digital twins, a virtual representation of physical systems, have emerged as a powerful tool in biomechanics and rehabilitation [6], [7]. These computational models simulate human gait biomechanics in controlled environments, eliminating the need to collect human motion data while providing valuable information on joint coordination, muscle activities, and gait balance [8], [9]. In addition, these models are particularly beneficial when developing wearable assistive devices or novel rehabilitation techniques [10]–[13]. Digital twins can model how these devices interact with the human body, offering a safe alternative to testing new control strategies directly on human subjects in physical settings. However, a significant challenge remains in ensuring that these digital twins accurately represent the real human body and its interactions with the environment, which is commonly referred as a sim-to-real gap [14], [15]. The fidelity of these models is vital for translating simulation results into practical applications, and ongoing research aims to bridge the gap between virtual simulations and real-world performance.

Significant efforts have been made within the biomechanics community to develop realistic simulation environments for human movement analysis. Among these, OpenSim [6], an open-source platform, is renowned for its comprehensive musculoskeletal models, enabling researchers to study joint dynamics and muscle forces. Despite its strong community support, OpenSim's relatively steep learning curve, high computational demands, and limited integration with machine learning (ML) frameworks present challenges for researchers looking to leverage data-driven approaches. Similarly, AnyBody [16], a proprietary system, offers detailed musculoskeletal modeling with robust industrial applications in ergonomics and orthopedics. However, its high cost and restricted accessibility hinder widespread adoption. Recent advancements, such as MyoSuite [17], have begun bridging these gaps by offering open-source musculoskeletal environments built on the multi-contact physics engine MuJoCo [18]. MyoSuite combines anatomical fidelity with seamless integration into widely used machine learning frameworks, making it well-suited for tasks such as musculoskeletal motor control using reinforcement learning; however, it is relatively underdeveloped compared to more established tools. These tools collectively demonstrate a spectrum of capabilities, catering to various research needs and priorities.

Accurately recreating human movements in virtual models is vital for analyzing gait biomechanics, as realistic simulation environments alone are insufficient. Replaying motion capture data alone is insufficient because it does not account for variations in human morphology (e.g., differences in height), tasks, and activities [19]. In addition, locomotive strategies often vary between individuals. To address these challenges, researchers have developed control policies for

* Y. Chiu and U. Lee contributed equally to the paper. Corresponding author: unghee@umich.edu.

[1]Y. Chiu, M. Hu, C. Song, and I. Kang are with the Department of Mechanical Engineering, Carnegie Mellon University, Pittsburgh PA 15213, USA.

[2]U. Lee is with the Department of Mechanical Engineering and the Department of Robotics, University of Michigan, Ann Arbor, MI 48109 USA.

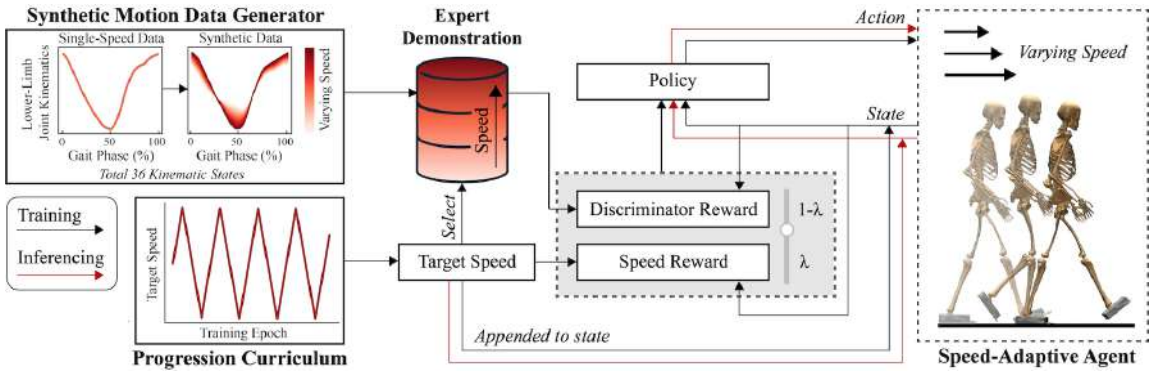


Fig. 1. Overview of our framework for training a speed-adaptive walking agent. The framework includes two main components: generating expert demonstrations and policy optimization. Expert demonstrations from motion data are used to train a discriminator that distinguishes expert- from policy-generated actions at different speeds. The reward function combines the discriminator's output with a speed reward (difference between the agent's target and actual center of mass speed). These rewards optimize the walking policy using trust region policy optimization. The target speed is part of the agent's observation space, with a progressive curriculum exposing the agent to a range of speeds during training. Evaluation tests the agent's ability to achieve the desired speed under varying conditions.

virtual skeletal humanoids to mimic human gait biomechanics. Techniques such as imitation learning and reinforcement learning have been employed to simulate human locomotion in virtual environments [20], [21]. However, these methods focus on training agents to replicate kinematic profiles for a single locomotor task or a single target speed [22], [23]. Such approaches lack generalizability for different tasks, speeds, and subjects, significantly limiting their applicability. This constraint undermines the utility of virtual models, restricting their use to narrow, task-specific scenarios rather than to the diverse applications that they are intended to support. Although there are ongoing efforts to train a single policy that can generalize across different speeds within specific activities, these studies typically employ agents with limited DOF compared to musculoskeletal models, reducing their potential for real-world interpretability [20], [21], [24].

In this work, we trained and validated a skeletal humanoid agent using imitation learning, capable of generalizing across various walking speeds using a high-fidelity physics engine. The key contributions of our study are as follows: (1) we developed a robust pipeline for generating synthetic lower-limb motion data derived from real-world lower-extremity gait biomechanics dataset, (2) using this synthetic dataset, we trained an agent with adversarial imitation learning that is capable of a natural and stable locomotion, (3) we performed an ablation study incorporating curriculum learning and an additional speed-based reward term to evaluate the agent's generalizability across speeds, and (4) we conducted comprehensive statistical analyses to compare the synthetic motion data-based agent's resulting kinematics and the original gait biomechanics dataset. Our work represents a significant step toward developing a digital twin that replicates human lower-limb gait biomechanics, with potential applications in biomechanical research, the design of wearable assistive devices, and rehabilitation. Our implementation of the proposed pipeline is publicly available at: `https://metamobility.cmu.edu/speed-adaptive-agent/`.

II. Methods

This study aims to develop a virtual locomotion agent capable of adapting to varying walking speeds while exhibiting gait profiles that closely resemble those of its biological counterpart. We designed a framework to train a speed-adaptive agent using imitation learning to replicate expert demonstrations derived from an open-source biomechanics dataset [25] (Fig. 1). This section outlines the simulation environment and skeletal model utilized, the training pipeline using our synthetic data generator, the learning algorithm via curriculum strategies, and the statistical analyses to compare the agent's performance against a baseline benchmark.

A. Environment and Task

We used LocoMuJoCo [26] as the simulation environment to train a walking skeletal agent. The simulation is designed to enable researchers to train and evaluate ML-based agents for locomotion tasks in realistic environments. LocoMuJoCo was selected because it offers high-DOF skeletal models that resemble human biomechanics, seamless ML integration, and realistic multi-contact dynamics via MuJoCo physics simulator [18].

Among the skeletal humanoid models available in LocoMuJoCo, we selected the one tailored to our study's focus on locomotion. LocoMuJoCo provides muscle and skeletal models and has four different categories of age groups. Specifically, we utilized an adult-sized skeletal model in which joint torques are directly actuated, bypassing the complexity of muscle contraction and the higher DOF present in muscle-actuated models. This model preserves the relevant joints (i.e., action and observation spaces) for walking while simplifying or omitting other components of the body (e.g., upper limb). The model, adapted from [27], represents an adult human with a total body mass of 86.62 kg. The upper body was fixed, and the foot structure is represented as a rigid box, omitting the subtalar and metatarsophalangeal joints. The observation space comprises 36 dimensions, which capture the angles and angular velocities of the lumbar,

hip, knee, and ankle joints, as well as the vertical position and velocity of the pelvis. The action space includes 13 dimensions, controlling the torques applied to the lumbar, hip, knee, and ankle joints. These abstractions maintain essential locomotion dynamics while improving computational efficiency.

LocoMuJoCo offers two locomotion tasks: walking and running. For the scope of our study, we selected the walking task. Additionally, the environment provide datasets for each task, and we utilized the dataset consists of a single subject walking for 15 minutes at a speed of 1.25 m/s, post-processed from a motion capture system [26].

B. Synthetic Motion Data Generator

We developed a synthetic motion data generator to approximate biomechanics across a diverse range of walking speeds. Humans adapt their walking patterns to environmental conditions (e.g., terrain context) and intentions (e.g., walking faster) by adjusting stride length, gait, and balance. Capturing these variations is crucial to creating a digital twin capable of producing human-like locomotion in everyday scenarios. However, most existing datasets only capture discrete conditions within a task (e.g., specific speeds or slope inclines), primarily due to the limitations of generating such conditions in lab settings with human subjects [28]–[30]. While collecting multi-speed motion capture data is feasible, it requires significant time and resources. To address these challenges, we designed the generator to produce synthetic yet biomechanically natural data, enabling the creation of realistic gait trajectories for training a virtual agent.

The synthetic motion data generator leverages an open-source lower-limb biomechanics dataset [25] that provides treadmill walking data from 22 subjects, covering speeds from 0.5 m/s to 1.85 m/s in 0.05 m/s increments. The dataset includes detailed lower-limb joint (i.e., hip, knee, and ankle) kinematics and kinetics, offering a comprehensive biomechanical representation of human gait. Using this dataset, we aggregated and averaged gait profiles across subjects within a gait cycle (heel strike to heel strike of the right leg) at each speed. We created synthetic gait kinematics by fitting a linear model to the open-source biomechanics dataset averaged across subjects. By applying the linear model to the LocoMuJoCo's single-speed walking dataset, we generated artificial data that vary across speeds. The use of synthetic kinematics instead of the open-source dataset ensured adherence to the model's physical morphology while maintaining realistic biomechanical correlations across varying speeds. Specifically, we first uniformly distributed 21 points within a gait cycle from the open-source biomechanics dataset, and then a linear model was fitted to each point as a function of walking speed. The number of points was determined to effectively capture the kinematic changes across different speeds while avoiding overfitting to the open-source dataset. Synthetic velocity data were derived by differentiating the synthetic position data.

The quality of the synthetic data was evaluated by comparing the gait profiles of the synthetic dataset to the open-source biomechanics dataset. The root mean square error (RMSE) and the coefficient of determination (R^2) were calculated for the hip, knee, and ankle joint kinematics, which were averaged over all gait cycles, providing a quantitative evaluation of the generated joint trajectories.

C. Training Speed-Adaptive Imitation learning Agent

We employed Variational Adversarial Imitation Learning (VAIL) to train the agent's control policy under varying speeds [24]. VAIL uses a Generative Adversarial Network structure—where the generator (policy π) competes with the discriminator D—with an encoder mapping outputs to a latent space to regularize training.

To facilitate the training of a speed-adaptive imitation learning agent, we incorporated the target speed into the observation space as a proxy of the human intent of desired walking speed, allowing the agent to dynamically adapt to varying speed commands. The agent processed the skeletal model's kinematics as inputs and returned joint torques as actions. The reward function was defined as follows

$$r = (1-\lambda)(-\log(1-\frac{1}{1+\exp(-D(\mathbf{z}))})) + \lambda r_{speed} \quad (1)$$

$$\mathbf{z} \sim E(\mathbf{z}|s,a) \quad (2)$$

where $D(\mathbf{z})$ is the discriminator output that measures the closeness of state and action pair of the agent to the expert demonstration, $\mathbf{z}$ is the encoding sampled from the latent space representation by the encoder given state s and action a, and r_{speed} is the speed reward which captures the difference between the target and simulated velocity. Specifically, speed reward was defined as the exponential of the negative error squared of the target speed and the current speed of the agent's center of mass (COM) velocity in the Sagittal plane. These two rewards were adjusted during training with a weighting ratio λ. This formulation allowed the agent to match its gait profiles with the expert demonstration (i.e., synthetic motion data) while simultaneously tracking the target speed. Trust Region Policy Optimization [31] was used to optimize the policy with reward as the objective. We trained the agent for 4000 epochs with 5000 environment steps per epoch. The policy was updated every 1000 steps and the discriminator was updated every 3000 steps.

1) Curriculum learning: Curriculum learning specifies the order of training data, which can improve the robustness and generalization of the model. In this study, we tested two curriculum approaches to train a walking agent: a random curriculum, where target speeds were randomly selected at the start of every epoch, and a progressive curriculum, where the target speed gradually cycled back and forth across the range of speeds. The range of target speeds were capped at the speeds available in the dataset, from 0.65 m/s to 1.85 m/s.

2) Balancing reward contributions: We also studied the balance between two reward streams: (1) speed rewards that represent how well the agent maintains the specified target speed and (2) discriminator rewards, which reflect how closely the agent matches the biomechanics in the dataset.

We tested the reward ratios of discriminator reward to speed reward, ranging from 0 to 1 in increments of 0.1 to determine the optimal balance for achieving the best performance.

3) Baseline agent: To evaluate our speed-adaptive agent training pipeline, from synthetic data generation to training with imitation learning, we configured a baseline agent. This baseline agent had limited access to multi-speed data from our synthetic generator, but was otherwise trained under identical conditions to the agent utilizing the full training pipeline with the optimal setting. Although the baseline agent had access to different speed information during the training process, this was only through the speed-based reward and the target speed state.

D. Model Evaluation and Analysis

To evaluate a fully trained agent against ground-truth kinematic data and its generalizability across different speeds, we conducted five simulation experiments. In each trial, the agent was evaluated over three episodes at each target speed, ranging from 0.65 to 1.85 m/s in 0.1 m/s increments. Each episode lasted for a maximum of 1000 time steps or until the agent fell, whichever occurred first. During these evaluations, we collected time series data of joint kinematics for analysis. The collected data were segmented into individual gait cycles by identifying the local minimum peaks at the hip joint in the Sagittal plane. To ensure reliable gait segmentation, we discarded gait cycle data that had a stride duration less than 60 time steps (0.6 seconds).

We evaluated the agent's performance by calculating the RMSE of the averaged differences in the hip, knee, and ankle joint angles between the synthetic dataset and the generated gait profiles of the trained agent across all speed conditions. We used R^2 to assess how closely the agent's predicted joint angle profiles matched the dataset. Additionally, we measured the agent's COM velocity and compared that to the target speed we prescribed during evaluation. The optimal configuration of the curriculum strategies and reward ratios was identified by the aggregated R^2 values, comparing synthetic data to the agent's kinematic output, across joint angles and speeds. We prioritized R^2 because RMSE values, expressed in different units (degrees and m/s), complicated cross-experiment comparisons.

To compare the agent's performance between the baseline and optimal settings, we performed statistical analyses using a paired sample t-test, with a significance level of 0.05. We also compared the agents' ability to track dynamic target speeds. During this test, we calculated the average measured speed over 10 episodes of 50-second inference with a time-varying sinusoidal target speed (i.e., chirp signal), where the frequency linearly increased from 0.01 Hz to 0.05 Hz.

III. Results

A. Synthetic Motion Data Generator

The kinematic gait profiles (i.e., joint angles) generated by the linear model demonstrated consistent variations and shapes across speeds for each lower-limb joints: hip, knee, and ankle (Fig. 2). Across all lower-limb joints, the synthetic data resulted in an RMSE of 8.10±0.16°and an R^2 of 0.59 compared to the biomechanical ground truth.

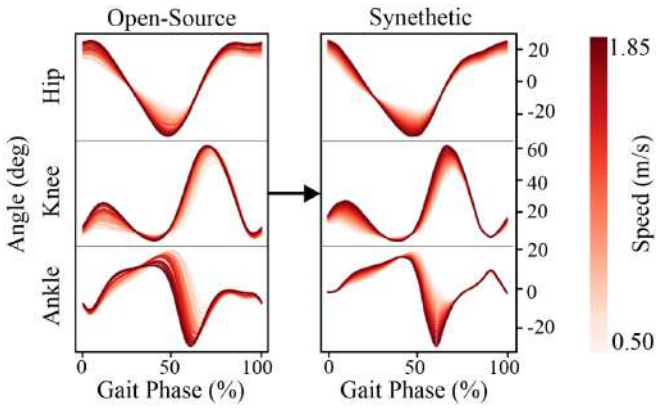


Fig. 2. Comparison of joint kinematics between open-source biomechanics and synthetic data across varying speeds. A linear model was fitted to joint kinematics from an open-source gait biomechanics dataset. This model was then used to generate synthetic kinematic profiles during training.

B. Effect of Curriculum Learning

We evaluated the differences in the joint angles between the synthetic data and the trained agent at various speeds using two curriculum strategies. In addition, we analyzed the differences between the target and the simulated COM speeds achieved by the agent under these conditions. The progressive curriculum strategy resulted in a 41.48±3.06% reduction in RMSE and a 47.77±4.37% increase in R^2 for joint angles compared to the random strategy (Fig. 3). Similarly, the progressive curriculum strategy achieved a 35.11±16.46% lower RMSE and a 5.67±2.31% higher R^2 for speed tracking compared to the random strategy.

C. Effect of Reward Contributions

We evaluated the joint angle differences between the synthetic dataset and the trained agent at various speeds under different ratios of two reward components: discriminator and speed (Table I). In addition, we evaluated the discrepancies between the target and the simulated COM speeds of the agent under these conditions. These differences were quantified using RMSE and R^2. Speed reward ratios of

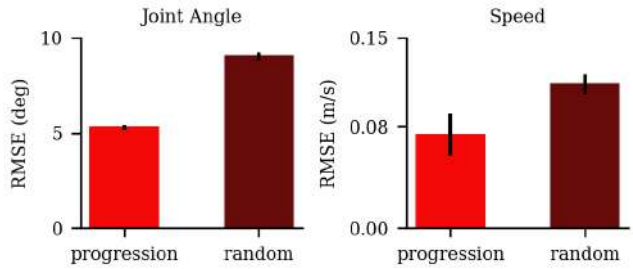


Fig. 3. Effect of curriculum learning on the walking agent's performance during training. The red plot represents the case for changing the target speed in a progressive way and the brown plot stands for a random case at every training epoch. Error bars indicate ±1 standard deviation.

0.4 and above 0.5 were excluded from our analysis due to the absence of viable samples after filtering gait cycles with values below 0.6 seconds, which exhibited unnatural gait patterns (Fig. 4). Among the included ratios, a speed reward ratio of 0.1 resulted in the lowest RMSE and the highest R^2 for joint angle differences, while the 0.5 ratio achieved the lowest RMSE and highest R^2 for speed comparisons.

TABLE I

EFFECT OF WEIGHTING OF THE REWARD CONTRIBUTIONS.

Reward Ratio		Target vs. Measured Speed		Ground Truth vs. Measured Joint Angle	
Discriminator	Speed	RMSE (m/s)	R^2	RMSE (°)	R^2
1	0	0.51±0.02	-0.85±0.14	5.42±0.16	0.80±0.01
0.9	0.1	0.19±0.01	0.73±0.02	**3.86±0.07**	**0.90±0.01**
0.8	0.2	0.13±0.01	0.88±0.01	4.97±0.06	0.85±0.01
0.7	0.3	0.08±0.02	0.95±0.02	5.38±0.15	0.81±0.01
0.6	0.4	0.07±0.01	0.96±0.01	-	-
0.5	0.5	**0.06±0.01**	**0.98±0.01**	5.24±0.08	0.83±0.01

Effect of varying speed and discriminator reward ratios during training. Results with bold fonts indicate the best walking performance for each evaluation criteria (i.e., target speed and kinematic profile).

D. Optimal Agent Settings

Based on the aggregated R^2 values across speed and joint angle comparison, the best-performing agent utilized a speed reward ratio of 0.5, a discriminator ratio of 0.5, and a progressive curriculum strategy. The agent with optimal settings significantly outperformed the baseline benchmark in both speed and joint angle metrics (p <0.05). Specifically, the optimal agent achieved an RMSE of 0.06±0.01 m/s and 5.24±0.09°, and an R^2 of 0.98±0.01 and 0.83±0.01 for speed and joint angles, respectively. In contrast, the baseline agent resulted in an RMSE of 0.24±0.01 m/s and 6.49±0.12°, and an R^2 of 0.59±0.01 and 0.70±0.02 for speed and joint angles, respectively. Lastly, the optimal agent outperformed the baseline in tracking dynamically changing speeds, accurately matching targets across all frequency ranges. In contrast, the baseline struggled to follow the target speeds, only approximating the rough trend (Fig. 5).

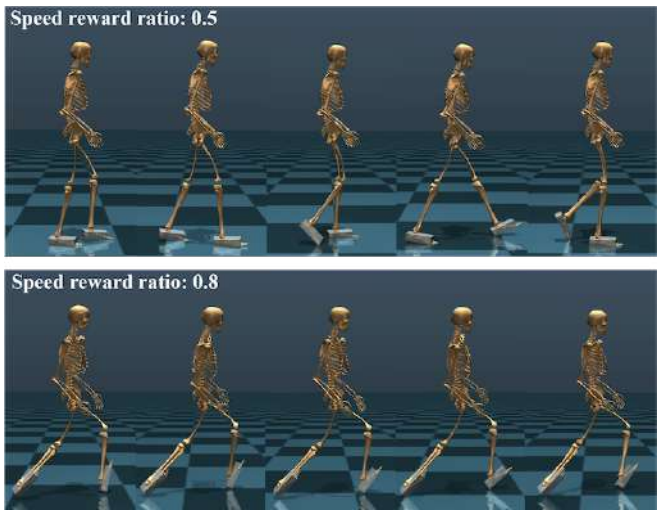


Fig. 4. Representative walking agent with optimal (top) and suboptimal (bottom) settings. Suboptimal agent (e.g., higher ratio of speed reward) exhibited abnormal gait patterns, such as irregular limb coordination, exaggerated dorsiflexion, and asymmetric range of motion.

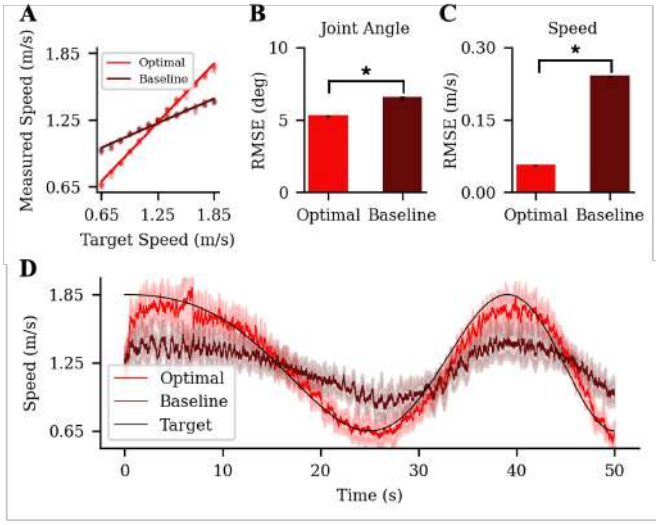


Fig. 5. Walking agent performance with optimal and baseline settings. (A) Target speed tracking performance across varying conditions. Tracking error for (B) joint angles and (C) COM speed relative to ground-truth data. (D) Walking agent's adaptability to dynamically changing walking speeds. Error bars and shaded regions indicate ±1 standard deviation, and asterisks indicate statistical significance ($p < 0.05$).

IV. DISCUSSION AND CONCLUSION

In this work, we presented a pipeline for optimizing a speed-adaptive walking agent using synthetic motion data and adversarial imitation learning, where our optimal agent achieved a stable, biomechanically plausible locomotion. The agent with optimal settings outperformed the baseline, highlighting the effectiveness of our pipeline. This included the synthetic data generator, underscoring the importance of speed-dependent data for producing biologically plausible gait while achieving target speeds. Furthermore, an evaluation of curriculum learning strategies showed that progressive speed transitions significantly outperformed random shuffling. We attribute this to frequent and abrupt changes in the target speed under the random strategy, which likely disrupted the agent's ability to establish a stable walking pattern. In contrast, the progressive curriculum facilitated a smoother transition between speeds, allowing enough time for the agent to develop stable walking dynamics without falling. Compared to prior methods on imitating human walking in simulation [32]–[34], our results not only achieved comparable kinematic profiles but also biomechanically plausible joint moments and powers (Fig. 6). These additional metrics provide deeper biomechanical insights, extending the analysis beyond kinematic comparison, and enhancing the framework's applicability to the real-world use case.

Despite these contributions, our framework has several limitations. First, the synthetic data generator uses a lin-

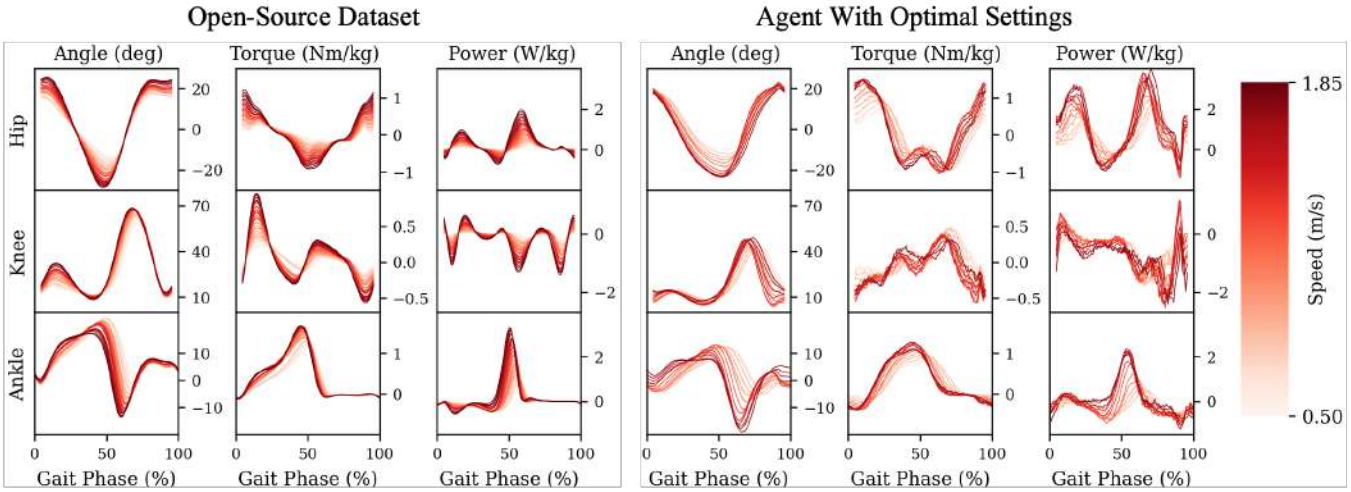


Fig. 6. Gait biomechanics comparison between the open-source dataset (left) and our optimal walking agent (right) across varying speeds. Each curve from the open-source dataset represents the average gait across all subjects in the dataset, while each curve from the optimal walking agent represents the average gait across 50 episodes of evaluation. Torque and power values were normalized by body mass.

ear model to capture gait trends, which may oversimplify the nonlinear behaviors seen at certain speeds (e.g., slow walking) and contribute to deviations from actual human biomechanics (Fig. 2), ultimately affecting the trained agent's gait profile (Fig. 6). Moreover, the linear model was fitted to the average data of 22 subjects, which filtered out individual variations in human gait dynamics. As a result, synthetic data may not adequately reflect the unique biomechanics of real individuals.

We investigated the use two reward components, the discriminator and the speed reward, to enable the agent to achieve a desired speed while exhibiting natural walking patterns. However, redundancy may have existed in our reward formulation, as the COM speed was already encoded in the discriminator, which evaluated kinematics against expert data at each speed. We hypothesized that an explicit speed reward would improve accuracy and our results supported this, with the RMSE decreasing as the speed reward ratio increased (Table I). However, beyond a 0.5 ratio, the agent produced unrealistic gait profiles, as shown by the RMSE trend and visual inspections (Fig. 4). This limitation is mainly due to the speed reward enforcing constant COM speed across gait cycles, which conflicts with the natural cyclic variations of human gait.

Although our optimal agent showed reduced kinematic deviations from the ground truth compared to the baseline agent, notable discrepancies were observed when compared to real human biomechanics (Fig. 6). For example, the agent's hip torque profile showed an additional extension peak around 50% of the gait cycle. Additionally, the agent's knee joint torque and power profiles deviated from those of biological counterparts. These discrepancies were mainly due to the gap in expert demonstrations using our synthetic data, which only provided joint kinematics but not corresponding kinetics. Lastly, a simplified box foot model, which reduces the complexity of contact dynamics, likely contributed to the additional sim-to-real gap. These limitations show that biomechanically plausible kinematics do not always translate into accurate interactions or contact physics, ultimately leading to differences in joint kinetics.

In future work, our aim is to develop a more representative human gait reward function to facilitate training schemes that produce a walking agent that is biomechanically plausible both kinematically and kinetically. Specifically, we plan to design rewards that assess the complete kinematic profile across the entire gait cycle, rather than evaluating it at individual time steps. This approach will address the previously discussed limitations of redundancy in the speed reward by dynamically assigning appropriate COM target speeds throughout the gait cycle. This enhanced reward function will incorporate lower-limb biomechanical metrics such as stride length, cadence, and stability, further improving the agent's ability to replicate human-like gait patterns. Additionally, we will explore the integration of our improved reward functions with adaptive curriculum strategies—such as Gaussian scheduling and self-paced learning—to ensure consistent intermediate reward signals within each gait cycle and further enhance training stability and performance.

There are several exciting directions from our work. First, we plan to extend our model to capture a broader spectrum of gait patterns across diverse demographics—including older adults and individuals with disabilities—by leveraging generative techniques (e.g., diffusion models [35], generative adversarial networks [36]) to create physically plausible gait trajectories from limited data. We also aim to integrate unsupervised clustering methods (e.g., Deep Embedded Clustering [37]) to identify latent subgroup characteristics, enabling the conditioning of our generative process on these features to produce tailored gait profiles that more accurately reflect natural variations in human locomotion. Second, we plan to extend the agent's task beyond level-ground walking to more complex locomotor activities such as sit-to-stand and

stair descent. Lastly, we are envisioning to utilize the walking agent for tuning control policies of wearable robots, such as exoskeletons. By incorporating real-world exoskeleton hardware into the simulation environment, we can rapidly iterate and test various control strategies without the need for human subject testing. Minimizing the sim-to-real gap will enable direct transfer of control parameters to physical systems or fine-tuning policies with minimal real-world training data. This approach is particularly advantageous for robotic prostheses, where robust control strategies are critical to ensure user safety and prevent potentially harmful failures.

REFERENCES

[1] W. A. Satariano, J. M. Guralnik, R. J. Jackson, R. A. Marottoli, E. A. Phelan, and T. R. Prohaska, "Mobility and aging: new directions for public health action," *American journal of public health*, vol. 102, no. 8, pp. 1508–1515, 2012.

[2] S. C. Webber, M. M. Porter, and V. H. Menec, "Mobility in older adults: a comprehensive framework," *The Gerontologist*, vol. 50, no. 4, pp. 443–450, 2010.

[3] Centers for Disease Control and Prevention, "Disability and health data system (dhds)," 2024.

[4] L. I. Iezzoni, E. P. McCarthy, R. B. Davis, and H. Siebens, "Mobility difficulties are not only a problem of old age," *Journal of General Internal Medicine*, vol. 16, no. 4, pp. 235–243, 2001.

[5] R. Baker, "Gait analysis methods in rehabilitation," *Journal of NeuroEngineering and Rehabilitation*, vol. 3, no. 1, p. 4, 2006.

[6] S. L. Delp, F. C. Anderson, A. S. Arnold, P. Loan, A. Habib, C. T. John, E. Guendelman, and D. G. Thelen, "Opensim: open-source software to create and analyze dynamic simulations of movement," *IEEE transactions on biomedical engineering*, vol. 54, no. 11, pp. 1940–1950, 2007.

[7] B. R. Barricelli, E. Casiraghi, and D. Fogli, "A survey on digital twin: Definitions, characteristics, applications, and design implications," *IEEE access*, vol. 7, pp. 167653–167671, 2019.

[8] S. L. Delp, J. P. Loan, M. G. Hoy, F. E. Zajac, E. L. Topp, and J. M. Rosen, "An interactive graphics-based model of the lower extremity to study orthopaedic surgical procedures," *IEEE Transactions on Biomedical engineering*, vol. 37, no. 8, pp. 757–767, 1990.

[9] C. F. Ong, T. Geijtenbeek, J. L. Hicks, and S. L. Delp, "Predicting gait adaptations due to ankle plantarflexor muscle weakness and contracture using physics-based musculoskeletal simulations," *PLoS computational biology*, vol. 15, no. 10, p. e1006993, 2019.

[10] M. Sreenivasa, M. Millard, M. L. Felis, K. Mombaur, and S. I. Wolf, "Optimal control based stiffness identification of an ankle-foot orthosis using a predictive walking model," *Frontiers in computational neuroscience*, vol. 11, p. 23, 2017.

[11] V. C. Kumar, S. Ha, G. Sawicki, and C. K. Liu, "Learning a control policy for fall prevention on an assistive walking device," in *2020 IEEE International Conference on Robotics and Automation (ICRA)*, pp. 4833–4840, IEEE, 2020.

[12] M. Tran, L. Gabert, S. Hood, and T. Lenzi, "A lightweight robotic leg prosthesis replicating the biomechanics of the knee, ankle, and toe joint," *Science robotics*, vol. 7, no. 72, p. eabo3996, 2022.

[13] I. Kang, H. Hsu, and A. Young, "The effect of hip assistance levels on human energetic cost using robotic hip exoskeletons," *IEEE Robotics and Automation Letters*, vol. 4, no. 2, pp. 430–437, 2019.

[14] E. Salvato, G. Fenu, E. Medvet, and F. A. Pellegrino, "Crossing the reality gap: A survey on sim-to-real transferability of robot controllers in reinforcement learning," *IEEE Access*, vol. 9, pp. 153171–153187, 2021.

[15] S. Sudhakar, J. Hanzelka, J. Bobillot, T. Randhavane, N. Joshi, and V. Vineet, "Exploring the sim2real gap using digital twins," in *Proceedings of the IEEE/CVF International Conference on Computer Vision*, pp. 20418–20427, 2023.

[16] M. Damsgaard, J. Rasmussen, S. T. Christensen, E. Surma, and M. De Zee, "Analysis of musculoskeletal systems in the anybody modeling system," *Simulation Modelling Practice and Theory*, vol. 14, no. 8, pp. 1100–1111, 2006.

[17] V. Caggiano, H. Wang, G. Durandau, M. Sartori, and V. Kumar, "Myosuite–a contact-rich simulation suite for musculoskeletal motor control," *arXiv preprint arXiv:2205.13600*, 2022.

[18] E. Todorov, T. Erez, and Y. Tassa, "Mujoco: A physics engine for model-based control," in *2012 IEEE/RSJ international conference on intelligent robots and systems*, pp. 5026–5033, IEEE, 2012.

[19] S. Corazza, L. Mündermann, E. Gambaretto, G. Ferrigno, and T. P. Andriacchi, "Markerless motion capture through visual hull, articulated icp and subject specific model generation," *International journal of computer vision*, vol. 87, pp. 156–169, 2010.

[20] T. Haarnoja, A. Zhou, P. Abbeel, and S. Levine, "Soft actor-critic: Off-policy maximum entropy deep reinforcement learning with a stochastic actor," in *International conference on machine learning*, pp. 1861–1870, PMLR, 2018.

[21] X. B. Peng, P. Abbeel, S. Levine, and M. Van de Panne, "Deepmimic: Example-guided deep reinforcement learning of physics-based character skills," *ACM Transactions On Graphics (TOG)*, vol. 37, no. 4, pp. 1–14, 2018.

[22] C. L. Dembia, N. A. Bianco, A. Falisse, J. L. Hicks, and S. L. Delp, "Opensim moco: Musculoskeletal optimal control," *PLOS Computational Biology*, vol. 16, no. 12, p. e1008493, 2020.

[23] A. Dashkovets and B. Laschowski, "Reinforcement learning for control of human locomotion in simulation," in *2024 10th IEEE RAS/EMBS International Conference for Biomedical Robotics and Biomechatronics (BioRob)*, pp. 43–48, IEEE, 2024.

[24] X. B. Peng, A. Kanazawa, S. Toyer, P. Abbeel, and S. Levine, "Variational discriminator bottleneck: Improving imitation learning, inverse rl, and gans by constraining information flow," *arXiv preprint arXiv:1810.00821*, 2018.

[25] J. Camargo, A. Ramanathan, W. Flanagan, and A. Young, "A comprehensive, open-source dataset of lower limb biomechanics in multiple conditions of stairs, ramps, and level-ground ambulation and transitions," *Journal of Biomechanics*, vol. 119, p. 110320, 2021.

[26] F. Al-Hafez, G. Zhao, J. Peters, and D. Tateo, "Locomujoco: A comprehensive imitation learning benchmark for locomotion," *arXiv preprint arXiv:2311.02496*, 2023.

[27] S. R. Hamner, A. Seth, and S. L. Delp, "Muscle contributions to propulsion and support during running," *Journal of biomechanics*, vol. 43, no. 14, pp. 2709–2716, 2010.

[28] B. Hu, E. Rouse, and L. Hargrove, "Benchmark datasets for bilateral lower-limb neuromechanical signals from wearable sensors during unassisted locomotion in able-bodied individuals," *Frontiers in Robotics and AI*, vol. 5, p. 14, 2018.

[29] T. Lencioni, I. Carpinella, M. Rabuffetti, A. Marzegan, and M. Ferrarin, "Human kinematic, kinetic and emg data during level walking, toe/heel-walking, stairs ascending/descending," *Figshare https://doi. org/10.6084/m9. figshare. c*, vol. 4494755, p. v1, 2019.

[30] L. Moreira, J. Figueiredo, P. Fonseca, J. P. Vilas-Boas, and C. P. Santos, "Lower limb kinematic, kinetic, and emg data from young healthy humans during walking at controlled speeds," *Scientific data*, vol. 8, no. 1, p. 103, 2021.

[31] J. Schulman, "Trust region policy optimization," *arXiv preprint arXiv:1502.05477*, 2015.

[32] P. Schumacher, T. Geijtenbeek, V. Caggiano, V. Kumar, S. Schmitt, G. Martius, and D. F. Haeufle, "Natural and robust walking using reinforcement learning without demonstrations in high-dimensional musculoskeletal models," *arXiv preprint arXiv:2309.02976*, 2023.

[33] S. S. Chan, M. Lei, H. Johan, and W. T. Ang, "Creation and evaluation of human models with varied walking ability from motion capture for assistive device development," in *2023 International Conference on Rehabilitation Robotics (ICORR)*, pp. 1–6, IEEE, 2023.

[34] S. Song, Ł. Kidziński, X. B. Peng, C. Ong, J. Hicks, S. Levine, C. G. Atkeson, and S. L. Delp, "Deep reinforcement learning for modeling human locomotion control in neuromechanical simulation," *Journal of neuroengineering and rehabilitation*, vol. 18, pp. 1–17, 2021.

[35] J. Ho, A. Jain, and P. Abbeel, "Denoising diffusion probabilistic models," *Advances in neural information processing systems*, vol. 33, pp. 6840–6851, 2020.

[36] I. Goodfellow, J. Pouget-Abadie, M. Mirza, B. Xu, D. Warde-Farley, S. Ozair, A. Courville, and Y. Bengio, "Generative adversarial networks," *Communications of the ACM*, vol. 63, no. 11, pp. 139–144, 2020.

[37] J. Xie, R. Girshick, and A. Farhadi, "Unsupervised deep embedding for clustering analysis," in *International conference on machine learning*, pp. 478–487, PMLR, 2016.

IdentiARAT: Toward automated identification of individual ARAT items from wearable sensors

1st Daniel Homm
TUM School of Computation, Information and Technology
Technical University of Munich
Garching, Germany
daniel.homm@tum.de

2nd Patrick Carqueville
Professorship of Sport Equipment and Sport Materials
Technical University of Munich
Garching, Germany
patrick.carqueville@tum.de / 0000-0001-7066-5225

3rd Christian Eichhorn
Research Group Augmented Reality
Technical University of Munich
Garching, Germany
christian.eichhorn@tum.de

4th Thomas Weikert
Data Analytics & Rehabilitation Technology (DART)
Lake Lucerne Institute
Vitznau, Switzerland
thomas.weikert@llui.org

5th Thomas Menard
Data Analytics & Rehabilitation Technology (DART)
Lake Lucerne Institute
Vitznau, Switzerland
thomas.menard@llui.org

6th David A. Plecher
Research Group Augmented Reality
Technical University of Munich
Garching, Germany
plecher@in.tum.de

7th Chris Awai Easthope
Data Analytics & Rehabilitation Technology (DART)
Lake Lucerne Institute
Vitznau, Switzerland
chris.awai@llui.org / 0000-0002-3602-7841

***Abstract*—This study explores the potential of using wrist-worn inertial sensors to automate the labeling of ARAT (Action Research Arm Test) items. While the ARAT is commonly used to assess upper limb motor function, its limitations include subjectivity and time consumption of clinical staff. By using IMU (Inertial Measurement Unit) sensors and MiniROCKET as a time series classification technique, this investigation aims to classify ARAT items based on sensor recordings. We test common preprocessing strategies to efficiently leverage included information in the data. Afterward, we use the best preprocessing to improve the classification. The dataset includes recordings of 45 participants performing various ARAT items. Results show that MiniROCKET offers a fast and reliable approach for classifying ARAT domains, although challenges remain in distinguishing between individual resembling items. Future work may involve improving classification through more advanced machine-learning models and data enhancements.**

***Index Terms*—ARAT, machine learning, ROCKET, IMU, time series classification, auto-labeling**

I. Introduction

Over 100 million people worldwide are living with the consequences of a stroke [1], a condition that frequently results in long-term motor impairments. Of stroke survivors, 85% present with initial upper limb impairments [2] and 60% of survivors report motor disabilities that persist even after rehabilitation [3]. Upper limb impairments span different domains and can include muscle weakness, changes in muscle tone, impaired motor control, and laxity of joints [4]. Importantly, these upper limb impairments lead to reductions in motor function, which consequently have a negative impact on quality of life. Clinically, standard assessments exist to evaluate both impairment and function. These are important both to track rehabilitation progress, as also to evaluate intervention efficacy and optimize therapy content. The Action Research Arm Test (ARAT) is a popular standard clinical assessment for motor function that evaluates the capacity to perform functional movements. The test consists of 19 movements (items) of different complexities for each arm (e.g. Fig. 1), which are sequentially performed and split into 4 subcategories (grasp, grip, pinch, gross). Each item is rated by an assessor on a scale of 0-3, based on the success, speed, and closeness to physiological motion. Scores are typically summed into subcategories to create a global score. The ARAT demonstrates good clinical properties with high interrater reliability, repeatability, and construct validity [5]. There is an ongoing discussion in the field as to what extent motor impairment may be approximated from the ARAT [6].

Given that the ARAT is well established in clinical routine and shows promise to measure both impairment and function,

there have been many approaches to investigate and better understand movement kinematics or at least statistical features of motion during the different movement items [7]–[9]. Instrumentation of the ARAT can give more details on the underlying kinematics, but at the same time, opens an opportunity for automation of the testing procedure. Automation is a necessary step for both clinical decision support and self-assessment, and a pre-requisite for any extension of ARAT measurements to the home. All of these topics are central pillars if rehabilitation as a field is to expand from a point-of-care to a continuum-of-care approach.

While motion capture systems and video recordings are well-suited to recognize human movements [10], these systems are expensive and can only be used in restricted environments. In contrast, wearable sensors such as inertial measurement units (IMUs) have no infrastructural requirements, are low-cost, and easy to use. These characteristics enable the use of IMUs at scale in a broad range of situations [11], including rehabilitation. Recent studies have demonstrated that IMU recordings are suitable for capturing essential characteristics of human movement across various tasks and activities [11]–[14]. Specifically, for upper limb movement assessments, IMU-based systems coupled with suitable analytics have been shown to deliver reliable and accurate results for many relevant movement metrics [4].

In terms of automation, previous work of our group has shown the ability to use wearable sensors to predict global ARAT assessor scores, achieving close to 80% accuracy over all domains [15]. In the next step, we investigate whether wearable sensor data can be used to automatically identify each of the 19 individual ARAT items from wearable sensor signals, specifically triaxial acceleration and gyroscope data in various different neurological populations. When working reliably, this automatic scoring proposal could be used as a clinical decision support system. For this purpose, we employ MiniROCKET [16], a method that can efficiently be executed in real-time on wearable devices, ensuring feasibility for practical applications.

This objective gives rise to two research questions:

RQ 1: With which mean accuracy are we able to automatically identify individual items of the ARAT?
RQ 2: To which extent does the impairment level affect the accuracy of the classification?

II. Method

A. Study design

We present a retrospective analysis (EKNZ 2024-00196) of instrumented ARAT data that was collected as part of the clinical routine at the cereneo - Center for Neurology and Rehabilitation from 1.1.2020 - 30.06.2024. All patients gave written informed general consent, which allowed their data to be used for retrospective analysis (EKNZ 2017-00730).

B. Data

The ARAT belongs to part of the core clinical assessment battery of this participating clinic and was routinely performed by trained and experienced physiotherapists on in-patients, often at multiple time points. In this analysis, we included only patients with a present upper limb impairment, represented by Fugl-Meyer scores between 12-59. In total, this led to a dataset containing 2,725 correctly performed and labeled ARAT items. Additionally, items not contributing to ARAT scores due to early starts or supervision uncertainties were relabeled as *junk*, adding 647 time sequences. However, this exceeded the number of each other label. To prevent the model from overfitting the junk data, we randomly removed junk sequences such that the number of junk labels was the same as that of the ARAT item with the most recordings. Of all the included individuals, 35 were men with a median age of 65 and 10 women with a median age of 70 years. The median height of all participants was 175 cm and the median weight was 55.2 kg. Five wearable sensors (Movella Dot) were mounted on each patient (Sensor location: left and right wrist, left and right middle of the upper arm, middle of the sternum), however, for all analyses presented here, only the two wrist sensors were used. These sensors were by far the best accepted and show the greatest promise for generalization to a home use case. The sensors recorded the following signals at a rate of 60 Hz: Triaxial acceleration [$\frac{m}{s^2}$], triaxial rotational acceleration [$\frac{deg}{s}$], and magnetic field strength [Gs]. Magnetometer data was discarded, as deemed too unreliable due to a measurement location close to a clinical MRI. Orientations were calculated as quaternions on board the device using the VQF (Versatile Quaternion-based Filter) magnetometer-free estimation [17]. Table II shows all further preprocessing steps that were tested.



Fig. 1. Patient performing ARAT item, Cube 10cm

C. Analytics

To distinguish and correctly classify the labels of each time sequence, the ROCKET [18] approach was used, as it is lightweight and well-suited to time series classification tasks. Specifically, we chose the MiniROCKET [16] adaptation as it is highly efficient, robust, and delivers comparable performance across diverse datasets [18]. Table I highlights the differences from the original ROCKET method. MiniROCKET has demonstrated the ability to effectively capture patterns in Human Activity Recognition time series data [16], [19]. As shown in Fig. 2, the method first applies 1-D convolutional kernels and extracts feature values with pooling operations.

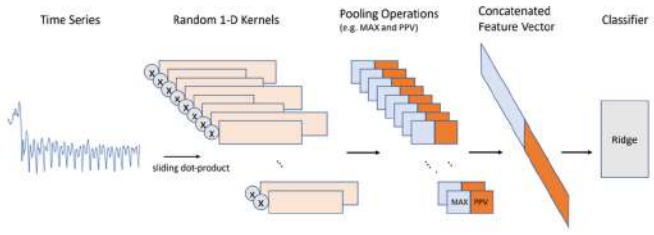


Fig. 2. RandOm Convolutional KErnel Transform (ROCKET) approach [20].

TABLE I
SETUP DIFFERENCES ROCKET AND MINIROCKET [16].

	ROCKET	MiniROCKET
length	$\{7, 9, 11\}$	9
weights	$\mathcal{N}(0, 1)$	{-1, 2}
bias	$\mathcal{U}$(-1, 1)	from convolution output
dilation	random	fixed (rel. to input length)
padding	random	fixed
features	PPV + max	PPV
number of features	20,000	10,000

The resulting feature vector is subsequently used as input for a classifier.

Table I shows the differences in the setup for ROCKET [18] and MiniROCKET [16]. The table illustrates that ROCKET kernels have random lengths from the set $\{7, 9, 11\}$. Each kernel is initialized with weights $\sim \mathcal{N}(0, 1)$, bias terms $\sim \mathcal{U}(-1, 1)$, random dilations, and random paddings. For each applied kernel, the proportion of predicted positives (PPV) and the maximum value are calculated. These result in a default total of 20,000 features [16].

With MiniROCKET [16], the randomness from ROCKET [18] is partially removed by using kernels with a fixed length of 9. Furthermore, weights are chosen from the set $\{-1, 2\}$. The authors show that kernels should be as small as possible to maximize computational efficiency. $2^9 = 512$ possible kernels can be chosen for a kernel length of 9 and two possible weights. In [16], an optimum of 84 is proposed to balance accuracy and computational cost. For a time series *X*, kernel W_d, and bias *b*, the PPV is given by Equation 1 [16].

$$PPV(X * W_d - b) = \frac{1}{N} \sum [(X * W_d - b) > 0] \quad (1)$$

For a kernel W_d, dilation spreads the kernel over the input by applying it to every dth element, where *d* is the dilation factor. In MiniROCKET, dilations are assigned from a fixed set based on the ratio of the input length and kernel length [16]. The bias values *b* are selected from the [0.25, 0.5, 0.75] quantiles of the convolution output for a given kernel *W* and dilation *d* on a randomly chosen training example. While this selection is random, the bias values themselves are derived from a fully deterministic convolution process, making MiniROCKET minimally random. Here, *N* refers to the number of elements in the transformed time series for one sample. The only randomness in MiniROCKET is the selection of training examples for sampling bias values.

TABLE II
THE TESTED DATA PREPROCESSING STEPS.

Preprocessing	**Values**
padding	Mean-padding; Zero-padding
Butterworth-filter frequencies	10Hz; 20Hz; No
freed acceleration	Yes; No
freed angular velocity	Yes; No
gaussian noise for acceleration	μ: 0 and σ: [0.1, 1]; no
gaussian noise for angular velocity	μ: 0 and σ: [1, 5]; no

The advantage of PPV is that this feature summarizes key statistical properties of the time series, which often contain sufficient discriminatory information for classification tasks. In addition, while more features can provide more information, they can also introduce noise and overfitting to the model. Only using PPV reduces the risk of overfitting, especially on small datasets, as it acts as a regularizer by focusing on a single, robust feature. In the end, MiniROCKET achieves almost the same accuracy as Rocket using a mostly deterministic and much faster procedure [16]. For these reasons, MiniROCKET was used for our further analysis [16].

III. EXPERIMENTS

For the experiments, the open-source library sktime [21] offers a built-in multivariate MiniROCKET implementation that was used for the classification tasks in this investigation.

A. Validation

We used a K-Fold Cross-validation (KFCV) with ten folds for all the experiments. This means we split the data into ten non-overlapping subsets (folds). Afterward, ten different models are trained on nine of the ten folds. For each model, the remaining tenth fold is subsequently used for validation. Here, the validation fold changes for each model until all folds are used exactly once for validation. Standard KFCV is not ideal for time series data where temporal ordering matters between multiple sequences. However, in this research, the data set consists of independent time sequences. Therefore, we can split the data into folds, including complete item executions. Before splitting the data into the folds, the time sequences were shuffled individually with a random seed of 42 to retain reproducibility.

B. Data Preprocessing

In the first experiment, we took all 19 ARAT items and junk as individual classes. To determine which data preprocessing method works best, we tested all the combinations from Table II on the data for the right and left wrists separately. Afterward, we chose the setup with the best mean accuracy for further investigation. During this process, we also observed the differences in the final accuracy. The model trained and tested on data from both wrists demonstrated the lowest accuracy. To provide an initial benchmark for potential performance on one wrist, we selected the wrist with the less accurate results as the focus for further investigation in this study.

C. Input Features

Having defined preprocessing and source data, we investigated which sensor recordings capture meaningful features for the classification task, therefore improving the model's performance and which input streams can be neglected to reduce computational costs. For this, the following three different sets of input streams were compared.

- 3-axis acceleration + 3-axis angular velocity
- 4-axis quaternions
- 3-axis acceleration + 3-axis angular velocity + 4-axis quaternions

D. Domain-Level Classification

Each ARAT item belongs to a specific movement domain, *Grasp, Grip, Gross,* and *Pinch*. Therefore, with the best-performing setup for all individual items, we also investigated the classification possibilities of the different ARAT domains. This classification assessment helps evaluate whether patterns from individual items can be generalized across the domains, offering a more comprehensive understanding of the model's capabilities.

E. Sequence Length Impact

Finally, due to the large variation in data segment lengths, we investigated to what extent especially long sequences from the distribution tail impact the performance of the classification. For this, we trained one model on only 75% of the shortest sequences.

IV. Results

The accuracies presented in this section refer to the average results of all ten models from the cross-validation. Due to the simplicity of MiniROCKET, calculating all embeddings and training a single model takes, on average, under 170 seconds on an Intel Core i5, 8th generation CPU, and 16GB RAM.

A. Data Preprocessing

The grid search for the best preprocessing resulted in the setups with the five best accuracies illustrated in Table III. The best result from Table III includes a mean padding and an applied Gaussian noise with a mean of 0 and a standard deviation of 0.5 for the acceleration and 3 for angular velocity. Furthermore, the data was not freed from gravity, and no low-pass filter was applied. The preprocessing steps with the best result were applied before all other experiments.

We proceeded with the experiments with the data from the left wrist since the models trained and validated on this data split achieved, with around 5% difference, less accurate results than models related to the right wrist data.

B. Input Features

The investigation of different input streams shows that including all available recording streams is beneficial. Using only acceleration and angular velocity as input features, the models were able to correctly classify about 42.7% of the classes. In comparison, when working only with the calculated quaternions, the performance dropped to around

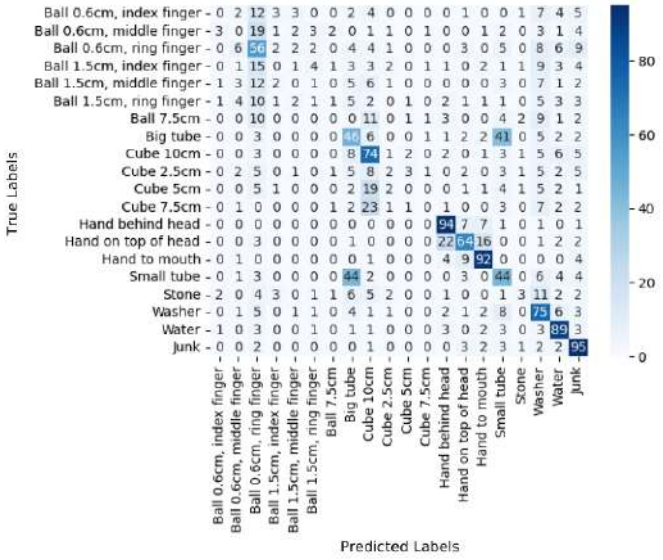


Fig. 3. Confusion matrix of the aggregated validation results for the all-item classification, using the complete left wrist



Fig. 4. Confusion matrix of the aggregated validation results for the item-domain classification, using the complete left wrist data.

34.3% accuracy. However, combining both sets of features improved the classification accuracy to 47.2%. Fig. 3 shows the confusion matrix for the best-performing model with all ten input features for the left wrist.

C. Domain-Level Classification

Even though these results do not seem promising for applied labeling of each item, Fig. 3 shows that most misclassifications belong to similar items. This leads to the result that for the classification of the domains, the same approach as for all 20 labels results in 82.3% accuracy and the confusion matrix illustrated by Fig. 4.

D. Sequence Length Impact

Discarding the 25% longest sequences, as the final step of this experiment, led to two main insights. The first main result

TABLE III
THE FIVE BEST DATA PREPROCESSING SETUPS AND THEIR MEAN ACCURACY RESULTS AVERAGED FOR BOTH ARMS. THE DATA WAS REDUCED TO 75% OF THE SHORTEST SEQUENCES TO REDUCE TIME CONSUMPTION.

Std. noise acceleration	Std. noise ang. vel.	Padding	Filter frequency acceleration ang. vel.	Freed sensors	Mean accuracy
0.5	3	Mean	0 / 0	False	64.5%
0	0	Zero	0 / 0	False	64.2%
0.5	1	Mean	0 / 0	False	63.6%
0.1	1	Zero	0 / 10	False	63.1%
0.1	3	Mean	20 / 20	False	62.9%

concerns the effects of data sequence length. Removing the longest time sequences reduced the number of time sequences that achieved the ARAT item scores zero or one from 16% to only 3%. For the 937 left-over sequences, the count of each ARAT item was reduced by similar amounts. Removing the longest sequences reduced the maximal sequence length to 318 ± 73 time steps. Consequently, all paddings were reduced to around 10% of the original length, reducing the run time by around 90%. Removing the longest time sequences and therewith the most strongly impaired movements, the classification facilitates significantly. We observe an increase in performance to around 61% accuracy for the classification of all ARAT items and to 93.9% for the domain classification.

V. DISCUSSION

The experiments of this investigation have demonstrated the possibilities of automatic ARAT item labeling using lightweight approaches.

A. Validation

In general, the KCFV approach allows us to use a large number of data for training. In addition, it provides a more stable and reliable estimation of the model's performance compared to a single train-test split by averaging the results of several train-test combinations. However, using an item-specific split leads to movement sequences of the same person being included in training and validation. While this can improve performance compared to the classification of a totally novel subject, it also favors models that overfit the training subjects.

B. Experimental Results

The first notable part of the preprocessing is that neither zero-padding nor mean-padding greatly impacts the resulting accuracy. This is because time series classification models like MiniROCKET primarily focus on patterns within observed data. MiniROCKET's kernel-based feature extraction is robust to padding due to its invariance to constant offsets and reliance on PPVs, which are robust to zero padding. Secondly, filtering high frequencies from the data and freeing acceleration or angular velocity recordings from gravity result in lower accuracies. One underlying reason for this may be that the frequency filter and the freed inputs reduces the information from essential features. The last observation concerning preprocessing is the possible model improvement through additional noise. Noise can be characterized by its statistical moments and the range of values it spans. It should relate to the data's range and statistical moments. Noise should not distort nor overwhelm the original data recordings, ensuring that the underlying patterns remain intact for accurate analysis. However, noise can result in a more generalizable model when applied correctly. This is because noise can introduce variability into the training data, preventing the model from overfitting the training samples [22].

With regard to the decision to use the left wrist data. The lower performance for left wrist data, compared to right wrist data, reflects its more diverse score distribution. This diversity represents a more balanced dataset and reduces the overfitting risks, supporting its use in this study. As scores were item- and side specific, there was no requirement to define an affected and unaffected side.

The experiments with different input streams demonstrate that while IMU readings and quaternions individually provide valuable activity recognition features, each has its limitations. However, when combined, the model's performance improves. We can assume that the input features complement each other. For future research, we would recommend integrating both inputs to enhance performance.

With regard to research question one (**RQ 1**), the final results indicate that while the current approach effectively disambiguates ARAT domains, fine-grained classification of individual items within a single domain remains limited. Addressing these challenges will require incorporating additional sensors, features, or enhancing feature extraction techniques in future work.

Fig. 4 demonstrates that the ARAT domains can be effectively distinguished with the current dataset using a lightweight and straightforward approach. The most frequently confused classes by the model are *Grasp* and *Pinch*. This is likely due to challenges in differentiating between certain *cube* items within the *Grasp* domain and *ball* items within the *Pinch* domain using only a wrist mounted IMU which encodes no information on the finger motion.

In terms of clinical utility, the current classification accuracy can only be considered as a proof of concept. The use of a minimal wearable sensor set reduces set up time and complexity, two very relevant aspects for clinical and home use. The addition of more wearable sensors will reduce feasibility. However, sensor fusion between video systems and wearable sensors may provide a straightforward solution to balancing data-greediness with practicality.

Regarding the second research question (**RQ 2**), the last experiment highlights the retaining large variance in the length of item sequences (ie. item duration) significantly

complicates the classification task. Long item sequences were mainly caused by inaccurate use of the start/stop function, which resulted in some sequences being 10x longer than the ARAT cutoff times. Slow executions are also frequently linked to greater impairment, hence our decision to remove the slowest 25% disproportionately affected scores 0 and 1, of which the relative proportion dropped drastically. This makes it very challenging to disentangle the confounding effects of decreased execution velocity and reduced movement quality. Adding well-understood hand-crafted metrics such as smoothness and trunk compensation metrics to the model may support do disentangle velocity effects through improved inference. None-the-less, reducing temporal variation of item length significantly boosted prediction accuracy for the current approach. This also would be a further incentive for examining ARAT item time cut-offs at an item-specific level, as opposed to the current "one-time-fits-all" approach.

C. Limitations and Future Work

In future work, we would aim to better disentangle execution velocity and compensation from movement quality. Furthermore, we would endeavor to develop multi-stage classification models to better handle class 0 & 1 scores, or add patient-specific priors that generalize across tasks. Finally, we would add additional sensing modalities to the data collection to be able to incorporate finger motion into our classification. This will allow us to improve the fine-grained item classification within single domains. From a model perspective, we would consider more data hungry approaches such as transformers which we would pre-train on public datasets or with synthetic data.

VI. Conclusion

We developed an auto-labeling model for individual ARAT items using two IMUs on the wrists. With its fast runtime and simplicity, MiniROCKET functions as a practical proof of concept to automatically classify ARAT items in neurological patients. The findings demonstrate that meaningful features can be effectively extracted from wrist-worn sensors. Despite the item classification still needing improvement, MiniROCKET allows for reliable differentiation between task domains. Finally, the analysis demonstrates that longer and more variable item sequences, typically associated with greater impairment levels, significantly decrease classification accuracy.

VII. Acknowledgments

We thank our clinicians: Alma Flueck, Migjen Shala, Elena Ruiz, Lisa Herndlhofer, our student team, and all participants.

References

[1] V. L. Feigin, M. Brainin, B. Norrving, S. Martins, R. L. Sacco, W. Hacke, M. Fisher, J. Pandian, and P. Lindsay, "World stroke organization (wso): Global stroke fact sheet 2022," *International Journal of Stroke*, vol. 17, p. 18–29, Jan. 2022.

[2] H. M. Feys, W. J. De Weerdt, B. E. Selz, G. A. Cox Steck, R. Spichiger, L. E. Vereeck, K. D. Putman, and G. A. Van Hoydonck, "Effect of a therapeutic intervention for the hemiplegic upper limb in the acute phase after stroke: A single-blind, randomized, controlled multicenter trial," *Stroke*, vol. 29, p. 785–792, Apr. 1998.

[3] G. Poomalai, S. Prabhakar, and N. Sirala Jagadesh, "Functional ability and health problems of stroke survivors: An explorative study," *Cureus*, Jan. 2023.

[4] A. Martino Cinnera, P. Picerno, A. Bisirri, G. Koch, G. Morone, and G. Vannozzi, "Upper limb assessment with inertial measurement units according to the international classification of functioning in stroke: a systematic review and correlation meta-analysis," *Topics in Stroke Rehabilitation*, vol. 31, p. 66–85, Apr. 2023.

[5] N. Yozbatiran, L. Der-Yeghiaian, and S. C. Cramer, "A standardized approach to performing the action research arm test," *Neurorehabilitation and Neural Repair*, vol. 22, p. 78–90, Apr. 2007.

[6] A. R. Fugl-Meyer, L. Jääskö, I. Leyman, S. Olsson, and S. Steglind, "The post-stroke hemiplegic patient. 1. a method for evaluation of physical performance," *Scandinavian journal of rehabilitation medicine*, vol. 7, no. 1, pp. 13–31, 1975.

[7] M. Saes, M. I. Mohamed Refai, B. J. F. van Beijnum, J. B. J. Bussmann, E. P. Jansma, P. H. Veltink, J. H. Buurke, E. E. H. van Wegen, C. G. M. Meskers, J. W. Krakauer, and G. Kwakkel, "Quantifying quality of reaching movements longitudinally post-stroke: A systematic review," *Neurorehabilitation and Neural Repair*, vol. 36, p. 183–207, Jan. 2022.

[8] A. Schwarz, C. M. Kanzler, O. Lambercy, A. R. Luft, and J. M. Veerbeek, "Systematic review on kinematic assessments of upper limb movements after stroke," *Stroke*, vol. 50, p. 718–727, Mar. 2019.

[9] A. M. Ponsiglione, C. Ricciardi, F. Amato, M. Cesarelli, G. Cesarelli, and G. D'Addio, "Statistical analysis and kinematic assessment of upper limb reaching task in parkinson's disease," *Sensors*, vol. 22, p. 1708, Feb. 2022.

[10] X. Suo, W. Tang, and Z. Li, "Motion capture technology in sports scenarios: A survey," *Sensors*, vol. 24, p. 2947, May 2024.

[11] O. D. Lara and M. A. Labrador, "A survey on human activity recognition using wearable sensors," *IEEE Communications Surveys & Tutorials*, vol. 15, no. 3, p. 1192–1209, 2013.

[12] S. Seenath and M. Dharmaraj, "Conformer-based human activity recognition using inertial measurement units," *Sensors*, vol. 23, p. 7357, Aug. 2023.

[13] F. Young, R. Mason, C. Wall, R. Morris, S. Stuart, and A. Godfrey, "Examination of a foot mounted IMU-based methodology for a running gait assessment," *Frontiers in Sports and Active Living*, vol. 4, Sept. 2022.

[14] J. P. O. Held, B. Klaassen, A. Eenhoorn, B.-J. F. v. Beijnum, J. H. Buurke, P. H. Veltink, and A. R. Luft, "Inertial sensor measurements of upper-limb kinematics in stroke patients in clinic and home environment," *Frontiers in Bioengineering and Biotechnology*, vol. 6, Apr. 2018.

[15] C. Werner, J. G. Schönhammer, M. K. Steitz, O. Lambercy, A. R. Luft, L. Demkó, and C. A. Easthope, "Using wearable inertial sensors to estimate clinical scores of upper limb movement quality in stroke," *Frontiers in Physiology*, vol. 13, May 2022.

[16] A. Dempster, D. F. Schmidt, and G. I. Webb, "Minirocket: A very fast (almost) deterministic transform for time series classification," in *Proceedings of the 27th ACM SIGKDD Conference on Knowledge Discovery & Data Mining*, KDD '21, ACM, Aug. 2021.

[17] D. Laidig and T. Seel, "Vqf: Highly accurate imu orientation estimation with bias estimation and magnetic disturbance rejection," *Information Fusion*, vol. 91, p. 187–204, Mar. 2023.

[18] A. Dempster, F. Petitjean, and G. I. Webb, "Rocket: exceptionally fast and accurate time series classification using random convolutional kernels," *Data Mining and Knowledge Discovery*, vol. 34, p. 1454–1495, July 2020.

[19] R. K. Bondugula, S. K. Udgata, and K. B. Sivangi, "A novel deep learning architecture and minirocket feature extraction method for human activity recognition using ecg, ppg and inertial sensor dataset," *Applied Intelligence*, vol. 53, p. 14400–14425, Oct. 2022.

[20] The aeon developers, "Convolution-based time series classification in aeon." https://www.aeon-toolkit.org/en/latest/examples/classification/convolution_based.html. Accessed: Aug. 13, 2024.

[21] M. Löning, A. Bagnall, S. Ganesh, V. Kazakov, J. Lines, and F. J. Király, "sktime: A unified interface for machine learning with time series," 2019.

[22] G. I. Kim and K. Chung, "Extraction of features for time series classification using noise injection," *Sensors*, vol. 24, p. 6402, Oct. 2024.

Mechatronic Design of a 2-DoF Wearable Robot for Wrist Stiffness Assessment

Giorgia Giovannetti[1], Alessia Noccaro[1], Nevio Luigi Tagliamonte[2], and Domenico Formica[1,3]

***Abstract*—Parkinson's Disease (PD) is a neurodegenerative disorder characterized by a variety of motor symptoms including joint rigidity, typically assessed through semi-quantitative clinical scales, which are subjective and low-reliable. To address the limitations of current methods, we introduce in this paper the PDMeter2, a portable, wearable device for objective, quantitative assessment of wrist rigidity along two coupled Degrees of Freedom (DoFs): Flexion-Extension (FE) and Radio-Ulnar Deviation (RUD). The system includes two actuators to deliver controlled and repeatable perturbations to the wrist, and simultaneously measures provided torques and joint motions necessary for estimating the stiffness, which is closely related to clinical rigidity. Its lightweight aluminum structure and 3D-printed interfaces prioritize wearability and comfort, facilitating assessments in non-clinical environments without clinicians' supervision. In this work we present the mechatronic design of the PDMeter2 and its functional characterization in terms of restrictions to the wrist Range Of Motion (ROM). Results suggest that wrist ROM is primarily reduced along the FE DoF; however, the available ROM remains suitable for effective stiffness assessment and ADLs performance. The PDMeter2 represents a significant step toward more accessible, objective, and cost-effective diagnostic and treatment management tools for Parkinson's Disease.**

***Index Terms*—Wearable Robot, Wrist Exoskeleton, 2-DoF Wrist Stiffness.**

I. Introduction

Parkinson's Disease (PD) is a chronic neurodegenerative disorder associated with significant health issues and high mortality rates [1]. Approximately 6.1 million people are diagnosed annually, with incidence rates ranging from 5 to $>$35 new cases per 100,000 individuals per year [2], [3]. PD is characterized by the progressive degeneration of dopamine-producing neurons and the formation of α-synuclein protein aggregates, particularly in the substantia nigra of the basal ganglia [1], [4]. This degeneration causes over-inhibition of efferent neural pathways, resulting in motor and non-motor symptoms. The cardinal motor symptoms include *bradykinesia* (slowness of movement), *joint rigidity* (increased resistance to passive joint motion), and *resting tremor* (involuntary and periodic body part oscillation) [1], [3], [4]. Nonmotor symptoms involve sleep behaviour disorder, depression, constipation, fatigue, hyposmia, anxiety, excessive daytime somnolence, and, in later stages, autonomic dysfunction, dementia and psychosis [1]–[3].

Although non-motor symptoms are equally prevalent and significantly affect the long-term course of PD, clinical diagnosis is only possible when motor symptoms manifest. Motor and non-motor symptoms are clinically evaluated using the semi-quantitative Unified Parkinson's Disease Rating Scale (UPDRS) [5]. However, while the clinical diagnosis for patients with fully developed motor features may seem straightforward, misdiagnosis is highly common [1]–[3]. In the early stages, error rates in the diagnosis can reach 24% even in specialised centres and can be affected by the clinician expertise [2], [6], [7]. This highlights the subjective and time-consuming nature of the semi-quantitative assessment based on the use of UPDRS and underscores the need for an objective and quantitative method for PD diagnosis [2], [6], [7].

Moreover, PD symptoms are currently managed with dopamine-targeting treatments such as L-DOPA, dopamine agonists, continuous L-DOPA infusion, or deep brain stimulation. These treatments cause varying dopamine levels, leading to significant symptom fluctuations, that are not easily detected in a single clinical evaluation. Therefore, continuous daily monitoring of motor parameters could be beneficial for treatment management [1]–[3].

To address these challenges, our research group previously developed a portable and wearable mechatronic device, known as the PDMeter [8]–[10], aimed to:

- Perform objective and quantitative evaluation of wrist rigidity along Flexion-Extension (FE), thus assisting PD diagnosis;
- Enable rigidity measurements during Activities of Daily Living (ADLs), to enhance understanding of the disease and associated motor control abnormalities;
- Enable multiple daily measurements, allowing continuous symptom monitoring and treatment optimization;
- Facilitate assessments in non-clinical environments, thereby reducing costs and required personnel time.

The focus on wrist rigidity arises from its prominence in UPDRS assessments [5], driven by the wrist's susceptibility to abnormal muscle tone and spasticity in neuromuscular disorders, as well as the central role of rigidity as a cardinal motor symptom of PD. The physical quantity that best fits with the clinical definition of rigidity is the stiffness, i.e., the static part of the joint torque-angle relationship. Hence, measuring wrist stiffness requires to gently perturb the joint while recording the delivered torques and related angular displacements [8], [9].

[1]Neurorobotics Lab, School of Engineering, Newcastle University, NE1 7RU, Newcastle Upon Tyne, United Kingdom.

[2]Research Unit of Advanced Robotics and Human-Centred Technologies, Universita' Campus Bio-Medico di Roma, 00128, Rome, Italy.

[3]NEXT: Neurophysiology and Neuroengineering of Human-Technology Interaction Research Unit, School of Medicine, Universita' Campus Bio-Medico di Roma, 00128, Rome, Italy.

Correspondence to: g.giovannetti2@newcastle.ac.uk

The main limitation of the PDMeter is its capability to measure wrist rigidity only along 1 Degree of Freedom (DoF), i.e. FE. However, natural wrist rotations occur in combination of 2 DoFs, i.e., Flexo-Extension and Radio-Ulnar Deviation (RUD), which are coupled through interaction forces deriving from stiffness [11]–[13]. A few studies have measured 2-DoF wrist stiffness and they have used bulky, general-purpose robotic systems [11], [14], [15]. These robots are typically limited to structured lab environments and lack portability. In contrast, manual systems are more compact and portable, and are designed for the assessment in a broader range of environments. However, they are non-actuated and rely on a human operator to produce mechanical perturbations, thus limiting the ability to provide consistent and objective measurements [9].

In this work, we present an evolution of the PDmeter design to include a second active DoF (i.e., RUD), with the aim of proposing a portable and wearable device for reliable 2-DoF wrist stiffness estimation in unstructured environments. Overcoming the limitations of the previous system, this new device, hereafter called PDMeter2, integrates two actuators to provide controlled and repeatable wrist perturbations along FE and RUD, with delivered torques estimated from motor currents and joint motion tracked via encoders. This paper presents the mechanical and electronic design of the device, as well as its functional characterization in terms of limitation to the wrist ROM.

II. Materials and Methods

A. Mechanical Design

Fig. 1 illustrates the mechanical structure and the kinematic sketch of the device. It consists of two kinematic chains, each one designed to actuate one human DoF and leave free the other one. The chain actuating the FE DoF is hereafter referred to as the *FE chain*, whereas the one actuating the RUD DoF is hereafter referred to as the *RUD chain*.

Each chain includes five revolute joints: *i)* one proximal active joint (blue in Fig. 1), which has an axis parallel to the one of the human DoF to be actuated; *ii)* three intermediate passive joints (purple in Fig. 1), which have their axes perpendicular to the one of the active joint, to allow the free movement around the other human DoF; *iii)* a distal passive joint (green in Fig. 1), whose axis is parallel to the one of the active joint. The two kinematic chains are secured to the hand through their distal links (link 6A and link 6B) and to the forearm through their proximal links (link 2 and link 10), connected to the active joints. They are functionally connected in parallel to the human (forearm-wrist-hand) chain to eventually create a closed-loop 2-DoF chain.

As shown in Fig. 2, each chain can be analyzed in two orthogonal planes: $PS-FE$ and $PS-RUD$, where PS refers to Prono-Supination. The RUD chain in the $PS-RUD$ plane is equivalent to the FE chain in the $PS-FE$ plane. With reference to Fig. 2, this planar mechanism is composed of three purple rotary joints (3R chain) and one grey human joint.

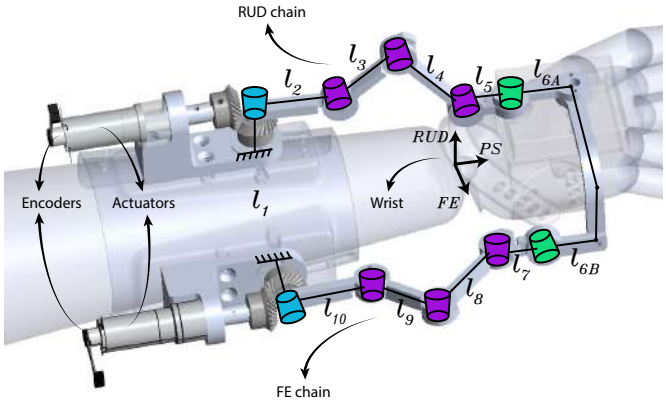


Fig. 1: Overview of the mechanical structure of the device. The frame (FE, RUD, PS) shows the rotation axes of the wrist DoFs. The kinematic sketch is superimposed: for each chain, the axes of the proximal active (blue) joint and of the distal passive (green) joint are parallel to the axis of the human DoF to be actuated (FE/RUD) whereas the axes of the intermediate passive (purple) joints are perpendicular to it, i.e., parallel to the DoF actuated by the other chain (RUD/FE). l_i are the links composing the kinematic structure, being l_1 the forearm and l_{6A} and l_{6B} secured to the hand.

The 3R chain can be represented as an equivalent prismatic joint in the corresponding orthogonal plane.

The RUD chain in the $PS-FE$ plane is equivalent to the FE chain in the $PS-RUD$ plane. With reference to Fig. 2, this planar mechanism is composed of two rotary joints (one active, in blue, and one passive, in green) and one purple prismatic joint (equivalent to the 3R chain in the corresponding orthogonal plane).

The number of DoFs F for each planar mechanism can be computed according to the Chebychev–Grübler–Kutzbach criterion [16]:

$$F = \lambda(l - j - 1) + \sum_{i=1}^{j} f_i, \tag{1}$$

where $\lambda = 3$ is the mobility parameter in the 2-dimensional space, l is the number of links, j is the number of joints and f_i is the number of DoFs of the $i-$th joint.

For each of the four planar chains of Fig. 2, $l = 4$, $j = 4$ and $f_i = 1$, leading to $F = 1$.

The actuation system was selected to optimize torque, speed and power requirements together with efficiency, weight, size, and cost. Previous studies on estimating wrist stiffness in healthy individuals conducted by our research group showed that the torque required for a passive wrist was less than 0.7 Nm [17]. Given that the rigidity typically observed in patients with PD would increase the torque needed to achieve the same motion, we designed the actuation system to have a nominal torque of 1 Nm in each actuated DoF [8]. To avoid triggering motor reflexes, the device must be operated in a smooth and slow manner. Previous studies in our group have implemented movement trajectories with an average velocity of 0.14 rad/s

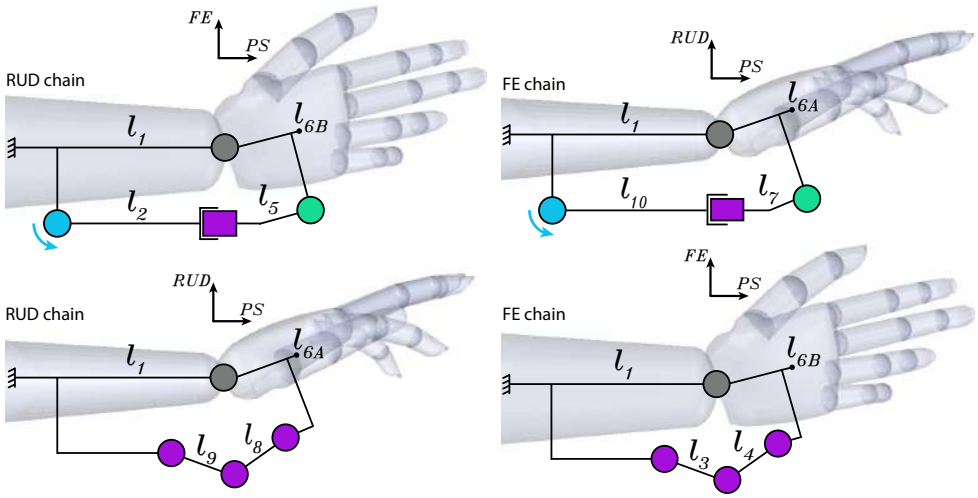


Fig. 2: Kinemtic sketches of the two chains: left) RUD chain, providing 1 actuated DoF (RUD) in the $PS-FE$ plane and 1 passive DoF (FE) in the $PS-RUD$ plane; right) FE chain, providing 1 actuated DoF (FE) in the $PS-RUD$ plane and 1 passive DoF (RUD) in the $PS-FE$ plane. Light blue arrows indicate actuated joints. Purple chains composed of three rotary joints in one plane can be represented as an equivalent prismatic joint in the orthogonal plane. Each chain represented in each plane has 1 DoF.

($\sim$1.33 rpm) [17]. However, to enable the device to assist with daily tasks and follow natural wrist movements, back-driveability of the system is also essential. Consequently, the device should be capable of passively following the user's motion when controlled in *transparent mode* (i.e., when stiffness is not being measured), increasing the required actuation speed to approximately 38 rpm [8].

Based on these criteria, we selected a commercial actuation system manufactured by Maxon Motors Inc., consisting of:

- a DC brushed motor: model DCX19S @ 12V, with a nominal torque of 11.4 mNm;
- a 3-stage planetary gearhead: model GPX22A, with a reduction ratio of 62 and an efficiency of 0.74;
- an incremental differential encoder: model ENX10 EASY 512IMP, with a count per turn of 512, providing a resolution of approximately 0.0028 deg [8].

To minimize encumbrance, the motors were positioned longitudinally to the forearm and connected to the proximal joint with high-efficiency bevel gears (ground spiral miter gears SMSG1-25R/L from MISUMI). Additionally, to reduce weight and size, the shape of the rigid links composing the kinematic chains was optimized with respect to the PDMeter [8], allowing the use of a single ball bearing for each revolute joint instead of two. Furthermore, to prevent exceeding users' ROM, critical rigid links were designed to be secured to interchangeable mechanical stops.

The material of the links was Al 6082 T651, selected for its smaller density compared to steel while still providing adequate strength for our application. In contrast, joint shafts were made of BS 1407 silver steel to ensure higher strength.

Ergonomic forearm and hand physical interfaces, shown in Fig. 3, were designed and 3D printed in Thermoplastic Polyurethane (TPU), a flexible material that enhances comfort and wearability. Specifically, the forearm interface houses the motors and incorporates two external skate buckles for easy donning and doffing, enabling the patient to wear the device autonomously. The hand interface was designed with a modular closure system, that allows adjustment for different hand sizes. This interface secures the hand from the dorsal side, with straps that wrap around the ulnar side of the hand and lateral thumb areas. Different sizes of this interface can be easily attached and detached from the device using a sliding system, which features a Polylactic Acid (PLA) component secured to Link 6A. Both the forearm and hand interfaces are internally coated with a foam layer to maximize comfort against the skin.

B. Electronic Design

An STM32F446RE microcontroller from ST Microelectronics Inc. was used to manage actuation control and data acquisition. To control the actuators, the microcontroller sends commands to two low-level drivers (Escon Module 24/2 by Maxon Motors Inc.), which ultimately adjust the voltage and current levels required to drive the actuators via a PWM signal. The microcontroller is also responsible for measuring motor rotation through the incremental encoder, utilizing the embedded Quadrature Encoder Interface (QEI). Current provided to the two motors through the Escon modules is converted with a 16-bit Analog-to-Digital Converter (ADC, model MAX1167 by Maxim Integrated Inc.) and used to estimate the torque applied by the actuators. The ADC communicates with the microcontroller via the SPI protocol. Finally, collected data, including measured currents, motor rotations, and desired torques, are transmitted to an external laptop via UART. A

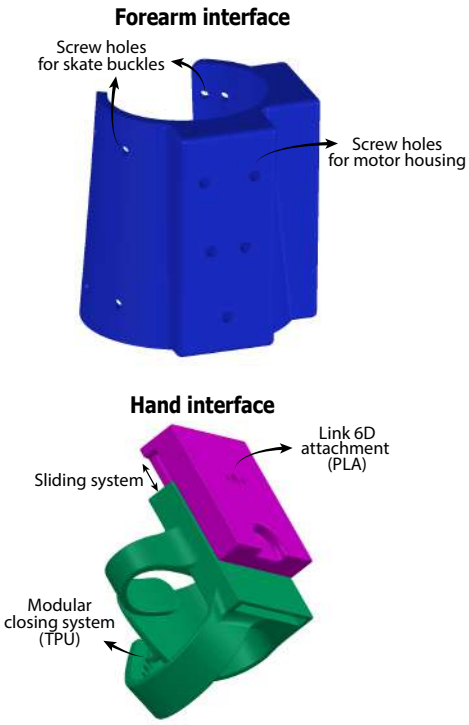


Fig. 3: Physical interfaces connecting the device to forearm and hand. The forearm interface is wrapped around through screwed skate buckles. The hand interface has a modular closure to adjust to different hand sizes and a sliding system to be easily attached and detached to the device. Drawings are not to scale.

scheme illustrating the architecture of the device electronics is shown in Fig. 4.

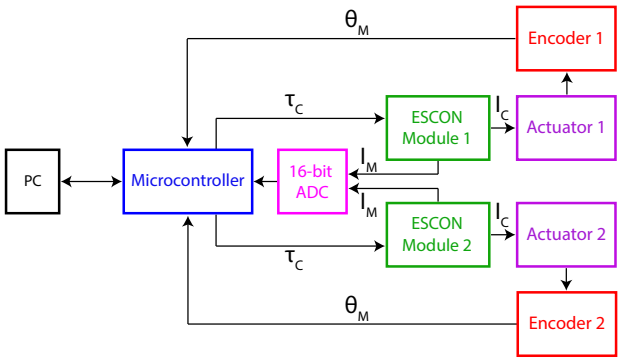


Fig. 4: Architecture of the PDMeter2 electronics. τ_C is the control torque, I_C is the control current, θ_M is the measured angle, I_M is the measured current.

We implemented a torque control based on a trapezoidal reference torque profile. This enables the two motors to operate individually for pure FE and RUD motions from a wrist neutral position to peripheral targets, or simultaneously to produce combined motions at 45 deg between the two. A GUI developed in the Qt environment allows users to select the desired ramp duration of the trapezoidal torque profile and the steady torque values, while the holding torque duration is fixed at 0.5 s.

C. Device Characterization

We characterized the device wearability and impact on natural wrist rotations in terms of maximum angular excursion of the wrist when performing FE and RUD motions with the exoskeleton, to identify any limitation to the movement due to its use.

1) Subjects: Four healthy volunteers (3 females; age range: 27-32) with no history of upper arm neuromuscular impairment were recruited. Written informed consent was obtained after participants were informed about the study's procedures. The experimental protocol was approved by Newcastle University's Ethics Committee (23-006-GIO) and conducted in line with the Declaration of Helsinki.

2) Experimental Setup & Protocol: Wrist motion data were acquired using an optical motion capture system (Motive OptiTrack, Natural Point Inc., Corvallis, OR, USA) with 5 infrared cameras and two rigid bodies positioned on the forearm and the hand, respectively. Fig. 5 shows the placement of the rigid bodies when performing wrist motions without (a) and with (b) the exoskeleton.

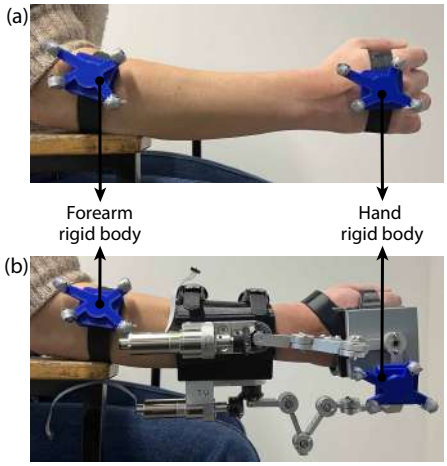


Fig. 5: Placement of the forearm and hand rigid bodies when performing wrist motions without (a) and with (b) the exoskeleton, during the functional characterization of the device. A set of 5 infrared cameras (not shown in the picture) were used to detect the rigid bodies motions.

Subjects sat on a chair with their right elbow resting on the chair's armrest and their forearm positioned horizontally, ensuring that the wrist could move freely and the device did not come into contact with the chair. Subjects were asked to move their wrist from a neutral position to eight peripheral targets representing pure FE, pure RUD, and combined motions at roughly 45 deg between them. The neutral position was defined according to the the International Society of Biomechanics recommendations [18], i.e., the long axis of the third metacarpal aligned with the long axis of the forearm.

Therefore, in each trial, participants were instructed to begin the movement by aligning middle finger knuckle to their forearm axis and to reach the maximum range of motion in each of the eight target directions. Three trials were performed while wearing the exoskeleton and three without it, with a rest of a few minutes in between, resulting in a total duration of the experiment of approximately 15 minutes.

3) Data Processing & Analysis: Data acquired from the cameras were resampled at a frequency of 100 Hz, low-pass filtered (5^{th} order Butterworth; cutoff frequency: 10 Hz) and cut to remove unnecessary information preceding and following the wrist motions.

Relative motions between the hand and the forearm rigid bodies were converted to wrist angles using a kinematic model of the human wrist [17]. Maximum angle values for flexion, extension, radial deviation, and ulnar deviation were extracted for each trial, as an indication of the ROM achievable along each direction. Extracted ROM data were then averaged per participant and finally analyzed with JASP software using a paired samples t-test, to identify any significant ROM differences with and without the device, after checking data normality with the Shapiro-Wilk test.

III. Results

After finalizing the design, the exoskeleton was manufactured in aluminum alloy (Fig. 6), with a total mass, including actuators and forearm/hand interfaces, of 1 kg.

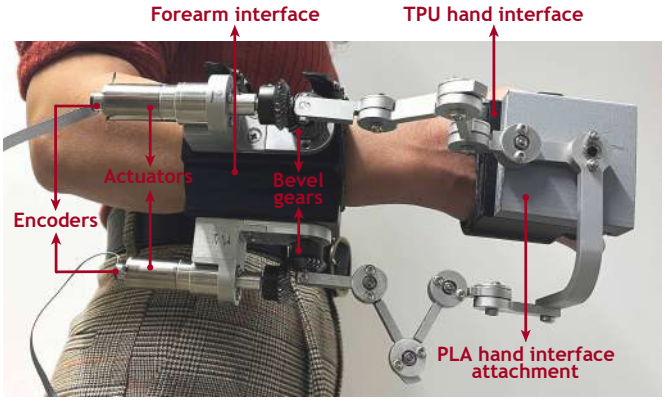


Fig. 6: Mechanical structure of the manufactured device.

Table I presents the mean ROM values achieved during extension, flexion, radial deviation, and ulnar deviation, both without and with the device, while Fig. 7 illustrates the results of the statistical analysis.

The results indicate that wearing the device impacts the achievable ROM to varying extents across the four directions of movement. Specifically, extension and flexion were the most affected. Extension exhibited a ROM reduction of approximately 56% (∼36 deg), while flexion showed a restriction of around 42% (∼34 deg). In contrast, radial deviation ROM showed no significant impact with or without the exoskeleton, while the ulnar deviation exhibited a percentage reduction of around 30% (∼14 deg), although no statistically significant differences were observed in this case.

MOTION	NO-EXO	EXO
EXTENSION	64 deg	28 deg
FLEXION	81 deg	47 deg
RADIAL D.	17 deg	21 deg
ULNAR D.	47 deg	33 deg

TABLE I: Mean ROM values achieved during extension, flexion, radial deviation, and ulnar deviation, without (NO-EXO) and with (EXO) the exoskeleton.

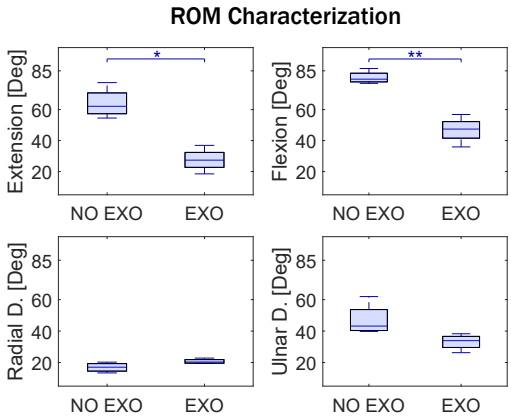


Fig. 7: Results of the statistical analysis conducted on the ROM values achieved during extension, flexion, radial deviation and ulnar deviation without (NO EXO) and with (EXO) the device. *: $p < 0.05$; **: $p < 0.005$.

IV. Conclusions

This work introduces the PDMeter2, a 2-DoF version of a wearable mechatronic device designed to measure wrist rigidity in PD patients along coupled FE and RUD. The device aims to support PD diagnosis by providing a quantitative and objective method to evaluate one of its cardinal symptoms. Such tool would facilitate reliable PD assessment even in the early stages, when current clinical methods still exhibit high error rates. Additionally, it enables treatment optimization through continuous symptom monitoring in non-clinical environments.

With respect to previous prototype [9], the system comprises two motors and two kinematic chains to deliver controlled and repetitive perturbations to the wrist along the FE and RUD DoFs, while simultaneously recording applied torques and joint motions to assess wrist rigidity. When not measuring stiffness, the device enables motion along the two DoFs, possibly allowing users to perform daily activities.

The device kinematic structure, made from aluminum alloy, is optimized to minimize weight and bulk. Additionally, 3D-printed body interfaces are designed to enhance both comfort and wearability.

We evaluated the restriction of wrist ROM caused by wearing the device compared to the natural ROM of the wrist during free movement. Results indicate that the most significant ROM limitations occur along the FE axis, where

the device allows a ROM of 28 deg and 47 deg in extension and flexion, respectively. While these values are significantly lower than the unrestricted ROM, they remain sufficient for stiffness assessment, which can be reliably conducted within a 20 deg motion range from the neutral position [11], [17], [19]. Moreover, ADLs such as personal hygiene and culinary tasks typically require approximately 35 deg of motion along FE and 25 deg along RUD [20], both of which are within the limits permitted by the PDMeter2.

The device affects ROM differently across the four movement directions, likely due to varying mechanical constraints during extending and bending of the kinematic chains. Additionally, the lack of a physical constraint on the neutral position may have introduced slight inter-trial variability, leading, for instance, to a radial deviation ROM with the device exceeding that without it, although the overall RUD ROM remains lower with the device. Future work will involve structural optimization to address ROM restrictions across the two DoFs and improvement of the experimental protocol.

Moreover, although not explicitly reported in the results, we noticed that the achievable ROM may slightly depend on the positioning of the forearm interface during the don procedure. This issue, likely due to the softness of the forearm's skin tissue, affects the level of extension of the kinematic chains and could be mitigated by optimizing the forearm interface design with an adjustable mechanism to customize fitting for each subject. However, ROM inter-subject variability remains minimal and does not affect stiffness assessment range, which always falls within the permitted limits.

To enhance wearability and simplify manufacturing, future work could explore replacing the aluminum kinematic links with 3D-printed plastic materials, which would reduce both weight and cost of the device. However, plastic presents certain drawbacks compared to aluminum, such as lower strength, reduced stiffness, and increased flexibility. As a result, the use of plastic materials would require a preliminary assessment of their suitability for motion transmission and reliability of the stiffness measurements due to the link deformation, as well as their resistance to fatigue loads and possible degradation. We anticipate that using plastic for the forearm and hand interfaces will not affect device performance. The forearm interface remains fixed, while the hand interface is rigidly attached to metal link 6A, minimizing any impact on motion transmission.

Initial testing of the device will involve healthy subjects to evaluate its reliability in assessing wrist rigidity. Following these tests, experimental trials will be conducted with PD patients to clinically validate the system's effectiveness.

After testing the device, future developments may include expanding the design to incorporate additional upper limb joints, e.g., the elbow, allowing for the simultaneous assessment of both joints in alignment with clinical UPDRS evaluations.

REFERENCES

[1] A. D. Halli-Tierney, J. Luker, and D. G. Carroll, "Parkinson disease," *American family physician*, vol. 102, no. 11, pp. 679–691, 2020.

[2] W. Poewe, K. Seppi, C. M. Tanner, G. M. Halliday, P. Brundin, J. Volkmann, A.-E. Schrag, and A. E. Lang, "Parkinson disease," *Nature reviews Disease primers*, vol. 3, no. 1, pp. 1–21, 2017.

[3] B. R. Bloem, M. S. Okun, and C. Klein, "Parkinson's disease," *The Lancet*, vol. 397, no. 10291, pp. 2284–2303, 2021.

[4] H. R. Morris, M. G. Spillantini, C. M. Sue, and C. H. Williams-Gray, "The pathogenesis of parkinson's disease," *The Lancet*, vol. 403, no. 10423, pp. 293–304, 2024.

[5] C. G. Goetz, B. C. Tilley, S. R. Shaftman, G. T. Stebbins, S. Fahn, P. Martinez-Martin, W. Poewe, C. Sampaio, M. B. Stern, R. Dodel *et al.*, "Movement disorder society-sponsored revision of the unified parkinson's disease rating scale (mds-updrs): scale presentation and clinimetric testing results," *Movement disorders: official journal of the Movement Disorder Society*, vol. 23, no. 15, pp. 2129–2170, 2008.

[6] G. Rizzo, M. Copetti, S. Arcuti, D. Martino, A. Fontana, and G. Logroscino, "Accuracy of clinical diagnosis of parkinson disease: a systematic review and meta-analysis," *Neurology*, vol. 86, no. 6, pp. 566–576, 2016.

[7] M. D. S. T. F. on Rating Scales for Parkinson's Disease, "The unified parkinson's disease rating scale (updrs): status and recommendations," *Movement Disorders*, vol. 18, no. 7, pp. 738–750, 2003.

[8] L. Raiano, G. Di Pino, A. Noccaro, D. Accoto, and D. Formica, "Design of a wearable mechatronic device to measure the wrist rigidity in parkinson's disease patients," in *2018 7th IEEE International Conference on Biomedical Robotics and Biomechatronics (Biorob)*. IEEE, 2018, pp. 497–502.

[9] L. Raiano, G. Di Pino, L. Di Biase, M. Tombini, N. L. Tagliamonte, and D. Formica, "Pdmeter: A wrist wearable device for an at-home assessment of the parkinson's disease rigidity," *IEEE Transactions on Neural Systems and Rehabilitation Engineering*, vol. 28, no. 6, pp. 1325–1333, 2020.

[10] L. Raiano, G. Di Pino, and D. Formica, "Flexion-extension wrist impedance estimation using a novel portable wrist exoskeleton: A pilot study," in *2020 8th IEEE RAS/EMBS International Conference for Biomedical Robotics and Biomechatronics (BioRob)*. IEEE, 2020, pp. 440–445.

[11] D. Formica, S. K. Charles, L. Zollo, E. Guglielmelli, N. Hogan, and H. I. Krebs, "The passive stiffness of the wrist and forearm," *Journal of neurophysiology*, vol. 108, no. 4, pp. 1158–1166, 2012.

[12] S. K. Charles and N. Hogan, "The curvature and variability of wrist and arm movements," *Experimental brain research*, vol. 203, pp. 63–73, 2010.

[13] ——, "Stiffness, not inertial coupling, determines path curvature of wrist motions," *Journal of neurophysiology*, vol. 107, no. 4, pp. 1230–1240, 2012.

[14] A. L. Pando, H. Lee, W. B. Drake, N. Hogan, and S. K. Charles, "Position-dependent characterization of passive wrist stiffness," *IEEE Transactions on Biomedical Engineering*, vol. 61, no. 8, pp. 2235–2244, 2014.

[15] S. Durand, C. P.-Y. Rohan, T. Hamilton, W. Skalli, and H. I. Krebs, "Passive wrist stiffness: the influence of handedness," *IEEE Transactions on Biomedical Engineering*, vol. 66, no. 3, pp. 656–665, 2018.

[16] J. J. Uicker, J. J. Uicker Jr, G. R. Pennock, and J. E. Shigley, *Theory of machines and mechanisms*. Cambridge University Press, 2023.

[17] G. Giovannetti, A. Noccaro, S. Buscaglione, and D. Formica, "Estimation of passive wrist stiffness across two coupled degrees of freedom using a kinematic model of the human wrist," in *2024 10th IEEE RAS/EMBS International Conference for Biomedical Robotics and Biomechatronics (BioRob)*. IEEE, 2024, pp. 1358–1363.

[18] G. Wu, F. C. Van der Helm, H. D. Veeger, M. Makhsous, P. Van Roy, C. Anglin, J. Nagels, A. R. Karduna, K. McQuade, X. Wang *et al.*, "Isb recommendation on definitions of joint coordinate systems of various joints for the reporting of human joint motion—part ii: shoulder, elbow, wrist and hand," *Journal of biomechanics*, vol. 38, no. 5, pp. 981–992, 2005.

[19] W. B. Drake and S. K. Charles, "Passive stiffness of coupled wrist and forearm rotations," *Annals of biomedical engineering*, vol. 42, pp. 1853–1866, 2014.

[20] A. K. Palmer, F. W. Werner, D. Murphy, and R. Glisson, "Functional wrist motion: a biomechanical study," *Journal of Hand Surgery*, vol. 10, no. 1, pp. 39–46, 1985.

Simultaneous Perturbation of Knee and Ankle Joints During Stance Phase of Walking: Towards Biological Joint Impedance Estimation

Michele Paravano*, Mohamed Irfan Refai, Herman van der Kooij, Massimo Sartori

***Abstract*—Characterization of lower limb joint impedance during locomotion is crucial for advancing our understanding of walking biomechanics, while also guiding the development of assistive technologies and rehabilitation strategies. Identification of impedance parameters is dependent on perturbation strategies which elicit measurable responses at the joint of interest. However current perturbation methodologies applied during locomotion either work in the swing phase or employ exoskeleton based setups which can add complexity and weight to the leg. This study introduces and evaluates a perturbation methodology using a custom-designed pusher system to elicit multi-joint-level torque and angular responses during the stance phase of gait for different conditions. Controlled perturbations applied behind the tibia revealed measurable dynamic response at the knee and ankle joint, while preserving the gait cycle's overall pattern. Torque-angle and torque-velocity graphs reveal insights into energy and power changes between perturbed and unperturbed gait cycles. The method can be adapted to various walking speeds, perturbation intensities, and durations, providing the first step for future estimation of joint impedance during locomotion.**

***Index Terms*—Joint impedance, joint stiffness, stance perturbation, rehabilitation, system identification.**

I. Introduction

Joint impedance, a fundamental biomechanical property, governs how human joints respond to external forces and is continuously regulated by the nervous system to enable effective interaction with the environment. It encompasses stiffness, damping, and inertia, capturing the dynamic relationship between changes in joint kinematics and the resulting torques.

State-of-the-art techniques for estimating joint impedance primarily rely on perturbation-based methods. Early pioneering studies focused on perturbations under static, time-invariant conditions [1], [2], estimating joint impedance around a fixed operating point. This was followed by advancements in time-varying system identification techniques [3]–[5], and allowed usage of dynamometer setups to perturb individual joints during motion [6]–[8].

The need to estimate joint impedance during locomotion and everyday activities has driven the development of perturbation techniques targeting walking gait. For instance, platform-based setups have been designed to induce controlled ankle angle changes during stance, providing insights into the dynamic modulation of joint impedance based on perturbation timing and intensity [9]. Exoskeleton-based setups have also been explored, such as the work by Nazon and Rouse, who investigated knee impedance during gait using controlled perturbations to characterize dynamic joint properties [10]. An earlier contribution by Sinkjaer et al. pioneered an exoskeleton-like perturbation method for simultaneous knee and ankle perturbations during stance [11].

While platform-based perturbation setups are commonly used to study joint dynamics, they primarily focus on single-joint responses, often neglecting the interplay between multiple joints during gait. Exoskeleton-based perturbations can introduce additional weight and complexity, which may alter natural walking patterns [12]. In contrast, pusher-based perturbation techniques offer a lightweight and minimally intrusive alternative by applying controlled forces to the leg through an external rod.

Van der Kooij et al. demonstrated the effectiveness of the LOPER system in perturbing the leg during the swing phase, enabling simultaneous estimation of knee and hip joint impedance [13]. However, their approach was limited to swing-phase perturbations, leaving stance-phase unexplored.

During the stance phase of gait, ground reaction forces anchor the foot, making it harder to apply effective perturbations than during the swing phase. Enhanced muscle activation and co-contraction further stiffen the joints, which reflects the body's strategy for maintaining stability under load. This work explores whether a pusher-based system can overcome these challenges and induce meaningful multi-joint perturbations during stance without disrupting the gait pattern.

This study assesses an extension to the perturbation method in [13] targeting the lower limb kinematic chain during stance. Controlled perturbations applied behind the tibia propagate through the kinematic chain, inducing measurable torque and angular responses at both the knee and ankle joints.

The primary contribution of this work is the design and validation of an experimental-robotic setup for controlled stance-phase perturbations. Data from one subject illustrate differences in joint kinetics between perturbed and unperturbed conditions. The study presents work loop and power loop analyses and discusses the future steps for joint stiffness estimation. To the best of our knowledge this is the first study providing a stance-perturbation strategy using a pusher setup. This work can potentially advance our capabilities of measuring joint biomechanical quantities during gait in

This work was supported by Horizon Europe RIA (Grant No. 101120408; S.W.A.G.). All authors are affiliated to the Department of Biomechanical Engineering, University of Twente, The Netherlands. *Corresponding author: m.paravano@utwente.nl.

multiple conditions and provides the base data acquisition process for lower limb joint impedance estimation.

II. METHODS

The lower limb perturbator (LOPER) design is extensively described in [13]. Here we present a brief overview. The experiments were conducted with the approval of the University of Twente Ethical Committee 241160, and participant provided written informed consent.

A. Experimental Setup

1) Hardware setup, as in Fig. 1:

- A split-belt instrumented treadmill Fig. 1 (**4.**) (Bertec FIT 5, USA) capable of independently measuring ground reaction forces (GRFs) and moments in three dimensions for each leg.
- A motion capture system Fig. 1 (**1.**) which records kinematic data for subsequent analysis to track limb motion (Qualisys AB, Sweden). The participant is equipped with 35 reflective markers placed on key anatomical landmarks used to scale the Gait2392 model of OpenSim.
- The participant's right leg is securely attached to a pusher rod via a brace strapped just below the knee. This location was selected for two primary reasons:
  - To maximize the moment arm for ankle perturbations.
  - To ensure proximity to the knee joint, allowing effective perturbations to be applied during the stance phase.

  A reflective marker is also placed on the pusher brace to track the location of the perturbation force with respect to the leg.
- The LOPER system Fig. 1 (**2.**) consists of a rod connected via a ball linkage to another link rigidly attached to a motor. This mechanical setup translates the motor's rotational torque into a linear push force applied to the participant's leg. Interaction forces between the pusher rod and the leg are measured using a load cell Fig. 1 (**3.**) (FUTEK FSH00086, USA) positioned between the motor's moment arm and the pusher rod. The load cell provides force measurements in three dimensions, enabling the implementation of real-time feedback control of interaction forces.
- For safety, the participant wears a ceiling-mounted harness designed to prevent falls in the event of tripping or loss of balance during the trials.

2) Software: All devices, including the treadmill, motion capture system, and pusher, are synchronized using a dedicated synchronization signal to ensure temporal alignment of all data streams. Motion capture data is acquired using the Qualisys system at a sampling frequency of 100 Hertz, while ground reaction forces and moments, are recorded at 2000 Hertz. Interaction forces from the pusher are sampled at 1000 Hertz and transmitted via the EtherCAT protocol, which is managed by TwinCAT on the main control PC. The control PC also runs a compiled Simulink model within TwinCAT, enabling real-time control of the pusher motor.

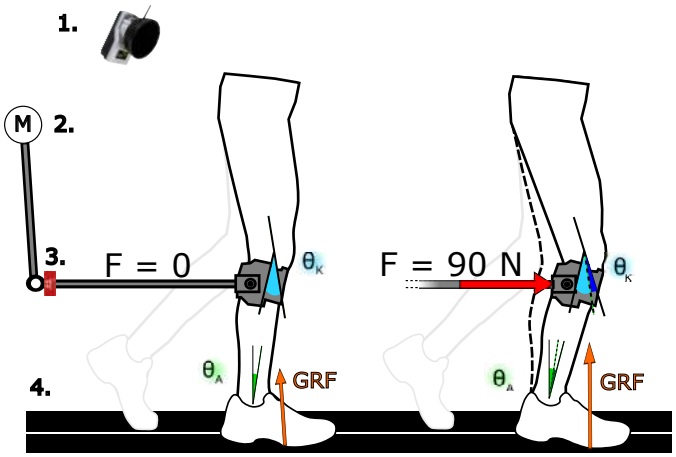


Fig. 1. Experimental setup for measuring joint impedance during locomotion, including a (1) motion capture system to track kinematics, (2) a LOPER pusher device to apply controlled perturbations, (3) a load cell to measure interaction forces, (4) and a split-belt treadmill for locomotion, with the left panel showing the unperturbed state (F=0) and the right panel depicting a 90 N perturbation force applied below the knee.

3) Control: The participant walks on the treadmill at a speed of $v = 0.8\,\text{m/s}$, which was determined to be a comfortable and normal gait speed by the participant. Before the start of the experiment the subject was given a test trial (5 min) to acclimate to the pusher interaction and the pushes. Heel strikes and toe-off timings are detected when the vertical ground reaction force exceeds 5% of the participant's body weight, as measured on the treadmill belt. A random perturbation is applied once within a range of 5 gait cycles to the participant's right leg, with a total of 20 perturbations delivered throughout the trial. Two separate trials are carried out, where perturbations are applied at the beginning of the stance phase and after 200 ms from heel strike. These instants correspond to $\approx 5\%$ (loading response) and $\approx 20\%$ of the gait cycle (mid-stance) respectively. The control strategy is divided into two modes:

- **Unperturbed gait**: Admittance control is implemented as described in [13] to minimize interaction forces between the pusher and the participant's leg, ensuring the system remains as transparent as possible. The control strategy aims to limit peak interaction forces to less than $20\,\text{N}$ and root mean square (RMS) forces to below $10\,\text{N}$. These thresholds are based on a study investigating the effects of adding inertia to the ankle, where $1.55\,\text{kg}$ resulted in changes in ankle and knee range of motion comparable to the natural variability across different subjects [14]. This mass was determined to be the upper limit for avoiding significant disruptions to natural gait. In contrast, a heavier mass of $3.5\,\text{kg}$ was shown to affect knee flexion and plantarflexion, which are more prominent during the swing phase rather than the stance phase. In addition, since the pusher in our setup is connected to

the shank rather than the ankle, these thresholds serve as conservative limits to ensure minimal gait disruption during perturbations.

- **Perturbed gait**: The pusher operates in admittance control mode until the perturbation instance. The perturbation signal is a square wave with duration $\Delta t_{\text{perturbation}} = 100\,\text{ms}$ and Intensity: $F = 90\,\text{N}$

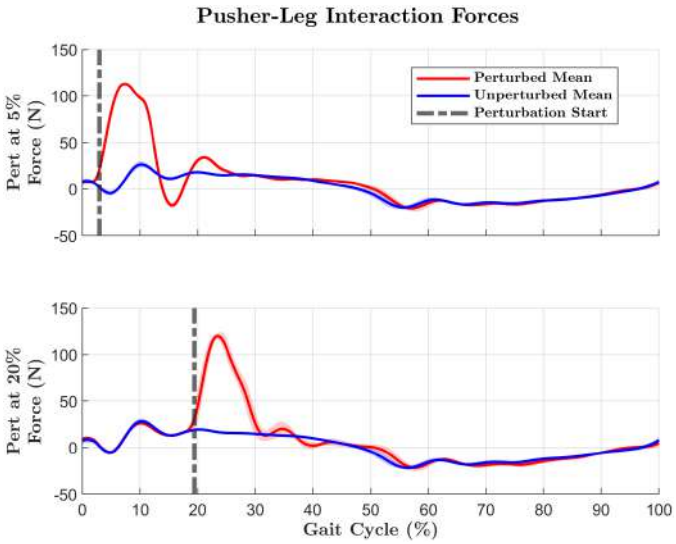


Fig. 2. Interaction forces between the leg and the pusher device during gait cycles. In blue, the interaction forces during unperturbed gait cycles, where the pusher's admittance controller aimed to minimize forces to achieve transparency. In red, the interaction forces during perturbed gait cycles. The top graph illustrates the average interaction forces when perturbations were applied during the loading response phase ($\approx 5\%$ of the gait cycle), while the bottom graph represents the interaction forces when perturbations occurred during the mid-stance phase ($\approx 20\%$). Shaded areas indicate the standard deviation (STD) around the mean for both perturbed and unperturbed trials. Pert stands for perturbation.

B. Data Processing

1) Pre-processing: Marker data is gap-filled using the Qualisys QTM software to address missing or incomplete data points, ensuring continuity in the recorded trajectories. The processed marker data is then exported into MATLAB format for further analysis. Both marker data and ground reaction forces (GRFs) are low-pass filtered using a 4th-order Butterworth filter to remove unwanted high-frequency noise while preserving the essential motion and force signals.

To ensure precise temporal alignment of all data streams, synchronization is performed using the previously mentioned synchronization signal. This step is necessary as the pusher data and the marker/GRF data streams do not share the same start time. Once synchronized, the pusher data is resampled at 2000 Hertz using a linear interpolation method to match the sampling frequency of the GRF data, allowing consistent analysis across all datasets.

2) Inverse Kinematics (IK) and Inverse Dynamics (ID): Marker trajectory data are processed using OpenSim, a biomechanical modeling software. OpenSim utilizes a scaled musculoskeletal model of the participant's skeleton to map marker positions to limb positions and joint angles (IK). During the IK process, the software minimizes the error between the experimentally observed marker positions and the corresponding virtual markers on the model by solving an optimization problem. This yields a time-series of joint angles that describe the participant's motion throughout the trial.

The joint angles derived from IK serve as inputs to the ID process, along with ground reaction forces (GRFs) and the interaction forces from the pusher. ID calculates joint torques by applying Newton-Euler equations of motion to the model.

3) Data Analysis: Inverse kinematics (IK) and inverse dynamics (ID) data were segmented into individual gait cycles based on heel-strike timing. To account for natural variations in gait cycle duration, all cycles were re-interpolated onto a fixed time vector for consistency. This standardization facilitates the visualization and comparison of gait cycles by ensuring they are of equal length. Additionally, gait cycles exceeding 1.5 seconds in duration were excluded from the analysis, as these were likely associated with treadmill acceleration or deceleration phases rather than steady-state walking. Finally, mean and standard deviation values were extracted from 60 unperturbed gait cycles and 20 perturbed gait cycles for each trial.

III. Results

A. Changes in Joint Angles and Torques Due to Perturbation

Fig. 2 illustrates the interaction forces between the pusher and the participant's right leg. During the unperturbed gait cycle (shown in blue), the interaction forces peaked at 28 N, with an RMS value of 13.7 N. Although the original perturbation signal is a square wave with an amplitude of 90 N, the interaction force exceeds this value, peaking at 117 N for perturbations occurring at 5% of the gait cycle and at 123 N for perturbations occurring at 20% of the gait cycle. Nonetheless this interaction force is consistent throughout multiple gait cycles, with little fluctuations around the mean value, which is crucial for ensuring reliable comparisons between cycles.

Fig. 3 presents the angular and torque responses at the ankle and knee joints during perturbed and unperturbed gait cycles for two different perturbation timings: at 5% and 20% of the gait cycle. Mean values are shown for both perturbed and unperturbed gait cycles. Perturbation can be seen to influence both joint kinematics and dynamics. Specifically:

- **Ankle Angle and Torque**: both trials (5% perturbation and 20% perturbation) present a higher range of dorsiflexion, both peaking at -0.25 rad but at different time instants. This corresponds to a significant increase in plantarflexion torque, where for both trials increases with a steeper slope than the unperturbed gait. The maximum difference in angle and torque between unperturbed and perturbed gait was 0.11 rad and 0.31 Nm/kg for the 5% trial and 0.09 rad and 0.36 Nm/kg for the 20% trial.
- **Knee Angle and Torque**: the perturbation introduces additional flexion in the knee joint, particularly around 15% and 30% of the gait cycle respectively. This increased

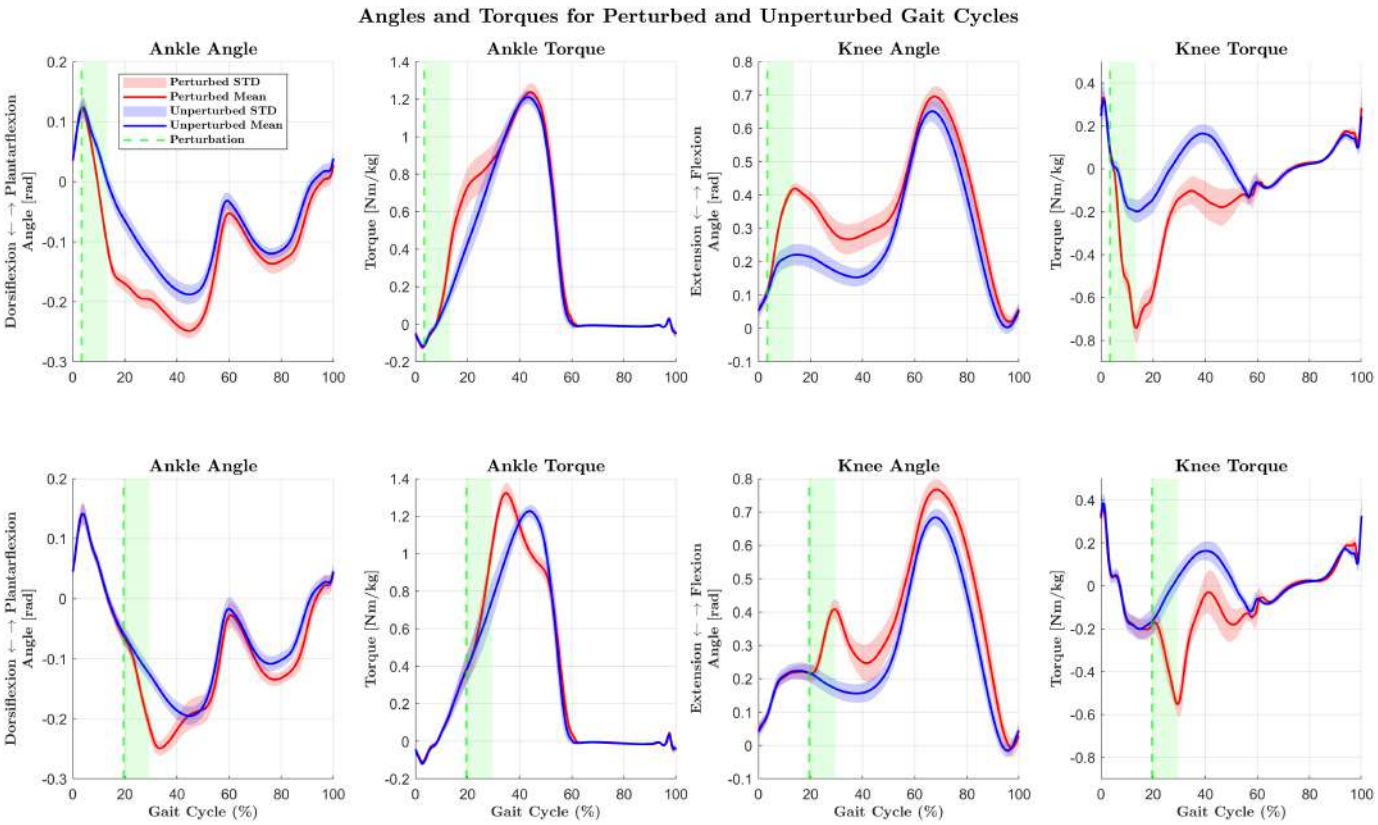


Fig. 3. Right leg joint angles and torques for perturbed and unperturbed gait cycles at the ankle and knee joints. The plots show mean values (solid lines) and standard deviations (shaded areas) for perturbed (red) and unperturbed (blue) conditions. The vertical dashed line indicate the onset of perturbation and the green shaded area represents the 100 ms duration of the perturbation. The top row illustrates ankle angle, ankle torque, knee angle, and knee torque when the perturbation onset is at $\approx 5\%$ of the gait cycle. The bottom row illustrates ankle angle, ankle torque, knee angle, and knee torque when the perturbation onset is at $\approx 20\%$ of the gait cycle. The x-axis represents the percentage of the gait cycle, while the y-axis indicates the respective joint angle (in radians) or torque (in Nm/kg).

knee flexion is accompanied by noticeable changes in the extension torque response, with peak timings matching the knee angle relative maximums. In addition, torque becomes increasingly more negative after the perturbation onset, contrary to the tendency of the unperturbed gait which is close to 0 or positive. The maximum difference in angle and torque between unperturbed and perturbed gait was 0.19 rad and 0.55 Nm/kg for the 5% trial and 0.23 rad and 1 Nm/Kg for the 20% trial.

B. Work and Power Loops

The work loops, as illustrated in Fig. 4, highlight the relationship between torque and angle (work loops) at the ankle and knee joints under perturbed and unperturbed conditions. Only the stance phase of the gait cycle is presented to avoid overcrowding the graphs. Additionally, the 100 ms duration corresponding to the perturbation is distinctly highlighted for better visualization and emphasis on the first affected segment of the curve.

- **Ankle Joint Work Loops:** The perturbed work loops exhibit a larger area compared to the unperturbed loops in the second quadrant for both trials. Perturbations occurring earlier in the gait cycle (5%) produce more pronounced deviations,with respect to the mid-stance (20%) perturbations.
- **Knee Joint Work Loops:** The knee perturbed work loops display a broader area under perturbed conditions in the 4th quadrant. Perturbation at 5% reach a higher peak torque at -0.78 Nm/kg.

The power loops, as illustrated in Fig. 5, highlight the relationship between torque and angular velocity (power loops) at the ankle and knee joints under perturbed and unperturbed conditions.

- **Ankle Joint Power Loops:** Earlier perturbation timing shows higher peak velocities (-3 rad/s). Both angle power loops present an increased activity in the 2nd quadrant with respect to unperturbed trials.
- **Knee Joint Power Loops:** The knee power loops demonstrate a similar trend, with enhanced activity in the 3rd and 4th quadrant. Angular velocity is higher after earlier perturbations, peaking at 5 rad/s, while only being 3.7 rad/s for mid-stance perturbation.

The analysis further highlights the ability of the perturbation method to elicit measurable responses that provide insight into joint behavior during dynamic tasks.

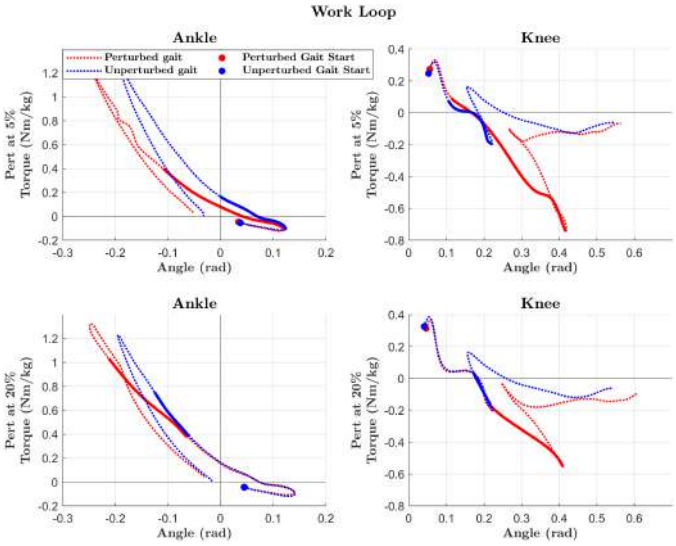


Fig. 4. Work loops of the stance phase for the ankle and knee joints under perturbed and unperturbed gait conditions. The red dashed lines represent the average of 20 perturbed gait cycles, while the blue dashed lines indicate the mean of 60 unperturbed gait cycles. Solid lines highlight the curve behavior during the perturbation. Solid dots mark the starting points for the perturbed (red) and unperturbed (blue) work loops. The top row shows the work loops for perturbations applied at $\approx 5\%$ of the gait cycle, with torque (Nm/kg) plotted against joint angle (rad). The bottom row illustrates the work loops for perturbations applied at $\approx 20\%$ of the gait cycle, highlighting timing-dependent variations in joint torque and angle behavior.

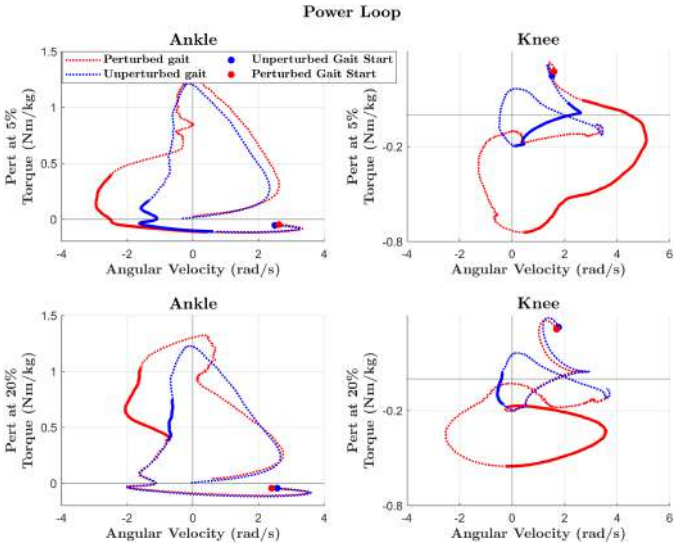


Fig. 5. Power loops of the stance phase for the ankle and knee joints under perturbed and unperturbed gait conditions. The red dashed lines represent the average of 20 perturbed gait cycles, while the blue dashed lines indicate the mean of 60 unperturbed gait cycles. Solid lines highlight the curve behavior during the perturbation. Solid dots mark the starting points for the perturbed (red) and unperturbed (blue) power loops. Thicker portions of the lines represent the variables during the perturbation duration (100 ms). The top row shows the power loops for perturbations applied at $\approx 5\%$ of the gait cycle, with torque (Nm/kg) plotted against angular velocity (rad/s). The bottom row illustrates the power loops for perturbations applied at $\approx 20\%$ of the gait cycle, emphasizing timing-dependent variations in joint torque and angular velocity behavior.

IV. Discussions

This study introduces and evaluates a perturbation method designed to elicit multi-joint-level torque and angular responses during the stance phase of the gait cycle. The proposed methodology effectively and consistently perturbs both the ankle and knee joints, as illustrated in Fig. 3, while preserving the gait cycle's overall pattern during unperturbed conditions. In addition, the pusher setup can offer a high versatility in terms of accessible perturbation conditions, being able to vary treadmill speed, perturbation timing and amplitude. The leg-pusher interaction forces demonstrate high repeatability in delivering consistent force-controlled perturbations. This consistency is important for ensuring the comparability of data across multiple trials.

The perturbation timing affects the amplitude and timing of angular and torque changes at the joints. Importantly, once the perturbation ends, the gait curves converge back to the original pattern, highlighting the leg's efficient recovery mechanism. A slight increase in the knee swing flexion angle was also observed for the perturbed gait, likely due to the compensatory behavior of the subject in response to the perturbation.

The work loops provide insights into the torque-angle behavior during the gait cycle. By examining the thick red lines, corresponding to perturbed conditions, a greater excursion in angle and torque over the same time period (100 ms) compared to unperturbed conditions (thick blue lines) can be observed.

The power loops further elucidate the joint behavior during perturbations. For the ankle, greater negative power is evident in the second quadrant during the perturbation, as the joint resists the imposed motion. This contrasts with the push-off phase in the first quadrant, where the ankle acts as an actuator producing positive power. Similarly, the knee exhibits negative power in the fourth quadrant, braking the fall of the leg and absorbing energy. Interestingly, after the perturbation subsides, the velocity switches sign, transitioning the power trajectory into the positive-power third quadrant. This indicates positive power production from the knee, which actively extends the leg after being forcefully flexed by the perturbation.

This study represents an initial step toward impedance estimation by developing a perturbation methodology specifically for the stance phase of gait. While previous methods employing a pusher system were limited to the swing phase, it was unclear whether a similar approach could be adapted for stance. Our findings confirm the feasibility of this adaptation, laying the groundwork for future studies on joint impedance parameter estimation during stance and expanding the potential for comprehensive gait analysis.

A. Limitations of the study

This study has certain limitations. Interaction forces during unperturbed gait cycles exceed the desired thresholds of 20 N peak and 10 N rms, indicating reduced pusher transparency during unperturbed gait.

The interpolation of gait cycles to a fixed length introduces minor distortions in the temporal characteristics of the data. However, given the treadmill's constant velocity and the

relatively small variation in gait cycle duration (14%), this adjustment was deemed acceptable for the purposes of visualization and comparison. Additionally, data were collected from a single participant, which limits the generalizability of the findings. To address this, future studies should incorporate a larger cohort to capture inter-individual variability in joint impedance responses.

Another limitation is the absence of electromyography (EMG) data, which would provide valuable insights into the neuromuscular contributions to joint dynamics during perturbations.

B. Future work

First, we will refine the admittance controller to improve transparency by reducing interaction forces during unperturbed gait. This will be done by retuning the controller's parameters. Additionally, we plan to implement feedforward control to further enhance system performance and responsiveness. Secondly, we will conduct a comparative analysis of the subject's joint angles during gait with and without the pusher to obtain a clearer assessment of its impact on natural movement. Thirdly we plan to investigate how joint kinetics correlate with perturbation duration and intensity. Most importantly, determining joint impedance from this data requires a system identification approach to relate changes in joint angle to corresponding changes in joint torque. Incorporating EMG data in future work could enhance our understanding of muscle activation patterns and the modulation of joint impedance. Furthermore, while this study focused on the ankle and knee joints, the methodology could be extended to include the hip, as perturbations are transmitted through the entire lower limb kinematic chain. This would allow for a more comprehensive analysis of lower limb dynamics. Further, these results can be used as a validation method to create model-based techniques as in [6], [15]–[17] for estimation of joint stiffness, which would not require perturbations.

V. Conclusions

In this study, we demonstrated the feasibility of eliciting joint-level angular and torque responses through a novel lower limb perturbation method applied during the stance phase of the gait cycle. Kinematic and dynamic data were collected from a single subject, providing a graphical comparison between perturbed and unperturbed gait cycles under two distinct perturbation timing conditions. The results confirmed the ability of the methodology to effectively perturb the lower limb. This approach shows good potential as a versatile testbed for evaluating various experimental conditions, walking speeds, and perturbation intensities. Furthermore, by enabling simultaneous perturbation of the ankle and knee, this methodology provides a useful tool for investigating joint impedance.

References

[1] I. Hunter and R. Kearney, "Dynamics of human ankle stiffness: variation with mean ankle torque," *Journal of Biomechanics*, vol. 15, no. 10, pp. 747–752, 1982.

[2] R. E. Kearney and I. W. Hunter, "Dynamics of human ankle stiffness: Variation with displacement amplitude," *Journal of Biomechanics*, vol. 15, no. 753, pp. 753–756, 1982.

[3] D. Ludvig and E. J. Perreault, "System identification of physiological systems using short data segments," *IEEE Transactions on Biomedical Engineering*, vol. 59, no. 12, pp. 3541–3549, 2012.

[4] Y. Xu and J. M. Hollerbach, "A robust ensemble data method for identification of human joint mechanical properties during movement," *IEEE Transactions on Biomedical Engineering*, vol. 46, no. 4, pp. 409–419, 1999.

[5] D. L. Guarin and R. E. Kearney, "Identification of a time-varying, box-jenkins model of intrinsic joint compliance," *IEEE Transactions on Neural Systems and Rehabilitation Engineering*, vol. 25, no. 8, pp. 1211–1220, 2016.

[6] C. P. Cop, G. Cavallo, R. C. van't Veld, B. F. Koopman, J. Lataire, A. C. Schouten, and M. Sartori, "Unifying system identification and biomechanical formulations for the estimation of muscle, tendon and joint stiffness during human movement," *Progress in Biomedical Engineering*, vol. 3, no. 3, p. 033002, 2021.

[7] A. M. Esteban, R. C. van't Veld, C. P. Cop, G. Durandau, M. Sartori, and A. C. Schouten, "Estimation of time-varying ankle joint stiffness under dynamic conditions via system identification techniques," in *2019 41st Annual International Conference of the IEEE Engineering in Medicine and Biology Society (EMBC)*. IEEE, 2019, pp. 2119–2122.

[8] K. L. Jakubowski, D. Ludvig, D. Bujnowski, S. S. Lee, and E. J. Perreault, "Simultaneous quantification of ankle, muscle, and tendon impedance in humans," *IEEE Transactions on Biomedical Engineering*, vol. 69, no. 12, pp. 3657–3666, 2022.

[9] E. J. Rouse, L. J. Hargrove, E. J. Perreault, and T. A. Kuiken, "Estimation of human ankle impedance during the stance phase of walking," *IEEE Transactions on Neural Systems and Rehabilitation Engineering*, vol. 22, no. 4, pp. 870–878, 2014.

[10] Y. Nazon and E. J. Rouse, "Estimation of knee impedance during exoskeleton assisted gait," *Dynamic Walking*, p. 1, 2021.

[11] J. B. Andersen and T. Sinkjær, "Mobile ankle and knee perturbator," *IEEE Transactions on Biomedical Engineering*, vol. 50, no. 10, pp. 1208–1211, 2003.

[12] X. Jin, Y. Cai, A. Prado, and S. K. Agrawal, "Effects of exoskeleton weight and inertia on human walking," in *2017 IEEE International Conference on Robotics and Automation (ICRA)*. IEEE, 2017, pp. 1772–1777.

[13] H. Van der Kooij, S. S. Fricke, R. C. van't Veld, A. V. Prieto, A. Q. Keemink, A. C. Schouten, and E. H. Van Asseldonk, "Identification of hip and knee joint impedance during the swing phase of walking," *IEEE Transactions on Neural Systems and Rehabilitation Engineering*, vol. 30, pp. 1203–1212, 2022.

[14] J. H. Meuleman, E. H. Van Asseldonk, and H. Van der Kooij, "The effect of directional inertias added to pelvis and ankle on gait," *Journal of neuroengineering and rehabilitation*, vol. 10, pp. 1–12, 2013.

[15] M. Sartori, M. Maculan, C. Pizzolato, M. Reggiani, and D. Farina, "Modeling and simulating the neuromuscular mechanisms regulating ankle and knee joint stiffness during human locomotion," *Journal of neurophysiology*, vol. 114, no. 4, pp. 2509–2527, 2015.

[16] C. P. Cop, A. C. Schouten, B. Koopman, and M. Sartori, "Electromyography-driven model-based estimation of ankle torque and stiffness during dynamic joint rotations in perturbed and unperturbed conditions," *Journal of Biomechanics*, vol. 145, p. 111383, 2022.

[17] C. P. Cop, K. L. Jakubowski, A. C. Schouten, H. Koopman, E. J. Perreault, and M. Sartori, "Can emg-driven musculoskeletal models estimate individual muscle displacements?" in *28th Congress of the European Society of Biomechanics, ESB 2023: Combining data-and knowledge-driven modeling: from measurements, through insights to decisions*, 2023.

Applying Palpation Forces on a Lower Jaw Model Using a Collaborative Robotic Arm

Sven Suppelt, Max Ulshöfer, Niklas Schäfer, Alexander A. Altmann, Yannick Châtelais, Julian Seiler, Jan Helge Dörsam, Bastian Latsch, and Mario Kupnik
Measurement and Sensor Technology Group, Technische Universität Darmstadt, Germany.
mario.kupnik@tu-darmstadt.de

***Abstract*—Traditional medical diagnostics heavily rely on the subjective expertise of physicians during palpation procedures, where muscles or tissues are examined by manually applying pressure. This work presents a robotic solution using a KUKA iiwa 14 R820 to replicate this diagnostic technique, for addressing the physician shortage, enhancing physician training, and integrating robotic arms into diagnostics. We emulate the palpation process, measure and analyze the forces applied by the robot on a test bench, and compare the uncertainty with palpation forces applied by physicians and the palpometer. As pain perception during palpation can indicate potential underlying conditions, we further incorporate a pain equivalence measurement into our system using a hand grip force sensor, completing it by developing a graphical user interface for visualization and control. Our results indicate that, while errors within the robot dominate the accuracy of the force application, a well-chosen robot configuration achieves comparable force application errors at typical palpation forces of approximately 5 N, 10 N, and 20 N. The resulting maximum errors are 1.24 N, 0.67 N, and 0.565 N, respectively, which are smaller for both larger forces than the palpation uncertainties of trained physicians. Our findings demonstrate that robotic systems can effectively emulate and refine palpation techniques, providing a foundation for their broader adoption in healthcare.**

***Index Terms*—Medical diagnostics, robotic palpation, force sensing, temporomandibular disorders (TMD).**

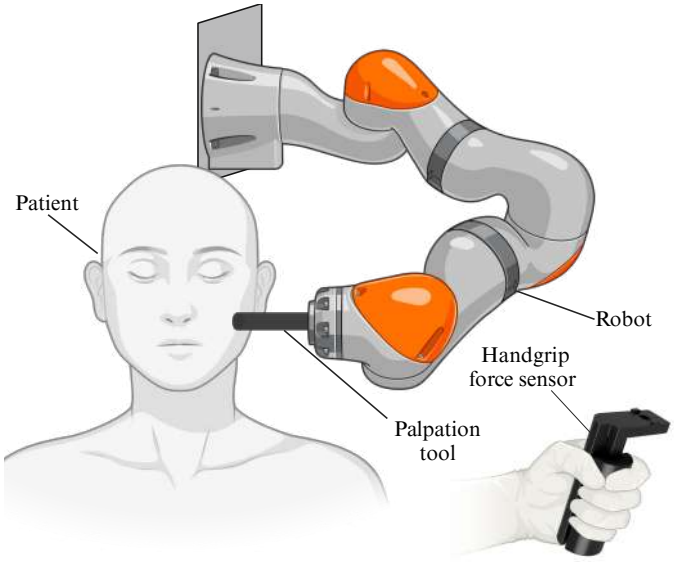


Fig. 1. Robotic palpation setup. The collaborative robot arm applies pressure to the region examined using a palpation tool, which is conventionally performed manually by a physician. The patient's handgrip force is measured as an objective pain equivalent. Figure created with BioRender.com.

I. Introduction

Palpation is a fundamental medical diagnostic technique where physicians use their hands to apply pressure to specific areas of a patient's body to detect abnormalities in texture, size, and consistency of underlying structures [1]. This hands-on method is crucial for assessing conditions that are not immediately visible through imaging or visual examination [2]. Palpation allows clinicians to detect abnormalities, assess organ sizes, evaluate tenderness, and determine the presence of fluid accumulations, among other diagnostic insights.

In dental medicine, palpation is particularly important as a primary diagnostic step for temporomandibular disorders (TMD), which encompass a range of conditions affecting the temporomandibular joint (TMJ), masticatory muscles, and associated structures [3], [4], [5], [6]. TMD includes various disorders such as muscle tenderness (myofascial pain syndrome), which involves pain and inflammation in the jaw muscles [7]; joint pain due to disc displacement, where the cushioning disc within the TMJ moves out of its normal alignment; and arthritis, which can cause degeneration of the joint tissues [8], [9]. These disorders are relatively common, affecting 3–19% of the population, with an estimated number of unreported cases reaching up to 40% due to underdiagnosis or misdiagnosis [10], [11], [12], [13].

The palpation process involves systematically searching the area for abnormalities by examining the area's texture, temperature, and elasticity, performing circular motions to locate the correct pressure position, and applying pressure within a specified force range while monitoring whether the patient feels pain. For the lower jaw, the applied pressure typically ranges from 3.92 N/cm^2 to 17.66 N/cm^2 [2], [14].

Consistent force application during palpation is crucial, as variations can affect pain perception. Efforts to measure and standardize the applied pressure, aimed at improving diagnostic accuracy, resulted in the development of the palpometer. This device allows the physician to recognize when the predetermined force threshold is reached, realized through a

This research received support from the Deutsche Forschungsgemeinschaft (DFG) under the grants 509096131 and 450821862, as well as from the Carl Zeiss Stiftung through the CZS Wildcard SOPHIMA project.

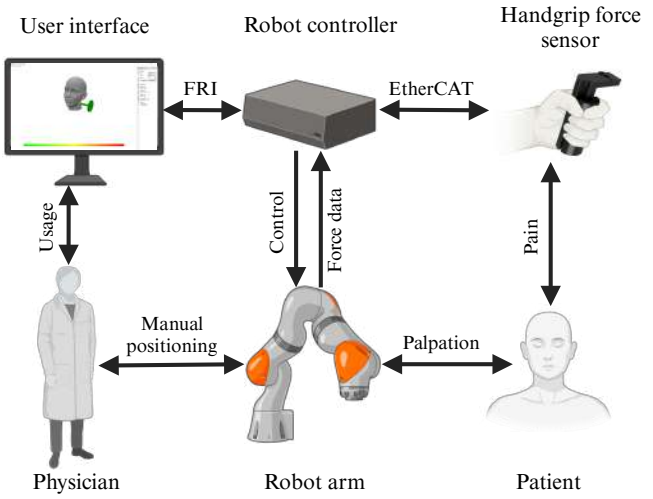


Fig. 2. Structure of the palpation system. The medical staff can control the program sequence with the help of a user interface. Palpation of the patient is carried out by the collaborative robotic arm, which can be manually positioned by the medical staff. At the same time, a handgrip force sensor is used to record the pain equivalent of the patient. Figure created with BioRender.com.

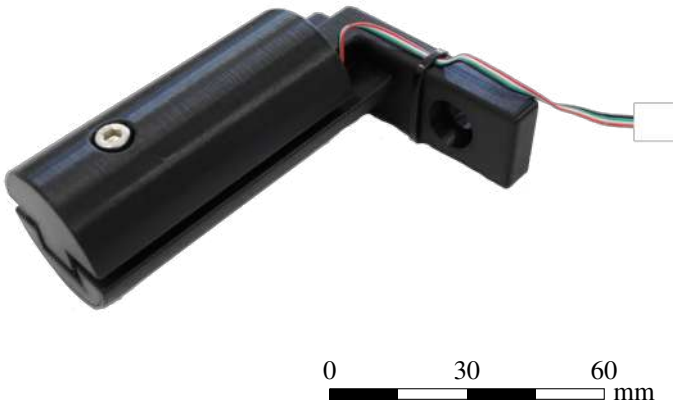


Fig. 3. Handgrip force sensor for measuring a pain equivalent during the palpation process. The current grip force, which is measured by an integrated load cell, is compared with the maximum grip force obtained during initial calibration. The ratio is taken as the measure for the pain.

tensioned spring and a tactile indicator at the device's rear end [1], [15].

Due to the complexity of palpation and the increasing physician shortage, robotic assistance presents a promising solution [16], [17], [18]. Recent research has demonstrated successful simulation and virtual performance of abdominal palpation using KUKA iiwa LBR robots, measuring forces with external sensors [19], [20]. However, practical implementation and efficacy assessment remain pending. Additionally, robotic systems have been explored for minimally invasive applications, such as texture discrimination using biomimetic prosthetic devices [21], and abdominal palpation with custom-designed robotic devices [22], [23].

In this work, we explore the potential of using a commercially available collaborative robot arm without external force sensing for dental palpation (Fig. 1) and discuss a complete palpation system comprising a user interface. We present a functional system that measures a patient's pain equivalent for diagnostic purposes in a model setup, and we then evaluate its force-application accuracy using a rigid test bench, comparing the results with those of trained physicians and the palpometer. By partially automating palpation, such systems can reduce physician workload, make training more uniform, and offer standardized diagnostics where experienced personnel may be limited.

II. Palpation System

The palpation system applies forces directly to the target area using a commercially available collaborative robotic arm (LBR iiwa 14 R820, KUKA AG, Germany) equipped with a palpation tool made of solid polylactic acid (PLA) with a probe area of 100 mm^2. The circular probe area of the palpation tool is identical to the palpometer, resulting in equivalent force application.

The robotic system consists of the robot arm and the robot controller. The robot controller runs the closed-loop controller for the robot arm and incorporates an integrated safety system. Being a collaborative robot, each joint contains torque sensors for real-time monitoring of external forces. If thresholds are exceeded, e.g., a sudden collision or a measured force higher than the desired palpation force, the robot stops. These safety features comply with relevant collaborative robot standards (e.g., ISO/TS 15066), which govern speed, force, and power limits for direct human-robot interaction. Medical staff can control the robot using a dedicated user interface on a computer, which communicates with the robot controller via the Fast Robot Interface (FRI), also providing visualization (Fig. 2).

During the palpation process, the robot operates in impedance mode, where the robotic controller simulates a spring-mass-damper system at the tool center point (TCP). The system consists of three translational springs for controlling position and three rotational springs for controlling orientation. The required force is set as an offset in the palpation direction, causing the robot to move with the specified offset force while maintaining position and orientation in other directions. Therefore, the stiffness of all springs is set to the maximum value (5000 N/m and 300 Nm/rad) except for the spring in the impact direction, which is deactivated, resulting in zero spring force. Gradual force application is critical to minimize discomfort [2]. Therefore, we ensure that the desired force is reached slowly by setting the rise time to 2 s, which prevents the robot arm from overshooting.

Measuring the handgrip force allows us to record patient pain during palpation, a method supported by literature for

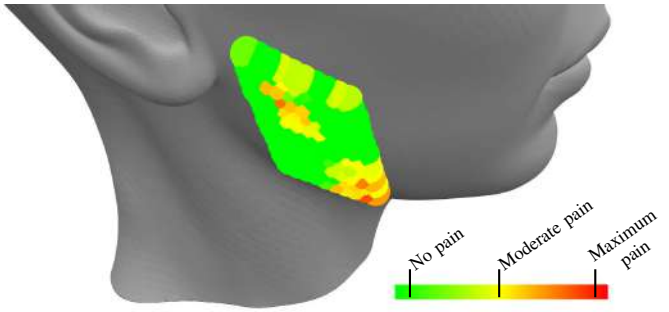


Fig. 4. A 3D head model is used to visualize the palpation results relative to the patient, with exemplary measurements performed on a styrofoam model. The individual palpated points are represented by a sphere in a 3D interface. The color of the sphere indicates the intensity of pain during the application of force. Perceived pain is quantified by the normalized handgrip force.

its linear relationship with perceived pain levels [24]. In this approach, no applied force represents a pain score of 0, increasing linearly to a score of 10 (NRS-11 scale), which corresponds to the patient's maximum handgrip force. The handgrip force sensor, comprising two hemispherical enclosing a load cell (CZL635-50Kg, CZL, China), is capable of measuring up to 600 N, accommodating the upper range of human handgrip force (Fig. 3) [25]. The output of the load cell is digitized by an EtherCAT module (EL3356-0010, Beckhoff Automation, Germany) and transmitted to the robot controller.

Medical staff can manually guide the robot in a handguiding mode to define the points or grids to be palpated and define the desired palpation force. For seamless integration into medical practice, the robotic system is designed to be user-friendly, eliminating the need for extensive training and experienced staff. Therefore, a simple user interface is created, allowing for definition of the target palpation force and grid sizes. Real-time display of the robot's position and the palpation results are provided, with each palpated point marked by a colored sphere, indicating the severity of the patient's pain (Fig. 4).

Accurate force application is crucial for effective palpation. The robot estimates the force at the TCP using torque sensors in its seven axes, which are processed through forward kinematics to calculate the forces acting on the TCP. However, the precision of this estimated force varies with the joint positions and drastically decreases in proximity to singularities.

III. Experiments

Using a 6-axis force sensor (K6D68, ME-Meßsysteme, Germany) and an evaluation unit (GSV-8DS, ME-Meßsysteme, Germany), the applied force is measured to evaluate the system's suitability for palpation. The sensor is positioned in different locations within the robot's workspace, and force is applied for 5 s (Fig. 5). During the experiment, the measured data from the force sensor and the robot arm's reported force values are recorded at a sampling frequency of 50 Hz.

The palpation tool attached to the robot's end-effector is aligned perpendicular to the force sensor to ensure accurate force transmission. Since human tissue is compliant and the force sensor is rigid, we estimate potential force overshoot

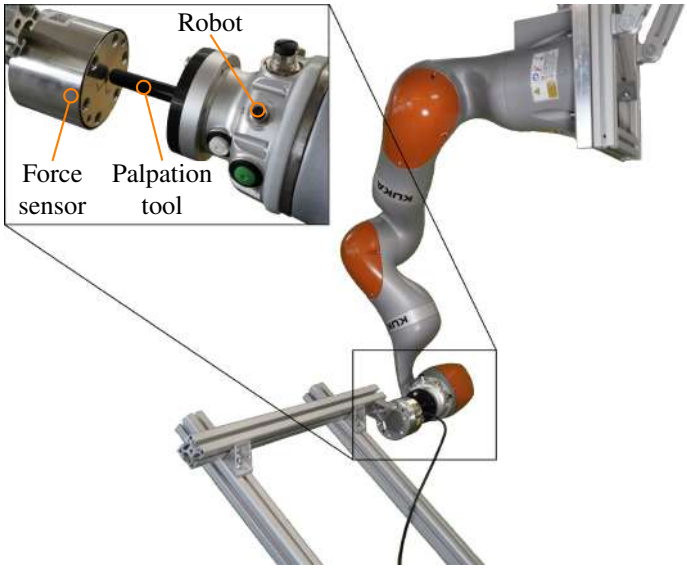


Fig. 5. Determining the uncertainty of our palpation system's force application involves mounting the robot horizontally and applying force to a rigidly mounted 6-axis force sensor using the palpation tool. The force sensor records the force in the direction of the robot's impact.

due to the robot's dynamics when interacting with a non-compliant surface. In order to overcome this overshoot, we filter out transient forces by discarding the initial 1 s of data and calculate the average of the remaining 4 s of sampled data for analysis.

Due to the robot's seven degrees of freedom, the robot controller allows movement within the nullspace, which means that the robot can adjust its joints while keeping the TCP fixed in position and orientation. To examine the influence of different joint configurations on the force output, we vary the dimensionless elbow parameter R in five increments across its permissible range in the robot's nullspace. We attempted to select these increments so that the elbow angle would change approximately linearly, but as the robot does not provide direct feedback on the exact value of R, slight deviations are possible. Nevertheless, these five nullspace configurations differ in the elbow region, which influences the robot's stiffness in the palpation direction and results in varying gravitational loads on the links. For each configuration, palpation is executed 400 times with a target force of 9.81 N and 100 times each with target forces of 4.9 N and 19.62 N. The target forces correspond to those used to verify the palpometer [15].

IV. Results and Discussion

It is essential to know whether the recorded applied palpation forces are normally distributed in order to compare it to other methods and to systematically determine sources of error, for which we use a Shapiro-Wilk test. Both the distribution over the entire measurement with different nullspace configurations (2000 measurements: $p = 2.3 \times 10^{-25}$) and each individual nullspace configuration (400 measurements: $p \leq 5 \times 10^{-16}$) are analyzed. The resulting p-values strongly reject the null

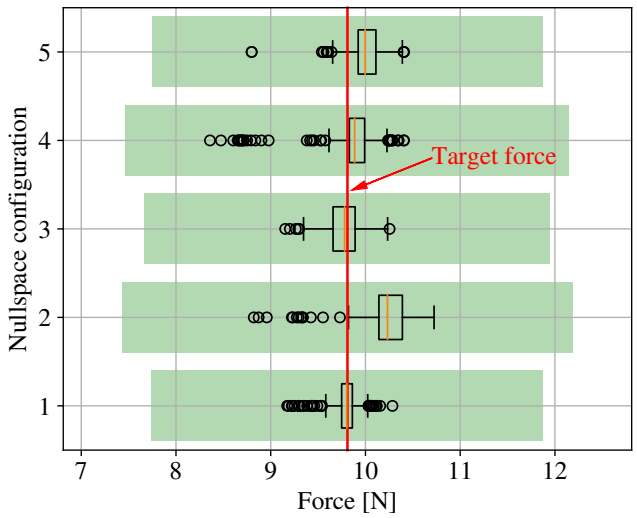


Fig. 6. Applied palpation forces (black) by the robot across five different nullspace configurations, each repeated 400 times, with a target force of 9.81 N (red). While the uncertainty differs across nullspace configurations, all measured forces lie within the uncertainty specified by the robot arm (green). These differences remain within the manufacturer-stated tolerance, indicating the system behaves as expected for a range of joint configurations.

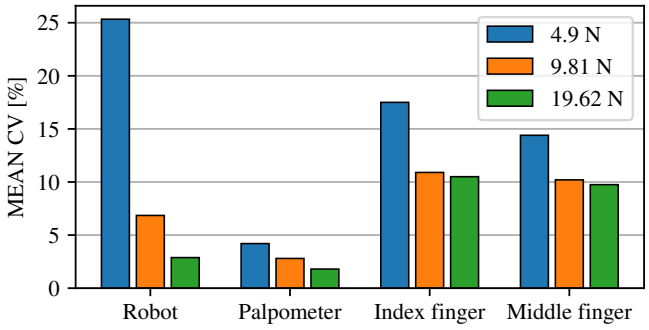


Fig. 7. Variability of palpation forces applied by the robotic arm compared to trained physicians using index and middle fingers as well as a palpometer [1], quantified by the mean coefficient of variation (CV). As the robot's force is non-normally distributed, the plot depicts the normalized maximum error for 95 % of the data. Notably, beyond a palpation force of 4.9 N, the robotic arm demonstrates lower uncertainty compared to trained physicians.

hypothesis of a normal distribution, indicating non-normality for all measurements.

The rejection of normality necessitates further investigation into the nature of the deviation. Therefore, the nullspace configurations are analyzed to identify whether they contribute to the observed deviations. Since the Shapiro-Wilk test strongly rejected normality, a non-parametric statistical approach was necessary. The Friedman test was chosen as it is a rank-based alternative to repeated measures ANOVA and is suitable for comparing multiple related groups when the normality assumption is violated.

The different nullspace configurations for the assembly position of the robot arm are evaluated to identify if the mean deviation differs across all nullspace configurations. The test yielded a statistic of 853 with a p-value of 2.4×10^{-183}, confirming a significant effect, which indicates that the nullspace configuration influences the error. This is also visually evident, as for some configurations (1 and 3) the applied median force to the target force is smaller than for others (Fig. 6). Since the robot's uncertainty varies with different nullspace configurations, it is reasonable to assume that it will also vary across different positions and orientations. The differing deviation from the target force suggests that the root cause lies within the robot arm itself, potentially due to imperfect alignment for gravity compensation or measurement uncertainties stemming from the individual torque sensors in the joints.

We compare the uncertainty of the applied palpation force over all nullspace configurations against the current state of the art to quantify the performance of our current palpation system. The deviations of trained physicians applying force with the index and middle finger [1] and those measured using the palpometer [1] are compared. Due to the non-normal distribution of the robot's values, the maximum error of 95 % of the measured data is evaluated. For mitigating the influence of outliers, we exclude the top and bottom 2.5 % of the data and normalize the maximum deviation to the target value (Fig. 7). In absolute values, the uncertainties are 1.24 N, 0.67 N, and 0.565 N for the palpation forces of 4.9 N, 9.81 N, and 19.62 N, respectively.

These uncertainties demonstrate a decreasing trend with increasing target force, which is consistent with the behavior observed for the palpometer [1]. At the lowest target force of 4.9 N, the uncertainty of our robotic system is much larger than that of the palpometer. This increased variability at lower force levels may be attributed to the limitations of the robot's torque sensors, which have reduced sensitivity and accuracy at lower torque values. At medium and high target forces (9.81 N and 19.62 N), our robotic system exhibits uncertainties that are lower than those observed when trained physicians use their fingers, but still slightly larger than those achieved with the palpometer. Thus, for forces around 10 N and 20 N, the system demonstrates sufficient precision that may be acceptable for clinical palpation ranges. However, direct comparison with prior literature must be interpreted cautiously, since the physician and palpometer data come from separate studies [1].

V. Conclusion and Outlook

In this work, we presented a test bench study of a robotic palpation system for the lower jaw, including a user interface and a handgrip sensor for measuring patient-reported pain equivalences. We found that the main source of uncertainty stems from the robot's indirect force measurement, relying on internal joint torque sensors prone to gravity-compensation errors and calibration drifts. These errors are inherent to the robot's method of force measurement, primarily attributed to two key factors: inadequate gravitational compensation and

measurement uncertainties associated with individual torque sensors. While our system achieved uncertainties smaller than those of trained physicians at higher forces ($\geq$9.81 N), it did not outperform the palpometer at the lowest tested level of 4.9 N.

An important future direction is to ensure that such a robotic palpation system complies with relevant medical regulations and standards. For future enhancements of robotic palpation systems, integrating external force sensors into the palpation tools will aim to improve measurement accuracy while addressing uncertainties related to tool positioning and nullspace interactions. Additionally, incorporating multimodal sensing capabilities, such as temperature and stiffness measurements, can enrich the diagnostic information obtained during palpation and can help to match the capabilities of physicians. This will enhance the diagnostic process for TMD, extend the application of robotic palpation to other medical fields, and potentially mitigate the impact of the physician shortage.

REFERENCES

[1] S. F. Kothari, M. Kothari, R. F. Zambra, L. Baad-Hansen, and P. Svensson, "Standardization of muscle palpation- methodological considerations," *The Clinical journal of pain*, vol. 30, no. 2, pp. 174–182, 2014. DOI: 10.1097/AJP.0b013e31828c893d.

[2] R. Bauer and S. Wolfram, *Palpationsatlas*. Berlin, Heidelberg: Springer Berlin Heidelberg, 2022. DOI: 10.1007/978-3-662-64241-2.

[3] H. J. M. von Piekartz and D. Andreotti, Eds., *Kiefer, Gesichts- und Zervikalregion [Jaw, facial and cervical region]: Neuromuskuloskeletales Assessment und Behandlungsstrategien [Neuromusculoskeletal assessment and treatment strategies]* (physiofachbuch), 2. edition. Stuttgart and New York: Georg Thieme Verlag, 2015. DOI: 10.1055/b-003-128259.

[4] E. Schiffman, R. Ohrbach, E. Truelove, J. Look, G. Anderson, J.-P. Goulet, et al., "Diagnostic criteria for temporomandibular disorders (dc/tmd) for clinical and research applications: Recommendations of the international rdc/tmd consortium network* and orofacial pain special interest group†," *Journal of oral & facial pain and headache*, vol. 28, no. 1, pp. 6–27, 2014. DOI: 10.11607/jop.1151.

[5] S. Suppelt, R. Chadda, N. Schäfer, A. A. Altmann, D. Gerovac, D. G. E. Thiem, P. Weigl, R. Sader, and M. Kupnik, "Multiparameter measurement system for analyzing the temporomandibular joint complex," *IEEE Sensors Journal*, vol. 25, no. 4, pp. 7263–7275, 2025. DOI: 10.1109/JSEN.2024.3524018.

[6] H. A. Gremillion and G. D. Klasser, *Temporomandibular Disorders*. Cham: Springer International Publishing, 2018. DOI: 10.1007/978-3-319-57247-5.

[7] B. Bentsianov, A. Francis, and A. Blitzer, "Botulinum toxin treatment of temporomandibular disorders, masseteric hypertrophy, and cosmetic masseter reduction," *Operative Techniques in Otolaryngology-Head and Neck Surgery*, vol. 15, no. 2, pp. 110–113, 2004. DOI: 10.1016/j.otot.2004.02.002.

[8] J. G. Travell, *Travell and simons' myofascial pain and dysfunction*. Lippincott Williams, 2018.

[9] T. A. Larheim and F. Flöystrand, "Temporomandibular joint abnormalities and bite force in a group of adults with rheumatoid arthritis," *Journal of oral rehabilitation*, vol. 12, no. 6, pp. 477–482, 1985. DOI: 10.1111/j.1365-2842.1985.tb01294.x.

[10] S. Nosouhian, A. Haghighat, I. Mohammadi, E. Shadmehr, A. Davoudi, and H. Badrian, "Temporomandibular joint hypermobility manifestation based on clinical observations," *Journal of international oral health : JIOH*, vol. 7, no. 8, pp. 1–4, 2015.

[11] G. D. Slade, R. Ohrbach, J. D. Greenspan, R. B. Fillingim, E. Bair, A. E. Sanders, et al., "Painful temporomandibular disorder: Decade of discovery from oppera studies," *Journal of dental research*, vol. 95, no. 10, pp. 1084–1092, 2016. DOI: 10.1177/0022034516653743.

[12] S. Suppelt, R. Chadda, T. Buchner, N. Schafer, R. Sader, and M. Kupnik, "Measurement system for human lateral mandibular forces," in *2022 IEEE Sensors*, IEEE, 2022, pp. 1–4. DOI: 10.1109/SENSORS52175.2022.9967072.

[13] G. Plato, "Gesichtsschmerz aus manualmedizinischer und kieferorthopädischer sicht [facial pain from a manual medical and orthodontic perspective]," *Manuelle Medizin*, vol. 39, no. 5, pp. 254–258, 2001. DOI: 10.1007/s003370170022.

[14] P. Małgorzata, K.-M. Małgorzata, C. Karolina, and A. Gala, "Diagnostic of temporomandibular disorders and other facial pain conditions-narrative review and personal experience," *Medicina (Kaunas, Lithuania)*, vol. 56, no. 9, 2020. DOI: 10.3390/medicina56090472.

[15] S. Futarmal, M. Kothari, E. Ayesh, L. Baad-Hansen, and P. Svensson, "New palpometer with implications for assessment of deep pain sensitivity," *Journal of dental research*, vol. 90, no. 7, pp. 918–922, 2011. DOI: 10.1177/0022034511402997.

[16] GBD 2019 Human Resources for Health Collaborators, "Measuring the availability of human resources for health and its relationship to universal health coverage for 204 countries and territories from 1990 to 2019: A systematic analysis for the global burden of disease study 2019," *Lancet (London, England)*, vol. 399, no. 10341, pp. 2129–2154, 2022. DOI: 10.1016/S0140-6736(22)00532-3.

[17] V. Winter, J. Schreyögg, and A. Thiel, "Hospital staff shortages: Environmental and organizational determinants and implications for patient satisfaction," *Health policy (Amsterdam, Netherlands)*, vol. 124, no. 4, pp. 380–388, 2020. DOI: 10.1016/j.healthpol.2020.01.001.

[18] X. Zhang, D. Lin, H. Pforsich, and V. W. Lin, "Physician workforce in the united states of america: Forecasting nationwide shortages," *Human resources for health*, vol. 18, no. 1, p. 8, 2020. DOI: 10.1186/s12960-020-0448-3.

[19] A. Shafikov, T. Tsoy, R. Lavrenov, E. Magid, H. Li, E. Maslak, and N. Schiefermeier-Mach, "Medical palpation autonomous robotic system modeling and simulation in ros/gazebo," in *2020 13th International Conference on Developments in eSystems Engineering (DeSE)*, IEEE, 2020, pp. 200–205. DOI: 10.1109/DeSE51703.2020.9450784.

[20] A. Shafikov, A. Sagitov, H. Li, N. Schiefermeier-Mach, and E. Magid, "Robotic palpation modeling for kuka lbr iiwa using gazebo simulator," *Proceedings of International Conference on Artificial Life and Robotics*, vol. 25, pp. 436–439, 2020. DOI: 10.5954/ICAROB.2020.OS18-3.

[21] D. Balamurugan, A. Nakagawa-Silva, H. Nguyen, J. H. Low, C. Shallal, L. Osborn, A. B. Soares, R. C. H. Yeow, and N. Thakor, "Texture discrimination using a soft biomimetic finger for prosthetic applications," *IEEE ... International Conference on Rehabilitation Robotics : [proceedings]*, vol. 2019, pp. 380–385, 2019. DOI: 10.1109/ICORR.2019.8779442.

[22] S. Davaria, F. Najafi, M. J. Mahjoob, and S. M. Motahari-Bidgoli, "Design and fabrication of a robotic tactile device for abdominal palpation," in *2014 Second RSI/ISM International Conference on Robotics and Mechatronics (ICRoM)*, IEEE, 2014, pp. 339–344. DOI: 10.1109/ICRoM.2014.6990924.

[23] M. Mir, J. Chen, A. Patel, M. R. Pinezich, B. A. Guenthart, G. Vunjak-Novakovic, and J. Kim, "A minimally invasive robotic tissue palpation device," *IEEE transactions on bio-medical engineering*, vol. 71, no. 6, pp. 1958–1968, 2024. DOI: 10.1109/TBME.2024.3357293.

[24] N. Wickboldt, G. Savoldelli, and B. Rehberg-Klug, "Continuous assessment of labour pain using handgrip force," *Pain research & management*, vol. 20, no. 3, pp. 159–163, 2015. DOI: 10.1155/2015/281976.

[25] N. M. Massy-Westropp, T. K. Gill, A. W. Taylor, R. W. Bohannon, and C. L. Hill, "Hand grip strength: Age and gender stratified normative data in a population-based study," *BMC research notes*, vol. 4, p. 127, 2011. DOI: 10.1186/1756-0500-4-127.

Sonomyography-Based Proportional Control For Isokinetic Movements: A Comparative Analysis of Features and Algorithms

Kavita Sharma
Centre for Biomedical Engineering
Indian Institute of Technology Delhi
New Delhi, India

Anne Tryphosa Kamatham
Centre for Biomedical Engineering
Indian Institute of Technology Delhi
New Delhi, India

Biswarup Mukherjee
Centre for Biomedical Engineering
Indian Institute of Technology Delhi
New Delhi, India
bmukherjee@iitd.ac.in

***Abstract*—Sonomyography is a technique that uses ultrasound imaging to measure muscle activity. Unlike traditional methods, sonomyography allows for real-time imaging of deeper muscles. Recent research has focused on developing wearable ultrasound devices to enable real-time muscle activity sensing, specifically for applications in proportional control systems. By tracking muscle movement intensity and dynamics, wearable sonomyography systems enable precise control in real-time applications, such as target tracking and robotic prosthetics, improving the functionality and user-friendliness of biomechatronic interfaces. In this paper, we explore the proportional control for target tracking using the sonomyography (SMG) signals, captured through a sensor array. We evaluated three feature extraction methods for comparison: peak location-based features, amplitude histogram features, and curve-fitting features. These features were used to train a regression model, which we evaluated for its effectiveness in controlling real-time gestures. The results demonstrate that the amplitude histogram feature set achieved the highest accuracy of 88.72$\pm$3.27 % when trained with an ensemble regression model during the target tracking proportional control task using the SMG signal.**

***Index Terms*—Sonomyography, Proportional control, Target tracking.**

I. INTRODUCTION

Prosthetic devices are important for rehabilitation, as well as assistive technology and intuitive control to improve mobility and quality of life. They are essential for restoring movement and improving life for people with limb loss [1]. Recent advancements in prosthetics have focused on achieving intuitive and seamless control, allowing users to perform both daily activities and complex motor tasks using various control strategies. Traditional myoelectric prostheses utilize surface electromyography (sEMG) signals for non-invasive muscle activation detection from two measurement sites, which limit control to only a few movements to interpret user intent and translate it into precise movements [2]–[4]. To enhance control capabilities, multi-channel and high-density EMG (HD-EMG) systems have been developed. These systems enable more advanced control methods, including simultaneous, sequential, and proportional control of multiple movements, as well as gesture recognition through pattern recognition and machine learning using muscle force, estimation of the joint forces [5], [6] and joint kinematics [7]. However, issues like limited spatial resolution, poor signal-to-noise ratio, and signal instabilities lead to inaccurate real-time control of the biomechatronic devices [8], [9]. Therefore, other noninvasive methods are being explored to overcome the limitations of EMG.

In recent years, sonomyography (SMG) has become popular for detecting muscle deformation through ultrasound imaging. It provides a non-invasive method which is capable of resolving individual muscles spacially, including deep-seated muscles, and detecting dynamic activity within various functional compartments in real-time [10], [11]. Previous studies on sonomyography methods for gesture classification and joint force estimation have focused on changes in muscle structure observed in ultrasound images. This is achieved either by tracking specific landmarks within the images or by analyzing patterns over time from the ultrasound images. For example, Shi et al. demonstrated that tracking muscle thickness [12] and pennation angle [13] from ultrasound images can accurately estimate wrist angle. Some studies have focused on pixel intensity [14] from B-mode images to measure muscle activity. B-mode ultrasound devices are often bulky, making them less suitable for wearable applications. In contrast, several studies have shown that A-mode ultrasound signals can effectively detect various muscle activities, making them more appropriate for wearables. Wearable ultrasound systems that utilize single-element transducers provide a compact solution for wearable applications that use features such as waveform length [15] and mean absolute value [16], which are extracted from specific depth regions of the A-mode ultrasound signal. However, X. Yang et al. presented a wearable ultrasound-based interface for decoding simultaneous and proportional wrist/hand kinematics, demonstrating superior performance over surface electromyography and the potential for intuitive position-based control of future prosthetic devices [17]. They used time-domain features and frequency-domain features to compare different regression models and find out that the

This work was funded in part by the Anusandhan National Research Foundation (ANRF) through a Core Research Grant - CRG/2021/004967 (PI:BM) and by the Department of Biotechnology, Government of India-BT/PR50638/MED/32/951/2023 (PI:BM).

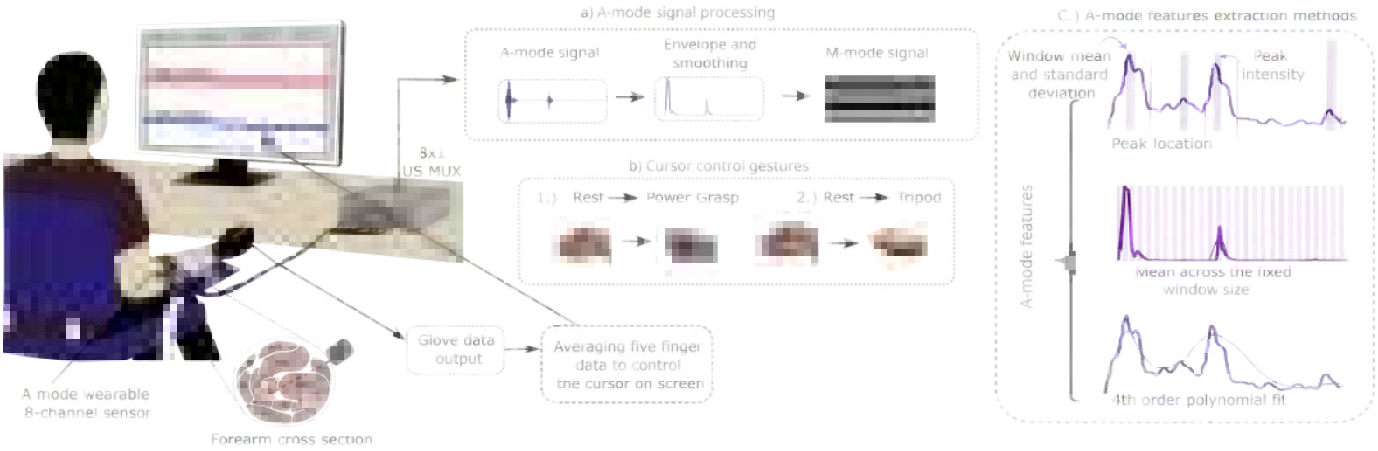


Fig. 1. Experimental setup for target tracking task during isokinetic movements and A-mode signal processing showing different feature extraction methods.

time histogram was outperforming. Similarly, another study used different feature sets to predict continuous isometric force levels using peak location features, mean, and standard deviation across those peaks [18] as features.

However, there has been no direct comparison of these feature sets for proportional control tasks. To address this gap, this paper evaluates three feature extraction methods peak location-based features, amplitude histogram features, and curve-fitting features by comparing their effectiveness in target tracking for proportional control. In the peak location-based approach, we identified significant peaks in the A mode signal and calculated the mean and standard deviation across these peaks to capture variability in muscle activity [18]. The amplitude histogram method analyzed the distribution of signal amplitudes by using an overlapping window size across the entire A mode signal. Finally, the curve-fitting approach modeled the SMG signal with a mathematical curve, using the coefficients from this model as features to train the proportional control model. These features were used to train various regression models, which we evaluated for their effectiveness during real-time movements.

II. Materials and Methods

A. Sensor Setup

In this study, an eight-channel wearable SMG sensor was used [19] which was made using lead zirconate titanate (PZT) transducers (SMD063T07R111, Steiner & Martins Inc., USA) and created using a piezoceramic disc with a diameter of 7 mm and thickness 0.7 mm. The resonant frequency of the transducer is 4.25 MHz, and the acoustic impedance is 33.7 MRayl. To improve the performance of the transducer and to dampen unwanted reverberations, an acoustic backing layer was created which consists of tungsten powder mixed with epoxy resin in a weight ratio of 4:1. Each transducer was connected to a matching circuit using a parallel L–C tank design (L = 5 µH, C = 511 pF). The fabricated transducer with a backing layer was tested using a pulse-echo method, as explained in [20] and [21]. They showed a bandwidth of about 470 ± 88 kHz and an axial resolution of 0.8 µm. Radial vibrations were greatly reduced, with improvements of over 100 dB after introducing the backing layer.

The eight sensors were placed in a custom 3D-printed case to hold the PZT elements and matching circuits. Each sensor was connected using 50 Ω RG-174 cables (model 8216 0101000, Belden Inc., USA), which were about 50 cm long. The transducers were then arranged within the enclosures and were sewn to the velcro band with an inter-transducer distance of 2 cm to form the wearable sonomyography transducer array. The sensors were attached to a fabric band, to fix them on the forearm.

B. Experimental Setup

In this study, we experimented to evaluate proportional control using A-mode data with various features. The primary aim was to compare different feature sets in controlling a cursor on a screen using hand gestures, specifically focusing on the power grasp and tripod grasp gestures. The experiment consisted of two phases: calibration and target tracking.

- *Calibration phase:* During the calibration phase, participants either rested or performed specific gestures for 10 s repeated three times to establish the signal range. The cursor movement corresponded to the average values from the fingers and this range was normalized between 0 (representing rest) and 1 (indicating full execution of the gesture). The signals recorded during both the resting and movement periods were saved as reference points.
- *Isokinetic target tracking phase:* In the target-tracking phase, participants controlled a cursor on the screen using their hand movements to follow a moving target, the cursor movement corresponded to the average of five finger values in real-time, which moved at a 10 %/s normalized velocity. The movements generated values normalized between ’0’ and ’1’, where 0 represented total relaxation of the hand and 1 indicated complete execution of the gesture. The cursor movement corresponded to the glove data values in real-time, which allowed participants to adjust their gestures to continuously track the target.

During the target tracking task, participants performed two types of hand movements: power grasp (PG) and tripod grasp (TG). These grasps were chosen because they are commonly used in everyday activities. The power grasp is used for holding large objects, while the tripod grasp is important for precise tasks like writing or picking up small items. Testing these movements helps evaluate how well different features from A-mode ultrasound data can control the cursor. Each movement was tested in five trials, with each trial including five target positions, repeated twice. This resulted in a total of 10 target positions, followed by 10 s rest intervals for power grasp as well as tripod experiment. The target positions were presented in a fixed order. The data collected from both hand gestures were used to compare the performance of various features extracted from the A-mode ultrasound data for proportional control.

C. Data Acquisition and Data Processing

Four healthy individuals (aged 29 $\pm$ 4 years) participated in the study. They were fully informed about the procedures and provided their consent to take part. All procedures were approved by the Institutional Ethics Committee at Indian Institute of Technology Delhi (Approval no. P021/050).

During the experiment, participants were asked to sit comfortably on a chair with their dominant arm resting on a handrest. A custom wearable sensor array for sonomyography was attached to their forearm approximately 4 cm from their olecranon process. The array was oriented such that four sensors imaged the flexors muscles while another four imaged the extensor muscle groups. The sensor array was connected to an eight-channel ultrasound pulser-receiver system (Lecoeur US-MUX, Lecoeur Electronique, France), which sent and received ultrasound signals using one transducer. The Lecoeur 8-channel US-MUX is designed for ultrasound acquisitions and measurements, featuring a transmitter that generates pulses with user-programmable voltage levels and widths, a receiver for signal amplification, and a digitizer with a 12-bit resolution capable of operating at frequencies at 80 MHz, which can function in either pulse-echo or pitch-and-catch mode, operates with a USB power supply and allows data acquisition using LabVIEW or MATLAB. The pulser was set to create a 90 V unipolar pulse that lasted 49.25 nanoseconds and repeated at a frequency of 15 kHz, allowing imaging up to 5 cm deep. We optimized the pulse width through acoustic testing to get the best possible signal strength [20]. The ultrasound echo signals were amplified using a time-gain compensation (TGC) amplifier, which increased the gain from 0 to 50 dB to help with tissue signal loss. The amplified signals were then digitized at a sampling rate of 80 MHz and sent to a computer (Intel Core i5-4790K, 16 GB RAM, 2 GB NVIDIA GeForce) via USB. A custom MATLAB application (Version 2022b, MathWorks Inc., Natick, MA, USA) processed these signals at a frame rate of 22 frames per second (fps) across all eight channels. A data glove (5DT Data Glove Ultra, Fifth Dimension Technologies, USA) was used for ground truth to measure the finger joint angles. Gesture tracking involved transitioning from rest to maximum motion and back.

The A-mode raw signals were recorded as 4000 points for a 5 cm depth. The data was manually verified for clear echoes from tissue changes during muscle movement. To analyze the raw data, the signal's envelope was extracted using the Hilbert transform with a window size of 25 points. All A-mode signals from the eight channels were combined into an array of 8×4000 for direct recording in MATLAB. Additionally, finger movement data from the data glove was recorded for all five fingers in both the resting and hand-closed positions. The average data for the five fingers was then normalized. Using this normalized average data, participants attempted to control a target-tracking cursor displayed on the computer screen, allowing for stable and accurate tracking of finger movements in real-time as they transitioned from open to closed in a continuous mode. After preprocessing the data, the next step was feature extraction, which involved deriving meaningful characteristics from the SMG signal for further analysis. In this study, three different feature extraction methods were applied to compare their effectiveness for proportional control.

- **Peak location-based features:** In the first approach, we identified the locations of significant peaks in the SMG signal and calculated the mean and standard deviation at these peak locations. These peaks help capture the variability of muscle activity during control tasks [18].
- **Amplitude histogram features:** The second approach focuses on creating an amplitude histogram from the SMG signal. This histogram is computed using both fixed window sizes and overlapping windows. Analyzing the distribution of signal amplitudes over time provides insights into muscle activation patterns during control tasks [17].
- **Curve Fitting Features:** The third approach is a polynomial-based curve-fitting technique to model the SMG signal. This method employs a mathematical equation that describes a set of data points using a 4th-order polynomial function. The coefficients obtained from this equation serve as features. These features create a continuous and smooth representation of the A-mode signal over time samples illustrating muscle activity [22].

The three feature sets were utilized to train various regression models, and their performance was compared through offline evaluations. The objective was to identify which feature extraction approach provides the most accurate and stable signal representation for proportional control tasks. To achieve this, the features were utilized to train different regression models using 5-fold cross-validation. In each fold, data from one trial was used for testing, while the data from the remaining four trials served as training data. Using training data models were trained and validation was performed on the test data, resulting in five-fold validation iterations. The average performance across the five folds for four subjects was then calculated. Four commonly used regression models were chosen for this analysis: Regression Tree Ensemble,

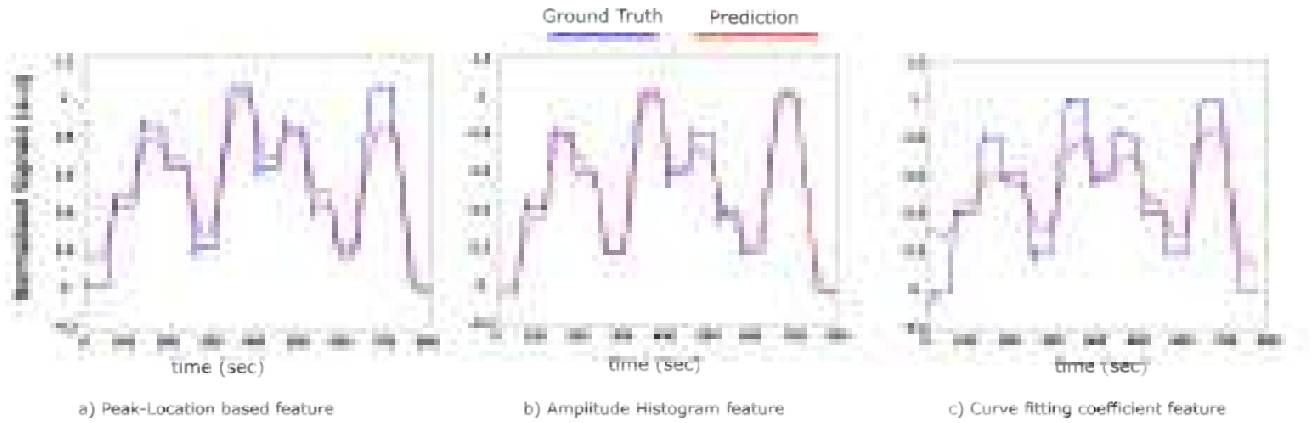


Fig. 2. Time series plot illustrating the measured and predicted outputs of the trained model for target tracking during proportional control for subject S1, using different feature extraction methods for power grasp and trained with ensemble tree regression.

Gaussian Process Regression, Support Vector Machine (SVM) Regression, and Linear Regression. For each model, the 5-fold cross-validation accuracy was computed as a measure of performance.

D. Statistical Testing

We performed a two-way Analysis of Variance (ANOVA) test using OriginPro (2020b, OriginLab Corporation, Northampton, Massachusetts, USA) with post-hoc Tukey comparison to assess the effect of feature type and regression model on the prediction performance.

III. Results and Discussion

The performance of various feature extraction methods and regression models were evaluated using 5-fold cross-validation to identify the most effective approach for the target tracking task during proportional control. Fig. 2 presents a time-series plot for the test trial, comparing the model prediction for ensemble regression model across three different feature extraction methods for a single fold and one representative subject. It demonstrates that amplitude histogram features exhibited the excellent tracking performance with an R^2 of 0.93 between the predicted and test data.

Since the models were trained separately for each grasp rather than distinguishing between them, the accuracy was first calculated for each grasp individually across different models. These values were then combined to obtain the final accuracy presented in Fig. 3. Fig. 3 displays a bar plot comparing all three feature extraction methods alongside all regression models across all subjects and grasp configurations. As a result, among all the regression models, the ensemble regression model achieved the highest mean accuracy of 88.72$\pm$3.27 % with amplitude histogram features. However, ensemble models underperformed with curve fitting features with the lowest accuracy of 68.5$\pm$7.08 %. This indicates that the ensemble regression model with amplitude histogram features offers superior predictive accuracy compared to the other models.

We conducted a two-way ANOVA test and found that the choice of features significantly affects predictive performance

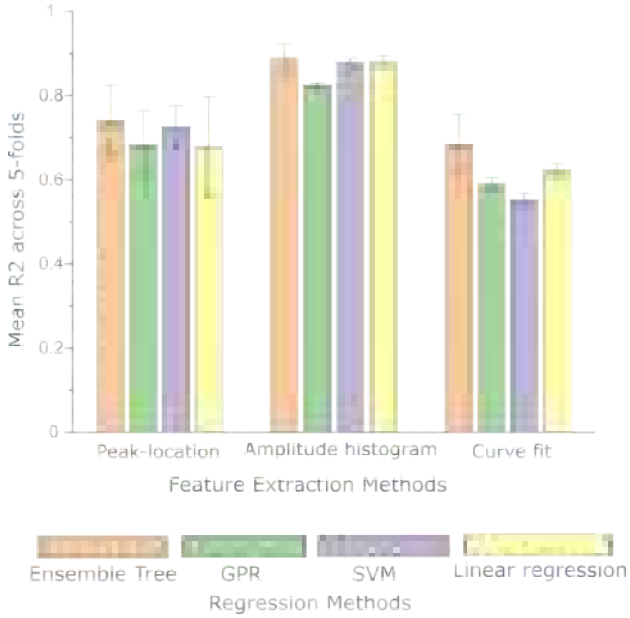


Fig. 3. Performance comparison of different feature extraction methods and regression models for target tracking task, showing the mean (R^2 value across 5-fold cross-validation, corresponding to each feature extraction method and different regression methods.

(F(2, 36) = 84.89, p $<$ 0.001). The type of regression model also has a significant influence on the accuracy (F(3, 36) = 3.54, p $<$ 0.024). However, we found no significant effect of the interaction of feature extraction methods and models (F(6, 36) = 1.42, p $<$ 0.232). Tukey's post-hoc comparisons also showed that the amplitude histogram method provides significantly better performance than the peak-location method (mean difference = 16.02, p $<$ 0.001) and the curve fitting method (mean difference = -25.47, p $<$ 0.001).

Conclusion and Limitations of the Approach

Wearable ultrasound-based human-machine interfaces have shown significant promise for the proportional control of modern biomechatronic devices. This study explored the role

of proper feature selection and the type of regression modeling methodology on the proportional control performance with three gestures. Our results demonstrate that the amplitude histogram method significantly outperforms both the peak-location and curve-fitting methods across all modeling techniques. The choice of regression model impacted the performance, with ensemble modeling outperforming other topologies. Our work only addresses isokinetic movements for a limited set of three gestures. A more comprehensive analysis involving proportional isometric and isotonic muscle contractions with an extended set of gestures will be explored in the future. Another limitation is that the study was done only on healthy subjects. Since the goal is to use this method for prosthesis control, future research will test individuals with trans-radial amputations to ensure the approach works well for them.

REFERENCES

[1] B. O'Keeffe, "Prosthetic rehabilitation of the upper limb amputee," *Indian J Plast Surg*, vol. 44, no. 02, pp. 246–252, Dec 2019.

[2] D. Quintero, E. Reznick, D. J. Lambert, S. Rezazadeh, L. Gray, and R. D. Gregg, "Intuitive clinician control interface for a powered knee-ankle prosthesis: A case study," *IEEE Journal of Translational Engineering in Health and Medicine*, vol. 6, pp. 1–9, 2018.

[3] M. Nowak, I. Vujaklija, A. Sturma, C. Castellini, and D. Farina, "Simultaneous and proportional real-time myocontrol of up to three degrees of freedom of the wrist and hand," *IEEE Transactions on Biomedical Engineering*, vol. 70, no. 2, pp. 459–469, 2023.

[4] R. Nasiri, M. Shushtari, and A. Arami, "An adaptive assistance controller to optimize the exoskeleton contribution in rehabilitation," *Robotics*, vol. 10, no. 3, 2021. [Online]. Available: https://www.mdpi.com/2218-6581/10/3/95

[5] R. A. Bogey, A. J. Gitter, and L. A. Barnes, "Determination of ankle muscle power in normal gait using an EMG-to-force processing approach," *J. Electromyogr. Kinesiol.*, vol. 20, no. 1, pp. 46–54, Feb. 2010.

[6] K. Koirala, M. Dasog, P. Liu, and E. A. Clancy, "Using the electromyogram to anticipate torques about the elbow," *IEEE Trans. Neural Syst. Rehabil. Eng.*, vol. 23, no. 3, pp. 396–402, May 2015.

[7] P. Qin and X. Shi, "A novel method for lower limb joint angle estimation based on semg signal," *IEEE Transactions on Instrumentation and Measurement*, vol. 70, pp. 1–9, 01 2021.

[8] E. A. Clancy, E. L. Morin, and R. Merletti, "Sampling, noise-reduction and amplitude estimation issues in surface electromyography," *J. Electromyogr. Kinesiol.*, vol. 12, no. 1, pp. 1–16, Feb. 2002.

[9] H. Daley, K. Englehart, L. Hargrove, and U. Kuruganti, "High density electromyography data of normally limbed and transradial amputee subjects for multifunction prosthetic control," *J. Electromyogr. Kinesiol.*, vol. 22, no. 3, pp. 478–484, Jun. 2012.

[10] X. Yang, Z. Chen, N. Hettiarachchi, J. Yan, and H. Liu, "A wearable ultrasound system for sensing muscular morphological deformations," *IEEE Transactions on Systems, Man, and Cybernetics: Systems*, vol. 51, no. 6, pp. 3370–3379, 2021.

[11] X. Yang, X. Sun, D. Zhou, Y. Li, and H. Liu, "Towards wearable a-mode ultrasound sensing for real-time finger motion recognition," *IEEE Trans. Neural Syst. Rehabil. Eng.*, vol. 26, no. 6, pp. 1199–1208, Jun. 2018.

[12] J. Shi, Q. Chang, and Y.-P. Zheng, "Feasibility of controlling prosthetic hand using sonomyography signal in real time: preliminary study," *J. Rehabil. Res. Dev.*, vol. 47, no. 2, pp. 87–98, 2010.

[13] J. Shi, Y.-P. Zheng, Q.-H. Huang, and X. Chen, "Continuous monitoring of sonomyography, electromyography and torque generated by normal upper arm muscles during isometric contraction: sonomyography assessment for arm muscles," *IEEE Trans. Biomed. Eng.*, vol. 55, no. 3, pp. 1191–1198, Mar. 2008.

[14] S. Sikdar, H. Rangwala, E. Eastlake, I. Hunt, A. Nelson, J. Devanathan, A. Shin, and J. Pancrazio, "Novel method for predicting dexterous individual finger movements by imaging muscle activity using a wearable ultrasonic system," *IEEE transactions on neural systems and rehabilitation engineering : a publication of the IEEE Engineering in Medicine and Biology Society*, vol. 22, 08 2013.

[15] P. Boyd and H. Liu, "A-mode ultrasound driven sensor fusion for hand gesture recognition," in *2020 International Joint Conference on Neural Networks (IJCNN)*, 2020, pp. 1–6.

[16] A. J. Fernandes, Y. Ono, and E. Ukwatta, "Evaluation of finger flexion classification at reduced lateral spatial resolutions of ultrasound," *IEEE Access*, vol. 9, pp. 24 105–24 118, 2021.

[17] X. Yang, Y. Zhou, and H. Liu, "Wearable ultrasound-based decoding of simultaneous wrist/hand kinematics," *IEEE Transactions on Industrial Electronics*, vol. 68, no. 9, pp. 8667–8675, 2021.

[18] A. T. Kamatham, M. Alzamani, A. Dockum, S. Sikdar, and B. Mukherjee, "Sparse sonomyography-based estimation of isometric force: A comparison of methods and features," *IEEE Transactions on Medical Robotics and Bionics*, vol. 4, no. 3, pp. 821–829, 2022.

[19] A. Kamatham, K. Sharma, S. Venkataraman, and B. Mukherjee, "Sparse wearable sonomyography sensor-based proprioceptive proportional control across multiple gestures," *IEEE Sensors Journal*, vol. PP, pp. 1–1, 06 2024.

[20] A. T. Kamatham and B. Mukherjee, "Design and optimization of a wearable sonomyography sensor for dynamic muscle activity monitoring," in *2023 IEEE Applied Sensing Conference (APSCON)*, 2023, pp. 1–3.

[21] A. T. Kamatham, A. Shariati, H. A. Wurdemann, and B. Mukherjee, "A multiplexed sonomyography system for proprioceptive proportional control of biomechatronic interfaces," in *2023 IEEE International Instrumentation and Measurement Technology Conference (I2MTC)*, 2023, pp. 1–6.

[22] S. Celin and K. Vasanth, "A novel method for ecg classification using polynomial based curve fitting," in *2019 IEEE International Conference on Electrical, Computer and Communication Technologies (ICECCT)*, 2019, pp. 1–9.

Robot-based assessment of dual task activities: investigating the impact of balance tasks on cognitive performance in older adults

E. Misley[1,+,*] and M.C. Delatto[1,+], M. Casadio[1,3], T. Falchi Delitala[2,3], V. Falzarano[2,3], G. Marchesi[2,3]
[1] *DIBRIS, University of Genoa, Genoa, Italy*
[2] *Movendo Technology srl, Genoa, Italy*
[3] *RAISE Ecosystem, Genova, Italy*
+ Shared first author contribution
**Correspondence: E. Misley; elisa.misley@edu.unige.it*

***Abstract*—Cognitive decline in older adults, even those without impairments, is well-established and becomes especially pronounced during dual-task situations. Advances in digital devices for cognitive assessment provide more precise evaluations compared to traditional oral or paper-based formats. However, most of these devices typically focus solely on cognitive performance without employing the Motor-Cognitive Dual-Task paradigm, which integrates cognitive tests with motor tasks. This study exploited such innovations by integrating digitalized cognitive tests with dynamic balance tasks, aiming to improve detection of age-related cognitive changes. Sixty-one participants completed Motor-Cognitive Dual-Task tests on a robotic platform under various balance conditions, both static and dynamic. The study validated the digital tests against their traditional counterparts and examined how age and balance conditions influenced cognitive performance. Results on cognitive performance showed how cognitive decline becomes more apparent with age, particularly in tasks requiring higher complexity. Both processing speed and working memory showed significant age-related reductions. Also, a deterioration in cognitive performance was shown in the most challenging balance scenarios, therefore revealing an effect of the balance task on cognitive performance. These findings suggest that combining dynamic balance tasks with cognitive assessments may effectively identify early cognitive changes.**

Keywords—motor-cognitive dual-task, cognitive performance, robotic-based assessment tests

I. Introduction

Cognitive decline is a common phenomenon observed in unimpaired older adults, often associated with age-related deficits that affect various cognitive functions, including memory, attention, processing speed, and executive function [1], [2]. As individuals age, structural and functional changes in the brain contribute to gradual reductions in cognitive abilities [3]. These changes can lead to challenges in daily functioning, impacting an individual's independence and quality of life [4]. Understanding the nature of age-related cognitive decline is essential for developing effective strategies to support aging populations and mitigate the impact of these deficits on physical and mental well-being.

Cognitive decline is commonly assessed using straightforward neuropsychological tests, typically administered in an oral or paper format. These tests are designed to be accessible and easy to administer, with outcomes measured through simple, quantifiable parameters such as the time taken to complete the test, the number of correct responses or the number of errors committed. Clinicians performing the tests directly record these parameters, providing immediate insight into cognitive performance. However, since clinicians manually compute these outcomes, they are subject to human error, which can introduce variability and limit the precision of these assessments. Traditional assessment tests also often rely on subjective interpretation, increasing the likelihood of variability between evaluators.

Over the past three decades, advancements in technology have led to the development of various devices and tablet-based applications for both the assessment and training of cognitive abilities [5], [6]. These digital tools offer various advantages, including automated data collection, standardized scoring, and the capacity to provide real-time, objective feedback [7]. By capturing a wider range of performance metrics, such as reaction times, error patterns, and response variability, these devices enable more accurate and comprehensive assessments of cognitive functions [8]. Although initially developed to target only cognitive functions, these devices can now be effectively integrated with motor assessment and training through Motor-Cognitive Dual-Task (MCDT) approaches. This integration is particularly valuable, as clinical research shows that older adults and individuals with neurological conditions frequently experience simultaneous cognitive and motor impairments [9].

The relationship between cognitive and motor functions is fundamentally bi-directional. Cognitive decline is often linked to motor impairments, manifesting as incoordination, balance instability, gait abnormalities, and an increased risk of falls [10]. This connection suggests that interventions addressing both cognitive and motor functions simultaneously may provide more effective support for both clinical populations and unimpaired older adults. Thus, in the last decade, there has been growing interest in the MCDT paradigm, an approach that involves performing a cognitive task simultaneously with a motor task. This increased focus on MCDTs due to its ability to reveal early cognitive impairments that may go unnoticed in single-task assessments. To this extent, a recent study highlighted how MCDT tests have shown promise as sensitive and objective tools for detecting early cognitive decline in patients with Parkinson's Disease [11]. The study's main finding was that MCDTs could identify subtle cognitive

XXX-X-XXXX-XXXX-X/XX/$XX.00 ©20XX IEEE

deterioration even before the onset of motor symptoms, making them a valuable tool for early detection and timely management of cognitive decline.

While the MCDT paradigm has been extensively investigated when standing in static conditions, a significant research gap remains in understanding the effects of dual-task (DT) challenges on dynamic balance. Indeed, evaluating dynamic balance is crucial because it mirrors more accurately real-world scenarios, involves more complex motor and cognitive processes, and can better inform injury prevention, training and rehabilitation strategies. Apart from gait-related conditions, among the studies concerning dynamic balance, only one study has used platforms to focus exclusively on movements in a single direction, either anterior-posterior or mediolateral. However, this did not address dual-task abilities. [12]. Therefore, our study aims to address this gap by exploring MCDT assessments across various balance conditions, including both static and dynamic scenarios. For the first time, we digitized versions of several commonly used cognitive assessment tests, that have been integrated within hunova [13], a medical robotic device developed by Movendo Technology (Genoa, Italy). Thanks to the device's versatile platforms we were able to combine the digitalized cognitive assessment tests with different platform movements, not limited to a single direction. With this study, we first validated the cognitive metrics we computed within the device algorithms and then, we analyzed how the balance conditions influenced cognitive performance in different age groups. Specifically, we conducted a trial with 61 unimpaired subjects from three distinct age groups: young adults (YA), middle-aged adults (MA) and older adults (OA), who performed both the newly developed digital MCDT tests and their corresponding traditional versions. Indeed, this study had a threefold objective:

1. Evaluate the correlation between the evaluators obtained from the newly developed digital tests and those derived from their traditional counterparts.
2. Assess the influence of age on cognitive performance of the MCDTs conducted under a single specific balance condition.
3. Assess the impact of age and balance conditions on cognitive performance during MCDTs performed under various balance scenarios.

II. Materials and Methods

A. Set up and protocol

This study utilized hunova, a medical robotic device for sensory-motor rehabilitation and evaluation of lower limbs and trunk (Fig. 1). It features two electromechanical platforms, one positioned under the feet and another under the seat, integrated with an inertial sensor to be placed on the sternum to track trunk motion [13]. This device enables balance assessment in both static and dynamic conditions. In this study, we examined performance across these balance conditions, utilizing the platform under the feet. Indeed, we included the following three balance tasks:

- Static. The platform remained parallel to the horizontal plane without any movement or tilting, providing a stable surface.
- Unstable. The platform simulated a plate with a central pivot, that tilted due to the user's weight shift, while an elastic force field, opposing the user's motion, attracts the platform to the horizontal position.
- Passive. The platform imposed an external perturbation as it moved independently from the subjects' sway, following a pre-programmed circular trajectory (as done in [14]).

These three balance tasks have been combined with the following cognitive tasks that required participants to physically interact with hunova's touchscreen:

- Stroop Color and Word Test. Includes three parts like the oral format: 1. Word Reading: participants are shown a stimulus on the screen, which is a color-word written in black ink. Below the stimulus are four buttons, each containing a color-word (also written in black ink). Participants are asked to press the button that matches the color-word of the stimulus. 2. Color Naming: participants are presented with the four buttons from part 1, but the stimulus now consists of a sequence of 'X's displayed in a specific ink color. They must select the button that represents the color of the ink used in the stimulus. 3. Interference: The same four buttons are used, but the stimulus consists of a color-word printed in a mismatched ink color (e.g., the word "red" written in blue ink). Participants must press the button that corresponds to the color of the ink (in this case, the correct response would be 'blue').
- Trail Making Test: consists of two parts: A and B. In part A participants are asked to connect a sequence of numbered circles in ascending order (e.g., 1-2-3...) as quickly as possible by moving their finger on the touchscreen. In part B participants must alternate numbers and letters in sequence (e.g., 1-A-2-B...). Throughout the whole duration of the test, participants are asked not to lift their finger from the screen when connecting the targets.
- Spatial Span Test: this is an adaptation of the Corsi Block Test [15]. Participants are presented with a visual grid where a specific sequence of squares is progressively highlighted. They are asked to remember and reproduce the sequence in the same order as it was shown. The task starts with a short sequence and gradually increases its length as participants answer correctly.

To avoid repeating the same cognitive exercise multiple times in the different motor configurations, we divided the MCDT activities into two protocols. Each participant was randomly assigned to one of the two protocols (details in Table I). Also, to validate the above presented digital MCDTs we also performed their corresponding traditional versions, either paper-based or oral. More specifically, in the original version of the Stroop test, participants responded verbally without

screen interaction, maintaining the division into three parts (as in the digital version). The Trail Making Test was administered in the paper-based format, mirroring its digital corresponding formats but using pen and paper. For the Spatial test, we selected the Digit Span test, where a clinician reads aloud a sequence of digits that participants must repeat in the same order. The sequence's length increases with each correct response. While the Stroop test was administered while standing on the robotic device across two balance conditions, all other classic cognitive tests were conducted in a seated position external to the device (full details in Table I).

B. Subjects

The study was approved by the local ethical committee of the University of Genoa (protocol n. 2023/93 approved on z14/12/2023). Sixty-one subjects with no history of neurological disease participated in the study: 20 subjects under 35 yo (26±3 yo, 11F), 20 subjects between 35 and 60 yo (51±5 yo, 11 F) and 21 over 60 yo (64±3 yo, 13 F).They were divided into two groups: one group, G1, performed Protocol 1, while the second group, G2, performed Protocol 2. Each group included both subjects under 35, between 35 and 60, and over 60: G1: 13 males (M), 17 females (F); 10 younger, 10 middle-aged and 10 older adults, G2: 13 M, 18 F; 10 younger, 10 middle-aged and 11 older adults.

TABLE I: COMPLTE LIST OF MCDTS PERFORMED IN BOTH DIGITAL AND TRADITIONAL FORMATS ACROSS BOTH PROTOCOLS

Cognitive task	Balance condition	Protocol 1	Protocol 2
Stroop Test digital	Static		✓
	Unstable	✓	
	Passive		✓
Stroop Test classic	Unstable	✓	
	Passive		✓
Trail Making Test digital	Passive	✓	
Trail Making Test classic	-	✓	
Spatial Span Test	Passive		✓
Digit Span Test	-		✓

C. Data and statistical analysis

The robotic device used in this study collects data from the platforms, the inertial sensor placed on the participants' chest, and the participants' interactions with the screen. Within this study, our analysis focused specifically on cognitive performance, prioritizing the data gathered from participants' screen interactions. To address our hypothesis, we calculated standard evaluation indices from the classic test formats as the primary outcome. Additionally, exploiting the advantages of the digital format, we identified secondary outcomes to gain a more comprehensive assessment of cognitive performance, decision-making and motor coordination that are not immediately evident from the primary outcomes . The primary outcomes considered in this study were:

- *Number of correct answers* in the Stroop test*:* the correct answers given, either verbally or by pressing the correct button on the screen, within 30 seconds for each section of the test.



Figure 1: Experimental set up: subjects were instructed to keep an upright stance on the platform beneath their feet. Depending on the task, they either kept their arms relaxed at their sides (during balance tasks) or interacted with the device's touchscreen (during certain dual-task tests) .

- *Completion time* in Trail Making Test*:* the time from the beginning to the end of the exercise.
- *Max span* in the Digit test*:* the number of squares highlighted in the longest sequence recalled by the participant in the Spatial Span test, and the number of digits recalled in the longest sequence.

To gain deeper insights into participants' cognitive performance, we computed secondary outcomes designed to reveal task engagement, information processing efficiency, and strategy approaches. Specifically, we analyzed:

- *Mean reaction* time in the Stroop test: the average reaction time calculated for all correct responses given
- *Number of* pauses during the Trail Making Test: the number of instances where a participant kept their finger in the same spot on the screen for more than one second.
- *Thinking time* during the Trail Making Test: the total time that the participants spent inside the circles.
- *Rate for correct answers* in the Spatial Span Test*:* the number of squares pressed per second, computed by dividing the total number of squares by the total duration of the correct sequence and averaged across all the correct attempts.
- *Rate for incorrect answers* in the Spatial Span Test: As the previous outcome but computed for the incorrect attempts.

To address our first objective, we determined whether there was a correlation between the digital tests and their corresponding oral or paper-based formats. The Spearman correlation coefficients were used for outcome measures (*completion time* and *max span*) not normally distributed according to the Shapiro-Wilk test, while the Pearson correlation coefficients for normally distributed data (*number of correct answers*). Correlation coefficients were categorized as follows: values below 0.20 were considered weak, those between 0.20 and 0.39 as moderate, between 0.40 and 0.59 as relatively strong, between 0.60 and 0.79 as strong, and 0.80 or higher as very strong correlations [16].
For our second objective, to analyze cognitive performance in the Stroop test, we performed a mixed-effects model with *the number of correct answers* and *reaction times* as dependent variables, balance condition, age group and cognitive task complexity factors as the independent

variables, and subject as the random factor. Meanwhile, general linear models were applied to the Trail Making Test, the Spatial and the Digit tests' data. The statistical analysis for these tests included an age factor, and for the Trail Making Test analysis we additionally included a task factor (part A and B).

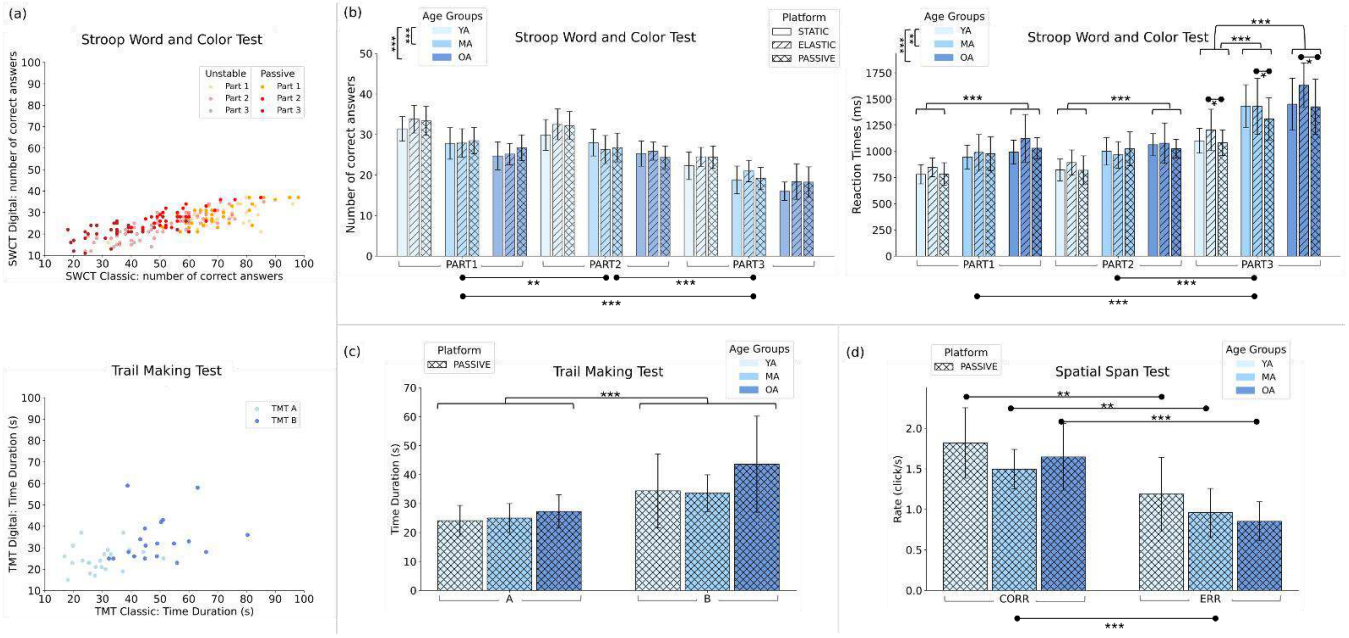


Figure 2: (a) Pearson's correlation between the number of correct answers for the classic and digital version of the Stroop test (top) and Spearman's correlation between the completion time of the classic and digital version of the Trail Making Test (bottom); (b): The number of correct answers (left) and reaction times (right) for each part of the Stroop test, across the three age groups and all three balance conditions; (c): Completion time for part A and B of the Trail Making Test; (d): Rates computed for both correct and incorrect answers for the Spatial Span Test. For all panels: * indicates a significant difference ($p<0.05$), ** indicates $p<0.01$, *** indicates $p<0.00$. Statistical significance for the main effects is indicated either below the bar plots, as in the case of the cognitive task complexity factor (done in (b)), or in the legend, as with the age factor (done in (b)). In contrast, the differences shown above the plots pertain to significant interactions (as for the right plot in (b), and the plots in (c) and (d)).

III. Results

A. Classic and digital tests correlations

Overall, the correlation between the digital versions of the MCDT tests and their traditional counterparts varied across tests. For the Stroop test, the *number of correct answers* revealed a positive strong correlation between the two versions ($r= 0.765$, $p < 0.001$, Fig. 2a - top). For the Trail Making Test, we calculated the correlation based on *completion time*, and results showed a relatively strong correlation ($\rho = 0.538$ and $p < 0.01$, Fig. 2b - bottom). Finally, for the Spatial test (and its classical format, the Digit test), the correlation based on the *max span* indicated a weak positive, not statistically significant ($\rho = 0.224$, $p = 0.24$) correlation between the two tests.

B. Cognitive performance

Stroop Color and Word Test

The Stroop test was administered across all three balance conditions, allowing us to assess the impact of age, cognitive task complexity and balance condition on cognitive performance. Both the *number of correct answers* (Fig. 1b – left) and *reaction times* (Fig. 1b - right) were influenced by age and cognitive task complexity. Specifically, age-related differences were relevant (both $p < 0.001$ for *reaction time* and *number of correct answers*), with post-hoc tests showing that YA consistently performed better, providing more and faster answers compared to both MA and OA (both $p < 0.001$). As expected, cognitive task complexity also impacted *reaction time* and *number of correct answers* (both $p < 0.001$) highlighting that when cognitive demands increased, subjects showed a longer response times with fewer correct responses. More specifically, the *number of correct answers* decreased between part 1 and 2 ($p = 0.009$) with no difference in *reaction times*. Differently, in part 1 to part 3 and part 2 to part 3 transitions, subjects showed both fewer correct answers and significantly longer *reaction times* (both transitions: *number of correct answers*, $p < 0.001$, *reaction time*, $p < 0.001$). In addition, the interaction between age and cognitive task complexity (age*cognitive task) significantly influenced *reaction times*. Post-hoc tests revealed that YA demonstrated consistently shorter *reaction times* compared to OA across all three Stroop test parts (part 1: $p < 0.001$, part 2: $p = 0.005$, part 3: $p < 0.001$). Moreover, in the most complex task condition (part 3), YA exhibited shorter reaction times than MA ($p < 0.001$).

Although both *reaction times* and *number of correct answers* were not directly affected by balance condition ($p > 0.050$), we found a significant interaction between cognitive task complexity and balance condition (*reaction times* $p = 0.005$, *number of correct answers*: $p = 0.045$). The post-hoc analysis

showed a main difference of balance condition in part 3: *reaction times* were longer for the unstable balance.

Trail Making Test

The Trail Making Test was performed only in the passive balance condition, therefore we assessed solely the impact of age and cognitive task complexity (part A and B) on cognitive performance. The *completion time* was only influenced by the task complexity ($p < 0.001$, Fig. 1c). As expected, *completion time* was significantly longer for part B compared to part A, and this difference was consistent across all three age groups (all $p < 0.001$). Similarly to the *completion time*, also the secondary outcomes (*number of pauses* (part A: YA: 1.1 ± 1.3, MA: 1.3 ± 1.8, OA: 2.4 ± 1.5, part B: YA: 5.8 ± 5.7, MA: 4.3 ± 3.2, OA: 7.2 ± 4.7) *and thinking time* (part A: YA: 9.25 ± 3.15 s, MA: 10.8 ± 3.22 s, OA: 12.95 ± 5.22 s, part B: YA: 19.5 ± 4.8 s, MA: 16.85 ± 4.45 s, OA: 25.5 ± 6.45 s), were both influenced only by the task factor (both $p < 0.001$). Consistent with the trend observed for *completion time*, these secondary outcomes were significantly higher in part B compared to part A.

Spatial Span Test

For the Spatial test we found that age significantly impacted the *max span* ($p = 0.006$). More specifically YA showed a larger span with respect to MA and OA (YA: 6.7 ± 0.94, MA: 5.4 ± 0.51, OA: 5.6 ± 1.07), with a significant decrease in *max span* between YA and MA ($p = 0.008$) and between YA and OA ($p = 0.028$). Differently, the secondary outcomes did not have an age effect neither for the *rate of correct answers* nor the *rate of incorrect answers*. However, for all subjects the *rate of incorrect answers* was significantly lower than the *rate of correct answers* ($p < 0.001$), meaning that subjects needed more time when they were unable to recall the sequence correctly.

IV. Discussion

In this study, we assessed cognitive performance using a robotic device that integrated cognitive tasks with both static and dynamic balance challenges. Within this study, we investigated how the cognitive performance is affected by age, cognitive task complexity and balance condition. This methodological approach can be also used to study the effect of cognitive tasks on motor performance. This innovative approach represents a significant advancement in rehabilitation research, as it allows for a comprehensive evaluation of the interplay between cognitive and motor functions. Integrating motor and cognitive evaluations provides deeper understanding of their interaction which is crucial for the definition of tailored rehabilitation strategies, that can focus on enhancing both cognitive and motor performance simultaneously.

A. Classic and digital tests correlations

The first objective of this study was to determine the validity and reliability of the digital MCDTs developed by comparing them to their oral/paper counterparts. Consistent with literature, the digital versions of the cognitive tests faithfully replicated the classic versions. Specifically, results showed a strong correlation for the Stroop test and a relatively strong correlation for the Trail Making Test, while weaker results were found for the Spatial Span test. For the Trail Making Test, the relatively strong correlation was expected, as it is in line with previous studies [15], [16], [17], [18]. In this case the digital version is an exact replica of the classic one, with the only difference that users need to use their finger instead of a pencil. Meanwhile, for both the Spatial Span test and the Stroop test the administration modality was different between the digital and classic versions. The Spatial test, which primarily assesses visual-spatial memory, was compared to the Digit test, which focuses on verbal working memory. Similarly, the digital Stroop test, which requires selecting answers from a screen, was compared to the classical Stroop test, which also involves verbal fluency. Although the administration methods differed in both cases, the Spatial Span test exhibited a weak correlation, whereas the Stroop test displayed a strong correlation, aligning with findings from previous studies [17], [18]. While participants achieved a higher number of correct answers in the original Stroop test format, the strong correlation suggests that the "Stroop effect" influenced participants consistently, regardless of whether they responded verbally or manually on the screen. In contrast, the memory tasks highlighted a key difference: humans tend to rely heavily on visual memory, which is generally considered easier to recall than abstract verbal information, such as numbers [15].

B. Cognitive performance

Overall, we found that age-related effects were evident across various MCDTs, reflecting their broad influence on cognitive performance. In the digital Stroop test, both age and task complexity significantly influenced performance. MA and OA showed a greater decline in *correct responses* and longer *reaction times* compared to YA, particularly in the most challenging task condition. These findings are consistent with previous literature [19], [20], [21]. Similarly, in the Spatial test, *max span* decreased significantly with age, highlighting age-related declines in working memory and processing speed, also in line with previous findings [22]. For the Trail Making Test, cognitive task complexity, rather than age, was the primary factor influencing performance. All groups took longer to complete the more challenging part B, which was also associated with more frequent pauses and extended thinking times. Balance conditions also influenced cognitive performance, particularly in the Stroop test, where unstable conditions resulted in slower *reaction times* but did not affect the *number of correct answers*, indicating that healthy subjects have robust cognitive function even under dynamic conditions.

Building on these findings, future research should further investigate the application of motor-cognitive dual-task (MCDT) exercises combined with the capabilities of robotic devices to potentially identify early cognitive decline in patient populations, including those with mild cognitive

impairment, Parkinson's disease, or dementia. Additionally, future studies should focus on examining the effects of MCDTs on balance performance, as this study primarily explored their impact on cognitive performance.

V. Conlusions

In this study we investigated the integration of digitalized cognitive assessments with dynamic balance tasks by exploiting a medical robotic device, *hunova*. The correlation between the digital and traditional tests confirmed the robustness of our methodology, showing very strong correlations for some tests and weaker ones for others. However, these findings align with the results reported in the literature. Also, by evaluating unimpaired participants across three age groups, we identified significant age-related differences in cognitive performance under various balance conditions. These findings suggest that dynamic balance tasks, combined with cognitive testing, may offer a valuable tool for detecting early cognitive changes. Future research should explore the impact of MCDTs on patient populations, where these assessment tests could be particularly effective in detecting subtle changes associated with cognitive decline.

Acknowledgment

Funded by the European Union—NextGenerationEU and by the Ministry of University and Research (MUR), National Recovery and Resilience Plan (NRRP), Mission 4, Component 2, Investment 1.5, project "RAISE—Robotics and AI for Socio-economic Empowerment" (ECS00000035).

References

[1] P. Sujitha and N. B. Swetha, "Impaired Cognition – A Menace to Aging," *Natl. J. Community Med.*, vol. 14, no. 2, pp. 118–123, 2023, doi: 10.55489/njcm.140220232125.

[2] T. del Ser *et al.*, "Dimensions of cognitive reserve and their predictive power of cognitive performance and decline in the elderly," *Front. Dement.*, vol. 2, 2023, doi: 10.3389/frdem.2023.1099059.

[3] E. B. H. Treichler and D. V. Jeste, "Cognitive decline in older adults: Applying multiple perspectives to develop novel prevention strategies," *Int. Psychogeriatrics*, vol. 31, no. 7, pp. 913–916, 2019, doi: 10.1017/S1041610219001121.

[4] N. P. W. P. Sari, "Cognitive Function and Quality of Life in Institutionalized Elderly: Each Predictors and Both Influences," *J. Educ. Heal. Community Psychol.*, vol. 12, no. 3, p. 717, 2023, doi: 10.12928/jehcp.v12i3.26124.

[5] K. Fouchenette, "Mobile Testing of Cognitive Function.," 2010.

[6] S. Bedyńska *et al.*, "Diagnostic tools for assessment of cognitive functioning in children and youth – the implementation project," *Przegląd Psychol.*, vol. 64, no. 2, pp. 97–111, 2021, doi: 10.31648/pp.7838.

[7] A. S. Atkins *et al.*, "Remote self-administration of digital cognitive tests using the Brief Assessment of Cognition: Feasibility, reliability, and sensitivity to subjective cognitive decline," *Front. Psychiatry*, vol. 13, no. August, pp. 1–11, 2022, doi: 10.3389/fpsyt.2022.910896.

[8] R. F. Buckley *et al.*, "Computerized Cognitive Testing for Use in Clinical Trials: A Comparison of the NIH Toolbox and Cogstate C3 Batteries," *J. Prev. Alzheimer's Dis.*, vol. 4, no. 1, pp. 3–11, 2017, doi: 10.14283/jpad.2017.1.

[9] O. Beauchet, J. Matskiv, Y. Rolland, A. M. Schott, and G. Allali, "Using Interaction between Cognitive and Motor Impairment for Risk Screening of Major Neurocognitive Disorders: Results of the EPIDOS Observational Cohort Study," *Brain Sci.*, vol. 12, no. 8, pp. 3–8, 2022, doi: 10.3390/brainsci12081021.

[10] H. M. Alharthi and M. M. Almurdi, "Association between cognitive impairment and motor dysfunction among patients with multiple sclerosis: a cross-sectional study," *Eur. J. Med. Res.*, vol. 28, no. 1, pp. 1–9, 2023, doi: 10.1186/s40001-023-01079-6.

[11] D. Szögedi, T. W. Stone, E. Dinya, and J. Málly, "Dual-Task Performance Testing As an Indicator of Cognitive Deterioration in Parkinson's Disease: A Pilot Study," *J. Psychiatry Psychiatr. Disord.*, vol. 07, no. 04, pp. 104–117, 2023, doi: 10.26502/jppd.2572-519x0190.

[12] R. Kiss, D. Brueckner, and T. Muehlbauer, "Effects of single compared to dual task practice on learning a dynamic balance task in young adults," *Front. Psychol.*, vol. 9, no. MAR, pp. 1–8, 2018, doi: 10.3389/fpsyg.2018.00311.

[13] J. A. Saglia *et al.*, "Design and development of a novel core, balance and lower limb rehabilitation robot: Hunova®," *IEEE Int. Conf. Rehabil. Robot.*, vol. 2019-June, pp. 417–422, 2019, doi: 10.1109/ICORR.2019.8779531.

[14] G. Marchesi *et al.*, "Assessment of trunk control and core stability in spinal cord injured subjects," *Gait Posture*, vol. 97, pp. 24–25, 2022, doi: 10.1016/j.gaitpost.2022.09.044.

[15] M. H. G. Claessen, I. J. M. Van Der Ham, and M. J. E. Van Zandvoort, "Computerization of the standard corsi block-tapping task affects its underlying cognitive concepts: A pilot study," *Appl. Neuropsychol.*, vol. 22, no. 3, pp. 180–188, 2015, doi: 10.1080/23279095.2014.892488.

[16] G. Marchesi *et al.*, "Modified functional reach test: Upper-body kinematics and muscular activity in chronic stroke survivors," *Sensors*, vol. 22, no. 1, pp. 1–15, 2022, doi: 10.3390/s22010230.

[17] J. A. Periáñez, G. Lubrini, A. García-Gutiérrez, and M. Ríos-Lago, "Construct validity of the stroop color-word test: Influence of speed of visual search, verbal fluency, working memory, cognitive flexibility, and conflict monitoring," *Arch. Clin. Neuropsychol.*, vol. 36, no. 1, pp. 99–111, 2021, doi: 10.1093/arclin/acaa034.

[18] S. Coelli *et al.*, "Assessment of the usability of a computerized Stroop Test for clinical" pp. 0–4, 2016.

[19] S. Test *et al.*, "タブレット版 Stroop 検査作成の試み," vol. 21, no. 1, pp. 19–25, 2023.

[20] N. A. Roque, I. Ferguson, E. T. Saulnier, and C. Anderson-Hanley, "Stroop for electronic touchscreen self-administration (eStroop) as used in the remote iPACES neuro-exergaming trial for Mild Cognitive Impairment (MCI): An initial validation report," *Alzheimer's Dement.*, vol. 19, no. S2, p. 65140, 2023, doi: 10.1002/alz.065140.

[21] D. Schoene, S. T. Smith, T. A. Davies, K. Delbaere, and S. R. Lord, "A Stroop Stepping Test (SST) using low-cost computer game technology discriminates between older fallers and non-fallers," *Age Ageing*, vol. 43, no. 2, pp. 285–289, 2014, doi: 10.1093/ageing/aft157.

[22] A. Wiechmann, J. R. Hall, K. Kelly, Ed Watkins, V. Campbell, and J. D. Meernik, "The Utility of the Spatial Span From the Wechsler Memory Scales," *Diss. Prep. degree Dr. Philos.*, pp. 17–18, 2010.

Arm Activity Feedback for Stroke Survivors – a User Needs Analysis for the Design of a Mobile Application

Laura Mayrhuber [1,†], Lea Roffler [1,†], Chris Awai Easthope [2,3], Roger Gassert [1,4], Olivier Lambercy [1,4]

***Abstract*—Involving end-users early in developing rehabilitation technologies is crucial, especially when designing solutions that aim to provide understandable and instructive feedback on activity or performance. This study explores user needs and preferences for a smartwatch and -phone application (app) to monitor and promote arm activity in stroke survivors. Semi-structured interviews with three stroke survivors and five healthcare professionals (HCPs) identified three key themes using reflexive thematic analysis: feedback, user interface, and motivational strategies. Both groups highlighted the need for an arm movement tracker, as existing commercial options primarily focus on lower limb activity, such as step counting. Stroke survivors preferred simple data representation and real-time tracking with daily and weekly summaries. Feedback was deemed essential, with stroke survivors valuing positive and corrective feedback to increase engagement. Participants emphasized the importance of personalizing the app, advocating for customizable features like font sizes, contrast, and feedback modes to meet varying needs. Moreover, remote HCP supervision was highlighted as a key motivational factor to promote accountability and support therapy planning. Further, incremental goal setting emerged as a potential key motivator. Together, these elements provide a roadmap for implementing more intuitive mobile apps to support arm rehabilitation after stroke.**

I. Introduction

Stroke is a significant cause of upper limb (UL) motor impairments worldwide [1]. Active and repetitive use of the affected arm is a critical part of rehabilitation to regain function, even in the chronic stage [2]. However, a large number of stroke survivors experience learned disuse, where the use of the affected arm is avoided [3]. This pattern becomes more pronounced as stroke survivors transition from rehabilitation clinics to their home environments [3]. The absence of external support through therapists, coupled with the challenges of using the impaired arm during daily life, can consequently lead to a functional decline and reduced motivation, creating a vicious circle of inactivity and further functional deterioration [4]. Therefore, it is crucial to develop supportive strategies that encourage active arm use of the affected side in stroke survivors beyond the clinical setting.

Wearable sensors have shown promise in continuously monitoring arm movements and providing feedback, for example, related to the amount of arm use [5], [6], [7], [8]. Such technology can help improve motivation and increase affected arm use by delivering feedback via different sensory channels. Feedback modalities can include visual displays of the performed activity, vibratory cues as reminders to move, or auditory signals to indicate goal completion [5], [6], [7], [8], [9], [10]. Furthermore, feedback can be provided in "real-time" with information updated during the day or as a summary, where users receive a report at the end of the day. While previous research indicates that activity tracking and feedback devices can effectively promote increased arm use, clinical implementation and usability challenges remain. Most existing solutions rely on dedicated research devices, which are often bulky and overly complex to use, limiting long-term adherence and upscaling [5], [6], [7], [10], [11].

While some studies evaluated the usability of arm activity trackers [10], [12], feedback modalities [9], [13], and report preferences [8], only a few included stroke survivors as the end-users and healthcare professionals (HCPs) as experts in the field, whose experiences with stroke patients of varying impairment levels can provide complementary insights. Specifically, there is a strong need to understand the requirements of stroke survivors regarding how and when feedback on arm use should be given and how these requirements may be fulfilled using consumer-grade devices such as smartphones or smartwatches.

This study focuses on collecting user needs and preferences for a mobile application (app) that processes wearable sensor data to assess and provide feedback about affected UL use. The goal is to improve user acceptance of both the app and the tracking device, thereby promoting consistent adherence to UL therapy at home. Semi-structured interviews with stroke survivors and HCPs explore relevant activity metrics to report (e.g., duration of arm use, activity counts), effective presentation methods and the granularity of the presented information, preferred feedback modalities (e.g., visual, vibratory, auditory), as well as factors for maintaining motivation, such as arm movement goals. These findings can guide the content of future smartwatch- and phone apps. Moreover, insights from the interviews indicate which aspects and motivational strategies are relevant and appropriate for users when designing feedback implementations to promote increased arm use. By engaging end-users early enough in the design and development process, we aim to identify important considerations to create a functional tool that aligns more closely with their expectations for smartwatch and -phone apps designed to monitor and increase the activity of the affected arm.

* Innosuisse is grateful acknowledged for funding the SwissNeuroRehab project (PFFS-21-64 / Agreement Nr. 2155009976) as part of their flagship initiative.

[1] Rehabilitation Engineering Laboratory (RELab), ETH Zurich, Switzerland (e-mail: laura.mayrhuber@hest.ethz.ch)

[2] Lake Lucerne Institue (LLUI), Switzerland

[3] Data Analytics & Rehabilitation Technology (DART), Lake Lucerne Institute, Switzerland

[4] Future Health Technologies program, Singapore - ETH Centre, Campus for Research Excellence and Technological Enterprise (CREATE), Singapore

[†] These authors contributed equally and share first authorship.

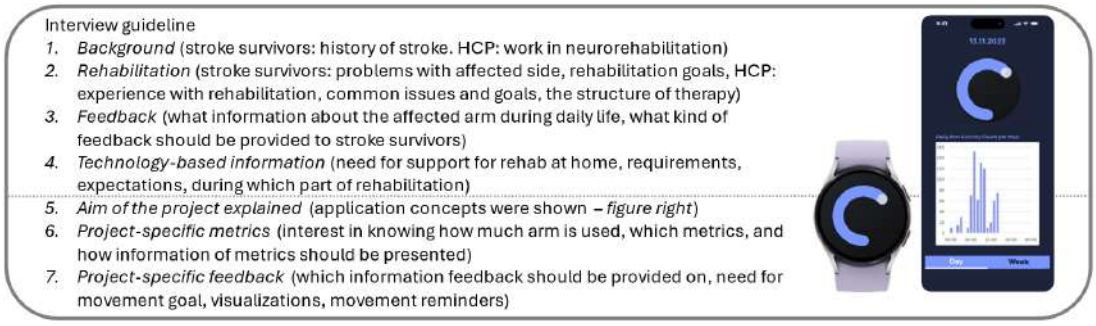


Figure 1. Guideline used during the semi-structured interviews (*left*) and visual representation examples of the application concepts, showing amount of arm activity on both a smartwatch and -phone application (*right*). To minimize bias during the initial part of the interviews, visual representation examples were only shown when the aim of the project was explained (point 5).

II. Methods

A. Study Design

Following a user-centered approach, semi-structured one-on-one interviews were conducted with stroke survivors and HCPs to identify and define user needs and app requirements. The interviews, lasting approximately 45 minutes, were conducted in person between October and November 2024 by LM and LR and were guided using a predefined interview guideline (Figure 1). Topics such as experience with rehabilitation, desired functionalities for a potential smartwatch and -phone app providing feedback on affected arm use, the challenges of smartphone interaction, the type of arm activity metrics to consider, and feedback preferences were addressed. After feedback preferences were identified, the project aim was explained, and the first concept of how the apps could look was presented (Figure 1). Each participant gave written consent for the study and audio recording before the interview started. This study was examined and approved by the Ethical Commission of the ETH Zurich (EK 2024-N-271).

B. Participants

The study population comprised stroke survivors and HCPs, including medical doctors, nurses, therapists, and caregivers. Participants were included if they were (1) above 18 years of age, (2) spoke German or English, and (3) able to provide written informed consent. Additionally, stroke survivors were included if they were in the (1) sub-acute or chronic stage and had a (2) residual unilateral hemiparesis. HCPs were included if they had regular professional contact with stroke survivors who have impairments of the UL following a stroke. Exclusion criteria were (1) major untreated depression, (2) severe cognitive impairment, (3) comprehensive aphasia, and (4) severe comprehension and/or memory deficits. Participants were recruited at the cereneo - Center for Neurology & Rehabilitation (Vitznau/ Hertenstein, Switzerland).

C. Data Analysis

The interview audio data was transcribed in German or English using MS Word Transcribe and checked by LM and LR. For the preparation of this manuscript, selected quotes were translated from German to English. Personal information was excluded from the transcripts to ensure anonymity. With a reflexive thematic analysis (RTA), the data was analyzed to fit the explorative nature of identifying user needs for a smartwatch and -phone app to track arm activity and feedback preferences [13]. RTA, based on Braun and Clarke, is a qualitative method that focuses on identifying, analyzing, and interpreting patterns (themes) within data [14]. A combined approach incorporating deductive and inductive methods was applied to identify themes [14]. Within a deductive approach, themes were established based on previous literature and interview topics. In contrast, an inductive approach involved examining the collected data for emerging patterns to extract themes. The analysis was conducted using the open-source software Taguette [15]. After re-reading the transcripts and familiarizing themselves with the data, LM and LR independently coded interview statements using RTA and subsequently grouped codes into sub-themes based on topic similarity through an iterative process. Corresponding sub-themes were further grouped into themes.

III. Results

In total, eight participants were included in the study (age: 41.5 (±14.7), gender: three females, five males). Three were stroke survivors, one of whom was supported by his son during the interview, and five HCPs. Table 1 provides further details on participants' demographics. The average interview time was 36 minutes (± 7). The RTA identified three themes and six subthemes (Figure 2). Statements from participants incorporated in this section are presented verbatim/direct.

TABLE I. PARTICIPANT CHARACTERISTICS

		Stroke survivors (n=3)	**Healthcare Professionals (n=5)**	
Sex (f/m)[a]	***Age (y)[b]***	***Stroke onset (m)[c]***	***Role***	***Experience (y)[b]***
m	57	8		
m	69	9		
f	36	25		
m	36		Assistant doctor in neurology/ Researcher	0.5/ 9
f	23		Nurse	2
m	43		Occupational therapist	17
m	33		Physiotherapist	4
f	35		Neurologist	6

[a]f = female, m= male, [b] y= years, [c] m= months at time of interview.

A. Theme 1 – Feedback Preferences

This theme provided an overview of what information participants would like stroke survivors to receive about their affected arm (e.g., movement metrics) and feedback preferences.

1) Parameters

Most participants expressed interest in stroke survivors receiving information about their affected arm during daily life. The underlying motivation for this, as reported by HCPs, included that it would give stroke survivors a better follow-up when leaving the rehabilitation clinic, as easy and objective monitoring of arm use is challenging at home, and there is a lack of guidance and feedback. Stroke survivors mentioned a lack of such devices and the importance of tracking progress over time. One stroke survivor mentioned: *"[I have] a manual activity tracker where [I] count [the] activity. [Information on arm use would be interesting] because [many] apps concentrate on the legs and feet but not on the arm or hand. […] I want to see how much I use my hand. Because in my life at home, I don't have the therapist, and I need to have the knowledge."*

The importance of notifying stroke survivors when they perform movements that could potentially cause harm was emphasized by HCPs and stroke survivors. Monitoring compensation movements was mentioned multiple times by HCPs as a critical aspect for stroke survivors to know and receive feedback on. Moreover, stroke survivors voiced that they would like a reminder to use their affected arm if they were inactive for an extended period, if they have not moved enough, and when they would rely too much on the less affected side. HCPs agreed and suggested that feedback should be provided to stroke survivors when the affected arm was not moving enough to meet daily targets or when it was time for a break. Additionally, most HCPs and stroke survivors mentioned that information transfer to stroke survivors on what type of movement was performed, such as grasping or reaching, would be appreciated. One stroke survivor who had almost no residual UL function, however, disagreed. He mentioned that he would not be interested in receiving information about arm use. One HCP supported this, noting that for stroke survivors who have practically no UL function, not much would be seen during the arm tracking.

HCPs suggested that not all detailed information on affected arm activity needs to be presented directly to stroke survivors. Instead, stroke survivors could be remotely monitored, and their data could be accessible to HCPs for clinical purposes. Considering the different use cases, most HCPs would then be interested in receiving detailed information on how stroke survivors performed their movements, whether it was voluntary, which part of the upper extremity was moving, and the variability and quality of the movement. One HCP reasoned: "*[I would like to know] which kind of movement [is performed]. Like if [they] pushed or moved up. Because then you [use] different muscles, and you can know which one has to work more. Because some patients do movements, but they do every time the same. Then you are using always the same muscle[s].*" Several HCPs highlighted their need to receive specific information on various activities of daily living (ADLs), such as the exact activities performed in a daily routine, the time spent on each ADL, the frequency of unilateral and bilateral movements, and whether stroke survivors performed the ADLs independently or required specific techniques or support. Additionally, HCPs addressed their need for information on the arm use ratio of the affected/ less affected side and the intensity of the movement. However, opinions varied on whether they would prefer the duration of arm movement or the number of movements.

2) Modalities

Participants described several possibilities for providing feedback on the affected arm use. Most HCPs agreed that a reminder to move in the form of an encouraging message or smiley emoji on the smartwatch or -phone would be beneficial. One HCP argued that a message on the phone may be more effective than the smartwatch as more people tend to look at their phones regularly. HCPs expected that stroke survivors would appreciate visual feedback to showcase their progress, though they noted that responses to feedback can vary. HCPs and stroke survivors expressed interest in receiving feedback through visual, vibration, and sound modalities.

Further, many stroke survivors elaborated on the benefits of receiving positive feedback when they did a correct movement, as well as negative when they needed to increase their arm activity. One HCP added that even negative feedback should be sent out in a positive format. Most HCPs agreed that positive feedback and an emphasis on reaching a portion of a daily arm movement goal would benefit most stroke survivors. However, it was mentioned multiple times that the feedback preferences are highly individual. One HCP emphasized: "*We generally know that positive feedback is more helpful. […] it's perhaps […] already very motivated by smaller successes, like saying you've only achieved 10% today.*"

Concerning the time and amount of feedback, participants shared a similar opinion. HCPs and stroke survivors both think it is essential that users receive feedback when the arm is not moved enough throughout the day. Participants preferred a gap (2-4 hours) between reminders. Regarding

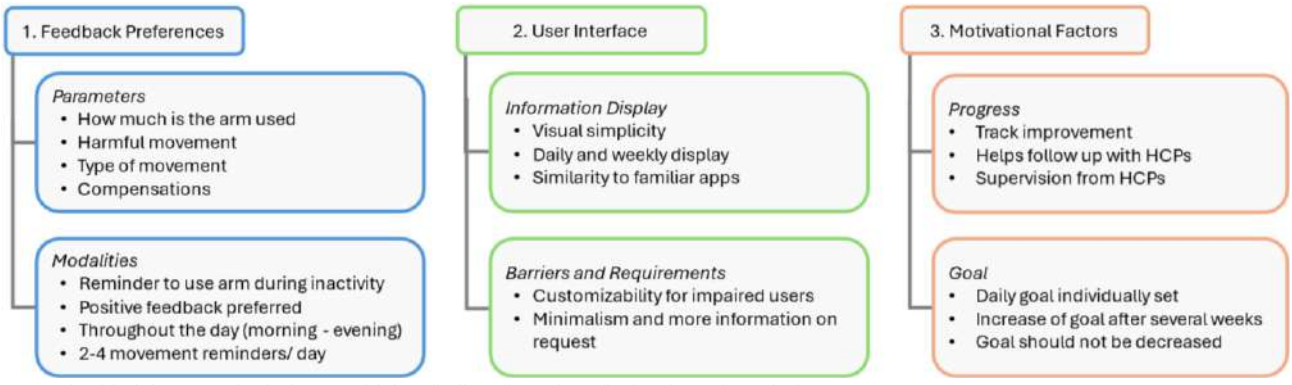


Figure 2. Identified themes and sub-themes with key findings from the reflexive thematic analysis.

when the reminder should be triggered, stroke survivors emphasized that they would like more activity throughout the day, so movement reminders in the morning, afternoon, and evening. Other participants mentioned that they would prefer reminders between 9 am and 5 pm and to have different settings for weekdays and weekends. Contrarily, HCPs suggested providing feedback during the whole wake time, but that stroke survivors should be able to set a time window when reminders are triggered. One stroke survivor remarked that a snooze function would be helpful, as sometimes the time when the reminder is triggered may not be convenient. One participant noted that movement reminders triggered too early in the day lose their effectiveness because they do not give patients sufficient time to move their arm before receiving the first reminder, suggesting that they be scheduled later in the afternoon or evening instead. HCPs indicated that a prolonged inactivity or deviation towards a specific daily arm movement goal should trigger a reminder. One HCP argued: "*If you see that you've maybe only done 200 by lunchtime, how are you going to manage the other 1800 […] by the evening? […] Now, you haven't done anything for half an hour or an hour, […] do your exercise program.*" Participants mentioned that a movement reminder should be triggered twice to four times daily. One HCP added that stroke survivors should be able to decide how many reminders they want to receive.

B. Theme 2 – User Interface

This theme explored what visualizations participants viewed as essential for effective feedback and design considerations critical to accessibility and ease of use.

1) Information Display

Almost all participants reported that they preferred graphical representations (e.g., bar charts and color-coded indicators) to text-heavy displays as they experienced these formats as being easier to understand. Visual simplicity was a key preference among HCPs and stroke survivors, with participants particularly favoring bar charts on an hourly timescale to view progress in real-time. This bar chart should also include the movement goal, as participants found it essential to track progress toward their targets throughout the day. One HCP stated the need for simplicity and visual representations as follows: "*[...]they [want], as I already said, as many graphics as possible [...] Basically very little text, titles maybe or not if they're not needed. And they want colors. They want big things to see and as little buttons as possible and as little windows as possible.*"

HCPs and stroke survivors favored simple metrics to support users' motivation and engagement, such as a daily overview of arm activity and a weekly summary showing which days the users achieved the activity goal. While some HCPs also expressed that stroke survivors may have an interest in monthly summaries for broader tracking, this interest was absent among stroke survivors. However, participants generally agreed that users should be able to interact with the app to get more detailed information if desired. Stroke survivors expressed that it should be similar to other health apps (e.g., Apple Health), as many were familiar with step-counters.

2) Barriers and Recommendations

Most HCPs agreed that too much information on the main display could be overwhelming, mainly since stroke survivors often contend with additional challenges beyond upper limb disability, such as neuropsychological disorders. Moreover, stroke survivors themselves mentioned the importance of customization in the interface, particularly for individuals with additional impairments. This adaptability should include options such as larger font size, adjustable contrast, or switching between visual and auditory feedback modes. One HCP mentioned: "*So it's important to understand for the type of patient […] the interface should be customized. For instance, if it's a patient with visual impairment, you should maybe zoom [in on] some aspects.*" Participants noted that older users could face difficulties with complex interfaces, mainly when the app contains too much information at once. One participant highlighted a common concern that overly complex technology might alienate some users, questioning whether elderly individuals would find smartwatches too challenging. Although some HCPs observed that older adults are becoming increasingly tech-savvy, many agreed that a simple, intuitive design is crucial to keep users from feeling overwhelmed or frustrated. HCPs emphasized simplicity in the design to reduce cognitive load and enhance usability. They advocated for a clear, consistent layout that employs color coding to differentiate essential information, making it easier for users to recognize their progress and goals.

C. Theme 3 – Motivational Factors

Various factors were captured in this theme that can influence the motivation and adherence to a technological rehabilitation intervention. The impact of monitoring the progress and setting a goal to increase motivation was discussed in detail.

1) Progress

Among the stroke survivors and HCPs, tracking the progress of arm use over multiple weeks and months was considered a strong motivational factor. Moreover, HCPs identified that monitoring the progress of arm use right after stroke may be advantageous for stroke survivors as the most significant progress usually occurs at the beginning of rehabilitation. One HCP argued that observing a positive change and seeing the improvement not only motivates but could also help the stroke survivor cope with the consequences of the stroke. The HCP stated: "*Progress is usually visible quite quickly at the beginning, and I think that patients probably get positive feedback from […]the first 3 to 6 months [which] are usually the most successful, and if you always have positive feedback the whole time, that you're always improving a little, I think that's much easier for the patients to deal with or cope with.*" Both stroke survivors and HCPs consider it essential that HCPs monitor the progress of arm use and support follow-ups, especially after discharge. Additionally, it provides information on whether the stroke survivor is improving the use of the affected arm or if it is deteriorating. Stroke survivors mentioned that the remote supervision of an HCP and knowing that someone is checking on their progress would be an additional motivational factor.

2) Goal

Overall, participants agreed that setting a goal value for using the affected arm would be motivating. Stroke survivors said they would like a daily goal to know the amount of arm activity expected and if they have done enough at the end of the day. Several participants further emphasized that the goal should be increased over time toward healthy values, with preferences ranging from expanding the goal every week after several weeks or months. HCPs stressed that the goal should be individually set, depending on patients' abilities, and that it should only be decreased for pathological reasons. One HCP explained: "*Maybe it's a good idea to have a first initial period like one week, two weeks in which you do monitoring and that's your assessment. Then you use that to define that your target is 20% more that over a certain amount of time, and then you see if you can increase [the target] over time.*" Contrarily, another HCP argued that the goal for stroke survivors should be to reach a balance of use between the affected and less affected side.

IV. Discussion and Conclusion

This study explored user needs and preferences to support the development of a mobile app that monitors and provides feedback on the activity of the affected arm in stroke survivors. Interview data from stroke survivors and HCPs offer considerations for the design and development of the apps.

Most participants expressed the need for an arm movement tracker, as few commercial options focus on arm use compared to step counting [15]. Stroke survivors and HCPs agreed on the importance of providing users with information on the types of arm movement performed. Both groups emphasized that stroke survivors should only receive the most relevant parameters on the apps, prioritizing the amount of arm activity. In parallel, HCPs should also be able to access more granular information remotely. Transferring information to HCPs would provide an opportunity for supervision post-discharge, therapy planning, early deterioration detection, and serve as a motivational factor. It has been shown that monitoring by HCPs is a crucial factor for long-term adherence to UL therapy at home, as stroke survivors feel accountable for doing their exercises and improving their progress [16].

Feedback was highly valued, with stroke survivors desiring positive reinforcement for achieving goals and corrective feedback for insufficient or harmful movements. Previous work used a smiley emoji's "happiness level" to indicate arm activity relative to the goal [7]. Positive or promotion-oriented feedback reinforces desirable behaviors, while negative or change-oriented feedback addresses areas that need improvement [17]. HCPs agreed but favored framing feedback positively, as evidence shows it is more effective than negative feedback in rehabilitation [18]. One participant, possibly due to his severe upper limb impairment, could not imagine using such a feedback tool. Literature indicates that stroke survivors with severe impairments often feel that their use of the affected arm is already at its maximum capacity, so additional feedback has a limited effect [8]. Feedback to avoid harmful movements is seen as beneficial, as pointed out by participants' preference for corrective feedback on potentially damaging actions. However, accurately detecting these movements with a single sensor setup can be challenging. Multi-sensor setups could improve harmful movement detection but may reduce practicality and long-term adherence [19].

The importance of visual feedback was emphasized throughout interviews, favoring simple visualizations like bar charts over text-heavy formats to reduce cognitive load [20]. It supports users in quickly identifying and understanding their performance without requiring extensive reading or interpretation [20]. Additionally, users are typically more comfortable using an app resembling familiar technologies, reducing learning barriers and making the app feel intuitive and accessible [21]. Overall, an interface communicating key information effectively using a consistent color scheme is preferred [20]. Simple metrics, like daily arm activity overviews and weekly summaries displaying goal achievement, were suggested to enhance user motivation and engagement. Observing real-time progress in the initial months following a stroke, when significant improvements in arm function often occur, enhances motivation through positive reinforcement [13], [22]. However, while tangible progress can be a strong motivator, a lack of visible improvement, common in the chronic stage, may lead to reduced motivation [16].

For situations requiring immediate feedback, such as inactivity, visual feedback on arm activity can be supported by vibratory or auditory cues [11]. Participants agreed that reminders should be triggered during inactivity or when goals are unmet, as seen in previous work [5], [6]. Different patterns of triggering movement reminders can be observed in the literature. The number of reminders per day ranged from 8 [5], [6] to 36 [13], with times between reminders including 10 minutes [13], 30 minutes [5], [6], or one to four hours [23]. Reminders were either triggered whenever inactivity was detected [5], [6], [23] or in a randomized manner [13]. Contrarily, participants in this study preferred a maximum of four reminders per day, distributed throughout the day, with fewer reminders in the morning and two to four hours between each. This aligns with existing literature showing that reminders in the afternoon tend to be more efficacious [13].

Goal setting emerged as a key motivator, emphasizing personalized movement goals and reminders to take breaks if the activity is excessive [11]. Personalized movement goals could support sustained engagement by fostering a sense of achievement and progress; however, they only seem effective if relevant to the stroke survivor [24]. Daily goals provide structure and reinforce a sense of accomplishment, especially if gradually adjusted based on individual progress [8]. Participants agreed on increasing the goal over time but differed on when it should increase, ranging from every week to several months. Previous literature suggested a daily increase of 3% of the past 30-day mean [5], [6]. Initial goals could be based on an assessment period of arm activity, with proposed increases of 20% over a selected timeframe or aiming for balance between the affected and less affected sides. Literature suggests setting the goal proportional to the impairment level assessed with clinical tests [7].

Developing an app to encourage arm use in stroke survivors must prioritize customization in design, feedback, and goal setting due to varying recovery needs and functional profiles [8]. The results of this study align with the literature,

highlighting that feedback must be tailored to individual recovery goals and daily routines [8]. A customizable approach to feedback, with flexibility in modality and frequency, may optimize user engagement and adherence.

Study limitations include a small sample size and an imbalance in stroke survivors and HCPs, relevant given the frequent differences in their perceptions. Moreover, while indications for developing a mobile app supporting arm use at home were identified, it is crucial to recognize that these generalizations may not reflect the opinions of every stroke survivor and HCP. Due to predefined interview guidelines and the presented app concepts, the interviews were focused on gathering specific insights and implications for an app currently under development, which may have biased some responses (Figure 1). The following steps of this research project involve developing and refining user interface prototypes based on interview insights and literature. Following a user-centered approach, these prototypes will undergo iterative design and usability testing with stroke survivors to optimize usability. Finally, interactive prototypes will be evaluated through task-based navigation assessments and standardized usability measures.

Overall, this study gathered valuable input based on user needs for developing a mobile app to monitor and increase the activity of the affected arm in stroke survivors. Key findings emphasize the need for real-time tracking, simple yet informative metrics, and detailed data for clinical use. Remote HCP supervision was highlighted as a key motivational factor in promoting accountability and supporting therapy planning. Personalization options, such as adjustable features and customizable feedback modes, are essential to accommodate varying impairments. Feedback strategies should balance positive reinforcement and corrective guidance, while incremental goal setting is crucial in maintaining motivation. These findings offer a foundation for developing intuitive and personalized apps to support arm rehabilitation after stroke.

ACKNOWLEDGMENT

The authors thank all study participants, Dr. Meret Branscheidt for assisting with patient recruitment, and Ioulia Barakou for supporting data analysis.

REFERENCES

[1] V. L. Feigin et al., "World stroke organization (WSO): global stroke fact sheet 2022," vol. 17, no. X, 2022, doi: 10.1177/17474930211065917.

[2] C. Winstein, B. Kim, S. Kim, C. Martinez, and N. Schweighofer, “Dosage matters.,” Stroke, vol. 50, no. 7, pp. 1831–1837, Jul. 2019, doi: 10.1161/STROKEAHA.118.023603.

[3] E. Taub, G. Uswatte, V. W. Mark, and D. M. M. Morris, "The learned nonuse phenomenon: implications for rehabilitation.," Eura. Medicophys., vol. 42, no. 3, pp. 241–256, Sep. 2006.

[4] B. R. Ballester, C. Winstein, and N. Schweighofer, "Virtuous and vicious cycles of arm use and function post-stroke," Front. Neurol., vol. 13, no. March, 2022, doi: 10.3389/fneur.2022.804211.

[5] L. Mayrhuber et al., Encouraging arm use in stroke survivors: the impact of smart reminders during a home-based intervention. 2024. doi: 10.21203/rs.3.rs-5002284/v1.

[6] L. Mayrhuber et al., "Movement reminders to encourage arm use during daily life in stroke patients," in 2023 International Conference on Rehabilitation Robotics (ICORR), 2023, pp. 1–6. doi: 10.1109/ICORR58425.2023.10304727.

[7] D. Schwerz de Lucena, J. B. Rowe, S. Okita, V. Chan, S. C. Cramer, and D. J. Reinkensmeyer, "Providing real-time wearable feedback to increase hand use after stroke: a randomized, controlled trial," Sensors, vol. 22, no. 18, pp. 1–17, 2022, doi: 10.3390/s22186938.

[8] M. Demers et al., "Understanding stroke survivors' preferences regarding wearable sensor feedback on functional movement: a mixed-methods study," J. Neuroeng. Rehabil., vol. 20, no. 1, p. 146, 2023, doi: 10.1186/s12984-023-01271-z.

[9] J. P. Held, B. Klaassen, B.-J. F. van Beijnum, A. R. Luft, and P. H. Veltink, “Usability Evaluation of a VibroTactile Feedback System in Stroke Subjects,” Front Bioeng Biotechnol, vol. 4, p. 98, 2016, doi: 10.3389/fbioe.2016.00098.

[10] S. F. M. Toh et al., “Usability of a wearable device for home-based upper limb telerehabilitation in persons with stroke: a mixed-methods study,” Digit. Heal., vol. 9, p. 20552076231153736, Jan. 2023, doi: 10.1177/20552076231153737.

[11] Q. Wang, P. Markopoulos, B. Yu, W. Chen, and A. Timmermans, "Interactive wearable systems for upper body rehabilitation: a systematic review," J. Neuroeng. Rehabil., vol. 14, no. 1, 2017, doi: 10.1186/s12984-017-0229-y.

[12] A. J. Langerak et al., "Requirements for home-based upper extremity rehabilitation using wearable motion sensors for stroke patients: a user-centred approach," Disabil. Rehabil. Assist. Technol., vol. 0, no. 0, pp. 1–13, 2023, doi: 10.1080/17483107.2023.2183993.

[13] N. E. J. Signal et al., "Haptic nudging using a wearable device to promote upper limb activity during stroke rehabilitation: exploring diurnal variation, repetition, and duration of effect," Behav. Sci. (Basel)., vol. 8, no. 12, p. e17036, 2023, doi: 10.3390/bs13120995.

[14] V. Braun and V. Clarke, "Using thematic analysis in psychology," Qual. Res. Psychol., vol. 3, no. 2, pp. 77–101, Jan. 2006, doi: 10.1191/1478088706qp063oa.

[15] K. Proudfoot, "Inductive/Deductive hybrid thematic analysis in mixed methods research," J. Mix. Methods Res., vol. 17, no. 3, pp. 308–326, Sep. 2022, doi: 10.1177/15586898221126816.

[16] R. Rampin and V. Rampin, "Taguette: open-source qualitative data analysis," J. Open Source Softw., vol. 6, no. 68, p. 3522, 2021, doi: 10.21105/joss.03522.

[17] A. Triantafyllidis et al., "Smartwatch interventions in healthcare: a systematic review of the literature," Int. J. Med. Inform., vol. 190, p. 105560, 2024, doi: 10.1016/j.ijmedinf.2024.105560.

[18] A. Mahmood, P. Nayak, G. Kok, C. K. English, N. Manikandan, and J. M. Solomon, "Factors influencing adherence to home-based exercises among community-dwelling stroke survivors in India: a qualitative study," Eur. J. Physiother., vol. 23, pp. 48–54, 2019, doi: 10.1080/21679169.2019.1635641

[19] J. Carpentier and G. A. Mageau, "When change-oriented feedback enhances motivation, well-being and performance: a look at autonomy-supportive feedback in sport," Psychol. Sport Exerc., vol. 14, no. 3, pp. 423–435, 2013, doi: 10.1016/j.psychsport.2013.01.003.

[20] Y. Arbel, A. Murphy, and E. Donchin, "On the utility of positive and negative feedback in a paired-associate learning task," J. Cogn. Neurosci., vol. 26, no. 7, pp. 1445–1453, Jul. 2014, doi: 10.1162/jocn_a_00617.

[21] Y. Wei, P. Zheng, H. Deng, X. Wang, X. Li, and H. Fu, "Design features for improving mobile health intervention user engagement: systematic review and thematic analysis.," J. Med. Internet Res., vol. 22, no. 12, p. e21687, Dec. 2020, doi: 10.2196/21687.

[22] A. Blair-Early and M. Zender, "User interface design principles for interaction design," Des. Issues, vol. 24, no. 3, pp. 85–107, Nov. 2008, doi: 10.1162/desi.2008.24.3.85

[23] N. F. Horgan, M. O'regan, C. J. Cunningham, and A. M. Finn, "Recovery after stroke: a 1-year profile," Disabil. Rehabil., vol. 31, no. 10, pp. 831–839, Jan. 2009, doi: 10.1080/09638280802355072.

[24] R. H. Da-Silva et al., "Prompting arm activity after stroke: a clinical proof of concept study of wrist-worn accelerometers with a vibrating alert function," J. Rehabil. Assist. Technol. Eng., vol. 5, p. 205566831876152, 2018, doi: 10.1177/2055668318761524.

[25] P. Maceira-Elvira, T. Popa, A.-C. Schmid, and F. C. Hummel, "Wearable technology in stroke rehabilitation: towards improved diagnosis and treatment of upper-limb motor impairment," J. Neuroeng. Rehabil., vol. 16, no. 1, p. 142, 2019, doi: 10.1186/s12984-019-0612-y.

Effects of Exoskeletons on Error between Marker and Markerless Motion Capture in Children with Crouch Gait: A Pilot Study

Noah Rubin[1], Jordan Dembsky[1], Diane L. Damiano[1], and Thomas C. Bulea[1]

Abstract— **This study evaluated if a lower-extremity exoskeleton affects error between marker-based (M^+) and markerless (M^-) motion capture in children with crouch gait. Two participants (P1: female, P2: male, ages 6 and 11 years old, cerebral palsy and spina bifida, both with assistive devices) walked with (Exo) and without (NoExo) an exoskeleton spanning the knee and ankle. Mean absolute difference (MAD) between M^+ and M^- of gait cycle normalized hip, knee, and ankle angles were analyzed. Key outcomes of an ongoing clinical trial including measures of sagittal knee angle and gait speed were also compared. M^- correlated with M^+ kinematics, but MAD ranged 1.57-17.0 deg. Except for sagittal (of P1) and frontal (of P2) hip angles, the Exo increased MAD (range 0.74-8.7 deg). M^- underestimated knee flexion at initial ground contact, peak knee extension in stance, and peak knee extension in swing. No significant difference in MAD (Exo vs NoExo) was observed except for total joint excursion which had distinct trends for P1 and P2. For peak knee extension, a primary endpoint of crouch gait severity, the Exo increased MAD beyond minimum clinically meaningful differences (5 deg). Gait speed was consistent, with MAD <0.03 m/s for all observations (NoExo vs Exo p=0.22). While M^- has potential to ease gait assessment, early results warrant caution for use with wearable devices, highlighting the need for kinematic estimation algorithms to accommodate diverse end users in clinical and research settings.**

Keywords – **Motion capture, markerless, exoskeletons, gait assessment.**

I. INTRODUCTION

Many techniques exist in the rehabilitation field to study biomechanics of human movement, and among them, measuring kinematic and spatiotemporal behavior is a vital, commonly utilized method. By using 3D gait assessment, treatment decisions may improve in accuracy, and with this, targeted interventions may be better informed to further improve patient outcomes [1].

The gold standard method for assessing kinematics in research and clinical settings is marker-based motion capture (M^+), where reflective markers placed on joints and limb segments permit fitting of quantitative models of the body and computation of joint angles in anatomical coordinate frames. While M^+ provides many benefits, it also brings its own set of challenges. Significant time with participants during gait studies is dedicated to precisely and securely placing markers. This burden is particularly amplified when working with individuals who use assistive or wearable robotic devices, as each new physical condition studied (such as walking barefoot with different shoes or orthoses or robotic devices) requires reconfiguration and recalibration. On top of this, marker setups are often cumbersome for individuals to wear and traverse in, especially for young participants. Accuracy can also be affected by marker movement, bumping into objects or other body parts, falling off the body, or being blocked from view, especially in children and those with pathology or devices, rendering some trials unusable. For infants and toddlers, markers may also pose a choking hazard.

To address these issues, many different markerless motion capture (M^∞) systems have been developed over the past several decades as a potential alternative. While open-source models that estimate pose based on video data have gained significant research popularity [2], [3], commercial development of proprietary datasets and algorithms using expert biomechanists for labeling based on multi-camera video data has occurred to streamline clinical gait analysis. These algorithms have shown promise in individuals without neurological or biomechanical impairments [4], [5]. As noted in a recent scoping review, though, few comparisons between M^+ and M^∞ in patient populations exist [6]. Indeed, a recent study showed mixed tracking results depending on which joint angles were observed for children with cerebral palsy [7]. As development of M^∞ for clinical gait assessment progresses, it is crucial to not only account for the impact of patient populations on M^∞ but also to evaluate how wearable devices may further influence these measures. One study examined pose tracking accuracy of M^∞ with a robotic gait trainer in typically developing children on a treadmill [8]. However, to our knowledge, no study has determined how exoskeletons affect M^∞ data during overground walking. Hence, this pilot study sought to determine if walking with a lower-extremity exoskeleton affects the ability of M^∞ to quantify gait biomechanics in children with crouch gait compared to M^+ as the gold standard.

II. METHODS

A. Participant Recruitment

Two participants (P1 female, P2 male, age 6 and 11 years, height 110 and 146 cm, mass 17.9 and 38.9 kg, using a walker and crutches, respectively) diagnosed with crouch gait from cerebral palsy and spina bifida (mid lumbar myelomeningocele and shunt) were recruited for this study. Both participants and their respective parents provided written informed consent prior to conducting study procedures. Data were collected within a larger ongoing clinical trial evaluating effects of training with an exoskeleton outside

This work was supported the by Intramural Research Program at the National Institutes of Health Clinical Center (NIH CC, protocol #001180).

[1]Rehabilitation Medicine Department, NIH CC, Bethesda, Maryland.

the clinic [9]. Data from P1 was included from two different visits three months apart. Data from P2 was from a single visit. Both participants were novice exoskeleton users before the study who acclimated to this device for three days prior to the first assessment. P1 then underwent 12-weeks of training with the device at home prior to the second assessment. Because all data analyzed involved error in kinematics within each trial, data from all visits were combined for later analysis.

B. Data Collection

The marker-based system used 12 infrared cameras (Vicon Vantage, Vicon Motion Systems, United Kingdom), and the markerless system (Theia3D, Theia Markerless, ON, Canada) used eight digital cameras (Sony RX 0II), all placed within approximately three meters of the workspace. Prior to data recording, M^{∞} and M^{+} were calibrated with an extrinsic chessboard and wand, respectively. For M^{+}, a custom 36 reflective marker set was used on the lower-extremities [10]. For the visit with P2, M^{∞} recorded at 60 Hz and M^{+} recorded at 100 Hz. For the two visits with P1, both systems recorded at 120 Hz.

C. Study Procedures

Steady-state walking without (NoExo) and with (Exo) an exoskeleton was recorded for each participant (Fig. 1A-B). In each walking trial, participants traversed an approximately 5-meter path multiple times until they completed at least ten strides for each condition. For the sake of time in setup and ordering of other assessments in the visit, participants always conducted the NoExo conditions first and the Exo conditions thereafter. NoExo conditions included walking barefoot (BF) or with a custom ankle-foot-orthosis (AFO) and shoes used in their daily life. Thereafter, the Exo conditions (always with shoes) were collected. For all conditions, P1 used a walker and P2 used crutches.

The exoskeleton (Fig. 1C-D) is based on a knee-ankle-foot orthosis (KAFO) architecture and therefore attaches to

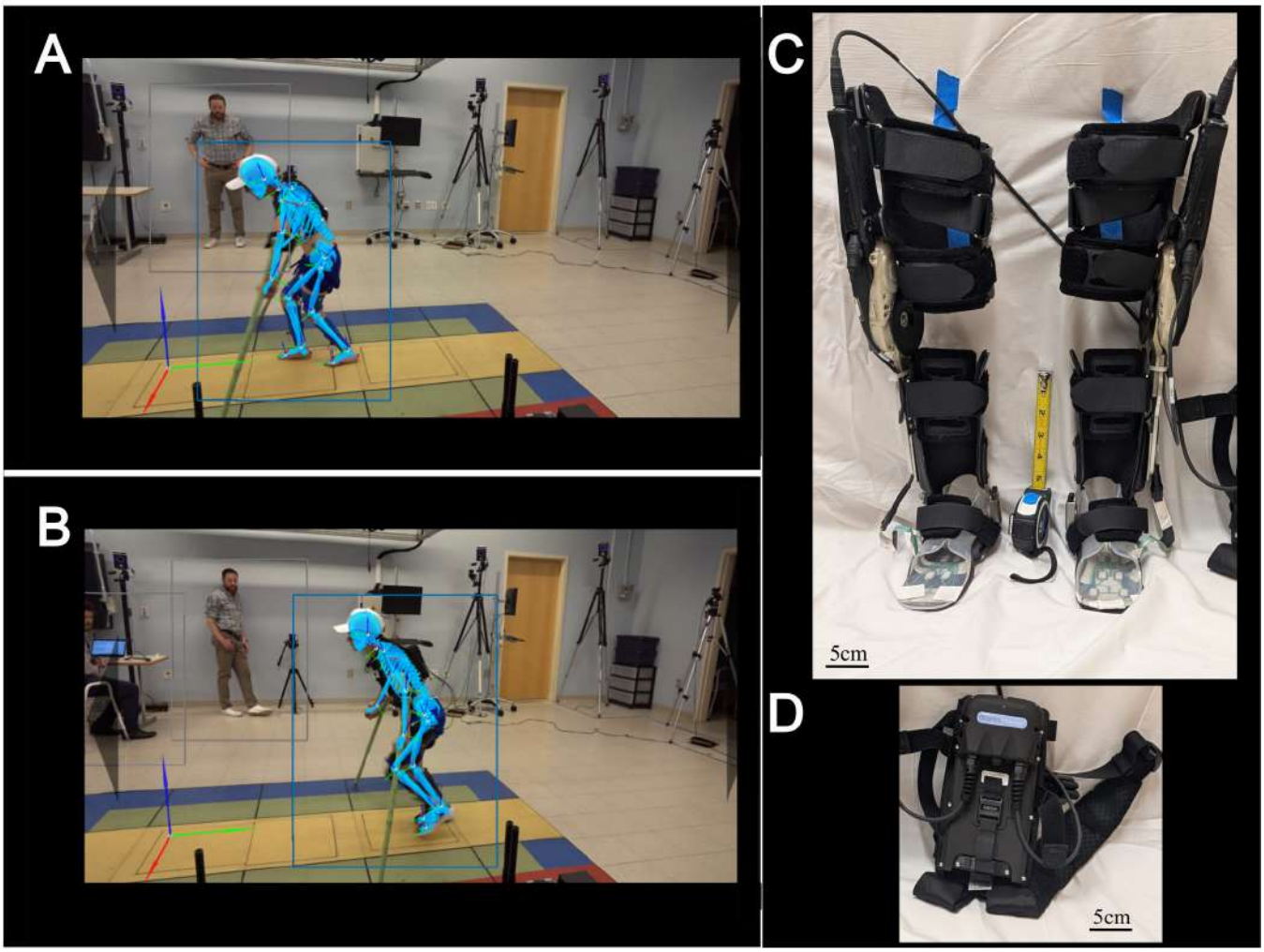


Fig. 1. Experimental setup. Images from one of eight cameras used for the markerless system (Theia3D) with the markerless model overlay are shown for the A) NoExo and B) Exo conditions. The C) bilateral exoskeleton consists of a single actuated degree of freedom at the knee joint in the sagittal plane that applies either flexion or extension torque (Agilik, Bionic Power Inc., Vancouver, Canada). The actuator is connected to a custom-fabricated orthosis (Ultraflex Systems Inc., Pottstown, PA) which has a passive ankle joint with adjustable stiffness independently in the plantar- and dorsi-flexion directions. The system is powered by a D) portable battary in a holster worn as a small backpack. Further device design details can be found in [9].

the thigh, shank and foot segments. The device is worn bilaterally, with a single actuated degree of freedom at the knee joint in the sagittal plane that applies either flexion or extension torque (Agilik, Bionic Power Inc., Vancouver, Canada). The actuator is connected to a custom-fabricated orthosis (Ultraflex Systems Inc., Pottstown, PA) which has a passive ankle joint with adjustable stiffness independently in the plantar- and dorsi-flexion directions. The exoskeleton controller implements a finite-state machine (5 states for early, mid, and late stance and early and late swing) with constant torque applied during each state. State estimation is based on knee angular velocity of an embedded encoder and a force sensitive resistor in the footbed. At least one of three control modes were used in each visit: Zero, Assist, and Interleaved. Zero mode applies a small amount of torque to compensate for inertia such that the device is transparent to the user. Assist mode provides assistive extension torque in both stance and late swing. Interleaved mode applies assistive and resistive torque in stance and late swing, respectively. Because participants must overcome resistance to complete steps, it is employed as a potential gait training tool to strengthen knee extensors and thereby combat knee extension deficiency [11]. Further device design details can be found in [9].

Between conditions, no changes were required for implementing M^{∞}. For M^{+}, markers that would be affected by shoes, an AFO, or the exoskeleton were removed and replaced as needed. Additionally, a 5-sec quiet standing static trial was conducted for each condition to allow for model calibration in post-processing.

D. Data Processing

Raw markerless pose data were processed in Theia3D. Details of the software are proprietary, but the overall architecture consists of a deep convolutional neural network that tracks human movement in 2D video frames to reconstruct 3D motion. The model was trained with over 500,000 images of humans in everyday settings, with at least two experts who labeled each image. Users input synchronized video data, and the model detects 51 anatomical features that are then used to estimate full-body motion through inverse kinematics. The system models the lower body with six degrees of freedom at the pelvis and three at the hip, knee, and ankle [12]. The default filter on pose data of M^{∞} was used (Generalized cross-validation with splines [13], low pass, 20 Hz cutoff). For M^{+}, gap filling of marker trajectories was processed in Vicon Nexus. Exported pose and marker data from each system (.c3d files) were then processed in Visual3D (C-Motion, Kingston, ON, Canada). Raw marker trajectories (prior to angle calculation) were lowpass filtered (4^{th} order Butterworth, 6 Hz cutoff), and joint angles for both systems were exported for analysis in MATLAB.

For each trial, the average delay between three instances of a common visual cue (phone camera flash in the field of view) was used to align the time of recorded frames between systems. Frames of gait events (initial and terminal floor contact of each limb) manually labeled based on digital video review were used to normalize data to each gait cycle with cubic spline interpolation. Individual strides were manually inspected and removed from further analysis if deemed atypical for the given participant or not in steady state. While the exoskeleton actuator applies torque in the sagittal plane, the brace constrains frontal plane motion, and wearing the device inherently changes visual features captured by markerless motion capture used to estimate pose, and by extension kinematics. Hence, mean absolute difference (MAD) between average gait cycle normalized data for each system in all three axes of rotation (sagittal, frontal, and transverse) were computed to evaluate overall performance. Because our current interventional study is evaluating the effect of this exoskeleton on crouch gait [9], we also computed four clinical knee joint kinematic measures (computed at each stride): 1) knee angle at initial ground contact (θ_{init}), 2) peak knee extension during stance (θ_{PKE}), 3) peak knee flexion during swing (θ_{PKF}), and 4) the absolute difference between peak extension and flexion, or total joint excursion (θ_{TJE}). Additionally, gait speed was computed as the mean velocity for pelvis center of gravity in the global Y-direction (along the walkway). Two-sample t-tests (or Mann-Whitney U tests if data not normally distributed, Kolmogorov-Smirnov test) on the absolute difference between M^{+} and M^{∞} in the NoExo and Exo conditions were conducted to determine if wearing the exoskeleton affects accuracy of M^{∞} (α=0.05).

III. RESULTS

The number of strides retained for analysis in each condition can be found in Table I. Both participants walked barefoot and with an AFO. P1 used the Zero and Interleaved modes, while P2 used the Assist and Interleaved modes, with torque magnitudes (normalized by participant body mass) ranging from 0 to 0.085 Nm/kg. Collectively, 116 and 62 strides were retained across both participants for analysis between the NoExo and Exo conditions, respectively.

TABLE I
NUMBER OF STRIDES ANALYZED BY CONDITION

	NoExo		**Exo**		
	BF	**AFO**	**Zero**	**Assist**	**Interleaved**
P1	54	23	8	0	26
P2	16	23	0	14	14

Figure 2 displays gait cycle normalized data from for the sagittal (X), frontal (Y), and transverse (Z) joint angles of the hip, knee, and ankle joints for P1 and P2 in the NoExo and Exo conditions. Across all conditions, kinematic profiles were reasonably correlated, but varied outcomes across the gait cycle were observed, with some angles exhibiting very close tracking while others exhibited large MAD. The sagittal hip angle MAD between M^{+} and M^{∞} for P1 (Fig. 2A) was higher in the NoExo (mean 10.7, range 6.9 to 14 deg) compared to Exo (mean 8.9, range 3.3-13 deg) condition. For P2, while M^{+} and M^{∞} performed similarly in the NoExo condition (mean 1.5, range 1.4-4.2 deg), the Exo amplified

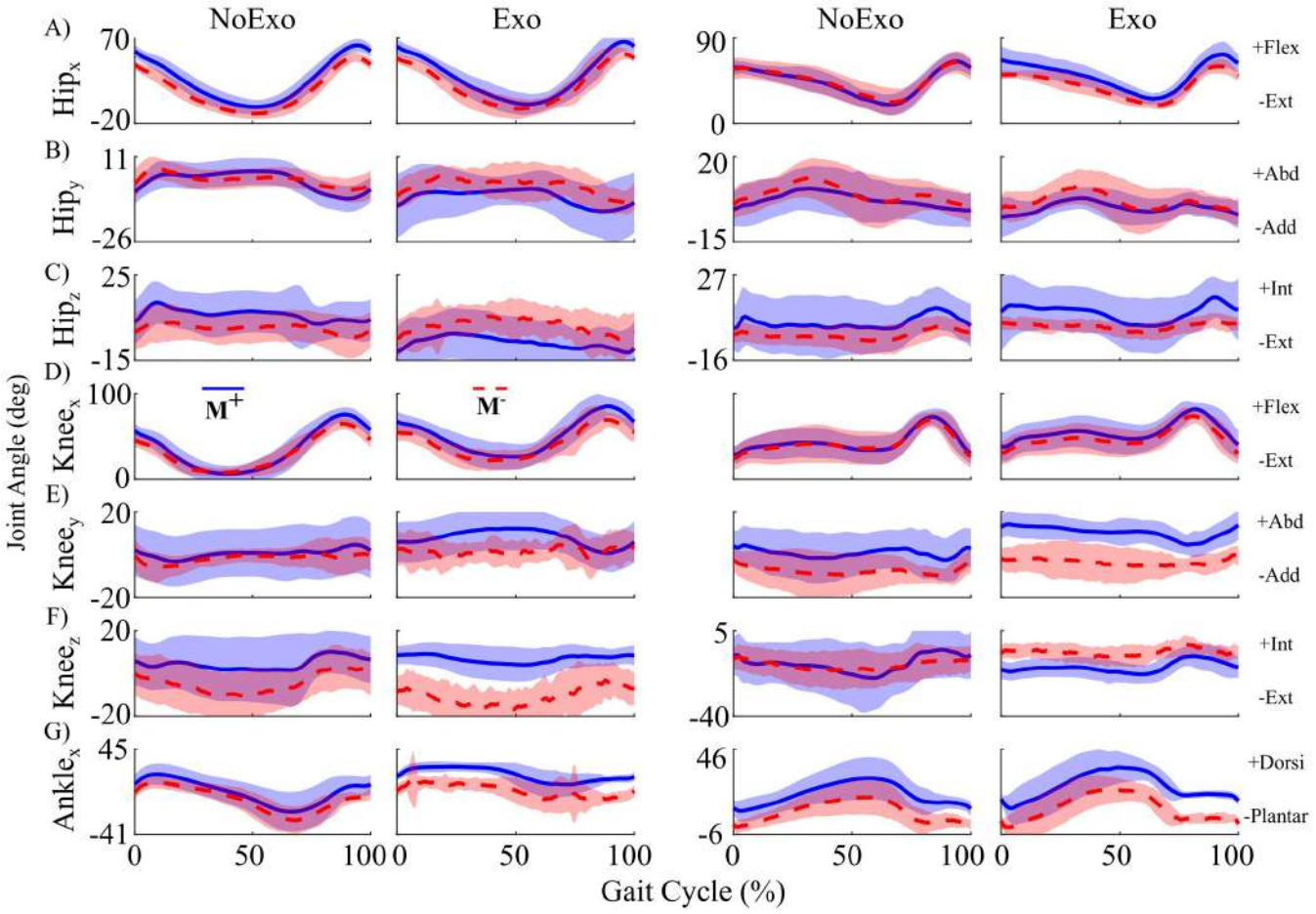


Fig. 2. Gait cycle normalized (0% and 100% initial contact) kinematic data for the sagittal (X), frontal (Y), and transverse (Z) joint angles of the hip, knee, and ankle joints are shown in each row. The first two and last two columns indicate data of the NoExo and Exo conditions from P1 and P2, respectively. Within each panel, the mean of the marker-based (M^+, blue) and markerless (M^-, dashed red) systems across all strides from both limbs are shown, with shades of ±1 standard deviation (SD). Sign conventions for each joint angle are indicated on the right of each row. Y-axis scales are maintained for each joint angle and subject to visualize within-subject differences between M^+ vs M^- and NoExo vs Exo.

MAD (mean 10.2, range 6.2-15 deg). For the sagittal ankle angle (Fig. 2G), M^∞ underestimated ankle dorsiflexion for both participants, where the Exo increased MAD for P1 substantially (NoExo 7.6 to Exo 16 deg) and to a smaller extent for P2 (10.6 to 13 deg). Whereas the Exo resulted in varied effects between participants at the hip and ankle, M^∞ estimated less knee flexion than M^+ with the Exo for both participants (Fig. 2D), and MAD across the gait cycle increased for both participants (P1: 4.3 to 9.5 deg, P2: 1.5 to 7 deg). This amplification was not limited to the sagittal plane of the knee joint. In the transverse plane (Fig. 2F), MAD across the gait cycle nearly doubled from NoExo to Exo for P1 (9.0 to 17.7 deg) and considerably increased for P2 (0.6 to 7.9 deg). Overall, except for the sagittal hip angle of P1 (1.7 deg decrease) and frontal hip angle of P2 (<0.1 deg increase), walking with the exoskeleton increased MAD between M^∞ and M^+ (range 0.74-8.7 deg).

A. Knee Kinematic Outcome Measures

After extracting normalized gait kinematics, clinical outcomes of our ongoing interventional study [9] from the sagittal knee and gait speed were derived for further analysis. For knee angle at initial contact (θ_{init}) in both participants and conditions, M^+ tended to estimate less extension than M^∞ (Fig. 3A). While no significant difference was observed in θ_{init} MAD (p=0.11, Fig. 3E) for both participants, MAD between M^+ and M^∞ slightly increased when wearing the Exo (11.1±4.9 deg) compared to NoExo (10.3±6.4 deg). A similar trend was observed for peak knee extension (θ_{PKE}) during stance phase (Fig. 3B). NoExo exhibited high variation centered near zero for P1 (0.99±7.7 deg) but walking with the Exo yielded overestimation of extension with M^∞ (-7.6±6.1 deg). For P2, a smaller shift in the same direction was seen from NoExo (-3.2±8.7 deg) to Exo (-7.3±5.7 deg). No significant difference was observed (p=0.07), but again θ_{PKE} MAD increased from NoExo (7.0±4.4 deg) to Exo (8.3±4.6 deg, Fig. 3F).

For peak knee flexion during swing (θ_{PKF}), in all cases, M^+ still tended to estimate greater flexion than M^∞. However, wearing the Exo (9.5±5.3 deg) slightly decreased MAD of θ_{PKF} compared to NoExo (10.4±6.0 deg), with no significant difference observed (p=0.29, Fig. 3G). For total

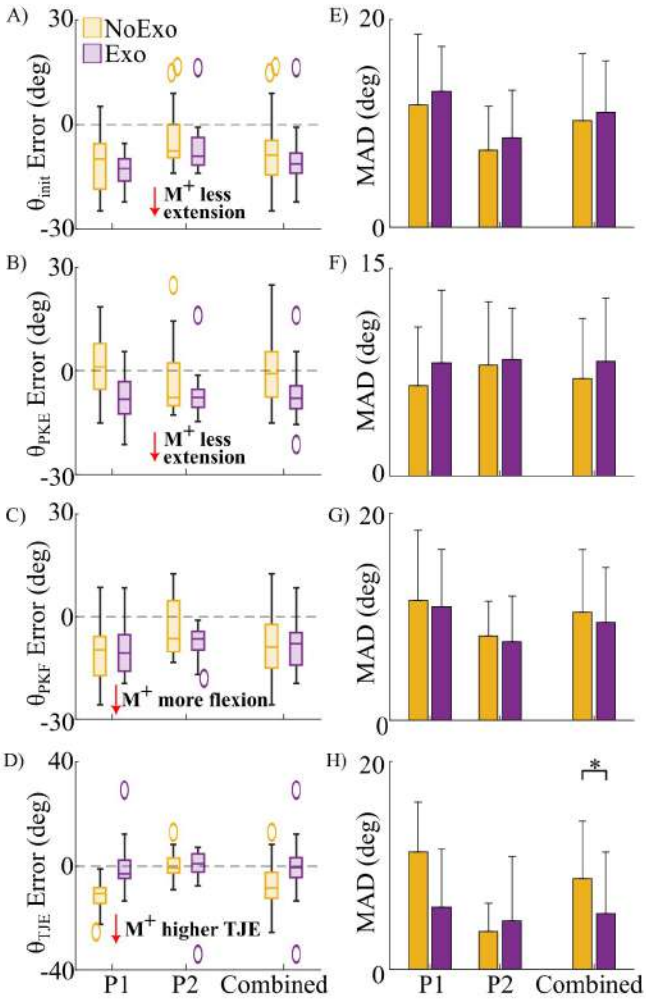


Fig. 3. Errors between motion capture systems for clinical kinematic outcome measures of the knee. Left and column right columns display raw error (M^- minus M^+) and mean absolute difference (MAD) ±1 SD, respectively. Each row corresponds to A) θ_{init}, angle at initial contact, B) θ_{PKE}, peak knee extension in stance, C) θ_{PKF}, peak knee flexion in swing, and D) θ_{TJE}, total joint excursion in the gait cycle. Data shown are from P1, P2, and combined in the NoExo (yellow) and Exo (purple) conditions. Significant differences between Exo and NoExo conditions are indicated with an asterisk ($p< 10^{-4}$).

joint excursion (θ_{TJE}), distinct trends were apparent within participants. M^+ estimated higher excursion in NoExo for P1 (Fig. 3D), but when wearing the Exo, a marked reduction in θ_{TJE} MAD occurred (Fig. 3H). P2, though, displayed similar distributions for both NoExo and Exo centered near zero. Combining participants, wearing the Exo significantly decreased θ_{TJE} MAD ($p < 10^{\infty 4}$).

B. Gait Speed

45 passes were analyzed to compute gait speed in each pass (26 NoExo, and 19 Exo). The MAD observed in gait speed between M^+ and M^∞ was remarkably low (Fig. 4), ranging less than 0.03 m/s across all passes. With this consistency, both systems yielded averages and standard deviations for each participant and condition with differences less than 0.01 m/s. P1 exhibited faster gait speed in the

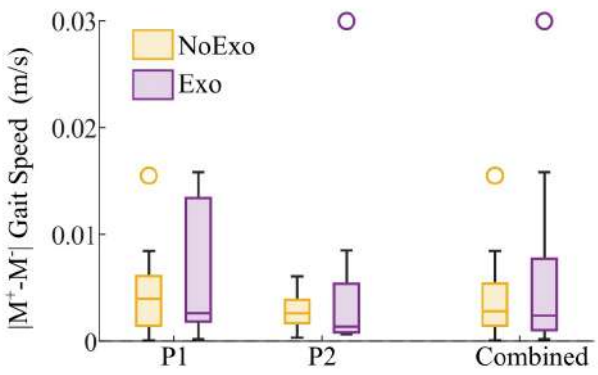


Fig. 4. Absolute difference between M^+ and M^- in gait speed for NoExo (yellow) and Exo (purple) conditions.

NoExo (0.77±0.29 m/s) than the Exo condition (0.57±0.29 m/s), while P2 maintained similar more consistent gait speed between conditions (0.58±0.12 and 0.57±0.07 m/s in NoExo and Exo, respectively). For both participants, no significant difference was observed in absolute difference of gait speed between NoExo and Exo conditions (p=0.74).

IV. DISCUSSION

To our knowledge, this pilot study is the first to evaluate outcomes between marker-based and markerless motion capture with an exoskeleton in overground walking. Given the clinical importance of accurate kinematic measures in gait assessment, we evaluated if wearing a lower-extremity exoskeleton spanning the ankle and knee joints (single knee actuator) affects error between markerless and marker-based motion capture in two children with crouch gait in normalized kinematic profiles, four sagittal knee kinematic outcomes measures, and gait speed.

Comparing normalized kinematic profiles (Fig. 2), M^∞ tended to follow M^+, but mean absolute difference across the gait cycle was highly variable between participants and all joint angles with and without the device (range 1.57-17 deg). In some cases, outcomes aligned with a prior study for children with cerebral palsy, such as consistent underestimation of ankle dorsiflexion with M^∞ [7]. In other cases, such as sagittal knee angle, we observed larger errors. That study recruited mostly individuals who did not require walking aids while both of our participants used an assistive aid (notably, these aids were the same across NoExo and Exo conditions), potentially contributing to this discrepancy. Across joint angles and participants, in most cases, MAD across the gait cycle increased when wearing an exoskeleton. The pose estimation model is a black box proprietary algorithm that to our knowledge has not been trained on data of the target population and has most likely not incorporated wearable devices, leading to possible model underfitting for our application. Incorporating a more diverse training set or implementing adjustable parameters to accommodate wearable device use may reduce potential model bias and improve results.

A primary purpose of quantitative gait analysis is to provide evidence for (or against) the effectiveness of emerging interventions. In this study, for both conditions and participants, M^{∞} consistently measured the knee at a more extended position than M^{+} for knee angle at initial contact, peak knee extension in stance, and peak knee flexion in swing, with MAD increasing when wearing the exoskeleton for outcomes in stance but decreasing for peak flexion in swing. The increased MAD in peak knee extension during stance (averaging 8.3 deg with the Exo) brings critical clinical implications, as this endpoint is frequently used as the primary measure for severity of crouch gait [9], with changes of 5 deg from an intervention often considered clinically meaningful. Thus, our results suggest markerless motion capture does not yet have sufficient accuracy to assess the effect of exoskeletons on crouch gait.

Considering other clinical measures in this study, while total joint excursion significantly reduced MAD with the Exo, distinct trends were observed between participants and differential effects were observed at peak flexion and extension in P1, requiring further investigation to shed light on this outcome. Importantly, the exoskeleton had minimal effect on gait speed, a secondary endpoint in our clinical trial [9]. This is likely due to a larger sampling (data from an entire pass instead of within single strides) which likely reduced variation. Additionally, the exoskeleton in this study does not span the pelvis, giving promise to high reliability in this outcome as reported in prior work [12].

There are several limitations to this study. Different sample rates for M^{+} and M^{∞} were used with P2. It is possible the lower frame rate of M^{∞} contributed to error observed, but given error also consistently increased from NoExo to Exo in P1, this is not likely to be driving observed effects. Movement of markers between conditions may have amplified error. Only two participants with variable physical configurations and device controllers were used. An imbalance in number of strides analyzed was present between NoExo and Exo because data were collected within a larger clinical trial [9]. Future studies with more participants, exoskeleton conditions, and balanced datasets are warranted.

In the long term, the prospect of markerless motion capture offers immense opportunity to ease the burden of clinical gait assessment, especially in children. Our preliminary results suggest strong caution for kinematic analysis with M^{∞} when wearing wearable robotic devices during overground walking. However, spatiotemporal parameters like gait speed may be highly reliable. The markerless system used here (Theia) utilizes supervised machine learning for pose estimation [4]; our results indicate the model's vital need to incorporate labeled gait data from clinical populations and walking with exoskeleton devices directly into the training datasets in order for the full capability of these markerless systems to be realized.

ACKNOWLEDGMENTS

The authors would like to thank Christopher Stanley and Kari Oppedal for their assistance in data processing.

REFERENCES

[1] T. A. Wren, C. A. Tucker, S. A. Rethlefsen, G. E. Gorton III, and S. Õunpuu, "Clinical efficacy of instrumented gait analysis: Systematic review 2020 update," *Gait & posture*, vol. 80, pp. 274–279, 2020.

[2] Z. Cao, T. Simon, S.-E. Wei, and Y. Sheikh, "Realtime multi-person 2d pose estimation using part affinity fields," in *Proceedings of the IEEE conference on computer vision and pattern recognition*, 2017, pp. 7291–7299.

[3] T. Nath, A. Mathis, A. C. Chen, A. Patel, M. Bethge, and M. W. Mathis, "Using deeplabcut for 3d markerless pose estimation across species and behaviors," *Nature protocols*, vol. 14, no. 7, pp. 2152–2176, 2019.

[4] R. M. Kanko, E. K. Laende, E. M. Davis, W. S. Selbie, and K. J. Deluzio, "Concurrent assessment of gait kinematics using marker-based and markerless motion capture," *Journal of biomechanics*, vol. 127, p. 110665, 2021.

[5] R. M. Kanko, E. Laende, W. S. Selbie, and K. J. Deluzio, "Inter-session repeatability of markerless motion capture gait kinematics," *Journal of Biomechanics*, vol. 121, p. 110422, 2021.

[6] M. Pardell, N. D. Dolgoy, S. Bernard, K. Bayless, R. Hirsche, L. Dennett, and P. Tandon, "Movement outcomes acquired via markerless motion capture systems compared with marker-based systems for adult patient populations: A scoping review," *Biomechanics*, vol. 4, no. 4, pp. 618–632, 2024.

[7] K. Wishaupt, W. Schallig, M. H. van Dorst, A. I. Buizer, and M. M. van der Krogt, "The applicability of markerless motion capture for clinical gait analysis in children with cerebral palsy," *Scientific reports*, vol. 14, no. 1, p. 11910, 2024.

[8] F. van Dellen, N. Hesse, and R. Labruyère, "Markerless motion tracking to quantify behavioral changes during robot-assisted gait training: A validation study," *Frontiers in Robotics and AI*, vol. 10, p. 1155542, 2023.

[9] T. M. Devine, K. E. Alter, D. L. Damiano, and T. C. Bulea, "A randomized cross-over study protocol to evaluate long-term gait training with a pediatric robotic exoskeleton outside the clinical setting in children with movement disorders," *PloS one*, vol. 19, no. 7, p. e0304087, 2024.

[10] Z. F. Lerner, D. L. Damiano, and T. C. Bulea, "A lower-extremity exoskeleton improves knee extension in children with crouch gait from cerebral palsy," *Science translational medicine*, vol. 9, no. 404, p. eaam9145, 2017.

[11] T. C. Bulea, V. Molazadeh, M. Thurston, and D. L. Damiano, "Interleaved assistance and resistance for exoskeleton mediated gait training: Validation, feasibility and effects," in *2022 9th IEEE RAS/EMBS International Conference for Biomedical Robotics and Biomechatronics (BioRob)*. IEEE, 2022, pp. 1–8.

[12] R. M. Kanko, E. K. Laende, G. Strutzenberger, M. Brown, W. S. Selbie, V. DePaul, S. H. Scott, and K. J. Deluzio, "Assessment of spatiotemporal gait parameters using a deep learning algorithm-based markerless motion capture system," *Journal of Biomechanics*, vol. 122, p. 110414, 2021.

[13] P. Craven and G. Wahba, "Smoothing noisy data with spline functions: estimating the correct degree of smoothing by the method of generalized cross-validation," *Numerische mathematik*, vol. 31, no. 4, pp. 377–403, 1978.

Design and Implementation of an Adaptive Robotic Head Support for Children with Low Head Control

Bradford Kerst
Mechanical Engineering
The University of Tulsa
Tulsa, Oklahoma, USA

Bryce Day
Mechanical Engineering
The University of Tulsa
Tulsa, Oklahoma, USA

Joshua Schultz
Mechanical Engineering
The University of Tulsa
Tulsa, Oklahoma, USA

***Abstract*—The recent growth of rehabilitation robots offers new opportunities to improve care for patients with low head control. Traditional cervical spine therapy equipment often restricts neck mobility, inadvertently leading to muscle weakness due to inactivity. This study introduces a novel 1-degree-of-freedom (DoF) Adaptive Robotic Head Support designed to aid recovery during light activity and strength training in head-neck therapy. This study measured the axial forces that simulate the physical human-robot interaction (66.1 ±3.91 N) exerted by the head support in 20 tests as the robot lifts a 2 kg medicine ball until the motor stalls (4.06 ±0.98 s). The Head Support allows full cervical rotation in the transverse plane while providing adjustable support for flexion and extension movements. This study presents a novel head-neck rehabilitation system and tests its ability to support the weight of a six-year-old's head and measure human-robot interaction forces during simulated head-lifting tasks. Our approach aims to address critical gaps in pediatric head neck rehabilitation robotics by reducing the physical burden on clinicians and enhancing rehabilitation capabilities.**

***Index Terms*—Cervical spine rehabilitation, robotic head support, head and neck, neuromuscular disorders, physical therapy**

I. Introduction

People with low head control, such as those with Cerebral Palsy (CP) at GMFCS Level V (Gross Motor Function Classification System), struggle to support the weight of their head for extended periods. This limits their opportunities to engage socially and perform activities of daily living (ADLs) [1]–[3]. Conditions such as low head control, dropped head syndrome (DHS), or forward head posture can be caused by weak neck extensor muscles or hypotonia due to neuromuscular disorders, spinal cord injuries, or other neurological and muscular causes [4], [5]. People who experience low head control spend most of their day in a reclined position, with limited rehabilitation options beyond surgery [6], [7].

Children with developmental delays who experience low head control have been a significant focus in head-neck rehabilitation [2]. Studies on pediatric head-neck assistive technology demonstrate improvements in quality of care during ADLs, including reduced head drops, increased active time, and changes in force measurements using a passive HeadPod head support [8], [9]. New physical therapy approaches were studied in games, trunk control, and individual muscle training that noted improvements in posture, ROM, and gaze [6], [10]. Patient outcome measurements have since become the focus of studies on new head-neck therapy tools, although there is no standard for evaluating head-neck rehabilitation technology. Although these studies are of vital importance to understand the benefits of new technology, there is a gap in research studying the physical interactions between the head and neck and the robotics used in therapy.

Preliminary interviews with pediatric physical and occupational therapists revealed that they use foam blocks or their own bodies to hold patients with low head control upright. Therapists are limited by the number of repetitions and intensity of exercises they can assist patients with before becoming fatigued [11]. Assistive technology plays an important role in reducing the physical demand placed on clinicians, allowing them to increase the intensity and number of repetitions necessary for effective therapy sessions [11], [12].

Cervical collars or similar braces designed to restrict cervical range of motion (CROM) are still used to treat patients with low head control [13]. Recent research has developed new robotic head supports for adults with DHS that uses rigid linkages [14]–[16]. However, these robotic solutions are designed for adults and are unsuitable for children because of differences in size and the force applied to the user's head. Exoskeleton head supports thus far are kinematically constrained; the only exception is the cable-driven platform of Bales and Zhang [17]. Bales and Zhang currently set the desired orientation for both torque control and orientation control using a manual joystick controller. Many users would be unable to use the joystick input without a caregiver due to spastic motion or upper extremity limitations.

This research constructs and programs a 1-DoF Adaptive Robotic Head Support system (Head Support) with assist-as-needed capabilities to augment treatment for children (up to age 6) with low head control. The Head Support is designed with parameters similarly outlined in Huang et al to (a) partially support the weight of a child's head, (b) fully support the weight of a child's head, (c) resist volitional motion away from an upright position, and (d) return the child's head to an upright position if the patient loses control [11]. To achieve (a) and (b), the head support simply needs to be able to sustain 20 N of distraction force at a constant strap length, which would act like the passive HeadPod head support [18]. To resist volitional motion (c), the Head

This research was funded by NSF DARE 1706428, Active Head Support for Children with Hypotonia

Support should be able to actuate with force greater than typical head motions (10-40 N) [9]. Returning the head to an upright position (d) can be demonstrated by raising the full weight of the head from an inferior position to a posterior position. Section II discusses other active head supports and some of the scenarios in which they are used. Section III details the novel mechanical design of the Head Support, including hardware components and sensing used to measure user interactions. Section IV outlines methods for prototype validation experiments to test mechanical functionality and usability prior to human-subject testing. Section V presents key results from lab experiments, while Section VI discusses the key findings, advantages, limitations, and clinical implications of the Head Support compared to other head supports. We present a new device with an operating principle not previously reported in the literature in (1) novel head-neck rehabilitation robot design and (2) physical interactions between rehabilitation robots and the human head-neck.

II. Existing Active Head Support Devices

A review of wearable assistive neck devices outlined the control mechanisms and active ranges of motion (AROM) in flexion, extension, and lateral bending for technology used in head and neck rehabilitation up to July 2023 [19]. Zhang et al. created a powered Robotic Neck Brace for adults with amyotrophic lateral sclerosis assists head motions in in-plane and off-plane angles, showing decreased error during prescribed motions with powered assistance compared to baseline support [16]. The position error measurement is used to guide patients through more ideal movement trajectories, which can help if the user controls motion better with some assistance. An active neck orthosis by Lozano et al examines trajectory tracking and the CROM restriction for a parallel robotic device [20]. The percentage of CROM restriction in this study is a common practice which measures the amount of immobilization from head-neck orthoses due to the constraints that rigid linkages have in cervical braces. A flex sensor measures the craniovertebral angle (CVA) for pneumatic artificial muscles with an augmenting force applied to the occiput and cervical vertebrae [21]. CVA measurements could be used to monitor variation from an upright pose while using varying types of head supports. Among the first cable-driven head supports is the CarNeck, which proposes a 3-DoF kinematic model and tension analysis to support head motions within the typical CROM [22]. Many of these studies have shown kinematic feasibility, patient outcome improvements, or a decrease in muscle activity required to move while using their head supports.

III. Construction of the Head Support

A cable-driven, Adaptive Robotic Head Support (Figure 1) has been designed and constructed to provide variable, programmable support of a 6-year-old child's full head mass (approximately 2 kg) while in a supported sitting position. Additional physical limitations were suggested by some suppliers which were implemented in the prototype design.

A. Design

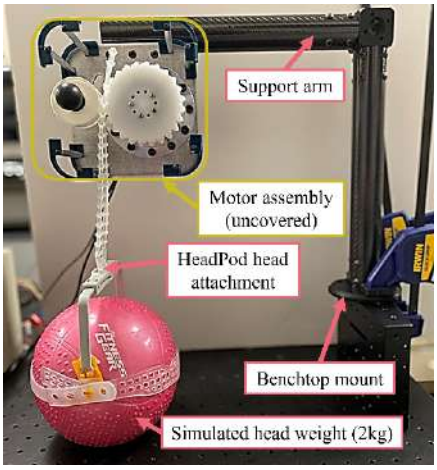
The Head Support utilizes a motor-driven wheel acting through a gear ratio of 100:1 to adjust the amount of tension applied to the user's head. A BLDC motor (Celera ULT-63-A-8-A-H-000) drives the support strap in either direction, with continuous torques (0.082 N-m) and maximum torque (0.245 N-m) that can lift the entire head weight without continuous resistance or overcome momentary resistance at its peak torque. Neck Injury Criteria (N_{ij}), the sum of normalized flexion and extension moment and axial load, is used as a safety measure in vehicle collision testing. The rotor inertia (7.9E-06 kg-m^2) was of particular concern, since an inertia that is too large could cause N_{ij} to exceed a safe value according to NHTSA Standards for vehicle collision safety [23]. Critical intercept tensions (2120 N) and extension moment (27 N-m) were selected from the scaled values to prevent injury in a 3-year-old Hybrid III crash test dummy [23]. Selected critical values are conservative estimates of what would cause injuries in tension, extension moment, or a combination of both.

To ensure that the Head Support moves the drive wheel at a safe speed, a reduction is needed between the motor and drive wheel. The Harmonic Drive (Beverly, MA CSD-14-100-2UH) in the Head Support acts as a compact, back-drivable, 100:1 gearbox with zero backlash. The gear ratio allows the BLDC motor to operate closer to the speed for which it is designed while maintaining continuous support forces up to 205 N with an expected max rpm of 7.5 rpm (3 drive wheel teeth per second). The Harmonic Drive manufacturer describes it as back-drivable, which is a useful feature as the user can temporarily overcome the resistance from the device. The maximum torque of the motor was set accordingly so that the motor torque would not damage the flex spline should the motor malfunction and run at full force. Similarly, the harmonic drive was chosen to minimize size and still output safe speed and sufficient torque to hold the head. A cross-sectional view of the motor assembly is shown in Figure 1c.

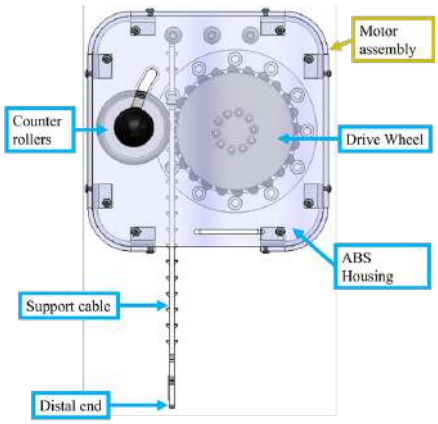
Two deep groove ball bearings resist the radial forces of the motor rotor, supporting the rotation of the motor hub, which connects the rotor to the harmonic drive wave generator. Although the rotor should impose only minimal axial forces, the wave generator does apply axial forces along the motor when accelerating, and the use of deep groove bearings is designed to resist these. The axial force (F_{axial}) applied by the wave generator is defined by Equation 1 provided by Harmonic Drive and can be calculated with the output torque of the harmonic drive (τ_{out}) and the size designation provided by Harmonic Drive ($size$).

$$F_{axial} = 2 * \frac{\tau_{out}}{size * 0.00254} * 0.07 * \tan(20^\circ) + 2.1 \quad (1)$$

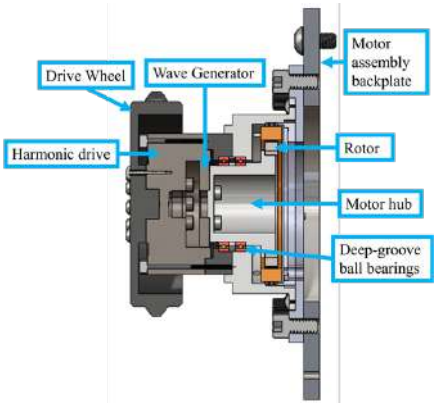
Using the peak motor torque with the 100:1 gear ratio to calculate the max output torque and the size 14 harmonic drive, a max axial force acting on the deep-groove ball bearings would be 37.2 N. Resisting axial and radial forces and moments are important for ensuring that the rotor does



(a) Constructed adaptive robotic head support that can be used in a supported sitting position.



(b) Main components of the motor assembly powering the movement of the support strap.



(c) Cross-sectional view of the motor assembly including a brushless DC Motor, Harmonic Drive, and custom drive wheel.

Fig. 1: Design and construction of the Head Support.

not run into the stator and that the wave generator of the Harmonic Drive does not leave the flex spline during use.

The drive wheel tooth profile was empirically tuned to match the silicone cable used as the adjustable support strap from the HeadPod device (Siesta Systems, Navarra, Spain). The head attachment consisting of the adjustable arc, occipital mesh, and silicone forehead straps, was conserved from HeadPod because it is designed to be biocompatible and flexible to allow cervical rotation while being able to feed the strap. The drive wheel tooth profile was initially sized based on the D-shaped holes in the strap, and notches were created between the teeth to grip the raised areas of the strap. Various laser-cut prototypes were cut varying the tooth profile parameter among them and each was evaluated for smoothness of feeding and ease of tooth engagement between segments. After settling on the best-performing profile for the drive wheel, the drive wheel was milled from Delrin on a 3-axis HAAS Mini Mill using a 24-segment dividing head. Two rigid skate wheels (McMaster-Carr, Elmhurst, IL) press the strap into the drive wheel.

TABLE I: Design Specifications

Parameter	Requirements	Justification
Motor continuous torque	0.082 N-m	Supports up to 205 N at drive wheel.
Motor maximum torque	0.245 N-m	Overcome momentary resistance without the possibility of injury.
Motor inertia	7.9E-06 kg-m^2	Prevent overcoming N_{ij}.
Motor speeds	750 rpm	Have a max drive wheel speed of 3 teeth per minute.
Harmonic drive gear ratio	100:1	Output safe motor speeds and torque.
Harmonic drive axial forces	37.2 N	Restricts the rotor from crashing into the stator and the wave generator from leaving the flexspline.

B. Mechatronics

An MSP430FR5994 (Texas Instruments, Dallas, Texas, USA) microcontroller controls the Head Support using a TI DRV8317HEVM motor driver. Researchers programmed custom Embedded C code to control the PWM signals to drive the BLDC motor, commutating within the firmware based on Hall sensor states for position or speed control using guidelines provided by Texas Instruments. Commands were sent via serial port from the PC for the testing performed in this study. The motor has a continuous current of 5.6 A, and the DRV8317HEVM limits the current to only 5.0 A as a secondary torque regulator to protect the motor from overheating and additional overexertion prevention during bench-top testing. The position of the drive wheel was controlled by a PID controller, with the PWM duty cycle to the motor being the control input to the system.

IV. Methods

Two main tests were performed to evaluate the performance of the active support device and to verify that it would safely deliver the intended function.

A. Test 1: Axial Loading on the Head

A test was devised to measure the distraction force applied to the head when the Head Support motor is run to stall an initially slack support. The purpose was to verify that sudden loads applied to the head would have a low probability of injury while holding the head. Distraction forces applied to the user's head are especially important, as the Head Support is designed for children with low head control. We assume that for children, there is a smaller range of effective forces (enough to lift the head without applying too much to cause injury) than is typically seen in adults. To measure these distraction forces in axial loading, we modified an MTS tensile testing machine to hold the support strap of the motor assembly in line with the load cell (Figure 2). The Head

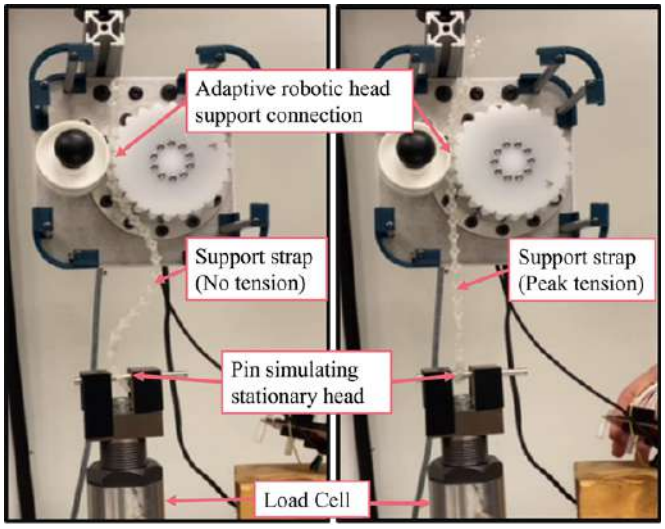


Fig. 2: Head Support mounted with the HeadPod support strap aligned above a load cell to measure axial loads that would be applied to the user's head. The test begins with no tension (left) in the support strap, and the maximum load is measured (right) when the motor stalls at its highest position.

Support positioned directly in line above the user's head to avoid additional moments applied while the patient is sitting upright. We mounted the Head Support to the top crossbeam and raised it 0.2 m above the load cell connection, the designed maximum height above the user's head. The distal end of the support strap is attached to a load cell (25 kN, 5 kHz) to measure the distractive forces that would be applied to the head in an upright position.

Twenty tests were performed from a starting point where the support strap was slack (0 N) and the strap was lifted by running the drive wheel with a simple position controller using the Hall sensor position until the motor stopped. The maximum position was held for approximately 5 seconds before a command returned the motor to its initial position.

B. Test 2: Position Tracking

Test 2 is designed to validate a position tracking method programmed to count Hall sensor events built into the Celera motor. A Polhemus Liberty magnetic motion tracking system (Colchester, VT, 240 Hz) tracked the position of the distal end of the support cable with one sensor in Figure 1b, and another sensor on the 2 kg ball where the user's forehead would be (Figure 3). Polhemus data are used to measure the actual Head Support strap length compared to the Hall sensor position tracking in the firmware. The strap length is calculated as the arc length with the drive wheel radius (44 mm). The difference between the number of Halls and initial position determines the central angle for this calculation.

Using the same Polhemus setup, a dataset for the approximate workspace of the robot was collected to measure the rotational CROM of the Head Support. The medicine ball was manually pushed until the support strap touched the anterior frame for the ABS housing. The medicine ball was then rotated clockwise along the transverse plane until it reached the proximal frame for the ABS housing, then continued the motion back to the anterior position. Workspace size during flexion, extension, and lateral bending will vary based on strap length. This workspace measurement is used to validate that our design can incorporate full cervical rotation within the transverse plane.

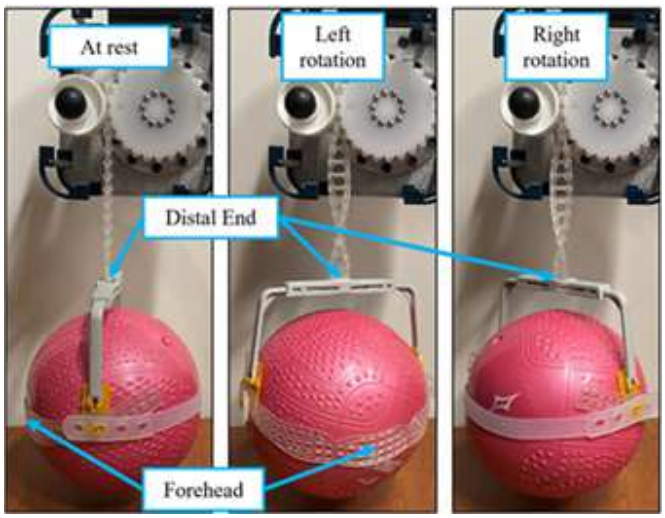


Fig. 3: Sensor probe positions for magnetic motion analysis at the start point of the test. Probes are placed on the forehead and the distal end of the support strap to estimate position.

V. Results

A. Test 1: Axial Loading Measurements

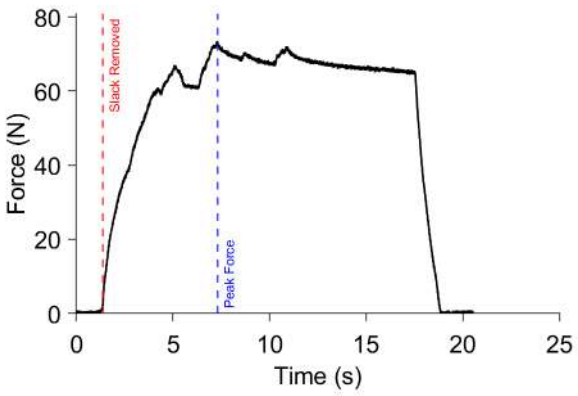


Fig. 4: Axial test 13, which reached the highest overall force magnitude (73.6 N). Constitutive curve of axial loading tests from the Head Support demonstrating the maximum force and time from cable slack to motor stall limit being reached.

TABLE II: Axial loading measurements (n=20) from lifting the Head Support with no tension until the motor stops.

Variable	Mean	Standard Deviation	Min.	Max.
Max Force (N)	66.1	3.91	60.3	73.6
Time to Stall (s)	4.06	0.98	3.31	6.65

The axial load that the device was able to provide was measured at a maximum value of 73.6 N in the 20 tests (Figure 4). The mean maximum force reached before the motor stalled was 66.1 ±3.91 N (Table II). The motor is rated for a continuous torque of 0.082 N-m, so the current limiter on the motor driver further limited the torque in this test. The rise time from when tension was applied to the motor stall was 4.06 ±0.98 s, with an overall maximum of 6.65 s.

B. Test 2: Position Measurements

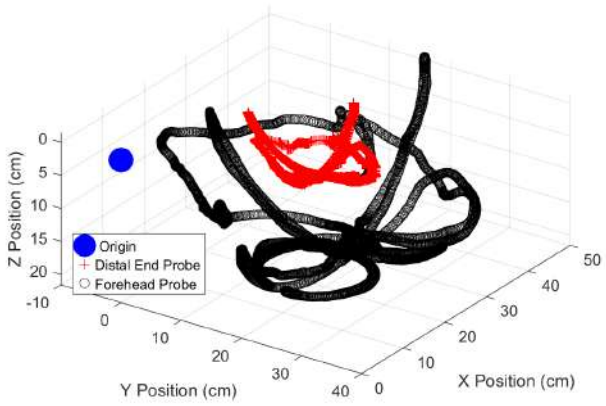


Fig. 5: Approximate workspace of the Head Support demonstrating unrestricted horizontal cervical range of motion due to the flexibility of the support strap.

The Head Support lifted (Hall sensor: 9.17 cm, Polhemus: 9.94 cm, Fig. 6a) and lowered (Hall sensor: 9.22 cm, Polhemus: 9.36 cm, Fig. 6c) the 2 kg mass for a 120-degree rotation of the drive wheel (see Figure 3). The Hall sensor position measurements, compared to the external Polhemus position measurements, had errors during lifting from the Distal End probe (-2.34 to 0.44 cm) and Forehead probe (-0.33 to 3.07 cm) (Fig. 6b). While lowering the support strap, errors were present from the Distal End probe (-0.01 to 4.78 cm) and the Forehead probe (-1.01 to 1.08 cm) (Fig. 6d). The Distal End probe error magnitude increased as the Head Support lowered the ball, though the Forehead probe error decreased as the Head Support stopped in both cases.

Additional Polhemus measurements rotated the medicine ball about the vertical axis to estimate CROM. A complete rotation around the vertical axis was performed while the medicine ball was hanging freely (Figure 5).

VI. Discussion

The Head Support needs to independently lift the weight of the head (approx. 20 N). It can supply peak distraction forces ranging between 60.3 and 73.6 N (66.1 ±3.91 N), demonstrating the Head Support's ability to provide a reasonable amount of resistance or the necessary assistance to return the child's head to an upright position. Previous work measured the forces exerted by children on the HeadPod passive head support with peak dynamic loads near 150 N, with typical use ranging between 10-40 N [9]. This means that the Head Support introduced in this research is capable of resisting most expected activity, similar to what children would impart on the device. The motor stopped at least at 60.3 N during our tests in the current control system, which would overcome most expected motions if the ability to resist voluntary or spastic motions is desired in a rehabilitation algorithm. This demonstrates the ability to partially or fully support the sustained weight of a 6-year-old's head. While position control was useful for bench-top experiments, force or torque control would enable higher precision of stall torque, rather than limiting this with electronics. The peak axial loads would fit well within a safe tolerance for use (F_{int}, 2120 N). Polymer creep observed during Test 1 may be a minor source of error.

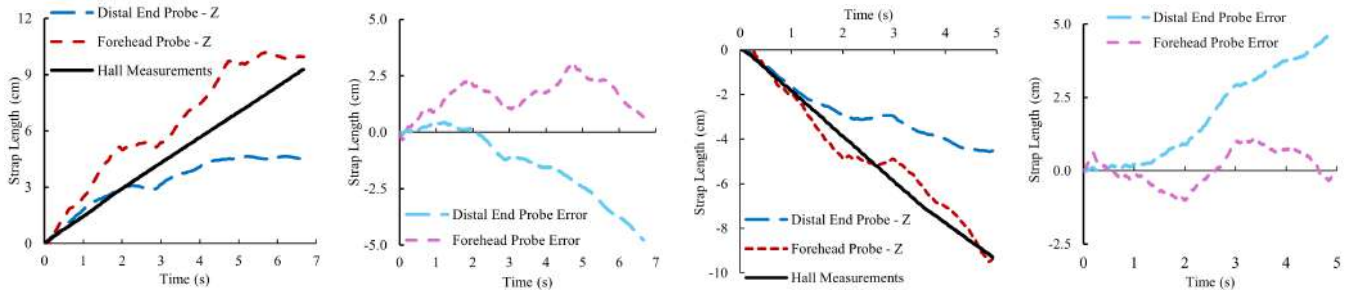
Preliminary usability testing revealed challenges with the toothed drive wheel when donning the head support. The drive wheel should interface with the HeadPod support strap's ridges and holes. The support strap often slipped when first loaded onto the drive wheel. Future iterations should affix the superior end of the strap to the drive wheel.

Test 2 demonstrates that Head Support Hall readings can approximate changes in height (Figure 6), though out-of-plane motion is not fully defined as in powered neck braces with rigid linkages. The curve deviates more when the medicine ball oscillated during both lifting and lowering. This caused additional out-of-plane movements in the motion capture data that were not captured in the Hall sensor data. The Forehead Probe error was lowest at the initial and final positions, which suggests that these oscillations caused most of the error. In human testing, users would be in a supported sitting position, so we would expect minimal error due to this oscillation. Rotating the medicine ball (Figure 3) with motion capture demonstrates a 180-degree horizontal rotation in both directions (Figure 5). Electric current, force, and torque sensing can be included to implement force and torque control as part of a rehabilitation algorithm.

VII. Conclusions

The Adaptive Robotic Head Support demonstrates mechanical capability to support the full or partial weight of the head, resist typical volitional movements, and assist in returning the user's head to an upright position. While current functionality relies on Hall sensor position tracking, future clinical applications may benefit from additional sensing functionality for better precision.

Future work should explore force and moment control to improve accuracy without relying on current limiting for torque management. Clinical evaluations involving therapists will provide feedback on usability and caretaker fatigue. Human-subject testing is essential to fully characterize the device's ROM in flexion, extension, rotation, and lateral bending. Incorporating activity monitoring, EMG data, intent detection, and patient outcome studies could further advance cervical spine rehabilitation and the role of physical human-robot interactions for head-neck mobility.



(a) Strap length while lifting, measured with Hall sensor and motion capture probes.

(b) Position error between Hall sensor and motion capture measurements while lifting.

(c) Strap length while lowering, measured with Hall sensor and motion capture probes.

(d) Position error between Hall sensor and motion capture measurements while lowering.

Fig. 6: Comparing external motion capture probes of the Head Support while lifting and lowering a 2 kg medicine ball to simulate lifting the entire weight of the head to validate internal Hall sensor measurements estimating vertical height.

REFERENCES

[1] L. Caruso, G. Barone, A. Farneti, and A. Caraffa, "Pedicle subtraction osteotomy for the treatment of chin-on-chest deformity in a post-radiotherapy dropped head syndrome: a case report and review of literature," *European Spine Journal*, vol. 23, no. 6, pp. 634–643, Oct. 2014. [Online]. Available: https://doi.org/10.1007/s00586-014-3544-z

[2] H. M. Lee and J. C. Galloway, "Early Intensive Postural and Movement Training Advances Head Control in Very Young Infants," *Physical Therapy*, vol. 92, no. 7, pp. 935–947, Jul. 2012, publisher: Oxford Academic. [Online]. Available: https://academic.oup.com/ptj/article/92/7/935/2735285

[3] F. Redstone and J. F. West, "The importance of postural control for feeding." *Pediatric nursing*, 2004.

[4] A. Z. Burakgazi, P. K. Richardson, and M. Abu-Rub, "Dropped head syndrome due to neuromuscular disorders: Clinical manifestation and evaluation," *Neurology International*, vol. 11, no. 3, p. 8198, Jun. 2019. [Online]. Available: https://www.ncbi.nlm.nih.gov/pmc/articles/PMC6763751/

[5] K. Işık, G. Morkavuk, and Z. Odabaşı, "Dropped Head Syndrome As a Presenting Sign of Different Diseases: Report of Three Cases," *Archives of Neuropsychiatry*, vol. 60, no. 2, pp. 185–187, May 2023. [Online]. Available: https://www.ncbi.nlm.nih.gov/pmc/articles/PMC10242275/

[6] T. Igawa, N. Isogai, A. Suzuki, S. Kusano, Y. Sasao, M. Nishiyama, H. Funao, and K. Ishii, "Establishment of a novel rehabilitation program for patients with dropped head syndrome: Short and intensive rehabilitation (SHAiR) program," *Journal of Clinical Neuroscience*, vol. 73, pp. 57–61, Mar. 2020. [Online]. Available: https://www.sciencedirect.com/science/article/pii/S0967586819319149

[7] P. L. Rosenbaum, R. J. Palisano, D. J. Bartlett, B. E. Galuppi, and D. J. Russell, "Development of the Gross Motor Function Classification System for cerebral palsy," *Developmental Medicine and Child Neurology*, vol. 50, no. 4, pp. 249–253, 2008, publisher: Blackwell Publishing Ltd.

[8] J. E. Brown, M. Thompson, and K. Brizzolara, "Head Control Changes after Headpod Use in Children with Poor Head Control: A Feasibility Study," *Pediatric Physical Therapy*, 2018.

[9] B. Kerst, L. Crouch, J. Fox, J. Wilson, and J. Schultz, "Effects of a Head Support on Children with Hypotonia in the Cervical Spine," in *Proceedings of the Annual International Conference of the IEEE Engineering in Medicine and Biology Society, EMBS*, vol. 2020-July, Jul. 2020, pp. 4783–4786. [Online]. Available: https://pubmed.ncbi.nlm.nih.gov/33019060/

[10] M. A. Velasco, R. Raya, L. Muzzioli, D. Morelli, A. Otero, M. Iosa, F. Cincotti, and E. Rocon, "Evaluation of cervical posture improvement of children with cerebral palsy after physical therapy based on head movements and serious games," *BioMedical Engineering Online*, 2017.

[11] V. S. Huang and J. W. Krakauer, "Robotic neurorehabilitation: a computational motor learning perspective," *Journal of NeuroEngineering and Rehabilitation*, vol. 6, no. 1, p. 5, Feb. 2009. [Online]. Available: https://doi.org/10.1186/1743-0003-6-5

[12] L. R. Keytel, J. H. Goedecke, T. D. Noakes, H. Hiiloskorpi, R. Laukkanen, L. van der Merwe, and E. V. Lambert, "Prediction of energy expenditure from heart rate monitoring during submaximal exercise," *Journal of Sports Sciences*, vol. 23, no. 3, pp. 289–297, Mar. 2005.

[13] K. Barati, M. Arazpour, R. Vameghi, A. Abdoli, and F. Farmani, "The Effect of Soft and Rigid Cervical Collars on Head and Neck Immobilization in Healthy Subjects," *Asian Spine Journal*, vol. 11, no. 3, pp. 390–395, Jun. 2017. [Online]. Available: https://www.ncbi.nlm.nih.gov/pmc/articles/PMC5481593/

[14] M. E.-H. Ibrahem, M. T. El-Wakad, M. S. El-Mohandes, and S. A. Sami, "Implementation and Evaluation of a Dynamic Neck Brace Rehabilitation Device Prototype," *Journal of Healthcare Engineering*, vol. 2022, pp. 1–12, Oct. 2022. [Online]. Available: https://www.hindawi.com/journals/jhe/2022/6887839/

[15] S. P. Torrendell, Y. Chen, H. Kadone, M. Hassan, and K. Suzuki, "Design of a Multi-Degree-of-Freedom Elastic Neck Exoskeleton for Persons with Dropped Head Syndrome," in *2023 IEEE International Conference on Soft Robotics (RoboSoft)*, Apr. 2023, pp. 1–8, iSSN: 2769-4534. [Online]. Available: https://ieeexplore.ieee.org/document/10122051

[16] H. Zhang, B.-C. Chang, P. Kulkarni, J. Andrews, N. A. Shneider, and S. Agrawal, "Amyotrophic Lateral Sclerosis Patients Regain Head-Neck Control Using a Powered Neck Exoskeleton," in *2022 9th IEEE RAS/EMBS International Conference for Biomedical Robotics and Biomechatronics (BioRob)*. Seoul, Korea, Republic of: IEEE, Aug. 2022, pp. 01–06. [Online]. Available: https://ieeexplore.ieee.org/document/9925452/

[17] I. Bales and H. Zhang, "A six degrees-of-freedom cable-driven robotic platform for head–neck movement," *Scientific Reports*, vol. 14, no. 1, p. 8750, Apr. 2024, publisher: Nature Publishing Group. [Online]. Available: https://www.nature.com/articles/s41598-024-59349-0

[18] S. Systems, "Siesta Systems HeadPod."

[19] A. S. Arockia Doss, P. K. Lingampally, G. M. T. Nguyen, and D. Schilberg, "A comprehensive review of wearable assistive robotic devices used for head and neck rehabilitation," *Results in Engineering*, vol. 19, p. 101306, Sep. 2023. [Online]. Available: https://www.sciencedirect.com/science/article/pii/S2590123023004334

[20] A. Lozano, M. Ballesteros, D. Cruz-Ortiz, and I. Chairez, "Active neck orthosis for musculoskeletal cervical disorders rehabilitation using a parallel mini-robotic device," *Control Engineering Practice*, vol. 128, p. 105312, Nov. 2022. [Online]. Available: https://www.sciencedirect.com/science/article/pii/S096706612200154X

[21] H. Kim, H. Park, W. Lee, J. Kim, and Y.-L. Park, "Design of wearable orthopedic devices for treating forward head postures using pneumatic artificial muscles and flex sensors," in *2017 14th International Conference on Ubiquitous Robots and Ambient Intelligence (URAI)*, Jun. 2017, pp. 809–814. [Online]. Available: https://ieeexplore.ieee.org/document/7992831

[22] M. Shoaib, E. Asadi, J. Cheong, and A. Bab-Hadiashar, "Cable Driven Rehabilitation Robots: Comparison of Applications and Control Strategies," *IEEE Access*, vol. 9, pp. 110 396–110 420, 2021. [Online]. Available: https://ieeexplore.ieee.org/document/9504529/

[23] R. Eppinger, E. Sun, F. Bandak, M. Haffner, N. Khaewpong, M. Maltese, S. Kuppa, T. Nguyen, E. Takhounts, R. Tannous, A. Zhang, and R. Saul, "Development of Improved Injury Criteria for the Assessment of Advanced Automotive Restraint Systems - II," 1999.

ARISE Control of an Uncertain Lower-Limb Hybrid Exoskeleton

Kislaya Mishra*, Sujata Basyal*, Jonathan Ting*, Brendon C. Allen*

***Abstract*—Neurological conditions (NCs) such as spinal cord injury, stroke, and Parkinson's disease have been affecting many individuals by deteriorating their standard of living by not letting them perform physical activities, resulting in inactive lifestyles that cause conditions such as diabetes, obesity, cardiovascular disease, etc. Thus, there is a need to overcome the inactive lifestyle caused by NCs. Many potential solutions have been introduced, but each are limited in someway. For example, functional electrical stimulation (FES), which bypasses typical neurological processes to activate an individual's muscles (active therapy), is one of the capable solutions, but it results in the patient becoming fatigued quicker than normal. In an effort to improve FES-based therapies, this paper develops a novel robust and adaptive control structure for a combined FES and robotic system called a hybrid exoskeleton. Specifically, for the first time, a recently developed ARISE control approach is modified for a hybrid exoskeleton. Furthermore, the control law is augmented with neural networks that learn uncertainties in the dynamic model. To evaluate the performance of the control system, a Lyapunov-based stability analysis is performed.**

***Index Terms*—Lyapunov methods, Nonlinear control, Neural network (NN), Robust and adaptive control.**

I. Introduction

Rehabilitation is vital for individuals suffering from movement disorders caused by neurological conditions (NCs) [1]. An important development in the field of rehabilitation is robot-aided therapy, known as rehabilitation robotics, which has been proven to facilitate recovery from NCs. For example, rehabilitation robots have assisted individuals recovering from a stroke to achieve beneficial health outcomes [2]. Moreover, the design of many rehabilitation robotics are reviewed in [3]. Though there are many advantages of robot-aided rehabilitation, active participation rather than passive movements from the affected individual is necessary for recovery [4]. Thus, finding a balance between the patient's and the robot's contribution is critical. Many techniques have been implemented in an effort to increase the patient's contribution and to achieve an optimal contribution from both the human and robot [5]. Functional electrical stimulation (FES) combined with robotics, also known as hybrid exoskeletons, is one of the more commonly used and actively researched techniques to increase human contribution and to achieve an optimal robot-human contribution split.

*Department of Mechanical Engineering, Auburn University, Auburn AL 36849-0001, USA Email: {kzm0074, szb0233, jat0076, bca0027}@auburn.edu

This research is supported in part by NSF award number 2230971. Any opinions, findings and conclusions, or recommendations expressed in this material are those of the author(s) and do not necessarily reflect the views of the sponsoring agency.

Hybrid exoskeletons are particularly effective for individuals with NCs, as hybrid exoskeletons apply FES to ensure muscle contractions while also providing an additional torque from the motor to assist the individual on an as-needed basis, helping to reduce the onset of fatigue. In fact, as shown in [6], hybrid exoskeletons can increase biceps strength by allowing patients to perform more repetitions of biceps curls till fatigue. However, hybrid exoskeletons have highly uncertain nonlinear dynamics with some uncertainties bounded by constants. Designing controllers to compensate for the uncertainties and nonlinearities associated with hybrid exoskeletons can be challenging. Many prior studies have been conducted in the field of nonlinear control theory, particularly for systems with uncertainties (cf. [7]).

One common control method is to combine high gain feedback with adaptive terms, but these methods are less optimal when unstructured disturbances exist that are bounded by constants. Consequently, other methods have been developed that combine robust high-gain terms with additional discontinuous terms, for example, sliding mode (SM) controllers [8]. Though SM often ensures great stability results, it requires an infinite frequency response from the actuator, making it physically unimplementable, or at least, unachievable. Moreover, SM controllers exhibit a chattering effect due to the discontinuous jumps that occur within the control input (typically when an error is driven towards 0), further hindering its practical use [9]. Desirous to develop a continuous controller that would mitigate the chattering effect and could compensate for unstructured terms bounded by constants, the authors developed the Auxiliary Robust Integral of the Sliding Mode (ARISE) controller, which can be implemented for a wide-class of uncertain smooth or nonsmooth dynamic systems [10].

In this paper, an ARISE controller is developed for the first time for a hybrid exoskeleton. To demonstrate the proposed approach, this preliminary work considers a one degree-of-freedom (DOF) leg extension exercise. All prior ARISE developments by the authors have considered a state-space model [10], and an Euler-Lagrange dynamic model [11]. Although the dynamic model presented in this work has similarities to the dynamic model in [11], several distinctions exist. Particularly, hybrid exoskeletons have motor and FES inputs, requiring the design of multiple controllers, and the control effectiveness that maps stimulation to torque output is unknown. Consequently, this work approximates the uncertain FES control effectiveness using a neural network (NN), increasing the optimality of the FES control design

and slowing the onset of fatigue. Furthermore, another NN is designed to approximate additional uncertainties in the dynamic model and ARISE is used to compensate for unstructured and time-varying disturbances, yielding an improved trajectory tracking performance. Additionally, a Lyapunov-based stability analysis was performed to ensure the stability and safety of the proposed control framework, proving semi-global exponential trajectory tracking towards an ultimate bound.

II. Dynamics

In this preliminary work, a lower-limb hybrid exoskeleton for leg extensions will be considered. The dynamics are unknown and nonlinear and can be modeled as[1]

$$M\ddot{x}+P(x,\dot{x})+G(x)+F\dot{x}+d(t) = \underbrace{g_m\left(x,\dot{x},t\right)u_m\left(t\right)}_{\tau_m(x,\dot{x},t)} + \underbrace{g_f\left(x,\dot{x},t\right)u_f\left(t\right)}_{\tau_f(x,\dot{x},t)}, \tag{1}$$

where $x : \mathbb{R}_{\geq 0} \to \mathbb{R}$ is the measurable knee joint angle coordinate, $\dot{x} : \mathbb{R}_{\geq 0} \to \mathbb{R}$ is the measurable angular velocity coordinate, $\ddot{x} : \mathbb{R}_{\geq 0} \to \mathbb{R}$ is the angular acceleration coordinate, $M \in \mathbb{R}_{>0}$ is the unknown constant inertia for the lower-limb about the knee, $P\left(x,\dot{x}\right) : \mathbb{R} \times \mathbb{R} \to \mathbb{R}$ is the unknown passive viscoelastic tissue effects, $G\left(x\right) : \mathbb{R} \to \mathbb{R}$ is the uncertain gravitational effects around the knee joint, $F \in \mathbb{R}$ is an uncertain viscous coefficient, and $d\left(t\right) : \mathbb{R}_{\geq 0} \to \mathbb{R}$ is an uncertain disturbance. In (1), $g_m : \mathbb{R} \times \mathbb{R} \times \mathbb{R}_{\geq 0} \to \mathbb{R}_{>0}$ and $g_f : \mathbb{R} \times \mathbb{R} \times \mathbb{R}_{\geq 0} \to \mathbb{R}_{>0}$ are a known motor control effectiveness term and an unknown lumped FES control effectiveness term, respectively, $u_m : \mathbb{R}_{\geq 0} \to \mathbb{R}$ and $u_f : \mathbb{R}_{\geq 0} \to \mathbb{R}$ are the motor and FES control inputs, respectively, and $\tau_m : \mathbb{R} \times \mathbb{R} \times \mathbb{R}_{\geq 0} \to \mathbb{R}$ and $\tau_f : \mathbb{R} \times \mathbb{R} \times \mathbb{R}_{\geq 0} \to \mathbb{R}$ are the generalized motor and FES input torques, respectively. Moreover, since muscle forces can only be applied unidirectionally, FES will be applied to the quadriceps and hamstrings muscle groups to enable full control about the knee joint. Specifically, the lumped FES control effectiveness is defined as

$$g_f\left(x,\dot{x},t\right) \triangleq g_q\left(x,\dot{x},t\right)\sigma_q\left(u_f\left(t\right)\right) + g_h\left(x,\dot{x},t\right)\sigma_h\left(u_f\left(t\right)\right),$$

$$\sigma_q \triangleq \begin{cases} 1, & u_f \geq 0 \\ 0, & u_f < 0 \end{cases} \quad \text{and} \quad \sigma_h \triangleq \begin{cases} 0, & u_f \geq 0 \\ -1, & u_f < 0 \end{cases},$$

where $g_q : \mathbb{R}\times\mathbb{R}\times\mathbb{R}_{\geq 0} \to \mathbb{R}_{>0}$ and $g_h : \mathbb{R}\times\mathbb{R}\times\mathbb{R}_{\geq 0} \to \mathbb{R}_{<0}$ are the control effectiveness terms for the quadriceps and hamstrings muscle groups, respectively, and σ_q and σ_h are switching signals for the activation of the quadriceps and hamstrings muscle groups, respectively. Note that the design of the switching signals' values, $\{0, 1, -1\}$, ensures that g_f remains continuous and positive for all time. Furthermore, note that the stimulation inputs into the quadriceps and hamstrings muscles groups are respectively defined as

$$u_q \triangleq \sigma_q\left(x,u_f\left(t\right)\right)u_f \quad \text{and} \quad u_h \triangleq \sigma_h\left(x,u_f\left(t\right)\right)u_f,$$

ensuring that FES inputs are always positive as is required. Additionally, below are common assumptions for the leg extension dynamics in (1).

Assumption 1. M can be bounded such that $c_m \leq M \leq c_M$, $\forall t \geq t_0$, where t_0 is the known initial time, and $c_m \in \mathbb{R}_{>0}$ and $c_M \in \mathbb{R}_{>0}$ are known positive constants.

Assumption 2. $P\left(x,\dot{x}\right)$ can be upper-bounded as $\left|P\left(x,\dot{x}\right)\right| \leq c_{P_1} + c_{P_2}\left|\dot{x}\right|, \forall t \geq t_0$, where $c_{P_1} \in \mathbb{R}_{>0}$ and $c_{P_2} \in \mathbb{R}_{>0}$ are known constants and $|\cdot|$ is the absolute value.

Assumption 3. $G\left(x\right)$ can be upper-bounded as $\left|G\left(x\right)\right| \leq c_G, \forall t \geq t_0$, where $c_G \in \mathbb{R}_{>0}$ is a known constant.

Assumption 4. F can be upper-bounded as $|F| \leq c_F, \forall t \geq t_0$, where $c_F \in \mathbb{R}_{>0}$ is a known constant.

Assumption 5. $d\left(t\right)$ can be upper-bounded as $\left|d\left(t\right)\right| \leq c_D, \forall t \geq t_0$, where $c_D \in \mathbb{R}_{>0}$ is a known constant.

III. Control Development

The control objective of the knee extension system in (1) is to track a bounded and smooth desired limb trajectory $x_d : \mathbb{R}_{\geq 0} \to \mathbb{R}$. The error signal, $e : \mathbb{R}_{\geq 0} \to \mathbb{R}$, can be quantified as

$$e\left(t\right) \triangleq x_d\left(t\right) - x\left(t\right). \tag{2}$$

Furthermore, a measurable auxiliary tracking error, $r : \mathbb{R}_{\geq 0} \to \mathbb{R}$, can be defined as

$$r \triangleq \dot{e} + \alpha_1 e + \alpha_2 e_f, \tag{3}$$

where $e_f : \mathbb{R}_{\geq 0} \to \mathbb{R}^n$ is an auxiliary filtered ARISE signal, and $\alpha_1, \alpha_2 \in \mathbb{R}_{>0}$ are user-implemented control gains. The filtered ARISE term, e_f, is derived by solving the auxiliary differential equation that is defined as

$$\dot{e}_f \triangleq -k_1 \text{sgn}\left(r\right) - k_2 r + \alpha_2 e - \beta_1 e_f, \tag{4}$$

where $\text{sgn}\left(\cdot\right)$ is a signum function (i.e., a SM term), $k_1, k_2, \beta_1 \in \mathbb{R}_{>0}$ are user-implemented control gains, and the initial condition of e_f is defined as $e_f\left(0\right) = 0$. The key feature of the ARISE control method is that the signum function is injected into the closed-loop error system for (3) through $\dot{e}_f$ rather than through the control input. As a result, the control input remains continuous, mitigating chattering and the need for infinite control frequency. Multiplying the derivative of (3) by M and substituting (1), (2), and (4) into the resulting product yields the open-loop error system as

$$M\dot{r} = M\ddot{x}_d + P + G + F\dot{x} + d - g_f u_f - g_m u_m + M\alpha_1\dot{e} + M\alpha_2\left[-k_1\text{sgn}\left(r\right) - k_2 r + \alpha_2 e - \beta_1 e_f\right]. \tag{5}$$

A goal of this paper is to learn uncertainties in the dynamic system. Numerous methods exist to approximate the

[1]For notational conciseness, all explicit dependence on time within the terms $x\left(t\right), \dot{x}\left(t\right), \ddot{x}\left(t\right)$ will be suppressed.

unknown FES control effectiveness. This paper will use a NN to approximate $g_f(x,\dot{x},t)\,u_f(t)$ (and ultimately just g_f); however, the universal function approximation theorem from [12] requires $g_f u_f$ to lie on a compact set to approximate $g_f u_f$ with almost complete accuracy and some residual error. Following a semi-global approach from [13], it will be proven that if x, $\dot{x}$, and u_f are initially bounded, they will remain bounded for all time, proving that they lie in a compact set. Furthermore, although time is unbounded, a nonlinear mapping, $f_g : [t_0,\infty) \to [0,1]$, is defined to map time, $[t_0,\infty)$, into a compact domain as

$$f_g(t) \triangleq \frac{k_g(t-t_0)}{k_g(t-t_0)+1},$$

where $k_g \in \mathbb{R}_{>0}$ is a user-defined constant. Note that time can be re-derived through an inverse mapping, $f_g^{-1} : [0,1] \to [t_0,\infty)$, that is defined as

$$f_g^{-1}(\xi) \triangleq \frac{k_g t_0(1-\xi)+\xi}{k_g(1-\xi)},$$

such that $f_g(t) = \xi$ and $f_g^{-1}(\xi) = t$. Therefore, $g_f\left(x,\dot{x},f_g^{-1}(\xi)\right)u_f$ can be treated as though it lies on a compact set and approximated using a NN. Specifically, the FES torque $\tau_f\left(x,\dot{x},f_g^{-1}(\xi),u_f\right) = g_f\left(x,\dot{x},f_g^{-1}(\xi)\right)u_f$ can be expressed as

$$\tau_f\left(x,\dot{x},f_g^{-1}(\xi),u_f\right) = W_f^T\varphi_f\left(V_f^T\phi_f\right)+\varepsilon_f, \quad (6)$$

where $W_f \in \mathbb{R}^{(F_1+1)\times 1}$ denotes the outer layer weights, $V_f \in \mathbb{R}^{5\times F_1}$ denotes the inner layer weights, $\varphi_f(\cdot) : \mathbb{R}^{F_1} \to \mathbb{R}^{F_1+1}$ denotes the inner layer activation functions defined as $\varphi = \left[\varphi_{f_1},...,\varphi_{f_{F_1}},1\right]^T$, $\phi_f(t) \in \mathbb{R}^5$ denotes the input vector to the NN defined as $\phi_f \triangleq \left[x,\dot{x},f_g^{-1}(\xi),u_f,1\right]^T$, $\varepsilon_f \in \mathbb{R}$ is the function approximation error, and $F_1 \in \mathbb{Z}$ denotes the number of neurons in the inner layer. Based on (6), the estimation of the FES generalized torque $\widehat{g}_f(x,\dot{x},t)\,u_f(t)$ can be represented as

$$\widehat{g}_f(x,\dot{x},t)\,u_f(t) = \widehat{W}_f^T\varphi_f\left(\widehat{V}_f^T\phi_f\right),$$

where $\widehat{W}_f \in \mathbb{R}^{(F_1+1)\times 1}$ denotes the estimated outer layer weights, $\widehat{V}_f \in \mathbb{R}^{5\times F_1}$ denotes the estimated inner layer weights, and $\widehat{g}_f$ is the estimate of g_f. To facilitate the subsequent design of the Lyapunov-based adaptive laws, the mismatch between the ideal and the estimated inner layer weights $\widetilde{V}_f : [t_0,\infty) \to \mathbb{R}^{5\times F_1}$ can be defined as

$$\widetilde{V}_f \triangleq V_f - \widehat{V}_f. \quad (7)$$

Similarly, the mismatch between the ideal and estimated outer layer weights $\widetilde{W}_f : [t_0,\infty) \to \mathbb{R}^{(F_1+1)\times 1}$ can be defined as

$$\widetilde{W}_f \triangleq W_f - \widehat{W}_f. \quad (8)$$

Using (6) and adding/subtracting $\widehat{W}_f^T\varphi_f\left(\widehat{V}_f^T\phi_f\right)$ and $W_f^T\varphi_f\left(\widehat{V}_f^T\phi_f\right)$ in (5) modifies the open-loop dynamics as

$$\begin{aligned} M\dot{r} &= M\ddot{x}_d + P + G + F\dot{x} + d - \varepsilon_f - g_m u_m + M\alpha_1\dot{e} \\ &\quad + M\alpha_2\left[-k_1\text{sgn}(r) - k_2 r + \alpha_2 e - \beta_1 e_f\right] \\ &\quad - W_f^T\left(\varphi_f\left(V_f^T\phi_f\right) - \varphi_f\left(\widehat{V}_f^T\phi_f\right)\right) \\ &\quad - \left(\widetilde{W}_f^T\right)\left(\varphi_f\left(\widehat{V}_f^T\phi_f\right)\right) - \widehat{W}_f^T\varphi_f\left(\widehat{V}_f^T\phi_f\right). \end{aligned} \quad (9)$$

To overcome the challenges associated with the nested structure of NN's, a Taylor series approximation was performed for $\varphi_f\left(V_f^T\phi_f\right)$ to yield

$$\varphi_f\left(V_f^T\phi_f\right) = \varphi_f\left(\widehat{V}_f^T\phi_f\right) + \varphi_f'\left(\widehat{V}_f^T\phi_f\right)\widetilde{V}_f^T\phi_f + \Theta_f,$$

where $\varphi_f' \in \mathbb{R}^{(F_1+1)\times F_1}$ denotes the partial derivative of the inner layer activation functions defined as $\varphi_f' \triangleq \frac{\partial\varphi\left(\boldsymbol{\nu}_f^T\phi_f\right)}{\partial\boldsymbol{\nu}_f^T\phi_f}$, and $\Theta_f \in \mathbb{R}^{F_1+1}$ denotes the higher order terms of the expansion. Adding/subtracting e and $\hat{W}_f^T\left(\varphi_f'\left(\hat{V^T}_f\phi_f\right)\widetilde{V}_f^T\phi_f\right)$, and simplifying (9) results in

$$\begin{aligned} M\dot{r} &= M\ddot{x}_d + P + G + F\dot{x} - g_m u_m + \chi_1 - e \\ &\quad + M\alpha_2\left[-k_1\text{sgn}(r) - k_2 r - \beta_1 e_f\right] \\ &\quad - \hat{g}_f u_f - \left(\widetilde{W}_f^T\right)\left(\varphi_f\left(\widehat{V}_f^T\phi_f\right)\right) \\ &\quad - \widehat{W}_f^T\left(\varphi_f'\left(\widehat{V}_f^T\phi_f\right)\widetilde{V}_f^T\phi_f\right), \end{aligned} \quad (10)$$

where $\chi_1 : \mathbb{R}_{\geq 0} \to \mathbb{R}$, is an auxiliary term defined as

$$\begin{aligned} \chi_1 &\triangleq M\alpha_1\dot{e} + \left(M\alpha_2^2+1\right)e - \varepsilon_f - W_f^T\Theta_f \\ &\quad - \widetilde{W}_f^T\left(\varphi_f'\left(\widehat{V}_f^T\phi_f\right)\widetilde{V}_f^T\phi_f\right) + d. \end{aligned} \quad (11)$$

Now a second NN will be developed to approximate the other uncertain dynamics in the system. To facilitate this NN approximation, the desired system dynamics, $q_d(x_d,\dot{x}_d)$, are defined as

$$q_d(x_d,\dot{x}_d) \triangleq P(x_d,\dot{x}_d) + G(x_d) + F\dot{x}_d, \quad (12)$$

where $x_d : \mathbb{R}_{\geq 0} \to \mathbb{R}$ is the desired angular position and $\dot{x}_d : \mathbb{R}_{\geq 0} \to \mathbb{R}$ is the desired angular velocity coordinate. Adding/subtracting q_d in (10), and simplifying will result in

$$\begin{aligned} M\dot{r} &= M\ddot{x}_d + q_d + S - g_m u_m + \chi_1 - e - \hat{g}_f u_f \\ &\quad + M\alpha_2\left[-k_1\text{sgn}(r) - k_2 r - \beta_1 e_f\right] \\ &\quad - \left(\widetilde{W}_f^T\right)\left(\varphi_f\left(\widehat{V}_f^T\phi_f\right)\right) \\ &\quad - \widehat{W}_f^T\left(\varphi_f'\left(\widehat{V}_f^T\phi_f\right)\widetilde{V}_f^T\phi_f\right), \end{aligned} \quad (13)$$

where S is the difference between the actual dynamics and the desired dynamics and is defined as

$$S \triangleq [P + G + F\dot{x}] - \underbrace{[P_d + G_d + F\dot{x}_d]}_{q_d}, \quad (14)$$

where P_d denotes $P(x_d,\dot{x_d})$ and G_d denotes $G(x_d)$. Considering the theory of universal function approximation from

[12], there exists activation functions and ideal layer weights such that $M\ddot{x}_d + q_d$ can be approximated with almost complete accuracy and some residual error such that

$$M\ddot{x}_d + q_d \triangleq W_l^T \varphi_l \left(V_l^T \phi_l(t)\right) + \varepsilon_l, \tag{15}$$

where $W_l \in \mathbb{R}^{(L_1+1)\times 1}$ is the outer layer weights , $V_l \in \mathbb{R}^{4\times L_1}$ is the inner layer weights, $\varphi_l(\cdot) : \mathbb{R}^{L_1} \to \mathbb{R}^{L_1+1}$ are the activation functions defined as $\varphi_l \triangleq \left[\varphi_{l_1}, ..., \varphi_{l_{L_1}}, 1\right]^T$, and $\phi_l(t) \in \mathbb{R}^4$ is the input vector defined as $\phi_l \triangleq [x_d(t), \dot{x}_d(t), \ddot{x}_d(t), 1]^T$, $\varepsilon_L \in \mathbb{R}$ is the function approximation error, and $L_1 \in \mathbb{Z}$ denotes the number of neurons in the inner layer. To facilitate the subsequent design of the Lyapunov-based adaptive laws, the mismatch between the ideal and the estimated inner layer weights $\widetilde{V}_l : [t_0, \infty) \to \mathbb{R}^{4\times L_1}$ can be defined as

$$\widetilde{V}_l \triangleq V_l - \widehat{V}_l. \tag{16}$$

Similarly, the mismatch between the ideal and estimated outer layer weights $\widetilde{W}_l : [t_0, \infty) \to \mathbb{R}^{(L_1+1)\times 1}$ can be defined as

$$\widetilde{W}_l \triangleq W_l - \widehat{W}_l. \tag{17}$$

Substituting (15) and adding/subtracting $W_l^T \varphi_l\left(\widehat{V}_l^T \phi_l\right)$ into (13) yields a modified open-loop error system as

$$\begin{aligned} M\dot{r} &= S - g_m u_m - e + \chi_1 - \hat{g}_f u_f \\ &\quad + M\alpha_2 \left[-k_1 \text{sgn}(r) - k_2 r - \beta_1 e_f\right] \\ &\quad - \left(\widetilde{W}_f^T\right) \varphi_f\left(\widehat{V}_f^T \phi_f\right) + W_l^T \varphi_l\left(\widehat{V}_l^T \phi_l\right) \\ &\quad - \widehat{W}_f^T \left(\varphi_f'\left(\widehat{V}_f^T \phi_f\right) \widetilde{V}_f^T \phi_f\right) \\ &\quad + W_l^T \left(\varphi_l\left(V_l^T \phi_l\right) - \varphi_l\left(\widehat{V}_l^T \phi_l\right)\right). \end{aligned} \tag{18}$$

Similar to the NN in (6), a Taylor series approximation was performed on φ_l to yield

$$\varphi_l\left(V_l^T \phi_l\right) = \varphi_l\left(\widehat{V}_l^T \phi_l\right) + \varphi_l'\left(\widehat{V}_l^T \phi_l\right) \widetilde{V}_l^T \phi_l + \Theta_l,$$

where $\varphi_l' \in \mathbb{R}^{(L_1+1)\times L_1}$ denotes the partial derivative of the inner layer activation functions defined as $\varphi_l' \triangleq \frac{\partial \varphi_l\left(\boldsymbol{\psi}_l^T \phi_l\right)}{\partial \boldsymbol{\psi}_l^T \phi_l}$, and $\Theta_l \in \mathbb{R}^{L_1+1}$ denotes the higher order terms of the expansion. Adding/subtracting $\hat{W}_l^T \left(\varphi_l'\left(\widehat{V}_l^T \phi_l\right) \widetilde{V}_l^T \phi_l\right)$ into (18) yields the open-loop error system as

$$\begin{aligned} M\dot{r} &= \chi_2 + S - g_m u_m - e + \chi_1 - \hat{g}_f u_f \\ &\quad + M\alpha_2 \left[-k_1 \text{sgn}(r) - k_2 r - \beta_1 e_f\right] \\ &\quad - \left(\widetilde{W}_f^T\right) \left(\varphi_f\left(\widehat{V}_f^T \phi_f\right)\right) + W_l^T \varphi_l\left(\widehat{V}_l^T \phi_l\right) \\ &\quad - \widehat{W}_f^T \left(\varphi_f'\left(\widehat{V}_f^T \phi_f\right) \widetilde{V}_f^T \phi_f\right) \\ &\quad + \hat{W}_l^T \left(\varphi_l'\left(\widehat{V}_l^T \phi_l\right) \widetilde{V}_l^T \phi_l\right), \end{aligned} \tag{19}$$

where $\chi_2 : \mathbb{R}_{\geq 0} \to \mathbb{R}$, is an auxiliary term defined as

$$\chi_2 \triangleq \widetilde{W}_l^T \left(\varphi_l'\left(\widehat{V}_l^T \phi_l\right) \widetilde{V}_l^T \phi_l\right) + \varepsilon_l + W_l^T \Theta_l \ . \tag{20}$$

Using (2), (3), 26-29 Assumptions 1-4, and Assumption 6 (stated below) $\chi_1 + \chi_2 + S$ can be denoted as $\chi \triangleq \chi_1 + \chi_2 + S$ for simplicity purposes and upper bounded as

$$\|\chi\| \leq \Phi + \rho(\|z\|) \|z\|, \tag{21}$$

where $\|\cdot\|$ is the Euclidean norm, $\Phi \in \mathbb{R}_{>0}$ is a known constant, $\rho(\cdot)$ is a positive, radially unbounded, and strictly increasing function, and $z : \mathbb{R}_{\geq 0} \to \mathbb{R}^3$ is a composite error vector defined as

$$z(t) \triangleq \begin{bmatrix} e & r & e_f \end{bmatrix}^T. \tag{22}$$

On the basis of an analysis of the open-loop error dynamics in (19), the control inputs u_f and u_m are designed as

$$u_f \triangleq \frac{1}{\hat{g}_f}(k_4 r), \tag{23}$$

$$\begin{aligned} u_m &\triangleq \frac{1}{g_m}\left(k_3 r - \left(k_2 + \hat{M}\alpha_2\beta_1\right) e_f \right. \\ &\quad \left. + \widehat{W}_l^T \varphi_l\left(\widehat{V}_l^T \phi_l\right)\right), \end{aligned} \tag{24}$$

where $\hat{M}$ is an estimated value for M and is defined by $\hat{M} \triangleq \frac{1}{2}(c_m + c_M)$, and $k_3 \in \mathbb{R}_{>0}$ is a user-defined control gain, and the inertial estimation error is defined as

$$\widetilde{M} \triangleq \widehat{M} - M. \tag{25}$$

Moreover, (25) can be bounded using Assumption 1 and (25) as $\left|\tilde{M}\right| \leq \frac{1}{2}(c_M - c_m) = c_M$, where $c_M \in \mathbb{R}_{>0}$ is a positive constant. Similarly, the NN parameter adaptive laws are designed as

$$\dot{\widehat{W}}_f = -\text{proj}\left(\Gamma_1 \varphi_f\left(\widehat{V}_f^T \phi_f\right) r\right), \tag{26}$$

$$\dot{\widehat{V}}_f = -\text{proj}\left(\Gamma_2 \phi_f r \widehat{W}_f^T \varphi_f'\left(\widehat{V}_f^T \phi_f\right)\right), \tag{27}$$

$$\dot{\widehat{W}}_l = \text{proj}\left(\Gamma_3 \varphi_l\left(\widehat{V}_l^T \phi_l\right) r\right), \tag{28}$$

$$\dot{\widehat{V}}_l = \text{proj}\left(\Gamma_4 \phi_l r \widehat{W}_l^T \varphi_l'\left(\widehat{V}_l^T \phi_l\right)\right), \tag{29}$$

where $\Gamma_1 \in \mathbb{R}^{(F_1+1)\times(F_1+1)}$, $\Gamma_2 \in \mathbb{R}^{5\times 5}$, $\Gamma_3 \in \mathbb{R}^{(L_1+1)\times(L_1+1)}$, and $\Gamma_4 \in \mathbb{R}^{4\times 4}$ are diagonal gain matrices that are positive definite, and $\text{proj}(\cdot)$ defines the smooth projection algorithm in [14] that ensures the bounding of the NN weight estimates. Moreover, the closed-loop error dynamics can be developed by substituting (23) and (24) into (19) to get

$$\begin{aligned} M\dot{r} &= \chi - k_3 r + \left(k_2 + \hat{M}\alpha_2\beta_1\right) e_f - k_4 r \\ &\quad + M\alpha_2 \left[-k_1 \text{sgn}(r) - k_2 r - \beta_1 e_f\right] \\ &\quad - \left(\widetilde{W}_f^T\right) \left(\varphi_f\left(\widehat{V}_f^T \phi_f\right)\right) - e \\ &\quad + \left(\widetilde{W}_l^T\right) \left(\varphi_l\left(\widehat{V}_l^T \phi_l\right)\right) \\ &\quad - \widehat{W}_f^T \left(\varphi_f'\left(\widehat{V}_f^T \phi_f\right) \widetilde{V}_f^T \phi_f\right) \\ &\quad + \widehat{W}_l^T \left(\varphi_l'\left(\widehat{V}_l^T \phi_l\right) \widetilde{V}_l^T \phi_l\right). \end{aligned} \tag{30}$$

The ideal weights of both the NNs are assumed to be bounded by known constants such that $\| V_f \| = \text{trace}\left(V_f^T V_f\right) \leq \overline{V_f}$, $\| W_f \| = \leq \overline{W_f}$, $\| V_l \| = \text{trace}\left(V_l^T V\right) \leq \overline{V_l}$, and $\| W_l \| \leq \overline{W_l}$. Similarly, the activation functions of the NNs and their derivatives, φ_f, φ_f', φ_l, and φ_l' are also assumed to be bounded.

IV. Stability Analysis

A Lyapunov-based analysis is carried out to ensure the safe implementation and the stability of the motor and FES controllers designed for knee extension exercises. A common Lyapunov function candidate is designed such that it is positive definite, and continuously differentiable, denoted by $V_q : \mathcal{D} \times \mathbb{R}_{\geq 0} \to \mathbb{R}_{\geq 0}$, is given as

$$\begin{aligned} V_q(y,t) \triangleq & \tfrac{1}{2}e^2 + \tfrac{1}{2}Mr^2 + \tfrac{1}{2}e_f^2 + \tfrac{1}{2}\left(\widetilde{W}_f^T \Gamma_1^{-1} \widetilde{W}_f\right) \\ & + \tfrac{1}{2}\text{trace}\left(\widetilde{V}_f^T \Gamma_2^{-1} \widetilde{V}_f\right) + \tfrac{1}{2}\left(\widetilde{W}_l^T \Gamma_3^{-1} \widetilde{W}_l\right) \\ & + \tfrac{1}{2}\text{trace}\left(\widetilde{V}_l^T \Gamma_4^{-1} \widetilde{V}_l\right), \end{aligned} \tag{31}$$

where $\mathcal{D} \subseteq \mathbb{R}^{\upsilon}$ is given as $\mathcal{D} \triangleq \{y \in \mathbb{R}^{\upsilon} \,|\, \|y\| < \gamma\}$, $\upsilon = 3 + (F_1 + 1) + 5F_1 + (L_1 + 1) + 4L_1$, $\gamma \in \mathbb{R}_{>0}$ is a known constant which satisfies the inequality $\gamma \leq \inf\left\{\rho^{-1}\left(\left(\sqrt{k_4}\delta, \infty\right)\right)\right\}$, $\delta \in \mathbb{R}$ is a known constant and is defined as $\delta \triangleq \min\left(\alpha_1, \frac{k_4}{2}, \frac{\beta_1}{2} - \frac{\varepsilon_2}{2}\right)$, and $\varepsilon_2 \in \mathbb{R}_{>0}$ is a user-selectable constant. Based on the subsequent stability analysis, $\mathcal{S}_{\mathcal{D}}$ denotes an acceptable set of initial conditions that is defined as

$$\mathcal{S}_{\mathcal{D}} \triangleq \left\{ y \in \mathbb{R}^{\upsilon} \,\middle|\, \sqrt{\lambda_2 \lambda_1^{-1}} \|y(t_0)\| \leq \gamma \right\}. \tag{32}$$

Additionally, V_q can be bounded such that

$$\lambda_1 \|y\|^2 \leq V_q \leq \lambda_2 \|y\|^2, \tag{33}$$

where

$$\begin{aligned} \lambda_1 \triangleq & \tfrac{1}{2}\min\left(1, c_m, \lambda_{\min}\left\{\Gamma^{-1}\right\}, \lambda_{\min}\left\{\Gamma_2^{-1}\right\}, \right. \\ & \left. \lambda_{\min}\left\{\Gamma_3^{-1}\right\}, \lambda_{\min}\left\{\Gamma_4^{-1}\right\}\right), \\ \lambda_2 \triangleq & \tfrac{1}{2}\max\left(1, c_M, \lambda_{\max}\left\{\Gamma^{-1}\right\}, \lambda_{\max}\left\{\Gamma_2^{-1}\right\}, \right. \\ & \left. \lambda_{\max}\left\{\Gamma_3^{-1}\right\}, \lambda_{\max}\left\{\Gamma_4^{-1}\right\}\right), \end{aligned}$$

where $\lambda_{\min}\{\cdot\}$ is the minimum eigenvalue of $\{\cdot\}$, $\lambda_{\max}\{\cdot\}$ is the maximum eigenvalue of $\{\cdot\}$, and $y : \mathbb{R}_{\geq 0} \to \mathbb{R}^{\upsilon}$ denotes a concatenated error vector defined as

$$y \triangleq \left[z^T, \quad \widetilde{W}_f^T \ , \text{vec}\left(\widetilde{V}_f\right)^T, \widetilde{W}_l^T, \text{vec}\left(\widetilde{V}_l\right)^T \right]^T. \tag{34}$$

Using (34), V_q can be further bounded as

$$\lambda_1 \|z\|^2 \leq V_q \leq \lambda_2 \|z\|^2 + v_1, \tag{35}$$

where v_1 is defined as

$$\begin{aligned} v_1 \triangleq & \tfrac{1}{2}\lambda_{\max}\left\{\Gamma_1^{-1}\right\} \left\|\widetilde{W}_f\right\|_{\max}^2 + \tfrac{1}{2}\lambda_{\max}\left\{\Gamma_3^{-1}\right\} \left\|\widetilde{W}_l\right\|_{\max}^2 \\ & + \tfrac{1}{2}\lambda_{\max}\left\{\Gamma_2^{-1}\right\} \left\|\text{vec}\left(\widetilde{V}_f\right)\right\|_{\max}^2 \\ & + \tfrac{1}{2}\lambda_{\max}\left\{\Gamma_4^{-1}\right\} \left\|\text{vec}\left(\widetilde{V}_l\right)\right\|_{\max}^2, \end{aligned} \tag{36}$$

Theorem 1. *If the knee extension dynamics in (1) satisfy Assumptions 1-4, the control inputs in (23) and (24), and the NN adaptation laws in (26), (27), (28), and (29) yield semi-global trajectory tracking to an ultimate bound in the sense that*

$$\begin{aligned} \|y(t)\|^2 \leq & \tfrac{\lambda_2}{\lambda_1}\|y(t_0)\|^2 \exp\left(-\delta(t - t_0)\right) \\ & + \tfrac{\upsilon}{\lambda_1 \delta}\left(1 - \exp\left(-\delta(t - t_0)\right)\right), \end{aligned} \tag{37}$$

$\forall t \in [t_0, \infty)$, where $\upsilon \triangleq \delta v_1 + \frac{k_1^2}{2\varepsilon_2}$, and ε_2 is a selectable constant, provided that $y(t_0) \in \mathcal{S}_{\mathcal{D}}$ and the following conditions are satisfied

$$c_m \alpha_2 k_1 \geq \Phi, \quad \sqrt{\frac{\upsilon}{\delta \lambda_1}} < \gamma \tag{38}$$

$$k_3 + c_m \alpha_2 k_2 \geq c_M \alpha_2 \beta_1 \frac{\varepsilon_1}{2}, \quad \frac{\beta_1}{2} \geq c_M \alpha_2 \beta_1 \frac{1}{2\varepsilon_1}, \tag{39}$$

Proof: Let $y : [t_0, \infty) \to \mathbb{R}^{\upsilon}$ be a Filippov solution to the differential inclusion $\dot{y} \in K[h](y)$, where $K[\cdot]$ is the differential inclusion operator given in [15], and $h : \mathbb{R}^{\upsilon} \to \mathbb{R}^{\upsilon}$ is defined as $h(y) \triangleq \left[\dot{e}, \quad \dot{r}, \quad \dot{e}_f, \quad \dot{\widehat{W}}_f^T \ , \text{vec}\left(\dot{\widehat{V}}_f\right)^T, \dot{\widehat{W}}_l^T, \text{vec}\left(\dot{\widehat{V}}_l\right)^T \right]^T$. As the closed-loop error dynamics in (30) are discontinuous, there exists a time derivative of V_q almost everywhere (a.e) such that $\dot{V}_q(y) \overset{\text{a.e.}}{\in} \dot{\tilde{V}}_q(y)$, where $\dot{\tilde{V}}_q(y)$ is the generalized time derivative of V_q and is defined based on [16, Equation 13] as $\dot{\tilde{V}}_q \triangleq \bigcap_{\xi \in \partial V_q(y)} \xi^T \left[K[h]^T(y), 1\right]^T$, where $\partial V_q(y)$ denotes the Clarke generalized gradient of V_q. Since V_q is continuously differentiable with respect to y, $\partial V_q(y) = \nabla V_q(y)$, where ∇ is the gradient operator. Thus, taking the generalized time derivative of V_q defined in (31), and substituting the closed-loop error dynamics in (30), the auxiliary error signal defined in (3), the filtered error signal defined in (4), and the NN update laws defined in (26)-(29)

yields

$$\begin{aligned}\dot{\tilde{V}}_q \quad \subseteq \quad & e\left[r-\alpha_1 e-K\left[\alpha_2 e_f\right]\right]+r\left[\chi-Cr\right.\\ & -k_3 r+\left(k_2+\hat{M}\alpha_2\beta_1\right)e_f-k_4 r-e\\ & +M\alpha_2\left[-k_1 K\left[\operatorname{sgn}(r)\right]-k_2 r-\beta_1 e_f\right]\\ & +\left(\widetilde{W}_l^T\right)\left(\varphi_l\left(\widehat{V}_l^T\phi_l\right)\right)-\left(\widetilde{W}_f^T\right)\left(\varphi_f\left(\widehat{V}_f^T\phi_f\right)\right)\\ & -\widehat{W}_f^T\left(\varphi_f'\left(\widehat{V}_f^T\phi_f\right)\widetilde{V}_f^T\phi_f\right)\\ & \left.+\widehat{W}_l^T\left(\varphi_l'\left(\widehat{V}_l^T\phi_l\right)\widetilde{V}_l^T\phi_l\right)\right]\\ & +e_f\left[K\left[-k_1\operatorname{sgn}(r)\right]-k_2 r+\alpha_2 e-K\left[\beta_1 e_f\right]\right]\\ & -\widetilde{W}_f^T\left[-\left(\varphi_f\left(\widehat{V}_f^T\phi_f\right)r\right)\right]\\ & -\widetilde{W}_l^T\left[\left(\varphi_l\left(\widehat{V}_l^T\phi_l\right)r\right)\right]\\ & -\widetilde{V}_f^T\left[-\left(\phi_f r\widehat{W}_f^T\varphi_f'\left(\widehat{V}_f^T\phi_f\right)\right)\right]\\ & -\widetilde{V}_l^T\left[\left(\phi_l r\widehat{W}_l^T\varphi_l'\left(\widehat{V}_l^T\phi_l\right)\right)\right].\end{aligned} \tag{40}$$

Implementing (21) to bound χ, using $-r^T K\left[\operatorname{sgn}(r)\right] \leq -|r|$ and $|K\left[\operatorname{sgn}(r)\right]| \leq 1$, canceling terms, and the definition of $\widehat{M}$ above (25), Assumption 1, and the gain conditions stated in (38) and (39), $\dot{V}_q$ can be bounded as

$$\begin{aligned}\dot{V}_q \quad \overset{\text{a.e.}}{\leq} \quad & -\alpha_1 e^2+r\|\chi\|-k_3 r^2-r\tilde{M}\alpha_2\beta_1 e_f\\ & -M\alpha_2 k_1|r|-M\alpha_2 k_2 r^2-k_4 r^2\\ & +k_1 e_f\left|K\left[\operatorname{sgn}(r)\right]\right|-\beta_1 e_f^2.\end{aligned} \tag{41}$$

Completing the squares and applying Young's Inequality allows (41) to be further bounded as

$$\begin{aligned}\dot{V}_q \quad \overset{\text{a.e.}}{\leq} \quad & -\alpha_1 e^2-\frac{k_4}{2}r^2-\left(\frac{\beta_1}{2}-\tfrac{\varepsilon_2}{2}\right)e_f^2\\ & +\frac{\rho^2\left(\|z\|\right)\|z\|^2}{2k_4}+\tfrac{k_1^2}{2\varepsilon_2}.\end{aligned} \tag{42}$$

Using the definitions of V from the theorem statement, the upper bound in (35), the gain values in (39), the inequality $\|y\| \geq \|z\|$, and the definitions of $\mathcal{D}$ and δ below (31), (42) can then be upper bounded as

$$\dot{V}_q \quad \overset{\text{a.e.}}{\leq} \quad -\delta V_q+v, \tag{43}$$

which can be solved to yield

$$\begin{aligned}V_q(t) \quad \leq \quad & V_q(t_0)\exp\left(-\delta\left(t-t_0\right)\right)\\ & +\tfrac{v}{\delta}\left[1-\exp\left(-\delta\left(t-t_0\right)\right)\right],\end{aligned} \tag{44}$$

provided that $y \in \mathcal{D}, \forall t \in [t_0, \infty)$. A sufficient condition for $y \in \mathcal{D}, \forall t \in [t_0, \infty)$ is that $y(t_0) \in S_D$ and the gain conditions in (39) is achieved. Using (33) with (44) yields the result in the theorem statement. Picking the gains k_1, k_2, k_3, k_4, α_1, α_2, and β_1, appropriately will ensure that $y \in \mathcal{S}_{\mathcal{D}}$ and that all the gain conditions are met in (38)-(39). Additionally, from (22), (34), and (37), combined with (2) and (3), it can be determined that $x, \dot{e}, \dot{x}, \hat{W}_f, \hat{V}_f, \hat{W}_l, \hat{V}_l \in \mathcal{L}_\infty$. It can further be proven that $u_f, u_m \in \mathcal{L}_\infty$. Since $y \in \mathcal{D}, \forall t \in [t_0, \infty)$ is proven to be true provided that $y(t_0) \in S_D$ and the gain conditions are satisfied, the prior assumption that x, $\dot{x}$, and u_f lie in a compact set is proven to be valid. ■

V. Conclusion

In this paper, NN- and ARISE-based controllers were designed for a hybrid exoskeleton that enables leg extension exercises for individuals with NCs, despite the FES control effectiveness matrix and other dynamic terms being unknown. In this work, the FES effectiveness and the dynamics were approximated using NNs. Moreover, Lyapunov-based adaptive laws were developed to estimate the NNs' ideal weights in real-time. A Lyapunov-based analysis was performed to prove semi-global exponential tracking of the knee joint angle to an ultimate bound. Future efforts will focus on experiments and modifications in the stability analysis to remove the ultimate bound from the current stability result.

References

[1] Adam Amorese and Alice Ryan. Home-based tele-exercise in musculoskeletal conditions and chronic disease: A literature review. *Front. in Rehab. Sci.*, 3, 02 2022.

[2] Mindy Lipson Aisen, H Igo Krebs, Neville Hogan, Fletcher McDowell, and Bruce T Volpe. The effect of robot-assisted therapy and rehabilitative training on motor recovery following stroke. *Archiv. Neuro.*, 54(4):443–446, 1997.

[3] R. Riener, T. Nef, and G. Colombo. Robot-aided neurorehabilitation of the upper extremities. *Med. Biol. Eng. Comput.*, 43(1):2–10, January 2005.

[4] S.A. Combs, S.P. Kelly, R. Barton, M. Ivaska, and K. Nowak. Effects of an intensive, task-specific rehabilitation program for individuals with chronic stroke: a case series. *Disabil. Rehabil.*, 32(8):669–78, 2010.

[5] Radhika Chemuturi, Farshid Amirabdollahian, and Kerstin Dautenhahn. Adaptive training algorithm for robot-assisted upper-arm rehabilitation, applicable to individualised and therapeutic human-robot interaction. *J. Neuroeng. Rehabil.*, 2013.

[6] M. Gomis, L.M. Gonzalez, F. Querol, J.E. Gallach, and J.L. Toca-Herrera. Effects of electrical stimulation on muscle trophism in patients with hemophilic arthropathy. *Arch Phys Med Rehabil*, 90(11):1924–30, November 2009.

[7] B. C. Allen, C. A. Cousin, C. A. Rouse, and W. E. Dixon. Robust cadence tracking for switched FES-cycling with an unknown time-varying input delay. *IEEE Trans. Control Syst. Tech.*, 30(2):827–834, 2022.

[8] K.K. Shyu and J.J. Yan. Robust stability of uncertain time-delay systems and its stabilization by variable structure control. *Int. J. Control*, 57(1):237–246, 1993.

[9] P. M. Patre, W. MacKunis, K. Kaiser, and W. E. Dixon. Asymptotic tracking for uncertain dynamic systems via a multilayer neural network feedforward and RISE feedback control structure. *IEEE Trans. Autom. Control*, 53(9):2180–2185, 2008.

[10] S. Basyal, J. Ting, and B. C. Allen. Rise-like saturated control for nonsmooth and switched nonlinear systems. In *ASME Int. Mech. Eng. Congr. Expo. (IMECE)*, 2023.

[11] K. Mishra, J. Ting, S. Basyal, and B. C. Allen. Robust control of a nonsmooth or switched Euler-Lagrange dynamic system using ARISE control. In *Proc. Conf. Decis. Control*, 2024.

[12] F. L. Lewis, A. Yesildirek, and K. Liu. Multi-layer neural network controller with guaranteed tracking performance. *IEEE Trans. Neural Netw.*, 7(2):388–399, March 1996.

[13] R. Sun, M. Greene, D. Le, Z. Bell, G. Chowdhary, and W. E. Dixon. Lyapunov-based real-time and iterative adjustment of deep neural networks. *IEEE Control Syst. Lett.*, 6:193–198, 2022.

[14] Z. Cai, M. S. de Queiroz, and D. M. Dawson. A sufficiently smooth projection operator. *IEEE Trans. Autom. Control*, 51(1):135–139, January 2006.

[15] B. E. Paden and S. S. Sastry. A calculus for computing Filippov's differential inclusion with application to the variable structure control of robot manipulators. *IEEE Trans. Circuits Syst.*, 34(1):73–82, January 1987.

[16] D. Shevitz and B. Paden. Lyapunov stability theory of nonsmooth systems. *IEEE Trans. Autom. Control*, 39 no. 9:1910–1914, 1994.

User field testing for robot wheelchairs: A mixed-method approach

Jorge L. Candiotti, Sivashankar Sivakanthan, Benjamin Gebrosky, Rosemarie Cooper, Rory A. Cooper, *Member, IEEE*

Abstract— **Enhancing mobility and independence for electric power wheelchair (EPW) users is often hindered by architectural barriers. Robotic wheelchairs with innovative mechanisms offer potential solutions, but current technologies are typically confined to lab evaluations with limited user input. This study employed a mixed-method approach to assess the effectiveness of a legged-wheel robotic wheelchair compared to standard EPWs in indoor and outdoor environments. Driving metrics, usability assessments, and user feedback were collected. EPW users found the robotic wheelchair challenging to learn, however, its overall usability and effectiveness in meeting their mobility needs were comparable to their EPWs. The robotic wheelchair also demonstrated improved stability and reduced vibration on uneven terrains. Feedback highlighted the benefits of robotic wheelchair applications when accessibility is not available compared to existing EPWs. Furthermore, participants suggested improvement of seating functions, better maneuverability in tight spaces, and enhanced indoor accessibility similar to EPWs. While standardized tools confirmed the robotic wheelchair's effectiveness compared to existing EPWs, user perceptions are essential to validate these findings. The study concludes that robotic wheelchairs can enhance outdoor safety and comfort but must integrate fundamental functions of existing EPWs to support users' health and indoor mobility.**

I. INTRODUCTION

Electric power wheelchairs (EPW) are essential for people with mobility impairments and the aging population, assisting with indoor navigation and daily activities. Approximately 80 million people need wheelchairs worldwide, with EPW becoming popular with advances in technology [1]. Despite its benefits for indoor maneuvering, architectural barriers in the community limit the mobility of EPW users and increase the risk of injury when navigating uneven terrains, curbs, or inclined surfaces [2-4].

Over the past 20 years, robotic wheelchairs have emerged in both research and market to enhance the mobility and independence of wheelchair users [5, 6]. These robotic wheelchairs incorporate features such as dynamic suspensions, additional degrees of freedom, and expanded ranges of motion to address architectural barriers [7]. Despite significant advances in the field, only a limited number of robotic wheelchairs have successfully transitioned to the market [8]. A key limitation in the development of robotic wheelchairs lies in the insufficient integration of participatory action design, which actively involves end-users in the development process, leading to devices that may not fully address real-world needs [5, 6, 8]. Additionally, much of the testing for robotic wheelchairs has been restricted to controlled laboratory settings, limiting potential evidence of practical use and effectiveness in everyday environments. Assistive technology competitions such as Cybathlon have promoted the innovation of robotic wheelchairs, particularly in navigating architectural barriers [9]. However, the focus on completing tasks in the shortest time may prioritize competition-specific performance over the translation of research into functional and user-centered designs suitable for daily use. Addressing these challenges requires a shift toward more inclusive design processes, real-world testing, and the development of standardized metrics to ensure that robotic wheelchairs meet the mobility and health needs of wheelchair users in everyday life.

The study aims to evaluate the effectiveness and usability of a testing robotic wheelchair, called Mobility Enhancement Robot (MEBot), in real-world indoor and outdoor environments with experienced EPW users. The primary objective is to explore the benefits and design limitations of MEBot through standardized assessment tools, complemented by end-users' feedback. Specifically, we hypothesize that (1) experienced EPW users will rate similar or better scores of usability and effectiveness of MEBot and their EPWs to meet mobility needs in daily environments, (2) MEBot will demonstrate higher stability and less discomfort than participants' EPWs in outdoor environments, and (3) the median NASA-TLX workload scores operating MEBot over curbs will be <40, indicating low workload demand. The findings aim to provide evidence of the MEBot's effectiveness for daily use while identifying potential improvements. The study seeks to refine standard assessment tools tailored to evaluate robotic wheelchairs, focusing on the ability to enhance users' mobility, health outcomes, and overall quality of life.

II. METHODS

A. Testing wheelchair: MEBot

MEBot [10] followed a participatory action design and engineering approach, incorporating feedback from EPW users throughout the design process to address their mobility challenges, particularly when navigating architectural barriers. Previous focus groups confirmed community mobility

*Research supported by the US Department of Veterans Affairs (VA) Career Development Awards (#A3806) and VA Senior Research Career Scientist (#A3916).

Jorge L. Candiotti and Rory A. Cooper are with the Department of Bioengineering, University of Pittsburgh, Pittsburgh, PA, USA

Rosemarie Cooper is with the Department of Rehabilitation Science and Technology, University of Pittsburgh, PA, USA

Jorge L. Candiotti, S. Sivakanthan, Ben Gebrosky, Rosemarie Cooper, Rory A. Cooper are with the Human Engineering Research Laboratories, VA Pittsburgh Healthcare Systems, Pittsburgh, PA, 15206 USA (phone: 412-822-3696, e-mail: jlc118@pitt.edu)

challenges, including the risk of tipping on uneven surfaces and steep inclines and restricted sidewalk access due to obstructed or unavailable curb cuts [4, 11]. These findings led to design requirements prioritizing dynamic adaptability to navigate such environments while maintaining stability and comfort [12].

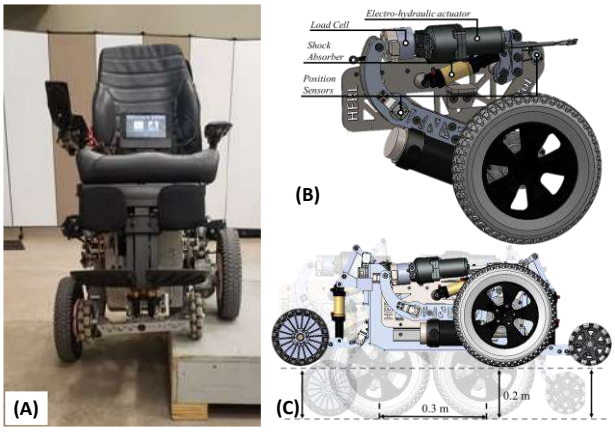


Fig 1: (A) *MEBot leveled* on an uneven surface (B) Side view of MEBot spring-elastic actuator mechanism and (C) MEBot Range of Motion

MEBot features four Series Elastic electro-hydraulic Actuators (SEA) connected to the wheels, enabling vertical motion and dynamic suspension on each side of the base. Two independently mounted driving wheels with separate carriages provide differential drive and horizontal repositioning along the base, allowing efficient maneuvering in tight spaces (Fig. 1). These combined mechanisms enable 5 unconstrained degrees of freedom for rotation and translation in three axes/planes. This design enhances stability on slopes up to 15° slope, shock absorption on uneven terrains, and curbs negotiation up to 20.3 cm high. MEBot also integrates an OEM power seating system, featuring a back and seat air cushion, trunk support, and actuated seat recline, tilt-in-space, and leg rest that can be adjusted by the researcher before the study.

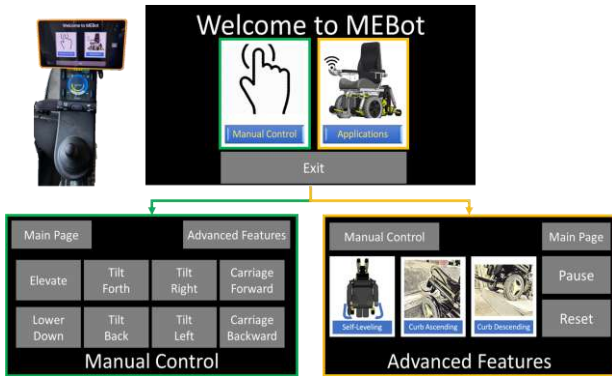


Fig 2. User Interface wireframe of MEBot mobility applications

A graphical user interface (GUI) enables users to select MEBot mobility applications via touchscreen (Fig. 2). The GUI wireframe includes a home screen with options for 'manual' and 'advanced' applications. Manual applications allow users to adjust basic mobility functions, such as wheelchair elevation, back-forth tilt, side tilt, and drive wheel configuration. Advanced applications include self-leveling and curb negotiation features, which users can activate or deactivate as needed. The self-leveling application keeps the seat horizontally level when driving on uneven surfaces by measuring the surface gradient (i.e. pitch and roll) [13] using an Inertial Measurement Unit (IMU) integrated into the frame. These measurements are then processed through a rotation transformation matrix to reposition the SEA mechanisms relative to a horizontal plane.

The curb negotiation application follows a two-step process 1) prompting the user to align perpendicular and adjacent to the curb, and 2) activating the application, allowing MEBot to take control. This autonomous process uses a finite state machine to operate each SEA mechanism, ensuring stability and safety at every stage [14, 15]. A preliminary usability evaluation with EPW users confirmed that MEBot's advanced mobility applications consistently overcome engineered tasks representing architectural barriers in the community [12, 16].

A. Study Procedure

Experienced EPW users were recruited at the National Veterans Wheelchair Games (NVWG) in Portland, Oregon. All participants provided informed consent. The Veterans Affairs Pittsburgh Healthcare System Institutional Review Board approved the study (Study ID: 1690689). After consent, participants completed a demographics questionnaire and information about their wheelchairs. They were then randomized to determine the order of using MEBot or their own EPW in the driving course. Before the study, researchers attached an IMU datalogger to each participant's EPW frame to measure vibration and seat angle changes. If the participants used MEBot, researchers configured its seating and driving parameters to match their EPWs, ensuring comfort and minimizing learning bias. Participants received MEBot training until they and the researcher felt confident in their familiarity with the device. Training for each participant took approximately 15 minutes. This included a checklist of tasks for demonstrating the user interface and applications, having participants replicate the tasks, and a driving session indoors, driving over an inclined surface, and up a curb.

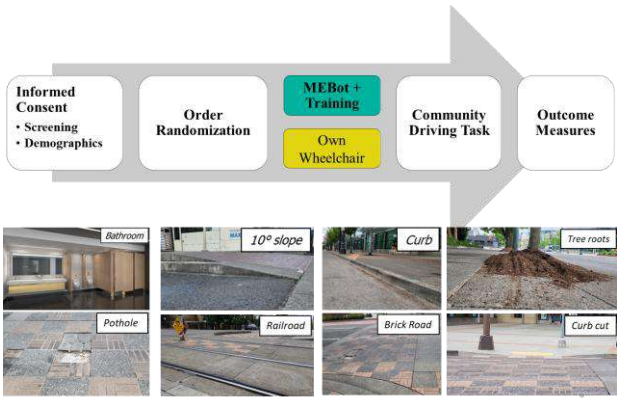


Fig 3. Protocol and Indoor and Outdoor mobility tasks

Participants navigated the driving course using both wheelchairs while maintaining an average speed of 1.2 m/s, comparable to a pedestrian crossing the street [17]. A researcher or clinician accompanied them throughout the course to ensure safety and provide pacing guidance. The driving course included real-world indoor and outdoor mobility tasks from current literature and prior focus groups (Fig. 3) [2, 18-20]. Each task was performed twice. Participants did not perform the last task of navigating a

standard curb height of 15 cm with their EPW due to manufacturer limitations (7.6 cm) and at risk of tipping.

At the end of the study, participants rated the ease of use and effectiveness of each wheelchair in meeting their mobility needs using the System Usability Scale (SUS) and the Assistive Technology Device-Predisposition Assessment (ATD-PA). Participants also rated the NASA Task Load Demand (NASA-TLX) for navigating curbs with MEBot and their daily driving with their EPW to serve as a baseline. Quantitative metrics such as seat angle changes and 3-axis accelerations were recorded throughout the driving course to assess the stability and vibration exposure of each wheelchair. Additionally, follow-up questions were asked about their responses to assessment tools to gather on the benefits, challenges, and areas for improvement of MEBot.

B. Outcome Measures

The SUS measures a device's usability in performing tasks. The questionnaire includes 10 questions rated on a 5-point Likert scale, from 1 (Strongly Disagree) to 5 (Strongly Agree). The overall score ranges from 0 to 100, with a SUS score of 69 considered an acceptable usability score in different studies [21, 22].

The Assistive Technology Device Predisposition Assessment (ATD-PA) tool evaluates user satisfaction with assistive technology based on their needs. It was adapted to assess participants' mobility, accessibility, positioning, and safety in daily environments. The tool included 12 questions rated on a 5-point scale [23].

The NASA-TLX measures the workload imposed by a given task [24, 25]. The short version used in this study consists of six questions, each addressing a unique dimension of workload: mental demand, physical demand, temporal demand, performance, effort, and frustration. Participants rated these six dimensions on a 0-100 scale. Each assessment tool included a comment section in each subscale for participants to describe their responses.

C. Data Analysis

Demographic questionnaire and wheelchair characteristics were described using mean and standard deviation. The SUS, ATD-PA, and NASA-TLX sub-scores were described with median and interquartile ranges since the data were not normally distributed. For hypothesis 1, the SUS and ATD-PA sub-scores were analyzed using a non-parametric Wilcoxon Signed Rank test for pairwise comparisons of usability and effectiveness between wheelchairs. Additionally, a minimum SUS score of 69 was considered an acceptable usability score. To test hypothesis 3, NASA-TLX median scores were calculated to ensure participants' task load demand to climb over curbs with MEBot was <40. A score of 40 falls within the lowest 25th percentile for tasks classified as 'robot operation' and 'medical tasks' [26]. The task load demand associated with their daily EPW driving was also recorded to create a baseline and facilitate a descriptive comparison, despite being a distinct task.

A datalogger with a built-in IMU was placed on the wheelchair frames to record acceleration and seat angles in three axes at a 100 Hz sampling rate for hypothesis 2. Discomfort was measured in terms of vibration exposure by calculating the total root-mean-square (RMS) and vibration dose value (VDV) following the ISO 2631 guidelines: Evaluation of human exposure to whole-body vibration [27]. The total RMS and VDV represented cumulative vibration and shock exposure over time. Seat stability was calculated by measuring the average magnitude of the peak seat angles in the pitch and roll directions during each driving task. The results were averaged and analyzed using within-subjects paired sample t-test to determine if MEBot significantly demonstrated higher seat stability and less discomfort than their EPWs on community driving tasks. The level of significance was set $\alpha = 0.05$ for all analyses. All statistical analyses were performed using Statistical Package for the Social Science (SPSS Inc., Chicago, IL). Participants' feedback was categorized into themes: Dimensions, Safety, Seating Functionality, Discomfort, Ease of Use, and Overall Effectiveness which encompassed SUS, ATD-PA, and NASA-TLX subscales and using NVivo 14 software.

III. RESULTS

A. Subjects

Ten experienced power wheelchair users (9 males, 1 female) aged 61.7 ± 10.9 years, with an average of 6.9 ± 5.4 years of EPW use, were recruited to evaluate the effectiveness and usability of MEBot compared to their existing EPWs in daily environments. Participants spent an average of 10.5 ± 3.3 hours per day in their wheelchairs and had impairments including Spinal Cord Injury (n=6), Multiple Sclerosis (n = 2), Stroke (n = 1), and Guillain-Barre (n =1). Their existing EPWs were evenly split between mid-wheel and front-wheel drive, featuring four seating functions (n = 9) and an EZ-lock mechanism (n =3) located under their EPWs for transportation securement. Participants with pressure injuries or those reporting back, pelvic, or thigh pain were excluded from the study. This criterion helps distinguish between discomfort caused by seating and discomfort from driving on uneven terrain. It also ensures that participants can tolerate sitting for the entire study duration.

B. Usability

Participants reported no significant difference in the usability of MEBot (75.8 ± 11.2) and their EPWs (91.8 ± 13.7) when navigating indoor and outdoor environments, both rated as having 'good' usability on the SUS scale. Participants

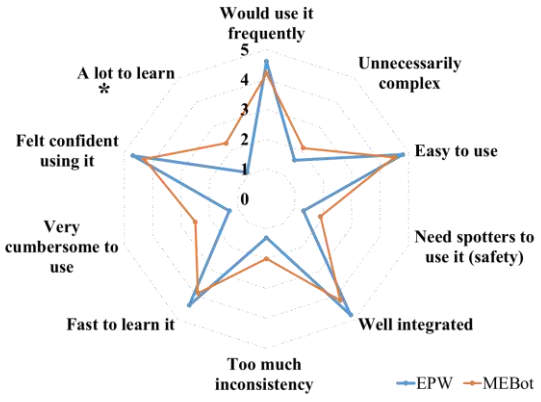


Fig 4. Usability Median sub-scores of MEBot and EPWs. *p <0.05

also indicated the need to learn more about the MEBot interface and applications compared to their EPWs (Figure 4).

C. *Effectiveness of wheelchairs to meet mobility needs*

Results showed no significant differences between MEBot and participants' EPWs in meeting their needs for mobility, accessibility, positioning, and safety in daily environments. Furthermore, participants rated both wheelchairs 4 or higher on each ATD-PA subscale. However, results indicated a coefficient of variation of 10% or higher in the subscales highlighted in Table I, suggesting variability in EPW users' preference to meet their mobility needs.

TABLE I. Effectiveness median and IQR sub-scores of MEBot and participants' EPW to meet users' mobility needs. No significant differences.

This device will	EPW	MEBot
Achieve my primary needs	5.0 [4.8 - 5.0]	5.0 [3.0 - 5.0]
benefit me and improve my Quality of life	5.0 [4.0 - 5.0]	4.5 [3.8 - 5.0]
give me confidence in using its features	5.0 [4.8 - 5.0]	5.0 [4.8 - 5.0]
make me feel more secure (safe) while using it	5.0 [4.0 - 5.0]	4.5 [3.0 - 5.0]
fit well with my routine	5.0 [4.0 - 5.0]	4.5 [3.8 - 5.0]
allow me to use it without stress/discomfort/fatigue	5.0 [4.0 - 5.0]	5.0 [4.0 - 5.0]
offer accommodations to use it successfully	5.0 [4.8 - 5.0]	5.0 [4.8 - 5.0]
physically fit the desired environments	4.5 [3.0 - 5.0]	4.5 [4.0 - 5.0]
make me feel comfortable using it around family	5.0 [4.8 - 5.0]	5.0 [5.0 - 5.0]
make me feel comfortable using it around friends	5.0 [4.8 - 5.0]	5.0 [5.0 - 5.0]
make me feel comfortable using it at work or school	5.0 [5.0 - 5.0]	5.0 [5.0 - 5.0]
make me feel comfortable using it around the community	5.0 [5.0 - 5.0]	5.0 [5.0 - 5.0]

D. *Task Load Demand when climbing over curbs*

Two participants rated a high mental demand, scoring over 40, when using MEBot to negotiate curbs. However, overall, the median NASA-TLX sub-scores met the hypothesis of being below 40. Participants also reported a low task load demand when negotiating curb with MEBot, similar to operating their EPWs in daily environments (Fig. 5).

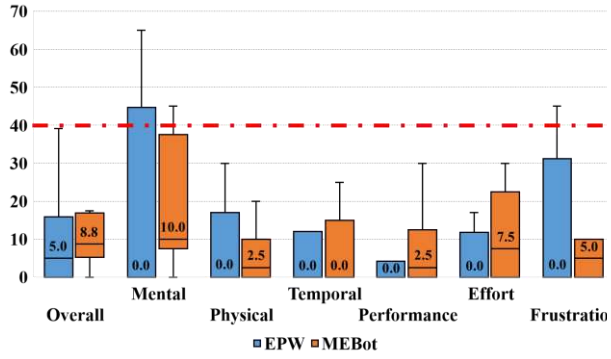


Fig 5. Median task load demand using MEBot to navigate curbs compared to daily EPWs use. Significant NASA-TLX sub scores >40.

E. *Stability and Discomfort Levels*

MEBot significantly reduced pitch and roll seat angle variations and discomfort, showing lower RMS acceleration than participants' EPWs in both indoor and outdoor environments (Table II). Both wheelchairs scored discomfort values below the ISO 2631 health caution safety threshold (RMS < 1.6 m/s^2, VDV < 9.0 m/s$^{1.75}$). Exceeding these values over one hour could pose risks to EPW users. These results were particularly representative of outdoor environments on uneven and inclined surfaces.

TABLE II. Overall stability and discomfort results of MEBot and participants' EPW in indoor and outdoor environments. *p <0.05

Wheel chair	RMS (m/s^2)	VDV (m/s$^{1.75}$)	Max pitch (deg)	Max roll (deg)
EPW	1.1 ± 0.4	6.6 ± 1.8	12.4 ± 4.4	12.7 ± 3.7
MEBot	0. 8 ± 0.2*	5.7 ± 6.6	7.8 ± 3.0*	7.7 ± 2.1*

F. *Participants feedback*

Participants' perception of MEBot's mobility applications and interface were categorized into the themes provided in Fig. 6. These themes combined subscales from the SUS, ATD-PA, and NASA-TLX assessment tools, along with a 'seating functionality' theme. Key codes highlighted areas for improvement in MEBot, including wheelchair footprint constraints, the need for power seating functions, positive feedback on the user interface, and the requirement for more time to assess safety and comfort when using the self-leveling and curb negotiation applications in outdoor environments.

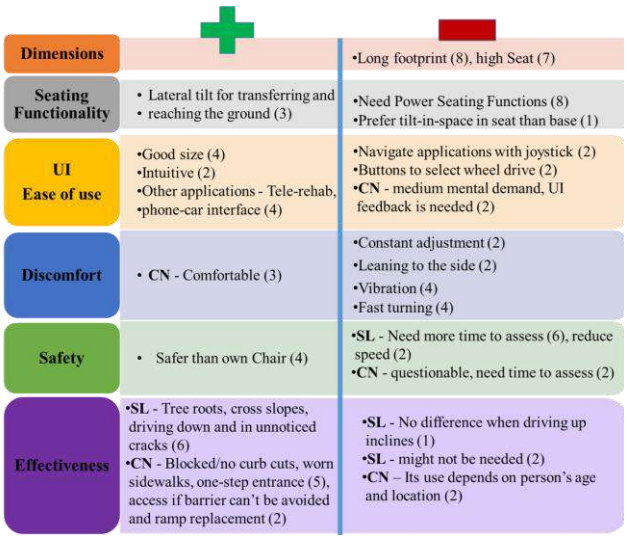


Fig 6. Participants' feedback on MEBot user interface (UI) and its mobility applications: self-leveling (SL) and curb negotiation (CN). Number of participants with similar feedback is indicated in parentheses.

IV. Discussion

The primary goal of the paper was to evaluate emerging robotic wheelchairs in real-world settings with the target population, focusing on their ability to meet mobility needs using both quantitative and qualitative outcome metrics. Specifically, the study assessed the usability and effectiveness of MEBot through a mixed-method approach, which

incorporated adapted assessment tools for robotic wheelchairs and gathered participants' perception of the device during navigation in real-world environments.

Participants reported that MEBot was similarly effective to their existing EPWs in meeting their mobility needs and improving their quality of life at home, work, and in the community. They also expressed high levels of confidence in operating MEBot and its potential to achieve their goals related to mobility, accessibility, safety, and repositioning. These results were further complemented by MEBot's higher stability and reduced discomfort compared to their EPW when navigating community environments. However, follow-up questions revealed additional insights that were not entirely aligned with the assessment tools responses. The findings were presented in themes related to the usability and feasibility of the device.

Dimensions: Although participants generally agreed that MEBot would physically fit desired environments better than their EPWs, eight out of ten participants experienced challenges maneuvering MEBot in indoor spaces such as toilet stalls and elevators due to its large footprint. In contrast, they were able to maneuver their EPW without issues.

Seat Functionality: Additionally, MEBot's seat height and lack of seating functions restricted participants from reaching bathroom sink counters. Although MEBot included seating functions available from the base using the 'manual screen'; its range of motion was comparatively less than their existing EPWs. This highlights the need for robotic wheelchair designs to incorporate the beneficial features of existing EPWs, including power seating functions and seating accommodations to meet user needs.

User interface Ease of use: MEBot demonstrated similar usability responses to participants' EPWs for operating its mobility applications and interface in indoors and in the community. Despite no statistical difference in SUS results, participants favored using their EPWs, likely due to their extensive experience using their wheelchair interface compared to the novelty of the MEBot interface. For example, while two participants found the MEBot interface intuitive to learn, three reported that it had complex features, indicating variability in preferences. Suggestions included reducing the number of screens and integrating all mobility applications into one screen. Additionally, dexterity is a crucial factor when developing touchscreen interfaces, as wheelchair users may have difficulties interacting with them. Two participants recommended alternative options for operating the MEBot interface, such as navigating and selecting applications with a joystick or using physical buttons, similar to the operation of their power seating functions.

Unexpected findings revealed that participants were comfortable with the dimensions of the 18 cm interface for visualizing options and did not expect physical interference with their daily activities. Furthermore, participants suggested that the large interface might offer additional applications for telerehabilitation or phone-car connection, similar to personal vehicles using Android Auto and CarPlay.

Effectiveness to meet mobility needs: When navigating in the community, more than half of the participants highlighted the potential benefits of self-leveling and curb negotiation applications enhancing safety and accessibility in challenging daily environments. More than half of participants suggested that the self-leveling can be useful for navigating over cracked sidewalks due to tree roots, cross slopes caused by driveway architecture, and for feeling safer and more stable when driving down steep streets. However, two participants felt that the self-leveling application was unnecessary due to the accessibility of their community, implying that MEBot applications might be less critical in urban areas with accessible infrastructure. On the other hand, participants who lived in rural areas acknowledged the benefits of MEBot applications where curb cuts are not commonly available and the likelihood of encountering uneven surfaces is higher.

Regarding the curb negotiation application, participants reported a great benefit of the application, specifically when curb cuts are less available due to construction or obstructed by crowds (e.g. at schools).

Safety and Discomfort: Participants concur with the autonomy of MEBot to complete the negotiation process but suggested visual or audio feedback when MEBot approaching the curb and while navigating over curb to reduce their mental demands and for situational awareness. Furthermore, one participant suggested locking the joystick to prevent unintentional use and human error.

Regarding the self-leveling application, participants suggested reducing the speed when descending slopes to minimize the risk of tipping forward. One participant noted no difference when driving up inclines compared to their EPW, suggesting that the actuation of the self-leveling application could be minimized in these scenarios. Participants did not report discomfort when operating the curb negotiation application but highlighted the constant adjustment and vibration sensation when driving outdoors with the self-leveling application activated. It was observed that the nature of the omnidirectional caster wheels to have gaps between their smaller wheels amplifies the vibration. The constant adjustment of the self-leveling can be optimized by increasing the tolerance of the inclination while keeping stability.

Most participants were not confident enough to assess the safety of both mobility applications in the driving course due to the limited time for the study and participants availability. This is a common concern for pilot studies evaluating the feasibility of the device. After addressing participants' feedback, the feasibility of the robotic wheelchair can be evaluated in participants' own environments for a longer period of time.

Limitations: The findings demonstrated that assessment tools may offer quantitative evidence to meet users' needs; however, there is evidence of ceiling effects, with participants rating high scores that reduce the tools' discriminatory power. Therefore, follow-up questions are important to gather the rationale of their responses, particularly to meet users' needs with different levels of impairment and living conditions.

The limited time and a small sample size were limitations in gathering in-depth feedback to address the mobility needs in their own environments and for people with different levels of impairment. For example, receiving only 15 minutes of training for a complex robotic wheelchair is likely inadequate.

Users may not have had sufficient time to become familiar with MEBot's controls and features, affecting their performance and perceptions. Furthermore, the novelty of MEBot compared to participants' EPWs could result in initial difficulties that skewed usability assessments unfavorably.

Existing EPWs are limited to overcome shallow curbs, restricting an effective assessment of MEBot curb negotiation application. For this case, efficacy and usability evaluation could be conducted a following a list of design criteria and through adapted standardized tools and new usability tools to evaluate novel mobility applications. With new technology rising, comparison could be performed between novel robotic wheelchairs

V. Conclusion

The findings highlighted the use of a mixed-methods approach to assess the usability and effectiveness of a robotic wheelchair in real-world environments. This study provides evidence of translational research addressing mobility needs unmet by existing EPWs, while also acknowledging the importance of incorporating the beneficial features of EPWs into the design of emerging robotics wheelchairs.

Future research should focus on developing adapted assessment tools tailored to individual mobility applications of this technology. Furthermore, longitudinal studies could offer deeper insight into the long-term effectiveness of robotic wheelchairs in enhancing the quality of life of wheelchair users.

Acknowledgment

The authors would like to thank the Human Engineering Research Laboratories' shop staff for their assistance with the design and development of the robotic wheelchairs, Ms. Nikitha Deepak for her support as the clinical coordinator for this study. This material is the result of work supported with resources and the use of facilities at the VA Pittsburgh Healthcare System. The contents do not represent the views of the U.S. Department of Veterans Affairs or the United States Government.

References

[1] W. H. Organization, *Wheelchair provision guidelines*. World Health Organization, 2023.

[2] S. Bennett, R. Lee Kirby, S. Bennett, R. Lee Kirby, and B. Macdonald, "Wheelchair accessibility: Descriptive survey of curb ramps in an urban area," *Disability and Rehabilitation: Assistive Technology,* vol. 4, no. 1, pp. 17-23, 2009.

[3] C. Torkia *et al.*, "Power wheelchair driving challenges in the community: a users' perspective," *Disability and Rehabilitation: Assistive Technology,* vol. 10, no. 3, pp. 211-215, 2015.

[4] B. Daveler, B. Salatin, G. G. Grindle, J. Candiotti, H. Wang, and R. A. Cooper, "Participatory design and validation of mobility enhancement robotic wheelchair," *J. Rehabil. Res. Dev,* vol. 52, no. 6, pp. 739-50, 2015.

[5] S. K. Sahoo and B. B. Choudhury, "A review on smart robotic wheelchairs with advancing mobility and independence for individuals with disabilities," *Journal of Decision Analytics and Intelligent Computing,* vol. 3, no. 1, pp. 221-242, 2023.

[6] J. Leaman and H. M. La, "A comprehensive review of smart wheelchairs: Past, present, and future," *IEEE Transactions on Human-Machine Systems,* vol. 47, no. 4, pp. 486-499, 2017.

[7] S. A. Sundaram, H. Wang, D. Ding, and R. A. Cooper, "Step-Climbing Power Wheelchairs: A Literature Review," *Topics in Spinal Cord Injury Rehabilitation,* vol. 23, no. 2, pp. 98-109, 2017.

[8] S. Sivakanthan *et al.*, "Mini-Review: Robotic Wheelchair Taxonomy and Readiness," *Neuroscience Letters,* p. 136482, 2022.

[9] L. Jaeger *et al.*, "How the CYBATHLON competition has advanced assistive technologies," *Annual Review of Control, Robotics, and Autonomous Systems,* vol. 6, no. 1, pp. 447-476, 2023.

[10] H. Wang *et al.*, "Mobility enhancement wheelchair," ed: Google Patents, 2017.

[11] B. Salatin, "Electrical Powered Wheelchair Driving Outdoors: The identification of driving obstacles & strategies and the development of an advanced controller," School of Health and Rehabilitation Sciences, University of Pittsburgh, Pennsylvania, etd-03282011-233924, 2011.

[12] J. L. Candiotti *et al.*, "Evaluation of Power Wheelchair Dynamic Suspensions for Tip Prevention in Non-ADA Compliant Surfaces," *Archives of physical medicine and rehabilitation,* vol. 104, no. 12, pp. 2043-2050, 2023.

[13] S. Sivakanthan *et al.*, "Usability evaluation of attitude control for a robotic wheelchair for tip mitigation in outdoor environments," *Medical Engineering & Physics,* vol. 82, pp. 86-96, 2020.

[14] J. L. Candiotti, B. J. Daveler, S. Sivakanthan, G. G. Grindle, R. Cooper, and R. A. Cooper, "Curb Negotiation With Dynamic Human–Robotic Wheelchair Collaboration," *IEEE Transactions on Human-Machine Systems,* vol. 52, no. 1, pp. 149-155, 2021.

[15] S. Sivakanthan *et al.*, "Automated curb recognition and negotiation for robotic wheelchairs," *Sensors,* vol. 21, no. 23, p. 7810, 2021.

[16] J. L. Candiotti *et al.*, "Usability Evaluation of a Novel Robotic Power Wheelchair for Indoor and Outdoor Navigation," *Archives of physical medicine and rehabilitation,* vol. 100, no. 4, pp. 627-637, 2019.

[17] K. Fitzpatrick, M. A. Brewer, and S. Turner, "Another look at pedestrian walking speed," *Transportation research record,* vol. 1982, no. 1, pp. 21-29, 2006.

[18] R. L. Kirby *et al.*, "Effectiveness of a wheelchair skills training program for powered wheelchair users: a randomized controlled trial," *Archives of physical medicine and rehabilitation,* vol. 96, no. 11, pp. 2017-2026. e3, 2015.

[19] A. L. Nelson *et al.*, "Wheelchair-related falls in veterans with spinal cord injury residing in the community: a prospective cohort study," *Archives of physical medicine and rehabilitation,* vol. 91, no. 8, pp. 1166-1173, 2010.

[20] R. Riener, "The Cybathlon promotes the development of assistive technology for people with physical disabilities," *Journal of neuroengineering and rehabilitation,* vol. 13, no. 1, p. 49, 2016.

[21] J. Brooke, "SUS-A quick and dirty usability scale," *Usability evaluation in industry,* vol. 189, no. 194, pp. 4-7, 1996.

[22] A. Bangor, P. Kortum, and J. Miller, "Determining what individual SUS scores mean: Adding an adjective rating scale," *Journal of usability studies,* vol. 4, no. 3, pp. 114-123, 2009.

[23] M. J. Scherer, C. Sax, A. Vanbiervliet, L. A. Cushman, and J. V. Scherer, "Predictors of assistive technology use: The importance of personal and psychosocial factors," *Disability and rehabilitation,* vol. 27, no. 21, pp. 1321-1331, 2005.

[24] D. Sharek, "A useable, online NASA-TLX tool," in *Proceedings of the Human Factors and Ergonomics Society Annual Meeting*, 2011, vol. 55, no. 1: SAGE Publications Sage CA: Los Angeles, CA, pp. 1375-1379.

[25] S. G. Hart and L. E. Staveland, "Development of NASA-TLX (Task Load Index): Results of empirical and theoretical research," *Advances in psychology,* vol. 52, pp. 139-183, 1988.

[26] R. A. Grier, "How high is high? A meta-analysis of NASA-TLX global workload scores," in *Proceedings of the Human Factors and Ergonomics Society Annual Meeting*, 2015, vol. 59, no. 1: SAGE Publications Sage CA: Los Angeles, CA, pp. 1727-1731.

[27] I. ISO, "2631-1: Mechanical vibration and shock-evaluation of human exposure to whole-body vibration-Part 1: General requirements," *Geneva, Switzerland: ISO,* 1997.

Pilot Testing of Dynamic Bayesian Optimization for Exoskeleton-Assisted Training of Propulsion Mechanics

GilHwan Kim, Haider Chishty, and Fabrizio Sergi

Abstract— **Human-in-the-loop (HIL) optimization has proven effective in assistive paradigms, but has yet to be translated to training paradigms. One challenge towards the implementation of HIL algorithms for training relates to the inability of conventional HIL optimization methods to account for neuromotor learning that can occur during training.**

In this work, we present our implementation of dynamic Bayesian optimization (DBO) in a single-parameter HIL optimization experiment targeting changes in propulsion mechanics - specifically an increase in the trailing limb angle (TLA). Five participants were exposed to exoskeleton-applied hip torque pulses while walking on an instrumented treadmill in user-driven walking conditions. Outcomes from this experiment were validated against an active control condition, where conventional Bayesian optimization (BO) was used.

Experimental results showed significant increases in TLA in both the early and late portions of the no torque, post-training session, under the DBO paradigm, while no significant increases were observed under BO; however, no significant increases in TLA were observed during training at the group level. A linear mixed model revealed a weak, albeit significant, effect of applied torque on the change in TLA relative to baseline, suggesting that modulation of TLA is not easily achievable under this paradigm. Future work will expand the optimization paradigm to use more parameters or target different metrics of propulsion mechanics.

I. INTRODUCTION

Robot-assisted gait training is attractive due to increased consistency, efficacy, and repeatability compared to standard approaches [1], [2]. During training, target outcomes can be met by applying a specific amount of assistance to the user; the optimal level of robotic assistance is often estimated based on previous observations of participant responses. The identification of this input-output relationship requires a large amount of observations; a primary limitation is efficiently gathering enough participant observations without inducing fatigue.

Previous approaches resolved the requirement for many observations by using group-averaged data to estimate participant responses [3]; unfortunately, group-averaged data eliminates the variability between participants, resulting in sub-optimal levels of assistance being applied during training to a specific individual. Human-in-the-loop (HIL) optimization has been introduced as a method to identify participant-specific optimal conditions in fewer observations by tuning control parameters in real time [4], [5]. This strategy has been successfully implemented using different optimization methods [6], [7], [8], [9].

HIL optimization has previously been implemented in assistive paradigms, seeking to minimize metabolic cost by modulating robot assistance; such paradigms require longer bouts of walking due to long measurement times required to establish metabolic-based metrics at each iteration [4], [6], [7], [8]. HIL optimization may also be beneficial in training paradigms that seek to modify motor coordination in desired directions with immediate outcomes established based on fewer observations. However, a limitation of conventional optimization techniques with regards to motor training and rehabilitation is that the dependency of participant response on training history is not considered. This flawed assumption limits the capacity of optimizers to account for changes in participant responses due to neuromotor learning, whereby participants modify their actions in response to external stimuli, resulting in changes that may persist when the stimulus is removed [10]. Therefore, there is a need to augment HIL optimization techniques to account for human learning dynamics, and to validate such techniques in walking-related outcomes [11].

One method for adapting existing HIL optimization algorithms to dynamic cases is to allow the optimizer to learn the time-dependence of the input-output relationship for a specific optimization problem. Dynamic Bayesian optimization (DBO) is a modification of Bayesian Optimization (BO) that heuristically corrects the covariance between different inputs based on when the inputs were applied in time [12], [13]. While DBO had previously been validated to address time-varying systems, it has yet to be validated for a HIL optimization training paradigm [12], [13], [14]. We have previously presented the application of DBO in simulated paradigms in the presence of learning [15]: our results suggest that DBO may improve the performance of HIL optimization over BO once a sufficient number of iterations had been evaluated.

The work presented here is an extension of our previous work on HIL optimization that also includes an experimental validation via a training paradigm with human participants. A suitable target for a robot-assisted training paradigm should be an indicator of walking function. In this work, we selected to target the kinematic component of propulsion, quantified by the trailing limb angle (TLA) [16]. We validate the efficacy of DBO by implementing it in an optimization algorithm seeking to increase participant TLA during training relative to a baseline.

G. Kim and H. Chishty are with the Department of Mechanical Engineering, University of Delaware, Newark, DE 19716, USA;

F. Sergi is with the Department of Mechanical and Biomedical Engineering, University of Delaware, Newark DE, 19713, USA; fabs@udel.edu

*This work is supported in part by NSF-CMMI-1934650 and in part by NIH-R01HD111071.

II. METHODS

A. Dynamic Bayesian Optimization

A detailed description of DBO is provided in our previous work [3], [15], but will be synthesized in this section. BO is a probabilistic approach to determining an (optimal) input value that minimizes a cost function based on the output of a system that is observed with measurement error [17]. Given these observations and a covariance function describing the relationship between changes in input to output, BO constructs a Gaussian process (GP) model which estimates outputs resulting from unobserved inputs. The GP model is used iteratively to identify the next input most likely to maximize some acquisition function, towards determining the optimal input relative to the cost function.

BO assumes the system to be stationary; i.e., repetitions of inputs are expected to result in similar outputs, an assumption that is inaccurate for the case of neuromotor learning. Thus, BO was augmented as DBO to account for system responses that may change with time. To that end, the covariance function $k(u, u')$ between inputs u and u' is modified by introducing the time variable t as $k((u,t),(u',t'))$, where t and t' are the corresponding time instances of inputs u and u' respectively. Assuming the time component of the covariance function to be separable [13], [18], the overall covariance function is described as a multiplication of the static component of the covariance function k_u with a dynamic component k_t, as

$$\begin{aligned} k((u,t),(u',t')) &= k_u(u,u') \cdot k_t(t,t') \\ &= \sigma^2 \cdot \exp\left[-\sum_{p=1}^{r} \frac{\tilde{u}_p^\top \cdot \tilde{u}_p}{2 \cdot l_p^2}\right] \cdot (1-\alpha)^{|t-t'|} \end{aligned} \quad (1)$$

where r is the number of input/control parameters and $\tilde{u}_p$ is the difference between the p-th input parameter of the input parameter arrays u and u' ($u_p - u'_p$). l_p is the p-th length scale hyperparameter, which influences the function's sensitivity to differences in parameter inputs, and σ^2 is the measurement variance. Finally, $\alpha \in [0, 1)$ is a hyperparameter that defines the time scale of the dynamic component of the covariance function.

B. Validation in Simulation

Validation of DBO was done in HIL simulations featuring a virtual human response based on a state-space model that we have previously established, capable of accounting for key features of human responses to exoskeleton-assisted training of propulsion [19], referred to as the modified use-dependent learning model (modified UDL). The validation will be summarized from the original paper [15].

HIL simulations were performed towards validating the performance of DBO relative to BO. Performance was defined in terms of convergence, by examining at which iterations error metrics using DBO became significantly lower than those using BO, if at all. In all simulations, the optimizers were only privy to system outputs, i.e., the optimizers were not aware of the true structure of the systems.

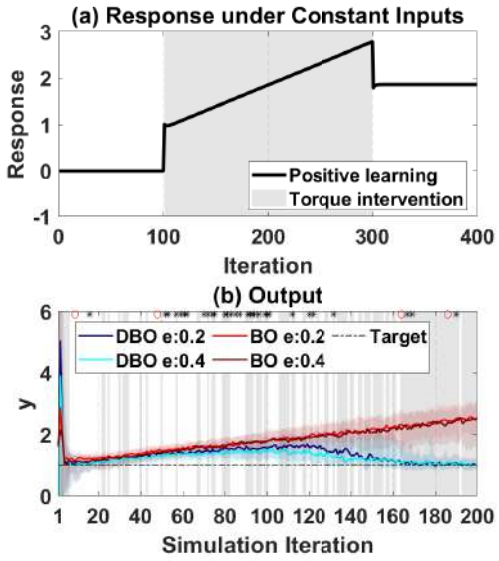


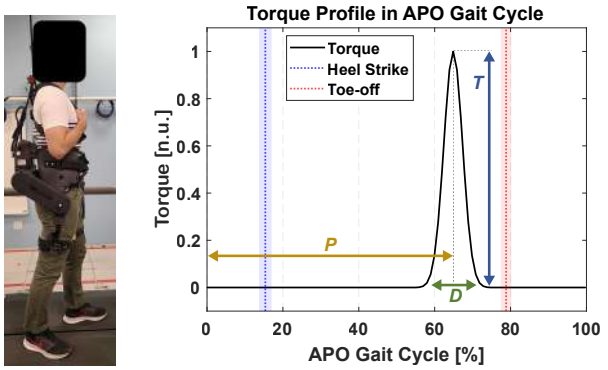
Fig. 1: Simulation results for the modified UDL model with "positive learning". (a) Model response before, during, and after constant input (u = 1) (b) Observed model output to HIL simulations: Solid lines represent the median output of each optimizer; corresponding shaded regions represent the 20th to 80th percentile over all repetitions. Shaded gray regions indicate iterations where optimizer type exhibited a significant difference ($p_{unc} < 0.05$). Different exploration-exploitation ratios (e:0.2 or 0.4) were also investigated during this validation.

One of the simulation models, "positive learning" model - where the response continuously increases with positive stimulus used in simulation - is presented in Fig. 1a for case where a continuous constant input is applied. 50 simulations were performed for the "positive learning" modified UDL model, each lasting for 200 iterations following three initial inputs, selected randomly but consistent across simulations. The goal of these optimizations was to achieve a response of $y = 1$ (i.e., minimize the cost function $g = (y-1)^2$). The response y can be interpreted as the hip extension or trailing limb angle of a participant during gait training. Fig. 1b shows the results of this validation: as is seen, DBO-based HIL optimization simulations eventually converged to the desired output value, in contrast to BO-based optimization simulations which continuously diverged from the desired output in presence of learning.

C. Experimental Methods

1) Equipment: Robot-assisted training was provided through an Active Pelvis Orthosis (IUVO, Pisa, Italy), or APO, a bilateral hip exoskeleton (Fig. 2a) with a weight of 6 kg. The APO features an onboard encoder used to measure the hip flexion/extension angle (resolution: 0.015 deg, log rate: 100 Hz).

Based on the measured hip joint angle, the APO predicts the participant's gait phase and total hip joint angular profile using adaptive oscillators [20], [21]. The gait phases are estimated individually for the left and right leg. Based on these predictions, the APO applies assistive/resistive torques to the hip joint as Gaussian shaped profiles. These profiles



(a) (b)

Fig. 2: (a) Experimental setup including the APO, instrumented treadmill, motion capture system, and safety harness. (b) Commanded torque profile in the APO Gait Cycle domain (0%: peak of hip flexion). Mean and std. of heel-strike and toe-off timings are provided by the blue and red distributions respectively. Control parameters that define the assistive profile are labeled.

are defined by three parameters: pulse amplitude (T), peak timing (P), and pulse duration (D) (Fig. 2b).

In this experimental study, participants experienced a single torque pulse profile on the right side at each stride. The duration of the applied torque profile D was set to 10% of the gait cycle, generating a brief torque pulse (pulse-width at half maximum: 5.9%). Timing of peak torque P was set to be 65% in the APO gait cycle (0%: peak of hip flexion), corresponding to the torque pulse being applied at the end of the stance phase. The amplitude of the torque pulse T was updated iteratively via a real-time controller in Simulink (MathWorks Inc., Natick, MA, USA) which communicated with the APO via a Serial Peripheral Interface connection at a frequency of 400 Hz; the update was performed during the swing phase (no torque applied), ensuring that it would be executed by the APO in the ensuing stance phase.

An instrumented, split-belt treadmill (Bertec Corp., Columbus OH, USA) was used to collect analog force/torque data via two force plates embedded within the treadmill. Control signals for the treadmill were sent from a Simulink-based controller running at a frequency of 400 Hz. To measure effects on propulsion mechanics in ecological conditions, we implemented a user-driven treadmill controller such that treadmill velocity changed in response to participant walking behavior [22].

Gait kinematics were assessed via motion capture, using a ten T40-S (Vicon Motion Systems Ltd, Oxford, UK) camera system, which tracked four retroreflective markers located on the right and left malleoli of the participant, and on the right and left side of the APO, coinciding with the exoskeleton's (and thus the user's hip) axis of rotation. Real-time marker location was recorded at 100 Hz and communicated in real-time to the Simulink-based controller for processing and optimization purposes. For safety, a harness system (Solo-Step Inc., North Sioux City, SD, USA) installed with an overhead track was used during all experiments.

2) Study Participants and Experimental Procedure: 5 healthy participants (3 female) of age (mean $\pm$ std) 25.4 $\pm$ 2.5 yrs, height 167.6 $\pm$ 8.6 cm, and mass 70.0 $\pm$ 14.7 kg were recruited for this study (protocol approved by the University of Delaware Institutional Review Board, protocol no. 1755609-7). Participants performed the experimental paradigm twice within the same day, separated by at least ten minutes of rest to avoid fatigue and reduce leftover training effects. The two experiments differed by which optimizer was used (DBO vs. BO), with the order randomized between participants.

Prior to the first experiment, the APO was fit to the participant such that the rotational axis of the device aligned with the user's hips. The device was secured once the participant confirmed comfort. Reflective markers were placed on the user and device, and a safety harness was secured. Participants then began a familiarization procedure to acclimate to walking with the exoskeleton on the user-driven treadmill.

Familiarization occurred for at least 150 strides. The treadmill was initially set to a constant speed of 1 m/s, switching to user-driven mode once 10 strides had been completed. During this session, the exoskeleton was set to transparent mode, minimizing interaction forces/torques between the user and device.

The experiments began once familiarization had been completed. Each experiment consisted of three consecutive sessions: a baseline session without robotic interventions, a training session featuring torque input from the exoskeleton, and an post-training session to evaluate post-training effects, in absence of robot input. During the baseline session, participants walked on the user-driven treadmill for 100 strides. The last 20 strides of this session were used to quantify baseline values for metrics of propulsion mechanics.

During training, the exoskeleton applied extension torques to the right hip joint towards increasing the trailing limb angle of the right leg relative to baseline. This session lasted for 40 iterations of optimization, with each iteration lasting for 6 to 7 strides (depending on HIL algorithm execution time). The torque applied to the user within each iteration was constant.

Following torque intervention, the post-training session lasted for 100 strides, with no torque being applied to the user, to quantify residual training effects left over from the robot assistance. Upon completion of this session, participants removed the exoskeleton and harness, and rested for at least ten minutes, before repeating the experimental procedure with the alternate optimizer.

3) Optimizer Setup: The objective of this HIL optimization paradigm was to increase the TLA of the right leg during stance by a target amount relative to baseline, ΔTLA^*, set to +3 degrees for this experiment. Thus, the optimizer cost function was defined as $c_i = |\Delta\text{TLA}_i - \Delta\text{TLA}^*|$, i.e., at iteration i, the absolute difference between the current change ΔTLA_i (relative to baseline), and the target change ΔTLA^*. Only the average of the first five strides at each iteration were considered for calculating ΔTLA_i, with the exoskeleton continuing to apply the same input later until the optimizer

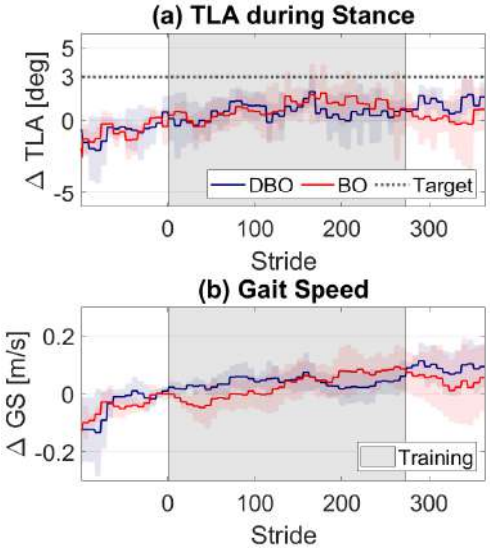


Fig. 3: Group analysis of the changes in (a) TLA, and (b) Gait speed (GS) compared to baseline for each stride. The solid line indicates the group mean at each iteration, repeated over strides, and the shaded area extends by one std. Stride numbering begins during the Training Session.

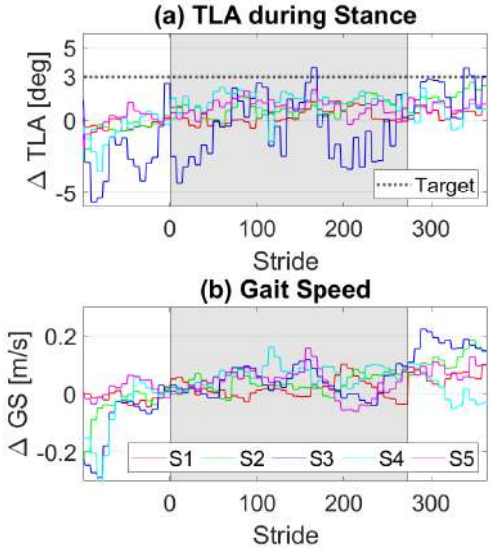


Fig. 4: Individual participant data under DBO for the change in (a) TLA, (b) GS, relative to baseline. Each color represents response from a participant.

identified a new solution for the new optimizer iteration. Computation of the following inputs took an additional 1-2 strides in our current setup.

The optimization pursued in this study was a single-parameter optimization with the only tunable parameter being torque pulse amplitude T, with bounds of 0 and 9 Nm, applied in the extension direction. To initialize the optimizer, the inputs applied in the first three iterations were fixed, such that the applied torques at these iterations were 0, 7, and 3 Nm respectively. Expected improvement was selected as the acquisition function of the optimization based on previous simulations [3]. Further, the exploration-exploitation ratio (e-ratio) was set to 0.4, also based on previous analysis [15]. This tunable ratio is bounded at [0 1], and promotes the optimizer to favor one optimization strategy over the other; a higher e-ratio results in greater exploration.

4) Data Processing and Analysis: Forceplate and retroreflective marker data were filtered in real-time during the experiment with low-pass Butterworth filters with cutoff frequencies of 100 and 60 Hz, respectively. Forceplate data were used in real-time to identify gait events and distinguish strides; kinematic marker data was used in real time to calculate TLA for each stride.

The angle between the vertical axis and the line connecting the hip and ankle markers in the sagittal plane [23] was calculated as a timeseries for each stride; we used the maximum angle over the stance phase of this time series as our measure of TLA.

Outlier removal was performed by removing TLA measurements outside of a $\pm$ 35 degrees range; after removing outliers, a median filter with 51 sample window size (127.5 ms) was applied.

Hip extension angle (HE) was determined based on encoder measurements from the APO, and the peak value during the stance phase was identified. Participant gait speed (GS) was defined as the average treadmill speed over each stride.

Baseline values of the above metrics of propulsion mechanics were defined as the average over the last 20 strides of the baseline session. Baseline values were subtracted from measured metrics to determine outcomes relative to baseline: ΔTLA, ΔHE, and ΔGS.

Individual participant responses were averaged within each iteration during training. For baseline and post-training sessions, responses from 7 strides were averaged for visualization. Individual participant responses were then averaged to construct group mean responses.

Baseline values were compared to the final 3 iterations of training, and both the initial and final 3 iterations of post-training to establish if either optimization algorithm induced changes in propulsion mechanics during and after training.

To study the mechanism under which robot-applied hip torque modulated TLA, we investigated the association between T and the change in TLA relative to baseline (ΔTLA) - the input and output of the training paradigm respectively - while controlling for changes in participant GS relative to baseline (ΔGS), as GS is a known covariate of TLA [24], [25]. This was done by building a linear mixed model with T, ΔGS, and their interaction as fixed effects, and participant as a random factor, which allowed us to study how these factors influence the outcome - ΔTLA.

III. Experiment Results

A. Training-induced changes in propulsion mechanics

Group level measures of changes in propulsion mechanics relative to baseline (ΔTLA and ΔGS) over each experimental session are displayed in Fig. 3.

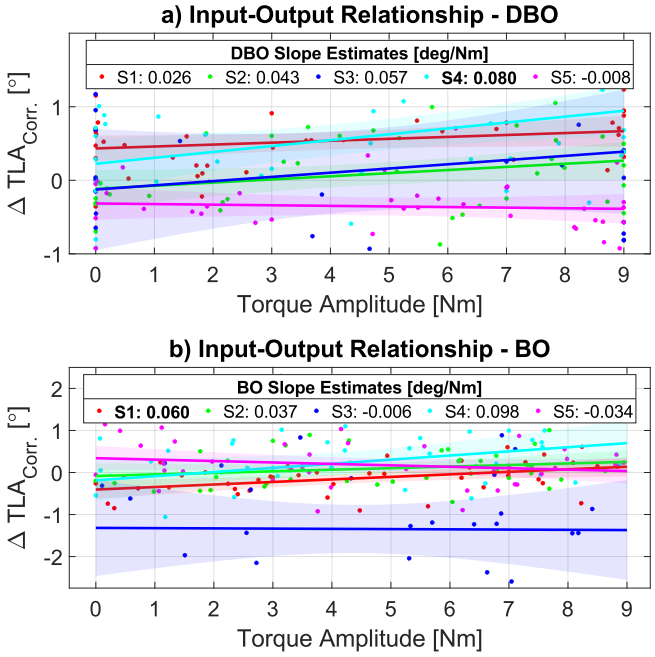


Fig. 5: Relationship between changes in TLA relative to baseline, corrected for the linear effect of GS, and T, for each iteration. Bolding in legends indicate which estimates are significant at the single-participant level ($p < 0.05$).

As is visible, neither optimizer was able to achieve the targeted 3 deg increase in TLA during training at the group level; however, significant increases were found in the post-training session. Notably, under DBO, TLA increased relative to baseline in both early and late portions of the post-training session (ΔTLA mean $\pm$ s.e.m: 1.039 $\pm$ 0.139 deg, $p = 0.002$, and 1.485 $\pm$ 0.367 deg, $p = 0.016$, for early and late post-training respectively). No significant effects were found under BO. Across optimizers, TLA significantly increased compared to baseline only during the early portion of post-training (0.721 $\pm$ 0.279 deg, $p = 0.029$).

Individual participant responses to DBO optimization are visible in Fig. 4, where the large variability of ΔTLA between iterations can be observed, even in the absence of torque inputs. It can also be observed that the desired increase in TLA was in fact achieved within a 1 deg accuracy in 4 out of 5 participants at some point during training. The largest participant-specific change in TLA observed during training under each optimizer is provided in Table I.

The effects of training on GS were qualitatively similar to those as TLA, in part as expected given that TLA scales positively with GS [24], [25]. Across optimizers, GS increased in the late portion of the training session (ΔGS mean $\pm$ s.e.m: 0.070 $\pm$ 0.018 m/s, $p = 0.004$), and the early portion of the post-training session (0.085 $\pm$ 0.018 m/s, $p = 0.001$).

At the optimizer-specific level, GS under DBO only significantly increased compared to baseline during the early portions of the post-training session (0.102 $\pm$ 0.016 m/s, $p = 0.003$), and under BO only significantly increased during the later portion of the training session (0.088 $\pm$ 0.030 m/s, $p = 0.041$).

TABLE I: Largest Change in TLA during Training for Participants

Participant	1	2	3	4	5
DBO (deg)	1.391	2.017	3.703	2.919	2.286
BO (deg)	2.414	1.846	7.144	3.438	1.432

B. *Effect of Torque Amplitude on Propulsion Mechanics*

The linear mixed model highlighted significant effects of both T and ΔGS on ΔTLA (Table II). This indicates that even after controlling for the known association between TLA and GS, the exoskeleton control input had an effect on the outcome. However, the strength of the association, while statistically significant ($p = 0.047$), was not very strong (slope = 0.032 deg/Nm, implying that even with a maximum applied torque of 9 Nm, TLA is only predicted to increase by about 0.3 deg after controlling for a linear effect of speed). For comparison, the same linear mixed model applied to the outcome of peak HE, yielded a stronger effect of T (p <0.001, slope = 0.801 deg/Nm).

Fig. 5 shows participant-specific associations between the T and ΔTLA, after correcting for changes in ΔTLA due to changes in ΔGS. This relationship was significant in only 1/5 participants when DBO was used, and 1/5 participants under BO.

TABLE II: Mixed Model Results: Fixed Effects for ΔTLA

Factor	Estimate	t ratio	Prob> $\|t\|$
T	0.032 [deg/Nm]	1.99	**0.047**
ΔGS	12.058 [deg·s/m]	12.72	**<0.001**
$T \cdot \Delta GS$	0.355 [deg·s/Nm^2]	1.31	0.189

IV. Discussion and Conclusions

This study builds upon our previous work towards validating the use of a dynamic HIL optimization algorithm (DBO) for robot-assisted training of propulsion. In this experiment, training was delivered by a hip exoskeleton that applied hip torques to the user's right leg. Training effects were compared to a no-torque baseline session, as well as a post-training session with no torque perturbations, to evaluate the effect of robot-training on the selected outcome measure.

Results of this pilot study indicate that the training paradigm was able to induce a positive increase in TLA in most participants during training, though this increase was not of the desired amplitude, nor was sustained during training. After training, TLA was significantly increased at the group level: across optimizers, TLA was significantly increased relative to baseline in the early portion of the post-training session, and under the DBO paradigm was significantly increased in both the early and late portions of the post-training session.

Statistical results from the linear mixed model indicate that the association between T and TLA is quite weak,

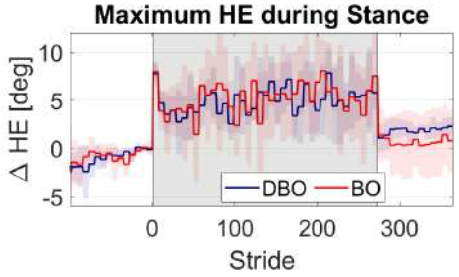


Fig. 6: Group analysis of the change in HE measured at each iteration, for both optimizers.

as evidenced by small estimated slopes and by the few significant cases at the participant level. This could indicate that the current target increase in TLA is too large for the current paradigm, and thus experimental modifications must be made before DBO can thoroughly be experimentally validated in a paradigm targeting TLA. One option is to open the optimization problem to more parameters, such as torque pulse timing (P) and duration (D) described in Fig. 2b, as done for assistive applications, which may lead to a stronger input-output control capability.

Alternatively. based on the strong association of T and increase in participant HE angle during training (Fig. 6), it may be beneficial to alter the paradigm to target HE instead. Performing the DBO validation on an HIL optimization paradigm with an output that is more reasonably sensitive to the applied inputs could better serve to evaluate the efficacy and necessity of using a history dependent optimizer.

One limitation of this study results from the lack of cross-validation trials, which prevented us from obtaining a direct comparison across optimizers that was not affected by the specific optimizer strategy at a given iteration. Cross-validation trials are critical for all applications of machine learning, but currently under-utilized in human-in-the-loop optimization methods [5]. In this work, online cross-validation can be done by incorporating sporadic validation iterations during training, where the estimated optimal input at that iteration is applied. This would allow for independent outcomes that can be compared across optimizers and will be explored in future work.

References

[1] A. Esquenazi and A. Packel, "Robotic-assisted gait training and restoration," *American journal of physical medicine & rehabilitation*, vol. 91, no. 11, pp. S217–S231, 2012.

[2] J. Mehrholz, S. Thomas, J. Kugler, M. Pohl, and B. Elsner, "Electromechanical-assisted training for walking after stroke," *Cochrane database of systematic reviews*, no. 10, 2020.

[3] G. Kim and F. Sergi, "Using bayesian optimization to identify optimal exoskeleton parameters targeting propulsion mechanics: A simulation study," in *2021 IEEE/RSJ International Conference on Intelligent Robots and Systems (IROS)*. IEEE, 2021, pp. 6225–6231.

[4] W. Felt, J. C. Selinger, J. M. Donelan, and C. D. Remy, "" body-in-the-loop": Optimizing device parameters using measures of instantaneous energetic cost," *PloS one*, vol. 10, no. 8, p. e0135342, 2015.

[5] P. Slade, C. Atkeson, J. M. Donelan, H. Houdijk, K. A. Ingraham, M. Kim, K. Kong, K. L. Poggensee, R. Riener, M. Steinert *et al.*, "On human-in-the-loop optimization of human–robot interaction," *Nature*, vol. 633, no. 8031, pp. 779–788, 2024.

[6] J. R. Koller, D. H. Gates, D. P. Ferris, and C. D. Remy, "'body-in-the-loop'optimization of assistive robotic devices: A validation study." in *Robotics: Science and Systems*, vol. 2016, 2016, pp. 1–10.

[7] J. Zhang, P. Fiers, K. A. Witte, R. W. Jackson, K. L. Poggensee, C. G. Atkeson, and S. H. Collins, "Human-in-the-loop optimization of exoskeleton assistance during walking," *Science*, vol. 356, no. 6344, pp. 1280–1284, 2017.

[8] Y. Ding, M. Kim, S. Kuindersma, and C. J. Walsh, "Human-in-the-loop optimization of hip assistance with a soft exosuit during walking," *Science robotics*, vol. 3, no. 15, p. eaar5438, 2018.

[9] M. Kim, Y. Ding, P. Malcolm, J. Speeckaert, C. J. Siviy, C. J. Walsh, and S. Kuindersma, "Human-in-the-loop bayesian optimization of wearable device parameters," *PloS one*, vol. 12, no. 9, p. e0184054, 2017.

[10] K. A. Leech, R. T. Roemmich, J. Gordon, D. S. Reisman, and K. M. Cherry-Allen, "Updates in motor learning: implications for physical therapist practice and education," *Physical therapy*, vol. 102, no. 1, p. pzab250, 2022.

[11] P. Kantharaju, S. S. Vakacherla, M. Jacobson, H. Jeong, M. N. Mevada, X. Zhou, M. J. Major, and M. Kim, "Framework for personalizing wearable devices using real-time physiological measures," *IEEE Access*, 2023.

[12] V. Aglietti, N. Dhir, J. González, and T. Damoulas, "Dynamic causal bayesian optimization," *Advances in Neural Information Processing Systems*, vol. 34, pp. 10 549–10 560, 2021.

[13] I. Bogunovic, J. Scarlett, and V. Cevher, "Time-varying gaussian process bandit optimization," in *Artificial Intelligence and Statistics*. PMLR, 2016, pp. 314–323.

[14] F. M. Nyikosa, M. A. Osborne, and S. J. Roberts, "Bayesian optimization for dynamic problems," *arXiv preprint arXiv:1803.03432*, 2018.

[15] G. Kim, H. A. Chishty, and F. Sergi, "Using dynamic bayesian optimization to induce desired effects in the presence of motor learning: a simulation study," *bioRxiv*, 2024.

[16] H. Hsiao, B. A. Knarr, J. S. Higginson, and S. A. Binder-Macleod, "Mechanisms to increase propulsive force for individuals poststroke," *Journal of neuroengineering and rehabilitation*, vol. 12, pp. 1–8, 2015.

[17] E. Brochu, V. M. Cora, and N. De Freitas, "A tutorial on bayesian optimization of expensive cost functions, with application to active user modeling and hierarchical reinforcement learning," *arXiv preprint arXiv:1012.2599*, 2010.

[18] T. Gneiting, M. G. Genton, and P. Guttorp, "Geostatistical space-time models, stationarity, separability, and full symmetry," *Monographs On Statistics and Applied Probability*, vol. 107, p. 151, 2006.

[19] G. Kim and F. Sergi, "Modeling neuromotor adaptation to pulsed torque assistance during walking," *accepted for presentation, IEEE RAS/EMBS Conference on Biomedical Robotics and Biomechatronics (BioRob 2024), pre-print available on bioRxiv*, pp. 2024–02, 2024.

[20] R. Ronsse, N. Vitiello, T. Lenzi, J. Van Den Kieboom, M. C. Carrozza, and A. J. Ijspeert, "Human–robot synchrony: flexible assistance using adaptive oscillators," *IEEE Transactions on Biomedical Engineering*, vol. 58, no. 4, pp. 1001–1012, 2010.

[21] T. Yan, A. Parri, V. Ruiz Garate, M. Cempini, R. Ronsse, and N. Vitiello, "An oscillator-based smooth real-time estimate of gait phase for wearable robotics," *Autonomous Robots*, vol. 41, pp. 759–774, 2017.

[22] S. Song, H. Choi, and S. H. Collins, "Using force data to self-pace an instrumented treadmill and measure self-selected walking speed," *Journal of NeuroEngineering and Rehabilitation*, vol. 17, pp. 1–14, 2020.

[23] D. Reisman, T. Kesar, R. Perumal, M. Roos, K. Rudolph, J. Higginson, E. Helm, and S. Binder-Macleod, "Time course of functional and biomechanical improvements during a gait training intervention in persons with chronic stroke," *Journal of Neurologic Physical Therapy*, vol. 37, no. 4, pp. 159–165, 2013.

[24] K. E. Zelik and P. G. Adamczyk, "A unified perspective on ankle push-off in human walking," *Journal of Experimental Biology*, vol. 219, no. 23, pp. 3676–3683, 2016.

[25] R. L. McGrath, M. L. Ziegler, M. Pires-Fernandes, B. A. Knarr, J. S. Higginson, and F. Sergi, "The effect of stride length on lower extremity joint kinetics at various gait speeds," *PloS one*, vol. 14, no. 2, p. e0200862, 2019.

Multi-Linear Regressor for Static Posturography Estimation Through an Instrumented Cane

Max Burns, Kaymie Shiozawa, and Neville Hogan, *Member, IEEE*

***Abstract*—Measuring static postural sway outside of the clinic could provide clinicians with long-term, continuous data on patient balance, offering a comprehensive view beyond infrequent in-clinic assessments. This paper presents a novel method to quantify balance ability through a regression algorithm that predicts postural sway velocity using only motion and force sensors. Data is acquired through sensors onboard an instrumented cane. The prediction algorithm's validity was demonstrated in a study of eight young unimpaired subjects and eight adults over 65. The subjects' balance was challenged with different stance widths and sight conditions while using an instrumented cane. In the younger subject cohort, balance was further challenged through an unstable platform. Together, these conditions allowed for variation of the tasks' difficulty levels and thus the range of measured sway velocity. Across subjects, sway velocity was demonstrated to be highly predictable (Younger Subjects $R^2 = 0.73$, Older Subjects $R^2 = 0.47$) using just the sensors onboard the instrumented cane. In particular, hand motion was shown to be important in predicting sway velocity. We also demonstrated the use of data features to estimate Romberg quotients of the older participants, suggesting the method's potential to track proprioceptive function over time (Correlation r = 0.82). This method offers a promising approach to continuous patient monitoring and could provide a long-term, quantitative assessment of balance ability.**

I. Introduction

Falls pose a serious threat to the health and autonomy of people. Persons over 65, a demographic that is rapidly growing, are disproportionately affected by fall-related injuries and fatalities and have greater difficulty recovering from fall injury [1, 2]. Younger adults also suffer from falls and resultant injuries but recover faster and are generally more robust [3, 4]. In 2018, 27.5% of American adults over 65, or 35.6 million people, reported at least one fall [5]. These falls led to 8.4 million injuries and approximately 32,000 deaths [5]. Falls are also the most common cause of traumatic brain injury [6] and can result in bone fractures and other bodily trauma [1].

Timely and accurate assessments are crucial to identify people with acute fall risk. Although many falls occur while the body is in motion, static balance analysis has been shown to be a valuable predictor of future fall risk [7-9]. The three most common functional balance and mobility tests administered by clinicians are the Timed Up and Go (TUG) test, the 30-second chair test, and the 4-stage balance test [10]. Unfortunately, recent work has suggested that the TUG and 4-stage balance tests are not adequate predictors of fall risk [7, 11]. Furthermore, clinical assessments require a clinician to be present to conduct the analysis, limiting the frequency at which a patient can be assessed.

Instead, static postural sway analysis has been shown to yield more effective predictions of fall risk [7-9]. This analysis is traditionally performed by measuring the center of pressure (CoP) with a force plate in different conditions. In particular, the velocity of the CoP (sway velocity) has been found to correlate with fall risk [7-9]. When subjects stood with their feet shoulder-width apart, Lin et al. observed an average sway velocity of 2.26 ± 0.95 cm/s in older adults compared to 1.43 ± 0.41 cm/s in younger adults [12]. Higher sway velocity is observed in older adults and younger adults when balance is challenged.

Romberg quotients can be calculated as part of postural sway analysis. A Romberg quotient is computed by dividing a measure of balance when a subject's eyes are closed, by the same measure when eyes are open. The ratio can highlight abnormal increases in instability when vision is removed, which can indicate poor proprioception [13]. Prior studies have shown that sway velocity Romberg quotients effectively classify populations with various balance-affecting conditions [13]. A sway velocity Romberg quotient over 2.0 may indicate a proprioceptive deficit; for adults without balance issues, the quotient is expected to be 1.2±0.3 [14].

Postural sway velocity and Romberg quotients can be combined for fall risk prediction [8]. A fall-risk classifier proposed by Howcroft et al. used the anterior-posterior (AP) component and magnitude of sway velocity, and the two corresponding Romberg quotients in a linear classifier [8]. The model achieved a classification accuracy of 84.9% for 47 fallers and 42 non-fallers, based on follow-up surveys six months after data collection [8].

However, similar to clinical balance assessments, sway velocity and Romberg quotient analyses are typically confined to a clinic or lab setting, as they require stationary equipment (a force plate). At the same time, the frequency of clinic visits by older adults has been declining over the past two decades [15], highlighting the necessity for continuous

Max Burns was with the Massachusetts Institute of Technology, Cambridge, MA 02139 USA, and was supported by the MIT UROP program and the MIT Department of Mechanical Engineering. He is now with Stanford University, Stanford, CA 94305 USA.

Kaymie Shiozawa is with the Massachusetts Institute of Technology, Cambridge, MA 02139 USA, and was supported by the Hugh Hampton Young Memorial Fund Fellowship and the Charles M. Vest Fellowship.

Neville Hogan is with the Massachusetts Institute of Technology, Cambridge, MA 02139 USA. This work was in part supported by the Eric P. and Evelyn E. Newman Fund.

balance monitoring tools to be used outside the clinic.

Instrumented mobility aids offer a promising solution for continuous balance assessment. Patients with poor balance are already prescribed walking aids, such as canes or walkers, to reduce their fall risk. As a result, nearly six million people in the United States use a walking cane, the most popular mobility aid [16]. Given the growth of the 65+ demographic, the number of cane users is projected to increase significantly by 2035 [2].

Instrumented walking canes in prior work typically feature an accelerometer near the handle, an axial force sensor in the tip, and sometimes a measure of handle grip force [17-20]. Instrumented walking canes have demonstrated near-perfect rates of fall identification after a fall has occurred using accelerometer readings [19, 20], classified the user's motion (walking, running, stair climbing, etc.) using machine learning [18], and found correlations between cane sensor data and functional gait assessment scores given by physical therapists [17]. However, as far as the authors are aware, instrumented canes have not been used for quiet balance assessment or for future fall prediction. For in-home assessments, static, rather than dynamic, analyses may be safer for the user, as they only require standing in place.

The work presented here aimed to predict both sway velocity and the Romberg quotient, which are typically measured with a force plate during quiet stance, using a novel data processing pipeline and regression model. The data were collected using the instrumented cane first described by Shiozawa et al. [21]. As a preliminary test, a healthy young subject was asked to balance on an unstable platform while using the instrumented cane under various quiet balance conditions. When the subject was more unstable, the instrumented cane demonstrated a greater mean acceleration in the plane parallel to the ground. This result suggested that instability could be assessed using data from the cane [21].

Machine learning methods have been used successfully to quantify stability in the past. Greene et al. used a combination of body-mounted inertial measurement units (IMUs) and data about the user's physical characteristics to improve the accuracy of the TUG test from 60% to 80% for 226 fallers and non-fallers [22]. The authors used a logistic regression model for the classifier and set a cutoff value which could classify patients as "at-risk" [22]. Sway Medical Inc. used smartphone sensors to assess postural sway, but the sway measurement accuracy is not publicly available [23].

In this work, we describe the design and validation of a novel regression algorithm which uses instrumented cane data features to predict postural sway velocity and estimate Romberg quotients in static balance. To evaluate the accuracy of these measurements, eight unimpaired young subjects and eight subjects over 65 were evaluated under four balance conditions while using the instrumented cane. The data gathered from these experiments were used to train our regression model and estimate Romberg quotients. This is the first algorithm that has been shown to predict postural sway ability using just the sensors in an instrumented mobility aid.

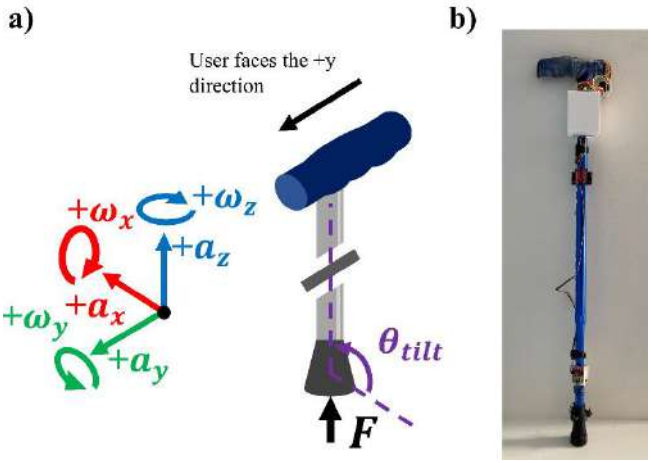


Fig. 1. a) An overview of cane sensor data outputs. Linear acceleration (a), angular velocity (ω), and orientation of the handle were collected from a 9-axis IMU. Absolute angle from the vertical axis (θ_{tilt}) was computed from the IMU's outputs. Axial force (F) was collected from a load cell inside of the cane tip. b) A photograph of the instrumented cane used in this study.

TABLE I. DATA VECTORS COMPUTED FROM COLLECTED DATA

Computed Data Vector	***Formula***
Acceleration Magnitude, a_{mag}	$a_{mag} = \sqrt{a_x^2 + a_y^2 + a_z^2}$
X-Y Acceleration, a_{xy}	$a_{xy} = \sqrt{a_x^2 + a_y^2}$
Angular Velocity Magnitude, ω_{mag}	$\omega_{mag} = \sqrt{\omega_x^2 + \omega_y^2 + \omega_z^2}$
Tilt Angular Velocity, ω_{tilt}	$\omega_{tilt} = \sqrt{\omega_x^2 + \omega_y^2}$
Tilt Angle, θ_{tilt}	*Quaternion Conversion*

II. CANE SYSTEM OVERVIEW

The design of the MIT Instrumented Cane and the data processing methods were based upon the instrumented cane system developed by Wade et al. [18]. A 1-axis load cell force sensor with a range of 0-250 N (FC2311-0000-0250-L, TE Connectivity Measurement Specialties) was connected to an amplifier (NAU7802 SparkFun Qwiic Scale) and installed within the ferrule of a commercially available walking cane to measure the force applied along the shaft of the cane. The range of the load cell was selected to encompass approximately 30% of a standard 75 kg subject's body weight [21]. A 9-axis inertial measurement unit (IMU) (SEN-14686 SparkFun VR IMU breakout) was fastened to the shaft next to the handle, which recorded 3-D linear acceleration, angular velocity, and orientation of the cane. Data were collected with a sampling frequency of 50 Hz. The raw data vectors gathered from the cane and their respective directions are indicated in Fig. 1. Four data vectors, which are outlined in Table I were computed with Python.

Data from the cane were recorded by an Arduino Leonardo, which transmitted the information to a nearby PC through USB Serial. A Python script on the acquisition PC was used to collect and organize the USB Serial input.

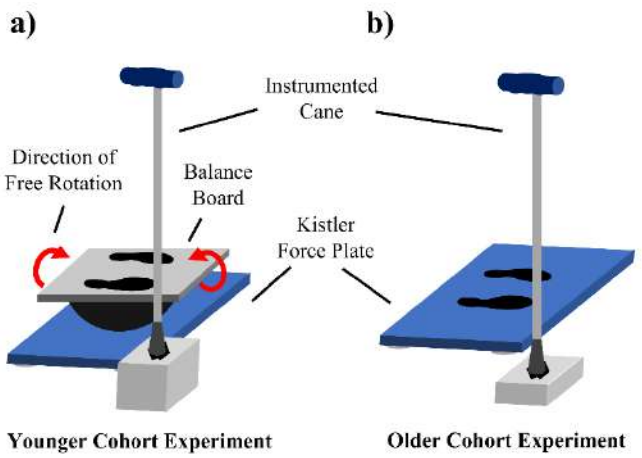


Fig. 2. Experimental setup. a) Young subjects were tasked with standing on an unstable balance board, which was placed on top of a force plate. b) Older subjects balanced directly on the force plate.

III. Experimental Data Collection

In this study, a measure of postural sway velocity and an estimate of a subject's Romberg quotient were sought. To validate that our algorithm can produce effective predictions of these measures, subjects participated in a balance experiment with the instrumented cane.

A. Participants

Eight young unimpaired human volunteers were recruited for this study, between the ages of 19 - 49 (Average: 25.4 ± 9.8 years). Young subjects were recruited to initially determine the validity of the prediction algorithms. All subjects in the younger cohort were inexperienced with using a cane and did not report any neurological or muscular issues which affected their balance. Subjects varied in height (1.65 ± 0.09 m) and mass (65.3 ± 13.2 kg), based on self-reported data. This experimental protocol was reviewed and approved by the Institutional Review Board of the Massachusetts Institute of Technology (protocol number 1912000067) on January 16, 2020.

Eight individuals over the age of 65 were also recruited to participate in a similar balance experiment to validate the instrumented cane's ability to quantify balance measures of the target population. Only community-ambulating individuals, who were able to walk a distance of 10 meters without assistance and stand in place for 5 minutes, were considered eligible for this study. Among these subjects, two were male (Age: 81.5 yrs, Mass: 77.3 kg, Height: 1.84m) and six were female (Age: 79 ± 6.9 yrs, Mass: 62.0 ± 7.1 kg, Height: 1.56 ± 0.12 m). Subjects ranged widely in age from 69-92 years at the time of collection. Six of the eight subjects were not affected by any self-reported balance conditions. Subjects varied in height (1.61 ± 0.12 m) and weight (67.3 ± 7.6 kg), based on self-reported data. This experimental protocol was reviewed and approved by the Institutional Review Board of the Massachusetts Institute of Technology (protocol number 2305000991) on June 15th, 2023.

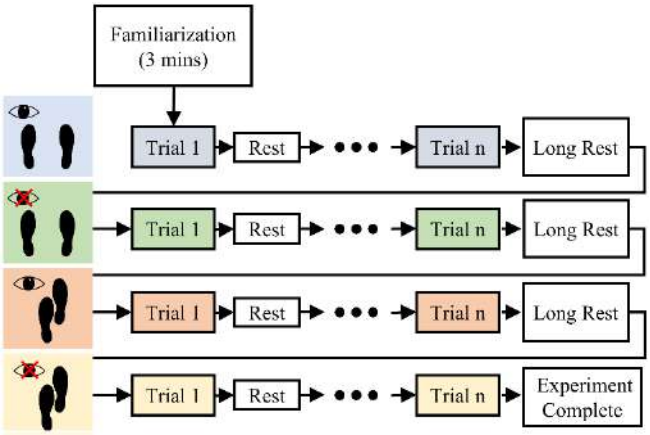


Fig. 3: The experimental protocol used in this study. Balance challenges are noted on the left, where the icons indicate the status of the eyes and positioning of the feet. A different number of trials, n, for each condition were performed by some subjects, based on subject ability and fatigue, summarized in Table II.

TABLE II. COMPLETED TRIALS BY SUBJECT & CONDITION

	Shoulder-Width		**Half-Tandem**		
Subject ID	***Eyes Open***	***Eyes Closed***	***Eyes Open***	***Eyes Closed***	***Total Windows***
Older 1	6	6	6	5	**138**
Older 2	6	6	6	6	**144**
Older 3	10	10	10	3	**198**
Older 4	6	6	6	6	**144**
Older 5	10	10	10	0	**180**
Older 6	6	6	6	6	**144**
Older 7	6	6	6	6	**144**
Older 8	6	6	6	6	**144**
Younger Cohort	10 ea.	10 ea.	10 ea.	10 ea.	**240 ea.**

B. Experimental Protocol

In the experiments, subjects in the younger cohort stood on top of an unstable platform with the cane in their dominant hand, which was placed on top of a Kistler force plate. The platform was free to rotate within the subjects' sagittal plane, allowing them to rock forward and back, as shown in Fig. 2. The unstable platform was used to artificially inhibit the balance ability of the participants, and not to imitate a specific balance condition. Subjects over 65 stood directly on the force plate with the cane in their dominant hand, as shown in Fig. 2. The distance between the cane and the center of the base of support was kept constant across trials and subjects.

During the experiment, all subjects were asked to assume two stances, the first with their feet shoulder-width apart and the second in the half-tandem orientation, where feet are close together and slightly offset in the sagittal plane. Subjects were instructed to stand in both stances with eyes open and then closed, yielding four experimental conditions. These conditions were selected to induce a high variation of stability and sway velocity. The condition order is shown in Fig. 3 and was not randomized because preliminary experiments suggested that transitioning between conditions too frequently decreased subject consistency. The number of trials and conditions varied for each subject, depending on their physical ability and fatigue, and is summarized in Table II. Each trial duration was 36 seconds, which was selected

based on preliminary data to maximize the number of data windows extracted without exhausting participants.

For each trial, center of pressure (CoP) data were collected from the force plate at a sampling frequency of 50 Hz. Then, the average speed of the subject's CoP, sway velocity, was calculated over a ten second time window. The CoP computation did not include the force on the cane, as it was small enough to be neglected (an average body weight borne of $3.08 \pm 2.07\%$ for the younger cohort, $2.26 \pm 1.18\%$ for the older).

IV. Balance Measure Prediction Algorithm

To predict body sway velocity using motion and force data from the instrumented cane, we used a feature extraction pipeline and linear regression model to fit data to true sway velocity collected with a force plate.

A. Linear Regression Model for Sway Velocity Prediction

The preparation of data for use in a linear regression model is summarized in Fig. 4. To create test and train sets, stratified three-fold cross-validation was used to divide each subject's trials into three equal bins. Data were divided by trials to avoid pollution between folds. In three-fold cross-validation, each bin (33% of data) is used once as the test set for a model trained with the two remaining bins (67% of data). The stratification process was applied to avoid class imbalance between the four balance challenges, which would interfere with model training due to the dissimilar test and train datasets.

1) Windowing

For each trial, a ten second sliding window was applied, with 48% overlap between windows. This overlap was selected based upon prior work to maximize the number of data points produced per trial without causing overfitting [18]. The sliding window produced six windows for each 36 second trial. The total number of windows varied by subject and is summarized in Table II.

Window length and number of features used were selected through a parameter sweep using the MIT SuperCloud computing system [24]. Window lengths between 2 and 17 seconds and total feature counts between 3 and 16 features were examined in a 2-dimensional parameter sweep. A window length of 10 seconds and a feature count of 10 produced acceptable and stable R^2 values across subjects.

2) Feature Computation and Selection

Features were extracted from the raw data recorded by the instrumented cane [18]. Each feature was computed by applying a statistical method to one window of raw data. For instance, the "mean axial force" feature was computed by applying the "mean" method to a window of "axial force" data. Each method was applied to each raw data vector such that 108 features (9 methods for each of the 12 raw data vectors) were extracted for each window. The functions used for feature production are summarized in Table III.

For each model, a feature selection process was employed to minimize overfitting and eliminate ineffective features. An optimizer was used to select features from the training data

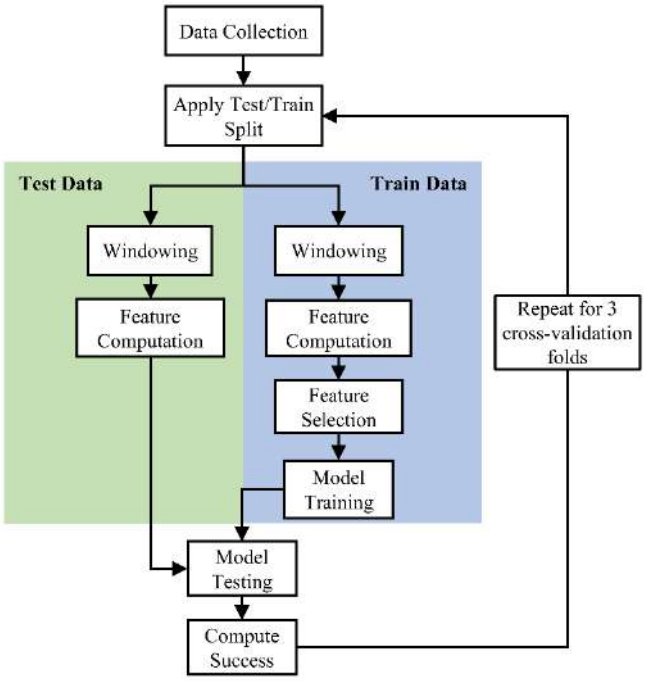


Fig. 4. A summary of the steps required to compute and evaluate the sway velocity regression model.

TABLE III. Data and Methods for Feature Computation

Data Vectors	Methods
X Acceleration, a_x	Mean
Y Acceleration, a_y	Median
Z Acceleration, a_z	Minimum
X Angular Velocity, ω_x	Maximum
Y Angular Velocity, ω_y	Range
Z Angular Velocity, ω_z	Interquartile Range
Axial Force, F	Standard Deviation
Tilt Angle, θ_{tilt}	Mean Absolute Deviation
Acceleration Magnitude, a_{mag}	Signal Energy
X-Y Acceleration, a_{xy}	
Angular Velocity Magnitude, ω_{mag}	
Tilt Angular Velocity, ω_{tilt}	

that strongly correlated with sway velocity while penalizing those that were closely correlated with each other, as described in Wade et al. [16]. This approach reduced redundancy and ensured that the chosen features were strong predictors of sway velocity. Feature selection was performed for each cross-validation fold based upon only training data to prevent contamination of test data. Using the methodology above, ten features were selected for use in linear regression. The feature selection process was conducted separately for the two cohorts, and training data from all subjects in a given cohort was used to select features for that cohort.

3) Model Training and Testing

Linear regression models were trained using each subject's feature data. While the training was specific to each individual's dataset, feature selection was based on data from the entire cohort for each cross-validation fold. Each model was then applied to the corresponding subject's test data set, and the predicted sway velocity was compared to the true sway velocity. Due to the random nature of the test-train split,

TABLE IV. PREDICTION RESULTS: 250 MODEL ITERATIONS

	Younger Cohort		Older Cohort	
Metric	R^2	$RMSE\left(\frac{mm}{s}\right)$	R^2	$RMSE\left(\frac{mm}{s}\right)$
SV (Mag)	0.73 ± 0.04	8.29 ± 0.51	0.47 ± 0.09	5.88 ± 0.37
SV (ML)	0.73 ± 0.04	6.43 ± 0.40	0.45 ± 0.09	4.71 ± 0.31
SV (AP)	0.57 ± 0.05	5.60 ± 0.36	0.36 ± 0.12	3.80 ± 0.24

TABLE V. "STRONG" FEATURES OBSERVED IN YOUNGER COHORT

Feature	Subjects with Correlation > 0.8	Avg. Correlation with Sway Velocity
ω_{tilt} Mean	8	0.88 ± 0.05
ω_{mag} Median	8	0.87 ± 0.05
ω_{tilt} Median	7	0.87 ± 0.05
ω_y Mean Abs. Deviation	7	0.84 ± 0.05
ω_y Interquartile Range	7	0.84 ± 0.05

TABLE VI. "STRONG" FEATURES OBSERVED IN OLDER COHORT

Feature	Subjects with Correlation > 0.8	Avg. Correlation with Sway Velocity
ω_{tilt} Mean	8	0.70 ± 0.10
ω_{tilt} Mean Abs. Deviation	8	0.69 ± 0.12
ω_{tilt} Interquartile Range	8	0.68 ± 0.13
ω_{tilt} Median	7	0.71 ± 0.12
ω_y Mean Abs. Deviation	7	0.66 ± 0.16

250 linear regression models were prepared for each subject, using test and train sets randomized through cross-validation. Average RMSE and R^2 values for the test data of each subject were calculated based on test set performance. [16]

B. *Identifying Common Important Features*

The selected features varied between models due to the variability of the test-train split. This variability made identification of common important features difficult. Instead, the Pearson correlation coefficient between sway velocity magnitude and each feature was computed for each subject. This correlation was not used for sway velocity prediction, so a test-train split was not applied. A feature with an absolute correlation of greater than 0.8 for the younger cohort, or 0.5 for the older cohort, was considered a "strong" feature for that subject. This process was repeated for each subject, and the strong features were recorded.

C. *Romberg Quotient Estimation*

Romberg quotients were obtained for the older subject cohort using the data from the instrumented cane. For this correlation analysis, no test-train split was applied. Romberg quotients were computed for all features, by dividing the feature vectors obtained during the eyes-closed trials by the feature vectors obtained during the eyes-opened trials. The correlation of these feature Romberg quotients to the true Romberg quotient (computed with the force plate sway velocity data) was evaluated for each subject. This analysis was confined to the shoulder-width stance condition, based on methods presented in prior work [13]. The quotient with the highest correlation was reported.

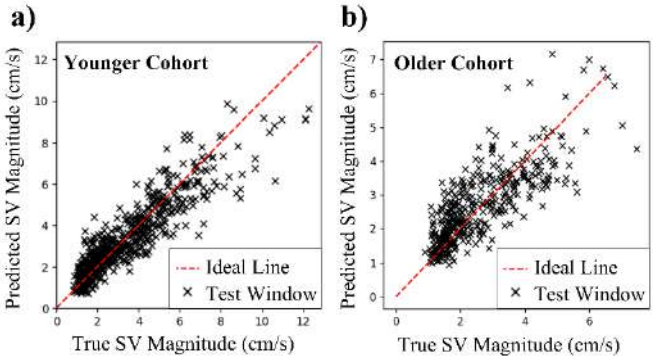


Fig. 5. Representative plots of the prediction of sway velocity magnitude for the a) younger and b) older subject cohorts. Each point is from one 10s window of test data from a subject. The diagonal line represents the ideal output, where the prediction error is zero.

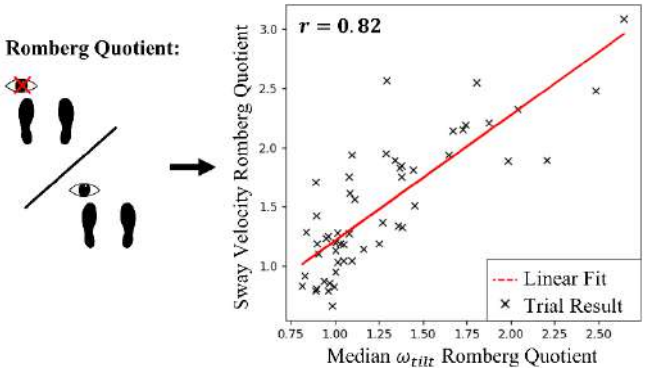


Fig. 6. A comparison between Romberg quotients computed from measured mean sway velocity and mean ω_{tilt} for older subjects in the shoulder-width stance. Each x icon represents the quotient computed from an eyes-open and eyes-closed trial for one subject. Data from all older subjects is displayed and used to compute the Pearson's correlation of $r = 0.82$ (p = 4e-14). A line of best fit, of which the slope was 1.06 ± 0.10 and the intercept was 0.15 ± 0.04, is shown.

V. RESULTS

Table IV summarizes the R^2 and RMSE values for each component of sway velocity, averaged across all subjects. For the younger cohort, an average R^2 value of 0.73 ± 0.04 was found between the linear regression result and the mean magnitude of sway velocity. For the cohort of subjects over 65, an average R^2 value of 0.47 ± 0.09 was observed for sway velocity magnitude. For the younger subjects, the highest average R^2 for sway velocity magnitude of an individual subject was 0.86 ± 0.05, while the lowest was 0.60 ± 0.12. For the older cohort, the highest average R^2 for a subject was 0.67 ± 0.13, and the lowest was 0.34 ± 0.31.

Fig. 5 demonstrates example models for the older and younger cohorts, which compared the predicted sway velocity magnitude of each data window to the true sway velocity magnitude for the younger and older cohorts respectively.

Tables V & VI summarize the features that displayed high Pearson's correlation with sway velocity magnitude for the two cohorts. Notably, features which described the magnitude and variability of ω_{tilt} (the angular velocity about the instrumented cane's base) were particularly well correlated with sway velocity magnitude for both subject cohorts.

For the older cohort, ω_{tilt} correlated most strongly (r-value of 0.82) with the true Romberg quotient in the shoulder-width stance. This Romberg quotient correlation across all older subjects is shown in Fig. 6.

VI. Discussion

Postural sway analysis can be used to estimate fall risk [8, 9] and quantify proprioceptive changes [13]. To our knowledge, this study is the first to estimate a user's sway velocity and Romberg quotient during quiet stance using only sensors onboard an instrumented mobility aid. Our results demonstrated that our algorithms were sufficient to both predict sway velocity and estimate the Romberg quotient across all participants using just instrumented cane data. Furthermore, aspects of the participants' hand motion were closely tied to body motion for all subjects. The Romberg quotients computed from instrumented cane metrics were found to have strong correlation with true Romberg quotients computed from sway velocity. This work provides support for future analysis of fall risk based upon long-term, continuous data from a portable, instrumented device.

In prior work, algorithms have been developed to classify activities or detect falls with instrumented cane data, but not to provide measures of balance health. The regression algorithm and Romberg estimation presented in this paper rely primarily on measurements from an IMU, and could be used to evaluate a user's balance throughout everyday life. This technology could bring dramatic change from the current standard of care, in which at-risk patients are evaluated for risk of falling a few times per year, if at all [10]. These estimations are accomplished by extracting useful feature information from the instrumented cane's data, which makes the models both easy to interpret and effective predictors of balance metrics. The features used in this work are static balance measures, but assessment of dynamic balance is a promising avenue for further investigation which could provide additional information. Future work could also conduct user-focused studies to assess adoption rates and preferences within older populations for this technology.

A promising relationship between predicted and actual sway velocity was observed, but predictions were strongest when sway variance was high. The younger cohort, likely more challenged due to the presence of the unstable platform and therefore exhibiting greater sway variance, achieved the highest average R^2 for sway velocity magnitude of 0.86; meanwhile, the older cohort's highest average R^2 was 0.67. Although older subjects displayed a smaller RMSE than younger subjects, their average R^2 values were lower. Similarly, the prediction accuracy for the AP sway velocity component was lower than for the medial-lateral (ML) component for all subjects. This result is also likely due to the greater variance of ML sway velocity across subjects and conditions. When sway velocity variance is low, the inherent noise between the true sway velocity signal and the interaction with the instrumented cane likely dominates. To improve predictive accuracy, future studies could collect more data to extract further useful feature information.

In both age cohorts, when subjects swayed more rapidly, it resulted in larger and more variable hand motion. Features with high correlation to sway velocity were primarily computed from ω_{tilt}, a measure of the planar motion of the hand. For example, mean ω_{tilt} had a very strong correlation with mean sway velocity (0.88 ± 0.05 for younger, 0.70 ± 0.10 for older), a finding that was consistent across all subjects (Tables V and VI). Three of the five strong features were shared between the two subject groups as well, and all strong features were computed from angular velocity components measured by the IMU. This is compelling evidence that hand motion and body sway are closely linked, and that this behavior is consistent across age and experience with assistive devices.

Median ω_{tilt} was found to correlate strongly with sway velocity magnitude for seven of the eight older subjects with an average correlation of $r = 0.71 \pm 0.12$ (Table VI). The Romberg quotient was computed for the older cohort, yielding an even stronger correlation of $r = 0.82$ between the Romberg quotients of mean sway velocity and the median ω_{tilt}. The Romberg quotient is a useful measure of abnormal proprioception. Therefore, the results suggest that data from the instrumented cane could quantify long-term proprioceptive trends, potentially signaling the need for intervention before a fall occurs. The older cohort's average Romberg quotient found from sway velocity (1.46 ± 0.52) was lower than the expected average for this population (1.94 ± 0.58, [13]), likely due to the cane's stabilizing effects.

Hand motion rather than force exerted on a cane may provide greater insight into the user's balance. Axial force features were not a strong indicator of sway velocity, and Romberg quotients computed from axial force exhibited poor correlation with true Romberg values. Since large forces applied to a walking cane are not necessary to provide greater stability [25], balance assessments using handheld assistive devices could focus on hand motion rather than force. The findings also agree with the work of Shiozawa et al., in which the mean acceleration, but not the mean axial force, of an instrumented cane was determined to be significantly different between various stability conditions [21]. Taken together, these insights suggest that the algorithms presented in this paper may only require IMU data to provide stability estimates.

One limitation of this study is that fewer trials were conducted for older adults compared to their younger counterparts to avoid fatigue. An average of 25.75 trials were collected per older subject, compared to 40 trials per younger subject. The larger dataset for younger subjects may have contributed to the higher variance accounted for compared to that of the older participants. Future studies could benefit from conducting multiple sessions with the same subjects to gather larger datasets and stronger predictions. Another limitation of this methodology is that using a cane artificially improves observed balance due to the physical support and haptic cues it provides [26]. Thus, it is important to note that this sway velocity estimate would be best applied by observing changes over time, rather than being used as a

stand-in for unsupported sway velocity.

Preliminary tests with nonlinear regression resulted in overfitting of the data and poor performance during test data evaluation. More advanced models trained with time series data may provide greater predictive ability for a larger dataset and are promising avenues for future work. Furthermore, the rate at which balance changes occur in an individual is a crucial area of future research. The algorithm presented in this work could be used to study daily changes in balance among a population of older individuals over months or years.

VII. Conclusion

This work demonstrated that the outputs of sensors onboard an instrumented cane can reliably estimate a user's postural sway velocity and Romberg quotient. Using a novel regression algorithm, the cane's motion data was crucial in predicting these measures for both unimpaired young subjects and those over 65.

Although the nature of falls is complex, postural sway velocity and the Romberg quotient are both important markers of a patient's balance health and can be incorporated into models to predict future fall risk [8]. The Romberg quotient, in particular, can indicate poor proprioception and overreliance on visual feedback for balance. Validating the proposed algorithm's ability to predict and compute these measures provides promising support for its eventual use as a tool to assess changes in balance ability. Equipped with the ability to predict balance performance via our custom regression model, the instrumented walking cane is envisioned to be an at-home monitoring device which measures a user's stability over the course of months or years, rather than during infrequent clinic visits. Such continuous monitoring could provide advance warnings of declining balance, potentially preventing falls. The proposed methods could complement a comprehensive balance assessment, informing physicians in developing treatment plans or determining the need for intervention.

Acknowledgment

The authors would like to thank Emily Skilling B.S. for her work developing the MIT instrumented cane hardware.

References

[1] Y. Dionyssiotis, "Analyzing the problem of falls among older people," *Int J Gen Med*, vol. 5, p. 805, 2012.

[2] U. C. Bureau, "2020 Census Will Help Policymakers Prepare for the Incoming Wave of Aging Boomers", Accessed: Aug. 10, 2023. [Online]. Available: https://www.census.gov/library/stories/2019/12/by-2030-all-baby-boomers-will-be-age-65-or-older.html

[3] M. J. H. Heijnen and S. Rietdyk, "Falls in young adults: Perceived causes and environmental factors assessed with a daily online survey," *Hum Mov Sci*, vol. 46, pp. 86–95, Apr. 2016.

[4] H. Y. Cho, M. J. H. Heijnen, B. A. Craig, and S. Rietdyk, "Falls in young adults: The effect of sex, physical activity, and prescription medications," *PLoS One*, vol. 16, no. 4, p. e0250360, Apr. 2021.

[5] B. Moreland, R. Kakara, and A. Henry, "Trends in Nonfatal Falls and Fall-Related Injuries Among Adults Aged ≥65 Years — United States, 2012–2018," *MMWR Morb Mortal Wkly Rep*, vol. 69, no. 27, pp. 875–881, Jul. 2023.

[6] T. E. Jager, H. B. Weiss, J. H. Coben, and P. E. Pepe, "Traumatic brain injuries evaluated in U.S. emergency departments, 1992-1994," *Acad Emerg Med*, vol. 7, no. 2, pp. 134–140, 2000.

[7] L. T. Southerland *et al.*, "Accuracy of the 4-Stage Balance Test and Sensor-Based Trunk Sway as Fall Risk Assessment Tools in the Emergency Department," *J Acute Care Phys Ther*, vol. 12, no. 2, pp. 79–87, Apr. 2021.

[8] J. Howcroft, E. D. Lemaire, J. Kofman, and W. E. McIlroy, "Elderly fall risk prediction using static posturography," *PLoS One*, vol. 12, no. 2, p. e0172398, Feb. 2017.

[9] A. Wiśniowska-Szurlej, A. Ćwirlej-Sozańska, A. Wilmowska-Pietruszyńska, and B. Sozański, "The Use of Static Posturography Cut-Off Scores to Identify the Risk of Falling in Older Adults," *Int J Environ Res Public Health*, vol. 19, no. 11, p. 6480, Jun. 2022.

[10] J. A. Mark, Y. K. Haddad, and E. R. Burns, "Differences in Evaluating Fall Risk by Primary Care Provider Type," *J Nurse Pract*, vol. 16, no. 7, pp. 528–532, Jul. 2020.

[11] E. Barry, R. Galvin, C. Keogh, F. Horgan, and T. Fahey, "Is the Timed Up and Go test a useful predictor of risk of falls in community dwelling older adults: A systematic review and meta- analysis," *BMC Geriatr*, vol. 14, no. 1, pp. 1–14, Feb. 2014.

[12] D. Lin, H. Seol, M. A. Nussbaum, and M. L. Madigan, "Reliability of COP-based postural sway measures and age-related differences," *Gait Posture*, vol. 28, no. 2, pp. 337–342, Aug. 2008.

[13] M. Gallamini *et al.*, "Revisiting the Instrumented Romberg Test: Can Today's Technology Offer a Risk-of-Fall Screening Device for Senior Citizens? An Experience-Based Approach," *Life (Basel)*, vol. 11, no. 2, pp. 1–20, Feb. 2021.

[14] S. Morioka, M. Okita, Y. Takata, S. Miyamoto, and H. Itaba, "Effects of Changes of Foot Position on Romberg's Quotient of Postural Sway and Leg Muscles Electromyographic Activities in Standing," *Journal of the Japanese Physical Therapy Association*, vol. 3, no. 1, p. 17, 2000.

[15] A. Rao, Z. Shi, K. N. Ray, A. Mehrotra, and I. Ganguli, "National Trends in Primary Care Visit Use and Practice Capabilities, 2008-2015," *Ann Fam Med*, vol. 17, no. 6, p. 538, Nov. 2019.

[16] N. M. Gell, R. B. Wallace, A. Z. Lacroix, T. M. Mroz, and K. V. Patel, "Mobility Device Use Among Older Adults and Incidence of Falls and Worry About Falling: Findings From the 2011–2012 National Health and Aging Trends Study," *J Am Geriatr Soc*, vol. 63, no. 5, p. 853, May 2015.

[17] J. W. Wade *et al.*, "Feasibility of Automated Mobility Assessment of Older Adults via an Instrumented Cane," *IEEE J Biomed Health Inform*, vol. 23, no. 4, pp. 1631–1638, Jul. 2019.

[18] J. Wade *et al.*, "Design and implementation of an instrumented cane for gait recognition," *Proc IEEE Int Conf Robot Autom*, vol. 2015-June, no. June, pp. 5904–5909, Jun. 2015.

[19] M. Lan, A. Nahapetian, A. Vahdatpour, L. Au, W. Kaiser, and M. Sarrafzadeh, "SmartFall: An automatic fall detection system based on subsequence matching for the smartcane," *BODYNETS 2009 - 4th International ICST Conference on Body Area Networks*, Nov. 2011.

[20] W. Wu *et al.*, "The SmartCane system: An assistive device for geriatrics," *BODYNETS 2008 - 3rd International ICST Conference on Body Area Networks*, Nov. 2011.

[21] K. S. Shiozawa, "Towards the Development of an Adaptive Rehabilitative Device," 2021.

[22] B. R. Greene, E. P. Doheny, C. Walsh, C. Cunningham, L. Crosby, and R. A. Kenny, "Evaluation of Falls Risk in Community-Dwelling Older Adults Using Body-Worn Sensors," *Gerontology*, vol. 58, no. 5, pp. 472–480, Aug. 2012.

[23] "Sway Medical." Accessed: Aug. 11, 2024. [Online]. Available: https://www.swaymedical.com/

[24] A. Reuther *et al.*, "Interactive Supercomputing on 40,000 Cores for Machine Learning and Data Analysis," *2018 IEEE High Performance Extreme Computing Conference, HPEC 2018*, Nov. 2018.

[25] M. Russo, J. Lee, N. Hogan, and D. Sternad, "Mechanical effects of canes on standing posture: beyond perceptual information," *J Neuroeng Rehabil*, vol. 19, no. 1, pp. 1–13, Dec. 2022.

[26] J. J. Jeka, "Light touch contact as a balance aid," *Phys Ther*, vol. 77, no. 5, pp. 476–487, 1997.

Development and Validation of a Low-Cost Open-Source Force Myography Band for Hand Gesture Recognition

Giancarlo K. Sagastume, Peyton R. Young, and Jonathon S. Schofield, *Member, IEEE*

Abstract— **Wearable systems for hand gesture recognition have gained significant attention in research and clinical applications due to advances in many hand-centric control interfaces for technologies such as upper limb prostheses, hand exoskeletons, and virtual reality for rehabilitation. However, common hand gesture recognition techniques are often associated with high costs and proprietary software which can reduce the accessibility of these devices. Thus, in this work we developed, and feasibility tested a low-cost open-source alternative in the form factor of a wearable forearm band. Our system leverages force myography (FMG) which recognizes patterns in the radial muscle forces at the skin's surface on the forearm when different hand gestures are performed. Our FMG band was validated through a participant-based study (N=15) where able-bodied individuals were instructed to perform repetition of 10 hand gestures. Offline classification analysis of the resulting muscle force data using a linear discriminant analysis showed the band achieved an average of 94.28% accuracy among all gestures across all participants. These results suggest that despite the FMG Band's low cost, its performance is comparable to similar gesture recognition technologies currently available for research, clinical, and consumer applications.**

INTRODUCTION

The recognition of hand gestures is a critical component in controlling many emerging rehabilitative and assistive technologies, such as upper limb prostheses, exoskeletons, and virtual reality rehabilitation systems [1], [2], [3]. Effective operation of these technologies can be facilitated by human-centric control interfaces—those that are intuitive and non-intrusive for the user. Various human interface technologies exist to decode user intentions from naturally occurring biological signals during attempted hand motions, enabling accurate prediction of hand gestures. These technologies can use a variety of sensing approaches, including electrophysiological [4], acoustic [5], and optical [6] methods, among others. However, despite increasing demand for intuitive hand-gesture decoding strategies, many techniques remain experimental. Those that are commercially available are often cost-prohibitive and rely on proprietary software, which can further limit their accessibility and utility in research and clinical environments. This is particularly true when constrained by research or clinical budgets or when requiring access to customize signal acquisition methods to meet specific data collection and equipment integration needs.

One relatively new approach with the potential to address accessibility limitations is Force Myography (FMG), the measurement of radial muscle forces at the surface of the forearm. Unlike Electromyography (EMG), a popular sensing modality which requires stable skin-electrode contact [4], FMG is a non-electrophysiological method that captures muscle activity through mechanical deformation. The surface of the forearm changes in response to the contraction and relaxation of underlying muscles when hand gestures are performed, resulting in unique force profiles that can be detected along the forearm's circumference. To capture these profiles and use them as control signals, FMG typically employs a series of pressure (or force) sensors placed around the circumference of the forearm. Although a variety of different pressure or force sensors can be used to accomplish the task of measuring these radial forces, the most common is the force sensitive resistor (FSR). FSRs are thin-film components that decrease in resistance as force is applied. Their popularity in numerous commercial and hobbyist applications has resulted in a low unit price when compared to other sensing modalities. Thus, FMG presents a low-cost sensing technology for potential applications in hand gesture recognition systems.

However, as an emerging technology, FMG remains a largely experimental control modality with few to no clinical or consumer systems available for purchase. As a result, those wishing to leverage FMG technologies in research or clinical applications are left to create custom systems drawing upon scientific literature reporting disparate quantities of force sensors, amplification and signal conditioning circuitry, and fitment solutions [7]. Thus, in addressing accessibility challenges, the objectives of this work are to develop and evaluate a low cost, open-source FMG system that takes the form factor of a wearable forearm band.

I. DESIGN METRICS

A literature search was conducted to survey trends in wearable technologies for hand gesture recognition. From this, three key design characteristics guided the development of our FMG band: *fitment*, *accessibility*, and *modularity*. These factors and their implications are further defined below and their impact on our prototype design are highlighted

*Research supported by UC Davis NXLR fund

G. K. Sagastume is with the Department of Electrical and Computer Engineering, University of California, Davis, Davis, CA 95616 USA

P. R. Young with the Department of Mechanical and Aerospace Engineering, University of California, Davis, Davis, CA 95616 USA

J. S. Schofield is with the Department of Mechanical and Aerospace Engineering, University of California, Davis, Davis, CA 95616 USA (phone: 530-754-1731; e-mail: jschofield@ucdavis.edu)

throughout the Electrical and Mechanical design section of this paper.

Fitment refers to how well a wearable device conforms to the users' anatomy. In the context of a wearable FMG system, fitment is critical because it directly affects the quality of contact between the force sensors and the user's forearm, which in turn impacts device performance. For instance, a band that fits too loosely may result in sensor contact loss or slippage on the forearm, leading to inconsistent or unreliable force measurements. Conversely, a band that is too tight may cause user discomfort and potentially saturate the sensors as they press with excessive force into the forearm tissue. These factors accentuate the impact of external forces and motion artifacts, making it a key quality to ensure signal reliability.

Accessibility was a primary consideration in our design and development process. We aimed to create an FMG device that leverages low-cost, off-the-shelf components and integrates existing open-source computational methods [8]. This approach ensures that the device remains affordable and widely accessible for various users and applications.

In the FMG literature, a range of force sensing modalities and fitment solutions have been reported [9]. To address this diversity, we prioritized modularity in our design. A modular system allows for easy removal and modification of sensor units, enabling compatibility with different sensor types, circuitry, and data acquisition systems. This flexibility supports the potential diverse needs of research and clinical applications. Furthermore, our design ensures that adjustments to fitment and mobility can be made with minimal effort by the end user (as described below).

II. Electrical and Mechanical Design

A. Electrical Design

FMG systems inherently rely upon force or pressure sensors to derive control signals from muscle activity. In literature, a variety of different sensor modalities have been reported to achieve this task. Barometric [10], capacitive [11], and strain transducer [12], technologies among others have all been used in previous works. However, we chose to develop our FMG system around force sensitive resistors (FSRs). FSRs are thin film, two-terminal sensors that decreases in resistance as force is applied to its surface. They are among the more common sensors in FMG applications owing to their widespread availability, low unit cost, low power draw, and reduced demand for complex circuits and signal conditioning when compared to other sensors [7], [13].

Toward the goal of designing an *accessible* system, our design used Interlink Electronic's FSR400. This choice was driven by the low cost and commercial availability of these sensors across multiple vendors internationally. Because FSRs are not active sensors, additional circuitry was required to acquire an analog output signal from these sensors. To obtain the difference in electric potential between ground and the FSR output, a voltage divider (VD) circuit was employed. The VD configuration comes with several benefits for use in FMG systems, such as its flexible voltage range, minimal-complexity design, and ease of tuning. In this configuration, an FSR is tied to the positive input voltage and its secondary lead is connected in series to a grounded reference resistor. The reference resistor controls the behavior of the FSR through limitation of current flow. Per manufacturer guidelines, a 7.5 kOhm reference resistor was selected to leverage the improved linearity in output voltage in response to an input force (force range 0-4N, pressure-voltage curve shown in [14]). Because of the VD's passive nature, input voltage was limited only by the FSR and resistor. While in this work we opted to use +5V, the FMG system can be powered through a wide range of voltage sources, including 3.3V. This further promoted our device's *modularity* by being capable integration with a wide variety of microcontrollers operating across this voltage range (Arduino, MSP432, etc.). An itemized bill of materials can be found in table 1, demonstrating the overall component cost of our system, being $162.60 USD.

B. Electrical Construction

Translation of the theoretical circuit design was done with consideration to reduce complexity. Following prior FMG literature, we opted to use 8 sensors [15] and thus, 8 VD channels (Fig. 1). The circuit was fabricated on a through-hole protoboard with accompanying resistors of the same style. Solder traces within the protoboard and jumper wires connected the components together. Two 10-pin DuPont connectors laid on the top and bottom of the board for quick connection of the FMG band and its analog output. Positive and ground jumper pins were soldered in place to feed the power supply voltage. A key aspect of this design is that the device can be used both in tethered or untethered fashion. This means that the analog output pins of the circuit can be fed to either a self-powered microcontroller or a benchtop power supply and data acquisition device (DAQ). In our validation study (described below), we chose to use the device in the tethered configuration. With the electrical portion completed, the FMG band itself could be constructed.

A. Mechanical Design

The mechanical design of the FMG band had the greatest impact on *fitment* and *modularity*. These two aspects governed the band's design as it needed to be able to fit a wide range of forearm sizes and accommodate other potential sensors.

The thin film composition of the FSR400 sensors lends to its small physical size and unobtrusive footprint. While this is helpful for physical space considerations and thus increasing the ability to incorporate additional sensors around a forearm, their construction required a custom designed housing to ensure effective measurement of forearm muscle forces. Sensor "cradles" were designed in SolidWorks to act as a hard backing for the FSRs, ensuring applied muscle forces would be directly translated into the FSR's sensing surface (Fig. 2). The cradles were designed with consideration to wiring management as each FSR requires a ground, voltage supply, and signal lead. This resulted in a T-shaped groove on the back of the cradles rear side and a negative shape of the FSR400 was cut from the front side of the cradle such that an FSR could rest flush with the top of the unit.

B. Mechanical Construction

Once printed, the cradles were outfit with FSR400 pressure sensors and accompanying wiring. To ensure consistent sensor

Item	Quantity	Cost Per Unit	Total Cost
FSR400	8	$2.99	$23.92
Velcro Strap	1	$8.49	$8.49
Velcro Adhesive Tape	1	$8.99	$8.99
30 AWG Flexible Cable	1	$12.99	$12.99
PCB Protoboard (x20)	1	$9.99	$9.99
ABS Resin	1	$44.09	$44.09
Copper Tape	1	$6.88	$6.88
PDMS Domes (x100)	1	$7.99	$7.99
7.5 kOhm Resistors (x100)	1	$5.49	$5.49
Wiring Sheath	1	$7.63	$7.63
Hot Glue Sticks (x10)	1	$2.92	$2.92
Solder	1	$5.79	$5.79
Dupont Connectors (x100)	1	$12.99	$12.99
Total Cost			**$162.60**

Table 1. Bill of materials for the FMG band. Costs provided in United States Dollars ($USD)

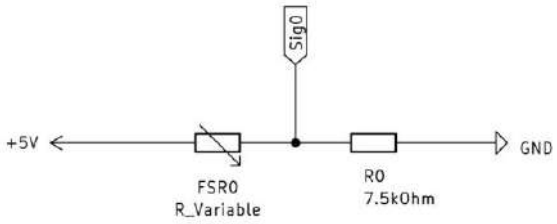


Fig. 1. A single channel of the VD circuit that was replicated 8 times on protobard. A benchtop power supply provides +5V (not pictured) connected to one lead of the FSR, followed by a grounded reference resistor. A NI DAQ measures and records the signal output from the sig0 wire junction.

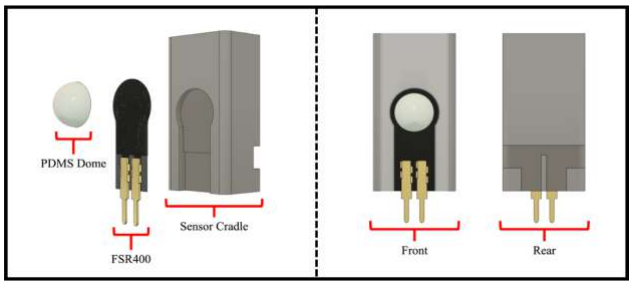


Fig. 2. Sensor cradle construction. From left to right: the exploded view of a single sensor cradle constructed of a PDMS dome, FSR400 sensor, and 3D printed housing; the front and rear view of an assembled sensor cradle.

placement, liquid adhesive was applied to affix the FSR in the appropriate position on the cradle. The sensing surface of each FSR was carefully fit with a small adhesive polydimethylsiloxane (PDMS) dome. This was done to ensure the even spread of applied forces across the sensor's active sensing region [16]. The FSR's solder tabs were bent at a 90-degree angle, laying on top of copper tape leading to the cradle's rear. This helps not only with wiring management but also to prevent solder joint damage from wire tension. On the rear, input and output wires are soldered to the copper tape and a thin layer of hot glue is applied to prevent unwanted movement. One inch Velcro adhesive backings were applied to the rear of the sensor units for individual sensor adjustment. Velcro was used as the band's base to allow for quick removal and replacement of sensor cradles, reducing the burden of resizing the device improving *fitment* by accommodating varying forearm sizes. In this work, our device was tethered to our data acquisition system. A bus cable of 9 wires was attached via DuPont connector to the outmost layer of the Velcro band. Fig. 3 shows the overall assembly. After final connections were made between the band, circuit, and benchtop equipment, the band was ready for feasibility testing.

III. Feasibility Testing

A hand gesture task was performed to evaluate the feasibility of our FMG band as a tool for hand gesture recognition. This offline hand gesture classification study required participants to complete a series of hand gestures while wearing the FMG band and we evaluated the accuracy to which a machine learning classifier could use the collected data to predict the performed gesture (described further below).

A. Experimental Setup

15 able-bodied subjects, aged 20 to 32 years old (mean age 23 ±3.2 years), participated in our study. 9 participants identified as male and 6 as female, with the majority (14) identifying as right-handed and 1 identifying as ambidextrous using the Edinburgh Handedness Inventory [17]. Study protocols were approved by the UC Davis Institutional Review Board (IRB) and all participants provided written informed consent.

Participants were seated at a table and were fit with the FMG band on the forearm of their dominant hand. Their hand and forearm were supported for comfort, but care was given to minimize limb movements during testing and ensure the FMG band was not in contact with any objects other than each participants' forearm. The FMG band was connected to the tethered VD circuitry resting on the table via bus cable connections. Following this, a +5V connection was made between the benchtop DC power supply (TekPower TP-3005D-3) and the VD circuit, and the signal outputs were sent to a National Instruments USB-6210 Data Acquisition System (NI DAQ). Following, a brief verification of sensor placement was conducted through a MATLAB test script in which the real-time sensor output was monitored and the investigators adjusted the band to maximize the sensor output when the participant contracted their muscles by making a fist. Fig. 4 shows the experimental setup. Once completed, the primary experiment began.

B. Experimental Procedure

Participants were tasked with performing a series of hand gestures. The 10 gestures seen in Fig. 5 [18]: Cylindrical Rotation (CR), Cylindrical Wrap (CW), Index Flexion (IF), Index Point (IP), Key Pinch (KP), Pulp Pinch (PP), Tripod

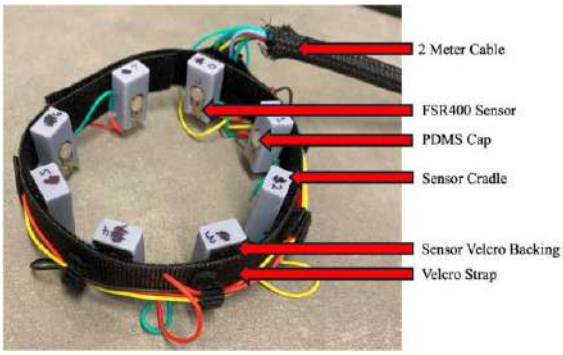


Fig. 3. The designed FMG band, comprised of a 2-meter long bus cable, 8 FSR400 sensors capped with PDMS domes, 3D printed cradles to house the sensors, and attachments to an outer Velcro band

Pinch (TP), Wrist Extension (WE), Wrist Flexion (WF), and Wrist Rotation (WR) are common to daily living. Testing began with the initial gesture being chosen at random. A MATLAB script would play an auditory tone for 3 seconds, indicating to the participant to perform the gesture, followed by silence, indicating a rest period (3 seconds long). During times of muscle contraction, the script would record FSR voltage responses through the NI DAQ's analog inputs at a rate of 2000 Hz. This sample rate was chosen as it was the most prevalent in FMG literature to captured appropriately rich data sets for gesture classification [7]. Each gesture was repeated 3 times; after which the next gesture was selected at random and this process repeated until all gestures were completed. In total, 10 MATLAB data files were generated (1 for each gesture), each time stamped data labels and the corresponding FSR voltages for each sensor in the FMG band.

C. Data Analysis

We employed an offline analysis approach in which participant FMG (voltage) data was processed through a classifier after the data collection had ended. While many metrics could be extracted from participant data, we chose to focus on hand gesture classification accuracy as our primary feasibility evaluation metric. Hand gesture classification accuracy refers to the accuracy at which our employed machine learning algorithms (described below) were able to use the voltage data collected using our FMG band to predict the user's performed hand gestures. Similar data collection and testing schemes are common in FMG literature [19] and reflect the FMG system's ability to measure relevant muscle forces generated during hand gestures for the specific context of hand gesture recognition in future real time device control applications. Our classification approach utilized a linear discriminant analysis classifier (LDA) paired with leave-one-out cross validation (LOOCV). To achieve this, MATLAB data files were input to a python script that isolated individual FSR voltage responses for each channel. These channels were then segmented into 200ms overlapping windows with 50ms time increments such that minute changes between points in time could be observed [20].

The mean absolute value (MAV) was calculated for each window, which served as the primary feature vector to train and test the LDA classifier using LOOCV [4], [21].

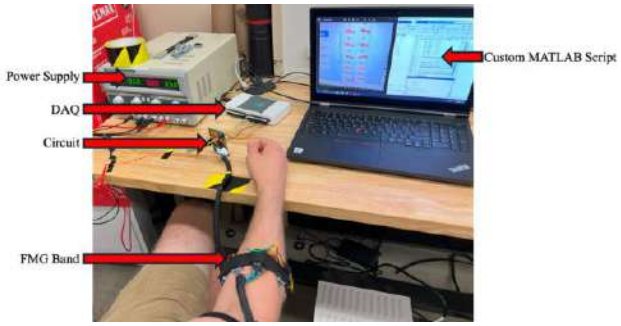


Fig. 4. The experimental setup of the FMG band validation testing. The FMG band is fit 2/3 the length of the participants forearm at a comfortable tension. A custom MATLAB script records the data for offline analysis and a TekPower TP-3005D-3 DC power supply powers the chosen circuit.

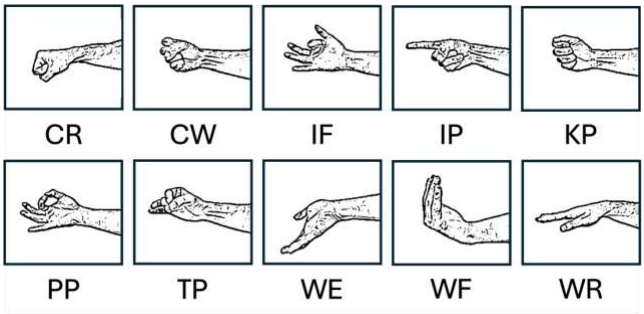


Fig. 5. The hand gestures participants were instructed to perform common to daily living. From left to right, top to bottom: Clockwise Rotation (CR), Cylindrical Wrap (CW), Index Flexion (IF), Index Point (IP), Key Pinch (KP), Pulp Pinch (PP), Tripod Pinch (TP), Wrist Extension (WE), Wrist Flexion (WF), Wrist Rotation (WR).

These feature vectors represented specific hand gestures and were labeled as such for use as the ground truth of the model. The LDA classifier was trained using the open source sklearn python package. A single feature vector (data from the completion of one single hand gesture movement) was removed from the dataset at random and the remainder were used to train the LDA classifier. Following a conventional LOOCV scheme a prediction using the removed data was then made, and this process was then repeated each time leaving a different hand gesture movement out and using it to test the prediction accuracy. The output of this pipeline was a series of predictions which were compared to the ground truth and used to create a confusion matrix. The classification accuracy of this confusion matrix was obtained to find the overall accuracy of the FMG system (Fig. 6).

The average accuracy across all participants for all hand grasps served as the summarizing metric of this work. This was found by summing the classification accuracies for each correctly predicted gesture (the diagonal elements of the confusion matrices), and dividing by the number of gestures performed (10), repeated for all participants. Standard deviations of this metric were also calculated.

IV. Validation Statistics

A. Classification Accuracies

The average classification accuracy of the FMG system was found to be 94.28% with a standard deviation across gestures

of ± 6.88%. Among all participants, the highest overall accuracy achieved was 100% (± 0%) for all hand gestures, and the lowest was 72.11% (± 31.39%). Fig. 6 illustrates the averaged confusion matrix and the average of the diagonal.

To evaluate the feasibility of our system in predicting hand gesture accuracy, we compared its performance to values reported in prior FMG literature as well as other modalities, including electromyography-based systems. While FMG systems—and other sensor modalities—represent heterogeneous datasets spanning diverse participant cohorts, sensing elements, circuitry, and even the underlying muscular phenomena being measured, FMG literature reports accuracy ranges from 91-96% [22]. EMG, a more mature measurement modality for hand gesture applications, has been suggested to require an accuracy threshold of >90% for reliable real-time control of external devices such as prostheses [23]. While FMG is more experimental, studies have shown it can produce classification accuracies similar to that of EMG-based control systems with less signal variance for participants with and without upper limb prostheses [7], [24]. Based on these benchmarks, the average performance of our FMG system meets or exceeds these values, supporting its feasibility as a low-cost, open-source option for hand gesture classification.

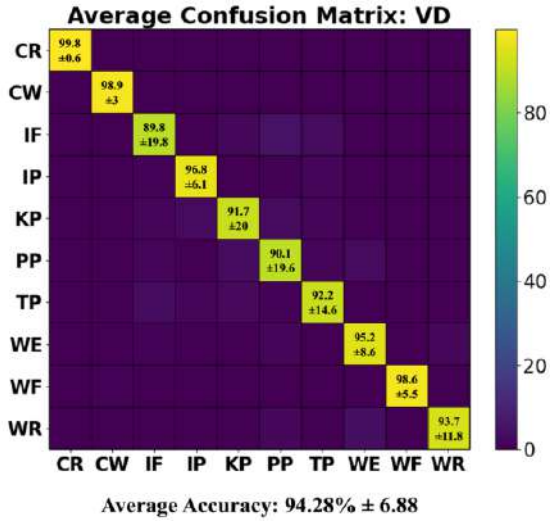


Fig. 6. Averaged classification accuracy in the style of a confusion matrix for the VD circuit. The hand gestures, Cylindrical Rotation (CR), Cylindrical Wrap (CW), Index Flexion (IF), Index Point (IP), Key Pinch (KP), Pulp Pinch (PP), Tripod Pinch (TP), Wrist Extension (WE), Wrist Flexion (WF), and Wrist Rotation (WR), display their actual (horizontal) versus predicted (vertical) classification accuracies within the matrix.

V. Discussion and Concluding Remarks

This work contributes an open-source low cost FMG wearable system designed to predict use's hand gestures from the radial muscle forces present in the forearm. To further promote the accessibility of our device, design files, a bill of materials, and accompanying fabrication documentation is available at https://github.com/BEAR-Labs.

Our prototype prioritized 3 primary considerations in shaping design decisions: *fitment, accessibility,* and *modularity*. Often, the *fitting* of a wearable system to a participant presents significant challenges in comfort and signal acquisition. Although the design of our FMG band still presents opportunities for further refinement, it was able to accommodate a wide range of forearm sizes across our participant cohort (circumference ranging from 21.5-29 cm). During our testing, it was anecdotally noted that no participants reported discomfort and all were successfully able to complete our study (approximately 45 minutes while wearing the FMG band) without any fit related or comfort related issues. Upon reviewing FSR voltage data, we found that voltages at the rest and contraction phases were clearly visually discernable. Distinct contraction and relaxation periods are a requisite condition needed to perform hand gesture classification analysis and further supporting that the FMG fitment allowed for appropriate sensor contact on the forearm skin and underlying muscle.

FSRs are one of many possible sensor types and sensing modalities used for hand gesture classification. Our system was designed to be *modular*, enabling integration with sensor technologies, circuitry, and data acquisition systems. Most significantly, the band can have its signal acquisition circuitry substituted for others that are commonly used in literature, such as the transimpedance amplifier or unity gain amplifier [25], [26]. This allows for the testing of unique signal profiles found from different circuit configurations. Furthermore, the Velcro-based band and mounting of sensors allows for the possible implementation of other force sensing modalities, sensory feedback or haptic actuators, sensor types, and more. This is of growing significance especially in research applications investigating sensor fusion and the impact of closed-loop feedback from wearable devices [27].

The overall component cost of the device was an important factor in making it *accessible*. Selection of readily available and off-the-shelf components resulted in the low cost of $162.60 USD (table 1). However, our feasibility data suggests that this low cost of componentry does not translate to poorer device performance when compared to other gesture recognition alternatives. Our offline classification analysis found an average classification accuracy upwards of 94%. While offline classification tends to produce more accurate results than real time classification, offline procedures are still highly prevalent in hand gesture classification research [23] and often reflective of efficacy in real time control applications. The *accessibility* of our system compounds with its *modularity* such that its low cost and ease of integration offers flexibility to accommodate a variety of clinical and research study demands.

For these reasons, future work aims to expand this study to a larger participant population to assess the device's efficacy across a greater range of physiological variances. Additionally, we aim to validate the device's ability to perform in real time control applications in an untethered fashion. This requires the creation of an adapted Python control script with optimized delay to overcome inaccurate classifications and motion artifacts, common in real time control. Collectively these changes could further promote the utility of our system and flexibility for use in a variety of

environment requiring larger dynamic movements and greater range of motion of the limbs, among many others.

REFERENCES

[1] D. Yungher and W. Craelius, 'Improving fine motor function after brain injury using gesture recognition biofeedback', *Disabil Rehabil Assist Technol*, vol. 7, no. 6, pp. 464–468, Nov. 2012, doi: 10.3109/17483107.2011.650782.

[2] E. Cho, R. Chen, L. K. Merhi, Z. Xiao, B. Pousett, and C. Menon, 'Force myography to control robotic upper extremity prostheses: A feasibility study', *Front Bioeng Biotechnol*, vol. 4, no. MAR, Mar. 2016, doi: 10.3389/fbioe.2016.00018.

[3] M. Sierotowicz *et al.*, 'Unobtrusive, natural support control of an adaptive industrial exoskeleton using force myography', *Front Robot AI*, vol. 9, 2022, [Online]. Available: https://www.frontiersin.org/journals/robotics-and-ai/articles/10.3389/frobt.2022.919370

[4] E. Scheme and K. Englehart, 'Electromyogram pattern recognition for control of powered upper-limb prostheses: State of the art and challenges for clinical use', *J Rehabil Res Dev*, vol. 48, no. 6, pp. 643–660, 2011, doi: 10.1682/JRRD.2010.09.0177.

[5] V. Nazari and Y. P. Zheng, 'Controlling Upper Limb Prostheses Using Sonomyography (SMG): A Review', Feb. 01, 2023, *MDPI*. doi: 10.3390/s23041885.

[6] E. Fujwara *et al.*, 'Design and Application of Optical Fiber Sensors for Force Myography', *2018 SBFoton International Optics and Photonics Conference, SBFoton IOPC 2018*, Jan. 2019, doi: 10.1109/SBFOTON-IOPC.2018.8610923.

[7] Z. G. Xiao and C. Menon, 'A Review of Force Myography Research and Development', *Sensors (Basel)*, vol. 19, no. 20, Oct. 2019, doi: 10.3390/S19204557.

[8] F. Pedregosa *et al.*, 'Scikit-learn: Machine Learning in Python', *Journal of Machine Learning Research*, vol. 12, Jan. 2012.

[9] Belyea et al., 'FMG vs EMG: A Comparison of Usability for Real-time Pattern Recognition Based Control', *TBME*, 2019.

[10] C. Marquardt, P. Weiner, M. Dezman, and T. Asfour, 'Embedded Barometric Pressure Sensor Unit for Force Myography in Exoskeletons', *IEEE-RAS International Conference on Humanoid Robots*, vol. 2022-November, pp. 67–73, 2022, doi: 10.1109/HUMANOIDS53995.2022.10000204.

[11] J. Rekimoto, 'GestureWrist and GesturePad: Unobtrusive wearable interaction devices', *International Symposium on Wearable Computers, Digest of Papers*, pp. 21–27, 2001, doi: 10.1109/ISWC.2001.962092.

[12] H. W. Ng, X. Jiang, L. K. Merhi, and C. Menon, 'Investigation of the Feasibility of Strain Gages as Pressure Sensors for Force Myography', *Lecture Notes in Computer Science (including subseries Lecture Notes in Artificial Intelligence and Lecture Notes in Bioinformatics)*, vol. 10208 LNCS, pp. 261–270, 2017, doi: 10.1007/978-3-319-56148-6_22.

[13] C. Castellini and V. Ravindra, *A wearable low-cost device based upon Force-Sensing Resistors to detect single-finger forces*. 2014. doi: 10.13140/2.1.2540.8008.

[14] Interlink, 'FSR® Integration Guide Interlink Electronics FSR ® Force Sensing Resistors ® FSR ® Integration Guide'. [Online]. Available: www.interlinkelectronics.com

[15] Z. G. Xiao and C. Menon, 'An Investigation on the Sampling Frequency of the Upper-Limb Force Myographic Signals', *Sensors 2019, Vol. 19, Page 2432*, vol. 19, no. 11, p. 2432, May 2019, doi: 10.3390/S19112432.

[16] T. R. Jensen, R. G. Radwint, and J. G. Webster, 'A CONDUCTIVE POLYMER SENSOR FOR MEASURING EXTERNAL FINGER FORCES', 1991.

[17] T. Charman *et al.*, 'Edinburgh Handedness Inventory', *Encyclopedia of Autism Spectrum Disorders*, pp. 1051–1054, 2013, doi: 10.1007/978-1-4419-1698-3_877.

[18] T. Feix, J. Romero, H. B. Schmiedmayer, A. M. Dollar, and D. Kragic, 'The GRASP Taxonomy of Human Grasp Types', *IEEE Trans Hum Mach Syst*, vol. 46, no. 1, pp. 66–77, Feb. 2016, doi: 10.1109/THMS.2015.2470657.

[19] M. Fora, B. Ben Atitallah, K. Lweesy, and O. Kanoun, 'Hand Gesture Recognition Based on Force Myography Measurements using KNN Classifier', in *2021 18th International Multi-Conference on Systems, Signals & Devices (SSD)*, 2021, pp. 960–964. doi: 10.1109/SSD52085.2021.9429514.

[20] S. Abbaspour, M. Lindén, H. Gholamhosseini, A. Naber, and M. Ortiz-Catalan, 'Evaluation of surface EMG-based recognition algorithms for decoding hand movements', *Med Biol Eng Comput*, vol. 58, no. 1, pp. 83–100, Jan. 2020, doi: 10.1007/s11517-019-02073-z.

[21] C. Ahmadizadeh, B. Pousett, and C. Menon, 'Investigation of Channel Selection for Gesture Classification for Prosthesis Control Using Force Myography: A Case Study', *Front Bioeng Biotechnol*, vol. 7, Dec. 2019, doi: 10.3389/FBIOE.2019.00331.

[22] P. Fang *et al.*, 'Fabrication, structure characterization, and performance testing of piezoelectret-film sensors for recording body motion', *IEEE Sens J*, vol. 18, no. 1, pp. 401–412, Jan. 2018, doi: 10.1109/JSEN.2017.2766663.

[23] S. Abbaspour, A. Naber, M. Ortiz-catalan, H. Gholamhosseini, and M. Lindén, 'Real-Time and Offline Evaluation of Myoelectric Pattern Recognition for the Decoding of Hand Movements', *Sensors (Basel)*, vol. 21, no. 16, p. 5677, Aug. 2021, doi: 10.3390/S21165677.

[24] M. Connan, E. Ruiz Ramírez, B. Vodermayer, and C. Castellini, 'Assessment of a Wearable Force- and Electromyography Device and Comparison of the Related Signals for Myocontrol', *Front Neurorobot*, vol. 10, 2016, [Online]. Available: https://www.frontiersin.org/journals/neurorobotics/articles/10.3389/fnbot.2016.00017

[25] D. Giovanelli and E. Farella, 'Force Sensing Resistor and Evaluation of Technology for Wearable Body Pressure Sensing', *J Sens*, vol. 2016, 2016, doi: 10.1155/2016/9391850.

[26] A. K. Godiyal, M. Mondal, S. D. Joshi, and D. Joshi, 'Force myography based novel strategy for locomotion classification', *IEEE Trans Hum Mach Syst*, vol. 48, no. 6, pp. 648–657, Dec. 2018, doi: 10.1109/THMS.2018.2860598.

[27] A. Ke, J. Huang, L. Chen, Z. Gao, and J. He, 'An ultra-sensitive modular hybrid EMG–FMG sensor with floating electrodes', *Sensors (Switzerland)*, vol. 20, no. 17, pp. 1–15, Sep. 2020, doi: 10.3390/S20174775.

SpasticMyoElbow: Physical Human-Robot Interaction Simulation Framework for Modelling Elbow Spasticity

Hao Yu[1,2,†], Zebin Huang[1,2], Yutong Li[3], Xinliang Guo[4], Vincent Crocher[4], Ignacio Carlucho[1], Mustafa Suphi Erden[1]

***Abstract*— Robotic devices hold great potential for efficient and reliable assessment of spasticity in post-stroke patients. However, the limited experimental data from patients with variable conditions has long posed a major barrier to quantitatively modelling spasticity with robotic measurements and fully validating robotic assessment techniques. As a result, spasticity is still assessed manually in current clinical settings. This paper presents a simulation framework developed to support the design and validation of elbow spasticity models and mitigate data problems. The framework consists of a simulation environment of robot-assisted spasticity assessment, two motion controllers for the robot and human models, and a stretch reflex controller. Our framework allows simulation based on synthetic data without experimental data from human subjects. Using this framework, we replicated the constant-velocity stretch experiment typically used in robot-assisted spasticity assessment and evaluated four types of spasticity models. Our results show that a spasticity reflex model incorporating feedback on both muscle fibre velocity and length more accurately captures joint resistance characteristics during passive elbow stretching in spastic patients than a force-dependent model. When integrated with an appropriate spasticity model, this simulation framework has the potential to generate extensive datasets of virtual patients for future research on spasticity assessment.**

I. Introduction

Statistics from the Global Burden of Disease Study show that there were approximately 12.2 million new stroke cases and 101 million prevalent cases worldwide in 2019 [1]. Spasticity is a common complication following stroke, referred to as a type of abnormal neuromuscular activity, with an incidence of 17%-38% in post-stroke patients [2]. Given the large number of stroke cases, the prevalence of spasticity is significant in society. The cost of treating stroke might be four times due to the influence of spasticity, making the assessment and therapy of spasticity an important research direction in post-stroke rehabilitation [3].

Pandyan et al. defined spasticity as a symptom of disordered sensorimotor control caused by an upper motor neuron (UMN) lesion, featuring intermittent or sustained involuntary activation of muscles [4]. They stratified the all-encompassing definition into multiple positive features of the UMN syndrome for practical study or measurement, including abnormal activation of muscles to an externally imposed stretch, spasms, clonus, and spastic dystonia [4]. In this paper, the term *spasticity* specifically refers to abnormal muscle reflexes to external stretches in the elbow.

In current clinical settings, clinicians use manual scales, e.g. the Modified Ashworth Scale, to assess spasticity, but these scales struggle with subjective judgement, ambiguous terminology, measurement errors, and inconsistencies in assessment results [5]. Consequently, a variety of robotic devices and instrumented assessment approaches have been developed to evaluate spasticity using biomechanical and neurophysiological measures [6], [7]. Beyond merely extracting statistic features from sensor measures, many physical models of spasticity were proposed to describe spasticity conditions with model parameters [8]. For example, impedance models can identify the viscoelasticity of spastic joints [9], [10], and threshold models represent the impaired ability to regulate the tonic stretch reflex thresholds [11].

Aiming to provide a more explainable approach to the characterisation of spasticity, some studies proposed neuromuscular spasticity models grounded in pathophysiology and realised numerical simulation. He et al. [12] developed the first neuromusculoskeletal model to simulate the pendulum test for knee spasticity, incorporating musculotendon actuators, motoneuron activation, and stretch reflex. Feng et al. [13] adapted He et al.'s model to simulate the pendulum test for elbow spasticity, and validated their simulation through experimental data of joint trajectories and muscle reflex activations from spastic patients. However, the models based on pendulum tests are unsuitable for patients with severe spasticity [14], as high muscle tone often causes their elbows to remain flexed. Consequently, Koo et al. [15] developed a neuromusculoskeletal model to simulate the stretch reflex response triggered by constant-velocity stretches in a spastic elbow.

With the advent of OpenSim [16], which offers well-developed musculoskeletal models and human motion simulation tools, researchers have developed feedback-dependent spasticity models in OpenSim to simulate the effects of spasticity during both passive and active leg movements. Krogt et al. [17] proposed a velocity-dependent reflex model to simulate the joint trajectories of a spastic knee during passive stretches, while, in subsequent research, Falisse et al. [18] demonstrated that a force-dependent reflex model outperformed a velocity-dependent model, as it better aligned

*This study was funded by the EPSRC Centre for Doctoral Training in Robotics and Autonomous Systems under the grant reference EP/S023208/1.

[1]School of Engineering and Physical Sciences, Heriot-Watt University, Edinburgh, UK.

[2]School of Informatics, the University of Edinburgh, Edinburgh, UK.

[3]School of Engineering, the Hong Kong University of Science and Technology, Hong Kong, China.

[4]Department of Mechanical Engineering, the University of Melbourne, Melbourne, Australia.

[†]Hao Yu is the corresponding author, e-mail: s2273711@ed.ac.uk

estimated muscle activity with experimental data of passive stretches and walking in children with spasticity. More recently, Veerkamp et al. [19] contradicted these findings, reporting that a velocity-dependent model outperformed a force-dependent model in simulating gait patterns of spastic patients. We did a detailed comparison of these modelling approaches and open-source code and found that, while all these studies used OpenSim, they used distinct optimisation algorithms in different simulation frameworks [17], [18]. Krogt et al. [17] obtained the optimal model parameters by matching predicted muscle excitability with experimental data, while Falisse and Veerkamp et al. [18], [19] realised the optimisation by fitting joint trajectory data. It is likely that their models achieved only a 'local optimum' within their respective datasets, optimisation targets, and simulation frameworks. To evaluate the optimised models, they also calculated the root mean square errors (RMSE) between the measured and predicted joint trajectories or qualitatively compared the real and simulated muscle activities, but the experimental data used for evaluation had been used in the optimisation process. In addition, these OpenSim-based spasticity simulation methods have been implemented and tested to date only on leg models, and they were computationally expensive, especially for testing combinations of spasticity model types [19].

In this paper, we present SpasticMyoElbow[1], a simulation framework that allows forward simulation of physical human-robot interaction in robot-assisted spasticity assessment, providing a transparent and physiologically grounded platform for validating and comparing different elbow spasticity models. This framework was implemented using MyoSuite [20], the latest simulator for musculoskeletal motion. We integrated a robotic controller and a stretch reflex controller into an exoskeleton-elbow environment provided by MyoSuite to simulate physical interactions occurring during robot-assisted elbow spasticity assessments (see Fig.1). With this simulation tool, we reproduced the constant-velocity stretch experiment and evaluated four types of elbow spasticity models. The main innovations of this study include:

- Developing an open and flexible simulation framework for testing and comparing elbow spasticity models;
- Comparing the performance of four prior models in describing the passive stretch resistance of spastic elbows;
- Exploring the application of physical interaction simulation between virtual patients and rehabilitation robots.

II. Methods

This work expanded on our prior study [21], in which we built a simulation tool for the physical interaction between an elbow and an exoskeleton in MyoSuite. We newly added a stretch reflex controller unit to the simulation tool to enable simulation of spasticity models on the virtual elbow. Afterwards, we simulated the robot-assisted constant-velocity stretch experiment for four types of elbow spasticity models.

[1]The repository can be accessed at: `https://github.com/myo-manipulation/SpasticMyoElbow.git`.

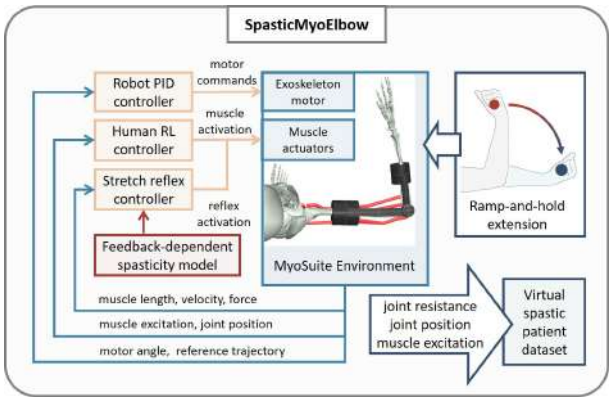


Fig. 1. Framework diagram of SpasticMyoElbow. The physical interaction between the robot and the musculoskeletal model during a ramp-and-hold extension can be simulated through the parallel control of the robot and human controllers in the simulation environment. The stretch reflex controller allows the elbow model to exhibit spasticity symptoms, simulating a virtual patient in the interaction. This setup provides a validation dataset for evaluating spasticity models.

A. Simulation framework

The foundation of the simulation framework is a simulation environment of a typical clinical setup for upper extremity rehabilitation [14], [15], [22], in which a seated person's elbow interacts with an exoskeleton robot, as shown in Fig.1. This simulation environment was adapted from the elbow-exoskeleton model provided by MyoSuite [23], which contains a human elbow skeleton with six muscle actuators (the long, lateral, and medial heads of the triceps brachii; the long and short heads of the biceps brachii (LHB, SHB); and the brachioradialis (BRD)) as well as a CAD model of the exoskeleton robot with a joint motor. In real-world laboratory settings, researchers might use other types of rehabilitation robots to apply controlled rotational motion to the elbow joint [14], [15], [22]. Nevertheless, the effect of other robots would be similar to that of the exoskeleton in the simulation.

The prior simulation tool [21] incorporates two controllers: a robot PID controller and a human controller, which respectively modulate the motor of the exoskeleton and the muscle activation of the elbow. The elbow musculoskeletal model, guided by its reinforcement learning (RL) controller, can simulate movements similar to those of a healthy real elbow. Meanwhile, the robot PID controller enables the exoskeleton to precisely track trajectories in position control or apply specific external torques in force control. This parallel control of the elbow and robot facilitates the simulation of their physical interactions in typical rehabilitation experiments, such as perturbation-based joint impedance identification experiments [21]. As the exoskeleton linkage is fixed on the arm model, there is no contact force interaction between them.

Building on this framework, we developed and integrated a stretch reflex controller into the simulation control loop. During each control cycle, the stretch reflex controller receives inputs of muscle fibre length, velocity, and force, simulating proprioceptor functions within muscles. It then generates a muscle reflex response based on proprioceptive feedback,

simulating the action of spinal motor neurons. This reflex is calculated using an equation-based model that describes the mechanics of muscle spasticity. The resulting spasticity-related muscle reflexes are then fused with the muscle activation outputs of the human RL controller, producing the final control commands for muscle actuators in the simulation environment. Muscle actuators produce torques around the elbow joint following the Hill-type musculotendon dynamic model [20]. When the human RL controller is disabled to simulate a completely relaxed elbow without voluntary control, muscle activations are driven solely by the stretch reflex controller, allowing for an isolated analysis of reflex-driven muscle behaviour.

B. Spasticity model and stretch reflex controller

Although no universal model can precisely describe the connections between spasticity pathophysiology and clinical symptoms, it is generally accepted that the abnormal stretch reflex in spasticity can be modelled as a dynamic function of exaggerated muscle excitation driven by proprioceptive feedback [8]. Spasticity is thought to arise from reduced inhibition of stretch reflex within the spinal cord, along with an increased reflex gain due to changes in the intrinsic properties of motoneurons [24]. On the one hand, the neural excitation underlying the stretch reflex originates from the firing rates of the muscle spindles, which are influenced by both the muscle length and the muscle velocity feedback. For a given spindle firing rate, a reduction in inhibitory inputs to the motoneurons can lead to higher levels of excitation [25]. This heightened excitation causes the stretch reflex to be elicited at lower velocities and shorter stretch distances. On the other hand, following a neurological injury, disrupted inputs to the motoneuron pool would activate persistent inward currents, which amplify inputs to motoneurons and cause self-sustained firing [24]. This process results in an exaggerated motoneuron response to incoming signals, contributing to the excessive reflex activity characteristic of spasticity.

In addition, there is evidence showing that spindle firing is proportional to muscle force and its derivative during passive stretches [26], so some researchers believed that spasticity could be related to the exaggerated response to spindle firing turned by the feedback of muscle force and its first-time derivative [18]. Given that, we implemented and tested force-, velocity- and length-dependent models of muscle spasticity and their combinations to comprehensively compare their capability to describe the characteristics of passive stretch resistance observed in elbows with spasticity.

To describe spasticity models incorporating different feedback mechanisms, we adapted the hybrid model equation for the muscle activation of a motoneuron proposed in [19]:

$$E(t) = C + G_l \cdot R_l(t) + G_v \cdot R_v(t) + G_f \cdot R_f(t) \quad (1)$$

where $E(t) \leq 1$; C represents the supraspinal drive modulated by the human RL controller, which is set to zero when simulating a completely relaxed elbow; R_l, R_v, and R_f denote the reflex activations contributed by muscle length, velocity, and force feedbacks within the afferent pathway; G_l, G_v, and G_f are the reflex gains of spasticity models, which can disable the corresponding model when set to 0. Similar to the modelling method of reflex thresholds used by He et al. [13], [27], the feedback-dependent reflex activations are calculated through normalisation functions with thresholds of corresponding feedbacks:

$$R_l(t+\tau) = \begin{cases} (l(t) - l_t)/(l_0 + l_r), & \text{if } l(t) \geq l_t \\ 0, & \text{if } l(t) < l_t \end{cases} \quad (2)$$

$$l_t = l_0 + \lambda_l \cdot l_r,\ 0 \leq \lambda_l \leq 1 \quad (3)$$

$$R_v(t+\tau) = \begin{cases} A \cdot (v(t) - v_t)/v_{max}, & \text{if } v(t) \geq v_t \\ 0, & \text{if } v(t) < v_t \end{cases} \quad (4)$$

$$v_t = \lambda_v \cdot v_{max},\ 0 \leq \lambda_v \leq 1 \quad (5)$$

$$R_f(t+\tau) = \begin{cases} A \cdot (f(t) - f_t)/f_{max}, & \text{if } f(t) \geq f_t \\ 0, & \text{if } f(t) < f_t \end{cases} \quad (6)$$

$$f_t = \lambda_f \cdot f_{max},\ 0 \leq \lambda_f \leq 1 \quad (7)$$

$$A = 3 \cdot l_r/(l_0 + l_r) \quad (8)$$

where $l(t)$, $v(t)$, and $f(t)$ are the proprioceptive feedbacks of fibre length, velocity, and tension force; l_t, v_t, and f_t are the reflex thresholds of muscle stretch length, velocity, and force; λ_l, λ_v, and λ_f are the factors to adjust the thresholds of the stretch reflex; l_0 is the starting muscle length of stretches; l_r is the range of muscle stretch; v_{max} is the maximal contracting velocity of a muscle, which was set as 1.5 times the optimal resting length of the muscle per second [28]; f_{max} is the maximal muscle force, which was set as 1.2 times the static maximal force [28]; τ is the stretch reflex delay, which was set as 30 ms [15]; A is the scaling factor that balances the reflex magnitudes of different models at a same level. In our simulation tool, we deployed three separate stretch reflex controllers based on the aforementioned feedback-dependent spasticity model to the LHB, SHB, and BRD muscles, respectively. As we only focused on the abnormal muscle reflexes to external stretches occurring in a relaxed elbow, the reflex mechanisms involved in voluntary movements, e.g. reciprocal inhibition, were not take in to account.

C. Robot-assisted elbow stretch experiment

The constant-velocity elbow stretch experiment is a typical biomechanical measurement method used in spasticity assessment research [14], [15], [22], [29]. This method involves using a robotic device to exert slow to fast constant-velocity stretching on the relaxed limb joint while recording the joint position and resistance over time. A fundamental assumption of this method is that when the stretching speed exceeds a threshold value, a spastic elbow will exhibit velocity-dependent stretch reflexes, demonstrating a lower reflex threshold and greater resistance compared to healthy individuals [29], [30]. In the early study proposing this

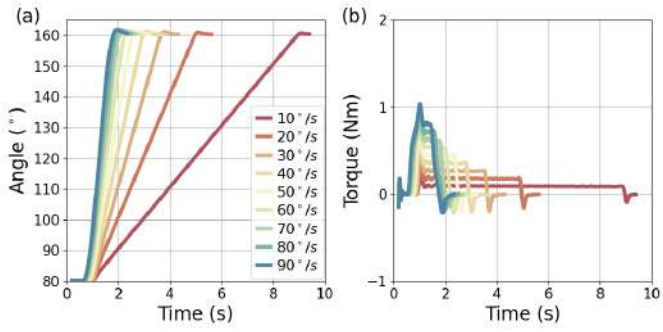


Fig. 2. Simulation data of the robot-assisted constant-velocity elbow stretch experiments: a) the angle profiles of the ramp-and-hold extension movements; b) the driving torques collected in the simulated elbow stretch experiment.

TABLE I

SPASTICITY PARAMETERS SET IN THE SIMULATION

Model	G_l	G_v	G_t	λ_l	λ_v	λ_f
Len.	$1 \sim 3$	0	0	0.1	0	0
Vel.	0	$1 \sim 3$	0	0	0.1	0
For.	0	0	$1 \sim 3$	0	0	0.1
Hybrid	$1 \sim 2$	$1 \sim 2$	0	$0.1 \sim 0.4$	$0.1 \sim 0.4$	0

method, researchers used a motor-driven beam connected to the forearm to apply ramp-and-hold extension and flexion movements to the elbow joint [14]. A ramp-and-hold movement includes a start phase that fixes the elbow at the initial position, a ramp phase that moves the elbow to the target position at a constant velocity, and a hold phase that stops the elbow at the target position. In recent studies by Guo et al. [22], this method was followed, but they used a planar forearm rehabilitation robot to conduct the experiment.

We reproduced Guo's experimental protocol in the simulation environment. The arm was attached to the robot with an initial posture of approximately 90° shoulder elevation and 70∼90° elbow angle (completely extending the elbow is 180°). The human RL controller was disabled to simulate a relaxed elbow, while the robot extended the elbow from the initial position to full extension at nine different angular velocities (ranging from 10 to $90°/s$). A sample of the experimental data is depicted in Fig.2. The stretch experiment was repeated on the virtual elbows with different model parameters in the simulation tool. The model parameters of the stretch reflex controllers set for the simulation are provided in TABLE I. By setting different combinations of gains and thresholds, the general spasticity model described by Eq.1 was transformed into the length-dependent model, velocity-dependent model, force-dependent model, and hybrid model of length and velocity muscle feedbacks. The muscle parameters used in all simulation experiments are the same, as listed in TABLE II, which were calculated by the internal parameters of the MyoSuite elbow model.

In the simulated experiments, virtual sensors within the simulation environment recorded the angle of the elbow joint θ and the driving torque T_{total}. According to Newton's third law, this driving torque represents the stretch resistance of the joint, which can be described as a function of joint angle.

TABLE II

MUSCLE PARAMETERS SET IN THE SIMULATION

Muscle	$l_0[m]$	$l_r[m]$	$v_{max}[m/s]$	$f_{max}[N]$
LHB	0.36	0.054	0.18	729
SHB	0.28	0.054	0.20	508
BRD	0.12	0.024	0.13	1171

For a spastic elbow joint, the stretch resistance is divided into passive resistance T_p contributed by the mechanical property of body inertia and soft tissues (muscles, tendons, ligaments, etc.) and reflex resistance T_s elicited by spasticity models [14]. The passive resistance can be further decomposed into the elastic torque T_e related to the joint displacement, viscous torque T_v dependent on the joint velocity, and inertial torque T_i [15], which accounts for accelerating and decelerating the body inertia:

$$T_{total}(\theta) = T_p(\theta) + T_s(\theta) \tag{9}$$

$$T_p(\theta) = T_e(\theta) + T_v(\theta) + T_i(\theta) \tag{10}$$

During the constant-velocity phase of each passive extension movement, the acceleration is zero, so inertial resistance is zero. The reflex torque elicited by the elbow flexors over this constant angular velocity range can be estimated by subtracting the passive elastic and viscous torques from the driving torque [15]. As shown in Fig.2(b), when the stretching speed increases, the joint resistance increases due to the increased viscous component, but the maximum peak viscous torque is approximately 1 Nm, which is relatively small compared to the reflex-induced torque in Fig.3. Although a more accurate value of the viscous torque can be estimated as the sum of the viscous components of all involved muscles using the method of Koo et al. [15], in our case, the viscous component is too small to influence our analysis results, so it is simplified. The passive elastic torque was estimated by the driving torque recorded at the lowest extension velocities when the reflex controller was disabled. We analysed the performance of different spasticity models by examining the reflex torque curves obtained in the simulation experiments.

III. RESULTS

We compared the reflex torque curves of the length-, velocity-, and force-dependent spasticity models, with reflex gains incrementally varying from 1 to 3. The results of the length-dependent spasticity model are shown in Fig.3 (a-d). As the elbow muscles are lengthened, the reflex torques gradually increase, reaching a plateau or slightly declining. This behaviour aligns with the intuitive understanding of a length-dependent model: as muscle length initially increases during stretching and then stabilises, the muscle excitation proportional to fibre length follows a similar pattern. The slight reduction at the end is attributable to the decreasing muscle velocity, as the force in a Hill-type muscle model is determined by the product of the length-tension and velocity-tension functions.

Fig.3 (e-h) presents the simulated results of the stretching experiment using the velocity-dependent spasticity model. It is evident that the peak of the reflex torque increases as

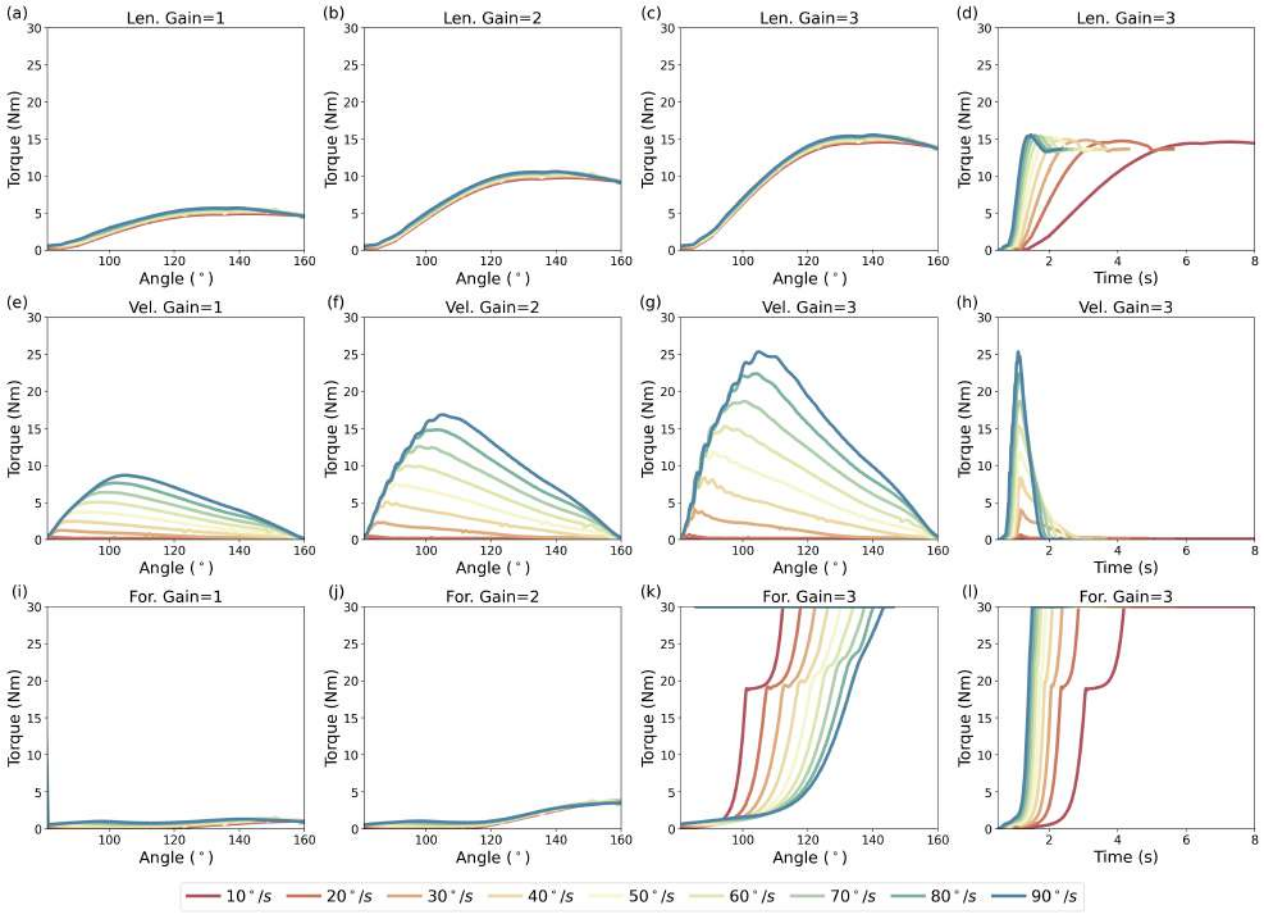


Fig. 3. (a-c) Reflex torque curves plotted against joint angle for the length-dependent spasticity model, with reflex gains ranging from 1 to 3. (e-g) Reflex torque curves plotted against joint angle for the velocity-dependent spasticity model, with reflex gains ranging from 1 to 3. (i-k) Reflex torque curves plotted against joint angle for the force-dependent spasticity model, with reflex gains ranging from 1 to 3. (d, h, l) Evolution of reflex torques over time for the length-, velocity-, and force-dependent spasticity models, with a reflex gain of 3.

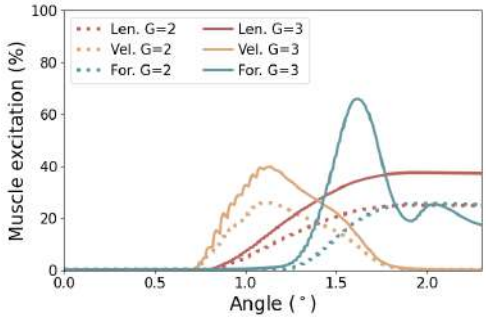


Fig. 4. Muscle excitations of the long head of the biceps brachii modulated by the length-, velocity-, and force-dependent spasticity models under a $90^{\circ}/s$ elbow stretch.

velocity increases. In addition, the resistance of the joint decreases after reaching the peak, even though the joint continues to move with a constant velocity. This reduction may be attributed to the decreasing stretch velocity of muscles as their moment arms change.

Fig.3 (i-l) shows the results of the extension experiment for the force-dependent spasticity model. When the gain is small, the force-dependent model induces an increase in resistance during the second half of stretching. However, when the spasticity gain is large, the reflex torque rapidly increases toward the limit value of the muscle force. It may be explained by the mathematical description of the model. The spasticity model causes greater reflex muscle forces and greater muscle forces also produce more intensive reflexes, so the elbow system cannot reach a stable state. We further plotted Fig.4 to compare the muscle excitation levels regulated by different models when G=2 and G=3. It can be observed that at G=2, the excitation peak values generated by the three models are quite close. However, at G=3, the force-dependent model shows a sharp increase and fluctuation in muscle excitation.

Previous studies have clearly analysed the trend of stretch reflex resistance in spastic elbows, where the most common pattern of resistance profiles is an initial increase followed by a plateau phase [14], [29], [30]. The rate of increase in resistance relative to joint angle (commonly referred to as reflex stiffness) and the onset of abnormally elevated resistance (typically called the reflex angle or catch angle) are both related to the severity of spasticity and the stretching velocity. In our simulation results, the length-dependent model does not exhibit velocity dependence, while the velocity-dependent model lacks a plateau phase in the resistance curve. As a result, we ultimately adopted a length-velocity

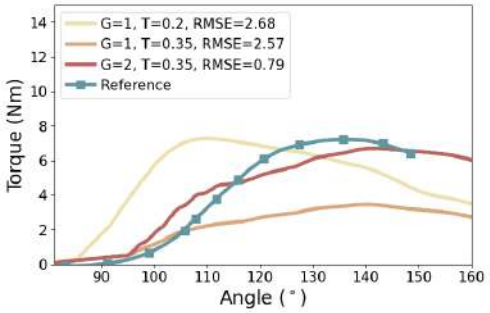


Fig. 5. Reflex torque curves plotted against joint angle for the hybrid spasticity model with different model parameters (G: gains, λ: threshold factor) at $90°/s$. The reference torque curve was extracted from McPherson et al. [29].

hybrid spasticity model and conducted simulation experiments using different model parameters listed in TABLE I. The gains and thresholds for length and velocity were set at identical values for simplification (G_l=G_v, λ_l=λ_v). As shown in Fig.5, when the gains are kept constant and the thresholds are increased, the onset of torque increase occurs later and the magnitude of the torque peak decreases. In contrast, increasing the gains while keeping the thresholds unchanged results in an obvious increase in the peak magnitude of the reflex torque curve. With appropriately selected model parameters (G=2, λ=0.35), the RMSE between the simulated and experimental data can reduce to 0.79 [29].

IV. Discussion

In this study, we proposed a simulation framework for modelling spasticity through passive stretch experiments based on the simulation of physical interaction between a rehabilitation robot and a human elbow. Unlike previous simulations of spasticity models, the realisation of the simulation in our framework does not rely on motion or electromyography data from real-life experiments, nor does it generate the simulation depending on optimal fitting to limited sample data. Instead, it leverages the advantages of the robotic simulator, combined with validated spasticity models, to perform forward simulations purely according to the physiological mechanism.

Our simulation examined length-, velocity-, and force-dependent models separately, all of which demonstrated unique characteristics, but none of the models alone could capture the full passive resistance curve observed in elbow stretches of spastic patients. Only when combining both velocity and length dependencies did the hybrid model display passive resistance patterns seen in a real spastic patient's elbow. This can be explained by the physiological origin of the stretch reflex, the muscle spindle, which contains Ia and II sensory fibres sensitive to muscle velocity and length, respectively. The activation of these sensory fibres in response to external stretch increases the afferent firing rate of the motoneuron, which can induce the stretch reflex [15]. Previous experimental evidence has shown that the muscle spindle in a spastic patient is not more sensitive than in a normal individual, and spasticity is more closely associated with a reduction in inhibition of motoneuron excitability within the spinal cord [24], [25]. Therefore, we infer that the weakening of afferent-related neural inhibition may lead to an abnormal stretch reflex exhibiting length- and velocity-dependent excitation originating from the muscle spindle.

In the study by Falisse et al. [18], spasticity models were described by state equations that incorporated reflex threshold and gain, with state variables of muscle feedbacks (length, velocity, acceleration, force, and force derivative), while the time course of muscle excitation was the simulation output. Optimisation of model parameters was performed to fit the simulated time course of muscle excitation with the electromyography data from real patients. However, the muscle force input of the model in their optimisation framework was generated from the real electromyography data, which might result in a fitting bias in that the force-dependent model has better optimisation results than the model based on other feedback. In contrast, our study directly simulates the force-dependent model without employing any optimisation techniques, allowing us to observe the model's behaviour without any pre-set bias from fitted data. Our findings reveal that models based solely on force variables lead to muscle system instability, producing physiologically unrealistic results.

Veerkamp et al. compared the velocity-dependent and force-dependent spasticity models in reproducing spastic patients' gait patterns [19]. Similar to our findings, the velocity-dependent model outperforms the force model under their simulation goals. Their simulation method consists of two layers of internal and external optimisation loops, and therefore the simulation is computationally intensive, so they failed to validate the spasticity model with multiple feedback combinations. In terms of computational cost, our proposed simulation tool is advantageous. It is true that adding optimisation of model parameters to our simulation tool to make it fit to the experimental data will introduce new computational costs. However, our simulation framework only requires one optimisation loop. Moreover, the simulation efficiency of MyoSuite is higher than that of OpenSim [20]. Therefore, we believe that the presented simulation tool has the potential to improve the computational efficiency of simulation of the spasticity model.

Due to space limitations, we have not included the simulation results for the full model incorporating all three reflex mechanisms in this paper. Our preliminary trial-and-error investigations indicate that the force-dependent reflex model actually degrades the agreement between model predictions and experimental data. Specifically, when the force gain is set to a low value, its contribution to the overall resistance torque is minimal; however, as the force gain increases, the total torque escalates to unreasonably high levels, corresponding to the phenomenon observed in Fig.3(i-k). In future work, once optimization techniques are employed, a more comprehensive search will be done to test the force-based feedback and and identify the most realistic reflex model.

V. Conclusion

It is undeniable that, due to the lack of clinical trial data, this study does not propose a rigorously validated spasticity model. The musculoskeletal model of the elbow requires improvement as it excludes the Brachialis muscle. However, our simulation framework provides new approaches and insights into some of the ongoing debates in spasticity modelling. The framework enables easier comparison of stretch resistance at the elbow joint across different types of spasticity models. The preliminary qualitative analysis results demonstrate the superiority of the length- and velocity-dependent hybrid spasticity model in explaining the abnormal elbow resistance caused by spasticity. Furthermore, while not covered in this paper, the effects of spasticity on active human motion can also be simulated, as the simulation tool includes a controller for active motion. In future research, one focus will be on gathering some real-patient data to develop a more precise and reliably validated spasticity model, thereby enhancing the simulation fidelity for spastic patients.

References

[1] V. L. Feigin, B. A. Stark, C. O. Johnson, G. A. Roth, C. Bisignano, G. G. Abady, M. Abbasifard, M. Abbasi-Kangevari, F. Abd-Allah, V. Abedi *et al.*, "Global, regional, and national burden of stroke and its risk factors, 1990-2019: a systematic analysis for the global burden of disease study 2019," *The Lancet Neurology*, vol. 20, no. 10, pp. 795–820, 2021.

[2] A. Brashear, E. Elovic, and K. E. Alter, *Spasticity: Diagnosis and Management*, 2nd ed. New York: Demos Medical, 2016, book section Why is Spasticity Treatment Important, pp. 3–4.

[3] E. Lundström, A. Smits, J. Borg, and A. Terént, "Four-fold increase in direct costs of stroke survivors with spasticity compared with stroke survivors without spasticity: The first year after the event," *Stroke*, vol. 41, no. 2, pp. 319–324, 2010.

[4] A. Pandyan, H. J. Hermens, and B. A. Conway, *Neurological rehabilitation: spasticity and contractures in clinical practice and research*. Boca Raton: CRC Press, 2018, book section Definition of Spasticity, pp. 2–24.

[5] F. Li, Y. Wu, and X. Li, "Test-retest reliability and inter-rater reliability of the modified tardieu scale and the modified ashworth scale in hemiplegic patients with stroke," *European Journal of Physical and Rehabilitation Medicine*, vol. 50, no. 1, pp. 9–15, 2014.

[6] X. Guo, R. Wallace, Y. Tan, D. Oetomo, M. Klaic, and V. Crocher, "Technology-assisted assessment of spasticity: a systematic review," *Journal of NeuroEngineering and Rehabilitation*, vol. 19, no. 1, p. 138, 2022.

[7] H. Yu, A. Nelson, and M. S. Erden, "A review of robot-assisted hand spasticity assessment," *IEEE Transactions on Human-Machine Systems*, vol. 54, no. 4, pp. 349–361, 2024.

[8] Y. Cha and A. Arami, "Quantitative modeling of spasticity for clinical assessment, treatment and rehabilitation," *Sensors (Basel, Switzerland)*, vol. 20, no. 18, p. 5046, 2020.

[9] H.-S. Park, J. Kim, and D. L. Damiano, "Haptic recreation of elbow spasticity," in *2011 IEEE International Conference on Rehabilitation Robotics*, pp. 1–6.

[10] V. Falzarano, G. Petrella, F. Marini, M. W. Holmes, L. Masia, P. Morasso, and J. Zenzeri, "Preliminary evaluation of a robotic measurement system for the assessment of wrist joint spasticity," in *2020 8th IEEE RAS/EMBS International Conference for Biomedical Robotics and Biomechatronics (BioRob)*, 2020, pp. 539–544.

[11] A. Calota, A. G. Feldman, and M. F. Levin, "Spasticity measurement based on tonic stretch reflex threshold in stroke using a portable device," *Clinical Neurophysiology: Official Journal of the International Federation of Clinical Neurophysiology*, vol. 119, no. 10, pp. 2329–2337, 2008.

[12] J. He, W. R. Norling, and Y. Wang, "A dynamic neuromuscular model for describing the pendulum test of spasticity," *IEEE Transactions on Biomedical Engineering*, vol. 44, no. 3, pp. 175–184, 1997.

[13] C. Feng and A. Mak, "Neuromuscular model for the stretch reflex in passive movement of spastic elbow joint," in *Proceedings of the 20th Annual International Conference of the IEEE Engineering in Medicine and Biology Society*, vol. 5, 1998, pp. 2317–2320.

[14] B. D. Schmit, Y. Dhaher, J. P. Dewald, and W. Z. Rymer, "Reflex torque response to movement of the spastic elbow: theoretical analyses and implications for quantification of spasticity," *Annals of Biomedical Engineering*, vol. 27, no. 6, pp. 815–829, 1999.

[15] T. K. K. Koo and A. F. T. Mak, "A neuromusculoskeletal model to simulate the constant angular velocity elbow extension test of spasticity," *Medical Engineering & Physics*, vol. 28, no. 1, pp. 60–69, 2006.

[16] S. L. Delp, F. C. Anderson, A. S. Arnold, P. Loan, A. Habib, C. T. John, E. Guendelman, and D. G. Thelen, "OpenSim: open-source software to create and analyze dynamic simulations of movement," *IEEE Transactions on Biomedical Engineering*, vol. 54, no. 11, pp. 1940–1950, 2007.

[17] M. M. van der Krogt, L. Bar-On, T. Kindt, K. Desloovere, and J. Harlaar, "Neuro-musculoskeletal simulation of instrumented contracture and spasticity assessment in children with cerebral palsy," *Journal of Neuroengineering and Rehabilitation*, vol. 13, no. 1, p. 64, 2016.

[18] A. Falisse, L. Bar-On, K. Desloovere, I. Jonkers, and F. De Groote, "A spasticity model based on feedback from muscle force explains muscle activity during passive stretches and gait in children with cerebral palsy," *PloS One*, vol. 13, no. 12, pp. 1–20, 2018.

[19] K. Veerkamp, C. P. Carty, N. F. Waterval, T. Geijtenbeek, A. I. Buizer, D. G. Lloyd, J. Harlaar, and M. M. van der Krogt, "Predicting gait patterns of children with spasticity by simulating hyperreflexia," *Journal of Applied Biomechanics*, vol. 39, no. 5, pp. 1–13, 2023.

[20] V. Caggiano, H. Wang, G. Durandau, M. Sartori, and V. Kumar, "Myosuite–a contact-rich simulation suite for musculoskeletal motor control," in *Proceedings of Machine Learning Research*, vol. 168, 2022, pp. 1–16.

[21] H. Yu, Z. Huang, Q. Liu, I. Carlucho, and M. S. Erden, "Replication of impedance identification experiments on a reinforcement-learning-controlled digital twin of human elbows," in *The IEEE World Congress on Computational Intelligence*, 2024.

[22] X. Guo, J. Tang, V. Crocher, M. Klaic, D. Oetomo, Q. Xie, M. P. Galea, C. M. Niu, and Y. Tan, "A practical post-stroke elbow spasticity assessment using an upper limb rehabilitation robot: A validation study," in *2022 44th Annual International Conference of the IEEE Engineering in Medicine & Biology Society (EMBC)*, pp. 4159–4162.

[23] H. Wang, V. Caggiano, G. Durandau, M. Sartori, and V. Kumar, "Myosim: fast and physiologically realistic mujoco models for musculoskeletal and exoskeletal studies," in *2022 International Conference on Robotics and Automation (ICRA)*, 2022, pp. 8104–8111.

[24] D. Burke, J. Wissel, and G. A. Donnan, "Pathophysiology of spasticity in stroke," *Neurology*, vol. 80, no. 3 Suppl 2, pp. S20–S26, 2013.

[25] C. Trompetto, L. Marinelli, L. Mori, E. Pelosin, A. Currà, L. Molfetta, and G. Abbruzzese, "Pathophysiology of spasticity: implications for neurorehabilitation," *BioMed Research International*, vol. 2014, p. 354906, 2014.

[26] K. P. Blum, B. Lamotte D'Incamps, D. Zytnicki, and L. H. Ting, "Force encoding in muscle spindles during stretch of passive muscle," *PLoS computational biology*, vol. 13, no. 9, pp. 1–24, 2017.

[27] J. He, "Stretch reflex sensitivity: Effects of postural and muscle length changes," *IEEE Transactions on Rehabilitation Engineering: a Publication of the IEEE Engineering in Medicine and Biology Society*, vol. 6, no. 2, pp. 182–189, 1998.

[28] E. Todorov, T. Erez, and Y. Tassa, "Introduction of muscle actuators in the mujoco documentation," accessible: 2024. [Online]. Available: https://mujoco.readthedocs.io/en/stable/XMLreference.html#actuator-muscle

[29] J. G. McPherson, A. H. A. Stienen, B. D. Schmit, and J. P. A. Dewald, "Biomechanical parameters of the elbow stretch reflex in chronic hemiparetic stroke," *Experimental Brain Research*, vol. 237, no. 1, pp. 121–135, 2019.

[30] D. G. Kamper, B. D. Schmit, and W. Z. Rymer, "Effect of muscle biomechanics on the quantification of spasticity," *Annals of Biomedical Engineering*, vol. 29, no. 12, pp. 1122–1134, 2001.

A low-cost, versatile, open-source, DIY partial body-weight support device

Dana L. Lorenz
Department of Physical Medicine and Rehabilitation
MetroHealth Systems and Case Western Reserve University
Cleveland, USA
dana.lorenz@case.edu

William Kozak
Department of Physical Medicine and Rehabilitation
MetroHealth Systems and Case Western Reserve University Systems
Cleveland, USA

Braedon Harris
Department of Mechanical Engineering
University of Texas at Austin
Austin, USA

Kyle Eaton
Department of Mechanical Engineering
University of Texas at Austin
Austin, USA

Amoagh Gopinath
Department of Mechanical Engineering
University of Texas at Austin
Austin, USA

Keven Hernandez
Department of Mechanical Engineering
University of Texas at Austin
Austin, USA

James Sulzer
Department of Physical Medicine and Rehabilitation
MetroHealth Systems and Case Western Reserve University
Cleveland, USA

***Abstract*—Partial body weight support during gait training and other tasks is a common practice. Approaches using robotic devices allow for a wide range of functions but at great cost and complexity. Based on constant force springs, we have created a low-cost body weight support system from off-the-shelf parts, with no tools required for assembly or maintenance, and it is easily integrated into any overhead support system. The design is presented as open source for future improvements. We evaluated the hysteresis using two different types of constant force springs, comprising clinically relevant levels of weight support, 61.2 N and 131 N. Force constancy during walking was examined. Hysteresis had noticeable effects on weight support, illustrating a potential challenge for future designs with body weight support through constant force springs. By providing the constant weight support, the most common type of body weight support, this device represents an accessible alternative to robotic dynamic body weight support tools.**

Keywords—Bodyweight support, gait, open-source tools, neuro-musculoskeletal rehabilitation, musculoskeletal

I. Introduction

In the U.S., 12.2% of adults have a mobility disability that makes tasks such as walking or climbing stairs more difficult [1]. To enable repetitive practice of these tasks for recovery, partial body weight support (BWS) devices have been developed for use in clinics [2]. A BWS device is a support system created with suspension that provides vertical support on the patient's pelvis and trunk, reducing the functional weight of the patient while they are training. It reduces mechanical demand on muscles and makes it easier for users to coordinate their movements. A study using body weight support along with standard of care in post-stroke patients found improved Functional Independence Measures over patients who only received the standard of care [3]. There have also been similar benefits of body weight support training seen in individuals with spinal cord injury [4], [5]. More testing on BWS systems in rehabilitation could lead to better outcomes for patients with musculoskeletal and neurological gait disorders.

BWS can be provided passively or actively. Passive BWS systems include the use of a weight stack and pulleys, extension springs, and bungees [6]. These methods have drawbacks. For example, a weight stack adds inertia and must be in a fixed location, and elastic elements provide height-dependent weight support. Active, robotic body weight support has become increasingly popular. A pioneering example is the ZeroG system (Aretech, Sterling VA), which travels actively along a rail with programmable BWS. The Bioness Vector (Bioness, Valencia, CA), based on Aretech's design, operates similarly. These devices cost approximately $200,000, not including the approximate $30,000 of renovation costs [7], making these inaccessible to most clinics.

Constant force springs, made from coiled stainless steel, provide a passive, low-cost cost alternative to BWS unhindered by inertia or changes in height. MacLean and Ferris used an arrangement of constant force springs to create a novel, low-cost BWS system. Their device can support up to 79% of the patient's body weight, and parts cost about $4000 [8]. A recent commercial device, the Levity by Ora Medical (Montreal, QC), integrates constant force spring modules of predetermined strengths into a novel pediatric gait trainer, as opposed to an overhead support. As a result, this device uniquely enables squatting, and other activities at different heights anywhere the gait trainer can travel at a cost of approximately $8000 [9].

The approach outlined in this paper moves further towards low cost and simplicity [10]. Our goal was to focus on easily sourced, off-the-shelf parts, versatility in usage, affordability to any clinic, no machining required, and easy adjustment and assembly by a non-expert. Our result is a device that costs under $100 in parts sourced from accessible vendors such as Amazon, McMaster-Carr, and Home Depot, can be assembled in under 10 minutes by a non-expert without tools (with the exception of sawing a PVC pipe), can adjust resistance just as easily, and can be used with any typical overhead support. Here, we describe the design, provide details on where to source the parts and perform a performance evaluation of the system. While robotic BWS has distinct advantages, including the ability to adjust BWS dynamically, the philosophy of this work is to prioritize accessibility, versatility, and ease of use when functionality lacks strict requirements.

II. Methods

A. Device Design

This project aimed to design an affordable BWS device that can be constructed with off-the-self parts that will require little to no additional machining. All components of this device, Table 1, can be bought off the shelf or delivered within 24 to 48 hours.

Constant force springs (McMaster-Carr) were chosen to provide the BWS due to their affordability, ease of replacement, and range of available force options. The system was designed to house the constant force springs to reduce the risk of the user coming into contact with the springs while also being easy to take apart to replace the springs at their end of life or change the level of assistance the device is providing. The component breakdown can be seen in Fig. 1, and the assembled device can be seen in Fig. 2. Two constant force springs are placed back-to-back, a configuration that prevents twisting and improves stability. The springs rotate around hex bolts that pass through mounting plates, with PVC pipe sections providing rigidity and preventing wear on the inner diameter of the springs. The mounting holes on the ends of the springs are connected with an S-hook, which then connects to a carabiner and eventually to the harness. A carabiner with a



Fig. 1 A disassembled BWS device 1. Swivel 2. Metal plate 3. Nuts 4. Wingnuts 5. Nuts 6. Oversized washers 7. PVC Pipe 8. Constant force springs 9. S-hook. The part numbers correspond to items in Table 1.



Fig. 2 Assembled BWS device (left) being used in two different conditions, a single point of contact (center) and two points of contact (right). Not pictured due to clarity are height adjustable lanyards that span between the device and the harness to allow adjustment to overhead mountings of different heights. Also not shown is a parallel lanyard that serves as a fall arrest system since the BWS device does not stop motion at end of range.

Table 1. Bill of materials

	Description	Quantity	Cost[a]	Vendor
1	Carabiners with swivels	1	$17.99	Amazon
2	Metal plate	2	$17.18	Amazon
3	1/4” – 20 bolts	3	$0.90	Home Depot
4	1/4” – 20 wingnuts (4 ct.)	1	$1.38	Home Depot
5	1/4” – 20 nuts	6	$0.54	Home Depot
6	1/4” Oversized washers (25 ct.)	1	$10.96	McMaster-Carr
7	1”x24” PVC pipe	1	$2.87[b]	Home Depot
8	Constant force springs	2	$10-$20[c]	McMaster-Carr
9	3/16”x1.5” Zinc S-Hook	1	$1.38	Home Depot
		Total Cost	**~$62 - $72**	

[a] Based-on prices as of November 2024, not including shipping
[b] The diameter of PVC depends on the spring diameter
[c] Cost of spring depends on force and excursion properties

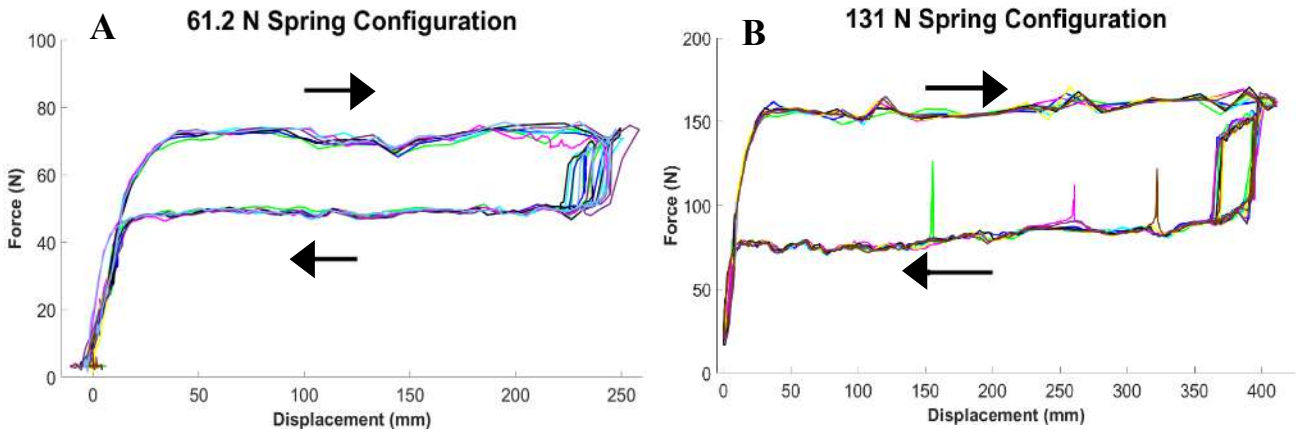


Fig. 3 (A) Hysteresis plot for the 61.2 N configuration (two 30.6 N springs), red arrows indicate the direction of motion of the applied force. (B) Hysteresis plot for the 131 N configuration (two 65.7 N springs). An increase in force over the initial, approximately 35 mm of the spring unraveling before leveling out to the constant force can be seen in both configurations. There is a decrease of force seen when the load begins to return to its starting point, with a quick decrease seen over the final, approximately 35 mm.

swivel connects to the top hole of the mounting plate via a hex bolt to connect to the overhead support. Wingnuts tighten the bolts by hand, and oversized washers prevent the springs from rubbing against the mounting plates. A full bill of materials and assembly instructions can be found on GitHub [11]. When weight is applied to constant force springs, there is no limit to their motion, and they will reach the end of the range of their excursion, so it is necessary to have a fall arrest lanyard parallel to the device for safety purposes.

B. Testing protocol

To validate the design of our device, we performed tests with two constant force spring strengths: 30.6 N and 65.7 N. Since the design requires a pair of springs, the two configurations account for 61.2 N and 131 N, respectively. The measurements, with the purpose of examining the mechanical properties of the device, were performed on author W.K. Given the design and goals of the study, no ethics approval was necessary according to local Institutional Review Board policy.

We first performed hysteresis testing on the device, where we applied a load to the springs over a distance to ensure the springs returned to their rest length. For the test, a known weight was attached to the springs, released to fall a distance, and then manually returned to the starting point; this was repeated 10 times for each spring strength. For the smaller springs, a load sufficient enough to extend the springs (75.6 N) was used, and for the larger springs, a load sufficient enough to extend the springs (164.6 N). An inline load cell, placed in series with the BWS device, measured the spring force (Futek, Irvine, CA). Data from the load cell were recorded using an NI USB-6009 and LabView 2024 (National Instruments, Austin, TX). The displacement of the springs was tracked using motion capture. Four reflective markers were placed on the device, with one being placed on the S-hook at the end of the springs. Motion capture data were recorded using Vicon Nexus 2.12 (Vicon Motion Systems Ltd., Oxford, UK). Both motion capture and the load cell readings were captured at a rate of 200 Hz.

We then performed a functional test of the device while walking on a Bertec instrumented treadmill with an overhead support structure (Bertec, Columbus, OH). A load cell was placed in line with the device during the trials where the BWS device was used in the same manner as during the hysteresis tests. The BWS device was then attached directly to a safety harness worn by a single participant. Fall arrest lanyards were also placed in parallel with the BWS device to allow the wearer to have enough movement so as not to alter their normal gait pattern but still prevent the springs from fully extending. The participant then walked on the treadmill at a comfortable walking speed of 1.0 m/s. Force plates embedded under the treadmill belts gathered ground reaction forces. Data from the treadmill were recorded at rate of 1000 Hz using Bertec Fit5 (Bertec, Colombus, USA). The participant walked at the speed of 1.0 m/s for three one-minute walking trials. The first trial was with no BWS; the following two trials were with the BWS device with the two different spring strengths mentioned previously.

C. Data Analysis

All analyses were performed using Matlab R2024b (Mathworks, Natick, USA). The data from the load cell and motion capture system were synchronized for analysis of the hysteresis data. The data from the displacement and force data were divided into cycles, with a cycle being defined starting when the marker starts moving (load is applied) and ending when the marker returns to its starting point (load has been removed).

For analysis of the functional walking data, the data from the force plates was down sampled to the load cell data. The load cell and force plates were then synchronized using a trigger point. The data were then divided into gait cycles using the heel strike of the participant's right foot. The average and standard error of the mean (SEM) were taken across the gait cycles for the left and right vertical ground reaction forces and the load cell. The mean was then plotted

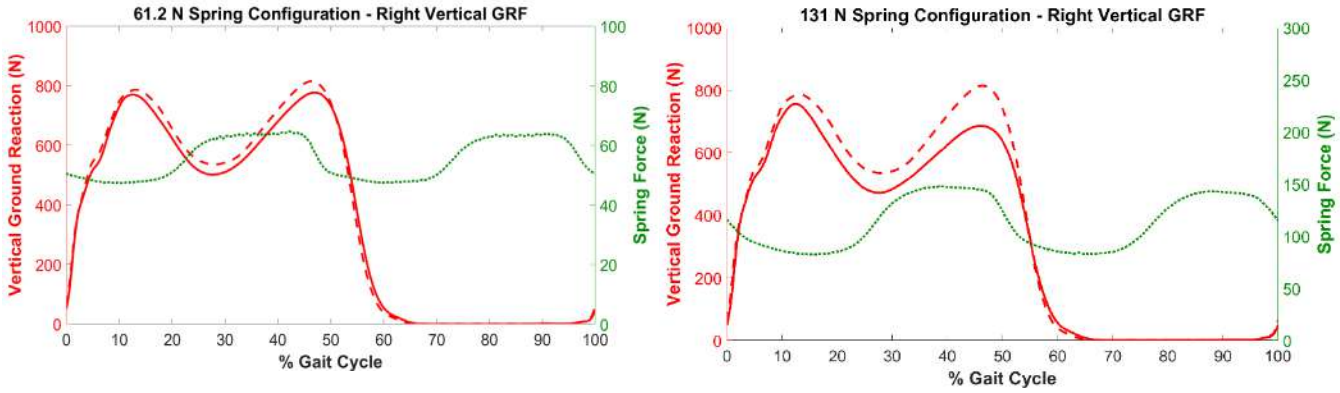


Fig 4 Average vertical ground reaction forces during gait of the right leg during unassisted walking (red-dashed) and assisted walking (red-solid) for the 61.2 N spring configuration (right) and 131 N spring configuration (left). The average force from the springs during the assisted walking (green-dotted) can also be seen throughout the gait cycle.

for the right and left vertical ground reaction forces along with the mean of the load cell.

III. Results

Both sets of springs showed hysteresis. The force vs. displacement graphs for the hysteresis tests can be seen in Fig. 3. In the small springs, Fig. 3A, a sharp increase in the force applied can be seen over the initial 35 mm of the spring unraveling before leveling out to the constant force. There is a decrease of about 20 N seen before the load begins to return to its starting point, with a quick decrease seen over the final 35 mm. A similar trend is seen in the hysteresis test of the large springs, Fig. 3B. There is, however, a larger decrease seen when returning the load to its starting point; this is a variation of about 60 N. There are also a few cycles that appear to have a spike in the applied load when returning to the start of the cycle. We attribute this to the experimenter's readjustment of the grip on the weight when moving it back to the beginning of the cycle.

The BWS device reduces the vertical ground reaction forces during walking, but the reduction varies (Fig. 4). The variation can be clearly seen after the loading response, but the decreased load is at the level that is expected until shortly before midstance when the unloading response begins. The load cell shows fluctuation in the support provided by the springs on the participant. The pattern seen by the load appears to follow what is seen in the vertical displacement of the center of mass (CoM) during walking [12].

IV. Discussion

This project aimed to develop a body-weight support device that was accessible, versatile, and easy to use. The product described in this paper meets these requirements. All components of our BWS device can be purchased off-the-shelf and delivered within 48 hours for less than $100, including shipping. The device can be assembled without tools by a layperson, with the only adaptation to any component being cutting PVC pipe to size. The springs can be easily replaced if worn out or other force levels are desired in minutes without tools. Due to its compact size, the device can be integrated into any overhead support frame. Unlike weights or bungees, the constant weight support does not suffer from inertial effects or displacement-dependent forces. In comparison to a similar device using constant force springs [8], the device of this paper costs an order of magnitude less, does not require any special manufacturing or custom parts, and has greater versatility of placement. Further, the design is open source, meaning that if others find better off-the-shelf solutions, the design can be updated. The low cost means that any clinic could easily purchase and manufacture this device, including individuals at home.

There is room for improvement in the design. While the S-hooks hold the springs, they sometimes require a crimp to ensure the springs remain in place. The springs are sheet metal, meaning that they have an exposed edge. We deal with this by connecting the device to the overhead support and then an inelastic lanyard in series connects to the user such that the exposed spring is far from the clinician or individual. A flexible cover, however, could help improve safety. The force adjustments are limited to the availability of springs with a geometry that fits within the mounting plate. Some versatility in spring force adjustments can be made by stacking the springs and using a longer hex bolt. It is also important to note that because the springs provide constant force, the springs can unwind with sufficient force. As such, a fall arrest lanyard must be used in parallel in any clinical setting. Since overhead support systems already have fall arrest lanyards, all that is required is setting the lanyard to a level of slack so that the BWS device has a range of operation. We tested a limited range of scenarios on a single participant, and it is possible other factors could be revealed through more comprehensive testing.

While we did find that the springs provided nominally constant force for most of their excursion, we observed

significant hysteresis. The force of the smaller springs was reduced by 33% when returning, and the larger springs were reduced by approximately 50%. This hysteresis was evident during walking trials, where spring force lowered by the measured hysteresis values when the vertical center-of-mass (CoM) moved upwards (loading response), and greater spring force was found when vertical CoM was moving downwards (mid-stance/pre-swing) [12]. This represents a potential issue with the functionality of constant force springs as a method of BWS. It is believed that this hysteresis seen in the working portion of the springs is because of friction of the springs. Characterization of constant force springs has shown a relationship between hysteresis and friction:

$$e = f * F_r 2R_d \quad (1)$$

where e is the hysteresis, f is the coefficient of friction in the roller, F_r is the roller reaction force, and R_d is the radius of the drum [13]. Based on these factors, hysteresis could be reduced with design change, for example, including ball bearings within the springs. However, this additional complexity would likely require machining expertise and cost. The clinical tolerance of weight support hysteresis would need to be determined to perform a cost-benefit analysis of making such design changes. There are few, constant force spring BWS systems currently available [8], [9], we are not aware of any published data on hysteresis reported in those devices, it would be interesting to see if they experience the same phenomenon. Likewise, we are not aware of any hysteresis evaluations of passive BWS devices. In its current configuration, due to the imprecise force production due to hysteresis, the device is most fit for clinical application as opposed to research.

One of the major motivations behind this work was to create accessible BWS. While the device itself is accessible, it still requires an overhead system to operate. This could be in the form of an overhead track system (e.g., Solostep, North Sioux City, SD), a two-degree-of-freedom support system (e.g., OASUS by Enliten, Newark, DE), a Universal Exercise Unit, an overground gait trainer (e.g., LiteGait, Tempe, AZ), or other equivalent overhead system. Clinically, BWS is provided as constant or nearly constant weight support [14]. In contrast to a robot that provides dynamic BWS, a passive, low-cost system could account for most of the applied usage at several orders of magnitude lower cost. Clinical trials should clarify in which scenarios such dynamic, robotic BWS is superior to the simpler design presented here.

An accessory like this device would typically be regulated by the FDA as a class I (low-risk) device. Providing the instructions to construct the device would classify one as a "specification developer" if those instructions were provided for commercial gain. However, providing those instructions open source for others to improve upon effectively eliminates the need for FDA regulation. While out of the scope of this work, it raises an interesting question on whether and how to regulate grass-roots "maker" initiatives, created to empower individuals over their own health and reduce undue costs and time using low-risk technologies. An example is a modified ride-on car for use in children with disabilities, a paradigm that has been found to improve socialization and mobility [15] In cases like these, the parent using the car assumes responsibility for its safe use, not the individual posting instructions on how to properly adapt the car. For the device considered here or for other solutions used by therapists, would need approval from clinical engineering, which in most hospitals only governs equipment plugged into the wall.

ACKNOWLEDGMENT

DL was supported by the NIH T32 Musculoskeletal Training Grant (AR007505)

REFERENCES

[1] "Disability impacts all of us infographic," Centers for Disease Control and Prevention. Accessed: Nov. 11, 2024. [Online]. Available: https://www.cdc.gov/ncbddd/disabilityandhealth/infographic-disability-impacts-all.html

[2] S. Ettema, G. H. Pennink, T. J. W. Buurke, S. David, C. A. M. van Bennekom, and H. Houdijk, "Clinical indications and protocol considerations for selecting initial body weight support levels in gait rehabilitation: a systematic review," *J Neuroeng Rehabil*, vol. 21, no. 1, p. 97, Jun. 2024, doi: 10.1186/s12984-024-01389-8.

[3] J. Huber, N. Elwert, E. S. Powell, P. M. Westgate, E. Hines, and L. Sawaki, "Effects of dynamic body weight support on functional independence measures in acute ischemic stroke: a retrospective cohort study," *J Neuroeng Rehabil*, vol. 20, no. 1, p. 6, Jan. 2023, doi: 10.1186/s12984-023-01132-9.

[4] E. S. Powell, J. Lopez, P. M. Westgate, E. Hines, and L. Sawaki, "Effects of Dynamic Overground Body Weight Support Training During Inpatient Rehabilitation After Traumatic Spinal Cord Injury," *Am J Phys Med Rehabil*, vol. 101, no. 2, pp. 196–200, Feb. 2022, doi: 10.1097/PHM.0000000000001828.

[5] A. L. Hicks *et al.*, "Long-term body-weight-supported treadmill training and subsequent follow-up in persons with chronic SCI: effects on functional walking ability and measures of subjective well-being," *Spinal Cord*, vol. 43, no. 5, pp. 291–298, May 2005, doi: 10.1038/sj.sc.3101710.

[6] J. Zhang, A. Zhu, P. Ma, C. Zheng, X. Zhang, and G. Cao, "Design and Evaluation of an Integrated Active and Passive Body Weight Support System for Variable Gravity and Inertia Compensation," *IEEE/ASME Transactions on Mechatronics*, vol. 29, no. 5, pp. 3706–3716, Oct. 2024, doi: 10.1109/TMECH.2024.3354335.

[7] R. Williams, "Safety System: Harness Will Prevent Falls During Rehab," The Ledger. Accessed: Nov. 11, 2024. [Online]. Available: https://www.theledger.com/story/news/2015/04/30/safety-system-harness-will-prevent/8220833007/

[8] M. K. MacLean and D. P. Ferris, "Design and Validation of a Low-Cost Bodyweight Support System for Overground Walking," *J Med Device*, vol. 14, no. 4, Dec. 2020, doi: 10.1115/1.4047996.

[9] "The Levity," ORA Medical. Accessed: Nov. 11, 2024. [Online]. Available: https://www.oramedical.ca/levity

[10] J. Sulzer and L. S. Karfeld-Sulzer, "Our child's TBI: a rehabilitation engineer's personal experience, technological approach, and lessons learned," *J Neuroeng Rehabil*, vol. 18, no. 1, Dec. 2021, doi: 10.1186/s12984-021-00862-y.

[11] D. L. Lorenz *et al.*, "Constant-Body-Weight-Support-Device," 2024. Accessed: Nov. 11, 2024. [Online]. Available:

https://github.com/jamessulzer/Constant-Body-Weight-Support-Device

[12] E. Al-Yahya *et al.*, "Gait adaptations to simultaneous cognitive and mechanical constraints," *Exp Brain Res*, vol. 199, no. 1, pp. 39–48, Oct. 2009, doi: 10.1007/s00221-009-1968-1.

[13] J. R. McGuire and J. A. Yura, "Advances in the analysis and design of constant-torque springs," in *Publication: 30th Aerospace Mechanisms Symposium*, 1996, pp. 205–220.

[14] J. Mehrholz, S. Thomas, and B. Elsner, "Treadmill training and body weight support for walking after stroke," *Cochrane Database of Systematic Reviews*, vol. 2017, no. 8, Aug. 2017, doi: 10.1002/14651858.CD002840.pub4.

[15] H.-H. Huang, Y.-M. Chen, H.-W. Huang, M.-K. Shih, Y.-H. Hsieh, and C.-L. Chen, "Modified Ride-On Cars and Young Children with Disabilities: Effects of Combining Mobility and Social Training," *Front Pediatr*, vol. 5, Jan. 2018, doi: 10.3389/fped.2017.00299.

Delivering Gait Training to Children at Home with a Robotic Knee Exoskeleton: Initial Findings on Feasibility and Patient Satisfaction*

Taylor M. Devine[1], Noah Rubin[1], Afua Asante-Otoo[1], Katharine Alter[1], Jeffrey Fairman[1], Diane L. Damiano[1], and Thomas C. Bulea[1]

Abstract— **Robotic exoskeletons offer the potential to increase gait training dosage by providing therapy outside the clinic. Exoskeleton use in naturalistic settings has been reported but under researcher supervision and for the purposes of assisting mobility. Here, we examined the feasibility of delivering a resistance-based exoskeleton gait training paradigm in the community setting. Five children aged 6-15 years with crouch gait/knee extension deficiency completed 12-weeks of gait training (5 days/week) at home with the exoskeleton as part of an ongoing interventional trial. Weekly telehealth check-ins were completed. Feasibility was assessed using patient-reported adherence to the prescribed dosage, number of adverse events, and exoskeleton hardware and software robustness during the intervention period. User satisfaction was assessed using the QUEST 2.0. No serious adverse events were reported. Participants completed between 44-57 of the targeted 60 sessions of gait training. Exoskeleton hardware and software were reliable with the most common controller adjustments involving tuning of underfoot sensing thresholds to detect stance and swing. Participant satisfaction with the exoskeleton (mean: 3.65/5) and service (4.7/5) were high. Thus, our findings indicate that resistive gait training with an exoskeleton in the real-world is safe and tolerable in children with neuromotor disorders and should be further investigated to determine effectiveness for improving functional mobility.**

Keywords - Exoskeletons, Wearable robotic systems, Usability

I. INTRODUCTION

Device-assisted gait training in children with neuromotor disorders, including full weight-bearing, body-weight support or guided robotic assistance paradigms, range in effectiveness with some studies reporting improvements in posture, gait speed, and endurance [1, 2]. Robotic-assisted gait trainers have gained prominence but are limited to the clinical setting, often coupled to a treadmill [3-5]. These challenges led to the expansion of wearable robotic exoskeleton technology to pediatric populations [6]. Initial cohort studies, conducted in clinical settings, demonstrated efficacy of exoskeletons as assistive devices for children with cerebral palsy (CP) [7-10]. Reduced muscle strength in children with CP is correlated with less locomotor ability [11]. Resistance training can be effective for improving knee extension deficiency [12]. Utilizing robotic exoskeletons and other wearable devices to apply resistance training during walking in clinic-based pilot studies has improved step length and knee extension among other measures [13-16]. These findings support use of robotic exoskeletons for gait therapy outside of the clinical setting to address the limitations of dosage and intensity.

Delivery of exoskeleton-based gait training outside the clinical environment has been very limited to date, especially in children. The Trexo Home (Trexo Robotics, Ontario, Canada), which combines a robotic exoskeleton spanning the hip and knee with an overground walker for safety and stability, was piloted for a non-ambulatory child with CP in the community setting [17]. The case study reported a high number of non-use days suggesting limitations in feasibility. Change in functional outcomes, including range of motion and spasticity, were variable suggesting the need for more controlled studies. The Trexo Home was subsequently analyzed in 70 elementary school age, non-ambulatory children with CP [18]. Usage was highly variable, ranging from 284-1795 steps/week split over 2-5 sessions. Nevertheless, this study indicates at least partial feasibility of exoskeleton use outside the clinical setting, potentially removing a major barrier to more frequent training.

Exoskeletons which target single joints are less encumbering and can be used by more functional individuals, increasing the potential for successful deployment in the real-world. For example, automatic personalized assistance to ambulation has been tested in an ankle exoskeleton resulting in meaningful benefits to gait speed and energetic costs of walking under naturalistic conditions in young healthy people [19]. A different ankle exoskeleton was capable of adapting assistance to real-world settings including uneven terrain [20]. An exoskeleton that assisted hip flexion reduced energy expenditure during uphill, outdoor hiking in healthy individuals and outdoor level walking on a track in adults greater than 60 years of age [21]. Additionally, a recent study of 8 individuals with CP spanning multiple levels of functional mobility (Gross Motor Function Classification System (GMFCS) I-III) demonstrated feasibility of using an ankle exoskeleton outdoors during level, incline and decline, and stair walking [22]. After 4 visits, participants significantly reduced their metabolic cost of walking, increased walking speed or both and all participants stated they preferred walking with rather than without the device. These results demonstrated rapid acclimation to the device with consistent improvement across sessions in most participants. Collectively, these studies demonstrate feasibility of deploying robotic exoskeletons across diverse naturalistic settings and

*This work was supported by the intramural research program of the National Institutes of Health Clinical Center

[1]T.M. Devine, N. Rubin, A. Asante-Otoo, K. Alter, J. Fairman, D.L. Damiano, and T.C. Bulea are with the Rehabilitation Medicine Department, National Institutes of Health Clinical Center, Bethesda, MD USA. thomas.bulea@nih.gov

user populations. Yet, these exoskeletons have all been used to assist, rather than train gait. Further, while experiments were completed in settings that reflected the real world by testing across multiple types of terrain, exoskeleton use was supervised by researchers who were present during each session. Therefore, the suitability of delivering gait training in a real-world setting, without the presence of clinicians or researchers, remains to be investigated.

We previously developed a robotic exoskeleton for over-ground use in children with knee extension deficiency [7, 8, 23, 24]. A next generation wearable robotic exoskeleton (Agilik®, Bionic Power, Inc., Vancouver, Canada) was later developed with an expanded target population to include children with CP, spina bifida (SB), muscular dystrophy (MD) or incomplete spinal cord injury (iSCI). The exoskeleton can apply torque to assist and/or resist knee movement. Initial findings from clinical evaluation of this exoskeleton showed that application of resistance during phases of knee extension was tolerable and increased extensor muscle activity during use, thereby providing the potential to strengthen muscles and improve function if used for an extended time [25]. Further, by interleaving assistive and resistive torques within the gait cycle, the resistance-based therapy could be extended to more affected individuals at elevated risk of mobility loss due to significant weakness and/or diminished motor control.

Based on these preliminary findings, we initiated a randomized interventional trial to evaluate the safety, feasibility and effectiveness of a 12-week resistance-based exoskeleton gait training regimen delivered in the home/community environment in children age 3-17 years with crouch gait from CP or knee extension deficiency from MD, SB or iSCI [26]. To our knowledge, this ongoing trial constitutes the first controlled study evaluating an exoskeleton that challenges users during walking outside of a clinical setting. The study includes primary outcome measures assessing changes in knee extension, gait speed, muscle activity during walking and strength. Importantly, feasibility, assessed as a measure of compliance with study parameters, safety, assessed as recorded adverse effects, and patient-reported usability are secondary or exploratory objectives of the ongoing protocol [26].

This manuscript aims to provide an initial analysis of the safety and feasibility of and participant satisfaction with the 12-week robotic intervention delivered outside the clinical setting. Our analysis encompasses data from five participants who completed the exoskeleton intervention. The goal is to fill the existing knowledge gap regarding suitability of unsupervised exoskeleton mediated gait training in the real world.

II. Methods

A. Intervention Description

The interventional study from which the data here were collected is a randomized crossover trial with two arms lasting 12 weeks each: (1) exoskeleton intervention and (2) standard therapy control. All participants completed both arms but the order in which they were completed was randomized. In this manuscript, only data from the first arm (the 12-week exoskeleton intervention period) was evaluated.

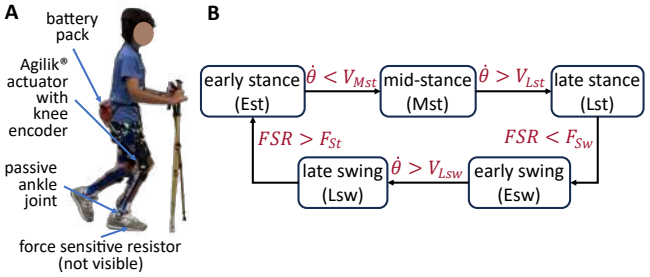


Fig. 1. A. The robotic knee exoskeleton utilized for delivery of gait training outside the clinic. B. The exoskeleton 5-state finite state machine that tracks user walking in real-time to deliver knee torque during walking.

The exoskeleton used for the intervention (Fig. 1) is based on a knee-ankle-foot orthosis (KAFO), with one actuated degree of freedom at the knee in the sagittal plane (Agilik®, Bionic Power, Vancouver, Canada) and a passive adjustable degree of freedom to control dorsi/plantar flexion stiffness and range of motion at the ankle (ADR®, Ultraflex Systems, Pottstown, PA). A custom KAFO is fabricated by a commercial orthotics manufacturer (Ultraflex) for each participant using a digital scan of their legs captured using a Structure Sensor Pro and an iPad. The knee actuator and ankle mechanism are attached to the lateral side of each KAFO. The actuator includes a motor encoder that measures knee angle and angular velocity (by differentiation) and force sensitive resistors (FSRs) mounted within the orthosis footbed detect foot-ground contact. The actuator also includes a Bluetooth modem which can connect to a software application on a laptop to stream, display and save sensor and actuator data at 100 Hz (Fig. 2, Fig. 3).

The exoskeleton parses the gait cycle into five discrete states in real-time (Fig. 1): early stance (Est), mid-stance (Mst), late stance (Lst), early swing (Esw), and late swing (Lsw) [25]. The swing-to-stance (foot contact) and stance-to-

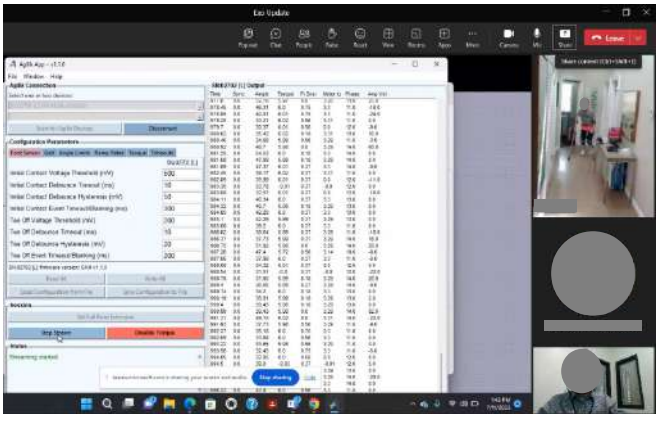


Fig. 2. Screenshot of a weekly telehealth visit. Left: The exoskeleton app streams real-time sensor data over the internet to the clinical team. Right: Live video of a participant walking with the exoskeleton at home while researchers monitor exoskeleton performance. Note: faces and names of the participant and study members have been obscured.

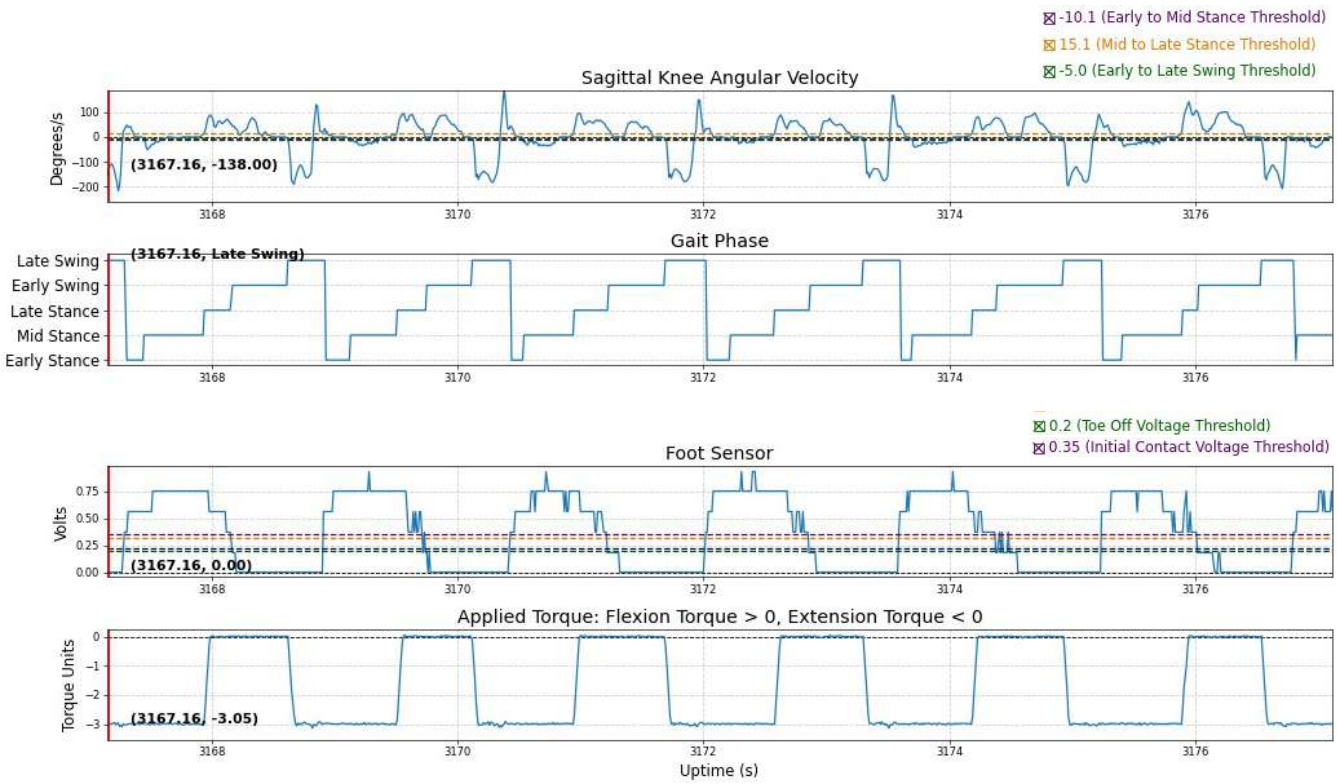


Fig. 3. Screen capture showing example data that are displayed in real-time by the app to facilitate adjustment of exoskeleton parameters if necessary. The top panel shows knee angular velocity in the sagittal plane and the angular velocity thresholds for early-to-mid-stance (V_{Mst}), mid-stance-to-late-stance (V_{Lst}), and early-to-late swing (V_{Lsw}) transitions. The second panel displays the output of the finite state machine. The third panel displays total voltage output of the underfoot FSR sensors and the thresholds for transition for foot contact (F_{St}) and foot off (F_{Sw}) events. The bottom panel displays applied torque.

swing (foot off) transitions are controlled by the underfoot FSR. Two separate thresholds are set for each participant, whereby when the FSR reading exceeds the first (F_{st}), the state machine transitions to stance, and when the FSR reading falls below the second (F_{sw}), it transitions to swing. States within stance and swing phase are determined by separate knee angular velocity thresholds for Est to Mst (V_{Mst}), Mst to Lst (V_{Lst}), and Esw to Lsw (V_{Lsw}) transitions. The Est to Mst and Esw to Lsw transitions occur when the knee angular velocity falls below the threshold governing each (extension velocity negative) whereas the Mst to Lst transition occurs when the angular velocity exceeds the threshold (flexion velocity positive). Within each gait phase, the exoskeleton can apply pre-tuned torque profiles up to 12 Nm in either the flexion or extension direction.

After custom exoskeleton fabrication, each participant completed 3-5 visits (up to 4 hours each) wherein the exoskeleton therapy was personalized to each individual and each family was educated on proper use of the device. The goal of the interventional study was to evaluate the ability of exoskeleton applied resistance to knee extension (i.e., a flexion torque) during walking to improve gait function. Briefly, the exoskeleton tracks the user's limbs as they walk and applies a resistive (flexor) torque during periods of knee extension in weight bearing (Mst) and/or swing (Lsw). These resistive torques have been previously shown to increase knee extensor muscle activity during walking [25]. The objective is to deliver this gait training at high dosages, with the hypothesis that doing so will increase knee extensor muscle strength and activation during walking, which can ultimately improve crouch gait.

After setup, participants completed 12 weeks of gait training using the exoskeleton at home or in the community. Participants were instructed to walk for 5 days/week for 1 hour/day using the exoskeleton. Participants were also provided a laptop to connect wirelessly to the exoskeleton through the app. Participants were requested to complete weekly telehealth visits (Microsoft Teams) with the study team during the 12-week intervention period (Fig. 2). During these visits researchers could view live video of the participant walking with the exoskeleton while its sensor data were streamed and recorded via the laptop app. Researchers also verbally reviewed the user's experiences during the past week's gait training sessions. Based on this information, researchers made changes to controller thresholds as necessary to ensure the exoskeleton was accurately tracking the user's gait phases and applying correct torques. Adjustment to torque magnitudes were also be made to progress (or dial back) the intervention intensity as needed. These changes were logged in text-based format (JSON file).

TABLE I

PARTICIPANT INFORMATION

Participant	Diagnosis	Gender	Age (yrs)	Height (cm)	Weight (kg)	GMFCS
P1	cerebral palsy	male	15	150	46.4	III
P2	cerebral palsy	male	14	162	41.2	II
P3	muscular dystrophy	female	10	143	41.3	-
P4	cerebral palsy	female	6	110	17.9	III
P5	spina bifida	male	11	146	38.6	-

B. Study Participants

Data were collected as part of an ongoing clinical trial [26]. The study was approved by the Institutional Review Board of the National Institutes of Health (protocol #001180) and is registered on clinicaltrials.gov (NCT05726591). Five participants (Table 1) who completed the 12 week home-based exoskeleton gait training intervention were included in this analysis. All participants and their parents/guardians completed informed assent and consent, respectively.

C. Objectives, Data Collection, and Outcomes

The primary objectives of this manuscript were to evaluate the initial feasibility and patient satisfaction with the resistance-based exoskeleton therapy delivered in the home environment over 12 weeks. Two aspects of feasibility were assessed. First, robustness of the exoskeleton during home use was quantified for hardware by the number of required maintenance events, and for the software/control system by the number of required adjustments to controller parameters during the intervention period. Second, participant adherence to the prescribed training protocol was assessed using patient self-reported exoskeleton use (dates and durations) as well as the occurrence of adverse events and side effects.

To assess participant satisfaction with the exoskeleton, we administered the QUEST 2.0 [27] which asks participants to rank their satisfaction with the exoskeleton in 8 categories (dimensions, size, adjustability, safety, durability, ease of use, comfort and effectiveness) and services related to the device in four categories (service delivery, repairs and servicing, professional services, and follow-up services).

III. RESULTS

A. Feasibility of Exoskeleton Gait Training in the Real-World

We completed regular, weekly telehealth visits with research participants during the 12-week intervention period. These visits typically lasted 20-40 minutes and included at least 1 clinical member (physical therapist) and one technical member (engineer) from the research team. During each visit, the participant walked with their exoskeleton while it was wirelessly connected to the app to stream, save and display data in real-time (Fig. 2, Fig. 3). Based on these data, the ability of the exoskeleton to track the 5 states of the gait cycle was assessed, and if necessary, thresholds that governed the transitions between states were adjusted to improve state machine tracking.

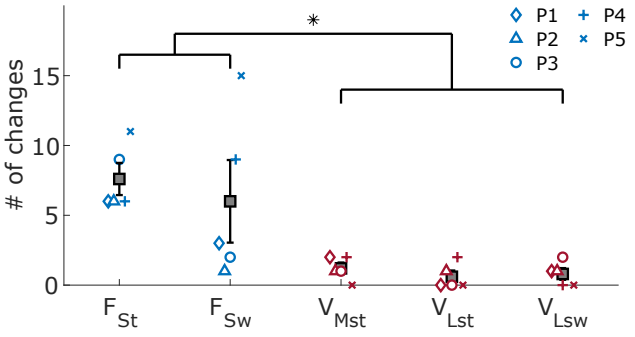


Fig. 4. The total number of changes of exoskeleton controller thresholds over the 12-week intervention period. Mean values for each threshold are shown as squares with error bars indicating 1 standard deviation. Individual data points show adjustments for each participant. Blue indicates FSR thresholds and red indicate angular velocity thresholds. * indicates significant difference between FSR and velocity thresholds.

We found that the 5-state finite state machine could robustly track user walking across the 12-week intervention period (Fig. 4). The majority of control parameters were stable with fewer than 3 adjustments during the entire intervention. The most frequent parameters requiring adjustment were the FSR based measures (F_{St} and F_{Sw}). In the majority of instances in which FSR thresholds were adjusted, the state transitions were still present but delayed. However, this was not the case in the two instances of FSR failure as described below. The knee angular velocity-based thresholds (V_{Mst}, V_{Lst}, and V_{Lsw}) had comparatively fewer adjustments than FSR-based thresholds. This result was statistically significant (paired t-test) with $p < 0.001$ (Fig. 4). We observed a correlation trend with participant age, wherein the younger participants (P3, P4, and P5) tended to require more adjustments than the older ones.

From a hardware perspective, the exoskeleton was robust across the intervention period. One actuator in one participant required repair due to a failure in the power supply circuitry. Three underfoot FSR sensors required replacement; one due to a loss of sensitivity and two due to complete failure. Mechanically, the KAFO design was robust with two participants reporting slight loosening of single fasteners that required manual tightening.

B. Participant Adherence to the Intervention

The exoskeleton delivered therapy applies resistance to knee extension during multiple points of the gait cycle, which is intended to make walking more difficult as an exercise. Although the trial is ongoing, our initial findings support the feasibility of our high dosage intervention design. Three of five participants have returned the self-reported usage log to date, reporting 44, 56, and 57 total walking sessions over the 12 weeks. Two of three completed at least 80% of the 60 session target and the one who did not experienced a medical event of a family member which disrupted therapy delivery. Within each day of training, participants reported 41.4 ± 3 mins (mean ± standard deviation) of walking. These initial findings indicate a high dosage of gait training

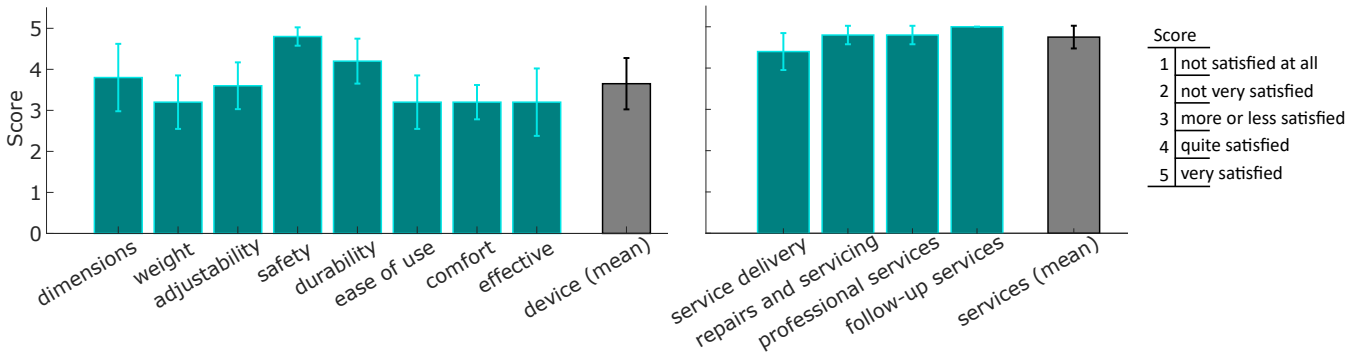


Fig. 5. Results of the QUEST 2.0 survey (n=5) to assess satisfaction with the exoskeleton device (left) and services (right). Green bars indicate mean for each item; gray bars indicate mean across the items for the device (left) and services (right). Error bars indicate 1 standard deviation.

is attainable, but the desired 60 minutes of walking was not fully achieved. Participants reported exoskeleton use across diverse settings including at home (overground and treadmill), in the community (sidewalks, streets and places of business), at public gyms, (overground and treadmill), physical therapy, school, and on an outdoor track.

To date, there have been no serious adverse events and no unanticipated problems with the exoskeleton intervention in participants who have completed the 12-weeks of therapy. One participant reported soreness of the knee extensor muscles and knee joint, which was an expected side-effect. This was addressed by providing several days of rest and a reduction in the resistance torque during walking for 1 week, after which the participant was able to return to their previous resistance level.

The goal of the intervention is to increase the delivered resistance torque over time if tolerated by the participant. We were able to achieve this goal in all 5 participants, with total increases in torque ranging from 0.5 to 2.5 Nm, constituting increases of 20-50% from their initial resistance levels.

C. Participant Satisfaction

Overall, participant satisfaction (n=5) with the exoskeleton device (QUEST 2.0) was good (Fig. 5), with a mean score of 3.65 and greater than half of responses to the 8-item device survey being either "quite satisfied" (4) or "very satisfied" (5). Importantly, safety was the most highly rated aspect of the exoskeleton with 4/5 scoring this aspect as "very satisfied" while 1 was "quite satisfied", thus indicating that participants felt secure using the exoskeleton delivered gait training in the home and community environments. Four areas received mean scores of "more or less satisfied": weight, ease of use, comfort and effectiveness. The first 3 categories suggest that design improvements which make the physical device as well as the user interface less cumbersome would be beneficial. Effectiveness was the only category in which a participant reported a score of 1 ("not satisfied at all"). It is possible scoring in this category was affected by the intended application: the purpose of the exoskeleton was for exercise, which makes walking more difficult. Multiple users reported disliking this effect, compared to walking without the exoskeleton. Given that the QUEST 2.0 asks "how effective your assistive device is", it is possible this incompatibility was driving the lower scores.

Compared with the physical device, participants were overall more satisfied with the services they received from the study team (Fig. 5). The mean score across the 4 categories was 4.7/5, with only 1 response scored as "more or less satisfied" (3), while all others were either "quite satisfied" (3/25 responses) or "very satisfied" (21/25).

IV. Discussion

There is emerging evidence to support feasibility of exoskeleton use in the real-world including multiple recent examples of assistive devices demonstrating mobility and energetic benefits in naturalistic settings in healthy individuals as well as aging and pediatric populations [19-22]. Yet, these studies have been done under researcher supervision and have focused, to our knowledge, on assisting mobility. Thus, the ability to deliver gait training that applies resistive torques to the limbs using a wearable exoskeleton in multiple settings remains unknown. Here we show the first evidence that this is feasible with a single joint knee exoskeleton in a diverse pediatric cohort.

Although the overall clinical trial is ongoing so we cannot yet assess the functional or biomechanical efficacy of the intervention, our preliminary findings show feasibility, safety and tolerability to support continued investigation of this approach. Importantly, in three participants, the exoskeleton intervention delivered assistance during midstance and resistance during late swing while the other two received resistance to knee extension during both phases. Further, all participants utilized assistive devices (such as trekking poles, lofstrand crutches or walkers) when walking overground. Thus, our findings indicate that our resistance and combined assistance and resistance approaches are well tolerated in a broad clinical population with neuromuscular disorders.

Many control strategies exist for delivery of exoskeleton torques during walking. Our findings indicate that the finite state machine approach is relatively stable across a 12-week intervention period in children with neuromotor disorders using assistive devices (i.e., walkers or crutches) in multiple environments. Notably, the thresholds related

to underfoot sensing were the most sensitive week-to-week (Fig. 4), whereas those for angular velocity were more stable. Taken together with the finding that the FSR was the most often replaced component, these results suggest removal of the FSR underfoot would enhance robustness. Potential alternatives include the use of IMUs to track foot ground contact, or alternately a continuous phase control approach [20] rather than a finite state machine.

Overall, protocol adherence was as forecasted in the initial study design [26]. Although some participants reported less satisfaction with certain aspects of the device, it was generally well tolerated. These high ratings are likely due to the interdisciplinary nature of the study team performing the clinical trial, which included physicians, physical therapists, recreation therapists, orthotists, and engineers. It is important to note this large of a team is not likely to be feasible for delivery of the intervention in typical clinical settings, so future studies are warranted to examine how to optimize intervention delivery. It will also be important to compare user perceptions of the device with the functional outcomes from the study. Other factors affecting home use not directly captured by the QUEST 2.0, such as ability to don/doff the device, operate the exoskeleton independently, and battery life should also be evaluated. Additional limitations include the relatively small size of the cohort to date, especially given the range in ages and statures, and the lack of a control condition, such as the home use of a wearable exoskeleton for assistance versus gait training. Importantly there were no serious adverse events or other safety concerns and no issues with major noncompliance. Thus, our findings provide initial evidence that gait training with a resistive exoskeleton paradigm in the real-world is safe and tolerable in a pediatric cohort, and should continue to be pursued in the future.

ACKNOWLEDGMENT

The authors thank Jesse Matsubara and Jordan Dembsky for their contributions to data collection and analysis, Brent Sperry for his pedorthotic services, and Robin Greenfield and Karen Perkins for providing recreation therapy services.

REFERENCES

[1] N. G. Moreau, et al., "Effectiveness of Rehabilitation Interventions to Improve Gait Speed in Children With Cerebral Palsy: Systematic Review and Meta-analysis," Physical Therapy, vol. 96, no. 12, pp. 1938-1954, 2016.

[2] I. Novak et al., "State of the Evidence Traffic Lights 2019: Systemic Review of Interventions for Preventing and Treating Children with Cerebral Palsy," Current Neurology and Neuroscience Reports, vol. 20, no. 3, 2020.

[3] S. Lefmann, R. Russo, and S. Hillier, "The effectiveness of robotic-assisted gait training for paediatric gait disorders: systematic review," Journal of NeuroEngineering and Rehabilitation, vol. 14, no. 1, 2017.

[4] B. H. Dobkin and P. W. Duncan, "Should Body Weight–Supported Treadmill Training and RoboticAssistive Steppers for Locomotor Training Trot Back to the Starting Gate?," Neurorehabil Neural Repair, vol. 26, no. 4, pp. 308-317, 2012.

[5] D. Žarkovic et al., "Gait Changes Following Robot-Assisted Gait Training in Children With Cerebral Palsy," Physiol. Res., vol. 70, 3, pp. S397-S408, 2021.

[6] M. Sarajchi, M. K. Al-Hares, and K. Sirlantzis, "Wearable Lower-Limb Exoskeleton for Children With Cerebral Palsy: A Systematic Review of Mechanical Design, Actuation Type, Control Strategy, and Clinical Evaluation," IEEE Trans Neural Syst Rehabil Eng, vol. 29, 2021.

[7] Z. F. Lerner, D. L. Damiano, and T. C. Bulea, "The Effects of Exoskeleton Assisted Knee Extension on Lower-Extremity Gait Kinematics, Kinetics, and Muscle Activity in Children with Cerebral Palsy," Nature Scientific Reports, vol. 7, no. 13512, 2017.

[8] Z. F. Lerner, D. L. Damiano, and T. C. Bulea, "A lower-extremity exoskeleton improves knee extension in children with crouch gait from cerebral palsy," Science Translational Medicine, vol. 9, no. 404, 2017.

[9] G. Orekhov, et al., "Ankle Exoskeleton Assistance Can Improve Over-Ground Walking Economy in Individuals with Cerebral Palsy," IEEE Trans Neural Syst Rehabil Eng, vol. 28, no. 2, pp. 461-467, 2020.

[10] C. Bayón et al., "Locomotor training through a novel robotic platform for gait rehabilitation in pediatric population: short report," Journal of NeuroEngineering and Rehabilitation, vol. 13, no. 98, 2016.

[11] N. G. Moreau, M. Falvo, and D. L. Damiano, "Rapid Force Generation is Impaired in Cerebral Palsy and is Related to Decreased Muscle Size and Functional Mobil," Gait Posture, vol. 35, no. 1, pp. 154-158, 2012.

[12] D. L. Damiano, L. E. Kelly, and C. L. Vaughn, "Effects of Quadriceps Femoris Muscle Strengthening on Crouch Gait in Children With Spastic Diplegia," Phys Ther, vol. 75, no. 8, 1995.

[13] B. C. Conner, et al., "Adaptive Ankle Resistance from a Wearable Robotic Device to Improve Muscle Recruitment in Cerebral Palsy," Ann Biomed Eng, vol. 48, no. 4, pp. 1309-1321, 2020.

[14] B. C. Conner, et al., "Wearable Adaptive Resistance Training Improves Ankle Strength, Walking Efficiency and Mobility in Cerebral Palsy: A Pilot Clinical Trial," IEEE Open Journal of Engineering in Medicine and Biology, vol. 1, pp. 282-289, 2020.

[15] M. Wu, et al., "Robotic Resistance/Assistance Training Improves Locomotor Function in Individuals Poststroke: A Randomized Controlled Study," Arch Phys Med Rehab, vol. 95, pp. 799-806, 2014.

[16] J. Kang, et al., "Robot-driven downward pelvic pull to improve crouch gait in children with cerebral palsy," Science Robotics, vol. 2, 2017.

[17] C. M. Diot, et al., "Robotic lower extremity exoskeleton use in a nonambulatory child with cerebral palsy: a case study," Disability and Rehabilitation: Assistive Technology, vol. 18, no. 5, pp. 497-501, 2021.

[18] C. M. Diot et al., "Robot-Assisted Gait Training with Trexo Home: Users, Usage and Initial Impacts," Children, vol. 10, no. 437, 2023.

[19] P. Slade, et al., "Personalizing exoskeleton assistance while walking in the real world," Nature, vol. 610, pp. 277-282, 2022.

[20] R. L. Medrano, et al., "Real-Time Gait Phase and Task Estimation for Controlling a Powered Ankle Exoskeleton on Extremely Uneven Terrain," IEEE Transactions on Robotics, vol. 39, no. 3, pp. 2170-2182, 2023.

[21] E. Tricomi et al., "Soft robotic shorts improve outdoor walking efficiency in older adults," Nature Machine Intelligence, vol. 6, pp. 1145-1155, 2024.

[22] E. A. Tagoe, Y. Fang, J. R. Williams, and Z. F. Lerner, "Walking on Real-World Terrain With an Ankle Exoskeleton in Cerebral Palsy," IEEE Transactions on Medical Robotics and Bionics, vol. 6, no. 1, 2024.

[23] Z. F. Lerner, D. L. Damiano, and T. C. Bulea, "A Robotic Exoskeleton to Treat Crouch Gait from Cerebral Palsy: Initial Kinematic and Neuromuscular Evaluation," Proc IEEE Eng Med Biol Soc, pp. 2214-2217, 2016.

[24] T. C. Bulea, Z. F. Lerner, and D. L. Damiano, "Repeatability of EMG activity during exoskeleton assisted walking in children with cerebral palsy: implications for real time adaptable control," Proc Int Conf IEEE Eng Med Biol Soc, pp. 2801-2804, 2018.

[25] T. C. Bulea, et al., "Interleaved Assistance and Resistance for Exoskeleton Mediated Gait Training: Validation, Feasibility and Effects," Proc 9th IEEE RAS/EMBS International Conference for Biomedical Robotics and Biomechatronics (BioRob), 2022.

[26] T. M. Devine, K. E. Alter, D. L. Damiano, and T. C. Bulea, "A randomized cross-over study protocol to evaluate long-term gait training with a pediatric robotic exoskeleton outside the clinical setting in children with movement disorders," PLoS ONE, vol. 19, no. 7, p. e0304087, 2024.

[27] L. Demers, R. Weiss-Lambrou, and B. Ska, "Development of the Quebec User Evaluation of Satisfaction with assistive Technology (QUEST)," Assistive Technology, vol. 8, no. 1, pp. 3-13, 1996.

Demographic-Driven Electromyography Analysis: Advancing Personalized Biosignal Interpretation

Maedeh Mohammadiazni, Yue Zhou, and Ana Luisa Trejos, *Senior Member, IEEE*

***Abstract*— The integration of rehabilitation robotics and surface electromyography (sEMG) offers a powerful approach for monitoring and enhancing recovery in patients with neuromuscular disorders. However, variability in baseline sEMG readings across individuals can limit its effectiveness. Factors such as age, height, and weight influence these baselines, and there is a lack of personalized baselines that account for demographic differences. This study proposes a novel model to estimate individualized baselines for one important sEMG parameter, Root Mean Square (RMS). Demographics and physiological data were collected from 30 healthy participants, and sEMG signals were recorded using four electrodes on the forearm muscles during a pushing task at two wrist positions. A Decision Tree Regression model was developed for each combination of the two wrist postures and four electrode locations, resulting in eight combinations, with optimal features identified using the Recursive Feature Elimination method. The regression models achieved accuracies ranging from 88.81% to 95.6%. A global sensitivity analysis using the Sobol method evaluated the importance of each input feature. Results indicate that gathering more comprehensive sEMG data for the most influential factors could improve model generalizability. The findings of this study offer a promising approach for individualized sEMG baselines, with potential applications in rehabilitation robotics to enable personalized recovery strategies for neuromuscular disorders.**

I. INTRODUCTION

Neuromuscular disorders include a range of conditions that impact the muscles and nervous system [1], [2]. Accurate diagnosis of these conditions is critical for effective management and treatment [3]. Surface Electromyography (sEMG) is a valuable tool in the diagnostic process, providing detailed insights into muscle and nerve function by analyzing the electrical signals generated during muscle activity [4]. Distinguishing between normal sEMG patterns and deviations is crucial for identifying changes associated with neuromuscular disorders, where normal sEMG refers to the expected sEMG value in the absence of neuromuscular impairments. This capability extends to applications in rehabilitation robotics, particularly in biofeedback systems that assist in neuromuscular recovery. By leveraging sEMG to detect and interpret abnormal muscle activation patterns, biofeedback devices can provide real-time feedback to patients, enabling them to adjust their movements to achieve more normative muscle activation.

As a standard practice, identifying abnormal sEMG signals has relied on visual inspection and comparison with normative values or baseline measurements from a population [5], [6]. However, a significant limitation of this approach is its failure to account for inter-individual variability, which can affect the accuracy of assessing neuromuscular disorders. Specifically, the features of the sEMG signal are influenced by individual factors such as age [7], [8], gender, and muscle mass—underscoring the limitations of using a single standard for normal sEMG features across all individuals. To address these challenges, such studies have attempted to use machine learning techniques [9]–[11]. By leveraging large datasets, these techniques aim to model the variability in sEMG signal features across different populations, enabling more personalized and precise analyses of sEMG signals. However, gathering large labeled datasets is often a major challenge, as it demands a considerable amount of annotated data for model training, which can be both time-consuming and expensive to acquire.

To overcome these challenges, this study proposes a novel method for developing models that estimate the normal sEMG characteristic of forearm muscles, personalized for each individual. By integrating individual demographic factors, including age, forearm length, forearm circumference, wrist circumference, height, and weight, along with physiological factors such as wrist sensory threshold and wrist motor threshold, the models aim to estimate personalized baselines for a key sEMG parameter, Root Mean Square (RMS), a measure of sEMG signal strength. RMS was selected as it reliably measures sEMG signal amplitude, directly associated with muscle activation, making it useful for assessing muscle function and detecting abnormalities in neuromuscular health [12], [13]. The objective of the proposed method is to address a critical limitation in the standard practice of using generalized normative values for sEMG analysis by accounting for variability in individual factors. This approach has the potential to enhance the accuracy of neuromuscular disorder assessments by estimating normal sEMG features in patients, providing a baseline for comparison after the onset of a neuromuscular disorder. Additionally, it can support applications in rehabilitation and biofeedback systems by enabling individualized assessments of muscle function.

This work was supported by the Natural Sciences and Engineering Research Council (NSERC) of Canada under grant RGPIN-2020-05648, by a WSS-CIHR Seed Grant from Western University, and by the Canada Research Chairs Program under File 950-233069.

Maedeh Mohammadiazni is with the School of Biomedical Engineering, Western University, London, ON N6A 5B9, Canada mmoha345@uwo.ca

Yue Zhou was with the School of Biomedical Engineering, Western University, London, ON N6A 5B9, Canada yzhou426@uwo.ca

Ana Luisa Trejos is with the Department of Electrical and Computer Engineering and the School of Biomedical Engineering, Western University, London, ON N6A 5B9, Canada atrejos@uwo.ca

II. METHODOLOGY

Surface EMG signals are influenced by multiple factors, necessitating a comprehensive approach to accurately model and interpret them [14]. In addition to individual differences, factors such as electrode placement and arm posture can significantly impact the quality and interpretation of sEMG signals [15]. The position of the electrodes can influence the recorded signal due to variations in the alignment of muscle fibers relative to the electrode. Similarly, arm posture can affect muscle activation patterns, altering their electrical activity. These factors contribute to additional variability, emphasizing the importance of considering electrode placement and arm posture when interpreting sEMG data. Accordingly, to achieve the objective, this study investigated two wrist postures and considered four electrode placements on the arm to account for these factors. For each combination of the two wrist postures and four electrode locations (corresponding to four channels, as shown in Fig. 2), one model has been developed, resulting in eight models. These models, which predict the RMS of the sEMG signal based solely on individual features, are built using the Decision Tree Regression (DTR) approach, with all models having the same architecture and parameters. The DTR approach was chosen due to its ability to capture complex relationships in the data and its robustness to outliers, making it well-suited for various regression tasks [16].

To develop the models and explore the relationship between the RMS of the sEMG signal and individual features, it was essential to identify which features were most relevant. Since it was uncertain whether the relationship involved all features, just one, or a combination of several, the Recursive Feature Elimination (RFE) technique [17] was employed. This method iteratively removes less important features, helping to identify the optimal set of predictors. By using RFE, the most influential features were selected, resulting in the best models for predicting RMS. For evaluation, the trained model predicts the RMS of the sEMG signal for individuals in the test group without accessing their actual RMS values. The predicted values are then compared to the actual values to calculate the accuracy. The global Sobol sensitivity analysis [18] was then conducted to assess the impact of each of the most influential features identified through RFE on the models' predictions, aiming to determine the extent to which each factor contributed to the variability in the predicted RMS. Fig. 1 provides a summary of the entire process of model development and sensitivity analysis.

A. Data Collection

To investigate the proposed approach, this study recruited thirty healthy participants (ethics approval was obtained from the Human Research Ethics Board at Western University, Project ID: 117923). Prior to participation, all individuals provided informed consent and were briefed on the study's procedures and goals. The demographics and physiological features of the participants (as listed in Table I) were collected and used as input parameters for the model. To measure wrist sensory and motor thresholds, participants were seated on a chair, with their arm resting on the armrest, as shown in Fig. 2. A pair of commercially available wet electrodes (KendallTM H590P, Fig. 2, #2) were used and placed on the muscle responsible for wrist flexion, identified through the palpation technique. One electrode was positioned approximately 5 cm distal to the medial epicondyle, and the second electrode was placed 1 cm distal to the first one along the longitudinal direction of the flexor carpi radialis. These two electrodes were connected to a transcutaneous electrical stimulator (TENS 210, Fig. 2, #1). A consistent series of electrical pulses were delivered to the electrodes. The pulse width was set to 200 μs and the pulse frequency to 50 Hz, following the parameters commonly reported in the literature (e.g., [19]). The stimulation current increased from 0 mA to the participant's sensory threshold and motor threshold, and the corresponding values were recorded.

For sEMG data collection, four pairs of sEMG electrodes were placed on the forearm muscles of the participants (as shown in Fig. 2, #3). Velcro straps securely positioned the electrodes, ensuring stable skin contact and minimizing movement interference. Participants were instructed to exert their maximum voluntary pushing force against a block that was securely held by the experimenter for a duration of 3 seconds. The block was adjustable, allowing for the achievement of various wrist flexion angles during the task. Data were collected in two wrist postures: one at 30 degrees and the other at maximum flexion.

B. Processing of sEMG Signal

Processing sEMG signals serves several purposes, including reducing noise from various sources such as electrical interference and movement artifacts. It also enhances the Signal-to-Noise Ratio (SNR) and enables the detection of muscle activity onset.

Initially, the raw sEMG signals were downsampled from 4 kHz into 1 kHz and then filtered using a bandpass filter to remove low and high frequencies. Specifically, a high-pass filter with a cutoff frequency of 10 Hz and a low-pass filter with a cutoff frequency of 400 Hz were employed. These cutoff frequencies are commonly used in sEMG signal processing [20]. To prevent the filtered sEMG signals from averaging to zero, rectification was applied, converting negative oscillations into positive values. To detect onsets, or sudden increases in muscle activation levels, the rectified sEMG signals were smoothed by applying a moving average filter. The onset point in the energy signal obtained with Teager-Kaiser energy operator (TKEO) [21] was identified as the point where the most significant increase in the RMS of the signal occurred. To detect offsets, the rectified sEMG signals were similarly analyzed; however, with a focus on the point where the RMS of the energy signal, calculated using the TKEO, dropped significantly after the onset. The TKEO equation is given as follows [22]:

$$\psi[e_n] = e_n^2 - (e_{n+1} \times e_{n\infty 1}) \,, \tag{1}$$

TABLE I

OVERVIEW OF PARTICIPANT DEMOGRAPHICS AND PHYSIOLOGICAL FEATURES

Age (years)	Forearm Length (cm)	Forearm Circumference (cm)	Wrist Circumference (cm)	Height (cm)	Weight (kg)	Wrist-Sensory Threshold (mA)	Wrist-Motor Threshold (mA)
27.56± 7.18	25.4± 2.06	24.78± 1.91	15.93± 1.28	171.25± 8.4	68.94± 10.29	11.5± 2.28	20.76± 8.12

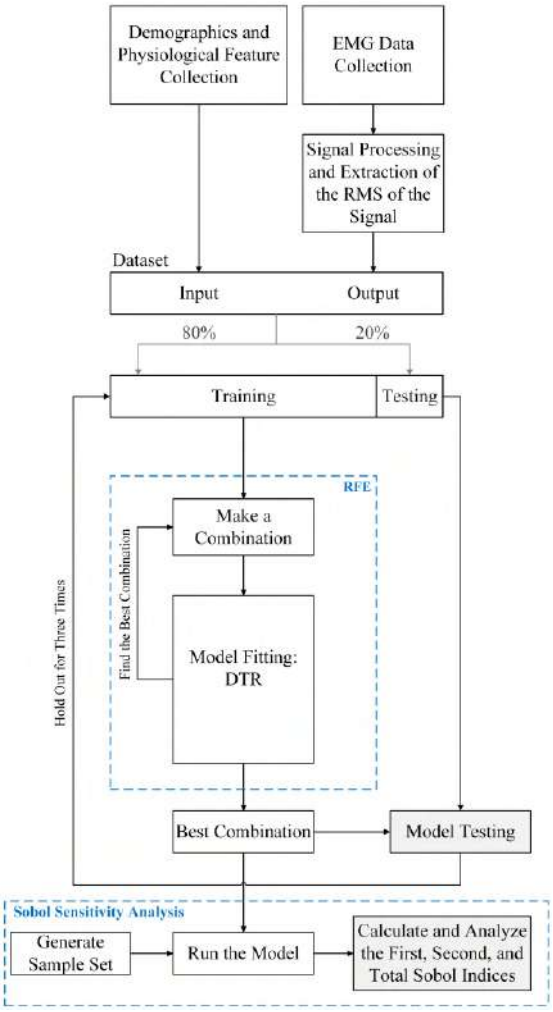


Fig. 1. The workflow of model development and Sobol sensitivity analysis involved the collection of demographics and physiological factors of individuals, which were considered as inputs for training. The sEMG signal was processed to compute its RMS, which was used as the output. The dataset was divided into training (80%) and testing (20%) subsets. RFE was applied to the DTR model to identify the optimal combination of input parameters for maximum accuracy. During testing, the model predicted the RMS of the sEMG signal without referencing the actual RMS value, and the predicted RMS was compared with the real RMS to evaluate model performance. The training and testing process was repeated three times using the holdout method with predefined, non-overlapping 20% test sets. The Sobol sensitivity analysis was then conducted, where samples were generated, the model was applied, and Sobol indices were calculated to assess the influence of input parameters. This entire process was repeated for each of the eight models, created from the combinations of two wrist postures and four electrode locations.

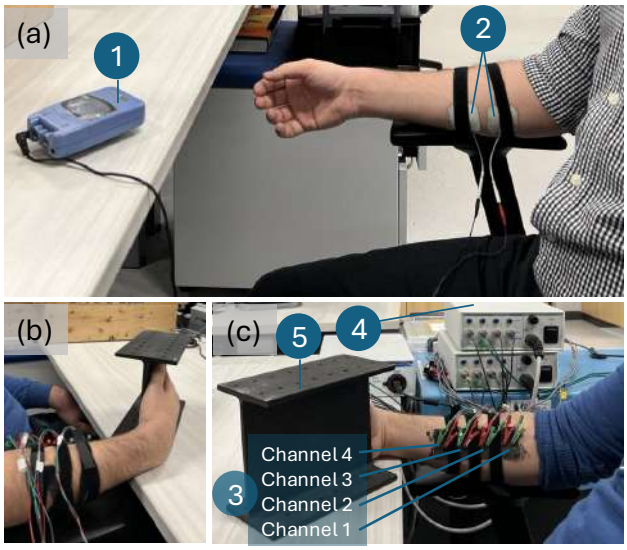


Fig. 2. (a) Experimental setup used for sensory and motor threshold measurements. (b) sEMG measurement setup with the wrist in maximum flexion, shown from the back view of the hand. (c) Front view of the hand during sEMG measurements. (1) Transcutaneous electrical stimulator (TENS 210). (2) Stimulation electrodes (KendallTM H590P). (3) sEMG electrodes. Each channel consists of two electrodes, with a 2 cm distance between adjacent channels. (4) sEMG data acquisition device (Intronix 2024F Isolated Amplifier). (5) The block was used in the experiment to create different wrist flexion angles.

where e represents the sEMG measurement and n denotes the data point number. Following the detection of onset and offset, the sEMG signal starting from the onset and ending at the offset was selected, and the RMS of this window was calculated for each individual.

C. Model Development

The aim of developing a DTR model is to predict the RMS of sEMG signals for individuals in the test group based on their unique features, without requiring actual sEMG data. To achieve this, the model was trained on a training group using normalized individual features, including age, forearm length, forearm circumference, wrist circumference, height, weight, and wrist sensory threshold as inputs, with the normalized RMS of sEMG signals as the output. The trained model was then tested on the test group to predict the RMS values of sEMG signals. To achieve this, the dataset was divided into two subsets using a hold-out validation approach: 80% for training and 20% for testing. To ensure robustness and minimize the impact of any specific data split, this process was repeated three times.

The optimal combination of individual features was selected

using the RFE technique. In DTR, data were split into smaller subsets based on feature values, creating a tree-like structure where each node represents a decision rule [16]. The DTR algorithm seeks to reduce variance to identify optimal splits, with the leaf nodes representing the predicted target values [16].

The combinations of input features that maximized the predictive accuracy of the DTR model were identified using RFE, and the model was subsequently evaluated using the Mean Absolute Percentage Error (MAPE) as the performance metric. MAPE measures the average percentage difference between the predicted and actual values, and is calculated as follows:

$$\text{MAPE} = \frac{1}{n}\sum_{i=1}^{n}\left|\frac{y_i - \hat{y}_i}{y_i}\right| \times 100 \ , \tag{2}$$

where y_i is the actual RMS value, $\hat{y}_i$ is the predicted RMS value, and n is the total number of observations. Eight regression models were developed using two wrist postures (30 degree flexion and maximum flexion) and four electrode placements on the forearm, resulting in 8 distinct models.

D. Sobol Sensitivity Analysis

A global sensitivity analysis was conducted to assess the influence of individual demographics and physiological factors used to develop the DTR model on its behavior. This analysis enables the exploration of the impact of both individual and combined changes in these parameters on variations in the RMS of sEMG signals. In this study, the Sobol sensitivity analysis method was applied, a widely used technique in uncertainty quantification and global sensitivity analysis [18], [24]. Considering the RMS of the sEMG signal (Y) as a function of the individual features, the relationship can be expressed as follows:

$$Y = f(\mathbf{Z}) \ , \tag{3}$$

where Z represents the set of model parameters, which correspond to the individual features in this study. The Sobol method determines the importance of each parameter by decomposing the variance of Y into components attributable to each input parameter. For a square-integrable function, this decomposition is given by the following [18]:

$$f(\mathbf{Z}) = f_0(\mathbf{Z}) + \sum_{s=1}^{n}\sum_{i_1<\cdots<i_S} f_{i_1\ldots i_S}(\mathbf{Z}_{i_1},\ldots,\mathbf{Z}_{i_S}) \ , \tag{4}$$

where f_0 is the expected value of f. It has been shown that the summands in the equation above can be recursively calculated using integrals. Further details on how these parameters can be computed are provided in [18], [24]. After performing the substitutions, the total variance is computed as follows:

$$D = \int f^2(\mathbf{Z})\, d\mathbf{Z} - f_0^2 \ . \tag{5}$$

Moreover, the partial variances are defined as follows:

$$D_{i_1,\ldots,i_S} = \int f^2_{i_1\ldots i_S}(\mathbf{Z}_{i_1},\ldots,\mathbf{Z}_{i_S})\, d\mathbf{Z} \ . \tag{6}$$

TABLE II

AVERAGE MAPE ACCURACY OF THE EIGHT MODELS FOR CHANNELS 1 TO 4 AT DIFFERENT WRIST ANGLES OVER THREE TEST SETS

Channel	Accuracy at 30° Flexion	Accuracy at Maximum Flexion
1	93.20 ± 3.75	91.05 ± 6.14
2	94.76 ± 0.77	95.41 ± 0.85
3	91.07 ± 2.49	94.01 ± 2.41
4	88.81 ± 1.26	95.60 ± 1.10

The Sobol indices are defined as follows [18]:

$$S_{i_1,\ldots,i_S} = \frac{D_{i_1,\ldots,i_S}}{D} \ . \tag{7}$$

The first-order Sobol index, which considers only a single input parameter, quantifies its individual effect, while higher-order Sobol indices capture interactions between multiple parameters. The total-order Sobol index for a given parameter i is the sum of all Sobol indices involving that parameter and is defined as follows:

$$S_i^T = 1 - S_{\sim i} \ . \tag{8}$$

The symbol $\sim i$ indicates that the variable i is excluded. The total-order Sobol index represents the overall contribution of a parameter to the output, including its interactions with other parameters. The Sobol sensitivity analysis was performed using the SALib library in Python [25], [26]. A normal distribution was assumed for all parameters in the Sobol sensitivity analysis procedure.

III. RESULTS

A. Model Development Results

The optimal feature combination that yields the best DTR learner was determined using the RFE method. The findings revealed that the optimal combination varies depending on wrist position and electrode location. Fig. 3 provides an example of the variability in results across different electrode locations (channel numbers shown in Fig. 2). As shown in Fig. 3, the highest accuracy for the best-performing combinations was achieved with five features for Channel 1, four features for Channel 2, five features for Channel 3, and three features for Channel 4. Fig. 4 illustrates the prediction MAPE accuracy of the optimal models (selected using RFE) for estimating the RMS of the sEMG signal across three test sets, with a total of eight models (2 wrist postures×4 sEMG channels). The average MAPE accuracy of the models for Channels 1 to 4 at two wrist postures is illustrated in Table II.

B. Sobol Sensitivity Analysis Results

After finding the optimal feature combination using RFE that results in the most accurate DTR model, those features underwent Sobol sensitivity analysis. The first-order, second-order, and total-order Sobol indices are shown in Fig. 5 for the wrist at 30 degree flexion and at maximum flexion. The first-order indices illustrate the effects of each input parameter on the output variations, the second-order indices

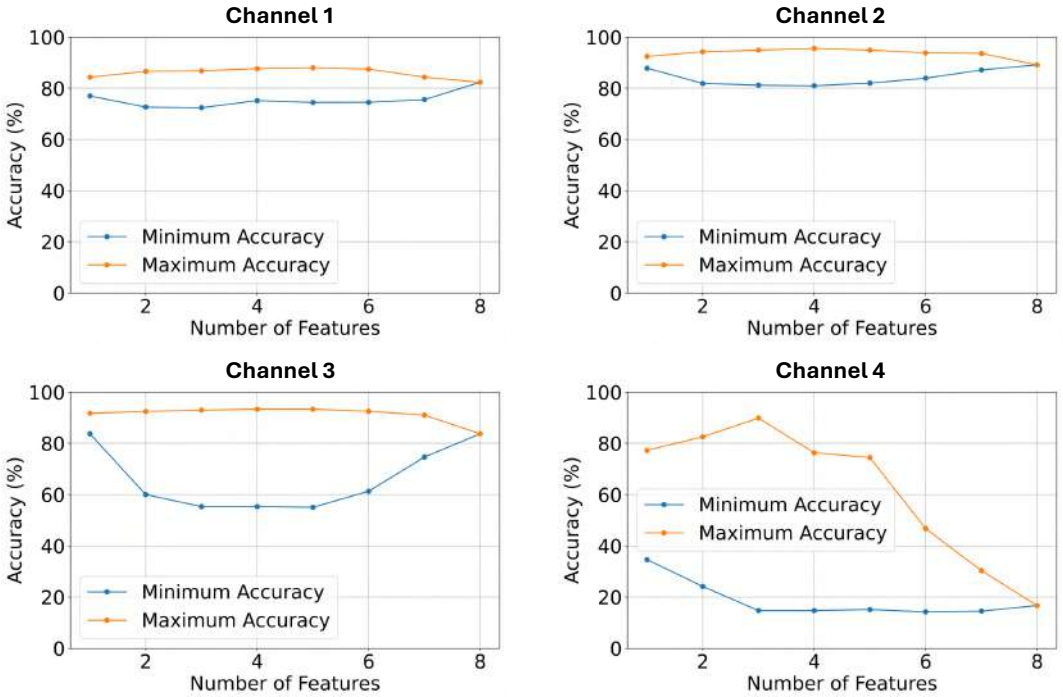


Fig. 3. The maximum and minimum MAPE accuracies among all possible feature combinations, where a separate model was developed for each combination, are shown in this figure for predicting the RMS values based solely on individual features for Channels 1 to 4 during 30-degree wrist flexion. The eight features are age, height, weight, arm length, arm circumference, wrist circumference, and sensory and motor thresholds. These accuracies are presented as a function of the number of input features, without access to the actual sEMG signal during estimation. The results indicate that increasing the number of input features does not necessarily improve accuracy.

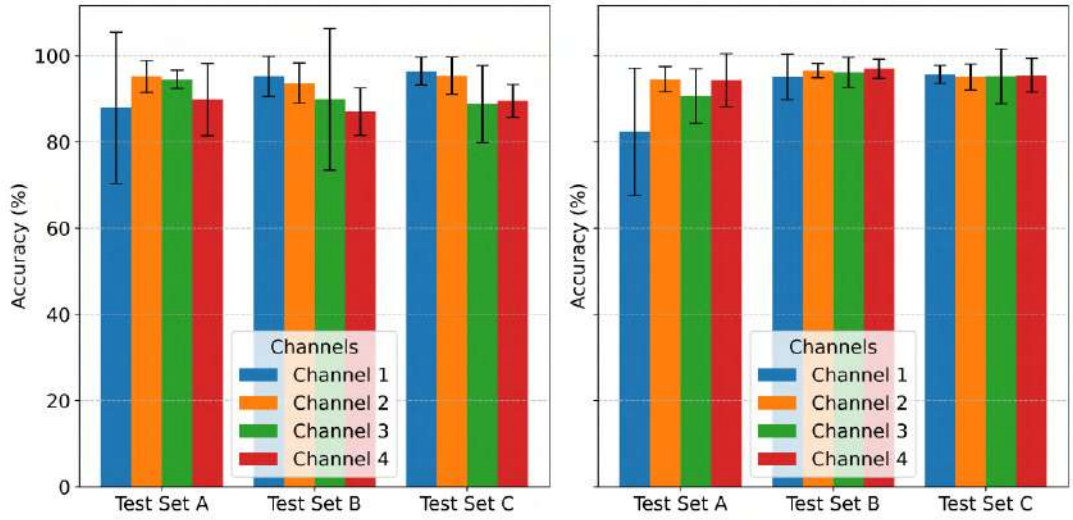


Fig. 4. The MAPE accuracy of the top-performing models (identified through RFE) reflects their ability to predict the expected RMS values based solely on individual features, evaluated across three separate test sets (each obtained through hold-out validation), without access to the actual sEMG signal during estimation. The left figure shows results for 30 degree wrist flexion, and the right figure depicts results for maximum wrist flexion. The channel numbers correspond to the electrode locations depicted in Fig. 2. With three test sets, four channels, and two wrist postures, a total of 24 results ($3 \times 4 \times 2$) are presented. The standard deviation reflects the variation in accuracy across the corresponding test set.

capture the interactions between pairs of input parameters and their joint contribution to the output variance, and the total-order indices capture both the direct effect of an input parameter and its interactions with other parameters.

The analysis of the total-order Sobol indices for wrist at 30 degree flexion, as shown in Fig. 5, revealed that age has the most significant direct effect on the RMS of the sEMG signal for Channels 1 to 4. The second-order Sobol indices for wrist at 30 degree flexion, shown in Fig. 5, highlight significant interactions between age and other demographic variables, including height for Channel 1, motor threshold for Channel 2, wrist circumference for Channel 3, and forearm circumference for Channel 4. The analysis of the RMS of the sEMG signal across four channels during maximum wrist flexion, as shown in Fig. 5 reveals that the total-order Sobol indices identify age, wrist circumference, height, and motor threshold as the most influential parameters for Channels 1 to 4, respectively. The second-order Sobol indices during maximum wrist flexion in Fig. 5 highlight significant interactions: for Channel 1, age and forearm length; for Channel 2, wrist circumference and forearm length; for Channel 3, height and age; and for Channel 4, motor threshold and height.

IV. DISCUSSION

This study introduced a method for predicting the RMS value of a normal sEMG signal in a personalized manner, assuming that the normal sEMG signal is not available due to factors such as a neuromuscular disorder. The purpose of this approach is to allow for better individualized comparisons between baseline and post-onset sEMG signals in neuromuscular disorders, improving the detection and monitoring of these conditions. This section discusses the importance of the findings of this study and identifies key areas for improvement to enhance the proposed approach.

The use of RFE to identify optimal individual features revealed that including more features does not necessarily lead to improved model accuracy. A meaningful relationship exists only between certain individual features and the sEMG signals. As shown in Fig. 3, for the best-performing combinations, the highest accuracy was achieved with different numbers of features for different channels. Additionally, the results highlight that both the number and type of features are critical for developing an optimal model. For example, while combinations with five, four, five, and three features for channels 1, 2, 3, and 4, respectively, yielded the highest accuracy, other combinations with the same number of features resulted in significantly lower accuracy: approximately 74% for Channel 1, 82% for Channel 2, 60% for Channel 3, and 12% for Channel 4.

In addition, the application of the Sobol method for global sensitivity analysis revealed that some features have a greater impact on the variability of the RMS values of the sEMG signal, offering a valuable tool for refining study designs and informing participant recruitment strategies. Researchers can broaden their recruitment to include a more diverse or targeted population that represents these key factors better. This makes it possible for the collected sEMG data to be more generalizable and relevant to a wider range of individuals, increasing the external validity of the study and improving the robustness of the findings.

Despite the promising results, several limitations must be acknowledged. One limitation is the relatively small sample size, which may restrict the generalizability of the findings. A larger sample would provide more robust data and increase confidence in the predictive capabilities of the model. Furthermore, the demographic variables included in this study were limited, focusing on eight factors. Other factors, such as sex, dominant hand, physical activity levels, or underlying medical conditions, could also influence baseline sEMG patterns and were not accounted for in this model. Although this study included 15 men and 15 women, sex was not considered as an influencing factor in the Sobol analysis due to limitations of the SALib library, which does not support categorical variables in its sensitivity analysis. As a result, the impact of sex could not be directly assessed or quantified using the Sobol analysis.

In addition, sEMG signals are influenced not only by muscle activity but also by the electrical properties of the skin between the electrodes and the muscles. For instance, changes in sweat levels, skin temperature, and ambient humidity can impact these properties, leading to variations in sEMG recordings [27], [28]. Future research should explore these factors to refine the model and enhance its applicability to diverse populations and conditions. Furthermore, while wrist posture was varied in this study, the analysis did not account for more complex movements or additional joint positions that could affect sEMG variability. The inclusion of other joint angles may provide a more comprehensive understanding of how these factors influence muscle activation across different functional tasks. Incorporating these variables in future studies could potentially refine the ability of the model to predict sEMG signal variations under real-world conditions. Future work should explore machine learning models beyond the DTR used in this study, assessing how different model structures and parameters influence the results. Additionally, a deeper investigation into the anatomical and biomechanical factors affecting EMG variability due to electrode placement is needed. Given the limitations of static models in capturing temporal dependencies, future research will also explore dynamic modeling approaches, such as recurrent neural networks, to improve predictive accuracy.

Nevertheless, this study demonstrates that it is possible to obtain an individualized prediction model for analyzing sEMG signals, offering valuable insights into personalized neuromuscular assessments. Furthermore, this approach has the potential to be applied in rehabilitation robotics, such as biofeedback systems, by leveraging individualized baseline sEMG predictions to adapt therapy to patients' specific needs. In individuals with neuromuscular disorders, the normal sEMG signal is often unavailable due to muscle damage. By using the predicted baseline RMS values, rehabilitation robots can tailor the intensity and type of feedback provided during physical therapy sessions, optimizing recovery strategies. However, limitations should be addressed in future

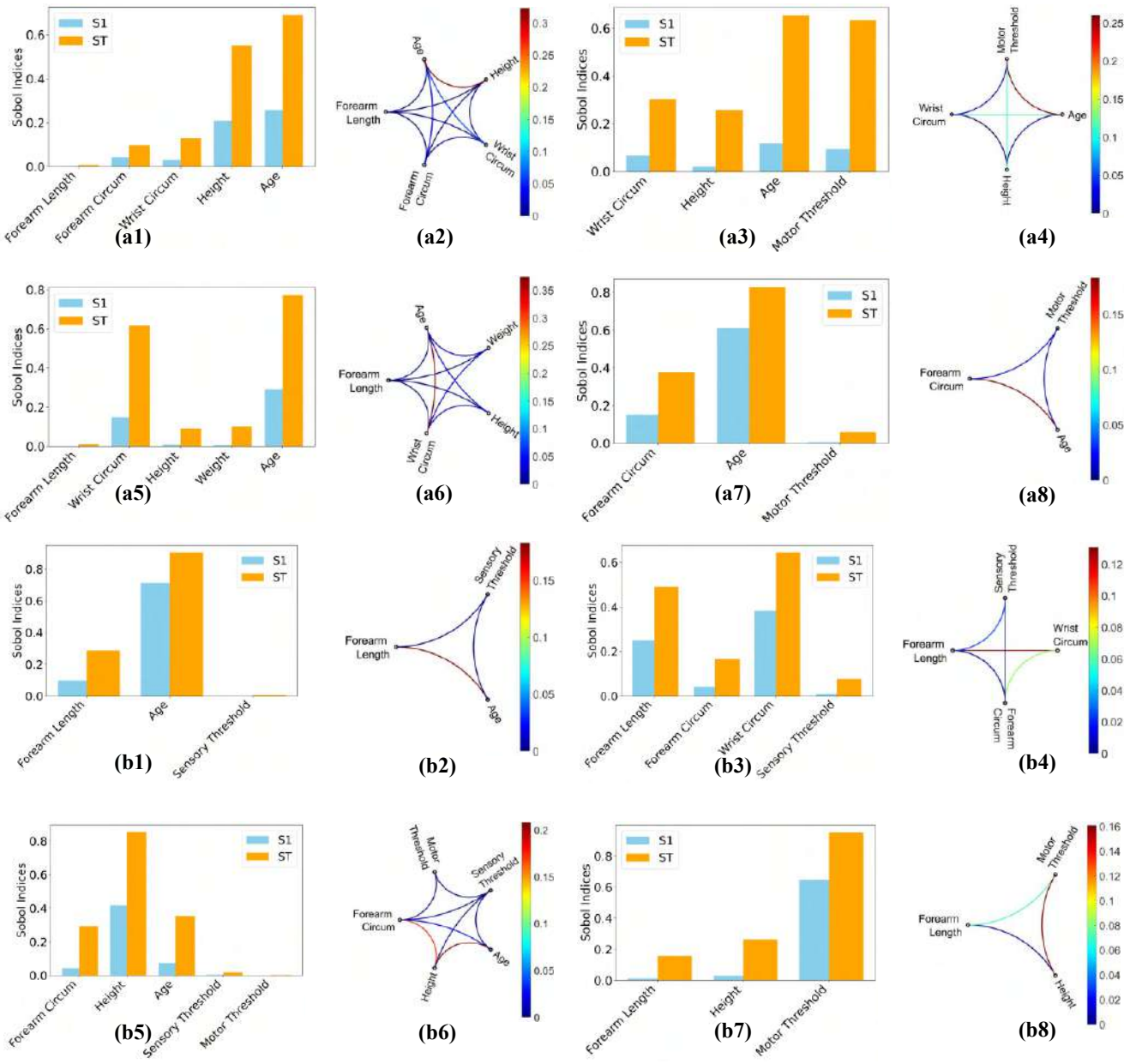


Fig. 5. The bar plots display the first-order (S1) and total-order (ST) Sobol indices for the RMS of the sEMG signal at 30 degree wrist flexion for (a1) Channel 1, (a3) Channel 2, (a5) Channel 3, and (a7) Channel 4, and at maximum wrist flexion for (b1) Channel 1, (b3) Channel 2, (b5) Channel 3, and (b7) Channel 4. The circular plots show the second-order Sobol indices for the RMS of the sEMG signal at 30 degree wrist flexion across (a2) Channel 1, (a4) Channel 2, (a6) Channel 3, and (a8) Channel 4, and at maximum wrist flexion across (b2) Channel 1, (b4) Channel 2, (b6) Channel 3, and (b8) Channel 4. The color bar indicates the magnitude of the interactions between pairs of input parameters, with red representing higher values (stronger interactions), blue representing lower values (weaker interactions), and intermediate colors representing values in between these extremes.

research to enhance the model's robustness and applicability. By doing so, the model could become more reliable and applicable across a wider range of patient populations, ultimately providing valuable tools for improving neuromuscular diagnoses and assessments in both clinical and research settings.

V. CONCLUSIONS

In conclusion, this study highlights the potential to develop a model capable of predicting individualized baseline features of sEMG signals. The model presented in this study combines individual demographic factors such as age, height, weight, arm length, arm circumference, and wrist circumference, along with physiological features including sensory and motor thresholds, to predict personalized baseline values of a key sEMG parameter, the RMS of the signal. Considering that sEMG patterns vary with arm posture and electrode placement, this study analyzed two wrist postures and four electrode positions on the arm to account for these factors. Eight DTR models were developed using various combi-

nations of two wrist postures and four electrode locations. For each model, the optimal configuration was obtained by applying the RFE technique, and the accuracy of these eight models ranged from 88.81% to 95.6%. A global Sobol sensitivity analysis was then performed to investigate the significance of each input parameter on the variability of the RMS of the sEMG signal. The use of RFE demonstrated that a meaningful relationship exists only between certain individual features and the sEMG signals, which contribute to the development of an accurate model. The results of the Sobol analysis offer valuable insights for future research, indicating that recruiting a more diverse population based on the factors identified in the analysis could lead to a more robust model. Overall, this research represents a significant step forward in the field of neuromuscular diagnostics, offering a promising avenue for the development of more precise and individualized clinical assessments. Future research should aim to incorporate a broader range of demographic factors, explore additional arm postures, and consider other sEMG features. These enhancements could provide deeper insights into neuromuscular assessments and contribute to the refinement of the model, ultimately improving its clinical applicability and accuracy in evaluating neuromuscular disorders. Additionally, by tailoring interventions based on individual features, this model could be effectively integrated into rehabilitation robotics, in the form of biofeedback systems to optimize therapeutic outcomes and support personalized recovery strategies.

ACKNOWLEDGMENT

We would like to express our gratitude to Intronix for providing the Intronix 2024F Isolated Amplifier used in our data collection.

REFERENCES

[1] B. Morrison, "Neuromuscular diseases," Seminars in Neurology, vol. 36, pp. 409–418, 2016.

[2] B. Katirji, H. Kaminski, and R. Ruff, "Neuromuscular disorders in clinical practice," Springer Science & Business Media, 2013.

[3] M. Putten, J. Hmeljak, A. Aartsma-Rus, and J. Dowling, "Moving neuromuscular disorders research forward: From novel models to clinical studies," Disease Models & Mechanisms, vol. 13, p. dmm044370, 2020.

[4] J. Hogrel, "Clinical applications of surface electromyography in neuromuscular disorders," Neurophysiologie Clinique/Clinical Neurophysiology, vol. 35, pp. 59–71, 2005.

[5] V. Medved, S. Medved, and I. Kovač, "Critical appraisal of surface electromyography (sEMG) as a taught subject and clinical tool in medicine and kinesiology," Frontiers in Neurology, vol. 11, p. 560363, 2020.

[6] A. Kotov-Smolenskiy, A. Khizhnikova, A. Klochkov, N. Suponeva, and M. Piradov, "Surface EMG: applicability in motion analysis and opportunities for practical rehabilitation," Human Physiology, vol. 47, pp. 237–247, 2021.

[7] R. Merletti, D. Farina, M. Gazzoni, and M. Schieroni, "Effect of age on muscle functions investigated with surface electromyography," Muscle & Nerve, vol. 25, pp. 65–76, 2002.

[8] A. Pradhan, G. Malagon, R. Lagacy, V. Chester, and U. Kuruganti, "Effect of age and sex on strength and spatial electromyography during knee extension," Journal of Physiological Anthropology, vol. 39, pp. 1–11, 2020.

[9] S. Jose, S. George, M. Subathra, V. Handiru, P. Jeevanandam, U. Amato, and E. Suviseshamuthu, "Robust classification of intramuscular sEMG signals to aid the diagnosis of neuromuscular disorders," IEEE Open Journal of Engineering in Medicine and Biology, vol. 1, pp. 235–242, 2020.

[10] I. Elamvazuthi, N. Duy, Z. Ali, S. Su, M. Khan, and S. Parasuraman, "Electromyography (EMG) based classification of neuromuscular disorders using multi-layer perceptron," Procedia Computer Science, vol. 76, pp. 223–228, 2015.

[11] M. Vallejo, C. Gallego, L. Duque-Muñoz, and E. Delgado-Trejos, "Neuromuscular disease detection by neural networks and fuzzy entropy on time-frequency analysis of electromyography signals," Expert Systems, vol. 35, p. e12274, 2018.

[12] K. Watanabe, M. Kouzaki, M. Ogawa, H. Akima, and T. Moritani, "Relationships between muscle strength and multi-channel surface EMG parameters in eighty-eight elderly," European Review of Aging and Physical Activity, vol. 15, pp. 1–10, 2018.

[13] S. Li, X. Luo, S. Zhang, Y. Tang, J. Sun, Q. Meng, H. Yu, and C. Sun, "Evaluation of multilevel surgeries in children with spastic cerebral palsy based on surface electromyography," Frontiers in Neuroscience, vol. 15, p. 680645, 2021.

[14] M. Mohammadiazni, J. G. C. Alfaro, and A. L. Trejos, "Mitigate the effect of arm posture on electromyography pattern recognition," IEEE Journal of Biomedical and Health Informatics, early access, doi: 10.1109/JBHI.2024.3518978, 2024.

[15] H. Wang, N. Li, X. Gao, N. Jiang, and J. He, "Analysis of electrode locations on limb condition effect for myoelectric pattern recognition," Journal of NeuroEngineering and Rehabilitation, vol. 21, p. 177, 2024.

[16] T. Guo, K. Kutzkov, M. Ahmed, J. Calbimonte, and K. Aberer, "Efficient distributed decision trees for robust regression," Machine Learning and Knowledge Discovery in Databases: European Conference, ECML PKDD 2016, Riva Del Garda, Italy, September 19–23, pp. 79–95, 2016.

[17] H. Jeon and S. Oh, "Hybrid-recursive feature elimination for efficient feature selection," Applied Sciences, vol. 10, p. 3211, 2020.

[18] I. Sobol, "Global sensitivity indices for nonlinear mathematical models and their Monte Carlo estimates," Mathematics and Computers in Simulation, vol. 55, pp. 271–280, 2001.

[19] M. Gonzalez, C. Nwokeabia, A. Vaskov, P. Vu, C. Lu, P. Patil, P. Cederna, C. Chestek, and D. Gates, "Electrical stimulation of regenerative peripheral nerve interfaces (RPNIs) induces referred sensations in people with upper limb loss," IEEE Transactions on Neural Systems and Rehabilitation Engineering, vol. 32, pp. 339–349, 2023.

[20] S. Muceli and R. Merletti, "Tutorial. Frequency analysis of the surface EMG signal: best practices," Journal of Electromyography and Kinesiology, vol. 79, p. 102937, 2024.

[21] S. Solnik, P. DeVita, P. Rider, B. Long, and T. Hortobágyi, "Teager–Kaiser operator improves the accuracy of sEMG onset detection independent of signal-to-noise ratio," Acta of Bioengineering and Biomechanics/Wroclaw University of Technology, vol. 10, pp. 65–68, 2008.

[22] J. Kaiser, "On a simple algorithm to calculate the 'energy' of a signal," International Conference on Acoustics, Speech, and Signal Processing, Albuquerque, New Mexico, USA, April 3–6, 1990, pp. 381–384, 1990.

[23] L. Hsiao and C. Cho, "The effect of aging on muscle activation and postural control pattern for young and older computer users," Applied Ergonomics, vol. 43, pp. 926–932, 2012.

[24] A. Ebrahimian, H. Mohammadi, and N. Maftoon, "Relative importance and interactions of parameters of finite-element models of human middle ear," The Journal of the Acoustical Society of America, vol. 154, pp. 619–634, 2023.

[25] T. Iwanaga, W. Usher, and J. Herman, "Toward SALib 2.0: Advancing the accessibility and interpretability of global sensitivity analyses," Socio-Environmental Systems Modelling, vol. 4, pp. 18155–18155, 2022.

[26] J. Herman and W. Usher, "SALib: An open-source Python library for Sensitivity Analysis," The Journal of Open Source Software, vol. 2, p. 97, 2017.

[27] J. I. P. Quesada, F. P. Carpes, R. R. Bini, R. S. Palmer, P. P'erez-Soriano, and R. Mª C. O. de Anda, "Relationship between skin temperature and muscle activation during incremental cycle exercise," Journal of Thermal Biology, vol. 48, pp. 28–35, 2015.

[28] M. Abdoli-Eramaki, C. Damecour, J. Christenson, and J. Stevenson, "The effect of perspiration on the sEMG amplitude and power spectrum," Journal of Electromyography and Kinesiology, vol. 22, pp. 908–913, 2012.

Effects of Hip Adduction-Abduction Exoskeleton-Controlled Step Width on Mediolateral Gait Balance during Walking

Soe Lin Paing[1], Abbas Alili[2], Varun Nalam[3] and He (Helen) Huang[3]

***Abstract*— Mediolateral balance during walking is a critical aspect of functional mobility, particularly in populations with neuromuscular disorders. Step width is one of the key gait parameters influencing balance, and mediolateral hip exoskeletons have emerged as potential tools to modulate step width for improved stability. This study investigated the effects of exoskeleton-controlled step width on mediolateral gait balance represented by various gait balance metrics, including trunk sway, margin of stability (MoS), net external moment, and step width variability, in healthy individuals. Using a reinforcement learning-based control framework, the exoskeleton achieved precise step width control with an average error of 0.46 cm. Results revealed that the step width has a strong positive correlation with trunk sway ($R^2 = 0.9795$), margin of stability ($R^2 = 0.8948$), and net external moment ($R^2 = 0.9188$), reflecting a trade-off between stability and effort. Step width variability was unaffected, suggesting no destabilizing impact from controlled step width adjustments. These findings provide valuable insights into the design and optimization of exoskeletons for enhancing mediolateral stability in clinical and rehabilitation settings.**

I. INTRODUCTION

Maintaining balance is a critical aspect of human mobility, enabling individuals to perform daily activities safely and efficiently [1]. Compromised balance affects a wide range of populations, including older adults, people with amputation, and individuals with neurological disorders, leading to significant health concerns such as an increased risk of falls, reduced mobility, loss of independence, and secondary complications like fractures, head injuries, and chronic pain [2], [3]. Given the wide range of daily tasks and environmental perturbations that can affect balance, humans employ distinct gait balance strategies in two anatomical directions: anteroposterior (AP) and mediolateral (ML). Specifically in the ML direction, humans employ active motor control to maintain gait balance [4]. Any disruption to the components involved in ML control is detrimental to frontal plane stability [5].

Active control of step width has been increasingly validated as a control strategy to maintain balance along ML direction during walking [6], [7]. Simulation studies show that ML balance is maintained by modulating the base of support based on center of mass behavior [8], and is achieved in bipedal locomotion by controlling step width [9], [10]. Reduced ability to control step width and increasing step width variability is observed in older populations and people with chronic neurological disorders, highlighting the role of step width in ensuring mediolateral balance [11], [12]. Hence, solutions must be developed that can effectively restore step width control in affected individuals.

While there is an increasing prevalence of exoskeletons developed for lower limb assistance, most devices primarily target assistance in the anteroposterior (AP) direction [13]–[15]. In order to address the increasingly apparent need for modulating ML balance, we have developed a bilateral mediolaterally active hip exoskeleton [16]. Investigations of the exoskeleton capabilities have shown that the device was able to significantly modulate step width by adjusting the stiffness simulated by the exoskeleton. [17]. Notably, this modulation was achieved without impacting other gait parameters such as step length or gluteus medius EMG activity, confirming that the changes in step width were directly induced by the exoskeleton. Motivated by these results, we have further developed a controller that can accurately control the step width of users during walking and have validated the approach through human subject testing [18]. The study has successfully shown that the developed exoskeleton could control the step width of users through a simple linear controller, paving the way for robot-aided balance assistance focused on ML direction.

Although step width control using a mediolateral hip exoskeleton has been successfully validated, the impact of this control on balance and stability is unclear. Multiple studies investigated and reported how larger step width in populations with neuromuscular deficits affects the gait balance metrics [19]–[21] but the step width changes were volitional and not robot-induced. It is imperative to understand the relationship between exoskeleton-induced step width and balance, as this would have implications for balance assistance. To address this gap, the present study investigated how controlled step width, facilitated by a hip exoskeleton, influences mediolateral gait balance. In this study, we established the relationship between exoskeleton-controlled step width and 4 mediolateral gait balance metrics: trunk sway, margin of stability (MoS), net external moment, and step width variability which could better inform the research on improving the mediolateral gait balance using hip exoskeleton. The research in this paper could provide insights into the feasibility of balance enhancement using exoskeletons and guide controller development.

This project is funded by NIDILRR #90REGE0017, NC Biotechnology Center #2023-TRG-0009.

[1]Soe Lin Paing is with the Department of Mechanical and Aerospace Engineering, NC State University, Raleigh, NC, 27606, USA. spaing@ncsu.edu

[2]Abbas Alili is with the Department of Electrical Engineering, NC State University, Raleigh, NC, 27606, USA. aalili@ncsu.edu

[3]Varun Nalam and He (Helen) Huang are with the Joint Department of Biomedical Engineering, UNC-Chapel Hill and NC State University, Raleigh, 27606, USA. vnalam@ncsu.edu; hhuang11@ncsu.edu;

II. METHODS

The goal of this study is to analyze the impact of exoskeleton-controlled step width on different balance metrics, specifically in the mediolateral direction. To achieve this, we conducted a study involving non-disabled human participants wearing an exoskeleton during walking. The study details are described below:

A. Participants

Three healthy male participants (mean age: 30.3 $\pm$ 1.5 years, mean weight: 82 $\pm$ 9.8 kg, mean height: 1.75 $\pm$ 0.05 m), with no known history of neuromuscular disorders, were recruited for this study. The research protocol was approved by the University of North Carolina at Chapel Hill (# 13-3028), and informed consent was obtained from all participants before the experiment.

B. Experimental Hardware

This study utilized a hip abduction-adduction exoskeleton developed by the Neuromuscular Rehabilitation Engineering Laboratory (NREL) to control participants' step width during walking [16]. The exoskeleton is equipped with two Maxon EC-60 brushless motors paired with 100:1 harmonic gearboxes (CSD-20100-2A-GR-SP674, Harmonic Drive, MA, USA) that generate torque at the hip joints to assist with abduction-adduction movements. Additionally, it includes passive joints to allow unrestricted flexion and extension of the legs. The device is capable of delivering a continuous torque output of 34 Nm and a peak torque of 57 Nm. Interaction torque between the user and the robot is measured using cantilevered load cells connected in parallel with the actuators, enabling precise force control. Figure 1 illustrates the mediolateral hip exoskeleton, highlighting key components such as the actuators, sensors, and other essential elements. The exoskeleton's limbs were securely attached to the participants' thighs using fabric cuffs during use.

C. Control Architecture

The control architecture [22] as illustrated in Figure 2 was implemented to regulate the step width of participants using the hip abduction-adduction exoskeleton.

The admittance controller [23], modeled as a second-order dynamic system characterized by stiffness (K), damping (B), and inertia (I) parameters, was used for the human-robot interaction control. The interaction torque $\tau(t)$ is given by Equation 1.

$$\tau(t) = K(\theta(t) - \theta_{eq}) + B\dot{\theta}(t) + I\ddot{\theta}(t) \tag{1}$$

where $\tau(t)$ is the interaction torque, K is the stiffness, B is the damping, and I is the inertia parameters. $\theta(t)$, $\dot{\theta}(t)$ and $\ddot{\theta}(t)$ are the hip abduction-adduction angle, velocity, and acceleration, respectively, and θ_{eq} is the equilibrium angle. Since the motors are configured to receive velocity commands from the admittance controller, we first compute the acceleration using Equation 2.

$$\ddot{\theta}(t) = \frac{\tau(t) - K(\theta(t) - \theta_{eq}) - B\dot{\theta}(t)}{I} \tag{2}$$

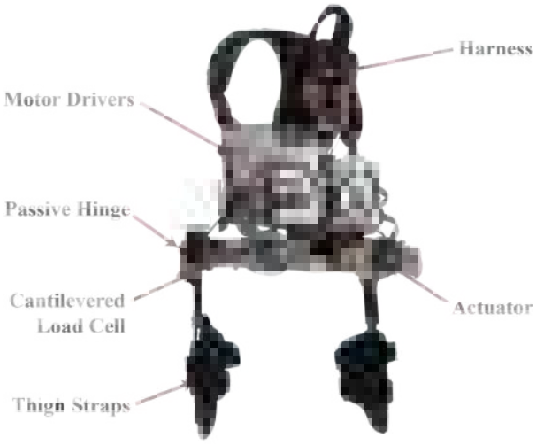


Fig. 1. Back view of the hip adduction-abduction exoskeleton with labeled components.

By integrating this acceleration, we obtain the corresponding velocity command to be sent to the motor in Equation 3.

$$\dot{\theta}(t) = \int_0^t \ddot{\theta}(\lambda)d\lambda \tag{3}$$

Throughout the trials, the equilibrium angle was kept constant at 15-degree abduction angle from the midline for both legs [17]. The admittance controllers were implemented separately for each motor in TwinCAT 3, operating at a frequency of 1 kHz. The admittance controller remains active throughout the entire gait cycle, applying torque to the legs during both the stance and swing phases [17].

Proportional-Integral-Derivative (PID) control was employed to regulate step width by adjusting the stiffness of the admittance controller based on step width error [18] using Equation 4 with the stiffness constrained between -10 Nm/rad and 80 Nm/rad.

$$K(t) = K_p e(t) + K_i \int_0^t e(\lambda)d\lambda + K_d \frac{de(t)}{dt} \tag{4}$$

where $K(t)$ represents the stiffness of the admittance control, $e(t)$ is the difference between the desired step width and the actual step width, and K_p, K_i, and K_d are proportional, integral, and derivative gains, respectively. However, achieving accurate control required manual fine-tuning of PID gains for each participant due to intersubject variability, a process that is both tedious and time-consuming. To overcome this challenge, a Deep Deterministic Policy Gradient (DDPG)-based Reinforcement Learning approach was introduced to dynamically update the PID gains and achieve optimal stiffness for admittance control [17]. The DDPG agent utilized input states including the desired step width, actual step width (measured using heel markers), the error signal (difference between desired and actual step width), and the integrated error signal. Using these inputs, the agent autonomously adjusted the PID gains every 2 seconds. Detailed descriptions of the architecture, training process, and implementation of the DDPG-based step width control

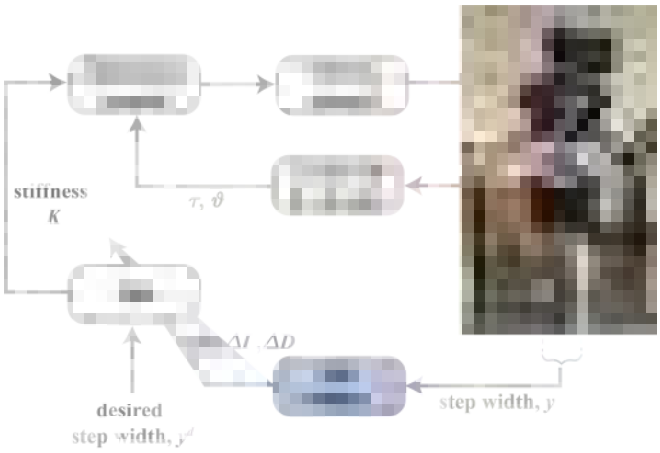


Fig. 2. Control framework for step-width modulation using the hip adduction-abduction exoskeleton. The RL DDPG agent controls step width (y) by adjusting the gains of the PID controller, which in turn regulates the stiffness (K) in the admittance control.

are available in [22]. This adaptive approach enhanced the exoskeleton's ability to achieve precise and efficient step width tracking across participants.

D. Experimental Setup

The setup includes the mediolateral exoskeleton, a motion capture system, and an instrumented split-belt treadmill. Participants began by donning the exoskeleton and having 38 retroreflective markers attached to their lower limbs, pelvis, and trunk. Their preferred walking speed was established by instructing them to walk on the instrumented treadmill while the exoskeleton operated in zero-stiffness mode where no external resistive or assistive torques were applied by the exoskeleton to the user's hip.

Following this, they underwent a 3-minute acclimation period walking with the exoskeleton still in zero stiffness control mode. During the experiment, three-dimensional kinematic data were collected at a sampling rate of 100 Hz using a VICON motion capture system (Oxford, U.K.) equipped with 12 cameras. Simultaneously, three-dimensional ground reaction force (GRF) data were recorded at 1000 Hz using the fully instrumented treadmill (Bertec Corp., Columbus, OH, USA).

E. Experimental Protocol

To establish the desired step widths for each participant, a baseline trial was conducted in which the participant walked on a treadmill at their preferred speed for two minutes with the exoskeleton operating in zero-stiffness mode. The average continuous step width during this trial was calculated and recorded as the baseline step width. Subsequently, the Deep Deterministic Policy Gradient (DDPG)-based controller was tuned to customize its parameters for each participant.

Based on the baseline step width, five desired step widths were defined as baseline step width, decreases of 20% and 10%, and increases of 20%, and 40% relative to the baseline. The selection of imbalanced desired step width levels (i.e., larger increases compared to decreases) was intentionally designed to minimize the risk of force plate crossing during narrower step widths. Force plate crossing can result in inaccurate measurements of ground reaction forces, compromising data reliability. The exoskeleton was then programmed to control the participant's step width to achieve each of these targets. Each trial lasted 2 minutes and was conducted twice for repeated measures, resulting in a total of 10 trials. The data recording was started only after the step width control reached a steady state. The order of the trials was completely randomized for each participant to mitigate potential bias. Sufficient rest was provided between trials to prevent fatigue.

F. Data Analysis

Kinematic data and ground reaction force (GRF) measurements were processed using a 4th-order Butterworth low-pass filter, with cutoff frequencies set at 10 Hz and 25 Hz, respectively. An 8-segment inverse dynamic model was developed in Visual3D software (C-Motion, Germantown, USA) to analyze key parameters, including the center of mass (CoM), the Center of Pressure (CoP), and gait events. To examine the relationship between step width and mediolateral gait balance, four mediolateral balance metrics were analyzed: (1) trunk sway, (2) margin of stability (MoS), (3) net external moment, and (4) step width variability.

In this study, step width was defined as the continuous displacement of heel markers between the left and right legs, rather than step width at heel strike, as the exoskeleton directly controlled this measure. Trunk sway in the frontal plane was quantified as the peak-to-peak displacement of a marker placed on the C7 vertebra, following the method outlined in [24], [25]. The margin of stability (MoS) was calculated using the method described by Hof et al. [26]. Net external moment was computed based on the approach described by Neptune et al. [20]. Step width variability was quantified as the standard deviation of the step width throughout the trial [27].

G. Statistical Analysis

A linear mixed-effects model was employed to assess the effects of step width on each gait balance metric [28]. Step width, treated as a continuous variable, was included as a fixed factor, while participant identity was modeled as a random factor to account for individual variability in the balance metrics. Before fitting the model for each balance metric, key assumptions of the linear mixed-effects model—including linearity, homoscedasticity, normality, and independence of errors—were evaluated to ensure the validity of the analysis.

III. Results

The results presented below illustrate the effects of exoskeleton-controlled step width on four mediolateral gait balance metrics: trunk sway, Margin of Stability (MoS), net external moment, and step width variability. In the accompanying figures, data points are distinguished by symbols representing the three participants: gray squares for Subject 1, green circles for Subject 2, and blue triangles for Subject 3.

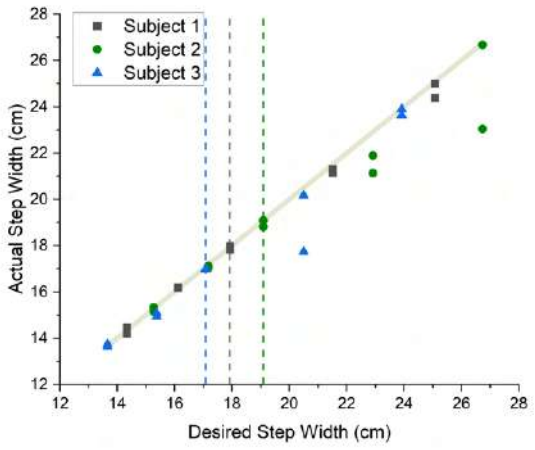


Fig. 3. The performance of step width control. The solid gray line depicts the ideal scenario where the participants' step width track the desired step width accurately. The vertical dashed lines denote each participant's preferred step width, as determined during the baseline trial. Each x-axis position contains two data points, representing the two trials conducted for each condition.

This visualization highlights both individual variability and overarching trends across the metrics.

A. Step Width Control

The exoskeleton effectively controlled participants' step widths in most trials, achieving high accuracy. As illustrated in Figure 3 which showcases the step width across all 10 trials. The average step width error across all trials was 0.46 cm, with a maximum deviation of 3.7 cm. This demonstrates the exoskeleton's ability to maintain step width control within a small margin of error relative to the desired values.

B. Trunk Sway

Trunk sway serves as an indicator of upper body stability and control during walking, providing insights into dynamic balance and postural regulation. As shown in Figure 4(a), trunk sway increased with an increase in step widths. Analysis using a linear mixed-effects model revealed that the effect of step width on trunk sway was statistically significant ($p < 0.0001$), with an R^2 value of 0.97954, indicating a strong relationship. The slope estimates and their corresponding confidence intervals are detailed in Table I.

C. Margin of Stability

The Margin of Stability (MoS) in the mediolateral direction quantifies the distance between the body's extrapolated Center of Mass (xCOM) and Center of Pressure (CoP) in the frontal plane, serving as a measure of the ability to maintain or recover balance during gait [26]. As depicted in Figure 4(b), the MoS also increased with an increase in step widths. Analysis using a linear mixed-effects model confirmed that the relationship between step width and MoS was statistically significant ($p < 0.0001$), with an R^2 value of 0.8948, indicating a strong association.

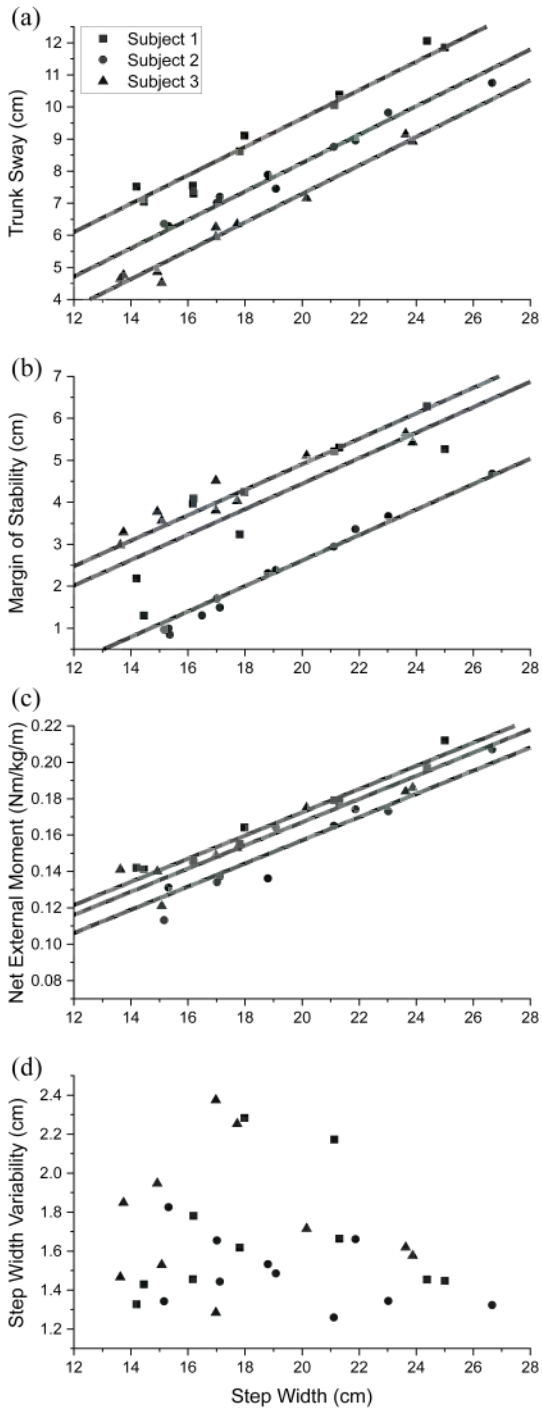


Fig. 4. Relationship between step width and gait balance metrics. (a) Trunk sway. (b) Margin of Stability. (c) Net external moment. (d) Step width variability. Fitted lines account for the random effect specific to each individual.

D. Frontal Plane Net External Moment

The net external moment represents the external forces acting on the body, providing insight into the mechanical effort required to maintain balance during gait. The frontal plane net external moment, normalized by participants' weight and height, is shown in Figure 4(c). Two trials from Subject 2 were excluded due to consistent cross strikes, where the

subject's foot landed across the boundary of two adjacent force plates. This led to inaccurate force measurements, as the data for left and right forces could not be reliably distinguished. The linear mixed-effects model revealed that step width had a statistically significant effect on the net external moment ($p < 0.0001$), with an R^2 value of 0.91884. This indicates a strong relationship between step width and the mechanical demands of maintaining balance.

E. Step Width Variability

Step width variability, which quantifies the consistency of step width during walking, serves as an indicator of stability and control in lateral balance. However, analysis using the linear mixed-effects model did not identify a significant linear relationship between step width variability and step width as shown in the 4(d). This suggests that controlling the step width using the hip exoskeleton does not directly impact the consistency either positively or negatively during gait under the conditions tested.

TABLE I
SUMMARY OF LINEAR MIXED-EFFECTS MODEL RESULTS FOR GAIT BALANCE METRICS

Gait Balance Metrics	***Model Estimate***	***p value***	R^2
Trunk Sway	0.4424	4.91e-21	0.9795
Margin of Stability	0.3034	4.95e-12	0.8948
Net External Moment	0.0064	2.3e-14	0.9188
Step Width Variability	-0.0108	0.4894	0.1160

IV. DISCUSSION

Step width is one of the key strategies for maintaining frontal plane stability during human gait. Populations with neuromuscular disorders often struggle to effectively control their step width, resulting in diminished mediolateral stability. This study shows how a mediolateral hip exoskeleton can influence balance metrics by modulating step width. While previous studies have examined gait balance metrics in individuals with neuromuscular disorders, often noting differences such as larger step widths and altered balance metrics compared to healthy populations [20], [21], no research to date has explored the specific effects of exoskeleton-controlled step width on mediolateral gait balance metrics. Studying whether the exoskeleton-assisted response aligns with or differs from human volitional behavior is crucial, as the findings could have significant implications for control development, rehabilitation strategies, and the understanding of the human neuromuscular system.

The results demonstrated that step width significantly influences mediolateral stability, as reflected by investigating the specified gait balance metrics. Each of these balance metrics focuses on a different aspect of balance. Reduced trunk sway and net external moment could reduce the energy required to stabilize individuals but could make individuals vulnerable to external perturbations. Increased MoS could help in reducing the effects of unexpected perturbations and thereby improving stability.

Trunk sway, Margin of Stability (MoS), and net external moment all increased with larger step widths across participants. While a larger step width enhances frontal plane stability by increasing the MoS, it simultaneously results in greater trunk sway and higher net external moments, indicating increased mechanical effort and upper body movement. This suggests that optimizing mediolateral stability requires a trade-off among MoS, trunk sway, and net external moment to achieve a balanced gait without resulting in high energetic costs. Step width variability, which reflects the consistency of foot placement, showed no apparent linear relationship with step width in this study. This indicates that controlled variations in step width did not negatively impact gait stability, as no destabilizing effects were observed in terms of variability. It could also imply that the torque interactions from the exoskeleton were not perceived as a disturbance by the individuals.

In the observed results, specifically, the net external moment showed similar trends to that observed in [19]. This could imply that the neuromuscular behavior of the individuals in both studies is similar with the exoskeleton contributing to the energy required to increase the step width rather than changing the mechanism by which wider step width is achieved. These results, therefore, imply that we can reduce the additional energetic exertion of ensuring balance through step width modulation implemented through this exoskeleton.

The use of a linear mixed-effects model in this study was motivated by the need to account for both fixed effects such as step width and random effects (individual variability among participants). This modeling approach allows us to capture the linear relationship between step width and gait balance metrics, and our experimental data exhibit a strong and statistically significant linear trend ($p < 0.0001$) across three gait balance metrics: trunk sway, margin of stability, and net external moment. Additionally, the linear mixed-effects model was chosen to analyze the relationship between step width and step width variability to assess whether the exoskeleton's control over step width had any destabilizing effects on gait stability. Although more complex relationships, such as nonlinearity and phase-dependent variations, could provide additional insights, our primary objective was to assess the overall trend in a robust and interpretable manner.

The limited sample size in this study poses challenges in establishing a definitive model that is generalizable to the broader healthy population. Additionally, the observed gait balance metrics results are likely influenced by the behavior of the torque applied to the hip joint by the exoskeleton. It is reasonable to hypothesize that variations in control mechanisms, such as different strategies for torque application or stiffness modulation, could result in differing effects on mediolateral gait balance. Future studies with larger and more diverse participant samples, as well as investigations into alternative control approaches, are essential to better understand these dynamics and enhance the generalizability of the findings. Additionally, further investigations of the

approach on people with balance deficits are essential to validate this approach as healthy individuals may have the ability to mitigate adverse effects of the applied torques, which people with balance deficits could not.

The preliminary results highlight the effects of controlled step width on gait balance in able-bodied individuals. These findings provide valuable insights that could inform the design and control strategies of exoskeletons aimed at enhancing mediolateral gait balance in populations with gait impairments. By understanding how step width modulation impacts balance metrics, future exoskeleton design and control architecture can be tailored to address specific needs, potentially improving stability and mobility for individuals with balance-related gait disabilities.

REFERENCES

[1] A. Shumway-Cook, "Motor control: Translating research into clinical practice," *Lippincoot Williams & Wilkins*, 2007.

[2] D. L. Sturnieks, R. St George, and S. R. Lord, "Balance disorders in the elderly," *Neurophysiologie Clinique/Clinical Neurophysiology*, vol. 38, no. 6, pp. 467–478, 2008.

[3] A. Ehrhardt, P. Hostettler, L. Widmer, K. Reuter, J. A. Petersen, D. Straumann, and L. Filli, "Fall-related functional impairments in patients with neurological gait disorder," *Scientific reports*, vol. 10, no. 1, p. 21120, 2020.

[4] A. D. Kuo, "Stabilization of Lateral Motion in Passive Dynamic Walking," *The International Journal of Robotics Research*, vol. 18, no. 9, pp. 917–930, Sep. 1999, publisher: SAGE Publications Ltd STM.

[5] S. Morrison, C. A. Rynders, and J. J. Sosnoff, "Deficits in mediolateral balance control and the implications for falls in individuals with multiple sclerosis," *Gait & Posture*, vol. 49, pp. 148–154, Sep. 2016.

[6] S. M. Bruijn and J. H. Van Dieën, "Control of human gait stability through foot placement," *Journal of The Royal Society Interface*, vol. 15, no. 143, p. 20170816, Jun. 2018.

[7] D. Winter, "Human balance and posture control during standing and walking," *Gait & Posture*, vol. 3, no. 4, pp. 193–214, Dec. 1995.

[8] M. Arvin, J. H. van Dieën, and S. M. Bruijn, "Effects of constrained trunk movement on frontal plane gait kinematics," *Journal of Biomechanics*, vol. 49, no. 13, pp. 3085–3089, Sep. 2016.

[9] C. E. Bauby and A. D. Kuo, "Active control of lateral balance in human walking," *Journal of Biomechanics*, vol. 33, no. 11, pp. 1433–1440, Nov. 2000.

[10] B. L. Rankin, S. K. Buffo, and J. C. Dean, "A neuromechanical strategy for mediolateral foot placement in walking humans," *Journal of Neurophysiology*, vol. 112, no. 2, pp. 374–383, Jul. 2014, publisher: American Physiological Society.

[11] L. Hak, H. Houdijk, P. Van Der Wurff, M. R. Prins, A. Mert, P. J. Beek, and J. H. Van Dieën, "Stepping strategies used by post-stroke individuals to maintain margins of stability during walking," *Clinical biomechanics*, vol. 28, no. 9-10, pp. 1041–1048, 2013.

[12] A. Skiadopoulos, E. E. Moore, H. R. Sayles, K. K. Schmid, and N. Stergiou, "Step width variability as a discriminator of age-related gait changes," *Journal of neuroengineering and rehabilitation*, vol. 17, pp. 1–13, 2020.

[13] C. L. Lewis and D. P. Ferris, "Invariant hip moment pattern while walking with a robotic hip exoskeleton," *Journal of Biomechanics*, vol. 44, no. 5, pp. 789–793, Mar. 2011.

[14] M. K. Ishmael, A. Gunnell, K. Pruyn, S. Creveling, G. Hunt, S. Hood, D. Archangeli, K. B. Foreman, and T. Lenzi, "Powered Hip Exoskeleton Reduces Residual Hip Effort Without Affecting Kinematics and Balance in Individuals With Above-Knee Amputations During Walking," vol. 70, no. 4, pp. 1162–1171. [Online]. Available: https://ieeexplore.ieee.org/abstract/document/9910473

[15] D. D. Molinaro, K. L. Scherpereel, E. B. Schonhaut, G. Evangelopoulos, M. K. Shepherd, and A. J. Young, "Task-agnostic exoskeleton control via biological joint moment estimation," *Nature*, vol. 635, no. 8038, pp. 337–344, Nov. 2024.

[16] V. Nalam, A. Alili, A. Fleming, X. Tu, M. Liu, and H. Huang, "Development of a hip abduction-adduction exoskeleton for mediolateral assistance," *techrxiv*, Mar. 2024.

[17] A. Alili, A. Fleming, V. Nalam, M. Liu, J. Dean, and H. Huang, "Abduction/Adduction Assistance From Powered Hip Exoskeleton Enables Modulation of User Step Width During Walking," *IEEE Transactions on Biomedical Engineering*, vol. 71, no. 1, pp. 334–342, Jan. 2024, conference Name: IEEE Transactions on Biomedical Engineering.

[18] A. Alili, V. Nalam, A. Fleming, M. Liu, J. Dean, and H. He Huang, "Closed-Loop Feedback Control of Human Step Width During Walking by Mediolaterally Acting Robotic Hip Exoskeleton," in *2023 IEEE/RSJ International Conference on Intelligent Robots and Systems (IROS)*, Oct. 2023, pp. 6097–6102, iSSN: 2153-0866.

[19] L. K. Molina, G. H. Small, and R. R. Neptune, "The influence of step width on balance control and response strategies during perturbed walking in healthy young adults," *Journal of Biomechanics*, vol. 157, p. 111731, Aug. 2023.

[20] R. R. Neptune and A. Vistamehr, "Dynamic Balance During Human Movement: Measurement and Control Mechanisms," *Journal of Biomechanical Engineering*, vol. 141, no. 7, pp. 0 708 011–07 080 110, Jul. 2019.

[21] A. Vistamehr, S. A. Kautz, M. G. Bowden, and R. R. Neptune, "Correlations between measures of dynamic balance in individuals with post-stroke hemiparesis," *Journal of Biomechanics*, vol. 49, no. 3, pp. 396–400, Feb. 2016.

[22] A. Alili, V. Nalam, J. Tacca, M. Liu, J. Si, and H. Huang, "Towards advancing mediolateral gait balance by hip exoskeletons: A reinforcement learning-based approach for proactive step width control," Feb. 2024.

[23] A. Q. Keemink, H. Van der Kooij, and A. H. Stienen, "Admittance control for physical human–robot interaction," *The International Journal of Robotics Research*, vol. 37, no. 11, pp. 1421–1444, 2018.

[24] J. McLoughlin, C. Barr, M. Crotty, S. R. Lord, and D. L. Sturnieks, "Association of Postural Sway with Disability Status and Cerebellar Dysfunction in People with Multiple Sclerosis," *International Journal of MS Care*, vol. 17, no. 3, pp. 146–151, 2015.

[25] J. F. Marsden, D. E. Playford, and B. L. Day, "The vestibular control of balance after stroke," *Journal of Neurology, Neurosurgery & Psychiatry*, vol. 76, no. 5, pp. 670–679, May 2005, publisher: BMJ Publishing Group Ltd Section: Paper.

[26] A. L. Hof, "The 'extrapolated center of mass' concept suggests a simple control of balance in walking," *Human Movement Science*, vol. 27, no. 1, pp. 112–125, Feb. 2008.

[27] A. Skiadopoulos, E. E. Moore, H. R. Sayles, K. K. Schmid, and N. Stergiou, "Step width variability as a discriminator of age-related gait changes," *Journal of NeuroEngineering and Rehabilitation*, vol. 17, no. 1, p. 41, Mar. 2020.

[28] A. Alili, V. Nalam, J. R. Tacca, and H. H. Huang, "Exploring the impact of continuous mediolateral torque application by hip exoskeleton on the gait balance of non-disabled individuals," *2024 46th Annual International Conference of the IEEE Engineering in Medicine and Biology Society (EMBC)*, pp. 1–4, 2024.

Analysis of Forces Exerted by Shoulder and Elbow Fabric-based Pneumatic Actuators for Pediatric Exosuits

Mehrnoosh Ayazi,[1] Ipsita Sahin,[2] Caio Mucchiani,[1] Elena Kokkoni,[2] and Konstantinos Karydis[1]

***Abstract*— To enhance pediatric exosuit design, it is crucial to assess the actuator-generated forces. This work evaluates the contact forces exerted by soft fabric-based pneumatic actuators in an upper extremity pediatric exosuit. Two actuators were examined: a single-cell bidirectional actuator for shoulder abduction/adduction and a bellow-type actuator for elbow extension/flexion. Experiments assessed the impact of actuator anchoring points and the adjacent joint's angle on exerted forces and actuated joint range of motion (ROM). These were measured via load cells and encoders integrated into a custom infant-scale engineered apparatus with two degrees of freedom (two revolute joints). For the shoulder actuator, results show that anchoring it further from the shoulder joint center while the elbow is flexed at 90° yields the highest ROM while minimizing the peak force exerted on the body. For the elbow actuator, anchoring it symmetrically while the shoulder joint is at 0° optimizes actuator performance. These findings contribute a key step toward co-optimizing the considered exosuit design for functionality and wearability.**

I. Introduction

Soft exosuits have shown significant promise in assistance, rehabilitation, and human augmentation across diverse applications. Existing efforts have targeted lower limb mobility, such as in walking [1], hip motion [2], knee function [3], [4], and ankle support [5], as well as upper limb mobility, including assistance at the shoulder joint [6], [7], elbow support [8], [9], wrist support [10], and hand function [11]. The vast majority of these efforts consider adult users; limited attention to devices specifically designed for children, particularly those that assist upper extremity (UE) movement in very young children, has been provided so far [12]–[14]. Given the potential of assistive technology to improve motor function [15], more research is needed in pediatric exosuits.

A key measure of exosuit performance is the force generation capability which has been examined mainly on devices aimed at adults [16]–[20]. Both the magnitude and direction of the exerted (contact) forces, as well as their point of application play a role. Excessive or improperly targeted amounts of force (or pressure) can restrict natural movement and cause skin problems, circulation problems, and injuries [16], [21]–[23], ultimately resulting in discomfort and reduced acceptance of the device [24]. As such, detailed profiling of contact forces can provide insight into actuator limitations and dynamic behaviors which in turn can be used to improve the device and its underlying controllers (e.g., [25], [26]). The *desired* force generation capacity of an exosuit is typically determined by the intended task and type of motion assistance (e.g., whole-arm reaching, fine manipulation), thereby guiding component selection and system design. The *achieved* force generation capacity is determined by multiple factors, crucially including among them the anchoring points of the actuators.

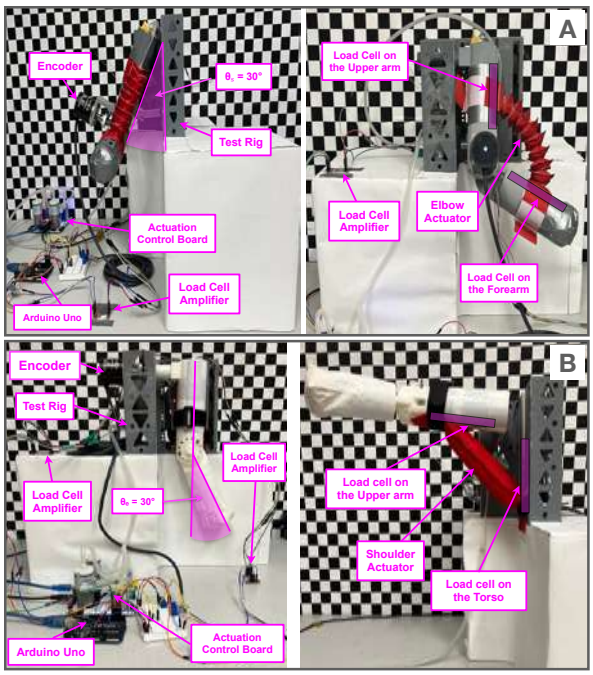


Fig. 1. Experimental setup for force profiling of a fabric-based pneumatic (A) shoulder and (B) elbow actuator. The setup allows various actuator anchoring points and non-actuated joint angle settings (locked in place).

The actuator anchoring points relative to the body can significantly influence joint kinematics and kinetics by facilitating force transfer to the body and stabilizing the body-exosuit interaction [27]–[30]. Our previous work [31] assessed the effect of varying the anchoring points of several different pneumatic actuators on end-effector kinematics, enabling an informed selection of the actuators used herein. A single-cell inflatable actuator [32] for the shoulder led to greater range of motion (ROM) and end-effector path length, while a 10-cell bellow-type actuator [33] with square cells was more appropriate for the elbow in terms of maximizing ROM. In both cases, kinematic performance (i.e. ROM, motion smoothness, etc.) was improved when the anchoring points intersect along the mid-auxiliary line of the body [31]. However, the previous work did not assess joint kinetics and the exerted forces on the body as anchoring points vary.

[1] Dept. of Electrical and Computer Engineering; [2] Dept. of Bioengineering, University of California, Riverside, 900 University Ave, Riverside, CA 92521, USA. Email:{mayaz004, isahi001, caiocesr, elenak, karydis}@ucr.edu. We gratefully acknowledge the support of NSF # CMMI-2133084. Any opinions, findings, and conclusions or recommendations expressed in this material are those of the authors and do not necessarily reflect the views of the National Science Foundation.

The goal of this paper was to assess the exerted forces from the aforementioned actuators on the torso, upper arm, and forearm of an engineered apparatus based on 12-month-old infant anthropometrics (Fig. 1). In addition, a preliminary assessment of the underlying relation between input pressure and exerted forces is provided for future automatic controller design. Experiments involved one joint's actuator being active while the other joint remained locked in place at different points. We analyzed the exerted forces and the actuated joint's ROM under varying the active actuator anchoring points and the non-actuated joint's locked angle value. Results reveal optimal actuator anchoring points and the cases where exerted forces are minimized and ROM is maximized for the same actuator input pressure. Taken together with our previous findings [31], this work provides key information about how to place actuators onto a soft pediatric exosuit to improve its function.

II. Materials and Methods

A. Experimental Setup

Two types of soft, fabric-based pneumatic actuators were selected for their range of motion, ease of manufacturing, and durability. A single-cell rectangular actuator [32] was used for shoulder abduction/adduction (achieved through inflation/deflation, respectively, with deflation-driven adduction due to reduced upper arm support). Elbow flexion/extension was facilitated via inflation and deflation, respectively, of a 10-cell bellow-type actuator [33].

Two 3D-printed test rigs (Fig. 1) were designed based on anthropometric data of 12-month-old infants in the 50th percentile [34], [35]. Each rig was configured to support a specific type of actuator (either shoulder or elbow) to study their individual force profiles. Both rigs consist of a base as the torso, an upper arm (UA), a forearm (FA), and a small part weighing 0.06 kg attached at the end of the FA in lieu of the hand. The UA (16.4 cm in length, 14.7 cm in circumference) was connected to the torso via a revolute joint, effectively allowing for shoulder adduction and abduction. The FA (10.85 cm in length and 14.51 cm in circumference) was attached to the UA through another revolute joint, allowing for elbow flexion and extension. Both UA and FA segments were hollow and filled in with sandbags to match a desired UE weight. The combined weight of UA and FA was set at 0.432 kg, based on anthropometrics of an infant of total body mass of 10.8 kg [36].

The primary distinction between the two rigs lies in the positioning of sensors, which are used to measure the normal force generated by the actuator as well as the respective joint angle.[1] Each test rig incorporated two load cells (YZC-133) with a capacity of 5 kg to gauge the contact force exerted by the actuators on the UA, torso, or FA. The placement of these load cells was determined based on the impact area of the actuator during operation. The shoulder actuator exerts forces on the torso and UA. In the rig designed for the shoulder actuator, one load cell was situated within the UA, aligned with the vertical centerline on its inner side. This load cell was coupled with a plate measuring 11.1×1.36 cm to effectively capture the force applied over the area covered by the plate. The second load cell was positioned at the torso of the rig, also aligned with the vertical centerline on the inner side facing the UA, and was attached to a 15.6×1.66 cm plate. Conversely, the elbow actuator exerts forces on the UA and FA. In the respective test rig, the load cells were installed and aligned with the UA and FA vertical centerlines on the front side. The plates connected to these load cells measured 11.6×1.66 cm for the UA and 8.85×1.66 cm for the FA. Each load cell was connected to an amplifier (HX711, Sparkfun) to convert the output data into a readable format at a frequency of 11 Hz, ultimately linked to the ADC pin of a microcontroller board (Arduino UNO). Additionally, a 1024 pulse per revolution rotary encoder (E6B2, Sparkfun) was integrated into the actuated joint to measure the respective joint angle. Encoder data were collected with the use of the microcontroller. The latter transmitted all collected data (amplified load cell and rotary encoder data) to a host computer for data logging and follow-on analysis.

The inflation and deflation of the actuators were managed using an external pneumatic board (Programmable-Air kit). This board features two compressor/vacuum pumps and three pneumatic valves to control the airflow at a rate of 2 L/min. The airflow is adjusted through the pump duty cycle in $[0 - 100]\%$. The pressure can vary between $[-50, 50]$ kPa. The board is equipped with a pressure sensor (SMPP-03) and its own microcontroller (Arduino Nano). The integrated Arduino allows for connectivity to the host computer via a serial-to-USB interface, enabling users to send commands to the pumps and valves and to log sensor data.

B. Experimental Protocol

A series of experiments were conducted to explore how two key elements affect joint ROM and force exertion of each actuator on the test rigs. The first element pertains to variations in the anchoring of the actuators. Two anchoring configurations were tested for the shoulder actuator: one at two-thirds (S1) and the other at one-half (S2) of the UA length, measured from its proximal end (Fig. 2A left panel). The other end of the actuator was attached to the torso. Three anchoring configurations were tested for the elbow actuator based on the distribution of the actuator's cells along the UA and FA: one symmetric (E2) and two asymmetric configurations (E1 and E3). In the E1 configuration, more cells extended on the UA (about 60%) than on the FA, while the opposite was true in E3. In E2, there was a symmetrical distribution of cells on both segments (Fig. 2B left panel). The second element refers to the effect the non-actuated joint being locked in place at different points can have on the active joint's ROM and force exertion of the actuators.

[1] By virtue of this work's actuator mechanical design and placement along the body's mix-auxiliary line, the normal force component is the one primarily contributing to mechanical work associated with the intended motion support as compared to a small but still present shear force component. For this reason, we prioritized the measurement and analysis of normal forces. The inclusion of shear forces is part of future work, as we delve into further motion support (e.g., shoulder flexion/extension).

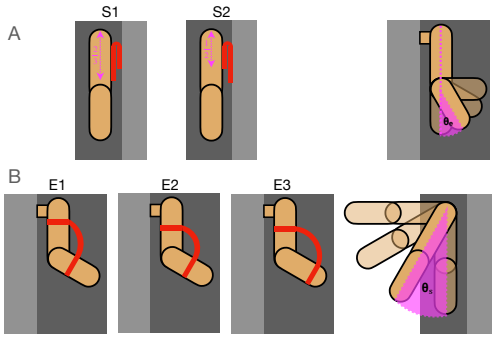


Fig. 2. (A) Schematic diagram of shoulder actuator anchoring: Two anchoring points (S1 at two-thirds and S2 at one-half of the upper arm length from the proximal end) and four fixed elbow angles (0°, 30°, 60°, and 90°). (B) Schematic diagram of elbow actuator anchoring: Twelve configurations with three anchoring points (E1, E2, E3) and four fixed shoulder angles (0°, 30°, 60°, and 90°). E1: Actuator cells distributed 6:4 (UA:FA), with attachment points at two-thirds (UA) and one-half (FA) of their lengths. E2: Cells distributed 1:1, with both attachment points at one-half of their lengths. E3: Cells distributed 4:6, with attachment points at one-half (UA) and four-fifths (FA) of their lengths. Actuators shown in thick (red) curves.

One of the test rigs allowed the elbow joint to be locked at four angles, $\theta_e \in \{0°, 30°, 60°, 90°\}$ (Fig. 2A right panel), while the other featured shoulder joint locking at four angles, $\theta_s \in \{0°, 30°, 60°, 90°\}$ (Fig. 2B right panel).

A total of 30 trials were performed for each configuration. Load cells and encoders integrated into the test rigs measured the exerted force and the angular displacement throughout each trial. Further, input pressure was collected from the pressure sensor on the pneumatic board. Before each trial, the load cell was set to zero with the actuator anchored but not actuated (to ensure that measured forces resulted solely from the actuation during the trials). Each trial for the shoulder actuator lasted 10 sec, consisting of a 5-sec inflation phase followed by a 5-sec deflation phase. The elbow actuator trials also lasted 10 sec each, containing a 5-sec deflation phase followed by 5 sec of inflation. To enable these 5-sec actuation phases, the pumps operated at a 100% duty cycle. [2]

C. Variables of Interest and Statistical Analysis

The computed variables were joint ROM (for both shoulder and elbow joints) and peak force exerted by each actuator on the relevant body segment. To assess how the actuator anchoring configurations and non-actuated locked joint angles affected these two variables, a series of separate non-parametric tests was performed for each factor and actuator (violation of normality was confirmed with the Kolmogorov-Smirnov test). For the shoulder actuator, Mann-Whitney U tests were conducted to identify significant differences in shoulder joint ROM and peak force between the two shoulder actuator anchoring configurations (S1, S2). Kruskal-Wallis H tests were performed to evaluate differences in shoulder joint ROM and peak force across the four non-actuated elbow joint locked angles θ_e. For the elbow actuator, Kruskal-Wallis H tests were conducted to assess significant differences in elbow joint ROM and peak force across the elbow actuator anchoring configurations (E1, E2, E3). Lastly, Kruskal-Wallis H tests were performed to evaluate differences in elbow joint ROM and peak force across the four non-actuated shoulder joint locked angles θ_s. Post-hoc pairwise comparisons were conducted as needed. The significance level at 0.05 was Bonferroni-adjusted to account for multiple comparisons. Statistical analyses were conducted with SPSS v.30.

[2] Achieving rapid actuation is important since infant reaching at this age can be fast, typically lasting about two sec [37]. Here we used 5-sec phases to facilitate analysis. However, as we will show shortly, the actuators can reach maximum ROM within three and two sec for the shoulder and elbow respectively, thus making the exosuit appropriate for our target application.

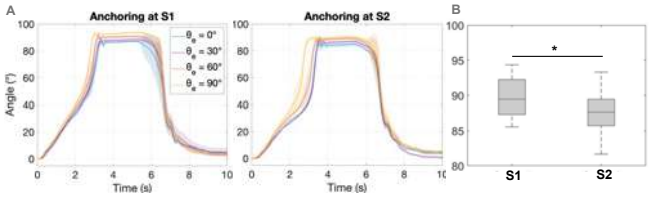


Fig. 3. (A) Changes in shoulder joint angle over time in the two shoulder actuator anchorings for different locked elbow angles. Shaded areas represent one standard deviation. (Best viewed in color.) (B) Boxplot comparing the shoulder joint angle between the S1 and S2 configurations.

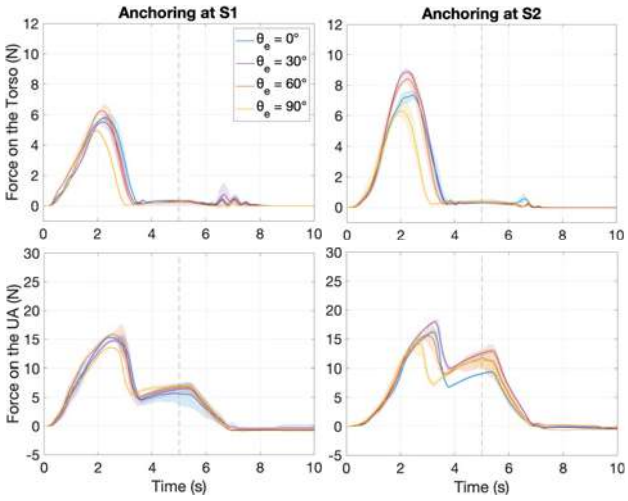


Fig. 4. Temporal evolution of the forces exerted by the shoulder actuator on the torso (Top) and UA (Bottom) for the two shoulder actuator anchorings and different locked elbow angles.

III. Results and Discussion

A. Shoulder Actuator Assessment

The change in shoulder joint angle throughout the trial and across the different non-actuated elbow joint angles for both shoulder actuator anchoring configurations is depicted in Fig. 3A. Overall, shoulder joint ROM was greater in S1 than S2 ($U = 4184$, $p < 0.001$; Fig. 3B). There was an effect of non-actuated elbow joint locked angles on ROM for both S1 ($\chi^2(3) = 102.281$, $p < 0.001$) and S2 ($\chi^2(3) = 83.999$, $p < 0.001$) configurations. Post-hoc tests demonstrated that locking the elbow angle at 60° and 90° leads to a greater shoulder joint ROM than being locked at 0° and 30° for both anchoring configurations ($p < 0.001$ for all comparisons).

The temporal evolution of the forces exerted by the shoulder actuator on the torso and UA across all pertinent configurations is illustrated in Fig. 4. When the actuator was anchored at S1, the peak force was exerted on the torso at 2.19 ± 0.15 sec and on the UA at 2.6 ± 0.18 sec.

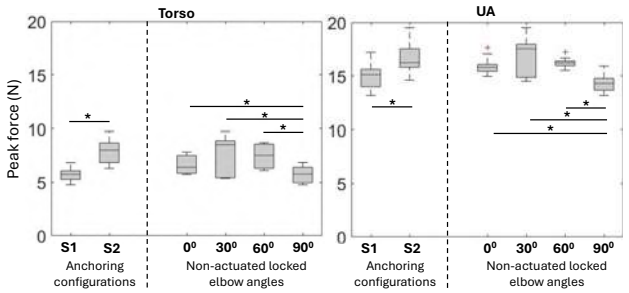


Fig. 5. Boxplots of the exerted peak force for the shoulder actuator on the torso and UA. Results show significant performance differences owing to different actuator configurations and non-actuated locked elbow angles.

When the actuator was anchored at S2, the peak force was exerted on the torso at 2.27 ± 0.15 sec and on the UA at 3.07 ± 0.25 sec. Statistical analysis showed a greater peak force exerted on the torso and UA in the S2 configuration compared to S1, regardless of the non-actuated elbow locked angle ($U_{\text{Torso}} = 13997.500$, $p < 0.001$; $U_{\text{UA}} = 11512.500$, $p < 0.001$); Fig. 5). In addition, the peak force exerted on the torso and UA was significantly different across the non-actuated elbow joint locked angles ($\chi^2{}_{\text{Torso}}(3) = 48.389$, $p < 0.001$; $\chi^2{}_{\text{UA}}(2) = 114.489$, $p < 0.001$). Post-hoc tests showed that locking the elbow at $90°$ leads to a lower peak force both on the torso and UA compared to the other three cases ($p < 0.001$ for all comparisons; Fig. 5). Visual inspection of Fig. 6 suggests that exerted forces appear to vary nonlinearly with the input pressure. When the actuator was anchored at S1, the peak forces on the UA and torso were observed at 16.73 ± 1.54 kPa and 13.45 ± 1.73 kPa, respectively. When the actuator was anchored at S2, the peak forces on the UA and torso were observed at 20 ± 2.44 kPa and 15.1 ± 2.03 kPa, respectively.

The previous results altogether allow for the following observations to be made. In configuration S1, ROM is larger and the peak force is smaller compared to S2. This can be explained by the fact that, when the actuator is placed farther from the shoulder joint center along the UA, the moment arm between its force application point on the UA and the shoulder joint increases. This helps generate more torque for the same actuator pressure. Similarly, when the elbow is mostly flexed (i.e. for $\theta_e = \{60°, 90°\}$) the moment arm between the center of mass of the FA and the shoulder joint's axis of rotation decreases. This reduces the mechanical work required for rotation for the same input pressure thereby increasing shoulder joint ROM. Lastly, it is worth noting that when the single-cell actuator is mounted onto the rig, it is folded into two sections that behave as separate cells initially. During inflation, these sections push outward, increasing force on both the torso and UA. Around mid-inflation, they merge into a single cell causing a discontinuity in the exerted force as well as a reduction in contact with the areas covered by load cells in both the torso (mainly) and UA. This effect may have led to the observed nonlinearities.

B. Elbow Actuator Assessment

The change in elbow joint angle throughout the trial and across the different non-actuated shoulder joint locked angles

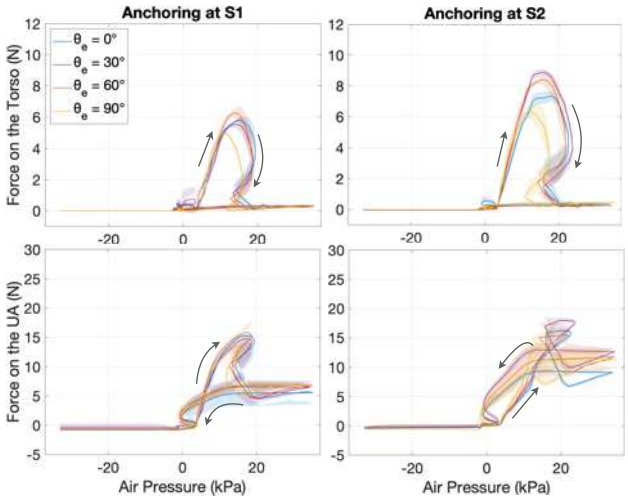


Fig. 6. Evolution of the shoulder actuator forces exerted on the torso (Top) and UA (Bottom) as the internal air pressure of the actuator varies, at different conditions. Arrows demonstrate the inflation-deflation cycle.

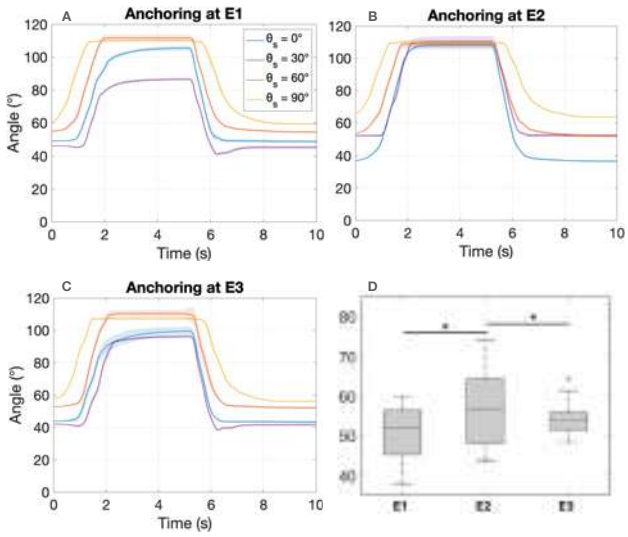


Fig. 7. (A, B, C) Changes in elbow joint angle over time in the three elbow actuator anchorings for different locked shoulder angles. (D) Boxplot showing elbow joint angles across the E1, E2, and E3 configurations.

for all elbow actuator anchoring configurations is depicted in Fig. 7 (A-C). Statistical analysis revealed that the elbow joint ROM was significantly different across the elbow actuator anchoring configurations ($\chi^2(3) = 28.580$, $p < 0.001$; Fig. 7D), with a greater ROM observed for E2 compared to E1 ($p < 0.001$) and E3 ($p = 0.012$). There was a statistically significant effect of non-actuated shoulder joint locked angles on the elbow joint ROM for the three elbow actuator anchoring configurations (E1: $\chi^2(3) = 101.544$, $p < 0.001$; E2: $\chi^2(3) = 102.782$, $p < 0.001$; E3: $\chi^2(3) = 83.809$, $p < 0.001$). Post-hoc tests showed that the smallest elbow joint ROM was observed at a locked shoulder joint angle of $90°$ for the E2 and E3 elbow actuator anchoring configurations, but not for E1 which was at a locked joint angle of $30°$ ($p < 0.001$ for all comparisons).

The temporal evolution of the forces exerted by the elbow actuator on the UA and FA for the three elbow actuator configurations and across the different non-actuated shoulder

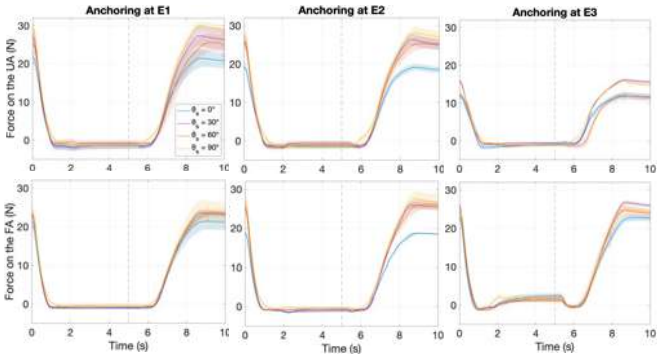


Fig. 8. Temporal evolution of the forces exerted by the elbow actuator on the UA (Top) and FA (Bottom) in all pertinent configurations.

joint locked angles is illustrated in Fig. 8. When the actuator was anchored at E1, the peak forces were exerted on the UA and FA at 8.51 ± 0.29 sec and 8.66 ± 0.34 sec, respectively. When anchored at E2, the peak forces were exerted on the UA and FA at 8.45 ± 0.26 sec and 8.53 ± 0.28 sec, respectively. In the E3 configuration, the peak forces were exerted on the UA and FA at 8.29 ± 0.21 sec and 8.45 ± 0.32 sec, respectively. Statistical analysis revealed that the peak force exerted on the UA and the FA was significantly different across the actuator anchoring configurations ($\chi^2_{\text{UA}}(2) = 243.053$, $p < 0.001$; $\chi^2_{\text{FA}}(2) = 36.783$, $p < 0.001$; Fig. 9). Post-hoc tests showed that the force exerted on the UA was significantly lower in the E3 configuration compared to the E1 ($p < 0.001$) and E2 ($p < 0.001$) ones, whereas, the force exerted on the FA was significantly lower for the E1 compared to the E2 ($p < 0.001$) and E3 ($p < 0.001$) configurations. In addition, the peak force exerted on the UA and FA was significantly different across the non-actuated shoulder joint locked angles ($\chi^2_{\text{UA}}(2) = 71.578$, $p < 0.001$; $\chi^2_{\text{FA}}(2) = 152.088$, $p < 0.001$; Fig. 9). Post-hoc tests showed that locking the shoulder at $\theta_s = 0^\circ$ led to the smallest peak force exerted on both UA and FA, compared to the other three cases ($p < 0.001$ for all comparisons). Visual inspection of Fig. 10 suggests that exerted forces demonstrate hysteresis to input pressure changes. Peak forces were observed at an average of 35.91 ± 0.72 kPa for the UA and 35.72 ± 0.65 kPa for the FA when the actuator was anchored at E1. When anchored at E2, the peak force was observed at 36.16 ± 0.68 kPa for the UA and 35.93 ± 0.65 kPa for the FA. Lastly, peak forces were observed at an average of 36.36 ± 0.7 kPa and 36.19 ± 0.71 kPa for the UA and FA, respectively, when the actuator anchored at E3.

The aforementioned results allow the following observations to be made. The symmetric configuration (E2) is the most efficient in terms of maximizing ROM. This can be explained by the mechanics of this actuator. When it is mounted between the UA and FA and inflated, it bends and attains an arc-like form. The bottom parts of its cells (i.e. the side closer to the body) come closer together while their top sides are being pulled away. Symmetry in the distribution of cells before and after the elbow joint center (i.e. number of cells over the UA and FA, respectively) enable the actuator to attain a more circular arc (compared to a more elliptical one

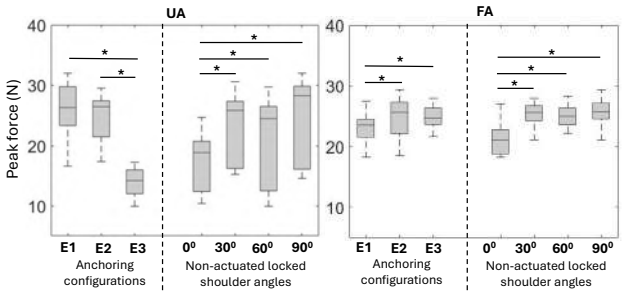


Fig. 9. Boxplots of the exerted peak force for the elbow actuator on the UA and FA. Results show significant performance differences owing to different actuator configurations and non-actuated locked shoulder angles.

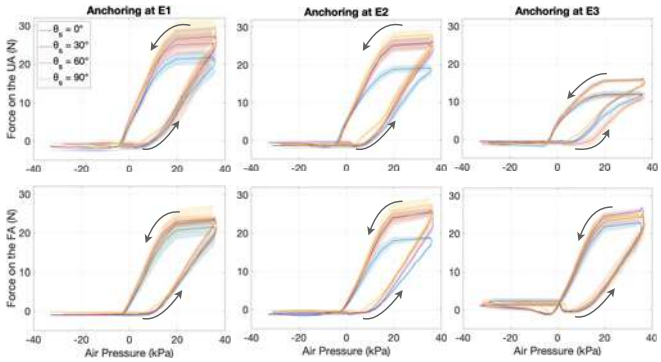


Fig. 10. Evolution of the elbow actuator forces exerted on the UA (Top) and FA (Bottom) as the internal air pressure of the actuator varies. Arrows indicate deflation (flexion) and inflation (extension).

when asymmetry is introduced), generating higher perpendicular force on the FA, increasing moment, and thus resulting in larger ROM. The asymmetric configurations bring some parts of the actuator closer together than others, reducing overall ROM but also reducing the peak force on the UA (E3; fewer cells over the UA) and FA (E1; fewer cells over the FA). The observed hysteresis may be caused by the binary (on/off) valves used in the pneumatic system; continuous flow valve could help remedy this effect. Besides the observed hysteresis, input pressure and exerted forces vary proportionally, while the transition between the deflation and inflation phases is smooth, highlighting the suitability of the elbow actuator in achieving its intended task.

IV. Conclusion

We investigated the contact forces generated by a single-cell actuator for shoulder abduction/adduction and a 10-cell bellow-type actuator for elbow flexion/extension using an infant-scale engineered apparatus. Extensive testing under various conditions revealed key information regarding actuator functionality. For the shoulder actuator: (1a) shifting it closer to the joint center can increase peak force while decreasing ROM, and (1b) increasing the elbow joint angle can help reduce the peak exerted force while improving ROM. For the elbow actuator: (2a) symmetric positioning can maximize ROM and result in equal peak forces exerted on the UA and FA, and (2b) larger shoulder joint angles can cause higher exerted forces and simultaneously reduce ROM.

The actuator anchoring findings (1a, 2a) give insight into how to improve the design for functionality and efficiency.

The findings relating to the effects of the adjacent joint when locked in a particular configuration (1b, 2b) can help create feedforward terms for an exosuit controller. For instance, if the task is to support primarily elbow function in terms of ROM, the underlying (admittance) controller should provide some input to the user to ensure the shoulder remains in a neutral position. A detailed treatise of such control design is part of future work. Further, the observed nonlinearity and hysteresis between actuator input pressure and exerted forces highlight the need for a dynamics-based analysis and modeling which is another direction of future work.

REFERENCES

[1] P. B. Banyarani, B. Tarvirdizadeh, and A. Hadi, "Design and fabrication of a soft wearable robot using a novel pleated fabric pneumatic artificial muscle (pfpam) to assist walking," *Sens. Actuators A. Phys.*, vol. 370, p. 115278, 2024.

[2] C. M. Thalman, L. Baye-Wallace, and H. Lee, "A soft robotic hip exosuit (sr-hexo) to assist hip flexion and extension during human locomotion," in *IEEE/RSJ Int. Conf. Intell. Robots Syst. (IROS)*, 2021, pp. 5060–5066.

[3] E. J. Park, T. Akbas, A. Eckert-Erdheim, L. H. Sloot, R. W. Nuckols, D. Orzel, L. Schumm, T. D. Ellis, L. N. Awad, and C. J. Walsh, "A hinge-free, non-restrictive, lightweight tethered exosuit for knee extension assistance during walking," *IEEE Trans. Med. Robot. Bionics*, vol. 2, no. 2, pp. 165–175, 2020.

[4] S. Sridar, P. H. Nguyen, M. Zhu, Q. P. Lam, and P. Polygerinos, "Development of a soft-inflatable exosuit for knee rehabilitation," in *IEEE/RSJ Int. Conf. Intell. Robots Syst. (IROS)*, 2017, pp. 3722–3727.

[5] J. Bae, C. Siviy, M. Rouleau, N. Menard, K. O'Donnell, I. Geliana, M. Athanassiu, D. Ryan, C. Bibeau, L. Sloot *et al.*, "A lightweight and efficient portable soft exosuit for paretic ankle assistance in walking after stroke," in *IEEE Int. Conf. Robot. Autom. (ICRA)*, 2018, pp. 2820–2827.

[6] C. Simpson, B. Huerta, S. Sketch, M. Lansberg, E. Hawkes, and A. Okamura, "Upper extremity exomuscle for shoulder abduction support," *IEEE Trans. Med. Robot. Bionics*, vol. 2, no. 3, pp. 474–484, 2020.

[7] C. T. O'Neill, N. S. Phipps, L. Cappello, S. Paganoni, and C. J. Walsh, "A soft wearable robot for the shoulder: Design, characterization, and preliminary testing," in *IEEE Int. Conf. Rehabil. Robot. (ICORR)*, 2017, pp. 1672–1678.

[8] D. Chiaradia, M. Xiloyannis, C. W. Antuvan, A. Frisoli, and L. Masia, "Design and embedded control of a soft elbow exosuit," in *IEEE Int. Conf. Soft Robot. (RoboSoft)*, 2018, pp. 565–571.

[9] C. M. Thalman, Q. P. Lam, P. H. Nguyen, S. Sridar, and P. Polygerinos, "A novel soft elbow exosuit to supplement bicep lifting capacity," in *IEEE/RSJ Int. Conf. Intell. Robots Syst. (IROS)*, 2018, pp. 6965–6971.

[10] K. Schäffer, Y. Ozkan-Aydin, and M. M. Coad, "Soft wrist exosuit actuated by fabric pneumatic artificial muscles," *IEEE Trans. Med. Robot. Bionics*, pp. 718–732, 2024.

[11] L. Ge, F. Chen, D. Wang, Y. Zhang, D. Han, T. Wang, and G. Gu, "Design, modeling, and evaluation of fabric-based pneumatic actuators for soft wearable assistive gloves," *Soft Robotics*, vol. 7, no. 5, pp. 583–596, 2020.

[12] B. Li, B. Greenspan, T. Mascitelli, M. Raccuglia, K. Denner, R. Duda, and M. A. Lobo, "Design of the Playskin Air^{TM}: A User-Controlled, Soft Pneumatic Exoskeleton," in *Des. Med. Dev. Conf.*, 2019, pp. 1–4.

[13] A. J. Arnold, J. L. Haworth, V. O. Moran, A. Abulhasan, N. Steinbuch, and E. Kokkoni, "Exploring the unmet need for technology to promote motor ability in children younger than 5 years of age: a systematic review," *Arch. Rehabil. Res. Clin. Transl.*, vol. 2, no. 2, p. 100051, 2020.

[14] E. Kokkoni, Z. Liu, and K. Karydis, "Development of a soft robotic wearable device to assist infant reaching," *J. Eng. Sci. Med. Diagn. Ther.*, vol. 3, no. 2, 2020.

[15] S. Henderson, H. Skelton, and P. Rosenbaum, "Assistive devices for children with functional impairments: impact on child and caregiver function," *Dev. Med. Child Neurol.*, vol. 50, no. 2, pp. 89–98, 2008.

[16] A. Schiele and F. C. Van der Helm, "Influence of attachment pressure and kinematic configuration on phri with wearable robots," *Appl. Bionics Biomech.*, vol. 6, no. 2, pp. 157–173, 2009.

[17] M. Xiloyannis, D. Chiaradia, A. Frisoli, and L. Masia, "Physiological and kinematic effects of a soft exosuit on arm movements," *J. Neuroeng. Rehabil.*, vol. 16, pp. 1–15, 2019.

[18] S. Bhardwaj, A. B. Shinde, R. Singh, and V. Vashista, "Manipulating device-to-body forces in passive exosuit: An experimental investigation on the effect of moment arm orientation using passive back-assist exosuit emulator," *Wearable Technol.*, vol. 4, p. e17, 2023.

[19] A.-M. Georgarakis, R. Stämpfli, P. Wolf, R. Riener, and J. E. Duarte, "A method for quantifying interaction forces in wearable robots," in *IEEE Int. Conf. Biomed. Robot. Biomechatron.(Biorob)*, 2018, pp. 789–794.

[20] D. Ito, Y. Funabora, S. Doki, and K. Doki, "Control system based on contact force distribution for wearable robot with tactile sensor," in *IEEE/SICE Int. Symp. Sys. Integr.(SII)*, 2019, pp. 259–263.

[21] A. F. Mak, M. Zhang, and E. W. Tam, "Biomechanics of pressure ulcer in body tissues interacting with external forces during locomotion," *Annu. Rev. Biomed. Eng.*, vol. 12, no. 1, pp. 29–53, 2010.

[22] A. Bringard, R. Denis, N. Belluye, and S. Perrey, "Effects of compression tights on calf muscle oxygenation and venous pooling during quiet resting in supine and standing positions," *J. Sports Med. Phys. Fitness*, vol. 46, no. 4, p. 548, 2006.

[23] H. N. Mayrovitz and N. Sims, "Effects of ankle-to-knee external pressures on skin blood perfusion under and distal to compression," *Adv. Skin Wound Care*, vol. 16, no. 4, pp. 198–202, 2003.

[24] A. K. Bright and L. Coventry, "Assistive technology for older adults: psychological and socio-emotional design requirements," in *Proceedings of the Int. Conf. Pervasive Technol. Relat. Assist. Environ.*, 2013, pp. 1–4.

[25] C. Mucchiani, Z. Liu, I. Sahin, J. Dube, L. Vu, E. Kokkoni, and K. Karydis, "Closed-loop position control of a pediatric soft robotic wearable device for upper extremity assistance," in *IEEE Int. Conf. Robot & Human Inter. Comm. (ROMAN)*, 2022, pp. 1514–1519.

[26] C. Mucchiani, Z. Liu, I. Sahin, E. Kokkoni, and K. Karydis, "Robust generalized proportional integral control for trajectory tracking of soft actuators in a pediatric wearable assistive device," in *IEEE/RSJ Int. Conf. Intell. Robots Syst. (IROS)*, 2023, pp. 559–566.

[27] J. L. Samper-Escudero, A. Gimenez-Fernandez, M. A. Sanchez-Uran, and M. Ferre, "A cable-driven exosuit for upper limb flexion based on fibres compliance," *IEEE Access*, vol. 8, pp. 153 297–153 310, 2020.

[28] J. Bae, L. N. Awad, A. Long, K. O'Donnell, K. Hendron, K. G. Holt, T. D. Ellis, and C. J. Walsh, "Biomechanical mechanisms underlying exosuit-induced improvements in walking economy after stroke," *J. Exp. Biol.*, vol. 221, no. 5, p. jeb168815, 2018.

[29] S. Kokubu, R. Nishimura, and W. Yu, "Deriving design rules for personalization of soft rehabilitation gloves," *IEEE Access*, 2024.

[30] M. Wehner, B. Quinlivan, P. M. Aubin, E. Martinez-Villalpando, M. Baumann, L. Stirling, K. Holt, R. Wood, and C. Walsh, "A lightweight soft exosuit for gait assistance," in *IEEE international conference on robotics and automation*, 2013, pp. 3362–3369.

[31] I. Sahin, M. Ayazi, C. Mucchiani, J. Dube, K. Karydis, and E. Kokkoni, "Evaluation of fabric-based pneumatic actuator enclosure and anchoring configurations in a pediatric soft robotic exosuit," *Front. Robot. AI*, vol. 11, p. 1302862, 2024.

[32] I. Sahin, J. Dube, C. Mucchiani, K. Karydis, and E. Kokkoni, "A bidirectional fabric-based pneumatic actuator for the infant shoulder: Design and comparative kinematic analysis," in *IEEE Int. Conf. Robot & Human Inter. Comm. (ROMAN)*, 2022, pp. 371–376.

[33] I. Sahin, M. Ayazi, C. Mucchiani, J. Dube, K. Karydis, and E. Kokkoni, "A fabric-based pneumatic actuator for the infant elbow: Design and comparative kinematic analysis," in *IEEE Int. Conf. Robot. Biom. (ROBIO)*, 2023, pp. 1–6.

[34] T. Edmond, A. Laps, A. L. Case, N. O'Hara, and J. M. Abzug, "Normal ranges of upper extremity length, circumference, and rate of growth in the pediatric population," *Hand*, vol. 15, no. 5, pp. 713–721, 2020.

[35] C. D. Fryar, M. D. Carroll, Q. Gu, J. Afful, and C. L. Ogden, "Anthropometric reference data for children and adults: United states, 2015-2018," *Vital Health Stat. 3*, 2021.

[36] K. Schneide and R. F. Zernicke, "Mass, center of mass, and moment of inertia estimates for infant limb segments," *J. Biomech.*, vol. 25, no. 2, pp. 154–148, 1992.

[37] J. Zhou and B. A. Smith, "Infant reaching in the first year of life: A scoping review of typical development and examples of atypical development," *Phys. Occup. Ther. Pediatr.*, vol. 42, no. 1, pp. 80–98, 2021.

Toward a Customizable Body Weight Support System with Interactive Treadmill for Patients with Diverse Gait Impairments

Yongjin Jo, Youjin Lee and Jonghyun Kim, *Member, IEEE*

***Abstract*— Stroke patients face significant gait rehabilitation challenges, including high physical demands and fall risks. While body weight support (BWS) systems assist recovery, conventional designs remain limited by space, cost, and adaptability. To address these issues, we developed a customizable two-cable driven BWS treadmill system with a movable cable adjustment module for adaptive rehabilitation. Users can configure the harness as a pelvic or overhead support, enabling two training protocols: (1) Performance-Focused Gait Training (PFGT) to enhance gait efficiency and (2) Stability-Focused Gait Training (SFGT) to improve postural control. Clinical testing showed that PFGT increased walking speed by up to 34.7% and step length by 44.7%, while SFGT reduced trunk tilt by 7.3°, promoting gait symmetry and stability. These results highlight the system's capability to provide customized unloading support for individualized gait training, enhancing rehabilitation accessibility and effectiveness.**

Keywords—Gait training, Body weight support, customization

I. Introduction

A significant proportion of stroke patients experience impaired walking ability as a result of residual effects, significantly affecting their activities of daily living [1]. Recovery of lower extremity motor function is crucial for these patients to facilitate a smooth reintegration into daily and social life [2]. However, achieving this recovery is often hindered by several challenges in gait rehabilitation training, including substantial physical and mental demands on both patients and therapists [3]. Furthermore, the risk of falls during training can induce fear in patients [4], which may lead to decreased participation in the rehabilitation process.

Various robotic devices, including wearable exoskeletons and treadmill-based trainers, have been developed to aid gait rehabilitation [5]. Exoskeletons like Ekso [6] and ReWalk [7] assist lower limb movement but face limitations such as poor adaptability to uneven terrains and user discomfort. To address these issues, body weight support (BWS) systems have been developed to enhance safety and reduce the physical burden by unloading body weight during gait training [8]. These systems facilitate natural overground walking [9], promote neuroplastic changes [10], and support the reintegration of walking skills into daily life. BWS systems also reduce fear of falls [11], improving patient engagement, and offer adjustable support levels to balance safety and challenge [12]. Overhead BWS systems, such as Zero-G and Float [13, 14], provide dynamic support via ceiling-mounted rails, enabling overground walking. However, their substantial spatial and financial demands limit their use in smaller clinics, and their lack of customization restricts applicability to patients with diverse gait abilities. To address these limitations of overhead BWS systems, a treadmill has been integrated into a BWS system, allowing patients easier access to training. However, as a trade-off, treadmill-based gait training differs from overground walking due to the treadmill's pre-determined speed, which can be a limitation for regaining independent walking ability in real-world environments [15].

To overcome these challenges, we developed a two-cable driven BWS system integrated with an interactive treadmill [16, 17], which combines the benefits of treadmill-based gait training with overground-like adaptability. Unlike conventional systems, our approach allows users to autonomously regulate walking speed based on real-time position feedback [18], facilitating a more dynamic and interactive training experience. Additionally, the system incorporates a custom harness with pelvic support configuration that enables natural pelvic movement, improving gait biomechanics while maintaining stability. Experimental validation demonstrated that the system effectively controlled unloading forces and provided a feasible training environment [16]. However, its reliance on an interactive treadmill and a wide walking range necessitates adequate trunk control, limiting its suitability to patients with moderate ambulatory abilities, such as those classified within Functional Ambulation Category (FAC) levels 3 to 4 [19]. Like many existing BWS systems, it struggles to accommodate patients with severe gait impairments, underscoring the need for further enhancements to improve clinical applicability and accessibility across a broader patient population.

In this paper, we propose a body weight support system designed to explore tailored gait training strategies for patients with varying levels of walking ability. The system features a movable cable adjustment module, allowing flexible modification of the assistance mechanism to accommodate different levels of trunk control. Using this adjustable assistance mechanism, we implemented two distinct training modes to investigate their effects on patients with different gait impairments. The first mode applies an anterior-posterior cable connection for targeted assistance in mild gait impairments, while the second resembles a

This study was supported by the Translational Research Program for Rehabilitation Robots (NRCTR-EX23004), National Rehabilitation Center, Ministry of Health and Welfare, Korea.

This work was supported by the Technology Innovation Program and Industrial Strategic Technology Development Program (20018256, Development of service robot technologies for cleaning a table).

Yongjin Jo, Youjin Lee and Jonghyun Kim are with the School of Mechanical Engineering, Sungkyunkwan University, Suwon, 16419, Republic of Korea. (e-mail: jonghyunkim@skku.edu)

conventional overhead BWS system, enhancing stability for more severe impairments. This study evaluates their feasibility and customized unloading support to inform individualized gait rehabilitation. Experimental evaluations with stroke patients were conducted to assess their clinical applicability.

II. Methods

A. System Hardware

1) *System framework*: The proposed system, which is shown in Fig. 1a, utilizes a two-cable driven body weight support (BWS) mechanism, designed to provide assistance during gait training. The system consists of the following key components:

- Actuation units : Each actuation unit facilitates power transmission through cables and comprises a winch drum, motor (EC-45, Maxon Inc., USA), gearbox (GP 32 HP, 69:1, Maxon Inc., USA), encoder (16 EASY, Maxon Inc., USA) and servo drive (EPOS 70-15, Maxon Inc., USA). These components work in coordination to regulate the force applied to the user, ensuring smooth and adaptive support.
- Tension Sensing Modules : To monitor the real-time tension in the cables, each tension sensing module is equipped with a load cell sensor (LPU-250, Transducer technique, USA). These sensors provide continuous feedback to maintain optimal force control.
- Cable Adjustment Modules : The system incorporates two cable adjustment modules, each featuring an encoder (E40S6, Autonics, Korea) to measure the angle of the cables connected to the user. This ensures accurate tracking of the user's movements and precise force application.

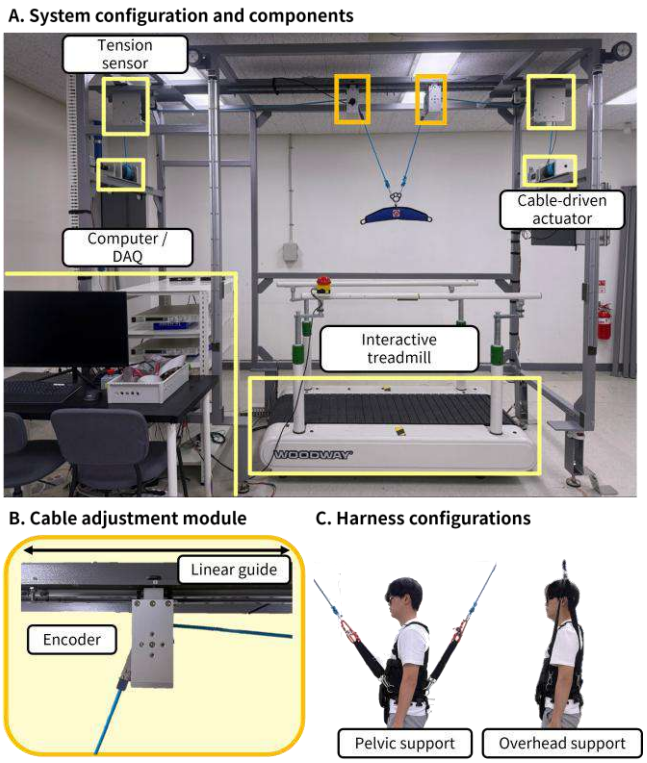


Fig. 1. System configuration and harness attachment types in the body weight support (BWS) system. (a) Overall hardware setup, including the cable-driven actuation system, interactive treadmill, and control units. (b) Detailed view of cable adjustment module with an encoder and linear guide for adaptive force application. (c) Comparison of two harness configurations: pelvic support, where cables are attached in a front-back orientation, and overhead support, where cables provide vertical support.

The two cables are connected in the anterior-posterior direction, delivering tension to the user under the following conditions.

$$\sum F_x = F_1 sin\theta_2 - F_2 \sin\theta_1 = 0 \quad (1)$$

$$\sum F_z = F_1 cos\theta_2 - F_2 \cos\theta_1 = F_r \quad (2)$$

where, F_x and F_z denote A/P and gravitational direction forces and F_1 and F_2 denote cable force connected to user in A/P direction. θ_1 and θ_2 are the angles of each cable. F_r is the reference unloading force. The desired forces of the two cables, denoted as $F_{1,d}$ and $F_{2,d}$, to satisfy Equations (1) and (2) can be calculated as follows:

$$F_{1,d} = \frac{F_r sin\theta_2}{\sin(\theta_1 + \theta_2)}, \quad F_{2,d} = \frac{F_r sin\theta_1}{\sin(\theta_1 + \theta_2)} \quad (3)$$

Feedback control is implemented to provide the desired force. The interactive treadmill adjusts the belt speed in response to changes in walking speed. Details on the system's operation can be found in our previous publication [17].

2) *Cable adjustment module*: The existing system was initially designed to connect cables in the anterior-posterior direction relative to the user, providing body weight support (BWS) while maintaining zero net force in the x-direction (Fig. 2a). To accommodate patients with reduced gait ability or impaired trunk control, we modified the system to also provide overhead BWS capabilities. Overhead BWS connects the cables above the user, increasing the vertical support ratio, which reduces the impact of anterior-posterior forces and enhances stability during walking. However, maintaining the original position of the cable adjustment modules for overhead BWS would lead to an increase of cable angle (θ_1, θ_2), as shown in Fig. 2b. This configuration alters the force distribution, increasing the horizontal force component relative to the vertical force component. Since the primary goal of the BWS is to provide unloading support through vertical forces, a steeper cable angle necessitates a higher overall cable tension to achieve the same vertical force. This, in turn, would require higher-performance actuators. To effectively implement overhead BWS using the current actuators, we installed linear guides on the ceiling, allowing the previously fixed cable adjustment modules to move along with these guides (Fig. 1b). If the module spacing is reduced from the original 1.2m to 0.45m, the required cable tension to provide the same unloading support can be reduced by 43%. This modification enables more efficient overhead support without necessitating enhanced actuators.

During training, the modules can be fixed in place by

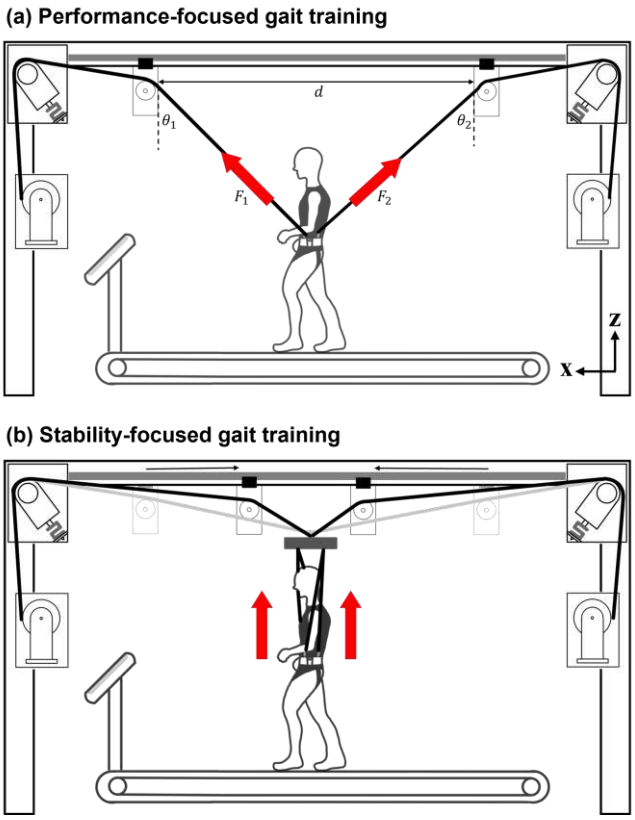


Fig. 2. (a) Wide spacing of cable adjustment module for Performance-focused gait training, (b) Reduced spacing of cable adjustment module for Stability-focused gait training

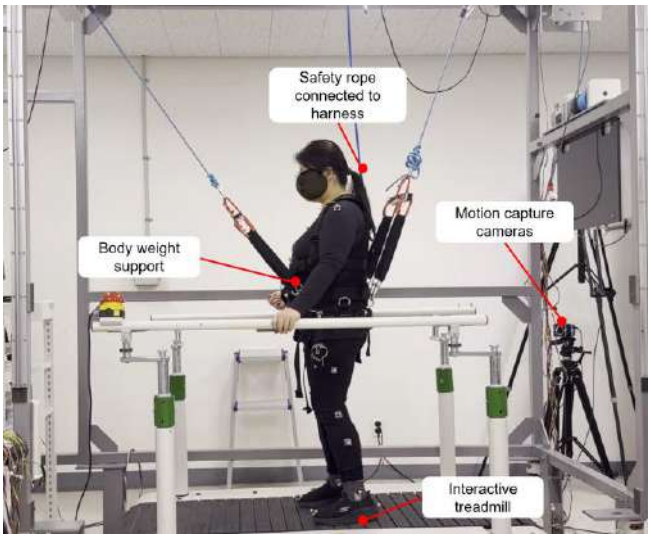


Fig. 3. Experimental setup for system evaluation with patients after stroke

inserting pins into holes arranged at 5 cm intervals, allowing the distance between modules to be freely adjusted. By customizing the assistance mechanism in this way, the pattern of support provided during training can be adjusted to suit individual needs. Adjusting the spacing of the modules also influences the user's walking range. If the user walks beyond the defined module spacing, the pendulum effect may occur, guiding the user back to stay within the designated walking range. Therefore, adjusting the module spacing provides a means of controlling the user's walking range, thereby optimizing the difficulty level of gait training to enhance both training efficiency and user safety.

B. Adaptive Training Modes Design

We designed training modes suitable for patients with varying gait abilities by utilizing the customizable assistance mechanism of the system.

1) Performance-focused gait training (PFGT): performance-focused gait training targets patients with relatively good gait abilities, specifically those at FAC levels 3 to 4. Rather than providing strong unloading support, this training is designed to guide patients to achieve a higher level of walking performance than they could achieve independently. The assistance mechanism of PFGT is shown in Fig. 2a. The cable adjustment module was set to a spacing of 1.2 m to enable gait training over a wide range, with two connection bars attached to cables from the front and rear to support natural movement. A harness with pelvic support configuration was used to avoid applying external force to the user's trunk, enabling natural body movement during walking. Additionally, an interactive treadmill was utilized, which dynamically adjusts to the user's movements, allowing the patient to select their own walking speed, thereby promoting active engagement and natural gait patterns.

2) Stability-focused gait training (SFGT): Stability-focused gait training is intended for patients with limited gait abilities, specifically those at FAC levels 1 to 2. These patients struggle with balance and shifting their center of gravity during walking [17], so the training focuses on maintaining stability while facilitating gait. To provide support in a manner similar to the conventional overhead BWS system, the cable adjustment module was set with a narrow spacing as shown in Fig. 2b. A harness with overhead support configuration was used to provide vertical support, with straps directly connecting the user's trunk to the connection bar. This configuration may restrict some natural trunk movement during walking, but it ensures a stable upward force to assist balance during gait. The module spacing was set to 0.45 m, covering approximately one-third of the total walking range (1.2 m). This setup is intended to support stable walking within a narrow range while reducing the occurrence of the pendulum effect. Although the assistance is provided similarly to a conventional BWS system, the user can still experience a distinct gait pattern. The direction of the assistance force remains upward, however, since the cables are connected to the user through an anterior-posterior arrangement via the connection bar, the benefits of the two-cable driven mechanism are retained. Consequently, as long as the user remains within the defined walking range, they can walk without experiencing the pendulum effect, thereby enhancing stability.

III. EXPERIMENTAL EVALUATION

A. Participants

Three participants with chronic stroke participated in the study. (see Table 1). Prior to the experiment, all participants were provided with a detailed explanation of the study procedures, including visual content describing the

TABLE 1. PARTICIPANTS BASELINE CHARACTERISTICS AND GAIT PERFORMANCE

Participants No.	Sex	Age (y)	Paretic side	Height (cm)	Weight (kg)	Assistive device	FAC level
SN01	Female	41	Right	158	68	None	4
SN02	Male	65	Right	165	60	None	4
SN03	Male	61	Right	172	65	Wheelchair	1

experiment. Medical clearance and written informed consent forms were obtained from all participants, in compliance with the guidelines approved by the Sungkyunkwan University Institutional Review Board (SKKU 2022-06-014).

B. Experimental Design

This study aimed to observe changes in gait patterns when patients with varying walking abilities are provided with different training protocols and levels of body weight support (BWS). Prior to the experiment, participants determined their preferred treadmill walking speed, which was then set as the speed for the interactive treadmill. For SN01 and SN02, gait training was conducted using an interactive treadmill set to their preferred speed under two distinct training modes: Performance-Focused Gait Training (PFGT) and Stability-Focused Gait Training (SFGT). To evaluate the effects of different levels of unloading support, gait patterns were observed under 30% and 50% BWS conditions, which were determined through preliminary experimentation to be the appropriate levels of assistance for effective gait training. Participant movements were recorded and analyzed using a motion capture system (VICON Nexus, UK). The detailed experimental setup can be found in Fig. 3.

The two participants first performed PFGT under 0% BWS (no unloading) for two trials, followed by two trials each under 30% BWS and 50% BWS conditions. Subsequently, they performed SFGT under 0%, 30%, and 50% BWS conditions, with two repetitions for each. Each walking trial lasted one minute, with a one-minute rest interval provided between trials to minimize fatigue. In contrast, SN03, who exhibited significantly lower walking ability compared to the other participants, was provided with different training protocols. Training under 0%, 30%, and 50% BWS conditions was not conducted due to the participant's inability to perform independent walking. Instead, based on preliminary assessments, an unloading support level of 85% BWS was identified as optimal for stable walking. Under this condition, SN03 completed four one-minute walking trials.

IV. RESULTS

In this section, we provide an analysis of the effects of the unloading support level from BWS on joint kinematics, spatiotemporal data, and each subject during assisted gait.

A. Spatiotemporal data

The spatiotemporal data of participants during gait are reported on Fig. 4. This analysis aims to determine whether there were any improvements in gait performance due to BWS assistance.

1) Performance-focused Gait Training: Participants who

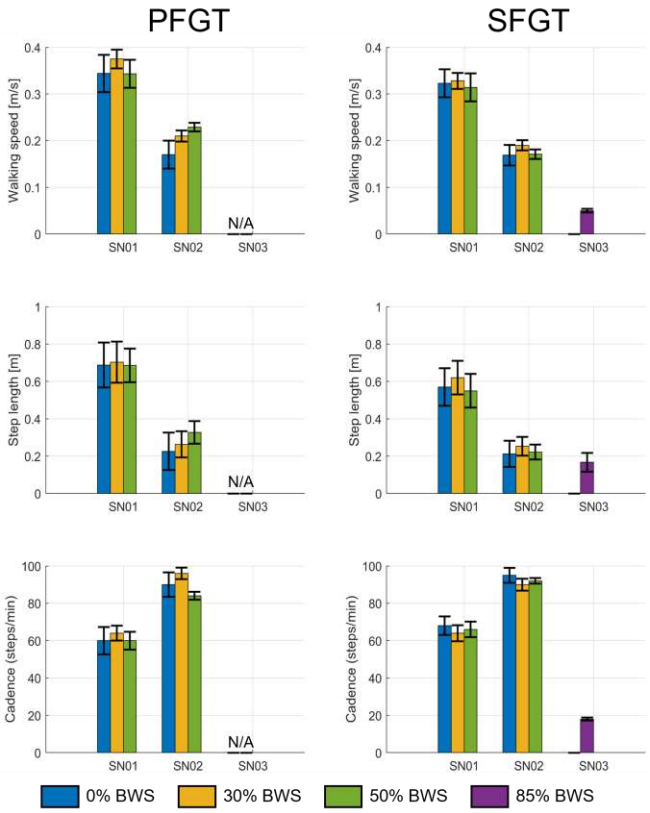


Fig. 4. Spatiotemporal gait parameters averaged across all participants for all the tested condition. (Top) Walking speed, (Middle) Step length, (Bottom) Cadence. SN03 was unable to complete total PFGT training and SFGT with 0% BWS, indicated by "N/A." In SFGT, SN03 achieved walking at 85% BWS. Error bars represent standard deviations.

performed PFGT demonstrated overall improvements in gait performance. Under a 30% BWS condition, compared to the 0% BWS, both participants were able to walk at an increased speed (SN01 - 9%, SN02 - 23.5%). Step length and cadence also increased (compared with 0% BWS) when 30% BWS was provided (SN01 – 2.18% for step length and 6.67% for cadence, SN02 – 16.3% for step length and 6.67% for cadence). Under the 50% BWS condition, SN01 showed a slight reduction in walking speed (-0.3%) and step length (-0.29%). SN02 showed the best walking performance (+34.7% for walking speed, +44.7% for step length and -6.7% for cadence compared to 0% BWS).

2) Stability-focused Gait Training: In PFGT, SN03 was unable to perform gait training even with assistance. However, in SFGT, SN03 successfully achieved independent walking when provided with 85% body weight support (BWS), reaching a walking speed of 0.05 m/s. For SN01 and SN02, no significant improvements in gait performance were observed during SFGT. Notably, under 30% BWS, walking

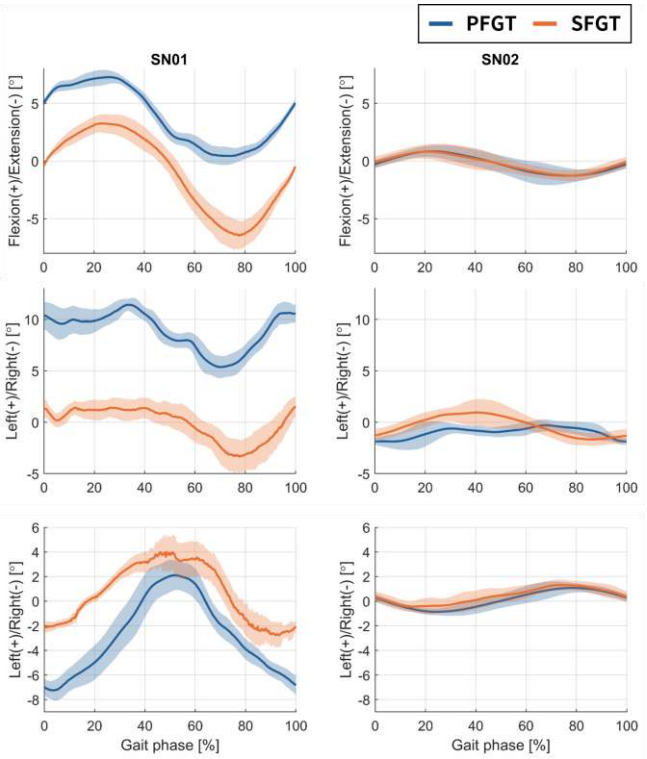


Fig. 5. kinematics during the gait cycle under different training protocols. The graphs compare joint movements for two subjects (SN01, SN02) in performance-focused gait training (PFGT, blue) and stability-focused gait training (SFGT, orange). The plots show variations in joint angles across the gait phase (%) in three planes: (Top) sagittal plane – trunk flexion/extension, (Middle) frontal plane – lateral movement, and (Bottom) transverse plane – rotational movement. Shaded areas represent standard deviations, illustrating variability in movement patterns.

speeds increased for both participants (SN01 by 2.16%, SN02 by 11.7%). Step length increased (SN01 by 8.77%, SN02 by 19.3%), whereas cadence decreased (SN01 by 5.88%, SN02 by 5.26%). Under 50% BWS, SN01 showed a reduction in gait performance (-2.78% for walking speed, -3.5% for step length and -2.94% for cadence). For SN02, there was a negligible difference compared to the 0% BWS condition (+1.18% for walking speed, +4.71% for step length and -2.94% for cadence).

B. Trunk kinematics

The trunk kinematics of the participants during gait are shown in Fig. 5. For SN03, due to environmental constraints that made it challenging to utilize the motion capture camera while ensuring participant safety, trunk kinematics data was only reported for SN01 and SN02. The analysis examines how trunk movement patterns change when two different training sessions are provided. The solid line represents the average trunk angle during gait, while the shaded area indicates the standard deviation. For SN01, when comparing SFGT to PFGT, trunk movement in the sagittal and frontal planes showed an average reduction of 7.3 degrees in both minimum and maximum values. Additionally, the mean position of movement decreased by 6.9 degrees. In the transverse plane, both the min/max values increased by an average of 3.19 degrees, and the mean position of movement increased by 3.5 degrees. In contrast, Participant SN02 exhibited changes of less than 1.3 degrees across all planes.

V. Discussion

In this study, we investigated how a customizable body weight support (BWS) system affects gait stability and performance in two stroke patients. The evaluation focused on trunk kinematics and spatiotemporal data to assess stability and gait performance. The spatiotemporal data indicated that SFGT could even make patients classified as FAC level 1 train using the BWS system. Participant SN03, who could not walk independently and struggled with trunk control, was unable to complete PFGT even with 85% BWS. However, SN03 successfully completed repeated gait training sessions using SFGT. This finding suggests that training can be provided to patients who were previously unable to benefit from the previous system.

For participants with relatively higher gait performance, SFGT did not significantly improve gait function in participants with higher initial performance levels. This might be due to SFGT focusing on stability enhancement, whereas these participants had already surpassed target performance levels. However, significant gains were observed during PFGT. Under the 30% BWS condition, improvements in all spatiotemporal metrics suggested better gait efficiency and safety. At 50% BWS, gait patterns diverged significantly between participants: SN01 experienced a general reduction in gait performance, while SN02 demonstrated the highest performance. These differing outcomes could stem from baseline gait strategies. SN02's improvement suggests that the assistance helped develop a more efficient gait strategy, addressing previously high cadence and short step length often seen as compensatory mechanisms for stability in elderly individuals [20]. The increase in walking speed, along with step length and reduced cadence, indicated enhanced gait efficiency and stability. In contrast, SN01's reduced performance may reflect over-reliance on the provided assistance, which can diminish engagement and overall performance [21]. These findings suggest that the most effective assistance level depends on individual needs.

The results for trunk kinematics also varied between participants. SN01 demonstrated distinct trunk movements between the two training types. When performing SFGT, an offset in trunk angles was observed compared to PFGT across all planes. Specifically, the average trunk angle during the gait phase approached zero in all planes during SFGT, which indicates that SFGT might improve gait symmetry and enhance stability during walking [22]. Even for participants demonstrating good gait capabilities, SFGT can help individuals with gait asymmetry train towards a gait pattern that more closely resembles regular walking. In contrast, SN02 exhibited no significant differences in trunk movement between the two training types. As SN02 had already adopted a stability-focused gait strategy even during PFGT, their trunk moved around a zero-degree position. Therefore, the effect of SFGT on improving trunk stability and symmetry might be diminished. These findings reinforce the importance of postural stability in gait training, further highlighting the potential benefits of tailored assistance for individuals with gait asymmetry.

Overall, our findings demonstrate that the proposed system, which enables customization of assistance

mechanisms based on individual needs, effectively supports diverse gait training strategies. Performance-Focused Gait Training (PFGT) enhances gait performance and efficiency, making it particularly beneficial for patients striving to regain natural walking patterns through increased speed and optimized gait mechanics. In contrast, Stability-Focused Gait Training (SFGT) promotes gait symmetry by reducing trunk tilt and prioritizing stability throughout training. By facilitating trunk control, SFGT extends the benefits of gait training to patients who previously lacked sufficient gait ability to engage in effective rehabilitation.

The findings indicate that different training protocols affect gait performance, highlighting the need for personalized rehabilitation strategies. By evaluating performance-focused and stability-focused gait training, this study provides insights into how adaptive assistance can enhance gait efficiency and postural control. Our system offers adaptable support by dynamically adjusting module distances, ensuring precise assistance tailored to rehabilitation needs. This flexibility improves accessibility in clinical settings, optimizing gait training outcomes.

While our system enables adaptability, this study primarily explores how different training protocols influence patient outcomes rather than implementing a fully individualized model. Instead of directly applying a customization framework, we establish foundational insights by analyzing spatiotemporal data and patient-specific factors. The findings suggest that spatiotemporal data, along with individual characteristics such as height and weight, could help classify patients into appropriate training categories, paving the way for a more adaptive, data-driven approach to personalized gait assistance.

A key limitation is the small and biased sample size (three patients: FAC levels 4, 4, and 1), which may have influenced the results. As the system is expected to benefit FAC levels 2 or 3, future studies should include a more diverse participant pool to validate its effectiveness across different mobility impairments. Additionally, further analysis using joint kinematics and muscle activity assessments is needed to uncover biomechanical changes affecting rehabilitation outcomes.

Despite these limitations, the system demonstrates strong potential for supporting personalized gait rehabilitation through adjustable walking range and assistance mechanisms. As training effects vary by gait pattern, refining adaptive control strategies will be crucial in optimizing assistance levels for individual users. Future advancements integrating real-time gait analysis and automated adaptation could further enhance rehabilitation effectiveness, making gait training more accessible and patient-specific.

REFERENCES

[1] H. S. Jørgensen, H. Nakayama, H. O. Raaschou, and T. S. Olsen, "Recovery of walking function in stroke patients: the Copenhagen Stroke Study," Archives of Physical Medicine and Rehabilitation, vol. 76, no. 1, pp. 27-32, 1995.

[2] S. L. Hitzig *et al.*, "Examination of social disconnectedness and perceived social isolation on health and life satisfaction in community-dwelling adults with dysvascular lower limb loss," *Prosthetics and Orthotics International*, vol. 46, no. 2, pp. 155–163, 2022.

[3] S.-Y. Ha and Y.-H. Sung, "Attentional concentration during physiotherapeutic intervention improves gait and trunk control in patients with stroke," Neuroscience Letters, vol. 736, p. 135291, 2020.

[4] C. Y. Chiu *et al.*, "Effect of physical exercise on fear of falling in patients with stroke: A systematic review and meta-analysis," *Clinical Rehabilitation*, vol. 37, no. 3, pp. 294–311, 2023.

[5] J. Hidler, D. Nichols, M. Pelliccio, and K. Brady, "Advances in the understanding and treatment of stroke impairment using robotic devices," Topics in stroke rehabilitation, vol. 12, no. 2, pp. 22-35, 2005.

[6] R. S. Calabrò *et al.*, "Shaping neuroplasticity by using powered exoskeletons in patients with stroke: A randomized clinical trial," *Journal of NeuroEngineering and Rehabilitation*, vol. 15, pp. 1–16, 2018.

[7] J. Kim, Y. Kim, and S.-J. Kim, "Biomechanical task-based gait analysis suggests ReWalk gait resembles crutch gait," *Applied Sciences*, vol. 12, no. 24, p. 12574, 2022.

[8] Z. Dong, J. V. S. Luces, and Y. Hirata, "Control and evaluation of body weight support walker for overground gait training," *IEEE Robotics and Automation Letters*, vol. 6, no. 3, pp. 4632–4639, 2021.

[9] S. Brunelli *et al.*, "Early body weight-supported overground walking training in patients with stroke in subacute phase compared to conventional physiotherapy: A randomized controlled pilot study," *International Journal of Rehabilitation Research*, vol. 42, no. 4, pp. 309–315, 2019.

[10] S. Hesse *et al.*, "Body weight-supported treadmill training after stroke," *Current Atherosclerosis Reports*, vol. 3, pp. 287–294, 2001.

[11] S. Huang *et al.*, "Body weight support-Tai Chi footwork for balance of stroke survivors with fear of falling: A pilot randomized controlled trial," *Complementary Therapies in Clinical Practice*, vol. 37, pp. 140–147, 2019.

[12] N. Maclean *et al.*, "Qualitative analysis of stroke patients' motivation for rehabilitation," *BMJ*, vol. 321, no. 7268, pp. 1051–1054, 2000.

[13] H. Vallery et al., "Multidirectional transparent support for overground gait training," presented at the 2013 IEEE 13th International Conference on Rehabilitation Robotics (ICORR), Seattle, Washington, USA, 2013.

[14] J. Hidler, D. Brennan, D. Nichols, K. Brady, T. Nef, *et al.*, "ZeroG: overground gait and balance training system," *J. Rehabil. Res. Dev.*, vol. 48, no. 4, 2011.

[15] A. P. Marsh *et al.*, "Effect of treadmill and overground walking on function and attitudes in older adults," *Medicine & Science in Sports & Exercise*, vol. 38, no. 6, pp. 1157–1164, 2006.

[16] J. Kim, S. Oh, Y. Jo, J. H. Moon, and J. Kim, "A robotic treadmill system to mimic overground walking training with body weight support," *Frontiers in Neurorobotics*, vol. 17, article 1089377, 2023.

[17] Kim, J., Oh, S., Kim, J., and Kim, J ., "A Two-Wire Body Weight Support System for Interactive Treadmill," *2019 IEEE 16th International Conference on Rehabilitation Robotics (ICORR)*, pp. 349-354, 2019.

[18] S. Oh, M. Song, and J. Kim, "Validating Attentive Locomotion Training Using Interactive Treadmill: An fNIRS Study," *Journal of NeuroEngineering and Rehabilitation*, vol. 15, pp. 1-11, 2018.

[19] G. Verheyden, L. Vereeck, S. Truijen, M. Troch, I. Herregodts, C. Lafosse, A. Nieuwboer, and W. De Weerdt, "Trunk performance after stroke and the relationship with balance, gait and functional ability," Clinical Rehabilitation, vol. 20, no. 5, pp. 451–458, 2006.

[20] L. Álvarez-Millán, D. Castillo-Castillo, R. Quispe-Siccha, A. Pérez-Pacheco, M. Angelova, J. Rivera-Sánchez, and R. Fossion, "Frailty Syndrome as a Transition from Compensation to Decompensation: Application to the Biomechanical Regulation of Gait," International Journal of Environmental Research and Public Health, vol. 20, no. 11, article 5995, 2023.

[21] J. Xu *et al.*, "A Rehabilitation Robot Control Framework with Adaptation of Training Tasks and Robotic Assistance," *Frontiers in Bioengineering and Biotechnology*, vol. 11, p. 1244550, 2023.

[22] D. E. Krebs, D. Wong, D. Jevsevar, P. O. Riley, and W. A. Hodge, "Trunk kinematics during locomotor activities," *Physical Therapy*, vol. 72, no. 7, pp. 505-514, 1992.

Real-time Continuous Calibration of an EMG-Informed Neuromusculoskeletal Model for Assistive Exoskeleton Control

Matthew J. Hambly, Matthew T.O. Worsey, David G. Lloyd, and Claudio Pizzolato

Abstract— **Accurate real-time neuromusculoskeletal (NMS) modeling is crucial for closed-loop neurorehabilitation. This study presents a novel electromyography (EMG)-informed NMS modeling framework with continuous real-time calibration for controlling an upper limb exoskeleton. Using an auto-differentiable NMS model, we implemented a sliding window online calibration to eliminate the need for model calibration prior to use. The framework was validated during a functional reaching task performed with an ArmeoPower exoskeleton. Model accuracy and exoskeleton control performance were compared across uncalibrated, offline calibrated, and continuously calibrated models. The continuously calibrated model achieved comparable accuracy to the offline calibrated model within just 15 movement cycles (110 seconds), eliminating the need for pre-session calibration. Furthermore, the continuous calibration approach provided physiologically plausible predictions of joint moments, enabling exoskeleton control performance comparable to the offline calibrated NMS model. An offline synergy-driven modelling approach was also examined, demonstrating potential to represent unrecorded excitations and improve moment prediction accuracy. By addressing the limitations of prior methods, this framework enhances the usability of EMG-informed NMS models in real-time applications, offering a personalized and adaptive solution for neurorehabilitation, able to dynamically adapt to physiological changes such as fatigue.**

I. Introduction

Motorized exoskeletons provide weight support and actuation to assist movement [1], enabling intensive and frequent rehabilitation for individuals with neurological impairments, such as spinal cord injury or stroke, without the dependence on a large team of therapists [2]. However, to optimize therapeutic outcomes, rehabilitation must effectively engage the user's neurophysiological and musculoskeletal systems [3], which can be achieved by incorporating the user's intent into the exoskeleton's control scheme [4]. Effective feedback mechanisms are therefore necessary to ensure seamless, synergistic interaction between the user and device.

Electromyography (EMG) is one of the most widely used biosignals for exoskeleton control [5, 6], offering insights into user's intent coded in their muscle excitations. Despite its advantages, EMG alone does not fully capture the complex muscle states and non-linear relationships between muscle excitations, muscle forces, joint moments, and movement. This makes EMG alone insufficient for estimating joint moments [7, 8], which can be used for effective exoskeleton control [9, 10]. Data-driven approaches, such as neural networks, have been employed to generate upper-limb exoskeleton control signals from EMG [11, 12] and kinematics [13]. While these methods can model complex relationships, they typically require large training datasets, lack inherent physiological and physical constraints, and do not provide insight into the underlying neuromusculoskeletal (NMS) mechanisms generating movement. Furthermore, coordinated muscle excitation patterns (i.e., EMG) change for the same joint moments and angles across people and even in the same person depending on control tasks, training, and disease state [14-16]. NMS models provide individual-specific representations of the skeletal, joint, muscular, and nervous systems, and predict physiologically plausible muscle forces and joint moments [7]. By incorporating EMG, NMS models can reflect individual-specific motor control [17] making them particularly promising for personalized rehabilitation. The long and continued development of calibrated EMG-informed NMS modelling has produced open-source software, known as CEINMS [18, 19], capable of real-time execution facilitating, for example, lower limb exoskeleton control [10].

To achieve appropriate personalization, the neuromuscular parameters of the model (e.g., optimal fiber length, tendon slack length) must first be calibrated for each individual before executing (i.e., using) the model [19, 20]. Calibration typically involves iteratively adjusting the model parameters to improve tracking of joint moments, while ensuring the model adheres to physiologically plausible solutions, such as maintaining muscle fiber lengths within the functional force-length range and enforcing consistent multi-joint muscle behavior [21]. This calibration process is typically time-intensive, often requiring several hours [22], severely limiting its practicality for real-time applications. Real-time simultaneous calibration and execution of NMS models could bypass the limitations of traditional offline calibration, enabling immediate adaptability and precision. We recently developed a differentiable physics NMS modelling framework that combines neural network optimization techniques with physics-based models [23], and could be extended to deploy real-time continuous calibration without compromising accuracy [24].

In this study, we present a neurally controlled upper limb exoskeleton system, designed for real-time continuous calibration and execution of an EMG-informed NMS model using differentiable physics. We demonstrate the feasibility of real-time continuous calibration and execution for predicting shoulder and elbow joint moments, which directly inform exoskeleton control. Our evaluation compares the prediction

This study was supported by the Motor Accident Insurance Commission, Queensland, Australia (BioSpine project) and by a Griffith University Postgraduate Research Scholarship.

Matthew J. Hambly, Matthew T.O. Worsey, David G. Lloyd, and Claudio Pizzolato are with The Australian Centre for Precision Health and Technology (PRECISE), Queensland, Australia, and the School of Health Sciences and Social Work, Griffith University, Queensland, Australia (correspondence e-mail: matthew.hambly@griffithuni.edu.au).

accuracy and movement precision of the continuously calibrated model with both uncalibrated and offline calibrated models. Additionally, we propose a synergy-informed approach to improve model prediction accuracy.

II. Methods

A. Subjects and apparatus

A single participant (age 23 years, body mass 66 kg, height 1.76 m) with no existing musculoskeletal or neurological injuries took part in this study, providing informed consent. This study was approved by the Griffith University Human Research Ethics Committee (GU ethics no 2022/664).

The sites on the skin for 11 surface EMG recordings were prepared following the SENIAM guidelines [25], with the signals sampled at 2,048 Hz (Quattrocento, OTBioelettronica, Torino, Italy). EMG was recorded from the deltoid (anterior, medial and posterior), pectoralis major (clavicular and sternal), infraspinatus, latissimus dorsi, biceps brachii short head, triceps brachii (lateral and long heads) and brachioradialis. To normalize EMG data, maximum voluntary contractions (MVC) were recorded for each muscle, whereby the participant was instructed to exert maximal effort against a fixed resistance under isometric conditions for three seconds for each muscle group [26]. For this study, we used the ArmeoPower upper limb exoskeleton (Hocoma, Switzerland), equipped with motorized weight support and movement assistance, along with encoders for joint angle measurement. The lengths of the participant's hand, forearm, upper arm, clavicle, and torso were measured to linearly scale a musculoskeletal model.

B. System design

The overall system design (Fig. 1) incorporates the participant using the ArmeoPower exoskeleton (Fig. 1A) and their corresponding models (Fig. 1B-F) modulating the ArmeoPower's assistance (Fig. 1G). The EMG-informed NMS model (Fig. 1E) predicted musculotendon unit (MTU) forces and joint moments from experimentally recorded muscle excitations, MTU lengths and moment arms. The NMS model was based on CEINMS [19], with updated mathematics and code restructuring for faster computation, while still retaining calibration to the individual and execution of the model [24]. EMG-informed execution can be EMG-driven, where the model is directly driven by EMG derived excitations [7], or where excitations of muscles with and without EMGs are adjusted or estimated, respectively, using various methods [19, 27], e.g., synergy-informed (see section IIE).

Muscle excitations were derived from processed EMG recordings (Fig. 1B), following well established procedures [28]. The raw EMG signals were band-pass filtered using a 3rd-order Butterworth filter (30-300 Hz) to reduce noise, then rectified and low-pass filtered at 5 Hz with a 4th-order Butterworth filter to extract the linear envelope. All filters were applied in the forward direction only to enable real-time operation. The processed EMG signals were normalized to the MVC trials to quantify muscle excitations and mapped to their corresponding MTUs in the NMS model [19]. MTU lengths and moment arms were estimated from ArmeoPower and upper limb musculoskeletal models.

ArmeoPower and upper limb musculoskeletal models were driven by the ArmeoPower's real-time angle measurements for the shoulder, elbow, forearm and wrist degrees of freedom (DOFs) via its built-in encoders (Fig 1A). However, these measured joint angles do not directly correspond to the person's anatomical joint angles due to motion between the exoskeleton and human arm. To address this, we developed a custom ArmeoPower model attached to an existing upper limb musculoskeletal model [29] (Fig. 1C) using OpenSim Creator (Version 0.5.16) [30] and OpenSim (Version 4.4) [31]. The musculoskeletal model contained 12 DOFs: three sternoclavicular, three acromioclavicular, three glenohumeral (shoulder plane, shoulder elevation, shoulder rotation), elbow flexion, forearm pronation and wrist flexion. The exoskeleton and musculoskeletal models were connected using slider joints at the humerus, forearm and hand, simulating the physical straps and handle of the exoskeleton. These slider joints allowed small, single-direction movements, preventing the model from being over constrained. So, the measured

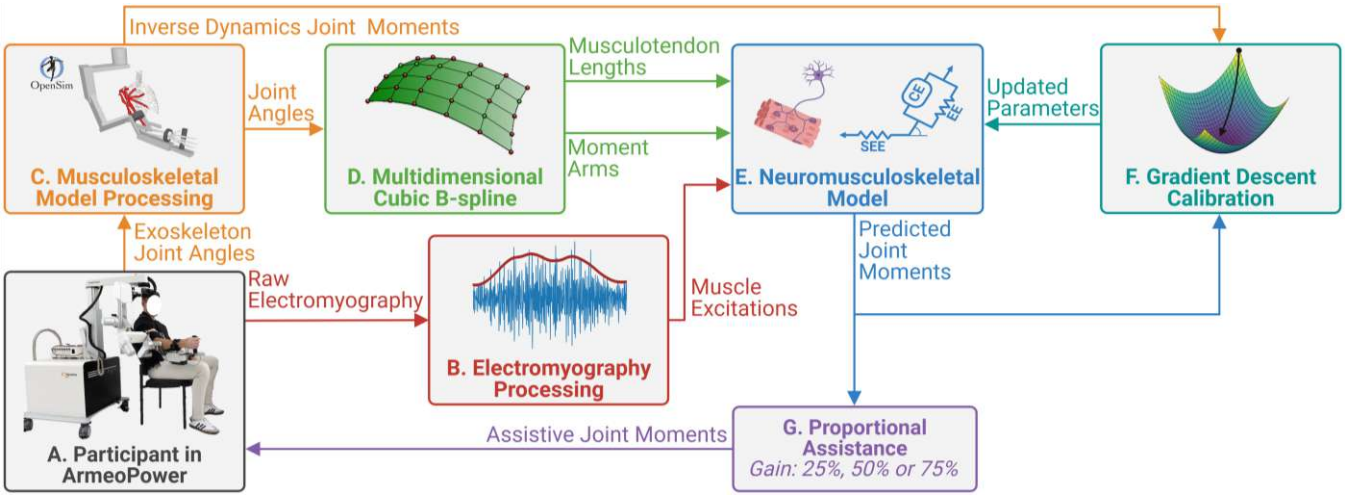


Fig. 1. Overview of the real-time EMG-informed NMS model-based exoskeleton control. (A) The participant is set up in the ArmeoPower exoskeleton, recorded joint angles and providing torque assistance. (B) Raw EMG signals are processed to obtain the muscle excitations. (C) Exoskeleton joint angles are processed through an OpenSim model providing anatomical joint angles and moments. (D) Multidimensional cubic B-splines are used to calculate the MTU lengths and moment arms. (E) The NMS model then predicts joint moments. (F) For continuous calibration, online calibration of model parameters is done using gradient descent. (G) NMS predicted joint moments informed proportional assistance through the exoskeleton motors.

exoskeleton joint angles drove the exoskeleton model kinematics, which in turn drove the musculoskeletal model to obtain the anatomical kinematics necessary to calculate the inputs for the NMS model. The NMS model contained four DOFs: shoulder plane, elevation and rotation, and elbow flexion, actuated by 14 MTUs, each driven by the recorded excitations. These were 3 deltoid, 3 pectoralis major, infraspinatus, latissimus dorsi, biceps brachii long and short heads, triceps brachii medial, lateral and long heads, and brachioradialis. The NMS model required inputs of MTU lengths and moment arms estimated via OpenSim. However, OpenSim cannot estimate these in real-time, so they were computed from MTU-specific multidimensional cubic B-splines (Fig. 1D), generated from the linearly scaled OpenSim model, enabling real-time computation [32].

Calibration requires minimizing the error between the inverse dynamics and NMS predicted joint moments. Real-time inverse dynamics were estimated using the OpenSim C++ API [33] driven by musculoskeletal model kinematics. These moments served as reference for the NMS model calibration (Fig. 1F). Calibration ensures the NMS model accurately represents individual physiology, calibrating model parameters (i.e., optimal fiber length, tendon slack length, strength coefficients and the activation dynamics) initialized from the linearly scaled OpenSim model. At each time step, the NMS model was executed in EMG driven mode (Fig 1E).

The new NMS model can perform separate or simultaneous calibration and execution, due to enhanced computational speed compared to CEINMS. This is possible using our previously validated auto-differentiable NMS modeling framework with efficient gradient-based optimization via backpropagation (Fig. 1F) [24]. To enhance computational efficiency, we adopted a stiff tendon model [34] that eliminated the need for one numerical integration step in the muscle dynamics solution. The NMS model was continuously calibrated using a sliding window approach. The most recent data, capturing approximately one movement cycles (i.e., four seconds) was used for calibration, with a single optimization iteration performed per window to maintain computational efficiency. During calibration, the following loss function was minimized:

$$Loss = \frac{1}{N_i}\sum_{i}^{N_i}\left[\frac{1}{N_d}\sum_{d}^{N_d}\left(\bar{M}_{i,d} - M_{i,d}\right)^2 + \sum_{m}^{N_m} P_{i,m}\left(\tilde{l}_m\right)\right] \quad (1)$$

$$P = \begin{cases} w(x^{min} - x)^2, & x < x^{min} \\ w(x - x^{max})^2, & x > x^{max} \\ 0, & otherwise \end{cases}$$

where N_i, N_d, and N_m are the number of time steps, DOFs and MTUs respectively, $\bar{M}$ and M are the inverse dynamics and NMS predicted joint moments, P is a penalty function for the normalized fiber length ($\tilde{l}_m$), penalizing values (x) outside of the operative range (x^{min}, x^{max}), applying a weighting (w). The loss function minimized joint moment tracking error, while penalizing normalized fiber length values outside of the range 0.5 to 1.5, ensuring physiologically plausible solutions [19]. After each calibration, updated model parameters were applied to the executing NMS model, and calibration restarted on the newest data window. A learning rate decay of 1% per iteration was implemented for gradual parameter adjustments over time.

The NMS predicted joint moments from execution were used in real-time to control the exoskeleton motors for four of its six DOFs, corresponding to the shoulder (plane, elevation and rotation) and elbow (flexion) (Fig. 1G). The predicted moments were scaled by a tunable gain factor (25%, 50% and 75%) and applied as torque outputs from the respective exoskeleton motors, augmenting the user's volitional movements. The remaining two DOFs (forearm supination and wrist flexion) were not actively assisted by the exoskeleton but allowed volitional movement. The ArmeoPower was configured to provide 50% weight support for the arm.

In summary, this computation framework enabled ArmeoPower control using uncalibrated, offline calibrated, and continuously calibrated NMS models. These models were all run using the same experimental protocol.

C. Experimental protocol

The participant performed the *Supermarket* exercise pre-programmed task on the ArmeoPower, selected because it actively engaged all four of the target control DOFs. The exercise required the participant to reach out and grasp a virtual item from a 3D space in front of them, then return the item to a centrally located basket. Upon completing a reaching task, a new target item was randomly selected for the participant to retrieve, ensuring varied and continuous movement. The participant was instructed to complete as many of these reaching tasks as possible within a two-minute period, comprising a single trial. The experiment included trials for each combination of control mode (i.e., uncalibrated model, offline calibrated model, and continuously calibrated model) and control gain (25%, 50%, and 75%), along with an unassisted trial to serve as a baseline. The order of control modes was randomized, and the participant was blinded to the condition sequence to minimize potential bias. A one-minute rest period was provided between trials to minimize fatigue.

During testing, the number of successful reaching cycles, kinematic data, EMG signals and NMS model outputs (i.e., muscle activations and forces, and joint moments) were recorded. For trials involving continuous calibration, the time required to complete each calibration window was also logged. These data were used for the calibration analyses.

D. Calibration analysis

These analyses compared the uncalibrated, offline calibrated, and continuously calibrated NMS models. The uncalibrated model provided a baseline with minimal personalization, while the offline calibrated model represented the conventional approach to obtaining optimal parameters. Offline calibration was performed using the new EMG-driven NMS approach [24], iterating over a recorded movement cycle until convergence, as indicated by no improvement in the loss over several iterations. Offline calibration data was collected from a single movement cycle recorded prior to the main data collection. The total time taken to complete the offline calibration was measured.

The recorded data were segmented into individual reaching tasks using a peak finding method applied to the grip strength data from the ArmeoPower handle, which identified when virtual items were grasped and released. A single movement cycle was defined as the period between two successive grip releases.

To evaluate the accuracy of the NMS models, root mean squared error (RMSE) between inverse dynamics and model predicted joint moments was calculated. The accuracy of the continuously calibrated model was compared against the uncalibrated and offline calibrated models. Additionally, we analyzed how the accuracy of the continuously calibrated model evolved across movement cycles, comparing it to the mean accuracy of the offline calibrated model to determine when their performance converged.

Exoskeleton control performance was assessed by counting the number of successful reaching tasks per trial and measuring the completion time for each task. Additionally, movement smoothness was quantified using the Spectral Arc Length (SPARC) [35] derived from the velocity profile of the hand based on kinematic data. SPARC was chosen in the current study over traditional jerk-based smoothness measures due to its lower sensitivity to measurement noise [35]. The SPARC measurement provides negatives values, with values closer to zero indicating smoother movements.

For analysis of the model calibration effects, data from trials under the different calibration modes were grouped across gain levels. Comparisons were made between the uncalibrated, offline calibrated, and continuously calibrated model-assisted conditions for model accuracy analysis, while the unassisted condition was included in the control analysis. Additionally, for the continuous calibration trials, the metrics from only the movement cycles occurring after the model reached accuracy comparable to offline calibration were analyzed, which was determined to be after the first 15 cycles.

E. Synergy NMS model and analysis

Pre-empting results of the EMG-driven NMS model, this approach did not achieve high joint moment accuracy, primarily due to the inability to record all experimental muscle excitations. To this end, further offline analysis was conducted using muscle synergies to synthesize missing excitations, incorporating additional MTUs that lacked recorded excitations (i.e., supraspinatus, subscapularis, teres minor, teres major, coracobrachialis, anconeus, and brachialis) into the NMS model. Muscle synergy-based NMS modelling approaches offer a promising method to reduce the number of required EMG recordings while maintaining accurate muscle excitation predictions [36].

The model was first calibrated using a synergy-hybrid approach [24], where synergies, comprising primitives and muscle weightings, were extracted using non-negative matrix factorization (NMF) [37] and subsequently optimized to synthesize excitations for MTUs without recorded signals. Calibration was performed on a single movement cycle. Following calibration, the primitives time series data for MTUs with recorded excitations were extracted from the remaining movement cycles using NMF. Excitations for unrecorded MTUs, computed using the calibrated weightings and extracted primitives, were combined with recorded excitations to drive the NMS model.

For this analysis, we used trials from the offline calibrated NMS model control condition. The model was calibrated on the first movement cycle of the trial, then executed on the two subsequent cycles. Only two cycles were used as the primitives and weightings vary over time, limiting the applicability of unrecorded muscle weightings beyond these cycles. This process was repeated for each gain level. For consistency, EMG-driven execution was performed on the same cycles using the synergy-hybrid calibrated model but was driven solely by the recorded excitations. RMSE was calculated between inverse dynamics and NMS model predictions from the EMG-driven and synergy-driven models. For analysis, data across gain levels were grouped together.

F. Statistical analysis

A Shapiro-Wilk test was conducted to assess normality of each dataset. For comparisons of model accuracy and exoskeleton control performance across the three calibration methods (uncalibrated, offline calibrated, and continuously calibrated), one-way ANOVA was applied to normally distributed data, while Kruskal-Wallis ANOVA was applied to non-normally distributed data. For the synergy execution analysis, independent sample t-tests were used for normally distributed data, and Mann-Whitney U tests were applied to non-normally distributed data. Statistical significance was set at $p<0.05$ for all analyses.

III. RESULTS

From the recorded data 20 individual movement cycles were extracted from the unassisted trial, 74 cycles from the uncalibrated trials, 81 from the offline calibrated trials, and 83 from the continuous calibration trials. For the three model control modes the cycles across all control gain level trials were combined.

For the continuous calibration method, RMSE decreased over time, requiring approximately 15 movement cycles to achieve accuracy comparable to offline calibration (Fig. 2 and Fig. 3). On average, a single calibration window took 7.3 seconds to run (110 seconds for 15 cycles), while the offline calibration process required 154 seconds.

The uncalibrated model produced significantly higher RMSE than both calibrated models (Fig. 3). When considering all continuous calibration cycles, the continuously calibrated model had significantly higher RMSE than the offline calibration for shoulder plane and elevation, and elbow flexion, but significantly lower shoulder rotation (Fig. 3). After 15 movement cycles, the continuously

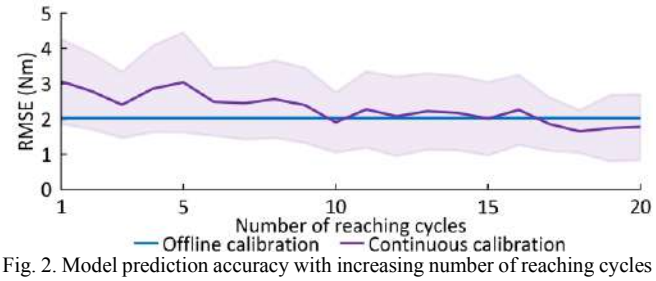


Fig. 2. Model prediction accuracy with increasing number of reaching cycles completed, averaged across all DOFs and control gain configurations.

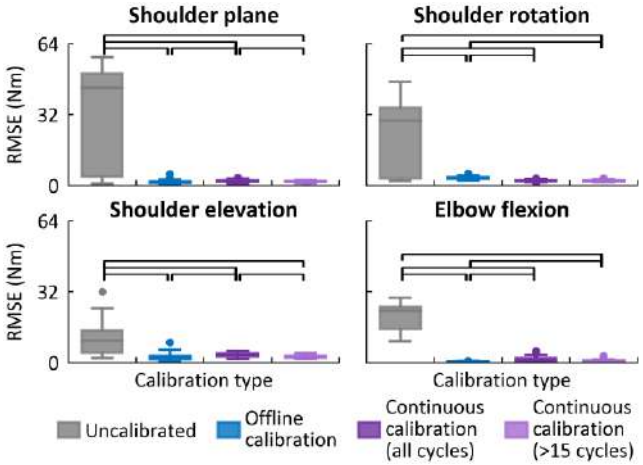


Fig. 3. Moment tracking accuracy using uncalibrated, offline calibrated and continuously calibrated models across all reaching tasks and control gain configurations. Horizontal bars signify a significant difference ($p<0.05$).

calibrated model showed significantly lower RMSE for shoulder plane and elevation compared to all cycles combined, significantly lower shoulder rotation RMSE than the offline calibration, and significantly higher RMSE for elbow flexion than the offline calibration (Fig. 3).

Regarding exoskeleton control performance, the offline calibrated model resulted in significantly higher (i.e., closer to zero) SPARC values compared to both the uncalibrated and continuously calibrated trials (Fig. 4). After 15 cycles, the continuously calibrated model produced significantly higher SPARC values than both the uncalibrated and continuously calibrated models when considering all cycles (Fig. 4). No significant differences were observed for other exoskeleton control performance metrics.

The synergy-driven model approach showed significantly lower shoulder rotation and elbow flexion moment RMSE compared to the EMG-driven method (Fig. 5).

IV. Discussion

Here we implemented a method for continuously calibrating an EMG-informed NMS model without prior calibration, using the predicted joint moments to control an upper limb exoskeleton. The approach was evaluated on a single participant performing functional reaching tasks to assess model prediction accuracy and control performance.

The uncalibrated NMS model consistently produced poor joint moment predictions, while the offline calibrated model provided the best overall moment prediction accuracy (Fig. 3), highlighting the importance of calibration. While the continuous calibration outperformed the uncalibrated model, its significantly higher RMSE compared to offline calibration (Fig. 3) may be due to a learning effect, where the model initially exhibits poor accuracy before improving over time. The continuous calibration method took less time, 15 movement cycles or 110 seconds (Fig. 2), to reach similar accuracy as the offline calibration (154 seconds). Importantly, the offline method also needs recording and processing data before commencing the calibration process, adding to the time required before being able to execute the model. Conversely, the continuous method calibrated the model parameters in a shorter time as the RSME plateaued around cycles 10–15 (Fig. 2), although this plateau had slight RMSE increases and decreases possibly reflecting transient adaptation effects from variability in movement execution, or challenges in navigating the complex solution space of the loss function before stabilizing. These findings underscore the potential of continuous calibration to replace offline calibration in time-sensitive applications. It should be noted that in this study the inverse dynamics moments were calculated without measured external forces, which may introduce ambiguity in the solution and could affect RMSE if unmodeled interaction forces were present.

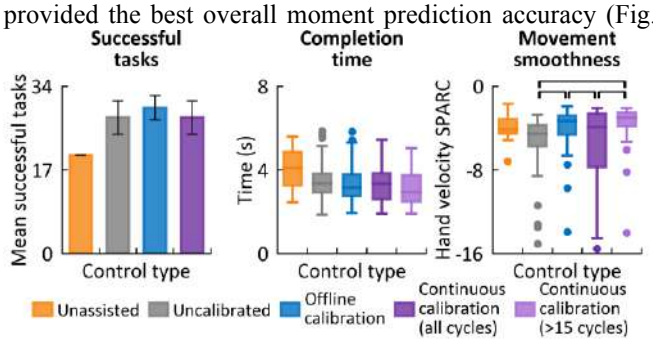


Fig. 4. Exoskeleton control performance using each model calibration type. Data for each control gain level were combined for each calibration type. Horizontal bars signify a significant difference ($p<0.05$).

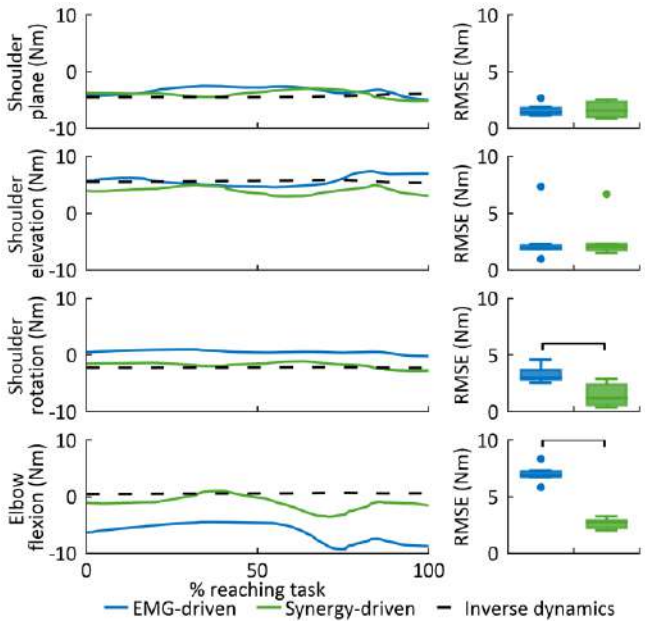


Fig. 5. Moment tracking accuracy with EMG- and synergy-driven approaches. Example time series data from movement cycle from the 25% gain control trial. RMSE was calculated from evaluated cycles across all gain conditions. Horizontal bars signify a significant difference ($p<0.05$).

Poor moment tracking across all methods for some DOFs, particularly shoulder rotation, was likely due to recorded excitations. To address this, we proposed and tested synthesizing physiologically plausible excitations for unrecorded muscles using muscle synergies. This synergy-informed approach improved joint moment predictions, particularly for DOFs with limited excitatory data (i.e., shoulder rotation) (Fig. 5). Future work should focus on adapting this synergy approach for real-time implementation, further enhancing the applicability of EMG-informed NMS modeling in dynamic environments. Continuously updating the weighting for the unrecorded excitations through calibration could also further enhance model prediction

accuracy, allowing the weightings for unrecorded muscles to best align with the time-varying primitives.

Exoskeleton control performance was evaluated across different calibration conditions, revealing that the offline calibrated model consistently delivered the best outcomes across all metrics (Fig. 4), underscoring the critical role of effective calibration in achieving the best control performance. In contrast, the uncalibrated model exhibited higher task completion times and less smooth movements (Fig. 4), likely stemming from poor model accuracy (Fig. 3), as its assistance often misaligned with participants' intentions. The continuous calibration method performed comparably to the offline calibrated model after initial adjustments, despite reduced accuracy at the onset of trials, demonstrated by a significantly higher SPARC value than the uncalibrated model and model continuously calibrated across all cycles (Fig. 4). The limited assistance level (capped at 75% of the user's volitional intent) may have mitigated differences between conditions, demonstrated by no significant differences in completion time between the different models, however, these findings demonstrate the feasibility of NMS model-driven robotic assistance in real-time applications.

Testing on an individual without neurological impairment here was a necessary first step to ensure safety and maintain experimental control. However, broader testing with individuals across a range of motor impairments, including spinal cord injury and stroke, and with a larger population, is essential to evaluate the system's adaptability and effectiveness. While the subject-specific and EMG-driven nature of the model should enable application across a wider population by accounting for neuromuscular differences, current limitations in NMS model accuracy remain a barrier to safe deployment in impaired populations. Additionally, our simple proportional controller may not provide sufficient adaptability and stability, particularly for users with neurological impairment. Since assistive joint moments influence muscle activation, there is a risk that reduced EMG due to assistance could, in turn, decrease assistance, creating a cycle that destabilizes support. These factors underscore the need for more advanced control strategies to be used in combination with NMS modelling, such as PID or adaptive controllers [10], which should be explored in future work.

Several approaches could be investigated to further improve the accuracy of the proposed methods. Firstly, muscle pathways from the underlying OpenSim musculoskeletal model are often simplified functions or geometries. These pathways can be highly sensitive to model scaling, potentially causing discontinuities in the MTU lengths used as input to the NMS model, leading to erroneous model predictions, particularly for the complex shoulder joint. The development of better representations of muscle pathways [38] may lead to improved NMS model predictions. Additionally, neural network surrogate models could improve setup and computational efficiency for calculating MTU lengths and moment arms compared to the multidimensional cubic B-spline method used in this study [39]. Another potential source of error lies in the recorded EMG signals, which can contain noise and crosstalk, particularly for muscles in close proximity of each other. While processing removes a large portion of the noise and the activation dynamics helps smooth the signal further, oscillations in the recorded signals will likely be present in the extracted primitive signals, and therefore in the synthesized excitations. To partially overcome these issues, the recorded muscle excitations could also be replaced with synergy reconstructed signals, similar to the commonly used EMG-assisted NMS model execution [19, 27]. While a stiff tendon model was used here for computational efficiency, incorporating an elastic tendon model could yield a more accurate representation of musculotendon behavior. Our previous work demonstrated the accuracy of an elastic tendon within a differentiable framework [24], although further optimization may be required for efficient real-time applications.

The ability to perform neural and muscle-level analyses through EMG-informed NMS modeling offers meaningful opportunities to understand and improve movement control. This approach enables detailed evaluation of individual muscle contributions during various motor tasks, which could inform personalized rehabilitation and training strategies. Real-time continuous calibration of NMS models, as demonstrated in this study, represents a step forward in adapting NMS models to dynamic physiological conditions, such as fatigue or recovery from injury [22], enhancing their clinical and real-world applicability. Integrating this technology with other assistive strategies, such as functional electrical stimulation (FES), could create hybrid rehabilitation systems, combining the benefits of each approach. While the exoskeleton provides mechanical assistance, FES can stimulate weakened muscles, promoting neuroplasticity and functional recovery. Subject-specific NMS models have shown potential in quantifying volitional contributions during FES [28], suggesting this integration could lead to improved monitoring and potentially even therapeutic outcomes. Beyond clinical applications, the insights provided by real-time NMS modeling could be applied to optimizing athletic performance and reducing injury risk.

V. Conclusion

In this study, we introduced a real-time continuous calibration and execution process for an EMG-informed NMS model to control an upper limb exoskeleton. The continuously calibrated model achieved comparable accuracy to an offline calibrated model after approximately 15 movement cycles, taking just 110 seconds. Offline analysis leveraging synthesized excitations from synergies for muscles with unrecorded EMG enhanced model accuracy. The proposed method delivered exoskeleton control performance comparable to the offline calibrated model, outperforming the uncalibrated model. By removing the initial calibration process, this approach enhances the practicality of EMG-informed NMS models for real-time applications, enabling personalized and physiologically valid predictions of muscle forces, and joint moments, making it a valuable tool for closed-loop neurorehabilitation systems.

References

[1] M. Mekki, A. D. Delgado, A. Fry, D. Putrino, and V. Huang, "Robotic rehabilitation and spinal cord injury: a narrative review," *Neurotherapeutics,* vol. 15, no. 3, pp. 604-617, 2018.

[2] J. Zariffa, N. Kapadia, J. Kramer, P. Taylor, M. Alizadeh-Meghrazi, V. Zivanovic, R. Willms, A. Townson, A. Curt, and M. Popovic,

"Feasibility and efficacy of upper limb robotic rehabilitation in a subacute cervical spinal cord injury population," *Spinal Cord,* vol. 50, no. 3, pp. 220-226, 2012.

[3] C. Pizzolato, D. J. Saxby, D. Palipana, L. E. Diamond, R. S. Barrett, Y. D. Teng, and D. G. Lloyd, "Neuromusculoskeletal Modeling-Based Prostheses for Recovery After Spinal Cord Injury," *Frontiers in Neurorobotics,* vol. 13, 2019.

[4] B. T. Volpe, M. Ferraro, D. Lynch, P. Christos, J. Krol, C. Trudell, H. I. Krebs, and N. Hogan, "Robotics and other devices in the treatment of patients recovering from stroke," *Current Atherosclerosis Reports,* vol. 6, no. 4, pp. 314-319, 2004.

[5] C. Lambelet, M. Lyu, D. Woolley, R. Gassert, and N. Wenderoth, "The eWrist—A wearable wrist exoskeleton with sEMG-based force control for stroke rehabilitation." pp. 726-733.

[6] W. Rong, W. Li, M. Pang, J. Hu, X. Wei, B. Yang, H. Wai, X. Zheng, and X. Hu, "A Neuromuscular Electrical Stimulation (NMES) and robot hybrid system for multi-joint coordinated upper limb rehabilitation after stroke," *Journal of neuroengineering and rehabilitation,* vol. 14, no. 1, pp. 1-13, 2017.

[7] D. G. Lloyd, and T. F. Besier, "An EMG-driven musculoskeletal model to estimate muscle forces and knee joint moments in vivo," *Journal of biomechanics,* vol. 36, no. 6, pp. 765-776, 2003.

[8] T. S. Buchanan, D. G. Lloyd, K. Manal, and T. F. Besier, "Neuromusculoskeletal modeling: estimation of muscle forces and joint moments and movements from measurements of neural command," *Journal of applied biomechanics,* vol. 20, no. 4, pp. 367-395, 2004.

[9] M. Sartori, D. G. Llyod, and D. Farina, "Neural data-driven musculoskeletal modeling for personalized neurorehabilitation technologies," *IEEE transactions on biomedical engineering,* vol. 63, no. 5, pp. 879-893, 2016.

[10] G. Durandau, D. Farina, G. Asín-Prieto, I. Dimbwadyo-Terrer, S. Lerma-Lara, J. L. Pons, J. C. Moreno, and M. Sartori, "Voluntary control of wearable robotic exoskeletons by patients with paresis via neuromechanical modeling," *Journal of neuroengineering and rehabilitation,* vol. 16, no. 1, pp. 1-18, 2019.

[11] J. Liu, Y. Ren, D. Xu, S. H. Kang, and L.-Q. Zhang, "EMG-based real-time linear-nonlinear cascade regression decoding of shoulder, elbow, and wrist movements in able-bodied persons and stroke survivors," *IEEE Transactions on Biomedical Engineering,* vol. 67, no. 5, pp. 1272-1281, 2019.

[12] C. G. McDonald, J. L. Sullivan, T. A. Dennis, and M. K. O'Malley, "A myoelectric control interface for upper-limb robotic rehabilitation following spinal cord injury," *IEEE Transactions on Neural Systems and Rehabilitation Engineering,* vol. 28, no. 4, pp. 978-987, 2020.

[13] Q. Liu, Y. Liu, Y. Li, C. Zhu, W. Meng, Q. Ai, and S. Q. Xie, "Path Planning and Impedance Control of a Soft Modular Exoskeleton for Coordinated Upper Limb Rehabilitation," *Frontiers in Neurorobotics,* vol. 15, 2021.

[14] T. S. Buchanan, and D. G. Lloyd, "Muscle activity is different for humans performing static tasks which require force control and position control," *Neuroscience Letters,* vol. 194, no. 1-2, pp. 61-64, 1995.

[15] C. Pizzolato, M. Reggiani, D. J. Saxby, E. Ceseracciu, L. Modenese, and D. G. Lloyd, "Biofeedback for gait retraining based on real-time estimation of tibiofemoral joint contact forces," *IEEE Transactions on Neural Systems and Rehabilitation Engineering,* vol. 25, no. 9, pp. 1612-1621, 2017.

[16] T. F. Besier, M. Fredericson, G. E. Gold, G. S. Beaupré, and S. L. Delp, "Knee muscle forces during walking and running in patellofemoral pain patients and pain-free controls," *Journal of biomechanics,* vol. 42, no. 7, pp. 898-905, 2009.

[17] A. Kian, C. Pizzolato, M. Halaki, K. Ginn, D. Lloyd, D. Reed, and D. Ackland, "Static optimization underestimates antagonist muscle activity at the glenohumeral joint: A musculoskeletal modeling study," *Journal of Biomechanics,* vol. 97, pp. 109348, 2019.

[18] M. Sartori, M. I. Refai, L. A. Gaudio, C. P. Cop, D. Simonetti, F. Damonte, D. G. Lloyd, C. Pizzolato, and G. Durandau, "CEINMS-RT: an open-source framework for the continuous neuro-mechanical model-based control of wearable robots," *Authorea Preprints*, 2024.

[19] C. Pizzolato, D. G. Lloyd, M. Sartori, E. Ceseracciu, T. F. Besier, B. J. Fregly, and M. Reggiani, "CEINMS: A toolbox to investigate the influence of different neural control solutions on the prediction of muscle excitation and joint moments during dynamic motor tasks," *Journal of biomechanics,* vol. 48, no. 14, pp. 3929-3936, 2015.

[20] A. Kian, C. Pizzolato, M. Halaki, K. Ginn, D. Lloyd, D. Reed, and D. Ackland, "The effectiveness of EMG-driven neuromusculoskeletal model calibration is task dependent," *Journal of Biomechanics,* vol. 129, pp. 110698, 2021.

[21] M. Sartori, M. Reggiani, D. Farina, and D. G. Lloyd, "EMG-driven forward-dynamic estimation of muscle force and joint moment about multiple degrees of freedom in the human lower extremity," *PloS one,* vol. 7, no. 12, pp. e52618, 2012.

[22] M. I. Mohamed Refai, A. Moya-Esteban, and M. Sartori, "Electromyography-driven musculoskeletal models with time-varying fatigue dynamics improve lumbosacral joint moments during lifting," *Journal of Biomechanics,* vol. 164, pp. 111987, 2024/02/01/, 2024.

[23] B. Ramsundar, D. Krishnamurthy, and V. Viswanathan, "Differentiable physics: A position piece," *arXiv preprint arXiv:2109.07573*, 2021.

[24] M. Hambly, M. Worsey, D. Lloyd, and C. Pizzolato, "Improving Calibration of EMG-Informed Neuromusculoskeletal Models Through Differentiable Physics and Muscle Synergies," nov, 2024.

[25] H. J. Hermens, B. Freriks, R. Merletti, D. Stegeman, J. Blok, G. Rau, C. Disselhorst-Klug, and G. Hägg, "European recommendations for surface electromyography," *Roessingh research and development,* vol. 8, no. 2, pp. 13-54, 1999.

[26] C. E. Boettcher, K. A. Ginn, and I. Cathers, "Standard maximum isometric voluntary contraction tests for normalizing shoulder muscle EMG," *Journal of orthopaedic research,* vol. 26, no. 12, pp. 1591-1597, 2008.

[27] M. Sartori, D. Farina, and D. G. Lloyd, "Hybrid neuromusculoskeletal modeling to best track joint moments using a balance between muscle excitations derived from electromyograms and optimization," *Journal of biomechanics,* vol. 47, no. 15, pp. 3613-3621, 2014.

[28] M. J. Hambly, A. C. C. De Sousa, D. G. Lloyd, and C. Pizzolato, "EMG-Informed Neuromusculoskeletal Modelling Estimates Muscle Forces and Joint Moments During Electrical Stimulation." pp. 1-6.

[29] W. Wu, P. V. Lee, A. L. Bryant, M. Galea, and D. C. Ackland, "Subject-specific musculoskeletal modeling in the evaluation of shoulder muscle and joint function," *Journal of biomechanics,* vol. 49, no. 15, pp. 3626-3634, 2016.

[30] A. Kewley, Beesel, J., & Seth, A. , "OpenSim Creator (0.5.16)," Zenodo, 2024.

[31] A. Seth, J. L. Hicks, T. K. Uchida, A. Habib, C. L. Dembia, J. J. Dunne, C. F. Ong, M. S. DeMers, A. Rajagopal, and M. Millard, "OpenSim: Simulating musculoskeletal dynamics and neuromuscular control to study human and animal movement," *PLoS computational biology,* vol. 14, no. 7, pp. e1006223, 2018.

[32] M. Sartori, M. Reggiani, A. J. van den Bogert, and D. G. Lloyd, "Estimation of musculotendon kinematics in large musculoskeletal models using multidimensional B-splines," *Journal of biomechanics,* vol. 45, no. 3, pp. 595-601, 2012.

[33] C. Pizzolato, M. Reggiani, L. Modenese, and D. Lloyd, "Real-time inverse kinematics and inverse dynamics for lower limb applications using OpenSim," *Computer methods in biomechanics and biomedical engineering,* vol. 20, no. 4, pp. 436-445, 2017.

[34] M. Sartori, D. G. Lloyd, M. Reggiani, and E. Pagello, "A stiff tendon neuromusculoskeletal model of the knee." pp. 132-138.

[35] S. Balasubramanian, A. Melendez-Calderon, A. Roby-Brami, and E. Burdet, "On the analysis of movement smoothness," *Journal of neuroengineering and rehabilitation,* vol. 12, no. 1, pp. 1-11, 2015.

[36] M. F. Rabbi, G. Davico, D. G. Lloyd, C. P. Carty, L. E. Diamond, and C. Pizzolato, "Muscle synergy-informed neuromusculoskeletal modelling to estimate knee contact forces in children with cerebral palsy," *Biomechanics and Modeling in Mechanobiology,* vol. 23, no. 3, pp. 1077-1090, 2024.

[37] M. F. Rabbi, C. Pizzolato, D. G. Lloyd, C. P. Carty, D. Devaprakash, and L. E. Diamond, "Non-negative matrix factorisation is the most appropriate method for extraction of muscle synergies in walking and running," *Scientific reports,* vol. 10, no. 1, pp. 1-11, 2020.

[38] B. Killen, S. Brito da Luz, D. Lloyd, A. Carleton, J. Zhang, T. Besier, and D. Saxby, "Automated creation and tuning of personalised muscle paths for OpenSim musculoskeletal models of the knee joint," *Biomechanics and Modeling in Mechanobiology,* vol. 20, pp. 521-533, 2021.

[39] B. M. Cornish, L. E. Diamond, D. J. Saxby, Z. Xia, and C. Pizzolato, "Real-time calibration-free musculotendon kinematics for neuromusculoskeletal models," *IEEE Transactions on Neural Systems and Rehabilitation Engineering*, 2024.

Somnomat Care: A Novel Robotic Bed for Vestibular Stimulation in Nursing Homes

Ricardo Manríquez-Cisterna[1], Oriella Gnarra[2,4], Ankit A. Ravankar[1†], Alexander Breuss[2], Tatsuya Yoshimi[3], Jose Victorio Salazar Luces[1], Diego Paez-Granados[2,4], Kenji Kato[3], Robert Riener[2,5], Yasuhisa Hirata[1]

***Abstract*—Sleep disorders affect one-third of the general population, with prevalence significantly increasing among the elderly. Rocking beds utilizing vestibular stimulation have shown promise as non-pharmaceutical interventions for improving sleep quality. However, existing designs lack the necessary features for retirement facilities, such as protective handles and reclining backrests, limiting their accessibility for elderly individuals who often experience markedly reduced sleep quality. In this work, we introduce Somnomat Care, an evolution of the long-running Somnomat sleep intervention project. While Somnomat Casa was designed for home use, Somnomat Care extends this concept to nursing homes and clinical environments, offering hospital-style functionality. Key enhancements include adjustable headrests, leg rests, and safety side rails, ensuring usability and safety for elderly residents. Preliminary feasibility testing with Somnomat Care demonstrated its viability and ease of integration into elderly care facilities or nursing homes. Combining innovative sleep robotics with tailored design for vulnerable populations, the newly designed robotic bed aims to enhance sleep quality, improving overall health and well-being in institutionalized elderly individuals. Future studies will validate its efficacy and assess long-term benefits, positioning Somnomat Care as a practical tool for improving sleep in geriatric care environments.**
Video: `https://youtu.be/OfjqR86ORLI`.

***Index Terms*—Sleep Robotics, Vestibular Stimulation, Robotic Bed, ROS, and System Integration.**

I. Introduction

Sleep is critical in maintaining overall health and well-being, particularly in vulnerable populations undergoing rehabilitation. During sleep, vital physiological processes, including memory consolidation, metabolic regulation, and tissue repair happen, which are essential for recovery and rehabilitation. Inadequate or poor-quality sleep is associated with various adverse health outcomes, such as cognitive decline, cardiovascular diseases, and reduced physical function, making it a crucial factor in rehabilitation programs [1].



Fig. 1. Overview of the Somnomat Care. Our contribution allows the introduction of a reclining frame and safety rails, taking into account safety and usability.

The global population is aging rapidly [2], resulting in a significant increase in the number of elderly individuals requiring rehabilitation care. This trend has placed considerable strain on the healthcare systems of many countries, which are already facing a shortage of healthcare professionals. In response, numerous countries are investing efforts to address this issue by introducing robotics and technology to assist with the decreasing workforce [3]–[6]. Among the many challenges with the aging, sleep disorders are particularly prevalent in older adults, with common issues including insomnia, sleep apnea, restless legs syndrome, and circadian rhythm disturbances [7]. These disorders not only impair sleep quality but also exacerbate comorbidities, reduce the effectiveness of rehabilitation programs, and diminish quality of life. Current pharmacological treatments for sleep disorders, while effective in some cases, often have undesirable side effects, particularly when used long-term. Such side effects include dependency, cognitive impairment, and residual daytime sleepiness, necessitating the exploration of alternative therapeutic approaches [8].

Vestibular Stimulation (VS), a non-pharmaceutical intervention, has emerged as a promising technique for improving sleep quality. It leverages the vestibular system, critical in regulating balance and spatial orientation, to promote relaxation and enhance sleep architecture [9]. Among the various applications of VS, rocking beds have shown particular promise in

[1] R. Manríquez C., A A. Ravankar, J.V. Salazar L., and Y. Hirata are with the Department of Robotics, Tohoku University, Sendai, Miyagi 980-8579, Japan {r.manriquez, ankit, j.salazar, hirata}@srd.mech.tohoku.ac.jp
[2] O. Gnarra, A. Breuss, D. Paez, and R. Riener are with Dept. of Health Sciences and Technology, ETH Zurich, Zurich, Switzerland {oriella.gnarra, alexander.breuss, diego.paez, robert.riener}@hest.ethz.ch
[3] T. Yoshimi and K. Kato are with the National Center for Gerontology and Geriatrics, Obu City, Aichi, Japan {yoshimit,kk0724}@ncgg.go.jp
[4] D. Paez and O. Gnarra are with the Swiss Paraplegic Research (SPF), Nottwil, Switzerland.
[5] R. Riener is with the Spinal Cord Injury Center, University Hospital Balgrist, Zurich, Switzerland.
†Corresponding Author: Ankit A. Ravankar
This work was partially supported by JST [Moonshot R&D] [Grant Number JPMJMS2034] and by the Japanese Society for Promotion of Science (JSPS).

inducing and sustaining sleep [10]. These systems gently rock the user, mimicking the natural motion experienced during infancy, which has been shown to enhance slow-wave sleep and improve sleep continuity [11]. Unlike other methods, these beds work overnight without requiring active participation.

Historically, rocking beds were designed primarily for short-term studies on the sleep-enhancing effects of VS in healthy individuals. Early examples include Woodward et al.'s 1990 parallel swing bed, suspended from the ceiling and powered by a motor [9], and Bayer et al.'s design, which used metal bars and an electric engine to generate horizontal oscillations [11]. Later, Morita et al. introduced a rocking chair replicating the soothing motions of a caregiver [12].

More recently, the Sensory-Motor Systems Lab at ETH Zurich developed advanced rocking beds, known as "Somnomat" to study the effects of VS on sleep under various conditions. These beds, capable of multidirectional movements, were used in studies showing significant benefits: enhanced sleep spindles in young adults, faster deep sleep transitions in older adults, and positive impacts on nap sleep architecture [13]–[15]. The first iteration of the Somnomat used a rope robot to move a bed with six Degrees of Freedom (DOF), demonstrating the concept's potential but facing challenges in practicality and scalability [16]. Subsequent iterations isolated individual DOF, but still, their large size and specialized requirements limited their use to controlled laboratory settings, preventing broader application in home environments or long-term studies [13]–[15]. The newest Somnomat, the Somnomat Casa, simplifies the system to a single DOF while ensuring safety and usability [17]. This bed also has a torque-limiting motor, pressure-sensing strips, and hinging panels to enhance safety and comfort in a system resembling a conventional bed [18].

Despite these advancements, the transition of the Somnomat system into healthcare environments, particularly nursing homes, required further adaptations. Nursing homes impose unique requirements, including enhanced safety mechanisms, adjustable components such as reclinable backrests and leg rests, and a compact design suitable for healthcare facilities. The design should also include safety provisions and quick intervention with the components in emergencies to isolate the user from the bed quickly and put them into critical care. This paper introduces the latest iteration, "Somnomat Care", which incorporates these adaptations to address the specific needs of nursing home residents while maintaining the core principles of vestibular stimulation (Figure 1). We detail key design features and technical modifications implemented in the Somnomat Care that further enhance its applicability compared to the previous iterations, highlighting its potential to improve sleep quality in elderly populations undergoing rehabilitation.

The rest of the paper is structured as follows: Section I gives a brief overview of Somnomat Casa, which forms the backbone for our new design, Somnomat Care. Section II describes the new structural design features, technical details and modifications, software architecture, ROS middleware integration, and safety features of Somnomat Care. Finally, Section III provides a brief discussion and conclusion for the article.

II. Somnomat Casa

In this section, we first give a brief overview of Somnomat Casa, which was designed at the Sensory-Motor Systems Lab at ETH Zurich, Switzerland. This design forms the inner core of our new robot bed, Somnomat Care. The following paragraphs provide a formal introduction to the key components of Somnnomat Casa.

The Somnomat Casa is a robotic bed that provides vestibular stimulation on the longitudinal axis and is intended for use in the home environment. It has a frequency range from $0.04\,\mathrm{Hz}$ to $0.4\,\mathrm{Hz}$ in a constant $10\,\mathrm{cm}$ amplitude. Previous literature shows that accelerations ranging from $0.2\,\mathrm{m\,s^{-2}}$ to $0.3\,\mathrm{m\,s^{-2}}$ show effectiveness at improving sleep, which falls in line with the accelerations attainable with Somnomat Casa, which are between $0.006\,\mathrm{m\,s^{-2}}$ to $0.63\,\mathrm{m\,s^{-2}}$ [19]. This motion is achieved by suspending the full top frame of the bed on 4 Roberts linkages [20, p. 11], special four-bar linkages that attain an approximate straight-linear motion in a small range. This top frame is connected to the bottom frame of the bed by a crank-slider mechanism, allowing for periodic motion. The crank is connected to a $400\,\mathrm{W}$ servo motor (EC60) produced by Maxon Switzerland AG motor and coupled to a 14:1 gearbox produced by IMS Gear SE Co. KGaA, Germany.

The designed bed measures $90\,\mathrm{cm} \times 200\,\mathrm{cm} \times 60\,\mathrm{cm}$, which is comparable to a regular single-size bed. The user interface is a simple two-button design meant for ease of use without any training required. One button toggles the rocking motion, and the second button turns on the handle light. This handle also incorporates two sensors: an ambient light sensor and an accelerometer.

The Somnomat Casa uses the handle-mounted light to communicate error states to the user. In the error state, the handle will turn red, indicating a problem with the bed. Similarly, for safety triggers, the robot incorporates 6 pressure-sensitive strips and two magnetic reed sensors; when triggered, the bed will stop the motion and signal red. The strips are placed on the ends of the bed and the top of the headboard and footboard; the reed sensors are placed near the pivot point of the head and footboard because they are hinged to prevent entrapment. as seen in Figure 2.

III. Somnomat Care: Design and Development

This section outlines the modifications implemented on the Somnomat Casa, forming the foundation of the proposed robotic bed. The following subsections detail the enhanced features and software upgrades significantly improving the system's capabilities.

A. Design Considerations

The development of the Somnomat Care system began with extensive consultations with nursing home staff and residents to ensure the design aligns with their needs. Key insights

were drawn from discussions with facilities accommodating individuals who, despite requiring assistance, retain partial independence. The inclusion criteria for potential users focused on adults with self-reported initial insomnia, characterized by prolonged sleep-onset latency exceeding 20–30 minutes. Additional requirements included the willingness to adhere to the study protocol and an absence of participation in concurrent sleep intervention studies. These insights informed the following technical specifications:

- **Reclinable Backrest and Leg Rest:** To enhance comfort and adaptability for diverse user needs.
- **Safety Restraints Compatibility:** Essential for ensuring the security of individuals with limited mobility or high fall risk.

Safety is a primary concern, particularly the need to rapidly convert the bed into a flat surface to facilitate emergency access. This requirement underscores the importance of designing a system that integrates seamlessly with existing caregiving protocols while maintaining ease of use for caregivers.

B. Safety Features

Implementing Somnomat Care prioritized safety, particularly given its intended use in environments with frail or disabled individuals. Building on the safety mechanisms of its predecessor, Somnomat Casa, which design incorporated multiple features to mitigate risks. Hinging panels with reed sensors were installed to halt the rocking motion upon collision detection. To further enhance safety, pressure sensors were positioned along the bed edges to prevent accidents involving the corners, and torque-limiting was employed in the main motor to reduce risks of entrapment. In the case of Somnomat Care, recognizing the importance of emergency response, the design ensures that all components above the mattress line can be quickly removed. This adjustment allows caregivers unobstructed access to users during critical situations, aligning the system with the requirements of healthcare environments. Although mandatory for emergency response, this feature also allows unobstructed caregiving day to day, for example to exchange bed sheets, change the users' clothes or to transfer the user.

C. Design Process

By evaluating the users' requirements, a plan was developed for modifying the existing Somnomat Casa and creating a new version suited for nursing care, subsequently named *Somnomat Care*. To comply with hospital and caregiving facilities standards, all accessories and parts have to be approved for medical use, and the bed should avoid having fixed components above the mattress line. Two options were considered: reclining frame conversion kits for home beds or dedicated care beds. However, conversion kits typically lack the ability to mount side rails, requiring an accessory rail installed under the mattress. This limitation makes them unsuitable for individuals who may face emergencies. Consequently, the second option was chosen: the Rento bed from Paramount Bed, Japan. Among its various sizes, the Mini 180 model was selected as it fits within the Somnomat Casa frame. After procurement, all measurements and geometries were verified, and installation confirmed no interferences between the components.

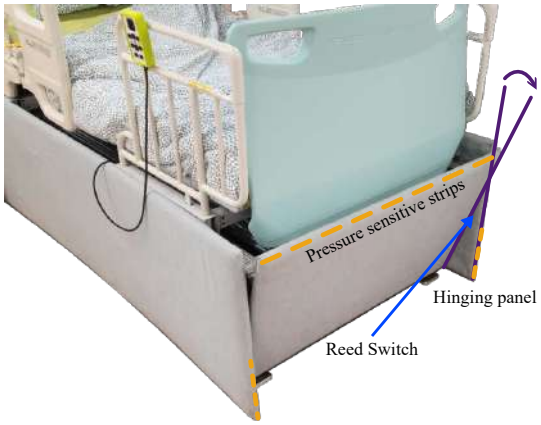


Fig. 2. Somnomat Casa safety sensors. Pressure-sensitive strips located around the hinging end panel provide safe operation in case of any possible collisions.

During the assembly of the new bed, concerns arose regarding cognitive load and ease of use. To address this, the control systems were integrated, enabling the entire robotic system to be operated from a single interface.

The original handle of the Somnomat Casa was removed to accommodate the new Paramount bed structure. This handle not only controlled functions such as activating the rocking mechanism and toggling the night light but also housed two important sensors: an illuminance sensor and an accelerometer. These sensors are valuable for sleep studies as they provide insights into the sleeping environment and detect movements on the bed. This required the design of a new remote control for the robotic system, allowing these sensors to be effectively incorporated.

D. Usability

When designing the system, consideration was taken of the target users, and it was defined that the system needs to be simple for elderly users regardless of their aging process. To achieve the goal, all systems were fused into a simple-to-use remote control that can be hung around the bed, replacing the Paramount bed remote and the Somnomat Casa handle because of the previously mentioned requirement of not having anything fixed above the mattress line (for safety and convenience reasons), both controllers needed to be merged into a single handheld operation interface. Another usability feature is the addition of folding casters, these allow the bed to be transported between rooms, this is necessary in the nursing care environment, and also allows studies to be conducted in the users' room, which should be less stressful for the person.

E. Remote Control Design

The proposed remote control was designed for reliability and ease of use, featuring a screen and 8 buttons to manage all connected systems (Figure 3). A handheld case, fitted



Fig. 3. New remote control for Somnomat Care, this control is designed to be simple to use and give adequate feedback to the user regardless of their impairments.

with a silicone cover, was sourced and machined to house the components: a piezo transducer for auditory feedback, an illuminance sensor replacing the one from the original handle, a screen to display system status for users or caregivers, button backlighting for nighttime use, and an ATSAMD51G19A microcontroller enabling double-buffered screen functionality. Icons were selected instead of text to support multilingual users, while auditory feedback was carefully designed with distinct tones—such as rising or falling pitches—to clearly convey actions like starting or adjusting bed positions.

A 3D-printed resin handle is mounted on the back of the remote. This handle serves two key functions: it allows the remote to be hung in convenient positions and acts as a light pipe to direct ambient light to the sensor below. This design prevents the sensor from being obstructed, whether the remote is hung or resting on a surface.

To overcome the limitations of the Somnomat Casa's error notification system—which signals issues only by changing the night light to red without offering guidance—the redesigned remote provides error messages and clear, actionable instructions. For instance, the interface guides users step-by-step to resolve the most common issue: realigning a triggered hinging panel.

A custom bus architecture and communication protocol were developed to ensure seamless interaction between system components. The remote communicates with the low-level controller via RS-232, enabling efficient data exchange and synchronized operation across the system.

F. System Architecture

Somnomat Care intends to integrate Somnomat Casa with a new reclinable hospital frame and a new set of sensors and controls. Somnomat Casa was designed as a main board where the main motor driver, a low-level controller, power supplies, and two Raspberry Pis connect together; the purpose of the Raspberry Pis is to do data logging and to host a Robot Operating System (ROS) subsystem to distribute the Somnomat's sensory information as standardized messages, as well as enabling its operation via ROS, making it readily available for integration with different robotic and/or IoT

TABLE I
COMMUNICATION PROTOCOL

Idx	**1**	**2**	**3**	**4**	**...**	**5+Len**	**6+Len**
Field	Header (S, M)		Command	Length	Data	CRC	Footer (T)
Example	S	M	0x10	0x00	0x00	0x22	T

systems. In the case of Somnomat Care, a low-level central controller was added, which we named the bottom controller; it communicates all the different systems, based on an ATSAMD21G18A, Microchip, USA; this micro-controller was selected because it includes many serial ports, making it ideal for our application. One of the serial ports is connected using I^2C to the Somnomat Casa Controller, another is connected using RS-485 to the Paramount Bed Controller, and a third one, using RS-232, is connected to the remote control that will command the full system. Additionally, another embedded Linux system was added, running on a Raspberry Pi, where an accelerometer connects to replace the one contained in the Somnomat Casa handle. This can be seen in Figure 4, where the protocols or methods are described in more detail. To replace the light, a new light bar was added that attaches using hangers to the headrest of the Paramount bed frame. This is also connected via USB to the embedded system. The main reason for adding new systems to the existing ones is to containerize responsibilities. As stated before, all the devices communicate via a common protocol defined for this system. The protocol is a simple message specification whose details can be seen in table Table I. From the protocol design, the use of error detection increases the reliability of the system, and it is flexible enough to add new commands in the future for more sensors or functionalities. On Table II, the different functions are listed, divided by their domain, and allow other parts of the system to instruct functions on the main bus. For example, the remote controller sends the ambient light value constantly and also listens for angle notifications to show on the screen; on an error from any system, the remote control can show it in a simple way to the user, providing pictorial information on how to solve the issue if it can be fixed by the user. It is this system that ties every component together and allows the robotic bed to work as a single unit.

G. ROS2

ROS2 is an open-source software development kit and a middleware for robotics. It builds on a set of industry-standard tools for communication, Data Distribution Service (DDS), a publisher-subscriber framework. For interface description, the Interface Description Language (IDL) is a programming language-independent description tool for interfaces between different software packages. Somnomat Care is built with ROS2 compatibility to enable deployment in different scenarios, such as integration with several sensors, robotic systems or triggers from different systems for more complex automation. The currently implemented topics are:

- Backrest and Leg Rest position
- Light color and status

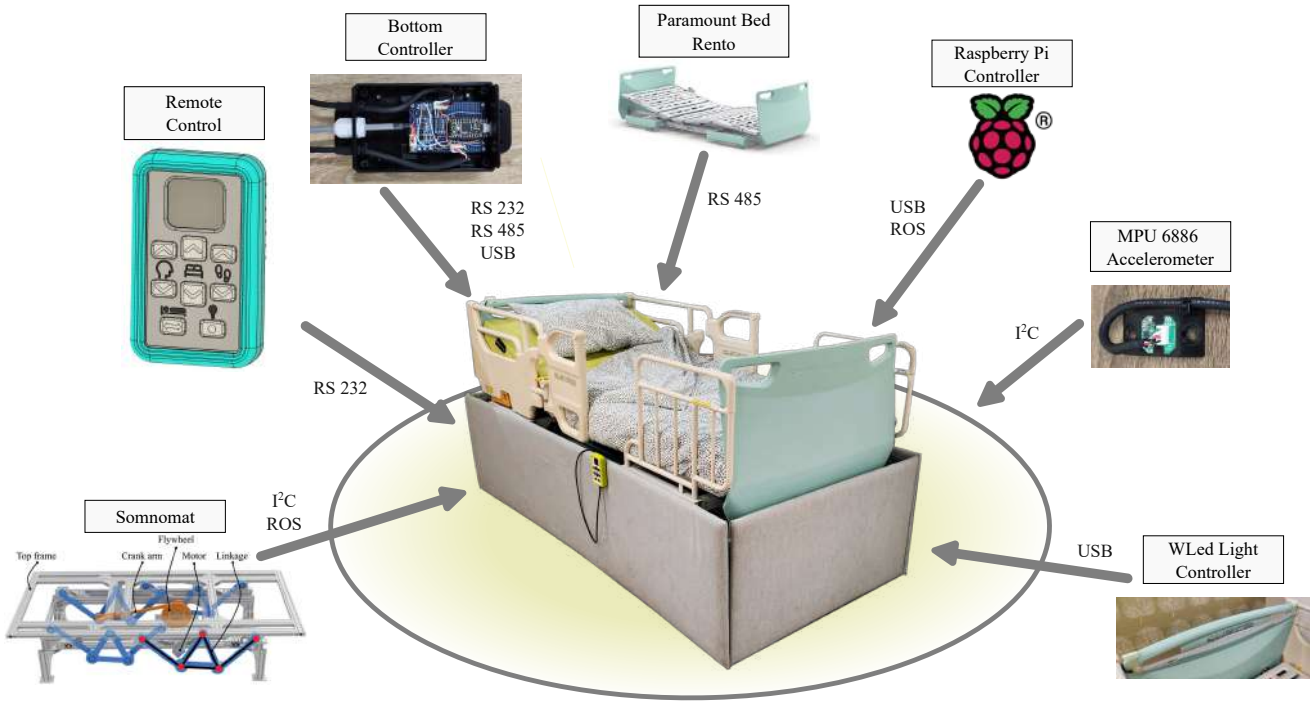


Fig. 4. System diagram: This figure shows the different interconnected parts that compose Somnomat Care. The objective is to allow Somnomat to be used safely in Healthcare environments.

TABLE II
PROTOCOL COMMANDS

Common	Ping	0x10
	Send datetime	0x11
	Send error	0x12
Paramount bed	Lift head	0x20
	Lower head	0x21
	Lift legs	0x22
	Lower legs	0x23
	Lift all	0x24
	Lower all	0x25
	Head angle notify	0x26
	Leg angle notify	0x27
	Set head position	0x28
	Set legs position	0x29
	Get head angle	0x2A
	Get legs angle	0x2B
Somnomat	Toggle rocking	0x30
	Toggle light	0x31
	Set speed	0x32
Sensors	Send lux value	0x40
Remote	Set remote brightness	0x50
	Activate alarm	0x51
	Toggle buzzer	0x52

- Ambient light measurement
- Acceleration measurement
- Toggle rocking
- Rocking speed
- Current error

With these topics, it is possible to integrate the robotic system with many different systems straightforwardly, thanks to the ROS standards, interconnection with disparate systems can be achieved with ease.

H. Future Enhancements

During the final phase of the system's design, additional functionalities were identified for potential integration. In particular, we propose the integration of a millimeter-wave (mmWave) sensor that enables non-invasive monitoring of bed occupancy, body poses, cardiovascular activity, and respiratory rate. This allows for a better understanding of the user's sleep patterns, and when vestibular stimulation is required, it also allows the user to toggle the lights or perform other interventions. A mmWave sensor shows a great fit for this application because of unobtrusiveness, ease of use, and the measured parameters fall within the range of commercial sensors during sleep, where, for example, the implemented sensor does not record heart rates above $100\,\mathrm{bpm}$.

An additional sensor under consideration is an ultrasound sensor for measuring bladder fullness. This sensor enables monitoring of the user's need to visit the toilet, potentially preventing unintended urination. It could be integrated into the system to trigger interventions, such as activating lights or more vigorous rocking, to awaken the user while simultaneously sending notifications to nursing staff. These functionalities aim to enhance the user's quality of life. However, a significant limitation of such sensors is the requirement for direct attachment to the user's body, which may lead to discomfort or rejection by some patients.

IV. Conclusion and Outlook

The Somnomat Care is the first robotic bed worldwide designed for elderly care facilities that allows for safe investigation of VS in the elderly. In this work, we presented a user-

centric design with advanced safety and usability features that address the unique challenges of nursing home environments.

We presented a new design update from the previous version that emphasizes user safety. This update includes new sensor integrations for improved and reliable data capture, user-friendly controls with ergonomic features, and advanced control through the Robot Operating System (ROS). These enhancements improve the overall design for conducting long-term vestibular studies in nursing care homes and expedite research on interventions for sleep disorders. Additionally, the new design supports modular plug-and-play sensor integration for future upgrades and facilitates ROS-based communication with other robotic systems, thereby bridging the gap for robot-based interventions.

Reliability testing revealed areas for improvement. After identifying potential failure points, some components were redesigned. Thanks to the modular architecture, these changes were easy to implement. Our goal is to develop a highly reliable system capable of operating in care environments for extended periods, even in the absence of specialized personnel.

Currently, efforts are ongoing to implement the first Somnomat Care in a Japanese nursing care facility. Japan represents an ideal environment for the implementation of Somnomat Care, given its demographic shift toward an aging population and the associated rise in age-related health challenges, particularly insomnia, which impacts more than 30% of the elderly.

We will first implement Somnomat Care in a study addressing sleep-onset insomnia. In a five-week study, residents of the elderly care facility will evaluate a combined approach of sleep hygiene recommendations and vestibular stimulation through Somnomat Care. The protocol includes a baseline week for monitoring natural sleep behaviors and EEG recordings, followed by an intervention phase where personalized sleep recommendations are implemented alongside vestibular stimuli. A two-week washout period will assess adherence to recommendations without interventions, concluding with follow-up EEGs to evaluate changes in sleep architecture. The study will then not only allow us to assess the feasibility and acceptance of the Somnomat Care as an interventional device in residents of elderly care facilities but also serve as a pilot for a future large-scale study to investigate the effects of VS on sleep quality, sleep onset latency, and daytime performance.

The initial deployment of Somnomat Care in Japanese nursing facilities will provide critical insights into its real-world efficacy. Data from these trials will inform iterative improvements and pave the way for broader adoption in healthcare settings globally. Future studies will explore the long-term impacts of vestibular stimulation on sleep architecture, comorbidities, and patient well-being, focusing on scalability and adaptability to diverse populations.

REFERENCES

[1] D. A. D. Worthington and Y. Melia, "Rehabilitation is compromised by arousal and sleep disorders: Results of a survey of rehabilitation centres," *Brain Injury*, vol. 20, no. 3, pp. 327–332, 2006, pMID: 16537274. [Online]. Available: https://doi.org/10.1080/02699050500488249

[2] M. Roser. (2024, Jul.) The global population pyramid: How global demography has changed and what we can expect for the 21st century. [Online]. Available: https://ourworldindata.org/global-population-pyramid

[3] A. A. Ravankar, S. A. Tafrishi, J. V. Salazar Luces, F. Seto, and Y. Hirata, "Care: Cooperation of ai robot enablers to create a vibrant society," *IEEE Robotics & Automation Magazine*, vol. 30, no. 1, pp. 8–23, 2023.

[4] "Harmony; Assistive robots for healthcare — harmony-eu.org," https://harmony-eu.org/, [Accessed 06-12-2024].

[5] J. Terayama, A. A. Ravankar, J. V. S. Luces, S. A. Tafrishi, and Y. Hirata, "Concept and prototype development of adaptive touch walking support robot for maximizing human physical potential," *IEEE Robotics and Automation Letters*, vol. 9, no. 8, pp. 6935–6942, 2024.

[6] Y. Hirata, J. V. S. Luces, A. A. Ravankar, and S. A. Tafrishi, "Cooperation of assistive robots to improve productivity in the nursing care field," in *The International Symposium of Robotics Research*. Springer, 2022, pp. 287–294.

[7] M. K. Pavlova and V. Latreille, "Sleep disorders," *American Journal of Medicine*, vol. 132, pp. 292–299, 3 2019.

[8] A. A. Perrault, A. Khani, C. Quairiaux, K. Kompotis, P. Franken, M. Muhlethaler, S. Schwartz, and L. Bayer, "Whole-night continuous rocking entrains spontaneous neural oscillations with benefits for sleep and memory," *Current Biology*, vol. 29, no. 3, pp. 402–411.e3, 2019. [Online]. Available: https://www.sciencedirect.com/science/article/pii/S0960982218316622

[9] S. Woodward, E. S. Tauber, A. J. Spielman, and M. J. Thorpy, "Effects of Otolithic Vestibular Stimulation on Sleep," *Sleep*, vol. 13, no. 6, pp. 533–537, 11 1990. [Online]. Available: https://doi.org/10.1093/sleep/13.6.533

[10] A. Subramaniam, A. K. Eberhard-Moscicka, M. Ertl, and F. W. Mast, "Rocking devices and the role of vestibular stimulation on sleep—a systematic review," *Clinical and Translational Neuroscience*, vol. 7, no. 4, 2023. [Online]. Available: https://www.mdpi.com/2514-183X/7/4/40

[11] L. Bayer, I. Constantinescu, S. Perrig, J. Vienne, P.-P. Vidal, M. Mühlethaler, and S. Schwartz, "Rocking synchronizes brain waves during a short nap," *Current Biology*, vol. 21, no. 12, pp. R461–R462, 2011. [Online]. Available: https://www.sciencedirect.com/science/article/pii/S0960982211005392

[12] Y. Morita, K. Yamaguchi, K. Ashida, R. Ikeura, and K. Yokoyama, "Verification of sleep-inducing effect by excitation apparatus simulating mother's embrace and rocking motion," in *9th International Workshop on Robot Motion and Control*, 2013, pp. 80–85.

[13] R. M. van Sluijs, Q. J. Rondei, D. Schluep, L. Jäger, R. Riener, P. Achermann, and E. Wilhelm, "Effect of rocking movements on afternoon sleep," *Frontiers in neuroscience*, vol. 13, p. 1446, 2020.

[14] R. van Sluijs, E. Wilhelm, Q. Rondei, X. Omlin, F. Crivelli, D. Straumann, L. Jäger, R. Riener, and P. Achermann, "Gentle rocking movements during sleep in the elderly," *Journal of sleep research*, vol. 29, no. 6, p. e12989, 2020.

[15] X. Omlin, F. Crivelli, L. Heinicke, S. Zaunseder, P. Achermann, and R. Riener, "Effect of Rocking Movements on Respiration," *PLoS One*, vol. 11, no. 3, p. e0150581, 2016.

[16] F. Crivelli, L. Heinicke, X. Omlin, and R. Riener, "Somnomat: A novel device to investigate the influence of vestibular stimulation on sleep," in *5th IEEE RAS/EMBS International Conference on Biomedical Robotics and Biomechatronics*, 2014, pp. 774–779.

[17] A. Breuss, M. Fujs, M. Müller, Z. Suter, N. Wyss, and R. Riener, "Design, development, and optimization of the somnomat casa: a rocking bed for sleep studies and nocturnal interventions in home settings," *at - Automatisierungstechnik*, vol. 72, no. 5, pp. 449–459, 2024. [Online]. Available: https://doi.org/10.1515/auto-2023-0219

[18] A. Breuss, Z. Suter, M. Fujs, and R. Riener, "Improving sleep through closed-loop autotuning of a robotic bed [accepted for publication]." *Proceedings on Automation in Medical Engineering*, 2023.

[19] K. Kompotis, J. Hubbard, Y. Emmenegger, A. Perrault, M. Mühlethaler, S. Schwartz, L. Bayer, and P. Franken, "Rocking promotes sleep in mice through rhythmic stimulation of the vestibular system," *Current Biology*, vol. 29, no. 3, pp. 392–401.e4, 2019. [Online]. Available: https://www.sciencedirect.com/science/article/pii/S0960982218316087

[20] J. M. McCarthy and G. S. Soh, *Geometric Design of Linkages*. Springer New York, 2011. [Online]. Available: http://dx.doi.org/10.1007/978-1-4419-7892-9

Preliminary results of a Multimodal Bidirectional Armband for Sensing and Feedback

Paolo Bianchino*
Rehab Technologies Lab
Istituto Italiano di Tecnologia
Genoa, Italy
paolo.bianchino@iit.it

Giulia Caserta*
Rehab Technologies Lab
Istituto Italiano di Tecnologia
Genoa, Italy
giulia.caserta@iit.it

Michele Canepa
Rehab Technologies Lab
Istituto Italiano di Tecnologia
Open University (ARC@IIT)
Genoa, Italy
michele.canepa@iit.it

Dario Di Domenico
Rehab Technologies Lab
Istituto Italiano di Tecnologia
Genoa, Italy
DET, Politecnico di Torino, Italy dario.didomenico@iit.it

Nicolò Boccardo
Rehab Technologies Lab
Istituto Italiano di Tecnologia
Open University (ARC@IIT)
Genoa, Italy
nicolo.boccardo@iit.it

Matteo Laffranchi
Rehab Technologies Lab
Istituto Italiano di Tecnologia
Genoa, Italy
matteo.laffranchi@iit.it

***Abstract*—This work presents a multimodal bidirectional armband that innovatively integrates sensing and feedback modules in an ergonomic, non-invasive design to enhance prosthetic functionalities. The armband is capable to deliver modality-matched force feedback while ensuring optimal skin adherence for electromyographic sensors, without interference. We performed a device characterization and evaluated its efficacy in improving users' ability to perceive object grasp while using the Hannes prosthetic hand. Moreover, we conducted an assessment to ensure the absence of interference between the feedback mechanism and the electromyographic acquisition system. Positive preliminary results demonstrate the armband's versatile design potential to fit into volume-adjustable sockets or in osteointegrated limb different subjects, enhancing prosthetic control and user experience, therefore providing a promising step toward advanced human-machine interaction.**

Keywords— prosthetic fitting, non-invasive feedback, EMG sensing, custom socket, upper limb prostheses.

I. INTRODUCTION

People with upper limb impairments often encounter significant obstacles when attempting routine activities. Prosthetics can help in restoring functional abilities and improve quality of life for individuals with limb absence. Despite potential advantages, many upper limb different subjects still choose not to use a prosthesis, due to issues with the socket or with the prosthetic end effector [1]. Although this latter can restore a significant portion of the missing hand functions, the absence of effective sensory feedback restoration greatly affects the user's ability to close the sensorimotor loop. Both invasive and non-invasive interfaces have been explored to convey proprioceptive [2], tactile [3] or thermal [4] information thereby improving control, increasing embodiment and reducing phantom limb pain [5]. Non-invasive methods rely on wearable haptic feedback devices, through skin-stretch [6], pressure [7], vibration [8] or electrical stimulation [9]. Force feedback is crucial for daily activities that require fine force modulation and precise pressure adjustments [10]. Feedback on grip force enables users to adjust the strength of their grasp in real-time, without relying on visual guidance only, which can require mental effort, especially in dynamic situations or when handling fragile objects [11]. Thus, developing a system integrating real-time force feedback could enhance both functional outcomes and the user's quality of life. Regarding the socket's issues, traditional solutions lack conformability, and may lead to electrode displacement, range of motion reduction, sweating, and skin irritation. These concerns limit user comfort, wear time, and complicate donning and doffing [12]. To this end, there is a clear need for advancements in materials and socket designs that prioritize stability, comfort [13], and functionality, ultimately improving the overall prosthetic experience [14]. Adjustable-volume prosthetic sockets, as the Socketless Socket from Martin Bionics, have been recently developed. These solutions simplify the fitting manufacturing [15], and overcome many of the previously mentioned limitations of traditional sockets, as sweating and skin irritation. While several research groups have distinctly explored upper limb signal extraction and haptic feedback [16], our work introduces a single armband that combines functionality with ergonomic design, simultaneously allowing non-invasive integration of myosensors with haptic feedback. In the field of upper limb prosthetics, surface electromyography (sEMG) is the main source of input for the device control. Many sEMG bracelets have been developed. One key distinction is the number of sensors: for instance, the MyoArm (Thalmic Labs) features eight sensors [17], while higher-density alternatives like EMaGer offer increased resolution [18]. Additionally, these devices vary in their construction materials, which may include rigid components, flexible elements, or a combination of both. Furthermore, some designs incorporate additional sensors, such as Inertial Measurement Units [19] or Force Myography sensors [20],

This work was supported by INAIL (Istituto Nazionale per l'Assicurazione contro gli Infortuni sul Lavoro) under Grant Agreement PR23-PAS-P1, Dexter Hand. The Open University Affiliated Research Centre at Istituto Italiano di Tecnologia (ARC@IIT) is part of the Open University, Milton Keynes, MK7, 6AA, United Kingdom.

* These authors equally contributed to this work.

to enhance functionality. Haptic feedback bracelet-like solutions are used to provide proprioception [2], contact pressure on fingers [7], or grip strength [21], mainly using vibromotors or squeezing cuff. Vibrotactile bracelets usually deliver information in a nonhomologous fashion. Squeezer bracelets, in contrast, can enhance feedback strategies by conveying grip strength as proportional compressive force to the upper limb. They generally differ in positioning (wrist, forearm, or bicep) and type of compression element (belts, Shape Memory Alloys materials, or pneumatic systems), typically controlled both in position/velocity or force/torque, employing various mechanisms [16]. While some devices integrate both sensing and feedback [22], they often lack customization, compactness and wearability. To address these gaps, we designed an innovative, customizable bidirectional armband, the Multimodal Bidirectional Armband for Sensing and Feedback (MBASF), that people with limb difference can wear comfortably, which provide both sensing and feedback. The armband could be integrated in an adjustable prosthetic socket, or it could totally replace it in case of osteointegration. Moreover, it has the potential to integrate multiple different feedback actuators. To this end, the proposed armband has been tested with the Hannes hand prosthesis for a preliminary validation in upper limb prosthetics field. The paper is organized as follows: Section II describes the MBASF system, while Section III explains the Experimental setup and Section IV the Validation methodology. Results are presented in Section V. Section VI and VII draw discussion and conclusions.

II. THE MBASF SYSTEM

MBASF integrates EMG sensing and haptic feedback into a single, wearable armband to enhance functionality and the user experience. It incorporates sEMG sensors, allowing proportional myocontrol of the prosthetic hand opening and closing based on muscle activity. Additionally, it features a custom-made squeezer for a real-time modality-matched feedback restitution of the prosthesis' grip force.

A. Design Requirements

A careful analysis of the challenges and user requirements led to the identification of several core objectives that guided the design evolution. The goal was to create a device not only functional, but also practical and comfortable. Specifically, the design aimed to achieve precise positioning, by ensuring optimal placement of the EMG sensors on the acquisition surface [23], and sufficient elasticity, allowing users to wear and remove it independently without assistance. At the same time, it was crucial to maintain an adequate rigidity to ensure that the sensors and the motorized constrictor remain stable and properly fixed during use.

B. Mechanics

The armband (Fig. 1.A) combines a rigid material (SLS-printed PA12) to provide structural support for the components, and a flexible material (SLS-printed TPU) to enable radial elasticity. This design allows for a comfortable adherence to any residual limb facilitating independent donning and doffing without assistance and ensures to hold both sensors and actuators in place. Ottobock's MyoBock sensors (13E200=50 AC) were chosen for reliable EMG signal acquisition. Five rigid housings were designed for hosting up to four EMG sensors, and the electronic board (data acquisition and processing unit). By design, it is possible to insert pairs of EMG sensors, typically used for dual-site control, into four housings. This, combined with the option to rotate the armband around the arm, provides flexible positioning to target the areas with the highest muscle activity, thereby enhancing signal quality. Moreover, thanks to the custom electronics receiving up to four EMG sensors, a machine learning-based control could be supported. The five housings are connected by two accordion-shaped stripes made with flexible material at high elastic recovery, assuring a firm EMG sensors-skin adherence. Additionally, the constrictive feedback component was designed around a motorized winch (Fig. 1.B). The winch-based system provides a proportional grip force sensation by tightening around the forearm, enabling a feedback loop that mimics natural grip pressure. The motorized constrictor stabilizes the position of the sEMG sensors on the user's arm by applying an initial preload force, selected by the experimenter. The mechanism employs a flat DC motor

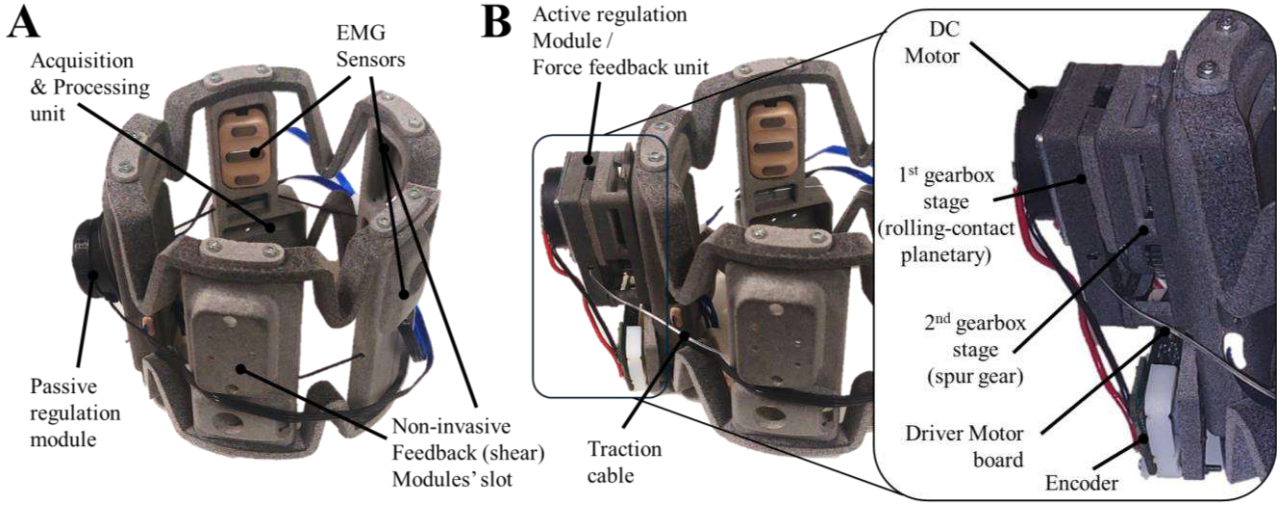


Fig. 1. MBASF mechanical architecture A) passive constrictor for regulation, B) active constrictor for non-invasive force feedback.

(Faulhaber DC motor 2607 6V) coupled with a two stages reductor (the first stage is based on a rolling-contact planetary 12.6:1, whilst the second one is based on spur gears 4:1). The entire mechanism exerts up to 315 mNm with an overall efficiency of around 0.5, therefore resulting in around 50 N winding force. The winding drum (11 mm diameter) hosts an on-axis magnet to provide absolute angle measurement via a magnetic digital encoder (AMS AS5045B). The drum has been engineered to perform one single rotation thus allowing the magnetic encoder to be reset during the bracelet's initial calibration phase hence resulting in an absolute measurement. Through this design it is possible to guarantee scalability and adaptability to any forearm sizes.

C. *Electronics and Control*

The proposed bracelet integrates two electronic modules, connected via CAN Bus, respectively responsible to acquire the sEMG sensors and to control the motorized constrictor (Fig. 2.A). From the control perspective, a proportional dual-site direct control mode is implemented for hand aperture and closure. Once the force feedback module is active, the current from the hand's motor directly correlates with the grip force exerted on the grasped object, allowing the system to restore a grip sensation on the residual limb as described in *(1),* where u_k denotes the position control command for the squeezer motor, I_k represents the motor current measured from the hand, I_{max} is the maximum current the motor can deliver, $\dot{x}$ indicates the velocity of the hand motor, and $\dot{x}_{th}$ is the threshold defined to activate the squeezer motor. The hand velocity ($\dot{x}_k$) calculated as difference between two consecutive position measurements over time, which are filtered using a low-pass filter with a cutoff frequency of 5 Hz. Muscle contraction regulates the closure speed of the prosthetic hand; upon encountering an object, sustained contraction leads to an increase in the motor's supply current (I_k) above a predefined threshold while the closing speed approaches zero. At this stage, electronic board detects that an object has been grasped and actuates the constrictor motor accordingly. As a consequence, the feedback module provides an intuitive, force-based response aligned with a modality-matching approach. In particular, the constriction force is proportional to the current delivered to the hand (I_k), reflecting the grasp force: higher currents indicate a stronger grip, prompting greater constriction, while lower currents signal a lighter grip and gentler constriction.

$$u_k = \begin{cases} \dfrac{I_k}{I_{max}} \cdot 100, & \dot{x}_k > \dot{x}_{th} \\ 0, & \dot{x}_k \leq \dot{x}_{th} \end{cases} \qquad (1)$$

III. EXPERIMENTAL SETUP

The testing setup (Fig. 2.B) consisted of three main components: a multimodal armband for sensing and feedback, the Hannes hand prosthesis, and a custom-designed sensorized object for measuring grip strength. The Hannes hand is an advanced biomimetic prosthetic hand developed by the Istituto Italiano di Tecnologia (IIT) and Centro Protesi INAIL. It combines myoelectric control with a unique mechanical differential system, allowing for versatile and adaptive grasping like a human hand. The prosthesis features a fast response time (full closure in less than 1 sec) and a maximum grasp force of 150 N. It is designed to perform a wide range of grips, from fine to power grips, enabling users to execute daily activities with ease [24]. Inspired by [25], we developed a standalone, sensorized 3D-printed object to characterize our squeezer. The object features a cylindrical shape designed for a comfortable grasp with the hand. It includes an on/off button, a LiPo battery pack (12V, 1500 mAh), an acquisition electronic board with embedded Bluetooth module, and five radially distributed compression load cells (FX293X-100A-0010-L with operative range 0÷5000 mV and 0÷45 N) strategically positioned to ensure that at least one cell is activated regardless of the grasping point. This custom-designed sensorized object measures and real-time streams via Bluetooth to a custom Unity-based Graphical User Interface (GUI) the exerted grip force (Unity GUI).

IV. VALIDATION METHODOLOGY

To evaluate the efficacy of the armband, we first conducted a device characterization followed by a twofold exploratory study using the Hannes hand prosthesis. This study involved ten healthy participants (five males and five females, aged between 26 and 35) and one trans-radial limb different subject (female, 29), for a preliminary feasibility study. Each participant provided written informed consent

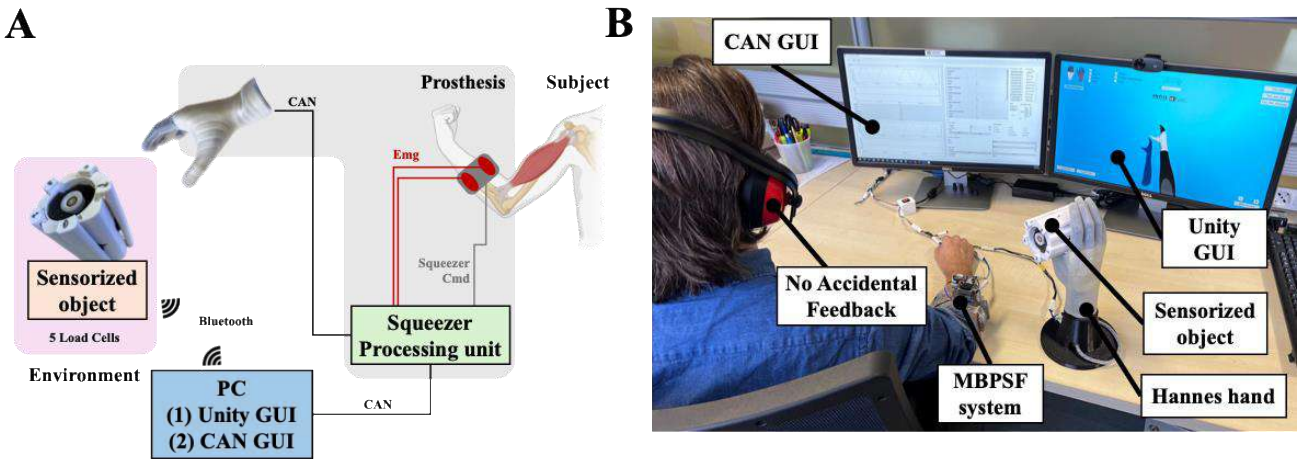


Fig. 2. Overall system and testing architecture A) MBPSF electrical architecture, B) Experimental setup with related testing architecture.

prior to the study, which followed the principles of the Declaration of Helsinki and received approval from the Territorial Ethics Committee of the Liguria Region (Protocol code: IIT_REHAB_HT01). Participants were seated in front of a table, blindfolded, and sound-isolated to eliminate sensory cues other than those provided by the armband. The right-handed Hannes prosthesis was fixed on the table, and the MBASF armband was positioned on each participant's right forearm, with EMG sensors aligned with wrist flexor and extensor muscles, to enable closing and opening of the prosthesis, respectively. Before starting the experimental session, the experimenter adjusts the tightness of the armband according to the forearm dimensions, hence ensuring a secure fit and consistent contact with the skin. Additionally, the EMG sensor thresholds were adjusted for each participant to ensure optimal controllability of the Hannes hand. Participants were then given five minutes of training with the constrictor in place to familiarize themselves with the feedback mechanism.

A. *MBASF System Characterization*

To validate the system, we started by characterizing the squeezer bracelet. To this aim, a sinusoidal reference signal (0.5 Hz, 10 repetitions) was imposed to the squeezer's DC motor (CAN GUI) while simultaneously recording the force exerted on a sensorized object placed inside the armband (Unity GUI). We then correlated the armband's constriction force with the squeezer motor current, as detailed in Subsection V.A. Notably, in real-life scenarios, the squeezer's DC motor is current-controlled using a remapped value proportional to the hand's DC motor absorbed current while grasping an object (Subsection II.C).

B. *Feedback efficacy test*

This test aimed at evaluating the efficacy of strength feedback. We expected that, during a blindfolded grasping task with the feedback device active, participants would achieve a high success rate in discerning whether an object is grasped. In this test, one experimenter controlled the Hannes closure trough the sliders on a custom made GUI (Fig. 2 - Unity GUI) to grasp the sensorized object, which may or may not have been placed in the prosthetic hand by a second experimenter. Participants were instructed to report, after each closure, whether they identified the grasped object, or a void closure based on the feedback information provided by the MBASF device. The test consisted of 10 trials per participant, with the presence or absence of the object randomly determined. The number of void closures was fixed for each participant (5) to minimize variability between subjects. The success rate was evaluated. Moreover, after completing the test, System Usability Scale (SUS) [26] was administered to the limb different participant to evaluate the system's usability.

TABLE I. Results for both healthy and limb different subjects.

Test	Healthy subjects	Trans-radial limb different subject	
	Success rate	*Success rate*	*SUS score*
Feedback efficacy	95%	90%	87.5
Sensing efficacy	100%	100%	-

C. *Sensing efficacy test*

To evaluate the accuracy of armband EMG sensing during active force feedback, a sensing efficacy test was also performed. The squeezer bracelet was controlled by sinusoidal reference (f = 0.4 Hz), inducing alternating squeezing-relaxing movements to simulate dynamic "real-world-like" conditions. Participants performed 10 voluntary closures and openings of the Hannes prosthesis via sEMG sensors, verbally stating 'open' or 'close' after each movement. This allowed the experimenter to verify sensors' functionality by ensuring the prosthesis responded correctly to the commands thus assessing any artifact generated by the skin-electrode interface. Performance was assessed by counting EMG sensor alterations, defined as instances where no signal or corresponding hand movement was detected, and calculating the success rate.

V. RESULTS

A. *MBASF System Characterization*

Fig. 3.A illustrates the system characterization. The curves should be interpreted in a counterclockwise direction. The constriction force of the armband exhibits an exponential relationship with the supply current, operating within a range of 0 to 900 mA for current and 0 to 32 N for force. Once the maximum constriction force of 32 N is generated (between 800 and 900 mA), the supply current drops immediately to zero.

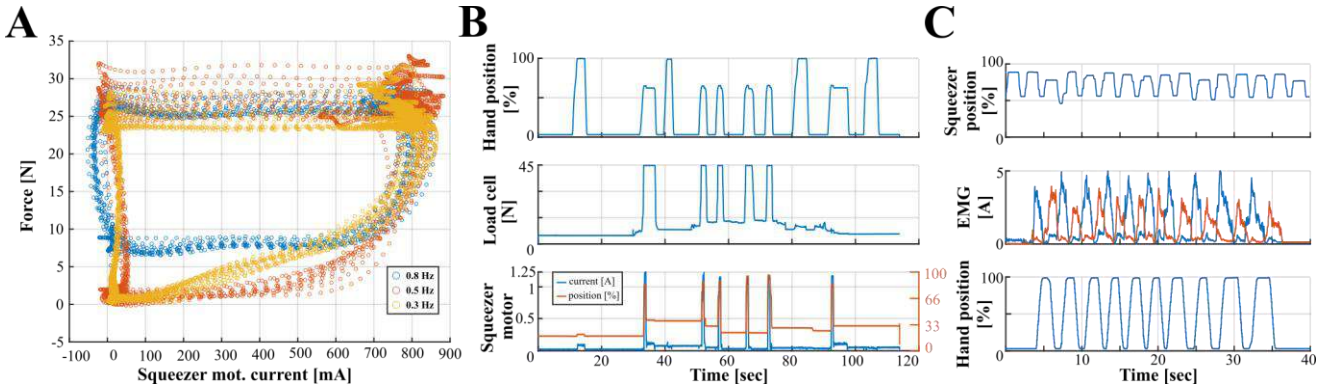


Fig. 3. Validation results A) MBAFS characterization; Single person example for B) Feedback efficacy test and C) Sensing efficacy test.

B. *Feedback efficacy test*

The healthy subjects performed a total of 100 trials. Five participants each made one error in recognizing a void grasp, giving an average success rate of 95% (TABLE I). The trans-radial limb different participant failed 1 time only on a total of 10 trials, again during a void grasp, resulting in a success rate of 90% (TABLE I). In Fig. 3.B, an example for a single participant illustrates the setup's measurements acquired during the test, such as the hand's encoder position, the load cell readings, and the squeezer motor current and position. The load cell subplot presents the value of the most activated load cell among the five available at every moment. Overall, this figure highlights the correlation between the exerted grip force by the hand (through the load cell) and the squeezer's DC motor current absorption. Moreover, regarding the SUS questionnaire, the trans-radial subject scored 87.5/100 points.

C. *Sensing efficacy test*

During the sensing efficacy test, no EMG sensor alterations were detected, either with healthy participants or limb different participant, achieving both a 100% success rate (TABLE I). In Fig. 3.C, as in Fig. 3.B it is possible to appreciate an example of results for a single participant. In this figure, during the sinusoidal operation of the squeezer, ten signals can be clearly identified for both the closure and aperture EMG sensors. These activations correspond to the hand closures and apertures, i.e., 100% and 0% of Hand position, respectively, as reported in Fig. 3.C.

VI. Discussion

The armband is designed to generate a squeezing force proportional to the hand's current *(1)*, starting from zero, when the hand is open, and gradually increasing during the object grasping. In Fig. 3A the blue curve does not return to zero because the system dynamics prevent full release at frequencies above 0.5 Hz. This occurs because constriction responds faster, while release relies on the passive elasticity of the armband, resulting in a noticeably slower response. From the feedback efficacy test (Fig. 3 B), the reaction time of the armband can be determined as the time difference between the initial increase in force, measured by the load cell in the sensorized object, and the moment the constrictor begins to close (approximately 10 ms). Meanwhile, 30 ms delay is measured in the release phase of the armband, which maintains the constriction force even in the absence of current. After this delay, the constrictor fully releases the wire, hence returning to a state of 0 N and 0 mA. These behaviours confirm the mechanical release dynamics of the actuation unit, which exhibit a slower response compared to the electrical constriction dynamics. Linking Fig. 3.A with Fig. 3.B, through the common variable squeezer motor current, it is possible to correlate the constriction force on the forearm with the hand grasping force. Moreover, the high success rate for both healthy (95%) and limb different subjects (90%) (TABLE I), demonstrates that the feedback offers an intuitive, force-based experience, hence allowing the user to easily understand when the object is grasped. As consequence, it is reasonable to suppose that this device could enhance the user's ability to proportionally modulate grip strength, improving both control and precision. The five errors in recognizing a void grasp may be caused by the armband, which must have tightened even though no object was grasped. This could be caused by two factors: the polyarticulated nature of the hand, which, may sometimes cause the fingers to touch each other, therefore increasing the motor current absorption and triggering the squeezer; or the armband's preset at zero value. For this latter, if any increase in arm volume occurs, the armband tries to return to its initial zero position, creating a tightening sensation even when the hand is not grasping an object. The SUS score of 87.5 (TABLE I), above average as greater than 68, indicates a satisfying level of usability. Moreover, according to the user's comment, MBASF is capable to evoke a grasping sensation like those of a natural limb. Indeed, the user stated that the constriction of the residual limb somehow evoked the perception of a strong contraction of both major muscle groups, like what occurs when gripping an object. Finally, in the sensing efficacy test, no alteration of the EMG sensors was registered, resulting in a success rate of 100% (TABLE I) for both healthy and limb different subjects. We can affirm that our armband successfully integrates sensing and feedback in a single wearable device as no interferences are generated by the constrictor while measuring sEMG signals.

VII. Conclusion

In this work, we explored the potential of a non-invasive human-machine interface, a multimodal armband, which combines sEMG sensing and feedback capabilities into a single wearable device. The development and design process of the armband is outlined, and we validated its efficacy through a device characterization and experimental tests with 10 healthy subjects and 1 limb different participant. Testing the armband with a final user provided first evidence of its usability. Considering the promising preliminary results, it is possible to hypothesize that the system should be able to allow users to sense grip force, offering an experience closer to the one perceived by the intact counterpart. Of course, we acknowledge that this assumption requires further analysis with the prosthesis worn by the user and tested in scenarios inspired by activities of daily living, also examining potential improvements in task performance. It will be interesting to explore if the user reduces reliance on visual feedback or improves fine force regulation. Overall, the multimodal bidirectional armband (MBASF) is easily customizable and can also be exploited as a platform for research development in both sensing and feedback strategies. The number of EMGs can be increased for machine learning-based control techniques [27] (Fig. 4.A), or direct control of hand and elbow for trans-humeral subjects with Targeted Muscle Reinnervation. Hence, the proposed armband could be easily deployed to people with limb difference at the trans-humeral level (Fig. 4.B). Furthermore, various feedback actuators can be added within the armband's housings to restore simultaneously

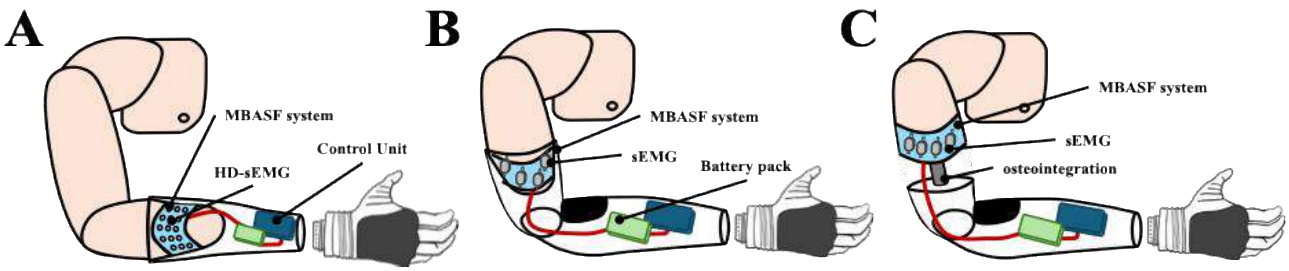


Fig. 4. Target scenarios of the MBASF armband integrated in standard sockets for A) trans-radial and B) trans-humeral, with C) osteointegration.

multiple sensations, such as touch [28], to decrease mental workload and improving human-machine interaction [29]. Finally, the armband could fit into the recently developed volume-adjustable prosthetic interfaces [15] for an everyday use or could substitute the socket in patients with osteointegration, to facilitate independent donning and doffing (Fig. 4.C). Although the small sample size of users in the experimental test, both in terms of number and types of limb difference, MBASF delivers modality-matched force feedback while ensuring optimal skin adherence for electromyographic sensors. This is a promising step toward advanced human-machine interaction, whose effectiveness could be in deep validated along with an extended clinical trial to quantitatively verify these preliminary results.

REFERENCES

[1] F. Cordella *et al.*, "Literature review on needs of upper limb prosthesis users," *Frontiers in neuroscience,* vol. 10, p. 209, 2016.

[2] A. Marinelli *et al.*, "A compact solution for vibrotactile proprioceptive feedback of wrist rotation and hand aperture," *Journal of NeuroEngineering and Rehabilitation,* vol. 21, no. 1, p. 142, 2024.

[3] F. M. Petrini *et al.*, "Six‐month assessment of a hand prosthesis with intraneural tactile feedback," *Annals of neurology,* vol. 85, no. 1, pp. 137-154, 2019.

[4] F. Iberite *et al.*, "Restoration of natural thermal sensation in upper-limb amputees," *Science,* vol. 380, no. 6646, pp. 731-735, 2023.

[5] S. J. Bensmaia, D. J. Tyler, and S. Micera, "Restoration of sensory information via bionic hands," *Nature Biomedical Engineering,* vol. 7, no. 4, pp. 443-455, 2023.

[6] J. Wheeler, K. Bark, J. Savall, and M. Cutkosky, "Investigation of rotational skin stretch for proprioceptive feedback with application to myoelectric systems," *IEEE Transactions on Neural Systems and Rehabilitation Engineering,* vol. 18, no. 1, pp. 58-66, 2010.

[7] M. R. Motamedi, D. Florant, and V. Duchaine, "A wearable haptic device based on twisting wire actuators for feedback of tactile pressure information," *Journal of Robotics and Mechatronics,* vol. 27, no. 4, pp. 419-429, 2015.

[8] L. Vargas, H. Huang, Y. Zhu, and X. Hu, "Object recognition via evoked sensory feedback during control of a prosthetic hand," *IEEE robotics and automation letters,* vol. 7, no. 1, pp. 207-214, 2021.

[9] M. Mulvey, H. Fawkner, H. Radford, and M. Johnson, "The use of transcutaneous electrical nerve stimulation (TENS) to aid perceptual embodiment of prosthetic limbs," *Medical hypotheses,* vol. 72, no. 2, pp. 140-142, 2009.

[10] C. Antfolk, M. D'alonzo, B. Rosén, G. Lundborg, F. Sebelius, and C. Cipriani, "Sensory feedback in upper limb prosthetics," *Expert review of medical devices,* vol. 10, no. 1, pp. 45-54, 2013.

[11] E. D'Anna *et al.*, "A closed-loop hand prosthesis with simultaneous intraneural tactile and position feedback," *Science Robotics,* vol. 4, no. 27, p. eaau8892, 2019.

[12] B. Peerdeman *et al.*, "Myoelectric forearm prostheses: State of the art from a user-centered perspective," *Journal of rehabilitation research and development,* vol. 48, no. 6, pp. 719-738, 2011.

[13] E. A. Biddiss and T. T. Chau, "Upper limb prosthesis use and abandonment: a survey of the last 25 years," *Prosthetics and orthotics international,* vol. 31, no. 3, pp. 236-257, 2007.

[14] A. Sturma *et al.*, "Long-term functional and clinical outcome of combined targeted muscle reinnervation and osseointegration for functional bionic reconstruction in transhumeral amputees: a case series," *Journal of Rehabilitation Medicine,* vol. 56, 2024.

[15] T. Klenow and J. Schulz, "Adjustable-volume prosthetic sockets: market overview and value propositions," *Canadian Prosthetics & Orthotics Journal,* vol. 4, no. 2, 2021.

[16] E. Pezent, P. Agarwal, J. Hartcher-O'Brien, N. Colonnese, and M. K. O'Malley, "Design, control, and psychophysics of tasbi: A force-controlled multimodal haptic bracelet," *IEEE Transactions on Robotics,* vol. 38, no. 5, pp. 2962-2978, 2022.

[17] S. Rawat, S. Vats, and P. Kumar, "Evaluating and exploring the MYO ARMBAND," in *2016 International Conference System Modeling & Advancement in Research Trends (SMART)*, 2016: IEEE, pp. 115-120.

[18] F. Chamberland *et al.*, "EMaGer: A Wearable Full-Circumference HD-EMG Sensor and Data Augmentation Method for Robust Hand Gesture Recognition," (in eng), *Annu Int Conf IEEE Eng Med Biol Soc,* vol. 2023, pp. 1-5, Jul 2023, doi: 10.1109/embc40787.2023.10340612.

[19] S. Jiang *et al.*, "Feasibility of wrist-worn, real-time hand, and surface gesture recognition via sEMG and IMU sensing," *IEEE Transactions on Industrial Informatics,* vol. 14, no. 8, pp. 3376-3385, 2017.

[20] S. Jiang, Q. Gao, H. Liu, and P. B. Shull, "A novel, co-located EMG-FMG-sensing wearable armband for hand gesture recognition," *Sensors and Actuators A: Physical,* vol. 301, p. 111738, 2020.

[21] F. Barontini *et al.*, "Evaluating the effect of non-invasive force feedback on prosthetic grasp force modulation in participants with and without limb loss," *PloS one,* vol. 18, no. 5, p. e0285081, 2023.

[22] M. A. Garenfeld *et al.*, "A compact system for simultaneous stimulation and recording for closed-loop myoelectric control," *Journal of NeuroEngineering and Rehabilitation,* vol. 18, no. 1, p. 87, 2021.

[23] A. Marinelli *et al.*, "Active upper limb prostheses: A review on current state and upcoming breakthroughs," *Progress in Biomedical Engineering,* 2022.

[24] M. Laffranchi *et al.*, "The Hannes hand prosthesis replicates the key biological properties of the human hand," *Science robotics,* vol. 5, no. 46, p. eabb0467, 2020.

[25] F. Cordella *et al.*, "Design and development of a sensorized cylindrical object for grasping assessment," in *2016 38th annual international conference of the IEEE Engineering in Medicine and Biology Society (EMBC)*, 2016: IEEE, pp. 3366-3369.

[26] J. Brooke, "SUS-A quick and dirty usability scale," *Usability evaluation in industry,* vol. 189, no. 194, pp. 4-7, 1996.

[27] D. Di Domenico *et al.*, "Long-Term Upper-Limb Prosthesis Myocontrol via High-Density sEMG and Incremental Learning," *IEEE Robotics and Automation Letters,* 2024.

[28] N. Boccardo *et al.*, "Identification of the Most Significant Tactile Sensing Pressure Points Towards Biomimetic Sensory Prosthetic Design," in *2024 10th IEEE RAS/EMBS International Conference for Biomedical Robotics and Biomechatronics (BioRob)*, 2024: IEEE, pp. 364-369.

[29] B. Stephens-Fripp, G. Alici, and R. Mutlu, "A review of non-invasive sensory feedback methods for transradial prosthetic hands," *IEEE Access,* vol. 6, pp. 6878-6899, 2018.

Automated Selectivity-Driven Algorithm for transcutaneous Spinal Cord Stimulation

Mouhamed Zorkot*[1] , Riccardo Carpineto[1], Solaiman Shokur[1,2], Silvestro Micera[1,2] and Mohamed Bouri [1]

***Abstract*—Spinal cord injury (SCI) impairs motor function and quality of life. Transcutaneous Spinal Cord Stimulation (tSCS) is a non-invasive method to restore motor function by activating spinal circuits below the lesion. However, its effectiveness is limited by individual variability, reliance on manual electrode placement, and offline muscle analysis. To address these challenges, we developed an online method for detecting spinal reflexes and muscle responses using two automated algorithms: the Ranking-Based Approach (binary method) and the Automated Selectivity-Driven Approach (leveraging a selectivity index), both designed to optimize electrode placement and stimulation amplitude for precise activation of proximal or distal muscles. In a study with six healthy participants in the supine position, the posterior root muscle test was performed automatically using tSCS across three rostrocaudal spinal electrodes. Our findings reinforce the evidence of the rostrocaudal tSCS selectivity, with rostral electrodes activating proximal muscles and caudal ones targeting distal muscles. Both algorithms identified optimal electrode positions and stimulation amplitudes, enhancing tSCS selectivity for lower-limb muscles. Our results suggest that the Automated Selectivity-Driven Approach is more appropriate for increasing selectivity for targeted muscle recruitment. These results highlight the potential of automated methods to improve tSCS selectivity for SCI rehabilitation and other conditions.**

***Keywords*-tSCS, Gait Rehabilitation, Rostrocaudal Selectivity, Muscle Recruitment, Automated Algorithm**

I. INTRODUCTION

Each year, over 500,000 people sustain spinal cord injuries (SCI), often resulting in significant mobility impairments and a lifelong need for rehabilitation [1]. Although existing therapies, such as traditional physical rehabilitation and technologies such as exoskeleton and functional electrical stimulation, offer some support [2], they often have limitations to restore natural movement and muscle coordination [2], [3]. An emerging technique for gait rehabilitation is Spinal Cord Stimulation (SCS), encompassing both invasive epidural (eSCS) and non-invasive transcutaneous (tSCS) methods, and has shown potential to enhance motor and neurorehabilitation by restoring voluntary movement, enhance sensory-motor recovery and promote supraspinal-spinal connectivity [3].

eSCS has been extensively studied over recent decades for its role in restoring voluntary movement after SCI [3] . Targeted activity programs combined with precise electrode placements have enabled patients with sensory-motor deficits to regain natural control over their legs, facilitating standing, walking, and stair climbing [3] . These advancements represent a breakthrough in neurorehabilitation; however, the clinical application of eSCS is limited by its invasive nature, which requires surgical intervention. In contrast, the non-invasive tSCS method offers broader clinical applicability. It probably activates similar neural structures in the spinal cord as eSCS[4] and, when combined with locomotor training, has shown promising functional improvements in SCI cases, improving locomotor activity, limb mobility, and walking function restoration [5], [6].

Standard tSCS clinical protocols typically use single-site, tonic stimulation with a surface electrode placed between T11-T12, delivering stimulation at 30 Hz frequency, 1 ms pulse width, and an amplitude set at 10% below the motor threshold as determined by the Posterior Root Muscle (PRM) reflex test [5], [6]. Conducted in a supine position, the PRM test evaluates short-latency spinal reflexes triggered by proprioceptive fibers in the posterior roots, activating motor neurons and producing muscle responses detectable via electromyography (EMG). This test is essential for understanding spinal cord responses to tSCS, guiding both electrode placement and stimulation amplitude selection [5].

Emerging research has explored enhancing tSCS selectivity through rostrocaudal electrode positioning along the spinal cord [7]. Studies with healthy participants in the supine position have demonstrated that this configuration can selectively recruit proximal and distal muscles [7], [8]. These findings suggest that optimizing electrode placement and stimulation parameters may enable precise motor neuron activation, supporting neurorehabilitation protocols aimed at improving joint-specific movements more effectively.

Identifying optimal electrode placement is often time-consuming and prone to suboptimal results due to individual variability across subjects and sessions. Moreover, conventional tSCS approaches rely on manual electrode positioning and offline muscle activity analysis, limiting their potential for precise and targeted selective activation [9]. Salchow-Hömmen et al. [9] proposed a binary algorithm for automated calibration using a multi-electrode spinal approach to determine the best-positioned electrode and stimulation amplitude that activates the largest number of lower-limb muscles. However, this method does not focus on optimizing tSCS selectivity.

To accelerate the process and enhance the precision of target muscle recruitment, an automated online protocol for spinal reflex detection and muscle responses induced by tSCS using electromyography (EMG). Furthermore, Two algorithms were developed and validated: a binary approach (Ranking-Based Approach), inspired and adapted from Salchow-Hömmen et al. [9]. and a novel selectivity-

[1]Swiss Federal Institute of Technology (EPFL), Translational Neural Engineering (TNE) lab and Rehabilitation and Assistive Robotics (REHAssist) lab, Lausanne, Switzerland. *Corresponding author: mouhamed.zorkot@epfl.ch

[2]Biorobotics Institute Scuola Superior Sant'anna, Pisa, Italy

driven approach (Selectivity-Driven Approach). These algorithms were developed to identify the optimal spinal electrode position and stimulation amplitude for effectively recruiting target muscles. The objective is to enable precise targeting of specific proximal or distal muscles by leveraging the rostrocaudal selectivity potential of tSCS and determine optimal parameters for single-site clinical applications.

II. Methods

A. Participants and experimental setup

We recruited 6 neurologically intact participants (5 male and female, age: 25.0 ± 3 years, height: 176.5 ± 13 cm, body mass: 69.0 ± 11.0 kg) who gave their consent to take part in this study that was reviewed and approved by EPFL Human Research Ethics Committee (HREC000477). tSCS was assessed using the PRM test [10] with three 2.5 cm electrodes placed centrally on the spinal cord between T10 - T11, T11-T12 and T12- L1 vertebrae. Stimulation was applied via a custom-made electrical stimulator (NeuroPulse), to deliver charge-balanced biphasic double pulses with a pulse width of 1ms, an interpulse interval of 50 ms. With respect to the abdominal electrodes, the selected stimulating electrode served as anode for the first phase and the cathode for the second phase of the biphasic pulses.

Muscle activity was recorded via EMG from four proximal muscles (Rectus Femoris [RF], Semitendinosus [ST], Vastus Lateralis [VL], and Vastus Medialis [VM]) and three distal muscles (Gastrocnemius [GASTRO], Tibialis Anterior [TA], and Soleus [SOL]) on both legs, using the Trigno Research+ system (Delsys, USA). The protocol was executed using a customized algorithm implemented in Python and integrated with the Delsys API.

Experimental Protocol: The PRM test was performed with an automated online protocol for spinal reflex detection developed (Section II.C). The algorithm continuously monitored muscle activity during stimulation (Sample Rate: 2148 Hz). Researchers set minimum and maximum amplitude thresholds, with each stimulation repeated three times at 5-second intervals. Amplitude increments began at 5 mA, and upon detecting a spinal reflex based on pre-established motor evoked potential (MEP) criteria, the increment was reduced to 2 mA for finer control. After detecting the first reflex for each electrode, fifteen additional stimulation amplitudes were applied, covering a range of up to 30 mA above the first reflex or the maximum amplitude tolerated by the participant. This protocol enabled detailed analysis of muscle recruitment categorized into proximal, distal, and optimal stimulation to recruit all muscles for conventional single-site tSCS approaches. Selectivity analysis focused on rostrocaudal selectivity based on spinal electrode placement, with recordings performed for each of the three electrodes (E1 to E3).

B. EMG Pre-Processing for online protocol

Pre-Processing: Online synchronization of stimulation and recording used 5-second EMG windows per repetition, relying on stimulation artifacts for precision. EMG signals

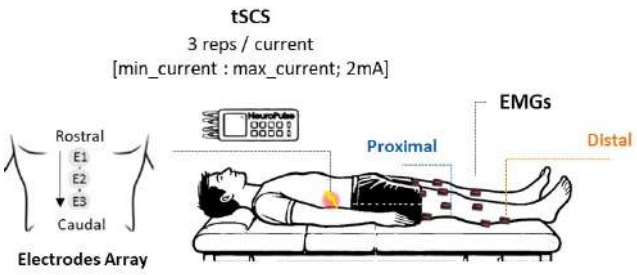


Fig. 1: **Experimental Setup:** Three electrodes (E1–E3) were placed rostrocaudally at T10-T11, T11-T12, and T12-L1. EMG data were recorded from proximal and distal muscles during automated tSCS with double-pulse stimulations every 5 seconds, repeated three times per amplitude.

were pre-processed by removing the median and detected artifacts to correct offsets and interference. Artifacts were blanked at -4 ms to 4 ms and 46 ms to 54 ms. A second-order notch filter (Butterworth, 43-47 Hz) and a first-order low-pass filter (Butterworth, 300 Hz) were applied. Noise levels for each muscle (i), amplitude (j), repetition (r), and electrode (n) were computed as the standard deviation of the signal during rest ($2.5\,\text{s} < t < 5\,\text{s}$), serving as a baseline threshold.

Artifact Detection: Stimulation artifacts were identified using a non-causal double differentiation method based on a discrete approximation of the Laplace operator. Artifacts from the first stimulus were flagged if: (1) peaks exceeded three times the noise standard deviation, (2) peaks at the interpulse interval (50 samples later) also surpassed this threshold, and (3) peak amplitudes were similar (ratio 0.8). Identified artifacts were used to synchronize EMG signals.

C. Automated tSCS Stimulation Protocol

1) ***Automatic Evaluation of Spinal Reflex****:* In MEP detection, peaks exceeding the noise threshold ($3SD \cdot emg_{\text{i,noise}}$) are identified within the time window $t_0 < t < t_0 + 40$. Upon detecting a peak, it is marked as t_{max}, and peak-to-peak amplitudes are calculated for the intervals $t_{max} - 8 < t < t_{max} + 15$ and $t_{max} + 42 < t < t_{max} + 65$, denoted as $amp_{1,i}(n, I)$ and $amp_{2,i}(n, I)$, respectively. The suppression level of the second response relative to the first is computed, and responses are classified as MEPs if the suppression level exceeds 70%, the amplitude $amp_{1,i}(n, I)$ is greater than 50μV, and it surpasses the threshold of $3SD \cdot emg_{\text{i,noise}}$.

2) ***tSCS Selectivity Analysis****:* For the selectivity analysis, recruitment curves were generated for each muscle across the three electrode configurations, using 2 mA increments in stimulation amplitude starting from the first detected reflex. At each amplitude level, three double-pulse stimulation repetitions were performed, and the average peak-to-peak value of the first pulse was calculated for repetitions exhibiting a spinal reflex. Evoked responses for each muscle were normalized to the average maximum evoked response across all three electrodes. If no response was observed at a specific amplitude but present at the previous one, the recruitment

value was maintained at the last detected level to ensure consistency in the area under the curve (AUC) calculations and minimize false negatives.

Muscle recruitment was quantified as the AUC of its recruitment curve, normalized to the maximum possible recruitment value. The selectivity index (SI) [8] was calculated to evaluate the normalized recruitment of a specific muscle relative to the average activation of all other muscles, expressed as:

$$SI_m = REC_m - \frac{\sum_{n \neq m}^{M} REC_n}{M-1}, \tag{1}$$

where REC_m is the normalized recruitment of the specific muscle, and the second term is the average normalized recruitment of the remaining $M-1$ muscles, excluding muscle m.

For this study, selectivity was analyzed based on target muscle groups (SI_T), categorized into proximal and distal muscles. The SI formula was adapted to account for these groups by averaging REC_m (REC_T)values across the target muscles (M_T) and comparing them to the average recruitment of non-target muscles. The selectivity index for the target muscle groups (SI_T) is then calculated as:

$$SI_T = REC_T - \frac{\sum_{n \in M_T}^{M} REC_n}{M - M_T}. \tag{2}$$

where M_T represents the set of all target muscles.

This index ranges from -1 to 1, providing clear interpretations:

- $SI_T = -1$: Target muscle group M_T is minimally recruited compared to non-target muscles.
- $SI_T = 0$: Target muscle group M_T is equally recruited as non-target muscles.
- $SI_T = 1$: Target muscle group M_T is maximally recruited compared to non-target muscles.

*3) **Automated Determination of Optimal Stimulation Position and Amplitude for tSCS**:* Two independent methods were developed to identify the optimal electrode position and stimulation amplitude. The first method, inspired by Salchow-Hömmen et al., [9], employs a Ranking-Based Approach using binary classification (presence or absence of reflex responses). The second method, known as the Selectivity-Driven Algorithm, enhances precision by targeting specific muscle groups through the application of the SI_T equation.

a) Ranking-Based Approach: This approach utilizes a hierarchical set of prioritized rules to determine the optimal electrode (n) and stimulation amplitude (I), based on the classification of reflex responses. The selection process follows these rules:

1) Only electrodes where at least 50% of target muscles exhibit reflex responses are considered (minimum criterion);
2) Among these, electrodes activating the highest number of target muscles are prioritized;
3) If multiple electrodes meet the above criteria, the one with the smallest difference between maximal (I) and first response (I') amplitudes is selected;
4) If still tied, the electrode requiring the lowest stimulation amplitude (I) is chosen.

The algorithm identifies the electrode (or electrodes, in case of a tie) and corresponding stimulation amplitude that best satisfy these conditions. For selectivity evaluation, the algorithm first determines the amplitude range where fewer than half of the non-target muscles are activated. Within this selective amplitude range, the same criteria (1–4) are applied exclusively to the target muscles. This process ensures that the algorithm selects the electrode that most effectively stimulates the target muscles while minimizing activation of non-target muscles. If no reflex responses are detected in the target muscles within the maximum selective amplitude, the electrode is classified as non-selective.

b) Automated Selectivity-Driven Approach :

This algorithm was developed to optimize tSCS selectivity for the targeted recruitment of proximal or distal muscle groups. The process leverages recruitment curves, AUC, and quantitative values of SI_T to determine the optimal spinal electrode position and stimulation amplitude required to achieve the desired muscle group activation.

The algorithm begins with the initial step of the Ranking-Based Approach, selecting electrodes that meet the minimum criterion of activating at least half of the target muscles before half of the non-target muscles are activated. It then calculates the mean selectivity for target muscle groups at each electrode using the SI_T formula to evaluate performance. Additionally, the stimulation amplitude is conditioned to ensure a minimum activation of at least 5% of the target muscles.

D. Statistical Analysis

Statistical analyses compared selectivity indices (SI_T) for proximal and distal muscle groups across spinal electrodes. As described by Bryson et al. [8], each participant provided one SI_T per electrode per condition, adhering to a *within-subject repeated-measures design*. Although SI_T is a single value per condition, it is derived from the mean peak-to-peak (P2P) amplitude of each target muscle across the full stimulation current range.

Data normality was first assessed with the *Kolmogorov-Smirnov test*. We applied the *Kruskal-Wallis test* ($\alpha = 0.05$) to evaluate differences in SI_T across electrodes. *Post-hoc Wilcoxon signed-rank tests* with *Benjamini-Hochberg correction*($\alpha = 0.05$) were used for pairwise comparisons, ensuring statistical rigor while accounting for repeated measures.

III. Results and Discussion

A. Online detection of spinal reflexes

The stimulation and recording setups were successfully implemented in all six participants without adverse events. To confirm a reflex, at least two out of three pulses must be identified as spinal reflexes. Online spinal reflex detection was compared with offline analysis, demonstrating consistent

recruitment curves. The online system provided effective feedback, reliably identifying spinal reflexes and ensuring robust synchronization during EMG recordings.

Spieker et al. [11] introduced a machine learning and mechanomyography-based method for automated spinal reflex detection using PRM, aiming to streamline setup and reduce time compared to EMG-based approaches, such as this study and that of Salchow-Hömmen et al. [9]. Although the EMG setup may take longer, it ensures greater reliability in muscle selectivity analysis, providing a more precise assessment of muscle responses than the acceleration data from mechanomyography.

Designed to streamline clinical applications, it supports automated stimulation protocols and enhances tSCS selectivity analysis, showing potential for optimizing therapy by targeting specific muscle groups.

B. Algorithm Prediction

After the online detection of spinal reflexes and the near-instantaneous creation of recruitment curves and normalized AUCs for all muscles for each electrode, two automated algorithms were developed: the **Ranking Approach**, inspired from Salchow-Hömmen et al. [9] and modified to assess rostrocaudal selectivity, is a binary method primarily aimed at maximizing the number of target muscles (proximal or distal). In contrast, the **Automated Selectivity-Driven Approach**, a novel method proposed in this study, utilizes quantitative values derived from SI_T (Eq. 9) while incorporating the conditions of the Ranking Approach sequentially (Section II.C3). Table (I) presents the results of both algorithms in determining the stimulation amplitude and the optimal spinal electrode positioned along the rostrocaudal axis to optimize selectivity for recruiting the target proximal or distal muscles.

		Target: Proximal			
		Ranking Based		Selectivity Driven	
		Electrode	Amp (mA)	Electrode	Amp (mA)
Subjects	S1	E3	30	E2	54
	S2	E3	44	E2	68
	S3	E3	30	E2	48
	S4	E2	60	E2	68
	S5	E2	58	E2	74
	S6	E2	58	E2	68

		Target: Distal			
		Ranking Based		Selectivity Driven	
		Electrode	Amp (mA)	Electrode	Amp (mA)
Subjects	S1	E3	30	E3	34
	S2	E2	44	E1	82
	S3	E3	44	E3	32
	S4	E3	38	E3	44
	S5	E1	66	-	-
	S6	E3	44	E3	48

TABLE I: Electrode and stimulation amplitude selected by ranking- and selectivity-based algorithms for optimal proximal or distal muscle activation..

Both approaches successfully identified the optimal electrode and stimulation amplitude to maximize recruitment of the target proximal or distal muscles. For participant S5, the **Automated Selectivity-Driven Approach** failed to identify an electrode that increased selectivity for the distal target muscle. This result is consistent, as SI_T for this participant only presented negative values for distal muscle recruitment (Table II). Although the two algorithms produced identical results for some participants (Proximal: S6; Distal: S3, S4, S6), divergences were observed in determining the optimal electrode and stimulation amplitude for the proximal and distal target muscles.

Our novel proposed approach, based on quantitative results SI_T, appears to be more robust in determining the optimal electrode and stimulation amplitude for the selective recruitment of the proximal target muscles. This robustness stems from the algorithm's ability to compare quantitative activation values across all muscles and stimulation amplitudes. The automated approach demonstrates potential for translational applications, particularly in the rehabilitation of specific lower-limb joints, reducing the time required for electrode placement, and minimizing errors associated with the identification of manual vertebrae and spinal variability. The comparison will be further analyzed and detailed in Section III.C, compared to the offline analysis of SI.

For single-site tSCS, the primary approach in clinical studies, the objective is the recruitment of all lower-limb muscles without selectivity. In this context, only the **Ranking Approach** was applied to identify the optimal electrode and stimulation amplitude, adhering to its criteria while targeting overall muscle activation. Although not shown in the table, results indicate a preference for caudal electrodes: E3 was selected for participants S1 (AMP = 29 mA), S3 (AMP = 27 mA), S5 (AMP = 45 mA), and S6 (AMP = 41 mA), while E2 was chosen for S2 (AMP = 65 mA) and S4 (AMP = 56 mA). This preference aligns with the anatomical enlargement of the lumbosacral region along the rostrocaudal axis [7], [8], [12].

C. RostroCaudal Selectivity

We investigated the rostrocaudal selectivity potential of tSCS using a multi-site automated stimulation protocol. Recruitment curves were generated, areas under the curves (AUC) calculated, and selectivity indices (SI) computed for individual muscles and proximal/distal muscle groups. Figure 2.a shows recruitment curves for subject S1, illustrating electrode placement along the rostrocaudal axis of the spinal cord. Electrode E1 (T10-T11) primarily recruited proximal muscles with higher AUC values, while electrode E3 (T12-L1) showed stronger recruitment and AUCs for distal muscles, consistent with prior studies [7], [8], [12] highlighting the effects of tSCS along the rostrocaudal axis, particularly in lumbosacral enlargement.

Normalized AUCs were used to compute the SI. Figure 2.b demonstrates that tSCS at T10-T11 selectively activates proximal muscles, while stimulation at T12-L1 targets distal muscles. While these findings align with recent studies, such as Bryson et al. [8], subject S1 exhibited a higher SI for proximal muscles when stimulated at E2 (T11-T12). This

discrepancy can be attributed to individual anatomical variations in the spinal cord [13], [10] or potential inaccuracies in electrode placement. Such inaccuracies may arise due to subject-specific variability and the limitations of manual vertebral identification and electrode positioning on the spinal cord [9].

As shown in Figure 2 .a, the selectivity of tSCS remains limited for recruiting single target muscles due to the manual application protocol and the inherent constraints of the non-invasive approach [4]. To address this limitation, we adapted the selectivity equation to group target muscles into distal or proximal categories (SI_T), as explained in Section II.C and defined in (2). Table (II) present the selectivity of target muscle groups (SI_T) for all subjects (S1 to S6) across each electrode.

		Spinal Electrodes		
		E1	E2	E3
Subjects	S1	0.351	0.585	0.554
	S2	0.103	0.235	0.153
	S3	0.198	0.553	0.204
	S4	0.230	0.386	0.251
	S5	0.008	0.289	0.103
	S6	0.076	0.482	0.362

Distal	< 0.250	0.250 - 0.500	> 0.500
Proximal	< 0.250	0.250 - 0.500	> 0.500

TABLE II: SI per subject and electrode,with positive values indicating greater selectivity for the target muscle group)

As expected, grouping the AUCs of distal and proximal muscle groups reveals a clear trend: SI_T increases for proximal muscles with stimulation at electrodes E1 or E2 and for distal muscles at electrode E3 (Table II). This confirms that tSCS at rostral positions selectively activates proximal muscles, while caudal positions, such as T12-L1, exhibit greater selectivity for distal muscles [7], [8], [12]. However, some variability was observed. Subject S2 showed greater selectivity for distal muscles at E1, while subject S5 exhibited no significant selectivity between muscle groups. These deviations may stem from limitations in manual electrode placement [9] or biophysical factors influencing tSCS conductivity, such as vertebral bones, skin, and adipose tissue tissue [13].

For the entire group ($S = 6$), SI_T analysis (Figure 3) using the Kruskal-Wallis test revealed significant differences in median SI_T values among electrodes for distal muscle groups. Since only two muscle groups were analyzed, the SI_T values and statistical results were identical for both proximal and distal groups; therefore, we present results for only one target muscle group. Post-hoc Wilcoxon pairwise comparisons with Benjamini-Hochberg correction identified significant differences between E1 vs. E2 ($p = 0.0312$) and E2 vs. E3 ($p = 0.0312$), while E1 vs. E3 showed no significant difference ($p = 0.1562$).

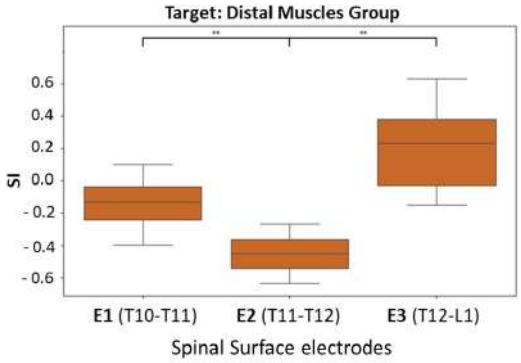


Fig. 3: Rostrocaudal Selectivity for Distal Muscles Group (S=6)

In the group analysis ($S = 6$), a rostrocaudal selectivity trend was observed: rostral electrodes showed greater selectivity for proximal muscles (E1 and E2), while the caudal electrode (E3) favored distal muscle recruitment [7], [8], [12]. However, both individual and group analyses of the selectivity index (SI) revealed that electrode E2 (T11-T12) exhibited higher proximal muscle selectivity than electrode E1 (T10-T11).

This partially contrasts with findings by Bryson et al. [8], likely due to several factors, including anatomical variations in the spinal cord, biophysical influences, and the limited sample size of our study. Additionally, our recruitment curves suggest that selectivity, whether proximal or distal, improves at lower stimulation amplitudes.

Ranking-Based vs. Selectivity-Driven Approach: A Comparative Analysis Based on Selectivity Results

When comparing the analyzed algorithms (Table I) and individual SI_T outcomes (Table II), differences between the **Selectivity-Driven Approach** and the **Ranking-Based Approach** become more evident. The Selectivity-Driven Approach consistently selects the electrode with the highest selectivity, while the Ranking-Based Approach, being binary, often chooses a suboptimal electrode for proximal (S1, S2, S3) or distal (S2, S5) muscle groups. Still, the Ranking-Based Approach remains useful for single-site tSCS, optimizing lower-limb recruitment while reducing setup time.

Additional sessions per subject and a larger sample are needed to fully assess robustness. However, based on muscle activity analysis and the direct SI equation, we suggest that the **Selectivity-Driven Approach** tends to better identify the electrode and stimulation current for optimal selectivity. Given that selective recruitment depends on electrode position and lower stimulation amplitudes, alternative methods beyond the AUC approach [13] and the binary algorithm [9] are essential for improving tSCS selectivity. The Selectivity-Driven Approach shows potential for clinical application, enhancing targeted muscle recruitment and rehabilitation outcomes.

Further validation is needed, but this approach can be translated into protocols using different stimulators, provided an EMG setup is available. Additionally, the algorithm features a user-friendly Graphic User Interface, facilitating

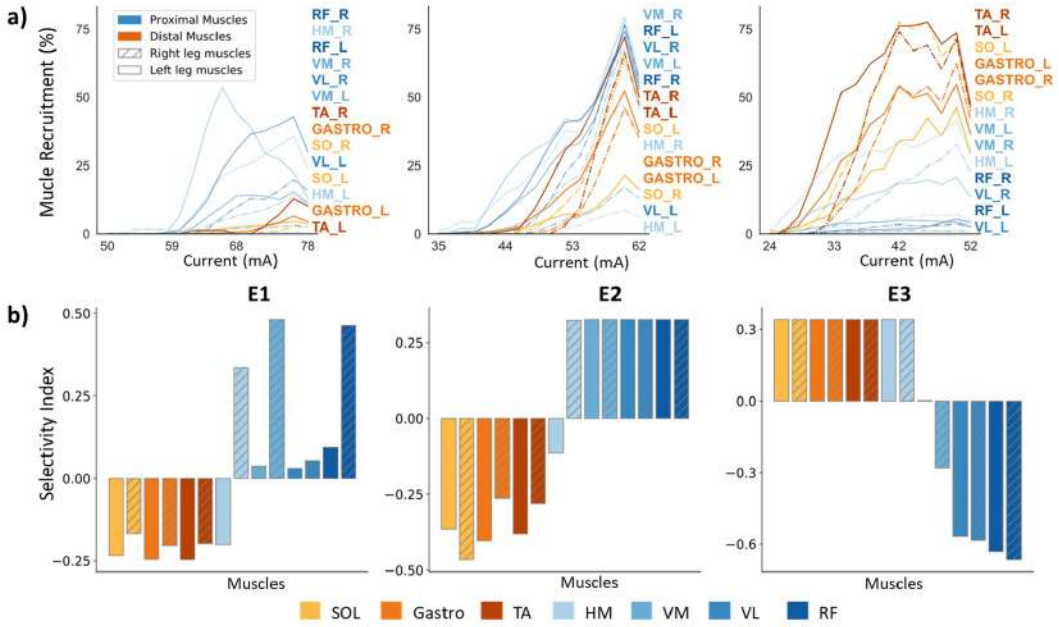


Fig. 2: a) Recruitment Curve and B) Rostro-Caudal Selectivity of S1 for Proximal and Distal Muscles.

clinician-driven parameter selection for targeted muscle recruitment via tSCS.

IV. MAIN FINDINGS

The observed rostrocaudal selectivity trend highlights the potential of multi-site tSCS for targeted muscle recruitment through precise electrode positioning. Rostral electrodes primarily activated proximal muscles, while caudal electrodes favored distal muscles. However, this trend varied in some cases, likely due to intersession variability and anatomical differences in spinal structures, underscoring the challenge of consistent electrode placement.

Both algorithms identified electrodes and stimulation currents for optimal selectivity, producing similar overall results but differing in specific choices. While additional sessions and participants are needed to assess algorithm robustness, we suggest the **Selectivity-Driven Approach** as the preferred method. By directly analyzing muscle activity rather than relying on binary classification and incorporating the SI equation, it offers greater precision in electrode selection, making it a promising tool for selective rehabilitation of specific joints and locomotor tasks.

REFERENCES

[1] M. K. Emami Maybodi, H. Hesarikia, M. Ghalamfarsa, M. M. Shater, S. Haji, M. H. Peypar, and M. Abdorrashidi, "Evaluation of spine and spinal cord injuries related to military personnel," *Trauma Monthly*, vol. 29, no. 3, pp. 1106–1113, 2024.

[2] A. Selfslagh, S. Shokur, D. S. Campos, A. R. Donati, S. Almeida, S. Y. Yamauti, D. B. Coelho, M. Bouri, and M. A. Nicolelis, "Non-invasive, brain-controlled functional electrical stimulation for locomotion rehabilitation in individuals with paraplegia," *Scientific reports*, vol. 9, no. 1, p. 6782, 2019.

[3] F. Wagner, J. Mignardot, C. Le Goff-Mignardot, R. Demesmaeker, S. Komi, M. Capogrosso, A. Rowald, I. Seáñez, M. Caban, E. Pirondini *et al.*, "Targeted neurotechnology restores walking in humans with spinal cord injury," *Nature*, vol. 563, pp. 65–71, 2018.

[4] T. S. Barss, B. Parhizi, J. Porter, and V. K. Mushahwar, "Neural substrates of transcutaneous spinal cord stimulation: neuromodulation across multiple segments of the spinal cord," *Journal of clinical medicine*, vol. 11, no. 3, p. 639, 2022.

[5] U. Hofstoetter, B. Freundl, S. Danner, M. Krenn, W. Mayr, H. Binder, and K. Minassian, "Transcutaneous spinal cord stimulation induces temporary attenuation of spasticity in individuals with spinal cord injury," *J. Neurotrauma*, vol. 37, pp. 481–493, 2020.

[6] C. Meyer, U. Hofstoetter, M. Hubli, R. Hassani, C. Rinaldo, A. Curt, and M. Bolliger, "Immediate effects of transcutaneous spinal cord stimulation on motor function in chronic, sensorimotor incomplete spinal cord injury," *Journal of Clinical Medicine*, vol. 9, p. 3541, 2020.

[7] D. G. Sayenko, D. A. Atkinson, C. J. Dy, K. M. Gurley, V. L. Smith, C. Angeli, S. J. Harkema, V. R. Edgerton, and Y. P. Gerasimenko, "Spinal segment-specific transcutaneous stimulation differentially shapes activation pattern among motor pools in humans," *Journal of Applied Physiology*, vol. 118, no. 11, pp. 1364–1374, 2015.

[8] N. Bryson, L. Lombardi, R. Hawthorn, J. Fei, R. Keesey, J. Peiffer, and I. Seáñez, "Enhanced selectivity of transcutaneous spinal cord stimulation by multielectrode configuration," *bioRxiv [Preprint]*, p. 2023.03.30.534835, Mar 31 2023, update in: J Neural Eng. 2023 Jul 07;: PMID: 37034788; PMCID: PMC10081184.

[9] C. Salchow-Hömmen, T. Schauer, P. Müller, A. Kühn, U. Hofstoetter, and N. Wenger, "Algorithms for automated calibration of transcutaneous spinal cord stimulation to facilitate clinical applications," *Journal of Clinical Medicine*, vol. 10, no. 22, p. 5464, 2021, published 2021 Nov 22.

[10] K. Minassian, B. Freundl, and U. S. Hofstoetter, "Chapter 18 - the posterior root-muscle reflex," in *Neurophysiology in Neurosurgery (Second Edition)*, second edition ed., V. Deletis, J. L. Shils, F. Sala, and K. Seidel, Eds. Academic Press, 2020, pp. 239–253. [Online]. Available: https://www.sciencedirect.com/science/article/pii/B9780128150009000186

[11] E. L. Spieker, A. Dvorani, C. Salchow-Hömmen, C. Otto, K. Ruprecht, N. Wenger, and T. Schauer, "Targeting transcutaneous spinal cord stimulation using a supervised machine learning approach based on mechanomyography," *Sensors*, vol. 24, no. 2, p. 634, 2024.

[12] K. Tran, A. Steele, R. Crossnoe, C. Martin, and D. G. Sayenko, "Multi-site lumbar transcutaneous spinal cord stimulation: When less is more," *Neuroscience Letters*, vol. 820, p. 137579, 2024.

[13] V. E. Binder, U. S. Hofstoetter, A. Rienmüller, Z. Száva, M. J. Krenn, K. Minassian, and S. M. Danner, "Influence of spine curvature on the efficacy of transcutaneous lumbar spinal cord stimulation," *Journal of clinical medicine*, vol. 10, no. 23, p. 5543, 2021.

Should Ankle Exoskeletons Also Provide Assistance During Swing Phase?

Karl Harshe
Dept. of Mechanical Engineering
Norhtern Arizona University
Flagstaff, AZ USA
kh2638@nau.edu

Ying Fang
College of Health Professions
Rosalind Franklin University of Med. and Sci.
North Chicago, IL, USA
ying.fang@rosalindfranklin.edu

Zachary F. Lerner
Dept. of Mechanical Engineering
Norhtern Arizona University
Flagstaff, AZ USA
zachary.lerner@nau.edu

Abstract— This work seeks to answer the question of whether adding swing phase dorsiflexion assistance further improves performance when walking with ankle exoskeletons providing standard powered stance phase plantar flexion assistance. The purpose of this study was to evaluate how novice exoskeleton users respond to stance phase plantar flexor assistance alone vs stance phase plantar flexor assistance combined with swing phase dorsiflexion assistance. We hypothesized that combining these assistance modalities would result in decreased metabolic power, reduced muscle activity, and improved gait mechanics. Participants performed walking trials with an untethered ankle exoskeleton under various conditions: plantar flexion assistance only or combined plantar flexion and dorsiflexion assistance. A baseline condition, where the exoskeleton was mechanically disconnected but with the same added mass, was also collected. While no significant differences were observed in steady-state metabolic power, muscle activity or toe clearance, there was a strong positive correlation (0.913) between the improvements in metabolic power across different assistance conditions. This suggests that individuals who benefited from one type of assistance also tended to benefit from the other, highlighting the potential for personalized exoskeleton design and control strategies.

Keywords— Exoskeleton, Powered Exoskeleton, Gait Mechanics

I. Introduction

Powered exoskeletons are often created with the intent to enhance human physical performance, but little research has been done on how motor patterns change when the exoskeleton is introduced [1], [2], [3]. Enhancing the efficiency of individual locomotion has been a challenging task, with only recent advancements allowing untethered exoskeletons to demonstrate a net metabolic benefit over not wearing the exoskeleton at all [4], [5], [6], [7], [8]. Many researchers have stated that a better understanding of the person wearing the exoskeleton is necessary to develop more comprehensive and impactful control strategies [9], [10].

Many of the most capable exoskeletons are currently tethered and are targeted to static research and rehabilitative settings [11], [12]. Untethered devices that have shown an ability to reduce metabolic power are rare and fewer than five are currently in the literature [1], [13]. It has been shown that merely copying the biological joint mechanics may be detrimental to metabolic power and that factors like optimal assistance onset timing and amplitude vary between individuals [12].

Extensive efforts have been dedicated to optimizing exoskeletons for walking in recent years; however, further research is warranted to assess the physiological response to fundamental modes of locomotion and assistance [14]. As exoskeletons improve metrics such as tracking error and bandwidth, we are now able to evaluate more nuanced control schemes [15]. The primary function of ankle exoskeletons is to assist in stance phase support and during push-off, providing positive ankle power to facilitate forward propulsion. For individuals with neuromuscular conditions, such as drop foot, swing phase dorsiflexion assistance from ankle exoskeletons can facilitate efficient walking. However, we are not aware of any research comparing individual responses to stance phase plantar flexor assistance with vs without swing phase dorsiflexion assistance in any study population. Our hope was that by providing the community with information on how novice users react to these two ankle assistance modes, the field can leverage this information to improve the effectiveness of new exoskeleton designs and controllers.

We sought to understand the effects of adding swing phase dorsiflexion assistance during walking with standard stance phase plantar flexion assistance, including the potential influence on motor learning [16], [17], in unimpaired adults to use a reference for future explorations in individuals with drop foot. We compared metabolic power, muscle activity, and joint kinetics during walking with (1) only stance phase plantarflexor assistance and (2) combined stance phase plantar flexion assistance with swing phase dorsiflexion assistance. The effects of acclimation and condition testing order were minimized using a repeated-reversal study design. We hypothesized that adding swing phase dorsiflexion assistance would result in decreased metabolic power and swing phase dorsiflexion muscle activity, as well as increased minimum toe clearance compared to only stance phase plantar flexion assistance [18]. The contribution of this work is the first exploration of swing phase dorsiflexion assistance

II. Methods

Ten unimpaired individuals (Table I) were enlisted from the broader Flagstaff, Arizona vicinity. The cohort comprised

This work was supported in part by Mary M. Winn-Radcliff and Gregory Winn via a gift to the Northern Arizona University Foundation.

nine novice exoskeleton users and one user with limited prior exoskeleton exposure (P10). This study was approved by the Institutional Review Board of Northern Arizona University (#986744).

TABLE I. PARTICIPANT DETAILS

	Age [years]	Sex	Mass [kg]	Leg length [m]	Walking speed [m/s]
P1	25	F	70.2	0.90	1.48
P2	24	M	70.3	0.94	1.52
P3	21	M	59.0	0.92	1.51
P4	27	M	79.3	0.96	1.53
P5	21	F	56.7	0.91	1.49
P6	20	M	70.3	0.94	1.52
P7	24	F	54.4	0.85	1.44
P8	25	F	70.4	0.89	1.48
P9	27	M	86.1	1.02	1.58
P10	22	M	68	0.93	1.51

A. The Exoskeleton

The exoskeleton was a lightweight bilateral, bidirectional battery-powered system that could assist the ankle joint in both plantar and dorsiflexion. Device characterization and sensor validation was reported previously [19], [20]. The mass of the device was approximately 2.6kg, the majority of which was housed on a waist assembly that transmitted force to a pulley that was co-located with the ankle joint. The device was powered by a 910 mAh LiPo battery housed in the waist assembly, and mechanical work done by two 24V Maxon (USA) brushless DC motors was transferred to the ankle assembly (Fig. 1 A) by steel cables housed in Bowden tubes. These cables rotated a pulley at the ankle, which drove a carbon fiber footplate. While in assistance modes, torque tracking error was 0.37-0.70 Nm [21]. Low level control was done onboard the device using an Arduino NanoBLE microcontroller connected to a custom printed circuit board. High level remote control of the device was done over Bluetooth Low Energy using a custom iOS application running on a tablet which also recorded the state data from the device in real-time.

B. Controller Description

The exoskeleton controller relied on two primary measurements: the force-sensitive resistor (FSR) values, which dictated the assistive torque assigned by a low-level controller. This torque was directly proportional to the FSR readings, with higher force levels corresponding to greater target torques. To validate these assigned torques, a custom aluminum sensor was integrated to enable real-time planar torque measurements. This sensor facilitated closed-loop proportional-derivative control, ensuring the safe operation of the system.

Furthermore, the controller for plantar and dorsiflexion assistance was synchronized with the FSR to identify each leg's stance phase. During this phase, the device provided plantar flexion assistance, while in the absence of stance phase detection, dorsiflexion assistance was activated (Fig. 1 B,C). Notably, dorsiflexion assistance was divided into two distinct

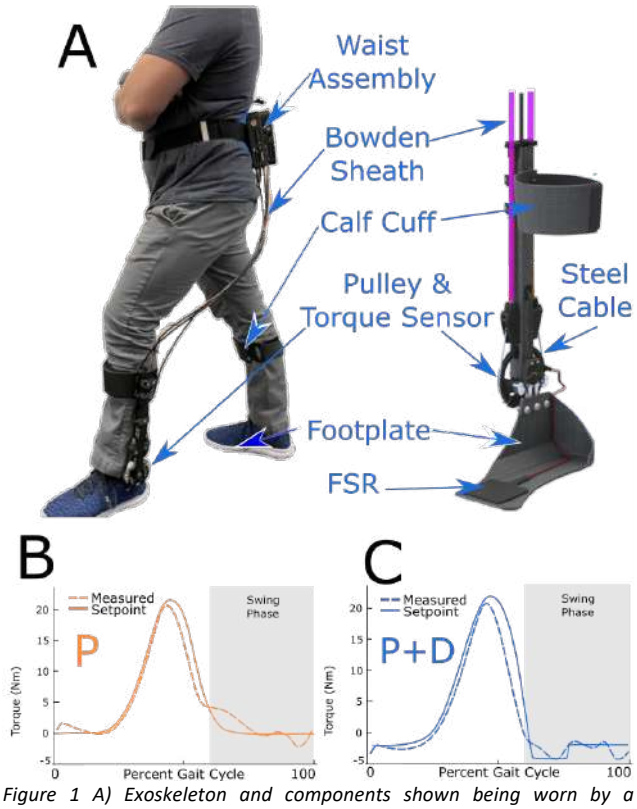


Figure 1 A) Exoskeleton and components shown being worn by a participant, B) Plantar-only torque profile for assistance, C) Plantar and Dorsiflexion torque assistance. Torque setpoints with values below zero indicate dorsiflexion assistance, while values above zero indicate plantarflexion assistance

target torques: one for early-swing phase and another for late-swing phase. The exoskeleton device defined early swing as the first 300ms after the foot left the ground, and the remainder of swing was considered late-swing. Enhancing the absolute assistance prescribed during early swing improved the overall quality of torque tracking for the device. This targeted assistance was subsequently applied from mid-swing through the initiation of stance.

C. Measurement Methods

Surface Electromyography (EMG) data was collected using lightweight Trigno Avanti sensors (Delsys Natick, MA USA). Eight such sensors were attached directly to the skin of each participant and assessed the lateral gastrocnemius, tibialis anterior, vastus lateralis and lateral biceps femoris on each leg. EMG data was synchronized with motion capture data. The final minute of each condition was selected so that the data most likely to be in steady-state conditions would be evaluated. Both peak and integrated EMG activity were evaluated during swing phase to identify changes in muscular activity while dorsiflexion assistance was in effect. Participants received no prompting or time calls.

Each subject was outfitted with 38 markers for 3-D motion capture calibration using an eight-camera Vicon system that had been previously validated [22]. Four calibration markers were removed for walking trials, but were located initially on the medial malleolus and medial condyles of each leg. Markers for motion tracking included four on the upper torso,

for on the hip, and each leg had two clusters as well as five joint markers. The four torso markers were located on the cervical spine C5, the xiphoid process of the sternum and on each of the acromioclavicular joints. The hip markers were located on each of the anterior superior iliac spines, and on the exoskeleton waist assembly in line with each posterior superior iliac spine. Each leg had two clusters of four markers located on the links of the leg. The upper cluster was placed in line with the lower 1/3 of the femur, while the lower cluster was centrally located on the tibia. Both clusters were oriented to face anteriorly with a slight external lateral bias. In addition to the clusters, each leg also had a marker on the lateral condyle and the lateral malleolus. Each foot was marked on the first and fifth toes and a posterior oriented marker was located on the calcaneus.

Gas exchange calorimetry using a Cosmed (Concord, CA USA) K5 was used to assess total energy expenditure. The device was a low-weight untethered system, and was calibrated each day within an hour of being donned. Primary analysis for this study was metabolic power, which was calculated according to a modified Brockway equation (1), normalized to body mass (M) [23]. The modified Brockway equation used values of the volumetric flow rate of expired oxygen $\dot{V}O^2$ and carbon dioxide $\dot{V}CO^2$ to estimate metabolic power.

$$MeT = \left(16.58 * \dot{V}O^2 + 4.51 * \dot{V}CO^2\right)/M \quad (1)$$

The participant's leg length was used to determine nondimensional walking speed for both visits [24]. We set a target nondimensional walking speed of 0.5, based off of a desire to see strenuous walking without approaching the walk-run threshold (0.72) [25]. The equation for nondimensional walking speed (2) normalized based on each participant's leg length (L) and accounted for stride-length being highly correlated with efficient walking speed [26], [27].

$$\text{Walking speed} = 0.50 * \sqrt{(9.81 * L)} \quad (2)$$

In an attempt to account for learning effects, each participant underwent an acclimation visit less than 36 hours before data collection was done. Order effects were mitigated through the double reversal condition ordering (Fig. 2). The level of assistance (torque) was based on the mass of the participant, and dorsiflexion was 10 percent of plantar flexion assistance [22].

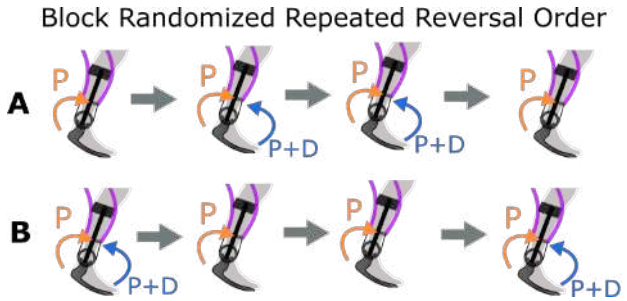


Figure 2 Participants were assigned to one of two study order groups A or B. Testing order went from left to right and only altered the mode of assistance that was delivered. This order of exposure was present in both the acclimation visit and the testing visit. "P" indicates plantar flexion assistance only, while "P+D" indicates both plantar and dorsiflexion assistance.

D. Protocol

Initially participants underwent a 30-45 minute acclimation visit in which they walked on the treadmill, donned the exoskeleton, walked for five minutes in each of the tested conditions, leg length was measured according to Carty and Bennett and were fitted for the calorimetry mask. This process allowed them to establish a comfort level with the laboratory environment and ask questions freely.

Prior to data collection, the participants underwent a 20-minute re-acclimation period where they walked in the exoskeleton a second time. The experimental protocol consisted of six bouts of walking with the exoskeleton, each lasting eight minutes with eight minutes of rest in between. Between conditions, there were eight-minute seated resting periods where conversation was kept to a minimum. Meyers et al. showed that 100 steps gave participants enough time to make biomechanical adjustments to steady-state walking [28], as a result we felt confident that prior conditions were not impacting subsequent tests. Each walking trial was monitored throughout by real time calorimetry, surface EMG and the first thirty seconds of the sixth minute was motion tracked.

Immediately prior to the first walking trial, a standing baseline was collected for no less than three minutes. Estimates of metabolic power during steady-state for each condition were calculated by taking the mean of all values of the final two minutes of the condition and comparison of conditions was done using the mean of similar conditions for each participant. Each trial was recorded in its entirety for both the EMG and calorimetry, however only the first half of the sixth minute of each trial was recorded with motion capture due to hardware limitations. This timing of motion capture was selected for its representative nature. Every participant initially experienced a mechanically disconnected scenario known as zero-torque where the ability of the device to impart torque to the ankle was removed.

The participants were split into two groups and experienced either the ``A" or the ``B" protocol (Fig. 2). Testing order ``A" corresponded to stance-phase plantar flexion only assistance followed by two plantar and dorsiflexion assistance conditions, with a stance-phase plantar flexion only condition to conclude assisted walking. Testing order ``B" was the inverse, with plantar only assistance making up the middle conditions. In both testing orders there was a zero-torque trial that preceded the testing and one that followed the testing.

E. Data Analysis

The measured metrics in this study were normalized metabolic power, EMG signals for the eight muscles observed, and the dynamics and kinematics of walking. Significance for all metrics was set at alpha = 0.05. We calculated the averages for each metric across different conditions and analyzed differences using repeated measures

t-tests, due to the exploratory nature of this research we chose not to adjust significance values for repeated measures. For each metric, the value associated with each condition was the average of the two trials conducted under that condition.

Metabolic power data and muscular activity were calculated based on the final minute of walking in each condition. EMG data were scaled relative to the average maximum peak in the initial zero-torque condition and metabolic data were scaled to the mean metabolic power of the initial zero-torque condition. Calculated metrics such as joint moments and powers were calculated using OpenSim [29]. To complete the analysis a previously validated custom model was employed, and data were not manipulated (scaled or filtered) prior to this analysis [30]. Exoskeleton data were recorded but were not used in the analysis of this study except to verify that tracking errors remained in the reported ranges. Due to the number of conditions that our participants underwent, ANOVA analysis was not done; the associated power of any test we could have run would have been under 0.10 and the results would have been uninformative [31].

III. Results

A. Metabolic Power

The zero torque conditions were not significantly different from one another and indicated that no group level fatigue occurred. There was an average decrease in metabolic power of 10.66% ($p = 0.003$) for plantar flexion-only assistance; combined plantar and dorsiflexion assistance resulted in a 12.51% improvement ($p < 0.001$) compared to the zero-torque condition. The cohort saw no significant change in metabolic power when comparing plantar flexion only assistance to combined plantar and dorsiflexion assistance ($p = 0.051$). Individual responses to additional assistance varied and a variety of positive and negative responses were observed (Fig. 3).

B. Joint Powers and Ranges

OpenSim was used to reconstruct joint mechanics. Step data were analyzed, and any outlying steps greater than two standard deviations from the median step curve were identified and removed using root-mean-square error. The mean step for the cohort in each condition was examined for differences in power. Fig.4 displays the powers for each joint (hip, knee and ankle) averaged over the observed steps and averaged across participants. This showed insignificant changes to hip ($p = 0.248$), knee ($p = 0.285$) and ankle ($p = 0.148$) excursion between the plantar and plantar with dorsiflexion assistance conditions.

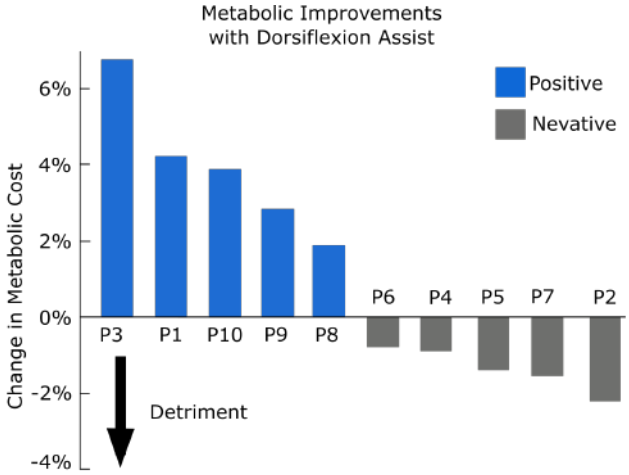


Figure 3 Relative change from in metabolic power for each participant.

C. Muscle Activity and Toe Clearance

The mean tibialis anterior activation for both legs was compared and we found that plantar and dorsiflexion assistance resulted in insignificant changes to both integrated ($p = 0.291$) and peak ($p = 0.085$) activation relative to plantarflexion only assistance. The lateral gastrocnemius, vastus lateralis and lateral biceps femoris also showed insignificant changes for both peak and integrated measures ($p > 0.05$). Minimum toe clearance did not differ significantly between the two conditions ($p = 0.311$).

IV. Discussion

This study compared metabolic power, muscle activity, and minimum toe-ground clearance when walking with stance phase plantar flexor assistance with and without swing phase dorsiflexion assistance. Despite no statistically significant

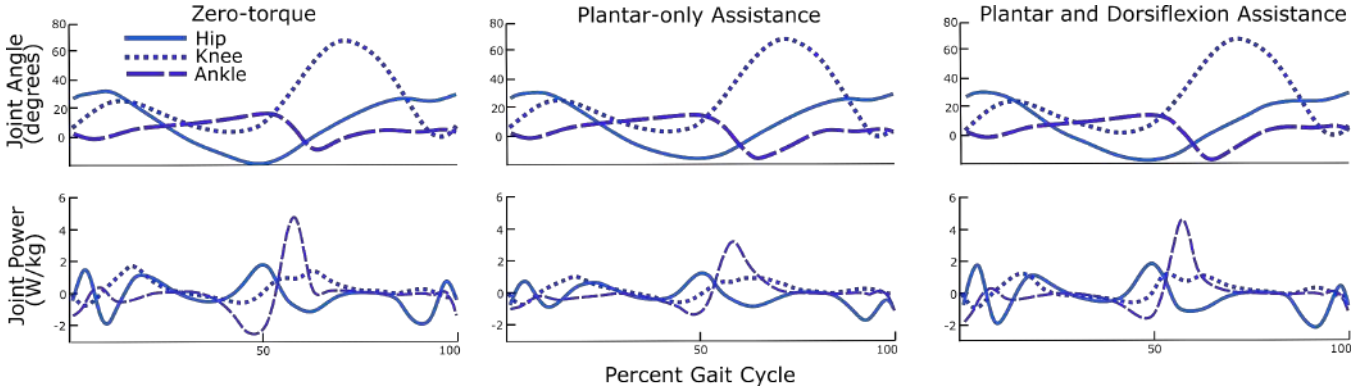


Figure 4 Joint kinematics and dynamics averaged across participants and conditions. No statistically significant differences were identified between these conditions at $p < 0.05$.

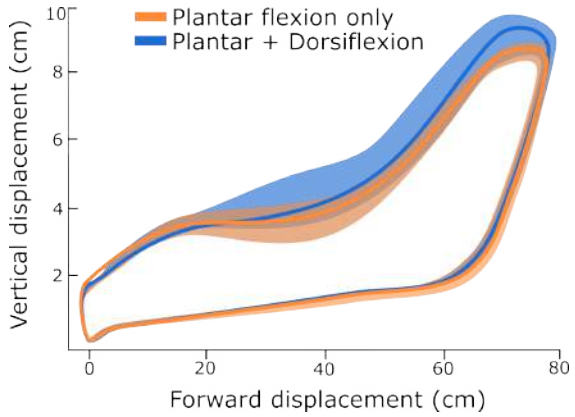


Figure 6 All participant toe paths (left and right) were averaged for each condition. Ground clearance decreased by at most 4.4% and increased by at most 23.9% for individuals.

changes in group-level metrics, individual-level analysis provided valuable insights. While the mean toe clearance was not significantly different between the assistance conditions, there was an increase in the mean value for 8 of the 10 participants; the high variability among participants, reflected in a standard deviation of 10.5%, overshadowed the small change in the mean (Fig. 5). This gives hope to future investigations for similar devices reducing trip risk.

When the tibialis anterior EMG was separated based on the metabolic responses seen in Fig. 6, it appeared that heightened levels of tibialis anterior activity near toe-off may have been beneficial, as those with the greatest positive response to the addition of dorsiflexion exhibited this muscular pattern. We examined this disparity using statistical parametric mapping, but due to the small sample size we did not find a statistical difference ($p = 0.116$). The results also suggest that the metabolic benefits observed in some participants may stem from the adoption of new movement strategies enabled by the exoskeleton. Training protocols that encourage exploration of optimized movement patterns could amplify the benefits of exoskeleton use. Furthermore, identifying and reinforcing key gait phases, such as pre-swing

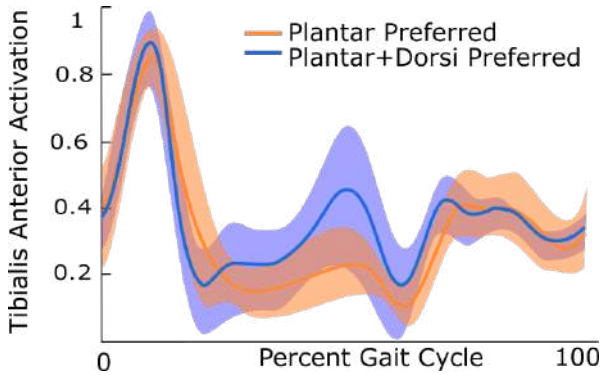


Figure 7 Plantar preferred individuals had lower metabolic power when only receiving plantarflexion assistance, while the Plantar +Dorsi preferred participants had lower metabolic power with assistance in both directions.

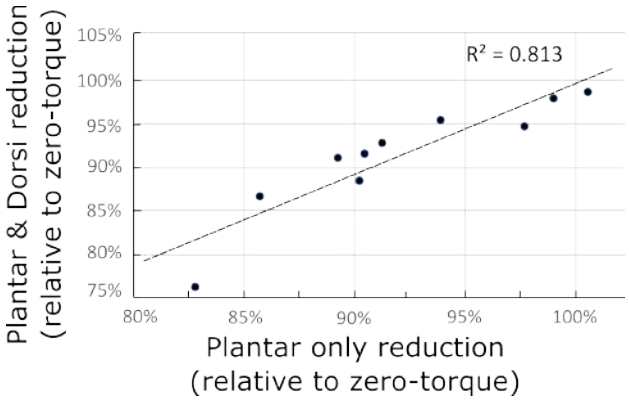


Figure 5 The impact of one mode of assistance from the exoskeleton was highly correlated with the impact of the other.

dorsiflexion, where assistance is most effective, could enhance the device's impact.

Finally, participants appeared to have related responses to the two different kinds of exoskeleton assistance. As Fig. 7 shows, the greater the improvement in metabolic power a participant had with plantar only assistance, the higher their improvement was likely to be when dorsiflexion assistance was included, the correlation coefficient of this relationship was 0.913 and a linear fit had an R^2 value of 0.834.

The variability in individual responses highlights the need for personalized assistance strategies in powered exoskeletons. While some participants demonstrated positive metabolic and muscle activity changes, others did not. This suggests that a one-size-fits-all approach may not be optimal for diverse users with varying neuromuscular and biomechanical profiles. Customizing the magnitude and timing of assistance based on individual gait mechanics, strength, and adaptability could enhance the exoskeleton's effectiveness. Adaptive control systems that dynamically adjust to the user's needs in real time may lead to more consistent benefits across users.

Future research into the effectiveness of dorsiflexion should incorporate the knowledge that novice users of powered exoskeletons have highly disparate responses and that large sample sizes would be needed to establish meaningful impacts. Additionally, we saw that individuals who were positively impacted by one control strategy may be more likely to respond positively to additional assistance. Validation of this observation would allow researchers to optimize different fundamental control strategies given a person's initial reaction to an exoskeleton. Such research could open the door for improving peak performance as well as creating controllers that may help even those who are initially less accepting of external assistance from a worn robotic system.

V. Conclusion

While no significant group-level differences were observed, individual responses revealed promising avenues

for future development. Personalized assistance, trust-building measures, and training protocols aimed at promoting beneficial movement strategies could significantly improve outcomes in powered exoskeleton use. These findings underscore the importance of tailoring exoskeleton systems to the unique needs and characteristics of users to maximize their potential for enhancing mobility and reducing metabolic cost.

Conflict of Interest

Z.F.L. is a co-founder with shareholder interest in a start-up company that is seeking to commercialize wearable exoskeleton technology related to this work.

References

[1] G. Bao *et al.*, "Academic review and perspectives on robotic exoskeletons," *IEEE Transactions on Neural Systems and Rehabilitation Engineering2*, vol. 27, no. 11, pp. 2294–2304, 2019.

[2] J. F. Veneman, R. Kruidhof, E. E. G. Hekman, R. Ekkelenkamp, E. H. F. Van Asseldonk, and H. Van Der Kooij, "Design and evaluation of the LOPES exoskeleton robot for interactive gait rehabilitation," *IEEE Transactions on Neural Systems and Rehabilitation Engineering*, vol. 15, no. 3, pp. 379–386, Sep. 2007, doi: 10.1109/TNSRE.2007.903919.

[3] H. Lee, W. Kim, J. Han, and C. Han, "The technical trend of the exoskeleton robot system for human power assistance," *International Journal of Precision Engineering and Manufacturing*, vol. 13, pp. 1491–1497, Jul. 2012.

[4] K. A. Witte, J. Zhang, R. W. Jackson, and S. H. Collins, "Design of two lightweight, high-bandwidth torque-controlled ankle exoskeletons," *Proc IEEE Int Conf Robot Autom*, vol. 2015-June, no. June, pp. 1223–1228, 2015, doi: 10.1109/ICRA.2015.7139347.

[5] M. Shepertycky, S. Burton, A. Dickson, Y.-F. Liu, and Q. Li, "Removing energy with an exoskeleton reduces the metabolic cost of walking." [Online]. Available: https://www.science.org

[6] S. Galle, P. Malcolm, S. H. Collins, and D. De Clercq, "Reducing the metabolic cost of walking with an ankle exoskeleton: interaction between actuation timing and power," *J Neuroeng Rehabil*, vol. 14, no. 1, Apr. 2017, doi: 10.1186/s12984-017-0235-0.

[7] P. Malcolm, W. Derave, S. Galle, and D. De Clercq, "A Simple Exoskeleton That Assists Plantarflexion Can Reduce the Metabolic Cost of Human Walking," *PLoS One*, vol. 8, no. 2, Feb. 2013, doi: 10.1371/journal.pone.0056137.

[8] D. J. Farris and G. S. Sawicki, "The mechanics and energetics of human walking and running: a joint level perspective," *The Royal Society Interface*, vol. 9, no. 66, Jan. 2011.

[9] B. Chen *et al.*, "Recent developments and challenges of lower extremity exoskeletons," *J Orthop Translat*, vol. 5, pp. 26–37, 2016, doi: 10.1016/j.jot.2015.09.007.

[10] A. Schiele, "An explicit model to predict and interpret constraint force creation in phri with exoskeletons," *Proc IEEE Int Conf Robot Autom*, pp. 1324–1330, 2008, doi: 10.1109/ROBOT.2008.4543387.

[11] G. S. Sawicki, O. N. Beck, I. Kang, and A. J. Young, "The exoskeleton expansion: Improving walking and running economy," *J Neuroeng Rehabil*, vol. 17, no. 1, pp. 1–9, 2020, doi: 10.1186/s12984-020-00663-9.

[12] P. W. Franks, G. M. Bryan, R. M. Martin, R. Reyes, A. C. Lakmazaheri, and S. H. Collins, "Comparing optimized exoskeleton assistance of the hip, knee, and ankle in single and multi-joint configurations," *Wearable Technologies*, vol. 2, 2021, doi: 10.1017/wtc.2021.14.

[13] Z. F. Lerner *et al.*, "An untethered ankle exoskeleton improves walking economy in a pilot study of individuals with cerebral palsy," *IEEE Transactions on Neural Systems and Rehabilitation Engineering*, vol. 26, no. 10, pp. 1985–1993, 2018, doi: 10.1109/TNSRE.2018.2870756.

[14] E. J. Harris, I. H. Khoo, and E. Demircan, "A Survey of Human Gait-Based Artificial Intelligence Applications," *Front Robot AI*, vol. 8, no. January, pp. 1–28, 2022, doi: 10.3389/frobt.2021.749274.

[15] N. Hogan *et al.*, "Motions or muscles? Some behavioral factors underlying robotic assistance of motor recovery," *J Rehabil Res Dev*, vol. 43, no. 5, pp. 605–618, 2006, doi: 10.1682/JRRD.2005.06.0103.

[16] G. Torres-Oviedo and A. J. Bastian, "Natural error patterns enable transfer of motor learning to novel contexts," *J Neurophysiol*, vol. 107, no. 1, pp. 346–356, 2012, doi: 10.1152/jn.00570.2011.

[17] D. Winter, "Biomechanical Motor Patterns in Normal Walking," *J Mot Behav*, vol. 15, no. 4, pp. 302–330, 1983.

[18] L. K. Drewes, P. O. McKeon, D. Casey Kerrigan, and J. Hertel, "Dorsiflexion deficit during jogging with chronic ankle instability," *J Sci Med Sport*, vol. 12, no. 6, pp. 685–687, Nov. 2009, doi: 10.1016/j.jsams.2008.07.003.

[19] G. Orekhov, Y. Fang, J. Luque, and Z. F. Lerner, "Ankle Exoskeleton Assistance Can Improve Over-Ground Walking Economy in Individuals with Cerebral Palsy," *IEEE Transactions on Neural Systems and Rehabilitation Engineering*, vol. 28, no. 2, pp. 461–467, 2020, doi: 10.1109/TNSRE.2020.2965029.

[20] G. Orekhov, Y. Fang, C. F. Cuddeback, and Z. F. Lerner, "Usability and performance validation of an ultra-lightweight and versatile untethered robotic ankle exoskeleton," *J Neuroeng Rehabil*, vol. 18, no. 1, pp. 1–16, 2021, doi: 10.1186/s12984-021-00954-9.

[21] G. Orekhov, I. Bioengineering, Z. F. Lerner, C. Ciocanel, R. Severinghaus, and M. Shafer, "THE DESIGN, VALIDATION, AND PERFORMANCE EVALUATION OF AN UNTETHERED ANKLE EXOSKELETON," 2022.

[22] Y. Fang, K. Harshe, J. R. Franz, and Z. F. Lerner, "Feasibility evaluation of a dual-mode ankle exoskeleton to assist and restore community ambulation in older adults," *Wearable Technologies*, vol. 3, 2022, doi: 10.1017/wtc.2022.12.

[23] J. M. Brockway, "Derivation of formulae used to calculate energy expenditure in man," *Hum Nutr Clin Nutr*, vol. 41, no. 6, pp. 463–471, 1987.

[24] C. P. Carty and M. B. Bennett, "The use of dimensionless scaling strategies in gait analysis," *Hum Mov Sci*, vol. 28, no. 2, pp. 218–225, 2009, doi: 10.1016/j.humov.2009.01.004.

[25] O. Pinzone, M. H. Schwartz, and R. Baker, "Comprehensive non-dimensional normalization of gait data," *Gait Posture*, vol. 44, pp. 68–73, 2016, doi: 10.1016/j.gaitpost.2015.11.013.

[26] T. Kobayashi, K. Sekiyama, Y. Hasegawa, T. Aoyama, and T. Fukuda, "Unified bipedal gait for autonomous transition between walking and running in pursuit of energy minimization," *Rob Auton Syst*, vol. 103, pp. 27–41, May 2018, doi: 10.1016/j.robot.2018.02.005.

[27] A. E. Martin and J. P. Schmiedeler, "Predicting human walking gaits with a simple planar model," *J Biomech*, vol. 47, no. 6, pp. 1416–1421, Apr. 2014, doi: 10.1016/j.jbiomech.2014.01.035.

[28] C. Meyer *et al.*, "Familiarization with treadmill walking: How much is enough?," *Sci Rep*, vol. 9, no. 1, pp. 1–10, 2019, doi: 10.1038/s41598-019-41721-0.

[29] S. L. Delp *et al.*, "OpenSim: Open-source software to create and analyze dynamic simulations of movement," *IEEE Trans Biomed Eng*, vol. 54, no. 11, pp. 1940–1950, 2007, doi: 10.1109/TBME.2007.901024.

[30] Y. Fang and Z. F. Lerner, "Feasibility of Augmenting Ankle Exoskeleton Walking Performance with Step Length Biofeedback in Individuals with Cerebral Palsy," *IEEE Transactions on Neural Systems and Rehabilitation Engineering*, vol. 29, pp. 442–449, 2021, doi: 10.1109/TNSRE.2021.3055796.

[31] K. R. Clarke and R. H. Green, "Statistical design and analysis for a 'biological effects' study," *Mar Ecol Prog Ser*, vol. 46, no. 1, pp. 213–226, Jun. 1988.

Effects of Deep Core Activation Method Using Wearable Cyborg HAL in a Supine Position for Ameliorating Defecatory Function: A Pilot Study

Hayato Tamai, Akira Uehara, Yoshiyuki Sankai, and Hiroaki Kawamoto, *Member, IEEE*

***Abstract*— Fecal evacuation disorder and incontinence are prevalent problems among patients with spinal cord injury (SCI) which greatly affect their quality of life. A major cause of these issues is well associated with weakness in their deep core muscular activity. Current programs for amelioration in their deep core muscles are either difficult to apply to patients with SCI or highly invasive. We have previously proposed a minimally invasive method using the wearable cyborg Hybrid Assistive Limb (HAL) for use by patients with SCI. In our proposed method, long-term repetition of supine HAL-assisted hip flexion is thought to activate deep core muscles potentially ameliorating deep core muscular activity. Here, we conducted a pilot study to validate that our methodology is applicable to a patient with SCI. A 24-year-old SCI patient with motor paralysis in his deep core muscles underwent four weeks of supine HAL-assisted hip flexion for thirty minutes, four times per week. To evaluate the effect of the intervention on the muscular activity, IAP measurement and sphincter electromyography were performed for seven days pre- / post-intervention. These assessments were repeated at a two-month follow-up after the intervention to verify the persistence of the effects. The increasing trends were observed in all periods of both IAP and in sphincter electromyogram. There was a significant increase in IAP and sphincter electromyogram between the pre-intervention and two-month follow-up ($p < 0.001$). These results demonstrate not only the applicability of our methodology to a patient with SCI but also the potential for ameliorating deep core muscular activity.**

I. Introduction

Neurogenic bowel dysfunction (NBD) is a major problem in patients with spinal cord injury (SCI) [1, 2]. The National Spinal Cord Injury Statistical Center Database [3] indicates that over 60% of patients with SCI currently experience bowel problems. Among various symptoms in NBD, fecal evacuation disorder and incontinence especially cause psychological stress for patients with SCI. Some literature suggests that the patients with NBD feel depression due to necessity of manual evacuation or incontinence concerns [4, 5]. Thus, an effective treatment program for NBD is urgently needed so that patients can live comfortably.

* This study includes the results of Cross-ministerial Strategic Innovation Promotion Program (SIP) 3rd Phase," Expansion of fundamental technologies and development of rules promoting social implementation to expand HCPS Human-Collaborative Robotics" promoted by Council for Science, Technology and Innovation (CSTI), Cabinet Office, Government of Japan. (Project Management Agency: New Energy and Industrial Technology Development Organization (NEDO), Project Code: JPJ012494, HCPS: Human-Cyber-Physical Space).

H.T. is with Ph.D. Program in Humanics, School of Integrative and Global Majors (SIGMA), University of Tsukuba, 1-1-1 Tennodai, Tsukuba, 305-8577, Japan. (e-mail: tamai_h@golem.iit.tsukuba.ac.jp).

H.K., A.U., Y.S., are with Institute of Systems and Information Technology and Center for Cybernics Research, University of Tsukuba, 1-1-1 Tennodai, Tsukuba, 305-8577, Japan. (e-mail: {sankai, kawamoto, uehara}@golem.iit.tsukuba.ac.jp)

To address the dysfunctions in patients with SCI, it is essential to ameliorate deep core muscular function. Vallès et al. identified the pathophysiological mechanisms underlying NBD in patients with SCI [2]. Patients experiencing significant evacuation difficulties were found to have an inability to increase intra-abdominal pressure (IAP) and a lack of voluntary anal relaxation during defecation. Those with severe incontinence lacked anal contraction in response to rectal distension. The IAP increase and anus contraction rely on the deep core muscles, which is the box-structured muscle group including the internal oblique (IO), transversus abdominis (TrA), and pelvic floor muscles (PFM) (Fig. 1). However, in patients with SCI, particularly those with a neurological level of injury at or above the lumbar level, have weakness in the deep core muscles contributing to these symptoms [6]. Therefore, the recovery of deep core muscular function is critical for the elimination of NBD.

Although previous studies have explored methods for restoring deep core muscle function, existing treatments are either difficult to apply to patients with SCI or highly invasive. One promising approach is PFM training, which involves techniques such as imagining moving the penis up and down for men or feeling the vagina pull upward and inward for women. However, because the PFM is not directly involved in joint motion, it is challenging to consciously contract these muscles. This often results in incorrect maneuvers, such as compensatory movements using other muscles—i.e., abdominal or gluteus [7]. While exercises combined with joint movement, such as Kegel exercises, are another option, these are impractical for most SCI patients as many of them have lower limb paralysis. Alternative includes electrical stimulation or biofeedback therapy. However, these options are highly invasive or requiring surgical intervention [8, 9]. Thus, to effectively treat NBD in patients with SCI, less invasive

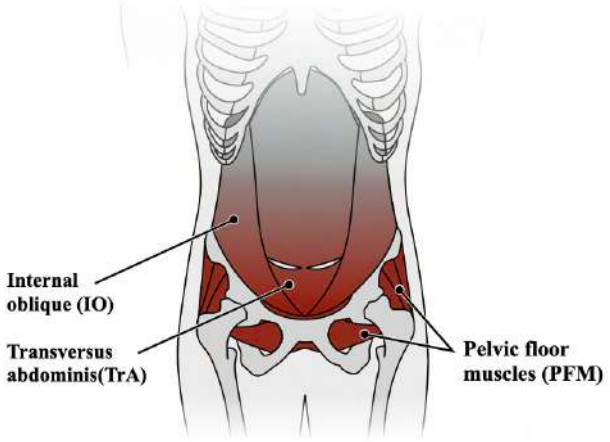


Figure 1. The specific segment of deep core which plays a crucial role for defecation.

therapies are needed that can also be applied to the physically impaired patients.

Cybernics treatment, on the other hand, can potentially ameliorate muscular functions with lower invasion in patients with SCI. Cybernics treatment is known as treatment strategy using wearable cyborg Hybrid Assistive Limbs® (HAL; CYBERDYNE Inc.) improving/regenerating motor functions in patients with various neurogenic dysmotility. The HAL detects wearer's motor intention by measuring bio-electrical signals (BES) from the electrodes attached on their skin surface. These signals control actuators in the HAL joints assisting exercise in unison with the wearer's intention. HAL-assisted motion generates sensory inputs from muscle spindles, ears, eyes, and other sensory receptors back to the wearer's brain. This intention-based sensory feedback loop activates the nervous system which in turn alters the patient's brain, nerves, and muscle function. Repeating this HAL-assisted motion has been considered to promote neural plasticity and sustain the effects of recovery on muscular function. Obviously, this technique is minimally invasive and can be applied to any individual, as long as their BES can be observed, even if the signals are weak. [10-12]

We have previously proposed a treatment methodology using wearable cyborg for deep core dysfunction based on the principle of cybernics treatment [13]. This method aims to activate the neural pathways controlling the deep core muscles by establishing a sensorimotor loop between brain and deep core muscles as the cybernics treatment. In this method, the wearable cyborg detects wearer's motor intention toward the deep core from the electrodes attached on their lower abdomen and lift their legs in a supine position (Fig. 2) [13]. In our hypothesis, the deep core muscles contract with fascial connected hip flexor during this process, and sensory feedback can be transmitted to the brain from deep core, thereby establishing the sensorimotor loop. Unlike conventional exercise therapy, this approach allows patients to recognize whether they are correctly contracting their deep core muscles during exercise. This is believed to prevent compensatory movements and facilitate the selective activation only of the deep core muscles. Furthermore, as the movement is assisted by the wearable cyborg, it can be performed even by patients with lower limb paralysis. After a long-term repetition of this robot-assisted supine hip flexion, it is thought that the neural pathways controlling the deep core muscles will undergo plasticity, enabling patients to regain deep core muscular function.

We have previously demonstrated the safety and applicability of this methodology in healthy individuals [13]. In this study, we conducted a one-month pilot trial for a patient with chronic SCI to confirm its applicability to the patient and the effect of amelioration in deep core muscle activity after a long-term intervention.

II. Materials and Methods

A. System Configuration

The system used for our method consisted of the HAL, a polypropylene sheet, and a urethane molded bed. The wearer attached electrodes to their fusion site of IO and TrA (IO-TrA) and connected them to the HAL (Fig. 2).

The surface electrodes on the IO-TrA can transmit the wearer's motor intention sent toward the deep core muscles to the HAL. As the deep core muscles move in coordination with each other [14] and some of their motor unit potentials leak from the IO-TrA [15, 16], the BES on the wearer's IO-TrA can be regarded as the motion intention toward the entire deep core muscles.

HAL has the actuators at both the hip and knee joints. Details of the HAL control algorithm is described in other literature [17]. Briefly, we used two control modes of HAL: Cybernic Voluntary Control (CVC) and Cybernic Impedance Control (CIC). The CVC mode determines the actuator torque based on the intensity of the wearer's BES. In contrast, the CIC mode determines the torque according to the angular velocity of joint motion. In our method, the hip joint was operated in CVC mode to reflect the BES from the IO-TrA into the hip flexion torque. The knee joint was controlled in CIC mode and to make it behave as a free axis.

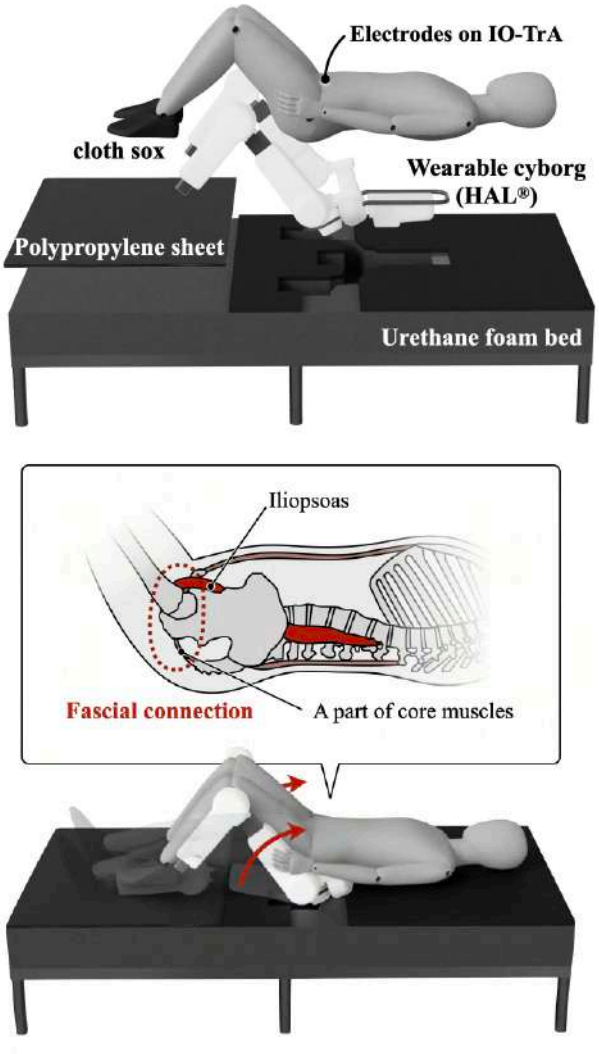


Figure 2. Overview of our method. HAL-assisted supine hip flexion establishes the sensorimotor loop between brain and deep core muscles. Repeating this exercise induces neural plasticity in their deep core, resulting in regaining muscular function.

A polypropylene sheet was placed under the wearer's feet to reduces friction with the ground. This prevents the wearer from stepping on the ground with the lower limbs during hip flexion. The sheet enables the wearer to perform hip flexion by selectively contracting the core muscles without relying solely on the compensatory movement of the lower extremity muscles.

B. Study Design

A case study was conducted involving a pre-clinical test and a four-weeks of HAL intervention. A preclinical test was performed to validate our methodology is applicable to a patient with SCI. Clinical assessments were carried out before, im-mediately after, and two months following the HAL intervention, each for one week, to verify the amelioration in deep core muscular activity (Fig. 3).

C. Participant

This case focused on a 24-year-old male patient (height, 178 cm; weight, 60 kg) who had injured his spinal cord due to a lumbar burst fracture at L1 four years before this study. The neurological level of injury (NLI), ASIA impairment scale (AIS), sensory zone of partial preservation (sensory ZPP), motor zone of partial preservation (motor ZPP) of the patient are presented in the following table (Table 1). Voluntary anal contraction was not preserved. The participant was not taking any medications or treatments for bowel control. The participant had undergone physical therapy for six months immediately following hospital discharge but had not received HAL training prior to this study.

Regarding his defecatory function, the participant exhibited a slight perception of the urge to defecate. However, due to paralysis of the deep core muscles especially in PFM, the participant was required to strain excessively in order to evacuate the stools. Frequently, even with straining, it was challenging to adequately expel the stool (Cleveland Clinic Constipation Score = 10). Although his voluntary anal contraction was not preserved, he had managed to control defecation by adhering to a scheduled toilet routine, resulting in the absence of incontinence episodes for three years (Wexner score = 0). The participant provided written informed consent before this study according to the Declaration of Helsinki.

D. Preclinical Test

A preclinical test was conducted to validate that our method was applicable to the participant by validating that HAL could achieve supine hip flexion based on his intention, engage all of the deep core muscles, and ensure that hip flexion is driven by the deep core muscles rather than by compensatory movements of the hip flexors.

Fig. 4 illustrates the experimental setup. The participant performed hip flexions with and without the HAL while measuring BES from IO-TrA, PFM, and rectus femoris (RF). Initially, surface electrodes (Vitrode; Nihon Koden) were attached to the IO-TrA and RF, and an intra-anal electrode (Anuform®; Neen) was inserted into the anal canal, where the PFM are concentrated. At first, in the configuration without the HAL, the participant lay supine. A speaker placed beside the participant played beeps every 5 s. The participant was instructed to engage his deep core muscles and perform hip flexion in order to achieve a hip angle of over 60 degrees only while the beep was sounding. This exercise was repeated three times. Subsequently, the participant donned the HAL and repeated the same test with HAL's assistance in the supine position. During both experimental sessions with and without the HAL, the electrodes on the IO-TrA were connected to the HAL and BES were recorded using its associated software (HAL Monitor; CYBERDYNE Inc.) at a sampling frequency of 1 kHz. The electrodes on the RF and PFM were connected to a recording computer, and BES was logged at a sampling rate of 500 Hz using a microcomputer (ESP32; Espressif Systems).

To determine that the HAL could achieve hip flexion based on the participant's motor intention, we verified the

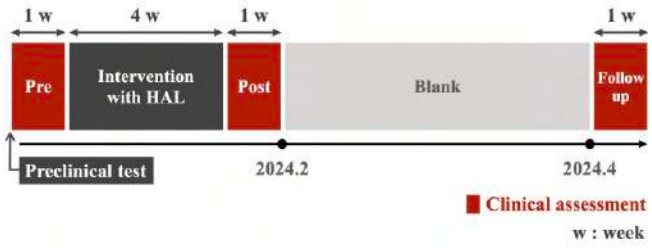


Figure 3. Assessment protocol.

TABLE I. PARTICIPANT'S INFORMATION.

		Diagnosis
NLI		L3
AIS		A
Sensory level	Left	L5
	Right	L3
Motor level	Left	L5
	Right	L3
Sensory ZPP	Left	S1
	Right	L4
Motor ZPP	Left	S1
	Right	L3

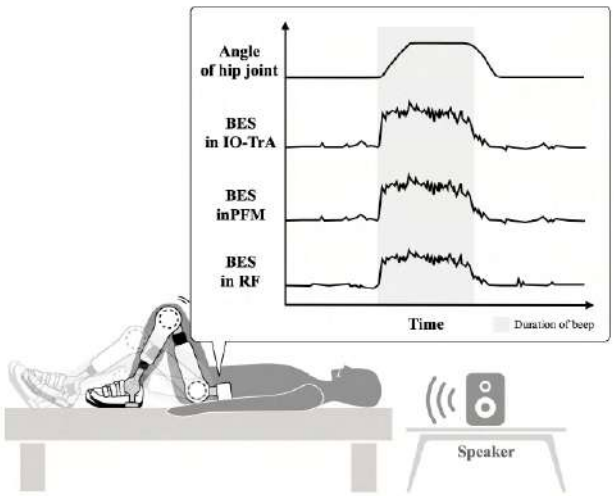


Figure 4. Overview of the experimental setup. The hip joint angle and the BES of IO-TrA, PFM, and RF were measured during hip flexion in both with- and without the HAL.

synchronization between the hip joint angle and the BES from the participant's IO-TrA during HAL-assisted hip flexion. Additionally, to ascertain whether all of the deep core muscles were engaged during the hip flexion, we confirmed the increase in the amplitude of BES in both IO-TrA and PFM during the beep playback. The BES was rectified by applying a low-pass filter with a cutoff frequency of 10 Hz and the root mean square over a time window of 10 ms. The mean amplitude was calculated from the signals during the middle 3 s of the 5 s hip flexion period, with the initial and concluding seconds excluded to minimize the impact of variability at the onset and offset of the signal. The mean values derived from three measurements were employed as representative values. The BES when the beep was not played was recorded as the baseline value with the same calculation procedure. Furthermore, to ensure that hip flexion is driven by the deep core muscles rather than by compensatory movements of the hip flexors, we measured the BES of one of the hip flexors, RF, and the deep core muscles (IO-TrA and PFM). The activity ratios of these muscles were compared between protocols with and without HAL. The muscle activity ratio was calculated by dividing the amplitude of IO-TrA, PFM, and RF with HAL assistance by their respective amplitudes without the HAL.

E. Intervention

The participant performed HAL-assisted supine hip flexions four times a week for a total of four weeks (Fig. 5). In the intervention program, the participant first attached electrodes to the IO-TrA and connected these electrodes to the HAL's hip actuator with cables. Subsequently, the participant engaged in approximately twenty to thirty repetitions of hip flexion while wearing the HAL, to familiarize himself with the wearable cyborg. The instruction for engaging the deep core muscles was as follows: "Please flex the hip over approximately 60 degrees while contracting the pelvic floor as if closing the anus." Subsequently, five sets of ten HAL-assisted hip flexions were carried out per session. The duration of each session with the HAL was approximately 30 mins.

The gain of the assistive torque for the HAL's hip actuator was set using the controller to enable the deep core to exert approximately 60–70% of the maximum force produced by the participant. This setting was informed by the literature which introduced pelvic floor muscle training [18, 19]. As the sessions progressed, the gain of the assistive torque gradually decreased as the participant became accustomed to the training.

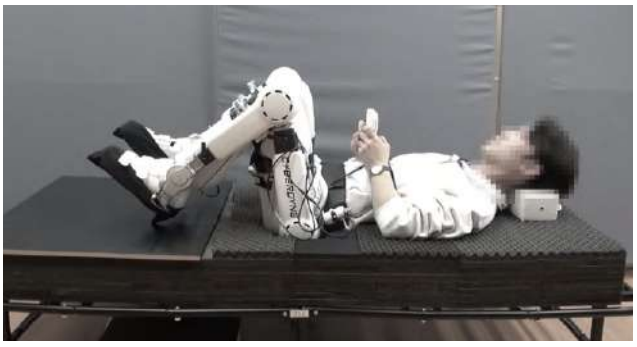


Figure 5. HAL-assisted hip flexion was performed by the participant for sixty minutes per a time, four times a week for a total of four weeks.

E. Outcome Measures

To determine the impact of the intervention on deep core muscular activity, two assessment indices were employed: IAP measurement and sphincter electromyography. These assessments were carried out at pre-, post-, and two-month follow-up of the HAL intervention for a week respectively to determine the persistence of the intervention effects.

F. IAP Measurement

One of the muscular activities that contributes to stool evacuation was evaluated by measuring the IAP increase during straining. The change in IAP is accurately reflected by the change in rectal pressure measured at a 10 cm depth of the anal canal [20]; thus, changes in rectal pressure at this depth were recorded and assessed as changes in IAP in this study. Rectal pressure measurement was carried out by inserting an air-filled balloon catheter into the participant's anal canal as previously described by Miller et al. [21]. The balloon catheter (Safired® Balloon Catheter; Terumo) was equipped with a transducer (2SMPP-02; Omron) connected to its balloon tube. The pressure change inside the balloon caused by the patient's straining was converted into discretized values by the transducer. The values were amplified by a differential amplifier circuit with a gain of 21x and recorded by a microcomputer (ESP32; Espressif Systems) at a sampling rate of 500 Hz. Prior to use, the measuring equipment was calibrated in a glass container connected to a gauge pressure sensor (MPS-C35R-NCA; CONVUM), which exhibited a linear response per unit rise in actual pressure.

In the left lateral position with the hip and knee flexed at 90 degrees, a catheter was placed 10 cm proximal from the participant's anal orifice, and 10 ml of air was injected into the balloon. Once the pressure within the balloon had reached equilibrium with the rectal pressure, the participant was instructed to strain for 5 s at a time, for a total of five repetitions, with a 5 s interval between each strain. To eliminate variations in amplitude during the onset and offset, the average pressure during the middle 3 s of each straining period was calculated, excluding the first and last 1 s. The median of the five measurements was used as the representative value. IAP measurements were conducted over seven days during each of the pre-, post-intervention, and two-month follow-up periods.

G. Sphincter Electromyography

The muscular function for maintaining fecal continence was assessed by using sphincter electromyography. Sphincter electromyography allows for the evaluation of motor unit potential recruitment during voluntary sphincter contraction, including denervation-reinnervation potentials [22, 23]. Therefore, in this study, sphincter electromyography via a transanal electrode was used to assess changes in neural activity in the sphincter. The change in potential while the participant was squeezing was obtained from the transanal electrode (Anuform®; Neen). These signals were amplified using a differential amplifier circuit with a gain of 220x and recorded by a microcomputer (ESP32; Espressif Systems) at a sampling rate of 500 Hz.

In the left lateral position with the hip and knee flexed at 90 degrees, a transanal electrode was inserted into the participant's anal canal. The participant was instructed to

perform a squeezing action for 5 s for a total of five repetitions with 5 s intervals between each. The acquired signals were processed by the BES and rectified by applying a low-pass filter with a cutoff frequency of 10 Hz and the root mean square over a time window of 10 ms. To eliminate variations in amplitude at the onset and offset of the signal, the average amplitude during the middle 3 s of each squeezing period was calculated. The median of the five measurements was used as the representative value. Sphincter electromyography was conducted over seven days during each of the pre-, post-intervention, and two-month follow-up periods.

H. Statistical Analysis

To assess the plausibility of the intervention effects on muscular activity, IAP measurement and sphincter electromyography data were statistically analyzed. The Dunn-Bonferroni multiple comparison test followed by the Kruskal-Wallis test were used to compare between pre- and post-intervention measurements, as well as pre-intervention and two-month follow-up measurements. Statistical significance for all measures was set at $p < 0.05$ after the Bonferroni adjustment. Given the small sample size, the effect size r was calculated as a standardized measure to assess the magnitude of the observed effects. Effect sizes were calculated by dividing the test statistic Z by the square root of the sample size n. Standardized effect sizes were categorized as small (r = 0.10), medium (r = 0.30), and large (r = 0.50) [24]. All statistical analyses were performed using SPSS software version 29.0 (SPSS Inc., Chicago, IL, USA).

III. Results

The participant completed preclinical test and all six-teen HAL-sessions. No intervention-related adverse events were observed.

A. Preclinical Test

Fig. 6 presents the representative time series data of hip joint angles and BES in IO-TrA during HAL-assisted hip flexion. The upper panel represents the hip joint angle, while the lower panel represents BES in IO-TrA. As the participant performed symmetrical movements for both legs, only the data for the right leg are shown as a representative result. The shaded area in the graph indicates the duration of the beep sound playing, signaling the participant to flex his hip joint. Fig. 7 shows the time series data of BES in IO-TrA, PFM, and RF during hip flexion both with and without HAL assistance. The red and blue lines represent the data obtained during hip flexion with- and without HAL assistance, respectively. Table 2 shows the average amplitude of BES in IO-TrA, PFM, and RF at the baseline and during hip flexion, both with- and without HAL assistance. Fig. 8 shows the ratio of muscle activity in IO-TrA, PFM, and RF with the HAL compared to without the HAL.

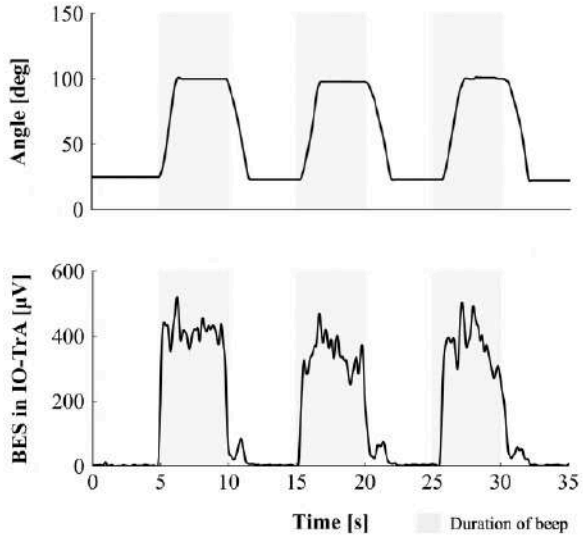


Figure 6. Time series data of the hip joint angle and BES in IO-TrA during HAL-assisted hip flexion. The shaded area indicates the duration of beep playing.

With HAL assistance, the hip joint angle and BES in the

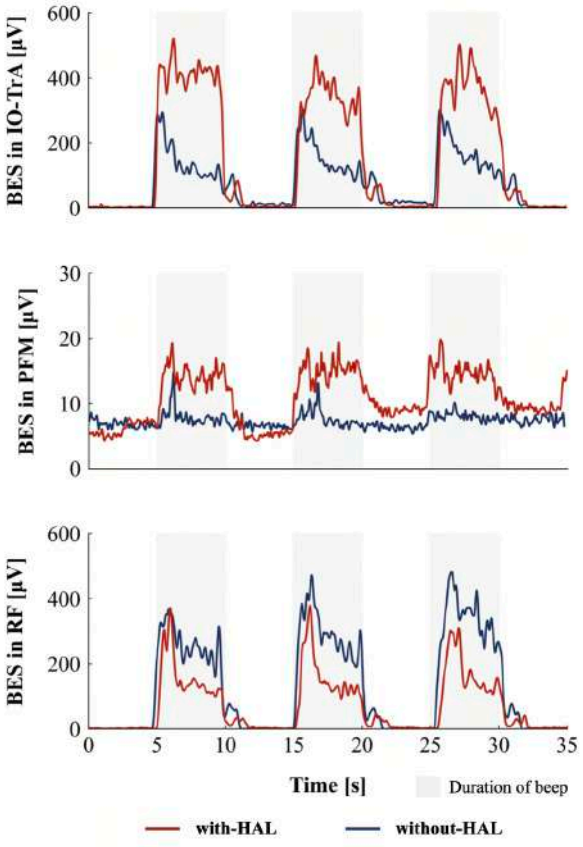


Figure 7. Time series data of BES in IO-TrA, PFM, and RF both with- and without-HAL assistance.

TABLE II. BES DURING BASELINE V.S HIP FLEXION

Measured area	***Baseline* [μV] (±SD)**	***Hip flexion* [μV] (±SD)**
IO-TrA (with-HAL)	13.49 (± 10.22)	385.1 (± 26.75)
IO-TrA (without-HAL)	10.37 (± 10.50)	147.7 (± 24.72)
PFM (with-HAL)	6.848 (± 1.918)	14.99 (± 0.543)
PFM (without-HAL)	6.661 (± 0.247)	8.309 (± 0.130)
RF (with-HAL)	9.268 (± 7.088)	185.0 (± 5.971)
RF (without-HAL)	1.750 (± 0.247)	309.8 (± 59.08)

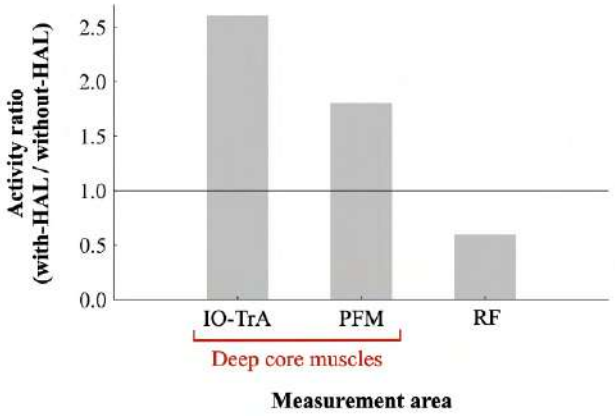


Figure 8. Activity ratio in IO-TrA, PFM, and RF with vs without HAL assistance during hip flexion.

IO-TrA were synchronized (Fig. 6). The BES increased in all measured areas at the onset of the beep. Thereafter, BES levels remained above baseline and then decreased to baseline levels after the beep stopped. Similarly, without HAL assistance, the BES showed comparable changes (Fig. 7, Table 2). The ratios of muscle activity in both IO-TrA and PFM were > 1.0. Conversely, the ratio in RF was < 1.0 (Fig. 8).

B. Pre / Post and Follow-up Comparison

Fig. 9 presents the median of the IAP measurements during the pre-intervention, post-intervention, and two-month follow-up periods. Error bars represent the 95% confidence intervals (95%CI) calculated using the bootstrap method. Increasing trends were observed in IAP (pre: Mdn = 2.96 kPa, 95%CI = [2.44, 3.43], post: Mdn = 4.55 kPa, 95%CI = [4.13, 5.65], follow-up: Mdn = 5.02 kPa, 95%CI = [4.83, 5.51]). Statistically significant increases and large effect sizes in IAP were observed both from pre- to post-intervention ($p = 0.0133$, $r = 0.72$) and from pre- to two-month follow-up ($p = 0.0006$, $r = 0.97$).

Fig. 10 illustrates the median of the sphincter electromyography values for the same periods along with their 95%CI. Increasing trends were observed (pre: Mdn = 0.05 μV, 95%CI = [0.09, 0.27], post: Mdn = 0.79 μV, 95%CI = [0.22, 1.42], follow-up: Mdn = 9.75 μV, 95%CI = [7.13, 11.9]). There were no significant differences between pre- and post-intervention ($p = 0.1548$). A significant increase and large effect size from pre-intervention to two-month follow-up was confirmed ($p = 0.0001$, $r = 1.08$).

Although a subjective outcome, the participant reported an improvement in ease of evacuation after the procedure. The Wexner Score remained unchanged at 0, while the Cleveland Clinic Constipation Score decreased from 10 to 8.

IV. Discussion

In the preclinical testing, we confirmed that HAL could realize hip flexion based on the wearer's motor intentions, resulting in all the deep core muscles working. The synchronized change in the hip joint angle and BES in IO-TrA during HAL-assisted hip flexion suggests that HAL successfully achieved hip flexion based on the participant's intention. The increase of the BES in all measured segments of the deep core at the onset of the beep sound indicates that the entire deep core musculature was engaged during HAL-assisted hip flexion.

Although the participant could perform hip flexion in a supine position without HAL, the increased activation ratio of IO-TrA and PFM, coupled with the decrease in that of RF, indicates that hip flexion without HAL predominantly involved compensatory actions using the hip flexors rather than the deep core, in contrast to HAL-assisted hip flexion. This demonstrates that HAL could selectively detected motion intentions directed towards the deep core and facilitate hip flexion accordingly. The finding suggests that the proposed methodology enabled the participant to consciously engage paralyzed muscles which were difficult for him to contract voluntarily. In other words, it can be assumed that the participant became able to relearn how to voluntarily contract the deep core muscles that he had previously forgotten the way to contract, through HAL-assisted hip flexion.

The significant increase in IAP with a large effect size from pre- to post-intervention suggests the participant seemingly relearned the correct way to strain. The significant difference in comparison between pre-intervention and two-month follow-up measurement allows us to assume that the proposed method enabled to repeat selective activation on the nerves related with deep core, which enhances its synaptic connections, resulting in the sustained effect on the participant's muscular activity under the principles of cybernics treatment [10-12]. Although there were no significant differences between pre- and post-intervention sphincter electromyography measurements,

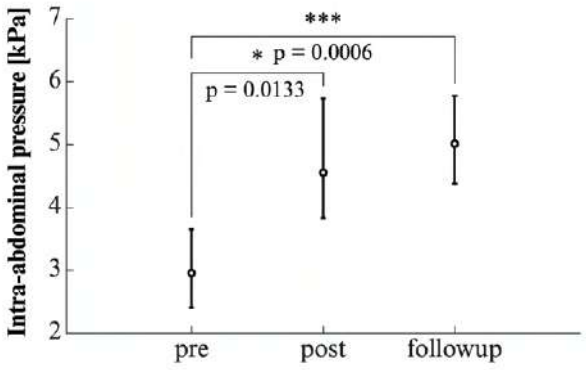


Figure 9. Pre/post and follow-up comparison in IAP measurements.

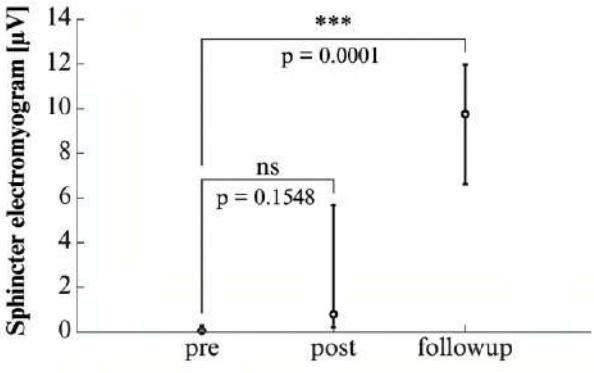


Figure 10. Pre/post and follow-up comparison in electromyography.

the post-intervention values showed non-zero values compared to the near-zero values observed pre-intervention. This implies that the intervention may have facilitated increased motor unit potential recruitment around the PFM. Moreover, even though the participant had not demonstrated voluntary anal contraction for over four years, the significant increase in sphincter electromyography observed at follow-up, compared to pre-intervention suggests that the intervention may have served as a catalyst for enhancing the neural pathways. We hypothesized that this neural enhancement provided the opportunity to move the deep core musculature in daily life after intervention and that the repetition of the voluntary muscular movement would have further enhanced the neural connections. This is reflected by the positive changes in IAP and sphincter electromyography values at follow-up vs. pre-intervention.

These findings confirm that the proposed deep core activation method is applicable for the participant with SCI and provides a sustained effect on ameriolation for deep core muscular activity. However, one limitation of this study is that the participant had relatively mild NBD, which makes the specific effects on improving bowel habits unclear. Furthermore, as this is a case study, it is unknown whether similar intervention effects can be achieved in patients with different types of SCI, such as supraconal or conal/infraconal injuries, or at different stages of injury, such as acute, subacute, or chronic.

Despite these limitations, HAL-assisted hip flexion has the potential to ameliorate not only deep core muscular activity but also the bowel habits at the same time. Several studies demonstrated that voluntary mild exercise in a supine position coordinate autonomic nervous system activity, such as in the vagus nerves [25, 26] which innervate the intestine, potentially improving colonic motility. Other studies proved that aerobic exercises seemingly regulate the autonomic nervous activity associated with colonic propulsion as well [27-29]. This suggests the possibility of improving the entire intestinal tract by performing the supine HAL-assisted exercise combined with proper breathing, which uses more oxygen. In terms of patients with SCI of different severities, our previous studies on cybernics treatment have demonstrated its application to SCI patients with different injury locations and stages [30], [31]. For patients whose BES cannot be appropriately measured from the skin surface, a pre-programmed control method called Cybernic Autonomous Control (CAC), which has been developed to automatically control the patient's lower limb and is now an alternative for them [17].

This pilot study does not allow for an assessment of the long-term sustainability of the clinical effects. Further studies with larger sample sizes and various injury types combined with the long-term assessment of bowel habit change are needed to confirm these assumptions. We intend to apply the proposed method to several patients with spinal cord injuries who also suffer from severe NBD. This will confirm the impact on the anorectum and gastrointestinal tract, which are innervated by both autonomic and somatic nerves. The results could eventually lead to the establishment of a completely new treatment for NBD.

V. Conclusion

We conducted a pilot trial to confirm that our proposed methodology is applicable to a patient with chronic SCI. A 24-year-old person with SCI accompanied by anorectal dysmotility underwent a four-week period of the supine HAL-assisted hip flexion for thirty minutes four times per week. Clinical assessments of its effect on deep core muscles were performed using IAP measurement and sphincter electromyography at pre-, post-intervention, and two-month follow-up periods. The results of the preclinical test confirmed that the proposed method enabled hip flexion based on the participant's motor intention and facilitated the engagement of the entire deep core musculature. Comparison of pre- / post-intervention measurements showed the increasing trends both in IAP and in sphincter electromyography. There were significant increases in IAP and sphincter electromyography between pre-intervention and two-month follow-up measurements. These results demonstrate not only the applicability of the proposed methodology, but also its potential for the amelioration on the deep core muscular activity in patients with chronic SCI.

Ethical declaration

This study was fully conducted in accordance with IEEE AUTHOR ETHICS GUIDELINES. In accordance with IEEE policy and my ethical obligations as a researcher, I disclose that all authors and one subject who participated in the experiments are past or present employees of CYBERDYNE Inc. and that I have fully disclosed these interests to IEEE.

References

[1] A. Lynch, C. Wong, A. Anthony, B. Dobbs, and F. Frizelle, "Bowel dysfunction following spinal cord injury: a description of bowel function in a spinal cord-injured population and comparison with age and gender matched controls," *Spinal Cord*, vol. 38, no. 12, pp. 717–723, 2000, doi: 10.1038/sj.sc.3101058.

[2] M. Vallès, J. Vidal, P. Clavé, and F. Mearin, "Bowel Dysfunction in Patients with Motor Complete Spinal Cord Injury: Clinical, Neurological, and Pathophysiological Associations," *Am. J. Gastroenterol.*, vol. 101, no. 10, pp. 2290–2299, 2006, doi: 10.1111/j.1572-0241.2006.00729.x.

[3] U. of A. at B. (UAB) D. of P. M. and Rehabilitation, "National Spinal Cord Injury Model Systems (SCIMS) Database." Accessed: May 01, 2023. [Online]. Available: https://www.nscisc.uab.edu/Public_Pages/Database

[4] K. Krogh, P. Christensen, and S. Laurberg, "Colorectal symptoms in patients with neurological diseases," *Acta Neurol. Scand.*, vol. 103, no. 6, pp. 335–343, 2001, doi: 10.1034/j.1600-0404.2001.103006335.x.

[5] S. S. C. Rao, A. K. Tuteja, T. Vellema, J. Kempf, and M. Stessman, "Dyssynergic Defecation: Demographics, Symptoms, Stool Patterns, and Quality of Life," *J. Clin. Gastroenterol.*, vol. 38, no. 8, pp. 680–685, 2004, doi: 10.1097/01.mcg.0000135929.78074.8c.

[6] K. Nas, L. Yazmalar, V. Şah, A. Aydın, and K. Öneş, "Rehabilitation of spinal cord injuries," *World J. Orthop.*, vol. 6, no. 1, pp. 8–16, 2015, doi: 10.5312/wjo.v6.i1.8.

[7] G. Dar and T. S. Saban, "The Perception of Pelvic Floor Muscle Function amongst Exercising Women Who Are Repeatedly Instructed to Contract Their Pelvic Floor Muscles," *Healthcare*, vol. 10, no. 9, p. 1768, 2022, doi: 10.3390/healthcare10091768.

[8] Y. Özin *et al.*, "Efficacy of combination of biofeedback therapy and pelvic floor muscle training in dyssynergic defecation," *Acta Gastro Enterol. Belg.*, vol. 84, no. 4, pp. 577–583, 2021, doi: 10.51821/84.4.008.

[9] R. P. MacDonagh, W. M. Sun, R. Smallwood, D. Forster, and N. W. Read, "Control of defecation in patients with spinal injuries by

stimulation of sacral anterior nerve roots.," *Br. Méd. J.*, vol. 300, no. 6738, p. 1494, 1990, doi: 10.1136/bmj.300.6738.1494.

[10] Y. Sankai and T. Sakurai, *Cybernics Treatment: Functional Treatment with Medical HAL Use, Regenerative Medicine and Rehabilitation (in Japanese)*. 2018.

[11] Y. S. and T. Sakurai and T. Sakurai, "Functional regenerative medicine: The dawn of 'Cybernic treatment," *The Japanese Society for Regenerative Medicine*, vol. 16.2, pp. 90–101, 2017.

[12] K. Saotome *et al.*, "Functional magnetic resonance imaging of brain activity during hybrid assistive limb intervention in a chronic spinal cord injury patient with C4 quadriplegia," *J. Clin. Neurosci.*, vol. 99, pp. 17–21, 2022, doi: 10.1016/j.jocn.2022.02.027.

[13] H. Tamai, H. Kawamoto, A. Uehara, and Y. Sankai, "Development of Anorectal and Core Activation Method with Wearable Cyborg HAL for Defecation Disorder Treatment" in *IEEE RAS EMBS 10th International Conference on Biomedical Robotics and Biomechatronics*, 1-4 Sep. 2024.

[14] R. Sapsford, "Rehabilitation of pelvic floor muscles utilizing trunk stabilization," *Man. Ther.*, vol. 9, no. 1, pp. 3–12, 2004, doi: 10.1016/s1356-689x(03)00131-0.

[15] S. McGill, D. Juker, and P. Kropf, "Appropriately placed surface EMG electrodes reflect deep muscle activity (psoas, quadratus lumborum, abdominal wall) in the lumbar spine," *J. Biomech.*, vol. 29, no. 11, pp. 1503–1507, 1996, doi: 10.1016/0021-9290(96)84547-7.

[16] P. Marshall and B. Murphy, "The validity and reliability of surface EMG to assess the neuromuscular response of the abdominal muscles to rapid limb movement," *J. Electromyogr. Kinesiol.*, vol. 13, no. 5, pp. 477–489, 2003, doi: 10.1016/s1050-6411(03)00027-0.

[17] S. K, K. Y, H. T, S. T, H. Y, and S. Y, "Intention-Based Walking Support for Paraplegia Patient," *2005 IEEE Int. Conf. Syst., Man Cybern.*, vol. 3, pp. 1–7, 2005, doi: 10.1109/icsmc.2005.1571559.

[18] M. Tanaka and Y. Aoki, "Fundamentals and practices for pelvic floor muscle training," *Jpn. J. Phys. Fit. Sports Med.*, vol. 71, no. 3, pp. 255–261, 2022, doi: 10.7600/jspfsm.71.255.

[19] M. Tanaka, "Assessment and approach to pelvic floor muscle group dysfunction (in Japanese)," *physical therapy*, vol. 35, no. 4, pp. 212–215, 2008, doi: 10.15063/rigaku.kj00004963396.

[20] T. A. McCarthy, "Validity of rectal pressure measurements as indication of intra-abdominal pressure changes during urodynamic evaluation," *Urology*, vol. 20, no. 6, pp. 657–660, 1982, doi: 10.1016/0090-4295(82)90326-0.

[21] R. Miller, D. C. C. Bartolo, D. James, and N. J. McC. Mortensen, "Air-filled microballoon manometr for use in anorectal physiology," *Br. J. Surg.*, vol. 76, no. 1, pp. 72–75, 1989, doi: 10.1002/bjs.1800760123.

[22] E. V. Carrington *et al.*, "Advances in the evaluation of anorectal function," *Nat. Rev. Gastroenterol. Hepatol.*, vol. 15, no. 5, pp. 309–323, 2018, doi: 10.1038/nrgastro.2018.27.

[23] J. Lefaucheur, "Neurophysiological testing in anorectal disorders," *Muscle Nerve*, vol. 33, no. 3, pp. 324–333, 2006, doi: 10.1002/mus.20387.

[24] A. MIZUMOTO and O. TAKEUCHI, "Basics and Considerations for Reporting Effect Sizes in Research Papers," *Study in English Language Teaching Vol.31*, pp. 57–66, Mar. 2008.

[25] V. F. Gladwell, G. R. H. Sandercock, and S. L. Birch, "Cardiac vagal activity following three intensities of exercise in humans," *Clin. Physiol. Funct. Imaging*, vol. 30, no. 1, pp. 17–22, 2010, doi: 10.1111/j.1475-097x.2009.00899.x.

[26] B. F. ROBINSON, S. E. EPSTEIN, G. D. BEISER, and E. BRAUNWALD, "Control of Heart Rate by the Autonomic Nervous System," *Circ. Res.*, vol. 19, no. 2, pp. 400–411, 1966, doi: 10.1161/01.res.19.2.400.

[27] A. J. Hautala, A. M. Kiviniemi, and M. P. Tulppo, "Individual responses to aerobic exercise: The role of the autonomic nervous system," *Neurosci. Biobehav. Rev.*, vol. 33, no. 2, pp. 107–115, 2009, doi: 10.1016/j.neubiorev.2008.04.009.

[28] S. Breit, A. Kupferberg, G. Rogler, and G. Hasler, "Vagus Nerve as Modulator of the Brain–Gut Axis in Psychiatric and Inflammatory Disorders," *Front. Psychiatry*, vol. 9, p. 44, 2018, doi: 10.3389/fpsyt.2018.00044.

[29] S. S. C. Rao, J. Beaty, M. Chamberlain, P. G. Lambert, and C. Gisolfi, "Effects of acute graded exercise on human colonic motility," *Am. J. Physiol.-Gastrointest. Liver Physiol.*, vol. 276, no. 5, pp. G1221–G1226, 1999, doi: 10.1152/ajpgi.1999.276.5.g1221.

[30] O. Jansen *et al.*, "Hybrid Assistive Limb Exoskeleton HAL in the Rehabilitation of Chronic Spinal Cord Injury: Proof of Concept; the Results in 21 Patients," *World Neurosurg.*, vol. 110, pp. e73–e78, 2018, doi: 10.1016/j.wneu.2017.10.080.

[31] A. Zieriacks, M. Aach, A. Brinkemper, D. Koller, T. A. Schildhauer, and D. Grasmücke, "Rehabilitation of Acute Vs. Chronic Patients With Spinal Cord Injury With a Neurologically Controlled Hybrid Assistive Limb Exoskeleton: Is There a Difference in Outcome?," *Front. Neurorobotics*, vol. 15, p. 728327, 2021, doi: 10.3389/fnbot.2021.728327.

Perspectives of Older Adults on Assistive Robot Support at Home

Samuel A. Olatunji
College of Applied Health Sciences
University of Illinois Urbana-Champaign
Champaign, IL, USA
olatunji@illinois.edu

Megan P. Bily
College of Applied Health Sciences
University of Illinois Urbana-Champaign
Champaign, IL, USA
mpbily2@illinois.edu

Megan A. Bayles
College of Applied Health Sciences
University of Illinois Urbana-Champaign
Champaign, IL USA
mbayles2@illinois.edu

Wendy A. Rogers
College of Applied Health Sciences
University of Illinois Urbana-Champaign
Champaign, IL, USA
wendyr@illinois.edu

***Abstract*—Assistive robots have tremendous potential to support older adults in their homes. The design of robots for home use is in its nascence, but broad commercial success will depend on the robot design and the older adults' willingness to adopt this technology in their homes. We aimed to understand older adults' perceptions about the potential for use of assistive robots in their homes. We grounded this exploration by understanding their views about aging independently. Using a mixed-methods approach, we interviewed 27 older adults (aged 60-79) about aging and assistive robots and assessed their technology and robot experience. Their views about aging independently revolved around living where they considered home and being able to do their activities on their own. They were open to a robot supporting them in their homes and shared activities the robot could support. We identified factors that should be considered when designing and deploying robots to support the autonomy of older adults.**

Keywords—Successful aging, human-robot interaction, acceptance

I. Introduction

In the United States, approximately 18 million adults over age 65 have difficulty or receive help with self-care, mobility, or household activities [1]. Technologies such as assistive robots have tremendous potential to support these individuals [2, 3, 4]. Robots might augment the person's capabilities, support their independence, enable functional activities, and ultimately lower healthcare costs associated with logistics for health screening, healthcare consultations, and monitoring [5, 6]. However, only a few robots with such capacity are commercially available and can be reliably operated remotely to support older adults in their homes [7].

Given that the design of robots for home use is in its early stages, it is important to understand older adults' openness to having them in their homes. Broad commercial success will depend on the robot design and the older adults' willingness to adopt this technology in their homes. Assistive robots, by definition, are meant to assist with everyday activities. As such, we first explored how older adults think about their independence. This approach primed them to think about what might be needed to support that independence and set the context for the discussion of their views about having an assistive robot in their own home. The research questions that guided the research were as follows:

1. What are the general perceptions of older adults about aging independently?
2. What are their views about using a robot in general to support aging independently?
3. How might older adults use an assistive robot to support their everyday home activities?
4. What are the facilitators and barriers to older adults' acceptance and use of an assistive robot in their homes?

II. Method

A. Participants

Participants were recruited from the TechSAge Participant Registry (TechSAgeRERC.org) and through word of mouth. Inclusion criteria were aged 60-79; access to internet and a video camera; and a score above 37 on the Modified Telephone Interview for Cognitive Status (TICS-M, [8]). Table 1 provides the socio-demographic characteristics for the 27 participants. Given that an estimated 25% of people over age 65 have a mobility disability [9], we oversampled this population as they might be more likely to benefit from having an assistive robot in their home. Reported mobility impairments were due to a range of conditions, including Parkinson's disease, multiple sclerosis, spina bifida, post-polio syndrome, and spinal cord injury.

B. Materials and Measures



Fig. 1. Stretch Research Edition robot (RE1) by Hello Robot (Hello Robot, 2020; https://hello-robot.com/product)

Robot Videos - We selected one assistive robot to use for the study to enable the participants to become familiar with its capabilities and to think deeply about the pros and cons of this type of assistive robot. The Stretch robot (Fig. 1, developed by Hello Robot Inc.) is a mobile manipulator robot designed to support everyday activities using a lightweight telescoping arm mounted on a mobile base [10]. We prepared a series of short video clips showing the Stretch robot's capabilities in home settings. The first video depicted Stretch completing various tasks in the home, such as vacuuming a couch, wiping a kitchen countertop, watering plants, or getting clothes from a dryer during laundry. The next set of video clips depicted Stretch completing tasks with the addition of a mounted tablet computer, such as medication reminding, delivery of a pillbox, or a cooking task. The last series of video clips showed Stretch supporting the activities of daily living (ADLs) of an individual with quadriplegia (e.g., Stretch supporting with self-feeding).

TechSAge Background Questionnaire - Participants were asked general demographic questions using the TechSAge Background Questionnaire (TSBQ, [11]) administered at the start of the interview. The TSBQ covers general demographics and health information, including current conditions, vision, hearing, and mobility capabilities.

Robot Trust Questionnaire - Participants were asked a series of questions to determine their trust in using robots, which was an adapted measure [12]. Participants responded to statements regarding trust in robots on a five-point Likert scale ranging from strongly disagree (1) to strongly agree (5).

Robot Familiarity and Use Questionnaire - Participants were asked about their familiarity with various types of robots [13]. For each robot listed, the participants responded on a five-point scale ranging from having no familiarity at all (1) with the robot to having used and operated the type of robot frequently (5).

Semi-Structured Interview - The interview questions explored understanding of aging independently and the implications of using robots at home. After each set of videos participants were queried about their impressions and opinions of the Stretch robot.

TABLE I. CHARACTERISTICS OF PARTICIPANTS (N=27)

Variables	Total	
	*n**	*%*
Gender		
Female	18	67
Male	9	33
Age		
60-65	9	33
66-72	14	52
73-79	4	15
Racial Group		
White/Caucasian	25	92
Black/African American	1	4
More than one race	1	4
Marital Status		
Single	2	7
Married	15	6
Separated	2	7
Divorced	3	11
Widowed	2	7
Do not wish to answer	3	11
Highest level of Education		
High school/GED	1	4
Vocational Training	2	8
In progress college / Associate's Degree	2	8
Bachelor's Degree (BA, BS)	9	38
Master's Degree (or other post-graduate training)	9	38
Doctoral Degree (PhD, MD, EdD. DDS, JD, etc.)	1	4
Income (US$)		
Less than 25,000	1	4
25,000-49,999	3	11
50,000-74,999	3	11
75,000 or more	14	52
Do not know for sure	1	11
Do not wish to answer	5	19
"With whom do you live?"		
Live alone	8	32
Roommate or Friend	1	4
Spouse or Partner	17	65
General Health (self-reported)		
Poor	0	0
Fair	4	15
Good	9	35
Very Good	8	31
Excellent	5	19
Mobility Impairment		
Yes	8	30
No	19	70

* Numbers do not always add to 27 due to missing data.

The questions also explored their perceptions about using the robot to support daily living activities. The study flow is presented in Fig. 2. The interview was conducted over Zoom. This was to make it easier for participants to participate in the study from the place that was convenient for them. It also provided participation opportunity for those who had more severe forms of mobility impairment who may not be able to travel to a specific study location.

C. Data Preparation and Analysis

Transcribing and Segmenting - After the interviews were completed, the research team edited the transcripts to ensure they matched the audio verbatim with personal information

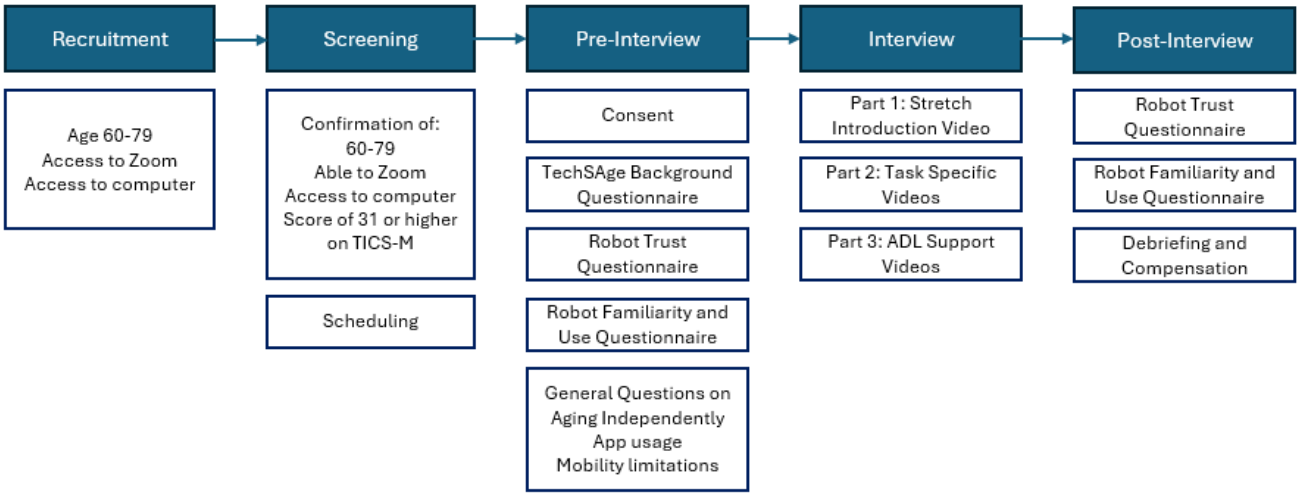


Fig. 2. Study flow diagram

omitted. Transcripts were segmented into analysis units, which were statements about participants' perceptions regarding using robots in their homes.

Coding Scheme Development - We used thematic coding to identify key topics and themes relevant to the research questions. We developed the coding scheme by reviewing a random sample of the transcripts and extracting key topics and common themes based on literature related to human-robot interaction (HRI) and the themes that emerged from the participants' comments [14]. This was an iterative strategy whereby categories were assigned using existing themes from the HRI literature and new categories were added based on the emerging themes. The authors reviewed the themes together.

III. Results

A. *What were the general perceptions of older adults about aging independently?*

Participants were asked, "What does aging independently mean to you?". We added this question after the first 10 participants to understand the common attitudes of older adults towards aging independently in general that had emerged spontaneously in the initial interviews. Thus 17 participants were asked this question directly and we observed three emergent themes (see Fig. 3). The theme "Person" referred to any discussion that revolved around being independent as a person, and not relying on another human for assistance as they age ("That means you can… You don't need anybody's help. That you can take care of yourself."). The theme "Place" was coded when the participant mentioned that staying in their preferred place was important to aging independently ("I guess it means living in one's own home with any necessary adaptive devices."). The "Tasks" theme referred to any comments that included being able to complete one's responsibilities ("…be able to do your day-to-day tasks. So daily activities would be very important"). As is evident in Fig. 3, participants often used a combination of themes ("That I'm able to live in a place by myself and do almost everything myself without having to depend on somebody else to come and do it for me").

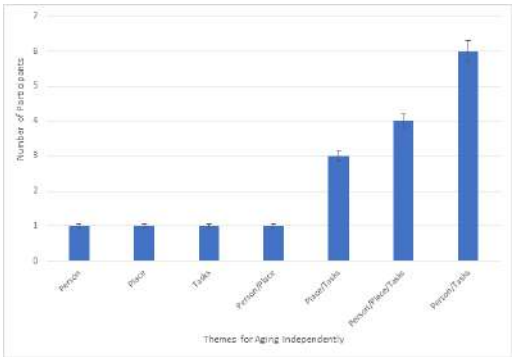


Fig. 3 Themes from "What does aging independently mean to you?" (n=17)

B. *What were older adults' views about using a robot, in general, to support aging independently?*

With respect to robot experience most participants answered, "Have only heard about or seen this robot" (M=2.74, SD=0.68) for the familiarity portion of the questionnaire, except for the remote presence robot, which had a majority answer of "Not sure what this is" (M=2.00, SD=0.90). With respect to robot trust the answers clustered around "Neither agree nor disagree" (M=3.36, SD=0.88). However, more than

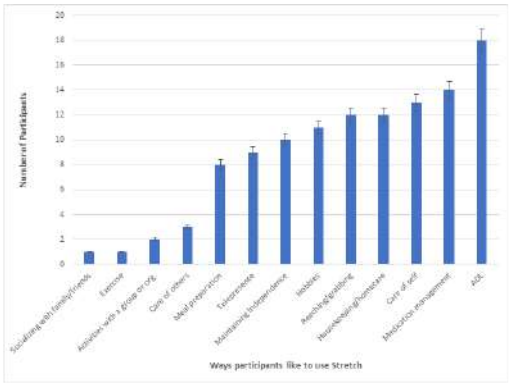


Fig. 4. Ways the older adult would like to use Stretch in their homes

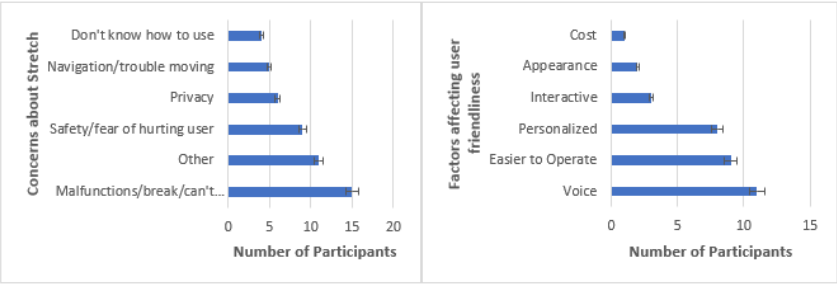


Fig. 5. (a) Concerns about Stretch (b) Ways to increase user friendliness.

half of the participants (19/27) agreed they would depend on a robot to support them. The majority of the participants expressed a willingness to have a robot to support aging independently: "*Oh yeah, I would, I would definitely, I would enjoy the cleaning up aspect. I hate to clean up, and I would employ a robot in a minute if it could clean things up like that. I have no problems with robots in general. I, I'm waiting, waiting for them*". After watching videos of Stretch assisting a man with quadriplegia with activities, participants were asked if they thought this robot could enhance independence for someone with a disability. All 27 participants answered with "yes". They were also asked, in the context of a robot working with somebody who has a disability, if they would trust this robot (Stretch) to help them. 26 participants answered "yes," with 1 answering "not sure" because they felt they did not have enough information to answer.

C. Initial Thoughts and Impressions of Stretch Robot

1) First Impressions

After watching the video demonstrations, participants were asked, "What is your first impression of Stretch?" and 25/27 had a positive first impression. They described Stretch as helpful, useful, and versatile. Other commonly shared first impressions include amusement from watching Stretch perform various tasks, being pleasantly surprised by Stretch's ability to complete many different tasks, and uncertainty about how Stretch was completing these actions, whether by automation or remote control. Furthermore, 4 participants stated explicitly that they wanted Stretch in their home or asked where to purchase it.

2) Appearance

With respect to appearance, 13/27 participants mentioned feeling neutral, neither positive nor negative: "*To me it [Stretch] just looked like a regular robot kind of thing*". Others (12/27) commented that the Stretch robot appeared very functional and mechanical and 7/27 mentioned that it had a very sleek, thin, or streamlined look that would have a "*small footprint... which you would need if you were going to use it in a house*". Some comments pointed to the fact that if the robot could successfully complete the tasks it was designed to do, that would be a higher priority for them than the robot's appearance.

3) How might older adults use Stretch robot to support their everyday home activities?

When asked if they could see themselves using this type of robot in their home, all 27 participants responded yes. Six participants elaborated on that, saying that they could see themselves using this robot in their homes, but only with the onset of mobility issues, disability, or greater need later in life. Fig. 4 shows participants' preferences about activities they felt Stretch could be used for in their homes. Participants without mobility impairments mentioned uses such as medication management and ADLs (dressing, bathing, toileting, grooming, etc...) whereas participants with mobility impairments focused on reaching/grabbing, meal preparation, and homecare. Participants who were wheelchair users commented about already having made adjustments so they could do things we showed Stretch doing, but that Stretch could be very helpful for levels of reach that they could not achieve. One noted, "*And myself who have had surgery or something of that sort and during recuperation the sort of go fetch function would be particularly useful if someone has either permanently or temporarily limited mobility.*"

D. What are the facilitators and barriers to acceptance and use of Stretch robot by older adults in their homes?

1) Ease of use

Over half of the participants (17/27) considered Stretch to likely be easy to use from the videos, but some participants (9/27) whose responses were coded as "other" or "not sure" noted that they could not be sure of Stretch's ease of use based solely on the videos alone. Only one participant responded with "no". They said they would need to try Stretch out themselves or they felt it could be easy to use with some practice.

2) Concerns

Concerns were related to functionality (see Fig. 5a), such as the robot breaking, and consequently not knowing how to fix it or not having an easy avenue to have robot fixed (n=15), a malfunction hurting the user (n=9), or generally not knowing how to use Stretch (n=4). Concerns related to privacy such as hacking and data storage were mentioned but less frequently (n=6).

3) User friendliness

The helpful additions mentioned most were about functionality, with 11/27 mentioning that adding voice communication (both to and from) and making Stretch easier to operate would increase its user-friendliness. However, this does not imply that they stated Stretch was not easy to use; rather, it simply suggests ways to make Stretch even easier to use (see Fig. 5b).

4) Adaptability through attachments

Participants (10/25) asked questions about items that were added onto Stretch to fulfill certain tasks (e.g., vacuum, washcloth, etc...) as well as how Stretch was controlled (e.g., remotely, autonomously, etc...). For example, "*Do those*

attachments come with Stretch?"; "*Do I need to know how to attach them myself?*"; "*How would I learn to operate Stretch?*". We posit that questions like these could be a barrier to the acceptance and adoption of Stretch but could be understood as facilitators to the adoption of Stretch for use in homes. The addition of the tablet received the most positive responses, with 16/25 participants expressing positive comments.

IV. Discussion

A. Perceptions about aging independently

Our goal was to understand older adults' perceptions about accepting assistive robots in their homes and to explore their views about such robot supporting their autonomy. We first explored their perceptions of aging independently to provide a foundation for them to consider how a robot could provide support. Similar to the pattern observed by [15] about definitions of aging in place, participants described common concepts of space, person, time, and their combinations. These concepts are consistent with the definition of aging in place as "One's journey to maintain independence in one's place of residence as well as to participate in one's community" [15].

The concepts of aging independently related to prioritizing tasks critical for an assistive robot to support. The older adults were open to the concept of using an assistive robot in their home and expressed positive expectations for the impact it could make. This supports the narrative in the literature about older adults desiring a robot that can help them do the things they want, in the way they want, when they want, with whom they want, where they want, and how they want it [16]. This perceptions they shared on aging independently grounded the discussion and set the context for understanding their views on the role robots could play in supporting independent aging.

B. Acceptance of robots for personal use in homes

All the participants affirmed that they would like to use the robot in their own homes irrespective of the differences in their background, socio-demographic status, initial perception of the robot, and health status. This is a testament to their willingness to accept the robot for personal use at home. The tasks they mentioned aligned with the existing literature about robotic support for older adults [17, 18]. The tasks we demonstrated to them through videos in the study were carefully selected and informed by literature [2, 3, 13, 18]. We showed the participants tasks supported by previous studies' findings and considered relevant to the target population. The participants related to these tasks, and provided more in-depth insights on how they would want the robot to support them.

We saw a positive response from the participants for various tasks that they would like the robot to support them with. In general, the need for assistance with ADLs is the most common among older adults who require a higher level of care [19]. This kind of support from robots will require more complex functions, sensing, and processing, such as identifying objects accurately and deciding on the most appropriate way to pick up these objects. This points to the delicateness of the support required in home environments, and how user satisfaction with these tasks impacts acceptance [3]. With the emergence of more advanced robots for domestic uses and home healthcare [20, 21], we foresee more applications of robots to support older adults with ADLs in their homes. These results point researchers, developers, and home healthcare teams to the openness of older adults regarding the idea of robot assistance as identified in the literature [22] and the use of the robot supporting them in their homes. When expressing their thoughts about acceptance, the older adults focused more on the functional ability of the robot as a priority rather than appearance, which is consistent with the findings from [23].

This was a major contribution that differentiated the study from previous work. Prior studies focused on what the robot could do to support older adults; the current study revealed how older adults would want the robot to support them through these tasks. We used data from the literature to inform the design and choice of the tasks that would be demonstrated to the participants in order to spur more ideas from the participants. The participants were able to relate to the tasks shown to them in the videos and then shared more insights on how they wanted these tasks executed and the impact this would have. This approach provided the opportunity for a more comprehensive discussion on how to make the robot's support in the home successful. We recommend this approach for further studies and for designers considering a starting point for the tasks to demonstrate the robot's capabilities and potential. Studies such as [2, 3, 13, 16, 18] have presented a collection of potential tasks that could demonstrate the robot's potential to support older adults in various contexts.

C. Understand the facilitators and barriers to acceptance.

Perception of the robot's usefulness in the homes stands out as a facilitator to the acceptance of an assistive robot. Most of the older adults mentioned that their ease of using the robot, including the ease of communicating with the robot will impact their willingness to use the robot in their own homes. This connects with technology acceptance model [24], wherein perceived usefulness and ease of use have been validated to impact the intention and actual use of a technology. Increasing user-friendliness is a facilitator that has been proven to support people's interaction with robots and to potentially influence acceptance of these robots [25, 26]. The most prominent element mentioned by the older adults that could contribute to user-friendliness was voice communication, which aligns with earlier propositions of voice communication to improve interpersonal communication and natural human-robot interactions [28, 29, 30]. It is critical to consider these facilitators alongside the concerns that the older adults expressed, such as ease of fixing malfunctions, safety, and privacy management.

V. Conclusion

In sum, our findings unveiled factors that could impact the adoption of robots by older adults in their homes. The older adults had an overall positive perception of a robot assisting them with a range of tasks. The insights they shared should be considered for future developments of robot design to facilitate more widespread adoption and use of these robots in homes. We provide these details to support designers, practitioners, and other researchers conducting similar forms of testing, participatory design, or deployment. Future research and development efforts should carefully consider how robots' actions can be adapted to meet the changing needs of individuals as they age to support their autonomy.

ACKNOWLEDGMENTS

This research was funded in part by the National Institute on Aging (National Institutes of Health) Small Business Innovation Research Grants, Phase I (R43AG072982) and Phase II (R44AG072982). We acknowledge the contributions of Travis Kadylak, the Hello Robot Research Team, especially Aaron Edsinger, Charles Kemp, and Vy Nguyen. We thank students in the Human Factors and Aging Laboratory who supported this project – Yi Cao, Jade Marks, and Zolzaya Byambasuren.

REFERENCES

[1] Assi, S., Morales, E. E. G., Windham, B. G., Lin, F. R., Bandeen-Roche, K., Shukla, A., ... & Martinez-Amezcua, P. (2023). Hearing Loss and Frailty among Older Adults: The Atherosclerosis Risk in Communities Study. Journal of the American Medical Directors Association, 24(11), 1683-1689.

[2] Beer, J. M., Fisk, A. D., & Rogers, W. A. (2015). Commanding Home Robots: A Comparison Between Older Adults With and Without Mobility Loss. In Proceedings of the Human Factors and Ergonomics Society Annual Meeting (Vol. 59, No. 1, pp. 70-74). Sage CA: Los Angeles, CA: SAGE Publications.

[3] Mitzner, T. L., Chen, T. L., Kemp, C. C., & Rogers, W. A. (2014). Identifying the potential for robotics to assist older adults in different living environments. International Journal of Social Robotics, 6(2), 213-227.

[4] Wu, Y. H., Cristancho-Lacroix, V., Fassert, C., Faucounau, V., de Rotrou, J., & Rigaud, A. S. (2016). The attitudes and perceptions of older adults with mild cognitive impairment toward an assistive robot. Journal of Applied Gerontology, 35(1), 3-17.

[5] Luo, C., Yuan, R., Mao, B., Liu, Q., Wang, W., & He, Y. (2024). Technology Acceptance of Socially Assistive Robots Among Older Adults and the Factors Influencing It: A Meta-Analysis. Journal of Applied Gerontology, 43(2), 115-128.

[6] Mann, D. M., Chen, J., Chunara, R., Testa, P. A., & Nov, O. (2020). COVID-19 transforms health care through telemedicine: evidence from the field. Journal of the American Medical Informatics Association, 27(7), 1132-1135.

[7] Kadylak, T., Uppalapati, N., Huq, A., Krishnan, G., & Rogers, W. A. (2023). Engaging Healthcare Providers to Design a Robot for Telehealth. Ergonomics in Design, 10648046231193287.

[8] Fong, T. G., Fearing, M. A., Jones, R. N., Shi, P., Marcantonio, E. R., Rudolph, J. L., ... & Inouye, S. K. (2009). Telephone interview for cognitive status: Creating a crosswalk with the Mini-Mental State Examination. Alzheimer's & Dementia, 5(6), 492-497.

[9] CDC (2020). Prevalence of Disabilities and Health Care Access by Disability Status and Type Among Adults — Centers for Disease Control and Prevention, 2016, United States. https://www.cdc.gov/ncbddd/disabilityandhealth/features/kf-adult-prevalence-disabilities.html

[10] Olatunji, S.A., Nguyen, V., Cakmak, M., Edsinger, A., Kemp, C.C., Rogers, W.A., & Mahajan, H.P. (2024). Immersive participatory design of assistive robots to support older adults. Ergonomics, 67, 717–731. https://doi.org/10.1080/00140139.2024.2312529

[11] Remillard, E. T., Griffiths, P. C., Sanford, J. A., Mitzner, T. L., & Rogers, W. A. TechSAge Background Questionnaire: Overview of Measures.

[12] Ullman, D., & Malle, B. F. (2018, March). What does it mean to trust a robot? Steps toward a multidimensional measure of trust. In Companion of the 2018 acm/ieee international conference on human-robot interaction (pp. 263-264).

[13] Mitzner, T. L., Smarr, C. A., Beer, J. M., Chen, T. L., Springman, J. M., Prakash, A., ... & Rogers, W. A. (2011). Older adults' acceptance of assistive robots for the home. Georgia Institute of Technology

[14] Braun, V., & Clarke, V. (2006). Using thematic analysis in psychology. Qualitative research in psychology, 3(2), 77-101.

[15] Rogers, W. A., Ramadhani, W. A., & Harris, M. T. (2020). Defining aging in place: The intersectionality of space, person, and time. Innovation in Aging, 4(4), 1–11. https://doi.org/10.1093/GERONI/IGAA036

[16] Lee, H. R., & Riek, L. D. (2018). Reframing assistive robots to promote successful aging. ACM Transactions on Human-Robot Interaction (THRI), 7(1), 1-23.

[17] Hall, A. K., Backonja, U., Painter, I., Cakmak, M., Sung, M., Lau, T., Thompson, H. J., & Demiris, G. (2019). Acceptance and perceived usefulness of robots to assist with activities of daily living and healthcare tasks. Assistive Technology, 31(3), 133–140. https://doi.org/10.1080/10400435.2017.1396565

[18] Smarr, C. A., Prakash, A., Beer, J. M., Mitzner, T. L., Kemp, C. C., & Rogers, W. A. (2012, September). Older adults' preferences for and acceptance of robot assistance for everyday living tasks. In Proceedings of the Human Factors and Ergonomics Society Annual meeting (Vol. 56, No. 1, pp. 153-157). Sage CA: Los Angeles, CA: Sage Publications.

[19] Mois, G., & Beer, J. M. (2020). Robotics to support aging in place. In Living with robots (pp. 49-74). Academic Press.

[20] Lee, H. R., Sun, F., Iqbal, T., & Roberts, B. (2023, March). Reimagining robots for dementia: From robots for care-receivers/giver to robots for carepartners. In Proceedings of the 2023 ACM/IEEE International Conference on Human-Robot Interaction (pp. 475-484).

[21] Vandemeulebroucke, T., Dzi, K., & Gastmans, C. (2021). Older adults' experiences with and perceptions of the use of socially assistive robots in aged care: A systematic review of quantitative evidence. Archives of Gerontology and Geriatrics, 95, 104399.

[22] David, D., Thérouanne, P., & Milhabet, I. (2022). The acceptability of social robots: A scoping review of the recent literature. Computers in Human Behavior, 137, 107419.

[23] Bayles, M. A., Lee, J., Kadylak, T., & Rogers, W. A. (2023). Understanding older adults' initial perceptions of robot appearance and function: Implications for acceptance. Gerontechnology, 22. https://doi.org/10.4017/gt.2023.22.2.bay.08

[24] Davis, F. D. (1989). Perceived usefulness, perceived ease of use, and user acceptance of information technology. MIS quarterly, 319-340.

[25] Salem, M., Rohlfing, K., Kopp, S., & Joublin, F. (2011). A friendly gesture: Investigating the effect of multimodal robot behavior in human-robot interaction. In 2011 RO-MAN (pp. 247-252). IEEE.

[26] Salem, M., Lakatos, G., Amirabdollahian, F., & Dautenhahn, K. (2015, March). Would you trust a (faulty) robot? Effects of error, task type and personality on human-robot cooperation and trust. In Proceedings of the tenth annual ACM/IEEE international conference on human-robot interaction (pp. 141-148).

[27] Torta, E., Werner, F., Johnson, D. O., Juola, J. F., Cuijpers, R. H., Bazzani, M., ... & Bregman, J. (2014). Evaluation of a small socially-assistive humanoid robot in intelligent homes for the care of the elderly. Journal of Intelligent & Robotic Systems, 76, 57-71.

[28] Rifinski, D., Erel, H., Feiner, A., Hoffman, G., & Zuckerman, O. (2021). Human-human-robot interaction: robotic object's responsive gestures improve interpersonal evaluation in human interaction. Human–Computer Interaction, 36(4), 333-359.

[29] Lee, O. E., Nam, I., Chon, Y., Park, A., & Choi, N. (2023). Socially assistive humanoid robots: effects on depression and health-related quality of life among low-income, socially isolated older adults in South Korea. Journal of Applied Gerontology, 42(3), 367-375.

[30] Werner, K., Oberzaucher, J., & Werner, F. (2012). Evaluation of human robot interaction factors of a socially assistive robot together with older people. In 2012 Sixth International Conference on Complex, intelligent, and Software-Intensive Systems (pp. 455-460). IEEE

Human-Centered Geodesics for Motion Planning

Francesco Bianchin[1], Davide Astarita[2], Lorenzo Amato[2], Emilio Trigili[2], Satoshi Endo[1], Sandra Hirche[1]

***Abstract*—This paper addresses the challenge of designing human-like reference trajectories for exoskeleton-aided rehabilitation, with a focus on mimicking human joint coordination while addressing clinical requirements. Redundant kinematic chains in human biomechanics pose challenges to trajectory planning: state-of-the-art algorithms often do not explicitly address the problem of replicating natural movements nor do they provide a suitable performance over a wide range of human motions. To address this challenge, this paper proposes a geodesics-based computational method that incorporates joint-level constraints, in addition to energy and level of comfort criteria to solve the problem of redundancy and better emulate human movements. Using upper-limb data retrieved with an exoskeleton platform, the advanced method demonstrated significant performance gains over standard approaches like the minimum-jerk model and cubic polynomial planning, and leads to human-like trajectories, while closely aligning with human demonstrations, both at the configuration (joints) and task-space (hand) level. In particular, we provide detailed comparisons across various motion types and subjects, demonstrating the versatility of the proposed method and its strong potential for application in clinical and assisted living settings.**

***Index Terms*—Trajectory planning, Exoskeleton rehabilitation, Human motion, Geodesics**

I. Introduction

An ongoing challenge in exoskeleton research is developing reference trajectories that recreate human-like motions in terms of joint coordination and velocity profiles, while also meeting the joint specific constraints required for rehabilitation tasks [1]. Achieving this is complex, as human motion often results from redundant kinematic chains [2]. When it comes to motion planning, kinematic redundancy is often exploited to address secondary objectives, but also introduces challenges in trajectory planning by increasing the solution space and complicating the selection of optimal joint configurations. This issue is particularly pronounced in inverse kinematics-based methods, which focus on inverting task-space trajectories but frequently overlook the intricate joint coordination required for human-like movement. This presents an opportunity to advance motion planning techniques by leveraging redundancy, not just for optimization, but to better replicate natural, human-like motion [1].

To address these limitations, researchers have explored different approaches that leverage kinematic redundancy to recreate natural human coordination [3]. These approaches generally fall into two main categories [4], namely analytical and computational methods on the one hand [5], [6], and data-driven methods, mainly traceable to the learning by demonstration subfield, on the other [7], [8].

In this work, we take a data-informed computational view on the problem, as we postulate a comprehensive set of criteria that capture the human optimization processes underlying motion generation and validate them with data. A commonly used computational approach involves the minimization of kinetic energy, as described in [9]. This method interprets human motion generation as the solution to an underlying geometric optimization problem, resulting in a geodesic path in the configuration space. It was originally proposed to model 3D pointing motions, where the kinetic energy criterion enhances performance compared to alternative methods, including Euclidean configuration-level planning [10] and the minimum torque-change model [11]. Geodesic-based trajectories have already been applied in exoskeleton-related research, as in [12], [13], where kinetic energy minimization is combined with considerations of scapulo-humeral rhythm to address limitations associated with assuming a fixed position of the shoulder's center of rotation. However, a thorough investigation of how to adapt the geodesics approach to a broader set of motions is still missing, as well as an exploration of how the underlying metric can be exploited for application-specific objectives.

In this work, we reformulate the trajectory generation approach by introducing novel optimization criteria—specifically, an anthropomorphism measure and potential energy minimization [14]—to enhance the human-like quality of the synthesized motion. Additionally, we extend the framework to accommodate constraints relevant to assistance and rehabilitation robotics. In particular, geodesic-based methods allow for modifications to the underlying Riemannian metric, enabling joint-level constraint satisfaction through the incorporation of barrier-function metric terms. We thus achieve the stated objective of generating human-compliant trajectories and exploit redundancy to reproduce key characteristics of natural human motion. To evaluate the effectiveness of our approach, we conducted an extensive validation using a dataset of real-world demonstrations from seven healthy subjects performing free-arm motion experiments. Joint trajectories

This study was part of the Innovation Network eXprt of the Technical University of Munich, funded by the Federal Ministry of Education and Research and the Free State of Bavaria under the Excellence Strategy of the Federal Government and the States. This work was supported by the EU Commission through the H2020 ReHyb project (Rehabilitation based on hybrid neuroprosthesis, Grant Agreement: 871767) and partially supported by the RIG – Robotics Institute of Germany, supported by the BMBF – Federal Ministry of Education and Research of Germany.

[1]Francesco Bianchin, Satoshi Endo and Sandra Hirche are with the School of Computation, Information and Technology, Technical University of Munich, Germany {francesco.bianchin, s.endo, sandra.hirche}@tum.de

[2]Davide Astarita, Lorenzo Amato and Emilio Trigili are with The BioRobotics Institute, Scuola Superiore Sant'Anna, Pontedera, Italy, and with the Department of Excellence in Robotics & AI, Scuola Superiore Sant'Anna, 56127 Pisa, Italy. {davide.astarita, lorenzo.amato,emilio.trigili}@santannapisa.it

were recorded using the NESM-γ exoskeleton system [15], [16]. The experimental trials focused on two main objectives: optimizing the parameters of our method to balance different optimization criteria effectively and performing a comparative evaluation against existing approaches. Specifically, we analyzed the performance of our geodesics-based method (GEO-HL) relative to minimum jerk (MJ), inverse kinematics (IK), and standard kinetic energy geodesics (GEO), assessing human-likeness based on configuration and end-effector error indicators. Empirical results demonstrate that our revised geodesic method outperforms conventional approaches, such as the minimum jerk model and cubic polynomial trajectory planning, in capturing human-like motion characteristics. The remainder of the paper is structured as follows. The motion planning problem is formulated in Section II. In Section III, we propose a novel geodesic-based approach to address typical rehabilitation-oriented requirements. The experimental trial setup is described in Section IV, while the data analysis is detailed in Section V. Section VI provides extensive comparisons between the proposed method and other approaches popular in the literature, and final remarks are presented in Section VII.

II. Problem Statement

In the context of our work, we define a motion planning task as follows. Given a known initial configuration $\mathbf{q}_0 \in Q$, where $Q \subseteq \mathbb{R}^n$ is the joint configuration space, and an end-effector target $\mathbf{x}_f \in \mathbb{R}^3$, we optimize over trajectories $\gamma : \lambda \in [0,1] \rightarrow \mathbf{q}(\lambda) \in Q$, where $\lambda \in \mathbb{R}$ is an affine parameter defining the level of trajectory completion. The basic requirement for a trajectory planning algorithm is that $\mathbf{q}(0) = \mathbf{q}_0$ and $\mathbf{x}_f = \mathbf{x}(\mathbf{q}_f) = \mathbf{x}(\mathbf{q}(1))$, i.e. the final joint configuration in the planned trajectory realizes the workspace target. In order to deal with the redundancy of the kinematic chains of interest, we perform a bi-level optimization procedure, i.e.:

1) Generate candidate trajectories $\gamma_{\boldsymbol{\alpha}}$ joining $\mathbf{q}_0$ and $\mathbf{q}_f(\boldsymbol{\alpha})$, where $\boldsymbol{\alpha} \in \mathbb{R}^p$ parameterizes the set of valid end-configurations, in accordance with the kinematic chain under analysis, having p redundancies.
2) Select $\gamma_{\boldsymbol{\alpha}^*}$ among candidate trajectories optimizing over a given cost J, i.e. $\gamma_{\boldsymbol{\alpha}^*} = \arg\min_{\boldsymbol{\alpha}} J(\gamma_{\boldsymbol{\alpha}})$

This work addresses the challenge of generating human-like trajectories by approximating typical human joint coordination. To achieve this, the cost function $J(\cdot)$ is designed to reflect human optimization principles, ensuring the synthesis of trajectories that are both natural and compliant with rehabilitation-related requirements, such as the satisfaction of prescribed joint limit constraints.

III. Geodesic-based Trajectory Generation

In this section, we briefly outline the basics of geodesics-based trajectory generation, as a means to attain phase 1 of the bi-level optimization. We then focus on metric augmentation strategies for application-oriented objectives and we address the issue of redundancy, to address phase 2 of the bi-level optimization.

When looking for geodesics, we formulate the problem of generating trajectories as an optimization problem on a suitably defined Riemannian space, as detailed in [9]. Given the configuration space Q and the configuration tuples $\mathbf{q} = [q_1, ..., q_n]^T \in Q$, which represent the joint variables and degrees of freedom (DoFs) involved, we note that a Riemannian manifold on Q is defined by means of a metric tensor $\mathbf{M}(\mathbf{q}) \in \mathbb{S}_n^+$, where S_n^+ is the set of symmetric positive definite matrices of size n, with components M_{ij}, such that the infinitesimal squared distance is given by

$$d\sigma^2 = \sum_{i=1}^{n}\sum_{j=1}^{n} M_{ij}(\mathbf{q}) dq_i dq_j \in \mathbb{R}^+ \tag{1}$$

where $d\sigma$ is the infinitesimal distance in the Riemannian manifold [17].

In [9] the metric is given by kinetic energy, which is a criterion often used in the human motion analysis field in order to interpret human planning strategy. It is given by

$$M_{ij}(\mathbf{q}) = \frac{\partial K(q, \dot{q})}{\partial \dot{q}_i \dot{q}_j} \tag{2}$$

where $K(\mathbf{q}, \dot{\mathbf{q}})$ represents the kinetic energy function associated to the kinematic chain under analysis, $\mathbf{q}$ represents the joint configuration and $\dot{\mathbf{q}}$ the joint velocity. One can see that the metric is configuration-dependent and relates to the inertial properties of the kinematic chain for the selection of desired configurations. Finding a geodesic path between two points in the configuration space using such metric means finding the shortest path according to the associated kinetic energy. Minimizing the distance between $\mathbf{q}_0$ and $\mathbf{q}_f(\boldsymbol{\alpha})$ with metric (2) inherently minimizes the kinetic energy expended along the path. As shown in [9], trajectories generated according to (2) are endowed with efficiency. When moving along kinetic energy geodesics, all accelerations act in direction tangential to the joint path, meaning that they minimize the torque required with respect to non-geodesic paths.

The use of exoskeletons for rehabilitation/assistance poses additional challenges beside efficiency, starting from joint constraints introduced by the mechanical structure of the robotic system, in terms of limited joint ranges of motion, due to mechanical stops [15], and the reduced range of motion of rehabilitation patients. We address this challenge by exploiting the Riemannian formulation, introducing a suitable change in the underlying metric $\mathbf{M}(\mathbf{q})$. In particular, if we take the joint limits to be of the type $[\mathbf{q}_m, \mathbf{q}_M]$, where $\mathbf{q}_m$, $\mathbf{q}_M$ are the minimum and the maximum attainable values for the joints as dictated by mechanical and patient-related constraints, one can modify the kinetic energy metric $\mathbf{M}(\mathbf{q})$ by adding a diagonal matrix term of the type

$$\begin{aligned} \mathbf{M}_1(\mathbf{q}) &= [\mathbf{M}_1(\mathbf{q})]_{ii} \\ &= -\frac{1}{t} log\left((q_i - q_{m,i})(q_{M,i} - q_i)\right) \\ &- \frac{2}{t} log\left(\frac{q_{M,i} - q_{m,i}}{2}\right) \end{aligned} \tag{3}$$

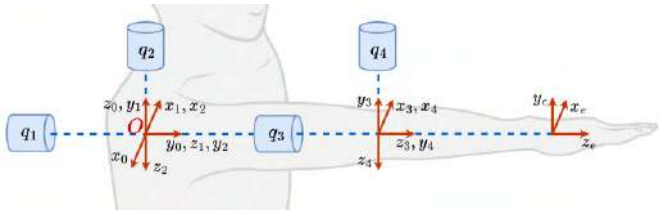


Fig. 1. Kinematic chain model for the 4DoF human arm and exoskeleton supporting system [15], with joint variables q_1, q_2, q_3 representing the shoulder's adduction/abduction, flexion/extension and internal/external rotation DoFs respectively, and q_4 representing the elbow's flexion/extension DoF.

where parameter $t \in \mathbb{R}_+$ can be used to modulate the barrier function terms $[\mathbf{M}_1(\mathbf{q})]_{ii}$, which are joint-specific and go to infinity for joint angles that are close to the limits. Considering that $\mathbf{M}_1(\mathbf{q}) \in S_n^+$, $\tilde{\mathbf{M}}(\mathbf{q}) = \mathbf{M}(\mathbf{q}) + \mathbf{M}_1(\mathbf{q}) \in S_n^+$ is still a valid metric tensor that combines the kinetic energy metric with a joint constraint term. Note that the efficiency inherent to $\mathbf{M}(\mathbf{q})$ is preserved, as the effect of term $\mathbf{M}_1(\mathbf{q})$ is significant only for areas of the manifold close to the joint limits.

The effect of $\mathbf{M}_1(\mathbf{q})$ can be easily exemplified by generating trajectories for the system considered for the experimental study, i.e. the 4-degree-of-freedom (4-DoF) arm model shown in Fig. 1. Trajectory generation between joint configurations is performed by solving the Euler-Lagrange equations derived from the metric, formulating it as a boundary value problem with the two configurations specified as the initial and final boundary conditions, as detailed in [9], [18]. In particular, consider trajectory generation between configuration $\mathbf{q}_0 = [50\ 50\ 15\ -20]^\circ$ and configuration $\mathbf{q}_f = [40\ 2\ -20\ -48]^\circ$, with joint constraints encoded by $\mathbf{q}_m = [0\ 0\ -50\ -50]^\circ$ and $\mathbf{q}_M = [50\ 50\ 20\ 0]^\circ$, which exemplify a reduced range of motion. Using metrics $\mathbf{M}(\mathbf{q})$ (pure kinetic energy) and $\tilde{\mathbf{M}}(\mathbf{q})$ (kinetic energy metric corrected by means of the joint limit metric), one obtains the trajectories shown in Fig. 2. One can see that the simple kinetic-energy metric leads to trajectories violating the imposed range of motion for the elbow (q_4), while the same does not happen when applying the modified metric.

In order to address phase 2 of the bi-level optimization procedure, one needs to select a suitable final configuration, in order to address the redundancy problem. After computing the geodesic path joining $\mathbf{q}_0$ and $\mathbf{q}_f(\boldsymbol{\alpha}) = \mathbf{q}(\boldsymbol{\alpha}; \mathbf{x}_f)$ for each candidate configuration $\mathbf{q}_f$ encoded by parameter $\boldsymbol{\alpha} \in \mathbb{R}^p$, one obtains the family of geodesics $\gamma_{\boldsymbol{\alpha}} : [0, 1] \to Q$. In order to select the optimal candidate among the ones codified by parameter α, we propose a multi-criteria cost with the purpose of achieving a human-like behaviour. To formulate the optimization problem, we first establish the key assumptions and postulates that motivate the structure of the cost function. The first assumption is kinetic energy expenditure minimization, according to an efficiency principle, as also argued in [9]. This is characterized by the term

$$E(\gamma_{\boldsymbol{\alpha}}) = \frac{1}{2}\int_0^1 \mathbf{q}'(\lambda,\boldsymbol{\alpha})^T \tilde{\mathbf{M}}(\lambda,\boldsymbol{\alpha})\mathbf{q}'(\lambda,\boldsymbol{\alpha})d\lambda \tag{4}$$

$$= \frac{1}{2}\Sigma^2(\boldsymbol{\alpha}) \tag{5}$$

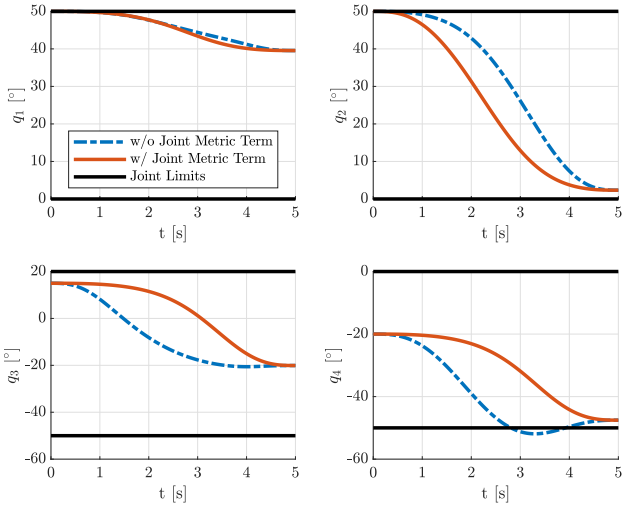


Fig. 2. A trajectory generation example where imposed constraints (black limits) would be violated without the joint constraint metric. Geodesics using $\mathbf{M}(\mathbf{q})$ are dashed blue, and those using $\tilde{\mathbf{M}}(\mathbf{q})$ are orange, shown for joint variables $q_1, \ldots, q_4$.

where $\tilde{\mathbf{M}}(\lambda, \boldsymbol{\alpha})$ is the metric tensor dependent on configuration and redundancy parameters. Along the same lines, we postulate potential energy to influence human motion preferences due to the additional metabolic cost associated with high-energy configurations. The corresponding term in the cost function is

$$U(\gamma_{\boldsymbol{\alpha}}) = U(\mathbf{q}_f(\boldsymbol{\alpha})) \tag{6}$$

where $U(\mathbf{q}_f)$ represents the potential energy of the final joint configuration. The third assumption is the preference for anthropomorphism in human movements, which translates into the tendency to avoid extreme joint angles to maintain comfort and residual mobility, in accordance with the end-state comfort hypothesis [19]. This concept is encapsulated in

$$\mathcal{A}(\gamma_{\boldsymbol{\alpha}}) = \mathcal{A}(\mathbf{q}_f(\boldsymbol{\alpha})) = \left\| \frac{2(\mathbf{q}_f(\boldsymbol{\alpha}) - \bar{\mathbf{q}})}{\mathbf{q}_M - \mathbf{q}_m} \right\| \tag{7}$$

where $\bar{\mathbf{q}} = \frac{\mathbf{q}_M + \mathbf{q}_m}{2}$ is the joint range mean value. Lower values of $\mathcal{A}(\cdot)$ indicate a configuration farther from joint limits, promoting mid-range postures. With these principles in place, the optimization problem is formulated as follows

$$\gamma_{\boldsymbol{\alpha}^*, GEO\text{-}HL} = \arg\min_{\boldsymbol{\alpha}} J_{GEO\text{-}HL}(\gamma_{\boldsymbol{\alpha}}) \tag{8}$$

where the composite cost function $J_{GEO\text{-}HL}$, emphasizing human-like geodesics, integrates the criteria

$$J_{GEO\text{-}HL}(\gamma_{\boldsymbol{\alpha}}) = E(\gamma_{\boldsymbol{\alpha}}) + w_u U(\gamma_{\boldsymbol{\alpha}}) + w_a \mathcal{A}(\gamma_{\boldsymbol{\alpha}}) \tag{9}$$

where w_u and w_a are weight parameters reflecting the relative importance of potential energy and anthropomorphism. These weights need to be tuned based on the kinematic chain under study, and we employ a data-driven approach for calibration, as exemplified for the 4-DoF arm model in experimental trials.

Computational Aspects

Generating trajectories via configuration-based geodesics involves solving a boundary value problem between $\mathbf{q}_0$ and $\mathbf{q}_f(\boldsymbol{\alpha})$ with a numerical solver, alongside optimizing valid final configurations $\mathbf{q}_f(\boldsymbol{\alpha})$. This high computational cost can limit real-time implementation. However, since most robot-assisted rehabilitation tasks require pre-designed trajectories for safety, this cost is usually not a bottleneck. The optimization process can also be made more efficient by seeking suboptimal solutions or reversing the approach—first identifying quasi-optimal end configurations in $\boldsymbol{\alpha}$, then generating fewer geodesics for these configurations.

IV. Experimental Trials: Objectives and Setup

The analysis based on experimental trials has two main objectives: (1) tuning the parameters w_u, w_a in the selection cost from Eq. (9) and (2) comparing existing methods (MJ, IK, GEO) with the proposed GEO-HL approach in terms of human-likeness. This is achieved through error measures evaluated against true recorded trajectories. Trajectory data collection was conducted using the NESM-γ exoskeleton platform [15], [16] in transparent mode, ensuring no external forces acted on subjects. NESM-γ is a powered upper-limb exoskeleton for motor rehabilitation, featuring four active revolute joints driven by series elastic actuators (SEAs) with compact custom-designed hollow springs. Transparent mode operation was maintained through low-level torque controllers applying zero reference torque while compensating for gravity and friction. The passive joints of the exoskeleton were fixed to ensure consistent results across subjects and to focus on the active joints' motions. A board with twelve targets was placed at a fixed distance from the subjects to allow unhindered arm movements. Target (3) was aligned with the robotic shoulder's center of rotation. The experiment was conducted using the right arm, as it was the dominant side for all subjects. Given the mirrored kinematic structure of the upper limbs, data collected from either side is applicable for the study's objectives. The selected tasks consist of predefined motion sequences that explore different joint coordination patterns within the 3D workspace. A distinction is made between tasks, which are considered as structured sets of movements, and individual motions, which correspond to specific trajectory segments between two postures (i.e. a task is generally made up of a sequence of multiple motions). Task subdivision was implemented to facilitate repetition. The evaluation focuses on individual motions (Motions 1-30), as they exhibit distinct acceleration and deceleration phases while targeting specific 3D workspace objectives. We study such motions, as we aim to provide a planning algorithm able to generate human-like trajectories starting from a known joint configuration and ending in a given 3D workspace objective. This can, in turn, be extended to planning composite tasks composed of multiple simple motions by concatenating the planned paths.

The following notation describes the movement postures: R: rest position on the side; K: rest position on the knee; M: mouth; S: contralateral shoulder; (1)-(12): numbered board targets. Fig. 3 illustrates the experimental setup, while Fig. 4 shows the target placements. The selected tasks are:

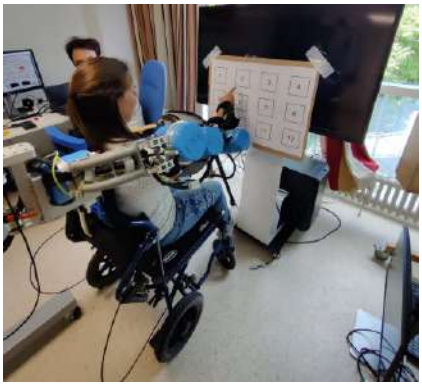


Fig. 3. Experimental setup showing one of the subjects performing free-motion tasks with the aid of a target board while wearing the NESM-γ exoskeleton in transparent mode.

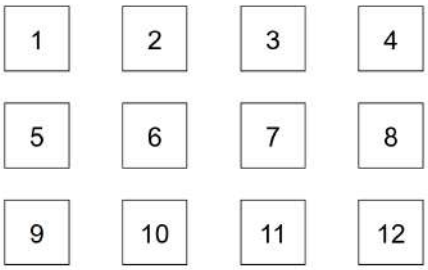


Fig. 4. Target board used as a visual aid for performing free-motion tasks.

- **Task 1 (Motions 1-6)**: Target reaching and diagonal planar motions R $\rightarrow$ (1) $\rightarrow$ (12) $\rightarrow$ R $\rightarrow$ (4) $\rightarrow$ (9) $\rightarrow$ R
- **Task 2 (Motions 7-12)**: Target reaching and top-bottom, left-right motions R $\rightarrow$ (2) $\rightarrow$ (10) $\rightarrow$ R $\rightarrow$ (9) $\rightarrow$ (11) $\rightarrow$ R
- **Task 3 (Motions 13-18)**: Bottom-up and right-left planar motions R $\rightarrow$ (10) $\rightarrow$ (2) $\rightarrow$ R $\rightarrow$ (11) $\rightarrow$ (9) $\rightarrow$ R
- **Task 4 (Motions 19-26)**: Pointing at board targets R $\rightarrow$ (1) $\rightarrow$ R $\rightarrow$ (3) $\rightarrow$ R $\rightarrow$ (9) $\rightarrow$ R $\rightarrow$ (11) $\rightarrow$ R
- **Task 5 (Motions 27-28)**: "Drinking" motion K $\rightarrow$ M $\rightarrow$ R
- **Task 6 (Motions 29-30)**: Shoulder touch K $\rightarrow$ S $\rightarrow$ K

Participant Information

Seven healthy subjects (4 male, 3 female) with normal limb function participated in the study. Their ages ranged from 25 to 31 years. Two participants had extensive experience with robotics, two had basic knowledge, and the remaining three had little to no prior exposure. All subjects completed the experimental protocol using their dominant right arm.[1]

Experimental Routine

A fixed target board ensured consistency across trials. Each subject repeated all six tasks 10 times, resulting in a total of

[1]The study was approved by the Ethics Committee of Scuola Superiore Sant'Anna (approval n. 18/2024), and experiments were conducted at Schön Klinik (Bad Aibling, Germany), following the principles stated in the Declaration of Helsinki. All participants signed informed consent.

420 task trajectory samples and 2100 motion trajectories[2]. The duration of each experimental session ranged from 30 to 45 minutes, depending on the participant.

V. Data Analysis Setup

For the analysis and comparison of trajectory generation methods, recorded experimental data serves as the ground truth for human likeness levels. Before detailing the analysis and results, we briefly introduce the methods being compared to our proposed approach, along with specifications for the human arm case. We use the swivel angle parametrization to characterize the redundant DoF of the 4DoF arm model [20]. This allows to represent valid joint configurations at a given 3D workspace position as:

$$\mathbf{q}_f(\alpha) = \mathbf{q}(\alpha; \mathbf{x}_f), \alpha \in I(\mathbf{x}_f) \tag{10}$$

where α is the swivel angle, and $I(\mathbf{x}_f) \subseteq \mathbb{R}$ represents the valid swivel angle range for a given 3D end-effector pose, defined by the joint limits. α is a free parameter representing the redundant DoF of the kinematic chain, with the choice of the most suitable final configuration $\mathbf{q}_f(\alpha)$ being part of the optimization process.

We now introduce the methods for comparison. Note that the temporal aspect of planning is excluded from this evaluation, as all trajectories were generated on a normalized time interval.

A. Human-like Geodesics (GEO-HL)

To validate the additional selection criteria in the composite index (9) and compare the proposed method to others, a tuning procedure is performed to find optimal parameters for weighing the components (i.e., w_u, w_a). A grid search is applied, evaluating joint trajectory fit over 66% of the dataset. The training set consists of 20 randomly selected motions from the 30 recorded (see Sec. IV), with the remaining 10 motions used for evaluation. This should provide evidence that the selected model configuration generalizes to motion categories not belonging to the ones covered by the training set.

In particular, as part of the grid search, we tested $w_u \in [0, 0.15]$ and $w_a \in [0, 1.2]$, in order to find the configuration of parameters to be used in the trajectory selection performed with Eq. 9, that guarantees a minimum of the joint fit index under evaluation, i.e.

$$RMSE_{joints} = \sum_{l=1}^{L} \sqrt{\frac{1}{4K} \sum_{j=1}^{K} \sum_{i=1}^{4} (q_i(j) - \hat{q}_i(j))^2} \tag{11}$$

where index $i = 1, ..., 4$ refers to the different joints and index j to the sample. Such index represents the root mean square error over the L tuning trajectories, to be computed as the deviation of the generated trajectory q with respect to the ground truth demonstration $\hat{q}$. We found a minimum to exist for $[\hat{w}_u, \hat{w}_a] \approxeq [0.08, 0.4]$ for the full "training" set, as shown in Fig. 5. The same figure highlights the importance of including additional selection criteria w.r.t. kinetic energy, as the value of total error across the training set significantly

[2]The dataset can be found at https://github.com/TUM-ITR/HuG-MP.git

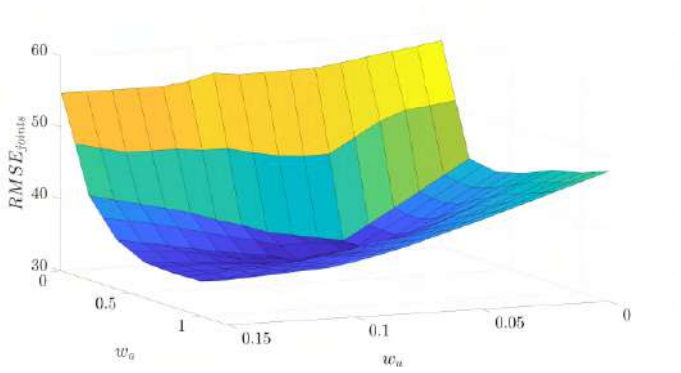


Fig. 5. $RMSE_{joints}$ behaviour as we vary selection parameters w_u, w_a.

decreases as we include both the potential energy and the anthropomorphism criteria. In particular, the anthropomorphism criterion is relevant for reducing the fit error, while the potential energy principle has an effect on the quality of fit, but only when used in combination with the anthropomorphism criterion.

B. Kinetic energy Geodesics (GEO)

We then take the base geodesics method into consideration. In particular, in the case of the human arm model, one has

$$\gamma_{\alpha^*, GEO} = \underset{\alpha \in I(\mathbf{x}_f)}{\arg\min}\, E(\gamma_\alpha) \tag{12}$$

Note that basic kinematic and dynamic parameters are technically required to compute the path kinetic energy $E(\gamma_\alpha)$. We omit a complete sensitivity analysis, but we note that the generated trajectories are mostly sensitive to kinematic parameters (i.e. upper arm and forearm lengths), which were accurately measured, with respect to dynamic parameters (i.e. inertias and masses), which were approximated.

C. Minimum Jerk Trajectories (MJ)

A prime candidate for trajectory generation is represented by the Minimum Jerk (MJ) model. It is one of the leading models in terms of representing the kinematics of human trajectories, originally introduced in [10], and then often exploited for trajectory planning for upper-limb exoskeletons [5], [21]. In particular, it is possible to compute the family of MJ trajectories ($\gamma_{\alpha,MJ} : [0, T] \rightarrow Q$) joining $\mathbf{q}_0$ and $\mathbf{q}_f(\alpha) = \mathbf{q}(\alpha; \mathbf{x}_f)$, $\alpha \in I(\mathbf{x}_f)$ (i.e. for each admissable final configuration). It is then straightforward to choose the global MJ solution as:

$$\gamma_{\alpha^*, MJ} = \underset{\alpha \in I(\mathbf{x}_f)}{\arg\min}\, J_{MJ}(\gamma_{\alpha,MJ})$$

where the cost function is the integral of the squared jerk across each candidate trajectory:

$$J_{MJ}(\gamma_{\alpha,MJ}) = \sum_{i=1}^{4} \int_{t_0}^{t_f} \left(\frac{d^3 q_i(\lambda)}{d\lambda^3}(\alpha) \right)^2$$

D. Inverse Kinematics-based Trajectories (IK)

We then considered trajectory generation based on the direct solution of the inverse kinematics problem. Advantages of the method are often related to the computational efficiency, as it does not consider the full spectrum of valid final configurations. Hence, the method remains a popular choice for trajectory generation in the context of upper-limb exoskeletons [22]. In our implementation, we first solve a generalized Inverse Kinematics problem for the final 3D objective, including the joint limits as constraints and the initial configuration $\mathbf{q}_0$ as an initial guess for the solver:

$$\mathbf{q}_f = gik(\mathbf{x}_f, \mathbf{q}_0, \mathbf{q}_m, \mathbf{q}_M) \tag{13}$$

The problem is solved by means of the MATLAB Robotic System Toolbox, exploiting the Broyden-Fletcher-Goldfarb-Shanno (BFGS) gradient projection algorithm. This is a basic approach to select the final configuration, as it just finds an objective-compliant configuration $\mathbf{q}_f(\alpha)$ that is close to the initial configuration $\mathbf{q}_0$, without additional criteria that relate to motion analysis. We then generate the full joint trajectories as cubic polynomial interpolants between configurations $\mathbf{q}_0$ and $\mathbf{q}_f$, similarly to what is done in [22], as to guarantee null initial and final velocities, in addition to a smooth behavior. This approach can be seen as providing a base performance for the task, since it achieves the desired objective with minimal joint variation and a reasonable velocity profile, but without exploiting any human-related optimization criteria.

E. Evaluation Setup and KPIs

We next proceed with a thorough evaluation of the postulated model on the motions not yet taken into consideration for tuning. We then compare its results with respect to those provided by competing methods. This evaluation data comprises 34% of the dataset, i.e. 700 trajectory samples across 7 subjects and 10 motion types[3]. This evaluation guarantees a fair comparison between the methods, and shows that the selected parameters in the tuning step generalize to motions not yet evaluated. The performance metrics used for comparison are summarized as follows:

1) Error at the Joint Level ($RMSE_{joints}$): The first and most relevant criterion is related to the accuracy attained by the methods at the joint level. This is because it best represents the human likeness of the generated trajectories, as they encode the coordination dynamics, which are not visible at the end-effector (hand) level. The evaluation criterion is mathematically defined as in Eq. 11.

2) Error of Final Configuration ($RMSE_{\mathbf{q}_f}$): Another relevant index is given by the root mean square error on the final configurations $\mathbf{q}_f$ attained for each motion, i.e. when subjects pause in order to perform the subsequent motion in the task sequence. The metric is expressed by:

$$RMSE_{\mathbf{q}_f} = \sqrt{\frac{1}{4}\sum_{i=1}^{4}(q_{f,i} - \hat{q}_{f,i})^2} \tag{14}$$

[3]Motions 2, 12, 14, 16, 21, 22, 24, 25, 26, 30 from Sec. IV

where i refers to the joint indexes 1 to 4.
This index is a direct measure of whether the generated trajectory mirrors the intention of the subject, as it approaches the workspace objective with a comparable configuration.

3) End-Effector Error (e_h): We finally consider the average end-effector error. The index is formulated as:

$$e_h = \frac{1}{K}\sum_{j=1}^{K}||x_h(j) - \hat{x}_h(j)||^2 \tag{15}$$

namely as the average euclidean distance between the predicted and true hand position across the whole trajectory.

VI. Results and Discussion

The presented approaches are copared by evaluating the accuracy they provide with respect to the ground truth trajectories (i.e. the experimental trials) in terms of a set of metrics. To test statistical significance, paired Wilcoxon signed-rank tests were employed, contrasting our proposed method GEO-HL against each one of the comparison approaches. The attained p-value is specified for each test.

Table I includes the $RMSE_{joints}$ values attained by the proposed methods (GEO-HL, GEO, MJ, IK) over the evaluation dataset, categorized by motion type. For each motion, we present the average performance and standard deviation of the $RMSE_{joints}$ index, in addition to the percentage improvement (or degradation) of the proposed approach GEO-HL with respect to the competing ones. One observes that our proposed method generally outperforms all other approaches, underperforming only for Motion 14 (bottom-up motion on the board). It should be noted that the standard deviation of the performance index for this motion is generally high across all methods under analysis, suggesting that Motion 14 is poorly repeatable and exhibits joint coordination dynamics that are difficult to model. This indicates the general validity of the method when it comes to reproducing human-like motions (which can be analysed at the joint level) and highlights how the GEO-HL provides a satisfactory performance on human motions not pertaining to the pointing class. Regarding this point, one can see that the GEO method performs adequately when it comes to motions belonging to the pointing class (i.e. 16, 21, 25), with a comparable performance to GEO-HL, which confirms the findings of [9]. Conversely, performance of base GEO downgrades for motions belonging to other classes, proving that the augmentation of the selection criteria done for GEO-HL was necessary in order to extend the applicability of the geodesics method in the context of human-like motion generation. Table II includes the $RMSE_{joints}$ index results in terms of subjects (1-7). One can observe how GEO-HL improves on the other methods for each of the subjects under consideration. When it comes to the full dataset, without any motion or subject distinction, GEO-HL attains an average value of $RMSE_{joints} = 0.123$ rad, which is a significant improvement over the base GEO method (-55.4%), but also with respect to both the MJ method (-23.03%) and the IK one (-26.25%). We provide a comprehensive performance overview of the methods on the evaluation dataset through

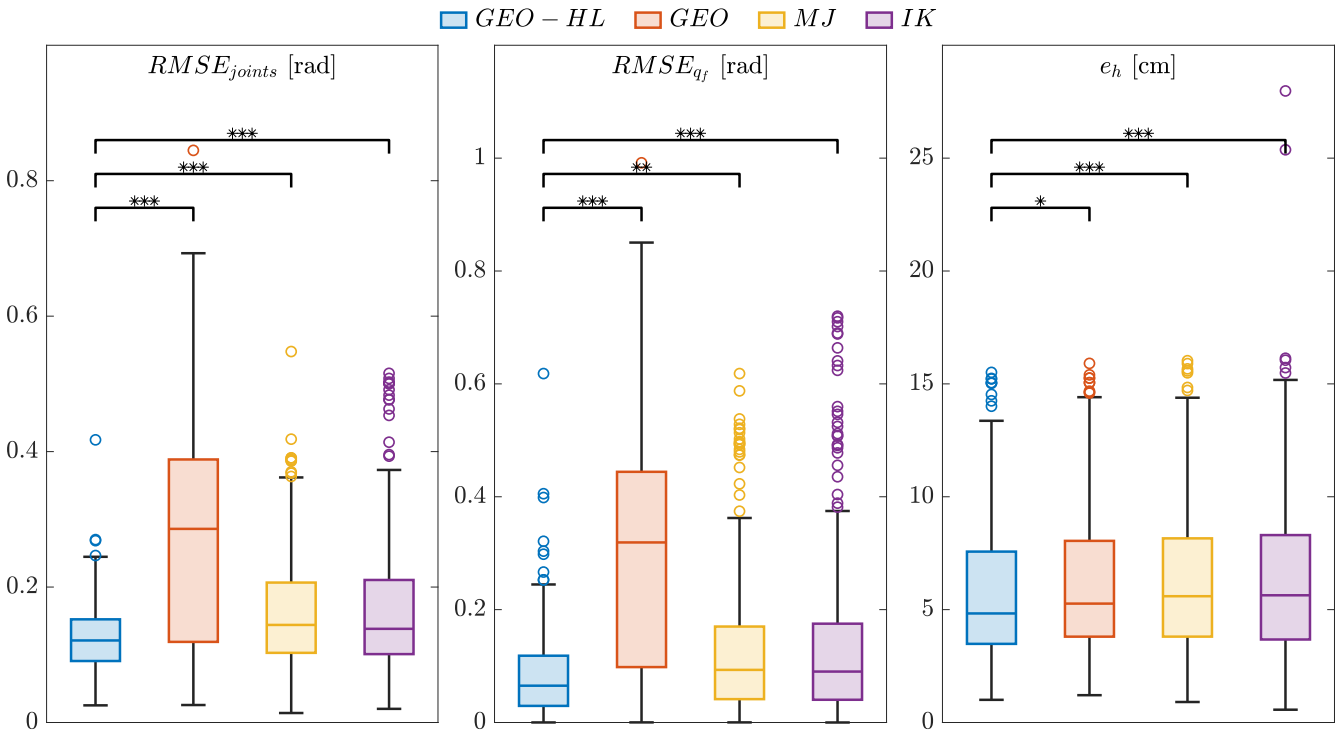


Fig. 6. Boxplots of the performance indexes attained by the GEO-HL (blue), GEO (orange), MJ (yellow), IK (purple) approaches across the whole evaluation dataset. On the left we present the boxplots for the $RMSE_{joints}$ index, representative of the error at the joint level; in the central panel we show the $RMSE_{q_f}$ results, indicating the final configuration error; the right panel includes the results for e_h, i.e. the end-effector error index. The p-value attained in the pair-wise Wilcoxon tests is shown according to the asterisk notation: * for $p < 0.05$, ** for $p < 0.01$, *** for $p < 0.001$.

the summary in Table III and the boxplots in Fig. 6 (left panel). They highlight the superior performance of GEO-HL across the entire dataset. The pairwise tests confirmed the statistical significance of the increase in performance of GEO-HL, with p-values of $p < 0.001$ in the comparisons against GEO, MJ and IK. Notably, GEO-HL exhibits a generally lower number of outlier trajectories that the method fails to represent accurately—compared to the other methods under consideration. This observation underscores the robustness and consistency of GEO-HL in capturing the underlying patterns of different motion types and subjects at the joint level.

When it comes to the end-configuration error ($RMSE_{\mathbf{q}_f}$, Fig. 6, central panel), our method GEO-HL showed significant improvement with respect to the other methods, improving on average on the base GEO method by -72.7% , and by -33.3%, and -39.0% over the competing approaches MJ and IK, respectively (see Table III). The improvement in performance is attested by the pairwise tests, with p-values of $p < 0.001$, $p < 0.01$, $p < 0.001$ against GEO, MJ and IK respectively.

Fig. 6 (right panel) reports the end-effector error distributions (e_h) achieved by the different methods, shown in the form of the associated boxplots, while Table III shows the average values obtained. Our method GEO-HL showed significant improvements with respect to the competing methods. In particular, GEO-HL achieved an average workspace error of 5.76 cm, which is a -6.9% improvement over GEO ($p < 0.05$), and a -7.0% ($p < 0.001$) and a -8.7% ($p < 0.001$) improvement against MJ and IK respectively. This metric is relevant for assessing the accuracy of motion in the workspace and the successful completion of tasks, as some studies suggest that movement is initially planned in the hand space (end-effector space) [23]. While it offers valuable insights into the overall correctness of the trajectory and is a common criterion for evaluating trajectory generation methods, end-effector error alone does not capture joint coordination, which is essential for achieving human-like motion, especially in rehabilitation

TABLE I
$RMSE_{joints}$ INDEX ATTAINED BY THE MODELS UNDER COMPARISON, ACCORDING TO MOTION TYPE.

$RMSE_{joints}$	GEO-HL	GEO	MJ	IK
Motion 2	0.098 ± 0.039	0.427 ± 0.068 -77.1%	0.105 ± 0.023 -7.1%	0.108 ± 0.024 -9.0%
Motion 12	0.102 ± 0.045	0.339 ± 0.068 -69.9%	0.130 ± 0.056 -21.5%	0.119 ± 0.048 -14.3%
Motion 14	0.140 ± 0.071	0.111 ± 0.067 26.2%	0.116 ± 0.086 20.0%	0.094 ± 0.039 48.6%
Motion 16	0.100 ± 0.030	0.091 ± 0.027 9.8%	0.115 ± 0.024 -12.8%	0.115 ± 0.023 -13.4%
Motion 21	0.162 ± 0.038	0.171 ± 0.058 -5.0%	0.257 ± 0.052 -36.8%	0.245 ± 0.053 -33.7%
Motion 22	0.133 ± 0.045	0.394 ± 0.083 -66.2%	0.193 ± 0.051 -31.1%	0.240 ± 0.215 -44.4%
Motion 24	0.133 ± 0.030	0.385 ± 0.094 -65.4%	0.161 ± 0.060 -17.3%	0.186 ± 0.077 -28.2%
Motion 25	0.109 ± 0.041	0.099 ± 0.038 9.9%	0.137 ± 0.040 -20.1%	0.136 ± 0.041 -19.6%
Motion 26	0.114 ± 0.031	0.347 ± 0.059 -67.1%	0.119 ± 0.049 -4.2%	0.113 ± 0.046 0.8%
Motion 30	0.134 ± 0.036	0.385 ± 0.150 -65.2%	0.259 ± 0.069 -48.2%	0.307 ± 0.099 -56.3%

TABLE II

$RMSE_{joints}$ INDEX ATTAINED BY THE MODELS UNDER COMPARISON, ACCORDING TO SUBJECT.

$RMSE_{joints}$	GEO-HL	GEO	MJ	IK
Subject 1	0.104 ± 0.046	0.313 ± 0.150	0.197 ± 0.091	0.209 ± 0.117
		-66.8%	-47.2%	-50.3%
Subject 2	0.131 ± 0.036	0.273 ± 0.134	0.138 ± 0.045	0.159 ± 0.135
		-52.1%	-5.6%	-17.9%
Subject 3	0.090 ± 0.043	0.243 ± 0.163	0.153 ± 0.068	0.161 ± 0.082
		-63.0%	-41.2%	-44.1%
Subject 4	0.118 ± 0.034	0.218 ± 0.099	0.169 ± 0.058	0.161 ± 0.052
		-45.7%	-30.1%	-26.6%
Subject 5	0.116 ± 0.033	0.282 ± 0.175	0.124 ± 0.062	0.125 ± 0.068
		-58.6%	-6.3%	-7.0%
Subject 6	0.141 ± 0.038	0.277 ± 0.145	0.144 ± 0.061	0.146 ± 0.139
		-49.2%	-2.0%	-3.6%
Subject 7	0.159 ± 0.054	0.320 ± 0.170	0.190 ± 0.108	0.203 ± 0.123
		-50.4%	-16.5%	-21.7%

TABLE III

SUMMARY OF THE AVERAGE INDEX VALUES OVER THE FULL EVALUATION DATASETS.

	GEO-HL	GEO	MJ	IK
$RMSE_{joints}$	0.123 ± 0.046	0.275 ± 0.153	0.159 ± 0.077	0.166 ± 0.110
		-55.4%	-23.0%	-26.3%
$RMSE_{q_f}$	0.082 ± 0.069	0.300 ± 0.203	0.123 ± 0.111	0.134 ± 0.158
		-72.7%	-33.3%	-39.0%
e_h	5.756 ± 3.085	6.185 ± 3.127	6.192 ± 3.133	6.306 ± 3.464
		-6.9%	-7.0%	-8.7%

contexts [24]. In summary, results show that our method generally achieves lower end-effector errors than the other methods, and does so while better encoding joint coordination, as demonstrated by its low $RMSE_{joints}$ and low $RMSE_{\mathbf{q}_f}$ values.

VII. CONCLUSIONS AND FUTURE WORK

In this study, we addressed the challenge of generating target-oriented human-like trajectories proposing a modified geodesics-based motion planning method. Our method was shown to excel at replicating the natural characteristics of human motion while combining motor efficiency with flexibility. The method is particularly well-suited for scenarios requiring constraints such as rehabilitation-oriented restrictions or adaptations to pathological conditions, ensuring that the generated trajectories remain both functional and human-like. Moreover, this method further improves the ability to capture the coordination typical of human movement. To validate its capabilities, we compared our method's performance against other popular methods and the standard implementation of geodesic trajectories using real-life human arm motion data. Our results showed that the proposed method not only achieved superior accuracy but also demonstrated an enhanced ability to replicate human-like motion patterns. Future research will explore higher-DoF models, advanced metric learning, and real-time exoskeleton testing for assistance.

REFERENCES

[1] T. Proietti, V. Crocher, A. Roby-Brami, and N. Jarrasse. Upper-Limb Robotic Exoskeletons for Neurorehabilitation: A Review on Control Strategies. *IEEE Rev Biomed Eng*, 9:4–14, 2016.

[2] F. A. Mussa Ivaldi, P. Morasso, and R. Zaccaria. Kinematic networks. *Biological Cybernetics*, 60(1):1–16, Nov 1988.

[3] G. Gulletta, W. Erlhagen, and E. Bicho. Human-like arm motion generation: A review. *Robotics*, 9(4), 2020.

[4] C. Nguiadem, M. Raison, and S. Achiche. Motion planning of upper-limb exoskeleton robots: A review. *Applied Sciences*, 10(21), 2020.

[5] C. Wang, L. Peng, Z.-G. Hou, J. Li, L. Luo, S. Chen, and W. Wang. Kinematic redundancy analysis during goal-directed motion for trajectory planning of an upper-limb exoskeleton robot. In *2019 41st Annual International Conference of the IEEE Engineering in Medicine and Biology Society (EMBC)*, pages 5251–5255, 2019.

[6] M. Ballesteros-Escamilla, D. Cruz-Ortiz, I. Salgado, and I. Chairez. Hybrid position/force output feedback second-order sliding mode control for a prototype of an active orthosis used in back-assisted mobilization. *Med Biol Eng Comput*, 57(9):1843–1860, June 2019.

[7] G. Averta, C. Della Santina, G. Valenza, A. Bicchi, and M. Bianchi. Exploiting upper-limb functional principal components for human-like motion generation of anthropomorphic robots. *Journal of NeuroEngineering and Rehabilitation*, 17(1):63, May 2020.

[8] C. Lauretti, F. Cordella, A. L. Ciancio, E. Trigili, J. M. Catalan, F. J. Badesa, S. Crea, S. M. Pagliara, S. Sterzi, N. Vitiello, N. Garcia Aracil, and L. Zollo. Learning by demonstration for motion planning of upper-limb exoskeletons. *Frontiers in Neurorobotics*, 12, 2018.

[9] A. Biess, D. G. Liebermann, and T. Flash. A computational model for redundant human three-dimensional pointing movements: integration of independent spatial and temporal motor plans simplifies movement dynamics. *J Neurosci*, 27(48):13045–13064, Nov 2007.

[10] T. Flash and N. Hogan. The coordination of arm movements: an experimentally confirmed mathematical model. *Journal of Neuroscience*, 5(7):1688–1703, 1985.

[11] Y. Uno, M. Kawato, and R. Suzuki. Formation and control of optimal trajectory in human multijoint arm movement. *Biological Cybernetics*, 61(2):89–101, Jun 1989.

[12] R. Soltani-Zarrin, A. Zeiaee, R. Langari, J. J. Buchanan, and N. Robson. Towards autonomous ergonomic upper-limb exoskeletons: A computational approach for planning a human-like path. *Robotics and Autonomous Systems*, 145:103843, 2021.

[13] R. Soltani-Zarrin, A. Zeiaee, R. Langari, and N. Robson. Reference path generation for upper-arm exoskeletons considering scapulohumeral rhythms. *IEEE Int. Conf. Rehabil. Robot.*, 2017:753–758, July 2017.

[14] Z. Li, W. Zuo, and S. Li. Zeroing dynamics method for motion control of industrial upper-limb exoskeleton system with minimal potential energy modulation. *Measurement*, 163:107964, 2020.

[15] J. Pan, D. Astarita, A. Baldoni, F. Dell'Agnello, S. Crea, N. Vitiello, and E. Trigili. Nesm-: An upper-limb exoskeleton with compliant actuators for clinical deployment. *IEEE Robotics and Automation Letters*, 7(3):7708–7715, 2022.

[16] J. Pan, D. Astarita, A. Baldoni, F. Dell'Agnello, S. Crea, N. Vitiello, and E. Trigili. A self-aligning upper-limb exoskeleton preserving natural shoulder movements: Kinematic compatibility analysis. *IEEE Trans. Neural Syst. Rehabil. Eng.*, 31:4954–4964, December 2023.

[17] J. W. Robbin and D. A. Salamon. Introduction to differential geometry. *ETH, Lecture Notes, preliminary version*, 18:52, 2011.

[18] M. P. Do Carmo and F. J. Flaherty. *Riemannian geometry*, volume 2. Springer, 1992.

[19] D. A. Rosenbaum, F. Marchak, H. J. Barnes, J. Vaughan, J. D. Slotta, and M. J. Jorgensen. Constraints for action selection: Overhand versus underhand grips. *Attention and performance 13: Motor representation and control*, page 321–342, 1990.

[20] H. Kim, L. M. Miller, N. Byl, G. M. Abrams, and J. Rosen. Redundancy resolution of the human arm and an upper limb exoskeleton. *IEEE Trans. Biomed. Eng.*, 59(6):1770–1779, June 2012.

[21] E. Takeshi, Y. Michi, N. Hiroyuki, A. Takaaki, N. Yutaka, and Y. Ken'ichi. Upper limb flexion assistance based on minimum-jerk trajectory using wearable motion-assist robot. *IFAC Proceedings Volumes*, 44(1):5962–5967, 2011. 18th IFAC World Congress.

[22] G. Li, Q. Fang, T. Xu, J. Zhao, H. Cai, and Y. Zhu. Inverse kinematic analysis and trajectory planning of a modular upper limb rehabilitation exoskeleton. *Technology and Health Care*, 27:123–132, 2019. S1.

[23] M. Desmurget, D. Pélisson, Y. Rossetti, and C. Prablanc. From eye to hand: Planning goal-directed movements. *Neuroscience Biobehavioral Reviews*, 22(6):761–788, 1998.

[24] J. van Kordelaar, E. E.H. van Wegen, and G. Kwakkel. Unraveling the interaction between pathological upper limb synergies and compensatory trunk movements during reach-to-grasp after stroke: a cross-sectional study. *Experimental brain research*, 221:251–262, 2012.

Design of an Active Sling-Suspension Robot for Adaptive Gravity Compensation of the Upper Limbs

Rodrigo Mendez[1], Aine Grady[1], Peter Snow[1], Rui Loureiro[1]

***Abstract*— This paper presents the design, prototyping, and preliminary evaluation of a novel active sling-suspension robot for gravity compensation of the upper limbs, developed for rehabilitation and assistive applications. The robot features a modular, scalable design with low inertia, achieved through a compact structure and optimized weight distribution. An admittance controller and a proportional controller were implemented to ensure effective gravity compensation and precise arm movement tracking, providing an always normal pulling force.**

Preliminary experimental results performing pick-and-place tasks demonstrated effective winch cable tension tracking while maintaining accurate position tracking with minimal error.

I. INTRODUCTION

Upper limb motor rehabilitation and assistance are critical for individuals with motor impairments, such as those resulting from stroke, spinal cord injuries (SCI), or neuromuscular diseases. These conditions can lead to significant functional limitations, including muscle weakness, impaired coordination, and reduced range of motion, which hinder the performance of everyday tasks [1]. For individuals affected by such impairments, regaining the ability to move and control their arms is essential for restoring independence in Activities of Daily Living (ADLs), such as eating, dressing, and personal hygiene [2]. Without effective rehabilitation, these motor deficits can result in long-term disability, decreased quality of life, and increased dependence on caregivers. Therefore, targeted interventions are vital not only for promoting physical recovery but also for enhancing patients' psychological well-being and overall quality of life [3].

Rehabilitation robotics has emerged as a promising approach to support upper limb motor recovery in patients with impaired mobility. By integrating robotics with therapeutic exercises, these systems can deliver consistent, intensive, and personalized rehabilitation sessions [4]. Unlike traditional manual therapy, robotic devices provide precise control over movement patterns, adjustable levels of assistance, and real-time feedback, enabling more engaging and interactive therapies [1].

During the delivery of robot-assisted rehabilitation for the upper limbs, gravity compensation, also referred to as weight support or antigravity assistance, is a common yet essential feature. Its primary purpose is to offset the torque generated by the weight of the impaired arm without interfering with the participant's natural movement patterns [5]. By reducing the muscular effort required to lift the limb, gravity compensation allows patients to focus on functional movement, thereby increasing the number of repetitions and enhancing Range of Motion (ROM) during therapy, which aids in the recovery of motor control [6].

Currently, there are various types of devices capable of providing gravity compensation, ranging from simple passive end-effector systems to sophisticated active exoskeletons. Passive devices primarily consist of mechanical systems that provide static balance through counterweights, springs, cams, or rubber bands [7]. Their main advantages include being lightweight, having low inertia, and utilizing low-cost materials, as these systems do not require actuators. However, most passive systems have a limited workspace, and the level of support they provide can only be adjusted manually, if at all [8].

In contrast, active devices are typically electromechanically actuated systems. Although these devices are more expensive, complex, and bulkier than passive ones, their advantages are considerable. For instance, active systems can automatically estimate the required level of support and adjust it in real-time. This capability is essential because the torque generated by the weight of the arm changes depending on its position. Without this adaptability, there is a risk of providing either excessive or insufficient support to the limb [9], [10].

In addition, sling-suspension devices are commonly designed specifically to provide gravity compensation and can be used either on their own or in combination with end-effector robots to offer an additional point of support for the arm's weight [11]. These systems are generally simpler than conventional end-effector robots and exoskeletons, as they primarily provide pulling forces. Despite this limitation, their simplicity makes them a more accessible and cost-effective alternative. However, most sling systems offer a fixed level of support that must be calibrated in advance, as seen in devices like the Dynamic Arm Support Sling FOCAL and the Helparm. This fixed support can lead to over- or under-compensation when the arm moves. Additionally, because the suspension cable is anchored to a fixed point, it may generate unwanted horizontal forces during arm movements [12].

The aim of this study is to present the design and proof-of-concept of a novel active sling-suspension robot for gravity compensation of the upper limbs. This device is designed to

This work was partly supported by ANID Chile through the Ph. D. scholarship 72210164

[1]R. Mendez, A. Grady, P. Snow, and R. Loureiro are with the Research Department of Orthopaedics and Musculoskeletal Science, and Aspire Centre for Rehabilitation Engineering and Assistive Technology, University College London, Royal National Orthopaedic Hospital, Brockley Hill, Stanmore, London, HA7 4LP, UK

Corresponding author: rodrigo.mendez.21@ucl.ac.uk



(a) (b) (c)

Fig. 1: Proposed working principle based on a two-axis structure: : a vertical rotational axis integrated with a horizontal axis (a), and examples of potential use-case scenarios (b)-(c).

follow the movement of the arm, continuously providing a normal pulling force and automatically adjusting the level of support as needed, all while minimizing inertia and complexity to preserve the key advantages of sling-suspension systems. The electromechanical and control system design of the first prototype will be detailed. Finally, a preliminary evaluation with a user performing pick-and-place tasks will be analyzed and discussed, providing insights for potential future work.

II. DESIGN CRITERIA AND CONCEPTUAL MODEL

The design of the active sling-suspension robot was driven by the goal of developing an engaging and interactive rehabilitation device that overcomes the main drawbacks of traditional sling-suspension systems, while minimizing the additional inertia and complexity typically associated with the integration of actuators. The following design criteria were established to achieve this goal and to ensure that the device meets functional and practical requirements of both clinicians and users,

- Adaptive Gravity Compensation: To avoid over- or under-compensation and provide interactive therapy, the system must deliver real-time adaptive support that adjusts based on the user's arm position, movement, or other desired rules.
- Minimal horizontal pulling force: The system must be able to follow the movement of the arm to continuously provide a normal pulling force.
- Modularity and scalability: The robot's design should be modular and scalable, allowing for easy adjustments, upgrades, and accommodations for diverse usage scenarios.
- Lightweight and low inertia: One of the primary objectives is to minimize the overall weight and inertia of the system for safety and feasibility reasons.
- Simplicity and cost-effectiveness: The design prioritizes simplicity to reduce manufacturing costs and improve accessibility.

Portability and ease of installation are not current priorities but will be considered in future iterations to facilitate use in various clinical environments or even at home.

After iterative design and testing, a novel concept was selected. The proposed design features a two-axis structure: a vertical rotational axis integrated with a horizontal axis, as depicted in Fig. 1. In addition to enabling rotational movement of the horizontal axis, the vertical axis is designed for easy integration into various use-case scenarios, such as use with a wheelchair, in sitting or standing positions, by the bedside, and more. The horizontal axis controls both the rotational and translational movements of a winch housed within it, but without mobile actuators. Instead, the actuators are placed and fixed on the vertical axis to minimize the device's overall inertia.

Thus, by combining the rotational movement of the vertical axis, and the translational and rotational movement of the winch in the horizontal axis, it is possible to provide an adaptive gravity compensation with a normal pulling force.

III. PROTOTYPE DESIGN

The testing and development of the proposed concept is divided into two main stages: the first focuses on the design and prototyping of the horizontal axis, while the second involves the design, prototyping, and integration of the vertical axis. This paper is focused on the first stage.

For the prototyping of the horizontal axis, the following requirements were considered:

- The device must support a load of up to 5 kg, which represents the weight of the arm for over 75% of the world's population following the World Health Organization data, resulting in a final design load of $F_L = 50$ N.
- The device must achieve a vertical (cable movement) and horizontal (winch translation along the horizontal axis) speed of 1 m/s, aligning with the capabilities of commercially available rehabilitation robots, such as the HapticMaster.
- The horizontal axis must have a length of 50 cm to accommodate tracking the arm during various ADLs.
- To facilitate rapid prototyping and cost reduction, commercially available, low-cost components and equipment are considered.

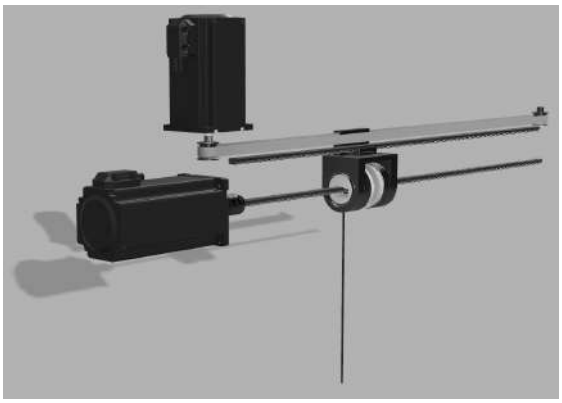


Fig. 2: The horizontal axis concept consists of a horizontally mounted motor with an extended shaft to control the rotational movement of the winch and a vertically mounted motor to drive the linear belt-driven mechanism.

A. Electromechanical Design

After iterative design and testing of the horizontal axis, the chosen mechanism utilizes a linear belt-driven actuator anchored to the winch to control its translational movement along the horizontal axis, and a motor with an extended shaft to control its rotational movement, thereby regulating the cable pulling force. The shaft must permit the translational movement of the winch along it while minimizing clearance between the shaft and the winch to ensure effective control of its rotation. Fig. 2 illustrates this concept.

1) Motor-winch mechanism: To size the motor $M1$ controlling the rotational movement of the winch, it is necessary first to design the diameter of the winch, which must integrate with the extended shaft. For rapid prototyping, a stainless-steel linear rail and carriage are used instead of manufacturing the extended shaft. The linear rail is coupled to the motor shaft, while the carriage is anchored to the 3D-printed winch. Fig. 3 summarize the main characteristics of the linear rail and carriage. The winch is designed with a diameter of 30 *mm*, considering the linear rail, carriage, and standard bearing dimensions, representing the most compact viable option.

Given the diameter of the winch, it is possible to verify that the carriage can support the defined maximum load F_L and appropriately size the motor.

Considering that the suspension robot must move the cable vertically at a speed of 1 *m/s*, this translates to the maximum required rotational speed for the motor,

$$\omega_{M1} = \frac{v_v}{r_w} \approx 640 \ [rpm] \tag{1}$$

where ω_{M1} represents the rotational speed of the motor $M1$ which controls the rotational movement of the winch, v_v represents the maximum vertical speed defined as 1 *m/s*, and r_w the radius of the winch designed as 15 *mm*.

With the winch's diameter, it is now possible to calculate the load torque,

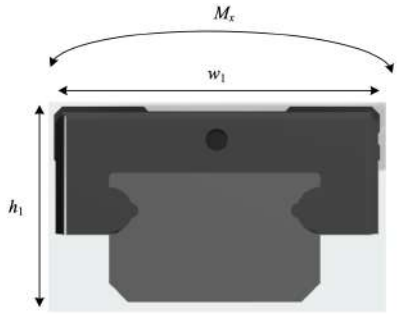


Fig. 3: Linear rail and carriage main characteristics: overall height $h_1 = 10$ *mm*, overall width $w_1 = 20$ *mm*, and maximum torsional torque allowed $M_x = 18.2$ *Nm*.

$$\tau_{M1_L} = r_w \cdot F_{M1_L} = 0.75 \ [Nm] \tag{2}$$

where τ_{M1_L} represents the load torque of $M1$, and F_{M1_L} its maximum load which is equal to F_L.

Considering the calculated speed and load torque, a stepper motor was chosen for this task, as these motors are generally more affordable and compact compared to others that provide the same speed and torque. Consequently, the acceleration torque is the only remaining variable needed to size the stepper motor, which can be approximated as,

$$\tau_{M1_a} = J_{M1_L} \cdot \frac{\pi}{30} \cdot \frac{\Delta\omega_{M1}}{\Delta t} \tag{3}$$

where τ_{M1_a} is the acceleration torque of $M1$, J_{M1_L} is the total inertia, $\Delta\omega_{M1}$ is equal to ω_{M1} in this case, and Δt is defined as 0.5 *s*.

The total inertia is calculated as follow,

$$J_{M1_L} = J_s + J_w \tag{4}$$

where J_s is the extended shaft inertia, approximated as a cuboid, and J_w is the winch inertia, which includes the load mass and is approximated as a hollow disc. The motor shaft and bearings inertia are neglected due to their small values compared to the total inertia.

The required torque, τ_{M1}, is calculated as the sum of the load torque, τ_{M1_L}, and the acceleration torque, τ_{M1_a}. Finally, the stepper motor $M1$ is selected to ensure it can provide the required torque τ_{M1} at the necessary speed, ω_{M1}. A Nema 24 stepper motor was chosen for this task.

2) Linear belt-driven actuator: To size stepper motor $M2$, which controls the translational movement of the winch, a conventional design of a linear belt-driven actuator is used, taking into account the defined load and the 3D-printed

TABLE I: Motor sizing summary. $M1$ controls the rotational movement of the winch, and $M2$ the belt-driven linear actuator.

Motor	Required speed ω (*rpm*)	Required torque τ (*Nm*)
$M1$	640	0.83
$M2$	477	0.11

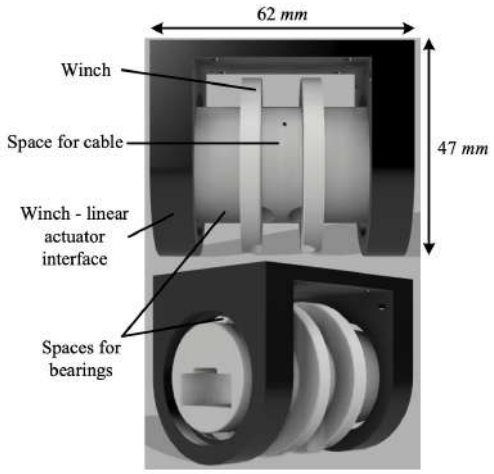


Fig. 4: Illustration of the winch and winch - linear actuator interface. This interface is the mechanism that enables the independent control of both the translational and rotational movements of the winch.

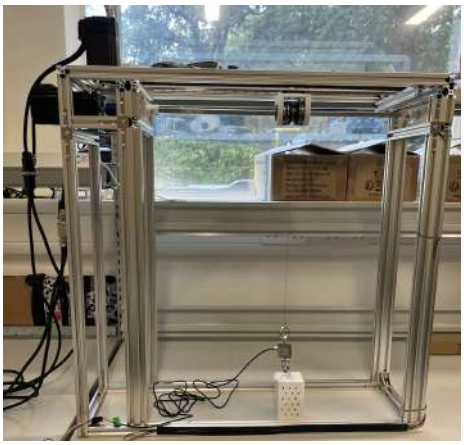


Fig. 5: The horizontal axis prototype is mounted on an aluminum profile frame for testing. It offers an approximate workspace of 500 *mm* horizontally and 590 *mm* vertically. The cable is connected to a weight for initial experiments.

interface depicted in Fig. 4, which anchors the winch to a linear rail and carriage mechanism.

To determine the required speed and torque, the belt and pulleys must be designed first. A GT3 timing belt with matching 20 mm diameter pulleys, one driving and one driven, are selected.

Based on the pulley diameter, the required speed is calculated as follows,

$$\omega_{M2} = \frac{v_h}{r_p} \approx 477 \ [rpm] \tag{5}$$

where ω_{M2} represents the required speed of motor $M2$, Mv_h the maximum horizontal speed defined as 1 m/s, and r_p the radius of the pulley.

The load and acceleration torques are approximated following the same approach presented for $M1$.

Finally, the stepper motor $M2$ is selected to ensure that it can provide the required torque at the necessary speed presented in Table I. A Nema 23 stepper motor was chosen for this task.

For testing purposes, the horizontal axis prototype is mounted on an aluminum profile frame, providing an approximate workspace of 500 mm horizontally and 590 mm vertically. Fig. 5 shows the implementation.

3) Sensors:

- A BNO055 absolute orientation sensor is placed at the end of the winch cable to track cable deviation and, consequently, arm movement.
- An S-beam load cell is integrated into the winch cable to measure tension.
- In addition, an optical encoder is used to monitor the rotational movement of the winch. For safety purposes, an ultrasonic sensor, limit switches, and an emergency stop are also included.

B. Control System Design

Initially, two independent closed-loop control systems were designed: one to track arm movement using the linear belt-driven actuator, and the other to control gravity compensation through the motor-winch mechanism.

1) Horizontal position control: Using the absolute orientation sensor, a conventional proportional control strategy is implemented with a cable deviation reference set to zero, where the control action determines the speed of the motor $M2$ driving the belt-driven mechanism.

2) Gravity compensation control: A conventional admittance controller without virtual stiffness is chosen to control the level of support provided. A gravity compensation estimator calculates the force reference, which can be adjusted based on arm position and other potential parameters, such as joint stiffness or challenge level. The integrated load cell in the cable is used to monitor its tension and close the control loop, while the controller generates a speed reference for the motor $M1$.

Fig. 6 illustrates the closed-loops and architecture of the control system, implemented using a master-slave architecture, with an Arduino Mega 2560 as the master controller and a second Arduino Mega 2560 as the slave to control the motors. The sampling frequency of the system is approximately 90 Hz, limited by the clock speed of the load cell voltage amplifier.

IV. PRELIMINARY EXPERIMENTAL RESULTS

To initially tune the controllers and assess the performance of the prototype, the winch was connected to a known 1 *kg* weight, nonetheless, this experiment is not intended to assess the biomechanical implications of using the device. The admittance and position controllers were empirically tuned based on the design criteria mentioned above, using a fixed gravity compensation reference. The goal was to maximize the speed response without introducing jerkiness, ensuring

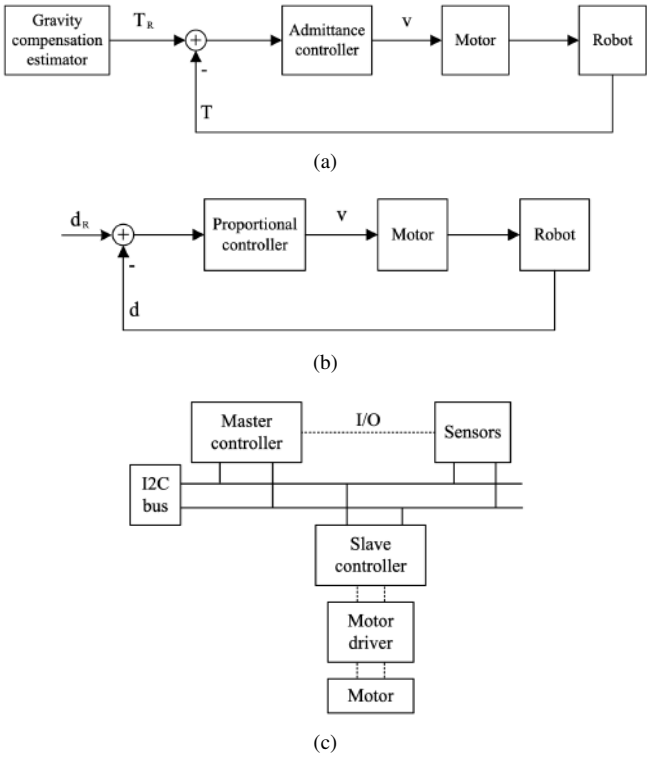


Fig. 6: Control system; gravity compensation (a) and horizontal position (b) control loops, where T represents the winch cable tension, d cable deviation angle, v control action, and the subscript R reference. (c) represents the control architecture.

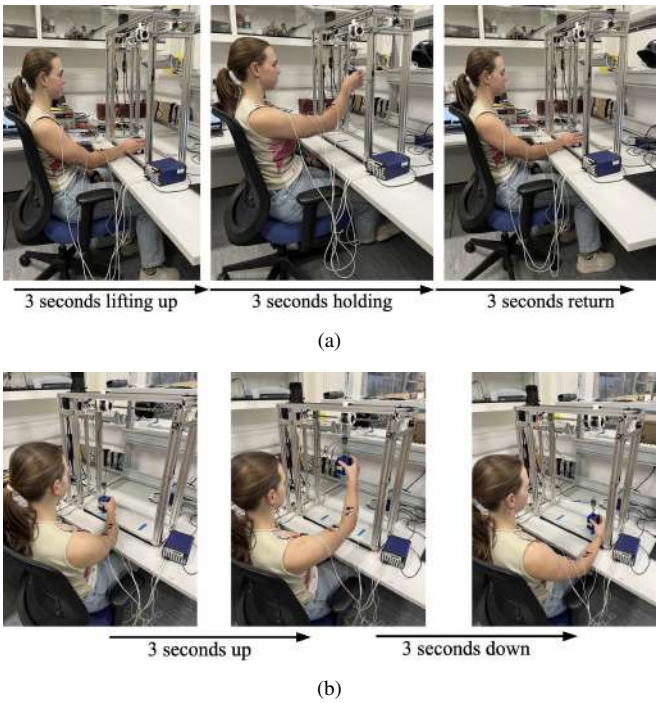


Fig. 7: Experimental setup for tuning and testing the controllers while the user performs pick-and-place tasks: (a) Task 1: describing an only vertical trajectory, and (b) Task 2: describing a parabolic trajectory.

comfort and safety. Subsequently, the device was tested with two different pick-and-place tasks, both with and without gravity compensation, while the user moved the weight at a fixed speed while seated in a fixed natural position, holding the weight with a fixed neutral hand angle. This setup simulated activities of daily living (ADLs) while maintaining consistent biomechanical conditions. One task involved only vertical movement to test the gravity compensation control, while the other followed a parabolic trajectory to test both gravity compensation and position control simultaneously,

- Task 1: the user lifted the weight vertically from the desk to the level of her nose in 3 seconds, held it there for 3 seconds, and returned it to the desk in 3 seconds.
- Task 2: the user lifted the weight from the desk to the level of her nose and returned it to the desk in 6 seconds, describing a parabolic trajectory similar to a pick-and-place task.

In addition to the control variables; cable tension and deviation angle, EMG data from the main muscles involved in the tasks [13]; anterior deltoid, biceps brachii, and brachioradialis, were recorded following SENIAM placement recommendations to provide additional insight about the control performance. Surface bipolar electrodes were used with a sampling rate of 512 Hz, collected using a TMSi Porti7 system. The data were processed as follows: high-pass filtered using a fourth-order 25 Hz Butterworth filter, filtered using a 50 Hz Notch filter, rectified, and low-pass filtered using a fourth-order 2 Hz Butterworth filter. Finally, all EMG data were normalized to maximum voluntary isometric contractions (MVC) [14].

Fig. 7 illustrates the setup of the experimental tests, while Table II and Fig. 8 present the results obtained, from which the following observations can be made,

- The admittance controller follows the reference with a Mean Square Error (MSE) of 0.08% and 0.13% for task 1 and task 2, respectively.
- The position controller tracks the reference with MSE of 0.14% for task 2. The peaks illustrate the effect of implementing a deadband and proportional controller. As expected, position tracking is not required for task 1.
- In both tasks, gravity compensation reduces the activation of all three muscles. Based on RMS values, gravity compensation decreases muscle activation by an average

TABLE II: RMS values of normalized EMG signals from the anterior deltoid (AD), biceps brachii (BB), and brachioradialis (BR) muscles during both tasks.

	Gravity Compensation	RMS Task 1	RMS Task 2
AD	No	16.6%	12.8%
	Yes	8.1%	8.1%
BB	No	4.0%	4.6%
	Yes	2.1%	2.9%
BR	No	6.4%	4.0%
	Yes	1.0%	1.2%

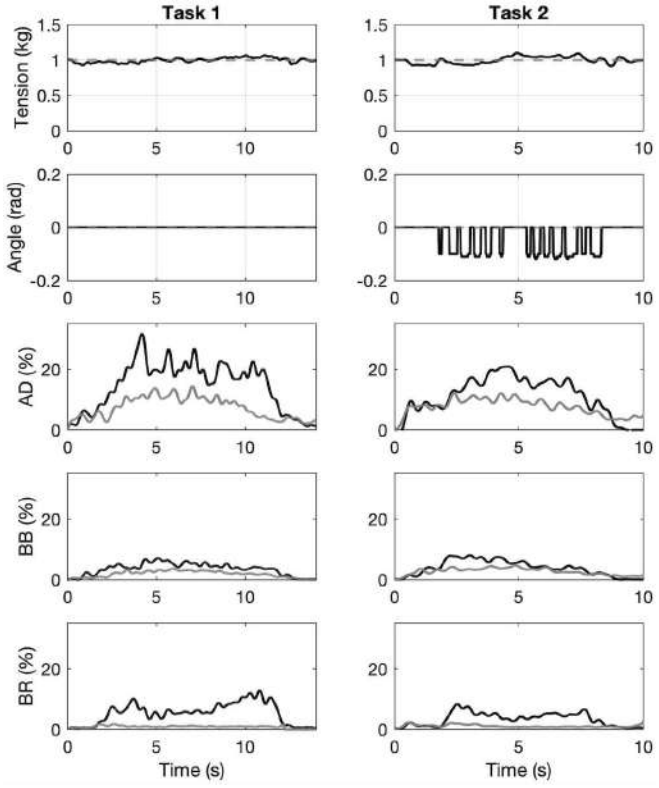


Fig. 8: Experimental results. The first and second rows show the performance of the admittance and position controllers respectively, where the dashed line indicates the reference. The third, fourth, and fifth rows display the normalized EMG data for the anterior deltoid (AD), biceps brachii (BB), and brachioradialis (BR) muscles, respectively. The black line represents the scenario without gravity compensation, while the gray line represents the scenario with gravity compensation..

of 44% for the AD, 42% for the BB, and 77% for the BR across both tasks.

This research was conducted with ethical approval from the UCL Research Ethics Committee (REC) under project ID number 6676/007, and all participants provided informed consent.

V. CONCLUSIONS

The design, prototyping, and initial experimental results of a novel active sling-suspension robot for gravity compensation of the upper limbs have been presented. The proposed concept is modular, scalable, and features low inertia, achieved through its compact design and optimized weight distribution. The flexibility of this concept enables the exploration and implementation of various gravity compensation approaches. For example, it facilitates the evaluation of fixed versus adaptive support and the comparison of providing support from a fixed position versus maintaining an always normal pulling force, unlike conventional sling-suspension devices.

While a comprehensive validation and usability studies are necessary to draw definitive conclusions, the experimental results provide initial insights into the effectiveness of this novel device. The results demonstrate that the robot effectively tracks the desired tension of the winch cable which significantly reduces anterior deltoid, biceps brachii, and brachioradialis muscles activation, while simultaneously providing an always normal pulling force following the arm's movement through monitoring the winch cable's deviation angle.

Future efforts will focus on conducting a validation and usability studies, performing an exhaustive control study, completing the design and integration of the vertical axis, and developing a VR environment to create a more engaging system.

REFERENCES

[1] K. Moulaei, K. Bahaadinbeigy, A. A. Haghdoostd, M. S. Nezhad, and A. Sheikhtaheri, "Overview of the role of robots in upper limb disabilities rehabilitation: a scoping review," *Archives of Public Health*, vol. 81, no. 1, p. 84, 2023.

[2] M. Manzano, S. Guégan, R. Le Breton, L. Devigne, and M. Babel, "Model-based upper-limb gravity compensation strategies for active dynamic arm supports," in *2023 International Conference on Rehabilitation Robotics (ICORR)*, pp. 1–6, IEEE, 2023.

[3] D. O'Flaherty and K. Ali, "Recommendations for upper limb motor recovery: an overview of the uk and european rehabilitation after stroke guidelines (2023)," in *Healthcare*, vol. 12, p. 1433, MDPI, 2024.

[4] S. H. Lee, G. Park, D. Y. Cho, H. Y. Kim, J.-Y. Lee, S. Kim, S.-B. Park, and J.-H. Shin, "Comparisons between end-effector and exoskeleton rehabilitation robots regarding upper extremity function among chronic stroke patients with moderate-to-severe upper limb impairment," *Scientific reports*, vol. 10, no. 1, p. 1806, 2020.

[5] S. Yang, L. Luo, M. Liu, J. Chen, W. C. Law, M. Yuan, L. Li, and W. T. Ang, "Adaptive gravity compensation framework based on human upper limb model for assistive robotic arm extender," in *2023 International Conference on Rehabilitation Robotics (ICORR)*, pp. 1–6, IEEE, 2023.

[6] R. O. Hailey, A. C. De Oliveira, K. Ghonasgi, B. Whitford, R. K. Lee, C. G. Rose, and A. D. Deshpande, "Impact of gravity compensation on upper extremity movements in harmony exoskeleton," in *2022 International Conference on Rehabilitation Robotics (ICORR)*, pp. 1–6, IEEE, 2022.

[7] J. Mukherjee, A. Chatterjee, S. Jena, N. Kumar, S. P. Muthukrishnan, S. Roy, and S. Bhasin, "Adaptive gravity compensation control of a cable-driven upper-arm soft exosuit," *arXiv preprint arXiv:2304.14823*, 2023.

[8] M. Demers, J. Rowe, and A. Prochazka, "Passive devices for upper limb training," *Neurorehabilitation Technology*, pp. 525–547, 2022.

[9] E. Hays, J. Slayton, G. Tejeda-Godinez, E. Carney, K. Cruz, T. Exley, and A. Jafari, "A review of rehabilitative and assistive technologies for upper-body exoskeletal devices," in *Actuators*, vol. 12, p. 178, MDPI, 2023.

[10] F. Just, Ö. Özen, S. Tortora, V. Klamroth-Marganska, R. Riener, and G. Rauter, "Human arm weight compensation in rehabilitation robotics: efficacy of three distinct methods," *Journal of neuroengineering and rehabilitation*, vol. 17, pp. 1–17, 2020.

[11] H. Bastiaens, G. Alders, P. Feys, S. Notelaers, K. Coninx, L. Kerkhofs, V. Truyens, R. Geers, and A. Goedhart, "Facilitating robot-assisted training in ms patients with arm paresis: a procedure to individually determine gravity compensation," in *2011 IEEE International Conference on Rehabilitation Robotics*, pp. 1–6, IEEE, 2011.

[12] R. C. Loureiro and T. A. Smith, "Design of the robin system: whole-arm multi-model sensorimotor environment for the rehabilitation of brain injuries while sitting or standing," in *2011 IEEE International Conference on Rehabilitation Robotics*, pp. 1–6, IEEE, 2011.

[13] Y. Hasegawa and S. Oura, "Exoskeletal meal assistance system (emas ii) for progressive muscle dystrophy patient," in *2011 IEEE international conference on rehabilitation robotics*, pp. 1–6, IEEE, 2011.

[14] W. Wu, J. Fong, V. Crocher, P. V. Lee, D. Oetomo, Y. Tan, and D. C. Ackland, "Modulation of shoulder muscle and joint function using a powered upper-limb exoskeleton," *Journal of biomechanics*, vol. 72, pp. 7–16, 2018.

Local Performance-based Control for End-effector Robots in Upper-arm Rehabilitation

Cristina Urdiales*, Manuel Fernández-Carmona*, Francisco J. Ruiz-Ruiz†, Jesús M. Gómez de Gabriel*
*Inst. de Investigación en Ingeniería Mecatrónica IMECH-UMA, Universidad de Málaga, Málaga, Spain
Emails: {mfc, jesus.gomez, acurdiales}@uma.es
†Human-Robot Interfaces and Interaction Lab, Istituto Italiano di Tecnologia, Genoa, Italy
francisco.ruiz@iit.it

***Abstract*—During physical Human-Robot Interaction (pHRI) for limb mobilization, humans and robots may contribute simultaneously to motion. Some Assist-As-Needed (AAN) strategies rely on models, while others are purely reactive. This paper presents a reactive AAN control for an end-effector robot in upper limb rehabilitation that weights commands dynamically based on local performance. Volunteers in tests followed a planar circular trajectory with visual feedback. Statistical analysis confirms that assistance is provided as needed, balancing performance across users and hands. Additionally, global metrics —including completion time, tracking errors, force, and disagreement— improve compared to standalone trajectories.**

***Index Terms*—Physical Human-Robot Interaction (pHRI), Reactive Shared Control, Adaptive Performance Weighting, Human-in-the-loop, collaborative robotics**

I. Introduction

Assistive robots can aid in the recovery from musculoskeletal and neurological conditions and support early mobilization after injury [1]. By operating more frequently than traditional care and continuously monitoring performance, they can better adapt treatment to patient needs. These robots fall into two main categories: wearables/exoskeletons and end-effector (EE) devices, both widely studied. EE devices assist users in developing motor skills and recovering limb function by constraining trajectory and/or force through repetitive maneuvers. All these systems require physical Human-Robot Interaction (pHRI), demanding careful mechanical design and control strategies since both human and robot contribute to motion. Ignoring human intent may reduce engagement and lead to physical harm. Excessive assistance may also hinder rehabilitation, as minimizing robotic intervention in patients with residual limb control enhances neural plasticity [2].

Shared Control (SC) strategies regulate autonomy levels, adjusting robot and human contributions dynamically [3]. Assist-As-Needed (AAN) controllers minimize assistance to maximize user engagement [4]. In structured tasks with clear targets, state-based models can be used [5], while other approaches assign user skill levels and adjust assistance accordingly [6]. Alternatively, linear blending (LB) of user and robot commands [7] in the absence of user models remains a popular choice. LB arbitration can also adapt reactively based on feedback errors [8].

This work presents an LB-based SC system for a robotic arm with a gripper for human limb mobilization, requiring i) a velocity-controlled manipulator with force sensing and ii) a compliant yet firm gripper. We implement this using a Franka arm equipped with the gripper in [9]. The system assists users in following a predefined path, a task common in Repetitive Task Training (RTT) [10], Mobilization with Movement (MWM) [11], and Occupational Therapy [12]. Human commands, extracted from interaction forces, are blended with robot commands to move toward the goal. Both contributions are continuously weighted by local performance, adapting assistance in real time.

Many AAN controllers focus on minimizing tracking errors [13]. Impedance-based AAN approaches [14], [15] introduce a torque-free region around the reference trajectory and corrective tangential forces [16], [17]. Instead, our AAN controller prioritizes progressive performance improvement over strict error minimization. Though tested only on healthy volunteers, results indicate reduced robot intervention and lower human resistance to assistance.

Section II in this paper presents the framework. Section III details the experiments and results, discussed in Section IV. Conclusions are summarized in Section V.

II. Shared Control Framework

A. Framework Overview

In a SC system, the command signal h is often a linear combination of human (u_h) and robot control (u_a) signals, weighted by α:

$$h(u_h, u_a) = \alpha u_h + (1-\alpha)u_a, \quad 0 \leq \alpha \leq 1. \tag{1}$$

In the proposed framework, h results from a weighted combination of u_h and the robot controller (u_r), further modulated by an overall performance factor η_s (Figure 1). The human and robot contributions are weighted based on their respective performances (η_h, η_r) in the given task.

The system employs a torque-sensitive robotic arm with a full dynamic model to compute external Cartesian forces $\boldsymbol{f}$ at its end-effector (EE). Many modern manipulators

This work has been funded by the "Agencia Estatal de Investigación" under project PID2021–127221OB-I00.

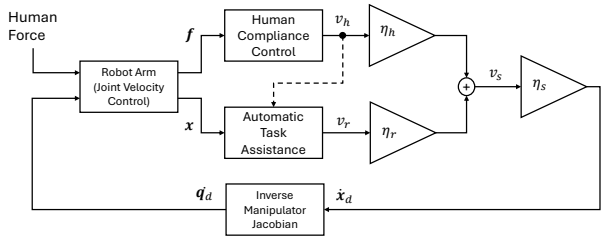


Figure 1: Block diagram of the proposed SC framework.

(e.g., Franka Research 3) offer this capability in real-time. Performance values $\eta(t)$ are computed based on how effectively human and robot commands contribute to achieving the goal [18].

B. Human Compliance Control

The estimated human-applied force $\boldsymbol{f}$ at the EE is used in a compliance model to regulate impedance during motion. This is implemented via an admittance model, as in (2), providing specific inertia and viscosity in Cartesian space:

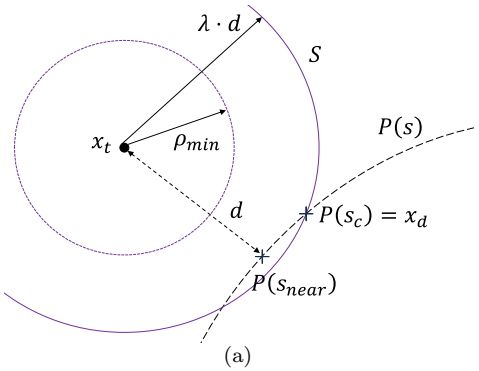
$$\boldsymbol{V}_h(s) = \frac{\boldsymbol{F}(s)}{\boldsymbol{M}s + \boldsymbol{B}} \tag{2}$$

where $\boldsymbol{M}, \boldsymbol{B} \in \mathbb{R}^{3\times3}$ are diagonal positive matrices representing virtual mass and damping, s is the Laplace variable, and $\boldsymbol{F}(s)$, $\boldsymbol{V}_h(s)$ are the Laplace transforms of the human Cartesian force $\boldsymbol{f}$ and velocity $\boldsymbol{v}_h$, respectively.

C. Automatic Task Assistance

The path follower continuously computes the desired Cartesian velocity v_a to reach the next goal from the current EE location.

1) Path Tracking: A spherical look-ahead approach determines the desired goal x_d along the trajectory (Figure 2).



(a)

Figure 2: The path follower selects the new objective point where the virtual sphere $\mathcal{S}$ intersects the path, advancing in the positive direction.

A virtual sphere $\mathcal{S}$ of dynamic radius ρ, centered at $\boldsymbol{x}$, is used to select the next target along a parameterized path $\mathcal{P}(s)$, where $s \in [0, 1]$. The system enlarges ρ (λ) while ensuring a lower bound (ρ_{min}) so that $\mathcal{S}$ intersects $\mathcal{P}(s)$ at least twice. The goal point in the task direction is chosen as $\boldsymbol{x}_d = \mathcal{P}(s_c)$.

2) Desired Automatic Velocity Computation: Let $\boldsymbol{x}$ be the EE position and $\boldsymbol{x}_d$ the goal Cartesian coordinates. The robot's velocity command $\boldsymbol{v}_r$ is given by:

$$\boldsymbol{V}r(s) = \frac{\boldsymbol{K}a}{\tau s + 1}\|\boldsymbol{v}_h\|(\boldsymbol{x}_d - \boldsymbol{x}), \tag{3}$$

where $\boldsymbol{K}_a$ is a diagonal positive matrix representing the attraction constant to the goal, and $\boldsymbol{x}_d - \boldsymbol{x}$ is the position error. A first-order low-pass filter with time constant τ modulates the robot's response.

To achieve AAN, the robot's assistance scales with the human-applied forces ($\|\boldsymbol{v}_h\|$), encouraging active user participation. The low-pass filter smooths noise in external force estimation.

D. Performance Computation

The proposed SC framework relies on local performance assessment, averaging multiple performance targets (e.g., smoothness, safety, precision, comfort). At any time, the performance $\eta_k \in [0, 1]$ of a command k (with $k = h, r, s$) is computed as a weighted combination of m partial performance factors η_{k_i}:

$$\eta_k = \frac{\sum_{i=1}^{m} w_i \eta_i}{\sum_{i=1}^{m} w_i}, \tag{4}$$

where w_i represents the weight of each factor. By default, weights are equal, but can be adjusted for specific task requirements (e.g., prioritizing smoothness or precision).

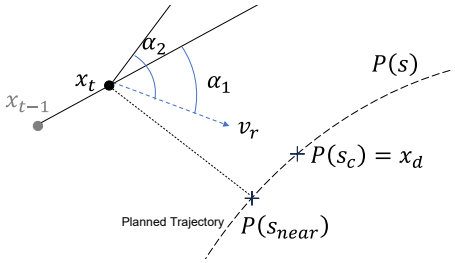


Figure 3: Computation of angles α_{k_1} and α_{k_2} for performance evaluation.

Following [18], we consider smoothness and directness as key performance factors ($m = 2$). The smoothness factor η_{k_1} penalizes abrupt direction changes, while directness η_{k_2} rewards commands that move toward the goal. These factors are computed as:

$$\eta_{k_j} = e^{-C_j|\alpha_{k_j}|}, \quad j = 1, 2 \tag{5}$$

where C_1 and C_2 adjust the sensitivity of each factor. The angle α_{k_1} measures deviation between consecutive commands, while α_{k_2} quantifies deviation from the optimal path (Figure 3). As with w_i, constants C_i can be heuristically tuned or set to 1 by default.

E. Shared Velocity Command (SVC) Computation

Once the human and robot propose commands to reach the target, the controller must combine them to obtain the final Shared Velocity Command (SVC) in two phases:

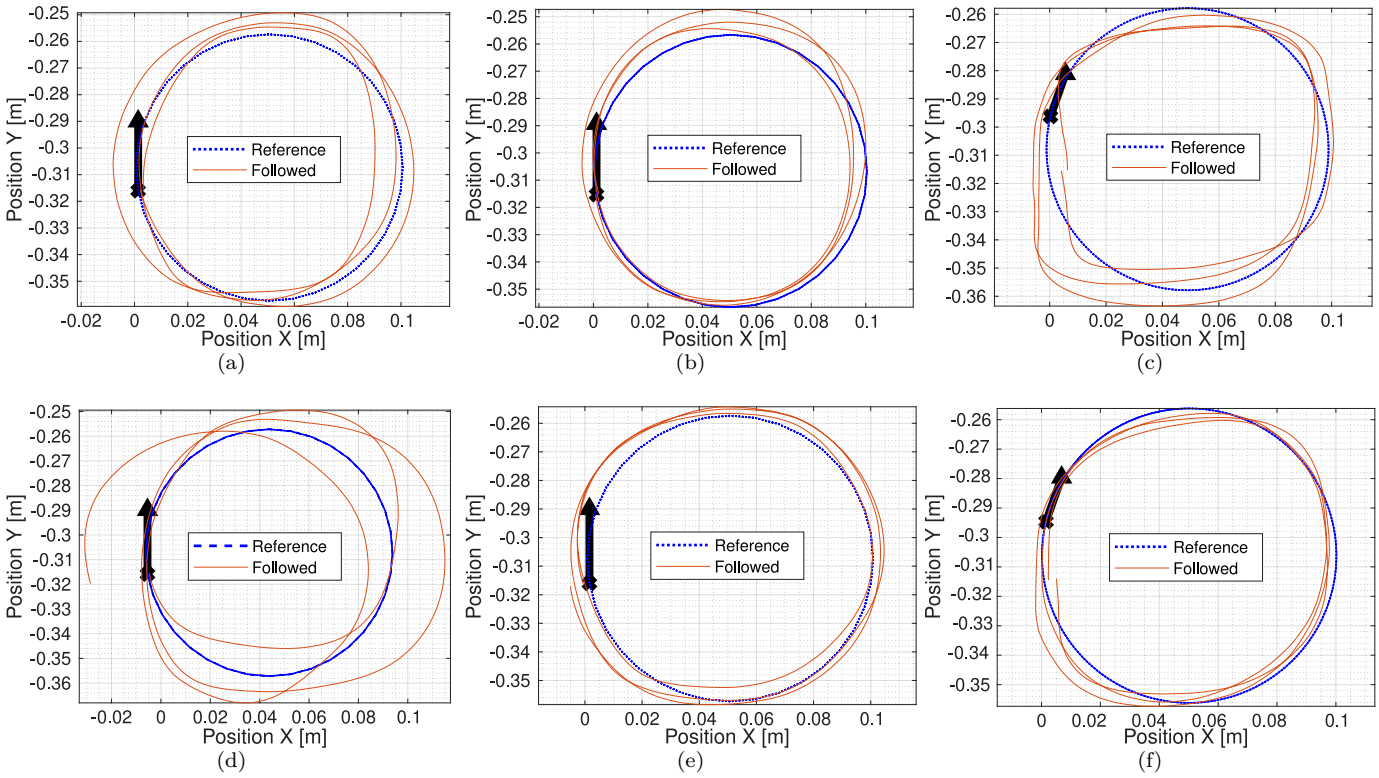


Figure 4: Paths in the XY plane performed by Volunteer 08: (a) DA, (b) DS, (c) DI, (d) NA, (e) NS, (f) NI.

1) Raw SVC Computation: $\hat{\boldsymbol{v}}_s$, is obtained as:

$$\hat{\boldsymbol{v}}_s = \eta_r \boldsymbol{v}_r + \eta_h \boldsymbol{v}_h, \tag{6}$$

where η_r and η_h represent the performance of the robot and human commands, respectively.

2) Performance-Weighted SVC: $\hat{\boldsymbol{v}}_s$ is scaled by its performance η_s, yielding the final command:

$$\dot{\boldsymbol{x}}_{\boldsymbol{d}} = \eta_s \hat{\boldsymbol{v}}_s. \tag{7}$$

Unlike traditional convex blending (1), where inputs are complementary, the weighting in (6) allows η_r and η_h to act independently.

F. Robot Arm Control

To ensure smooth motion, $\dot{\boldsymbol{x}}d$ is saturated if its norm exceeds the maximum Cartesian velocity allowed at the EE, $vmax$. The final velocity command is then transformed into joint velocities using the inverse Jacobian matrix before being sent to the arm's joint controller:

$$\dot{\boldsymbol{q}}_{\boldsymbol{d}} = J(q)^{-1} \dot{\boldsymbol{x}}_{\boldsymbol{d}} \tag{8}$$

This command incorporates admittance to external forces, so motion remains compliant with user interaction.

III. Experiments and Results

A. Experimental Setup

The setup consists of an underactuated gripper [9] attached to a Franka Research 3 robot arm, running a Cartesian velocity controller to assist in tracing a circular path [10]. Since robots typically outperform humans in precision, volunteers were expected to improve their tracing performance collaboratively.

1) Parameters: The admittance parameters $\mathbf{M}$ and $\mathbf{B}$ were set to $\mathrm{diag}(1,1,1)$ kg and $\mathrm{diag}(83.3, 83.3, 83.3)$ Ns/m [19]. $\boldsymbol{K}a$ was set to identity for a good user experience. Since both smoothness and directness are crucial for circular path tracing, performance weights were equal ($w_1 = w_2 = 0.5$), and $C_1 = C_2 = 1$ (Section II-D). The path follower parameters were $\lambda = 1.02$ and $\rho_{min} = 0.015$ m.

2) Participants & Procedure: Ten healthy volunteers (7 male, 3 female) of different ages and backgrounds participated under the Declaration of Helsinki principles[1]. Each completed six tests: standAlone (A), SC mode (S), and Impedance (I) control-based AAN [15], using both dominant (**D**) and non-dominant (**N**) hands. Volunteers, unaware of assistance conditions, traced a 5 cm radius circle clockwise, viewing their trajectory on a screen. Each test consisted of four loops. Figure 4 illustrates typical trajectories, demonstrating that the SC mode resulted in the best curvature outcomes for all loops in both hands.

3) Hypotheses: In order to study the benefits of the system, the following hypotheses were proposed:

- H1: Shared mode improves performance.

[1]CEUMA 7-2023-H

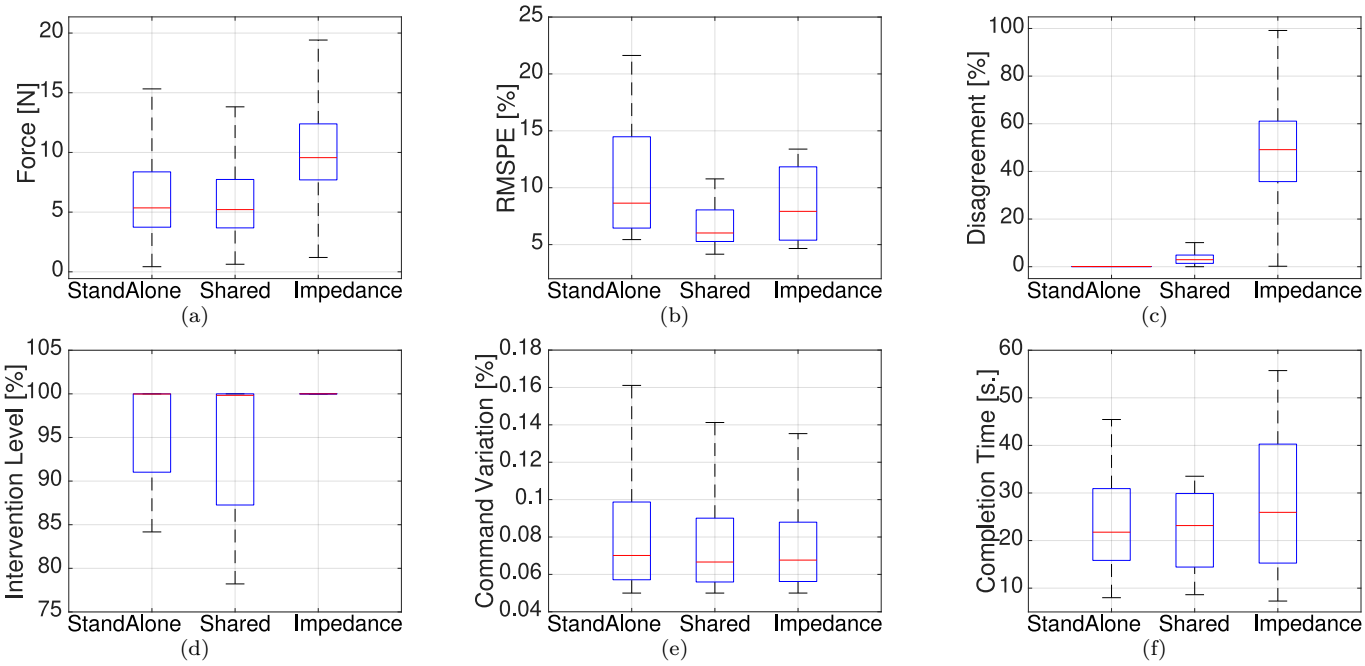


Figure 5: Average tests performance.

- H2: Root Mean Square Percentage Error (RMSPE) decreases in shared mode.
- H3: SC equalizes performance between hands.
- H4: SC reduces RMSPE variance, improving precision.
- H5: Participants feel comfortable with assistance (questionnaire).

B. Result Analysis

Table I presents ANOVA results for the hypotheses in Section III-A. All hypotheses were validated except H3, which aimed to show that SC equalizes performance between dominant and non-dominant hands. This rejection might be due to some users naturally performing equally well with both hands, so we reformulated this hypothesis to consider only users with significant hand performance differences (upper tercile, H_i'). Under these circumstances, ANOVA test confirms that SC significantly reduces performance gaps for "imbalanced" users.

Table I: ANOVA test results.

Hyp.	Data	Factor	ANOVA
H1	user performance	standalone/shared	0.0143
H2	average RMSPE	standalone/shared	0.0423
H3	$\Delta\eta_{hand}$ (per user)	standalone/shared	0.848
H3'	$\Delta\eta_{hand}$ (per user)	standalone/shared	0.0421
H4	RMSPE variance	standalone/shared	0.0347
H5	command variation	standalone/shared	0.0395

Additional statistics of several performance metrics were obtained and are summarized in Figure 5. From these results, the following key findings can be stated:

- SC improves task performance (H1), figure fit (H4), and reduces both RMSPE and cognitive load variance (H2, H5).
- RMSPE decreases in SC mode due to adaptive haptic feedback, though IC introduces higher error variance (see Figure 5b).
- Intervention Level (Figure 5d) is consistently high across modes. In SC, command variation is more controlled, while in IC, users struggle more with the robot, leading to increased force and completion time variability.
- IC mode results in higher forces as users counteract corrections, whereas in SC, disagreement remains low, and performance improves with lower exertion (see Figure 5a).
- SC maintains an effective trade-off between performance and disagreement, keeping force levels moderate. In contrast, IC disrupts these relationships, increasing struggle. This can be observed in the scatter plots in Figure 6, which state dependencies between force, performance, and disagreement across control modes.
- SC provides adaptive assistance, helping users when necessary while maintaining smooth and consistent control. IC, however, alters force-disagreement-performance dynamics, often leading to inefficiency.

IV. Discussion

Our SC law dynamically blends human and robot commands based on local performance, estimated in terms of smoothness and directness. This results in continuous and natural motion, while trajectories remain globally smooth and precise. Moreover, even metrics not explicitly considered in the control function—such as RMSPE, disagreement, cognitive load, and completion time—show

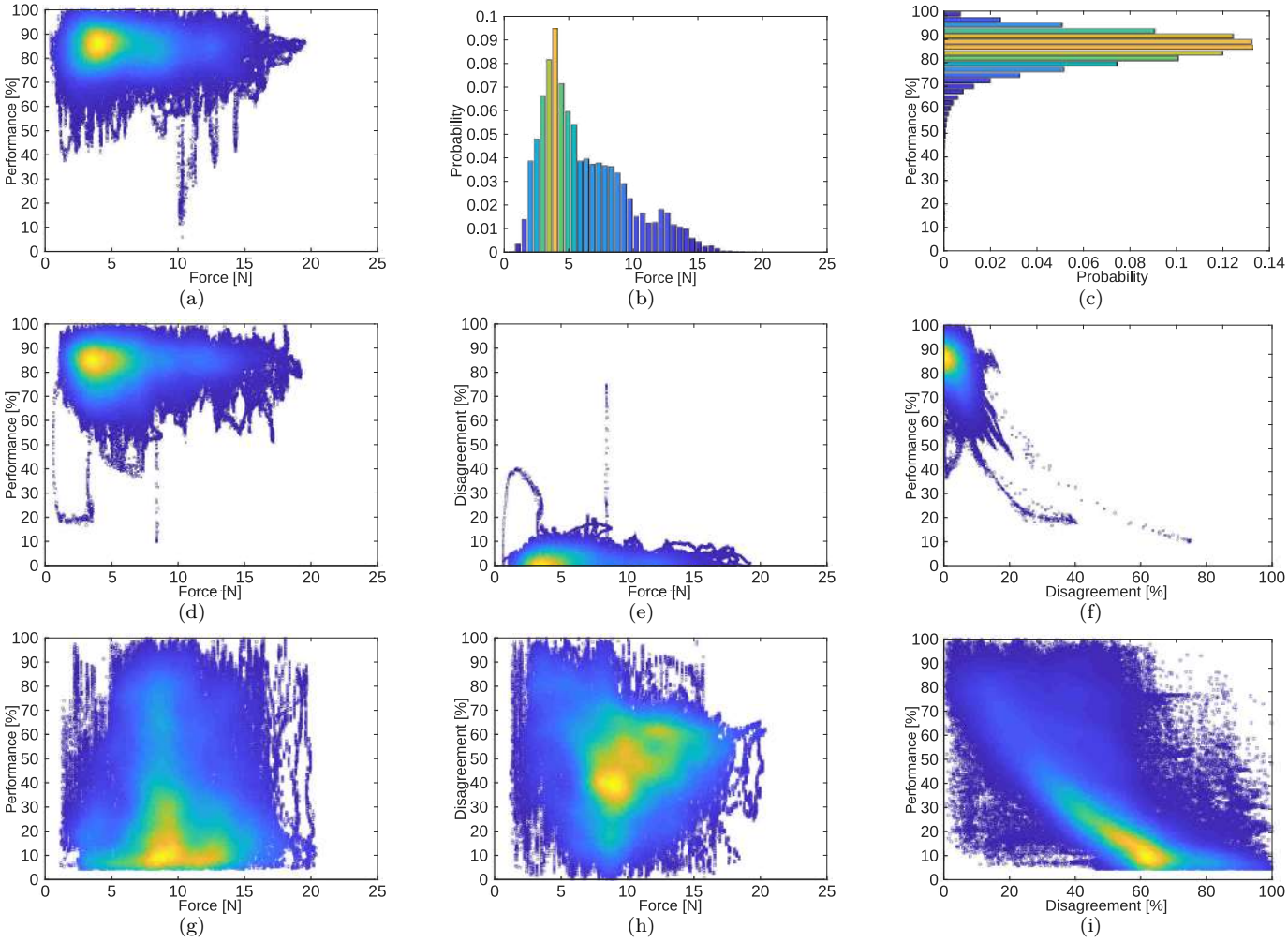


Figure 6: Scatter plots of all Standalone (top row), SC (middle row), and IC (bottom row) tests comparing force vs. performance (left column); force vs. disagreement[1] (mid column); and disagreement vs. performance (right column)[1]. Light-colored areas are more likely to happen.

positive trends in SC mode.

We compared SC against Standalone human control and a classical IC in tests with healthy volunteers. SC improves local performance, reduces RMSPE variance and average error, likely by stabilizing user input and gradually increasing resistance when deviations occur. One of the most notable effects of SC is a significant reduction in performance variance, both across participants and between dominant and non-dominant hands. This indicates that SC adapts to individual needs. Performance homogenization was an intended effect of performance-weighted assistance: rather than elevating performance to robot levels, SC enhances human execution to a consistent and competent standard.

Assistance in SC is well accepted. Lower Disagreement values suggest that human and robot commands align better than in other modes, contributing to improved accuracy and task efficiency. Although users were unaware of the control mode during trials, most reported feeling more comfortable in SC. By contrast, Disagreement was highest in IC mode, where many volunteers described control as jagged. Notably, high Disagreement often occurred when the hand was closer to the body, suggesting difficulties in certain postures.

SC also reduces the number of corrections, as indicated by increased variance in the Intervention Level and lower command variation. Since corrections often correlate with cognitive effort, SC may lower mental workload, though further analysis would be needed to confirm this. Additionally, SC minimizes completion time variation. Observations suggest that some users, especially those less familiar with robots, initially applied insufficient force—perhaps out of concern for damaging the system. In Standalone and IC modes, this sometimes led to intermittent stops, followed by overcompensation, creating oscillatory force patterns. This issue was less pronounced in SC mode.

Regarding system stability, the control loop gains are modulated in real-time based on performance indices

[1]In Standalone control, the user command matches the shared command, resulting in a 1-D histogram instead of a 2-D scatterplot

$\eta_i \in [0, 1]$ which provide direct feedback on task execution. These indices adjust the gains for both robot path-following and human admittance control, reducing them when performance declines (e.g., in terms of smoothness or directness). This approach improves upon conservative passivity-based methods. Additionally, a low-pass filter and saturation on the desired velocity reference enhance stability, considering the limited bandwidth of human arm motion (below 2 Hz) [20].

V. Conclusions

This paper has introduced a novel SC method for pHRI rehabilitation robots, designed to enable continuous human-robot collaboration. SC dynamically blends human and robot commands based on local performance, ensuring smooth motion while allowing users to contribute as much as their abilities permit. By adapting assistance to individual needs, SC effectively homogenizes performance across different users and between dominant and non-dominant hands.

Experimental results demonstrate that SC improves performance while reducing both variance and tracking error. The Intervention Level confirms that users remain actively involved in motion, while low command variation suggests that this occurs without increased cognitive load. Volunteers generally reported higher comfort in SC mode, despite variations in individual preferences. While Disagreement fluctuated with body and arm positioning, it remained lower in SC mode overall. Notably, more skilled users exhibited slightly higher average Disagreement in SC mode, likely due to their tendency to assert greater control. Across all assessed metrics, SC consistently outperformed both Standalone and IC.

Future work will focus on deploying this SC approach in hospitals and nursing homes to evaluate its effectiveness in real-world rehabilitation after ethical approval. Additionally, we aim to incorporate safety constraints for more complex collaborative maneuvers in 3D space and refine robot navigation strategies to better align with human preferences. Beyond rehabilitation, we also envision extending this SC framework to critical pHRI applications, such as rescue, first aid, and nursing robots, where human safety and adaptive assistance are paramount.

References

[1] B. D. Argall, "Autonomy in rehabilitation robotics: An intersection," *Annual Review of Control, Robotics, and Autonomous Systems*, vol. 1, no. 1, pp. 441–463, 2018.

[2] E. T. Wolbrecht, V. Chan, D. J. Reinkensmeyer, and J. E. Bobrow, "Optimizing compliant, model-based robotic assistance to promote neurorehabilitation," *IEEE Trans. on Neural Systems and Rehabilitation Engineering*, vol. 16, no. 3, pp. 286–297, 2008.

[3] M. Laghi, M. Maimeri, M. Marchand, C. Leparoux, M. Catalano, A. Ajoudani, and A. Bicchi, "Shared-autonomy control for intuitive bimanual tele-manipulation," in *2018 IEEE-RAS 18th International Conference on Humanoid Robots (Humanoids)*, 2018, pp. 1–9.

[4] A. U. Pehlivan, D. P. Losey, and M. K. O'Malley, "Minimal assist-as-needed controller for upper limb robotic rehabilitation," *IEEE Trans. on Robotics*, vol. 32, no. 1, pp. 113–124, 2016.

[5] H. Jeon, D. Losey, and D. Sadigh, "Shared autonomy with learned latent actions," in *Proceedings of Robotics Science and Systems*, 2020, p. 10.

[6] N. Enayati, G. Ferrigno, and E. De Momi, "Skill-based human–robot cooperation in tele-operated path tracking," *Autonomous Robots*, vol. 42, 06 2018.

[7] C. Ezeh, P. Trautman, D. Louise, V. Bureau, M. Babel, and T. Carlson, "Probabilistic vs linear blending approaches to shared control for wheelchair driving," *IEEE International Conference on Rehabilitation Robotics*, vol. 2017, pp. 835–840, 07 2017.

[8] Y. Li, K. P. Tee, W. Chan, R. Yan, Y. Chua, and D. Limbu, "Continuous role adaptation for human–robot shared control," *IEEE Trans. on Robotics*, vol. 31, pp. 1–10, 06 2015.

[9] F. J. Ruiz-Ruiz, J. Ventura, C. Urdiales, and J. M. G. de Gabriel, "Compliant gripper with force estimation for physical human–robot interaction," *Mechanism and Machine Theory*, vol. 178, p. 105062, 2022.

[10] T. Krabben, B. Molier, A. Houwink, J. Rietman, J. Buurke, and G. Prange, "Circle drawing as evaluative movement task in stroke rehabilitation: An explorative study," *Journal of neuroengineering and rehabilitation*, vol. 8, p. 15, 03 2011.

[11] K. Satpute, S. Reid, T. Mitchell, G. Mackay, and T. Hall, "Efficacy of mobilization with movement (mwm) for shoulder conditions: a systematic review and meta-analysis," *Journal of Manual & Manipulative Therapy*, vol. 30, pp. 1–20, 08 2021.

[12] D. Nilsen, G. Gillen, M. Arbesman, and D. Lieberman, "Occupational therapy interventions for adults with stroke," *The American Journal of Occupational Therapy*, vol. 69, no. 5, 09 2015.

[13] A. Cherubini, R. Passama, A. Crosnier, A. Lasnier, and P. Fraisse, "Collaborative manufacturing with physical human-robot interaction," *Robotics and Computer-Integrated Manufacturing*, vol. 40, pp. 1–13, 2016.

[14] M. Mihelj, T. Nef, and R. Riener, "A novel paradigm for patient-cooperative control of upper-limb rehabilitation robots," *Advanced Robotics*, vol. 21, no. 8, pp. 843–867, 2007.

[15] L. Zhang, S. Guo, and F. Xi, "Performance-based assistance control for robot-mediated upper-limbs rehabilitation," *Mechatronics*, vol. 89, p. 102919, 2023.

[16] S. Kana, K.-P. Tee, and D. Campolo, "Human-robot comanipulation during surface tooling: A general framework based on impedance control, haptic rendering and discrete geometry," *Robotics and Computer-Integrated Manufacturing*, vol. 67, p. 102033, 2021.

[17] H. Wang, J. Peng, F. Zhang, H. Zhang, and Y. Wang, "High-order control barrier functions-based impedance control of a robotic manipulator with time-varying output constraints," *ISA Transactions*, vol. 129, pp. 361–369, 2022.

[18] M. Fernández-Carmona, J. M. Peula, C. Urdiales, and F. Sandoval, "Towards a shared control navigation function: Efficiency based command modulation," in *Advances in Computational Intelligence*. Springer International Publishing, 2015, pp. 185–198.

[19] D. Reyes-Uquillas and T. Hsiao, "Safe and intuitive manual guidance of a robot manipulator using adaptive admittance control towards robot agility," *Robotics and Computer-Integrated Manufacturing*, vol. 70, p. 102127, 2021.

[20] E. J. Perreault, R. F. Kirsch, and P. E. Crago, "Effects of voluntary force generation on the elastic components of endpoint stiffness," *Experimental brain research*, vol. 141, pp. 312–323, 2001.

Development and Pre-Clinical Validation of Tendon Driven 2 Degree-of-freedom Powered Ankle-Foot Orthosis for Heuristic Algorithm Based on Gait Stability

Kyeongwon Kang[1], Sehee Jung[2], Minseok Lim[2], and Ho Seon Choi[1,*], *Member, IEEE*

Abstract— **In the field of rehabilitation, Powered Ankle-Foot Orthoses (PAFO) are often used, which are wearable robots designed to rehabilitate the mobility of individuals with reduced walking stability, such as the elderly. Previous studies have developed a 2-degree-of-freedom PAFO capable of assisting both the talocrural and subtalar joints of the ankle. However, the use of pneumatic artificial muscles (PAMs) as actuators resulted in low control capacity(low cutoff frequency). To address this limitation, this study developed a tendon-driven device that offers higher cutoff frequencies through a motor system driven by cables. Furthermore, we did pre-clinical experiment, and it showed the possibility of enhancing walking stability with our heuristic-based algorithm for human-in-the-loop optimization. This algorithm was based on the activity of antagonistic muscles to those targeted for assistance at both ankle joints and walking stability was evaluated through Gaussian ellipsoid.**

I. INTRODUCTION

Populations with decreased walking stability, such as the elderly, can enhance their walking function through rehabilitation. Decreased walking stability is usually associated with impaired ankle function [1]. The ankle joint comprises two primary joints: the talocrural joint and the subtalar joint, each with two degrees of freedom [2]. The talocrural joint facilitates plantar flexion and dorsiflexion, while the subtalar joint enables eversion and inversion movements [2]. Among these, eversion movement of subtalar joint plays a crucial role in maintaining walking stability [3]. Therefore, improving eversion movement through training or rehabilitation can potentially enhance overall walking stability.

Various rehabilitation systems are being developed to prevent fall, and powered ankle–foot orthosis (PAFO) is one of them. PAFOs are wearable robots designed to assist the human body by incorporating actuators into exoskeletons worn on the ankle [4]. Most PAFOs are typically designed with one degree-of-freedom (*dof*), primarily assisting the talocrural joint of the ankle [4]. However, the ankle comprises two joints—the talocrural and subtalar joints, and the eversion movement of the subtalar joint plays an important role in walking stability. To address this, in this paper, we selected 2-*dof* PAFO that can assist the two joints of the ankle simultaneously using pneumatic artificial muscles (PAMs) [5]. However, this had the drawback of insufficient transmission efficiency. To address this, we have chosen a tendon-driven mechanism to assist the user's bilateral ankle movements. This method mimics tendons by utilizing cables for actuation.

Despite advancements, current PAFOs often face challenges in effectively assisting users in achieving their intended purpose. A promising approach to address this is human-in-the-loop optimization, which enhances human performance by dynamically adjusting device control based on interactions between the exoskeleton and the user [15]. While numerous studies have explored human-in-the-loop optimization [6], it remains a complex and challenging task due to the intricacy and variability of the human motor control system. Walking strategies while using exoskeletons exhibit unique characteristics and patterns for each individual, making it highly difficult to predict user-specific responses or determine optimal assistive patterns [7].

Therefore, this study aims to develop human-in-the-loop optimization of PAFO to improve walking stability. Previous research has designed such algorithms based on heuristic approaches [8]. This algorithm is also designed based on the muscles to be assisted and the muscles that act collaboratively and antagonistically. For example, during plantar flexion assistance, if the activity of the Soleus (SOL), an agonist muscle, increases, additional torque is applied. Conversely, if the activity of the Tibialis Anterior (TA), an antagonistic muscle, increases, less torque is applied. However, these algorithms are limited to assisting plantar flexion of the talocrural joint and primarily focus on improving walking performance rather than walking stability. In reality, walking stability is closely associated with eversion motion, which also requires assistance for the elderly. The muscles involved in this movement include the Peroneus Longus (PL) as a agonist muscle and the TA as an antagonist. In this study, we utilized a 2-dof PAFO capable of assisting both plantar flexion and eversion movements of the ankle joints. At this time, assisting both ankle joints requires an understanding of their interdependent movements and twisted rotational positions, which must be considered in the design and control of the robot. Therefore, this study developed and simply validated a human-in-the-loop optimization algorithm based on heuristics to enhance gait stability by assisting both ankle movements.

* This project is currently supported by the National Research Foundation of Korea(NRF) grant funded by the Korea government (MSIT) (RS-2024-00452977) and the IITP(Institute of Information & Communications Technology Planning & Evaluation)-ICAN(ICT Challenge and Advanced Network of HRD) grant funded by the Korea government(Ministry of Science and ICT)(IITP-2024-RS-2024-00436528)

[1]Kyeongwon Kang and [1,*]Ho Seon Choi are with the Department of Artificial Intelligence and Robotics and Biomechatronics Lab, Sejong University, Seoul, Korea ([*]Corresponding author: choihoseon@sejong.ac.kr).

[2]Sehee Jung and Minseok Lim are with the Department of Intelligent Mechatronics Engineering and Biomechatronics Lab, Sejong University, Seoul, Korea

II. 2 Degree-of-Freedom Powered Ankle-Foot Orthosis

A. Description of orthosis

We conducted the study with the 2-*dof* PAFO developed in the previous study [5]. The developed PAFO has two joints of the ankle through anatomical data and uses the two PAMs as actuators to simultaneously assist in plantarflexion and eversion movements. However, we replaced the PAM with a motor drive system connected with cables as shown in Fig. 1(c) for higher cutoff frequencies. In the proposed drive system, one end of the Bowden cable (made of Teflon-coated material) is attached to an ankle-foot orthosis (AFO), emulating the positioning of the tendons of the soleus and peroneus longus (PL) muscles, as shown in Fig. 1. The exoskeleton frame, excluding the knee brace, is fabricated using a 3D printer with polycarbonate (PC) material [16]. The other end of the Bowden cable is connected to an external motor–load cell–spring assembly, in Fig. 2. The rotation of the BLDC motor (DC 24V, rated current: 11.5 A, rated power: 205 W, encoder: 1000 PPR) transmits force through the Bowden cable, while a spring (experimentally selected at 21.57 N/mm) is positioned at the end of the load cell (LCM201-500N) to eliminate motor backlash. This design enables the proposed drive system to achieve more precise force control and faster responsiveness compared to conventional PAM-based drive mechanisms.

Four types of sensors were used in the experiment: IMU (Inertial Measurement Unit, EBIMU-9DFV5-R3; E2BOX), EMG (Electromyography, AM530), FSR (Force Sensitive Resistor, UX 402; Interlink), and encoder (AMT103). The PAFO was equipped with two encoders to measure the angles of the two ankle joints and one FSR sensor to detect heel strikes for gait cycle analysis. These sensors were connected to an external microcontroller via CAN communication. The IMU sensor was attached to a vest and worn at the trunk position of the body. It measured the acceleration in the x- and z-axis directions, calculated the left-right and front-back acceleration of the body, respectively, and was low-pass filtered with a cut-off frequency of 40 Hz. For the EMG sensor, signals were non-invasively recorded from three muscles (soleus, peroneus longus, and tibialis anterior). The signals were firstly high-pass filtered at a cut-off frequency of 200 Hz, and then low-pass filtered with cut-off frequency of 10 Hz. And filtered signals were finally processed using a moving average filter for smoothing and to extract the meaningful data.

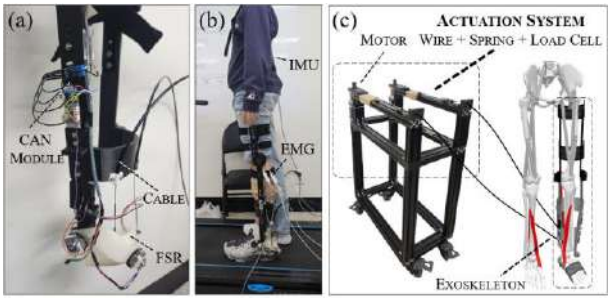


Figure 1. The overall system and experimental environment. (a) PAFO image, (b) the experimental setup, (c) actuation system

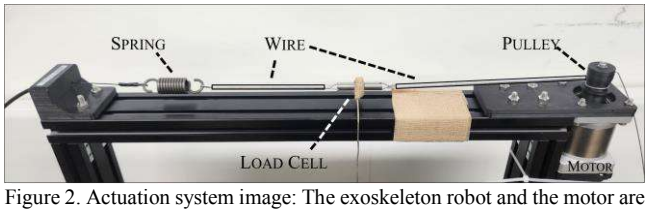


Figure 2. Actuation system image: The exoskeleton robot and the motor are connected by a cable, with a spring, wires, and a load cell in a row.

B. Workspace validation

To determine the workspace of the exoskeleton, the end-effector position was calculated through kinematic analysis. The global coordinate system was set at the Talocrural joint, as shown in Fig. 3, and the DH(Denavit Hartenberg) parameters were derived using the encoder angles as variables. In addition, the end of the exoskeleton sole structure was set as the end effector and plotted in a three-dimensional space. The green area is an operable area(workspace), and the blue dots mean a profile of the end effector during the gait cycle. Since each encoder corresponds to the position of the ankle joints, the coordinates of the end-effector were calculated by substituting the biological ankle joint angles during the gait cycle into the encoder angle variables. As the end-effector trajectory during the gait cycle falls within the operable workspace, the exoskeleton robot is capable of adequately covering human ankle movements during walking.

C. Link Adjustment

There are a total of three links corresponding to the length of the shin of the exoskeleton, and it is designed so that the length can be adjusted. We designed the link by dividing the height of a person into 160, 170, and 180 cm. According to the measurement method proposed by Harless, the ratio of the shin segment according to the height of the person is 0.2484H (H = height) [9]. Therefore, if the shin lengths of a person with heights of 160 cm, 170 cm, and 180 cm are measured as 39.52 cm, 41.99 cm, and 44.46 cm respectively, the corresponding shin lengths for the exoskeleton parts are determined as three. As shown in Fig. 4, the knee brace and PAFO are connected in three ways for the length of the link corresponding to each height. It is designed to fit the length of the shin corresponding to each height, and if the height is 180 cm, the upper two holes of the knee brace link are connected to the red-marked holes on the AFO link, as shown in Fig. 4. For a height of 160 cm, the yellow-marked holes are connected, and for 170 cm, the lower two holes of the knee brace link are connected to the green-marked holes in Fig. 4. Each link length is designed to accommodate height variations within ±3 cm for each target height, allowing for greater flexibility.

III. Control Validation

A. Load cell calibration

The load cell used in the actuation system was calibrated in Newton(N). All motors for controlling PAFO are defined based on torque. To compute the torque for system control, it is essential to determine the tension applied to the motor, which is measured by the load cell. However, since the load cell was obtained through Analog to Digital Converter(ADC) of microcontroller, it must be corrected in the unit of load.

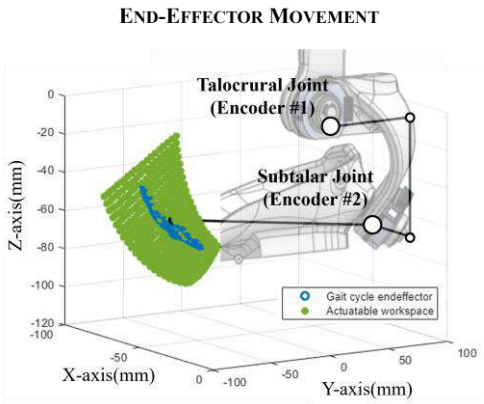


Figure 3. Calculated workspace of the designed PAFO. The green dots indicate the actuatable workspaces, respectively.

Since the manufacturer specified that there is a linear relationship between the load cell and the ADC output value, 1-50kg was measured and linear fitting was performed through MATLAB to calibrate the load cell.

B. Control method

In this study, the performance of the actuator control system must be validated, as it is crucial for assisting two ankle movements during walking through cables while facilitating interaction between the human and the robot. Accordingly, the two cables must meet the required performance level to assist ankle movements appropriately. The performance of Cable 1 and Cable 2, as shown in Fig. 6 was validated compared using commonly used controllers and torque profiles of the elderly and young individuals, respectively.

Cable 1 was evaluated using a commonly used controller as it assists the plantar flexion movement of the ankle. Plantar flexion directly impacts walking dynamics, and there are already many preceding studies. Therefore, we verified the controller performance through the Proportional Myoelectric Controller (PMC), a method that leverages soleus EMG signals to adapt to individual walking patterns[10]. Since this study intends to develop an algorithm that allows the wearer to interact with each other based on muscle activity, this is an appropriate control method to verify the controller performance. The walking speed was determined at 1.2 m/s with reference to another PAFO study, and the profile obtained above was Fast Fourier Transform(FFT) [11]. The results of FFT are shown in Fig.6.

In the case of Cable 2, there are not many prior studies, so the controller performance was verified through the torque difference between the elderly and the young. Cable 2 affects both plantar flexion and eversion movements, but to improve walking stability, assistance for the eversion movement is centered. Since cable2 mainly plays a role of assisting the eversion movement, and there have not been many prior studies on the controller of PAFO that assist this movement. Liu et al. it can be seen that the profile of the eversion-related moments differs between the elderly and the young during the walking cycle [12]. Therefore, we verified the controller performance by setting the profile through the difference in the torque profile that occurred while walking between the elderly and the young through the difference between the two profiles. At this time, the distance between the rotation axis and the

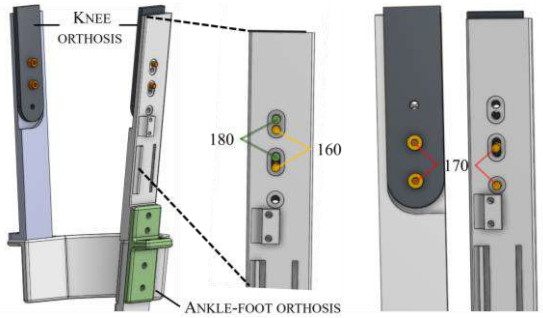


Figure 4. The connection method of the exoskeleton link for individuals with heights of 160 and 180 is shown on the left, while the right figure corresponds to a height of 170.

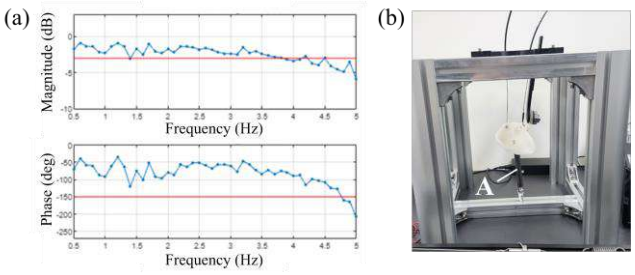


Figure 5. (a) Bode plot result when the amplitude of cable2 is 75N. (b) Closed-loop frequency response experimental setup; A is a spring.

action point where the event torque of the aid occurred was approximately 0.1m, and it was expressed as a force profile, and as shown in cable1, the walking speed was set at 1.2m/s to FFT. This is indicated by AET (Ankle eversion torque) in Fig.6, which shows the torque during the eversion movement.

C. Closed-loop frequency response and results

We conducted closed-loop frequency response experiments for Cable 1 and Cable 2. The target force profiles for these experiments were determined by the peak forces required for the PAFO to assist in ankle torque. The typical population with impaired walking stability is the elderly, whose ankle function gradually declines, leading to reduced walking stability [13]. Svoboda et al. compared the degree of muscle loss in the elderly and found that peak torque decreased by 35.60% for plantar flexion and 33.80% for eversion. Additionally, during walking, the elderly exhibited a 28.0% decrease in plantar flexion torque and a 40.0% decrease in eversion torque compared to younger individuals [12]. Fatigue accumulation also contributes to muscle strength reduction, further impairing walking stability. According to Gutierrez et al., fatigue caused a decrease in peak torque of 18.86% for plantar flexion and 11.86% for eversion [14]. Based on these findings, we determined that a 40% reduction in peak ankle torque during walking in healthy individuals would be sufficient for rehabilitation aimed at improving walking stability. The peak ankle torque during walking for a healthy individual was measured as 88.23 N·m for plantar flexion and 30.37 N·m for eversion. Assuming a moment arm of 0.1 m, we calculated the peak forces for plantar flexion and eversion to be 352.92 N and 11.48 N, respectively. Therefore, in this study, we set the peak force for Cable 1 at 50 N, 75 N, 100 N, 150 N, 200 N, 250 N, 300 N, and 350 N, and for Cable 2 at 50 N, 75 N, 100 N, and 122 N. These forces were used to conduct the frequency response experiments. PID control was applied to the cable system, and the cutoff frequencies of -3 dB and -

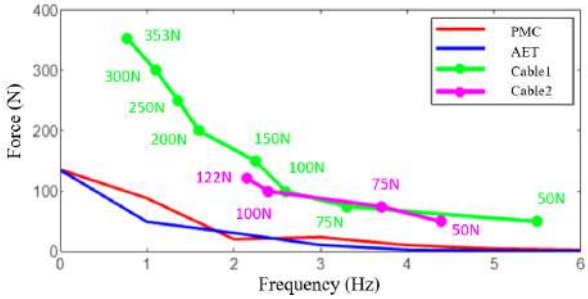


Figure 6. Results of FFT of Proportional Myoelectric Controller (PMC) and Ankle eversion torque difference between young and elderly individuals (AET) and cutoff frequencies of each amplitude from the closed-loop frequency response of the two cables.

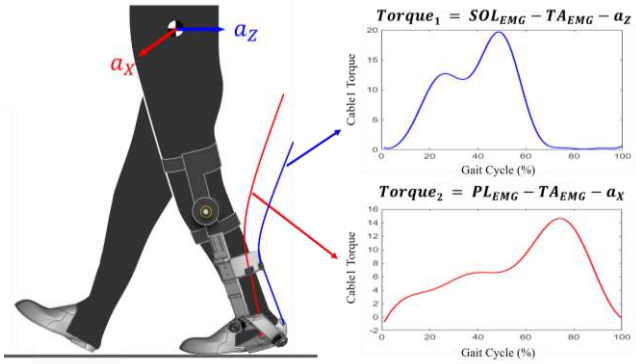


Figure 7. The process of generating torque profiles : It derived from muscle activity and acceleration, are shown in red for cable 1 and blue for cable 2.

150° phase shift were calculated for all experiments, as shown in Fig. 5. In Fig. 5(a), the amplitude of the sinusoidal function is plotted on the y-axis, while the cutoff frequency is shown on the x-axis. For the dynamic changes of the cable during the experiment, we connected a spring to part A of the PAFO, as illustrated in Fig. 5(b). The spring used had a spring constant of 7.75 N/mm.

As a result of the closed-loop frequency response experiment, the cutoff frequencies for cable1 at amplitudes of 50N, 75N, 100N, 150N, 200N, 250N, 300N, and 350N were 5.5, 3.3, 2.6, 2.25, 1.6, 1.36, 1.1, and 0.77 Hz, respectively. For cable2, at amplitudes of 50N, 75N, 100N, and 122N, the cutoff frequencies were 4.4, 3.7, 2.4, and 2.15 Hz, respectively. As shown in Fig 6, the cutoff frequencies of each cable are plotted. Here, cable1 includes the control bandwidth of PMC, and cable2 includes the control bandwidth of AET.

IV. Algorithm Development

We developed a heuristic-based algorithm to enhance walking stability. The algorithm is founded on two fundamental principles: (1) when the muscle to be assisted is activated, more torque is applied, and (2) when both the muscles to be assisted and the antagonistic muscles are activated, the torque is reduced. For example, in the case of assisting plantar flexion, the SOL muscle is the muscle to be assisted, while the TA muscle is the antagonistic muscle. If the activity of the SOL muscle increases, the muscle is considered unassisted, and if the TA muscle is activated, it is deemed over-assisted, leading to a reduction in torque. As illustrated in Fig. 7, we assist both movements of the ankle, including the corresponding antagonistic muscle pairs. Additionally, since the focus is on improving walking stability, acceleration is also

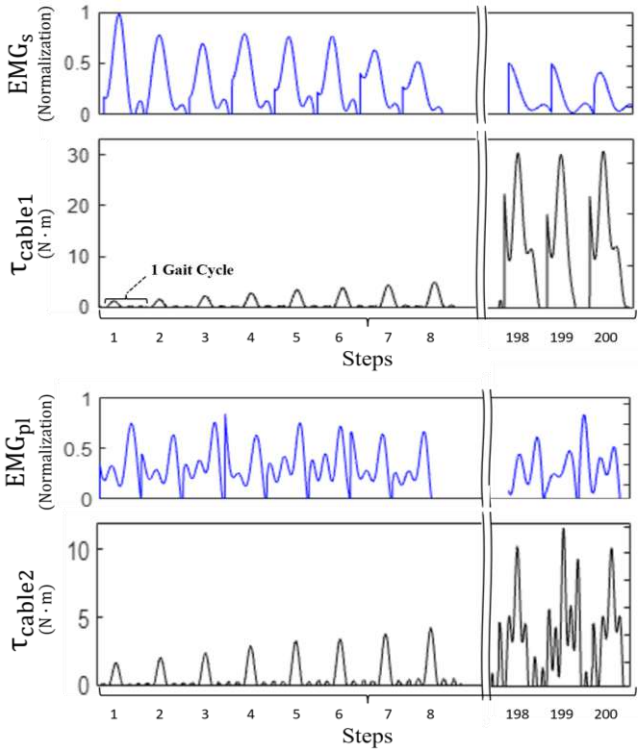


Figure 8. This is an example of how the EMG and torque profiles evolve for two cables. The EMG is normalized to its peak value. (EMG_s and EMG_{pl} mean EMG amplitude signals of soleus and peroneus longus, respectively.)

taken into account. In this context, the z-axis of the acceleration sensor represents the front-back shaking of the body, while the x-axis represents the left-right shaking.

A. Algorithm Formulation

We formulated an equation for each of the two cables. τ_{cable} refers to the torque applied to each cable, n represents the current step, and i represents the index of a particular step. (1) describes the (n+1)th step, which is an adaptive evolutionary algorithm influenced by the nth step. And then, $d\tau_{cable}$ denotes a term that adjusts the torque from the previous step, with a threshold applied to $d\tau_{db}$. Therefore, by adding a memory component to the stepping sequence, the torque profile is designed to converge, as shown in Fig. 8, with the torque gradually increasing at each step until $d\tau_{db}$ no longer changes. Additionally, (1) and (2) apply to cable1, while (3) and (4) apply to cable2.

The term $d\tau_{cable}(i,n)$ represents the muscle activity to be assisted, the antagonistic muscle activity, the previous torque, and the acceleration magnitude, and is designed for both cable1 and cable2. In the case of cable1, $EMG_s(i+d,n)$ is added as a positive term to increase the torque when the SOL muscle activity increases. Additionally, a delay d between muscle activation and the algorithm's operation time was incorporated. To prevent rapid torque increases, $\langle EMG_s(n)\rangle^{-m}$ is introduced to distribute the average EMG value over one step. For antagonistic muscle TA, $EMG_t(i+d,n)$ is included as a negative term to reduce the torque when TA activity increases. Since co-activation of SOL and TA muscles, which are opposite, positively impacts walking stability, the section where EMG_t is not greater than EMG_s is considered as co-activity, and the torque is not reduced. The

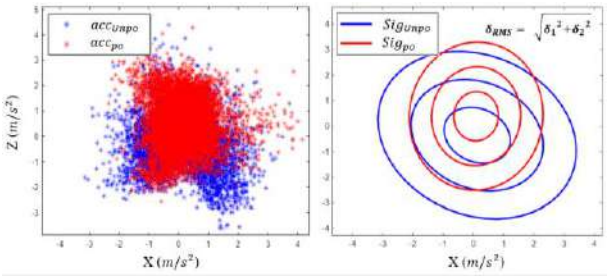


Figure 9. Trunk accelerations was plotted with Gaussian ellipsoid for quantification. The left graph represents the acceleration distribution, while the right one plots the probability circles with standard deviations.

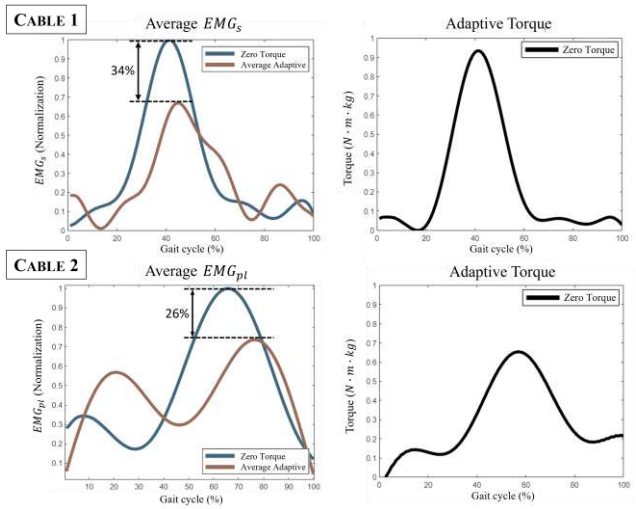


Figure 10. Average EMG profile and average torque profile for the subjects. Different profiles are shown for each of the two cables. The left graph represents the EMG profiles when wearing the exoskeleton in a zero-torque state and after applying the heuristic algorithm. And the right graph shows the torque profile generated after applying the heuristic algorithm.

term $\tau_{cable}(i,n)$ is designed to gradually reduce the influence of previous adjustment patterns on the current torque pattern of the exoskeleton, helping stabilize the system through equilibrium criteria. Finally, a positive term for acceleration along the z-axis is added, as it was found that increased body swaying leads to reduced walking stability, prompting an increase in torque which has threshold at c_{a_z}.

$$\tau_{cable1}(i,n+1) = \tau_{cable1}(i,n) + sgn\big(d\tau_{cable1}(i,n)\big) \cdot \max(|d\tau_{cable1}(i,n)| - d\tau_{db}, 0) \quad (1)$$

$$d\tau_{cable1}(i,n) = k_1 \cdot EMG_s(i+d,n) \cdot \langle EMG_s(n)\rangle^{-m} - k_2 \cdot \max(EMG_t(i+d,n) - EMG_s(i+d,n), 0) - k_3 \cdot \tau_{cable1}(i,n) + k_4 \cdot \max(|\langle a_z(n)\rangle| - c_{a_z}, 0) \quad (2)$$

$$\tau_{cable2}(i,n+1) = \tau_{cable2}(i,n) + sgn\big(d\tau_{cable2}(i,n)\big) \cdot \max(|d\tau_{cable2}(i,n)| - d\tau_{db}, 0) \quad (3)$$

$$d\tau_{cable2}(i,n) = k_5 \cdot EMG_{pl}(i+d,n) \cdot \langle EMG_{pl}(n)\rangle^{-m} - k_6 \cdot \max\big(EMG_t(i+d,n) - EMG_{pl}(i+d,n), 0\big) - k_7 \cdot \tau_{cable2}(i,n) + k_8 \cdot \max(|\langle a_x(n)\rangle| - c_{a_x}, 0) \quad (4)$$

In the case of Cable2, it was designed with the same structure as Cable1, where the muscle to be assisted is the PL, and the antagonistic muscle is the TA, represented by EMG_{pl} and EMG_t, respectively. Additionally, since Cable2 primarily assists with the eversion movement, the acceleration along the x-axis, corresponding to the left and right direction of the body, was applied. At this time, the constant k in the equation was determined experimentally.

V. Experimental Validation

A. Stability Measurements

In this study, stability was assessed using the acceleration values from an IMU sensor attached to the body. The acceleration values along the X-axis and Z-axis were compared using a Gaussian ellipsoid, as shown in Fig. 9. This approach compares the values probabilistically rather than simply using the maximum radius. An ellipse was drawn by calculating the covariance of the two-dimensional acceleration values obtained from the IMU sensor and computing the corresponding eigenvalues. The resulting ellipsoid represents the standard deviation and typically employs the three ratios of Gaussian ellipsoid: 1δ (39%), 2δ (68%), and 3δ (99%). This allows for a quantitatively reliable comparison, and the stability was calculated as the root mean square (δ_{RMS}) of the acceleration values along the X-axis and Z-axis for 1δ. It can be observed that walking stability decreases as δ_{RMS} increases.

B. Experimental Protocol

Three healthy subjects (2 men and 1 woman; 22.7 ± 2.0 yo; 68.3 ± 9.4 kg; 1.75 ± 0.05 m) participated in the experiment. The subjects walked at 0.95 m/s, wearing the brace only on their left leg. Initially, to allow the subjects to become accustomed to the brace, they walked on a treadmill for 5 minutes. Then, adjustment time was provided, and sufficient rest was taken to reduce any effects on the experiment. For the first phase, the PAFO was not powered, and walking data were collected for 5 minutes as a baseline for comparison with the powered condition. Following this, an additional 6 minutes of rest was provided. Afterward, the algorithm interacted with the subjects to create profiles, and the treadmill walking was conducted for 10 minutes. Each subject performed the heuristic-based algorithm three times, with 6 minutes of rest between each trial to minimize fatigue. And this experimental Protocol was approved by the Institutional Review Board of Sejong University. (IRB number: SUIRB-HR-2024-023)

C. Result

EMG values were normalized based on the peak value, and the torque was normalized according to the subjects' body weight. The average data across all subjects was then calculated. As shown in Fig. 10, for cable1, the EMG peak value of the SOL muscle decreased by 34% compared to the previous measurement, and for cable2, the EMG peak value of the PL muscle decreased by 26%. The final torque profiles were then generated, as depicted in Fig. 10.

As a result of calculating the gait stability based on the values measured through the IMU using a Gaussian ellipsoid, the stability data for the three subjects is presented in Table 1. When comparing the stability of each subject before and after applying power to the PAFO, it can be observed that δ_{RMS} decreased. Specifically, the δ_{RMS} decreased by 6%, 21%, and 26%, respectively, with an average decrease of 17%. This confirms that walking stability was impaired.

TABLE I. STABILITY OF THE SUBJECTS BEFORE AND AFTER POWERING TO THE PAFO

Stability		Participants		
		Subject A	***Subject B***	***Subject C***
δ_{RMS}	Pre	1.915	1.545	2.002
	Post	1.789	1.216	1.481

VI. DISCUSSION

This study aims to design and control a 2-*dof* PAFO system and to develop and apply a heuristic-based algorithm to enhance walking stability As a result of the experiment, the performance of design and control was proved, and it was confirmed that walking stability was enhanced.

To address the limitation that exoskeleton robots can only be worn by individuals with a specific shin length, we designed the link to accommodate a wider range of shin lengths. The link is adjustable in three lengths based on body segments corresponding to individuals of 160, 170, and 180 cm in height. As a result of actual trials, individuals with heights within ±3 cm of the target could wear the exoskeleton, and the misalignment between the robot and human joint axes was minimized. However, this design is based on standardized body segment measurements, and individuals of the same height may have different shin lengths, meaning that the link lengths might not be optimal for all users and should be addressed with more precise adjustment of the link length.

In addition, we replaced the actuator from PAM to motor control via cable to achieve a higher cutoff frequency than the existing 2-*dof* PAFO, which was confirmed through experimentation. By plotting the cutoff frequency in two dimensions through a closed-loop frequency response experiment, it was confirmed that cable1 includes the control bandwidth of the PMC from previous studies, and cable2 encompasses the control bandwidth associated with the torque differences between the elderly and the general population. This demonstrated that our driving system has a sufficiently high cutoff frequency to control the PAFO, which is crucial for rehabilitation purposes aimed at improving walking stability. Furthermore, it suggests that the difficulty in implementing mobility with conventional pneumatic actuators can be addressed through cable-driven motor control, which may contribute to future commercialization and mobilization.

Pre-clinical experiments confirmed the possibility that the heuristic-based algorithm developed in this study could improve gait stability of the wearers. Gait stability was assessed by analyzing body sway while walking with the PAFO equipped with the algorithm. Comparing the trunk acceleration values using a Gaussian ellipsoid showed that δ_{RMS} decreased by an average of approximately 17%, confirming the algorithm's positive impact on gait stability.

As a result of applying the heuristic-based algorithm developed in this experiment, it showed that the torque profile evolved and the muscle activity of the target muscle had trends of decrease, as intended. However, in terms of the torque profiles, adapting to the wearer and achieving body balance in each experiment proved challenging, with cases where the torque either continuously increased or increased irregularly. This suggests that errors caused by noise in the EMG sensors and the need for additional terms to improve the algorithm's interaction with the wearer. The algorithm was able to prevent the continuous increase of the torque profile by including a term for the muscle activity of the antagonistic muscle and the previous torque; however, this term had limited effectiveness because the TA muscle activity was not well measured during the experiment. To address this, it would be necessary to incorporate an additional negative term to adjust the torque changes more smoothly. Therefore, future studies could focus on integrating foot kinematics, such as the joint angles.

VII. CONCLUSION

We redesigned the drive system of the 2-dof PAFO for higher cutoff frequencies and developed a heuristic-based control algorithm to improve walking stability and reduce body shaking. However, further research is needed to refine the algorithm and establish a stable steady-state torque profile.

REFERENCES

[1] Tinetti, Mary E., Mark Speechley, and Sandra F. Ginter. "Risk factors for falls among elderly persons living in the community." New England journal of medicine 319.26 (1988): 1701-1707.

[2] Brockett, Claire L., and Graham J. Chapman. "Biomechanics of the ankle." Orthopaedics and trauma 30.3 (2016): 232-238.

[3] A.M. van Leeuwen, "The effect of external lateral stabilization on ankle moment control during steady-state walking," Journal of Biomechanics, Vol 142, September 2022.

[4] K. E. Gordon, D. P. Ferris, "Learning to walk with a robotic ankle exoskeleton", Journal of Biomechanics vol 40, Issue 12, 2007.

[5] Choi, Ho Seon, Chang Hee Lee, and Yoon Su Baek. "Design and validation of a two-degree-of-freedom powered ankle-foot orthosis with two pneumatic artificial muscles." Mechatronics 72 (2020): 102469.

[6] Zhang, Juanjuan, et al. "Human-in-the-loop optimization of exoskeleton assistance during walking." Science 356.6344 (2017): 1280-1284.

[7] J. R. Koller, D. A. Jacobs, D. P. Ferris, and C. D. Remy, "Learning to walk with an adaptive gain proportional myoelectric controller for a robotic ankle exoskeleton," J. Neuroeng. Rehabil., vol. 12, p. 97, Nov. 2015.

[8] Jackson, Rachel W., and Steven H. Collins. "Heuristic-based ankle exoskeleton control for co-adaptive assistance of human locomotion." IEEE transactions on neural systems and rehabilitation engineering 27.10 (2019): 2059-2069.

[9] Park, Se Jin, et al. "Biomechanical parameters on body segments of Korean adults." International Journal of Industrial Ergonomics 23.1-2 (1999): 23-31.

[10] Koller, Jeffrey R., et al. "Learning to walk with an adaptive gain proportional myoelectric controller for a robotic ankle exoskeleton." Journal of Neuroengineering and Rehabilitation 12 (2015): 1-14.

[11] Choi, Ho Seon, and Yoon Su Baek. "Effects of the degree of freedom and assistance characteristics of powered ankle-foot orthoses on gait stability." PloS one 15.11 (2020): e0242000.

[12] Liu, Jian, and Thurmon E. Lockhart. "Comparison of 3D joint moments using local and global inverse dynamics approaches among three different age groups." Gait & posture 23.4 (2006): 480-485.

[13] Svoboda, Zdenek, et al. "Effect of aging on the association between ankle muscle strength and the control of bipedal stance." PLoS One 14.10 (2019): e0223434.

[14] Gutierrez, Gregory M., et al. "Effect of fatigue on neuromuscular function at the ankle." Journal of sport rehabilitation 16.4 (2007): 295-306.

[15] Slade, Patrick, et al. "On human-in-the-loop optimization of human–robot interaction." Nature 633.8031 (2024): 779-788

[16] Korean Council of Professors of Anatomy Physiology, Human Anatomy (3rd Edition) (HardCover). 2012.

Multimodal Sensor System for Continuous Monitoring in Elderly Care: A Pilot Study

Oriella Gnarra[1], Mehdi Ejtehadi[1], Sabrina Amrein[1], Daiki Shimotori[2], Tatsuya Yoshimi[2], Kenji Kato[2], Diego Paez-Granados[1]

***Abstract*—The growing prevalence of chronic health conditions in aging populations highlights the need for innovative solutions in rehabilitation and long-term care. We propose a multimodal system designed to automatically classify Activities of Daily Living (ADLs) and, in the future, support the prevention of secondary health conditions in institutionalized elderly individuals. This system continuously integrates six commercially available wearable and nearable sensors to monitor ADLs over two weeks, ensuring data completeness and maintaining high data quality throughout the trial. In this study, we present pilot data from two residents of a Japanese elderly care facility, demonstrating the proposed system's feasibility and usability. The collected data was comprehensive and robust, with residents showing strong acceptance of the wearable and nearable technologies for long-term use. These findings underscore the potential of multimodal sensory systems to enhance rehabilitation strategies by enabling continuous health monitoring. Integrating ADLs monitoring into rehabilitation programs may facilitate early detection of health changes and support personalized interventions, building on the success of digital health tracking in other clinical domains.**

***Index Terms*—Wearables, Nearables, Data Completeness, Data Quality, Activities of Daily Living**

I. Introduction

The demographic shift towards an aging population creates unprecedented challenges in global healthcare systems. Current projections indicate that the population pyramid will become increasingly concentrated with individuals over 65 within the next five decades [1]. This demographic trend is accompanied by a significant rise in chronic health conditions, including stroke, Parkinson's disease, Alzheimer's disease, and Spinal Cord Injury (SCI). These conditions require long-term, often lifelong, rehabilitation, spanning months to years [2], [3]. Effective management of chronic conditions in an aging society necessitates innovative approaches beyond traditional healthcare models.

Previous research has emphasized predicting morbidities in chronic conditions using data from self-reported surveys and healthcare records [3], [4]. The International Classification of Functioning, Disability, and Health (ICF), established by the World Health Organization (WHO), offers a standardized framework for assessing health and disability in individuals [5]. It provides a holistic approach by evaluating an individual's bodily functions, activities, and participation alongside environmental and personal factors influencing their health. In nursing homes, the ICF is applied through structured assessments conducted by multidisciplinary teams, including physicians, physiotherapists, and occupational therapists. These assessments map ADLs to the ICF framework, enabling tailored interventions to optimize functional health and promote independence among elderly residents [6]. Such frameworks are critical in addressing the complex interplay of aging, chronic conditions, and rehabilitation needs.

While these methodologies provide valuable insights, they have inherent limitations. Self-reported surveys and healthcare records present low-frequency data, which fail to capture dynamic, real-time changes in an individual's physiological or behavioral state. This limitation is particularly critical for individuals with chronic conditions, where early detection of secondary health complications can significantly affect outcomes. Despite its holistic approach, the ICF framework also has limitations. It may not fully capture the subjective experiences of individuals with disabilities, as it focuses on observable functioning. The framework's complexity can make it challenging to implement consistently and objectively across different healthcare settings and professionals. Additionally, the ICF may not adequately capture the temporal aspects of disability, as functioning can fluctuate over time.

In response to these limitations, the field of digital health has emerged, leveraging advanced technologies to facilitate high-frequency data collection and integrating real-world physiological and behavioral metrics into healthcare management [7]. However, tracking health conditions outside controlled environments remains a formidable challenge, especially for populations requiring continuous monitoring [8], such as those with SCI or neurodegenerative diseases [9].

Our collaborative efforts with the Swiss Paraplegic Center in Nottwil, Switzerland, aim to address these challenges by developing digital biomarkers for detecting Secondary Health Conditions (SHCs) in individuals with SCI living in community settings [10]. SHCs, including pressure injuries, cardiovascular diseases, and urinary tract infections, frequently exacerbate existing functional limitations, adversely impacting the quality of life and independence [11]. Monitoring ADLs has proven to be a promising avenue for early detection and progression tracking of SHCs, as changes in ADLs performance often

[1]O. Gnarra, M. Ejtehadi, S. Amrein, and D.Paez-Granados are with Dept. of Health Sciences and Technology, ETH Zurich, 8092 Zurich, Switzerland, and with the Swiss Paraplegic Research (SPF), 6207 Nottwil, Switzerland. {oriella.gnarra, mehdi.ejtehadi, sabrina.amrein, diego.paez}@hest.ethz.ch

[2]D.Shimotori, T. Yoshimi, and K. Kato are with the Laboratory of Clinical Evaluation with Robotics, Assistive Robot Center, National Center for Geriatrics and Gerontology Research Institute, Obu, Aichi, Japan. {d-shimotori, yoshimit, kk0724}@ncgg.go.jp

This research project was supported by the JST Moonshot R&D Program, Grant Number JPMJMS2034.

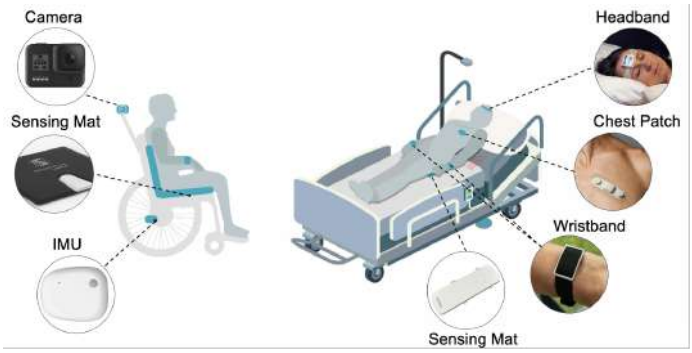


Fig. 1. The multimodal monitoring system comprises three wearables (two wristbands, one chest patch), three nearables (IMU, pressure mat, piezoelectric mat), and two reference systems (video camera, portable EEG).

reflect the onset of health complications [12].

Building on recent advancements in activity monitoring [13], [14], our research has focused on leveraging video-based classification systems and translating these insights into wearable sensor-based monitoring systems for continuous ADLs assessment. Moreover, this approach is not unique to SCI; similar SHCs and activity-based interventions are relevant in other chronic conditions, including stroke, Parkinson's disease, and dementia, which are increasingly prevalent among the elderly population [15].

The Life-logging study, part of the Moonshot program, extends this work by integrating multimodal wearable and nearable sensors into a comprehensive data collection framework for elderly residents in Japanese nursing homes. Our approach includes the future development of algorithms to classify ADLs, map them to the ICF framework, and improve sleep detection through advanced machine-learning techniques. This study aims to contribute to the body of knowledge on managing chronic health conditions and aging populations by providing actionable insights into real-world health monitoring. In this paper, we emphasize the importance of data completeness and quality in longitudinal monitoring, which is critical for reliable ADLs classification, ICF mapping, and sleep detection.

II. Methods

The study was conducted with approval from the National Center of Geriatrics and Gerontology Institutional Review Board (approval number 1692-2023). It involved two male participants aged 73 and 87, both wheelchair users residing in Ai-ko Home Obu, Japan. The first participant had a stroke that affected the mobility of his left, non-dominant (ND) arm; the second participant was diagnosed with Parkinson's disease. Data collection was performed over five consecutive days during two successive weeks, enabling a longitudinal analysis of the participants' ADLs and sleep patterns in a real-world community setting.

A. Sensor System

A multimodal sensor system was employed to capture the participants' physiological data. The system was designed based on prior work in SCI populations, emphasizing user-friendliness, unobtrusiveness, and measurement reliability [7]. The system consisted of three wearable and three nearable sensors, alongside two reference systems, as shown in Tab. I and Fig. 1. Fig. 1 is an updated version of our previously published work [16].

TABLE I
Wearables and Nearables Integrated in the Sensor System.
ECG - Electrocardiography; **PPG** - Photoplethysmography

Sensor	Manufacturer	Modality	Frequency
Headband	HomeSleepTest SOMNOmedics, Germany AG	EEG Acceleration	256 HZ 100 Hz
Chest patch	SDK01 VivaLNK, Campball CA, USA	Acceleration ECG Heart Rate Respiration Rate	5 Hz 128 Hz 1 Hz 1 Hz
Wristband	CardioWatch 287-2 Corsano Health In., Cambridge MA, USA	Acceleration Bioimpedance Emography PPG Respiration Rate	32 Hz 32Hz 1/minute 128 Hz 1 Hz
Piezoelectric Mat	Nemuri SCAN Paramount, Japan	Sleep Stages Activity Respiration Rate Heart Rate	1/minute
IMU	MMS+ Mbient MbientLab Inc, San Francisco, USA	Acceleration Angular Velocity	50 Hz 50 Hz 2000°/s
Pressure Mat	Sensomative, Rothenburg, Switzerland	Pressure Distribution	20Hz
Videocamera	Hero 9 Black GoPro Inc., San Mateo CA, USA	Video	24 Fps

The wearable sensors included two wristbands, one per wrist, for monitoring physiological data such as acceleration, bioimpedance, heart rate, and respiratory rate, and one chest patch for capturing cardiac and respiratory parameters. The nearable sensors included a pressure mat placed on the wheelchair seat to measure pressure distribution, a Inertial Measurement Unit (IMU) mounted on the wheelchair right wheel to track mobility dynamics, and a piezoelectric mat positioned on the bed to assess sleep-related metrics. The reference systems included a video camera, used to record participant activities and serve as ground truth for ADLs classification, and a Electroencephalography (EEG) headband, which provided high-fidelity sleep stage recordings.

This multimodal system was carefully selected to balance comprehensive data collection with participant comfort.

B. Study Protocol

The study protocol comprised three phases: synchronization, training, and longitudinal data collection.

During the synchronization phase, a standardized movement was performed at the beginning and end of each week to ensure accurate alignment of multi-modal sensor data. This

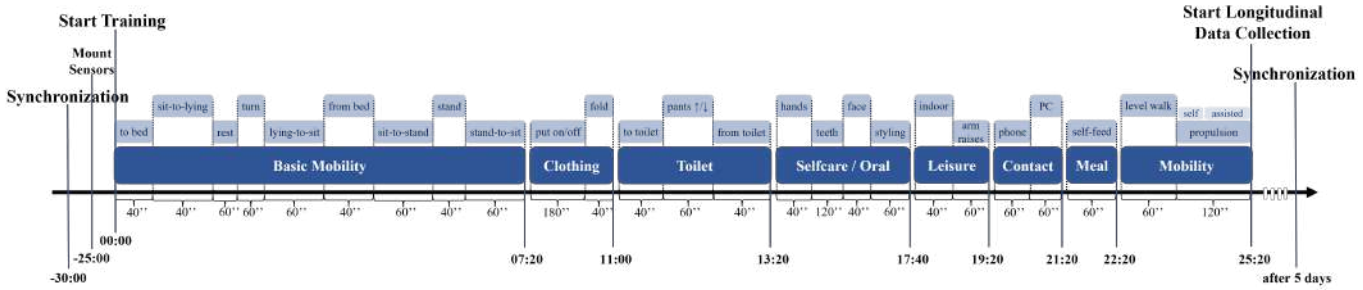


Fig. 2. The study protocol starts with the system time synchronization, followed by the training phase where ADLs are performed, ending with longitudinal data collection and end of synchronization.

movement created patterns across acceleration and pressure signals across all sensors, facilitating precise post-processing synchronization.

In the training phase, participants performed a predefined set of ADLs under the supervision of a researcher. The activities were derived from the ICF core set for SCI [17] and adapted for the elderly population in collaboration with clinical experts. As shown in Fig. 2, the activities were divided into basic mobility (turning in bed, lying to sit, transferring to bed, sitting to stand), grooming (clothing, toileting, self-caring), social activities (leisure and communication or contacts), self-feeding and other mobilities like self or assisted propulsion and level walking. The researcher logged each activity's start and end times using a custom mobile application while the camera recorded video data for validation. This phase lasted approximately 30 minutes. The video camera was removed after the training to minimize intrusiveness.

Participants continued their daily routines during the longitudinal data collection phase while wearable and nearable sensors collected continuous data. This phase extended over five days per week across two consecutive weeks.

C. Data Pipeline

The data pipeline was developed to manage the acquisition, transmission, and processing of multimodal sensor data, as shown in Fig. 3. Most sensors transmit data directly to a smartphone mounted on the wheelchair's backrest. For certain sensors, data was uploaded to the cloud before being relayed to a centralized server, while others routed data through our custom-made mobile application. Efforts are ongoing to standardize and automate this transmission process across all devices. Sensor data was parsed into a unified format and stored in a secure, study-specific database. This pipeline ensured robust data acquisition and storage, supporting the development of advanced algorithms for ADLs classification and sleep stage detection.

D. Data Preprocessing and Feature Extraction

We first filtered the time-series data using a second-order, low-pass Butterworth filter, applying a 3 Hz cut-off to preserve frequency components relevant to human motion activities. We then segmented each signal with a 5-second sliding window and a step size of 0.5 seconds. From each window, we extracted a broad range of time-domain features—including basic statistics (mean, standard deviation, range), amplitude metrics (avarage (avg) amplitude change, magnitude area), energy/entropy measures (logarithm (log) of energy, singular value decomposition (svd) entropy), and fractal descriptors (Higuchi fractal dimension)—alongside frequency-domain features computed via Fast Fourier Transform (FFT) and Welch's method (spectral absolute (abs) deviation order 1, spectral bandwidth order 3, spectral coefficient of variability (var), spectrum log slope, and band-limited power). These features were obtained using the TIFEX-Py toolbox [18]. Subsequently, the extracted features and their corresponding activity labels (level walking vs. assisted propulsion) were evaluated through one-way ANOVA for feature ranking. The resulting F-values were employed to quantify how effectively each feature discriminated between the two activities. In particular, a high F-value indicates that the between-group variance (i.e., the difference across activity labels) substantially exceeds the within-group variance, making that feature a strong candidate for distinguishing between the classes.

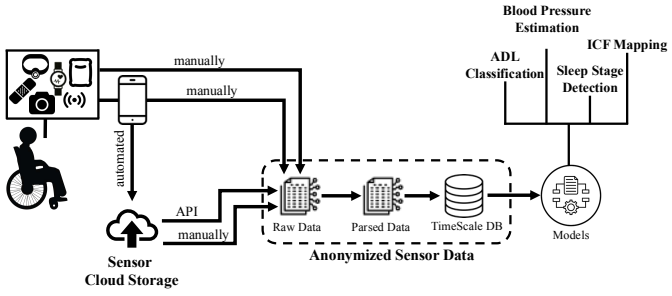


Fig. 3. Data collected by the wearables and nearables are transmitted to the server and parsed for analysis.

E. From ICF to the R4 scale system

The ICF, standardized by the WHO, provides a comprehensive taxonomy to describe functioning and disabilities related to health conditions; however, its practical application is limited by the complexity of its classification system, which includes over 1,400 codes. The Japan Association of Geriatric

Health Services Facilities (Roken Facilities) developed the R4 system as a structured care management system. It is divided into four stages: Assessment (R1): Conducting a multifaceted evaluation of the user's needs and daily functions; Care Plan Development (R2): Formulating individualized care plans based on assessment results; Implementation and Verification of Care Plan (R3): Delivering services in line with the care plan and confirming their execution; Monitoring and Change Evaluation (R4): Regularly monitoring changes in the user's condition and adjusting the care plan as necessary. This process enables an objective understanding of the user's condition, facilitating the provision of appropriate care. Okochi et al. [19] developed two scales to stage mobility and walking functions in elderly individuals based on the ICF codes. To address this issue, the authors selected 33 ICF codes related to mobility, transfer, and walking. They analyzed them using the Rasch model [20] to identify items suitable for a Guttman-type scale, which organizes items hierarchically by difficulty. Two scales were constructed: a *basic mobility* scale and a *walking* scale, each comprising four ICF codes. The scales classify functional performance into five stages, enabling rapid and standardized assessments. Validation demonstrated their applicability across settings, such as nursing homes and day-care centers, without significant differences in sex, age, or study location. The R4 System is designed for all professionals working in Roken facilities, including doctors, nurses, caregivers, rehabilitation specialists, and nutritionists. By tracking user condition changes, the system reflects the ideal state of Roken facilities, contributing to high-quality care.

III. Results

A. Data Completeness

Data completeness was assessed for all sensor modalities, participants, and weeks of recording to evaluate the reliability and feasibility of the multimodal monitoring system in a real-world nursing home environment. Results revealed variation in data completeness across different sensors and participants, with several factors influencing sensor performance, including device misplacement, battery life, and user adherence.

For the first participant during the first week, the chest patch reports 50% of data completeness, with missing data attributed to improper placement or detachment during daily activities. The right (dominant (D)) wristband achieved 97% completeness across all measured modalities, with 3% of data missing due to the daily charging period (approximately 30 minutes per day). In contrast, the left (non-dominant) wristband exhibited a lower completeness rate of 75%, with the final day of recording missing entirely. Only three out of four nights of sleep data were successfully captured. The piezoelectric mat achieved 100% data completeness, demonstrating the robustness and reliability of stationary nearable sensors. The IMU recorded 47% completeness, with significant data loss due to insufficient initial battery charge. The pressure mat reported 99% data completeness, indicating high reliability in pressure distribution measurement during seated activities.

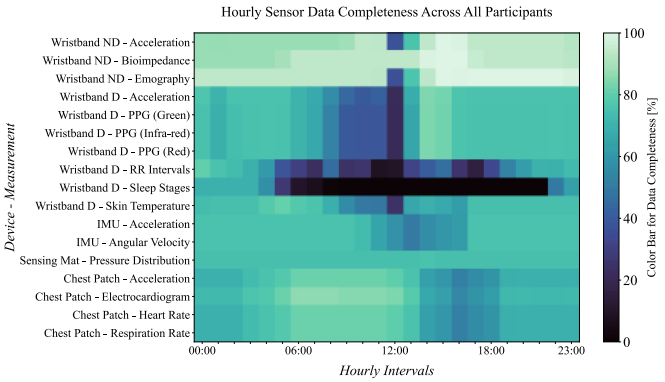


Fig. 4. The heatmap represents data completeness across modalities and participants.

In the second week, the chest patch improved performance with 95% data completeness, suggesting better device placement or participant adaptation over time. Both wristbands performed comparable to the first week, with the right (dominant) wristband achieving 95% completeness and the left (non-dominant) wristband achieving 65%. Extended charging periods accounted for the missing data in the wristband on the non-dominant arm. The piezoelectric mat maintained 100% completeness, reinforcing its reliability across recording periods. The IMU improved to 94%, indicating adjustments in the protocol, such as better initial battery preparation. The pressure mat consistently reported 99% completeness.

For the second participant during the first week, the chest patch demonstrated moderate performance with 55% completeness, similar to the first participant in the first week. The dominant wristband achieved 83% completeness, while the left wristband showed lower reliability at 55%, with only two out of four nights of sleep data successfully captured. The piezoelectric mat retained 100% data completeness, underscoring the value of non-contact sensing for sleep and activity monitoring. The IMU fell below 50%, primarily due to battery life constraints during extended use. The pressure mat maintained high performance with 99% completeness.

In the second week, the chest patch improved to 85% completeness, paralleling trends observed in the first participant. The wristband on the dominant arm achieved 80% completeness, while the wristband on the non-dominant side recorded 68%, with occasional charging issues impacting data continuity. Notably, the left wristband missed the third night of recording. The piezoelectric mat retained 100% completeness, further validating its robustness. The IMU improved significantly to 94%, reflecting protocol adjustments. The pressure mat consistently reported 99% completeness.

Across all recording sessions, the chest patch showed an average completeness of 52%. The right wristband achieved 88.75%, while the left wristband recorded 65.75%. The piezoelectric mat achieved 100%, the IMU reached 71.25%, and the pressure mat maintained high reliability at 99%. These results are visualized in a heatmap (Fig. 4). The heatmap

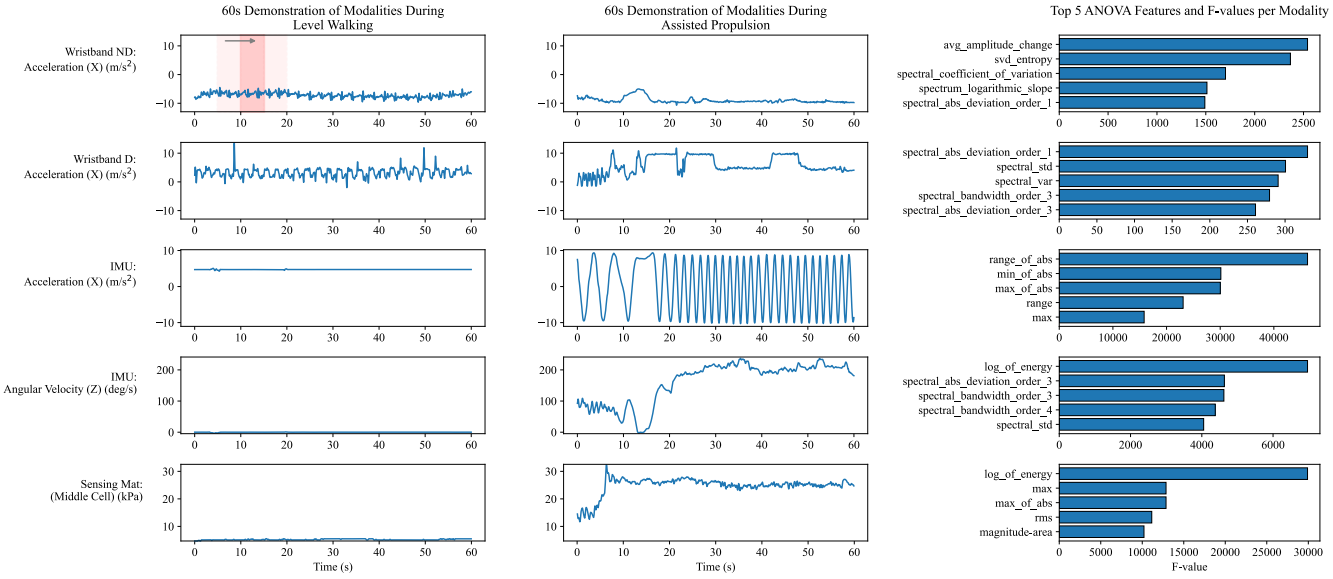


Fig. 5. On the left, selected sensor modalities show different signal patterns according to the performed activities. On the right are the five most discriminative extracted features.

reveals distinct patterns, such as the expected absence of sleep modality data during daytime hours. Devices requiring daily charging, such as wristbands, exhibited predictable data interruptions, typically occurring around 12:00 PM. Notably, some modalities, such as bioimpedance, continued to record intermittent data even when the sensor was not actively worn.

B. Data Quality

Data quality was evaluated by visualizing sensor outputs during the training protocol and inspecting signal integrity across 2 key activities. Figure 5 presents 60-second windows from multiple sensor modalities: wristband accelerometers (X-axis), the IMU on the wheel (X-axis acceleration and angular velocity), and the sensing mat (central pressure cell), during two activities: level walking and assisted propulsion and the top five discriminative features. All modalities were synchronized within each activity.

This figure aims to demonstrate the distinctive characteristics of the sensor modalities for these activities. The top discriminative features collectively capture the signals' amplitude distribution, variability, and frequency content.

Notably, during level walking, the wrist accelerometers show the repetitive hand movements that distinguish the activity, while the periodicity is lacking during self-propulsion. For the wheel IMU, acceleration data indicate wheel rotation, and the gyroscope's Z-axis (normal to the wheel) confirms angular velocity during propulsion, which is absent during level walking when the wheelchair is stationary. Finally, the pressure mat data show zero values during level walking, indicating the wheelchair is unoccupied, while non-zero values during propulsion confirm the participant's presence.

These visual differences, supported by extracted features, highlight the discriminatory power of the sensor modalities for classifying ADLs. This visualization is intended as an illustrative example and is not exhaustive.

C. R4 Scoring

The R4 mapping system, commonly used in Japanese long-term care health facilities, is designed following the ICF and is characterized by its ability to stage and assess individuals' activity and participation levels. Trained staff in the nursing home assigned scores based on observed performance across standardized tasks (Fig. 6). The first participant (Subj_A) scored 2/5 in "Walking", reflecting dependence on a wheelchair with the ability to take a few assisted steps. This participant scored 5/5 for dressing and undressing ("put on/off"), demonstrating full independence in these tasks. The second participant (Subj_B) also scored 2/5 in "Walking" but received a slightly lower score of 4/5 for "put on/off", indicating occasional need for assistance. The R4 scores provided a valuable framework for correlating sensor data with functional outcomes, enabling a deeper understanding of participant capabilities and limitations.

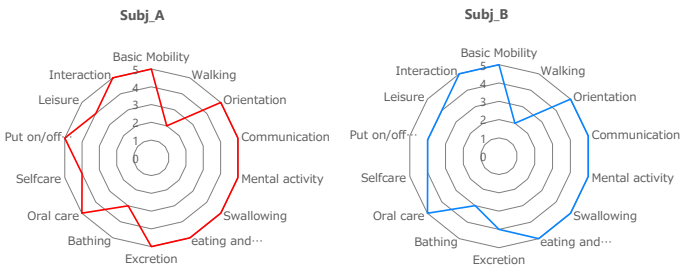


Fig. 6. R4 scoring results for two participants, highlighting differences in functional independence.

IV. Discussion

This study highlights the feasibility of utilizing a multimodal wearable and nearable sensor system for longitudinal monitoring in a nursing home environment. The observed data completeness across sensors demonstrates the practicality of the system, with specific sensors, such as the piezoelectric mat and pressure mat, achieving near-perfect data capture. This underscores the reliability of stationary sensors for continuous monitoring, while wearable sensors showed high variability influenced by device placement, user adherence, and charging requirements. Notably, the system's unobtrusive design and high acceptance among participants align with the broader goal of integrating seamless monitoring solutions in real-world settings.

The findings also emphasize the need for a larger dataset to address the limitations posed by the small sample size in this pilot study. Ongoing efforts to collect data from additional residents will enhance the robustness of our findings, enabling more comprehensive analyses. Specifically, future work will focus on developing machine learning algorithms for automatically classifying ADLs mapped to the ICF. This approach will facilitate objective and standardized assessments of functional health, which are critical for evaluating rehabilitation outcomes.

In parallel, improvements to sleep stage classification algorithms will be pursued, leveraging transfer learning techniques to enhance accuracy and adaptability across diverse populations. By refining these models, we aim to extend the system's applicability to broader use cases, including the early detection and management of SHCs. Ultimately, this work represents a significant step towards integrating multimodal sensing technologies in personalized rehabilitation strategies, addressing the complex needs of aging and chronically ill populations.

Acknowledgment

We thank the National Center for Geriatrics and Gerontology team for their support in the data collection, the Japanese Society for Promotion of Science (JSPS), and the Japan Science and Technology Agency (JST) Moonshot for their financial support in performing the study. We thank the nurses and the residents at the Ai-ko nursing home in Obu, Japan, for participating in the data collection.

References

[1] M. Roser. (2024, Jul.) The global population pyramid: How global demography has changed and what we can expect for the 21st century. [Online]. Available: https://ourworldindata.org/global-population-pyramid

[2] M. French, R. T. Roemmich, K. Daley, M. Beier, S. Penttinen, P. Raghavan, P. Searson, S. Wegener, and P. Celnik, "Precision rehabilitation: Optimizing function, adding value to health care," *Arch. Phys. Med. Rehabil*, vol. 103, p. 1233–1239, 2022.

[3] G. I. Correa, M. Fuentes, X. Gonzalez, F. Cumsille, J. L. Piñeros, and J. Finkelstein, "Predictive factors for pressure ulcers in the ambulatory stage of spinal cord injury patients," *Spinal Cord*, vol. 44, pp. 734–739, 2006.

[4] A. Tarekegn, F. Ricceri, G. Costa, E. Ferracin, and M. Giacobini, "Predictive modeling for frailty conditions in elderly people: Machine learning approaches," *JMIR Med. Inform.*, vol. 8, p. e16678, 2020.

[5] S. Mishra, E. S. Rotarou, C. B. Peterson, D. Sakellariou, and N. A. Muscat, "The who european framework for action to achieve the highest attainable standard of health for persons with disabilities 2022–2030," *The Lancet Regional Health - Europe*, vol. 25, p. 100555, 2023. [Online]. Available: https://www.sciencedirect.com/science/article/pii/S2666776222002514

[6] E. Huber, A. Tobler, T. Gloor, E. Grill, and B. Gut, "The icf as a way to specify goals and to assess the outcome of physiotherapeutic interventions in the acute hospital." *Journal of Rehabilitation Medicine*, vol. 43, no. 2, p. 174–177, Oct. 2010.

[7] J. S. Marwaha, A. B. Landman, G. A. Brat, T. Dunn, and W. J. Gordon, "Deploying digital health tools within large, complex health systems: key considerations for adoption and implementation," *Npj Digit. Med.*, vol. 5, p. 13, 2022.

[8] O. Gnarra, J. van der Meer, J. D. Warncke, L. G. Fregolente, E. Wenz, K. Zub, U. Nwachukwu, Z. Zhang, R. Khatami, S. von Manitius, S. Miano, J. Acker, M. Strub, R. Riener, C. L. A. Bassetti, and M. H. Schmidt, "The swiss primary hypersomnolence and narcolepsy cohort study: feasibility of long-term monitoring with fitbit smartwatches in central disorders of hypersomnolence and extraction of digital biomarkers in narcolepsy," *Sleep*, vol. 47, no. 9, p. zsae083, 03 2024. [Online]. Available: https://doi.org/10.1093/sleep/zsae083

[9] P. Daniore, V. Nittas, C. Haag, J. Berard, R. Gonzenbach, and V. von Wyl, "From wearable sensor data to digital biomarker development: ten lessons learned and a framework proposal," *NPJ digital medicine*, vol. 7(1), p. 161, 2024.

[10] S. Bensland, A. Paul, L. Grossmann, I. E. Hoogland, R. Riener, and D. Paez-Granados, "Healthcare monitoring for sci individuals: Learning activities of daily living through a slowfast neural network," *IEEE/SICE International Symposium on System Integration (SII), Atlanta, GA, USA*, pp. 1–7, 2023.

[11] Y. Cao, D. Murday, E. H. Corley, N. D. DiPiro, and J. S. Krause, "Rehospitalization during the first 5 years after the onset of traumatic spinal cord injury: A population-based study using administrative billing records," *Arch Phys Med Rehabil*, vol. 103, no. 7, pp. 1263–1268, 2022. [Online]. Available: https://www.ncbi.nlm.nih.gov/pubmed/35218708

[12] J. A. Piatt, S. Nagata, M. Zahl, J. Li, and J. P. Rosenbluth, "Problematic secondary health conditions among adults with spinal cord injury and its impact on social participation and daily life," *J Spinal Cord Med*, vol. 39, no. 6, pp. 693–698, 2016. [Online]. Available: https://www.ncbi.nlm.nih.gov/pubmed/26833021

[13] M. Ejtehadi, S. Amrein, I. E. Hoogland, R. Riener, and D. Paez-Granados, "Learning activities of daily living from unobtrusive multimodal wearables: Towards monitoring outpatient rehabilitation," *Int. Conf. Rehabil. Robot. ICORR*, pp. 1–6, 2023.

[14] J. Bickenbach, S. Rubinelli, C. Baffone, and G. Stucki, "The human functioning revolution: implications for health systems and sciences," *Front. Sci.*, vol. 1, p. 1118512, 2023.

[15] J. Okochi, T. Takahashi, K. Takamuku, and R. Escorpizo, "Staging of mobility, transfer and walking functions of elderly persons based on the codes of the international classification of functioning, disability and health," *BMC Geriatr.*, vol. 13, p. 16, 2013.

[16] O. Gnarra, S. Amrein, M. Ejtehadi, T. Yoshimi, K. Kato, and D. Paez-Granados, "Wearables in long-term monitoring for chronic conditions: Learning adls for elderly care," in *Converging Clinical and Engineering Research on Neurorehabilitation V*, J. L. Pons, J. Tornero, and M. Akay, Eds. Cham: Springer Nature Switzerland, 2024, pp. 476–480.

[17] I. Kirchberger, A. Cieza, F. Biering-Sørensen, M. Baumberger, S. Charlifue, M. W. Post, R. Campbell, A. Kovindha, H. Ring, A. Sinnott, N. Kostanjsek, and G. Stucki, "Icf core sets for individuals with spinal cord injury in the early post-acute context," *Spinal Cord*, 2009.

[18] M. Ejtehadi, G. E. Graham, C. Ringstrom, E. Du, R. Riener, and D. Paez-Granados, "Tifex-py: Time-series feature extraction for python in a human activity recognition scenario," in Proceedings of the International Consortium for Rehabilitation Robotics (ICORR), Chicago, USA, May 12–16, 2025, accepted.

[19] J. Okochi, T. Takahashi, K. Takamuku, and R. Escorpizo, "Staging of mobility, transfer and walking functions of elderly persons based on the codes of the international classification of functioning, disability and health," *BMC Geriatrics*, vol. 13, 2013.

[20] D. K. Luigi Tesio, Antonio Caronni and S. Scarano, "Interpreting results from rasch analysis 1. the "most likely" measures coming from the model," *Disability and Rehabilitation*, vol. 46, no. 3, pp. 591–603, 2024, pMID: 36740739.

Measuring Muscle Activation with the HRX-1 Wrist Manipulation Robot

Joshua Brown[1,7], Aaron Yurkewich[2,7], Maryam Zardbani[3], Lucille Cazenave[4,5], Etienne Burdet[4,7], Ildar Farkhatdinov[6,7]

***Abstract*— A portable robotic system, such as the HRX-1 robot designed for neuromechanics and rehabilitation research, enables motor assessment and training across diverse settings including clinics, laboratories, and home environments. This study presents the findings of wrist muscle activation measurements conducted using the HRX-1 robot in conjunction with surface electromyography (sEMG) electrodes on a cohort of fifteen healthy participants. Participants were seated and instructed to resist and maintain wrist flexion and extension against torques applied to their hand by the robot. Muscle activation data were recorded using two 32-channel high-density surface EMG electrodes placed on the forearm to capture activity from the flexor and extensor muscle groups. The analysis focuses on identifying the number of active regions within the recorded muscle activations under each experimental condition. As expected, flexor muscles were most active during wrist flexion and extensor muscles were most active during wrist extension. There was also no statistically significant change in the number of muscle regions active when torque was increased in each configuration.**



Fig. 1: The prototype 1-DoF joint manipulation robot

I. Introduction

A key effect of musculoskeletal (MSK) trauma and neurological illness is the loss of reliable upper limb function which can have a devastating impact on patients' quality of life. Grasping and manipulating everyday objects is made much more difficult by low muscle power, tremors, spasticity, unilateral weakness and low range of movement. Approximately 5% of the global population experience lasting loss of upper limb function due to stroke [1], while the prevalence of Parkinson's disease, which increases with age, reaches up to 4.8% in those aged 80 or over [2]. Alongside these serious and prevalent conditions, waiting times for physical therapy are increasing in many major healthcare systems [3] due to increasing patient numbers [4] and reduced gatekeeping via primary care [5], [6], whilst early intensive interventions remain essential to enhancing patient outcomes [7], [8].

Robot-assisted rehabilitation has long been proposed as a solution to many of these challenges [9]. Robots can apply forces and torques to resist and assist users, taking the physical role of a therapist, whilst guiding a patient through exercises either autonomously [10], [11] or under the remote control of a therapist [12], [13]. The ability to provide physical therapy without the need for a therapist to be present allows therapy to take place in non-clinical settings such as patients' homes, driving improved patient engagement [14] and increasing access in remote locations such as low- and middle-income countries that often do not have extensive networks of physical therapists or rehabilitation clinics [15].

Robots used in rehabilitation may take many forms, but have some common requirements in terms of power delivery (at least as much force/torque output as their intended user requires), haptic transparency (reduced friction/inertia when not driven, allowing the user to move freely) and ergonomics (must be comfortable to use, matching the user's biomechanics, range of movement and degrees of freedom). Many rehabilitation robots exist as research prototypes and are targeted at specific joints/body parts and specific conditions. For example, MIT's Skywalker robotic treadmill [16] and Imperial College's Hi5 dual-wrist robot [17] are both high cost, high performance room-scale research setups - ideal for scientific exploration of neuromechanics and robotic rehabil-

[1]Department of Surgery & Cancer, Imperial College of Science, Technology and Medicine, London, UK joshua.brown@imperial.ac.uk

[2]Department of Automotive & Mechatronics Engineering, Ontario, Canada aaron.yurkewich@ontariotechu.ca

[3]School of Engineering and Materials Science, Queen Mary University of London, London, UK

[4]Department of Bioengineering, Imperial College of Science, Technology and Medicine, London, UK e.burdet@imperial.ac.uk

[5]AI for Healthcare Centre for Doctoral Training, Department of Bioengineering, Imperial College of Science, Technology and Medicine, London, UK lucille.cazenave16@imperial.ac.uk.

[6]School of Biomedical Engineering and Imaging Sciences, King's College London, London, UK. ildar.farkhatdinov@kcl.ac.uk

[7]Human Robotix Ltd., London, UK

Declaration of conflict of interest: I. Farkhatdinov, J. Brown, E. Burdet and A. Yurkewich are co-founders of Human Robotix Ltd

L. Cazenave and E. Burdet were supported in part by the UKRI CDT in AI for Healthcare EP/S023283/1 and the EC H2020 project ReHyb (ICT 871767).

itation strategies, but not at all suitable for quick clinical or research deployment due to their design, mechanical structure and dimensions. More portable and light weight robotic solutions are required for faster and efficient preparation of neuromechanical and motor rehabilitation research. Desktop-scaled hand exercisers can resist the movement of the wrist and fingers [18]; however, the intricate mechanisms required to apply different forces and movements to different fingers would be difficult to maintain in real-world use.

Using interactive robots for physical therapy also raises the possibility of connecting the robot's sensors (i.e. user movement data) to computer games to promote engagement and reduce nonadherence, a serious limitation of traditional physical therapy [19]. This gamified rehabilitation has been demonstrated extensively with stroke patients, and a variety of upper limb exoskeletons [20], resistance machines [21] but also in contexts such as paediatric cerebral palsy [22] and recovery from hand injuries [23].

This paper presents the application of a portable lightweight HRX-1 robot for applying torques to the wrists of healthy human-participants, allowing biosignals such as muscle activation to be measured and studied. The HRX-1 robot's primary function is to generate controlled wrist flexion/extension torque, however compared to other similar devices [17], [24], [25], HRX-1 robot's key advantage is portability and compact design which enables fast integration, easy transportation and deployment. This paper presents the results of muscle activation from fifteen healthy participants which used the HRX-1 robot for wrist flexion and extension tasks. Surface electromyography recordings were analysed to identify number of muscle activation regions.

II. HRX-1 ROBOT DESIGN

There is clearly a need for a high-performance, portable, easily adaptable haptic robot that can be used in a variety of different rehabilitation and research contexts. A 1-DoF torque feedback robot has been designed based on Imperial College's Hi5 wrist manipulation robot [17]. This offers high torque, position and torque sensing and a variety of control modes in a compact robotic platform, whilst also being modifiable to work with a number of other joints. The HRX-1 robot measures approximately $280\times200\times115$ mm when collapsed for transportation, and weighs approximately 4 kg.

The below describes the design and construction of such a robot that can be used in many different scenarios.

A. Mechanical Design of HRX-1 robot

The key requirement of a portable, modular joint manipulation robot is the ability to exert strong, comfortable, measurable and controllable torques on specific joints, while maintaining high backdrivability. To achieve output torques that can be useful in human movement research, the robot is directly driven by the 600W Maxon EC90 series brushless direct current motor. Torque exerted against the robot by the user is measured with a Transducer Techniques TRT-100 torque sensor mounted on a flanged coupling to the motor shaft. This coupling has a large eccentric protrusion shaped

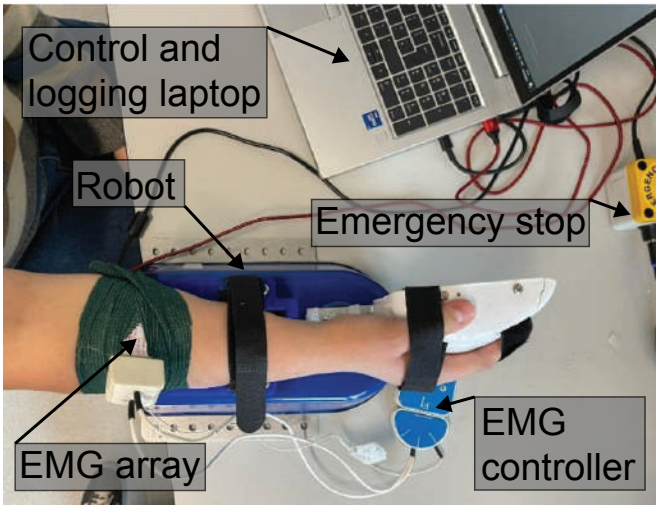


Fig. 2: The experiment setup used to capture s-EMG data of participants using the joint manipulation robot

to interfere with two endstop screws located on a circle around the motor shaft, which can be adjusted depending on the desired range of motion. The handle is mounted to the top side of the torque sensor such that the sensor measures the torque difference between the motor shaft and handle. The handle consists of a thin aluminium frame, ergonomically shaped plastic hand rest (designed for an open palm as this shape is known to minimise contraction in the forearm) and velcro straps to ensure good contact during abduction. The handle is shaped such that for an average-sized hand, the wrist joint will align with the axis of the motor which is essential for safe and comfortable transfer of torque. An arm rest with 8, 80 mm spaced stages of adjustment is mounted on the top of the robot in line with the handle, with more velcro straps to constrain the forearm position and ensure that only the wrist joint is able to move and exert torque against the motor. The robot's key ergonomic features are highlighted in Figure 1.

The need for a portable robot raises the competing goals of low weight and durability. Mechanically, the robot has a steel and aluminium skeleton which secures all load-bearing components, minimizing weight (a low volume of metal overall) whilst maximising rigidity and robustness. This consists of a lower plate to which the motor controller and drive circuit are mounted, and an upper plate which secures the motor and mainboard. Two socket head screws with plastic bumpers are screwed into this top plate, providing range of motion limits that can be adjusted for different users, joints or tasks. Steel supports above the second plate secure a thin, durable plastic cover and the arm rest. This ensures that there is a rigid metal support for the arm, allowing the robot to easily take its weight and keep it in a fixed position relative to the motor.

B. Electronic Configuration

The robot's motion is controlled by a Maxon EPOS4 70/15 controller which offers closed-loop position, velocity and

current control, the latter being most useful and most common in rehabilitation, neuromechanics and pHRI (physical human-robot interaction) use cases. The torque sensor output is calibrated and amplified with a Mantracourt ICA2H signal amplifier. This is delivered to the general-purpose analog/digital input/output ports on the controller which can be read by PC-based software, and exposed to other electronic devices/dataloggers via an I/O connector on the back of the robot.

The motor/handle position is read by a Maxon 6400 cpt (counts per turn) encoder which is fixed to the top of the motor. This is again wired to the motor controller and exposed to custom controllers and other hardware via I/O. The robot connects to a computer over USB and is powered by a standard 19.5 V laptop power adapter, both connected to ports on the back of the robot. The power supply can optionally be routed through an emergency stop button which will open the power supply circuit and disengage the motor in the event of a problem.

C. Software Integration and Control System

By default, the robot's onboard motor controller can receive torque output commands from either Maxon's C++ SDK or the EPOS4MATLAB wrapper, allowing the robot to be easily integrated with MATLAB's other scientific computing tools and supported data acquisition hardware. The robot's onboard torque sensor and encoder can also be read in this way, allowing the user's exertion on the handle and joint position to be measured and logged or used in interactive applications. Either method runs over a USB connection to a computer at up to 500 Hz which is sufficient for applications where, for example, the robot needs to produce pre-defined torque curves or impulses, which are common in neuromotor rehabilitation exercises.

III. Electromyography Evaluation of Wrist HRX-1 Robot

To evaluate the robot's ability to exert controllable torque on joints, a user study was performed using surface EMG to measure muscle activation in participants trying to resist the robot's manipulation. Fifteen adult participants were recruited to take part in this study (male and female, ages 20-35). Two participants were left-handed. None self-reported any neurological or musculoskeletal impairment. All participants gave informed consent prior to taking part. The study received ethical approval from the Imperial College Research Ethics Committee with certificate number 21IC6935.

A. Setup

The prototype force feedback robot was placed on a standard-height work desk in front of and to the right of the participant. It was connected to a laptop computer running Windows 10 and MATLAB over USB. Two 32-channel HD surface EMG electrodes (GR10MM0804e electrodes, Sessantaquattro acquisition system, OT Bioelettronica) were attached to the participant's forearm to record flexor and extensor muscle group activation at 2 kHz. The participant's forearm was strapped to the arm rest of the robot, and their hand strapped to the open palm handle. The experiment setup is shown in Figure 2.

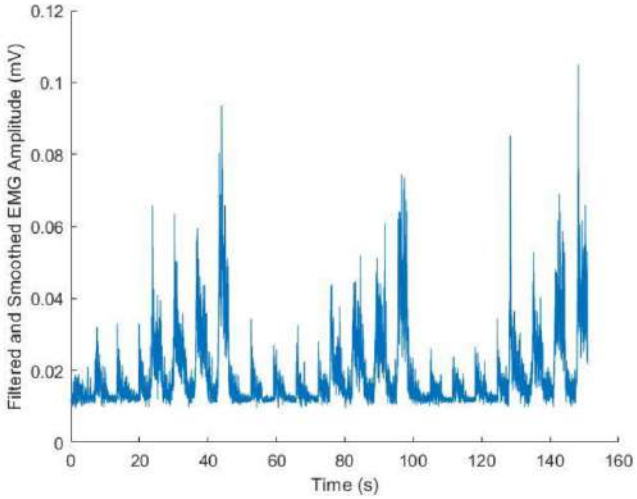


Fig. 3: Sample participant data showing an increasing EMG amplitude during wrist manipulation target tracking tasks at increasing resistance levels

B. Procedure

The initial calibration consisted of three repeats of wrist extension and flexion at a fixed angle of 30° while resisting an increasing torque at four different levels: 0.4 Nm, 0.8 Nm, 1.2 Nm, 1.6 Nm. Each repeat starts off by flexion exercises, holding at each torque level for 3.5 s with 3 s of relaxation between trials to prevent fatigue. After flexion at the highest resistive torque level, the extension trials start (no rest when switching from flexion to extension). Again, wrist extensions are held for 3.5 s at each increasing torque level with 3 s of rest between trials. The rest period is increased to 6.5 s between repeated blocks of trials.

C. Signal Processing and Data Preparation

All data processing has been done in MATLAB. First, a high-pass filter with a passband frequency of 5 Hz is applied on the raw EMG data. Then, outliers are eliminated using a Hampel filter where data points more than two standard deviations away from the local median within a window size of seven are replaced by that local median. At this stage, an envelope filter is applied using the root-mean-square method with a sliding window of 101 data points. The upper envelope signal is what is used for all further investigations. The data was sectioned into trials, separating each trial of each repeat at each torque level and wrist movement. Regional maxima are found by averaging the EMG amplitude recorded by each channel in each of these trials. Heatmaps were created by smoothing and interpolating the data using MATLAB's imresize and imshow commands. The regions corresponding to the top 25% mean EMG amplitude in each case were considered as the number of active regions for that trial.

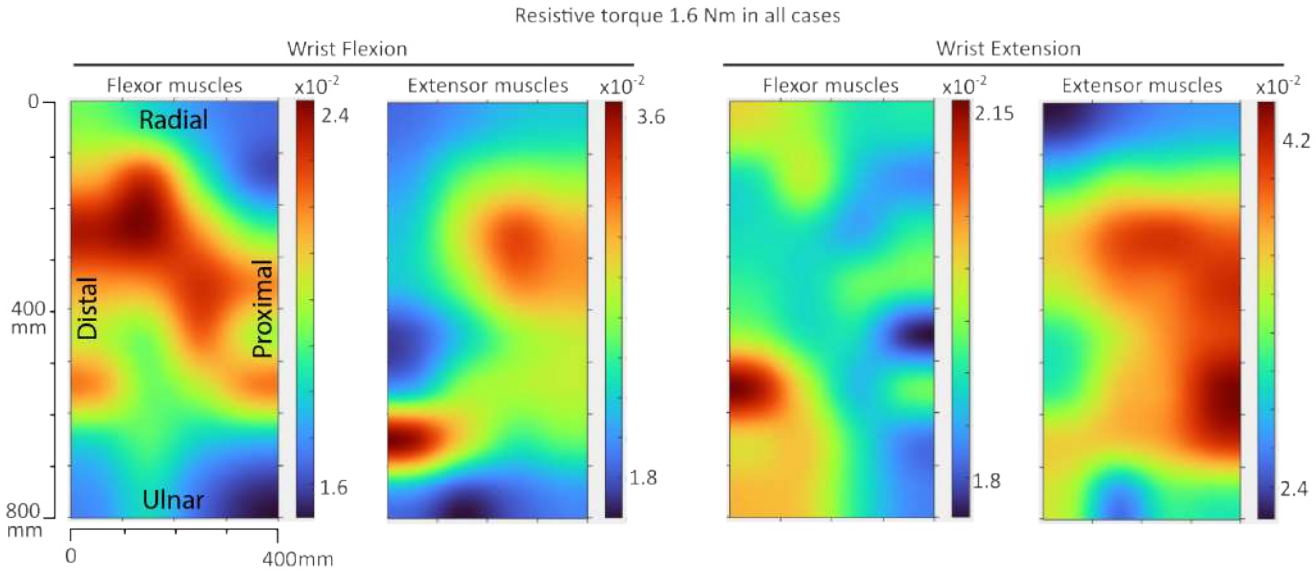


Fig. 4: EMG array heatmaps from electrode arrays positioned across the dorsal (extensor) and ventral (flexor) side of the forearm during wrist flexion and extension tasks

D. Results

Each participant's EMG signal for an active region electrode, after the filtering approach described above, is shown in Figure 3. The main parameter of interest in this study was the average number of active muscle regions when performing the same task at increasing torque levels. The heatmaps of EMG array data and the active region computed are shown in Figures 4 and 5. These heatmaps show that the greatest EMG activity is generated in the flexor muscles during wrist flexion and the extensor muscles during wrist extension. During wrist flexion, the flexor activity is greatest nearest to the elbow (proximal end of the forearm, top of image), suggesting that the flexor carpi muscles that control wrist motion are engaged more than the flexor digitorum muscles that control finger motion. One-way ANOVA tests were performed and there was no statistically significant difference between any of the groups ($p>0.3$ in all cases), showing that the number of active regions does not on average differ when the resistive torque is increased. The results show that the robot targets the wrist muscles specifically and the average number of active regions in the forearm does not increase when the resistive torque is increased, suggesting that the user continues to employ the same motor strategy.

IV. Discussion

The key objectives of the HRX-1 robot are: to be portable, such that it can be easily moved to clinical research sites or patients homes; powerful enough to use for human movement research; and easily connected to other sensors and equipment.

The design of the HRX-1 robot is substantially more compact and lighter than existing comparable systems. For example, whilst the Hi5 bimanual torque feedback robot does not have published size or weight characteristics it is a room-scale device [17], whilst the EDUSA Pro-R (the commercial successor to the IIT WristBot) measures $75\times129\times90$ cm and weighs 65 kg, including a permanently connected computer and display [26]. The smaller size and weight of the HRX-1 means that it can be comfortably carried in a large backpack when walking or cycling, or in hand luggage with most airlines. This supports the robot being used at multiple study locations for clinical or in-home research, as well as used at conferences and exhibitions for live demonstrations of research projects.

Published data on human wrist strength is highly variable, however values up to 12 Nm have been reported for midpronated (neutral) male wrist flexion and extension [27], [28]. Wrist strength in populations with musculoskeletal or neurological illness is known to be substantially lower, with conditions such as stroke reducing wrist flexion/extension torque to values in the range of 2.5 Nm or lower [29], [30], and ageing by up to 40% [31]. Whilst the 4 Nm generated by the HRX-1 would not be able to match or overpower a healthy user's wrist, it can produce meaningful resistance (or assistance) to movement and is well scaled for unwell or aged users. Torque outputs from existing wrist manipulation robots are known to be lower, with the MIT-MANUS having a maximum published 1.43 Nm flexion/extension torque [32] and a more recent, lightweight wrist robot based on twisted string actuation offering up to 2.4 Nm [33]. Recent applications of the HRX-1 robot for combined physical assistance and functional electrical stimulation demonstrated promising results for the robot to be used as a rehabilitation device in clinical settings [34], [35], as well as a research tool for human-robot interaction research [36], [37], [38].

Integration with other sensors is supported by built-in analog and digital input/output connections to the robot

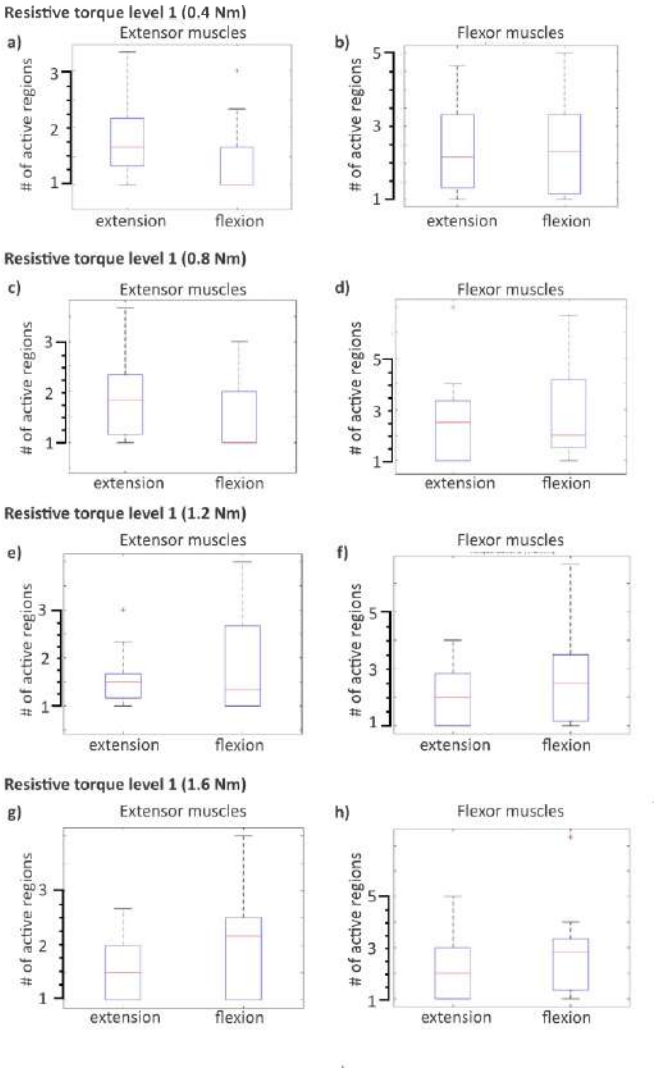


Fig. 5: Boxplots showing the number of identified active EMG regions for extensor and flexor muscles during wrist flexion and extension tasks at increasing levels of torque resistance.

controller, allowing a range of sensors to be directly connected and read. The use of a MATLAB programming environment also allows the robot and more complex PC-connected sensors to be controlled via the same software program, with the option of synchronising datastreams from the robot and sensors in hardware using pulses from the robot's built in input/output. Whilst it would be impossible to achieve compatibility with every possible external sensor, these approaches allow the robot to be used harmoniously with many popular accelerometers, gyroscopes, EMG, EEG, force/torque and pressure sensors.

V. Conclusion

The one-degree-of-freedom wrist manipulation robot presented in this study was evaluated through surface electromyography measurement tasks. The findings demonstrate that the HRX-1 robot satisfies the requirements for a portable, high-performance, and modular torque feedback robotic system. The device successfully generated sufficient torque to support experimental studies involving sEMG recordings in healthy participants.

Integration of the wrist robot with a multi-channel sEMG measurement system provided reliable data acquisition and facilitated research-relevant analyses. Specifically, the system enabled the identification and localization of activation regions corresponding to the extensor and flexor muscle groups during wrist movements.

References

[1] F. Aggogeri, T. Mikolajczyk, and J. O'Kane, "Robotics for rehabilitation of hand movement in stroke survivors," *Advances in Mechanical Engineering*, vol. 11, no. 4, 4 2019.

[2] T. Pringsheim, N. Jette, A. Frolkis, and T. D. Steeves, "The prevalence of Parkinson's disease: A systematic review and meta-analysis," *Movement Disorders*, vol. 29, no. 13, pp. 1583–1590, 11 2014.

[3] M. Rastall and B. Fashanu, "Hospital Physiotherapy Outpatient Department Waiting Lists," *Physiotherapy*, vol. 87, no. 11, pp. 563–572, 11 2001.

[4] L. A. Passalent, M. D. Landry, and C. A. Cott, "Wait Times for Publicly Funded Outpatient and Community Physiotherapy and Occupational Therapy Services: Implications for the Increasing Number of Persons with Chronic Conditions in Ontario, Canada," *Physiotherapy Canada*, vol. 61, no. 1, pp. 5–14, 1 2009.

[5] M. Yang, A. Bishop, J. Sussex, M. Roland, S. Jowett, and E. C. Wilson, "Economic evaluation of patient direct access to NHS physiotherapy services," *Physiotherapy*, vol. 111, pp. 40–47, 6 2021.

[6] M. Gallotti, B. Campagnola, A. Cocchieri, F. Mourad, J. D. Heick, and F. Maselli, "Effectiveness and Consequences of Direct Access in Physiotherapy: A Systematic Review," *Journal of Clinical Medicine*, vol. 12, no. 18, p. 5832, 9 2023.

[7] S. Murtagh, A. Touloumis, G. Olivier, J. Butterworth, and U. Hammerbeck, "Physiotherapy Outcomes Are Associated With Shorter Waiting Times, More Treatment Sessions and Younger Age: Analysis of a Clinical Database," *Musculoskeletal Care*, vol. 22, no. 3, 9 2024.

[8] S. Deslauriers, J. Déry, K. Proulx, M. Laliberté, F. Desmeules, D. E. Feldman, and K. Perreault, "Effects of waiting for outpatient physiotherapy services in persons with musculoskeletal disorders: a systematic review," *Disability and Rehabilitation*, vol. 43, no. 5, pp. 611–620, 2 2021.

[9] J. Laut, M. Porfiri, and P. Raghavan, "The Present and Future of Robotic Technology in Rehabilitation," *Current Physical Medicine and Rehabilitation Reports*, vol. 4, no. 4, pp. 312–319, 12 2016.

[10] A. Garcia-Gonzalez, R. Q. Fuentes-Aguilar, I. Salgado, and I. Chairez, "A review on the application of autonomous and intelligent robotic devices in medical rehabilitation," *Journal of the Brazilian Society of Mechanical Sciences and Engineering*, vol. 44, no. 9, p. 393, 9 2022.

[11] A. B. Payedimarri, M. Ratti, R. Rescinito, K. Vanhaecht, and M. Panella, "Effectiveness of Platform-Based Robot-Assisted Rehabilitation for Musculoskeletal or Neurologic Injuries: A Systematic Review," *Bioengineering*, vol. 9, no. 4, p. 129, 3 2022.

[12] G. Ganesh, A. Takagi, R. Osu, T. Yoshioka, M. Kawato, and E. Burdet, "Two is better than one: Physical interactions improve motor performance in humans," *Scientific Reports*, vol. 4, no. 1, p. 3824, 1 2014.

[13] Y. Liu, S. Guo, Z. Yang, H. Hirata, and T. Tamiya, "A Home-based Tele-rehabilitation System With Enhanced Therapist-patient Remote Interaction: A Feasibility Study," *IEEE Journal of Biomedical and Health Informatics*, vol. 26, no. 8, pp. 4176–4186, 8 2022.

[14] G. Postolache, R. Oliveira, I. Moreira, and O. Postolache, "Why, What and When in-Home Physiotherapy?" 2017, pp. 215–246.

[15] K. S. Jayawardana, G. Crowfoot, H. Janssen, P. Nayak, J. M. Solomon, and C. K. English, "Comparing the physical activity of stroke survivors in high-income countries and low to middle-income countries," *Physiotherapy Research International*, vol. 26, no. 4, 10 2021.

[16] C. J. Bosecker and H. I. Krebs, "MIT-Skywalker," in *2009 IEEE International Conference on Rehabilitation Robotics*. IEEE, 6 2009, pp. 542–549.

[17] A. Melendez-Calderon, L. Bagutti, B. Pedrono, and E. Burdet, "Hi5: A versatile dual-wrist device to study human-human interaction and bimanual control," *IEEE International Conference on Intelligent Robots and Systems*, pp. 2578–2583, 2011.

[18] L. Dovat, O. Lambercy, B. Salman, V. Johnson, T. Milner, R. Gassert, E. Burdet, and T. C. Leong, "A technique to train finger coordination and independence after stroke," *Disability and rehabilitation: Assistive technology*, vol. 5, no. 4, pp. 279–287, 2010.

[19] K. Lohse, N. Shirzad, A. Verster, N. Hodges, and H. F. M. Van der Loos, "Video Games and Rehabilitation," *Journal of Neurologic Physical Therapy*, vol. 37, no. 4, pp. 166–175, 12 2013.

[20] K. W. Lee, S. B. Kim, J. H. Lee, S. J. Lee, and J. W. Kim, "Effect of Robot-Assisted Game Training on Upper Extremity Function in Stroke Patients," *Annals of Rehabilitation Medicine*, vol. 41, no. 4, p. 539, 2017.

[21] T. Alves, R. S. Gonçalves, and G. Carbone, "Serious Games Strategies With Cable-Driven Robots for Bimanual Rehabilitation: A Randomized Controlled Trial With Post-Stroke Patients," *Frontiers in Robotics and AI*, vol. 9, 2 2022.

[22] J. E. Cifuentes-Zapien, J. A. Valdez-Aguilar, F. J. Rojas-Correa, J. E. Chong-Quero, and A. Pineda-Olivares, "A video game for an upper limb rehabilitation robotic system for children with cerebral palsy," in *2011 Pan American Health Care Exchanges*. IEEE, 3 2011, pp. 189–193.

[23] H. Taheri, J. B. Rowe, D. Gardner, V. Chan, K. Gray, C. Bower, D. J. Reinkensmeyer, and E. T. Wolbrecht, "Design and preliminary evaluation of the FINGER rehabilitation robot: Controlling challenge and quantifying finger individuation during musical computer game play," *Journal of NeuroEngineering and Rehabilitation*, vol. 11, no. 1, pp. 1–17, 2014.

[24] I. Farkhatdinov, A. Garnier, and E. Burdet, "Development and evaluation of a portable mr compatible haptic interface for human motor control," in *2015 IEEE World Haptics Conference (WHC)*. IEEE, 2015, pp. 196–201.

[25] I. Farkhatdinov, A. Garnier, T. Arichi, H. Bleuler, and E. Burdet, "Evaluation of a portable fmri compatible robotic wrist interface," in *2022 44th Annual International Conference of the IEEE Engineering in Medicine & Biology Society (EMBC)*. IEEE, 2022, pp. 2535–2539.

[26] ReWing s.r.l, "Edusa pro-r technical data," https://rewingtech.com/products/edusa-pro-r, 2025, accessed: 18-02-2025.

[27] G. Loren, S. Shoemaker, T. Burkholder, M. Jacobson, J. Fridén, and R. Lieber, "Human wrist motors: Biomechanical design and application to tendon transfers," *Journal of Biomechanics*, vol. 29, no. 3, pp. 331–342, 3 1996.

[28] Y. Yoshii, H. Yuine, O. Kazuki, W. l. Tung, and T. Ishii, "Measurement of wrist flexion and extension torques in different forearm positions," *BioMedical Engineering Online*, vol. 14, no. 1, pp. 1–10, 2015.

[29] J. Kim, W. Park, and J. Kim, "Quantitative Evaluation of Stroke Patients' Wrist Paralysis by Estimation of Kinematic Coefficients and Machine Learning," *Sensors and Materials*, vol. 32, no. 3, p. 981, 3 2020.

[30] K. L. de Gooijer-van de Groep, E. de Vlugt, H. J. van der Krogt, Helgadóttir, J. H. Arendzen, C. G. Meskers, and J. H. de Groot, "Estimation of tissue stiffness, reflex activity, optimal muscle length and slack length in stroke patients using an electromyography driven antagonistic wrist model," *Clinical Biomechanics*, vol. 35, pp. 93–101, 6 2016.

[31] K. Keller and M. Engelhardt, "Strength and muscle mass loss with aging process. Age and strength loss." *Muscles, ligaments and tendons journal*, vol. 3, no. 4, pp. 346–50, 10 2013.

[32] H. I. Krebs and N. Hogan, "Therapeutic Robotics: A Technology Push: Stroke rehabilitation is being aided by robots that guide movement of shoulders and elbows, wrists, hands, arms and ankles to significantly improve recovery of patients." *Proceedings of the IEEE. Institute of Electrical and Electronics Engineers*, vol. 94, no. 9, pp. 1727–1738, 9 2006.

[33] V. Skvortsova, S. Nedelchev, J. Brown, I. Farkhatdinov, and I. Gaponov, "Design, characterisation and validation of a haptic interface based on twisted string actuation," *Frontiers in Robotics and AI*, vol. 9, no. September, pp. 1–9, 2022.

[34] L. Cazenave, M. Einenkel, A. Yurkewich, S. Endo, S. Hirche, and E. Burdet, "Hybrid robotic and electrical stimulation assistance can enhance performance and reduce mental demand," *IEEE Transactions on Neural Systems and Rehabilitation Engineering*, 2023.

[35] L. Cazenave, A. Yurkewich, C. Höhler, T. Keller, C. Krewer, K. Jahn, S. Hirche, S. Endo, and E. Burdet, "Hybrid functional electrical stimulation and robotic assistance for wrist motion training after stroke: Preliminary results," in *2023 International Conference on Rehabilitation Robotics (ICORR)*. IEEE, 2023, pp. 1–6.

[36] H. Kavianirad, S. Endo, T. Keller, and S. Hirche, "Emg-based volitional torque estimation in functional electrical stimulation control," in *2022 IEEE-EMBS Conference on Biomedical Engineering and Sciences (IECBES)*. IEEE, 2022, pp. 171–176.

[37] B. Berret, D. Verdel, E. Burdet, and F. Jean, "Co-contraction embodies uncertainty: An optimal feedforward strategy for robust motor control," *PLOS Computational Biology*, vol. 20, no. 11, p. e1012598, 2024.

[38] M. Cecamore, I. Gaponov, S. C. Miller, and I. Farkhatdinov, "Design and validation of a haptic ankle platform for physical human-machine interaction," in *2024 10th IEEE RAS/EMBS International Conference for Biomedical Robotics and Biomechatronics (BioRob)*. IEEE, 2024, pp. 1301–1306.

Design of a Low-cost VR-Based Robotic Pedal System with Dynamic Resistance and Muscle Activity Feedback

Claudia Simon Rueda[1], Peter Snow[1], Rodrigo Mendez[1] and Rui C.V. Loureiro[1]

***Abstract*— This paper presents the design and usability evaluation of an affordable, virtual reality (VR)-integrated robotic pedal system aimed at enhancing lower-limb rehabilitation through interactive gaming. Key features include real-time cadence monitoring, dynamic resistance adjustment, and muscle activity tracking via electromyography (EMG) sensors. A usability study with 7 healthy participants, demonstrated increased cadence and symmetry scores in VR conditions. Clinician feedback supports the device's potential for at-home rehabilitation, though EMG sensor calibration remains a key improvement area.**

I. INTRODUCTION

As global demographics shift, the aging population continues to grow rapidly, with over 10% of individuals worldwide aged 65 or older in 2022, projected to increase to 25% by 2100 [1]. Age-related declines in mobility, muscle strength, and coordination significantly impact independence and quality of life for many older adults, raising the demand for effective, accessible neurorehabilitation solutions [2]. Neurorehabilitation, historically reliant on conventional methods such as range-of-motion (ROM) and muscle-strengthening exercises, has evolved to include advanced, sensor-driven approaches aimed at improving motor function and engagement [3].

Pedaling-based rehabilitation was first introduced to neurorehabilitation protocols during the mid-20th century, gaining attention for its ability to engage multiple lower-limb muscle groups in rhythmic, repetitive motion conducive to neuromuscular adaptation [4]. Studies have shown that pedaling stimulates the primary motor cortex and cerebellum, helping restore coordinated muscle activities that support motor recovery [5]. Cycling metrics, including cadence (RPM), speed, and symmetry, are commonly used to assess exercise intensity, endurance, and coordination, all critical to optimizing outcomes in cycling-based rehabilitation [6], [7].

Current pedaling-based devices vary in accessibility, interactivity, and cost. Basic pedaliers are affordable (under £50) and portable, yet they lack adjustable resistance and feedback mechanisms, limiting their rehabilitative effectiveness [8]. Stationary bikes offer an intermediate option, with prices around £200 and simple metrics like cadence. However, they lack the adaptability and immersive feedback critical for effective rehabilitation, particularly in at-home settings [9]. Some smart exercise bikes with integrated gaming, provide real-time feedback and multiplayer functionality but are costly (often over £1,000) and subscription-based, making them inaccessible for many patients and lacking specialized rehabilitation features such as electromyography (EMG)-based muscle biofeedback [10].

At-home, low-cost solutions offer substantial potential for addressing these gaps, supporting effective rehabilitation by reducing costs, improving accessibility, and increasing adherence [11]. These devices must be designed to accommodate various user needs and capacities, incorporating real-time feedback, low-power sensors, and intuitive interfaces to maintain user engagement. By integrating features like dynamic resistance and VR-enhanced biofeedback, low-cost devices can bring essential therapy tools into the home, supporting routine rehabilitation and potentially alleviating strain on healthcare systems [12].

This study introduces a VR-integrated robotic pedal-based rehabilitation device that combines an affordable cadence sensor with a dynamic resistance system and EMG-based feedback for real-time monitoring of muscle activity. Unlike existing low-cost devices, this system dynamically adjusts pedal resistance in response to virtual terrain changes, creating a more realistic and engaging experience, allowing different exercise intensities throughout the session. By integrating EMG sensors to assess muscle activation and provide symmetry feedback, the system encourages balanced specific muscle engagement rather than just exerted force like other devices. As an experimental device, there was interest in seeing muscle activity. This design addresses gaps in cost, functionality, effectiveness, modularity, and usability, aiming to improve patient adherence and outcomes through gamified, accessible rehabilitation.

II. USER REQUIREMENTS AND DESIGN SPECIFICATIONS

The VR-based pedal rehabilitation device was developed in response to user needs for affordability, ease of setup, and seamless integration with virtual environments. Key user requirements included a low-cost, adaptable design suitable for a range of seating configurations (e.g., bed, wheelchair, bench) as well as a setup that could support both leg and arm exercises.

In designing to meet these requirements, a comprehensive review of existing cost-effective pedaling devices revealed limitations in current models, particularly regarding the lack of real-time biofeedback. To address this, the device was

This work was supported by the La Caixa Postgraduate Fellowship, awarded to Claudia Simon Rueda, and University College London.

[1]Claudia Simon Rueda, Peter Snow, Rodrigo Mendez and Rui C.V. Loureiro are with Aspire Centre for Rehabilitation Engineerinf and Assistive Technologies, University College London, WC1E 6BT London, UK {claudia.rueda.23, p.snow, rodrigo.mendez.21, r.loureiro}@ucl.ac.uk

created with modular, replaceable components and constructed from low-cost materials and additive manufacturing techniques, ensuring accessibility while allowing for customization and potential upgrades. The device's configuration minimizes loose wiring, enabling simple assembly and disassembly for various therapeutic settings.

III. System Design and Methods

The centralized control hub is an Unreal Engine 4 (UE4) cycling game that processes sensor inputs and adjusts the virtual environment and pedal resistance in real time, as seen in Fig. 1. It consists of a SparkFun microcontroller and an Arduino Nano interface with EMG sensors and a motorized gear system to monitor muscle activity and dynamically modify resistance. Using two microcontrollers allows for efficient handling of the separate demands and ensures precise, real-time responsiveness. Additionally, a Bluetooth Low Energy (BLE) cadence sensor transmits data to a Python script, which synchronizes the user's pedaling with the avatar's movement in UE4. The system, compatible with a Windows Mixed Reality HMD for 3D immersion, exports session data for research analysis or clinician review.

A. Hardware

The hardware design integrates sensors and actuators in a pedalier [13] that work in conjunction with the VR environment to capture user metrics and dynamically adjust resistance as seen in Fig. 2.

1) Cadence: A Magene S3+ Speed/Cadence Dual-Mode sensor [14] was chosen for measuring pedaling cadence due to its Bluetooth Low Energy (BLE) capability, which ensures low power consumption and stable data transmission at a rate of 2 Hz. The sensor is mounted on the crank arm of the pedal system, transmitting real-time RPM data to a Python script that processes and forwards this information to the VR interface in Unreal Engine (UE). The cadence data determines the speed of the virtual cycling avatar, providing a responsive and realistic experience for the user.

The system's cadence detection performance was analyzed by measuring the delay and accuracy of cadence data transmission from the BLE cadence sensor to Python and later to the VR environment in Unreal Engine 4 (UE4) and averaging the results of 3 trials. Accuracy was assessed by pedalling to a metronome at 30, 40, 50, and 60 BPM. Delay measurements were obtained by recording timestamps at three points—when pedaling began, when Python registered non-zero cadence, and when Unreal Engine (UE) did the same.

2) Motor-driven gear mechanism: The system uses 2 hybrid NEMA 17 0.44Nm stepper motors [15], chosen for their optimal size-to-torque ratio, paired with A4988 drivers [16] to control pedal resistance. This dual-motor setup was necessary to generate enough torque to fully screw the resistance knob in to notice the change in resistance. Adjusting resistance enables dynamic simulation of terrain changes, enhancing the VR experience by simulating uphill

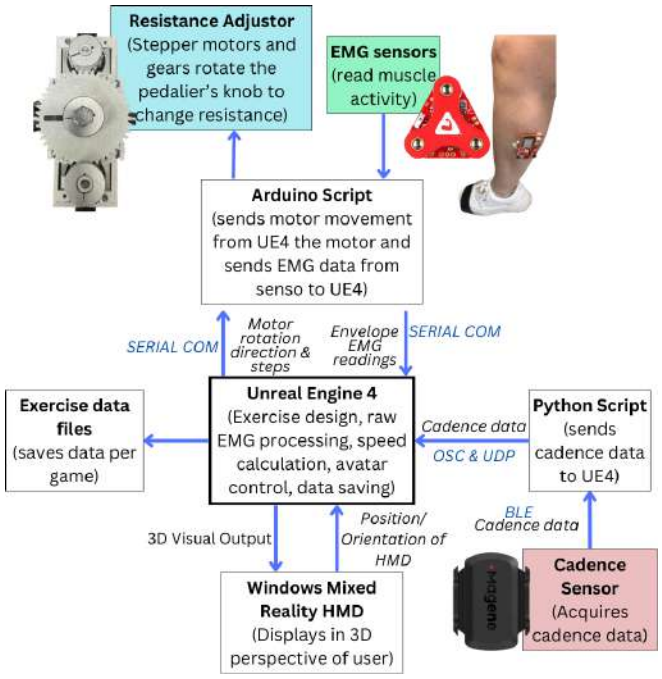


Fig. 1. System architecture illustrating the interaction between hardware components (cadence sensor, EMG sensors, motor-driven gear system) and software elements (Arduino and Python scripts, Unreal Engine 4, Windows Mixed Reality HMD). Data flows through serial communication, Bluetooth, BLE and OSC/UDP protocols to synchronize user inputs with the VR cycling environment.



Fig. 2. Hardware configuration of the VR cycling system, showing key components including the Magene S3+ cadence sensor, motor-driven gear mechanism, and adjustable resistance knob. Collar shafts securely attach the PLA gears to the motors and knob, and the electronics storage box secures the Arduino and motor drivers.

or downhill resistance. The motors are powered by a 24V external power source, while an Arduino Nano microcontroller handles motor control, synchronizing resistance levels with the virtual terrain in real time.

A 3:1 spur gear mechanism transfers the rotation from the motors to the pedal resistance knob, with this ratio enhancing the mechanical advantage and providing enough torque to allow the precise control of resistance levels. The PLA gear mechanism is encased in a 3D-printed housing of the same material designed to provide stability. Each slope condition in the game is encoded within Unreal Engine and transmitted to the Arduino Nano via serial communication, instructing the motor to rotate clockwise or counterclockwise to adjust resistance based on the simulated terrain.

3) EMG: Muscle activity is monitored through two Myoware 2.0 Muscle wireless sensors [17], [18] positioned

on the gastrocnemius lateralis of each leg. These low-cost wireless sensors (70 $) are more affordable than expensive commercial EMG systems designed for intense exercise. Given the altered biomechanics in the seated position on the chair, this muscle plays a primary role in generating plantarflexion torque, which is central to pedaling dynamics in this setup [19]. These sensors, attached via disposable electrodes, provide real-time muscle activation data, highlighting any asymmetries in leg use. The Myoware sensors are connected to a SparkFun Thing Plus ESP32 microcontroller, which transmits data to the VR environment through Bluetooth.

To analyze symmetry, the system computes a symmetry score based on the normalized difference in activation levels between the left and right legs. The EMG signals are first smoothed using a moving average to reduce noise and capture consistent muscle activation trends. The symmetry score is then calculated as [20]:

$$\text{Symmetry Score} = \left(1 - \frac{|EMG_{\text{left}} - EMG_{\text{right}}|}{EMG_{\text{left}} + EMG_{\text{right}}}\right) \times 100 \quad (1)$$

This score, expressed as a percentage, provides real-time feedback visualized within the VR environment to encourage balanced muscle engagement and support users in achieving their rehabilitation goals.

B. Software: VR environment

The software component combines real-time data processing and VR simulation to create an interactive rehabilitation experience. Data from the cadence and EMG sensors feed into the VR game developed in Unreal Engine 4.27.

The VR cycling game, developed using the Unreal Engine Vehicle Advanced Pack, features an animated bike and cyclist, where the avatar's pedaling speed is directly controlled by the user's cadence input. This synchronization between physical pedaling and virtual speed provides realistic feedback, enhancing immersion and engagement. The cycling path includes hills up and down, which trigger resistance changes and encourage users to adapt their pedaling speed, simulating real-world cycling conditions.

To increase user motivation and adherence, the VR environment incorporates gamification features such as coin-collecting boosters and speed multipliers, all providing auditory feedback. These boosters are activated when users collect designated items during the game. For instance, collecting a speed booster doubles the avatar's speed for 10 seconds, encouraging users to take advantage of it and pedal faster to get more coins. These features align with gamification principles by providing a balance of challenge and reward, fostering long-term engagement and helping users reach their rehabilitation goals [11]. Fig. 3 shows the game environment as seen from the cyclist perspective.

C. Usability Study

After prototyping, a usability study aimed to evaluate the system's usability, user experience, and performance with seven healthy participants (4 men, 3 women) recruited with



Fig. 3. Game main screen. Coin related features and active multipliers (if any) on the left top corner. Time, distance and a time progress bar are centered at the top. Speed, cadence and symmetry score on the top right corner. Below is a symmetry bar - green with symmetric scores and red with a "Dominant" label if asymmetric. The bottom left graph shows the evolution in speed and the bottom right graph the evolution of muscle activity for both right (red) and left (green) legs.

UCL ethical approval (ID: 6676/007). Participants had no lower limb injuries and completed two randomized 5-minute pedaling sessions: one in a VR environment and one non-gamified, to simulate typical at-home rehabilitation settings.

The study protocol included electrode placement and EMG calibration exercises, followed by a randomized sequence of two pedaling sessions and a 5-minute rest in between. Performance data on cadence, muscle activity, and a symmetry score were recorded, while additional VR-specific data (e.g., distance traveled, terrain type) provided further insights. User experience was assessed with a 17-question electronic questionnaire focusing on comfort, ease of use, engagement, and motivation.

The usability study included a comparative analysis of VR-enabled pedaling sessions against non-gamified sessions. Quantitative metrics collected, including cadence consistency and symmetry score from EMG data, showed marked differences between the two conditions.

Data analysis was divided into two primary components:

1) Comparison of VR vs. Non-gamified experience: Paired t-tests were conducted on cadence, EMG values, and symmetry to quantify differences in physiological responses between VR and non-gamified pedaling conditions. Motivation, engagement and user preference were further analyzed with questionnaire responses to assess user-perceived differences.

2) VR Environment Evaluation: ANOVA tests were applied to examine variations in cadence and EMG values across different in-game terrains - thus distinct resistance levels -, and under conditions with or without in-game speed and coin multipliers. Symmetry progression over time was also analyzed to understand the impact of this live feedback on symmetry correction. Additionally, subjective evaluations of ease of use, ease of learning, and user satisfaction provided insights into system usability and participant experience.

Feedback from a post-study interview with a physical therapist offered professional insights into the system's potential applications in rehabilitation and highlighted opportunities

for gamified therapy advancements.

IV. Results

A. Hardware Performance

*1) **Cadence Delay and Accuracy**:* High accuracy was shown at faster pedaling speeds (40–60 BPM) with errors under 0.7%, but dropped significantly at 30 BPM (error 16.26%), suggesting a poor performance at lower speeds.

The average delay between real-time activation and detection in Python was 2.62 seconds, aligning closely with the 3-second delay specified by the vendor—a typical lag in cadence sensors due to their inherent data-processing mechanisms. As seen in Fig. 4, further delay from Python to UE is under 0.2s, ensuring near-seamless integration with the VR system.

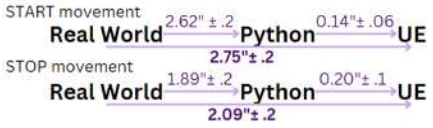


Fig. 4. Cadence latency breakdown for when initiating and stopping movements across the Real World, Python processing, and UE, with times indicated in seconds

*2) **Cycling Pattern in muscle activity**:* The cycling pattern was evaluated to assess how closely the system emulated a natural cycling movement. The data collected on pedal strokes, measured by both cadence sensor readings and muscle activation levels, aligned closely with established cycling biomechanics literature. Specifically, the cadence readings and leg muscle activation profiles, as seen in Fig. 5 mirrored the general trend reported by [21], who documented ideal cycling form characteristics for rehabilitation contexts. The system's ability to replicate a realistic cycling pattern supports its potential utility in rehabilitation settings where the simulation of natural movement is essential.

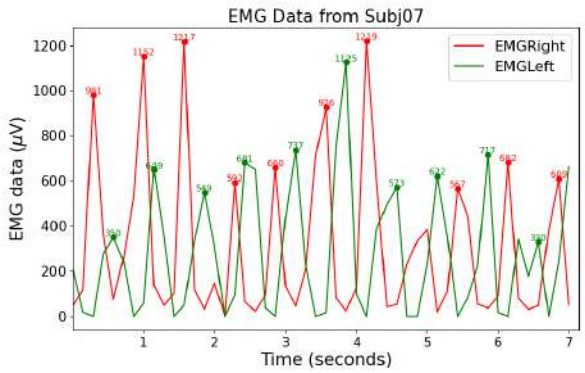


Fig. 5. Pedaling EMG data: Muscle activation patterns for the right and left legs during pedaling, recorded from Subject 07. The EMG data illustrate periodic activation peaks corresponding to pedal strokes

TABLE I
Comparison of VR and Non-Gamified Metrics

Metric	VR	Non-gamified	P-value
Cadence (rpm)	88.02	83.34	0.041*
EMG (μV)	208.94	153.51	0.106
Symmetry Score (%)	72.06	60.22	0.007
Engagement (out of 5)	4.1	2.4	0.0009*

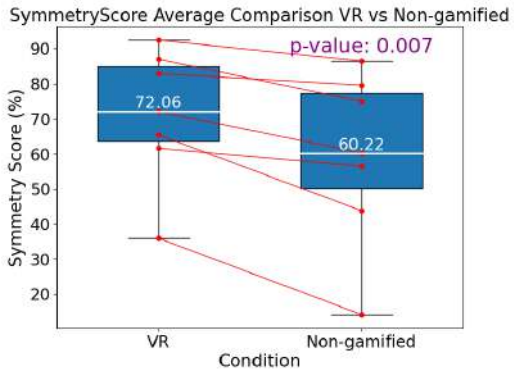


Fig. 6. Box plot with overlaid individual data points comparing average symmetry scores between VR and non-gamified conditions with a paired t-test.

B. Usability Testing of the System

*1) **Comparison of VR vs. Non-gamified experience**:* The comparison between VR and non-gamified metrics seen in Table I shows that VR significantly increased cadence, with a value of 88.02 rpm compared to 83.34 rpm for non-gamified ($p = 0.041 < 0.05$). This represents a 5.6% increase in cadence when using VR. Symmetry score was also significantly higher (p=0.007) for VR (72.06%) than for non-gamified (60.22%) as seen in Fig. 6. Mean muscle activity did not differ significantly between the two conditions ($p = 0.106$). Notably, VR also led to a higher engagement score (4.1 out of 5 for VR vs. 2.4 for non-gamified, $p = 0.0009$), with all users explicitely selecting the VR experience. These results suggest that VR increases cadence and engagement compared to non-gamified pedaling sessions. The observed evolution in Symmetry Score for participants throughout the session is very variable and there is no evidence of a clear trend of improvement in neither of the pedaling sessions.

*2) **VR Environment evaluation**:* Cadence and electromyography (EMG) values were evaluated across downhill, flat, and uphill terrains as seen in Table II. Cadence values showed no significant difference between terrains, with averages of 69.01 rpm (downhill), 67.25 rpm (flat), and 66.30 rpm (uphill) ($p = 0.425$). In contrast, EMG activity exhibited significant variation, with the highest median values recorded for the uphill condition (229.33 μV), followed by downhill (197.77 μV), and the lowest on flat terrain (160.28 μV), showing a statistically significant difference ($p = 0.0031$) as seen in Fig. 7. These findings suggest that while terrain type does not significantly influence cadence, it has a substantial impact on muscle activation.

TABLE II

CADENCE AND EMG VALUES ACROSS DIFFERENT TERRAINS

	Downhill	Flat	Uphill	P-value
Cadence (rpm)	69.01	67.25	66.30	0.425
EMG (µV)	197.77	160.28	229.33	0.0031*

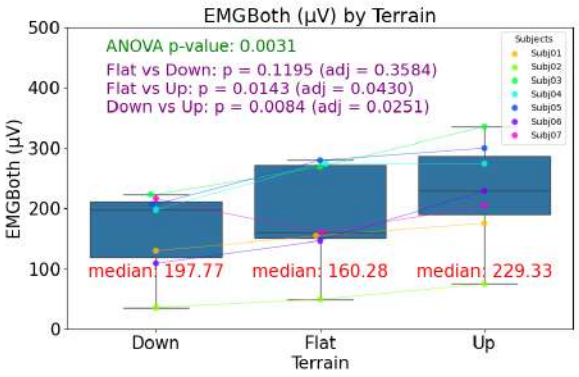


Fig. 7. EMG by terrain

TABLE III

CADENCE AND EMG METRICS ACROSS MULTIPLIER CONDITIONS

Metric	None	Both M	Coin M	Speed M	P-value
Cadence (rpm)	88.09	71.00	70.50	63.13	0.09
EMG (µV)	204.59	232.03	178.78	208.05	0.17

Table III presents cadence and EMG metrics across different multiplier conditions: no multiplier, both multipliers, coin multiplier, and speed multiplier. Neither cadence nor EMG values showed statistically significant differences across these conditions (p = 0.09 for cadence and p = 0.17 for EMG), indicating that the presence or type of multiplier did not substantially impact these metrics. Although the data suggest slight trends—such as a decrease in cadence with the speed multiplier (63.13 rpm) and higher EMG with both multipliers (232.03 µV)—these variations were not strong enough to reach significance. This suggests that multiplier conditions, as tested, may not have a meaningful effect on cadence or muscle activation. However, participants reported that the multipliers provided additional incentive during the activity, showing that such features have motivational benefits even if they do not significantly impact physiological metrics.

*3) **User experience**:* Qualitative feedback from the participant questionnaire highlighted positive reception towards the VR game's immersive and interactive aspects. All participants noticed the increased resistance when pedaling uphill, rating it 3.8/5 smooth and realistic and all but one (85%) noticed the decreased resistance going downhill, with 3.07/5. Participants reported that visual feedback (e.g., avatar movement, graphs) and game elements (e.g., boosters, coins) enhanced their motivation, which aligns with principles of gamification shown to improve engagement in physical therapy contexts [22].

C. Clinician feedback

Clinical feedback highlighted the potential of the device not only for at-home but also for inpatient rehabilitation, noting that it could be especially valuable in hospital settings where patients often risk muscle waste due to prolonged periods of inactivity. This portable device could be used directly from a patient's room—or even from the bed if mounted appropriately—reducing the need for visits to the hospital gym with a fixed schedule. The clinician emphasized that many patients lack motivation to exercise independently, often finding solo pedaling sessions boring and difficult to sustain without supervision.

They saw value in the EMG monitoring feature, as targeted muscle activity tracking could enhance patient awareness and facilitate a stronger mind-body connection.

Additionally, they suggested a mobile app version of the system, eliminating the VR component, to increase adaptability and make the device easier to integrate into inpatient settings where resources may be limited.

V. DISCUSSION AND CONCLUSION

The cadence sensor performs with high accuracy ($< 0.7\%$ relative error) at moderate to high cadences (≥ 40 rpm), making it well-suited for users with standard cycling speeds. However, it becomes less reliable at very low cadences (16.3% error at 30 rpm), limiting its applicability for certain rehabilitation patients with lower pedaling rates. While accuracy is not specified by the vendors, further comparisons with other models and sensors, such as IMUs, could expand its potential user base.

The data transfer to the system adds minimal additional delay. The delay is primarily noticeable at the start and end of pedaling, but does not impact the session itself. Additionally, a 3-second countdown at the beginning of the game effectively masks the initial lag, helping synchronize initial pedaling with virtual movement.

The muscle activity sensors captured gastrocnemius lateralis activation, with alternating muscle activity between legs resembling literature´s ranges of values [21]. Although basic calibration was undertaken for this project, further work will be carried out on implementing additional filters and calibration to normalize sensor readings and enhance measurement consistency.

The system successfully integrates the hardware components with the software, leveraging communication protocols that allow seamless data transfer between the VR environment and sensors and motors. The cadence sensor continuously monitors the user's pedaling speed, relaying real-time data to the game, which adjusts the in-game avatar's movement to match the user's cadence. This synchronization ensures that the virtual experience mirrors the user's real-world performance. Additionally, the resistance adjustments based on terrain changes—uphill or downhill—through the stepper motors, offers users an immediate physical response,

increasing or decreasing the effort required to pedal. The real-time feedback displayed on-screen, including visual cues related to muscle activity and symmetry, allows users to track their progress during the session. This immediate feedback and dynamic interaction create an immersive experience, enhancing user engagement and motivation, as stated by all participants. Overall, participants were satisfied with the VR session and preferred this to the non-gamified experience.

Results on pedaling performance show that the inclusion of VR elements significantly increase the user's cadence and symmetry. This agrees with [22], who demonstrates that a VR environment can increase exercise adherence and intensity by lowering perceived exertion that encourages users to push beyond their usual physical limits. It is also consistent with research [23], which found that interactive and feedback-rich environments can help correct asymmetries in motor function, likely through real-time visual and auditory feedback that encourages even effort distribution between limbs. With these results, developing a game specifically for upper limb rehabilitation could significantly enhance the system's versatility. For instance, designing virtual environments that simulate rowing, swimming, or other upper body movements could broaden the applicability of the system, making it more inclusive for different pathological conditions. This approach aligns with findings that demonstrated the potential of VR-based robotic rehabilitation systems to engage patients in targeted upper limb therapies [24].

Within the VR experience, there were significant variations in muscle activity with changes in resistance, particularly increasing during uphill terrain. These resistance changes did not alter cadence, with participants possibly focusing on keeping a constant cadence while increasing or reducing their effort. This ability to modulate resistance and thus muscle activation, allows for targeted strengthening and endurance training, enabling rehabilitation programs to be designed with varying intensities that adjust both muscle activity and resistance throughout the session and rehabilitation scheme, ensuring progression while preventing overexertion.

The system's ability to export session data opens future possibilities to integrate it into clinical practice. By providing detailed records of cadence, resistance, muscle activity, and symmetry, therapists could monitor progress, tailor rehabilitation plans, and enable remote adjustments, supporting the expanding field of tele-neurorehabilitation. Cybersickness was not specifically studied, it was unlikely to be an issue due to the seated position and short session duration. Future research could explore its impact on prolonged use.

Overall, the usability study and performance evaluations underscore the effectiveness of a VR-enhanced cycling system in promoting balanced, consistent pedaling mechanics. By providing real-time feedback and utilizing gamification elements, the system demonstrates significant potential as a therapeutic tool for neurorehabilitation and at-home exercise regimens.

REFERENCES

[1] United Nations Department of Economic and Social Affairs, Population Division, "World population prospects 2022: Summary of results," Report UN DESA/POP/2022/TR/NO. 3, 2022.

[2] M. Grimmer, R. Riener, C. J. Walsh, and A. Seyfarth, "Mobility related physical and functional losses due to aging and disease - a motivation for lower limb exoskeletons," *Journal of NeuroEngineering and Rehabilitation*, vol. 16, Jan 2019.

[3] W. Deng, I. Papavasileiou, Z. Qiao, W. Zhang, K.-Y. Lam, and S. Han, "Advances in automation technologies for lower extremity neurorehabilitation: A review and future challenges," *IEEE Reviews in Biomedical Engineering*, vol. 11, p. 289–305, 2018.

[4] T. Fujiwara, M. Liu, and N. Chino, "Effect of pedaling exercise on the hemiplegic lower limb," *Am. J. Phys. Med. Rehabil.*, vol. 82, pp. 357–363, May 2003.

[5] L. N. Sattler, W. A. Hing, and C. J. Vertullo, "Pedaling-based protocol superior to a 10-exercise, non-pedaling protocol for postoperative rehabilitation after total knee replacement: A randomized controlled trial," *J. Bone Joint Surg. Am.*, vol. 101, pp. 688–695, Apr. 2019.

[6] K. Watanabe, T. Sato, T. Mukaimoto, W. Takashima, M. Yamagishi, and T. Nishiyama, "Electromyographic analysis of thigh muscles during track cycling on a velodrome," *Journal of Sports Sciences*, vol. 34, p. 1413–1422, Nov 2015.

[7] F. Hug and S. Dorel, "Electromyographic analysis of pedaling: A review," *Journal of Electromyography and Kinesiology*, vol. 19, p. 182–198, Apr 2009.

[8] T. G. Hornby, C. R. Kinnaird, C. L. Holleran, M. R. Rafferty, K. S. Rodriguez, and J. B. Cain, "Kinematic, muscular, and metabolic responses during exoskeletal-, elliptical-, or therapist-assisted stepping in people with incomplete spinal cord injury," *Physical Therapy*, vol. 92, p. 1278–1291, Oct 2012.

[9] A. Mahlovanyy, O. Kunynets, I. Grygus, and O. Ivanochko, "The influence of dosed physical exercise on indicators of the cardiovascular system of persons who have lost limbs," - *(Rehabilitation recreation)*, 2023.

[10] A. B.M. Hasan, A. F. El-Sheikh, and N. E. Mohamed, "Pedaling exercise as a rehabilitation for children with cerebral palsy (a review article)," *Egyptian Journal of Applied Science*, vol. 38, p. 126–141, Sep 2023.

[11] K. Robson, K. Plangger, J. H. Kietzmann, I. McCarthy, and L. Pitt, "Is it all a game? understanding the principles of gamification," *Business Horizons*, vol. 58, no. 4, pp. 411–420, 2015.

[12] Government Office for Science, "Future of an ageing population," 2016.

[13] Mobiclinic, "Pedal exerciser: Arms and legs exerciser: Adjustable: Sendero: Mobiclinic," 2024.

[14] Magene, *Bike Speed/Cadence Sensor 2-in-1: Model S3+*, 2017.

[15] R. Pro, "Rs pro hybrid stepper motor, 0.44nm torque, 2.8v, 0.9°, 42.3 x 42.3mm frame, 5mm shaft," 2024.

[16] Pololu, "Pololu 8-35v 2a single bipolar stepper motor driver a4988," 2024.

[17] Myoware, "Myoware 2.0 muscle sensor," 2024.

[18] Myoware, "Myoware 2.0 wireless shield," 2024.

[19] D. J. Sanderson, P. Martin, G. Honeyman, and J. Keefer, "Gastrocnemius and soleus muscle length, velocity, and emg responses to changes in pedalling cadence," *Journal of Electromyography and Kinesiology*, vol. 16, p. 642–649, Dec 2006.

[20] A. S. B. M. M. K. S. O. Susan M. Linder, Anson B. Rosenfeldt and J. L. Alberts, "Improved lower extremity pedaling mechanics in individuals with stroke under maximal workloads," *Topics in Stroke Rehabilitation*, vol. 25, no. 4, pp. 248–255, 2018. PMID: 29447080.

[21] D. M. Rouffet and C. Hautier, "Emg normalization to study muscle activation in cycling," *Journal of electromyography and kinesiology*, vol. 18, Oct 2008.

[22] K. Hoolahan, "A preliminary investigation into the effects of gamified virtual reality on exercise adherence, perceived exertion, and health," *International Journal of Virtual and Augmented Reality*, 2020.

[23] N. Hamzeheinejad, D. Roth, S. Monty, J. Breuer, A. Rodenberg, and M. E. Latoschik, "The impact of implicit and explicit feedback on performance and experience during vr-supported motor rehabilitation," *2021 IEEE Virtual Reality and 3D User Interfaces (VR)*, pp. 382–391, 2021.

[24] P. W. Snow, I. Sedki, M. Sinisi, R. Comley, and R. C. Loureiro, "Robotic therapy for phantom limb pain in upper limb amputees," in *2017 International Conference on Rehabilitation Robotics (ICORR)*, pp. 1019–1024, 2017.

Muscle synergies during gait of functionally-dependent subacute stroke survivors before and after robotic rehabilitation

Agnese Cherubini, Clara Sánchez Del Valle, Natacha León, Jesús Tornero, Juan C. Moreno, Clara B. Sanz-Morère

Abstract— **Stroke affects the neuromuscular control of humans, influencing muscle coordination and consequently gait patterns. Robotic devices can be useful to improve walking function and kinematics after stroke, but there is not much research related to muscle coordination through muscle synergies. This is the first study in which muscle synergies have been studied in functionally-dependent subacute post-stroke patients (FAC <2) in a robotic rehabilitation context. We analyzed muscle synergies during gait of three post- stroke patients before and after 2 months of robotic rehabilitation and correlated the results with functional improvements and kinematic changes. After the rehabilitation, patients walked faster, more independently, with normalized gait patterns and different muscle coordination. However, the results obtained underline the importance of a patient- specific therapeutic approach guided by the combination of multi-level metrics.**

I. INTRODUCTION

Stroke is an age-associated neurological condition that will drastically increase in the next decades due to the worldwide extended life expectancy (1,2). Stroke is the second most common cause of death and the first cause of disability worldwide (1). Post-stroke patients present lower walking speed, stance and swing time variations and an altered coordination of lower limb muscle activity, which are essential for balance and stability (3,4). Stroke also has a significant impact on the reduction of quality of life (5). For motor recovery of post-stroke patients, many technological devices have been developed for rehabilitation (2). Robotic rehabilitation is an increasingly used type of gait training, as it shows many advantages for both patients and therapists, increasing the frequency of repetitions of the walking therapy and consequently leading to improvements in locomotor functions (6). The effects of robotic rehabilitation on post-stroke patients have been studied using various metrics, such as functional improvements, kinematics, muscle activity, and corticomotor excitability (7). Another possible biomarker to study the effects of rehabilitation on post-stroke patients is muscle coordination, studied by deriving muscle synergies for electromyographic signals (3,7). Muscle synergies are the result of the synergistic activation of several muscles as a single functional unit. Research suggests that the central nervous system simplifies the simultaneous activation of different muscles, allowing them to function in a coordinated manner with a common specific goal (8). Currently, many studies have analyzed muscle synergies during gait in both healthy (8,9) and stroke patients (10,11). Post- stroke patients exhibit poor neuromuscular control, which leads to a reduced inter-muscular coordination characterized by altered muscle activation patterns (10). These alterations are associated with changes in muscle synergies number, electromyography (EMG) reconstruction and Variance Accounted for (VAF) (7). Research has shown that alterations of muscle synergies in post-stroke patients correlate with deficits in both biomechanical and clinical assessments (2,4,10). However, most of the studies have been conducted with stroke patients who underwent conventional therapy (12) and analyzed muscle synergies mainly while walking on a treadmill (4,5,10). Only a reduced number of research studies have examined muscle synergies changes in the context of robotic rehabilitation, and only four were related to lower limb rehabilitation (2,13–15). Of those, none were related to subacute stroke survivors, as two were related to chronic patients with high motor functions, which were able to walk independently with minimal supervision (13,14) and two explored muscle synergies in acute post-stroke patients (10-18 days after the stroke) with limited walking independence (2,15). The limited use of muscle synergies as a biomarker for stroke rehabilitation may be due to 1) the technical complexity of measuring EMG activity in patients with reduced gait abilities, 2) the complexity of analyzing intersubject variabilities due to the different neurophysiological conditions between each patient (7), 3) the need of additional complementary biomarkers such as kinematics or corticomotor excitability to understand muscle synergies in a global rehabilitation framework. Thus, though muscle synergies during gait have been widely accepted as an indicator for motor coordination (3,7), several aspects related to their utility in stroke rehabilitation assessment are still unclear.

In this research, we analyzed muscle synergies during gait of three subacute post-stroke patients with low functional abilities before and after two months of robotic rehabilitation. The main goal of this paper is to analyze and quantify how motor coordination can be modified in subacute post-stroke patients after a robotic therapy and to study whether this approach could be a viable means of tracking motor control changes and to observe progress in subacute stroke patients

This research is part of the NIMBLE project PID2021-123657OB-C31, funded by MCIN/AEI/10.13039/501100011033 and by the European Regional Development Fund.. Co-funded by grant RED2022-134319-T and by the European Union with grant DTS23/00047, funded by MCIN/AEI/ 10.13039/501100011033. A.C, N.L and J.T are with Hospital Los Madroños (Madrid, Spain). C.S-d-V, J.C.M and C.B.S-M are with the Center for Robotics and Automation of the Spanish National Research Council (Madrid, Spain). Corresponding author: C.B.S-M (clara.sanzmorere@csic.es; 918711900).

with low motor functions. Finally, we aim to determine if muscle synergies during gait are related to functional outcomes and kinematics improvements, following a multi-level approach (2,16).

Our hypotheses include that after the rehabilitation 1), patients will obtain higher scores on clinical scales, 2) patients will modify kinematics walking patterns, 3) patients will modify their muscle coordination and motor control during gait, considering both time-dependent and time-independent components. Finally, the analysis of these multi-level metrics may provide a clearer understanding of the clinical meaning of the modified muscle coordination.

II. Materials and Methods

A. Protocol design

Three subacute stroke participants were enrolled for a 2-month clinical study in which they received robotic gait therapy with the Walkbot Premium (P&S Mechanics, Seoul, Korea), a robot-assisted locomotor training system (6) and daily conventional prescribed rehabilitation, including physical, occupational, speech and cognitive therapy. Robotic rehabilitation was carried out five times a week, for 45 minutes, in which they received at least 30 minutes of active walking therapy. Assessment sessions were carried out before the start of the study (PRE) and at the end of the study (POST). The assessments included the Functional Ambulation Category (FAC), Functional Independence Measure (FIM), the 10-meter walking test (10MWT), and electromyography activity (EMG) and kinematic data collection during natural overground walking. For the 10MWT, two runs were carried out at the patient's self-selected speed. Patients walked on a 14-meter corridor, but only the 10 central meters were considered to avoid the acceleration and deceleration phases. EMG data were recorded during the 10MWT from 16 bilateral muscles: Gluteus Medius (GlMe), Rectus Femoris (ReFe), Vastus Lateralis (VaLa), Biceps Femoris (BiFe), Semitendinosus (Sem), Tibialis Anterior (TiAn), Gastrocnemius Medialis (GaMe) and Soleus (Sol) by means of the wireless Trigno Research + system (Delsys Inc., Boston, MA) integrated in Xsens MVN (Movella Inc., Henderson, NV). Though most of the studies in literature measured EMG activity using optoelectronics gait analysis systems, we selected a system based on inertial measurement units (IMUs) that provide practical and faster setting up, suitable for patients with lower motor functions that need physical support by a physical therapist. EMG sensors were placed based on the SENIAM recommendations (17).

B. Patient recruitment

Inpatients whom have experienced a single stroke event between 28 and 200 days prior to enrollment, present with hemiparesis, have a minimum cognitive level (Token Test > 8), and were at least 18 years old were eligible for recruitmentPatients could not participate if they had any orthopedic, cardiorespiratory or neurological pathology that could limit walking (painful arthritis, osteoporosis, heart failure, uncontrolled hypertension, severe cognitive damage…). Other exclusion criteria for gait training with the robotic Walkbot device included non-healing ulcers or active infections, a maximum height of 200 cm and a maximum weight of 135 kg. The study was accepted on the 12th of April 2023 by the Ethical Committee of the Severo Ochoa University Hospital with the code NIMBLE_Stroke_HLM.

C. Data analysis

Kinematic data of the sagittal plane of hip, knee and ankle joints were recorded at 60 Hz with the Xsens MVN (Movella Inc., Henderson, NV) and segmented based on left and right heel strike events, manually indicated by expert researchers based on kinematics and acceleration signals obtained from the IMUs. Data from each gait cycle were resampled with 100 samples and averaged between steps.

EMG data were recorded at 2.148 kHz and were filtered with a 4th-order Butterworth high-pass filter at 20 Hz and a 4th-order Butterworth low-pass filter at 400 Hz. Additionally, the EMG data were de-meaned, rectified, and then re-filtered with a 5 Hz low-pass filter to obtain the envelopes. Finally, as kinematics and EMG data were synchronized, EMG data were segmented based on the same events obtained for kinematics. For all patients, the 20 central cycles of the smoothest walking run were selected.

Muscle synergies were computed separately for the most affected side of each patient using the SynergyLAB interface developed by Barroso et al., 2014 (18). This software applies the Non-Negative Matrix Factorization and delivers the time-dependent (H) and time-independent (W) coefficients calculated from the EMG data. The optimal number of synergies was selected by studying the quality of the reconstruction with the Variability Accounted For (VAF) for each muscle (VAFmuscle) and the total (VAFtotal). Based on literature, the threshold chosen was 75% for VAFmuscle and 90% for VAFtotal (19).

III. Results

Three subacute post-stroke patients were enrolled for this study (Table 1). Clinical scales are summarized in Figure 1.

Table 1.Characteristics of the patients. Stroke type H refers to hemorrhagic and I to ischemic.

	Patient 1	Patient 2	Patient 3
Gender	F	M	M
Age	76	68	76
Affected side	R	L	L
Days from stroke	58	134	107
Stroke type	H	I	I
Initial FAC	1	1	0
Initial FIM	93	104	107

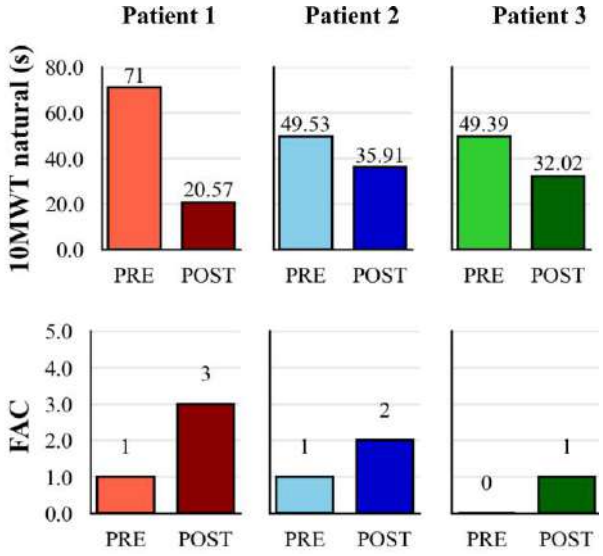


Figure 1 Clinical Scales outcomes during the PRE and POST sessions of all three patients for the 10-meter walking test (10mWT) and the Functional Ambulation Category (FAC).

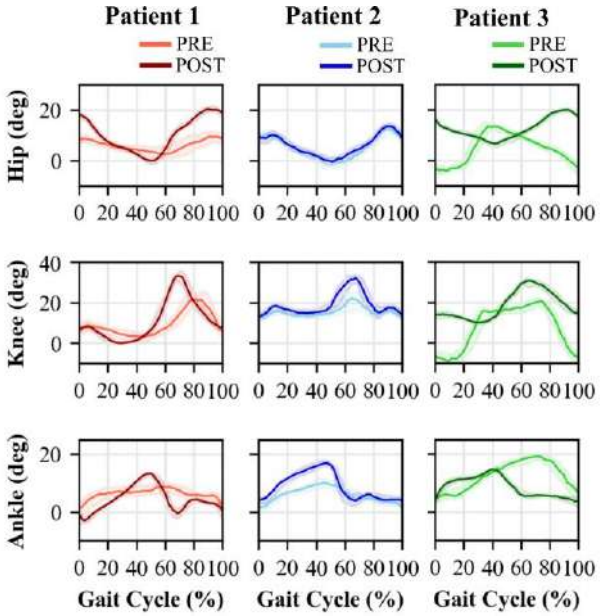


Figure 2 Sagittal kinematics for the Hip, Knee and Ankle of the affected side of each Patient throughout the gait cycle during the PRE and POST sessions of all three patients.

All patients improved their walking speed by 72%, 27% and 35% and FAC by 2, 1 and 1 respectively.

The sagittal kinematics of the affected side of all patients are shown in Figure 2. The RoM of Patient 1 and Patient 2 changed from the PRE to the POST session. For Patient 1, notable improvements included an increased hip, knee and ankle RoM (respectively by 55, 30 and 35%). Patient 2 did not show changes in the hip RoM, but we observed changes of 38 and 43% in the knee and ankle RoM, respectively. The walking patterns of all patients were more physiological after the rehabilitation. They showed a higher knee flexion during the swing phase, a more pronounced ankle dorsiflexion during the stance phase and, for Patient 1, a higher hip flexion at heel strike. The kinematics patterns of Patient 3 at the level of the hip and the knee were inverted compared to a normalized gait pattern during the PRE session, but they were normalized after the rehabilitation with a positive knee flexion and a flexed hip at heel strike.

Regarding muscle synergies, as shown in Table 2 the optimal number obtained was 4 for Patient 1, as 3 synergies did not allow for an accurate EMG reconstruction (the VAFtotal was lower than 90 % and a VAFmuscle lower than 75% in the PRE). On the other hand, for both Patients 2 and 3, 3 synergies would have been enough for a precise reconstruction of muscle synergies. However, to allow the comparison between the 3 patients, we selected 4 synergies for the analysis. Figure 3 summarizes the results of the muscle synergies analysis. The time- dependent variable H shown in Figure 3A, changed between the PRE and the POST sessions in all 3 patients. For Patient 1, anticipation of muscle activation was observed in Synergies 1, 2 and 3: the peak activity in the POST session occurred at 3% of the gait cycle, compared to 19% in the PRE session for Synergy 1; at 40% instead of 48% for Synergy 2 and at 62% instead of 72 % for Synergy 3.For Patient 2, an extra peak of activation occurred in the Synergies 1 and 3 in the POST session compared to the PRE at 64% and 39% of the gait cycle, while Synergy 2 and 4 remained similar. For Patient 3, the pattern of the synergies changed considerably. In Synergy 1, an anticipated activation occurred shifting from the peak of activation from 31% of the gait cycle in PRE to 8% of the gait cycle in the POST session. Moreover, the activation peaks were more pronounced in the POST session for Synergy 2 and 3. Figure 3B shows the time-independent variable W. For Patient 1 and Patient 2, the patterns of activation remained similar throughout the rehabilitation process in all 4 synergies. Patient 2 showed a co-activation of ReFe, VaLa, GaMe and Sol can be observed in Synergy 2 with a Synergy 1 mainly dedicated to GlMe. In contrast, for Patient 3 we observed an activation of the GlMe in Synergy 1 during the PRE session that shifted to Synergy 4 in the POST session.

IV. Discussion

In this research, we analyzed the effects of a 2-months robotic therapy in the muscle synergies of the affected leg of 3 subacute stroke patients with low gait independence and mobility (FAC of 1 for both Patient 1 and 2, and FAC of 0 for Patient 3 at admission) during overground walking. To the best of the authors' knowledge, this is the first time muscle synergies have been studied for this type of patient after robotic gait rehabilitation. Moreover, muscle synergies were related to the functional and kinematic changes observed during the rehabilitation program, as part of the

Table 2 Variability Accounted For (VAF) in % for all muscles (VAFtotal) and for the minimum VAFmuscle of all 8 muscles. Bold indicates the values that are below the quality threshold of 90% for VAFtotal and 75% for VAFmuscle.

VAF (%)		PRE		POST	
		3 syn	4 syn	3 syn	4 syn
Total	Patient 1	**87**	93	93	96
	Patient 2	92	95	91	94
	Patient 3	90	94	92	95
Muscle	Patient 1	**74**	86	89	92
	Patient 2	82	92	86	89
	Patient 3	76	77	80	91

multi-level characterization of the recovery process of stroke survivors proposed by the NIMBLE project (16).

Clinical scales and kinematics showed 1) a higher walking speed, 2) a more independent ambulation, 3) a higher sagittal RoM and (4) a normalized sagittal gait pattern. These results are consistent with the observed functional improvements after robotic rehabilitation (20).

The number of muscle synergies chosen was 4, even though for Patients 2 and 3, it would have been more appropriate to select 3 synergies according to the VAFtotal and VAFmuscle of both PRE and POST sessions. This decision was made to allow the comparison between patients, as in previous studies (2,8,10). Muscle synergies evolved throughout the rehabilitation process for all patients, though the changes observed were different for each patient. Patient 1 showed mainly changes in the time dependent component H, Patient 2 in both dependent H and independent component W and Patient 3 mainly in the independent component W. Patient 1 presented an earlier activation of Synergy 1, 2, 3, consistent with the changes in muscle synergies observed in the literature when increasing walking speed (5). Also, we observed a higher activation peak of Synergy 2 and 4, during the stance phase, which could be related to a stronger activation of hamstrings and triceps surae muscle due to an increased body weight loading on the affected leg, leading to a better preparation for the swing phase (15). For Patient 2 we observed a modified activation of Synergy 1, which mainly represented the GlMe activation. In the POST session, a second peak appeared during the initial swing phase, probably due to the hip abduction carried out by the patient to compensate for his limited knee flexion (around 30 deg), a characteristic pattern in post-stroke patients known as hip hiking (21). A higher activation of Synergy 3, related to TiAn, was also observed during the stance phase of the POST session. This could be a compensatory strategy to increase the propulsion force that seems to be lost due to the reduced

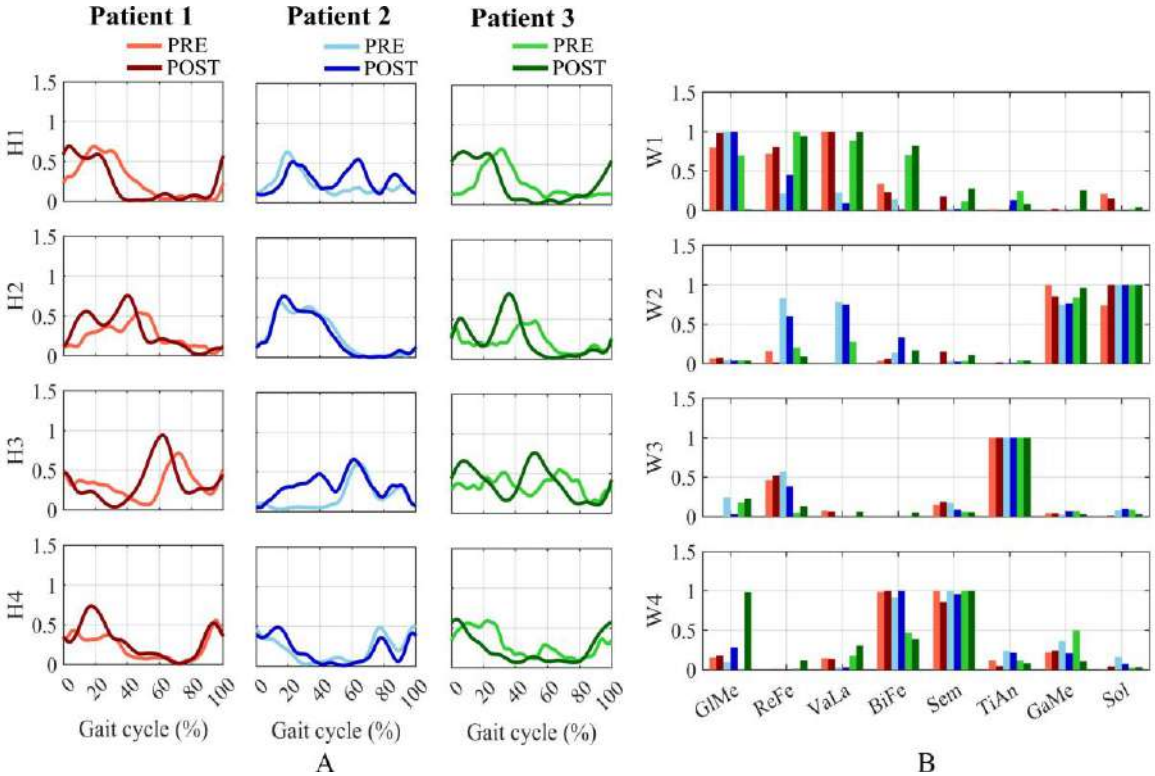


Figure 3 A. Time- dependent variable (H) across 4 synergies throughout the gait cycle during the PRE and POST sessions of all three patients. B. Time- independent variable (W) showing muscle activation patterns across 4 synergies during the PRE and POST sessions of all three patients. Red, blue and green colors refer to the affected side of Patient 1, 2 and 3 respectively. H equal to 1 refers to a synergy being 100% active during that Gait cycle %. W equal to 1 refers to the muscle being 100% part of that specific synergy.

hip extension during stance (5). Patient 3 exhibited a synergy shift of the time-independent component W of the GlMe from Synergy 1 to Synergy 4 from PRE to POST. This is an unexpected change that could be explained by the inability of Patient 3 to control individual muscles, leading to a strategy of simultaneous multiple-muscle activation to maintain control during the stance phase (12). This could also explain the similarity of the time-dependent components H, which are very similar between Synergy 1 and Synergy 4. These changes are consistent with the changes observed in the kinematics of Patient 3, who walked with a flexed knee and hip and has a tendency of ankle dorsi-flexion during the stance phase and plantar flexion during the swing phase.

The comparison of the current results with the literature is not straightforward. First, only two studies have analyzed muscle synergies of subacute stroke survivors during a single session. One was related to overground curved walking, which might affect the muscle coordination, and the other analyzed merged muscle synergies (12,22).Though it is beyond the scope of this research, considering the classification presented in (12), we can consider Patient 2 as Subtype 1, where GaMe and Sol are merged with quadriceps activation and Patient 3 as Subtype 3, with a slight coactivation of GlMe, hamstrings and quadriceps in early stance. The subtypes of these patients did not change after the rehabilitation. However, the subtype classification was mainly based on the time-independent component W and does not consider the time-dependent component H where some positive changes were observed for Patients 2 and 3 post-treatment. Some studies have analyzed the effects of rehabilitation on stroke survivors with several devices such as a treadmill with body weight support (10,23), an exoskeleton (2,14,15) or a Functional Electrical Stimulator (24). Most of them conclude that the optimal number of synergies changes after rehabilitation from 3 to 4 synergies and that, if the synergy number does not change, it might be related to a change in improved synergy timing (10). Though the optimal number of synergies did not change in our study, we observed changes in the time-dependent component H which is consistent with the literature. It is noteworthy that most of these studies are related to chronic patients (10,14,23,24) or assessments are carried out on a treadmill (11,25). Only two studies, in the literature, were conducted with acute post-stroke patients with low motor function (FAC < 3 and FIM < 78) and a similar multi-level approach protocol. They found the number of muscle synergies was similar between limbs in the POST session with an increased similarity between lateral synergies of patients after robotic intervention. They associated these improvements with better walking speed, step cadence, stance duration percentage of gait cycle. Comparing the muscle synergies of Patients 1, 2, and 3 with the healthy subjects of Gizzi et al. (8), we observe a tendency towards more normalized patterns in the POST session. However, the comparison of our results with the literature is not straightforward. In fact, most research studies tend to have specific protocols such as: 1) different sets of muscles (for example including the adductor muscles or not including the soleus), 2) different number of cycles, 3) different algorithms for synergy extraction. Standardizing the measuring protocols might be practical to compare results between research groups. This study presents several limitations. First, this study was tackled as a case study due to the limited sample size. Increasing the sample sizes could help generalize findings to a greater subacute stroke population. Moreover, to record the kinematics of these patients, IMUs synchronized with surface EMG sensors were employed. Although this is not the gold-standard strategy typically used in research, this approach enabled data collection in these patients, as they needed continuous or intermittent physical therapists help during the PRE session. One study analyzed muscle synergies during overground walking with low-mobility patients while measuring kinematics with the optoelectronic gold-standard method. They used the All in one Walking Trainer body weight support device for safety, allowing patients to walk independently and avoiding marker occlusion. However, considering that with FAC lower than 3 external assistance for walking is needed, it might be possible that, in that study, patients were being held by the body weight support, reducing the weight of the patient, increasing balance, modifying the natural walking pattern and thus affecting muscle synergies. Employing IMUs could have affected kinematics accuracy and gait cycle segmentation, as kinematics and acceleration signals were used instead of marker position, which is a more accurate method. However, IMUs allowed patients to walk with external assistive devices, since in the POST session, they all switched to a cane or walker, which could have influenced their stability and security, and subsequently impact their walking pattern, walking speed and muscle coordination. Though great care was taken to correctly place the electrodes in the same place in every session by the same physical therapist, it is not possible to determine whether results might be affected by sensor placement, crosstalk or uncommon muscle coordination due to the stroke. Additionally, the comparisons with the less affected side and with a control group were not carried out in this study (2). Similarly, our multi-level approach considered functional and kinematics changes for a global understanding of the effects of muscle synergies in patients' walking abilities, but other metrics such as gait scores (28) or corticomotor excitability (13,16). These three aspects could be considered in future research.

Our robotic-assisted gait therapy incorporates the two main conditions to promote functional neural recovery. In addition to movement repetition for intensive training, it enables task- specific practice, which may drive central nervous adaptations (26). Further research could be carried out to isolate robot-dependent and activity-dependent plasticity to provide additional insights into the optimal rehabilitation treatment for each patient.

V. Conclusion

Our research presents for the first time the muscle synergy of low-mobility post-stroke patients during overground walking after a gait rehabilitation treatment with a robotic exoskeleton. Even if results are not generalizable, our hypotheses were verified: (1) patients walked faster with higher independence after the rehabilitation, (2) the kinematics patterns were normalized after the therapy, (3) muscle modules were modified, each patient responding differently to the rehabilitation. The addition of functional and kinematics metrics allowed for a more comprehensive understanding of muscle synergies. In this study we observed meaningful changes in the time-dependent and time-independent components of muscle synergies, all consistent with the kinematics patterns of the patients, patient-specific muscle coordination and muscle adaptations during rehabilitation. This emphasizes the importance of patient-specific approaches in gait therapy guided by the identification of multi-level metrics. Finally, the therapy proved to be effective in improving functionality, kinematics, and muscle coordination of subacute stroke survivors.

Acknowledgment

We would like to thank Elena De Eusebio Rubio; Elena Orcajo, MD; Melina Longoni, MD; Filipe Barroso, PhD and the remaining therapists and personnel of the Advanced Neurorehabilitation Unit of Hospital Los Madroños.

References

1. Feigin VL, Stark BA, Johnson CO, Roth GA, Bisignano C, Abady GG, et al. Global, regional, and national burden of stroke and its risk factors, 1990–2019: a systematic analysis for the Global Burden of Disease Study 2019. Lancet Neurol. 2021 Dec;20(10):795–820.
2. Tan CK, Kadone H, Watanabe H, Marushima A, et al. Lateral symmetry of synergies in Lower Limb muscles of acute post-stroke patients after robotic intervention. Front Neurosci. 2018 Dec;12(APR).
3. Criekinge T Van, Vermeulen J, Wagemans K, Schröder J, Embrechts E, Truijen S, et al. Lower limb muscle synergies during walking after stroke: a systematic review. Disabil Rehabil. 2020 Dec;42(20):2836–45.
4. Hashiguchi Y, Ohata K, Kitatani R, Yamakami N, Sakuma K, Osako S, et al. Merging and fractionation of muscle synergy indicate the recovery process in patients with hemiplegia: The first study of patients after subacute stroke. Neural Plast. 2016;2016.
5. Barroso FO, Torricelli D, Molina-Rueda F, Alguacil-Diego IM, et al. Combining muscle synergies and biomechanical analysis to assess gait in stroke patients. J Biomech. 2017 Dec;63:98–103.
6. Kim SY, Yang L, Park IJ, Kim EJ, Park MS, You SH, et al. Effects of innovative WALKBOT robotic-assisted locomotor training on balance and gait recovery in hemiparetic stroke: A prospective, randomized, experimenter blinded case control study with a four-week follow-up. IEEE Transactions on Neural Systems and Rehabilitation Engineering. 2015 Dec;23(4):636–42.
7. Hong YNG, Ballekere AN, Fregly BJ, Roh J. Are muscle synergies useful for stroke rehabilitation? Vol. 19, Current Opinion in Biomedical Engineering. Elsevier B.V.; 2021.
8. Gizzi L, Nielsen JF, Felici F, Ivanenko YP, Farina D. Impulses of activation but not motor modules are preserved in the locomotion of subacute stroke patients. Hart and Giszter. 2011;106:202–10.
9. Kautz SA, Bowden MG, Clark DJ, Neptune RR. Comparison of motor control deficits during treadmill and overground walking poststroke. Neurorehabil Neural Repair. 2011 Dec;25(8):756–64.
10. Routson RL, Clark DJ, Bowden MG, Kautz SA, Neptune RR. The influence of locomotor rehabilitation on module quality and post-stroke hemiparetic walking performance. Gait Posture. 2013 Dec;38(3):511–7.
11. Coscia M, Monaco V, Martelloni C, Rossi B, Chisari C, Micera S. Muscle synergies and spinal maps are sensitive to the asymmetry induced by a unilateral stroke. J Neuroeng Rehabil. 2015 Dec;12(1).
12. Mizuta N, Hasui N, Nishi Y, Higa Y, Matsunaga A, Deguchi J, et al. Merged swing-muscle synergies and their relation to walking characteristics in subacute post-stroke patients: An observational study. PLoS One. 2022 Dec;17(2 February).
13. Krishnan C, Ranganathan R, Kantak SS, Dhaher YY et al. Active robotic training improves locomotor function in a stroke survivor. 2012.
14. Zhu F, Kern M, Fowkes E, Afzal T, Contreras-Vidal JL, Francisco GE, et al. Effects of an exoskeleton-assisted gait training on post-stroke lower-limb muscle coordination. J Neural Eng. 2021 Dec;18(4).
15. Tan CK, Kadone H, Watanabe H, Marushima A, Hada Y, et al. Differences in Muscle Synergy Symmetry Between Subacute Post-stroke Patients With Bioelectrically-Controlled Exoskeleton Gait Training and Conventional Gait Training. Front Bioeng Biotechnol. 2020 Dec;8.
16. Cherubini A, del Valle CS, Sanz-Morere CB, Herranz-Calero E, De-Eusebio-Rubio E, González-Expósito S, et al. Multi-level characterization of the recovery process of a stroke survivor after 2 months of robotic therapy with the Walkbot robot. 2024 10th IEEE RAS/EMBS International Conference for Biomedical Robotics and Biomechatronics (BioRob). 2023;(62):183–209.
17. Stegeman DF, Hermens HJ. Standards for surface electromyography: the European project "Surface EMG for non-invasive assessment of muscles (SENIAM)."
18. Barroso FO, Torricelli D, Moreno JC, Taylor J, Gomez-Soriano J, Bravo-Esteban E, et al. Shared muscle synergies in human walking and cycling. J Neurophysiol. 2014;112.
19. Turpin NA, Uriac S, Dalleau G. How to improve the muscle synergy analysis methodology? Eur J Appl Physiol. 2021;121(4):1009–25.
20. Hu M miao, Wang S, Wu C qin, Li K peng, Geng Z hui, Xu G hui, et al. Efficacy of robot-assisted gait training on lower extremity function in subacute stroke patients: a systematic review and meta-analysis. J Neuroeng Rehabil. 2024;21(1):165.
21. Kerrigan DC, Frates EP, Rogan S, Riley PO. Hip Hiking and Circumduction. Am J Phys Med Rehabil. 2000 Dec;79(3):247–52.
22. Lee JH. Characteristics of muscle synergy extracted using an autoencoder in patients with stroke during the curved walking in comparison with healthy controls. Gait Posture. 2024 Dec;107:225–32.
23. Young DR, Banks CL, McGuirk TE, Patten C. Evidence for shared neural information between muscle synergies and corticospinal efficacy. Sci Rep. 2022 Dec;12(1).
24. Ferrante S, Bejarano NC, Ambrosini E, Nardone A, Turcato AM, Monticone M, et al. A personalized multi-channel FES controller based on muscle synergies to support gait rehabilitation after stroke. Front Neurosci. 2016 Dec;10(SEP).
25. Clark DJ, Ting LH, Zajac FE, Neptune RR, Kautz SA. Merging of healthy motor modules predicts reduced locomotor performance and muscle coordination complexity post-stroke. J Neurophysiol. 2010 Dec;103(2):844–57.
26. Fisher BE, Sullivan KJ. Activity-dependent factors affecting poststroke functional outcomes. Top Stroke Rehabil. 2001;8(3):31–44.
27. Mayr A, Kofler M, Quirbach E, Matzak H, Fröhlich K, Saltuari L. Prospective, blinded, randomized crossover study of gait rehabilitation in stroke patients using the Lokomat gait orthosis. Neurorehabil Neural Repair. 2007 Jan;21(4):307–14.
28. Schwartz MH, Rozumalski A. The gait deviation index: A new comprehensive index of gait pathology. Gait Posture. 2008;28(3):351–7.

A Body-Powered Wrist-Driven Supernumerary Robotic Finger

Alyssa N. Maguina
Biomedical Engineering Program PUCP-UPCH
Pontificia Universidad Catolica del Peru
Lima, Peru
0009-0006-3621-3472

Renato Mio
Chair of Digital Health
University of Bayreuth
Bayreuth, Germany
0000-0001-8419-2633

Sebastian Caballa
Mechanical Engineering Section
Pontificia Universidad Catolica del Peru
Lima, Peru
0000-0002-8356-2003

***Abstract*—Individuals with grasping impairments face significant challenges in performing daily tasks due to reduced hand function. Existing supernumerary robotic fingers (SRFs) often rely on electronic components that limit their usability through added weight and power constraints. This work introduces the first body-powered wrist-driven SRF (bpSRF), a design that addresses these limitations by removing all electronic components. The proposed bpSRF weighs 52 g and is mostly made of 3D printed parts. Using body-powered actuation principles, the extra finger is driven by wrist movements, offering a practical, affordable, and lightweight solution for hand augmentation. The bpSRF has two degrees of freedom, enabling users to perform enhanced grasping techniques with minimal learning curve. Experimental validation with five healthy participants showed high success rates and rapid learning of novel grasping patterns for tasks involving large or multiple objects that typically require two hands. The design offers a workspace volume approximately three times larger than a human thumb, potentially expanding users' manipulation capabilities. This research contributes to a new paradigm in assistive technology, presenting a lightweight, cost-effective, and open source SRF that can enhance grasping abilities for individuals with motor impairments while also offering augmentation possibilities for healthy users.**

***Index Terms*—supernumerary robotic finger, assistive technology, body-powered, hand augmentation, 3D printing**

I. Introduction

Individuals with grasping difficulties face constant challenges, as impairments in hand dexterity and strength hinder their ability to perform daily tasks. Spinal cord injuries [1], trauma, stroke, cerebral palsy, and other neurological pathologies result in motor impairment [2], further contributing to the loss of manipulation ability. Up to 60% of stroke patients experience loss of hand sensory and/or motor function. In addition, chronic motor disorders make it difficult to utilise the hand for everyday functional tasks, such as donning shirts, tying laces, and gripping objects. [3].

Currently, a variety of assistive technologies are available to aid people with grasping difficulties. Hand exoskeletons [4] and soft gloves [5] are used in to assist the movement of finger joints, with the latter being safer and more comfortable for the hand. Recently, supernumerary robotic fingers (SRFs) have emerged as a promising alternative. SRFs are a type of wearable technology that, by adding one or more extra robotic fingers to the hand, can compensate for the lack of fingers mobility in persons with hand impairment or, in healthy persons, augment standard human manipulation with novel 6-fingered or 7-fingered grasp patterns [6].

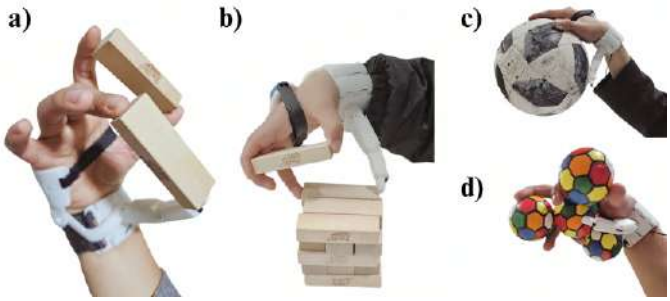


Fig. 1. The bpSRF prototype in different grasping tasks: (a) double pinch grasp, (b) augmented spherical grasp, (c) Double pinch grasp in Jenga tower building task and (d) grasping multiple objects in one hand.

SRFs are typically wrist-mounted, working alongside the natural fingers for grasping assistance and augmentation [7]–[23]. For patients with grasping limitations, such as those suffering from hemiparesis due to a stroke, SRFs usually act as a surrogate artificial thumb [7]–[12]. For example, patients can grip objects by forming a cylindrical grasp between the SRF and the palm. Additionally, in healthy individuals, SRFs extend the natural capabilities of the hand, making it possible to form grasp patterns capable of holding large objects or manipulating several small ones [13]–[23], feats that are normally attainable bimanually. Therefore, SRFs can enhance the capabilities not only in people with grasping disabilities but also in healthy individuals.

Current SRFs offer many advantages, but their widespread adoption could also be limited by the inconveniences associated with the electronic components they require. The actuators and batteries, which are often placed outside the SRF itself [8], [18], considerably increase the weight and limit the time it can be worn before causing discomfort. For example, in [11], the actuation system accounts for 146g, representing 51% of the total weight. Similarly, in [7], the actuator alone comprises 69.5% of the SRF's total weight. In the context of assistive applications, it is crucial to minimise the weight of SRFs to prevent discomfort and potential orthopedic injuries to users.

A potential workaround to current electronics size and

weight limitations could be drawn from the principles of body-powered prosthetics. Body-powered upper-limb prostheses draw power from healthy limb movements through cables that control the closing and opening of the terminal device, which could be a hook [24] or an artificial anthropomorphic hand [25]. In fact, over the last decade, 3D-printed body-powered prostheses have gained wide popularity due to their low-cost and ease of replication [26]. Even without electronics and complex controllers, body-powered prostheses offer high functionality and intrinsic force feedback via the driving cable reaction forces over the wearer's body. Crucially, at the Cybathlon 2016 Arm Prosthesis Race, a body-powered device defeated even the most advanced bionic prostheses in the world [27]. In the same manner, a body-powered SRF would also offer the advantage of minimal weight and intrinsic feedback while keeping their functionality.

Although recently developed SRFs have experimented with novel design strategies, none of these devices are driven by the body. A manually actuated SRF was also proposed [14], but driving it required the use of the contralateral hand. This could prove cumbersome for the user and defeats the purpose of movement augmentation, which is to add extra degrees of freedom (DoFs).

To address current limitations and promote more widespread and continuous use of SRFs, this paper proposes a novel body-powered wrist-driven SRF (see Fig. 1). The body-powered SRF (bpSRF) does not require any electronic components or external power, weighs only 52 g, and can be easily manufactured by 3D printing. It is driven by wrist flexion/extension and abduction/adduction movements through a cable mechanism. This design can potentially improve the capabilities of users with grasping impairments, but who preserve wrist mobility. In healthy individuals, the bpSRF offers the possibility to execute novel grasping patterns and expand the workspace volume of the hand as shown in Fig. 1. To our knowledge, this is the first SRF that fully utilises body-powered actuation, setting it apart from all previous designs.

II. Design Process

The bpSRF mechanism was designed to operate directly through the user's own body movements, dramatically reducing the complexity of the system and its weight compared to externally powered SRFs. This simplicity leads to a shorter learning curve, allowing users to quickly adapt and integrate the bpSRF into their hand control motor strategies. Intrinsic haptic feedback will occur naturally through the physical interaction between the bpSRF and the user's hand and wrist, as it happens with body-powered prostheses [28]. Furthermore, the body-powered principle provides immediate actuation with no latency between user command and device motion.

Maintaining a lightweight design without compromising performance is a crucial design goal for a wearable SRF. Previous SRFs weigh between 100-286 g for one additional robotic finger [8], [10], [12], [15], [19], [21], [29], between 229-650 g for two additional robotic fingers [7], [16], [18], [30], [31], and 96 g for one additional manually-actuated robotic finger [14]. Common approaches to lower the overall weight of the system include underactuation [11], [14], the use of soft materials [9], and even origami-inspired structures [10]. In contrast, the bpSRF proposed weighs only 52g, comprising mostly 3D-printed parts of easy assemble, driving cables, and Velcro straps for attaching it to the user's hand (see Fig. 3).

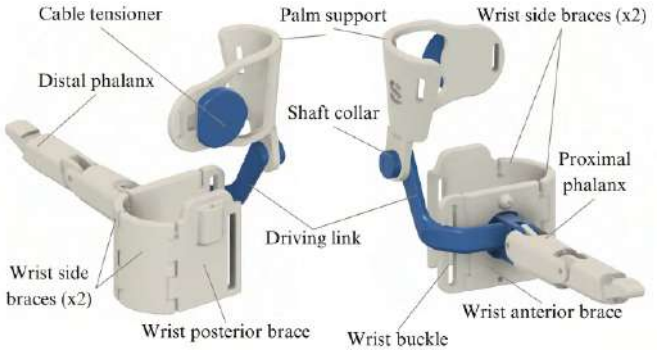


Fig. 2. Components of bpSRF: Featuring the wrist mount, linkage connector, lateral hand-shaped piece, tension adjustment piece and the proximal and distal links

A. Body-powered actuation

The bpSRF design is highly inspired by the model from [25], in which the prosthetic fingers form a 4-bar linkage mechanism that is actuated by cables. The 4-bar linkage was chosen for its ability to emulate natural finger movements and requiring less cable excursion to achieve full finger flexion while maintaining simplicity in its mechanical design. The bpSRF features two degrees of freedom (DoFs): flexion-extension and abduction-adduction, both driven by wrist movements. It is actuated through a cable mechanism in a similar fashion to wrist-driven partial hand prostheses [26]. When the wrist is flexed, the actuation cable is pulled and the finger is flexed. Conversely, wrist extension allows the bpSRF to return to its initial extended position due to the elastic cable (see Figure 3). The actuation cable is fixed in the distal phalanx, passes through the proximal phalanx, then enters the wrist

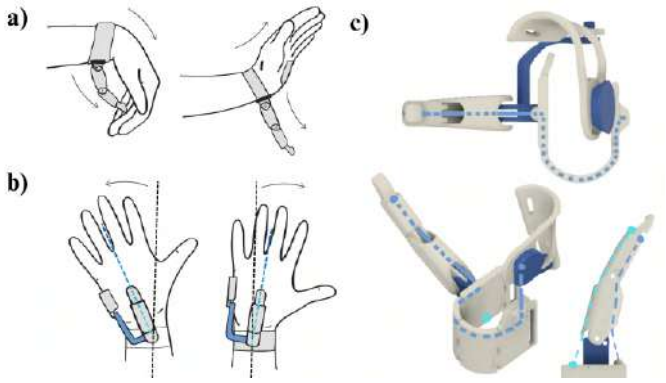


Fig. 3. Body-powered driving principle of the bpSRF. (a) By flexing the wrist, the bpSRF also flexes and by extending the wrist, the bpSRF also extends, (b) The second DoF of the bpSRF is akin to finger abduction-adduction and is driven by the wearer's palm when moving in ulnar or radial deviation, (c) Driving cable path through the 3D-printed components.

anterior brace and the side braces, and then exits through the wrist posterior brace. Finally, the cable can be manually tensioned with the cable tensioner in the dorsum of the hand over the palm support. Proper cable tension is important in body-powered devices as it directly influences the actuation force distribution across the mechanism. Adjustable tension allows users to fine-tune the device according to their own strength and comfort level, ensuring that the robotic finger moves in harmony with their natural fingers.

B. Ergonomy

The bpSRF was designed to integrate ergonomically with the hand. Anthropometric data from adult male hands guided the dimensions of the proximal and distal phalanges, ensuring effective grasping assistance while minimizing strain. Its grasp diameter range accommodates the size of objects that users typically interact with in their daily activities, including common household objects such as utensils and tools.

Most SRFs are positioned on the ulnar or radial side of the wrist. In this case, the placement of the base of the finger was carefully considered to avoid interference with the natural fingers. By positioning the bpSRF on the anterior side of the wrist and opposite to the palm, we allow a natural interaction between the bpSRF and the user's hand, minimizing obstruction and promoting its intuitive use as an additional 'thumb'. Moreover, this positioning leverages wrist flexion-extension and radial-ulnar deviation, translating these movements into the two DoFs of the bpSRF.

The parts in contact with the hand are meant to fit a variety of sizes and shapes of human hands. The palm support was designed in small (S), medium (M) and large (L) sizes. Each of them varies slightly in length and width to prevent discomfort during prolonged use. The wrist bracelet, as it is made of rigid plastic, was divided into four sections with relative movement that can adjust better to the compliant skin tissue.

C. Kinematics

Fig. 4 shows the two DoFs of the bpSRF about its base: flexion-extension and abduction-adduction. These DoFs have ranges of motion of approximately 60° and 50°, respectively, although these would depend on subject-specific mobility. As seen in Fig. 4a, the bpSRF flexion-extension DoF is driven by the palm support and the driving link in blue. In this manner, 15° of wrist flexion are converted through the cable tension and the 4-bar linkage in the robotic finger into a 60° finger flexion. Additionally, the robotic finger is capable of abduction and adduction about its rotating base, a movement driven by the ulnar and radial deviation movements of the wrist. This second DoF enhances the ability to grasp and manipulate objects by accommodating different orientations of the fingers in the coronal plane. Although the driving link mechanism allows for full 360° rotation of the robotic finger around its base, in this representation only the angles corresponding to the maximum radial and ulnar deviations according to [32] are shown.

The motion trajectory of the bpSRF, defined by a four-bar mechanism, moves from maximum extension (opening) to maximum flexion (closing) until it comes into contact with the palm. Fig. 5a illustrates the trajectory of the fingertip during flexion-extension. The blue shaded area represents a circular object grasped between the fingertip of the middle finger and the distal tip of the bpSRF, which could have a diameter of about 208 mm. For this estimation, it was assumed that the geometric center of the circular object must be within the boundary marked by straight perpendicular lines that represent the normal forces from each fingertip. Objects with slightly larger diameters could also be grasped by applying greater gripping forces.

Based on the bpSRFs estimated ranges of motion, its working volume was computed as a three-dimensional mesh (see Fig. 5b). This method yields a workspace volume of approximately 97.64 cm³. In comparison, the standard range of motion of a human thumb has an estimated functional workspace of 32-73 cm³ [33]. Hence, the bpSRF provides an increase in workspace volume ranging from 34% up to 205% compared to a natural human thumb.

III. Prototype Implementation

The majority of parts of the bpSRF can be 3D printed. The assembly of the different parts only requires metal pins, Velcro straps, and fishing braid wire. The metal pins are all 2.5 mm in diameter but with variable lengths depending on the parts it connects. To ensure friction-free movement between adjacent and connecting parts, a tolerance was added to several dimensions of the bpSRF before 3D printing. Table I presents a comprehensive summary of the materials and printing specifications, as well as the mechanical features of the resulting prototype.

For donning, the device is secured using Velcro straps, with the bpSRF base positioned on the anterior side of the wrist. The shaft of the driving link is inserted in the palm support. Then, the rigid cable is wrapped around the cable tensioner until it is sufficiently tightened and correctly positioned. For doffing, the cable tensioner is released, the palm support is removed from the pin, the Velcro straps are unfastened. All the files required for 3D printing components, a detailed list of

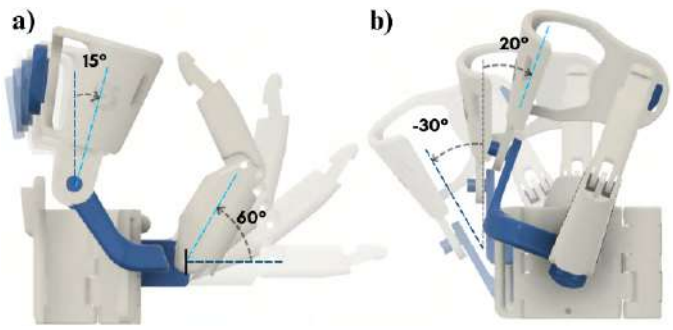


Fig. 4. Mechanical design and range of motion of the bpSRF. (a) Lateral view showing the flexion/extension range from 0° to 90°. (b) Frontal view illustrating adduction/abduction, with side-to-side motion across angles of -30° to 20°.

TABLE I
MATERIALS AND MANUFACTURING SPECIFICATIONS FOR THE BPSRF

Parameter	Specification
Materials	- PLA (3D printed). - 1.2 cm-width velcro straps. - 3.5 cm-width velcro straps - 2.5 mm⌀ galvanised aluminum pins for joints in four lengths: 5 x 33 mm, 1 x 17 mm, 1 x 14 mm, 2 x 8 mm. - 2 mm⌀ elastic wire. - 0.36 mm⌀ fishing braid wire.
Printing Parameters	- Layer height: 0.2 - 0.24 mm. - Infill percentage: 15%. - Print speed: 60 mm/s. - Support structure: Tree.
Mechanical specifications	- Total weight: 52g. - Assembled finger length: 93 mm. - Wrist brace dimensions (when unfolded): 138L x 50H x 5T mm.

materials and assembly instructions are available as an open repository at https://github.com/RenatoMio/bpSRF.

IV. EXPERIMENTS

A. Payload Characterization

The performance of the bpSRF was evaluated using a digital portable dynamometer (Opalux, OP-607) to quantify the actuation force (i.e., cable tension) and the payload relationship. The setup consisted of disconnecting the driving cable from the cable tensioner and instead tying it to the hook of the dynamometer with minimal initial tension (see Fig. 6a). Additionally, a MPU6015 inertial measurement unit (IMU) was placed on the hand side and used to verify that the hand palm was aligned with gravity (see Fig. 6b). The dynamometer was stabilised on the hand dorsum and zeroed, and the orientation of the hand was verified through the IMU reading before taking measurements (see Fig. 6c).

In this experiment, the resistive vertical force during an augmented cylindrical grasp between the palm and the bpSRF was measured. The trials were performed in three conditions, one per each bpSRF size (S, M, and L), and with five repetitions per condition. The payload consisted of a plastic bottle attached to calibrated metal weights, which increased

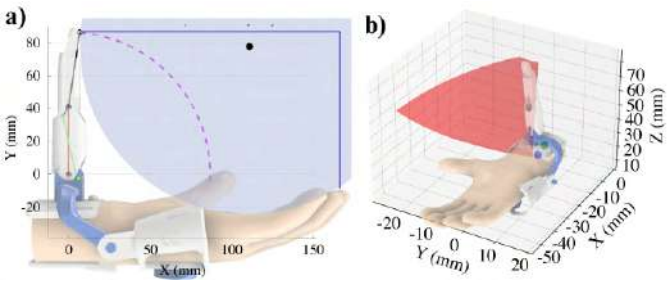


Fig. 5. Kinematics of the bpSRF. (a) Sagital view of the fingertip of the bpSRF trajectory during flexion. The shaded circular area represents the largest graspable object. (b) Angular workspace of the bpSRF.

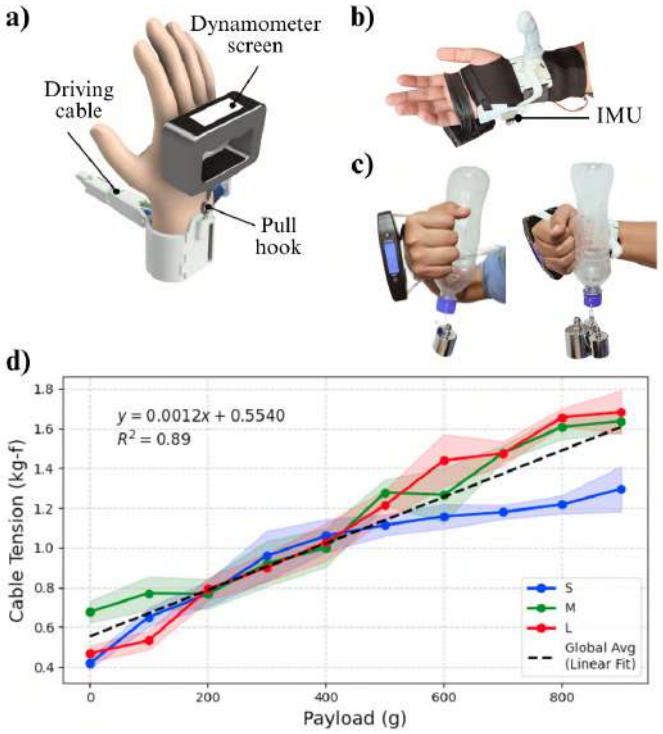


Fig. 6. Performance characterization. a) Digital dynamometer setup. b) View of the setup before adding payload with inertial sensor over the side of the palm. c) Setup after adding payloads of 200g and 800g. d) Payload vs Cable tension characterisation for each size version of the bpSRF. The shaded areas represent standard deviations (n=5) and the dashed line represents the result of linear regression across all trials.

from 0 g (no added weight) to 900 g in increments of 100 g. In this range, there is a linear relationship (coefficient of determination $R^2 = 0.89$) between the payload and the actuation tension of the cable (see Fig. 6d). At no added weight, 0.4 kilograms-force (kg-f) of tension are the minimum required to fully close the bpSRF, while at 900g of payload an average tension of 1.6 kg-f is used. This equates to an increase of 0.12 kg-f in tension per 100 g of payload, which highlights the efficiency of cable routing.

B. Grasping assessments

Pick-and-place experiments were conducted with five healthy participants (mean age = 23.2 ± 2.71 years, 2 females). All participants were right-handed and reported no neurological or motor impairments. The experiments were carried out in accordance to the Declaration of Helsinski and with approval of The Ethics Committee from the Pontifical Catholic University of Peru, with code 002-2023-CEICVyTech/PUCP. The grasps considered were previously described in [6] and are as follows:

- Augmented spherical grasp: a collaborative grasping technique in which both natural fingers and the SRF work together to grasp a large spherical object. The goal is to open the entire hand and fingers to maximise contact area, allowing for a better grip on the object. In our experiment,

we used a soccer ball with a diameter of 16 cm and a weight of 433 g.

- Augmented cylindrical grasp: a collaborative grasping technique in which both natural fingers and the SRF work together to grasp a large cylindrical object. Instead of the natural thumb, the SRF performs the opposition again the palm to grasp the object. In our experiment, we used a 3 liter empty bottle with a diameter of 19 cm.
- Simultaneous multi-grasp: When the natural fingers and SRF work together to execute two distinct conventional grasps in the augmented hand. In our experiment, participants performed a pinch grasp on a Jenga wooden block using the SRF and an adduction grasp on a standard playing card simultaneously.

In these tasks, only the augmented hand is used and the participant must remain seated. Each task lasts 1 minute, with a 30-second break in-between (see Fig. 7a). The objects are initially placed at Point A and must be moved to Point B (see Fig. 7). Participants were positioned midway between the starting and target locations. They are required to pick up, lift, and move each object as quickly as possible from A to B and from B to A. The task begins when the user starts a stopwatch and ends when the time runs out. A trial is considered a failure if it is not completed, if the correct grasp is not performed, or if the object falls. In any of these cases, the participant must restart the trial from their last position (A or B).

In general, all participants became proficient in executing the augmented grasps with just one minute of practice per task. On average, participants succeeded on 8.8 ± 2.9, 11.4 ± 3.6 and 7.2 ± 3.0 attempts per minute with average success rates per task of 81.5%, 91.0% and 98.5% for the ball, bottle, and multi-object grasping tasks respectively. Moreover, as shown in Fig. 8, participants kept reducing the time required to complete an attempt, with average durations of 5.38 ± 1.79s, 4.11 ± 0.95s and 6.96 ± 1.65s over their last three attempts for the ball, bottle, and multi-object grasps tasks, respectively. These results are an indication of early stages of motor learning in hand and bpSRF coordination. Finally, all participants reported minimal fatigue overall during this short experiment, although many grasping cycles were performed, which supports the idea that wrist-driven actuation was comfortable to use.

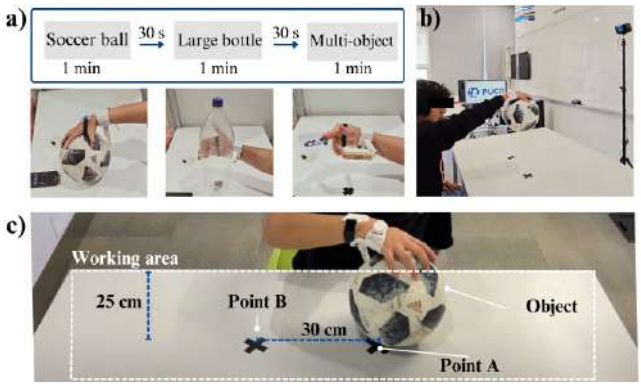


Fig. 7. Grasping experiments protocol. a) Tasks and times per task. b) Side and c) top views of the experimental setup.

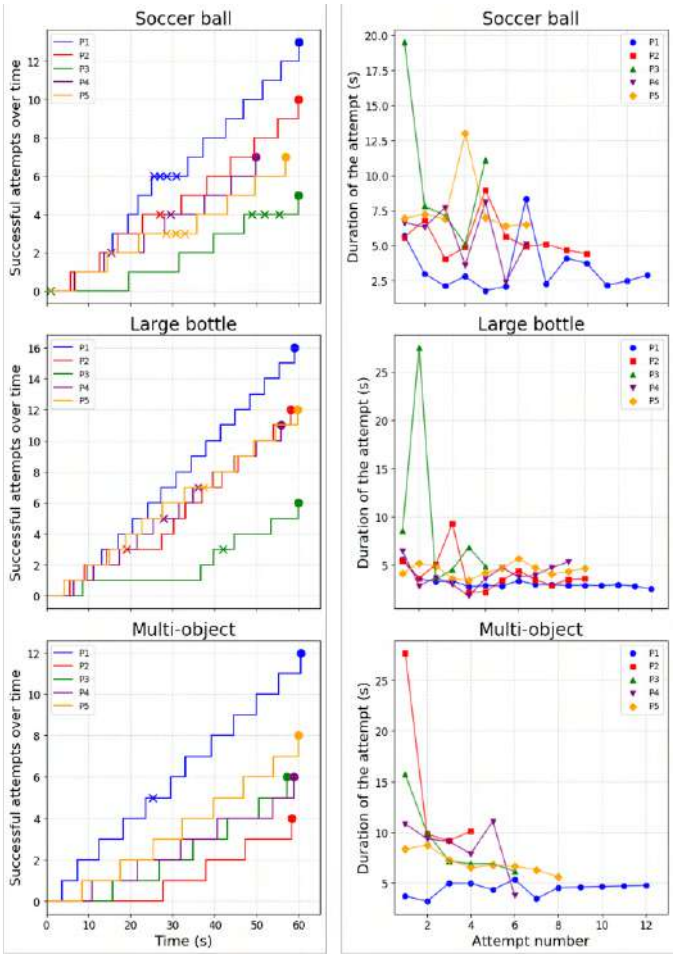


Fig. 8. Results from the grasping experiments. Each line represents a participant. On the cumulative attempts plots, the circles at the end of each line represent the ending time (last successful attempt within the allotted 60 seconds) while the X's represent instances in which participants droped the object and had to star over from the initial position

V. Discussion & Conclusions

The results confirm that the bpSRF effectively addresses key limitations of previous SRFs, particularly in terms of weight, simplicity, and usability. Its lightweight design of only 52g, achieved through 3D printing and body-powered actuation, sets it apart from electronically powered counterparts that typically weigh more than 100g and up to 286g-325g per added finger. Eliminating electronic components also reduces maintenance requirements, making the bpSRF a practical and low-cost option for both assistance and augmentation.

The assessments demonstrated the mechanical reliability of the bpSRF in terms of cable force transmission and its ability to support various manipulation tasks. The intuitive, wrist-driven operation of the bpSRF naturally integrates with hand biomechanics, enabling users to learn and apply novel grasping patterns with minimal effort. In particular, the multi-grasp tasks highlight its potential for applications requiring coordination between natural fingers and the SRF.

As the first body-powered SRF, this work introduces a novel approach to hand augmentation by removing the reliance on electronic components. The open source release of the bpSRF also provides a platform for further research into the biomechanical and neurocognitive effects of movement augmentation. Future work will explore long-term usability, its effects on upper-limb kinematics, and durability in diverse real-world tasks.

ACKNOWLEDGMENT

This work was supported by the Pontificia Universidad Católica del Perú (PUCP) through grant number FAI-064–2023.

REFERENCES

[1] C. L. McDonald, S. Westcott-McCoy, M. R. Weaver, J. Haagsma, and D. Kartin, "Global prevalence of traumatic non-fatal limb amputation," *Prosthetics and orthotics international*, vol. 45, no. 2, pp. 105–114, 2021.

[2] J. Allen, M. Brenner, J. Hauer, E. Molloy, and D. McDonald, "Severe neurological impairment: A delphi consensus-based definition," *European Journal of Paediatric Neurology*, vol. 29, pp. 81–86, 2020.

[3] D. A. Nowak, "The impact of stroke on the performance of grasping: usefulness of kinetic and kinematic motion analysis," *Neuroscience & Biobehavioral Reviews*, vol. 32, no. 8, pp. 1439–1450, 2008.

[4] S. Park, M. Fraser, L. M. Weber, C. Meeker, L. Bishop, D. Geller, J. Stein, and M. Ciocarlie, "User-driven functional movement training with a wearable hand robot after stroke," *IEEE Transactions on Neural Systems and Rehabilitation Engineering*, vol. 28, no. 10, pp. 2265–2275, 2020.

[5] Y. Zhu, W. Gong, K. Chu, X. Wang, Z. Hu, and H. Su, "A novel wearable soft glove for hand rehabilitation and assistive grasping," *Sensors*, vol. 22, no. 16, p. 6294, 2022.

[6] A. N. Maguina and R. Mio, "Augmented grasps: Supernumerary robotic fingers and their practical uses," in *Latin American Conference on Biomedical Engineering*. Springer, 2022, pp. 519–529.

[7] M. Malvezzi, Z. Iqbal, M. C. Valigi, M. Pozzi, D. Prattichizzo, and G. Salvietti, "Design of multiple wearable robotic extra fingers for human hand augmentation," *Robotics*, vol. 8, no. 4, p. 102, 2019.

[8] I. Hussain, M. Anwar, Z. Iqbal, R. Muthusamy, M. Malvezzi, L. Seneviratne, D. Gan, F. Renda, and D. Prattichizzo, "Design and prototype of supernumerary robotic finger (srf) inspired by fin ray® effect for patients suffering from sensorimotor hand impairment," in *2019 2nd IEEE International Conference on Soft Robotics (RoboSoft)*. IEEE, 2019, pp. 398–403.

[9] L. Tiziani, A. Hart, T. Cahoon, F. Wu, H. H. Asada, and F. L. Hammond, "Empirical characterization of modular variable stiffness inflatable structures for supernumerary grasp-assist devices," *The International Journal of Robotics Research*, vol. 36, no. 13-14, pp. 1391–1413, 2017.

[10] I. Hussain, L. Meli, C. Pacchierotti, and D. Prattichizzo, "A soft robotic supernumerary finger and a wearable cutaneous finger interface to compensate the missing grasping capabilities in chronic stroke patients," in *2017 IEEE World Haptics Conference (WHC)*. IEEE, 2017, pp. 183–188.

[11] I. Hussain, G. Salvietti, G. Spagnoletti, and D. Prattichizzo, "The soft-sixthfinger: a wearable emg controlled robotic extra-finger for grasp compensation in chronic stroke patients," *IEEE Robotics and Automation Letters*, vol. 1, no. 2, pp. 1000–1006, 2016.

[12] H. Kai Yap, J. Cho Hong Goh, and C.-H. Yeow, "A low-profile soft robotic sixth-finger for grasp compensation in hand-impaired patients," *Journal of Medical Devices*, vol. 10, no. 3, p. 030914, 2016.

[13] S. Weijun, X. Yong, G. Shuyan, and L. Lingxiao, "Kinematic modeling and prototype experiment of flexible supernumerary robotic finger," in *2024 8th International Conference on Robotics, Control and Automation (ICRCA)*. IEEE, 2024, pp. 13–17.

[14] L. Franco, D. Prattichizzo, and G. Salvietti, "A manually actuated robotic supernumerary finger to recover grasping capabilities," in *2021 IEEE International Humanitarian Technology Conference (IHTC)*. IEEE, 2021, pp. 1–4.

[15] X. Lin, X. Xiao, and Z. Guo, "Mechanical design of a supernumerary robotic finger for grasping abilities compensation," in *2021 IEEE International Conference on Robotics and Biomimetics (ROBIO)*. IEEE, 2021, pp. 1792–1797.

[16] R. Mio and A. Morveli, "Supernumerary robotic fingers for assistance in cylindrical and pinch grasps," in *2023 5th International Conference on Bio-engineering for Smart Technologies (BioSMART)*. IEEE, 2023, pp. 1–4.

[17] P. Kieliba, D. Clode, R. O. Maimon-Mor, and T. R. Makin, "Robotic hand augmentation drives changes in neural body representation," *Science robotics*, vol. 6, no. 54, p. eabd7935, 2021.

[18] J. D. Setiawan, M. Ariyanto, M. Munadi, M. Mutoha, A. Glowacz, and W. Caesarendra, "Grasp posture control of wearable extra robotic fingers with flex sensors based on neural network," *Electronics*, vol. 9, no. 6, p. 905, 2020.

[19] J. Cunningham, A. Hapsari, P. Guilleminot, A. Shafti, and A. A. Faisal, "The supernumerary robotic 3 rd thumb for skilled music tasks," in *2018 7th IEEE International Conference on Biomedical Robotics and Biomechatronics (Biorob)*. IEEE, 2018, pp. 665–670.

[20] F. Y. Wu and H. Asada, "Bio-artificial synergies for grasp posture control of supernumerary robotic fingers," *Robotics: Science and Systems X*, 2014.

[21] D. Prattichizzo, M. Malvezzi, I. Hussain, and G. Salvietti, "The sixth-finger: a modular extra-finger to enhance human hand capabilities," in *The 23rd IEEE International Symposium on Robot and Human Interactive Communication*. IEEE, 2014, pp. 993–998.

[22] N. S. Meraz, H. Shikida, and Y. Hasegawa, "Auricularis muscles based control interface for robotic extra thumb," in *2017 International Symposium on Micro-NanoMechatronics and Human Science (MHS)*, 2017, pp. 1–3.

[23] M. Ariyanto, R. Ismail, J. D. Setiawan, and Z. Arifin, "Development of low cost supernumerary robotic fingers as an assistive device," in *2017 4th International Conference on Electrical Engineering, Computer Science and Informatics (EECSI)*, 2017, pp. 1–6.

[24] J. T. Belter, B. C. Reynolds, and A. M. Dollar, "Grasp and force based taxonomy of split-hook prosthetic terminal devices," in *2014 36th Annual International Conference of the IEEE Engineering in Medicine and Biology Society*. IEEE, 2014, pp. 6613–6618.

[25] M. Bustamante, R. Vega-Centeno, M. Sánchez, and R. Mio, "[regular paper] a parametric 3d-printed body-powered hand prosthesis based on the four-bar linkage mechanism," in *2018 IEEE 18th International Conference on Bioinformatics and Bioengineering (BIBE)*, 2018, pp. 79–85.

[26] J. Ten Kate, G. Smit, and P. Breedveld, "3d-printed upper limb prostheses: a review," *Disability and Rehabilitation: Assistive Technology*, vol. 12, no. 3, pp. 300–314, 2017.

[27] Fillauer TRS Prosthetics, "Cybathlon winner: Bob radocy," (accessed: Nov. 12, 2024). [Online]. Available: https://www.trsprosthetics.com/cybathlon-winner-bob-radocy/

[28] J. D. Brown, T. S. Kunz, D. Gardner, M. K. Shelley, A. J. Davis, and R. B. Gillespie, "An empirical evaluation of force feedback in body-powered prostheses," *IEEE Transactions on Neural Systems and Rehabilitation Engineering*, vol. 25, no. 3, pp. 215–226, 2017.

[29] I. Hussain, G. Salvietti, G. Spagnoletti, M. Malvezzi, D. Cioncoloni, S. Rossi, and D. Prattichizzo, "A soft supernumerary robotic finger and mobile arm support for grasping compensation and hemiparetic upper limb rehabilitation," *Robotics and Autonomous Systems*, vol. 93, pp. 1–12, 2017.

[30] S. Liu, Y. Zhu, Z. Zhang, Z. Fang, J. Tan, J. Peng, C. Song, H. H. Asada, and Z. Wang, "Otariidae-inspired soft-robotic supernumerary flippers by fabric kirigami and origami," *IEEE/ASME Transactions on Mechatronics*, vol. 26, no. 5, pp. 2747–2757, 2021.

[31] F. Y. Wu and H. H. Asada, ""hold-and-manipulate" with a single hand being assisted by wearable extra fingers," in *2015 IEEE International Conference on Robotics and Automation (ICRA)*. IEEE, 2015, pp. 6205–6212.

[32] R. Drake, A. W. Vogl, and A. W. Mitchell, *Gray's anatomy for students E-book*. Elsevier Health Sciences, 2009.

[33] P. F. Curran, A. M. Bagley, M. Sison-Williamson, and M. A. James, "Three-dimensional functional workspace of thumb prehension," *Clinical Biomechanics*, vol. 63, pp. 63–72, 2019.

A Shared Control Approach to Safely Limiting Patient Motion Based on Tendon Strain During Robotic-Assisted Shoulder Rehabilitation

Italo Belli[1,2,*], Yuxuan Hu[1], J. Micah Prendergast[1], David Abbink[1,3], Ajay Seth[2], and Luka Peternel[1]

***Abstract*— Combining biomechanical modeling with robotic physiotherapy is a promising direction to provide real-time insights during the rehabilitation of patients with musculoskeletal injuries, such as rotator-cuff tears. One aspect is to prevent re-injuries caused by high strain in the injured tissues while allowing patients to perform the required rehabilitation exercises. In this paper, we propose a novel shared control method for robots to limit unsafe patient movements, through physical guidance based on a strain-space representation of the human rotator cuff. The method provides motion corrections through two complementary predictive modules. The first module exerts a lower degree of intervention and is analogous to rumble strips or speed bumps for cars on the road. In this case, an impedance controller induces variable damping to slow down the patient's movement when a danger zone is approached. The second module produces a higher degree of intervention and is analogous to lane-assist in cars. In this case, the robot plans an optimal deflection trajectory and temporarily takes over control of the movement to avoid an unsafe situation. We performed experiments with a healthy participant acting as a patient and evaluated the effect of different human-robot interaction modalities on the resulting human movement in terms of avoidance of high-strain areas of the rotator-cuff tendons and contact forces exchanged.**

I. Introduction

Musculoskeletal injuries can occur during many daily activities, ranging from workplace and household tasks to sports. Such injuries negatively affect the quality of life of those who suffer from them, limiting their comfort, mobility, agency and productivity in their daily life as well as at workplaces. Elderly populations are particularly susceptible to such injuries due to weakening of the musculoskeletal system and general reduction in muscle mass that occurs with age. One of the most typical injuries occurs in rotator cuff muscles that keep the upper arm (humerus) in the socket of the shoulder blade (glenoid of the scapula). The prevalence of rotator cuff injuries is estimated to be as high as 22% in the general population [1].

Traditional therapy in treating injuries to the shoulder involves sessions with human physiotherapists. Nevertheless, re-injuries are common [2], and demand for the therapy often exceeds physiotherapists' capacity, which can further affect the recovery times and completeness of recovery. To this end, robots provide a good solution to augment the capacity of human physiotherapists. Existing works in robotics for physiotherapy enable the generation of prescribed rehabilitation movements [3], as well as learning these movements from expert human demonstrations [4]. These strategies are excellent in automating the movements of human physiotherapists.

Authors are with the Cognitive Robotics[1], BioMechanical Engineering[2] and Sustainable Design Engineering[3] departments at Delft University of Technology, Delft, The Netherlands.

* corresponding author (i.belli@tudelft.nl)

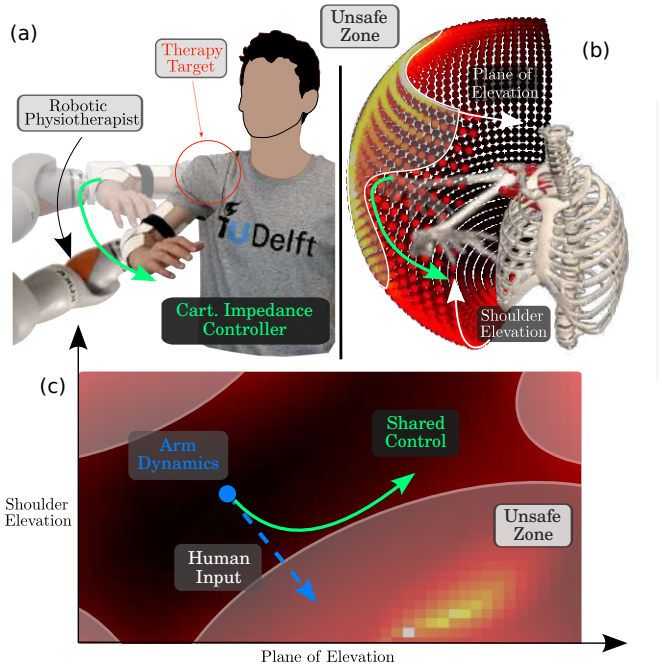


Fig. 1. An overview of the proposed robot-assisted shoulder physiotherapy system. (a) The robot end effector is connected to the human elbow with a customized brace, allowing the robot to limit human motion when necessary. (b) Shoulder strain map is pre-calculated from a high-fidelity musculoskeletal model to determine unsafe movement zones. (c) The current and predicted human arm pose are projected in the strain map to formulate the planning scene. When potential injury is detected, optimal movement in the elbow is achieved through shared control from the robot physiotherapist.

Nevertheless, repeating prescribed or learned movements can be limiting when addressing the specific needs of every patient.

Musculoskeletal models are a valuable addition to the robot motion and force sensors, enabling personalized insights into what is happening inside the human body during the interaction [5]. Most of the existing studies employ models offline, for example, to quantify assistance needed by a human operator [6]–[8] or reduce human metabolic cost in walking-assistive devices [9]–[11]. Some recent studies also explore the use of models in an online manner, where they are integrated into the robot control loops for real-time adjustments of robot assistive movements [12]–[15].

Our previous work [13] developed a method that mapped tendon strains on the human state space using an OpenSim musculoskeletal model to create so-called "strain maps", which chart the high-strain areas where re-injury could occur. The approach employed an offline optimization to create the low-strain therapy trajectories used to navigate the strain maps in real time. A significant advancement was recently made with BATON [16], which enabled an online

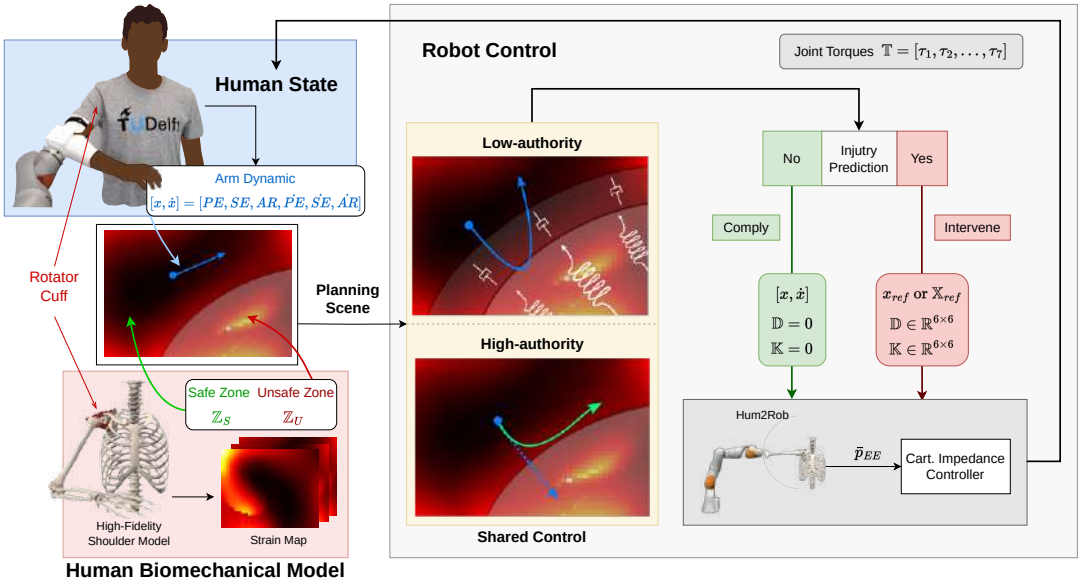


Fig. 2. Diagram of the proposed real-time system for safely limiting human motion during rehabilitation, on the basis of a high-fidelity OpenSim shoulder model. The two shared control modules receive the current state of the human shoulder and their corresponding strain maps to identify dangerous situations and output commands for variable impedance control of the robotic arm. Low-authority guidance is achieved by damping human velocities approaching unsafe high-strain zones. High-authority guidance relies on deflecting human motion away from the danger zones by actively tracking an optimized reference trajectory. These modules are complimentary and can be selected based on the therapy requirements and user preferences.

trajectory optimization and accounted for real-time changes in strain space by considering both the strain behavior and the human arm dynamics. Notably, these approaches focused on optimizing robot-led therapy, which is suitable for early-stage shoulder rehabilitation. Since patients take a more active role as therapy progresses [17], safety and potential re-injury concerns should be addressed while specifically promoting patient-led exercises. In this context, shared control is a promising solution that allows the patient to retain authority over the movement [18], [19], while a robot therapist monitors and potentially intervenes to limit unsafe motions. A simple solution to patient-robot interaction during rotator-cuff rehabilitation was proposed in [15], where the robot provided a "safety net" during physiotherapy by segmenting the dangerous high-strain zones and generating haptic boundaries around them, thus preventing patients or therapists from entering these unsafe regions. Although this offered a promising first step toward a biomechanics-aware safety approach to patient-led physiotherapy, potentially unsafe situations could still occur if a haptic boundary was contacted with high velocity or at a high angle. Therefore, an open challenge is how to predict potential impacts with high-strain zones in advance and avoid them before they occur.

To address this challenge, we developed a method based on shared control that allows the user to perform rehabilitation movements freely, with the robot intervening whenever an incursion into a high-strain danger zone or a high-impact collision with a haptic boundary is about to occur. We propose two distinct predictive modules, each handling the robot's intervention in a different manner. In the first module, the robot exerts lower authority, similar to "rumble strips" or "speed bumps" for cars on the road. In this case, the impedance controller induces variable damping when a danger zone is approached in a potentially unsafe direction to slow down the movement. In contrast, the second module exerts higher authority, akin to lane departure correction autopilot (e.g., "lane assist" or "lane centering") in cars. In this case, the robot plans an optimal deflection trajectory and temporarily takes over control of the movement to avoid an unsafe situation. The two modules are complementary, where the advantage of the first is that it takes away less control from the patient/therapist, while the second module provides a smarter and more assertive way of avoiding unsafe situations. Each module can be selected based on the specific exercise, stage of therapy, user confidence, etc. To demonstrate the key aspects of each, we performed experiments with a healthy participant acting as a patient and evaluated the effect of the different human-robot interactions on the resulting human movement in terms of avoidance of high-strain areas and contact forces exchanged.

II. Methods

Figure 2 illustrates the proposed system with key elements. The human modeling and strain map computation element provide insight into the human musculoskeletal system and allow the physiotherapy robot to navigate away from dangerous high muscle strains. Human state estimation is performed in real-time from the robot's onboard sensors, to monitor human safety. The robot controller implements our two novel modules for predictive guidance to avoid dangerous zones in the strain maps, leveraging a low-level impedance controller that governs physical human-robot interaction. Finally, we present our experimental setup. Each of the key elements is described in the following subsection.

A. Human Biomechanical Model and Strain Maps

To capture the biological properties of the human shoulder, we employ a high-fidelity musculoskeletal model of the

human shoulder complex [20] developed in OpenSim [21], [22]. In particular, we are interested in the behavior of the rotator cuff tendons, spanning the glenohumeral joint and connecting the humerus to the shoulder blade. Therefore, we obtained a reduced-order model of the human shoulder, capturing the mobility of the glenohumeral joint alone in terms of three rotational coordinates (PE: plane of elevation, SE: shoulder elevation, and AR: axial rotation), while retaining the information about the relevant muscles and tendons contained in the original model. As such, the variables that define the configuration of the human model are:

$$\boldsymbol{x} = [\boldsymbol{q},\ \dot{\boldsymbol{q}}]^\top, \quad \text{with} \quad \boldsymbol{q} = [PE, SE, AR]^\top \tag{1}$$

where PE, SE, and AR are defined as the Y-X'-Y'' sequence of intrinsic Euler angles in the fixed shoulder reference frame [20], and $\dot{PE}, \dot{SE}$ and $\dot{AR}$ are their corresponding derivatives with respect to time. Similar to our previous work [13], [16], we employ the OpenSim functionalities to pre-compute the relationship between human pose and strain σ of the tendon(s) of interest, generating "strain maps" that carry the same information as the original model, but much quicker to access. By defining a threshold on the strain value, we leverage this data to identify elliptical unsafe zones $\mathbb{Z}_U$ on the map, corresponding to configurations of the human arm that should be avoided during therapy. Since rehabilitation mostly occurs with a limited speed of movement, the dependency between the fiber velocity and the strain level was neglected.

Movement in the human state space obeys the equations of motion of the corresponding multibody skeletal system. As OpenSim natively provides this information only numerically, we resorted to OpenSimAD [23] as an instrumented version of OpenSim to automatically generate differentiable outcomes and functions from our reduced-order shoulder model. We obtained a differentiable representation of the forward and inverse dynamics functions relating the evolution of the human state $\boldsymbol{x}$ to the generalized torques $\boldsymbol{u} \in \mathbb{R}^3$ applied to the model's degrees of freedom:

$$\dot{\boldsymbol{x}} = f_{\mathrm{FD}}(\boldsymbol{x}, \boldsymbol{u}), \tag{2}$$

$$\boldsymbol{u} = f_{\mathrm{ID}}(\boldsymbol{x}, \dot{\boldsymbol{x}}) \tag{3}$$

The use of model-based human skeletal dynamics was recently proposed as a strategy for real-time planning of biomechanical-aware trajectories on strain maps [16] and brings the benefit of accounting for subject-specific parameters both regarding tendon behavior and human inertial properties.

B. Human State Estimation

We developed a human state estimation module to inform our control algorithms about the current state of the human subject during therapy. Our subject wore a custom-made brace during our experimental validation, connecting them rigidly to the robot's end-effector (Fig. 2). As such, the estimation of the current human state $\hat{\boldsymbol{x}}_t = [\hat{\boldsymbol{q}}_t,\ \hat{\dot{\boldsymbol{q}}}_t]^\top$ can be achieved based on the Cartesian pose $\boldsymbol{p}_{\mathrm{EE}} \in \mathbb{R}^6$ of the end-effector (EE), assuming a fixed orientation of the human torso and negligible movement of the scapula. The interested reader is referred to our previous work for a full derivation of the human pose and velocities ([16], Section II.D).

C. Robot Control

The interaction between our rehabilitation robot and the human subject is shaped with an impedance controller [24] running at 200 Hz, whose parameters are adjusted in real time according to the estimated human state. Specifically, the commanded force at the end-effector $\boldsymbol{F}_{\mathrm{EE}} \in \mathbb{R}^6$ can be defined as:

$$\mathbf{F}_{\mathrm{EE}} = \mathbf{K}_t(\overline{\mathbf{p}}_{\mathrm{EE}} - \mathbf{p}_{\mathrm{EE}}) - \mathbf{D}_t\dot{\mathbf{p}}_{\mathrm{EE}} \tag{4}$$

where the end-effector reference and actual pose are $\overline{\mathbf{p}}_{\mathrm{EE}}$ and $\mathbf{p}_{\mathrm{EE}}$, respectively, and $\mathbf{K}_t,\ \mathbf{D}_t \in \mathbb{R}^{6\times 6}$ are the desired, time-dependent stiffness and damping matrices in Cartesian space. The selection of $\overline{\mathbf{p}}_{\mathrm{EE}}$, $\mathbf{K}_t$, and $\mathbf{D}_t$ ultimately determines the level of authority of the robotic therapist on the movement performed by the human subject, and modifies the control authority of the human during therapy. As such, we present two different modules for tuning the controller's parameters and, effectively, the robot's intervention authority. Both modules combine a prediction of the future human state based on the current human state and determine if future movements will be safe. If the predicted motion will be unsafe (resulting in higher tendon strains), the robot physiotherapy will provide force-based feedback/corrections to the human subject, with lower or higher authority.

1) Low-Authority Shared Control: The human subject retains control of their movements as much as possible, provided that they stay within the safe boundaries defined by the strain maps. In addition to the safe and unsafe zones, we also introduce "damped zones" which represent regions in the human state space that are near, but not yet within, an unsafe zone. At time step t, we perform a biomechanical-safety check on estimated human pose $\hat{\boldsymbol{q}}_t$, projecting it on the strain maps to assess if it lies in a safe, damped, or unsafe zone. Accordingly, we define three conditions (captured in Algorithm 1):

- if $\hat{\boldsymbol{q}}_t$ is safe, then stiffness and damping of the controller are set to zero, permitting free subject movement;
- if the subject's pose lies in a damped zone, then we analyze their velocity $\hat{\dot{\boldsymbol{q}}}_t$. If $\hat{\dot{\boldsymbol{q}}}_t$ points away from the closest unsafe zone, then the movement is safe, and free movement is enabled. Otherwise, the damping in the physical human-robot interaction is increased, setting low stiffness $\mathbf{K}_{\mathrm{low}}$ associated with damping exceeding the critical one $\mathbf{D}_t = 2r\sqrt{\mathbf{K}_{\mathrm{low}}}$ (where we employ the ratio $r > 1$). In this way, the subject receives haptic information for safer direction of movement;
- if $\hat{\boldsymbol{q}}_t$ lies within an unsafe zone, the closest point on the elliptical contour $\mathbb{C}_U$ of the zone is set as a reference point in human coordinates, and tracked with $\mathbf{K}_t = \mathbf{K}_{\mathrm{high}}$, $\mathbf{D}_t = 2\sqrt{\mathbf{K}_{\mathrm{high}}}$. In this way, the human subject is pushed to the nearest safe point by the robot intervention (similar to [15]).

2) High-Authority Shared Control: This modality uses a kinematic prediction of the future human state based on the current human state $\hat{\boldsymbol{x}}_t$, performed over a receding time

Algorithm 1 Low-Authority Shared Control

Given: Unsafe Zone $\mathbb{Z}_U$, Damped Zone $\mathbb{Z}_D$
Input: Human State $\boldsymbol{x}_t = [\boldsymbol{q}_t, \dot{\boldsymbol{q}}_t]$
if $\boldsymbol{q}_t \in \mathbb{Z}_D \setminus \mathbb{Z}_U$ **AND** $\dot{\boldsymbol{q}} \to \mathbb{Z}_U$ **then**
  $\boldsymbol{K}_t \leftarrow \boldsymbol{K}_{low}$
  $\boldsymbol{D}_t \leftarrow 2r\sqrt{\boldsymbol{K}_{low}}$
  $\boldsymbol{x}_{\text{ref}} = \boldsymbol{x}_t$
else if $\boldsymbol{q} \in \mathbb{Z}_U$ **then**
  $\boldsymbol{K}_t \leftarrow \boldsymbol{K}_{high}$
  $\boldsymbol{D}_t \leftarrow 2\sqrt{\boldsymbol{K}_{high}}$
  $\boldsymbol{x}_{\text{ref}} = \boldsymbol{x}^\star$, with $\boldsymbol{x}^\star = \textbf{argmin}_{\boldsymbol{x}}$ distance$(\boldsymbol{x}_t, \mathbb{C}_U)$
else
  $\boldsymbol{K}_t \leftarrow \boldsymbol{0}$
  $\boldsymbol{D}_t \leftarrow \boldsymbol{0}$
end if
Return: $[K,\ D,\ \boldsymbol{p}_{\text{EE}}(\boldsymbol{x}_{\text{ref}})]$ to Robot Control

horizon T, to find the estimated future subject's trajectory $\hat{\boldsymbol{X}} = [\hat{\boldsymbol{x}}_{t+1},\ \hat{\boldsymbol{x}}_{t+2}, ...,\ \hat{\boldsymbol{x}}_{t+T}]^\top$. The future trajectory is analyzed to determine whether it intersects any unsafe zone. When $\hat{\boldsymbol{X}}$ is entirely safe, free movement is enabled by setting zero Cartesian stiffness and damping matrices, similarly to II-C.1. If, instead, the current movement leads the subject to any unsafe zones, the algorithm determines an alternative trajectory $\boldsymbol{X}^\star$ by defining an optimization problem that minimally deflects the predicted trajectory but ensures that no unsafe configuration is reached. The robot temporarily takes control of the motion, setting $\mathbf{K}_t = \mathbf{K}_{\text{high}}$, $\mathbf{D}_t = 2\sqrt{\mathbf{K}_{\text{high}}}$, and tracks $\boldsymbol{X}^\star$ so the human is deflected to a safe configuration where free movement is enabled again (see Algorithm 2).

Below, we specify the cost function and constraints that constitute the optimal control problem to be solved over the generic time interval $[t, t+T]$ to find $\boldsymbol{X}^\star$.

Cost Function: we propose three terms that an optimal deflection of the human movement should minimize, ensuring that the latest human intention is respected as much as possible and that forces and accelerations be low to mitigate human discomfort:

- $L_1(\boldsymbol{x}_t, \hat{\boldsymbol{x}}_t) = w_{\text{pos}}\gamma^t||\hat{\boldsymbol{q}}_t - \boldsymbol{q}_t||_2^2 + w_{\text{vel}}||\hat{\dot{\boldsymbol{q}}}_t - \dot{\boldsymbol{q}}_t||_2^2$, which weights the distance between a given human state and the predicted one, potentially with different weights for the human coordinates position and velocities. Note that a discount factor $\gamma < 1$ is employed, to permit larger deviations as time progresses;
- $L_2(\hat{\boldsymbol{x}}_t, \boldsymbol{u}_t) = w_{\text{torq}}||\boldsymbol{u} - f_{\text{ID}(\boldsymbol{x}_t, \boldsymbol{0})}||_2^2$, accounting for the difference between the generalized torques exerted on the human model and the torques that would guarantee equilibrium of the future trajectory;
- $L_3(\dot{\boldsymbol{x}}_t) = w_{\text{acc}}||\dot{\boldsymbol{q}}_t||_2^2$, weighting the instantaneous acceleration of the human model.

Constraints: the set of constraints that we employ formalize the requirements that $\boldsymbol{X}^\star$ should satisfy:

- *Initial Condition*: Trivially, the deflected trajectory should start from the current human state;
- *Tendon Safety*: The human pose should not cause excessive strain on the healing tendon(s), leading to the requirement $\boldsymbol{q}_t \notin \mathbb{Z}_U$;
- *Dynamic consistency*: For each instant in time, the system's accelerations need to respect the dynamics of the human skeletal system, resulting in $\dot{\boldsymbol{x}}_t = f_{\text{FD}}(\boldsymbol{x}_t, \boldsymbol{u}_t)$;
- *Terminal Conditions*: At the end of the optimization interval, we require that the human speed be zero and that the torques on the human model match the equilibrium ones. This results in $|\dot{\boldsymbol{q}}_T| \leq \varepsilon_{\text{vel}}$, $||\boldsymbol{u}_T - f_{\text{ID}}(\boldsymbol{x}_T, \boldsymbol{0})||_2^2 \leq \varepsilon_{\text{torq}}$, where suitable tolerances $\varepsilon_{\text{vel}}, \varepsilon_{\text{torq}}$ are used. Moreover, the final human state should be far enough from the contour of the closer unsafe zone, to guarantee that the movement can be continued safely by the human subject: dist$(\boldsymbol{x}_T, \mathbb{C}_U) \geq \delta$.

Through orthogonal collocation techniques [25], the problem formalized above is cast into an equivalent Non-Linear Programming problem (NLP) that structure-exploiting solvers can solve.

For slow movements and relatively short T, the human skeletal dynamics specified by (2)-(3) could introduce more involved computations without significantly affecting the quality of the optimal deflection $\boldsymbol{X}^\star$. We tested this hypothesis by considering an alternative version of the NLP where the strain maps are navigated by a virtual point-mass system instead, actuated by ideal forces. The accuracy of this approximation, evaluated through computer simulations, is presented in Section III-A.

Algorithm 2 High-Authority Shared Control

Given: Unsafe Zone $\mathbb{Z}_U$
Input: Human State $\boldsymbol{x}_t$
$\hat{\boldsymbol{X}} \leftarrow$ **pathPrediction**$(\boldsymbol{x}_t)$
if $\exists \boldsymbol{x}_i \in \hat{\boldsymbol{X}} \mid \boldsymbol{x}_i \in \mathbb{Z}_U$ **then**
  $\boldsymbol{K}_t \leftarrow \boldsymbol{K}_{high}$
  $\boldsymbol{D}_t \leftarrow 2\sqrt{\boldsymbol{K}_{high}}$
  $\boldsymbol{X}^\star_{ref} \leftarrow \textbf{argmin}_{\boldsymbol{X}_{\text{ref}}} \mathcal{L}(\boldsymbol{X}, \boldsymbol{X}_{\text{ref}})$
else
  $\boldsymbol{K}_t \leftarrow \boldsymbol{0}$
  $\boldsymbol{D}_t \leftarrow \boldsymbol{0}$
end if
Return: $[K,\ D,\ \boldsymbol{p}_{\text{EE}}(\boldsymbol{X}^\star_{\text{ref}})]$ to Robot Control

D. Initial User Testing

Before conducting proof-of-concept experiments, we solicited the input of a physiotherapist for qualitative feedback on the interaction. Initial trials with the PT were deemed to be overly "aggressive" during motion correction. To account for this, steps were taken to better tune the controller parameters, (i.e., tuning the weights in the cost function and increasing the sampling frequency of the reference trajectory) to avoid this perceived behavior.

E. Experimental setup

A healthy subject participated in our experiments and interacted with a KUKA LBR iiwa 7 through our custom arm brace, allowing simultaneous human state estimation and physical human-robot collaboration during a simulated rehabilitation session. Our experimental protocol was approved by the Human Research Ethics Committee of TU

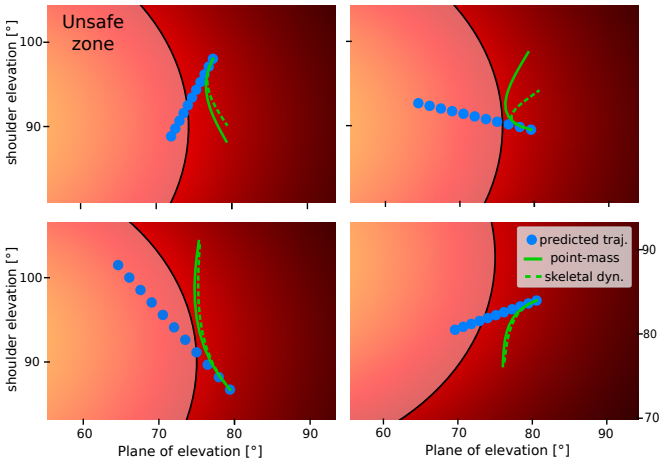


Fig. 3. Simulation comparison of optimal deflections generated by the high-authority module, contrasting the results when using the human model's dynamics (dashed green) versus a virtual point mass (solid green) for navigating the strain map.

Delft. To demonstrate the key functionalities of our method and ensure the repeatability of the experiments, we locked the AR degree of freedom and considered a custom strain map with one time-invariant unsafe zone. The subject was instructed to maintain a constant torso orientation during the interaction to satisfy the assumption of Section II-B. We selected $k_{high,t} = 400\frac{N}{m}$ and $k_{high,r} = 20\frac{N}{[rad]}$ as high translational and rotational stiffness respectively, while low values were set to $k_{\mathrm{low,t}} = 20\frac{N}{m}$ and $k_{\mathrm{low,r}} = 5\frac{N}{[rad]}$.

By removing the damped zone in the low-authority module, we effectively recreated the haptic boundaries considered in our previous work [15], to measure the performances of this baseline controller in terms of robot-commanded forces when the unsafe zone was reached (Section III-B). Then, we set $r = 4$ to increase the damping of the controller, so that our subject could receive anticipatory haptic feedback before impacting the unsafe zone. In the high-authority module, we selected $T = 1$ s and divided it into 10 discrete steps, and up-sampled the resulting optimal deflection to the required frequency for the controller. When the deflection was executed, the system also played a sound to promptly inform the subject that they should comply with the robot's corrective movement.

During these proof-of-concept experiments, the subject interacted with the robot by moving their arm through a natural range of motion. They were then directed to move towards the prescribed unsafe region while the resulting trajectory and forces were recorded. The subject repeated this for both deflection modalities to analyze the effectiveness of our method. Computations were performed on a Dell Latitude 7420 laptop with an i7-1185G7 processor, interfaced with a Dell workstation with an Xeon W-2123 processor dedicated to the impedance controller. Our code is available at *https://github.com/itbellix/biomechanical_safe_deflection*.

III. Results

A. Evaluation of the approximated dynamics

We employed computer simulations to evaluate the differences between the optimal deflections produced by the NLP presented in Section II-C.2 when the strain maps are navigated with the human model's dynamics or by the virtual point mass. We selected 100 random initial conditions for human poses and velocities, to represent the different ways that a subject would move toward an unsafe zone, and computed the optimal deflection proposed by the NLP in the two cases. Figure 3 exemplifies the results obtained, given the kinematic prediction of the human trajectory computed from the randomly selected initial state. Overall, we observed a RMSE of about $2°$ between the last point of the two trajectories. The NLPs employing human skeletal dynamics required an average solution time of 740 ms (failing to converge in $4/100$ instances), whereas the NLPs with virtual point mass approximation could be solved in 12 ms on average, with 100% convergence rate. For these reasons, we opted to use the second approximation in the experiments performed with our physical robot, the results of which we present next.

B. Baseline controller

We ran our baseline controller [15] and recorded the forces generated by the robot on the human as a consequence of collisions with the unsafe zone during subject-led movements. The peak force magnitude that we observed exceeded 17 N, with the subject executing similar movements as during the rest of our experiments, but receiving no feedback or deflection from the robot before hitting the unsafe zone.

C. Shared control modalities

We analyzed our two shared controllers during physical human-robot interaction, mimicking a physiotherapy session. In both cases, the human subject moved their arm, and the robot behavior was dictated alternatively by one of the two algorithms presented in Sections II-C.1, II-C.2. As the movement started from a safe region, initially both modules guaranteed minimal interaction force. On the contrary, the behavior was different as the unsafe zone was approached. The lower authority module (Figure 4) damped the human movement as the subject entered the damped zone, generating a dragging force opposing human velocities pointing towards the unsafe zone. The subject continued their movement and entered the unsafe zone, triggering the algorithm to pull them toward the closest point on the zone contour. Finally, the subject left the unsafe zone and moved away from it, receiving no further robot intervention in virtue of the safe direction of movement.

Regarding the higher authority module (Figure 5), the subject could move undisturbed closer to the unsafe zone until their predicted future trajectory was no longer safe. At this stage, the algorithm proposed a minimal deflection of the original trajectory, triggering the robot to lead the human subject toward a position where they could move safely again. For both cases, we analyzed the magnitude of the Cartesian forces that were commanded to the human subject and found that the first control method led to a peak interaction force of about 8 N, while a maximum force of about 6 N was reached with the second control method.

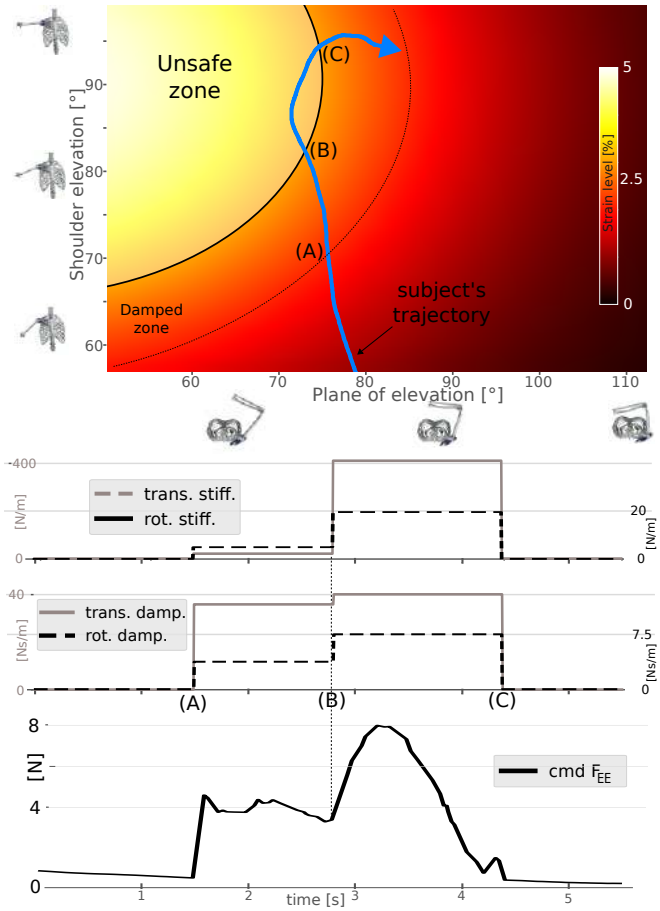


Fig. 4. Low-authority shared control module behavior, during physical human-robot interaction. Top: strain map in which the subject moved, with skeletal poses detailing the axes. The subject approached the unsafe zone: (A) first, the "damped zone" was encountered, then (B) they entered the "unsafe zone" and experienced higher robot correction before leaving the zone and continuing with their free movement (C). Evolution of the controller's stiffness and damping and resulting interaction force are highlighted.

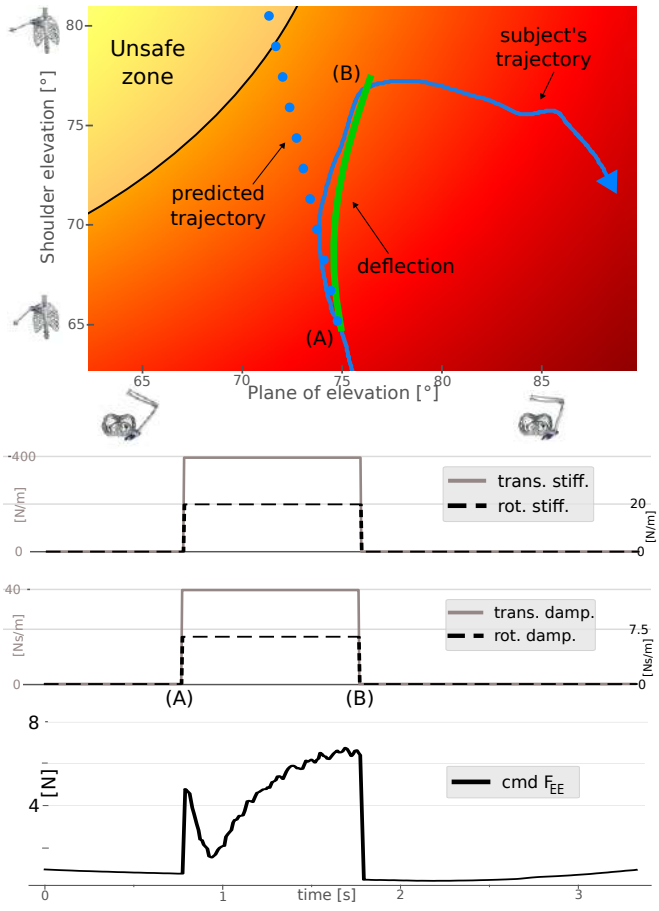


Fig. 5. High-authority shared control module behavior, during physical human-robot interaction. Top: strain map in which the subject moved, with skeletal poses detailing the axes. The subject approached the unsafe zone, triggering the system to impose a short deflection on their movement (A). After that (B), control was given back to the human, who could independently continue their free motion. The evolution of the controller's stiffness and damping and the resulting interaction force are highlighted.

IV. Discussion and Conclusions

We have presented two shared control modalities that allow a robot to limit unsafe human movement during robotic-assisted shoulder rehabilitation, using information from a high-fidelity biomechanical model. Both modules permit human-led movements to maximize patients' independent exploration of their shoulder range of motion, safeguarding their users against reaching shoulder configurations that could generate unsafe levels of strain in injured/healing tendons. When the current human action is deemed unsafe, our controller intervenes with different degrees of authority to shape the resulting human movement. The use of the shared control paradigm expands our previous contributions, in which the robotic therapist unilaterally dictated the therapeutic motion [16] and did not anticipate human intentions [15].

In the present work, the low-authority control modality, designed to allow the human subject to retain greater agency over the resulting movement, was capable of providing state-dependent haptic feedback during human motion. The system produced a force field that can allow the user to avoid unsafe zones autonomously (Figure 4). While entering such zones is still possible, the maximum robot-commanded force was smaller than what was observed when no predictive damping was provided to the user for similar movements, since higher unsafe velocities were limited. The high-authority control modality, on the other hand, is expected to reduce the autonomy of the human subject, as it temporarily takes over the movement, to reposition the human in a pose where they can safely continue their therapy. This approach allowed the system to avoid our experimental unsafe zone better, with lower force produced by the robot, by guaranteeing initial alignment between the human intention and the robot's deflection. Moreover, our real-robot results validated the initial simulation findings reported in Figure 3, showing that the subject can be smoothly deflected without accounting for the specific human skeletal dynamics, for the type of rehabilitation movements considered.

Simplifying human inertia also allows for reduced computational costs. Comparing the optimal deflections obtained with and without accounting for the human skeletal dynamics highlighted minor differences in our simulation results (see Figure 3), likely due to different relative weighting of

the torque terms in the cost function. Indeed, the inertial parameters of virtual point mass navigating across the strain map were not tuned to our participant since only the human kinematics was employed by the robot's impedance controller. Identifying the human-arm inertia at the robot's end-effector and using these parameters in the point mass approximation could enhance the alignment between the two methods under low accelerations, as in our case. This approach could also enable integrating optimized generalized torques from the human model into the robot controller, such as for personalized gravity compensation [16].

While our findings demonstrate the potential of the proposed shared control modalities, there are limitations that warrant consideration and open avenues for interesting research. In this work, we considered a stationary exemplary strain map, purely dependent on the human shoulder pose, which simplified the demonstration of our control modalities. However, the effects of tendon fiber velocity and muscle activation on the resulting strain are currently ignored, and their inclusion will be necessary in the future, as was demonstrated previously [26]. Including rapid estimation of the muscle activation through dedicated solvers such as [27] is an interesting future direction, as it would improve the quality of the strain estimations by accounting directly for the effect of the interaction wrenches that are exchanged between the human and the robot during their physical interaction.

We are also planning to further explore the control modality that potential users/stakeholders (both patients and therapists) might prefer, allowing us to better define the most effective way to share control of therapy between human and robotic agents. As noted in the methodology, to gather feedback on the system during development, we have conducted a preliminary interactive session with one of the leading experts in orthopedic physiotherapy in the Netherlands. The response was generally very positive, and the main takeaway was to make the shared control system slightly less aggressive. We accounted for this feedback prior to doing experiments for this paper, but our future work will need to focus on testing the method on multiple healthy participants first, to further explore the user experience before moving to tests in more clinical settings.

ACKNOWLEDGMENTS

We thank Michael J. Davidson for the useful discussions about the PTbot project at TU Delft. We acknowledge the support from the transdisciplinary research and innovation centre FRAIM and the Chan Zuckerberg Initiative DAF, an advised fund of Silicon Valley Community Foundation through grants 2020-218896 and 2022-252796.

REFERENCES

[1] H. Minagawa, N. Yamamoto, H. Abe, M. Fukuda, N. Seki, K. Kikuchi, H. Kijima, and E. Itoi, "Prevalence of symptomatic and asymptomatic rotator cuff tears in the general population: from mass-screening in one village," *J. Orthop.*, vol. 10, no. 1, 2013.

[2] F. V. Sciarretta, D. Moya, and K. List, "Current trends in rehabilitation of rotator cuff injuries," *Sicot-j*, vol. 9, 2023.

[3] Y. Cen, J. Yuan, S. Ma, J. Luo, and H. Wang, "Trajectory optimization algorithm of trajectory rehabilitation training mode for rehabilitation robot," in *IEEE ROBIO)*, IEEE, 2022.

[4] B. Luciani, L. Roveda, F. Braghin, A. Pedrocchi, and M. Gandolla, "Trajectory learning by therapists' demonstrations for an upper limb rehabilitation exoskeleton," *IEEE RA-L*, 2023.

[5] C. Fang, L. Peternel, A. Seth, M. Sartori, K. Mombaur, and E. Yoshida, "Human modeling in physical human-robot interaction: A brief survey," *IEEE RA-L*, 2023.

[6] M. G. Carmichael and D. Liu, "Estimating physical assistance need using a musculoskeletal model," *IEEE TBME*, vol. 60, no. 7, 2013.

[7] B. Ghannadi, N. Mehrabi, R. S. Razavian, and J. McPhee, "Nonlinear model predictive control of an upper extremity rehabilitation robot using a two-dimensional human-robot interaction model," in *IEEE/RSJ IROS*, IEEE, 2017.

[8] A. Zignoli, F. Biral, K. Yokoyama, and T. Shimono, "Including a musculoskeletal model in the control loop of an assistive robot for the design of optimal target forces," in *IEEE IECON*, vol. 1, IEEE, 2019.

[9] J. Fang and Y. Yuan, "Human-in-the-loop optimization of wearable robots to reduce the human metabolic energy cost in physical movements," *Robot. Auton. Syst.*, vol. 127, 2020.

[10] D. F. Gordon, C. McGreavy, A. Christou, and S. Vijayakumar, "Human-in-the-loop optimization of exoskeleton assistance via online simulation of metabolic cost," *IEEE T-RO*, vol. 38, no. 3, 2022.

[11] K. Li, M. Tucker, R. Gehlhar, Y. Yue, and A. D. Ames, "Natural multicontact walking for robotic assistive devices via musculoskeletal models and hybrid zero dynamics," *IEEE RA-L*, vol. 7, no. 2, 2022.

[12] P. K. Jamwal, S. Hussain, Y. H. Tsoi, and S. Q. Xie, "Musculoskeletal model for path generation and modification of an ankle rehabilitation robot," *IEEE Trans. Hum.-Mach. Syst.*, vol. 50, no. 5, 2020.

[13] J. M. Prendergast, S. Balvert, T. Driessen, A. Seth, and L. Peternel, "Biomechanics aware collaborative robot system for delivery of safe physical therapy in shoulder rehabilitation," *IEEE RA-L*, vol. 6, no. 4, 2021.

[14] G. Clark and H. B. Amor, "Learning ergonomic control in human–robot symbiotic walking," *IEEE T-RO*, vol. 39, no. 1, 2022.

[15] S. Balvert, J. M. Prendergast, I. Belli, A. Seth, and L. Peternel, "Enabling patient-and teleoperator-led robotic physiotherapy via strain map segmentation and shared-authority," in *IEEE-RAS Humanoids*, IEEE, 2022.

[16] I. Belli, J. M. Prendergast, A. Seth, and L. Peternel, "Biomechanics-aware trajectory optimization for navigation during robotic physiotherapy," *arXiv preprint*, 2024.

[17] T. A. Sgroi and M. Cilenti, "Rotator cuff repair: post-operative rehabilitation concepts," *Curr Rev Musculoskelet Med*, vol. 11, 2018.

[18] D. A. Abbink, T. Carlson, M. Mulder, J. C. De Winter, F. Aminravan, T. L. Gibo, and E. R. Boer, "A topology of shared control systems—finding common ground in diversity," *IEEE Trans. Hum.-Mach. Syst.*, vol. 48, no. 5, 2018.

[19] D. P. Losey, C. G. McDonald, E. Battaglia, and M. K. O'Malley, "A review of intent detection, arbitration, and communication aspects of shared control for physical human–robot interaction," *Applied Mechanics Reviews*, vol. 70, no. 1, 2018.

[20] A. Seth, M. Dong, R. Matias, and S. Delp, "Muscle contributions to upper-extremity movement and work from a musculoskeletal model of the human shoulder," *Front. neurorob.*, vol. 13, 2019.

[21] S. L. Delp, F. C. Anderson, A. S. Arnold, P. Loan, A. Habib, C. T. John, E. Guendelman, and D. G. Thelen, "Opensim: open-source software to create and analyze dynamic simulations of movement," *IEEE TBME*, vol. 54, no. 11, 2007.

[22] A. Seth, J. L. Hicks, T. K. Uchida, A. Habib, C. L. Dembia, J. J. Dunne, C. F. Ong, M. S. DeMers, A. Rajagopal, M. Millard, *et al.*, "Opensim: Simulating musculoskeletal dynamics and neuromuscular control to study human and animal movement," *PLoS Comput. Biol.*, vol. 14, no. 7, 2018.

[23] A. Falisse, G. Serrancolí, C. L. Dembia, J. Gillis, and F. De Groote, "Algorithmic differentiation improves the computational efficiency of opensim-based trajectory optimization of human movement," *PLoS One*, vol. 14, no. 10, 2019.

[24] N. Hogan, "Impedance control: An approach to manipulation," in *American control conference*, IEEE, 1984.

[25] D. Garg, M. Patterson, W. Hager, A. Rao, D. R. Benson, and G. T. Huntington, "An overview of three pseudospectral methods for the numerical solution of optimal control problems," *hal-01615132*, 2017.

[26] I. Beck, I. Belli, L. Peternel, A. Seth, and J. M. Prendergast, "Real-time tendon strain estimation of rotator-cuff muscles during robotic-assisted rehabilitation," in *IEEE Humanoids*, IEEE, 2023.

[27] I. Belli, S. Joshi, J. M. Prendergast, I. Beck, C. Della Santina, L. Peternel, and A. Seth, "Does enforcing glenohumeral joint stability matter? a new rapid muscle redundancy solver highlights the importance of non-superficial shoulder muscles," *PLoS one*, vol. 18, no. 11, 2023.

Handling kinematic features in an action observation task to optimize a Brain Computer Interface-based rehabilitation training*

F. Patarini, C. Maronati, J. Manuello, L.F. Cuturi, M. Monti, G. Savina, E. Ferrari, I. Iarrobino, C. Iani, S. Rubichi, A. Ciaramidaro, L. Astolfi, A. Cavallo and J. Toppi

***Abstract*—Brain-Computer Interface (BCI) technology promotes neuroplasticity mechanisms which favor the functional motor recovery in stroke survivors. Patients' residual motor abilities determine the intention, which, once detected by the BCI is fed back via an effector. The majority of studies aimed at optimizing the feedback branch, but not enough attention has been posed to supporting patient in the movement intention that should be detected by the BCI system. The inclusion of a visual motor priming (observed action before a task) in a BCI could promote the retrieval of movements from the patient's own impaired motor repertoire. None of the motor priming proposed until so far have been tailored to the patients' residual motor ability, although it is well known that the human brain recognizes movements closer from a kinematic perspective to its own repertoire more easily. The aim of this study was to investigate how individual motor style in an action observation task would affect the observer's cortical excitability. EEG signals were recorded from 10 individuals during an action observation task where different levels of motor distance between the observer and the agent were modulated. EEG-based group spectral activations shown an involvement of bilateral parietal areas in beta band in case of more unpredictable kinematics. The results would open the way for the design of a kinematic-based visual motor priming to be embedded in a BCI system for post-stroke rehabilitation.**

I. Introduction

Brain computer Interfaces (BCIs) are one of several technology-based approaches used to restore upper limb motor function after stroke [1]. BCIs establish a real-time bi-directional coupling between central and peripherical nervous systems which enhances recovery by driving the brain reorganization towards improved motor function [2], [3]. In fact, BCI systems collect and process in real-time the physical correlates of brain activity (e.g. recorded by electroencephalography-EEG or electrocorticography-ECoG) to provide feedback to the user regarding the modulation of their brain activity. The feedback most often consists of a sensory stimulus, e.g. visual, auditory, tactile, or could be translated in a more complex design that allows the patient to complete/execute the movement through the BCI-based activation of an external device such as a robotic prosthesis or a functional electrical stimulator (FES) [4]. In the context of motor rehabilitation, the BCI task is usually based on motor imagery (MI) or motor execution (ME) depending on the patient's residual motor abilities. Both BCI tasks involve the primary motor cortex and when the patients' mental activity produces event-related desynchronization (ERD) of the sensorimotor rhythm, they receive specific feedback that, by closing the loop, induces neuroplasticity's mechanisms crucial for functional recovery [5]. As a result, most of research efforts were focused on the optimization of the BCI feedback to maximize plasticity phenomena [6], [7]. However, little or no attention was devoted to supporting the patient in the execution of the task required by the BCI, being it MI or ME.

Providing structured support for these processes could represent an effective method of enhancing neural excitability within the patient's brain, which in turn may strengthen the closed-loop effect. This approach could simultaneously promote the retrieval and reactivation of motor patterns from the patient's own impaired motor repertoire, fostering a more effective neurorehabilitation process. In fact, stroke survivors often experience a phenomenon known as "learned non-use," in which the prolonged inactivity of the affected limb leads to a gradual decline in motor function. This not only results in the deterioration of upper extremity motor skills but may also contribute to a weakening or even loss of cognitive motor control schemes specifically related to the movement of the impaired side. Over time, the neural representations associated with voluntary movement may become less accessible, making it even more challenging for patients to regain functional use of the affected limb. Therefore, integrating strategies that actively engage patients in MI or ME tasks while providing appropriate guidance and reinforcement could help counteract these negative effects [8].

Such support to the patients could be provided by integrating the BCI system with a visual motor priming, where the motor response is facilitated by an observed action (i.e. representing an action before a task [9])) that it has been shown to increase corticospinal excitability [10], [11], leading to

*Research was partially supported by the Italian Ministry of University and Research (PRIN MUR 20207S3NB8) and by Sapienza University of Rome-Progetti di Ateneo (LEAF, RM123188F229EC72 and RP123188F7621611)

F. Patarini is with Sapienza University of Rome, Rome, Italy and IRCCS Fondazione Santa Lucia, Rome, Italy (corresponding author to provide e-mail: francesca.patarini@uniroma1.it).

C. Maronati, J. Manuello and A. Cavallo are with University of Turin, Turin, Italy (e-mail: camilla.maronati@unito.it, jordi.manuello@unito.it, and andrea.cavallo@unito.it).

L.F. Cuturi is with University of Messina, Messina Italy and Italian Institute of Technology, Genoa, Italy (e-mail: luigifelice.cuturi@unime.it).

M. Monti is with University of Bologna, Bologna, Italy (e-mail: melissa.monti4@unibo.it).

G. Savina, L. Astolfi and J. Toppi are with Sapienza University of Rome, Rome, Italy and IRCCS Fondazione Santa Lucia, Rome, Italy (e-mail: giulia.savina@uniroma1.it, laura.astolfi@uniroma1.it and jlenia.toppi@uniroma1.it).

E. Ferrari, I. Iarrobino, C. Iani, S. Rubichi and A. Ciaramidaro are with University of Modena and Reggio Emilia, Reggio Emilia, Italy (e-mail: e.ferrari@unimore.it, igor.iarrobino@unimore.it, cristina.iani@unimore.it, srubichi@unimore.it and aciarami@unimore.it).

improved motor outcomes. However, none of the motor priming proposed until now have been tailored to the patients' residual motor ability as assessed by kinematics and thus selected according to the specific patient's motor repertoire. Indeed, it has been shown how the human brain is better at recognizing the kinematics of a movement when it falls within their own range of expertise [12], [13], [14] . In this context, we conducted a preliminary study to investigate how individual motor and perceptual characteristics (i.e. individual motor style [15]) would affect the cortical excitability, expressed in terms of ERD, induced by observing an action performed by an agent with a dissimilar or similar motor style to that of the observer. This would help the design of a kinematic-based visual motor priming to be embedded in a BCI system for post-stroke rehabilitation. Specifically, we leveraged on the metric of motor distance to quantify motor (dis)similarities between agents and observer, in an action observation paradigm [16]. We hypothesize that the kinematic characteristics of the observed movement influence the ERD patterns. To this end, ten individuals without motor impairment were subjected to an action observation paradigm where motor distance factor was manipulated while their EEG signals were recorded.

II. MATERIAL AND METHODS

A. Visual stimuli creation

We employed a dataset of 2093 movements obtained by recording naïve participants grasping either a light (150g) or a heavy (510g) bottle. From the reach-to-grasp phase of each action we extracted the following kinematic parameters: wrist velocity (mm/s), wrist acceleration (mm/s2), wrist jerk (mm/s3), grip aperture (mm) and wrist height (mm) and used them to quantify the motor distance by using a novel technique proposed by [16], that leverages on the Procrustes transformation to compare couples of movements. Notably, this approach allowed to jointly operate on the 5 selected kinematic features, rather than on one variable at a time, so that the computed motor distance reflects a global representation of the movement.

B. Participants

Ten subjects (6 M, aged 22-34 years; mean age = 26,7; SD = 2,53) who had previously taken part in a reach-to-grasp action execution task (section II.A), were recruited in an action observation study. All participants were right-handed, with normal or corrected-to-normal vision, with no history of either psychiatric or neurological disorders, with no motor impairment and with no current medications. Handedness was assessed in all participants by means of the short form the Edinburgh Handedness Inventory (EHI) [17] and they had to score at least 61 to be considered as right handers and being enrolled. The dataset used for the purposes of this study was obtained within a research project approved by the bioethics committee of the University of Turin (approval number: 0260704). All the participants signed an informed consent.

C. Experimental design

Participants were presented with video-clips of reach-to-grasp movements described in section A. With the intent of manipulating the motor distance between the participant (i.e. observer) and the agent performing the action in the video clips, we classified the experimental pool videos in four

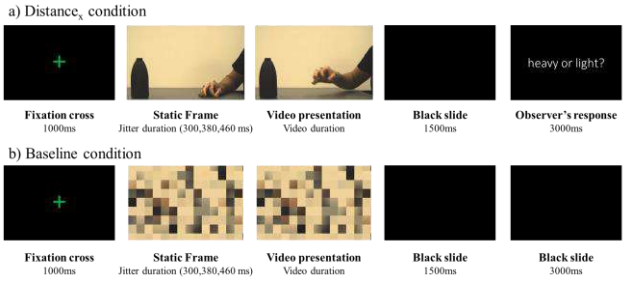


Fig.1 Frames' sequence of a trial during Distance$_x$ condition (a) and a trial during baseline condition (b).

classes depending on the motor similarity, expressed in kinematic terms, in the execution of the reach-to-grasp movement. Specifically, for each observer we selected: i) 10 videos of movements falling within the first quartile of the motor distance distribution (Distance 1; i.e., highly similar kinematics between the observer and the agent); ii) 10 videos of movements falling between the first and the second quartile of the motor distance distribution (Distance 2); iii) 10 videos of movements falling between the second and the third quartile of the motor distance distribution (Distance 3); iii) 10 videos of movements falling above the third quartile of the motor distance distribution (Distance 4; i.e., highly different kinematics between the observer and the agent). 10 additional stimuli were created by randomly selecting 10 videoclips within the experimental stimuli pool and by scrambling the pixels' position at each frame of the video. In this way, these baseline stimuli were no kinematically informative, but of duration and pixels colour comparable to those of the videos of other conditions.

Participants were seated in a comfortable chair in front of a monitor at a distance of 50cm, in which were presented the videos, and a response keyboard was placed at a distance of 15cm from their body midline. Additionally, black panels were placed around the experimental setting to create an isolated and quiet environment for the observers. Before the start of the action observation paradigm, participants were requested to execute 10 reach-to-grasp movements, 5 directed toward a light object and 5 toward a heavy object, to familiarize again with the objects that they manipulated during the action execution task. During the action observation paradigm, participants were presented with the reach-to-grasp video clips extracted by the custom selection based on their motor distances. The experiment was administered according to a block design approach including 6 blocks of 50 trials each, with a break among them. In each block, were administered 10 videos for each motor distance (Distance 1, Distance 2, Distance 3, Distance 4) and 10 baseline videos. The presentation's order of the stimuli was randomized within blocks and each video was shown once per block. Each trial began with the presentation of a green cross fixation with duration of 1000ms, followed by the videoclip of the movement. To avoid anticipation and to keep subjects focused, a static frame of pseudo-random duration was added at the beginning of each clip. Possible duration values were: 300ms, 380ms and 460ms. After the video presentation there was an interstimulus interval with duration of 1500ms and, after this, participants were asked to indicate accurately if

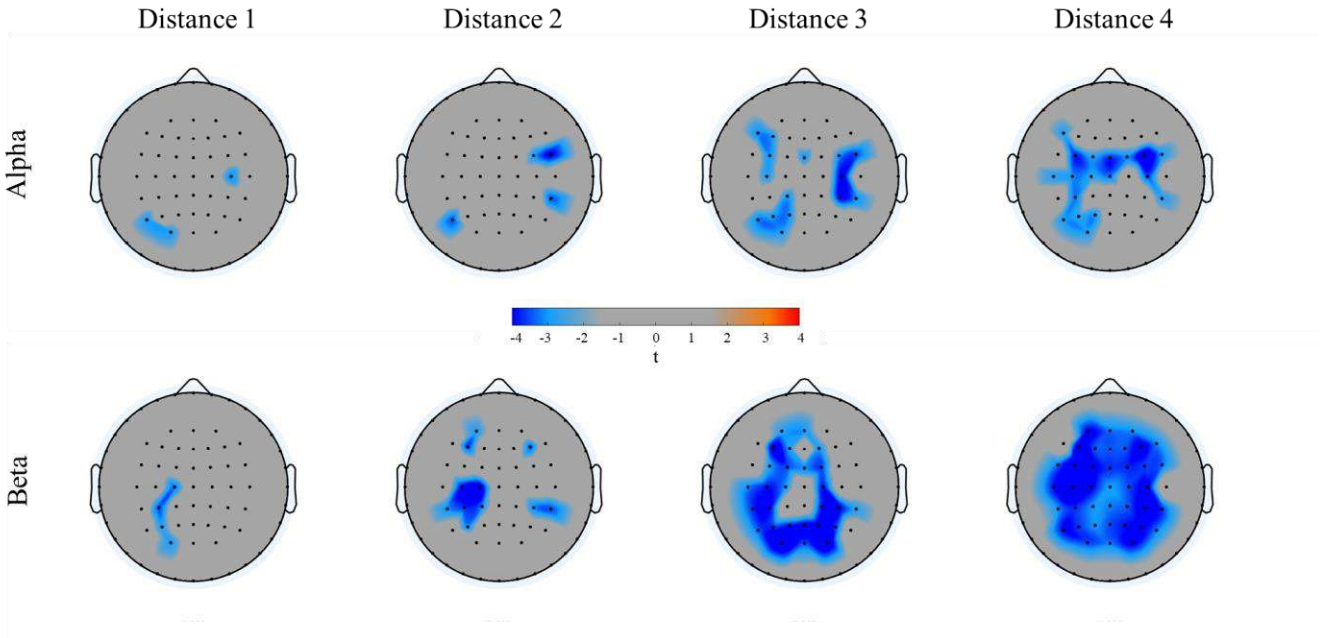


Fig. 2 Topographical scalp maps in alpha and beta bands obtained performing a paired t-test ($\alpha = 0.05$, False Discovery Rate correction), comparing the PSD values obtained in each of the four experimental condition (i.e. Distance 1, Distance 2, Distance 3, Distance 4) vs those obtained for Baseline condition. Results are mapped over a 2D scalp model with the nose pointing the upper part of the page. Pixels color codes for t-values obtained for the different channels. T-values below statistical threshold were represented in gray. Red pixels codes for significant synchronizations (t-values when condition$_x$ > baseline) while blue colobar for desynchronizations (t-value when condition$_x$ < baseline).

the grasped object was heavy or light by using the keyboard. Participants were instructed to respond within a maximum of 3000ms, during the response slide. In baseline condition, this frame was replaced by a black slide with a duration of 3000 ms. After the response an inter-trial interval, represented by a black slide, was shown for 500ms. The sequence of frames of a trial during the presentation of a video falling in Distance$_x$ condition and in baseline condition is depicted in Fig.1. No feedback about the correctness of their responses was provided to participants. The entire experimental session lasted approximately 40 minutes and was managed using E-prime V3.0 software (Psychology Software Tools, Inc, Sharpsburg, PA, USA).

D. EEG data collection

EEG data were acquired during the paradigm administration and sampled at 500Hz. EEG signals were recorded from the scalp by means of a 61-channel active electrodes system (LiveAmp, Brain Products GmbH, Germany) positioned according to an extension of the 10-20 International System. The ground and reference were placed on the right and left mastoid respectively. Markers related to the different experimental conditions were delivered to the EEG amplifier through the BrainVision TriggerBox (Brain Products GmbH, Germany).

E. EEG data analysis

An ad-hoc EEG pre-processing pipeline was implemented to maximize the signal information extrapolated from the noise. First of all, EEG signals were down-sampled to 250 Hz using a spline interpolation to minimize data manipulation. Sequentially, the data were band-pass filtered [1- 45] Hz by means of an 8th order zero-phase shift Butterworth IIR filter and also a 50 Hz notch filter was applied to remove power line interference. The noisy channels were identified and excluded from further analysis. Eye artefacts (i.e. blinks and saccades) were removed using the independent component analysis (ICA). EEG data of each subject were re-referenced to the Common Average Reference and segmented according to the different experimental conditions (i.e. Distance 1, Distance 2, Distance 3, Distance 4 and Baseline). Only the video-related trials with a duration between 500 and 1100 ms were selected. Channels located at the scalp edge were excluded from further analyses being mostly subjected to the presence of artifacts. A voltage semi-automatic threshold criterion (±100 μV) was applied to highlight residual artefacts. In particular, if we found more than five channels which exceeded the threshold in a trial, we removed it, otherwise we interpolated the bad channels by means of a spherical interpolation including all the other channels. Only artefact-free epochs were considered for further analyses.

F. Grand Average Spectral Maps

The power spectral density (PSD) was computed by means of Welch periodogram (Hann's window of 1100ms duration and with 0% overlap) for each electrode, experimental condition (i.e. Distance 1, Distance 2, Distance 3, Distance 4 and Baseline) and participant. We applied the decibel (db) transformation of PSD values, and we averaged them in the two frequency bands more related to motor tasks: Alpha [8-12] Hz and Beta [13-30] Hz.

In order to identify the spectral activations solely associated with the observation of motor actions and thus discard all that could be associated to confounding factors such as the environment or the use of a monitor to administer the stimuli, we designed a statistical test in which PSD values,

obtained during the observation of videos labelled by different motor distances, were compared with those obtained in the baseline condition. Such condition was in fact planned as reference since it contains all the brain activations related to the context of the experiment except for the motor content. In particular, we compared the PSD values for each motor distance level with the baseline by performing a paired t-test ($\alpha = 0.05$, False Discovery Rate correction) across the participants (N=10) for each electrode. The t-values resulting from the statistical test were then filtered using statistical thresholds derived from the theoretical t-student distribution ($\alpha = 0.05$), thereby yielding grand-average statistical spectral maps at the scalp level between each condition and the baseline. These results are illustrated in Fig. 2.

G. Assessing the effect of motor distance on ERD

In order to confirm what was qualitatively noticed at the group level by means of statistical mapping and thus to evaluate how the motor distance would affect the level of desynchronization of specific brain areas, we computed at single subject level the ERD for each experimental condition (Distance 1, Distance 2, Distance 3, Distance 4) in alpha and beta frequency bands and for each channel, as follows:

$$\frac{PSD_{condition}\text{-}PSD_{baseline}}{PSD_{baseline}} \quad (1)$$

Since we hypothesized that motor distance in the observed videos could modulate the level of desynchronizations of specific brain areas of the observer mainly in the beta band, we designed a statistical test comparing ERD values between the two experimental conditions associated to the extreme values of motor distance (1 and 4) where we expected the higher size of the effect. We then compared the ERD values computed in Distance 4 and Distance 1 conditions by performing a paired t-test ($\alpha = 0.05$) for each band and each channel.

III. RESULTS

A. Grand Average spectral maps

In Figure 2 we reported the grand-average statistical spectral maps obtained for alpha and beta bands obtained by comparing the PSD values for each experimental condition with those related to baseline. The effect of the motor distance manipulation is evident on spectral activations in both frequency bands. Specifically, as for alpha band, in case of high motor distance (Distance 3 and 4) spectral desynchronizations are located over the bilateral sensorimotor areas and in left parietal area. When the observer was exposed to motor actions kinematically closer to them (Distance 1 and 2) the desynchronizations are more focal over the right central area. As for beta band, we obtained the activation of bilateral sensori-motor areas more spread in left hemisphere (that is contralateral to the side used to perform the motor action shown in the videos) independently on the applied motor distance manipulation. Moreover, observations of videos exhibiting kinematic movement dissimilar between the agent and observer (i.e. Distance 3 and Distance 4 conditions) revealed the activation of bilateral parietal areas.

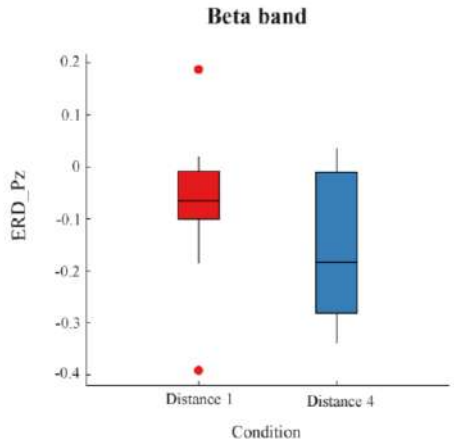


Fig. 3 Boxplot reporting the result of paired t-test ($\alpha = 0.05$) comparing the distribution of ERD values between Distance 4 and Distance 1 condition computed in beta band for Pz channel

B. Assessing the effect of motor distance on ERD

As for the comparison of ERD values between Distance 4 and Distance 1 conditions, we obtained a statistically significant difference for the Pz channel in the beta band, as shown in the Fig.3. In particular, the degree of desynchronization is significantly greater at maximum motor distance (Distance 4) than to at minimum motor distance (Distance 1). This result confirms quantitatively what we have described from grand average spectral maps.

IV. DISCUSSION AND CONCLUSION

In this preliminary study, we proposed to evaluate the effect of kinematic-based motor distance on neural activity in a group of subjects without motor impairment and neurological disorders during an action observation paradigm in order to design a kinematic-based visual motor priming to be embedded in a BCI system for post-stroke rehabilitation.

The grand-average statistical spectral maps reveal different neural activations depending on the frequency band considered. In both alpha and beta bands we found significant desynchronizations over the bilateral sensorimotor areas (centro-parietal electrodes), even if more lateralized over the left hemisphere, when the kinematic-based motor distance computed between the observer and the actor in the video is low (Fig. 1). This result is in line with what is already known about the role of such areas in motor tasks. In fact, motor and pre-motor areas are active not only when an individual performs a movement but also when such movement is imagined or observed, even if with a reduced level of desynchronization [18]. The lateralization over the left hemisphere is explained by the fact that the videos shown to the participants were played by individuals performing motor actions with right limb, thus an activation localized over the contralateral hemisphere is expected [5]. The effect of motor distance handling in action observation task was more evident in beta band. In particular, when participants observed videos characterized by a motor content kinematically unexpected (Distance 3 and Distance 4 conditions) activations over the bilateral parietal areas resulted. This is also confirmed by the

result of the paired t-test performed on the ERD scores, in which a higher desynchronization in Pz was found when observing movement with kinematics far from their internal mental motor representation with respect to the closer one (Fig.3). These results are consistent with previous studies that have shown how the kinematic characteristics and biological plausibility of observed movement has an influence on the brain activations [19]. In fact, an fMRI study shown how sensorimotor parietal regions are modulated when observing a movement with kinematics different from what is considered plausible [20].

In conclusion, this preliminary study demonstrates how the manipulation of kinematics-based motor distance in an action observation task influences observer's neural activation highlighting how the motor action shown to the observer should be closer to their motor repertoire otherwise it is perceived as unexpected and unpredictable. This is a key information to be taken into account if we are interested in the design of a motor priming for BCI systems, that supports patients in accomplishing the request to attempt/execute a motor action [11], [21]. The use of a kinematic-based motor priming preceding the request to the patients to attempt a movement supported by BCI would increase corticospinal excitability thus facilitating the recognition of the motor pattern ultimately promoting plasticity phenomena related to the use of a closed-loop rehabilitation approach. Priming presupposes, in fact, that enhanced neural activity before training could facilitate the activation of long-term potentiation-like mechanisms supporting synaptic plasticity [22]. To the best of our knowledge, none of the motor priming included in the available BCI systems has been tailored to the residual motor ability of the patient as assessed by kinematics. Adapting the motor priming to the specific patient's kinematics would allow to bring them to a level of corticospinal excitability where they would benefit the most from BCI intervention. In addition, such tailored priming would support the patient in movement attempt/execution helping them in the recall of movements from their own impaired motor repertoire and not from a general repertoire which could be perceived as unrelated.

REFERENCES

[1] J. R. Wolpaw, N. Birbaumer, D. J. McFarland, G. Pfurtscheller, e T. M. Vaughan, «Brain–computer interfaces for communication and control», Clin. Neurophysiol., 2002.

[2] E. López-Larraz, A. Sarasola-Sanz, N. Irastorza-Landa, N. Birbaumer, e A. Ramos-Murguialday, «Brain-machine interfaces for rehabilitation in stroke: A review», NeuroRehabilitation, vol. 43, fasc. 1, pp. 77–97, Jan. 2018, doi: 10.3233/NRE-172394.

[3] F. Pichiorri e D. Mattia, «Brain-computer interfaces in neurologic rehabilitation practice», in Handbook of Clinical Neurology, vol. 168, Elsevier, 2020, pp. 101–116. doi: 10.1016/B978-0-444-63934-9.00009-3.

[4] S. Silvoni et al., «Brain-Computer Interface in Stroke: A Review of Progress», Clin. EEG Neurosci., vol. 42, fasc. 4, pp. 245–252, Oct. 2011, doi: 10.1177/155005941104200410.

[5] G. Pfurtscheller e F. H. Lopes Da Silva, «Event-related EEG/MEG synchronization and desynchronization: basic principles», Clin. Neurophysiol., vol. 110, fasc. 11, pp. 1842–1857, Nov. 1999, doi: 10.1016/S1388-2457(99)00141-8.

[6] D. Camargo-Vargas, M. Callejas-Cuervo, e S. Mazzoleni, «Brain-Computer Interfaces Systems for Upper and Lower Limb Rehabilitation: A Systematic Review», Sensors, vol. 21, fasc. 13, Art. fasc. 13, Jan. 2021, doi: 10.3390/s21134312.

[7] E. Colamarino et al., «A Scoping Review of Technology-Based Approaches for Upper Limb Motor Rehabilitation after Stroke: Are We Really Targeting Severe Impairment?», J. Clin. Med., vol. 13, fasc. 18, Art. fasc. 18, Jan. 2024, doi: 10.3390/jcm13185414.

[8] P. Raghavan, «Upper Limb Motor Impairment After Stroke», Phys. Med. Rehabil. Clin. N. Am., vol. 26, fasc. 4, pp. 599–610, Nov. 2015, doi: 10.1016/j.pmr.2015.06.008.

[9] E. Scaliti, K. Pullar, G. Borghini, A. Cavallo, S. Panzeri, e C. Becchio, «Kinematic priming of action predictions», Curr. Biol. CB, vol. 33, fasc. 13, pp. 2717-2727.e6, July 2023, doi: 10.1016/j.cub.2023.05.055.

[10] D. J. Wright, J. Williams, e P. S. Holmes, «Combined action observation and imagery facilitates corticospinal excitability», Front. Hum. Neurosci., vol. 8, Nov. 2014, doi: 10.3389/fnhum.2014.00951.

[11] M. E. Stoykov e S. Madhavan, «Motor Priming in Neurorehabilitation», J. Neurol. Phys. Ther., vol. 39, fasc. 1, p. 33, Jan. 2015, doi: 10.1097/NPT.0000000000000065.

[12] S. M. Aglioti, P. Cesari, M. Romani, e C. Urgesi, «Action anticipation and motor resonance in elite basketball players», Nat. Neurosci., vol. 11, fasc. 9, pp. 1109–1116, Sept. 2008, doi: 10.1038/nn.2182.

[13] A. Cavallo, A. Koul, C. Ansuini, F. Capozzi, e C. Becchio, «Decoding intentions from movement kinematics», Sci. Rep., vol. 6, fasc. 1, Art. fasc. 1, Nov. 2016, doi: 10.1038/srep37036.

[14] R. C. Jackson, S. Warren, e B. Abernethy, «Anticipation skill and susceptibility to deceptive movement», Acta Psychol. (Amst.), vol. 123, fasc. 3, pp. 355–371, Nov. 2006, doi: 10.1016/j.actpsy.2006.02.002.

[15] P.-P. Vidal e F. Lacquaniti, «Perceptual-motor styles», Exp. Brain Res., vol. 239, fasc. 5, pp. 1359–1380, May 2021, doi: 10.1007/s00221-021-06049-0.

[16] J. Manuello, C. Maronati, M. Rocca, R. Guidotti, T. Costa, e A. Cavallo, «Motor styles in action: developing a computational framework for operationalization of motor distances», Behav. Res. Methods.

[17] J. F. Veale, «Edinburgh Handedness Inventory – Short Form: A revised version based on confirmatory factor analysis», Laterality, vol. 19, fasc. 2, pp. 164–177, Mar. 2014, doi: 10.1080/1357650X.2013.783045.

[18] J.-R. Duann e J.-C. Chiou, «A Comparison of Independent Event-Related Desynchronization Responses in Motor-Related Brain Areas to Movement Execution, Movement Imagery, and Movement Observation», PLOS ONE, vol. 11, fasc. 9, p. e0162546, Sept. 2016, doi: 10.1371/journal.pone.0162546.

[19] N. Syrov, D. Bredikhin, L. Yakovlev, A. Miroshnikov, e A. Kaplan, «Mu-desynchronization, N400 and corticospinal excitability during observation of natural and anatomically unnatural finger movements», Front. Hum. Neurosci., vol. 16, Sept. 2022, doi: 10.3389/fnhum.2022.973229.

[20] M. Costantini et al., «Neural Systems Underlying Observation of Humanly Impossible Movements: An fMRI Study», Cereb. Cortex, vol. 15, fasc. 11, pp. 1761–1767, Nov. 2005, doi: 10.1093/cercor/bhi053.

[21] S. Dorsch, V. Nicholson, E. Roman, E. Fanayan, e S. Chagpar, «Motor imagery priming improves activity and impairment outcomes in people after stroke but the effects of other types of priming are unclear: a systematic review», J. Physiother., vol. 70, fasc. 4, pp. 275–287, Oct. 2024, doi: 10.1016/j.jphys.2024.08.007.

[22] U. Ziemann e H. R. Siebner, «Modifying motor learning through gating and homeostatic metaplasticity», Brain Stimulat., vol. 1, fasc. 1, pp. 60–66, Jan. 2008, doi: 10.1016/j.brs.2007.08.003

Effectiveness and Adherence of a Robot-Enhanced Imitation Therapy in Autistic Children

Gabriele Fassina
NEAR-Lab, DEIB, Politecnico di Milano
Milan, Italy
gabriele.fassina@polimi.it

Silvia Annunziata
IRCCS Fondazione don Carlo Gnocchi
Milan, Italy
sannunziata@dongnocchi.it

Michelle Brivio
IRCCS Fondazione don Carlo Gnocchi
Milan, Italy
mibrivio@dongnocchi.it

Laura Santos
NEAR-Lab, DEIB, Politecnico di Milano
ISR, Universidade de Lisboa
Lisbon, Portugal
laurajoana.espinosa@polimi.it

Emilia Ambrosini
NEAR-Lab, DEIB, Politecnico di Milano
Milan, Italy
emilia.ambrosini@polimi.it

Anna Cavallini
IRCCS Fondazione don Carlo Gnocchi
Milan, Italy
ancavallini@dongnocchi.it

Alessandra Pedrocchi
NEAR-Lab, DEIB, Politecnico di Milano
Milan, Italy
alessandra.pedrocchi@polimi.it

***Abstract*—Robot-Enhanced Therapies (RET) are gaining recognition in autism interventions, though limited empirical evaluations of their effectiveness exist. This study introduces a novel RET focused on imitation training to promote social skills, incorporating gestures from children's songs to enhance engagement. This work presents preliminary findings from eight autistic children who underwent a 12-week intervention, assessing improvements in adaptive abilities using the Adaptive Behavioral Assessment Scale (ABAS-II) and *Primo Vocabolario del Bambino* (PVB), with the Social Adaptive Domain (SAD) of ABAS-II as the primary outcome. Treatment adherence is measured as the proportion of correctly imitated gestures, which is also quantified by leveraging a CNN-based gesture recognition algorithm. While results show overall trends of improvement, the primary outcome does not reach statistically significant. However, adherence was significantly higher in subjects with improved social skills, underscoring the importance of active participation The gesture recognition algorithm achieved an F1-score of 0.57. While findings are promising, the comparison with a control group will permit differentiating the outcomes of the therapy protocol and the developmental trajectory. Future efforts should focus on improving the gesture-imitation algorithm and refining adherence assessment tools.**

***Index Terms*—Robot-Enhanced Therapy, Autism, Social skills**

I. Introduction

Autism Spectrum Disorder (ASD) is a neurodevelopmental condition characterized by restricted and repetitive behaviors as well as social and communication deficits [1]. The prevalence of autism is increasing, with an estimated 1 in 36 children diagnosed with ASD in the U.S. [2]. Existing interventions are designed to promote the development of socio-communicative skills, addressing the core symptoms and their influence on child's development and easing inclusion in a neurotypical society [3]. Advancements in Artificial Intelligence (AI) and robotics have fostered a growing interest towards their applications for autism [4]. Specifically, HRI research on autism primarily follows a medical model, highlighting robots' role in ASD interventions [5]. The rationale underpinning robots' use in ASD therapy is rooted in their predictability, which can reduce discomfort elements for autistic children compared to human-human interaction [6]–[8]. Several robot-mediated approaches have been explored in ASD intervention. For instance, Marino and colleagues proposed the use of robots to improve emotion recognition skills [9]; Javed et al, utilized a humanoid robot to address sensory processing difficulties in ASD children [10]; Cao et al, developed a Robot-Enhanced Therapies (RET) for joint attention training [6]. Additionally, some studies have investigated the use of robots for imitation training [11], [12], given that gesture imitation plays a crucial role in empathy development [13] and serves as a social function by facilitating engagement in social and emotional contexts. Moreover, gesture imitation has been found to positively correlate with joint attention [14].

In all forms of intervention, active involvement of the child is essential to achieve therapeutic outcomes [15]. The measurement of adherence to the protocol is thus crucial to determine whether the observed changes can be imputable to the proposed intervention. In this direction, Rakhymbayeva et al. proposed quantifying adherence using a 1-5 Likert scale [16] based on the number of prompts needed to complete the task. However, this method is prone to inter-operator variabil-

This research was funded within the MUSA – Multilayered Urban Sustainability Action – project, funded by the European Union – NextGenerationEU, under the National Recovery and Resilience Plan (NRRP) Mission 4 Component 2 Investment Line 1.5: Strenghtening of research structures and creation of R&D "innovation ecosystems", set up of "territorial leaders in R&D".

ity and lacks sensitivity to subtle changes. Alternatively, van den Berk-Smeekens and colleagues assessed adherence as the percentage of therapy sessions in which participants accepted the use of the NAO robot, reflecting sufficient motivation to complete the interaction [17]. Nonetheless, their approach did not account for the child's effective participation in the therapy protocol.

In order to sustain engagement, researchers have explored integrating music and dance to stimulate spontaneous communication [18]. Music, in particular, is widely acknowledged as an effective tool for promoting communication within therapeutic settings [19].

Various quantitative approaches have been proposed to measure engagement during therapy. Gaze direction has been identified as a biomarker for detecting engagement [20], while Joint Attention Behaviors have been used to estimate the level of child involvement [21]. Additionally, more advanced multi-modal methods combining gaze features with emotion recognition have been explored [22].

In this work, we propose a Robot-Enhanced Therapy (RET) centered on gesture imitation and empowered by the introduction of songs in the imitation activities, with the aim of permitting the engagement of children with moderate or high levels of autism. The primary research question of this study is to evaluate the effectiveness of the proposed intervention in terms of adaptive abilities with a particular focus on social skills. A secondary research question examines whether differences in outcome measures are associated with children's adherence to the intervention protocol. The final research question explores whether an automatic quantitative algorithm can assess adherence to the therapy.

II. Materials and Methods

A. Study Design

This study presents preliminary results from a Randomized Controlled Trial (RCT) currently underway at IRCCS Fondazione Don Carlo Gnocchi, Milan, Italy. Specifically, a subset of participants from the experimental group has been analyzed. Eligibility criteria include a confirmed autism diagnosis via the Autism Diagnostic Observation Schedule, Second Edition (ADOS-2) [23] and an age of under six years at recruitment. Participants completed 12 weekly sessions of Robot-Enhanced Therapy, each lasting approximately 20 minutes, as detailed in Section II-C. The study protocol was approved by the Ethical Committees of Politecnico di Milano (approval number 34/2022, dated 16/09/2022) and Fondazione Don Gnocchi (approval number 07/2023, dated 29/03/2023). All parents provided written informed consent before the intervention, and participants were free to withdraw at any time.

B. Setup

The therapy setup includes a NAO (6th version) humanoid robot, developed by Aldebaran Robotics, integrated with a Microsoft Azure Kinect camera to track participants' movements. A serial communication protocol is established between the robot and the camera through a dedicated computer. A tablet-based Graphical User Interface (GUI) enables the therapist to control the robot.



Fig. 1. Gestures included in the current protocol for each song [26].

C. Therapy protocol

The therapy protocol is based on a triadic interaction involving the therapist, the child, and the NAO robot, which serves as a mediator to promote socio-communicative skills between the two human partners. Sessions begin with a familiarization phase, during which the robot interacts with the child with sensory stimuli such as lights, sounds, and simple movements. Once the child feels comfortable with NAO, the therapist transitions to the core phase, which centers on gesture imitation. Body movements and gesture imitation are believed to help establish an effective communication channel between the child and the therapist [24]. A previous pilot study included only semantic gestures related to daily living activities [25]. However, as children with severe autism often struggled to engage with these tasks, the protocol was expanded to incorporate gestures from popular children's songs. Specifically, *Noah's Song* (*L'arca di Noè*), *Baby Shark*, and *Crocodile Song* (*Il coccodrillo come fa?*) were introduced, with corresponding gestures selected based on the lyrics, as illustrated in Figure 1.

The imitation interaction begins with the therapist selecting a song through the GUI, considering the child's verbal and non-verbal preferences and requests. The robot starts singing the song and it demonstrates the gestures related to the lyrics when the specific part associated with that gesture is sung. After the demonstration, the robot repeats the same segment without showing the gesture anymore. In this phase, the therapist structures the triadic interaction by encouraging imitation but does not provide additional prompts beyond those given by the robot. This pattern continues till the end of the song. Besides gesture training, this protocol is aimed to exercise the turn-taking skills of the children and to enhance their social interaction with the therapist. Although parents are allowed to be present during therapy, children typically participate independently.

D. Outcome measurements

The Griffiths Mental Development Scales III (GMDS-III) [27] are administered at the baseline to evaluate each child's Global Developmental Quotient (GDQ), which ranges between 20 and 150. To evaluate the effectiveness of the therapy protocol, two assessment scales are employed: The Adaptive Behavior Assessment Scale - Second Edition (ABAS-II) [28] and the Italian adaptation of the MacArthur-Bates Communicative Development Inventories, *Primo Vocabolario Del Bambino* (PVB) [29]. The ABAS-II is a parent-reported questionnaire that measures the adaptive abilities by assessing the presence and frequency of specific behaviors. The scale provides a Global Adaptive Composite Score (GAC), ranging from 37 to 170, along with three subdomain scores. The Conceptual Adaptive Domain (CAD), ranging from 41 to 150, assesses communication skills and self-regulation. The Social Adaptive Domain (SAD), with a range of 49 to 148, measures socialization abilities, including interactions with peers and adults. Lastly, the Practical Adaptive Domain (PAD), spanning 44 to 149, evaluates self-care and school-related skills. In all cases, higher scores indicate better adaptive skills. Given that the therapy protocol primarily targets socio-relational development, the SAD subdomain was selected as the primary outcome measure. The PVB scale is a questionnaire aimed to assess children's communication skills. Specifically, its *Gestures and Words* subtest quantifies the words and phrases understood and pronounced, as well as the gestures observed and acquired, providing insights about the development of their receptive and expressive abilities. The scale ranges between 0 and 63. Both questionnaires are administered at T0, before the beginning of the intervention, and at T1, the week after its conclusion.

E. Adherence Assessment

Although the therapy protocol is designed to offer standardized interaction possibilities, with the inclusion of the robot further enhancing the consistency of the intervention, each session differs from the others by the number of stimuli provided. These variations primarily depend on the child's willingness to engage during the session. Therefore, adherence to the conceived therapeutic protocol can be quantified by the proportion of gestures imitated by the child compared to the total amount of stimuli presented. Specifically, the number of gestures imitated during each therapy session is recorded and divided by the total number of stimuli provided along the whole session. This latter is defined as the sum of the gestures presented in each song multiplied by the number of times each song was played during the session.

F. Automatic Method for Adherence Assessment

Despite the robustness of the proposed metric for assessing the impact of child adherence on therapy outcomes, the manual annotation of all sessions is highly time demanding. To overcome this limitation, an automatic gesture recognition algorithm was implemented. The algorithm builds upon our previous work [26], processing kinematic data acquired via the Azure Kinect camera. This data is fed into a set of binary classifiers — one per gesture — based on Convolutional Neural Networks (CNNs), which determine whether the child performed the expected gesture or not. In our previous study, gestures were precisely segmented via manual video observation, achieving high classification accuracy. However, to enable a fully automatic computation, in this work manual segmentation was avoided and an automated alternative was implemented [30].

Only sessions in which at least one gesture was proposed have been included in the automatic analysis. Indeed, during some sessions, no imitation activities were proposed due to technical issues (e.g. Kinect cable disconnections or Wi-Fi instability affecting the Graphical User Interface) or to child's complete refusal to interact with NAO.

G. Data analysis

To answer the first research question, the General Composite Score of the ABAS-II scale, as well as all its subdomains and the PVB were assessed both before and after the intervention for all children. The Wilcoxon test with a significance of 0.05 was used to assess the statistical significance of the differences found at the two time points. A deeper analysis was performed by dividing the cohort into two subpopulations depending on the variations in the SAD subdomain score: a first one defined as *Respondent Group* which encompasses those children presenting a positive change in the SAD scale and a second one, named *Non-Respondent Group*, that comprehends those subjects with no change in the SAD subdomain. To answer the second research question, the Mann-Whitney U test was applied to compare the mean percentage of imitated gestures between the *Respondent* and *Non-Respondent* subjects. The performance of the automatic method for adherence assessment was evaluated using the F1-score, considering class imbalances. Moreover, in order to better investigate the performances of each classifier, each gesture's dataset was artificially balanced by sourcing the additional false samples from the true representations of the other classes and the accuracy for the specific dataset is considered [26].

III. Results

A. Participants

Eight participants (3 females and 5 males; mean age 52.1 ± 12.9 months) completed the Robot Enhanced Therapy protocol and underwent the assessment phases. Table I summarizes their demographic and clinical characteristics. Since the minimum value of the GDQ as reported by the GMDS-III score is 20, children who scored below this threshold are reported as < 20. ADOS-2 comparison scores assess the level of symptoms related to Autism Spectrum Disorders, with values between 5 and 7 indicating a moderate evidence of autism-related symptoms and between 8 and 10 indicating a high level of symptoms.

Patient ID	Sex	Age (months)	GDQ	ADOS
DG01	F	52	56	9
DG02	M	42	<20	10
DG03	M	38	63	9
DG04	F	55	42	6
DG08	M	61	<20	7
DG10	F	63	<20	7
DG12	M	71	<20	6
DG13	M	35	73	9

TABLE I

DEMOGRAPHIC AND CLINIC CHARACTERISTICS OF CHILDREN INCLUDED IN THE STUDY. THE AGE IS REPORTED AT THE TIME OF T0 ASSESSMENT. GLOBAL DEVELOPMENTAL QUOTIENT (GDQ) IS ASSESSED THROUGH THE GMDS-III. ADOS-II COMPARISON SCORE IS REPORTED TO ACCOUNT FOR AUTISM SEVERITY (5-7 MODERATE; 8-10 HIGH LEVEL OF SYMPTOMS).

Scale	T0	T1	p-value
GAC	41 [37-51]	49 [39-68]	**0.04**
CAD	45.5 [41-60]	56 41-78]	0.3
SAD	49 [49-61]	56 [49-66]	0.3
PAD	46 [44-61]	57.5 [49-68]	**0.04**
PVB	38.5 [34-35]	42.5 [37-54]	0.1

TABLE II

MEDIAN [INTER-QUARTILE RANGE] RESULTS OF THE ABAS-II SCALE GENERAL ADAPTIVE COMPOSITE (GAC) AND ITS SUBDOMAINS, NAMELY THE CONCEPTUAL ADAPTIVE DOMAIN (CAD), THE SOCIAL ADAPTIVE DOMAIN (SAD) AND THE PRACTICAL ADAPTIVE DOMAIN (PAD) AND OF THE *Primo Vocabolario del Bambino* (PVB). THE LAST COLUMN REPORTS THE P-VALUE OBTAINED AT THE WILCOXON TEST AND SIGNIFICANT RESULTS ARE HIGHLIGHTED IN BOLD

B. Clinical Scales

Table II presents the median and interquartile ranges for the scores obtained across these scales and their respective subdomains. The results indicate that while the median values of all considered metrics improved, statistical significance was found only for the General Adaptive Composite score ($p = 0.04$) and for the Practical Adaptive Domain ($p = 0.04$).

Since the proposed treatment primarily targets social aspects, individual changes in the SAD subdomain were further analyzed, with the results depicted in Figure 2. The population can be distinctly clustered into two subgroups: a *respondent* one, consisting of individuals who exhibit an improvement in the SAD score during the intervention, and a *non-respondent* group, comprising children who do not present any pre to post-treatment change.

C. Adherence Assessment

Our second research question investigates whether active engagement by the child during therapy positively impacts treatment effectiveness. We hypothesize that the proportion of gestures imitated by the child could serve as a meaningful parameter to assess adherence to the proposed therapeutic approach.

The percentage of gestures imitated by the child during each session computed by manual annotation is illustrated in Figure 3. The distinction between *respondent* and *non-respondent* groups presented in Section III-B is maintained to highlight behavioral differences between the two groups. Specifically, the left panel depicts the *respondent* group, while the right one

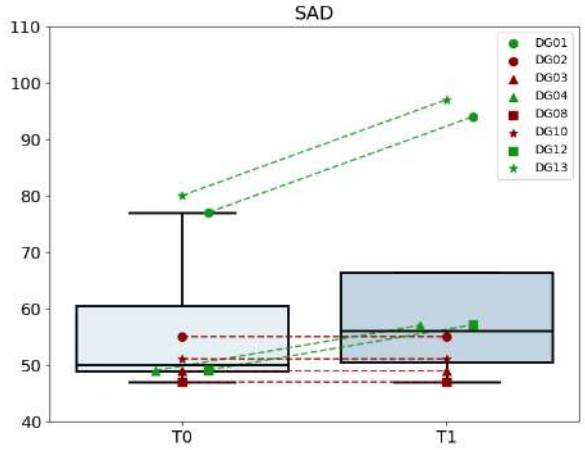


Fig. 2. Results in the Social Adaptive Domain (SAD) of the ABAS-II scale at T0 and T1. Each points represents a specific subject. Green points represent *respondent* subjects while red ones indicate *non-respondent* children.

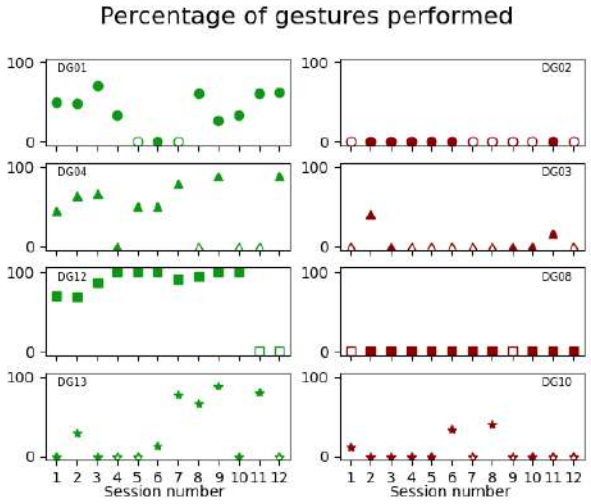


Fig. 3. Percentage of gestures imitated by each child. Green symbols represent children in the *respondent* group while red symbols represent the *non-respondent* group. Empty symbols indicate the sessions excluded from the analysis, i.e. when no gestures were proposed.

represents the *non-respondent* group. Notably, only respondents actively engaged in the imitation task, while the non-responders demonstrated a marked absence of participation in imitation activities throughout all sessions. The difference in the average number of imitated gestures between the two groups was statistically significant, as confirmed by the Mann-Whitney U test ($p = 0.02$).

D. Automatic Method for Adherence Assessment

Of the 96 sessions conducted in this study, 67 (70%) were included in the analysis. The dataset consists of 316 stimuli, defined as instances when the child was expected to replicate a gesture demonstrated by the robot. The dataset is imbalanced, with 216 gestures manually labeled as correct imitations and 100 classified as incorrect imitations. Given this imbalance,

the F1-score was used to evaluate the method's performance, yielding a result of 0.57, with a precision of 0.66 and a recall of 0.55. To further analyze classifiers' performances, each gesture's dataset was artificially balanced by adding true representations pertaining to the other classes, and the accuracy of the algorithm was computed separately for each gesture, as detailed in Table III.

Gesture	True samples	False samples	Total samples balanced	Accuracy
baby	18	11	36	0.64
boh	8	6	16	0.5
bye	19	12	38	0.45
daddy	24	4	48	0.67
drink	8	5	16	0.38
eagle	19	4	38	0.71
eat	9	5	18	0.5
elephant	14	9	28	0.57
mommy	24	7	48	0.58
no	24	12	48	0.54
orangutan	16	8	32	0.69
sad	10	4	20	0.5
swim	18	12	36	0.47
walk	4	1	10	0.6
Total	**216**	**100**	**432**	

TABLE III
TRUE AND FALSE SAMPLES INDICATE THE ORIGINAL DATASET DISTRIBUTION. ACCURACY WAS COMPUTED AFTER BALANCING EACH GESTURE'S DATASET.

IV. DISCUSSION

The primary research question of this study investigates the effectiveness of the proposed Robot Enhanced Therapy, based on gesture imitation. To assess this, we analyzed the General Adaptive Composite (GAC) score of the ABAS-II scale and its subdomains, along with the *Primo Vocabolario del Bambino*. While all metrics indicated a median improvement from T0 to T1, only the GAC and PAD subdomains reached statistical significance. Since the intervention primarily targets social skills, the Social Adaptive Domain (SAD) of the ABAS-II scale was selected as the primary outcome. Four children (DG01, DG04, DG12, DG13) showed improvement, forming the *respondent group*, while the remaining four exhibited no pre-post variation and were categorized as *non-respondents*. Notably, the two children with the highest SAD scores at T0 are also the ones who showed a more marked improvement. The other two respondents displayed better interaction skills at the baseline, although they did not stand out in clinical scales. Conversely, three of the non-respondents had a GDQ below the minimum threshold. These findings may suggest that this RET could be more effective for children with a minimum level of social skills at baseline.

To explore the impact of adherence on therapy outcomes, we computed the percentage of imitated gestures. Only children who actively engaged in imitation tasks showed improvement in the SAD score, indicating that participation is crucial for achieving therapeutic benefits. Interestingly, DG13, the youngest participant, initially exhibited low adherence, which gradually increased from session 7 onward. This might suggest that younger children may require a longer adaptation period. Conversely, the severity of ASD symptoms, appears to have no correlation with either therapy effectiveness or adherence level.

Given the time-intensive nature of manual adherence assessment, we propose the use of an automatic gesture recognition algorithm. Results reveal the challenges of applying this method with autistic children data, as reflected in the low F1-score. This is probably due to the fact that ASD children move a lot during the acquisition without maintaining the expected standing pose. In fact, the training set of the Gesture Recognition Algorithm was composed of neurotypical individuals, both adults and children, without including any autistic child. Moreover, these results are lower than the ones reported in [26] probably because in the present work the algorithm has been applied following an online approach in order to avoid the need for manual segmentation, which was in turn done when the algorithm was tested in the previous work. To gain further information on this result, each gesture dataset was balanced, and the corresponding recognition accuracies were computed. Gestures involving broader movements (*daddy*) and those primarily occurring in the frontal plane (*orangutan*, *eagle*) achieved higher recognition rates. This aligns with previous research indicating that the Azure Kinect performs well under these conditions but struggles with sagittal-plane movements and gestures with limited amplitude [31].

V. CONCLUSION

In this study, we proposed a new Robot-Enhanced Therapy protocol based on imitation training of gestures derived from children's songs, with the objective of enhancing participant engagement. While a general trend of improvement across all metrics suggests potential benefits of the proposed treatment, the primary outcome measure, the Social Adaptive Domain (SAD) of the ABAS-II scales, did not demonstrate statistical significance between pre- and post treatment. The subsequent analysis of the data involved the establishment of two distinct subgroups: those who exhibited a positive response to the intervention and those who did not, based on the primary outcome. To address the second research question, the adherence to treatment was quantified using the percentage of gestures imitated by the child. The obtained results indicate that only those children who actively engaged in the imitation activity demonstrated a performance improvement in the main outcome metric. In conclusion, given the significant time investment required for manual computation of the percentage of imitated gestures, we implemented of an automatic algorithm, which yielded an F1-score performance of 0.57, underscoring the necessity for further research in this domain.

Although the results of this study are encouraging, several limitations must be acknowledged. Firstly, the RET was evaluated on a small sample of eight children from the experimental group. A larger dataset and a control group will permit drawing more robust conclusions about the effectiveness of the proposed intervention. Secondly, adherence was assessed solely based on the percentage of gestures imitated by the children, without considering other aspects of engagement not directly tied to the therapy protocol. Future studies should

incorporate additional measures, such as motor abilities, eye gaze, and emotion recognition, to provide a more comprehensive understanding of the child's engagement. Lastly, gesture recognition was used to automate adherence assessment. While this approach demonstrated feasibility, further refinements are needed to enable full automation, facilitating adherence assessment in larger cohorts.

ACKNOWLEDGMENT

We would like to acknowledge the therapists Arianna Caglio and Eleonora Santini who carried out the interventions.

REFERENCES

[1] A. P. Association, *Diagnostic and Statistical Manual of Mental Disorders - 5th edition*.

[2] R. P. Walensky, R. Bunnell, C. K. Kent, A. J. Gottardy, M. A. Leahy, J. C. Martinroe, S. R. Spriggs, T. Yang, Q. M. Doan, P. H. King, T. M. Starr, M. Yang, T. F. Jones, M. L. Boulton, M. Carolyn Brooks, M. A. Virginia Caine, J. E. Fielding, M. W. David Fleming, W. E. Halperin, M. Jewel Mullen, M. Jeff Niederdeppe, P. Quinlisk, M. L. Patrick Remington, M. Carlos Roig, M. William Schaffner, M. Bobb Swanson, B. Ian Branam, K. Cohen, S. Hairston, L. Hamlin, and L. Johnson, "Morbidity and Mortality Weekly Report Prevalence and Characteristics of Autism Spectrum Disorder Among Children Aged 8 Years-Autism and Developmental Disabilities Monitoring Network, 11 Sites, United States, 2020 Surveillance Summaries Centers for Disease," *MMWR Surveill Summ*, vol. Summer, no. 2, 2023.

[3] M. Sandbank, K. Bottema-Beutel, S. Crowley, M. Cassidy, K. Dunham, J. I. Feldman, J. Crank, S. A. Albarran, S. Raj, P. Mahbub, and T. G. Woynaroski, "Project AIM: Autism intervention meta-analysis for studies of young children," *Psychological Bulletin*, vol. 146, no. 1, pp. 1–29, 2020.

[4] L. Santos, S. Annunziata, A. Geminiani, A. Ivani, A. Giubergia, D. Garofalo, A. Caglio, E. Brazzoli, R. Lipari, M. C. Carrozza, E. Ambrosini, I. Olivieri, and A. Pedrocchi, "Applications of Robotics for Autism Spectrum Disorder: a Scoping Review," *Review Journal of Autism and Developmental Disorders*, 2023.

[5] N. Rizvi, W. Wu, M. Bolds, R. Mondal, A. Begel, and I. Munyaka, "Are Robots Ready to Deliver Autism Inclusion?: A Critical Review," *Conference on Human Factors in Computing Systems - Proceedings*, 2024.

[6] B. H.-l. Cao, P. G. Esteban, M. Bartlett, P. Baxter, T. Belpaeme, E. Billing, H. Cai, M. Coeckelbergh, C. Costescu, D. David, A. D. Beir, D. Hernandez, J. Kennedy, H. Liu, S. Matu, A. Mazel, and A. Pandey, "Robot-Enhanced Therapy," pp. 49–58, 2019.

[7] J. DiPietro, A. Kelemen, Y. Liang, and C. Sik-Lanyi, "Computer-and robot-assisted therapies to aid social and intellectual functioning of children with autism spectrum disorder," *Medicina (Lithuania)*, vol. 55, no. 8, pp. 1–18, 2019.

[8] H. Hodges, C. Fealko, and N. Soares, "Autism spectrum disorder: Definition, epidemiology, causes, and clinical evaluation," *Translational Pediatrics*, vol. 9, no. 8, pp. S55–S65, 2020.

[9] F. Marino, P. Chilà, S. T. Sfrazzetto, C. Carrozza, I. Crimi, C. Failla, M. Busà, G. Bernava, G. Tartarisco, D. Vagni, L. Ruta, and G. Pioggia, "Outcomes of a Robot-Assisted Social-Emotional Understanding Intervention for Young Children with Autism Spectrum Disorders," *Journal of Autism and Developmental Disorders*, vol. 50, no. 6, pp. 1973–1987, 2020.

[10] H. Javed, R. Burns, M. Jeon, A. M. Howard, and C. H. Park, "A Robotic Framework to Facilitate Sensory Experiences for Children with Autism Spectrum Disorder," *ACM Transactions on Human-Robot Interaction*, vol. 9, no. 1, pp. 1–26, 2020.

[11] W.-C. So, M. K.-Y. Wong, C. K.-Y. Lam, W.-Y. Lam, A. T.-F. Chui, T.-L. Lee, H.-M. Ng, C.-H. Chan, and D. C.-W. Fok, "Using a social robot to teach gestural recognition and production in children with autism spectrum disorders.," *Disability and rehabilitation. Assistive technology*, vol. 13, pp. 527–539, aug 2018.

[12] A. S. Ivani, A. Giubergia, L. Santos, A. Geminiani, S. Annunziata, A. Caglio, I. Olivieri, and A. Pedrocchi, "A gesture recognition algorithm in a robot therapy for ASD children," *Biomedical Signal Processing and Control*, vol. 74, no. December 2021, p. 103512, 2022.

[13] T. Field, J. Nadel, and S. Ezell, "Imitation Therapy for Young Children with Autism," *Autism Spectrum Disorders - From Genes to Environment*, 2011.

[14] B. Ingersoll, "The Social Role of Imitation in Autism," *Infants Young Children*, vol. 21, no. 2, pp. 107–119, 2008.

[15] C. S. Albaum, T. Sellitto, N. Vashi, Y. Bohr, and J. A. Weiss, "Treatment Engagement as a Predictor of Therapy Outcome Following Cognitive Behaviour Therapy for Autistic Children," *Journal of Autism and Developmental Disorders*, pp. 3575–3586, 2023.

[16] N. Rakhymbayeva, A. Amirova, and A. Sandygulova, "A Long-Term Engagement with a Social Robot for Autism Therapy," *Frontiers in Robotics and AI*, vol. 8, no. June, pp. 1–14, 2021.

[17] I. van den Berk-Smeekens, M. van Dongen-Boomsma, M. W. De Korte, J. C. Den Boer, I. J. Oosterling, N. C. Peters-Scheffer, J. K. Buitelaar, E. I. Barakova, T. Lourens, W. G. Staal, and J. C. Glennon, "Adherence and acceptability of a robot-assisted Pivotal Response Treatment protocol for children with autism spectrum disorder," *Scientific Reports*, vol. 10, no. 1, pp. 1–11, 2020.

[18] H. Javed and C. H. Park, "Promoting Social Engagement With a Multi-Role Dancing Robot for In-Home Autism Care," *Frontiers in Robotics and AI*, vol. 9, no. June, pp. 1–15, 2022.

[19] J. M. Beer, M. Boren, and K. R. Liles, "Robot assisted music therapy: A case study with children diagnosed with autism," *ACM/IEEE International Conference on Human-Robot Interaction*, vol. 2016-April, pp. 419–420, 2016.

[20] B. Silva, L. Santos, C. Barata, A. Geminiani, G. Fassina, A. Rita Gonzalez, S. Ferreira, B. Barahona-Corrêa, I. Olivieri, A. Pedrocchi, and J. Santos-Victor, "Attention Analysis in Robotic-Assistive Therapy for Children with Autism," *IEEE Transactions on Neural Systems and Rehabilitation Engineering*, vol. 32, no. Figure 1, pp. 2220–2229, 2024.

[21] D. O. David, C. A. Costescu, S. Matu, A. Szentagotai, and A. Dobrean, "Developing Joint Attention for Children with Autism in Robot-Enhanced Therapy," *International Journal of Social Robotics*, vol. 10, no. 5, pp. 595–605, 2018.

[22] H. Javed and C. H. Park, "Promoting Social Engagement With a Multi-Role Dancing Robot for In-Home Autism Care," *Frontiers in Robotics and AI*, vol. 9, no. June, pp. 1–15, 2022.

[23] L. PC, "The autism diagnostic observation schedule-generic: a standard measure of social and communication deficits associated with the spectrum of autism," *J Autism Dev Disord*, vol. 30, pp. 205–223, 2000.

[24] A. Taheri, A. Meghdari, and M. H. Mahoor, "A Close Look at the Imitation Performance of Children with Autism and Typically Developing Children Using a Robotic System," *International Journal of Social Robotics*, pp. 6–10, 2020.

[25] S. Annunziata, L. Santos, A. Caglio, A. Geminiani, E. Brazzoli, E. Piazza, I. Olivieri, A. Pedrocchi, and A. Cavallini, "Interactive mirrOring Games wIth sOCial rObot (IOGIOCO): a pilot study on the use of intransitive gestures in a sample of Italian preschool children with autism spectrum disorder," *Frontiers in Psychiatry*, vol. 15, no. June, pp. 1–15, 2024.

[26] G. Fassina, L. Santos, E. Zorzella, A. Caglio, S. Annunziata, A. Cavallini, A. Pedrocchi, and E. Ambrosini, "Song Gesture Recognition for a Robot-Enhanced Imitation Therapy," *2024 33rd IEEE International Conference on Robot and Human Interactive Communication (ROMAN)*, pp. 1815–1820, 2024.

[27] G. E, S. L, B. S, C. J, F. C, H. K, and Others, *Griffiths scales of child development*. Oxford: Hogrefe, 2016.

[28] T. Oakland and P. L. Harrison, "Chapter 1 - Adaptive Behaviors and Skills: An Introduction," in *Adaptive Behavior Assessment System-II* (T. Oakland and P. L. Harrison, eds.), Practical Resources for the Mental Health Professional, pp. 1–20, San Diego: Academic Press, 2008.

[29] C. MC, B. A, R. R, S. S, and P. P, "Il Primo Vocabolario del Bambino: Gesti, Parole e Frasi. Valori di riferimento fra 8 e 36 mesi delle Forme complete e delle Forme brevi del questionario MacArthur-Bates CDI," *Franco Angeli Edition*, vol. 8, 2015.

[30] G. Fassina, L. Santos, A. Geminiani, A. Caglio, S. Annunziata, I. Olivieri, and A. Pedrocchi, "Development of an Interactive Total Body Robot Enhanced Imitation Therapy for ASD children.," *IEEE International Conference on Rehabilitation Robotics*, vol. 2022-July, pp. 2–7, 2022.

[31] C. Brambilla, R. Marani, L. Romeo, M. Lavit Nicora, F. A. Storm, G. Reni, M. Malosio, T. D'Orazio, and A. Scano, "Azure Kinect performance evaluation for human motion and upper limb biomechanical analysis," *Heliyon*, vol. 9, no. 11, p. e21606, 2023.

Psychophysical Evaluation of A Mechanotactile Haptic Feedback Device

Deep Roshan
Centre for Biomedical Engineering
Indian Institute of Technology Delhi

Azadeh Shariati
Department of Mechanical Engineering
University College London

Kamyar Motaghedolhagh
Department of Mechanical Engineering
University College London

Helge A. Wurdemann
Department of Mechnanical Engineering
University College London

Biswarup Mukherjee
Centre for Biomedical Engineering
Indian Institute of Technology Delhi
bmukherjee@iitd.ac.in

***Abstract*—Sensory feedback enhances the intuitive operation of upper limb prostheses. However, most modern commercial prosthetic devices lack sensory feedback mechanisms due to the difficulty of integration and added complexity. Mechanotactile haptic feedback provides a non-invasive and low-cost alternative to traditional electromechanical haptic feedback modalities. While mechanotactile haptic feedback systems have been studied for their mechanical behaviour, their practical integration in prosthetic devices and associated human factors still remain to be investigated. Therefore, in this paper, we perform a psychophysics study to investigate the perceptual thresholds associated with a mechanotactile feedback system. We use a mechanotactile sensory system and feedback device to provide force feedback on the forearm of healthy volunteers. We systematically assess the optimal placement of the feedback devices and the minimum perceptible forces at each position. We found that the minimum perceptible force that a user can perceive range lies in the range of 0.39 N to 1.36 N at various points on the forearm. The distal forearm was found to have higher perception sensitivity compared to the proximal forearm. Our results shed light on the perception thresholds achievable with mechanotactile haptic elements. Results also indicate that proper placement and site selection of the mechanotactile feedback elements are crucial to enhance force perception accuracy.**

***Index Terms*—Mechano-tactile feedback, psychophysical measurement**

I. Introduction

The human hand is one of the most complex structures in nature, showcasing remarkable flexibility, dexterity, and sensory capabilities. It operates within a closed-loop sensory feedback system that is essential for maintaining precise control over its movements and interactions with the environment [1]. The sense of touch in the human hand is achieved by different types of mechanoreceptors present in the skin [2]. However, individuals with upper-extremity amputation who utilize upper limb prosthetic devices lack the ability to perceive sensory information related to touch. Therefore, crucial information required to execute simple tasks, grasping and holding objects without slipping or crushing them often exhibits poor force modulation and high failure rates [3], [4]. As a result, a vast majority of prosthetic users end up abandoning their devices and often cite the lack of sensory feedback as a key determinant [5], [6].

Several techniques have been adopted to sense distal tactile interactions and to provide haptic feedback to users to restore the sense of touch in prosthetic devices [7]. Several groups have reported resistive, capacitive and optical systems to sense the interaction forces on the fingertips of prosthetic devices and robotic grippers. BioTac, employed a conductive fluid enclosed in an elastomeric chamber to measure changes in electrical impedance due to tactile interactions [8].

On the other hand, sensory feedback can also be delivered through multiple modalities, including vibration, compressive and shear forces (skin stretch) and electrotactile feedback [9]. Invasive methods involving the implantation of neural interfaces have been successful in eliciting illusory sensory percepts in phantom limbs, providing highly realistic feedback to individuals with amputation [10]. However, the high risk of surgery and coupled with poor long-term stability of neural interfaces, has led to limited adoption [11].

Shi et al. developed a purely mechanical haptic feedback and sensing system [12], [13]. Briefly, the system utilizes a fluid-filled mechanotactile system, which has three main components: a fingertip sensor, an actuator, and a tube. This system senses the force on the fingertip sensor and transfers the force through the fluid to the actuator to produce modality-matched tactile stimuli. Unlike traditional approaches, the sensing element and the haptic feedback element are purely mechanical in nature, obviating the need for electrical connections or signal processing. Therefore, mechanotactile haptic systems are uniquely suited for integration into passive prosthetic devices and devices with limited electrical and electronic hardware resources. However, a systematic psychophysical measurement is required to understand the relationship between sensory input and perceived stimuli, i.e. the perception thresholds for mechanotactile haptic systems [14], [15].

Therefore, in this paper, we perform a thorough psychophysical evaluation of the mechanotactile systems reported by Shi et. al [12], [13]. First, we conducted an experiment to identify

This work is funded in part by a grant from the Department of Biotechnology, Government of India- BT/PR50638/MED/32/951/2023 (PI: Biswarup Mukherjee) and by IIT Delhi-University College London MFIRP grant - MI02264G (PIs: Biswarup Mukherjee and Helge A. Wurdemann.)

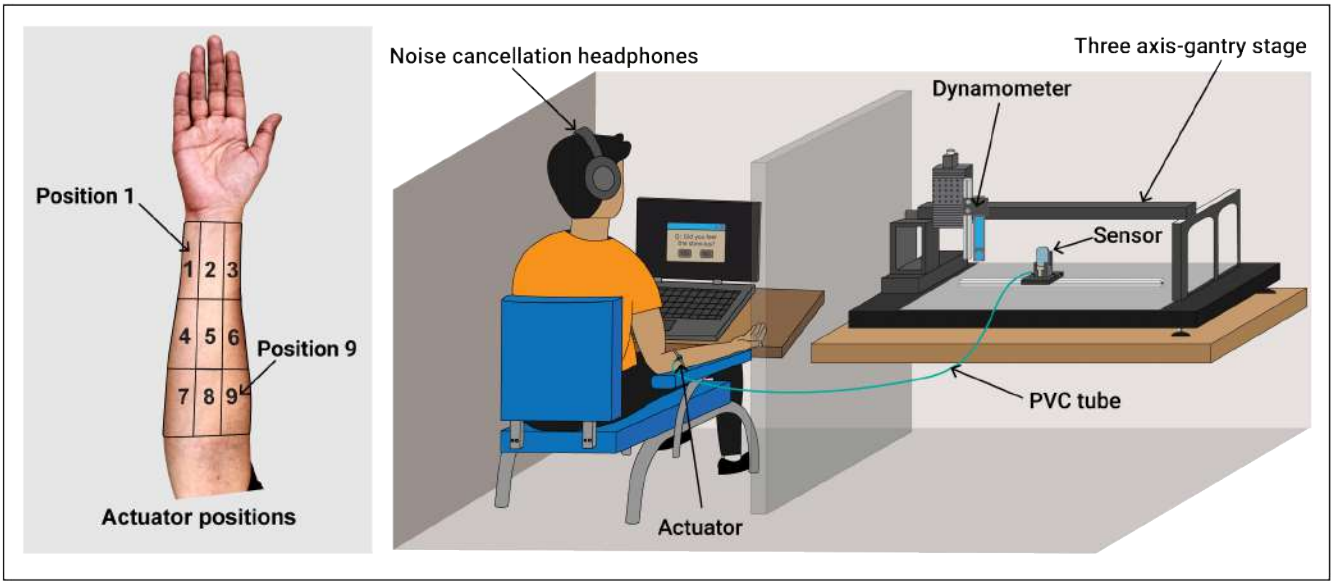


Fig. 1. The experimental setup for the psychophysical evaluation of mechano-tactile haptic device. The feedback actuator was placed on the Participant's forearm, and the fingertip sensor was fixed on the gantry. A curtain was placed between the gantry setup and the subject, and noise-cancellation headphones were used to avoid visual and audio bias.

the most suitable position for placing the mechanotactile actuator on the forearm. In a follow-up experiment we also assess the smallest perceptible force.

II. Methods

A. Participants

We recruited six non-disabled participants for this study. The mean age of all participants was 27$\pm$6. All the participants self-reported being right-hand dominant with no history of injury to the dominant arm. All procedures reported here were approved by the Institute's ethics committee (IEC) at the Indian Institute of Technology, Delhi, New Delhi. Participants provided written consent prior to participating in the study.

B. Experimental setup

The main components of the experimental setup include a three-axis-gantry stage (by Holmarc), dynamometer (Go Direct by Vernier), mechanotactile haptic system [12], Laptop with intel i7 processor 32 GB RAM Windows 11 64-bit, one external monitor, noise cancellation headphones. The mechanotactile sensing system was filled with water and assembled. The fingertip sensor was fixed on the gantry platform with the help of the custom-designed 3D printed holder, as shown in Fig. 2. The use of the gantry in the experiment ensures precise control and repeatably for every trial and across the subjects. The dynamometer was attached to the moving arm of the gantry such that it could be pressed against the sensing element with a pre-calibrated force. The actuator of the mechanotactile system was placed on the forearm of the participant at various locations (discussed in the next section).The outer diameter of the actuator is 20 mm, and the membrane diameter is 12 mm, the thickness of the actuator is 8mm. From the palmer side of the fingertip sensor, the width of the sensor is around 12mm, height is around 32 mm, and the thickness of the sensor is around 20 to 25 mm. The sensor and actuator are connected via a water-filled 3mm diameter PVC pipe, which transfers the force. The three-axis-gantry stage and dynamometer are connected to the Laptop using USB. The experiment was run on a custom-developed MATLAB script (The MathWorks, Inc., Natick, MA).

C. Experiment Procedure

Experiment one was conducted to obtain the minimum perceptible forces at each position and identify the most suitable position for placing the mechanotactile actuator on the forearm. One mechanotactile actuator element is placed in nine different positions on the glabrous side of the forearm (palmar aspect). The feedback actuators were placed on the forearm by measuring the length of the forearm and dividing it into three equal portions from distal to proximal with a 2 cm margin from wrist and elbow joints.

A noise-cancellation headphones (Bose Quiet Comfort 15, Bose Corporation, USA) with brown noise sound was used to avoid any external disturbance. Additionally, an opaque curtain was used between the subject and the gantry to remove any effect of direct visual feedback.

The experiment sequence used in this experiment was as follows: the actuator was placed at one of the positions on the forearm and secured using a velcro strap. The random sequence of the six different force levels (0, 0.4, 1, 1.2, 2, 2.2) N, including sham, are presented one by one. All these forces are pre-measured by indentation of the fingertip sensors from 1 mm to 3.5 mm displacement with a difference of 0.5 mm by moving the dynamometer with the speed of 16 mm/s. The range of displacement for this experiment was restricted to

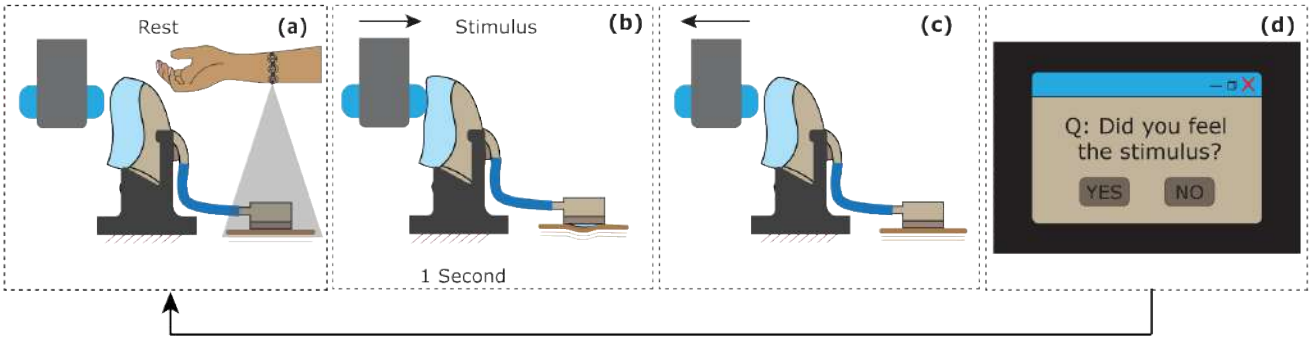


Fig. 2. Experiment sequence. (a) The dynamometer is in rest condition (no tactile feedback on the forearm). (b) The dynamometer moves and applies force on the fingertip sensor, holding it for one second. (c) The dynamometer returns to its resting condition. (d) A pop-up window appears on the screen with the question, "Did you feel the stimulus? Yes/ No".

3.5 mm to prevent the fingertip sensor from any physical damage.

As shown in Fig. 2(a), the dynamometer is on rest condition (no stimulus is applied); after 2 s, the dynamometer is translated by the gantry and exerted the pre-determined force on the actuator and was held for a period of 1 s as shown in Fig. 2(b). The gantry was then moved back to its original position to release the force stimulus, as shown in Fig. 1(c). Immediately following the release of the stimulus, the MATLAB control interface was programmed to pose the following question to the user: "Did you feel the stimulus?". The user was allowed to verbally respond - 'Yes' or 'No', as shown in Fig. 2 (d). the verbal response was recorded by the experimenter. After entering the response, the next force stimulus in the random sequence was presented, and the process was repeated till all force values had been presented. A total of ten trials were conducted at each position on the forearm.

The experiment two is the follow-up experiment of the first study. This study only includes the proximal position on the forearm. The mechanotectile actuator was placed in the best suitable position that was found in experiment one. The criteria for choosing the most suitable position on the proximal side was based on the minimum absolute force value on the forearm out of three positions from medial to lateral. In this study, another force value, 1.6 N, was introduced between 1.2 N and 2 N to improve the resolution of the psychometric curve above the 90% of the proportion of perceived stimuli. The experiment setup of this experiment is shown in Fig. 1. The noise-cancellation headphones and the opaque curtain were used the same as the previous experiment, as shown in Fig. 1. The sequence used in this experiment was as follows: the mechanotactile actuator was placed on position 8 (between medial and lateral on the proximal side) shown in the Fig. 1. The random sequence of the six different force levels (0, 0.4, 1, 1.2, 1.6, 2) N, including sham, are presented one by one. As illustrated in Fig. 2 (a), the dynamometer is on rest condition (no stimulus is applied); after 2 s, the dynamometer is translated by the gantry and exerted the pre-determined force on the actuator and was held for a period of 1 s as shown in Fig. 2(b). The gantry was then moved back to its original position to release the force stimulus, as shown in Fig. 1(c). Immediately following the release of the stimulus, the MATLAB control interface was programmed to pose the following question to the user: "Did you feel the stimulus?". The user was allowed to verbally respond - 'Yes' or 'No', as shown in Fig. 2 (d). the verbal response was recorded by the experimenter. After entering the response, the next force stimulus in the random sequence was presented, and the process was repeated till all force values had been presented. A total of ten trials were conducted on signal position.

III. Result

The recorded response data for all the positions were processed through a custom MATLAB script by taking the mean and standard deviation of all ten trials for each force level. The sigmoidal model with the logistic fit function was used to fit the psychometric curve. The psychometric curve was generated with 95% confidence interval for each position. The logistic fit function is mentioned in the Equation (1) [16].

$$y = \frac{A_1 - A_2}{1 + \left(\frac{x}{x_0}\right)^p} + A_2 \tag{1}$$

Where y is the proportion of perceived stimuli, x is the force in Newton (N) , A_1 and A_2 represent the initial and final values of the proportion of perceived stimuli, x_o is the centre or midpoint between minimum and maximum values of response, and p is the power it determines slope of the curve. The absolute force thresholds were calculated by taking the force value at 50% of the proportion of perceived stimuli. The equation for calculating absolute force thresholds is given in Eq (2) by rearranging Eq (1)

$$x = x_0 \cdot \left[\frac{A_1 - A_2}{y - A_2} - 1\right]^{1/p} \tag{2}$$

where: $y = (A_1 + A_2)/2$ for 50% of the proportion of perceived stimuli.

The absolute force distribution for all nine positions on

the forearm is shown in Fig. 3. The results show that the minimum and maximum absolute force thresholds on the forearm are 0.39 N (0.14 N, 0.43 N: 95% CI) and 1.36 N (0.99 N, 1.46 N: 95% CI) at positions 2 and 5 respectively (see Fig. 1).

However, considering our target population of individuals with amputation, distal placement of actuators may not be possible depending on the length of the residuum. At the proximal end, position 8, demonstrated the lowest absolute force perception threshold of 0.51 N (0.43 N, 0.63 N: 95% CI). Therefore, we conducted experiment 2, at position 8, by repeating the psychophysical evaluation with 5 additional participants.

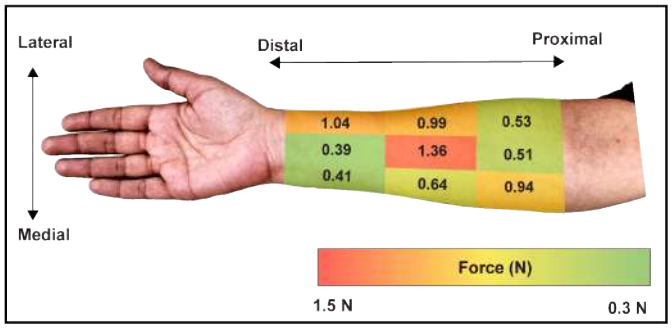


Fig. 3. Absolute force discrimination threshold obtained with the mechanotactile haptic feedback unit across the volar aspect of the forearm .

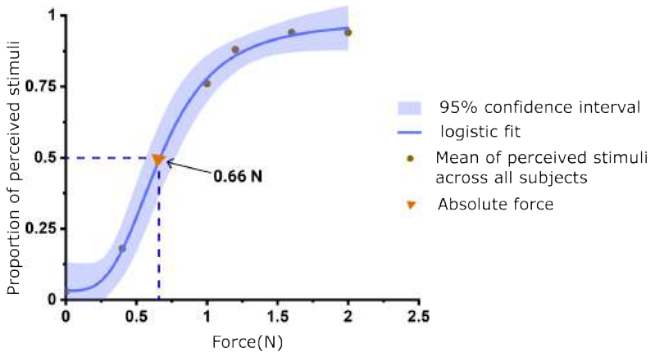


Fig. 4. Psychometric curve showing responses to the absolute force discrimination task of Experiment 2.

For Experiment 2, all five subject responses were processed through a custom MATLAB script, and the mean and standard deviation across all ten trials for each subject were calculated individually. A psychometric curve was plotted using the sigmoidal model with a logistic fit function as mentioned in Eq 1. The psychometric curve with 95% of CI for position eight is shown in Fig. 4. The absolute force threshold was calculated by taking the force at 50% of the proportion of perceived stimuli. As mentioned in the Fig. 4 the calculated absolute force threshold is 0.66 N (0.56 N, 0.77 N: 95% CI).

IV. Discussion and Future Work

In this study, we conducted two experiments. In the first experiment, a pilot study was conducted to determine the distribution of the absolute force perception threshold of the mechanotactile haptic unit for the volar aspect of the forearm. Our findings indicate that while the distal regions of the forearm exhibit perception thresholds as low as 0.39 N, the proximal portion of the forearm may be more appropriate for individuals with an upper limb amputation. In the follow-up experiment, we also investigated the minimum perceptible force values that the user could perceive at a single position with five subjects. For experiment 2, we found that at the proximal forearm, the minimum force perceptible was approximately 0.66 N.

This study has a few critical limitations. The study was conducted with a sample size of six, one for the initial and five for the follow-up experiment. Further, we used only one mechanotactile device for this study, requiring repositioning of the feedback actuator at each step possibly leading to minor errors in placement over repeated trials. In future work, more mechanotactile devices will be used to reduce the duration of the experiment. In a follow-up study, we also intend to determine the discriminability of two closely matched forces exerted through the mechanotactile units. This experiment will further shed light on the minimum achievable and perceptible force resolution with the mechanotactile haptic units.

V. Conclusion

In this paper, we performed a psychophysical evaluation to investigate the relationship between physical force and perceived force in mechanotactile haptic devices. First, we placed feedback actuators at various positions along the forearm and applied different force stimuli randomly. Based on the participants' responses, we determined the perceptible minimum force values at each position and found that the distal sensitivity was as low as 0.39 N while the perceptibility was 0.51 N at the proximal forearm.

Acknowledgment

This project is supported in part by the University College London-IIT Delhi (UCL-IITD) Strategic Partnership MFIRP grant from the Industrial Research and Development Unit, Indian Institute of Technology Delhi and from the Department of Biotechnology, Ministry of Science and Technology, Government of India.

References

[1] N. Lan, C. M. Niu, M. Hao, C.-H. Chou, and C. Dai, "Achieving neural compatibility with human sensorimotor control in prosthetic and therapeutic devices," *IEEE Transactions on Medical Robotics and Bionics*, vol. 1, no. 3, pp. 122–134, 2019.

[2] K. O. Johnson, "The roles and functions of cutaneous mechanoreceptors," *Current Opinion in Neurobiology*, vol. 11, no. 4, pp. 455–461, 2001.

[3] S. Raspopovic, G. Valle, and F. M. Petrini, "Sensory feedback for limb prostheses in amputees," *Nature Materials*, vol. 20, no. 7, pp. 925–939, 2021.

[4] E. D'Anna, G. Valle, A. Mazzoni, I. Strauss, F. Iberite, J. Patton, F. M. Petrini, S. Raspopovic, G. Granata, R. D. Iorio, M. Controzzi, C. Cipriani, T. Stieglitz, P. M. Rossini, and S. Micera, "A closed-loop hand prosthesis with simultaneous intraneural tactile and position feedback," *Science Robotics*, vol. 4, no. 27, p. eaau8892, 2019.

[5] L. Jabban, S. Dupan, D. Zhang, B. Ainsworth, K. Nazarpour, and B. W. Metcalfe, "Sensory feedback for upper-limb prostheses: Opportunities and barriers," *IEEE Transactions on Neural Systems and Rehabilitation Engineering*, vol. 30, pp. 738–747, 2022.

[6] M. A. Abd, J. Ingicco, D. T. Hutchinson, E. Tognoli, and E. D. Engeberg, "Multichannel haptic feedback unlocks prosthetic hand dexterity," *Scientific reports*, vol. 12, no. 1, p. 2323, 2022.

[7] P. Svensson, U. Wijk, A. Björkman, and C. Antfolk, "A review of invasive and non-invasive sensory feedback in upper limb prostheses," *Expert review of medical devices*, vol. 14, no. 6, pp. 439–447, 2017.

[8] N. Wettels and G. E. Loeb, "Haptic feature extraction from a biomimetic tactile sensor: Force, contact location and curvature," in *2011 IEEE International Conference on Robotics and Biomimetics*, 2011, pp. 2471–2478.

[9] A. Masteller, S. Sankar, H. B. Kim, K. Ding, X. Liu, and A. H. All, "Recent developments in prosthesis sensors, texture recognition, and sensory stimulation for upper limb prostheses," *Annals of biomedical engineering*, vol. 49, pp. 57–74, 2021.

[10] G. Dhillon and K. Horch, "Direct neural sensory feedback and control of a prosthetic arm," *IEEE Transactions on Neural Systems and Rehabilitation Engineering*, vol. 13, no. 4, pp. 468–472, 2005.

[11] N. Malešević and C. Antfolk, "Sensory feedback in upper limb prosthetics: advances and challenges," *Nature Reviews Neurology*, vol. 20, no. 8, pp. 449–450, 2024.

[12] G. Shi, A. Palombi, Z. Lim, A. Astolfi, A. Burani, S. Campagnini, F. G. C. Loizzo, M. L. Preti, A. M. Vargas, E. Peperoni, C. M. Oddo, M. Li, J. Hardwicke, M. Venus, S. Homer-Vanniasinkam, and H. A. Wurdemann, "Fluidic haptic interface for mechano-tactile feedback," *IEEE Transactions on Haptics*, vol. 13, no. 1, pp. 204–210, 2020.

[13] G. Shi, A. Shariati, I. Eames, and H. Wurdemann, "Modelling the compression of a soft ellipsoid fingertip," *Soft Matter*, vol. 18, pp. 9076–9085, 2022.

[14] L. A. Jones and H. Z. Tan, "Application of psychophysical techniques to haptic research," *IEEE Transactions on Haptics*, vol. 6, no. 3, pp. 268–284, 2013.

[15] S. Alvarado, B. Kanter-Braem, K. Manz, P. Masciopinto, E. McKenna, D. Nelson, C. Williams, K. Korek, and W. Wozniak, "Sensation and perception: a unit lesson plan for high school psychology teachers," *National Standards for High School Psychology Curricula*, pp. 1–46, 2011.

[16] OriginLab, *Logistic Fit Function*, OriginLab Corporation, n.d., accessed: December 5, 2024. [Online]. Available: https://www.originlab.com/doc/origin-help/logistic-fitfunc

Intertwined digital human and robot modeling-driven development of REHAROB 3.0: the quad-arm functional upper limb rehabilitation robot system*

A. Tóth[1], T. Pilissy[1], J. Kocsis[1], M. O. Bauer[1], D. Simon[1], I. Tavaszi[2], K. Sándor[2], G. Fazekas[2,3]

1 Budapest University of Technology and Economics, Faculty of Mechanical Engineering, Department of Manufacturing Science and Engineering, Budapest, Hungary
2 Semmelweis University, Rehabilitation Clinic, Department of Rehabilitation Post-Stroke, Budapest, Hungary
3 University of Szeged, Department of Rehabilitation Medicine, Szeged, Hungary

***Abstract* — Mass-produced industrial and service robots have been used to build therapeutic rehabilitation robots since the 1990s. REHAROB 1.0, the dual-arm upper limb rehabilitation robot prototype, was among the pioneers. The industrial collaborative robot is a new type of robot in terms of safety, appearance, performance, and cost, thanks to which it is proving itself in more and more applications. To take advantage of these benefits, the REHAROB 3.0 Robotic Trainer for Activities of Daily Living, also updated in its name, was designed and built using two industrial collaborative robots and two uniquely developed robotic fingers. The goal of our study was to introduce an iterative design and simulation process in which digital human modeling is intertwined with digital robot modeling, leading to an upper limb rehabilitation robot system targeting outstanding performance features such as synchronous exercising of every upper limb anatomical joint and training reaching and grasping Activities of Daily Living with real objects in a real environment.**

I. Introduction

It was an epoch-making milestone in the era of robotics when an international standards body, the International Organization for Standardization defined the term "industrial robot" in the standard ISO 9283:1990 Manipulating industrial robots - Performance criteria and related test methods. The second milestone of similar significance is related to the 2016 standard defining collaborative industrial robots [1]. Due to their versatility, reliability, accuracy, and cost, ordinary and collaborative industrial robots have gained an essential presence in the construction of non-industrial robot applications.

For a long time, our goal has been to see if industrial robots can be used effectively for upper limb movement rehabilitation. The aim of the research presented in this article was to design an upper limb movement rehabilitation system built from industrial collaborative robots. The innovation lies in the design method, where the system model is subjected to iterative simulation and assessment in an integrated digital human and robot simulation software environment.

* This work was done in the confines of Project no. K_125263/125357 and 2017-2.3.7-TÉT-IN-2017-00048 supported by the National Research, Development and Innovation Fund of Hungary.

II. Review of industrial robots and Collaborative Robots Used in Medical Applications

This chapter reviews commercial and experimental industrial robot- and cobot-based medical robot systems, first in a broader spectrum and second, those that comply with the RACA [2] or the surgical robot [3] safety standards. Two pioneering medical robotic systems were developed using industrial robots in the late 20th century. The CASPAR (Computer Assisted Surgical Planning and Robotics) system used a Stäubli RX90CR industrial robot for the autonomous implantation of knee prostheses [4]. The upper limb rehabilitation robot MIME (Mirror-Image Motion Enabler) was based on a Westinghouse PUMA 560 industrial robot [5].

Currently, nine commercial and eight laboratory medical robotic systems demonstrate the use of industrial robots. The CyberKnife® System [6], is a robot-driven alternative to conventional radiotherapy, where the radiation unit is mounted on a KUKA KR 240 industrial robot. Various ROSA™ systems [7] support robot-assisted Total Knee Arthroplasty: cranial and spinal surgery. ROSA™ uses the Stäubli TX2-60 industrial robot. The actuator of the YOMI® dental robotic system [8] holds the tool, and later, the implant is a SCHUNK POWERBALL LWA 4P lightweight industrial robot arm. ARTAS iX™[9] is a robotic hair restoration system with a KUKA LBR MED medically certified cobot. The Sculptura™[10] integrated with a KUKA LBR Med cobot is a mobile platform focusing on robot-assisted intraoperative radiation therapy. The CARLO® system [11] incorporates a KUKA LBR Med cobot to perform orthopaedic surgical operations with cold ablation robot-guided laser osteotome. The TMS-Cobot [12] is a robot-assisted Transcranial Magnetic Stimulation system that integrates a UR5 cobot of Universal Robots Inc. Modus V™[13] uses a UR5 cobot to precisely move and keep in pose the digital microscope during neurosurgical operations. The iYU Pro [14] uses a KUKA LBR MED cobot to massage the neck and back by moving and pressing the massaging pad on the client's body part. EMMA[15] is a robotic massaging system developed to provide Traditional Chinese Massage assessment and professional therapeutic massage services. EMMA integrates

* The research reported in this paper and carried out at BME has been supported by the NRDI Fund (TKP2022 EGA, Grant No. BME-EGA-BIO) based on the charter of bolster issued by the NRDI Office under the auspices of the Ministry for Innovation and Technology.

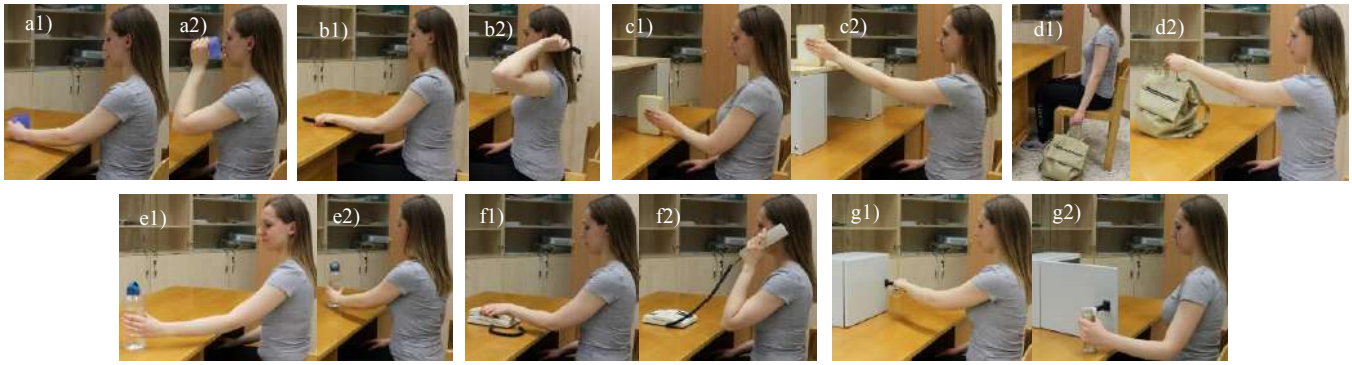


Figure 1. Seven reach-and-grasp type Activity of Daily Living exercises defined for REHAROB 3.0 (1-grasping, 2-target of motion): a) drinking from a glass, b) combing with a hairbrush, c) putting a book on the shelf, d) lifting a bag, e) moving a bottle to the side, f) picking up a phone, g) opening a door

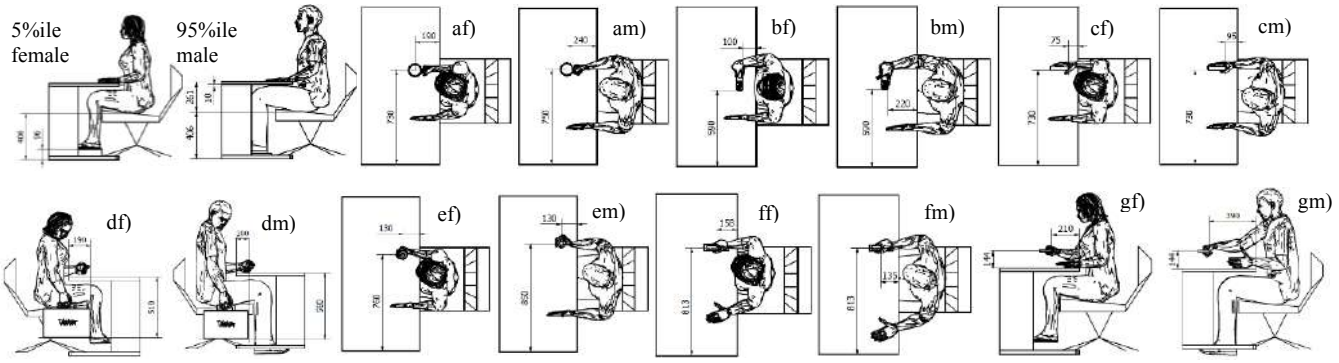


Figure 2. Reach-and-grasp type Activities of Daily Living exercises and setup modeled and simulated for 5%ile female (f) and 95%ile male (m): a) drinking from a glass, b) combing with a hairbrush, c) putting a book on the shelf, d) lifting a bag, e) moving a bottle, f) picking up a phone, g) opening a door

a UR5 cobot to precisely move and press multiple massaging rollers and pads on the client's body. The ROBERT®[16] movement rehabilitation robot assists health professionals with numerous tasks, including lower limb motion therapy. ROBERT®, in its early prototype, used the UR10 cobot, but the current version applies a KUKA LBR MED cobot. ALEX [17] is a dual-arm robotic massaging system with two UR10 cobots to deliver safe full-body massage therapy. RAINER (Universal RoboTrainer) [18] with a UR10 cobot is designed to help patients with repetitive functional movements as part of their rehabilitation process. The Cobot with Prismatic Compliant Joint Intended for Doppler Sonography [19] is a master-slave robotic diagnostic system, which integrates the 7 DoF cobot Panda of Franka Emika AG. BROCA [20] uses three UR5 cobots to assist surgeons with laparoscopy procedures. The Chinese robot dentist [21] with a UR5 cobot fits implants in the patient's mouth without any human involvement. The inRehaRob [22] uses a KUKA LBR MED cobot to guide the stroke patient's forearm in repetitive exercise scenarios. The VELYS™ Active Robotic-Assisted System [23] applies a KUKA LBR MED cobot for use in planning and instrumenting spinal fusion procedures in the cervical, thoracolumbar and sacroiliac spine. The NaoTrac [24] applies a UR5 cobot for neurosurgical navigation. The REHAROB Therapeutic System is a dual-arm robot-assisted movement therapy system that integrated IRB140 and IRB400H industrial robots of ABB in its version 1.0 [25,26] and IRB140 and IRB1600 robots in its version 2.0 [27].

III. Functional Task Definition and Digital Human Modeling

The REHAROB motion therapy process focused on the application of functional tasks with real objects already in version 2.0 [27]. To radically reduce size and weight and improve functionality, we decided to replace industrial robots with industrial cobots in the new REHAROB 3.0 Robotic Trainer for Activities of Daily Living. We have transitioned to a fully digital design and testing process, leveraging the latest developments in Digital Human Modeling (DHM) and offline robot programming (OLP) technologies. For the first time in the history of developing a movement rehabilitation system, we applied the Siemens® Tecnomatix Process Simulate software platform [28].

The set of five REHAROB 2.0 reach-and-grasp type Activitiy of Daily Living (ADL) exercises [27] has been increased to seven with movements of greater difficulty levels at the side of the body and at the head (Figure 1). Then, we designed and modeled the exercises with the extreme size 5%ile female and 95%ile male mannequins in the Process Simulate Human environment (Figure 2). Using the semi-automatic toolsets of Process Simulate: Task Simulation Builder and Human Control Panel, the ADL exercises, including grasping and manipulating of objects were modeled with validated human ergonomics (Figure 3). The ADL exercises were made uniform in terms of their anatomical joint trajectory, so that each patient moved along a standard anatomical reference trajectory, regardless of size.



Figure 3. ADL exercise design in Process Simulate Human environment

IV. Robot Selection and 3D Layout Design

A. Selection of the Industrial Collaborative Robots for Dual-Arm Upper Limb Therapy

Unlike at REHAROB 1.0 and 2.0 systems, an industrial collaborative robot arm A) with at least 6DOF, load capacity of at least 10 kg, and a reach of approximately 1400 mm to move the hand therapy module [29] and the human hand; and B) with at least 6DOF, load capacity of at least 5 kg, and reach of approximately 800 mm to move the human elbow were sought. In addition to structural requirements, eligible cobots must have built-in force/torque sensors and a controller that allows continuous streaming of the trajectory by an external device. Only Universal Robot Inc. has met the stringent requirements listed with its UR10e and UR5e cobots and the ability to stream 500 Hz externally. Like us, Cai et al. chose Universal Robot cobots, but unlike us, they used two identical UR5e industrial collaborative robots in their unilateral upper limb rehabilitation robotic system [30]. One of their UR5e cobots moves the patient's lower arm, and the other UR5e cobot moves the upper arm. Although the patient's upper limb can be connected to two UR5e robots, its anatomical Range of Motion is severely limited when using two identical robots. REHAROB, on the contrary, insists on its structural hypothesis that the size of the robotic arms used in two-arm end-effector-type rehabilitation robots should be two to three times the distance between the actuated body point and the shoulder.

B. Definition of the Tool Center Point Frame trajectories

The unsurpassed advantage of the Siemens® Tecnomatix Process Simulate software is that it integrates full-fledged Digital Human Modeling and offline robot programming toolsets in a shared environment. This allowed for simultaneous simulation of the movements of the human mannequin, the UR5e/UR10e cobots, and the robot fingers of the hand module. First, the UR5e and UR10e cobots were placed in temporary locations. To emulate the offset between the Tool Center Point Frame (TCPF) and the actuated body point, suitably sized boxes were attached to the hand and elbow (Figure 4). The digital human simulator was then started and stopped to create a green frame of the virtual box. In our case, an ADL trajectory contains approximately 200-300

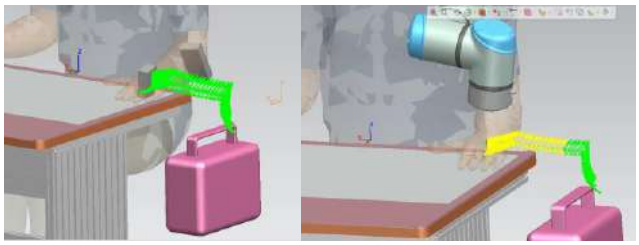


Figure 4. Trajectory generation of ADL tasks (series of green frames) and of robot TCPFs (series of yellow frames)

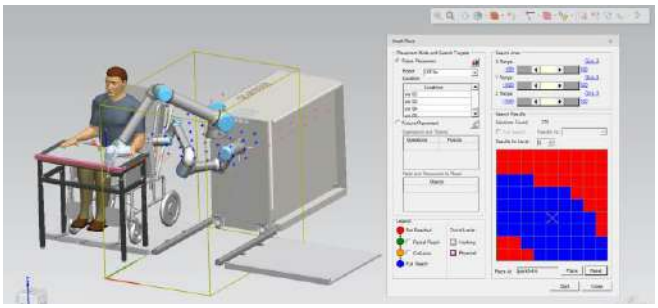


Figure 5. Use of the Smart Place function to find the suitable placement locations of the UR10e cobot at the lifting a bag ADL exercise

frames. The robot simulator also started, and the yellow TCPF of the selected cobot was aligned automatically to the last created green frame (right side of Figure 4). If the alignment failed due to workspace, collision, singularity, or configuration issues, the affected cobot had to be relocated, and the layout planning procedure restarted. The success of this procedure depends on the skills of the simulation engineer.

C. Determining the Ideal Location for the Two Cobots

The advantage of the applied digital human-robot intertwined modeling method becomes apparent when we need to locate the UR5e and UR10e cobots relative to the patient without compromising the ADL environment described in Figure 2. The challenge is that in the ideal layout, both cobots simultaneously avoid collisions, joint range, velocity, acceleration limits, and singularities, and neither cobot changes configuration. Process Simulate can help solve this challenge with Smart Place service. This tool can classify robot placement grids distributed in a box-shaped spatial domain. Figure 5 shows entirely suitable cobot placement locations in blue, collisions in orange, misorientation in green, and unusable robot placement locations with a red cursor.

We further filtered the suitable placement locations according to robot configurations. On the left panel of Figure 6, all eight possible inverse kinematics solution configurations are listed for the UR10e cobot at a given target location. The highlighted elbow-down configuration is unacceptable. The right elbow-up configuration is also available in this case (right side of Figure 7). Only those suitable placement locations where all seven ADL exercises can be performed in fixed UR5e and UR10e inverse kinematics solution configurations are acceptable.

Finally, simulation diagnostic reports were obtained from Process Simulate Robot Viewer for all remaining suitable placement locations. The software logs and visualizes information such as the joint range of motions, the joint

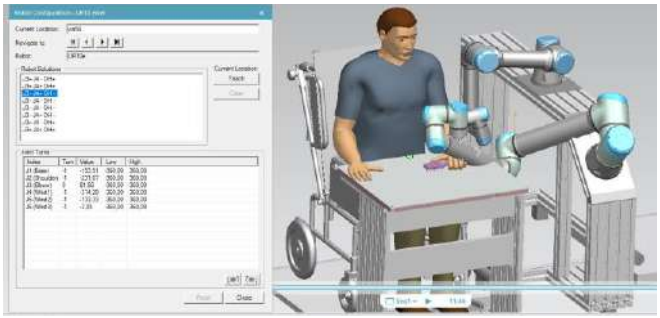


Figure 6. An unacceptable elbow-down configuration of the UR10e cobot

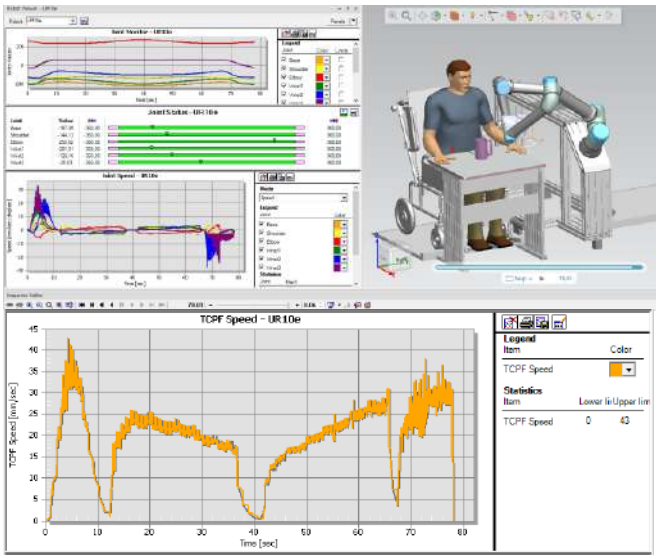


Figure 7. Robot diagnostic report about the simulation of the drinking ADL with UR5e cobot

speeds, joint accelerations, and the speed of the tool-center point. Figure 7 shows the diagnostic report of the UR10e robot about the simulation of the drinking ADL.

V. Industrial and Mechanical Design of the REHAROB 3.0 Robot System

We also started the industrial and mechanical design process in parallel with the digital human and robot modeling.

The design requirements focused on elements derived from the critical review of the REHAROB 1.0 and 2.0 systems. The dimensions and weight of the system must be reduced to such an extent that the REHAROB 3.0 rehabilitation robot can be easily moved manually from one ward to another. Two wheelchair docking platforms allow for unilateral therapies. These docking platforms should be foldable platforms that, when folded down, ensure the mechanical stability of the system during treatment and, when folded up, do not make the system unstable during manual transport. The central cabinet holds the two industrial collaborative robots, the two wheelchair docking platforms and includes all electrical and control components. Depending on the treatment side, the ADL desk connects to the left or right docking platform.

The images in Figure 8 a)-d) show some initial design concepts. Images e)-f) show the detailed design of the central cabinet and wheelchair docking platforms, which was later discarded. The final industrial design of the REHAROB 3.0 system is shown in image g). The free-body diagrams show the centers of mass in the transport (image h) and handling (image i) conditions. Mechanical stability is achieved in all use cases, but the calculations themselves are not disclosed.

The mechanical, electrical, electronic and control designs have been prepared following the RACA standard [2] and the Medical Device Regulation (MDR) of the European Union. Python, polyscope, microcontroller and PLC codes have been completed for the high-level control PC, UR robot controllers, hand module controller and SICK safety PLC.

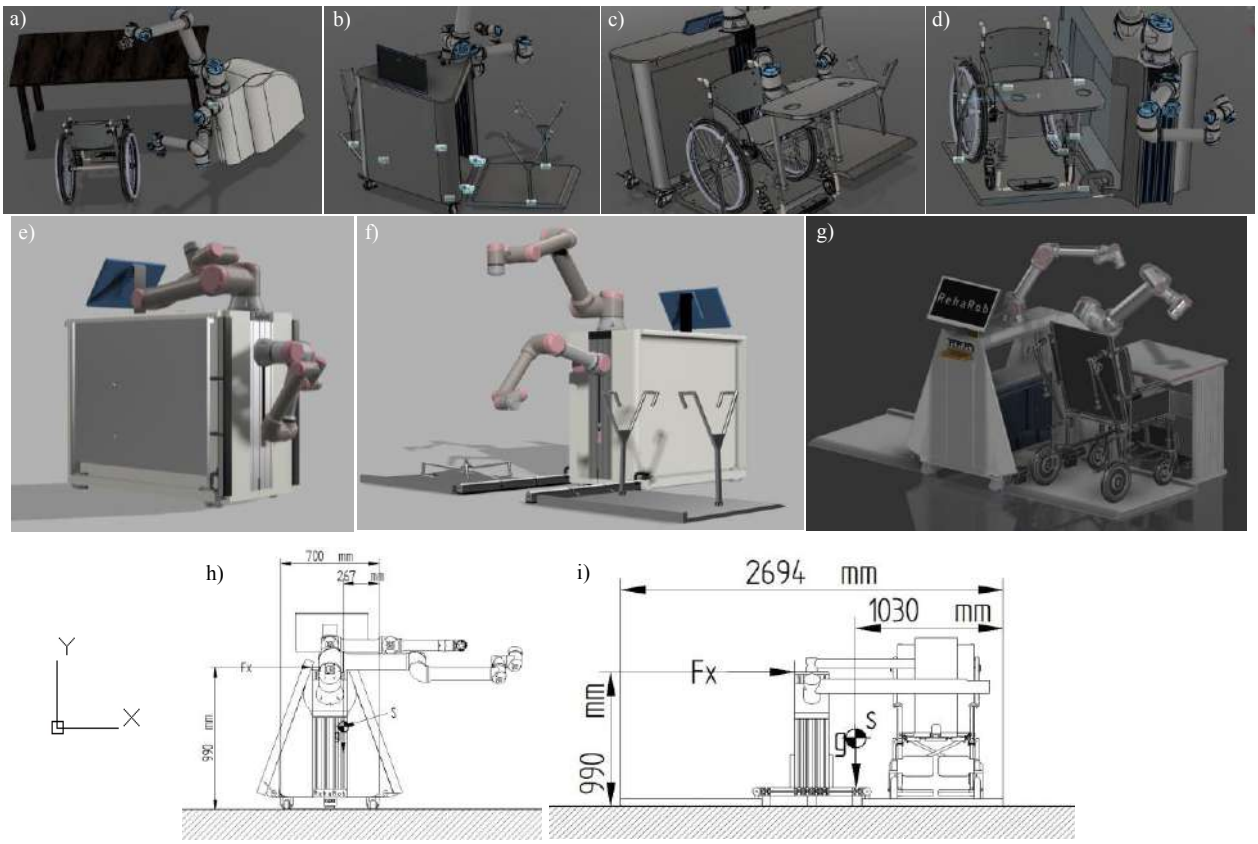


Figure 8. Various concepts for a)-b)-c) left-right symmetry, d) wheelchair docking platform, e) ready for transfer, f) platforms folded down, g) ADL desk, h) static stability during transfer when the docking platforms are folded-up, i) static stability during therapy when the docking platforms are folded-down

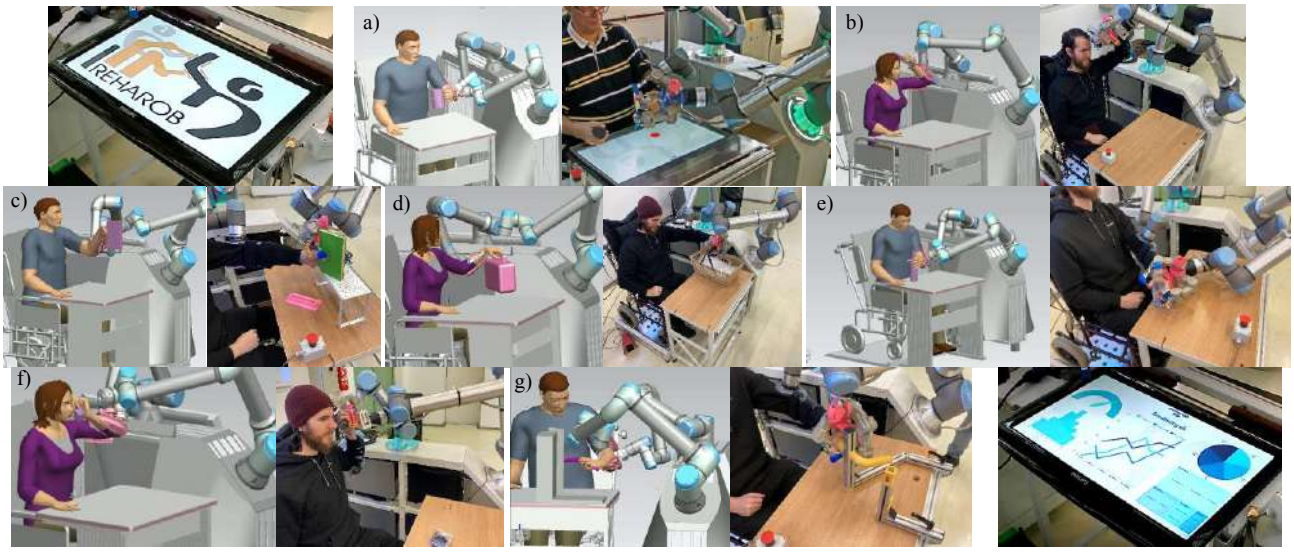


Figure 9. The REHAROB 3.0 reach-and-grasp type Activities of Daily Living exercises simulated in Process Simulate® environment for 5%ile female/95%ile male and tested with 95%ile male healthy volunteers: a) drinking from a glass, b) combing with a hairbrush, c) putting a book on the shelf, d) lifting a bag, e) moving a bottle, f) picking up a phone, g) opening a door

VI. Acceptance and Usability Testing

The development of the REHAROB 3.0 rehabilitation robot took five years from compiling the requirements list to completing the prototype. The acceptance testing of the REHAROB 3.0 prototype began with a sensorized dummy upper limb we developed for this purpose [31]. In the next step, physiotherapists tested the system by having one of them play the role of the patient and the other the physiotherapist, and then they switched roles. Finally, we tested all seven ADL exercises with a 95%ile male volunteer who had better control over the geometric operating extremes of the system than a 5%ile female (Figure 9). One suggestion was to transform the ordinary desktop board into a digital Human Machine Interface dashboard for both the patient and the physiotherapist (first and third images in the first row, last image in the third row of Figure 9). While the REHAROB 3.0 system performed excellently in all three test batteries (see also Video Appendix), with the exception of the digital dashboard, the invaluable experience gained can be utilized in future product development.

In the reach-and-grasp type movement therapy with real objects, the REHAROB 3.0 hand module, which contains two robotic fingers and moves human fingers, plays an equally important role as the two robotic arms that move the hand and elbow. Although we have previously reported on the development of the REHAROB 3.0 robotic fingers [29], the hand module with the robotic fingers, the tool changer, the finger and hand orthoses shown in Figure 9 is a brand-new achievement.

Similar to the clinical testing of the REHAROB 1.0 and 2.0 systems, we are also planning a clinical trial of the 3.0 system.

Conclusions

The presented iterative design approach, in which digital human modeling is intertwined with offline robot programming, has proven to be extremely effective in overcoming geometric and kinematic deficiencies, anthropometric scaling, layout planning and collision avoidance in an upper limb rehabilitation robotic system. The key is to use a professional simulation environment, in our case, the Siemens Tecnomatix Process Simulate®, which integrates a validated human and robot modeling toolset in the same scene. The simulation engineering skill-driven process (Figure 10) radically shifts design iterations from the physical to the digital world. As a result, the REHAROB 3.0 Robotic Trainer for Activities of Daily Living has the following technical data:

- Intended for adult patients from 5%ile female to 95%ile male (ANSUR II),
- Anatomical joints simultaneously treated in the upper limb: shoulder complex, elbow, wrist, all joints of the thumb, MCP and PIP joints of the index/middle/ring fingers, altogether 19 DOFs,
- Free exercises: 3D continuous passive,
- Active exercises: Seven reach-and-grasp ADL exercises with real objects: passive, active assisted-guided-resisted,
- Two wheelchair docking platforms at the sides of the cabinet for the left and right side treatments,

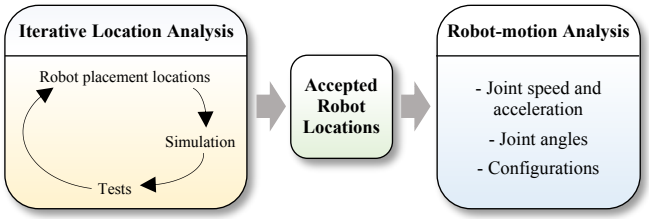


Figure 10. The process of 3D robot placement optimization

- Actuator A connected to the elbow: min 6 active DOFs, min reach 850 mm, axis 1 aligned by Y axis, base placed 830 mm (-X) from the sagittal YZ plane of the wheelchair, 754 mm (+Y) from the wheelchair seat, 405 mm (+Z) from the wheelchair backrest,

- Actuator B connected to the hand: min 6 active DOFs, min reach 1300 mm, axis 1 tilted 45 around axis X, base placed 0 mm (X), 206 mm (-Y), 644.5 mm (+Z) from the base of actuator A,
- Actuator C mounted on Actuator B and connected to the index/middle/ring fingers: min 3 active DOFs,
- Actuator D mounted on Actuator B and connected to the thumb: min 2 active DOFs and min 3 passive DOFs,
- Real objects for ADL exercises: glass, hairbrush, bag or basket, book, bottle, phone, door mockup with handle

Based on the REHAROB 1.0, 2.0 and 3.0 upper limb rehabilitation robot systems, we develop the geometric law of two-arm end-effector type rehabilitation robots, i.e. the length of each actuator must be proportional to the distance between the actuated body point and the shoulder.

UTILITY MODEL

The examination of the Utility Model application number U 25 000xx, entitled *End-effector type quad-arm robotic system for unilateral upper limb movement rehabilitation*, submitted on 21 February 2025 to the Hungarian Intellectual Property Office, is in progress.

ACKNOWLEDGMENT

A. Tóth, T. Pilissy, and M. O. Bauer thank Nándor Bánvölgyi for his contribution to ADL object and exercise design, and László Péter Sándor for his contribution to concepting and industrial design of the frame structure. G. Fazekas thanks Zsófia Markó for her contribution to ADL definition and presentation.

VIDEO APPENDIX

This 84-second-long film briefly summarizes how REHAROB 3.0 Robotic Trainer for Activities of Daily Living works: https://tinyurl.com/reharob3short. For a deeper insight, eight short film clips showcase the capabilities of REHAROB 3.0 at https://tinyurl.com/reharob3 1. Continuous Passive Motion training with 95%ile male, 2. patient GUI process flow for ADL training, 3. ADL drinking - generated trajectory - passive training - dry run, 4. ADL drinking - generated trajectory - active training - dry run, 5. ADL drinking - generated trajectory - passive training with 95%ile male, 6. ADL drinking - generated trajectory - active training with 95%ile male, 7. master hand cobot – slave elbow cobot admittance control demonstration: elbow swiveling, 8. master hand cobot – slave elbow cobot admittance control demonstration: the physiotherapist teaches an exercise by moving the hand only.

REFERENCES

[1] ISO/TS 15066:2016 Robots and robotic devices — Collaborative robots.
[2] IEC 80601-2-78:2019 Medical electrical equipment — Part 2-78: Particular requirements for basic safety and essential performance of medical robots for rehabilitation, assessment, compensation or alleviation
[3] IEC 80601-2-77:2019 Medical electrical equipment — Part 2-77: Particular requirements for the basic safety and essential performance of robotically assisted surgical equipment
[4] D. Meister, P. Pokrandt and A. Both, "Milling accuracy in robot assisted orthopaedic surgery," IECON '98. Proceedings of the 24th Annual Conference of the IEEE Industrial Electronics Society (Cat. No.98CH36200), Aachen, Germany, 1998, pp. 2502-2505 vol.4, doi: 10.1109/IECON.1998.724120.
[5] P.S. Lum, C.G. Burgar, H.F. M. Van der Loos, "The use of a robotic device for post-stroke movement therapy," ICORR 1997, Proceedings of the International Conference on Rehabilitation Robotics. April 14-15, 1997. Bath, U.K., p. 79-82
[6] https://www.kuka.com/en-my/industries/solutions-database/2020/02/cyberknife
[7] https://www.zimmerbiomet.com/medical-professionals/knee/product/rosa-knee-system.html
[8] https://www.neocis.com/
[9] https://www.venusconcept.com/en-gl/artas-ix.htm
[10] https://www.kuka.com/en-us/industries/solutions-database/2020/04/sensus-healthcare
[11] https://aot.swiss/en/carlo/
[12] https://www.axilumrobotics.com/en/tms-robot/
[13] https://www.synaptivemedical.com/products/modus-v/
[14] https://store.iyu.care/
[15] https://www.aitreat.com/about-emma
[16] https://www.lifescience-robotics.com/
[17] http://massagerobotics.com
[18] http://www.en.patientathome.dk/projects/rehabilitation-using-industrial-robots-universal-robotrainer.aspx
[19] Cobot with Prismatic Compliant Joint Intended for Doppler Sonography by Juan Sandoval, Med Amine Laribi, Saïd Zeghloul, Marc Arsicault and Jean-Michel Guilhem, Robotics 2020, 9(1), 14; https://doi.org/10.3390/robotics9010014
[20] https://www.universal-robots.com/about-universal-robots/news-centre/universal-robots-ur5-chosen-for-the-broca-project-the-first-surgical-robot-made-in-spain/
[21] https://www.scmp.com/news/china/article/2112197/chinese-robot-dentist-first-fit-implants-patients-mouth-without-any-human
[22] https://www.ame.rwth-aachen.de/cms/AME/Forschung/RPE-Rehabilitations-und-Praeventionst/Rehabilitation/~pkfb/Roboter-[assistierte-Rehabilitation/?lidx=1
[23] https://www.jnjmedtech.com/en-US/news-events/depuy-synthes-launches-its-first-active-spine-robotics-and-navigation-platform
[24] https://brainnvai.com
[25] Arz, G ; Tóth, A ; Fazekas, G ; Bratanov, D ; Zlatov, N Three-Dimensional Anti-Spastic Physiotherapy with the Industrial Robots of "REHAROB" In: Anon (ed.) Proceedings of the 8th International Conference on Rehabilitation Robotics (ICORR 2003) Seoul, Dél-Korea : Seoul National University (2003) pp. 215-218. , 4 p.
[26] A. Toth, G. Arz, G. Fazekas, D. Bratanov, N. Zlatov (2004) Poststroke shoulder-elbow physiotherapy with industrial robots. In: Zenn Bien Z, Dimitar Stefanov (eds) Advances in rehabilitation robotics, human-friendly technologies on movement assistance and restoration for people with disabilities. LNCIS series, Springer Verlag, Berlin, Germany, pp 391–411, ISBN: 3-540-21986-2
[27] Tavaszi, I., Tóth, A., Pilissy, T., Bauer, M., Hodosán, Z., Stépán, G., Magyar, B., Fazekas, G. "Robotic Fingers in Reach-to-Grasp Tasks of Rehabilitation", Periodica Polytechnica Mechanical Engineering, 66(4), pp. 273–281, 2022. https://doi.org/10.3311/PPme.17484
[28] https://www.dex.siemens.com/plm/tecnomatix/process-simulate-human
[29] Bauer, M. O., Vizi, M. B., Galambos, P., & Szalay, T. (2021). Direct drive hand exoskeleton for robot-assisted post stroke rehabilitation. Acta Polytechnica Hungarica, 18(5), 37-54.
[30] S. Cai, W. Wu and L. Xie, "Dual-Arm Upper Limb Rehabilitation Robot: Mechanism Design and Preliminary Experiments," *2020 6th International Conference on Control, Automation and Robotics (ICCAR)*, Singapore, 2020, pp. 80-86, doi: 10.1109/ICCAR49639.2020.9108019.
[31] Tóth, A., Pilissy, T., Bauer, M. O., Al-Absi, G., Dávid, S. and Fazekas, G., "Testing the Limit Range of Motion Safety Function of Upper Limb Rehabilitation Robots with an Anthropometrically Adjustable and Sensorized Dummy Limb*," 2022 International Conference on Rehabilitation Robotics (ICORR), 2022, pp. 1-6, doi: 10.1109/ICORR55369.2022.9896575.

FES-induced and voluntary-induced fatigue in a rehabilitation-like task

Lucille Cazenave[1, 2], Nuria Peña-Pérez[3], Aaron Yurkewich[4], and Etienne Burdet[1]

Abstract— **In the context of FES-based rehabilitation and assistance tasks, there is a growing interest in managing the induced fatigue, which is an obvious limiting factor in training duration. However, it is unclear whether and how fatigue may develop in tasks commonly used in stroke rehabilitation. This work explored the effect of FES- or volition- induced movements on EMG-based effort and M-wave metrics that characterise fatigue, during a continuous wrist target-tracking task completed by 22 unimpaired participants. We found no significant changes in the mechanical and electrical responses of the muscles during the Volition-only, FES-only, and Volition-FES conditions, suggesting that during this task, FES did not induce muscular fatigue, while both mental and physical demands were reported as low. Our results thus suggest that it may not be necessary to consider FES-induced fatigue during such continuous FES-assisted tasks, that can be used in post-stroke motor rehabilitation training.**

I. Introduction

Functional electrical stimulation (FES) training often leads to rapid muscle fatigue due to the constant motor unit recruitment, unlike the naturally varying recruitment pattern seen in voluntary movements [1]–[5]. This fatigue is evident in tasks like the Cybathlon cycling race [6], where pilots with spinal cord injuries experience a decline in pedal power over time. Physical rehabilitation after stroke commonly uses FES and might thus be affected by muscle fatigue, however it is usually applied as an assistive device, in conjunction with voluntary movement, and involves frequent breaks [7]. To explore how fatigue develops during such activities, we investigated the effects of FES-induced and voluntary motion in a simple target-tracking task designed to simulate motor rehabilitation training [8], [9].

Various metrics have been employed to characterise muscle fatigue during specific volitional or FES-induced contractions. Traditionally, EMG-based effort and fatigue metrics include time-domain measures such as EMG envelope amplitude, reciprocal activation, and cocontraction. In the frequency domain, metrics such as mean and median frequency are commonly used to assess muscle fatigue [10], [11]. On the other hand, the muscle's response to electrical stimulation can be used to estimate muscle fatigue. This so-called M-wave represents the total electrical activity of all motor units depolarized within the stimulation electrodes' range [12], where its amplitude, duration, and area can be used as fatigue measures [12]–[15]. However, the literature presents discrepancies regarding which M-wave parameters best quantify muscle fatigue, as the underlying mechanisms are not fully understood. Some studies report a decrease in M-wave peak-to-peak amplitude with fatigue [13], [14], [16], and the extent of this change may be influenced by stimulation parameters and muscle type [15], [17]. Conversely, other research highlights an increase in M-wave duration (or a decrease in frequency) or area with fatigue [13], [18]–[20].

In light of these inconsistent findings, some researchers have focused on the biphasic characteristic of the M-wave, extracting parameters from each of the two phases separately. It is believed that these phases are differently affected by the physiological processes of fatigue [12], [19], [21], [22]. Studies suggest that the second phase of the M-wave may be influenced by changes in muscle architecture, such as shortening muscle length or relative positional changes between the muscle and recording electrodes, making it less suitable for fatigue analysis [12], [21]. However, recent findings indicate that the first phase of the M-wave may remain unaffected by such structural changes and may reflect more accurately fatigue-related mechanisms [22]. Thus, separate analysis of the two M-wave phases is recommended [12].

However, most studies using fatiguing protocols have focused on isometric contractions induced by voluntary or FES input [12]. These are not typically used in a stroke rehabilitation scenario where continuous movements, through the patient's range of motion, are often preferred. To investigate how fatigue develops in such a task, we investigated these EMG-based effort and M-wave metrics during FES and/or volitionally induced muscle contractions, both in an isometric and dynamic (target-tracking) scenario. We recorded kinematic data to assess tracking performance, EMG data to extract effort and fatigue metrics, and NASA-TLX questionnaire responses, with a focus on mental and physical demand. We hypothesised that muscle fatigue would be more prominent in the presence of FES compared to the volition-only condition.

II. Methods

A. Experimental design

Twenty-two unimpaired individuals (11 female, 3 left-handed), aged 21-30 years old, participated in this experiment, approved by the Research Ethics Committee of Imperial College London (approval number: 21IC6935). Participants completed three block conditions of 25 trials of target-tracking task (Fig. 1 B). In each 30 s-trial they tracked a target moving pseudo-randomly along the horizontal axis with their right wrist flexion/exte?ZXx'nsion motions [23]. The

This work was supported in part by the UKRI CDT in AI for Healthcare EP/S023283/1 and the EC H2020 project ReHyb (ICT 871767).

[1] LC and EB are with Imperial College of Science, Technology and Medicine, London, UK. {lucille.cazenave16, e.burdet}@imperial.ac.uk.

[2] LC is with the AI for Healthcare CDT of Imperial College London.

[3] NPP is with Institute of Automatic Control, RWTH Aachen, Germany.

[4] AY is with Mechatronics Engineering dept, Ontario Tech U, Canada.

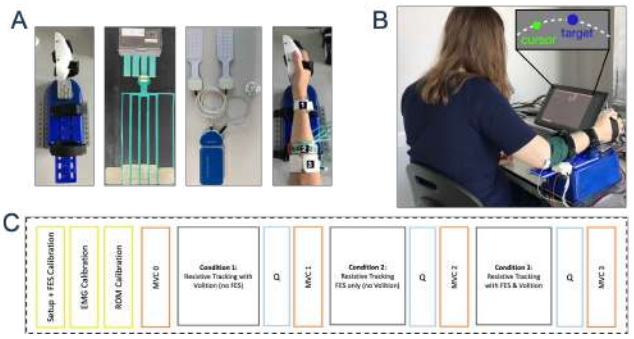


Fig. 1: Experiment description. **A.** Wrist robot-FES interface (left to right): HRX-1 wrist robotic device; FES device with 16-electrode array; EMG recording device with ground electrode and two high-density 32-channel electrode arrays; Device set-up, where the FES anode electrode (1), was placed on the dorsal side of the wrist near the ulnar head and the cathode electrodes array (2), were around the arm inline with the wrist flexor and extensor muscle belly with the EMG electrodes placed distally (3). **B.** Unimpaired individuals track a randomly moving target on-screen with wrist flexion/extension. **C.** Experimental protocol for the study on fatigue with unimpaired participants. The three conditions were presented in random order for each participant and consisted of 25 trials of a 30-second wrist target-tracking task. MVC refers to three repetitions of maximum voluntary wrist flexion and extension, followed by three repetitions of maximum flexor and extensor stimulation while participants were instructed to relax.

conditions, presented in a random order, required participants to: (i) track the target as accurately as possible, (ii) remain relaxed while FES was applied to their wrist flexor/extensor muscles to track the target, and (iii) track the target as accurately as possible while they received the same FES assistance as in (ii). The randomisation was designed to ensure that all six possible sequences of experimental conditions were presented, with each sequence carried out by at least three participants to maintain balanced exposure across conditions. The general difficulty of the task was increased by adding damping to the robot ($D = 0.0068\,Nm\,s/^\circ$).

The FES assistance was implemented with stimulation intensity proportional to the difference between the target position and the participant's wrist position $e(t)$. Prior to carrying out these experimental conditions, an FES calibration was conducted to determine the optimal location for the stimulation electrodes and the maximum comfortable amplitude for the flexor (s_f^{max}) and extensor (s_e^{max}) muscle stimulation, and the sensory thresholds s_f^{min} and s_e^{min}, which altogether provided the stimulation range to use throughout the experiment. This was followed by a range of motion (ROM) calibration, used to determine the amplitude range of the target, set to 85% of the participants' ROM.

The amplitudes of the stimulation provided to the wrist flexor $s_f(t)$ and extensor $s_e(t)$ muscles were computed as:

$$\begin{cases} s_e(t) = -\kappa\, e(t) \;+\; s_e^{min} & e(t) < 0 \\ s_f(t) = \kappa\, e(t) \;+\; s_f^{min} & e(t) \geq 0 \end{cases} \tag{1}$$

Here, κ is the FES control stiffness (in mA/°) for the flexor and extensor stimulation and (after calibration) is equivalent to a robot control stiffness $K = 0.0097\,Nm/^\circ$ [24].

After completion of each condition, participants filled the NASA-TLX questionnaire and performed a maximum voluntary contraction (MVC) exercise, where they were asked to flex and extend their wrist for 3.5 s as forcefully as possible three times on each side. Following this, they were instructed to relax while the maximum calibrated FES was applied for 3.5 s to their wrist flexor (s_f^{max}), followed by their wrist extensor (s_e^{max}), three times as well. For this step, the same calibrated FES intensity was used throughout the experiment.

B. FES and robotic device

The electrical stimulation device used was a 16-electrode array (Tecnalia Research & Innovation, Spain), where the anode was placed on the dorsal side of the wrist near the ulnar head and the cathode on the wrist flexor and extensor muscle belly to ensure comfortable and effective muscle contraction (Fig. 1 A). The frequency of the stimulation was set to 35 Hz, the pulse width to 300 μs and the amplitude of the stimulation varied during the experiment (with 1 mA resolution) (see Eq. 1). The robotic interface used was the HRX-1 one degree-of-freedom wrist robotic interface (HumanRobotiX, UK), which is actuated by a brushless low-friction motor and contains an embedded optical encoder (0.01 ° resolution) recorded the wrist angle (Fig. 1 A). Muscle activity was recorded using two 32-channel EMG electrode arrays (GR10MM0804, OT Bioelettronica, Italy) with a Sessantaquattro amplifier (OT Bioelettronica, Italy).

C. Data analysis

To analyse whether the target-tracking task induced fatigue, either with or without FES, we focused on five key aspects: i) the perceived mental and physical demand, ii) changes in EMG envelope amplitude during MVC, iii) changes in FES-induced torque and M-wave characteristics during continuous maximum stimulation, iv) tracking error, and v) cocontraction, and reciprocal activation of the flexor and extensor muscles during the condition trials. For evaluating metrics within each condition block, the first three trials used for familiarisation were excluded from the analysis, hence the remaining 22 trials were considered.

EMG pre-processing: EMG was recorded from the participants' wrist flexor and extensor muscles at a frequency of 2000 Hz. Mains noise was attenuated using a notch filter (Matlab function *iirnotch* with a notch at 50 Hz). A band-pass second order Butterworth filters (cut-off frequencies of 10 Hz and 500 Hz) were applied in the forward and reverse directions, so without inducing delay. An adaptive filter designed for EMG-based torque estimation under stimulation of wrist flexor and extensor with the same setup as here [25] was used to filter out the FES artifact and M-wave contribution for the in-trial EMG. The EMG signal was then rectified, and the envelope was obtained using a low-pass second-order Butterworth filter with a cut-off frequency of 5 Hz. The amplitude of the EMG envelope was normalised by the mean EMG envelope during the first MVC in flexion/extension (MVC0 condition in Fig. 1 C), so muscle activity is reported as a ratio of this maximum MVC amplitude. For subsequent analyses, the channel on the extensor and flexor arrays with the highest envelope amplitude during the EMG calibration

was selected. EMG metrics are reported for N = 21, as the EMG data for one participant were corrupted.

Metrics computation: Perceived effort was assessed based on the mental and physical demand items from the TLX-NASA questionnaire. To evaluate a potential decrease in MVC, we calculated the difference in muscle activity during the MVC performed before and after each condition. The average EMG value over the peak 1 s window of the 3.5 s MVC was used to characterize the MVC and the normalization value [26]–[28].

Similarly, to assess changes in FES-induced torque and M-wave characteristics, we computed the difference in mean torque and M-wave metrics during 3 s of continuous stimulation performed before and after each condition. The first 0.5 s of stimulation were excluded from the analysis to account for the delay between stimulation onset and muscle contraction. For M-wave analysis, the 3 s EMG signal was divided into pulse windows, each containing a stimulus artifact that marked the start of the window, followed by the corresponding M-wave. Within each window, we extracted the amplitude, area, and duration of each M-wave phase, averaging these metrics across the 3 s stimulation period for each M-wave phase separately [22]. Since this task is dynamic and can thus induce changes in muscle length and in the relative position of the recording and stimulating electrodes, the two M-wave phases were analysed separately (as previous work found that the first M-wave phase may be less affected by these structural changes [22]). We also analysed these metrics for the full M-wave by summing the parameters extracted from each phase to obtain the overall M-wave amplitude, duration, and area, as these are also commonly used to assess muscular fatigue [12]–[15].

We evaluated effort within trials using the cocontraction and the reciprocal activation of the wrist flexor and extensor normalised EMG envelope as described above, where co-contraction was defined as the minimum envelope amplitude between the flexor and extensor and the reciprocal activation as their difference. The tracking performance in each trial was evaluated using the Root Mean Square Error (RMSE) between the participant's and target trajectories.

Statistics: To compare perceived mental and physical demands, MVC levels, FES-induced torque, M-wave parameters, performance metrics, and EMG-based metrics during conditions, we used a one-way repeated measures ANOVA, or a non-parametric Friedman test when data were not normally distributed. Normality was assessed using the Shapiro-Wilk test. For pairwise comparisons of these metrics between conditions, we used paired sample t-tests or paired Wilcoxon signed-rank tests, controlling for the family-wise error rate using the Bonferroni-Holm correction. To determine whether differences in MVC torque, FES-induced torque, and M-wave parameters before and after each condition differed from a distribution with a mean of zero, we applied one-sample t-tests or Wilcoxon signed-rank tests for each condition individually. Moreover, for these differences, we performed this statistical analysis on the metrics distributions based on the chronological order in which the conditions were presented, regardless of their types, to identify any temporal changes in the metrics. We also conducted the same analysis after categorising the data by condition labels (FES, Volition, Volition-FES) to investigate differences associated with the specific condition types.

To explore whether tracking performance and EMG changed over time, we (i) explored trends within conditions using a linear mixed-effects model (LME) with restricted maximum likelihood, with the trial number as a fixed effect (slope) and a random intercept for each participant; and (ii) examined differences between the first and last three trials of each condition (excluding familiarisation trials), both across and within conditions. We used a one-way ANOVA or Friedman test and corresponding post-hoc tests to compare across conditions, and we used a one-sample t-test or Wilcoxon signed-rank test to compare the distribution of the metric within one condition, to one with a zero mean.

III. Results

A. Perceived mental and physical demand

We observed a significant effect of the condition on the NASA-TLX responses for the questions: "How physically demanding was this task?" ($\chi^2(2)$ = 26.66, $p < 0.001$) and "How mentally demanding was this task?" ($\chi^2(2)$ = 30.34, $p < 0.001$), where the mean for the Volition and Volition-FES conditions is below 6/10, and for the FES condition below 3/10, for both items. When participants were asked to relax while FES was applied, the task was perceived as the least demanding. In contrast, no differences were observed between the Volition and Volition-FES conditions in physical ($p = 0.73$) or mental demand ratings ($p = 0.45$).

B. MVC differences

Changes in MVC during the condition (a negative difference indicates a decrease in MVC) are reported in Fig. 2. No significant differences in MVC change across conditions were observed (MVC EMG flexor: $\chi^2(2)$ = 1.52, $p = 0.467$; MVC EMG extensor: $\chi^2(2)$ = 0.10, $p = 0.954$). Additionally, none of the conditions induced a significant change in MVC compared to zero (all $p > 0.1924$). We also investigated the chronological evolution of the MVC throughout the experiment by computing the difference between the current MVC and the previous one, independently of the condition order, and found a significant effect of the condition for the flexor MVC ($\chi^2(2)$ = 9.09, $p = 0.0106$), but no significant pairwise comparisons between conditions (all $p > 0.276$). There was no effect of the condition on the extensor MVC ($\chi^2(2)$ = 0.09, $p = 0.956$).

C. FES-induced torque differences

Similarly, we explored changes in the torque generated under maximum comfortable stimulation intensity (calibrated at the start of the experiment) while participants were at rest, across conditions. Fig. 2 shows the difference between FES-induced torque before and after each condition to assess potential decreases in this induced torque (where a negative difference indicates a decrease). No significant differences

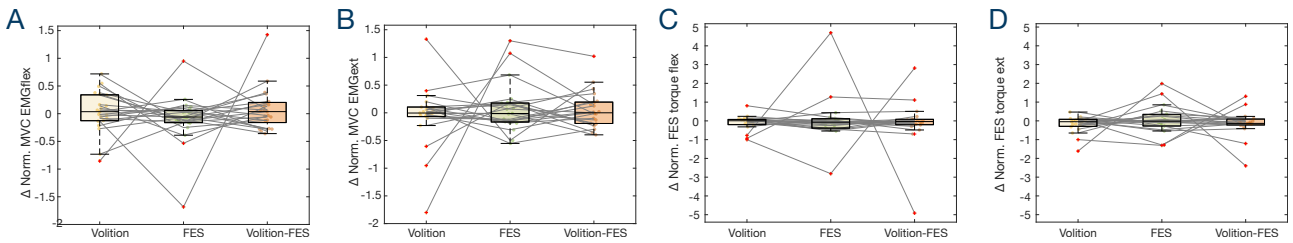


Fig. 2: Difference in mean normalised EMG during MVC trials for the flexor MVC (A) and extensor MVC (B), and in mean normalised FES-induced torque for the flexor stimulation (C) and extensor stimulation (D), for each condition. A negative difference indicates a decrease in MVC or FES-induced torque after the condition compared to before the condition.

in FES-induced torque changes across conditions were observed (FES torque flexor: $\chi^2(2)$ = 4.11, $p = 0.1284$; FES torque extensor: $\chi^2(2)$ = 0.42, $p = 0.8102$). Additionally, there were no significant changes (different from zero) in FES-induced torque within any condition (all $p > 0.1842$). When investigating chronological evolution of this metric, where conditions are considered in the order they were presented to the participants, we did not find an effect of the condition either (FES torque flexor: $\chi^2(2)$ = 3.26, $p = 0.1956$; FES torque extensor: $\chi^2(2)$ = 0.74, $p = 0.6918$).

D. M-wave parameters differences

Additionally, we evaluated the changes of various parameters characterising the M-wave recorded during maximum comfortable stimulation intensity while participants were at rest. We explored differences between the current M-wave peak-to-peak amplitude, duration and area, before and after each condition to assess potential changes in these metrics. There was no significant effect of the condition type on these metrics (MW amplitude flexor: $\chi^2(2)$ = 0.4, $p = 0.8187$; MW amplitude extensor: $\chi^2(2)$ = 0.11, $p = 0.9487$; MW duration flexor: $\chi^2(2)$ = 0.7, $p = 0.7047$; MW duration extensor: $\chi^2(2)$ = 5.05, $p = 0.08$; MW area flexor: $\chi^2(2)$ = 0.7, $p = 0.7047$; MW area extensor: $\chi^2(2)$ = 2.63, $p = 0.2683$). We also examined changes in parameters for each phase of the M-wave separately but found no significant effect of the condition (all $p > 0.0648$). When assessing whether changes within each condition differed from zero, no significant results were found for any full M-wave parameters across conditions (all $p > 0.062$). However, in the Volition-FES condition, significant changes were observed in the MW2 amplitude ($p = 0.0442$) and MW2 area ($p = 0.0329$) during extensor stimulation. Similarly when considering the data chronologically, regardless of the condition type, no effect of the condition was observed (MW amplitude flexor: $\chi^2(2)$ = 0.3, $p = 0.8607$; MW amplitude extensor: $\chi^2(2)$ = 2.63, $p = 0.2683$; MW duration flexor: $F(2)$ = 1.94, $p = 0.1536$; MW duration extensor: $\chi^2(2)$ = 0.95, $p = 0.6227$; MW area flexor: $\chi^2(2)$ = 1.3, $p = 0.5220$; MW area extensor: $F(2)$ = 0.15, $p = 0.8648$).

E. Changes in performance metrics across conditions

Fig. 3 A shows the changes in RMSE across trials for each condition. In the Volition and FES conditions, we observed a significant effect of trial number on RMSE, with a positive slope indicating a slight decrease in tracking performance (Volition: slope = 0.0275, $t(461) = 2.282$, $p = 0.023$; FES: slope = 0.0278, $t(461) = 5.171$, $p < 0.001$). In contrast, the Volition-FES condition showed no significant slope (slope = 0.0027, $t(461) = 0.245$, $p = 0.806$). When investigating the difference in RMSE between the last three trials and the first three trials for each condition, we found no significant effect of condition ($\chi^2(2)$ = 0.27, $p = 0.87$). We also considered each condition individually and evaluated whether the change in RMSE across each condition is significantly different from zero. There, we found that RMSE change during the FES condition is significantly different from zero ($p = 0.0112$), with a positive median, indicating a decrease in tracking performance throughout the condition.

F. Changes in effort across conditions

We examined how the mean cocontraction (CC) and reciprocal activation (RA) of the wrist flexor and extensor varied over trials in each condition, to measure voluntary effort (Fig. 3 B, C). For the CC, we observed a significant negative effect of the trial number on the FES (slope = -0.0004, $t(437) = -2.125$, $p = 0.0341$) and Volition-FES (slope = -0.0016, $t(437) = -4.344$, $p < 0.001$) conditions, suggesting adaptation and learning. However, the slope was not significant in the Volition condition (slope = -0.0003, $t(440) = -0.991$, $p = 0.322$). For RA, a significant positive slope was observed in the Volition-FES condition (slope = 0.0004, $t(437) = 2.811$, $p < 0.0052$), while non-significant effects were found in the other two conditions (Volition: slope = -0.0005, $t(440) = -1.491$, $p = 0.137$; FES: slope = 0.0002, $t(437) = 1.931$, $p = 0.0541$). Additionally, in the (relaxed) FES condition, the median of the normalised RA and CC was lower compared to the other two conditions, where participants actively followed the target (Fig. 3 B, C). We also investigated whether changes in mean CC and RA, over trials differed across conditions by computing the difference between the last three and first three trials and did not find a significant effect of condition type (CC: $\chi^2(2)$ = 2.67, $p = 0.264$; RA: $\chi^2(2)$ = 0.38, $p = 0.827$).

IV. Discussion

The aim of this study was to determine whether FES-assisted tasks, similar to those used in rehabilitation, induce muscular fatigue, and how this should inform the design of FES-based motor rehabilitation systems. We explored the effects of FES-induced and voluntary motion on perceived and muscular fatigue, performance, and effort during a continuous target-tracking task.

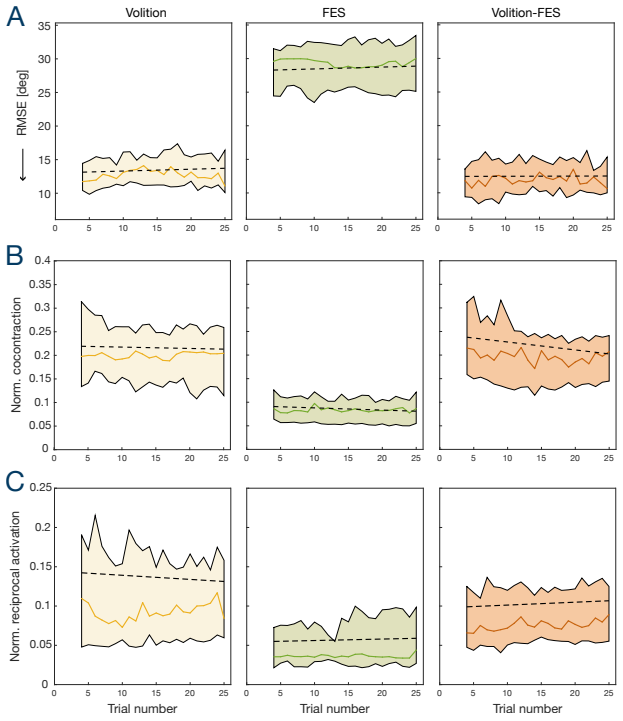


Fig. 3: Evolution of performance metrics across trials for each condition: RMSE between the participant's and target positions (A), cocontraction of the wrist flexor and extensor (B), reciprocal activation of the wrist flexor and extensor (C). The lines represent the median of each metric computed over all participants and the shaded areas represents the data from the first to third quartile of the metric. The first three trials are excluded as they were used as familiarisation trials.

A. Subjective, mechanical and electrical responses after condition

We did not observe significant changes in mechanical responses following each training block involving FES-induced and/or voluntary wrist motion aimed at tracking a continuously moving target, as was indicated by consistent MVC torque output across all conditions (Fig. 2 A, B). Similarly, no significant changes were detected in the electrical response, as assessed by the M-wave response to maximum stimulation and the constant FES-induced torque across conditions (Fig. 2 C, D). Since fatigue is typically characterised by a reduction in maximal power or force output [29], the absence of changes in MVC before and after each condition suggests that fatigue did not develop over time in this study. The M-wave parameters measured under maximum comfortable stimulation after each condition also remained stable, indicating that the muscle's electrical response was unaffected by the tracking task conditions. Even when separating the M-wave phases to compute these parameters—which has been found to be more suitable for fatigue estimation during tasks involving changes in muscle architecture—we did not find any changes across conditions [12], [21]. These findings contradict our initial hypothesis that the Volition-FES condition would result in greater fatigue compared to the Volition condition.

Indeed, previous research has shown that fatigue tends to be greater in conditions involving electrical stimulation, potentially due to the unnatural recruitment patterns and the early recruitment of fast and fatigable muscle fibres under FES [3]. However, despite the task being designed to simulate an FES-assisted rehabilitation scenario, and involving continuous stimulation for 25 trials of 30 seconds each, it did not induce noticeable muscular fatigue. This may be attributed to the task not being sufficiently challenging or tiring for participants. The mean questionnaire ratings indeed suggest that the task was not physically demanding, with ratings consistently lower than or equal to 6/10 across conditions. Literature on fatiguing protocols typically involves more intense conditions, such as 1-5 minutes of MVC or 1-3 minutes of tetanic stimulations [12]. This may also be related to the electrode configuration used for stimulation in this experiment, which may not have been optimal for extracting parameters from the M-wave, as a monopolar (belly-tendon) configuration is typically recommended. In this study, we used the FES electrode placement recommended by our clinical collaborators and employed in our clinical studies [23]. This choice may have made the recordings more susceptible to crosstalk and positional shifts, particularly since the wrist flexor and extensor muscles of interest are relatively small [12]. On the other hand, the aim of this study was to explore whether FES-assisted motor training, relevant for post-stroke rehabilitation, induces fatigue, and while muscle fatigue might manifest differently in stroke patients, it was not observed in the unimpaired participants in this scenario. The mechanical and electrical response of stroke patients' muscles following FES-based rehabilitation exercise should be further investigated to confirm whether these findings translate to the target clinical population.

B. Performance and effort across conditions

We also investigated the evolution of metrics potentially associated with muscle fatigue over time, including tracking performance, cocontraction, and reciprocal activation (Fig. 3). Tracking performance decreased over trials in both the Volition and FES conditions (Fig. 3 A). This was also confirmed by the increase in tracking error between the first three and last three trials in the FES condition. This suggests that, over time, the stimulation became less effective at contracting the muscles to follow the target trajectory, consistent with previous studies on FES during continuous tasks [30]. It is also possible that the decrease in tracking performance is related to variations in the electromechanical delay between stimulation and motion onset [31], resulting in a delayed motion response relative to the target. This decrease in performance may thus be in part due to fatigue and could be used as a marker of fatigue in a closed-loop control system.

In contrast, the EMG metrics did not show significant performance degradation. A decrease in cocontraction over trials was found in the Volition-FES and FES conditions, together with an increase in reciprocal activation in the Volition-FES condition (Fig. 3). This decrease in cocontraction suggests learning and adaptation, where participants reduce their muscle activation over time and learn to interact

with FES assistance [32], [33]. The increased reciprocal activation could suggest that muscle usage became more efficient and movement directionality more pronounced. On the other hand, although no significant decrease in performance and MVC was observed in the Volition-FES condition, the slight increase in reciprocal activation could constitute an early sign of muscle fatigue or a fatigue management mechanism [34].

When further examining the effect of condition on changes in tracking performance and effort from the first to the last trials, we found no significant differences across conditions. This suggests that no single condition led to greater performance reduction or effort alteration compared to others. This outcome was unexpected given the differing physiological processes underlying voluntary and FES-induced muscle contractions [3]. Despite observing higher tracking error and lower muscle activity in the relaxed FES condition, no significant difference in performance or effort changes was found across conditions. This discrepancy may be due to the experimental task design, which did not involve long-duration MVCs or tetanic stimulations as seen in studies reporting fatigue [3], [12]. Overall, these results suggest that continuous FES-assisted tasks, which could be used in post-stroke motor rehabilitation, may be suitable and may not induce significant muscular fatigue.

V. Conclusion

We investigated the impact of FES-induced and/or voluntary movement during a continuous target-tracking task on perceived fatigue, performance, effort, and muscular fatigue in unimpaired participants. Our findings revealed no significant changes in the mechanical and electrical responses of the muscles across any of the three conditions, suggesting that the task did not induce muscular fatigue, although we observed a larger decline in tracking performance in the FES condition, which may indicate that the movement resulting from stimulation could be altered over time without necessarily leading to fatigue. Together, these findings suggest that for this type of continuous FES-assisted task, that can be used in post-stroke rehabilitation, FES-induced fatigue may not be a major factor to be considered.

References

[1] A. S. Gorgey *et al.*, "Effects of Electrical Stimulation Parameters on Fatigue in Skeletal Muscle," *J Orthop Sports Phys Ther*, 2009.

[2] N. A. Maffiuletti, "Physiological and methodological considerations for the use of neuromuscular electrical stimulation." *Eur J App Physiol*, 2010.

[3] C. S. Bickel, C. M. Gregory, and J. C. Dean, "Motor unit recruitment during neuromuscular electrical stimulation: a critical appraisal," *Eur J Appl Physiol*, 2011.

[4] N. Miura and T. Watanabe, "Potential of M-Wave Elicited by Double Pulse for Muscle Fatigue Evaluation in Intermittent Muscle Activation by Functional Electrical Stimulation for Motor Rehabilitation," *J Med Eng*, 2016.

[5] Q. Zhang *et al.*, "FES-Induced Torque Prediction With Evoked EMG Sensing for Muscle Fatigue Tracking," *IEEE/ASME Trans Mechatronics*, 2011.

[6] R. Riener and L. J. Seward, "Cybathlon 2016," in *IEEE Int Conf Syst Man Cybern*, 2014.

[7] J. Eraifej *et al.*, "Effectiveness of upper limb functional electrical stimulation after stroke for the improvement of activities of daily living and motor function: a systematic review and meta-analysis," *Sys Reviews*, 2017.

[8] G. Alon, "Functional Electrical Stimulation (FES): Transforming Clinical Trials to Neuro-Rehabilitation Clinical Practice- A Forward Perspective," 2013.

[9] A. Nehrujee *et al.*, "Long-term Usability and Feasibility of Home-Based Hand Therapy With the Plug-And-Train Hand Rehabilitation Robot(PLUTO)," *Arch Phys Med Rehab*, 2023.

[10] F. B. Stulen and C. J. De Luca, "Frequency Parameters of the Myoelectric Signal as a Measure of Muscle Conduction Velocity," *IEEE Trans Biomed Eng*, 1981.

[11] L. Arendt-Nielsen *et al.*, "Changes in muscle fiber conduction velocity, mean power frequency, and mean EMG voltage during prolonged submaximal contractions," *Muscle & Nerve*, 1989.

[12] J. Rodriguez-Falces and N. Place, "Determinants, analysis and interpretation of the muscle compound action potential (M wave) in humans: implications for the study of muscle fatigue," *Eur J App Physiol*, 2018.

[13] N. C. Chesler and W. K. Durfee, "Surface EMG as a fatigue indicator during FES-induced isometric muscle contractions," *JEK*, 1997.

[14] D. Tepavac and L. Schwirtlich, "Detection and prediction of FES-induced fatigue," *JEK*, 1997.

[15] M. Badier *et al.*, "M-wave changes after high- and low-frequency electrically induced fatigue in different muscles," *Muscle & Nerve*, 1999.

[16] J. Mizrahi *et al.*, "EMG as an indicator of fatigue in isometrically FES-activated paralyzed muscles," *IEEE Trans Rehab Eng*, 1994.

[17] M. Vromans and P. D. Faghri, "Functional electrical stimulation-induced muscular fatigue: Effect of fiber composition and stimulation frequency on rate of fatigue development," *JEK*, 2018.

[18] N. Dimitrova *et al.*, "Estimate of M-wave changes in human biceps brachii during continuous stimulation," *JEK*, 2005.

[19] J. Heasman *et al.*, "Detection of fatigue in the isometric electrical activation of paralyzed hand muscles of persons with tetraplegia," *IEEE Trans Rehab Eng*, 2000.

[20] M. Hayashibe *et al.*, "Evoked EMG-based torque prediction under muscle fatigue in implanted neural stimulation," *JNER*, 2011.

[21] Z. C. Lateva *et al.*, "Anatomical and electrophysiological determinants of the human thenar compound muscle action potential," *Muscle & Nerve*, 1996.

[22] J. Rodriguez-Falces and N. Place, "Muscle excitability during sustained maximal voluntary contractions by a separate analysis of the M-wave phases," *Scand J Med Sci Sports*, 2017.

[23] L. Cazenave *et al.*, "Hybrid Functional Electrical Stimulation and Robotic Assistance for Wrist Motion Training After Stroke: Preliminary Results," in *IEEE ICORR*, 2023.

[24] E. Ivanova *et al.*, "For Motion Assistance Humans Prefer to Rely on a Robot Rather Than on an Unpredictable Human," *IEEE Open J Eng Med Biol*, 2020.

[25] H. Kavianirad *et al.*, "EMG-Based Volitional Torque Estimation in Functional Electrical Stimulation Control," in *IEEE EMBS*, 2022.

[26] H. Nieminen *et al.*, "Normalization of electromyogram in the neck-shoulder region," *Eur J Appl Physiol*, 1993.

[27] B. Castelein *et al.*, "Optimal Normalization Tests for Muscle Activation of the Levator Scapulae, Pectoralis Minor, and Rhomboid Major: An Electromyography Study Using Maximum Voluntary Isometric Contractions," *Arch Phys Med Rehab*, 2015.

[28] R. A. Ekstrom *et al.*, "Normalization procedures using maximum voluntary isometric contractions for the serratus anterior and trapezius muscles during surface EMG analysis," *JEK*, 2005.

[29] N. K. Vøllestad, "Measurement of human muscle fatigue," *J Neurosci Methods*, 1997.

[30] B. C. Allen *et al.*, "Characterization of the Time-Varying Nature of Electromechanical Delay During FES-Cycling," *IEEE TNSRE*, 2020.

[31] R. J. Downey *et al.*, "The Time-Varying Nature of Electromechanical Delay and Muscle Control Effectiveness in Response to Stimulation-Induced Fatigue," *IEEE TNSRE*, 2017.

[32] K. A. Thoroughman *et al.*, "Electromyographic Correlates of Learning an Internal Model of Reaching Movements," *J Neurosci*, 1999.

[33] D. W. Franklin *et al.*, "Adaptation to Stable and Unstable Dynamics Achieved By Combined Impedance Control and Inverse Dynamics Model," *J Neurophysiol*, 2003.

[34] B. Prilutsky and R. Gregor, "Analysis of muscle coordination strategies in cycling," *IEEE TRE*, 2000.

Towards Unsupervised Incremental and Proportional Myocontrol based on Higher-Density Surface Electromyography

Alisa Schulz[1], Fabio Egle[1], Marius Osswald[2], Alessandro Del Vecchio[2] and Claudio Castellini[1,3]

***Abstract*— Upper limb differences present tremendous challenges for autonomy in daily living, and current prostheses often face high abandonment rates due to complexity and lack of functionality. This study investigates fully unsupervised incremental myocontrol using higher-density surface EMG. Utilizing incremental sparse non-negative matrix factorization (ISNMF), we employed two 32-channel sEMG bracelets to incrementally extract muscle synergies from EMG signals in real-time. Eight able-bodied participants underwent this unsupervised training paradigm with an increasing number of target synergies and were evaluated with a virtual target achievement control (TAC) test. Participants demonstrated up to six independently controllable synergies in full-intensity tasks, exceeding the current state of the art. However, proportional control remained challenging, reflected in a median success rate of 10% for half-intensity targets. Subjective feedback across the number of synergies showed only small variations in cognitive and physical workload despite increased complexity. This approach shows promise for enabling fully unsupervised myocontrol, but further refinement of training protocol and hyperparameters, as well as testing on users with limb differences, are necessary to validate and improve this approach.**

I. INTRODUCTION

Congenital anomalies of the upper limb affect approximately one in 500 births [1]. Italy and the UK report 3500 and 5200 upper limb amputations per year, respectively [2]. Furthermore, due to an aging population and increasing prevalence of diabetes and cardiovascular disease, the number of people with upper limb amputation in the US is expected to double by 2050 [3]. Individuals with limb difference (LD) face challenges in autonomy and daily functioning as well as a heightened risk to their psychological well-being, including anxiety and depression [4].

Despite the considerable advances in the field of upper limb prosthesis (ULP) in the last decades, prosthesis abandonment is still very high [5]. The reasons for this include comfort, lack of functionality, and complex control systems [6]. Methods based on pattern recognition (PR) have been developed in the last decades to approach the latter two reasons [7], [8]. One of the main issues with the developed prosthesis control methods is the non-stationarity of surface electromyography (sEMG) signals due to sweat, muscle fatigue, sensor shift, and user adaptation [9]. To overcome this problem and to foster the co-adaptation process between the user and system, incremental learning approaches providing regression or classification have been developed and tested in recent years [10]–[12]. While these methods empower the user to voluntarily update their model, they are still limited by the requirement for the user to provide accurate labels. These labels can be provided either by a contralateral data acquisition [13], by following a visual reference [14], or by training on a steady-state, e.g., a certain percentage of the maximum contraction. Providing these labels can be especially challenging for people with LD, as this requires dedicated pre-prosthetic user training and data acquisition protocols [15]. Unsupervised myocontrol (UM) allows continuous adaptation without labels, thus potentially solving this problem. Furthermore, instead of only using small portions of labeled data, it allows a stream of (interaction) data to update the model continuously.

In 2009, Jiang et al. [16] applied the non-negative matrix factorization (NMF) as a myocontrol algorithm to achieve both proportional and simultaneous control of multiple degrees of freedom (DOFs). Building on this, Lin et al. proposed a NMF algorithm with additional sparsity constraints for the control signal, thereby simplifying the training and even allowing arbitrary movements during the training phase [17]. Yeung et al. [18] designed an incremental NMF that can adapt to changes and counteract performance degradation. Gigli et al. [19] developed this approach further by adding an arbitrary motor mapping, which eliminates the necessity for labeled data. Finally, [20] adapted the method to add muscle synergies progressively during the training process.

This work investigates the feasibility and potential of combining incremental unsupervised learning with higher-density sEMG as previously used in such unsupervised myocontrol paradigms. For this, we implemented the incremental sparse NMF (ISNMF) approach described by Gigli et al. [19] in combination with two 32-channel sEMG dry electrode bracelets. Although sEMG setups with higher number of electrodes, in many cases high-density (interelectrode distance <= 10 mm) electrode grids have previously been used for real-time myocontrol in experimental conditions [14], [21]–[23], most of these works rely either on supervised approaches, the use of computationally demanding neural networks, adhesive electrode grids applied to the skin with conductive paste limiting their usefulness in real-world settings, or a combination of the above.

*This work was partially supported by the European Commission's Horizon Europe Framework Program with the project IntelliMan (AI-Powered Manipulation System for Advanced Robotic Service, Manufacturing and Prosthetics) under Grant Agreement 101070136.

[1]Assistive Intelligent Robotics Lab, Department Artificial Intelligence in Biomedical Engineering, Friedrich-Alexander Universität Erlangen-Nürnberg, 91052 Erlangen, Germany

[2]n-squared Lab, Department Artificial Intelligence in Biomedical Engineering, Friedrich-Alexander Universität Erlangen-Nürnberg, 91052 Erlangen, Germany

[3]Institute of Robotics and Mechatronics, German Aerospace Center, 82234 Wessling, Germany

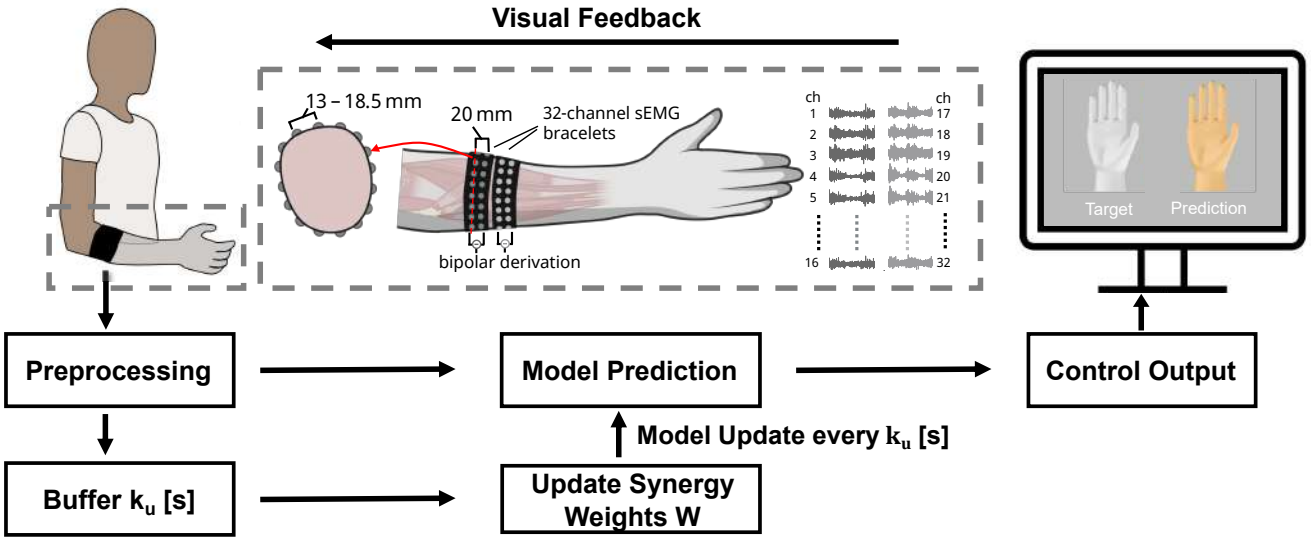


Fig. 1. *Experimental setup of the online myocontrol experiment.* Two 32-channel dry electrode bracelets were placed around the participant's forearm. Each electrode bracelet consisted of two rows of 16 electrodes. The bipolar configuration of the monopolar signals was derived for each pair of electrodes in the longitudinal direction of the arm, resulting in an output of 16 EMG signals per bracelet. Interelectrode distance in the transversal and longitudinal direction is shown in the bottom panel. Signals were preprocessed (see Methods) and then simultaneously fed into a buffer and the latest prediction NMF model. The collected data in the buffer was used to update the currently extracted weights W at defined intervals k_u. The model's prediction controlled a virtual hand on a monitor, that gave the user feedback on the model´s current prediction.

We tested our developed system in an online myocontrol experiment with eight able-bodied (AB) participants. During the experimental sessions, the subjects had to train a number of muscle synergies incrementally, increasing the number of synergies by one each round. After each round, the participants performed a target achievement control (TAC) test as an objective and filled in the NASA-TLX questionnaire as a subjective measure of perceived workload. To the author's knowledge, no dry electrode setup with such an electrode density as used in this work has been used for fully unsupervised and incremental online myocontrol to this date.

II. METHODS

A. Processing and Incremental Unsupervised Myocontrol

In order to extract the participants' movement intention from their sEMG signals, the ISNMF algorithm proposed by Gigli et al. [19] was implemented. The standard NMF algorithm aims to minimize the difference between the input EMG $V \in \mathbb{R}_+^{s\times n}$ consisting of s n-dimensional samples and WH. Where $W \in \mathbb{R}_+^{r\times n}$ contains r extracted synergies and $H \in \mathbb{R}_+^{r\times s}$ holds the activation coefficients. The ISNMF model uses iterative multiplicative updates on input batches of V based on Formula 1 and 2 to extract and refine muscle synergies in the m-th update. The matrices A and B are history matrices and eliminate the necessity of storing the entire training data set. While the forgetting factor μ reduces the contribution of the previous training batches. [19].

$$W^m \leftarrow W^m \circ \frac{\mu A^{m-1} + V_m H_m^{mT}}{\mu W^m B^{m-1} + W^m H_m^m H_m^{mT} + \frac{\mu(1-\mu^m)}{(1-\mu)}\beta W^m} \quad (1)$$

To compute the activation coefficients, H is optimized based on Formula 2.

$$H_m^m \leftarrow H_m^m \circ \frac{W^{mT} V_m}{W^{mT} W^m H_m^m + \gamma (H_m^m)^{-0.5}} \quad (2)$$

To improve the sparsity of the predictions, H is regularised with an $L_0.5$ norm weighted by γ, while W is regularised with an L_2 norm weighted by β.

For the online application, two ISNMF models were run in parallel, one for computing the predictions and one performing the updates, to guarantee that predictions were computed in real-time without disruptions through model updates, as shown in Figure 1. Each muscle synergy in W is arbitrarily mapped to a predefined myocontrol action of the hand model. The activation coefficients are normalized to a range of [0, 1] based on the historical 95th percentile of previous activations [19].

B. Hardware

For sEMG acquisition, two 32-channel sEMG bracelets (HD20MM1602B, OT Bioelettronica, Turin, Italy) were placed around the forearm of the participants. The electrodes of the sEMG bracelets are arranged in two columns of 16 electrodes each, with a longitudinal interelectrode distance (IED) of 20 mm between the columns and 13-18.5 mm IED in transversal direction, depending on the participants´ forearm circumference (20.8 - 29.5 cm in this study) (Fig. 1). Signals were sampled at 2000 Hz by a commercially available, wireless amplification system (MUOVI, OT Bioelettronica, Turin, Italy).

C. sEMG Preprocessing

To improve signal stability, the bipolar derivation of each pair of electrodes in the longitudinal direction of the arm was computed and used for further processing, resulting in 16 sEMG signals per bracelet. Then, the EMG was amplified by a factor of 100 and filtered with a bandpass filter over a frequency range of 20 Hz to 90 Hz and a bandstop filter over a frequency range of 45 Hz to 55 Hz. Finally, the root mean square (RMS) was calculated over a sliding window of 500 ms with a step size of 50 ms.

D. Online Myocontrol Experiment

1) Participants: The study was conducted with eight AB subjects (sex: $2f$, $6m$; age: 26.6 ± 3.0, range $[20, 30]$). Participants 1 and 5 had prior experience in myocontrol-based study designs.

2) Experimental Setup: As visualized in Figure 1, two sEMG bracelets, as described in II-B, were placed around the participants' forearm, targeting all superficial extrinsic hand and wrist muscles. The recorded sEMG was preprocessed as described in II-C. Due to limited space available, the wrist, hand, and fingers were not fixed with an orthosis. The participants were placed in front of a monitor that displayed a target hand, and the control hand. The target hand displayed the desired hand postures during the TAC test. While the control hand performed the hand movements according to the currently detected synergy activation and arbitrary motor mapping.

3) ISNMF: The value of the forget factor μ, was fixed at 0.9 throughout the course of the online trials. The tolerance ε was set to 10^{-5}, and the maximum number of iterations per update and prediction was limited to 200. In each trial, the number of extracted synergies, r, was increased from the initial value of $r = 3$ to a maximum of $r = 7$. The training batch size k_u was set to $10s$ for $r = [3,4]$, $15s$ for $r = [5,6]$, and $20s$ for $r = 7$. The initial values of the regularization terms β and γ were set to 10, although these could be modified by the experimenter if, for example, extracted synergies diminished repeatedly.

4) Study protocol: Each participant trains multiple ISNMF models with an increasing number of synergies, starting with three synergies. Each model is trained for a maximum time of ten minutes. Afterward, the ISNMF model was no longer updated, and a TAC test was performed, which requested the participant to reach a specific target position and hold them for 2 seconds with a maximal myocontrol error of 0.2. Thereby the myocontrol error is defined as the maximum component of the elementwise absolute difference between the target and the predicted pose [20]. The target poses require the activation of single synergies at *half-* and *full-intensity* to assess proportional control. Between the training and test phases of the models controlling more than three synergies, the NASA-TLX questionnaire (p. 1) is filled out by the participant. If a new synergy (four or later) could not be correctly activated at all, the experiment was terminated. The study was conducted following the WMA Declaration of Helsinki, participants provided informed consent, and the experiment was approved by the Ethics Committee of FAU Erlangen-Nürnberg (No. 22-275-S) before the experiments were carried out.

5) Data Analysis: The objective evaluation of the myocontrol of the participants was conducted through the analysis of the TAC test results, i.e. the success rate and task completion time. Each participant's success rate was calculated as the number of successfully reached and held target poses divided by the total number of target poses. In the case of a successful trial, the task completion time was calculated. Furthermore, both metrics are again provided for *half-intensity tasks* and *full-intensity tasks* separately (see II-D.4). For further use, the metrics from single-task trials are aggregated as a mean on a TAC level per participant. Missing values due to early termination (see II-D.4) were filled with the success rate of the last synergy minus the tasks corresponding to the new synergy. This approach assumes that the participant would have successfully achieved the same number of synergies again but would not have been able to control the subsequent synergy. The workload, assessed by the NASA-TLX part 1, was evaluated as a mean of the single categories [24] Due to a data loss during the acquisition of the participant, $S5$ was excluded from the study.

III. RESULTS

A. Objective Measurements

Figure 2 shows the success rate during the TAC tests for the increasing number of synergies across all targets. Missing values (see II-D.5) were anticipated for $S2(7)$, $S7(6,7)$, $S8(7)$, $S9(7)$. A downward trend of the success rate with an increasing number of synergies is visible, except for S3. It is also visible that all participants performed equally or better in TAC 4 than in TAC 3. The success rates of target poses with *half-* and *full-intensity* clearly show that the *full-intensity* poses were performed much better in comparison to the *half-intensity* targets. Furthermore, while the *half-intensity* targets commonly decrease for all participants except for S3, the *full-intensity* targets heavily differ between participants. There, it is particularly noteworthy that three of the participants achieved test results of 100% for $r = 5$ and two reached $\geq 80\%$. For $r = 6$ still, one participant reached 100% success, and three other subjects reached scores $\geq 80\%$.

TABLE I
TASK COMPLETION TIME OF SUCCESSFUL TASKS PER NUMBER OF SYNERGIES r IN [S] (MEAN AND STANDARD DEVIATION)

r	Target intensity		
	all	*full*	*half*
3	6.70 ± 1.62	5.96 ± 2.07	7.36 ± 2.34
4	6.14 ± 0.69	5.72 ± 0.93	7.53 ± 1.34
5	6.69 ± 1.70	6.21 ± 1.42	10.95 ± 4.66
6	7.44 ± 2.64	6.85 ± 2.61	10.96 ± 4.28
7	6.79 ± 1.24	6.58 ± 1.32	7.66 ± 1.50

Also, the time to task completion of successful tasks shown in Tab. I shows substantially longer task completion times for *half-* compared to *full-intensity targets* across all

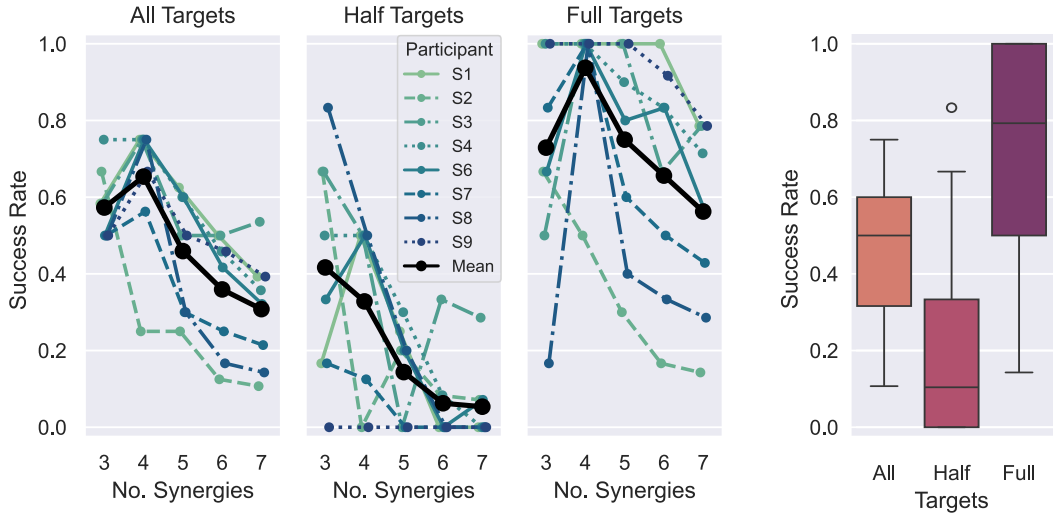


Fig. 2. *TAC test performance.* Left: Mean success rate (black) and each participant's success rate across the number of synergies r and targets (*all targets*, *only half-intensity targets*, and *only full-intensity* targets). Right: Box plot shows the success rates across target categories with median and IQR across all participants. Absent values for $S2(7)$, $S7(6,7)$, $S8(7)$, $S9(7)$ were filled as described in II-D.5

synergies. An overall increasing trend in completion time is visible from $r = 3$ to $r = 6$.

B. Subjective Measurement

The results of the NASA-TLX are shown in Fig. 3. Of all TLX dimensions combined, $r = 6$ received the highest scores and thus the highest perceived workload. Amongst the individual dimensions, Temporal Demand (TD) and Frustration (F) received, with the exception of 7 synergies (only $n = 4$), the lowest scores. Mental demand (MD), Effort (E), and Performance (P) were scored higher across most synergies. Physical Demand (PD) stayed relatively consistent across synergies.

IV. DISCUSSION AND CONCLUSION

A. Objective Measurements:

The main goal of this work was to improve current state-of-the-art results on incremental unsupervised online myocontrol by leveraging higher-density electrode setups as previously used. In comparison, Gigli et al. achieved success rates of 80% with a maximum of 4 separately controllable synergies [20]. We were able to reach similar success rates with 5-6 independently controllable synergies as shown in Figure 2. At four synergies, near-perfect *full-intensity* target scores were reached in all but one participant. Multiple participants even reached rates of ˜80% with seven controllable synergies (*S1*, *S3*, *S4*, *S9*). The significantly lower success rates at 3 active synergies compared to 4, 5, 6, and 7 synergies suggest a strong need for familiarisation and customization of the participants with the protocol and the interaction with the prediction model. The decrease in success rate in *full-intensity* target control at 5, 6, and 7 synergies can be attributed to the increased model complexity and the model's difficulty in identifying and separating new muscle synergies that were independent of the existing ones. Prominently, the high success rates in full-intensity target control could not be replicated in *half-intensity* target control, where success rates of less than 50% were achieved even at 3 and 4 synergies by all participants. One potential explanation for this might have been a too strong regularization of the activation coefficients by the ISNMF, or issues in the scaling of the coefficients. A hyperparameter optimization optimized towards the TAC test's demands could have also improved proportional control. A further possibility is that, in order to activate a myofunction with a half-intensity, the EMG amplitude must be maintained within a specific amplitude range. Conversely, for a full activation, the EMG amplitude merely needs to reach a certain threshold value. Notably, in two participants (*S6, S7*), significant model degradation was observed between the model training phase and the TAC tests in higher synergies numbers, suggesting a shift in electrode placement during the completion of the NASA-TLX questionnaire.

Given the much higher number of electrodes used in this study compared to previous work and the high number of controllable synergies in multiple participants, we hypothesize a high possible number of reliably and independently controllable synergies given further optimized hyperparameters and experimental protocol, including longer familiarization with the prediction model and setup, and increased duration of model training before the TAC tests.

B. Subjective Measurements

Similar to Gigli et al. [20], the results of the NASA-TLX scores presented in Figure 3 suggest no consistent decrease or increase of physical demand, mental demand, or frustration with increasing number of synergies despite decreasing success rates towards higher synergy numbers. This suggests that the higher familiarity with the system might be counteracted by the increased difficulty of controlling more myocontrol actions.

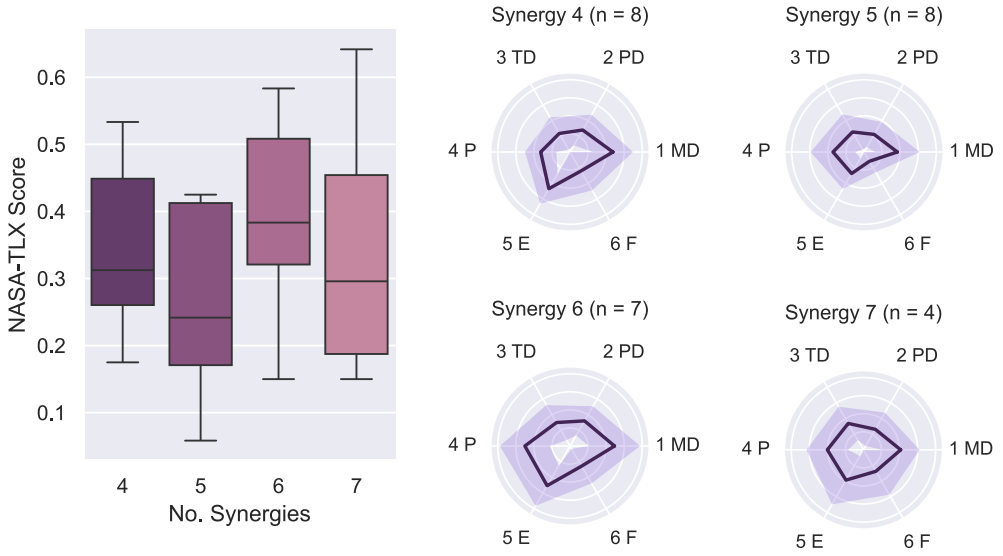


Fig. 3. *Results of the NASA-TLX questionnaire.* Left: NASA-TLX score for the number of synergies. Right: Each questionnaire subcategory result averaged across participants for synergies 4 to 7 with circular ticks from 0 to 0.8, with 0.8 corresponding to a high perceived workload. Subcategories: Temporal Demand (TD), Physical Demand (PD), Mental demand (MD), Frustration (F) Effort (E), and Performance (P). Only the number of participants n who successfully performed the previous synergy TAC test completed the respective NASA-TLX questionnaire.

C. Limitations

All participants in this study were non-disabled individuals. Furthermore, the wrist, hand, and fingers were not constrained with an orthosis. Both factors limit the generalizability to individuals with LD. Since it has been shown that limiting non-disabled subjects to isometric muscle contractions makes them more comparable with individuals with LD [25]. In Addition, this study was conducted in a controlled laboratory setting, which may not fully replicate the complexities and variabilities of daily life scenarios. Furthermore, the TAC-tests did not include simultaneous actions, therefore not evaluating combined control. The gradual increase in controllable Myocontrol functions influenced the results due to familiarisation. However, future users will also start with limited functions and increase the complexity over time. The sequential method therefore models the real use cases.

D. Outlook

Increasing the number of sEMG channels and, therefore, input dimensions not only increases the information density and possibly achievable prediction accuracy but also increases computational demand and model complexity, especially when dealing with the processing of raw EMG signals at high sampling frequencies.

We show that an unsupervised NMF-based control system, such as the one used in this work, can extract a considerable number of muscle synergies from higher-density dry electrode grids. Such a control system could also be used to extract movement intents in an unsupervised fashion from motor unit activation patterns. Motor unit activity extraction was recently shown to be possible in real-time scenarios [26]–[28]. Research suggests, that specific motor unit recruitment patterns encode distinct DoFs that could pose as lightweight but reliable input signals to the NMF model [29]–[31].

The optimal values for the hyperparameters β and γ, which are used to regulate W and H, directly affect myocontrol quality and vary between individuals. Standardized methods to determine the best hyper-parameters for proportional control for each individual are essential to ensure optimal user satisfaction.

The ISNMF algorithm has the capability to counteract model degradation from sEMG non-stationarities, such as user adaptation, without requiring stored training data or calibration procedures [18]. Moreover, it enables closed-loop co-adaptive learning, thereby enhancing its usability for individuals with congenital LD [32]. Additionally, the progressive and incremental NMF proposed by Gigli et al., allows an increase in the number of extracted synergies, thus enabling the integration of newly learned motor skills [20]. This study confirmed that muscle synergies extracted by ISNMF have the potential to control multiple myocontrol actions (which can be mapped to DOFs) without labeling and calibration procedures. Therefore, it could be used as a myocontrol algorithm for upper limb prosthesis control for individuals with a LD, especially a congenital LD. Furthermore, it allows the identification of distinct muscle synergies with minimal supervision, making it a suitable method for periprosthetic training.

E. Conclusion

This study investigated the feasibility of transferring unsupervised incremental myocontrol to HD-EMG. While preliminary studies based on sEMG and unsupervised incremental

learning demonstrated control over four actions, we showed that it is possible to archive more controllable actions by increasing the number of electrodes.

Nevertheless, the study has certain limitations. It was conducted in a controlled environment and was tested with non-disabled participants. These factors may affect the generalizability of the results for individuals with LDs. Future research should aim to validate these findings with a representative target group and increase the number and density of electrodes even further.

REFERENCES

[1] H. Giele, C. Giele, C. Bower, and M. Allison, "The incidence and epidemiology of congenital upper limb anomalies: A total population study," *The Journal of Hand Surgery*, vol. 26, no. 4, pp. 628–634, Jul. 2001.

[2] F. Cordella, A. L. Ciancio, R. Sacchetti, A. Davalli, A. G. Cutti, E. Guglielmelli, and L. Zollo, "Literature Review on Needs of Upper Limb Prosthesis Users," *Frontiers in Neuroscience*, vol. 10, May 2016.

[3] K. Ziegler-Graham, E. J. MacKenzie, P. L. Ephraim, T. G. Travison, and R. Brookmeyer, "Estimating the Prevalence of Limb Loss in the United States: 2005 to 2050," *Archives of Physical Medicine and Rehabilitation*, vol. 89, no. 3, pp. 422–429, Mar. 2008.

[4] S.-H. Jo, S.-H. Kang, W.-S. Seo, B.-H. Koo, H.-G. Kim, and S.-H. Yun, "Psychiatric understanding and treatment of patients with amputations," *Yeungnam University Journal of Medicine*, vol. 38, no. 3, pp. 194–201, Jul. 2021.

[5] S. Salminger, H. Stino, L. H. Pichler, C. Gstoettner, A. Sturma, J. A. Mayer, M. Szivak, and O. C. Aszmann, "Current rates of prosthetic usage in upper-limb amputees – have innovations had an impact on device acceptance?" *Disability and Rehabilitation*, vol. 44, no. 14, pp. 3708–3713, Jul. 2022.

[6] P. Capsi-Morales, C. Piazza, L. Sjoberg, M. G. Catalano, G. Grioli, A. Bicchi, and L. M. Hermansson, "Functional assessment of current upper limb prostheses: An integrated clinical and technological perspective," *PLOS ONE*, vol. 18, no. 8, p. e0289978, Aug. 2023.

[7] A. Marinelli, N. Boccardo, F. Tessari, D. Di Domenico, G. Caserta, M. Canepa, G. Gini, G. Barresi, M. Laffranchi, L. De Michieli, and M. Semprini, "Active upper limb prostheses: a review on current state and upcoming breakthroughs," *Progress in Biomedical Engineering*, vol. 5, no. 1, p. 012001, Jan. 2023.

[8] A. Phinyomark and E. Scheme, "EMG pattern recognition in the era of big data and deep learning," *Big Data and Cognitive Computing*, vol. 2, no. 3, p. 21, Aug. 2018.

[9] I. Kyranou, S. Vijayakumar, and M. S. Erden, "Causes of Performance Degradation in Non-invasive Electromyographic Pattern Recognition in Upper Limb Prostheses," *Frontiers in Neurorobotics*, vol. 12, Sep. 2018.

[10] A. Gijsberts, R. Bohra, D. Sierra González, A. Werner, M. Nowak, B. Caputo, M. Roa, and C. Castellini, "Stable myoelectric control of a hand prosthesis using non-linear incremental learning," *Frontiers in Neurorobotics*, vol. 8,

[11] F. Egle, D. Di Domenico, A. Marinelli, N. Boccardo, M. Canepa, M. Laffranchi, L. De Michieli, and C. Castellini, "Preliminary Assessment of Two Simultaneous and Proportional Myocontrol Methods for 3-DoFs Prostheses Using Incremental Learning," in *2023 International Conference on Rehabilitation Robotics (ICORR)*. Singapore, Singapore: IEEE, Sep. 2023. doi: 10.1109/ICORR58425.2023.10304813

[12] D. Di Domenico, N. Boccardo, A. Marinelli, M. Canepa, E. Gruppioni, M. Laffranchi, and R. Camoriano, "Long-Term Upper-Limb Prosthesis Myocontrol via High-Density sEMG and Incremental Learning," *IEEE Robotics and Automation Letters*,

[13] A. Hagengruber, U. Leipscher, B. M. Eskofier, and J. Vogel, "A New Labeling Approach for Proportional Electromyographic Control," *Sensors*, vol. 22, no. 4, p. 1368, Jan. 2022.

[14] R. C. Sîmpetru, D. I. Braun, A. U. Simon, M. März, V. Cnejevici, D. S. d. Oliveira, N. Weber, J. Walter, J. Franke, D. Höglinger, C. Prahm, M. Ponfick, and A. D. Vecchio, "MyoGestic: EMG Interfacing Framework for Decoding Multiple Spared Degrees of Freedom of the Hand in Individuals with Neural Lesions," "

[15] C. Widehammar, K. Lidström Holmqvist, and L. Hermansson, "Training for users of myoelectric multigrip hand prostheses: a scoping review," *Prosthetics and Orthotics International*, vol. 45, no. 5, p. 393, Oct. 2021.

[16] Ning Jiang, K. Englehart, and P. Parker, "Extracting Simultaneous and Proportional Neural Control Information for Multiple-DOF Prostheses From the Surface Electromyographic Signal," *IEEE Transactions on Biomedical Engineering*, vol. 56, no. 4, pp. 1070–1080, Apr. 2009.

[17] C. Lin, B. Wang, N. Jiang, and D. Farina, "Robust extraction of basis functions for simultaneous and proportional myoelectric control via sparse non-negative matrix factorization," *Journal of Neural Engineering*, vol. 15, no. 2, p. 026017, Apr. 2018.

[18] D. Yeung, I. M. Guerra, I. Barner-Rasmussen, E. Siponen, D. Farina, and I. Vujaklija, "Co-Adaptive Control of Bionic Limbs via Unsupervised Adaptation of Muscle Synergies," *IEEE Transactions on Biomedical Engineering*, vol. 69, no. 8, pp. 2581–2592, Aug. 2022.

[19] A. Gigli, A. Gijsberts, and C. Castellini, "Unsupervised Myocontrol of a Virtual Hand Based on a Coadaptive Abstract Motor Mapping," in *2022 International Conference on Rehabilitation Robotics (ICORR)*. Rotterdam, Netherlands: IEEE, Jul. 2022. doi: 10.1109/ICORR55369.2022.9896414

[20] A. Gigli, A. Gijsberts, M. Nowak, I. Vujaklija, and C. Castellini, "Progressive unsupervised control of myoelectric upper limbs," *Journal of Neural Engineering*, vol. 20, no. 6, p. 066016, Nov. 2023.

[21] F. I. Serdana, S. Muceli, and D. Farina, "Using High Density EMG to Proportionally Control 3D Model of Human Hand," *International Journal on Advanced Science, Engineering and Information Technology*, vol. 13, no. 3, pp. 1118–1126, Jun. 2023.

[22] M. Barsotti, S. Dupan, I. Vujaklija, S. Došen, A. Frisoli, and D. Farina, "Online Finger Control Using High-Density EMG and Minimal Training Data for Robotic Applications," *IEEE Robotics and Automation Letters*, vol. 4, no. 2, pp. 217–223, Apr. 2019.

[23] R. C. Sîmpetru, M. März, and A. Del Vecchio, "Proportional and Simultaneous Real-Time Control of the Full Human Hand From High-Density Electromyography," *IEEE Transactions on Neural Systems and Rehabilitation Engineering*, vol. 31, pp. 3118–3131, 2023.

[24] S. G. Hart and L. E. Staveland, "Development of NASA-TLX (Task Load Index): Results of Empirical and Theoretical Research," in *Advances in Psychology*, ser. Human Mental Workload, P. A. Hancock and N. Meshkati, Eds. North-Holland, Jan. 1988, vol. 52,

[25] M. B. Kristoffersen, A. W. Franzke, C. K. van der Sluis, R. M. Bongers, and A. Murgia, "Should Hands Be Restricted When Measuring Able-Bodied Participants to Evaluate Machine Learning Controlled Prosthetic Hands?" *IEEE Transactions on Neural Systems and Rehabilitation Engineering*, vol. 28, no. 9, pp. 1977–1983, Sep. 2020.

[26] J. Rossato, F. Hug, K. Tucker, C. Gibbs, L. Lacourpaille, D. Farina, and S. Avrillon, "I-Spin live: An open-source software based on blind-source separation for real-time decoding of motor unit activity in humans," *eLife*, vol. 12, Sep. 2024.

[27] D. Y. Barsakcioglu and D. Farina, "A real-time surface EMG decomposition system for non-invasive human-machine interfaces," in *2018 IEEE Biomedical Circuits and Systems Conference (BioCAS)*, Oct. 2018. doi: 10.1109/BIOCAS.2018.8584659

[28] Y. Wen, S. Avrillon, J. C. Hernandez-Pavon, S. J. Kim, F. Hug, and J. L. Pons, "A convolutional neural network to identify motor units from high-density surface electromyography signals in real time," *Journal of Neural Engineering*, vol. 18, no. 5, p. 056003, Apr. 2021.

[29] A. Grison, J. I. Pereda, S. Muceli, A. Kundu, F. Baracat, G. Indiveri, E. Donati, and D. Farina, "Intramuscular High-Density Micro-Electrode Arrays Enable High-Precision Decoding and Mapping of Spinal Motor Neurons to Reveal Hand Control," "

[30] S. Tanzarella, S. Muceli, M. Santello, and D. Farina, "Synergistic Organization of Neural Inputs from Spinal Motor Neurons to Extrinsic and Intrinsic Hand Muscles," *The Journal of Neuroscience*, vol. 41, no. 32, pp. 6878–6891, Aug. 2021.

[31] M. Oßwald, A. L. Cakici, D. S. d. Oliveira, D. I. Braun, and A. D. Vecchio, "Mechanical Hand Synergies during Dynamic Hand Movements are Mostly Controlled in a Non-Synergistic Way by Spinal Motor Neurons," *bioRxiv*, p. 2023.07.25.550369, Jul. 2023.

[32] C. Igual, L. A. Pardo, J. Hahne, and J. M. Igual, "Myoelectric Control for Upper Limb Prostheses," *Electronics*, vol. 8, no. 11, p. 1244, Oct. 2019.

Does gait assistance modulate reflex excitability in those with spasticity? A preliminary study

Ricardo Siu
Physical Medicine and Rehabilitation
Case Western Reserve University
Cleveland, United States
ricardo.siu@case.edu

Dana Lorenz
Physical Medicine and Rehabilitation
Case Western Reserve University
Cleveland, United States
dxl954@case.edu

Jake Stahl
Biomedical Engineering
Case Western Reserve University
Cleveland, United States
jas703@case.edu

Mark Waschak
Metrohealth Center for Rehabilitation Research
Metrohealth Hospital
Cleveland, United States
mwaschak75@gmail.com

Donald Johnson
Metrohealth Center for Rehabilitation Research
Metrohealth Hospital
Cleveland, United States
donclar@yahoo.com

Juliet Zakel
Metrohealth Center for Rehabilitation Research
Metrohealth Hospital
Cleveland, United States
jzakel@metrohealth.org

Aiko Thompson
Health Sciences and Research
Medical University of South Carolina
Charleston, United States
thompsai@musc.edu

David Cunningham
Physical Medicine and Rehabilitation
Case Western Reserve University
Cleveland, United States
dxc536@case.edu

James Sulzer
Physical Medicine and Rehabilitation
Case Western Reserve University
Cleveland, United States
jss280@case.edu

***Abstract*— Stiff-Knee gait (SKG) is a common post-stroke impairment, marked by insufficient knee flexion during the swing phase, which reduces toe clearance, increases fall risk, and requires compensatory movements that can have adverse biomechanical effects. To address muscle weakness and paresis in SKG, assistive technologies, such as functional electrical stimulation (FES) and robotic exoskeletons, have been introduced. However, robotic assistance may inadvertently increase spinal reflex excitability by activating muscle stretch receptors, potentially worsening SKG. Previous studies suggest that SKG may stem from quadriceps hyperreflexia, particularly in the rectus femoris (RF) muscle. As such, assistive interventions could exacerbate, rather than alleviate, this condition via artificial activation of stretch receptors. In this study, we examined the impact of two FES modalities, plantarflexor and knee flexor assistance, on RF reflex excitability at rest and during gait in six post-stroke individuals with SKG. Results showed that, at rest, plantarflexor FES facilitated the RF reflex excitability, while knee flexor FES led to a slight inhibition. During gait, we observed that some individuals exhibited changes in reflex excitability during FES, but this effect was not as consistent as during rest. These preliminary results suggest that assistive technology such as FES modulates reflex excitability dependent on context.**

Keywords—H-reflex, stroke, gait, functional electrical stimulation, reflex excitability, exoskeleton

I. INTRODUCTION

Approximately 80% of stroke survivors experience gait impairments (Duncan, 2005), with 25–75% of these individuals developing Stiff-Knee gait (SKG)[1], [2]. Characterized by reduced peak knee flexion during swing phase, SKG limits foot clearance, raising fall risk[3] and leading to asymmetric gait patterns that impact joint loading and energy efficiency [4]. These consequences often translate to more sedentary lifestyles, reduced community engagement, social isolation, depression, and heightened fear of falls among stroke survivors.

Mechanical assistance devices, such as exoskeletons, and functional electrical stimulation (FES) can potentially compensate for weakness, offering insights into SKG mechanisms. Our prior research applied a lightweight exoskeleton to assist knee flexion during pre-swing in individuals with chronic SKG[5]. Contrary to our expectations, this assistance increased quadriceps reflex excitability, potentially due to elevated RF fiber stretch velocity and subsequent Ia afferent activation[6]. Notably, RF hyperreflexia, measured as evoked H-reflex potentials [7], [8], correlated strongly with reduced peak knee flexion angle ($R = -0.92$)[9]. This finding aligns with prior hypotheses linking quadriceps hyperreflexia to SKG [10], [11], supported by studies demonstrating reduced quadriceps reflex excitability following fatigue [12], [13].

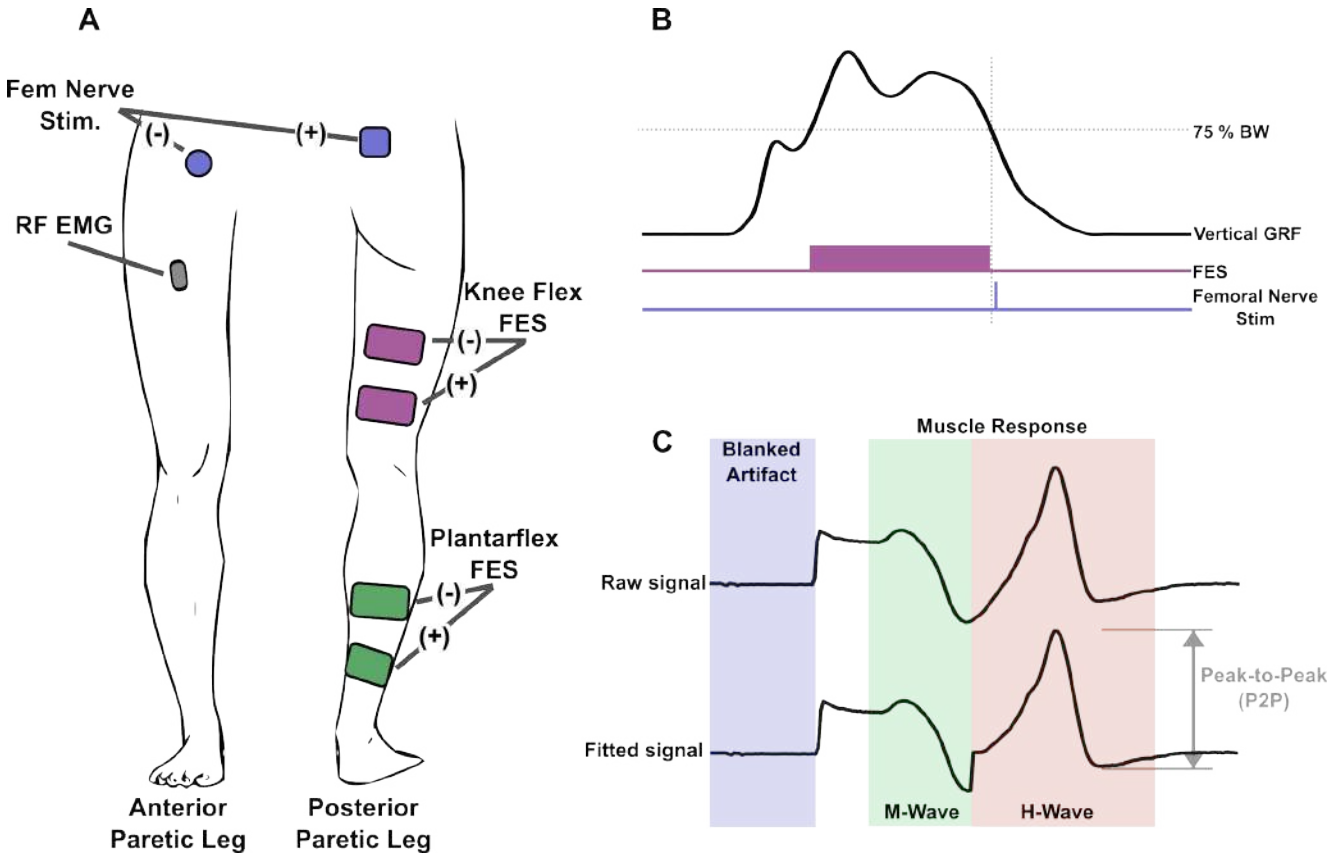


Fig. 1. Experimental setup for assessing spinal reflexes during FES-assisted gait in post-stroke survivors. (A) FES electrodes were placed on the posterior aspect of the paretic limb to evoke functional contractions of the plantarflexors and knee flexors. An EMG electrode positioned on the RF muscle recorded the H-reflex, elicited by transcutaneous stimulation of the femoral nerve. (B) FES activation and H-reflex probing pulses were synchronized with gait phases using ground reaction force data collected from an instrumented treadmill. The probing pulse was delivered during the pre-swing phase, corresponding to 25% body weight unloading. (C) EMG responses were processed to isolate the H-wave by subtracting residual depolarization from the overlapping M-wave using a fitted exponential decay function. The peak-to-peak amplitude of the processed H-wave was used as a measure of reflex excitability.

While interventions like FES have shown promise, they can have complex effects on the spinal reflex system, particularly in SKG. For example, Tenniglo et al. (2018)[14] applied FES to the hamstrings of post-stroke individuals with SKG, achieving modest yet significant improvements in knee flexion range following five weeks of training, although responsiveness varied. Unlike exoskeletons, which primarily stretch antagonist muscle spindles, FES induces excitation of Ia afferents, impacting both homonymous and heteronymous pathways [15] and creating complex excitatory and inhibitory effects across the lower limbs[16], [17]. Beyond Ia pathways, FES can stimulate Golgi tendon organ (Ib) afferents and Renshaw cells, introducing further inhibitory influences across quadriceps and soleus muscles [18], [19]. Task context, muscle state, and other afferent inputs also modulate reflex excitability, with stroke leading to distinctive alterations in both heteronymous and monosynaptic pathways [20], [21]. Given these intricate spinal adaptations, understanding FES and exoskeleton interactions with spinal reflexes is essential for optimizing therapeutic efficacy.

To address this gap, we investigated RF H-reflex behavior in response to FES-assisted gait in post-stroke SKG survivors, applying plantarflexor or knee flexor FES during gait pre-swing and at rest. By probing these reflex circuits, we aim to refine FES protocols that leverage heteronymous pathways to enhance locomotor outcomes and provide mechanistic insights for improving FES-based therapies and optimized integration with hybrid exoskeleton systems.

II. Methods

Six post-stroke survivors with chronic hemiparetic locomotor impairments presenting with SKG were recruited for this study. A licensed physical therapist confirmed the presence of SKG in all participants. Written informed consent was obtained following procedures approved by the local Institutional Review Board. The presence of the RF H-reflex was verified prior to beginning FES testing. Participants' level of quadriceps spasticity was clinically assessed using the Modified Ashworth Scale (MAS). Additionally, two functional measures were used: the peak knee flexion angle difference between the paretic and nonparetic limb [22], where a larger difference indicates more pronounced SKG, and the quadriceps reflex threshold angle (QRTA) from the quadriceps pendulum test, where a lower first inflection angle reflects greater quadriceps spasticity [23]. Table 1 shows

Table 1. Participant information showing sex, time since stroke incident, Modified Ashworth Scale (MAS) score for the quadricep muscles, treadmill speed used during gait assessments, the difference between peak knee angles between the paretic and nonparetic side, the quadriceps reflex threshold angle during a pendulum test, and the average percent change (%Δ) from control trials for each tested condition. The MAS, peak knee flexion angle difference, and quadriceps reflex threshold angle can serve as indicators of quadriceps hyperreflexia severity.

Participant	Sex	Time post-stroke (yrs)	Treadmill Speed (m/s)	MAS Score (Knee Extensors)	Peak Knee Flexion Angle Difference (Δ°)	Quadriceps Reflex Threshold Angle (°)	Rest PF FES (%Δ)	Rest KF FES (%Δ)	Gait PF FES (%Δ)	Gait KF FES (%Δ)
P1	M	0.5	0.6	2	27.33 ± 3.74	26.6 ± 12.3	-3.8	-21.2	+29.5	+44.2
P2	M	4.5	0.6	1	3.10 ± 1.50	57.3 ± 14	+3.4	-7.9	+2.1	-21.9
P3	M	1.7	0.24	0	18.36 ± 4.74	52.9 ± 0.5	-43.6	-63.8	+34	-44.6
P4	M	12.1	0.64	0	10.29 ± 3.09	56.4 ± 0.4	+50.8	-31.3	-32.4	-40.6
P5	M	4.9	0.42	0	16.07 ± 1.70	48.6 ± 2.4	+85.1	+49.2	+21.2	+22.7
P6	M	2.3	0.28	2	15 ± 2.44	45.3 ± 12.6	+0.3	-14.2	+47.2	+11.2

participant demographics as well as a summary of their results.

A recording electrode was positioned on the RF muscle to capture responses from femoral nerve stimulation. An EMG amplifier (CED 1408, Cambridge Electronics Design Ltd, Cambridge, UK) with blanking capabilities was used to eliminate stimulation artifacts and prevent amplifier saturation. Ground reaction force (GRF) data were collected via an instrumented treadmill (FIT 5 Instrumented Treadmill, Bertec Inc, Columbus, OH). EMG and GRF data were sampled at 5 kHz using custom MATLAB software, and MATLAB Simulink Desktop Real-Time was utilized to achieve real-time stimulation during gait.

For femoral nerve stimulation, a cathode electrode (1", Axelgaard Valutrode, Axelgaard Manufacturing Co Ltd, Fallbrook, CA) was placed on the skin above the femoral nerve, while an anode electrode (2"x2", Axelgaard Valutrode) was positioned over the ipsilateral sacrum (Figure 1A). For plantarflexor FES, cathode electrodes (2x3.5", Axelgaard Valutrode) were placed on the distal gastrocnemius, with an anode positioned above the malleolus. Knee flexor FES involved placing cathode electrodes on the biceps femoris muscle mid-thigh, with the distal cathode approximately 2" above the knee crease. Femoral nerve stimulation pulses were biphasic (cathodic first) square pulses with 500 μs phase duration and a 50 μs interphase interval. FES stimulation followed similar pulse parameters, adjusted only in amplitude, and was delivered at 40 Hz. Both femoral nerve stimulation and FES were administered via an external stimulator (DS8R, Digitimer Ltd, Welwyn Garden City, UK) connected to a switchbox for multichannel stimulation with precise temporal control.

The femoral nerve stimulation amplitude was determined by generating a recruitment curve and selecting a level that evoked 50% of the maximum H-reflex along the ascending phase. For FES, amplitude was set at twice the motor threshold to ensure functional muscle contraction; if this level was uncomfortable, it was reduced to a level the participant found tolerable.

At rest, six responses were collected for each condition: control (no FES), plantarflexor FES, and knee flexor FES. During gait trials, where variability was higher, ten responses were collected per condition. The femoral nerve stimulation interval was set to at least 10 seconds to reduce potential homosynaptic depression effects [24]. For at rest FES trials, femoral nerve stimulation was delivered 1.5 seconds after initiating FES, at which point the FES was deactivated. During walking assessments, femoral nerve stimulation was triggered based on ground reaction forces measured by the instrumented treadmill described above. Participants were asked to walk for up to 3 minutes at a time with the option of a seated rest between trials. Stimulation occurred during the pre-swing phase, defined as the downward phase of the vertical GRF reaching 75% of the participants body weight (BW). FES was active throughout stance for both modalities, where stance was defined as vertical GRF exceeding 75% of the standing vertical GRF (Figure 1B).

The primary outcome measure was the percent change in the peak-to-peak RF H-reflex response. The peak-to-peak value was determined as the difference between the maximum and minimum amplitudes within a visually selected window, starting approximately 20 ms after stimulation onset and lasting approximately 30 ms. Given the RF muscle's close proximity to the spinal cord, the M-wave and H-wave responses occasionally overlapped. To address this, an exponential decay function was fitted from the end of the M-wave to the end of the H-wave (Figure 1C). This fitted decay curve was subtracted from the original signal, isolating the H-wave and removing any M-wave artifacts [9]. An arbitrary threshold of 10% was used to qualitatively determine if modulation was present within each condition for each participant.

Statistical analysis was not conducted due to the small sample size and significant inter-individual variability observed among participants. With only six participants, the study lacked the statistical power needed to detect meaningful differences between conditions. Additionally, the high variability in responses, both within and across participants, highlighted the heterogeneity of neurological impairments and their effects on reflex modulation. As a result, descriptive

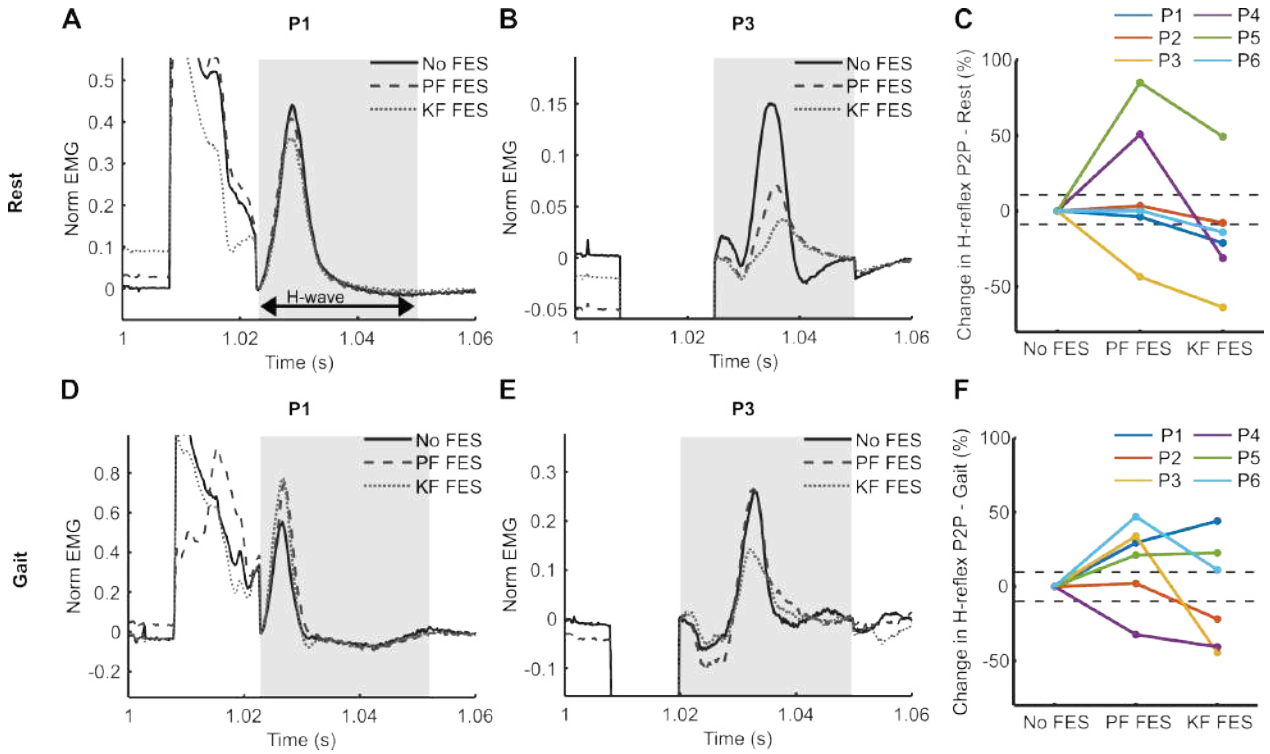


Fig. 2. Modulation of RF H-reflex by heteronymous muscle group stimulation at rest and during gait in post-stroke survivors with stiff-knee gait. (A, B) Reflex responses from two participants (P1 and P3) at rest without FES (solid), with PF FES (dashed), and with KF FES (dotted). Shaded region depicts the H-wave analysis window. P1 exhibited minimal changes across conditions, while P3 showed substantial inhibition with both PF FES and KF FES, with greater inhibition during KF FES. (C) Percent change in peak-to-peak H-reflex amplitude relative to No FES for all participants at rest highlights inter-individual variability. Dashed line at 10% represents modulation threshold. (D, E) Reflex responses during gait for P1 and P3 under the same conditions. P1 showed facilitation with both FES modalities, whereas P3 exhibited significant inhibition with KF FES and minimal facilitation with PF FES. (F) Percent change in H-reflex amplitude during gait demonstrates considerable variability in responses across participants.

analyses were prioritized to qualitatively examine trends and patterns, providing preliminary insights to guide future studies with larger, more homogeneous samples. Nonetheless, a preliminary Spearman's rank correlation analysis was performed to explore potential relationships between participants' level of spasticity, measured by the reflex threshold angle, and the percent change in RF H-reflex amplitude across tested conditions.

III. Results

At rest, the effects of FES on the RF H-reflex varied across participants, as shown in representative responses in Figures 2A and 2B. In Participant 1 (P1), PF FES had no discernible effect on the H-reflex (-4%), while KF FES led to slight inhibition (-21%). In contrast, Participant 3 (P3) demonstrated substantial modulation of the H-reflex amplitude by both FES modalities, with KF FES producing greater inhibition (-63%) than PF FES (-43%). Figure 2C summarizes the percent change in peak-to-peak H-reflex amplitude across all participants during rest. PF FES facilitated the H-reflex in two of six participants (P4, 51%; P5, 85%), caused minimal changes (<10%) in three (P1, -4%; P2, 4%, P6, 0.3%), and inhibited the response in one (P3, 44%). KF FES, on the other hand, consistently either inhibited or resulted in minimal changes in all (P1, -21%; P2, -8%; P3, -64%; P4, -31%, P6, -14%) but 1 participant (P5, 49%). These findings highlight notable inter-individual variability, as indicated by the wide distribution of data points across conditions, but show a trend towards inhibition during KF FES.

During gait, the effects of FES on RF H-reflex modulation were even more variable between participants. Figures 2D and 2E depict responses from P1 and P3, respectively. In P1, both PF FES and KF FES increased H-reflex amplitude compared to the no-FES condition, suggesting an overall facilitatory effect of FES during walking. Conversely, in P3, PF FES produced slight facilitation, whereas KF FES caused approximately 45% inhibition relative to the no-FES baseline. The aggregated percent changes in H-reflex amplitude across participants during gait are shown in Figure 2F. Three participants exhibited facilitation with both PF FES (P1, 30%; P5, 21%, P6, 47%) and KF FES (P1, 44%; P5, 23%, P6, 11%), one showed facilitation with PF FES (P3, 34%) and inhibition with KF FES (P3, -45%), one demonstrated inhibition with both PF FES (P4, 32%) and KF FES (P4, 41%), and one showed less than 10% change with PF FES (2%) and inhibition with KF FES (P2, 22%). Similar to the rest condition, large inter-individual variability was evident. Overall, no consistent pattern of facilitation or inhibition

emerged across the cohort, underscoring the participant-specific nature of FES effects during gait.

Preliminary correlation analysis using Spearman's rank method revealed varying relationships between the QRTA and the percent change in RF H-reflex amplitude across different conditions. During rest, a weak positive correlation was observed with PF FES (r_s = 0.31), suggesting a limited association between spasticity and reflex facilitation. In contrast, KF FES at rest showed no meaningful relationship (r_s = -0.03). During gait, PF FES exhibited a moderate negative correlation (r_s = -0.66), indicating that higher spasticity levels may correspond to greater reflex inhibition. Similarly, KF FES during gait showed a strong negative correlation (r_s = -0.71), suggesting a more pronounced inhibitory effect with increased spasticity. These findings suggest that spasticity, as measured by reflex threshold angle, may differentially influence H-reflex modulation depending on the condition and stimulation modality.

IV. Discussion

This preliminary study investigated the effects of functional electrical stimulation (FES) on the modulation of the rectus femoris (RF) H-reflex at rest and during gait in post-stroke individuals with Stiff-Knee gait (SKG). These preliminary findings revealed substantial inter-individual variability in H-reflex responses, both at rest and during gait, suggesting that FES effects are highly participant-specific and may depend on individual characteristics, including severity of spasticity and sensorimotor capabilities.

At rest, PF FES predominantly facilitated the RF H-reflex in a subset of participants, likely due to heteronymous facilitation, a spinal mechanism where anatomically distinct muscles activate synergistically to enhance motor functionality [15]. In contrast, KF FES exhibited predominantly inhibitory or negligible effects, potentially mediated by reciprocal inhibition, where antagonistic muscle activation reduces excitability in the quadriceps motor pool [25]. During gait, these patterns became less consistent, with some participants exhibiting facilitation and others showing inhibition or variable responses across conditions. This variability underscores the dynamic and task-dependent nature of spinal reflex modulation during locomotion, driven by interactions between central pattern generators, descending motor control, and sensory feedback [26], [27]. These findings highlight the complexity of generalizing FES effects across a heterogeneous population of post-stroke individuals with SKG, as gait-specific mechanisms likely override reflex responses elicited during rest.

The correlations between reflex threshold angle and H-reflex percent change further emphasize the influence of spasticity on reflex modulation. While PF FES at rest showed a weak positive correlation, suggesting a limited role of spasticity under static conditions, the strong negative correlations observed during gait, particularly with KF FES, highlight the impact of spasticity in dynamic contexts. Spasticity-related reflex excitability may amplify during functional tasks like walking, reducing the efficacy of therapeutic interventions [9], [28]. These results underscore the importance of tailoring FES parameters to individual spasticity profiles, as well as the need to develop approaches that adaptively account for spasticity-driven reflex changes.

Robotic exoskeletal assistance presents a promising strategy to address these challenges. By offering precise control over joint movement and muscle activation, exoskeletons equipped with advanced sensors and real-time feedback systems could coordinate adaptively with FES to enhance reflex modulation while mitigating excessive facilitation or inhibition. Future studies should investigate whether the facilitatory and inhibitory mechanisms observed here interact with those seen during robotic-assisted gait in individuals with SKG [5], and explore their potential to improve gait biomechanics through personalized, context-specific interventions.

While these findings provide valuable insights, several limitations must be addressed in future studies. The small sample size in this preliminary trial and lack of an age-matched control group limits generalizability and introduces potential bias, particularly for such a heterogeneous population. A larger randomized clinical study would allow for a more comprehensive evaluation of FES effects and account for inter-individual variability. Additionally, future research should explore key factors not addressed in this study, including the relationship of RF H-reflex modulation with other measures of spasticity, the dose-response relationship of FES on reflex modulation, the long-term rehabilitative effects of repeated FES sessions, and the impact of FES on reflex modulation during walking on non-level surfaces, better reflecting real-world mobility challenges.

In conclusion, this study underscores the highly participant-specific nature of FES effects on RF H-reflex modulation, reflecting the complexity of spinal reflex dynamics in post-stroke individuals with SKG. These preliminary findings highlight the need for tailored stimulation protocols that account for individual neuromuscular profiles and the interplay between reflex mechanisms and functional tasks. Future research should prioritize the refinement of FES parameters, the integration of multimodal assistive technologies such as robotic exoskeletons, and the identification of reliable biomarkers to predict FES responsiveness. These efforts will be essential for advancing personalized therapeutic strategies aimed at optimizing locomotor outcomes and enhancing quality of life in individuals with SKG.

Acknowledgment

The authors would like to thank Shreya Ramani for assistance during data collection, Sebastian Correa for insightful feedback during the conceptualization process, and Kristine Hansen for participant selection, recruitment, and coordination.

References

[1] A. Merlo and I. Campanini, “Impact of instrumental analysis of stiff knee gait on treatment appropriateness and associated costs in stroke

patients," *Gait & Posture*, vol. 72, pp. 195–201, Jul. 2019, doi: 10.1016/j.gaitpost.2019.06.009.

[2] F. Chantraine, C. Schreiber, J. A. C. Pereira, J. Kaps, and F. Dierick, "Classification of Stiff-Knee Gait Kinematic Severity after Stroke Using Retrospective k-Means Clustering Algorithm," *Journal of Clinical Medicine*, vol. 11, no. 21, Art. no. 21, Jan. 2022, doi: 10.3390/jcm11216270.

[3] G. G. Stoquart, C. Detrembleur, S. Palumbo, T. Deltombe, and T. M. Lejeune, "Effect of Botulinum Toxin Injection in the Rectus Femoris on Stiff-Knee Gait in People With Stroke: A Prospective Observational Study," *Archives of Physical Medicine and Rehabilitation*, vol. 89, no. 1, pp. 56–61, Jan. 2008, doi: 10.1016/j.apmr.2007.08.131.

[4] M. D. Lewek, C. E. Bradley, C. J. Wutzke, and S. M. Zinder, "The Relationship Between Spatiotemporal Gait Asymmetry and Balance in Individuals With Chronic Stroke," *Journal of Applied Biomechanics*, vol. 30, no. 1, pp. 31–36, Feb. 2014, doi: 10.1123/jab.2012-0208.

[5] J. S. Sulzer, R. A. Roiz, M. A. Peshkin, and J. L. Patton, "A Highly Backdrivable, Lightweight Knee Actuator for Investigating Gait in Stroke," *IEEE Trans Robot*, vol. 25, no. 3, pp. 539–548, Jun. 2009, doi: 10.1109/TRO.2009.2019788.

[6] T. Akbas, R. R. Neptune, and J. Sulzer, "Neuromusculoskeletal Simulation Reveals Abnormal Rectus Femoris-Gluteus Medius Coupling in Post-stroke Gait," *Front. Neurol.*, vol. 10, p. 301, Apr. 2019, doi: 10.3389/fneur.2019.00301.

[7] R. W. Angel and W. W. Hofmann, "The H Reflex in Normal, Spastic, and Rigid Subjects: Studies," *Archives of Neurology*, vol. 8, no. 6, pp. 591–596, Jun. 1963, doi: 10.1001/archneur.1963.00460060021002.

[8] M. Knikou, "The H-reflex as a probe: Pathways and pitfalls," *Journal of Neuroscience Methods*, vol. 171, no. 1, pp. 1–12, Jun. 2008, doi: 10.1016/j.jneumeth.2008.02.012.

[9] T. Akbas *et al.*, "Rectus femoris hyperreflexia contributes to Stiff-Knee gait after stroke," *J NeuroEngineering Rehabil*, vol. 17, no. 1, p. 117, Dec. 2020, doi: 10.1186/s12984-020-00724-z.

[10] S. J. Piazza and S. L. Delp, "The influence of muscles on knee flexion during the swing phase of gait," *Journal of Biomechanics*, vol. 29, no. 6, pp. 723–733, Jun. 1996, doi: 10.1016/0021-9290(95)00144-1.

[11] D. C. Kerrigan, R. S. Roth, and P. O. Riley, "The modelling of adult spastic paretic stiff-legged gait swing period based on actual kinematic data," *Gait & Posture*, vol. 7, no. 2, pp. 117–124, Mar. 1998, doi: 10.1016/S0966-6362(97)00040-4.

[12] J. Boudarham *et al.*, "Relationship between neuromuscular fatigue and spasticity in chronic stroke patients: a pilot study," *J Electromyogr Kinesiol*, vol. 24, no. 2, pp. 292–299, Apr. 2014, doi: 10.1016/j.jelekin.2013.11.006.

[13] K. Fujita *et al.*, "Pedaling improves gait ability of hemiparetic patients with stiff-knee gait: fall prevention during gait," *Journal of Stroke and Cerebrovascular Diseases*, vol. 29, no. 9, p. 105035, Sep. 2020, doi: 10.1016/j.jstrokecerebrovasdis.2020.105035.

[14] M. Tenniglo, J. Buurke, E. Prinsen, A. Kottink, A. Nene, and J. Rietman, "Influence of functional electrical stimulation of the hamstrings on knee kinematics in stroke survivors walking with stiff knee gait," *J Rehabil Med*, vol. 50, no. 8, pp. 719–724, 2018, doi: 10.2340/16501977-2367.

[15] S. Meunier, E. Pierrot-Deseilligny, and M. Simonetta, "Pattern of monosynaptic heteronymous Ia connections in the human lower limb," *Exp Brain Res*, vol. 96, no. 3, pp. 534–544, 1993, doi: 10.1007/BF00234121.

[16] H. Hultborn, S. Meunier, E. Pierrot-Deseilligny, and M. Shindo, "Changes in presynaptic inhibition of Ia fibres at the onset of voluntary contraction in man," *J Physiol*, vol. 389, pp. 757–772, Aug. 1987, doi: 10.1113/jphysiol.1987.sp016681.

[17] C. K. Mummidisetty, A. C. Smith, and M. Knikou, "Modulation of reciprocal and presynaptic inhibition during robotic-assisted stepping in humans," *Clin Neurophysiol*, vol. 124, no. 3, pp. 557–564, Mar. 2013, doi: 10.1016/j.clinph.2012.09.007.

[18] C. Cuadra, A. De Boef, S. Luong, S. L. Wolf, T. R. Nichols, and M. A. Lyle, "Reduced inhibition from quadriceps onto soleus after acute quadriceps fatigue suggests Golgi tendon organ contribution to heteronymous inhibition," *Eur J Neurosci*, vol. 60, no. 3, pp. 4317–4331, Aug. 2024, doi: 10.1111/ejn.16438.

[19] M. A. Lyle, C. Cuadra, and S. L. Wolf, "Quadriceps muscle stimulation evokes heteronymous inhibition onto soleus with limited Ia activation compared to femoral nerve stimulation," *Exp Brain Res*, vol. 240, no. 9, pp. 2375–2388, Sep. 2022, doi: 10.1007/s00221-022-06422-7.

[20] V. Dietz, "Proprioception and locomotor disorders," *Nat Rev Neurosci*, vol. 3, no. 10, pp. 781–790, Oct. 2002, doi: 10.1038/nrn939.

[21] J. B. Nielsen and T. Sinkjaer, "Afferent feedback in the control of human gait," *Journal of Electromyography and Kinesiology*, vol. 12, no. 3, pp. 213–217, Jun. 2002, doi: 10.1016/S1050-6411(02)00023-8.

[22] J. Lee, R. K. Lee, B. A. Seamon, S. A. Kautz, R. R. Neptune, and J. Sulzer, "Between-limb difference in peak knee flexion angle can identify persons post-stroke with Stiff-Knee gait," *Clinical Biomechanics*, vol. 120, p. 106351, Dec. 2024, doi: 10.1016/j.clinbiomech.2024.106351.

[23] Y.-W. Kim, "Clinical Usefulness of the Pendulum Test Using a NK Table to Measure the Spasticity of Patients with Brain Lesions," *Journal of Physical Therapy Science*, vol. 25, no. 10, pp. 1279–1283, 2013, doi: 10.1589/jpts.25.1279.

[24] H. Hultborn, M. Illert, J. Nielsen, A. Paul, M. Ballegaard, and H. Wiese, "On the mechanism of the post-activation depression of the H-reflex in human subjects," *Exp Brain Res*, vol. 108, no. 3, pp. 450–462, Mar. 1996, doi: 10.1007/BF00227268.

[25] J. Nielsen and Y. Kagamihara, "The regulation of presynaptic inhibition during co-contraction of antagonistic muscles in man," *J Physiol*, vol. 464, pp. 575–593, May 1993, doi: 10.1113/jphysiol.1993.sp019652.

[26] C. Capaday and R. B. Stein, "Amplitude modulation of the soleus H-reflex in the human during walking and standing," *J. Neurosci.*, vol. 6, no. 5, pp. 1308–1313, May 1986, doi: 10.1523/JNEUROSCI.06-05-01308.1986.

[27] E. B. Simonsen and P. Dyhre-Poulsen, "Amplitude of the human soleus H reflex during walking and running," *The Journal of Physiology*, vol. 515, no. Pt 3, p. 929, Mar. 1999, doi: 10.1111/j.1469-7793.1999.929ab.x.

[28] M. Faist, M. Ertel, W. Berger, and V. Dietz, "Impaired modulation of quadriceps tendon jerk reflex during spastic gait: differences between spinal and cerebral lesions," *Brain*, vol. 122, no. 3, pp. 567–579, Mar. 1999, doi: 10.1093/brain/122.3.567.

Enhancing Human Walking Economy Through a Biomimetic Cable-Driven Ankle Exoskeleton*

Xianyu Zhang, Kotaro Hinuma, Zhengguang Wang, Zhenzhi Ying, Naohiko Sugita, Shihao Li

Abstract— **Enhancing the walking economy is a primary goal in the application of exoskeletons for gait assistance. However, traditional exoskeletons often face challenges due to rigid designs and the additional distal mass they introduce, limiting their effectiveness. In this study, inspired by the muscle-tendon complex of the human calf, we present a cable-driven ankle exoskeleton designed to provide targeted assistance during plantarflexion movements at the ankle joint. The proposed exoskeleton integrates a compact, lightweight actuation unit with a flexible fabric shank sleeve, ensuring efficient torque transmission from the motor to the ankle joint. A feedback-based cascaded repetitive control system, combined with a multi-sensor fusion communication framework, was developed to achieve precise force control. The system's actuation performance was evaluated through benchtop experiments, demonstrating a bandwidth of approximately 13.5 Hz and a force tracking error of 5% under position disturbances. Treadmill experiments further validated the effectiveness of the exoskeleton, showing a 7.53% improvement in walking economy compared to no-assistance conditions. These findings highlight the potential of the proposed design to advance the development of cable-driven exoskeletons for improved gait assistance.**

I. Introduction

Through millions of years of evolution, humans have refined bipedal locomotion, achieving remarkable efficiency in walking. This evolution has optimized energy-efficient gaits by fine-tuning factors such as cadence and stride length, supported by biomechanical strategies like arm swinging [1]. Despite these advancements, walking remains a metabolically demanding activity. For a typical adult, walking consumes approximately 2.5 J/kg/m at a speed of 4.5 km/h, with energy expenditure increasing at higher speeds [2]. Given that daily life involves thousands of steps, walking becomes one of the most energy-intensive activities. While this metabolic cost is manageable for healthy individuals, it poses challenges for those with mobility impairments or in contexts requiring sustained walking, where reducing energy expenditure is critical for improving performance and quality of life [3]. As a result, recent research has increasingly focused on developing assistive technologies to assist human walking and enhance walking efficiency.

*Research supported by the Japan Society for the Promotion of Science (JP24KJ0940).

S. Li is with the Department of Mechanical Engineering, The University of Tokyo, Tokyo 113-8656, Japan (corresponding author, phone: +81-3-5841-6336; e-mail: lsh@mfg.t.u-tokyo.ac.jp).

X. Zhang, K. Hinuma, Z. Wang, Z. Ying, and N. Sugita are with the same department (e-mail: zhangxy@mfg.t.u-tokyo.ac.jp, Hinuma-kotaro4649@g.ecc.u-tokyo.ac.jp, zhengguangwang@g.ecc.u-tokyo.ac.jp, ying@mfg.t.u-tokyo.ac.jp, sugi@mfg.t.u-tokyo.ac.jp).

A promising approach for enhancing walking efficiency involves the use of lower limb exoskeletons (LLEs), which are wearable devices designed to deliver targeted assistance to specific joints [4]. Over the past decade, the diversity of LLEs has grown substantially. Among these, passive LLEs, which emulate the function of biological muscle tendons through the use of springs and clutches for energy storage and release, have gained attention for their simplicity and cost-effectiveness [5]. Despite these advantages, passive LLEs are limited by their static assistance, which is dictated by the inherent properties of their elastic components and lacks dynamical adaptability. To overcome these limitations, active LLEs equipped with sensing and control systems have been developed to regulate the provided assistance [6]. Active LLEs typically employ electric motors to drive joint movements., with notable examples including the Berkeley Lower Extremity Exoskeleton [7] and the Hybrid Assistive Limb exoskeleton [8]. Traditional active LLEs often rely on rigid frames to transmit actuator forces to the target joints. This design not only restricts the wearer's natural movements but also introduces challenges related to misalignment. Additionally, the non-ignorable distal mass of these systems diminishes some of the benefits provided by the exoskeleton, ultimately hindering improvements in the gait economy.

In recent years, there has been an increasing trend toward designing soft LLEs that merge the advantages of being lightweight and structurally simple with the capability for adjustable assistance [9]. These soft LLEs primarily adopt cable-driven mechanisms, specifically designed for joints including the hip [10], knee [11], and ankle [12][13]. In these configurations, heavy components like actuators and batteries are strategically placed in more proximal body regions to minimize the impact of distal mass. Assistance is transmitted through cables connected to anchors embedded in functional textiles attached to the limbs. By adjusting the distance between adjacent anchors, the mechanism mimics muscle contraction and delivers support. However, challenges persist with cable-driven LLEs, particularly in the magnitude and precision of the torque delivered. This issue arises mainly from the inherent elasticity of the cables and friction losses within the transmission system [14]. Furthermore, despite cable-driven LLEs holding promise, comprehensive evidence demonstrating their effectiveness in enhancing the walking economy remains limited.

During walking, the ankle and hip joint are the primary contributors to mechanical work, ranking first and second, respectively [15]. In the push-off phase, the ankle joint generates the largest forward propulsion through plantar flexion driven by calf muscle contraction [16]. Inspired by this, we propose a cable-driven exoskeleton aligned with the posterior calf's muscle-tendon units to reduce muscle efforts

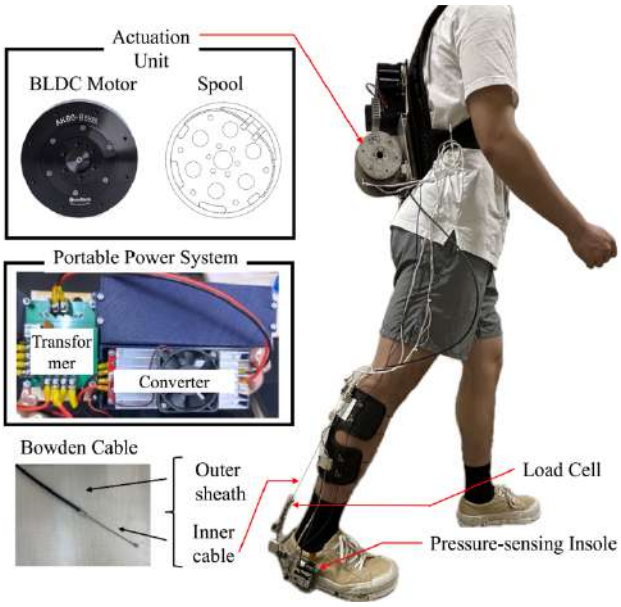


Figure 1. The proposed cable-driven ankle exoskeleton and its components.

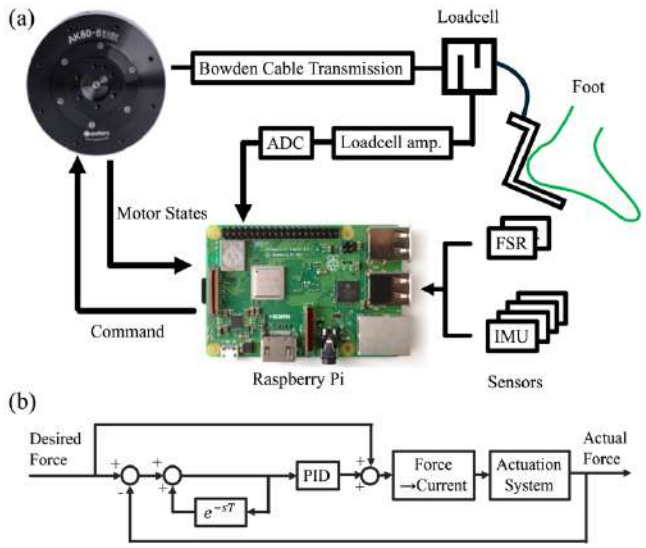


Figure 2. Communication and control framework of the proposed device. (a) Information flow, (b) Feedback-based cascaded repetitive control.

and enhance walking economy. The contributions of this study are as follows. A compact, lightweight actuation unit was developed, reducing the system weight to 4.2 kg while delivering high pulling forces and effectively managing cable tension and slack through a self-aligning spool design. A feedback-based cascaded repetitive control system was implemented, achieving precise tension control (± 5%) without additional mechanisms. The exoskeleton's ability to improve walking economy was validated through treadmill experiments, demonstrating significant performance gains (7.53%). The remainder of this paper is organized as follows. Section II details the design of the exoskeleton. Section III describes the treadmill experiment setup, results, and analysis. Section IV discusses the advantages and limitations, and Section V concludes this study.

II. Exoskeleton Design and Characterization

This section presents a detailed description of the structure design of the proposed cable-driven ankle exoskeleton, along with its integrated sensing and control system. Additionally, benchtop experiments were conducted to evaluate and characterize the performance of the actuator unit.

A. Mechanical Design

The proposed cable-driven exoskeleton mimics the contraction of the soleus muscle-Achilles tendon complex by aiding during the ankle's plantarflexion movement in the propulsion phase of walking (50–65% of the gait cycle). During this phase, the motor activates, winding the inner cable around the spool to emulate the contraction of the soleus muscle. This reduces the workload on the user's calf muscles and improves walking economy. Designed for lightweight portability and sufficient force output, the system comprises a compact actuation unit and a fabric-based wearable interface, as illustrated in Fig. 1.

The actuation unit generates mechanical power through a brushless DC motor equipped with an 8:1 planetary gearhead (AK80-8, CubeMars, China), featuring a weight of 0.57 kg, a rated torque of 10 Nm, a peak torque of 25 Nm, and a rated speed of 243 rpm. To minimize distal mass, the heavier components, including the actuation unit, are strategically positioned on the user's back. To transmit the actuator's torque to the ankle joint, a Bowden cable (XA507100, Nippon Flex Controls, Japan) is employed as the force transmission medium. It comprises an inner steel cable (diameter: 1.2 mm, load capacity: 390 N) and an outer resin sheath (external diameter: 4.2 mm, inner diameter: 2.3 mm). The output shaft of the gearhead is directly coupled to a custom-designed spool made of aluminum alloy, with an effective radius r of 40 mm and a weight of 0.16 kg. The spool is specifically designed for winding the inner cable and features smooth grooves and strategically placed anchor points to facilitate cable installation and prevent derailment. The distal end of the inner cable is anchored to a metal rod extending from the heel, with an effective length l of approximately 120 mm. The force applied to the ankle joint is related to the gearhead's output torque through the following equation:

$$F_{applied} = \frac{\eta \tau_{gear}}{r} \quad (1)$$

Here, η denotes the transmission efficiency, which accounts for losses such as friction within the Bowden cable. Its value was determined to be 0.8 based on experimental verification.

The fabric-based wearable interface includes a customized shank sleeve and a backpack. The shank sleeve is specifically designed to securely fix the distal end of the Bowden cable sheath to the user's calf, preventing sliding while ensuring comfort and ease of wear. Constructed from soft materials such as OK fabric and cow leather, it features a rubber inner layer to enhance friction with the skin, thereby improving stability. Sponge padding is added at key areas with thinner subcutaneous fat to reduce shear forces and distribute pressure evenly. The outer leather surface incorporates metal fixtures attached with stitching and bolts. Additionally, a lacing system (L7-1, Fitgo, China) enables quick donning and doffing with a dial rotation, allowing precise tension adjustment for an optimal fit. The final design weighs less than 0.1 kg per leg.

The backpack houses heavy components such as the actuation units, controller, and power supply system. Adapted from a commercially available motorcycle protective backplate, it includes extensive padding for cushioning and prolonged comfort. The backpack is securely mounted on the user's back using shoulder and waist straps for stability and ergonomic support. Weighting 4.04 kg in total, it comprises two actuation units (0.73 kg each), a lithium battery (1.65 kg), a Raspberry Pi-based control circuit (0.08 kg), and a harness system (0.85 kg), offering a lightweight and practical solution.

B. Sensing and Control System

An appropriate sensing and control system is essential for achieving improved human-robot interaction. As shown in Fig. 2(a), a Raspberry Pi is chosen as the upper-level controller, with the main loop operating at 100 Hz. A load cell (MCDW-50L, Toyo Sokki, Japan) is mounted on the posterior side of the heel to measure cable tension. The measured signal is then sent to the amplifier (LA-1024A-2-EXC5V-500Hz, Toyo Sokki, Japan) and converted into a digital signal via an A/D converter (MCP3208-CI/P, Microchip Technology, USA), which is subsequently received by the Raspberry Pi. Additionally, the built-in controller within the motor performs lower-level closed-loop control while also monitoring motor states such as angle and current. To enhance the perception of the wearer's motion state, two IMU sensors (LSM9DS0, STMicroelectronics, Switzerland) are placed on the shank sleeve and shoes. The global link angles are calculated using the Extended Kalman Filter algorithm [17]. A pressure sensing insole (RPPS-45, LEGACT Technology, China), positioned beneath the wearer's foot inside the shoes, is used to approximate the ground reaction force and segment the gait cycle based on the right heel strike event. Communication between the motor, sensors, and the Raspberry Pi is established through the CAN protocol. Considering portability, a 24V lithium-ion battery is chosen as the power supply module. It is coupled with both a boost and buck converter to provide output voltages of 48V, 24V, and 5V, which power the motor, amplifier, and sensors, respectively.

To achieve precise tension control, we designed a dual-layer cascaded closed-loop control system based on sensor feedback, as illustrated in Fig. 2(b). Given that the Bowden cable is designed to mimic the contraction of the muscle-tendon complex and apply a desired force profile throughout the gait cycle, the outer layer implements force control, while the inner layer employs current control. In the outer layer, the desired force, derived from our previous research [18], serves as the input. The error between this desired force and the actual tension measured by the load cell is processed by a proportional-integral-derivative (PID) controller. Then, a feedforward term of the desired force is incorporated before transmitting the command to the inner layer. To further enhance force tracking performance, a delay-based repetitive control (RC) mechanism is introduced, leveraging the cyclic nature of walking. In this delay term, T corresponds to the duration of the gait cycle, which is estimated from the preceding three consecutive gait cycles. The outer layer operates at a frequency of 100 Hz, generating the current command for the inner layer. The inner layer, running at 500 Hz, precisely adjusts the motor's actual current to meet the command requirements.

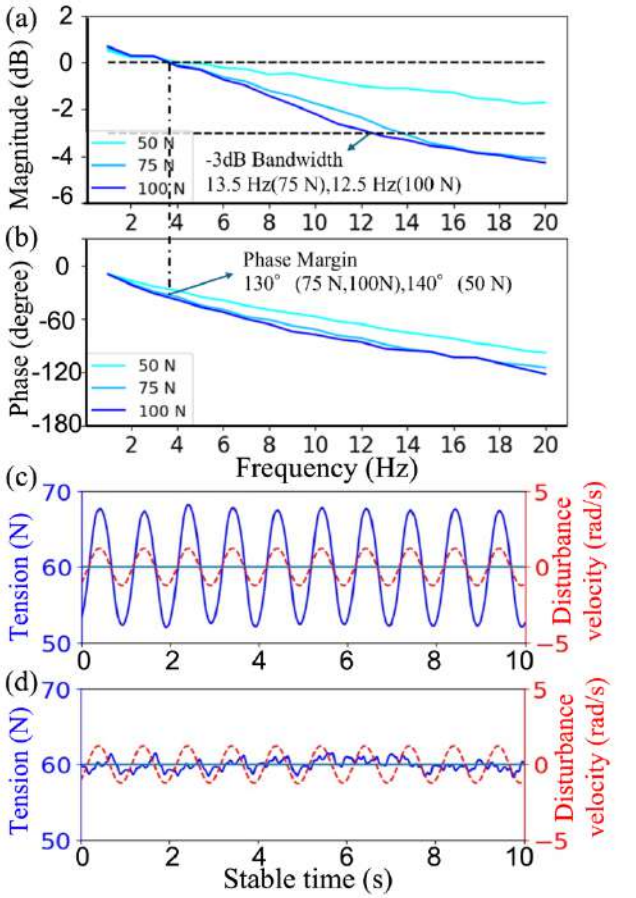


Figure 3. Benchtop experiment results. (a) and (b) Bandwidth test results of the system, (c) and (d) Dynamic disturbance experiment results. (c) shows the result of the traditional PID controller, while (d) presents the result of the repetitive controller.

C. Actuation Performance Characterization

To evaluate the performance of the proposed exoskeleton, a dedicated test platform was constructed, and a series of characterization experiments were performed. To assess active force tracking capability, a bandwidth test was conducted. In this experiment, the load cell was fixed, and sinusoidal force signals with amplitudes of 50 N (peak-to-peak 100 N), 75 N, and 100 N were applied, with frequencies sweeping from 1 Hz to 20 Hz. These force amplitudes were chosen based on practical application requirements. Each amplitude test was repeated three times, with each trial maintaining over 20 seconds at each frequency, ensuring at least 20 complete cycles were available for analysis. The experimental results are presented in Fig. 3(a) and 3(b). The -3 dB bandwidth was undetectable at 50 N, approximately 13.5 Hz at 75 N, and 12.5 Hz at 100 N. The phase margin was measured at approximately 140° for 50 N and 130° for both 75 N and 100 N. These results confirm that the device's is significantly higher than the typical frequency spectrum of human motion.

To assess the impact of disturbances caused by human motion on force control accuracy, dynamic experiments were conducted. An additional identical actuation unit was employed as a towing system to drive the distal end of the Bowden cable in a sinusoidal, periodic reciprocating motion.

This motion simulated the ankle joint's behavior during a gait cycle, operating at a frequency of 1 Hz, approximately corresponding to the natural walking frequency. During this experiment, the desired force was maintained at a constant value of 60 N. The force control performance of a traditional PID controller was compared with that of a RC controller, PID parameters are the same for both controllers. The results, showing the steady-state control performance of both controllers, are presented in Fig. 3(c) and Fig. 3(d). The measured tension exhibited periodic variations around the target value. Potential causes for these fluctuations include backlash in the Bowden cable and gearbox, as well as the stiffness and friction of the cable. Initially, the fluctuation range was 60 ± 8 N, with the period of variation aligning with the disturbance motion. However, when repetitive control was implemented, the amplitude of the fluctuations gradually decreased over time, ultimately stabilizing at a reduced range of 60 ± 3 N (±5%).

III. Walking Experiment and Results

The exoskeleton aims to assist walking and enhance the walking economy. For safety considerations, an off-board version of the exoskeleton was used during the treadmill experiments. The power supply and actuation unit were placed beside the treadmill, and participants only wore the shank sleeve. This setup ensured that the added mass was negligible and did not interfere with metabolic cost measurements. This section summarizes the experimental protocol, apparatus, and results of the human walking assistance tests.

A. Experimental Protocol

To evaluate the device's walking assistance (unilateral) performance, treadmill experiments were conducted with approval from the University of Tokyo's Research Ethics Committee (No. KE24-129). Two healthy young participants (details in Table 1), without movement disabilities were recruited. Written informed consent was obtained before participation. Each participant completed a two-day protocol: a two-hour familiarization session on day one and a formal testing session on day two. Three conditions were evaluated—no assistance, low assistance (peak force of 30 N), and high assistance (peak force of 50 N). The desired torque profiles, derived from previous studies [18][19], and shown in Fig. 4(b), were adjusted based on safety considerations and feedback from the familiarization session. Timing parameters for each participant were derived from our previous research [18] and further refined during the familiarization session.

For each assistance condition, participants were instructed to stand still on the treadmill for 90 seconds before the treadmill was started at a speed of 4 km/h, a typical walking speed. Participants then walked for 6 minutes under each condition. After completing one condition, participants rested for 12 minutes to minimize the effects of fatigue before proceeding to the next condition. The order of the three conditions was randomized in each trial. Upon completing all conditions in a trial, participants rested for one hour before repeating the trial. Each trial was repeated three times in total.

B. Apparatus and Data Process

During the treadmill experiments, in addition to the sensors embedded in the exoskeleton, additional wearable sensors

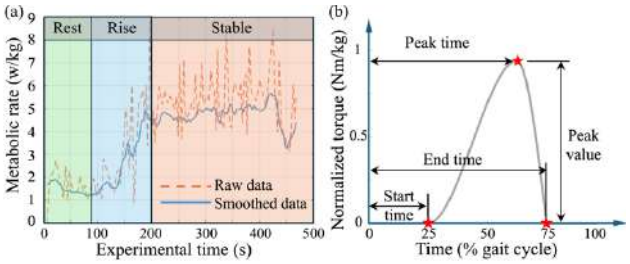


Figure 4. (a) Example of the test results from the respiratory mask in the treadmill experiment, (b) Torque profile applied during the experiment.

TABLE I. Subject Specific Information

Subject	Gender	Age(yrs)	Weight(Kg)	Height(m)
01	Male	22	84	1.83
02	Male	26	73	1.75

were utilized to assess the participants' walking performance. A respiratory mask (PNOE metabolic analysis system, PNOE, USA) was employed to measure the oxygen uptake (*VO2*) and carbon dioxide production (*VCO2*) rates. The metabolic consumption rate was indirectly estimated using an empirical model from [20], expressed by the following equation:

$$r = 16.58\,VO_2 + 4.51VCO_2 - 5.90N \qquad (2)$$

where *VO2* is the oxygen uptake in L/s; *VCO2* is the carbon dioxide production in L/s; *N* is the nitrogen in g; *r* is the metabolic rate in *W*. However, respiratory measurements often exhibit instability due to low sampling rates and delayed responses. As shown in Fig. 4(a), it typically takes 1–2 minutes for changes in physical activity to appear in respiratory gas readings, consistent with previous studies [19]. To address this, the sensor mask was calibrated before each experiment, and a moving average filter with a 20-sample window was applied to the collected data.

Two 64-channel high-density surface electromyography (HDsEMG) sensors (GR08MM1305, OT Bioelettronica, Italy) were placed on the lateral and medial gastrocnemius muscles, which are pivotal for ankle plantarflexion and easily accessible for activation monitoring. Before placement, the skin was shaved and cleaned to enhance signal quality. In accordance with SENIAM recommendations [21], each sensor grid was centered on the muscle belly with its long axis parallel to the fibers. Electrolyte paste was applied, and the grid was secured with double-sided tape and an elastic bandage for added stability during walking. EMG signals were recorded at 2 kHz and initially processed with a comb filter to remove 50 Hz power line noise and its six harmonics. The data were then band-pass filtered within a frequency range of 20–500 Hz. The envelope of each channel was computed using a Hilbert transform. For refinement, the envelope from the center channel and its eight neighbors were averaged. Finally, the resulting signal was smoothed with a 200-millisecond moving average filter.

C. Experimental Results

Metabolic cost is widely recognized as the gold standard

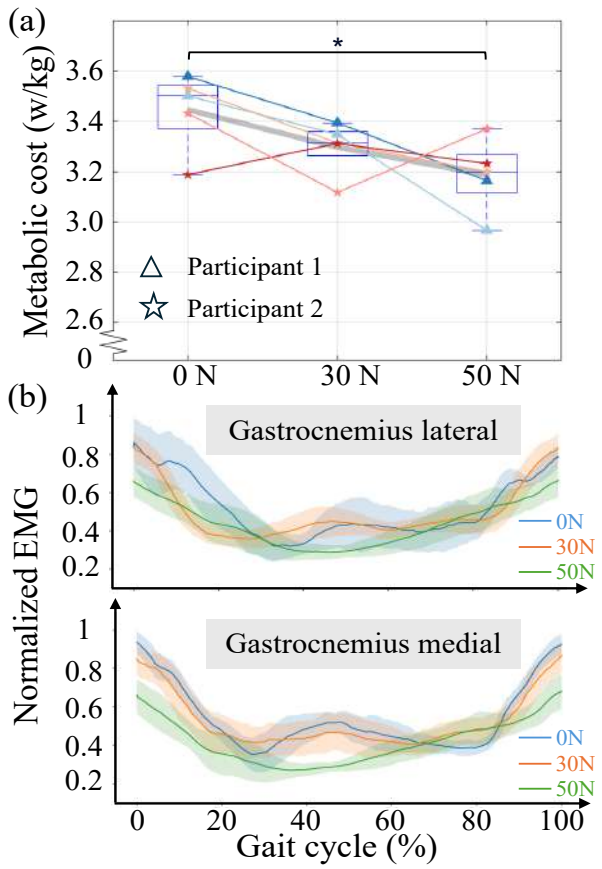


Figure 5. Treadmill experiment results under different assistance conditions: (a) metabolic consumption, (b) EMG intensity of the lateral and medial gastrocnemius muscles.

TABLE II. PEAK AND MEAN EMG VALUES OF LATERAL AND MEDIAL GASTROCNEMIUS MUSCLES UNDER DIFFERENT ASSISTANCE CONDITIONS

	Lateral		Medial	
	Peak	Mean	Peak	Mean
0N	1	0.5132	1	0.5357
30N	0.9189	0.4902	0.9529	0.5202
50N	0.7562	0.4361	0.7771	0.4153

for evaluating walking economy [22]. The metabolic cost under different assistance conditions is presented in Fig. 5(a), representing the increase in metabolic cost during walking relative to baseline standing. The resting metabolic rate was averaged over the first 60 seconds, while the active metabolic rate during walking was calculated over 250–400 seconds. Values were normalized to each participant's weight for comparison. Triangles and stars in Fig. 5(a) indicate data for different participants, with one trial for Participant 2 excluded due to equipment issues, leaving two valid data sets. The measured metabolic cost was 3.45 ± 0.15 W/kg for no assistance, 3.30 ± 0.11 W/kg for 30 N assistance, and 3.19 ± 0.15 W/kg for 50 N assistance. Compared to no assistance, the metabolic cost decreased by 0.15 W/kg (4.35%) under 30 N assistance and by 0.26 W/kg (7.53%) under 50 N assistance. The reduction in metabolic cost became more pronounced with increasing assistance levels. An ordinary one-way analysis of variance analysis showed a statistically significant difference ($p < 0.1$) only between the 0 N and 50 N conditions, with no significant differences observed between other conditions.

The average EMG curves of the lateral and medial gastrocnemius muscles over one gait cycle under different assistance conditions are illustrated in Fig. 5(b). The gait cycle was segmented based on the peak EMG signals of the respective muscles, rather than the conventional heel strike events. Solid lines represent the mean EMG signals recorded from the two participants during a 1-minute interval (340-400 seconds), while shaded regions indicate standard deviations. EMG signals were normalized to the peak values under the no-assistance condition. As summarized in Table 2, both the lateral and medial gastrocnemius muscles exhibited reduced peak and mean EMG values with assistance when compared to the no-assistance condition. For the lateral gastrocnemius, EMG peak values decreased by 8.11% and 24.38%, and mean values by 4.48% and 15.02%, respectively. Similarly, for the medial gastrocnemius, peak values decreased by 4.71% and 22.29%, and mean values by 2.89% and 22.47%, respectively. These results indicate that higher assistance levels lead to greater reductions in muscle activation, demonstrating the enhanced effect of assistance.

IV. DISCUSSION

In this study, we present a biomimetic cable-driven ankle exoskeleton designed to provide plantarflexion assistance to the ankle joint. Through a series of benchtop tests and treadmill experiments, we validated both the actuation performance of the exoskeleton and its effectiveness in enhancing walking economy. Compared to existing designs [13][23], the proposed exoskeleton features a compact, lightweight structure, with each actuation unit weighing approximately 0.7 kg and a total weight (including the battery) of 4 kg. Powered by a BLDC motor coupled with a gearbox and lever mechanism, it can deliver a maximum assistive force of 500 N, achieving a high torque-to-weight ratio. The cascaded repetitive control system enables precise force control with an error margin of ±5%, eliminating the need for additional components such as clutch in [13]. Benchtop tests confirmed a force control bandwidth of 13.5 Hz under a 50 N load, far exceeding the 1~2 Hz typically required for human walking. To prevent cable derailment and slack, the spool groove was designed with a self-aligning cross-section, ensuring the cable automatically centers upon entry. Anti-slip flanges at the groove edges further enhance stability. To avoid slack without complex tensioning mechanisms [12][13], the controller applies a small tensioning force when the target torque is zero, maintaining consistent cable tension. Additionally, an integrated communication and sensing system improves motion perception, enhancing practicality in real-world applications.

To assess the exoskeleton's effectiveness in enhancing the walking economy, treadmill experiments were conducted using a respiratory mask and HDsEMG sensors for

quantitative analysis. Unilateral assistance was employed due to the availability of single-leg hardware, with plans for bilateral assistance. The results showed significant improvement in the walking economy, with higher assistance levels providing greater benefits. Remarkably, a 50 N assistance level achieved a 7.53% improvement in the economy with unilateral assistance. In comparison, a previous study [24] reported a 6.2 kg cable-driven ankle exoskeleton that achieved a 5.6% improvement under bilateral assistance. Our exoskeleton, weighing 4.2 kg, achieved a comparable 7.53% improvement with unilateral assistance. IMU data analysis confirmed that unilateral assistance preserved gait symmetry, as joint angle patterns remained consistent with no-assistance conditions. Combined with EMG results, these findings suggest that the metabolic cost reduction primarily stems from decreased muscle activation in the assisted leg. Given the inherent symmetry of walking, it can be inferred that bilateral assistance could potentially improve the economy by over 15%.

However, this study has several limitations. In the treadmill experiments, the maximum assistance level was limited to 50 N to ensure safety, which is considerably below the exoskeleton's designed maximum capacity. In future work, we plan to reinforce mechanical structures and components to safely explore higher assistance levels. Additionally, the treadmill experiments involved only two participants and were conducted at a fixed walking speed of 4 km/h. This small sample size and single walking condition may introduce variability and limit the generalizability of the findings. To address these, future studies will recruit more participants, explore a broader range of walking conditions, and incorporate overground walking experiments to improve the reliability and applicability of the findings. Although this study did not include EMG measurements of the non-assisted leg, we recognize the potential value of such data in understanding compensatory mechanisms and will consider incorporating these measurements in future research. While the current exoskeleton is relatively lightweight, future iterations will aim to further reduce its weight through structural optimization and the use of lighter materials. Additionally, expanding the exoskeleton to assist multiple joint movements simultaneously will be considered in future work.

V. Conclusion

In conclusion, we present a biomimetic cable-driven ankle exoskeleton designed to provide plantarflexion assistance to the ankle joint. Experimental results demonstrated that even with unilateral assistance, the device effectively improved walking economy by 7.53%.

References

[1] M. Y. Zarrugh, F. N. Todd, and H. J. Ralston, "Optimization of energy expenditure during level walking," *Eur. J. Appl. Physiol. Occup. Physiol.*, vol. 3, pp. 293–306, 1974.

[2] P. E. di Prampero, "The energy cost of human locomotion on land and in water," *Int. J. Sports Med.*, vol. 7, no. 2, pp. 55–72, 1986.

[3] K. R. Westerterp, "Physical activity and physical activity-induced energy expenditure in humans: Measurement, determinants, and effects," *Front. Physiol.*, vol. 4, p. 90, 2013.

[4] A. J. Young and D. P. Ferris, "State of the art and future directions for lower limb robotic exoskeletons," *IEEE Trans. Neural Syst. Rehabil. Eng.*, vol. 25, no. 2, pp. 171–182, 2016.

[5] S. H. Collins, M. B. Wiggin, and G. S. Sawicki, "Reducing the energy cost of human walking using an unpowered exoskeleton," *Nature*, vol. 522, no. 7555, pp. 212–215, 2015.

[6] A. M. Dollar and H. Herr, "Lower extremity exoskeletons and active orthoses: Challenges and state-of-the-art," *IEEE Trans. Robot.*, vol. 24, no. 1, pp. 144–158, 2008.

[7] H. Kazerooni, A. Chu, and R. Steger, "That which does not stabilize, will only make us stronger," *Int. J. Robot. Res.*, vol. 26, no. 1, pp. 75–89, 2007.

[8] Y. Sankai, "HAL: Hybrid assistive limb based on cybernics," in Proc. *13th Int. Symp. Robotics Res. (ISRR)*, Berlin, Germany: Springer, 2011, pp. 25–34.

[9] A. M. Khomami and F. Najafi, "A survey on soft lower limb cable-driven wearable robots without rigid links and joints," *Robot. Auton. Syst.*, vol. 144, p. 103846, 2021.

[10] X. Wang, S. Guo, and S. Bai, "A cable-driven parallel hip exoskeleton for high-performance walking assistance," *IEEE Trans. Ind. Electron.*, vol. 71, no. 3, pp. 2705–2715, 2023.

[11] S. Yu et al., "Bio-inspired design of a self-aligning, lightweight, and highly-compliant cable-driven knee exoskeleton," *Front. Hum. Neurosci.*, vol. 16, p. 1018160, 2022.

[12] Q. Zhang et al., "Evaluation of a fused sonomyography and electromyography-based control on a cable-driven ankle exoskeleton," *IEEE Trans. Robot.*, vol. 39, no. 3, pp. 2183–2202, 2023.

[13] M. Xu et al., "Bio-inspired cable-driven actuation system for wearable robotic devices: Design, control and characterization," *IEEE Trans. Robot.*, vol. 39, no. 2, pp. 1567–1578, 2023.

[14] A. T. Asbeck et al., "Stronger, smarter, softer: Next-generation wearable robots," *IEEE Robot. Autom. Mag.*, vol. 21, no. 4, pp. 22–33, 2014.

[15] P. DeVita, J. Helseth, and T. Hortobagyi, "Muscles do more positive than negative work in human locomotion," *J. Exp. Biol.*, vol. 210, no. 19, pp. 3361–3373, 2007.

[16] M. Meinders, A. Gitter, and J. M. Czerniecki, "The role of ankle plantar flexor muscle work during walking," *Scand. J. Rehabil. Med.*, vol. 30, no. 1, pp. 39–46, 1998.

[17] M. I. Ribeiro, "Kalman and extended Kalman filters: Concept, derivation and properties," *Inst. Syst. Robot.*, vol. 43, no. 46, pp. 3736–3741, 2004.

[18] X. Zhang et al., "Integrating musculoskeletal simulation and machine learning: A hybrid approach for personalized ankle-foot exoskeleton assistance strategies," *Front. Bioeng. Biotechnol.*, vol. 12, p. 1442606, 2024.

[19] J. Zhang et al., "Human-in-the-loop optimization of exoskeleton assistance during walking," *Science*, vol. 356, no. 6344, pp. 1280–1284, 2017.

[20] J. M. Brockway, "Derivation of formulae used to calculate energy expenditure in man," Hum. Nutr. Clin. Nutr., vol. 41, no. 6, pp. 463–471, 1987.

[21] D. Stegeman and H. Hermens, "Standards for surface electromyography: The European project surface EMG for non-invasive assessment of muscles (SENIAM)," *Enschede: Roessingh Res. Develop.*, vol. 10, pp. 8–12, 2007.

[22] O. S. Mian et al., "Metabolic cost, mechanical work, and efficiency during walking in young and older men," *Acta Physiol.*, vol. 186, no. 2, pp. 127–139, 2006.

[23] X. Tan et al., "A time-independent control system for natural human gait assistance with a soft exoskeleton," *IEEE Trans. Robot.*, vol. 39, no. 2, pp. 1653–1667, 2022.

[24] C. Khazoom, et al., "Design and control of a multifunctional ankle exoskeleton powered by magnetorheological actuators to assist walking, jumping, and landing," *IEEE Robot. Autom. Lett.*, vol. 4, no. 3, pp. 3083–3090, 2019.

A Qualitative Exploration of EMG Visual Feedback for Spinal Cord Injury Rehabilitation*

Janelle Aikens, Aaron Tabor, Kevin Englehart, *Fellow, IEEE*, Erik Scheme, *Senior Member, IEEE*

***Abstract*—Sustaining motivation during hand function rehabilitation after a Spinal cord injury (SCI) can be challenging, particularly when natural movement feedback is impaired. Augmented feedback, such as through visual feedback of electromyography (EMG) muscle activity, may support motor (re-) learning and user motivation, but its impact on SCI rehabilitation remains underexplored. This study involved the design of an EMG-based visual feedback tool and an exploration of its suitability in rehabilitation and potential impact on user motivation. Using a qualitative approach informed by Self-Determination Theory (SDT) and a custom-developed EMG visualization interface, data were collected through semi-structured interviews with five quadriplegic participants and a focus group with seven occupational therapists (OT). Findings revealed that EMG visual feedback functions as an extrinsic motivator, providing tangible progress indicators, and has the potential to enhance intrinsic motivation by fostering enjoyment and aligning with personal interests. Themes highlight EMG feedback's potential in various rehabilitation contexts, from pre-functional muscle awareness to improved patient-therapist communication, offering a promising tool for advancing SCI rehabilitation.**

***Keywords*—EMG, electromyography biofeedback, visual feedback, spinal cord injury, rehabilitation, motivation**

I. Introduction

Spinal cord injuries (SCI) can result in significant impairments in movement, sensation, and visceral functions below the level of injury. Rehabilitation aims to re-learn muscle control and enhance mobility and independence but requires substantial effort and motivation [1], [2], [3], [4]. Because of the nature of these injuries, natural movement feedback—like visual coordination and proprioception (the sense of body position)—is often impaired.

Due to this impaired ability to receive natural feedback during movement, individuals with SCI may benefit from augmented feedback mechanisms that provide external sensory cues, such as visual or auditory signals, to compensate for this loss. By allowing individuals to "see" or "hear" their movement efforts in real-time, augmented feedback can help restore part of this essential feedback loop [5]. This not only plays a role in motor learning and the underlying mechanisms of neuroplasticity but also plays an integral role in driving and sustaining the learner's motivation [6].

*All authors are with the Institute of Biomedical Engineering, Fredericton, New Brunswick, Canada.

J. Aikens (phone: 506-458-7703; e-mail: jaikens@unb.ca).

A. Tabor (e-mail: aaron.tabor@unb.ca).

K. Englehart (e-mail: kengleha@unb.ca).

E. Scheme (e-mail: escheme@unb.ca).

Among augmented feedback modalities, visual feedback of muscle activity is widely recognized [7], [8]. In this type of feedback, electromyography (EMG) signals produced by muscle contractions are recorded and used, translating even subtle movement intentions into visual data.

Existing research, however, has predominantly focused on post-stroke patients, employing traditional methods that rely on muscle signals from single muscles or pairs, which presents challenges when working with populations with limited voluntary muscle activation. Although post-stroke studies have shown positive outcomes, such as improved hand function [9], enhanced EMG signals [10], and reduced spasticity [11], similar studies in SCI remain inconclusive [12], [13], [14]. Therefore, this study investigates how diverse forms of EMG-based visual feedback could influence motivation and support hand-function rehabilitation in individuals with SCI.

II. Methods

A. Study Design and Setting

This qualitative descriptive study was conducted in New Brunswick, Canada, involving participants recruited from a local rehabilitation center. The EMG feedback tool was developed through an iterative process, incorporating clinician input to refine its functionality and usability. After a pilot session with a patient participant, a focus group and individual interviews were conducted to explore user experiences. All participants provided informed consent as approved by the research ethics boards of the rehabilitation center (#2023-3284) and the University of New Brunswick (#2023-139).

B. Study Tool

The EMG Visualizer App is a Python-based desktop application that leveraged early features of the now open-source library LibEMG [15]. It was designed to enable the real-time exploration of EMG signals streamed from the Myo Armband (Thalmic Labs) in various formats. Its core functionality includes multiple visualization options such as time-series graphs, signal amplitude bars, and multi-channel muscle activity indicators for the forearm. Users can also record trials representing different motion classes (e.g. wrist flexion or hand open) to enable more pattern-based explorations of contractions and muscle synergies. Fig 1. illustrates some of the available screens. Key features include real-time signal smoothing, a snapshot of activation history from the most recent repetition ("max bar"), and adjustable y-axis scaling for enhanced focus on smaller signals.

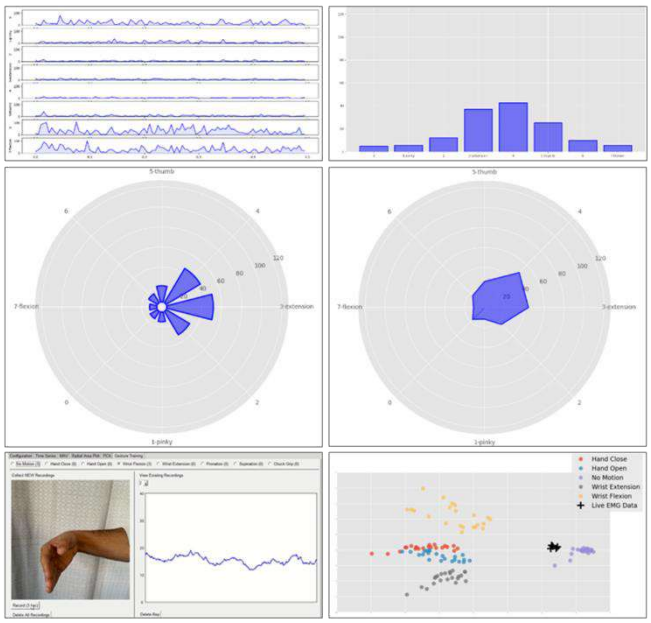


Fig. 1 Examples of the EMG data representations explored (from left to right, top to bottom): EMG time-series; Signal amplitude (MAV) bars; MAV radial bars; Radial area; Self-paced screen-guided training; and PCA-projected feature space.

C. Data Collection

1) Focus Group

Seven occupational therapists (OT) from a local rehabilitation center participated in a 1.5-hour focus group. The group included six females and one male (ages 22–56) with 2–20 years of experience. Four had no prior exposure to visual feedback, and three had limited experience. The discussion, guided by pre-determined questions, focused on motor learning, feedback interpretability, and potential use cases. Participants viewed a brief presentation featuring pilot EMG session excerpts before the discussion, which was audio-recorded and facilitated by the principal investigator (PI) with research team support.

2) Semi-Structured Interviews

Five male participants with quadriplegia (Table 1) were recruited through the participating OTs. Sessions included a guided exploration of EMG visualizations and a flexible interview and the audio, video, and screen were recorded. Interviews explored how EMG visual feedback could influence motivation, along with usability and general user feedback. Example questions included: *What motivates you in rehabilitation and how has it changed over time? What is challenging about understanding what's happening in your muscles since your injury? What were your thoughts on the amount of information on the screen? How would you describe your experience with the visualization—did you feel in control of it, or did it feel more like passively watching a screen? How do you feel about the idea of using visual feedback independently at home? What would make it useful or challenging for you? In what ways do you think a tool like this could impact your communication with your therapist? Can you think of any specific scenarios where it would be helpful?* The patient sessions were conducted with the PI and an OT present.

a) Patient Session Protocol

The Myo Armband was placed around the participants' upper forearm of their choice. Participants were prompted through verbal and visual cues to perform various forearm muscle contractions and hand movements while interacting with different EMG visualizations displayed on a monitor. Each EMG session lasted approximately 1.5 to 2 hours.

D. Data Analysis

Audio recordings were transcribed using Whisper [16], an AI-based audio-to-text software, run on a local server and manually deidentified. Transcripts were checked against the recordings for accuracy and coded by a single researcher. Thematic analysis was conducted following the six phases outlined by Braun and Clarke [17], employing both inductive and deductive approaches. Video and screen recordings were included in the analysis. NVivo software version 14 was used to manage data.

1) Establishing Trustworthiness

To ensure trustworthiness in this qualitative study, we applied the criteria outlined in [18]: credibility, dependability, confirmability, and transferability. Credibility was achieved through pilot interviews, expert-reviewed interview guides, verbatim quotes, and data triangulation. Dependability was ensured by providing a detailed study protocol and following the six phases of thematic analysis. Confirmability was supported by a rich description of methods and data triangulation. Transferability was addressed by collecting demographic information, offering a detailed context description, and using purposive and convenience sampling.

2) Theoretical Framework

This study is grounded in the Self-Determination Theory of Motivation (SDT) [19], a framework well-suited for exploring various behaviors in individuals with SCI, including participation in daily and social activities [20], engagement in physical activity [21], goal setting during rehabilitation [22], and health-related motivational processes [23]. SDT posits a continuum of motivation, ranging from amotivation (absence of intent), through extrinsic motivation (driven by external factors), to intrinsic motivation (driven by inherent satisfaction and enjoyment), with distinct regulatory styles influencing behavior along this continuum [19].

III. Findings

Our analysis identified multiple themes, organized into two broad categories: A) Motivation Along a Continuum, and B) Use Cases and Considerations.

A. Motivation Along a Continuum

In our study, EMG visual feedback functioned as an extrinsic motivator by providing tangible evidence of progress and clear benchmarks to work toward. At the same time, it demonstrated the potential to enhance intrinsic motivation by fostering enjoyment and aligning with personal interests.

1) Tangible Evidence as a Source of Hope

EMG visual feedback has the potential to provide participants with emotional reassurance by offering tangible

evidence of muscle activity, which could instill hope and encourage continued effort in rehabilitation. For some, it could be a powerful source of hope. P2 shared: "*If I could see [the visual feedback] moving a little bit, I could see [my muscles are] firing [...] [and they have the] possibility to improve*." Similarly, P1 noted that seeing a signal on the screen, even when physical sensation was absent, could provide reassurance: "*If I'm contracting and didn't feel my arm, seeing that there is a signal would be super positive*." A clinician in the focus group emphasized the value of objective data in sustaining motivation:

> *Something cool about this is you have concrete data... You may not see the difference looking at your hand [or it may not] feel like a huge difference, but objectively you have progressed.*

Conversely, the absence of feedback has made it harder to stay hopeful. P5 shared, "*When you don't know you have it, it makes it difficult [...] I'm not getting any feedback. I'm not getting encouragement*."

These insights suggest that real-time EMG feedback could serve as a powerful tool to validate patient efforts, rekindle hope, and support emotional resilience, which may enhance engagement in rehabilitation activities.

2) Thresholds, Numerical Markers, and Personal Bests

EMG visual feedback could also offer motivational benefits by enabling patients to track concrete, measurable progress. P3 explained that visualizing improvements, such as increased signal amplitude, could motivate patients more effectively than vague encouragement: "*It's a tool that therapists could use to motivate people to work [...] harder than just saying, 'if we do this, something may happen*.'"

Thresholds and numerical markers in EMG feedback can be powerful motivators by providing clear, measurable targets, and fostering both extrinsic and intrinsic motivation. These features turn rehabilitation exercises into structured tasks with defined goals, promoting focus and engagement. Before the max bar threshold feature was introduced, participants recognized its potential. A focus group member suggested, "*Even having a threshold of where they should achieve [...] if they had a threshold or a goal that you could change and vary*." P1 found the max bar threshold meaningful, saying, "*There's something for me to get at. For those lines to mean something to me*." Similarly, P3 stated, "*I like working towards an achievable, visual goal*." By offering adjustable goals and visual benchmarks, EMG feedback provides extrinsic motivation, helping users stay focused on incremental progress and surpass established targets.

Incorporating personal challenges, such as surpassing previous results or achieving personal bests, further enhanced motivation. P5 found excitement in outperforming his own results, sharing, *"It motivated me to try to beat what I was seeing on the screen."* He went on to say:

Similarly, P2 enjoyed the aspect of self-competition, stating, *"I like storing your high score. And beating your high score."* P3 echoed these sentiments, appreciating how visual goals made the exercises more satisfying. These insights suggest that EMG feedback systems designed with thresholds, numerical markers, and self-competition features can inspire both extrinsic motivation through structured goals and intrinsic motivation by fostering personal mastery and enjoyment.

> *When you told me there were numbers, I was way more motivated, like, 'Oh, so I'm only at a 50? Well, give me a week, and I'll show you—I'll be at 60.'* (P5)

3) Enjoyment

A key aspect of intrinsic motivation is the enjoyment derived from the activity itself. In this study, P4 expressed excitement when engaging with the real-time visual feedback: "*Just to see that play out in front of me, like see all the waves in real time, that's exciting enough for me*" (P4). The real-time nature of the feedback provided a tangible connection to his efforts, making the activity enjoyable.

Similarly, P3 contrasted exercises with and without visual feedback, describing the latter as tedious and unengaging while the former made him enthusiastic about participation: "*It's black and white. You know, it's 180 degrees. I hate doing that. I like doing this*." Even repetitive tasks sometimes led to states of flow. For instance, P3 completed 20 repetitions of an exercise while exclaiming, "*Yeah, that's incredible*," as the research team noted his sustained energy and motivation throughout the task.

4) Aligning with Personal Interests

Intrinsic motivation is closely tied to personal interests and values. When rehabilitation tools aligned with participants' interests, they found greater motivation to engage. For example, P2, a sports enthusiast, likened the EMG feedback system to sports data analytics, describing how it resembled baseball pitching trends and provided a similar sense of feedback and progress. He explained, "*It kind of gives you that feedback of what spot you're hitting and how you're getting there.*" These personal connections underscored how tailoring rehabilitation tools to individual preferences can enhance engagement.

A. Use Cases and Considerations

In our exploration, we identified several use cases where this tool shows promise and important factors to consider.

1) Pre-Functional Muscle Awareness

EMG visual feedback has the potential to be used in helping patients recognize sub-functional muscle activity and fostering muscle awareness, particularly in the early stages of rehabilitation.

TABLE 1. SCI PARTICIPANT DEMOGRAPHICS

ID	Age	Sex	Lesion Level	Lesion Classification	Years since injury	Hand used	Experience with VF (1-5)[a]
P1 (pilot)	46	M	C4	Incomplete[b]	10	R	1
P2	51	M	C2	Motor Incomplete	2	R	1
P3	50	M	C5	Complete	17	R	1
P4	58	M	C4	Motor Incomplete	2	L	1
P5	46	M	C5	Motor Incomplete	27	R	2

a. Level of experience with visual feedback (VF) of EMG activity on a scale of 1 to 5. 1 = no experience and 5 = highly experienced. b. Lesion classification undetermined

A clinician highlighted how visual feedback could support patients when functional tasks are still unattainable:

> *I can picture it being helpful [during] that hard time when someone first comes in [and] can't do anything functional yet, just trying to [build] awareness of when they're activating what and they're frustrated.*

By providing real-time insights into muscle activation, EMG feedback may motivate patients by making even minimal progress visible, reinforcing the value of small achievements in their rehabilitation journey.

2) Muscle Isolation

Visual feedback demonstrated potential in helping participants isolate specific muscle groups during exercises, addressing a common challenge in traditional rehabilitation. A clinician described the difficulty of isolating muscles during therapy:

> *Getting them to see if they're activating the wrong thing and fighting themselves, I find really challenging... I don't think I ever found a way to get some visual feedback on that besides looking at their hand.*

P1 struggled with co-contraction of opposing forearm muscles during wrist extension, limiting his movement. The study team asked him to extend his wrist while monitoring the visual display of muscle activity. The Study OT instructed, "*Look at the flexion bar and try to extend your wrist while keeping it low*." This feedback helped P1 relax his flexors during wrist extension. Reflecting on the experience, he shared: *"There's feedback. I had no idea that [points to forearm] this was a thing."* For participants like P1, real-time feedback highlighted unintended co-contractions, allowing them to make corrective adjustments and refine their muscle control. As P1 explained:

> *I liked the isolation [pointing to the MAV bars] to work on what you want me to work on and relax when I'm supposed to relax. Otherwise, I'd probably still do the same bad habit... using both my muscle groups instead of what I'm supposed to use. (P1)*

3) Spasticity Management

Spasticity management is a significant challenge for individuals with SCI, and visual feedback of muscle activity could be a valuable tool for both patients and therapists. The study OT noted, "*The thing about muscles firing at the same time, especially with spasticity, [it] is such an incredibly difficult concept to understand*." A clinician added, "*Spasticity [management]... we spend a lot of time doing that [...] It's [that] they're over-recruiting*." A visual feedback tool could help identify where spasticity persists and guide interventions.

Patients often struggle to determine if they are successfully relaxing their muscles. For example, P1 expressed frustration, saying, "*Yes, [I'm asked to relax] all the time, but my muscles don't relax. At least I don't think [they] do*." Seeing the feedback gave P1 clarity, reinforcing that muscle relaxation is achievable and measurable: *"So seeing that feedback happen is definitely a lot more helpful than me guessing whether this is relaxed or not*." EMG feedback could help address spasticity-related challenges in identifying muscle activation, leading to more effective strategies for relaxation.

4) Informing Clinical Decisions: Breaking Tenodesis Grip

Deciding when to break the tenodesis grip in SCI rehabilitation is a critical and nuanced decision for therapists. Tenodesis grasp is a technique used to create a passive grip by extending the wrist, causing the fingers to bend towards the palm. This grasp is essential for patients with certain levels of SCI who lack the muscle strength for an active grip. In these cases, avoiding overstretching of the fingers is important. However, if muscle strength returns, there may come a point in the rehabilitation process when patients could grasp naturally, prompting a discussion about whether to break the tenodesis grasp:

> *We often have talks about when clients need to break their tenodesis or not. So, I wondered if we had visual feedback to know, 'okay, there's a muscle group waking up, but because they're using their tenodesis, we are not breaking it'.*

This tool could offer a more precise understanding of whether a patient's muscle activity is strong enough to shift from a passive grip to an active one, potentially allowing them to make more informed decisions.

5) Focused Rehabilitation and Remote Monitoring

In rehabilitation, particularly when patients are sent home with exercises, compliance and oversight become crucial elements of ensuring progress. Visual feedback tools could enhance rehabilitation by providing structured protocols and enabling oversight during home exercises. A therapist emphasized its potential:

> *If they have visual feedback, we could coach them and say, 'This is exactly what we want the screen to look like when you're trying to activate your wrist.'*

Participants also appreciated the potential to track progress and connect with their OT remotely. P5 envisioned:

> *Say we weren't together, but somehow you could connect [through the EMG feedback system] like, 'Hey, can I check in on your strength? How have you been doing?' (P5)*

This remote monitoring could reduce in-person visits while maintaining engagement. By setting thresholds for home exercises, therapists could ensure patients adhere to proper techniques, even outside the clinic. The benefits extend beyond compliance. Visual feedback offers insights into patient performance that verbal reporting cannot capture. One therapist noted:

> *You could look at this as a therapist and say, 'You did your homework, but this really didn't go well,' which that's not the insight you always get.*

6) Improved Patient-Clinician Communication

Some participants recognized that visual feedback tools could improve communication with therapists. P3 noted that such tools would help articulate bodily sensations during rehabilitation, enabling more precise discussions about progress and challenges. He explained:

> *Yeah, I could explain what's happening... '[sensor] number 5 is working more than number 4, and that's not the way I want it' [...] you could articulate more what the problem was and what your goals were. (P3)*

P1 echoed similar sentiments, describing how visual aids could make it easier to communicate his experiences to healthcare professionals. He said:

> *It would be much easier because instead of me trying to figure things out on my own and trying to convey that information to the doctor or to physio. (P1)*

These insights suggest that visual feedback could help bridge communication gaps and strengthen therapeutic relationships by fostering a shared understanding between patients and therapists.

7) Feedback Modalities and Focus Strategies

In SCI rehabilitation, various feedback modalities, including visual, tactile, and auditory, offer distinct benefits depending on the patient's condition and task. Visual feedback, such as real-time muscle activity on a screen, is useful but may not always be ideal, especially for patients with functional movement. As a focus group member noted, patients who had functional control of their limb may prefer focusing on their limb rather than a screen: "*If someone is functional or they're expecting some functional [movement], their focus is gonna be here [on their limb], not on the screen.*" Similarly, P1 found actual limb movement more effective than screen-based feedback: "*Seeing the actual action happen... would probably be better feedback than seeing the numbers [on a screen].*"

Tactile feedback plays a critical role in helping patients locate and activate specific muscles. P5 shared that physical touch greatly improves his ability to fire muscles that are harder to engage:

> *I get way better reaction. You rubbed your finger over the inside of my arm [and] as soon as someone triggers that my brain's like, 'ohh' there's where it is. (P5)*

Tactile feedback serves as a reminder, helping patients identify the correct muscle pathways and improve activation. P5 described this as "pathfinding," where physical touch aids in locating and firing the intended muscle. Similarly, P3 found it helpful when the experimenter placed a finger on the back of his wrist during an exercise, saying, *"It gave me a focus."* This subtle input helped him direct his attention more precisely, improving control.

Auditory feedback can complement visual focus, providing simultaneous guidance, especially for patients who struggle with movement awareness. As one therapist explained, *"Some people do not have great insight into what their movement is like... [with] auditory feedback, they can do both at once."*

For some patients, visual feedback can hinder relaxation, particularly when they need to engage internal sensations for muscle activation. P5 found closing his eyes helped him focus on muscle recruitment without visual distractions: *"If I shut my eyes, it's mostly pathway finding... it helps me channel to silence everything else and completely focus."* P5 also found visual feedback frustrating when it interfered with relaxation: *"Watching it made me intently focus on trying to calm it down, which is probably the opposite of what [my muscles] needed."* Similarly, P3 preferred closing his eyes, saying, *"Each time you do it, you can kind of hone in on it a little more precisely."* Too much feedback, whether visual or otherwise, can overwhelm patients and detract from the rehabilitation goal. P3 noted:

> *With just the two [channels of feedback], I was less prone to close my eyes because I wasn't being overwhelmed with all of the information. (P3)*

8) Functional Movements in Occupational Therapy

In discussions with OTs, it was reiterated that functional movements are a primary focus in occupational therapy, with the goal of helping patients regain the ability to perform daily tasks. In contrast, during our sessions with EMG feedback, participants were often directed to focus on specific muscle groups, such as their wrist "flexors", rather than engaging in functional tasks like reaching for a bottle. P1 reflected, "*I've never been told to focus on a specific muscle group if I'm doing an [exercise]. It's always been like 'pick the blocks up.*'" This highlights a potential gap between what clinicians focus on and what the current EMG visual feedback system may be able to reinforce. As seen in our findings, our tool has the potential to support functional recovery by targeting subtasks such as muscle isolation and improved synergies—key elements essential for most functional movements. However, aligning the protocol gestures more closely with everyday tasks could further enhance outcomes. There may be opportunities for more targeted interventions that connect functional tasks with the muscle activity required.

9) Importance of Clinician's Guidance

The study highlights the essential role of clinicians in the rehabilitation process, particularly in coaching patients using visual feedback systems for muscle activity. While technology can offer some independence, the clinician's presence is crucial for effective learning and muscle control. For example, during a session with P3, the OT used verbal cues and physical guidance, such as visualizing flexor muscles as a "loose rubber band" and extensor muscles as a "tight rubber band." This coaching technique helped P3 better understand muscle dynamics and improve his wrist extension. The therapist's tailored approach, based on the patient's needs, was key in enhancing muscle engagement and relaxation.

IV. Discussion

This study examined the impact of visual feedback of EMG activity on motivation and its role in supporting hand function goals in SCI rehabilitation. Our findings, in conjunction with literature from stroke rehabilitation, sports psychology, and gaming, provide deeper insights into the potential of EMG visual feedback in enhancing SCI rehabilitation outcomes.

A. Motivation Along a Continuum

Extrinsic motivation, driven by external rewards or feedback, plays a crucial role in SCI rehabilitation, particularly in the early stages when progress may be slow or difficult to perceive [24]. Our findings suggest that visual feedback has the potential to provide participants with tangible markers of muscle activity and progress. This form

of objective validation may help foster hope and reduce the risk of hopelessness and demotivation often associated with slow recovery [4]. Furthermore, our findings align with previous observations [4], emphasizing participants' preference for objective reinforcement over verbal positive feedback from clinicians. By offering concrete metrics of effort and improvement, feedback systems address the doubts and frustrations that may arise when verbal reinforcement is the sole source of encouragement.

Visual feedback systems can incorporate game-like features, such as progress markers and goal setting, to further enhance motivation—an approach supported by findings in both rehabilitation and gaming research [25], [26], [27]. For example, numerical feedback, like EMG signal amplitude, enabled participants in our study to set personalized goals akin to game mechanics, promoting engagement and fostering a sense of achievement.

Self-competition emerged as a particularly effective motivator. Participants were driven to surpass their personal benchmarks, demonstrating a strong desire for self-directed improvement. This aligns with sports psychology literature, which highlights the role of personal records in boosting self-efficacy, a critical factor for sustained effort [22], [28]. In our study, participants' enthusiasm for improving their scores underscored the importance of incorporating self-directed challenges into rehabilitation to maintain motivation and foster a growth mindset.

Research further suggests that optimal challenges—goals that are achievable but not overly easy—enhance feelings of competence, a central element of intrinsic motivation [19]. The visual feedback system introduced concrete challenges, such as regulating muscle activity and meeting strength thresholds, which maintained participants' engagement. By tailoring rehabilitation activities to the right level of challenge, the system not only has the potential to boost competence but also support long-term adherence to rehabilitation efforts [29].

Intrinsic motivation, driven by inherent enjoyment or interest, plays a critical role in long-term SCI rehabilitation. Studies emphasize its importance in healthcare, where intrinsically motivated behaviors contribute to better adherence and outcomes [19], particularly when visible progress plateaus and extrinsic rewards lose their impact [4]. While extrinsic motivation is crucial during the early stages of recovery, sustaining motivation in later rehabilitation stages requires individuals to find personal value in the process.

Our study found that visual feedback tools could enhance participant engagement and enjoyment, even during repetitive tasks. Although it is uncommon for individuals to inherently enjoy rehabilitation [4], these tools appear to bridge the gap between extrinsic rewards and intrinsic motivation by making the process more interactive and intrinsically rewarding. Participants noted that they were more motivated when rehabilitation activities aligned with their interests, reinforcing the idea that intrinsic motivation is heightened when activities hold personal significance [19], [30].

B. Use Cases and Considerations in SCI Rehabilitation

Rehabilitation following an SCI focuses on restoring muscle control to enhance mobility, with hand function playing a key role in quality of life [31], [32], [33], [34].

Participants in this study reported that visual feedback enhanced their muscle awareness by highlighting sub-functional muscle activity, such as minor wrist extensions. This type of feedback could foster motivation during early rehabilitation and support motor learning [6], [26], [35]. For individuals with impaired proprioception, visual feedback could compensate as a form of "sensory substitution," reinforcing the brain-body connection and anchoring neuroplastic processes through the "use it or lose it" principle to prevent functional decline [36].

The tool showed potential to aid in muscle isolation, addressing challenges in traditional rehabilitation. Minimizing co-activation has been shown to enhance motor function [37], [38], and participants in our study successfully reduced co-activation that hindered movement. Additionally, visual feedback could help manage spasticity by improving awareness of over-activation, enabling patients to adjust and work with therapists to refine muscle relaxation strategies. Research supports the effectiveness of EMG feedback in improving spasticity management and motor function in persons living with stroke [11].

The tool could also inform decisions about tenodesis grip, a technique enabling passive grip in SCI rehabilitation. EMG visual feedback provides insights into whether muscle activity is sufficient to transition from passive to active grip, aiding clinicians in modifying rehabilitation strategies [39].

Participants noted that EMG visual feedback could improve rehabilitation by enabling real-time progress tracking and exercise adjustments, promoting error correction and goal calibration. Our EMG feedback system uses abstract visualizations, such as lines or bars, that are effective for motor learning [7]. Participants also expressed interest in remote therapist check-ins, underscoring the value of tools that extend rehabilitation beyond clinical settings. Research demonstrates a positive correlation between therapy duration and clinical outcomes, with more sessions yielding greater recovery in stroke survivors [40]. Aligned with Activity-Based Therapy (ABT) principles—repetition, intensity, and task specificity—the EMG feedback tool supports neuroplasticity-driven rehabilitation and promotes habit formation and flexibility for home use [41], [42].

Furthermore, participants emphasized that visual feedback strengthens communication with therapists by enabling clearer articulation of challenges and progress, which fosters a therapeutic alliance associated with improved outcomes [43].

While EMG visual feedback shows promise in SCI rehabilitation, its integration requires consideration of individual preferences. None of our participants had prior experience with EMG feedback, emphasizing the need for a personalized introduction. Some may benefit from focusing directly on limb movements, while others may prefer visual, auditory (e.g., tones), or tactile (e.g., vibrations) feedback, or combinations of these modalities [7]. Tailoring feedback to individual needs could optimize outcomes.

In SCI, where sensory and motor impairments limit proprioceptive feedback, visually observing the limb becomes crucial. Internal Focus of Attention (IFA), where individuals focus on their movements and sensations, can enhance muscle awareness, but excessive reliance on IFA may hinder performance [44]. While IFA can be beneficial in certain contexts, such as increasing awareness of muscle activation, excessive reliance on this focus may hinder motor performance and learning [44]. Van Vliet & Wulf [44] suggest that an External Focus of Attention (EFA), concentrating on the effects of one's movements on the environment, improves task performance, highlighting its relevance in SCI rehabilitation. In our study, participants with more functional movement preferred observing their limbs directly, while those with greater motor impairment found EMG feedback more useful, suggesting that feedback should match individual impairments and preferences.

Auditory feedback, such as tones, can help patients track muscle activity without solely relying on visual cues, though it may be distracting for some [45]. Tactile feedback, such as vibration, has also been reported to enhance muscle recruitment and focus, supporting its potential as a complementary modality alongside visual and auditory feedback.

Functional recovery, particularly in gripping and dexterity, is a core goal of SCI rehabilitation [46]. While our EMG feedback tool focused on basic movements, such as wrist flexion, extension, and hand opening, these movements are vital for restoring function. A strength of the tool was its ability to visualize antagonistic muscle pairs, helping participants refine control and isolate muscles. Aligning the gestures more closely with everyday tasks could further improve outcomes. Future versions could allow customization, enabling clinicians to tailor exercises to functional goals.

Clinicians are crucial in helping patients use visual feedback systems effectively. While these tools promote independence, prescriptive feedback in the early stages is essential for progress [7]. In this study, the lack of prescriptive capabilities in the EMG feedback system required participants to rely on guidance from the research team, highlighting the importance of clinician support in maximizing the tool's effectiveness in SCI rehabilitation.

C. *Beyond Visualizations – Games and Device Control*

As an extension of visual feedback of EMG activity, EMG amplitude and patterns of activation can be leveraged to control a curser in a game environment or serve as input to assistive devices. Pattern-recognition techniques have shown promise in detecting and decoding movement intent from subfunctional muscle contractions, with successful applications in individuals with SCI [47][48]. Over the past decade, rehabilitation games targeting post-stroke populations have gained significant research attention due to their potential to boost patient motivation, enhance motor skills, and provide effective pain management through positive distraction [49][50].

V. Conclusion

This exploratory study highlights the significant potential of EMG visual feedback in enhancing motivation and supporting the rehabilitation of hand function in individuals with SCI. By expanding access to remote and cost-effective care, this technology has the potential to improve patient outcomes and provide essential early, intensive, and consistent rehabilitation.

References

[1] R. Colombo et al., “Design strategies to improve patient motivation during robot-aided rehabilitation,” J Neuroeng Rehabil, vol. 4, pp. 1–12, Feb. 2007, doi: 10.1186/1743-0003-4-3.

[2] Z. K. Güngör, “Rehabilitation of Spinal Cord Injury,” in Traumatic Brain Injury - Challenges, I. Mavroudis and A. Ciobica, Eds., IntechOpen, Oct. 2024. doi: 10.5772/intechopen.1007372.

[3] K. Nas, L. Yazmalar, V. Sah, A. Aydin, K. Ones, “Rehabilitation of Spinal Cord Injuries,” World Journal of Orthopedics, vol. 6, no. 1, pp. 8–16, Jan. 2015, doi: 10.5312/wjo.v6.i1.8.

[4] T. Yoshida, Y. Otaka, R. Osu, M. Kumagai, S. Kitamura, and J. Yaeda, “Motivation for Rehabilitation in Patients With Subacute Stroke: A Qualitative Study,” Frontiers in Rehabilitation Sciences, vol. 2, no. 664758, pp. 1–10, Jun. 2021, doi: 10.3389/fresc.2021.664758.

[5] M. M. Yassin, M. N. Saad, A. M. Khalifa, and A. M. Said, “Advancing clinical understanding of surface electromyography biofeedback: bridging research, teaching, and commercial applications,” Expert Review of Medical Devices, vol. 21, no. 8, pp. 709-726, Jul. 2024, doi: 10.1080/17434440.2024.2376699.

[6] R. A. Schmidt, T. D. Lee, C. J. Winstein, G. Wulf, and H. N. Zelaznik, Motor control and learning: A behavioral emphasis 6th ed. Champaign, Il: Human Kinetics, 2019.

[7] R. Sigrist, G. Rauter, R. Riener, and P. Wolf, “Augmented visual, auditory, haptic, and multimodal feedback in motor learning: A review,” 2013, Psychonomic Bulletin & Review, vol. 20, no. 1, pp. 21-53, Nov. 2012, doi: 10.3758/s13423-012-0333-8.

[8] A. Sturma, L. A. Hruby, C. Prahm, J. A. Mayer, and O. C. Aszmann, “Rehabilitation of upper extremity nerve injuries using surface EMG biofeedback: Protocols for clinical application,” Frontiers in Neuroscience, vol. 12, Dec. 2018, doi: 10.3389/fnins.2018.00906.

[9] A. B. Gámez, J. J. Hernandez Morante, J. L. Martínez Gil, F. Esparza, and C. M. Martínez, “The effect of surface electromyography biofeedback on the activity of extensor and dorsiflexor muscles in elderly adults: a randomized trial,” Scientific Reports, vol. 9, no. 1, Sep. 2019, doi: 10.1038/s41598-019-49720-x.

[10] O. Armagan, F. Tascioglu, and C. Oner, “Electromyographic Biofeedback in the Treatment of the Hemiplegic Hand: A Placebo-Controlled Study,” Am J Phys Med Rehabil, vol. 82, no. 11, pp. 856–861, Nov. 2003, doi: 10.1097/01.PHM.0000091984.72486.E0.

[11] M. Doan-Aslan, G. F. Nakipolu-Yüzer, A. Doan, I. Karabay, and N. Özgirgin, “The effect of electromyographic biofeedback treatment in improving upper extremity functioning of patients with hemiplegic stroke,” Journal of Stroke and Cerebrovascular Diseases, vol. 21, no. 3, pp. 187–192, Apr. 2012, doi: 10.1016/j.jstrokecerebrovasdis.2010.06.006.

[12] R. B. Stein, B. S. Brucker, and D. R. Ayyar, “Motor units in incomplete spinal cord injury: Electrical activity, contractile properties and the effects of biofeedback,” J Neurol Neurosurg Psychiatry, vol. 53, no. 10, pp. 880–885, Oct. 1990, doi: 10.1136/jnnp.53.10.880.

[13] K. J. Klose, B. M. Needham, D. Schmidt, J. G. Broton, and B. A. Green, “An assessment of the contribution of electromyographic biofeedback as an adjunct therapy in the physical training of spinal cord injured persons,” Arch Phys Med Rehabil, vol. 74, no. 5, pp. 453–456, May. 1993, doi: 10.1016/0003-9993(93)90103-H.

[14] B. S. Brucker and N. V. Bulaeva, “Biofeedback effect on electromyography responses in patients with spinal cord injury,” Arch Phys Med Rehabil, vol. 77, no. 2, pp. 133–137, Feb. 1996, doi: 10.1016/S0003-9993(96)90157-4.

[15] E. Eddy, E. Campbell, A. Phinyomark, S. Bateman, and E. Scheme, “LibEMG: An Open Source Library to Facilitate the Exploration of Myoelectric Control,” IEEE Access, vol. 11, pp. 87380–87397, Jan. 2023, doi: 10.1109/ACCESS.2023.3304544.

[16] A. Radford, J. W. Kim, T. Xu, G. Brockman, C. McLeavey, and I. Sutskever, "Robust speech recognition via large-scale weak supervision," Proc. 40th Int. Conf. Mach. Learn. (ICML'23), vol. 202, article 1182, pp. 28492–28518, 2023. JMLR.org.

[17] V. Braun and V. Clarke, “Using thematic analysis in psychology,” Qual Res Psychol, vol. 3, no. 2, pp. 77–101, Jul. 2006, doi: 10.1191/1478088706qp063oa.

[18] Y. Lincoln and E. Guba, Naturalistic Inquiry, 1st ed. London: Sage Publications, 1985.

[19] R. M. Ryan and E. L. Deci, “Intrinsic and extrinsic motivation from a self-determination theory perspective: Definitions, theory, practices, and future directions,” Contemp Educ Psychol, vol. 61, Apr. 2020, doi: https://doi.org/10.1016/j.cedpsych.2020.101860.

[20] E. Michalovic, M. Rocchi, and S. N. Sweet, “Motivation and participation in daily and social activities among adults with spinal cord injury: Applying self-determination theory,” Disabil Health J, vol. 12, no. 3, pp. 489–494, Jul. 2019, doi: 10.1016/j.dhjo.2018.11.015.

[21] M. Saebu, M. Sørensen, and H. Halvari, “Motivation for physical activity in young adults with physical disabilities during a rehabilitation stay: A longitudinal test of self-determination theory,” J Appl Soc Psychol, vol. 43, no. 3, pp. 612–625, Feb. 2013, doi: 10.1111/j.1559-1816.2013.01042.x.

[22] R. J. Siegert and W. J. Taylor, “Theoretical aspects of goal-setting and motivation in rehabilitation,” *Disabil Rehabil*, vol. 26, no. 1, pp. 1–8, Jan. 2004, doi: 10.1080/09638280410001644932.

[23] J. Y. Y. Ng et al., “Self-Determination Theory Applied to Health Contexts: A Meta-Analysis,” Perspectives on Psychological Science, vol. 7, no. 4, pp. 325–340, Jun. 2012, doi: 10.1177/1745691612447309.

[24] T. W. Malone, “Toward a Theory of Intrinsically Motivating Instruction*,” Cognitive Science, vol. 5, no. 4, pp. 333–369, Oct. 1981, doi: https://doi.org/10.1207/s15516709cog0504_2.

[25] D. R. Flatla, C. Gutwin, L. E. Nacke, S. Bateman, and R. L. Mandryk, “Calibration games: Making calibration tasks enjoyable by adding motivating game elements,” Proceedings of the 24th Annual ACM Symposium on User Interface Software and Technology - UIST’11, pp. 403–412, 2011, doi: 10.1145/2047196.2047248.

[26] M. Sailer and L. Homner, “The Gamification of Learning: a Meta-analysis,” Educ Psychol Rev, vol. 32, no. 1, pp. 77–112, Aug. 2019, doi: 10.1007/s10648-019-09498-w.

[27] D. L. Kappen, P. Mirza-Babaei, and L. E. Nacke, “Gamification of Older Adults’ Physical Activity: An Eight-Week Study,” Proceedings of the 51st Hawaii International Conference on System Sciences, 2018, doi: https://doi.org/10.24251/hicss.2018.149.

[28] R. J. Siegert and W. M. M. Levack, Rehabilitation Goal Setting: Theory, Practice, and Evidence. Boca Raton: CRC Press/Taylor & Francis Group, 2015.

[29] K. Kingston, D. Jenkins, and G. Kingston, “Promoting adherence to rehabilitation through supporting patient well-being: A self-determination perspective,” Essentials of exercise and sport psychology: An open access textbook, pp. 759–782, Jan. 2021, doi: 10.51224/b1032.

[30] K. A. Renninger and S. E. Hidi, “Interest: A unique affective and cognitive motivational variable that develops,” in Advances in Motivation Science, vol. 9, Elsevier, 2022, ch. 6, pp. 179–239.

[31] R. de la Rosa, A. Carrera, A. Alonso, B. Peñasco-Martín, A. Gil-Agudo, and E. J. Abril, “Myoelectric gaming in the rehabilitation of patients with C7 spinal cord injury,” Applied Sciences, vol. 9, no. 9, May 2019, doi: 10.3390/app9091912.

[32] K. Ganguly and M. Poo, “Activity-Dependent Neural Plasticity from Bench to Bedside,” *Neuron*, vol. 80, no. 3, pp. 729–741, Oct. 2013, doi: https://doi.org/10.1016/j.neuron.2013.10.028.

[33] M. G. Bowden, M. L. Woodbury, and P. W. Duncan, “Promoting neuroplasticity and recovery after stroke: Future directions for rehabilitation clinical trials,” *Curr Opin Neurol*, vol. 26, no. 1, pp. 37–42, 2013, doi: 10.1097/WCO.0b013e32835c5ba0.

[34] H. Hoffman *et al.*, “Rehabilitation of hand function after spinal cord injury using a novel handgrip device: a pilot study,” *J Neuroeng Rehabil*, vol. 14, no. 1, Mar. 2017, doi: 10.1186/s12984-017-0234-1.

[35] J. Hattie and H. Timperley, “The power of feedback,” Review of Educational Research, vol. 77, no. 1, pp. 81-112, Mar. 2007, doi: 10.3102/003465430298487.

[36] P. Lynch, P. Broderick, and K. Monaghan, “Sensory substitution for orthopaedic gait rehabilitation: A systematic review and meta-analysis for clinical practice guideline development,” Heliyon, vol. 8, no. 10, Oct. 2022, doi: 10.1016/j.heliyon.2022.e10986.

[37] M. L. Latash, “Muscle coactivation: Definitions, mechanisms, and functions,” J Neurophysiol, vol. 120, no. 1, pp. 88–104, Jul. 2018, doi: 10.1152/jn.00084.2018.

[38] J. Chae, G. Yang, B. K. Park, and I. Labatia, “Muscle Weakness and Cocontraction in Upper Limb Hemiparesis: Relationship to Motor Impairment and Physical Disability,” Neurorehabil Neural Repair, vol. 16, no. 3, pp. 241–248, Sep. 2002, doi: 10.1177/154596830201600303.

[39] S. Pripotnev, J. Bruce, C. B. Novak, C. R. Kennedy, and I. K. Fox, “Quantifying Tenodesis Hand Function in Cervical Spinal Cord Injury: Implications for Function,” The Journal of Hand Surgery, vol. 48, no. 7, pp. 700–710, Jul. 2023, doi: https://doi.org/10.1016/j.jhsa.2023.04.004.

[40] A. J. Song, L. Lugo, J. Muccini, M. Mlynash, and M. G. Lansberg, “EngageHealth: a mobile device application designed to deliver stroke rehabilitation exercises using asynchronous video recordings,” Frontiers in Stroke, vol. 3, Sep. 2024, doi: 10.3389/fstro.2024.1418298.

[41] A. L. Behrman, E. M. Ardolino, and S. J. Harkema, “Activity-Based Therapy: From Basic Science to Clinical Application for Recovery after Spinal Cord Injury,” in Journal of Neurologic Physical Therapy, pp. S39–S45, Jul. 2017, doi: 10.1097/NPT.0000000000000184.

[42] E. Swaffield et al., “Perspectives of people living with a spinal cord injury on activity-based therapy,” Disabil Rehabil, vol. 44, no. 14, pp. 3632–3640, Feb. 2021, doi: 10.1080/09638288.2021.1878293.

[43] L. K. Truong, A. D. Mosewich, C. J. Holt, C. Y. Le, M. Miciak, and J. L. Whittaker, “Psychological, social and contextual factors across recovery stages following a sport-related knee injury: A scoping review,” British Journal of Sports Medicine, vol. 54, no. 19, pp. 1149-1156, Feb. 2020, doi: 10.1136/bjsports-2019-101206.

[44] P. Van Vliet, “Attentional focus of feedback and instructions in the treatment of musculoskeletal dysfunction: A systematic review,” Manual Therapy, vol. 18. No. 6, pp. 458-467, Dec. 2013, doi: 10.1016/j.math.2013.07.002.

[45] A. W. Shehata, E. J. Scheme, and J. W. Sensinger, “Audible Feedback Improves Internal Model Strength and Performance of Myoelectric Prosthesis Control,” *Sci Rep*, vol. 8, no. 1, Dec. 2018, doi: 10.1038/s41598-018-26810-w.

[46] American Occupational Therapy Association, “Occupational therapy practice framework: Domain and process (3rd edition),” American Journal of Occupational Therapy, vol. 68, no. 1, pp. S1–S48, Sep. 2014, doi: https://doi.org/10.5014/ajot.2014.682006.

[47] N. Seth, R. C. D. Freitas, M. Chaulk, C. O’Connell, K. Englehart, and E. Scheme, “EMG pattern recognition for persons with cervical spinal cord injury,” IEEE International Conference on Rehabilitation Robotics, vol. 2019-June, pp. 1055–1060, 2019, doi: 10.1109/ICORR.2019.8779450.

[48] D. S. Oliveira et al., “You Will Grasp Again: A Direct Spinal Cord/Computer Interface with the Spared Motor Neurons Restores the Dexterous Control of the Paralyzed Hand after Chronic Spinal Cord Injury,” Sep. 10, 2022. doi: 10.1101/2022.09.09.22279611.

[49] N. T. Hung et al., "Wearable myoelectric interface enables high-dose, home-based training in severely impaired chronic stroke survivors," Annals of Clinical and Translational Neurology, vol. 8, no. 9, pp. 1895–1905, 2021. doi: 10.1002/acn3.51442.

[50] E. M. Mugler et al., "Myoelectric computer interface training for reducing co-activation and enhancing arm movement in chronic stroke survivors: A randomized trial," Neurorehabilitation and Neural Repair, vol. 33, no. 4, pp. 284–295, 2019. doi: 10.1177/1545968319834903.

Biplanar Ankle Assistance for Dropfoot Gait Post-Stroke with Multi-objective Human-in-the-Loop Optimization: A Case Study

Xiaochen Zhang[1], Axel Fredriksen[2], Susanne Palmcrantz[2], and *Elena M. Gutierrez-Farewik[1,3]

***Abstract*— Exoskeletons are frequently explored for their efficacy in rehabilitation and in assisting in daily activities in people with motor disorders, yet relatively few have convincing evidence for use, nor do many aim to personalize assistance for maximum benefit of each user. Here, we describe a cable-driven ankle exoskeleton that assists persons with dropfoot and excessive inversion after stroke. We propose a multi-objective human-in-the-loop optimization that simultaneously adjusts exoskeleton assistive profiles to minimize two independent gait quality indices: foot kinematics deviation and step length asymmetry. This optimization proposes, rather than a single solution, a group of solutions that minimize both indices. We present experimental findings from one participant with chronic stroke, specifically the feasibility of the device in assisting ankle motion in two anatomical planes, the resulting gait pattern and individualized optimal assistive profiles. Following the design goals, the exoskeleton improved the dropfoot and excessive inversion gait pattern; with the exoskeleton, the participant's foot inclination angle at initial contact increased from -2° to 10°, ankle inversion angle decreased from 2° to 0°, foot clearance during swing increased from 31 mm to 44 mm, and step length asymmetry decreased from 12% to 6%. The optimal solutions are an inventory of profiles from which the user can choose based on priorities. We believe the device and approach have a large potential in achieving individualized assistance.**

I. INTRODUCTION

Exoskeletons and exosuits for gait are developed with increasing frequency, with objectives often focusing on a single, albeit complex, criterion [1], e.g. strength augmentation, reduced target muscle activation [2], normalized joint kinematics, or reduced metabolic cost of transport [3]. Outcome and compliance, however, often depend on the user's perception and subjective experience [4]. Goals to improve gait quality, furthermore, often rely on an individualized approach [5] and on gait metrics that are of a more holistic nature [6], such as walking speed or symmetry. An approach that considers several gait metrics simultaneously may have to strike an optimal balance between different metrics.

The gait pathology in focus in this study is dropfoot, or the inability to dorsiflex the foot during swing and to position the foot for heel contact [7]. Dropfoot is a common secondary gait disorder after a stroke or other neurological injury that affects motor control. It is often accompanied by excessive subtalar inversion due to spasticity of the tibialis posterior [8]. Together, these symptoms can affect stability in stance and risk of falling [9]. Addressing these can vastly improve the quality of life and promote independence [10], [11] in the large post-stroke population. While exoskeletons have shown promise in improving mobility after stroke [11], existing devices largely focus on sagittal plane assistance, neglecting frontal plane malalignments that are also crucial for stability.

Thanks to approaches such as human-in-the-loop (HIL) optimization, significant progress has been made in recent years in customizing exoskeleton control [4], [12]. To date, these efforts have predominantly targeted non-disabled individuals; few attempts have been made to optimize exoskeleton control for individuals with motor disorders, leaving a critical gap in addressing the unique needs of this population. Furthermore, metabolic cost or muscle activity reduction has typically been the pre-defined physiological objective [13]–[15], whereas for people with motor disorders, performance metrics related to gait quality can be more relevant [16]. Evaluation of gait quality generally involves multiple, rather than single, outcome measures, including but not limited to temporospatial symmetry and kinematics of specific joints or segments.

We recently proposed a cable-driven ankle exoskeleton that can simultaneously guide the foot in the sagittal and frontal planes, and thereby increase foot clearance height and stabilize the foot and ankle in initial contact [17]. We also recently proposed a multi-objective HIL optimization to improve foot segment kinematics in swing and initial contact as well as step length symmetry and pilot-tested it on a group of nondisabled adults [18].

This paper presents a case study of one woman with chronic stroke and a dropfoot gait pattern, with aims to evaluate the exoskeleton's feasibility and effectiveness in two criteria: minimizing step length asymmetry and foot kinematic deviations in swing and initial contact. The key contributions presented in this study are as follows: 1) In a participant in the chronic phase after stroke and a dropfoot gait pattern, we demonstrated performance enhancements in two gait quality indices simultaneously, achieved through an ankle exoskeleton and multi-objective HIL protocol. 2) We introduce a flexible decision-making individualization framework that can tailor assistive solutions to individual goals and abilities.

*This work was generously funded by the Promobilia Foundation (ref 23010, 23010-2, and 23300), by the Swedish Research Council (ref 2018-00750) and by Digital Futures (ref KTH-RPROJ-0146472). The work of Xiaochen Zhang was also supported by the China Scholarship Council (CSC).

*Corresponding author is Elena M. Gutierrez-Farewik, lanie@kth.se.

[1]KTH MoveAbility, Department of Engineering Mechanics, KTH Royal Institute of Technology, Stockholm, Sweden.

[2]Department of Clinical Sciences Danderyd Hospital, Karolinska Institutet, Stockholm, Sweden.

[3]Department of Women's and Children's Health, Karolinska Institutet, Stockholm, Sweden.

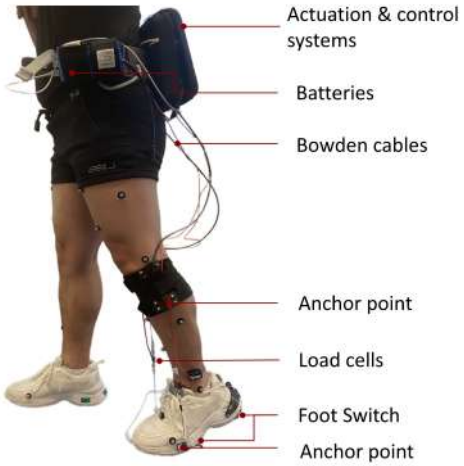


Fig. 1. The cable-driven ankle exoskeleton. The exoskeleton, designed to dorsiflex and evert the foot, consists of an actuation and control system, two Bowden cables that span to anchor points on the medial and lateral forefoot, textile components, and sensors.

II. MATERIALS AND METHODS

A. Device design and control

Our active soft ankle exoskeleton (Fig. 1) consisted of a waist unit, a calf wrap, a pair of shoes, cables, and sensors, with a total mass of 3.1 kg. The waist unit houses the actuation module, which consists of two brushless DC motors (Maxon, max torque 5.54 Nm), 3D printed pulleys, and Bowden cables with a maximum retraction force of 396 N. A microcomputer (Raspberry Pi 4B) controls the actuators by sending control signals to motor drivers, and can be monitored and controlled remotely. Encoders mounted on the motors monitor motor positions. Each Bowden cable is aligned in series with a load cell (Futek) and amplifier, which measure cable tension and transmit values to the controller. The two Bowden cables span distally to the shoe via anchors on the medial and lateral sides of the calf wrap, to hooks in the medial and lateral shoe forefoot. A set of foot switches (Cometa), with 4 force sensitive resisters under each foot detect foot-floor contact. Movement information is extracted from sensors, the microcomputer sends control signals to the motor drivers, and the actuators are driven to follow the control profiles.

In the high-level controller, the foot switch information is used to identify the stance and swing phases. In the mid-level controller, assistance profiles are generated as two parameters – t_p: the combined torque generated by two motors, and r_{lm}: the torque ratio between lateral and medial motors, wherein a larger ratio results in more cable tension on the lateral than the medial side. Ramp ascent and descent timing of the current profiles were based on swing phase duration and were the same for both motors. The low-level controller drives the motors to follow the assistive profiles defined by the mid-level controller precisely.

B. Multi-objective HIL optimization protocol

We integrated a multi-objective optimization algorithm into the HIL protocol to identify exoskeleton assistive profiles, defined by [t_p, r_{lm}], with two objectives: improving segment kinematics and enhancing overall performance.

1) Variable and constraints: Two variables, the sum of the torque magnitude of the two motors t_p and the torque ratio between lateral and medial motors r_{lm}, determined the assistive profile, and were set to 57 ± 12 Nmm/kg and 1.15 ± 0.1, respectively.

2) Multiple objective functions: Two independent gait quality metrics were minimized in the optimization approach; 1) deviation of paretic side foot segment kinematics compared to nonparetic side, characterized by two parameters: foot inclination angle in the sagittal plane at initial contact and foot clearance height during swing, as per Eq. 1, and 2) minimal step length asymmetry, as per Eq. 2.

$$\mathrm{Dev}_{\mathrm{foot}} = \left(\left|\frac{\alpha_{\mathrm{p}} - \alpha_{\mathrm{np}}}{\alpha_{\mathrm{np}}}\right| + \left|\frac{H_{\mathrm{p}} - H_{\mathrm{np}}}{H_{\mathrm{np}}}\right|\right) \times 100\% \quad (1)$$

$$\mathrm{ASI}_{\mathrm{SL}} = \left|\frac{L_{\mathrm{step,p}} - L_{\mathrm{step,np}}}{0.5 \cdot (L_{\mathrm{step,p}} + L_{\mathrm{step,np}})}\right| \times 100\% \quad (2)$$

where $\mathrm{Dev}_{\mathrm{foot}}$ is the deviation index of the foot's kinematics of the paretic side compared to the non-paretic side, α_{p} and α_{np} are the foot inclination angle at initial contact for paretic and non-paretic sides, respectively, in the sagittal plane, H_{p} and H_{np} are the clearance height of the paretic and non-paretic feet during swing, $\mathrm{ASI}_{\mathrm{SL}}$ is the step length asymmetry index, $L_{\mathrm{step,\,p}}$ and $L_{\mathrm{step,\,np}}$ are step length of paretic and non-paretic sides [16], [19], defined as the distance between the ipsilateral and contralateral heel marker at initial contact in the direction of walking.

3) Optimization algorithm: A non-dominated sorting genetic algorithm II (NSGA-II) was used for multi-objective optimization in the HIL framework. Three generations, each comprising 10 assistive profiles constrained by t_p and r_{lm}, were tested, with crossover and mutation rates set to 0.7 and 0.3, respectively.

C. Participant

One participant with chronic stroke, a 47-year-old woman, 159 cm, 73 kg, participated in this study. Her left side was affected following a stroke nearly 5 years previously. She habitually used an AFO but could walk without it. Her Fugl-Meyer Lower Extremity scores were 25 (out of 34) for motor function and 9 (out of 12) for sensory function. She presented with spasticity according to the Modified Ashworth Scale of 2 in the rectus femoris, 2 in the soleus, and 0 in the gastrocnemius. Her dorsiflexion passive range of motion was -2 degrees, with the knee extended. The Swedish Ethical Review Authority granted approval for this experiment (Dnr. 2023-02891-01). The participant provided informed written consent before the experiment.

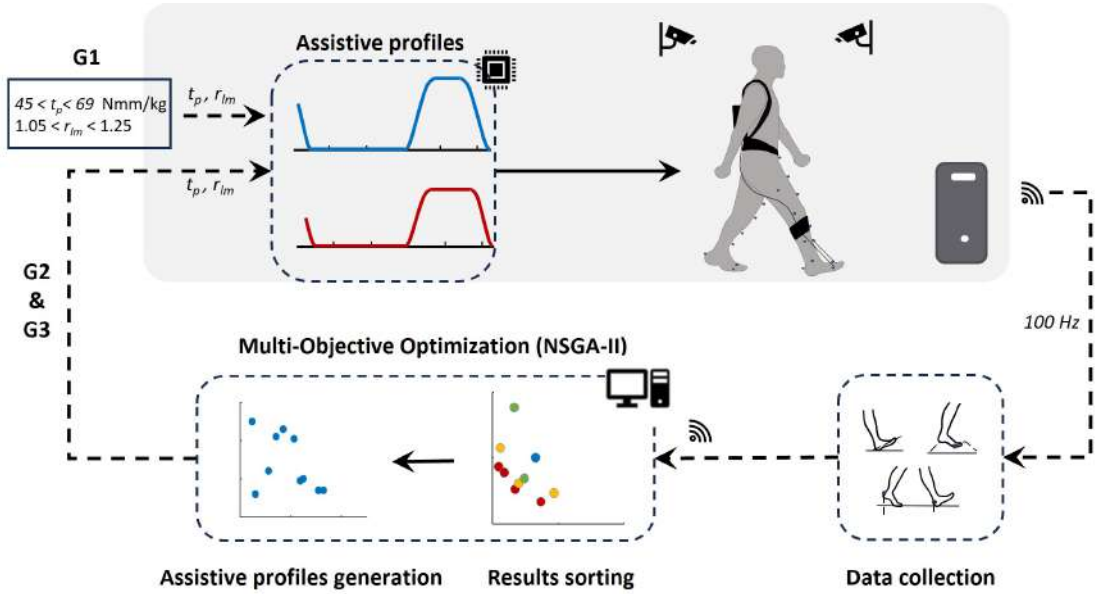


Fig. 2. The experimental setup for multi-objective HIL optimization. The participant underwent three generations of assistance trials, each consisting of two 10-meter trials. Kinematic and spatiotemporal parameters were collected by the motion capture system, and the two optimization functions were computed - deviation of foot segment kinematics and step length asymmetry. NSGA-II was used to sort the assistive profiles after each generation, and new assistive profiles were generated for the subsequent generation.

D. Experiments

The experiment was conducted in the Promobilia Move-Ability Lab, in overground walking along a 10-meter walkway. Markers were placed on the lower extremity and trunk according to a common model (CGM 2.4) and their trajectories were captured with a 10-camera motion capture system (Vicon V16, UK) at 100 Hz.

Equipped with markers, the participant walked at her preferred speed in the following conditions:

- NoExo: walking with regular shoes, e.g. no exoskeleton or AFO, to establish the participant's baseline gait.
- Familiarization: The participant donned the exoskeleton and walked with it for 20-30 minutes, during which several different assistive profiles were randomized. No specific instructions about modifying the walking strategy were given, so that the participant could respond naturally to the device.
- UnpowExo: The participant wore the exoskeleton unpowered and with the cables detached, to evaluate the effect of donning the exoskeleton but independent of active assistance or passive device resistance.
- PowExoHIL: The participant walked with the powered exoskeleton, through 3 generations of ten assistive profiles each and HIL optimization.

For Generation 1 of PowerExo, the range of assistance profiles was constrained to: $45<t_p<69$ Nmm/kg as per suggestion [10] and $1.05<r_{lm}<1.25$, with a uniform distribution. A 1-minute interval for rest was provided between different profiles. Immediately after Generation 1 experiments, the two objective functions (Eq. 1 and Eq. 2) were computed from all solutions in the generation. The NSGA-II algorithm sorted the objective function results into multiple fronts, wherein the Pareto front represents the optimal solutions for this generation. It then generated a new set of assistive profiles, subject to the same constraints for t_p and r_{lm}, which formed Generation 2. This process was iterated again, and the experiment concluded after Generation 3.

After the experiment, the participant answered the Quebec User Evaluation of Satisfaction with Assistive Technology 2.0 (QUEST 2.0) [20] pertaining to the device's dimensions, weight, stability and security, comfort, and effectiveness. The answers were given on a 5-point scale, with 5 indicating "very satisfied," and 1 indicating "not satisfied at all," so that a grade of 1-2 can be defined as negative, 3 as neutral, and 4-5 as positive.

III. Results

During the HIL optimization, the solutions progressed towards better gait quality metrics, specifically lower foot segment deviation and step length asymmetry. (Fig. 3), wherein both indices converged towards 0. The solutions from Generation 3 on the Pareto front can be seen as the optimal solutions for this participant and these two defined optimization criteria.

Compared to NoExo, with the PowExoHIL optimal solutions, the ankle joint kinematics were normalized; a first/heel rocker occurred after initial contact, and the ankle was in dorsiflexion throughout the stance. The key gait metrics improved; at initial contact, the foot inclination angle increased from -2° to 11°, and the ankle inversion angle decreased slightly from 2° to around 0°. Foot clearance height in swing increased from 31 mm to 43 mm, and step length asymmetry reduced from 12% to 6%.

We also observed slight differences between the NoExo and UnpowExo conditions, indicating that the structure itself

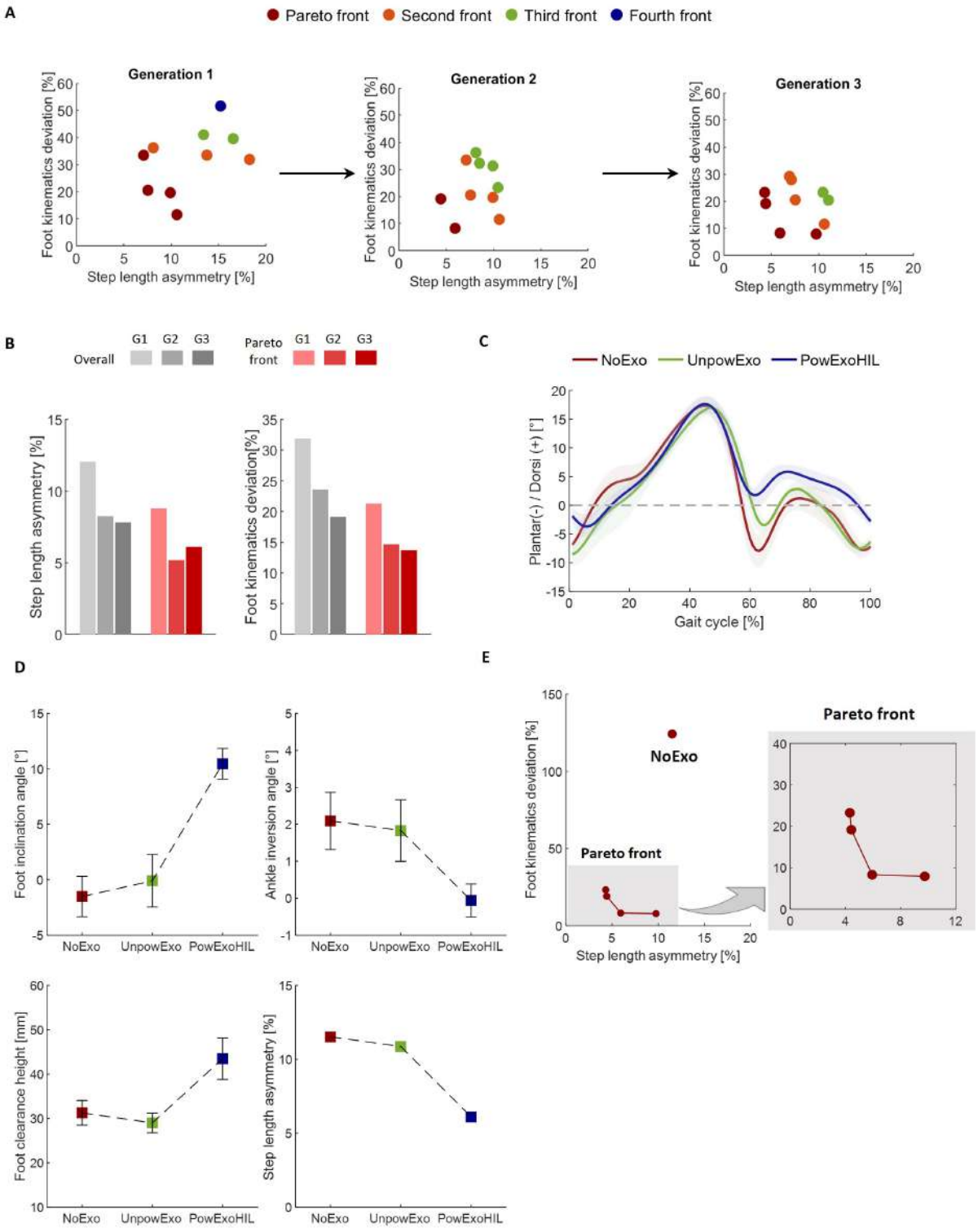


Fig. 3. A. Resulting gait quality metrics during the multi-objective HIL optimization process for the participant across three generations. B. Mean gait quality metrics of the overall solutions and the solutions on the Pareto front across three generations. C. The participant's ankle joint kinematics without the exoskeleton (NoExo), with the exoskeleton but no cables or power (UnpowExo), and with the exoskeleton and optimal assistance (PowExoHIL). D. The participant's gait metrics in NoExo, UnpowExo, and PowExoHIL conditions. Four metrics are listed: Foot inclination angle at initial contact, Ankle inversion angle at initial contact, Foot clearance height during swing, and step length asymmetry. E. Subject-specific Pareto front illustrates the trade-off between gait deviation and step length asymmetry for the participant. The metrics in the NoExo condition are shown in the inset at the top left for comparison.

has some effect, but this difference was small compared to the improvements observed with optimal assistance (PowExoHIL).

The gait metrics with solutions on the Pareto front illustrate the improvements in both metrics with assistance. These solutions can all be seen as optimal, even though trade-offs among them can be observed. No single solution minimized both gait quality metrics; the solution that minimizes step length symmetry resulted in a much lower foot kinematics deviation than the baseline NoExo, but was not minimum, and vice versa. The optimal assistive profiles that correspond to the gait quality indices on the Pareto front in Fig. 3E from left to right are [64.4, 1.07], [62.9, 1.10], [68.1, 1.17], and [60.8, 1.11] (Nmm/kg, /).

The participant was satisfied with the device's weight (5/5), stability and security (4/5), and effectiveness (4/5), neutral to the dimension (3/5), and not satisfied with the device's comfort (2/5).

IV. Discussions

In this study, we evaluated the feasibility and potential efficacy of a cable-driven ankle exoskeleton and a multi-objective HIL framework, which were designed to improve gait quality in persons with dropfoot and excessive inversion following a stroke. This evaluation included both objective biomechanical metrics and subjective perception of the user. The simultaneous improvements in multiple gait quality metrics, namely foot kinematics deviation and step length asymmetry, were achieved with the exoskeleton and the HIL framework. The generated Pareto front represents, instead of one optimal solution, a diverse set of optimal solutions that all improve the gait quality metrics in the optimization algorithm. These findings highlight the exoskeleton's ability to effectively address pathological gait patterns while demonstrating the effectiveness of the individualized control framework. This approach offers versatile solutions to accommodate varying individual needs, suggesting a new perspective to personalize the assistance.

The improvements in both gait quality metrics support the effectiveness of the multi-objective HIL optimization introduced in our previous study [18], which was previously only tested on non-disabled subjects with simulated impairments. This study, therefore, addresses three key gaps in the state-of-the-art: individualizing assistance for people with motor disorders, using gait quality kinematic metrics as optimization objectives, and incorporating multiple objectives in the optimization process.

Foot clearance in swing, appropriate pre-positioning of the foot for initial contact, stability in stance, and adequate step length are 4 of the 5 prerequisites of normal and efficient gait, as defined by Gage [21]. Perry has described the importance of the heel rocker mechanism in early stance [9] for stable and efficient gait. Swing phase gait deviations and a forefoot initial contact, with or without excessive ankle inversion, are commonly observed in persons with a dropfoot gait following stroke [8]. They disrupt an efficient gait pattern, commonly requiring compensatory movements to achieve clearance and weight acceptance, and can lead to instability and fall risk [6], and are thus a common target for orthotic treatment [22]. Our exoskeleton and the optimal control solutions improved these features in the participant, as illustrated by the more dorsiflexed ankle position during swing, the greater ankle dorsiflexion and foot segment inclination at initial contact, the presence of a heel rocker in early stance, i.e. the short phase of plantarflexion movement immediately following initial contact, the increased foot clearance height during swing, and the correction of ankle inversion at initial contact. These results are encouraging for the exoskeleton's potential effectiveness in the biplanar assistance required to improve swing phase quality and stability in stance in a post-stroke population, despite its relatively simple design and control concepts.

Gait asymmetry is commonly observed in hemiplegic gait following a stroke [23], [24], and was thus also targetted in this study, here specifically as step length asymmetry. This metric was chosen since its improvement would suggest a positive effect on whole-body kinematics, promoting a more balanced and efficient walking pattern [19], and would also demonstrate that ankle joint assistance can potentially contribute to holistic enhancements in gait quality.

The optimal solutions that make up the Pareto front served as a foundation for individualization of assistance. Each solution can be considered beneficial and unique in that they demonstrated substantial improvements in both gait quality indices compared to without the exoskeleton and presumably contributed to increased stability and efficiency. The multiple, rather than singular, nature of the Pareto front solutions enables each individual to prioritize among the predefined objectives according to goal, preference, and subjective experience; it is conceivable that one solution can be preferable in some walking situations, or that one of the objectives is perceived as more important than the other. This adaptability provides greater flexibility and supports dynamic decision-making during the post-processing stage, making a multi-objective protocol more flexible than traditional single-objective approaches, even those in which the single objective function consists of a weighted sum of different objectives [25].

Thanks to the HIL approach, the solutions identified in this participant are personalized. It can be expected that variations exist in a larger population with dropfoot gait following stroke, as the extent of inability to dorsiflex the ankle and evert the foot will vary. Numerous interesting questions arise regarding how much individual optimal solutions would vary in a larger population, and whether the exoskeleton with this HIL approach can further personalize assistive exoskeleton control.

It can furthermore be expected that the optimization approach would produce entirely different solutions if tasked with optimizing other gait quality and/or performance metrics; the objectives in this study were carefully selected for the targetted gait problem and patient population, and can be constructed instead with different objectives, as deemed appropriate for a specific gait pathology or performance goal.

The participant's overall feedback from the questionnaire was relatively positive and comparable with the subjective feedback reported from other studies [26], [27], indicating that the device largely met their expectations. The only reported point of dissatisfaction was related to comfort, which was attributed to the placement of the EMG transmitter under the relatively tight calf wrap. An interesting point to explore in the future is whether the user's subjective assessment of each assistance profile corresponds to its efficacy in improving gait quality, and whether it can further personalize the device's assistance.

There are, of course, some limitations in this study. The UnpowExo condition was designed to isolate the effects of assistance and assess the impact of the exoskeleton hardware itself on the participant. While slight effects were observed in some metrics, they were not considered to be of a substantial impact, indicating minimal interference from the device. In the HIL framework, three generations comprising 30 assistive profiles in total were tested, which is fewer compared to the four generations used in our previous study [18]. The main reason for this adjustment was practical; the participant reported being tired after 1–2 hours of testing. Drastically reduced walking endurance can be expected in a population post-stroke [28], so the experimental protocol should be kept as short as possible. However, the convergence of mean values for the Pareto front between the second and third generations, along with participant endurance status, suggest that three generations was sufficient for this participant and may be sufficient for a post-stroke population. Furthermore, in this study, we only evaluated the exoskeleton's efficacy in short-term use and in a controlled laboratory setting; its efficacy to improve gait in real-world environments over a long time should be addressed in future studies, as should the clinical significance of improving these gait quality metrics. This is an ongoing study; we only present the findings of one participant in this study and will be able to make firmer conclusions after more participants have been included.

V. Conclusions

To the best of our knowledge, this is the first active exoskeleton device to successfully provide assistance for individuals with dropfoot gait in two anatomical planes with a relatively simple, lightweight, and largely soft design, using an individualized human-in-the-loop approach that seeks the optimality of two objectives simultaneously. The generated family of optimal solutions represents possible choices for an individualized plan for a specific person. Future work will explore additional objectives, including participants' subjective assessments of different assistance profiles.

References

[1] C. Siviy, L. M. Baker, B. T. Quinlivan, F. Porciuncula, K. Swaminathan, L. N. Awad, and C. J. Walsh, "Opportunities and challenges in the development of exoskeletons for locomotor assistance," *Nature Biomedical Engineering*, vol. 7, no. 4, pp. 456–472, 2023.

[2] T. Lenzi, D. Zanotto, P. Stegall, M. C. Carrozza, and S. K. Agrawal, "Reducing muscle effort in walking through powered exoskeletons," in *2012 Annual International Conference of the IEEE Engineering in Medicine and Biology Society*. IEEE, 2012, pp. 3926–3929.

[3] S. H. Collins, M. B. Wiggin, and G. S. Sawicki, "Reducing the energy cost of human walking using an unpowered exoskeleton," *Nature*, vol. 522, no. 7555, pp. 212–215, 2015.

[4] J. Zhang, P. Fiers, K. A. Witte, R. W. Jackson, K. L. Poggensee, C. G. Atkeson, and S. H. Collins, "Human-in-the-loop optimization of exoskeleton assistance during walking," *Science*, vol. 356, no. 6344, pp. 1280–1284, 2017.

[5] G. Durandau, D. Farina, G. Asín-Prieto, I. Dimbwadyo-Terrer, S. Lerma-Lara, J. L. Pons, J. C. Moreno, and M. Sartori, "Voluntary control of wearable robotic exoskeletons by patients with paresis via neuromechanical modeling," *Journal of neuroengineering and rehabilitation*, vol. 16, pp. 1–18, 2019.

[6] L. H. Sloot, L. M. Baker, J. Bae, F. Porciuncula, B. F. Clément, C. Siviy, R. W. Nuckols, T. Baker, R. Sloutsky, D. K. Choe *et al.*, "Effects of a soft robotic exosuit on the quality and speed of overground walking depends on walking ability after stroke," *Journal of neuroengineering and rehabilitation*, vol. 20, no. 1, p. 113, 2023.

[7] P. M. Kluding, K. Dunning, M. W. O'Dell, S. S. Wu, J. Ginosian, J. Feld, and K. McBride, "Foot drop stimulation versus ankle foot orthosis after stroke: 30-week outcomes," *Stroke*, vol. 44, no. 6, pp. 1660–1669, 2013.

[8] C. Beyaert, R. Vasa, and G. E. Frykberg, "Gait post-stroke: Pathophysiology and rehabilitation strategies," *Neurophysiologie Clinique/Clinical Neurophysiology*, vol. 45, no. 4-5, pp. 335–355, 2015.

[9] J. Perry and J. M. Burnfield, "Gait analysis. normal and pathological function 2nd ed," *California: Slack*, 2010.

[10] L.-F. Yeung, C. C. Lau, C. W. Lai, Y. O. Soo, M.-L. Chan, and R. K. Tong, "Effects of wearable ankle robotics for stair and over-ground training on sub-acute stroke: a randomized controlled trial," *Journal of NeuroEngineering and Rehabilitation*, vol. 18, pp. 1–10, 2021.

[11] L. N. Awad, J. Bae, K. O'donnell, S. M. De Rossi, K. Hendron, L. H. Sloot, P. Kudzia, S. Allen, K. G. Holt, T. D. Ellis *et al.*, "A soft robotic exosuit improves walking in patients after stroke," *Science Translational Medicine*, vol. 9, no. 400, p. eaai9084, 2017.

[12] Y. Ding, M. Kim, S. Kuindersma, and C. J. Walsh, "Human-in-the-loop optimization of hip assistance with a soft exosuit during walking," *Science Robotics*, vol. 3, no. 15, p. eaar5438, 2018.

[13] D. F. Gordon, C. McGreavy, A. Christou, and S. Vijayakumar, "Human-in-the-loop optimization of exoskeleton assistance via online simulation of metabolic cost," *IEEE Transactions on Robotics*, vol. 38, no. 3, pp. 1410–1429, 2022.

[14] H. Han, W. Wang, F. Zhang, X. Li, J. Chen, J. Han, and J. Zhang, "Selection of muscle-activity-based cost function in human-in-the-loop optimization of multi-gait ankle exoskeleton assistance," *IEEE Transactions on Neural Systems and Rehabilitation Engineering*, vol. 29, pp. 944–952, 2021.

[15] V. Nalam, X. Tu, M. Li, J. Si, and H. H. Huang, "Admittance control based human-in-the-loop optimization for hip exoskeleton reduces human exertion during walking," in *2022 International Conference on Robotics and Automation (ICRA)*. IEEE, 2022, pp. 6743–6749.

[16] S. Y. Shin, R. K. Lee, P. Spicer, and J. Sulzer, "Does kinematic gait quality improve with functional gait recovery? a longitudinal pilot study on early post-stroke individuals," *Journal of Biomechanics*, vol. 105, p. 109761, 2020.

[17] X. Zhang, Y.-X. Liu, R. Wang, and E. M. Gutierrez-Farewik, "Soft ankle exoskeleton to counteract dropfoot and excessive inversion," *Frontiers in Neurorobotics*, vol. 18, p. 1372763, 2024.

[18] X. Zhang, "Design and control parameter optimization of soft ankle exoskeleton for people with dropfoot and excessive inversion," Ph.D. dissertation, KTH Royal Institute of Technology, 2023.

[19] J. Bae, S. M. M. De Rossi, K. O'Donnell, K. L. Hendron, L. N. Awad, T. R. T. Dos Santos, V. L. De Araujo, Y. Ding, K. G. Holt, T. D. Ellis *et al.*, "A soft exosuit for patients with stroke: Feasibility study with a mobile off-board actuation unit," in *2015 IEEE International Conference on Rehabilitation Robotics (ICORR)*. IEEE, 2015, pp. 131–138.

[20] L. Demers, R. Weiss-Lambrou, and B. Ska, "Quebec user evaluation of satisfaction with assistive technology versione 2.0," *The Institute for Matching Persons and Technology: Webster, NY*, 2000.

[21] J. R. Gage, M. H. Schwartz, S. E. Koop, and T. F. Novacheck, *The identification and treatment of gait problems in cerebral palsy*. John Wiley & Sons, 2009, vol. 180.

[22] J. A. Blaya and H. Herr, "Adaptive control of a variable-impedance ankle-foot orthosis to assist drop-foot gait," *IEEE Transactions on*

Neural Systems and Rehabilitation Engineering, vol. 12, no. 1, pp. 24–31, 2004.

[23] Q. Zhang, X. Tu, J. Si, M. D. Lewek, and H. H. Huang, "A robotic assistance personalization control approach of hip exoskeletons for gait symmetry improvement," 2023.

[24] B. Zhong, K. Guo, H. Yu, and M. Zhang, "Toward gait symmetry enhancement via a cable-driven exoskeleton powered by series elastic actuators," *IEEE Robotics and Automation Letters*, vol. 7, no. 2, pp. 786–793, 2021.

[25] A. Lakmazaheri, S. Song, B. B. Vuong, B. Biskner, D. M. Kado, and S. H. Collins, "Optimizing exoskeleton assistance to improve walking speed and energy economy for older adults," *Journal of NeuroEngineering and Rehabilitation*, vol. 21, no. 1, p. 1, 2024.

[26] B. Noronha, C. Y. Ng, K. Little, M. Xiloyannis, C. W. K. Kuah, S. K. Wee, S. R. Kulkarni, L. Masia, K. S. G. Chua, and D. Accoto, "Soft, lightweight wearable robots to support the upper limb in activities of daily living: a feasibility study on chronic stroke patients," *IEEE Transactions on Neural Systems and Rehabilitation Engineering*, vol. 30, pp. 1401–1411, 2022.

[27] J. de Miguel-Fernández, C. Pescatore, A. Mesa-Garrido, C. Rikhof, E. Prinsen, J. M. Font-Llagunes, and J. Lobo-Prat, "Immediate biomechanical effects of providing adaptive assistance with an ankle exoskeleton in individuals after stroke," *IEEE Robotics and Automation Letters*, vol. 7, no. 3, pp. 7574–7580, 2022.

[28] L. N. Awad, P. Kudzia, D. A. Revi, T. D. Ellis, and C. J. Walsh, "Walking faster and farther with a soft robotic exosuit: Implications for post-stroke gait assistance and rehabilitation," *IEEE open journal of engineering in medicine and biology*, vol. 1, pp. 108–115, 2020.

Organizing and prioritizing user needs for upper limb prostheses

Palma Borracci, Robinson Guachi, Linda Paternò, *Member, IEEE,* Irene Mannari, Flavio Napoleoni and Marco Controzzi, *Member, IEEE*

***Abstract*—Upper limb amputation leads to severe restrictions in daily activities and psychosocial difficulties, which can dramatically reduce the quality of life of affected people. Despite the significant scientific and engineering effort in building advanced robotic prostheses, their abandonment rates suggest a discrepancy between user needs and device performance. To address this gap, we present an initial step in identifying, harmonizing, and prioritizing the needs of people with limb loss. Using the PRISMA methodology, we analysed 73 papers on the topic. Using a bottom-up approach, we clustered the needs identified in different surveys into categories and macro-categories based on a taxonomy derived from the terms identified in the literature. We then prioritized the needs after a normalization of the major surveys. We believe that this work will provide both a high-level and low-level understanding of the needs of people with limb loss, thereby helping to guide the design of more user-friendly prostheses. In the future, combining these results with the definition of technical specifications will enable the identification of needs that can be satisfied through personalized design, particularly considering recent advances in manufacturing processes.**

I. Introduction

Hands are our primary elements of interaction with the world, enabling us to perform a wide range of tasks, from daily essentials like opening a bottle of water to more complex activities such as self-feeding [1]. In addition to their functional role, hands also play a key part in expressing identity, second only to the face in their ability to convey emotions for most individuals [2]. Thus, hand amputation represents a devastating event that limits one's ability to carry out daily activities and hinders social participation. Globally, approximately 5 million people live with upper limb amputations [3], with trauma being the leading cause. The prevalence of amputations varies by region, with trauma accounting for more than 80% of cases in areas affected by conflict, while vascular diseases, including diabetes, are more common causes in other regions. Cancer also contributes, although less frequently [3]. Given these causes, the number of people living with upper limb amputations is expected to rise due to ongoing conflicts, the increasing prevalence of vascular diseases, and the global rise in diabetes [3]. Post-amputation rehabilitation is a complex process that involves a multidisciplinary team. From an engineering perspective, prostheses aim to restore both functionality and aesthetics, improving patients' quality of life and enabling reintegration into social and work life [4]. Upper limb prostheses can be classified into two categories: passive and active. Passive prostheses include cosmetic devices, which replicate the limb's appearance, and functional devices, which feature interchangeable tools for specific tasks. Active prostheses are

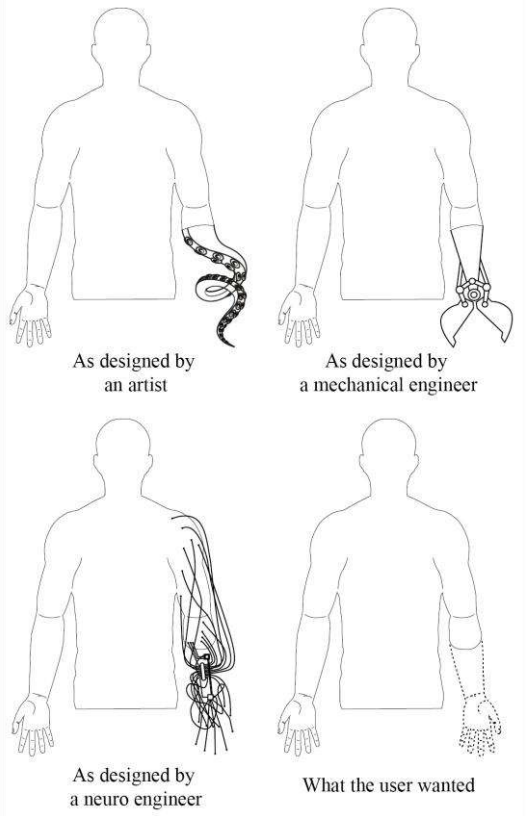


Figure 1 Understanding the prosthesis need, adapted from [15]. The illustration depicts the contrast between prosthetic design perspectives and user expectations. Top left: conceptual design by an artist, focusing on creativity. Top right: engineering-driven design, emphasizing mechanical functionality. Bottom left: electronic system design, highlighting complexity of wiring to record bio-signals. Bottom right: the user's ideal prosthetic, prioritizing simplicity, usability, and human-like functionality.

*This work was financially supported by the Italian Ministry of University and Research (MIUR) through the PRIN (Progetto di Rilevante Interesse Nazionale) "Calliope: lattiCe bAsed uLtra Light SensOrized upper limb ProsthEsis" (CUP J53D23002380001) and partially supported by the European Union's Horizon 2020 research and innovation programme under grant Brain-Connected inteRfAce TO machineS (B-Cratos grant agreement N° 965044).

P. Borracci, R. Guachi, L. Paternò, I. Mannari, F. Napoleoni and M. Controzzi are with The BioRobotics Institute, Scuola Superiore Sant'Anna, Pisa, Italy, and with the Department of Excellence in Robotics & AI, Pisa, Scuola Superiore Sant'Anna, Italy (MC corresponding author +39 050 883 100; e-mail: marco.controzzi@santannapisa.it).

R.G. is also with Department of Mechatronics, International University of Ecuador, Quito, Ecuador.

further divided into body-powered, which utilize the motion of the residual limb, and myoelectric, which are battery-powered and controlled via surface electromyography [5]. Despite technological advancements, many users still prefer passive prostheses. Body-powered devices provide a reliable, lightweight, and intuitive experience, while aesthetic prostheses are favored for their ability to symmetrically replicate the missing arm. However, myoelectric prostheses may offer, on the paper, greater functional restoration of the missing hand. Despite this advantage, 20% to 50% of users abandon these devices [4]-[8]. These factors point to a significant gap in prosthetic design that hampers user satisfaction and long-term usage [9], [10]. Numerous surveys have explored the needs of individuals with limb loss (here a recent review [3]), yet translating these insights into practical prosthetic solutions remains unsatisfactory. State-of-the-art robotic prostheses still face significant limitations, including poor controllability and functionality, lack of sensory feedback, inadequate aesthetics, and discomfort during wear [4]-[11]. These shortcomings result in unintuitive devices that many users perceive as impractical for daily use. So, it stands to reason that a fundamental misunderstanding of user needs is a primary reason for the high abandonment rates of hand prostheses (Figure 1). The limited adoption of co-creation models, such as the one proposed by Jones et al. in 2021 [12], is probably a key factor contributing to this issue. Given the individualized nature of prosthetic requirements, user-centered design is crucial in prosthesis development. For example, the HAAT - Human Activity Assistive Technology model demonstrates how integrating human, technological, and environmental factors can enhance user experience and prosthesis functionality [13]. Prostheses must accommodate different levels of amputation by incorporating compatible, commercially available components. For example, trans-humeral amputations require not only a hand but also a wrist, an elbow, and appropriate connection components. Some of the prosthetic elements are highly personalized to account for the specificity of the single patient. This is the case for the socket, whose primary function is to offer a secure anchoring of the prosthesis to the body and is molded based on the cast of the residual limb. In contrast, off-the-shelf components should be designed to accommodate a broader user base while maintaining affordability through an optimal balance of engineering specifications. In various industrial sectors, one of the most widely used approaches for generating engineering specifications is Quality Function Deployment (QFD), developed in the 1970s [14]. This framework prioritizes customer needs and constructs a House of Quality (HoQ) to map the relationship between user desires and the engineering specifications required to fulfill them. To narrow the gap between user expectations and upper limb prostheses, we apply the QFD framework to this field. Specifically, this paper explores the complex and challenging process of identifying "universal" user needs as inputs for the QFD process to enhance prosthetic design. We hypothesize that adopting a more user-centered approach and integrating frameworks like QFD can better align user desires with the engineering specifications necessary for functional and comfortable upper limb prostheses.

The paper is structured as follows: the first section reviews the QFD methodology and its proposed adaptation for application in the prosthetic field. The second section employs the PRISMA methodology to systematically review the state-of-the-art regarding amputees' needs. The third section details how these needs were organized into categories and macro-categories, culminating in the development of a taxonomy that assigns relative importance to each. Finally, both the categories and macro-categories were prioritized using various methods. This structured approach provides a comprehensive overview of the population's needs, enabling targeted interventions to address the most critical areas effectively.

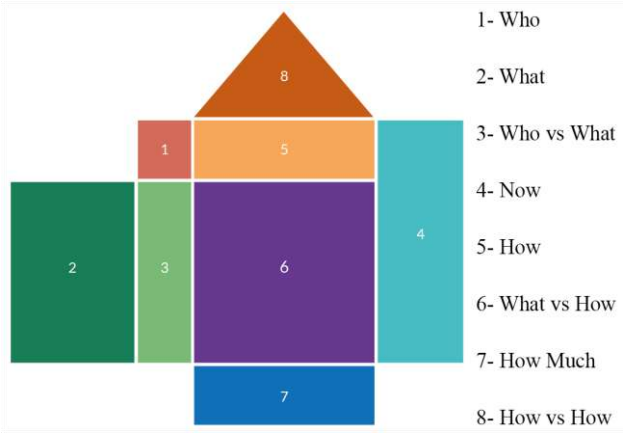


Figure 2 Organization of the House of Quality (i.e. QFD diagram). The diagram is organized in rooms, each containing information that are used to translate the customers' requirements into engineering specifications.

II. Background

A. Overview of the Quality Function Deployment (QFD)

The QFD method helps generate the necessary information during the engineering product definition phase of the design process through the creation of a HoQ (Figure 2). Each room in the diagram represents a step in the methodology for building the relationship between customer desires and the engineering specifications necessary to meet those desires. The framework is flexible and can be adapted to accommodate advancements in prosthetic technologies and emerging innovations. Specifically, in the technical specifications section of the HoQ, customizable specifications can be activated, deactivated, or added, ensuring that the design process evolves alongside technological progress and remains aligned with current user needs and capabilities.

The first step is identifying *who* (room 1) the customers are and *what* (room 2) they want the product to do. In developing this information, we also determine to whom the "*what*" is important—*who versus what* (room 3). Then it is important to identify how the problem is solved *now* (room 4), in other words, what the competition is for the product being designed. This information is compared to *what* the customers desire—*now versus what* (room 4)—to find out where there are opportunities for an improved product. Next, one of the more challenging steps in developing the house is determining *how* (room 5) you are going to measure the product's ability to satisfy the customers' requirements. *How* refers to the engineering specifications, and their correlation to the customers' requirements is given by *what versus how* (room 6). Target information—*how much* (room 7)—is developed in

the basement of the house and indicates the extent to which each technical requirement must be achieved to satisfy customer needs. Finally, the interrelationship between the engineering specifications is noted in the roof of the house—*how versus how* (room 8).

We aim to exploit the QFD [15] as a methodology to cluster the users' requirements and in future, through the requirements, identify the technical specifications for advance the design of upper limb prostheses.

B. Applications of the QFD for rehabilitation engineering

The QFD methodology has been previously applied in prosthetic design, such as in the 1994 study by Jacques et al. on child-sized myoelectric prosthetic hands [16]. The study involved multiple stakeholders—amputees, parents, and prosthetists—and used questionnaires to define functional requirements, rate their importance, and assess satisfaction with different models. The study highlighted the importance of including the amputee in the design process and identified the potential misalignment of prosthesis designs with patient needs due to varying interpretations of customer requirements.

C. Objective of the study

Our goal is to unify and prioritize the needs of amputees while also identifying those that can be personalized, considering advancements in manufacturing technologies. For the first time, we attempt to cluster needs identified in existing literature into a taxonomy, followed by their prioritization. The process was completed in three phases. First, we clustered 657 individual needs from the literature into 21 categories based on semantic similarity. Then, these 21 categories were further organized into 6 macro-categories for a higher-level understanding of user needs. Finally, we prioritized the categories based on term frequency in the literature and prioritized the macro-categories using insights from two major studies.

III. Application of QFD to the Design of Prosthetic Hands

In this work, we focus on room 1, 2, and 3 of the HoQ [15].

A. WHO: Identify the customers

The first step is the identification of the customers [15]. As with many products, prosthetics have more than one type of customer. For example, depending on a country's health services, the consumer (individuals with limb loss) may be different from the buyer, which could be a hospital or an orthopedic workshop. Given the prosthesis's lifespan, we identify five classes of customers: consumers, buyers, prosthetists, caregivers, and service technicians and clinicians. For the scope of this study, the primary customers are individuals who have lost an upper limb, focusing specifically on adults who wish to use a myoelectric prosthesis, which can restore both aesthetic and functional aspect.

B. WHAT: the amputees' requirements

Once the customers have been identified, the second step of the QFD method is to determine what aspects of the prosthesis need to be designed or improved—specifically, understanding customer needs [15]. In this step, we focus on identifying requirements, which refer to customer needs, rather than specifications, which are the detailed, often technical descriptions of how those needs will be met. To achieve this, we structured the process into three key stages: (i) performing a systematic literature review, (ii) categorizing customer needs into a taxonomy, and (iii) linking the identified needs to the relevant components of the prosthesis.

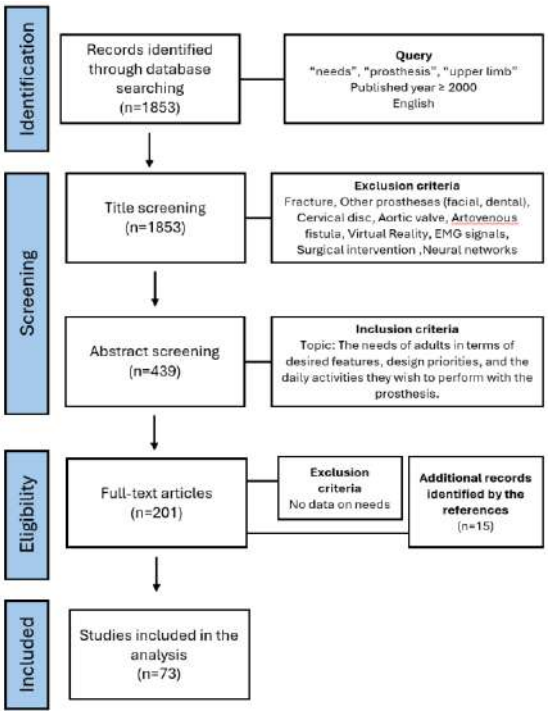


Figure 3 Flow diagram according to the PRISMA method.

Identification and screening of the needs

We systematically reviewed the scientific literature about the needs of individuals with limb loss according to the 'Preferred Reporting Items for Systematic Reviews and Meta-Analyses' (PRISMA) guidelines [17]. The flow diagram showing the process is depicted in Figure . The bibliography was retrieved by searching the Scopus database through query results on three words ("needs", "prosthesis", "upper limb") and their synonyms. The search encompassed conference papers, articles, book chapters, and reviews published between 2000 and 2023 in English. The search results were collected on October 25, 2023. The search yielded 1853 papers, which were subjected to an initial screening based on their titles. Then, records were selected according to the inclusion or exclusion criteria. This process reduced the output to 439 articles, which were subsequently divided into different groups based on topics. We then restricted the initial set to 201 papers considering only studies addressing the needs of adults in terms of desired features, design priorities, and the daily activities they wish to perform with the prosthesis. Based on the abstract, we excluded 143 papers since they did not report data on needs retrieved by questionnaires. This resulted in the identification of 58 papers [3], [4], [9], [10], [12], [17]-[69], that were deemed eligible for inclusion. Additionally, 15 papers [1], [6]-[8], [70]-[80], were included during this phase since cited by the studies and judged relevant according to our inclusion criteria. The final set of papers in our analysis

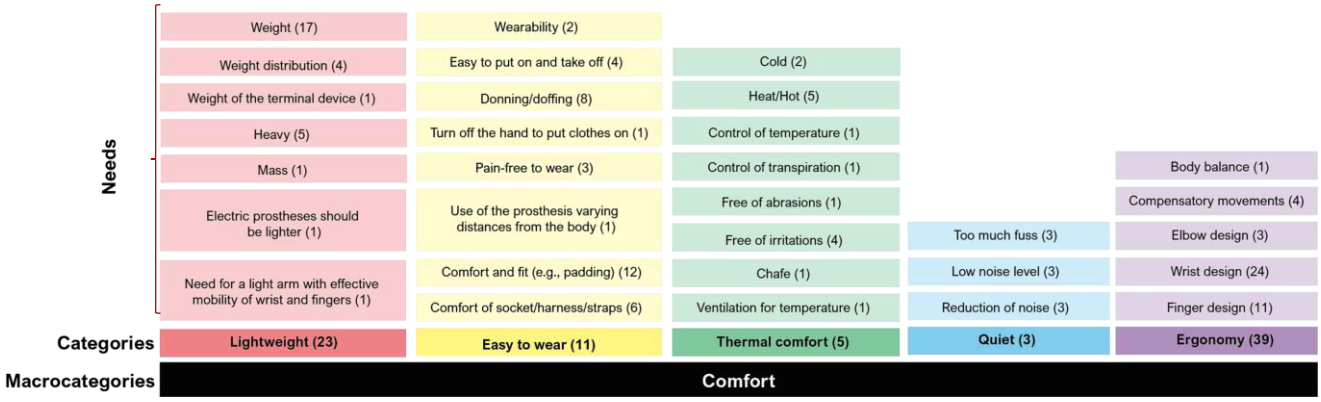


Figure 4 Rationale of the taxonomy of needs. The taxonomy is organized in three layers. The first layer is composed by all the needs that are semantically grouped into specific categories (second layer). The third layer is represented by the macro categories, which can provide a high-level understanding of the needs. In this example we report how the needs related to the macro category "Comfort".

consists of 73 papers. This set considered approximately 6646 amputees who were subjected to the questionnaires and the collected needs comprised 657 items.

Organization of the needs following a taxonomy

The taxonomy is structured into three hierarchical layers for clarity and usability (Figure 4). The first layer consists of all the individual needs, which are semantically grouped based on their similarities. Among the 657 needs identified, 470 can be considered as 470 user needs, while 127 are needs related to consequences and technical specifications. To maintain a focused analysis, we restricted our study to the 470 user needs, as they directly reflect the desires and priorities of the customers. In the second layer, these grouped needs are organized into specific categories, each representing a distinct aspect of the broader requirements. These were clustered semantically according to three main criteria: same denomination, synonym, or related concept. The clustering process resulted in 21 categories, leading to the taxonomy depicted in yellow in Table 1 (column 10). To better understand the process, here we report a description of the first five categories and examples of needs that were clustered within each category.

"Lightweight" describes the need to reduce the weight of prostheses, making them easier to use, and in turn enhancing comfort and mobility for the user. This category derives from prosthetic needs reported by users, such as for instance, "Weight", "Mass", "Heavy", "Weight distribution".

"Easy to wear" emphasizes the need for comfort, which includes the wearing process of the prosthesis and clothes. The terms selected underline the importance of the design to consider the wearer's daily life and activities, ensuring the prosthesis is not only functional but also comfortable and convenient to use. This category was defined based on needs reported as, for instance, "Comfort and fit", "Donning/Doffing", "Wearability".

"Thermal comfort" pertains to the desire to maintain a comfortable temperature at the residual limb and occurs as the need for "temperature regulation". The terms selected refer to the prosthetic's ability to prevent excessive heat buildup and promote adequate ventilation, ensuring that the area in contact with the residual limb remains at a comfortable temperature. This aspect is crucial for preventing discomfort, sweating and potential skin issues.

"Quiet" underlines the need for a prosthesis that operates without producing loud or disruptive sounds. This ensures that the user can move and interact without being disturbed or stressed by noise or feeling embarrassed during use.

"Ergonomics" refers to the needs aimed at reducing compensatory movements in activities of daily living caused, for instance, by a poor kinematic matching of the prosthesis. This is usually mentioned by amputees in surveys using terms like "Wrist design" or "Elbow design".

To provide a high-level understanding of the needs, the 21 categories have been further clustered into 6 macro-categories, as their combination represents a complex and interconnected system of user needs (Table 1, column 3). The clustering rationale followed a definition of each macro category:

- **Comfort** is a sense of physical or psychological ease, often characterized as a lack of hardship.
- **Function** describes what the product must do.
- **Control** pertains to the ease of controlling the prosthesis.
- **Appearance**: refers to the way the prosthesis looks, and how someone looks while wearing the prosthesis.
- **Reliability** pertains to the capability to perform its intended functions without issues e.g. unplanned movements, slipping of objects, failure/malfunction, breakage.
- **Cost & Service** includes the costs of purchasing and maintaining the prosthesis.

Division of needs within the components of the prosthesis

In upper limb prostheses, most of the engineering efforts focus on the design of the terminal device or on the development of algorithms inferring the user's intention. However, the prosthesis comprises different components,

each impacting a subset of needs. Therefore, the identification of the correlation between needs and components of the prosthesis plays a fundamental role. In this regard, we divided the prosthesis into four main elements, envisioning a trans humeral fitting: suspension system (socket and interface), elbow, wrist, and terminal device (hand) (Table 1, columns 4-7). By considering the comfort category, we note for instance that the need "Lightweight" refers to all components, while the category "Easy to wear" is mainly affected by the suspension system.

C. *WHO vs WHAT: Prioritization*

The third step in the QFD technique is to assess the relative importance of each customer requirement. This is achieved by assigning a weighting factor to each requirement. The weighting factor helps prioritize the level of effort, time, and resources needed to address each requirement [15]. The importance of the 6 macro categories was based on a subset of studies which included at least six needs related to our six macro categories. This led us to consider the papers Biddis et al. [21], and Nagaraja et al. [43]. Each of them reports its own prioritization in the form of a ranked list of needs: Biddis et al. [21] reports 14 needs, prioritized to a 10-point scale (including *ex aequo*), while Nagaraja et al. [43] reports 6 needs, prioritized to 6-point scale. We normalized the prioritization of the Biddis et al. needs to a 6-point scale. Then, the importance of the macro categories was retrieved using *Reciprocal Rank Fusion (RRF)* [82] algorithm, this technique combines multiple search systems or classifiers to generate a final ranking by assigning a score based on the position of each result in the rankings of the models used, following the equation:

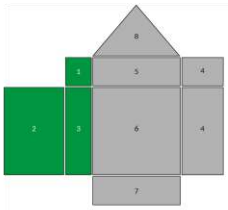
$$RRF = \sum \frac{1}{r(d)}$$

Where $r(d)$ is the rank/position of the macro categories. Based on the *RRF*, the macro categories can be ranked on a 6-point scale, where 1 indicates the least important and 6 the most important (Table 1, column 2). Finally, these values were converted into percentages (Table 1, column 1) using the following formula:

$$\frac{Rank_i}{All} \times 100$$

Where $Rank_i$ is the rank of the macro category i, and All is the sum of all categories. Concerning the prioritization of the needs (here clustered in 21 categories), we hypothesized that the frequency of the terms (Table 1, column 9) provides an index of urgency. In other words, the more frequently a need is cited by amputees, the higher its priority should be in prosthesis design. For the computation of the frequencies, we analysed all the 73 papers included in this study, and we computed the occurrences of the items within each category. These values were converted into the relative percentage within the macro category (Table 1, column 8) using the following formula:

$$\frac{f_j}{\sum f_j} \times 100$$



WHO										
Adult who has lost an arm and uses a myoelectric prosthesis										
WHAT										
1	2	3	4	5	6	7	8	9	10	11
% Relative Weight Macrocategories	Re-Ranking	Macrocategories	Suspension System	Elbow	Wrist	Terminal Device	% Relativa Weight Categorie	Frequency	Categories	% Importance
14,3%	3	COMFORT	■	■	■	■	28,4%	23	Lightweight	4,1%
			■				13,6%	11	Easy to wear	1,9%
			■	■	■	■	6,2%	5	Thermal comfort	0,9%
				■	■	■	3,7%	3	Quiet	0,5%
			■	■	■	■	48,1%	39	Ergonomy	6,9%
23,8%	5	COST & SERVICE	■	■	■	■	41,2%	7	Affordable	9,8%
			■	■	■	■	23,5%	4	Cost-effective	5,6%
			■	■	■	■	11,8%	2	Purchase condition	2,8%
			■	■	■	■	23,5%	4	Assistance	5,6%
28,6%	6	FUNCTION			■	■	50,0%	18	Precision and stability	14,3%
						■	25,0%	9	Powerful	7,1%
						■	25,0%	9	Operating time	7,1%
19,0%	4	RELIABILITY	■	■	■	■	61,3%	19	Robustness	11,7%
			■	■	■	■	22,6%	7	Durability - Maintenance	4,3%
			■	■	■	■	12,9%	4	Cleanable	2,5%
			■	■	■	■	3,2%	1	Safety	0,6%
4,8%	1	APPEARANCE	■	■	■	■	58,6%	17	Aesthetically pleasing	2,8%
			■	■	■	■	41,4%	12	Anatomically proportionate	2,0%
9,5%	2	CONTROL			■	■	32,4%	11	Versatility	3,1%
					■	■	23,5%	8	Usability	2,2%
					■	■	44,1%	15	Feedback	4,2%

Table 1 Customers, importance of needs and taxonomy of the amputee's needs. The data are rounded to the nearest whole number.

Where f_j is the frequency of the need j, and $\sum f_j$ is the sum of the frequency within the macro category considered. Finally, the absolute importance of each need (Table 1, column 11) is computed by combining its percentage within the macro category (Table 1, column 8) with the percentage of the macro category itself (Table 1, column 1) relative to the others.

IV. Discussion

We identified key user needs based on a broad cohort of studies addressing the needs of amputees. These needs were synthesized into a taxonomy organized into three hierarchical layers. This process serves two purposes: 1) standardizing terminology for needs within the scientific community, enhancing communication and comparison across studies, and 2) providing both high-level and detailed understanding of these needs. We integrated and followed different but established methodologies to ensure a rigorous prioritization. The importance of the macrocategories was obtained using two important studies (Biddis et al. [21] and Nagaraja et al. [43]) whose prioritization rankings were normalized to a common scale. We applied Reciprocal Rank Fusion (RRF) to reduce potential inconsistencies arising from variations in these rankings. For prioritizing the 21 categories, we assumed that needs that are frequently mentioned are also of higher concern to users. This method aligns with the guidelines of the PRISMA used to identify key themes [17]. Finally, we computed the absolute importance of each need by combining its relative percentage within its macro-category with the weight of the macro-category itself to ensure consistency.

"Function" emerged as the primary macro-area for improvement in myoelectric prostheses, with users reporting a lack of "precision and stability" in grasping. From an engineering perspective, addressing this issue requires enhancements in both hand design (e.g., increasing finger grip and adaptability to different shapes) and the user-prosthesis interface. Myoelectric prosthetic hands are typically controlled using two-channel surface myoelectric signals, whose performance depends on the activity of residual muscles that may not be accurate and reliable over time. "Cost & Service" is the second macro-area requiring major attention, particularly regarding the "affordability" of devices and the availability of "assistance." Affordability is a significant concern, especially for multi-grip hands, which cost approximately seven times more than single-grip hands. The demand for better "assistance" is closely linked to another macro-category, "Reliability", where users emphasize the importance of device "robustness". "Comfort" is primarily associated with the need for "ergonomics" and "lightweight" prostheses. The demand for ergonomics is driven by the compensatory movements amputees must adopt during daily activities, mainly due to limited wrist mobility or thumb abduction. Weight remains a well-known issue across the entire prosthetic system—hand, battery, and ancillary components often weigh more than the natural limb, with perceived weight further increased by common suspension systems like sockets. "Appearance" was considered less critical in the context of myoelectric prostheses. Without proper functionality, a myoelectric prosthesis serves only as a passive aesthetic device, adding unnecessary weight and cost. However, this may strongly depend on context and culture. It is not uncommon for amputees to use multiple prostheses for different situations—for instance, a task-specific or body-powered prosthesis for daily activities and a cosmetic hand for social events.

During the analysis of the results, we identified two main limitations of our work. First, the survey respondents were predominantly from Western contexts, which may have influenced the prioritization of needs. For example, cost may be a more pressing issue in developing countries. Second, merging needs from different surveys may have led to some needs being overemphasized. Further research is needed to ensure that these needs are fairly represented across different cultural contexts. Despite these limitations, we believe that the identified needs reflect the core requirements of users, as they appear consistently across various studies and patient populations, even in different cultural contexts. This demonstrates their universal relevance, marking a significant contribution in harmonizing previously fragmented findings into a unified set of prioritized requirements.

V. Conclusions and Future works

This article aims to consolidate previous efforts through the analysis of 73 articles. The goal—and the novelty of this study—is to systematically unify the needs of amputees and organize them into a taxonomy. The next steps involve completing the subsequent rooms of the House of Quality, focusing on the following tasks: i) Translating the needs into technical specifications that can be quantified; ii) Identifying the relationships between needs and technical specifications; iii) Benchmarking of off-the-shelf prostheses and components; iv) Identifying the needs and specifications that can be personalized for the individual, also considering the potential of new manufacturing processes, such as additive manufacturing technologies. These steps will establish a structured framework to guide prosthetic development, ensuring that design closely aligns with user needs. Specifically, we aim to identify which parts of the prosthesis can be easily personalized (e.g., cosmetic appearance) and adapt the HoQ to reflect user preferences. In the future, an online questionnaire integrated with the QFD framework will enable amputee users to regularly provide feedback on factors such as demographic data, emerging needs, and satisfaction with their prostheses. Specifically, we propose developing an online questionnaire structured within the QFD framework, allowing users to continuously share feedback on general factors, needs, and satisfaction, ensuring an ongoing update process. The ultimate goal of this work is to develop a new, personalized prosthesis. By integrating user preferences into the design process, we can ensure that the prosthesis not only meets functional requirements but also aligns with individual user needs and preferences.

Acknowledgment

The authors would like to thank Leandro Giordani for the insightful discussion on the House of Quality as well as the reviewers for their valuable suggestions for improvement.

REFERENCES

[1] C. H. Jang *et al.*, "A Survey on Activities of Daily Living and Occupations of Upper Extremity Amputees," pp. 907–921, 2011.

[2] B. Munari, "Il corpo parlante," *Suppl. al Diz. Ital.*, no. May 2021, pp. 303–320, 2017, doi: 10.2307/j.ctv1p6hpvz.27.

[3] F. Cordella *et al.*, "Literature review on needs of upper limb prosthesis users," *Front. Neurosci.*, vol. 10, no. MAY, pp. 1–14, 2016, doi: 10.3389/fnins.2016.00209.

[4] E. Biddiss and T. Chau, "Upper-limb prosthetics: Critical factors in device abandonment," *Am. J. Phys. Med. Rehabil.*, vol. 86, no. 12, pp. 977–987, 2007, doi: 10.1097/PHM.0b013e3181587f6c.

[5] F. Don and C. Gnocchi, "Ausili tecnici per persone disabili Classificazione EN ISO 9999," pp. 1–79.

[6] L. R. Id *et al.* "A national study of Veterans with major upper limb amputation : Survey methods , participants , and summary findings," pp. 1–24, 2019, doi: 10.1371/journal.pone.0213578.

[7] S. M. Engdahl *et al.* "Surveying the interest of individuals with upper limb loss in novel prosthetic control techniques," *J. Neuroeng. Rehabil.*, vol. 12, no. 1, pp. 1–11, 2015, doi: 10.1186/s12984-015-0044-2.

[8] M. Yamamoto *et al.*, "Cross-sectional International Multicenter Study on Quality of Life and Reasons for Abandonment of Upper Limb Prostheses," *Plast. Reconstr. Surg. - Glob. Open*, vol. 7, no. 5, p. E2205, 2019, doi: 10.1097/GOX.0000000000002205.

[9] E. Biddiss and T. Chau, "Upper limb prosthesis use and abandonment: A survey of the last 25 years," *Prosthet. Orthot. Int.*, vol. 31, no. 3, pp. 236–257, 2007, doi: 10.1080/03093640600994581.

[10] N. Kerver *et al.*, "The multi-grip and standard myoelectric hand prosthesis compared: does the multi-grip hand live up to its promise?," *J. Neuroeng. Rehabil.*, vol. 20, no. 1, pp. 1–18, 2023, doi: 10.1186/s12984-023-01131-w.

[11] S. Sansoni *et al.*, "The aesthetic appeal of prosthetic limbs and the uncanny valley: The role of personal characteristics in attraction," *Int. J. Des.*, vol. 9, no. 1, pp. 67–81, 2015.

[12] H. Jones *et al.*, "Co-creation and User Perspectives for Upper Limb Prosthetics," *Front. Neurorobot.*, vol. 15, no. July, pp. 1–10, 2021, doi: 10.3389/fnbot.2021.689717.

[13] A. M. Cook, J. M. Polgar, and P. Encarnação, "Principles of Assistive Technology: Introducing the Human Activity Assistive Technology Model," *Assist. Technol.*, pp. 1–15, 2020.

[14] Y. Akao and G. H. Mazur, "The leading edge in QFD: Past, present and future," *Int. J. Qual. Reliab. Manag.*, vol. 20, no. 1, pp. 20–35, 2003, doi: 10.1108/02656710310453791.

[15] D. G. Ullman, *The Mechanical Design Process*.

[16] G. E. Jacques *et al.*, "Application of Quality Function Deployment in Rehabilitation Engineering," *IEEE Trans. Rehabil. Eng.*, vol. 2, no. 3, pp. 158–164, 1994, doi: 10.1109/86.331565.

[17] M. J. Page *et al.*, "The PRISMA 2020 statement: An updated guideline for reporting systematic reviews," *BMJ*, vol. 372, 2021, doi: 10.1136/bmj.n71.

[18] J. Davidson, "A survey of the satisfaction of upper limb amputees with their prostheses, their lifestyles, and their abilities," *J. Hand Ther.*, vol. 15, no. 1, pp. 62–70, 2002, doi: 10.1053/hanthe.2002.v15.01562.

[19] I. Dudkiewicz *et al.*, "Evaluation of prosthetic usage in upper limb amputees," *Disabil. Rehabil.*, vol. 26, no. 1, pp. 60–63, 2004, doi: 10.1080/09638280410001645094.

[20] F. V. Wright, "MEASURES," vol. 18, no. 2, 2006.

[21] E. Biddiss, D. Beaton, and T. Chau, "Consumer design priorities for upper limb prosthetics," *Disabil. Rehabil. Assist. Technol.*, vol. 2, no. 6, pp. 346–357, 2007, doi: 10.1080/17483100701714733.

[22] E. Biddiss and T. Chau, "The roles of predisposing characteristics, established need, and enabling resources on upper extremity prosthesis use and abandonment," *Disabil. Rehabil. Assist. Technol.*, vol. 2, no. 2, pp. 71–84, 2007, doi: 10.1080/17483100601138959.

[23] C. Pylatiuk, S. Schulz, and L. Döderlein, "Results of an internet survey of myoelectric prosthetic hand users," *Prosthet. Orthot. Int.*, vol. 31, no. 4, pp. 362–370, 2007, doi: 10.1080/03093640601061265.

[24] W. Hill *et al.*, "Working Group and Their Findings," *J. Prosthetics Orthot.*, no. 21, pp. P69-82, 2009.

[25] W. Hill *et al.*, "Functional outcomes in the WHO-ICF model: Establishment of the upper limb prosthetic outcome measures group," *J. Prosthetics Orthot.*, vol. 21, no. 2, pp. 115–119, 2009, doi: 10.1097/JPO.0b013e3181a1d2dc.

[26] V. Wright, "Prosthetic outcome measures for use with upper limb amputees: A systematic review of the peer-reviewed literature, 1970 to 2009," *J. Prosthetics Orthot.*, vol. 21, no. SUPPL. 9, 2009, doi: 10.1097/JPO.0b013e3181ae9637.

[27] H. Y. N. Lindner, B. S. Nätterlund, and L. M. N. Hermansson, "Upper limb prosthetic outcome measures: Review and content comparison based on International Classification of Functioning, Disability and Health," *Prosthet. Orthot. Int.*, vol. 34, no. 2, pp. 109–128, 2010, doi: 10.3109/03093641003776976.

[28] L. Resnik *et al.*, "Development and Evaluation of the Activities Measure for Upper Limb Amputees," vol. 6, 2013, doi: 10.1016/j.apmr.2012.10.004.

[29] J. Bouffard *et al.*, "Interactions between the phantom limb sensations, prosthesis use, and rehabilitation as seen by amputees and health professionals," *J. Prosthetics Orthot.*, vol. 24, no. 1, pp. 25–33, 2012, doi: 10.1097/JPO.0b013e318240d171.

[30] K. Ostlie *et al.*, "Prosthesis use in adult acquired major upper-limb amputees: Patterns of wear, prosthetic skills and the actual use of prostheses in activities of daily life," *Disabil. Rehabil. Assist. Technol.*, vol. 7, no. 6, pp. 479–493, 2012, doi: 10.3109/17483107.2011.653296.

[31] G. Jarl, M. Holmefur, and L. M. N. Hermansson, "Test-retest reliability of the Swedish version of the Orthotics and Prosthetics Users' Survey," *Prosthet. Orthot. Int.*, vol. 38, no. 1, pp. 21–26, 2014, doi: 10.1177/0309364613485113.

[32] S. NiMhurchadha *et al.*, "Identifying successful outcomes and important factors to consider in upper limb amputation rehabilitation: An international web-based Delphi survey," *Disabil. Rehabil.*, vol. 35, no. 20, pp. 1726–1733, 2013, doi: 10.3109/09638288.2012.751138.

[33] K. E. Waldera *et al.*, "Assessing the prosthetic needs of farmers and ranchers with amputations," *Disabil. Rehabil. Assist. Technol.*, vol. 8, no. 3, pp. 204–212, 2013, doi: 10.3109/17483107.2012.699994.

[34] E. J. Ligthelm and S. C. D. Wright, "Lived experience of persons with an amputation of the upper limb," *Int. J. Orthop. Trauma Nurs.*, vol. 18, no. 2, pp. 99–106, 2014, doi: 10.1016/j.ijotn.2013.08.018.

[35] L. Resnik, S. L. Klinger, and K. Etter, "User and clinician perspectives on DEKA Arm: Results of VA study to optimize DEKA Arm," *J. Rehabil. Res. Dev.*, vol. 51, no. 1, pp. 27–38, 2014, doi: 10.1682/JRRD.2013.03.0068.

[36] S. L. Carey, P. M. Stevens, and M. J. Highsmith, "Prostheses : Systematic Literature Review Update 2013 – 2016," *Am. Acad. Orthotists Prosthetists*, pp. 17–20, 2017.

[37] M. Luchetti *et al.*, "Impact of Michelangelo prosthetic hand: Findings from a crossover longitudinal study," *J. Rehabil. Res. Dev.*, vol. 52, no. 5, pp. 605–618, 2015, doi: 10.1682/JRRD.2014.11.0283.

[38] E. Pröbsting *et al.*, "Ease of activities of daily living with conventional and multigrip myoelectric hands," *J. Prosthetics Orthot.*, vol. 27, no. 2, pp. 46–52, 2015, doi: 10.1097/JPO.0000000000000058.

[39] G. Smit, D. H. Plettenburg, and F. C. T. Van Der Helm, "The lightweight Delft Cylinder hand: First multi-articulating hand that meets the basic user requirements," *IEEE Trans. Neural Syst. Rehabil. Eng.*, vol. 23, no. 3, pp. 431–440, 2015, doi: 10.1109/TNSRE.2014.2342158.

[40] U. Wijk and I. Carlsson, "Forearm amputees' views of prosthesis use and sensory feedback," *J. Hand Ther.*, vol. 28, no. 3, pp. 269–278, 2015, doi: 10.1016/j.jht.2015.01.013.

[41] H. L. Benz *et al.*, "Upper extremity prosthesis user perspectives on unmet needs and innovative technology," *Proc. Annu. Int. Conf. IEEE Eng. Med. Biol. Soc. EMBS*, vol. 2016-Octob, pp. 287–290, 2016, doi: 10.1109/EMBC.2016.7590696.

[42] M. Hofmann *et al.*, "Helping hands: Requirements for a prototyping methodology for upper-limb prosthetics users," *Conf. Hum. Factors Comput. Syst. - Proc.*, pp. 1769–1780, 2016, doi: 10.1145/2858036.2858340.

[43] V. H. Nagaraja *et al.*, "Examining the needs of affordable upper limb prosthetic users in India: A questionnairebased survey," *Technol. Disabil.*, vol. 28, no. 3, pp. 101–110, 2016, doi: 10.3233/TAD-160448.

[44] T. Jiralerspong *et al.*, "Experimental study of real-time classification of 17 voluntary movements for multi-degree myoelectric prosthetic hand," *Appl. Sci.*, vol. 7, no. 11, 2017, doi: 10.3390/app7111163.

[45] J. Fajardo *et al.*, "User-prosthesis interface for upper limb prosthesis based on object classification," *Proc. - 15th Lat. Am. Robot. Symp. 6th Brazilian Robot. Symp. 9th Work. Robot. Educ. LARS/SBR/WRE 2018*, pp. 396–401, 2018, doi: 10.1109/LARS/SBR/WRE.2018.00076.

[46] E. M. Janssen *et al.*, "Identifying and prioritizing concerns associated with prosthetic devices for use in a benefit-risk assessment: a mixed-methods approach," *Expert Rev. Med. Devices*, vol. 15, no. 5, pp. 385–398, 2018, doi: 10.1080/17434440.2018.1470505.

[47] T. W. Armstrong *et al.*, "Psychological distress among persons with upper extremity limb loss," *Br. J. Health Psychol.*, vol. 24, no. 4, pp. 746–763, 2019, doi: 10.1111/bjhp.12360.

[48] M. Davidson, C. Bodine, and R. F. f. Weir, "User surveys support designing a prosthetic wrist that incorporates the Dart Thrower's Motion," *Disabil. Rehabil. Assist. Technol.*, vol. 14, no. 3, pp. 312–315, 2019, doi: 10.1080/17483107.2018.1447607.

[49] N. Kerver *et al.*, "User-relevant factors determining prosthesis choice in persons with major unilateral upper limb defects: A meta-synthesis of qualitative literature and focus group results," *PLoS One*, vol. 15, no. 6 June, pp. 1–25, 2020, doi: 10.1371/journal.pone.0234342.

[50] C. L. McDonald *et al.*, "Perceptions of ability among adults with upper limb absence: impacts of learning, identity, and community," *Disabil. Rehabil.*, vol. 42, no. 23, pp. 3306–3315, 2020, doi: 10.1080/09638288.2019.1592243.

[51] S. Salminger *et al.*, "Current rates of prosthetic usage in upper-limb amputees–have innovations had an impact on device acceptance?," *Disabil. Rehabil.*, vol. 44, no. 14, pp. 3708–3713, 2022, doi: 10.1080/09638288.2020.1866684.

[52] K. Šosterič, H. Burger, and G. Vidmar, "Adjustment and satisfaction with prosthesis among people after upper limb amputation in Slovenia," *Ortop. Traumatol. Rehabil.*, vol. 22, no. 2, pp. 85–93, 2020, doi: 10.5604/01.3001.0014.1165.

[53] B. Stephens-Fripp *et al.*, "A survey on what Australians with upper limb difference want in a prosthesis: justification for using soft robotics and additive manufacturing for customized prosthetic hands," *Disabil. Rehabil. Assist. Technol.*, vol. 15, no. 3, pp. 342–349, 2020, doi: 10.1080/17483107.2019.1580777.

[54] M. J. Walker *et al.*, "Towards Including End-Users in the Design of Prosthetic Hands: Ethical Analysis of a Survey of Australians with Upper-Limb Difference," *Sci. Eng. Ethics*, vol. 26, no. 2, pp. 981–1007, 2020, doi: 10.1007/s11948-019-00168-2.

[55] U. Wijk *et al.*, "Sensory Feedback in Hand Prostheses: A Prospective Study of Everyday Use," *Front. Neurosci.*, vol. 14, no. July, pp. 1–13, 2020, doi: 10.3389/fnins.2020.00663.

[56] L. C. Smail *et al.*, "Comfort and function remain key factors in upper limb prosthetic abandonment: findings of a scoping review," *Disabil. Rehabil. Assist. Technol.*, vol. 16, no. 8, pp. 821–830, 2021, doi: 10.1080/17483107.2020.1738567.

[57] H. Jones *et al.*, "Towards User-Centred Prosthetics Research Beyond the Laboratory," *Front. Neurosci.*, vol. 16, no. April, pp. 1–11, 2022, doi: 10.3389/fnins.2022.863833.

[58] L. J. Resnik *et al.*, "Measuring Satisfaction With Upper Limb Prostheses: Orthotics and Prosthetics User Survey Revision That Includes Issues of Concern to Women," *Arch. Phys. Med. Rehabil.*, vol. 103, no. 12, pp. 2316–2324, 2022, doi: 10.1016/j.apmr.2022.05.008.

[59] M. R. Fossati *et al.*, "From Robotics to Prosthetics: What Design and Engineering Can Do Better Together," *ACM Trans. Human-Robot Interact.*, vol. 12, no. 2, 2023, doi: 10.1145/3588323.

[60] A. Marinelli *et al.*, "Active upper limb prostheses: a review on current state and upcoming breakthroughs," *Prog. Biomed. Eng.*, vol. 5, no. 1, 2023, doi: 10.1088/2516-1091/acac57.

[61] X. Zhang *et al.*, "Factors influencing perceived function in the upper limb prosthesis user population," *PM R*, vol. 15, no. 1, pp. 69–79, 2023, doi: 10.1002/pmrj.12697.

[62] P. J. Kyberd *et al.*, "and the United Kingdom".

[63] P. J. Kyberd and W. Hill, "Survey of upper limb prosthesis users in Sweden, the United Kingdom and Canada," *Prosthet. Orthot. Int.*, vol. 35, no. 2, pp. 234–241, 2011, doi: 10.1177/0309364611409099.

[64] C. Murray, *Amputation, prosthesis use, and phantom limb pain: An interdisciplinary perspective*. 2010. doi: 10.1007/978-0-387-87462-3.

[65] K. Østlie *et al.*, "Adult acquired major upper limb amputation in Norway: Prevalence, demographic features and amputation specific features. A population-based survey," *Disabil. Rehabil.*, vol. 33, no. 17–18, pp. 1636–1649, 2011, doi: 10.3109/09638288.2010.541973.

[66] R. D. Lipschutz *et al.*, "Use of two-axis joystick for control of externally powered shoulder disarticulation prostheses," *J. Rehabil. Res. Dev.*, vol. 48, no. 6, pp. 719–737, 2011, doi: 10.1682/JRRD.2010.08.0161.

[67] S. L. Carey, D. J. Lura, and M. J. Highsmith, "Systematic literature review," *Lit. Rev. Mod. Methods Investig. Sci. Technol. Knowl.*, vol. 52, no. 3, pp. 19–30, 2021, doi: 10.1007/978-3-030-75722-9_3.

[68] J. A. Tello, M. Zapata, and D. Paillacho, "Advances in Additive Manufacturing, Modeling Systems and 3D Prototyping," vol. 975, pp. 108–118, 2020, doi: 10.1007/978-3-030-20216-3.

[69] N. Ju *et al.*, "A user-driven approach to prosthetic upper limb development in Korea," *Healthc.*, vol. 9, no. 7, pp. 1–13, 2021, doi: 10.3390/healthcare9070839.

[70] G. H. Kejlaa, "Consumer concerns and the functional value of prostheses to upper limb amputees," pp. 157–163, 1993.

[71] H. Burger *et al.*, "Original Report Validation Of The Orthotics And Prosthetics User Survey Upper Extremity Functional Status Module In People With Unilateral Upper Limb Amputation," pp. 393–399, 2008, doi: 10.2340/16501977-0183.

[72] G. Cavallari and C. Costantino, "Riabilitazione in esiti di amputazione degli arti superiori," *EMC - Med. Riabil.*, vol. 15, no. 2, pp. 1–15, 2008, doi: 10.1016/S1283-078X(08)70223-2.

[73] A. Saradjian, A. R. Thompson, and D. Datta, "The experience of men using an upper limb prosthesis following amputation : Positive coping and minimizing feeling different," vol. 30, no. 11, pp. 871–883, 2008, doi: 10.1080/09638280701427386.

[74] E. Schaffalitzky *et al.*, "Identifying the values and preferences of prosthetic users : A case study series using the repertory grid technique," vol. 33, no. June, pp. 157–166, 2009, doi: 10.1080/03093640902855571.

[75] L. V Mcfarland *et al.*, "Unilateral upper-limb loss: Satisfaction and prosthetic-device use in," vol. 47, no. 4, pp. 299–316, 2010, doi: 10.1682/JRRD.2009.03.0027.

[76] C. A. Chestek *et al.* , "Priorities for the design and control of upper limb prostheses : A focus group study," vol. 12, pp. 706–711, 2019, doi: 10.1016/j.dhjo.2019.03.009.

[77] L. R. and A. M. D. A. J. Spiers, J. Cochran, "Quantifying Prosthetic and Intact Limb Use in Upper Limb Amputees via Egocentric Video :," vol. 3, no. 2, pp. 463–484, 2021, doi: 10.1109/TMRB.2021.3072253.

[78] J. D. Brown, "Supplementary Materials for Touching reality : Bridging the user-researcher divide in upper-limb prosthetics," vol. 9421, 2023, doi: 10.1126/scirobotics.adk9421.

[79] P. Departments and S. G. Hospital, "Upper limb traumatic," 1997.

[80] E. Biddiss, *Need-Directed Design of Prostheses and Enabling Resources. In: Murray, C. (eds) Amputation, Prosthesis Use, and Phantom Limb Pain.*, vol. 11, no. 1. New York, NY, 2019.

[81] W. H. M. Atkins, Diane J. OTR1; Heard, Denise C Y MSE2; Donovan, *Epidemiologic Overview of Individuals with Upper-Limb Loss and Their Reported Research Priorities. J*. 1996.

[82] G. V. Cormack, C. L. A. Clarke, and S. Buettcher, "Reciprocal rank fusion outperforms condorcet and individual rank learning methods," *Proc. - 32nd Annu. Int. ACM SIGIR Conf. Res. Dev. Inf. Retrieval, SIGIR 2009*, pp. 758–759, 2009, doi: 10.1145/1571941.1572114.

Abnormal Synergies and Muscle Weakness Identified in Stroke Survivors via Wrist Position Probability Distributions

Adith V. Srivatsa[1,2], Partha Ryali[1,2], Courtney Celian[2], Valentino Wilson[1,2], Leah O'Shea[2], Mac Camardo[1,2], Arturo Ramirez[1,2], Dongwon Kim[1,2], and James L. Patton[1,2]

[1] Richard and Loan Hill Department of Biomedical Engineering, University of Illinois at Chicago, Chicago, IL, United States

[2] RobotLab, Center for Neural Plasticity, Shirley Ryan AbilityLab, Chicago, IL, United States

Abstract— **Stroke significantly impairs motor function, often causing abnormal synergies and muscle weakness. Clinical assessments are vital for diagnosing impairment and guiding treatments but are labor-intensive and time-consuming. Moreover, the supply of clinicians cannot keep pace with the growing number of individuals affected by stroke. This study presents a more efficient strategy to assess motor function, substantially reducing the time and effort required for assessment while eliminating the need for direct accessor involvement. Our proposed method leverages wrist position probability distribution during two minutes of free upper-extremity movements of individuals with chronic stroke, tracked by a markerless motion capture system. Two probabilistic models, rectilinear and icosahedron-based, revealed stroke survivors spend significantly less time in four posterior zones and more time in the anterior-inferior-medial zone. The icosahedron model identified abnormal flexion synergies in 10 stroke survivors (52.6%), two more than the rectilinear model. Conversely, the rectilinear model demonstrated stronger associations with clinical scores, with three zones showing strong correlations (R>0.70) compared to one in the icosahedron model. These findings highlight the promise of wrist position probability distribution models as tools to detect movement deficits and abnormal synergies in stroke survivors. Future work could integrate joint angles to improve clinical insights.**

Keywords—stroke rehabilitation, abnormal synergies, markerless joint tracking, probability distribution, human movement analysis, biomechanics and robotics in physical rehabilitation

I. INTRODUCTION

Each day, more data is coming in and we do not know how to use it. As stroke is a debilitating event that can damage the ipsilesional corticospinal tract and hence volitional controls, large data sets of volitional actions are of interest. A variety of robotic, wearable technology can track and store full body and large free actions of such large body actions, but a critical question is how we might reliably analyze such data to answer questions about disease mechanisms and recovery pathways.

Stroke often leads to reliance on alternative pathways including the reticulospinal tract [1], [2]. Those neuroanatomical changes lead to significant motor impairment, including abnormal coactivation across muscles, termed the flexion synergy and extension synergy, in the extremities [3], [4], [5]. These abnormal synergies involve functional limitations in hand/arm manipulation by binding the motions of more distal joints with that of the shoulder joint. Since abnormal synergies provide critical insight into the neuroanatomical progress in each individual with stroke and guide therapy, the need for a quantitative and effective assessment has arisen [6].

Current methods of evaluating upper extremity range of motion consume valuable therapy time. Occupational therapists use a variety of upper extremity assessments to assess motor function impairment [7] and stroke-caused abnormal synergies [8], and fine and gross motor ability [9], [10]. Yet, some of these assessments can take upwards of 45 minutes, they are not appropriate for cognitively impaired participants, and using only the aforementioned capacity measures are insufficient at measuring rehabilitation effectiveness [11], [12] and underlying muscle synergies.

Many have turned to the use of technology to aid in the measurement of upper extremity impairment, but it oftentimes falls short. Sensors in electromyography (EMG) can objectively quantify upper extremity impairment and synergies [13], [14], [15], [16]; but sensor placement can be time consuming, it requires a skilled user, and they are prone to noise in dynamic movements. IMUs can assess movement diversity and longitudinal use of arms and hands, [17], [18] but they also run into accuracy challenges because of their sensitivity to noise. The gold-standard for robustness in kinematic measurements, marker-based joint tracking, is far too expensive and the complex setup in a lab space make it inaccessible to clinics [19].

Here, we present a markerless joint tracking analysis to explore movement impairments in stroke survivors with hemiplegia. We hypothesize that probability distribution analysis of two minutes of free exploration wrist position data will reveal underlying abnormal synergies and identify limited mobility regions in chronic stroke survivors. Prior work employed rectilinear-based models to convert position data into probability distributions for upper extremity and tongue movement [20], [21]. Since the shoulder is a ball-and-socket joint and thus wrist range of motion follows a spherical shape, a more anatomically aligned model could better identify clinically relevant deficits. To our knowledge, we are the first to propose an icosahedron instead be used to segment the spherical wrist position data about the shoulder joint.

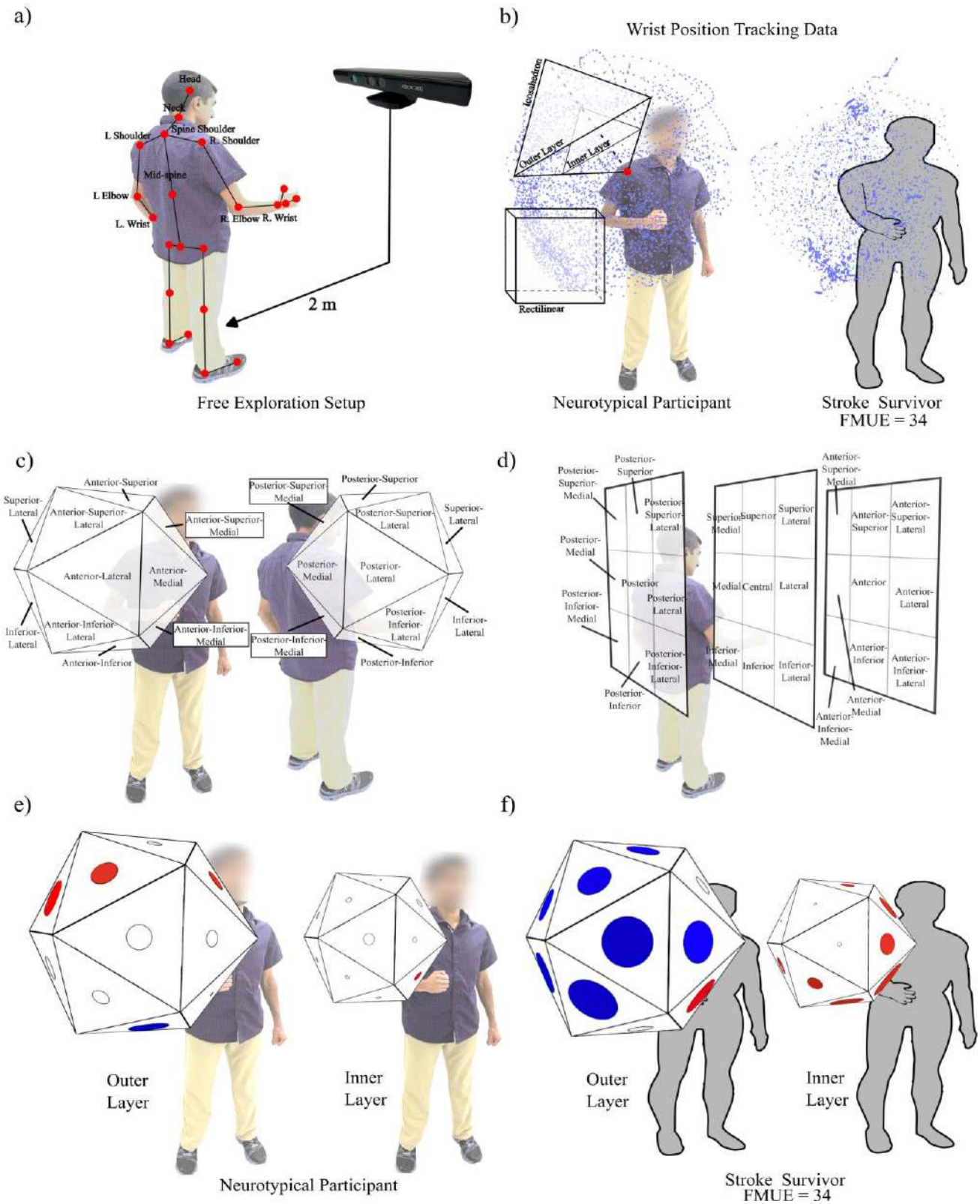


Figure 1: (a) Participant performs two minutes of free exploration in front of Kinect v2. (b) 3D wrist position sample frame data for a neurotypical individual and a stroke survivor (FMUE=34). (c) Icosahedron-based model's wrist position compartments labeled as anatomical zones. (d) Rectilinear-based model's wrist position compartments labeled as anatomical zones. (e) Sample probability distribution of neurotypical participant. Icosahedron faces categorize each wrist position frame into 20 zones. Half radius further splits zones into outer and inner layers. Probability calculated as percent time per zone. Red filled circles reflect that participant spent significantly more time than neurotypical individuals. Blue filled circles reflect significantly less time. Difference from neurotypical median is represented by circle radii. (f) Sample probability distribution of a stroke survivor (FMUE=34).

II. Materials and Methods

A. Study Design

19 chronic stroke survivors (7 female, 8 right side impaired, age: 53.4 +/- 12.3 [standard deviation] years) and nine neurotypical individuals with no history of stroke (5 female, 7 right-handed, age: 31.9 +/- 15.2 years) were recruited, and all gave written informed consent. The experiment was approved under the Institutional Review Board of Northwestern University (STU00216062).

Stroke survivors and neurotypical participants completed a free upper-extremity exploration task with their dominant arm, or affected extremity for 2 minutes, respectively. During the task, they were asked to move their arm towards all reachable areas with their upper extremity, as much as possible, at their own selected speed (Fig 1a) [15].

B. Data Acquisition and Analysis

We collected kinematic data using Kinect v2 (Microsoft, Seattle, WA), a markerless motion capture system, placed about two meters in front of the participant. The Body2Basics software provided estimates of 3-dimensional positions for 24 joints of the upper extremity, including the bilateral shoulders and wrists. Data were low-pass filtered using a 5th-order Butterworth filter with a cutoff frequency of 6 Hz . Cutoff frequency was selected based on literature recommendations for analyzing faster arm movements [22]. Data from participants left-impaired or dominant were reflected across the sagittal plane. All joints were then translated such that the shoulder joint of the affected arm (stroke group) or dominant arm (neurotypical group) was set as the origin.

To partition the wrist position data based on an icosahedron model, we first calculated a radius equal to the furthest point of the wrist from the shoulder during free exploration. The vertices of the icosahedron were determined using the golden ratio and scaled by the radius. Each of its 20 faces serves as the base of a tetrahedron with the shoulder joint as the apex. The radius is also used to categorize the wrist position data into two layers – inner and outer – with a cutoff set at half the radius. The combination of 20 tetrahedrons and two layers form 40 zones from which probability distribution is calculated as the percentage of time an individual spends in each of these zones.

To segment the wrist position data in the 3-dimensional rectilinear model, a maximum distance from the gleno-humeral joint is calculated, and the x, y, and z axes are bounded by this distance with the shoulder as the origin. This cube-shape is then split into 27 zones with equal volume by splitting each axis into 3 layers (Fig 1b). Probability distribution is then calculated as percent time a participant's wrist is in each of these zones.

We used Python SciPy library to calculate 95% confidence intervals (CI) for the percent time spent in each zone based on data from neurotypical participants. A stroke survivor was considered significantly higher or lower than neurotypical individuals if their percent time fell outside these CIs. The number of participants with stroke outside the CI was counted and categorized as higher or lower for each zone. The Cochran-Armitage test was performed to determine if stroke survivors were more likely to spend less time in superior zones compared to inferior zones, suggesting sensitivity to gravity. In the icosahedron model, flexion synergies were identified if a stroke survivor spent more time in two of the following zones: inferior-lateral, anterior-inferior-lateral, anterior-lateral, and anterior-superior-lateral. In the rectilinear model, flexion synergies were present if more time was spent in the central zone.

To compare zone probabilities between stroke survivors and neurotypical individuals, unpaired Welch's t-tests with unequal variances were conducted using the Python SciPy library. We performed nonparametric correlation analyses to evaluate the associations between specific zone probabilities and clinical scores including Fugl-Meyer Upper Extremity (FMUE) score, FMUE synergy sub score (FMUE-SS), and Action Research Arm Test (ARAT) score. The significance level was set at 0.05.

III. Results

In the icosahedron-based model, neurotypical participants spent most time in the outer layer's anteroinferior (12.81 ± 6.40%), anterior-inferior-lateral (9.96 ± 4.92%), and posterior-inferior-lateral (9.57 ± 7.46%) zones. They spent the least amount of time in the posterior-medial-inferior zone (0.01 ± 0.02%), superomedial (0.03 ± 0.08%), and inferomedial (0.03 ± 0.08%) zones. They spent 89.47 ± 6.51% of the two minutes in the outer layer. When segmented by the rectilinear model, neurotypical participants spent most time in the anterior (16.69 ± 8.22%), inferior (13.48 ± 8.49%), and inferolateral (10.57 ± 7.21%) zones, and spent least time in the posterior-superior-medial (0%), posterior-inferior-medial (0.01 ± 0.02%), and posterior-medial (0.03 ± 0.08%) zones.

A. Muscle Weakness

Per icosahedron-based model, Participants with stroke spent most time in the outer layer's anteroinferior (18.91 ± 13.19%) and anterior-inferior-lateral (12.74 ± 8.94%) zones. On average, they differed significantly compared to neurotypical individuals in five zones: the anterior-inferior-medial (9.46% vs. 5.12%, respectively; $p<0.01$), the posterior-inferior-lateral (3.03% vs. 9.57%, respectively; $p=0.03$), posterior-superior (0.43% vs. 2.45%, respectively; $p=0.04$), posterior-superior-lateral (0.52% vs. 2.74%, respectively; $p=0.02$), and posterior-lateral (0.26% vs. 1.13%, respectively; $p=<0.01$) zones (Fig 2a). Other outer layer zones and all inner layer zones were not significantly different.

When comparing four inferior zones (anterior-inferior-medial, anterior-inferior, anterior-inferior-lateral, and inferolateral) with their corresponding superior zones (anterior-superior-medial, anterior-superior, anterior-superior-lateral, and superolateral), stroke survivors were more likely to fall below the neurotypical CI in superior zones than in their inferior counterpart. In the anterior-inferior-lateral zone, 5 stroke survivors were lower and 8 higher whereas the superior counterpart had 11 lower and 2 higher ($Z=2.78$, $p=0.01$). For the anterior-inferior zone, 4 were lower and 9 higher, while the superior zone had 12 lower and 3 higher ($Z=3.01$, $p<0.01$). In the anterior-

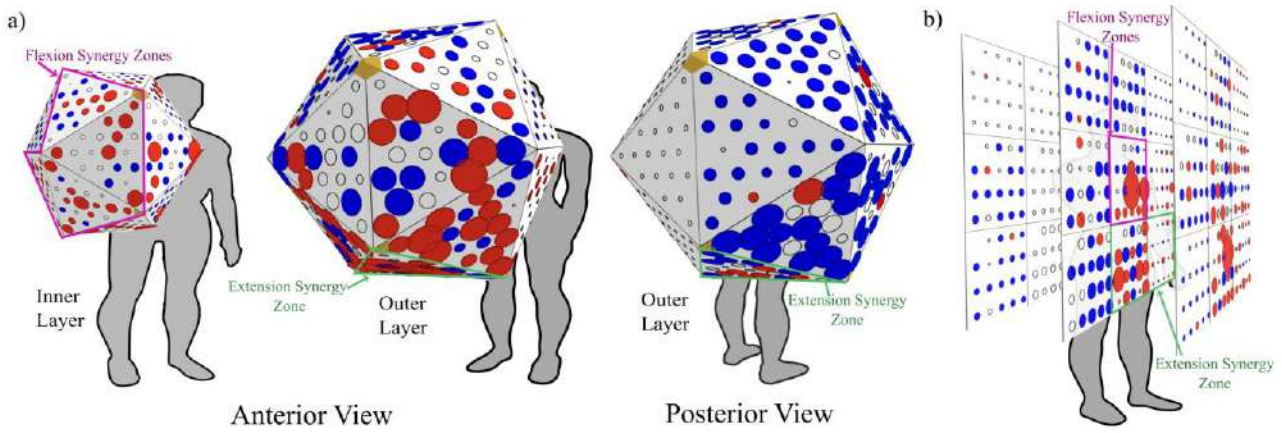


Figure 2: (a) All stroke survivors' probability distributions of wrist position partitioned by icosahedron where individuals have the same location on each face. Orientation marked by golden triangles. Red filled circles convey significantly more time than neurotypical individuals. Blue filled circles represent less time. Anterior view's inner and outer layer and posterior view's outer layer is presented. (b) All stroke stroke survivors' probability distribution of wrist position when segmented by the rectilinear model. Participants have same location in each zone.

inferior-medial zone, 6 participants were lower and 12 higher than the CI compared to 6 lower and 6 higher in the corresponding superior zone ($Z=1.14$, $p>0.05$). Finally, in the inferolateral zone, 11 were lower and 1 higher compared to 13 lower and 1 higher in the superolateral zone ($Z=0.55$, $p>0.05$).

Per rectilinear model, stroke survivors spent most time in the inferior (18.35 ± 13.21%) and anterior (17.45 ± 9.08%) zones. On average, they spent less time than neurotypical participants in four zones: superior (2.66% vs. 6.33%, respectively; $p=0.04$), superolateral (1.18% vs. 3.84%, respectively; $p<0.01$), posterior-lateral (0.73% vs. 2.73%, respectively; $p=0.02$), posterior-inferior-lateral (0.51% vs. 2.06%, respectively; $p=0.03$). Stroke survivors spent more time in the anterior-inferior-medial zone (2.11% vs. 0.56%, respectively; $p=0.02$) (Fig 2b).

In the anterior-inferior-medial zone, 10 stroke survivors were higher than the 95% CI and 4 lower, while the corresponding superior zone had 5 higher and 0 lower ($Z=0.35$, p=ns). In the anterior-inferior zone, 12 were higher and 4 lower whereas the anterior-superior zone had 3 higher and 10 lower ($Z=3.26$, $p<0.01$). The anterior-inferior-lateral zone had 1 higher and 14 lower, and the corresponding superior zone had 1 higher but 12 lower ($Z=-0.56$, p=ns). The inferolateral zone had 1 higher and 13 lower, and the superolateral zone had 2 higher and 16 lower ($Z=0.58$, p=ns).

B. Abormal Synergy

With the icosahedron model, 10 stroke survivors spent more time than the 95% CI in at least two of the inner layer's inferolateral, anterior-inferior-lateral, anterior-lateral, or anterior-superior-lateral zones. While, on average, stroke survivors did not spend more time than neurotypical participants in these four zones (7.10% vs. 4.37%, respectively; p=ns), these 10 stroke survivors did (11.49% vs. 4.37%, respectively; $p < 0.001$). Five in this group spent more time with their wrist in the posterior-inferior zone, and five spent more time in the anterior-inferior zone. Seven of the 10, however, spent less time in the outer layer's inferolateral zone (Fig 2a).

Per the rectilinear model, eight stroke survivors spent more time than the 95% CI in at least two of the middle layer's central, inferior, and inferomedial zones. Of these eight stroke survivors, two spent over 75% of the time here, and six of them were significantly less likely to have their wrist in the inferolateral zone. Seven of them overlapped with the 10 stroke survivors identified by the icosahedron model. On average, stroke survivors did not spend more time in these four zones compared to neurotypical participants (32.23% vs. 18.72%, respectively; p=06), but the eight stroke survivors did (52.78% vs. 18.72%, $p<0.01$) (Fig 2b).

C. Association to Clinical Scores

Six zones in the outer layer of the icosahedron model were positively associated with FMUE and ARAT scores. Of the zones in the outer layer, the percent time spent in the posterior-superior-lateral zone demonstrated strong positive correlation to FMUE ($R=0.70$, $p<0.0001$), FMUE-SS ($R=0.71$, $p<0.0001$), and ARAT ($R= 0.73$, $p<0.0001$). Percent time in the superior-lateral zone was moderately correlated with FMUE ($R = 0.57$, $p<0.01$), FMUE-SS ($R=0.59$, $p<0.001$), and ARAT ($R=0.58$, $p<0.01$), and time in posterior-superior zone was also moderately correlated with FMUE ($R=0.59$, $p<0.001$), FMUE-SS ($R=0.63$, $p<0.001$), and ARAT ($R=0.56$, $p<0.001$). The posterior-inferior-lateral, posterior-lateral, and inferior-lateral zones also had moderate correlation with all clinical scores (Fig. 3). The anterosuperior zone was moderately correlated with FMUE ($R=0.52$, $p<0.001$) and FMUE-SS ($R=0.55$, $p<0.001$), but not ARAT. The anterior-superior-lateral zone was also moderately correlated with FMUE ($R=0.44$, $p=0.02$), FMUE-SS ($R=0.51$, $p<0.01$), but not ARAT. Time in the anterior- inferior zone was negatively associated with ARAT ($R=-0.41$, $p=0.03$).

When segmented by the rectilinear model, percent time in the superolateral zone was strongly correlated with FMUE ($R=0.72$, $p<0.0001$), FMUE-SS ($R=76$, $p<0.0001$), and moderately correlated with ARAT ($R=0.69$, $p<0.0001$). Percent time in the anterior-superior-lateral zone was also strongly correlated with FMUE ($R=0.70$, $p<0.0001$), FMUE-SS ($R=0.72$, $p<0.0001$), and moderately correlated

with ARAT (R=0.61, p<0.001). The time in posterior-superior-lateral zone was strongly associated with ARAT (R=0.74, p<0.0001) and moderately associated with FMUE (R=0.64, p<0.001), FMUE-SS (R=0.66, p<0.001). In the posterior layer, percent time in the posterior-lateral, posterior, posterior-inferior-lateral, and posterior-inferior zones all had moderate association with all three clinical scores. In the anterior layer, time in the anterior-superior, anterior-lateral, anterior-inferior-lateral, and the anterior-inferior zones had moderate correlation to some of the three clinical scores. In the middle layer, the superior, superior-medial, and inferolateral zones had moderate correlation to some of the clinical scores (Fig. 3).

IV. Discussion

This study analyzed wrist position data during 2-minute upper-extremity free exploration in nine neurotypical individuals and 19 stroke survivors. An icosahedron-based model and a rectilinear-based model were then applied to segment the data and calculate probability distributions for each participant. Each model's identification of muscle weakness and abnormal synergies, and the correlation of probability in each zone to clinical scores was assessed.

Both the icosahedron and rectilinear model capture the tendencies of neurotypical participants to explore the inferior zones more during the 2-minute period. The over 10% discrepancy in probability between some lateral and medial zones in both models is likely due to the participant's body being positioned inferomedial to the shoulder joint, obstructing wrist movement in these regions. The approximately 70% difference in the icosahedron model between the outer and inner layer may be categorizing wrist position data with <90 degrees elbow flexion into the outer layer.

A. Muscle Weakness

Though stroke survivors showed the highest probabilities in the anterior-inferior and anterior-inferior-lateral zones, both the icosahedron and recitlinear models did show a significant drop in percent time in several posterior zones, including the posterior-lateral, posterior-inferior-lateral, posterior-superior-lateral, and posterior-superior zones. While the rectilinear model indicates that deficits are in the superior and the superior-lateral zones, the icosahedron-model clarifies that these deficits are specifically in the posterior direction. It identifies the posterior-superior-lateral zone to be the strongest movement deficit, on average, with an about 2% difference between neurotypical participants and stroke survivors. The results suggest the weakness of muscles involved in the flexion and abduction of the shoulder [23]. Both models agreed that stroke survivors compensate for decreases in percent time in the posterior regions with increase in percent time spent in the anterior-inferior-medial zone. This may be a generic sign of weakness in stroke survivors whose range of motion has been shown to decrease after stroke.

We expected the stroke survivor group to spend less time in the anterior-superior zones compared to neurotypical participants, but this was not the case. Still, compared to the 95% CIs of percent time based on

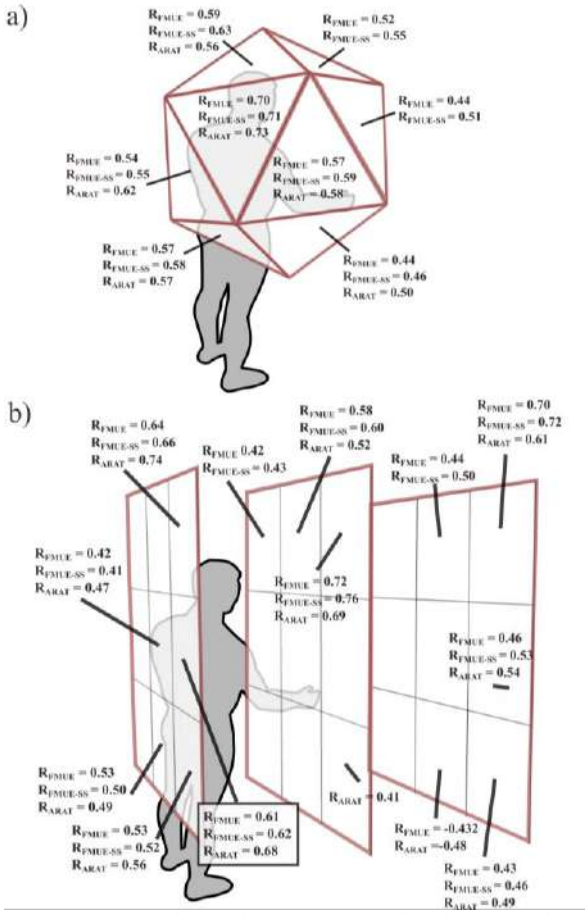


Figure 3: a) The eight icosahedral zones significantly correlated with FMUE, FMUE-SS, and/or ARAT are presented with their Spearman's correlation coefficient. The anterior-inferior zone not shown here had moderate negative correlation. All other zones were not significant when tested. b) The 14 rectilinear-based zones significantly correlated with clinical scores are displayed. Zones without Spearman's correlation coefficient displayed were not significant when tested.

neurotypical participant data in the icosahedron model, individual stroke survivors were more likely to fall below the interval in the anterior-superior and anterior-superior-lateral zones, spending more time in their inferior counterparts. The rectilinear model was aligned with the results in the anterior-superior direction. These results suggest that stroke survivors were more affected by gravity compared to neurotypical participants, indicating muscle weakness even in the anterior field. The icosahedron model identified muscle weakness in the anterior-superior-lateral. Meanwhile, the rectilinear model failed to detect it. This discrepancy may be due to the rectilinear model's grid-based structure, which likely struggles to capture the spherical data's corners effectively. The icosahedron model may offer an advantage due to its superior directional specificity in these regions.

B. Abnornal Synergy

Per the icosahedron model, 10 stroke survivors were found to spend significantly more time in at least two of the inner layer's inferolateral, anterior-inferior-lateral, anterior-lateral, and anterior-superior-lateral zones. These results may originate from the influence of the flexion synergy. As

literature suggests [24], this abnormal movement pattern can be observed as involuntary elbow flexion when the shoulder is abducted, which the icosahedron model reveals as higher percent time in the inner layer in these four regions. Meanwhile, abnormal synergies in the other 9 stroke survivors were not identified. This may be due to the inner layer's radius being small or too exclusive. Adding joint angle data of the shoulder abduction and elbow flexion may be beneficial to confirm this or improve the diagnostic quality of this model. The model also identifies that five of the 10 stroke survivors whose flexion synergy may have been observed spend more than the 95% CI in the posterior-inferior and anterior-inferior zones. This may be a sign of the extensor synergy in this group, which previous studies predict overlap in patients with the flexion synergy [1], [3] or it may be a sign of muscle weakness. However, though these subjects are able to flex their shoulders in the anterior zones, seven of the 10 stroke survivors could not abduct their shoulder to even the inferolateral zone. The combination of their flexion synergy where elbow flexion is seen with shoulder abduction and the extensor synergy where elbow extension is paired with shoulder adduction may be the cause of stroke survivors' inability to reach this inferolateral zone.

The rectilinear model found eight stroke survivors who spent more than the 95% CI in two of the middle layer's following zones: central, inferior, inferomedial. This model also found that six of the eight participants spent significantly less time in the inferolateral zone. The combination of these findings may be a sign of the flexion and extension synergies. Of note, seven of these eight overlapped with the icosahedron model, indicating that these models observe the same abnormal synergies in slightly different perspectives. The large difference of about 35% between these eight survivors in comparison to neurotypical participants may be due to the rectilinear model's single central zone which sums all the icosahedron's inner layer's zones into one. However, the icosahedron model's splitting of this zone may have allowed it to find a couple more stroke survivors who exhibit these stereotypical movement patterns. Overall, the icosahedron model is potentially more sensitive at identifying synergistic behaviors in stroke survivors.

C. Association to Clinical Scores

In the icosahedron model, eight zones were associated with FMUE and ARAT with one zone, posterior-superior-lateral, having a strong correlation of greater than 0.70. A few zones including the posterior-superior and the superior-lateral had correlations greater than 0.60. Other zones like the anterior-superior showed moderate correlation linked possibly by muscle weakness in these stroke survivors. The consistent compensation of stroke survivors in the anterior inferior medial zone was again identified here with a moderate negative correlation to ARAT.

The rectilinear model, meanwhile, related 14 zones to these clinical scores. Two zones (superolateral and anterior-superior-lateral) demonstrated strong association with FMUE and ARAT of greater than 70. Unlike the icosahedron model, the posterior-superior-lateral zone only strongly correlated well with ARAT. Six of the 14 zones showed significant but less than 0.50 association to the clinical scores maybe due to the generalized weakness as well. The consistent relation of rectilinear-based zones may suggest a superiority to the icosahedron model for clinical score prediction. Both models had a higher correlation with FMUE-SS in comparison to FMUE, which may indicate that both models' segmentation of the data are capturing how different muscles work independently of one another via wrist position in each zone.

D. Limitations and Future Work

In this analysis, with the group of nine neurotypical participants and 19 stroke survivors, flexion and extension synergy patterns are claimed to have been identified. The small sample size may limit however the generalizability of these patterns. Also, while Welch's t-tests accounted for unequal variances, the imbalance in group sizes may still introduce bias, potentially overestimating the differences between groups. Additionally, the repeatability of the free exploration data is unchecked. Future work may compare each participants' probability distributions to other instances of free exploration in follow up data collection. The study is also retroactively performed so the instructions of free exploration may have been unclear and the intention of subjects when they are they are in regions claimed to signify synergistic patterns cannot be ascertained.

Weakness and synergistic patterns are inferred in this analysis based on clinical presentation and FMUE scores. Confirmation using EMG was not performed, which may limit the validity of the findings. This analysis could be performed in future work. All data were assessed in comparison to the glenohumeral joint with left impaired stroke survivors or left dominant neurotypical individuals' wrist position reflected across the sagittal plane. This potentially misses shoulder movement and trunk compensation, which may have strengthened the link to flexion and extension synergies. Future work may consider joints external to the wrist in the context of joint angles to corroborate the hypotheses made in this study. Findings from this paper suggest that differences in probability distributions can be used across various movements to identify movement deficits and evaluate the effectiveness of new devices designed to assist other movements such as supination and plantar flexion [25], [26].

V. Conclusion

This study compared icosahedron-based and rectilinear-based probability distributions for identifying arm movement deficits in stroke survivors using wrist position data from two minutes of upper extremity free exploration. While both models revealed shoulder flexion weakness in the zones directly anterior to the body and shoulder abduction weakness, the icosahedron-based model identified an additional flexion movement deficit anterolaterally in stroke survivors. Furthermore, this model detected abnormal flexion and extension synergies in 10 stroke survivors, two more than the rectilinear model. However, the rectilinear-based model demonstrated superiority in predicting clinical scores with 14 zones correlating to FMUE or ARAT compared to just 8 in the icosahedron model.

The icosahedron model's alignment with anatomical movement makes it a promising framework for

individualized upper extremity assessment. Meanwhile the rectilinear model's performance in correlating to clinical scores highlight its utility in broader score-based evaluations. A hybrid of both models may equip therapists to identify movement deficits and to estimate clinical score within two minutes of evaluation, saving them time to treat patients effectively, potentially improving care and reducing therapist burnout. A key limitation of this study was the unchecked repeatability of the data and a relatively small sample size. Future research could address these limitations by validating results in follow up free exploration data and incorporating joint angles to contextualize wrist position further.

ACKNOWLEDGMENT

This study was funded by NIDLRR grant 90REGE0005-01. The authors thank the members of the RobotLab, the Northwestern and UIC IRBs, and the Shirley Ryan AbilityLab.

REFERENCES

[1] J. G. McPherson, A. Chen, M. D. Ellis, J. Yao, C. J. Heckman, and J. P. A. Dewald, "Progressive recruitment of contralesional cortico-reticulospinal pathways drives motor impairment post stroke," *J. Physiol.*, vol. 596, no. 7, pp. 1211–1225, 2018, doi: 10.1113/JP274968.

[2] H. Karbasforoushan, J. Cohen-Adad, and J. P. A. Dewald, "Brainstem and spinal cord MRI identifies altered sensorimotor pathways post-stroke," *Nat. Commun.*, vol. 10, no. 1, p. 3524, Aug. 2019, doi: 10.1038/s41467-019-11244-3.

[3] A. J. C. McMorland, K. D. Runnalls, and W. D. Byblow, "A Neuroanatomical Framework for Upper Limb Synergies after Stroke," *Front. Hum. Neurosci.*, vol. 9, p. 82, Feb. 2015, doi: 10.3389/fnhum.2015.00082.

[4] T. E. Twitchell, "The Grasping Deficit in Infantile Spastic Hemiparesis," *Neurology*, vol. 8, no. 1, pp. 13–13, Jan. 1958, doi: 10.1212/WNL.8.1.13.

[5] D. Kim *et al.*, "Correlations in abnormal synergies between the upper and lower extremities across various phases of stroke," *J. Neurophysiol.*, vol. 132, no. 1, pp. 87–95, Jul. 2024, doi: 10.1152/jn.00102.2024.

[6] S. FACCIORUSSO *et al.*, "Muscle synergies in upper limb stroke rehabilitation: a scoping review," *Eur. J. Phys. Rehabil. Med.*, vol. 60, no. 5, pp. 767–792, Nov. 2024, doi: 10.23736/S1973-9087.24.08438-7.

[7] C. E. Lang, J. M. Wagner, A. W. Dromerick, and D. F. Edwards, "Measurement of Upper-Extremity Function Early After Stroke: Properties of the Action Research Arm Test," *Arch. Phys. Med. Rehabil.*, vol. 87, no. 12, pp. 1605–1610, Dec. 2006, doi: 10.1016/j.apmr.2006.09.003.

[8] D. J. Gladstone, C. J. Danells, and S. E. Black, "The Fugl-Meyer Assessment of Motor Recovery after Stroke: A Critical Review of Its Measurement Properties," *Neurorehabil. Neural Repair*, vol. 16, no. 3, pp. 232–240, Sep. 2002, doi: 10.1177/154596802401105171.

[9] C. S. A. Oliveira, "Use of the Box and Block Test for the evaluation of manual dexterity in individuals with central nervous system disorders: A systematic review," *Use Box Block Test Eval. Man. Dexterity Individ. Cent. Nerv. Syst. Disord. Syst. Rev.*, vol. 14, pp. 0–0, Dec. 2016, doi: 10.17784/mtprehabJournal.2016.14.436.

[10] G. M. Johansson and C. K. Häger, "A modified standardized nine hole peg test for valid and reliable kinematic assessment of dexterity post-stroke," *J. NeuroEngineering Rehabil.*, vol. 16, no. 1, p. 8, Jan. 2019, doi: 10.1186/s12984-019-0479-y.

[11] C. E. Lang, M. D. Bland, R. R. Bailey, S. Y. Schaefer, and R. L. Birkenmeier, "Assessment of upper extremity impairment, function, and activity after stroke: foundations for clinical decision making," *J. Hand Ther.*, vol. 26, no. 2, pp. 104–115, Apr. 2013, doi: 10.1016/j.jht.2012.06.005.

[12] C. E. Lang *et al.*, "Improvement in the Capacity for Activity Versus Improvement in Performance of Activity in Daily Life During Outpatient Rehabilitation," *J. Neurol. Phys. Ther.*, vol. 47, no. 1, pp. 16–25, Jan. 2023, doi: 10.1097/NPT.0000000000000413.

[13] M. Al-Ayyad, H. A. Owida, R. De Fazio, B. Al-Naami, and P. Visconti, "Electromyography Monitoring Systems in Rehabilitation: A Review of Clinical Applications, Wearable Devices and Signal Acquisition Methodologies," *Electronics*, vol. 12, no. 7, Art. no. 7, Jan. 2023, doi: 10.3390/electronics12071520.

[14] M. C. Tresch, V. C. K. Cheung, and A. d'Avella, "Matrix factorization algorithms for the identification of muscle synergies: evaluation on simulated and experimental data sets," *J. Neurophysiol.*, vol. 95, no. 4, pp. 2199–2212, Apr. 2006, doi: 10.1152/jn.00222.2005.

[15] P. Ryali *et al.*, "Evaluation of a passive wearable arm ExoNET," *Front. Robot. AI*, vol. 11, p. 1387177, Jul. 2024, doi: 10.3389/frobt.2024.1387177.

[16] C. Celian, P. Ryali, V. Wilson, A. Srivatsaa, and J. L. Patton, "A wearable anti-gravity supplement to therapy does not improve arm function in chronic stroke: a randomized trial," May 07, 2024, *arXiv*: arXiv:2405.04707. doi: 10.48550/arXiv.2405.04707.

[17] G. Cornella-Barba, S. Okita, Z. Li, and D. J. Reinkensmeyer, "Real-Time Sensing of Upper Extremity Movement Diversity Using Kurtosis Implemented on a Smartwatch," *Sensors*, vol. 24, no. 16, Art. no. 16, Jan. 2024, doi: 10.3390/s24165266.

[18] A. Martino Cinnera, P. Picerno, A. Bisirri, G. Koch, G. Morone, and G. Vannozzi, "Upper limb assessment with inertial measurement units according to the international classification of functioning in stroke: a systematic review and correlation meta-analysis," *Top. Stroke Rehabil.*, vol. 31, no. 1, pp. 66–85, Jan. 2024, doi: 10.1080/10749357.2023.2197278.

[19] A. Casile *et al.*, "Quantitative Comparison of Hand Kinematics Measured with a Markerless Commercial Head-Mounted Display and a Marker-Based Motion Capture System in Stroke Survivors," *Sensors*, vol. 23, no. 18, Art. no. 18, Jan. 2023, doi: 10.3390/s23187906.

[20] V. Bratland *et al.*, "Statistical evaluation of tongue capability with visual feedback," *J. NeuroEngineering Rehabil.*, vol. 21, no. 1, p. 2, Jan. 2024, doi: 10.1186/s12984-023-01293-7.

[21] Z. A. Wright, J. L. Patton, F. C. Huang, and E. Lazzaro, "Evaluation of force field training customized according to individual movement deficit patterns," in *2015 IEEE International Conference on Rehabilitation Robotics (ICORR)*, Singapore, Singapore: IEEE, Aug. 2015, pp. 193–198. doi: 10.1109/ICORR.2015.7281198.

[22] R. Bartlett, *Introduction to sports biomechanics: analysing human movement patterns*, Second edition. London ; New York: Routledge, Taylor & Francis Group, 2007.

[23] G. L. Santos, L. F. García-Salazar, M. B. Souza, A. B. Oliveira, P. R. Camargo, and T. L. Russo, "Torque steadiness and muscle activation are bilaterally impaired during shoulder abduction and flexion in chronic post-stroke subjects," *J. Electromyogr. Kinesiol.*, vol. 30, pp. 151–160, Oct. 2016, doi: 10.1016/j.jelekin.2016.07.003.

[24] M. D. Ellis, Y. Lan, J. Yao, and J. P. A. Dewald, "Robotic quantification of upper extremity loss of independent joint control or flexion synergy in individuals with hemiparetic stroke: a review of paradigms addressing the effects of shoulder abduction loading," *J. NeuroEngineering Rehabil.*, vol. 13, no. 1, p. 95, Oct. 2016, doi: 10.1186/s12984-016-0203-0.

[25] M. Camardo *et al.*, "Design Evaluation of a Passive Ankle Exoskeleton for Gait Training," in *International Conference on Rehabilitation Robotics (ICORR)*, Chicago, IL, USA: IEEE, May 2025, p. Accepted. doi: Pending.

[26] V. Wilson *et al.*, "Structural Optimization of a Passive ExoNET for Forearm Supination," in *International Conference on Rehabilitation Robotics (ICORR)*, Chicago, IL, USA: IEEE, May 2025, p. Accepted. doi: Pending.

Mapping the Neural Control of Force and Impedance of Wrist Movements Using Robotics and fMRI

Kristin Schmidt and Fabrizio Sergi

***Abstract*—While robots are becoming increasingly valuable tools in neurorehabilitation, our limited understanding of the brain's response during human-robot interaction tasks restricts advancements in training programs to restore neural pathways after injury. Co-contraction is characteristic of several neuromuscular disorders, such as stroke and cerebral palsy, and it is often targeted by assessments or rehabilitation programs. Despite its importance, the neural mechanisms underlying co-contraction remain poorly understood. To address this gap, this study investigates the neural substrates of muscle co-contraction via functional magnetic resonance imaging (fMRI) during a dynamic motor task with an MR-compatible wrist robot.**

To establish suitable fMRI experimental conditions, we first conducted a behavioral study assessing muscle activity during a wrist-pointing task with four participants. Participants reached toward a target while experiencing four main perturbation conditions (no force, divergent force, constant force up, and constant force down), designed to elicit distinct force and impedance responses. Following this behavioral validation, five additional participants performed the wrist-pointing task during fMRI. Our results suggest localization of force and impedance control within the cortico-thalamic-cerebellar network. These findings provide new insights into the neural mechanisms of co-contraction, supporting the development of neurorehabilitation paradigms.

I. Introduction

Motor control is essential for performing skilled movements in daily life, yet disruptions in this ability are associated with several neuromuscular conditions, such as stroke and cerebral palsy [1]. These neuromuscular disorders often feature altered muscle activation strategies, such as excessive co-contraction of agonist and antagonist muscles. This lack of precise regulation of muscle groups impairs movement efficiency and increases fatigue, making everyday activities more challenging. As a result, physical therapists sometimes target a reduction in muscle co-contraction as a goal for rehabilitation [1]. However, current therapeutic approaches to regulating muscle co-contraction are limited by our lack of understanding of how muscle co-contraction is controlled at the neural level. Addressing this gap is critical for identifying therapeutic targets and developing effective interventions to optimize muscle coordination and restore motor function.

Co-contraction plays an important role in maintaining joint stability [2], resisting external disturbances during movement [3], and may also facilitate the learning of new skills [4]. However, it is a metabolically demanding control strategy and is generally reserved for tasks that demand increased joint stiffness, such as those that are unpredictable or unstable. Conversely, tasks that involve learnable dynamics allow the central nervous system to predict dynamics with an accurate internal model, enabling a more efficient control strategy through the reciprocal activation of agonist muscles. Reciprocal activation generates direction-specific joint torques, which is useful for opposing forces with a predictable direction. While co-contraction and reciprocal activation are distinct motor strategies, they often occur simultaneously [5], [6], necessitating careful task design to isolate their control. Ultimately, disentangling these mechanisms at the neural level can enable more targeted therapeutic approaches in neurorehabilitation.

In this work, we first validate a set of experimental task conditions in a wrist-pointing task designed to decouple co-contraction and reciprocal activation, as estimated by electromyography (EMG). This EMG validation ensures the task conditions reliably differentiate between these mechanisms, a crucial step for distinguishing their underlying neural processes. Following this behavioral validation, we conduct an fMRI study using the same task conditions to investigate the neural correlates associated with torque and stiffness control. This work provides preliminary insights into the neural mechanisms responsible for muscle co-contraction and reciprocal activation during dynamic motor tasks, with potential implications for improving rehabilitation strategies.

II. Materials and Methods

In this work, we present findings from two studies, a behavioral study and a neuroimaging study, with similar methodologies; the primary distinction between the two studies is that the behavioral study was conducted in a mock MRI scanner with EMG, while the neuroimaging study took place in a real MRI scanner without EMG. In both studies, participants performed wrist-pointing movements using the MR-SoftWrist [7], an MR-compatible wrist robot, while lying supine (Fig. 1). The MR-SoftWrist enables wrist movements in flexion-extension (FE) and radial-ulnar deviation (RUD).

A. Participants

Four healthy young adults (2 male, 27.5±3.11 years) were recruited for the behavioral study, and five healthy young adults (3 male, 27.2±3.19 years) were recruited for the neuroimaging study. Participants had no history of neuromuscular disorders. This study was approved by the Institutional Review Board of the University of Delaware, IRB no. 1936400-3.

B. Experimental Setup

Participants' right hand was secured in the handle of the MR-SoftWrist, which enclosed the knuckles without limiting

FS (corresponding author - fabs@udel.edu) and KS are with the Human Robotics Laboratory, Departments of Biomedical and Mechanical Engineering, University of Delaware, Newark, DE, 19713 USA. This work is supported by the National Science Foundation under Award 194712 and the University of Delaware Graduate College through the Doctoral Fellowship for Excellence.

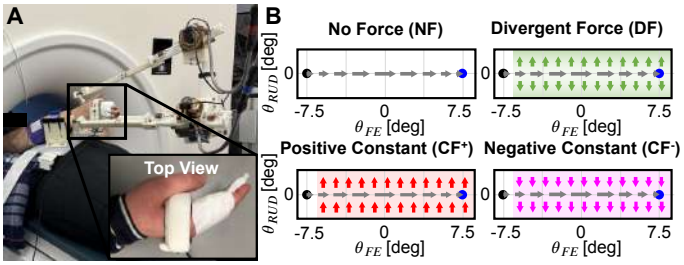


Fig. 1. A. MR-SoftWrist pictured in its operating condition. The enlarged image shows a top view of the handle with the paddle insert and tape around the participant's fingers. B. Experimental force conditions.

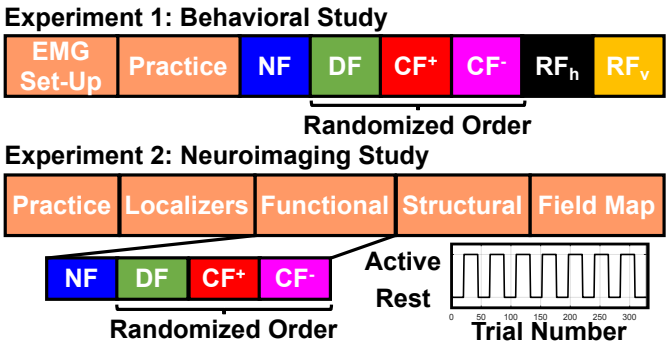


Fig. 2. Experimental protocol of the behavioral and neuroimaging studies.

finger movement. To promote a slightly flexed finger posture and reduce extraneous finger muscle contraction, their fingers were taped to a small paddle inserted into the handle (Fig. 1A). They were instructed to focus on making wrist movements while keeping their fingers and thumb relaxed. Their forearm rested on a rigid arm support placed on their stomach, with additional padding for shoulder and upper arm support. Participants viewed the task on a monitor through glasses with angled mirrors in the behavioral study or through an angled mirror attached to the imaging head coil during neuroimaging.

In all tasks, the goal was to move in a straight line between two circular targets. For horizontal tasks, these were located at ($\pm$7.5,0) deg, and for vertical tasks, these were located at (0,$\pm$7.5) deg, relative to the neutral hand posture in the FE and RUD axes, respectively. Each trial began with the target changing color from black to blue. After the participant moved the cursor 1 deg away from the starting target, the cursor was hidden to reduce corrections on real-time feedback. At the end of each trial, speed feedback was displayed by a change in target color to red if too slow (>0.45 s), green if too fast (<0.2 s), or black if within the desired time window. Error feedback was also displayed via a yellow cursor at the position of the maximum deviation from the straight-line trajectory.

During these movements, the robot applied forces perpendicular to the primary movement direction. The main force conditions used in this study were no force (NF), divergent force (DF), constant force up (CF$^+$), and constant force down (CF$^\infty$) (Fig. 1B). These conditions were all oriented as horizontal movements, so forces were applied in the RUD direction. NF was intended to assess baseline performance. In DF, the robot applied RUD perturbation torques proportional to the RUD wrist angle, up to a maximum torque, τ_m, such that $\tau_{RUD} = \min(k_v\theta_{RUD}, \tau_m)$, with $k_v = 0.085$ Nm/deg and $\tau_m = 1$ Nm. This unstable condition was designed to up-regulate muscle co-contraction [3]. In the CF conditions, torque was applied to push the wrist in the radial (positive, against gravity) direction (CF$^+$: $\tau_{RUD} = 0.3$ Nm) or in the ulnar (negative, with gravity) direction (CF$^\infty$: $\tau_{RUD} = -0.3$ Nm). These CF conditions were included to provide a clearer interpretation of DF, as the effects observed during DF could result from either the independent control of individual muscles or a higher-order mechanism regulating co-contraction [6]. Specifically, CF controls for radial muscle activation (u_R), primarily in response to CF$^\infty$, and ulnar muscle activation (u_U), primarily in response to CF$^+$.

1) Behavioral Study: EMG was used in the behavioral study only. We used Delsys Trigno Duo electrodes (sampling frequency: 2148 Hz), and the EMG signal was time-synced to task performance data (sampling frequency: 1000 Hz) via a common analog signal sent at the onset of each trial. EMG sensors were placed on the participant's four major wrist muscles: flexor carpi radialis (FCR), flexor carpi ulnaris (FCU), extensor carpi ulnaris (ECU), and extensor carpi radialis (ECR). The forearm was prepared for electrode placement by shaving the arm hair and cleaning the skin with alcohol. Electrode placement was checked by observing large bursts of agonist muscle activity. A force-torque sensor (ATI mini40, ATI Industrial Automation, Apex, NC, USA) in the device handle was used to measure user-applied torques.

2) Neuroimaging Study: The neuroimaging study took place at the University of Delaware Center for Biomedical and Brain Imaging with a Siemens Prisma 3T scanner and 64-channel head coil. All functional images were acquired using a multiband T_{2*}-weighted EPI sequence (spatial resolution: 2×2×2 mm^3, 60 slices, TE=30ms, TR=1s, acceleration factor=4, Image Size=[110 110 60]). We also acquired a T1-weighted anatomical image (1×1×1 mm^3, TE=3.02ms, TR=2.3s, Image Size=[160 256 256]) for image registration and normalization and a GRE-field map (3×3×3 mm^3, TE=4.92ms, TR=400ms) for unwarping due to magnetic field inhomogeneities. We monitored physiological signals with an MR-compatible pulse oximeter and respiration belt (Siemens Physiology Monitoring Unit).

C. Protocol

After participants were positioned on the bed with the robot, they practiced the task in a transparent (NF) condition. During this time, they were instructed to practice making straight point-to-point movements within the cued time window. Participants were able to self-select when they felt comfortable enough with the task instructions and felt ready to end the practice session, after typically no more than 100 trials.

1) Behavioral Study: After familiarization, participants performed six blocks of 200 trials each, with about five minutes

of rest between blocks to reduce fatigue (Fig. 2). All but the final task block featured horizontal movements, and the final block featured vertical movements. The goal of the task was always the same, but the robot was commanded in different force modes across blocks. The first block was always an NF task to assess baseline task performance, followed by three randomly ordered DF, CF^{+}, and CF$^{\infty}$ blocks (Fig. 2). The final two blocks were added for EMG calibration, where participants were subject to viscous resistive forces (RF) during horizontal (RF$_h$: $\tau_{FE} = -\alpha_R \dot{\theta}_{FE}$ Nm) and vertical (RF$_v$: $\tau_{RUD} = -\alpha_R \dot{\theta}_{RUD}$ Nm) movements, where α_R=0.050 Nm/deg. The RF tasks were intended to elicit strong agonist activation in each direction, improving the signal-to-noise ratio for improved EMG calibration.

2) Neuroimaging Study: In the neuroimaging study, participants performed four tasks during functional imaging (Fig. 2). Each task consisted of 168 active trials divided evenly into seven blocks, interspersed with 19.5 s passive blocks. During these passive blocks, the robot locked in its current position, and participants were instructed to watch the virtual cursor make straight point-to-point movements between the targets. This condition acts as our visual control to match the visual stimulus seen during task performance. Within each task, all active trials were controlled under the same force mode, which corresponded to the same conditions used in the first four blocks of the behavioral EMG study. The first block was always NF, followed by a random order of DF, CF^{+}, and CF$^{\infty}$. The neuroimaging session also consisted of localizers and anatomical scans for image registration and unwarping.

D. Data Analysis

1) Trial Onset and Normalization: To consistently analyze data collected over multiple trials, we established three specific time windows: Early, Middle, and Late. The Early window spanned from 150 ms before trial onset ($t_{\propto 150}$) and lasted until trial onset (t_0). In our analysis, t_0 was defined as the instant when the cursor exceeded a position threshold of 1 deg away from the starting target in the direction towards the cued target. The Middle time window started at t_0 and ended at the point of maximum velocity (t_{vmax}). Finally, the Late time window covered the period from t_{vmax} until the end of the trial (t_{end}), defined as the time when the cursor reached a lateral position within 1 deg of the ending target. Task kinematics, kinetics, and EMG were normalized via resampling so that the instants of $t_{\propto 150}$, t_0, t_{vmax}, and t_{end} coincided across participants.

2) EMG-based Joint Torque and Stiffness Estimation: EMG signals were bandpass filtered at 30-500 Hz, rectified, and the envelope was taken via a 10 Hz low-pass, zero-shift 4th order Butterworth filter. Muscle moment arms (ρ) were obtained at each joint position using OpenSim [8].

For each muscle, we time-shifted the EMG signal (m) to synchronize with kinematic data, accounting for the electromechanical delay. We then related this delayed EMG signal ($m(t-t_d)$) to muscle forces (F_m) via a muscle-specific scaling factor (γ) (Eqn. 1). While this simplistic EMG-force relationship neglects the position and velocity-dependent effects of muscle activation, these effects may be negligible in our task because movements are small amplitude (range < 20 deg) and slow during the main region of interest (quasi-static in the Early window, $t_{\propto 150} : t_0$). Within this range, the peak active muscle force is predicted to change by 0.6-45%, as predicted by the force-length curves in the OpenSim wrist model [8]. We are primarily interested in relative differences across force conditions, where the muscle lengths and velocities are similar, so estimation errors across conditions should be comparable.

We calibrate γ at the joint level by relating task dynamics and predicted user-generated torques (τ_{pred}) to the force-torque sensor measured torques (τ_{meas}) via linear regression (Eqn. 2-3). For the calibration procedure, we included all active trials across all six force conditions.

$$F_{m_i}(t) = \gamma_i m_i(t - t_d), t_d = 90 \text{ ms} \tag{1}$$

$$\tau_{pred,j}(t) = I_j \ddot{\theta}_j(t) + b_j \dot{\theta}_j(t) + \sum_{i=1}^{4} \rho_{j,i}(\gamma_i m_i(t - t_d)) \tag{2}$$

$$\boldsymbol{\tau_{pred} - \tau_{meas} = 0} \tag{3}$$

In these equations, j refers to the degree of freedom (FE or RUD) and i refers to the muscle (FCR, FCU, ECU, or ECR). The system dynamics are modeled in Eqn. 2 as an inertial term ($I\ddot{\theta}$) with viscosity ($b\dot{\theta}$) and human-applied torque (ρF_{m_i}). The coefficients I, b, and γ are estimated by minimizing prediction errors via linear regression (Eqn. 3). Once γ was estimated for each muscle, we calculated human-generated torques in the radial direction only (u_R), ulnar direction only (u_U), and net RUD torque (τ_{RUD}) as:

$$u_R = \rho_{2,FCR}\gamma_{FCR}m_{FCR} + \rho_{2,ECR}\gamma_{ECR}m_{ECR} \tag{4}$$

$$u_U = \rho_{2,FCU}\gamma_{FCU}m_{FCU} + \rho_{2,ECU}\gamma_{ECU}m_{ECU} \tag{5}$$

$$\tau_{RUD} = u_R - u_U \tag{6}$$

where $\rho_{2,i}$ refers to the muscle moment arm in RUD.

Muscle stiffness is typically a function of its mechanical properties (i.e., stiffness of its cross-bridges), length, and cross-sectional area. However, it has been found experimentally that muscle stiffness within a small range can be directly related to force via a scaling constant α/l_0, where α=23.4 [n.u.] and l_0 is the optimal muscle fiber length at maximum activation [9]. We used this relationship to estimate muscle-level stiffness (Eqn. 7) and related it to joint-level stiffness via its moment arms (Eqn. 8), where $\boldsymbol{J}$ is the Jacobian matrix comprised of the muscle moment arms from OpenSim [8].

$$\kappa_{SRS,i} = \frac{\alpha}{l_0} F_{m,i} \tag{7}$$

$$\boldsymbol{\kappa} = \boldsymbol{J}\ \text{diag}(\boldsymbol{k}_{SRS})\ \boldsymbol{J}^T \tag{8}$$

$\boldsymbol{\kappa}$ reflects the force opposed by the participant when a unit displacement is applied, such that the magnitude of stiffness along a specific direction, *p*, is described as

$$\kappa_p = ||\boldsymbol{\kappa} \cdot [\Delta\theta_{FE}, \Delta\theta_{RUD}]^T|| \tag{9}$$

Thus, we extract RUD stiffness as $\kappa_{RUD} = ||\boldsymbol{\kappa} \cdot [0,1]^T||$.

Group-level differences were assessed using the average across all trials and analyzed using a linear mixed model. Significant force condition effects were followed by pairwise student's t-tests ($p < 0.05$). Statistics were computed using only the Early window ($t_{\propto 150} : t_0$) to assess anticipatory motor commands, with full-trial data included for visualization.

3) Statistical Analysis of Imaging Data: Neuroimaging data was preprocessed using SPM12 [10], following a standard pipeline: unwarping, field map correction, realignment, MNI normalization, and smoothing with an 8mm Gaussian kernel.

The neural response was modeled as

$$y = \beta_1 H_1 + \beta_2 H_2 + \beta_3 H_3 + \beta_4 H_4 + \beta_{nui} H_{nui} + \beta_0 \quad (10)$$

where H_1, H_2, H_3, and H_4 represent the task regressors for active blocks of NF, DF, CF$^+$, and CF$^\infty$ trials convolved with the standard hemodynamic response function. H_{nui} is a set of 25 nuisance regressors (18 physiological noise regressors, 6 head movement regressors, and 1 linear signal drift regressor). Physiological noise regressors were modeled using the RETROICOR algorithm via the TAPAS PhysIO Toolbox [11].

Analysis of the General Linear Model (GLM) (Eqn. 10) yielded maps of beta-weights, relating signal measured in each voxel to each regressor of interest (β_1, β_2, etc.). We report voxels that activate more in one condition relative to others, based on linear contrasts c_i of the extracted β coefficients. Due to the study's limited number of participants, we report voxels with t-scores exceeding 4. This threshold was selected as a representative level for significance found in our prior work with larger study sizes [12], [13]. Activation regions were labeled using the Juelich Histological atlas for cortical regions [14], Harvard-Oxford atlas for subcortical regions [15], and MNI FNIRT atlas for the cerebellum [16].

For ease of notation, we define four activation maps to describe voxels related to the physiological phenomena of interest, i.e. brain areas associated with force and impedance. Specifically, the K map identifies voxels that contribute to stiffness modulation, which we define as those whose BOLD signal is upregulated more during DF compared to NF ($c_K = \beta_{DF} - \beta_{NF}$). The u_R and u_U maps reflect torque regulation in the radial or ulnar direction, respectively, compared to baseline ($c_{u_R} = \beta_{CF^-} - \beta_{NF}$, $c_{u_U} = \beta_{CF^+} - \beta_{NF}$). The $|T|$ map isolates voxels specific to torque in any direction ($c_{|T|} = \beta_{CF^-} - \beta_{CF^+}$, where both positive and negative statistical parametric coefficients are evaluated). Finally, the CC map, related to co-contraction control, identifies voxels with greater activation in DF relative to baseline, that exceeds the upregulation due to CF conditions ($c_{CC} = (\beta_{DF} - \beta_{NF}) - (\beta_{CF^-} - \beta_{NF}) - (\beta_{CF^+} - \beta_{NF}) = \beta_{DF} - \beta_{CF^-} - \beta_{CF^+} + \beta_{NF}$). With this formulation, the intersection of the K and CC maps reflects voxels that tune to co-contraction.

III. Results

A. Behavioral Results

As confirmation of reasonable EMG to torque estimation, τ_{RUD} levels in the Early window ($t_{\propto 150} : t_0$) differed significantly across conditions in the expected directions ($p = 0.002$) (Fig. 3). Torque generated in CF$^\infty$ was significantly greater than all other conditions (CF$^\infty$–NF: $p = 0.002$, CF$^\infty$–DF: $p = 0.011$, CF$^\infty$–CF$^+$: $p < 0.001$), while τ_{RUD} was not significantly different between NF and DF conditions ($p = 0.263$). Torque in CF$^+$ was lower than both DF ($p = 0.026$) and CF$^\infty$ ($p = 0.002$), but not different than NF ($p = 0.176$).

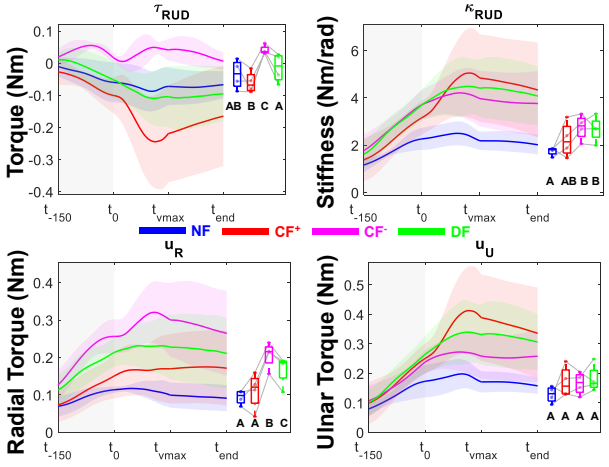


Fig. 3. Group-level torque and stiffness estimates. The boxplots show the distribution of each subject's mean activity in the shaded time window ($t_{-150} : t_0$). Significance is expressed in the connecting letters format, where pairs of conditions that do not share a letter are significantly different.

The torque relationships in the radial direction (u_R) follow a similar pattern (Fig. 3). The largest u_R magnitude occurred in the CF$^\infty$ condition, significantly exceeding NF ($p < 0.001$), DF ($p = 0.007$), and CF$^+$ ($p < 0.001$). There was no significant difference between NF and CF$^+$ ($p = 0.158$). However, despite aiming to match u_R levels between DF and CF$^\infty$ to test the muscle-level control hypothesis of co-contraction, u_R was significantly smaller in DF ($p = 0.007$).

For torque in the ulnar direction (u_U), there were no significant differences across conditions ($p = 0.218$) (Fig. 3). The desired relationship would be to match u_U levels between DF and CF$^+$ (where ulnar activation is agonist), and we are correctly not observing any significant difference between them. However, ideally we would like to see higher levels of u_U in CF$^+$ compared to CF$^\infty$ or NF to confirm that significant ulnar activation is necessary for the CF$^+$ task. In its current state, the gravitational force may be canceling out much of the applied force, requiring only small ulnar activation.

Stiffness (κ_{RUD}) was also significantly modulated by force condition ($p = 0.020$) (Fig. 3). While there was no significant difference in κ_{RUD} across pairs of the non-zero force conditions (CF$^+$–CF$^\infty$: $p = 0.097$, CF$^\infty$–DF: $p = 0.795$, CF$^+$–DF: $p = 0.148$), κ_{RUD} was smaller in NF than CF$^\infty$ ($p = 0.006$) and DF ($p = 0.009$). There was no significant difference between NF and CF$^+$ ($p = 0.115$).

B. Neuroimaging Results

Group-level fMRI results are shown in Fig. 4 and Table I. Activation for stiffness modulation (K map, green clusters in

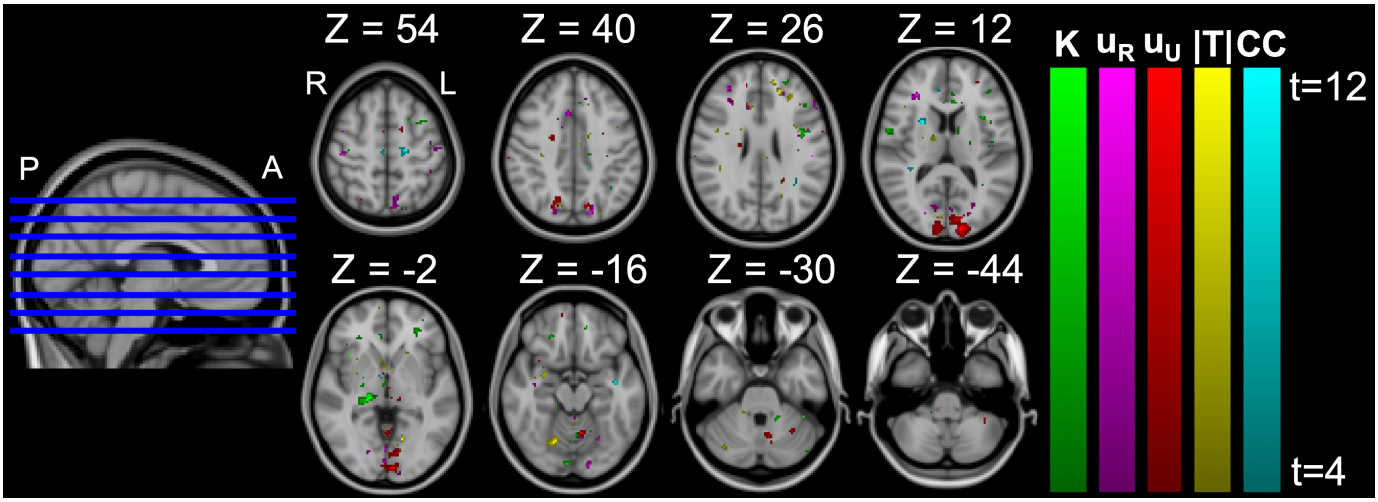


Fig. 4. Group-level t-score activation maps for task-based regressors. These maps refer to contrasts $c_K > 0$, $c_{u_R} > 0$, $c_{u_U} > 0$, $c_{|T|} = 0$,and $c_{CC} > 0$. For visualization of the t-score gradients, each contrast was thresholded between t={4,12}. Z coordinates refer to axial slices in MNI152 coordinates in mm.

Fig. 4) localized in the bilateral premotor cortices (Brodmann's Area 6), cerebellum (left V and vermis VI lobules), and the thalamus and subthalamic region across both hemispheres, including the pallidum, amygdala, and caudate. We also observed some activation clusters in the occipital lobe. Torque-related maps (u_R (magenta), u_U (red), and $|T|$ (yellow)) showed large regions of activation in the cerebellum and visual areas, including the lateral occipital cortex and visual cortex V2 (Brodmann's Area 18). The CC map (cyan), which describes the control of co-contraction, primarily resulted in active voxels in the bilateral premotor cortices, thalamus, and subthalamic regions (putamen, pallidum, and amygdala).

C. Task Performance Results

Task errors did not significantly differ between the two studies ($p = 0.660$, Fig. 5), suggesting that muscle activation in the behavioral experiment generally reflects the behavior during neuroimaging. While force condition had a significant effect on task errors ($p < 0.001$), there was no significant effect of interaction between force condition and study ($p = 0.055$).

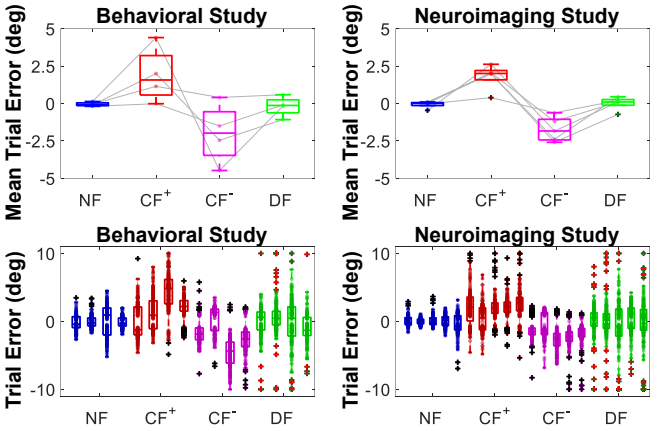


Fig. 5. Trial errors displayed at the end of each trial. The top row shows the distribution of each subject's average error in each force condition, and the bottom row shows the within-subject distribution of error across trials and conditions, where each boxplot represents one subject.

IV. Discussion and Conclusion

Our primary objective was to examine the neural substrates associated with force and impedance control during dynamic wrist-pointing. We showed that our task significantly modulates stiffness (κ_{RUD}) in DF relative to NF (Fig. 3), enabling the use of c_K to study stiffness modulation, albeit coupled with effects of increased muscle activation. To isolate torque generation in the radial or ulnar direction, we included the CF conditions to match agonist activation levels with those in DF. However, u_R was significantly greater in CF$^{\infty}$ than DF, despite our aim to match levels. Additionally, CF^{+} produced a weak u_U response due to gravity reducing the applied force magnitude. This suggests our contrasts c_{u_R} and c_{u_U} may not fully compensate for the effects of agonist activation. In the future, we will increase the instability of DF to provide more stiffness modulation relative to the CF conditions and a better match of u_R between DF and CF^{+}. We also plan to increase the magnitude of CF^{+} to overcome gravity. These changes should improve the relationships across conditions.

Our fMRI study revealed activation within the cortico-thalamic-cerebellar network (Fig. 4, Table I). Consistent with prior studies [17], clusters related to torque generation (u_R, u_U, and $|T|$ maps) were observed in the dorsal premotor cortex. We also observed activation clusters in the ventral premotor cortex in the K, u_R, u_U, and $|T|$ maps, supporting its role in voluntary co-contraction [17]. The overlap of the K and CC maps, reflecting co-contraction, identified only a few common voxels (left thalamus, left amygdala, and anterior intra-parietal sulcus). We will need additional participants to understand if these areas are truly significant. Additionally, cerebellar activation in the K, u_R, u_U, and $|T|$ maps aligns with the cerebellum's proposed role in managing complex

TABLE I
SELECTED PEAK ACTIVATION VOXELS

Map	Anatomical Region	x	y	z	Cluster Size	T Score
K	Premotor Cortex BA6 R	30	-20	70	16	6.732
K	Premotor Cortex BA6 L	-14	-10	46	16	10.636
K	Premotor Cortex BA6 L	-42	-14	52	5	5.075
K	Right Thalamus	18	-24	-2	142	20.937
K	Right Pallidum	22	-10	-4	12	14.223
K	Left Amygdala	-22	-12	-12	13	8.315
K	Left Caudate	-8	6	8	6	5.227
K	Vermis VI (Cerebellum)	2	-66	-18	16	7.458
K	Left V (Cerebellum)	-18	-44	-28	45	7.136
K	Occipital Fusiform Gyrus	10	-88	-20	58	15.193
K	Lateral Occipital Gyrus	-16	-72	52	32	12.651
u_R	Frontal Pole	32	42	28	81	17.209
u_R	Premotor Cortex BA6 L	-60	0	24	7	10.560
u_R	Superior Parietal Lobule 5Ci R	14	-30	48	8	7.799
u_R	Left V (Cerebellum)	-4	-62	-18	25	11.086
u_R	Left VI (Cerebellum)	-10	-62	-18	25	8.294
u_R	Lateral Occipital Cortex	16	-82	44	68	26.445
u_R	Visual Cortex V2 BA18 L	-10	-95	13	234	11.926
u_U	Premotor Cortex BA6 L	-38	-14	60	37	9.998
u_U	Premotor Cortex BA6 L	-12	-8	48	11	7.140
u_U	Right Thalamus	16	-6	4	19	7.816
u_U	Left Thalamus	-8	-24	2	31	7.557
u_U	Left V (Cerebellum)	-6	-58	-16	55	10.423
u_U	Left I-IV (Cerebellum)	-6	-52	-8	55	9.404
u_U	Visual Cortex V2 BA18 L	45	5	39	873	31.491
u_U	Lateral Occipital Cortex	-14	-80	48	81	9.747
$\lvert T \rvert$	Premotor Cortex BA6 L	-24	-20	56	41	14.701
$\lvert T \rvert$	Broca's Area BA44 L	-46	4	10	13	10.336
$\lvert T \rvert$	Superior Parietal Lobule 7A L	-6	-60	50	66	-6.077
$\lvert T \rvert$	Right Thalamus	12	-10	18	25	14.069
$\lvert T \rvert$	Right Amygdala	30	-2	-16	9	-7.442
$\lvert T \rvert$	Left Putamen	-24	20	2	11	8.280
$\lvert T \rvert$	Right Crus I (Cerebellum)	30	-58	-36	71	-24.588
$\lvert T \rvert$	Left I-IV (Cerebellum)	-2	–46	-14	15	-11.391
$\lvert T \rvert$	Occipital Fusiform Gyrus	20	-68	-14	123	12.261
$\lvert T \rvert$	Visual Cortex V1 BA17 L	-20	-62	2	48	6.676
CC	Premotor Cortex BA6 L	-18	-18	54	27	36.783
CC	Premotor Cortex BA6 L	-2	-16	68	9	7.314
CC	Premotor Cortex BA6 R	4	-20	54	9	6.332
CC	Somatosensory Cortex BA3 L	-24	-36	50	7	8.228
CC	Left Thalamus	-2	-20	6	40	12.961
CC	Right Putamen	24	8	12	18	11.786
CC	Right Pallidum	24	-4	-2	28	6.450
CC	Right Amygdala	26	-4	-10	28	9.792
CC	Optic Radiation L	-38	-48	6	20	10.160

x,y,z coordinates are defined in mm in MNI152 standard space. Clusters are thresholded at t=4, and cluster size represents the number of 8 mm^3 voxels.

dynamics [18], [19].

We observed large activation clusters in the visual cortex in the u_R and u_U maps. This activation may result from inadequate matching across conditions of the error feedback displayed at the end of each trial. Because error magnitude and direction differed across conditions (Fig. 5), the feedback cursor appeared at a different location on the screen, invoking a unique visual response. For future studies, we will improve the visual control condition shown during rest by displaying errors that are representative of actual task performance and incorporating explicit error regressors into the GLM (Eqn. 10).

In conclusion, we demonstrated that the DF condition sufficiently modulates stiffness relative to NF, and the CF conditions properly modulate torque. However, while these relationships are sufficient to interpret joint-level neural activation, we need to refine the magnitudes of these conditions to fully control for muscle-specific activation (u_R and u_U). Our fMRI study revealed activation within the cortico-thalamic-cerebellar network, with notable areas including the premotor cortex, thalamus, and cerebellum.

REFERENCES

[1] M. L. Latash, "Muscle coactivation: definitions, mechanisms, and functions," *Journal of Neurophysiology*, vol. 120, pp. 88–104, 3 2018.

[2] N. Hogan, "Adaptive Control of Mechanical Impedance by Coactivation of Antagonist Muscles," *IEEE Transactions on Automatic Control*, vol. 29, no. 8, pp. 681–690, 1984.

[3] E. Burdet, R. Osu, D. W. Franklin, T. E. Milner, and M. Kawato, "The central nervous system stabilizes unstable dynamics by learning optimal impedance," *Nature*, vol. 414, pp. 446–449, 11 2001.

[4] J. B. Heald, D. W. Franklin, and D. M. Wolpert, "Increasing muscle co-contraction speeds up internal model acquisition during dynamic motor learning," *Scientific Reports*, vol. 8, 12 2018.

[5] A. J. Farrens, K. Schmidt, H. Cohen, and F. Sergi, "Concurrent Contribution of Co-Contraction to Error Reduction During Dynamic Adaptation of the Wrist," *IEEE Transactions on Neural Systems and Rehabilitation Engineering*, vol. 31, pp. 1287–1296, 2023.

[6] K. Schmidt, B. Berret, and F. Sergi, "Development of an Experimental Protocol to Study the Neural Control of Force and Impedance in Wrist Movements with Robotics and fMRI," in *IEEE RAS/EMBS International Conference for Biomedical Robotics and Biomechatronics*, pp. 1334–1339, IEEE, 9 2024.

[7] A. Erwin, M. K. O'Malley, D. Ress, and F. Sergi, "Kinesthetic Feedback during 2DOF Wrist Movements via a Novel MR-Compatible Robot," *IEEE Transactions on Neural Systems and Rehabilitation Engineering*, vol. 25, pp. 1489–1499, 9 2017.

[8] K. R. Saul, X. Hu, C. M. Goehler, M. E. Vidt, M. Daly, A. Velisar, and W. M. Murray, "Benchmarking of dynamic simulation predictions in two software platforms using an upper limb musculoskeletal model," *Comput Methods Biomech Biomed Engin*, vol. 18, p. 1445, 10 2015.

[9] X. Hu, W. M. Murray, and E. J. Perreault, "Muscle short-range stiffness can be used to estimate the endpoint stiffness of the human arm," *J Neurophysiol*, vol. 105, pp. 1633–1641, 2 2011.

[10] J. Ashburner, G. Barnes, C.-C. Chen, J. Daunizeau, G. Flandin, K. Friston, D. Gitelman, V. Glauche, R. Henson, C. Hutton, A. Jafarian, S. Kiebel, J. Kilner, V. Litvak, J. Mattout, R. Moran, W. Penny, C. Phillips, A. Razi, K. Stephan, S. Tak, A. Tyrer, and P. Zeidman, "SPM12 Manual," 2021.

[11] L. Kasper, S. Bollmann, A. O. Diaconescu, C. Hutton, J. Heinzle, S. Iglesias, T. U. Hauser, M. Sebold, Z. M. Manjaly, K. P. Pruessmann, and K. E. Stephan, "The PhysIO Toolbox for Modeling Physiological Noise in fMRI Data," *J Neurosci Methods*, vol. 276, pp. 56–72, 1 2017.

[12] A. J. Farrens, S. Vahdat, and F. Sergi, "Changes in resting state functional connectivity associated with dynamic adaptation of wrist movements," *J Neuroscience*, 3 2023.

[13] A. Zonnino, A. J. Farrens, D. Ress, and F. Sergi, "Measurement of stretch-evoked brainstem function using fMRI," *Scientific Reports*, vol. 11, 12 2021.

[14] S. B. Eickhoff, T. Paus, S. Caspers, M. H. Grosbras, A. C. Evans, K. Zilles, and K. Amunts, "Assignment of functional activations to probabilistic cytoarchitectonic areas revisited," *NeuroImage*, vol. 36, pp. 511–521, 7 2007.

[15] R. S. Desikan, F. Ségonne, B. Fischl, B. T. Quinn, B. C. Dickerson, D. Blacker, R. L. Buckner, A. M. Dale, R. P. Maguire, B. T. Hyman, M. S. Albert, and R. J. Killiany, "An automated labeling system for subdividing the human cerebral cortex on MRI scans into gyral based regions of interest," *NeuroImage*, vol. 31, pp. 968–980, 7 2006.

[16] J. Diedrichsen, J. H. Balsters, J. Flavell, E. Cussans, and N. Ramnani, "A probabilistic MR atlas of the human cerebellum," *NeuroImage*, vol. 46, pp. 39–46, 5 2009.

[17] M. Haruno, G. Ganesh, E. Burdet, and M. Kawato, "Differential neural correlates of reciprocal activation and cocontraction control in dorsal and ventral premotor cortices," *J Neurophysiol*, vol. 107, pp. 126–133, 2012.

[18] T. E. Milner, D. W. Franklin, H. Imamizu, and M. Kawato, "Central control of grasp: Manipulation of objects with complex and simple dynamics," *NeuroImage*, vol. 36, pp. 388–395, 6 2007.

[19] S. Babadi, S. Vahdat, and T. E. Milner, "Neural substrates of muscle co-contraction during dynamic motor adaptation," *J Neuroscience*, vol. 41, 6 2021.

Measuring actual arm use during soft-robotic glove use at home: single-case experimental design in patients with hand limitations

Anke I. R. Kottink, Leendert Schaake, Erik C. Prinsen, Johan S. Rietman and Gerdienke B. Prange

Abstract— **Patients with persistent hand function limitations in a chronic phase of their traumatic hand injury or neurologic disorder can benefit from wearable robotics to assist in their activities of daily life (ADL). Use of a grip-supporting soft-robotic glove as assistive device at home for six weeks has a therapeutic effect in addition to the direct assistance, with improved grip strength and hand function. The effect is thought to be related to an increase in actual arm use in daily life. This is investigated in an ongoing single-case experimental design (SCED) study among three patients with traumatic hand injury or a neuromuscular disorder. Actual arm use was measured using an accelerometer worn around each wrist for a week before, during and after six weeks of glove use at home.**

Three participants started concurrently. Two participants completed the study in compliance with the protocol, indicating feasibility for an SCED study in this setting. However, it needs attention during recruitment for participants' capacity to follow an intensive study schedule. Actual arm use increased during soft-robotic glove use in both participants, although to varying degrees, and decreased after cessation of glove use. This indicates that the arms/hands were used more intensively in daily activities during the period when the soft-robotic glove was worn. Further analysis is needed to assess whether a relation with hand function improvement and/or perceived benefit exists.

I. Introduction

Patients with persistent hand function limitations after traumatic hand injuries or due to neurologic disorders experience a permanent decline of their ability to perform activities of daily living (ADL), affecting their independence and wellbeing. Often hand strength is affected, resulting in a decreased ability to handle objects, which is crucial for ADL.

Technological advancements in wearable robotics (WR) have generated devices that are increasingly suitable to be used in daily life. Particularly, soft WRs are promising to improve uptake of wearable robots in daily life, due to their advantage regarding comfort, weight and bulkiness over rigid WRs [1], [2]. This enables prolonged use of a WR in daily life, providing direct support for assistance during ADL by supporting the patient's movement. By allowing longer or better performance of functional tasks, assistive WRs may also have a potential training effect, improving functioning without WR support [3].

This work was funded as part of the FutureGlove study under the Eurostars program, grant E!114821.

A. I. R. Kottink, E. C. Prinsen, J. S. Rietman, and G. B. Prange-Lasonder, are with Roessingh Research and Development, and University of Twente, Enschede, the Netherlands. L. Schaake is with Roessingh Research and Development, Enschede, the Netherlands. Corresponding author is G. B. Prange-Lasonder (g.prange@rrd.nl).

Recently, we demonstrated that use of a wearable soft-robotic glove as assistive device for 1,5 months during ADL by patients with hand function limitations resulted in a training effect on grip strength and the ability to perform functional tasks with the affected arm/hand (without the glove) [4], [5]. One of the hypotheses of the beneficial effect of assistive glove use in that clinical trial, as reported by the involved healthcare professionals, was that it stimulates increased use of the more-affected arm/hand in daily tasks instead of relying on the less-affected side, essentially reversing learned non-use. Therefore, in a consecutive study (as part of the FutureGlove study), we are investigating whether actual arm use changes during and/or after use of the soft-robotic glove at home (Figure 1).

Objectively measuring actual arm use, without having to rely on subjective recall of arm use by users themselves, of both arms separately can be done by employing accelerometers on the wrists [6], [7]. By wearing accelerometers on a wristband for multiple days, a good impression of actual arm activity in daily life can be obtained, including distinction between activity of the more- and less-affected arm and hand.



Figure 1. Soft-robotic glove Carbonhand (Bioservo, SV; bioservo.com)

The study design considered to be most appropriate for assessing whether increase in actual arm use is one of the mechanisms that can explain a therapeutic effect of assistive soft-robotic glove use in ADL, was a single-case experimental design (SCED). Since we already know that assistive soft-robotic glove use has a therapeutic effect on hand function from previous studies [4], [5], a large-scale clinical trial replicating a complex and expensive multicenter trial,



Figure 2. Single-case experimental design for measuring arm activity (using MotionWatch8, CamNTech UK) in daily life before, during and after use of a soft-robotic glove (Carbonhand, Bioservo SV) at home.

involving many patients with relatively few assessments, is not suitable for the objective of the current study. Instead, we are interested in more fine-grained information about actual arm use to better understand the potential underlying mechanisms. A study design increasingly advocated as method to examine the effect of rehabilitation or health interventions is an SCED [8], [9]. One of the main advantages of SCEDs for studying rehabilitation interventions is the ability to deal with a heterogeneous and small sample, and to detect an effect in a situation of (large) variability within an individual, as opposed to a more traditional form of evaluation in which only a few snapshots (e.g., pre, post, follow-up) are taken [8]. The evaluation of technological innovations has also been proposed as a particularly fitting application for SCEDs [10], making it a particularly interesting method for assessing interventions involving rehabilitation robotics in patients.

Therefore, in this paper we apply a SCED to measure accelerometry-based arm activity in daily life and assess its differences during and after use of a soft-robotic glove at home, in the first two participants with hand function limitations due to traumatic or neurologic disorders.

II. METHODS

A. Participants

Participants were patients (between 16 and 90 years) experiencing difficulties in performing ADL due to a trauma-related injury or neurologic disorder affecting hand function. Participants were recruited via the local rehabilitaton center and the rehabilitation department of the local hospital. They had to be in the chronic stage with stable hand function, to live independently, and to be able to activate the soft-robotic glove by grasping an object. They must not receive physical therapy specifically focused on arm/hand function during their participation in the study.

B. Study design

The SCED in the present study is a randomized multiple baseline variant, consisting of three phases (Fig. 2), a baseline phase (control condition) of 2-4 weeks, followed by a 6-week intervention phase, consisting of use of an assistive soft-robotic glove during ADL at home, and a subsequent follow-up phase of 4 weeks without glove use to assess retention. The duration of the baseline phase was determined randomly per participant after inclusion, by a random number generator, picking a number between 14 and 28 days. A concurrent multiple baseline process (i.e., the baseline phase starts at the same time for individual participants, while the duration of the baseline phase randomly varies between participants) is implemented to improve validity. As commonly recommended for multiple baseline SCEDs involving one change condition, at least 5 datapoints for each phase are collected [11]. Repeated assessment of grip strength, perceived functional ability and wellbeing was done at home throughout the three phases, remotely via (video) call contact between participant and researcher. Three additional pre-, post- and follow-up assessments were scheduled at the end of each phase with an extended set of clinical tests related to functional ability, perceived arm use and quality of life. The study was approved by Medical-Ethical Research Committee East-Netherlands, reviewed against Medical Device Regulation procedures. It is registered with ClinicalTrials.gov as NCT06033027.

In this paper only the methods and outcomes related to arm activity monitoring of the first participants of this ongoing study are detailed. Arm activity was monitored at the beginning of each phase for 7 consecutive days by wearing accelerometers around both wrists. During the arm activity monitoring weeks, the researcher verified during the home assessments whether the wrist bands were being worn, were operational and whether the right wrist bands were worn on the right sides.

C. Intervention

Participants used a soft-robotic glove at home for six weeks, during self-selected activities for a self-selected duration and frequency. The soft-robotic glove is an existing tendon-driven device (Fig. 1), Carbonhand (Bioservo; Kista, Sweden). It supports and empowers grip strength by actuating flexion of the thumb, middle and ring finger. The amount of flexion force is modulated proportionally via pressure detected by sensors in the fingertips, positioned at the finger tips, along the finger's ventral surface and in the palm of the hand, below metacarpal-phalangeal (MCP) joint 2. Release of actuation is achieved via the proportional force modulation: reducing pressure on the sensors reduces flexion forces generated by the glove, which essentially means that relaxing an active grip turns off the grip support gradually. The three actuators and batteries are located in the control unit, which can be worn with a hip belt (see Fig. 1) or as a small backpack. Glove settings

(e.g. maximum force, sensitivity, gain) per finger are tuned individually for each user via an app prior to the intervention by a trained researcher. Participants were contacted by the researchers between one and three times per week, depending on the study phase, via (video) call to check in on them and administer the home assessments of the SCED remotely (which are out of consideration for this analysis).

D. Outcome measures and data analysis

Actual arm use during daily life was measured by two MotionWatch8 devices (CamNtech; Cambridgeshire, UK), containing a 3D accelerometer, one around each wrist (Figure 3). They were worn for 7 consecutive days, to include both week and weekend days, during the first week of each phase (baseline, intervention, follow-up). The MotionWatches were worn day and night, and didn't need to be taken off during bathing. If participants did take them off during bathing or sleeping, they had to make sure to put the same MotionWatch on the same wrist each time. For this, the MotionWatches were labeled with a red sticker to denote right side and a white sticker to denote left side. During the home assessments via videocall, the researcher visually verified correct placement of the two MotionWatches.



Figure 3. Accelerometer on wristband for measuring arm activity (MotionWatch8, CamNtech, UK; camntech.com)

For processing of the activity data, the same method as in [6] was used. Even though the current version of MotionWatch has a 3D accelerometer, the option for collecting the 1D signal was used to align with the methods from [6]. From the accelerometer signal, the highest peak within each consecutive second was identified. Next, signal amplitudes for every 2 consecutive peaks are summed, resulting in units of 'counts'. Intensity of use is defined as the sum of counts (signal intensity per data point) within a given time epoch, thus producing the 'area under the curve'. For both the affected arm-hand and the unaffected arm-hand, intensity of use was calculated for each day (daily intensity). Data of the middle 5 days (day 2 – day 6) of the measurement period were summed to calculate total intensity, excluding days where the MotionWatches were potentially not worn for a full day. No distinction is made between weekdays and weekend. The ratio between total intensity of the affected arm and total intensity of the unaffected arm was calculated too, where 1 indicates equal intensity of use and values <1 indicate that the affected arm is used less than the unaffected arm.

Data analysis in an SCED concerns assessing changes over time on a case-by-case basis, and is done first and foremost via visual analysis of the time-series data: in this case analyzing whether actual arm use changes during and/or after glove use. During visual analysis, attention is paid specifically to potential differences in level and mean of data points around phase transitions, as well as the overall pattern in the results, the amount of variability within and between phases, and the number of replications of effects across participants [10]. This was quantified by calculating the average level of arm activity per day across all measurement days for each phase per participant, as well as its slope (i.e., slope of linear regression line through all datapoints per phase and per participant). Statistical methods can be used to assist in visual analysis of SCED data, but due to the limited number of participants in this study currently, analysis in this paper is limited to visual and descriptive analysis.

III. RESULTS

A. Participants and study compliance

Three participants have started the multiple baseline SCED concurrently. Two have had trauma-related hand injury with persistent symptoms (P01, female of 51 years old, and P02, male of 54 years old), both with their left hand affected (while right-hand dominant). P03 (female of 74 years old) had a neuromuscular disorder with the right (dominant) hand as more affected side, and the left arm affected to a lesser extent. P01 and P02 wore the glove on their left hand, P03 on her right hand. The randomized duration of the baseline phase was 22 days for P01 and P03, and 30 days for P02 (randomized as 28, but the associated visits were scheduled 30 days apart due to not scheduling visits during a weekend).

One participant (P01) dropped out after the second week of the intervention phase, due to the intensive study schedule (in particular the large number of (remote) assessments and different expectations of the trial and the glove). The other two participants completed the study in compliance with the protocol, with at least five datapoints collected (i.e., home assessments administered) per phase, having used the glove for at least six weeks and worn the wristbands for arm activity monitoring for at least seven consecutive days. The remote assessments were well tolerated by the participants, of which one was familiar with remote videocalls and one was not, and took between 5 and 10 minutes per assessment.

Arm activity monitoring using the MotionWatches worn via a wristband on both wrists was feasible and acceptable for

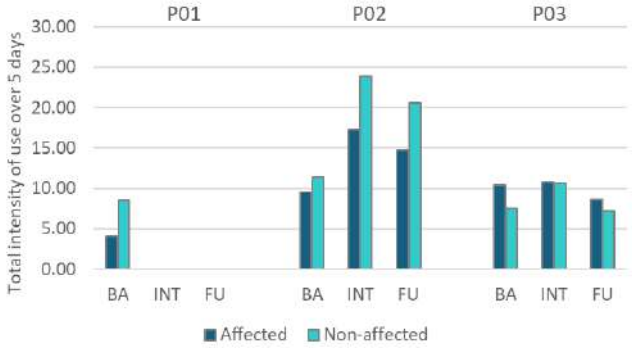


Figure 4. Sum of arm activity during ADL across 5 days during baseline (BA), intervention (INT) and follow-up (FU) per participant, for the affected and non-affected hand (glove was worn on affected hand: left hand for P01 and P02, right for P03).

all participants. The wristbands were worn continuously for at least seven days without issues, in three instances eight days of activity data was available. However, participant 01 developed a rash under the wristband, gradually during the last days of the baseline measurement period. After the wristband was removed, the redness and itch disappeared within a day. A wristband of different material was available but not used before the participant dropped out.

B. Intensity of arm use

The participants who were left-side affected (P01 and P02) showed higher intensity of use of the right (dominant unaffected) arm and hand (Fig. 4). P03 who had their dominant hand as more affected side demonstrated slightly higher intensity of use of the affected arm than the unaffected arm. This is also reflected in lower ratios of affected-to-unaffected arm use intensity in P01 and P02 compared to P03 (Table I).

Total intensity of arm use for both arms summated increased in both participants from baseline to intervention (Table I). This indicates that the arms/hands were used more intensively in daily activities during the period when the soft-robotic glove was worn compared to their activity between two and four weeks before the intervention. The increase was much more pronounced in P02 than in P03. In P02 intensity of use increased for both the affected (gloved) hand and the unaffected hand, whereas in P03 intensity of use of the more affected (gloved) hand remained roughly the same between baseline and intervention and predominantly the unaffected hand was used more intensively (Fig. 4). In both participants, intensity of arm use decreased from intervention to follow-up in both arms.

When looking at intensity of arm use per day across the study phases on a case-by-case basis (Fig. 5 and Table II), data of P02 shows an increase in average level of daily intensity of arm use from baseline to intervention, as well as a change in slope across days, with a more positive slope during the intervention phase compared to baseline. Towards follow-up, a decrease in both average level and slope can be observed, but to a lesser extent than during baseline. This is underlined by the changes in average phase level of intensity of arm use per day in P02, with a marked increase from baseline to intervention and a smaller decrease from intervention to follow-up (Table II). Also, differences in quantified slope of daily arm use intensity between phases underline the visual observations: a negative slope during baseline is followed by a positive slope during intervention, further suggesting a stimulation of arm use intensity when the soft-robotic glove was used. During follow-up, the slope of arm activity per day is negative, although to a smaller degree than during baseline. When looking at the time-series data for left and right arms separately, it is observed that both arms follow the same pattern of increased arm activity during intervention and a partial decrease during follow-up, although in the unaffected arm those changes are slightly more pronounced.

In P03, differences between phases are much less pronounced, although the quantified average level of arm activity per phase does show a small increase from baseline to intervention and decrease during follow-up. The slope of arm activity per day changes from slightly negative during baseline (close to 0, indicating roughly constant arm use per day during baseline) to a steeper negative during intervention, indicating a decline in arm activity during the first week of the glove use period. Since the average level of the intervention phase is slightly higher than baseline, this suggests a decline from an initially higher intensity of arm use at the beginning of the measurement period during the intervention, although this is not very clear in visual observation of the time-series data. During follow-up, arm activity increases across days as reflected in a positive slope. Visual analysis of the time-series data for left and right arms separately indicates that the observed pattern is more pronounced in the unaffected arm than in the affected arm.

TABLE I. TOTAL INTENSITY OF USE OF BOTH ARMS OVER 5 DAYS

ID	Phase	Total intensity L+R (activity counts x10^5)	Ratio total intensity (affected/unaffected)
P01	***BA***	12.7	0.48
	INT	-	-
	FU	-	-
P02	***BA***	20.9	0.84
	INT	41.2	0.72
	FU	35.4	0.72
P03	***BA***	18.0	1.38
	INT	21.3	1.01
	FU	15.8	1.20

ID=subject code; L=left, R=right; BA = baseline, INT = intervention, FU = follow-up

TABLE II. LEVEL AND SLOPE OF TIME-SERIES DATA OF INTENSITY OF USE OF BOTH ARMS SUMMATED

ID	Phase	Average level of arm activity per day (x10^5)	Slope of arm activity per day (x10^5)
P01	***BA***	2.3	1.6
	INT	-	-
	FU	-	-
P02	***BA***	4.1	-0.7
	INT	8.4	0.7
	FU	6.8	-0.4
P03	***BA***	3.5	-0.2
	INT	4.1	-1.4
	FU	3.1	3.6

ID=subject code; L=left, R=right; BA = baseline, INT = intervention, FU = follow-up

IV. DISCUSSION

The present study applies an SCED to collect fine-grained information about actual arm use in daily life before, during and after soft-robotic glove use in ADL, as well as functional outcomes and patient-reported outcomes on their hand function and wellbeing. With this information, we aim to better understand underlying mechanisms of the therapeutic effect of assistive use of a soft-robotic glove at home as

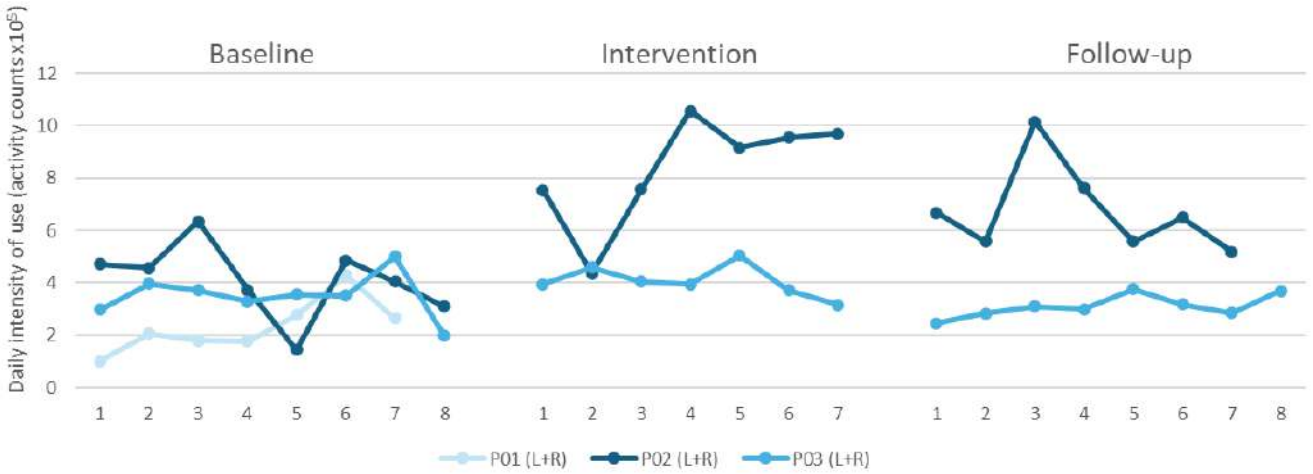


Figure 5. Time-series data of intensity of arm use per day per participant, left and right arm summated, in each study phase

demonstrated earlier [4], [5]. The present findings show that measuring actual arm use in daily life is feasible and enables gathering of valuable information that can be used to improve understanding of the potential mechanisms involved in the effect of the soft-robotic glove.

Study execution among the first three participants shows that compliance to the SCED study set-up was high in both participants who completed the study, following the intervention schedule as planned and without missing assessments. However, one out of the first three participants dropped out due, at least partly, to the intensive and relatively complex study schedule. This suggests on one hand that the choice for an SCED can limit who can and wants to participate in such a trial, increasing the risk for selection bias. Practically, this means that specific attention should be given to the ability of the candidate to comprehend the study logistics and adhere to its schedule during selection of suitable candidates for participation, especially considering the small sample size involved in SCEDs. On the other hand, the advantages of a SCED in understanding how a technological intervention influences patients' functioning and activity in much more detail [10], balances a potentially increased selection bias, as long as this is taken into account with interpretation and generalization of results. Especially in populations and/or outcomes that show a high variability, this approach has its merits [9]. The intra-subject variation in the time-series data of intensity of arm use (Figure 5) emphasizes this merit and highlights the limitations of a pre-post design with fewer data points.

Actual arm use as measured in the first participants of the current ongoing study indicates that intensity of arm use during ADL increases during soft-robotic glove use in both participants, although to varying degrees. Intensity of arm use decreased after cessation of glove use in both participants, but in one participant the activity level remained higher during follow-up than the activity level during baseline. This suggests that arm activity in daily life is stimulated when the soft-robotic glove is used in the present two participants. Differences in population (neuromuscular disorder and traumatic hand injury) might contribute to the differences observed between participants. Also, personal factors and differences in environment and events are likely to influence the outcomes of this SCED. For instance, P02 participated in the study during the time that a home renovation project was carried out, which might have influenced the amount and type of arm use with respect to their average behavior.

It is notable that in both participants intensity of use of the unaffected side seems to be stimulated to a slightly larger degree than the affected side on which the soft-robotic glove is worn. This may suggest that use of the soft-robotic glove promotes engaging in bimanual tasks more than unimanual use of the affected (gloved) hand. On the other hand, this could also indicate that P03 didn't extend their affected arm use to other or more activities when wearing the glove, while P02 started doing more and/or other activities with the affected hand when using the soft-robotic glove. Further analysis of affected vs unaffected arm use intensity (distinguishing between uni- and bimanual activity), including duration of use, and assessing changes in functional outcomes and (perceived) gains in capacity or performance of the arm and hand, is needed to obtain a full understanding of mechanisms involved in the effect of soft-robotic glove use.

The current observations so far are not dismissive of the hypothesis that use of the soft-robotic glove is associated with an increase in actual arm use. If this coincides with hand function improvement and/or perceived benefit, this may be one of the mechanisms underlying the therapeutic effect of assistive glove use demonstrated in previous studies [4], [5].

Performance in daily life must be assessed when evaluating effects of (neuro)rehabilitation interventions in addition to clinical measures of functioning (capacity) [12]. This includes perceived performance, for instance using patient-reported outcomes, and actual performance [13]. Measuring actual arm use in daily life is important to extend clinical measures of capacity and performance with ecologically valid measures of real-life arm activity [14]. Accelerometry has been proposed as a valid, practical and objective measure for actual arm use

in daily life since over a decade [7], [13], [15], however, standardized methods don't exist (yet). It has only been applied as outcome measure in a limited number of studies of upper extremity rehabilitation, mostly stroke [6], [16], [17].

To the best of our knowledge, only one other study investigated actual arm use in context of robot-assisted interventions for the upper extremity, showing no change in intensity and duration of arm use after robot-assisted task-oriented training in chronic stroke patients [6]. This contrasts the preliminary findings of the present paper. Besides a different population, a different intervention context may play a role, where application of the soft-robotic glove is intended to integrate robot-assisted 'exercises' in daily life activities at home as opposed to dedicated robot-assisted training sessions in a clinical setting, with potential differences in treatment dose and exercise content as well.

The findings presented in this paper are limited to intensity of arm use and are based on only the first two participants in this ongoing study. This obviously prevents conclusions to be drawn about changes in actual arm use in daily life due to soft-robotic glove use. Data of at least three participants is needed to increase SCED data validity [10]. Besides potential selection bias of participants capable to understand and adhere to the SCED protocol, the Hawthorne effect can also influence outcomes when people alter their behavior (e.g., use their affected arm more) when they know they are being observed.

This paper provides initial and promising information about the feasibility of measuring intensity of arm use continuously in daily life for seven days, and corresponding considerations and limitations. Currently we have no reference values of intensity of arm use to consider whether our findings constitute high or low intensity of arm use for the populations involved in this study and whether observed differences between phases are related to functional and/or perceived improvements in hand function. Investigating duration of arm use additionally, distinguishing between week and weekend days, and analyzing unimanual vs bimanual activity will improve interpretation of findings. These topics will be addressed as next steps in the ongoing study.

V. Conclusion

Actual arm use as measured in the first participants of the current ongoing study suggests that intensity of arm use during ADL increased during soft-robotic glove use in two participants, although to varying degrees. Intensity of arm use decreased after cessation of glove use in both participants. The current observations so far are in line with the hypothesis that use of the soft-robotic glove is associated with an increase in actual arm use. Further analysis should assess whether this coincides with hand function improvement and/or perceived benefit, before we can conclude whether increase of actual arm use is one of the mechanisms underlying the therapeutic effect of assistive soft-robotic glove use.

Acknowledgment

We thank K. Kuijpers, MD, for recruitment of participants, and C. Rikhof, PhD, for preparing data analysis methods.

References

[1] M. Xiloyannis *et al.*, "Soft Robotic Suits: State of the Art, Core Technologies, and Open Challenges," *IEEE Trans Robot*, vol. 38, no. 3, pp. 1343–1362, 2022, doi: 10.1109/TRO.2021.3084466.

[2] J. Babič *et al.*, "Challenges and solutions for application and wider adoption of wearable robots," *Wearable Technol*, vol. 2, 2021, doi: 10.1017/wtc.2021.13.

[3] A. Rodríguez-Fernández, J. Lobo-Prat, and J. M. Font-Llagunes, "Systematic review on wearable lower-limb exoskeletons for gait training in neuromuscular impairments," *J NeuroEngineering Rehabil 2021 181*, vol. 18, no. 1, pp. 1–21, Feb. 2021, doi: 10.1186/S12984-021-00815-5.

[4] B. Radder *et al.*, "Home rehabilitation supported by a wearable soft-robotic device for improving hand function in older adults: A pilot randomized controlled trial," *PLoS One*, vol. 14, no. 8, 2019, doi: 10.1371/journal.pone.0220544.

[5] A. Kottink *et al.*, "Therapy effect on hand function after home use of a wearable assistive soft-robotic glove supporting grip strength," *PLoS One*, vol. 19, no. 7, p. e0306713, 2024, doi: 10.1371/journal.pone.0306713.

[6] R. J. M. Lemmens *et al.*, "Accelerometry Measuring the Outcome of Robot-Supported Upper Limb Training in Chronic Stroke : A Randomized Controlled Trial," *PLoS One*, vol. 9, no. 5, p. e96414, 2014, doi: 10.1371/journal.pone.0096414.

[7] C. E. Lang, M. D. Bland, R. R. Bailey, S. Y. Schaefer, and R. L. Birkenmeier, "Assessment of upper extremity impairment, function, and activity after stroke: Foundations for clinical decision making," *J Hand Ther*, vol. 26, no. 2, pp. 104–115, Apr. 2013, doi: 10.1016/j.jht.2012.06.005.

[8] A. Krasny-Pacini and J. Evans, "Single-case experimental designs to assess intervention effectiveness in rehabilitation: A practical guide," *Ann Phys Rehabil Med*, vol. 61, no. 3, pp. 164–179, 2018, doi: 10.1016/J.REHAB.2017.12.002.

[9] L. Yang, S. Armijo-Olivo, and D. P. Gross, "Single-case experimental design in rehabilitation: Basic concepts, advantages, and challenges," *Am J Phys Med Rehabil*, vol. 102, no. 5, pp. 454–460, 2023, doi: 10.1097/PHM.0000000000002215.

[10] J. Dallery, R. N. Cassidy, and B. R. Raiff, "Single-case experimental designs to evaluate novel technology-based health interventions," *J Med Internet Res*, vol. 15, no. 2, p. e22 p1-17, 2013, doi: 10.2196/jmir.2227.

[11] A. Krasny-Pacini and J. Evans, "Single-case experimental designs to assess intervention effectiveness in rehabilitation: A practical guide," *Ann Phys Rehabil Med*, vol. 61, no. 3, pp. 164–179, May 2018, doi: 10.1016/J.REHAB.2017.12.002.

[12] G. Kwakkel *et al.*, "Motor rehabilitation after stroke : European Stroke Organisation (ESO) consensus-based definition and guiding framework," 2023, doi: 10.1177/23969873231191304.

[13] R. J. M. Lemmens, A. A. A. Timmermans, Y. J. M. Janssen-potten, and R. J. E. M. Smeets, "Valid and reliable instruments for arm-hand assessment at ICF activity level in persons with hemiplegia : a systematic review," 2012.

[14] G. B. Prange-Lasonder *et al.*, "European evidence-based recommendations for clinical assessment of upper limb in neurorehabilitation (CAULIN): data synthesis from systematic reviews, clinical practice guidelines and expert consensus," *J NeuroEngineering Rehabil 2021 181*, vol. 18, no. 1, pp. 1–12, Nov. 2021, doi: 10.1186/S12984-021-00951-Y.

[15] M. Alt Murphy, C. Resteghini, P. Feys, and I. Lamers, "An overview of systematic reviews on upper extremity outcome measures after stroke.," *BMC Neurol*, vol. 15, p. 29, Mar. 2015, doi: 10.1186/s12883-015-0292-6.

[16] J. A. Franck, R. J. E. M. Smeets, and H. A. M. Seelen, "Changes in actual arm-hand use in stroke patients during and after clinical rehabilitation involving a well-defined arm-hand rehabilitation program : A prospective cohort study," *PLoS One*, vol. 14, no. 4, p. e0214651, 2019.

[17] G. J. Kim *et al.*, "Feasibility of a Self-directed Upper Extremity Training Program to Promote Actual Arm Use for Individuals Living in the Community With Chronic Stroke," *Arch Rehabil Res Clin Transl*, vol. 6, p. 100316, 2024, doi: 10.1016/j.arrct.2023.100316.

An advantageous array of air springs that attenuates aerial inherent nonlinearities for force sensing

Dongwon Kim, Jaeho Shin and Leah M. O'Shea

***Abstract*—Despite the inherent leakage issue, pneumatics is advantageous for device development in some respects. The use of air secures power transmission flexibility while it could alleviate structural complexity depending on the design objectives. Since air is compressible and can act as a spring, it is worth utilizing this for the development of a force sensing device. However, air's inherent nonlinearities cause a decreased linear relationship between the imposed force and deformation even at low frequencies. Those lead to irregular responses and eventually energy dissipation. We note that a serial deployment of two air springs can reduce the effect of aerial inherent nonlinearities since the arithmetic summation of the stiffnesses of the two air springs in the proposed deployment becomes linear over a wide range of displacement. In this study, we investigated the influences of the serial deployment of air springs in reducing the effect of aerial inherent nonlinearities. The Lyapunov exponent is employed to characterize the behaviors of air springs in response to external excitation. We found that the serial deployment efficiently promotes the linear relationship between the imposed force and deformation, indicated by a lower value of the Lyapunov exponent. These results suggest that the effect of aerial inherent nonlinearities is mitigated, in particular, at low frequencies where contacts with humans are considered to occur primarily. Experimental validation was performed.**

Keywords*—Air, force sensing, Lyapunov exponent, energy dissipation

I. Introduction

Typically, we estimate interaction forces through the relationship between the imposed force and corresponding deformation/displacement, often with the procedure of calibration. For example, series elastic actuators, which were specifically devised for safe interactions between the robot and the environment [1], [2], [3], use the deformation of their series elasticity measured with optical encoders to estimate the interaction force in the control loop [4].

Air is compressible and can act as a spring. Indeed, air is used in vehicle suspensions or exoskeletons to realize elasticity to minimize the effects of unwanted interactions from the environment or the power source [5], [6], [7], [8], [9]. Though air shows highly nonlinear properties, mathematical models of deformation relating to the pressure imposed on the system have been well developed [6], [7], [10]. Those models enable us to estimate the interaction force on the system by measuring the change in the volume of the contained air.

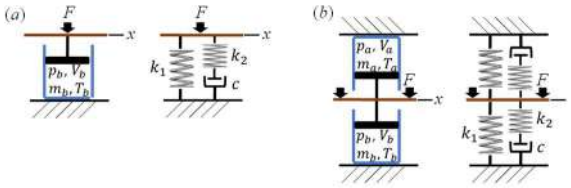
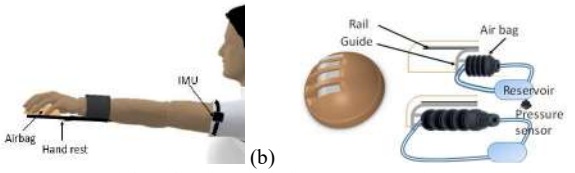


Fig. 1. Schematics of air springs and their linear models: (a) Case I- air spring with a single chamber and (b) Case II- air spring with two chambers connected in series and the plate on which an external excitation is imposed is placed in between.

However, the use of pneumatic elasticity is always followed by issues resulting from aerial inherent nonlinearities [8]. Such nonlinearities degrade the linear relationship between the imposed force and deformation, as well as, they lead to irregular responses, and eventually energy dissipation [11]. Force sensors that are exposed to irregular responses and energy dissipation may exhibit a low accuracy of force estimation that is achieved using the value of the deformation, especially when contacts occur irregularly and frequently. Since irregular responses and energy dissipation originate from air's properties, it is impossible to reduce energy dissipation, unless we change the volume, contact area, or temperature of the contained air. Meanwhile, we note that a certain structural deployment of air springs possibly reduces the effect of aerial inherent nonlinearities. The stiffness of air springs is a strictly increasing function of the displacement [8], which is primarily associated with inherent nonlinearities. If we deploy two air springs with chambers of the same volume and contact area such that one air spring is expanded while the other one is compressed (see Fig. 1(b)), the resultant stiffness, which is the arithmetic summation of the stiffnesses of the two air springs, can become linear over a wide range of displacement. This deployment could effectively reduce the effect of the inherent nonlinearities of air.

In this study, we demonstrate the beneficial aspects of the serial deployment of air springs in reducing the effect of inherent nonlinearities through a mathematical model. The Lyapunov exponent is employed to characterize the behaviors of air springs in response to external excitation at a

Dongwon Kim is with Shirley Ryan AbilityLab, Chicago, United States, dkim04@sralab.org, Jaeho Shin is with Korea Electronics Technology Institute, South Korea, jayh@keti.re.kr, and Leah M. O'Shea is with Shirley Ryan AbilityLab, Chicago, United States, loshea@sralab.org.



(a) (b)

Fig. 2. Our potential application with force sensing using pneumatics (a) A schematic of the proposed system and (b) its hand part. An air reservoir is installed in the pneumatic circuit to modulate the driving-point impedance of the airbags. A pressure sensor measures the pressure of the internal air. Tubing is connected to both sides of the airbags. An inertial measurement unit (IMU) is used to estimate arm movement and configuration.

range of frequencies of interest. This measure enables us to investigate whether responses of air springs are periodic transient to aperiodic or chaotic behaviors [11], [12]. The Lyapunov exponent can be an indicator of irregularity and energy dissipation in air springs resulting from the inherent nonlinearities of air. This study will form the basis for developing a force sensing device using pneumatics. Fig. 2 depicts our potential application with force sensing using pneumatics. This device is designed to measure involuntary finger flexion during upper-extremity movement after a neurological damage (e.g., stroke).

II. MODEL DERIVATION

1. Nonlinear model

A. CASE I

First, we derive a model of the air spring with a single chamber (Fig. 1(a)) that entraps air with its pressure, volume, mass, and temperature of the entrapped air defined as P_b, V_b, m_b, and T_b, respectively. The equation of energy equilibrium can be derived as

$$\alpha A(T_{atm} - T_b) - p_b\dot{V}_b = \dot{m}_b C_v T_b + m_b C_v \dot{T}_b, \quad (1)$$

where α, $C_v$denote the heat transfer coefficient and constant volume-specific heat capacity, respectively. A and T_{atm} denote the area of the piston and the temperature of the environment, respectively. We assume that energy does not transfer through the walls of the chamber.

We employ the gas equation of state

$$P_b V_b = m_b R T_b, \quad (2)$$

where R is the universal gas constant,

and derivate it with respect to time:

$$p_b\dot{V}_b + \dot{p}_b V_b = \dot{m}_b R T_b + m_b R\dot{T}_b. \quad (3)$$

Assuming that $\dot{m}_b = 0$ (closed system), the combination of Eqs. (1) and (3) leads to

$$\frac{\alpha A}{C_p}(T_{atm} - T_b) - \frac{1}{R}\left(\frac{\dot{p}_b V_b}{\gamma} + p_b\dot{V}_b\right) = 0, \quad (4)$$

where C_p denotes constant pressure specific heat capacity and γ is defined as the ratio of C_p with C_v.

The volume of the air chamber can be obtained as

$$V_b = V_{b0} - Ax, \quad (5)$$

where V_{b0} is the initial volume and x denotes the displacement of the piston.

The force applied to the piston can be calculated as

$$F = A(p_b - p_{atm}), \quad (6)$$

where p_{atm} denotes the pressure of the environment. We assume that the area on which the pressure of the entrapped air is imposed is the same as that on which the pressure of the environment is imposed for convenience.

The relationship *F-x* can be obtained through combinations of Eqs. (1) to (6).

B. CASE II

Similarly, we derive a model of the air spring with two chambers deployed in series (Fig. 1(b)). Another chamber is added to Case I, with its pressure, volume, mass, and temperature defined as P_a, V_a, m_a, and T_a, respectively. The equation of energy equilibrium can be derived as, respectively,

$$\alpha A(T_{atm} - T_a) - p_a\dot{V}_a = \dot{m}_a C_v T_a + m_a C_v \dot{T}_a, \quad (7)$$
$$\alpha A(T_{atm} - T_b) - p_b\dot{V}_b = \dot{m}_b C_v T_b + m_b C_v \dot{T}_b. \quad (8)$$

The derivatives of the gas equation of state with respect to time for each chamber are obtained as Eq. (3) and

$$p_a\dot{V}_a + \dot{p}_a V_a = \dot{m}_a C_v T_a + m_a \mathrm{R}\dot{T}_a. \quad (9)$$

Assuming that $\dot{m}_a = 0$, the combinations of those equations lead to the following pair of equations:

$$\frac{\alpha A}{C_p}(T_{atm} - T_b) - \frac{1}{R}\left(\frac{\dot{p}_b V_b}{\gamma} + p_b\dot{V}_b\right) = 0, \quad (10)$$
$$\frac{\alpha A}{C_p}(T_{atm} - T_a) - \frac{1}{R}\left(\frac{\dot{p}_a V_a}{\gamma} + p_a\dot{V}_a\right) = 0. \quad (11)$$

The volume of each chamber varying with the displacement of the piston is calculated as

$$V_a = V_{a0} + Ax, \quad (12)$$
$$V_b = V_{b0} - Ax, \quad (13)$$

where V_{a0}, V_{b0} denote the initial volume of each chamber.

Finally, the resultant force applied to the pistons that are rigidly connected with each other is obtained as

$$F = A(p_a - p_b). \quad (14)$$

The pressures p_a, p_b are calculated from the gas equations of state and Eqs. (10) and (11).

2. Linear model

We present linear models of Case I and Case II to feature the nonlinear models as well as to address their appropriateness.

A. CASE I

Air springs with one chamber (Case I) can be modeled as a pure spring k_1 connected in parallel with a group of a spring k_2 and damper c connected in series, neglecting nonlinearities including the coupling term of the chamber pressure and piston velocity (see Fig. 1) [6], [7]. The derivation was presented elsewhere [6]. The resultant stiffness can be obtained in the frequency domain as

$$K(s) = k_1 + \frac{1}{\frac{1}{k_2}+\frac{1}{cs}} = \frac{(k_1+k_2)cs+k_1k_2}{cs+k_2}, \quad (15)$$

where s is a complex variable.

Eq. (15) suggests that at low frequencies ($s \to 0$), the resultant stiffness appears as k_1. At high frequencies ($s \to \infty$), the resultant stiffness appears as $(k_1 + k_2)/k_2$. The frequency where the transition of the resultant stiffness occurs is around k_2/c (rad/s). The transition frequency is proportional to $\alpha A/m_b C_v$ [6], suggesting that an air spring with a greater mass leads to the transition of the resultant stiffness at a lower frequency. Meanwhile, k_1 is proportional to $m_b \mathrm{R} T_b A^2/(V_{b0} - Ax)^2$, k_2 is proportional to $\gamma p_{b0} A^2/V_{b0}$, and c is proportional to $k_2 m_b C_v/\alpha A$ The equivalent stiffnesses and damping coefficient depend on the entrapped air's initial pressure, mass, and volume.

B. CASE II

For Case II, we obtain the stiffness by simply doubling K:

$$K'(s) = 2K(s) = \frac{2(k_1+k_2)cs+2k_1k_2}{cs+\ _2}, \quad (16)$$

Note that the stiffness is different from that of two springs in series. Eq. (16) suggests that at low frequencies ($s \to 0$), the resultant stiffness appears as $2k_1$. At high frequencies ($s \to \infty$), the resultant stiffness appears as $2(k_1 + k_2)/k_2$. The transition frequency is around k_2/c (rad/s).

Parameters	***Value***	***Unit***
α	15.5 [7]	W/m^{2}K
C_v	0.718	kJ/kgK
C_p	1.005	kJ/kgK
γ	1.3928	-
T_{atm}	298	K
p_{atm}	101325	N/ m^2
R	0.286	kJ/kgK
A	3.1416* 0.01^2	m^2

Table I. System parameters.

III. NUMERICAL SIMULATION

The mathematical model for Case I is found excellent in reproducing the behaviors of real pneumatic systems at a wide range of frequencies [7], [10]. The stiffnesses of air springs follow a strictly increasing curve; the primary stiffness component k_1 is proportional to $m_b \mathrm{R} T_b A^2/(V_{b0} - Ax)^2$. Those stiffnesses nonlinearly increase as the deformation increases [8]. However, linearization eliminates such nonlinear properties, although those should be considered in analyzing air springs. We analyze the frequency-domain responses (F) to a chirp input (x) at a wide range of frequencies undergoing the thermodynamics addressed above, without linearization.

The behaviors of F versus x in the frequency domain are investigated using the *iddata* and *fft* functions in Matlab 2018a. Numerical integration is performed through the 4th-order Runge-Kutta method. The sampling time is set as 0.001 s, with step size 0.0001 s. The system parameters with fixed values are summarized in Table 1. We add variations to the initial volumes of the chambers to produce various stiffnesses: A×0.1, 0.3, 0.6, and 1.2 (m). The mass of the entrapped air in each chamber is calculated using the gas equation of state with the temperature and pressure of the environment. For Case II, the air springs of both chambers are assumed pre-loaded by compressing the entrapped air with a certain amount of displacement (0.02 m). This imposes simultaneous loading and unloading on the air springs of both chambers. The volumes of the chambers are reduced and expanded at the same time, while their masses remain the same (closed system). A chirp input with an amplitude of 0.01 m and an increment of 0.01 rad/s^2 is applied to the displacement for 10000 s.

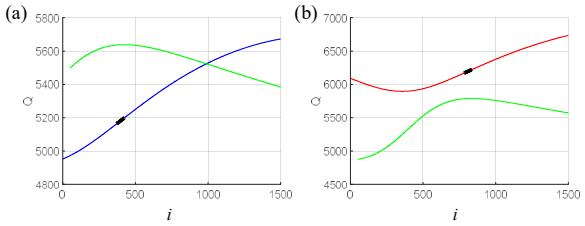


Fig. 3. Values of Q in Eq. (18) for (a) Case I (blue) and (b) Case II (red), with a chamber volume of A×0.1 (m), A is the piston area. The green curves are the slopes of the curves of 50 points of Q, amplified with an arbitrary constant gain to identify i that gives the maximum slope. The largest Lyapunov exponents are obtained from Q between K_{Min} and K_{Max} where the maximum slopes of the curves of Q is achieved. The black lines are a line connecting two points at $i = K_{Min}$ and $i = K_{Min} + 50$ ($= K_{Max}$).

Beyond the transition frequencies, a greater effect of hysteresis appears [7]. Obviously, significant energy dissipation is caused, because the damping effect is pronounced. In our study, we focus on responses under the transition frequencies. The Lyapunov exponent is employed to investigate whether the effect of aerial inherent nonlinearities on energy dissipation reduces, in particular, at the range of frequencies where the stiffness component of the air spring is dominant (i.e. low frequencies). The value of the

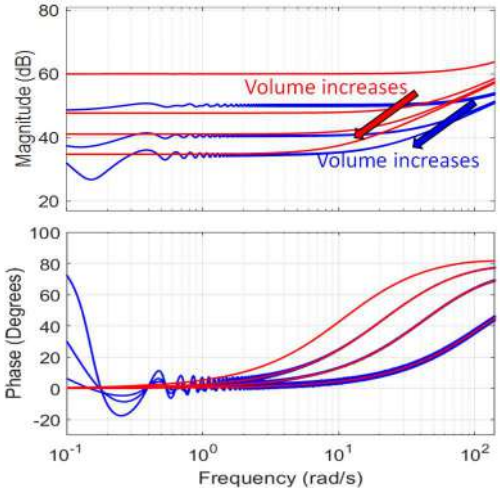


Fig. 4. Frequency-domain responses of the force over the displacement, for Case I (blue) and Case II (red). Chamber volumes are changed to produce various air stiffnesses: A×0.1, 0.3 and 0.6 (m) for Case I and A×0.1, 0.3, 0.6, and 1.2 (m) for Case II, where A is the piston area.

Lyapunov exponent is an indicator of the rate of convergence or divergence of the infinitesimally close trajectories (Fig. 3). A negative value of the Lyapunov exponent indicates convergence, while a positive value of the Lyapunov exponent indicates divergence and aperiodic behaviors. Responses of air springs that are transient to aperiodic behaviors mean that energy dissipation occurs. We assess the Lyapunov exponent of responses to a periodic input with its frequency varying. The varying frequencies emulate realistic contacts by a human with a force sensor. The value of the Lyapunov exponent is calculated as [13]:

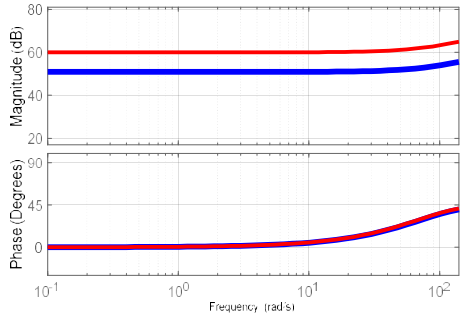


Fig. 5. Frequency-domain responses of the force over the displacement of the linear models, for Case I (blue) and Case II (red). Those models replicate the responses of the nonlinear models with a chamber volume of A×0.1 (m) for Case I and Case II, respectively, where A is the piston area.

$$\mathrm{LE} = \frac{1}{N}\sum_{i=1}^{N} Q(i), \tag{17}$$

$$Q(i) = \left(\frac{f}{K}\sum_{K=K_{Min}}^{K_{Max}} ln\frac{\|Y_{i+K}-Y_{i^*+K}\|}{\|Y_i-Y_{i^*}\|}\right), \tag{18}$$

where f is the sampling frequency and i^* denotes the nearest neighbor point of i outside the reciprocal of the mean frequency that satisfies min $\|Y_i-Y_{i^*}\|$. N is the number of the points of $Q(i)$.

We search the largest LE between K_{Min} and $K_{Min}+50$ ($\triangleq K_{Max}$) such that the coefficient of determination of the regression line forming the points of $Q(i)$ between K_{Min} and K_{Max} is greater than 0.98 (refer to Fig. 2). The search range is set as $1 \le K_{Min} \le 1450$, because it is recognized that the

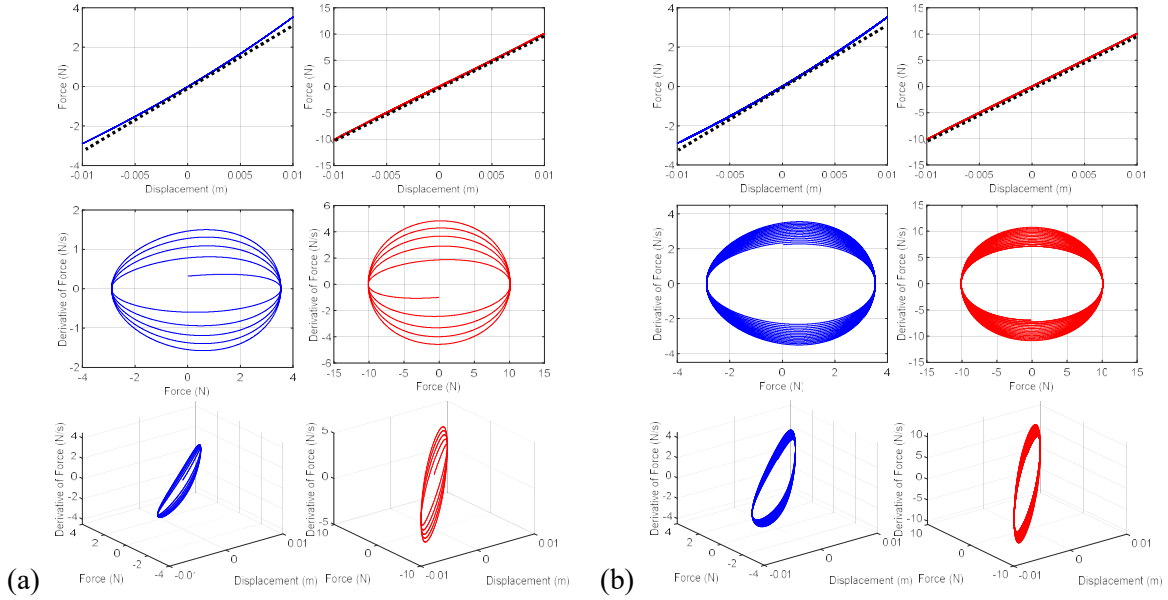


Fig. 6. Phase portraits of the force versus the displacement, the derivative of the force versus the force, and the derivative of the force versus the force and displacement, for Case I (blue) and Case II (red) in response to excitations with frequencies of (a) 0.1-0.3 rad/s and (b) 0.7-0.9 rad/s. The black dotted lines are to assess linearity of the relationship of the force versus the displacement. The largest LE=0.2765 (Case I):0.2257 (Case II) for frequencies of 0.1-0.3 rad/s. and the largest LE=2.1587 (Case I):1.1483 (Case II) for frequencies of 0.7-0.9 rad/s. The nonlinear models with a chamber volume of A×0.1 (m) for Case I and Case II, respectively, where A is the piston area, are used.

Frequency	0.1-0.3 rad/s				0.4-0.6 rad/s				0.7-0.9 rad/s			
Volume	*A*×0.1	*A*×0.3	*A*×0.6	*A*×1.2	*A*×0.1	*A*×0.3	*A*×0.6	*A*×1.2	*A*×0.1	*A*×0.3	*A*×0.6	*A*×1.2
Case I	0.2765	0.2399	0.2312	0.2244	1.8895	1.8079	1.6962	1.4453	2.1587	1.1849	1.7886	1.2207
Case II	0.2257	0.2256	0.2221	0.2240	1.8307	1.7587	1.6361	1.5206	1.1483	1.2029	1.1442	0.9544

Table 2. Largest Lyapunov exponent of Case I and Case II. *A* is the piston area.

largest LE is detected within this range for Case I and Case II, respectively. N in Eq. (17) is 50.

Lastly, the influence of asymmetry in the initial volumes of the two air chambers is investigated. We evaluate how responses change depending on the degree of asymmetry in the chamber volumes (1:1, 0.95:1, and 0.90:1).

IV. Simulation Results

Fig. 4 shows the frequency-domain responses of the force over the displacement, for Case I and Case II, respectively, with the chamber volumes changing. The resultant stiffness of Case II is greater than that of Case I even when those use chambers of the same dimensions are employed. However, the frequencies where the transitions of the resultant stiffness occur are similar regardless of Case I and Case II. Those transition frequencies mainly depend on the initial mass of the entrapped air in one chamber (see the Model derivation section). Fig. 4 shows that as the initial mass, which mainly depends on the initial chamber volumes, increases, the transition frequency decreases.

We replicate the results of the nonlinear models using the linear models (Fig. 5). The apparent resultant stiffness of Case II in low frequencies ($\approx 2k_1$) for the linear model is set as 1000 N/m, while that of Case I ($\approx k_1$) is set as 350 N/m. The secondary stiffness k_2 is set as 1500 and 2250 N/m for each single chamber for Case I and Case II, respectively. The damping coefficient c is set as 3 and 4.5 N/ms for each chamber for Case I and Case II, respectively. Those settings lead to the same transition frequencies of 500 rad/s for Case I and Case II. Though the same chambers are used, the secondary stiffness k_2 and damping coefficient c, as well as the primary stiffness k_1, that characterize the behaviors of the air springs are not the results of the arithmetic summation of the stiffnesses between Case I and Case II. These results originate from how much the air springs are pre-loaded for Case II. Indeed, the equivalent stiffnesses and damping coefficient depend on the entrapped air's initial pressure and volume (see the Model derivation section).

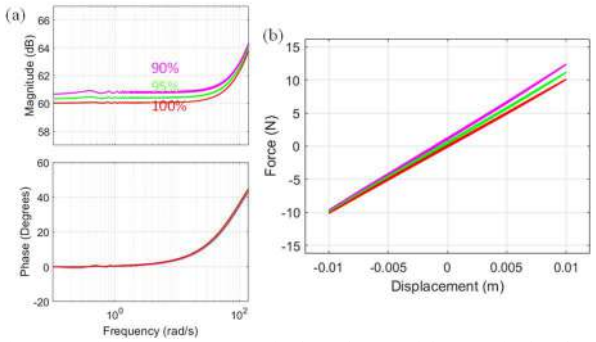


Fig. 7. Sensitivity to asymmetry in the volumes of the two air chambers for Case II: (a) Frequency responses and (b) overlapped curves of the force over the displacement. The percentage indicates the ratio of the volumes. The nonlinear models with a chamber volume of *A*×0.1 (m) for Case I and Case II, respectively, where *A* is the piston area, are used.

We note that the responses of Case I with the nonlinear model below the transition frequency are quite wavy and irregular in comparison to those of Case II (Fig. 4). Such responses were observed experimentally in the authors' previous study [5]. Those phenomena are impossible to observe with the linear models (Fig. 5). This response feature may originate from the inherent nonlinearities of air. We observe that the trajectories of the force over the displacement of Case I are curvy (strictly increasing). Such a nonlinear relationship is observed experimentally [6], [7]. Meanwhile, those of Case II are fairly linear, as seen in Fig. 6. The largest Lyapunov exponent suggests that generally, the transition to aperiodic behaviors occurs more strongly in Case I in response to periodic inputs, especially, at low frequencies, as presented in Table 2. The Poincaré maps (i.e. plot of the force and its derivative) show asymmetrical trajectories for Case I while showing fairly symmetrical trajectories for Case II. Also, the 3D plots of the derivative of the force versus the force and displacement exhibit that the bundles of circular trajectories for Case I tend to be a little bit bent in comparison to those for Case II. These results imply that more energy dissipation occurs in Case I. The trajectory of the response of Case I are transformed due to a change in energy (mainly through dissipation) within the system. This change may eventually result from aerial inherent nonlinearities. From these results, we could conclude that the serial deployment of air springs is effective in alleviating the effect of the inherent nonlinearities.

The sensitivity to asymmetry in the volumes of the two air chambers for Case II is presented (Fig. 7). We found that the linear relationships between the imposed force and deformation preserve even in the presence of asymmetry in the volumes of the two air chambers. However, we found that responses at low frequencies become more wavy as the degree of asymmetry increases. An increase in asymmetry in the volumes of the two air chambers leads to an increase in the effect of the inherent nonlinearities, as in an air spring with a single chamber.

V. Experimental Validation

We conducted experimental validation to evaluate the enhanced linearity in the relationship of the force versus the displacement for Case II. Enhanced linearity implies that the proposed deployment of air springs is effective in reducing irregular responses and energy dissipation. 3D-printed air chambers (made of Acrylonitrile Butadiene Styrene) were created, and airbags were used to entrap air. We ensured that

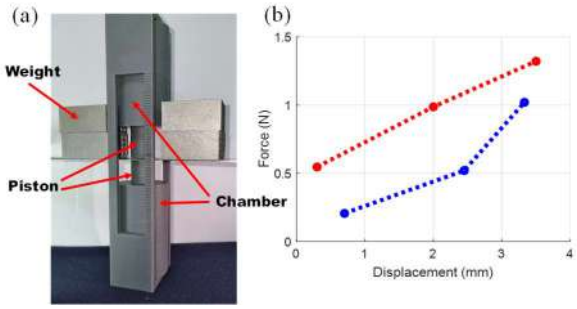


Fig. 8. (a) Experimental setup to assess the relationship of the force versus the displacement and (b) plot of the force versus the displacement for Case I (blue) and Case II (red). Changes in the force and displacement are caused by different 3 weights (filled dot).

no energy was used for expansion of the airbag surface. The friction effect between the piston and the wall of the chambers was minimized by giving a gap between them, while the piston prevented the airbag from escaping behind the piston. The radii of the chamber and piston were 10 and 9.9 mm, respectively. The inner depth of each chamber was 80 mm. Each piston weighed 21 g. For Case II, the airbag of each air chamber was preloaded (30 mm) using a structure that limited the total length of the two chambers in series. Three different weights were used to load the piston for Case I and Case II, respectively. Loading was imposed very slowly to guarantee low-frequency responses. For Case II, we considered all loading components that imposed load on the airbag inside the bottom chamber, including the airbag inside the top chamber, two pistons, weights, and their rest. For Case I, we considered loading components, including one piston, weights, and their rest. The displacement of the piston was measured using a ruler and a high-resolution camera. The experiment was conducted under a temperature of 298.15 K.

Fig. 8 shows the experimental setup and results of Case I and Case II. We found that Case II showed enhanced linearity in the relationship of the force versus the displacement in comparison to Case I. In Case II, the air springs were preloaded and the volumes of the two airbags were not exactly the same, so the force did not start at the origin. Based on these preliminary results, we will develop a force sensing system to measure the force imposed by a human finger for our future study (Fig. 2).

ACKNOWLEDGMENT

The authors declare no competing financial and/or non-financial interests in relation to the work described. Kim declares the ownership of EpicWide, LLC. This work was partially supported by the Korea Electronics Technology Institute (KETI) of the Republic of Korea (No. 401C3901)

REFERENCES

[1] M. Yokoyama, R. A. B. Petrea, R. Oboe, and T. Shimono, "External Force Estimation in Linear Series Elastic Actuator without Load-Side Encoder," *IEEE Trans. Ind. Electron.*, vol. 68, no. 1, pp. 861–870, 2021, doi: 10.1109/TIE.2020.3013791.

[2] T. Zhang, M. Tran, and H. Huang, "Admittance shaping-based assistive control of SEA-driven robotic hip exoskeleton," *IEEE/ASME Trans. Mechatronics*, vol. 24, no. 4, pp. 1508–1519, 2020, doi: 10.1109/TMECH.2019.2916546.

[3] G. A. Pratt and M. M. Williamson, "Series elastic actuators," in *Proceedings 1995 IEEE/RSJ international conference on intelligent robots and systems. Human robot interaction and cooperative robots*, IEEE, 1995, pp. 399–406.

[4] D. Kim, K. Koh, G. R. Cho, and L. Q. Zhang, "A Robust Impedance Controller Design for Series Elastic Actuators using the Singular Perturbation Theory," *IEEE/ASME Trans. Mechatronics*, vol. 25, no. 1, pp. 164–174, 2020, doi: 10.1109/TMECH.2019.2951417.

[5] R. B. Gillespie, D. Kim, J. M. Suchoski, B. Yu, and J. D. Brown, "Series elasticity for free free-space motion for free," *IEEE Haptics Symp. HAPTICS*, pp. 609–615, 2014, doi: 10.1109/HAPTICS.2014.6775525.

[6] M. Y. Wu, H. Yin, X. B. Li, J. C. Lv, G. Q. Liang, and Y. T. Wei, "A new dynamic stiffness model with hysteresis of air springs based on thermodynamics," *J. Sound Vib.*, vol. 521, no. May 2021, 2022, doi: 10.1016/j.jsv.2021.116693.

[7] F. Löcken and M. Welsch, "The dynamic characteristic and hysteresis effect of an air spring," *Int. J. Appl. Mech. Eng.*, vol. 20, no. 1, pp. 127–145, 2015, doi: 10.1515/ijame-2015-0009.

[8] D. Kim and J. Lee, "Robust control of a system with a pneumatic spring," *J. Franklin Inst.*, 2021, doi: 10.1016/j.jfranklin.2020.10.037.

[9] D. Kim, "Design and Analysis of an Origami-structured Actuator for Backdriveability and Power Amplification," *IEEE/ASME Trans. Mechatronics*, vol. 24, no. 3, pp. 1002–1010, 2019, doi: 10.1109/TMECH.2019.2907982.

[10] T. Vo-Minh, T. Tjahjowidodo, H. Ramon, and H. Van Brussel, "A new approach to modeling hysteresis in a pneumatic artificial muscle using the Maxwell-slip model," *IEEE/ASME Trans. Mechatronics*, vol. 16, no. 1, pp. 177–186, 2011, doi: 10.1109/TMECH.2009.2038373.

[11] K. Zaki, S. Noah, K. R. Rajagopal, and A. R. Srinivasa, "Effect of nonlinear stiffness on the motion of a flexible pendulum," *Nonlinear Dyn.*, vol. 27, no. 1, pp. 1–18, 2002, doi: 10.1023/A:1017512317443.

[12] D. Kim and P. H. Chang, "A new butterfly-shaped chaotic attractor," *Results Phys.*, vol. 3, pp. 14–19, 2013, doi: 10.1016/j.rinp.2012.12.001.

[13] M. T. Rosenstein, J. J. Collins, and C. J. De Luca, "A practical method for calculating largest Lyapunov exponents from small data sets," *Phys. D Nonlinear Phenom.*, vol. 65, no. 1–2, pp. 117–134, 1993, doi: 10.1016/0167-2789(93)90009-P.

Real-Time Rehabilitation Tracking by Integration of Computer Vision and Virtual Hand

Parham Ahmadpanah[1] and Soroush Korivand[1]

***Abstract*— Rehabilitation is a critical component of healthcare services that often requires prolonged monitoring to achieve optimal outcomes. One of the major challenges in rehabilitation tracking is the necessity for patients to visit medical centers, which can be costly and time-consuming, especially for individuals in remote areas. Although telehealth solutions such as video conferencing have been introduced, they are predominantly qualitative and do not provide precise rehabilitation tracking. Consequently, there is a need for a robust, accessible, and accurate method for rehabilitation monitoring. To address this need, we introduce a quantified, easily accessible framework for extracting and analyzing human finger joint torques to enable virtual hand interaction. Hand landmarks from MediaPipe are integrated with the MANO hand model in PyBullet. The hand positions, rotations, and joint angles extracted from the landmarks are used as controller inputs to mirror human hand movements in a virtual environment. A PID controller was designed to accurately track joint angle trajectories, with its parameters optimized using genetic algorithms. The torques extracted from the metacarpophalangeal and proximal interphalangeal joints were validated, achieving mean squared errors of $4.346 \times 10^{-4}(N.m)^2$ and $1.506 \times 10^{-5}(N.m)^2$, respectively. This quantification and accessibility of human joint dynamics information is highly desirable for tracking rehabilitation progress using exoskeleton robotics.**

I. INTRODUCTION

Exoskeletons have become pivotal in rehabilitation engineering due to their ability to provide precise, controlled assistance during therapeutic exercises, thereby enhancing motor recovery outcomes [1], [2]. Specifically, finger exoskeletons address the critical need for restoring fine motor skills essential for daily activities such as grasping, writing, and manipulating objects. Impairments in finger function—often resulting from neurological conditions such as stroke, spinal cord injury, or neurodegenerative diseases—can significantly diminish a person's independence and quality of life [3]. By facilitating targeted, repetitive, and task-specific movements, finger exoskeletons promote neuroplasticity and motor relearning, which are essential for functional recovery [4]. Recent advancements have demonstrated that integrating finger exoskeletons into rehabilitation programs enhances the effectiveness of therapy, leading to improved dexterity and functional independence for patients [5].

To maximize the benefits of finger exoskeletons in rehabilitation, effective recovery also necessitates continuous monitoring and tracking of patient progress. Rehabilitation tracking is crucial for evaluating the efficacy of therapeutic interventions and for tailoring treatment plans to individual needs [6]. By systematically assessing improvements in motor function, clinicians can make informed decisions to adjust therapy intensity, duration, and specific exercises [7]. In the context of finger rehabilitation, accurate tracking allows for the optimization of exoskeleton parameters to match the patient's evolving capabilities, thereby enhancing the rehabilitation process [8]. Moreover, rehabilitation tracking provides valuable data that contribute to evidence-based practices, ultimately improving patient outcomes [9].

Within this framework, torque analysis emerges as a critical component for optimizing therapeutic outcomes in finger exoskeleton applications. The metacarpophalangeal (MCP) and proximal interphalangeal (PIP) joints are primarily responsible for the flexion and extension movements essential for hand functionality [10]. By analyzing the torques generated at these joints, clinicians and engineers can gain deeper insights into the biomechanical demands of finger movements, allowing for the customization of exoskeleton assistance to meet individual patient needs [10]. Accurate torque measurements at the MCP and PIP joints enable the development of precise control algorithms that can adapt real-time to a patient's capabilities, thereby enhancing the effectiveness of rehabilitation interventions [11]. Recent research has demonstrated that incorporating torque analysis into rehabilitation protocols significantly improves motor recovery and functional independence in patients with hand impairments [10]–[12]. Therefore, focusing on torque analysis at these critical joints not only advances the design and control of finger exoskeletons but also contributes substantially to the efficacy of rehabilitation programs. Despite the clear benefits of rehabilitation tracking and torque analysis, traditional methods often require patients to visit medical centers for assessments, which can be expensive and time-consuming [13]. This requirement poses significant challenges for individuals in remote areas or those with mobility limitations, potentially hindering consistent participation in rehabilitation programs. Consequently, there is a pressing need for innovative methodologies that facilitate remote rehabilitation tracking without sacrificing accuracy or effectiveness. Recent advancements in technology, such as computer vision and virtual simulation environments, offer promising solutions by enabling accessible and cost-effective monitoring of patient progress outside clinical settings. Unlike traditional exoskeletons that rely on embedded sensors, our approach leverages computer vision to extract joint torques, eliminating the need for additional hardware and improving accessibility for home-based rehabilitation. Additionally, this quantified data can help optimize exoskeleton

[1] Michael W. Hall School of Mechanical Engineering, Mississippi State University, MS, 39762, USA sa1983@msstate.edu, skorivand@me.msstate.edu

control strategies for personalized assistance. By integrating these technologies, it is possible to develop rehabilitation systems that reduce the burden on patients and healthcare providers while maintaining high-quality care. To address the mentioned challenges, researchers have explored various methods to facilitate remote rehabilitation tracking. In this regard, wearable sensor devices like data gloves equipped with flex sensors [14] or inertial measurement units [15] have been developed to capture hand movements for rehabilitation purposes. However, these methods often rely on specialized hardware that can be expensive and cumbersome for patients to use at home, limiting their accessibility and practicality. In addition, while some studies have utilized depth cameras and infrared sensors to track hand gestures without physical markers, these approaches may lack the precision required for detailed torque analysis of the MCP and PIP joints, which is crucial for customizing exoskeleton assistance.

Furthermore, computer vision-based techniques have gained attention for their potential in remote rehabilitation. Systems leveraging standard RGB cameras and algorithms can track hand movements and recognize gestures. However, many of these solutions focus primarily on high-level gesture recognition or qualitative assessments rather than extracting precise biomechanical data such as joint torques and angles. Consequently, they do not fully address the need for accurate, quantitative tracking necessary for optimizing exoskeleton control algorithms and enhancing therapeutic outcomes.

To address these gaps and challenges, in this study, we propose and verify a novel framework for extracting human finger joint torques by combining motion capture data from MediaPipe [16] with a simulated robotic hand model based on MANO hand model [17] in PyBullet environment [18]. Precise control of the hand model was achieved by employing a proportional–integral–derivative (PID) controller, with its gains optimized through genetic algorithms. This approach facilitates accurate modeling of human hand dynamics and provides valuable data for further advancements in rehabilitation and human-computer interaction. Moreover, because this method utilizes readily available open-source software and requires only a single camera, it is both cost-effective and accessible, making it suitable for telehealth and telerehabilitation tracking.

II. METHODOLOGY

The framework of the proposed system is divided into several stages, as shown in Fig 1. (a) Initially, MediaPipe is employed to detect hand landmarks for gesture recognition. (b) These detected landmarks are then utilized to compute the input joint angles. (c) A controller calculates the necessary torques for each joint by comparing the input angles with the simulation angles. (d) Genetic algorithms are subsequently applied to optimize these torques using validation data, thereby enhancing their accuracy to emulate human-like finger joint torques. (e) The optimized torques are integrated into the MANO hand model within the PyBullet simulation environment. The final outcome is the user-controlled virtual hand, which allows for the extraction of finger joint torques.

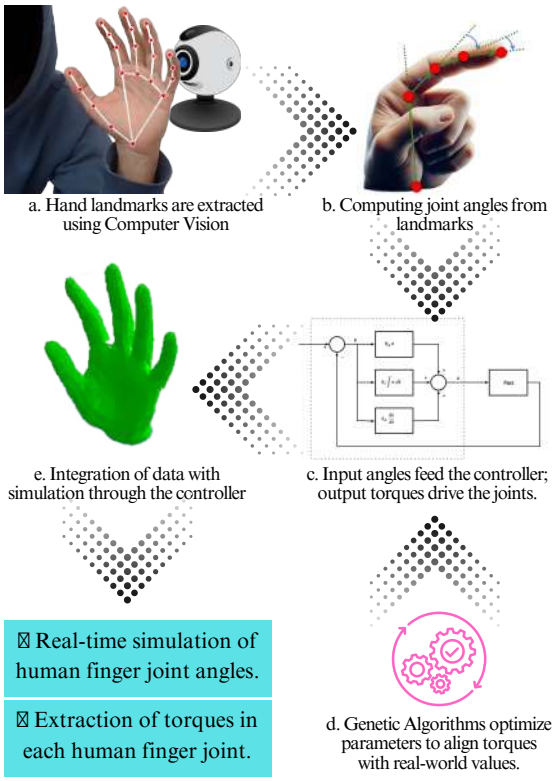


Fig. 1. Framework of the Proposed System. The system integrates hand gesture recognition (a), pose estimation (b), torque computation (c), and optimization (d) to simulate and control the virtual hand model (e), with extraction of human hand finger joint torques.

A. Simulation Environment

The simulation environment was developed using PyBullet [18], a robust physics engine widely employed in robotics and simulation research. PyBullet supports rigid body dynamics, collision detection, and advanced robotic control features, enabling seamless integration and testing of diverse robotic models within a unified framework. By applying joint torques and tracking the resulting model responses, this environment provided a realistic, real-time platform for analyzing hand dynamics.

In this simulation environment, we integrated the MANO hand model [17] to emulate hand movements. MANO is a parametric hand model that provides a detailed representation of both hand shape and motion. Its capacity to capture inter-individual shape variations and a wide range of pose configurations has led to its widespread adoption in hand pose estimation, virtual reality interactions [19], and imitation learning for robotic manipulation [20]. In this study, the MANO model was integrated with PyBullet [21], utilizing three degrees of freedom for each finger and six degrees of freedom for the overall position and rotation of the hand.

B. Hand Landmarks and Poses

MediaPipe was used to extract 21 hand landmarks with a built-in laptop's single 720p HD camera at 15 frames per second. These landmarks included the wrist, as well as

the MCP, PIP, DIP, and fingertip points of each finger, as illustrated in Fig. 2. This figure also depicts the joint angles, their anatomical locations, and the corresponding directions. Positional data were obtained directly from an individual landmark, while rotational information was derived using three key landmarks: the wrist, index MCP, and pinky MCP.

To compute joint angles, displacement vectors were formed between consecutive landmarks, and the angles between these vectors were subsequently calculated. Using landmarks of wrist, MCP, PIP, DIP, and fingertip, vectors are constructed between consecutive landmarks. These vectors are wrist (**w**), MCP (**m**), PIP (**p**), and DIP (**d**) which are illustrated in Fig 2.

By connecting a given joint to its two adjacent joints, we define two vectors $\mathbf{v}_1$ and $\mathbf{v}_2$. The angle θ between these vectors can be computed as:

$$\theta = \arccos\left(\frac{\mathbf{v}_1 \cdot \mathbf{v}_2}{\|\mathbf{v}_1\|\|\mathbf{v}_2\|}\right) \tag{1}$$

For instance, the angle at the PIP joint is obtained by:

$$\theta_{\text{PIP}} = \arccos\left(\frac{(\mathbf{m}) \cdot (\mathbf{p})}{\|\mathbf{m}\|\|\mathbf{p}\|}\right) \tag{2}$$

The calculated joint angles were employed as input trajectories for the controller, guiding the simulated hand's movements within the virtual environment.

Each finger's joint—MCP, PIP, and DIP—has a range of motion in the simulation that reflects its biomechanical role in the hand dynamics. The initial joint angles in the fully extended position are close to 0° for all joints. As the finger flexes, the joint angles increase to follow the natural biomechanics of the hand. The min and max possible values for the range of motion of each joint in the simulation are summarized in Table I. This information is crucial for defining motion trajectories and evaluating joint function.

TABLE I
RANGE OF POSSIBLE MOTION FOR FINGER JOINTS IN THE SIMULATION

Joint	Minimum Angle (°)	Maximum Angle (°)
MCP	-10	90
PIP	-4	100
DIP	0	90

C. Torque Extraction

With the extracted input angles and the MANO dynamic model, a PID controller is used to compute the torques required to drive the virtual hand. In other words, the controller continuously tracks the input joint angles of the user by comparing them with the simulated joint angles and calculating the error between the two. This error serves as the controller's input, while its output torques adjust joint positions accordingly, effectively simulating the forces a human would exert to control finger joints.

The PID controller's gains are optimized to minimize discrepancies between the simulated and real-world behaviors, employing a genetic algorithm to iteratively refine the gains. A fitness function evaluates both the accuracy of angle tracking and the fidelity of the torque output relative to that of an actual human joint. After 50 iterations, the algorithm selects the best set of PID gains. Table II summarizes the resulting gain values for the MCP and PIP joints of the index finger, and Fig. 2 provides a visualization of the joint angles, their locations, and directions.

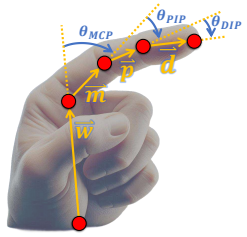


Fig. 2. Illustration of the MCP, PIP, and DIP finger joints, highlighting their angular configurations, anatomical locations, and directions.

TABLE II
OPTIMIZED PID CONTROLLER GAINS FOR THE MCP AND PIP JOINTS OF THE INDEX FINGER

Parameter	Kp	Ki	Kd
MCP	3.446×10^{-1}	9.440×10^{-3}	4.784×10^{-3}
PIP	3.772×10^{-2}	8.911×10^{-4}	4.620×10^{-4}

This methodology facilitates precise and responsive control of the simulated hand's motion through the use of input joint angles. Although these angles are initially derived from MediaPipe landmarks, for validation purposes, they are obtained from the reference dataset [22], ensuring a robust evaluation of system performance.

D. Validation Experiment

To validate our results, we used torque data from Agarwal et al. [22], which represents the torque at each joint of the index finger over multiple movement cycles. This data was extracted using an exoskeleton device on the index finger. It was used both for validating our results and optimizing the system parameters. The resulting torque outputs simulated human-applied forces at the MCP and PIP joints, enabling controlled movement and facilitating the evaluation of rehabilitation strategies and joint torque behaviors.

For the comparison, similar to the reference model, our simulation was programmed to follow sinusoidal trajectories with identical frequencies and durations over a predefined period. Torque profiles at the MCP and PIP joints were measured and analyzed to assess tracking performance and the accuracy of torque generation. Consistent movement patterns are maintained across both models to enable a direct comparison of torque outputs and control effectiveness.

III. RESULTS

A. Validation

The torques at the MCP joint and the PIP joint of the index finger are extracted and compared between the simulation

and the validation data. The actual torques for the validation data are obtained from [22]. The simulated torques are computed using the proposed methodology in Section II.

Based on the input joint angles from the validation data, the simulated joint angles are shown in Fig 3. This plot illustrates the cyclic motion of the index finger, from an open hand to a fist, repeated over four cycles in an 8-second interval. The corresponding torques from the validation data and the simulation for the index MCP and PIP joints are shown in Fig 4. These torque plots directly relate to the input angles displayed in Fig 3.

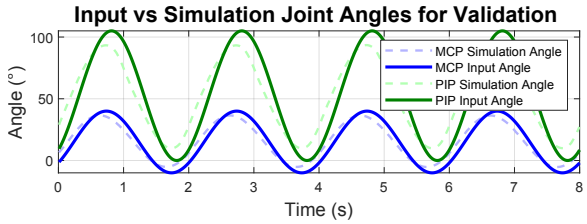


Fig. 3. The input angles from the validation data and the joint angles from the simulation over four cycles within an eight-second interval.

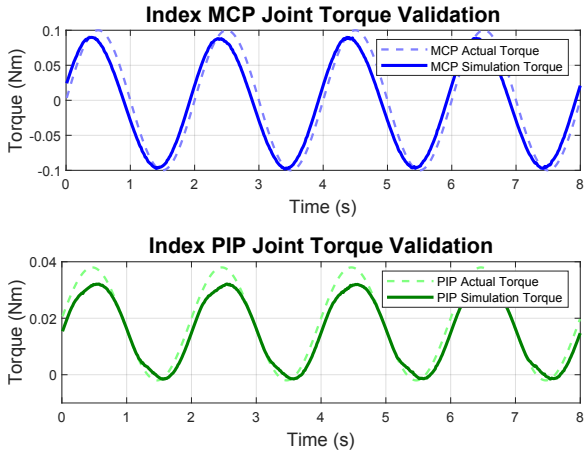


Fig. 4. Comparison of torque measurements of validation data with simulated torque outputs for the MCP and PIP joints. The simulated torque, derived from the input angles shown in Fig. 3, represents the controller's output and corresponds to the torque extracted from the human finger joints.

The simulated torque for the MCP joint closely follows the validated actual torque, achieving a mean squared error (MSE) of 4.346×10^{-4} and an accuracy of 91.32%. This demonstrates the effectiveness of the system in simulating human hand finger joint torques. Although minor deviations are observed during peak torque phases, the overall torque trends remain consistent. This is because the errors are primarily caused by the lag between the actual amount and the simulated amount, rather than a lack of accuracy. These results validate the simulation's accuracy in replicating the torque profiles of the MCP joint under sinusoidal motion trajectories. Similarly, the PIP joint of the index finger demonstrates a comparable trend to that of the MCP joint. The MSE values for both torque and angle errors in the index finger are presented in Table III.

TABLE III
MSE AND DIFFERENCE OF MAXIMUM VALUES FOR THE MCP AND PIP JOINTS IN THE INDEX FINGER

Parameter	MSE	Difference of Max Values
MCP Joint Torque	4.346×10^{-4}	$1.014 \times 10^{-2}(N.m)$
PIP Joint Torque	1.506×10^{-5}	$5.899 \times 10^{-3}(N.m)$
MCP Joint Angle	8.654×10^{-3}	$6.043 \times 10^{-2}(rad)$
PIP Joint Angle	6.357×10^{-2}	$2.010 \times 10^{-1}(rad)$

B. Torque Simulation for Other Finger Joints

After validating our results with the available experimental data for the index finger, the MCP, PIP, and DIP joints of the index, middle, ring, and pinky fingers were simulated using the input angles illustrated in Fig. 5. This figure depicts a single cycle of joint motion over a 4-second interval, serving as the input trajectory for each finger.

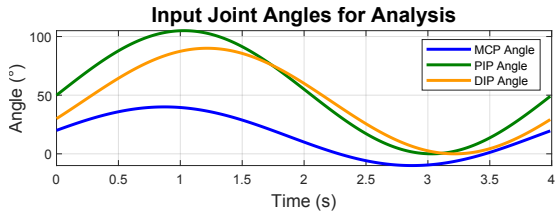


Fig. 5. MCP, PIP, and DIP joint input angles over one oscillation in 4 seconds for extracting torques of different fingers.

The resulting torque profiles for the MCP and PIP joints of the index, middle, ring, and pinky fingers are presented in Fig. 6. These plots compare the simulated torques across different fingers, highlighting the dynamic behavior of each joint under the specified input angles. The observed variations in torque among the MCP and PIP joints can be attributed to the distinct biomechanics and functional roles inherent to each finger.

The index and middle fingers exhibit higher torque values due to their primary roles in precision and power grips [23]. Additionally, these fingers possess stronger musculature and tendon connections [24], which contribute to their increased torque generation. In contrast, the ring and pinky fingers demonstrate lower torque values, reflecting their secondary roles in grip stabilization and support. These findings illustrate the simulation's capability to generalize and accurately model the dynamics of multiple finger joints, underscoring its potential for broader applications in rehabilitation and human-computer interaction.

IV. DISCUSSION

Accurate estimation of MCP and PIP joint torques and angles is essential for effective rehabilitation tracking with exoskeletons. Precise measurement enables personalized rehabilitation programs that adapt to patient progress, ensuring appropriate assistance or resistance. This aids in tracking motor recovery for neurological injury patients, such as stroke survivors [25]–[27]. Integrating torque and angle estimation also allows real-time feedback and adaptive control

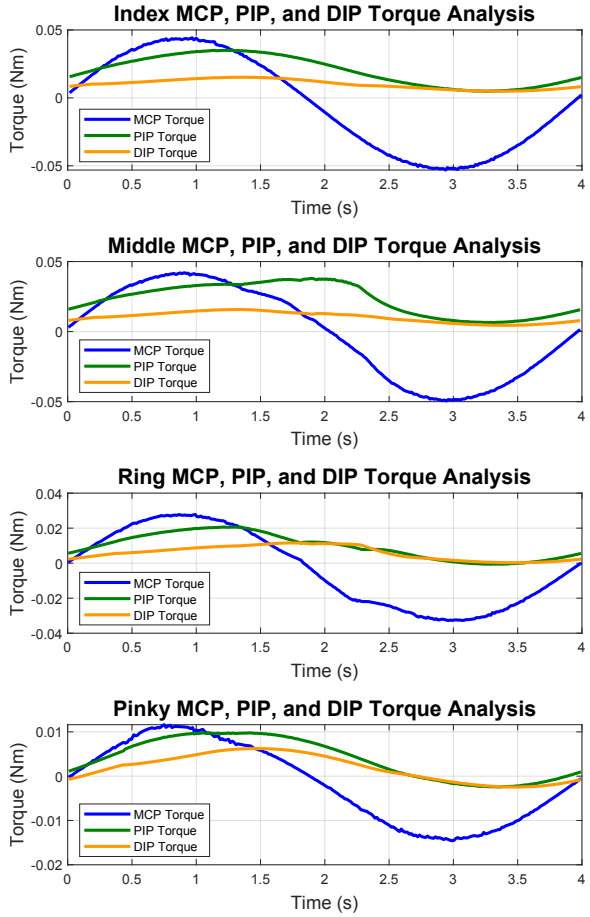


Fig. 6. MCP, PIP, and DIP joint torques analysis based on the input angles in Fig 5 for index, middle, ring, and pinky fingers.

in exoskeletons, which leads to efficient motor learning and recovery while providing clinicians with quantitative data for optimizing rehabilitation outcomes.

However, current methods for measuring MCP and PIP joint angles and torques, such as optical motion capture, electromagnetic tracking, and instrumented sensor gloves, face significant limitations. These systems require expert supervision, specialized medical facilities, and controlled environments, making routine clinical use and home rehabilitation impractical. Additionally, high costs, sensitivity to interference, calibration requirements, and user discomfort further restrict their accessibility. While these technologies provide valuable insights into joint kinematics, their real-time capabilities are largely confined to basic angle calculation, limiting their applicability for dynamic rehabilitation scenarios that require the key component of torque estimation. Advanced imaging techniques such as MRI and ultrasound offer precise structural and biomechanical measurements but remain expensive and unsuitable for frequent monitoring.

The proposed novel method employing a virtual hand model integrated with computer vision techniques has demonstrated a high degree of agreement between the estimated MCP and PIP joint torques and those obtained from previous experimental studies. Specifically, the MSE of our method is 4.346×10^{-4} for MCP torque and 1.506×10^{-5} for PIP torque when comparing with experimental results. This strong correlation validates the reliability and accuracy of our methodology in extracting human joint dynamics.

The system relies on a camera (e.g., laptop) with no complex calibration, requiring only basic data on hand size and mass. The distance to the camera is not critical as long as the resolution is sufficient to extract hand landmarks. The user simply positions the camera to capture the area above and places their hand within the frame. The successful estimation of MCP and PIP torques underscores the potential of our approach as a viable alternative to traditional measurement methods, often constrained by the need for direct expert supervision, specialized equipment, and clinical settings.

The validation data from Agarwal et al. [22] represents controlled finger movements within a typical range of motion and speed relevant to rehabilitation applications. Compared to daily activities, where finger motion speeds can vary significantly—from slow, precise manipulations (e.g., typing, grasping small objects) to rapid dynamic movements (e.g., gripping, flicking)—the speeds used in our study fall within a moderate range. While higher speeds could introduce additional challenges, such as increased torque fluctuations and motion blur in vision-based tracking, our approach is designed to adapt to varying movement speeds through its physics-based modeling. Preliminary tests indicate that the system can estimates joint torques at different speeds, but further validation is needed to assess its performance across a broader spectrum of daily activity motions.

In prosthetic design, torque data plays a pivotal role in developing devices that closely replicate natural hand movements, thereby enhancing adaptability and functionality for users. Understanding these forces also aids in optimizing material properties and actuation mechanisms, leading to improvements in efficiency and user comfort.

In the realm of robotic hand control, extracted torque data is essential for designing algorithms that replicate human-like movements. Integrating computer vision allows various hand models, including pre-built robotic hands, to be incorporated into the control system. Additionally, this setup supports training reinforcement learning models, enabling robots to learn precise and efficient hand motions. These advancements enhance applications in assistive technology, automation, and human-robot interaction, resulting in more responsive and functional robotic systems.

Although the proposed approach offers several advantages, it is subject to certain limitations. A primary constraint is the reliance on a single camera for data acquisition, which restricts the ability to capture the full range of hand poses, particularly during movements where occlusions occur. However, this limitation can be partially mitigated if the user follows predefined movement protocols to maintain optimal visibility. Additionally, unintentional hand displacement beyond the camera's field of view may disrupt continuous tracking, potentially reducing the reliability of the extracted motion data. While future enhancements, such as multi-camera fusion or depth estimation techniques, could improve

robustness and mitigate these challenges, they introduce a trade-off with the simplicity and ease of deployment that make the current approach accessible and user-friendly.

Furthermore, patients with significant movement limitations may exhibit restricted joint displacement, reducing the accuracy of estimated torques due to lower variation in extracted kinematic data. While our approach provides a markerless, vision-based solution for rehabilitation tracking, it is not inherently designed to support patients with severely impaired mobility unless integrated with an exoskeleton device. In such cases, our system could complement exoskeleton-assisted rehabilitation by tracking joint dynamics in response to robotic assistance, enabling more precise monitoring of rehabilitation progress. However, without direct access to an exoskeleton, the applicability of our setup for patients with minimal voluntary movement remains limited.

For future work, we aim to enhance the system by incorporating multiple cameras, sensor fusion, and intelligent camera placement algorithms to improve joint angle estimation and mitigate occlusions when tracking complex movements involving additional joints (e.g., spinal cord, knee, shoulder, wrist). While the single-camera setup remains the primary low-cost solution, multi-camera configurations and additional sensors (e.g., electromyography, stereo vision cameras) will serve as optional enhancements for clinical or research applications requiring higher accuracy. AI-driven occlusion handling techniques will further optimize tracking without significantly increasing hardware complexity. However, these improvements introduce a trade-off with simplicity, ease of deployment, and cost-effectiveness. Future efforts will focus on maintaining this balance to enhance tracking while preserving the system's practicality for remote rehabilitation.

REFERENCES

[1] J. Mehrholz, M. Pohl, T. Platz, J. Kugler, and B. Elsner, "Electromechanical and robot-assisted arm training for improving activities of daily living, arm function, and arm muscle strength after stroke," *Cochrane database of systematic reviews*, no. 9, 2018.

[2] S. Korivand, X. Zhu, N. Jalili, K. Koh, L.-Q. Zhang, and J. Gong, "Short: Toward personalized rehabilitation employing classification, localization, and visualization of brain–arm movement relationships," *Smart Health*, vol. 28, p. 100397, 2023.

[3] P. Heo, G. M. Gu, S.-j. Lee, K. Rhee, and J. Kim, "Current hand exoskeleton technologies for rehabilitation and assistive engineering," *International Journal of Precision Engineering and Manufacturing*, vol. 13, pp. 807–824, 2012.

[4] V. W. Mark and E. Taub, "Constraint-induced movement therapy for chronic stroke hemiparesis and other disabilities," *Restorative neurology and neuroscience*, vol. 22, no. 3-5, pp. 317–336, 2004.

[5] P. Tran, S. Jeong, K. R. Herrin, and J. P. Desai, "Hand exoskeleton systems, clinical rehabilitation practices, and future prospects," *IEEE Transactions on Medical Robotics and Bionics*, vol. 3, no. 3, pp. 606–622, 2021.

[6] B. H. Dobkin and A. Dorsch, "The promise of mhealth: daily activity monitoring and outcome assessments by wearable sensors," *Neurorehabilitation and neural repair*, vol. 25, no. 9, pp. 788–798, 2011.

[7] J. Chen, W. Jin, X.-X. Zhang, W. Xu, X.-N. Liu, and C.-C. Ren, "Telerehabilitation approaches for stroke patients: systematic review and meta-analysis of randomized controlled trials," *Journal of Stroke and Cerebrovascular Diseases*, vol. 24, no. 12, pp. 2660–2668, 2015.

[8] J. M. Veerbeek, A. C. Langbroek-Amersfoort, E. E. Van Wegen, C. G. Meskers, and G. Kwakkel, "Effects of robot-assisted therapy for the upper limb after stroke: a systematic review and meta-analysis," *Neurorehabilitation and neural repair*, vol. 31, no. 2, pp. 107–121, 2017.

[9] D. Steins, H. Dawes, P. Esser, and J. Collett, "Wearable accelerometry-based technology capable of assessing functional activities in neurological populations in community settings: a systematic review," *Journal of neuroengineering and rehabilitation*, vol. 11, pp. 1–13, 2014.

[10] G. Li, L. Cheng, and N. Sun, "Design, manipulability analysis and optimization of an index finger exoskeleton for stroke rehabilitation," *Mechanism and Machine Theory*, vol. 167, p. 104526, 2022.

[11] E. Peperoni, S. L. Capitani, T. Fiumalbi, E. Capotorti, A. Baldoni, F. Dell'Agnello, I. Creatini, E. Taglione, N. Vitiello, E. Trigili *et al.*, "Self-aligning finger exoskeleton for the mobilization of the metacarpophalangeal joint," *IEEE Transactions on Neural Systems and Rehabilitation Engineering*, vol. 31, pp. 884–894, 2023.

[12] G. Alonso-Linaje, A. Cisnal, J. C. Fraile, and J. P. Turiel, "Design and analysis of the m3rob: A robotic platform for wrist and hand rehabilitation," *IEEE Access*, vol. 12, pp. 30 472–30 481, 2024.

[13] S. C. Cramer, L. Dodakian, V. Le, J. See, R. Augsburger, A. McKenzie, R. J. Zhou, N. L. Chiu, J. Heckhausen, J. M. Cassidy *et al.*, "Efficacy of home-based telerehabilitation vs in-clinic therapy for adults after stroke: a randomized clinical trial," *JAMA neurology*, vol. 76, no. 9, pp. 1079–1087, 2019.

[14] S. Thangam, A. C. Reddy, G. Varun, M. Hemasri, J. J. J. Kumari *et al.*, "Flex sensor data analysis for hand rehabilitation using wearable glove," in *2024 Third International Conference on Electrical, Electronics, Information and Communication Technologies (ICEEICT)*. IEEE, 2024, pp. 1–8.

[15] S. Korivand, N. Jalili, and J. Gong, "Inertia-constrained reinforcement learning to enhance human motor control modeling," *Sensors*, vol. 23, no. 5, p. 2698, 2023.

[16] C. Lugaresi, J. Tang, H. Nash, C. McClanahan, E. Uboweja, M. Hays, F. Zhang, C.-L. Chang, M. G. Yong, J. Lee *et al.*, "Mediapipe: A framework for building perception pipelines," *arXiv preprint arXiv:1906.08172*, 2019.

[17] J. Romero, D. Tzionas, and M. J. Black, "Embodied hands: Modeling and capturing hands and bodies together," *arXiv preprint arXiv:2201.02610*, 2022.

[18] E. Coumans and Y. Bai, "Pybullet, a python module for physics simulation for games, robotics and machine learning," 2016.

[19] M. Duver, N. Wiederhold, M. Kyrarini, S. Banerjee, and N. K. Banerjee, "Vr-hand-in-hand: Using virtual reality (vr) hand tracking for hand-object data annotation," in *2024 IEEE International Conference on Artificial Intelligence and eXtended and Virtual Reality (AIxVR)*. IEEE, 2024, pp. 325–329.

[20] K. Li, D. Chappell, and N. Rojas, "Immersive demonstrations are the key to imitation learning," in *2023 IEEE International Conference on Robotics and Automation (ICRA)*. IEEE, 2023, pp. 5071–5077.

[21] ikalevatykh, "mano_pybullet: Mano hand model integration with pybullet," https://github.com/ikalevatykh/mano_pybullet, 2023, accessed: 2024-04-27.

[22] P. Agarwal, J. Fox, Y. Yun, M. K. O'Malley, and A. D. Deshpande, "An index finger exoskeleton with series elastic actuation for rehabilitation: Design, control and performance characterization," *The International Journal of Robotics Research*, vol. 34, no. 14, pp. 1747–1772, 2015.

[23] V. M. Zatsiorsky, R. W. Gregory, and M. L. Latash, "Force and torque production in static multifinger prehension: biomechanics and control. i. biomechanics," *Biological cybernetics*, vol. 87, pp. 50–57, 2002.

[24] M. El-Badawi, M. Butt, A. Al-Zuhair, and R. Fadel, "Extensor tendons of the fingers: Arrangement and variations-ii," *Clinical Anatomy: The Official Journal of the American Association of Clinical Anatomists and the British Association of Clinical Anatomists*, vol. 8, no. 6, pp. 391–398, 1995.

[25] P. De Pasquale, M. Bonanno, S. Mojdehdehbaher, A. Quartarone, and R. S. Calabrò, "The use of head-mounted display systems for upper limb kinematic analysis in post-stroke patients: A perspective review on benefits, challenges and other solutions," *Bioengineering*, vol. 11, no. 6, p. 538, 2024.

[26] S. Korivand, N. Jalili, and J. Gong, "Experiment protocols for brain-body imaging of locomotion: A systematic review," *Frontiers in Neuroscience*, vol. 17, p. 1051500, 2023.

[27] D. E. T. A. U. Tarihoran, I. Daryanti Saragih, I. S. Saragih, and H.-M. Tzeng, "Effects of videoconferencing intervention on stroke survivors: A systematic review and meta-analysis of randomised controlled studies," *Journal of Clinical Nursing*, vol. 32, no. 17-18, pp. 5938–5947, 2023.

Implementing and Testing the Novel REHAB-PAL System on Unimpaired Population: Towards Rehabilitation Engagement at Home with a Socially Assistive Robot for Pediatric Adherence

Matilde Antonj, Giulia Corniani, Kathy Piela, Leonard Eusebi, Maura Casadio, Alessandra Sciutti and Paolo Bonato

***Abstract*— This study introduces the REHAB-PAL system, an interactive solution for home-based rehabilitation in children with cerebral palsy. To verify its functioning and usability, the system was tested with physical therapists and rehabilitation specialists simulating patient roles. The system was evaluated for its ability to track users' movements during rehabilitation exercises and assess the quality of their performance. A look-up table was developed to correlate kinematic movement characteristics with clinical scores that quantify exercise quality. To enhance exercise performance and promote adherence, the system integrates NAO social robot, programmed to provide verbal instructions, demonstrate exercises, and deliver personalized feedback based on users' movement quality. Feedback delivery was guided by a decisional strategy, prioritizing specific kinematic variables tracked by the system. Participants were asked to perform a rehabilitation session under three experimental conditions: 1) Interaction with the physical NAO robot, 2) Interaction with a virtual robot displayed on a computer screen, and 3) Receiving instructions without the use of a robot. The REHAB-PAL system accurately detected participants' kinematics and automatically generated correct movement scores. Questionnaires revealed participants' preference for the interaction with the physical robot, associated with highest levels of engagement and seen as the most effective means of delivering exercise instructions.**

I. Introduction

Cerebral palsy (CP) is the most common motor disability in childhood, affecting 500,000 children under the age of 18 only in the United States, and 10,000 babies born each year are diagnosed with this pathology [1]. Cerebral palsy originates from an injury that occurs during the brain development in the prenatal, perinatal, or postnatal period [2]. Due to this neurological condition, patients are affected by motor disabilities, often accompanied by potential sensory and cognitive impairments; therefore, repeated sessions of rehabilitation are prescribed for the improvement in balance [3], gait [4], posture [5] and flexibility [6]. Every year, a substantial number of children require sessions of rehabilitation to improve their motor skills. However, the limited time of physical therapy in the hospitals and the families' support in terms of time and funding is challenging [7]. At-home sessions of rehabilitation could help children with cerebral palsy perform extensive and repetitive rehabilitative exercise, promoting the adherence to the therapy [8].

Unfortunately, maintaining adherence with at-home rehabilitation is often difficult: for this reason, new methods of training have been developed and tested to increase the level of engagement in children with motor impairment. Video games for rehabilitation have been demonstrated to be a valid alternative to increase users' engagement with therapy and to induce motor learning [9]. As well as encouraging the improvement of motor skills, results from playing with Active Video Game (AVG) revealed that children with cerebral palsy could achieve specific therapeutic goals with a low-cost and commercially available technology [10]. However, AVG lacks socially interactive skills, which could help engage users in their motor exercises through human-like abilities, such as speech and gestures. Socially Assistive Robots (SARs) aim at covering this gap in rehabilitative technologies [11]: by benefiting human social drives, children could increase their level of engagement through interaction with a robot characterized by social attitudes [12]. Although the use of virtual agents has already helped children maintain focus on rehabilitation, SAR has been demonstrated to induce greater effects on users' engagement and motor performance [13]. Novel methods of rehabilitation have been developed with the use of social robots that could encourage children with CP during their training [14]. Thanks to Socially Assistive Robots, children with cerebral palsy could be motivated in performing repetitive physical exercises [15], promoting the improvement of their non-verbal communication with their peers and caregivers [16]. However, current solutions do not involve comprehensive systems aimed at coaching patients during the training, establishing social interaction through customized feedback during the performance, and retrieving

The research was supported by a Starting Grant from the European Research Council (ERC) under the European Union's Horizon 2020 research and innovation programme. G.A. No 804388, wHiSPER, and partially supported by the grant title "Rehabilitation Engagement at Home with a socially Assistive roBot for Pediatric Adherence (REHAB-PAL)", National Institutes of Health (R43 HD106834-01).

Matilde Antonj is with DIBRIS & CONTACT, University of Genoa & Italian Institute of Technology, Genoa, Italy (corresponding author to provide e-mail: matilde.antonj@iit.it).

Giulia Corniani, Kathy Piela and Paolo Bonato are with Dept. of Physical Medicine & Rehabilitation, Harvard Medical School & Spaulding Rehabilitation Hospital, Boston, MA, USA (e-mail: gcorniani@mgh.harvard.edu, kpiela@mgb.org, pbonato@mgh.harvard.edu).

Leonard Eusebi is with Human-Centered Artificial Intelligence, Charles River Analytics, Inc., Arlington, MA USA (email: leusebi@cra.com).

Maura Casadio is with DIBRIS, University of Genoa, Genoa, Italy (e-mail: maura.casadio@unige.it).

Alessandra Sciutti is with CONTACT, Italian Institute of Technology, Genoa, Italy (e-mail: alessandra.sciutti@iit.it).

movement assessments of the rehabilitation, which could be reviewed by parents or physical therapists remotely.

To address the aforementioned problem, this study presents the implementation and testing of the REHAB-PAL system, a novel solution that assists children with cerebral palsy in at-home rehabilitation through the interaction with the social robots NAO [17], maintaining high levels of engagement during the training. Through tight collaboration with physical therapists, a look-up table was developed to associate kinematic characteristics with a score reflecting the quality of movement. Therefore, the REHAB-PAL system was developed to track users' movement during the interaction and generate a movement assessment in real-time during the training. Moreover, during rehabilitation sessions, the robot was programmed to show the exercise to perform and provide users with customized feedback to achieve the correct position. Physical therapists and rehabilitation specialists participated in an experiment to test the system functioning and evaluate the results of tracking, movement assessment and delivery of feedback. Moreover, these stakeholders tested the system through the interaction with the physical robot NAO, with the virtual robot, and without robot, to demonstrate that the interaction with the physical robot could increase users' engagement during the exercise execution.

II. METHODS

A. REHAB-PAL system

The REHAB-PAL system is designed to engage patients in motor skills training at home, without the need for direct supervision by physical therapists. The system integrates a variety of rehabilitative exercises with the humanoid robot NAO. The interaction between the robot and the patient aims to replicate the experience of working with a physical therapist. To achieve this goal, the system tracks patients' movements, provides performance feedback, and stores movement assessment, based on joint angles during rehabilitation sessions.

The setup prioritizes simplicity to facilitate future deployment in patients' homes. It consists of a PC with pre-installed software, a screen, the NAO robot, and an external camera positioned in front of the participant. To enhance usability, the system features an intuitive graphical user interface that allows parents to easily initiate rehabilitation sessions. The interface also offers customization options, such as entering the patient's personal details and selecting the types and number of exercise repetitions.

The REHAB-PAL system is developed in Python, utilizing PyGame to create an engaging and colorful interface designed to appeal to children. The interface transitions through shades of green to orange, evoking a game-like experience. This interface is displayed on a screen positioned behind the NAO robot and in front of the participant. Key training information is clearly shown on the screen, including a yellow counter indicating the remaining focus time. In the center, real-time tracking of the participant's movements is displayed. The name of the exercise appears at the top of the screen, while the robot's vocal feedback is transcribed at the bottom to assist participants in completing the exercises.

B. Target Population and Stakeholders

The system is designed to target children with cerebral palsy aged 7–14 years and classified at levels I or II of the Gross Motor Function Classification System (GMFCS) [18]. Impaired population was involved in the pilot study in order to decide the rehabilitative exercises to implement in the system and define a consistent method for the movement assessment.

Once the development was completed, 11 stakeholders (i.e., physical therapists and rehabilitation specialists) tested the functioning and usability of the system.

The study was approved by the Institutional Review Board at Mass General Brigham (protocol number 2021P002424).

C. Upper Body Movement Assessment

Since children with cerebral palsy present impaired range of motion [19], during rehabilitation sessions active exercises have been demonstrated to improve their motor abilities [20]. In collaboration with physical therapists, three upper-body exercises were selected for rehabilitation training to ensure broad applicability and focus on motor skills (Fig. 1):

- *Hands Up*: raising both hands towards the ceiling;
- *Hands T*: extending both arms outward to form the shape of the letter T;
- *Hands Y*: raising both arms upward and outward to form the shape of the letter Y.

Following the inclusion criteria of the target population, in a pilot study six pediatric patients performed these rehabilitation exercises for one repetition and maintained the position for 30 seconds. Due to high variability in patients' motor skills, above all, their capability of standing up, these exercises were chosen to target the upper body and to make the rehabilitation accessible to most patients while being suitable for home-based use.

To quantify movement performance during these exercises, the study utilized the MediaPipe Pose Landmarker [21], a pre-trained machine learning model that tracks 33 key body landmarks from video captured by a front-facing camera. The movement of the upper body was assessed considering the shoulders, elbows, wrist, and hip position, associated with MediaPipe skeleton landmarks. Each performance was evaluated in terms of shoulder abduction, elbow flexion, and shoulder tilt in the 2D experimental scene. Shoulder abduction was calculated for each side of the body as the

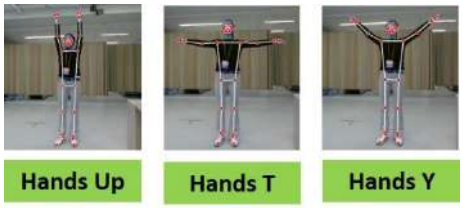


Figure 1. Rehabilitative exercises in REHAB-PAL system. Three different positions, considering the upper body, were selected as rehabilitative training for motor skills in the REHAB-PAL system: Hands Up, Hands T, Hands Y.

joint angle between the elbow, shoulder, and hip. Elbow flexion was measured as the joint angle between the wrist, elbow, and shoulder. Additionally, shoulder tilt was determined by measuring the vertical displacement between the right and left shoulders. Through a tight collaboration with physical therapists, participants' movements were inspected by analyzing joint angles: both normative and compensatory strategies were identified and used to develop a look-up table (TABLE I). This table associates performance levels—accurate, mild, moderate, and severe—with quantitative measures of joint angles and body displacements. Each each clinical label was associated with a score from 0 to 3: the smallest value corresponded to a severe label, while the highest number to the correct one. The system was designed to provide real-time feedback on performance, enabling parents and remote physical therapists to immediately assess the effectiveness of the motor training. Through this process, the REHAB-PAL system was refined to autonomously evaluate upper-body motor performance, offering a clinically informed and practical tool for home-based rehabilitation.

TABLE I. LOOK-UP TABLE FOR MOVEMENT ASSESSMENT

Physical Exercise	Shoulder Abduction	Elbow Flexion	Shoulder Tilt
Hands Up	**[170° , 180°]**	**[0°, 9.9°]**	**[0, 0.0049]**
	[165°, 169.9°]	**[10°, 14.9°]**	**[0.005, 0.0099]**
	[160°, 164.9°]	**[15°, 19.9°]**	**[0.01, 0.019]**
	[0°, 159.9°]	**[20°, 150°]**	**> 0.02**
Hands T	**[85°, 94.9°]**	**[0°, 9.9°]**	**[0, 0.0049]**
	[80°, 84.9°] & [95°, 99.9°]	**[10°, 14.9°]**	**[0.005, 0.0099]**
	[70°, 79.9°] & [100°, 109.9°]	**[15°, 19.9°]**	**[0.01, 0.019]**
	[0°, 69.9°] & [110°, 180°]	**[20°, 150°]**	**> 0.02**
Hands Y	**[130°, 139.9°]**	**[0°, 9.9°]**	**[0, 0.0049]**
	[125°, 129.9°] & [140°, 144.9°]	**[10°, 14.9°]**	**[0.005, 0.0099]**
	[115°, 124.9°] & [145°, 154.9°]	**[15°, 19.9°]**	**[0.01, 0.019]**
	[0°, 114.9°] & [155°, 180°]	**[20°, 150°]**	**> 0.02**

Label	Accurate	Mild	Moderate	Severe
Score	3	2	1	0

D. *Customized Feedback*

To emulate the interaction between the patient and the physical therapist, the system was endowed with the capability of providing participants with customized suggestions. To choose simple and effective feedback, a physical therapist was involved in the decision of the appropriate feedback for pediatric rehabilitation. During the exercise, suggestions were given every 5 seconds so that participants had the time to receive the comments of the system and fix their erroneous position. The same tracking modality used for the development of the look-up table was implemented, in order to track participants' movement in each instant of the interaction (II.C). Relying on the assessment of patients' performance during the training, the REHAB-PAL system provided different instructions in real-time, which suggested the way to correct specific body angles or tilt (i.e., shoulder abduction, elbow flexion, and shoulder tilt). In case of multiple errors during the execution of the exercise, the delivery of suggestions was prioritized: first, participants could receive suggestions on the position of their shoulders, then on the location of their elbows, and eventually on the alignment of their shoulders. After the feedback was delivered, the system continued tracking the participant's movement: if they did not manage to correct the position, participants were provided with the following suggestion in the scale of priorities (See Fig. 2 for the complete decisional strategy of feedback delivery implemented in REHAB-PAL system). In this way, the REHAB-PAL system could avoid patients' frustration in hearing the same feedback two consecutive times and maintain children's engagement. If patients performed the exercise correctly, they were encouraged to maintain the position, thanks to the delivery of variable words of exhortation. At the end of each exercise, participants received a score for the performance, considering the number of times shoulder abduction, elbow flexion, and

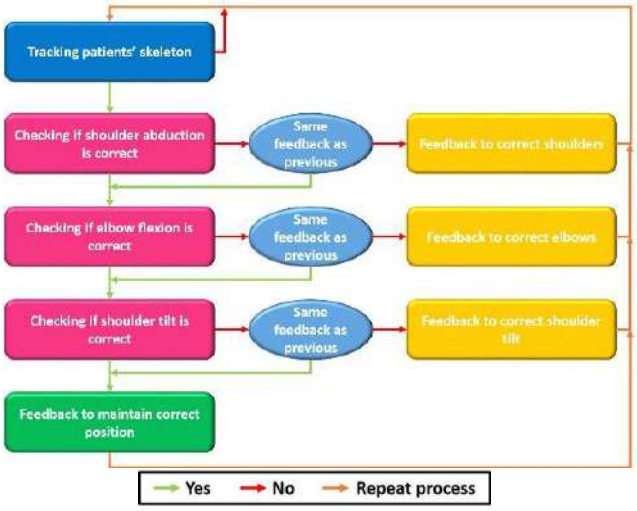


Figure 2. The decisional strategy of feedback delivery implemented in REHAB-PAL. At each instant of the interaction, the REHAB-PAL system tracked participants' movement and, every 5 seconds, provided them with customized feedback according to their performance. Feedback was delivered by prioritizing shoulder abduction, followed by elbow flexion and shoulder tilt, but two identical consecutive suggestions were avoided to maintain subjects' engagement.

shoulder tilt were associated with each label: the more accurate labels were gathered during the execution of the movement, the higher the score obtained. Over the trials, points were accumulated, and the total score was communicated to participants at the end of the training.

E. Robot Characterization

To enhance engagement during rehabilitation sessions, the REHAB-PAL system was integrated with the humanoid robot NAO, developed by Aldebaran – United Robotics Group. At the start of each session, the robotic agent greeted participants and provided instructions for the exercises. Leveraging its 25 degrees of freedom, the robot could demonstrate the exercises and perform them alongside the participants to encourage active participation (Fig. 3). The robot's movements were programmed using the Choregraphe application. Initially, the actions were created, tested, and refined on the corresponding virtual robot. Once finalized, these actions were recreated on the physical robot, enabling it to replicate the three rehabilitative positions – Hands Up, Hands T, and Hands Y – with a human-like appearance. During the exercises, participants were instructed to replicate the movements of the robot, striving to achieve the correct positions as accurately as possible. During participants' performance, the REHAB-PAL system tracked their movements and communicated to the robot the customized feedback to deliver. In this way, each time, the human-robot interaction could vary, according to participants' performance, with the final result of increasing engagement in the rehabilitation session. To increase engagement and improve the execution of the exercises, the robot informed participants of the score computed by the system at the end of each performance and the total amount of points when the training finished.



Figure 3. The interaction with the robot NAO, realized by the REHAB-PAL system. The image shows the interaction between a participant and the robot NAO: the embodied agent shows the Hands Up position and the subject has to replicate its movement. Thanks to the customized feedback of the robot, participants can adjust the position to correct the erroneous movement.

F. Testing System

The novel system REHAB-PAL was tested on 11 unimpaired adults, enrolled among physical therapists and rehabilitation specialists, to verify the functioning of the system and gathering feedback from a potential stakeholder population. Participants performed each exercise (i.e., Hands Up, Hands T and Hands Y) in three different trials in the following order:

1. *Accurate round*: participants had to achieve the position in the most accurate way;
2. *Correction round*: subjects were asked to display shoulder abduction in Hands T, elbow flexion in Hands Up, and elbow flexion and shoulder tilt in Hands Y, and correct their position, following the feedback of the system;
3. *Erroneous round*: participants performed the exercise by varying their joint angles and tilt without achieving the correct position.

Thanks to the structure of this experiment, participants could test the system functioning in detecting participants' movement, the association of clinical labels to their joint angles and tilt during the performance, and the delivery of feedback.

To have additional proof that the implemented interaction with the robot was perceived as an engaging tool for rehabilitative sessions, the experiments were repeated in three different modalities:

- *Physical robot*: the embodied agent performs the exercises in front of the participant and, through vocal comments, corrects participants' movements with tailored feedback;
- *Virtual robot*: an artificial virtual agent shows the motor exercise and provides customized feedback by displaying a textual comment on the screen;
- *No robot*: participants interacted just with the feedback and information reported on the graphical user interface without any virtual or physical agent.

The order of the three conditions was randomized among participants. Within each session, 30-second exercises were executed in the same sequence: all the three positions were performed in each round, avoiding consecutive repetitions to increase engagement in the training. To avoid differences in the understanding of the exercise, the positions were shown before starting the whole experiment.

G. Skeleton and Questionnaire Data

For each participant, the positions of MediaPipe skeleton landmarks were collected, and joint angles and tilt for the upper body were computed and saved at each instant of the experiment with a sampling rate of 30 Hz. To avoid outliers, clinical scores in the first and last 5 seconds of interaction were excluded. Shoulder abduction, elbow flexion, and shoulder tilt were inspected to verify how the association of clinical labels worked during the experiment: in particular, participants' performance was verified to be associated with the clinical labels, corresponding to the instructions of the round. First, each participant's mean clinical scores were computed, considering all three different conditions (i.e., without, virtual robot, and physical robot), and mean values among participants were found for each joint angle and tilt. In addition, since no detection of skeleton data corresponded to missing movement assessment (i.e., labels and scores), number of times the system identified the users' body landmarks were calculated. Moreover, at the end of each condition, participants were asked to evaluate the type of interaction with a Likert scale from 1 (minimum score) to 7 (maximum score), considering 5 different items: enjoyment, usefulness, encouragement, helpfulness, and fun. Since the three different interactions shared the same content in the customized feedback, at the end of the whole experiment, participants were also provided with a questionnaire aimed at evaluating the system, using Likert scales from 1 (minimum score) to 7 (maximum score) and general questions to gather impressions about the system. In particular, in the final questionnaire, participants had to rate the usefulness and the engagement associated with the delivery of customized feedback, the usefulness in priority of feedback, the rewarding method (i.e., communication of individual scores at the end of the exercise and the total amount at the end of the condition) and accuracy in associating labels to joints.

III. Results

This study led to the development and testing of the novel REHAB-PAL system: through a tight collaboration with physical therapists, a new method to provide rehabilitation sessions was created through the interaction of the humanoid robot NAO. During the training, the embodied agent showed the rehabilitative exercise and gave customized feedback according to the participants' performance. Moreover, the novelty of the system consists of having a real-time movement assessment of the exercise execution: the user's joint angles and shoulder tilt could be associated with four different levels of performance and motor impairment (i.e., accurate, mild, moderate, and severe). Participants performed the exercises in front of the robot and the camera: the system managed to detect their joint angles 100% of the time, and associate a clinical label, confirming the stability of the method.

A. Testing Movement Assessment

In the first round of exercises, participants had to perform the three exercises for the upper body (i.e., Hands Up, Hands T, Hands Y) in the most accurate way. The system was tested to verify if participants' performance was associated to clinical labels, corresponding to accurate motor behavior. Results showed that in the execution of the Hands Up position, the association of clinical labels worked correctly: as shown in Fig. 4, mean clinical score for each joint and tilt varied between score 2 and 3, indicating a mild-accurate behavior (left shoulder: 2.1 (0.2 SE), right shoulder: 2.4 (0.2 SE), left elbow: 2.6 (0.2 SE), right elbow: 2.5 (0.2 SE), shoulder tilt: 2.9 (0.1 SE)). Although the exercise was shown before starting the experiment, participants often slightly decreased their joint angles for shoulders and elbows, also caused by the long duration of exercises. The same analysis was carried out also for the other two positions: the Hands T was demonstrated to be a more intuitive exercise to perform, particularly in the alignment of the shoulders. Also in this case, the system was able to assess correctly participants' performance from mild to accurate behavior (left shoulder: 2.6 (0.1 SE), right shoulder: 2.6 (0.1 SE), left elbow: 2.8 (0.1 SE), right elbow: 2.2 (0.2 SE), shoulder tilt: 3.0 (0.01 SE)). For what concerned Hands Y, results showed that the system correctly assessed a mild-moderate behavior (left shoulder: 1.5 (0.3 SE), right shoulder: 1.5 (0.3 SE), left elbow: 2.7 (0.2 SE), right elbow: 2.7 (0.2 SE), shoulder tilt: 2.9 (0.1 SE)) because participants challenged to find the accurate position, by varying the width of the Y shape. To prove the consistency of the system, results in the first round were compared to the last two series of exercises. Results demonstrated that the clinical score, associated with participants' performance, correctly decreased their value. Considering Hands Up as representative position, the assessment of the system was compared among the three rounds of exercises: in the second repetition, participants' shoulder abduction was meanly categorized as severe-

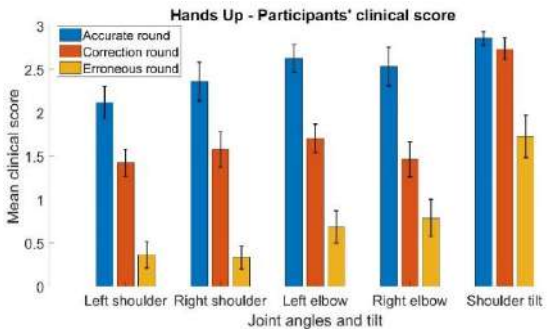


Figure 4. Comparison of clinical score in Hands Up among the three rounds. This image compares the clinical score in the different rounds: blue bars represent participants' performance in the accurate round, while orange and ocher graphs refer to their scores, in the correction and erroneous round, respectively. Left and right shoulder abduction, left and right elbow flexion and shoulder tilt achieved higher results in the first round, where the system managed to evaluate their performance as a mild-accurate behavior. In the second round, participants had to perform Hands Up position varying the elbow flexion, which also led to the variation of the shoulder abduction and tilt. During the performance, participants had the possibility of correcting their position. Results showed that the system categorized their behavior in a severe-moderate mode for the shoulders and a moderate-mild behavior for the elbows and shoulder tilt. In the last round, participants never corrected their position: the system correctly evaluated their behavior as severe-moderate for shoulders and elbows, with a slight variation of shoulder tilt remaining in a moderate-mild mode. The black error bars identify the standard error of the mean.

moderate behavior, while elbow flexion and shoulder tilt were associated with moderate-mild labels (left shoulder: 0.9 (0.2 SE), right shoulder: 0.9 (0.2 SE), left elbow: 1.9 (0.2 SE), right elbow: 1.7 (0.2 SE), shoulder tilt: 1.6 (0.1 SE)). Clinical score significantly decreased in the last round, where participants have not the possibility to correct their position, moving closer to severe behavior, with a slight modulation of the shoulder tilt (left shoulder: 0.4 (0.2 SE), right shoulder: 0.4 (0.1 SE), left elbow: 0.8 (0.2 SE), right elbow: 0.8 (0.2 SE), shoulder tilt: 1.6 (0.1 SE)). These differences in movement assessment among rounds were verified through a Repeated Measures ANOVA (all p's < 0.001).

B. System Evaluation

The aim of performing different rounds of the exercises consisted of letting participants understand how the REHAB-PAL system could provide them with useful suggestions in case of error or just with encouraging comments to maintain the correct position. In the evaluation of the entire system, questionnaire results showed that participants rated the delivery of customized feedback with a mean score of 5.7 for its usefulness and 5.3 for its engagement, with the suggestion of incrementing the number of feedback for more challenging positions, such as Hands Y. Most of the participants highlighted the importance of giving priority to the different body parts with the final goal of achieving the correct positions: indeed, they averagely evaluated the usefulness of priority in feedback delivery with 5.6. Since each participant obtained a score at the end of each exercise, in the questionnaire they were asked to evaluate this rewarding method: the assessment reached the mean value of 5.3, also proposing a visualization method to help children visualize their improvement over time. Only for this experiment clinical labels for each joint were displayed on the screen so that participants could evaluate how the clinical assessment was working during the trials. Participants were satisfied with the association of correct clinical labels to each joint, evaluating the method with a mean score of 6.

C. Interaction Evaluation

To assess how the system was engaging for the target population, at the end of the whole experiment, participants were asked which type of interaction they preferred: 100% of participants confirmed that the interaction with the robot was more appropriate to achieve the goal, compared to the interaction with the virtual robot or without robot. Moreover, participants' questionnaire results were analyzed for the evaluation of the interaction in different conditions: computing the mean values for each item, in Fig. 5 results showed that participants rated the highest values for all the items, belonging to the interaction with the physical robot (enjoyment: 6.7 (0.2 SE), usefulness: 6.6 (0.2 SE), encouragement: 6.3 (0.3 SE), helpfulness: 6.3 (0.3 SE), fun: 5.9 (0.3 SE)). On the contrary, participants rated with lower scores the interaction with the virtual robot (enjoyment: 5 (0.4 SE), usefulness: 5.8 (0.4 SE), encouragement: 5 (0.4 SE), helpfulness: 5.5(0.4 SE), fun: 4.4 (0.4 SE)), followed by the score achieved without robot (enjoyment: 4.8 (0.4 SE), usefulness: 4.8 (0.4 SE), encouragement: 4.4 (0.5 SE), helpfulness: 4.6 (0.3 SE), fun: 3.5 (0.4 SE)). These results demonstrated that the presence of the robot NAO, able to show the movement and give useful suggestions during the performance of the exercises, was fundamental in the engagement of the training (Repeated Measures ANOVA, all p's < 0.001).

IV. Discussion and Conclusions

The implementation of REHAB-PAL system presents a novel method to deliver sessions of rehabilitation for children with cerebral palsy, with the final aim of improving their motor skills for the upper body. The system was developed to imitate the interaction between patients with physical therapists. Therefore the system integrated the humanoid robot NAO: the embodied agent was manipulated to show the motor exercises to replicate. Thanks to a tight collaboration with physical therapists, the REHAB-PAL system was endowed with the capability of creating a real-time movement assessment of participants' performance: shoulder abduction, elbow flexion, and shoulder tilt were associated with clinical labels, according to their performance during the execution of the task. Moreover, in case of errors, the robot was able to give customized suggestions in order to help participants achieve the correct position. By testing the REHAB-PAL system with a group of physical therapists and rehabilitation experts, the movement assessment was demonstrated to work properly during the session of rehabilitation. The customized feedback was appreciated by participants when they had to correct their position: for most challenging exercises, an increase in the number of feedback was suggested. To demonstrate the importance of the interaction with robots for engagement in rehabilitation, the system was compared in three different modalities: with the physical robot, with the virtual robot and without robot. All the participants evaluated the interaction with the physical robot as superior to the other two conditions, in terms of enjoyment, usefulness, encouragement, helpfulness, and fun. In line with previous findings [22], these results confirmed the benefit of physical appearance in users' environment during an

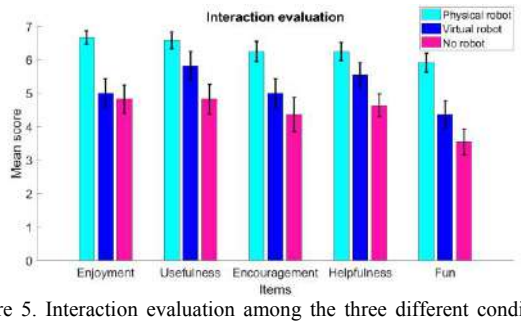


Figure 5. Interaction evaluation among the three different conditions. Participants had to evaluate the interaction with the REHAB-PAL system in the three different modalities: with the physical robot, the virtual robot and without robot. The interaction with the robot was assessed with highest scores (cyan bars), followed by the interaction with the virtual robot (blue bars). On the contrary, the modality without robot received the lowest scores (magenta bars). The black error bars represent the SE of mean score.

interaction, demonstrating the potential increase of engagement in rehabilitation settings. In comparison to the existing technology [23], the REHAB-PAL system simultaneously covers the rehabilitation needs of training users' motor abilities, establishing an engaging interaction through customized feedback, and providing a movement assessment, which could be reviewed by physical therapists and parents. Based on the results of this research, the system will be further evaluated in terms of validity and usability with the target population (i.e., children with cerebral palsy). Although the use of a social robot could seem a financial barrier for at-home rehabilitation, their presence could provide impaired population with distant care [24]: therefore, an effective rehabilitation with REHAB-PAL system could reduce the financial burden of families in physical therapy and optimize the hospital workflow. In conclusion, this study proposed a new comprehensive method aimed at the delivery of at-home rehabilitation for children with cerebral palsy through interaction with a socially assistive robot able to show the exercises, give customized feedback, and store the movement assessment obtained during the training.

ACKNOWLEDGMENT

The authors would like to thank all the participants in the pilot study and in the experiments for their commitment.

REFERENCES

[1] MyChild at CerebralPalsy.org, "Prevalence of Cerebral Palsy," CerebralPalsy.org, 2024. https://www.cerebralpalsy.org/about-cerebral-palsy/prevalence-and-incidence.

[2] Krigger, Karen W. "Cerebral palsy: an overview." American family physician 73.1 (2006): 91-100.

[3] Shumway-Cook, A., Hutchinson, S., Kartin, D., Price, R., & Woollacott, M. (2003). Effect of balance training on recovery of stability in children with cerebral palsy. Developmental medicine and child neurology, 45(9), 591-602.

[4] Booth, A. T., Buizer, A. I., Meyns, P., Oude Lansink, I. L., Steenbrink, F., & van der Krogt, M. M. (2018). The efficacy of functional gait training in children and young adults with cerebral palsy: a systematic review and meta‐analysis. Developmental Medicine & Child Neurology, 60(9), 866-883.

[5] Dewar, R., Love, S., & Johnston, L. M. (2015). Exercise interventions improve postural control in children with cerebral palsy: a systematic review. Developmental Medicine & Child Neurology, 57(6), 504-520.

[6] Wiart, L., Darrah, J., & Kembhavi, G. (2008). Stretching with children with cerebral palsy: what do we know and where are we going?. Pediatric physical therapy, 20(2), 173-178.

[7] Tonmukayakul, U., Shih, S. T., Bourke-Taylor, H., Imms, C., Reddihough, D., Cox, L., & Carter, R. (2018). Systematic review of the economic impact of cerebral palsy. Research in developmental disabilities, 80, 93-101.

[8] Novak, I., & Cusick, A. (2006). Home programmes in paediatric occupational therapy for children with cerebral palsy: where to start?. Australian Occupational Therapy Journal, 53(4), 251-264.

[9] Lohse, K., Shirzad, N., Verster, A., Hodges, N., & Van der Loos, H. M. (2013). Video games and rehabilitation: using design principles to enhance engagement in physical therapy. Journal of neurologic physical therapy, 37(4), 166-175.

[10] Howcroft, J., Klejman, S., Fehlings, D., Wright, V., Zabjek, K., Andrysek, J., & Biddiss, E. (2012). Active video game play in children with cerebral palsy: potential for physical activity promotion and rehabilitation therapies. Archives of physical medicine and rehabilitation, 93(8), 1448-1456.

[11] Feil-Seifer, D., & Mataric, M. J. (2005, June). Defining socially assistive robotics. In 9th International Conference on Rehabilitation Robotics, 2005. ICORR 2005. (pp. 465-468). IEEE.

[12] M. J. Matarić and B. Scassellati, "Socially Assistive Robotics," in Springer Handbook of Robotics, 2016, pp. 1973–1994.

[13] Winkle, K., Caleb-Solly, P., Turton, A., & Bremner, P. (2018, February). Social robots for engagement in rehabilitative therapies: Design implications from a study with therapists. In Proceedings of the 2018 acm/ieee international conference on human-robot interaction (pp. 289-297).

[14] Buitrago, J. A., Bolaños, A. M., & Caicedo Bravo, E. (2020). A motor learning therapeutic intervention for a child with cerebral palsy through a social assistive robot. Disability and Rehabilitation: Assistive Technology, 15(3), 357-362.

[15] Fridin, M., & Belokopytov, M. (2014). Robotics agent coacher for cp motor function (rac cp fun). Robotica, 32(8), 1265-1279.

[16] Dennler, N., Yunis, C., Realmuto, J., Sanger, T., Nikolaidis, S., & Matarić, M. (2021, August). Personalizing user engagement dynamics in a non-verbal communication game for cerebral palsy. In 2021 30th IEEE International Conference on Robot & Human Interactive Communication (RO-MAN) (pp. 873-879). IEEE.

[17] Shamsuddin, S., Ismail, L. I., Yussof, H., Zahari, N. I., Bahari, S., Hashim, H., & Jaffar, A. (2011, November). Humanoid robot NAO: Review of control and motion exploration. In 2011 IEEE international conference on Control System, Computing and Engineering (pp. 511-516). IEEE.

[18] Palisano, R., Rosenbaum, P., Walter, S., Russell, D., Wood, E., & Galuppi, B. (1997). Gross motor function classification system for cerebral palsy. Dev Med Child Neurol, 39(4), 214-23.

[19] De Bruin, M., Smeulders, M. J. C., & Kreulen, M. (2013). Why is joint range of motion limited in patients with cerebral palsy?. Journal of Hand Surgery (European Volume), 38(1), 8-13.

[20] Clutterbuck, G., Auld, M., & Johnston, L. (2019). Active exercise interventions improve gross motor function of ambulant/semi-ambulant children with cerebral palsy: a systematic review. Disability and rehabilitation, 41(10), 1131-1151.

[21] Pose landmark detection guide, "Models", Google AI for Developers, https://ai.google.dev/edge/mediapipe/solutions/vision/pose_landmarker

[22] Li, J. (2015). The benefit of being physically present: A survey of experimental works comparing copresent robots, telepresent robots and virtual agents. International Journal of Human-Computer Studies, 77, 23-37.

[23] Malik, N. A., Hanapiah, F. A., Rahman, R. A. A., & Yussof, H. (2016). Emergence of socially assistive robotics in rehabilitation for children with cerebral palsy: a review. International Journal of Advanced Robotic Systems, 13(3), 135.

[24] Ragno, L., Borboni, A., Vannetti, F., Amici, C., & Cusano, N. (2023). Application of social robots in healthcare: Review on characteristics, requirements, technical solutions. Sensors, 23(15), 6820.

Impedance-Controlled Knee Orthosis: Transitional Movements and their Effect on Knee Kinematics and Muscular Activity

Marc-Anton Scheidl[1], Hannah Braun[1], İsmail Berkay Akarsu[1], Claudio Castellini[1,2]

***Abstract*— This study investigated the effects of an impedance-controlled active knee orthosis on knee kinematics and muscle activation during transitional movements, focusing on Sit-To-Stand and Step-Up tasks. A custom hardware and software setup employed an EMG-driven impedance controller to modulate joint stiffness real-time. Four healthy participants performed Sit-To-Stand and Step-Up tasks under assisted and non-assisted conditions. The results indicated that the orthosis reduced muscle activity in stable, bilateral tasks like Sit-To-Stand, leading to lower average EMG amplitudes in the assisted leg. In contrast, for more unstable, unilateral tasks such as Step-Up, changes in velocity and muscle activity were more variable. Inter-participant differences in body mass and movement strategy influenced outcomes, and the device's interference with normal muscle patterns highlighted the need for improved sensor attachment and personalized parameter tuning. These findings underscore that while EMG-based impedance control can lessen physical effort under certain conditions, its benefits depend on the task's nature and individual user characteristics. Future work should refine hardware stability, improve data quality, and explore adaptive algorithms for personalized assistance.**

I. Introduction

Active knee orthoses (AKOs), in particular, have gained increasing attention over the last few years as assistive devices for individuals with lower-limb weakness [1], [2]. Mobility-related disabilities, such as hemiplegia, cerebral palsy, hemiparesis, diplegia, and spinal cord injuries, often require the use of lower limb orthotics to stabilize, support, and even reduce energy expenditure [3], [4]. Addressing structural joint issues and reducing strain on the lower limbs can also benefit an aging population in tasks of daily living, reducing the risk of injury while potentially alleviating geriatric issues such as cartilage degeneration [5], [6], [7], [8].

These systems are designed to augment knee extension during demanding activities such as standing up from a chair or climbing stairs [9], [10], [11], which require significant knee torques $0.38 - 0.9\,\mathrm{Nm/kg}$ [12], [13]. Therefore, these cannot always compensate for the entire load due to technical limitations and trade-offs [9].

Impedance control, based upon a variety of high to low-level control paradigms and even advanced biomechanical model approaches, allows an attached exoskeleton or AKO to modulate its stiffness and damping in response to the user's movements, ensuring safe and adaptive human-robot interaction [14], [15], [16]. To achieve intuitive user control, recent studies propose the usage of electromyography (EMG) signals from the user's muscles to adjust assistance in real time [17] and provide feedback on biomechanics and muscle recruitment [18], [19]. In a post-stroke case study, proportional EMG control with a knee exoskeleton significantly decreased muscle effort and improved balance metrics by up to 29.3% during sit-to-stand attempts [20]. Similarly, a lightweight AKO reduced EMG activity by roughly 19% on average during step-up trials in healthy adults [2]. Such findings indicate that EMG-driven augmentation of knee joint torques in active knee orthoses can effectively compensate for deficits in muscle strength arising from aging, injury, or neurological conditions, facilitating recovery by promoting neuroplasticity and restoring motor function [21].

This paper explores the application of impedance control in AKOs to reduce muscle strain during Sit-To-Stand and Step-Up exercises in four healthy participants. By leveraging EMG signals to dynamically adjust the joint's impedance, our system delivers intuitive, user-centered assistance that minimizes muscular effort. Additionally, our device requires minimal calibration, is lightweight, and is based on a CE-certified, medical-grade knee orthosis that utilizes off-the-shelf components to keep costs low and maintain minimal weight. In the following sections, we present the methodology, experimental setup, and initial findings of our study.

II. Methodology

A. Hardware-Setup

The core component of our setup (Figure 1) is a modified Sporlastic GENUDYN® CI STEP THRU Knee Orthosis [22] equipped with an electric actuator (AK80-9, CubeMars) [23], which provides industry-grade torque, position, and velocity sensing capabilities thanks to the MAB Robotics MD80 v2.1 controller [24] with a peak torque of $18\,\mathrm{Nm}$ and $9\,\mathrm{Nm}$ sustained ($\approx 2\,\mathrm{kg}$ total, Orthosis incl. $1.4\,\mathrm{Ah}$ 6s Lipo and AK80-9). The actuator is mounted to the orthosis's center of rotation via a specifically designed and custom-built 3D-printed brace, which is available open-source [25]. Since the gear shape of the orthosis mimics the changing center of rotation of a knee joint, the brace employs a linear element to adjust for transitional changes during movement while maintaining easy movability and proper torque transmission.

Eight Trigno® Avanti sEMG sensors from Delsys Inc. were fitted to the participant's anterior and posterior side of the thighs to monitor muscle activity. The placement of EMG

[1]Marc-Anton Scheidl, Hannah Braun, İsmail Berkay Akarsu and Claudio Castellini are with the Assistive Intelligent Robotics Lab, FAU Erlangen-Nürnberg, Erlangen, Germany. Email: marc.scheidl@fau.de.

[2]Claudio Castellini is also with the Assistive Intelligent Robotics Lab, Friedrich-Alexander-Universität Erlangen-Nürnberg, Institute of Robotics and Mechatronics, German Aerospace Centre, Erlangen/Oberpfaffenhofen, Germany. Email: claudio.castellini@fau.de.

This study was conducted with ethical approval (no. 23-350-B) from the Friedrich-Alexander-Universität Erlangen-Nürnberg Ethics Commission.



Fig. 1. Experimental hardware setup during a Step-Up task.

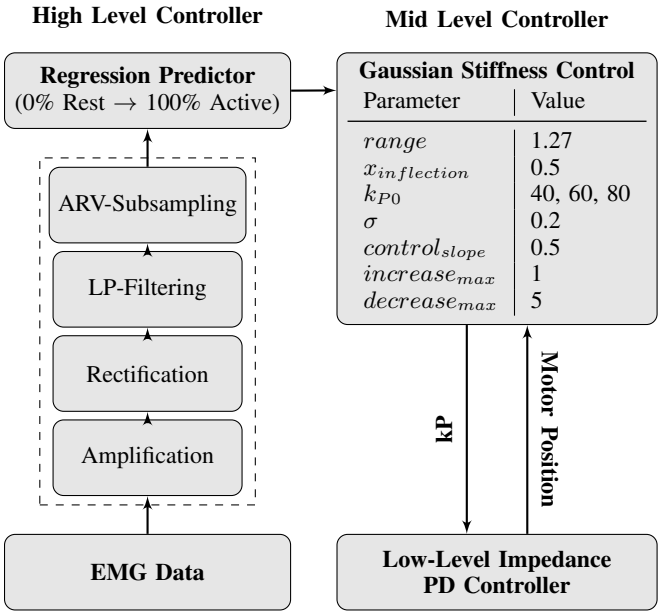


Fig. 2. Signal processing and controller flowchart.

sensors followed the SENIAM guidelines to ensure accurate and consistent signal acquisition. Sensors were positioned on four key muscles of the lower limb: the Rectus Femoris, Vastus Lateralis, Biceps Femoris, and Semitendinosus. The electrodes were aligned with the muscle fibers and placed using anatomical reference points (see Figure 1) with the limitation of occlusion by the orthosis in mind [26], [27].

B. Software-Setup

The EMG signals are sampled at 2148 Hz, amplified, rectified, and low-pass filtered at a cut-off frequency of 1 Hz. The Average Rectified Value (ARV) was down-sampled to 50 Hz and forwarded into a ridge regression algorithm to map resting and maximum voluntary contraction (MVC) of the right leg extensor muscles into a continuous high-level control signal $(0-1)$ (see Figure 2). Further, this is used as $control_{EMG}$, indicating muscle activation levels for the mid-level control.

A custom control policy was implemented to manage the impedance controller based on the EMG prediction. Figure 2 shows the control parameters for the Gaussian stiffness modulation, which aims to define an adaptive stiffness modulation policy for a motorized actuator. The weighted stiffness (k_P) is dynamically adjusted based on the actuator's position and user intent through muscle activation, while the derivative gain k_D was held constant at 0.3. The baseline stiffness $k_{P,0}$ was varied to examine the effect of different stiffness levels on user comfort and the system's range of assistive torque.

1) **Gaussian-Based Stiffness Calculation:** The stiffness profile is modeled using a Gaussian function centered at the midpoint of the motion range (μ), with $x_{inflection}$ shifting the peak stiffness forward or backward. This allows us to tune the point of maximum amplitude in the output function. σ determines the spread of the Gaussian, controlling the rate at which stiffness decreases as the motor position (θ) moves away from μ.

$$\mu = \frac{range}{2} * (1 + x_{inflection}) \tag{1}$$

$$k_P(\theta) = k_{P,0} \exp\left(-\frac{(\theta-\mu)^2}{2\sigma^2}\right) \tag{2}$$

2) **Scaling Factor:** An empirically determined scaling factor modifies the stiffness based on the motor position's relative distance to μ. $control_{slope}$ shapes how stiffness changes as the motor moves away from μ. High values cause sharper stiffness decay (or increase), providing a steeper gradient.

$$k_{P,scale} = k_P(\theta)\left(\frac{\theta}{\mu}\right)^{control_{slope}} \tag{3}$$

3) **EMG-Control Signal Influence:** The overall stiffness is linearly scaled by $control_{EMG}$. This allows the stiffness to reflect the user's muscle activation and intent proportionally.

$$k_{P,final} = k_{P,scaled} \times control_{EMG} \tag{4}$$

4) **Ramping Logic:** The algorithm limits the rate of stiffness change between consecutive calculations to ensure smooth transitions and prevent abrupt changes in stiffness.

$$\Delta k_{P,increase} = k_{P,prev} + increase_{max} \tag{5}$$

$$\Delta k_{P,decrease} = k_{P,prev} - decrease_{max} \tag{6}$$

5) **Boundary Conditions:** Finally, the stiffness values are clamped to non-negative values to maintain system stability and safety of the participants:

$$k_{P,final} = \max(0, k_{P,final}) \tag{7}$$

A Graphical User Interface (GUI) was implemented to allow participants to select between different exercise modes and to guide them through the movements. Two progress bars provide participants with information about when to begin the exercise and the appropriate speed for progressing through the movements, as well as when to take a break. This interface was designed to assist participants, promoting consistent, uniform movement across all exercises and repetitions by visually separating transitions and resting phases.

C. Study Protocol

Four healthy participants, with a 50:50 gender distribution and a mean age of 28.75 ± 3.5 years, participated in the study. Additional information about height ($177 \pm 10.2\,\mathrm{cm}$), weight ($80.2 \pm 19.8\,\mathrm{kg}$), and thigh circumference ($55.5 \pm 3.9\,\mathrm{cm}$) were collected to examine their potential influence on the study results (see Table I).

TABLE I
DEMOGRAPHIC INFORMATION OF PARTICIPANTS

	Age	**Height** (cm)	**Weight** (kg)	**Thigh Circ.** (cm)	**Femur** (m)
A	34.00	190.00	108.00	61.00	0.50
B	27.00	166.00	67.00	55.00	0.50
C	27.00	179.00	81.00	54.00	0.50
D	27.00	173.00	65.00	52.00	0.50

The orthosis is calibrated by fully extending the leg to establish the reference position (Position 0) and resting the leg with a 90-degree angle (Position 1) while seated. For each position, $3.00\,\mathrm{s}$ of EMG signal is acquired to train the Ridge Regression predictor. In the Sit-To-Stand exercise, participants sit on a standard chair with feet flat on the ground and knees at a 90-degree angle. They are instructed to stand up fully, within the timeframe given by the trajectory guidance GUI, maintain the standing position, and then sit back down in a controlled manner. This sequence constitutes one complete repetition. Each participant performs five repetitions. This is repeated with five different conditions, *No Orthosis*, *Orthosis OFF*, and *Orthosis ON* with stiffness gains of 40, 60, and 80 Nm/rad with resting phase after each repetition of the movement. Each phase is set to last 1.3 seconds. The second exercise, forward Step-Up, evaluates the activation isolated to the right leg under increased load. Participants stand next to a $30\,\mathrm{cm}$ elevated platform. They start by resting the right leg on the platform (see Figure 1). Then, they follow the same procedure as in the Sit-To-Stand, while data on muscular activity, position, velocity, and torque are collected. The metrics analyzed included the ARVs and right leg encoder kinematics.

III. RESULTS

A. ARV Analysis of Activities: Sit-to-Stand and Step-Up

Evaluation of the normalized muscle activity across every participant during the full Sit-To-Stand activity, displayed in Table II and Figure 3, suggests a significantly decreased muscle activity from the extensor muscles of the assisted leg (right) when the device is worn and increasing slightly from there with the stiffness gain. Compared to the non-assisted leg (left), the ARVs are reduced slightly ($\approx 10\%$), as well as the variance in the signal, suggesting some degree of compensation. The standard deviation of the right leg increases with the device attached.

TABLE II
SUMMARY OF THE EMG DATA (LEFT/RIGHT). IQR OUTLIER CURATION REMOVED $\approx 9\%$. THE MODE COLUMN LISTS ALL TRAIL CONDITIONS WITH NO ORTHOSIS WORN (-), ORTHOSIS OFF (IDLE), AND THE STIFFNESS GAIN VARIATIONS k_P.

	Left Leg		**Right Leg**	
Mode	**Mean ± Std**	**Median**	**Mean ± Std**	**Median**
-	1.000 ± 0.305	0.934	1.000 ± 0.438	1.158
Idle	0.932 ± 0.182	0.940	0.784 ± 0.621	0.657
$k_{P,40}$	0.899 ± 0.092	0.926	0.842 ± 0.636	0.710
$k_{P,60}$	0.906 ± 0.089	0.926	0.861 ± 0.681	0.750
$k_{P,80}$	0.909 ± 0.087	0.922	0.845 ± 0.640	0.674

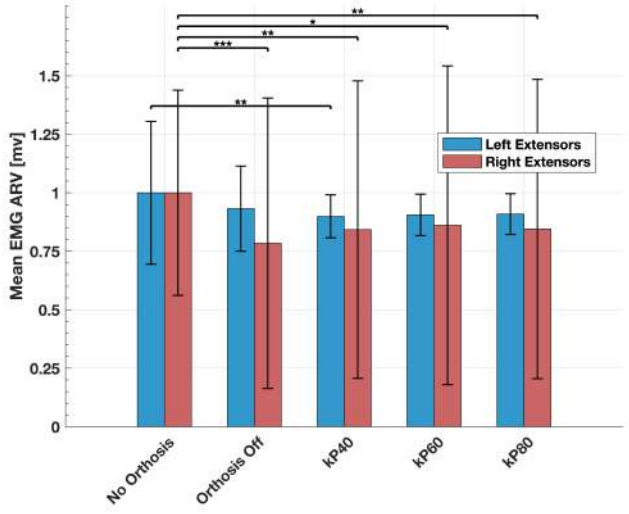


Fig. 3. Average Rectified Muscle Activity (ARV) in the non-assisted leg (left) vs. the assisted leg (right) of the knee extensor muscles during the Sit-To-Stand exercise across all participants. Whiskers indicate the standard deviation. IQR outlier curation removed $\approx 9\%$

B. Inter-Phase Assistance Comparison

The activities are segmented into the transitioning states *Sit-To-Stand* (Up-Phase: P1) and *Stand-To-Sit* (Down-Phase: P2) as illustrated in Figure 4 for the Sit-To-Stand and Step-Up activities, focusing on the most physically demanding phases. The conditions evaluated included *No Orthosis*, *Orthosis OFF*, and *Orthosis ON* with spring stiffness gains of 40, 60, and 80 $k_{P,0}$. Participants C and D had to be excluded due to significant velocity variability during testing that are especially pronounced when isolating the phases. The complete comparison can be retrieved from Table III.

All data consistently failed the Shapiro–Wilk normality test ($p < 0.05$), so nonparametric Kruskal–Wallis tests were

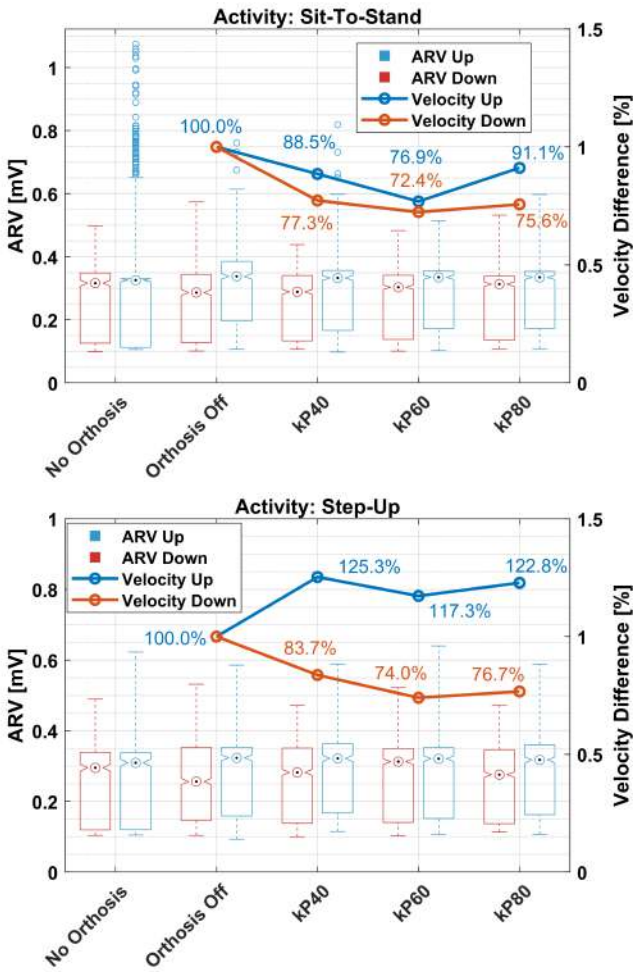


Fig. 4. Assisted leg extensor muscle ARVs of Participant A and B, with no Orthosis, Orthosis Off and Orthosis On conditions comparing the Stand-To-Sit: Down (red) and Sit-To-Stand: Up (blue) phases during Sit-To-Stand (top) and Step-Up (bottom) activities. The solid lines show the normalized mean velocities relative to Orthosis OFF.

employed. Table IV provides sample p-values for Velocity and ARVs, separately for Up-Phase (P1) and Down-Phase (P2), across both Sit-to-Stand and Step-Up activities.

1) Sit-To-Stand Activity: Figure 4 (top) and Table III compare *No Orthosis*, *Orthosis Off*, and various *Orthosis On* conditions (with stiffness gains $k_{P,40}, k_{P,60}, k_{P,80}$) for the Sit-to-Stand activity. From the velocity perspective, introducing orthosis assistance shows a trend of around a 20% decrease in mean velocity (particularly noticeable at $k_{P,60}$) compared to the Orthosis Off idle condition. In the Up-Phase (Stand-To-Sit), these velocity reductions are less consistent overall, but still hover around 9–13%. Simultaneously, ARVs in the Up-Phase tend to be higher under orthosis assistance (by up to 13% in some cases), whereas in the Down-Phase the ARVs remain comparatively lower to the baseline measurement. Statistical tests (Table IV) confirm that most velocity and ARV metrics in the Up-Phase (P1) differ significantly between the reference idle conditions (Orthosis Off) and the higher stiffness gains. Conversely, the Down-Phase (P2) often does not

TABLE III

METRICS FOR SIT-TO-STAND AND STEP-UP ACTIVITIES ACROSS DIFFERENT STIFFNESS GAINS, SEGMENTED BY UP-PHASE P1 (SITTOSTAND / ASCENDING) AND DOWN-PHASE P2 (STANDTOSIT / DESCENDING).

	Sit-to-Stand				Step-Up			
	Velocity		ARV		Velocity		ARV	
Mode	**P1**	**P2**	**P1**	**P2**	**P1**	**P2**	**P1**	**P2**
-	-	-	0.326	0.316	-	-	0.309	0.295
Idle	1.00	1.00	0.338	0.286	1.00	1.00	0.323	0.256
$k_{P,40}$	0.885	0.773	0.333	0.289	1.253	0.837	0.322	0.282
$k_{P,60}$	0.769	0.724	0.335	0.303	1.173	0.740	0.321	0.313
$k_{P,80}$	0.911	0.756	0.335	0.313	1.228	0.767	0.317	0.276

TABLE IV

SIGNIFICANCE ANALYSIS (P-VALUES) FOR SIT-TO-STAND AND STEP-UP ACROSS DIFFERENT STIFFNESS GAINS BY SIT-TO-STAND UP-PHASE (P1) AND STAND-TO-SIT DOWN-PHASE (P2). SHOWN ARE GLOBAL VALUES FOR VELOCITY AND ARV.

	Sit-to-Stand				Step-Up			
	Velocity		ARV		Velocity		ARV	
Mode	**P1**	**P2**	**P1**	**P2**	**P1**	**P2**	**P1**	**P2**
k_{P40}	0.0053	0.0029	$< 10^{-10}$	0.11	0.656	0.025	$< 10^{-6}$	$< 10^{-6}$
k_{P60}	0.0120	0.0042	$< 10^{-8}$	0.10	0.6556	0.0696	0.0005	0.0000
k_{P80}	0.05	0.01	$< 10^{-5}$	0.12	1.000	0.40	0.0000	0.0000

reach significance in ARVs, implying that the leg-muscle activation during the descent is less affected by these stiffness variations.

2) Step-Up Activity: Figure 4 (bottom) and Table III illustrate the Step-Up movement under the same orthosis conditions. Here, ARV medians across the Up-Phases remain close, yet higher than the baseline with no orthosis, with only subtle differences among the stiffness gains. In contrast, the Down-Phase shows overall lower ARVs during assistance. While the ARVs do generally increase somewhat under assistance, pairwise statistical tests still show significant contrasts between the references and certain stiffness levels. For velocity, the Up-Phase increases under orthosis assistance (by up to 25%), whereas the Down-Phase velocity decreases by up to 26%. According to Table IV, these Down-Phase velocity changes are often significant, while the Up-Phase velocity differences do not consistently reach significance. Thus, the orthosis stiffness exerts a more evident effect on the descending movement than on the ascent during the Step-Up task.

IV. DISCUSSION

A. Assessment of Data Quality

Initial observations indicate that the motorized knee orthosis effectively reduces muscle activity (see Figure 3); nevertheless, a closer inspection of the ARV distributions

(see Figure 4) suggests that, in certain conditions, the device may interfere with normal muscle activation, paradoxically increasing overall ARV. Several factors likely contribute to this outcome. First, the adhesive-based Trigno® Avanti EMG sensors frequently detached when the skin was stretched near rigid orthosis contact points, necessitating repeated trials. Second, unintended device contact introduced noise, especially if the orthosis slipped on participants with smaller leg circumferences (see Table I). These challenges underscore the inherent limitations of EMG in mechanically demanding setups rather than an issue specific to our study. Future real-world applications should explore gel electrodes, alternative sensor placements, or complementary sensing technologies to mitigate these artifacts.

B. Assessment of the Study Design

Beyond data quality, the overall study design was largely exploratory, aiming to dynamically adjust joint stiffness for high-demand tasks without rigid state machines. This approach inherently involves a learning component, as users may gain finer control with repeated exposure. Nevertheless, EMG signals are still prone to noise, especially under external pressure, suggesting that multi-pronged control strategies could yield more robust performance in future studies. To isolate user adaptation effects, it may be worthwhile to hold assistance levels constant across trials or gradually increase them over weeks based on each participant's MVC. Moreover, participant weight differences highlight the importance of hardware sizing: heavier users require stronger actuation, whereas lighter individuals could be overburdened by excessive hardware bulk. Finally, although Sit-to-Stand is already a strenuous task, Step-Up may be too challenging for clinical populations. Future experiments might prioritize more straightforward activities like walking and shifting the focus to gait parameters rather than EMG reduction alone.

C. Efficiency of Motorized Assistance

The motor hardware provides up to $18\,\mathrm{Nm}$ of sustained, controller-enforced torque, which translates into roughly 37% offloading for an average-weight participant (assuming $0.6\,\mathrm{Nm/kg}$ for Sit-To-Stand. Although this is a noticeable contribution, it remains relatively modest for high-demand movements. The device's $1.57\,\mathrm{rad}$ range of motion means that the chosen stiffness gains ($k_{P,0} = 40, 60, 80$) primarily shape the slope of assistance rather than pushing the upper torque limit. As such, the orthosis offers measurable torque augmentation but does not fully compensate for the user's total effort during Sit-to-Stand. These parameters reflect a design philosophy favoring simplicity, low cost, and minimal weight. Future designs requiring more substantial support for heavier or more impaired users may need significantly higher torque capacity, potentially at the cost of increased mass or complexity. In its current iteration, the system is thus best suited for torque augmentation rather than complete torque compensation.

D. Stable vs. Unstable Activities

Building on our ARV findings, we compared Sit-to-Stand and Step-Up tasks to see how activity stability affects motion execution. For healthy participants, Sit-to-Stand generally offers bilateral support and load-sharing, making it relatively stable, whereas Step-Up is inherently more unstable due to unilateral load and higher balancing demands. Additionally, the Up-Phase of each activity relies heavily on knee and hip extensors to overcome gravity, while the Down-Phase requires deliberate braking to ensure accuracy and prevent abrupt descent.

In the stable Sit-to-Stand, participants did not appear to leverage the orthosis's additional power effectively, only showing significant ARV reduction during descent (see Table IV). Overall, the movement velocity was reduced significantly in both phases, contributing to the picture of slow and controlled movement. By contrast, the unstable Step-Up saw a clearer response to the device: the extra power in the Up-Phase led to higher velocities, whereas the Down-Phase velocity was significantly slowed or dampened. This suggests that impedance modulation may offer the greatest benefits in tasks where dynamic adjustments are crucial, and a strategy combining higher stiffness during ascent with additional damping during descent could be promising.

It is worth noting that all participants here were able-bodied and performed the movements with relative ease. Individuals with mobility impairments may not exhibit the same adaptive strategies or might struggle to complete a Step-Up at all, underscoring the need to tailor tasks and parameters for clinical populations.

Moreover, our velocity metrics in the Step-Up activity showed lower statistical significance than accomplished by the ARV measure (see Table IV), indicating that orthosis stiffness had a limited effect on gross movement speed. The dominant influences of gravity and high load appear to overshadow any velocity changes the orthosis can augment. While the device effectively modulates the force response for stability and control, its ability to substantially alter velocity remains constrained in unilateral, high-demand scenarios.

E. Implications for Rehabilitation Robotics

The results from both stable and unstable tasks demonstrate the motorized knee orthosis's potential to reduce muscular effort, especially in activities that demand precise, real-time control. However, differences in users' muscle strength, body weight, and movement strategies underscore the importance of tailored parameter tuning to maintain both efficiency and comfort. By carefully calibrating stiffness and damping thresholds in response to each individual's biomechanics, the system can better accommodate the unique demands of different bodies and tasks.

Looking ahead, efforts should focus on refining adaptive assistance that updates in real-time based on EMG or kinematic signals, thereby minimizing variability and aligning torque output with the requirements of specific movement phases. Designing control architectures that learn from changing user inputs over longer periods can also refine

stiffness modulation, promising more effective support in rehabilitation programs. At the same time, it will be critical to widen the participant pool, especially to older adults or individuals with severe motor impairments, to confirm the suitability of these technologies in broader clinical contexts. As sensor attachment and device stability remain central challenges, future prototypes must incorporate improved electrodes or supplementary sensing modalities to ensure that movement artifacts do not undermine performance or comfort in day-to-day tasks. By integrating these improvements, next-generation knee orthosis systems could offer robust, user-specific assistance and help a wider range of patients perform challenging tasks with greater safety and independence.

V. Conclusion

Our pilot results suggest that EMG-driven impedance control can reduce muscle effort and enhance movement efficiency, especially under high-load conditions. However, further testing and improved hardware are necessary to validate these benefits for a wider population.

ACKNOWLEDGMENT

This work was (partially) supported by the German Federal Ministry of Education and Research (BMBF) under the Robotics Institute Germany (RIG).

Special acknowledgment goes to OT Baßler GmbH Erlangen for supporting this research with expert knowledge and orthopedic equipment.

References

[1] J.-H. Kim, M. Shim, D. H. Ahn, B. J. Son, S.-Y. Kim, D. Y. Kim, Y. S. Baek, and B.-K. Cho, "Design of a Knee Exoskeleton Using Foot Pressure and Knee Torque Sensors," *International Journal of Advanced Robotic Systems*, vol. 12, no. 8, p. 112, Aug. 2015.

[2] G. Choi, D. Lee, I. Kang, and A. J. Young, "Effect of Assistance Timing in Knee Extensor Muscle Activation During Sit-to-Stand Using a Bilateral Robotic Knee Exoskeleton," *Annual International Conference of the IEEE Engineering in Medicine and Biology Society. IEEE Engineering in Medicine and Biology Society. Annual International Conference*, vol. 2021, pp. 4879–4882, Nov. 2021.

[3] H. A. Dereshgi, H. Dal, D. Demir, and N. F. Türe, "Orthoses: A systematic review," *Journal of Smart Systems Research*, vol. 2, no. 2, pp. 135–149, 2021.

[4] G. S. Balkman, B. J. Hafner, R. E. Rosen, and S. J. Morgan, "Mobility experiences of adult lower limb orthosis users: a focus group study," *Disability and rehabilitation*, vol. 44, no. 25, pp. 7904–7915, 2022.

[5] A. B. Sánchez, A. B. Ortega, E. M. Rayón, F. A. G. Becerra, A. A. Pliego, R. C. Amezcua, and C. H. G. Valdivia, "State of the art review of active and passive knee orthoses," *Machines*, vol. 10, no. 10, p. 865, Sep. 2022. [Online]. Available: https://www.mdpi.com/2075-1702/10/10/865

[6] H. Huang, J. Chen, and C. Huang, "Toward the gait analysis and control of a powered lower limb orthosis in ascending and descending stairs," *Procedia Engineering*, vol. 79, pp. 417–426, 2014.

[7] M. Mohaddis, S. A. Maqsood, E. Ago, S. Singh, Z. Naim, and S. Prasad, "Enhancing functional rehabilitation through orthotic interventions for foot and ankle conditions: A narrative review," *Cureus*, vol. 15, no. 11, p. e49103, Nov. 2023.

[8] A. C. D. M. de Brito, P. Kutilek, J. Hejda, P. Smrcka, and V. Havlas, "Design of smart orthosis of upper limb for rehabilitation," in *World Congress on Medical Physics and Biomedical Engineering 2018*, L. Lhotska, L. Sukupova, I. Lacković, and G. S. Ibbott, Eds. Springer Singapore, 2019, pp. 773–778.

[9] Z. Zhang, J. Fan, H. Jin, T. Zheng, S. Zhao, S. Ma, J. Zhao, and Y. Zhu, "Active knee joint exoskeleton for stair ascent augmentation," *Science China Information Sciences*, vol. 64, no. 3, p. 139204, Mar. 2021.

[10] M. K. Shepherd and E. J. Rouse, "Design and Validation of a Torque-Controllable Knee Exoskeleton for Sit-to-Stand Assistance," *IEEE/ASME Transactions on Mechatronics*, vol. 22, no. 4, pp. 1695–1704, Aug. 2017.

[11] S. V. Sarkisian, M. K. Ishmael, G. R. Hunt, and T. Lenzi, "Design, Development, and Validation of a Self-Aligning Mechanism for High-Torque Powered Knee Exoskeletons," *IEEE Transactions on Medical Robotics and Bionics*, vol. 2, no. 2, pp. 248–259, May 2020.

[12] F. Sibella, M. Galli, M. Romei, A. Montesano, and M. Crivellini, "Biomechanical analysis of sit-to-stand movement in normal and obese subjects," *Clinical Biomechanics*, vol. 18, no. 8, pp. 745–750, Oct. 2003.

[13] T. Kotake, N. Dohi, T. Kajiwara, N. Sumi, Y. Koyama, and T. Miura, "An analysis of sit-to-stand movements," *Archives of Physical Medicine and Rehabilitation*, vol. 74, no. 10, pp. 1095–1099, Oct. 1993.

[14] W. Huo, H. Moon, M. A. Alouane, V. Bonnet, J. Huang, Y. Amirat, R. Vaidyanathan, and S. Mohammed, "Impedance Modulation Control of a Lower-Limb Exoskeleton to Assist Sit-to-Stand Movements," *IEEE Transactions on Robotics*, vol. 38, no. 2, pp. 1230–1249, Apr. 2022.

[15] L. Liu, M. Luken, S. Leonhardt, and B. J. E. Misgeld, "Emg-driven model-based knee torque estimation on a variable impedance actuator orthosis," in *2017 IEEE International Conference on Cyborg and Bionic Systems (CBS)*, 2017, pp. 262–267.

[16] A. C. Villa-Parra, D. Delisle-Rodriguez, J. Souza Lima, A. Frizera-Neto, and T. Bastos, "Knee Impedance Modulation to Control an Active Orthosis Using Insole Sensors," *Sensors (Basel, Switzerland)*, vol. 17, no. 12, p. 2751, Nov. 2017.

[17] N. Karavas, A. Ajoudani, N. Tsagarakis, J. Saglia, A. Bicchi, and D. Caldwell, "Tele-impedance based assistive control for a compliant knee exoskeleton," *Robotics and Autonomous Systems*, vol. 73, pp. 78–90, Nov. 2015.

[18] C. Fleischer, C. Reinicke, and G. Hommel, "Predicting the intended motion with emg signals for an exoskeleton orthosis controller," in *2005 IEEE/RSJ International Conference on Intelligent Robots and Systems*, 2005, pp. 2029–2034.

[19] A. K. Mishra, A. Srivastava, R. P. Tewari, and R. Mathur, "Emg analysis of lower limb muscles for developing robotic exoskeleton orthotic device," *Procedia Engineering*, vol. 41, pp. 32–36, 2012.

[20] S. V. Sarkisian, A. J. Gunnell, K. Bo Foreman, and T. Lenzi, "Knee Exoskeleton Reduces Muscle Effort and Improves Balance During Sit-to-Stand Transitions After Stroke: A Case Study," in *2022 International Conference on Rehabilitation Robotics (ICORR)*, Jul. 2022, pp. 1–6.

[21] R. Momosaki, M. Abo, S. Watanabe, W. Kakuda, N. Yamada, and S. Kinoshita, "Effects of ankle-foot orthoses on functional recovery after stroke: a propensity score analysis based on japan rehabilitation database," *PLoS One*, vol. 10, no. 4, p. e0122688, Apr. 2015.

[22] Sporlastic. GENUDYN® CI STEP THRU. [Online]. Available: https://www.sporlastic.de/produkt/artikel/genudyn-ci-step-thru/

[23] CubeMars. AK80-9. [Online]. Available: https://www.cubemars.com/goods-982-AK80-9.html

[24] MABRobotics. MD80 v2.1 motor controller. [Online]. Available: https://www.mabrobotics.pl/product-page/md80-V20-motor-controller

[25] M.-A. Scheidl, İ. B. Akarsu, F. Mehrkens, K. Schuh, and C. Castellini, "The AIROB-active-knee-orthosis," Dec. 2024. [Online]. Available: https://doi.org/10.5281/zenodo.14286202

[26] H. J. Hermens, B. Freriks, C. Disselhorst-Klug, and G. Rau, "Development of recommendations for SEMG sensors and sensor placement procedures," *Journal of Electromyography and Kinesiology*, vol. 10, no. 5, pp. 361–374, Oct. 2000.

[27] M. Barbero, R. Merletti, and A. Rainoldi, *Atlas of Muscle Innervation Zones*. Milano: Springer Milan, 2012.

A Passive Mechanical Add-on for Treadmill Exercise (P-MATE) in Stroke Rehabilitation

Irene L. Y. Beck[1, 2,*], Belle C. Hopmans[1, 3], Bram Haanen[1], Levi Kieft[1], Heike Vallery[2, 3, 4], Laura Marchal-Crespo[1, 2], and Katherine L. Poggensee[1, 2, 3]

***Abstract*— Robotic rehabilitation can deliver high-dose gait therapy and improve motor function after a stroke. However, for many devices, high costs and lengthy setup times limit clinical adoption. Thus, we designed, built, and evaluated the Passive Mechanical Add-on for Treadmill Exercise (P-MATE), a low-cost passive end-effector add-on for treadmills that couples the movement of the paretic and non-paretic legs via a reciprocating system of elastic cables and pulleys. Two human-device mechanical interfaces were designed to attach the elastic cables to the user. The P-MATE and two interface prototypes were tested with a physical therapist and eight unimpaired participants. Biomechanical data, including kinematics and interaction forces, were collected alongside standardized questionnaires to assess usability and user experience. Both interfaces were quick and easy to attach, though user experience differed, highlighting the need for personalization. We also identified areas for future improvement, including pretension adjustments, tendon derailing prevention, and understanding long-term impacts on user gait. Our preliminary findings underline the potential of the P-MATE to provide effective, accessible, and sustainable stroke gait rehabilitation.**

I. Introduction

Stroke is one of the leading causes of disability worldwide, affecting twelve million people annually [1]. Up to 75 % of people who have had a stroke are left with lower-limb somatosensory and motor impairments three months post-stroke [2]. Individuals with more severe impairments experience a greater negative impact on their quality of life and participation in everyday activities [2].

High-dose physical therapy can enhance motor recovery following a stroke [3]. However, individuals often receive less therapy than recommended due to, among other factors, a shortage of trained personnel [4]. Conventional gait interventions—where therapists physically assist or resist an individual's limb movements—often require more than one therapist per patient [2]. Work-related injuries can result from the physical demands placed on therapists [5]. These shortcomings in current lower-limb rehabilitation practices are expected to worsen with an aging population and global physician shortage [6].

This work was supported by the Health and Technology Convergence Alliance of TU Delft, Erasmus MC, and Erasmus University Rotterdam and the H2020-MSCA-RISE project CoSP- GA No 101106071 and Hocoma provided the Lokomat.

[1]Dept. of Cognitive Robotics, TU Delft, Delft, Netherlands.
[2]Dept. of Rehabilitation Medicine, Erasmus MC, Rotterdam, Netherlands.
[3]Dept. of Biomechanical Engineering, TU Delft, Delft, Netherlands.
[4]Institute of Automatic Control, RWTH Aachen University, Aachen, Germany.
Corresponding author: I.L.Y.Beck@tudelft.nl

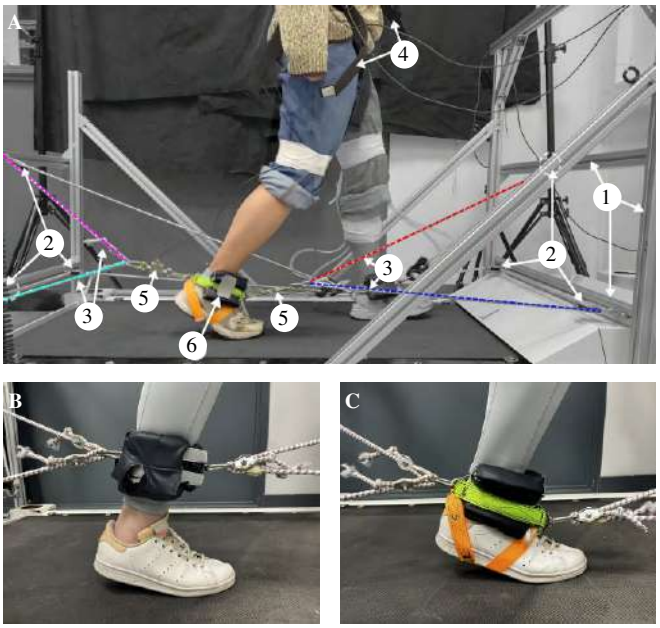


Fig. 1: The mechanical design of the P-MATE. **A**: An overview of all parts of the system with the 1) frame, 2) six pulleys, 3) two anterior and two posterior elastic tendons, 4) safety harness, 5) anterior and posterior load sensors, and 6) human-device interface. The two prototypes of the interface are highlighted in **B**: the cuff around the shank and **C**: the bandage around the foot.

Robotic rehabilitation provides a promising solution to these challenges by delivering high-intensity therapy while reducing physical demands on therapists. Several robotic devices have already been developed to support gait rehabilitation, offering controlled, high-intensity training as a way to lower therapists' workload while objectively tracking patient progress [7], [8]. However, factors such as set-up time and cost hinder the introduction and adoption of robotics into the clinic, calling for more affordable and simpler devices [5]. Despite advances in the design of lightweight exoskeletons [9], these current robotic solutions can limit the active participation of patients, which is crucial to enhance neurorehabilitation [7], [10].

Tendon-based devices also show promise in providing effective resistance and assistance for gait rehabilitation [5], [11], [12], although how to best route the cables without impeding the unimpaired leg's range of motion is still an open question. One option is to attach a single tendon to the

impaired leg, which tensions a spring in a controlled way during the stance phase of the impaired leg and subsequently releases the stored energy during swing [13]. However, the mechanism still requires an active brake, electronics, and control to compensate for the movement of the impaired leg during stance and to avoid tensioning of the spring during the entire stance phase.

We aimed to address the aforementioned challenges by designing and evaluating a purely mechanical solution that exploits the reciprocating movement of both legs to assist in the gait rehabilitation of the paretic leg. This is done by attaching both legs to elastic tendons, guided by a set of pulleys optimally located around a treadmill to leverage the movement of the non-paretic leg and the treadmill. This low-cost system could be implemented on existing treadmills, does not require any actuators or control, and allows for the individual's active participation.

II. Design

A. System Overview

We developed the Passive Mechanical Add-on for Treadmill Exercise (P-MATE) for use in stroke gait rehabilitation. The P-MATE was designed to provide support during treadmill walking, particularly for individuals with hemiparesis, a condition that affects gait symmetry by impairing one side of the body. The add-on combines four elastic tendons attached to both legs and guided by pulleys. The pulleys are optimally located around a treadmill to assist the paretic leg as needed during the swing phase while the non-paretic leg is moved backward by the treadmill during stance, but without impeding physiological leg motion. A schematic overview of the P-MATE's working principle is presented in Fig. 1A.

Two human-device interfaces were designed to attach the elastic tendons to different points on the user: one at the shank (*cuff prototype*) and the other at the foot (*bandage prototype*), see Figs. 1B and 1C, respectively. The entire system was designed and evaluated via two datasets, both of which were approved by the Human Research Ethics Committee of TU Delft, and all participants provided written informed consent prior to the start of the study.

B. Pulley Location Optimization

The goal of the P-MATE was to assist the paretic foot's movement in the three translational degrees of freedom, with coordinate directions forward (x), lateral (y), and upward (z) (Fig. 2). Therefore, at least four elastic tendons are required due to the underconstrained behavior of tendons (i.e., only pulling) [14]. Furthermore, to promote gait symmetry, the pulley and tendon arrangement is symmetrical across the sagittal plane.

The P-MATE was designed to avoid interfering with unimpaired gait, i.e., in the case of natural walking, no resistive nor assistive forces should be transmitted to the participant. To achieve this, a simulation-based optimization was run to determine the optimal pulley locations that minimize the "parasitic" forces, i.e., any forces (in all directions) acting on the legs during "normal gait" for six participants. The optimization used a cost function that minimized the sum of the root mean square of each of the Cartesian forces (in x-, y- and z-directions) acting on the left and right legs over time. At each frame (collected at $100\,\mathrm{Hz}$), the Cartesian forces were derived from the "parasitic" tendon forces, which were computed using a Jacobian based on the location of the legs and the pulleys.

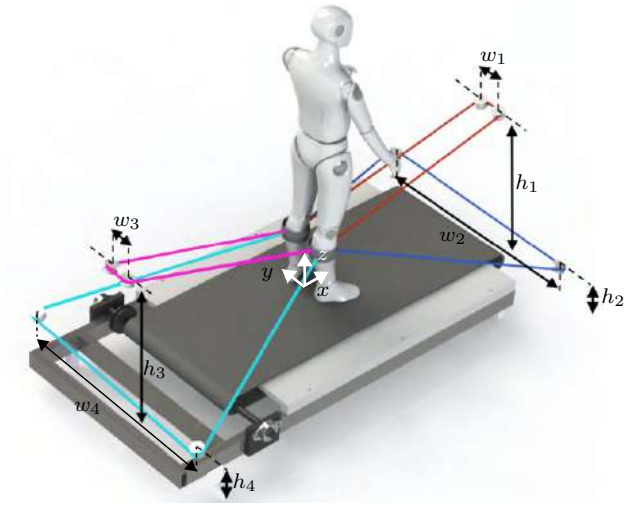


Fig. 2: The optimization setup with the eight parameters to determine optimal pulley location.

These "parasitic" tendon forces originate from the elongation of the elastic tendons during unimpaired walking. Based on preliminary research of commercially-available elastic ropes, we chose to set all tendons to the same stiffness of $300\,\mathrm{N/m}$. The slack length, or the length at zero-force, of each tendon was chosen as the shortest tendon length observed per participant.

The optimization parameters describe the locations of eight pulleys around the treadmill, two pulleys per each of the four tendons, while a simulated human was placed in the center of the treadmill. The pulley locations were assumed constant in the x-direction at $0.75\,\mathrm{m}$ in front of and behind the individual, based on conventional treadmill length. Additionally, the location of each pair of pulleys was assumed to be the same height. These assumptions reduce the optimization parameters to only the distances between the pulleys per pair in y-direction (w_j) and their heights (h_j) (see Fig. 2), resulting in four widths and four heights. The search space of the parameters was constrained to $w_{1,3} \in [0, 0.1]$, $w_{2,4} \in [0.4, 0.8]$, $h_{1,3} \in [0.5, 1.0]$, and $h_{2,4} \in [0.1, 0.3]\,\mathrm{m}$. Initial conditions were set to the average of each constraint bound. The optimization of the pulleys was executed for lower-body optical motion capture data collected from six unimpaired young adults walking on a treadmill at $1.0\,\mathrm{m/s}$ (see Table I). We used the genetic algorithm function (`ga`) from the Optimization Toolbox in MATLAB (R2023b, Mathworks, USA). The optimization stopped after 100 generations or when the average relative change in the cost function was smaller than $1 \times 10^{\circledast 6}\,\mathrm{N}$.

TABLE I: Demographic information for pulley location optimization training dataset.

ID	**Sex**	**Age/**yr	**Height/**m	**Mass/**kg
A	F	30	1.55	51.0
B	M	26	1.73	63.7
C	M	25	1.76	63.6
D	F	23	1.71	56.2
E	M	30	1.87	72.5
F	M	30	1.81	71.0

TABLE II: The optimal pulley locations for each participant from the simulation-based optimization and the final implemented values (Imp) in the mechanical design. All measurements are in meters.

ID	w_1	h_1	w_2	h_2	w_3	h_3	w_4	h_4
A	0.00	0.50	0.40	0.10	0.00	0.74	0.56	0.10
B	0.00	0.50	0.40	0.10	0.00	0.76	0.40	0.10
C	0.00	0.57	0.80	0.10	0.00	0.69	0.80	0.10
D	0.00	0.50	0.74	0.10	0.00	0.62	0.40	0.10
E	0.00	0.56	0.40	0.10	0.00	0.78	0.80	0.10
F	0.00	0.56	0.40	0.10	0.00	0.79	0.55	0.10
Imp	0.00	0.50	0.80	0.13	0.00	0.50	0.80	0.13

The main contributors to the cost function were the forces in x-direction, with median anterior and posterior forces of $28.4\,\mathrm{N}$ and $34.0\,\mathrm{N}$, respectively. The optimal pulley location parameters per participant are shown in Table II. The optimal solution for both w_1 and w_3, i.e., the width between the two sets of upper pulleys, was $0.00\,\mathrm{m}$ for all participants, reducing the overall system from eight to six pulleys.

C. Mechanical Design

1) Frame: A frame was built to fit around a modified Lokomat (Hocoma AG, Switzerland) treadmill to realize the P-MATE based on the optimization results. The frame consists of extruded aluminum Profile 8 40x40 profiles (item, Germany) of various lengths anchored to the treadmill frame. The total dimensions of the P-MATE were $1.8\,\mathrm{m}$ long by $1.0\,\mathrm{m}$ wide by $1.2\,\mathrm{m}$ high.

2) Pulleys: Based on the optimal solutions found in the simulation, six pulleys were used (diameter $50\,\mathrm{mm}$, groove $6\,\mathrm{mm}$) (105140, Waelbers, Netherlands). Three pulleys were attached to the front part of the frame, and three pulleys to the back, with one higher pulley in the middle and with two pulleys just above treadmill height on either side of the participant. The implemented pulley locations (Imp in Table II) were kept as close to the optimal solution, subject to the setup constraints. This included a slight increase in the height of the lower lateral pulleys and lowering of the upper back pulley, while the x-position of all pulleys was increased to $\pm 0.9\,\mathrm{m}$. The final layout of the pulleys was symmetrical in the sagittal and coronal planes.

3) Elastic tendons: The elastic tendons are commercially available with a diameter of $8\,\mathrm{mm}$ (5411387036028, Ledent, Corbeo NV, Belgium), chosen in an effort to match the assumptions from the simulation. Four stainless steel carabiners (432712, Seilflechter, Germany) connected the elastic tendons to the human-device interface. The slack length of the elastic tendons can be adjusted via a rope tightener for each elastic tendon (CAMJAM™ XT™, Nite Ize, USA).

4) Safety harness: The harness of the Lokomat's body weight support (BWS) system was used to ensure safety against falls with enough slack to allow for free movement. However, any safety harness or BWS system could be used in combination with the P-MATE.

5) Human-device interface: The P-MATE requires a human-device interface to effectively transfer the elastic tendons' forces to the user while promoting comfort, ease of use, and adjustability. To identify user requirements for the interface, observations of training sessions and interviews with a neurorehabilitation physical therapist ($27\,\mathrm{years}$ experience) were conducted at a stroke rehabilitation center (Rijndam Revalidatie, the Netherlands). These activities indicated a need for a quick and easy setup for rehabilitation devices to maximize the therapy time. This included not only a maximum of five minutes for the donning and doffing of the system on the patient but also reduced complexity compared to existing robotic exoskeletons. Additionally, the system should accommodate patients typically seen in the clinic, ranging in demographics and severity of disease. We therefore designed two prototypes, namely a *cuff* and a *bandage* design. The cuff prototype encloses the shank via an aluminum C-shaped profile around the back of the shank and a rectangular aluminum plate at the front (Fig. 1B). The aluminum is covered by a layer of cold foam padding with an exterior layer of synthetic leather to allow for a comfortable but close-fitting attachment to the participant's leg. The bandage prototype (see Fig. 1C) consists of two straps, one around the ankle and one in a figure-eight pattern wrapping around the sole of the foot. To mitigate shearing between the strap and the ankle, cold foam padding covered in synthetic leather was added.

The amount of Velcro used to secure both prototypes to the participant was chosen to withstand the worst-case scenario, i.e., where the participant was at the limits of the treadmill and the pulling forces were the highest. To facilitate donning and doffing, stainless steel buckles at the front and back of the interfaces secured the elastic tendons using carabiners.

III. Experiment

A. Experimental Protocol

We conducted a feasibility study with eight adults without physical impairments (see Table III) to evaluate the P-MATE and the two interface prototypes. Each participant received a demonstration from the experimenter on how to don and doff the two prototypes while sitting comfortably in a chair. They were then invited to walk on the treadmill and select their comfortable walking speed and pretension. They were then asked to walk at their selected speed for five minutes while wearing the safety harness but without any prototype (baseline). Following the five-minute baseline, participants took a minimum five-minute rest while seated, during which

the experimenter attached one of the prototypes to the participant.

Participants then walked for $20\,\mathrm{minutes}$ at their chosen speed with each prototype, in a randomized order. After each session, participants completed three questionnaires to evaluate the prototype's design while resting for at least five minutes. During this break, the experimenter doffed the first prototype and donned the second, timing each transition.

After both walking sessions, participants practiced donning and doffing each prototype independently. The experimenter timed these actions, and participants completed the final section of the questionnaires.

The neurorehabilitation physical therapist, who helped identify user requirements, also participated in a shortened experimental protocol. Baseline walking measurements were taken for one minute, followed by ten-minute walking sessions with each prototype. At the therapist's request, a second ten-minute session with the bandage prototype was conducted with lengthened anterior elastic tendons.

B. Outcome Metrics

During the baseline and the two walking sessions, biomechanical data regarding the right leg were collected. In particular, forces at the front and back of the leg were recorded with two load sensors (KD40S 1000N, ME-Meßsysteme, Germany). One load sensor was positioned between the two anterior tendons and the human-device interface on the front of the right leg, and the other between the two posterior elastic tendons and the same interface on the right leg.

To evaluate whether the P-MATE changed the participants' gait, a depth camera (ZED mini Stereo Camera, StereoLabs, USA) with the onboard software detecting anatomical landmarks was used to capture the kinematics of the right leg in the sagittal plane. Step length and step height were extracted from this kinematic data and averaged over the trial. The force and kinematic data were synchronized offline. Additionally, the first and last minute of the sessions were disregarded as warm-up and cool-down periods, so early and late periods were defined as minute 2 and 19, respectively.

To evaluate setup time, the experimenter timed every donning and doffing action, either performed by the experimenter themselves or the participant. Data on participants' user experience and acceptance of the prototypes, and system usability were collected using three questionnaires: the Van Der Laan Acceptance Questionnaire [15] (AQ), the System Usability Scale (SUS) [16], and a modified version of the User Experience Questionnaire (UEQ) [17], respectively. The questions in the UEQ were modified to target the experience with the P-MATE. The AQ and UEQ were answered on a Likert scale from -2 to +2, with -2 indicating a negative response (e.g., "useless") and +2 a positive response (e.g., "useful"). The SUS was answered on a Likert scale from 1 to 5: 1 indicating "Strongly disagree" and 5 "Strongly agree," resulting in an overall score between 0 and 100. Each questionnaire was filled out for both interface prototypes. The experimenter also wrote down any comments made by the participants during the study.

TABLE III: Demographic data of experiment participants and their chosen treadmill walking speed. T: Therapist

ID	**Sex**	**Age/**yr	**Height/**m	**Mass/**kg	**Speed/**$\mathrm{km/h}$
1	F	63	1.60	79	3.0
2	F	23	1.65	70	3.0
3	M	26	1.85	72	2.5
4	M	61	1.73	79	3.5
5	M	22	1.86	94	3.5
6	M	24	1.91	86	3.5
7	F	24	1.67	70	3.0
8	F	60	1.63	71	2.5
T	M	49	1.81	73	3.0

C. Experimental Results

For both prototypes, the highest anterior tendon forces occurred at toe off (determined as the instance the foot was farthest back), while the highest posterior tendon forces were recorded near heel strike (conversely the instance the foot was farthest forward). In the cuff prototype, the highest average peak anterior and posterior forces across all participants were $118\,\mathrm{N}$ and $110\,\mathrm{N}$, respectively. For the bandage prototype, these forces reached $141\,\mathrm{N}$ and $114\,\mathrm{N}$, respectively.

All participants showed larger differences between the maximum and minimum forces with the bandage prototype compared to the cuff prototype. Over time, comparing early and late in the session, the cuff prototype visually appeared to exert consistent forces at the front and back of the leg, whereas the forces from the bandage prototype started higher and tended to decrease as time passed.

Preliminary kinematic analysis indicated a reduced step length for both prototypes: the median of the average was $0.58\,\mathrm{m}$ at baseline, compared to $0.53\,\mathrm{m}$ with the cuff and $0.53\,\mathrm{m}$ with the bandage. Step height also changed with the system: the median of the average at baseline was $0.16\,\mathrm{m}$, compared to the cuff at $0.15\,\mathrm{m}$ and the bandage at $0.10\,\mathrm{m}$.

Donning and doffing for both prototypes took under five minutes. Experimenter donning times improved with practice: cuff prototype times decreased from $135\,\mathrm{s}$ to $74\,\mathrm{s}$, and bandage times from $235\,\mathrm{s}$ to $127\,\mathrm{s}$ (Fig. 3A). Doffing times remained consistent between $30\,\mathrm{s}$ to $40\,\mathrm{s}$. Participants averaged $87\,\mathrm{s}$ to don the cuff and $217\,\mathrm{s}$ for the bandage (Fig. 3B), with doffing averaging $30\,\mathrm{s}$ for the cuff and $41\,\mathrm{s}$ for the bandage (Fig. 3C).

The questionnaire results are presented in Fig. 4. Both prototypes received generally positive feedback on user experience (UEQ), with median scores of 0.8 for the cuff and 0.6 for the bandage prototype, indicating a more favorable user experience with the cuff. Based on the responses on usability (SUS), the cuff prototype was rated as highly usable, scoring 85 out of 100, while the bandage prototype scored lower at 62.5 out of 100. Similar to the other questionnaires, both prototypes generally received positive ratings on both usefulness and satisfaction ($\mathrm{AQ_U}$ and

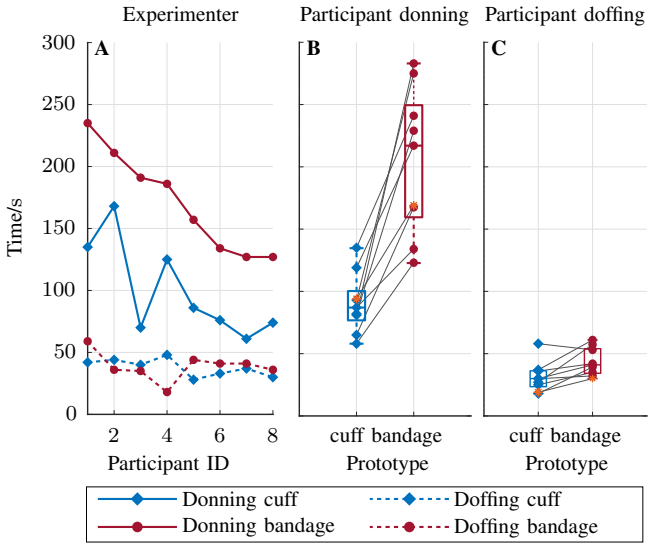


Fig. 3: Donning and doffing time of both prototypes. **A**: Donning (solid) and doffing (dashed) by the experimenter over time for the cuff (blue diamond) and bandage (red circle) prototype. Donning (**B**) and doffing (**C**) of the two prototypes by the participants and therapist (orange star) are also shown.

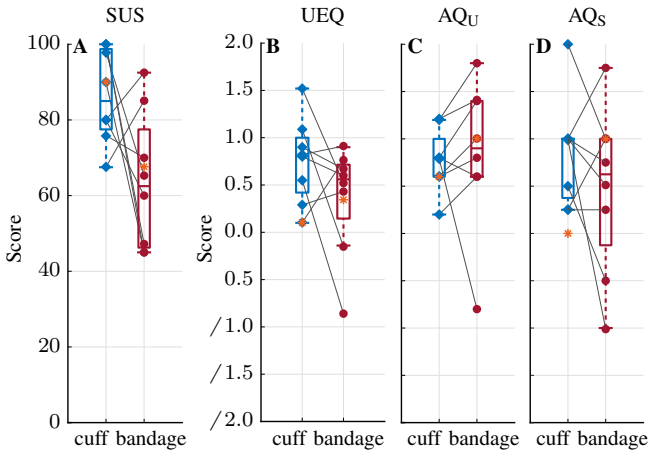


Fig. 4: Questionnaire results for the cuff (blue diamond) and bandage (red circle) prototypes and therapist (orange star). The System Usability Scale (SUS) (**A**) is ranked on a scale from 0 to 100, and the User Experience Questionnaire (UEQ) (**B**), Acceptance Questionnaire on Usability (AQ_U) (**C**) and Satisfaction (AQ_S) (**D**) on a scale from -2 to 2.

AQ_S), with the cuff prototype rated more highly than the bandage prototype. In the study, one participant lost balance within the first minute of using the bandage prototype. Analysis of the kinematics indicated that the participant was taking longer steps just before the loss of balance, generating a strong forward pulling force from the elastic tendons (235.6 N), causing instability in the subsequent step. Following this incident, the study was temporarily paused, and the participant restarted with an elongated anterior tendon and a reduced treadmill speed. No further incidents occurred for the remainder of the study.

While the therapist liked the bandage prototype more than the cuff, both were preferred over a rigid exoskeleton due to their greater freedom of movement and more natural gait. Walking in both prototypes became "easier with practice," though he "needed to adjust the gait timing" with the cuff prototype to align with the P-MATE. He also recommended moving the front attachment of the bandage prototype closer to the toes, noting that the lengthened elastic tendon provided "more guidance than control" over foot placement.

IV. Discussion

In this study, we designed, built, and evaluated two prototypes of the Passive Mechanical Add-on for Treadmill Exercise (P-MATE). This system could assist stroke patients during their gait rehabilitation by leveraging the non-paretic leg to facilitate the swing phase of the paretic leg using an elastic tendon-and-pulley system. The system was optimized in simulation to minimize parasitic forces acting on the user during natural treadmill walking.

The optimization aimed to determine the optimal pulley locations. However, due to setup constraints, the final configuration deviated from these results. Furthermore, we decided to focus the optimization on the pulley locations for assistive rehabilitation rather than exploring configurations for resistive treatment. We also chose a single, constant-stiffness tendon pretension for the optimization, but relaxing these constraints may allow for more targeted, personalized rehabilitation.

Results from a feasibility study with eight adults without physical impairments and one physical therapist indicate differences in user experience between the two human-device interfaces. Higher anterior pulling forces were measured with the bandage prototype compared to the cuff interface. This aligns with the therapist's observation of "feeling more guided" using the cuff and a "more controlling" perception when wearing the bandage prototype.

Some design elements of the current setup could be improved further. A general solution for the location of the pulleys was applied for all participants. However, variations in user experience, pretension, and walking speed preferences suggest that incorporating user-specific configurations could improve the experience of using the P-MATE for gait rehabilitation. Additionally, the pulleys have a fixed orientation, which prevents dynamic adjustments of the guiding of elastic tendons throughout the gait cycle. This limitation may cause friction and wear on the tendons, potentially affecting both their durability and the user's kinematics.

The initial pretension differed per participant, influencing the interaction forces of the P-MATE. In the case of the participant who lost their balance and the therapist, the anterior tendons were lengthened to reduce the pretension. Both the participant and therapist reported feeling in more control with the longer tendons compared to the original

tendon length, possibly as a result of the reduced forces from the device. All participants claimed that walking became easier with practice, particularly when using the bandage prototype, in line with the observed reduction in the interaction forces. A future system should allow for rapid customization of the pulley locations and pretension of the elastic tendons to maximize the clinical impact of the system.

While the depth camera allowed for a quick and cheap data collection, we likely need to optimize the setup and use different sensors to collect more meaningful data. First, the current experimental setup only collected kinematic data from the right leg, limiting insights into the full impact of the P-MATE prototypes on the overall gait pattern. There are indications that participants adapted to the system, as illustrated by changes in interaction forces throughout the trial and between prototypes. However, the specific mechanisms of this adaptation cannot be determined from this setup, particularly because the camera did not consistently and reliably track the ankle position. It is also important to note the two load cells used in this study measured the combined forces from the two anterior and two posterior elastic tendons, respectively, making it impossible to distinguish the individual pulling force contributions from each tendon acting on the leg. Participant feedback also suggested biomechanical changes that could not be validated by our dataset, including perceiving changes in balance and energy expenditure, so relevant sensors should be added to the future protocols.

Further research is needed to better understand the P-MATE's impact on the gait of people who have had a stroke. Insights from these experiments would help assess whether P-MATE promotes healthy muscle engagement, which is essential for motor learning and rehabilitation while ensuring active participation from users. Additionally, the long-term effects of the P-MATE on both the quantity of training and quality of movement should be considered to ensure that the P-MATE does not lead to negative outcomes, such as over-reliance on the device or compensatory movement patterns that could hinder recovery.

V. Conclusion

We presented the design and evaluation of a passive mechanical treadmill add-on, the P-MATE, for gait rehabilitation following a stroke. The system employs elastic tendons, pulleys, and treadmill actuation to create a dynamic connection between legs, in order to leverage the movement of the non-paretic leg to assist the paretic limb. The P-MATE was evaluated on kinematics and forces alongside unimpaired participants' feedback on the system acceptance, usability, and user experience.

Although differences were observed between normal treadmill walking kinematics and walking with both P-MATE human-device interfaces, participants responded positively regarding the usability and overall experience with the device, showing promise toward accessible gait therapy. However, several design aspects require refinement, including addressing pulley derailing, optimizing tendon pretension, and conducting a more detailed kinematic analysis. Future work will also focus on further improving usability and clinical impact.

References

[1] V. L. Feigin, M. Brainin, B. Norrving, S. Martins, R. L. Sacco, W. Hacke, M. Fisher, J. Pandian, and P. Lindsay, "World Stroke Organization (WSO): Global stroke fact sheet 2022," *International Journal of Stroke*, vol. 17, no. 1, pp. 18–29, 2022.

[2] B. H. Dobkin, "Rehabilitation after stroke," *New England Journal of Medicine*, vol. 352, no. 16, pp. 1677–1684, 2005.

[3] J. Tollár, F. Nagy, B. Csutorás, N. Prontvai, Z. Nagy, K. Török, E. Blényesi, Z. Vajda, D. Farkas, B. E. Tóth, I. Repa, M. Moizs, D. Sipos, A. Kedves, Árpád Kovács, and T. Hortobágyi, "High frequency and intensity rehabilitation in 641 subacute ischemic stroke patients," *Archives of Physical Medicine and Rehabilitation*, vol. 102, no. 1, pp. 9–18, 2021.

[4] N. Foley, J. A. McClure, M. Meyer, K. Salter, Y. Bureau, and R. Teasell, "Inpatient rehabilitation following stroke: amount of therapy received and associations with functional recovery," *Disability and Rehabilitation*, vol. 34, no. 25, pp. 2132–2138, 2012.

[5] S. A. Foley and E. P. Washabaugh, "Applying elastic resistance bands for gait training: A simulation-based study to determine how band configuration affects gait biomechanics and muscle activation," *Gait & Posture*, vol. 108, pp. 320–328, 2024.

[6] A. Haakenstad, C. M. S. Irvine, M. Knight, C. Bintz, A. Y. Aravkin, P. Zheng, V. Gupta, M. R. Abrigo, A. I. Abushouk, O. M. Adebayo *et al.*, "Measuring the availability of human resources for health and its relationship to universal health coverage for 204 countries and territories from 1990 to 2019: A systematic analysis for the Global Burden of Disease Study 2019," *The Lancet*, vol. 399, no. 10341, pp. 2129–2154, 2022.

[7] A. Pennycott, D. Wyss, H. Vallery, V. Klamroth-Marganska, and R. Riener, "Towards more effective robotic gait training for stroke rehabilitation: A review," *Journal of NeuroEngineering and Rehabilitation*, vol. 9, no. 1, p. 65, Sep. 2012.

[8] P. Langhorne, J. Bernhardt, and G. Kwakkel, "Stroke rehabilitation," *The Lancet*, vol. 377, no. 9778, pp. 1693–1702, 2011.

[9] L. N. Awad, J. Bae, K. O'Donnell, S. M. M. D. Rossi, K. Hendron, L. H. Sloot, P. Kudzia, S. Allen, K. G. Holt, T. D. Ellis, and C. J. Walsh, "A soft robotic exosuit improves walking in patients after stroke," *Science Translational Medicine*, vol. 9, no. 400, p. eaai9084, 2017.

[10] J. de Miguel-Fernández, J. Lobo-Prat, E. Prinsen, J. M. Font-Llagunes, and L. Marchal-Crespo, "Control strategies used in lower limb exoskeletons for gait rehabilitation after brain injury: a systematic review and analysis of clinical effectiveness," *Journal of NeuroEngineering and Rehabilitation*, vol. 20, no. 1, Feb. 2023.

[11] R. Hidayah, L. Bishop, X. Jin, S. Chamarthy, J. Stein, and S. K. Agrawal, "Gait adaptation using a cable-driven active leg exoskeleton (C-ALEX) with post-stroke participants," *IEEE Transactions on Neural Systems and Rehabilitation Engineering*, vol. 28, no. 9, pp. 1984–1993, 2020.

[12] X. Jin, A. Prado, and S. K. Agrawal, "Retraining of human gait - Are lightweight cable-driven leg exoskeleton designs effective?" *IEEE Transactions on Neural Systems and Rehabilitation Engineering*, vol. 26, no. 4, pp. 847–855, 2018.

[13] M. Tomc and Z. Matjačić, "Harnessing energy of a treadmill for push-off assistance during walking: In-silico feasibility study," *Frontiers in Bioengineering and Biotechnology*, vol. 10, 2022.

[14] S. Fang, *Design, Modeling and Motion Control of Tendon Based Parallel Manipulators*, ser. Fortschritt-Berichte VDI. VDI-Verlag, 2005.

[15] J. D. Van Der Laan, A. Heino, and D. De Waard, "A simple procedure for the assessment of acceptance of advanced transport telematics," *Transportation Research Part C: Emerging Technologies*, vol. 5, no. 1, pp. 1–10, 1997.

[16] J. Brooke, "SUS: A quick and dirty usability scale," *Usability Evaluation in Industry*, vol. 189, 11 1995.

[17] B. Laugwitz, T. Held, and M. Schrepp, "Construction and evaluation of a user experience questionnaire," in *HCI and Usability for Education and Work*, A. Holzinger, Ed. Berlin, Heidelberg: Springer Berlin Heidelberg, 2008, pp. 63–76.

Ground Perturbation Detection via Lower-Limb Kinematic States During Locomotion

Maria T. Tagliaferri[1], Leonardo Campeggi[1], Owen N. Beck[2], and Inseung Kang[1]

***Abstract*— Falls during daily ambulation activities are a leading cause of injury in older adults due to delayed physiological responses to disturbances of balance. Lower-limb exoskeletons have the potential to mitigate fall incidents by detecting and reacting to perturbations before the user. Although commonly used, the standard metric for perturbation detection, whole-body angular momentum, is poorly suited for exoskeleton applications due to computational delays and additional tunings. To address this, we developed a novel ground perturbation detector using lower-limb kinematic states during locomotion. To identify perturbations, we tracked deviations in the kinematic states from their nominal steady-state trajectories. Using a data-driven approach, we optimized our detector with an open-source ground perturbation biomechanics dataset. A nine-subject cross-validation demonstrated that our model distinguished perturbed from unperturbed gait cycles with 95.5% accuracy and only a delay of 33.1% within the gait cycle, outperforming the benchmark by 49.4% in detection accuracy. The results of our study offer exciting promise for our detector and its potential utility to enhance the controllability of robotic assistive exoskeletons.**

***Index Terms*— Ground Perturbation Detection, Lower-Limb Kinematics, Locomotion, Gait Stability**

I. Introduction

Dynamic postural control during locomotion is regulated by anticipatory and reactive neuromuscular mechanisms that work to maintain stability [1]. During daily ambulation tasks, these physiological systems handle occasional perturbations (i.e., sudden changes in walking stability) caused by factors such as unexpected changes in environmental contexts [2], [3]. Maintaining stability in response to disturbances requires the rapid integration of sensory inputs and motor outputs to execute gait pattern adjustments, reducing the risk of falling [4], [5]. Fall prevention strategies for older adults must compensate for delayed reaction times by detecting disturbances and initiating gait stabilization adjustments faster than the physiological response [6], [7]. Lower-limb exoskeletons designed for balance correction offer a promising solution to achieve this type of fall prevention [8]–[10]. However, progress is limited by the lack of consensus on a standard metric for detecting ground perturbations during locomotion [11], [12].

A simple approach to detect walking perturbations is to identify when the person's body center of mass (COM) moves outside the area bounded by both feet [12], [13]. However, this detection mechanism is unsuitable for exoskeleton control due to the challenge in defining consistent boundaries throughout the gait cycle (e.g., single vs. double stance) during locomotion [14]. Whole-body angular momentum (WBAM) is commonly proposed as an alternative metric to detect perturbations during walking [15]. WBAM represents the combined rotational momentum of all body segments around the person's COM. Humans tightly regulate WBAM during steady-state walking; therefore, perturbations can be identified by observing a sudden increase in WBAM [16], [17].

While this metric is effective for perturbation detection in retrospective gait analyses, it is not well suited for real-time control of exoskeletons [15]. Calculating WBAM involves complex kinematic analyses to determine the momentum of each limb segment in the sagittal and frontal planes. This requires substantial time and computational resources, leading to delays when monitoring the instantaneous value of WBAM [17]. Another drawback is that steady-state WBAM varies significantly between walking conditions (e.g., incline walking) and subjects. Therefore, WBAM must be normalized by each subject's walking speed, body mass, and body height to maintain its accuracy [18]. Thus, in the context of perturbation detection for assistive exoskeletons, a large amount of additional gait data may be required to calibrate a WBAM perturbation threshold across subjects and walking speeds [19].

Direct tracking of lower-limb kinematic states can be a promising solution to ground perturbation detection for exoskeleton control [1]. The key anatomical points involved in walking balance, such as the foot and COM, exhibit predictable patterns during stable locomotion. Deviations in the position and velocity of these points, relative to their steady-state trajectories, serve as clear indicators of disturbances during locomotion. These deviations can be quantified with minimal time and computation using data from motion capture systems or wearable sensing [20].

In this paper, we propose a novel ground perturbation detector during level-ground walking. Our model tracks 16 lower-limb kinematic states in a local coordinate system and quantifies the variation of each state from its value during steady-state walking. For our detector, we use a single threshold value to identify the perturbation onset timing across subjects and perturbation types. We evaluated our model's detection performance in 64 unique ground perturbations. We hypothesize that a ground perturbation detector using lower-limb kinematic states will outperform a WBAM-based model by achieving faster and more accurate detection. Our underlying rationale is that the kinematic states are highly

[1]M. T. Tagliaferri, L. Campeggi, and I. Kang are with the Department of Mechanical Engineering, Carnegie Mellon University, Pittsburgh, PA, 15213 USA (e-mail: mtagliaf@cmu.edu).

[2]O. N. Beck is with the Department of Kinesiology and Health Education, The University of Texas at Austin, Austin, TX, 78712 USA.

sensitive to gait disturbances, allowing efficient and accurate tracking in real-time with minimal computation [21], [22]. The development of an improved walking perturbation detector will directly support advancements in balance-assistive exoskeletons and potentially reduce the risk of falls in aging adults.

II. Methods

A. Open-Source Gait Perturbation Dataset

We utilized an open-source gait biomechanics dataset to investigate how individuals respond to ground translation perturbations during locomotion [23]. This dataset contained motion capture marker data, ground reaction forces, and whole-body angular momentum for 11 able-bodied subjects (4 females, age of 24.5±3.4 years, height of 175.1±7.2 cm, leg length of 91.3±5.1 cm, and body mass of 73.3±11.0 kg). The trial conditions included three sessions of 96 unique ground translation perturbations. The perturbations were varied in eight directions with three distinct magnitudes (i.e., ground translations of 5, 10, and 15 cm) using a 6 degrees of freedom actuated platform. Ground perturbations occurred at varying points within the gait cycle: 1) 50% of the double stance phase and 2) 25%, 50%, and 75% of the single stance phase. Gait phase was varied because it directly impacts subject's response to perturbations [23]. Our post-hoc analysis revealed that, in response to 5-cm magnitude perturbations induced in the direction of walking, the kinematic states largely remained within their nominal trajectories. Consequently, we focused on medium- and large-magnitude perturbations and excluded all 5-cm perturbation trials from analysis. Additionally, two subjects were omitted because they exhibited jump responses to perturbation.

B. Tracking Kinematic States in a Local Coordinate System

Humans tightly regulate the relative distance between the COM and the foot, as well as the velocity of each, to maintain stability during locomotion [24], [25]. Therefore, we tracked the relative position and velocity of the COM and both feet to detect the perturbation onset. A local coordinate system was chosen to minimize the effect of natural global positional drift during walking and to automatically scale the tracked kinematic states to the anthropomorphic dimensions of each subject (Fig. 1).

To track the state of each foot, we used the subject's heel markers. The heel position was calculated within a coordinate system centered at the global COM in 3 axes (Fig. 1). The global COM position was calculated as the average of the positions of four pelvic markers (right/left anterior/posterior superior iliac spine markers). The relative COM position was determined by projecting the global COM vertically downward onto a coordinate system centered at the instantaneous midpoint between the feet in the horizontal plane (Fig. 1). The vertical axis was omitted because the vertical position of the COM is minimally sensitive to ground translation perturbations [12], [24]. The velocity states were calculated by differentiating the global position over time. A dimensionality reduction technique using Principal Component

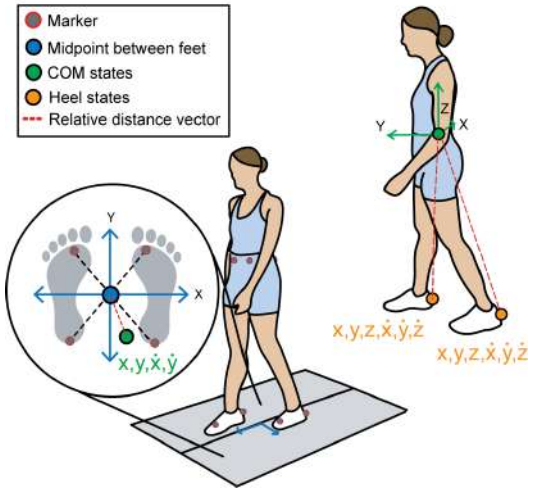


Fig. 1. Kinematic state-based perturbation detection. The relative distance between the body's COM and each foot was calculated to track the kinematic state (right). Eight relative position states and eight velocity states were tracked. A local coordinate system was established at the estimated midpoint between the feet in the horizontal plane. The COM position was then projected into this coordinate system, with a vector (red dashed lines) tracking the relative distance between the COM and the feet over time (left).

Analysis (PCA) was implemented. This analysis provided a simplified visual inspection of the overall state response to perturbations (Fig. 2). It also provided qualitative validation of our prediction that the selected states would exhibit rapid and distinct deviations from steady-state behavior following a perturbation. Two different perturbation trials from the open-source dataset, one in the mediolateral direction (Fig. 2A) and one in the anteroposterior direction (Fig. 2B), were chosen for visual evaluation.

C. Quantifying Kinematic State Variance

The mean and standard deviation of each state were calculated as a function of the gait cycle using state values from 3 steady-state walking cycles. We chose 3 cycles given that the current gait literature states that 2-3 strides are sufficient to capture the natural variance of healthy gait [26]. For subsequent gait cycles, the current value of each state was compared to the mean and standard deviation to quantify variance using Eq. 1,

$$\alpha_i = \begin{cases} 0, & \text{if } |\bar{x}_i - x_i| \leq 2\sigma_i, \\ x_i - (\bar{x}_i \pm 2\sigma_i), & \text{otherwise.} \end{cases} \quad (1)$$

where $\bar{x}$ and σ represent the mean and standard deviation of the current state at a given time point, α denotes the deviation of the individual state from its natural range of variance, and i indicates the current time step. During walking, α was assigned a value of zero if the current state value was within ± 2 standard deviations of the mean. Otherwise, α was calculated as the Euclidean distance from the current state value to 2 standard deviation above or below the mean (Fig. 2C). A value of α close to zero indicates that the subject's kinematic states are within a stable basin, corresponding to steady-state walking.

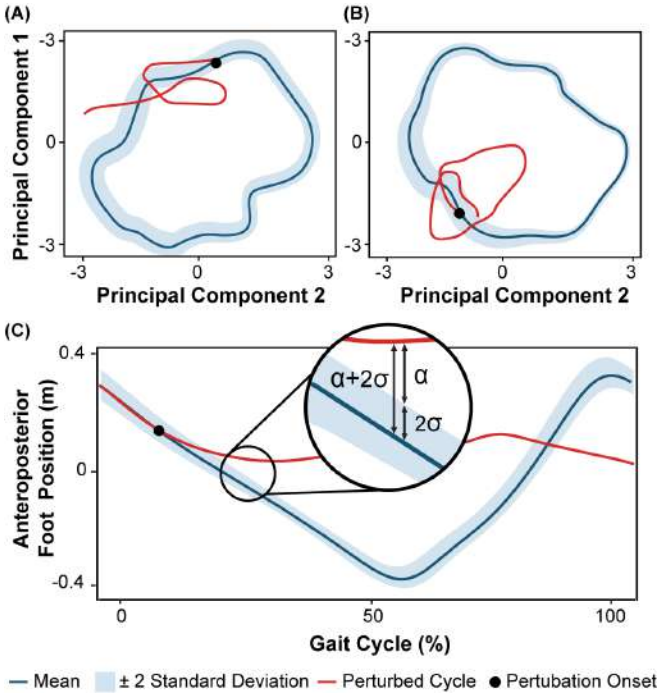


Fig. 2. (A) Principal Component Analysis for a single representative trial of an (A) anteroposterior and (B) mediolateral perturbation. For both cases, perturbations with a magnitude of 15 cm occurred during the double stance phase. (C) Visual representation of state variance calculation (Eqs. 1 and 2). α is the Euclidean distance between the current state value and the edge of 2 standard deviations (σ) from the mean.

Next, α was used to calculate an instantaneous ratio of current to natural state variance (Fig. 2C). This ratio ensured that a state with a lower natural variance contributed more significantly to the total stability deviation value and prevented a state with a large natural variance from disproportionally skewing the total value. The standard deviation of each state was normalized using the coefficient of variation formula, Eq. 2a,

$$C_i = \frac{\sigma_i}{\bar{x}_i} \tag{2a}$$

to account for the differences in unit and scale between states [27]. C represents the coefficient of variation. The ratio for each state was then computed and linearly aggregated using Eq. 2b,

$$\varphi_i = \frac{1}{n}\sum_{j=1}^{n} \frac{\alpha_i}{2C_i + \alpha_i} \tag{2b}$$

where φ represents a single stability deviation value that characterizes the subject's perturbation state and n is the total number of tracked kinematic states. By monitoring the single variable, φ, we determined whether a subject was perturbed (i.e., deviating from their natural variance) by selecting an appropriate threshold value.

D. Threshold Optimization

To calculate the optimal threshold value for φ, which denotes a perturbation onset, we conducted a parameter sweep using the open-source perturbation dataset [23]. Values increasing by a step size of .001 from 0.5 to 4 were used as a threshold for perturbation detection. Detection performance was evaluated on accuracy and delay at each threshold. We determined accuracy by calculating the number of gait cycles that were correctly labeled as perturbed or unperturbed. We defined delay as the percentage of the gait phase that elapsed between the onset of the perturbation and the time when φ crossed the detection threshold. For parameter sweep, we rewarded threshold values that minimized false detections (false positives) and undetected perturbations (false negatives), aligning with the target application of our approach for lower-limb exoskeleton control. Incorrect exoskeleton stability assistance, whether unnecessarily initiated due to false detection of a perturbation or omitted due to an undetected perturbation, carries a significant risk of user injury [28].

E. Baseline Benchmark Implementation

A perturbation detection model using WBAM was implemented and evaluated as a baseline comparison for our model [15], [29]. We replicated this method using the instantaneous sagittal and frontal WBAM values provided in the open-source perturbation dataset. For each trial, the mean and standard deviation of WBAM were calculated using data from the 3-5 steady-state gait cycles that preceded the induced perturbation. A detection threshold of ± 4 standard deviations was chosen according to the recommendations of a previous literature on WBAM [29]. Perturbation detection occurred when the instantaneous WBAM value exceeded this threshold. We evaluated the performance of this model on both the detection accuracy and the delay.

F. Cross Validation

We conducted a nine-subject cross-validation using the open-source perturbation biomechanics dataset to evaluate the model's performance. Following a leave-one-out approach, one subject was systematically withheld at a time. The perturbation threshold was then optimized using data from all 64 perturbation types of the remaining eight subjects, following the threshold optimization method outlined previously. The optimized threshold was subsequently applied to the withheld subject to assess the model's accuracy and detection delay. This procedure provided a measure of the model's generalizability.

III. Results

A. Perturbation Detection Performance Using Cross Validation

Across all nine leave-one-out cross-validations, the average optimal threshold for φ was determined as 0.131 (Fig. 3). The model classified gait cycles as either perturbed or unperturbed for each withheld subject, achieving an average per-subject accuracy of $94.10 \pm 1.46\%$ and detection delay of $33.14 \pm 0.91\%$ of the gait cycle (Fig. 4A). When aggregating all gait cycles across the nine subjects into a single confusion matrix, the overall model accuracy was 95.52% (Fig. 4B).

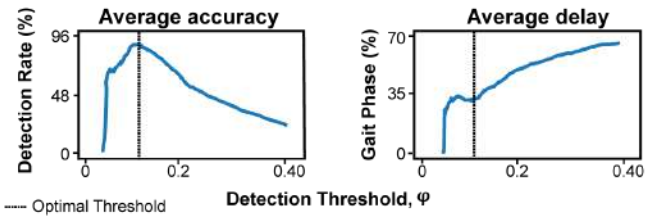


Fig. 3. Parameter sweep result to determine a perturbation detection threshold, φ. A threshold value of 0.131 (black dashed lines) was determined as the average optimal value following cross validation.

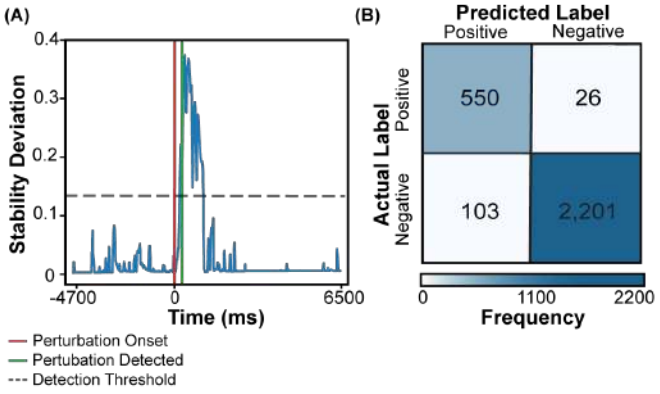


Fig. 4. (A) A representative trial of our model performance in the ground perturbation biomechanics dataset. The red line represents the perturbation onset and the green line represents the time when our model detects the perturbation (detection threshold shown with the dashed grey line). (B) A confusion matrix summarizing our model performance across all leave-one-out validations. Positive and negative labels indicate perturbed and unperturbed gait cycles, respectively.

B. Baseline Model Comparison

Implementation of the baseline WBAM-based model performed with 49.4% less accuracy than our method for the open-source dataset. However, it resulted in a 21.1% faster detection within the gait cycle. The WBAM-based results were obtained by taking the average across sagittal and frontal planes to provide a representative analysis (Fig. 5) [29].

IV. Discussion

In this paper, we proposed a novel perturbation detection model, which utilizes 16 lower-limb kinematic states and their deviations from steady-state gait dynamics. We established a local coordinate system to track relative positions to avoid misinterpreting natural drift in the state during walking. Using a data-driven approach, we optimized a

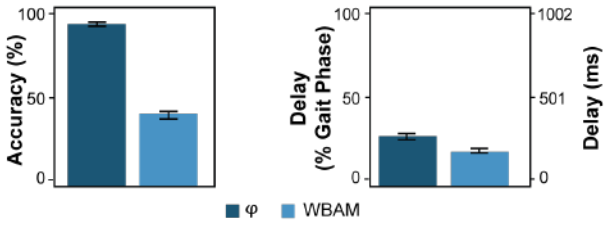


Fig. 5. Perturbation detection performance result using our model (dark) and the WBAM-based benchmark (light) on accuracy (left) and delay (right). Error bars indicate ± 1 standard deviation.

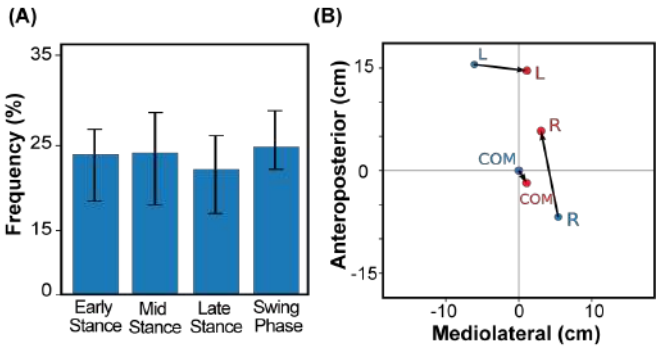


Fig. 6. (A) Average perturbation timing across subjects: early stance (0-10% and 90-100% of the gait cycle), mid stance (10-30% of the gait cycle), late stance (30-50% of the gait cycle), and swing phase (50-90% of the gait cycle) of the right leg. Error bars indicate ± 1 standard deviation. (B) Visual illustration of tracking of positional states. Blue dots represent expected positional states and red dots show actual states values during a perturbation. Black arrows indicate a distance vector between expected and actual states.

single threshold value to detect ground perturbations, φ. We hypothesized that our kinematic state-based detection model would outperform the WBAM-based model under varying perturbation conditions across subjects. To test this hypothesis, we evaluated the performance of our model and the WBAM-based benchmark in detecting 64 ground translation perturbations. Our study results corroborate our initial hypothesis that the ground perturbation detection model using kinematic states detected perturbations more accurately than the WBAM-based model. In the open-source dataset analysis, our model showed a 49% improvement in detection accuracy compared to that of the WBAM-based model (Fig. 5). However, contrary to our initial hypothesis, the WBAM-based model outperformed our model in the detection delay, demonstrating a faster response on average by 21% earlier within the gait cycle. It is important to note that this delay was only calculated in instances of successful perturbation detections and may not be representative of the remaining 54% of perturbations that the WBAM-based model failed to detect. Furthermore, since this was an offline analysis, it did not consider the time required to calculate WBAM.

The generalizability of our model across subjects and perturbation conditions showcased the potential benefit of integrating our approach into lower-limb exoskeleton control (Fig. 6A). The average stride duration across subjects in the open source dataset was 1002.5 ± 7.2 ms. Biomechanics literature states that older adults can require up to 469 ms to complete a stabilizing step in response to perturbations. Given that the detection timing of our model was 332 ms, our result indicated that the detection was early enough for an exoskeleton to respond (with assistance) within a single stride [3], [4], [30]. Moreover, the generalizability of our model and its consistent performance across subjects showed that the system can potentially be deployed to exoskeletons with minimal user-specific tuning [31]. In future work, we aim to make our model fully autonomous by tracking kinematic states using on-board wearable sensors (e.g,. inertial measurement units) from an exoskeleton.

Additionally, we plan to extend our model to determine

both the direction and magnitude of each perturbation. The instantaneous sign and magnitude of each α value can provide an estimate of the direction in which the individual's feet and COM were perturbed as well as the relative magnitude of the perturbation (Fig. 6B). We will evaluate the accuracy of these estimations and explore their potential to enhance the precision of perturbation responses in lower-limb exoskeletons. We will also evaluate our model under diverse ground perturbation conditions and subject demographics in real-time to improve the generalizability. Although our model was trained on healthy young subjects, its performance at the same walking speed is likely comparable in healthy older adults. Given their longer reaction times, our method could be especially valuable for assisting balance in older adults [32]. However, additional data collection from older adult subjects is needed to evaluate the model's performance in this target population.

V. Conclusion

We developed a novel perturbation detection model by tracking lower-limb kinematic states and their deviations from steady-state gait dynamics during walking. Our model employed a weighted sum of state deviations and used a data-driven threshold to detect ground perturbations. In a nine-subject cross-fold validation, our model achieved 95.5% detection accuracy with a delay of 33.1% within a gait cycle after a perturbation onset, outperforming the benchmark WBAM-based model. These results highlight the potential of our model to enable lower-limb exoskeletons to provide fast and precise balance support, particularly for older adult users.

References

[1] S. M. Bruijn, O. G. Meijer, P. J. Beek, and J. H. van Dieën, "Assessing the stability of human locomotion: a review of current measures," *Journal of the Royal Society Interface*, vol. 10, p. 20120999, 2013.

[2] S. M. Bruijn and J. H. Van Dieën, "Control of human gait stability through foot placement," *Journal of The Royal Society Interface*, vol. 15, no. 143, p. 20170816, 2018.

[3] J. Y. Lim, "Choice stepping reaction time under unstable conditions in healthy young and older adults: A reliability and comparison study," *J Kor Phys Ther*, vol. 33, no. 6, pp. 265–271, 2021. Published online December 31, 2021.

[4] R. M. Hardwick, A. D. Forrence, M. G. Costello, K. Zackowski, and A. M. Haith, "Age-related increases in reaction time result from slower preparation, not delayed initiation," *Journal of neurophysiology*, vol. 128, no. 3, pp. 582–592, 2022.

[5] A. van den Bogert, M. Pavol, and M. Grabiner, "Response time is more important than walking speed for the ability of older adults to avoid a fall after a trip," *Journal of Biomechanics*, vol. 35, no. 2, pp. 199–205, 2002.

[6] O. N. Beck, M. K. Shepherd, R. Rastogi, G. Martino, L. H. Ting, and G. S. Sawicki, "Exoskeletons need to react faster than physiological responses to improve standing balance," *Science robotics*, vol. 8, no. 75, p. eadf1080, 2023.

[7] C. McCrum, *A Trip to Remember: Assessing and Improving Walking Stability in Older Adults*. PhD thesis, Maastricht University, 2019.

[8] I. Kang, D. Molinaro, S. Duggal, Y. Chen, P. Kunapuli, and A. Young, "Real-time gait phase estimation for robotic hip exoskeleton control during multimodal locomotion," *IEEE Robotics and Automation Letters*, vol. PP, pp. 1–1, 02 2021.

[9] J. K. Leestma, S. Mathur, M. D. Anderton, G. S. Sawicki, and A. J. Young, "Dynamic duo: Design and validation of an autonomous frontal and sagittal actuating hip exoskeleton for balance modulation during perturbed locomotion," *IEEE Robotics and Automation Letters*, vol. 9, no. 5, pp. 3995–4002, 2024.

[10] D. D. Molinaro, I. Kang, and A. J. Young, "Estimating human joint moments unifies exoskeleton control, reducing user effort," *Science Robotics*, vol. 9, no. 88, p. eadi8852, 2024.

[11] H. Shimada, S. Obuchi, N. Kamide, Y. Shiba, M. Okamoto, and S. Kakurai, "Relationship with dynamic balance function during standing and walking," *American Journal of Physical Medicine and Rehabilitation*, vol. 82, no. 7, pp. 511–516, 2003.

[12] C. Curtze, T. J. Buurke, and C. McCrum, "Notes on the margin of stability," *Journal of biomechanics*, vol. 166, p. 112045, 2024.

[13] A. L. Hof, "The 'extrapolated center of mass' concept suggests a simple control of balance in walking," *Human movement science*, vol. 27, no. 1, pp. 112–125, 2008.

[14] A. L. Hof, M. G. Gazendam, and W. E. Sinke, "The condition for dynamic stability," *Journal of biomechanics*, vol. 38, no. 1, pp. 1–8, 2005.

[15] S. Shokouhi, P. Sritharan, and P. V.-S. Lee, "Recovering whole-body angular momentum and margin of stability after treadmill-induced perturbations during sloped walking in healthy young adults," *Scientific Reports*, vol. 14, no. 1, p. 4421, 2024.

[16] M. van Mierlo, *Recovering linear and angular momentum during walking*. Phd thesis - research ut, graduation ut, University of Twente, Netherlands, May 2023.

[17] J. Zhang, M. van Mierlo, P. Veltink, and E. van Asseldonk, "Estimation of sagittal-plane whole-body angular momentum during perturbed and unperturbed gait using simplified body models," *Human Movement Science*, vol. 93, p. 103179, 2024.

[18] M. Liu, A. Naseri, I.-C. Lee, X. Hu, M. D. Lewek, and H. Huang, "A simplified model for whole-body angular momentum calculation," *Medical Engineering and Physics*, vol. 111, p. 103944, 2023.

[19] L. Wang, X. Li, Y. Peng, J. Han, and J. Zhang, "Balance evaluation based on walking experiments with exoskeleton interference," *Bioengineering (Basel, Switzerland)*, vol. 11, no. 4, p. 386, 2024.

[20] C. Karakasis and P. Artemiadis, "Real-time kinematic-based detection of foot-strike during walking," *Journal of Biomechanics*, vol. 129, p. 110849, 2021.

[21] U. Lugrís, M. Pérez-Soto, F. Michaud, and J. Cuadrado, "Human motion capture, reconstruction, and musculoskeletal analysis in real time," *Multibody System Dynamics*, vol. 60, no. 1, pp. 3–25, 2024.

[22] L. Jiang, S. Kasahara, T. Ishida, Y. Koshino, A. Chiba, Y. Wei, M. Samukawa, and H. Tohyama, "Effect of suspensory strategy on balance recovery after lateral perturbation," *Human Movement Science*, vol. 94, p. 103184, 2024.

[23] J. K. Leestma, P. R. Golyski, C. R. Smith, G. S. Sawicki, and A. J. Young, "Linking whole-body angular momentum and step placement during perturbed human walking," *Journal of Experimental Biology*, vol. 226, no. 6, p. jeb244760, 2023.

[24] M. S. Redfern and T. Schumann, "A model of foot placement during gait," *Journal of Biomechanics*, vol. 27, no. 11, pp. 1339–1346, 1994.

[25] H. F. Bagce, S. Saleh, S. V. Adamovich, J. W. Krakauer, and E. Tunik, "Corticospinal excitability is enhanced after visuomotor adaptation and depends on learning rather than performance or error," *Journal of Neurophysiology*, vol. 109, no. 4, pp. 1097–1106, 2013.

[26] R. A. Mann, J. L. Hagy, V. White, and D. Liddell, "The initiation of gait," *The Journal of Bone and Joint Surgery. American Volume*, vol. 61, pp. 232–239, March 1979.

[27] Z. Jalilibal, A. Amiri, P. Castagliola, and M. B. Khoo, "Monitoring the coefficient of variation: A literature review," *Computers and Industrial Engineering*, vol. 161, p. 107600, 2021.

[28] M. Raitor, S. W. Ruggles, S. L. Delp, C. K. Liu, and S. H. Collins, "Lower-limb exoskeletons appeal to both clinicians and older adults, especially for fall prevention and joint pain reduction," *IEEE Transactions on Neural Systems and Rehabilitation Engineering*, vol. 32, pp. 1577–1585, 2024.

[29] D. Martelli, V. Monaco, and S. Micera, "Detecting falls by analyzing angular momentum," in *2011 IEEE International Conference on Rehabilitation Robotics*, pp. 1–7, IEEE, 2011.

[30] I. Jiang and B. Hannaford, "Comparison of reaction times while walking," in *2015 IEEE International Conference on Rehabilitation Robotics (ICORR)*, pp. 345–349, 2015.

[31] I. Kang, D. D. Molinaro, G. Choi, J. Camargo, and A. J. Young, "Subject-independent continuous locomotion mode classification for robotic hip exoskeleton applications," *IEEE Transactions on Biomedical Engineering*, vol. 69, no. 10, pp. 3234–3242, 2022.

[32] D. B. Coelho, M. B. Silva, A. C. d. Lima-Pardini, A. R. Martinelli, T. d. S. Baptista, R. T. Ramos, and L. A. Teixeira, "Young and older adults adapt automatic postural responses equivalently to repetitive perturbations but are unable to use predictive cueing to optimize recovery of balance stability," *Neuroscience Letters*, 2023.

Rehabilitation of Chronic Stroke Using Neurofeedback, Functional Electrical Stimulation and Cerebrospinal Direct Current Stimulation

Teodiano Bastos-Filho, Aura Ximena Gonzalez-Cely *Student Member, IEEE*, Sheida Mehrpour, Fernanda Souza, Ana Cecilia Villa-Parra, Fernando Cabral

***Abstract*— This work presents the application of a rehabilitation protocol using a novel Non-Invasive Brain Stimulation (NIBS) technique, called cerebrospinal Direct Current Stimulation (csDCS), together with the use of a Brain-Computer Interface (BCI) based on Motor Imagery (MI) with Neurofeedback (NFB), and applying Functional Electrical Stimulation (FES) plus the use of a pedal exerciser. This protocol uses the concept of Alternating Treatment Design (ATD), in which a chronic post-stroke subject is submitted to these techniques to recover his left hand and leg movements. The rehabilitation progress was verified through metrics, such as Fugl Meyer Assessment (FMA), Functional Independence Measure (FIM), Ashworth Scale, Muscle Strength Grading (MSG), and surface Electromyography (sEMG). Results from these metrics include a 41% gain in hand function recovery, a 5% gain in performance in motor and cognitive/social domains, and a 50% improvement in both wrist extensor muscle strength and finger extensor muscle strength. In addition, there was a 17% gain of Maximum Voluntary Contraction (MVC) for the tibialis anterior muscle of the patient's left leg. On the other hand, there was a worsening in some values of EMG, probably due to the participant having received application of botulinum toxin in his hand.**

I. Introduction

A study by the United Nations forecasts that, by 2050, the population of individuals aged 65 and older will reach 1.5 billion, constituting 16% of the total population [1]. This demographic shift is accompanied by an increase in age-related health concerns, notably stroke, as the likelihood of experiencing a stroke doubles roughly every 10 years after turning 55 [2]. Stroke, a clinical condition marked by insufficient blood flow to the brain, leads to cell death. Stroke can be ischemic (80% of cases), caused by reduced blood flow, or hemorrhagic, due to bleeding, whose impact largely depends on the location and its severity. Individuals recovering from a stroke may face varying degrees of neural injury affecting motor functions in both upper- and lower-limbs [3].

The effects of a stroke on the upper limb can be a weakness (hemiparesis) or paralysis (hemiplegia) on one side of the body (often seen on the opposite side to where the stroke occurred); loss of fine motor skills of fingers and hands; spasticity (increased muscle tone or stiffness in the affected arm); sensory changes (such as numbness, tingling, or a "pins and needles" sensation); and difficulty with the coordination of shoulder, elbow, wrist, and fingers. On the other hand, the lower limb effects can be weakness or paralysis (similar to the upper-limb) in one leg, affecting the ability to walk and perform weight-bearing activities; impaired balance and coordination while standing and walking, increasing the risk of falls; spasticity (due to tightness and stiffness in the muscles of the affected leg, making walking and movement challenging); foot drop (the foot cannot be lifted properly due to weakness or paralysis of the muscles that control dorsiflexion (lifting the foot upwards), which can lead to dragging the foot while walking); and altered gait patterns (such as a limp, scissoring gait – legs crossing over each other –, or circumduction – swinging the leg out to the side while walking). After a stroke, rehabilitation for impairments in both the upper and lower limbs typically consists of a blend of physical therapy, occupational therapy, and sometimes speech therapy. The goal is to improve strength, range of motion, coordination, and functional abilities to enhance independence in Activities of Daily Living (ADL) [4],[5].

Early intervention is vital for optimal outcomes in upper- and lower limb rehabilitation, capitalizing on the brain's adaptability known as "neuroplasticity". Traditional therapies focus on strength, range of motion, motor control, and ADL performance [6]. Such therapies form the foundation, but advancements like technology-enhanced therapies offer new possibilities for optimizing training intensity, repetition, progress evaluation, and patient-specific treatment [7].

Recent years have shown innovations that can transform stroke rehabilitation, such as the use of robot-assisted therapy, which provides feedback and tracks progress for personalized rehabilitation [7],[8]. Rehabilitation involving a Brain-Computer Interface (BCI) is another innovation that provides a groundbreaking approach. In fact, BCI establishes direct communication between the brain and the rehabilitation equipment [9]. Moreover, studies have shown that BCIs based on Motor Imagery (MI) of upper- and lower-limb movements can improve motor learning and increase neural plasticity [10],[11]. These motor patterns can be analyzed through Event-Related Synchronization (ERS)/Desynchronization (ERD), which are associated to indicate neural changes, specifically a power increase or decrease in the brain's electrical signals, respectively [12]. Thus, BCIs can translate these detected MI into commands for external devices, enhancing motor function and independence for stroke

*Research supported by CAPES, CNPq, and FAPES, all from Brazil.

Teodiano Bastos-Filho, Aura Ximena Gonzalez-Cely, Sheida Mehrpour, Fernanda Souza, and Fernando Cabral are with the Federal University of Espirito Santo, Vitoria, Brazil (corresponding author to provide e-mail: teodiano.bastos@ufes.br).

Ana-Cecilia Villa Parra is with Biomedical Engineering Research Group–GIIB, Universidad Politécnica Salesiana, Cuenca, Ecuador

survivors [5]. As part of such MI-BCI therapy, the inclusion of Neurofeedback (NFB) has shown improvements in neuroplasticity, as this technique measures and shows to the subject their brain wave activity to help them self-regulate their brain function and enhance specific targets [13].

Another novelty in this field is the use of Functional Electrical Stimulation (FES) to induce peripheral activation to enhance muscle contraction, through suitable pulse amplitude, duration and frequency, to generate stimuli triggering action potentials in intact peripheral nerves [14]. As well as a new Non-Invasive Brain Stimulation (NIBS) technique (cerebrospinal Direct Current Stimulation –csDCS), which is a promising novelty to exciting, simultaneously, the brain and the spinal cord. This technique uses a low-level continuous current (2 mA) to modulate the activity of the brain and spinal cord. This technique uses a pair of electrodes, where the anode is placed on the M1 region of the affected hemisphere, and the cathode is placed on the spinous apophysis of the thoracic vertebra over T11 (T10-T12) upon palpation.

We present here the results from the application of this novel NIBS technique together with the use of a MI-BCI with NFB, and applying FES plus the use of a pedal exerciser. It is worth mentioning that our protocol uses the concept of Alternating Treatment Design (ATD), in which a chronic post-stroke subject is submitted to these techniques to recover his left hand and leg movements. The evaluation of his rehabilitation progress was conducted using typical metrics used in this field, such as Fugl Meyer Assessment (FMA), Functional Independence Measure (FIM), Ashworth Scale, Muscle Strength Grading (MSG), and Electromyography (EMG).

II. Study Design

This study is based on the concept of ATD, which is a single-case research design study that typically involves a single subject, later replicated individually in other research participants. In this kind of study design a baseline assessment phase is used to track the problem before intervention or treatment. Different interventions are applied in a randomized, semi-randomized order, or predetermined sequence, to assess whether one treatment is more effective than the other and, further, making decisions to determine the specific treatment being implemented. In this method the participant acts as both the control and the treatment group [15], i.e., each participant is considered as his/her own control in sham phase.

In our recent study [16], we explored the rationale behind the ATD as a suitable research design for neurorehabilitation objectives. As the most common concern with NIBS trials is related to incomparable outcomes, the ATD adopted here allows for future comparison of the outcomes with other studies. We consider that such an approach may help to some extent to address the study of a single subject. Additionally, we consider results from recent studies after stroke, which claim that the total brain volume decreases in a heterogeneous manner, which is known as brain atrophy rates [17],[18]. From such studies it was inferred that the brain atrophy rates may impact the density current distribution and, in turn, the cortical excitability during stimulation. Therefore, based on our previous studies [19], in this study it was postulated that using a subject-specific stimulation protocol that varies the current intensity and duration of intervention, depending on the brain tissue volume for the subject, would reduce the variability of the NIBS results. Using this justification, the approach used here employs a single-case research design in which the same participant receives both the real and the sham stimulations. Thus, it is believed that the influence of brain atrophy rates can potentially be mitigated by examining the stimulation (real or sham) on a single case, leading to more reliable and comparable outcomes [16].

III. Matherials And Methods

A. Brain-Computer Interface (BCI)

Given its broad adoption and accessibility, all the protocols presented here rely on the use of an electroencephalography (EEG) cap, enabling the real-time streaming of EEG data. Following an initial stage of signal pre-processing, a stage of feature extraction, and a final stage of classification, control signals are transmitted to the NFB system on a computer screen as well as to the FES device, which is applied to the paretic arm of the participant (Fig. 1).

The BCI used in our study is composed of an EEG wireless board (Open BCI Cyton-Daisy, OpenBCI, USA). This electronic board samples, at 125 Hz, the signals that are acquired from sixteen EEG electrodes located on: FP1, FP2, F3, F4, FC3, FCz, FC4, C5, C3, C1, C2, C4, C6, CP3, CPz, CP4, including two references at earlobes (A1 and A2). It is important to emphasize that we modified the original locations of the original EEG cap, so that the electrodes used in our research are grouped on the Supplementary Motor Area (SMA), Primary Motor Cortex (M1), and Pre-Motor Area (PMA) of the brain motor area, which are related to motor mental tasks (Fig. 1). These EEG channels were selected because the signals recorded from these channels show a tight relationship to activity of the most relevant sensorimotor areas. In our protocol, scalp-electrode impedances are maintained below 20 kΩ, which is suitable to have a good quality of the EEG signals, in addition to accelerating the participant preparation time.

B. Neurofeedback (NFB)

NFB was implemented here to provide the subject with his success rate related to the MI recognition in both calibration and online stages while he imagined performing limb movements. For that, his EEG signals were processed using a 1-s window, and Relative Power Changes (RPC) were calculated in mu and beta bands, using a Laplacian filter around C_3 and C_4 electrodes, such as done by [20], [21]. Using this method, an RPC value is generated, which is translated to the screen in front of the subject to show him, as on-line feedback, the success rate in recognizing his MI, thus

motivating him to improve his performance in generating high RPC values.

To detect the MI, first there is a calibration stage (with the subject in rest) using the EEG dataset as input to recognize MI and resting classes, where the period of baseline is considered as the resting class. The calibration stage considers the use of a 5-fold cross-validation to avoid overfitting, data leaking, and generalize better the system, such as done by [20], [22], [23]. This stage generates the classification model to be used in the online stage.

In a second stage there is a data segmentation to split the dataset into 80% for training, and 20% for testing. From the previous 80%, a new split is performed to obtain new training and validation datasets. With each segment of data, a 1-s sliding window (with 50% overlap) is applied to segment the data for processing, as done in [20], [24], [25]. Using each window of data, a Butterworth zero-phase band-pass filter is used between 7 to 30 Hz to isolate the mu and beta bands [3]. In the final stage, the technique of Riemannian Geometry (RG) is used for feature extraction, as done in [20], [23], and Linear Discriminant Analysis (LDA) is used for classification, such as done by [20], achieving a mean ACC of 0.72, while recognizing MI and resting classes.

C. Participant recruitment

Before recruiting the post-stroke participant for our study, specific inclusion and exclusion criteria were established. The participant of our study was required to have a diagnosis of stroke resulting in hemiparesis of their upper and/or lower limbs, the ability to maintain balance in a seated position, and the capacity to perform passive movements with the paretic limb in both the upper and/or lower limbs. Participants with a clinical history indicating other neurological diseases, two or more stroke episodes, uncontrolled blood pressure or angina, and a history of convulsions were excluded from our study. Additionally, the participant was required to meet another inclusion criterion: he needed to have sufficient auditory, visual, cognitive, and language skills to understand and follow instructions. Based on such criteria, a 59 years-old man affected by chronic ischemic stroke on December 22, 2021 was chosen for our experiments. His stroke caused hemiparesis in his left hand and leg, with distal brachial predominance.

The participant voluntarily participated in the experiments and signed the informed consent in accordance with the Declaration of Helsinki and the experimental protocol approved by the Ethics committee of the Federal University of Espirito Santo (UFES/Brazil) under the number CAAE: 39410614.6.0000.5060.

D. Experiments

Before starting our protocol, the participant was injected 1000 units of botulinum toxin (brand Dysport) into his left hand to relax his hand muscles and joints, in a single application, due to his high hand muscle stiffness provoked by the stroke. Afterwards, the participant was submitted, for two weeks, to the hand protocol using MI-BCI-NFB plus FES (Fig. 1).

In this protocol the participant was worn with the EEG cap and instructed to imagine his paretic arm movement. Thus, once the BCI was able to recognize his MI, the NFB calculation was performed, and the participant was able to watch on the screen in front of him the RPC value. A FES device (Balego EMS Digital Neuromuscular) was used to target the flexor muscles of the fingers and wrist, and the extensor muscles, simultaneously, with the following parameters: synchronous mode, 1-s ramp, 7-s on-time, 8-s off-time, frequency of 20 Hz, and pulse width of 200 μs. The stimulation intensity was adjusted based on the participant's comfort level.

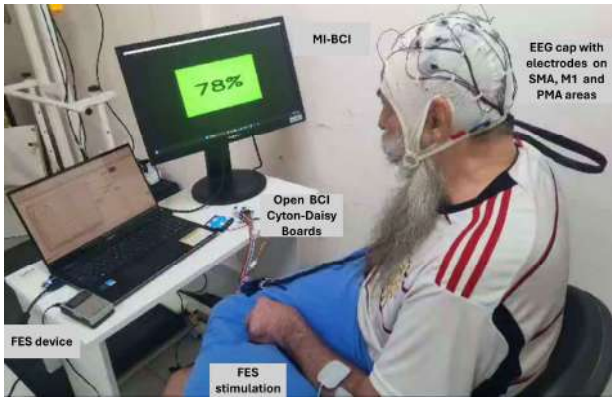
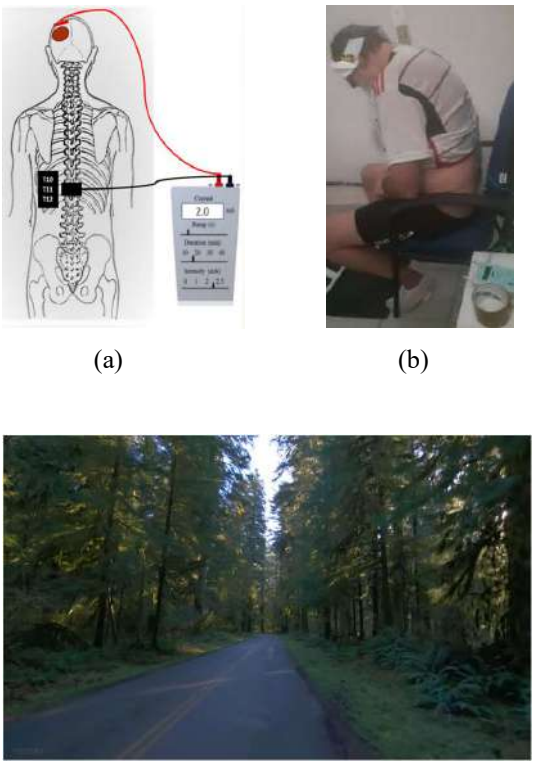


Fig. 1. Neurofeedback provided to the subject, according to his performance in generating MI values.

Fig. 1 shows the participant during the experiment, in which he is verbally guided to focus on the MI task, in order to increase the RPC value during NFB. This procedure was also held five times a week for two weeks.

After that, the leg protocol started (Fig. 2), in which csDCS was applied to the participant for 20 min (five days a week, for two weeks, with current intensity of 2 mA, and fade-in and fade-out periods of 30 s each) via two conductive-rubber electrodes (35 cm^2) enclosed in perforated sponges pocked soaked with saline connected to the equipment (DC-Stimulator Plus, NeuroConn, Ilmenau, Germany). In this technique one electrode (anode) is located on the M1 region of the affected hemisphere, and the other electrode (cathode) is located on the spinous process of the thoracic vertebra over T11 (T10-T12) by palpation. It is worth mentioning that during the cerebrospinal stimulation (20 min) the participant watched a video projected in front of him with pedaling content, and was instructed to imagine himself pedaling (to strength his mu and beta bands related to MI), in addition to pedaling a pedal exerciser (Mini Exercise Bike, from Himaly, USA). Fig. 2 shows the participant receiving csDCS through electrodes in specific location, and a screenshot of the video projected on the wall to stimulate the participant to generate his MI.

To evaluate the efficacy of our protocol, the patient was assessed by an experienced physiotherapist, using the same methodology to ensure reliability, at the beginning, middle and the end of the experiment, using the following metrics: Fugl Meyer Assessment (FMA), Functional Independence Measure (FIM), Ashworth Scale, Muscle Strength Grading (MSG), and surface Electromyography (sEMG). The sEMG data were acquired with a wireless Miotec device (New Miotool Face model), 16-bit resolution, between 20 and 500 Hz, at 3k samples per second.



(a) (b)

(c)

Fig. 2. Aplication of cerebrospinal Direct Current Stimulation (csDCS): a) Eletrode position; b) Participant with electrodes; c) Screenshot of the video.

IV. RESULTS

A. *For Upper-Limb*

- Fugl Meyer Assessment (FMA)

A 41% gain in the left participant's hand function recovery was observed in terms of functionality, range of motion, sensitivity, pain, proprioception and speed (Fig. 3).

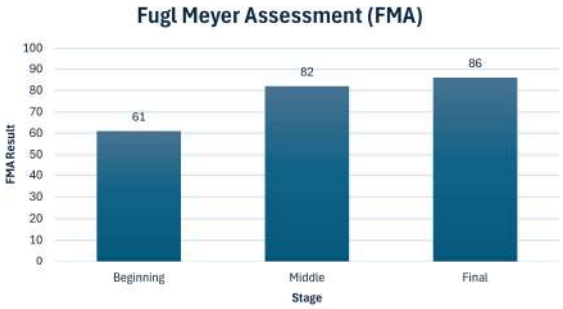


Fig. 3. Results for Fugl Meyer Assessment (FMA).

- Functional Independence Measure (FIM)

A 5% gain was observed in performance in motor and cognitive/social domains in the following aspects: eating, personal hygiene, bathing, dressing the upper half of the body, dressing the lower half of the body, using the toilet, controlling urine, controlling feces, transferring to bed, chair, wheelchair, transferring to toilet, transferring to bathtub or shower, locomotion, locomotion on stairs, understanding, expression, social interaction, problem solving, and memory. Fig. 4 shows the results obtained for the metric FIM.

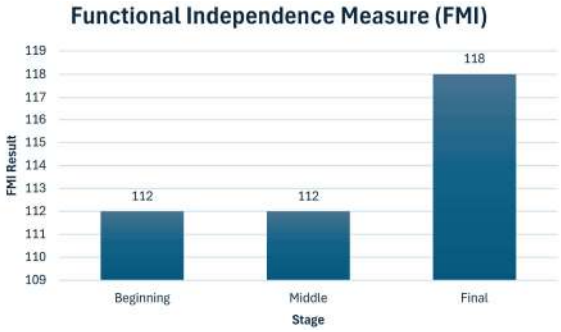


Fig. 4. Results for Functional Independence Measure (FIM).

- Ashworth Scale

In this metric, which assesses the intensity of hypertonia and therapeutic response, there was a 33% improvement in the values measured at the beginning and the end of the protocol, which indicates a decrease in the patient's level of spasticity. Fig. 5 shows the three values of the Ashworth scale measured along the protocol.

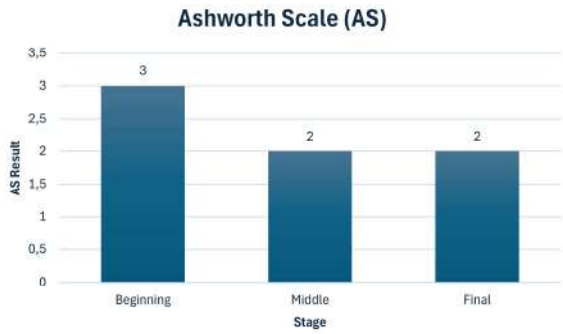


Fig. 5. Results for Ashworth Scale.

- Muscle Strength Grading (MSG)

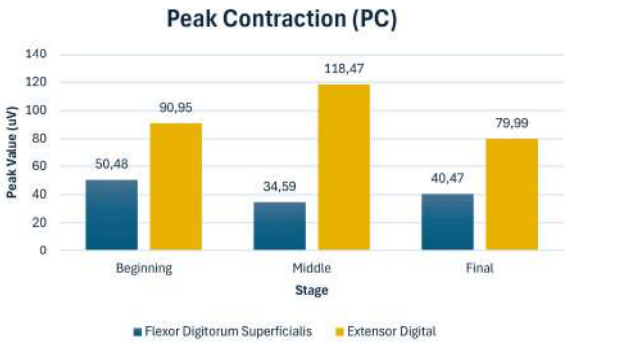
This metric assesses the muscle strength of the wrist flexors, wrist extensors, finger flexors and finger extensors. There was no improvement either in wrist flexor strength or in finger flexor muscle strength, but there was a 50% improvement in both wrist extensor strength and finger extensor muscle strength, such as shown in Fig. 6.



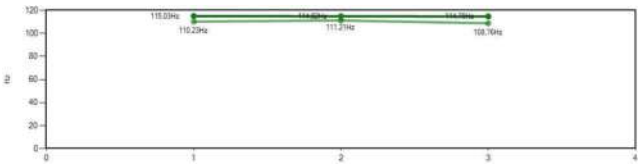
Fig. 6. Results for Muscle Strength Grading (MSG) of wrist flexor muscle strength, finger flexor muscle strength, wrist extensor muscle strength and finger extensor muscle strength.

- surface Electromyography (sEMG)

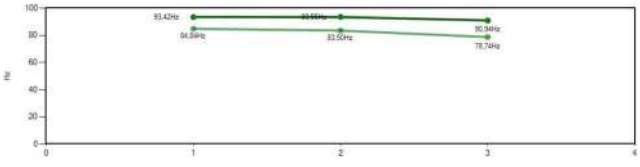
Such as shown in Fig. 7, after an improvement of 30% in the peak of flexor contraction of the fingers (flexor digitorum superficialis), there was a worsening of 32%. In relation to the contraction of the extensor digitorum muscle, there was also a worsening of 32% in its peak. In addition, no significant variation was observed in the mean and median frequency. We believe that this was due to the application of botulinum toxin in the left arm of the participant.



(a)



(b)



(c)

Fig. 7. Results for surface Electromyography (sEMG): a) peak value (μV) for flexor digitorum superficialis muscle and extensor digitorum muscle; b) Mean (dark green) and median (light green) frequencies for flexor digitorum superficialis muscle; c) Mean (dark green) and median (light green) frequencies for extensor digitorum muscle.

B. *Lower-Limb*

Regarding the lower limb, there was a 17% gain of Maximum Voluntary Contraction (MVC) for both the left extensor and flexor tibialis anterior muscles of the participant. Fig. 8 shows the results for these muscles.

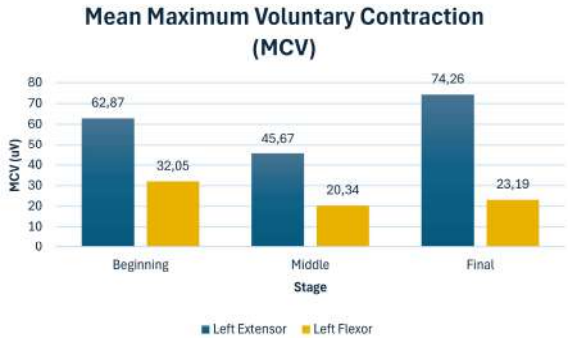


Fig. 8. Results for Maximum Voluntary Contraction (MVC) for the left tibialis muscle.

V. Conclusions

This work presented the application of a rehabilitation protocol using csDCS together with the use of MI-BCI-NFB, and applying FES. This protocol used the concept of ATD, in which a chronic post-stroke subject was submitted to these techniques to recover his left hand and leg movements. Results from these metrics showed a 41% gain of the participant's left hand function recovery, a 5% gain in performance in motor and cognitive/social domains, and a 50% improvement in both wrist extensor and finger extensor muscle strength.

Regarding the lower limb, there was a 17% gain of Maximum Voluntary Contraction (MVC) for the left tibialis anterior muscle. We believe these improvements were due to our therapy, which facilitated neuromodulation, enhancing the excitability of the motor cortex and improving muscle activation, as well as reducing spasticity and allowing for greater voluntary contraction during assessments. It is worth commenting that there is a limitation in this study, which evaluated only a single participant. On the other hand, this study does not present comparisons with other studies, as we believe that this is the first study using a combination of csDCS, MI-BCI-NFB and FES for post-stroke rehabilitation, therefore, more studies are needed to confirm the results with a wider sample, as well as conducting the research by blinded evaluators. Following this therapy, the next step of this research is to include transcranial Alternate Current Stimulation (tACS) and Transcranial Magnetic Stimulation (TMS) in our protocol.

ACKNOWLEDGMENT

T. Bastos-Filho acknowledges the financial support from CNPq and FAPES, Brazil. Aura Ximena Gonzalez-Cely acknowledges the financial support from CAPES/Brazil. Ana Cecilia Villa-Parra acknowledges the financial support from Universidad Politécnica Salesiana /Ecuador.

REFERENCES

[1] World population ageing 2020 highlights: Living arrangements of older persons. United Nations Dept. Economic Social Affairs, Population Division, Herndon, VA, 2020.

[2] CDC Homepage: Know your risk for stroke, https://www.cdc.gov/stroke/risk_factors.htm#:~:text=The%20chance%20of%20having%20a,65%20years%20also%20have%20strokes.&text=In%20fact%2C%20about%20one%20 in,adults%20ages%2015%20to%2049, last accessed 2024/11/20.

[3] CDC Homepage: About stroke, https://www.cdc.gov/stroke/about.htm#:~:text=A%20stroke%2C%20sometimes%20called%20a,term%20disability%2C%20or%20even%20death, 2024/11/20.

[4] V. Cardoso et al., "Effect of a brain-computer interface based on pedaling motor imagery on cortical excitability and connectivity," Sensors, vol. 21, 2020.

[5] T. Bastos-Filho, T., Introduction to non-invasive EEG-based brain-computer interfaces for assistive technologies. CRC Press, Boca Raton, 2020.

[6] A. Pollock et al., "Interventions for improving upper limb function after stroke," Cochrane Database Syst Rev., vol. 12(11), p. CD010820, 2014.

[7] R. Loureiro et al., "Advances in upper limb stroke rehabilitation: a technology push," Medical & Biological Engineering & Computing, vol. 49(10), pp. 1103-18, 2011.

[8] A. Aguilera-Rubio et al., "Feasibility and efficacy of a virtual reality game-based upper extremity motor function rehabilitation therapy in patients with chronic stroke: a pilot study," International Journal of Environmental Research and Public Health, vol. 19(6), p. 3381, 2022.

[9] S. Soekadar et al., "Brain-machine interfaces in neurorehabilitation of stroke," Neurobiology of Disease, vol. 83, pp. 172-179, 2015.

[10] N. Heena et al., "Effects of task complexity or rate of motor imagery on motor learning in healthy young adults," Brain Behav., vol. 11, p. e02122, 2021.

[11] C. Ruffino, C. Papaxanthis, and F. Lebon F., "Neural plasticity during motor learning with motor imagery practice: Review and perspectives," Neuroscience, vol. 26, pp. 61-78, 2017.

[12] G. Pfurtscheller, and F. H. Lopes, "Event-related EEG/MEG synchronization and desynchronization: basic principles," Clinical neurophysiology, vol. 110, pp. 1842–1857, 1999.

[13] M. Mihara et al., "Effect of neurofeedback facilitation on poststroke gait and balance recovery: a randomized controlled trial," Neurology, vol. 96, pp. e2587–e2598, 2021.

[14] H. Shin et al, "Therapeutic Effects of Functional Electrical Stimulation on Physical Performance and Muscle Strength in Post-stroke Older Adults: A Review," Annals of Geriatric Medicine and Research, vol. 26(1), p. 16-24, 2022.

[15] M. A., Lobo et al., " Single-case design, analysis, and quality assessment for intervention research," J Neurol Phys Ther., vol. 41(3), pp. 187-197, 2017.

[16] S. Mehrpour et al., "A review about synergistic effects of transcranial direct current stimulation (tDCS) in combination with motor imagery (MI)-based brain computer interface (BCI) on post-stroke rehabilitation," *Res. Biomed. Eng.*, vol. 40, pp. 43–67, 2024.

[17] A. Brodtmann et al., "Neurodegeneration over 3 years following ischaemic stroke: findings from the cognition and neocortical volume after stroke study," Frontiers in neurology, vol. 12, p. 754204, 2021.

[18] N. Bu et al., "Early brain volume changes after stroke: subgroup analysis from the axis-2 trial," Frontiers in neurology, vol. 12, p. 747343, 2022.

[19] T. Bastos, et al., "Towards upper- and lower-limb rehabilitation of post-stroke patients through brain-computer interface, cerebrospinal stimulation and robotic devices," in *6th International Conference on NeuroRehabilitation (ICNR2024)*, 2024, pp. 689–692.

[20] C. F. Blanco-Diaz et al., "A gait imagerybased brain-computer interface with visual feedback for spinal cord injury rehabilitation on lokomat," IEEE Transactions on Biomedical Engineering, pp. 1–10, 2024.

[21] E. Lopez-Larraz et al., "Control of an ambulatory exoskeleton with a brain–machine interface for spinal cord injury gait rehabilitation," Frontiers in Neuroscience, vol. 10, p. 359, 2016.

[22] V. Quiles et al., "Brain-machine interface based on transfer-learning for detecting the appearance of obstacles during exoskeleton-assisted walking," Frontiers in Neuroscience, vol. 17, p. 1154480, 2023.

[23] F. Lotte et al., "A review of classification algorithms for EEG-based brain–computer interfaces: a 10 year update," Journal of Neural Engineering, vol. 15(3), p. 031005, 2018.

[24] M. Ortiz et al., "An EEG database for the cognitive assessment of motor imagery during walking with a lower-limb exoskeleton," Scientific Data, vol. 10(1), p. 343, 2023.

[25] M. Ortiz et al., "Sensory integration in human movement: A new brain-machine interface based on gamma band and attention level for controlling a lower-limb exoskeleton," Frontiers in Bioengineering and Biotechnology, vol. 8, p. 735, 2020.

Comparative Analysis of Temporal Difference Learning Methods to Learn General Value Functions of Lower-Limb Signals

Sonny T. Jones, Grange M. Simpson, Wyatt M. J. Young,
Kylee North, Patrick M. Pilarski, Ashley N. Dalrymple

***Abstract*— Millions of people in the United States suffer from paralysis, resulting in significant deficits in motor function. Restricted mobility due to these deficits and the lack of adaptive rehabilitative solutions make traversing complex and challenging terrains unsafe. Exoskeletons offer a promising solution, but their effectiveness could be greatly enhanced by incorporating reinforcement learning algorithms for real-time adaptation to changing environments and the user's unique gait biomechanics. This study explored different temporal difference learning methods for predicting signals recorded from sensors on the lower-limbs, including muscle activation from electromyography, underfoot pressure, and joint angles from goniometers. Specifically, the performance of the temporal difference learning methods TD(λ), TOTD, and SwiftTD to quickly and accurately predict these signals was examined. From initial findings, SwiftTD generally converged faster, while TOTD typically achieved lower convergence errors. These outcomes varied depending on the specific signal that was being predicted, highlighting the need for careful consideration of algorithm choice depending on the signal, accuracy, and speed. The results, therefore, support the informed selection of specific algorithms for providing predictive knowledge to adaptive, machine learning-controlled assistive rehabilitative technologies. These findings will enable the selection of appropriate predictive algorithms, leading to the development of better exoskeletons and other assistive devices to enhance the mobility and quality of life of individuals with motor paralysis.**

I. Introduction

There are an estimated 5.4 million individuals currently in the United States who suffer from motor paralysis, with stroke and spinal cord injury as the leading causes [1]. People with impaired motor function often suffer from muscle stiffness, muscle spasms, and altered muscle activation, including weakness, impaired coordination, and reduced endurance [2]. Many individuals adapt to their restricted mobility, but experience difficulties while walking on more complex terrains such as slopes, curbs, stairs, uneven surfaces, and while turning. There is a critical need to provide personalized adaptive solutions to navigate changing and challenging terrains. The lack of adaptive solutions for rehabilitative devices to navigate changes in terrain transitions limits safe, reliable ambulation in complex environments. Developing responsive rehabilitative solutions can improve overall autonomy and mobility in people with motor impairments.

Current state-of-the-art control methods rely on static approaches such as state machines or kinematic models to define control parameters, which are not predictive and cannot anticipate changes of terrain in dynamic environments [3], [4]. Reinforcement Learning (RL) is a type of machine learning that can both learn and adapt sensorimotor predictions over time [5]. Because of this property, RL-based controllers for exoskeleton control promise to enable adaptation to individual users and varying environmental conditions [6], [7]. RL utilizes a trial-and-error learning paradigm that chooses the best actions and behavior based on learned expectations about future success (i.e., reward) [5]. This allows behavior to beneficially change before future events occur. RL also facilitates adaptation to unforeseen events via mechanisms of exploration and meta-learning [8]. Therefore, RL holds promise for more adaptable exoskeleton control, especially in dynamic environments [7]. Adaptability is particularly important for community ambulation, where individuals encounter various terrains and obstacles that require real-time adjustments to maintain stability and safety.

For adaptable RL-based controllers of exoskeletons, accurate and real-time signal prediction is essential. Temporal difference (TD) learning—the main learning process underpinning RL in both animals and machines [5]—has been shown to learn reliable predictions of various gait-related signals, including electromyography (EMG), underfoot pressure, and joint angles, for applications in prosthesis and exoskeleton control, as well as spinal cord stimulation [9]–[11]. However, there remains a gap in identifying the most effective TD algorithms for approximating these gait-relevant sensor signals. Closing this gap is necessary for enhancing the accuracy and functionality of RL-based controllers that rely on these predictions for real-time decision-making.

This present study explores and compares different TD learning algorithms for the prediction of walking kinetic and kinematic signals relevant to exoskeleton control, including muscle activation from EMG, underfoot pressure, and joint angles. The approach aims to predict these complex biomechanical signals while people walk across different terrains. By providing methods to determine the most appropriate algorithm for this task, groundwork can be laid for future applications that leverage the predictive capabilities of RL to anticipate transitions between different types of terrains dur-

We thank the Departments of Biomedical Engineering and Physical Medicine and Rehabilitation for funding this study. PMP was supported by NSERC, Amii, and the Canada CIFAR AI Chairs program. We also thank our participants who volunteered their time.

S. T. Jones (corresponding author e-mail sonny.jones@utah.edu), G. M. Simpson, W. M. J. Young, and K. North are with the Department of Biomedical Engineering, University of Utah, Salt Lake City, UT, USA.; P. M. Pilarski is with the Alberta Machine Intelligence Institute (Amii), and the Department of Medicine and Department of Computing Science, University of Alberta, Edmonton, Alberta, Canada; A. N. Dalrymple (corresponding author e-mail ashley.dalrymple@utah.edu) is with the Department of Biomedical Engineering and the Department of Physical Medicine and Rehabilitation, University of Utah, Salt Lake City, UT, USA.

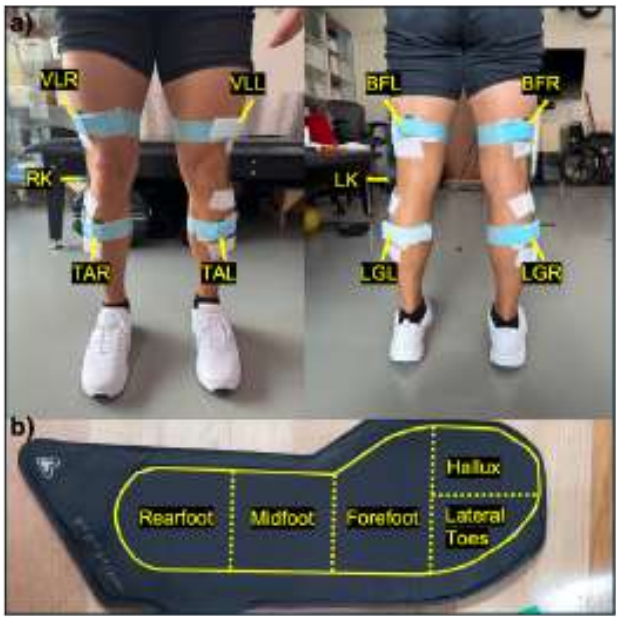


Fig. 1. Experimental setup showing a study participant equipped with the sensor suite. a) EMG sensors are placed on the TAL, TAR, LGL, LGR, VLL, VLR, BFL, and BFR to capture muscle activations during walking. Goniometers are placed on the LK and RK to capture joint angles. b) Pressure insoles with the divided bins.

ing walking. The goal is to create adaptive control strategies for lower-limb exoskeletons that adapt to the user's unique biomechanics and facilitate safe gait over variable terrains.

II. Methods

A. Participants

Nine healthy participants (3 female, aged 19 - 31 years) with no known neuromuscular deficits were recruited for this study. All participants provided written informed consent following the University of Utah Institutional Review Board (IRB00171076).

B. Data Acquisition and Processing

Participants were fitted with 8 wireless EMG sensors, 2 wireless goniometers (Trigno, Delsys, Natick, MA, USA), and 2 wireless pressure-sensing insoles (XSensor, Calgary, AB, Canada). EMG sensors were placed bilaterally on the tibialis anterior (TAL/TAR), lateral gastrocnemius (LGL/LGR), vastus lateralis (VLL/VLR), and biceps femoris (BFL/BFR), with 'L' or 'R' at the end of each abbreviation indicating the left or right leg, respectively. Before sensor placement, each muscle belly was cleaned with abrasive gel and alcohol (LemonPrep, Mavidon, Flat Rock, NC) and treated with conductive electrode gel (Signagel, Parker, Fairfield, NJ). Sensors were secured with double-sided Delsys adhesive and Medipore medical tape (3M, Saint Paul, MN). Each EMG sensor sampled data at 1926 Hz. Goniometers were placed bilaterally on the lateral knee joint (LK and RK) with Medipore tape and sampled joint angle data at 519 Hz. Pressure insoles were placed in the participant's shoes and sampled underfoot pressure at 33 Hz. The sensor setup is illustrated in Figure 1a. Hardware and data collection were controlled using a custom graphical user interface (GUI) built in Python (version 3.8.1, Python Software Foundation, Wilmington, DE) running on a computer with an Intel Core i7 CPU and 32 GB of RAM. Data were collected online and saved for offline analysis.

EMG data were processed using a 4th-order Butterworth bandpass filter (10 Hz high pass, 450 Hz low pass, the function *scipy.signal.filtfilt* doubles filter order). The filtered signal was rectified, and a moving average (window size of 0.1 times the EMG sampling rate) was applied to obtain the signal envelope. The resulting envelope was down-sampled to 33 Hz to match the insole sampling rate. EMG data were normalized to each muscle's maximum voluntary contraction (MVC), where participants maximally contracted the muscle isometrically [12]. Pressure data were normalized to the participant's weight. The pressure insoles contain 235 total sensors. The foot was divided into 5 different regions, and the average value of each region was taken at each time step (Figure 1b) [13]. Pressure signals were smoothed using an exponential moving average with a filter size equal to 11 samples. Goniometer data were down-sampled to 33 Hz and were normalized to [0, 1].

C. Machine Learning Approach

1) Selective Kanerva Coding: Selective Kanerva Coding (SKC) is a function approximation method to reduce a high-dimensional continuous state space into a binary feature vector, shown to be useful with stochastic sensor data in rehabilitation settings [10], [11], [14]. Thirty sensor signals formed the state space: 8 EMG signals, 20 underfoot pressure signals (regions and moving averages), and 2 goniometer signals [10]. Sensor signals were normalized to [0, 1].

SKC was initialized by randomly distributing $K = 2500$ prototypes across the state space. Prototype positions were held constant after initialization. The c closest prototypes to the current state were found according to the Euclidean distance between the current state and the prototypes, sorted with Hoare's quickselect [14]. 3-c values were utilized, such that the resulting binary feature vector had a length equal to $len(c)*K$ long with $sum(c)$ active features, for more flexible representations and more granularity of the state space [10].

2) General Value Functions: Traditionally, RL allows an agent to explore an environment, learning to assign value to actions and states according to the expected, or predicted, future reward. [5]. The value function approximates the expected return, the future cumulative discounted sum of rewards an agent can expect from a particular state. Value functions can also be used to estimate the future values of any arbitrary signal of interest, called the cumulant (Z) [15], [16]. These functions are called General Value Functions (GVFs; [16]). GVFs have previously been used to quickly predict walking-related signals, including EMG, ground reaction forces, and angular velocity [9], [10].

3) Temporal Difference (λ) Learning: Temporal Difference (TD) learning is a fundamental RL algorithm where an agent learns from experience without relying on a model

of the environment [17]. TD learning is the key method used to update predictions of GVFs [16]; it provides good performance and low computational complexity [5], [18]. TD learning adapts the predicted future rewards for a specific state. It uses the observed reward for the current state and the predicted value of the next state to adjust the current prediction, making it closer to the observed reward plus the discounted value of the next state. The core component of this update is the TD error (δ), which calculates the difference between the current state estimate (V) and an estimate of the future state (V'). TD learning uses a discount factor (γ, $0 \leq \gamma \leq 1$) that determines whether the algorithm estimated more immediate or long-term reward.

TD(λ) extends basic TD learning by introducing an additional decaying parameter (λ, $0 \leq \lambda \leq 1$) that determines whether the algorithm prioritizes previous learning or current value estimations to update the predictions [5]. This decaying parameter is combined with an eligibility trace (e) to assign credit to previous states for the current reward or error. The TD(λ) algorithm is outlined in black in Algorithm 1. While TD(λ) is powerful, it can be sensitive to divergence in the online setting from the mathematically optimal solution in settings where function approximation is used, especially with larger step sizes. [18]. TD(λ) uses an accumulated trace to update e, which can lead to unbounded updates. The combination of unbounded updates and large step sizes causes the learning algorithm to become unstable, leading to divergence and poor prediction performance.

4) True Online Temporal Difference Learning: True Online Temporal Difference (TOTD) learning solves the divergence problem of TD(λ) learning by adding extra terms to the update rule for the eligibility trace and weight vectors [18]. The additional components introduced by TOTD are shown in red in Algorithm 1. Specifically, TOTD uses a Dutch trace to update the eligibility trace, which bounds the eligibility update. Additionally, TOTD introduces a TD error correction to account for the change in the estimates of the predictions over time. This correction helps to maintain consistency with the online mathematical update, leading to more accurate predictions without divergence. These improvements enable more stable learning, particularly with larger step sizes. TOTD is also computationally more efficient than TD(λ), especially with larger state spaces [18].

5) SwiftTD: SwiftTD aims to improve TD(λ) learning by introducing adaptive step sizes with maximum bounds that decay over time [19]. This approach solves the problem of large step size sensitivity in TD methods, allowing faster learning while maintaining stability. Instead of updating the weight vector with a single step size, this algorithm uses a custom step size to adjust each weight. SwiftTD dynamically adjusts each step size based on the magnitude of previous updates, helping to overcome slow learning from small updates. A meta-step size (θ) is employed to update the step sizes of the weights. A step size bound (η) and decay (ϵ) are introduced to combat divergence from overly large updates. The additional components added by SwiftTD are highlighted in blue in Algorithm 1.

Algorithm 1 Learning GVFs with TD Methods

Indicators: TD(λ), TOTD, SwiftTD
Input: $\lambda, \gamma, \alpha, \theta, \epsilon, \eta, \alpha_{init}$
Initialize: $w, x, V_{old}, S, e, \bar{e}, p, h \leftarrow 0, \beta \leftarrow \alpha_{init}$
Repeat every time-step:
Generate next state S' and cumulant Z'
$x' \leftarrow SKC(S')$
$V \leftarrow w^T x$, $V' \leftarrow w^T x'$
$\delta \leftarrow Z + \gamma V' - V$ {TD Error}
$T \leftarrow e^T x$
$E \leftarrow max(\eta, \alpha^T x^2)$
$V_{diff} \leftarrow V - V_{old}$
$e \leftarrow \gamma\lambda e + x - \alpha\gamma\lambda(e^T x)x$ {TD(λ), TOTD}
$w \leftarrow w + \alpha(\delta + V_{diff})e - \alpha V_{diff} x$ {TD(λ), TOTD}
for i = 1, 2, ..., n **do**
  $\alpha_i \leftarrow e^{\beta_i}$
  $e_i \leftarrow \gamma\lambda e_i + \frac{\eta}{E}\alpha_i x_i - \alpha_i\gamma\lambda T x_i$
  $w_i \leftarrow w_i + \delta e_i - \alpha_i x_i V_{diff}$
  $p_i \leftarrow \gamma\lambda p_i + x_i h_i$
  $\beta_i \leftarrow \beta_i + \frac{\theta}{\alpha_i + e^{-8}}\delta h_i$
  $\bar{e}_i \leftarrow \gamma\lambda\bar{e}_i + \alpha_i x_i[1 - \gamma\lambda T - \gamma\lambda x_i \bar{e}_i]$
  $k \leftarrow h_i$
  $h_i \leftarrow h_i[1 - \alpha_i x_i^2] - h_i^{old} x_i[e_i - x_i\alpha_i] + \delta\bar{e}_i - x_i\alpha_i V_{diff}$
  $h_i^{old} \leftarrow k$
  $if(E > \eta \; and \; x_i \neq 0) \; : \; \beta_i = \beta_i - ln(\epsilon)$
end for
$V_{old} \leftarrow V', x \leftarrow x'$

TABLE I
LEARNING PARAMETERS FOR TD ALGORITHMS

Parameter	TD(λ)	TOTD	SwiftTD
λ	0.5	0.5	0.9
α	0.015	0.015	NA
α_{init}	NA	NA	0
θ	NA	NA	-2
ϵ	NA	NA	0.9
η	NA	NA	0.2

6) Learning Parameter Selection: The learning parameters used for each algorithm were selected using a grid search on a subset of data to minimize prediction error, comparing the predicted GVF and the actual return on a subset of the data (Table 1).

D. Experimental Protocol

Participants performed MVCs for each muscle group for EMG signal normalization. Participants walked across designated tracks with various terrains, including even ground, uneven ground, up and down ramps, upstairs, downstairs, and left and right turns (Figure 2). The experiment was comprised of a total of 10 trials. Participants first walked across Track 1 four times, then three times across Track 2, and concluded by walking across Track 3 three times. Continuous data were collected from all sensors while participants transversed the terrains during the walking trials. Transitions between terrains were synchronously marked when the participant first stepped onto a new terrain surface.

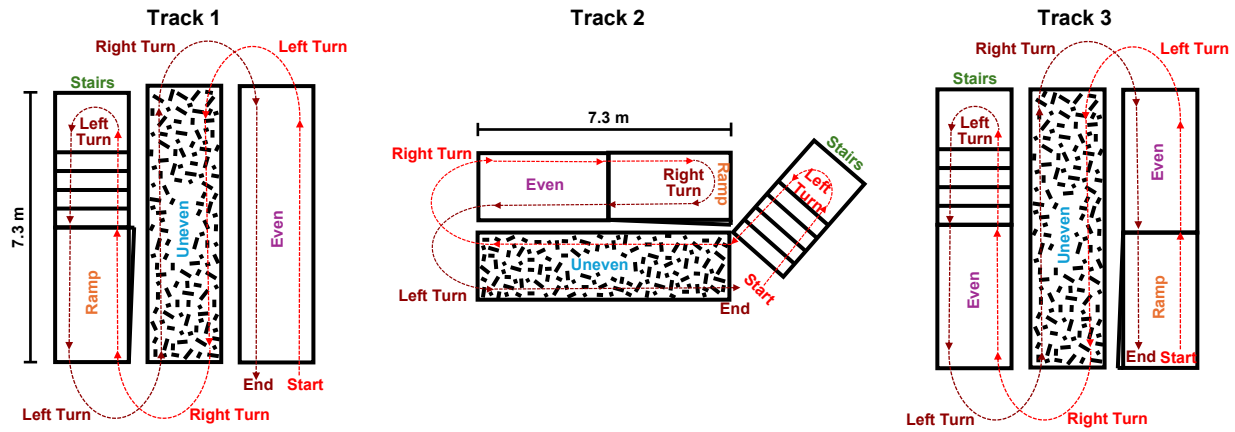


Fig. 2. Participants begin walking on the track from the 'Start' and follow the arrows until the 'End' mark. The straight portion of the terrain track was 7.3 m long. Terrain tracks include even ground, uneven ground, up and down ramps, upstairs, downstairs, and left and right turns. Participants first began walking on track 1 four times, followed by three times on track 3, and finished with three times on track 3.

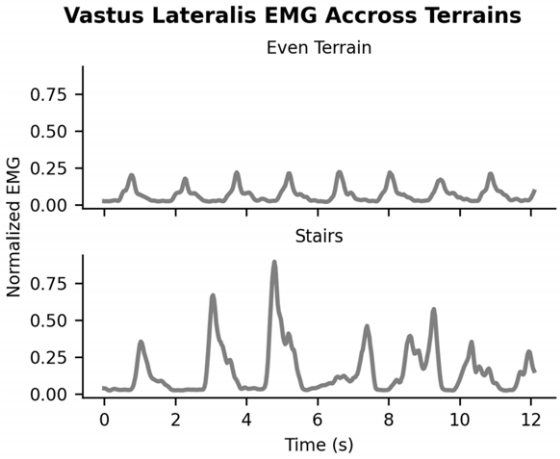


Fig. 3. Representative EMG captured from the VLL muscle from P3 walking on different terrains, showing larger VLL activation on stairs compared to even ground.

E. Analyses and Statistics

Each TD learning method was used to obtain GVFs for EMG, pressure, and goniometer signals as cumulants at multiple time scales: 0.25, 0.5, 1.0, and 2.0 seconds. In total, 360 GVFs were learned in parallel [16]. The γ values were calculated using $\gamma = 1 - \frac{1}{T}$ where $T = fs * timescale$ and were 0.879, 0.940, 0.970, and 0.985, respectively [10]. These time scales capture the immediate and longer-term dynamics of the sensor signals.

The performance of each algorithm was evaluated by comparing the convergence time and the root mean squared error (RMSE) between the expected and predicted returns. [15], [20]. This was done by fitting the learning curve with a single breakpoint piecewise regression, where the second line was fitted to the flat, stabilized error of the learning curve. The x-value, corresponding to timesteps, at 10% along the second fitted line was taken as the convergence time, and the y-intercept was taken as the convergence error. This enabled the assessment of the speed and accuracy of learning GVFs using each TD learning method.

Normality was assessed using the Shapiro-Wilk Test. Data were found to be non-normally distributed; therefore, the Kruskal-Wallis test was used to compare the convergence times and errors between the TD learning methods. Metrics were compared using Dunn's Test with a Holms-Sidak correction to correct for multiple comparisons.

III. Results and Discussion

The time to featurize the data and obtain predictions using GVFs was 9.8 $\pm$ 0.8 ms for TD(λ), 13.9 $\pm$ 0.9 ms for TOTD, and 22.3 $\pm$ 1.6 ms for SwiftTD. Therefore, the computation times allow for real-time implementation within our 33 Hz (30.3 ms) loop time.

A. Sensor Signals Differ Between Different Walking Terrains

As participants walked across the terrains, the sensor signals exhibited distinct differences in shape and amplitude. For example, during stair ascent, larger activations of the VL muscle were required to lift the individual up the stairs (Figure 3). Larger VL activation was additionally associated with an increase in underfoot pressure towards the forefoot and hallux as they pushed off the ball of their foot during stair ascent. Although this was the most noticeable example, there were differences in all signals between terrains.

B. SwiftTD Outperforms TOTD in Convergence Time But Can Have Higher Convergence Error When Learning GVFs

The expected return was compared to the predictions of the raw signal by the TD methods (Figs. 4 and 5). Figure 5 shows the raw signal, expected return, and predicted return from the TD learning algorithms. The expected return represents a temporal abstraction of the cumulative discounted signal, which TD learning methods try to predict [15]. Generally, the expected return anticipated the rise and fall of the raw signal, demonstrating successful signal prediction.

Convergence error and time were derived from RMSE curves, comparing the predicted signal to the expected return for each sensor signal. The predictions for TD(λ) and TOTD were nearly identical (Figure 5), and there was no statistical difference in convergence time and error between both methods; therefore, TD(λ) was excluded from further

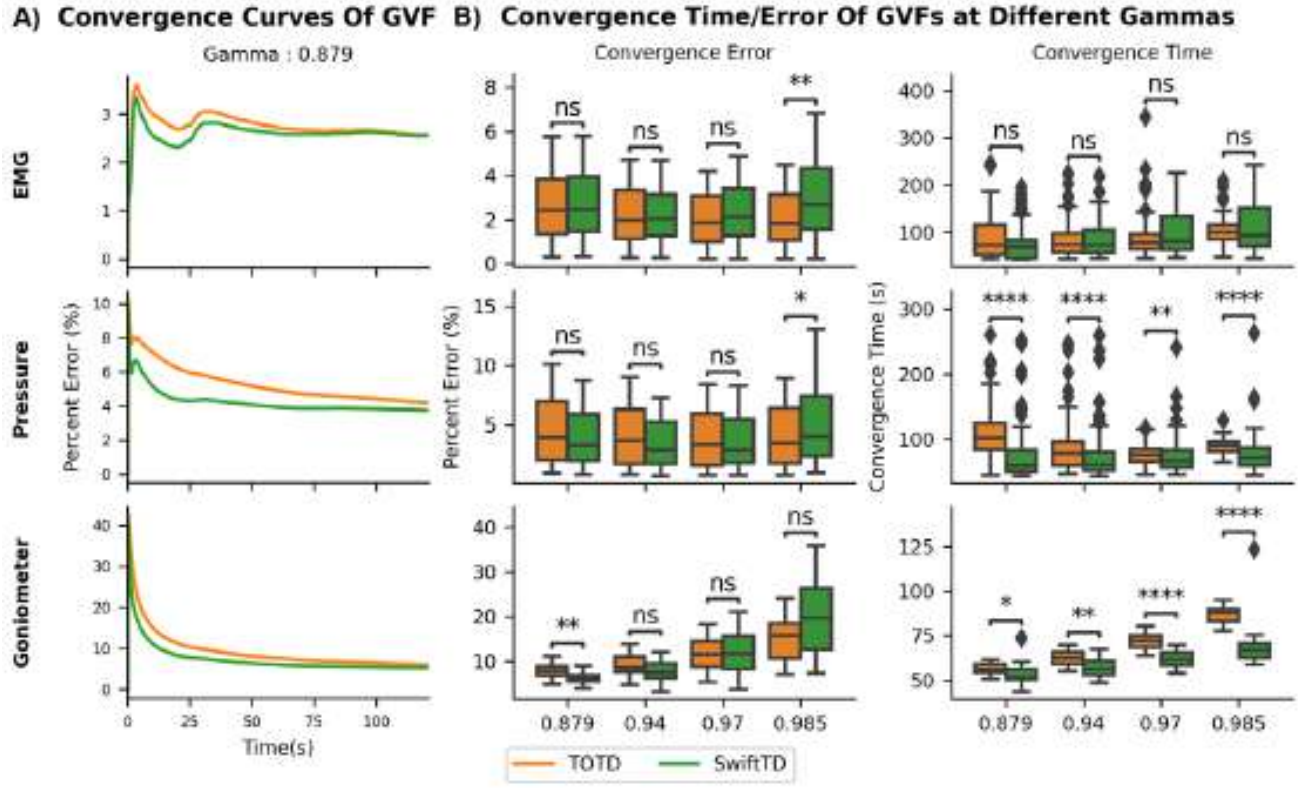


Fig. 4. Convergence error and convergence time performance metrics for evaluating TD learning algorithms. (A) The average RMSE convergence curves for EMG, underfoot pressure, and goniometer signals at the discount factor (γ) of 0.879. Error is reported as the percentage of the maximum cumulant value. (B) Boxplots contain the convergence errors and times for EMG, underfoot pressure, and goniometer signals (ns: $p \geq 0.05$, *: $p < 0.05$, **:$p < 0.01$, ***: $p < 0.001$, ****:$p < 0.0001$). Statistical annotations done using the *Statsannotation* package (v0.2.3) [21]

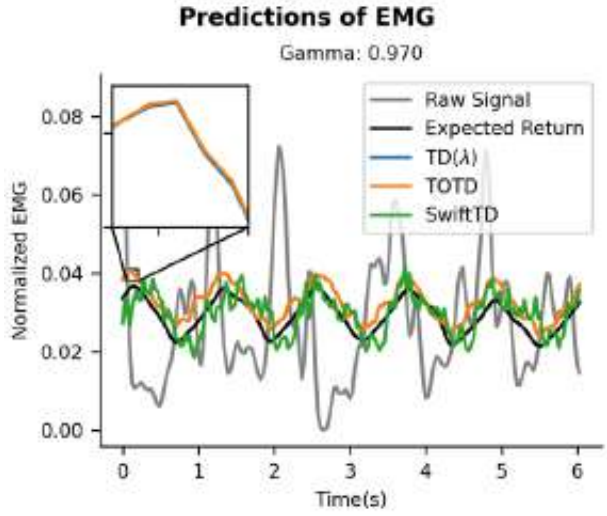


Fig. 5. Comparison of representative EMG signal, the expected return of predictions, and predictions made by three TD learning algorithms (TD(λ), TOTD, and SwiftTD) of P2's TAL muscle. Note the varying degrees of accuracy and anticipatory behavior exhibited by each algorithm compared to the expected return. TD(λ) predictions overlap the TOTD predictions.

analyses, and all comparisons were made between TOTD and SwiftTD. Figure 4A illustrates the convergence curves from TOTD and SwiftTD for three different sensor signals.

For EMG prediction, no significant differences in convergence error were observed across γ values of 0.879 (0.25s), 0.94 (0.5s), and 0.97 (1s) ($p = 0.996$, $p = 0.931$, $p = 0.267$). At γ = 0.985 (2s), however, TOTD demonstrated a 27.0% lower error than SwiftTD ($2.08\% \pm 1.2\%$ vs $2.85\% \pm 1.6\%$) ($p = 0.007$). Convergence times for both algorithms were not different across all γ values ($p = 0.495$, $p = 0.870$, $p = 0.516$, $p = 0.895$). TOTD generally minimized error when learning GVFs on EMG signals with higher γ values. The lack of difference in convergence time indicates that both algorithms sufficiently learned GVFs of EMG signals.

Convergence errors for predicting underfoot pressure were not different across γ values of 0.879 (0.25s), 0.94 (0.5s), and 0.97 (1s) ($p = 0.216$, $p = 0.246$, $p = 0.975$). However, at γ = 0.985 (2s), TOTD outperformed SwiftTD with a 21.4% lower convergence error ($3.98\% \pm 2.50\%$ vs. $5.06\% \pm 3.25\%$, $p = 0.034$). SwiftTD converged faster than TOTD in all cases, with the largest performance increase at γ = 0.879, where SwiftTD converged 33.9% faster ($71.0s \pm 36.4s$ vs $105.5s \pm 40.6s$) ($p = 0.003$, $p < 0.001$, $p < 0.001$, $p < 0.001$). Based on these results, GVFs of pressure signals learned using TOTD at γ = 0.985 minimized the convergence error. For lower γ values, SwiftTD minimized the convergence time with errors similar to those of TOTD.

The most noticeable convergence error difference for predicting joint angle signals was at γ = 0.879 (0.25s), where SwiftTD converged with a 20.5% lower average error compared to TOTD ($6.31\% \pm 1.27\%$ vs $7.94\% \pm 1.58\%$) ($p = 0.009$). SwiftTD converged faster than TOTD in all cases, with the biggest performance increase at γ = 0.985,

with SwiftTD converging faster by 19.1% ($69.7s \pm 13.8s$ vs $86.2s \pm 5.2s$) ($p < 0.001$). These results suggest that a lower γ value of 0.879 for the joint angle prediction task was suitable for minimizing convergence error with SwiftTD. Additionally, SwiftTD excelled in convergence time. For learning GVFs of goniometer signals at higher γ values, SwiftTD minimized convergence time with similar convergence errors compared to TOTD.

These results extend prior work using TD methods for predicting kinetic and kinematic signals [9], [10]. The current work showed that choices in prediction timescale and learning algorithms affect prediction accuracy and learning time of GVFs. Convergence error increased with higher γ values, indicating a potential trade-off between temporal abstraction and prediction accuracy. This highlights the importance of careful algorithm selection and parameter tuning based on the application requirements and type of signal.

Although valuable insights are extracted from this comparative analysis, it is important to acknowledge some limitations. This analysis compared convergence speed and error as primary evaluation metrics, but other factors may be relevant in real-world applications. For example, the computational complexity of each algorithm is not discussed but may be pertinent to real-time implementation. Additionally, the TD algorithms chosen for this comparison were a focused subset of those currently in use. Future studies could add other TD algorithms, such as Gradient TD, for a more comprehensive analysis. Future research will assess the prediction performance across each terrain to understand how a changing environment impacts learning.

IV. Conclusion

There currently remains a gap in empirical evidence regarding the most effective TD algorithms for predicting lower-limb sensor signals during walking. This study assessed the performance of TD learning algorithms for predicting walking-related sensor signals during walking tasks relevant to the control of exoskeletons and related standing-and-walking rehabiltiation technology. As a main contribution, evidence was found in this setting that SwiftTD favors learning efficiency, while TOTD favors learning accuracy. Careful consideration of TD learning algorithms is essential to balance the trade-off between accuracy and temporal abstraction when deployed. Future work includes assessing the impact of TD-learned predictive knowledge online in an exoskeleton controller to provide adequate and timely assistance for individuals with motor deficits. These findings reinforce the idea that an exoskeleton controller integrated with RL could adapt to an individual's unique biomechanics, paving the way for truly personalized assistive technologies.

References

[1] B. S. Armour, E. A. Courtney-Long, M. H. Fox, H. Fredine, and A. Cahill, "Prevalence and causes of paralysis—united states, 2013," *American journal of public health*, vol. 106, no. 10, pp. 1855–1857, 2016.

[2] C. M. Cirstea, "Gait rehabilitation after stroke: should we re-evaluate our practice?" pp. 2892–2894, 2020.

[3] D. Archangeli, B. Ortolano, R. Murray, L. Gabert, and T. Lenzi, "A Lightweight Powered Hip Exoskeleton with Parallel Actuation for Frontal and Sagittal Plane Assistance," *IEEE Transactions on Robotics*, pp. 1–17, 2025. [Online]. Available: https://ieeexplore.ieee.org/document/10874165/

[4] S. A. Murray, K. H. Ha, C. Hartigan, and M. Goldfarb, "An Assistive Control Approach for a Lower-Limb Exoskeleton to Facilitate Recovery of Walking Following Stroke," *IEEE Transactions on Neural Systems and Rehabilitation Engineering*, vol. 23, no. 3, pp. 441–449, May 2015. [Online]. Available: https://ieeexplore.ieee.org/document/6876184/

[5] R. S. Sutton, "Reinforcement learning: An introduction," *A Bradford Book*, 2018.

[6] M. Tucker, M. Cheng, E. Novoseller, R. Cheng, Y. Yue, J. W. Burdick, and A. D. Ames, "Human preference-based learning for high-dimensional optimization of exoskeleton walking gaits," in *2020 IEEE/RSJ International Conference on Intelligent Robots and Systems (IROS)*. IEEE, 2020, pp. 3423–3430.

[7] Q. Zhang, J. Si, X. Tu, M. Li, M. D. Lewek, and H. Huang, "Toward task-independent optimal adaptive control of a hip exoskeleton for locomotion assistance in neurorehabilitation," *IEEE Transactions on Systems, Man, and Cybernetics: Systems*, 2024.

[8] A. Nagabandi, I. Clavera, S. Liu, R. S. Fearing, P. Abbeel, S. Levine, and C. Finn, "Learning to adapt in dynamic, real-world environments through meta-reinforcement learning," *arXiv preprint arXiv:1803.11347*, 2018.

[9] P. M. Pilarski, T. B. Dick, and R. S. Sutton, "Real-time prediction learning for the simultaneous actuation of multiple prosthetic joints," in *2013 IEEE 13th International Conference on Rehabilitation Robotics (ICORR)*. IEEE, 2013, pp. 1–8.

[10] A. N. Dalrymple, D. A. Roszko, R. S. Sutton, and V. K. Mushahwar, "Pavlovian control of intraspinal microstimulation to produce over-ground walking," *Journal of neural engineering*, vol. 17, no. 3, p. 036002, 2020.

[11] P. Faridi, J. K. Mehr, D. Wilson, M. Sharifi, M. Tavakoli, P. M. Pilarski, and V. K. Mushahwar, "Machine-learned adaptive switching in voluntary lower-limb exoskeleton control: Preliminary results," in *2022 International Conference on Rehabilitation Robotics (ICORR)*. IEEE, 2022, pp. 1–6.

[12] G. Avdan, S. Onal, and B. K. Smith, "Maximum voluntary contraction (MVC) techniques to normalize lower limb muscle groups in young healthy subjects," *IIE Annual Conference Proceedings*, 2022.

[13] A. Searle, M. J. Spink, C. Oldmeadow, S. Chiu, and V. H. Chuter, "Calf muscle stretching is ineffective in increasing ankle range of motion or reducing plantar pressures in people with diabetes and ankle equinus: A randomised controlled trial," *Clinical biomechanics*, vol. 69, pp. 52–57, 2019.

[14] J. B. Travnik and P. M. Pilarski, "Representing high-dimensional data to intelligent prostheses and other wearable assistive robots: A first comparison of tile coding and selective kanerva coding," in *2017 International Conference on Rehabilitation Robotics (ICORR)*. IEEE, 2017, pp. 1443–1450.

[15] A. White, "Developing a preditive approach to knowledge," Ph.D. dissertation, University of Alberta, 2015.

[16] R. S. Sutton, J. Modayil, M. Delp, T. Degris, P. M. Pilarski, A. White, and D. Precup, "Horde: A scalable real-time architecture for learning knowledge from unsupervised sensorimotor interaction," in *The 10th International Conference on Autonomous Agents and Multiagent Systems-Volume 2*, 2011, pp. 761–768.

[17] R. S. Sutton, "Learning to predict by the methods of temporal differences," *Machine learning*, vol. 3, pp. 9–44, 1988.

[18] H. Van Seijen, A. R. Mahmood, P. M. Pilarski, M. C. Machado, and R. S. Sutton, "True online temporal-difference learning," *Journal of Machine Learning Research*, vol. 17, no. 145, pp. 1–40, 2016.

[19] K. Javed, A. Sharifnassab, and R. S. Sutton, "SwiftTD: A fast and robust algorithm for temporal difference learning," *Reinforcement Learning Journal*, vol. 2, pp. 840–863, 2024.

[20] A. Kearney, A. J. Koop, and P. M. Pilarski, "What's a good prediction? challenges in evaluating an agent's knowledge," *Adaptive Behavior*, vol. 31, no. 3, pp. 197–212, 2023.

[21] F. Charlier, M. Weber, D. Izak, E. Harkin, M. Magnus, J. Lalli, L. Fresnais, M. Chan, N. Markov, O. Amsalem, S. Proost, A. Krasoulis, getzze, and S. Repplinger, "Statannotations," 2022. [Online]. Available: https://doi.org/10.5281/zenodo.7213391

Effort generation capabilites mapping for personalized robotic assistance of the elbow

Maël Gallois[1], Maxime Manzano[2], Sylvain Guegan [3], Nicolas Vignais [4], Marie Babel [2] and Charles Pontonnier[1]

***Abstract*— This study explores the use of a robotic aid to improve the mobility of people with neuromuscular or neurodegenerative disorders, who have reduced motor skills. It aims to compare the use of either a musculoskeletal model or a torque-angle joint model in a shared control framework of an upper limb exoskeleton in order to assists elbow flexion/extension movements. The method consists of measuring the effort-generating capacities of the elbow using an isokinetic ergometer. Data were then used to calibrate the two models. Both were integrated into an exoskeleton control law to estimate online user isometric capacities during a mass-holding task performed in various positions. Four experimental conditions were compared: without exoskeleton, with exoskeleton without assistance, with assistance computed from the quadratic model and from the musculoskeletal model. In order to test the method against individual variability, the study was conducted with nine participants. The results show a decrease in muscular activity for the biceps in both assistance conditions. In extrapolating effort-generating capacities outside the ergometer's measured range, the musculoskeletal model is more robust than the torque-angle joint model. Its estimations are more consistent with the literature, while torque-angle joint model errors induces unintended triceps activation. In conclusion, this study highlights the potential of combining a musculoskeletal model with shared control for assisting elbow.**

I. INTRODUCTION

Upper limb assistance is essential for individuals with neuromuscular or neurodegenerative disorders, which hinder their ability to perform daily tasks and reduce their autonomy. Robotic assistance can then help restore independence by partially or fully supporting the user's actions.

Currently, shared control is a widely used approach in the field of robotic assistance. This collaborative method involves to share the control responsibility between the human and the robot during task execution. An effective implementation requires accurately interpreting the user's intentions and generating commands tailored to the task and the user's specific needs. Admittance control is a common strategy of shared control for assitive robotic: it adjusts the robot position or velocity in response to the measured interaction forces or torques [1].

However, designing efficient shared control systems requires to adapt the provided assistance to the user capabilities, and can be challenging in particular for users that face multiple mobility impairments. To alleviate this issue, one solution is to accurately estimate the effort-generating capacity of users and take this information into account in the assistive control, thus enhancing user experience [2].

Incorporating user capability estimates into exoskeleton control effectively adapts assistance, as it has been shown in a walking-assistance systems [3]. A similar strategy could benefit upper-limb assistance. In this case, for instance, effort capability estimators have been used in minimal assist-as-needed (mAAN) controllers for static poses [4]. However, the personalization of these estimations in the field of upper limb assistive robotics remains unexplored in the literature.

Nonetheless, works have already been made to represent effort generation capabilities. For example, joint torque generation capabilities have been represented as joint torque-angle relationships [5], specifically as a quadratic function in the case of the elbow [6]. Alternatively, such works have been used to calibrate musculoskeletal models with individualized parameters from experimental measurements [7], [8]. These models could then be used to estimate effort-generating capacities of the user [9]. In turn, these biomechanical representations can be used to personalize robotic assistance.

Here, we aim to integrate a personalized estimator of the user's effort generation capabilities into the shared control of an upper-limb exoskeleton. The objective of this study is then to compare two force capabilities representations, i.e. torque-angle model and musculoskeletal model. For instance, we focused in the context of elbow assistance. In Section II, we present two estimators based on experimental measurements. The first is a quadratic torque-angle model (TAM). The second is a personnalized musculoskeletal model (MSM) based on the Saul et al. upper limb model [10]. Then, a control law derived from these two effort generation capabilities representations is introduced and an experimental evaluation is proposed. Section III presents and discusses the evaluation results. Finally, Section IV provides a conclusion.

II. MATERIALS AND METHODS

This section presents two methods of effort generation capabilities estimators. Subsequently, an assistive control law utilising a effort estimator is described, as well as a proposed experimental protocol.

A. Torque-angle joint model (TAM)

The objective is to obtain the torque-angle relationship of the elbow. This requires to measure the maximum isometric

[1]Univ Rennes, Inria, CNRS, IRISA - UMR 6074, F-35000 Rennes, France, mael.gallois@inria.fr

[2]Univ Rennes, INSA Rennes, Inria, CNRS, IRISA - UMR 6074, F-35000 Rennes, France

[3]Univ Rennes, INSA Rennes, LGCGM, F-35000 Rennes, France

[4]M2S Laboratory, Rennes 2 Université, École Normale Supérieure de Rennes, F-35000 Rennes, France

torque τ_{isom} in flexion ($\tau_{isom} > 0$) and extension ($\tau_{isom} < 0$) over the joint amplitude. Directly measuring isometric torque for each position in the workspace is time-intensive and may cause significant fatigue for the participant. To optimize the process and limit fatigue, we proposed to conduct isokinetic tests, i.e. at a constant speed. However, as muscles capacities are non-linearly coupled with speed values, these tests inherently alter the elbow torque values. To address this issue, we performed tests in two distinct configurations for each direction of efforts (flexion and extension), namely concentric (effort in the direction of movement) and eccentric (effort opposing the movement). These measurements τ_{mes} are obtained using an isokinetic ergometer (see Figure 1), a device designed for rehabilitation that measures joint capacities using a torque sensor aligned with the rotational axis of the participant's joint. The ergometer imposed a constant speed of 30 degrees per second, which was considered to be sufficiently low to ensure a near-linear relationship between torque and speed variation [5]. This linearity allowed us to approximate the isometric torque curve by averaging the results of both concentric and eccentric tests. Each of the four configurations was repeated three times, and for each elbow angle, we retained the maximum value measured.



Fig. 1. The isokinetic ergometer used for joint torque measurements (ConTrex, Medimex).

The experiment was validated by the Operational Committee for the Evaluation of Legal and Ethical Risks (COERLE) of the Inria institute. Nine participants took part in the study (height in cm: 175.3 ± 5.4, weight in kg: 70.3 ± 9.54, age in years : 25.8 ± 8.6). The joint range of elbow motion varied between participants, with a mean range of 60.2±3.2 to 126.8±5.8 degrees. Using the collected data, we fit two quadratic TAMs to the experimental isometric torque curves for both flexion and extension

B. Personnalized musculoskeletal model (MSM)

The MSM is composed of two layers. The first layer consists of an osteoarticular model describing geometrical and inertial properties of the upper limb. It is represented as a two-dimensional system composed of three rigid bodies: the trunk (considered as a fixed reference frame), the arm, and the forearm/hand. These rigid bodies are connected by two revolute joints, simulating the flexion/extension motions of the shoulder and elbow. The joint angles are denoted as q_1 (shoulder) and q_2 (elbow).

The second layer of the MSM is the actuation model, consisting in muscles lines attached to the osteoarticular model. The muscles behavior is based on the Hill-Zajac model [11], ans the model incorporates $N_m = 12$ muscles. Their insertion points and physiological properties following the description made by Saul et al. [10]. Each muscle line $j \in \{1; N_m\}$ is composed of three elements:

- a passive element modeling the tendon with a length of l_{sj}, assumed to be non-deformable to reduce computational complexity;
- an active element of lenght l_{mj} represents the contractile active force generated by the muscle F_{aj};
- parallel to the active element, a nonlinear spring models the passive properties of the muscle fiber producing F_{pj}.

The total muscle line j force is therefore $F_{aj} + F_{pj}$, and its total length is $l_{mj} + l_{sj}$.

Muscle lengths vary according to the position of the osteoarticular model. The force-length characteristic is defined by its maximum voluntary force F_{0j}, and the muscle length at which it can be produce, i.e. the optimal muscle fiber length l_{0j}. We define $\tilde{l}_{mj} = \frac{l_{mj}}{l_{0j}}$ as the normalized muscle fiber length. As did [12] and [7], we also defined the minimum (resp. maximum) length of the force-length characteristic: $\tilde{l}_{minj}$ (resp. $\tilde{l}_{maxj}$). This two length parameterize the shape of the characteristic without modifying the anatomic values of l_{0j} and l_{sj}, so that

$$F_{aj}(\tilde{l}_{mj}) = \begin{cases} F_{0j}\left(\frac{\tilde{l}_{minj}^2(\tilde{l}_{minj}-3)}{(\tilde{l}_{minj}-1)^3} + \frac{6\tilde{l}_{minj}}{(\tilde{l}_{minj}-1)^3}\tilde{l}_{mj} - \frac{3(\tilde{l}_{minj}+1)}{(\tilde{l}_{minj}-1)^3}\tilde{l}_{mj}^2 \right. \\ \qquad \left. + \frac{2}{(\tilde{l}_{minj}-1)^3}\tilde{l}_{mj}^3\right) \qquad \text{if } \tilde{l}_{mj} < 1 \\ F_{0j}\left(\frac{\tilde{l}_{maxj}^2(\tilde{l}_{maxj}-3)}{(\tilde{l}_{maxj}-1)^3} + \frac{6\tilde{l}_{maxj}}{(\tilde{l}_{maxj}-1)^3}\tilde{l}_{mj} - \frac{3(\tilde{l}_{maxj}+1)}{(\tilde{l}_{maxj}-1)^3}\tilde{l}_{mj}^2 \right. \\ \qquad \left. + \frac{2}{(\tilde{l}_{maxj}-1)^3}\tilde{l}_{mj}^3\right) \qquad \text{if } \tilde{l}_{mj} \geq 1 \end{cases} \tag{1}$$

for active forces, and

$$F_{pj}(\tilde{l}_{mj}) = \begin{cases} 0 \qquad \text{if } \tilde{l}_{mj} < 1 \\ F_{0j}\left(\frac{5}{4(\tilde{l}_{maxj}-1)^2} - \frac{5}{2(\tilde{l}_{maxj}-1)^2}\tilde{l}_{mj} + \frac{5}{4(\tilde{l}_{maxj}-1)^2}\tilde{l}_{mj}^2\right) \\ \qquad \text{if } \tilde{l}_{mj} \geq 1 \end{cases} \tag{2}$$

for passive forces. The figure 2 shows the normalized characteristic behavior of this Hill-Zajac model. Then, each muscle $j \in \{1; N_m\}$ exerts a torque around joint $i \in \{1; 2\}$ defined as

$$\tau_{i,j}^{model} = \left[F_{aj}(\tilde{l}_{mj}) + F_{pj}(\tilde{l}_{mj})\right]\frac{\partial l_{mj}}{\partial q_i}. \tag{3}$$

In order to personalize this MSM, two successive steps were implemented. First, segment and muscle paths were scaled simultaneously, adjusting muscle length parameters (l_{0j} and l_{sj}) to match participant segment sizes (Figure 3). Maximum voluntary forces F_{0j} were then linearly adjusted based on the initial Saul model's torque maximal capacity and the ergometer's maximal measured torque, ensuring consistency between model geometry and muscle capacities. The scaling used the same measurements as those defining the TAM in II-A.

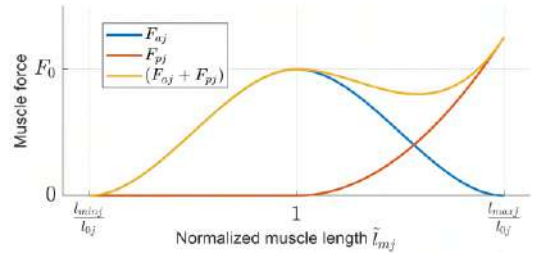


Fig. 2. Normalized force-length characteristic of a muscle line model [7].

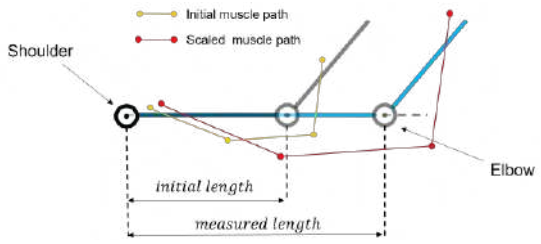


Fig. 3. Schematic diagram of arm scaling and muscle pathway scaling.

The second step consists of calibrating muscle parameters $\tilde{l}_{minj}$ and $\tilde{l}_{maxj}$ using ergometer torque measurements. This involved an optimization process to minimize the difference between the measured torque τ_{mes} and the MSM estimated muscle torques around the elbow, such that

$$\min_{\mathbf{F_0},\tilde{\mathbf{l}}_{\mathbf{min}},\tilde{\mathbf{l}}_{\mathbf{max}}} \left(\tau_2^{model} - \tau_{mes}\right)^2, \quad \text{with } \tau_2^{model} = \sum_{j=1}^{N_m} \tau_{2,j}^{model}. \quad (4)$$

$\{\mathbf{F_0}, \tilde{\mathbf{l}}_{\mathbf{min}}, \tilde{\mathbf{l}}_{\mathbf{max}}\} = \{(F_{0j}), (\tilde{l}_{minj}), (\tilde{l}_{maxj})\}_{i=1}^{N_m}$ are the optimisation variables. As they do not have the same same order of magnitude, we successively optimized the length parameters and the force parameters until the problem converged.

C. Assistance control law

The control scheme employs an admittance filter for torque control. Furthermore, two modes have been implemented: transparent and assisted.

Transparent mode, as defined by W. van Dijk et al. [13], eliminates the interaction forces between the user and the robot, ensuring the robot does not resist against user movements. To do that, two strategies are discussed in the literature [14]. The first aims to compensate the dynamics of the exoskeleton. In this work, only the exoskeleton gravity $\mathbf{G}(\mathbf{q})$ was computed and compensated. The second strategy is to use force measurement to impose a zero interaction force. The control scheme shown in figure 4 was therefore used for this work, where J is the exoskeleton Jacobian. In the case of transparent mode, the reference torque input τ^* is set to 0.

The assisted mode (with a non zero τ^*) aimed to provide assistance according to the effort required by a task, in order to limit the user's contribution to a predefined percentage of their maximum force. The torque required for the task τ_{task} was estimated statically with

$$\tau_{task} = g(m_{obj}L_f + m_f L_{fmc}), \quad (5)$$

knowing the mass of the object carried by the user m_{obj} and the mass of his forearm m_f. The forearm length L_f was measured at the start of the experiment and the lever arm of the forearm's center of mass L_{fmc} was known from the osteoarticular model. g is the gravity acceleration.

The assistance principle is illustrated in Figure 5 and is obtained by computing

$$\tau^* = \begin{cases} 0 & \text{if } |\tau_{task}| < 0.03 \times |\tau_2^{model}| \\ \tau_{task} - 0.03 \times \tau_2^{model} & \text{otherwise.} \end{cases} \quad (6)$$

This combines the advantages of a transparent mode (preserved user control) and a physical assistance (reduced fatigue). We set this threshold at 3% of the maximum voluntary force τ_2^{model} estimated by either the TAM or MSM. This threshold is lower than the recommendations of [15], which suggest a maximal value of 10% to avoid fatigue. This value remains then completely adjustable. Effort generation capacities are then estimated in real time using either the TAM or the MSM according to equation (3).

D. Experimental setup

Nine participants, whose elbow torque generation capabilities were measured (II-A), sat in a stationary power wheelchair on which the exoskeleton is attached. The setup included an optoelectronic motion capture system (Nine Qualisys Miqus) sampled at 100 Hz. Fifteen markers, each with a diameter of 14 mm, were placed on the participant at standardized anatomical landmarks following the guidelines of the International Society of Biomechanics [16]. The exoskeleton is capable of assisting the abduction of the shoulder and the flexion of both the shoulder and the elbow [17]. In the present case study, shoulder movements are locked. Figure 6 illustrates the experimental setup. In addition, electromyographic sensors (EMG) were placed on the following muscles, according to the SENIAM standard [18]: Triceps Long Head, Anterior Deltoid, Posterior Deltoid, Medial Deltoid, Biceps. These sensors operated at 1259Hz. Once installed in the wheelchair, the participant's arm was positioned in the exoskeleton using a 3D-printed support in which the arm rests, and the forearm was positioned using a 3D-printed orthosis. A screen was positioned in front of the participant. This screen displayed feedback on the angular position of the elbow and a target zone. For position feedback, data from the encoder of the exoskeleton were used. The position feedback delay was less than 20ms. The control was fully implemented in a dSPACE system running at 5 kHz. Motion capture and EMGs were not used for control, but only for evaluation. F_{mes} is measured with a NF742 force sensor.

Participants were asked to perform a task involving moving/holding a cylindrical object with a mass of 1kg. The set trajectory comprised five consecutive 10 seconds steps at 20°, 60°, 100°, 60° and 20°. It was performed in 4 configurations:

- No-Exo mode: the participant performs the task without the exoskeleton;
- Transparent mode: the reference torque τ^* is set to 0;
- Torque-Angle based Control (TAC) mode: the reference torque τ^* is computed from the TAM;

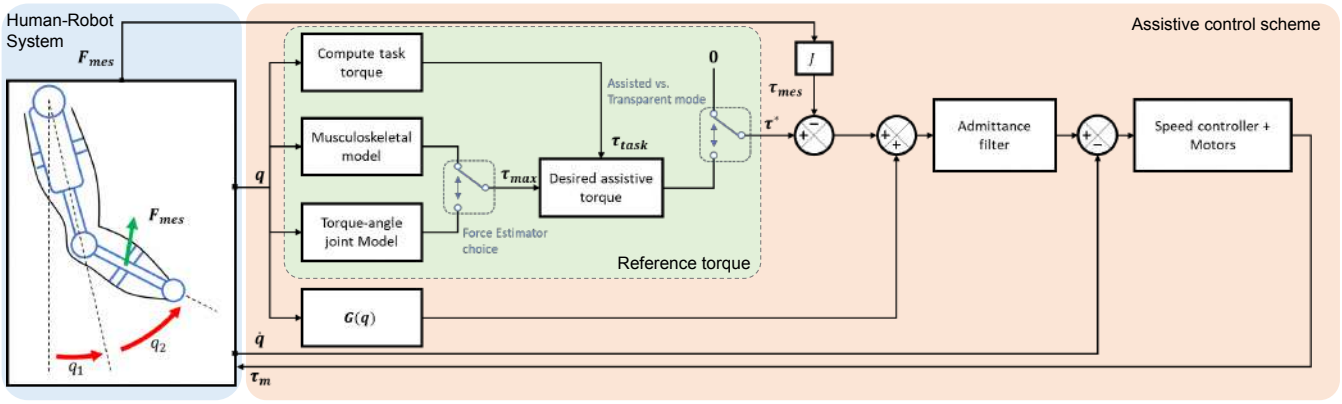


Fig. 4. Architecture of the assistive control. Human-robot interaction force is measured for torque control, and robot gravity is compensated. J is the exoskeleton Jacobian.

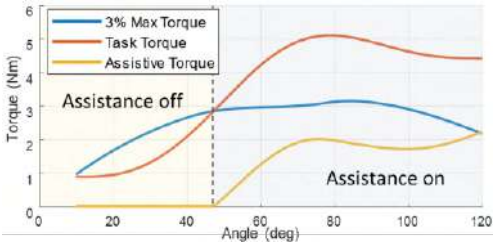


Fig. 5. Principle of the assistance provided by the exoskeleton according to the torque required by the task.

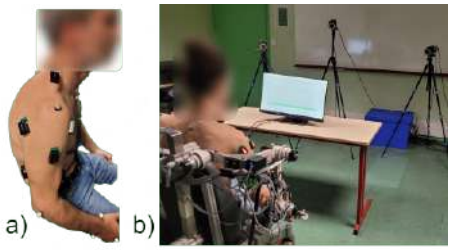


Fig. 6. a) Six EMG on arm and shoulder muscles and markers. b) Experimental setup. The participant is positioned in the exoskeleton, which is mounted on an power wheelchair. A display shows the angle to be reached with feedback on the position in real time.

- Musculoskeletal based Control (MSC) mode: the reference torque τ^* is computed from the MSM.

E. Data processing

The EMG data were rectified and filtered with a Root Mean Squared (RMS) filter to obtain the signal envelope with a 500ms window. The filter window was deliberately chosen to correspond to slow or static tasks, as recommended in the literature [19]. For each participant and for each EMG sensor, the signal was normalized to the highest value of the envelope recorded during the No-Exo test.

Data from the optoelectronic system were converted into joint angles using the OpenSim software [20]. The osteoarticular model used for this step is the one developed by Seth *et al.* [21]. This kinematic model enables the investigation of potential shoulder translational motion when the subject wears the exoskeleton.

An estimate of the torque provided by the participant was made by taking the difference between the torque of the task τ_{task} and the measurement of the torque exerted by the exoskeleton. It is given by

$$\tau_p = \tau_{task} - \tau_{mes}. \tag{7}$$

All the data set was temporally normalized over the duration of one repetition of the task. As the timing was imposed, identically lasting 50 seconds.

Finally, we conducted a statistical analysis for each of the levels (20°, 60°, and 100°) to compare the control modes. According to the Shapiro-Wilk test, the distribution of the data was not normal ($p > 0.15$). We therefore compared the situations two by two using a Mann-Whitney test.

III. RESULTS AND DISCUSSIONS

Figure 7 displays the personalized MSM parameters $\{\mathbf{l_s}, \mathbf{l_0}, \mathbf{F_0}\}$ for the elbow muscles. The parameters' values remained consistent with to the parameters defined in the Saul model [10] and with values reported in the literature. However, the triceps muscles appeared to be more powerful (bigger F_{0j}) in our study compared to those described in the Saul model. This inconsistency was likely due to the testing position in the ergometer, in which participants were able to lean against the machine, artificially increasing the measured torque values. Figure 8 illustrates the mean estimated torques for the MSMs and TAMs. The torque-angle relationships generated by the two estimators were closely aligned within the range of experimental measurements. However, outside this range of measures, the estimations given by the two models divergeds. Near the lower limit of elbow joint motion, the TAM produced inconsistent effort-generating capacities, even changing sign for some participants. In contrast, the MSM exhibited a curve shape that is more closely aligned with the original Saul model that appears to be consistent with the actual capabilities of the elbow [5].

Figure 9 illustrates the estimated torque results for the participants. In both assisted configurations (TAC and MSC), as expected, the average torque supplied by the participants was lower than the one provided in the transparent configuration. During static phases, the 3% user effort limit was better maintained compared to the dynamic phases. Indeed one of the main challenges of admittance control is improving reactivity while ensuring stability, as noted by [1].

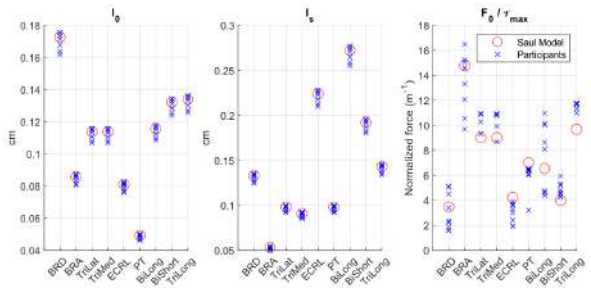


Fig. 7. Muscle characteristics of customized MSMs for muscles acting on the elbow. For each participant, each F_0 parameter is normalized to the maximum torque τmax that a participant can produce. Muscles are Brachioradialis (BRD), Brachialis (BRA), Triceps Lateral head (TriLat), Triceps Medial head(TriMed), Extensor Carpi Radialis Longus (ECRL), Pronator Teres (PT), Biceps Long head (BiLong), Biceps Short head (BiShort) and Triceps Long head(TriLong).

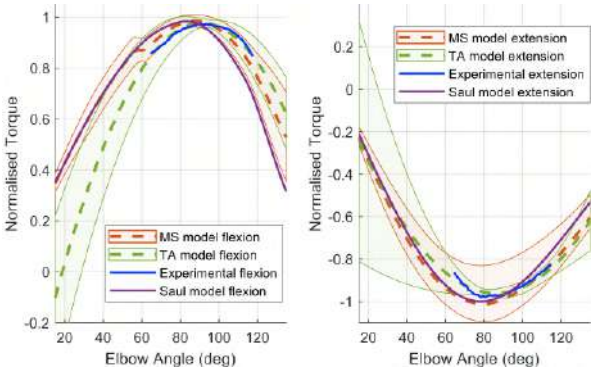


Fig. 8. Torque-angle relationships in flexion (left) and extension (right) obtained from the ergometer measurements. Torque is normalized by its maximum value, then averaged over all participants. Standards deviations of the MSM and TAM are plotted as a zone.

Figure 10 illustrates the mean EMG envelopes for biceps and triceps during the normalized cycle. The capacity estimators' values also differed, particularly at low elbow angles: this deviation was reflected in the biceps EMG envelopes. A low threshold has been set to highlight the effects of control, but it could be personalized depending on the endurance/fatigue of each individual or based on ergonomic criteria. The EMG data indicated increased triceps activation in the assistance with TAC, with this effect being more pronounced at low elbow angles. This may be explained by the fact that the torque estimator tended to over-assist the task by pushing the forearm upwards when it underestimated the effort-generating capacity for flexion. This imbalance shifted the workload between the flexor and extensor muscles, requiring the extensors to compensate by pulling the forearm down. The MSC therefore has a more robust behavior outside the model calibration range, and therefore a wider validity range. As illustrated in Figure 11, the statistical study of the biceps EMG reveals a significant decrease when comparing the TAC and MSC modes with the No-Exo mode.

In the transparent configuration, the EMG envelopes for the biceps and triceps were lower compared to the No-Exo configuration, despite the fact that the transparent mode was not assisting the user. Figure 12 illustrates the EMG envelopes for the shoulder deltoids. A similar reduction was observed for the anterior (DA) and medial (DM) deltoids.

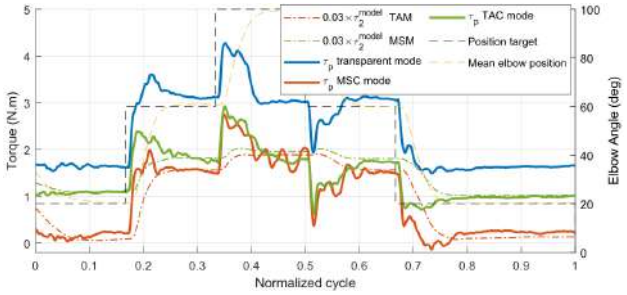


Fig. 9. Limit torques ($0.03 \times \tau_2^{model}$) averaged over all participants for TAM and MSM estimators. τ_p is averaged over all participants for transparent, TAC and MSC modes as a function of the normalized cycle.

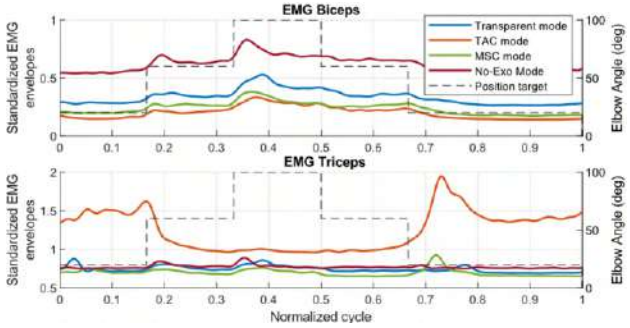


Fig. 10. EMG envelope averages for biceps (top) and triceps (bottom) and for each of the transparent, TAC, MSC and No-Exo modes.

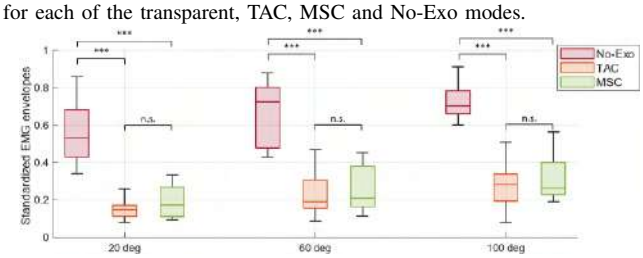


Fig. 11. EMG biceps results across the angles target and the control modes. The p-value of the Mann-Whitney test is indicated : '***' mean $p < 0.001$; 'n.s.' mean 'not significant' and $p > 0.2$.

In contrast, the posterior deltoid (PD) was more active with the exoskeleton. This can be explained by two factors: 1) the exoskeleton passive structure supported the shoulder,thus altering muscle stabilization, and 2) joint angle reconstruction showed differing shoulder positions between conditions (Figure 13), thus affecting muscle force capacity and complicating EMG comparisons. The reduction in EMG envelopes between transparent and assisted modes is therefore a more accurate representation of the assistance provided.

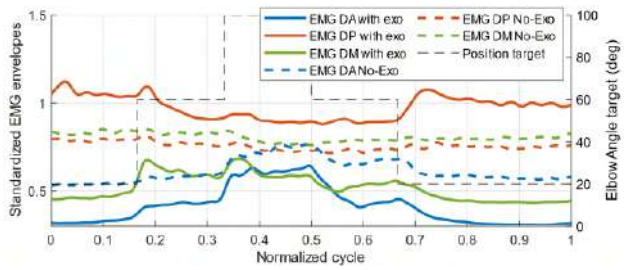


Fig. 12. EMG envelope averages normalized for Deltoid Anterieur (DA), Deltoid Medial (DM) and Deltoid Posterieur (DP) with the exoskeleton and whitout (No-Exo mode).

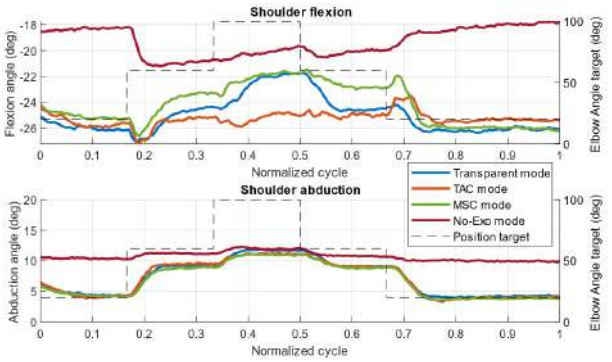


Fig. 13. Averaged shoulder flexion (top) and extension (bottom) for all participants and for each of the transparent, TAC, MSC and No-Exo modes.

Other limitations may be considered in this work. First, this study focused solely on static estimation. Effort generation capabilities are known to change dynamically during motion [11], and it raised issues in the admittance control during movement phases. A more accurate detection of intention therefore is then necessary. In addition, dynamic assistance requires on-line estimation of the user's kinematic state, that could be achieved by a reconstruction using inertial units or using a recurrent neural network or using a recurrent neural network for example. Secondly, the comparison between the joint model and the MSM was restricted to a single joint. As noted by [5], [6], the elbow torque capacity is significantly influenced by the shoulder position. However, linking joints within an articular model with a reasonable number of measurements is challenging. Consequently, MSMs may perform better when multiple joints are considered simultaneously. Lastly, we assumed a known object mass throughout the study. In real-world applications, estimating the mass of the object directly from the exoskeleton measurement will be essential. An auto-calibration phase could solve this problem in the future. Another possibility would be to use a sensor dedicated to the recognition of the grasped object, such as a force sensor in the hand or a RGBD camera [22].

IV. CONCLUSION

Incorporating an effort-generating capacity estimator into shared control systems allows for assistance tailored to the user's needs. Here, we compared two estimators: torque-angle joint model and musculoskeletal model. Both estimators were designed using an assistance control and evaluated with nine participants. The results showed similar performance when movements rely within the calibration range. However, outside this range, the torque-angle joint model proved less robust results than the musculoskeletal model, leading to unintended demands on antagonistic muscles. This preliminary study highlights the limitations of the torque-angle model and highlights the advantages of adopting more sophisticated approaches, such as musculoskeletal modeling.

V. ACKNOWLEDGMENT

This work was supported by the Inria as part of the Exploratory Action MusMaps and the CONTINUUM project.

REFERENCES

[1] A. Q. Keemink, H. Van der Kooij, and A. H. Stienen, "Admittance control for physical human–robot interaction," *The International Journal of Robotics Research*, vol. 37, no. 11, pp. 1421–1444, 2018.

[2] T. Proietti, N. Jarrassé *et al.*, "Adaptive control of a robotic exoskeleton for neurorehabilitation," in *2015 7th International IEEE/EMBS Conference on Neural Engineering (NER)*. IEEE, 2015, pp. 803–806.

[3] L. Rose, M. C. Bazzocchi, and G. Nejat, "A model-free deep reinforcement learning approach for control of exoskeleton gait patterns," *Robotica*, vol. 40, no. 7, pp. 2189–2214, 2022.

[4] M. G. Carmichael and D. Liu, "Estimating physical assistance need using a musculoskeletal model," *IEEE Transactions on Biomedical Engineering*, vol. 60, no. 7, pp. 1912–1919, 2013.

[5] L. A. Frey-Law, A. Laake *et al.*, "Knee and elbow 3d strength surfaces: peak torque-angle-velocity relationships," *Journal of applied biomechanics*, vol. 28, no. 6, pp. 726–737, 2012.

[6] D. Haering, C. Pontonnier *et al.*, "Using torque-angle and torque–velocity models to characterize elbow mechanical function: Modeling and applied aspects," *Journal of Biomechanical Engineering*, vol. 141, no. 8, p. 084501, 2019.

[7] A. Muller, D. Haering *et al.*, "Non-invasive techniques for musculoskeletal model calibration," in *Congrès Français de Mécanique*, 2017.

[8] W. Wu, P. V. Lee *et al.*, "Subject-specific musculoskeletal modeling in the evaluation of shoulder muscle and joint function," *Journal of biomechanics*, vol. 49, no. 15, pp. 3626–3634, 2016.

[9] A. Skuric, V. Padois *et al.*, "On-line feasible wrench polytope evaluation based on human musculoskeletal models: an iterative convex hull method," vol. 7, no. 2, pp. 5206–5213, 2022.

[10] K. R. Saul, X. Hu *et al.*, "Benchmarking of dynamic simulation predictions in two software platforms using an upper limb musculoskeletal model," *Computer methods in biomechanics and biomedical engineering*, vol. 18, no. 13, pp. 1445–1458, 2015.

[11] F. E. Zajac, "Muscle and tendon: properties, models, scaling, and application to biomechanics and motor control." *Critical reviews in biomedical engineering*, vol. 17, no. 4, pp. 359–411, 1989.

[12] B. A. Garner and M. G. Pandy, "Estimation of musculotendon properties in the human upper limb," *Annals of biomedical engineering*, vol. 31, pp. 207–220, 2003.

[13] W. van Dijk, H. van der Kooij *et al.*, "Improving the transparency of a rehabilitation robot by exploiting the cyclic behaviour of walking," in *2013 IEEE 13th International Conference on Rehabilitation Robotics (ICORR)*, 2013, pp. 1–8.

[14] D. Verdel, A. Farr *et al.*, "Human movement modifications induced by different levels of transparency of an active upper limb exoskeleton," *Frontiers in Robotics and AI*, vol. 11, p. 1308958, 2024.

[15] J. Steven Moore and A. Garg, "The strain index: a proposed method to analyze jobs for risk of distal upper extremity disorders," *American Industrial Hygiene Association Journal*, vol. 56, no. 5, pp. 443–458, 1995.

[16] G. Wu, F. C. Van der Helm *et al.*, "Isb recommendation on definitions of joint coordinate systems of various joints for the reporting of human joint motion—part ii: shoulder, elbow, wrist and hand," *Journal of biomechanics*, vol. 38, no. 5, pp. 981–992, 2005.

[17] M. Manzano, S. Guégan *et al.*, "Force-triggered control design for user intent-driven assistive upper-limb robots," in *IEEE/RSJ Int. Conf. on Intelligent Robots and Systems, IROS'24*, 2024.

[18] H. J. Hermens, B. Freriks *et al.*, "European recommendations for surface electromyography," *Roessingh research and development*, vol. 8, no. 2, pp. 13–54, 1999.

[19] P. Konrad, "The abc of emg," *A practical introduction to kinesiological electromyography*, vol. 1, no. 2005, pp. 30–5, 2005.

[20] S. L. Delp, F. C. Anderson *et al.*, "Opensim: open-source software to create and analyze dynamic simulations of movement," *IEEE transactions on biomedical engineering*, vol. 54, no. 11, pp. 1940–1950, 2007.

[21] A. Seth, R. Matias *et al.*, "A biomechanical model of the scapulothoracic joint to accurately capture scapular kinematics during shoulder movements," *PloS one*, vol. 11, no. 1, p. e0141028, 2016.

[22] A. Ceglia, K. Facon *et al.*, "Real-time, accurate, and open source upper-limb musculoskeletal analysis using a single rgbd camera—an exploratory hand-cycling study," *Computers in Biology and Medicine*, vol. 184, p. 109434, 2025.

Unseen and Unheard Potential: Visual and Auditory Cues Affect Motor Plans and Coordination

1st Cecilia De Vicariis
DIBRIS
University of Genoa
Genoa, Italy
cecilia.devicariis@unige.it

2nd Mitchell D.L. McDermott
EECS
Queen Mary University
London, United Kingdom
m.d.l.mcdermott@se22.qmul.ac.uk

3rd Giada Parodi
DIBRIS
University of Genoa
Genoa, Italy
giada.parodi@edu.unige.it

4th Ludovica Viola
DIBRIS
University of Genoa
Genoa, Italy
ludovica.viola@edu.unige.it

5th Laura Bandini
DIBRIS
University of Genoa
Genoa, Italy
laura.bandini@edu.unige.it

5th Vittorio Sanguineti
DIBRIS
University of Genoa
Genoa, Italy
vittorio.sanguineti@unige.it

6th Etienne Burdet
Department of Bioengineering
Imperial College
London, United Kingdom
e.burdet@imperial.ac.uk

7th Ekaterina Ivanova
EECS
Queen Mary University
London, United Kingdom
e.ivanova@qmul.ac.uk

***Abstract*—During daily life activities we not only gather information regarding the environment, but also regarding other humans which are performing similar actions. Even if not specifically required by the task, people affect other motion plans through different sensory modalities and may align their plans in a subtle way even if not required. This study explores the role of visual and auditory feedback in tasks with a sensory connection between partners. We used a dual robotic interface to test various visual and auditory coupling modalities, translating the spatial dynamics of the partners into distinctive feedback. Results from visual experiment showed that the explicit representation of the partner position along with own position greatly improves coordination between them. The auditory experiment emphasized the effectiveness of binaurally presented spatio-temporally discrete auditory cues. The current study provides insights relevant to the design of novel enriched rehabilitative protocols which rely on the mechanisms underlying interaction.**

***Index Terms*—Emergent coordination, planning, visual coupling, auditory coupling**

I. Introduction

The exchange of sensorimotor information between humans is crucial to efficiently interact and succeed in achieving a shared goal [1], [2]. For instance, during rehabilitation, a therapist communicates verbally while assessing the patient's posture and movements through vision and feels their strength through haptics. Coordination was found in joint action, but not in parallel action [3], suggesting that participants that receive visual information regarding the partner's action represents a collective goal motorically. However, even if people are not interacting in a joint task with a partner, it has been found that humans unintentionally coordinate their movements when performing rhythmic tasks facing a partner who is doing the same task [4]–[6]. Therefore, people observing the other people tend to imitate them even when not required by the task [7].

When pairs of participants, unaware of being interacting with another person in a reaching task, had incompatible subgoals [8], [9], the addition of the visual feedback, regarding the other agent, to a haptic connection greatly increase motor plans coordination. Also, in rehabilitative settings [10] dyads of patients and healthy individuals as well as healthy-healthy dyads coupled by visual link displayed on a screen coordinated in a force production game using sensor-based GripAble devices.

While much research demonstrated the role of visual and haptic cues in interaction [11], the role of auditory cues still needs to be explored.Non-speech sounds are information-rich, yet unintrusive way to communicate in interactive settings [12]. However, auditory cues may convey subtle information which affect others' motion plans even if not required to or necessary.

Music theory informs how different sound elements – such as tempo, rhythm, pitch, and harmony – can be manipulated to create various types of auditory feedback. Each feedback type carries distinct implications for cognitive processing and motor coordination [13], [14]. Stroke rehabilitation may benefit from a deeper understanding of how auditory feedback regarding others' action affect individual motor plans. Music and robot-aided therapy can significantly benefit motor training within the rehabilitation context [15].

This work aims at investigating the impact of visual and auditory feedback, from another person action, on individual motor plans.

We conducted two experiments to study various types of visual and auditory representations of partner during a via-

This research was supported by ICT 871803 CONBOTS, the Italian Ministry of Research, under the complementary actions to the NRRP "Fit4MedRob - Fit for Medical Robotics" Grant (# PNC0000007), and IES 2\232331 International Exchange Grant of The Royal Society.

point motor task. We investigate (i) whether the presence of visual or auditory information about the partner increases the motor plans alignment in space and time;(ii) which type of feedback leads to better coupling; and (iii) which feedback is preferred by participants the two modalities.

II. Materials and Methods

A. Participants

All participants signed the consent form before starting the experiment. We recruited a total of 20 participants (aged $21-34$ yo). Ten performed in the visual experiment and ten in the auditory experiment.

B. Experimental apparatus and protocol

The experimental setup consisted of two 2-DoF haptic interfaces (H-Man, Articares [16]), each with a separate control computer and a 28-inches LCD display for the presentation of visual feedback - see Figure 1a. Participants were seated in front of their individual planar robotic interface H-MAN and were separated by a curtain. They wore a noise-cancelling headset to prevent any auditory communication beside the presented sounds for the auditory group.

Each trial began with participants positioning their handle at a starting point, demarcated by a red arrow. After receiving the 'Go!' signal they were instructed to execute planar point-to-point movements, through four via-points in a clockwise direction, before returning to the initial starting position.

The protocol is presented in Figure 1b. In the first familiarization phase of 12 trials, participants received a visual cue representing a possible trajectory that they could use to solve the task. The displayed trajectory was different for the two players to manipulate their individual motor plans. For one subject, a 'circle' shape, and for the other – a 'diamond' shape was presented - see Figure 1a. In this initial phase, they received no sensory feedback from the other participant. In the auditory experiment, during this familiarization,in addition to the visual cue regarding a possible trajectory and the visualization of own moving cursor, participants were cued with an ambisonic pink noise that correlated with their cursor position.

After the familiarization phase, the training phase began (a total of 144 for visual and 96 for auditory). In the visual experiment we tested six visual feedback. While in the auditory we tested four conditions in a corresponding number of blocks. Each block consisted of a training part (18 trials), in which participants received either visual or auditory feedback, regarding their partner's position, and a wash-out part (three trials) without a connection with the partner. Wash-out trials in the auditory study included ambisonic pink noise. After the coupled phase and the wash-out, a post-test consisting of three trials without any visual or auditory feedback but in which the trajectory cue was presented again as in the familiarization. After completing all trials, participants in the two experiments ranked all forms of visual/auditory feedback, measuring their preferences among modalities.

C. Visual feedback conditions

We explored six different types of visual feedback representing the partner's position during a joint via-point task (see Figure 1c). These visual feedback conditions were designed to assess how different visual cues and the amount of information they provide about the partner's actions can influence joint coordination. The order of the visual modalities V1 to V6 was specified as shown in Figure 1c.

In the *'Cursor'* condition, (V1 in Figure 1c), the subjects' own hand position was represented on the screen as a green cursor. This minimal visual feedback was introduced as a control, to assess the participants' behavior in the absence of further visual information about the partner. In the *'Cursor + Line'* condition (V2 in Figure 1c), in addition to the cursor representing the player's position, a grey line was shown, indicating the distance and orientation between the participant and the other player.

In the third condition, called *'Cursor + Cloud'* (V3 in Figure 1c), participants saw their cursor and a noisy representation of the distance between partners visualized as a cloud of eight gray randomly moving dots, which introduced greater uncertainty on the perception of the partner's position as in [17].

The fourth to sixth conditions introduced a more complex visual feedback by adding specific information about the partner's position. In *'Cursor + Cursor'* (V4 in Figure 1c), participants could see two separate cursors representing the positions of the two players' hands position - the player's position in green and the partner's in gray. In *'Cursor + Line + Cursor'* condition (V5 in Figure 1c), participants could see a line representing the distance between the two players and a cursor for each player. Finally, in *'Cursor + Cloud + Cursor'* condition (V6 in Figure 1c), participants could see the two cursors representing the players positions on the workspace together with a points cloud, representing the distance between the two subjects with greater uncertainty respect to V5.

D. Auditory feedback conditions

We tested four different auditory conditions. Each mode presented unique auditory feedback which was chosen based on existing theories about the relationship between auditory stimuli and human behavior. The order of the four auditory conditions was specified, with similar modalities grouped together, and temporal and pitch-dependent tasks spaced out.

In the *Distance Pitch Dissonance* condition (A1), the distance between the two partners' positions is translated into dissonance between two pitches, achieved using three sine wave oscillators. When the distance is zero, the three pitches are identical, resulting in the perception of a single, stable pitch. As the distance increases, the pitches are detuned to increase dissonance. This design choice relies on the understanding that adults typically associate consonance with pleasantness and dissonance with unpleasantness [18]–[22]. Therefore, the increasing dissonance may be an intuitive signal for the subjects to adjust their positions.

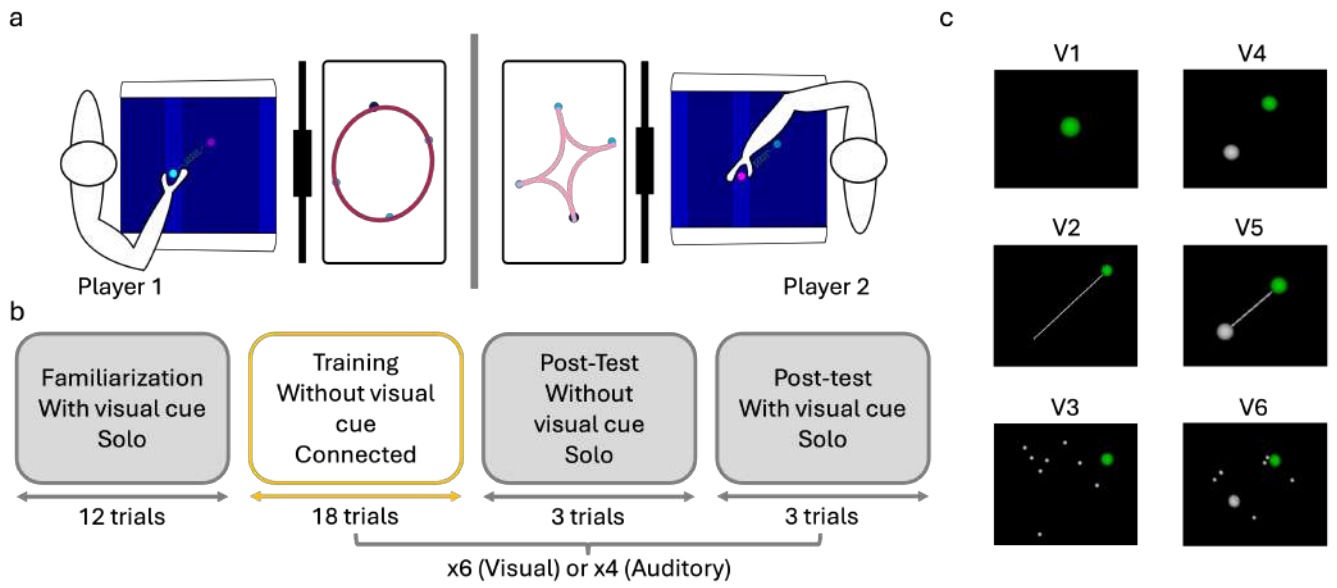


Fig. 1. Set-up and protocol. a) Two participants sat in front of a computer screen and a planar manipulandum. Participants were asked to perform reaching movement using the robotic handle from a start point (dark blue point on the left), by crossing a sequence of via-points in a clockwise order and finishing the movement at the endpoint (start point = endpoint). b) The protocol consists of a familiarization phase (12 trials) during which players receive a visual cue of a suggested solution ('circle' or 'star') before the 'Go!' signal. During the training phase players performed the same task without a solution cue, and with different visual/auditory feedback from their partner. During the post-test phase, players were not connected. This phase was divided into 3 trials without and 3 trials with the initial visual cue of a solution. c) Six modalities for visual feedback of the partner's positions. In V1 own cursor in green is shown. In V2 and V3 in addition to their own cursor a grey line and a cloud of dots, indicating the distance between the partners, are added respectively. In V4 own (green) and partner (grey) cursors are displayed. In V5 and V6, the two cursor configurations and a grey line (in V5) or a cloud (in V6) are displayed.

Visual Mode	**Input**	**Visual Cue**
V1) Cursor	own hand position	continuous cursor movement
V2)Cursor + Line	own hand position and partner hand position	own cursor and an attached line directed toward partner's hand position, whose length depends on distance from partner, are continuously displayed during the motion
V3) Cursor + Cloud	own hand position and partner hand position	own cursor and a dots' cloud directed toward partner's position, whose spread depends on distance from partner, are continuously displayed during the motion
V4) Cursor + Cursor	own hand position and partner hand position	own and partner's cursors are continuously displayed during motion
V5) Cursor + Line + Cursor	own hand position and partner hand position	own and partner's cursors are continuously displayed during motion and are linked by a line connecting the two
V6) Cursor + Cloud + Cursor	own hand position and partner hand position	own and partner's cursors are continuously displayed during motion and linked by a cloud of dots connecting the two

TABLE I
VISUAL FEEDBACK SUMMARY

In the *Distance Rhythmic Synchrony* modality (A2), the distance of the subjects' hand position correlates with changes in rhythmic synchronization achieved using a stereo percussive drum loop. When the distance is zero, the drum rhythms synchronize, resulting in a coordinated and musical pattern. As the distance increases, the signal in the right ear delays progressively, leading to an increasingly chaotic and unmusical rhythm. This design is grounded in the understanding that humans inherently perceive a regular pulse or beat in an auditory signal, a phenomenon referred to as 'tactu' in music theory, which aids in synchronizing movements with each other [23]. Furthermore, the salience of a pulse sensation, which is most prominent at moderate tempos, plays a crucial role in distinguishing musical rhythm from nonrhythm [24]. As such, manipulating the salience of the pulse sensation through the synchronization or desynchronization of the drum loop could significantly impact the subjects' perception of rhythm and their ability to coordinate their actions.

The *Target Impact Chime* condition (A3) employs a distinct bell sound when participants cross via-points. In particular, upon crossing a via-point, participants hear a distinct bell sound tuned to specific pitches: C3 for own crossing and E3 for the partner's crossing. Chimes are spatially presented through the application of ambisonics, allowing participants to distinguish the pace-based positioning of one another. The central hypothesis is that introducing discrete-time visually-linked auditory stimuli can increase spatial consciousness and rhythm in a joint task. The efficacy of such a mechanism relies heavily on the concept of crossmodal interactions and the consequential influence that auditory stimuli can impose on spatial perception. Increasing attention is being given to

exploring multisensory integration and the co-influence of auditory and tactile senses in spatial and non-spatial domains [25]–[29].

In the *Speed-Adaptive Tempo* condition (A4), each participant's progressing along path dynamically modulates a rhythmic drum beat's tempo. Those advancing faster experience a slowing drum tempo, signaling the need to decelerate and maintain synchrony with their partner. Conversely, those lagging, hear a progressively quickened drum beat, suggesting to fasten their pace. The change in tempo is scaled to the distance between the participants, creating a sonically intuitive guide for movement coordination. Previous studies [30] observed that faster music could lead subjects to cover longer distances on an exercise bike. Conversely, slower beats led to diminished walking distances [31], illustrating the direct impact tempo can have on the velocity of physical motion. Also, background music's speed can dictate the pace of motor behaviors [32]–[34].

Auditory mode	**Input**	**Auditory cue**
A1) Distance Pitch Dissonance	distance between hands position	sine wave frequencies alignment
A2) Distance Rhythmic Synchrony	distance between hands position	drums rhythms synchronization
A3)Target Impact Chime	discrete via-points crossing events	bell sound with different pitches for the two players
A4)Speed Adaptive Tempo	reciprocal velocity differences	continuous rhythmic signal

TABLE II
AUDITORY FEEDBACK SUMMARY

E. Coordination Metrics

To investigate temporal and spatial coordination within dyads, we analyzed asynchrony and Dynamic Time Warping (DTW). *Temporal asynchrony* assessed the synchronization of the times of crossing start and via-points. For each player i, with $i = \{1, 2\}$, the via-point j crossing time CT_{ij}, with $j = \{1, 2, 3\}$, was calculated as the time in which the player reached the (minimal) distance D_{ij} from via-point. We computed the absolute value of the differences of start time $\Delta ST = |ST_1 - ST_2|$ and the differences for each crossing time at each via-point $\Delta CT_j = |CT_{1j} - CT_{2j}|$. In the analysis, we considered the average of these timing differences. Small values of asynchrony indicate well-coordinated movements. To evaluate coordination in space, we considered *DTW*, which characterizes the distance between two-time series [35]. In our case, the input time series are the planar trajectories used by the two participants in each trial. Low values indicate that trajectories are similar in space.

F. Statistical Analysis

To understand whether receiving different visual or auditory cues about another person action affect motion plans leading to unintende coordination we considered the last twelve trials for each condition including the familiarization block as a control. A Shapiro-Wilk test showed that both metrics in both experiments were not normally distributed. We conducted one-way ART (Aligned Rank Transform) ANOVA using a linear mixed-effects model. For all dependent variables, we fitted a model with the fixed effect on the block and the random intercepts for the subject number. In case the block factor was significant, post-hoc comparisons using t-test contrasts with a Holm–Bonferroni adjustment were employed.

III. RESULTS

A. Plans alignment with visual feedback from partner

In the experiment in which participants received information regarding partner's action through vision, the type of the given feedback influenced both temporal asynchrony ($F(5, 410) = 28.736$, $p < 0.0001$) and DTW ($F(5, 410) = 21.78$, $p < 0.0001$) - see Fig. 2. In the familiarization, in which participants were cued with different path shapes before motion and did not receive visual signals regarding the partner, participants within dyads were less coordinated compared to all feedback conditions in terms of both time and space (all $p < 0.0001$). When participants could only see their own cursor (V1), they coordinated less in both space (DTW) and time (asynchrony) their movements within the dyads compared to the other conditions, in which they could see their and the partners' cursors as well as a connection between them (DTW: V1 vs. V5: $t(409) = 3.345$, $p = 0.0099$, V1 vs. V6: $t(409) = 4.771$, $p < 0.0001$; asynchrony: V1 vs. V5: $t(409) = 4.819$, $p < 0.0001$, V1 vs. V6: $t(409) = 6.041$, $p < 0.0001$). Even seeing the partners' position alone improved temporal alignment compared to its absence (V1 vs. V4: $t(409) = 2.835$, $p = 0.0348$). Moreover, in both conditions without explicit representation of the partner's position – own cursor and line (V2) or noise (V3) – participants were less coordinated in terms of DTW and temporal asynchrony with respect to those in which partner's cursor was displayed ($p < 0.05$ for all comparisons V2/V3 vs. V5/V6). Regarding asynchrony, noisy connection with both cursors increased alignment compared to the cursors representation (V4 vs. V6: $t(409) = 3.205$, $p = 0.0131$). No other differences between conditions were detected ($p > 0.05$).

B. Coordination with auditory feedback from partner

In the experiment in which participants received information regarding the partner's action through hearing, the temporal ($F(4, 291) = 26.477$, $p < 0.0001$, see Fig. 2) and spatial motion plans alignment ($F(4, 291) = 30.555$, $p < 0.0001$, see Fig. 2) was affected by the feedback type. The alignment in both metrics, DTW and asynchrony, was lower in the initial familiarization trials and increased when the auditory feedback was provided (all $p < 0.0001$ for pairwise comparisons between A1-A4 and familiarization). Analysis of DTW metric (coordination in space) showed that pitch dissonance modality (A1), which gave feedback on the distance between partners' positions, and target impact chime (A3), which presented a discrete auditory cue every time a participant or their partner crossed the via-point,

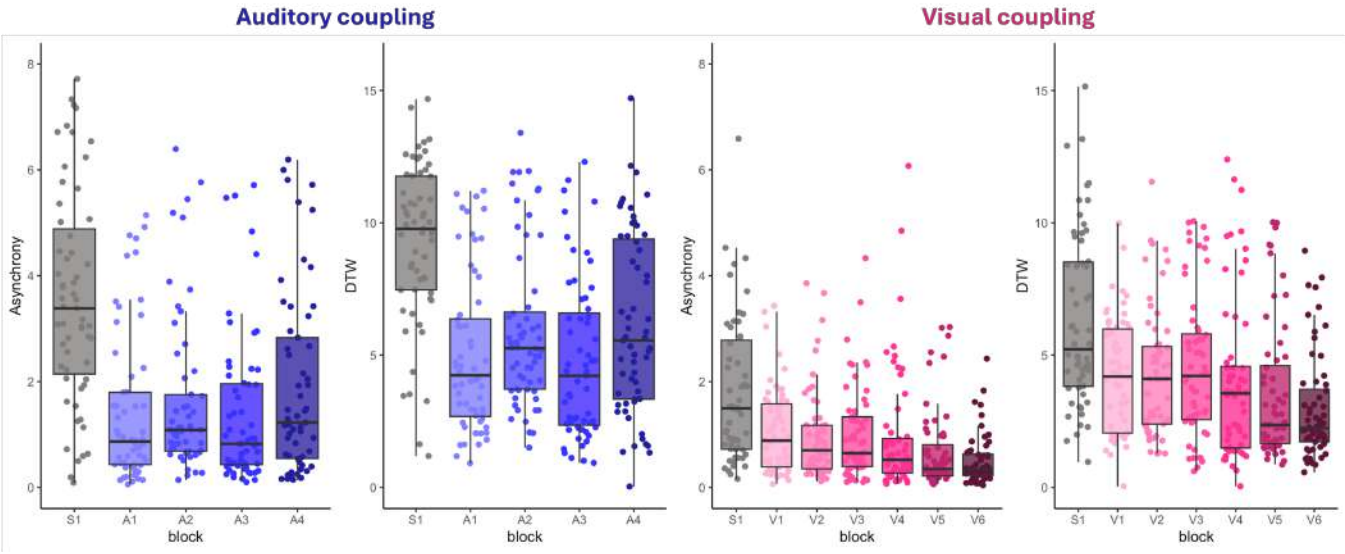


Fig. 2. Motion plans alignment results. Boxplots are reported for the two experiments. Points represent data for each trial included in the analysis. We reported in blue tints data related to the auditory experiment and in pink tints data related to visual experiments. Different tints in the two groups denote different experimental blocks corresponding to different feedback conditions.

increased the spatial coordination within a dyad compared to the speed-adaptive tempo (A1 vs. A4: $t(291) = -2.894$, $p = 0.0205$, A3 vs. A4: $t(291) = -3.098$, $p = 0.0128$) and distance rhythmic synchrony (A2) conditions (A1 vs. A2: $t(291) = -2.573$, $p = 0.0317$, A2 vs. A3: $t(291) = 2.778$, $p = 0.0233$). Similarly, for temporal asynchrony, speed-adaptive tempo condition (A4) resulted in a lower temporal coordination than distance pitch dissonance (A4 vs A1: $t(291) = -2.994$, $p = 0.0179$) and target impact chime (A4 vs A3$t(291) = -2.776$, $p = 0.0293$). Moreover, distance rhythmic synchrony (A2) leads to a higher asynchrony than distance pitch dissonance (A2 vs A1: $t(291) = -2.621$, $p = 0.0369$).

C. Ranking regarding preference of the feedback

At the end of the trial, we asked participants to rank all of the modalities in both experiments. In the visual study, six of ten people choose the 'Cursor + Line + Cursor' (V5) as their first preference. In the auditory experiment, nine of ten participants indicated the target impact chime (A3) as their preferred option. The majority of the subjects explained their ranking with the clarity of the feedback in these two conditions.

IV. Discussion

The goal of this research was to investigate the effect of visual and auditory cues regarding partner actions in a motor task. In particular, we were interested in understanding whether the various cues lead participants to align their plans, showing to be more effective in conveying information related to the partner's actions. We compared various types of visual and auditory representation in two different experiments where participants were required to perform the same via-points motor task that allowed spatial and temporal flexibility for both partners.

Consistent with previous literature [5]–[7], we observed that participants tended to coordinate their actions even if not required by the task when visual feedback was provided regarding another person's actions with respect to the solo conditions. However, with our study we also attempted to analyze which feedback mode was more efficient. This is crucial in rehabilitation [10] as it may provide insights for the design of more efficient interactive rehabilitation tools and enrich the interaction and the patient experience. We found that the preferred feedback is similar to the one used by [8] together with haptic feedback. Confirming that not only a cue regarding the distance and connection between interacting agents but also having full information regarding the partner's position is crucial for achieving a stronger alignment.

In the auditory study, pitch dissonance and target impact chime significantly increased coordination between participants, with the latter being the most preferred. This preference likely stems from its clear and simple feedback, which directly signaled when participants crossed the via-point. Conversely, speed-adaptive tempo hindered coordination, possibly because its mapping caused confusion—when one participant overtook the other, the beat slowed down. Similarly, distance rhythmic synchrony also reduced coordination, suggesting that rhythm-based feedback might be less effective. A key factor could be mental load, as continuous sound in most conditions (except target impact chime) may have increased cognitive demand, aligning with prior studies showing that background noise can impair performance in various tasks [36]–[38]. Additionally, it has been found that auditory signals reduced reaction time when presented before movement initiation [37]. This may explain why the target impact chime was so effective, as its discrete feedback helped

participants synchronize their movements precisely when crossing the via-point.

In general, both visual and auditory feedback about the partner's position lead to spatial and temporal alignment compared to the first solo block, supporting similar findings in the context of solo motor learning [39]. We observed a higher level of coordination when visual cues were presented, which can be explained by the dominance of the visual modality in perception [40] and the mapping complexity of the auditory feedback provided [39].

REFERENCES

[1] C. Vesper, R. P. R. D. van der Wel, G. Knoblich, and N. Sebanz, "Making oneself predictable: reduced temporal variability facilitates joint action coordination," *Exp Brain Res*, vol. 211, pp. 517–30, Jun 2011.

[2] G. Pezzulo, F. Donnarumma, and H. Dindo, "Human sensorimotor communication: a theory of signaling in online social interactions," *PLoS One*, vol. 8, no. 11, p. e79876, 2013.

[3] F. della Gatta, F. Garbarini, M. Rabuffetti, L. Viganò, S. A. Butterfill, and C. Sinigaglia, "Drawn together: When motor representations ground joint actions," *Cognition*, vol. 165, pp. 53–60, 2017.

[4] R. C. Schmidt and B. O'Brien, "Evaluating the dynamics of unintended interpersonal coordination," *Ecological Psychology*, vol. 9, no. 3, pp. 189–206, 1997.

[5] M. J. Richardson, K. L. Marsh, and R. C. Schmidt, "Effects of visual and verbal interaction on unintentional interpersonal coordination.," *Journal of experimental psychology. Human perception and performance*, vol. 31 1, pp. 62–79, 2005.

[6] O. Oullier, G. C. de Guzman, K. J. Jantzen, J. Lagarde, and J. A. S. Kelso, "Social coordination dynamics: measuring human bonding," *Soc Neurosci*, vol. 3, no. 2, pp. 178–92, 2008.

[7] R. Li, N. Mayseless, S. Balters, and A. L. Reiss, "Dynamic inter-brain synchrony in real-life inter-personal cooperation: A functional near-infrared spectroscopy hyperscanning study," *NeuroImage*, vol. 238, p. 118263, 2021.

[8] V. T. Chackochan and V. Sanguineti, "Incomplete information about the partner affects the development of collaborative strategies in joint action," *PLoS Comput Biol*, vol. 15, p. e1006385, Dec 2019.

[9] C. De Vicariis, V. T. Chackochan, L. Bandini, E. Ravaschio, and V. Sanguineti, "Computational joint action: Dynamical models to understand the development of joint coordination," *PLOS Computational Biology*, vol. 20, pp. 1–27, 10 2024.

[10] M. Mace, N. Kinany, P. Rinne, A. Rayner, P. Bentley, and E. Burdet, "Balancing the playing field: collaborative gaming for physical training," *Journal of neuroengineering and rehabilitation*, vol. 14, pp. 1–18, 2017.

[11] H. Bekkering, E. R. De Bruijn, R. H. Cuijpers, R. Newman-Norlund, H. T. Van Schie, and R. Meulenbroek, "Joint action: Neurocognitive mechanisms supporting human interaction," *Topics in Cognitive Science*, vol. 1, no. 2, pp. 340–352, 2009.

[12] W. W. Gaver, "The sonicfinder: An interface that uses auditory icons," *Human–Computer Interaction*, vol. 4, no. 1, pp. 67–94, 1989.

[13] M. R. Jones, "Time, our lost dimension: toward a new theory of perception, attention, and memory.," *Psychological review*, vol. 83, no. 5, p. 323, 1976.

[14] S. Proksch, D. C. Comstock, B. Médé, A. Pabst, and R. Balasubramaniam, "Motor and predictive processes in auditory beat and rhythm perception," *Frontiers in Human Neuroscience*, vol. 14, p. 578546, 2020.

[15] T. Särkämö, M. Tervaniemi, S. Laitinen, A. Forsblom, S. Soinila, M. Mikkonen, T. Autti, H. M. Silvennoinen, J. Erkkilä, M. Laine, *et al.*, "Music listening enhances cognitive recovery and mood after middle cerebral artery stroke," *Brain*, vol. 131, no. 3, pp. 866–876, 2008.

[16] D. Campolo, P. Tommasino, K. Gamage, J. Klein, C. M. L. Hughes, and L. Masia, "H-man: a planar, h-shape cabled differential robotic manipulandum for experiments on human motor control," *J Neurosci Methods*, vol. 235, pp. 285–97, Sep 2014.

[17] A. Takagi, F. Usai, G. Ganesh, V. Sanguineti, and E. Burdet, "Haptic communication between humans is tuned by the hard or soft mechanics of interaction," *PLoS Comput Biol*, vol. 14, p. e1005971, Mar 2018.

[18] S. Koelsch, S. Jentschke, D. Sammler, and D. Mietchen, "Untangling syntactic and sensory processing: An erp study of music perception," *Psychophysiology*, vol. 44, no. 3, pp. 476–490, 2007.

[19] M. Rigg, "Musical expression: an investigation of the theories of erich sorantin.," *Journal of Experimental Psychology*, vol. 21, no. 4, p. 442, 1937.

[20] D. Sammler, M. Grigutsch, T. Fritz, and S. Koelsch, "Music and emotion: electrophysiological correlates of the processing of pleasant and unpleasant music," *Psychophysiology*, vol. 44, no. 2, pp. 293–304, 2007.

[21] J. P. van de Geer, W. J. Levelt, and R. Plomp, "The connotation of musical consonance," *Acta Psychologica*, vol. 20, pp. 308–319, 1962.

[22] L. Wedin, "A multidimensional study of perceptual-emotional qualities in music," *Scandinavian journal of psychology*, vol. 13, no. 1, pp. 241–257, 1972.

[23] I. Winkler, G. P. Háden, O. Ladinig, I. Sziller, and H. Honing, "Newborn infants detect the beat in music," *Proceedings of the National Academy of Sciences*, vol. 106, no. 7, pp. 2468–2471, 2009.

[24] R. Parncutt, "A perceptual model of pulse salience and metrical accent in musical rhythms," *Music perception*, vol. 11, no. 4, pp. 409–464, 1994.

[25] M. Eimer, D. Cockburn, B. Smedley, and J. Driver, "Cross-modal links in endogenous spatial attention are mediated by common external locations: evidence from event-related brain potentials," *Experimental Brain Research*, vol. 139, pp. 398–411, 2001.

[26] V. Jousmäki and R. Hari, "Parchment-skin illusion: sound-biased touch," *Current biology*, vol. 8, no. 6, pp. R190–R191, 1998.

[27] D. M. Lloyd, N. Merat, F. Mcglone, and C. Spence, "Crossmodal links between audition and touch in covert endogenous spatial attention," *Perception & Psychophysics*, vol. 65, pp. 901–924, 2003.

[28] C. Spence, M. E. Nicholls, N. Gillespie, and J. Driver, "Cross-modal links in exogenous covert spatial orienting between touch, audition, and vision," *Perception & psychophysics*, vol. 60, no. 4, pp. 544–557, 1998.

[29] C. E. Sherrick, "Basic and applied research on tactile aids for deaf people: Progress and prospects," *The Journal of the Acoustical Society of America*, vol. 75, no. 5, pp. 1325–1342, 1984.

[30] N. Becker, S. Brett, C. Chambliss, K. Crowers, P. Haring, C. Marsh, and R. Montemayor, "Mellow and frenetic antecedent music during athletic performance of children, adults, and seniors," *Perceptual and motor skills*, vol. 79, no. 2, pp. 1043–1046, 1994.

[31] N. Becker, C. Chambliss, C. Marsh, and R. Montemayor, "Effects of mellow and frenetic music and stimulating and relaxing scents on walking by seniors," *Perceptual and motor skills*, vol. 80, no. 2, pp. 411–415, 1995.

[32] J. Edworthy and H. Waring, "The effects of music tempo and loudness level on treadmill exercise," *Ergonomics*, vol. 49, no. 15, pp. 1597–1610, 2006.

[33] R. Kuribayashi and H. Nittono, "Speeding up the tempo of background sounds accelerates the pace of behavior," *Psychology of Music*, vol. 43, no. 6, pp. 808–817, 2015.

[34] A. Szabo, A. Small, and M. Leigh, "The effects of slow-and fast-rhythm classical music on progressive cycling to voluntary physical exhaustion," *Journal of sports medicine and physical fitness*, vol. 39, no. 3, p. 220, 1999.

[35] T. K. Vintsyuk, "Speech discrimination by dynamic programming," *Cybernetics*, vol. 4, no. 1, pp. 52–57, 1968.

[36] X. Jiang and A. K. Sengupta, "Effect of music and induced mental load in word processing task," in *2011 IEEE International Conference on Systems, Man, and Cybernetics*, pp. 3261–3266, IEEE, 2011.

[37] A. W. Van Gemmert and G. P. Van Galen, "Auditory stress effects on preparation and execution of graphical aiming: A test of the neuromotor noise concept," *Acta Psychologica*, vol. 98, no. 1, pp. 81–101, 1998.

[38] D. Bläsing and M. Bornewasser, "Influence of complexity and noise on mental workload during a manual assembly task," in *Human Mental Workload: Models and Applications: 4th International Symposium, H-WORKLOAD 2020, Granada, Spain, December 3–5, 2020, Proceedings 4*, pp. 147–174, Springer, 2020.

[39] R. Sigrist, "Visual and auditory augmented concurrent feedback in a complex motor task," *Presence*, vol. 20, no. 1, pp. 15–32, 2011.

[40] D. Stokes and S. Biggs, "The dominance of the visual," *Perception and its Modalities*, pp. 350–378, 2014.

Evaluating Cognitive Workload with the Auditory Stroop Task While Using a Lower Limb Prosthesis: A Feasibility Study

Xiaolu Bai
Department of Psychology
North Carolina State University
Raleigh, USA
xbai23@ncsu.edu

Joshua R. Tacca
Joint Department of Biomedical Engineering
NC State University and UNC-Chapel Hill, Raleigh, USA
jrtacca@ncsu.edu

Ming Liu
Joint Department of Biomedical Engineering
NC State University and UNC-Chapel Hill, Raleigh, USA
mliu10@ncsu.edu

Elizabeth D. Buxton
Department of Rehabilitation Therapies
UNC Hospitals
Chapel Hill, USA
elizabeth.buxton@unchealth.unc.edu

Michael D. Lewek
Department of Health Sciences,
UNC-Chapel Hill, Chapel Hill, USA
mlewek@med.unc.edu

Jing Feng
Department of Psychology
North Carolina State University,
Raleigh, USA
jfeng2@ncsu.edu

He (Helen) Huang
Joint Department of Biomedical Engineering
NC State University and UNC-Chapel Hill, Raleigh, USA
hhuang11@ncsu.edu

***Abstract*— This study explored the feasibility of using the auditory Stroop task to assess cognitive workload in a dual-task paradigm. Performance on two tasks—counting backward by 3 and the auditory Stroop task—was measured across two conditions: participants' own passive device and a direct EMG-controlled (dEMG) device. Results based on individual participants' data indicated that the auditory Stroop task effectively captured more consistent dual-task costs under cognitively demanding conditions, whereas the backward counting task exhibited minimal and less consistent performance deterioration. Participant interviews suggested that the backward counting task might be less sensitive to workload because participants could use strategies, while no strategies were reported for the auditory Stroop task. Although the findings are promising, this study was limited by a small sample size, which precluded statistical analysis. Future research should involve larger samples to confirm the auditory Stroop task's validity for measuring cognitive workload while using a lower limb prosthesis.**

Keywords— cognitive workload, dual-task paradigm, evaluation methods

I. Introduction

Like other rehabilitation robotics, lower limb prosthetics are using increasingly sophisticated mechanisms, such as direct electromyography control and finite state machine-based impedance control, to improve motor function for amputees. There is encouraging evidence of these advanced control methods replicating the natural limb control mechanism and increasing the sense of agency [1]. However, one of the significant challenges that comes with these newer prosthetic control methods is that it demands substantial cognitive resources to use them (for a review, see [2]). This poses difficulty as prosthesis wearers must consciously monitor and adjust their movements to ensure stability, especially during complex tasks like walking on uneven surfaces or navigating stairs [3, 4]. The increased cognitive load can lead to fatigue and impaired walking mechanics [5]. Studies have shown that attention and cognitive efforts are crucial for prosthesis users to manage both their movements and the external environment [4]. As a result, developing advanced lower limb prostheses that are easy, safe, and comfortable to use requires a precise way to measure cognitive workload during walking. Despite this strong need, there is currently limited methods for a precise, real-time, and continuous measure of cognitive workload associated with lower limb prosthesis usage.

Existing methods for quantifying cognitive workload during walking with a lower limb prosthesis face various challenges, such as not being real-time or precise, or facing high equipment and data processing barriers. Specifically, questionnaire measures such as the NASA-TLX [6] are valid and easy to use but can only be used to capture overall workload at the end of a session or condition. Physiological measures, like eye tracking and brain activity monitoring [7, 8], offer more precision but require significant investment in equipment setup and extensive data processing (i.e., high capability but also high equipment demand). The dual-task paradigm, which involves having participants perform a secondary task while simultaneously walking. This approach assesses the cognitive workload of walking by analyzing how well participants can manage both tasks simultaneously. It provides an alternative that balances the need for accurate cognitive workload measurement with the constraints of equipment feasibility. However, it still poses challenges in terms of selecting appropriate secondary tasks that effectively simulate real-world demands. Therefore, a balanced task is needed to achieve a better compromise between measurement capability and equipment demand.

This study was supported by the National Institutes of Health (NIH award # 1R01HD110519 - 01A1 and 02S1) to HH, JF and ML

In this paper, we discuss the literature background, including relevant methods and challenges in measuring cognitive workload using the dual-task paradigm in the context of lower limb prosthesis use. We then introduce auditory Stroop task that strikes a balance between equipment demand and measurement capability, presenting preliminary evidence of its effectiveness through data from three pilot amputee participants.

A. Dual-Task Paradigm

The dual-task paradigm is a commonly used approach to assess cognitive workload. This method involves having participants perform two tasks simultaneously, with one being the primary task, such as "time up and go" test (TUG), and the other as secondary cognitive task, such as solving arithmetic problems [9]. Depending on the instruction of task prioritization (i.e., ensure good performance on either the primary or the secondary task), the extent to which performance on the other task deteriorates indicates a dual-task cost. Studies have used dual-task cost to reveal cognitive workload with prosthesis use. For example, Shaw et al. [10] found that transfemoral amputees showed reduced performance on a visual secondary task while walking compared to sitting, whereas those with transtibial amputations displayed consistent secondary task performance in both seated and walking conditions. This suggests that walking with a prosthesis places greater cognitive workload on individuals with more proximal amputations.

While dual-task paradigms are widely used in previous studies, the selection of an appropriate secondary task requires careful consideration. For instance, visual secondary tasks used to evaluate cognitive workload can interfere with walking, limiting their feasibility to controlled environments like treadmill-based simulations [10]. Therefore, it is essential to identify a secondary task that enables precise measurement and continuous monitoring during walking.

B. A Clinical Task: Counting Backward

Counting backward is frequently used as a secondary task in the dual-task paradigm to introduce an additional cognitive demands because of its simplicity and capacity to challenge cognitive resources [11, 12]. In this task, participants are typically given a starting number and are asked to keep reporting the next numbers by continuously subtracting another number. For example, starting with 89 and counting backward by 3 would lead to answers 82, 79, 76, 73, 70, 67, and so on. This task involves cognitive components such as attention and working memory, and it is favored in clinical settings as a secondary task to identify risks in mobility and walking safety. For example, Vance et al. [13] found that adding counting backward to TUG improved the identification of fall risk in people with Parkinson's disease. In the context of amputation rehabilitation, Frengopoulos et al. [14] found that using counting backward as a secondary task affected amputees' walking performance similarly, regardless of their etiology, levels of amputation and time with the prosthesis.

Despite its usefulness, using counting backward to assess cognitive workload has limitations that impact measurement accuracy and precision. Potential confounding variables, such as individual math ability and stress-related math anxiety, could pose problems. For low performance individuals, it may be difficult to differentiate due to the floor effect. Given the participant has already performing poorly at baseline, there is little room to show the effect of increasing primary task demand leading to even worse performance. Furthermore, final counts of correct responses instead of response times are usually used as the performance measure for convenience, leading to issues of missing information about the workload dynamics. Given these limitations, it is perhaps not surprising that in some studies (e.g., [9]), no differential cognitive workloads were reflected in the counting backward task, even when participants perceived significantly different cognitive burdens. This suggests the possible lack of sensitivity of the task for evaluating the cognitive workload associated with different lower limb prosthesis technologies. As such, while counting backward is convenient, its limitations suggest the need for alternative or supplementary methods to provide a more precise and continuous assessment.

C. An Alternative Lab-Based Task: Auditory Stroop

The auditory stroop task presents a promising alternative to the counting backward task for assessing cognitive workload as the secondary task in dual-task walking. The auditory Stroop task requires participants to process conflicting auditory information, such as hearing the word "high" spoken in a low pitch and responding based on the pitch rather than the word's meaning [15]. The cognitive demand of resolving such conflicts taps into attention and executive function, making it a suitable concurrent task with walking [16]. In the context of prosthesis use, the auditory Stroop task has been shown to cause wider steps in participants with transfemoral amputation using microprocessor knees [17], suggesting increased cognitive workload associated with the dual-task condition as compared to the single task (i.e., walking-only) condition. Compared to counting backward, the auditory Stroop task minimizes potential impact from individual variability related to math skills. It is also highly relevant to daily tasks that require resolving conflicts among perceptual information. Furthermore, it maintains a predetermined timing of trials so sampling rate of response time and accuracy data can remain consistent throughout the walking task, instead of potential loss of data sample due to strategy use when performing the counting backward task (e.g., participant stopped doing the counting due to difficulty in counting or walking).

While existing evidence and considerations point to the promise of the auditory Stroop task, much remains to be examined. For example, to use this task to compare different prosthesis technologies, the task prioritization instruction needs to emphasize the walking performance being the priority. Then by observing participants performance on the Stroop task, we can quantify the cognitive workload associated with each prosthesis technology. Second, feasibility studies are needed to find out a proper setting of the auditory Stroop task, such as the pace of trials, to ensure the task effectively captures cognitive workload under different walking conditions. Third, the psychometric properties, such as sensitivity, need to be ensured. In the case of using auditory Stroop task to evaluate cognitive workload, sensitivity indicates how well the task can accurately capture changes in cognitive workload [18]. By comparing the results of the auditory Stroop task under different imposed workload

conditions, we can evaluate how sensitive the task detects the cognitive changes across varying conditions. Additionally, observations from prosthesis wearers are essential to validate the findings. These considerations call for expanded investigation of the feasibility and effectiveness of the auditory Stroop task as a cognitive workload measure in the dual-task paradigm.

D. The Current Study

The study aimed to explore the feasibility of using the auditory Stroop task as a tool to assess cognitive workload in a dual-task paradigm. Specifically, participants completed two tasks—counting backward by 3 and the auditory Stroop task—while operating two devices: their own passive device and a direct EMG-controlled (dEMG) device. In addition to task performance, interviews were conducted to gain qualitative insights into participants' experiences.

II. Methods

A. Participants

Three participants with transtibial amputations were recruited for this study (1 male, 2 females). Participants' age ranged from 29 to 70 years, the height ranged from 1.64 meters to 1.80 meters, and years of amputation were 5 to 18 years. The reason for amputation was edema, cancer, or trauma. All participants were recruited from the community.

B. Measures

1) Timed Up and Go (TUG)

Participants began the task by standing up from a chair, then walked 3 meters to a line marked on the floor, turned around, walked back, and sat down. They were instructed to walk as quickly and safely as possible. The time from standing up to sitting down was recorded using a stopwatch.

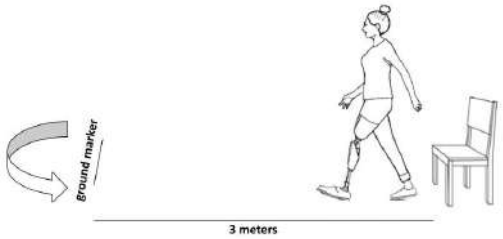


Fig. 1. Timed up and go setup.

2) Counting Backward by 3

Participants were instructed to count backward by threes from a randomly selected number. In the single-task condition, participants counted backward for 30 seconds. In dual-task condition, participants counted backward during the duration of the TUG. The number of correct responses were recorded and used to calculate accuracy. Counting speed was determined by dividing the total number of responses by the counting duration.

3) Auditory Stroop Task

The auditory Stroop task was programmed using OpenSesame [19]. Each trial began with a 200-millisecond break, followed by a 350-millisecond auditory beep, then a 150-millisecond interval. Participants then heard the word "high" or "low" spoken in either a high or low pitch. Then participants heard the word "high" or "low" spoken in either a high pitch or a low pitch. Using a clicker with up and down arrows, participants responded by pressing the up arrow for high-pitch sounds and the down arrow for low-pitch sounds.

Trials were organized into blocks. Each block consisted of four trials with unique combinations of words and pitches, presented in a random order. In the single task condition, participants completed four blocks, resulting in a total of 16 trials. In the dual-task condition, participants were asked to respond while performing the TUG. Therefore, the number of completed trials varied based on their TUG performance. The reaction time for each trial and the number of correct answers were recorded as measures of performance.

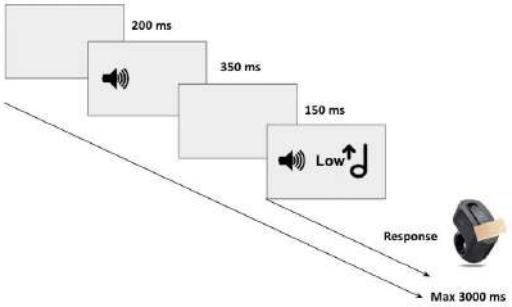


Fig. 2. Auditory Stroop task. The condition shown in the figure presents the word *low* in a high pitch, and the participant needed to respond by pressing the upper arrow on the clicker.

4) Dual-Task Cost

Participants were instructed to primarily focus on walking. Dual-task cost was defined as the percent change in performance relative to an individual's single-task performance [20]. A greater dual-task cost implicates greater performance deterioration under dual-task conditions. To reflect the cost in accuracy for the counting backward and auditory Stroop task, the dual-task cost was calculated as follows (1):

$$\frac{(single_task - dual_task)}{single_task} * 100\% \quad (1)$$

For speed and response time (2), dual-task cost was calculated as follows:

$$\frac{(dual_task - single_task)}{single_task} * 100\% \quad (2)$$

C. Procedure

The study protocol was approved by the Institutional Review Board of the university, and written informed consent was obtained from each amputee participant. The study was conducted as part of a larger investigation to understand the effects of a direct EMG-controlled (dEMG) powered prosthetic ankle compared to their prescribed passive prosthesis. Participants underwent performance evaluations through a series of clinical, cognitive, and biomechanical assessments using both their passive device and the dEMG device. Evaluations for the passive and dEMG devices were conducted on separate days. The reason for including both passive and dEMG devices is to examine measurement

sensitivity by comparing the two different cognitive measures. Patients are known to experience difficulties using dEMG devices without prior exposure [21]. If the measurement can detect these difficulties, it would demonstrate good sensitivity.

During the cognitive assessments, participants were evaluated on their performance in the TUG, counting backward by 3, and the auditory Stroop task. They also completed dual-task conditions, in which they performed the TUG concurrently with the counting backward or the auditory Stroop task. For all dual-task conditions, participants were asked to prioritize their focus on walking. Participants first practiced the TUG, followed by two trials to assess their performance. They then practiced counting backward by 3 and completed a 30-second counting task only while sitting as the baseline. Afterward, participants performed two trials of counting backward by 3 while simultaneously completing the TUG. After a brief break, participants were asked to practice and then perform the auditory Stroop task only while sitting, which was used as the baseline. Next, they practiced and completed two dual-task trials, combining the TUG with the Stroop task.

III. Results

Since each participant performed every task twice, the best performance was selected for analysis. For the cognitive tasks, the trial with the highest accuracy was chosen. If two trials had the same accuracy, the trial with the faster reaction time was selected.

A. TUG

1) Participant 1

For passive device, the TUG time was 17.50 seconds; with counting it was 23.00 seconds; and with Stroop was 20.20 seconds.

For dEMG device, the TUG time was 34.34 seconds When performed with counting, the TUG time was 33.00 seconds, and when combined with the auditory Stroop task, the time was 31.28 seconds.

2) Participant 2

Using the passive device, the TUG completion time was 7.95 seconds. With counting backward, the TUG time increased to 13.80 seconds. With the auditory Stroop task, the TUG time was 11.14 seconds.

With the dEMG device, the TUG time was 11.98 seconds. When performed with the counting backward task, the TUG time was 15.30 seconds, and with the auditory Stroop task, it was 12.55 seconds.

3) Participant 3

For the passive device, the TUG time was 9.78 seconds. With counting backward, the TUG time increased to 10.89 seconds. When combined with the auditory Stroop task, the TUG time was 11.96 seconds.

For the dEMG device, the TUG time was 14.08 seconds. With counting, the TUG time was 13.32 seconds, and with the auditory Stroop task, the TUG time was 14.07 seconds.

In summary, the pattern was consistent across all three participants, with both the passive and dEMG devices showing that walking speed was impacted by the dual-task conditions. Using dEMG device took longer than using their own passive device to walk (Fig. 3, upper panels).

B. Counting Backward by 3

1) Participant 1

For passive device, the baseline accuracy was 89% (8/9) and the counting speed was 3.33 seconds per number. When performed with the TUG, the accuracy was 100% (9/9) and the speed was 2.78 seconds per number. The dual-task cost of accuracy was -0.12, and the cost of speed was -0.17.

dEMG baseline showed a 100% accuracy (11/11) with a counting speed of 2.73 seconds per number. When performing with the TUG, this participant had 100% accuracy (7/7) and the speed was 4.71 seconds per number. The dual-task cost was 0% on accuracy and 73% on speed.

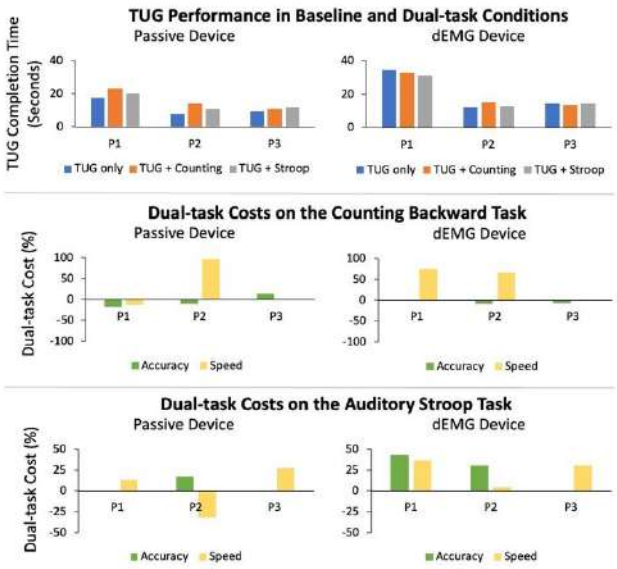


Fig 3. Performance on the Timed Up and Go (TUG) task and dual-task costs on the counting backward task and the auditory Stroop task from each of the three participants (P1, P2, P3) when wearing their own passive devices or a dEMG device. The upper panels show participants' TUG task completion time in the basline (TUG only) and dual-task conditions (TUG + Counting, TUG + Stroop). The middle panels show the dual-task costs (%) on the counting backward task. The lower panels show the dual-task costs (%) on the auditory Stroop task. A positive dual-task cost suggests the dual-task having a lower accuracy or taking longer to complete than the single task. Opposite directions of costs on speed and accuracy suggests a speed-accuracy trade-off (e.g., P33 on the counting backward task for both devices, and on the auditory Stroop task for the passive device). A greater and positive dual-task cost suggests an overall more demanding task condition (e.g., the dEMG device poses higher demand than the passive device for P1 as shown on the auditory Stroop task). Fewer negative costs and more consistent cost patterns across participants comparing the passive and dEMG devices suggest higher criterion validity and external validity of a measure. In general, based on this preliminary data from three participants, the auditory Stroop task presents more consistent and meaningful dual-task costs.

2) Participant 2

Using passive device, participant counted 11 numbers in 30 seconds with 1 error at the baseline. Accuracy was 91%. On average, the counting speed was 2.72 seconds per number. In the dual-task condition, participant counted 3 numbers with no error. Accuracy was 100% with a counting speed of 5.33 seconds per number. The dual-task cost was -10% for

accuracy and 96% for speed, meaning that this participant had higher accuracy but slower speed in the dual-task condition as compared to the baseline.

Using dEMG, participants counted 13 numbers in 30 seconds and had 1 error at the baseline. Accuracy was 92% with a speed of 2.31 seconds per number. In the dual-task condition, the participant counted 4 numbers with no error. Accuracy was 100%. The counting speed was 3.83 seconds per number. The dual-task cost was -9% for accuracy and 65% for speed.

3) Participant 3

In passive device, baseline accuracy was 100% for the 19 total counted numbers (19/19). Counting speed was 1.58 seconds per number. In the dual-task condition, this participant counted 7 numbers with 1 error (i.e., accuracy was 86%) with a speed of 1.56 seconds per number. The dual-task cost was 14% for accuracy and -1% for speed.

For dEMG device, the baseline accuracy for counting was 94% (17/18). The speed was 1.67 seconds per number. In the dual-task condition, this participant had 100% accuracy (i.e., all correct for the 8 total counted numbers), and a speed of 1.66 numbers per second. The dual-task cost was -6% for accuracy and -1% for speed.

In summary, the dual task costs for accuracy and speed varied across participants. Only one participant showed meaningful dual-task cost in accuracy, and two participants showed dual-task cost in speed. Many results showed improved performance under the dual-task conditions (Fig. 3, middle panels), suggesting weak sensitivity and measurement stability of this task.

C. Auditory Stroop Task

1) Participant 1

For passive device, the baseline accuracy was 50%, and the response time was 780 milliseconds. With TUG, the accuracy was 50% and response time was 883 milliseconds Therefore, the dual-task cost was 0% for accuracy and 13% for speed.

For dEMG device, of the baseline accuracy was 70% with a response time of 1219 milliseconds. In the dual-task condition, the accuracy dropped to 40% and the response time increased to 1651 milliseconds. Therefore, the dual-task cost was 43% for accuracy and 36% for speed.

2) Participant 2

When using the passive device, on the baseline, the participant had 100% accuracy and an average response time of 707 milliseconds. When performed with the TUG, the accuracy dropped to 83.33%, although with a shorter average response time of 484 milliseconds. The dual-task cost was 17% for accuracy and -32% for speed.

Using dEMG device, on the baseline, participant had an accuracy of 95% and an average response time of 696 milliseconds. When performing with the TUG, participant had an accuracy of 66.67% and average response time of 725 milliseconds. The dual-task cost was 30% for accuracy and 4% for speed.

3) Participant 3

In the baseline condition using the passive device, the participant was 100% accurate with 590 milliseconds response time. In the dual-task condition, it was 100% accuracy with 758 milliseconds response time. The dual-task cost was 0% for accuracy and 28% for speed.

dEMG baseline showed 100% accuracy and 665 milliseconds response time. In the dual-task condition, the participant had 100% accuracy and 864 milliseconds response time. The dual-task cost was 0% for accuracy and 30% for speed.

In summary, the results showed dual-task costs in both response time and accuracy, except one participant had faster responses when using the passive device as compared to baseline. The general patterns across the three participants also suggest consistently greater dual-task costs when using the dEMG device compared to the passive device (Fig. 3, lower panels). Overall, the Stroop task data captured consistent and meaningful dual-task costs.

D. Interview

Participants were asked to reflect on their experience with counting backward and auditory Stroop task, including the strategy they used, as well as the challenges and the difficulties they encountered.

For the strategies used during the tests, all three participants reported using strategies to assist with counting backward by 3. Two participants described using mental strategies to identify numerical patterns. For example, participant 3 explained, *"when we were counting backward from three, if we went down ten numbers, we would be hitting the same numbers … I was just trying to remember that."* Similarly, participant 1 noted, *"I've tried not to practice, but I'm getting a pattern in my head now."* Participant 2 explicitly recalled slowing down the pace and using fingers to aid in counting backward. In contrast, no participant reported any strategies used in the auditory Stroop task.

Regarding difficulties and challenges, participants 2 and 3 identified the mathematical aspect of the counting backward as particularly demanding, noting it was more challenging than the auditory Stroop task. Both participants attributed this to their mathematical abilities. For example, participant 2 mentioned, *"Maybe I'm not good at numbers, and it was all in your head". Similarly,* participant 3 stated, *"Numbers are not my thing … I had to think a lot more [than the auditory Stroop task] while I was doing it."* Participant 1 found the auditory Stroop task was more difficult than counting backward, remarking, "*I could argue with the voices sometimes.*" In addition to the cognitive demands, participants 1 and 3 pointed out issues with the clicker, especially when managing other physical demands. Participant 1 stated, "*The clicker is the most frustrating thing, because you're holding on to the walker and holding on [to it] and having to push a button at the same time.*"

IV. Discussion

The findings of the current study provide preliminary evidence that the auditory Stroop task could potentially become a valuable tool for measuring cognitive workload in a dual-task paradigm. Compared to the counting backward task, the auditory Stroop task demonstrated a consistent pattern of capturing greater dual-task costs under more

cognitively demanding conditions (i.e., using the dEMG device). In contrast, performance in the counting backward task did not show much deterioration during dual-task performance and the patterns were quite inconsistent across participants when comparing the passive and the dEMG devices. This aligns with previous research [9], which suggests that cognitive workload may not be effectively reflected in the counting backward task. While counting backward has proven to be an effective task for adding load in clinical assessments of mobility and safety, preliminary results from the current study suggest it may not be the most suitable method for evaluating cognitive workload for prosthetic technologies. Instead, the auditory Stroop task appears to be a more promising alternative.

Interviews further supported that as participants reported employing strategies by identifying patterns while performing the backward counting task, which may have contributed to its insensitivity in reflecting changing cognitive workload. For future studies, the setup of the auditory Stroop task can be enhanced. In the current study, participants used a presentation clicker to respond, and all participants reported that the clicker made the task more challenging. Addressing this usability issue may improve the task's effectiveness and participant experience.

As an initial feasibility study to explore the use of the auditory Stroop task in assessing cognitive workload with the dEMG device, the findings are promising. However, a key limitation of this study is its small sample size even though the participants were amputees, which precluded the possibility of conducting statistical analyses. Future research should address this limitation by incorporating a larger sample size to enable statistical testing.

ACKNOWLEDGMENT

The authors would like to thank Avery Murray, Austin Mituniewicz, Brendan Driscoll, and Pinar Onal from North Carolina State University, as well as Derek Frankena from Atlantic P&O for their assistance with the preparation and data collection for this study.

REFERENCES

[1] P. D. Marasco *et al.*, "Illusory movement perception improves motor control for prosthetic hands," Sci. Transl. Med., vol. 10, no. 432, p. eaao6990, Mar. 2018, doi: https://doi.org/10.1126/scitranslmed.aao6990.

[2] X. Bai, J. Yuan, M. Liu, H. Huang, and J. Feng, "Human factors considerations of Interaction between wearers and intelligent lower-limb prostheses: a prospective discussion," J Neuroeng Rehabil, vol. 21, no. 1, Oct. 2024, doi:https://doi.org/10.1186/s12984-024-01475-x.

[3] M. Li et al., "Gaze Fixation Comparisons Between Amputees and Able-bodied Individuals in Approaching Stairs and Level-ground Transitions: A Pilot Study," 2019 41st Annual International Conference of the IEEE Engineering in Medicine and Biology Society (EMBC), Berlin, Germany, 2019, pp. 3163-3166, doi: 10.1109/EMBC.2019.8857388.

[4] W. C. Miller, A. Barry. Deathe, M. Speechley, and J. Koval, "The influence of falling, fear of falling, and balance confidence on prosthetic mobility and social activity among individuals with a lower extremity amputation," *Archives of Physical Medicine and Rehabilitation,* vol. 82, no. 9, pp. 1238–1244, Sep. 2001, doi: https://doi.org/10.1053/apmr.2001.25079.

[5] A. L. Pruziner *et al.*, "Biomechanical and neurocognitive performance outcomes of walking with transtibial limb loss while challenged by a concurrent task," *Experimental Brain Research*, vol. 237, no. 2, pp. 477–491, Feb. 2019, doi: https://doi.org/10.1007/s00221-018-5419-8.

[6] Hart, S. G. "Development of NASA-TLX (Task Load Index): Results of empirical and theoretical research." *Advances in Psychology,* vol. 52, pp. 139-183, 1988.

[7] S. Manz *et al.,* "Using mobile eye tracking to measure cognitive load through gaze behavior during walking in lower limb prosthesis users: A preliminary assessment," *Clinical Biomechanics*, vol. 115, pp. 106250–106250, Apr. 2024, doi: https://doi.org/10.1016/j.clinbiomech.2024.106250.

[8] R. Rackerby, S. Lukosch, and D. Munro, "Understanding and measuring the cognitive load of amputees for rehabilitation and prosthesis development," *Archives of Rehabilitation Research and Clinical Translation*, vol. 4, no. 3, p. 100216, Sep. 2022. doi:10.1016/j.arrct.2022.100216

[9] R. M. Williams *et al.*, "Does Having a Computerized Prosthetic Knee Influence Cognitive Performance During Amputee Walking?," *Archives of Physical Medicine and Rehabilitation*, vol. 87, no. 7, pp. 989–994, Jul. 2006, doi: https://doi.org/10.1016/j.apmr.2006.03.006.

[10] E. P. Shaw *et al.*, "A Comparison of Mental Workload in Individuals with Transtibial and Transfemoral Lower Limb Loss during Dual-Task Walking under Varying Demand," *Journal of the International Neuropsychological Society,* vol. 25, no. 09, pp. 985–997, Aug. 2019, doi: https://doi.org/10.1017/s1355617719000602.

[11] M. F. Folstein, S. E. Folstein, and P. R. McHugh. "'"Mini-mental state": a practical method for grading the cognitive state of patients for the clinician." *Journal of psychiatric research,* vol 12, no. 3, pp. 189 – 198, 1975.

[12] O. Spreen and E. Strauss, A compendium of neuropsychological tests : administration, norms, and commentary. New York: Oxford University Press, 1998.

[13] R. C. Vance, D. G. Healy, R. Galvin, and H. P. French, "Dual Tasking With the Timed 'Up & Go' Test Improves Detection of Risk of Falls in People With Parkinson Disease," *Physical Therapy*, vol. 95, no. 1, pp. 95–102, Jan. 2015, doi: https://doi.org/10.2522/ptj.20130386.

[14] C. Frengopoulos, M. W. C. Payne, J. D. Holmes, R. Viana, and S. W. Hunter, "Comparing the Effects of Dual-Task Gait Testing in New and Established Ambulators With Lower Extremity Amputations," *PM&R*, vol. 10, no. 10, pp. 1012–1019, Apr. 2018, doi: https://doi.org/10.1016/j.pmrj.2018.03.018.

[15] K. Kestens, S. Degeest, M. Miatton, and H. Keppler. "An auditory Stroop test to implement in cognitive hearing sciences: development and normative data." *International Journal of Psychological Research*, vol. 14, no. 2, pp. 37-51, 2021.

[16] S. Janssen *et al.*, "Validation of the Auditory Stroop Task to increase cognitive load in walking tasks in healthy elderly and persons with Parkinson's disease," *PLOS ONE*, vol. 14, no. 8, p. e0220735, Aug. 2019, doi: https://doi.org/10.1371/journal.pone.0220735.

[17] S. J. Morgan, B. J. Hafner, and V. E. Kelly, "The effects of a concurrent task on walking in persons with transfemoral amputation compared to persons without limb loss," *Prosthetics & Orthotics International*, vol. 40, no. 4, pp. 490–496, Aug. 2016, doi: https://doi.org/10.1177/0309364615596066.

[18] Trevethan R., "Sensitivity, specificity, and predictive values: foundations, pliabilities, and pitfalls in research and practice," *Frontiers in Public Health,* vol. 5, no. 307, 2017, doi: https://doi.org/10.3389/fpubh.2017.00307

[19] S. Mathôt and D. Schreij, and J. Theeuwes, "OpenSesame: an open-source, Graphical Experiment Builder for the Social Sciences," *Behavior Research Methods*, vol. 44, no. 2, pp. 314–324, Nov. 2012, doi: https://doi.org/10.3758/s13428-011-0168-7.

[20] B. Abernethy, "Dual-task methodology and motor skills research: some applications and methodological constraints," *J Human Movement Studies*, vol. 14, pp.101-132, 1988.

[21] Fleming A, Huang S, Buxton E, Hodges F, Huang HH. "Direct continuous electromyographic control of a powered prosthetic ankle for improved postural control after guided physical training: A case study." *Wearable Technologies*, vol. 2, 2021, doi: https://doi.org/10.1017/wtc.2021.2.

Fabric Sensing of Intrinsic Hand Muscle Activity

Katelyn Lee[1], Runsheng Wang[1], Ava Chen[1], Lauren Winterbottom[2], Ho Man Colman Leung[3], Lisa Maria DiSalvo[3], Iris Xu[3], Jingxi Xu[3], Dawn M. Nilsen[2,4], Joel Stein[2,4], Xia Zhou[3,4] and Matei Ciocarlie[1,4]

***Abstract*—Wearable robotics has the capacity to assist and rehabilitate hand function in stroke survivors. Many devices that use surface electromyography (sEMG) for control rely on extrinsic hand muscle signals, since sEMG sensors are relatively easy to place on the forearm without interfering with hand function. In this work, we target the intrinsic muscles of the thumb, which are superficial to the skin and thus potentially more accessible via sEMG sensing. Traditional, rigid electrodes can not be placed on the hand without adding bulk and affecting hand functionality. We thus present a novel sensing sleeve that uses textile electrodes to measure sEMG activity of intrinsic thumb muscles. We evaluate the sleeve's performance on detecting thumb movements and muscle activity during both isolated and isometric muscle contractions of the thumb and fingers. This work highlights the potential of textile-based sensors as a low-cost, lightweight, and non-obtrusive alternative to conventional sEMG sensors for wearable robotics.**

I. Introduction

Stroke-induced hemiparesis can cause chronic upper limb weakness and reduced hand dexterity [1][2], which can hinder a stroke survivor's mobility and independence. Wearable robotic devices can aid stroke survivors by assisting hand function and providing rehabilitation therapy. Because continued, active use of the paretic hand is a key element of effective robotic rehabilitation [3], there is great interest in developing devices that promote this active engagement.

Surface electromyography (sEMG) sensors can measure residual muscle activity during active use of the paretic hand, enabling ipsilateral, robotic orthosis control. These robotic orthoses commonly place sEMG sensors on the forearm to capture activity from extrinsic hand extensor and flexor muscles, which are responsible for many gross hand movements. This data is then processed by machine learning models to infer user intent [4][5]. While these methods work well on healthy participants, stroke complications like muscle spasticity, abnormal muscle co-activation, and neurological disorders [6], introduce challenges for sEMG-based intent inferral on stroke survivors.

Beyond the forearm, the intrinsic muscles in the hand offer an alternate sEMG sensing region for intent inferral. Muscles in the thenar eminence (TE) are responsible for some thumb movements during grasping and fine motor movements [7].

This work was supported in part by the National Institutes of Health (R01NS115652, F31HD111301), National Science Foundation (IIS-2202553), and a Columbia RISE award.

[1] Dept. of Mechanical Engineering, Columbia University, NY, NY 10027, USA.{katelyn.lee, matei.ciocarlie}@columbia.edu

[2] Dept. of Rehabilitation and Regenerative Medicine, Columbia University, NY, NY 10032, USA.

[3] Dept. of Computer Science, Columbia University, NY, NY 10027, USA.

[4] Co-Principal Investigators

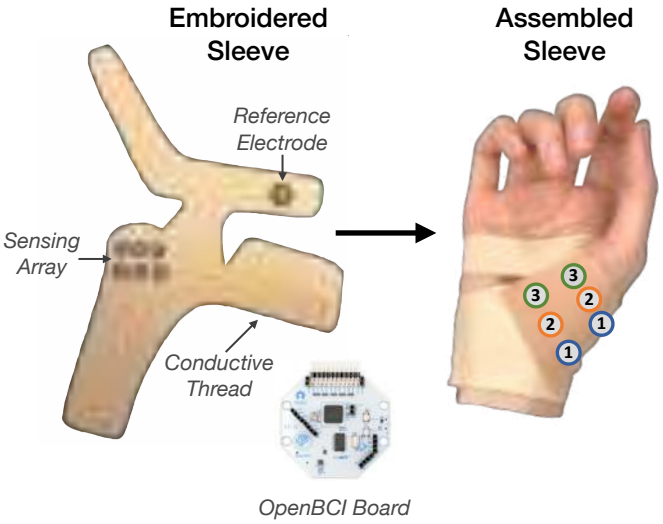


Fig. 1. The fabric sensing sleeve. After embroidering the fabric electrodes and conductive thread, which act as wires to connect the sleeve to the OpenBCI board, the sleeve is assembled into a wearable form. The sensor array is positioned on the thenar eminence of the thumb to detect when the thumb moves into abduction.

Research has suggested that in stroke survivors, the *abductor pollicis brevis* (APB) in the TE has reduced spasticity compared to other muscles in the hand [8], which highlights the TE's potential as a sensing region for stroke survivors.

Despite its advantage as a localized, grasping-specific muscle sensing region, the TE is underexplored due to its small size on a curved contour of the palm. Conventional sEMG sensors are often bulky and use stiff, adhesive pads that, when placed on the TE, can interfere with grasping and restrict thumb movement.

Textile sensors, made from conductive fabrics and threads, are an alternative sensing platform that is low-profile, non-adhesive, and comfortable for extended wear. Unlike conventional sEMG sensors, fabric electrodes are flexible and can conform to curved surfaces without adhesives on the skin.

In this pilot study, we introduce a novel, textile sensing array embroidered in a fabric sleeve to measure sEMG activity of the intrinsic thumb muscles. Our main contributions are:

- To the best of our knowledge, we are the first to use fabric sensors to measure surface EMG activity of intrinsic hand muscles. The fabric sensors are built with off-the-shelf fabrics and are optimized to mitigate motion artifacts and improve skin-contact quality without adhesive pads.
- We demonstrate that the textile sensors can distinguish

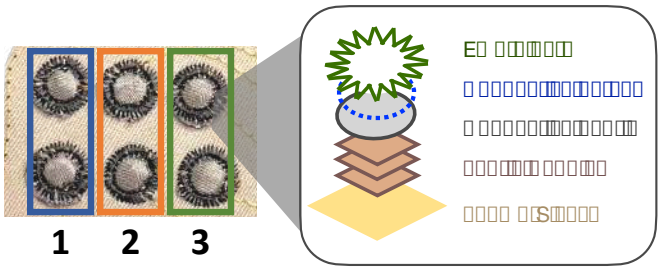


Fig. 2. The 3-channel textile sensing array, labeled by color and channel number. Each textile electrode is made of conductive fabric embroidered to a fabric substrate with internal padding to improve skin-electrode contact. Conductive thread is stitched around the perimeter of the electrode to connect the electrode to the bioamplifier board.

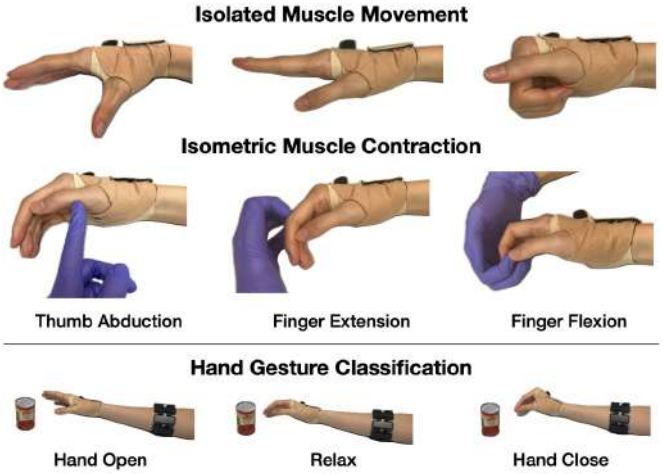


Fig. 3. Schematic of experimental protocol. During the Isolated Muscle Movement task, participants moved their thumb or fingers from rest to an engaged position as shown. The Isometric Muscle Contraction task required participants to resist external force from the experimenter's hand to engage the relevant muscles for the movement. Hand Gesture Classification data collection involved participants opening and closing their hands into a lumbrical grasp, as shown.

thumb muscle activity from finger movements. In addition, training a classifier with only the 3-channel sensing array achieves promising classification accuracy for detecting hand opening and closing.

- Our results demonstrate the fabric sensing sleeve's potential as an effective sEMG sensor for intent inferral, highlighting the value of intrinsic muscle sensing modalities for improving model classification performance in future work.

II. Related Work

Surface EMG sensing for intent inferral has been explored with various sensor configurations. Tacca et al. combined forearm sEMG sensing with a non-EMG data glove in a multi-modal system for hand gesture recognition [9]. Previous works with conventional sEMG sensors combined extrinsic and intrinsic hand muscle sensing for post-stroke rehabilitation exercises [10] and hand gesture recognition [11]. Multiple groups built fabric sleeves with textile electrodes for the forearm to measure extrinsic muscle activity for hand gesture recognition [12][13]. Lara et al. developed a PCB sEMG electrode array with a flexible polyamide substrate for intrinsic hand muscle sensing, though this system requires custom adhesive pads for use [14]. Across these works, however, intrinsic hand muscle sensing in a soft, wearable system remains underexplored.

To our knowledge, the only works related to fabric sensing of intrinsic hand muscles are a piezoresistive strain fabric sensor that measures muscle strain of the APB [15] and a graphite composite sEMG sensor extruded on a fabric substrate that measures APB muscle activity [16]. However, [15] measures muscle strain rather than sEMG activity, and [16] uses fabric as a substrate, rather than a sensing modality. This distinction highlights how fabric sEMG sensors for intrinsic hand muscles have not yet been directly explored, which our work aims to address.

III. Fabric Sensing Sleeve Design

The fabric sleeve presented in this work is a prototype 3-channel, fabric sEMG sensing sleeve that measures the intrinsic muscle activity of the thumb. The materials for fabricating the sleeve are off-the-shelf and low-cost (<$5 per sleeve) and takes about 2 hours to assemble, which enables modular design for project-specific sensing array customization and scalability.

The biopotential sensing electrode is made of a layer of conductive fabric [17] embroidered to an elastic fabric substrate. Three layers of fabric padding are placed between the conductive fabric and fabric substrate to increase electrode concavity and improve skin-electrode contact (Fig. 2). The reference electrode is 8 mm in diameter, and each sensing electrode is 6 mm in diameter, with a center-to-center electrode distance per channel of 9 mm. The electrodes were sized to fit comfortably on the TE and reduce motion noise during thumb movement.

We designed the fabric sleeve to place the 3-channel sensing array over the TE of the palm, with the reference electrode placed on the back of the hand (Fig. 1). The 3-channels array wraps around the curved TE to maintain skin contact and, similar to high-density electromyography methods, enable simultaneous sEMG measurements of one muscle for increased spatial resolution [14]. Each fabric electrode routes to a bioamplifier board (Cyton, OpenBCI) [18] via machine-sewn conductive thread [19], which is positioned on the outside of the sleeve and insulated with sports kinesiology tape to reduce noise reduce impedance and cross talk between wires and prevent off-target skin contact. Previous work using this conductive fabric as a biosensor found the material is robust to changes in signal strength after 50 wash cycles [20]. We confirmed the connectivity between the fabric electrode and the wiring adapter with a multimeter and measured an average resistance of $46.3\ \Omega \pm 3.3\ \Omega$ across all electrodes and conductive thread wires.

IV. Methods

We designed two experiments to evaluate the fabric sleeve's performance on nine healthy participants and one stroke participant. Our first objective was to determine

whether the sleeve could distinguish thumb-specific movements from overall finger movements and movement noise. The tasks chosen to evaluate this aspect included both dynamic and static thumb and finger movement conditions to isolate intrinsic thumb muscle activity. Our second objective was to explore whether signals measured by the fabric sleeve could be used for intent inferral. To test this, we trained a machine learning classifier to detect hand opening and hand closing from sEMG signals measured by the fabric sleeve.

A. Isolated Muscle Movement Task

The Isolated Muscle Movement Task distinguished between dynamic, thumb-only movement and coordinated finger movement. Participants moved either their thumb or all four fingers from rest into an engaged position with moderate effort for about 5 seconds (Fig. 3). To assess thumb-specific muscle activity, participants moved their thumb from rest into abduction. For finger-specific muscle activity, participants simultaneously moved all four fingers from a resting position into either extension or flexion.

B. Isometric Muscle Contraction Task

The Isometric Muscle Contraction Task targeted thumb-specific muscle activity in a static position. Participants performed the same actions as the Isolated Muscle Movement task with added resistance from the experimenter (Fig. 3). To minimize movement artifacts, participants resisted the external force for 5 seconds, without moving their thumb or fingers. For the thumb, the experimenter applied pressure with their finger to the lateral side of the participant's thumb MCP joint. For finger extension, the experimenter applied resistance on the dorsal side of their fingers at the head of the proximal phalanx. For finger flexion, the experimenter applied resistance on the palmar side of the participant's fingertips.

C. Hand Gesture Classification

To test whether signals from the fabric sleeve could be used for intent inferral, we collected data while participants performed a series of hand gestures. We instructed participants to open and close their hand as if they were to grasp a metal can, which we provided as a visual aid to encourage thumb abduction in a lumbrical grasp (Fig. 3). We collected two datasets for training and testing, during which the participant opened and closed their hand 8 times, each for 5 seconds, with 5 seconds of rest between each movement. The stroke participant performed an abbreviated set of 3 hand movements instead of 8.

D. Data Collection and Analysis

During data collection, participants were seated with their forearms resting on the table and elbows bent at a 90 degree angle. Participants donned both the fabric sensing sleeve and the commercial, 8-channel forearm sEMG armband (Myo, Thalmic Labs). Before donning the fabric sensing sleeve, we prepped the participant's hand by wiping their skin with a moist towelette and adjusted the position of the sensing array to lie over the TE of the thumb.

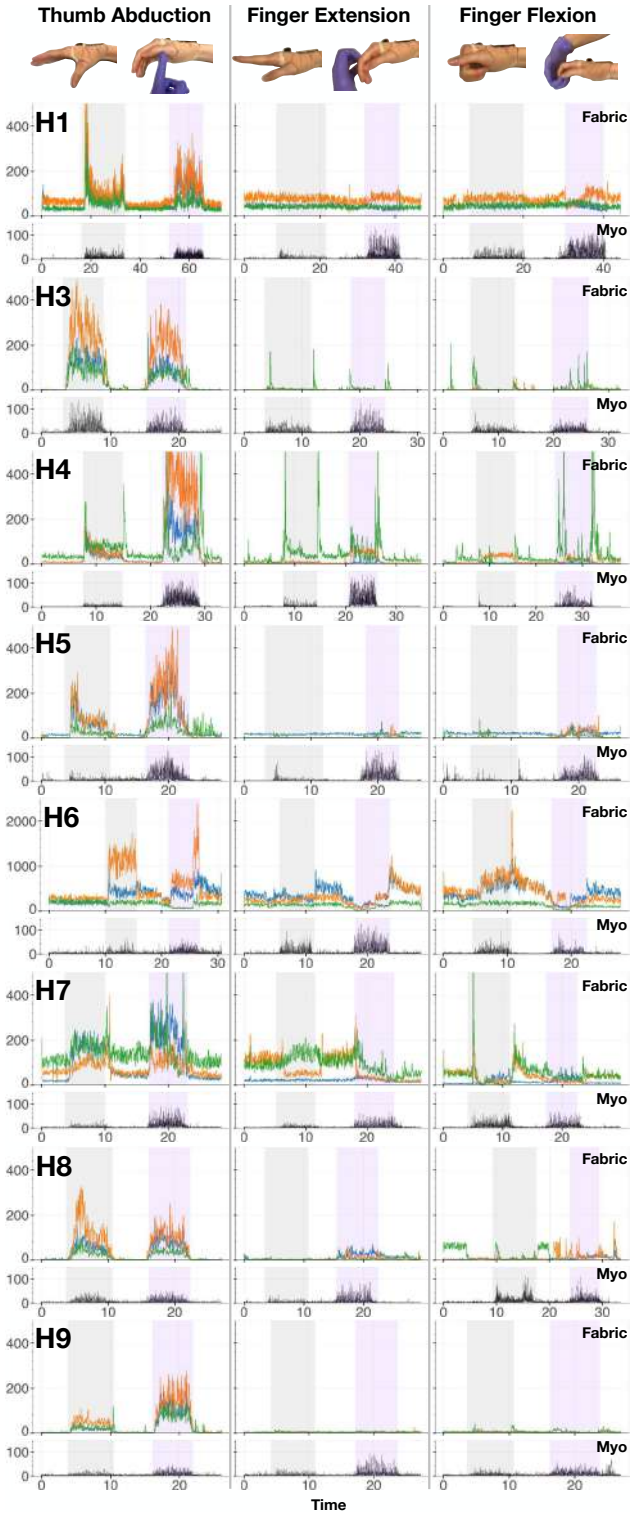


Fig. 4. (best seen in color) Data from our fabric sensing sleeve and commercial armband (Myo) during the Isolated Muscle Movement and Isometric Muscle Contraction tasks over time (s). Grey bars denote isolated movement, and purple bars denote isometric contraction. Each row depicts data from one healthy participant, and each column corresponds to a hand movement (Fig. 3). For each figure, the top plot shows the fabric sensor activity in μV_{rms} (blue = Channel 1, orange = Ch. 2, green = Ch. 3). Y-axis limit is 500 μV except for H6 (2,500 μV), and all cut-off peaks are below 1,000 μV. Bottom plot depicts corresponding Myo sensor activity in proprietary values (a.u.), with all 8 channels plotted in black.

Using the OpenBCI software, we measured the skin-electrode impedance to ensure sufficient contact and monitored the contact throughout the session. We collected raw voltage sEMG data from the fabric sleeve at 250 Hz and 1x amplification and used a 4th order Butterworth bandpass filter from 50 Hz to 115 Hz with a notch filter at 50 Hz and 60 Hz to eliminate environmental powerline noise. We collected sEMG data from the Myo armband at 200 Hz and did not perform any additional filtering of the output signal.

For the Isolated Muscle Movement and Isometric Muscle Contraction Tasks, we needed to to quantify changes in muscle activity between rest and active phases. To achieve this, we first rectified the raw EMG signal and passed it through a 40 Hz low-pass filter. Next, we found the average signal amplitude per sensing channel (3 channels in the fabric sensing sleeve and 8 channels in the commercial armband) to calculate the ratio of signal amplitude between the resting phase and the active phase of each of the two tasks.

For hand gesture classification, we processed the raw output from the OpenBCI board by extracting overlapping sliding windows of size 250 (1 second) with an offset of 10 samples. Each window was labeled with the ground truth at the end of the window, indicating the intent. From each window, we extracted both time-domain and frequency-domain features from each channel in each window, including Mean Absolute Value, Root Mean Square, Variance, Waveform Length, Zero Crossing Rate, Mean Frequency, Median Frequency, and Total Power. After feature extraction, we standardized features by removing the mean and scaling to unit variance using the training set.

We then trained three machine learning models to classify the extracted features: Linear Discriminant Analysis (LDA), Random Forest (RF), and a Multi-layer Perceptron (MLP). LDA was chosen for its simplicity and effectiveness with lower-dimensional data, RF for its ability to capture nonlinear relationships, and MLP for its capability to model more complex patterns. Each model was trained using subject-specific data, with distinct training and test sets.

E. Participants

We recruited nine healthy participants (five male, four female, ages 22-27)[1]. We also recruited a single stroke participant with chronic hemiparesis (male, right-hand impaired, scores of 1+ elbow flexors and 1 finger flexor on the Modified Ashworth Scale) for feasibility testing in a clinical setting under the supervision of an occupational therapist. Testing with all participants was approved by the Columbia University Institutional Review Board (IRB-AAAS8104).

V. Results & Discussion

We evaluated the sensor performance by finding the ratio between the average signal amplitude during the resting phase and the active phases. The raw data is visualized in Fig. 4[2], and Table I shows the average ratio values across all sensing channels measured by the fabric sleeve. In Table I, the hand movement labels are abbreviated: Thumb for thumb abduction, FE for finger extension, and FF for finger flexion.

TABLE I
Average Change in Signal Amplitude of Fabric Sensing Sleeve Relative to Relaxed State

Participant	Isolated Finger Movement			Isometric Muscle Contraction		
	Thumb	FE	FF	Thumb	FE	FF
H1	**2.2**	1.0	1.1	**2.4**	0.9	1.2
H3	**88.5**	4.1	2.1	**66.6**	2.9	2.6
H4	**4.9**	2.5	2.4	**18.9**	5.7	2.5
H5	**13.2**	1.2	1.1	**30.9**	3.5	4.8
H6	**2.4**	1.0	1.5	**1.9**	0.7	0.5
H7	**3.7**	1.0	1.4	**5.2**	0.8	1.6
H8	**20.5**	0.8	0.9	**22.0**	4.3	2.1
H9	**11.6**	1.2	1.4	**39.3**	1.2	1.2
Avg	**18.4**	1.6	1.5	**23.4**	2.5	2.1

We did not control for uniform force output exerted by each participant during the movement, so we posit that individual strength differences may have contributed to the varying sEMG signal amplitudes. Other factors that can be explored in future work include measurements of skin conditions and overall engagement with the task.

A notable outlier in signal quality from Fig. 4 was H6, whose baseline signal and overall signal amplitude was larger than all other participants. As a simple proxy for TE size, we measured the depth of the TE for each healthy participant between the palmar and dorsal sides of the hand. H6 had a TE depth of 25 mm, compared to the average TE depth of 34 ± 3.9 mm among all other healthy participants. Furthermore, we observed that H6 had drier skin compared to other participants. Thus, H6's hand size and skin condition could have affected skin-electrode contact with the fabric sleeve for reduced performance.

A. Isolated Muscle Movement Results

During the Isolated Muscle Movement Task, we observed the largest increase in signal amplitude during thumb abduction. For the thumb abduction condition, we report an average increase in signal amplitude by a factor of 18.4 from the relaxed position across all healthy participants. In contrast, the average signal amplitude change for the finger conditions were much smaller, with a factor of 1.6 for finger extension and 1.5 for finger flexion.

The difference in average signal magnitude between the thumb condition and the finger conditions demonstrated that the fabric sensing sleeve measured high activity during thumb activity and low activity when thumb movement was absent. Even during finger movement, the fabric sensors detected low activity as long as the thumb was not engaged.

To confirm the low activity detected by the fabric sensors during finger movement was not due to a lack of effort, we recorded the commercial sEMG armband values of concurrent extrinsic muscle activity in the forearm during finger extension and flexion (Fig. 4). The sustained peaks in signal activity measured by the commercial sEMG armband suggested greater activation of the extrinsic muscles than the

[1]H2 was later excluded from the study due to insufficient sEMG activity measured by the commercial armband.

[2]H1 performed a slightly extended active period of about 10 seconds for all tasks.

intrinsic muscles. During the finger movement conditions of the Isolated Muscle Movement task, the fabric sensor did not detect sustained activation during the 5 second period, indicating that the sensor was more sensitive to TE muscle activity than to finger movements.

We observed that three healthy participants had transient peaks at the start and end of each movement. However, the lack of sustained activation as observed in the thumb movement tasks supported the conclusion that the sensor primarily detected thumb muscle activity. These transient peaks could also be attributed to the participant's ability to maintain a relaxed thumb position during both the isolated finger movements.

B. Isometric Muscle Contraction Results

The Isometric Muscle Contraction Task focused on measuring TE muscle activity without finger movement to mitigate potential motion noise. With isometric muscle contraction alone, the results aligned with those of the Isolated Muscle Movement Task–the thumb abduction condition exhibited the largest change in average signal amplitude from the relaxed phase. Across the healthy participants, we report an average increase in signal amplitude by a factor of 23.4 for the thumb abduction condition, compared to a factor of 2.5 and 2.1 increase from relaxed during the finger extension and flexion conditions, respectively.

During the thumb abduction condition, a visible and sustained peak in signal during both Isolated Muscle Movement and Isometric Muscle Contraction indicated its sensitivity to thumb activity, whether from movement or muscle engagement (Fig 4). While muscle shape changes during contraction could affect the contact surface with the sensors, the sustained peak during isometric muscle contraction—where no thumb movement occurred—indicated that the signal was likely due to muscle activation rather than motion artifacts.

C. Classification Performance

Using the simultaneously collected fabric sensor and commercial sEMG armband data, we trained three machine learning models (LDA, RF, MLP) with the fabric sensor and the commercial armband separately to assess their classification accuracy. The results are shown in Table II, with the highest classification accuracy per sensing modality marked in bold. For the fabric sensor, the highest classification accuracy of 92.6% was achieved with the LDA model. The commercial sEMG armband achieved a maximum classification accuracy of 91.1% with the RF model.

The classification accuracy of the fabric sensing sleeve highlighted its potential as a viable sensor for intent inferral. For half of the participants, the 3-channel fabric sensing sleeve achieved a maximum classification accuracy within 5% of the commercial armband. This comparison is not intended to suggest the fabric sensing sleeve could replace the commercial forearm sEMG sensor. Rather, this suggests that sEMG signals from TE activity alone captured sufficient signal information for intent inferral. These results suggest the fabric sensing sleeve could augment a forearm sEMG sensing setup to improve intent inferral in future work.

TABLE II
CLASSIFICATION ACCURACY OF FABRIC SENSING SLEEVE AND MYO ARMBAND ACROSS 3 CANDIDATE MODELS

Hx	**Fabric Sensor**			**Myo Armband**		
	LDA	**RF**	**MLP**	**LDA**	**RF**	**MLP**
H1	**70.1%**	68.6%	65.1%	84.6%	**84.7%**	80.4%
H3	**84.7%**	83.8%	79.4%	**84.1%**	83.1%	82.1%
H4	**84.4%**	80.8%	83.0%	**86.6%**	86.3%	81.5%
H5	**81.9%**	69.6%	66.7%	78.7%	**84.8%**	79.0%
H6	13.0%	**67.5%**	42.0%	77.3%	**81.3%**	74.6%
H7	70.1%	46.5%	**70.6%**	88.2%	**91.1%**	89.9%
H8	**92.6%**	91.1%	87.7%	89.3%	**90.7%**	90.0%
H9	77.5%	78.6%	**80.3%**	86.8%	**87.4%**	83.3%
Avg	71.8%	73.3%	71.9%	84.4%	86.2%	82.6%
Std	24.9%	13.6%	14.5%	4.3%	3.4%	5.2%

D. Preliminary Testing with Stroke Participant

We performed a modified version of this protocol with one stroke survivor who had limited active thumb movement. We performed only the thumb movement of the Isolated Muscle Movement and the Isometric Muscle Contraction Tasks and an abbreviated Hand Gesture Classification data collection set due to stroke participant fatigue.

For the thumb-only Isolated Muscle Movement and Isometric Muscle Contractions, we observed a 0.8 change in signal amplitude from resting for both tasks. Unlike the healthy participants, we did not observe increased signal amplitude with the fabric sleeve during thumb engagement. However, the participant had a 3.9 factor increase in signal amplitude measured by the commercial sEMG armband during isolated thumb movement, and a 2.6 factor increase in signal amplitude during isometric thumb muscle contraction. The lack of signal activity measured by the fabric sleeve could be because the stroke survivor had difficulty isolating fine-motor movement of the thumb from overall hand engagement.

During overall hand engagement, however, the fabric sleeve captured some signals from the stroke participant. The fabric sensor had a maximum classification accuracy of 74.5% with the RF model, and the commercial sEMG armband had a maximum classification accuracy of 86.7% with the MLP model. While the fabric sleeve may not distinguish isolated thumb movement in stroke survivors, this result shows potential for its use with a commercial armband for intent inferral.

E. Future Work & Limitations

The modularity of the textile sensor design presents an opportunity to integrate additional, targeted sEMG sensors on the body for improved intent inferral. A future direction of this work would be integrating additional textile sensors to create an entirely fabric-based sensing sleeve to measure intrinsic and extrinsic muscle activity. Developing a multimodal machine learning model to leverage both intrinsic and extrinsic muscles would be a logical next step toward improving classification accuracy for intent inferral.

Limitations of this work include the small sample size of stroke participants. For the stroke participant, we could not rule out that the activation may have been from *flexor pollicis brevis* rather than APB, as stroke survivors may have difficulty distinguishing between these motions. Expanding the number of stroke participants in the work would allow us to draw more conclusions on using intrinsic hand muscle activity for intent inferral and the use of textile sensors to detect abnormal muscle signals from impaired individuals.

Further research will focus on characterizing the textile sensors, including a comparison of its performance to commercial sEMG systems on the TE, evaluating the sensors' dynamic response, and skin-electrode contact quality. As seen with participant H6, two factors—hand size and skin condition—motivates multiple fabric sleeve sizes and testing sEMG preparation gel to improve skin-electrode contact. Exploring different skin conditions and methods could help address the fluctuations in signal quality observed among healthy participants to ensure better sensor performance.

VI. Conclusion

In this work, we present a textile sEMG sensing array to measure muscle activity of intrinsic hand muscles in the TE. To the best of our knowledge, this is the first fabric sensing sleeve that uses textile sensors to measure intrinsic hand muscle sEMG activity. With a 3-channel sensing array on the thenar eminence, we demonstrate that the textile sensors can effectively discriminate intrinsic thumb movements from extrinsic finger movements during both Isolated Muscle Movement and Isometric Muscle Contraction Tasks. Furthermore, we show that the fabric sleeve alone can achieve promising classification accuracy in classifying hand poses for intent inferral. For assistive robotics, where wearability and comfort are key aspects of device design, textile sensors offer a non-obtrusive interface for muscle sensing.

References

[1] A. J. Barry, D. G. Kamper, M. E. Stoykov, K. Triandafilou, and E. Roth, "Characteristics of the severely impaired hand in survivors of stroke with chronic impairments," *Top. Stroke Rehabil.*, vol. 29, pp. 181–191, 2022.

[2] D. G. Kamper, H. C. Fischer, E. G. Cruz, and W. Z. Rymer, "Weakness is the primary contributor to finger impairment in chronic stroke," *Arch. Phys. Med. Rehabil.*, vol. 87, pp. 1262–1269, 2006.

[3] N. Hogan et al., "Motions or muscles? some behavioral factors underlying robotic assistance of motor recovery," *J. Rehabil. Res. Dev.*, vol. 43, pp. 605–618, 2006.

[4] C. Meeker, S. Park, L. Bishop, J. Stein, and M. Ciocarlie, "EMG pattern classification to control a hand orthosis for functional grasp assistance after stroke," *IEEE Int. Conf. Rehabil. Robot.*, pp. 1203–1210, 2017.

[5] Z. Lu, K.-Y. Tong, X. Zhang, S. Li, and P. Zhou, "Myoelectric pattern recognition for controlling a robotic hand: A feasibility study in stroke," *IEEE Trans. Biomed. Eng.*, vol. 66, pp. 365–372, 2019.

[6] L. C. Miller and J. P. A. Dewald, "Involuntary paretic wrist/finger flexion forces and EMG increase with shoulder abduction load in individuals with chronic stroke," *Clin. Neurophysiol.*, vol. 123, pp. 1216–1225, 2012.

[7] C. I. I. Long, P. W. Conrad, E. A. Hall, and S. L. Furler, "Intrinsic-extrinsic muscle control of the hand in power grip and precision handling: AN ELECTROMYOGRAPHIC STUDY," *J. Bone Joint Surg. Am.*, vol. 52, p. 853, 1970.

[8] J. Towles, D. G. Kamper, and W. Z. Rymer, "Lack of hypertonia in thumb muscles after stroke," *J. Neurophysiol.*, vol. 104, pp. 2139–2146, 2010.

[9] N. Tacca et al., "Wearable high-density EMG sleeve for complex hand gesture classification and continuous joint angle estimation," *Sci. Rep.*, vol. 14, p. 18564, 2024.

[10] X. L. Hu, K. Y. Tong, X. J. Wei, W. Rong, E. A. Susanto, and S. K. Ho, "The effects of post-stroke upper-limb training with an electromyography (EMG)-driven hand robot," *J. Electromyogr. Kinesiol.*, vol. 23, pp. 1065–1074, 2013.

[11] M. Chen, L. Cheng, F. Huang, Y. Yan, and Z.-G. Hou, "Towards robot-assisted post-stroke hand rehabilitation: Fugl-meyer gesture recognition using sEMG," in *IEEE 7th Annu. Int. Conf. on CYBER Technol. in Automat., Control, and Intell. Syst.*, 2017, pp. 1472–1477.

[12] E. N. Kamavuako, M. Brown, X. Bao, I. Chihi, S. Pitou, and M. Howard, "Affordable embroidered EMG electrodes for myoelectric control of prostheses: A pilot study," *Sensors (Basel)*, vol. 21, p. 5245, 2021.

[13] H. Wang, P. Huang, T. Xu, G. Li, and Y. Hu, "Towards zero retraining for multiday motion recognition via a fully unsupervised adaptive approach and fabric myoelectric armband," *IEEE Trans. Neural Syst. Rehabil. Eng.*, vol. 30, pp. 217–225, 2022.

[14] J. E. Lara, L. K. Cheng, O. Rohrle, and N. Paskaranandavadivel, "Muscle-specific high-density electromyography arrays for hand gesture classification," *IEEE Trans. Biomed. Eng.*, vol. 69, pp. 1758–1766, 2022.

[15] C. Xing et al., "Silk fabric functionalized by nanosilver enabling the wearable sensing for biomechanics and biomolecules," *ACS Appl. Mater. Interfaces*, vol. 16, pp. 51 669–51 678, 2024.

[16] T. E. Paterson et al., "Monitoring of hand function enabled by low complexity sensors printed on textile," *Flex. Print. Electron.*, vol. 7, p. 035003, 2022.

[17] Mission Darkness, "Mission darkness titanrf faraday tape," Amazon, ASIN: B07CRLCGCH, 2024.

[18] OpenBCI, https://shop.openbci.com/products/cyton-biosensing-board-8-channel, 2024.

[19] MadeIRA USA, "Hc-12-sp highly conductive embroidery thread 12," https://www.madeirausa.com/hc-12-sp-highly-conductive-embroidery-thread-12.html, 2024.

[20] Q. Shao et al., "Joey: Supporting kangaroo mother care with computational fabrics," in *Proc. 22nd Annu. Int. Conf. on Mobile Syst., Appl. and Services*. ACM, 2024.

Automated prediction of item-level ARAT scores from wearable sensors

Thomas Weikert[1,2,3], Yanke Li[2,3], Diego Paez-Granados[2,3], Chris Awai Easthope[1]
[1]*Data Analytics & Rehabilitation Technology (DART), Lake Lucerne Institute, Switzerland*
[2]*Spinal Cord and Artificial Intelligence (SCAI) Lab, ETH Zurich, Switzerland*
[3]*Swiss Paraplegic Research (SPF), Switzerland*
thomas.weikert@llui.org, yanke.li@hest.ethz.ch, diego.paez@hest.ethz.ch, chris.awai@llui.org

***Abstract*—The demand for neurorehabilitation is projected to increase drastically over the next decades, creating a need to automate and enhance the efficiency of clinical processes. Clinical assessments are important to track treatment effectiveness and to tailor therapy approaches. We here develop a scoring prediction system for the Action Research Arm Test (ARAT), a common clinical assessment for upper limb function in stroke. To predict each of the 19 movement items individually, we use a raw time series of 5 wearable movement sensors. A general classification model was trained on 100 ARAT tests from various neurological disorders and achieved a mean balanced accuracy across all closely related movement items of 80% (range: 59%-91%). Training disorder-specific models for stroke and Parkinson's disease did not improve accuracy but yielded specific feature maps that can inform future research. This study demonstrates the feasibility of predicting ARAT scores at the item level, preparing the ground for clinical decision support systems or even automated ARAT scoring.**

***Index Terms*—Wearable Sensing, Clinical Assessments**

I. Introduction

Stroke and Parkinson's Disease (PD) are among the most common and fastest-growing neurological disorders. Between 1990 and 2015, deaths from neurological disorders rose by 36.7%, showing their growing impact despite medical progress [1]. Both disorders lead to impaired motor function, negatively affecting quality of life. Despite rehabilitation leading to improvements in function, upper limb impairments persist in 55% to 75% of stroke survivors, and many persons with Parkinson's [2], [3]. Concurrently, health systems have enormous pressure to develop more cost-efficient and scalable pathways for providing rehabilitation [4], [5]. Precision rehabilitation, which relies on granular quantification of individual patients' health status, is an emerging approach to improve treatment outcomes [6]. To make precision rehabilitation more accessible, health assessments need to be rapid and highly automated.

Standardized clinical assessments such as the Action Research Arm Test (ARAT) and Fugl-Meyer Assessment (FMA) are regularly used to evaluate motor recovery and upper limb function. While the FMA measures impairment, the ARAT focuses on functional movement items such as grasping and pinching, aligning with the International Classification of Functioning (ICF) [7]. These assessments are resource-intensive, requiring trained personnel and manual observational scoring, limiting their usefulness for frequent or remote use [8]. Wearable inertial measurement units (IMUs) combined with machine learning provide a promising approach to automate clinical assessments like the ARAT. [9] demonstrated that kinematic features derived from motion sensors could reliably capture movement quality and correlate with clinical outcomes. Similarly, recent studies leveraging kinematic data from IMUs achieved approximately 80% accuracy in predicting ARAT subscale scores, aggregations of multiple movement item scores, with strong correlations to clinical ratings (R^2 = 93%) [10]. Other studies have explored IMU-based predictions of upper-limb function, achieving comparable accuracies. For example, [11] used motion capture to estimate ARAT scores with an R^2 of 67%, highlighting the potential of kinematic metrics such as smoothness and trunk displacement. [12] and [13] also used IMUs to predict motor function scores, achieving R^2 values up to 97%, however, these were limited to subscales of broader assessments such as the Wolf Motor Function Test or CAHAI. Score prediction systems can be useful tools to reduce inter-rater variability, enhance objectivity, and enable scalable, location-independent tracking of impairments, addressing key challenges in neurorehabilitation.

Despite these advances, there is need for further improvement when using wearable sensors to predict ARAT scores in clinical routine. Firstly, current work only enables scoring prediction at a domain level, leading to a functional score prediction that subsumes multiple movement items. In the clinical assessment workflow, however, scores are allocated by an assessor on a single item level sequentially per item. Hence, for a decision support to be useful, a prediction would need to take place on an item level. Secondly, it is unclear whether models specific to neurological disorders are necessary to accurately distinguish adjacent ARAT scores (e.g., scores of 2 and 3) at an item level. Differences in movement patterns, severity of impairments, and compensatory strategies between populations, such as stroke and PD, pose challenges to developing generalizable models, particularly for subtle distinctions critical to optimize therapy content. This paper directly addresses these possible improvements, resulting in two research questions.

- **RQ 1:** How accurately can we predict closely related ARAT scores at an item level?
- **RQ 2:** Do disorder-specific models result in higher classi-

fication accuracy compared to a general model?

II. Methods

A. Study Design and Procedure

This investigation is a retrospective analysis of ARAT assessments collected as part of clinical routine at Cereneo - Center for Neurology & Rehabilitation between 2020 - 2024 and was approved by the Ethics Committees of Northwest and Central Switzerland (EKNZ 2024-00196). All participants had previously provided written informed consent for data reuse per general consent (EKNZ 2017-00730).

B. Participants

To be included in this retrospective analysis, participants had to be at least 18 years old. Participants were excluded if they had: (1) neurological conditions linked to dementia, cognitive impairment, or central motor dysfunction, (2) severe sensory aphasia, (3) a history of arm paresis prior to the current condition, (4) were taking sedatives or neuroleptics, or (5) had significant hearing loss. The analysis included 37 participants (8 females, 29 males) undergoing neurorehabilitation, with a mean age of 63 ± 16 years and an average weight of 83 ± 23 kg. Of these, 14 were diagnosed with stroke, 11 with Parkinson's disease, and 12 with other neurological conditions. 26 of the participants had a left paretic side, while 13 had a right paretic side. The dataset comprised a total of 100 ARAT tests, as some participants performed multiple tests.

C. Action Research Arm Test (ARAT)

The Action Research Arm Test (ARAT) is a widely recognized clinical assessment to assess motor function in individuals with stroke that has strong inter-rater and test-retest reliabilities [14]. Its simplicity and robust psychometric properties make it a popular instrument for assessing motor recovery in clinical settings [15]. The ARAT is composed of 19 movement items categorized into four domains: grasp, grip, pinch, and gross motor movements. Each item is scored by a trained human assessor on a 4-point ordinal scale, ranging from 0 ("no movement") to 3 ("movement performed normally"), leading to a total possible score of 57. The differentiation between score 2 ("adapted movement") and score 3 ("normal movement") is made based on two criteria: Item completion time under 5s, and "normal movement quality". In standard clinical use, the ARAT employs a hierarchical scoring method, allowing assessors to assess the most challenging item within a subscale first. If the item is performed at full points, all simpler items in that subscale are scored accordingly; otherwise, additional items are evaluated to determine the appropriate score [16]. The assessments that constitute the data set were conducted using standardized ARAT materials (as shown in Figure 1) and procedures, with each movement item scored by trained professionals with over 5 years of experience to ensure consistent and reliable ratings. Assessor scores were entered into a digital ARAT application on a tablet, and exported as *.csv for further analysis. Wearable sensor data was streamed at 60Hz to the tablet from 5 synced sensors, respectively mounted at the sternum, on both upper arms, and each wrist (Dot, Xsens, NL). Assessments were typically performed at patient intake and discharge, and in some cases during the rehabilitation period if clinically indicated.



Fig. 1: (A) A depiction of the ARAT setup, including item objects arranged on a standardized table. (B) Screenshot of the scoring interface on a tablet, allowing the therapist to connect wearable sensors and rate movement item performance.

The dataset was unbalanced due to the uncontrolled nature of the data acquisition. Scores 0 and 1 were strongly underrepresented (10%), and were hence removed from this analysis. All classifications are therefore binary, predicting only score 2 or score 3. Scores 2 & 3 were also unbalanced (1113 observations vs 2096 observations over all items). To address class imbalances, the Synthetic Minority Oversampling Technique (SMOTE) was applied to balance the sample distribution across classes 2 & 3 on an item level, ensuring more robust and equitable metric calculations [17]. SMOTE generates synthetic data points for minority classes rather than simply duplicating existing samples, thereby improving model training and reducing bias.

D. Feature Extraction

Accurate movement item classification relies on features that are able to encode differences between movement patterns. Analysis was performed using data from IMU sensors and demographic data. From the IMU, raw acceleration (m/s^2) and raw gyroscope (°/s) time series in three axes were used to extract a wide range of time and frequency domain features. Key time-domain metrics such as mean, standard deviation, skewness, kurtosis, median absolute deviation, inter-quartile range, and root mean square were used to represent movement stability and variability, while features like range represented motion extremes [15]. Frequency-domain features, including dominant frequency, spectral power, peak power, signal-to-noise ratio, and spectral entropy encapsulated aspects of signal complexity [14], [16]. Additionally, jerk magnitude (mean and root-mean-square) and sample entropy represented aspects of motion smoothness and irregularity. Together, these features offered a multifaceted representation of motion patterns, providing rich substance

for the model to learn differentiation between ability levels.

E. Classification

To predict ARAT scores from IMU time-series data, we used traditional machine learning models with 5-fold cross-validation on a participant level and grid search for hyper-parameter optimization. By removing a complete participant from the fold, we ensure that no data from the same individual - also over multiple assessments - is used in the training of this fold. All features across the dataset were included for each analysis, with min-max normalization performed within each fold separately.

- **Random Forest (RF)** [18]: An ensemble method combining decision trees to capture non-linear relationships.
- **AdaBoost** [19]: A boosting algorithm that iteratively improves weak classifiers.
- **Gradient Boosting** [20]: An ensemble method minimizing residuals to reduce prediction errors.
- **K-Nearest Neighbors (KNN)** [21]: A distance-based algorithm assigning class labels from nearest neighbors.
- **Logistic Regression** [22]: A linear model offering interpretable results but limited for complex patterns.
- **Neural Network (NN)** [23]: Interconnected layers of neurons capturing complex, non-linear patterns.
- **Support Vector Classifier (SVC)** [24]: A kernel-based classifier handling non-linearities in the feature space.

To address **RQ2**, we used the same classification approach on subsets of the overall data. One model was trained only on the stroke data, and one model was only trained on the Parkinson's data.

F. Evaluation

Performance was evaluated using balanced accuracy, precision, recall, F1 score, and ROC AUC, calculated from the difference between human-assigned ARAT item scores and the corresponding estimated scores. Balanced accuracy accounts for class imbalance, while precision and recall measure the correctness and completeness of positive predictions. The F1 score balances these two metrics, and ROC AUC assesses the model's ability to distinguish between classes.

To evaluate the error distribution, item-level ARAT scores for each arm were summed per measurement.

III. Results

A. Predict Action Research Arm Test Item Score

All 7 models were trained on each of the 19 movement items across all neurological disorders. Of all trained models, the Random Forest (RF) demonstrated the highest mean performance across all movement items, achieving a balanced accuracy of 80%, ROC AUC of 89%, precision of 77%, and recall of 87% (Table I). Concerning the individual movement items, (Figure 2A) indicates robust performance in fine motor items such as GRASP Ball 7.5, GRASP Cube 7.5, and PINCH Cube 0.6 Middle Finger, with all evaluation metrics

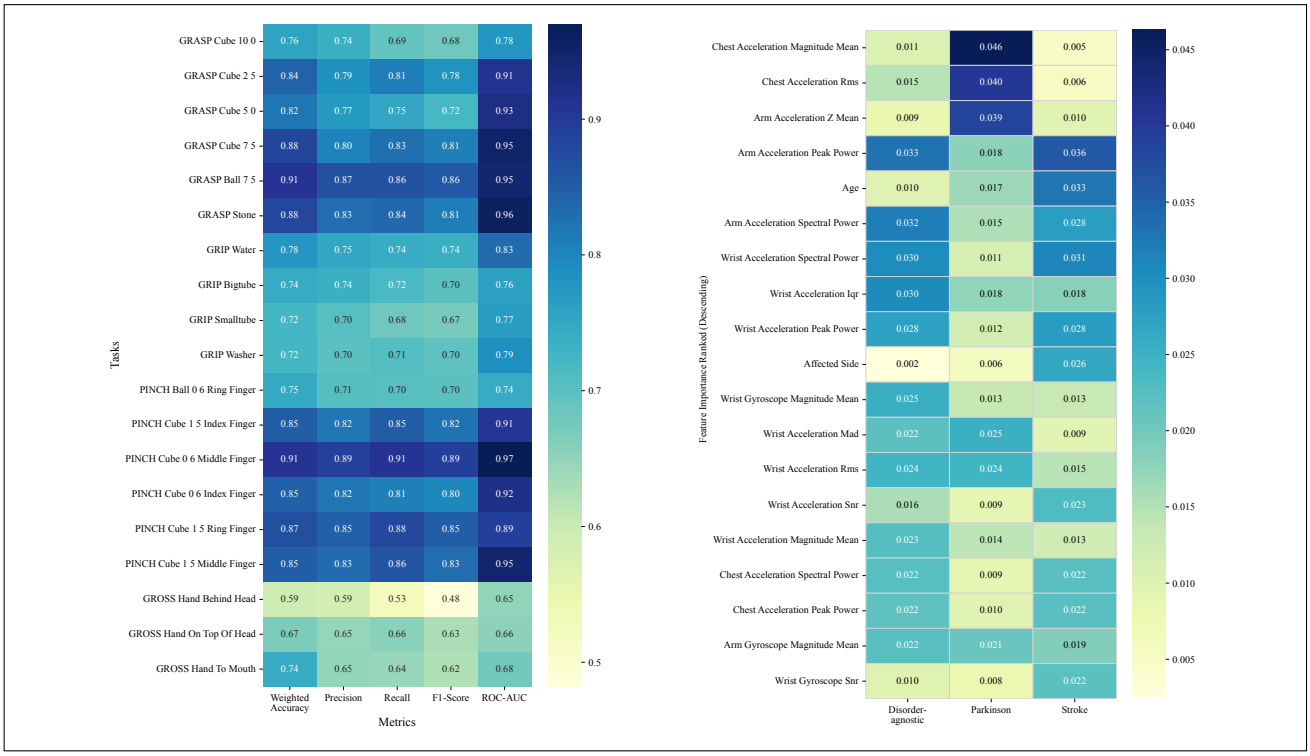


Fig. 2: (A) Performance metrics across movement items: Weighted accuracy, Precision, Recall, F1-Score, and ROC-AUC of the highest performing disorder-agnostic model for each movement item. (B) Feature importance for disorder-agnostic and disorder-specific models: Note that feature maps are quite different between models, indicating that there are disorder-specific patterns underlying the change between scores 2 & 3.

TABLE I: Model Performance Across Datasets.

Model	Overall Dataset					Parkinson's Dataset					Stroke Dataset				
	Weighted Accuracy	Precision	Recall	F1-Score	ROC-AUC	Weighted Accuracy	Precision	Recall	F1-Score	ROC-AUC	Weighted Accuracy	Precision	Recall	F1-Score	ROC-AUC
RandomForest	**0.7959**	**0.7620**	**0.7611**	**0.7412**	**0.8415**	0.7346	**0.6370**	0.6924	0.6269	0.7421	**0.7737**	0.6783	0.7203	0.6639	**0.8287**
AdaBoost	0.7661	0.7242	0.7260	0.7092	0.7991	0.6940	0.6155	0.6230	0.5800	0.6389	0.7651	0.6930	0.7258	0.6730	0.7865
GradientBoosting	0.7663	0.7344	0.7053	0.6941	0.7933	0.7137	0.5617	0.6142	0.5532	0.7059	0.7499	0.6733	0.6829	0.6328	0.7865
K-Nearest Neighbors	0.7273	0.7014	0.6474	0.6299	0.7251	0.7016	0.4979	0.5862	0.5122	0.6097	0.7130	0.6047	0.6407	0.5699	0.7001
LogisticRegression	0.7315	0.6839	0.6071	0.5816	0.5058	0.6969	0.4813	0.5886	0.5062	0.3447	0.7257	0.5457	0.5933	0.5320	0.4130
NeuralNetwork	0.7134	0.6573	0.6036	0.5809	0.4971	0.6962	0.5056	0.5868	0.5140	0.3407	0.7112	0.5432	0.5870	0.5220	0.3818
SVC	0.7751	0.7403	0.7508	0.7171	0.7919	**0.7611**	0.6165	**0.7039**	**0.6295**	**0.7503**	0.7640	**0.6933**	**0.7477**	**0.6825**	0.7758

Seven different model architectures were evaluated for classification performance over all 19 movement items of the ARAT. Reported values are means over all movement items. This process was performed once on the combined dataset, that contains data from multiple neurological disorders, and on two subsets of data, containing only stroke patients or only Parkinson's patients. The highest performing metrics are highlighted in bold.

exceeding 85%. These items involve grasping or pinching objects of varying sizes and shapes (e.g. grasping a ball of the size 7.5 cm), assessing controlled hand movements and dexterity. Movement items such as the GRIP Washer demonstrated moderate performance, with metrics ranging from 68% to 79%, whereas gross motor items, including GROSS Hand Behind Head, exhibited the lowest performance, with metrics falling below 60%.

B. Impact of Neurological Disorders on Classification Accuracy

To investigate the robustness of a general classification model over different disorders, we trained disorder-specific models for Parkinson's and stroke, and compared the overall accuracy to the general, random forest classification model. An SVC model trained only on the Parkinson's dataset achieved a balanced accuracy of 76%. A Random Forest classifier trained only on the stroke dataset resulted in a balanced accuracy of 77%. For the combined dataset, as reported above, the model attained a balanced accuracy of 80% (Figure 3). Despite slightly different model architectures performing best in the different populations, there was only around 5% difference in accuracy between architectures. The error distribution reveals a narrower spread for the Parkinson's dataset compared to the combined and stroke datasets, indicating more consistency in the prediction. To understand differences between the models, we ranked the importance of individual features for each model by maximum importance contribution (Figure 2). In the Parkinson's-specific model, the highest ranked features were *chest acceleration magnitude mean* and *chest acceleration root-mean-square*. In the stroke-specific model, *arm acceleration peak power and wrist acceleration peak power* were the highest ranked time-series features. The *affected side* and *age* were observed as distinguishing features for stroke, whilst these played little role for Parkinson's or the combined dataset. Notably, *arm* and *wrist acceleration spectral power* consistently emerged as a key feature across all models, underscoring its relevance in predicting ARAT scores irrespective of the underlying neurological disorder.

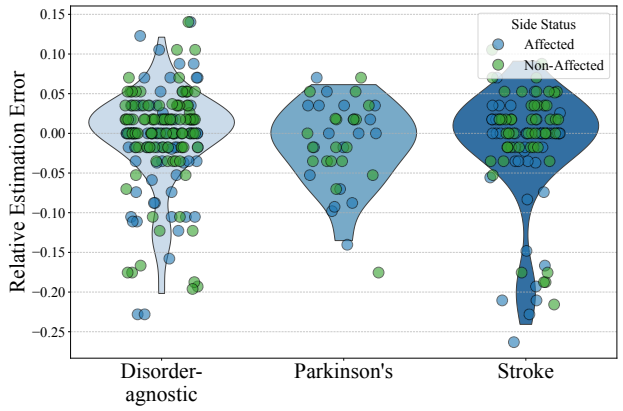


Fig. 3: Violin plots showing the distribution of the estimation error of ARAT score prediction for a disorder-agnostic, Parkinson's-specific, and stroke-specific model. Each point represents a single ARAT measurement with both the affected and non-affected sides.

IV. Discussion

The objective of this work was to evaluate to what extent data captured from wearable sensors during an ARAT assessment can be used to predict clinical ARAT scores. In contrast to previous work [10], we aimed to predict ARAT scores at the item level (**RQ1**) and to investigate the impact of neurological disorders on classification accuracy (**RQ2**). For this, we used raw acceleration and gyroscope data from wrist, arm, and chest sensors in combination with a machine-learning-based classification. Over the complete dataset of 100 ARAT assessments, our disorder-agnostic classifier achieved a mean balanced accuracy over all items of almost 80%. Models trained specifically for stroke or Parkinson's did not demonstrate a major improvement in classification accuracy. In summary, we demonstrate the feasibility of a generalizable classifier for ARAT score prediction at an item level and

identify areas for future improvement

To investigate how accurately ARAT scores can be predicted in neurological disorders using wearable sensors at an item level (**RQ1**), we trained and evaluated seven popular machine learning model architectures for each of the 19 ARAT movement items. Of the evaluated architectures, the RF classifier achieved the highest mean balanced accuracy of 80%. The RF classifier is an ensemble learning method that constructs multiple decision trees on bootstrapped subsets of the data, randomly selecting a subset of features at each split to reduce impurity and find the best decision boundary. It aggregates predictions from all trees to optimize for balanced accuracy, reduce overfitting, and improve generalization. RF works well here because it effectively captures complex, nonlinear feature interactions and is robust to noise and imbalanced datasets. Nonetheless, as shown in Table I, the maximum spread between architectures is 8%, indicating that all models effectively capture the underlying feature contributions. At the level of a single movement item, the accuracies achieved by the RF classifier ranged between 59% and 91%. The classifier achieved the greatest accuracies on items within the subscales GRASP and PINCH, ranging from 76% to 91%. These movement items are quite similar in execution - the main difference being the size and shape of an object that is picked up and moved to a predefined target location. Despite the most distal sensor being mounted at the wrist and hence not capturing finger motion, these signals seem to capture sufficient aspects of the movement pattern to predict scores quite well. Classifier performance on items from the GRIP subscale was slightly lower, with accuracies ranging from 72% to 78%. Movement items of the GRIP subscale include highly skilled movements, such as removing hollow tubes from one support and threading them onto a second support, or pouring water from one cup into another. The classifier achieves the lowest accuracies of 59% to 74% on the GROSS subscale, which entails macro movements such as touching the back of the head with the hand. These very global movements are variable in execution even in a healthy population, which leads to a larger variation in both the visual scoring and in the movement features that are considered healthy. Notably, the classifier is less accurate for larger, more difficult movements (ie. hand behind head) and accuracy increases in smaller, easier movement items (ie. hand to mouth).

Another key factor contributing to performance variation is the imbalance in the distribution of observations across score classes, particularly in movement items such as those in the GRASP subscale, where higher scores were disproportionately represented. While oversampling techniques like SMOTE were applied to address this imbalance, the generated synthetic data may not fully replicate the complexity of real-world observations, leading to reduced classification performance.

Compared to previous work, our mean balanced accuracy of around 80% at a single item level is comparable to estimations made by [10] at a subscale level. As there are no universally accepted minimal clinically important differences (MCIDs) for individual ARAT items, we cannot make any claims about our accuracy in terms of clinically meaningful values. However, we have demonstrated the feasibility of predicting individual item scores between 2 and 3 with a relatively small and heterogeneous dataset.

Our disorder-agnostic classifier trained on data across multiple neurological disorders achieved a mean balanced accuracy of 80%. Disorder-specific classifiers achieved comparable accuracies (stroke: 76%; Parkinson's: 77%), despite using much smaller datasets (stroke: n=14; Parkinson's: n=11). The trade-off between data volume and variability is not clear, hence we cannot answer RQ2 conclusively at this time. However, there are some indications that disorder-specific models will outperform a general model. First, despite the smaller data volume, accuracies are comparable to the overall dataset. Second, error distribution is more constrained in the disorder-specific models, indicating that these models may perform better when trained on larger datasets. Third: The ranking of feature importance is quite different between the disorder-specific models, indicating that individual disorders may result in degradation of disorder-specific movement features. This is something already well-described in clinical perspective, with certain movement patterns being stereotypically associated with disorders. Specifically, for Parkinson's disease, features reflecting movement variability and wrist control, such as *wrist acceleration mean absolute deviation* and *chest acceleration inter-quartile range*, were the most predictive. In contrast, for stroke patients, features that captured arm stability and compensatory strategies, like *chest acceleration signal-to-noise ratio* and *mean arm angular acceleration* in frontal plane, played a larger role. Furthermore, side-specific features were more prominent in stroke datasets, aligning with the typically asymmetric impairments observed in stroke patients.

This study demonstrates that using only statistical features of raw acceleration and angular velocity data in time and frequency domains, which are provided by most inertial sensors, encapsulates sufficient movement information to classify item scores. This approach is more accessible and potentially less biased than methods requiring pre-selection and computation of specific kinematic features, such as endpoint smoothness or joint angles [25], [26]. However, the constrained feature space may limit classification performance. Adding further features, such as joint angle trajectories and spatial information may result in increased performance. Furthermore, inherent limitations arise from using clinical scores as reference data for training machine learning models, as these models are constrained to reproduce the information encoded in the clinical scores. These observational scores may not fully capture all aspects of function at a granular level, which may cause divergent score predictions from the more sensitive sensor system.

With larger and more homogeneous datasets, we expect improved automated predictions of ARAT scores from wearable sensors. This may lead to a clinical decision support

system to support less experienced assessors, perhaps accelerating training times and reducing variability between raters. In the future, automated scoring may be sufficiently accurate for patients to perform self-assessment of upper limb function also at home using ARAT or ARAT-like movements. To support this, future research should investigate the interaction between impairment and function, and strive to determine a minimal set of movements that can inform on both constructs. Secondly, alternative technologies to wearable sensors should be considered that create more feature-rich datasets, such as markerless motion capture. Finally, sensor-based metrics need to be placed within the clinical reasoning framework in a meaningful manner, as to enable a more fine-grained distinction between assessment scores and the allocation of tailored interventions.

V. Conclusion

This study aimed to predict clinical scores for closely related individual ARAT movement items using wearable sensors. We demonstrated that item-level ARAT score predictions can be achieved across disorders with almost 80% accuracy. Disorder-specific models did not improve prediction accuracy, however, differences in the feature maps indicate that accuracy could be improved with larger datasets. By combining raw sensor data with machine learning algorithms, we aim to develop clinical decision support systems for ARAT scoring, ultimately leading to sensitive, objective, automated self-assessment tools in clinics and at home. These tools are a necessary part of the framework needed for precision rehabilitation, enabling fine-grained monitoring of motor recovery across the continuum of care.

Acknowledgment

We would like to thank the clinicians and students involved in this study: Alma Flueck, Elena Ruiz, Migjen Shala, Lisa Herndlhofer, Anna Schmitt, Leah Schulz, and Loic Kreienbuehl. We thank the patients who generously participated in this research, and our funders: SwissNeuroRehab InnoSuisse Flagship Project (SP3).

References

[1] V. L. Feigin, A. A. Abajobir, K. H. Abate, F. Abd-Allah, A. M. Abdulle, S. F. Abera, G. Y. Abyu, M. B. Ahmed, A. N. Aichour, I. Aichour, *et al.*, "Global, regional, and national burden of neurological disorders during 1990–2015: a systematic analysis for the global burden of disease study 2015," *The Lancet Neurology*, vol. 16, no. 11, pp. 877–897, 2017.

[2] D. S. Nichols-Larsen, P. Clark, A. Zeringue, A. Greenspan, and S. Blanton, "Factors influencing stroke survivors' quality of life during subacute recovery," *Stroke*, vol. 36, no. 7, pp. 1480–1484, 2005.

[3] S.-M. Lai, S. Studenski, P. W. Duncan, and S. Perera, "Persisting consequences of stroke measured by the stroke impact scale," *Stroke*, vol. 33, no. 7, pp. 1840–1844, 2002.

[4] World Health Organization, "Over 1 in 3 people affected by neurological conditions, the leading cause of illness and disability worldwide," 2021.

[5] World Health Organization, "Rehabilitation 2030: A call for action," 2017.

[6] D. J. Reinkensmeyer, E. Burdet, M. Casadio, J. W. Krakauer, G. Kwakkel, C. E. Lang, S. P. Swinnen, N. S. Ward, and N. Schweighofer, "Computational neurorehabilitation: modeling plasticity and learning to predict recovery," *Journal of NeuroEngineering and Rehabilitation*, vol. 13, pp. 1–25, 2016.

[7] World Health Organization, *International Classification of Functioning, Disability and Health (ICF)*. Geneva: World Health Organization, 2001.

[8] M. Alt Murphy, C. Willén, and K. S. Sunnerhagen, "Movement kinematics during a drinking task are associated with the activity capacity level after stroke," *Neurorehabilitation and Neural Repair*, vol. 26, no. 9, pp. 1106–1115, 2012.

[9] L. Saes, R. Billiet, S. Herregodts, P. Feys, T. Van der Stede, and N. Wenderoth, "Kinematics extracted with inertial sensors accurately reflect clinical upper limb scales across different tasks," *IEEE Journal of Translational Engineering in Health and Medicine*, vol. 6, pp. 1–8, 2018.

[10] C. Werner, J. G. Schönhammer, M. K. Steitz, O. Lambercy, A. R. Luft, L. Demkó, and C. A. Easthope, "Using wearable inertial sensors to estimate clinical scores of upper limb movement quality in stroke," *Frontiers in Physiology*, vol. 13, p. 877563, 2022.

[11] M. Alt Murphy and C. Häger, "Kinematic analysis of a daily activity drinking from a glass: A pilot study," *Journal of NeuroEngineering and Rehabilitation*, vol. 9, p. 29, 2012.

[12] S. Patel, H. Park, P. Bonato, L. Chan, and M. Rodgers, "A wearable sensor technology for assessing stroke patients," in *IEEE Engineering in Medicine and Biology Society*, pp. 1082–1085, IEEE, 2010.

[13] C. P. Adans-Dester, K. Scanlan, S. J. Fodeh, and P. Bonato, "A framework for individualized predictions of motor performance during rehabilitation therapy using wearable sensor data," *Nature Biomedical Engineering*, vol. 4, no. 12, pp. 1213–1220, 2020.

[14] J. H. Van Der Lee, H. Beckerman, G. J. Lankhorst, and L. M. Bouter, "The responsiveness of the action research arm test and the fugl-meyer assessment scale in chronic stroke patients," *Journal of Rehabilitation Medicine*, vol. 33, no. 3, pp. 110–113, 2001.

[15] S. Pike, N. A. Lannin, K. Wales, and A. Cusick, "A systematic review of the psychometric properties of the action research arm test in neurorehabilitation," *Australian Occupational Therapy Journal*, vol. 65, no. 5, pp. 449–471, 2018.

[16] N. Yozbatiran, L. Der-Yeghiaian, and S. C. Cramer, "A standardized approach to performing the action research arm test," *Neurorehabilitation and Neural Repair*, vol. 22, no. 1, pp. 78–90, 2008.

[17] N. V. Chawla, K. W. Bowyer, L. O. Hall, and W. P. Kegelmeyer, "Smote: Synthetic minority over-sampling technique," *Journal of Artificial Intelligence Research*, vol. 16, pp. 321–357, 2002.

[18] L. Breiman, "Random forests," *Machine learning*, vol. 45, no. 1, pp. 5–32, 2001.

[19] Y. Freund and R. E. Schapire, "A decision-theoretic generalization of on-line learning and an application to boosting," *Journal of Computer and System Sciences*, vol. 55, no. 1, pp. 119–139, 1997.

[20] J. H. Friedman, "Greedy function approximation: a gradient boosting machine," *Annals of statistics*, pp. 1189–1232, 2001.

[21] N. S. Altman, "An introduction to kernel and nearest-neighbor nonparametric regression," *The American Statistician*, vol. 46, no. 3, pp. 175–185, 1992.

[22] D. R. Cox, "The regression analysis of binary sequences," *Journal of the Royal Statistical Society: Series B (Methodological)*, vol. 20, no. 2, pp. 215–232, 1958.

[23] Y. LeCun, Y. Bengio, and G. Hinton, "Deep learning," *Nature*, vol. 521, no. 7553, pp. 436–444, 2015.

[24] C. Cortes and V. Vapnik, "Support-vector networks," *Machine learning*, vol. 20, no. 3, pp. 273–297, 1995.

[25] E. V. Olesh, S. Yakovenko, and V. Gritsenko, "Use of a low-cost, portable motion capture system for upper extremity rehabilitation," *Journal of Rehabilitation Research and Development*, vol. 51, no. 6, pp. 949–960, 2014.

[26] H.-J. Kim, Y.-K. Lee, I.-B. Lee, K.-H. Cho, and E.-K. Park, "Kinematic analysis of upper extremity movements during activities of daily living in stroke patients," *Journal of Physical Therapy Science*, vol. 28, no. 12, pp. 3253–3258, 2016.

Validating predictive simulation-derived electrical stimulation cycling in a person with spinal cord injury

Alexandre B. Peres, Gabriel G. Carmona, Carlos Gonçalves,
Ana Carolina C. de Sousa and Roberto de S. Baptista

***Abstract*— Functional electrical stimulation (FES) is commonly used in rehabilitation for its ability to activate muscle groups and functionally apply them. One of the most popular applications of FES is cycling for its safety and proven increase in users' health and quality of life. However, some challenges are intrinsic to the cycling application, among them, finding the best parameters of electrical stimulation to optimize the benefits for each user. While studies have focused on determining the optimal timing for stimulation with a bang-bang control strategy, there has been comparatively less research on its stimulation profile. This study develops and tests a predictive simulation-derived stimulation profile for FES cycling. We applied fully predictive simulations of FES cycling models following a straightforward framework consisting of (1) building torque-driven and muscle-driven models, (2) defining and solving an optimal control problem, (3) converting the optimal solution result to applicable FES control signal, (4) implementing the signal in an experimental setting, and lastly, (5) validating the control signal on a volunteer with spinal cord injury. The results, when compared to a bang-bang control strategy, increased in power output, cadence, and balance in all trials. As far as we know, this is the first study to successfully implement such a strategy. Our results show the potential of predictive simulations to improve the effectiveness of FES cycling rehabilitation.**

I. INTRODUCTION

Electrical stimulation is a rehabilitation technique that invokes muscles' contraction through electrical current resembling physiological activation [1]. By providing functionality to the generated joint movement, such as for cycling, we can refer to it as functional electrical stimulation (FES). FES significantly improves the quality of life for users with spinal cord injury (SCI) by increasing bone density and muscle mass, and improving cardiovascular health [2].

Nevertheless, many factors should be considered when implementing the exercise with patients, such as finding the optimal muscle stimulation timing [3], and its stimulation profile for each individual. Previous studies developed techniques to determine optimal electrical stimulation timing, meaning when to turn it on and off, including PID control [4], fuzzy logic [5], neural network [6], or a combination of methods [7], being it mostly focused on a bang-bang (BB) control and dependent of constant feedback or a previously collected dataset.

There is great potential in digital twins studies through musculoskeletal (MSK) modeling and simulation [8], [9], allowing for a deeper and non-invasive understanding of human motion biomechanics [10]. MSK modeling can also be integrated with optimal control theory and direct collocation. The optimal control theory is a mathematical framework for determining the control inputs to a system that minimize or maximize a cost function while satisfying dynamic and operational constraints. Meanwhile, in the context of simulations, direct collocation solves optimal control problems by discretizing time, approximating states and controls with polynomials, and enforcing system dynamics at specific collocation points, transforming the problem into a unified optimization framework [11]. A recent cycling study [12] has implemented this combination and developed a framework for optimal control simulation. Another study [13] validated the use of direct colocation by comparing its results with experimental electromyography data. These mentioned studies had as limitations their need for previously collected data from able-bodied subjects, which is not possible for people with SCI.

The integration of MSK modeling, optimal control theory, and direct colocation also enables fully predictive simulations [14]. These simulations provide insights and predictions without requiring prior experimental datasets, focusing on controlling and optimizing a specific objective function problem. For instance, previous studies [15] evaluated the effects of posture and cadence while cycling in the leg muscle activation patterns, showing the versatility and practicality of predictive simulations, but did not implement its findings in an experimental setting, and [16] introduced an electrical stimulation profile with varied intensities throughout the cycle, but was still limited due to its model simplicity, composed by only two ideal actuators in the leg, not taking into consideration the characteristics and complexities of MSK models.

Therefore, the objectives of this study are to (1) determine an optimal stimulation timing, along with its profile, suitable for experimental implementation through a simulation pipeline, and (2) evaluate the movement in an experimental FES cycling setup with a participant with SCI, comparing it to a previously used trial and error BB stimulation pattern

*The study received support from the Coordenação de Aperfeiçoamento de Pessoal de Nível Superior (CAPES - Brazil), the Fundação de Apoio à Pesquisa do Distrito Federal (FAPDF - Brazil), the Beatriu de Pinós Fellowship (Spain), and the Agència de Gestió d'Ajuts Universitaris i de Recerca (AGAUR - Spain).

Alexandre B. Peres, Gabriel G. Carmona, and Roberto de S. Baptista are with the Dept. of Electrical Engineering, Universidade de Brasília, Brasília, Brazil alexandre.peres@aluno.unb.br

Carlos Gonçalves is with the Faculty of Physical Education, Universidade de Brasília, Brasília, Brazil

Ana Carolina C. de Sousa is with the Institute for Research and Innovation in Health (IRIS), Universitat Politècnica de Catalunya - Barcelona Tech, Barcelona, Spain

[17]. This framework may shed new light on the application of simulations, while also paving the way for future work that can improve the comprehension of FES cycling muscle activation.

II. METHODS

This study followed a multi-step methodology to develop, implement, and validate predictive simulation-derived stimulation profiles for FES cycling in a participant with SCI. The process (Fig. 1) involved (1) creating cycling models in an MSK simulation environment, (2) solving an optimal control problem to derive stimulation profiles, (3) extracting and processing the stimulation profile, and (4) implementing and testing these signals in an experimental setup.

A. Cycling models creation

We used OpenSim [18], an open-source tool for simulating MSK structures, for modeling and neuromusculoskeletal analysis. The human model used is one of the human default models within OpenSim's library, the *Gait10dof18musc*[1], which has ten degrees of freedom and eighteen muscles in the lower limbs. The *rectus femoris* (RF) and *vastus intermedius* (VI) in the model are a simplified generalization of the quadriceps muscle group. The cycling model is the human model positioned for recumbent cycling in relation to a crank model based on a crank-pelvis relation seen in Fig. 1(a). In addition, there are pedals with the same dimensions as the experimental setup, to which the model's ankles are attached and immobilized to represent the use of orthopedic boots, ensuring the safety of the user during sagittal cycling movement. The cycling model's design was based on our previous studies [19], [20], where it was developed and is publicly available[2], with adaptations to better fit this study's predictive simulations context. A recent update in OpenSim Moco required replacing locked joints in the cycling model with weld joints to improve computation efficiency. Therefore, we modified the upper body joints accordingly, ensuring the model's compatibility with the updated framework while maintaining its biomechanical accuracy.

Two different versions of the base cycling model were created: a torque-driven and a muscle-driven. In the torque-driven model, all muscles were removed and replaced with ideal torques at the hip and knee joints, capable of generating up to 40 Nm, which is enough for the desired simulated cycling intensity based on [13]. For the muscle-driven model, all muscles but the RF and VI were deactivated. This selection was chosen to better represent a previous FES cycling control system [17], where a possible setup is to have only the quadriceps muscle group experience direct activation. Nevertheless, the passive forces and tendon compliance of all other muscles are preserved in the model.

B. Optimal control problem definition and solution

We used OpenSim Moco [21], a toolkit within OpenSim to optimize motion and control of the simulations, and OpenSim Moco, which initiates *CasADI* [22] within *(MocoCasADI)*, converting the problem into a nonlinear programming problem. Then, Moco uses IPOPT [23] to find an optimal solution to the problem.

Similarly to [20], we defined an optimal control problem to be solved (Fig.1(b)). The problem was formulated to simulate a range of cycling data and represent the gear resistance present in the experimental setup. The torque-driven model was required to complete four full revolutions within 7 seconds, encountering a crank resistance moment of 8 Nm. The revolutions requirement was made to obtain cycling data from a steady state regime, while the crank resistance was slightly exaggerated aiming for more expressive muscle activations in the simulations. To prevent the crank from spinning backward and simulate an average performance from the volunteer, its speed must remain within the range of 0°/sec to 240°/sec. The initial position of the crank is fixed at 0°, meaning the left crank arm is at the top dead center (Fig. 1(a)). The model is free to assume initial speeds for the crank, hips, and knee joints as long as they are maintained within the set crank speed. The simulation will be deemed successful if it meets these conditions, along with a convergence tolerance of 10^{-2} and constraint tolerances set at 10^{-4}, while also aiming to minimize the cost function in Eq. (2). The cost function weights were set by balancing the time to execute the movement and its use of torque and are represented by $w_{time} = 6$ and $w_{actu} = 2$ respectively. The eq. (1) minimizes the duration of the movement (t_{sim}) and the sum of each actuator's (x) total energy (J_{actu}) during the torque-driven movement.

$$J_{actu} = \int_0^{t_{sim}} \sum_{i \in actu} |x_i(t)|^2 \, dt \tag{1}$$

$$J_{total} = w_{time}\, t_{sim} + w_{actu}\, J_{actu} \tag{2}$$

Next, we addressed the muscle redundancy problem [24] using the muscle-driven model. To solve this problem, we employed the *MocoInverse* function, which utilized the kinematics from the torque-driven simulation as a reference. This approach helped us determine a combination of muscle activations that could reproduce the kinematics with the available actuators, i.e., the RF and VI muscles. The *MocoInverse* function was beneficial not only for identifying the desired sequence of muscle activations but also for its ease of implementation and computational efficiency, allowing for quick verification of results throughout the development process.

C. Optimal control signal extraction

Once the simulations were finished, the final product was a muscle-driven file containing a time stamped list of all the RF and VI muscle activations ranging from 0 to 1, where the latter represents maximum muscle activation, that contributed to the cycling motion described in Section II-B. To enhance the overall quality of the data, the first revolution was discarded because its motion was not yet stable.

[1]The model can be found at: Gait10dof18musc.

[2]Currently being developed and maintained at: FES-cycling project.

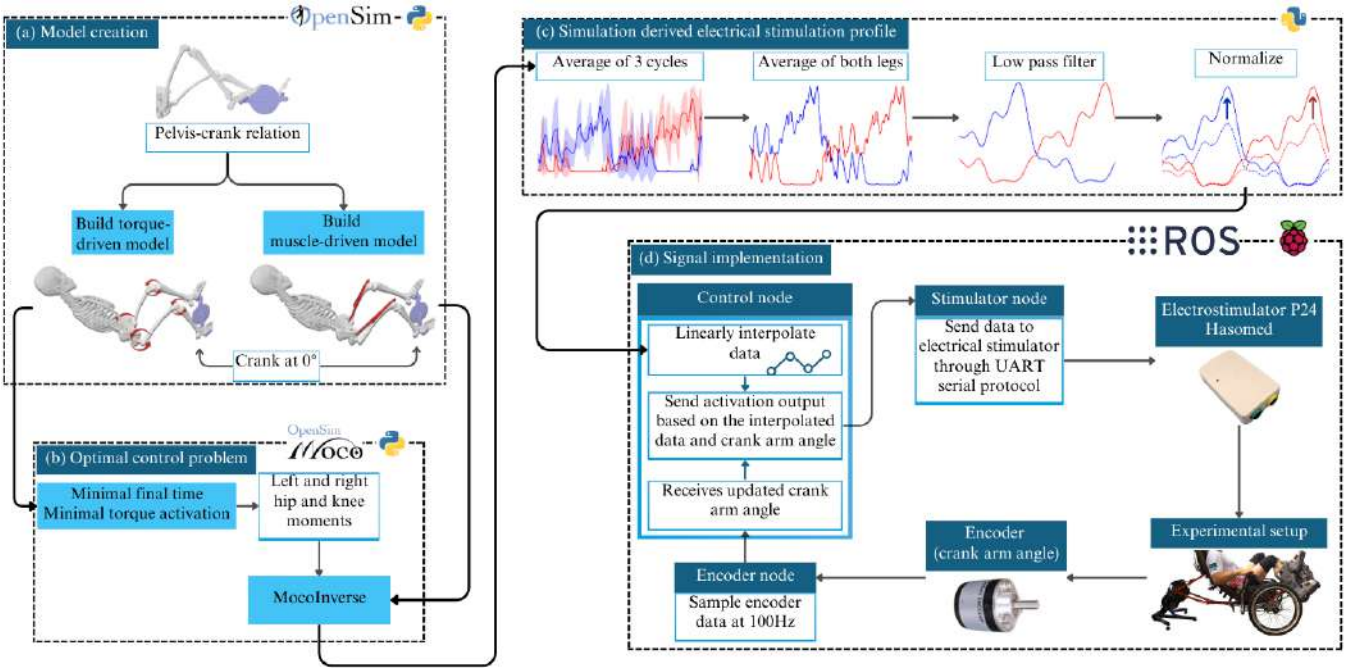


Fig. 1: Framework for generating muscle activation from predictive simulations. (a) Model creation: torque-driven and muscle-driven models were developed using the pelvis-crank relationship from the physical setup. (b) Optimal control problem: simulations that minimize movement time and joint effort using predictive algorithms. (c) Simulation-derived electrical stimulation profile: the necessary steps to obtain the stimulation profile from the simulated data. (d) Signal implementation: the control node receives the stimulation profile and data from the encoder, where angle values are processed and interpolated to generate the stimulation signal, which is then sent to the stimulation topic for delivery via the electrical stimulator.

Therefore, the three remaining revolutions were organized into separate files, where the data was interpolated to ensure consistent resolution. This process allowed for the extraction of an average stimulation pattern for each leg over the three cycles (Fig. 1(c)). Next, to ensure a symmetrical stimulation signal, we calculated the average stimulation from both legs. Furthermore, the signal was filtered using a 5^{th} order Butterworth low-pass filter to achieve a smoother signal and more easily implement it in an experimental setting. Lastly, we normalized the signal, as the simulation results assumed direct muscle fiber activation, which is not replicable through superficial stimulation. All the torque-driven and muscle-drive simulations and data processing were performed on a Ryzen 9 5950X CPU with 64GB of RAM.

D. Optimal control signal implementation

The Fig.1(d) illustrates the setup used in [17] and to validate the study, which is an embedded system consisting of a Raspberry Pi 4 Single Board Computer utilizing the ROS2 (Robot Operating System) framework, an encoder model E38S6G5-600B-G24N from SHARVi Electronics, and an electrical-stimulator model Rehastim P24 from Hasomed. ROS2 facilitates code modularization, creating modules named nodes, which separate input angle data, control logic, and stimulation output into topics that can be subscribed to and published by the respective nodes [25].

We modulated the current according to the interpolation of the simulated result while having the pulse width fixed at 450μs. The stimulation signal was interpolated using a linear model, allowing angle values to have different frequencies from the simulation ones. The control node receives the encoder's angle at a sample rate of 100 Hz. After interpolating, the output is multiplied by the desired current and then published to the stimulation topic, which sends the stimulation pattern current value in a fixed pulse width. The final stimulation signal follows the encoder's sample rate, therefore a control signal sample is generated for every encoder sample.

E. Experimental protocol

We followed a protocol consisting of three non-consecutive days of data collection. Each day of data collection started with 20 minutes of stretching, followed by 20 minutes of electrical stimulation warm-up. Two $8cm$ x $13cm$ electrodes were positioned in each leg over the quadriceps muscle group with the supervision of a physiotherapist similarly to [26]. On the first day, we implemented the unnormalized control signal (uCS) obtained after the filtering step. This signal assumes that the simulated signal is directly applied to the muscles. The normalized simulated control signal (CS) was used on the subsequent data collection days. On the second and third days, four sets of data were collected, with 5 minutes of rest between each set, alternating between the new proposed CS and the BB. The pulse width was set at 450 μs and the current, starting from 30mA, was increased manually in steps of 2mA every 10 seconds

TABLE I: Summary of data collection protocols, including the type of control signal (uCS or CS) and the sequence of trials conducted over three non-consecutive days

day 1	1 set of data	uCS
day 2	4 sets of data	CS_1, BB_1, CS_2, BB_2
day 3	4 sets of data	BB_3, CS_3, BB_4, CS_4

for a safe and cautious approach until a maximum value of 100mA, which is the maximum current the volunteer is used to. From this point on no assistance was given and one minute of data was collected (Table I).

For later data analysis, we collected power (P), crank arm angular velocity (V), and the symmetry of the left and right legs during the motion (B). Two sensors were used for the data collection: (1) instrumented pedals (WAHOO POWRLINK ZERO) to measure P, V, and B at a sample rate of 1Hz, and (2) an instrumented bike trainer WAHOO Kickr V6 that can control resistance to simulate different cycling conditions. Furthermore, during the data collection we connected to *Indievelo*, a virtual cycling environment to better replicate the volunteer's weight and a flat cycling surface and assist with data collection.

F. Compliance with ethical requirements

The volunteer is a 46-year-old male, 170cm tall, 78kg, with a complete SCI (T9 AIS A), meaning no voluntary lower limb muscle contraction, agreed to participate in the study via written consent. The experiments were performed under the ethics committee from the University of Brasília code CAAE: 75441323.4.0000.8093.

III. Results

A. Fully predictive simulations

The problem (Section II-B) was implemented and solved with fully predictive simulations and MSK modeling taking approximately 6 minutes for each simulation. The torque-driven motion was then tracked for the muscle-driven problem and we generated the muscle activations for RF and VI, resulting in the sequence of muscle activation capable of performing the optimal solution to the problem. However, it was noticed that the RF activation patterns are a lot more expressive when compared to the VI, which only activates simultaneously with its correspondent RF but with less intensity. As the VI activations were much lower than the RF, the used signals were the predicted RF activations. but as mentioned in section II-C, only the RF contributions were considered (Fig. 2).

B. Control signal implementation

The predictive simulation-based pattern implementation of the CS was successful. The uCS was used on the first day, and the volunteer could not perform the cycling motion unassisted due to an insufficient current magnitude. Therefore, P, V, and B were not measured (Table II - day 1). On the second and third days (Table II - days 2 and 3), the normalized signal (CS) was used and the cycling motion was performed.

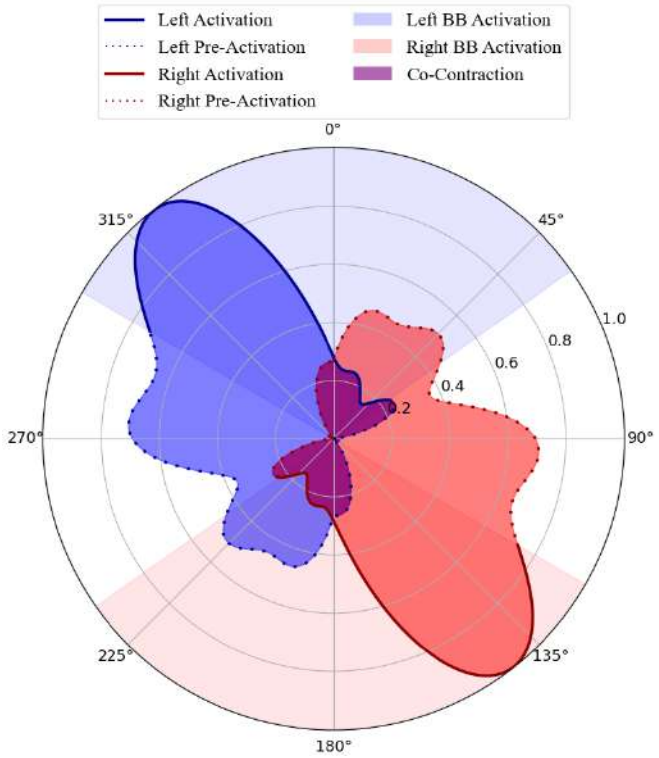


Fig. 2: Rectus femoris (RF) activations for the left (blue) and right (red) legs. The blue and red graphs indicate normalized muscle activation, with the perimeter corresponding to the crank position. The dark blue and red graphs indicate de simulation-derived stimulation profile. The background shades follow the same color code and scale and represent the bang-bang (BB) stimulation pattern used by Project EMA. The dotted lines are outside what is considered mechanically advantageous muscle activation, hence, referred to as pre-activation. The purple area indicates muscle co-contraction, where both RF muscles are activated simultaneously, even during the opposite leg's high activation moments.

There was an increase in all three observed variables when compared to the BB signal. For instance, during the second trial of Day 2 (CS_2 vs BB_2), the power output increased from 11.9 W to 15.2 W (27% higher), the speed rose from 41.3 RPM to 49.0 RPM (18% higher), and the balance improved from 27.1% to 44.0% (62% higher). A high improvement in balance, especially for rehabilitation in SCI patients, could indicate better muscle coordination and safety during cycling. In Fig. 3 is possible to see the 1 minute of non-assisted cycling performed in sequence (CS_4 and BB_4).

IV. Discussion

We successfully created and implemented a framework to predict muscle activations required for FES cycling using fully predictive simulations. We also successfully implemented the simulated-derived CS in an experimental setting, not only working but achieving better results (Table II). This type of conclusion was only achievable by considering

TABLE II: Results of cycling performance metrics collected during experimental trials. Variables include average power output in W, crank angular velocity in RPM, and left-right balance in %, organized by trial and day of collection.

	$\overline{Power}$	$\overline{Velocity}$	$\overline{Balance}$
Day 1 of data collection			
uCS	—	—	—
Day 2 of data collection			
CS_1	13.7	44.1	44.1
BB_1	12.7	42.3	34.6
CS_2	15.2	49.0	44.0
BB_2	11.9	41.3	27.1
Day 3 of data collection			
BB_3	13.2	39.4	35.6
CS_3	14.2	40.9	54.7
BB_4	13.4	40.5	40.1
CS_4	16.3	43.7	48.8

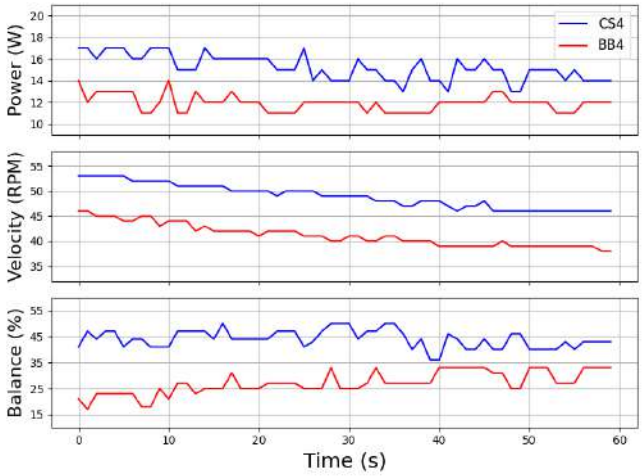


Fig. 3: Comparison of cycling performance during one minute of unassisted cycling between CS_4 and BB_4 trials. Variables shown include power (top), cadence (middle), and left-right balance (bottom), based on data from Table II.

the complete analysis of the dynamics of movement, made possible through the use of fully predictive simulations.

It can be seen in Fig. 2 that the control signal indicated by the simulation overlaps the stimulation pattern utilized by Project EMA in its peak point, but for the most part, it keeps the RF pre-activated with considerably less intensity. Pre-activation, although it may initially seem counterproductive, is commonly observed in high-performance athletes and has been shown to reduce force loss during less energy-efficient stages of cycling [27]. The improved equilibrium between the legs observed during the experiment could be attributed to the decreased muscle reaction time facilitated by RF pre-activation (Fig. 2), which likely contributed to a more balanced and synchronized cycling motion [28].

A second phenomenon present in the simulated FES pattern (CS) is the co-contraction of both RF (Fig. 2). Co-contraction of antagonist muscles is well described [29]–[31], and has an important role in movement stabilization and consequently protection of the joints from elevated stress [32]. In the context of simulations, it is also a result of excessive passive forces from the hip and knee extensors [33]. However, since this is not a factor in the cost function, the co-contraction can be understood as a product of the bi-articulated properties of the RF [34], being not only responsible for knee extension but also the sole responsible for hip flexion throughout the model's movement. Additionally, it is also a mechanism to prevent the crank from exceeding its maximum speed.

We believe a collective of pre-activation, co-contraction, and the optimized control signal is responsible for the increase in average power, cadence, and balance seen in the results. In the rehabilitation context, power is directly related to the user's mass and strength gains, making it the most commonly used metric for evaluating performance and motor recovery when applicable [35]. The crank angular velocity indicates the intensity of cardiovascular exercise as well as work efficiency [36]. Finally, balance is an important indicator of lower limb symmetry [37]. However, further studies need to validate the control signal over longer trials evaluating the effects on fatigue development caused by the longer stimulation periods. Additionally, we recognize that the modeling and simulations presented can be improved to more accurately represent FES cycling conditions, since the validity of the methods relies on the assumption that the models accurately represent SCI conditions. Future work involves grouping muscles within the quadriceps. This is important because superficial non-invasive electrical stimulation can not selectively target specific muscle fibers such as the *rectus femoris* and *vastus intermedius*. When this is implemented in simulations, it's expected to observe a decrease in the overall activation signal, due to the improved use of VI contributions to the movement.

V. Conclusion

As far as we know, this is the first study to successfully implement the results of a fully predictive simulation pipeline in an individual with a complete spinal cord injury. The predictive simulation-derived stimulation patterns outperformed the traditional bang-bang control strategy in terms of power output, cadence, and balance. This was achieved through the integration of musculoskeletal modeling, optimal control theory, and direct collocation techniques, which enabled a comprehensive analysis of movement dynamics and muscle activation. These findings highlight the potential of predictive simulations to enhance FES cycling rehabilitation and provide a solid foundation for future research aimed at further optimizing stimulation strategies and improving clinical outcomes.

Acknowledgment

We would like to express our thanks to Estevão Lopes for volunteering to participate in this study.

Conflict of Interests

The authors declare that they have no conflict of interest.

REFERENCES

[1] Marquez-Chin Cesar, Popovic Milos R.. Functional electrical stimulation therapy for restoration of motor function after spinal cord injury and stroke: a review *BioMedical Engineering OnLine.* 2020;19.

[2] Scheer Jan W., Goosey-Tolfrey Victoria L., Valentino Sydney E., Davis Glen M., Ho Chester H.. Functional electrical stimulation cycling exercise after spinal cord injury: a systematic review of health and fitness-related outcomes *Journal of NeuroEngineering and Rehabilitation.* 2021;18.

[3] McDaniel John, Lombardo Lisa M., Foglyano Kevin M., Marasco Paul D., Triolo Ronald J.. Cycle Training Using Implanted Neural Prostheses: Team Cleveland *European Journal of Translational Myology.* 2017;27.

[4] de Sousa Ana Carolina Cardoso, Ramos Felipe Moreira, Narvaez Dorado Marien Cristina, da Fonseca Lucas Oliveira, Lanari Bó Antônio Padilha. A Comparative Study on Control Strategies for FES Cycling Using a Detailed Musculoskeletal Model *IFAC-PapersOnLine.* 2016;49:204-209. Cyber-Physical Human-Systems CPHS 2016.

[5] Farhoud Aidin, Erfanian Abbas. Fully Automatic Control of Paraplegic FES Pedaling Using Higher-Order Sliding Mode and Fuzzy Logic Control *IEEE Transactions on Neural Systems and Rehabilitation Engineering.* 2014;22:533-542.

[6] Wannawas Nat, Diaz-Pintado Clara, Narayan Jyotindra, Faisal A. Aldo. Accessible FES Cycling: Leveraging Cost-Effective Crank Angle Measurement and Reinforcement Learning for Stimulation Optimization in *2024 10th IEEE RAS/EMBS International Conference for Biomedical Robotics and Biomechatronics (BioRob)*:1529–1534IEEE 2024.

[7] Wang Guangyu, Zhao Yucheng, Sun Mingxu, Dong Wenhua, Zhu Shiwei. Different Control Methods for FES Cycling:Review in *2024 IEEE 24th International Conference on Software Quality, Reliability, and Security Companion (QRS-C)*:759-766 2024.

[8] Fregly Benjamin J.. A Conceptual Blueprint for Making Neuromusculoskeletal Models Clinically Useful *Applied Sciences.* 2021;11.

[9] Uhlrich Scott D, Uchida Thomas K, Lee Marissa R, Delp Scott L. Ten steps to becoming a musculoskeletal simulation expert: a half-century of progress and outlook for the future *Journal of biomechanics.* 2023;154:111623.

[10] Kainz Hans, Falisse Antoine, Pizzolato Claudio. Neuromusculoskeletal modeling in health and disease *Brazilian Journal of Motor Behavior.* 2024;18.

[11] Kelly Matthew. An Introduction to Trajectory Optimization: How to Do Your Own Direct Collocation *SIAM Review.* 2017;59:849-904.

[12] Park Sangsoo, Caldwell Graham E., Umberger Brian R.. A direct collocation framework for optimal control simulation of pedaling using OpenSim *PLOS ONE.* 2022;17:1-17.

[13] Clancy Caitlin E., Gatti Anthony A., Ong Carmichael F., Maly Monica R., Delp Scott L.. Muscle-driven simulations and experimental data of cycling *Scientific Reports.* 2023;13.

[14] Febrer-Nafría Míriam, Nasr Ali, Ezati Mahdokht, Brown Peter, Font-Llagunes Josep M., McPhee John. Predictive multibody dynamic simulation of human neuromusculoskeletal systems: a review *Multibody System Dynamics.* 2022;58:299–339.

[15] Gfohler M., Lugner P.. Dynamic simulation of FES-cycling: influence of individual parameters *IEEE Transactions on Neural Systems and Rehabilitation Engineering.* 2004;12:398-405.

[16] Kim Chul-Seung, Eom Gwang-Moon, Hase Kazunori, et al. Stimulation Pattern-Free Control of FES Cycling: Simulation Study *IEEE Transactions on Systems, Man, and Cybernetics, Part C (Applications and Reviews).* 2008;38:125-134.

[17] S. Baptista Roberto, C. C. Moreira Marina, D. M. Pinheiro Lucas, et al. User-centered design and spatially-distributed sequential electrical stimulation in cycling for individuals with paraplegia *Journal of NeuroEngineering and Rehabilitation.* 2022;19.

[18] Delp Scott L., Anderson Frank C., Arnold Allison S., et al. OpenSim: Open-Source Software to Create and Analyze Dynamic Simulations of Movement *IEEE Transactions on Biomedical Engineering.* 2007;54:1940-1950.

[19] Sousa A., Sousa F., Baptista R., Bó A.. Passive knee orthoses assistance in functional electrical stimulation cycling in an individual with spinal cord injury *IEEE transactions on neural systems and rehabilitation engineering.* 2021;29:690–698.

[20] Sousa Ana Carolina Cardoso, Font-Llagunes Josep M.. Predictive Framework for Electrical Stimulation Cycling in Spinal Cord Injury *IFAC-PapersOnLine.* 2024;58:332–337.

[21] Dembia Christopher L., Bianco Nicholas A., Falisse Antoine, Hicks Jennifer L., Delp Scott L.. OpenSim Moco: Musculoskeletal optimal control *PLOS Computational Biology.* 2020;16:e1008493.

[22] Andersson Joel A. E., Gillis Joris, Horn Greg, Rawlings James B., Diehl Moritz. CasADi: a software framework for nonlinear optimization and optimal control *Mathematical Programming Computation.* 2018;11:1–36.

[23] Wächter Andreas, Biegler Lorenz T.. On the implementation of an interior-point filter line-search algorithm for large-scale nonlinear programming *Mathematical Programming.* 2005;106:25–57.

[24] De Groote Friedl, Kinney Allison L., Rao Anil V., Fregly Benjamin J.. Evaluation of Direct Collocation Optimal Control Problem Formulations for Solving the Muscle Redundancy Problem *Annals of Biomedical Engineering.* 2016;44:2922–2936.

[25] Macenski S, Foote T, Gerkey B, Lalancette C, Woodall W. Robot Operating System 2: Design, architecture, and uses in the wild *Science Robotics.* 2022;7:eabm6074.

[26] Scott Wayne, Adams Cheryl, Fisher Jason, Fisher Stephanie, Jones Kayla, Mathieu Brian. Electrically elicited quadriceps muscle torque: Comparison at three knee angles *Physiotherapy Theory and Practice.* 2019;37:729–735.

[27] Hering Gernot O., Bertschinger Raphael, Stepan Jens. A quadriceps femoris motor pattern for efficient cycling *PLOS ONE.* 2023;18:1-28.

[28] Kimura Ken, Imanaka Kuniyasu, Kita Ichiro. The effects of different instructions for preparatory muscle tension on simple reaction time *Human Movement Science.* 2002;21:947-960. Current issues in motor control and coordination.

[29] Bautmans Ivan, Vantieghem Stijn, Gorus Ellen, et al. Age-related differences in pre-movement antagonist muscle co-activation and reaction-time performance *Experimental Gerontology.* 2011;46:637-642.

[30] Hug François, Turpin Nicolas A., Couturier Antoine, Dorel Sylvain. Consistency of muscle synergies during pedaling across different mechanical constraints *Journal of Neurophysiology.* 2011;106:91–103.

[31] Turpin Nicolas A., Watier Bruno. Cycling Biomechanics and Its Relationship to Performance *Applied Sciences.* 2020;10.

[32] So Raymond C.H., Ng Joseph K.-F., Ng Gabriel Y.F.. Muscle recruitment pattern in cycling: a review *Physical Therapy in Sport.* 2005;6:89–96.

[33] Lai Adrian K. M., Arnold Allison S., Wakeling James M.. Why are Antagonist Muscles Co-activated in My Simulation? A Musculoskeletal Model for Analysing Human Locomotor Tasks *Annals of Biomedical Engineering.* 2017;45:2762–2774.

[34] Ryan Mary M., Gregor Robert J.. EMG profiles of lower extremity muscles during cycling at constant workload and cadence *Journal of Electromyography and Kinesiology.* 1992;2:69-80.

[35] Frazão Murillo, Gomes Figueiredo Thainá, Cipriano Gerson. Should We Use the Functional Electrical Stimulation-Cycling Exercise in Clinical Practice? Physiological and Clinical Effects Systematic Review With Meta-analysis *Archives of Physical Medicine and Rehabilitation.* 2024.

[36] Hunt K.J., Fang J., Saengsuwan J., Grob M., Laubacher M.. On the efficiency of FES cycling: A framework and systematic review *Technology and Health Care.* 2012;20:395–422.

[37] Ambrosini Emilia, Ferrante Simona, Ferrigno Giancarlo, Molteni Franco, Pedrocchi Alessandra. Cycling Induced by Electrical Stimulation Improves Muscle Activation and Symmetry During Pedaling in Hemiparetic Patients *IEEE Transactions on Neural Systems and Rehabilitation Engineering.* 2012;20:320-330.

Assessing Stylistic Differences in the Underlying Biomechanical Objectives of Walking using Simulation-Based Observational Gait Analysis

McKenna C. Everett
Walker Department of Mechanical Engineering
The University of Texas at Austin
Austin, USA
mceverett@utexas.edu

Wentao Li
Walker Department of Mechanical Engineering
The University of Texas at Austin
Austin, USA
wentao.li@utexas.edu

Ann Majewicz Fey
Walker Department of Mechanical Engineering
The University of Texas at Austin
Austin, USA
ann.majewiczfey@utexas

Nicholas P. Fey
Walker Department of Mechanical Engineering
The University of Texas at Austin
Austin, USA
nfey@utexas.edu.edu

***Abstract*—Observational gait analysis and categorical ratings are commonly used by clinicians to assess pathologies. The purpose of this study was to determine the capacity of novice observers to characterize the gait behavior underlying biomechanical performance objectives using stylistic labels. We hypothesized that visual characterization of physics-based musculoskeletal predictive simulations of walking would be sensitive to the biomechanical objective employed by individuals, as well as the visual perspective. We developed 75 full-body muscle-driven predictive gait simulation videos, corresponding to five subject models, five biomechanical objectives, and three visual perspectives. Subject models were constructed for five individuals performing straight line walking, with optimal tracking simulations generated for each using computed muscle control. Direct collocation was used to apply five different objectives to each individual's nominal behavior including metabolic cost, summed and squared muscle activations, time-integrated whole-body angular momentum, time-integrated bilateral ground reaction forces, and an equally weighted multi-objective cost function summing the individual objectives. 100 crowd workers characterized each simulation on a 1-5 scale using stylistic labels corresponding to each objective. Multinomial logistic regression analysis revealed that loading and activation ratings were significant predictors of muscle activation-optimized movements, while activation ratings were significant predictors of movement perspective. Balance ratings were significant for the frontal view alone, suggesting that balance indicators are more easily distinguished in the frontal plane. Collectively, the wisdom of crowds could distinguish motion associated with some biomechanical objectives, but due to the redundancy of motor control strategies used by individuals, the resolution of this observational approach is limited.**

Keywords— gait analysis, predictive simulation, crowdsourcing

I. Introduction

Determining accurate assessments of gait performance is key in preventing falls among individuals with limb loss, neurologic conditions, and the elderly [1]. However, current laboratory and clinically based assessment methods can be expensive, lengthy and suboptimally diagnose comorbidities or subclinical presentations [2]. Pathological gaits are difficult to assess due to the overlapping symptoms underlying multiple gait disorders [1] as well as high gait pattern variability both within and across individuals [3]. These factors make it difficult to determine appropriate interventions from single metrics or clinical assessments, and instead suggest that assessment based on a variety of multi-modal metrics by multiple assessors is needed.

Qualitative, semiquantitative, and quantitative metrics are all used as modes of gait assessment. Qualitative assessments rely on clinical observation, which can be subjective [4, 5], and while useful for assessing severity and risk do not provide much information on specific gait mechanics [2, 6]. Quantitative sensors can be costly and less practical, and while some diagnoses correlate with factors such as self-selected gait speed, these quantitative metrics are often less applicable to geriatric individuals [3], individuals with neurologic gait patterns [7], or those with nonspecific gait abnormalities [4]. Semiquantitative techniques often involve rating scales, such as the Tinetti Mobility Test (TMT) and the Gait Abnormality Rating Scale (GARS) [7, 8], and require extensive gait observation by an experienced clinician [6]. Subjectivity of clinician judgement, gait variability, and gait comorbidities can make it difficult to identify objective quantitative evidence for gait disorders or provide accurate diagnoses [1]. The prevalence of these methods supports the existence of visible indicators of kinematic and postural factors in a patient's motion that are implicitly used to diagnose underlying ailments [9], and suggests that assessment techniques based around these visible indicators provides viable quantitative data. In addition, multifactorial analyses that include both kinematic and postural factors may improve the overall accuracy of diagnosis for those with comorbid or subclinical presentations [10].

Prior work has demonstrated the feasibility of simulation-based and videotaped observational gait analysis (VOGA) to diagnose and assess the severity of gait disorders including multiple sclerosis [11], post-stroke hemiplegia [12], rheumatoid arthritis [4], and Parkinson's disease [13]. These studies were each performed at a small scale, with concerns about the inter-rater reliability of untrained individuals [4, 12]. The inter-rater reliability of VOGA has been shown to vary across studies [14, 15], but also exceeds that of real-time observational assessments [16]. The intra-rater reliability of VOGA also varies, with cases of worse reliability than in-

person assessments [17], as well as moderate reliability regarding the presence of gait characteristics, but a lower reliability when making judgements about their severity [18]. A study on post-stroke gait found a negligible difference in observations made by novice and experienced physical therapists, with visual observations equally reliably made by less experienced individuals [5]. Another study in surgical robotics found a positive correlation between biometric data and both clinician and crowd estimations of the experience level of surgeons based on their performance [19], suggesting crowd workers were able to distinguish surgical skill levels and indicate this via a lexicon of contrasting adjective pairs.

The purpose of this study was to determine the capacity of novice observers (i.e., crowd workers) to characterize gait behavior corresponding with the biomechanical performance objectives underlying an individual's motor control strategy using a lexicon of contrasting adjective pairs. We test the hypothesis that visual characterization of physics-based musculoskeletal predictive simulations of walking would be sensitive to the biomechanical objective (i.e., cost function optimization) used by individuals, as well as the visual perspective (sagittal, frontal, or 3D views).

II. Methods

A. Crowd Worker Video Assessment

Simulated gait videos [20] were generated of a full-body musculoskeletal model completing one full gait cycle. Gait patterns were constructed using subject-specific tracking and ground reaction force (GRF) data from an IRB-approved experiment [21, 22]. Scaled musculoskeletal models of each subject were developed in Visual3D (C-Motion, Inc.) and OpenSim with 21 degrees of freedom, a locked MTP joint, and 92 Hill-type musculotendon actuators [23]. Predicted gait patterns were optimized for each of five biomechanical objectives (metabolic cost, summed and squared muscle activations, time-integrated whole-body angular momentum, time-integrated bilateral ground reaction forces, equal weight multi-objective) [20] in MATLAB (MathWorks, Inc.) as an optimal control problem using direct collocation [20, 24]. Videos presented each unique motion from each of three different views (frontal, 3D, and sagittal) for all five subjects, for a total of 75 videos. Images of the activation-optimized gait model from all three views are shown in Fig. 1.

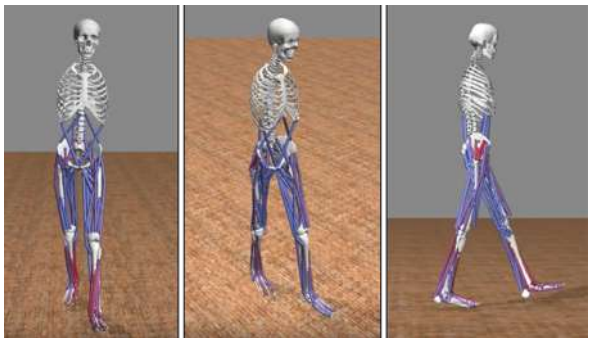


Fig. 1. Visualized time steps of a subject simulation walking with an activation optimized controlled gait from frontal, 3D, and sagittal views.

This work is supported by DOD grant W81XWH2211091.

TABLE I. Lexicon of Gait Objective Adjective Pairs

Category	Qualitative Ratings	
	Low Rating (1)	***High Rating (5)***
Energy	Lethargic	Swift
Activation	Stiff	Casual
Balance	Unstable	Controlled
Loading	Heavy	Light
Normal	Unrealistic	Realistic

This gait assessment technique was evaluated by comparing crowd worker assessments of perceived gait characteristics to underlying gait mechanics. The 75 simulated gait videos were posted on Amazon Mechanical Turk and rated by 100 untrained crowd workers on five objectives (energy, muscle activation, balance, loading, and normal appearance) on a 1-5 semantic differential rating scale using a lexicon of contrasting adjective pairs (Table I), with a rating of "1" corresponding to "negative" terms, and "5" with "positive" ones.

B. Average Crowd Worker Responses and Normalization

The mean and standard deviation of the 100 crowd worker ratings were determined for each objective and simulation view combination, resulting in 15 unique groups. Mean ratings for the characteristics corresponding to biomechanical objectives were Z-score normalized by the "Normal" ratings to discern variations between each simulated gait by their perceived viability as a realistic gait pattern. The mean ratings for each objective were compared with associated quantitative metrics provided by these physics-based simulations [20], including normalized metabolic energy, sum of muscle activations, lower-limb loading, and whole-body angular momentum.

C. Multinomial Logistic Regression Models

Multinomial logistic regression (MLR) was used to determine statistically significant predictors of each gait objective and simulation view from crowd worker ratings, with each gait objective and view representing separate unordered dependent variables. The individual objective probabilities were compared to the multi-objective probability (π_multi) and the views probabilities were compared to the sagittal probability ($\pi_sagittal$), as shown in (1-a) and (1-b). In the equations, a is the intercept and b is the logistic coefficient of each objective and view respectively, where i denotes gait characteristics including: metabolic energy, muscle activation, balance, limb-loading, and normal appearance, respectively. P-values under 0.05 were considered statistically significant.

$$\ln\left(\frac{\pi_objective}{\pi_multi}\right) = a + \sum_{i=1}^{n} b_i x_i \qquad \text{(1-a)}$$

$$\ln\left(\frac{\pi_view}{\pi_sagittal}\right) = a + \sum_{i=1}^{n} b_i x_i \qquad \text{(1-b)}$$

Additional multinomial logistic regression curves were used to predict biomechanical gait objectives (1-a) using the

crowd worker ratings for each individual view to determine which simulation view(s) provided statistically significant results. All data analyses were conducted in MATLAB.

III. Results

A. Crowd Worker Video Assessment

The responses of 100 crowd workers to 75 simulated gait videos resulted in 7500 total ratings for each gait characteristic (Fig. 2). The loading and metabolic energy characteristics received the lowest mean ratings across all simulations, at 2.49±0.05 and 3.26±0.04 respectively, regardless of the optimization or view utilized in the video. The balance characteristic received the highest mean ratings, at 3.62±0.05, for all simulations regardless of biomechanical objective or simulation view shown. These results are also reflected in the normalized values, where the balance Z-scores were positive, and the limb-loading and metabolic energy scores negative, suggesting that crowd workers found the gaits to be mildly controlled, slightly swift, and mildly heavy (Table I) regardless of their optimized objective.

The "normal" metric was also similar across all simulations, at a mean rating of 3.48±0.04. The overall mean rating across all assessments was 3.28±1.03, with few "1" ratings. Maximum (5) and minimum (1) scale values made up only 5.1% and 9.1% of the total ratings respectively. Non-extreme response styles have been observed for semantic differential rating scales [25], with respondents tending towards non-extreme responses when the scale labels are more ambiguous [26]. This infrequency of extreme rating responses could be due to the crowd workers' lack of familiarity with the survey, VOGA or the lexicon of gait characteristics.

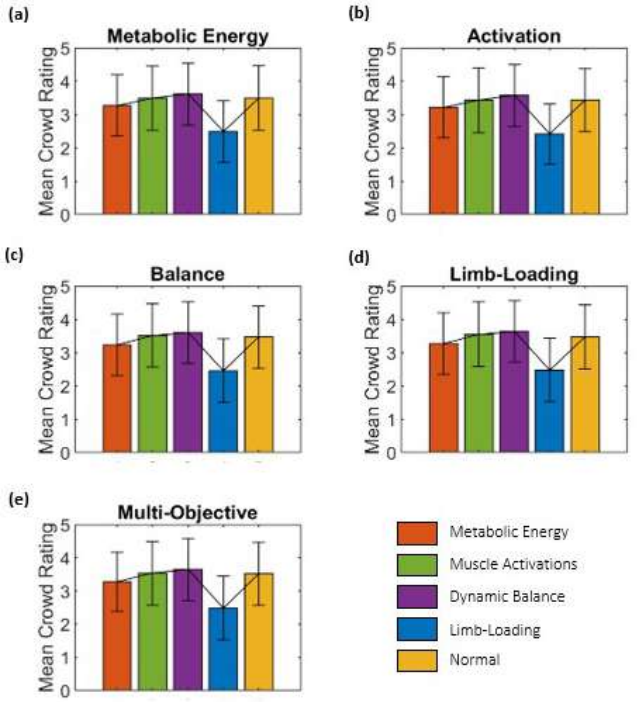


Fig. 2. Mean and standard deviations of raw crowd worker ratings for each simulation optimized for (a) metabolic energy, (b) activation, (c) balance, (d) limb-loading, and (e) multi-objective biomechanical objectives.

B. Comparisons with Biomechanical Simulation Data

Results from the previous simulation study [20] showed that the simulations minimizing muscle activations also had lower normalized metabolic energies [20]. This is reflected in the energy ratings for the muscle activations-optimized simulation, which was rated as the most lethargic on average (3.22±0.05). The activation optimized simulations were also rated as appearing the most unstable (3.58±0.05), stiff (3.43±0.05), heavy (2.42±0.02), and unrealistic (3.44±0.01). Crowd workers rated the multi-objective simulation as appearing to have the greatest metabolic energy (3.29±0.01), the swiftest on average across all three views, followed by the metabolic energy and limb-loading optimized simulations. These gait patterns were also rated as the most controlled (3.65±0.04), and realistic (3.53±0.004). The metabolic energy optimized gait was rated as the lightest (2.49±0.03), and the loading optimized gait as appearing the most casual (3.55±0.06).

The whole-body angular momentum in the transverse plane is significantly lower across all gaits than in the other planes [20]. The wisdom of crowds rated that the 3D view, activation-optimized gait appeared the least balanced, or most unstable, with the 3D view rated as the most unstable view for the balance and loading-optimized gaits as well. Interestingly, the multi-objective optimized gait was rated as the most unstable from the frontal view, and the metabolic energy optimized gait rated as the most unstable from the sagittal view (Fig. 3).

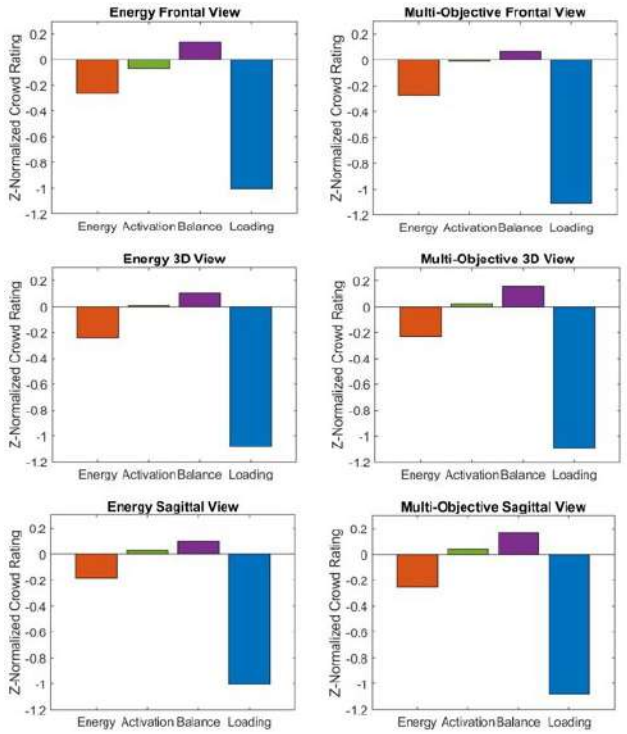


Fig. 3. Comparison of the Z-normalized mean ratings for the metabolic energy and multi-objective optimized gaits.

C. Multinomial Logistic Regression Models

The biomechanical objective MLR model predicts (p=0.002) the logistic probability of each objective compared to the multi-objective probability from all 7500 crowd worker ratings (Fig. 4). The crowd worker ratings for activation (p=0.003) and loading (p=0.001) provided statistically significant indicators for predicting if a simulation was optimized for muscle activation levels. This suggests that crowd worker perceptions of how "casual" vs. "stiff" and "light" vs. "heavy" a gait appeared were statistically relevant in determining if the gait modeled minimized the summed muscle activations as opposed to the multi-objective cost function. MLR analysis also revealed that the crowd worker ratings for normal gait appearance (p=0.016) were a significant indicator of simulations optimized for lower-limb loading.

The simulation views multinomial logistic regression model (p=0.01) determined the logistic probability of each view compared to the sagittal view probability. This model found that activation ratings were a significant predictor of a simulation having a 3D or frontal view rather than a sagittal one. Loading ratings were also identified as a significant predictor for the frontal view.

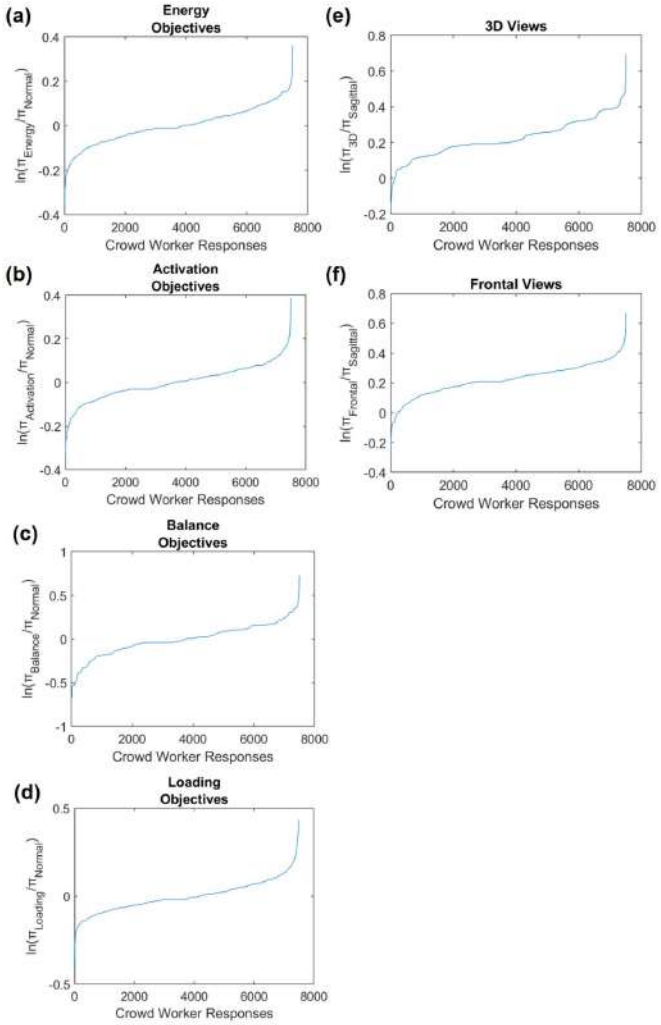


Fig. 4. Multinomial logistic regression models of crowd worker ratings predicting each gait simulation's biomechanical objective (a-d) and simulation perspective view (e-f).

TABLE II. FRONTAL VIEW MULTINOMIAL LOGISTIC REGRESSION

	Value	SE	tStat	pValue
Muscle Activation				
a_Intercept	1.863	0.467	3.989	6.65E-05
b1_Balance	-0.195	0.085	-2.301	0.021
b2_Activation	-0.134	0.087	-1.535	0.125
b3_Energy	-0.104	0.091	-1.152	0.249
b4_Loading	-0.222	0.079	-2.816	0.005
b5_Normal	0.051	0.089	0.576	0.564
Dynamic Balance				
a_Intercept	1.085	0.464	2.338	0.019
b1_Balance	-0.093	0.085	-1.101	0.271
b2_Activation	0.062	0.087	0.710	0.478
b3_Energy	-0.067	0.090	-0.743	0.458
b4_Loading	-0.185	0.077	-2.394	0.017
b5_Normal	-0.084	0.088	-0.962	0.336
Metabolic Energy				
a_Intercept	0.416	0.461	0.901	0.367
b1_Balance	-0.082	0.085	-0.962	0.336
b2_Activation	0.000	0.087	0.000	1.000
b3_Energy	-0.024	0.090	-0.271	0.787
b4_Loading	-0.052	0.076	-0.687	0.492
b5_Normal	0.026	0.088	0.295	0.768
Lower-Limb Loading				
a_Intercept	0.896	0.462	1.942	0.052
b1_Balance	-0.113	0.085	-1.341	0.180
b2_Activation	0.012	0.087	0.135	0.893
b3_Energy	0.020	0.090	0.225	0.822
b4_Loading	-0.079	0.077	-1.035	0.301
b5_Normal	-0.114	0.087	-1.318	0.188

Separate multinomial logistic regression models were constructed for the frontal, 3D, and sagittal views, with 2500 observations for each view. The most statistically significant gait characteristic predictors of biomechanical objectives were found in simulation videos from the frontal view (p=0.049). The results for the frontal view MLR analysis conducted to identify significant predictors for each biomechanical objective cost function can be found in Table II, including the logistic intercept (a) and coefficients (b) used in Equation (1-a) for each objective. Significant predictors are highlighted. Two significant gait characteristics were identified for predicting that a gait simulation was optimized for muscle activations: the balance ratings and limb-loading

ratings. Limb-loading was found to be the single significant gait characteristic for predicting a dynamic balance-optimized simulation. For videos from the 3D view (p=0.020), balance ratings were found to be a significant indicator in predicting whether a simulation was optimized for lower-limb loading. The logistic model for the sagittal view did not yield statistically significant results (p=0.287).

IV. Discussion

In this study, simulated musculoskeletal gait simulations optimized for five different biomechanical objectives and shot from three different views were rated by the wisdom of crowds based on the quality of five gait characteristics: energy, muscle activation, balance, loading, and normal appearance using a provided lexicon of contrasting adjective pairs given in Table I. The purpose of this study was to determine the capacity of novice observers to characterize the gait behavior underlying biomechanical performance objectives using stylistic labels. We hypothesized that visual characterization of physics-based musculoskeletal predictive simulations of walking would be sensitive to the biomechanical objective (i.e., cost function optimization) used by individuals, as well as the visual perspective. In general, we accept these hypotheses. The wisdom of crowds found that the multi-objective gait simulation appeared the most realistic, or "normal" in appearance. This suggests that from a strictly visual perspective, gait patterns optimized for multiple objectives were recognized as more realistic than those optimizing any one biomechanical objective. The gait simulations used in this study are of straight-line walking with no perturbations, differing from previous studies where multi-objective gaits were prioritized in performing perturbed or lateral movements [27], [28], but crowd workers still identified a multi-objective gait optimization as more realistic to the appearance of self-selected walking patterns than that of a metabolically optimal gait.

The muscle activation optimized simulations were rated on average as the least controlled, energetic, and realistic, and the most heavy and stiff, which is supported by the MLR findings that limb-loading and activation ratings were significant predictors of an activation-optimized gait. Balance ratings were not significant predictors overall but were significant when predicting from the frontal view simulations alone, suggesting the visual indicators of balance between the activation and multi-objective simulations were more easily distinguished in the frontal plane. Crowd workers rated the activation characteristic lower for the sagittal view across all simulations except the metabolic energy optimization, where the mean rating was slightly greater than that of the frontal view. The activation ratings were also found to be the sole significant predictor of a 3D or frontal view rather than a sagittal one in MLR analysis. Whole-body angular momentum is greater in the sagittal plane than the frontal plane across biomechanical objectives, but with the greatest disparity in muscle activation and metabolic energy optimizations [20]. This suggests that crowd workers were able to identify the shift in perspective and associate it with the "casual" and "swift" stylistic labels. Conversely, frontal view simulations were rated as appearing the most activated, or "stiff", and low energy, or "lethargic", well as the most normal, or "realistic". This may be due to the frontal view's omission of sagittal information, where joint excursions are greatest during normal walking.

The observed crowd worker response style indicates that the design of the videotaped observational gait analysis (VOGA) survey provided insufficient clarity for the tasks to be accurately completed by untrained crowd workers, and that clarification of the task and semantic rating scale may provide more significant rating deviations between biomechanical objective optimizations [29, 30]. The crowd worker ratings were indicative of a non-extreme response bias typical of surveys with unclear or ambiguous instructions or rating scales. A second potential bias was the wisdom of crowds' limb-loading ratings where a higher, or "lighter" rating was attributed to gait simulations with lower GRFs. The loading ratings were inverted in post analysis to align with the other gait characteristics due to the lower rating of "heavy" carrying a "negative" connotation. The wisdom of crowds demonstrated the capacity to distinguish motion associated with some biomechanical objectives, but we expect that for novice observers, unfamiliarity with this assessment format and the redundancy of motor control strategies used by individuals limit the resolution of this observational approach. Future VOGA assessment methods using the wisdom of crowds should assign clear and comprehensive stylistic labels, use intermediate rating scale labels, and standardize high vs. low ratings across scales.

Future VOGA of gaits shown from the transverse view could be used to determine if the balance characteristic ratings are lower for this perspective across biomechanical objective optimizations, as suggested by the lower whole-body angular momentum observed in the transverse plane [20]. This hypothesis would further the conclusion that visual characterization of walking is sensitive to the perspective view used. These results stem from crowd worker VOGA of simulated, optimized gait patterns, and future work is needed to verify if the wisdom of crowds can accurately characterize these same biomechanical objectives in real healthy and pathological gaits. This method of gait analysis may also be applied in the visual characterization of experimental human gait patterns representing a multi-objective cost function with unknown and uneven biomechanical objective weights [31], which can be used to determine an individual's biomechanical objective strategy. In-clinic, crowd worker trained classification of specific, visually identifiable gait patterns may be used alongside clinician observation to validate diagnoses and suitable interventions in rehabilitative therapy settings [32].

V. Conclusions

This study demonstrates the feasibility of using the wisdom of crowds to characterize some underlying biomechanical objectives. It suggests that specific adjectives are better for distinguishing certain biomechanical objectives, and that specific viewing perspectives are better for visually assessing muscle activation changes within a person. Collectively, this work supports the idea that due to a redundancy of muscle and motor control strategies, visually

assessing the underlying biomechanical objective strategy used by individuals is very difficult. We expect that for this reason, how and why specific individuals respond favorably to specific interventions (e.g., control strategies or design characteristics of wearable devices) is also difficult to predict using standard analysis and movement science techniques.

REFERENCES

[1] J. M. Hausdorff, "Gait variability: methods, modeling and meaning," *J Neuroeng Rehabil*, vol. 2, no. 1, p. 19, 2005, doi: 10.1186/1743-0003-2-19.

[2] M. W. Creaby and M. H. Cole, "Gait characteristics and falls in Parkinson's disease: A systematic review and meta-analysis," *Parkinsonism Relat Disord*, vol. 57, pp. 1–8, 2018, doi: https://doi.org/10.1016/j.parkreldis.2018.07.008.

[3] A. Gabell and U. S. L. Nayak, "The effect of age on variability in gait," *J Gerontol*, vol. 39, no. 6, pp. 662–666, Nov. 1984, doi: 10.1093/geronj/39.6.662.

[4] M. E. Eastlack, J. Arvidson, L. Snyder-Mackler, J. V Danoff, and C. L. McGarvey, "Interrater reliability of videotaped observational gait-analysis assessments," *Phys Ther*, vol. 71, no. 6, pp. 465–472, Jun. 1991, doi: 10.1093/ptj/71.6.465.

[5] J. L. McGinley, P. A. Goldie, K. M. Greenwood, and S. J. Olney, "Accuracy and reliability of observational gait analysis data: judgments of push-off in gait after stroke," *Phys Ther*, vol. 83, no. 2, pp. 146–160, Feb. 2003, doi: 10.1093/ptj/83.2.146.

[6] M. Saleh and G. Murdoch, "In defence of gait analysis. Observation and measurement in gait assessment," *J Bone Joint Surg Br*, vol. 67-B, no. 2, pp. 237–241, 1985, doi: doi:10.1302/0301-620X.67B2.3980533.

[7] N. B. Alexander, "Differential diagnosis of gait disorders in older adults," *Clin Geriatr Med*, vol. 12, no. 4, pp. 689–703, 1996, doi: https://doi.org/10.1016/S0749-0690(18)30196-4.

[8] J. Vanswearingen, K. Paschal, P. Bonino, and J. Yang, "The modified gait abnormality rating scale for recognizing the risk of recurrent Falls in Community-Dwelling Elderly Adults," *Phys Ther*, vol. 76, pp. 994–1002, Oct. 1996, doi: 10.1093/ptj/76.9.994.

[9] R. Rucco *et al.*, "Spatio-temporal and kinematic gait analysis in patients with Frontotemporal dementia and Alzheimer's disease through 3D motion capture," *Gait Posture*, vol. 52, pp. 312–317, 2017, doi: https://doi.org/10.1016/j.gaitpost.2016.12.021.

[10] M. L. Corradini, S. Fioretti, T. Leo, and R. Piperno, "Early recognition of postural disorders in multiple sclerosis through movement analysis: a modeling study," *IEEE Trans Biomed Eng*, vol. 44, no. 11, pp. 1029–1038, 1997, doi: 10.1109/10.641330.

[11] M. Liparoti *et al.*, "Gait abnormalities in minimally disabled people with Multiple Sclerosis: A 3D-motion analysis study," *Mult Scler Relat Disord*, vol. 29, pp. 100–107, 2019, doi: https://doi.org/10.1016/j.msard.2019.01.028.

[12] R. Wellmon, A. Degano, J. A. Rubertone, S. Campbell, and K. A. Russo, "Interrater and intrarater reliability and minimal detectable change of the Wisconsin Gait Scale when used to examine videotaped gait in individuals post-stroke," *Arch Physiother*, vol. 5, no. 1, p. 11, 2015, doi: 10.1186/s40945-015-0011-z.

[13] K. Eguchi *et al.*, "Gait video-based prediction of unified Parkinson's disease rating scale score: a retrospective study," *BMC Neurol*, vol. 23, no. 1, p. 358, 2023, doi: 10.1186/s12883-023-03385-2.

[14] E. C. Field-Fote *et al.*, "The spinal cord injury functional ambulation inventory (SCI-FAI)," *J Rehabil Med*, vol. 33, no. 4, pp. 177–181, 2001, doi: 10.1080/165019701750300645.

[15] D. E. Krebs, J. E. Edelstein, and S. Fishman, "Reliability of observational kinematic gait analysis," *Phys Ther*, vol. 65, no. 7, pp. 1027–1033, Jul. 1985, doi: 10.1093/ptj/65.7.1027.

[16] J. Brunnekreef, C. Uden, S. van Moorsel, and J. Kooloos, "Reliability of videotaped observational gait analysis in patients with orthopedic impairments," *BMC Musculoskelet Disord*, vol. 6, p. 17, Feb. 2005, doi: 10.1186/1471-2474-6-17.

[17] H. de Bruin, D. J. Russell, J. E. Latter, and J. T. Sadler, "Angle-angle diagrams in monitoring and quantification of gait patterns for children with cerebral palsy," *Am J Phys Med*, vol. 61, no. 4, pp. 176–192, 1982, [Online]. Available: https://www.ncbi.nlm.nih.gov/pubmed/7102828

[18] K. A. Hughes and F. Bell, "Visual assessment of hemiplegic gait following stroke: pilot study," *Arch Phys Med Rehabil*, vol. 75, no. 10, pp. 1100–1107, 1994, doi: https://doi.org/10.1016/0003-9993(94)90085.

[19] M. Ershad, R. Rege, and A. M. Fey, "Meaningful assessment of robotic surgical style using the wisdom of crowds," *Int J Comput Assist Radiol Surg*, vol. 13, no. 7, pp. 1037–1048, 2018, doi: 10.1007/s11548-018-1738-2.

[20] W. Li and N. P. Fey, "Relating underlying performance objectives of overground walking to observable walking mechanics using predictive musculoskeletal simulations," in *2022 International Conference on Rehabilitation Robotics (ICORR)*, 2022, pp. 1–6. doi: 10.1109/ICORR55369.2022.9896553.

[21] W. Li and N. P. Fey, "Neuromechanical control strategies of frontal-plane angular momentum of human upper body during locomotor transitions," in *2018 7th IEEE International Conference on Biomedical Robotics and Biomechatronics (Biorob)*, 2018, pp. 984–989. doi: 10.1109/BIOROB.2018.8487920.

[22] W. Li, N. Pickle, and N. Fey, "Time evolution of frontal plane dynamic balance during locomotor transitions of altered anticipation and complexity," *J Neuroeng Rehabil*, vol. 17, Jul. 2020, doi: 10.1186/s12984-020-00731-0.

[23] S. Delp, J. P. Loan, M. Gross, F. Zajac, E. Topp, and J. Rosen, "An interactive graphics-based model of the lower extremity to study orthopaedic surgical procedures," *IEEE Trans Biomed Eng*, vol. 37, pp. 757–767, Sep. 1990, doi: 10.1109/10.102791.

[24] M. Ackermann and A. J. van den Bogert, "Optimality principles for model-based prediction of human gait," *J Biomech*, vol. 43, no. 6, pp. 1055–1060, 2010, doi: https://doi.org/10.1016/j.jbiomech.2009.12.012.

[25] M. Liu, A. G. Harbaugh, J. R. Harring, and G. R. Hancock, "The effect of extreme response and non-extreme response styles on testing measurement invariance," *Front Psychol*, vol. 8, 2017, [Online]. Available: https://www.frontiersin.org/articles/10.3389/fpsyg.2017.00726

[26] N. Schwarz, B. Knäuper, H.-J. Hippler, E. Noelle-Neumann, and L. Clark, "Rating scales numeric values may change the meaning of scale labels," *Public Opin Q*, vol. 55, no. 4, pp. 570–582, Jan. 1991, doi: 10.1086/269282.

[27] K. McDonald, J. Cusumano, P. Peeling, and J. Rubenson, "Multi-objective control in human walking: insight gained through simultaneous degradation of energetic and motor regulation systems," *J R Soc Interface*, vol. 16, p. 20190227, Sep. 2019, doi: 10.1098/rsif.2019.0227.

[28] A. C. Dzewaltowski, P. Antonellis, A. Mohammadzadeh Gonabadi, S. Song, and P. Malcolm, "Perturbation-based estimation of within-stride cycle metabolic cost," *J Neuroeng Rehabil*, vol. 21, no. 1, p. 131, 2024, doi: 10.1186/s12984-024-01424-8.

[29] D. R. Heise, "Some methodological issues in semantic differential research.," *Psychol Bull*, vol. 72, no. 6, pp. 406–422, 1969, doi: 10.1037/h0028448.

[30] L. A. Suskie, Questionnaire Survey Research: What Works. 1996.

[31] V. Q. Nguyen, R. T. Johnson, F. C. Sup, and B. R. Umberger, "Bilevel optimization for cost function determination in dynamic simulation of human gait," *IEEE Transactions on Neural Systems and Rehabilitation Engineering*, vol. 27, no. 7, pp. 1426–1435, 2019, doi: 10.1109/TNSRE.2019.2922942.

[32] R. T. John N. A. Bianco, and J. M. Finley, "Patterns of asymmetry and energy cost generated from predictive simulations of hemiparetic gait," *PLoS Comput Biol*, vol. 18, no. 9, pp. e1010466-, Sep. 2022, [Online]. Available: https://doi.org/10.1371/journal.pcbi.1010466.

Face Validity and Usability Evaluation of a Wearable Upper-Limb Motion Sensing System for Home Use

Jaspreet Kalsi, Yue Zhou, *Member, IEEE*, Mary E. Jenkins, Lorie Donelle, Ana Luisa Trejos, *Senior Member, IEEE*, Michael D. Naish, *Member, IEEE*

***Abstract*— Comprehensive, real-world data are required to inform the design of more effective rehabilitation strategies and assistive devices for individuals with Parkinson's disease (PD). Parkinsonian tremor, a common symptom affecting the upper limbs, significantly impairs daily activities and quality of life. Traditional clinical assessments of tremor are limited in frequency and scope, often failing to capture the full variability of tremor experienced in daily life. To address this gap, this paper presents a robust, user-friendly wearable upper-limb motion sensing system designed for home use. It incorporates 23 six-axis inertial measurement units to monitor the motion of 21 joints in the hand and upper limb continuously over extended periods. By enabling continuous home-based monitoring, the system can provide valuable insights into the daily impact of tremor and other upper limb pathologies, facilitating personalized treatment plans. The device was tested on seven healthy participants over 48 hours. To complement the quantitative data, participants maintained an activity log and provided qualitative feedback on the device. The results demonstrate that meaningful data can be collected outside a laboratory or clinic. They further inform several recommendations to improve the design of wearable devices for the upper limb. These findings underscore the potential of wearable technology in rehabilitation robotics for long-term monitoring and management of motor symptoms in PD.**

I. Introduction

Parkinson's disease (PD) is the second most common neurodegenerative disease, with over 10 million diagnosed individuals worldwide [1]. The most common symptom, experienced by 80% of individuals with PD, is tremor [2]. The involuntary oscillatory motion of parkinsonian tremor predominantly occurs in the upper limb, specifically in the hand and wrist [3]. It can have a large impact on an individual's ability to perform activities of daily living (ADL), particularly those that require fine motor skills.

This work was supported by the Natural Sciences and Engineering Research Council (NSERC) of Canada and the Canadian Institutes of Health Research (CIHR) through a Collaborative Health Research Projects (CHRP) grant #396234, by the NSERC Discovery Grant Program under grant RGPIN-04998-2022, and by the Canada Research Chairs Program under File #950-233069.

J. Kalsi and Y. Zhou were with the School of Biomedical Engineering (BME), Western University, London, ON, Canada

M. E. Jenkins is with the Movement Disorders Program, Western University, London, ON, Canada, email: mary.jenkins@lhsc.on.ca

L. Donelle is with the College of Nursing, University of South Carolina, Columbia, SC, USA, email: ldonelle@mailbox.sc.edu

A. L. Trejos is with the Dept. of Electrical and Computer Engineering (ECE) and BME, Western University, London, ON, Canada, email: altrejos@uwo.ca

M. D. Naish is with the Dept. of Mechanical and Materials Engineering, ECE, and BME, Western University, London, ON, Canada, email: mnaish@uwo.ca

The standard method of assessing tremor uses Part 3 of the Movement Disorder Society-Unified Parkinson's Disease Rating Scale (MDS-UPDRS). It can only be conducted by a neurologist [2] and relies on visual observation in the clinic rather than quantitative evaluation [4]. The motor exam is done in 15 minutes or less and is typically performed 1–4 times a year. This limited assessment does not allow for full characterization of the variation in an individual's tremor and the impact that it may have on their ADL. Further, individuals may be nervous in the clinic and show varied motor skills and tremor patterns compared to what they experience in their daily lives.

The development of new treatments and devices to manage parkinsonian tremor requires a more complete understanding of the general nature of tremor over time, how it can vary between and within individuals, and how it is influenced by activity, sleep, medication, and stress. The first step in improving understanding is the ability to capture quantitative tremor data throughout the day.

The voluntary or intentional motions of people with PD are often superimposed with tremor. Voluntary motion typically has a frequency of around 1–2 Hz [5]. Resting tremor occurs when a body part is at rest against gravity and usually has a frequency of 3–7 Hz [6]. Postural tremor occurs when an individual holds a position against gravity and has a frequency between 5–12 Hz [6].

Inertial Measurement Unit (IMU) sensors are an effective way to measure movement data related to voluntary motion and tremor. These typically use a combination of MEMS-based accelerometers, gyroscopes, and/or magnetometers to measure multiple degrees of freedom (DOF).

A variety of IMU-based wearable motion sensing devices have been developed by researchers to help understand the nature of voluntary motion and tremor. Lin et al. [7] and Fang et al. [8] placed 18 9-DOF IMU sensors on a thin glove. Connolly et al. [9] developed a device with 16 9-DOF IMU sensors that were placed inside a glove. Zhou et al. [10] and Kortier et al. [11] taped IMUs (5 9-DOF IMUs and 16 6-DOF IMUs and 3 magnetometers, respectively) directly to the skin. All of these devices were designed to operate in the controlled environment of a lab for a short time. The sensors and electronics were not covered for protection.

Das et al. [12] developed a simple system to track PD motor symptoms during ADL in a home setting. The system consisted of 5 3-DOF accelerometers that were strapped to the wrists, ankles, and waist. The device batteries were charged at night, allowing data to be collected over several

days. Participants were also asked to log their symptoms and times when medication was taken for PD within a 20-minute range. While able to operate outside of a lab environment, the system only measured wrist motion, which is inadequate to properly characterize tremor and other upper-limb motions.

To date, no devices have been designed that are able to measure the motion of all of the upper limb joints throughout the day. Most have been designed for supervised lab or clinic use. They are not easy to put on and take off, do not protect the electronics and wires, and are not intended for data collection over extended periods. Further, while many measure the joints of the fingers and thumb, the wrist and elbow are often excluded.

This paper presents a wearable motion sensing device that is suitable for home use. It collects data from the elbow and all joints of the hand and wrist to capture a complete picture of upper-limb motion. It adopts a modular design for robustness to failure of one or more IMUs. All wiring and electronics are covered for protection and to prevent them from snagging. The device can operate for at least two days without any intervention from the user, i.e., there is no need to recharge the battery or transfer data from it. Beyond providing a platform that can collect the data necessary to understand the nature of tremor and other upper-limb pathologies better, the data collected by this device is expected to provide insights into the design and use of wearable devices. Specifically, it can help to identify which joints are the most important to measure for particular symptoms or activities, and how long they should be measured for. With this information, future devices can be designed with a minimum number of sensors and power sources optimized for the required operating time.

II. Device Design

To operate within a home setting, the device must be portable, comfortable, and be easy enough for participants to don and doff. It should be able to measure the motion of all joints of the upper limb from the elbow to the fingertips and be able to operate over a two-day period. The proposed device consists of custom-designed and commercially-available electronics that are attached to a glove and sleeve system.

The device hardware consists of a LPC1768 microcontroller unit (MCU) (NXP Semiconductors) that is interfaced with 23 LSM6DS1 IMU sensors (ST Microelectronics) soldered onto 23 custom printed circuit boards (PCBs), with six different variations; a DS1307 real-time clock (RTC) module (Maxim Integrated); a micro-SD card module (Geekstory); and a 10000 mAh 5V battery pack (EAFU). The PCBs are connected with 32-gauge wires. The connected components are shown in Fig. 1.

The IMUs are placed on both sides of the following joints: the interphalangeal (IP), metacarpophalangeal (MCP), and trapeziometacarpal (TMC) joints of the thumb; the distal interphalangeal (DIP), proximal interphalangeal (PIP), and carpometacarpal (CMC) joints of the index, middle, ring, and pinky fingers; the radiocarpal joint (wrist), and the elbow joint.

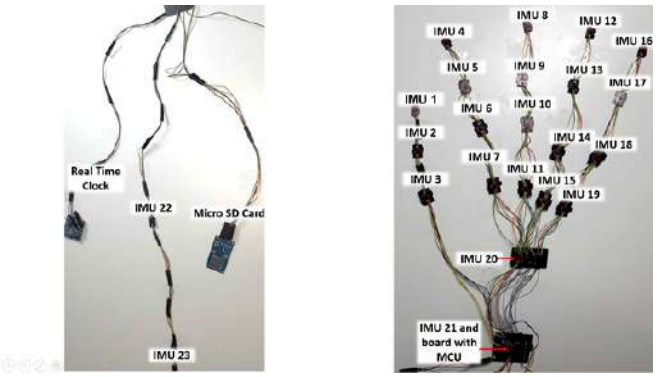


Fig. 1. The connected hardware of the device.

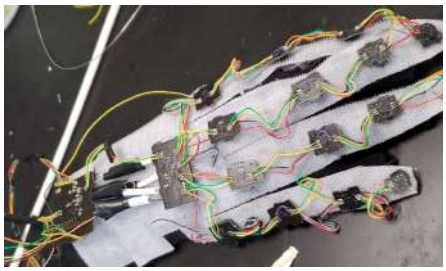


Fig. 2. The hardware attached to the base layer of the glove.

The device has a glove component that consists of a fingerless compression glove and two-way stretch polyester blend fabric. The compression glove has hook-and-loop fastening strips (Velcro) to connect the hand/wrist IMUs (21 total), as shown in Fig. 2. For this initial evaluation, two gloves were developed: one for small hands and one for large hands. Both gloves are right-handed. The hardware is covered by a polyester blend fabric with fingertips that easily lift and attach to hook-and-loop fastening strips on the compression glove. This layer of fabric helps to keep the sensors and wires in place and adds protection.

The sleeve component of the device extends from the biceps to the wrist, where it connects with the glove. It consists of a thin, breathable, nonslip compression sleeve with hook-and-loop fastening strips to attach the two elbow IMU sensors and other electronics. These are covered by the same polyester blend fabric used for the glove to protect the hardware. In addition, an adjustable armband (GoZone) is placed over the compression sleeve on the biceps to hold the battery pack in place. The complete device with the glove, sleeve, and armband on a participant is shown in Fig. 3. The device without the battery pack has a mass of 260 g and the battery pack used for testing weighs 185 g.

III. Experimental Design

The device was evaluated by collecting motion data from healthy participants with the same experimental procedure that is intended for individuals with PD. The experimental procedure was approved by the Health Sciences Research Ethics Board (HSREB) at Western University, Project 118552. Prior to the trial, each participant reviewed a Letter

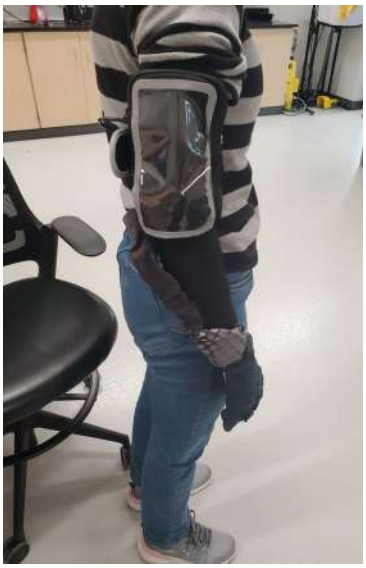


Fig. 3. The complete device on a participant.

of Information. Following consent, participants visited the Wearable Biomechatronics Laboratory at Western University, where the study details were explained in person, measurements of the hand and arm were obtained, the dominant hand was noted, device care instructions were given, and an ADL Log and a Participant Feedback Questionnaire were provided and explained.

Prior to fitting, the IMU sensors were individually validated to ensure that they were performing as expected. For each participant, the 21 IMU sensors on the glove and two IMU sensors around the elbow were positioned according to anatomical landmarks on either side of the target joints. The battery pack was placed over the sleeve, and the participant was shown how to put on the device and take it off.

Data collection took place over a 48 hour period within the home of each participant. Participants were asked to wear the device while performing their typical ADL. For wet tasks, participants could put a rubber/nitrile glove over the device when feasible; otherwise (e.g., showering or submersion), participants were told to remove the device to prevent damage to the electronics. The device was also expected to be removed during sleep.

IMU data were sampled and saved to a micro-SD card every 35 ms as a human-readable comma-separated values (CSV) file. Each data entry included the time, IMU number, and a 16-bit decimal value for each axis—angular velocity about the x, y, and z axes, and linear acceleration along the x, y and z axes. A new CSV file was created every 15 minutes to minimize data loss in the event of power disruption. Since the maximum frequency of typical voluntary motion is 4 Hz [5] and tremor is generally less than 12 Hz [6], the sampling frequency (28.6 Hz) is sufficient to capture both types of motion [13].

Entries in the ADL Log were completed by each participant a minimum of once every two hours. The log serves to record the activity that the participant is performing, the time of occurrence, and the approximate duration. A Participant Feedback Questionnaire was filled out after one hour, at the midpoint (24 hours), and after the trial had finished (48 hours). The Participant Feedback Questionnaire used an 11-point Likert scale to assess the comfort and the ability to perform ADL throughout the trial. At the end of the trial, participants were also asked to rate their overall impression of the device, its ease of donning and doffing, and convenience. Space for additional written feedback was also provided.

A total of 7 healthy subjects (3 male and 4 female, with ages ranging from 23–52) participated in this study. When each trial was complete, the device, ADL Log, and the Participant Feedback Questionnaire were collected from each participant. The remaining battery life was noted and the recorded data were transferred from the micro-SD card to secure cloud-based storage. The IMU data were processed using a 2nd-order low-pass Butterworth filter with a 10 Hz cutoff frequency to extract voluntary motion. Note that studies with individuals exhibiting tremor would use a higher cutoff frequency to extract tremor motion.

IV. Results and Discussion

The performance of the device is reported in this section, along with the qualitative feedback that was received from the participants.

A. Face Validity

The device was able to reliably record data from all 23 IMUs. Clear differences were evident in the IMU data when an individual was engaged in different ADL. Tasks that were associated with rest include sitting, phone calls, laying down, and watching television. In comparison, tasks that were associated with movement include typing on a computer, walking, eating, writing, cooking, and driving. Example angular velocities of the index finger DIP joint for one participant engaged in different tasks are shown in Figs. 4–6. Figs. 7–9 show the angular velocities of the wrist. Similar motion profiles were observed for all joints, with differences resulting from different joints and activities.

The capacity of the selected battery pack was sufficient for every trial. The average battery life remaining after 48 hours for the seven trials was 59%. This indicates that a battery pack with lower capacity could be used to supply power to the device, allowing the device to be smaller, lighter, and more comfortable to wear.

B. ADL Log

The ADL Log documents the tasks that the participants performed during their trials. The participants were asked to log their ADL a minimum of once every two hours, but ideally as often as possible. The ADL Log can be used to correlate the IMU data to specific tasks. Some participants did not fill out the ADL Log for every activity performed, or they estimated the times at which activities took place. The most common ADL performed during the 7 individual trials were using a computer or typing, resting or sitting,

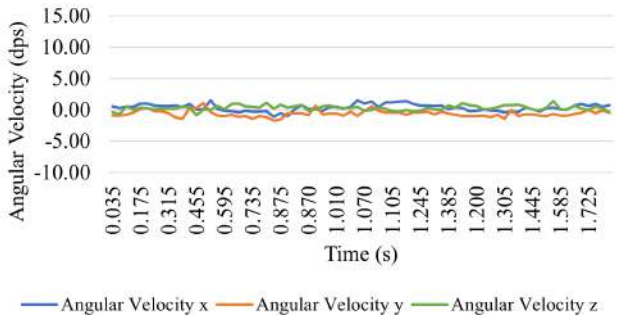


Fig. 4. Example index finger DIP joint angular velocity during rest.

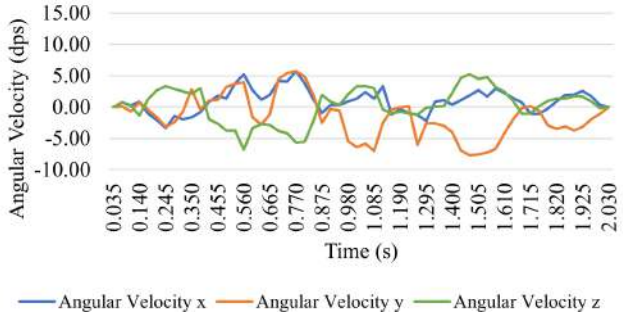


Fig. 5. Example index finger DIP joint angular velocity when using a computer.

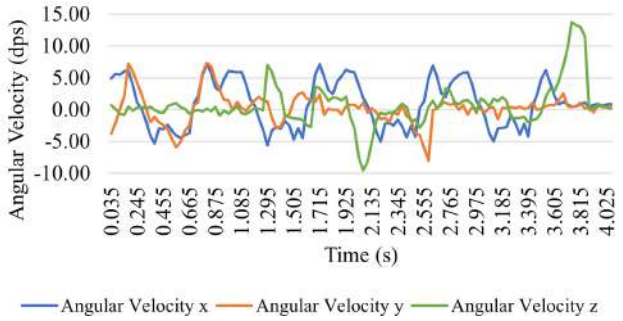


Fig. 6. Example index finger DIP joint angular velocity when walking.

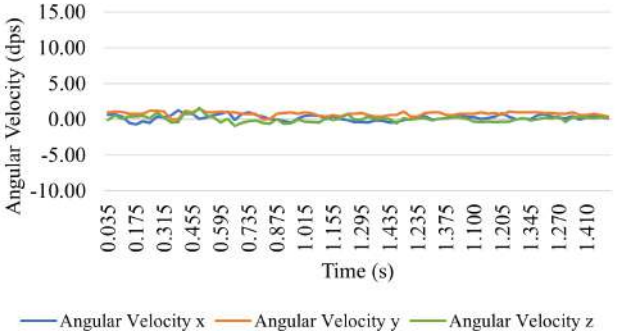


Fig. 7. Example angular velocities of the wrist during rest.

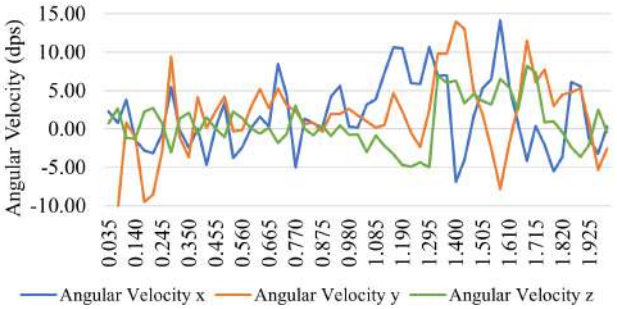


Fig. 8. Example angular velocities of the wrist when using a computer.

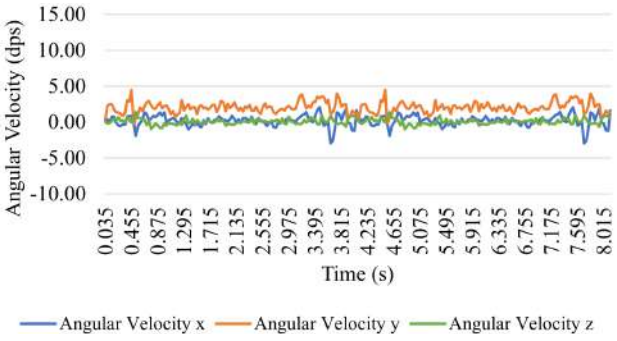


Fig. 9. Example angular velocities of the wrist when walking.

walking, talking on the phone, and eating or drinking. The task breakdown during the trials can be seen in Table I.

Note that ADL were not logged an average of 13.93% of the time. Some participants struggled to update the ADL log for different ADL performed. In addition to providing a timed prompt to users to record their activity, programmable interrupts in the IMUs could be used to detect motion and provide a prompt. Additionally, it may be more convenient for some users to record an audio log on their smartphone than to write their activities on a log sheet.

C. Participant Feedback Questionnaire

The Participant Feedback Questionnaire was filled out by the participants after 1 hour, 24 hours, and at the end of the trial. The mean comfort rating was 6.00 $\pm$ 1.63 after one hour (range: 3–8), 6.14 $\pm$ 1.57 after 24 hours (range: 4–8), and 7.43 $\pm$ 1.27 after 48 hours (range: 5–9), as shown in Fig. 10. Based on the feedback provided, it appears that

TABLE I

THE AVERAGE TIME SPENT ON ADL SORTED BY PREVALENCE.

ADL	Average ADL Time (%)
Using a computer or typing	46.99
Time where ADL not logged	13.93
Resting or sitting	12.42
Walking	7.38
Talking on the phone	4.46
Eating and drinking	4.24
Other	2.55
Driving	1.73
Cooking or food preparation	1.59
Doing laundry	1.41
Texting or scrolling on a mobile phone	1.09
Using the washroom	0.96
Cleaning	0.66
Laying down	0.48
Standing up	0.06
Outdoor work	0.04

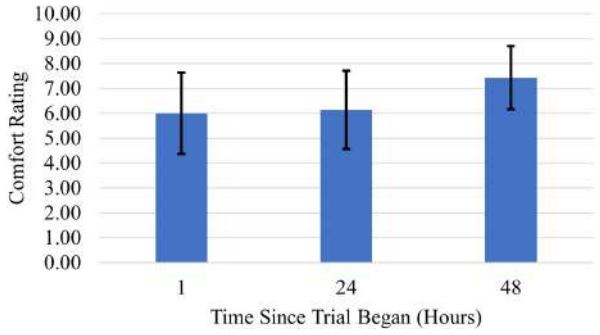


Fig. 10. Mean participant comfort ratings after 1, 24, and 48 hours. The bars show standard deviation.

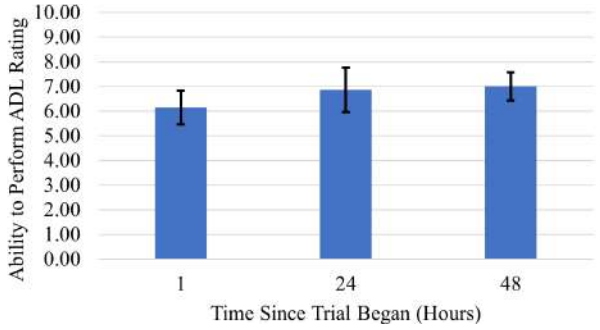


Fig. 11. Mean participant ratings of ability to perform ADL ratings after 1, 24, and 48 hours. The bars show standard deviation.

the participants found the device to be more comfortable the longer it was worn.

Participants scored the ability to perform ADL while wearing the device, with an average rating of 6.14 $\pm$ 0.69 after one hour (range: 5–7), 6.86 $\pm$ 0.9 after 24 hours (range: 5–8), and 7.00 $\pm$ 0.58 after 48 hours (range: 7–8), as shown in Fig. 11. Similar to comfort, the participants found that they were able to perform ADL better as they gained experience with the device.

At the end of the trial, participants were asked to indicate how they felt about the trial, the device, and their overall experience. The average rating for the participants' feelings about wearing the device was 6.43 $\pm$ 2.07 (range: 2–8). The average rating for ease of donning and doffing was 8.60 $\pm$ 0.89 (range: 7–9). The average rating for the convenience of wearing the device was 6.57 $\pm$ 1.90 (range: 3–9). These ratings are summarized in Fig. 12. Overall, the results show that most participants did not dislike the device and felt better than indifferent about wearing the device, but most did not enjoy wearing the device during their trial.

In addition to the ratings, participants provided written comments that provide further insights into how the device performed and highlight areas that would benefit from refinement. These are summarized below:

- In general, participants found the device to be more comfortable on the second day of the trial.
- Most found it difficult to perform ADL at first, but learned to adapt over time.
- The battery became noticeably heavy after 3–4 hours for everyone. Some had a feeling of their arm falling asleep, even when the band holding it to the biceps was loose, and developed a sore arm after 24 hours. In addition, the size of the battery was cumbersome for some tasks.
- The device negatively affected delicate tasks such as writing, typing (seeing a 50% reduction in productivity for some), and tying shoes. It also affected cooking and rummaging though a bag to find an object.
- Drinking and eating were affected by the stiffness of the hook-and-loop fastening strips.
- Driving and other ADL could be performed easily.
- The fabric in contact with the skin was drying for some and caused minor irritation.
- The multiple layers of fabric were very warm, reducing comfort.

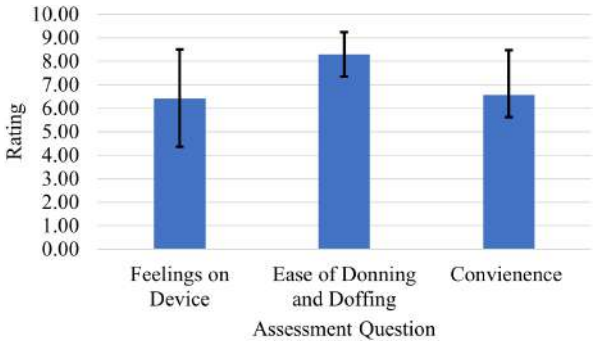


Fig. 12. Mean ratings for the assessment questions. The bars show standard deviation.

V. Recommendations

As this work has demonstrated, designing devices for the upper limb that are worn for extended periods of time presents many challenges. Future designs may benefit by considering the following recommendations:

1) Reduce bulk: The overall size of the device has a significant impact on whether ADLs can be performed normally or not. This is particularly important at the distal end of the fingers, where the sensors, wires, and fabrics must be as small and thin as possible. Consider the use of flexible printed circuit boards and use the smallest components available.
2) Fabric choices: Select materials that are thin and conform to individual anatomy. Thicker fabrics, in addition to adding bulk, tend to impede motion and reduce sensation. Consider biased materials that stretch for comfort while maintaining sensor position over anatomy. Instead of multiple full layers, use pockets and channels to minimize the amount of fabric required for protection and enhance breathability. Cooling fabrics may also be used. Ideally, fabrics in contact with the skin should not cause irritation or drying. Beyond comfort, the materials should provide a degree of water resistance, resist staining, and be easily washed should they become soiled.

3) Free fingertips: Delicate tasks that rely on subtle tactile cues or that require direct interaction with the finger will be impaired less if the fingertips are exposed. Glove should adopt a "fingerless" design.
4) Customize to individuals: While hook-and-loop fastening strips (i.e., Velcro) allows the fit of a device and the placement of sensors to be easily adjusted, it can significantly reduce the comfort of the device, particularly when worn for extended periods of time. Instead, devices should be designed as garments that are sewn to fit the anatomy of a specific user.
5) Power supply location: For portability a battery is necessary; however, it is typically the largest and heaviest part of an unactuated wearable device. If worn on the arm, a battery should closely match the overall power consumption of the device, so that it is not larger than necessary. If a larger battery is necessary, consider locating it on an area of the body that can bear more weight, such as the legs or hips, although the power cable may become cumbersome.

Overall, these recommendations aim to make the device as transparent to the user as possible, with the ultimate goal of feeling like ordinary clothing. Since this may not be achievable, it may be worthwhile to design systems that are as balanced and symmetrical as possible. As the size and weight of the device increases, it may be necessary to add bilateral components to limit imbalances to the overall musculoskeletal system of the wearer.

VI. Conclusion

The device presented in this paper is the first portable device that can collect motion data from 21 upper-limb joints in a home setting over a two-day period. The ability to operate at home is significant because it allows extensive ADL data to be collected. By capturing the full rhythm of the day, it is possible to observe activities and nuances that are not possible in a lab or clinic. Further, the device underscores the potential of wearable technology in rehabilitation robotics, offering a scalable solution for long-term monitoring and management of motor symptoms in PD.

Since the device has now been validated on healthy participants, the next steps are to improve the device and then conduct trials on individuals with PD to capture tremor data. This will lead to a better understanding of how tremor impacts the daily life of people living with PD and their ability to perform ADL. By studying tremor in a home setting, data on individual tremor behavior, how tremor impacts ADL, and how often an individual's tremor occurs in a typical day can be determined. The collected tremor data can also be used to improve our understanding of the characteristics of tremor, such as frequency patterns and power spectral density, leading to better modelling, estimation, and control. The data could be used by a neurologist to better manage PD. It can also be used to design customized wearable assistive devices and adapt their performance to the peculiarities of each person and the changes that their tremor may undergo over time. Further, the data may be used to identify which joints are most important to monitor, allowing the size, weight, and complexity of future devices to be reduced.

Acknowledgment

Technical support from Eugen Porter and the commitment of the study participants, as well as all members of the WearME Lab who supported this work, is greatly appreciated.

References

[1] Parkinson's Foundation. Statistics. Accessed: Nov. 21, 2024. [Online]. Available: https://www.parkinson.org/understanding-parkinsons/statistics

[2] American Physical Therapy Association. Unified Parkinson's Disease Rating Scale (UPDRS), Movement Disorders Society (UP) Modified Unified Parkinson's Disease Rating Scale (MDS-UPDRS). Accessed: Nov. 21, 2024. [Online]. Available: https://www.apta.org/patient-care/evidence-based-practice-resources/test-measures/unified-parkinsons-disease-rating-scale-updrs-movement-disorders-society-mds-modified-unified-parkinsons-disease-rating-scale-mds-updrs

[3] American Parkinson Disease Association. Tremor. Accessed: Nov. 21, 2024. [Online]. Available: https://www.apdaparkinson.org/what-is-parkinsons/symptoms/tremor/

[4] International Parkinson and Movement Disorder Society. (2008) MDS-UPDRS the MDS-sponsored revision of the unified Parkinson's disease rating scale. Accessed: Nov. 21, 2024. [Online]. Available: https://www.movementdisorders.org/MDS-Files1/PDFs/Rating-Scales/MDS-UPDRS_English_FINAL.pdf

[5] C. Riviere, R. Rader, and P. Khosla, "Characteristics of hand motion of eye surgeons," in *Proceedings of the 19th Annual International Conference of the IEEE Engineering in Medicine and Biology Society*, vol. 4, 1997, pp. 1690–1693.

[6] S. Morrison, G. Kerr, and P. Silburn, "Bilateral tremor relations in Parkinson's disease: Effects of mechanical coupling and medication," *Parkinsonism & Related Disorders*, vol. 14, no. 4, pp. 298–308, 2008.

[7] B. Lin, I. Lee, S. Yang, Y. Lo, J. Lee, and J. Chen, "Design of an inertial-sensor-based data glove for hand function evaluation," *Sensors*, vol. 18, no. 1545, pp. 2–17, 2018.

[8] B. Fang, F. Sun, H. Liu, and D. Guo, "Development of a wearable device for motion capturing based on magnetic and inertial measurement units," *Sensors*, vol. 2017, no. 7594763, pp. 1–11, 2017.

[9] J. Connolly, J. Condell, B. O'Flynn, J. Sanchez, and P. Gardiner, "IMU sensor-based electronic goniometric glove for clinical finger movement analysis," *IEEE Sensors*, vol. 18, no. 3, pp. 1273–1281, 2018.

[10] Y. Zhou, A. Ibrahim, K. G. Hardy, M. E. Jenkins, M. D. Naish, and A. L. Trejos, "Design and preliminary performance assessment of a wearable tremor suppression glove," *IEEE Transactions on Biomedical Engineering*, vol. 68, no. 9, pp. 2846–2857, 2021.

[11] H. G. Kortier, V. I. Slutier, D. Roetenberg, and P. H. Veltink, "Assessment of hand kinematics using inertial and magnetic sensors," *Journal of Neuroengineering and Rehabilitiation*, vol. 11, no. 70, pp. 1–14, 2014.

[12] S. Das, B. Amoedo, F. De la Torre, and J. Hodgins, "Detecting Parkinsons' symptoms in uncontrolled home environments: A multiple instance learning approach," in *2012 Annual International Conference of the IEEE Engineering in Medicine and Biology Society*, 2012, pp. 3688–3691.

[13] Y. Zhou, M. E. Jenkins, M. D. Naish, and A. L. Trejos, "Characterization of parkinsonian hand tremor and validation of a high-order tremor estimator," *IEEE Transactions on Neural Systems and Rehabilitation Engineering*, vol. 26, no. 9, pp. 1823–1834, 2018.

An exoskeleton 'teacher-student' gait rehabilitation control system using real-time joint posture acquisition: A feasibility study.

Robert E. Trott, *Member, IEEE,* Jonathan T. Wheare, *Member, IEEE,* Michael P. Russo, Timothy J. Kleinig, Susan L. Hillier, Karen J. Reynolds, David A. Hobbs

***Abstract*—Recovering the ability to walk following the events of a stroke is important for community participation. For patients that are unable to weight bear, rehabilitation is difficult, for both themselves and for therapists that must manipulate their lower limbs. Exoskeletons can reduce the reliance on a patient's capability and reduce the exertion that therapists must provide to deliver manual rehabilitation. Providing intuitive methods of control is important to ensure that users have the inputs they need. We have implemented a simple joint acquisition system to be used in a 'teacher-student' paradigm, that can attach to a therapist's leg (teacher) to measure their hip and knee posture to then control the equivalent joints of an exoskeleton worn by a patient (student). This would provide a therapist with direct control of their patient's leg, which they can manipulate under supervision, to guide a patient through trajectories they would otherwise provide manual support to achieve. The feasibility of the system is demonstrated with one subject as the teacher and the exoskeleton (without a user) as the student. Using motion capture we assess the reference tracking error and the phase delay in the system through single leg standing gait using three different gains. With high proportional gain the mean (SD) phase delay was 11.1 (0.7) ms and 8.4 (4.9) ms for the hip and knee, respectively. Using the same gain the joints were tracked through normal gait ROM with a mean (SD) error of 7.7 (6.1) degrees and 7.6 (5.4) degrees for the hip and knee, respectively. This early-stage feasibility study demonstrated that a low cost 'teacher-student' control system could control a lower limb exoskeleton.**

I. Introduction

Gait is central to mobility and enhances community participation [1]. Hence, in a world where we are often faced with complex mobility scenarios, restoring or improving a person's mobility post-injury is a critical effort and recovery of a person's gait, where possible, is often cited as a high priority [1]. There are few activities that can easily be completed without having a period of gait in between. Gait is often accompanied by activities such as sit-to-stand and stair ascent/descent, reflecting the complexity of the environments we live in [2].

* Research supported by the Medical Device Future Fund Cardiovascular Health Mission – 2021 (Grant #2017290)

R. E. Trott and K. J. Reynolds are with the Medical Device Research Institute (MDRI), College of Science and Engineering (CSE), Flinders University, Adelaide, Australia (robert.trott@flinders.edu.au)

J. Wheare is with the CSE of Flinders University of Adelaide, Australia

M. P. Russo is with the Biomechanics and Implants Laboratory, MDRI, CSE of Flinders University, Adelaide Australia

T. J. Kleinig is with the Royal Adelaide Hospital, Adelaide, Australia

S. L. Hillier is with the Allied Health & Human Performance,

Innovation, IMPlementation and Clinical Translation (IIMPACT) in Health, University of South Australia (UniSA), Adelaide, Australia

D. A. Hobbs. is with the MDRI, CSE, Flinders University, Adelaide, Australia, and with IIMPACT in Health, UniSA, Adelaide, Australia

A variety of therapies that aim to restore gait exist, ranging from manual therapies that manipulate a patient's limbs, treadmill training, Body Weight Support (BWS) overground walking and their combinations, through to robotic assisted therapy using exoskeletons. The goal of these therapies is to improve conditioning of the limb and to stimulate the neuroplasticity that is inherent in learning [3], [4], [5], [6]. Across these therapies there is a common theme of kinetic support, where the demands of gait are supported to promote training.

Therapy must focus on the fundamental principles of motor learning [3]; among these principles patients should receive adequate controlled repetitions and intensity delivered across multiple sessions that are relevant to the task, collectively known as dosage [7], [8], [9]. The same principles that promote recovery can also apply maladaptively and it is important to practice good quality movements, and discourage movement strategies that may initially be beneficial, but detrimental in the long term [10].

Therapy is a taxing and repetitious endeavor for both the person and therapist [11], [12], [13], requiring hours of physical work and learning. Within the dosage of rehabilitation, there is a threshold to what an individual can tolerate that needs to be carefully managed so that therapies are sufficiently challenging without being detrimental. Conventional and treadmill training type rehabilitation techniques have a high degree of manual input from up to three therapists, placing a strain on the therapists [14], [15]. Prolonged strain and excessive overwork can limit the amount of therapy they themselves can deliver, and increase the risk of developing musculoskeletal disorders [11], [12], [13]. Variations within and between therapists can also limit the treatment consistency a patient receives [16].

Exoskeleton technology, that was initially intended for industrial applications, has been quickly adapted for the rehabilitation setting. Exoskeletons offer the promise of high rehabilitation dosage with improved consistency, by increasing the number of repetitions and the intensity a patient receives [12], [17], while simultaneously reducing therapist burden as the manual work is applied by the machine. Despite these advantages, exoskeletons have never been considered a substitute for conventional therapies [11], [18]. They have only recently been recognised as complementary to conventional therapy [19], [20].

Therapists and exoskeleton wearers have different methods that they can use to control an exoskeleton. These methods often focus on the initiation of a movement profile that is then completed with or without input from the exoskeleton wearer. For example, buttons can be used to

trigger a step that is completed without user intention [21]. Such strategies are good for general mobility but lack critical engagement from the wearer and may not maximally stimulate intended rehabilitation outcomes [22].

Upper limb pairing between two devices, one as a student and the other as a teacher, has been demonstrated a number of times and may help boost engagement [23]. Despite the critical need to restore gait, this paradigm has been sparsely applied in the lower limbs [24], [25]. The former [24], demonstrated haptic coupling between two users wearing exoskeletons and the ability of their system to control the strength of that coupling and feedback torque between the wearers. The latter [25] used motion capture to measure hip angles from oner person (teacher) and apply these to another person (student) wearing an artificial pneumatic muscle. Coupling a teacher to a student may leverage the advantages of conventional and exoskeleton mediated gait rehabilitation. An exoskeleton guided by the therapist in a consistent manner may be used to recreate a gait cycle and provide the manual input otherwise provided by a therapist, reducing their burden. An initial barrier for such a configuration is the cost of entry, as motion capture technology [25], or two exoskeletons are needed, along with technical challenges to integrate the systems. There are, however, a variety of options that can be used to affordably and simply capture the basic kinematics of a therapist (teacher) for application on an exoskeleton, which in most cases are sagittally constrained.

Here we aim to demonstrate the basic feasibility of a lower limb exoskeleton coupling using a 'teacher-student' paradigm. Sagittal kinematics are captured from the teacher device using readily available sensors to capture hip and knee flexion and extension, and these kinematics are applied to a powered lower limb exoskeleton without an occupant (the student). Our system lacks the haptic coupling offered by dual exoskeleton paradigms [24], but reduces the complexity and cost, and doesn't rely on motion capture [25]. We assess the accuracy of capturing the kinematics from the teacher and their application on the student, and the phase delay between the two.

II. Methods

A. System description

A lower limb exoskeleton (Fourier Intelligence, ExoMotus-X2 exoskeleton) with minor modifications (student) was paired with a joint acquisition system (henceforth, teacher system) composed of a microcontroller (Seeed, Seeeduino Xiao) [26] and two rotary potentiometers (Panasonic EVW-AE4001B14) (Figure 1). The exoskeleton has 4 total active degrees of freedom for the left and right hip and knee, respectively, and 2 passive degrees of freedom at the ankles. The teacher system potentiometers were fixed to custom 3D printed brackets with a bearing to isolate axial and transverse forces from the potentiometer and allow free rotation. Acrylic arms with slots were fixed to the brackets (Figure 1). The potentiometers were located over the center of rotation of the right hip and knee, respectively.

Communication within the exoskeleton components is managed using the open-source software CANOpen Robot Controller (CORC) [27], which uses the Robot Operating System (ROS1) [28], CANbus, and C++. The CORC controller updates the system at 333 Hz. The teacher system uses a Seeeduino Xiao (clock speed 48 MHz), sampled by an ADC at 350 ksps and an effective resolution of 16-bits per channel for both the hip and the knee sensors [26].

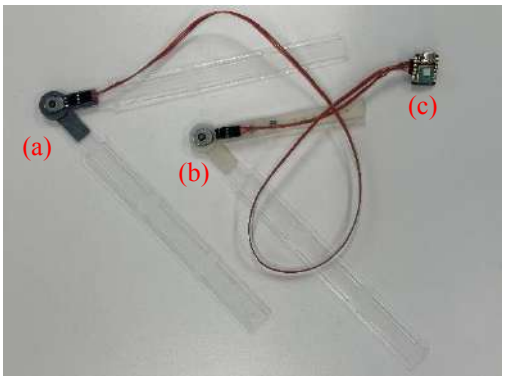


Figure 1. The teacher system with: (a) knee joint, (b) hip joint with waist bracket, and (c) Seeeduino Xiao Microcontroller.

These hip and knee angles were published to the CORC interface as ROS topics using the rosserial [29] Arduino library. CORC also received joint angle information from the exoskeleton via CANbus, and this information was used by both the controller and published via ROS topics. A custom feedback controller in CORC generated the motor velocity targets by multiplying the difference between the teacher and student joint positions by a proportional gain that is varied based on the trial condition as expressed in eq 1. The CORC node then sent these velocity targets to the exoskeleton via CANbus.

$$\dot{X} = k_p \cdot (X_{teacher} - X_{student}) \quad \text{- (1)}$$



Figure 2. The Fourier Intelligence ExoMotus X2 used in this study (left) and the teacher system worn on the subject during piloting (right).

B. Experimental Set-Up

The system was set up in the Rehabilitation and Motion Analysis Laboratory of Flinders University. Ten Vicon 3D motion capture cameras (Vicon Motion Systems, Oxford, United Kingdom) were used to acquire 3D kinematics at 100 Hz. Motion capture was used to determine the phase delay between the teacher and when that motion was applied on the exoskeleton. The exoskeleton was suspended from a BWS system in a neutral standing position above the ground in the center of the room and connected to a PC running CORC and

the teacher system. Retro-reflective markers (Ø10 mm) were placed on both the left and right sides of the exoskeleton over the center of rotation of the ankle, knee, and hip, with two additional markers on the hip motor cover (Figure 2, left).

Retro-reflective markers (Ø10 mm) were also placed on a single subject from the research team (teacher) using the Vicon plug-in-gait pipeline to obtain hip and knee joint angles (Figure 3). Medial knee markers were added to better define the knee axis. The hip joint sensor of the teacher system was approximately placed over the center of rotation of the hip, and the knee joint was placed under the lateral plug-in gait knee marker. The teacher system was fixed to the user using strapping and further fixed using adhesive tape. The top of the hip system slipped over the subject's waist band and was fixed to the user using strong adhesive tape to reduce relative motion between the system and the wearer.

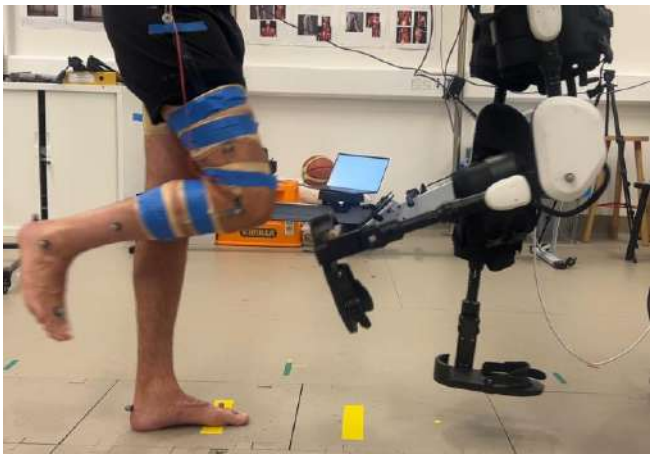


Figure 3. Video image taken during data collecton with both the subject/teacher (left) and the exoskeleton/student (right) with retro-reflective markers. The subject is wearing the teacher system, and the exoskeleton responds to the subject's posture.

C. Data Acquisition

The motion capture system was calibrated on the day, immediately prior to data collection. The subject and exoskeleton were marked up as described in the experimental set-up. The teacher system was fitted to the subject and the system started. The exoskeleton used a hand controller configured as a dead-man switch to enable motion of the system. The state of this controller as well as the internal communications between the exoskeleton and joint capture were captured using the rosbag [30] system, which provided time-stamped recordings of all published ROS messages. Information captured in these recordings included the hand controller status, the target angles of the teacher system, the reported angles of the student exoskeleton, and the reported effort of the exoskeleton motors. The session was broken into three trials of single leg standing gait using both the hip and knee, with three different proportional gains. The gain controlled how aggressively the system attempted to track the reference provided by the teacher system. The three proportional gains, k_p, are referred to as low, medium, and high and correspond to values of 3, 5, and 10.

The three cyclic gait activities were intended to characterise the ability of the system to track both joints and to model the assistance that a therapist would otherwise provide in an assisted walking rehabilitation task. In all activities the subject remained in the center of the room and gripped the exoskeleton for stability and to prevent it from rotating and swinging the BWS. Locating the subject behind the exoskeleton allowed the teacher to supervise both the exoskeleton and a live terminal output of the angles reported by the teacher system. Observation of the exoskeleton is similar to how a therapist responds to a patient's posture during rehabilitation. Between trials the user adjusted the teacher system if necessary. Generally, each trail used the following structure:

1. Subject/teacher was positioned in the middle of the room behind the exoskeleton in neutral stance;
2. Exoskeleton/student was positioned in a neutral stance and held by subject/teacher;
3. Motion recording was started;
4. ROS data collection was started;
5. Exoskeleton/student enabled using dead-man switch;
6. Subject/teacher conducted prescribed movements; and
7. All recordings were stopped in reverse order.

D. Analysis

All motion capture data was processed in Vicon Nexus 2.12 and imported into MATLAB (R2022b The MathWorks Inc, Natick, MA, USA). Teacher sagittal angles were outputted from the Vicon plug-in gait model. Data were trimmed close to the beginning and cessation of a trial. Exoskeleton knee flexion-extension was calculated using vectors made from the ankle, knee, and hip markers. While hip flexion-extension was calculated using vectors made from the knee, hip and one of the additional markers on the hip motor cover. An exoskeleton referred normal vector was produced from two opposing markers at the left and right hip motor cover. Sagittal joint angles were calculated by taking the vector projection on the sagittal normal plane using first principles. Peak angles were automatically detected and erroneous values manually excluded. Both the tracking error and the phase delay were calculated from the teacher to student for like joints. The tracking error was defined as mean absolute joint angle difference, and the phase delay was defined as the timing difference between when a peak value occurred.

III. Results

Figures 4 and 5 show the hip and knee angles for both the subject and the exoskeleton during cyclic gait at low and high gain, respectively. Considering low gain first, the hip performs well around neutral stance and in extension, however, cannot track the joint accurately into flexion. The system is better at tracking the knee, though less so toward extension. Across 10 cycles the mean (SD) tracking error was 12.7° (9.6°) for the hip and 17.4° (11.9°) for the knee. The mean (SD) hip and knee phase delay of the system was 32.0 (3.4) ms and 27.1 (6.3) ms, respectively. There is an offset between the exoskeleton and subject hip joint at stance and this persists and is amplified at the peak flexion. An offset was apparent between the respective knee joints at the beginning of the trial, however, at this time the exoskeleton was prohibited from moving.

For both the hip and knee, compared to the low gain, medium gain improved the mean (SD) phase delay, 19.3 (0.9) ms and 17.1 (5.1) ms, and reduced the tracking error, 9.4° (6.5°) and

13.2 ° (10.2°), respectively. Using a high gain, the mean (SD) tracking error for the hip and knee was 7.7° (6.1°) and 7.6° (5.4°), respectively, and the phase delay was 11.1 (0.7) ms and 8.4 (4.9) ms, respectively. The high gain resulted in much better performance (see Figure 5). The exoskeleton gait profile was able to closely follow the subject at the knee and capture the slight knee flexion that typically occurs through the stance phase of gait despite the unconstrained nature of this task. The exoskeleton hip again closely followed the subject into extension, though still had difficulty tracking the peaks in subject hip flexion. Again, the offset between the respective hip joints persists with high gain. The results for all joint tracking errors and phase lags are summarised in Table I.

TABLE I – Summary of the gait cycle phase delay and tracking errors.

	Phase delay (ms, peak to peak)			Mean Absolute Joint Error (degrees)		
Gain	Low	Medium	High	Low	Medium	High
Hip (Mean, (sd))	32 (3.4)	19.3 (0.9)	11.1 (0.7)	12.7 (9.6)	9.4 (6.5)	7.7 (6.1)
Knee (Mean (sd))	27.1 (6.3)	17.1 (5.1)	8.4 (4.9)	17.4 (11.9)	13.2 (10.2)	7.6 (5.4)

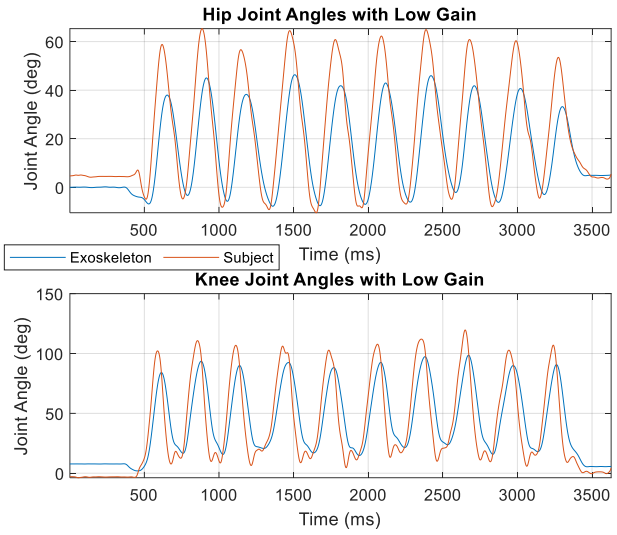


Figure 4. Subject/Teacher (orange) and exoskeleton/student (blue) motion capture angles with low gain.

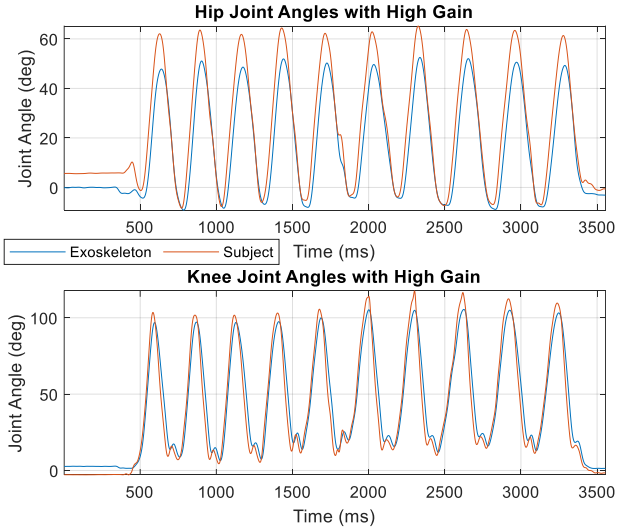


Figure 5. Subject/Teacher (orange) and exoskeleton/student (blue) motion capture angles with high gain.

To better understand the source of the error, the joint values captured from the teacher system, as opposed to motion capture, and those of the exoskeleton in the high gain scenario were compared (Figure 6). The CORC system updates at 333Hz and data was captured after motion capture had commenced, but before the subject began the task. Figure 6 shows close alignment between the acquired joint angles and those of the exoskeleton and the mean (SD) tracking error for the hip and knee were 4.1° (2.6°) and 6.8° (4.4°) respectively.

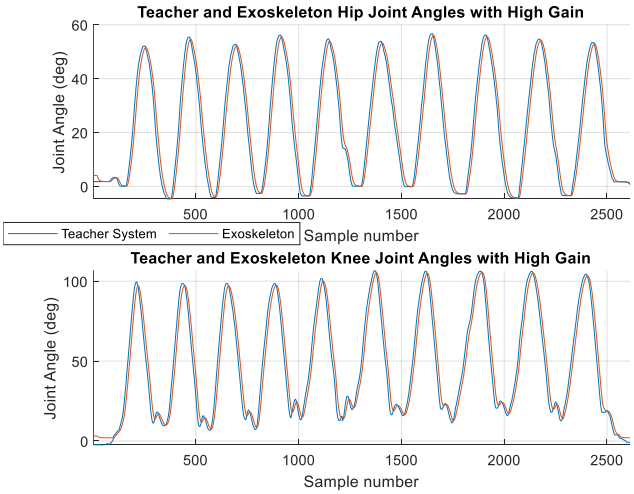


Figure 6. Subject/Teacher (orange) and exoskeleton/student (blue) system angles when using high gain. Angles are aquired from the system, not motion capture.

IV. Discussion

In this proof-of-concept pilot study we developed a system to capture the hip and knee posture of a single subject (teacher) and used that posture to provide a control reference to the same joints on a lower limb exoskeleton (student). We used motion capture, using the plug-in gait protocol as a validation tool, to acquire the subject's lower limb posture while simultaneously capturing the joint postures of the exoskeleton (angles calculated using first principles). From this we were able to characterise the error between the posture of the teacher and the exoskeleton (student) tracking the reference and the phase delay between capture and reproduction between the two. Others have used motion capture to acquire subject posture and apply that posture to an exoskeleton [25], or have used two of the same exoskeletons with differing strengths of feedback between their two postures [24].

Using soft pneumatic actuators the system in [25] achieved a hip angle error of approximately 5° with a phase delay of 400ms, and with joint angle prediction were able to reduce the phase delay to 100ms [25]. In comparison our system experienced higher error (7.7° at the hip), between the motion capture and the subsequent exoskeleton motion, with a lower phase delay (11.1 ms), though their exoskeleton was worn by a person. The system in [24] passed haptic feedback between able bodied users so that one user could feel the intention of the other and try to follow. With a hard stiffness between the two exoskeletons, they were able to achieve 3° mean absolute joint angle difference at the hip and knee, compared to our 7.7° and 7.6°, and did not characterize phase delay, though it appeared to be minimal [24]. The error we report is between

the human state captured through motion capture, not that the teacher system sensors, and the exoskeleton. The system in [25] uses motion capture as the input to their control system and reports the error as the difference, and [24] reports the error between two sets of exoskeleton joints. But importantly no system, including ours, characterizes the error between the two humans. Subsequent analysis showed our teacher system captured angles were faithfully reproduced on the exoskeleton (4.1° and 6.8° tracking error, for the hip and knee, respectively), implying the source of our error came from the teacher system configuration and its fit on the wearer. Generally, this means that while there were errors between the angles measured using plug-in gait and the exoskeleton, there was good agreement between the system driving the exoskeleton (teacher system) and the exoskeleton, indicating reliability in the teacher system).

The error between the respective joints on the subject and the exoskeleton might not be as important as it seems. Minimal clinically important differences (or MCIDs) in hip and knee flexion/extension measurement have been reported as 5.8° [31] and 6.4° [32], respectively, in osteoarthritis patients. Exoskeletons do not align perfectly with the user. The revolute joint at the knee is incapable of recreating the sliding hinge mechanism of the human knee and there will always be a need for some compliance between an exoskeleton and it's wearer. Our system uses supervised control, that is, the teacher is able to alter the state of the exoskeleton according to their posture, but can use visual feedback to alter the student posture to a desired state. Similar to how a therapist guides a patient's limb in overground walking treadmill training, the teacher can alter their posture to induce a change in the student, irrespective of the error between the two.

Our system differentiates from [24] and [25] in its accessibility and affordability, and the use of motion capture to validate performance of the system. We found that when the exoskeleton was set with a high gain there was good agreement between the exoskeleton posture and the subject through motion capture, and the phase delay between the two was low, demonstrating the viability of the joint capture system. As expected, when using a low gain, the exoskeleton was not able to track the subject's posture as well. There was apparent relative motion between the subject and the hip joint of the teacher system. The teacher system was strapped to the thigh and shank using acrylic arms, however, at the hip joint the superior arm was slipped over the shorts of the wearer and secured using tape. There was no mechanism to prevent the shorts from moving relative to the subject and this likely contributed to the error in peak flexion between the subject and the exoskeleton.

Therapist burden is a problem in rehabilitation [11], [12], [13] and can be limiting of the therapy time a patient receives when there is increased emphasis on delivering adequate dosage [7], [8], [9]. Exoskeletons can be difficult to access in a rehabilitation setting, and their efficacy and status as being complimentary to and not a substitute for conventional rehabilitation may be limiting their adoption [19]. Using exoskeletons differently by providing therapists and patients with more intuitive control may boost engagement, and rehabilitation outcomes. Using an exoskeleton to unburden a therapist by providing the therapist with intuitive and direct control may be helpful in these instances.

Our study is limited in that it was applied with a single user, and the exoskeleton was used without an operator. In practice an exoskeleton wearer must adopt a degree of passivity and move with the device, and this may be difficult in instances where the user has motor deficits or experiences spasticity [33]. An exoskeleton with a user will have more mass and this will likely affect the ability of the exoskeleton to track a reference and add further phase delay between the teacher and the student coupling. The joint tracking system used rotary potentiometers, and these were applied in this system without addressing linearity and this may have affected the ability of the system to track joint angles at the extremes, and may have contributed further to tracking the error near peak hip flexion.

An issue this system does not address is feedback to the person controlling the exoskeleton, which can be dangerous for the exoskeleton wearer [24]. The method that we have demonstrated has no impedance between the teacher system and how the exoskeleton responds, an idea that has been addressed by others [24]. Communication between patient and clinician is an important part of rehabilitation and is essential in this model where the clinician is in control of their patient. Exoskeletons are expensive and paradigms that use two exoskeletons, one as teacher and the other as a student, doubly so. Our teacher system is economical (material cost, AUD$30), uses a straightforward implementation, and may reduce the financial barriers to exoskeleton adoption, and increase utility.

The error in hip posture was likely a result of relative motion between the shorts, where the sensor arm was adhered, and the subject. Future iterations of the design and fixation method should focus on this as it was likely the largest source of error in the system. The knee posture obtained through plug-in gait also needs to be considered cautiously. The skin site for the lateral right retroreflective marker was identified, and the potentiometer was placed over this site, but left floating. The reflective motion capture marker was then placed over this site and would have been able to move relative to the site marked. This doesn't seem to have affected the results significantly and at high gain the knee was the better performing joint. The knee has a sliding center of rotation, which a stationary marker on the skin also cannot track. Future iterations of the design will benefit from having a reusable fixation method and instructions that don't rely on expert positioning of the system elements.

V. Conclusion

In this paper we present a low-cost system for capturing hip and knee joint posture of a subject (teacher) and used those postures as the tracking reference for the same limb of a powered lower limb exoskeleton (student). The premise for this type of control is to give therapists an intuitive mechanism for manipulating a person's limbs in rehabilitation settings, to gain precise control and reduce the physical exertion required to deliver gait rehabilitation therapy. Our proof-of-concept system used a single subject and an unworn exoskeleton to characterise the tracking error and the phase delay between the subject (teacher) and the exoskeleton (student). The phase delay was low when a high gain was applied. In the future, we intend on replicating this work with the exoskeleton worn on

a person(s) as the student, and the teacher system applied to both lateralities of the teacher to control both limbs. Furthermore, we aim to investigate and characterise the exoskeleton/user interface.

ACKNOWLEDGMENT

This work was funded through the Medical Device Future Fund (MRFF) Cardiovascular Health Mission – 2021 (Grant #2017290). The authors would like to thank the Flinders University Engineering Services Team for their expert unwavering and enthusiastic support.

REFERENCES

[1] World Health Organisation, ICF : International classification of functioning, disability and health. Geneva: Geneva : World Health Organization, 2001.

[2] A. Kralj, R. J. Jaeger, and M. Munih, "Analysis of standing up and sitting down in humans Definitions and normative data presentation," J Biomech, vol. 23, no. 11, pp. 1123–1138, 1990.

[3] J. A. Kleim and T. A. Jones, "Principles of Experience-Dependent Neural Plasticity: Implications for Rehabilitation After Brain Damage," 2008, [Rockville, MD] : doi: 10.1044/1092-4388(2008/018).

[4] R. J. Nudo, "Recovery after brain injury: mechanisms and principles," Front Hum Neurosci, vol. 7, no. December, pp. 1–14, 2013, doi: 10.3389/fnhum.2013.00887.

[5] B. Kolb and A. Muhammad, "Harnessing the power of neuroplasticity for intervention," Front Hum Neurosci, vol. 8, no. June, pp. 1–13, 2014, doi: 10.3389/fnhum.2014.00377.

[6] W. H. R. Miltner, "Plasticity and reorganization in the rehabilitation of stroke: The Constraint-Induced Movement Therapy (CIMT) example," Zeitschrift fur Psychologie / Journal of Psychology, vol. 224, no. 2, pp. 91–101, 2016, doi: 10.1027/2151-2604/a000243.

[7] A. Esquenazi and A. Packel, "Robotic-assisted gait training and restoration," Am J Phys Med Rehabil, vol. 91, no. 11 SUPPL.3, 2012, doi: 10.1097/PHM.0b013e31826bce18.

[8] M. Gilliaux et al., "Upper limb robot-assisted therapy in cerebral palsy: A single-blind randomized controlled trial," Neurorehabil Neural Repair, vol. 29, no. 2, pp. 183–192, Mar. 2015, doi: 10.1177/1545968314541172.

[9] S. E. Fasoli, B. Ladenheim, J. Mast, and H. I. Krebs, "New horizons for robot-assisted therapy in pediatrics," 2012. doi: 10.1097/PHM.0b013e31826bcff4.

[10] J. W. Krakauer, S. T. Carmichael, D. Corbett, and G. F. Wittenberg, "Getting Neurorehabilitation Right," Neurorehabil Neural Repair, vol. 26, no. 8, pp. 923–931, Oct. 2012, doi: 10.1177/1545968312440745.

[11] A. Rodríguez-Fernández, J. Lobo-Prat, and J. M. Font Llagunes, "Systematic review on wearable lower-limb exoskeletons for gait training in neuromuscular impairments," J Neuroeng Rehabil, vol. 18, no. 1, pp. 1–21, 2021, doi: 10.1186/s12984-021-00815-5.

[12] I. Díaz, J. J. Gil, and E. Sánchez, "Lower-Limb Robotic Rehabilitation: Literature Review and Challenges," Journal of Robotics, vol. 2011, no. i, pp. 1–11, 2011, doi: 10.1155/2011/759764.

[13] S. Zabel et al., "Physiotherapy students' perspectives on the use and implementation of exoskeletons as a rehabilitative technology in clinical settings," Disabil Rehabil Assist Technol, vol. 0, no. 0, pp. 1–8, 2020, doi: 10.1080/17483107.2020.1818139.

[14] S. Fisher, L. Lucas, and T. Adam Thrasher, "Robot-Assisted Gait Training for Patients with Hemiparesis Due to Stroke," Top Stroke Rehabil, vol. 18, no. 3, pp. 269–276, May 2011, doi: 10.1310/tsr1803-269.

[15] E. Y. Y. Cheung, T. K. W. Ng, K. K. K. Yu, R. L. C. Kwan, and G. L. Y. Cheing, "Robot-Assisted Training for People With Spinal Cord Injury: A Meta-Analysis," Arch Phys Med Rehabil, vol. 98, no. 11, pp. 2320-2331.e12, 2017, doi: 10.1016/j.apmr.2017.05.015.

[16] S. Hesse, A. Waldner, and C. Tomelleri, "Innovative gait robot for the repetitive practice of floor walking and stair climbing up and down in stroke patients," J Neuroeng Rehabil, vol. 7, no. 1, pp. 1–10, 2010, doi: 10.1186/1743-0003-7-30.

[17] S. Hesse, C. Tomelleri, A. Bardeleben, C. Werner, and A. Waldner, "Robot-assisted practice of gait and stair climbing in nonambulatory stroke patients," J Rehabil Res Dev, vol. 49, no. 4, pp. 613–622, 2012.

[18] J. Mehrholz, S. Thomas, C. Werner, J. Kugler, M. Pohl, and B. Elsner, "Electromechanical-assisted training for walking after stroke," Cochrane Database of Systematic Reviews, pp. 188–189, May 2017, doi: 10.1002/14651858.CD006185.pub4.

[19] J. Mehrholz, M. Pohl, J. Kugler, and B. Elsner, "Electromechanical-Assisted Training for Walking After Stroke: Update of the Evidence," May 01, 2021, Wolters Kluwer Health. doi: 10.1161/STROKEAHA.120.033755.

[20] M. Talaty and A. Esquenazi, "Feasibility and outcomes of supplemental gait training by robotic and conventional means in acute stroke rehabilitation," J Neuroeng Rehabil, vol. 20, no. 1, Dec. 2023, doi: 10.1186/s12984-023-01243-3.

[21] M. Bortole, A. J. del Ama, E. Rocon, J. C. Moreno, F. Brunetti, and J. L. Pons, "A robotic exoskeleton for overground gait rehabilitation," Proc IEEE Int Conf Robot Autom, pp. 3356–3361, 2013, doi: 10.1109/ICRA.2013.6631045.

[22] J. Vaughan-Graham, D. Brooks, L. Rose, G. Nejat, J. L. Pons, and K. Patterson, "Exoskeleton use in post-stroke gait rehabilitation: A qualitative study of the perspectives of persons post-stroke and physiotherapists," J Neuroeng Rehabil, vol. 17, no. 1, pp. 1–15, 2020, doi: 10.1186/s12984-020-00750-x.

[23] E. B. Küçüktabak, S. J. Kim, Y. Wen, K. Lynch, and J. L. Pons, "Human-machine-human interaction in motor control and rehabilitation: a review," Dec. 01, 2021, BioMed Central Ltd. doi: 10.1186/s12984-021-00974-5.

[24] E. B. Kucuktabak, Y. Wen, M. Short, E. Demirbas, K. Lynch, and J. Pons, "Virtual Physical Coupling of Two Lower-Limb Exoskeletons," in IEEE International Conference on Rehabilitation Robotics, IEEE Computer Society, 2023. doi: 10.1109/ICORR58425.2023.10304601.

[25] T. Tagami et al., "Development of Master-slave Type Lower Limb Motion Teaching System," in 2018 IEEE/RSJ International Conference on Intelligent Robots and Systems (IROS), 2018, pp. 2762–2767. doi: 10.1109/IROS.2018.8593737.

[26] Microchip, 2021, SAM D21/DA1 Family, URL: https://ww1.microchip.com/downloads/en/DeviceDoc/SAM-D21DA1-Family-Data-Sheet-DS40001882G.pdf

[27] Fong J., Küçüktabak E, Crocher V, Tan Y, Lynch K, Pons J, Oetomo D, Moreno J, Masood J, Schneider U, Maufroy C, Pons J, 2022. CANopen Robot Controller (CORC): An Open Software Stack for Human Robot Interaction Development. In: Moreno, J.C., Masood, J., Schneider, U., Maufroy, C., Pons, J.L. (eds) Wearable Robotics: Challenges and Trends. WeRob 2020. Biosystems & Biorobotics, vol 27. Springer, Cham.

[28] Quigley M, Conley K, Gerkey B, Faust J, Foote T, Leibs J, Wheeler R, Ng AY. ROS: an open-source Robot Operating System. InICRA workshop on open source software 2009 May 12 (Vol. 3, No. 3.2, p. 5).

[29] Ferguson M., 2024, rosserial URL: https://wiki.ros.org/rosserial

[30] Field T., Leibs J., Bowman J., Thomas D., Perron J., 2024, rosbag URL: https://wiki.ros.org/rosbag

[31] Guzik, A., Drużbicki, M., Perenc, L., Wolan-Nieroda, A., Turolla, A. and Kiper, P. (2021) 'Establishing the Minimal Clinically Important Differences for Sagittal Hip Range of Motion in Chronic Stroke Patients', Frontiers in Neurology, 12. Available at: https://doi.org/10.3389/fneur.2021.700190.

[32] Silva, M.D.C., Woodward, A.P., Fearon, A.M., Perriman, D.M., Spencer, T.J., Couldrick, J.M. and Scarvell, J.M. (2024) 'Minimal clinically important change of knee flexion in people with knee osteoarthritis after non-surgical interventions using a meta-analytical approach', Systematic Reviews, 13(1). Available at: https://doi.org/10.1186/s13643-023-02393-0.

[33] A. Ekelem and M. Goldfarb, "Supplemental Stimulation Improves Swing Phase Kinematics During Exoskeleton Assisted Gait of SCI Subjects With Severe Muscle Spasticity," Front Neurosci, vol. 12, no. June, pp. 1–9, Jun. 2018, doi: 10.3389/fnins.2018.00374.

From Lab to Life: Correlating Lab-based Motion Capture and Field-based Wearable Sensor Metrics to Assess Motor Impairments in people with Multiple Sclerosis

Paula Villa Fulton[1], Valerie Thorbecke[1], Benedikt Becker[2], Philipp Gulde[1], Joachim Hermsdörfer[1]

***Abstract*— Understanding the relationship between lab-based kinematic metrics and real-world wearable sensor data offers valuable insights into motor dysfunction in multiple sclerosis (MS). This study explores the correlations between task specific metrics derived from motion capture systems during Tea Making and Drinking tasks and wrist-worn inertial measurement units (IMU). Path length hand differences (PL_Diff) in lab tasks exhibited strong correlations with the Expanded Disability Status Scale (EDSS)(r = 0.64, adjusted p = 0.02), indicating their potential as markers of disease severity. Consistent correlations between lab-based kinematics and wearable sensor metrics across different activities of daily living highlight the potential of IMU data for real-world motor impairment monitoring. This emphasizes the role of wearable assessments in improving the sensitivity and scalability of MS progression tracking.**

I. INTRODUCTION

Multiple Sclerosis (MS) is a chronic and progressive autoimmune disease affecting the central nervous system, with peak onset typically occurring in early adulthood [1]. Even when symptoms appear mild, maximum performance tests can detect underlying impairments [2]. However, commonly used clinical tools such as the Expanded Disability Status Scale (EDSS) [3] primarily assess static or isolated functional deficits, failing to capture the dynamic motor challenges people with MS (pwMS) face in real-world environments.

Motor impairments often manifest in subtle, task-specific ways. Submaximal tasks, performed at less than maximal effort, are particularly relevant because many real-world activities do not require peak performance but instead demand sustained coordination, precision, and adaptability. Submaximal behaviors, such as Activities of Daily Living (ADL), may reveal latent motor dysfunctions, making them crucial for real-world monitoring.

Despite the importance of ADLs, their relationship with MS-related motor impairments remains poorly understood [4]. While EDSS effectively quantifies neurological deficits, it does not fully capture how these impairments impact daily task performance. In contrast, wearable sensors and kinematic analyses provide a more comprehensive assessment by continuously monitoring movement dynamics in both structured and spontaneous activities. These technologies have demonstrated sensitivity to subtle motor changes that standard clinical tests may overlook [5]. Prior studies have shown their efficacy in detecting motor differences in populations such as young adults, the elderly, and stroke survivors [6], [7], yet their application to ADL performance in pwMS remains largely unexplored.



Fig. 1. Living laboratory setup with 9 Qualisys motion capture cameras.

This study bridges the gap between traditional clinical assessments and real-world functionality by integrating lab-based kinematic data with real-world inertial measurement unit (IMU) metrics. Laboratory-based ADL kinematics, obtained via state-of-the-art motion capture systems, provide high-resolution insights into motor performance under controlled conditions, while IMU-derived metrics offer scalable, continuous monitoring in free-living environments. Together, these approaches allow for the identification of both task-specific movement patterns and task-independent biomarkers of disease severity, complementing clinical scores such as EDSS.

Since kinematic parameters, such as movement smoothness, are highly task-dependent [8], we examine two ADLs with differing complexities: Tea Making task, a multi-step task requiring coordination and planning, and drinking from a glass, a simpler motor action. By identifying robust kinematic markers across these tasks, we aim to enhance the sensitivity of motor assessments, ultimately improving real-world disease monitoring and MS management.

This study was funded by the Federal Ministry of Education and Research and the Free State of Bavaria under the Federal Government's Excellence Strategy.

Ethical approval: All procedures performed in studies involving human participants were in accordance with the ethical standards of the Ethics Committee of the Technical University of Munich (reference number: 2023-212-S-KH).

[1]Chair of Human Movement Sciences, Technical University of Munich, Munich, Germany

[2]Neuro-Kopf-Zentrum, Department of Neurology, Rechts der Isar Hospital, Munich, Germany

II. Materials & Methods

A. Participants

This study involved 21 pwMS and 21 age-matched healthy controls. The pwMS group had a mean age of 46.2 ± 11.4 years (22-62 years), while the control group averaged 44.7 ± 10.6 years (24-60 years). Both groups included 61.9% females. MS participants exhibited mild to moderate disability, with an average EDSS score of 2.3 ± 1.7 (0-6).

The study is part of the TUM Innovation Network, eXprt, and received ethical approval from the Ethics Committee of the Technical University of Munich (reference: 2023-212-S-KH). Written informed consent was obtained from all participants prior to their participation.

B. Clinical Assessments

Participants completed clinical assessments to evaluate motor and functional abilities:

- **Nine-Hole Peg Test (PEG):** Trial duration [s].
- **Box and Blocks Test (BB):** Blocks transported per minute [1/min].
- **Grip Strength (GRIP):** sex-specific z-scores based on kilogram force [kg].
- **Tapping Tasks (TAP):** Finger tapping speed [Hz].
- **Reaction Task (REACT):** Average reaction speed [ms].
- **Two-Point Discrimination (DISCR):** Minimal detectable distance [mm] on the index finger.

Higher values generally indicate better performance, except for PEG, DISCR and REACT. Results for dominant and non-dominant upper limbs were averaged, and a laterality index was calculated to reflect performance asymmetry, with higher values indicating greater lateralization of impairments.

The Normalized Difference quantifies the performance asymmetry between the dominant (DL) and non-dominant (NDL) limbs:

$$\text{Normalized Difference} = \frac{|\text{DL} - \text{NDL}|}{(\text{DL} + \text{NDL})/2}$$

C. Lab-Based Kinematics

Motor performance was assessed through two everyday activities: preparing a cup of tea [6], [7] and drinking from a glass [9]. These tasks mimic real-world demands while enabling precise kinematic measurements. Hand movements were recorded using an optoelectronic motion capture system with nine Miqus cameras (Qualisys Inc., Gothenburg, Sweden), tracking reflective markers at 120 Hz. Extracted kinematic parameters included:

- **Trial Duration (TD):** Time to complete the task, excluding the water boiling wait [s].
- **Path Length (PL):** Length of hand trajectories [m].
- **Relative Activity (RA):** Time one hand exceeds a velocity of 0.05 m/s [s].
- **Mean Peak Velocity (MP):** Average velocity peaks over 0.05 m/s [m/s].
- **Number of Peaks per Meter (NP):** Velocity peaks per meter [1/m].
- **Bimanual Quotient (BQ):** Ratio of non-dominant to dominant hand path lengths.
- **Bimanual Cooperation (BC):** Time both hands exceed a velocity of 0.05 m/s [s].

The absolute difference and normalized difference (laterality) of hand-specific measures was computed for PL, RA and NP, respectively (PL_Diff, RA_lat and NP_lat).

D. Real-World Wearable Sensor Metrics

Participants wore inertial measurement units (IMUs) on both hands for seven days following the lab assessments. IMUs captured kinematic data at a sampling rate of 64 Hz, with features categorized as:

- **Time-Domain Features:** Task duration (TD), maximum and mean acceleration and gyroscopic values (A_Max, G_Max, A_Mean, G_Mean).
- **Smoothness Features:** Spectral Arc Length from acceleration and gyroscopic signals (A_SPARC and G_SPARC).
- **Variability Features:** Standard deviation (STD) of acceleration, gyroscopic values, and derived metrics.
- **Laterality:** The normalized difference of hand-specific measures was also computed.

E. IMU Data Processing

IMU data was processed using the 2MPAC algorithm [10], with analysis restricted to a four-hour segment of sensor data collected from wrist-worn IMUs between 12:00 and 16:00 on the second day of wear. The algorithm identifies activity onset and offset by detecting acceleration and angular velocity thresholds, thus segmenting independent of activity duration. Movements exceeding a minimum acceleration (0.5 m/s²), angular velocity (60°/s), and duration (400 ms) are classified as valid activities, with pauses within activities limited to 1 second. This approach aims to capture both short and fragmented movements while filtering out noise and inactivity.

F. Statistical Analysis

Differences between MS and control groups were assessed using ANOVA, with sex interaction included for GRIP. Linear associations between kinematic features and EDSS scores for MS participants were examined using Pearson correlation. Statistical significance was set at $\alpha = 0.05$, with Benjamini-Hochberg corrections applied to account for multiple comparisons and control the false discovery rate.

III. Results

A. Group Differences and Laterality

Group differences were analyzed for absolute values and symmetry measures, including laterality (normalized differences) and absolute differences (e.g., Path Length). As illustrated in Fig. 2, significant group-level differences were observed in laterality measures for the Nine-Hole Peg Test (PEG_lat) (p = 0.01, η^2 = 0.76) and Two-Point Discrimination (DISCR_lat) (p = 0.02, η^2 = 0.71), emphasizing the sensitivity of these assessments in detecting motor asymmetry.

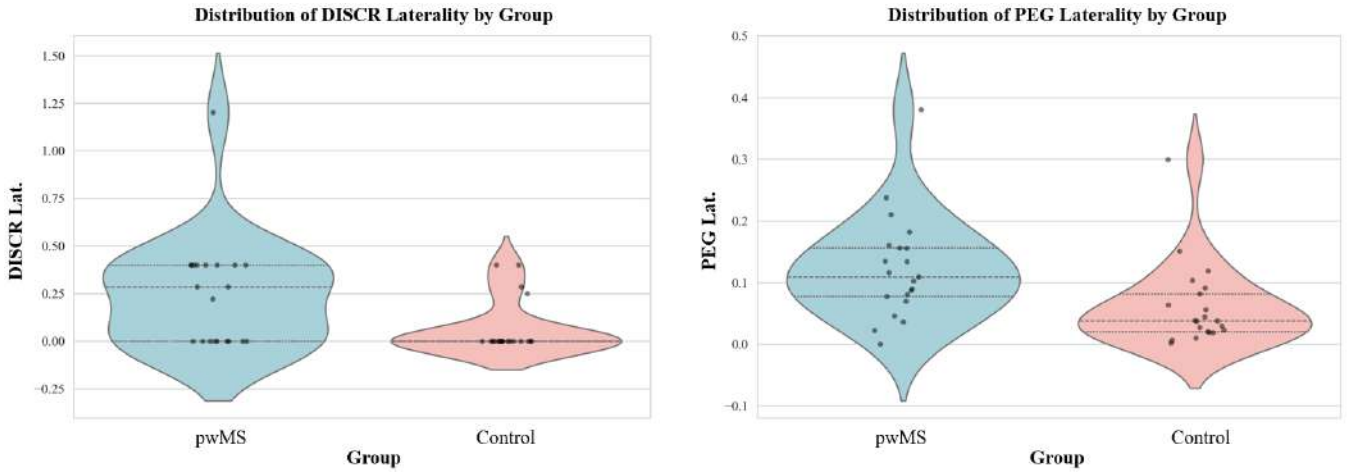


Fig. 2. Statistically significant differences between groups.

However, other metrics did not reach statistical significance (Table I), suggesting that gross motor speed and force-based measures may be less sensitive to mild impairments compared to assessments requiring fine motor control and sensory processing.

Despite these significant group differences in clinical assessments, no significant group differences were observed in field-based IMU-derived metrics or lab-based kinematic parameters from Tea Making and Drinking tasks. This indicates that while traditional clinical assessments can detect motor impairments, IMU and motion capture metrics may require more refined analytical approaches or complementary measures to better reflect functional deficits observed in clinical assessments.

TABLE I
CORRECTED P-VALUES, EFFECT SIZES, AND BENJAMINI–HOCHBERG (BH) SIGNIFICANCE FOR CLINICAL FEATURES

Feature	Corr. P-Value	Effect Size (η^2)	BH Significant
PEG_lat	0.01	0.76	True
DISCR_lat	0.02	0.71	True
REACT	0.05	0.21	False
GRIP_lat	0.09	0.67	False
BB_lat	0.44	0.58	False
TAP_lat	0.91	0.001	False

[a]Group differences were significant for a subset of clinical measures.

B. Correlations with Disease Severity

To evaluate the sensitivity of kinematic lab-based and IMU field-based features to disease severity, Pearson correlations with EDSS scores were analyzed. The difference between hand path lengths (PL_Diff) showed a strong positive correlation with EDSS in the Tea Making task, with a Pearson correlation coefficient of r=0.64 (p=0.002, adjusted p=0.02), as seen in Fig. 3.

C. Relationships Between Lab and Real-World Data

We conducted an exploratory analysis to examine the relationships between kinematic features measured in lab-based motion capture tasks and field-based IMU data. The aim was to uncover consistent patterns and correlations that could inform the development of hypothesis-driven studies in the future. By comparing features across two distinct ADL, Tea Making and Drinking tasks, we sought to identify task-specific and task-independent markers of motor impairment.

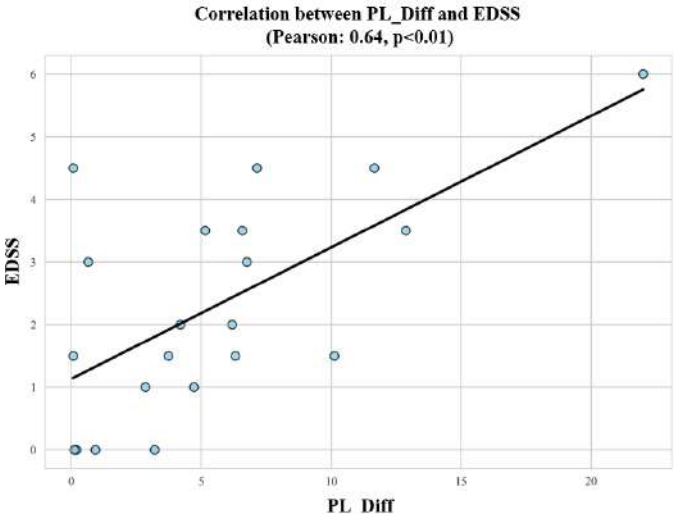


Fig. 3. Observed correlation between the absolute path length difference between hands (PL_Diff) and EDSS scores.

Absolute values (e.g., path length, velocity) and their symmetry metrics (e.g., laterality or absolute differences) were evaluated for correlations between lab-based kinematics and field-based IMU-derived measures.

Rather than examining single-task correlations, we specifically identified features that were significantly correlated between lab and IMU metrics across both the Tea Making and Drinking tasks. This approach was designed to pinpoint robust, task-independent relationships.

While individual task correlations varied, only two feature pairs consistently correlated across both Tea Making and Drinking tasks (Table II, as seen in Fig 4). Lab-based Path

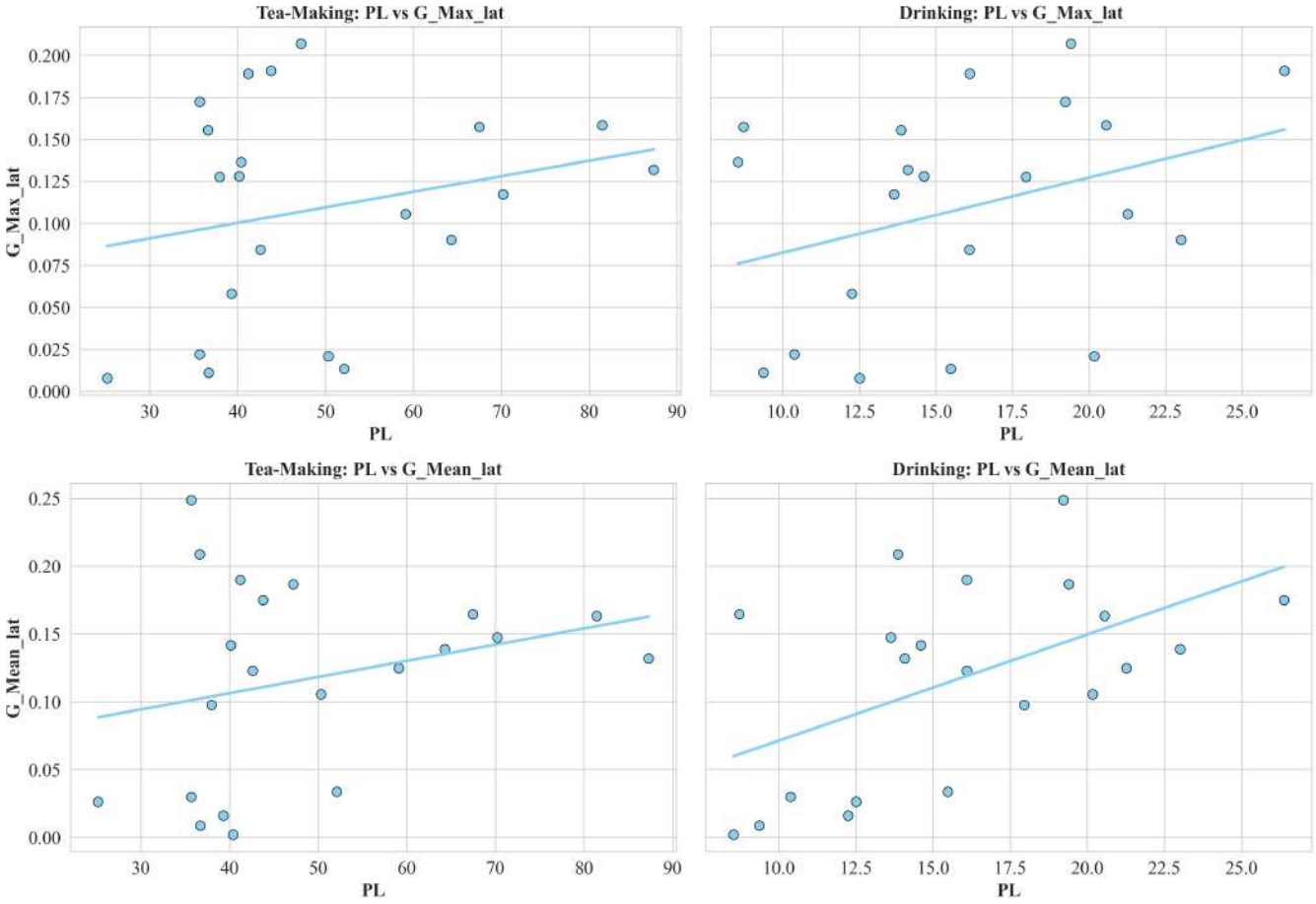


Fig. 4. Consistent relationships were observed between lab-based kinematics and field-based IMU metrics across Tea Making and Drinking tasks. Regarding the laterality of the mean angular velocity signal (G_Mean_lat), significant correlations were found for Tea Making task (r = 0.41, p< 0.001) and drinking (r = 0.52, p< 0.001). Similarly, the laterality of the maximum angular velocity signal (G_Max_lat) showed correlations for Tea Making task (r = 0.39, p = 0.011) and drinking (r = 0.36, p = 0.018).

Length (PL) correlated significantly with the laterality of the mean angular velocity signal (G_Mean_lat: Tea Making task r=0.41, p< 0.001, drinking r=0.52, p< 0.001), and laterality of the maximum angular velocity signal (G_Max_lat: Tea Making task r=0.39,p=0.011, drinking r=0.36,p=0.018). The consistency of these correlations highlights their potential as task-independent biomarkers for assessing motor impairments in free-living environments.

TABLE II
CORRELATIONS BETWEEN ADL AND IMU FEATURES ACROSS TASKS

ADL Feature	IMU Feature	Correlation	P-Value	Task
PL	G_Mean_lat	0.41	< 0.001	Tea
PL	G_Mean_lat	0.52	< 0.001	Drink
PL	G_Max_lat	0.39	0.01	Tea
PL	G_Max_lat	0.39	0.02	Drink

IV. DISCUSSION

This study highlights the importance of assessing submaximal behaviors in ADL using IMU and motion capture data. Submaximal tasks may not always detect functional limitations when impairments are mild. This is reflected in the lack of significant group differences and the weak associations with EDSS. These findings emphasize the need for task-independent metrics capable of capturing subtle motor impairments in real-world settings.

We explored the potential of combining lab-based kinematics with field-based IMU-derived metrics to assess motor impairments in pwMS. Correlations between lab-based path length (PL) and IMU-derived angular velocity metrics across tasks suggest these features may serve as robust, task-independent markers of motor behavior (Table II). Path length differences between hands have been shown to distinguish pwMS from controls [11], likely due to MS-related demyelination, even in mild cases [12]. Meanwhile, gyroscopic metrics capture rotational hand dynamics, offering complementary insights into motor performance. Their strong correlations across tasks suggest they are sensitive and robust for real-world disease monitoring (Fig. 4).

Prior studies have shown that kinematic markers detect early motor impairment in stroke and Parkinson's disease, but their use in upper limb analysis for MS remains limited. Our findings align with recent research emphasizing move-

ment asymmetry as an indicator of disease severity in MS [13]. The strong correlation between EDSS and PL_Diff in the Tea Making task (Fig. 3) supports prior evidence that unilateral deficits are an early hallmark of MS-related motor dysfunction and may reflect compensatory or pathological strategies in MS. However, its clinical implications require further validation, as PL_Diff alone may not fully encapsulate the nuances of daily motor deficits, reinforcing the need for more granular kinematic analyses.

The consistency of path length correlations with IMU features across tasks (Table II) highlights their potential as task-independent biomarkers, allowing for scalable assessments in home settings. This correlation likely arises because both Tea Making and Drinking require coordinated wrist rotations for object manipulation, which increase the total angular displacement captured by gyroscopes; correspondingly, the wrist travels a greater distance in space, thereby elevating the measured path length in lab-based tasks. IMU-based tracking could complement clinical evaluations and reduce the need for frequent hospital visits. However, a key question remains: Do these markers provide insights beyond traditional clinical assessments? Addressing this will be crucial for integrating IMU-based monitoring into clinical practice.

Despite strong correlations with disease severity, the lack of significant group-level differences suggests some individuals with MS retain near-normal task performance, likely due to the mild symptoms of this cohort. While features like PL_Diff showed high sensitivity to disease severity, they lacked discriminative power between groups. This highlights the need to select kinematic features based on specific research or clinical goals—whether for tracking disease progression or detecting early impairments.

Although correlations with EDSS suggest that IMU metrics reflect disease severity, they do not inherently establish their added clinical value. Given EDSS's broad, ordinal nature, IMU-based assessments should ideally provide more refined functional insights. Without a well-established clinical parallel, standalone interpretation of these metrics remains challenging, reinforcing the need for further validation.

Future research should prioritize validating IMU-derived features against more detailed functional assessments. Longitudinal studies could determine whether these metrics serve as early indicators of motor or cognitive decline. Refining data segmentation algorithms and task-specific movement analyses may also enhance IMU-based sensitivity to subtle impairments.

While IMU metrics showed limitations in cross-sectional analysis due to the lack of group-level differences, their potential for continuous, remote disease monitoring remains promising. With further refinement, IMU-based tracking could become a valuable tool for personalized rehabilitation and real-world disease management.

V. Conclusion

This study explored the integration of lab-based kinematic analyses and field-based IMU metrics to assess motor impairments in pwMS. Correlations between path length and gyroscopic measures across tasks of different complexities suggest the potential utility of these features as task-independent markers of motor behavior. While the findings highlight the promise of combining lab precision with wearable sensor scalability, further research is necessary to validate these relationships and assess their broader applicability in monitoring disease progression and real-world motor performance.

References

[1] W.-J. Huang, W.-W. Chen, and X. Zhang, "Multiple sclerosis: Pathology, diagnosis and treatments," Exp. Ther. Med., vol. 13, no. 6, pp. 3163-3166, Jun. 2017, doi: 10.3892/etm.2017.4410.

[2] C. Solaro, R. Di Giovanni, E. Grange, D. Marengo, et al., "Box and Block Test, Hand Grip Strength, and 9-Hole Peg Test: Correlations between Three Upper Limb Objective Measures in Multiple Sclerosis," *Eur. J. Neurol.*, vol. 27, no. 12, Jun. 2020, doi: 10.1111/ene.14427.

[3] J. F. Kurtzke, "Rating neurologic impairment in multiple sclerosis: an expanded disability status scale (EDSS)," Neurology, vol. 33, no. 11, pp. 1444-1452, Nov. 1983, doi: 10.1212/wnl.33.11.1444.

[4] M. Pau, M. Porta, G. Spinicci, J. Frau, L. Lorefice, G. Coghe, and E. Cocco, "Change in upper limb function in people with multiple sclerosis treated with nabiximols: a quantitative kinematic pilot study," *Neurol. Sci.*, vol. 44, no. 2, pp. 685-691, Feb. 2023. doi: 10.1007/s10072-022-06456-3.

[5] M. Bigoni, et al. , "Does kinematics add meaningful information to clinical assessment in post-stroke upper limb rehabilitation? A case report," J. Phys. Ther. Sci., vol. 28, no. 8, pp. 2408-2413, Aug. 2016, doi: 10.1589/jpts.28.2408.

[6] P. Gulde and J. Hermsdörfer, "Both hands at work: the effect of aging on upper-limb kinematics in a multi-step activity of daily living," Exp. Brain Res., vol. 235, pp. 1337-1348, Feb. 2017. doi: 10.1007/s00221-017-4907-0.

[7] P. Gulde, S. Schmidle, A. Aumüller, and J. Hermsdörfer, "The effects of speed of execution on upper-limb kinematics in activities of daily living with respect to age," Exp. Brain Res., vol. 237, pp. 1383-1395, Mar. 2019. doi: 10.1007/s00221-019-05512-3.

[8] S. Balasubramanian, A. Melendez-Calderon, A. Roby-Brami, and E. Burdet, "On the analysis of movement smoothness," J. NeuroEng. Rehabil., vol. 12, Dec. 2015. doi: 10.1186/s12984-015-0090-9.

[9] M. A. Murphy, K. S. Sunnerhagen, B. Johnels, and C. Willen, "Three-dimensional kinematic motion analysis of a daily activity drinking from a glass: a pilot study," *J. NeuroEngineering Rehabil.*, vol. 3, p. 18, Aug. 2006. doi: 10.1186/1743-0003-3-18.

[10] P. Gulde, H. Vojta, S. Schmidle, P. Rieckmann, and J. Hermsdörfer, "The association of upper limb sensorimotor capacity, everyday inpatient behavior, and the effects of neurorehabilitation in persons with multiple sclerosis and stroke: A mixed-design study," *J. NeuroEng. Rehabil.*, 2025.

[11] C. M. Kanzler, R. Sylvester, R. Gassert, J. Kool, O. Lambercy, and R. Gonzenbach, "Goal-directed upper limb movement patterns and hand grip forces in multiple sclerosis," Mult. Scler. J. Exp. Transl. Clin., vol. 8, no. 3, Aug. 2022. doi: 10.1177/20552173221116272.

[12] S. Groppa, G. Gonzalez-Escamilla, A. Eshaghi, S. G. Meuth, and O. Ciccarelli, "Linking immune-mediated damage to neurodegeneration in multiple sclerosis: could network-based MRI help?," Brain Commun., vol. 3, no. 4, 2021, Article fcab237. doi: 10.1093/braincomms/fcab237.

[13] C. J. Shanahan, F. M. C. Boonstra, L. E. Cofré Lizama, M. Strik, B. A. Moffat, F. Khan, T. J. Kilpatrick, A. van der Walt, M. P. Galea, and S. C. Kolbe, "Technologies for Advanced Gait and Balance Assessments in People with Multiple Sclerosis," *Front. Neurol.*, vol. 8, Feb. 2018. doi: 10.3389/fneur.2017.00708.

Skeleton-Based Transformer for Classification of Errors and Better Feedback in Low Back Pain Physical Rehabilitation Exercises

Aleksa Marusic[1], Sao Mai Nguyen[1] and Adriana Tapus[1]

***Abstract*— Physical rehabilitation exercises suggested by healthcare professionals can help recovery from various musculoskeletal disorders and prevent re-injury. However, patients' engagement tends to decrease over time without direct supervision, which is why there is a need for an automated monitoring system. In recent years, there has been great progress in quality assessment of physical rehabilitation exercises. Most of them only provide a binary classification if the performance is correct or incorrect, and a few provide a continuous score. This information is not sufficient for patients to improve their performance. In this work, we propose an algorithm for error classification of rehabilitation exercises, thus making the first step toward more detailed feedback to patients. We focus on skeleton-based exercise assessment, which utilizes human pose estimation to evaluate motion. Inspired by recent algorithms for quality assessment during rehabilitation exercises, we propose a Transformer-based model for the described classification. Our model is inspired by the HyperFormer method for human action recognition, and adapted to our problem and dataset. The evaluation is done on the KERAAL dataset, as it is the only medical dataset with clear error labels for the exercises, and our model significantly surpasses state-of-the-art methods. Furthermore, we bridge the gap towards better feedback to the patients by presenting a way to calculate the importance of joints for each exercise.**

I. INTRODUCTION

Physical rehabilitation plays a crucial role in helping patients recover from injuries, surgeries, and various medical conditions that affect their movement and functional abilities. Low back pain (LBP), which is the focus of our research, is a leading cause of disability globally, affecting over 50% of the population at some point in their lives. Consequently, healthcare providers face substantial challenges in managing the increasing number of LBP patients [1]. The success of rehabilitation exercises depends significantly on how accurately and consistently they are performed. Throughout the weeks or even months of a rehabilitation program, patients often have to carry out exercises at home without direct oversight from healthcare professionals. The absence of supervision and timely feedback from healthcare providers diminishes patient engagement in rehabilitation. Additionally, incorrect movements can not only delay the rehabilitation process but also increase the risk of further injuries [2]. Thus, there is a critical need for accurate and automated movement analysis methods to support patients and clinicians in monitoring rehabilitation exercises.

*This work was supported by ENSTA Paris

[1]Autonomous Systems and Robotics Lab, Computer Science and System Engineering (U2IS), ENSTA Paris, Institut Polytechnique de Paris, 828 Blvd des Maréchaux, 91120 Palaiseau, France, name.surname@ensta-paris.fr

The primary objective of automated monitoring systems for physical rehabilitation is to identify the activity being performed, evaluate its quality, and offer detailed information on errors and potential improvements. Current movement analysis methods in rehabilitation typically provide a general quality score that reflects how well an exercise is executed [3], [4], [5] While these scoring systems provide useful feedback, they represent only the initial step toward a fully automated and practical monitoring system.

A more detailed analysis, which not only evaluates the overall quality of movement but also identifies and localizes specific errors, would be highly beneficial for both patients and clinicians. This detailed feedback can help patients adjust their movements more precisely, keep them motivated throughout the rehabilitation sessions, and allow clinicians to more accurately monitor patients' progress while in-home rehabilitation [6], [7].

Human activity analysis is an evolving field that tackles the complex challenge of interpreting body movements based on data collected from various sources such as videos, images, or wearable sensors. While using data from wearable sensors directly as input is the dominant approach, recently, human pose estimation to estimate joint coordinates from videos has become a promising approach to analyze human movement. Given that skeletons can be naturally modeled as graphs, it is not surprising that Graph Convolutional Networks (GCNs) have become a leading method for skeleton-based action recognition. By representing the body as a graph of joints and their spatial-temporal relationships, skeleton-based methods effectively capture movement dynamics and remain resilient to changes in appearance and environmental conditions, while capturing spatial and temporal relationships during exercise performance [8], [9].

Furthermore, Transformer models, originally developed for natural language processing tasks, have shown remarkable success in various applications, such as recognition of daily activities in smart homes [10]. Their ability to model long-range dependencies and capture contextual information makes them well-suited for analyzing sequential data, such as skeleton sequences in rehabilitation exercises [11].

For automated feedback allowing physical rehabilitation patients to improve their performance, this paper offers two key innovations: error classification and movement analysis. Unlike previous methods that focus solely on providing a quality score, our approach requires a more precise model, thus we utilize a skeleton-based transformer model. Through self-attention mechanism, our model is able to better learn spatial and temporal relations between skeleton

joints. Specifically, our model is designed to:

- Classify errors: Identify and categorize different types of errors that may occur during the performance of rehabilitation exercises.
- Biomechanical attention: Identify the most important joints in human body skeleton for a specific movement, thus providing better feedback to the patient.

The remainder of this paper is organized as follows: Section II reviews related work on movement analysis in rehabilitation and skeleton-based action recognition models. After outlining the data we used in Section III, Section **??** describes the architecture of our skeleton-based transformer model and the methods for error classification and localization. Section V details our experimental setup and results, and discusses the implications of our findings. Finally, Section VI summarizes our main contributions, acknowledges the limitations of our approach, and suggests potential directions for future research..

II. RELATED WORK

A. Skeleton-based Action Recognition

Skeleton-based action recognition is a dynamic and rapidly evolving research area. Early studies depended on handcrafted features that utilized relative 3D rotations and translations between joints [12], [13]. However, the field has experienced significant advancements in recent years, largely driven by Deep Learning algorithms [8]. These Deep Learning methods for skeleton-based action recognition can be categorized into three primary groups, based on their approaches to extracting features from skeleton data for classification:

- Recurrent Neural Networks (RNNs), which consider skeleton data primarily as a temporal sequence of continuous features. Some of the examples are [14] that introduced a hierarchical recurrent neural network, and [15] that proposed Context-Aware Attention LSTM Networks.
- Convolutional Neural Networks (CNNs), [16], [17] apply CNNs on pseudo-images obtained from skeleton data [16], [17]. In this way, they capture spatial relations between joints in a frame.
- Graph Neural Networks (GNNs): Skeleton data naturally corresponds to a graph structure, with joints as vertices and bones as edges. As a result, Graph Convolutional Networks have become increasingly popular as they can extract both spatial relationships and be combined with temporal data [18], [19].

B. Physical Rehabilitation Assessment

Qualitative exercise assessment is essential for effective home-based rehabilitation systems, aiming to provide patients with informative feedback and enhance their performance. Early research on exercise evaluation applied traditional machine learning methods for classification, such as Adaboost, K-Nearest Neighbors (KNN), or Bayesian classifiers. Some approaches also utilized distance function-based models [20], [21]. Later studies adopted probabilistic models like Hidden Markov Models (HMMs) and Gaussian Mixture Models (GMMs) [6], [22]. While these models capture the stochastic nature of human motion and provide a quality score for movement accuracy, they do not fully exploit given information, such as joint or spatial connections between body parts.

Liao et al. [23] introduced a deep neural network model that generates quality scores for movements. They proposed a deep learning architecture for hierarchical spatio-temporal modeling, combining GMMs, CNNs, and LSTMs to compute a quality score. With the advent of Graph Neural Networks (GNNs), it is now possible to exploit spatial information through the skeletal graph structure. The authors in [24] and [25] applied Graph Convolutional Networks (GCNs) to assess physical rehabilitation, achieving state-of-the-art results on popular datasets such as KIMORE and UI-PRMD. Additionally, Yu et al. [26] employed an ensemble of two GCNs, one for position and one for orientation features of the skeletal joints, to further improve performance.

While existing methods primarily focus on quality scoring, a few studies have explored error classification and localization. For example, dynamic time warping (DTW) was used in [27] to compare patient movements with reference movements and identify phases with significant deviations. Devanne et al. [7] added on top of DTW, a GMM model to analyse the likelihood per body part and per time segment to localize the error. However, its accuracy remains modest. On the other hand, our approach leverages the power of Deep Learning and Transformer models to capture the spatial-temporal dynamics of movements and provide actionable feedback with error classification and localization.

In the following sections, we describe our methodology in detail, including the architecture of our skeleton-based transformer model and the approaches for error classification and movement analysis.

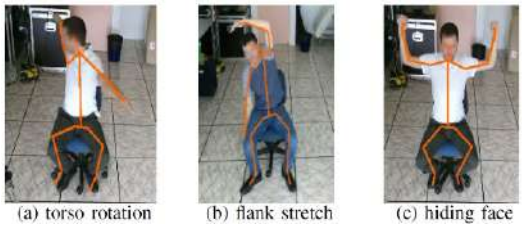
III. DATA PROCESSED

A. Dataset

We evaluate our model on the Keraal dataset [28], as it is the only one of the available rehabilitation datasets that fits into our problem setting and has error labels. TRSP [29] is the only other rehabilitation dataset, to our knowledge, with error labels, but they only use two types of simple reaching motions.

In the Keraal dataset, participants performed each of 3 predefined exercises, and the movements were recorded with Microsoft Kinect V2 and Vicon Recordings are annotated by physiotherapists in detail, with assessment of correctness, recognition of errors, and spatio-temporal localization of errors. In our model we used Kinect data as input, since it is a non-invasive system we would like to focus on.

The three exercises, chosen in agreement with medical experts, are namely torso rotation, flank stretch, and hiding face, which are illustrated in Figure 1. For each exercise therapists identified three most common errors, and each labeled recording was classified either as correct or as one of these 3 errors. As can be seen on Figure 2, the common



(a) torso rotation (b) flank stretch (c) hiding face

Fig. 1: The three rehabilitation exercises in the Keraal dataset. Image sourced from [28].



Fig. 2: Errors descriptions for all three exercises in the Keraal dataset. Image sourced from [28].

mistakes for exercise (a) torso rotation are: 1) Arms are not raised enough, 2) The torso's rotation is not sufficient, 3) The body is leaned on the side; for exercise (b) flank stretch: 1) Opposite arm is not along the body, 2) Body is not tilted, 3) The above arm is not bent; and for exercise (c) hiding face: 1) Arms are not raised enough, 2) Arms are not outspread enough, 3) Arms are not raised enough.

The Keraal dataset was recorded during a clinical rehabilitation study that included Low Back Pain patients, aged 18 to 70 years. The dataset includes recordings from both healthy subjects and 12 rehabilitation patients, from three groups of participants:

- Group 1 where patients performed exercises
- Group 2 where healthy participants performed exercises without specific intructions
- Group 3 where trained healthy participants performed exercises while simulating errors.

Groups 1 and 2 were labeled by physiotherapists, while Group 3 was implicitly labeled as participants simulated errors.

B. Data representation

The data of the Keraal dataset recorded exercises at a fixed frame rate, capturing the spatial information of key skeletal joints in the human body, either in two or three dimensions. The data include joint positions and sometimes their orientations (in our case we use only 3D joint positions).

Consider a tracking system that monitors V key points (joints) on a person's body. When someone performs one repetition of an exercise, the system records data across a certain number of time frames. Since that number can vary from recording to recording even for the same exercise type, we interpolate each recording to T timeframes. For each frame, we collect the positions of all V joints in a vector $x(i), i \in [1 \dots T]$. This vector has the dimension $D = V \times C$, where C equals either 2 or 3, depending on whether we are working with 2D or 3D data. When we combine these vectors from all frames, we create a three-dimensional tensor $X \in \mathbb{R}^{T \times V \times C}$, which represents the complete movement data from a single repetition.

C. Evaluation scenarios

Our goal is to classify a performed movement into one of four categories: correct, error1, error2, or error3. To achieve this, we train a separate model for each exercise. The primary metrics used for evaluation are the F1 score and accuracy.

We consider three cases:

- Scenario 1: Initial scenario where we train the models on trained professionals simulating errors (group 3), and evaluate on healthy subjects and patients (groups 2A and 1A). This setup is critical as it demonstrates the model's performance on unseen data, closely simulating real-life application conditions.
- Scenario 2: In the second scenario, data from all three groups are combined and split into training and testing sets, in proportion 80:20. Also, it is important to note that the split is stratified, meaning the proportion of class labels is approximately the same in both training and test splits. This second scenario highlights the model's full potential by showing the level of performance achievable with sufficient data for both training and validation.
- Scenario 3: The scarcity of labels for certain exercises in the first scenario prompted us to design a third scenario. We still wanted to have unseen patient data in the test set to simulate real-life conditions, but we added a portion of healthy participants in the test set as well, so that we better evaluate our model. In this setup, the test set is made from patient data (group 1) and 15% of the combined data from groups 2 and 3, while the training set consists of the remaining 85% of the healthy participants' data (split is stratified in this case as well).

IV. Algorithm

A. Self-attention

Self-attention in Transformers was originally developed to identify and map relationships between words in a text, whether they are close together or far apart in a sentence. This mechanism helps the network prioritize important parts of the input data [30], [31].

We can adapt this same concept to analyze human movement patterns captured through skeletal tracking. Just as Transformers process relationships between words in a text, we can process relationships between body joints in motion. Individual joint positions can be seen as words and each

frame of movement as a sentence. By applying the self-attention mechanism, we can more effectively learn both local (between nearby joints or sequential frames) and distant relationships (between far-apart joints or temporally distant frames) in the motion sequence.

Consider a given input sequence $X = (x_1, x_2, \ldots, x_n)$ where each x_i represents an input token. Each token x_i is transformed into three vectors: Query vector q_i, Key vector k_i, and Value vector v_i. These vectors are obtained by applying learned projection matrices to each token, transforming them into new representations suited for computing attention. Essentially, these projections allow the model to learn more complex spatial relations of the input data.

For each token x_i, its attention score is computed relative to every other token in the sequence x_j, including itself. The attention score is calculated by applying a softmax function on the dot product A_{ij} between the query vector q_i of token i and the key vector k_j of token j:

$$A_{ij} = q_i \cdot k_j^{\top} \tag{1}$$

To capture more complex relationships, an extension called Multi-Head Self-Attention (MHSA) is added [31]. With multiple attention heads, the model learns different kinds of spatial relations between the joints, in parallel.

B. Model architecture

The main processing idea is inspired by a novel algorithm - Hyperformer [32]. It has achieved state-of-the-art results on well-known human action recognition (HAR) benchmarks, proving it can learn complex relations between joints in the movement. However, unlike HAR datasets, we are not interested in distinguishing different types of actions, but different types of errors in one specific action. Thus, we are looking for much more subtle differences in motions during the same actions and trying to classify each motion accordingly. We train one model per exercise (action), compared to HAR algorithms which train one model in total to classify actions.

Furthermore, we have only a few classes (for errors), and even more importantly, very limited medical data to train the model, which emphasizes the need for a better understanding of spatio-temporal relations between the joints. That was another reason to choose Hyperformer as our basis, since it is one of the smallest HAR algorithms available (by number of trainable parameters).

One of the key novelties of Hyperformer is utilizing hypergraphs - dividing the initial skeleton graph into subgraphs in order to obtain more precise relations between the joints. In our paper we propose a different split of the skeleton graph, more tailored to our problem setting. We split 25 joints into 6 different groups: left and right forearm and hand (with wrists and fingers), legs and spine with head, as can be seen on the left part of Figure 3. We give particular importance to arms as they are one of the key parts in all exercises from the dataset used, as opposed to legs which do not move much during the exercises.

The overall model architecture can be seen on the right part of Figure 3 The input data is passed through a certain

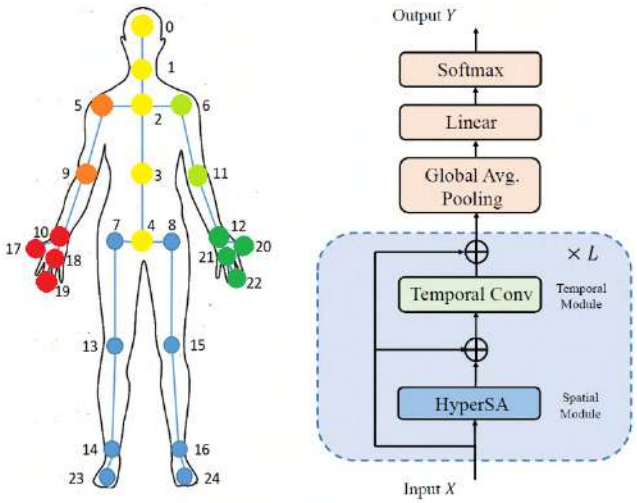


Fig. 3: Groups of skeletal joints (hypergraphs) on the left and model overview on the right. Right part taken from [32]

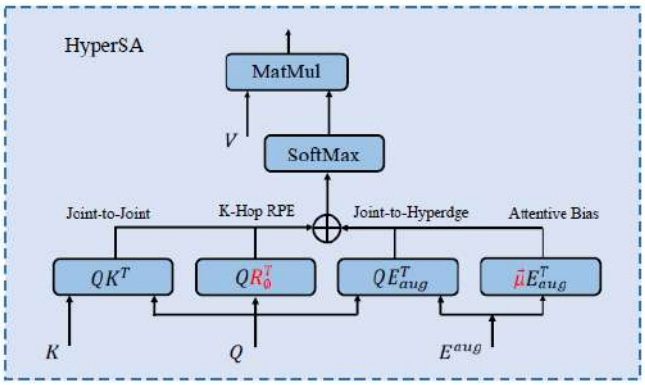


Fig. 4: Overview of the hyper self-attention module [32].

number of layers (10 in our case). Each layer consists of a custom self-attention layer followed by Multi-Scale Temporal Convolution. Global pooling, a linear activation and softmax functions are added at the end. The model is trained via backpropagation through a cross-entropy loss function by comparing $\hat{\mathbf{y}}$ with the true label $\mathbf{y}$ - a class labeled by the physiotherapists.

The main part of the layer is a custom self-attention module, as depicted in Figure 4. It consists of 4 parts :

- Joint-to-joint attention. Projection matrices used to get q, k, v vectors are obtained with 2D convolutions. Attention is calculated as described in IV-A.
- Joint-to-subgraph attention. Learns relations between joints and subgraphs, calculated the same way
- Relative positional embedding. Incorporates structural information of the skeleton, obtained with the Shortest Path Distance between the joints
- Attentive bias. Assigns the same amount of attention to each joint that belongs to a certain subgraph, enforcing independence of the query position.

V. RESULTS & DISCUSSION

In this section, we present the results of comprehensive comparative experiments conducted to assess the perfor-

mance of our model. We provide a comparison between our proposed approach and the current state-of-the-art, as well as some guidelines for further improvement.

A. Implementation details

Python 3.10 and the PyTorch 2.3 + CUDA 12.1 framework were used to develop the model. The system is equipped with an Intel Core i9-9900KF Silver 4215R CPU, 32GB of RAM, and an Nvidia RTX 2080 Ti 11GB. The model was trained with the Adam optimizer for 600 epochs, with a learning rate set to 25×10^{-4}, and using a batch size of 10. Performance measures were recorded for each run and averaged to ensure accuracy. Our code is based on the Hyperformer code repository and is available at `https://github.com/aleksamarusic/hyperphysio/`

B. Comparison with state-of-the-art

Table I shows that out model reaches higher accuracies in Scenario 1, outperforming the models benchmarked in [28].

TABLE I: Accuracies of our model and benchmark from [28]

Exercise	Ours	LSTM best	LSTM mean	GMM
Torso rotation	**73.17 %**	64.44 %	53.89 %	27.78 %
Flank stretch	**64.10 %**	43.04 %	31.64 %	25.32 %
Hiding face	**74.28 %**	56.19 %	49.1 %	33.33 %

Additionally, we present confusion matrices for the classification of rehabilitation movements, comparing three described scenarios

The confusion matrices for the first case are presented in Figure 5, with true labels on the left and predicted labels on the bottom. The values in the matrices represent the percentage of exercises classified as a certain class. For instance, in Figure 5a, the first row indicates that 71% of "Correct" exercises are classified as correct, 28% as error2, and 1% as error3. Consequently, the sum of any row in these matrices should be 1. Exceptionally, rows with all zeros mean that the corresponding error is not present in the test set. The value in brackets next to the left-side labels denote the frequency of the corresponding class in the test set.

For the torso rotation exercise, it is very hard to evaluate the model performance as we have 72 "correct" labels, only 4 of error1 and 6 of error2, while error3 is not present in the test set.

Similarly, the scarcity of labels for errors 1 and 3 in the flank stretch exercise poses significant challenges for accurately evaluating the model's performance. Error2 exhibits some confusion with correct exercises, which can be explained by the general challenge to determine that the body is not tilted enough solely based on joint positions.

For hiding face, error2 has only 1 example in the test set, and we need more to properly evaluate. Also, it can be noticed that error3 shows misclassification with both correct and error1 categories. These can be also attributed to a general challenge as errors 1 and 3 are quite similar, and both are hard to distinguish from the correct performance as it is only a matter of a few pixels on the image whether they would be classified as one or the other. These issues could potentially be mitigated with the inclusion of additional training and validation data, and with more precise data.

Confusion matrices for the second case can be seen in Figure 6. As explained, we randomly sample 20% of the dataset for testing, keeping the proportion of the labels in the test set. This scenario obtained better performance, which confirms the model's potential to perform significantly better when having more training data.

The confusion matrices for the third case are shown in Figure 7. While the majority of movements are correctly classified, some confusion can be observed between "correct" and "error3" in the flank stretch exercise . This may be attributed to the limited number of sequences labeled as correct by the medical expert and the subtle differences between correct movements and error2. The latter occurs when the body is not sufficiently tilted, a distinction that can be challenging to detect solely through skeleton joint data.

C. Visualization of joints' importance

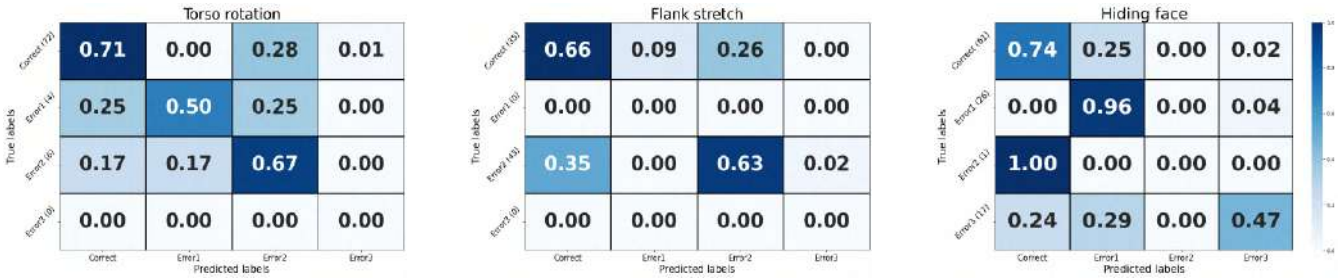
The described visualization aims to analyze and compare the attention weights learned during the training and evaluation phase. By analyzing attention matrices, we can identify important joints in each exercise.

From our model, we can obtain the self-attention weights, which are quite comprehensive as we have weights for every layer, frame, and head (of multi-head attention) from every batch and input sequence. However, by averaging across these dimensions, we can obtain self-attention map that shows the attention weights for each body joint to every other body joint (since we have 25 joints, it is represented as $25 * 25$ matrix). Further, the joint role can be computed by the column-wise summation over that map. Additionally, we also notice that is important to look at differences in self-attention maps obtained from correct and incorrect exercises. This way we can more easily obtain information on which joints play an important role in the exercise.

Looking at Figure 8, we can notice that arm joints play an important role in all exercises, contrarily to the legs, as the exercises relate to the upper body. Additionally, Torso rotation and Hiding face give more importance to the angles of the shoulders and elbows, contrarily to Flank stretch. This is expected as the two former exercises require keeping the upper arm horizontal, while Flank stretch leaves the arm free, focusing more on the flank. These observations align with key joint patterns seen in the exercises (Figure 1), confirming the ability of the model to provide accurate and useful feedback to patients.

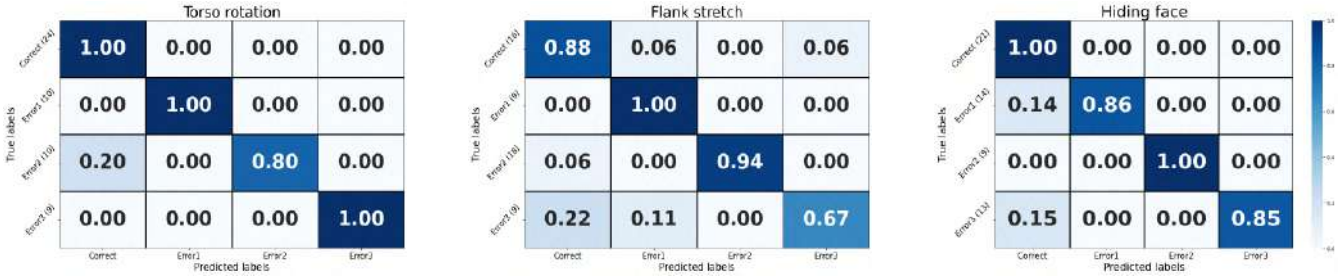
VI. CONCLUSION

In this paper, we present a Transformer-based model for classifying errors in physical rehabilitation exercises. The model takes skeleton joint positions as input and classifies movement as either correct or one of the predefined errors. Inspired by the Hyperformer algorithm, our approach divides



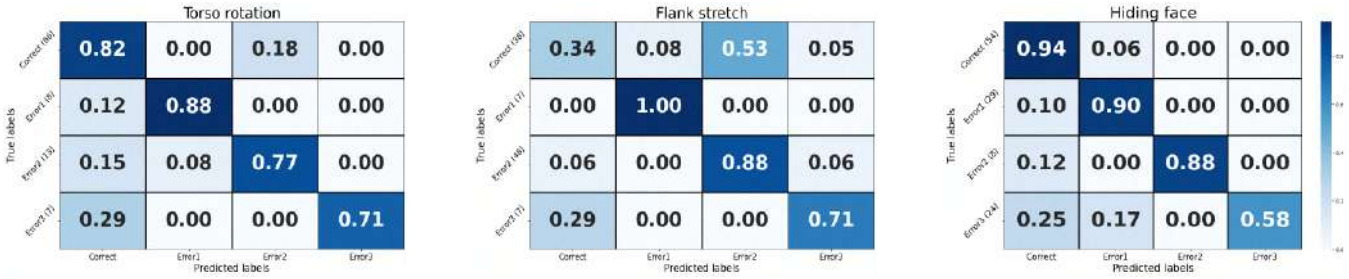
(a) Torso rotation confusion matrix (b) Flank stretch confusion matrix (c) Hiding face confusion matrix

Fig. 5: Confusion matrices for each of 3 exercises for the first case (trained on group3 and tested on groups 2A and 1A). Rows full of 0.00 mean that the corresponding error is not present in the test set.



(a) Torso rotation confusion matrix (b) Flank stretch confusion matrix (c) Hiding face confusion matrix

Fig. 6: Confusion matrices for each of 3 exercises for the second case (all groups combined and then data split into train and test sets).



(a) Torso rotation confusion matrix (b) Flank stretch confusion matrix (c) Hiding face confusion matrix

Fig. 7: Confusion matrices on test for each of 3 exercises for the third case (trained on most 85% healthy (groups 2 & 3) and tested on patients (group 1) and 15% of groups 2 & 3 combined.

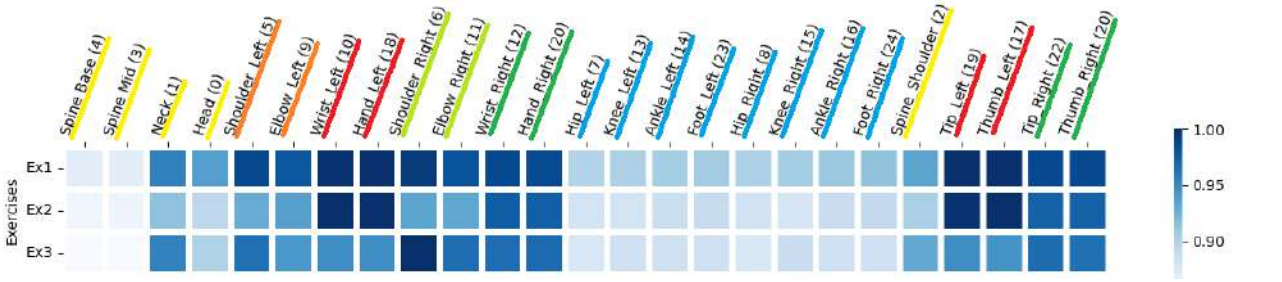


Fig. 8: An illustration of the joints' importance calculated from attention weights. Each row represents importance values for each of 25 skeleton joints during a specific exercise. Ex1 : Torso rotation, Ex2 : Flank stretch, and Ex3 : Hiding face. Each column corresponds to a joint, designated by its name and its joint order (numbers in brackets next to labels), that are underlined with a color matching its group from Fig 3

the skeleton graph into subgraphs to enhance the learning of complex spatial joint relations using the self-attention mechanism. We evaluate our model on the Keraal dataset, focusing on low back pain rehabilitation, which is the only dataset suitable for this error classification task. We can draw several conclusions:

- Our model achieves significant improvements over benchmark algorithms and sets new state-of-the-art re-

sults. This proves the ability to better capture spatial and temporal relations with the self-attention module, and sets a new direction for automated rehabilitation assessment

- We also calculate the importance of specific joints in performed exercises. This information can be used to detect which joints are wrongly moved, leading to enhanced feedback provided to the patients.
- Since we were interested in subtle differences in motions during the same exercise, it was necessary to train one model for each exercise type. In a scenario in which patients are trained by a coach, the system knows which exercise is being performed and the focus was on the assessment method. A more comprehensive model integrating exercise detection, can be a future research direction.
- One of the key limitations lies in the limited data available. While the Keraal dataset has detailed annotations, medical datasets are unfortunately limited in number.
- The imbalance of the dataset makes it harder to evaluate the model for underrepresented classes. Exploring data augmentation methods could lead to better classification and is a potential research direction for further studies.
- Some of the further research directions are temporal localization of errors, as well as more precise instructions on how to fix errors. These are essential for qualitative feedback to a patient.

REFERENCES

[1] A. Wu, L. March, X. Zheng, J. Huang, X. Wang, J. Zhao, F. M. Blyth, E. Smith, R. Buchbinder, and D. Hoy, "Global low back pain prevalence and years lived with disability from 1990 to 2017: estimates from the global burden of disease study 2017," *Annals of Translational Medicine*, 2020.

[2] S. F. Bassett and H. Prapavessis, "Home-based physical therapy intervention with adherence-enhancing strategies versus clinic-based management for patients with ankle sprains," *Physical Therapy*, 2007.

[3] S. Sardari, S. Sharifzadeh, A. Daneshkhah, B. Nakisa, S. W. Loke, V. Palade, and M. J. Duncan, "Artificial intelligence for skeleton-based physical rehabilitation action evaluation: A systematic review," *Computers in Biology and Medicine*, 2023.

[4] A. Marusic, L. Annabi, S. M. Nguyen, and A. Tapus, "Analyzing data efficiency and performance of machine learning algorithms for assessing low back pain physical rehabilitation exercises," in *2023 European Conference on Mobile Robots (ECMR)*, 2023.

[5] Y. Mourchid and R. Slama, "D-stgcnt: A dense spatio-temporal graph conv-gru network based on transformer for assessment of patient physical rehabilitation," *Computers in Biology and Medicine*, vol. 165, p. 107420, 2023.

[6] M. Devanne and S. M. Nguyen, "Multi-level motion analysis for physical exercises assessment in kinaesthetic rehabilitation," in *2017 IEEE-RAS 17th International Conference on Humanoid Robotics (Humanoids)*, 2017.

[7] M. Devanne, S. M. Nguyen, O. Remy-Neris, B. Le Gales-Garnett, G. Kermarrec, and A. Thepaut, "A co-design approach for a rehabilitation robot coach for physical rehabilitation based on the error classification of motion errors," in *IEEE International Conference on Robotic Computing (IRC)*, Jan 2018, pp. 352–357.

[8] V.-T. Le, K. Tran-Trung, V. T. Hoang, and H. Chen, "A comprehensive review of recent deep learning techniques for human activity recognition," *Intell. Neuroscience*, Jan. 2022.

[9] J. Shin, N. Hassan, A. S. M. Miah1, and S. Nishimura, "A comprehensive methodological survey of human activity recognition across divers data modalities," 2024.

[10] D. Bouchabou, J. Grosset, S. M. Nguyen, C. Lohr, and X. Puig, "A smart home digital twin to support the recognition of activities of daily living," *Sensors*, 2023.

[11] W. Xin, R. Liu, Y. Liu, Y. Chen, W. Yu, and Q. Miao, "Transformer for skeleton-based action recognition: A review of recent advances."

[12] R. Vemulapalli, F. Arrate, and R. Chellappa, "Human action recognition by representing 3d skeletons as points in a lie group," *2014 IEEE Conference on Computer Vision and Pattern Recognition*, pp. 588–595, 2014.

[13] M. E. Hussein, M. Torki, M. A. Gowayyed, and M. El-Saban, "Human action recognition using a temporal hierarchy of covariance descriptors on 3d joint locations," ser. IJCAI 2013.

[14] Y. Du, W. Wang, and L. Wang, "Hierarchical recurrent neural network for skeleton based action recognition," in *2015 IEEE Conference on Computer Vision and Pattern Recognition (CVPR)*, 2015.

[15] J. Liu, G. Wang, L. yu Duan, K. Abdiyeva, and A. C. Kot, "Skeleton-based human action recognition with global context-aware attention lstm networks," *IEEE Transactions on Image Processing*, vol. 27, pp. 1586–1599, 2017.

[16] Q. Ke, Bennamoun, S. An, F. Sohel, and F. Boussaïd, "A new representation of skeleton sequences for 3d action recognition," *IEEE Conference on Computer Vision and Pattern Recognition*, 2017.

[17] M. Liu, H. Liu, and C. Chen, "Enhanced skeleton visualization for view invariant human action recognition," *Pattern Recognition*, 2017.

[18] S. Yan, Y. Xiong, and D. Lin, "Spatial temporal graph convolutional networks for skeleton-based action recognition," ser. AAAI'18/IAAI'18/EAAI'18. AAAI Press, 2018.

[19] F. Ye, S. Pu, Q. Zhong, C. Li, D. Xie, and H. Tang, "Dynamic gcn: Context-enriched topology learning for skeleton-based action recognition," ser. MM. ACM, 2020.

[20] I. Ar and Y. S. Akgul, "A computerized recognition system for the home-based physiotherapy exercises using an rgbd camera," *IEEE Transactions on Neural Systems and Rehabilitation Engineering*, vol. 22, no. 6, pp. 1160–1171, 2014.

[21] R. Houmanfar, M. Karg, and D. Kulić, "Movement analysis of rehabilitation exercises: Distance metrics for measuring patient progress," *IEEE Systems Journal*, vol. 10, 2016.

[22] A. Vakanski, J. Ferguson, and S. Lee, "Mathematical modeling and evaluation of human motions in physical therapy using mixture density neural networks," *Journal of Physiotherapy Physical Rehabilitation*.

[23] Y. Liao, A. Vakanski, and M. Xian, "A deep learning framework for assessing physical rehabilitation exercises," *IEEE Transactions on Neural Systems and Rehabilitation Engineering*, 2020.

[24] S. Deb, M. F. Islam, S. Rahman, and S. Rahman, "Graph convolutional networks for assessment of physical rehabilitation exercises," *IEEE Transactions on Neural Systems and Rehabilitation Engineering*, vol. 30, pp. 410–419, 2022.

[25] C. Du, S. A. Graham, C. A. Depp, and T. Q. Nguyen, "Assessing physical rehabilitation exercises using graph convolutional network with self-supervised regularization," *International Conference of the IEEE Engineering in Medicine & Biology Society*.

[26] B. X. Yu, Y. Liu, X. Zhang, G. Chen, and K. C. Chan, "Egcn: An ensemble-based learning framework for exploring effective skeleton-based rehabilitation exercise assessment," in *Proceedings of International Joint Conference on Artificial Intelligence 2022*.

[27] X. Chen, Y. Liu, and Q. Huang, "Real-time error detection and feedback for physical rehabilitation exercises using kinect and dtw," 2016.

[28] S. M. Nguyen, M. Devanne, O. Remy-Neris, M. Lempereur, and A. Thepaut, "A medical low-back pain physical rehabilitation dataset for human body movement analysis," in *International Joint Conference on Neural Networks*, 2024.

[29] E. Dolatabadi, Y. X. Zhi, B. Ye, M. Coahran, G. Lupinacci, A. Mihailidis, R. Wang, and B. Taati, "The toronto rehab stroke pose dataset to detect compensation during stroke rehabilitation therapy," 2017.

[30] D. Bahdanau, K. Cho, and Y. Bengio, "Neural machine translation by jointly learning to align and translate," *CoRR*, 2014. [Online]. Available: https://api.semanticscholar.org/CorpusID:11212020

[31] A. Vaswani, N. Shazeer, N. Parmar, J. Uszkoreit, L. Jones, A. N. Gomez, L. Kaiser, and I. Polosukhin, "Attention is all you need," in *Proceedings of the 31st International Conference on Neural Information Processing Systems*, 2017.

[32] Z. Hu, V. Gutiérrez-Basulto, Z. Xiang, R. Li, and J. Z. Pan, "Hyperformer: Enhancing entity and relation interaction for hyper-relational knowledge graph completion," 2023.

Effects of Visual and Verbal Feedback on Active Patient Participation during Robot-Assisted Gait Training

F. Di Tommaso[1,*], M. Ferrara[1], F. Patarini[2,3], S. Mohebban[2,3], A. Bigioni[5], G. Serratore[5], M. Lorusso[5], F. Cincotti[2], G. Scivoletto[5], D. Mattia[3], F. Tamburella[4,5], J. Toppi[2,3], F. Pichiorri[3], N. L. Tagliamonte[1,5]

***Abstract*—Robot-Assisted Gait Training (RAGT) is a widely adopted neurorehabilitation approach for individuals with Spinal Cord Injury (SCI). In this context, active patient participation is a key factor to improve the success of the therapy. Previous works with the robotic trainer Lokomat have shown that real-time visual feedback and verbal instructions from a physical therapist effectively enhance active participation. However, the optimal type of visual feedback and its potential synergy with verbal indications remain unclear. This study investigates how different visual feedback types influence active participation when combined with therapist verbal instructions. Nine participants with SCI underwent RAGT sessions with three types of visual feedback (*chart*, *emoticon*, *game*) and two levels of patient-therapist verbal interaction (*high*, *low*). Active participation was quantified from a biomechanical point of view through the human-robot interaction work in four joints (left/right hip and knee) during the stance and swing phases of the gait cycle. Results showed that feedback *chart* was the most effective in promoting positive, symmetric performance, as opposed to feedback *game* and *emoticon* which, though probably more engaging, exhibited heterogeneous results. *High* therapist interaction significantly improved the performance of the limb with the highest muscular strength for the hip during the swing phase, whereas the effects on the limb with the lowest muscular strength were less clear.**

***Index Terms*—Robot-assisted gait training, visual feedback, patient-therapist verbal interaction, spinal cord injury.**

I. Introduction

Gait rehabilitation for individuals with neurological disorders, such as stroke, Spinal Cord Injury (SCI), and traumatic brain injury, has evolved significantly over the past decades. In particular, Robot-Assisted Gait Training (RAGT) has transformed traditional therapeutic approaches [1] based on the manual assistance from physical therapists or the use of a treadmill with a weight-unloading system. Although effective [2], conventional methods required significant physical effort from both therapists and patients [3]. The introduction of lower-limb robotic systems has overcome these limitations by offering intensive, repetitive, task-specific, and goal-oriented rehabilitation sessions, reducing the physical burden on therapists while preserving patient engagement and therapeutic effectiveness [3], [4]. The adoption of RAGT has gained prominence in neurorehabilitation due to the possibility of providing controlled assistance and collecting objective performance metrics [5]. Furthermore, consistent, biomechanically accurate and meaningful movements of the limbs can contribute to providing the useful sensory input required to stimulate spinal neural circuits, promoting brain plasticity [6] and allowing activation of lower limb muscles that cannot be voluntarily controlled [7].

A widely adopted device for RAGT is the Lokomat (Hocoma AG, Switzerland), which consists of a treadmill, a Body Weight Support (BWS) that modulates weight-bearing effects and a bilateral robotic orthosis that assists the hip and knee joints in flexion/extension [8]. Several studies have highlighted the therapeutic efficacy of the system when integrated with traditional gait rehabilitation approaches, for pathologies affecting the central nervous system [9], [10]. A relevant contribution to successful clinical outcomes lies in the ability to ensure active patient participation during the movement, which has been widely shown to be crucial for motor learning and rehabilitation [11], [12]. In this context, providing visual feedback on real-time task-related metrics is a fundamental aspect, as it compensates for the loss of information on the patient's contribution to the task due to the lack of physical interaction with the therapist. Hence, visual feedback represents both an assessment and motivational tool for the therapist and the patient, respectively [13]. Specifically, it supports patients' intrinsic feedback mechanisms, which may be compromised due to impaired somatosensory pathways [14], and complements the extrinsic feedback provided by the therapist. This combination facilitates a better understanding of the task and encourages movement corrections aligned with the therapeutic goals [13], [15]. Additionally, the effectiveness and enjoyment of the functional training can be enhanced by incorporating gamification strategies, such as virtual environments [16], [17].

The Lokomat can provide visual feedback based on human-robot joint interaction torques measured via force sensors embedded in its linear actuators. Specifically, interaction torques are multiplied by corresponding weighting functions for each joint to provide positive feedback values when the patient is performing therapeutically desired movements, and negative values in case of passive or resistive contributions, depending on the specific phase of the gait cycle [13]–[15]. Despite the robot-mediated physical guidance, the role of therapists remains indispensable in bridging the gap between the visual feedback and the patient's comprehension. By interpreting robot-generated feedback, offering verbal support and empa-

[1]Research Unit of Advanced Robotics and Human-Centred Technologies, Università Campus Bio-Medico di Roma, Rome, Italy.

[2]Department of Computer, Control and Management Engineering, University of Rome La Sapienza, Italy.

[3]Neuroelectrical Imaging and Brain Computer Interface Lab, IRCCS Fondazione Santa Lucia, Rome, Italy.

[4]Department of Life Sciences, Health and Health Professions, Link Campus University Rome, Italy.

[5]Laboratory of Robotic Neurorehabilitation, Neurorehabilitation 1 Department, Fondazione Santa Lucia, Rome, Italy.

[*]Corresponding Author: f.ditommaso@unicampus.it.

thetic encouragement, therapists ensure the correct execution of the movements and promote active participation [16]. Nevertheless, determining the optimal balance between robotic feedback and therapist intervention remains a significant challenge, as patients often rely on the therapists' expertise to fully comprehend their performance, properly exploit the robotic assistance and translate it into meaningful movements.

This study explores how the combination of different types of visual feedback and verbal interactions influences the active participation of SCI patients during RAGT with the Lokomat. To the best of our knowledge, these two factors have always been considered separately in previous relevant studies on Lokomat-assisted training, despite their synergy representing an essential ingredient to implement effective and engaging rehabilitation protocols. In a recent study, we have already investigated the effects of visual and verbal feedback on attention and emotional engagement by using eye-tracking and EEG metrics [18]. In this paper, we shift the focus to the biomechanical quantification of patient participation by analyzing physical metrics based on human-robot joint interaction data.

II. Materials and Methods

A. Recruitment of Participants

Nine participants (6 females, age 62.9 ± 14.7 y.o.) were recruited from the Spinal Cord Injury Unit of the Neurorehabilitation 1 Department at Fondazione Santa Lucia (Rome, Italy). The study was approved by the local Ethics Committee (protocol number: PROT.CE/PROG.883). Inclusion criteria were defined as: *i)* incomplete spinal cord injury classified as AIS C or D according to the American Spinal Injury Association Impairment Scale (ASIA); *ii)* lesion level at or above D12; *iii)* traumatic or non-traumatic aetiology; *iv)* subacute or chronic phase; *v)* age between 18 and 85 years; *vi)* absence of severe cognitive impairments, assessed with the Montreal Cognitive Assessment (MoCA, cut-off > 26) [19]; *vii)* absence of severe psychiatric conditions, assessed with the Beck Depression Inventory (BDI-II, cut-off < 30, severe depression) [20] and the State-Trait Anxiety Inventory (STAI, cut-off < 40) [21]. All participants underwent RAGT in addition to conventional therapy. Epidemiological data and neurological features of recruited participants are reported in Tab. I. The lower limbs of each participant were evaluated using the Lower Extremity Motor Score (LEMS) from the International Standards for Neurological Classification of SCI [22], [23], whose values account for the strength of five key lower limb muscles. Hereafter, we will refer to the limb with the highest and lowest LEMS as *High Strength Limb* (HSL) and *Low Strength Limb* (LSL), respectively.

The RAGT sessions were carried out by 3 different research physical therapists (2 females, age 32.66 ± 5.50 y.o.) with at least 6 years of experience in neurorehabilitation and fully trained on the use of the Lokomat, including the visual feedback types, from at least 1 year.

B. Experimental Setup

1) Robotic Device: The study was carried out with the robotic gait trainer Lokomat. The device assists the movements of the hip and knee in the sagittal plane and the pelvis rotation, whereas passive spring-based foot lifters support ankle dorsiflexion. The user's limbs are fixed to the orthosis by cuffs with Velcro straps and their motion is assisted by a stiffness controller, whose reference trajectory is defined by the physical therapist together with the Gait Speed (GS). The level of assistance, (Guidance Force, GF), is typically decided according to the user's needs in a range from 0% (no robotic assistance) to 100% (full robotic assistance).

2) Visual Feedback: Three types of visual feedback were selected among those available from the manufacturer [14], referred to in this paper as *chart*, *emoticon* and *game* (Fig. 1). Despite their different visual formats, they are all derived from human-robot interaction torques, with positive and negative torques corresponding to the user flexing or extending a joint, respectively [15]. The interaction torques are processed with joint-specific weighting functions, defined following two principles: *i*) to reward distinctive intervals of the gait cycle and neglect the possible detrimental effects of transitory phases that might not capture the real patient's intention of movement [13] and *ii*) to account for the assumption that meaningful joint interaction torques are expected to have the same sign as the joint angular velocity (*i.e.* they should point in the same direction of the desired movement), except the knee during stance, in which extensive action counteracting weight loading is desired [24]. Additional details regarding the weighting functions are reported in [13]–[15], [24], [25]. The weighted torques are then averaged over each gait cycle, separately for the stance and swing phases, yielding eight values per stride: right and left values for the hip and knee joints during the stance and swing phases. In summary, positive feedback values indicate active participation, whereas negative values suggest passive behaviour or resistance to robot assistance.

Feedback *chart* displays the eight feedback values in four time-series graphs for the left and right hip and knee joints, with separate lines for stance and swing phases. Each data point corresponds to the value from a single stride, and participants are instructed to walk actively to produce positive values. Feedback *game* provides a virtual environment where the patient's movements are mapped onto an avatar: the hip and knee values are averaged for the left and right limbs and used to control the avatar, allowing it to navigate along a walking path to collect coins as rewards. Finally, in the *emoticon* modality, the average of the eight feedback values represents the overall performance and is visually depicted by a cartoon face, whose degree of smiling or frowning corresponds to the patient's performance relative to a threshold set during a calibration phase. The goal is to achieve a full smile, reflecting positive and consistent engagement.

3) Data Acquisition: The Lokomat was configured in *Research Mode* to export, through the *Research Output* module, real-time analogue data, specifically joint angles and

ID	Age	Gender	Mass [kg]	AIS	Aetiology	Lesion level	Left LEMS	Right LEMS	Condition
P1	36	F	70	D	Tr	C4	20	21	Sub
P2	81	F	80	D	NTr	T12	17	21	Chr
P3	62	F	59	C	NTr	T10	14	5	Sub
P4	83	F	69	D	NTr	C5	17	20	Chr
P5	68	M	76	C	NTr	T9	1	5	Sub
P6	59	F	65	D	NTr	C4	21	15	Sub
P7	65	F	83	C	NTr	T12	18	16	Sub
P8	64	M	75	D	Tr	C5	8	21	Sub
P9	48	M	96	D	NTr	C5	12	23	Sub

TABLE I: Epidemiological and neurological data of the enrolled participants. M/F: Male/Female, AIS: ASIA Impairment Scale, Tr/NTr: Traumatic/Non-Traumatic, C/T: Cervical/Thoracic, LEMS: Lower Extremity Motor Score, Chr/Sub: Chronic/Subacute.

interaction torques. Data were collected with a National Instruments USB-6218 acquisition board (National Instruments, Austin, TX, USA) and recorded with MATLAB Analog Input Recorder tool at 500 Hz.

C. Experimental Protocol

1) Experimental Manipulation: Two experimental factors, visual feedback (*feedback*) and patient-therapist verbal interaction (*interaction*), were randomly varied to create different training conditions (Fig. 1). Factor *feedback* included three levels (*chart*, *emoticon*, *game*), as detailed in Sec. II-B2, whereas factor *interaction* consisted of three levels (*high*, *medium*, *low*). At the *high* interaction level, the physical therapist provided continuous verbal support, enhancing the information conveyed by the visual feedback, such as translating it into specific instructions when incorrect movements were observed, assigning focused tasks to targeted joints during specific gait phases, and maintaining motivation to encourage active participation throughout the exercise. At the *medium* interaction level, the therapist set a predefined task for the participant, *e.g.* focusing on a specific joint, while relying on the visual feedback, but only intervened upon request for clarification or assistance. At the *low* level, verbal communication between the therapist and the participant was limited to non-technical aspects, such as inquiring on perceived comfort, leaving the participant to rely solely on the visual feedback.

2) Training Sessions: All participants completed an initial familiarization session (SS0) to adjust the device parameters according to their needs, such as the robot dimensions, based on anthropometric measurements, and the values of BWS, GS and GF. Once configured, these settings remained unaltered throughout the subsequent training sessions. For the entire cohort of participants, the average selected parameters were BWS = $60.1 \pm 15.0\%$, GS = 1.24 ± 0.30 km/h, GF = $89.70 \pm 9.96\%$. The study involved six training sessions (SS1-SS6), each lasting approximately 45 minutes and covering an average of two weeks as part of the rehabilitation plan defined by the medical team. Each visual feedback type was used for two consecutive sessions, during which the therapist alternated the three interaction levels every 5 minutes. In odd-numbered sessions, the sequence of interaction levels followed a predefined order (*high–medium–low*), while in even-numbered sessions, the order was randomized. This approach ensured that participants experienced all the combinations of feedback modalities and interaction levels in a balanced manner. Data from Lokomat were not recorded during these sessions.

3) Assessment Session: After the last training session, participants' performance was evaluated in a final assessment session (SS7). First, participants completed a 5-minute warm-up walking with the Lokomat without any specific task or feedback. Then, all three visual feedback types were administered in a randomized order, with only *high* and *low* levels of patient-therapist verbal interaction adopted for each visual feedback type. We excluded the *medium* interaction level during this phase because its characteristics might not have been clearly different from those of the other levels and easily standardized among therapists and sessions. Nonetheless, the reason for its inclusion in the training sessions lies in the need to provide patients with a gradual and smooth transition from a continuous technical interaction (*high*) to none (*low*), avoiding the risk of generating possible confusion. The session followed a block design, where each visual feedback type was presented in a 5-minute block. Each block was evenly divided into two halves, corresponding to *high* and *low* interaction. The sequence of blocks was randomized across participants to minimize order effects. During this session, we collected Lokomat data to evaluate the effects of visual feedback and verbal interaction on participants' performance after six RAGT sessions, as described in Sec. II-B3.

D. Data Analysis

Data processing and statistical analysis were performed in MATLAB (Mathworks, Natick, MA, USA).

1) Biomechanical Quantification of Participation: Joint angles data were differentiated to obtain angular velocity profiles and human-robot interaction torques were normalized to the body mass to account for inter-participant variability. Then, data were smoothed by using a third-order, zero-lag Butterworth low-pass filter with a cutoff frequency of 5 Hz. The dataset for each trial was segmented based on heel strike events and time-normalized to express all variables as a function of the percentage of the gait cycle. For each gait cycle, joint interaction torques were multiplied by the corresponding angular velocities to compute the interaction power. The angular velocity was used directly for the knee, while for the hip it was quenched during mid-swing by using a cosine function. This approach, motivated by the need to mitigate the potential contribution from passive factors, such

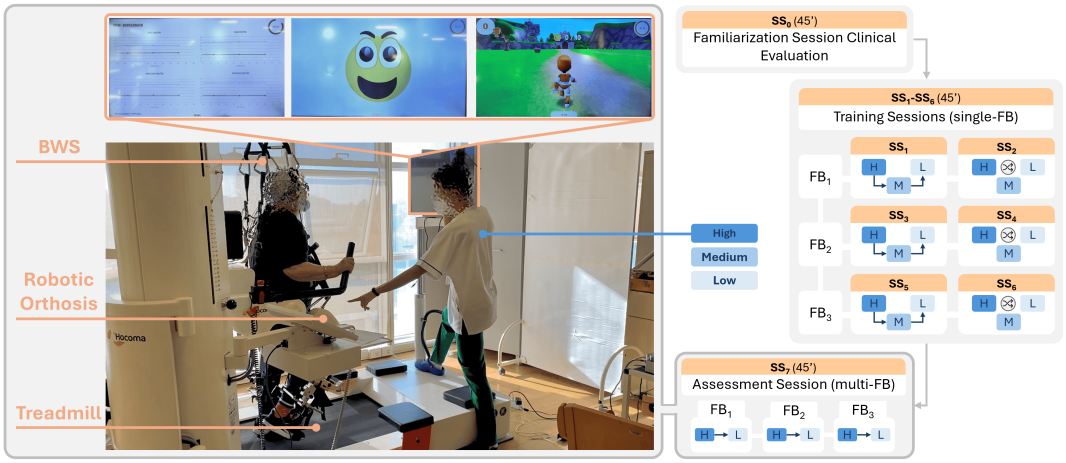


Fig. 1: Experimental setup and protocol for RAGT sessions with three visual feedback types (*chart*, *emoticon*, *game*). A representative participant is depicted during the assessment session with *high* patient-therapist verbal interaction.

as gravity, that could otherwise have inflated the interaction power, was suggested in [14], [15]. The interaction power was then integrated over specific windows of the gait cycle to calculate the work for the stance and swing phases. In accordance with [15], the window for the stance phase was defined as 0-50% of the gait cycle for both joints; the window for the swing phase was defined as 55-82% for the hip and 51-90% for the knee. By definition, positive work values indicate active contribution while negative values represent passive or even resistive behaviour. This process yielded eight values for each stride: hip and knee stance and swing for both sides.

2) Statistical Analysis: The distribution of the data was assessed for normality by using the Shapiro-Wilk test (significance level $\alpha = 0.05$). Results indicated a non-normal distribution, thus non-parametric statistical tests were employed to analyze the differences in the work values with respect to three factors: *feedback* (3 levels: *chart*, *emoticon*, *game*), *interaction* (2 levels: *high*, *low*), and *impairment* (2 levels: HSL, LSL).

For factor *feedback*, Friedman tests were employed to detect differences in the dependent variables across the three levels ($\alpha = 0.05$). In case of significant results, post-hoc pairwise comparisons were conducted by using Tukey's test to identify specific differences. For factors *interaction* and *impairment*, Wilcoxon signed-rank tests were applied to compare results between the two levels of each factor and Bonferroni correction was used for multiple comparisons.

III. Results

Fig. 2a shows the physical variables (angular velocity $\dot{\theta}$, torque τ and power P) used to compute the work W within the highlighted windows, and Fig. 2b shows the resulting work values for the stance and swing phases of the gait cycle for hip (W_{hip}) and knee (W_{knee}) separately.

The analysis of the aggregated data in Fig. 3a revealed that participants were able to generate positive work across most conditions, except for knee during the swing, for which median negative values were observed regardless of feedback type, interaction, or more impaired side.

1) Effects of Impairment: Participants delivered significantly more positive, or less negative, work with the joints of the HSL compared to the LSL (hip stance: $\Delta W = 1.38$ J/kg, $+65\%$, $p = 0.003$; hip swing: $\Delta W = 1.13$ J/kg, $+72\%$, $p < 0.001$; knee stance: $\Delta W = 0.56$ J/kg, $+45\%$, $p < 0.001$; knee swing: $\Delta W = 2.15$ J/kg, $+122\%$, $p < 0.001$). This trend was especially pronounced under specific conditions. For instance, during hip stance with feedback *game*, the average work for the HSL was 1.73 J/kg, compared to -1.03 J/kg for the LSL ($\Delta W = 2.76$ J/kg, $+788\%$), highlighting a marked performance discrepancy. Similarly, during hip swing with feedback *emoticon*, the work for the HSL was 1.79 J/kg, compared to 0.58 J/kg for the LSL ($\Delta W = 1.22$ J/kg, $+102\%$). For the knee joint, the differences were generally smaller though exceptions were noted, such as for knee swing with feedback *emoticon* ($\Delta W = 1.93$ J/kg, $+98\%$). In contrast, conditions that minimized discrepancies between HSL and LSL were predominantly associated with feedback *chart*: hip stance ($\Delta W = 0.63$ J/kg, $+25\%$), hip swing ($\Delta W = 0.28$ J/kg, $+21\%$), and knee stance ($\Delta W = 0.27$ J/kg, $+20\%$). A similar effect was observed in knee swing with feedback *game* ($\Delta W = 0.17$ J/kg, -6%).

2) Effects of Verbal Feedback: When patient-therapist verbal interaction was set to *high*, participants generally produced more positive work with the HSL compared to conditions with interaction *low*, significantly for hip swing ($\Delta W = 0.48$ J/kg, $+23\%$, $p = 0.008$). Other examples include hip stance with feedback *chart* ($\Delta W = 0.86$ J/kg, $+30\%$) and knee swing with feedback *emoticon* ($\Delta W = 1.15$ J/kg, $+350\%$). The only exceptions, where interaction *low* yielded slightly better performance, were hip stance ($\Delta W = 0.32$ J/kg, $+18\%$) and hip swing ($\Delta W = 0.29$ J/kg, $+16\%$) with feedback *emoticon*, though these differences were minor. For the LSL, factor interaction yielded heterogeneous results. Even if higher work was generally observed with interaction *high* for feedback

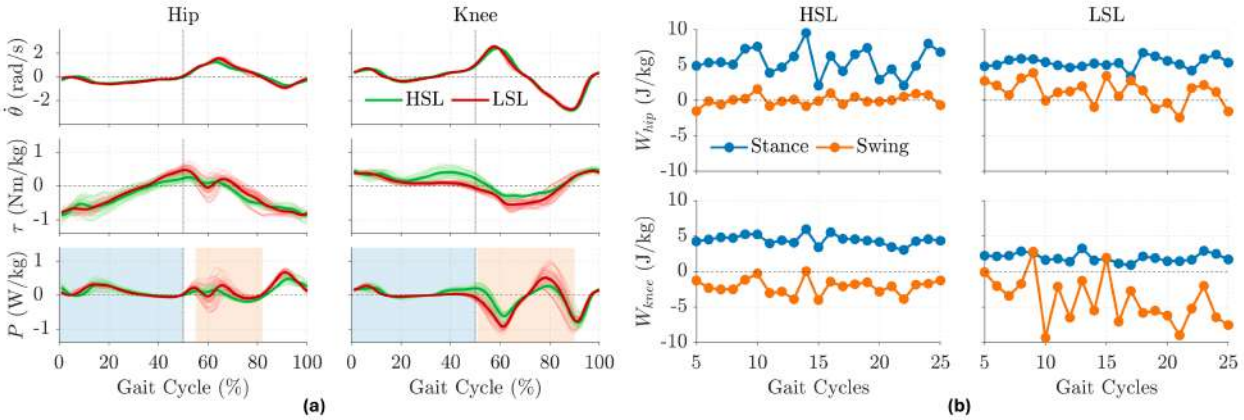


Fig. 2: Data from a representative participant (P7 in Tab. I). (a) Angular velocity $\dot{\theta}$, interaction torque τ and power P, time-normalized to the gait cycle duration, for the High Strength Limb (HSL) and Low Strength Limb (LSL). Blue and orange shaded areas represent the windows of integration for the stance and swing phases, respectively. (b) Stride-by-stride work for hip (W_{hip}) and knee (W_{knee}) calculated for stance and swing phases.

chart (hip stance: $\Delta W = 1.75$ J/kg, $+78\%$; hip swing: $\Delta W = 0.17$ J/kg, $+19\%$; knee stance: $\Delta W = 0.34$ J/kg, $+27\%$; knee swing: $\Delta W = 0.83$ J/kg, $+40\%$), under feedback *emoticon* and *game* participants sometimes produced comparable or higher work with interaction *low*. The most remarkable example of this result was found for hip stance with feedback *emoticon* ($\Delta W = 2$ J/kg, $+164\%$).

3) Effects of Visual Feedback: Overall, the results indicated that feedback *chart* was the most effective in promoting positive work, followed by feedback *emoticon* and *game*. This trend was consistent across all joints and phases, but statistically significant only for hip swing ($p = 0.032$), for which post-hoc analysis confirmed that feedback *chart* was significantly more effective than feedback *game* ($\Delta W = 1.22$ J/kg, $+63\%$, $p = 0.026$) in eliciting positive work.

Regarding the variability of the work (Fig. 3b), the hip and the knee during the stance phase exhibited the highest and lowest variability across all conditions, respectively (average median values around 2 J/kg for the hip and 0.5 J/kg for the knee). Although no statistically significant differences were observed with factors interaction or impairment during the stance phase, a significant effect of factor feedback was identified for both the hip ($p = 0.008$) and knee ($p = 0.013$), for which post-hoc analysis revealed that variability was significantly higher for feedback *game* compared to *emoticon* (hip: $\Delta W = 1.44$ J/kg, $+74\%$, $p = 0.006$; knee: $\Delta W = 1.33$ J/kg, $+71\%$, $p = 0.013$). During the swing phase, the variability was more comparable between the hip and knee, with median values around 1 J/kg. For both joints, the HSL demonstrated higher variability with interaction *high* compared to *low*, but significantly for knee only (hip: $\Delta W = 0.28$ J/kg, $+23\%$; knee: $\Delta W = 0.28$ J/kg, $+23\%$, $p = 0.002$). Additionally, the hip during swing showed significantly higher variability for the HSL compared to the LSL, regardless of the level of interaction ($\Delta W = 0.27$ J/kg, $+25\%$, $p < 0.001$).

IV. Discussion

This study examined the effects of visual feedback and patient-therapist interaction on the active participation of individuals with SCI during RAGT with the Lokomat. Previous research has demonstrated that Lokomat-assisted training with visual feedback produces similar performance as verbal instructions from a therapist for healthy participants and SCI patients [13]–[15], [25]. Building on these findings, we focused on identifying the most effective type of visual feedback for eliciting active patient participation and investigated whether combining visual feedback with an empathetic and supporting human component would enhance performance. From a biomechanical perspective, active participation during RAGT with Lokomat has been described with different, yet rather similar, approaches [13]–[15], [17], [24], [25]. In our work we referred to the interaction energy between participants and the robot, calculated as the integral of the pointwise multiplication between the weight-normalized interaction torques and angular velocities or, in other words, the normalized interaction power.

A. Role of visual and verbal feedback

One relevant result is the efficacy of feedback *chart* in promoting positive work. Across nearly all conditions and joints, it yielded smaller discrepancies between the HSL and the LSL, suggesting its capacity to promote symmetric performance. Moreover, it elicited higher median values with respect to the other feedback types, even if only significantly better than feedback *game* during hip swing. This suggests that the structured and detailed nature of feedback *chart* may provide patients with a clearer, more practical understanding of their performance, enabling them to focus on generating positive work. In contrast, feedback types like *game* and *emoticon* displayed heterogeneous results. Even though they likely foster engagement and motivation, their qualitative and abstract

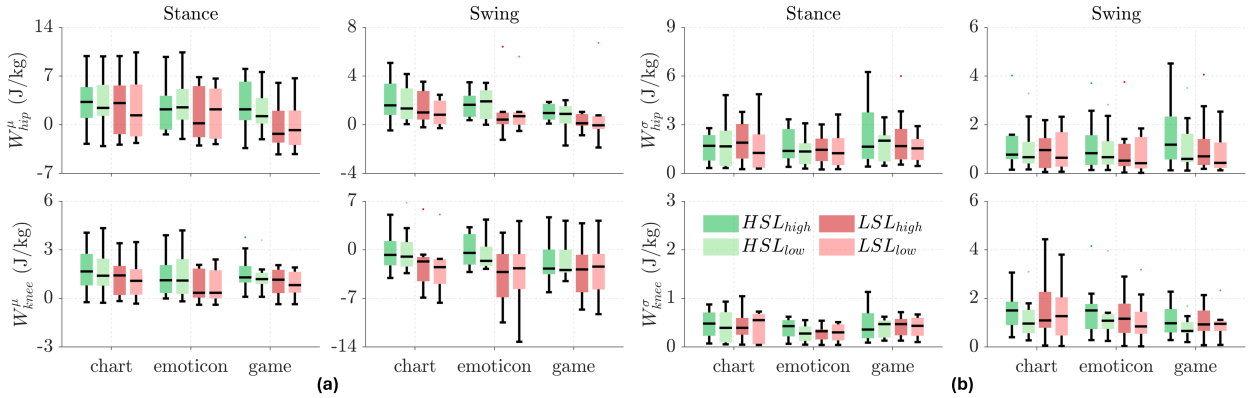


Fig. 3: Aggregated work values across participants and strides for hip/knee during stance/swing phases. Green and red boxes represent the High Strength Limb (HSL) and the Low Strength Limb (LSL), respectively. Darker and lighter shades indicate *high* and *low* patient-therapist verbal interaction, respectively. (a) Mean work W^{μ}. (b) Standard deviation of the work W^{σ}.

Factor		$W^{\mu}_{hip,st}$	$W^{\mu}_{hip,sw}$	$W^{\mu}_{knee,st}$	$W^{\mu}_{knee,sw}$	$W^{\sigma}_{hip,st}$	$W^{\sigma}_{hip,sw}$	$W^{\sigma}_{knee,st}$	$W^{\sigma}_{knee,sw}$
feedback		0.459	0.032^{*}	0.459	0.062	0.008^{*}	0.09	0.013^{*}	0.641
	chart vs emoticon		0.613			0.142		0.085	
	chart vs game		0.026^{*}			0.466		0.759	
	emoticon vs game		0.255			0.006^{*}		0.013^{*}	
interaction		0.792	$< 0.001^{*}$	0.04	0.859	0.014^{*}	0.005^{*}	0.103	$< 0.001^{*}$
	HSL	0.828	0.008^{*}	0.258	0.648	0.102	0.032	0.107	0.002^{*}
	LSL	0.665	0.018	0.068	0.754	0.057	0.084	0.548	0.035
impairment		0.003^{*}	$< 0.001^{*}$	$< 0.001^{*}$	$< 0.001^{*}$	0.223	$< 0.001^{*}$	0.205	0.332
	high	0.034	$< 0.001^{*}$	0.002^{*}	$< 0.001^{*}$	0.773	0.013	0.290	0.301
	low	0.043	$< 0.001^{*}$	0.003^{*}	$< 0.001^{*}$	0.118	0.017	0.361	0.718

TABLE II: Results of the statistical analysis for visual feedback, patient-therapist interaction, and impairment for hip/knee average work (W^{μ}) and standard deviation (W^{σ}) during stance/swing phases. The symbol * indicates significant results.

nature may have introduced ambiguities in how patients interpreted and responded to the task, despite the dedicated training sessions before the assessment. For example, with feedback *game*, discrepancies in work between HSL and LSL were high during hip stance, and for feedback *emoticon*, the LSL sometimes performed better with interaction *low* compared to *high*. These inconsistencies suggest that while these feedback types may promote enthusiasm and playfulness, their lack of specificity might limit their effectiveness in supporting targeted performance improvements. This hypothesis is consistent with our previous findings, which suggested that feedback *game* elicits lower mental and physical demands [18].

As for patient-therapist verbal interaction, the level *high* was generally associated with better performance of the HSL, particularly during hip swing. This suggests that verbal cues and a closer engagement may have provided support and motivation for the participants, encouraging them to focus on specific goals. However, the impact of interaction level was less clear for the LSL, with level *low* resulting in higher work in some cases, such as hip stance with feedback *emoticon*.

B. Limitations and future works

A critical consideration in interpreting these results is the generic nature of the instructions given to participants during the experiment. Participants were encouraged to enhance their performance across all joints and phases rather than focusing separately on specific sub-tasks. This approach, even if realistic for clinical training scenarios, may have diluted the measurable differences among conditions specifically for the LSL. Indeed, in the absence of specific instructions, patients likely directed their efforts more consistently toward the HSL, given that it is the limb with greater muscular strength. This broad approach could have partially masked the full impact of the interventions, especially for the LSL in which we expect higher inter- and intra-subject variability. To address this limitation, future studies should explore a more task-specific approach: by isolating individual sub-tasks, for example, the knee of the LSL during the stance phase, patients could be given clearer, more focused goals. This might enhance their ability to respond to visual feedback and better highlight the benefits of different modalities and interaction levels. Additionally, this approach could allow for a more detailed evaluation of how feedback and interaction strategies influence specific impairments, ultimately leading to more effective rehabilitation protocols. In the envisioned scenario, feedback *chart* is likely the most useful among the

investigated options, as it provides information on all joints and gait phases separately, as opposed to feedback *game*, which only discriminates between left and right limbs, and feedback *emoticon*, which cumulatively considers all joints and gait phases, thus providing very generic feedback. On the other hand, our previous work hypothesized that feedback *chart* likely elicited a higher mental demand due to the concurrent amount of displayed information, but a frustration level comparable to the other types [18]. In this context, we believe that the role of the therapist's verbal instructions can be determinant in facilitating the conveyance of information.

Overall, these results suggest the need for feedback mechanisms that balance motivational benefits with clear, consistent guidance to maximize performance. At the same time, besides the type of visual feedback and therapist's verbal instructions, the nature of the task seems likewise important. A generic task with broad, non-specific instructions may only partially highlight the therapist's contribution. In contrast, a more specific task with clearly targeted requests and instructions could better boost the benefits of therapist's role, potentially enhancing the rehabilitation outcomes.

V. Conclusions

The study highlights the role of patient-therapist verbal interaction combined with different types of visual feedback, to enhance the active participation of individuals with SCI during RAGT. Specifically, it shows that providing patients with a quantitative measure of their performance while verbally interacting with the physical therapist results in more evident participation. We also argue that the type of visual feedback and the level of verbal interaction with the therapist are not the only factors influencing the active patient participation. Indeed, the role of the selected task and the specific requests deserve further investigation in dedicated experiments.

Acknowledgment

This work was partially supported by: *i)* Italian Ministry of Health (GR2019-12369207); *ii)* Sapienza University of Rome (RM123188F229EC72); *iii)* Italian Ministry of University and Research under the National Recovery and Resilience Plan, Mission 4, Component 2, Investment 1.1, Call for tender No. 104, funded by the EU (NextGenerationEU), Project Title 202254EAA5 - Exoskeleton-assisted walking for prehabilitation and active aging.

References

[1] R. Gassert and V. Dietz, "Rehabilitation robots for the treatment of sensorimotor deficits: A neurophysiological perspective," *Journal of NeuroEngineering and Rehabilitation*, vol. 15, p. 46, 06 2018.

[2] V. Dietz, M. Wirz, A. Curt, and G. Colombo, "Locomotor pattern in paraplegic patients: Training effects and recovery of spinal cord function," *Spinal cord*, vol. 36, pp. 380–90, 07 1998.

[3] S. Hesse, D. Uhlenbrock *et al.*, "A mechanized gait trainer for restoration of gait," *Journal of rehabilitation research and development*, vol. 37, no. 6, pp. 701–708, 2000.

[4] T. G. Hornby, D. D. Campbell, J. H. Kahn, T. Demott, J. L. Moore, and H. R. Roth, "Enhanced gait-related improvements after therapist-versus robotic-assisted locomotor training in subjects with chronic stroke: a randomized controlled study," *Stroke*, vol. 39, pp. 1786–1792, 2008.

[5] F. Di Tommaso, F. Tamburella, M. Lorusso, L. Gastaldi, M. Molinari, and N. L. Tagliamonte, "Biomechanics of exoskeleton-assisted treadmill walking," in *2023 International Conference on Rehabilitation Robotics (ICORR)*. IEEE, 2023, pp. 1–6.

[6] G. Morone, S. Paolucci, A. Cherubini, D. D. Angelis, V. Venturiero, P. Coiro, and M. Iosa, "Robot-assisted gait training for stroke patients: current state of the art and perspectives of robotics," *Neuropsychiatric Disease and Treatment*, vol. 13, pp. 1303 – 1311, 2017. [Online]. Available: https://api.semanticscholar.org/CorpusID:2702241

[7] G. Colombo, M. Joerg, R. Schreier *et al.*, "Treadmill training of paraplegic patients using a robotic orthosis," *Journal of rehabilitation research and development*, vol. 37, no. 6, pp. 693–700, 2000.

[8] G. Colombo, M. Wirz, and V. Dietz, "Driven gait orthosis for improvement of locomotor training in paraplegic patients," *Spinal cord*, vol. 39, no. 5, pp. 252–255, 2001.

[9] L. Wu, G. Xu, and Q. Wu, "The effect of the lokomat® robotic-orthosis system on lower extremity rehabilitation in patients with stroke: a systematic review and meta-analysis," *Frontiers in Neurology*, vol. 14, p. 1260652, 2023.

[10] A. R. Alashram, G. Annino, and E. Padua, "Robot-assisted gait training in individuals with spinal cord injury: A systematic review for the clinical effectiveness of lokomat," *Journal of Clinical Neuroscience*, vol. 91, pp. 260–269, 2021.

[11] M. Lotze, C. Braun, N. Birbaumer, S. Anders, and L. G. Cohen, "Motor learning elicited by voluntary drive," *Brain*, vol. 126, pp. 866–872, 2003.

[12] A. Kaelin-Lang, L. Sawaki, and L. G. Cohen, "Role of voluntary drive in encoding an elementary motor memory," *Journal of neurophysiology*, vol. 93, no. 2, pp. 1099–1103, 2005.

[13] R. Riener, L. Lunenburger, S. Jezernik, M. Anderschitz, G. Colombo, and V. Dietz, "Patient-cooperative strategies for robot-aided treadmill training: first experimental results," *IEEE transactions on neural systems and rehabilitation engineering*, vol. 13, no. 3, pp. 380–394, 2005.

[14] L. Lünenburger, G. Colombo, and R. Riener, "Biofeedback for robotic gait rehabilitation," *Journal of neuroengineering and rehabilitation*, vol. 4, pp. 1–11, 2007.

[15] R. Banz, M. Bolliger, G. Colombo, V. Dietz, and L. Lünenburger, "Computerized visual feedback: an adjunct to robotic-assisted gait training," *Physical therapy*, vol. 88, no. 10, pp. 1135–1145, 2008.

[16] F. Tamburella, J. C. Moreno, M. Iosa, I. Pisotta, F. Cincotti, D. Mattia, J. L. Pons, and M. Molinari, "Boosting the traditional physiotherapist approach for stroke spasticity using a sensorized ankle foot orthosis: a pilot study," *Topics in stroke rehabilitation*, vol. 24, pp. 447–456, 2017.

[17] A. Koenig, X. Omlin, J. Bergmann, L. Zimmerli, M. Bolliger, F. Müller, and R. Riener, "Controlling patient participation during robot-assisted gait training," *Journal of neuroengineering and rehabilitation*, vol. 8, pp. 1–12, 2011.

[18] F. Patarini, F. Tamburella, F. Pichiorri, S. Mohebban, A. Bigioni, A. Ranieri, F. Di Tommaso, N. Tagliamonte, G. Serratore, M. Lorusso *et al.*, "On the role of visual feedback and physiotherapist-patient interaction in robot-assisted gait training: an eye-tracking and hd-eeg study," *Journal of NeuroEngineering and Rehabilitation*, 2024.

[19] A. L. Krill and S. M. Platek, "Working together may be better: Activation of reward centers during a cooperative maze task," *PloS one*, vol. 7, no. 2, p. e30613, 2012.

[20] B. D. INVENTORY-II, "Beck depression inventory-ii," *The Corsini Encyclopedia of Psychology, Volume 1*, vol. 1, p. 210, 2010.

[21] Z. S. Nasreddine, N. A. Phillips, V. Bédirian, S. Charbonneau, V. Whitehead, I. Collin, J. L. Cummings, and H. Chertkow, "The montreal cognitive assessment, moca: a brief screening tool for mild cognitive impairment," *Journal of the American Geriatrics Society*, vol. 53, no. 4, pp. 695–699, 2005.

[22] A.-B. Meseguer-Henarejos, J. Sánchez-Meca, J.-A. López-Pina, and R. Carles-Hernández, "Inter-and intra-rater reliability of the modified ashworth scale: a systematic review and meta-analysis." *European journal of physical and rehabilitation medicine*, vol. 54, 2017.

[23] F. M. Maynard Jr, M. B. Bracken, G. Creasey, J. F. Ditunno Jr, W. H. Donovan, T. B. Ducker, S. L. Garber, R. J. Marino, S. L. Stover, C. H. Tator *et al.*, "International standards for neurological and functional classification of spinal cord injury." *Spinal cord*, vol. 35, no. 5, 1997.

[24] R. Banz, M. Bolliger, S. Muller, C. Santelli, and R. Riener, "A method of estimating the degree of active participation during stepping in a driven gait orthosis based on actuator force profile matching," *IEEE Transactions on Neural Systems and Rehabilitation Engineering*, vol. 17, no. 1, pp. 15–22, 2008.

[25] L. Lunenburger, G. Colombo, R. Riener, and V. Dietz, "Biofeedback in gait training with the robotic orthosis lokomat," in *The 26th Annual International Conference of the IEEE Engineering in Medicine and Biology Society*, vol. 2. IEEE, 2004, pp. 4888–4891.

Development of a Real-Time Neural Controller using an EMG-Driven Musculoskeletal Model

Joel Biju Thomas and Brokoslaw Laschowski

Abstract – **Here we present the development of a novel real-time neural controller based on an EMG-driven musculoskeletal model, designed for volitional control of robots and computers. Our controller uniquely enables motion control during both isometric and non-isometric muscle contractions. We address several key challenges in EMG control system design, including accuracy, latency, and robustness. Our approach combines EMG signal processing, neural activation dynamics, and Hill-type muscle modeling to translate neural commands into muscle forces, which can enhance robustness against electrode variability and signal noise. Additionally, we integrate muscle activation dynamics with impedance control, inspired by the human motor control system, for smooth and adaptive interactions. As a proof of concept, we demonstrate that our system can control a robotic actuator across a range of lower-limb movements, both static and dynamic, and at different operating speeds, achieving high reference tracking performance and state-of-the-art processing time of 2.9 ms, important for real-time embedded computing. This research helps lay the groundwork for next-generation neural-machine interfaces that are fast, accurate, and adaptable to diverse users and control applications.**

I. Introduction

Surface electromyography (EMG) is a non-invasive neural interface that can be used to volitionally control robots and computers by translating feedforward neural commands from the brain (i.e., that encode information about motor intent) into actionable control signals. Despite this potential, the development of reliable EMG neural controllers faces significant challenges, particularly in terms of system accuracy, latency, and adaptability to diverse users [1]. Applications in patients with amputation require precise control during isometric muscle contractions, while controllers for able-bodied persons need to also support dynamic, non-isometric contractions for natural, functional movements. High accuracy and low latency, which are critical to optimal user experience, remains an open problem for these neural controllers [2]-[5].

Two of the main paradigms used for EMG neural control are data-driven classification models and neuromusculoskeletal models. Data-driven methods typically use machine learning algorithms to classify, or decode, the joint movement from EMG signals [6]-[7] such as quadratic discriminant analysis used by [6] for patients with amputation. While these models have shown success, they often make simplifying assumptions about the underlying data distributions, which can limit their robustness given the inherent non-Gaussian nature of EMG data. Factors such as noise, muscle fatigue, and inter-subject variability also pose significant challenges to these classification models for long-term operation [7]-[8], including requiring long user training times. More complex models such as convolutional or recurrent neural networks could help eliminate these assumptions but could compromise real-time inference with low latency.

In contrast, neuromusculoskeletal modelling approaches model muscle forces and joint dynamics more directly, thus allowing for improved accuracy in muscle force prediction and system adaptability. Previous research [5] has used these computational models to simulate muscle-generated forces from EMG signals. However, they tend to lack an EMG-to-activation model, which can limit their robustness to variations in sensor placement and EMG signal-to-force mapping accuracy, constraining their practical utility. Despite progress in both machine learning and neuromusculoskeletal modelling EMG controllers, the focus has been on isometric control for amputees, with less attention given to the general population (i.e., able-bodied users) and to dynamic, non-isometric movements [5]-[7], which can be more technically challenging.

To address these gaps, here we present the development of a novel EMG neural controller driven by a musculoskeletal model. We include an EMG-to-activation model to improve robustness and to more accurately map EMG signals to muscle forces. Our controller uniquely handles both isometric and non-isometric muscle contractions, expanding functionality over previous work [5]-[7]. By combining the strengths of neuromusculoskeletal modeling with a more accurate EMG signal-to-force mapping model, our research helps lay the foundation for next-generation neural-machine interfaces that can support diverse users and control applications. While the focus of this study was on the control system design, as a proof-of-concept, we demonstrate that our EMG neural controller can be used to accurately and in real-time control a robotic actuator across a range of operating speeds using neural commands to leg muscles (see Fig. 1).

II. Methods

A. Signal Processing

We used standard EMG processing to enhance our signal quality and to reduce unwanted artifacts [9], including a 200x gain amplifier, hardware bandpass filter between 20-498 Hz, signal rectification, and offset removal. We also performed envelope detection using a linear, passive first-order filter with a cutoff frequency of 3.6 Hz. This filter has a frequency response characterized by a -20 dB/decade attenuation, capturing the slow-varying envelope of the rectified EMG signal [9]. To further enhance clarity, we amplified the envelope using a secondary gain amplifier and digitized the signal with an Arduino

*Research supported by the Schroeder Institute for Brain Innovation and Recovery, Canada.

J. B. Thomas is with the Department of Electrical and Computer Engineering, University of Toronto, Toronto, ON, Canada (e-mail: jb.thomas@mail.utoronto.ca).

B. Laschowski is with the Department of Mechanical and Industrial Engineering, University of Toronto, Toronto, ON, Canada, and KITE Research Institute, Toronto Rehabilitation Institute, Toronto, ON, Canada (e-mail: brokoslaw.laschowski@utoronto.ca).

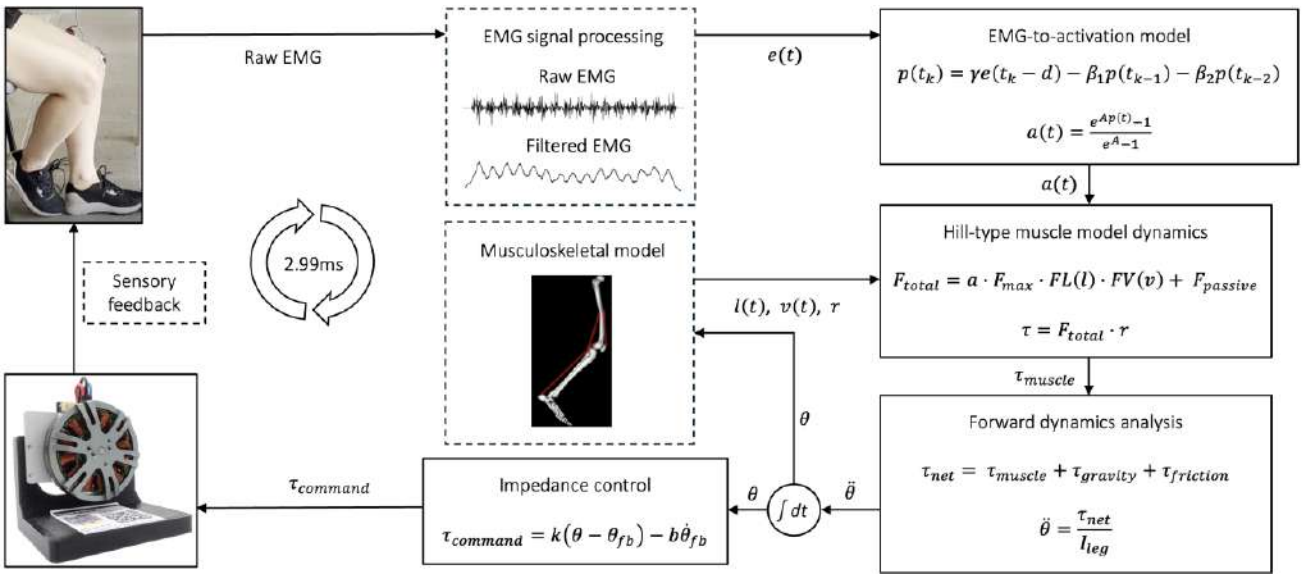


Fig. 1 System diagram of our real-time neural controller using an EMG-driven musculoskeletal model. We process and convert raw EMG signals into neural activations, which drive our muscle and musculoskeletal dynamics models to produce joint torques and movement. We also developed an impedance controller to generate torque commands for our motor actuator, which takes as input the simulated joint kinematics. The control loop is closed by the user receiving visual feedback of the rotating motor.

Uno R3 as an ADC, sampling at 1400 Hz with a baud rate of 115,200. The digitized EMG signals were sent to Raspberry Pi using USB UART for further processing. We normalized the signal to a 0–1 range to enable consistency across subjects using maximal voluntary contraction (MVC) and minimum EMG amplitude during full muscle flexion and relaxation. This minimizes variations in amplitude due to individual physiology, which allow for more accurate cross-subject and experimental comparisons [10].

B. Neural Activation Model

The biological tissue between the EMG electrode and muscle filters the neural signals produced by the muscles before they are recorded. This can pose an issue where factors such as the positioning of the electrodes, ambient temperature, skin condition, and electrical impedance can influence filtering [11]. To reduce this effect of tissue filtering, we developed an EMG-to-activation model to interpret the EMG signals and estimate muscle forces, accounting for physiological delays and nonlinearities in muscle activations, thus enhancing precision.

The EMG-to-activation model begins with activation dynamics, which transforms the processed EMG signals $e(t)$ into neural activations $p(t)$ [12]. This process addresses the time delay between EMG onset and muscle force generation, as well as the longer durations of muscle forces compared to EMG signals [11]. Unlike previous work [5], our controller includes this EMG-to-activation model for a more reliable muscle force estimation by taking into account biological delays and nonlinearities. We used a critically-damped linear second-order differential system to model the delayed muscle twitch response, which occurs when a single action potential stimulates an individual muscle fiber [12]. In its discrete form, see Equation 1, the second-order system can be expressed recursively to compute $p(t)$, providing a more accurate representation of the muscle's force generation based on the input EMG neural signal.

$$p(t_k) = \gamma e(t_k - d) - \beta_1 p(t_{k-1}) - \beta_2 p(t_{k-2}) \quad (1)$$

$$a(t) = \frac{e^{Ap(t)}-1}{e^{A}-1} \quad (2)$$

where $e(t)$ is the filtered EMG signal, d is the electromechanical delay, and γ, β_1, and β_2 are coefficients governing the second-order system dynamics. To ensure a positive and stable outcome, we enforced specific constraints: $\beta_1 = C_1 + C_2$ and $\beta_2 = C_1 C_2$, with the conditions $|C_1| < 1$ and $|C_2| < 1$. Furthermore, to preserve the filter's gain, we must satisfy $\gamma - \beta_1 - \beta_2 = 1$. We used a nonlinear conversion between the neural activations $p(t)$ and muscle activations $a(t)$, see Equation 2, to address the non-linear relationship between the EMG signal and muscle force generation at low-force and high twitch frequencies [12].

C. Muscle Model

We developed a Hill-type muscle model to mathematically model the muscle force generation based on the relationships between muscle length, contraction speed, and activation dynamics. Our Hill-type muscle model combines active forces from neural activations with the passive forces from muscle stretching for a more biofidelic representation of biological muscle dynamics. We used the force-length factor to model how the muscle force generation depends on its length relative to optimal length, with maximum force at the optimal length and an exponential decrease as the muscle length deviates.

$$FL(l) = e^{-\left(\frac{l - l_{opt}}{0.5 \cdot l_{opt}}\right)^2} \quad (3)$$

where $FL(l)$ is the muscle force-length factor, l is the current muscle length, and l_{opt} is the optimal muscle length [13]. For concentric muscle contractions, where velocity is greater than

or equal to 0, we used a linear force-velocity relationship. For eccentric muscle contractions, where the velocity is less than zero, we used a nonlinear force-velocity relationship.

$$FV(v) = \begin{cases} 1 - \frac{v}{v_{max}} & if\ v \geq 0 \\ N - (N-1) \cdot e^{\frac{v}{v_{ecc} \cdot l_{opt}}} & if\ v < 0 \end{cases} \quad (4)$$

where $FV(v)$ is the muscle force-velocity factor, v is the muscle velocity, v_{max} is the maximum shortening velocity, N is the eccentric muscle force factor, and V_{ecc} is the characteristic velocity of eccentric muscle contractions [13]. Active force (F_{active}) is defined as the product of the muscle activation, maximum isometric force, force-length factor, and the force-velocity factor, and is represented by:

$$F_{active} = a \cdot F_{max} \cdot FL(l) \cdot FV(v) \quad (5)$$

where a is the muscle activation level, ranging from 0 to 1, and F_{max} is the maximum isometric force. We derived muscle length and velocity from the joint angle and angular velocity using our musculoskeletal model. We calculated the muscle length by converting the joint angle into radians, adjusting for deviations from the reference angle, and scaling by moment arm. We calculated muscle velocity by converting the joint angular velocity into radians and scaling using the moment arm. Passive forces $(F_{passive})$ are generated when the muscle stretches beyond its optimal length, increasing quadratically with stretch. We assume no passive muscle force is produced below the optimal length, but beyond that, the force grows exponentially and is defined by the maximum isometric force and a passive stiffness coefficient $(C_{passive})$ [13].

$$F_{passive} = F_{max} \cdot C_{passive} \cdot \left(\frac{l - l_{opt}}{l_{opt}}\right)^2 \quad if\ l > l_{opt} \quad (6)$$

We calculated the total force F_{total} generated by the muscle using the sum of the active F_{active} and passive $F_{passive}$ muscle forces. The resultant joint torque τ generated by the muscle was calculated using the product of the total force F_{total} and the moment arm r.

D. Forward Dynamics

We used forward dynamics analysis to calculate the joint motion from the applied muscle torques, gravitational forces, and joint friction in our musculoskeletal system model.

$$\tau_{muscle} = \tau_{quad} - \tau_{ham} \quad (7)$$

where τ_{muscle} is the net joint torque, which is the difference between the joint torques generated by the quadricep muscles τ_{quad} and the hamstring muscles τ_{ham}. We estimated the joint torque generated from gravity acting on the leg $\tau_{gravity}$ using Equation 8:

$$\tau_{gravity} = m_{leg} \cdot g \cdot \frac{l_{leg}}{2} \cdot sin\left(\theta_{joint} + 90°\right) \quad (8)$$

where m_{leg} is the estimated mass of the leg, g is acceleration due to gravity, l_{leg} is the length of the leg, and θ_{joint} is the instantaneous joint angle. We estimated the frictional torque in the joint using $\tau_{friction} = -b \cdot \dot{\theta}$, where b is the biological damping coefficient and $\dot{\theta}$ is the angular velocity of the joint. The net joint torque τ_{net} is the sum of τ_{muscle}, $\tau_{gravity}$ and $\tau_{friction}$, and the resulting angular acceleration $\ddot{\theta}$ is calculated as $\ddot{\theta} = \frac{\tau_{net}}{I_{leg}}$, where I_{leg} is the estimated moment of inertia of the leg derived from anthropometric measurements. When calculating τ_{net} for isometric contractions, we set $\tau_{gravity}$ and the muscle velocity to 0. We did this so that the EMG signal is used to generate an angular velocity, which means that the motor will only actuate when the muscles are contracting and is stationary when the muscles are relaxed. This is important for downstream applications in patients with amputation, for example, to minimize fatigue while operating our controller. We assume a constant muscle length.

E. Kinematics

We used kinematic analysis to continuously track the joint angular velocity and position over time based on the initial conditions and integrals. We calculated joint angular velocity $\dot{\theta}(t) = \dot{\theta}(t_0) + \int_{t_0}^{t} \ddot{\theta}(t')\ dt'$ using the initial velocity $\dot{\theta}(t_0)$ and the cumulative angular acceleration $\ddot{\theta}(t')$. We calculated the joint angular position $\theta(t) = \theta(t_0) + \int_{t_0}^{t} \dot{\theta}(t')\ dt'$using the initial position $\theta(t_0)$ and the integrated velocity.

F. Impedance Control

We developed an impedance controller for our low-level controller to convert joint motion (input) to torque (output). Impedance control is widely used in robotics to control the interaction between force and motion by adjusting mechanical impedance. This control paradigm is inspired by human motor control, where the nervous system regulates muscle stiffness and compliance for smooth and adaptive physical interactions with the environment. Research has consistently shown that myoelectric impedance control outperforms conventional velocity-based controllers in constrained motion tasks [4]. Our impedance controller is expressed as:

$$\tau_{command} = k\left(\theta - \theta_{fb}\right) - b\dot{\theta}_{fb} \quad (9)$$

where $\tau_{command}$ is the torque command to the field-oriented controller of our motor actuator, θ is the joint position of our musculoskeletal model, θ_{fb} is the motor position, $\dot{\theta}_{fb}$ is motor velocity, and k and b are stiffness and damping, respectively. Here we assumed that k and b are fixed constants that do not change based on muscular co-contraction.

G. Experiments

As a proof of concept to evaluate the performance of our EMG neural controller, we tested the ability of a single user to volitionally control a robotic actuator, specifically a brushless DC electric motor, during isometric (static) and non-isometric (dynamic) muscle contractions. We determined accuracy of our controller based on the root mean square error (RMSE) with reference joint angle trajectories, and we measured latency to assess responsiveness and real-time control.

For EMG acquisition, we used EMG sensors in bipolar configuration with the help of surface Ag/AgCl electrodes. We prepared the EMG recording sites similar to [2]. To locate the

Table 1. Comparison of our EMG neural controller with the previous state-of-the-art [6]. We evaluated performance based on the RMSE in joint angles for isometric and non-isometric muscle contractions across different movement frequencies.

	0.50Hz	**0.33Hz**	**0.25Hz**	**0.20Hz**	**Avg.**
Previous SOTA (isometric)	-	5.6°	-	7.9°	6.8
Our controller (isometric)	9.4°	9.7°	8.2°	9.5°	9.2°
Our controller (non-isometric)	9.3°	9.7°	7.9°	9.7°	9.2°

best electrode position, we had the user fully extend their leg and perform maximum quadricep contractions while we palpated the muscle. Two electrodes, ~25 mm apart, were placed on the quadricep muscle. We used a similar procedure for the hamstrings when the knee was flexed. We had the user perform maximum voluntary contraction and relaxation of their quadricep and hamstring muscles and we recorded the maximum and minimum EMG signals for normalization. In a seated posture, we instructed the user to flex and extend their instrumented leg with the goal of controlling the motor angle to follow a reference video displayed on a computer. The user practiced with our controller for ~10 minutes before results were recorded. The user performed non-isometric, sinusoidal knee flexion and extension, followed by isometric contractions with a fixed knee joint angle.

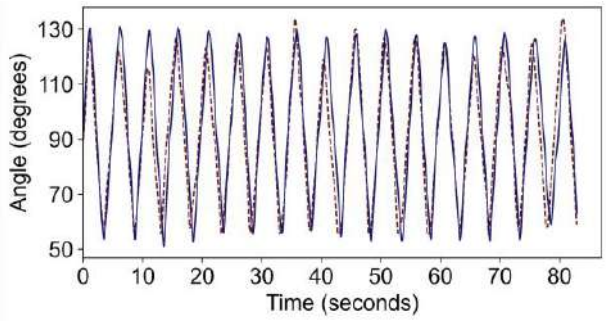


Fig. 2 Trajectory tracking of our EMG neural controller for isometric, sinusoidal movements at 0.2 Hz frequency. The red dashed signal is the reference joint angle, and the blue dashed signal is the motor angle of our neural-controlled actuator.

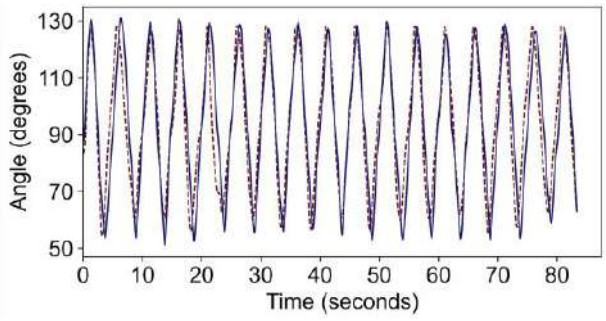


Fig. 3 Trajectory tracking of our EMG-driven neural controller for non-isometric, sinusoidal movements at 0.2 Hz frequency. The red dashed signal is the reference joint angle, and the blue dashed signal is the motor angle of our neural-controlled actuator.

We evaluated accuracy of our EMG neural controller by calculating the RMSE between the neural-controlled motor angles as measured by the motor controller (moteus r4.11 controller connected to mj5208 brushless motor) and the calculated knee joint angles from the reference video displayed on the computer. We conducted 80-second trials to test different movement frequencies at 0.2 Hz, 0.25 Hz, 0.33 Hz, and 0.5 Hz, with RMSE selected for direct comparisons with the previous state-of-the-art [6]. We developed the reference video by recording the user flex and extent their leg at the specified frequencies, guided by a metronome. We calculated the joint angles using Vicon motion tracker with 16 passive markers on the leg sampled at 100 Hz and the Vicon ProCalc software. Lastly, we measured our controller's latency by combining the processing times from the Arduino and Raspberry Pi during a motor controller update.

III. Results

Table 1 shows the accuracy of our EMG neural controller across different movement frequencies, ranging from 0.50 Hz (2 seconds) to 0.20 Hz (5 seconds). For isometric muscle contractions, our controller achieved the lowest RMSE of 8.2° at 0.25 Hz and the highest RMSE of 9.7° at 0.33 Hz (Fig. 2). Non-isometric muscle contractions followed a similar trend, with the lowest RMSE of 7.9° at 0.25 Hz and highest RMSE of 9.7° at both 0.33 Hz and 0.20 Hz (Fig. 3). Our controller achieved an average RMSE of 9.2° across all conditions, demonstrating a relatively consistent accuracy for a diverse set of motion control. Moreover, our controller achieved a state-of-the-art end-to-end processing time of 2.9 ms, showcasing its responsiveness and real-time control.

IV. Discussion

In this study, we developed a new real-time neural controller using an EMG-driven musculoskeletal model. Our system enables intuitive and responsive control for both isometric and non-isometric movements. Using processed EMG signals, we dynamically drive a muscle model to translate the user's intent into precise motor control with minimal latency. As a proof-of-concept, we demonstrate that our system can use feedforward neural commands to leg muscles for accurate real-time control of a robotic actuator across a range of different movements and operating speeds. This performance is partially due to our incorporation of muscle activation dynamics and a Hill-type muscle model with impedance control. Motivated by these promising results, our controller could be used to support the development of next-generation neural-machine interfaces for diverse users and control applications.

Our EMG neural controller achieved an average RMSE of 9.2° over 80-second experiments for both isometric and non-isometric movements. In comparison, [6] achieved 6.2° RMSE in patients with leg amputation. For 3- and 5-second isometric movement frequencies, our controller achieved an RMSE of 9.7° and 9.5°, whereas [6] achieved an RMSE of 5.6° and 7.9°, respectively. Although we achieved slightly lower accuracy, our controller can uniquely support both isometric and non-isometric motion control, whereas [6] focused on patients with amputation, and thus limited to isometric movements. Given that joint proprioception accuracy in healthy adults is ~2.5° [14], our controller's instantaneous error difference is arguably imperceptible, especially as RMSE reflects cumulative error.

Our study is one of few to develop an EMG neural controller for both isometric and non-isometric movements. Moreover, our use of a neuromusculoskeletal model can enhance our system's robustness compared to [6], which used a data-driven model. Our controller also requires significantly less training time, achieving intuitive control with only 10 minutes of user familiarization, whereas [6] required one-hour of training per session, repeated three times a week. Most notably, our controller achieved state-of-the-art processing speed of 2.9 ms, compared to 10 ms times for other two-channel EMG systems [3].

Despite these advantages, our controller has limitations. It cannot not seamlessly transition between isometric and non-isometric states as it lacks a learning algorithm for movement classification, operating in discrete controllers rather than continuously. Moreover, while our neuromusculoskeletal model offers flexibility via tunable parameters, this can lead to inconsistent accuracy across users such that optimizing our model for one user may yield suboptimal results for another unless calibrated. While muscle co-contractions are common in patients with amputation [6], our controller does not include signal processing to account for this, which would otherwise benefit our controller. Although our EMG-to-activation model can theoretically improve system robustness to uncertainty in electrode placement, we did not explicitly test this. Another limitation of our study was that the experiments were based on one user. However, the focus of this research was on the engineering control system design, while the user testing was to demonstrate an initial proof-of-concept.

Future research could expand our control system design to also include a classification algorithm to detect isometric and non-isometric movements, advancing toward a more universal EMG neural controller. Incorporating additional processing to manage muscle co-contraction—such as principal component analysis used by [6], or unsupervised learning algorithms like k-means clustering—could improve accuracy. Other neural sensors such as electroencephalography (EEG) could also be used to decode different movements and tasks [15]-[16]. Adding sensors like accelerometers or computer vision could help supplement our neuromusculoskeletal model by providing data on gravitational directionality for better control in variable orientations [17]-[20]. Overall, future research is needed to explore generalizability of our control system to novel users and tasks.

In conclusion, we developed a new EMG neural controller driven by neuromusculoskeletal model. As a proof-of-concept, we showed that our controller could achieve accurate and consistent motion control of a robotic actuator across a range of different movements and operating speeds, in addition to state-of-the-art processing speed, important for real-time embedded computing. With further development, our controller could be used to interact with and control robots and computers, providing an intuitive neural-machine interface.

ACKNOWLEDGMENT

This research study is dedicated to the people of Ukraine in response to Russia's ongoing invasion. We thank Stephen Yang and Yume Yamamoto for their assistance.

REFERENCES

[1] R. A. Fleming, N. Stafford, S. Huang, X. Hu, D. P. Ferris, and H. Huang, "Myoelectric control of robotic lower limb prostheses: a review of electromyography interfaces, control paradigms, challenges and future directions," *Journal of Neural Engineering*, vol. 18, no. 4, p. 041004, Aug. 2021.

[2] R. R. Posh, J. P. Schmiedeler, and P. M. Wensing, "Finite-state impedance and direct myoelectric control for robotic ankle prostheses: Comparing their performance and exploring their combination," *IEEE Transactions on Neural Systems and Rehabilitation Engineering*, vol. 31, pp. 2778–2788, 2023.

[3] A. Cimolato, J. J. M. Driessen, L. S. Mattos, E. De Momi, M. Laffranchi, and L. De Michieli, "EMG-driven control in lower limb prostheses: a topic-based systematic review," *Journal of NeuroEngineering and Rehabilitation*, vol. 19, no. 1, p. 43, May 2022.

[4] C. D. Hoover and K. B. Fite, "A configuration dependent muscle model for the myoelectric control of a transfemoral prosthesis," *IEEE International Conference on Rehabilitation Robotics (ICORR)*, Jun. 2011, pp. 1–6.

[5] S. K. Wu, G. Waycaster, and X. Shen, "Electromyography-based control of active above-knee prostheses," *Control Engineering Practice*, vol. 19, no. 8, pp. 875–882, Aug. 2011.

[6] K. H. Ha, H. A. Varol, and M. Goldfarb, "Volitional control of a prosthetic knee using surface electromyography," *IEEE Transactions on Biomedical Engineering*, vol. 58, no. 1, pp. 144–151, Jan. 2011.

[7] L. J. Hargrove, A. M. Simon, R. Lipschutz, S. B. Finucane, and T. A. Kuiken, "Non-weight-bearing neural control of a powered transfemoral prosthesis," *Journal of NeuroEngineering and Rehabilitation*, vol. 10, no. 1, p. 62, 2013.

[8] R. V. Schulte, M. Zondag, J. H. Buurke, and E. C. Prinsen, "Multi-day EMG-based knee joint torque estimation using hybrid neuromusculoskeletal modelling and convolutional neural networks," *Frontiers in Robotics and AI*, vol. 9, p. 869476, Apr. 2022.

[9] D. A. Winter, *Biomechanics and motor control of human movement*, 4th ed. Hoboken, N.J: Wiley, 2009.

[10] R. E. Alcaide-Aguirre, D. C. Morgenroth, and D. P. Ferris, "Motor control and learning with lower-limb myoelectric control in amputees," *Journal of Rehabilitation Research and Development*, vol. 50, no. 5, p. 687, 2013.

[11] D. G. Lloyd and T. F. Besier, "An EMG-driven musculoskeletal model to estimate muscle forces and knee joint moments in vivo," *Journal of Biomechanics*, vol. 36, no. 6, pp. 765–776, Jun. 2003.

[12] M. Hayashibe and D. Guiraud, "Voluntary EMG-to-force estimation with a multi-scale physiological muscle model," *BioMedical Engineering OnLine*, vol. 12, no. 1, p. 86, 2013.

[13] T. K. Uchida, S. Delp, and D. B. Delp, *Biomechanics of movement: the science of sports, robotics, and rehabilitation*. Cambridge, Massachusetts: The MIT Press, 2020.

[14] B. C. Stillman, E. A. Tully, and J. M. McMeeken, "Knee joint mobility and position sense in healthy young adults," *Physiotherapy*, vol. 88, no. 9, pp. 553–560, Sep. 2002.

[15] O. Shevchenko, S. Yeremeieva, and B. Laschowski, "Comparative analysis of neural decoding algorithms for brain-machine interfaces," *bioRxiv*, Dec. 2024.

[16] A. Dempster and B. Laschowski, "Domain adaptation for decoding brain dynamics using mixture models," *bioRxiv*, 2025.

[17] D. Kuzmenko, O. Tsepa, A. G. Kurbis, A. Mihailidis, and B. Laschowski, "Efficient visual perception of human-robot walking environments using semi-supervised learning," *IEEE International Conference on Intelligent Robots and Systems (IROS)*, Dec. 2023.

[18] B. Ivanyuk-Skulskiy, A. G. Kurbis, A. Mihailidis, and B. Laschowski, "Sequential image classification of human-robot walking environments using temporal neural networks," *IEEE International Conference for Biomedical Robotics and Biomechatronics (BioRob)*, Oct. 2024.

[19] D. Rossos, A. Mihailidis, and B. Laschowski, "AI-powered smart glasses for sensing and recognition of human-robot walking environments," *IEEE International Conference for Biomedical Robotics and Biomechatronics (BioRob)*, Oct. 2024.

[20] A. G. Kurbis, D. Kuzmenko, B. Ivanyuk-Skulskiy, A. Mihailidis, and B. Laschowski, "StairNet: Visual recognition of stairs for human-robot locomotion," *BioMedical Engineering OnLine*, Feb. 2024.

Lower Limb Muscle Activities and Contractility during Stepping Response to Unexpected Waist-Pull Perturbations

Oluwasegun Akinniyi[1], *Graduate Student Member, IEEE*, Maxwell Gainey[1], Dario Martelli[2], Qiang Zhang[1*], *Member, IEEE*

***Abstract*— Reactive balance responses, which involve corrective and protective strategies, are highly dependent on rapid muscle activation to restore postural stability. Although electromyography (EMG) is commonly used to measure muscle activity, it has limitations such as signal interference, particularly during fast responses to external disturbances. Ultrasound imaging (US), in contrast, provides visualization of both superficial and deep muscles. Combining EMG and US imaging offers complementary insight into muscle behavior during reactive balance tasks. In this study, we investigated muscle activation and fascicle length changes in the medial gastrocnemius (MGS), lateral gastrocnemius (LGS), and soleus (SOL) muscles of the dominant (stepping) leg during stepping responses to unexpected low-amplitude (57.6 ± 5.8 N) and high-amplitude (123.4 ± 11.1 N) waist-pull perturbations in the anterior and posterior directions. Five young male adults (age: 25.2 ± 5.5 years) participated in the study. Results showed that perturbation amplitude significantly affected the EMG activation of both the MGS and SOL muscles in both directions, consistent with previous studies. Similarly, perturbation amplitude impacted fascicle length shortening in the LGS and SOL muscles. Significant differences in MGS and SOL activation were observed between high-amplitude and low-amplitude perturbations in both directions. Fascicle shortening in the LGS also differed significantly between perturbation amplitudes, whereas SOL fascicle shortening did not. By combining EMG and US imaging within the same participants, this study provides new insights into the neuromuscular mechanisms underlying balance control. These findings may inform the development of improved control strategies for neurorehabilitation devices and fall-prevention systems.**

I. Introduction

Falls and fall-related injuries are a growing medical concern among older adults [1]. Most falls result from internally generated errors or external disturbances that cause undesired movement of the center of mass (CoM), often occurring when an individual cannot recover from a loss of balance due to missteps, slips (backward falls), or trips (forward falls) [2], [3]. While physical injuries are the most noticeable outcome of falls, the fear of falling may also cause individuals to reduce their activity levels, leading to a decline in function and potentially increasing their risk of future falls [4].

*This work was supported by the FOAP at the University of Alabama #13009-214271-200. Corresponding author: Qiang Zhang (qiang.zhang@ua.edu).

[1]O. Akinniyi, and M. Gainey are with the Department of Mechanical Engineering, and Q. Zhang is also with the Department of Chemical and Biological Engineering, the University of Alabama, Tuscaloosa, AL 35401, USA.

[2]D. Martelli is with the Orthopedics/Sports Medicine Department, MedStar Health Research Institute, Baltimore, MD 21218, USA.

Timely and appropriate postural adjustments are crucial to preventing falls, such as keeping the CoM within the base of support (BoS). Reactive balance response describes how individuals respond to unexpected external disturbances (perturbations), this involves the selection of the most appropriate strategy based on the magnitude of the disturbance [5], [6]. For small disturbances, corrective strategies, such as the ankle strategy, help maintain the BoS, while for larger or limited BoS disturbances, the hip strategy is more effective [7]. Protective strategies, including stepping, are considered last resort responses, used when the CoM moves outside the BoS, requiring active movements to restore balance [8]. These reactive strategies depend on muscle activation to maintain postural stability following the detection of a disturbance by the central nervous system. Hence, studying how lower limb muscles rapidly respond to external perturbations to help maintain balance is important to preventing falls.

To study the human response to perturbations, researchers simulate fall conditions (slips, trips, and missteps) in the laboratory, applying perturbations to various parts of the body, such as the foot [9], pelvis / waist [10] and shoulder [11] to alter the original postural balance of individuals in static or dynamic positions. These perturbations are applied using robotic devices/platforms like waist-pull perturbation systems and instrumented treadmills. Waist-pull perturbation systems are mostly cable-driven devices used to apply a pull force to the pelvis in different directions (forward, backward, and sideways). Their application includes perturbation training [6], locomotor adaptation studies [12], prediction of protective stepping response [13], and stability. In such studies, reactive balance strategies are examined by assessing metrics such as whole-body sway, lower limb kinematics and kinetics, and muscle activation and contraction.

Surface electromyography (EMG) is used to measure muscle electrical activities, it provides information about the timing and magnitude of muscles activities. However, its signals suffer from interference from adjacent muscles, particularly during rapid unexpected external disturbances. Another challenge with EMG is its inability to measure activations of deep-layer muscles [14], [15]. In contrast, ultrasound (US) imaging enables non-invasive visualization of the targeted muscle's musculature. For instance, a two-dimensional brightness mode (B-mode) ultrasound imaging device allows us to see both superficial and deep muscle layers simultaneously. Common architectural features derived from US images include muscle thickness [16], pennation angle [17], fascicle length [18], and cross-sectional area [19].

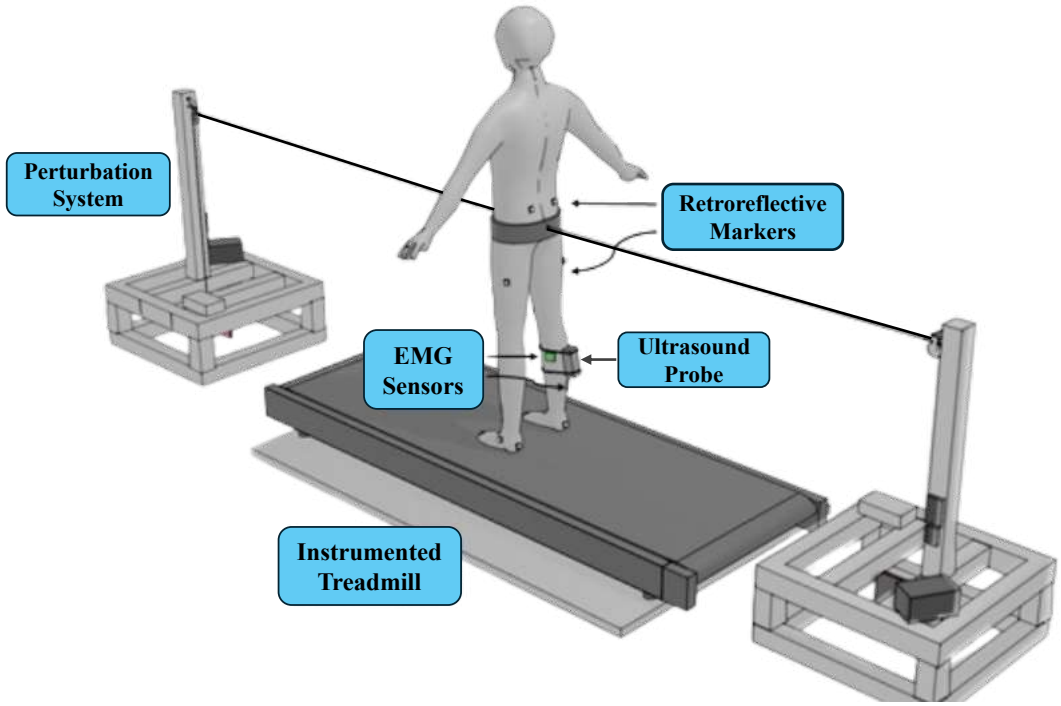


Fig. 1: Experimental setup showing the perturbation system and measurement sensors attached to a participant.

These features have been associated with joint kinematics and kinetics during various static and dynamic tasks [20]. To overcome the shortcomings of both EMG and US imaging, several studies have proposed multi-modal fusion of both technologies to estimate human hand force [21], develop control framework for ankle exoskeleton assistance [22], predict ankle moment [23], and predict plantarflexion force during dynamic cycling tasks [24]. EMG signals and US imaging may offer complementary information, and their combination could reduce interference effects from neighboring EMG signals, and minimize image drift in US imaging caused by cumulative errors from misaligned probes during limb movement [25]. Several studies have investigated lower limb muscle activity during reactive balance, using EMG [26]–[29], however, the use of US imaging to study lower limb muscle architecture during reactive balance is less explored. To the best of the authors' knowledge, no study has investigated the lower limb muscles using both EMG and US imaging during waist-pull human balance perturbation. This study investigated the relationship between the electrical activity (muscle activation) and architectural feature (fascicle length changes) of the calf muscles during protective stepping responses to bidirectional waist-pull perturbations of varying amplitudes delivered while standing. The findings from this study may contribute to improved control mechanisms for neurorehabilitation devices, and enhanced fall-prevention strategies.

II. Materials and Method

A. Participants and Protocol

Five male participants with no record of musculoskeletal or neurological deficits (age: 25.2 ± 5.5 years; height: 174.7 ± 4.9 cm; weight: 83.9 ± 8.4 kg) volunteered for the study. Table I shows the demography of the participants. All participants provided written informed consent according to the guidelines approved by the Institutional Review Board of the University of Alabama (21-06-4695-R2).

A cable-driven perturbation system was used in this study to induce waist-pull disturbances (perturbations), as illustrated in Fig. 1. The system comprises a modular aluminum frame (80/20, IN, USA), an actuation unit with a brushless EC motor (EC 90, Maxon Group, Switzerland), a pulling cable, a waist belt, and additional hardware components. Designed for compactness and versatility, the system can be easily mounted to a wall using screws and adjusted for various experimental setups. A lightweight force sensor connects the waist belt to the pulling cable, which is guided through a pulley to the motor, ensuring precise force application. For participants' safety, a breakaway cable is incorporated to automatically disconnect the system in the event of excessive force. An adaptive closed-loop controller implemented in a MATLAB-Simulink (MathWorks, Natick, MA, USA) program controls the actuation unit of the perturbation system. The program sends force commands to the perturbation system which translates into a pulling force applied to the participants. The perturbation system has been previously validated and detailed in [30].

TABLE I: Participant demographics and perturbation levels

LF = Low Perturbation (7 %BW), HP = High Perturbation (15 %BW)					
Participant	Mass (kg)	Height (cm)	BMI	LP (N)	HP (N)
S01	90.7	177.8	28.7	62.3	133.4
S02	81.4	167.6	29.0	55.9	119.8
S03	81.6	172.7	27.4	56.0	120.1
S04	93.4	180.3	28.7	64.1	137.4
S05	72.3	175.2	23.6	49.6	106.3

B. Experimental procedure

Participants stood on an instrumented treadmill (Bertec Corp., Columbus, OH, USA) embedded with two force plates, with their feet positioned approximately hip-width apart, each foot placed on a separate force plate. The positions of their feet were marked on the platform surface to ensure consistent foot placement across all sessions. Participants were asked to maintain a normal, relaxed stance while standing and to respond naturally to the perturbations. They were instructed to take a step with their dominant leg if they lose their balance to avoid falling. We recommended that after taking a step, they remain in that position for about 5 seconds to regain stability before returning to the initial position. Horizontal waist-pull perturbations were induced using an adaptive-controlled, cable-driven waist-pull perturbation system described in detail previously. During the experiment, all participants wore a commercially available harness system attached to the ceiling to prevent falls during the experiment. Additionally, an emergency stop switch, accessible to both the experimenter and participant, was available to stop the system in case of malfunction. Force-impulse perturbations [31] were applied anteriorly and posteriorly to participants' pelvis region while they stood on the treadmill. Two levels of perturbation were administered: low-amplitude perturbation (7% body weight (BW)) (57.6 ± 5.8 N) and high-amplitude perturbation (15% BW) (123.4 ± 11.1 N) levels, with 10 repetitions for each level [32]. The interval time between successive perturbations (10–16 seconds) was pseudo-randomized for each participant, while the order of perturbation level was also randomized. Participants were blinded from the sequence of perturbation throughout the experiment. We ensured that all participants regained their stability and returned to the initial position before applying the next perturbation. A rest time of 5 minutes was observed between each perturbation level to prevent fatigue. Data collection began once the participant was prepared and the measurement equipment setup, as described below, was completed.

C. Experimental Measurement and Analyses

Throughout the experiment, we recorded muscle activities from the medial gastrocnemius (MGS) and soleus (SOL) muscles of each participant's dominant leg using the Trigno wireless biofeedback system (Trigno, Delsys Inc., Natick, MA, USA) at 1000 Hz. EMG wireless sensors were placed longitudinally over the muscles following skin preparation using published recommendations [33]. Eight cameras (Vicon Motion Systems Ltd., Yarnton, UK) were used to capture lower limb kinematics at 100 Hz. The Plug-in Gait Lower-body Model was used, with 16 retroreflective markers affixed to anatomical landmarks on both legs, including the anterior superior iliac spine, posterior superior iliac spine, thigh, knee, tibia, ankle, heel, and the second metatarsal head of the feet. After data collection, each trial's EMG data was bandpass filtered (20 Hz - 400 Hz), rectified (full-wave), low-pass filtered at 6 Hz, and normalized to each subject's maximum peak value across all trials. The variable of interest is the peak muscle activation amplitude during stepping response. For EMG processing, the perturbation onset (time point when a pull-force is applied to a participant) was defined as the point when the signal exceeded three times the resting activity level for at least 50 ms.

To measure individual muscle fascicles, a B-mode ultrasound diagnostic system (ArtUs EXT-2H, Telemed, Lithuania) was used to capture cine B-mode images of individual muscle fascicles through LGS and SOL muscles of the dominant leg of participants at 60 frames per second, with an imaging depth of 40 mm (Fig. 2). The start and stop times of the perturbation system, VICON motion capture, EMG recording, and ultrasound image recording were synchronized using a custom MATLAB Simulink multi-system controller running on a computer system with a data acquisition system (Quanser Q8-USB, ON, Canada). To minimize inter-investigator variability, the same investigator processed all ultrasound data, the same for all data processing. In the case of fascicle length processing, the perturbation onset was defined as the point when the fascicle length shortens below three times the resting activity level for at least 50 ms. After the definition of a resting activity level before perturbation onset, a region of interest was defined around the muscle bellies and aponeuroses of the lateral gastrocnemius (LGS) and SOL muscles. An affine optical flow algorithm (Ultratrack) [34] was used to quantify the time series of LGS and SOL fascicle lengths from the perturbation onset to stepping. The tracking results were filtered using a 4th-order low-pass Butterworth filter with a 6 Hz cutoff frequency.

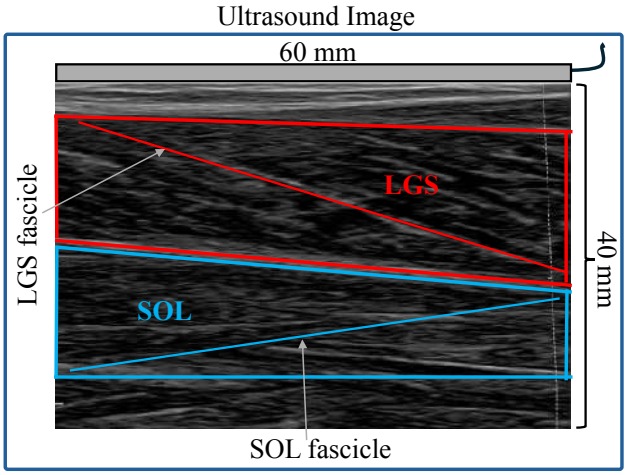


Fig. 2: Ultrasound image recorded from the LGS and SOL muscles during the experiment

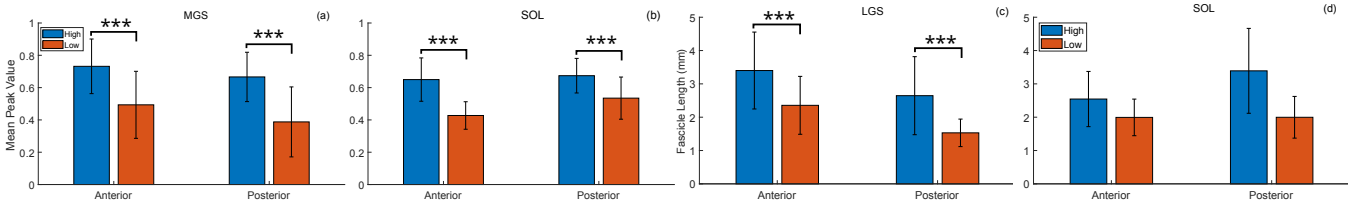


Fig. 3: Mean and standard deviation of peak EMG activation and fascicle length shortening following perturbation onset across all perturbation conditions and trials. (a) Mean and standard deviation of MGS peak values across all subjects (b) Mean and standard deviation of SOL peak values across all subjects (c) Mean and standard deviation of LGS fascicle shortening across all subjects (d) Mean and standard deviation of SOL fascicle shortening across all subjects. Error bars represent the standard deviation of the mean. "High" represents high-amplitude perturbation, and "Low" represents low-amplitude perturbation. Asterisks (*) indicate significant differences $P < 0.05$

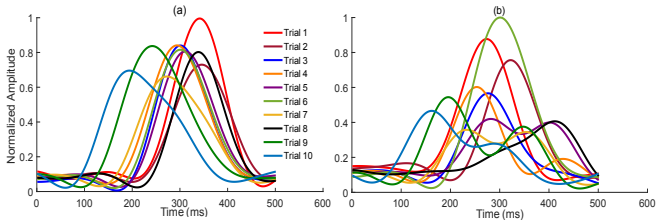


Fig. 4: EMG activity for a representative participant during low-amplitude anterior perturbation across ten perturbation trials. (a) MGS muscle activity (b) SOL muscle activity, each plot represents the muscle activity following perturbation onset

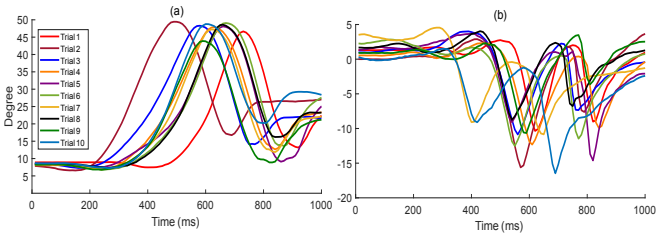


Fig. 5: Joint angles of the dominant leg of a representative participant during low-level anterior perturbation across ten trials. Each plot represents the joint angle trajectory during a step response: (a) Knee joint angles, (b) Ankle joint angles

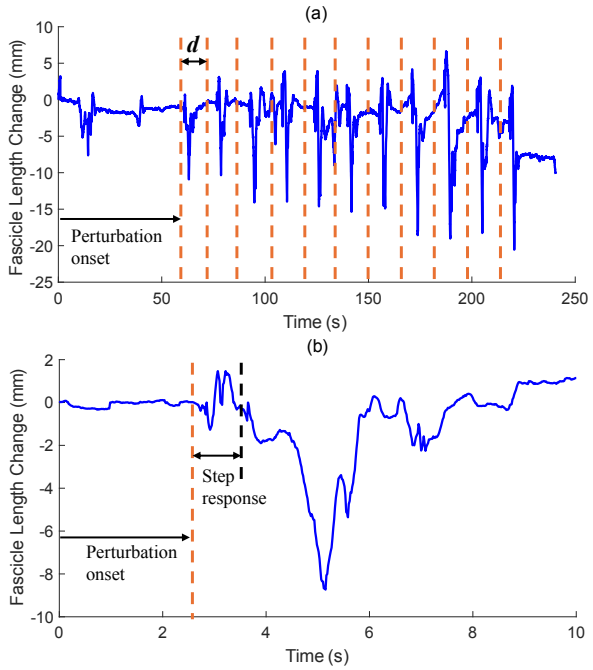


Fig. 6: US Imaging for a representative participant during low-amplitude anterior perturbation showing the (a) relative fascicle length change of the LGS muscle across ten perturbation trials, d represents the delay between each perturbation (10-14 s) (b) relative fascicle length change of the LGS muscle during a perturbation

Paired t-tests were conducted to examine differences in MGS and SOL muscle activation, as well as LGS and SOL fascicle length changes, between low-amplitude and high-amplitude perturbations in both anterior and posterior directions. A significance level of $P < 0.05$ was used.

III. Result and Discussion

A. Experimental Outcomes

Paired t-tests revealed a significant difference in MGS activation between high-amplitude and low-amplitude perturbations in both the anterior direction ($p < 0.0001$), and posterior direction ($p < 0.0001$) (Fig. 3a). Similarly, SOL activation showed a significant difference between high-amplitude and low-amplitude perturbations in the anterior direction ($p < 0.0001$), and the posterior direction ($p < 0.001$) (Fig. 3b). For fascicle length changes, a significant difference was observed in LGS length shortening between high-amplitude and low-amplitude perturbations in both anterior direction ($p < 0.001$), and posterior directions ($p < 0.0001$). However, SOL length shortening did not differ significantly between high-amplitude and low-amplitude perturbations in either the anterior or posterior directions (Fig. 3c,d).

B. Discussion

The main goal of this study is to investigate the relationship between muscle activity (muscle activation) and

architecture (fascicle length change) across both the gastrocnemius and soleus muscles during a stepping response to waist-pull perturbations in different directions (anterior and posterior) and amplitudes (high and low). Several studies have investigated how the lower limb muscles respond to unexpected balance perturbation, with all aiming at several goals including the effect of perturbation profile, perturbation magnitude, varying time intervals in perturbation, and motor adaption. These studies use only EMG for analyzing the lower limb muscle activity. We combined EMG and US imaging to analyze the gastrocnemius and soleus muscles during stepping response to an unexpected waist-pull perturbation under different perturbation conditions. In this study, MGS and SOL muscle electrical activities were recorded with EMG sensors while an ultrasound probe recorded the architecture of the LGS and SOL muscles [35].

We observed a notable increase in EMG activation in the MGS and SOL muscles during high-amplitude perturbations in both anterior and posterior directions. This increased activation reflects the contribution of these muscles in maintaining postural stability under substantial external disturbances. The increased muscle activity likely reflects the recruitment of additional motor units to generate the necessary force to counteract the destabilizing effect of the perturbation. In response to anterior perturbations, the MGS and SOL muscles act to decelerate forward motion and restore balance by producing greater plantarflexion forces. Conversely, during posterior perturbations, the increased muscle activation is essential for preventing backward falls by resisting the posterior shift of the CoM. Notably, a relatively high activation was observed in the SOL muscle during posterior perturbations, emphasizing its specific contribution to stabilizing the ankle joint during backward stepping. These findings are consistent with previous studies, which have demonstrated that enhanced activation of the ankle plantarflexors (gastrocnemius and soleus muscles) serves as a compensatory mechanism to maintain stability during balance recovery tasks involving external perturbations [36], [37]. Furthermore, evidence of motor adaptation was observed during perturbation trials [38], as reflected in EMG activation. The activation levels varied with repeated perturbation, leading to an adaptation trend across trials. As shown in Fig. 4(a,b), the EMG activation during the initial trials was notably higher, while subsequent trials showed more consistent and reduced amplitudes. This pattern suggests that participants adapted to the repeated perturbations, likely through improved neuromuscular control and optimized motor responses over time. Similar trend was observed in the knee and ankle joint angle trajectories of participants (Fig. 5 a,b).

Our US imaging results showed fascicle length shortening following perturbation onset (Fig. 6 a,b) indicative of muscle contraction during stepping responses to unexpected external disturbances. We observed greater shortening of LGS and SOL fascicle lengths during high-amplitude perturbations in both anterior and posterior directions, reflecting increased muscle contractions in response to higher perturbations. These findings on muscle architecture align with the observed EMG activity patterns. However, Hodges et al. [39] reported a nonlinear relationship between EMG activity and muscle architecture. In contrast, Narici et al. [40] found a linear relationship between muscle activity and architecture in certain muscles such as MGS. Results from these studies suggest that the relationship between muscle activity and architecture varies across different muscles, and is influenced by muscle-specific factors such as innervation [41], [42].

This study has several limitations. First, only the calf muscles were investigated; the tibialis anterior (TA), a key contributor to ankle dorsiflexion and foot stability during protective stepping, may be included in future studies to provide a more comprehensive analysis of muscle activity and contractility during reactive balance. Second, in ultrasound imaging, we examined only the lateral region of the soleus muscle, which may differ significantly from other compartments of the muscle. Investigating additional architectural features and muscle geometry, such as muscle thickness, pennation angle, and cross-sectional area, could offer deeper insights into muscle architectural properties during stepping. Furthermore, we did not analyze the EMG activity or muscle architecture of the non-dominant leg. Future studies could explore muscle responses in the non-dominant leg to better understand its role during the stepping response.

IV. Conclusion

We investigated both muscle electrical activation and fascicle length changes in MGS, LGS, and SOL muscles of the dominant (stepping) leg during stepping responses to unexpected low-amplitude and high-amplitude waist-pull perturbations in the anterior and posterior directions. By combining EMG and US imaging, we provided complementary insights into muscle activation and fascicle length changes of the calf muscles. Our findings show that waist-pull perturbation amplitude has significant effect on the EMG activation of both MGS and SOL muscle, and fascicle length shortening of both LGS and SOL muscle. Our next study will investigate the neuromuscular responses of the lower limb using EMG and US imaging during combined perturbation methods, such as platform translations and waist-pull perturbations.

Aknowledgement

The authors extend their gratitude to Yun Chen, Zhiyu Zhang, and Johnnie Reed for assisting with data collection preparations.

References

[1] I. Nurmi and P. Lüthje, "Incidence and costs of falls and fall injuries among elderly in institutional care," *Scandinavian journal of primary health care*, vol. 20, no. 2, pp. 118–122, 2002.

[2] Y.-C. Pai, B. Maki, K. Iqbal, W. McIlroy, and S. Perry, "Thresholds for step initiation induced by support-surface translation: a dynamic center-of-mass model provides much better prediction than a static model," *Journal of biomechanics*, vol. 33, no. 3, pp. 387–392, 2000.

[3] L. Z. Rubenstein, "Falls in older people: epidemiology, risk factors and strategies for prevention," *Age and ageing*, vol. 35, no. suppl_2, pp. ii37–ii41, 2006.

[4] M. E. Tinetti, D. Richman, and L. Powell, "Falls efficacy as a measure of fear of falling," *Journal of gerontology*, vol. 45, no. 6, pp. P239–P243, 1990.

[5] A. J. Devasahayam, K. Farwell, B. Lim, A. Morton, N. Fleming, D. Jagroop, R. Aryan, T. M. Saumur, and A. Mansfield, "The effect of reactive balance training on falls in daily life: an updated systematic review and meta-analysis," *Physical therapy*, vol. 103, no. 1, p. pzac154, 2023.

[6] D. Kim and J.-M. Hwang, "Responses to external repeated perturbations vary with time intervals," *IEEE Transactions on Human-Machine Systems*, 2024.

[7] F. B. Horak and L. M. Nashner, "Central programming of postural movements: adaptation to altered support-surface configurations," *Journal of neurophysiology*, vol. 55, no. 6, pp. 1369–1381, 1986.

[8] A. Shumway-Cook, "Motor control," *Theory and practical applications*, 2001.

[9] C. Z.-H. Ma and W. C.-C. Lee, "A wearable vibrotactile biofeedback system improves balance control of healthy young adults following perturbations from quiet stance," *Human movement science*, vol. 55, pp. 54–60, 2017.

[10] M. Inacio, R. Creath, and M. W. Rogers, "Effects of aging on hip abductor-adductor neuromuscular and mechanical performance during the weight transfer phase of lateral protective stepping," *Journal of biomechanics*, vol. 82, pp. 244–250, 2019.

[11] N. Kanekar and A. S. Aruin, "Aging and balance control in response to external perturbations: role of anticipatory and compensatory postural mechanisms," *Age*, vol. 36, pp. 1067–1077, 2014.

[12] V. Vashista, D. Martelli, and S. K. Agrawal, "Locomotor adaptation to an asymmetric force on the human pelvis directed along the right leg," *IEEE Transactions on Neural Systems and Rehabilitation Engineering*, vol. 24, no. 8, pp. 872–881, 2015.

[13] Y.-C. Pai, M. W. Rogers, J. Patton, T. D. Cain, and T. A. Hanke, "Static versus dynamic predictions of protective stepping following waist–pull perturbations in young and older adults," *Journal of biomechanics*, vol. 31, no. 12, pp. 1111–1118, 1998.

[14] L. J. Hargrove, K. Englehart, and B. Hudgins, "A comparison of surface and intramuscular myoelectric signal classification," *IEEE transactions on biomedical engineering*, vol. 54, no. 5, pp. 847–853, 2007.

[15] D. L. Crouch, L. Pan, W. Filer, J. W. Stallings, and H. Huang, "Comparing Surface and Intramuscular Electromyography for Simultaneous and Proportional Control Based on a Musculoskeletal Model: A Pilot Study," *IEEE Transactions on Neural Systems and Rehabilitation Engineering*, vol. 26, no. 9, pp. 1735–1744, 2018.

[16] E. Hodson-Tole and A. Lai, "Ultrasound-derived changes in thickness of human ankle plantar flexor muscles during walking and running are not homogeneous along the muscle mid-belly region," *Scientific reports*, vol. 9, no. 1, p. 15090, 2019.

[17] E. M. Strasser, T. Draskovits, M. Praschak, M. Quittan, and A. Graf, "Association between ultrasound measurements of muscle thickness, pennation angle, echogenicity and skeletal muscle strength in the elderly," *Age*, vol. 35, pp. 2377–2388, 2013.

[18] Q. Zhang, A. Iyer, K. Kim, and N. Sharma, "Evaluation of non-invasive ankle joint effort prediction methods for use in neurorehabilitation using electromyography and ultrasound imaging," *IEEE Transactions on Biomedical Engineering*, vol. 68, no. 3, pp. 1044–1055, 2020.

[19] J.-Y. Guo, Y.-P. Zheng, H.-B. Xie, and X. Chen, "Continuous monitoring of electromyography (emg), mechanomyography (mmg), sonomyography (smg) and torque output during ramp and step isometric contractions," *Medical engineering & physics*, vol. 32, no. 9, pp. 1032–1042, 2010.

[20] M. H. Jahanandish, N. P. Fey, and K. Hoyt, "Lower-Limb Motion Estimation Using Ultrasound Imaging: A Framework For Assistive Device Control," *IEEE Journal of Biomedical and Health Informatics*, pp. 1–10, 2019.

[21] Y. Zou, L. Cheng, and Z. Li, "A multimodal fusion model for estimating human hand force: Comparing surface electromyography and ultrasound signals," *IEEE Robotics & Automation Magazine*, vol. 29, no. 4, pp. 10–24, 2022.

[22] Q. Zhang, K. Lambeth, Z. Sun, A. Dodson, X. Bao, and N. Sharma, "Evaluation of a fused sonomyography and electromyography-based control on a cable-driven ankle exoskeleton," *IEEE Transactions on Robotics*, vol. 39, no. 3, pp. 2183–2202, 2023.

[23] Q. Zhang, N. Fragnito, J. R. Franz, and N. Sharma, "Fused ultrasound and electromyography-driven neuromuscular model to improve plantarflexion moment prediction across walking speeds," *Journal of Neuroengineering and Rehabilitation*, vol. 19, no. 1, p. 86, 2022.

[24] T. J. Dick, A. A. Biewener, and J. M. Wakeling, "Comparison of human gastrocnemius forces predicted by hill-type muscle models and estimated from ultrasound images," *Journal of experimental biology*, vol. 220, no. 9, pp. 1643–1653, 2017.

[25] Q. Zhang, W. H. Clark, J. R. Franz, and N. Sharma, "Personalized fusion of ultrasound and electromyography-derived neuromuscular features increases prediction accuracy of ankle moment during plantarflexion," *Biomedical Signal Processing and Control*, vol. 71, p. 103100, 2022.

[26] W. J. Hurd, T. L. Chmielewski, and L. Snyder-Mackler, "Perturbation-enhanced neuromuscular training alters muscle activity in female athletes," *Knee Surgery, Sports Traumatology, Arthroscopy*, vol. 14, pp. 60–69, 2006.

[27] S. Wang, Y.-C. Pai, and T. Bhatt, "Neuromuscular mechanisms of motor adaptation to repeated gait-slip perturbations in older adults," *Scientific Reports*, vol. 12, no. 1, p. 19851, 2022.

[28] H. K. Kim and L.-S. Chou, "Lower limb muscle activation in response to balance-perturbed tasks during walking in older adults: a systematic review," *Gait & Posture*, vol. 93, pp. 166–176, 2022.

[29] R. T.-L. Zhu, P.-Z. Lyu, S. Li, C. Y. Tong, Y. T. Ling, and C. Z.-H. Ma, "How does lower limb respond to unexpected balance perturbations? new insights from synchronized human kinetics, kinematics, muscle electromyography (emg) and mechanomyography (mmg) data," *Biosensors*, vol. 12, no. 6, p. 430, 2022.

[30] O. Akinniyi, M. Sharifi, D. Martelli, and Q. Zhang, "Development and control of a cable-driven robotic platform for studying human balance and gait," in *2024 IEEE International Conference on Advanced Intelligent Mechatronics (AIM)*. IEEE, 2024, pp. 58–63.

[31] M. Paterna, Z. Dvir, C. De Benedictis, D. Maffiodo, W. Franco, C. Ferraresi, and S. Roatta, "Center of pressure displacement due to graded controlled perturbations to the trunk in standing subjects: the force–impulse paradigm," *European Journal of Applied Physiology*, vol. 122, no. 2, pp. 425–435, 2022.

[32] B. W. Schulz, J. A. Ashton-Miller, and N. B. Alexander, "Compensatory stepping in response to waist pulls in balance-impaired and unimpaired women," *Gait & posture*, vol. 22, no. 3, pp. 198–209, 2005.

[33] H. J. Hermens, B. Freriks, R. Merletti, D. Stegeman, J. Blok, G. Rau, C. Disselhorst-Klug, and G. Hägg, "European recommendations for surface electromyography," *Roessingh research and development*, vol. 8, no. 2, pp. 13–54, 1999.

[34] D. J. Farris and G. A. Lichtwark, "Ultratrack: Software for semi-automated tracking of muscle fascicles in sequences of b-mode ultrasound images," *Computer methods and programs in biomedicine*, vol. 128, pp. 111–118, 2016.

[35] W. H. Clark, R. E. Pimentel, and J. R. Franz, "Imaging and simulation of inter-muscular differences in triceps surae contributions to forward propulsion during walking," *Annals of biomedical engineering*, vol. 49, pp. 703–715, 2021.

[36] J. J. Eng, D. A. Winter, and A. E. Patla, "Strategies for recovery from a trip in early and late swing during human walking," *Experimental brain research*, vol. 102, pp. 339–349, 1994.

[37] F. B. Horak and J. M. Macpherson, "Postural orientation and equilibrium," *Comprehensive physiology*, pp. 255–292, 1996.

[38] T. D. Welch and L. H. Ting, "Mechanisms of motor adaptation in reactive balance control," *PloS one*, vol. 9, no. 5, p. e96440, 2014.

[39] P. Hodges, L. Pengel, R. Herbert, and S. Gandevia, "Measurement of muscle contraction with ultrasound imaging," *Muscle & Nerve: Official Journal of the American Association of Electrodiagnostic Medicine*, vol. 27, no. 6, pp. 682–692, 2003.

[40] M. V. Narici, T. Binzoni, E. Hiltbrand, J. Fasel, F. Terrier, and P. Cerretelli, "In vivo human gastrocnemius architecture with changing joint angle at rest and during graded isometric contraction." *The Journal of physiology*, vol. 496, no. 1, pp. 287–297, 1996.

[41] K. Kubo, Y. Kawakami, and T. Fukunaga, "Influence of elastic properties of tendon structures on jump performance in humans," *Journal of applied physiology*, vol. 87, no. 6, pp. 2090–2096, 1999.

[42] C. N. Maganaris, "In vivo measurement-based estimations of the moment arm in the human tibialis anterior muscle-tendon unit," *Journal of Biomechanics*, vol. 33, no. 3, pp. 375–379, 2000.

A Task-Agnostic Hip Exoskeleton for Osteoarthritis Pain Relief: Energetic Control Across Activities of Daily Life

Jiefu Zhang, Nikhil V. Divekar, Ernesto Hernandez Hinojosa, and Robert D. Gregg

***Abstract*— Hip osteoarthritis (OA) affects millions worldwide, yet effective conservative (non-surgical) treatments are still limited. Conventional hip braces cannot reduce painful joint loads associated with contractile forces from flexors and extensors during locomotion. Powered hip exoskeletons could potentially reduce biological hip moments by applying flexion/extension torques, thus attenuating muscle forces that contribute to OA pain. Here, we present a novel task-agnostic controller for a backdrivable hip exoskeleton that relieves hip OA pain across the primary activities of daily life. Inspired by the energy shaping method, this controller utilizes biomechanics-based components to assist with level walking, ramp and stairs ascent/descent, and sit-to-stand transitions, which can be customized to different populations, like hip OA. In a pilot study with three hip OA participants, the hip exoskeleton holistically reduced pain and perceived difficulty during a multi-activity test (except difficulty of level walking). The exoskeleton also increased hip range of motion during walking, with subject-specific improvements in walking speed. This pilot study suggests that hip exoskeletons may offer a promising new intervention for managing hip OA.**

I. Introduction

Hip osteoarthritis (OA) is a degenerative joint disease that affects millions worldwide, yet effective conservative treatments are still limited. While total hip arthroplasty (THA) is considered the gold standard for late-stage hip OA patients, it is economically unjustifiable for less severe cases [1]. Pharmacologic treatments such as non-steroidal anti-inflammatory drugs (NSAIDs) [2] and intra-articular injection [3] are common treatments for mild OA. However, prolonged use of NSAIDS can have adverse effects [2], and masking pain without addressing root causes can result in further joint damage [4]. Exercise is typically recommended to counter muscle atrophy/dysfunction [5] that contributes to abnormal joint loading and pain [6]–[8]. However, pain often forces patients to avoid strenuous activities like stair climbing and limit themselves to low-impact exercises like walking. Restricted mobility can perpetuate a detrimental cycle where muscle weakness and physical inactivity contribute to the worsening of OA symptoms [9].

Hip unloading braces can reduce pain caused by hip OA by restricting frontal plane motions and thus reducing hip joint load [10], [11], but their effectiveness was subject-dependent. This can be potentially attributed to the bulkiness and rigidity of current braces, which are essential for motion restriction but negatively affect their usability [12]. Moreover, they neglect flexion/extension moments that also cause OA pain [13], since unloading forces by restricting motion in the sagittal plane is not an option, given the necessary range of motion (RoM) for locomotion.

Powered exoskeletons, which apply external torque to joints, offer a promising approach to reduce joint compression forces [14] and associated pain in lower-limb OA. These devices have been shown to effectively decrease joint moments [15] and muscle effort [16] during various activities. Since joint compression forces during dynamic movements are primarily caused by muscle contractions generating internal joint moments [17], powered exoskeletons can potentially benefit OA patients by providing external torques that partially reduce the requisite muscle activation. Simulation studies [14] have suggested that knee exoskeletons applying pure torque can decrease joint loading across different walking speeds. However, the effects of hip exoskeletons on OA patients remain to be investigated.

In order for hip exoskeletons to help manage OA pain on a daily basis, they must be sufficiently versatile to support the various activities of daily life (ADLs). However, existing commercial hip exoskeletons like Samsung GEMS [18], [19] typically use task-specific controllers that must first identify the activity being performed before applying pre-programmed torque profiles. This approach proves problematic in real-world applications due to the unpredictable and varied nature of daily activities. For instance, studies with the highly-geared Keeogo knee exoskeleton [20] failed to show immediate improvements for knee OA patients, likely due to the lengthy user adaptation needed to effectively use the task recognition-based controller. While neural networks trained with unimpaired human data can enhance task adaptability by estimating normative biological hip moments across various activities [15] (referred to as a *task-agnostic* controller), the lack of tunability limits customization for specific patient populations like hip OA. Moreover, the "black box" nature of neural networks raises safety concerns when used with impaired populations due to the possibility of unpredictable behavior outside training scenarios.

Our previous research on energy shaping-based controllers has shown promise in providing task-agnostic, biomimetic torque assistance with improved safety and stability guarantees [21]–[24]. However, the optimization over hundreds of non-intuitive torque bases made these methods susceptible to over-fitting the training data and impractical to tune for more effective assistance, resulting in limited interpretability

This work was supported by the National Institute of Biomedical Imaging and Bioengineering of the NIH under Award Number R01EB031166. The content is solely the responsibility of the authors and does not necessarily represent the official views of the NIH.

The authors are with the Department of Robotics, University of Michigan, Ann Arbor, MI 48109, USA. Corresponding author: Robert D. Gregg. Contact: {zjiefu, ndivekar, ehdz, rdgregg}@umich.edu

and customizability. In [25], an energy shaping controller was designed using physically-meaningful components like virtual springs and dampers, which are inherently passive and intuitive but not necessarily biomimetic. This idea was extended in [16] by optimizing physically-meaningful energetic components to match human data followed by manual tuning to maximize quadriceps assistance during lifting, lowering, and carrying tasks. By moving away from purely data-driven optimization of abstract torque bases, this approach has demonstrated superior effectiveness in improving physical performance and reducing muscle effort across various activities while maintaining customizability. The use of intuitive parameters also makes the controller more practical to tune and adapt for individual needs. While the results in [16] are promising for healthy individuals, this technology may also have impact for people with hip OA.

In this paper, we designed and implemented an energy shaping-inspired hip exoskeleton controller based on the approach in [16] for individuals with hip OA. Fig. 1 provides a high-level overview of our controller, which utilizes virtual springs modulated by kinematic variables such as joint angles and velocities, featuring physically-meaningful parameters that can be customized. This design represents our first key contribution, offering task-agnostic assistance for common ADLs with improved interpretability and customizability. Our second major contribution lies in investigating the effects of powered hip exoskeleton assistance on the hip OA population, hypothesizing that it could reduce pain and decrease the difficulty of performing ADLs. To validate this, three participants with hip OA performed various activities both with and without our hip exoskeleton at different assistance levels. Results demonstrated significant pain and difficulty reductions during hip-intensive tasks across all subjects, along with subject-specific improvements in walking speed accompanied by increased hip RoM. These promising outcomes reveal the potential of powered hip exoskeletons as an effective treatment option for individuals with hip OA.

II. Controller Design and Implementation

In our previous hip exoskeleton controller design [23], assistive torque was formulated as a linear combination of trigonometric basis functions, whose coefficients were determined through off-line optimization using normative human data. This approach presents challenges for impaired populations like hip OA patients, primarily due to its heavy dependence on data and the use of non-intuitive basis functions. Designing controllers for impaired populations is complicated by the scarcity of rich population-specific datasets, leading to the use of datasets with less subjects and activities, thus increasing the risk of overfitting. Furthermore, patient datasets often consist of pathological movement patterns, which will be reproduced by a purely data-driven controller, leading to suboptimal assistance. For example, hip OA patients typically exhibit reduced range of motion during walking, partly stemming from insufficient hip extension moment [8]. A controller developed using such patient data would reproduce these limited movement

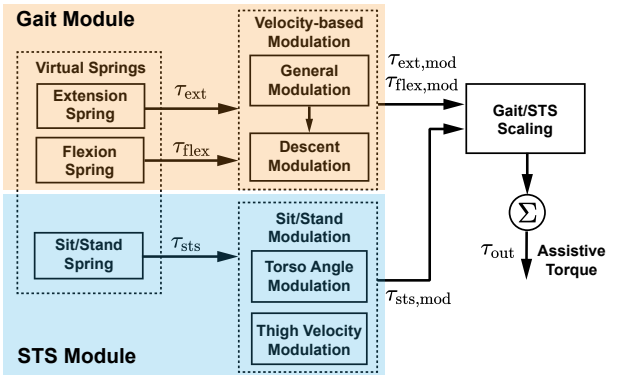


Fig. 1. High-level overview of the controller. Torque generated by virtual springs is modulated based on joint kinematics, and then scaled and summed to obtain the output assistive torque.

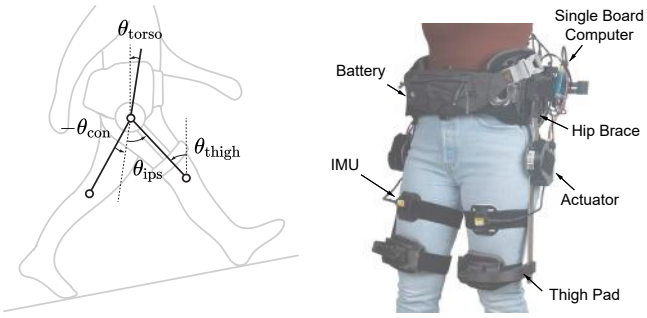


Fig. 2. **Left:** Definitions of angles used in the controller. Black-outlined circles represent the centers of hip and knee joints. $\theta_{\mathrm{torso}}, \theta_{\mathrm{thigh}}, \theta_{\mathrm{ips}}$, and θ_{con} denote torso angle, thigh angle, ipsilateral hip angle, and contralateral hip angle respectively. **Right:** Picture of the modified M-BLUE hip module. For clarity only one of the inertia measurement units (IMUs), actuators, and thigh pads are labeled.

patterns, resulting in insufficient torque. Unintuitive control parameters would also prevent heuristic fine-tuning based on user feedback, often essential in clinical settings. To address these limitations, in this paper we propose a biomechanics-informed controller, which incorporates virtual springs modulated by human kinematics. This new design can provide task-agnostic assistance for hip OA patients, while remaining tunable.

A. Physical Component-based Controller Design

The physical component-based controller comprises two modules: the gait module that generates torque for gait activities (level walking, ramp and stairs ascent/descent), and the sitting/standing (STS) module that generates torque for sit-to-stand transitions. The gait module includes two unidirectional virtual torsion springs—the extension spring and the flexion spring, modulated by joint velocity. The STS module consists of one unidirectional virtual torsion spring—the STS spring, modulated by the torso angle and thigh velocity. The torque from the two modules is scaled and combined to provide the output assistive torque. The definition of joint angles used in the controller is shown in Fig. 2 (left). The counterclockwise (flexion) direction is defined as positive.

1) Gait Module: In the gait module, the extension spring and flexion spring provide extension and flexion torque

during gait activities. The torques generated by the two springs are given by

$$\begin{aligned}\tau_{\text{ext}} &= \min\left(0,\ k_{\text{ext}} \cdot (\theta_{\text{ips}} - \theta_{\text{ext,eq}})\right) \\ \tau_{\text{flex}} &= \max\left(0,\ k_{\text{flex}} \cdot (\theta_{\text{flex,eq}} - \theta_{\text{ips}})\right),\end{aligned} \tag{1}$$

where $k_{\text{ext}},\ k_{\text{flex}}$ are the constant spring stiffness values of the extension and flexion springs, θ_{ips} is the ipsilateral hip angle, and $\theta_{\text{ext,eq}}$, $\theta_{\text{flex,eq}}$ are the equilibrium angles of extension and flexion springs respectively. The $\min(\cdot)$ and $\max(\cdot)$ functions ensure that springs are unidirectional and only provide torque in the intended direction.

We want to predict biomimetic torques using measurable input kinematics (e.g., angles and velocities) across multiple ADLs, which is not feasible with virtual springs alone, since similar hip angles may correspond to dissimilar biological hip moments in different activities and gait phases. For example, a vertical thigh orientation during mid-stance and mid-swing corresponds to conflicting extension and flexion biological moments, respectively. Prediction power can be substantially improved by modulating the torque from two springs using joint velocity (the general modulation block in Fig. 1). In early-to-mid stance, the flexion spring torque is attenuated due to large negative hip velocity, providing extension torque aligned with leg movement. This attenuation continues until late stance, when hip velocity is slightly negative, signaling the need for overall negative power for braking. Similarly, in early-to-mid swing, the extension spring torque is attenuated based on large positive hip velocity until late swing. This velocity-based modulation strategy for general gait activities enables precise control of torque application timing across gait phases. Due to the smoothness and boundedness of sigmoid function, we chose it as the nonlinear modulation function:

$$\sigma(x, w, \phi) = \frac{1}{1 + e^{-w \cdot x + \phi}}\ , \tag{2}$$

where x is the input argument, and w, ϕ are parameters that determine the slope and horizontal shifts of the sigmoid function. Let x be the angular velocity $\dot{\theta}$, then (2) maps $\dot{\theta} \in \mathbb{R}$ to $[0, 1]$, ensuring the boundedness of the modulation. By adjusting w and ϕ, the timing of assistive torque and its sensitivity to velocity can be tuned.

The general modulation factors can then be determined by

$$\begin{aligned}\eta_{\text{ext}} &= \sigma(\dot{\theta}_{\text{ips}}, w_{\text{ext}}, \phi_{\text{ext}})\ , \\ \eta_{\text{flex}} &= \sigma(\dot{\theta}_{\text{ips}}, w_{\text{flex}}, \phi_{\text{flex}})\ ,\end{aligned} \tag{3}$$

where $\dot{\theta}_{\text{ips}}$ is the ipsilateral hip angular velocity, and $w_{\text{ext}}, w_{\text{flex}}, \phi_{\text{ext}}, \phi_{\text{flex}}$ are parameters to be determined.

For certain descent tasks, such as stair descent, modulations solely based on velocity direction are insufficient to generate biomimetic assistive torque. During mid-swing, the concentric contraction of the hip flexors swings the leg forward. On the other hand, a hip flexion velocity is also observed during stance in descending tasks, associated with the eccentric contraction of hip extensors, to allow a "controlled lowering" of body center-of-mass. In this case, the exoskeleton needs to provide torque against the leg's motion to brace the user from collapsing, which is challenging with existing modulations since they tend to provide torque that aligns with the leg motion's direction (or sign of the velocity). By analyzing normative kinematics of descending tasks, we observed that during early to mid-stance, the ipsilateral hip flexes for lowering, while the contralateral hip flexes to swing the leg forward. This pattern allows us to further introduce descent modulation for effective assistance during descending tasks, determined by the descent modulation factor

$$\begin{aligned}\eta_{\text{desn}} = \sigma(\dot{\theta}_{\text{ips}}, w_{\text{ips}}, \phi_{\text{ips}}) \cdot \sigma(\dot{\theta}_{\text{con}}, w_{\text{con}}, \phi_{\text{con}}) \\ \cdot \text{step}(\theta_{\text{ips}} - \theta_{\text{con}} - \theta_{\text{th}})\end{aligned} \tag{4}$$

where $\dot{\theta}_{\text{con}}$ is the contralateral hip angular velocity, step$(\cdot)$ is the step function, θ_{con} is the contralateral hip angle, and θ_{th} is the angle difference limit. Parameters $w_{\text{ips}}, \phi_{\text{ips}}, w_{\text{con}}, \phi_{\text{con}}$ are designed such that both sigmoid functions converge to 1 when velocities are positive and to 0 when velocities are negative. The multiplication acts as a proxy of the "AND" logic operation, allowing $\eta_{\text{des}} \to 1$ only when both thighs are flexing, an indicator of descent activities. The step function further restricts the descent modulation to only be applied in a certain range of joint angle.

Combining (1), (3), and (4) gives the extension and flexion torques from the gait module:

$$\begin{aligned}\tau_{\text{ext,mod}} &= \tau_{\text{ext}} \cdot \left[\eta_{\text{desn}} \cdot C_{\text{ext}} + (1 - \eta_{\text{desn}}) \cdot \eta_{\text{ext}}\right]\ , \\ \tau_{\text{flex,mod}} &= \tau_{\text{flex}} \cdot \left[\eta_{\text{desn}} \cdot C_{\text{flex}} + (1 - \eta_{\text{desn}}) \cdot \eta_{\text{flex}}\right]\ ,\end{aligned} \tag{5}$$

where C_{ext} and C_{flex} are constant parameters to be chosen. General modulation and descent modulation together comprise velocity-based modulation, which changes the angle to torque mapping of extension and flexion springs to angle-velocity to torque, improving versatility and allowing more task-adaptive, biomimetic assistance from simple virtual springs.

2) STS Module: Due to the differences between sit-to-stand transitions and other walking tasks, the STS module is designed separately and operates in parallel with the gait module. The core of the STS module is the STS spring, a unidirectional virtual torsion spring with equilibrium angle at $\theta_{\text{thigh}} = 0°$, where θ_{thigh} is the ipsilateral thigh angle, as defined in Fig. 2. An extension restoring torque is generated when the thigh is flexed, determined by

$$\tau_{\text{sts}} = \min(0,\ -k_{\text{sts}} \cdot \theta_{\text{thigh}})\ . \tag{6}$$

Similar to the gait module, solely relying on the thigh angle leads to large extension torque at the end of the stand-to-sit transition and while seated. Therefore, to reduce torque while the user is seated, τ_{sts} is first modulated based on the torso angle θ_{torso}, as defined in Fig. 2 (left). The torso angle is a key differentiator between the sit-to-stand transition and a sitting posture, where the sit-to-stand transition exhibits an anterior torso lean ($\theta_{\text{torso}} > 0$). Furthermore, to reduce bracing during the late stand-to-sit transition, hip velocity is used to taper down extension torque when the thigh is flexing, indicating a stand-to-sit transition. Combining the

two modulations, the modulation factors for STS torque are determined by

$$\begin{aligned} \eta_{\text{sts,torso}} &= \sigma(\max(0, \theta_{\text{torso}}), w_{\text{torso}}, \phi_{\text{torso}}) \ , \\ \eta_{\text{sts,vel}} &= \sigma(\dot{\theta}_{\text{ips}}, w_{\text{vel}}, \phi_{\text{vel}}) \ . \end{aligned} \tag{7}$$

The maximum function $\max(0, \theta_{\text{torso}})$ allows the STS spring to only engage when $\theta_{\text{torso}} > 0$ (forward torso lean). Combing (6) and (7) gives the modulated STS torque:

$$\tau_{\text{sts,mod}} = \tau_{\text{sts}} \cdot \eta_{\text{sts,torso}} \cdot \eta_{\text{sts,vel}} \ .$$

3) Module Integration: To create seamless transitions between the gait module and the STS module, the torque from both modules is scaled based on the symmetry of bilateral kinematics, serving as a strong indicator of walking and STS activities. The scaling factor is determined by

$$\beta = \sigma(|\theta_{\text{ips}} - \theta_{\text{con}}|, w_{\text{sc}}, \phi_{\text{sc}}) \cdot \text{step}(|\dot{\theta}_{\text{ips}} - \dot{\theta}_{\text{con}}| - \omega_{\text{th}}) \ ,$$

where ω_{th} is the velocity difference limit. The step function ensures that β is nonzero only when the bilateral velocity is below the threshold determined by ω_{th}, implying symmetric bilateral velocities. By modifying $w_{\text{sc}}, \phi_{\text{sc}}$, and ω_{th}, one can adjust the sensitivity to asymmetry. Subsequently, the torques from the walking and STS modules are combined as a convex combination to produce the output torque

$$\tau_{\text{out}} = \beta \cdot \tau_{\text{sts,mod}} + (1 - \beta) \cdot (\tau_{\text{ext,mod}} + \tau_{\text{flex,mod}}) \ .$$

B. Parameter Optimization

Our biomechanics-informed design offers enhanced flexibility, enabling parameter adjustments beyond the original data-driven optimization process—a capability our previous design [23] lacked. Similarly to our previous work, we use normative datasets to inform the initial parameters (providing a *warm start*), which were later tuned based on pilot subject feedback. We formulate the parameter design problem as an optimization problem using normative human data from open-source multi-activity datasets [26] [27]. By minimizing the difference between estimated assistive torque (given normative input kinematics) and biological joint moment, we obtain parameters that serve as an improved starting point for further fine-tuning.

The parameters to be optimized are $w_{(\cdot)}, \phi_{(\cdot)}$ in (3), and $C_{\text{ext}}, C_{\text{flex}}$ in (5). The objective function is

$$\begin{aligned} J = \sum_{i \in T} \ & (\gamma_i \cdot \|\tau^i_{\text{out}} - \tau^i_{\text{bio}}\| + \gamma_2 \cdot \|\tau^0_{\text{out}}\| \\ & + \gamma_3 \cdot \|\text{sgn}(\tau^i_{\text{out}}) - \text{sgn}(\tau^i_{\text{bio}})\|) \ , \end{aligned}$$

where T is the set of activities used in the optimization, τ^i_{bio} is the scaled biological hip moment, and τ^i_{out} is the estimated assistive torque for activity i. The biological hip moment is scaled to 35% since the actuators can only provide around 1/3 of normative hip moment. τ^0_{out} denotes the estimated torque when all kinematics are zero, which corresponds to the configuration of standing still. $\text{sgn}(\cdot)$ is the sign function. γ_i is the task-dependent weight, and γ_2, γ_3 are constant weights. The first term of the objective function minimizes the difference between assistive torque and biological moment, with activity-dependent weight to emphasize hip demanding activities. The second term minimizes the static torque to prevent discomfort, and the third term minimizes the sign difference between τ^i_{out} and τ^i_{bio} to penalize assistive torque in the wrong direction.

To cover a range of ADLs, we used data from six subjects performing the following activities as our training set: level walking at 0.85 and 1.15 m/s, ascending and descending ramps at 5.2° and 11°, ascending and descending stairs with step heights of 5 and 7 inches (12.7 and 17.8 cm), and rising from a chair. The optimization problem was solved in MATLAB R2023b using the "`fmincon`" function, with physically reasonable lower and upper bounds. Figure 3 compares the estimated torque from the optimized controller, based on normative kinematics, to the corresponding scaled biological hip moment. Although data from healthy individuals were used, the optimized parameters served only as an initial guess and were further fine-tuned through feedback from pilot tests. Once determined, parameters remained fixed throughout the study.

C. Hardware Implementation

The controller was implemented on a bilateral hip exoskeleton shown in Fig. 2 (right), which is an improved hip module of the M-BLUE system [28]. The hip exoskeleton combines off-the-shelf hip braces (Breg T Scope Hip) with two highly backdrivable actuators (T-motor AK80-9 with Dephy FASTER driver) that provide 25 Nm peak torque with low reflected inertia (92.1 kg $\cdot$ cm^2). During the study, the maximum torque was limited to 20 Nm. Three IMUs (Microstrain 3DM-GX5 AHRS) were directly attached to thighs and torso to acquire: sagittal thigh, torso, and hip angles, and their angular velocities. The real-time controller ran on a Raspberry Pi 5 8 GB at 300 Hz. Hip angular velocity and commanded torque were filtered with second-order Butterworth low-pass filters with cutoff frequencies of 10 Hz and 5 Hz respectively. The system was powered by a 24 V, 2 Ah power tool battery (Kobalt 24-V Lithium Battery) and weighs approximately 4.3 kg. For safety, a remote e-stop switch was implemented to cut power to the motor if needed.

III. Hip Osteoarthritis Pilot Study

A. Experimental Design

To investigate the effect of the exoskeleton/controller on hip OA patients' physical performance and perceived pain and difficulty during different activities, we designed a study consisting of a multi-activity test approved by the Institutional Review Board at University of Michigan (HUM00201957). As a proof of concept, we enrolled three participants diagnosed with hip OA. Participant 1 was diagnosed with bilateral hip OA (S1: female, age-53, weight-52 kg, height-1.65 m), while participant 2 and 3 were diagnosed with unilateral hip OA (S2: male, age-32, weight-70 kg, height-1.71 m; S3: female, age-64, weight-78 kg, height-1.68 m). All participants gave written consent before participation. Participants were required to wear a safety harness to prevent falling during the study.

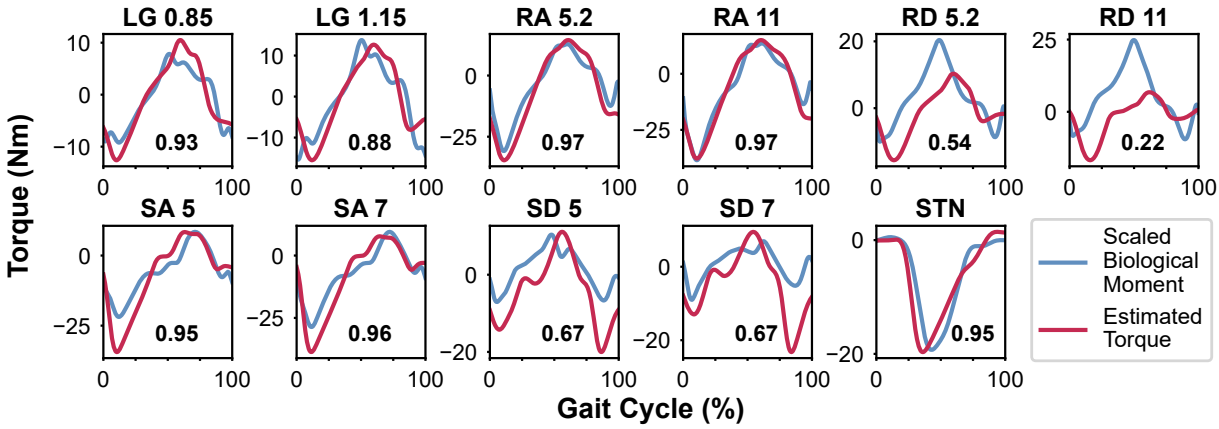


Fig. 3. *In silico* comparison between controller estimated torque and scaled biological hip moment. Estimated torque is computed using across-subject average kinematics with optimized parameters, and biological moment is the average hip moment scaled to 35%. Activities include LG (level-ground walking) at 0.85 and 1.15 m/s, RA (ramp ascent) and RD (ramp descent) on 5.2° and 11° ramps, SA (stairs ascent) and SD (stairs descent) on 5 and 7-inch step height stairs, and standing. Bold numbers in the subfigures denote the cosine similarity between the estimated torque and the scaled hip moment for the corresponding task [23].

Before the tests, participants underwent an acclimation session in which they performed different activities with the exoskeleton under different levels of assistance (LoA) until they were confident with the device. Participants also indicated the maximum LoA that they felt comfortable with across activities, which was used later in the test. To investigate the effect of exoskeleton assistance the test was performed under the following conditions: no exoskeleton (No-Exo), passive exoskeleton (0% Exo), 50% active exoskeleton (50% Exo), and 100% active exoskeleton (100% Exo), where 100% denotes the maximum comfortable LoA indicated during acclimation. Note that in the No-Exo condition, participants wore a low-profile data collection setup, with IMUs attached to body segments using elastic straps to measure kinematics.

In the multi-activity test, participants performed ADLs including level-ground walking (LG), ramp ascent (RA), ramp descent (RD), stairs ascent (SA), stairs descent (SD), sit-to-stand (STN), and stand-to-sit (SIT) on a multi-terrain circuit comprising a 3.7-m ramp inclined at 15°, a short level platform of 2 m, and a 5-step staircase with 7-inch (18 cm) step height. We repeated each activity multiple times until obtaining at least 10 gait/task cycles with average speeds within $\pm 10\%$ of their baseline values measured during the acclimation. Pain and difficulty were assessed using a modified Western Ontario and McMaster Universities Arthritis Index (WOMAC) questionnaire, in which participants rated their perceived pain and difficulty on a scale of 0-4, corresponding to "None", "Slight", "Moderate", "Very", and "Extremely". Additionally, participants performed a 10-meter walk test (10MWT) at their comfort and fast speeds with three repetitions each, and the average of these repetitions was recorded as their comfort or fast 10MWT speed.

B. Results

Each participant's pain and difficulty ratings across activities for each condition are shown in Table I and Table II. Additionally, Fig. 4 compares the effect of the active exoskeleton on pain and difficulty with No-Exo, where the best rating out of 50% and 100% LoA was chosen for the active condition. Compared to No-Exo, the active exoskeleton reduced the across-subject average pain rating for all tasks. Similarly, average difficulty ratings were lower with the active exoskeleton for all tasks except LG.

TABLE I

PAIN RATINGS FOR ACTIVITIES UNDER DIFFERENT CONDITIONS (NO-/0%/50%/100% EXO). BOLD ENTRIES DENOTE THE BEST ACTIVE EXOSKELETON RATINGS.

Paricipant	LG	RA	RD	SA	SD	SIT	STN
S1	1/0/**0/0**	1/1/**0/0**	1/1/1/**0**	2/1/1/**0**	1/1/**0/0**	1/2/**0/0**	1/1/1/**0**
S2	1/2/1/**0**	1/0/**0/0**	1/1/**1/1**	2/2/2/**1**	2/1/**1**/2	2/3/2/**1**	2/1/**1/1**
S3	1/2/**2/2**	2/2/**2/2**	1/2/**1/1**	3/2/2/**1**	2/2/**2/2**	2/2/2/**1**	2/2/2/**1**

TABLE II

DIFFICULTY RATINGS FOR ACTIVITIES UNDER DIFFERENT CONDITIONS (NO-/0%/50%/100% EXO). BOLD ENTRIES DENOTE THE BEST ACTIVE EXOSKELETON RATINGS.

Paricipant	LG	RA	RD	SA	SD	SIT	STN
S1	0/0/**0/0**	1/1/**0/0**	1/1/1/**0**	2/1/1/**0**	2/1/**0/0**	1/2/**0**/1	1/2/**0**/1
S2	1/2/**0/0**	1/1/**0/0**	1/1/**1/1**	2/1/2/**0**	1/1/**1**/2	2/2/1/**0**	2/1/**0**/1
S3	1/2/**2/2**	2/2/**2/2**	1/2/**1/1**	2/3/2/**1**	2/2/**2**/3	1/2/**1/1**	1/2/1/2

The average and individual speed changes of 10MWT in the Exo conditions compared to No-Exo condition are shown in Fig. 5. Both average comfort and fast speeds in 100% Exo condition increased compared to No-Exo condition, but with large inter-participant variation.

For comfort speed 10MWT, results from three exoskeleton conditions (0%, 50%, and 100% Exo) were compared to the No-Exo condition. S1's comfort speeds were 1.55, 1.56, and 1.52 m/s in the respective exoskeleton conditions, corresponding to changes of +0.98%, +1.63%, and -0.98% compared to the No-Exo condition (1.54 m/s). S2's comfort speeds were 1.40, 1.32, and 1.79 m/s, representing changes of -0.99%, -7.06%, and +26.46% compared to the No-Exo condition (1.42 m/s). S3's comfort speeds were 1.32, 1.36,

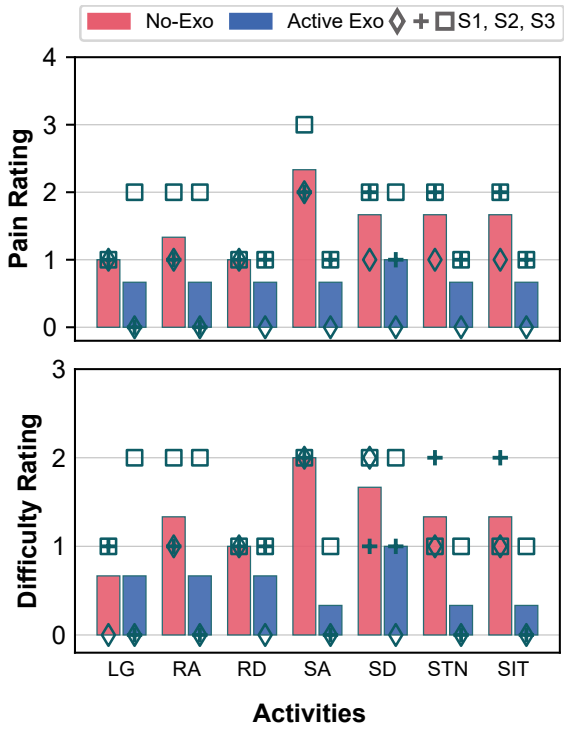


Fig. 4. Across-subject average and individual pain and difficulty ratings of activities under no exoskeleton (No-Exo) and active exoskeleton (Active Exo) conditions. Bar plots and scatter plots show the average and individual ratings.

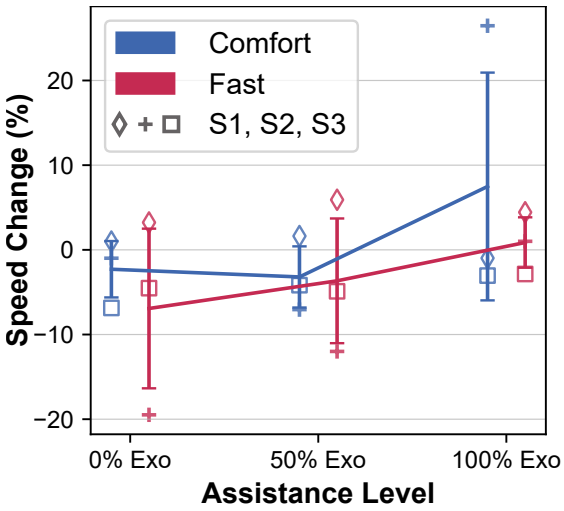


Fig. 5. Across-subject average and individual 10MWT speed changes relative to the No-Exo condition. Points where lines intersect error bars (± 1 standard deviation) indicate the mean values, and scatter plots denote individual data points. Positive numbers indicate faster speeds.

and 1.37 m/s, corresponding to changes of -6.86%, -4.17%, and -2.9% compared to the No-Exo condition (1.41 m/s).

For fast speed 10MWT, results from three exoskeleton conditions were compared to the No-Exo condition. S1's fast speeds were 1.89, 1.93, and 1.91 m/s in the respective exoskeleton conditions, corresponding to changes of +3.23%, +5.91%, and +4.44% compared to the No-Exo condition (1.83 m/s). S2's fast speeds were 1.84, 2.01, and 2.31 m/s, representing changes of -19.48%, -12.00%, and +1.01% compared to the No-Exo condition (2.28 m/s). S3's fast speeds were 1.54, 1.54, and 1.57 m/s, corresponding to changes of -4.52%, -4.89%, and -2.85% compared to the No-Exo condition (1.61 m/s).

As an exploratory result, Fig. 6 shows participants' hip joint angle over a gait cycle during 10MWT at comfort speed under No-Exo, 0% and 100% Exo conditions, overlaid with the commanded torque from the 100% Exo condition. Compared to No-Exo, hip RoM increased in 100% Exo for all participants. Specifically, the hip RoM of S1 was (-11.5°, 42.9°) in No-Exo, (-14.4°, 36.7°) in 0% Exo, and (-16.5°, 41.7°) in 100% Exo. This corresponds to 3.8° RoM increase in 100% Exo compared to No-Exo. The hip RoM of S2 was (-10.5°, 36.7°) in No-Exo, (-17.4°, 35.2°) in 0% Exo, and (-18.8°, 40.2°) in 100% Exo. This corresponds to a 11.8° RoM increase in 100% Exo compared to No-Exo. The hip RoM of S3 was (-12.0°, 40.6°) in No-Exo, (-21.2°, 30.3°) in 0% Exo, and (-22.8°, 39.3°) in 100% Exo. This corresponds to a 9.5° RoM increase in 100% Exo compared to No-Exo.

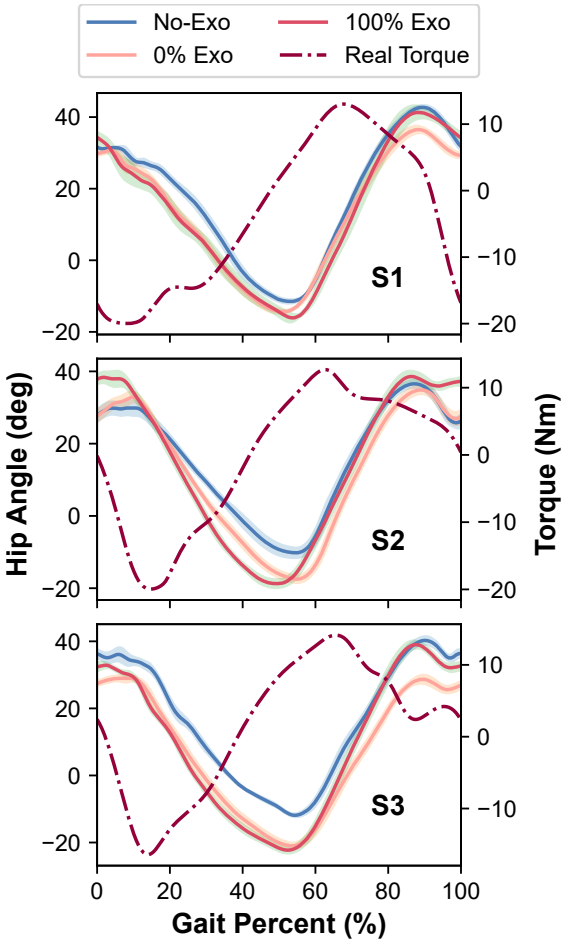


Fig. 6. Participants' hip joint angle over a gait cycle during comfortable speed 10MWT, under No-Exo, 0% Exo, and 100% Exo conditions. Solid lines represent the mean value, and shaded areas represent ±1 standard deviation. Dashed lines represent the commanded actuator torque. Positive values indicate flexion.

IV. Discussion

We hypothesized that our powered hip exoskeleton can reduce pain and difficulty in the hip OA population when performing various activities, due to reduced internal joint moments. The results of this study support our hypothesis. Across-subject pain ratings reduced across all tasks with the active exoskeleton, and the average difficulty ratings decreased for all tasks except LG. Pain and difficulty were most reduced in hip-intensive tasks like SA, STN and SIT. The small reductions in pain and difficulty in RA, an activity that requires large hip extension moment, was unexpected. A possible explanation is that participants adopted an altered gait that requires less hip effort during RA, due to muscle weakness and pain—such gait adaptations have been reported in the knee OA population during stair climbing [29]. This can also explain the lower pain/difficulty ratings in RA compared to SA in No-Exo condition. However, inverse dynamics will be needed to verify this hypothesis, which is outside the scope of this initial study.

The effect of LoA on pain and difficulty was as expected. In general, higher LoA led to the same or reduced pain and difficulty. However, for certain tasks like SD and STN, less reduction in pain or difficulty was reported in 100% Exo condition compared to other LoAs. During SD, the exoskeleton mainly does negative power, which causes resistance to leg motion, potentially leading to more difficulty. During STN, large bilateral assistive torque in the same direction needs to be applied in a short time, which leads to a large rate of torque increase. This might have increased the difficulty in 100% Exo condition, compared to milder and smoother assistive torque rates in the 50% Exo condition. The discrepancies in LoA preferences show the importance of customizability in exoskeleton control. Although we left the controller unchanged across participants in this study, the design of our controller allows user-based customization and task-specific fine-tuning to maximize the benefits of the exoskeleton in managing hip OA.

The passive exoskeleton (the 0% Exo condition) had mixed effects compared to No-Exo. In some tasks like SA, the passive exoskeleton induced benefits, likely because the underlying post-op hip brace provides hip stabilization and restricts frontal plane motions (a common strategy in OA treatment). On the other hand, increased pain and difficulty with the passive exoskeleton can still be observed in other activities, which indicates the potential penalty due to the weight and/or restrictions of the exoskeleton. Note that due to the backdrivable actuators, the penalty caused by the backdrive torque (1-2 Nm) is likely negligible. Overall, the mixed effect of the passive exoskeleton condition reflects the limited benefit of passive braces, further demonstrating the value of powered exoskeletons for OA treatment.

Slower walking speed has been observed in the hip OA population compared to the control group [30]. In this study, we compared the comfort/fast speeds during 10MWT between conditions, observing increases on average for the 100% Exo condition compared to No-Exo condition. However, large inter-subject variation exists: S1 and S2 responded well to active exoskeleton and had increases in both comfort and fast speed, while S3 did not have any speed increase with the exoskeleton. This large variability might be caused by inter-subject differences in sensorimotor factors other than muscle strength and pain; including balance, reaction time, and proprioception [31]. Although the exoskeleton can compensate for muscle strength loss and reduce pain, the assistance can also cause disruption of underlying physiology and negatively affect their gait. Therefore, acclimation is usually required for exoskeleton users to experience the most benefit. However, becoming fully acclimated to exoskeletons takes several hours, and older age further slows motor adaptation to walking with exoskeletons [32]. Therefore, it is possible that the senior most participant in our cohort (S3) did not fully acclimate to the exoskeleton, although they indicated confidence during acclimation. This may have prevented them from benefiting more from assistance compared to the younger participants.

Reduced hip RoM is a typical gait characteristic of the hip OA population during walking. This compromised gait may lead to abnormal joint load patterns at the hip and other lower extremity joints, further causing joint degeneration and chronic pain [33]. In this study, the active exoskeleton condition was associated with notably higher hip RoM compared to No-Exo. The most probable reason is the effect of the assistive extension torque of the active exoskeleton. This likely enabled participants to walk with a high peak hip extension by overcoming the effects of weak hip extensors and possible flexion contractures. On the other hand, pain arising from the higher joint forces associated with a larger step length could lead to a reduced hip RoM. The force and pain reduction capabilities of the active exoskeleton could have offset these effects, thereby encouraging larger steps and RoM. While hip RoM and walking speed are generally correlated, S1 and S3 had larger RoM despite slower speed in the 100% Exo condition. This indicates that the holistic increase in hip RoM is not simply a by-product of changes in walking speed.

The effect of the exoskeleton's assistance is evident in the commanded torque shown in Fig. 6. Across all participants, significant extension torque was provided during early-to-mid stance, which can compensate for the decreased hip extension moment associated with OA. It is important to note that normative extension torque during slow walking is typically small compared to hip-intensive activities such as ramp or stair ascent. As a result, a purely data-driven controller based on normative data would likely generate insufficient extension torque for hip OA populations, who require greater extension assistance than healthy individuals. In contrast, our controller produced large extension torques, with peak values approaching 20 Nm (the maximum allowable torque), demonstrating its ability to assist impaired populations without relying on population-specific data.

V. Conclusion

In this paper, we presented a novel biomechanics-informed, task-agnostic hip exoskeleton controller designed to address hip OA-related mobility challenges. Inspired by energy shaping principles, the controller utilizes virtual springs modulated by joint kinematics, allowing improved customizability. A pilot study with three hip OA patients showed that our hip exoskeleton and controller can reduce pain and difficulty across activities, increase hip RoM during walking, and improve 10MWT speed on an individual basis. These promising results suggest that hip exoskeletons may provide a novel conservative intervention for managing hip OA to improve patient mobility and quality of life.

Acknowledgment

The authors thank Emily Keller for assisting experiments.

References

[1] B. S. Ferket, Z. Feldman, J. Zhou, E. H. Oei, S. M. Bierma-Zeinstra, and M. Mazumdar, "Impact of total knee replacement practice: cost effectiveness analysis of data from the osteoarthritis initiative," *BMJ*, vol. 356, 2017.

[2] T. Towheed, L. Maxwell, M. Judd, M. Catton, M. C. Hochberg, and G. A. Wells, "Acetaminophen for osteoarthritis," *Cochrane database of systematic reviews*, no. 1, 2006.

[3] K. L. Bennell, D. J. Hunter, and R. S. Hinman, "Management of osteoarthritis of the knee," *BMJ*, vol. 345, 2012.

[4] M. Henriksen, E. B. Simonsen, T. Alkjær, H. Lund, T. Graven-Nielsen, B. Danneskiold-Samsøe, and H. Bliddal, "Increased joint loads during walking–a consequence of pain relief in knee osteoarthritis," *The Knee*, vol. 13, no. 6, pp. 445–450, 2006.

[5] O. A. Uthman, D. A. Van Der Windt, J. L. Jordan, K. S. Dziedzic, E. L. Healey, G. M. Peat, and N. E. Foster, "Exercise for lower limb osteoarthritis: systematic review incorporating trial sequential analysis and network meta-analysis," *BMJ*, vol. 347, 2013.

[6] J. M. Hootman, S. FitzGerald, C. A. Macera, and S. N. Blair, "Lower extremity muscle strength and risk of self-reported hip or knee osteoarthritis," *J. Physical Activity and Health*, vol. 1, no. 4, pp. 321–330, 2004.

[7] T. B. Birmingham, K. A. Marriott, K. M. Leitch, R. F. Moyer, A. L. Lorbergs, D. M. Walton, K. Willits, R. B. Litchfield, A. Getgood, P. J. Fowler *et al.*, "Association between knee load and pain: within-patient, between-knees, case–control study in patients with knee osteoarthritis," *Arthritis care & Res.*, vol. 71, no. 5, pp. 647–650, 2019.

[8] D. Hurwitz, C. Hulet, T. Andriacchi, A. Rosenberg, and J. Galante, "Gait compensations in patients with osteoarthritis of the hip and their relationship to pain and passive hip motion," *J. Orthopaedic Res.*, vol. 15, no. 4, pp. 629–635, 1997.

[9] J. Dekker, P. Tola, G. Aufdemkampe, and M. Winckers, "Negative affect, pain and disability in osteoarthritis patients: the mediating role of muscle weakness," *Behav. Res. Ther.*, vol. 31, no. 2, pp. 203–206, 1993.

[10] N. Shiba, Y. Tagawa, Y. Nakashima, S. Matsuo, K. Yamamoto, Y. Watanabe, F. Higuchi, and A. Inoue, "Biomechanical effect and clinical application of the hip joint moment reduction brace," *Clinical Orthopaedics and Related Research®*, vol. 351, pp. 149–157, 1998.

[11] A. Nérot and M. Nicholls, "Clinical study on the unloading effect of hip bracing on gait in patients with hip osteoarthritis," *Prosthetics and Orthotics Int.*, vol. 41, no. 2, pp. 127–133, 2017.

[12] E. Squyer, D. L. Stamper, D. T. Hamilton, J. A. Sabin, and S. S. Leopold, "Unloader knee braces for osteoarthritis: do patients actually wear them?" *Clinical Orthopaedics and Related Res.*, vol. 471, no. 6, pp. 1982–1991, 2013.

[13] T. G. Sutlive, H. P. Lopez, D. E. Schnitker, S. E. Yawn, R. J. Halle, L. T. Mansfield, R. E. Boyles, and J. D. Childs, "Development of a clinical prediction rule for diagnosing hip osteoarthritis in individuals with unilateral hip pain," *J. Orthopaedic & Sports Physical Therapy*, vol. 38, no. 9, pp. 542–550, 2008.

[14] R. L. Medrano, E. J. Rouse, and G. C. Thomas, "Biological joint loading and exoskeleton design," *IEEE Trans. Med. Robot. and Bionics*, vol. 3, no. 3, pp. 847–851, 2021.

[15] D. D. Molinaro, I. Kang, and A. J. Young, "Estimating human joint moments unifies exoskeleton control, reducing user effort," *Sci. Robot.*, vol. 9, no. 88, p. eadi8852, 2024.

[16] N. V. Divekar, G. C. Thomas, A. R. Yerva, H. B. Frame, and R. D. Gregg, "A versatile knee exoskeleton mitigates quadriceps fatigue in lifting, lowering, and carrying tasks," *Sci. Robot.*, vol. 9, no. 94, p. eadr8282, 2024.

[17] D. A. Winter, *Biomechanics and motor control of human movement*. John Wiley & Sons, Ltd, 2009.

[18] I. Kang, D. D. Molinaro, S. Duggal, Y. Chen, P. Kunapuli, and A. J. Young, "Real-time gait phase estimation for robotic hip exoskeleton control during multimodal locomotion," *IEEE robotics and automation letters*, vol. 6, no. 2, pp. 3491–3497, 2021.

[19] D.-S. Kim, H.-J. Lee, S.-H. Lee, W. H. Chang, J. Jang, B.-O. Choi, G.-H. Ryu, and Y.-H. Kim, "A wearable hip-assist robot reduces the cardiopulmonary metabolic energy expenditure during stair ascent in elderly adults: a pilot cross-sectional study," *BMC geriatrics*, vol. 18, pp. 1–8, 2018.

[20] C. McGibbon, A. Sexton, A. Jayaraman, S. Deems-Dluhy, E. Fabara, C. Adans-Dester, P. Bonato, F. Marquis, S. Turmel, and E. Belzile, "Evaluation of a lower-extremity robotic exoskeleton for people with knee osteoarthritis," *Assistive Technol.*, vol. 34, no. 5, pp. 543–556, 2022.

[21] J. Lin, N. V. Divekar, G. C. Thomas, and R. D. Gregg, "Optimally biomimetic passivity-based control of a lower-limb exoskeleton over the primary activities of daily life," *IEEE Open J. Control Syst.*, vol. 1, pp. 15–28, 2022.

[22] K. Walters, G. C. Thomas, J. Lin, and R. D. Gregg, "An energetic approach to task-invariant ankle exoskeleton control," in *IEEE/RSJ Int. Conf. on Intelligent Robots and Syst. (IROS)*, 2023, pp. 6082–6089.

[23] J. Zhang, J. Lin, V. Peddinti, and R. D. Gregg, "Optimal energy shaping control for a backdrivable hip exoskeleton," in *2023 Amer. Control Conf. (ACC)*. IEEE, 2023, pp. 2065–2070.

[24] J. Lin, G. C. Thomas, N. V. Divekar, V. Peddinti, and R. D. Gregg, "A modular framework for task-agnostic, energy shaping control of lower limb exoskeletons," *IEEE Trans. Control Syst. Technol.*, vol. 32, no. 6, pp. 2359–2375, 2024.

[25] J. Lin, N. Divekar, G. Lv, and R. D. Gregg, "Energy shaping control with virtual spring and damper for powered exoskeletons," in *2019 IEEE 58th Conference on Decision and Control (CDC)*, 2019, pp. 3039–3045.

[26] B. Laschowski, R. Sharif Razavian, and J. McPhee, "Measurement and simulation of human sitting and standing movement biomechanics," 2019. [Online]. Available: https://dx.doi.org/10.21227/9cqv-w712

[27] J. Camargo, A. Ramanathan, W. Flanagan, and A. Young, "A comprehensive, open-source dataset of lower limb biomechanics in multiple conditions of stairs, ramps, and level-ground ambulation and transitions," *J. Biomech.*, vol. 119, p. 110320, 2021.

[28] C. Nesler, G. Thomas, N. Divekar, E. J. Rouse, and R. D. Gregg, "Enhancing voluntary motion with modular, backdrivable, powered hip and knee orthoses," *IEEE Robot. and Automat. Lett.*, vol. 7, no. 3, pp. 6155–6162, 2022.

[29] J. L. Asay, A. Mündermann, and T. P. Andriacchi, "Adaptive patterns of movement during stair climbing in patients with knee osteoarthritis," *J. Orthopaedic Research*, vol. 27, no. 3, pp. 325–329, 2009.

[30] D. Schmitt, A. Vap, and R. M. Queen, "Effect of end-stage hip, knee, and ankle osteoarthritis on walking mechanics," *Gait & posture*, vol. 42, no. 3, pp. 373–379, 2015.

[31] M. L. Callisaya, L. Blizzard, M. D. Schmidt, J. L. McGinley, S. R. Lord, and V. K. Srikanth, "A population-based study of sensorimotor factors affecting gait in older people," *Age and Ageing*, vol. 38, no. 3, pp. 290–295, 2009.

[32] A. Lakmazaheri, S. Song, B. B. Vuong, B. Biskner, D. M. Kado, and S. H. Collins, "Optimizing exoskeleton assistance to improve walking speed and energy economy for older adults," *J. NeuroEng. and Rehabil.*, vol. 21, no. 1, p. 1, 2024.

[33] M. Murray, D. R. Gore, and B. Clarkson, "Walking patterns of patients with unilateral hip pain due to osteo-arthritis and avascular necrosis," *JBJS*, vol. 53, no. 2, pp. 259–274, 1971.

Identification of Neuromotor Patterns Associated with Hand Rehabilitation Movements from EMG and EEG signals

Michelle Soto-Florido[1], Elkin Garcia-Cifuentes[2], Angela M. Irragorri[2], Ivan F. Mondragon[1], Diego Mendez[1], Julian D. Colorado[1], Catalina Alvarado-Rojas[1]

***Abstract*— Stroke rehabilitation is essential for restoring upper limb function, impaired in nearly 85% of stroke survivors. Accurate classification of movement intention and execution can enhance rehabilitation through improved patient monitoring and robotic assistance. This study explores integrating electroencephalography (EEG) and electromyography (EMG) signals to classify five hand movements commonly used in rehabilitation therapy: four finger pinches and full hand closure. Biological signals were acquired from 22 healthy participants using a synchronized setup of EEG and EMG systems. Signal processing methods were applied to extract frequency and connectivity features from EEG and muscle activity metrics from EMG. These features were used to train machine learning models, including Ensemble Bagged Trees, neural networks, and SVMs, for classifying movement intention and execution. Results demonstrated that the Ensemble Bagged Trees model achieved the highest accuracy classified 5 classes, particularly when employing EEG power spectral density features, with 84.7% and 67.4% accuracy for movement execution and intention, respectively. Correlation analysis identified distinct motor-related brain connectivity patterns, offering insights into neuromotor processes. These findings support the integration of EEG-EMG analysis with machine learning to enhance stroke rehabilitation, improving patient monitoring and robotic-assisted therapy.**

Keywords—Hand rehabilitation, EEG signals, EMG signals, Signal Processing, Machine Learning

I. INTRODUCTION

Stroke is one of the leading causes of death and disability worldwide, placing a significant burden on healthcare systems and patients alike. According to the World Health Organization (WHO), approximately 12.2 million new cases of stroke were reported in 2022, with an estimated 101 million individuals living with its aftermath [1]. Moreover, it is estimated that one in four individuals over the age of 25 will experience a stroke during their lifetime. Stroke typically results from an interruption of blood flow to the brain—either due to an obstruction (ischemic stroke) or a rupture of a blood vessel (hemorrhagic stroke)—leading to cellular death and significant neurological impairment [2]. Notably, up to 85% of stroke survivors experience upper limb dysfunction, highlighting the critical need for effective rehabilitation strategies to restore hand functionality and improve activities of daily living [3].

Since the dominant hand is essential for daily activities. Stroke can severely limit independence and participation in task that requiring precision, coordination an strength. With up to 80% of individuals being right-handed and nearly half of all strokes affecting the left hemisphere, a significant portion of stroke survivors experience right-hand paresis. Studies suggest that the dominant hand benefits from greater motor efficiency, muscle endurance, and refined motor programs due to lifelong use. Therefore, effective rehabilitation strategies must prioritize restoring right-hand function to maximize recovery and maintain quality of life.[4], [5]

Early and intensive rehabilitation is crucial for maximizing recovery, particularly within the first three months following a stroke. Rehabilitation programs are most effective when they are tailored to the individual, often combining initial in-hospital therapy with subsequent outpatient sessions designed to address the specific motor deficits of each patient [6] [7]. Recently, there has been growing interest in incorporating technology-assisted therapies, such as robotic exoskeletons, to complement traditional rehabilitation methods. These devices not only support the restoration of motor function but also offer enhanced patient monitoring and personalized therapeutic interventions [8], [9]

Furthermore, advances in biomedical signal processing have enabled the integration of electroencephalography (EEG) and electromyography (EMG) to monitor both neural and muscular activity during rehabilitation. Several studies have demonstrated the utility of EEG and EMG signals in decoding movement intention and execution, which can significantly improve the control of robotic devices in therapeutic settings [10][11]. By leveraging machine learning algorithms to analyze these signals, it is possible to develop more adaptive and responsive exoskeleton-assisted rehabilitation systems that cater to individual patient needs. This innovative approach enhances the efficacy of rehabilitation but also accelerates the recovery process for stroke survivors.

* This work was Funded by the project "iREHAB: Sistema inteligente de Rehabilitación usando un Exoesqueleto para recuperar Habilidad motora en discapacidades post-ACV, usando señales Biológicas del paciente" sponsored by The Ministry of Science Technology and Innovation (MinCiencias), program 918-2022 under GRANT CTO: 622-2022, Award ID: 91805.

[1]*School of Engineering,* Pontificia Universidad Javeriana, Bogotá,110231 Colombia.

[2]*School of Medicine,* Pontificia Universidad Javeriana, Bogotá, 110231 Colombia.

Soekadar et al.[12] research on brain computer interfaces (BCIs) for motor recovery, showing that EEG-based systems can facilitate functional restoration through neuroplasticity driven mechanisms. In this way other studies have demonstrated the effectiveness of combining EEG and EMG signals for movement classification in rehabilitation applications. Aly et al. [13] utilized deep learning approaches, such as CNNs with 192 layers and 24,576 neurons, achieving 95% accuracy for classifying wrist and hand movements. Similarly, Yang et al. [14] employed Pearson correlation coefficients and graph convolutional networks (GCN) to analyze EEG and EMG data, achieving 80.7% accuracy in distinguishing between hand opening, closing, and wrist movements. These findings underscore the potential of EEG and EMG integration for neuromotor rehabilitation.

In this study, we explore the integration of EEG and EMG signal analysis with machine learning techniques to classify hand movements commonly used in rehabilitation therapy. Our approach aims to provide a robust framework for understanding neuromotor processes and facilitating the development of intelligent robotic systems for stroke rehabilitation, but it also represents the first step toward understanding the evolution of cortical behavior in patients during therapy process.

II. Methods

In this work, we aim to analyze electrophysiological signals, such as electroencephalography and electromyography, during the execution of movements related to hand rehabilitation therapies in healthy subjects. Due to the importance of complex movements of the hand for activities of daily life and the scarce literature in dexterous movements, the exercises selected for this study were 4 individual finger pinches and hand closing. For this purpose, the experimental setup consists of synchronous acquisition of biological signals (EEG, EMG), followed by signal processing to extract features relevant to movements of interest, and intention/execution classification of the 5 movements (Fig. 1).

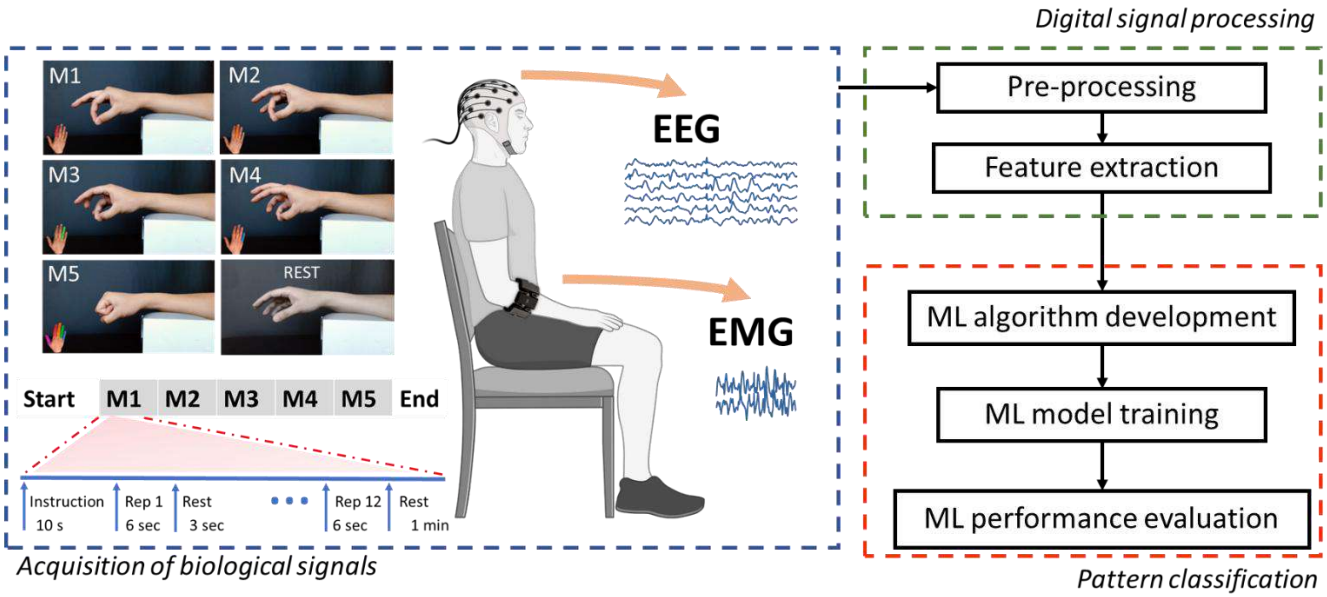


Fig. 1 General methodology diagram. The diagram outlines the sequential steps of the study, beginning with the synchronous acquisition of EEG and EMG signals from healthy subjects performing five hand movements (four individual finger pinches and a full hand closure)

A. Acquisition of Biological Signals

Twenty-two right-handed healthy subjects (12 males - 10 females; age 18 - 30 years) volunteered to participate in the study. From all of them, the informed written consent was obtained, following the approval of the Ethics Committee of the School of Engineering at Pontificia Universidad Javeriana, Bogotá, Colombia. The electroencephalography (EEG) data were collected with the USBAmp system (g.tec medical engineering, GmbH, Austria). A total of 28 electrodes were acquired at a sampling rate of 256Hz. The electrodes covered the frontal (F1-F4, FC1-FC4), motor (FCC3-FCC6, C1-C4), somatosensory (CCP3-CCP6), and parietal (CP1-CP4, P1-P4) cortical areas according to the 10-10 system. The electromyographic (EMG) signals were recorded with the Myo ARMBAND (Thalmic Labs, Canada) device. The 8 electrodes of the sensor were located superficially on the forearm and sampled at 200Hz (Fig. 2).

1) Experimental Procedure

Participants were asked to perform 5 different movements of the hand: 4 finger pinches (index, middle, ring, and little, all with the thumb), and full hand closure. The five distinct hand gestures are frequently used in rehabilitation therapy. To guide the participant along the experiment, the sequence of movements was presented in a video. Each movement was repeated 12 times, with each repetition lasting for 6 seconds followed by 3 seconds of rest between repetitions of the same movement, and 1 minute of rest between movements. Those times are based on previous project work [15].Therefore, we obtained 60 observations of 6 seconds per participant. The segments of 6 seconds were further divided into 2 segments of 3 seconds, one segment before and one segment after the

gesture execution. The signals were segmented into 3-second windows for movement intention classification (60 events), and 3-second windows for movement execution classification (60 events). Finally, the acquisition systems were synchronized using Universal Time Coordinated (UTC) to ensure precise alignment between EEG, EMG and movements.

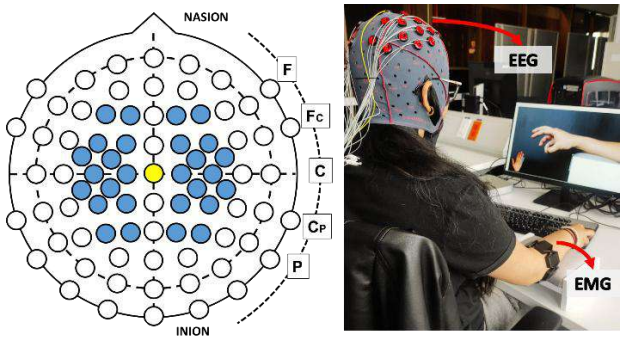


Fig. 2. Montage Acquisition, 28 channels F1-F4, FC1-FC4, FCC3-FCC6, C1-C4, CCP3-CCP6, CP1-CP4, P1-P4. And experimental Procedure set up.

B. Digital Signal Processing

1) EEG Signal Processing

The EEG signals were preprocessed, and features related to frequency and brain connectivity were extracted (TABLE I). To compute the frequency content of the signals, the power spectral density (PSD) was computed using Welch's method for each channel, and the mean power in 5 physiological frequency bands was computed for theta (4-8 Hz), alpha (8-12 Hz), low beta (12-18 Hz), high beta (18-30 Hz) and gamma (30-100 Hz) Fig. 3. Thus, the power for the 3-sec windows was obtained for 28 channels and 5 frequency bands, giving a total of 140 frequency features for classification purposes.

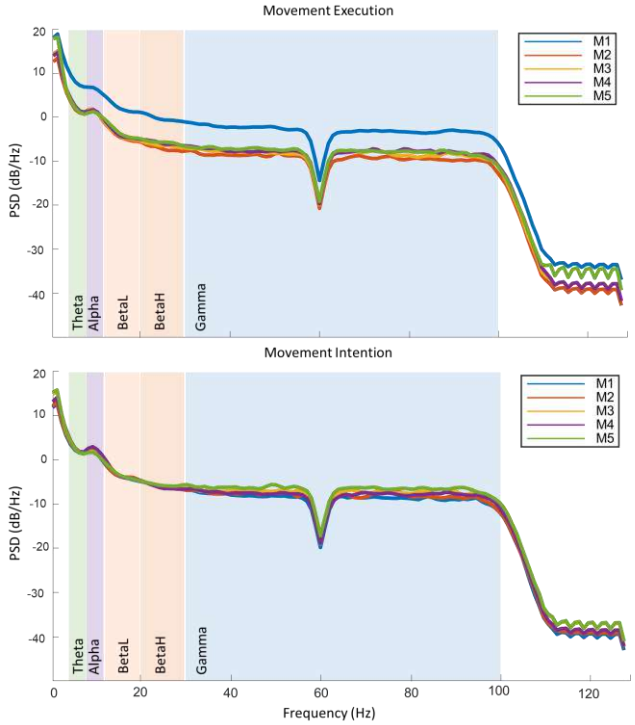


Fig. 3. Mean PSD for C3 channel of all Subjects, to each movement execution an intention.

The EEG signals were then filtered to divide the physiological bands and analyze brain networks, by means of brain connectivity measures. To filter the signals, Butterworth bandpass filters (n=4) were implemented for each physiological band. Moreover, power line interference at 60 Hz was removed using a notch filter. Subsequently, the Pearson's correlation was calculated from the filtered signal to determine the connectivity strength between different pairs of EEG electrodes. The weighted connectivity matrix was constructed, pairing all combinations of channels. (28x28). Then, we reduced the connectivity matrix into predefined regions of interest related to motor control processes, with electrodes grouped according to 3 anatomical locations: premotor, sensorimotor and sensory association cortices for left and right hemispheres (6x6). The values were averaged to obtain regional connectivity measures. Finally, graph theory metrics based on weights, such as clustering coefficient, path length, and node degree, were derived from the connectivity matrices (28x28) with the *Brain Connectivity Toolbox* from MATLAB. We then obtained a total of 420 brain connectivity features for classification purposes.

TABLE I
EEG FEATURES

Features	Equation
PSD	$PSD(f_m) = \frac{1}{N\Delta t}\lvert X_m^2\rvert\,;\ \Delta t = \frac{1}{fs}$
Pearson	$\lVert r_{ij}\rVert = \left\lVert \frac{Cov(X_i X_J)}{\sqrt{varX_i}\sqrt{varX_j}} \right\rVert$
Clustering coefficient	$k^w = \sum_{j\in N} W_{ij}$
Path lengh	$d_{ij}^w = \sum_{a_{uv}\in gi^w \leftrightarrow j} f(w_{uv})$
Node degree	$C^{\rightarrow} = \frac{1}{n}\sum_{i\in N} \frac{2t_i^w}{k_i(k_i-1)}$

2) EMG Signals Processing

On the other hand, the EMG signals were analyzed to extract features focused on measures to known to capture muscle activation dynamics (TABLE II) like mean absolute value (MAV), zero crossing rate (ZC), waveform length (WL), and variance (VAR). those related to the activity and frequency of muscle activation. These measures were computed for each of the 8 electrodes, obtaining a total of 40 features for EMG signals. These measures are highly reported in literature[16], [17], [18] and were previously used by our group[19], [20].

TABLE II
EMG FEATURES

Features	Equation
MAV	$\frac{1}{N}\sum_{i=1}^{N}\lvert x_i\rvert$
WL	$\sum_{i=1}^{N-1}\lvert x_{i+1} - x_i\rvert$
VAR	$\frac{1}{N-1}\sum_{i=1}^{N} x_i^2$
WAMP	$\sum_{i=1}^{N-1} f(\lvert x_i - x_{i+1}\rvert);$ $f(x) = \begin{cases} 1, si\ x \geq Threslhold \\ 0, si\ x < Threslhold \end{cases}$
ZC	$\sum_{i=1}^{N-1} f(x_i - x_{i+1}),$ $f(x_i, x_{i+1}) = \begin{cases} 1, if\ x_{i+1} > 0\ y\ x_i < 0 \\ 1, if\ x_{i+1} < 0\ y\ x_i > 0 \\ 0, in\ other\ case \end{cases}$

C. *Movement Classification*

Initially, the extracted features from both EEG and EMG initially analyzed separately to assess the individual contributions of each modality. Subsequently, these features were merged into a combined Feature matrix to get complementary information from neural and muscular signals. The resulting features matrices were partitioned into 70% for training and 30% for testing. To ensure robustness, k-fold cross-validation (k=5) was applied to the training set.

In the first phase, various machine learning models, such Ensemble Bagged Trees, Neural Networks, and SVMs, were evaluated to identify those with significant performance. The top-performing models from this inial evaluation advanced toi the hyperparameter optimization phase. During optimization, 20 variants of each ensemble tree type were generated using methods such as Bagging, RUSBoost, and AdaBoostM2. For SVMs, hyperparameters including box constraint level (ranging from 0.5 to 930), encoding type (one-vs-one and one-vs-all), and kernel scale (ranging from 150 to 700) were adjusted. For neural networks, the number of hidden layers and of epochs were modified to optimize performance. Finally, the model with the best performance was selected for different combinations of input features, including PSD and connective metrics for EEG and the features extracted for EMG.

III. Results

The preprocessing, feature extraction and classification methods were applied to the dataset collected from 22 healthy volunteers. After segmenting the signals, each subject contributes 60 events for identifying movement intention and 60 executions were obtained per subject. This gives a total of 2640 events. 1320 events for movement intention and 1320 events for movement execution used to train and test the algorithms.

Using Pearson's correlation, 28 x 28 channel feature matrix were obtained for different movements and frequency bands. The results of these matrices are shown in Fig. 4a where some regions exhibit a correlation coefficient of 1. To reduce the dimensionality of the matrix obtained and facilitate the physiological analysis, two strategies were applied: grouping by regions and extracting graph features, as was described in the previous section. Fig. 4b shows the connectivity matrices after grouping electrodes by neuroanatomical functions: premotor, sensorimotor and sensory cortex. The average value of the electrodes corresponding to each section was calculated. The motor region includes electrodes located at F and FC, the sensory-motor region includes the central line and adjacent positions FCC and CCP, and the sensory-association region includes CP and P. This was done for both hemispheres, obtaining 6 regions, as shown in Fig. 4b. The matrices shown are the average for the 12 repetitions of the subject, which shows a consistent network's behavior for some regions, in specific movements and frequency bands.

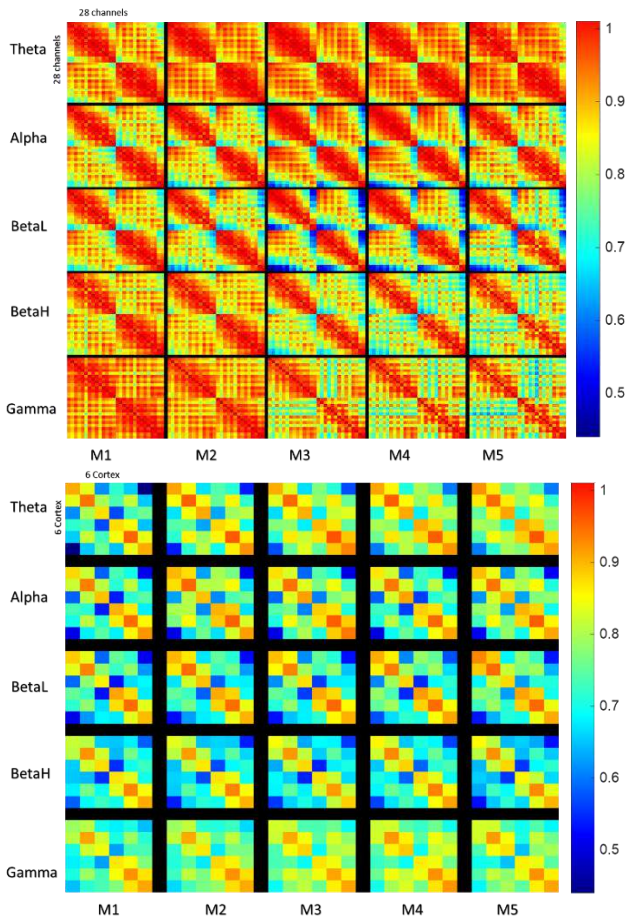


Fig. 4. a. Average Correlation Matrix from volunteer 14. All gestures all Band. b. Grouping Matrix From volunteer 14.

The extracted features were combined to train and test the selected machine learning algorithms. The initial models included Ensemble Bagged Trees, neural networks (medium and wide), and SVM, with accuracy being the primary comparison criterion, as it was a balanced dataset as shown on TABLE III. The Ensemble Bagged Trees model consistently showed better results, especially with brain connectivity and PSD features.

TABLE III
RESULTS FROM CLASSIFICATION LEARNER EXPLORATION

	Model	Movement Intention		Movement Execution	
		Training (%)	*Test (%)*	*Training (%)*	*Test (%)*
PSD	Ensemble Bagged trees	51.7	54.5	52.7	53
	Medium Neural network	38.2	36.4	38.2	39.9
	Wide Neural network	39.1	40.4	39.4	37.9
	SVM	39.4	38.9	38.6	37.6
Regions	Ensemble Bagged trees	38.3	38.4	34.8	39.4
	Medium Neural network	33.2	33.1	31.8	32.3
	Wide Neural network	34.0	37.4	30.7	33.8
	SVM	33.3	38.1	32.1	33.3
Graph	Ensemble Bagged trees	35.0	36.9	35.6	37.6
	Medium Neural network	33.4	31.8	31.2	32.3
	Wide Neural network	31.8	34.3	32.3	29.0
	SVM	31.9	31.3	30.2	36.6
EMG	Ensemble Bagged trees	66.2	65.8	82.1	85.6
	Medium Neural network	59.4	66.1	84.5	90.1
	Wide Neural network	67.4	72.2	85.8	86.3
	SVM	66.2	72.9	86.4	87.6

Subsequently, hyperparameters were optimized for Ensemble Bagged Trees (using methods such as Bagging, RUSBoost, and AdaBoostM2), SVM (adjusting box constraint level, multiclass coding, and kernel scale), and neural networks (varying the number of hidden layers and epochs). The top five optimized models for each approach were selected based on metrics such as accuracy, precision, recall, and F1-score. After the optimization, the best-performing model was Ensemble Bagged Trees with AdaBoostM2, configured with 464 learning cycles, a learning rate of 0.8642, and a minimum leaf size of three. This was the selected model to analyze different sets of features (Fig. 5), implicated in Movement Intention and Movement Classification.

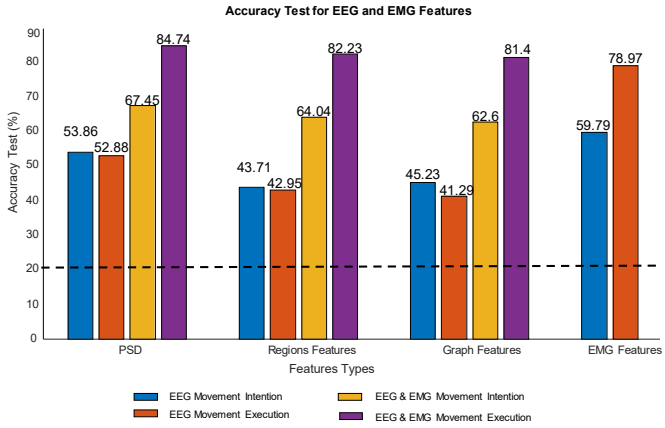


Fig. 5. Comparative accuracy chart of the optimized model using individual and combined EEG and EMG feature matrices.

IV. Discussion

In this work, we developed signal processing and machine learning techniques on EEG and EMG signals, to classify 5 hand gestures commonly used in rehabilitation therapy after stroke that involves global finger extension and flexion [21]. The aim is to advance the study of biological signals that could eventually help to understand neuromotor processes during movement and rehabilitation of the hand function. Moreover, the control of robotic devices to assist during therapies of the patients using biological signals is of great interest in research and clinical contexts. The models trained in this study outperformed the expected random chance level (20%) for 5-class classification. The Ensemble Bagged Trees model achieved the highest accuracy, with 84.74% for movement execution and 67.45% for movement intention. After a feature analysis, the power extracted from the PSD was the most effective for classification purposes.

The EEG analysis revealed significant differences between motor activity and resting states. Volunteers exhibited more random signals during rest and synchronized signals with pronounced peaks during execution, often reporting moments of drowsiness or relaxation. Correlation matrices revealed higher correlation patterns within brain hemispheres, with intra0-hemispheric interactions being more pronounced in the theta band and less pronounced in the low beta range. Furthermore, central EEG electrodes (FC to CP) showed the greatest interaction, highlighting the recruitment of neuronal groups near the motor region, these findings align with previous research indicating that theta and alpha waves play a crucial role in motor control and planning [10]. Theta and alpha waves exhibited more inter-hemispheric interaction, while frontal and parietal electrodes showed the least correlation, suggesting shorter signal transmission pathways.

Regional correlation matrices aligned with theoretical expectations. The left motor and sensory regions exhibited higher correlation values, particularly with alpha waves (mu waves), which diminish during movement execution. Significant interaction was observed between the primary motor-sensory and premotor regions in the left hemisphere for theta and alpha waves, increasing as movements were executed. Gestures involving the ring and pinky fingers consistently showed stronger correlations, which could be due to the increased effort to perform fewer common movements. Finally, comparisons between the classification of movement intention and movement execution patterns showed similar connectivity patterns, but lower values for movement intention. hese results suggest that early neural signatures of movement can be captured before execution, which is critical for rehabilitation strategies involving brain-computer interfaces and assistive robotics.

EMG signals exhibited rapid changes during movement execution, reflecting the action of agonist and antagonist muscles during hand opening and closing. The extracted EMG features, including MAV, WL, and ZC, contributed to the classification accuracy by capturing muscle activation dynamics. The integration of EEG and EMG features provided complementary information, reinforcing the potential of multimodal signal analysis for decoding movement intention and execution in neurorehabilitation contexts.

Our results match previous studies showing that theta and alpha brain waves are important for movement control and planning [10]. Higher theta wave connections between brain hemispheres may help prepare for movement, while lower alpha waves (mu suppression) happen when a movement is actively performed. These findings agree with Seta et al.[22], who used beta-wave brain signals to classify movements with 85% accuracy, highlighting the value of EEG connectivity in understanding and predicting movement.

Overall, these results suggest that classification of hand movements is possible with EEG and EMG signals, in different moments such as movement intention and execution. This approach holds great promise for rehabilitation applications, as it can support patient monitoring after a stroke and enhance the control of robotic exoskeletons during therapy. Future work should extend this analysis to stroke patients to validate its clinical applicability and explore adaptive models that personalize rehabilitation strategies based on individual neurophysiological responses.

V. References

[1] V. L. Feigin *et al.*, "World Stroke Organization (WSO): Global Stroke Fact Sheet 2022," *International Journal of Stroke*, vol. 17, no. 1, pp. 18–29, Jan. 2022, doi: 10.1177/17474930211065917/FORMAT/EPUB.

[2] "Centros para el control y la prevención de enfermedades." Accessed: Nov. 22, 2023. [Online]. Available: https://www.cdc.gov/stroke/about_esp.htm

[3] S. M. Lai, S. Studenski, P. W. Duncan, and S. Perera, "Persisting consequences of stroke measured by the Stroke Impact Scale," *Stroke*, vol. 33, no. 7, pp. 1840–1844, 2002, doi: 10.1161/01.STR.0000019289.15440.F2.

[4] J. E. Harris and J. J. Eng, "Individuals with the dominant hand affected following stroke demonstrate less impairment than those with the non-dominant hand affected," *Neurorehabil Neural Repair*, vol. 20, no. 3, p. 380, Aug. 2006, doi: 10.1177/1545968305284528.

[5] V. S. Hedna *et al.*, "Hemispheric Differences in Ischemic Stroke: Is Left-Hemisphere Stroke More Common?," *J Clin Neurol*, vol. 9, no. 2, p. 97, Apr. 2013, doi: 10.3988/JCN.2013.9.2.97.

[6] C. Benaim *et al.*, "Cognitive assessment scale for stroke patients (CASP): A multicentric validation study," *Ann Phys Rehabil Med*, vol. 65, no. 3, p. 101594, May 2022, doi: 10.1016/J.REHAB.2021.101594.

[7] S. R. Belagaje, "Stroke Rehabilitation," *Continuum (Minneap Minn)*, vol. 23, no. 1, Cerebrovascular Disease, pp. 238–253, Feb. 2017, doi: 10.1212/CON.0000000000000423.

[8] A. Pollock *et al.*, "Interventions for improving upper limb function after stroke," *Cochrane Database of Systematic Reviews*, vol. 2014, no. 11, Nov. 2014, doi: 10.1002/14651858.CD010820.PUB2.

[9] E. López-Larraz, A. Sarasola-Sanz, N. Birbaumer, and A. Ramos-Murguialday, "Unveiling Movement Intention after Stroke: Integrating EEG and EMG for Motor Rehabilitation," *bioRxiv*, p. 2024.02.22.581596, Feb. 2024, doi: 10.1101/2024.02.22.581596.

[10] A. Y. Paek, H. A. Agashe, and J. L. Contreras-Vidal, "Decoding repetitive finger movements with brain activity acquired via non-invasive electroencephalography," *Front Neuroeng*, vol. 7, Mar. 2014, doi: 10.3389/fneng.2014.00003.

[11] S. M. Sarhan, M. Z. Al-Faiz, and A. M. Takhakh, "A review on EMG/EEG based control scheme of upper limb rehabilitation robots for stroke patients," *Heliyon*, vol. 9, no. 8, p. e18308, Aug. 2023, doi: 10.1016/J.HELIYON.2023.E18308.

[12] S. R. Soekadar, N. Birbaumer, M. W. Slutzky, and L. G. Cohen, "Brain-machine interfaces in neurorehabilitation of stroke," *Neurobiol Dis*, vol. 83, pp. 172–179, Nov. 2015, doi: 10.1016/J.NBD.2014.11.025.

[13] H. Aly and S. M. Youssef, "Bio-signal based motion control system using deep learning models: a deep learning approach for motion classification using EEG and EMG signal fusion," *J Ambient Intell Humaniz Comput*, vol. 14, no. 2, pp. 991–1002, Feb. 2023, doi: 10.1007/S12652-021-03351-1/TABLES/6.

[14] S. Yang, M. Li, and J. Wang, "Fusing sEMG and EEG to Increase the Robustness of Hand Motion Recognition Using Functional Connectivity and GCN," *IEEE Sens J*, vol. 22, no. 24, pp. 24309–24319, Dec. 2022, doi: 10.1109/JSEN.2022.3221417.

[15] D. Bonilla *et al.*, "Progressive Rehabilitation Based on EMG Gesture Classification and an MPC-Driven Exoskeleton," *Bioengineering (Basel)*, vol. 10, no. 7, Jul. 2023, doi: 10.3390/BIOENGINEERING10070770.

[16] C. L. Kok, C. K. Ho, F. K. Tan, and Y. Y. Koh, "Machine Learning-Based Feature Extraction and Classification of EMG Signals for Intuitive Prosthetic Control," *Applied Sciences*, vol. 14, no. 13, p. 5784, Jul. 2024, doi: 10.3390/app14135784.

[17] A. Phinyomark, P. Phukpattaranont, and C. Limsakul, "Feature reduction and selection for EMG signal classification," *Expert Syst Appl*, vol. 39, no. 8, pp. 7420–7431, Jun. 2012, doi: 10.1016/j.eswa.2012.01.102.

[18] A. Phinyomark, S. Hirunviriya, C. Limsakul, and P. Phukpattaranont, "Evaluation of EMG Feature Extraction for Hand Movement Recognition Based on Euclidean Distance and Standard Deviation." Accessed: Dec. 05, 2024. [Online]. Available: https://ieeexplore.ieee.org/stamp/stamp.jsp?tp=&arnumber=5491586

[19] M. V. Arteaga, J. C. Castiblanco, I. F. Mondragon, J. D. Colorado, and C. Alvarado-Rojas, "EMG-driven hand model based on the classification of individual finger movements," *Biomed Signal Process Control*, vol. 58, p. 101834, Apr. 2020, doi: 10.1016/j.bspc.2019.101834.

[20] D. Bonilla *et al.*, "Progressive Rehabilitation Based on EMG Gesture Classification and an MPC-Driven Exoskeleton," *Bioengineering*, vol. 10, no. 7, p. 770, Jun. 2023, doi: 10.3390/bioengineering10070770.

[21] G. Mesplié, "Hand and Wrist Therapy: Clinical Examination and Advanced Rehabilitation Tools," *Hand and Wrist Therapy: Clinical Examination and Advanced Rehabilitation Tools*, pp. 1–252, Jan. 2022, doi: 10.1007/978-3-030-94942-6/COVER.

[22] V. de Seta *et al.*, "Cortico-muscular coupling to control a hybrid brain-computer interface for upper limb motor rehabilitation: A pseudo-online study on stroke patients," *Front Hum Neurosci*, vol. 16, Nov. 2022, doi: 10.3389/fnhum.2022.1016862.

Towards an Optimal Model of Post-Stroke Sensorimotor Control

Erica L. Waters[1], Reem Azar[2], Joana Opong-Duah[3], Samuel Gaardsmoe[4], Alwyn Johnson[5], Rochelle J. Mendonca[6], Pamela Z. Cacchione[7], Michelle J. Johnson[8]

***Abstract*— After stroke, motor control deficits are a common cause of disability. An optimal control model could provide insight into how motor and cognitive impairments influence post-stroke sensorimotor control. We present an initial attempt at modeling how post-stroke individuals perform a robot-based preview tracking task. Specifically, we fit a feedback controller with added delay and position bias to the impaired and less-impaired limbs of 11 stroke patients. We use an inverse linear quadratic regulator (LQR) to find the cost function for each participant. We also use linear regression to determine relationships between model parameters and clinical assessments of motor and cognitive impairments. Our main findings are that post-stroke sensorimotor control can be modeled as an optimal feedback controller and adding a delay and bias constant may improve the performance of this model. We also comment on how model parameters may be related to clinical assessments via linear regression. Future work should model more individuals and evaluate kinematic performance.**

I. Introduction

Stroke is a leading cause of disability among older adults [1]. Upper-extremity impairments are a common contributor to post-stroke disability [2]. Motor control deficits can be observed in kinematic performance of tasks [3], and these deficits persist even among stroke patients who demonstrate near or full recovery of sensorimotor function on standard assessments [4]. Despite the pervasive nature of motor control deficits, recovery of motor control is essential for true motor recovery. Deficits in motor control are particularly detrimental to functional task performance [5]. Improvements in motor control typically occur early after stroke incidence but can continue into the chronic phase [6]. A more complete understanding of post-stroke sensorimotor control would better inform post-stroke rehabilitation.

A model of post-stroke upper-extremity movement could provide insight into post-stroke sensorimotor control. Modeling post-stroke impairment, however, is complex. Stroke related sensorimotor impairments are highly heterogeneous, affecting both the contralesional ("impaired") and ipsilesional ("less-impaired") limbs [7]. Furthermore, post-stroke deficits on motor tasks may be influenced by cognitive impairments [8], [9], which are common post-stroke [10]. Modeling post-stroke motor control, therefore, requires a patient-specific approach that considers both limbs and accounts for cognitive deficits.

Optimal control modeling is commonly used to understand motor control. Over two decades ago, Todorov and Jordan proposed that human sensorimotor control is an optimal feedback control process in which goals may be quantified as cost functions that the human seeks to minimize [11]. Since then, researchers have employed optimal control techniques to model healthy human motor control on a variety of movements including posture control [12], reaching movements [13], and saccadic eye gaze [14]. Optimal control models are less studied for individuals with impairments, but a few models exist for impaired movements. For example, an optimal control model that accounts for Parkinson's tremors with a modeled delay [15] and an optimal control model of older adults with mild cognitive impairment in a walking obstacle crossing task [16]. Specific to stroke, Asghari et al. introduced a planar neuro-musculoskeletal arm model based on optimal control with "muscle significance factors" that modify the contribution of each muscle to the movement [17]. This model showed promising results but was only assessed on a simple point-to-point reaching movement. The model was also not assessed in the context of specific motor and cognitive impairments. Another interesting application of optimal control techniques to stroke modeling is to model the pre-stroke optimal behavior that stroke patients would have performed in order to create a biomechanical index that compares the impaired limb to the modeled pre-stroke limb [18]. To our knowledge, there has not been an attempt to model post-stroke individuals' motor control of a complex task featuring motor and cognitive components.

In this study, we propose an optimal control model of post-stroke sensorimotor control. We model the impaired

Research reported in this publication was supported by the Eunice Kennedy Shriver National Institute Of Child Health & Human Development of the National Institutes of Health under Award Number F31HD116597 and under Award Number R42HD104325. The content is solely the responsibility of the authors and does not necessarily represent the official views of the National Institutes of Health. Dr. Michelle Johnson and Dr. Rochelle Mendonca have a patent that uses devices inspired by the device being evaluated through this research. Dr. Michelle Johnson, Alwyn Johnson, and Dr. Rochelle Mendonca are co-founders of Recupero Robotics LLC. Samuel Gaardsmoe is an employee of Recupero Robotics LLC.

[1] Erica Waters is a PhD candidate in Mechanical Engineering & Applied Mechanics at the University of Pennsylvania waterica@seas.upenn.edu

[2] Reem Azar is a PhD student in Bioengineering at the University of Pennsylvania

[3] Joana Opong Duah is a research assistant in the Rehabilitation Robotics Lab at the University of Pennsylvania

[4] Samuel Gaardsmoe is the lead engineer at Recupero Robotics LLC.

[5] Alwyn Johnson is the CTO at Recupero Robotics LLC.

[6] Dr. Rochelle J. Mendonca is Assistant Professor in the Department of Rehabilitation & Regenerative Medicine/Programs in Occupational Therapy at Columbia University

[7] Pamela Z. Cacchione is a Professor of Geropsychiatric Nursing at the University of Pennsylvania School of Nursing

[8] Dr. Michelle J. Johnson is an Associate Professor at the University of Pennsylvania with a primary appointment in Physical Medicine & Rehabilitation and secondary appointments in Bioengineering and Mechanical Engineering & Applied Mechanics johnmic@pennmedicine.upenn.edu

TABLE I: Demographic Information and Clinical Assessment Scores

ID	Demographic Info				Cognitive Scores				Motor Scores				
	Age	Impaired Side	Group		MoCA	MoCA-EF	CT1	CT2	Impaired			Less-impaired	
			Impaired	Less-Impaired					FM	BBT	GP	BBT	GP
002	66	Left	MMI/MCI	MMI/MCI	13	1	-5.68	-13.21	61	-6.66	-17.44	-7.90	-19.88
003	65	Right	MMI/MCI	LMI/MCI	15	0	-2.45	-1.52	66	-4.28	-4.14	-2.87	-4.22
004	75	Left	MMI/MCI	LMI/MCI	18	1	-6.79	-7.34	52	-4.08	-16.46	-3.38	-0.08
005	80	Right	MMI/MCI	MMI/MCI	8	1	-7.70	-3.19	23	-8.17	-16.16	-5.51	-17.38
006	64	Left	MMI/LCI	MMI/LCI	22	4	-4.10	-3.71	55	-5.37	-16.16	-4.24	-9.61
007	72	Left	MMI/LCI	LMI/LCI	17	3	-9.34	-3.71	47	-4.21	-16.16	-3.51	-17.22
008	72	Right	MMI/MCI	MMI/MCI	9	2	-3.05	-3.71	43	-7.80	-17.44	-5.90	-3.78
010	67	Right	LMI/MCI	LMI/MCI	14	2	-0.97	-4.84	52	-3.86	-16.16	-1.33	-1.30
011	66	Right	LMI/LCI	LMI/LCI	25	4	0.44	-0.42	51	-2.45	-2.28	-2.74	-2.07
012	61	Right	MMI/MCI	MMI/MCI	14	1	-8.07	-2.45	47	-4.69	-16.46	-4.75	-0.24
014	68	Right	MMI/LCI	LMI/LCI	26	5	-1.15	-1.63	59	-4.03	-7.28	-2.38	-4.58

*Note: MoCA is reported out of 30, MoCA-EF is reported out of 5, FM is reported out of 66; all other metrics are reported as normalized z-scores.

and less-impaired limbs of 11 post-stroke participants and correlate various model parameters with clinical assessments of motor and cognitive function. We seek to (1) verify that an optimal control model is feasible for modeling post-stroke sensorimotor control on a tracking task and (2) understand how model parameters related to post-stroke motor and/or cognitive impairments.

II. Methods

A. Human Data

The data for this study come from the Rehabilitation Using Community-Based Affordable Robotic Exercise Systems (Rehab CARES) clinical trial (phase II), which aims to validate a robotic gym of 1-DOF TheraDrive rehabilitation robots for providing effective, affordable post-stroke upper limb rehabilitation in a community-based setting [19]. This protocol was approved by the Institutional Review Board of the University of Pennsylvania (protocol 853607).

This study is ongoing and plans to recruit 36 post-stroke individuals. Participants will complete therapy either with the robotic gym or standard of care over a period of 4-6 weeks. The study includes several pre- and post-clinical and robot-based assessments. In this paper, we analyze the pre-assessment data of the 11 participants enrolled in the study at the time of publication, including clinical evaluations and a robot-based assessment—trajectory tracking.

1) Participants: To enroll in the study, participants must be 55 or older, a requirement of the clinical location, with an official diagnosis of stroke at least 3 months prior to study start. All participants must have a CT Scan or MRI Scan completed post-stroke onset. All participants must have hemiplegia, with a Fugl-Meyer Upper Extremity (FM) score between 15 and 60. Participants are excluded if they present severe spasticity, greater than moderate language difficulties, or greater than moderate depression.

At the time of this paper, 11 participants are included in the study. This group is used as preliminary data for the development of the proposed optimal control model. These participants completed the pre-assessment phase of the study, including clinical assessments and robot-based assessments.[1] Table I shows participants' demographic information.

[1]Participant 012 did not complete the trajectory tracking task with their impaired limb. All other participants completed the task with both limbs.

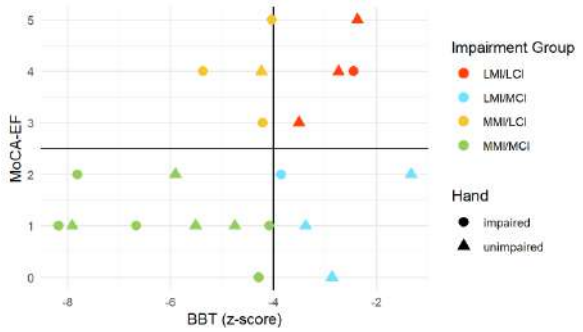


Fig. 1: Participants' impaired and less-impaired limbs sorted into impairment group by normalized BBT and MoCA-EF. A BBT cut-off score of four standard deviations below the norm (BBT z-score = 4) indicates moderate motor impairment; a MoCA-EF cut-off score of 2.5 out of 5 possible points indicates moderate cognitive impairment.

2) Clinical Assessment: A battery of cognitive and motor assessments are used to determine the level of functioning. Figure 1 shows participants sorted according to motor and cognitive impairment levels. Cognitive assessments include the Montreal Cognitive Assessment (MoCA), which targets multiple domains of cognitive function, including visuospatial/executive function, naming, memory, attention, language, abstraction, delayed recall, and orientation [20]. A score of 26 out of 30 indicates normal cognitive functioning across these domains. An executive function subscore—MoCA-EF—is also calculated out of 5 [20]. Participants also complete the Color Trails parts 1 and 2. This pair of tests are used to determine impairment in selective attention, sequencing, visual-spatial skills, mental flexibility, and motor speed. Performance is assessed as the time taken to complete each task; a shorter time indicates better performance [21]. The motor assessments include the Blocks & Box task (BBT), which assesses gross motor function by asking participants to move blocks from one side of a box to the other in one minute [22]. The Grooved Pegboard (GP) task is used to assess fine motor skills with an added cognitive component, and a lower completion time equals a better performance [23]. An occupational therapist administers the FM assessment to the impaired limb. Table I provides the clinical scores for all participants.

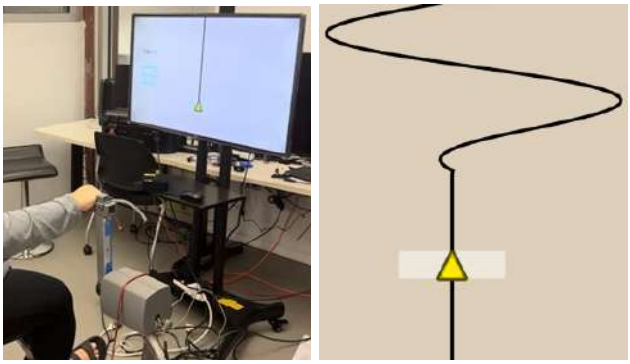


Fig. 2: TheaBot robot and trajectory tracking task

For analysis purposes, participants' hands are sorted into four impairment groups: low motor impairment and low cognitive impairment (LMI/LCI), low motor impairment and moderate cognitive impairment (LMI/MCI), moderate motor impairment and low cognitive impairment (MMI/LCI), and moderate motor impairment and moderate cognitive impairment (MMI/MCI). The motor impairment group is defined by normalized BBT because BBT is a measure of gross motor function and is performed on both hands. The cognitive impairment group is defined by MoCA-EF because MoCA-EF is sensitive to cognitive deficits relevant to the trajectory tracking task [9]. Figure 1 shows the participants' hands sorted into each of these four groups.

3) Robotic Interface: TheaBot, developed by Recupero Robotics, LLC, is based on the Haptic TheraDrive robot [24]. TheaBot is now a standalone robot mounted on a movable base and is interfaced with a custom assessment and therapy gaming suite developed in collaboration with EnAble Games, LLC. The 1-DOF robot is equipped with Picasso Intelligence Gemini motors. The robot is re-configurable and can be placed in 3 positions that cover shoulder, elbow, and wrist range of motion from 135 degrees to -135 degrees. These positions can be adjusted based on participant need. Figure 2 shows the TheaBot robot in position 1.

4) Trajectory Tracking Task: The trajectory tracking motor task is designed to assess motor performance by asking the player to follow a pseudo-sinusoidal wave [9], [24]. In a single trial, the user moves the crank arm forward and backward to follow the path for 15 seconds. Figure 2 shows the trajectory tracking task and a user performing the task. Participants complete 15 trials of this task. The displayed trajectory is the same each time. To account for effects of learning and fatigue, only the middle five trials are used to fit the models described in the next section.

B. Modeling Approach

1) System State Equations: For this initial implementation, we simplify the system dynamics to a point mass in discrete time such that the dynamics may be represented as in Equation 1.

$$x_{k+1} = Ax_k + Bu_k \tag{1}$$

In Equation 1 x_k is the system state and u_k is the control output or torque applied by the human operator to the robot at time step k. We define A and B in Equation 2 and Equation 3 where Δt represents the time step.

$$A = \begin{bmatrix} 1 & \Delta t \\ 0 & 1 \end{bmatrix} \tag{2}$$

$$B = \begin{bmatrix} 0 \\ \Delta t \end{bmatrix} \tag{3}$$

We recognize that this simplified model will not capture the full complexity of human sensorimotor control, but we believe that it may be sufficient to represent the overall behavior in this preview tracking task. Furthermore, a similar simplified representation has been used to model healthy participants in a pursuit tracking task [25].

2) Feedback Control Model: The human model is based on a simple feedback controller with a gains on error in position (K_p) and velocity (K_v), similar to Takagi et al. [25]. We modify the model to better represent post-stroke impairment. Specifically, we adjust the target trajectory with two constants: a delay term (γ) and a bias term (ζ).

The feedback controller is in Equation 4.

$$u_k = -Kx_k = -\begin{bmatrix} K_p & K_v \end{bmatrix} \begin{bmatrix} \theta_{t,k+\gamma} - \theta_{h,k} + \zeta \\ \dot{\theta}_{t,k+\gamma} - \dot{\theta}_{h,k} \end{bmatrix} \tag{4}$$

In Equation 4, $\theta_{h,k}$ and $\dot{\theta}_{h,k}$ represent the angle and angular velocity of the human while $\theta_{t,k}$ and $\dot{\theta}_{t,k}$ represent the desired angle and angular velocity of the target.

TABLE II: Feedback control models

Model	Description	Tuned Parameters
M1	standard model ($\zeta = 0$, $\gamma = 0$)	K_p, K_v
M2	bias model ($\gamma = 0$)	K_p, K_v, ζ
M3	delay model ($\zeta = 0$)	K_p, K_v, γ
M4	bias and delay model	K_p, K_v, ζ, γ

Table II shows the four model variations that we explore. The most basic is M1, which only tunes the feedback control gains. Some participants, however, present with a clear bias to one side such that their trajectory is not centered around zero, and M1 fails to solve (Figure 3B). We propose M2 to account for bias, which is calculated by finding the average of the medians of the participant's trajectories. The displayed trajectory has a median of zero, so a median other than zero may indicate a shifted range of motion—i.e. a "bias" to one side or the other. We likewise observe that some participants follow the trajectory but are delayed in their response (Figure 3C). M3 accounts for delay by finding the average lag corresponding to the maximum cross correlation between the participant's trajectory and the target trajectory. M4 combines M2 and M3 with both bias and delay. Feedback control gains for all models are tuned with least squares to minimize the error in position and velocity. Delay and bias terms are added to the model prior to this optimization for M2, M3, and M4.

3) Inverse Optimal Control: We define the inverse optimal control problem as an inverse linear quadratic regulator (LQR) problem. In LQR, we may seek to minimize the cost function in Equation 5 such that we obtain an optimal set

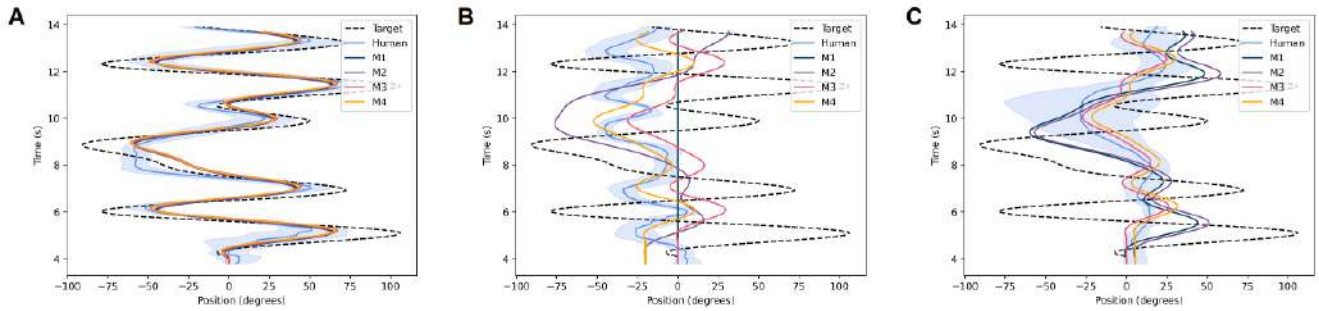


Fig. 3: Exemplar plots of 3 participants' actual and modeled trajectories. The blue line represents the average actual trajectory, and the shaded area represents the standard deviation across all 5 trials. **A:** Participant 011, impaired arm in the LMI/LCI group; all models perform similarly. **B:** Participant 003, less-impaired arm in the LMI/MCI group; M4 performs best. **C:** Participant 002, less-impaired arm in the MMI/MCI group; the M3 and M4 models perform best.

of control gains K for the feedback controller described in Equation 4 with $Q \succeq 0$ and $R \succ 0$, where Q is the state cost matrix and R is the control cost matrix.

$$J = \sum_{k=0}^{\infty} x_k^T Q x_k + u_k^T R u_k \tag{5}$$

This optimal value of K may be computed according to Equation 6.

$$K = (B^T P B + R)^{-1}(B^T P A) \tag{6}$$

We define P as the unique, positive definite solution to the discrete time algebraic Riccati equation in Equation 7.

$$A^T P A - P - (A^T P B)(B^T P B + R)^{-1}(B^T P A) + Q = 0 \tag{7}$$

We may solve the inverse LQR problem according to the linear matrix inequality and gradient descent method employed by Priess et al. [12]. In this method, they describe using linear matrix inequalities to ensure uniqueness of solution. Their problem formulation in discrete time is provided in Equation 8 – Equation 12.

$$(\hat{Q}, \hat{R}, \hat{P}, \hat{\alpha}) = \arg \min_{Q,R,P,'\alpha} \alpha^2 \quad s.t. \tag{8}$$

$$P \succeq 0 \tag{9}$$

$$A^T P A - P - A^T P B K + Q = 0 \tag{10}$$

$$B^T P A - (B^T P B + R) K = 0 \tag{11}$$

$$I \preceq \begin{bmatrix} Q & 0 \\ 0 & R \end{bmatrix} \preceq \alpha I \tag{12}$$

If Equation 8 is infeasible (no exact solution exists for the inverse LQR problem), then they suggest approximating the cost function parameters by using gradient descent to reduce the error between the actual control gains K and the estimated control gains $\hat{K}$ according to the minimization problem in Equation 13 with $\zeta = [Q_{11}, Q_{12}, Q_{22}, R_{11}]$.

$$\hat{\zeta} = \arg\min_{\zeta} \|\hat{K}(\zeta) - K\|_F^2 \tag{13}$$

We then use the analytical gradient of the cost in Equation 13 to minimize the difference between the estimated control gains $\hat{K}$ and the actual control gains K; more information about this problem formulation is available in their original publication [12].

C. Data Analysis

1) Feedback Control Model Selection: Performance of the four feedback models is assessed with root mean square error (RMSE) between the modeled trajectory and the average human trajectory across the five trials, for each participant/hand. The feedback controller (M1, M2, M3, or M4) with the best RMSE is selected for all other analyses.

2) Inverse Optimal Control Analysis: The inverse optimal control approach is analyzed by comparing the feedback controller gains that were initially found with least squares and then approximated with LQR. Specifically, we use a paired Mann-Whitney U test to compare the controller gains (Kp or Kv) between each method of gain fitting.

3) Linear Regression Analysis: The influence of motor and cognitive impairment on various model parameters are assessed with linear regressions. The model parameters include: elements of the state cost matrix (Q_1, Q_2, Q_3), the response cost (R), the delay constant, and the bias constant. The four parameters associated with the optimal controller (Q_1, Q_2, Q_3, R) are cube root transformed to create a more even distribution. Due to a low sample size (impaired limb n = 10 and less-impaired limb n = 11), only one metric is used to predict each parameter for the separate analyses. The independent variable for each model is selected based on which clinical assessment score had the highest correlation with the dependent variable. Prediction strength is set at $r^2 \geq 0.25$ for a mild prediction, $r^2 \geq 0.5$ for a moderate prediction, and $r^2 \geq 0.75$ for a strong prediction.

III. Results

A. Model Performance

Figure 3 shows the actual and modeled trajectories for three exemplar participants/hands (011 impaired, 003 less-impaired, 002 less-impaired). Figure 4 shows the performance of the four models. From the figure, it is clear that although all models perform fairly well for the LMI/LCI participant (011 impaired) but M4 performs better for the LMI/MCI participant (003 less-impaired) and MMI/MCI participant (002 less-impaired). Figure 4 shows that all of the models have fairly similar performance in terms of RMSE with no significant differences, but M4 performs slightly

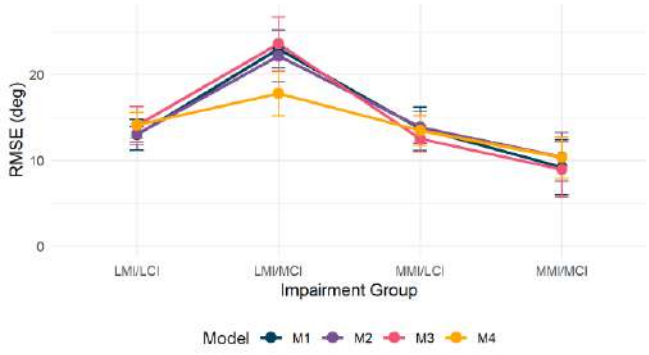


Fig. 4: Median and standard error of model RMSE for all modeled participants/hands separated by impairment groups

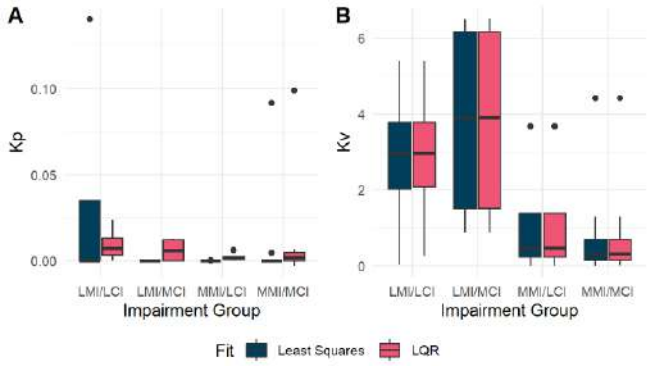


Fig. 5: Box plots comparing the control gains tuned with least squares fit and calculated with LQR. **A**: K_p gains are close to zero for all groups, regardless of fit. **B**: K_v gains are similar for both Least Squares fit and LQR fit. K_v is higher for the LMI groups compared to the MMI groups.

better for the LMI/MCI group. For this reason, M4 is selected to proceed in the analysis.

B. Inverse Optimal Control Analysis

Figure 5 shows the feedback gains for each impairment group. The paired Mann-Whitney U shows no significant differences between the feedback gains (Kp and Kv) fitted with the least squares and inverse LQR approaches. As shown in Figure 5, Kp is overall very low, with the mean for all groups falling very close to zero. Furthermore, Kv tends to be higher for the higher motor function groups (LMI/LCI and LMI/MCI) than the lower motor function groups (MMI/LCI and MMI/MCI).

C. Linear Regression Analysis

Figure 6 shows the Pearson correlation coefficients (r) between all clinical assessments and all model parameters for both the impaired and less-impaired limbs. The clinical assessment score with the highest correlation is chosen as the independent variable in the linear regression model for each model parameter (Q_1, Q_2, Q_3, R, delay, bias). $Q1$'s highest correlation is moderate (CT1, $r = 0.65$) in the impaired limb and mild (BBT, $r = 0.24$) in the less-impaired limb. $Q2$ has moderate correlations with cognitive metrics in both limbs with CT2 ($r = 0.56$) for the less-impaired limb and MoCA-EF for the more impaired limb ($r = -0.52$). $Q3$ likewise has mild correlations with cognitive metrics in the less-impaired limb (MoCA, $r = -0.34$) and impaired limb (MoCA-EF, $r = -0.28$), respectively. R also has mild correlations with cognitive metrics for the less-impaired limb (CT2, $r = 0.31$) and the impaired limb (CT1, $r = -0.35$). Bias is most related to a cognitive metric (MoCA-EF, $r = -0.5$) for the less-impaired limb, but for the impaired limb, it is most related to a motor metric (FM, $r = -0.71$). Delay is most correlated with BBT in both the less-impaired limb ($r = -0.52$) and the impaired limb ($r = -0.74$).

Figure 7 shows the linear regression results for the less-impaired limb. BBT is a poor predictor of Q_1 with the model explaining less than 6% of the variance in Q_1 ($r^2 = 0.0567$). MoCA and CT2 are likewise poor at predicting Q_3 and R, respectively ($r^2 = 0.118$, $r^2 = 0.095$). $CT2$, $MoCA - EF$, and BBT are mildly predictive of $Q2$, bias, and delay, respectively ($r^2 = 0.315$, $r^2 = 0.249$, $r^2 = 0.272$).

Figure 8 shows the linear regression results for the impaired limb. MoCA-EF and CT1 are poor predictors of Q_3 and R, respectively ($r^2 = 0.0774$ and $r^2 = 0.123$). CT1 and MoCA-EF are mild predictors of Q_1 and Q_2, respectively ($r^2 = 0.426$, $r^2 = 0.275$). CT1 explains 43% of the variance in Q_1, and MoCA-EF explains 28% of the variance in Q_2. Bias and delay each have a moderately predictive model. FM-UE explains 50% of the variance in bias ($r^2 = 0.504$), and BBT explains 55% of the variance in delay ($r^2 = 0.548$).

IV. Discussion

We present an inverse optimal control model of post-stroke sensorimotor control on a preview tracking task. Our results indicate that a subset of post-stroke participants can be represented by a simple feedback control model with a delay and bias constant. All four feedback control models perform similarly in this analysis, but M4 shows a modest improvement in RMSE for the LMI/MCI group, Figure 4.

The difference in model performance across groups may be explained by the fact that only some participants exhibit a delay or a bias term. Figure 3A shows that a participant/hand with low motor and cognitive impairment, like 011's impaired limb, may not have a large bias or delay. Because M1 is the same as M4 just with bias and delay set to zero, these values being low in M4 will result in very similar trajectories between M1 and M4. The model, however, shows noticeable improvements for participants with delay or bias. Participant 002's less-impaired limb in Figure 3C displays a pronounced delay. M1 approximates the movement, but M3 and M4 show much better fits with the actual behavior. The addition of a bias term in M2, however, does not improve performance over M1 for this participant due to low bias in the behavior. Conversely, as shown in Figure 3B, 003's less-impaired limb has a pronounced bias to the negative side. This bias seems to prevent M1 from solving at all, resulting in a trajectory with no movement. M2, however, uses the bias to adjust and achieves non-zero movement. Participant 003 also has a clear delay; the addition of a delay term in M3 results in

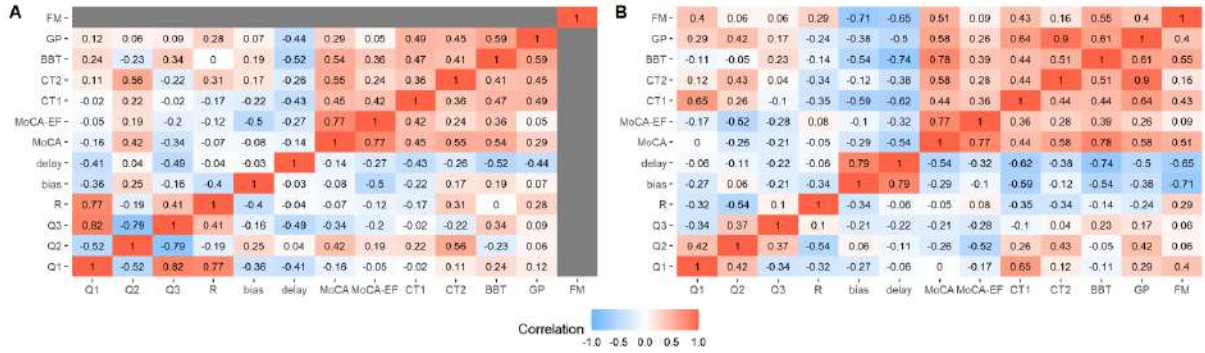


Fig. 6: Heat map of Pearson correlations between model parameters and clinical assessments. (A) Correlations for the less-impaired limb (B) Correlations for the impaired limb

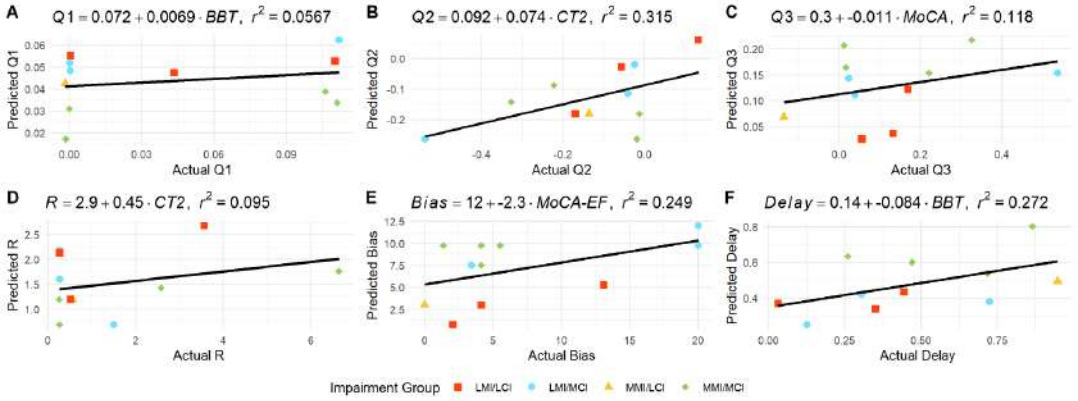


Fig. 7: Linear regression results for less-impaired limb model parameters

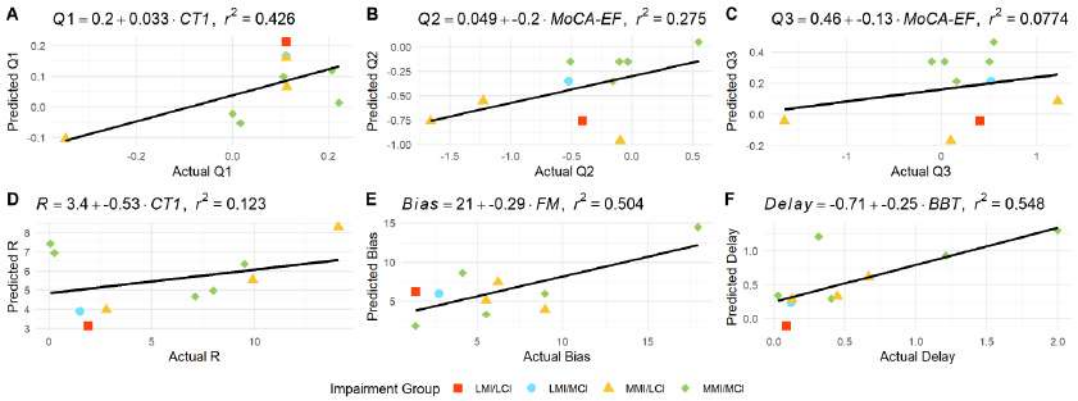


Fig. 8: Linear regression results for impaired limb model parameters

better performance than M1. The combination of both bias and delay terms in M4 allows the best fit. Taken together, these results suggest that the bias and delay terms in M4 may help to account for differences in tracking behavior due to motor and cognitive impairments.

This paper also supports that inverse optimal control can be used to identify a cost function employed by individuals with varying levels of post-stroke motor and cognitive impairment. The inverse optimal control method performs well, producing feedback control gains that are almost identical to the least squares fit feedback controller. The control gains are close to zero for the gain on position K_p, which may indicate that post-stroke participants rely on target velocity more than the position in a preview tracking task.

The linear regression analysis shows mixed results at predicting model parameters. Interestingly, the linear regression analyses perform better for the impaired limb than for the less-impaired limb. This result could be due to less overall spread in the motor assessment data for the less-impaired limb. Another explanation is a learning bias affecting performance in the less-impaired limb influencing model fit. During assessment, participants perform the trajectory tracking task with their less-impaired arm first, meaning they are still familiarizing themselves with the task, which may lead to higher motor variability across trials. By the time they complete the task with the impaired arm, they have

completed fifteen trials with the less-impaired arm and better understand the task, which may reduce motor variability.

The delay model has moderate predictive power for the less-impaired limb and mild predictive power for the impaired limb. Interestingly, delay is correlated with BBT for both limbs. Although BBT is a motor assessment, it is time-based and may involve a cognitive component [8]. The bias model also performs better for the impaired limb than the less-impaired limb with moderate and mild predictive powers, respectively. Interestingly, bias is associated with a motor impairment metric (FM) in the impaired limb but a cognitive metric (MoCA-EF) in the less-impaired limb. Similarly, models for $Q1$ show mild predictive power for the impaired limb but very poor predictive power for the less-impaired limb. The models of $Q2$ are moderately predictive for both limbs. Finally, models for $Q3$ and R are not highly predictive, indicating that a larger sample size and/or expanded set of clinical assessments may be necessary. We note that with the exception of the less-impaired $Q1$ model, all cost function parameters are most highly correlated with cognitive assessment scores. This result highlights the extent to which cognition influences sensorimotor control.

Limitations include a small sample size, exclusion of healthy participants, and a lack of severely motor impaired participants. Future work should investigate the model with a larger population. Likewise, more in-depth system identification, including tasks with higher movement frequency, could increase the complexity and fit of the model. Finally, a more robust and complete analysis of the model, perhaps on a kinematic level that considers limb dominance is necessary.

ACKNOWLEDGMENT

We want to thank members of the Rehabilitation Robotics Lab, our collaborators at Recupero Robotics LLC, and our colleagues at enAble Games LLC. We also want to thank the Department of Physical Medicine and Rehabilitation.

REFERENCES

[1] T. Vos, S. S. Lim, C. Abbafati, K. M. Abbas, M. Abbasi, M. Abbasifard, M. Abbasi-Kangevari, H. Abbastabar, F. Abd-Allah, A. Abdelalim, *et al.*, "Global burden of 369 diseases and injuries in 204 countries and territories, 1990–2019: a systematic analysis for the Global Burden of Disease Study 2019," *The lancet*, vol. 396, no. 10258, pp. 1204–1222, 2020.

[2] L. A. Simpson, K. S. Hayward, M. McPeake, T. S. Field, and J. J. Eng, "Challenges of estimating accurate prevalence of arm weakness early after stroke," *Neurorehabilitation and Neural Repair*, vol. 35, no. 10, pp. 871–879, 2021.

[3] M. Alt Murphy, C. Willén, and K. S. Sunnerhagen, "Responsiveness of upper extremity kinematic measures and clinical improvement during the first three months after stroke," *Neurorehabilitation and neural repair*, vol. 27, no. 9, pp. 844–853, 2013.

[4] G. Thrane, K. S. Sunnerhagen, H. C. Persson, A. Opheim, and M. A. Murphy, "Kinematic upper extremity performance in people with near or fully recovered sensorimotor function after stroke," *Physiotherapy theory and practice*, 2019.

[5] N. Lodha, P. Patel, A. Casamento-Moran, E. Hays, S. N. Poisson, and E. A. Christou, "Strength or motor control: what matters in high-functioning stroke?," *Frontiers in neurology*, vol. 9, p. 1160, 2019.

[6] J. van Kordelaar, E. E. van Wegen, R. H. Nijland, A. Daffertshofer, and G. Kwakkel, "Understanding adaptive motor control of the paretic upper limb early poststroke: the explicit-stroke program," *Neurorehabilitation and neural repair*, vol. 27, no. 9, pp. 854–863, 2013.

[7] G. H. Kitsos, I. J. Hubbard, A. R. Kitsos, and M. W. Parsons, "The ipsilesional upper limb can be affected following stroke," *The Scientific World Journal*, vol. 2013, no. 1, p. 684860, 2013.

[8] D. J. Lin, K. S. Erler, S. B. Snider, A. K. Bonkhoff, J. A. DiCarlo, N. Lam, J. Ranford, K. Parlman, A. Cohen, J. Freeburn, *et al.*, "Cognitive demands influence upper extremity motor performance during recovery from acute stroke," *Neurology*, vol. 96, no. 21, pp. e2576–e2586, 2021.

[9] K. D. Bui, B. Lyn, M. Roland, C. A. Wamsley, R. Mendonca, and M. J. Johnson, "The impact of cognitive impairment on robot-based upper-limb motor assessment in chronic stroke," *Neurorehabilitation and neural repair*, vol. 36, no. 9, pp. 587–595, 2022.

[10] H. Delavaran, A.-C. Jönsson, H. Lövkvist, S. Iwarsson, S. Elmståhl, B. Norrving, and A. Lindgren, "Cognitive function in stroke survivors: a 10-year follow-up study," *Acta Neurologica Scandinavica*, vol. 136, no. 3, pp. 187–194, 2017.

[11] E. Todorov and M. I. Jordan, "Optimal feedback control as a theory of motor coordination," *Nature Neuroscience*, vol. 5, pp. 1226–1235, Nov 2002.

[12] M. C. Priess, R. Conway, J. Choi, J. M. Popovich, and C. Radcliffe, "Solutions to the inverse LQR problem with application to biological systems analysis," *IEEE Transactions on Control Systems Technology*, vol. 23, no. 2, pp. 770–777, 2015.

[13] B. Berret, E. Chiovetto, F. Nori, and T. Pozzo, "Evidence for composite cost functions in arm movement planning: an inverse optimal control approach," *PLoS computational biology*, vol. 7, no. 10, p. e1002183, 2011.

[14] H. El-Hussieny and J.-H. Ryu, "Inverse discounted-based LQR algorithm for learning human movement behaviors," *Applied Intelligence*, vol. 49, pp. 1489–1501, 2019.

[15] C. R. Kelley and J. L. Kauffman, "Optimal control perspective on parkinson's disease: Increased delay between state estimator and controller produces tremor," *IEEE Transactions on Neural Systems and Rehabilitation Engineering*, vol. 28, no. 10, pp. 2144–2152, 2020.

[16] T.-W. Lu, S.-H. Lu, C.-H. Yu, K.-W. Wu, and Y.-C. Kuan, "A multi-objective optimal control approach to motor strategy changes in older people with mild cognitive impairment during obstacle crossing," *Journal of NeuroEngineering and Rehabilitation*, vol. 21, no. 1, p. 200, 2024.

[17] M. Asghari, S. Behzadipour, and G. Taghizadeh, "A planar neuromusculoskeletal arm model in post-stroke patients," *Biological cybernetics*, vol. 112, pp. 483–494, 2018.

[18] M. Abedi and S. Behzadipour, "A novel biomechanical index for quality assessment of the upper-extremity movements in post-stroke patients," *Computers in Biology and Medicine*, vol. 179, p. 108875, 2024.

[19] U. N. L. of Medicine, "Rehab CARES in USA: Clinical trial (nct05542121)," 2024. Accessed: 2024-10-28.

[20] Z. S. Nasreddine, N. A. Phillips, V. Bédirian, S. Charbonneau, V. Whitehead, I. Collin, J. L. Cummings, and H. Chertkow, "The Montreal Cognitive Assessment, MoCA: a brief screening tool for mild cognitive impairment," *Journal of the American Geriatrics Society*, vol. 53, no. 4, pp. 695–699, 2005.

[21] L. Messinis, A.-C. Malegiannaki, T. Christodoulou, V. Panagiotopoulos, and P. Papathanasopoulos, "Color Trails Test: Normative data and criterion validity for the Greek adult population," *Archives of Clinical Neuropsychology*, vol. 26, no. 4, pp. 322–330, 2011.

[22] V. Mathiowetz, G. Volland, N. Kashman, and K. Weber, "Adult norms for the Box and Block Test of manual dexterity," *The American journal of occupational therapy*, vol. 39, no. 6, pp. 386–391, 1985.

[23] K. A. Tolle, A. M. Rahman-Filipiak, A. C. Hale, K. A. Kitchen Andren, and R. J. Spencer, "Grooved Pegboard Test as a measure of executive functioning," *Applied Neuropsychology: Adult*, vol. 27, no. 5, pp. 414–420, 2020.

[24] M. J. Johnson, R. Rai, S. Barathi, R. Mendonca, and K. Bustamante-Valles, "Affordable stroke therapy in high-, low- and middle-income countries: From Theradrive to Rehab CARES, a compact robot gym," *Journal of Rehabilitation and Assistive Technologies Engineering*, vol. 4, 2017.

[25] A. Takagi, M. Hirashima, D. Nozaki, and E. Burdet, "Individuals physically interacting in a group rapidly coordinate their movement by estimating the collective goal," *Elife*, vol. 8, 2019.

Manipulation of sensory information in competitive scenarios induces adaptive changes in action selection: insights for neurorehabilitation

Laura Bandini, Cecilia De Vicariis,Vittorio Sanguineti

Dept. Informatics, Bioengineering, Robotics and Systems Engineering, University of Genoa, Genoa (ITALY)
Email: laura.bandini@edu.unige.it, cecilia.devicariis@unige.it, vittorio.sanguineti@unige.it

***Abstract*—Competitive settings may be promising for neurorehabilitation as they may lead to stronger patient motivation. However, the mechanisms underlying the development of an interaction in competitive settings are not well understood. We use a dyadic haptic interface to investigate the dynamics of competitive interaction. Pairs of participants engaged in a ball game (a penalty kick challenge), with an attacker and a defender. To explore how the participants adapt to each other over game iterations, we manipulated the amount of information available to each one about the location of their opponent. We found that under the different experimental conditions, the participants adjusted their behavior in response to their opponents' strategy change. These observations are consistent with simulations with a computational model assuming that during interaction the participants use optimal (Bayesian) perception and action selection (based on game theory). Taken together, experiments and simulations suggest that the participants develop and update a flexible, adaptive predictor of their opponents next action, which helps them adjust their behavior to optimize performance. These findings provide a foundation for further research into the mechanisms that drive adaptive behavior in competitive scenarios, and provide new insights into how competitive environments can be used in rehabilitation.**

***Index Terms*—competitive games, joint action, optimal control**

I. Introduction

Neuromotor recovery is facilitated by repeated task-oriented movements of the impaired limb. Stroke survivors typically perceive using the impaired limb as more costly than using the intact limb or, more in general, than using compensatory strategies that rely on the spared body movements [1]. Therefore, the exercises used in neuromotor rehabilitation should not only focus on training the impaired limb, but also need to be sufficiently engaging to counteract their perceived greater cost.

Competitive games have high potential in neurorehabilitation due to their ability to maintain motivation and adherence to treatment [2]. Competitive games involving two players have been reported to be more effective than similar tasks in single-player mode in maintaining a high level of engagement and exercise intensity [3], [4]. Likewise, dyadic haptic communication in a competitive scenario may lead to a greater active effort than in a similar cooperative task [5]. Game modality also influences the physiological response. It has been suggested [6] that training through a competitive two-player game modality resulted in higher physiological responses when compared to the single-player and cooperative modes. A study on different forms of therapeutic games with subacute stroke patients underlined that patients preferred competitive modalities to cooperative ones both in terms of engagement and intensive game play [7]. Moreover, the use of serious games that can adapt the difficulty based on the patient strategy could be a valuable approach in the upper limb rehabilitation to improve training outcomes [8], [9]. A review on human-machine-human interaction in motor control and rehabilitation settings [10] revealed that, although the benefits of different interaction modalities and partner characteristics are still unclear, the study of optimal personalized interaction may lead to the development of more effective exercise protocols.

In joint action in general and competitive scenarios in particular, the actions of each participant are determined by the (predicted) reaction of their opponent. The emerging coordination strategy is influenced by the amount of information that each player has available about their partner [11], [12].

Dyadic haptic interfaces are useful tools to study these mechanisms as all aspects of interaction (haptic, visual) can be manipulated. For instance, haptic coupling between two participants can lead to an improvement of the performance of the partner that initially exhibits poorer performance [5]. Likewise, haptic coupling during an ankle tracking task improves the performance of the worst partner [13].

While cooperative dyadic tasks have been extensively studied, competitive interactions remain less understood. In a competitive scenario, humans accumulate sensory evidence to predict the action intentions of their opponents [14]. The behavior of baseball batters, for instance, has been interpreted [15] in terms of Bayesian models, showing that they manage

The work is supported by #NEXTGENERATIONEU and funded by the Ministry of University and Research (MUR), National Recovery and Resilience Plan (NRRP), in the framework of the Extended Partnership on Neuroscience and Neuropharmacology (PE12); project *MNESYS - A Multiscale integrated approach to the study of the nervous system in health and disease*. C.D.V is supported by the Italian Ministry of Research, under the complementary actions to the NRRP "Fit4MedRob - Fit for Medical Robotics" Grant (#PNC0000007)

pitch uncertainty by optimally integrating prior information with real-time observations.

The study of the mechanisms underlying how, in competitive games, each player understands (perceives) and predicts (takes decisions) the opponent's actions may lead to new insights in the developpent of rehabilitation games that can adapt the difficulty on the patient action selection strategy and use principles of optimality in the interaction.

The aim of this study is to understand how two players change their own action selection in a competitive scenario according to the behavior of the partner. In particular, we use a haptic version of a ball game (penalty kick) to study whether and to what extent competitors account for the sensory information (knowledge about partner location) they have available about their partner.

II. Materials and Methods

A. Task and experimental protocol

The task involves two players, an attacker (A) and a defender (D). They cannot see and hear each other. Each player sits in front of a computer screen and grasps the handle of a robot manipulandum (H-MAN, Articares) [16], as in Fig. 1. Both are constrained to move within a horizontal line (implemented as a haptic channel). On the computer screen each participant sees the game state in a subjective view by displaying their location along a horizontal line on the lower portion of the screen and the opponent on the upper portion of the screen; see Fig. 1. An elastic force (virtual spring) pulls each handle toward the center of each player's horizontal line, thus creating a preferred region for both participants. Each competitor is also aware of the position of the opponent's elastic force thanks to a green spring displayed above the opponent's line to provide a prior information about the partner.

At the beginning of each trial, both players are asked to move to a start position right at the center of their horizontal line. At the start of the trial, both the attacker and the defender are free to move along the horizontal line. The attacker's goal is to shoot a ball (yellow circle) in a vertical direction. The ball is fired by exerting a vertical force on the wall of the haptic channel. The defender must try to intercept the ball before it crosses the horizontal line. The attacker may shoot the ball at any time. Once shot, the ball moves at a constant speed of 3 m/s, too high to be trackable by the defender by reactive movements. However, the defender can try to predict where the attacker will shoot the ball and elicit a corrective movement to compensate for its own displacement from the attacker at the time instant when the ball is shot. After the ball is shot each player receives the information about the partner's location at that trial and at the moment of shooting/receiving (depending on the role) the ball, as in Fig. 2. In particular, the attacker sees the receiving defender's position on the upper horizontal line on the screen. The defender sees the ball once it is shot, which is equal to seeing the attacker's position since the ball is fired on a vertical line.

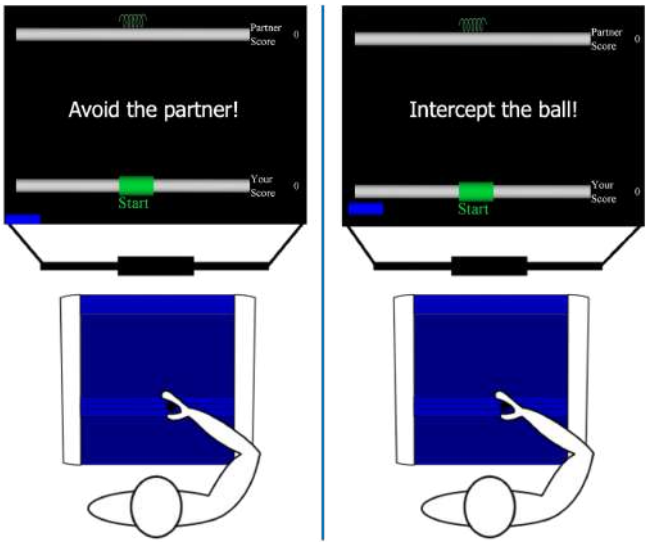


Fig. 1. Experimental apparatus and task. Attacker (left) and defender views (right)

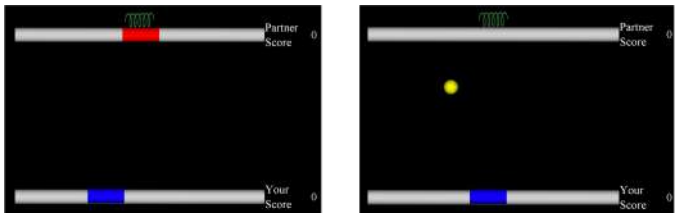


Fig. 2. Attacker (left) and defender (right) views after the ball is shot (Z-Z condition, i.e. each player has a perfect view of their opponent)

To understand if the performance is affected by the uncertainty about partner location (sensory information), in different experimental blocks we varied the uncertainty Σ_y on the visual display of the position of the opponent for player A or the ball for player D: (i) Zero (Z): opponent/ball location is fully visible ($\Sigma_y = 0$); (ii) Low (L): opponent/ball location displayed a cloud of random dots with a Gaussian distribution ($\Sigma_y = 0.08$) on the horizontal axis; (iii) Inf (I): opponent/ball location not visible ($\Sigma_y = \infty$).

We recruited 12 participants (five male and seven female, aged 24-27 yo) and randomly assigned them to each dyad. All participants signed a consent form before starting the experiment. Each participant played one fixed role, either A or D. The experimental protocol was organized into blocks (epochs) of 30 trials each, with a randomized block design. A familiarization block with $\Sigma_y = 0$ of a pass ball game was followed by nine blocks of competitive play (total 300 trials). Within each epoch, we varied the sensory information (Σ_y^A and Σ_y^D) of both players.

B. Computational model

We used a probabilistic computational model [12] to simulate the time series of the attacker and the defender actions under all experimental conditions. The model uses a trial-by-trial development to describe the joint coordination and the

time series of players; in this case, we modeled it as a non-cooperative game.

Specifically, the model assumes that each agent (i) uses Bayesian principles (Kalman filter) to predict the next action of their opponent, and (ii) selects the action minimizing their expected cost, given the expected action of their opponent; see Figure 3. Each player knows their own goals but not their opponent's and has imperfect information about their opponent's actions. On each trial t, the i-th player chooses their action, $u_i(t)$, based on the expected opponent action, $x_i(t) = \hat{u}_{\infty i}(t)$. Both players collect information $y_i(t)$ about their own and their partner's actions through their sensory systems, and use such information to update their prediction of the action of their opponent, which is taken into account when selecting the next action.

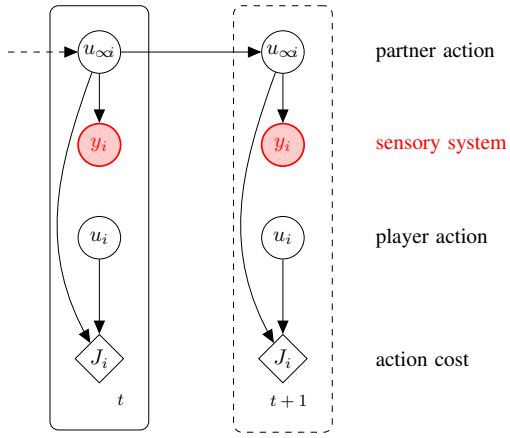


Fig. 3. Probabilistic graphical model (influence diagram) of a player in a generic joint action game. At each time step, Player i receives information about partner action (u_{-i}) through their sensory system (y_i). The player assumes that opponent actions depend on previous actions and combines this prior information with sensory feedback to predict the opponent's next action. Action selection involves minimizing a cost function (J_i) which depends on both own (u_i) and partner's action (u_{-i}). See [12] for details

The model is very general, and a specific task is encoded by the players' cost function. To model the competitive scenario, we assumed that the attacker's goal is to maximize the distance from the defender's position, while the defender's goal is to minimize the distance from the attacker's position. In addition, both players try to minimize their effort (spring force, i.e. the distance from the workspace center). The cost functions are defined as:

$$\begin{aligned} J_A(u_A, u_D) &= -\frac{1}{2} w_A |u_A - u_D|^2 + \frac{1}{2} r_A |u_A|^2 \\ J_D(u_A, u_D) &= \frac{1}{2} w_D |u_A - u_D|^2 + \frac{1}{2} r_D |u_D|^2 \end{aligned} \quad (1)$$

where parameters w_A and w_D control the minimum displacement from the partner to score the goal, whereas r_A and r_D control the weight of each player's effort. The sensory system is defined as:

$$y_i(t) = u_{\infty i} + v_i(t) \quad (2)$$

where

$$v_i(t) \sim N(0, \Sigma_y^i)$$

is the sensory (measurement) noise of the i-th player, with covariance Σ_y^i. In the simulations, we varied the sensory noise of each player among the three conditions: (i) Zero, $\Sigma_y^i \to 0$; (ii) Low, $\Sigma_y^i = 0.08$; (iii) Infinite, $\Sigma_y^i \to \infty$.

Based on the computational model of interaction and the experimental task we expected that each player uses principles of optimality to choose their strategy. The action selection at each trial would be balanced between the minimization of the effort (try not to move so far from the virtual spring that pulls the handle toward the center of the workspace) and the achievment of each competitor's goal.

C. Data analysis

The study aimed to understand how much players account for the differences in the visual display of the partner location (sensory system) giving some prior information about the preferred partner's region in the workspace.

In both experiments and simulations, we focused on the spatial distribution of A and D actions within the workspace. We took the attacker action u_A as the position in the horizontal line when the ball is shot. Likewise, we took the defender's action u_D as the horizontal position when the ball crosses the gate line. For each block, as the players were not informed about the changing conditions, the first five trials were excluded from the analysis.

We used a Gaussian mixture model to describe the joint probability density function of attacker and defender, $p(u_A, u_D)$. For each dyad and each experimental condition, we tested different variants of the model, with a different number of clusters (one, two, three or four) and different covariance structures (diagonal, non-diagonal). We used Akaike's Information Criterion (AIC) and Bayesian Information Criterion (BIC) to select the optimal model.

III. Results

A. Experiments

The scoring probability was similar in all dyads and in all experimental conditions ($87\% \pm 3\%$ for the attacker and $13\% \pm 3\%$ for the defender).

The morphology of the action distribution in the joint workspace is similar in all dyads. The attacker tends to shoot on either the left or the right of the defender, thus resulting in a bimodal distribution. On the contrary, the defender tends to cover the whole workspace, thus resulting in a (approximately central) unimodal distribution. The optimal model for the joint distribution – qualitatively similar in all conditions – is a mixture of two Gaussians, with non-diagonal covariances. However, in most conditions the covariances' principal directions are aligned along the vertical direction; see Fig. 4.

For each dyad, we took the inter-cluster distance $\Delta\mu_A$ and the dispersion σ_D^2 to quantify attacker (A) and defender (D) performance within each experimental condition.

A 2-way ANOVA (factors: Σ_y^A and Σ_y^D) revealed that the reliability of their own sensory information had no significant effects on their performance. However, in the defender behavior alone we observed a significant effect (p=0.025) of the

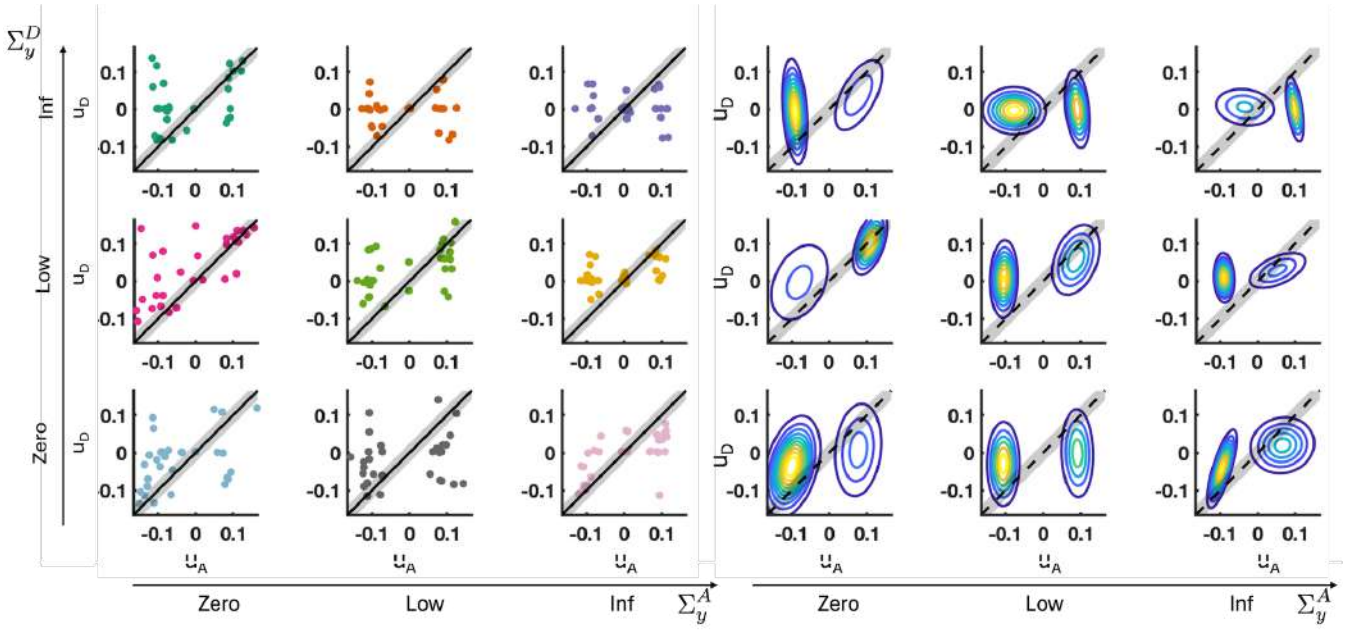


Fig. 4. Joint distribution of the A and D actions in a typical dyad, displayed as a scatter plot (left) and a Gaussian mixture model (right). Each subplot panel corresponds to one of the nine experimental conditions resulting from the manipulation of the sensory noise of both players. The grey area denotes the region where the attacker and the defender are within half the cursor size (5 cm), corresponding to the case when the defender catches the ball

attacker's sensory information. If the latter is more reliable, the defender tends to increase the dispersion of their actions. A similar trend, though not statistically significant, was observed in the attacker. These results are summarised in Fig. 5.

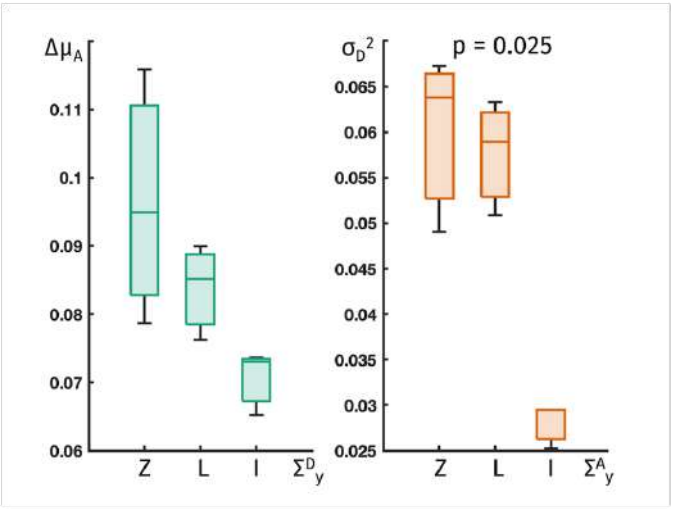


Fig. 5. Attacker ($\Delta\mu_A$, left) and defender performance (σ_D^2, right) as a function of the sensory uncertainty of their respective opponents, i.e. Σ_y^D (left) and Σ_y^A (right)

B. Simulations

Model simulations qualitatively reproduce the observed behavior. In particular, the joint distribution of the actions is qualitatively similar to the experimental results; see Fig. 6. We analyzed the simulated data in the same way as the experimental results using a Gaussian mixture model. We found that $\Delta_{\mu A}$ has greater values when the defender has more reliable information about the position of the attacker, in the same way the σ_D^2 is wider when the attacker has more reliable information about the defender's location. The simulation results are summarized in Fig. 7.

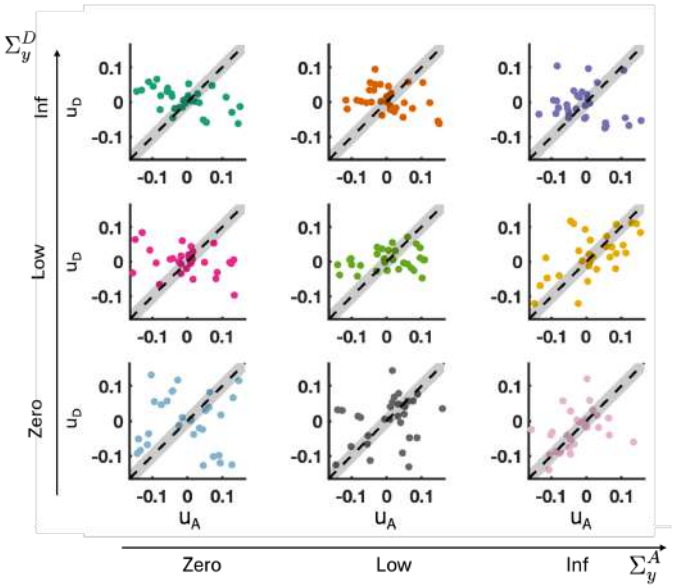


Fig. 6. Joint distribution (scatter) of the simulated players' actions in all experimental conditions (one simulation). Gray area as in Fig. 4

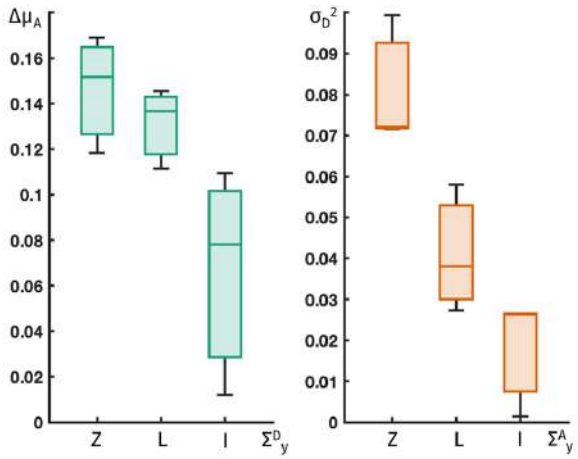


Fig. 7. Attacker ($\Delta\mu_A$, left) and defender performance (σ_D^2, right) as a function of the sensory uncertainty of their respective opponents, i.e. Σ_y^D (left) and Σ_y^A (right). The same model was used to simulate each dyad's randomized block order

IV. Discussion

Overall, these preliminary results suggest that each player strategically uses the information about their opponent's actions to develop a representation of their strategy and this enables them to continuously adapt their own actions accordingly. Players seem to rely on their observations of the opponent's behavior to adjust their strategy and make more informed action selections in the game.

Kucuktabak et al. [10] suggested that a deeper understanding of optimal personalized interaction can play a crucial role in the development of more effective rehabilitation protocols. Simulations conducted using a computational model designed around optimal action selection principles align with the experimental observations. These results suggest that players are using optimal strategies (in the game-theoretic sense) when choosing their next actions.

Our findings suggest that, in a competitive rehabilitation context, a patient can be encouraged to increase their range of motion (action dispersion) by manipulating the information available about their partner's location. For instance, adjusting sensory information could be used to dynamically modify the task's difficulty level, tailored to the patient's specific needs. More specifically, such manipulation could directly influence the patient's action selection strategy, pushing them to increase their action dispersion.

The competitive nature of the game can help patients maintain a high level of engagement and focus throughout their rehabilitation. Additionally, the ability to control and adjust the difficulty level of the task allows for a more personalized approach, attempting that motor improvements are maximized.

In the context of the rehabilitation game, patients may engage in training sessions either with another patient, a therapist, or even a simulated human-like partner. The use of the computational model proposed that can replicate human-like behaviors could be a promising tool. Such a model could be used as a simulated partner that adapts the action selection strategy in response to the patient's behavior by manipulating the sensory noise on the patient's position. By doing so, it allows the task to dynamically adjust to the patient's progress, helping to maintain the necessary level of challenge to promote improvement.

This adaptive approach can be beneficial in maintaining patient engagement and providing a more personalized rehabilitation experience.

References

[1] H. Nguyen, T. Phan, R. Shadmehr, and S. W. Lee, "Choice of arm use in stroke survivors is largely driven by the energetic cost of the movement," *Neurorehabil Neural Repair*, vol. 37, pp. 183–193, Apr 2023.

[2] M. Goršič, I. Cikajlo, N. Goljar, and D. Novak, "A multisession evaluation of an adaptive competitive arm rehabilitation game," *Journal of NeuroEngineering and Rehabilitation*, vol. 14, Dec. 2017.

[3] M. Goršič, I. Cikajlo, and D. Novak, "Competitive and cooperative arm rehabilitation games played by a patient and unimpaired person: effects on motivation and exercise intensity," *Journal of NeuroEngineering and Rehabilitation*, vol. 14, no. 1, p. 23, 2017.

[4] D. Novak, A. Nagle, U. Keller, and R. Riener, "Increasing motivation in robot-aided arm rehabilitation with competitive and cooperative gameplay," *Journal of NeuroEngineering and Rehabilitation*, vol. 11, no. 1, p. 64, 2014.

[5] A. Takagi, C. Bagnato, A. Melendez-Calderon, N. Jarrasse, G. Ganesh, and E. Burdet, "Competition increases the effort put into a physical interaction task.," *IEEE Trans Haptics*, vol. 16, pp. 719–725, Oct-Dec 2023.

[6] J. Catalán, J. García-Pérez, A. Blanco, D. Martínez, L. D. Lledó, and N. García-Aracil, "Differences in physiological reactions due to a competitive rehabilitation game modality.," *Sensors (Basel)*, vol. 21, May 2021.

[7] K. Baur, P. Wolf, V. Novak, D. Boering, S. Hörner, C. Dahlen, J. Berger, R. Riener, and V. H. V. Novak, "Competitive versus cooperative forms of therapeutic gaming with subacute stroke patients," *IEEE Transactions on Medical Robotics and Bionics*, vol. 5, no. 4, pp. 956–965, 2023.

[8] I. Doumas, G. Everard, S. Dehem, and T. Lejeune, "Serious games for upper limb rehabilitation after stroke: a meta-analysis," *Journal of neuroengineering and rehabilitation*, vol. 18, pp. 1–16, 2021.

[9] N. Hocine, A. Gouaïch, S. A. Cerri, D. Mottet, J. Froger, and I. Laffont, "Adaptation in serious games for upper-limb rehabilitation: an approach to improve training outcomes," *User Modeling and User-Adapted Interaction*, vol. 25, pp. 65–98, 2015.

[10] E. B. Küçüktabak, S. J. Kim, Y. Wen, K. Lynch, and J. L. Pons, "Human-machine-human interaction in motor control and rehabilitation: a review," *Journal of NeuroEngineering and Rehabilitation*, vol. 18, no. 1, p. 183, 2021.

[11] V. T. Chackochan and V. Sanguineti, "Incomplete information about the partner affects the development of collaborative strategies in joint action," *PLoS Comput Biol*, vol. 15, p. e1006385, Dec 2019.

[12] C. De Vicariis, V. T. Chackochan, L. Bandini, E. Ravaschio, and V. Sanguineti, "Computational joint action: Dynamical models to understand the development of joint coordination.," *PLoS Comput Biol*, vol. 20, p. e1011948, Oct 2024.

[13] M. R. Short, D. Ludvig, E. B. Kucuktabak, Y. Wen, L. Vianello, E. J. Perreault, L. Hargrove, K. Lynch, and J. L. Pons, "Haptic human-human interaction during an ankle tracking task: Effects of virtual connection stiffness," *IEEE Transactions on Neural Systems and Rehabilitation Engineering*, vol. 31, pp. 3864 – 3873, 2023.

[14] R. Lokesh, S. Sullivan, J. A. Calalo, A. Roth, B. Swanik, M. J. Carter, and J. G. A. Cashaback, "Humans utilize sensory evidence of others' intended action to make online decisions," *Sci Rep*, vol. 12, p. 8806, May 2022.

[15] J. A. Brantley and K. P. Körding, "Bayesball: Bayesian integration in professional baseball batters," *bioRxiv*, 2022.

[16] D. Campolo, P. Tommasino, K. Gamage, J. Klein, C. M. L. Hughes, and L. Masia, "H-man: a planar, h-shape cabled differential robotic manipulandum for experiments on human motor control," *J Neurosci Methods*, vol. 235, pp. 285–97, Sep 2014.

Ankle Power Biofeedback Augments Wearable Resistance for Improved Push-off Power and Muscle Recruitment

Emmanuella A. Tagoe
Department of Mechanical Engineering
Northern Arizona University
Flagstaff, US
eat277@nau.edu

Karl Harshe
Department of Mechanical Engineering
Northern Arizona University
Flagstaff, US
kh2638@nau.edu

Collin D. Bowersock
Department of Mechanical Engineering
Northern Arizona University
Flagstaff, US
collin.bowersock@nau.edu

Zachary F. Lerner
Department of Mechanical Engineering
Northern Arizona University
Flagstaff, US
zachary.lerner@nau.edu

***Abstract*— Ankle push-off power generated by the plantar flexor muscles is essential for efficient walking but is often impaired in individuals with cerebral palsy (CP), leading to inefficient walking. Both powered and passive (i.e., motor- and spring-based) wearable resistance devices are being developed for targeted training. This study explored the use of ankle power biofeedback across powered and passive wearable resistive devices to improve muscle recruitment and push-off power in individuals with CP. Seven individuals with CP completed walking sessions under the following conditions: (1) baseline (no device), (2) spring resistance with and without biofeedback, and (3) motor resistance with and without biofeedback. Push-off power and muscle recruitment were compared between biofeedback vs no-biofeedback conditions for both devices, and to baseline. Combined spring resistance and biofeedback increased soleus activity by 40% compared to the spring resistance only ($p = 0.004$) and by 48% compared to baseline ($p = 0.002$). Similarly, spring resistance and biofeedback increased peak ankle power by 32% relative to the spring resistance only ($p = 0.009$) and by 33% compared to baseline ($p = 0.010$). In contrast, motorized resistance and biofeedback did not significantly increase peak soleus activity or peak ankle power relative to motor resistance only ($p = 0.544$; $p = 0.544$). These findings show that ankle power biofeedback can augment spring resistance to elicit increased muscle recruitment and power during push-off in CP.**

***Keywords*— Ankle power, Gait, Rehabilitation Robotics**

I. Introduction

Ankle push-off power plays a significant role in human walking. It is the burst of positive power generated by the ankle plantar flexor muscles at the end of the stance phase of the gait cycle that facilitates the transition into the swing phase, propels the body forward, and initiates the progression from one leg to the other [1]. Impaired ankle plantar flexor muscle recruitment, therefore, can significantly reduce push-off power, and negatively affect walking ability. This diminished push-off power can place a greater demand on the hip joint, resulting in an inefficient walking pattern [2], [3]. Over time, the extra demand on the hip joint can lead to hip pain, especially for individuals with cerebral palsy (CP), the most prevalent lifelong cause of childhood disability [4], [5].

This work was supported in part by the National Science Foundation under Grant 2045966.

Several gait rehabilitation interventions have been implemented to address gait impairments experienced by individuals with CP [6]. Among these, functional resistance training with robotic devices has emerged as a highly effective approach. In recent years, robotic resistance has been shown to significantly improve ankle muscle recruitment and strength for individuals with CP [7], [8], [9]. Robotic devices offer a more effective method of delivering the intensity, duration, and progressive training to targeted joints, facilitating better mobility outcomes when compared to conventional or manual therapy [10], [11], [12].

Robotic devices are available in both powered and passive forms. Powered robotic devices use motors to provide resistance, while passive devices utilize springs. Powered robotic devices for resistance training have typically targeted the ankle joint, and previous research demonstrated that powered ankle resistance can improve soleus muscle recruitment in individuals with CP by 45% [7]. Conversely, passive robotic devices for resistance training have typically focused on the knee rather than the ankle. For example, Washabaugh et al. showed that passive knee resistance improved hamstring and quadriceps muscle recruitment in a healthy individual [13], though the effects in individuals with CP remain uncertain.

Audio-visual biofeedback systems have also been increasingly combined with resistance training to enhance the benefits of rehabilitation. These systems provide real-time feedback on specific gait parameters that align with rehabilitation goals. For instance, audio-visual biofeedback targeting step length, when paired with resistance training has been showed to improve step length in individuals with CP [14]. Similarly, biofeedback using electromyography (EMG) and plantar pressure have demonstrated to increase plantar flexor muscle activation [15]. These improvements are likely to be further amplified when paired with resistance training. Additionally, ankle power biofeedback has also showed to improve ankle push-off power in individuals with CP [16]. Given that plantar flexor muscles are the primary contributors to ankle push-off power, it raises an important question: Could ankle power biofeedback lead to increased muscle

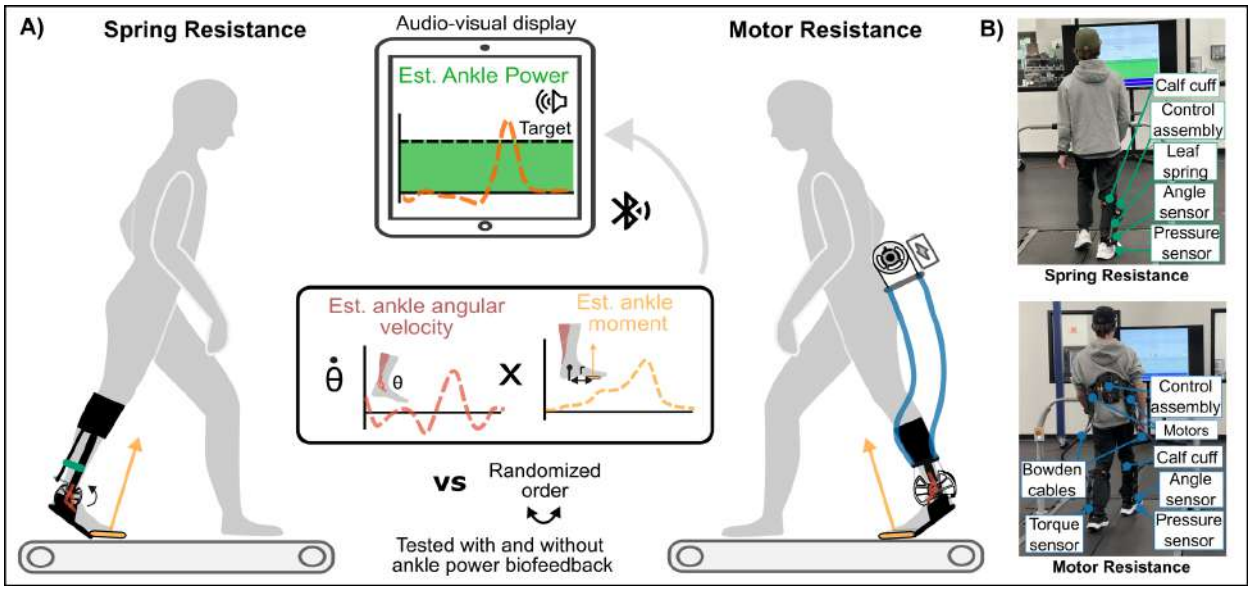


Figure 1: A) Depiction of ankle power biofeedback system and its operation as used in the experimental protocol B) Participant pictured wearing the ankle exoskeleton with motorized resistance and the ankle device with spring resistance.

recruitment and improved ankle power when its benefits are significantly enhanced by pairing it with resistance training?

We previously developed a powered ankle exoskeleton and passive ankle device capable of provide plantar flexor resistance via motors and springs, respectively. This study aimed to explore the use of ankle power biofeedback across powered and passive wearable resistive devices to enhance plantar flexor recruitment and push-off power in individuals with CP. We hypothesized that combining ankle power biofeedback with resistance would result in greater plantar flexor muscle recruitment and increased ankle push-off power compared to resistance alone, for both motor- and spring-based resistive devices. We also hypothesized that both the combination of ankle power biofeedback with resistance and resistance alone during training would increase plantar flexor muscle recruitment and ankle push-off power relative to baseline.

II. METHODS

A. Ankle Power Biofeedback System

We developed a biofeedback system that utilized on-board sensors on our wearable devices to provide feedback on estimated net ankle power (i.e. device and biological ankle power). The biofeedback system leveraged force sensitive resistors (FSRs), and angle sensors embedded in the ankle devices to estimate ankle power in real-time. Ankle power was calculated as the product of ankle angular velocity and the ankle moment estimated from FSR data [17]. Real-time audio-visual biofeedback on ankle power was provided to participants during the biofeedback conditions via a 65-inch television placed in front of them for clear visibility (Figure 1). An iOS application (Biomotum, Portland, US) received, processed, and streamed the ankle power data via Bluetooth, projecting it onto the television. This setup was similar to those described in prior studies [15], [18]. The real-time estimated ankle power displayed on the screen was for the participant's more affected limb only. The television also displayed a horizontal target line, set as a 10% increase of the participant's peak ankle power during walking without resistance or biofeedback. When the estimated peak ankle power exceeded the target line, the system displayed a green background with confetti and played an audible 'ding' as a reward to reinforce the desired performance.

B. Ankle Device with Spring Resistance

We used a simple ankle device that employed a carbon fiber leaf spring to deliver targeted plantarflexion resistance. The device consisted primarily of an ankle assembly, which included the carbon fiber leaf spring, a custom 3D-printed slider with carbon fiber reinforcement (Onyx, Markforged) to adjust the pivot point of the spring and modulate its effective length for varying resistance, a neutral angle adjuster, a footplate with an embedded force-sensitive resistor (FSR), Hall-effect angle sensor (AS5600, AMS OSRAM), a calf cuff, and a pulley. The leaf spring was a 6.35 mm thick 0/90 ply carbon fiber bar (8194K111, McMaster-Carr) with a functional length of 115 mm. It generated a maximum peak resistive torque of 0.073 Nm/kg. The timing for spring

TABLE I
PARTICIPANTS CHARACTERISTICS

	Age (Years)	Mass (kg)	Height (m)	GMFCS Level	Preferred speed (m/s)
P1	40	72.0	1.80	II	0.60
P2	17	58.3	1.70	II	0.60
P3	14	58.0	1.71	I	0.85
P4	13	47.0	1.49	II	0.45
P5	18	52.0	1.67	I	0.65
P6	15	53.0	1.62	II	0.75
P7	13	56.2	1.70	I	0.85

GMFCS: Gross Motor Function Classification System. PF: Plantarflexion. Participants were all males and had their right side more affected by CP.

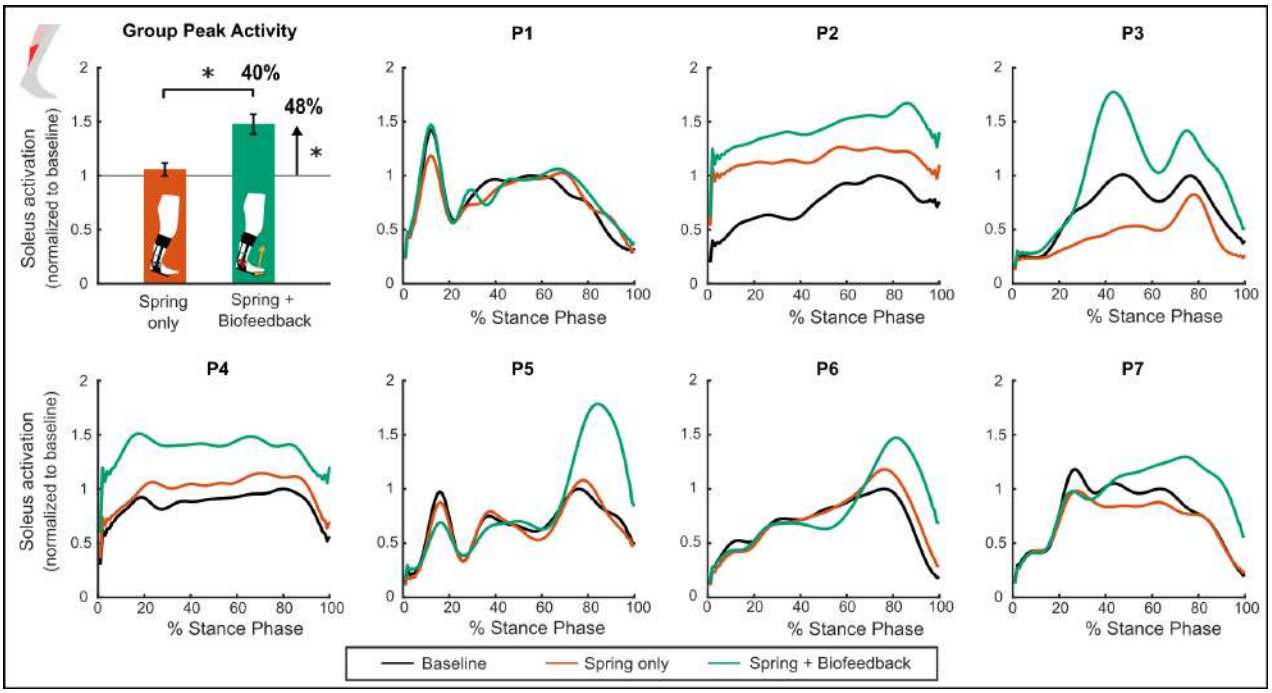


Figure 2: *First plot:* Group level peak propulsive phase soleus activation relative to baseline for walking with spring resistance only (orange) and spring resistance plus biofeedback (green) and *Remaining plots:* Soleus activation curves (average across all gait cycles) for baseline walking (black), walking with spring resistance only (orange) and spring resistance plus biofeedback (green); Error bars represent standard error of the mean, bracket represent pairwise comparison between walking spring resistance only and spring resistance plus biofeedback, upward arrow indicate pairwise comparison between baseline walking and walking with spring resistance plus biofeedback, and * indicates statistical significance (p-value) less than 0.05.

engagement was customized for each participant using the neutral angle adjuster, allowing the spring to engage at the onset of plantarflexion. This adjuster consisted of a barrel adjuster and a steel coupling nut, interfacing with the spring via a steel cable that terminated at an ankle pulley.

C. Ankle Exoskeleton with Motor Resistance

The ankle exoskeleton used in this study was untethered, battery-powered and capable of adaptive control, as previously described in [19], [20] (Figure 1). The device comprised waist and ankle assemblies connected via Bowden cables. The waist assembly housed two DC motors (T-Motor, AK60v1.1), a custom printed circuit board, microcontrollers, and an 1800mAh lithium-ion battery. The ankle assembly included footplates embedded with force sensitive resistors (FSRs; Tekscan, FlexiForce A502), custom torque sensors, angle sensors (Hall-effect; AS5600, AMS OSRAM), a pulley, and calf cuffs. The accuracy and reliability of the custom torque sensor has been shown in our prior work [21]. The exoskeleton applied plantarflexion resistance by using its motors to drive a chain-and-sprocket transmission, which interfaced with a Bowden cable system terminating at the ankle pulley. Its control strategy provided resistive torque proportional to the real-time estimated biological ankle joint moment [7], [19]. Torque sensors in the ankle assembly measured the applied resistive torque, enabling closed-loop torque feedback control. FSRs in the footplates informed a finite state machine to differentiate between stance and swing phases of the gait cycle. The peak torque setpoint was set to 0.08 Nm/kg, providing resistance similar to highest spring resistance.

D. Study Approval and Participants

This study was approved by the Institutional Review Board of Northern Arizona University (#2137266). Seven individuals with CP (ages 13 – 40 years) completed this study (Table I). Inclusion criteria were a diagnosis of CP, Gross Motor Function Classification System (GMFCS) level I, II, or III, and the ability to walk on a treadmill continuously with or without support for at least six minutes. Exclusion criteria included orthopedic surgery within the past six months, any botulinum toxin injections within the past six months, and any other conditions that would prevent safe participation. A licensed physical therapist completed a physical evaluation with each participant to assess function and confirm eligibility. All adult participants and the parents of participants below the age of 18 provided their informed written consent before participation. Minor participants provided verbal assent as well.

E. Experimental Protocol

First, we obtained participants' preferred walking speed while they walked on the treadmill without any devices. Then, participants walked with both motor and spring resistance devices, with ankle power biofeedback to familiarize themselves with the biofeedback system and

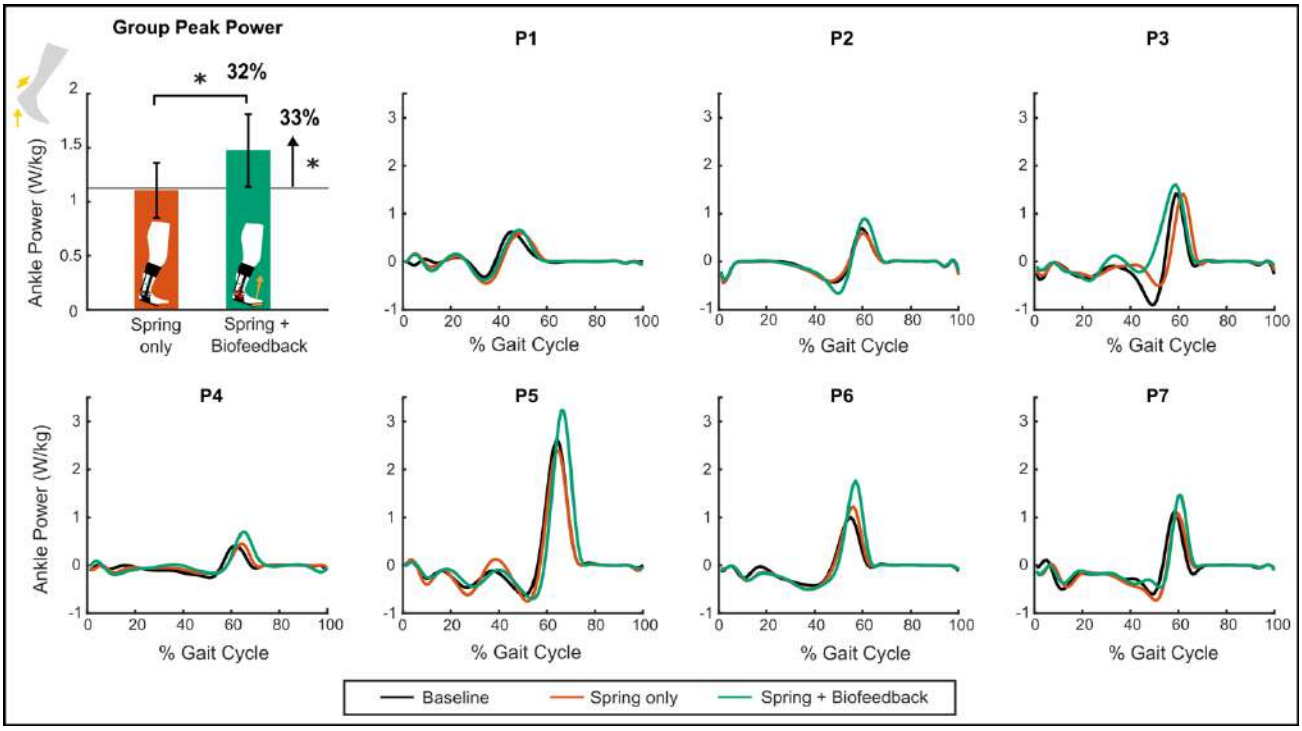


Figure 3: *First plot:* Group level peak ankle power for walking with spring resistance only (orange) and spring resistance plus biofeedback (green) and *Remaining plots:* Ankle power curves (average across all gait cycles) for baseline walking (black), walking with spring resistance only (orange) and spring resistance plus biofeedback (green); Error bars represent standard error of the mean, bracket represent pairwise comparison between walking with spring resistance only and spring resistance plus biofeedback, upward arrow indicate pairwise comparison between baseline walking and walking with spring resistance plus biofeedback, and * indicates statistical significance (p-value) less than 0.05.

acclimate to the devices. Participants walked continuously until they hit the target line for ten consecutive steps and for a minimum of four minutes in each device. Following this acclimation period, each participant had a seated rest for twenty minutes.

We then placed wireless EMG sensor (Trigno, Delsys, Natick, MA) on the soleus and medial gastrocnemius muscles of the more affected limb of participants, and reflective markers on participants' lower legs to define the foot and shank segments. Participants then walked at their preferred speed with no device *(Baseline)* for two minutes and either the ankle device with spring resistance for two minutes first with no biofeedback *(Spring only)* and another two minutes with biofeedback *(Spring + Biofeedback) or* ankle device with motor resistance for two minutes first with no biofeedback *(Motor only)* and another two minutes with biofeedback *(Motor + Biofeedback)* in a randomized order. A four-minute seated resting period was included between each condition. During each condition, we recorded EMG data at 1200 Hz and lower limb kinematic data at 120 Hz using an eight-camera capture system (Vicon, Oxford, UK). A trigger system synchronized with Vicon Nexus system was used to separate between the first and last two minutes of walking conditions with devices. Walking with the ankle device with spring resistance was completed in low, medium and high spring configurations, corresponding to effective spring lengths of 115mm, 65mm, and 15mm, respectively. The motor resistance was matched with the high spring resistance configuration.

F. Data Analysis

To assess our objective of evaluating how ankle power biofeedback affects walking across passive vs powered resistance systems, we analyzed measurable outcomes for conditions with the high spring resistance, motor resistance and baseline. EMG data were bandpass filtered (15 - 380 Hz, 4th order Butterworth), rectified, and lowpass filtered (7 Hz, 4th order Butterworth) to generate the linear envelope. The linear envelope was then normalized by the peak value from the baseline condition. We calculated the peak EMG during the push-off phase of the gait cycle (51-100% of the stance phase [22]). Gait events were identified using Vicon Nexus.

We used OpenSim 4.4 to calculate the sagittal plane joint kinematics and kinetics [23]. A 3D generic musculoskeletal model was first scaled for each participant, and then ankle angles and moments were computed using inverse kinematics and inverse dynamics, respectively. Inertia properties from each device were integrated into their respective OpenSim models by rigidly attaching the ankle assemblies to the tibia and the waist assembly to the pelvis for the ankle device with motor resistance. Ankle power was calculated as the product

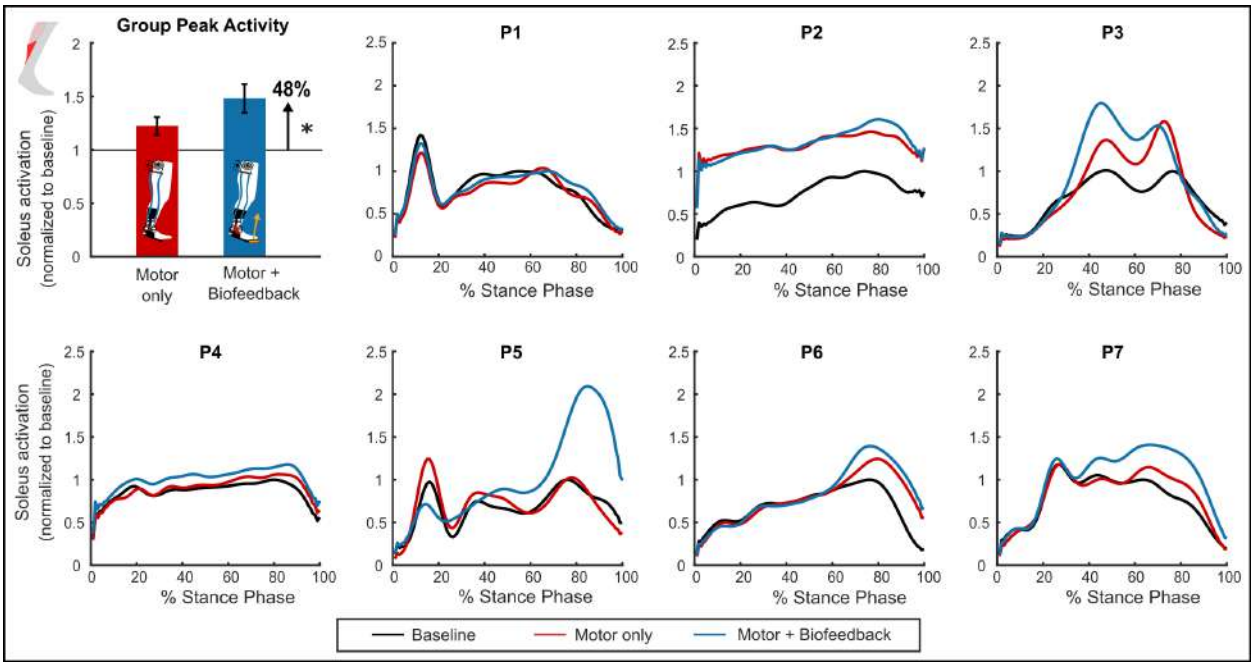


Figure 4: *First plot:* Group level peak propulsive phase soleus activation relative to baseline for walking with motor resistance only (red) and motor resistance plus biofeedback (blue) and *Remaining plots:* Soleus activation curves (average across all gait cycles) for baseline walking (black), walking with motor resistance only (red) and motor resistance plus biofeedback (blue); Error bars represent standard error of the mean, upward arrow indicate pairwise comparison between baseline walking and walking with motor resistance plus biofeedback, and * indicates statistical significance (p-value) less than 0.05.

of the ankle moment (excluding resistive torque from devices) and the respective ankle angular velocity.

G. Statistical Analysis

To validate our first objective of evaluating how ankle power biofeedback affects outcomes during walking with passive resistive devices, we used one-way repeated measures ANOVA to compare measured outcomes between the *Baseline*, *Spring only*, and *Spring + Biofeedback* conditions (p-value set at 0.05). Prior to this, we conducted normality tests on the differences between pairs for measured outcomes using the Shapiro-Wilks test; all data passed normality tests. Pairwise comparisons were made using paired two-tailed t-tests with Holm-Bonferroni correction for multiple comparisons (adjusted significance level set at 0.05).

To validate our second objective of evaluating how ankle power biofeedback affects outcomes during walking with motorized resistive devices, we used Friedman test to compare measured outcomes between the *Baseline, Motor only, and Motor + Biofeedback* conditions (p-value set at 0.05). Prior to this, we conducted normality tests on the differences between pairs for all measured outcomes using the Shapiro-Wilks tests; some data did not pass normality tests. Pairwise comparisons were made using Wilcoxon signed rank test with Holm-Bonferroni correction for multiple comparisons (adjusted significance level set at 0.05).

III. RESULTS

A. Effect of Ankle Power Biofeedback on Spring Resistance

There was a significant effect of walking condition on peak soleus activity ($p < 0.001$, Fig 2). Pairwise comparisons showed that the spring resistance plus biofeedback condition significantly increased peak soleus activity relative to the spring resistance only condition by 40% ($p = 0.004$) and baseline by 48% ($p = 0.002$). There was no difference between baseline and spring resistance only conditions ($p = 0.377$).

There was a significant effect of walking condition on peak ankle power ($p = 0.001$, Fig 3). Pairwise comparisons showed that the spring resistance plus biofeedback condition significantly increased peak ankle power relative to the spring resistance only condition by 32% ($p = 0.009$) and baseline by 33% ($p = 0.010$). There was no difference between baseline and spring resistance only conditions ($p = 0.773$).

B. Effect of Ankle Power Biofeedback on Motor Resistance

There was a significant effect of walking condition on peak soleus activity ($p = 0.002$, Fig 4). Pairwise comparisons showed that the motor resistance plus biofeedback condition significantly increased peak soleus activity relative to baseline by 48% ($p = 0.002$). The motor resistance plus biofeedback condition did not significantly increase peak soleus activity relative to motor resistance only ($p = 0.544$). There was also no difference between baseline and motor resistance only conditions ($p = 0.098$).

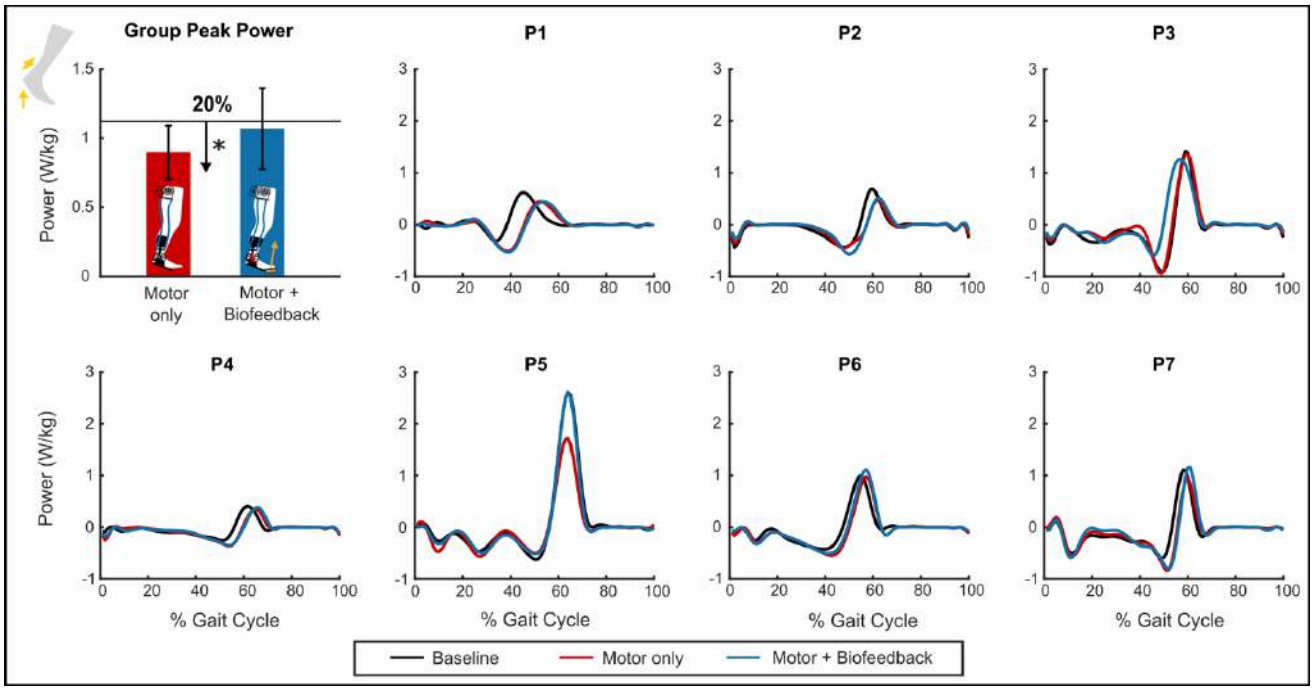


Figure 5: *First plot:* Group level peak ankle power for walking with motor resistance only (red) and motor resistance plus biofeedback (blue) and *Remaining plots:* Ankle power curves (average across all gait cycles) for baseline walking (black), walking with motor resistance only (red) and motor resistance plus biofeedback (blue); Error bars represent standard error of the mean, downward arrow indicate pairwise comparison between baseline walking and walking with motor resistance only, and * indicates statistical significance (p-value) less than 0.05.

There was a significant effect of walking condition on peak ankle power ($p = 0.028$, Fig 5). Pairwise comparisons showed that the motor resistance only condition decreased peak ankle power relative to baseline by 20% ($p = 0.023$). The motor resistance plus biofeedback condition did not significantly increase peak ankle power relative to motor resistance only ($p = 0.544$). There was no difference between baseline and motor resistance plus biofeedback conditions ($p = 0.544$).

IV. DISCUSSION

The purpose of this study was to implement an ankle power biofeedback system paired with motor- and spring-based resistance training modalities to improve plantar flexor muscle engagement push-off power in individuals with cerebral palsy (CP) relative to resistance alone. We partially confirm our hypothesis combining ankle power biofeedback with resistance would result in greater plantar flexor muscle recruitment and increased ankle push-off power compared to resistance alone, for both motor and spring resistance devices – ankle power biofeedback improved plantar flexor muscle engagement and push-off power for the spring device only.

Improvements in peak soleus activity and peak ankle power for walking with resistance plus biofeedback compared to resistance alone were observed, but for only the spring device. It is surprising that no difference was observed between motor resistance only and motor resistance plus biofeedback, as prior research showed that combining plantar pressure biofeedback with motor resistance improved both peak and mean soleus activity relative to resistance alone [18]. For plantar pressure biofeedback, participants typically respond by simply applying plantar pressure into the ground during gait training. However, ankle power biofeedback requires participants not only to apply plantar pressure but also to quickly rotate their ankle. While participants appeared to successfully perform this during acclimation, the added complexity of ankle rotation may have made it more challenging to effectively improve muscle recruitment. Future studies should explore whether additional training can mitigate the complexity associated with ankle power biofeedback and enhance its effectiveness in improving muscle recruitment.

There remains an unmet need for effective gait rehabilitation tools for individuals with CP. In this study, combining ankle power biofeedback with spring resistance led to improved peak push-off soleus activity and power compared to spring resistance alone. A passive spring-based ankle gait rehabilitation system would likely be a simpler and more cost-effective option than its powered alternative. This system can potentially facilitate faster clinical adoption [24] and broader applications, including use in at-home training.

This study has several limitations that need to be considered. First, the sample size was small ($n = 7$). Although this is similar to other exploratory intervention studies in CP [15], [25], our findings cannot be generalized to the broader CP population. Secondly, this study focused on an immediate effect of the intervention following only a brief of acclimation. It is still unclear how additional acclimation may affect our results. Future studies are needed to further investigate how additional training would affect muscle recruitment and power.

V. CONCLUSION

This study demonstrates that ankle power biofeedback can augment spring resistance to elicit both increased plantar flexor muscle recruitment and ankle power during push-off in individuals with CP. This approach offers a promising strategy to improve two key biomechanical outcomes necessary for efficient human walking. Its relatively simpler design also holds promise in facilitating clinical translation and practical at-home training. Future research will explore the long-term effects of functional training with the combined spring resistance and ankle power biofeedback, with focus on sustained improvements.

ACKNOWLEDGMENT

This work was supported in part by the National Science Foundation under Grant 2045966. The authors thank all the participants and their families for their participation in this study. Z. F. Lerner is a co-founder with shareholder interest in Biomotum, Inc., a university start-up company, seeking to commercialize the devices used in this study. He also has intellectual property inventorship rights covering aspects of the design and control of the exoskeleton. Z. F. Lerner and E. A. Tagoe have an application for a patent covering the aspects of the design and control of the spring device used in this study. All other authors have no competing interests.

REFERENCES

[1] K. E. Zelik and P. G. Adamczyk, "A unified perspective on ankle push-off in human walking," *J. Exp. Biol.*, vol. 219, no. 23, pp. 3676–3683, Dec. 2016, doi: 10.1242/jeb.140376.

[2] A. D. Kuo and J. M. Donelan, "Dynamic Principles of Gait and Their Clinical Implications," *Phys. Ther.*, vol. 90, no. 2, pp. 157–174, Feb. 2010, doi: 10.2522/ptj.20090125.

[3] T. P. Huang, K. A. Shorter, P. G. Adamczyk, and A. D. Kuo, "Mechanical and energetic consequences of reduced ankle plantar-flexion in human walking," *J. Exp. Biol.*, vol. 218, no. 22, pp. 3541–3550, Nov. 2015, doi: 10.1242/jeb.113910.

[4] H. K. Graham *et al.*, "Cerebral palsy," *Nat. Rev. Dis. Primer*, vol. 2, p. 15082, Jan. 2016, doi: 10.1038/nrdp.2015.82.

[5] P. Haak, M. Lenski, M. J. C. Hidecker, M. Li, and N. Paneth, "Cerebral palsy and aging," *Dev. Med. Child Neurol.*, vol. 51, no. 0 4, pp. 16–23, Oct. 2009, doi: 10.1111/j.1469-8749.2009.03428.x.

[6] D. L. Damiano, "Rehabilitative therapies in cerebral palsy: the good, the not as good, and the possible," *J. Child Neurol.*, vol. 24, no. 9, pp. 1200–1204, Sep. 2009, doi: 10.1177/0883073809337919.

[7] B. C. Conner, J. Luque, and Z. F. Lerner, "Adaptive Ankle Resistance from a Wearable Robotic Device to Improve Muscle Recruitment in Cerebral Palsy," *Ann. Biomed. Eng.*, vol. 48, no. 4, pp. 1309–1321, Apr. 2020, doi: 10.1007/s10439-020-02454-8.

[8] J. Laut, M. Porfiri, and P. Raghavan, "The Present and Future of Robotic Technology in Rehabilitation," *Curr. Phys. Med. Rehabil. Rep.*, vol. 4, no. 4, pp. 312–319, Dec. 2016, doi: 10.1007/s40141-016-0139-0.

[9] P. van Vliet and A. M. Wing, "A new challenge--robotics in the rehabilitation of the neurologically motor impaired," *Phys. Ther.*, vol. 71, no. 1, pp. 39–47, Jan. 1991, doi: 10.1093/ptj/71.1.39.

[10] D. L. Damiano, "Activity, Activity, Activity: Rethinking Our Physical Therapy Approach to Cerebral Palsy," *Phys. Ther.*, vol. 86, no. 11, pp. 1534–1540, Nov. 2006, doi: 10.2522/ptj.20050397.

[11] O. Verschuren, M. D. Peterson, A. C. J. Balemans, and E. A. Hurvitz, "Exercise and Physical Activity Recommendations for People with Cerebral Palsy," *Dev. Med. Child Neurol.*, vol. 58, no. 8, pp. 798–808, Aug. 2016, doi: 10.1111/dmcn.13053.

[12] M. R. Spiess, F. Steenbrink, and A. Esquenazi, "Getting the Best Out of Advanced Rehabilitation Technology for the Lower Limbs: Minding Motor Learning Principles," *PM R*, vol. 10, no. 9 Suppl 2, pp. S165–S173, Sep. 2018, doi: 10.1016/j.pmrj.2018.06.007.

[13] E. P. Washabaugh, T. E. Augenstein, A. M. Ebenhoeh, J. Qiu, K. A. Ford, and C. Krishnan, "Design and Preliminary Assessment of a Passive Elastic Leg Exoskeleton for Resistive Gait Rehabilitation," *IEEE Trans. Biomed. Eng.*, vol. 68, no. 6, pp. 1941–1950, Jun. 2021, doi: 10.1109/TBME.2020.3038582.

[14] Y. Fang and Z. F. Lerner, "Feasibility of Augmenting Ankle Exoskeleton Walking Performance With Step Length Biofeedback in Individuals With Cerebral Palsy," *IEEE Trans. Neural Syst. Rehabil. Eng.*, vol. 29, pp. 442–449, 2021, doi: 10.1109/TNSRE.2021.3055796.

[15] B. C. Conner, Y. Fang, and Z. F. Lerner, "Under pressure: design and validation of a pressure-sensitive insole for ankle plantar flexion biofeedback during neuromuscular gait training," *J. Neuroengineering Rehabil.*, vol. 19, no. 1, p. 135, Dec. 2022, doi: 10.1186/s12984-022-01119-y.

[16] A. T. Booth, A. I. Buizer, J. Harlaar, F. Steenbrink, and M. M. van der Krogt, "Immediate Effects of Immersive Biofeedback on Gait in Children With Cerebral Palsy," *Arch. Phys. Med. Rehabil.*, vol. 100, no. 4, pp. 598–605, Apr. 2019, doi: 10.1016/j.apmr.2018.10.013.

[17] S. S. P. A. Bishe, T. Nguyen, Y. Fang, and Z. F. Lerner, "Adaptive Ankle Exoskeleton Control: Validation Across Diverse Walking Conditions," *IEEE Trans. Med. Robot. Bionics*, vol. 3, no. 3, pp. 801–812, Aug. 2021, doi: 10.1109/TMRB.2021.3091519.

[18] B. C. Conner and Z. F. Lerner, "Improving Ankle Muscle Recruitment via Plantar Pressure Biofeedback during Robot Resisted Gait Training in Cerebral Palsy," *IEEE Int. Conf. Rehabil. Robot. Proc.*, vol. 2022, pp. 1–6, Jul. 2022, doi: 10.1109/ICORR55369.2022.9896581.

[19] G. M. Gasparri, J. Luque, and Z. F. Lerner, "Proportional Joint-Moment Control for Instantaneously Adaptive Ankle Exoskeleton Assistance," *IEEE Trans. Neural Syst. Rehabil. Eng.*, vol. 27, no. 4, pp. 751–759, Apr. 2019, doi: 10.1109/TNSRE.2019.2905979.

[20] K. Harshe, E. Tagoe, C. Bowersock, and Z. F. Lerner, "Priming Robotic Plantarflexor Resistance With Assistance to Improve Ankle Power During Exoskeleton Gait Training," *IEEE Robot. Autom. Lett.*, vol. 9, no. 11, pp. 10511–10518, Nov. 2024, doi: 10.1109/LRA.2024.3477093.

[21] G. Orekhov, Y. Fang, C. F. Cuddeback, and Z. F. Lerner, "Usability and performance validation of an ultra-lightweight and versatile untethered robotic ankle exoskeleton," *J. NeuroEngineering Rehabil.*, vol. 18, no. 1, p. 163, Nov. 2021, doi: 10.1186/s12984-021-00954-9.

[22] J. S. Gottschall and R. Kram, "Energy cost and muscular activity required for propulsion during walking," *J. Appl. Physiol. Bethesda Md 1985*, vol. 94, no. 5, pp. 1766–1772, May 2003, doi: 10.1152/japplphysiol.00670.2002.

[23] S. L. Delp *et al.*, "OpenSim: open-source software to create and analyze dynamic simulations of movement," *IEEE Trans. Biomed. Eng.*, vol. 54, no. 11, pp. 1940–1950, Nov. 2007, doi: 10.1109/TBME.2007.901024.

[24] A. Bertolazzi, V. Quaglia, and R. Bongelli, "Barriers and facilitators to health technology adoption by older adults with chronic diseases: an integrative systematic review," *BMC Public Health*, vol. 24, no. 1, p. 506, Feb. 2024, doi: 10.1186/s12889-024-18036-5.

[25] L. van Noort, N. Van Crey, E. J. Rouse, I. Martínez-Caballero, E. H. F. van Asseldonk, and C. Bayón, "A usability study on the inGAIT-VSO: effects of a variable-stiffness ankle-foot orthosis on the walking performance of children with cerebral palsy," *J. NeuroEngineering Rehabil.*, vol. 21, no. 1, p. 132, Aug. 2024, doi: 10.1186/s12984-024-01433-7.

TIFEX-Py: Time-series Feature Extraction for Python in a Human Activity Recognition Scenario

Mehdi Ejtehadi
SCAI Lab, D-HEST
ETH Zurich, Swiss Paraplegic Research
Zurich, Switzerland
mehdi.ejtehadi@hest.ethz.ch

Gloria Edumaba Graham
Dept. of Computer Engineering
KNUST
Kumasi, Ghana
gegraham2@st.knust.edu.gh

Cailin Ringstrom
D-MAVT,& SCAI-Lab
ETH Zurich
Zurich, Switzerland
cringstrom@student.ethz.ch

Elisa Du
Dept. of Neurology, & SCAI-Lab
University of Zurich
Zurich, Switzerland
elisa.du@uzh.ch

Robert Riener
Dept. of Health Sciences and Technology
ETH Zurich, Balgrist University Hospital
Zurich, Switzerland
robert.riener@hest.ethz.ch

Diego Paez-Granados
SCAI Lab, D-HEST
ETH Zurich, Swiss Paraplegic Research (SPF)
Zurich, Switzerland
diego.paez@hest.ethz.ch

***Abstract*—Human Activity Recognition (HAR) is a valuable tool for healthcare and rehabilitation, enabling applications like remote patient monitoring and rehabilitation progress assessment. This paper introduces `TIFEX-Py`, a comprehensive Python toolbox designed for time series feature extraction in HAR. `TIFEX-Py` offers a rich set of 195 feature extraction methods across statistical, amplitude, spectral, and time-frequency domains. To evaluate its effectiveness, `TIFEX-Py` was applied to 11 publicly available HAR datasets: *DSADS*, *HHAR*, *MHEALTH*, *MotionSense*, *PAMAP2*, *REALDISP*, *RealWorld*, *UniMiBSHAR*, *USC-HAD*, *WARD*, and *WISDM*. Machine learning pipelines utilizing `TIFEX-Py` features, evaluated under both random and subject-stratified cross-validation settings, consistently achieved performance that is competitive with or superior to state-of-the-art (SOTA) benchmark performances available for the datasets. In 11 out of 11 random split cross-validation scenarios, our pipeline surpassed or matched SOTA performance. For stratified by subject cross-validation, this was the case for more than half of the datasets. These results highlight the power of `TIFEX-Py`'s feature space in representing time series data. `TIFEX-Py` is open-source and publicly available for researchers in rehabilitation and movement analysis fields.**

***Index Terms*—Time Series, Feature Extraction, Classification, Python, Human Activity Recognition**

I. Introduction

Human activity recognition (HAR), the automatic detection of activities through sensor data analysis, is a critical tool in healthcare and rehabilitation [1]–[3]. HAR has various applications, including remote patient monitoring and evaluation of rehabilitation progress [2], [4]. For example, for elderly individuals, HAR systems enable the monitoring of activity patterns, the identification of critical events such as falls, and the promotion of independent living [1], [2]. In the context of e-health, HAR holds immense potential for remote care, tracking rehabilitation outcomes, and monitoring physical and mental health [1], [4].

While automated feature extraction (AutoFE) in deep learning (DL) models, such as convolutional neural networks (CNNs), has significantly advanced HAR, manual feature extraction (ManFE) in statistical learning (SL) and traditional machine learning (ML) approaches remains highly competitive, especially when paired with well-crafted feature representations [5]–[8]. Specifically, studies show that ensemble learners can match or even surpass DL models on specific HAR datasets, particularly in classification performance (e.g., accuracy and precision) [9]–[11]. However, constructing an effective feature space remains challenging, requiring domain expertise and careful feature selection.

This paper presents `TIFEX-Py`, a comprehensive compilation of feature extraction methods from the literature for **Ti**me series **Fe**ature **Ex**traction in **Py**thon, specifically tailored for HAR applications in healthcare and rehabilitation. By incorporating a diverse set of statistical, spectral, and time-frequency feature extraction methods, `TIFEX-Py` provides a rich and structured feature representation of time-series data, facilitating its effective use in ML pipelines. The toolbox is benchmarked on various HAR datasets, offering a robust resource for extracting meaningful features that can enhance classification performance. By enabling accurate activity classification, it supports key rehabilitation tasks such as ADL monitoring, rehab progress assessment, fall detection, and managing secondary medical conditions [3].

II. Materials and Methods

Fig. 1 outlines the experimental workflow, including time-series pre-processing, sliding window segmentation, feature extraction with `TIFEX-Py`, and model evaluation via k-fold cross-validation against SOTA benchmarks. Each step is detailed in the following subsections.

A. *TIFEX-Py*

As walked through in Fig. 1, `TIFEX-Py` is a Python 3 toolbox developed for time series feature extraction across

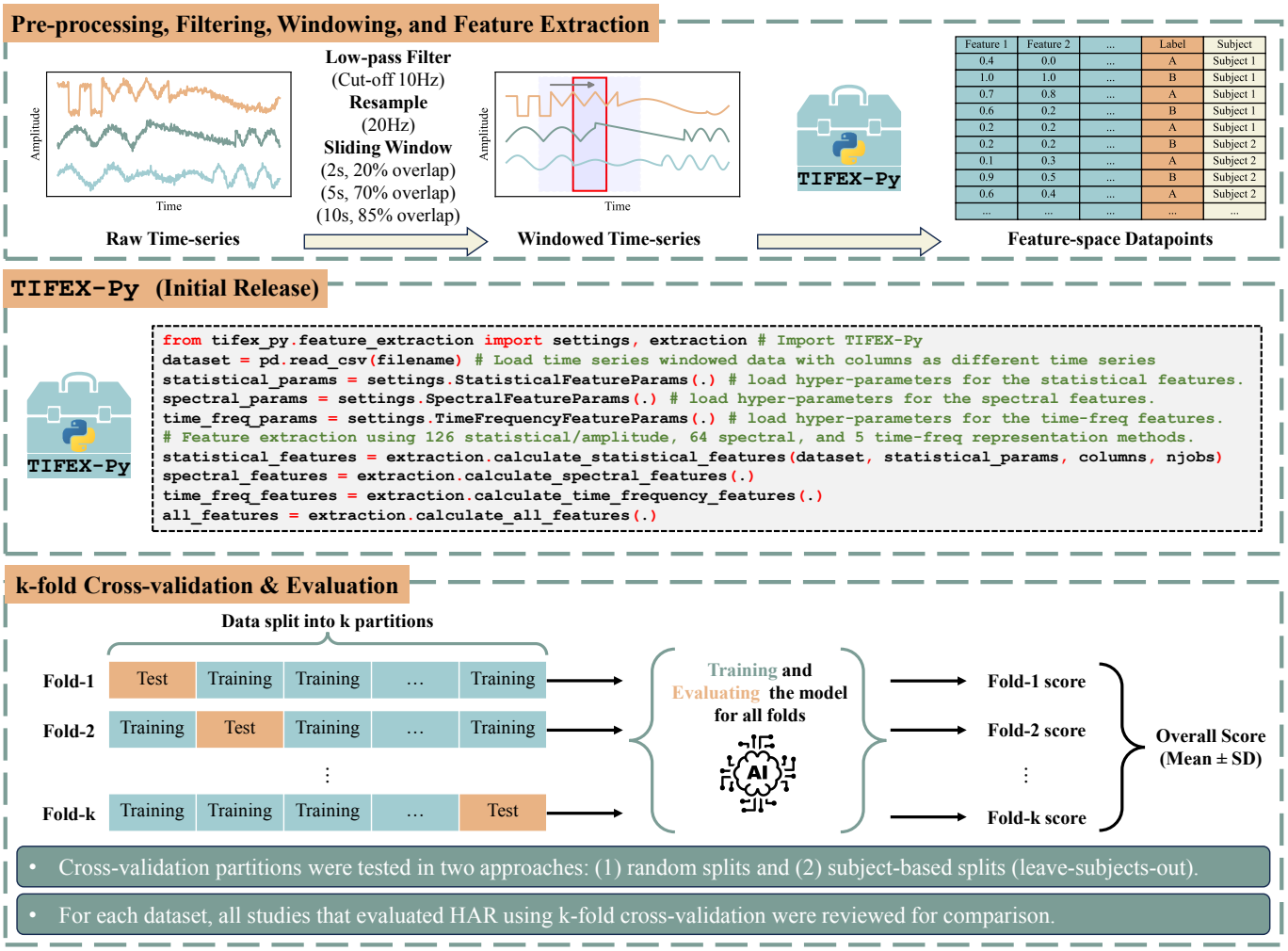


Fig. 1. Flow diagram of the pre-processing (filtering, resampling, windowing), feature extraction (including snippets from TIFEX-Py used for extracting features in statistical/amplitude, spectral, and time-frequency domains), and evaluation stages (including the cross-validation diagrams).

statistical and amplitude (125 methods), spectral (64 methods), and time-frequency (5 methods) domains. This extensive compilation makes TIFEX-Py the most comprehensive Python package for time series feature extraction. Several Python-based toolboxes for time series feature extraction exist, including *TSFEL* [12], which offers over 60 methods, and *tsfresh* [13], which provides 64 feature extraction methods. By offering a broader range of features, TIFEX-Py extends the capabilities of these toolboxes and, when combined with effective feature selection and hyperparameter tuning, has the potential to improve time series representation and classification performance.

TIFEX-Py is built upon widely used Python data analysis libraries such as NumPy and Pandas, ensuring compatibility with standard data processing workflows. The toolbox is open-source and publicly available[1]. Documentation, tutorials, feature implementations, feature references, computation time benchmarks, and additional details are available in the repository. The current paper corresponds to the initial release of the toolbox, which is archived in the ETH Data Archive[2].

With the current version of TIFEX-Py, users are responsible for: (1) pre-processing the input time series data (e.g., normalizing, filtering, and resampling), (2) feature selection, as TIFEX-Py compiles features available in the literature, but their selection should be incorporated into machine learning pipelines, and (3) hyperparameter tuning, as many feature extraction methods include adjustable parameters that can be fine-tuned to optimize performance for specific datasets.

B. Data

A total of 11 open-source HAR datasets were employed to evaluate the effectiveness of TIFEX-Py in generating representative features for time series data. These datasets included accelerometer and gyroscope data collected from various body locations, encompassing a diverse range of activities and events relevant to rehabilitation, such as ADLs,

[1] TIFEX-Py repository: https://github.com/mehdieji/tifex-py.

[2] TIFEX-Py initial release archive: https://doi.org/10.5905/ethz-1007-861.

physical exercises, and fall-related events. ADLs include sitting, standing, lying supine, lying on the side, stair climbing, walking, jogging, running, cycling, rowing, ironing, vacuuming, watching television, working on a computer, driving, and folding laundry. Recreational and sports activities include playing basketball, playing soccer, and exercises such as trunk twisting and forward bending. Fall-related events involve falling backward from standing, falling backward while seated, falls with protective strategies, falling forward, and lateral falls to the right or left. Additional scenarios include syncope (loss of consciousness), collisions with obstacles during falls, and wheelchair propulsion. Table I summarizes the datasets used in this study.

C. Pre-processing & Feature Extraction

Accelerometer and gyroscope time series data from all datasets were processed using a 5th-order Butterworth low-pass filter with a cut-off frequency of 10Hz [3]. The filtered time series were then resampled to 20Hz to reduce computational complexity. The pre-processed time series data were segmented using a sliding window approach. Based on the evaluation of SOTA methods across the datasets, optimal window sizes ranged from 1s to 10s. To ensure comparability with SOTA, this study utilized three window sizes: 2s, 5s, and 10s, with sliding windows overlapping by 20%, 70%, and 85%, respectively, to ensure a comparable number of resulting windowed datapoints, enabling fair comparisons between different window sizes. The `TIFEX-Py` default features (detailed on the repository) were extracted for each windowed segment. The concatenated features from all time series within a segment constituted the feature space input to the model.

D. Experiments & Evaluation

The feature-space datapoints were used to train and evaluate an ML model. This study employed an XGBoost (XGB) model [51] due to its proven effectiveness in feature selection and HAR performance [3]. The evaluation used a k-fold cross-validation (CV) approach with two splitting strategies based on the literature: 1) random split and 2) stratified by subjects [7]. The value of k was set to 10, or 5 when the number of subjects in the dataset was insufficient for 10 folds. In this study, no hyper-parameter tuning was performed, and the default parameters of the XGB model and `TIFEX-Py` were used. Classification metrics [52], including accuracy, balanced accuracy, precision, recall, and F1-score, were calculated for each fold and averaged across all folds.

Under both splitting strategies, experiments were conducted for three window sizes (2s, 5s, and 10s). The results were compared against AutoFE- and ManFE-based SOTA benchmarks, considering all studies that utilized k-fold cross-validation. However, only the highest reported performance for each dataset is reported in this paper. The comparison is fair as it follows similar evaluation metrics, including cross-validation and window size. By centering the evaluation on classification performance, this study provides a direct assessment of `TIFEX-Py`'s effectiveness in time-series representation. Notably, if an XGB model, even without hyperparameter tuning, achieves performance comparable to or surpassing existing SOTA benchmarks, it highlights the strength of `TIFEX-Py`'s feature space in capturing meaningful patterns for classification.

III. Results & Discussion

Fig. 2 presents the mean and standard deviation (SD) of classification metrics across all datasets and window sizes (window size of 10s was not possible for REALDISP due to its provided length of activities), evaluated using CV with randomly shuffled splits, compared to SOTA benchmarks (where available) with similar splitting strategy. Similarly, Fig. 3 shows the results for the subject-stratified split CV.

In both figures, comparisons with SOTA were conducted separately for each classification metric, as different studies report only a subset of these metrics. For each metric, the highest reported benchmark from SOTA was used for comparison. Where SOTA values were unavailable for specific metrics or datasets, results are marked as N/A. A review of SOTA performance reveals no clear advantage between AutoFE- and ManFe-based methods, supporting the effectiveness of manual feature extraction in achieving competitive results compared to automated feature learning.

Examining both random and subject-stratified split results shows that larger window sizes generally improve performance across most datasets. This improvement may result from the richer information and enhanced spectral representation provided by larger windows. However, DSADS and MHEALTH in the subject-stratified setting deviate from this trend, indicating that optimal window size selection might depend on activity types and inter-subject variability in activity durations.

For random splits in (Fig. 2), where the test subjects' data is partially used for training the model, our pipeline consistently outperforms or matches SOTA across all datasets and classification metrics, achieving mean values close to 100% for all metrics. This is particularly valuable for cases where the model needs to be adapted to new subjects, by training partially on the new subjects' movement data (adaptation data). Moreover, the low SD values indicate the robustness and consistency of the feature set combined with the XGB model, when the model is provided with adaptation data for the test subjects.

In contrast, the subject-stratified results in Fig. 3 (with no adaptation data for test subjects), generally underperform compared to the random split results, a trend also observed in the corresponding SOTA results. This is expected, as the subject-stratified setup introduces a domain shift due to subject-specific variability. Furthermore, the higher SD values for subject-stratified metrics highlight the challenges in achieving robust performance for completely unseen subjects' data.

To evaluate the contribution of different feature extraction methods, we computed feature importance scores output by XGB classifier across 11 datasets. For each dataset, the importance values were first averaged over folds and then normalized to account for scale differences. By mapping

TABLE I

OVERVIEW OF THE HAR DATASETS USED IN THIS STUDY, INCLUDING THE NUMBER OF ACTIVITIES, TIME SERIES, SUBJECTS, AND AVERAGE DURATION PER ACTIVITY. FOR EACH DATASET, THE HIGHEST-PERFORMING SOTA BENCHMARKS WERE IDENTIFIED BY REVIEWING ALL PUBLISHED STUDIES THAT UTILIZED THE DATASET. WHILE ONLY THE TOP-PERFORMING METHODS ARE REPORTED, A BROADER RANGE OF APPROACHES WAS CONSIDERED.

Dataset	No. Activities	No. Time series	No. Subjects	Avg. Duration per Activity (s)	Benchmark ManFE SOTA Model	Benchmark AutoFE SOTA Model
DSADS [14]	19	30	8	2400	SVM, RF [8]	MLP, Bi-GRU, MBi-GRU [8], [15], [16]
HHAR [17]	6	6	9	27882	k-NN, SVM [10], [17]	BiGRU, DeepConvLSTM [18], [19]
MHEALTH [20]	12	15	10	571	RF, XGB, LGBM [8], [21], [22]	CNN, CNN-LSTM [5], [8], [22]–[24]
MotionSense [25]	6	6	24	4709	RF, XGB [26], [27]	CNN-LSTM, CNN-FCM-LSTM [27]–[29]
PAMAP2 [30]	12	18	9	1619	SVM, RF [8], [31]	Conv2D, Self-Att, MLP [8], [32]
REALDISP [33]	33	54	17	431	RF [11]	-
RealWorld [34]	8	6	15	57012	RF, k-NN [34]–[37]	HMGAN, DeepConvLSTM+LLM, LSTM [34]–[39]
UniMiBSHAR [40]	9	3	30	1046	MBoss, RF [9], [41]	PCNN-Transformer, ResNet [6], [42], [43]
USC-HAD [44]	12	6	14	2343	RF [35]	ResNet, DeepConvLSTM + LLM [5], [45], [46]
WARD [47]	13	25	20	2208	-	-
WISDM [48]	6	3	36	15628	RF [7]	LSTM-CNN, ResNet, Bi-GRU [5], [43], [49], [50]

individual features to their corresponding extraction methods, we aggregated these normalized scores to obtain a representative importance for each method. The methods were ranked based on their mean normalized importance across datasets. The top 100 methods were selected for further analysis. As shown in Fig. 4, we used boxplots to display the distribution of importance scores: the upper subplot shows the top 50 methods, while the lower subplot shows those ranked 51–100. The boxplots illustrate not only the median importance for each method but also the variability across different datasets and iterations. A Kruskal–Wallis test revealed statistically significant differences in the distributions of importance scores (H = [H-statistic], p = [p-value]) across datasets. This figure also provides an example of useful feature extraction methods for HAR tasks. The ranking highlights that effective features come from diverse domains, including fractal features such as Higuchi's fractal dimension, which captures the complexity of signals, amplitude-based features like minimum and maximum values, statistical features such as mean and variance, and other features, including autocorrelation, spectral characteristics derived from Fourier analysis, and wavelet-based features. A key takeaway from these results is that no single feature extraction method is universally optimal. Instead, different datasets or modalities benefit from different feature sets, emphasizing the need for dataset-specific feature selection.

It is important to note that this study did not include hyper-parameter tuning or feature selection based on unseen subjects' data, which could further improve performance in this setting. Despite this limitation, the results confirm that a comprehensive feature extraction approach, as made possible by `TIFEX-Py`, when combined with an effective feature selection strategy, leads to classification performance that is comparable to SOTA methods. However, it is important to note that the comparison with SOTA methods in this study is limited to those previously evaluated on the 11 selected datasets, and the evaluation metrics reported in SOTA studies. A more comprehensive analysis could extend beyond these datasets to include a broader range of existing SOTA approaches, also ensuring identical CV splits of data among all approaches. This would enable a more exhaustive comparison between SOTA methods and the ManFE-based approach leveraging `TIFEX-Py`, providing deeper insights into its generalizability and effectiveness across diverse HAR tasks.

IV. CONCLUSION

This paper introduced `TIFEX-Py`, the most extensive Python toolbox for time series feature extraction, specifically designed to support HAR applications in healthcare and rehabilitation. `TIFEX-Py` enables researchers to extract a diverse set of informative features across statistical, amplitude, spectral, and time-frequency domains. This comprehensive feature space allows for the development of robust and efficient HAR systems, capable of matching or surpassing SOTA automated feature learning approaches, such as DL models. In rehabilitation, the use of handcrafted features enhances interpretability, providing clinicians with more explainable insights into movement patterns from wearable sensors. Such insights can aid in optimizing rehabilitation plans and improving patient outcomes. Future work will focus on expanding `TIFEX-Py` by integrating feature selection techniques and predefined feature extraction settings. These enhancements will further streamline the analysis pipeline and strengthen its applicability in healthcare and rehabilitation.

ACKNOWLEDGMENT

This study was partially funded by the Schweizer Paraplegiker Stiftung (SPS) and the ETH Zürich Foundation through the 2021-HS-348 ETH-SPS Digital Transformation in Personalized Healthcare for SCI individuals. The authors would also like to thank Kang Wang and Amelie Schopper for their valuable input and assistance during this research.

REFERENCES

[1] L. Schrader, A. Vargas Toro, S. Konietzny *et al.*, "Advanced sensing and human activity recognition in early intervention and rehabilitation of elderly people," *Population Ageing*, vol. 13, pp. 139–165, 2020. [Online]. Available: https://doi.org/10.1007/s12062-020-09260-z

[2] L. Bibbò and M. M. B. R. Vellasco, Eds., *Human Activity Recognition (HAR) in Healthcare*. MDPI, 2024.

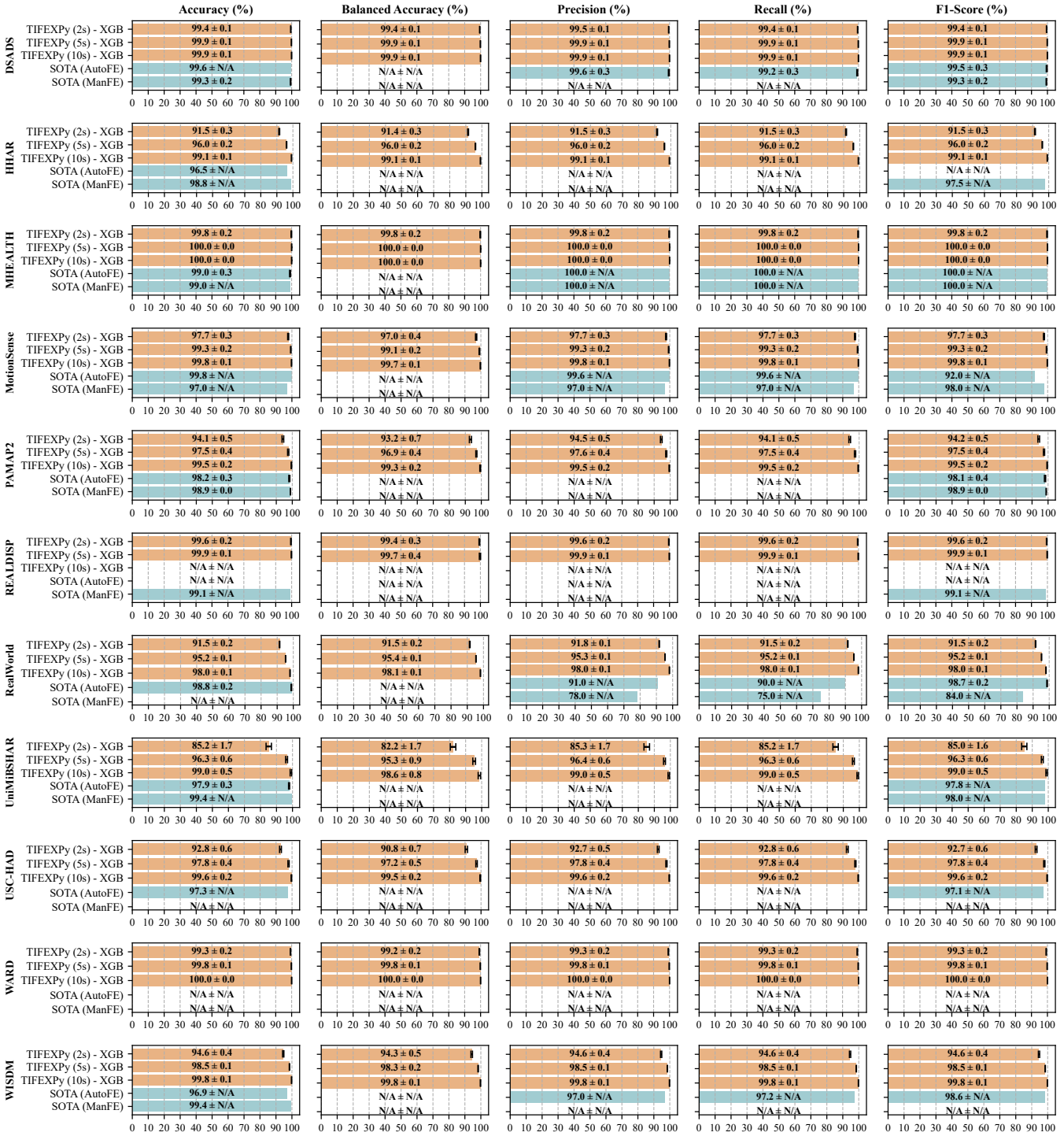


Fig. 2. Mean values (± (SD) where available) of classification metrics — Accuracy, Balanced Accuracy, Precision, Recall, and F1-score — obtained from a k-fold cross-validation pipeline with **random splits**. Metrics are reported for each dataset and window size (2s, 5s, and 10s) and compared against AutoFE- and ManFE-based SOTA benchmarks: DSADS [15], [16] (AutoFE) and [8] (ManFE); HHAR [18] (AutoFE) and [10], [17] (ManFE); MHEALTH [5], [22] (AutoFE) and [8], [22] (ManFE); MotionSense [27]–[29] (AutoFE) and [27] (ManFE); PAMAP2 [8] (AutoFE & ManFE); REALDISP [11] (ManFE); RealWorld [34], [36], [37] (AutoFE & ManFE); UniMiBSHAR [42] (AutoFE) and [9], [41] (ManFE); USC-HAD [45] (AutoFE); and WISDM [5], [43], [50] (AutoFE) and [7] (ManFE). Missing metrics are reported as N/A.

[3] M. Ejtehadi, S. Amrein, I. E. Hoogland, R. Riener, and D. Paez-Granados, "Learning activities of daily living from unobtrusive multimodal wearables: Towards monitoring outpatient rehabilitation," in *2023 International Conference on Rehabilitation Robotics (ICORR)*, 2023, pp. 1–6.

[4] F. Serpush, M. B. Menhaj, B. Masoumi, and B. Karasfi, "Wearable

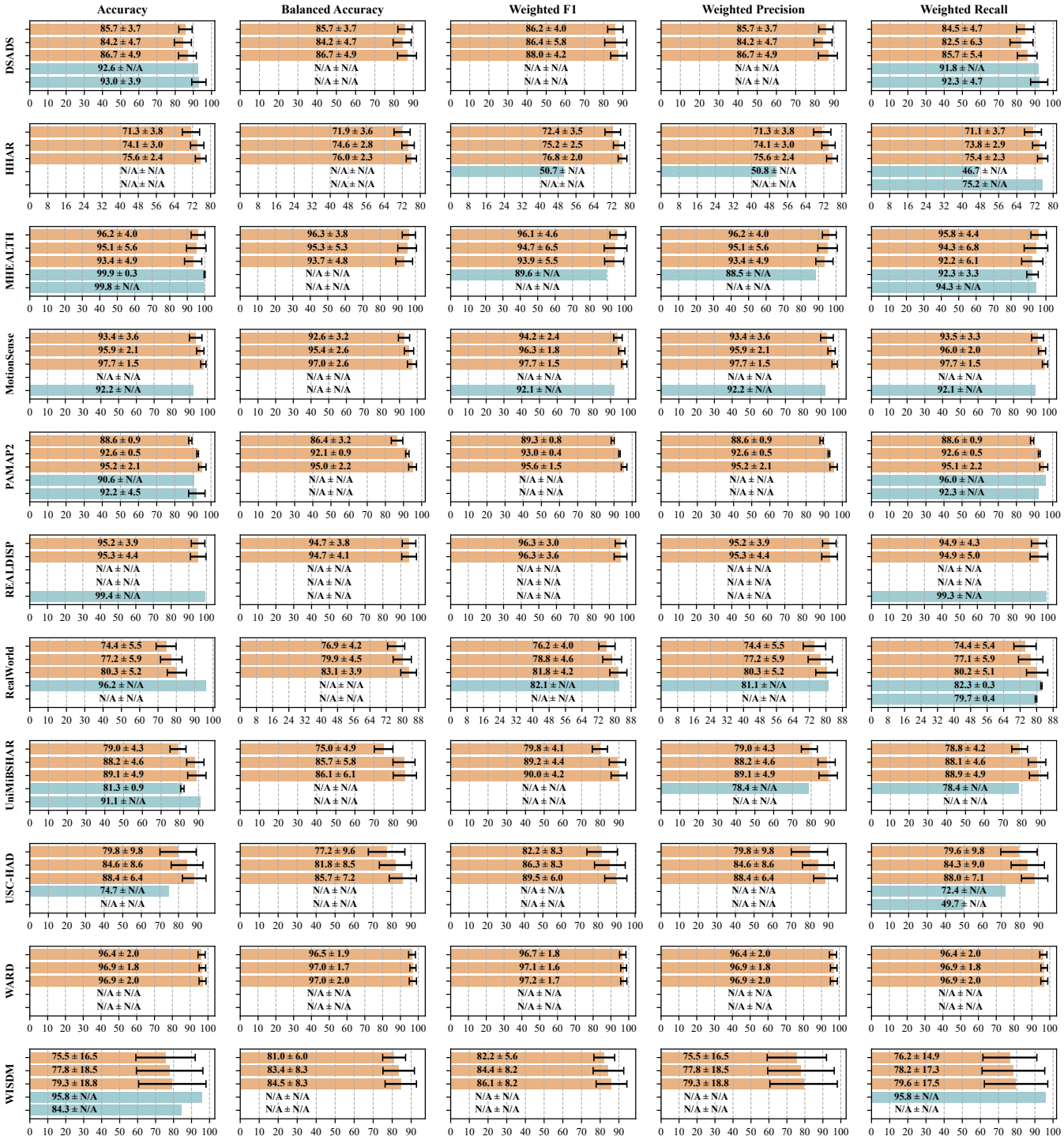


Fig. 3. Mean values (± (SD) where available) of classification metrics — Accuracy, Balanced Accuracy, Precision, Recall, and F1-score — obtained from a k-fold cross-validation pipeline with **subject-stratified splits**. Metrics are reported for each dataset and window size (2s, 5s, and 10s) and compared against AutoFE- and ManFE-based SOTA benchmarks: DSADS [8] (AutoFE & ManFE); HHAR [19] (AutoFE) and [17] (ManFE); MHEALTH [8], [23], [24] (AutoFE) and [8], [21] (ManFE); MotionSense [26] (ManFE); PAMAP2 [8], [32] (AutoFE) and [8], [31] (ManFE); REALDISP [11] (ManFE); RealWorld [35], [38], [39] (AutoFE) and [35] (ManFE); UniMiBSHAR [6], [43] (AutoFE) and [9] (ManFE); USC-HAD [5], [46] (AutoFE) and [35] (ManFE); and WISDM [49] (AutoFE - no CV) and [7] (ManFE). Missing metrics are reported as N/A.

sensor-based human activity recognition in the smart healthcare system," *Computational Intelligence and Neuroscience*, vol. 2022, no. 1, p. 1391906, 2022. [Online]. Available: https://onlinelibrary.wiley.com/doi/abs/10.1155/2022/1391906

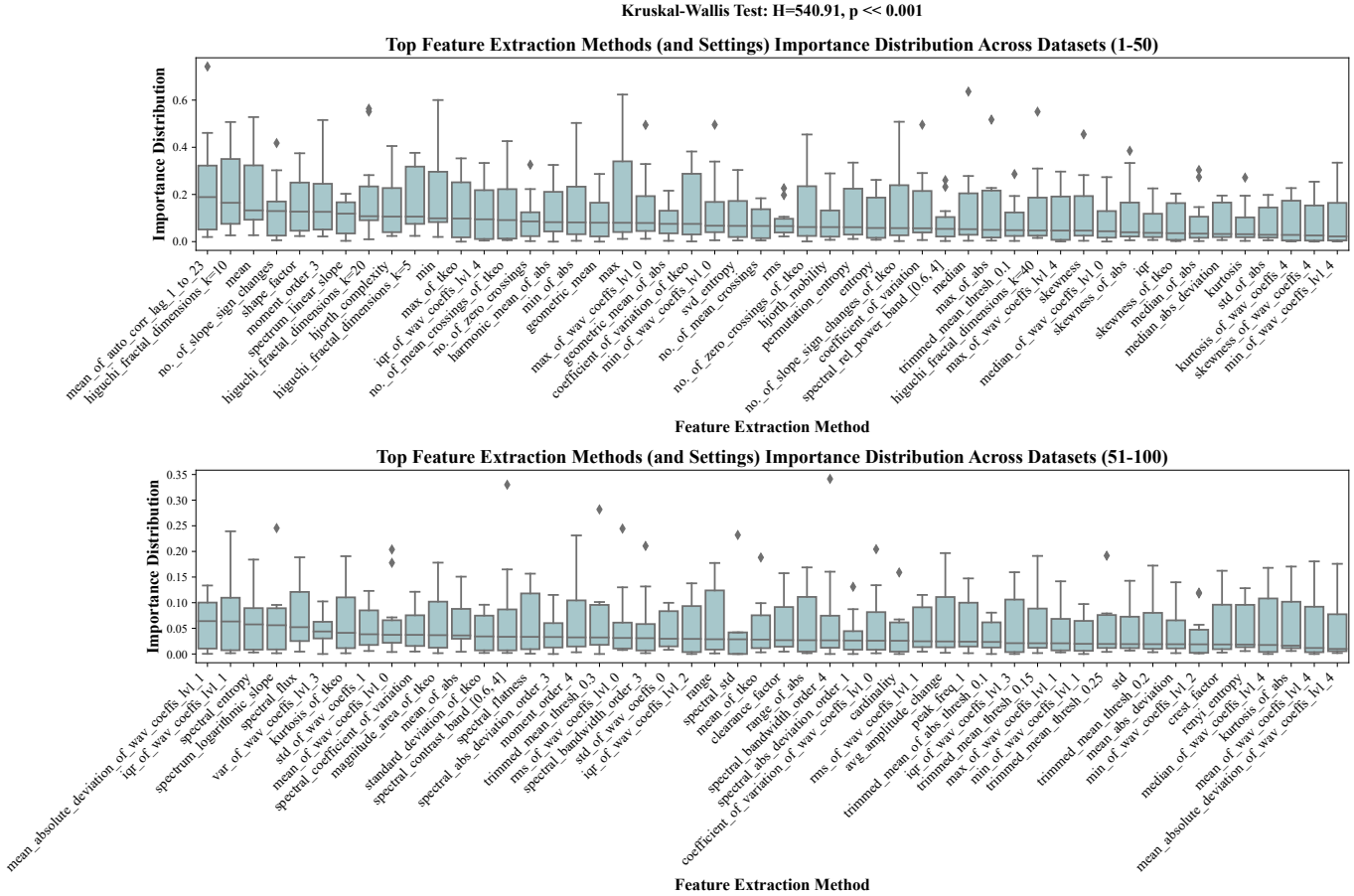


Fig. 4. Boxplot distributions of normalized feature importance scores for feature extraction methods aggregated across 11 datasets. The top 100 methods (ranked by their mean normalized importance) are shown, with the upper subplot displaying the top 50 methods and the lower subplot displaying those ranked 51–100. Each boxplot summarizes the median, interquartile range, and variability of the importance scores computed over 25 training iterations. A Kruskal–Wallis test confirmed significant differences among the methods (H = [H-statistic], p = [p-value]), indicating that the choice of feature extraction method substantially influences model performance.

[5] R. Abdel-Salam, R. Mostafa, and M. Hadhood, *Human Activity Recognition Using Wearable Sensors: Review, Challenges, Evaluation Benchmark*. Springer Singapore, 2021, p. 1–15.

[6] J. Yu, L. Zhang, D. Cheng, W. Huang, H. Wu, and A. Song, "Improving human activity recognition with wearable sensors through bee: Leveraging early exit and gradient boosting," *IEEE Transactions on Neural Systems and Rehabilitation Engineering*, vol. 32, pp. 3452–3464, 2024.

[7] H. Bragança, J. G. Colonna, H. A. B. F. Oliveira, and E. Souto, "How validation methodology influences human activity recognition mobile systems," *Sensors*, vol. 22, no. 6, 2022. [Online]. Available: https://www.mdpi.com/1424-8220/22/6/2360

[8] Z. Yang, M. Qu, Y. Pan, and R. Huan, "Comparing cross-subject performance on human activities recognition using learning models," *IEEE Access*, vol. 10, pp. 95 179–95 196, 2022.

[9] M. H. Khan, H. Shafiq, M. S. Farid, and M. Grzegorzek, "Encoding human activities using multimodal wearable sensory data," *Expert Systems with Applications*, vol. 261, p. 125564, 2025. [Online]. Available: https://www.sciencedirect.com/science/article/pii/S095741742402431X

[10] M. Bennasar, B. A. Price, D. Gooch, A. K. Bandara, and B. Nuseibeh, "Significant features for human activity recognition using tri-axial accelerometers," *Sensors*, vol. 22, no. 19, 2022. [Online]. Available: https://www.mdpi.com/1424-8220/22/19/7482

[11] J. Zhu, R. San-Segundo, and J. M. Pardo, "Feature extraction for robust physical activity recognition," *Human-Centric Computing and Information Sciences*, vol. 7, p. 16, 2017. [Online]. Available: https://doi.org/10.1186/s13673-017-0097-2

[12] M. Barandas, D. Folgado, L. Fernandes, S. Santos, M. Abreu, P. Bota, H. Liu, T. Schultz, and H. Gamboa, "Tsfel: Time series feature extraction library," *SoftwareX*, vol. 11, p. 100456, 2020. [Online]. Available: https://www.sciencedirect.com/science/article/pii/S2352711020300017

[13] M. Christ, N. Braun, J. Neuffer, and A. W. Kempa-Liehr, "Time series feature extraction on basis of scalable hypothesis tests (tsfresh – a python package)," *Neurocomputing*, vol. 307, pp. 72–77, 2018. [Online]. Available: https://www.sciencedirect.com/science/article/pii/S0925231218304843

[14] B. Barshan and M. C. Yüksek, "Recognizing daily and sports activities in two open source machine learning environments using body-worn sensor units," *The Computer Journal*, vol. 57, no. 11, pp. 1649–1667, 2014.

[15] S. Mekruksavanich and A. Jitpattanakul, "Multimodal wearable sensing for sport-related activity recognition using deep learning networks," *Journal of Advances in Information Technology*, vol. 13, no. 2, pp. 132–138, April 2022.

[16] A. J. Sakorn Mekruksavanich, "Sport-related activity recognition from wearable sensors using bidirectional gru network," *Intelligent Automation & Soft Computing*, vol. 34, no. 3, pp. 1907–1925, 2022. [Online]. Available: http://www.techscience.com/iasc/v34n3/47942

[17] A. Stisen, H. Blunck, S. Bhattacharya, T. S. Prentow, M. B. Kjærgaard, A. Dey, T. Sonne, and M. M. Jensen, "Smart devices are different: Assessing and mitigatingmobile sensing heterogeneities for activity recognition," in *Proceedings of the 13th ACM Conference on Embedded*

Networked Sensor Systems, ser. SenSys '15. New York, NY, USA: Association for Computing Machinery, 2015, p. 127–140. [Online]. Available: https://doi.org/10.1145/2809695.2809718

[18] S. Mekruksavanich, P. Jantawong, N. Hnoohom, and A. Jitpattanakul, "Heterogeneous recognition of human activity with cnn and rnn-based networks using smartphone and smartwatch sensors," in *2022 3rd International Conference on Big Data Analytics and Practices (IBDAP)*, 2022, pp. 21–26.

[19] M. Bock, A. Hölzemann, M. Moeller, and K. Van Laerhoven, "Improving deep learning for har with shallow lstms," in *2021 International Symposium on Wearable Computers*, ser. UbiComp '21. ACM, Sep. 2021. [Online]. Available: http://dx.doi.org/10.1145/3460421.3480419

[20] O. Banos, R. Garcia, J. A. Holgado-Terriza, M. Damas, H. Pomares, I. Rojas, A. Saez, and C. Villalonga, "mhealthdroid: A novel framework for agile development of mobile health applications," in *Ambient Assisted Living and Daily Activities*, L. Pecchia, L. L. Chen, C. Nugent, and J. Bravo, Eds. Cham: Springer International Publishing, 2014, pp. 91–98.

[21] E. Zdravevski, P. Lameski, V. Trajkovik, A. Kulakov, I. Chorbev, R. Goleva, N. Pombo, and N. Garcia, "Improving activity recognition accuracy in ambient-assisted living systems by automated feature engineering," *IEEE Access*, vol. 5, pp. 5262–5280, 2017.

[22] N. A. Choudhury and B. Soni, "In-depth analysis of design & development for sensor-based human activity recognition system," *Multimedia Tools and Applications*, vol. 83, pp. 73 233–73 272, 2024. [Online]. Available: https://doi.org/10.1007/s11042-023-16423-5

[23] D. M. Burns and C. M. Whyne, "Personalized activity recognition with deep triplet embeddings," 2020. [Online]. Available: https://arxiv.org/abs/2001.05517

[24] D. Gholamiangonabadi, N. Kiselov, and K. Grolinger, "Deep neural networks for human activity recognition with wearable sensors: Leave-one-subject-out cross-validation for model selection," *IEEE Access*, vol. 8, pp. 133 982–133 994, 2020.

[25] M. Malekzadeh, R. G. Clegg, A. Cavallaro, and H. Haddadi, "Protecting sensory data against sensitive inferences," in *Proceedings of the 1st Workshop on Privacy by Design in Distributed Systems*, ser. W-P2DS'18. New York, NY, USA: Association for Computing Machinery, 2018. [Online]. Available: https://doi.org/10.1145/3195258.3195260

[26] S. B. u. d. Tahir, A. B. Dogar, R. Fatima, A. Yasin, M. Shafiq, J. A. Khan, M. Assam, A. Mohamed, and E.-A. Attia, "Stochastic recognition of human physical activities via augmented feature descriptors and random forest model," *Sensors*, vol. 22, no. 17, 2022. [Online]. Available: https://www.mdpi.com/1424-8220/22/17/6632

[27] N. A. Choudhury, S. Moulik, and D. S. Roy, "Physique-based human activity recognition using ensemble learning and smartphone sensors," *IEEE Sensors Journal*, vol. 21, no. 15, pp. 16 852–16 860, 2021.

[28] N. A. Choudhury and B. Soni, "An adaptive batch size-based-cnn-lstm framework for human activity recognition in uncontrolled environment," *IEEE Transactions on Industrial Informatics*, vol. 19, no. 10, pp. 10 379–10 387, 2023.

[29] R. Bodhe, S. Sivakumar, G. Sakarkar *et al.*, "Outdoor activity classification using smartphone based inertial sensor measurements," *Multimedia Tools and Applications*, vol. 83, pp. 76 963–76 989, 2024. [Online]. Available: https://doi.org/10.1007/s11042-024-18599-w

[30] A. Reiss and D. Stricker, "Introducing a new benchmarked dataset for activity monitoring," in *2012 16th International Symposium on Wearable Computers*, 2012, pp. 108–109.

[31] A. K. Chowdhury, D. Tjondronegoro, V. Chandran, and S. G. Trost, "Physical activity recognition using posterior-adapted class-based fusion of multiaccelerometer data," *IEEE Journal of Biomedical and Health Informatics*, vol. 22, no. 3, pp. 678–685, 2018.

[32] S. Mahmud, M. T. H. Tonmoy, K. K. Bhaumik, A. K. M. M. Rahman, M. A. Amin, M. Shoyaib, M. A. H. Khan, and A. A. Ali, "Human activity recognition from wearable sensor data using self-attention," 2020. [Online]. Available: https://arxiv.org/abs/2003.09018

[33] O. Baños, M. Damas, H. Pomares, I. Rojas, M. A. Tóth, and O. Amft, "A benchmark dataset to evaluate sensor displacement in activity recognition," in *Proceedings of the 2012 ACM Conference on Ubiquitous Computing*, ser. UbiComp '12. New York, NY, USA: Association for Computing Machinery, 2012, p. 1026–1035. [Online]. Available: https://doi.org/10.1145/2370216.2370437

[34] T. Sztyler and H. Stuckenschmidt, "On-body localization of wearable devices: An investigation of position-aware activity recognition," in *2016 IEEE International Conference on Pervasive Computing and Communications (PerCom)*, 2016, pp. 1–9.

[35] Z. Leng, A. Bhattacharjee, H. Rajasekhar, L. Zhang, E. Bruda, H. Kwon, and T. Plötz, "Imugpt 2.0: Language-based cross modality transfer for sensor-based human activity recognition," 2024. [Online]. Available: https://arxiv.org/abs/2402.01049

[36] U. Azmat, Y. Y. Ghadi, T. a. Shloul, S. A. Alsuhibany, A. Jalal, and J. Park, "Smartphone sensor-based human locomotion surveillance system using multilayer perceptron," *Applied Sciences*, vol. 12, no. 5, 2022. [Online]. Available: https://www.mdpi.com/2076-3417/12/5/2550

[37] L. Chen, R. Hu, M. Wu, and X. Zhou, "Hmgan: A hierarchical multi-modal generative adversarial network model for wearable human activity recognition," *Proc. ACM Interact. Mob. Wearable Ubiquitous Technol.*, vol. 7, no. 3, Sep. 2023. [Online]. Available: https://doi.org/10.1145/3610909

[38] T. Huynh-The, C.-H. Hua, N. A. Tu, and D.-S. Kim, "Physical activity recognition with statistical-deep fusion model using multiple sensory data for smart health," *IEEE Internet of Things Journal*, vol. 8, no. 3, pp. 1533–1543, 2021.

[39] M. Bock, A. Hoelzemann, M. Moeller, and K. Van Laerhoven, "Investigating (re)current state-of-the-art in human activity recognition datasets," *Frontiers in Computer Science*, vol. 4, p. 924954, 2022. [Online]. Available: https://doi.org/10.3389/fcomp.2022.924954

[40] D. Micucci, M. Mobilio, and P. Napoletano, "Unimib shar: A dataset for human activity recognition using acceleration data from smartphones," *Applied Sciences*, vol. 7, no. 10, 2017. [Online]. Available: https://www.mdpi.com/2076-3417/7/10/1101

[41] K. G. Montero Quispe, W. Sousa Lima, D. Macêdo Batista, and E. Souto, "Mboss: A symbolic representation of human activity recognition using mobile sensors," *Sensors*, vol. 18, no. 12, 2018. [Online]. Available: https://www.mdpi.com/1424-8220/18/12/4354

[42] M. A. Al-qaness, A. Dahou, M. Abd Elaziz, and A. M. Helmi, "Human activity recognition and fall detection using convolutional neural network and transformer-based architecture," *Biomedical Signal Processing and Control*, vol. 95, p. 106412, 2024. [Online]. Available: https://www.sciencedirect.com/science/article/pii/S1746809424004701

[43] S. Wang, Y. Sun, Y. Sha, G. Yang, D. Cheng, L. Zhang, H. Wu, and A. Song, "Robust human activity recognition via wearable sensors using dynamic gaussian kernel learning," *IEEE Sensors Journal*, vol. 24, no. 6, pp. 8265–8280, 2024.

[44] M. Zhang and A. A. Sawchuk, "Usc-had: a daily activity dataset for ubiquitous activity recognition using wearable sensors," in *Proceedings of the 2012 ACM Conference on Ubiquitous Computing*, ser. UbiComp '12. New York, NY, USA: Association for Computing Machinery, 2012, p. 1036–1043. [Online]. Available: https://doi.org/10.1145/2370216.2370438

[45] M. Yao, L. Zhang, D. Cheng, L. Qin, X. Liu, Z. Fu, H. Wu, and A. Song, "Revisiting large-kernel cnn design via structural re-parameterization for sensor-based human activity recognition," *IEEE Sensors Journal*, vol. 24, no. 8, pp. 12 863–12 876, 2024.

[46] A. Bolatov, A. Yessenbayeva, and A. Yazici, "Glula: Linear attention-based model for efficient human activity recognition from wearable sensors," *Wearable Technologies*, vol. 5, p. e10, 2024.

[47] A. Yang, R. Jafari, S. Sastry, and R. Bajcsy, "Distributed recognition of human actions using wearable motion sensor networks," *JAISE*, vol. 1, pp. 103–115, 01 2009.

[48] J. R. Kwapisz, G. M. Weiss, and S. A. Moore, "Activity recognition using cell phone accelerometers," *SIGKDD Explor. Newsl.*, vol. 12, no. 2, p. 74–82, mar 2011. [Online]. Available: https://doi.org/10.1145/1964897.1964918

[49] K. Xia, J. Huang, and H. Wang, "Lstm-cnn architecture for human activity recognition," *IEEE Access*, vol. 8, pp. 56 855–56 866, 2020.

[50] L. Tong, H. Ma, Q. Lin, J. He, and L. Peng, "A novel deep learning bi-gru-i model for real-time human activity recognition using inertial sensors," *IEEE Sensors Journal*, vol. 22, no. 6, pp. 6164–6174, 2022.

[51] T. Chen and C. Guestrin, "Xgboost: A scalable tree boosting system," *CoRR*, vol. abs/1603.02754, 2016. [Online]. Available: http://arxiv.org/abs/1603.02754

[52] M. Grandini, E. Bagli, and G. Visani, "Metrics for multi-class classification: an overview," 2020. [Online]. Available: https://arxiv.org/abs/2008.05756

Adaptive Negative Damping Control for User-Dependent Multi-Terrain Walking Assistance with a Hip Exoskeleton

Giulia Ramella[1,2], Auke Ijspeert[2], and Mohamed Bouri[1,3]

***Abstract*— Hip exoskeletons are known for their versatility in assisting users across varied scenarios. However, current assistive strategies often lack the flexibility to accommodate for individual walking patterns and adapt to diverse locomotion environments. In this work, we present a novel control strategy that adapts the mechanical impedance of the human-exoskeleton system. We design the hip assistive torques as an adaptive virtual negative damping, which is able to inject energy into the system while allowing the users to remain in control and contribute voluntarily to the movements. Experiments with five healthy subjects demonstrate that our controller reduces the metabolic cost of walking compared to free walking (average reduction of 7.2%), and it preserves the lower-limbs kinematics. Additionally, our method achieves minimal power losses from the exoskeleton across the entire gait cycle (less than 2% negative mechanical power out of the total power), ensuring synchronized action with the users' movements. Moreover, we use Bayesian Optimization to adapt the assistance strength and allow for seamless adaptation and transitions across multi-terrain environments. Our strategy achieves efficient power transmission under all conditions. Our approach demonstrates an individualized, adaptable, and straightforward controller for hip exoskeletons, advancing the development of viable, adaptive, and user-dependent control laws.**

I. Introduction

Hip exoskeletons for walking assistance are gaining popularity for their versatility to assist users across diverse contexts. Initially designed for rehabilitation purposes, these wearable devices are now increasingly used to assist healthy users. In recent years, there have been significant advancements, but developing control strategies that seamlessly synchronize with users remains a major challenge [1]. This is particularly critical with healthy users, where the exoskeleton's assistive actions must align with voluntary movements and individual intentions. To achieve a synchronized assistance, control algorithms must account for individual gait patterns, terrain variability, and diverse walking styles [2].

Multiple control approaches have been proposed to achieve a compliant human-exoskeleton interaction. Adaptive oscillators [3] and fixed-shape torque profiles [4] are effective, but do not address individual walking patterns. Human-in-the-loop optimizations achieve highly personalized control [5], but they involve computationally-intensive and time-demanding procedures. Energy-shaping methods [6] are precise and effective, but demand complex modeling of the system. Previously, researchers used the GEMS exoskeleton to implement a delayed output feedback control that relies on hip joint angular positions [7]. However, this approach requires manual tuning of delays, as these signals do not naturally align with hip torques. Similarly, assisting users with estimated biological hip torques is a highly advanced technique but requires tuning of delay parameters [8]. Overall, further explorations are needed to address the following research question: how can a hip exoskeleton control strategy be designed to align the assistance with the wearer's voluntary movements while adapting to individual gait patterns across diverse terrains?



Fig. 1: The user-dependent and multi-terrain walking assistance with the hip exoskeleton eWalk. Participants walked on treadmill and in varied unstructured environments.

When designing control strategies, researchers widely agree on the importance of the positive mechanical power transmitted from the exoskeleton to the user [5], [7], [9]. To regulate the energy transfer, existing research has explored a virtual modification of the mechanical impedance of the human-exoskeleton system [10]–[12]. For instance, negative damping has been used to modulate the dynamic response of the human-exoskeleton system, while keeping the wearer in control of the movements [10], [11]. Knowing that damping naturally causes energy dissipation, providing

Giulia Ramella received funding from the European Union's Horizon 2020 research and innovation program under the Marie-Sklodowska-Curie Grant Agreement No. 945363.

[1] Giulia Ramella and Mohamed Bouri are with the REHAssist group, Ecole Polytechnique Federale de Lausanne (EPFL). giulia.ramella@epfl.ch

[2] Giulia Ramella and Auke Ijspeert are with the BioRobotics Laboratory, Ecole Polytechnique Federale de Lausanne (EPFL).

[3] Mohamed Bouri is with the TNE Laboratory, Institute of Neuro-X, Ecole Polytechnique Federale de Lausanne (EPFL).

negative damping can inject energy into the system. As damping is proportional to the joint velocities, the resulting assistance is inherently dependent on the wearer's motion. In theory, negative damping alone introduces positive feedback, risking instability and torque escalation. However, in the practical case of human-exoskeleton interaction, these issues are prevented thanks to pendulum dynamics, musculoskeletal damping, and torque limits. Preliminary implementations with a knee exoskeleton [10], [11] suggest that bounded negative damping holds great promise to provide partial assistance with wearable devices.

In this work, we design a negative damping control for the hip exoskeleton eWalk. With this approach, the exoskeleton torques assist wearers according to their own volitional movements. We experimentally evaluate the impact of our control strategy on users' walking energetics by comparing the assisted and the exoskeleton-free conditions. To assess the synchronization between the users' movements and the exoskeleton torques, we compute the transmitted mechanical powers. This quantity is defined as the product of the exoskeleton torque and the user's hip angular velocity, and positive powers indicate alignment between the users' movements and the assistive torques. Moreover, we measure the lower-limbs kinematics to analyze if the exoskeleton assistance preserves the natural walking movements.

Afterwards, we evaluate our controller's ability to assist users in unstructured environments (Figure 1). During multi-terrain locomotion, exoskeletons must dynamically adapt the assistance strength to meet varying demands across terrains [13]–[15]. Existing studies have proposed terrain recognition algorithms based on the data from onboard sensors [16]–[18], but these methods are prone to misclassification. In contrast, we propose a Bayesian Optimization framework to adjust the assistance level to different scenarios (flat walking and stairs descending/ascending) relying only on the exoskeleton's kinematic signals observed over a defined time window.

In summary, we present a novel control approach that injects energy into the human-exoskeleton system. We design an adaptive virtual negative damping control, where the assistive torques are generated based on the users' hip kinematics. Compared to existing works, our algorithm encompasses both individualization and terrain adaptation, while maintaining a straightforward and versatile approach. The main contributions are: (i) the design of the hip assistive torque profile based on the wearer's volitional movements; (ii) an experimental evaluation of the efficacy of our control to reduce the metabolic cost of walking, while preserving individual walking kinematics; and (iii) a validation of the adaptability of our control across varied locomotion terrains.

The rest of this paper is organized as follows. In Section II we describe our algorithm for hip exoskeleton assistance, and the methodologies to validate our strategy. Section III presents the results and discussion for the experiments performed on a treadmill and on unstructured environments. Section IV presents the conclusions and the future directions of this study.

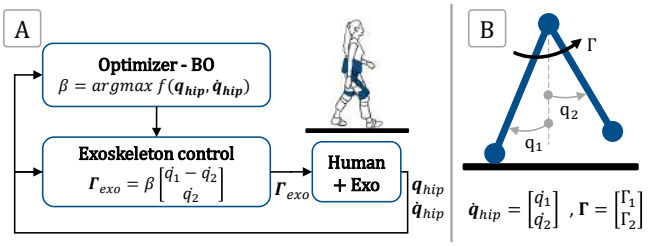


Fig. 2: (A) Schematic representation of our control framework. The torque profile is defined by a control law consisting of a Virtual Adaptive Negative Damping. The multiplicative coefficient (β) for the assistance strength is optimized with a Bayesian Optimization (BO). (B) Schematic representation of the compass-gait model and its main variables, where q_1 represents the hip angle of the stance leg, and q_2 the hip angle of the swing leg.

II. Methods

A. Assistive Control Law

We designed the torque profile provided by our hip exoskeleton eWalk as a virtual negative damping. This approach is able to inject energy into the system, while keeping the user in control of the movements [10], [11]. In order to apply the control action, a model for human locomotion is required. Although human walking has been described by diverse models of varied complexity [19], we opted for the simple compass-gait biped [20], where the legs are represented as rigid links connected at the hip joint. This approach has demonstrated a remarkable ability to capture fundamental characteristics of bipedal locomotion [21]–[24], the legs coupling [25], and the energy exchanges in human-exoskeleton interactions [6]. This method assumes no foot dynamics, and describes walking as a series of alternating swing and stance phases. At each heel-strike event, the stance and swing leg roles are switched between the feet.

The model's state variables consist of the hip joint positions and velocities for the stance and swing legs, denoted by q_1 and q_2 respectively ($\mathbf{q}_{hip} = [q_1; q_2]$). The hip input torques are defined as $\boldsymbol{\Gamma} = [\Gamma_1; \Gamma_2]$, as shown in Figure 2B. The control is implemented as the product of the coupling matrix $\mathbf{R} = [1 \;\; -1 \;; 0 \;\; 1]$ (inspired from [20]), and the user's hip joints angular velocity vector $\dot{\mathbf{q}}_{\mathbf{hip}}$ measured by the exoskeleton motor encoders at each sampling time. A damping factor β (Nms/rad) allows to modulate the strength of the assistive torques. The resulting the total expression is $\boldsymbol{\Gamma}_{\mathbf{exo}} = \beta \mathbf{R} \dot{\mathbf{q}}_{\mathbf{hip}}$ ("Exoskeleton control" in Figure 2A). The value of β is bounded to prevent the exoskeleton assistance from disrupting the movements or overpowering the users. The control torque is computed in real time at each sampling step by the exoskeleton's embedded controller.

At heel-strike, the swing leg becomes the new stance leg, causing a reset in the velocities and joint configuration. The coordinate change from before (-) to after (+) the heel-strike event is expressed as: $q^+ = [0\ 1; 1\ 0] q^\infty$. To detect the stance and swing leg, we analyzed the signs of the hip angular velocities as suggested in a previous study [26]. We avoided using joint angular positions to eliminate the ambiguity caused by the surjective mapping of joint angles to gait phases [1]. Instead, we relied on hip joint angular velocities that can differentiate the stance and swing legs based on their

opposite signs during continuous locomotion. We represented the hip flexion with positive increasing angles. The leg with hip extension (negative velocities), and counter-leg in flexion (positive velocities), was identified as q_1 (stance), and the other leg as q_2 (swing).

The exoskeleton assistive torques are designed to inject energy into the system, and the resulting total energy of the human-exoskeleton system can be expressed as $E_{tot} = E_{human} + E_{exo}$. By ensuring that E_{exo} remains bounded and lower than the human energy contribution, the exoskeleton assistance synchronizes with the user's walking cycle. Adjusting and limiting the assistive strength (β) allows the control to dynamically support natural cyclic motion without disrupting the user's gait.

In order to incorporate the hip angular velocities in the control law, we filtered the signals measured be the exoskeleton motors encoders, as suggested in previous research [7], [27]. Pilot testings were performed to define the cutoff frequency that could reduce the signal peaks while preserving the majority of its frequency components. A power-spectrum analysis guided our choice to filter joint velocities at $4Hz$. Filtering also ensures that quasi-static movements and static standing (with quasi-zero joint velocity) do not result in a jittery assistance, but keep the torque values close to zero.

B. Torque Amplitude Optimization

To modulate the assistance strength across varied locomotion scenario, we implemented a real-time optimization procedure to adapt the multiplicative coefficient β (where $\beta \in [1.0, 2.5]$, with bounds tuned experimentally). With the Optuna framework [28], [29], we developed a Bayesian Optimization algorithm based on features computed from the hip exoskeleton kinematics ("Optimizer - BO" in Figure 2A). Unlike traditional mapping approaches, this optimization framework enables iterative updates of the algorithm based on the system's status and conflicting objectives. Additionally, designing the optimization based solely on kinematic variables eliminates the need for complex terrain-recognition algorithms or continuous manual tuning of torque coefficients [17], [30].

Our real-time multi-objective optimization balances two objectives. On one hand, we need to increase the torque during larger hip range of motion (ROM, the difference between minimum and maximum measured hip angles), as in stair or slope ascending [31]. On the other hand, we want to limit the transmitted torque in case of increased movement jerkiness (where the jerk is computed as the derivative of the acceleration). The resulting objective is expressed as $f_{obj} = q_{rom} - \ddot{q}_{mean}$. At the end of a fixed 2 s observation window, the Bayesian Optimization maximizes the value of the kinematics-based objective function, providing as output the optimal value of β.

C. Experimental Protocol

Five healthy subjects volunteered to participate in the study (age: 29 ± 2.8 yrs old, height: 1.73 ± 0.10 m, weight: 65.8 ± 6.4 kg). The experimental procedures were approved by the human research ethics committee of Canton de Vaud (CER-VD) under the protocol number 2023-02305. Participants provided an informed consent before the experimental evaluation, and the study was conducted in compliance with the principles of the Declaration of Helsinki.

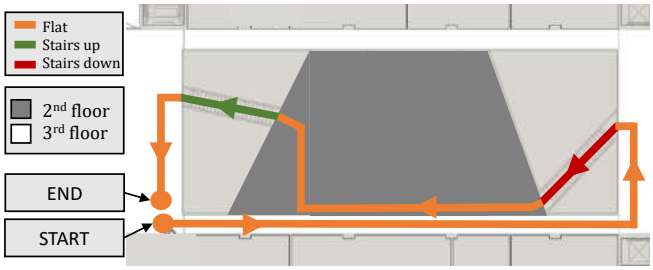


Fig. 3: Representation of the walking path for the varied terrain locomotion session (top view). The terrain consists of stairs (up and down), flat bouts, and changes of direction.

The experimental evaluation was divided into two sessions. Initially, we evaluated the performance of our controller in steady-state walking conditions on a treadmill. Participants were first familiarized with the exoskeleton assistance by walking with the device for 10 minutes on a treadmill. Then, they performed two 5-minute treadmill walking tests, one without the device and one with the exoskeleton assistance. Subjects walked at a fixed speed of $1.1\ m/s$, and the experimental conditions were proposed in a randomized order. In the assisted condition, the same value of $\beta = 2.3$ was used to facilitate intra-subject comparisons.

In a second session, we investigated the adaptability of our control in an unstructured environment. Participants walked with the assistive device in a varied terrain, consisting of flat sections, stairs ascending/descending, changes in direction, and variations in the walking speed. The duration of each segment was timed and kept consistent across participants, with the total duration set to 90 s. One of the buildings of EPFL was used for this scenario, and the walking path (from a top view) is represented in Figure 3.

D. Measurement Setup

In our study, we used the hip exoskeleton eWalk [14], an active hip orthosis developed in a collaboration between the BioRob-REHAssist group of EPFL and the company Sonceboz. This exoskeleton provides partial assistance during walking, with an actuated joint to assist hip flexion/extension and a passive degree of freedom for hip abduction to facilitate natural walking movements [32]. The version of the device used in this study weighs 4.4 kg, and it is attached to the user's body with a corset and two thigh attachments. eWalk is actuated by two DC servo motors (PowerSolutions, X8 Pro, maximum torque 32 Nm and reduction ration 1:9, China), and controlled by an embedded computer (BeagleBoneBlack, Texas Instruments, USA) running at 500 Hz.

To record the kinematic data of the lower limbs during walking, we used the portable motion capture system XSens (XSens, Movella, The Netherlands). The system has a custom interface to collect and process IMU data and to reconstruct the body movements. Data collection was performed at

$100Hz$, and the IMUs were calibrated for each participant according to the recommended procedure.

We measured the walking energetics in real-time through indirect calorimetry, by using the Q-NRG MAX metabolic monitoring device (COSMED Srl, Rome, Italy).

During the experiments, we used two separate computers. The first one was used to collect kinematic data in real-time with the XSens software. A second device was connected to the exoskeleton via Wi-Fi in order to monitor the exoskeleton data from a custom GUI. This second computer was also used to perform the optimization during the unstructured walking session.

E. Metrics

After the experiments, the collected data was processed in custom routines in MATLAB 2023b (The MathWorks, Natick, MA, USA). Before the analysis in MATLAB, XSens data was pre-processed in the custom software in order to reconstruct the walking kinematics of each user. We computed dedicated metrics for all participants, indicated as S1, S2, S3, S4, and S5. For treadmill walking trials, data was collected from the exoskeleton, XSens, and the indirect calorimetry device. For the walking session in the unstructured environment, we recorded data from the exoskeleton.

1) Exoskeleton data - treadmill: From the exoskeleton data, we extracted the applied torque profiles, the values of hip joint angular positions and velocities measured by the motor encoders, and the values from the inertial measurement unit on the exoskeleton corset. These kinematic signals were segmented into individual gait cycles with an algorithm developed in our laboratory [33]. These signals were averaged across gait cycles and between legs to derive the mean profiles for each participant. Finally, we computed the maximum torque value normalized by the weight of each user ($\frac{\Gamma_{exo,max}}{weight}$, in Nm/kg).

Power profiles were calculated by multiplying the joint angular velocities ((t), rad/s) by the torque applied by the exoskeleton ($\Gamma_{exo}(t)$, Nm), according to the formula $P(t) = \quad (t) \cdot \Gamma_{exo}(t)$, for $0 \leq t \leq T_{\text{gait cycle}}$. The resulting power profiles were averaged across gait cycles, and then normalized by each user's weight. We also evaluated the power transmission efficiency between the exoskeleton and the wearer. To this end, we computed the positive power, representing efficient energy transmission, and the negative power, an indicator of energy losses. To quantify power losses, we calculated the percentage of the negative power area relative to the total area under the power profiles.

2) Walking energetics data: To compute the metabolic energy expenditure, we integrated into the Weir equation [34] the values of oxygen and carbon dioxide measured by indirect calorimetry. For each treadmill trial, with and without the exoskeleton, we calculated the mean energy consumption during the final two minutes. Then, we subtracted the resting metabolic rate measured during the two minutes prior to the start of the experiment. This procedure allowed to isolate the activity-related energetic expenditure. Finally, we determined the percentage reduction in metabolic cost (MC) between the two experimental conditions as $\frac{(MC_{exo} \infty MC_{noexo})}{MC_{noexo}} * 100$.

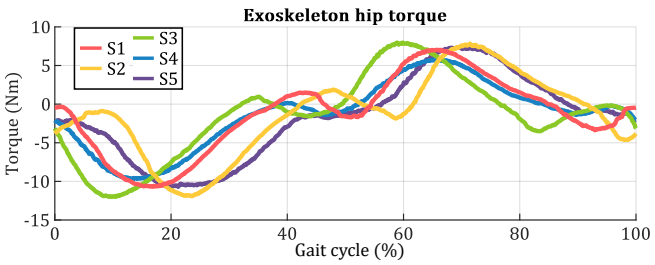


Fig. 4: Hip exoskeleton torque profiles resulting from our control strategy, for each participant to the experiment, when walking on the treadmill.

3) Kinematic data: Lower-limbs kinematic data was extracted from the XSens software after being processed to reconstruct individual movements. We extracted the vertical displacement of the center of mass (COM) and the flexion/extension angles of the hip joint. Then, we segmented the data using the heel-strike information of XSens, and computed the mean values for each subject. We also calculated the cadence ratio between exoskeleton-assisted and device-free walking conditions. Finally, we computed the ratio between the stance time and the swing time, and verified the statistical significance ($\alpha < 0.05$) between the two experimental conditions for each participant.

4) Exoskeleton data - unstructured terrain: When subjects walked in the unstructured environment, we recorded the applied torques, and the hip joint angular positions and velocities measured by the exoskeleton. From this data, we analyzed the torque profiles resulting from our optimization framework across the various walking conditions. To evaluate the efficiency of the power transmission, we calculated the negative power area (representing power losses) as a percentage of the total power area.

III. Results and Discussion

In our study, we successfully developed a hip exoskeleton control strategy that assists the wearers based on their volitional movements. The exoskeleton assistance adapts to individual gait patterns, and dynamically adjusts the support across various terrains. In this section, we first discuss the resulting user-specific hip torque assistive profiles. Then, we analyze the effectiveness of the assistive control strategy to reduce the walking energetics, while preserving individual kinematic patterns. Finally, we demonstrate the adaptability of the control framework to assist users in a variety of locomotion terrains.

1) Exoskeleton data - treadmill: We succeeded in generating exoskeleton hip torques to assist users during walking. The exoskeleton torques supported participants during both hip flexion and extension, with smooth transitions between gait cycles. Participants exhibited varied hip assistive torques profiles depending on their individual walking pattern and corresponding joints kinematics (Figure 4). The obtained torque profiles closely resemble the exoskeleton hip torques obtained with human-in-the-loop optimization techniques [5]. However, our approach did not require extensive tuning,

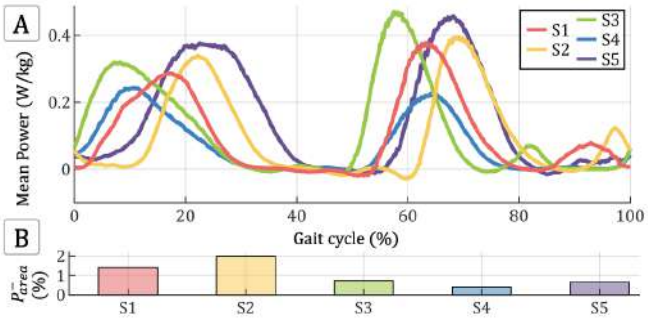


Fig. 5: (A) Power profiles calculated as the product of the hip exoskeleton torque and the hip joint angular velocities, for each participant. (B) Percentage of negative power area with respect to the total power area.

TABLE I: Metrics of our experiment.

Metric	*S1*	*S2*	*S3*	*S4*	*S5*
$\frac{(MC_{exo}-MC_{noexo})}{MC_{noexo}} * 100$ (%)	-5.6	-7.7	-3.9	-7.7	-11.0
$\frac{\Gamma_{exo,max}}{weight}$ ($\frac{Nm}{kg}$)	0.17	0.17	0.18	0.13	0.19
$\frac{Cadence_{exo}}{Cadence_{noexo}}$ ( )	1.00	1.04	1.01	1.02	0.97

as the torque curves were derived directly from the users' movements.

The peak torque timings varied between participants, but they were generally consistent with previous results in the literature [5], [15], [27], [35]. Most importantly, these timings were not manually adjusted for each participant. Instead, torque profiles were automatically synchronized with users' movements by incorporating joint angular velocities, thus the movements direction, into the control law. This is a crucial aspect because modifying the timing of assistive torques has been proven to affect the total power transferred from the exoskeleton to the user [5], [35], [36].

The power profiles shown in Figure 5A further emphasize the user-dependent nature of our control strategy. These profiles show peaks at different phases of the gait cycle, reflecting individual movements and torque profiles. Participants showed power profiles with peaks timings similar to the biological powers reported in the literature [37]. Conversely, the exoskeleton torque profiles appeared to be delayed compared to their biological counterparts [37], [38].

The power curves remained positive for most of the gait cycle, indicating that our control strategy remained aligned with users' movements. This efficient power transmission is further supported by the percentage of negative power remaining below 2% for all participants during the gait cycle (Figure 5B). Negative power indicates torques are not synchronized with the wearers' movements, therefore minimizing this value is essential to ensure seamless human-exoskeleton interaction [5], [7], [9], [35].

2) Walking energetics data: All participants exhibited reduced metabolic cost when walking with the exoskeleton against the condition without the device (Table I). In our experiments, we achieved an average reduction of $7.2 \pm 2.6\%$. This result demonstrates that the energy delivered into the human-exoskeleton system by our negative damping control can lead to a decreased energetic demand for the wearer.

The variability in the metabolic cost reductions may

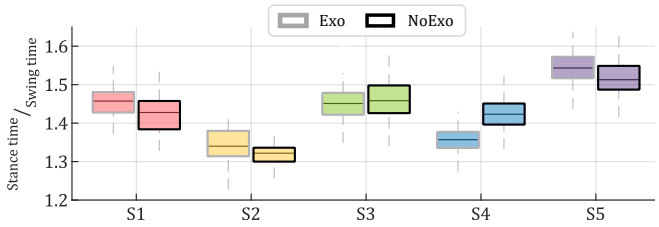


Fig. 6: The stance-to-swing ratio for each participant, and for each of the two experimental conditions.

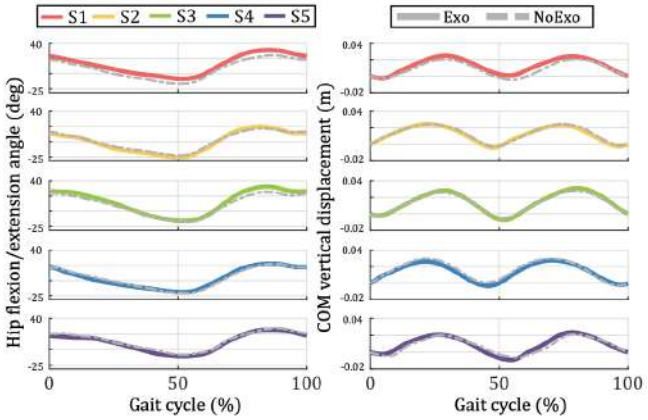


Fig. 7: Kinematic variables during the assisted and unassisted walking conditions. The center of mass (COM) vertical displacement and the hip flexion/extension angles are shown for each participant to the experiment.

be attributed to differences in participants' anthropometric characteristics. This is because, despite using the same β for all participants, the exoskeleton transmitted the mechanical power differently to each user. Consequently, the shortest participant experienced the greatest decrease in metabolic cost (S5, Table I). This user also received the greatest power relative to their body weight (Figure 5), and the highest peak torque normalized by body weight (Table I).

3) Kinematic data: During the assisted and unassisted walking conditions, participants adopted a similar walking strategy. This is demonstrated by the consistent stance-to-swing time ratio (Figure 6), and the cadence ratio close to 1.0 for all subjects (Table I). This finding confirms that our control strategy could assist users without causing forced movements. Conversely, disruptions of wearers' walking kinematics may occur in case of non-synchronized or excessively strong torque profiles [13].

The stance-to-swing time ratio was further analyzed using statistical methods, and a Friedman non-parametric test revealed significant differences between participants. This result can be attributed to the fixed treadmill speed used for all users, which led subjects to adjust their walking strategies accordingly. For instance, we observed that shorter participants adopted a longer stance time to increase stability [38]. These results are consistent with previous research showing that gait phase durations are influenced by anthropometric dimensions [39] and deviations from individual preferred walking speed [40]. On the other hand, within each subject, pairwise post-hoc comparisons indicated no significant difference between assisted and unassisted conditions.

Furthermore, for all subjects, the hip joint angle and the

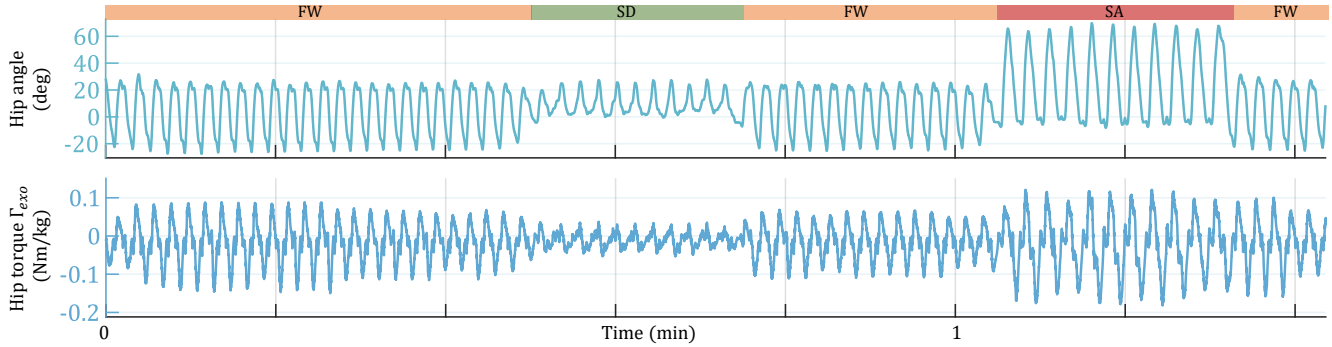


Fig. 8: Data collected during the varied environment walking trial. The user's hip flexion extension angle is shown, along with the hip assistive torque resulting from our control strategy. Tags: FW = flat walking, SD = stairs descending, SA = stairs ascending.

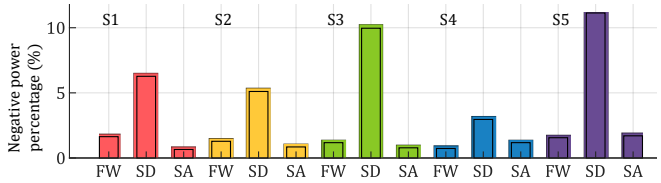


Fig. 9: Negative power area percentages for each subject in each unstructured environment. Center tags: FW = flat walking, SD = stairs descending, SA = stairs ascending.

vertical displacement of the center of mass (COM) remained unchanged in the two experimental conditions (Figure 7). Avoiding increases or decreases in the COM movement is crucial to avoid higher energetic cost during walking [21], [41], [42]. This finding also consolidates our results on the decreased metabolic cost measured when walking with the exoskeleton. With our approach, we achieved energetic cost reductions through efficient exoskeleton power transmission and without altering the users' walking kinematics.

4) Exoskeleton data - unstructured terrain: Our control strategy succeeded in assisting users in diverse walking conditions. The exoskeleton provided smooth support during gait transitions, and adapted the assistance to changes in terrain and walking directions (Figure 8). The assistance strength was dynamically adjusted in real-time through the designed optimization. Our multi-objective Bayesian optimizer remained unaware of the specific walking conditions, and, rather than performing a terrain classification, it relied only on the user's kinematics. The optimizer increased the torque strength during stairs ascending, a condition characterized by higher hip power demands [31], [43]. Conversely, intermediate assistive torques were applied during flat walking, while the assistance strength was decreased during stair descent. Our findings align with previous research on unstructured walking with hip exoskeletons [7], [14], [15], reinforcing the importance of modulating assistance strength across different conditions. Achieving this adaptability is essential for delivering seamless exoskeleton support across varied terrains and gait styles transitions [17].

The mechanical power exchanged between the users and the exoskeleton varied depending on the walking scenario (Figure 9). During flat walking and stairs ascent, the exoskeleton assistance generated low negative power, implying that the exoskeleton's assistive torque was synchronized with the wearers' movements. In contrast, stairs descent exhibited slightly higher negative power (still below 11% of the total power area), despite the lower assistance strength in this walking condition. These results are consistent with previous findings [7], and highlight the ability of our control framework to provide adaptive and synchronized assistance across varying terrains.

IV. Conclusion

In this work, we present a novel adaptive and user-dependent control strategy for the hip exoskeleton eWalk. We design the assistive torque as an adaptive virtual negative damping, capable of injecting energy into the human-exoskeleton system while keeping the users in charge of the movements. Our approach results in a torque profile that smoothly follows individual gait patters. Additionally, our control strategy reduces the energy expenditure of walking while preserving the natural joint kinematics. When tested in unstructured environments, our multi-objective Bayesian Optimization framework modulates the assistance strength by relying only on the exoskeleton kinematic variables. Notably, the exoskeleton assistance remains synchronized with users' movements across different terrains, as indicated by the low percentages of negative mechanical power transmitted from the device. In future work, we will evaluate the efficacy of the control with a wider population, test other dynamic optimization techniques, and evaluate our control on more unstructured terrains.

In conclusion, we introduce a simple but powerful strategy to provide partial walking assistance with the hip exoskeleton eWalk. Our control strategy provides individualized and adaptable assistance in various walking scenarios, without the need for extensive modeling or coefficients tuning. Overall, our approach contributes to advancing the development of viable, adaptive, and used-dependent control strategies for hip exoskeletons.

References

[1] R. Baud, A. R. Manzoori, A. Ijspeert, and M. Bouri, "Review of control strategies for lower-limb exoskeletons to assist gait," *Journal of NeuroEngineering and Rehabilitation*, vol. 18, p. 119, Dec. 2021.

[2] P. Slade, M. J. Kochenderfer, S. L. Delp, and S. H. Collins, "Personalizing exoskeleton assistance while walking in the real world," *Nature*, vol. 610, pp. 277–282, Oct. 2022.

[3] K. Seo, J. Lee, Y. Lee, T. Ha, and Y. Shim, "Fully autonomous hip exoskeleton saves metabolic cost of walking," in *2016 IEEE International Conference on Robotics and Automation (ICRA)*, (Stockholm, Sweden), pp. 4628–4635, IEEE, May 2016.

[4] A. R. Manzoori, D. Malatesta, J. Primavesi, A. Ijspeert, and M. Bouri, "Evaluation of controllers for augmentative hip exoskeletons and their effects on metabolic cost of walking: explicit versus implicit synchronization," *Frontiers in Bioengineering and Biotechnology*, vol. 12, p. 1324587, Mar. 2024.

[5] G. M. Bryan, P. W. Franks, S. Song, A. S. Voloshina, R. Reyes, M. P. O'Donovan, K. N. Gregorczyk, and S. H. Collins, "Optimized hip–knee–ankle exoskeleton assistance at a range of walking speeds," *Journal of NeuroEngineering and Rehabilitation*, vol. 18, p. 152, Dec. 2021.

[6] J. Zhang, J. Lin, V. Peddinti, and R. D. Gregg, "Optimal Energy Shaping Control for a Backdrivable Hip Exoskeleton," in *2023 American Control Conference (ACC)*, (San Diego, CA, USA), pp. 2065–2070, IEEE, May 2023.

[7] B. Lim, J. Jang, J. Lee, B. Choi, Y. Lee, and Y. Shim, "Delayed Output Feedback Control for Gait Assistance and Resistance Using a Robotic Exoskeleton," *IEEE Robotics and Automation Letters*, vol. 4, pp. 3521–3528, Oct. 2019.

[8] D. D. Molinaro, I. Kang, and A. J. Young, "Estimating human joint moments unifies exoskeleton control, reducing user effort," *Science Robotics*, vol. 9, p. eadi8852, Mar. 2024.

[9] B. T. Quinlivan, S. Lee, P. Malcolm, D. M. Rossi, M. Grimmer, C. Siviy, N. Karavas, D. Wagner, A. Asbeck, I. Galiana, and C. J. Walsh, "Assistance magnitude versus metabolic cost reductions for a tethered multiarticular soft exosuit," *Science Robotics*, vol. 2, p. eaah4416, Jan. 2017.

[10] G. Aguirre-Ollinger, J. E. Colgate, M. A. Peshkin, and Ambarish Goswami, "A 1-DOF assistive exoskeleton with virtual negative damping: effects on the kinematic response of the lower limbs," in *2007 IEEE/RSJ International Conference on Intelligent Robots and Systems*, (San Diego, CA, USA), pp. 1938–1944, IEEE, Oct. 2007.

[11] G. Aguirre-Ollinger, J. E. Colgate, M. A. Peshkin, and A. Goswami, "Active-Impedance Control of a Lower-Limb Assistive Exoskeleton," in *2007 IEEE 10th International Conference on Rehabilitation Robotics*, (Noordwijk, Netherlands), pp. 188–195, IEEE, June 2007.

[12] A. Ortlieb, R. Baud, T. Tracchia, B. Denkinger, Q. Herzig, H. Bleuler, and M. Bouri, "An Active Impedance Controller to Assist Gait in People with Neuromuscular Diseases: Implementation to the Hip Joint of the AUTONOMYO Exoskeleton," in *2018 7th IEEE International Conference on Biomedical Robotics and Biomechatronics (Biorob)*, (Enschede), pp. 537–543, IEEE, Aug. 2018.

[13] I. Kang, H. Hsu, and A. Young, "The Effect of Hip Assistance Levels on Human Energetic Cost Using Robotic Hip Exoskeletons," *IEEE Robotics and Automation Letters*, vol. 4, pp. 430–437, Apr. 2019.

[14] A. R. Manzoori, D. Malatesta, A. Mortier, J. Garcia, A. Ijspeert, and M. Bouri, "Adaptive Hip Exoskeleton Control using Heart Rate Feedback Reduces Oxygen Cost during Ecological Locomotion," June 2024.

[15] D. D. Molinaro, K. L. Scherpereel, E. B. Schonhaut, G. Evangelopoulos, M. K. Shepherd, and A. J. Young, "Task-agnostic exoskeleton control via biological joint moment estimation," *Nature*, vol. 635, pp. 337–344, Nov. 2024.

[16] J. Lin, R. D. Gregg, and P. B. Shull, "Improving Task-Agnostic Energy Shaping Control of Powered Exoskeletons With Task/Gait Classification," *IEEE Robotics and Automation Letters*, vol. 9, pp. 6848–6855, Aug. 2024.

[17] I. Kang, D. D. Molinaro, G. Choi, and A. J. Young, "Continuous locomotion mode classification using a robotic hip exoskeleton," in *2020 8th IEEE RAS/EMBS International Conference for Biomedical Robotics and Biomechatronics (BioRob)*, (New York City, NY, USA), pp. 376–381, IEEE, Nov. 2020.

[18] E. Tricomi, M. Mossini, F. Missiroli, N. Lotti, X. Zhang, M. Xiloyannis, L. Roveda, and L. Masia, "Environment-Based Assistance Modulation for a Hip Exosuit via Computer Vision," *IEEE Robotics and Automation Letters*, vol. 8, pp. 2550–2557, May 2023.

[19] S. Faraji and A. J. Ijspeert, "3LP: a linear 3D-walking model including torso and swing dynamics," May 2016. arXiv:1605.03036 [cs].

[20] M. Spong, J. Holm, and D. Lee, "Passivity-Based Control of Bipedal Locomotion," *IEEE Robotics & Automation Magazine*, vol. 14, pp. 30–40, June 2007.

[21] P. G. Adamczyk and A. D. Kuo, "Redirection of center-of-mass velocity during the step-to-step transition of human walking," *Journal of Experimental Biology*, vol. 212, pp. 2668–2678, Aug. 2009.

[22] O. Darici, H. Temeltas, and A. D. Kuo, "Anticipatory Control of Momentum for Bipedal Walking on Uneven Terrain," *Scientific Reports*, vol. 10, p. 540, Jan. 2020.

[23] O. Darici and A. Kuo, "Humans plan for the near future to walk economically on uneven terrain," *Proceedings of the National Academy of Sciences*, vol. 120, p. e2211405120, May 2023.

[24] H. Ohtsu, K. Hase, K. Sakoda, S. Aoi, S. Kita, and S. Ogaya, "A powered simple walking model explains the decline in propulsive force and hip flexion torque compensation in human gait," *Scientific Reports*, vol. 13, p. 14770, Sept. 2023.

[25] A. D. Kuo, "A Simple Model of Bipedal Walking Predicts the Preferred Speed–Step Length Relationship," *Journal of Biomechanical Engineering*, vol. 123, pp. 264–269, June 2001.

[26] M. Grimmer, K. Schmidt, J. E. Duarte, L. Neuner, G. Koginov, and R. Riener, "Stance and Swing Detection Based on the Angular Velocity of Lower Limb Segments During Walking," *Frontiers in Neurorobotics*, vol. 13, p. 57, July 2019.

[27] B. Lim, B. Choi, C. Roh, S. Hyung, Y.-J. Kim, and Y. Lee, "Parametric Delayed Output Feedback Control for Versatile Human-Exoskeleton Interactions During Walking and Running," *IEEE Robotics and Automation Letters*, vol. 8, pp. 4497–4504, Aug. 2023.

[28] T. Akiba, S. Sano, T. Yanase, T. Ohta, and M. Koyama, "Optuna: A Next-generation Hyperparameter Optimization Framework," in *Proceedings of the 25th ACM SIGKDD International Conference on Knowledge Discovery & Data Mining*, (Anchorage AK USA), pp. 2623–2631, ACM, July 2019.

[29] G. Bellegarda, M. Shafiee, M. E. Özberk, and A. Ijspeert, "Quadruped-Frog: Rapid Online Optimization of Continuous Quadruped Jumping," in *2024 IEEE International Conference on Robotics and Automation (ICRA)*, (Yokohama, Japan), pp. 1443–1450, IEEE, May 2024.

[30] L. Grazi, E. Trigili, N. Caloi, G. Ramella, F. Giovacchini, N. Vitiello, and S. Crea, "Kinematics-Based Adaptive Assistance of a Semi-Passive Upper-Limb Exoskeleton for Workers in Static and Dynamic Tasks," *IEEE Robotics and Automation Letters*, vol. 7, pp. 8675–8682, Oct. 2022.

[31] J. R. Montgomery and A. M. Grabowski, "The contributions of ankle, knee and hip joint work to individual leg work change during uphill and downhill walking over a range of speeds," *Royal Society Open Science*, vol. 5, p. 180550, Aug. 2018.

[32] R. Baud, A. Ortlieb, J. Olivier, M. Bouri, and H. Bleuler, "HiBSO Hip Exoskeleton: Toward a Wearable and Autonomous Design," in *New Trends in Medical and Service Robots* (M. Husty and M. Hofbaur, eds.), vol. 48, pp. 185–195, Cham: Springer International Publishing, 2018. Series Title: Mechanisms and Machine Science.

[33] A. R. Manzoori, T. Ye, D. Malatesta, C. Lugaz, O. Pajot, A. Ijspeert, and M. Bouri, "Gait Phase Estimation in Steady Walking: A Comparative Study of Methods Based on the Phase Portrait of the Hip Angle," in *2023 International Conference on Rehabilitation Robotics (ICORR)*, (Singapore, Singapore), pp. 1–6, IEEE, Sept. 2023.

[34] J. B. D. V. Weir, "New methods for calculating metabolic rate with special reference to protein metabolism," *The Journal of Physiology*, vol. 109, pp. 1–9, Aug. 1949.

[35] G. Ramella, A. Ijspeert, and M. Bouri, "Rapid Online Learning of Hip Exoskeleton Assistance Preferences," in *2025 IEEE International Conference on Robotics and Automation (ICRA)*, p. in Press, IEEE, 2025.

[36] J. Lee, K. Seo, B. Lim, J. Jang, K. Kim, and H. Choi, "Effects of assistance timing on metabolic cost, assistance power, and gait parameters for a hip-type exoskeleton," in *2017 International Conference on Rehabilitation Robotics (ICORR)*, (London), pp. 498–504, IEEE, July 2017.

[37] E. Reznick, K. R. Embry, R. Neuman, E. Bolívar-Nieto, N. P. Fey, and R. D. Gregg, "Lower-limb kinematics and kinetics during continuously varying human locomotion," *Scientific Data*, vol. 8, p. 282, Oct. 2021.

[38] D. Winter, "Human balance and posture control during standing and walking," *Gait & Posture*, vol. 3, pp. 193–214, Dec. 1995.

[39] M. Iosa, G. Morone, F. Bini, A. Fusco, S. Paolucci, and F. Marinozzi, "The connection between anthropometry and gait harmony unveiled through the lens of the golden ratio," *Neuroscience Letters*, vol. 612, pp. 138–144, Jan. 2016.

[40] C. A. Fukuchi, R. K. Fukuchi, and M. Duarte, "Effects of walking speed on gait biomechanics in healthy participants: a systematic review and meta-analysis," *Systematic Reviews*, vol. 8, p. 153, Dec. 2019.

[41] S. R. Wurdeman, P. C. Raffalt, and N. Stergiou, "Reduced vertical displacement of the center of mass is not accompanied by reduced oxygen uptake during walking," *Scientific Reports*, vol. 7, p. 17182, Dec. 2017.

[42] S. Faraji, A. R. Wu, and A. J. Ijspeert, "A simple model of mechanical effects to estimate metabolic cost of human walking," *Scientific Reports*, vol. 8, p. 10998, July 2018.

[43] R. W. Nuckols, K. Z. Takahashi, D. J. Farris, S. Mizrachi, R. Riemer, and G. S. Sawicki, "Mechanics of walking and running up and downhill: A joint-level perspective to guide design of lower-limb exoskeletons," *PLOS ONE*, vol. 15, p. e0231996, Aug. 2020.

The Relationship Between Stroke-Related Cognitive Impairment and Robotic Proprioceptive Assessment

Caitlin M. Callaghan, Christopher A. Johnson, Piyashi Biswas, Jill See, Lucy Dodakian, Vicky Chan, Po T .Wang, Steven C. Cramer, Zoran Nenadic, An H. Do, and David J. Reinkensmeyer, *Senior Member, IEEE*

***Abstract*— The interplay between proprioceptive and cognitive impairment following stroke is not well understood, along with the implications it may have on the design of robotic proprioception assessments. To examine the relationship between proprioceptive and cognitive impairments, we used a robotic device to measure ankle proprioception in 37 chronic stroke patients. Participants also completed the Montreal Cognitive Assessment (MoCA) and NIH stroke scale (NIHSS). We found that overall MoCA score was correlated with both active (R_s = -0.32 p=0.034) and passive proprioception ability (R_s = -0.52, p = 0.01). When we examined the MoCA subscores, we found that the Visuospatial/Executive subscore was moderately correlated with measures of both active (R_s = -0.57, p=0) and passive (R_s = -0.42, p=0.01) ankle proprioception ability. When we removed 5 individuals who were identified as having unilateral neglect using the NIHSS, the correlations remained significant. The Attention subtest was also weakly correlated with active proprioception ability (R_s = -0.36, p=0.03). Thus, proprioception ability is interrelated with specific cognitive impairments after stroke besides neglect. This suggests that cognitive tests should be conducted alongside robotic proprioceptive tests after stroke, to identify where cognitive factors may be contributing to measured proprioceptive error.**

I. Introduction

Over half of people who have experienced a stroke exhibit proprioception impairment [1]. These impairments predict functional ability of the upper [2] and lower extremities [3], [4] as well as ability of the upper extremity to benefit from rehabilitation therapy [5], [6], [7]. Further, proprioceptive impairment itself is treatable with targeted training after stroke [8]. Despite this, few rehabilitation therapists routinely assess proprioception [9]. The sparse technological landscape for clinical proprioceptive testing likely contributes to this situation. Clinical assessments are coarse, and there is a lack of practical technologies for sensitively measuring proprioception in the clinic or at home.

Given this need, there is increasing interest in developing technologies, including robotic devices, that enable routine, quantitative testing of proprioceptive ability after stroke [10], [11]. A challenge in developing these technologies, however, is that it is currently unclear which aspects of proprioception they should measure. Proprioception is a complex skill involving an array of different types of biological sensors, multiple brain areas that integrate information from those sensors, and complex computational processes that form the dynamic body models used for proprioceptive decision making [12], [13]. As a result, although over 1000 proprioceptive testing procedures have been developed, they rarely produce results that generalize between themselves [11].

It is clear that cognitive ability must play a role in proprioceptive ability. At a minimum, proprioceptive assessments require individuals to pay attention to the test and to internally model the sensed body movements. Over half of people who have experienced a stroke exhibit cognitive impairments [14], [15]. Despite this, there is limited information about how various aspects of cognitive impairment impact proprioceptive ability after stroke. Specifically, while it has been established that post-stroke individuals with unilateral neglect often show worse proprioception [16], the role of other cognitive abilities, such as attention and spatial reasoning is less clear.

One recent study found no significant correlation between a common test of cognitive ability, the Montreal Cognitive Assessment (MoCA), and wrist position sense measured with a quantitative testing paradigm [17]. Another group recently included participant data in a paper that described a study that

C Callaghan is with the Mechanical and Aerospace Engineering Department, University of California Irvine, Irvine, CA USA., callaghc@uci.edu

C Johnson is with the Rancho Los Amigos National Rehab Center with the Rancho Research Institute, Downey, CA, USA Johnson4@uci.edu

P Biswas is with the Mechanical and Aerospace Engineering Department, University of California Irvine, Irvine, CA USA. piyashib@uci.edu

J See is a PT at the Department of Rehabilitation Service at the University of California Irvine Medical Center, Irvine CA jsee@hs.uci.edu

L Dodakian is an OT at the Department of Rehabilitation Service at the University of California Irvine Medical Center, Irvine CA, LDodak@uci.edu

V Chan is a PT at the Department of Rehabilitation Service at the University of California Irvine Medical Center, Irvine CA vchan2@hs.uci.edu

P Wang is a postdoctoral scholar with the Biomedical Engineering Department, University of California Irvine, Irvine, USA, ptwang@uci.edu

S Cramer is with the School of Medicine Department of Neurology, University of California, Los Angeles, Los Angeles CA USA, scramer@uci.edu

Z Nenadic is with the Biomedical Engineering Department, University of California Irvine, Irvine, CA 92617 USA znenadic@uci.edu

A Do is with the School of Medicine Department of Neurology at the University of California Irvine, Irvine, CA USA. and@hs.uci.edu

D Reinkensmeyer is with the with the Departments of Mechanical and Aerospace Engineering and Anatomy and Neurobiology, University of California Irvine, Irvine, CA USA, dreinken@uci.edu

Research supported by NIDILRR Grant 90REGE0010 and NIH Grant HD095457. Biorobotics Lab, Department of Mechanical and Aerospace Engineering, University of California Irvine.

tracked proprioceptive recovery of the fingers after stroke using a robotic device. This allowed us to perform our own analysis of the relationship between the MoCA and finger proprioceptive ability [18], which showed no correlation.

The goal of this study was to quantify the interplay of cognitive and proprioceptive impairment after stroke, with a view toward gaining insight on how to optimize robotic technology for assessment of proprioception. We asked 37 people in the chronic phase following stroke to perform active and passive proprioceptive tasks with the ankle using a novel robotic device, as part of a larger study focused on rehabilitating foot drop. We assessed cognitive ability with the MoCA, identifying subscores on different subsections as well.

II. Methods

A. Participants and clinical assessments

These data were collected as part of a clinical trial designed to evaluate the efficacy of a brain-computer-interface, functional electrical stimulation system for treating foot drop in chronic stroke participants [4]. Inclusion and exclusion criteria can be found in [19]. The local ethics committee approved this study, and written informed consent was obtained from each participant prior to participating, following procedures established by the University of California Irvine Institutional Review Board. For this study we only used baseline measurements.

We evaluated cognitive ability with the MoCA, a widely-used and validated screening tool for mild and moderate dementia [20], [21]. The MoCA tests eight areas of cognition: Visuospatial/Executive Ability, Naming, Memory, Attention, Language, Abstraction, and Delayed Recall. The MoCA is scored out of 30 points; scores of 26+ indicate normal cognition, 18-25 indicate mild cognitive deficits, 10-17 moderate deficits, and <16 severe cognitive deficits. [20]

B. Robotic Proprioceptive Assessments

The robotic proprioceptive assessments were completed using the Ankle Measuring Proprioceptive Device (AMPD, Fig. 1) [22], a custom-designed device for which the foot platforms have two impedance states, mechanically rigid and mechanically transparent. These impedance states are achieved by engaging and disengaging a rack and pinion system driven by a motorized lead screw. Rotary encoders were used to measure ankle rotation at 200 Hz. Participants sat with their shank perpendicular to the ground and the ankle flexion/rotation center aligned to foot pedal shaft.

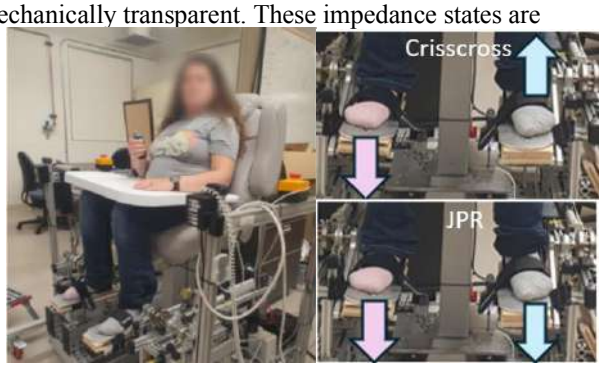


Figure 1: AMPD allows robot-driven or user-driven ankle movement for each pedal. For the Crisscross assessment (top right), the passive feet are robot-driven past each other and the participant must push a button when they cross. For the Joint Position Reproduction (JPR) assessment (bottom right), the impaired foot is robot-driven and the participant tracks it with the unimpaired foot. JPR involves dynamic and static periods. During static periods, the participant adjusts the feet to match if needed and then pushes the handheld button to signal readiness to return to dynamic tracking. Participant view of feet was obfuscated with a removable table top.

We used AMPD to measure two forms of proprioception. Passive proprioception is one's sense of limb position and movement when muscles are relaxed. Passive proprioception sense is built from sensory signals from the muscles, tendons, joint capsules, and skin. Active proprioception refers to body sense during voluntary movement, utilizing the same sensors as well as an estimate of joint movement derived from an internal forward model [12], [23].

We measured passive ankle proprioceptive ability using the Crisscross test originally developed by the UCI Biorobotics Lab for the fingers after stroke [4], [24], [25]. This involved AMPD in its mechanically rigid state moving the ankles in opposing directions to the participant's maximum dorsiflexion and plantarflexion, and participants pressing a handheld button when they believed their ankles aligned (Fig. 1). Passive range of motion was measured by a trained therapist and set as the limits. Crossing speed and position were randomized. Crisscross error was defined as the absolute angular difference between ankles at button press, averaged across trials.

We measured active ankle proprioceptive ability using a joint position reproduction (JPR) task. A range of JPR tasks have been developed for both the upper and lower extremities, testing the ability to reproduce an active or passively imposed movement. JPR has good test-retest reliability [26], [27]. The JPR task implemented here was a contralateral passive-active task with periods of dynamic position tracking mixed with periods of static position matching. Dynamic tracking involved AMPD moving the passive, impaired foot 5 deg/s through its passive ROM. Participants were instructed to actively move their unimpaired foot to match the movement of their impaired foot. Following a dynamic tracking period of random duration, the robot stopped moving and participants were instructed to adjust their unimpaired ankle to align with their impaired one, as needed, and then press the button once they believed the feet were aligned, at which point the dynamic tracking task resumed. Dynamic JPR error was quantified as the mean absolute difference between the ankle angles during dynamic periods. Static JPR error was the angle difference at button press.

TABLE I. Participant Characteristics (N = 37)

	Mean ± SD
Age (years)	60 ±12
Time Post Stroke (months)	35.6 ± 31.7
NIH Stroke Scale Severity (0 42)	6 ± 3
Sex M/F	23/14
Side Affected L/R	11/26
Ischemic/Hemorrhagic/Both	19/15/3
Montreal Cognitive Assessment (MoCA) (0 30)	24 ± 5
10M Walking Test (m/s)	0.43 ± 0.19

C. Data Analysis

MoCA subtests scores are ordinal data. Shapiro-Wilk testing of the MoCA subtests indicated that the MoCA scores were not normally distributed. Therefore, two-sided Spearman correlation was used for correlation analysis with alpha = 0.05. Group comparisons were performed using Kruskal-Wallis tests, also with alpha = 0.05.

III. Results

We measured ankle proprioception ability of 37 post-stroke individuals using a robotic device. We compared their proprioception error for active and passive tests to the overall MoCA score and to selected subscores. Of the 39 original participants, one was excluded due to an incomplete MoCA test, and one for an incomplete proprioception test, resulting in 37 participants. Table I provides an overview of participant characteristics as well as several clinical assessments given at baseline by an experienced therapist.

A. Proprioception error was correlated with overall MoCA score

Overall MoCA score was weakly and negatively correlated with Crisscross error ($p = 0.034$, Spearman's Correlation $R_s = -0.35$) and moderately correlated with JPR dynamic error ($p = 0.01$, $R_s = -0.42$, Fig. 2), using common correlation strength descriptors [28].

As unilateral neglect is common after stroke and known to affect proprioception assessments [7], we identified five individuals with neglect using the 'Extinction and Inattention" subscore of the NIHSS (formerly the Neglect score). When we omitted these five participants, these correlations were still significant for both Crisscross Error ($p = 0.047$, $R_s = -0.35$) and JPR dynamic error ($p = 0.002$, $R_s = -0.52$).

B. Proprioception error was correlated with two MoCA subscores: Visuospatial/Executive and Attention

The total MoCA score is obtained by adding subscores on the 7 subtests that are scored: Visuospatial/Executive, Naming, Attention, Language, Abstraction, Delayed Recall, and Orientation. The Memory task is used to scaffold the Delayed Recall task and does not contribute to the total score. We found that subscores on two of these tests were correlated with ankle proprioceptive error. First, the subscore on the Visuospatial/Executive (VSE) subtest was negatively correlated with error for the passive Crisscross Task (Fig. 4, $p < 0.001$, $R_s = -0.55$), as well as both the static and dynamic portions of the JPR task ($p < 0.0001$, $R_s = -0.47$, and $p=0.01$ $R_s = -0.57$, respectively). Omitting the five participants with neglect slightly weakened this correlation for all metrics, but the correlations remained significant. Crisscross error ($p = 0.006$, $R_s = -0.48$), JPR static error ($p = 0.017$, $R_s = -0.42$), and JPR dynamic error ($p = 0.001$, $R_s = -0.55$) all remained moderately negatively correlated with VSE score.

The Score on the Attention subtest was weakly correlated with JPR dynamic error ($p = 0.03$, $R_s = -0.36$, Fig. 2). Omitting participants with neglect strengthened this correlation ($p=0.003$, $R_s = -0.51$).

C. Neglect and robotic proprioceptive assessment

Although omitting individuals with neglect did not change the correlation results, we were interested in whether individuals with neglect had worse proprioception. We therefore compared proprioception error for the 5 individuals identified using the NIHSS as having neglect to those without neglect. Only dynamic JPR error was significantly different ($p = 0.037$, Table II), though for all metrics participants with detected neglect had equal or higher error than those without detected neglect. Neglect comes in multiple forms depending on lesion location and severity [29]. NIHSS emphasizes visual and tactile aspects of neglect, while the Clock Drawing task used in the MoCA Visuospatial/Executive subtest measures spatial awareness. In the Clock Drawing task, spatial neglect is indicated by digit clustering on one side of the clock [30]. None of the clock drawings of the participants who were identified by NIHSS as having neglect showed digit clustering (Fig. 3).

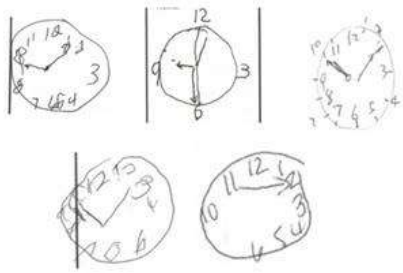


Figure 3: Clock Drawing Task results for 5 participants indicated by NIHSS as having neglect. None showed digit clustering on one side of clock.

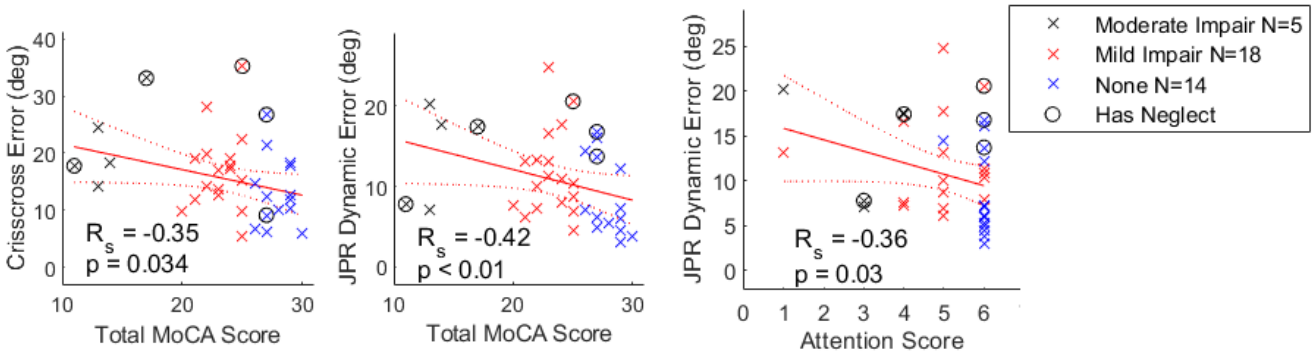


Figure 2. Proprioceptive error for the Crisscross test (left) and JPR Dynamic test (center) was significantly correlated with the total MoCA score. JPR Dynamic Test Error (right) was also correlated with the MoCA Attention score. Circled points are individuals identified as having neglect on the NIHSS.

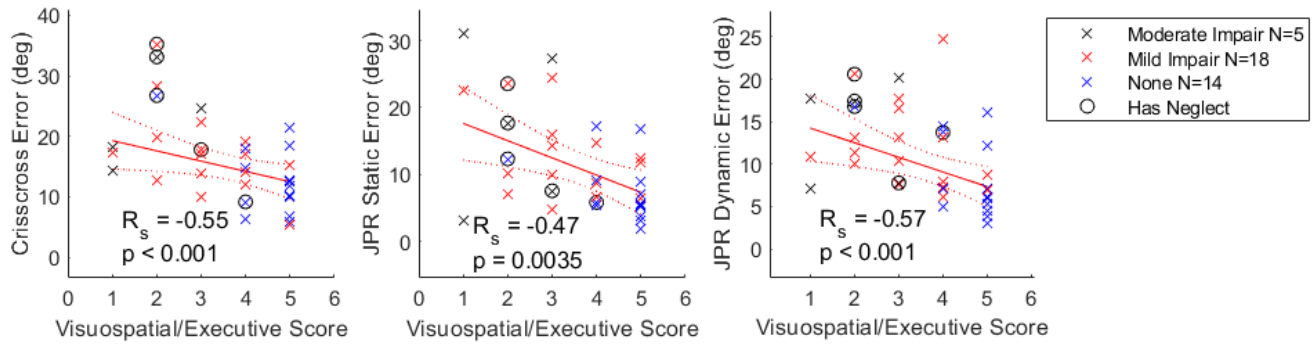


Figure 4. Proprioceptive error for the Crisscross test (left), JPR Static test (middle), and JPR Dynamic test (right) was significantly correlated with the VisuoSpatio subscore of the MoCA test. Circled points are individuals identified as having unilateral neglect on the NIHSS.

TABLE II. COMPARISON OF PROPRIOCEPTION ERROR FOR INDIVIDUALS WITH AND WITHOUT UNILATERAL NEGLECT ON THE NIHSS.

Proprioception Metric	***No Neglect (N=32)***	***Neglect (N=5)***	***p***
CC Error (deg)	14.9 ± 5.46	24.4 ± 10.9	0.068
JPR Static Error (deg)	10.9 ± 7.3	13. 4 ± 7.3	0.33
JPR Dynamic Error (deg)	10.2 ± 5.3	15.3 ± 4.8	0.037

IV. DISCUSSION

Proprioception assessment involves cognitive processes such as attention, but little is known about how cognitive impairment affects proprioceptive assessment after stroke. Here we found that the overall MoCA score was significantly correlated with active and passive ankle proprioception error after stroke. Two of the MoCA subscores, the Visuospatial/Executive and Attention subscores, accounted for this correlation. We discuss these results now plus limitations and directions for future research.

A. Overall cognitive impairment and proprioception impairment after stroke

Although it is well known that individuals with unilateral neglect after stroke exhibit worse proprioception [16], only a few studies to our knowledge have looked at how overall cognitive ability relates to proprioception impairment. A recent study found that hand proprioception ability was not correlated with total MoCA score [17], a finding at odds with the results of this study. The difference could arise due to the difference in joints tested (hand vs. ankle), or the difference in proprioceptive testing protocol. In individuals with multiple sclerosis [31] and mild cognitive impairment [32], proprioception ability was found to be correlated with MoCA score. Future research should seek to understand which aspects of proprioception at which joints and for what types of stroke most closely relate to overall cognitive impairment.

B. Specific aspects of cognitive impairment that correlated with proprioception impairment

The correlation with overall MoCA score most likely arose from the correlations present with subscores related to the Attention and Visuospatial/Executive (VSE) subsections. The finding that attention is related to proprioceptive error is not surprising: proprioception tests, including the ones used here, require the participant to pay continuous attention to their limbs. Further, attention deficits are common among stroke patients, and are associated with proprioception-related injuries such as heightened risk of fall injury [13]. However, the attention subscore positively correlated only with JPR dynamic error, not Crisscross or JPR static error. Dynamic JPR may be a more attention-demanding test than either passive proprioception (Crisscross), or matching static limb position (Static JPR), because active position tracking requires constant updates to both the passively-generated estimate of impaired side ankle position and motor planning to match that position with the other ankle.

The finding that VSE subscore was correlated with ankle proprioception was surprising and the reason is unclear. VSE ability is measured in the MoCA by completing three drawing tasks with the unimpaired hand: an alphanumeric "connect-the-dots" task, cube drawing, and clockface drawing. It is unclear why performance on these tasks is related to ankle proprioceptive performance. However, the fact that the tasks were completed with the unimpaired hand, whereas we measured proprioception of the impaired ankle, suggests that a higher-level cognitive process required for both types of tasks, joints, and sides is involved.

One possibility is that unilateral neglect plays a role. Unilateral neglect, the lack of awareness of stimuli on one side of the body, measurably affects 30% of chronic stroke patients [7]. Neglect has several modalities: visual, tactile, auditory, spatial, motor, or personal inattention [8], [9], [10]. Proprioception losses are associated with spatial neglect, typically associated with damage to the parietal lobe, especially for lesions in the nondominant hemisphere [11][16]. However, the correlations observed here were robust to omitting participants indicated by the NIHSS to have neglect. Neglect-style symptoms among chronic stroke patients are self-reported at a higher rate than neglect tests actually detect [33], which suggests neglect that does not meet the level of clinical detection may be common among stroke survivors. Thus, more subtle forms of neglect could still have played a role in the results of the current study. Future studies should assay neglect with more sensitive instruments to determine if it accounts for the findings here.

If neglect too mild to be detected by existing techniques is a contributing factor to both cognitive and proprioceptive assessment results, this would motivate future research into

using combinations of proprioceptive and cognitive assessments in the development of new, highly sensitive techniques for detection of neglect. Given the heightened injury risk associated with neglect, identifying mild cases may be important for assessing patient injury risk factors.

C. Limitations, Future Directions, and Clinical Implications

Participants handedness was not recorded at intake. Patients with stroke in the dominant hemisphere have significantly lower scores in the MoCA [34], and this may have added noise to the VSE subscores that we did not account for. Though the affected side and type of stroke were recorded, location of lesion was not. Spatial neglect is most common in participants with parietal lobe damage in the non-dominant hemisphere [24]; knowledge of lesion location could have indicated participants likely to experience neglect-type symptoms even if the NIHSS did not detect it.

Side-affected was not controlled for equal distribution. For MoCA distribution, the parent study for this paper had a minimum cutoff of 22, but the protocol allowed for the possibility of lowering this cutoff at the discretion of the clinical team for individuals with aphasia, which was done for eight participants. As a result, there were low MoCA score participants in this study, but relatively few of them (8 such participants, mean MoCA score 16 +- 4). Low MoCA score is frequently used as an exclusion criterion in proprioceptive studies; this may have limited the ability of studies to detect a relationship between cognitive impairment and proprioception. The selected statistical tests – Spearman Correlation and Kruskal-Wallis test – were selected for robustness against outliers as well as their tolerance for non-normally distributed ordinal data, but inclusion of more participants with severe and moderate cognitive impairment is an important direction for future research.

We asserted that the finding of correlation between a drawing task performed with the unimpaired side with impaired-side proprioception for a different limb suggests a higher-level cognitive process is at play in both assessments. This assertion would be strengthened by performing similar analysis on proprioceptive studies on other joints. The sparsity of proprioception studies that are inclusive of participants with low MoCA scores may require design of studies specifically targeting this relationship through a battery of proprioceptive assessments suitable for participants with a wide range of MoCA scores.

Future research will analyze the different drawing tasks that comprise the VSE subtest to identify which is most predictive of proprioceptive error. Though the clock drawing task is well known in neglect assessment, the other tasks may offer further insights into why the VSE subtest is correlated with proprioception ability.

We also plan in future research to include dual-tasking to modulate the attention load during proprioception assessment. Augmenting the attention load through the addition of a simultaneous task stressing a sensory pathway not involved in the proprioception task, such as visual or audio signal interpretation, could indicate how much influence attention load has on active and passive proprioception assessment results, and whether active proprioception truly is more sensitive to heightened global attention load. Further, identifying the influence of task-specific attention demands on proprioceptive assessment results would provide insight into appropriate assessment design for patients with attention deficits.

That proprioception of the ankle and VSE score correlations were weakened by the omission of subjects identified to have neglect by NIHSS suggests non-detected neglect may still be contributing to both tasks. More sensitive tests for neglect may have detected its presence in more of our subjects. Future research that compares performance on other tests for spatial neglect, such as Semi-structured Scale for Functional Evaluation of Hemi-inattention [35], to proprioceptive assessment results, would indicate the importance of detecting and controlling for neglect in both proprioceptive and cognitive assessments.

Finally, an important clinical implication is accounting for cognitive factors in proprioceptive assessment. At a minimum, the current results suggest that robotic proprioceptive tests should be performed alongside cognitive tests, as cognitive impairment may explain some aspects of proprioceptive error. Proprioception assessments rely on attention and memory while common cognitive assessments rely on sensory motor control of the hand (to draw pictures, for example). Therefore, it is conceivable that impairments in one area may be confounded as impairments in the other. Designing a minimally viable set of quantitative, clinical tests that comprehensively characterizes the essential elements of proprioceptive skill is an important goal for rehabilitation practice.

V. Conclusion

Overall MoCA score, as well as the Visuospatial/Executive and Attention subscores, were correlated with proprioception ability of the ankles after stroke. This implies the existence of a shared neural impairment (or impairments) that affects performance on both proprioceptive and cognitive assessments. New technologies for clinical proprioception testing after stroke should determine how to account for the interplay of cognitive impairment with proprioception impairment, given the high frequency of cognitive impairment after stroke.

References

[1] Y. Yu, Y. Chen, T. Lou, and X. Shen, "Correlation Between Proprioceptive Impairment and Motor Deficits After Stroke: A Meta-Analysis Review," *Front. Neurol.*, vol. 12, p. 688616, Jan. 2022, doi: 10.3389/fneur.2021.688616.

[2] D. Rand, "Proprioception deficits in chronic stroke—Upper extremity function and daily living," *PLoS ONE*, vol. 13, no. 3, p. e0195043, Mar. 2018, doi: 10.1371/journal.pone.0195043.

[3] F. S. Chia, S. Kuys, and N. Low Choy, "Sensory retraining of the leg after stroke: systematic review and meta-analysis," *Clin Rehabil*, vol. 33, no. 6, pp. 964–979, Jun. 2019, doi: 10.1177/0269215519836461.

[4] C. A. Johnson *et al.*, "The weak relationship between ankle proprioception and gait speed after stroke a robotic assessment study," Feb. 16, 2024, *arXiv*: arXiv:2402.11110. doi: 10.48550/arXiv.2402.11110.

[5] M. L. Ingemanson, J. R. Rowe, V. Chan, E. T. Wolbrecht, D. J. Reinkensmeyer, and S. C. Cramer, "Somatosensory system integrity explains differences in treatment response after stroke," *Neurology*, vol. 92, no. 10, pp. e1098–e1108, Mar. 2019, doi: 10.1212/WNL.0000000000007041.

[6] J. B. Rowe, V. Chan, M. L. Ingemanson, S. C. Cramer, E. T. Wolbrecht, and D. J. Reinkensmeyer, "Robotic Assistance for Training Finger Movement Using a Hebbian Model: A Randomized Controlled Trial," *Neurorehabil Neural Repair*, vol. 31, no. 8, pp. 769–780, Aug. 2017, doi: 10.1177/1545968317721975.

[7]S.-W. Park, S. L. Wolf, S. Blanton, C. Winstein, and D. S. Nichols-Larsen, "The EXCITE Trial: Predicting a Clinically Meaningful Motor Activity Log Outcome," *Neurorehabil Neural Repair*, vol. 22, no. 5, pp. 486–493, Sep. 2008, doi: 10.1177/1545968308316906.
[8]H. G. Seo, S. J. Yun, A. J. Farrens, C. A. Johnson, and D. J. Reinkensmeyer, "A Systematic Review of the Learning Dynamics of Proprioception Training: Specificity, Acquisition, Retention, and Transfer," *Neurorehabil Neural Repair*, vol. 37, no. 10, pp. 744–757, Oct. 2023, doi: 10.1177/15459683231207354.
[9]J. E. Hoh, M. R. Borich, T. M. Kesar, D. S. Reisman, and J. A. Semrau, "Limitations in utilization and prioritization of standardized somatosensory assessments after stroke: A cross-sectional survey of neurorehabilitation clinicians," *Top Stroke Rehabil*, vol. 31, no. 1, pp. 29–43, Jan. 2024, doi: 10.1080/10749357.2023.2200304.
[10] J. E. Aman, N. Elangovan, I.-L. Yeh, and J. Konczak, "The effectiveness of proprioceptive training for improving motor function: a systematic review," *Front Hum Neurosci*, vol. 8, p. 1075, Jan. 2015, doi: 10.3389/fnhum.2014.01075.
[11] Á. Horváth, E. Ferentzi, K. Schwartz, N. Jacobs, P. Meyns, and F. Köteles, "The measurement of proprioceptive accuracy: A systematic literature review," *J Sport Health Sci*, vol. 12, no. 2, pp. 219–225, Mar. 2023, doi: 10.1016/j.jshs.2022.04.001.
[12] K. E. Cullen and O. A. Zobeiri, "Proprioception and the predictive sensing of active self-motion," *Current Opinion in Physiology*, vol. 20, pp. 29–38, Apr. 2021, doi: 10.1016/j.cophys.2020.12.001.
[13] B. P. Delhaye, K. H. Long, and S. J. Bensmaia, "Neural Basis of Touch and Proprioception in Primate Cortex," in *Comprehensive Physiology*, 1st ed., Y. S. Prakash, Ed., Wiley, 2018, pp. 1575–1602. doi: 10.1002/cphy.c170033.
[14] N. K. Al-Qazzaz, S. H. Ali, S. A. Ahmad, S. Islam, and K. Mohamad, "Cognitive impairment and memory dysfunction after a stroke diagnosis: a post-stroke memory assessment," *Neuropsychiatric Disease and Treatment*, vol. 10, pp. 1677–1691, Sep. 2014.
[15] G. M. Nys, M. J. van Zandvoort, P. L. de Kort, B. P. Jansen, E. H. de Haan, and L. J. Kappelle, "Cognitive disorders in acute stroke: prevalence and clinical determinants," *Cerebrovascular Diseases*, vol. 23, no. 5, pp. 408–416, Apr. 2007.
[16] G. Fisher, C. Quel de Oliveira, A. Verhagen, S. Gandevia, and D. Kennedy, "Proprioceptive impairment in unilateral neglect after stroke: A systematic review," *SAGE Open Med*, vol. 8, p. 2050312120951073, Aug. 2020, doi: 10.1177/2050312120951073.
[17] B. M. Young *et al.*, "Wrist Proprioception in Adults with and without Subacute Stroke," *Brain Sci*, vol. 13, no. 1, p. 31, Dec. 2022, doi: 10.3390/brainsci13010031.
[18] M. Zbytniewska-Mégret *et al.*, "The Evolution of Hand Proprioceptive and Motor Impairments in the Sub-Acute Phase After Stroke," *Neurorehabil Neural Repair*, vol. 37, no. 11–12, pp. 823–836, Dec. 2023, doi: 10.1177/15459683231207355.
[19] P. Biswas *et al.*, "A single-center, assessor-blinded, randomized controlled clinical trial to test the safety and efficacy of a novel brain-computer interface controlled functional electrical stimulation (BCI-FES) intervention for gait rehabilitation in the chronic stroke population," *BMC Neurol*, vol. 24, no. 1, p. 200, Jun. 2024, doi: 10.1186/s12883-024-03710-3.
[20] Z. S. Nasreddine *et al.*, "The Montreal Cognitive Assessment, MoCA: A Brief Screening Tool For Mild Cognitive Impairment," *J American Geriatrics Society*, vol. 53, no. 4, pp. 695–699, Apr. 2005, doi: 10.1111/j.1532-5415.2005.53221.x.
[21] C.-Y. Wu, S.-J. Hung, K. Lin, K.-H. Chen, P. Chen, and P.-K. Tsay, "Responsiveness, Minimal Clinically Important Difference, and Validity of the MoCA in Stroke Rehabilitation," *Occupational Therapy International*, vol. 2019, pp. 1–7, Apr. 2019, doi: 10.1155/2019/2517658.
[22] C. A. Johnson, D. S. Reinsdorf, D. J. Reinkensmeyer, and A. J. Farrens, "Robotically quantifying finger and ankle proprioception: Role of range, speed, anticipatory errors, and learning," in *2023 45th Annual International Conference of the IEEE Engineering in Medicine & Biology Society (EMBC)*, Sydney, Australia: IEEE, Jul. 2023, pp. 1–5. doi: 10.1109/EMBC40787.2023.10340566.
[23] R. C. Miall and D. M. Wolpert, "Forward Models for Physiological Motor Control," *Neural Networks*, vol. 9, no. 8, pp. 1265–1279, Nov. 1996, doi: 10.1016/S0893-6080(96)00035-4.
[24] D. S. Reinsdorf, E. E. Mahan, and D. J. Reinkensmeyer, "Proprioceptive Gaming: Making Finger Sensation Training Intense and Engaging with the P-Pong Game and PINKIE Robot," *Annu Int Conf IEEE Eng Med Biol Soc*, vol. 2021, pp. 6715–6720, Nov. 2021, doi: 10.1109/EMBC46164.2021.9631041.
[25] M. L. Ingemanson, J. B. Rowe, V. Chan, E. T. Wolbrecht, S. C. Cramer, and D. J. Reinkensmeyer, "Use of a robotic device to measure age-related decline in finger proprioception," *Exp Brain Res*, vol. 234, no. 1, pp. 83–93, Jan. 2016, doi: 10.1007/s00221-015-4440-4.
[26] M. Bertrand-Charette, C. Dambreville, L. J. Bouyer, and J.-S. Roy, "Systematic review of motor control and somatosensation assessment tests for the ankle," *BMJ Open Sport Exerc Med*, vol. 6, no. 1, p. e000685, Jul. 2020, doi: 10.1136/bmjsem-2019-000685.
[27] N. Elangovan, A. Herrmann, and J. Konczak, "Assessing Proprioceptive Function: Evaluating Joint Position Matching Methods Against Psychophysical Thresholds," *Phys Ther*, vol. 94, no. 4, pp. 553–561, Apr. 2014, doi: 10.2522/ptj.20130103.
[28] P. Schober, C. Boer, and L. A. Schwarte, "Correlation Coefficients: Appropriate Use and Interpretation," *Anesthesia & Analgesia*, vol. 126, no. 5, pp. 1763–1768, May 2018, doi: 10.1213/ANE.0000000000002864.
[29] A. E. Hillis, "Neurobiology of Unilateral Spatial Neglect," *Neuroscientist*, vol. 12, no. 2, pp. 153–163, Apr. 2006, doi: 10.1177/1073858405284257.
[30] D. Tranel, D. Rudrauf, E. P. M. Vianna, and H. Damasio, "Does the Clock Drawing Test have focal neuroanatomical correlates?," *Neuropsychology*, vol. 22, no. 5, pp. 553–562, 2008, doi: 10.1037/0894-4105.22.5.553.
[31] D. A. Henning, J. M. Huisinga, S. Lynch, and N. E. Fritz, "Cognition and proprioception in persons with multiple sclerosis and healthy controls: Nascent findings," *Multiple Sclerosis and Related Disorders*, vol. 68, p. 104372, Dec. 2022, doi: 10.1016/j.msard.2022.104372.
[32] K. Li, K. A. Pickett, H. Fu, and R. Chen, "Proprioceptive and olfactory deficits in individuals with Parkinson disease and mild cognitive impairment," *Acta Neurol Belg*, vol. 124, no. 2, pp. 419–430, Apr. 2024, doi: 10.1007/s13760-023-02420-w.
[33] E. S. Grattan, B. Hounshel Smith, K. Mullen, and M. L. Woodbury, "Unilateral Spatial Neglect May Not Be Detected by Performance-Based Functional Neglect Assessment," *The American Journal of Occupational Therapy*, vol. 78, no. 2, p. 7802180200, Mar. 2024, doi: 10.5014/ajot.2024.050497.
[34] A. Esmael, M. Elsherief, and K. Eltoukhy, "Prevalence of cognitive impairment in acute ischaemic stroke and use of Alberta Stroke Programme Early CT Score (ASPECTS) for early prediction of post-stroke cognitive impairment," *Neurol Neurochir Pol.*, vol. 55, no. 2, pp. 179–185, Apr. 2021, doi: 10.5603/PJNNS.a2021.0006.
[35] P. Plummer, M. E. Morris, and J. Dunai, "Assessment of Unilateral Neglect," *Physical Therapy*, vol. 83, no. 8, pp. 732–740, Aug. 2003, doi: 10.1093/ptj/83.8.732.

Evaluation of the Human-like Robotic Touch: A User Study.

Yucheng Tang[1,2]
[1]*Proximity Robotics & Automation GmbH*
[2]*Karlsruhe University of Applied Sciences*
Pfinztal, Germany
tang@proximityrobotics.com

Tara Chand[3,4]
[3]*Friedrich Schiller University Jena*
[4]*O.P. Jindal Global University*
Sonipat, India
tara.chand@jgu.edu.in

Ilshat Mamaev[1,2]
[1]*Proximity Robotics & Automation GmbH*
[2]*Karlsruhe University of Applied Sciences*
Pfinztal, Germany
mamaev@proximityrobotics.com

Björn Hein[2]
[2]*Karlsruhe University of Applied Sciences*
Karlsruhe, Germany
bjoern.hein@h-ka.de

Ilona Croy[3]
[3]*Friedrich Schiller University Jena*
Jena, Germany
ilona.croy@uni-jena.de

***Abstract*—Affective touch is crucial for human development, social bonding, and emotional support, while physical interaction plays a key role in rehabilitation, aiding motor recovery and well-being. Although AI has advanced verbal and non-verbal communication, replicating human-like physical interaction remains a challenge. This paper explores whether robots can convey emotional touch. Using a soft brush as a haptic transfer mediator, we isolated temporal and spatial touch characteristics to assess their impact on human perception.**

We implemented Cartesian dynamic movement primitives to replicate the human touch and adapt it to individuals by sampling geometric points on the forearm. Questionnaire analysis revealed that robotic touch at $3\,\mathrm{cm/s}$ was more effective in replicating the pleasurable sensations of human touch compared to $0.3\,\mathrm{cm/s}$. Our findings indicate that the human-like quality of robotic touch depends more on temporal factors than spatial trajectories. However, robotic touch was still distinguishable from human touch, with 75.71% of participants correctly identifying it as robotic.

These results contribute to robotic rehabilitation by improving the understanding of affective touch, with potential applications in motor recovery, sensory stimulation, and emotional well-being.

***Index Terms*—Affective Touch, Robotic Touch, Human-Robot Interaction, Haptic Transfer Interface, Humanization of Robot Touch**

I. Introduction

Humans are social beings and rely on cooperation with each other to survive. Such cooperation builds on verbal and non-verbal interaction processes with affective touch being one of them. Affective touch is friendly interpersonal contact and it fosters the initiation and maintenance of human bonds [1] [2]. This type of touch typically involves the activation of a specialized set of cutaneous nerve fibers, known as C-tactile fibers, leading to a pleasant or calming sensation and an accompanying decrease in physiological arousal [1] [3], especially in the face of stress [4].

The involvement of C-tactile nerve fibers in the transmission of affective touch has been identified through microneurography studies, which revealed that slow stroking stimulation activates this specific set of touch-processing fibers, whose response characteristics differ fundamentally from other cutaneous fibers involved in somatosensation [5]. Specifically, slow stroking with velocities of 1, 3 or $10\,\mathrm{cm/s}$ CT activates those fibers more, and is perceived as more pleasant, as compared to stroking with 0.1, 0.3 or $30\,\mathrm{cm/s}$ [6]. The experiments underlying this finding are typically performed by stroking with a soft goat hair brush over a participant's forearm and the inverted U-shaped curve of pleasantness perception has been replicated multiple times in group results, although it cannot be found in each single individual [7]. Interestingly, slow stroking with C-tactile nerve fiber targeted velocities does not only lead to feeling pleasant, but also more "human" than stroking at other velocities [8] [9].

This finding leads us and other researchers to believe that touch speed may be one of the important features reshaping interpersonal touch. A similar situation exists in the spatial characteristics of touch, where trajectories tend to be deterministic for robots, whereas human behavior is relatively more uncertain, e.g., it is difficult for humans to draw a straight line. Therefore, if the robot will only deliver fixed trajectories as in previous studies (e.g. linear haptic stimulators - Dancer design), comparing it to human-to-human interaction becomes challenging. We aim to introduce more flexible and relatively random trajectories of robotic touch to better assess the emotional impact of robot-applied touch on humans and compare it to human behavior.

Overall, the goal of this work is to use spatial and temporal (trajectory and velocity) to investigate whether robots can create natural, pleasurable experiences for humans. The study aimed to test whether we could: a) replicate typical inverted U-shaped velocity-related pleasantness with touch provided by a fully robotic arm; and b) whether participants could distinguish between touch provided by humans and robots.

II. Related Works

A. Affective Robotic Touch

Most haptics-related algorithms for robot motion planning or control currently focus on the industrial sector to perform better assembly tasks or to make robots more flexible so that they can share workspaces with humans [10]. On the other hand, research on affective social touch has rarely focused on human-like tactile reproduction or motion planning of robots.

1) Vibration or Other Actuators without Robot Arm and Hand: Specific actuators can stimulate the receptors for emotional touch, even if they do not yet provide the exact sensation of a fully realistic human touch. For example, vibrotactile [11], air pressure [12], or specially designed mechanical stimuli [13] can stimulate different mechanoreceptors.

2) NAO: The NAO robot has been utilized in numerous studies to achieve robotic touch. For example, it was employed to comfort people by trying to touch the shoulder or big arm of the experimenter for $10 - 40$ seconds while some scary scenes were shown [14] [15]. However, neither test mentions specific robot-related data.

3) PR2: Previous iterations of HuggieBot [16] focused on static hugs, identifying hug firmness, duration, and joint angle during the hug as key factors. Inspired by the human prolonged hugs, attention was shifted to several different contact features on HuggieBot 3.0, including rubbing, patting, and squeezing [17]. However, no advanced stroking mechanisms were implemented. The PR2 robot executed rubbing movements by changing the shoulder joint angle. Law et al. [18] conducted several studies on robotic touch, primarily involving a robot assisting a human when the screen suddenly goes black. Most experiments indicated that people felt more comfortable in situations where the robot was in contact with them (by placing its hand on the experimenter's shoulder), yet no specific robot-related data is mentioned in the text. It is assumed that the usual software and hardware configuration of PR2 was used.

4) Human-like Contacts: Guidelines on how robots touch humans were proposed at an early stage [19]. Zheng et al [20] used the female robot Erica to explore the effects of touch on participant arousal and whether the robot was able to convey specific emotions by varying the type of touch (touch or tap), the length of the path of the touch, and the location of the touch (hand or fingers). Teyssier et al. [21] define four important parameters of robotic touch: spatial (position of contact), temporal (length of contact), dynamic (pressure or vibration), and other parameters (e.g. temperature, texture, and softness). In the study, they also evaluated each type of parameter and chose eight specific dynamic touches to explore the effects of robotic touch on human emotions. However, they did not compare the robot touch with the human touch and used only classical robot control algorithms in their experiments. The study closest to the goal of this work is [22], which researched the effect of touch exerted by humans, the Nao robot, a mannequin arm, and a plastic tube on human comfort. Stroking touches at a velocity of ca. 3 cm/s were rated as the most pleasant, which is similar to the results of the human touch study [6]. Robot touch was not rated as significantly more pleasant than touches applied with the mannequin hand or tube and was lower than human-applied touch. However, participants evaluated the comfort and pleasantness of the touch through a video in which the participant was not actually being touched.

To the best of our knowledge, a gap still exists in the comparison between human and robotic touch, which is the focus of this work. As Teyssier states, the parameter space for human touch is too large (including, but not limited to the four-parameter types he summarized), and to better enable robots to replicate human-like touch, we use a brush as a mediator to limit the touch parameter space to spatial, temporal parameters.

B. Motion Planning and Control for Human-like Robotic Touch

The field of robotic movement and its adaptation from human behaviors has garnered considerable attention, aiming to endow robots with the capability to perform tasks with human-like dexterity and adaptability. Among the techniques explored, Dynamical Movement Primitives (DMPs) have emerged as a potent method for modeling and replicating human movements, facilitating the teaching and execution of complex motor tasks in robots.

Key contributions include the foundational framework that introduced DMPs for capturing and replicating motor behaviors, demonstrating their potential for robotic applications [23]. Pastor et al. furthered this by showing how robots could learn and generalize motor skills from demonstrations, highlighting the versatility of DMPs [24].

DMPs were applied to robot table tennis, showcasing their adaptability in dynamic sports environments [25], while Ude et al. expanded DMPs to include orientation tasks [26]. Force feedback modulation was also introduced into DMPs, allowing for real-time adjustment based on environmental interactions [27].

At the control level, Ishikura et al. [28] used impedance control and a hand modeled on a human to perform a gentle stroke on the back, which has positive emotional effects in tactile care. However, the pressure and speed of the end effector also remain constant. Contact with constant force can hardly be defined as human-like contact and therefore has an impact on the evaluation of the social touch imparted.

In general, DMPs are well suited to the needs of affective robotic touch scenarios as an important method for encoding human behavior and enabling the robot to reproduce it. Therefore, we use DMPs in the Cartesian coordinate system as the basis of this work and eliminate as much as possible the influence of the robot's dynamic touch features (force or acceleration, etc.) on human perception by using a soft brush.

III. Affective Robotic Touch

Based on our research objectives, we propose the following hypotheses:

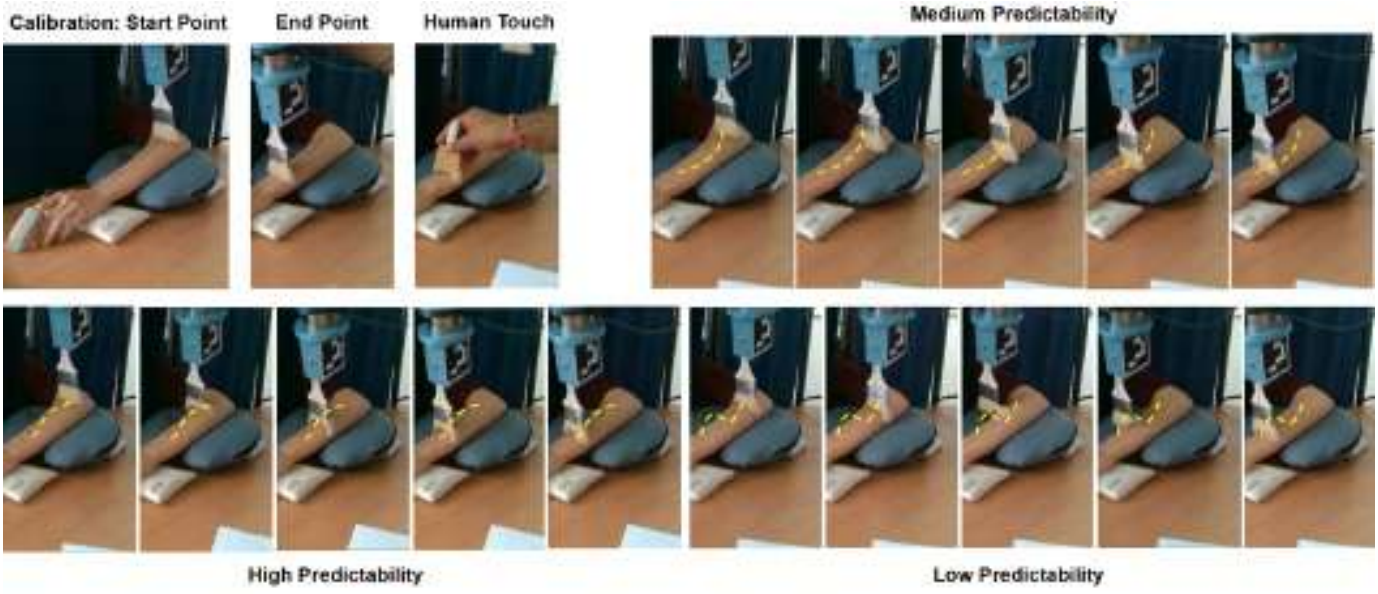


Fig. 1. **Spatial Characteristic (Trajectory) of the stroking:** At the beginning of the experiment, the robot will first calibrate the forearm of the experimenter, which involves collecting pose data on the start and end points. Trajectories resembling straight lines are defined as having high predictability. In contrast, curvilinear trajectories with three waypoints are considered to have medium predictability, and S-shaped trajectories with four waypoints are deemed to have low predictability.

- **H1:** Stroking at a velocity of $3\,\mathrm{cm/s}$ will be perceived as more pleasant than stroking at $0.3\,\mathrm{cm/s}$, regardless of whether the stroking is performed by a human or a robot.
- **H2:** The predictability of stroking trajectories will influence the perceived pleasantness, with higher predictability leading to more pleasant experiences.
- **H3:** Participants will be able to distinguish between human and robotic touch, and this ability will be influenced by the trajectory predictability.

As we want to explore the spatial and temporal characteristics of touch, short-duration spatially invariant touch patterns such as tapping will not be explored in this work. The focus of the experiments will be on long-distance strokes with different trajectories, while uncertainty (which can also be called randomness or predictability) similar to human behavior will also be introduced in the trajectory chapter. For clarity, within the context, the spatial characteristics of touch will be synonymous with the trajectories of the robot's Tool Center Point (TCP).

A. Stroking with a Robotic Arm

In this section, we will detail how different stroking can be realized with a robotic arm. As mentioned in the introduction, our objective is to investigate whether the spatial and temporal characteristics of stroking influence the perception and effect of affective touch, while it is also a very worthwhile question for robotics to explore whether it is possible to produce a touch effect comparable to that of a human utilizing a robotic arm. In the experimental scenarios, affective touch was achieved through a soft brush, which simplifies the haptic problem for robots in reproducing human-to-human touch. Therefore, this section will concentrate on explaining the choice of robots and sensors as well as the choice of motion planning and control algorithms in reproducing affective touch.

1) Hardware Setup: Our primary objective was an arm-stroking motion produced by the robot that closely approximates the characteristics of human motion. Therefore some hardware prerequisites are necessary, including providing joint torque feedback, a torque control interface for compliant manipulation, and the capacity to record human strokes as references. Regarding the robotic arm, we chose to use a 7-DoF Franka Panda robot (as shown in Fig. 2). It only has a $3\,\mathrm{kg}$ payload, but it meets the needs of our touch experiment. It has a maximum reach of $855\,\mathrm{mm}$. The maximum linear speed in Cartesian coordinate system can reach $2\,\mathrm{m/s}$, and the repeatability is $\pm 0.1\,\mathrm{mm}$.

The main reason we chose this robot was its high precision, joint torque feedback, and integrated control algorithm. Franka is equipped with high-resolution joint encoders, allowing them to execute precise motions. Furthermore, Franka is also equipped with torque sensors at all 7 axes to provide the necessary feedback for the touch. Libfranka and franka_ros provide state-of-the-art control algorithms, and the torque control interface allows the Franka to move compliantly.

From our experience, the force on the end-effector of a robotic arm can be calculated from joint torque feedback, it is prone to errors due to external disturbances and abrupt changes in motion. The compliance of Franka's joints may introduce additional instability. For safety, we incorporated an additional force-torque sensor at the end-effector. The sensor not only records the precise downforce during the experiment for subsequent analysis but also supports contact detection and

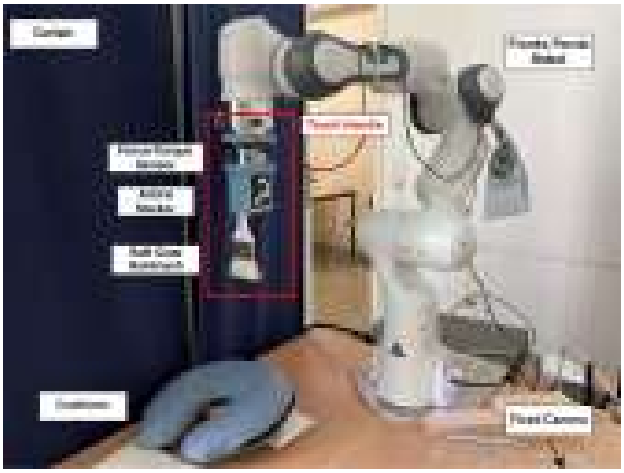
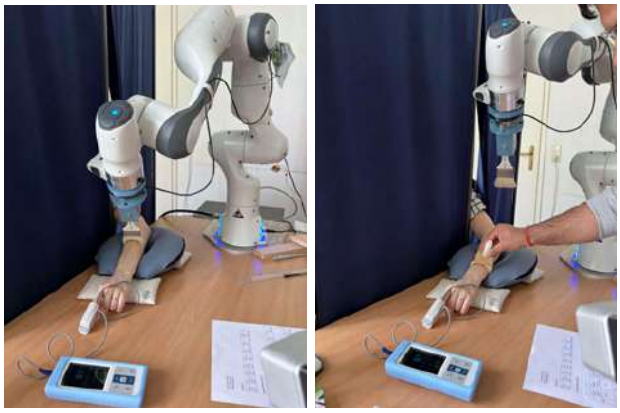


Fig. 2. **Affective robotic touch experiment setup**: The touch handle consists of a force-torque sensor, ArUco Marker, 3D printed components, and a soft goat hairbrush. It can be used to apply human touch alone or mounted on a robot to apply robotic touch. The fixed FRAMOS D400e camera records RGB-D video for capturing touch trajectories and for archiving experimental data.



(a) (b)

Fig. 3. **Robots and humans perform strokes:** physiological information such as heartbeat is recorded while the experimenter is applying the strokes, and an evaluation is required at the end of each stroke. The entire procedure is recorded by a fixed camera. When a human applies a stroke, the robot provides a reference trajectory directly above it, while ensuring that the noise of the robot's movement is present during each stroking motion.

force control, ensuring the robot does not exert excessive force.

To capture the trajectory and force of human stroking movements, we designed a handle with force-torque-sensor and ArUco marker. A soft wool brush for stroking was mounted underneath the handle. We plan to record the Cartesian trajectory of stroking through the FRAMOS D400e camera and the ArUco marker, as well as the 6D force information of stroking through the force-torque-sensor. This is used as a reference value for the robot to reproduce the touch. So far the experimental table composed of a robotic arm, force sensor, the camera fixed on the table, ArUco code, and soft brush is completed (as shown in Fig. 2).

During the preparation of the experiment, we observed that the camera and ArUco marker solution introduced additional errors, leading to unreasonable waypoints in the trajectories. To mitigate this issue, we mounted the brush handle on the robot, allowing the person providing the reference stroking trajectory to use the robot's interactive mode. This setup enabled stroking on the experimenter's arm while recording waypoints in the Cartesian coordinate system.

2) Selecting the Methods: Considering the uniqueness of each individual—variances in forearm diameter, surface curvature, hardness, and even sitting position and reactions to stroking intensity—our technical goal was to deliver as consistent a touch as possible to each subject. Since all human-initiated touches in the experiments were also delivered by a single individual, we aimed for the 8 different variants share common characteristics, such as downward pressure on the forearm surface, which can also be interpreted as a relatively consistent position of the brushes perpendicular to the forearm. This allows for a better validation of whether robotic touch is distinguishable from human touch.

We chose the Cartesian DMPs [26] [29] with given feature points as our motion planning method. DMP can encode and reproduce movement patterns from demonstration, which means once reference trajectories are available, the generated trajectories could be the same type of shape but with specific characteristics (Size, starting point and goal. . .). The Cartesian DMPs can capture complex Cartesian trajectories and are therefore suitable for mimicking human stroking movements, which involve coordinated movements in multiple dimensions.

At the beginning of the experiment, we sample the start and end points of the stroking motion of the subject's forearm so that we can implicitly obtain information such as forearm position, inclination, diameter, etc. Cartesian DMPs can combine the reference stroke trajectory we recorded and the start and end positions to produce a forearm stroking trajectory that is appropriate for the subject.

3) Trajectory: We use Moveit Cartesian Interpolator [30] as the interface between the DMPs and the controller. It is the default Cartesian Interpolator functionality in MoveIt, which provides a greedy interpolation between the waypoints defined by the user. Furthermore, when this function tries to get the IK solution of the waypoints, it will pass these points plus a random noise within tolerance, rather than pass the exact waypoints position to the IK solver. This is done to deal with situations where a particular IK solution may be sensitive to initial conditions. However, this situation also gives us unpredictable computational results, for which we can influence the randomness of the whole generated trajectory by defining different numbers of reference trajectory waypoints.

Also, since the algorithm used is greedy interpolation, which means the trajectory between waypoints is not optimized for factors like joint limits, kinematic singularities, or collision avoidance. This can result in suboptimal trajectories. The number of waypoints affects the results of the IK solver and thus changes the predictability of the whole trajectory. In short, if the whole trajectory is given only the start and end points, then the randomness of the trajectory is defined only by the

random values attached to the start and end points at the time of solving and the randomness of the two IK solver processes. At the same time, the predictability is greatly improved due to the relatively smooth point-to-point trajectory. As the number of waypoints increases, the randomness of the entire trajectory increases, and more standing points can make the robot's trajectory elusive.

In our experiments, we defined trajectories close to straight lines as high predictability, curvilinear trajectories with three waypoints as medium predictability, and s-shaped trajectories with four waypoints as low predictability (Fig. 1).

IV. Experiment Details

A. Participants

34 female participants aged $19 - 25$ (20.70 ± 1.69) were tested. All of them were students and received course credits or a small financial compensation for participation. None of the participants reported any mental health issues as screened by PHQ4 [31] questionnaire (3.61 ± 1.84). According to the questionnaire on touch experiences and attitudes (TEAQ [32]), participants had a normal attitude to interpersonal touch (62.32 ± 8.05). The first six participants tested were not included in the final analysis due to initial technical issues with the robotic arm, leading the brush to lose contact with the participant's arm.

B. Study Instructions to Participants

Participants were informed that the study involves interacting with a robot designed to replicate affective touch. They were briefed on the nature of the touch (soft brush strokes on the forearm) and that their reactions and perceptions would be recorded via questionnaires after each interaction. Instructions emphasized that their participation was voluntary, and they could withdraw at any time without penalty. Our procedures were designed to prioritize participant comfort and privacy, including measures to de-identify data and protect participant anonymity.

C. IRB Approval

This study was approved by the local ethical committee (FSV 22/102), ensuring adherence to ethical guidelines for research involving human participants.

D. Informed Consent

All participants provided informed consent before participating in the study. The consent process involved explaining the study's purpose, procedures, potential risks, and benefits, ensuring participants were fully informed. Participants were also assured of their right to withdraw from the study at any time.

E. Procedure

After informed consent, participants were asked to answer demographic and health-related questions, the short version of the questionnaire on touch experiences and attitudes (TEAQ), and the brief Patient Health Questionnaire (PHQ-4). For the experiment participants were placed on a comfortable chair in front of a computer screen. They placed their left forearm on a soft cushion behind a curtain to avoid seeing the stroking agent. The participants were stroked in 8 different conditions on their left forearm. The stroking material was always a soft goat hairbrush ($3\,\mathrm{cm}$ width). Three of the conditions were performed by a human and five by the robot arm. The order of presentations was randomized, and each presentation was repeated twice. Two of the robot conditions included linear stroking with a velocity of 3 or $0.3\,\mathrm{cm/s}$, and the other three included non-linear stroking with small, medium, and large deviation (low, medium, high predictability) from linear movement and a velocity of $3\,\mathrm{cm/s}$. The manipulation of trajectory was included to enhance ecological validity, as natural touch typically does not follow strict linear movements [33]. As mentioned above (Fig. 1), we show the randomness, predictability, and degree of deviation of the trajectories by defining different numbers and poses of waypoints. The human experimenter stroked with linear with a velocity of 3 or $0.3\,\mathrm{cm/s}$, and non-linear with a velocity of $3\,\mathrm{cm/s}$. The linear (straight line) trajectories were visualized on the participants' forearm using a kajal pen, the non-linear (medium deviation) trajectory will be displayed by the robot above. This ensured stroking reliability, which was further facilitated by the experimenter following the movement of the robot, which ran at the same time but did not touch the participant. Hence, there was always a sound of the robot's arm, so the participants could not differentiate human vs robot conditions based on sound effects.

F. Assessment of Stroking Perception

After each of the 16 stroking events, the participant was asked to rate the pleasantness, intensity, and human-likeness on a VAS with the endpoints from "not at all pleasant/intense/human-like" (0) to "very pleasant/intense/human-like" (10). In addition, the receiver was asked to decide for each stroke whether it was performed by a human or by a robot.

G. Statistical Analysis

First, we calculated the mean pleasantness, humanness, and intensity score over repetitions for each condition (Tab. I). Then, we conducted separate statistical analyses using R (version 4.2.3). To test whether stroking with $3\,\mathrm{cm/s}$ was rated more pleasant than stroking with $0.3\,\mathrm{cm/s}$ (H1), we computed an ANOVAs for repeated measurements with the within-subject factors velocity (2) and agent (2). We repeated the analysis for the dependent variable of "human-like". To test whether the predictability of stroking is related to the perceived pleasantness (H2), we computed an ANOVA for repeated measurements with the within-subject factor trajectory (3), using the three non-linear robot conditions. Post-hoc-Tests were performed with paired t-tests and are presented Bonferoni-corrected. The analysis was repeated for the dependent variable of "human-like". Finally, we explored whether participants could distinguish robot from human touch and

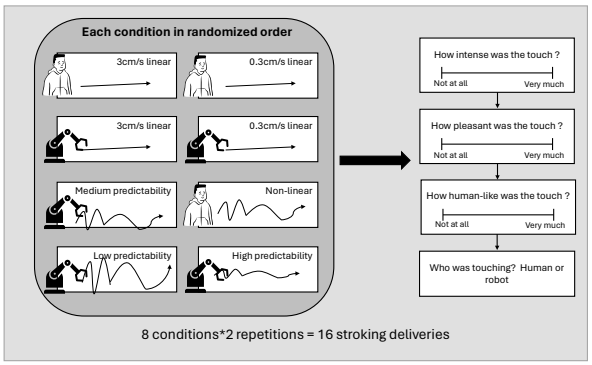


Fig. 4. **Experiments design**: The participants were stroked in 8 different conditions on their left forearm by a soft goat hairbrush. Three of the conditions were performed by a human and five by a robot. Two of the human touch conditions included linear stroking with a velocity of 3 or $0.3\,\mathrm{cm/s}$, the third condition included non-linear stroking. Two of the robot conditions included linear stroking with a velocity of 3 or $0.3\,\mathrm{cm/s}$, the other three included non-linear stroking with low, medium, and high predictability.

whether this related to predictability (H3) and determined for all conditions, whether choices deviated significantly from the 50% chance using χ^2 tests.

V. Results

We confirmed previous results showing higher pleasantness ratings for $3\,\mathrm{cm/s}$ as compared to the slower 0.3 cm/s stroking conditions ($F(1,27) = 51.15, p < .001, \eta^2 = 0.31$, Figure 5). There was no significant effect of agent ($F(1,27) = 0.51, p = 0.481 \eta^2 = 0.002$) and no significant velocity by agency interaction ($F(1,27) = 2.73, p = 0.11 \eta^2 = 0.017$), indicating that robot and human-delivered touch were not perceived as different in pleasantness (H1).

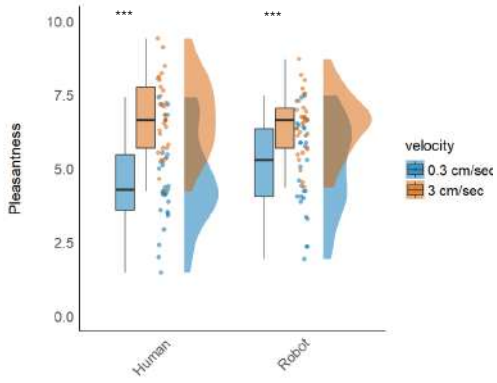


Fig. 5. **Pleasantness ratings in human and robot touch.** There was a significant effect of the main effect of the velocity ($p < 0.001$)

For human-likeness, we observed no significant effect of velocity ($F(1,27) = 0.69, p = 0.413, \eta^2 = 0.008$, Figure 6) and not significant velocity by agency interaction ($F(1,27) = 0.35, p = 0.55, \eta^2 = 0.002$). A significant effect of agency ($F(1,27) = 5.71, p = 0.024, \eta^2 = 0.051$, Figure 6) however indicates that the human-delivered touch was perceived as more human-like than the robot-delivered touch.

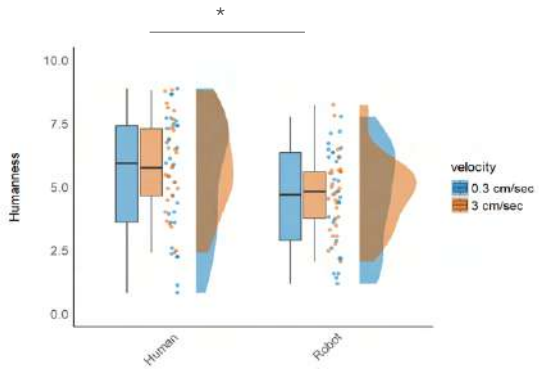


Fig. 6. **Humanness ratings in human and robot touch.** There was a significant effect of the main effect of the agent ($p < 0.05$) and the touch performed by the human was perceived as more human-like as compared to the robot touch.

For the different stroking trajectories, we observed a significant effect of trajectory on pleasantness ($F(2,54) = 9.52, p < .001, \eta^2 = 0.15$), but not on humanness ($F(2,54) = 1.87, p = .163, \eta^2 = 0.034$). Post-hoc-Test revealed reduced pleasantness perception during the low predictable conditions as compared to the high ($t(27) = -3.85, p < 0.001$) and medium ($t(27) = -3.13, p = 0.004$) ones (H2).

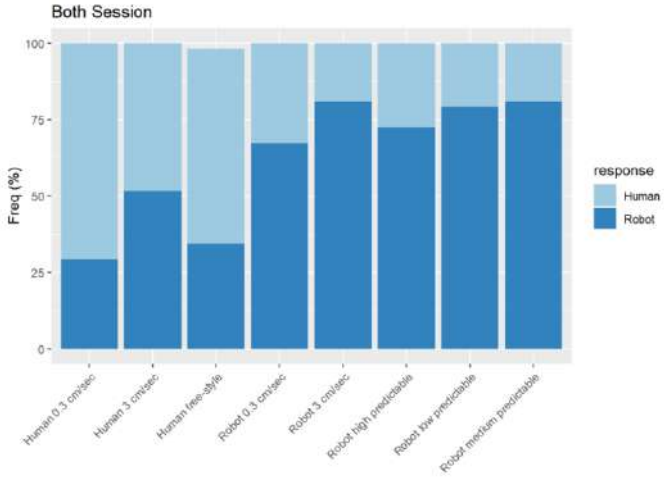


Fig. 7. **The percentage of the touch recognition delivered by agents**

Over all conditions, 75.71% of the participants correctly recognized the robotic touch as delivered by the robot ($\chi^2 = 26.45; p < 0.001$), and 60.12% of the participants correctly recognized the human touch as delivered by human ($\chi^2 = 4.37; p = 0.036$, Figure 7) (H3).

The recognition of robot touch (H3) did not relate to the trajectory ($\chi^2 = 1.70; p = 0.427$). For the human touch, correct recognition related to the touch characteristics and exceeded chance level for the linear $0.3\,\mathrm{cm/s}$ ($\chi^2 = 15.44, p < 0.001$) and non-linear 3cm/s ($\chi^2 = 9.38, p = 0.002$) conditions.

TABLE I
MEAN VALUES OF THE PLEASANTNESS, INTENSITY, AND HUMANNESS SCORES GENERATED AT THE DIFFERENT VELOCITIES AND CONDITIONS.

		Pleasantness		Intensity		Humanness	
Agent	**Condition**	**Mean**	**SD**	**Mean**	**SD**	**Mean**	**SD**
Human	0.3 cm/sec, linear	4.65	2.04	5.31	1.98	5.36	2.73
	3 cm/sec, linear	6.82	1.52	5.16	1.88	5.87	2.24
	3 cm/sec, medium deviation	6.67	1.51	5.13	1.64	6.18	1.97
Robot	0.3 cm/sec, linear	5.13	2.22	3.56	2.21	4.62	2.5
	3 cm/sec, linear	6.59	1.33	4.86	1.63	4.82	2.13
	3 cm/sec, small deviation (high predictability)	6.53	1.41	5.00	1.46	4.93	2.05
	3 cm/sec, large deviation (low predictability)	5.29	1.62	5.52	1.96	4.2	2.09
	3 cm/sec, medium deviation (medium predictability)	6.29	1.61	5.32	1.48	4.62	2.05

VI. DISCUSSION AND CONCLUSION

In this paper, we employ the Cartesian DMPs to emphatically replicate the spatial and temporal characteristics of human stroking. Thanks to the use of a soft brush as an intermediate transmitter of touch, we can eliminate as many other touch characteristics as possible, such as material, texture, temperature, etc., and even the dynamic characteristic (strength, pressure, acceleration) of the touch can be neutralized by the brush. As a result, we can more clearly analyze the influence of stroke velocity and stroke trajectory on the interpersonal haptic experience, and also analyze whether the robot can perfectly reproduce human strokes from these two perspectives alone.

Our results show that we were able to replicate the typical pleasurable sensations associated with human touch when the robot touched at a speed of 3 cm/s compared to the slow speed of 0.3 cm/s.

The results of robotic touch recognition show that the degree of humanization of robotic strokes is independent of trajectory. The speed of touch (a temporal parameter) played a role in participants' ability to predict the initiator of the touch, but a human-initiated touch at 3 cm/s had nearly a 50% chance of being predicted as robotic, whereas the probability of a robot-initiated touch being judged correctly exceeded 70% for all touches. It can be concluded that spatial and temporal parameters alone are not sufficient for the replicative reconstruction of human touch and that the strength and intensity of touch need to be the next focus of research in future work. For the robotic scope, the hybrid position and force controller and Cartesian compliant DMPs may serve as a tool for reproducing the dynamic parameters of touch.

Meanwhile, the main reason why human behavior is more easily confounded is that we did not extract features from the individual human who applied the touch, which resulted in the touch applied by the robot being based more on the forearm geometry of the person being touched than on the touch habits of the person applying the touch itself. The fact that humans are more adaptable than robots when applying strokes also leads to experimental bias as humans involuntarily mimic the stroking behavior of the robot above them. Enhancing video capture capabilities to precisely record the human operator's touch velocity and trajectory could facilitate future studies in achieving a more accurate mimicry of human touch.

In conclusion, affective touch holds great promise for advancing robotic rehabilitation by supporting motor recovery, enhancing sensory stimulation, and improving the emotional well-being of patients. Robotic affective touch could play a transformative role in clinical applications, such as stroke rehabilitation, where controlled stroking movements may facilitate sensory relearning and neuroplasticity. Furthermore, robotic touch therapy presents exciting opportunities for neuropathic pain management and as a non-invasive approach to reducing anxiety in hospitalized patients. With continued research and development, these innovations could significantly enhance patient care and well-being.

REFERENCES

[1] F. McGlone, J. Wessberg, and H. Olausson, "Discriminative and Affective Touch: Sensing and Feeling," *Neuron*, vol. 82, no. 4, pp. 737–755, May 2014. [Online]. Available: https://www.sciencedirect.com/science/article/pii/S0896627314003870

[2] A. Gallace and C. Spence, "The science of interpersonal touch: An overview," *Neuroscience & Biobehavioral Reviews*, vol. 34, no. 2, pp. 246–259, Feb. 2010. [Online]. Available: https://www.sciencedirect.com/science/article/pii/S0149763408001723

[3] A. Schirmer, I. Croy, and R. Ackerley, "What are C-tactile afferents and how do they relate to "affective touch"?" *Neuroscience & Biobehavioral Reviews*, vol. 151, p. 105236, Aug. 2023. [Online]. Available: https://www.sciencedirect.com/science/article/pii/S0149763423002051

[4] B. Ditzen, I. D. Neumann, G. Bodenmann, B. Von Dawans, R. A. Turner, U. Ehlert, and M. Heinrichs, "Effects of different kinds of couple interaction on cortisol and heart rate responses to stress in women," *Psychoneuroendocrinology*, vol. 32, no. 5, pp. 565–574, Jun. 2007. [Online]. Available: https://linkinghub.elsevier.com/retrieve/pii/S0306453007000698

[5] A. Vallbo, H. Olausson, J. Wessberg, and U. Norrsell, "A system of unmyelinated afferents for innocuous mechanoreception in the human skin," *Brain Research*, vol. 628, no. 1, pp. 301–304, Nov. 1993. [Online]. Available: https://www.sciencedirect.com/science/article/pii/000689939390968S

[6] L. S. Löken, J. Wessberg, I. Morrison, F. McGlone, and H. Olausson, "Coding of pleasant touch by unmyelinated afferents in humans," *Nature Neuroscience*, vol. 12, no. 5, pp. 547–548, May 2009, publisher: Nature Publishing Group. [Online]. Available: https://www.nature.com/articles/nn.2312

[7] I. Croy, A. Bierling, U. Sailer, and R. Ackerley, "Individual Variability of Pleasantness Ratings to Stroking Touch Over Different Velocities," *Neuroscience*, vol. 464, pp. 33–43, Jun. 2021.

[8] R. H. Watkins, J. Wessberg, H. Backlund Wasling, J. P. Dunham, H. Olausson, R. D. Johnson, and R. Ackerley, "Optimal delineation of single C-tactile and C-nociceptive afferents in humans by latency slowing," *Journal of Neurophysiology*, vol. 117, no. 4, pp. 1608–1614, Apr. 2017, publisher: American Physiological Society. [Online]. Available: https://journals.physiology.org/doi/full/10.1152/jn.00939.2016

[9] U. Sailer, M. Hausmann, and I. Croy, "Pleasantness Only?: How Sensory and Affective Attributes Describe Touch Targeting C-Tactile Fibers," *Experimental Psychology*, vol. 67, no. 4, pp. 224–236, Jul. 2020. [Online]. Available: https://econtent.hogrefe.com/doi/10.1027/1618-3169/a000492

[10] M. Deniša, T. Petric, A. Gams, and A. Ude, "A Review of Compliant Movement Primitives," Oct. 2016.

[11] S.-Y. Kim, K.-b. Kim, J. Kim, and K.-u. Kyung, "A Film-Type Vibrotactile Actuator for Hand-Held Devices," in *Haptic and Audio Interaction Design*, I. Oakley and S. Brewster, Eds. Berlin, Heidelberg: Springer, 2013, pp. 109–116.

[12] R. Sodhi, I. Poupyrev, M. Glisson, and A. Israr, "AIREAL: interactive tactile experiences in free air," *ACM Transactions on Graphics*, vol. 32, no. 4, pp. 134:1–134:10, Jul. 2013. [Online]. Available: https://doi.org/10.1145/2461912.2462007

[13] A. A. Stanley and K. J. Kuchenbecker, "Design of body-grounded tactile actuators for playback of human physical contact," in *2011 IEEE World Haptics Conference*. Istanbul: IEEE, Jun. 2011, pp. 563–568. [Online]. Available: http://ieeexplore.ieee.org/document/5945547/

[14] C. J. A. M. Willemse, A. Toet, and J. B. F. van Erp, "Affective and Behavioral Responses to Robot-Initiated Social Touch: Toward Understanding the Opportunities and Limitations of Physical Contact in Human–Robot Interaction," *Frontiers in ICT*, vol. 4, May 2017, publisher: Frontiers. [Online]. Available: https://www.frontiersin.org/articles/10.3389/fict.2017.00012

[15] C. J. A. M. Willemse and J. B. F. van Erp, "Social Touch in Human–Robot Interaction: Robot-Initiated Touches can Induce Positive Responses without Extensive Prior Bonding," *International Journal of Social Robotics*, vol. 11, no. 2, pp. 285–304, Apr. 2019. [Online]. Available: https://doi.org/10.1007/s12369-018-0500-9

[16] A. E. Block, "HuggieBot: An interactive hugging robot with visual and haptic perception," Ph.D. dissertation, ETH Zürich, Zürich, Aug. 2021, department of Computer Science.

[17] A. E. Block, H. Seifi, O. Hilliges, R. Gassert, and K. J. Kuchenbecker, "In the arms of a robot: Designing autonomous hugging robots with intra-hug gestures," *J. Hum.-Robot Interact.*, vol. 12, no. 2, Mar. 2023. [Online]. Available: https://doi.org/10.1145/3526110

[18] T. Law, B. F. Malle, and M. Scheutz, "A Touching Connection: How Observing Robotic Touch Can Affect Human Trust in a Robot," *International Journal of Social Robotics*, vol. 13, no. 8, pp. 2003–2019, Dec. 2021. [Online]. Available: https://doi.org/10.1007/s12369-020-00729-7

[19] J. B. V. Erp and A. Toet, "How to Touch Humans: Guidelines for Social Agents and Robots That Can Touch," in *2013 Humaine Association Conference on Affective Computing and Intelligent Interaction*. Geneva, Switzerland: IEEE, Sep. 2013, pp. 780–785. [Online]. Available: http://ieeexplore.ieee.org/document/6681537/

[20] X. Zheng, M. Shiomi, T. Minato, and H. Ishiguro, "What Kinds of Robot's Touch Will Match Expressed Emotions?" *IEEE Robotics and Automation Letters*, vol. 5, no. 1, pp. 127–134, Jan. 2020. [Online]. Available: https://ieeexplore.ieee.org/document/8865356/

[21] M. Teyssier, G. Bailly, C. Pelachaud, and E. Lecolinet, "Conveying Emotions Through Device-Initiated Touch," *IEEE Transactions on Affective Computing*, vol. 13, no. 3, pp. 1477–1488, Jul. 2022. [Online]. Available: https://ieeexplore.ieee.org/document/9139211/

[22] C. J. A. M. Willemse, G. Huisman, M. M. Jung, J. B. F. Van Erp, and D. K. J. Heylen, "Observing Touch from Video: The Influence of Social Cues on Pleasantness Perceptions," in *Haptics: Perception, Devices, Control, and Applications*, F. Bello, H. Kajimoto, and Y. Visell, Eds. Cham: Springer International Publishing, 2016, vol. 9775, pp. 196–205, series Title: Lecture Notes in Computer Science. [Online]. Available: http://link.springer.com/10.1007/978-3-319-42324-120

[23] A. J. Ijspeert, J. Nakanishi, H. Hoffmann, P. Pastor, and S. Schaal, "Dynamical Movement Primitives: Learning Attractor Models for Motor Behaviors," *Neural Computation*, vol. 25, no. 2, pp. 328–373, Feb. 2013. [Online]. Available: https://direct.mit.edu/neco/article/25/2/328-373/7850

[24] P. Pastor, H. Hoffmann, T. Asfour, and S. Schaal, "Learning and generalization of motor skills by learning from demonstration," in *2009 IEEE International Conference on Robotics and Automation*. Kobe: IEEE, May 2009, pp. 763–768. [Online]. Available: http://ieeexplore.ieee.org/document/5152385/

[25] K. Mülling, J. Kober, O. Kroemer, and J. Peters, "Learning to select and generalize striking movements in robot table tennis," *The International Journal of Robotics Research*, vol. 32, no. 3, pp. 263–279, Mar. 2013. [Online]. Available: http://journals.sagepub.com/doi/10.1177/0278364912472380

[26] A. Ude, B. Nemec, T. Petric, and J. Morimoto, "Orientation in Cartesian space dynamic movement primitives," in *2014 IEEE International Conference on Robotics and Automation (ICRA)*. Hong Kong, China: IEEE, May 2014, pp. 2997–3004. [Online]. Available: http://ieeexplore.ieee.org/document/6907291/

[27] A. Gams, B. Nemec, L. Zlajpah, M. Wachter, A. Ijspeert, T. Asfour, and A. Ude, "Modulation of motor primitives using force feedback: Interaction with the environment and bimanual tasks," in *2013 IEEE/RSJ International Conference on Intelligent Robots and Systems*. Tokyo: IEEE, Nov. 2013, pp. 5629–5635. [Online]. Available: http://ieeexplore.ieee.org/document/6697172/

[28] T. Ishikura, A. Yuguchi, Y. Kitamura, S.-G. Cho, M. Ding, J. Takamatsu, W. Sato, S. Yoshikawa, and T. Ogasawara, "Toward an Affective Touch Robot: Subjective and Physiological Evaluation of Gentle Stroke Motion Using a Human-Imitation Hand," Dec. 2020, arXiv:2012.04844 [cs]. [Online]. Available: http://arxiv.org/abs/2012.04844

[29] A. Fabisch, jkklemm, maotto, wujiajun, B. Busch, and E. Eberhard, "dfki-ric/movement_primitives: 0.7.0," Nov. 2023. [Online]. Available: https://zenodo.org/doi/10.5281/zenodo.6491361

[30] D. Coleman, I. Sucan, S. Chitta, and N. Correll, "Reducing the Barrier to Entry of Complex Robotic Software: a MoveIt! Case Study," Apr. 2014, arXiv:1404.3785 [cs]. [Online]. Available: http://arxiv.org/abs/1404.3785

[31] K. Kroenke, R. L. Spitzer, J. B. W. Williams, and B. Löwe, "An ultra-brief screening scale for anxiety and depression: the PHQ-4," *Psychosomatics*, vol. 50, no. 6, pp. 613–621, 2009.

[32] P. D. Trotter, F. McGlone, R. L. E. P. Reniers, and J. F. W. Deakin, "Construction and Validation of the Touch Experiences and Attitudes Questionnaire (TEAQ): A Self-report Measure to Determine Attitudes Toward and Experiences of Positive Touch," *Journal of Nonverbal Behavior*, vol. 42, no. 4, pp. 379–416, 2018.

[33] C. Lo, S. T. Chu, T. B. Penney, and A. Schirmer, "3D Hand-Motion Tracking and Bottom-Up Classification Sheds Light on the Physical Properties of Gentle Stroking," *Neuroscience*, vol. 464, pp. 90–104, Jun. 2021.

Analysis of Induced Muscle Activations by an Affordable, Reconfigurable Robot for Comprehensive Post-Stroke Rehabilitation

Nova Y. Meng*[1], Erica L. Waters*[2], Gary Lin[3], Samuel Gaardsmoe[4], Alwyn Johnson[5], Laura A. Hallock[6], Rochelle J. Mendonca[7], Pamela Z. Cacchione[8], and Michelle J. Johnson[9]

***Abstract*— Post-stroke upper-limb impairments affect millions of people worldwide. Low-degree-of-freedom (DoF) end-effector (EE) rehabilitation robots have the potential to provide more affordable and accessible rehabilitation, but there is concern that sacrificing complexity could reduce the efficacy of robotic rehabilitation. In this paper, we present preliminary evidence that a 1-DoF EE rehabilitation robot with multiple configurations can provide comprehensive upper limb exercise. Specifically, we introduce the reconfigurable Rehab CARES system, an expansion of the Haptic TheraDrive robot, and analyze muscle activation data (as measured by surface electromyography, or sEMG) from 11 post-stroke participants performing range of motion (ROM) movements in 3 different robot positions, each of which simulates a different activity of daily living. Our findings indicate that collectively, these positions elicit comprehensive activation of the arm muscles in post-stroke individuals, and that induced motor patterns differ across both positions and levels of user impairment, some of which are likely reflective of compensatory movement strategies. We conclude that with smart reconfiguring, a 1-DoF EE robot is capable of inducing different muscle activation patterns, but does not prevent the user from employing these undesirable compensatory strategies, suggesting that such robots are a promising platform for low-cost rehabilitation exercise and characterizing pathological synergistic movements.**

Research reported in this publication was supported by the Eunice Kennedy Shriver National Institute Of Child Health & Human Development of the National Institutes of Health under Award Number F31HD116597 and Award Number R42HD104325. The content is solely the responsibility of the authors and does not necessarily represent the official views of the National Institutes of Health. Dr. Michelle Johnson has a patent that uses devices inspired by the device being evaluated in this research. Dr. Michelle J. Johnson, Alwyn Johnson, and Dr. Rochelle J. Mendonca are co-founders and Samuel Gaardsmoe is an employee of Recupero Robotics LLC.

*Indicates equal contribution.

[1]Nova Y. Meng is a graduate of the University of Pennsylvania with a B.S. in Bioengineering.

[2]Erica L. Waters is a PhD candidate in Mechanical Engineering & Applied Mechanics at the University of Pennsylvania. waterica@seas.upenn.edu

[3] Gary Lin is a graduate of the University of Pennsylvania with an M.S.E. in Robotics.

[4] Samuel Gaardsmoe is the lead engineer at Recupero Robotics LLC.

[5] Alwyn Johnson is the CTO of Recupero Robotics LLC.

[6] Dr. Laura A. Hallock is an Assistant Professor in the Department of Mechanical Engineering and an Adjunct Assistant Professor in the Department of Physical Medicine & Rehabilitation at the University of Utah.

[7] Dr. Rochelle J. Mendonca is Assistant Professor in the Department of Rehabilitation & Regenerative Medicine/Programs in Occupational Therapy at Columbia University.

[8]Pamela Z. Cacchione is a Professor of Geropsychiatric Nursing at the University of Pennsylvania School of Nursing.

[9] Dr. Michelle J. Johnson is an Associate Professor at the University of Pennsylvania with a primary appointment in Physical Medicine & Rehabilitation and secondary appointments in Bioengineering and Mechanical Engineering & Applied Mechanics. johnmic@pennmedicine.upenn.edu

I. Introduction

Globally, over 12.2 million people experience a stroke each year [1]. Upper-limb impairments are common following a stroke, with prevalence estimates ranging from 40–80% [2], and these impairments are associated with a lower quality of life [3]. Effective and accessible rehabilitation methods are crucial for these individuals to regain functional independence. Rehabilitation robots are one solution for post-stroke upper-limb exercise and are capable of delivering affordable, high-quality therapy that is tailored to individual needs. Rehabilitation robots can be categorized into two types based on their mechanical structure: end-effector (EE) robots, which interact with the hand or distal limb to move the entire arm, and exoskeleton (Exo) robots, which are wearable devices that support and guide arm movement.

Single degree-of-freedom (DoF) EE robots are cost effective compared with complex EE and Exo robots, making them a desirable option for affordable care [4]. Stroke survivors who train with low-DoF EE robots may actually increase activity and participation compared with stroke survivors who train with Exo robots [5]. However, the lack of control at specific joints can allow users to rely on compensatory movements. Meta-analysis of randomized controlled trials with rehabilitation robots show that they can significantly reduce motor impairment but often do not result in significant improvements in motor capacity or performance of activities of daily living (ADL) compared with standard of care therapy [6]. This disparity between improvements in motor impairment measures and lack of improvement in ADL performance could be the result of compensatory strategies [6]. Post-stroke individuals often rely on compensatory strategies such as trunk movements [7] or abnormal muscle synergies, especially between the shoulder and elbow [8]. Although compensatory strategies can help people regain functional performance after a stroke, the long-term use of such strategies can be maladaptive and detrimental to motor recovery [9]. Therefore, it is necessary to understand which muscles stroke survivors recruit during robot-based exercise to better understand whether such exercises train "normal," healthy movement strategies or reinforce maladaptive compensatory strategies.

Due to the limited motion patterns they enable, 1-DoF robots may be less effective in activating all the important muscle groups required for upper limb therapy compared with multi-DoF robots. A survey of rehabilitation robots, for example, highlighted multiple-single-active-DoF robots,

including eleven targeting elbow flexion/extension, one targeting the forearm pronation/supination, and four targeting wrist flexion/extension, but the survey found no 1-DoF robots that assisted whole arm movements [10]. 1-DoF robots that can be configured in multiple positions may provide a solution that maintains affordability while also exercising a variety of muscle groups. The MIT Manus was one of the first reconfigurable rehabilitation robots and can provide both arm and wrist rehabilitation [11]. Other 1-DoF reconfigurable rehabilitation robots include the Bi-Manu-Track [12], which provides bimanual forearm pronation/supination and wrist flexion/extension, and the CR2-Haptic [13], which targets ten different movements of the shoulder, elbow, forearm, wrist and hand. Training with these robots allowed stroke survivors to improve on clinical metrics [12], [13], but the effectiveness of a 1-DoF reconfigurable rehabilitation robot at inducing different muscle activations has not been investigated.

In this study, we assess the ability of a 3-configuration, 1-DoF EE rehabilitation robot, the TheraDrive to activate muscle groups of the arm by analyzing surface electromyography (sEMG) muscle activation patterns during standardized movements. We analyze sEMG data from the impaired limbs of 11 post-stroke participants who completed a 1-day exercise protocol with the TheraDrive as part of the Rehabilitation Using Community-Based Affordable Robotic Exercise Systems (Rehab CARES) clinical trial [14]. Specifically, we investigate muscle activation patterns in three distinct configurations of the robot: a simulated reach-to-grasp movement (Pos. 1), a standard planar movement involving shoulder abduction/adduction (Pos. 2), and a wrist pronation/supination movement (Pos. 3), for both mildly and moderately/severely impaired individuals, as measured by the Fugl-Meyer assessment of the upper extremity.

Note that this is a preliminary publication on the Rehab CARES system, and analyses of many aspects of the system and data collection protocol are beyond the scope of this paper, as noted in future sections. In particular, the protocol we describe includes participants performing a number of assessment tasks and therapy games, which are discussed in another publication [15]. In this paper, we restrict our analyses to the sEMG activation and kinematic data collected during standardized range of motion (ROM) movements performed on the robot in different configurations.

II. Rehab CARES System Design

The Rehab CARES project is a community-based approach to rehabilitation that uses multiple affordable, reconfigurable 1-DoF TheraDrive robots to provide solo and group therapy to individuals after stroke. The Rehab CARES robot gym approach has been tested in both Mexico and the USA [16]. More information about the updated Rehab CARES system is available in our collaborators' publication [15].

In previous work, the TheraDrive was primarily investigated in a single configuration—a simulated reach to grasp movement (Position 1). The present study investigated the TheraDrive in three distinct positions, shown in Figure 1.

A. Position 1 – Reach-to-Grasp

Figure 1a shows the TheraDrive in Position 1 (Pos. 1). In this configuration, the robot is positioned to the side of the user with the workspace parallel to the sagittal plane. The EE for this configuration is a cylindrical handle that attaches perpendicular to the crank arm. In this position, we expect the user to exhibit flexion/extension of the shoulder and elbow. This configuration of the robot simulates a reach-to-grasp task, replicating movements typically used in opening cabinets and closets.

B. Position 2 – Shoulder Abduction/Adduction

Figure 1b shows the TheraDrive in Position 2 (Pos. 2). This position was designed to involve more abduction/adduction of the shoulder than Pos. 1. To achieve this movement, the robot is positioned vertically with the workspace along the user's transverse plane. The same EE from Pos. 1 is used. Pos. 2 replicates the movements used for wiping down a table or a window, and mimics the planar motion studied in much of the rehabilitation literature.

C. Position 3 – Wrist Pronation/Supination

Figure 1c shows the TheraDrive in Position 3 (Pos. 3). This position was designed to target wrist and forearm pronation/supination. For this position, the robot is in the horizontal position, and the user is turned to face the robot so that the robot workspace falls along the user's frontal/coronal plane. The EE is replaced with a handle parallel to the crank-arm. This new handle allows the user to perform internal/external arm rotations and replicates wrist movements used to turn faucets and door handles.

III. Methods

We outline our methodology to assess differences in muscle activations across positions in a pilot cohort of post-stroke users, including data collection, processing, and analysis.

A. Participants

Patients were recruited from Good Shepherd Penn Partners and stroke support groups at the University of Pennsylvania hospitals. Our inclusion criteria for the participants were that the patients must be: 18 years or older, clinically diagnosed with hemiparesis resulting from a stroke, at least 3 months post-stroke, able to undergo therapy, and having some level of voluntary activity on the impaired side, evidenced by some active elbow ROM and some finger flexion.[1] Participants were excluded if they had cerebellar stroke, seizures before stroke, had depression scores on the NeuroQoL Depression measure of > 32, or pain measure of > 4. This protocol was approved by the Institutional Review Board of the University of Pennsylvania (protocol 849090). For the initial evaluation of the rehabilitation platform, 11 stroke survivors (60 ± 10 years, 4F/7M) were recruited, presenting varying degrees of motor and cognitive impairment, as detailed in Table I.

[1]Participants unable to grip the handle were not excluded; a passive grip assist was used for those unable to maintain grip.



(a) Position 1 (Reach-to-Grasp)

(b) Position 2 (Shoulder Abduction/Adduction)

(c) Position 3 (Wrist Pronation/Supination)

Fig. 1: The Rehab CARES TheraDrive robot in each of its 3 ADL-inspired configurations. The TheraDrive's 1-DoF EE reconfigurable design allows the device to remain affordable while supporting a variety of motor rehabilitation tasks.

TABLE I: Participant Clinical Assessment Scores

ID	MoCA	CT1	CT2	UE-FM	BBT	9-HP
001	24	0.90	-0.51	65	61	19.09
003	29	0.90	1.25	65	52	19.03
004	23	-0.13	0.53	65	71	16.72
005	15	-6.51	-6.45	57	43	64
007	17	-7.09	-9.98	33	8	DNC
009	22	-0.11	-1.11	65	40	25.53
010	22	–	–	56	40	43.97
011	24	0.19	0.31	30	23	131.37
012	25	-7.62	-3.36	51	27	52.23
013	17	-1.62	-2.35	54	37	40.47
014	12	-2.70	-7.93	13	0	DNC

BBT and 9-HP are reported only for the affected limb. BBT is reported as the number of blocks and 9-HP is reported as time in seconds. CT1 and CT2 are reported as z-scores.

TABLE II: Sensor Placement and Activating Motions

ID	Location	Expected Activating Motions
1A	biceps brachii	shoulder flex, elbow flex, wrist sup
1B	posterior deltoid	shoulder (ext, ex-rot)
1C	anterior deltoid	shoulder (flex, in-rot)
1D	middle deltoid	shoulder abd
2A	triceps brachii (long head)	shoulder (ext, add), elbow ext
2B	wrist flexor bundle	wrist flex
2C	wrist extensor bundle	wrist ext
2D	brachioradialis	elbow flex, wrist (pro, sup)

Activating motion abbreviations: flexion (flex), extension (ext), adduction (add), abduction (abd), external rotation (ex-rot), internal rotation (in-rot), pronation (pro), supination (sup)

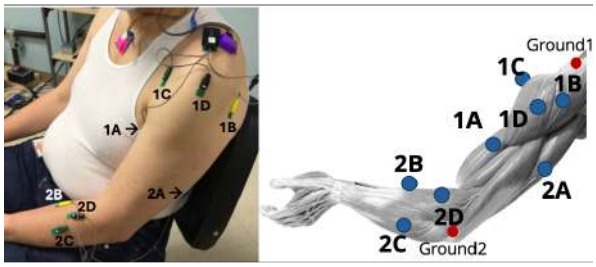


Fig. 2: Placement of sEMG sensors on the impaired arm.

B. Experimental Protocol

The data analyzed in this paper were collected during a larger validation study consisting of 3–4 experimental days for each participant: 1 clinical assessment day; 1–2 days performing robot-based assessments tasks, ROM movements, and therapy games; and 1 day of qualitative interviews on their experiences with the robot. If a second robot exercise day was necessary, data were re-collected at each ROM position to ensure consistent sEMG placement. Only the clinical assessments and a selection of the robot exercise tasks are analyzed in this work and are discussed below.

1) Clinical Assessment Day: On the day of the clinical assessment, participants worked with a trained occupational therapist to complete cognitive and motor assessments. The cognitive assessments included the Montreal Cognitive Assessment (MoCA), Color Trails 1 (CT1), and Color Trails 2 (CT2). Motor assessments included the Fugl-Meyer Upper Extremity Assessment (UE-FM), the Box and Block Test (BBT), and the 9-hole Pegboard Assessment (9-HP). Table I reports the results of the clinical evaluation for all participants.

2) Robot Exercise Day(s): The robot exercise day(s) consisted of two main phases: first, sensorization; and second, data collection during sensor calibration, ROM movements, assessment tasks, and therapy games.

a) Sensorization Phase: Participants were outfitted with sEMG sensors, 2 inertial measurement unit (IMU) sensors, a galvanic skin response (GSR) sensor, and a heart rate (HR) sensor [15]. Surface EMG data were collected from the subject's impaired arm via two four-channel sensor motes (Trigno Quattro, Delsys, Inc., Natick, MA, USA), each of which also contained an associated 6-DoF IMU. Targeted muscles were selected to comprehensively probe joint motions of interest induced by TheraDrive interaction and grounding sensors (and internal IMUs) were placed atop nearby bones (the acromion at the shoulder and olecranon at the elbow) as recommended by the manufacturer. A list of all sensor placements and associated motion(s) is shown in Table II; an image of all sensor placements is shown in Figure 2. Sensors were adhered to the subject using Trigno adhesives (Delsys, Inc., Natick, MA, USA) and transparent "transpore" surgical tape. Data were collected at 222 Hz via Trigno Discover software (Delsys, Inc., Natick, MA, USA).

b) Data Collection Phase: Once sensorized, participants performed the tasks outlined in Figure 3, including sensor calibration, ROM movements, assessment tasks, and therapy games while all sensor data described above were collected. All study days began with collection of a trial in

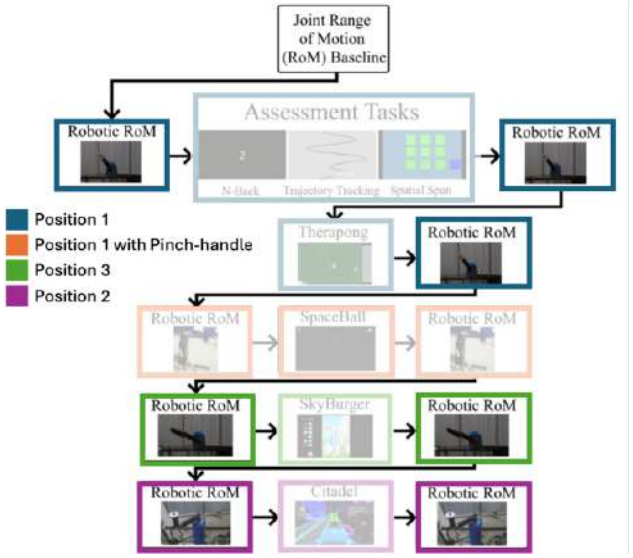


Fig. 3: Experimental workflow during robot exercise. Participants performed assessment tasks and therapy games, interleaved with ROM movements, at each position shown in Figure 1. Only the ROM movements are used in this work to analyze muscle activations in each position..

which the participant sat unmoving, with their eyes closed, and in silence, to establish a baseline for GSR and HR sensors.[2] The participant was then moved over to the haptic robot in Pos. 1 and completed a ROM task, in which the patient was instructed to move the handle of the robot as far as possible in both directions with their affected limb, in a rhythmic pattern while guided by a video, as shown in Figure 4. Participants first performed this task while unrestrained, and then again while restrained to their chair with a harness to prevent compensatory trunk motions. They then performed several assessment tasks (previously described for individuals with both HIV and stroke [17]). The robotic ROM task was then completed again after the assessment tasks in reverse order (restrained, then unrestrained), a therapy game was played in this position (Therapong), and a final unrestrained ROM trial collected.

All remaining activities were completed while unrestrained. This pattern—move to a new position, perform an initial ROM task, followed by a therapy game, followed by a final ROM task—persisted for all remaining experimental activities.[3] Each position had an associated therapy game developed by collaborators at enAble Games LLC; analysis of these games is the subject of a recent publication [15].

In this work, we analyze only the sEMG and associated IMU data collected during ROM trials at each position. The ROM trials are highly controlled movements that serve as an ideal starting point for initial understanding of what muscle activation patterns are induced in each of the three positions.

[2]Some participants also completed joint ROM tasks, but these tasks were ultimately eliminated from the protocol because they were too time-intensive.

[3]The Pos. 1 with pinch-handle trials were not analyzed due to the handle malfunctioning in many of the trials.

C. Data Processing

To compare muscle activations across participants (who performed ROM motions at inconsistent rates) and robot positions, sEMG data were clipped at the start of the first movement and at the end of the last movement. The beginning and end of the ROM movement was determined based on the accelerometer data from the y-axis of the elbow IMU, which showed the cleanest motion onset and end, as illustrated in Figure 4. Once segmented, the raw sEMG data were then put through a high pass filter at 10 Hz to remove any low frequency noise. Baseline offset was removed by subtracting the median of the overall signal. The resulting signal was then rectified and passed through an envelope with a window size of 80 samples (320 ms) to smooth the data. A rolling window outlier removal method was applied with a window size of 100 samples (3 s) and a threshold of 3 standard deviations away from the mean of the window. Lastly, for each subject, each of the eight channels were normalized to the highest signal value recorded for that channel across all ROM trials for that particular subject.[4]

D. Data Analysis

The primary metric used to quantify muscle activation was the area under the curve (AUC) for each muscle, calculated over the entire ROM during the movement cycle. The AUC of the clipped data was normalized by dividing it by the total number of samples throughout the movement, ensuring that the final activation metric was expressed as a percentage of the maximum possible activation [18], [19].

To examine the overall activations, we analyzed the AUC of each muscle across the factors of robot position and impairment group. Impairment group was defined by score on the UE-FM. Specifically, participants were classified as having "mild impairment" if they had a UE-FM > 50 and "moderate/severe impairment" if they had a UE-FM ≤ 50.

Due to small sample size and non-normality, we used the Mann Whitney U nonparametric test for all data comparisons. We first investigated if there were differences between initial and final AUC for each muscle and position with a paired Mann Whitney U. This test revealed no significant effects, so we chose to combine the initial and final AUC for all subsequent analyses. Next, we analyzed each position with an unpaired Mann Whitney U between impairment groups for each muscle. We also used an unpaired Mann Whitney U to compare the AUC of different muscles across positions (data collapsed across impairment groups). Bonferroni adjustment was used to account for multiple comparison.

IV. Results

We outline preliminary differences in muscle activation patterns across robot positions and impairment levels.

[4]We note that Subject 3 only completed the movements in Pos. 1. Additionally, some trials were removed due to excess noise, such as varying offsets that could not be removed. Some trials were also lost due to sensor malfunction at the time of data collection. Based on their statistical similarity (noted below), we combined initial and final ROM trials in our analysis. Subjects 5 and 9 did not have any data for Pos. 1. All other participants had either (or both) initial and final ROM for all positions.

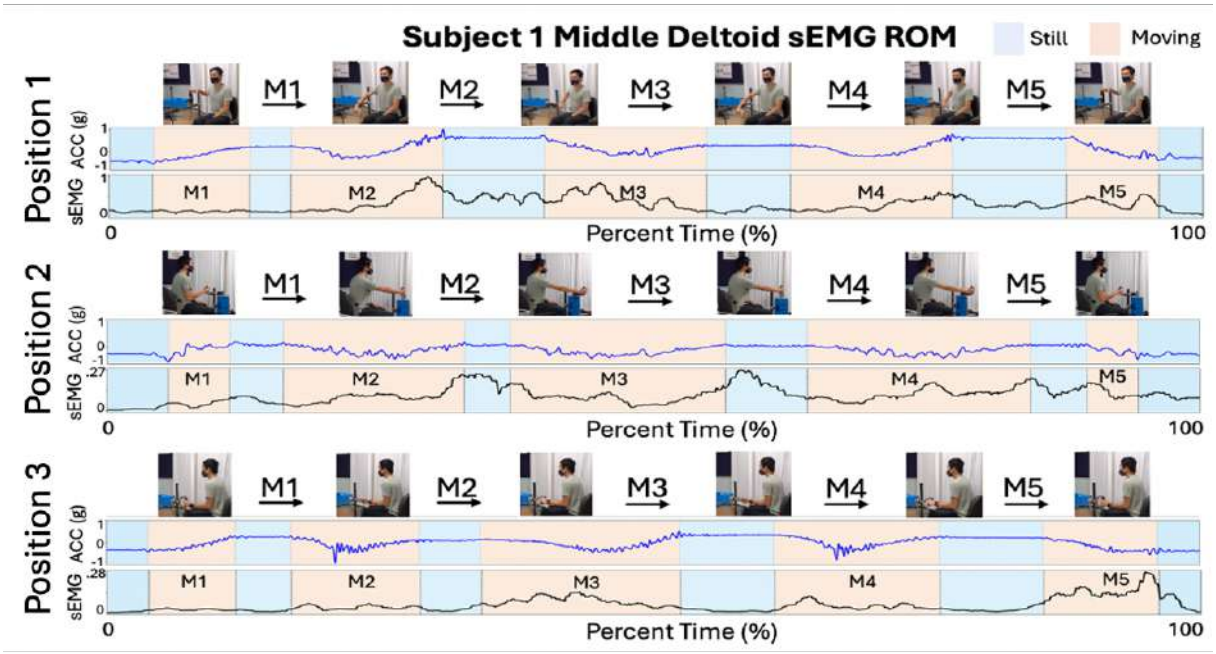


Fig. 4: Example normalized sEMG plots of the middle deltoid activation during ROM movements at each robot position from Subject 001. To compare data across participants performing this motion at various speeds, movement divisions are determined by kinematic data from the y-axis accelerometer.

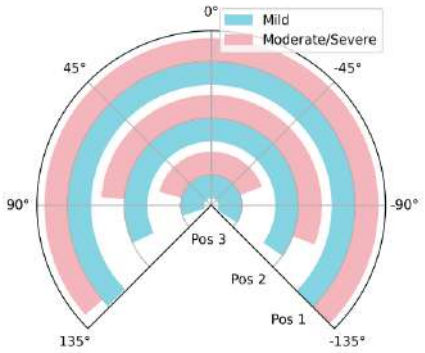


Fig. 5: Average ROM for three positions of the TheraDrive robot. Note that the moderate/severe impairment group has reduced ROM compared to the mild impairment group.

A. Variation Across Impairment

Figure 5 shows the average ROM for the different impairment groups in the three positions. The moderate/severe impairment group has a smaller ROM than the mild impairment group, which is particularly pronounced in Pos. 2 and Pos. 3. Figure 6 shows the observed variation in activation across levels of impairment at each robot position.

1) Position 1 – Reach-to-Grasp: As shown in Figure 6a, the brachioradialis AUC showed a significant difference between impairment groups when analyzed with a Mann Whitney U. Specifically, the mild impairment group (median AUC $= 22.1 \pm 6.92$) had significantly higher brachioradialis AUC than the moderate/severe impairment group (median AUC $= 12.7 \pm 6.05$), $z = 45,\ p = 0.036$.

2) Position 2 – Shoulder Abduction/Adduction: As shown Figure 6b, the biceps and middle deltoid showed significant differences in AUC between impairment groups when analyzed with a Mann Whitney U. For the biceps, the mild impairment group (median AUC $= 21.4 \pm 6.11$) had significantly higher biceps AUC than the moderate/severe impairment group (median AUC $= 10.8 \pm 6.49$), $z = 38,\ p = 0.042$. For the middle deltoid, the moderate/severe impairment group (median AUC $= 23.0 \pm 8.25$) had significantly higher middle deltoid AUC than the mild impairment group (median AUC $= 11.1 \pm 7.61$), $z = 6,\ p = 0.029$.

3) Position 3 – Wrist Pronation/Supination: As shown in Figure 6c, the anterior deltoid showed a significant difference in AUC between impairment groups when analyzed with a Mann Whitney U. Specifically, the mild impairment group (median AUC $= 28.8 \pm 9.74$) had significantly higher anterior deltoid AUC than the moderate/severe impairment group (median AUC $= 13.8 \pm 8.99$), $z = 56,\ p = 0.0202$.

B. Variation Across Position

Figure 7 shows the Mann Whitney U comparison between positions for each muscle's AUC. As shown, several muscles exhibit varied activations across positions: in particular, the middle deltoid and wrist extensor show significant differences in AUC across positions. Pos. 1 (median AUC $= 25.9 \pm 12.6$) had significantly higher middle deltoid AUC than Pos. 3 (median AUC $= 10.3 \pm 4.79$), $z = 217,\ p = 0.001$. Likewise, Pos. 2 (median AUC $= 18.1 \pm 9.52$) had significantly higher middle deltoid AUC than Pos. 3 (median AUC $= 10.3 \pm 4.79$), $z = 180,\ p = 0.029$. For the wrist extensor, Pos. 2 (median AUC $= 25.6 \pm 8.47$) had significantly higher activation AUC than Pos. 1 (median AUC $= 8.23 \pm 8.37$), $z = 35,\ p = 0.005$. No other muscles showed significant differences across positions.

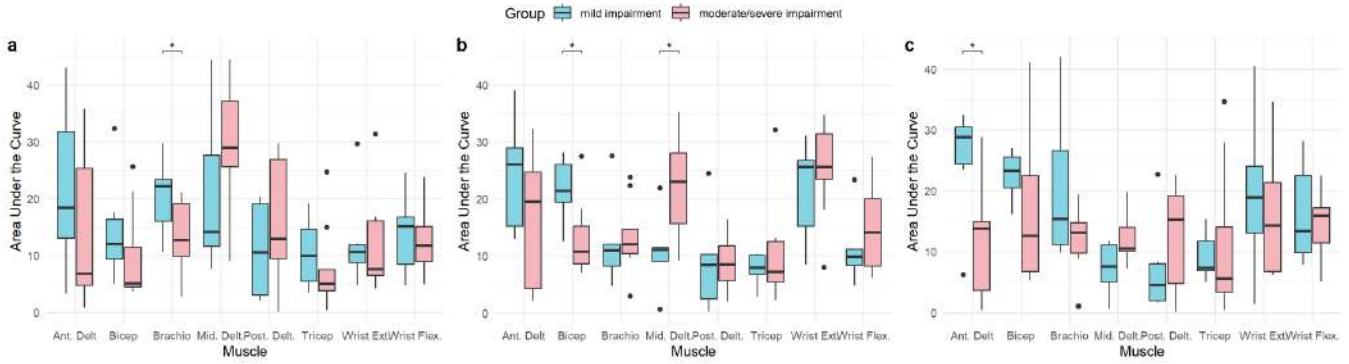


Fig. 6: AUC-quantified muscle activations for all three positions. **a:** Pos. 1; more severely impaired individuals show increased activation of the middle deltoid and decreased activation of the brachioradialis. **b:** Pos. 2; more severely impaired individuals show even more increased activation of the middle deltoid than observed in Pos. 1. **c:** Pos. 3; more severely impaired individuals show increased activation of the posterior deltoid and decreased activation of the anterior deltoid.

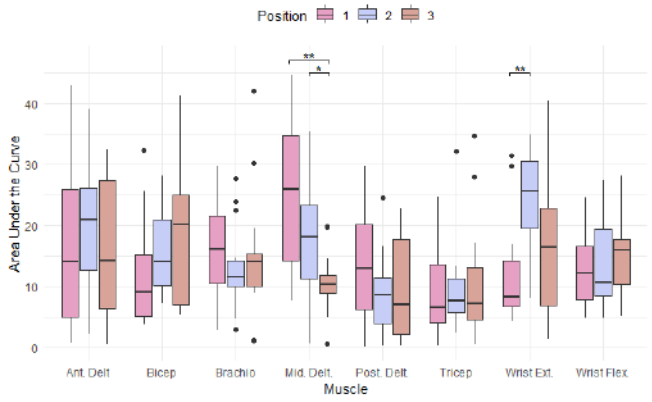


Fig. 7: Activation of each arm muscle, as quantified by AUC of the sEMG signal, at each position of the robot. Observed muscle activations vary substantially across positions (most saliently, the middle deltoid and wrist extensors).

V. Discussion

Prior to data collection, an occupational therapist outlined the expected movements for each position; we discuss the results above in the context of those expected behaviors to assess the TheraDrive's efficacy in activating expected motor patterns and identify potential compensatory strategies in users. Many participants had limited ROM due to their impairments. Figure 5 illustrates the variation in robot ROM angles across subjects and positions. The moderate/severe impairment group had relatively lower ROM in both Pos. 2 and Pos. 3 but were still able to attain the desired movements, indicating that the robot configurations are usable for rehabilitation. Notably, the moderate/severe impairment group's lower ROM suggests that reduced muscle activation may be influenced by the distance moved.

The expected movement for Pos. 1 is the flexion/extension of the shoulder and elbow, which involves the biceps, posterior deltoid, anterior deltoid, triceps, and the brachioradialis. As shown in Figure 6a, the mild impairment group showed significantly higher activation of the brachioradialis, suggesting that the moderate/severe impairment group may struggle with activating this muscle, compensating instead with shoulder abduction, as is indicated by greater middle deltoid activation. Although not significant, the moderate/severe impairment group showed greater middle deltoid activation than the mild impairment group. Middle deltoid activation is associated with shoulder abduction, which has been shown to correlate with motor impairment of the shoulder and elbow [20]. This result suggests that individuals with greater motor impairments may compensate with the middle deltoid in order to complete the reach-to-grasp movement of Pos. 1.

In Pos. 2, the expected movement is shoulder abduction/adduction, primarily involving the middle deltoid and triceps. As shown in Figure 6b, both impairment groups exhibited activations of the biceps, anterior deltoid, and wrist extensors. The moderate/severe impairment group demonstrated greater activation of the middle deltoid, indicating use of shoulder abduction, which aligns with the expected movement. However, given the over activity of the middle deltoid in Pos. 1, compensatory movement cannot be ruled out as a contributing factor. The mild impairment group exhibited higher activation in the biceps and the anterior deltoid, indicating that the shoulder flexes and the elbow bends simultaneously—an abnormal synergy commonly observed in post-stroke patients with hemiparesis [21]. The mild impairment group's co-activation is unexpected when compared with the more severely impaired group. Video data of the Pos. 2 ROM task, however, show that the more severely impaired subjects tend to use trunk compensation to complete the movement while maintaining a straighter arm. This reliance on trunk compensation could reduce bicep activation in the mild impairment group.

The expected movement for Pos. 3 involves forearm pronation and supination, which primarily activates the brachioradialis and biceps. The results shown in Figure 6c show that both groups display moderate activation of the wrist flexors and extensors, likely indicating wrist stiffening to better control the movement. The moderate/severe impairment group showed nonsignificant greater activation of the middle deltoid and the posterior deltoid, possibly due to compensatory shoulder twisting, while the mild impairment group relied more on the anterior deltoid and biceps.

In Figure 7, a comparison of muscle activation across positions shows significantly lower activation of the middle deltoid during Pos. 3, which aligns with the expected muscle activation pattern for wrist pronation/supination. We also found higher activation of wrist extensors in Pos. 2, suggesting that this position may involve wrist stiffness to stabilize the handle. In general, muscle activation varied across positions, with Pos. 1 activating the middle deltoid, posterior deltoid, and brachioradialis, Pos. 2 primarily activating the anterior deltoid and wrist muscles, and Pos. 3 showing the highest activation of the biceps and wrist flexors. An additional finding was the consistently low activation of the triceps across all positions, despite their expected activation during Pos. 1 and Pos. 2. Challenges with electrode placement on the triceps may have led to data inaccuracies.

VI. Conclusion

The Rehab CARES system effectively activates diverse muscle patterns across a range of motions that mimic daily activities through its three configurations. However, sEMG activation patterns suggest the presence of compensatory behaviors in all three positions, especially in the moderate/severe impairment group. Without a control group, it is difficult to definitively determine whether muscle activation in each position corresponds to the intended movement or reflects compensatory strategies. Future work could use the TheraDrive to compare pathological and healthy movements.

This study represents a first attempt at understanding how different positions of a reconfigurable 1-DoF robot activate muscles in a post-stroke population. This initial work has several limitations, including small sample size, low sampling frequency of the sEMG, and low task complexity. Future work may involve a more in-depth analysis of agonist–antagonist muscle pairings to characterize compensatory behaviors and more advanced analytical techniques, such as statistical parametric mapping, which enables time-resolved comparison of muscle activation across the movement cycle, or an analysis of muscle synergies. Additionally, a longitudinal study of behavior during the core assessment tasks and therapy games will be necessary to evaluate the long-term effectiveness of the rehabilitation system. This study—part of the Phase I Rehab CARES clinical trial—provides preliminary data on muscle activation patterns in each position, informs strategies to prevent compensatory behavior, and helps to assess the system's overall impact on muscle activation.

Acknowledgement

We want to thank the Rehab Robotics Lab and collaborators at Recupero Robotics LLC and enAble Games LLC.

References

[1] World Stroke Organization, "WSO Global Stroke Fact Sheet," 2022. Accessed: 2024-10-28.

[2] L. A. Simpson, K. S. Hayward, M. McPeake, T. S. Field, and J. J. Eng, "Challenges of estimating accurate prevalence of arm weakness early after stroke," *Neurorehabilit. Neural Repair*, vol. 35, no. 10, pp. 871–879, 2021.

[3] M. Franceschini, F. La Porta, M. Agosti, M. Massucci, *et al.*, "Is health-related-quality of life of stroke patients influenced by neurological impairments at one year after stroke?," *Eur. J. Phys. Rehabil. Med.*, vol. 46, no. 3, pp. 389–399, 2010.

[4] A. Demofonti, G. Carpino, L. Zollo, and M. J. Johnson, "Comparisons between end-effector and exoskeleton rehabilitation robots regarding upper extremity function among chronic stroke patients with moderate-to-severe upper limb impairment," *IEEE Trans. Med. Robot. Bionics*, vol. 3, no. 1, pp. 11–20, 2021.

[5] S. H. Lee, G. Park, D. Y. Cho, H. Y. Kim, J.-Y. Lee, S. Kim, S.-B. Park, and J.-H. Shin, "Comparisons between end-effector and exoskeleton rehabilitation robots regarding upper extremity function among chronic stroke patients with moderate-to-severe upper limb impairment," *Scientific Reports*, vol. 10, no. 1, p. 1806, 2020.

[6] G. Kwakkel, B. J. Kollen, and H. I. Krebs, "Effects of robot-assisted therapy on upper limb recovery after stroke: A systematic review," *Neurorehabilit. Neural Repair*, vol. 22, no. 2, pp. 111–121, 2008.

[7] M. C. Cirstea and M. F. Levin, "Compensatory strategies for reaching in stroke," *Brain*, vol. 123, pp. 940–953, May 2000.

[8] P. H. McCrea, J. J. Eng, and A. J. Hodgson, "Saturated muscle activation contributes to compensatory reaching strategies after stroke," *Journal of Neurophysiology*, vol. 94, pp. 2999–3008, Nov. 2005.

[9] T. A. Jones, "Motor compensation and its effects on neural reorganization after stroke," *Nature Reviews Neuroscience*, vol. 18, pp. 267–280, May 2017.

[10] P. Maciejasz, J. Eschweiler, K. Gerlach-Hahn, A. Jansen-Troy, and S. Leonhardt, "A survey on robotic devices for upper limb rehabilitation," *Journal of Neuroengineering and Rehabilitation*, vol. 11, pp. 1–29, 2014.

[11] H. I. Krebs, B. T. Volpe, D. Williams, J. Celestino, S. K. Charles, D. Lynch, and N. Hogan, "Robot-aided neurorehabilitation: A robot for wrist rehabilitation," *IEEE Trans. Neural Syst. Rehabilitation Eng.*, vol. 15, no. 3, pp. 327–335, 2007.

[12] S. Hesse, G. Schulte-Tigges, M. Konrad, A. Bardeleben, and C. Werner, "Robot-assisted arm trainer for the passive and active practice of bilateral forearm and wrist movements in hemiparetic subjects," *Archives of Physical Medicine and Rehabilitation*, vol. 84, no. 6, pp. 915–920, 2003.

[13] K. X. Khor, P. J. H. Chin, C. F. Yeong, E. L. M. Su, A. L. T. Narayanan, H. Abdul Rahman, and Q. I. Khan, "Portable and reconfigurable wrist robot improves hand function for post-stroke subjects," *IEEE Trans. Neural Syst. Rehabilitation Eng.*, vol. 25, no. 10, pp. 1864–1873, 2017.

[14] U. N. L. of Medicine, "Rehab CARES in USA: Clinical trial (nct05542121)," 2024. Accessed: 2024-10-28.

[15] Y. Shang, S. Bahrami, S. Gaardsmoe, A. Johnson, M. J. Johnson, and P. Diefenbach, "General purpose haptic/biometric-based dynamic difficulty adjustment for post-stroke upper-limb rehabilitation games," in *2025 19th IEEE/RAS-EMBS International Conference on Rehabilitation Robotics (ICORR 2025)*, 2025.

[16] M. J. Johnson, R. Rai, S. Barathi, R. Mendonca, and K. Bustamante-Valles, "Affordable stroke therapy in high-, low- and middle-income countries: From Theradrive to Rehab CARES, a compact robot gym," *Journal of Rehabilitation and Assistive Technologies Engineering*, vol. 4, 2017.

[17] K. D. Bui, C. A. Wamsley, F. S. Shofer, D. L. Kolson, and M. J. Johnson, "Robot-based assessment of HIV-related motor and cognitive impairment for neurorehabilitation," *IEEE Trans. Neural Syst. Rehabilitation Eng.*, vol. 29, pp. 576–586, 2021.

[18] E. Stålberg, H. van Dijk, B. Falck, J. Kimura, C. Neuwirth, M. Pitt, S. Podnar, D. I. Rubin, S. Rutkove, D. B. Sanders, M. Sonoo, H. Tankisi, and M. Zwarts, "Standards for quantification of EMG and neurography," *Clinical Neurophysiology*, vol. 130, no. 9, p. 1682–1683, 2019.

[19] J. Finsterer, "EMG-interference pattern analysis," *Journal of Electromyography and Kinesiology*, vol. 11, no. 4, pp. 1688–1729, 2001.

[20] M. Y. Lee, J. W. Park, R. J. Park, J. H. Hong, S. M. Son, S. H. Ahn, Y. W. Cho, and S. H. Jang, "Cortical activation pattern of compensatory movement in stroke patients," *NeuroRehabilitation*, vol. 25, no. 4, pp. 255–260, 2009.

[21] J. Deward, P. Pope, and D. Given, "Abnormal muscle coactivation patterns during isometric torque generation at the elbow and shoulder in hemiparetic subjects," *Brain*, vol. 118, pp. 495–510, 1995.

Improving Active Range of Motion in the Arm after Stroke with a Body-Mounted Shoulder Exoskeleton

Joel C. Perry, Alex C. Stella, Cody I. Russell, Cole Bailey, Shay Albrecht, and Christopher K. Bitikofer
Assistive Robotics Lab, Mechanical Engineering Department
University of Idaho
Moscow, ID, USA
jperry@uidaho.edu, {stel7656, russ3194, bail9993, albr5703}@vandals.uidaho.edu, bitikofer@uidaho.edu

***Abstract* -** Arm use and arm function are inextricably linked; nonuse leads to a decline in fuctionality, while proper and consistent usage maintains functionality and can lead to further improvement. Many individuals with impairment are discharged from therapy with functional levels that are too low to promote self-use of arm and hand function at home. However, with gravitational support to the arm, some of these same individuals could experience immediate improvements in reachable workspace. To increase arm function and usage, we developed a custom wearable shoulder exoskeleton with variable levels of gravitational support and evaluated its effect on three participants with chronic impairment from stroke, measuring planar reach area during a single session (assisted vs unassisted). We also measured baseline arm use at home with wrist-mounted activity trackers to evaluate the amount of use vs. nonuse of the impaired limb during daily activities. With exoskeleton assistance, participants achieved average gains in planar reach area of 11%, 1.3%, and 14.2% in the transverse, sagittal, and frontal planes, respectively, relative to unimpaired function. Baseline unassisted arm usage was also measured by numerically integrated accelerometry activity counts which may offer a quantitative way to compare the difference in arm usage with and without provision of an assistive exoskeleton.

Keywords—activity tracking, arm, assistance, body-mounted, exoskeleton, gravity-balancing, shoulder, wearable

I. Introduction

Cerebral damage from stroke leaves about half of survivors with long-term impairment in the arm and hand, leading to significant disability in activities of daily living (ADLs) [1]. One-sided impairment (hemiparesis) is one of the most common post-stroke symptoms, marked by weakness and abnormal muscle synergies (groups of muscles that contract together). During active self-support of the impaired arm against gravity, the flexion synergy causes simultaneous contraction of biceps, forearm supinators, wrist flexors, and finger flexors. When severe, the combined contraction pattern restrains the hand close to the torso, limiting the ability to reach for objects.

Intensive rehabilitation, even in the chronic phase (>6 months post-stroke), leads to better functional outcomes [2]. However, gains in performance are often used to justify continuation of care, and many clinical assessment scores plateau (due to insensitivity of metrics) before functional recovery can be fully reached. Particularly evident in the US, the need for rehabilitation services is outpacing the supply of physical and occupational therapists, putting strain on the rehabilitative care system [3, 4]. Despite growing workforce shortages, it is known that function at discharge significantly impacts future recovery trends. Patients discharged with higher function have been shown to be more likely to enter a positive cycle of continued use and recovery. In comparison, those with lower function are more likely to enter a negative cycle of disuse and decline [5].

Given these facts, it is probable that early discharge of partially rehabilitated patients increases the population of individuals with long-term impairment who are unable to incorporate their affected arm into ADLs without external assistance. These individuals develop (and are taught in therapy) compensation strategies that rely on the unimpaired limb [6]. Unfortunately, this approach contributes to the decline and further neglect of motor function in the impaired limb [5]. This trend creates an opportunity for wearable assistive exoskeletons to bridge the gap between function and performance. Provision of gravity support to the hemiparetic arm can, in many cases, improve active (i.e., self-driven) range of motion (AROM), facilitating greater functional use of the arm [7, 8]. Gravity support effectively lowers the barrier to spontaneous use of the impaired limb and, if available in the home setting, has the potential to increase arm use and thereby maintain or improve function.

Chair- and table-mounted mobile arm supports (MASs) have been used by wheelchair-bound individuals for decades to increase range of motion and function, but commercial MASs are not available as wearable body-mounted systems. Only a few prototypes have been directly mounted to impaired users, such as the WREX [9] and the WREX Mini [10]. The reported limitations of body-mounting are device size and weight [11, 12], aesthetics (e.g., profile and appearance) [13-15], and/or a

Funded by an award from the National Institute of General Medical Sciences (NIGMS), National Institutes of Health (NIH) under grant number U54 GM104944.

low level of perceived benefit considering the limitations [13, 16]. Within the last decade, a number of lightweight wearable exoskeletons have finally reached the market, but so far, these devices have been targeted toward able-bodied users in industrial settings only [17-19], aiming to reduce bilateral shoulder strain during repetitive overhead tasks. While their acceptance in the workplace continues to grow, similar wearable products have not yet emerged for individuals with impairment.

Successful implementation of body-mounted systems intended for long-term use at home necessitates design improvements to ensure that devices are lightweight, durable, easy to use, comfortable and safe, particularly since they are intended to be used in environments with little or no professional supervision. Creating user independence and establishing ease of use for donning/doffing and adjustment is a high priority since patients at home may not have access to assistance. Toward this objective, a wearable shoulder exoskeleton has been under development at the University of Idaho [20, 21]. The device aims to provide gravity support to a single arm, adjustable from no support to full support, reducing shoulder effort and the undesirable synergies that typically impede reaching after neurological impairment.

In this paper, we report on preliminary experiments with a body-mounted exoskeleton to improve the active range of motion in the arm of individuals with chronic hemiparesis from stroke. We also explore a method of analyzing arm use metrics in individuals with impairment using off-the-shelf wrist-mounted activity trackers as a means to evaluate the effectiveness of assistance provision at home.

II. Methods

A wearable shoulder exoskeleton (Fig. 1) is designed and built from custom and off-the-shelf components. Structural links are created from carbon fiber rods and 3D-printed thermoplastics; energy storing springs are constructed from natural latex rubber tubes [22]; and low-stretch Vectran™ cables.

Four subjects with arm impairment were recruited to participate in an arm mobility and usage study, with three of the four subjects participating in both parts. Subjects had experienced a single stroke that occurred between 14 and 51 months prior and demonstrated limited ability to elevate the arm against gravity.

A. Testing Procedure

The testing protocol was approved by the University of Idaho's Institutional Review Board (IRB Protocol #23-041). Testing included a set of intake measures followed by two substudies: 1) AROM sub-study, measuring active range of motion with and without external assistance from a body-mounted exoskeleton; and 2) Spontaneous Arm Use sub-study, measuring normal arm use in the home setting. The AROM sub-study was conducted in a laboratory setting during an initial 90-minute session, starting with informed consent, anthropometric measures, and baseline functional assessment tests. In preparation for the AROM sub-study, subjects provided input through trial and error on the level of assistance that they felt best facilitated their arm range of motion. For the Spontaneous Arm Use sub-study, each subject was sent home with two Axivity AX6 data loggers (3-axis accelerometer and 3-axis gyro). These devices were worn on each wrist for 3–5 days to measure daily usage of the impaired and non-impaired arm. The data loggers are contained in waterproof silicone straps, enabling continuous wear by subjects in all daily activities (e.g., showering, washing dishes, etc.).

B. Intake Measures and Baseline Assessments

Intake measures included subject age, gender, height, weight, approximate time since stroke, 60-sec Box and Blocks test (BBT) scores, grip strength, and finger-thumb pinch strength (TABLE I). Two subjects were primarily wheelchair-bound and did not perform strength tests due to the severity of tone in their affected hands; one of these two was also self-withdrawn from the AROM sub-study due to

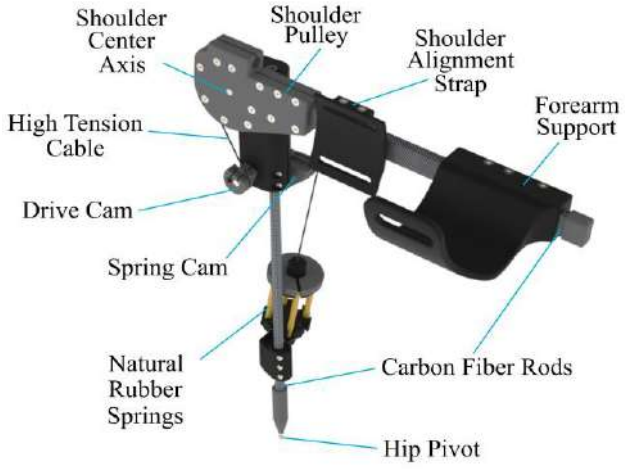


Fig. 1. Wearable shoulder exoskeleton prototype

TABLE I. Subjects intake measures. Box and Blocks Test (BBT) scores as well as Grip and Pinch strengths provided for impaired (I) and unimpaired (U) sides.

Subject Number	Age (yrs)	Time Since Stroke (mos)	Sex	Weight (kg)	Height (m)	Months Post Stroke	Affected Arm	BBT Score I/U	Grip I/U (kg)	Pinch I/U (kg)
M4601	78	51	M	97.5	1.78	55	L	0 / -	-	-
M6603	58	14	M	86.2	1.75	14	R	0 / 53	1.7 / 36	0.7 / 8.8
M5704	67	28	M	99.8	1.88	28	R	16 / 62	11.6 / 48.5	2 / 5.4



Fig. 2. A subject performing arm reach range of motion tests without (LEFT) and with (RIGHT) assistance by a wearable shoulder exoskeleton prototype. Red, green, and blue coordinate system denotes the X, Y, and Z axes of the origin (white dot).

the level of tone and spasticity present in the affected arm on the day of testing.

C. AROM Substudy: Active Range of Motion Evaluation

Subjects were seated and secured with a 4-point harness to an experimental chair [23] and then fit with a custom glove-based marker set (Fig. 2). The marker set forms a rigid body around the hand with a centroid located approximately along the grip line of the palm at the level of the metacarpophalangeal (MCP) joint. This point represents the reach distance for the subject (i.e., their unimpaired reach work area). Subjects were instructed to perform a planar reach motion to circumscribe the largest area possible in each of three planes (transverse, sagittal, and frontal). The movements were demonstrated on video and in-person, and subjects were allowed to practice them as needed. The movements were performed first with the unimpaired side, allowing confirmation that the subject understood the task instructions, and were then repeated with the impaired side. Movements in each plane were repeated 3 to 5 times, depending on the level of difficulty for the subject. Each movement was recorded and analyzed. Impaired-side range of motion trials were repeated with and without assistance from the body-mounted exoskeleton, where the level of assistance had been previously determined with input from each subject.

A 5-camera motion capture setup (OptiTrack with 5 Flex13 cameras) recorded hand movements at 120 Hz using OptiTrack's Motive software. Movement data was processed in MATLAB to compute the planar reach area. The outline of the reach works areas were smoothed using *smoothdata()* (moving average filter with window size N = 50) and the areas were calculated using polyarea(). For comparison between subjects, the smoothed reach areas are plotted (Fig 3), illustrating the differences in size, shape, and relative location of subject reaching ability with and without exoskeleton assistance. Range of motion of the

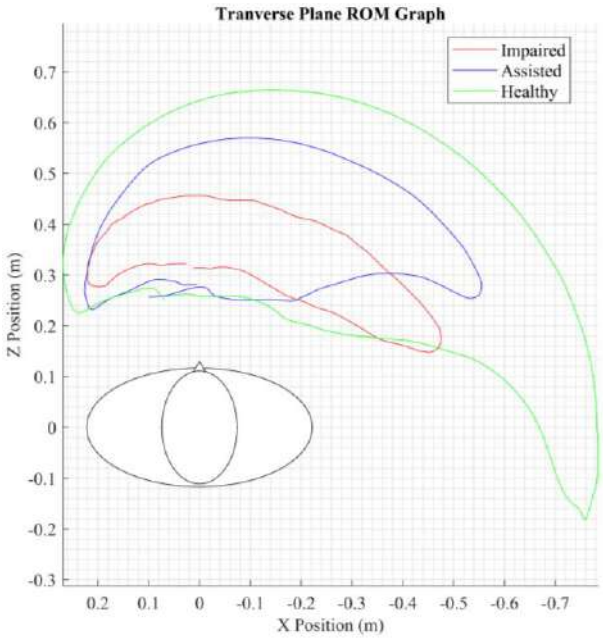


Fig. 3. Active range of motion area for impaired-unassisted (red), impaired-assisted (blue), and healthy (green) arm reach for subject M5704 as measured by hand displacement in the transverse plane. Healthy side (left arm) AROM has been mirrored across the sagittal plane for comparison.

unimpaired arm was mirrored across the sagittal plane to provide a reference for impaired-side range of motion.

D. Arm Use Substudy: Evaluation of Spontaneous Arm Use

An AX6 multi-sensor data logger is attached to each wrist (left and right) via a silicone wristband to be worn at home during the subject's normal activities. The set of onboard sensors are pre-configured via Open Movement's OpenGUI subject identifiers, sensor attachment locations, and recording start and stop times. Data collection rates were set to 100Hz with sensitivities set to ±8g for linear acceleration and 500 degrees per second (dps) for angular velocity. The recording duration depended on the subject, but all subjects provided at least 3 days (72 hours) of continuously recorded data. Subjects were instructed to always keep the sensors on if possible and to set the AX6 devices on a stationary surface if removed.

After completion of the 3–5-day accelerometry collection, data was downloaded via the OpenGUI software, and data files were converted from raw measures into activity counts using *cwa-to-counts*, a Windows command script available in Open Movement's open-source repository [24]. The converted data is imported into MATLAB to apply a moving average with a window size of 10 minutes via the *envelope()* function. Finally, MATLAB's *trapz()* function is used to compute the discrete integration of the accelerometry data to estimate the average overall activity level in order to compare the datasets of impaired and non-impaired arm usage.

III. Results

At the time of writing, four subjects were enrolled in the overall study, and three were eligible to participate in the AROM sub-study. One subject was removed due to the reasons described in Section II B.

A. Arm Range of Motion Evaluation (AROM Sub-study)

Providing gravity assistance to the shoulder of individuals with significant impairment in the arm and hand produced varying changes in active range of motion. Subject M6603 saw the highest relative gains in reach range of motion (relative to baseline performance), while subject M5704 saw the highest absolute gains (relative to healthy performance). Both subjects M6603 and M5704 had similar absolute gains with percentage increases relative to their unimpaired arms of 14-20% in the transverse and frontal planes while the most severely impaired of the three (subject M4601) had more modest improvements of 1.5-3.5% of healthy ROM in these planes (Fig. 4 and TABLE II). Although one subject achieved gains in all three planes, two of the three saw slight decreases in sagittal plane ROM. For all subjects, shoulder assistance increased AROM in the frontal plane the most, followed by transverse AROM, and then the sagittal AROM. Subject M5704 achieved a 20% improvement in the frontal plane and an 18% improvement in the transverse plane, both with respect to full range of motion of the subject's healthy (left) arm. The frontal plane AROM task is shown in Fig. 5 with a

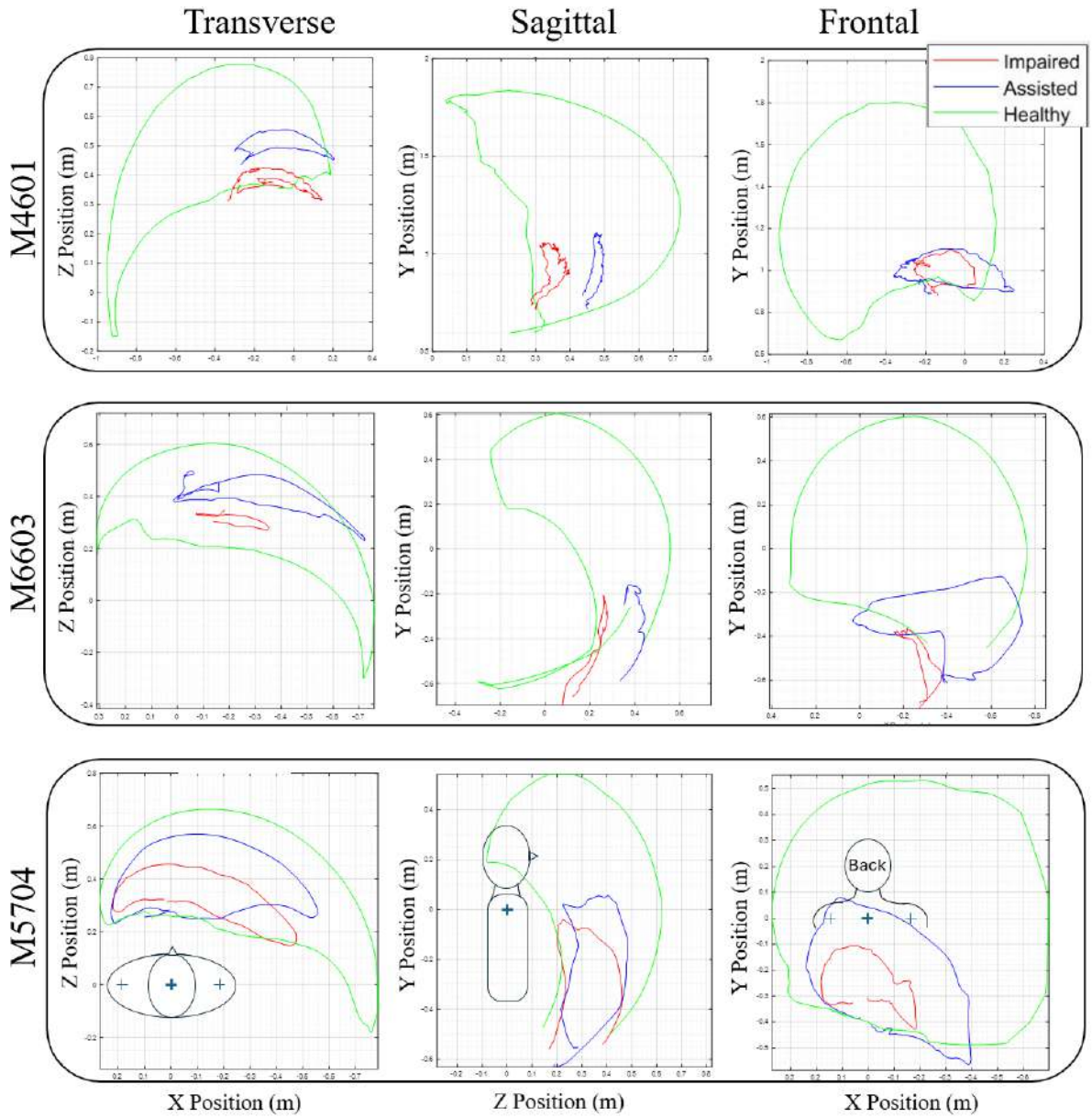


Fig. 4. Active range of motion for impaired arm-unassisted (red), impaired arm-assisted (blue), and healthy arm (green), in the transverse (LEFT column), sagittal (MIDDLE column), and frontal (RIGHT column) planes for subjects M4601 (TOP row), M6603 (MIDDLE row), and M5704 (BOTTOM row). Subplots for M5704 included approximation of human torso locations based on measurements from shoulder markers included in the mocap. Shoulder locations for M4601 and M6603 datasets were not recorded, and therefore healthy data (green plots) may not be accurately mirrored relative to the impaired data; however, the relative sizes of work areas within each subplot are accurate and comparable for scale.

TABLE II. Active arm reach range of motion measures in three planes without assistance (Unassisted) and with assistance (Assisted) expressed in cm^2 and as a percent of range of motion of the subject's healthy (H) side. Relative change in range of motion area also provided with respect to (w.r.t.) the unassisted (U) area and the healthy (H) side area.

Subj. Num.	Motion Plane	Range of Motion Area				Relative Change	
		Unassisted		*Assisted*		*w.r.t. U*	*w.r.t. H*
		(cm^2)	*w.r.t H (%)*	*(cm^2)*	*w.r.t H (%)*	*(%)*	*(%)*
M4601	Transv.	17.3	4.1	23.6	5.6	36	1.5
	Sagittal	12.0	2.6	9.5	2.2	-20	-0.5
	Frontal	39.0	4.4	70.7	7.9	81	3.5
M6603	Transv.	64.2	1.8	561	15	774	14
	Sagittal	74.1	1.6	293	6.6	295	4.9
	Frontal	156	1.8	1812	21	1062	19
M5704	Transv.	975	24	1738	42	78	18
	Sagittal	1037	24	1012	24	-2	-0.5
	Frontal	603	6.7	2297	25	281	20
					Average	287	8.9

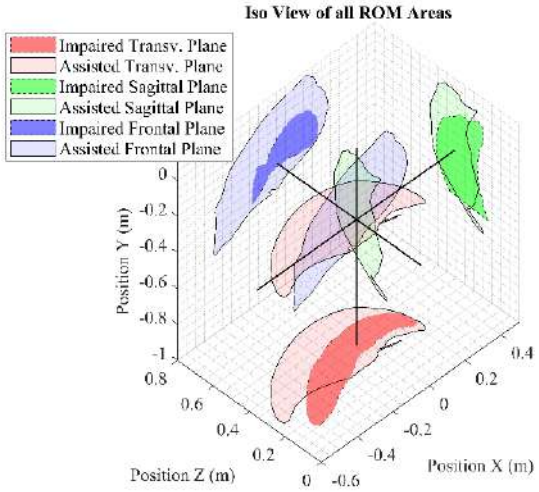


Fig. 6. AROM data from subject M5704 in transverse (red), frontal (blue), and sagittal (green) planes without (dashed line, darker fill) and with (solid line, lighter fill) assistance from a wearable shoulder exoskeleton. Assisted range of motion results are also overlaid in the center to illustrate the 3D volume reachable for the subject with exoskeleton assistance.

sequence of images that illustrate, left-to-right, the progression of movement and top-to-bottom the relative difference between unassisted and assisted workspaces. In Fig. 5, transverse planar AROM areas are compared for impaired (assisted and unassisted) and healthy sides. Without assistance, the impaired side is able to achieve 24% of the full unimpaired AROM, but with partial gravity assistance from the exoskeleton, transverse AROM increases by 18 percentage points (with respect to the healthy arm) to 42% of healthy range of motion. Fig. 6 illustrates the difference between assisted (solid) and unassisted (dashed) AROM for the same subject in each of the three planes.

B. Spontaneous Arm Use Evaluation (Arm Use Sub-study)

The amount of recorded activity in impaired extremities was significantly less than the unimpaired extremity for all subjects. Fig. 7 shows recorded activity from subject M5704 over a 24-hour period starting and ending at midnight. The numerically integrated counts for the impaired (right) side totaled 4.35×10^4, while the non-impaired (left) side totaled 61.2×10^4 counts. TABLE III shows integrated count values, representing the total amount of use of each arm, as well as a ratio between the level of impaired vs. unimpaired arm use for all subjects.



Fig. 5. Task progression of a subject performing arm reach range of motion task in the frontal plane without (TOP row) and with assistance (BOTTOM row). Timeline progresses left to right with the starting pose shown in the left-most image.

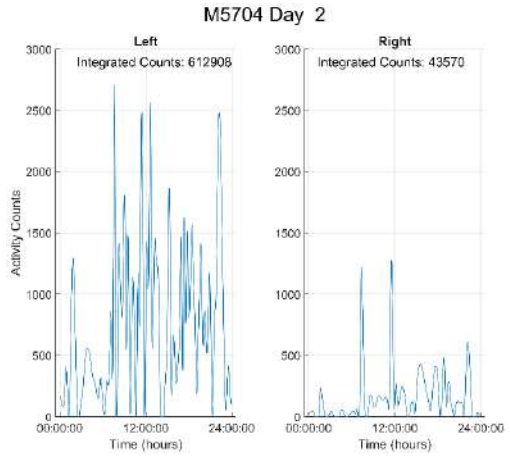


Fig. 7. Activity comparison between left (unimpaired) and right (impaired) of subject M5704 for a 24-hour period.

TABLE III. Activity counts comparison between impaired (I) and unimpaired (U) arms.

Subject Number	Day	I Counts (x 10^4)	U Counts (x 10^4)	I/U Activity Ratio (%)	I/U Average Activity Ratio (%)
M4601	1	8.08	116	6.97	6.53
	2	5.08	80.1	6.34	
	3	4.72	68.9	6.85	
	4	4.94	84.5	5.85	
F7302	1	2.82	52.5	5.37	6.8
	2	10.7	150	7.13	
	3	10.8	152	7.11	
	4	-	-	-	
M6603	1	25.0	136.94	18.26	20.07
	2	39.68	198.73	19.97	
	3	46.26	213.59	21.66	
	4	19.78	101.98	19.40	
M5704	1	1.53	17.2	8.90	6.73
	2	4.35	61.2	7.11	
	3	2.39	45.8	5.22	
	4	1.25	17.3	7.23	

Fig. 8 shows a side-by-side comparison of integrated counts between impaired and unimpaired arms for all subjects over a 24-hour period. The average activity ratio varied greatly per subject, with the lowest at 6.53% and the highest at 20.07%. It can be seen that the common range of activity ratios for subjects measured at the time of writing is 6-7%.

IV. Discussions and Conclusions

A wearable exoskeleton was developed to lessen the shoulder effort required to support the arm against gravity with the goal of increasing active range of motion post-stroke. AROM of the impaired arm with and without the exoskeleton assistance was evaluated in a laboratory setting through motion capture. Three subjects participated in the laboratory evaluation, and four also took part in an at-home assessment of arm use measured by wrist-mounted wearable trackers.

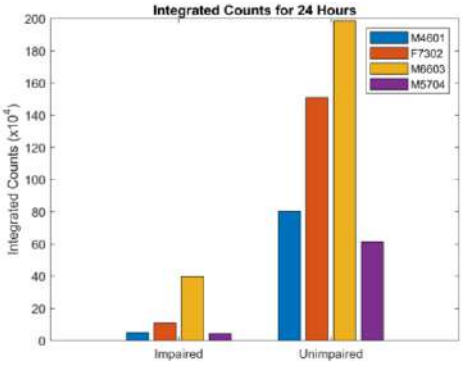


Fig. 8. Comparison of impaired and unimpaired integrated counts over 24 hours (midnight to midnight) for all subjects.

While wearing the exoskeleton, all subjects saw significant improvement in the frontal and transverse planes. Changes in the sagittal plane were more varied, with two subjects showing decreased AROM in that plane when using the exoskeleton. There are two reasons for this effect: 1) The exoskeleton spring support design does not take into account elbow angle and will under-support the arm when the elbow is extended and over-support when the elbow is flexed. 2) the direction of the range of motion task can either work with or against this under/over-support limitation. The subjects in this experiment were asked to perform the motion in the direction that would work against the support limitation, minimizing the resulting range of motion. This resulted in reduced range of motion over the unassisted condition for two of the subjects, the change was negligible for one, and the third subject still achieved an increased range of motion. Future subjects will perform the sagittal plane AROM tasks in both directions to compare AROM capabilities when taking advantage of the device's ability to over-support when lifting and under-support when lowering the arm. It can also be seen that there is a portion of the unassisted AROM that lies outside of the assisted AROM for some; this can be attributed to a range of motion limitation in the exoskeleton version used in this study which prevented full shoulder adduction. A redesign is underway to address this adduction limit.

Other constraints imposed by the current design are a limited ROM and inability to actively move the limb. The design currently limits the range of assistance to between 17 and 90 degrees of elevation from the side. As a passive device, it can only amplify the subject's already existing motion capabilities, so AROM increases are dependent on the subject's strength prior to testing. This can be seen by comparing the average activity ratio and the relative increases in AROM in each subject. Those with a higher average activity ratio had higher relative changes in assisted AROM values.

It was observed during testing that the wearable exoskeleton can make useage of the impaired arm less strenuous. This was not a metric that we originally intended to measure, but after this observation the study protocol was modified to allow measurement of electromyography

(EMG) during the AROM assessment to evaluate muscular effort along with AROM. Regardless of whether improvements are in AROM or effort, there is potential for these improvements to increase subject motivation and ability to use their impaired arm in daily life. The goal is to adequately match user impairment with the proper assistance level from the exoskeleton to maximize impaired arm use at home.

The preliminary work in measuring arm use at home clearly shows a difference in arm use and establishes a baseline against which to compare future measurements of arm use at home with exoskeleton assistance. Future steps of this study will send participants home with the assistive exoskeleton and monitor changes in the impaired-to-unimpaired arm use activity ratio. Following the preliminary results of Section IV, we expect exoskeleton assistance to produce increased activity levels in the impaired extremity, and higher scores in standardized functional assessment tests.

In conclusion, the designed exoskeleton provides immediate improvement of subject AROM in the frontal and transverse planes of motion, and we believe it will also provide increased sagittal plane AROM if the characteristics of the gravity support are properly leveraged. We believe these preliminary results provide strong, positive evidence of the potential benefits of wearable exoskeletons for stroke rehabilitation.

ACKNOWLEDGMENT

The authors would like to thank Jeremiah Schroeder and Zhihui Wang for their prior contributions to the design and development of the shoulder exoskeleton prototype, and Abishek Rathod for his contributions to spring characterization.

REFERENCES

[1] Doyle, S., Bennett, S., Fasoli, S. E., & McKenna, K. T. (2010). Interventions for sensory impairment in the upper limb after stroke. *Cochrane Database of Systematic Reviews*, (6).

[2] Housman, S. J., Le, V., Rahman, T., Sanchez, R. J., & Reinkensmeyer, D. J. (2007, June). Arm-training with T-WREX after chronic stroke: preliminary results of a randomized controlled trial. In *2007 IEEE 10th international conference on rehabilitation robotics* (pp. 562-568).

[3] Zimbelman, J. L., Juraschek, S. P., Zhang, X., & Lin, V. W. H. (2010). Physical therapy workforce in the United States: forecasting nationwide shortages. *PM&R*, *2*(11), 1021-1029.

[4] Lin, V., Zhang, X., & Dixon, P. (2015). Occupational therapy workforce in the United States: Forecasting nationwide shortages. *PM&R*, *7*(9), 946-954.

[5] Hidaka, Y., Han, C. E., Wolf, S. L., Winstein, C. J., & Schweighofer, N. (2012). Use it and improve it or lose it: interactions between arm function and use in humans post-stroke. PLoS computational biology, 8(2), e1002343.

[6] Nakayma, H., Jørgensen, H. S., Raaschou, H. O., & Olsen, T. S. (1994). Compensation in recovery of upper extremity function after stroke: the Copenhagen Stroke Study. Archives of physical medicine and rehabilitation, 75(8), 852-857.

[7] Reinkensmeyer, D. J., Zondervan, D. K., & Andrés, M. C. (2022). Upper-Extremity Movement Training with Mechanically Assistive Devices. In *Neurorehabilitation Technology* (pp. 649-662). Cham: Springer International Publishing.

[8] Perry, B., Sivak, J. and Stokic, D., 2021. Providing unloading by exoskeleton improves shoulder flexion performance after stroke. Experimental Brain Research, 239, pp.1539-1549.

[9] Rahman, T., Sample, W., Jayakumar, S., & King, M. M. (2006). Passive exoskeletons for assisting limb movement. Journal of rehabilitation research and development, 43(5), 583.

[10] Batkuldinova, K., Abilgaziyev, A., Shehab, E., & Ali, M. H. (2021). The recent development of 3D printing in developing lower-leg exoskeleton: A review. Materials Today: Proceedings, 42, 1822-1828.

[11] Ates, S., Haarman, C.J. and Stienen, A.H., 2017. SCRIPT passive orthosis: design of interactive hand and wrist exoskeleton for rehabilitation at home after stroke. Autonomous Robots, 41(3), pp.711-723.

[12] Lund, K., Brandt, R., Gelderblom, G.J. and Herder, J.L., 2009, June. A user-centered evaluation study of a mobile arm support. In Rehabilitation Robotics, 2009. ICORR 2009. IEEE International Conference on (pp. 582-587).

[13] Herder, J.L., Vrijlandt, N., Antonides, T., Cloosterman, M. and Mastenbroek, P.L., 2006. Principle and design of a mobile arm support for people with muscular weakness. Journal of rehabilitation research and development, 43(5), p.591.

[14] Dunning, A.G. and Herder, J.L., 2013, June. A review of assistive devices for arm balancing. In Rehabilitation Robotics (ICORR), 2013 IEEE International Conference on (pp. 1-6).

[15] Kooren, P.N., Dunning, A.G., Janssen, M.M., Lobo-Prat, J., Koopman, B.F., Paalman, M.I., de Groot, I.J. and Herder, J.L., 2015. Design and pilot validation of A-gear: a novel wearable dynamic arm support. Journal of neuroengineering and rehabilitation, 12(1), p.83.

[16] Rahman, T., Sample, W., Seliktar, R., Alexander, M. and Scavina, M., 2000. A body-powered functional upper limb orthosis. Journal of rehabilitation research and development, 37(6), pp.675-680.

[17] Pinho, J. P., Americano, P. P., Taira, C., Pereira, W., Caparroz, E., & Forner-Cordero, A. (2020, July). Shoulder muscles electromyographic responses in automotive workers wearing a commercial exoskeleton. In *2020 42nd Annual International Conference of the IEEE Engineering in Medicine & Biology Society (EMBC)* (pp. 4917-4920).

[18] Pacifico, I., et al. (2020). An experimental evaluation of the proto-mate: a novel ergonomic upper-limb exoskeleton to reduce workers' physical strain. *IEEE robotics & automation magazine*, *27*(1), 54-65.

[19] Renner, T. (2018). Exoskeleton with lightweight plastic components finds applications in medicine, manufacturing, and agriculture. *Plastics Engineering*, *74*(3), 30-35.

[20] Schroeder, J. S., & Perry, J. C. (2018). Development of a series wrapping cam and energy-storing spring system for application in wearable robotic arm supports. *Technology & Innovation*, *20*(1-2), 21-36.

[21] Stella, A., et al. (2024). Development of Wearable Shoulder Exoskeleton for Stroke Rehabilitation Using Series Wrapping Cams. Idaho Conference on Undergraduate Research, July 3, 2024, Boise, Idaho.

[22] J. C. Perry, A. Rathod, "Energy density and hysteresis comparison in natural rubber tube springs for wearable exoskeleton applications," in *Proc. 2019 IEEE 16th Int. Conf. Rehabilitation Robotics (ICORR)*, Toronto, Canada, Jun. 2019, pp. 1-3, 27.

[23] Stump, J. A. (2024). *Design and Integration of Anthropometric Adjustments and Hand Control Developments Toward Full-arm Rehabilitation with an Exoskeleton* (Master's thesis, University of Idaho).

[24] OpenMovement Project, "OMConvert: Cut Points," *GitHub*. [Online]. Available: https://github.com/openmovementproject/omconvert#cut-points.

Fabrication and Evaluation of Woven and Crocheted Strain Sensors for Soft Rehabilitation Robots

Meghan Newkirk, J. Guillermo Colli Alfaro, and Ana Luisa Trejos, *Senior Member, IEEE*

***Abstract*— Recent advancements in technology have made possible the use of soft wearable mechatronic devices for musculoskeletal rehabilitation. Soft sensors are crucial components of these devices, as they are used for user data collection and device control. However, current fabrication methods are expensive, complex, and not available to those in low resource communities. To address this issue, this paper presents advances in low-cost textile sensors created using either crocheting or weaving. The performance of four different types of sensors was evaluated in terms of working range, linearity, hysteresis, sensitivity, and repeatability. The results showed that a fully crocheted sensor made with elastic and silver-plated conductive thread performed the best. This sensor demonstrated high repeatability, an excellent working range (49.76%), and relatively good hysteresis (20.12 $\pm$ 19) and linearity (R^2 of 0.7741 $\pm$ 0.03). Overall, these results indicate that soft textile strain sensors created using simpler techniques, such as crocheting, have the potential to be used in applications requiring tracking of human motion, meaning that they could be used as integral components of soft wearable robots. This low-cost approach could make soft wearable rehabilitation technologies more accessible and affordable, paving the way for broader implementation and improved patient outcomes.**

***Index Terms*— textile sensors, crocheted materials, strain sensors, soft robotics, wearable sensors, rehabilitation robotics.**

I. Introduction

The use of soft wearable mechatronic devices in musculoskeletal rehabilitation is a research topic that has been gaining traction in recent years. Within these devices, sensors are one of the most important elements, as they can be used to collect data from activities of daily living [1], to estimate forces exerted by wearable robots during walking [2], and to control the behaviour of the robotic device [3] by detecting changes in the position of the wearer [4].

To comply with the soft aspect of the wearable mechatronic device, recent studies have explored the use of textile sensors due to their comfortable fit and easy integration into everyday clothing. These sensors are often fabricated using carbon-based techniques [5]–[7], screen-printed with conductive inks [8], or using chemical-based methods [9]. Although these manufacturing techniques show promise, they require specialized equipment and complex processes, limiting access and widespread availability. Simplifying the manufacturing process and reducing material costs may be sufficient for regions with limited funds to be able to produce functional textile wearable sensors.

To make these solutions widely available, low-cost manufacturing processes that provide high-quality measurements are essential. Methods such as sewing, and embroidering [10]–[12] use simpler techniques, but still require specialized machinery that might limit accessibility in under-resourced communities. On the other hand, two low-cost manufacturing alternatives are weaving and manual crocheting, with crocheting offering the lowest cost solution. Woven sensors are created by interlacing a set of threads perpendicularly to a different set of threads. In woven structures, the set of threads arranged vertically are known as warp threads, and the horizontal threads are known as weft threads (Fig. 1a). Crocheting, on the other hand, consists of interlocking loops of threads to create rows of a tightly bundled structure (Fig. 1b). By using weaving and crocheting in combination with conductive threads and elastic materials, textile sensors can be designed to meet specific needs. For example, it can be possible to substitute or combine multiple rows of the crochet structure with a conductive thread to detect changes in resistance when the crochet structure is stretched. Similarly, for woven sensors the warp and weft threads can be substituted by an elastic element and a conductive thread, respectively, to create a strain sensor.

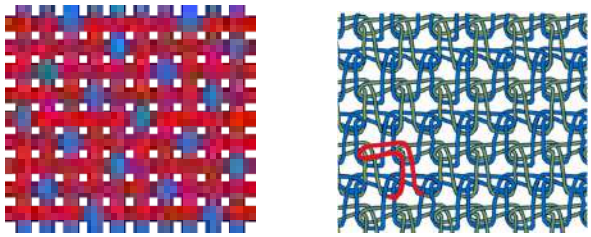
Unfortunately, the use of weaving and crocheting for the development of textile strain sensors has only been explored in few studies. For example, in [13] an elastic crochet structure was created using non-conductive threads. This piece of material was then coated with a conductive polymer to create a strain sensor. Similarly, in [14] a strain textile sensor was created using a weaved structure, which was made of fibres that had been previously coated with a conductive polyurethane. Although effective, these methods relied on a chemical process to provide electrical characteristics to the sensors. In another study [15], a simple textile strain sensor was created using a double crochet pattern. This sensor was used to measure elbow joint motions. However, the double crochet pattern created a structure with wide gaps, which affected the performance of the sensor over time.

This work was supported by the Natural Sciences and Engineering Research Council (NSERC) of Canada under grant RGPIN-2020-05648; by the Canadian Foundation for Innovation (CFI), by the Ontario Research Fund (ORF), and in part by the Canada Research Chairs Program under File #950-233069. M. Newkirk is funded by a summer internship from the Frugal Biomedical Innovations Program, Western University. J.G. Colli Alfaro is funded by the Western Innovation Fund, Western University.

M. Newkirk is in the Mechatronic Systems Engineering Program and in the School of Biomedical Engineering, Western University, London, ON N6A 5B9, Canada (e-mail: mnewkirk@uwo.ca).

J.G. Colli Alfaro is with the Department of Electrical and Computer Engineering, Western University, London, ON N6A 5B9, Canada (e-mail: jcollial@uwo.ca).

A.L. Trejos is with the Department of Electrical and Computer Engineering and the School of Biomedical Engineering, Western University, London, ON N6A 5B9, Canada (phone: 519-661-2111 ext. 89281; e-mail: atrejos@uwo.ca).



(a) (b)

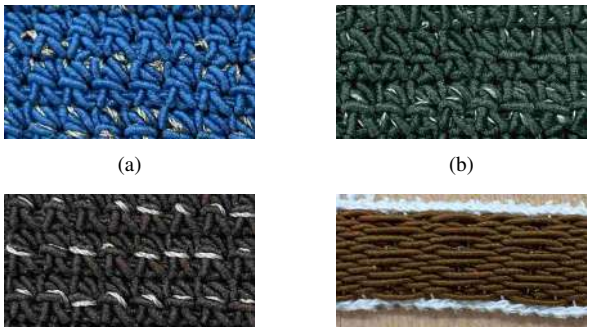
Fig. 1. a) Path of threads in a woven material, using the satin weave pattern. The red lines represent the weft threads, and the blue lines represent the warp threads. b) Path of the threads in the single crochet sensor. The blue lines represent the base, elastic thread and the green lines represent the elastic and conductive threads crocheted together. One single crochet stitch is outlined in red.

While some efforts have been made towards the development of textile strain sensors using the crochet and weaving techniques, fabrication and affordability issues still need to be addressed before they can be fully integrated into soft wearable mechatronic devices. Therefore, this study focuses on the development and assessment of textile strain sensors using the crochet and weaving techniques. The main objective of this study is to compare both techniques, and to provide a low-cost alternative for the development of stretchable textile strain sensors that can be potentially used during robot assisted therapies.

II. Materials and Methods

In order to achieve this objective, four different types of sensors were constructed and tested using a Madeira HC-40 silver-plated thread, a Bekinox VN14/1x90/100Z stainless steel conductive thread, and VistorHies elastic thread (model #CIDSTECA_3276258350). All of the crochet sensors were manually fabricated, whereas the woven sensors were created using an eight-shaft table loom (Ashford Handicrafts Ltd.). To assess variability, four sensors of each of the following types of sensors were created:

1) *Silver-plated full crochet (SPFC)*: These sensors were fully crocheted, 25 stitches long and 11 rows high. Silver-plated conductive thread was crocheted with the elastic thread every third row. This left a two-row buffer of elastic thread between rows where conductive thread had been used (Fig. 2a).
2) *Stainless steel full crochet (SSFC)*: These sensors had the same pattern and dimensions as SPFC, but used stainless steel as the conductive thread (Fig. 2b).
3) *Silver-plated backstitch (SPBS)*: A 25 stitch by 11 row sensor was made using only elastic thread. Silver-plated conductive thread was then sewn into the sensor using the backstitch. The backstitches were made by looping the conductive thread around the v-shaped pattern of the crocheted material, as shown in Fig. 2c. The stitching was completed for every other row on the crochet material for a total of five rows.
4) *Silver-plated satin weave (SPSW)*: A woven sensor made with the satin weave pattern was created in order to directly compare the crocheted sensors to woven sensors. The sensors were made with one row of plain weave, and four sets of the satin weave pattern, making 20 rows of satin weave, and then 1 row of plain weave at the end (Fig. 2d). The rows of plain weave allow for the pairs of warp thread to be tied off surrounding the last weft thread, keeping everything in place. There were 9 rows of conductive thread in the sensor. They were placed after every 2 rows of satin weave and embedded in the sensor using a plain weave. There is no layer of conductive thread after the last 2 rows of satin weave as it would slide out of place. A layer of fabric glue was applied to the edges of the sensor, to keep the warp threads from loosening when cut.



(a) (b) (c) (d)

Fig. 2. Four types of sensors created: a) Silver-plated conductive thread crocheted with elastic thread sensor; b) Stainless steel conductive thread crocheted with elastic thread sensor; c) Elastic thread crocheted base with silver-plated conductive thread embedded through a backstitch; and d) Satin weave sensor with silver-plated conductive thread embedded.



(a) (b)

Fig. 3. a) Crochet end pieces attached to one end of the sensor. b) Non-stretch nylon strips were sewn to the crochet end pieces. A piece of conductive fabric and snap were attached to the nylon, providing a contact point for the ends of the silver-plated or stainless steel thread.

Along the edge of each sensor, 12 rows of 10 single crochet stitches were added, as shown in Fig. 3a. Two layers of cotton sewing thread (Cansew Inc. model CG 24/4 6) were used on these ends, in order to give the end pieces more strength when pulled. Also, a non-stretch nylon strip was sewn onto the crocheted end pieces, with a patch of conductive fabric on top Fig. 3b. This conductive patch served as an interface between the conductive thread and a metal snap, which was used to connect the sensor to a data collection device.

The resistance of the sensor was recorded with a Rigol DM3058E Digital Multimeter (DMM) (RIGOL Technologies Inc., Portland, OR, USA) by attaching alligator clips at the ends of the sensors. Note that the added resistance value from the conductive fabric and snap shown in Fig. 3b was initially measured and removed from the resistance values

TABLE I

INITIAL SENSOR RESISTANCE VALUES. THE LAST COLUMN REPRESENTS THE DIFFERENCE IN RESISTANCE BETWEEN THE SENSOR WITH AND WITHOUT THE METAL SNAPS ATTACHED.

Sensor	Sensor Base Resistance (Ω)	Sensor Resistance With Snaps (Ω)	ΔR (Ω)
SPFC1	21.02	22.22	1.2
SPFC2	17.48	19.23	1.75
SPFC3	14.65	16.3	1.74
SSFC1	131.81	134.61	2.8
SSFC2	122.27	129.22	6.95
SSFC3	115.21	119.52	4.32
SPBS1	51.45	52.73	1.59
SPBS2	48.58	51.62	3.05
SPBS3	53.27	55.73	2.46
SPSW1	22.89	26.78	3.89
SPSW2	31.76	33.78	2.02
SPSW3	12.52	19.41	6.88

(a)

(b)

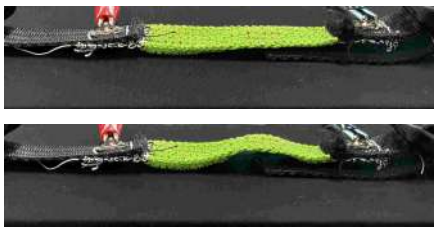


Fig. 4. a) Crochet sensor after being stretched 6 cm and relaxed. This was the maximum length that this type of sensor could be stretched without permanent deformation. b) The same crochet sensor after being stretched 7 cm. After the sensor was stretched to this length, it could no longer be restored back to its initial form.

obtained throughout testing. The initial resistance for each sensor is shown in Table I.

III. PERFORMANCE EVALUATION

In order to evaluate their performance, each sensor was stretched for 100 cycles while measuring the resulting change in resistance. All fo the sensors were tested in a dry, cool environment, at approximately 22.5 ± 0.5 °C. One property of the elastic thread is that its cross sectional area decreases when stretched. This allows the loops in the crocheted stitches to be pulled closer together, as the thread is thinner. The result is an increase in the length of the sensor, as the extra thread that used to be in the loops is now spacing out the stitches. When the tension is removed from the sensor, the extra length causes ductile deformation to occur. For example, Fig. 4a shows a sensor that was stretched but did not start to buckle, while Fig. 4b shows a sensor that was stretched past this maximum amount resulting in buckling.

One of the four sensors made for each pattern was used to determine the maximum distance that the sensor could be stretched before permanently deforming the material. This was done by stretching and relaxing the sensor in one centimeter increments. The maximum deformation that the sensor could withstand was determined to be about one centimeter below the permanent deformation distance. The remaining three sensors of the same pattern were stretched to this length for 100 cycles. Table II shows the average strain values applied to each sensor.

TABLE II

AVERAGE STRAIN VALUE APPLIED TO EACH TYPE OF SENSOR.

Type of Sensor	Average Initial Length (mm)	Distance Stretched (mm)	Average Strain (%)
SPFC	74.66	60	80.36
SSFC	73.91	30	40.59
SPBS	65.87	35	53.13
SPSW	95.52	20	20.94

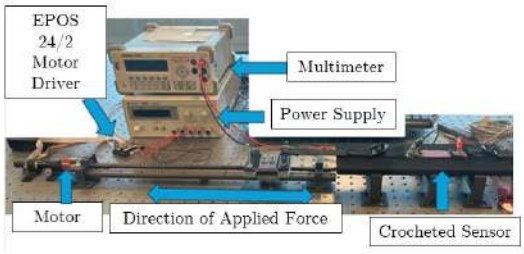


Fig. 5. Testing set-up used to stretch the sensors for 100 cycles.

The nylon strips were attached to the testing set-up using buckles, Fig. 5. The motor was set to rotate at 2000 revolutions per minute (rpm) and the DMM recorded the resistance of the sensor at a frequency of 2.5 Hz. The table under the sensor supported the weight of the buckles and DMM clamps, keeping all parts of the sensor level.

After the cycling was complete, the following properties were measured:

1) Working Range: This is the range over which the resistance changes due to the strain progression acting on the sensors. The range begins at the strain percentage where the loading and unloading cycles have a consistent decreasing or increasing monotonic behaviour, and extends to where the monotonic behaviour changes.
2) Sensitivity: The sensitivity of the sensors refers to the resolution and range that the sensors can measure [10]. To determine the sensitivity, the gauge factor (GF) was used, which relates the change in resistance (ΔR) with respect to the applied strain. A higher gauge factor indicates that a smaller amount of strain is needed to observe a change in the resistance. This is given by the gauge factor, as follows:

$$GF = \frac{\Delta R/R_0}{\varepsilon}, \tag{1}$$

where R_0 is the initial sensor resistance, and ε is the applied strain, which refers to the change in length (ΔL) of the sensor with respect to its initial length (L_0). The strain is given as follows:

$$\varepsilon = \frac{\Delta L}{L_0}. \tag{2}$$

3) Hysteresis: This is a measure of the difference in energy as a load is applied and released from a material. Ideal sensors would have no hysteresis. This would mean that the sensors show no loss of energy between

loading and unloading in the form of friction [10]. For these sensors, strain is used to measure hysteresis. The following formula is used:

$$H = \frac{\Delta\varepsilon_h}{\varepsilon_{max} - \varepsilon_{min}} \times 100, \quad (3)$$

where H denotes the hysteresis value in percentage units, $\Delta\varepsilon_h$ is the maximum difference in strain between the loading and unloading cycles, and ε_{max} and ε_{min} are the maximum and minimum applied strain, respectively. Since there were slight variations in the maximum and minimum positions recorded for each cycle, the average of the 100 cycles was used to calculate the hysteresis of each sensor.

4) Repeatability: The repeatability of a sensor represents the ability to maintain electrical and elastic properties over an extended number of cycles. Changes in the sensor performance over time are known as drift. The repeatability can be evaluated by comparing the resistance values of each cycle and how these values change as the cycling progresses.
5) Linearity: The linearity is given by the R^2 value. As the R^2 value approaches 1, the data set becomes more linear, demonstrating a higher level of consistency and energy retention in the sensors.

IV. Results

After collecting data from each sensor, the performance metrics outlined in the previous section were obtained for each sensor pattern. The results of these performance metrics are presented in the following paragraphs.

For each sensor sample, the working range was assessed on the 2nd, 11th, 30th, 75th, and 100th stretching cycles. This was done to observe the change of the working range of each pattern over each stretching cycle. It is important to mention that the first 10 stretching cycles were excluded from the analysis due to the Mullins effect, which relates to the stress softening of rubber materials [16].

The working range of each sensor sample of each pattern is illustrated in Fig. 6. For the SPFC and SSFC sensors, a decrease in the working range was observed before stabilizing around the 30th cycle. For example, for the SPFC1, an initial 68% working range was observed before decreasing to a 54% working range by the 30th cycle. On the other hand, the working range of the SPBS sensors stabilized around the 10th cycle. However, of all the patterns analyzed, the SPSW showed an inconsistent working range across all of its sensor samples. For SPSW1, a working range between 14–21% strain was observed from the 2nd to the 100th stretching cycle. This was not the case for SPSW2 and SPSW3, with the latter showing a working range that stabilized around the 75th cycle.

The second metric assessed was the gauge factor. This metric was calculated by first averaging the response of each of the sensor samples on cycles 11 to 100. Then the gauge factor was computed over this averaged data and over the working range found in the previous section. The gauge

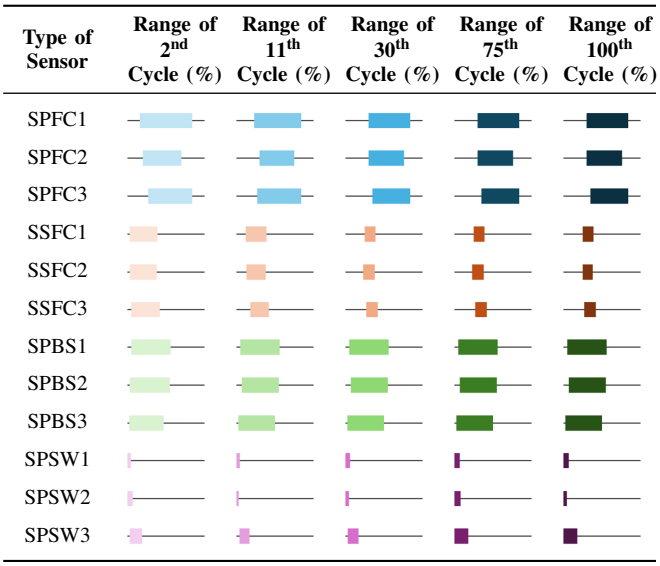


Fig. 6. Working range of the 2nd, 11th, 30th, 75th, and 100th cycle of each sensor. Each horizontal line represents a 0 to 100% range. The total working range of each sensor pattern is represented by the coloured boxes on the horizontal lines. The upper limit of each box is the maximum strain applied to that sensor.

TABLE III

Performance evaluation metrics for the tested sensors.

Sensor Number	Gauge Factor	Hysteresis (%)	Linearity (R^2)
SPFC1	1.12	28.21	0.8002
SPFC2	1.09	2.340	0.7405
SPFC3	0.954	39.80	0.7815
Average	**1.05 ± 0.09**	**20.12 ± 19**	**0.7741 ± 0.03**
SSFC1	1.00	38.25	0.6910
SSFC2	0.958	47.96	0.6558
SSFC3	0.425	38.23	0.6538
Average	**0.795 ± 0.3**	**41.48 ± 5.6**	**0.6669 ± 0.02**
SPBS1	0.276	24.16	0.6669
SPBS2	0.407	16.09	0.5905
SPBS3	0.191	44.25	0.5940
Average	**0.291 ± 0.1**	**28.17 ± 15**	**0.6171 ± 0.04**
SPSW1	2.000	0.89	0.9141
SPSW2	3.34	2.74	0.8553
SPSW3	10.6	6.250	0.9223
Average	**5.3133 ± 4.6**	**3.293 ± 2.7**	**0.8972 ± 0.04**

factor of each sensor sample and each pattern is shown in Table III. From this table, it can be observed that a gauge factor between 0.795 and 1.05 was obtained for the SPFC and SSFC sensors, with the SPFC sensors showing a more consistent value. The worst overall gauge factor was obtained for the SPBS sensors. However, these sensors showed less variation when compared with the SPSW sensors, which showed varying gauge factors between 2 and 10.6.

The hysteresis measurements were computed using the same averaged data used to compute the gauge factor. The hysteresis of each sensor pattern can be observed in Fig. 7. Note that this figure shows the sensor response of each pattern averaged across cycles 11 to 100, and across all of the three sensor samples. On the other hand, the individual hysteresis value of each sensor sample is shown

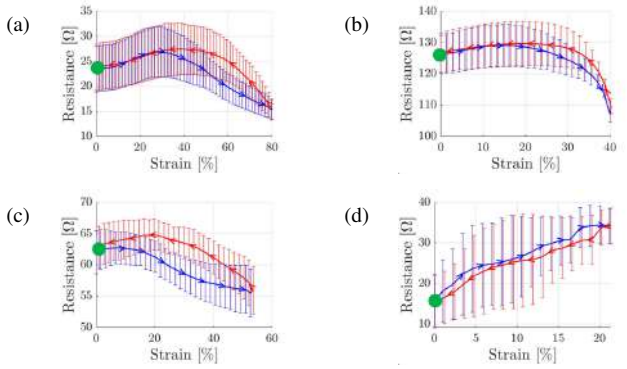


Fig. 7. Average sensor response of each sensor pattern. a) SPFC b) SSFC c) SPBS d) SPSW. Data from cycles 11–100 were averaged among the three sensors samples made from each pattern. The error bars show the standard deviation of the three patterns for the stretching (blue) and relaxing (red) portions of the cycles. The green dot shows where the cycles started and ended, and the direction of the arrows represents the path of motion.

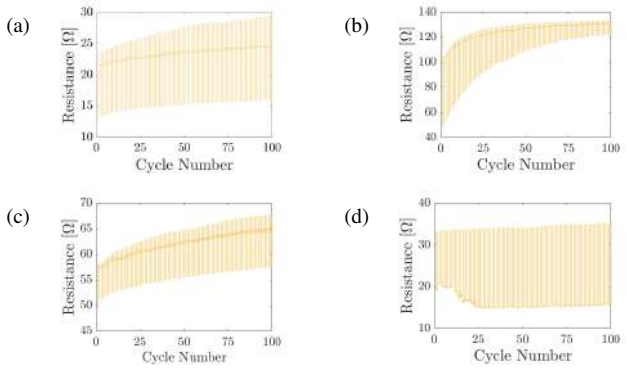


Fig. 8. Resistance readings as a function of cycle number for the average values across the three sensors made from each pattern. a) SPFC b) SSFC c) SPBS d) SPSW. The cycle number increases in increments of 1. The darker line in the middle or at the bottom of the graphs are where the data switch between cycle numbers. This change in resistance shows the readings at the beginning of each cycle.

in Table III. For each pattern, hysteresis varied within each sensor sample, with the SPSW sensors showing the lowest overall hysteresis and the SSFC having the highest hysteresis. However, the SSFC sensor hysteresis varied less between the sensor samples (38.23–47.96%), compared to the SPFC, which showed high hysteresis variability with values between 2.34% and 39.8%. A similar performance was observed for the SPBS sensors, whose hysteresis values ranged between 16.09% and 44.25%.

The next metric assessed was the repeatability of each sensor pattern. This metric was obtained by averaging the sensor resistance readings of each cycle across all of the three sensor samples of each pattern. The resulting data are shown in Fig. 8. All of the sensor patterns showed a drifting behaviour that trended upwards. *i.e.*, the sensor base resistance drifted towards higher values after each stretching cycle. Another important aspect that was observed among the sensor patterns is how their resistance range changed over time. The SPSW sensor pattern showed a major increase on its resistance range during the first stretching cycles that stabilized around the 25th stretching cycle. Also, this sensor pattern showed a minor drifting behaviour (Fig. 8d). In contrast, the SPBS sensor pattern showed an increased drifting behaviour between stretching cycles. However, no reduction on its resistance range was observed (Fig. 8c). A similar drifting behaviour was observed for the SPFC pattern, which showed no variability on its change in resistance between cycles but a positive drifting trend (Fig. 8a). Interestingly, the SSFC pattern showed little to no drift after the 40th stretching cycle. Unfortunately, it also showed the greatest reduction on its resistance range (Fig. 8b).

The last metric computed for each sensor pattern was the sensor linearity. The linearity values are displayed in Table III, and were calculated as the R^2 value obtained over the working range of each sensor sample. The linear response of each sensor pattern did not show high variability among their sensor samples. For example, an overall R^2 of 0.8972 $\pm$ 0.04 was found for the SPSW sensor pattern. The second best linear response was achieved by the SPFC pattern, whose sensor samples showed an average R^2 of 0.7741 $\pm$ 0.03. This was followed by the SSFC and the SPBS sensor patterns with R^2 of 0.6669 $\pm$ 0.02 and 0.6171 $\pm$ 0.04, respectively.

V. Discussion

The results of this study show that the crochet and woven sensors demonstrate good performance characteristics, which can be advantageous when integrated into soft wearable rehabilitation robots. Among the four sensor patterns, the SPFC and SPBS sensors demonstrated an average working range between all of its three sensor samples of 49.67% and 48.83%, respectively, after 100 stretching cycles. These working ranges are more than the suggested 30% for measuring joint data that can be used to control a wearable mechatronic device [17], which makes these patterns a great candidate for these applications. Although it would be expected to observe a similar behaviour across all of the three crochet sensor patterns, the SSFC was not able to achieve a usable working range. This can be observed in Fig. 8b, where the change in resistance of the sensor decreases drastically over time. This reduction on resistance has a direct impact on the working range performance of the sensor. This behaviour can be attributed to the stainless steel conductive thread used for the fabrication of this pattern. As opposed to the silver-plated thread, the stainless steel thread is composed of staple fibres that fray when being tensioned. Furthermore, whenever the stainless steel thread is stretched, the staple fibres tend to create new contact points that reduces the overall resistance of the conductive material [10].

Regarding the SPSW sensor pattern, the poor performance on the working range can be attributed to how the silver-plated thread behaves under tension. Differently to the SPFC pattern whose change in resistance occurs due to an increase in the number of contact points when the loops of the crochet pattern tighten, the change in resistance of the SPSW happen due to axial forces acting on the surface of the conductive thread. As its name implies, the silver-plated thread consists of a non-conductive thread (typically nylon), that has been coated with a conductive layer. Whenever this thread is

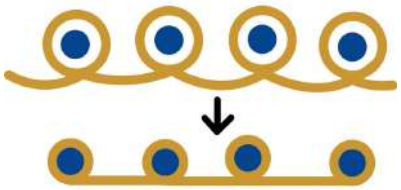


Fig. 9. Change in the crochet backstitch's conductive thread when stretched. The gold lines represent the conductive thread and the blue dots represent the posts of the crochet material the conductive thread wraps around. As the sensor is stretched (bottom), the number of points where the thread touches itself increases.

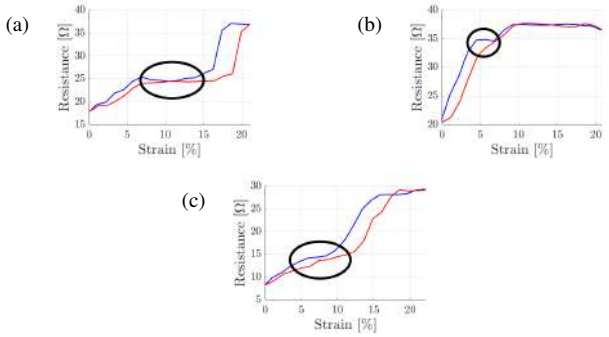


Fig. 10. a) SPSW1 b) SPSW2 c) SPSW3. All graphs compare the resistance readings to the displacement applied to the sensors. The region of limited change in resistance readings is circled in black. The stretching portion of the sensor is shown in blue and the relaxing is shown in red.

put under axial tension, cracks form on the surface of this conductive layer, which increases the overall resistance of the conductive thread [18]. However, because the thread is not elastic, there is a limit on how much it can be stretched. This is the reason why the working range of the SPSW pattern is less than 30%.

Regarding the gauge factor, the sensor that showed the lowest performance was the SPBS. This is because when fabricating this sensor pattern, the backstitches looped around the posts of the crocheted stitch base. When the sensor is stretched, the loops of the conductive thread tighten around the crocheted post as seen in Fig. 9. This increases the number of contact points in the conductive thread, reducing the overall resistance of the sensor. This limits the sensitivity of the sensor, as a larger amount of strain is required for change in resistance to be detected.

Compared to the SPBS, the SPFC and the SSFC had a larger number of initial contact points in the conductive thread. Therefore, only a smaller amount of strain was required to create a change in the sensor resistance. The exception was for the SSFC3, where the gauge factor was approximately half as small as the SSFC1 and SSFC2 sensor samples. This was because the initial length of SSFC3 sensor sample was shorter than the others. To account for this difference in length and to keep consistency during testing, the SSFC3 sensor had to be stretched to a distance that matched the length of SSFC1 and SSFC2 sensor samples. Since a larger value of strain was applied before testing, the amount of effective strain achieved by this sensor sample was reduced, which in turn affected the overall sensitivity.

As for the SPSW pattern, the large variation in the gauge factor among its sensor samples can also be explained by the initial lengths of the sensor samples, and by the inconsistent crack formation on the surface of the conductive thread. The change in resistance is then a function of the number of cracks, and the width and length of each crack [19]. Due to these inconsistencies, the sensor response varied among each of the sensor samples of the SPSW pattern (Fig. 10).

With respect to the linearity and hysteresis, the SPSW pattern showed the lowest hysteresis among all of the 4 sensor patterns and a consistent R^2 across all sensor samples. This was expected, as the underlying behaviour of these sensors was based on the crack propagation of the conductive thread, and not on the number of contact points at any given time. For the SPFC, SSFC, and SPBS sensors the hysteresis observed was due to the elastic thread used during the fabrication of these sensors. Since the elastic thread is made of rubber, it losses energy due to the viscoelasticity of the material [20]. The hysteretic behaviour on these crochet sensors can also be attributed to the number of contact points between the conductive thread. After stretching the sensors, the restoring force of the elastic band causes loosening of the conductive thread that was looped around the crochet stitches. This creates a sudden increase in the resistance of the sensor before it stabilizes to the base resistance. This behaviour can be observed better on Figs. 7a to 7c, in which during the unloading phase of the crochet sensors, higher resistance values can be observed compared to the resistance values during the loading phase. In contrast, the woven sensor showed lower resistance values during the unloading phase compared to the resistance values observed during stretching of the sensor, Fig. 7d.

Finally, all of the sensor patterns displayed a drifting behaviour. Similar to the other metrics, the SPSW sensors showed the lowest drift among the sensor patterns. This was thanks to the cracks on the surface of the conductive thread that created the drift in the resistance readings. When these cracks are formed, the initial resistance of the sensors cannot be reached again. As the sensor undergoes through more stretching cycles, more cracks are formed until a maximum number of cracks are created.

As for the crochet sensors, both the SPFC and the SPBS sensor patterns shown a similar upwards drift. During the experiments, it was observed that the conductive thread on the crochet sensor deviated from its original position. This was caused by the elastic band used during the fabrication of these sensors. When the sensors were stretched, the cross-sectional area of the elastic material decreased. This caused the sensors to slide across the crochet structure and thus, loosening the loops of the conductive thread. Regarding the SSFC, the other phenomenon that affected the repeatability of these sensors was the composition of the stainless steel thread. As the stainless steel conductive thread rubbed against itself, small fibres that form the stainless steel thread are pulled or broken out of place, causing a drift in the sensor resistance.

Overall, the best performing sensor pattern was the SPFC sensor due to its high repeatability and consistent gauge factor among its sensor samples. Regarding the hysteresis and linearity of this sensor pattern, they could be improved by implementing simple algorithms, such as neural networks, during the data processing step [21]. Similarly, the gauge factor can be improved even more by implementing a self-compensating Wheatstone bridge [18] in a diagonal bridge configuration.

VI. Conclusions and Future Work

This work provided an evaluation of different types of textile strain sensors manufactured using weaving and crocheting for applications involving soft robot assistive devices. Three crochet sensor patterns and one woven sensor pattern were created and evaluated. These sensors were assessed in terms of linearity, working range, sensitivity, hysteresis, and repeatability. The results of this study found that the sensor that performed best was the SPFC sensor—a fully crocheted sensor made of elastic thread and a conductive thread embedded every third row. However, before being able to be integrated into a soft wearable mechatronic device, the sensor design needs to be improved in terms of hysteresis and linearity. The SPSW sensor (a woven sensor made with the satin weave pattern) showed the second best performance among the four tested patterns. Although the working range of this sensor pattern is limited due to the inherent woven structure, this sensor may be used in applications where the sensing of a wide range of motions is not required. Some of these applications include early stages of rehabilitation, where joint mobility is limited.

In future work, the linearity and hysteresis performance of these sensors will be improved by implementing some deep learning models as part of the data processing algorithms. After improving these performance metrics, the sensors will be tested on human subjects and under different testing conditions, such as under different temperature and humidity settings. Although the sensors presented in this study show potential for applications involving monitoring of human motion, the performance of these sensors should be assessed against similar sensors in the literature. Beyond the low-cost aspect, this assessment would provide an insight regarding the similarities between crochet sensors and chemical-based sensors. These comparisons should be accompanied by a statistical analysis to highlight the differences between sensors. Similarly, future work should focus on the development and testing of different crochet patterns (*e.g.*, double crochet and chain crochet) to see whether the performance metrics assessed can be improved. Also, it is important to test the sensors under different conditions such as torsion and bending motions. Finally, in this study, sensors were stretched for 100 cycles, which is similar to the testing conditions presented in other studies. However, it would be important to increase the number of stretching cycles to more than 1000. This would allow observing if the performance of the sensors changes over time, and also to assess the fatigue of the sensors.

Overall, the sensors presented in this study provide an accessible alternative to traditional soft sensors. By implementing simpler manufacturing methods, it will be possible to make soft wearable rehabilitation robots accessible in communities with limited resources.

References

[1] K. Minami, Y. Akiyama, *et al.*, "Motion classification with embroidery bend sensors using multiple zigzag-stitch for loose-fitting garments," *IEEE Access*, vol. 13, pp. 2982–2993, 2025.

[2] C. Basla, A. M. Georgarakis, *et al.*, "A stretchable sensor for force estimation in soft wearable robots," in *IEEE International Conference on Rehabilitation Robotics (ICORR)*, Rotterdam, Netherlands, July 25–29, 2022, pp. 1–6.

[3] T. Desplenter, Y. Zhou, *et al.*, "Rehabilitative and assistive wearable mechatronic upper-limb devices: a review," *Journal of Rehabilitation and Assistive Technologies Engineering*, vol. 7, p. 2055668320917870, 2020.

[4] K. Zhu, B. Sharma, *et al.*, "Development of a smart textile-driven soft spine exosuit for lifting tasks in industrial applications," in *IEEE/SICE International Symposium on System Integration (SII)*, Ha Long, Vietnam, January 8–11, 2024, pp. 13–18.

[5] D. Kamireddi, R. M. Street, *et al.*, "Electrospun nanoyarns: a comprehensive review of manufacturing methods and applications," *Polymer Engineering & Science*, vol. 63, no. 3, pp. 677–690, 2023.

[6] A. A. Smith, R. Li, *et al.*, "A narrative review of in-textile sensors in human health applications," *Advanced Materials Technologies*, p. 2302141, 2024.

[7] R. K. Seidu and S. Jiang, "Functional performance of low-cost electronic yarn for e-textiles," *MRS bulletin*, pp. 1–16, 2024.

[8] G. Wu, L. Wu, *et al.*, "Research progress of screen-printed flexible pressure sensor," *Sensors and Actuators A: Physical*, p. 115512, 2024.

[9] A. Sankauskaite, R. Pauliukaite, *et al.*, "Smart textile with integrated wearable electrochemical sensors," *Current Opinion in Electrochemistry*, p. 101410, 2023.

[10] J. G. Colli Alfaro and A. L. Trejos, "Design and fabrication of embroidered textile strain sensors: An alternative to stitch-based strain sensors," *Sensors*, vol. 23, no. 3, p. 1503, 2023.

[11] M. Martínez-Estrada, I. Gil, *et al.*, "An alternative method to develop embroidery textile strain sensors," *Textiles*, vol. 1, no. 3, pp. 504–512, 2021.

[12] R. Aigner, A. Pointner, *et al.*, "Embroidered resistive pressure sensors: a novel approach for textile interfaces," in *Proceedings of the 2020 CHI Conference on Human Factors in Computing Systems*, Honolulu, Hawai, USA, April 25–30, 2020, pp. 1–13.

[13] T. Alam, F. Saidane, *et al.*, "Smart-textile strain sensor for human joint monitoring," *Sensors and Actuators A: Physical*, vol. 341, p. 113587, 2022.

[14] H. Cheng, T. Zuo, *et al.*, "High sensitive, stretchable and weavable fiber-based PVA/WPU/MXene materials prepared by wet spinning for strain sensors," *Journal of Materials Science*, vol. 58, no. 34, pp. 13 875–13 887, 2023.

[15] M. Bobin, H. Amroun, *et al.*, "SVM based approach for the assessment of elbow flexion with smart textile sensor," in *IEEE International Conference on Systems, Man, and Cybernetics (SMC)*, Banff, AB, Canada, October 5–8, 2017, pp. 2129–2134.

[16] B. Fazekas and T. J. Goda, "Constitutive modelling of rubbers: mullins effect, residual strain, time-temperature dependence," *International Journal of Mechanical Sciences*, vol. 210, p. 106735, 2021.

[17] K. M. Jansen, "Performance evaluation of knitted and stitched textile strain sensors," *Sensors*, vol. 20, no. 24, p. 7236, 2020.

[18] J. G. Colli Alfaro and A. L. Trejos, "Analysis of embroidered strain sensors in the presence of dynamic forces," *IEEE Sensors Journal*, vol. 25, no. 2, pp. 2422–2431, 2025.

[19] J. Wang, P. Xue, *et al.*, "Strain sensing behavior of electrically conductive fibers under large deformation," *Materials Science and Engineering: A*, vol. 528, no. 6, pp. 2863–2869, 2011.

[20] W. Luo, Y. Huang, *et al.*, "Fatigue life assessment of filled rubber by hysteresis induced self-heating temperature," *Polymers*, vol. 12, no. 4, p. 846, 2020.

[21] R. Aigner and A. Stöckl, "Machine learning based compensation for inconsistencies in knitted force sensors," *IEEE Sensors Journal*, 2024.

Pupillometry for Arm and Hand Motor Intent Detection

Shane Forbrigger
Dalhousie University
Department of Mechanical Engineering
Faculty of Computer Science
Halifax, NS, Canada
s.forbrigger@ieee.org

Thomas Trappenberg
Faculty of Computer Science
Dalhousie University
tt@cs.dal.ca

Ya-Jun Pan
Department of Mechanical Engineering
Dalhousie University
yajun.pan@dal.ca

***Abstract*—Rehabilitation robots and assistive devices that detect the motor intent of their users can provide more intuitive and effective control. Pupil dilation occurs when people perform motor activities, but its utility for detecting motor intent has not been explored previously. In this work, a human participant research study is conducted to determine if pupillometric data can be used to differentiate between a person's intent to pick up or observe an object. Thirty participants were recruited to perform 120 trials of picking up and observing objects while their pupil dilation was recorded by an eye tracking headset. Features were extracted from the time series data and used to train a neural network classifier. The classifier was tested using leave-one-out cross-validation. The classifier achieved an average accuracy of 59.4% and F1 score of 0.578 across the thirty test datasets. The performance varied significantly depending on the participant used for testing, suggesting that the pupillometric approach to intent detection may be better suited to some participants than others. Future work should determine whether intent detection can be improved with more advanced machine learning methods, such as convolutional neural networks (CNN), and whether intent detection can be performed in real time.**

***Index Terms*—Human-machine interfaces; Assistive robotics; Control in rehabilitation robotics; Intent detection**

I. Introduction

Stroke survivors often lose the ability to move one of their arms because of brain damage. They can recover by participating in rehabilitation therapy. The most effective therapy engages the patient's effort and relates to activities of daily life, but this kind of therapy is difficult for patients with severe arm impairment. Rehabilitation robots can assist such patients in therapy activities; however, they must ensure that the patient is always engaged and making an effort [1].

Although the user of a rehabilitation robot or assistive device could manually indicate their engagement, such as by pressing a button or giving a verbal command, this results in a slow and awkward interface. Ideally, these devices would react automatically to the user's intent as if reading their mind, thus creating a seamless experience that simulates the natural behaviour of their limb. This approach is called intent detection: the robot only activates its assistance when it can detect an intent to act from the user. In literature, robots have been designed to measure brain activity, muscle activity, and forces applied by the patient to detect intent [2]. Brain activity is the most relevant signal for intent, since intent originates in the brain. However, it is difficult to isolate the signals of interest and sensor placement is difficult for an untrained user. Muscle activity is the next most relevant signal, but it is only appropriate if the user is able to produce measurable, voluntary muscle activations. Force measurements are the furthest removed from intent but are the easiest to isolate. They require that the user can produce sufficient force in a controlled manner to reliably indicate what they are attempting to do. Disabled people want more intuitive interfaces [3], but due to the limitations of automatic intent detection, most assistive devices in practice use joysticks or manual control.

Eye tracking has been explored as an interface for controlling assistive devices. A person's gaze contains information about their intended interactions in an environment: they tend to look at objects before manipulating them [4], [5]. Existing assistive device interfaces focus on eye motion, tracking fixations, smooth pursuit motions, or saccades [6]. These methods suffer from the "Midas Touch Problem" [7], where eye movements to gather information (observations) are interpreted incorrectly as eye movements to interact (actions). Previous approaches to solve this intent detection problem include adding additional confirmation dialogs [8], requiring more complex eye gestures [9], or adding a separate input device, such as a switch, to confirm actions [10].

The use of pupillometry (pupil dilation measurement) and gaze information is an unexplored approach to intent detection. The pupil dilates slightly when a person performs, or even imagines performing, an action like reaching for an object [11], [12]. To the authors' knowledge, no previous research has attempted to use pupil diameter as a method of determining motor intent for controlling an assistive device. Detecting arm and hand motor intent from gaze tracking and pupillometry could therefore present several advantages: it precedes object manipulation, meaning it could anticipate intent before muscle activity or force sensing methods; it could be used to distinguish between fixations for observing an object versus physically interacting with an object; it could work even if the person has no voluntary movement of their arm; and it is easier to set up an eye tracking system than surface electroencephalogram (EEG) or electromyogram (EMG) sensors. A disadvantage of pupillometry is the pupil's sensi-

tivity to other stimuli, such as lighting conditions, emotional state, medications, and even cognitive load. Nonetheless, it could still be useful in controlled environments or when combined with other sensor data.

The purpose of this work is to determine the potential effectiveness of pupillometry for arm and hand motor intent detection. This work contributes to the understanding of motor intent and its relation to pupil dilation. A pupil response dataset is collected from human participants and analyzed, and important features and differences in pupil response between participants are discussed. A classifier is trained based on features extracted from the pupil data and its performance and generalizability are analyzed. The classifier demonstrates a proof of concept for novel pupillometric intent detection systems. Limitations of this approach are discussed as well as potential areas for improvement.

II. Study Design

Human participants were recruited to gather eye tracking and pupillometry data. The study was approved by the Dalhousie University Social Sciences and Humanities Research Ethics Board (Study #2024-7211).

A. Target Population and Recruitment

The target population was healthy people aged 18 years or older with normal or corrected to normal vision and hearing. Healthy adults were chosen as a target population to determine if a reliable, measurable pupillometric differences exist before involving a more vulnerable population like stroke survivors. Normal or corrected-to-normal vision is required because vision impairments could result in different gaze behaviours among the participants. Participants were considered to have normal vision if they could comfortably read the number off of a die at arms-length without squinting or straining. The eye-tracking hardware used in this study, the PupilLabs Pupil Core headset, does not fit over glasses but other corrections such as contact lenses were permitted.

Participants were excluded if they had muscular or neurological impairments, or an inability to follow auditory instructions. Muscular impairments of the eye, head, or neck could lead to compensatory movement that affects the way that a participant gazes at their environment. Neurological impairments could have a similar effect and could also change the responsiveness of the pupil.

Participants were recruited through word of mouth, physical posters, and advertisements shared via departmental email lists at Dalhousie University. A $15 honorarium was offered as an incentive to all participants.

B. Participant Demographics

Thirty-two people were recruited, of which two did not participate. One chose not to participate after the briefing, and one had an eye impairment that required them to be excluded. All participants gave informed consent before participating in the study. The demographics of the 30 participants are presented in Table I.

Approximately 73% of the participants were men and 23% were women. Half of the participants were in the 18 - 24 age group, and the next largest group was the 25-44 age group. All participants except one were right-handed.

TABLE I
Participant Demographics

Age Group	18 - 24 15 (50%)	25 - 44 12 (40%)	45 - 64 3 (10%)
Dominant Hand	Right 29 (97%)	Left 1 (3%)	
Gender ID	Man 22 (73%)	Woman 7 (23%)	Nonbinary 1 (3%)



Fig. 1. The participants' view of the experiment setup. Four dice are placed in a square on a small platform on top of a table. A computer monitor provides a neutral background with the gaze starting position (cross). Two speakers provide auditory instructions to the participant. A set of AprilTags are placed at the corners of the platform to allow post-experiment calibration and head movement tracking. The calibration marker is in the bottom right.

C. Experiment Procedure

Participants were asked to perform a series of tasks with and without motor action while their gaze and pupil dilation were recorded by an eye-tracking headset. All participants were briefed on the purpose and process of the experiment beforehand and their consent was recorded.

Experiments were conducted in a windowless room with ceiling-mounted lights. The experiment setup is shown in Fig. 1. Participants were seated at a table covered by a black tablecloth with four dice placed on a raised platform. The dice were placed in a square approximately $14\,\mathrm{cm}$ on a side. The dice were numbered one to four, left to right, top to bottom. Multiple dice were used to encourage different eye movements within the participant's field of view. AprilTags were placed at the corners of the platform to allow head movement tracking and post-recording calibration if necessary, but they were not used in this work.

Participants donned a PupilLabs Pupil Core headset [13]. The headset was calibrated with the calibration marker, shown in the bottom right of Fig. 1, placed in the center of the square of dice. Calibration was considered successful if the resulting model accuracy, the difference between the

predicted gaze position of their eye and the actual position, was less than or equal to 2.5° and the calibrated field of view encompassed all four dice and the cross on the background.

Participants were asked to perform one of two tasks selected at random: pick up one of the dice or read the number value on one of the dice without touching it. These two tasks represented the desired classes to differentiate: looking at an object with motor intent and action (an **Action** task) versus looking at an object without motor intent or action (an **Observation** task). Each trial began with the participant looking at the cross on the background. The experimenter triggered the start of each trial when the participant's gaze stayed on the cross for a few seconds. One second of data was recorded as a baseline [14], then an audio instruction would begin to play from the speakers. The audio instruction was either "Pick up" (**Action**) or "Read off" (**Observation**), followed by a number corresponding to the die with which to interact. The number of the die was randomized for each trial. In an **Action** task, the participant would reach with their dominant hand to pick up the commanded die, lift it from the platform and place it on the table, then return it to its original position. The recording would end once the participant placed the die on the table. In an **Observation** task, the participant would look at the commanded die without moving their hand and report the number to the experimenter. The recording would end once the participant reported the die number. After reporting the number, the participant would wait approximately two seconds, pick up the die, roll it on the table to get a new number, and then return it to its place on the platform. The dice were rolled to ensure that the participant would not be able to memorize the number on each die over the course of the experiment. Participants were asked to avoid reading or memorizing the dice numbers between trials. If the participant made a mistake, such as interacting with the wrong die or getting distracted, the trial would be repeated.

Tasks were assigned at random until the participant had done each task 60 times, for a total of 120 trials. The headset was re-calibrated every 30 trials to ensure that it had not slipped and was still reporting accurate eye measurements. The total experiment duration was approximately one hour.

III. Data Processing and Analysis

A. Data Processing

The data recorded by the Pupil Core headset consists of estimates of pupil diameter and pupil direction based on 2D image tracking of the eye mapped to a 3D eye model. Each estimate has a confidence measure from zero to one based on the goodness of fit between the detected ellipse in the camera frame and the eye model. The estimates are performed in real time, resulting in an inconsistent sample rate as some frames take slightly more time to process than others. A consistent sampling rate simplifies other processing steps, such as filtering, so the data was resampled to a fixed sample rate of 100 Hz. This rate was selected because 99% of samples were found to have $10\,\mathrm{ms}$ or less between them. The resampling was performed using a weighted average of all samples within each $10\,\mathrm{ms}$ period, with the confidence of each sample as the sample weight. In rare cases were no samples fell within a resampling period, a zero-order hold was used based on the value of the previous timestep.

After resampling, low-confidence samples were removed from the dataset. The Pupil Core documentation recommends discarding samples with less than 0.6 confidence. Removed samples were replaced by linear interpolation [14]. Two out of the 3600 total trials had a large amount of samples with less than 0.6 confidence and were discarded.

Another necessary data transformation involved the pupil diameter estimate. The Pupil Core measures each eye with a single camera, therefore there is no way to get an absolute measure of the pupil's diameter. To provide its estimate in millimetres, the Pupil Core's 3D algorithm fits a sphere of known diameter to the eye measurements during calibration. This can result in pupil diameter estimates that vary between eyes and between calibrations. Therefore, it is useful to normalize the pupil diameter in each trial to a baseline to allow comparisons between eyes and between trials. As described in Section II-C, the first $1\,\mathrm{s}$ of data in each trial was a baseline measurement, where the participants observed a neutral background before receiving their instructions. Therefore, the average pupil diameter for $0 \leq t \leq 1$, $d_{baseline}$, could be used to normalize the rest of the data in the trial according to,

$$d_{norm}(t) = \frac{d(t)}{d_{baseline}} - 1, \tag{1}$$

where $d(t)$ is the pupil diameter at time t. The value d_{norm} therefore represents the proportional change in pupil diameter relative to the baseline over the course of the trial.

Finally, the discrete pixels of the camera images and the nature of the pupil tracking algorithm leads to some "wobble" in the tracked pupil. The maximum frequency of interest for pupillometric data is approximately 9 Hz [14], therefore an $18\,\mathrm{Hz}$ low-pass, 3rd-order Butterworth filter was applied to the data to smooth this sensor noise.

B. Pupil Diameter Analysis

Representative, normalized eye diameter trendlines for each task type from four participants are shown in Fig. 2. The time range in which the participants received the instruction, from 1.0 to $2.5\,\mathrm{s}$, is labelled in each plot. The most common behaviour is illustrated by Fig. 2a: at the start of the instruction, the pupil diameter begins to increase for both task types, with a greater increase over time for the **Action** task. This behaviour was observed in 12 out of 30 participants. Fig. 2b shows the second most common behaviour, observed in 11 participants: the average pupil diameter increases for both tasks without a clear difference between them. The third most common behaviour, shown in Fig. 2c, where the pupil diameter increases more for the **Observation** tasks than the **Action** tasks, was only observed in three participants. Fig. 2d illustrates a behaviour observed in two participants: on average the pupil diameter increases for the **Action** trials but stays nearly constant for the **Observation** trials. Finally, one participant not illustrated in Fig. 2 showed negligible average

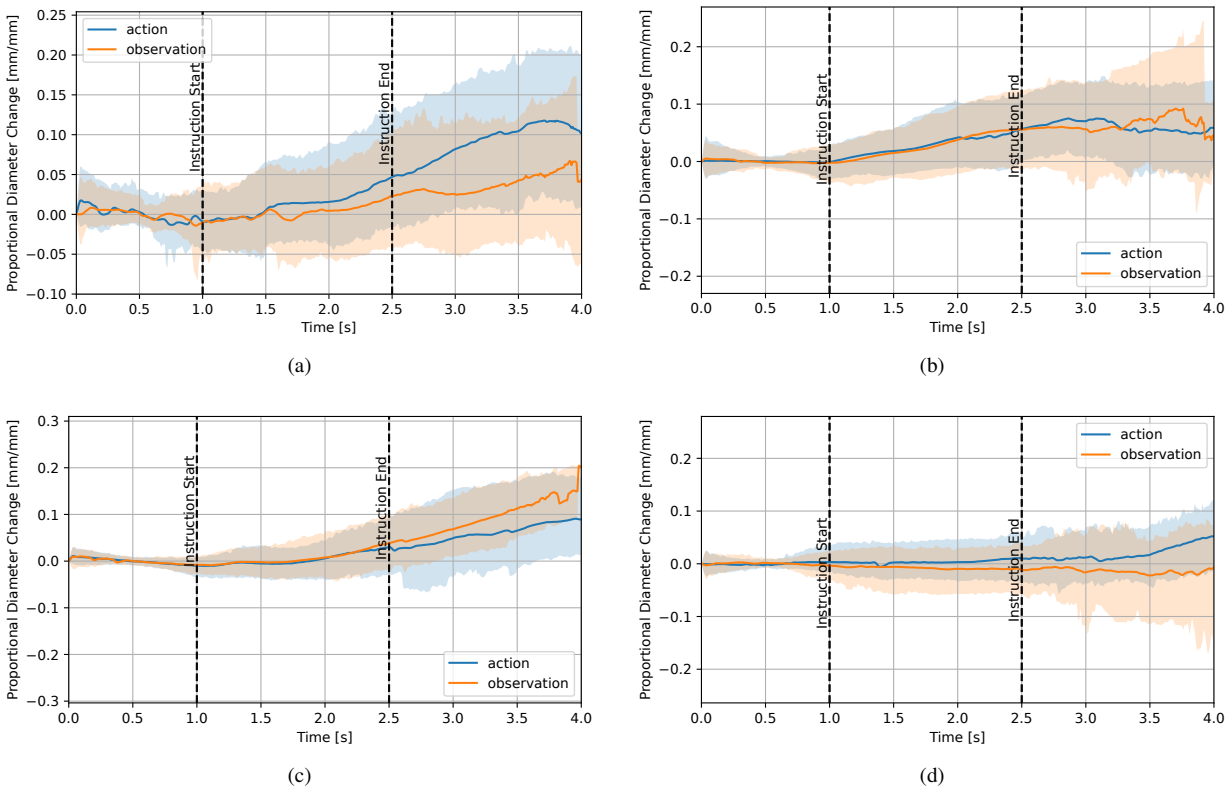


Fig. 2. Selected plots of average proportional pupil diameter change (d_{norm}) over all trials for several participants. The shaded regions show the 5th and 95th percentile ranges of the pupil diameter. (a) P23, showing a higher diameter for **Action** trials, (b) P06, showing a minimal difference between trial types, (c) P21, showing an increase in diameter for **Observation** trials compared to **Action** trials, and (d) P30, showing a difference without an increase in diameter for **Observation** trials

pupil diameter change for either task type, and one participant showed a decrease in pupil diameter of approximately the same amount on average for both task types.

IV. Classifier Design and Results

A. Classifier Design and Training

To train a simple classifier, features must be extracted from the normalized pupil diameter trajectory of each trial. Four features were selected for both eyes, for eight features in total. The selected features were: the mean normalized pupil diameter, the maximum normalized pupil diameter, the mean of the absolute value of the rate of change of normalized pupil diameter ($\left|\frac{d_{norm}}{dt}\right|$), and the maximum rate of change of normalized pupil diameter. These features were calculated from the post-baseline data in each trial, in other words for $t > 1$ s. Histograms of the selected features for Eye 0 (the right eye) are presented in Fig. 3. Each feature shows a noticeable difference between the **Action** and **Observation** task types, with **Action** tasks being biased to higher magnitudes.

A multi-layer perceptron classifier with two hidden layers of 50 neurons each using ReLU activation functions implemented in Scikit-learn [15] was trained on the selected features. The model was tested using leave-one-out cross-validation: 30 separate models were trained on the dataset where a different participant was left out of the training data for each model. The data of the left-out participant were then used to test the respective model.

B. Classifier Results

The classifiers were able to achieve results better than random chance for most of the testing data. The average confusion matrices for the training and testing data in Fig. 4 show an average accuracy of 67.3% on the training data and 59.4% on the testing data, with an approximately equal number of false positives and false negatives.

Fig. 5 provides a further breakdown of accuracy and F1 score across all 30 test sets. The accuracy histogram, Fig. 5a, shows three distinct clusters of results: the classifier achieved approximately 70-80% accuracy on 13 of the test sets, slightly better than random chance on 10 of the test sets, and at or worse than chance on 7 of the test sets. The F1 score histogram, Fig. 5b, shows a cluster of five test sets on which the classifier performed particularly poorly.

V. Discussion

The distribution of classifier performance in Fig. 5 demonstrates that the performance depends very strongly on which participant's data was set aside for testing. These results align with the observations in Section III-B that the participants' pupil responses could be classified into four main groups with clear differences. The features chosen for classification were particularly well suited for classifying the pupil responses

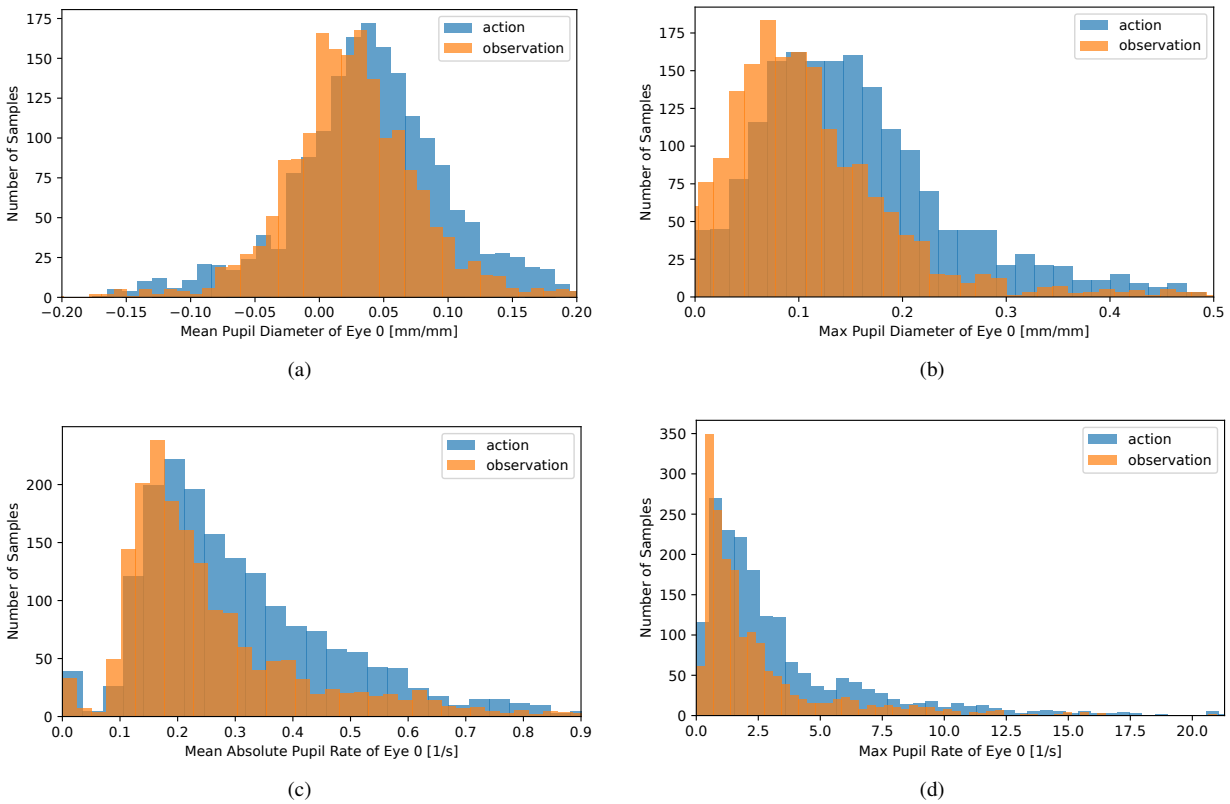


Fig. 3. Histograms showing the distribution of the four selected features used to train the model across all participants (3598 samples in total) for Eye 0 (the right eye). The plots for the other eye are similar. The distributions each show a small difference in bias between **Action** and **Observation** task types. (a) The mean pupil diameter for each trial. (b) The maximum pupil diameter for each trial. (c) The average absolute value of the rate of change of pupil diameter for each trial. (d) The maximum rate of change of pupil diameter for each trial.

in the first group: those who showed a larger pupil dilation for **Action** tasks versus **Observation** tasks. Since that group was the largest of the identified groups, it would dominate the training data and the classifier would be expected to perform better on participants with similar pupil responses. This would explain the distribution of classifier performance.

Other factors that could have impacted the results include fatigue over the course of the experiment and whether the participants were using any medications that affect pupillary response. The lack of gender diversity in the participants also prevents conclusive analysis of gender effects on the pupillometric data, if those effects exist.

The distribution of the classifier results suggests a few possible considerations for applying pupillometry to intent detection. Intent detection much better than random chance, in some cases up to 80% accuracy, can be achieved for some people. For those people that pupillometry works well, it could serve as a useful tool for intent detection. Stroke survivors and therapists have advocated for seeking a variety of approaches to rehabilitation technology rather than looking for a 'one-size-fits-all' solution [16], so pupillometry being a poor approach to some potential users does not disqualify its utility.

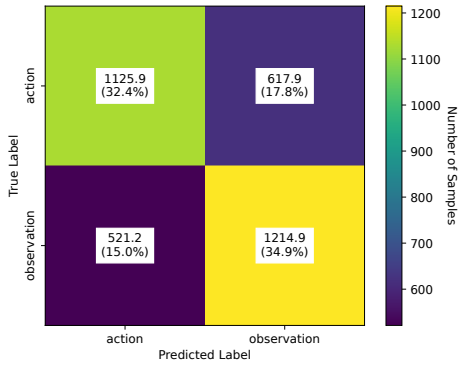
In this work the feature extraction was performed heuristically, using statistics that seemed to differentiate different classes. However, there may be other features within the time series data that are not as visible that could result in more effective classification. There are also additional time series signals, such as pupil orientation, that could be incorporated into the classifier. The training parameters and other properties of the neural network could also be tuned to provide better performance. Other network types could also be applied: convolutional neural networks and transformers are specialized for extracting features out of sequential data like time series [17] and could provide better performance.

To make the classification of the users intent useful, it must be performed in real time and quickly after the intent forms. Therefore, future investigation is necessary to determine if a classifier can work well on strictly causal data and how quickly it can identify intent after that intent forms in the mind.

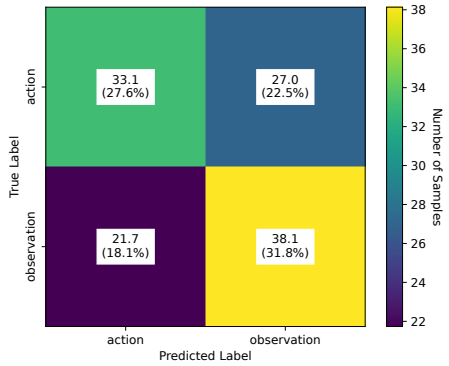
Finally, this work demonstrated the potential of this approach using healthy, mostly young participants. It remains to be seen how effective this approach will be for stroke survivors, which tend to be older and may have conditions that affect the reactivity of their eyes and pupils.

VI. Conclusions

Intent detection using pupillometric data shows mixed results. For some participants in the study it performed very well, while for others it performed poorly. This approach may not be suitable for all potential users of rehabilitation robots

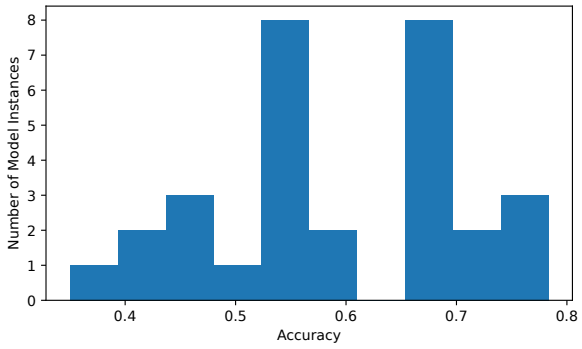


(a)

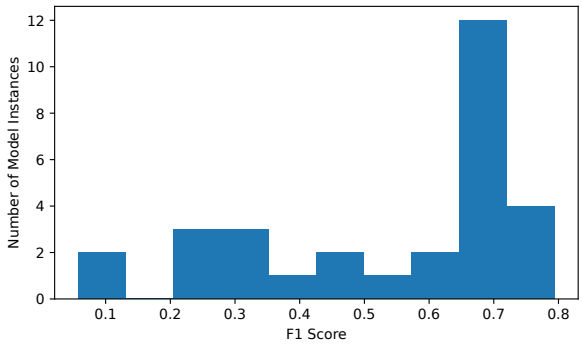


(b)

Fig. 4. Average Confusion matrices for (a) Training and (b) Testing of the neural net classifier.



(a)



(b)

Fig. 5. Distribution of (a) accuracy and (b) F1 score for all 30 classifiers.

or assistive devices, but it could serve as another tool in a broader intent detection toolbox. Better performance could be achieved with more advanced classification methods.

Acknowledgment

Thanks to the financial support of the Natural Sciences and Engineering Research Council of Canada (NSERC) and the Donald Hill Family Postdoctoral Fellowship Fund.

References

[1] A. A. Blank, J. A. French, A. U. Pehlivan, and M. K. O'Malley, "Current trends in robot-assisted upper-limb stroke rehabilitation: Promoting patient engagement in therapy," *Current Physical Med. and Rehabil. Reports*, vol. 2, pp. 184–195, 2014.

[2] D. P. Losey, C. G. McDonald, E. Battaglia, and M. K. O'Malley, "A review of intent detection, arbitration, and communication aspects of shared control for physical human–robot interaction," *Appl. Mech. Rev.*, vol. 70, p. 010804, 2018.

[3] J. Gantenbein, J. T. Meyer, L. Jager, R. Sigrist, R. Gassert, and O. Lambercy, "An analysis of intention detection strategies to control advanced assistive technologies at the cybathlon," in *Proc. of the Int. Conf. on Rehabil. Robot. (ICORR)*, 2022, pp. 1–6.

[4] M. Land, N. Mennie, and J. Rusted, "The roles of vision and eye movements in the control of activities of daily living," *Perception*, vol. 28, pp. 1311–1328, 1999.

[5] M. F. Land, "Eye movements and the control of actions in everyday life," *Prog. Retinal Eye Res.*, vol. 25, pp. 296–324, 5 2006.

[6] M. O. B. Wibowo, S. A. I. Alfarozi, and S. Wibirama, "Pros and cons of fixation and smooth pursuit interaction in assistive technology: A review," in *Proc. of the 8th Int. Conf. on Sci. and Tech. (ICST)*, 2022, pp. 1–6.

[7] R. J. K. Jacob, "What you look at is what you get: eye movement-based interaction techniques," in *Proc. of the SIGCHI Conf. on Human Factors in Comput. Syst.* New York, NY, USA: Association for Computing Machinery, 1990, p. 11–18.

[8] P. Mohan, W. B. Goh, C.-W. Fu, and S.-K. Yeung, "DualGaze: Addressing the midas touch problem in gaze mediated VR interaction," in *Proc. of the IEEE Int. Symp. on Mixed and Augmented Reality Adjunct (ISMAR-Adjunct)*, 2018, pp. 79–84.

[9] A. Mansour and J. Orlosky, "Approximated match swiping: Exploring more ergonomic gaze-based text input for XR," in *IEEE Int. Symp. on Mixed and Augmented Reality Adjunct (ISMAR-Adjunct)*, 2023, pp. 141–145.

[10] Y. K. Meena, H. Cecotti, K. Wong-Lin, and G. Prasad, "A multimodal interface to resolve the midas-touch problem in gaze controlled wheelchair," in *Proc. of the 39th Int. Conf. of the IEEE Eng. in Med. and Biol. Soc. (EMBC)*, 2017, pp. 905–908.

[11] D. Rozado, M. Lochner, U. Engelke, and A. Dünser, "Detecting intention through motor-imagery-triggered pupil dilations," *Human–Computer Interaction*, vol. 34, pp. 83–113, 2019.

[12] D. Voudouris, I. Schuetz, T. Schinke, and K. Fiehler, "Pupil dilation scales with movement distance of real but not of imagined reaching movements," *J. Neurophysiol.*, vol. 130, pp. 104–116, 7 2023.

[13] Pupil Labs GmbH. "Pupil Core - Open source eye tracking platform". Accessed: Dec. 6, 2024. [Online]. Available: https://pupil-labs.com/products/core

[14] S. R. Steinhauer, M. M. Bradley, G. J. Siegle, K. A. Roecklein, and A. Dix, "Publication guidelines and recommendations for pupillary measurement in psychophysiological studies," *Psychophysiology*, vol. 59, 2022.

[15] F. Pedregosa, G. Varoquaux, A. Gramfort, V. Michel, B. Thirion, O. Grisel, M. Blondel, P. Prettenhofer, R. Weiss, V. Dubourg, J. Vanderplas, A. Passos, D. Cournapeau, M. Brucher, M. Perrot, and E. Duchesnay, "Scikit-learn: Machine learning in Python," *J. Mach. Learn. Res.*, vol. 12, pp. 2825–2830, 2011.

[16] S. Forbrigger, M. Liblong, T. Davies, V. DePaul, E. Morin, and K. Hashtrudi-Zaad, "Considerations for at-home upper-limb rehabilitation technology following stroke: Perspectives of stroke survivors and therapists," *J. Rehabil. and Assistive Technol. Eng.*, vol. 10, 2023.

[17] N. M. Foumani, L. Miller, C. W. Tan, G. I. Webb, G. Forestier, and M. Salehi, "Deep learning for time series classification and extrinsic regression: A current survey," *ACM Comput. Surveys*, vol. 56, pp. 1–45, 2024.

Investigating kinematic and kinetic asymmetries during sit/stand movements with a powered knee-ankle prosthesis: a pilot study

Kellen Waters
Biomedical Engineering
University of Colorado Boulder
Boulder, CO
kellen.waters@colorado.edu

Benson Zou
Mechanical Engineering
University of Colorado Boulder
Boulder, CO
benson.zou@colorado.edu

T. Kevin Best
Robotics
University of Michigan
Ann Arbor, Michigan
tkbest@umich.edu

Robert D. Gregg
Robotics
University of Michigan
Ann Arbor, Michigan
rdgregg@umich.edu

Cara Gonzalez Welker
Mechanical Engineering
University of Colorado Boulder
Boulder, CO
cara.welker@colorado.edu

***Abstract*—Individuals with lower-limb amputation often experience significantly decreased daily activity due to difficulty in completing sitting and standing tasks. Additionally, due to the lack of power provided by their passive prosthetic limb, their movements are typically asymmetric, leading to increased rates of osteoarthritis and lower back pain. A study by Welker et al. introduced a novel data-driven controller implemented on a powered knee-ankle prosthesis to aid individuals with transfemoral amputation in sitting and standing by providing a biologically inspired torque to both the knee and ankle, which saw reductions in ground reaction force loading asymmetries. The purpose of this study is to further investigate asymmetry in kinematics and kinetics when wearing the powered prosthesis with the same novel controller. For our study, two participants performed various sit/stand tasks at three stool heights and two speeds. Using optical motion capture and ground reaction forces to determine inverse kinematics and inverse dynamics revealed significant differences between the intact and prosthesis side hip and knee torques, but still showed reduced asymmetry in kinematics and kinetics compared to previous literature with passive and powered prostheses. These results suggest the controller's potential to alleviate secondary conditions like osteoarthritis by improving these asymmetries.**

I. Introduction

An estimated one million Americans are currently affected by amputation of the lower limb [1], with over 150 thousand undergoing amputation every year [2]. Lower-limb prosthesis users (LLPUs) typically compensate by loading their intact limb more than the affected limb during walking [3, 4], sitting, and standing, resulting in kinetic and kinematic asymmetries [5, 6, 7]. As a result, many LLPUs experience secondary conditions from these compensatory mechanisms, including osteoarthritis, back pain, and reduced mobility, resulting in decreased quality of life [8]. Where only 2-11% of the general population experience knee or hip osteoarthritis, 16–60% experience knee osteoarthritis [9], and 14% experience hip osteoarthritis in the LLPU population [10]. Osteoarthritis in all populations leads to increased joint pain, stiffness, and reduced mobility [11], which has a greater impact on populations with limited mobility.

During the day, the average adult transitions between sitting and standing 60 times a day [12]. An impaired ability to stand up from a seated position predisposes the LLPU population to a sedentary lifestyle, where more than 61% are "not sufficiently active," and 30% are classified as sedentary [13].

Currently, most LLPUs wear passive prostheses that cannot provide net power. The lack of power in passive devices has caused LLPUs to move slower, less efficiently, and less symmetrically than healthy individuals [14]. In Teater et al. [15], transtibial passive prosthesis users generated peak knee torques $\sim$300% greater on the intact limb than the prosthesis limb with only 36-48% greater peak ground-reaction force asymmetry. Although studies in this population have been limited, it is likely that these asymmetries would be even more exaggerated for individuals with above-knee amputation, given their missing knee joint. Even though LLPUs wearing passive prostheses have significantly worse clinical metrics during sit/stand transitions [5], powered prosthesis controller design in this area of research remains understudied [16], and it is unclear which types of asymmetries lead to secondary conditions. Our goal is to explore these asymmetries further using a novel-powered prosthesis controller.

Although limited, previous work has shown benefits of wearing a powered prosthesis compared to a passive prosthesis when performing sit/stand transitions. Highsmith et al. [6] investigated the commercially available first-generation Power Knee (Össur. Reykjavik, Iceland), which has a quadriceps-mimicking function to provide some assistance in both sit-to-stand and stand-to-sit motions. Compared to the LLPUs' prescribed passive device, they found that even though users of the Power Knee did not fully activate the torque capabilities of

TABLE I
PARTICIPANT DEMOGRAPHICS

Participant	Sex	Age	Body Mass (kg)	Height (cm)	Side of Amputation	Residual Limb Length (cm)	Time since Amputation (years)	Prescribed Prosthesis (knee/ankle)	Etiology	Device Experience
1	M	26	108.8	192	L	26.8	26	C Leg 4/Triase	Congenital	Moderate
2	M	40	79.2	180	L	38	23	Rheo Knee/Freedom Maverick Xtreme AT	Cancer	Low

the controller, affected limb hip moment production was found not to be significantly different than the unaffected control group [6]. However, [6] also found a degree of asymmetry ($\overline{DoA}$) of 124% for peak knee torques during sit-to-stand and 87% during stand-to-sit comparing the intact and affected limb. It is also important to note that during the study, some subjects used armrests while performing sit/stand tasks, reducing the reliability of their results.

Powered prostheses frequently use impedance control

$$\tau = \kappa(\theta_{eq} - \theta) - \beta\dot{\theta} \tag{1}$$

which determines joint torque as a function of the joint's angular position and velocity, and parameterized by a stiffness κ, damping β, and equilibrium coefficient θ_{eq} [18, 19]. This controller design typically involves manually tuning the coefficients for segments of the sit/stand transition per individual and has been found to reduce asymmetry in peak vertical acceleration compared to a passive prosthesis [19]. Although these results are promising, manual tuning can extend prosthesis fittings by multiple hours [19].

Other sit/stand controllers are designed without impedance control, yet still involve manual tuning [20]. Hunt et al. [20] designed a sit-to-stand quasistiffness controller with a look-up table to match the prosthesis knee torque output based on the relationship of knee-flexion position to knee torque output seen in able-bodied biomechanics. During their study, subjects increased the peak knee torque output on the prosthesis side during sit-to-stand movements compared to their passive prosthesis [20]. They also found improvements in asymmetric loading, stand-up duration, and vastus medialis activation when subjects used the powered prosthesis compared to their passive device [20]. However, towards the end of the movement, there were increases in kinematic asymmetries and weight-bearing asymmetry with increasing torque magnitude assistance from the powered prosthesis.

In recent literature, phase-based controller design has made progress in limiting asymmetries during gait and sit/stand loading [21, 22]. Best et al. [21] designed a novel controller for adaptive speed and incline walking. This minimal tuning controller design focuses on a data-driven approach, using able-bodied data and an optimization problem (Eqn. 2) to estimate continuous knee and ankle impedance parameters across a given motion. The optimization problem identifies the set of impedance parameter coefficients $\kappa^*_{\chi_p}$ for each task χ_p that best reproduces the dataset's mass-normalized joint torques τ with given kinematics $(\theta, \dot{\theta})$ over all n data points at χ_p:

$$\begin{aligned} \kappa^*_{\chi_p} &= \arg\min \frac{1}{n}||\tau - \hat{\tau}||_2^2, \\ \text{where } \hat{\tau} &= \kappa_{\chi_p}\Big]\theta_{\text{eq},\chi_p} - \theta\Big) - \beta_{\chi_p}\dot{\theta}. \end{aligned} \tag{2}$$

When using this controller for sitting and standing tasks, participants experienced significant reductions in average ground reaction force loading asymmetry and decreased time to complete sit-to-stand and stand-to-sit at multiple stool heights and trial speeds compared to the participants' prescribed passive device [22]. However, their study only investigated loading and lacked further investigation of the powered prosthesis's kinematic and kinetic effects.

Currently, multiple outcomes and metrics are used to measure impact when comparing powered and passive prostheses. Various papers only report significant changes in loading [22, 20], kinematics [20], or kinetics [6], but it is unclear which asymmetries are the largest cause of negative secondary conditions and how they may be related. The goal of this manuscript is to perform a preliminary investigation of the impact of the same novel sit/stand prosthesis controller from [22] on asymmetries when comparing the unaffected and affected side for kinematics and kinetics and to compare these same metrics with prior work in passive and powered prostheses.

II. METHODS

A. Participants

The Institutional Review Board of the University of Michigan (HUM00166976) approved this protocol. To validate the experimental controller designed by Welker et al. [22] for improving kinematic and kinetic asymmetries, three participants completed a series of tasks while wearing a powered knee-ankle prosthesis [23], with the implemented novel sit/stand controller. During the trials, participants wore a ceiling-mounted safety harness, and a certified prosthetist was available and assisted in the fitting of the powered prosthesis. Three participants completed the study; however, due to extreme motion-capture recording artifacts, Participant 3's data was unusable and excluded from analyses. The demographics of the two remaining participants are described in Table I. Both participants had previous experience wearing a powered prosthesis. Participant 1 had previous experience in both a walking study and a sit/stand study with an earlier version of the controller, and Participant 2 had participated in only a walking study prior to this data collection.

B. Controller Design

The controller previously designed by Welker et al. [22] was implemented on the powered prosthesis worn by participants

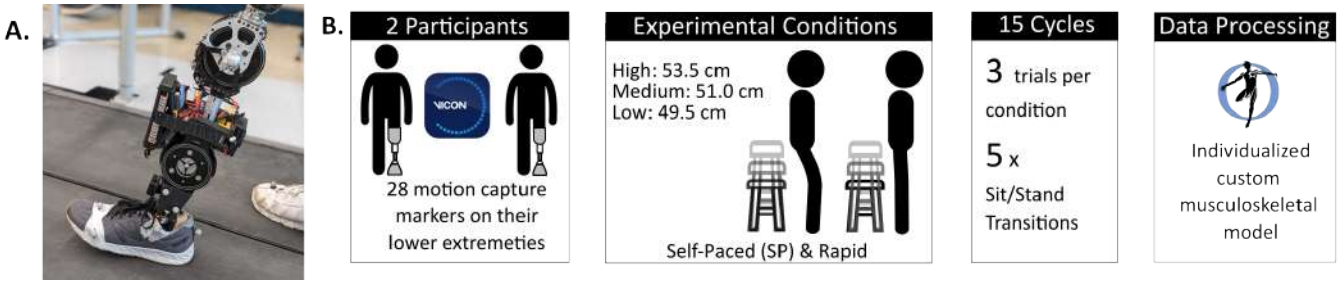


Fig. 1. **A.** Detailed marker placement on the prosthetic limb. The markers shown are the lateral knee, two shank markers, the lateral ankle, two toe markers, and the heel. **B.** Protocol overview showing two participants wearing their powered prosthesis for three stool heights (49.5, 51.0, and 53.5 cm) and two speeds, performing 15 sit/stand movements per condition. The VICON Nexus motion capture data was analyzed using OpenSim [17] and an individualized custom musculoskeletal model for each participant.

during the study. This controller takes a novel approach using a phase variable to determine the progression of the user's sitting or standing motion. Global thigh angle was used as this phase variable due to its monotonic decreases during sit-to-stand and increases during stand-to-sit. This allows the phase variable to accurately predict the direction of the movement and only requires one controller for sit-to-stand and stand-to-sit. Using experimental data [24] combined with the optimization problem model from Equations 1 and 2 and able-bodied kinematics and kinetics during sit-to-stand and stand-to-sit at a self-selected pace, impedance parameter functions were optimized for both the knee and ankle [22]. This controller was then implemented on a powered knee-ankle prosthesis previously validated for open-loop impedance control [23].

C. Experimental Protocol

Participants completed the experimental protocol while wearing the powered prosthesis with the implemented novel controller after being fit by a certified prosthetist. During the trials, ground-reaction forces were recorded from two in-ground force plates (AMTI, MA, USA) at 250 Hz and lower-body kinematics were recorded at 100 Hz using a 32-camera motion capture system (Vicon, UK). 28 reflective markers were worn along the lower extremities of each participant, which were affixed to the hip (6), thighs (7), knees (2), shanks (5), ankles (2), and feet (6). On the intact side, markers were attached to the lateral malleolus, the calcaneus tuberosity, and the first and second metatarsal head. On the prosthesis side, as seen in Fig. 1A, markers were placed at the powered ankle joint, at the same height as the calcaneus marker, and estimated toe markers on the shoe based on the intact side. For the tibial markers, markers were placed just above the powered prosthesis ankle joint due to geometric limitations.

Participants were given 15 minutes of training with a loading symmetry visual aid (see details in [22]), including 5 minutes of exploratory training, 5 minutes where they were instructed to increase their asymmetry by loading the biological limb as they would while using their passive prosthesis, and 5 minutes where they were instructed to try to minimize their asymmetry. Once training was completed, the visual aid was removed, and participants began the study. Participants performed sitting and standing tasks at two different speed conditions (self-paced and rapid) and three stool height conditions (low, medium, and high, at 48.5 cm, 51.0 cm, and 53.5 cm), totaling six different conditions. All self-paced trials involved cues to sit or stand at a comfortable pace, and rapid trials had the participants perform the five-times sit/stand movements as fast as they comfortably could. For each trial, participants completed five sit-to-stand movements at the specified stool height and assigned speed for three trials, totaling 15 sit-to-stand movements per condition. Participants were asked to keep their hands across their chest and prevent themselves from using their arms to aid in the movement.

D. Modeling

Marker trajectories and ground reaction force data were filtered using Butterworth low-pass filters at 2 Hz and 6 Hz, respectively, as in [22]. Using custom-scaled musculoskeletal models modified from [25], the VICON motion capture data from each trial was processed in OpenSim [17] to calculate joint angles and joint torques. The mass, moment of inertia, and center of mass of each biological body segment in the musculoskeletal model were scaled for each individual based on segment lengths. Following an adapted protocol of Willson et al. [26], the mass of the residual limb (the femur) was scaled to 55% of the mass of the intact limb, and the center of mass was shifted to be closer to the hip joint by 30%. The prosthetic device model was scaled alongside the musculoskeletal model to match the length of the device and then manually changed to the experimentally determined mass of the shank and foot of the powered prosthesis. The center of mass and moment of inertia for each prosthesis segment (foot and shank) were estimated from a CAD model of the prosthesis [23].

E. Segmentation

Sit-to-stand and stand-to-sit segments were isolated using peak detection for the prosthesis knee angle velocity, where peak positive and negative velocities indicated a movement transition (Fig. 2). Steady-state knee angular velocities found before and after the detected peaks were then used to determine initiation and completion events. Specifically, in sit-to-stand segments, an initiation event was marked when knee-angle velocity first fell outside of a threshold where it was less than zero but greater than -1.0 deg/sec, and sit-to-stand completion was determined as the last instance when knee

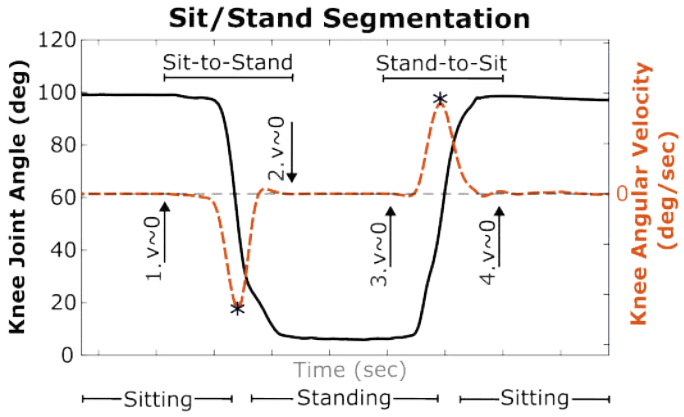


Fig. 2. Example segmentation for both sit/stand movements. Segments were initially isolated using peak detection for knee angle velocity (indicated by the asterisk), which marks that a movement event is occurring. The labels 1-4 show the initiation and completion events of sit-to-stand and stand-to-sit, when the knee velocity either left or entered a steady state of approximately zero.

velocity was greater than -1.0 deg/sec before reaching a steady state angular velocity of zero. During stand-to-sit designated segments, initiation was determined when knee velocity first fell outside of a threshold where it was greater than zero, but less than 1.0 deg/sec, and completion was marked as the last occurrence of the knee velocity being greater than 1.0 deg/sec. Joint angles and joint torques were segmented for every trial using the time points from the segmentation above.

F. Symmetry Calculations

There has been little work done quantifying kinematic asymmetries during sit-to-stand, but [20] recently reported kinematic asymmetries while wearing a powered prosthesis controller. In order to directly compare to their values, we adapted their approach as follows. The sit/stand segmentation described in Section IIE includes a stationary period at rest, whether sitting or standing, allowing us to examine torques generated before the movement initiates. However, this sit/stand segmentation prevents the joint angle transitions from being monotonic as typically investigated [20]. Adding a secondary segmentation for kinematics allows us to find the joints' start and end positions for monotonic movements. Then, to quantify the kinematic differences between the intact and prosthetic sides, each side was independently normalized to a start and end position (0-100), as in [20]. Calculating the normalized difference between each joint allows for a direct comparison between the biological and affected limb for the entirety of the motion and provides greater insight into kinematic asymmetries. Kinematic asymmetry peak-to-peak estimates were calculated from the difference between the maximum and minimum normalized difference of each trial and then averaged across trials.

For every participant, joint torques were normalized by body mass. Peak extension moments were found for each sit/stand transition and individual limb. The degree of asymmetry ($\overline{DoA}$) was calculated between the intact and prosthesis sides for knee and hip torques. $\overline{DoA}$ was calculated as

$$\overline{DoA} = (Intact - Pros.)/(Intact + Pros.) * 100 \quad (3)$$

where positive $\overline{DoA}$ corresponds to a larger value on the intact side, and a negative value indicates a larger magnitude on the prosthesis side. For all reported kinematic and kinetic profiles, outliers three standard deviations outside the mean were removed (an average of 0.5% of data points were considered outliers across trials for joint angles and torques).

G. Statistical Analysis

A linear mixed effects model was fit to determine differences in maximum torque at each joint for each sit/stand movement at each speed (self-paced or rapid). The fixed effects for each model were stool height and leg side (intact or prosthesis side), and the random effect was the participant, which included a subject-specific intercept. Statistical significance was determined using Bonferroni corrections. Due to two comparisons being made (stool height and leg side), the significance was set to $p<0.025$.

III. Results

Fig. 3 and Fig. 4 show the mean joint angles and torques during both sit-to-stand and stand-to-sit for the knee and hip. From these curves, we were able to calculate kinematic asymmetries in Fig. 5 and torques in Fig. 6.

A. Kinematics

Fig. 5 shows that for sit-to-stand, the prosthesis side had a greater rate of change for most of the sit-to-stand transition in both the knee and hip until the end of the trial, where the intact limb began to progress quicker. For the highest stool height, the sit-to-stand movement remained more symmetric than both the medium and low stool heights. During stand-to-sit trials, the limbs moved fairly symmetrically until about 40% through the movement, when the prosthesis side started to progress more quickly.

Kinematic peak-to-peak values were calculated to determine the range of asymmetry across the trial, as in [20]. Sit-to-stand self-paced trials had an average kinematic peak-to-peak difference of 7.66±2.5% in the hip and 7.01±1.75% in the knee. There was a slight increase in the rapid trials, with the hip averaging 8.4±1.24% and the knee 8.84±0.95%. These ranges increased for stand-to-sit, with self-paced averaging at 11.94±2.07% for the hip and 7.49±2.85% for the knee and rapid trials averaging 11.4±1.27% for the hip and 8.69±2.21% for the knee.

B. Kinetics

Peak hip extension torques were calculated for each condition for both sit-to-stand and stand-to-sit movements. For sit-to-stand trials, participants experienced a greater average maximum hip torque on the intact side than on the prosthesis side (0.90±0.02 Nm/kg vs 0.63±0.13 Nm/kg) for self-paced trials, with an average $\overline{DoA}$ of 17.05±4.12%. For rapid trials, participants experienced an increased average maximum hip

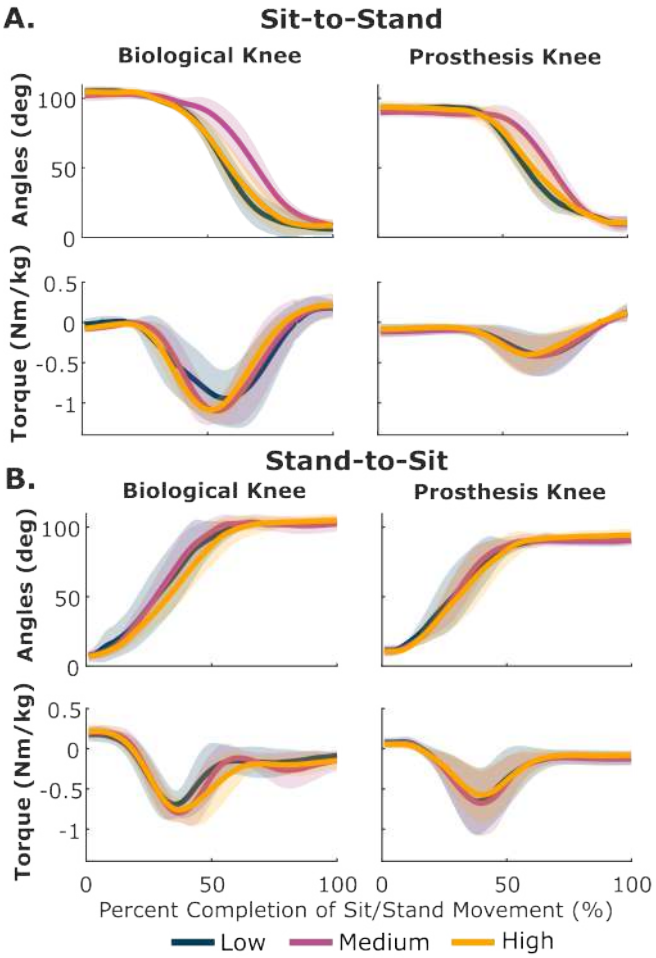


Fig. 3. Kinematic and kinetic knee profiles for self-paced trials on each the intact and prosthesis side, during sit-to-stand **(A.)** and stand-to-sit **(B.)** movements. The shaded region on each curve represents one standard deviation from the mean. Knee flexion is represented in the positive direction and knee extension is in the negative direction.

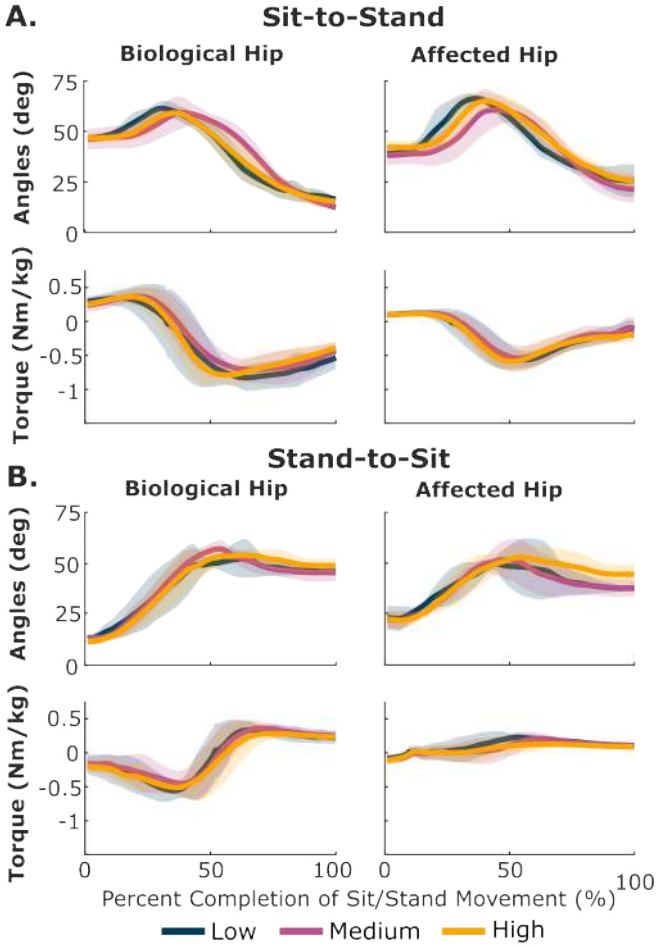


Fig. 4. Kinematic and kinetic hip profiles for self-paced trials on the intact and prosthesis (affected) side, during sit-to-stand **(A.)** and stand-to-sit **(B.)** movements. The shaded region on each curve represents one standard deviation from the mean. Hip flexion is represented in the positive direction and hip extension is in the negative direction.

torque and similar prosthesis side torque 0.97±0.21 Nm/kg vs. 0.63±0.16 Nm/kg to the self-paced trials, with an average $\overline{DoA}$ of 21.55±10.47%. During stand-to-sit trials, the self-paced maximum hip torque of the intact limb (0.59±0.06 Nm/kg) was lower than the sit-to-stand trials, as well as for the rapid trials (0.59±0.26 Nm/kg), but the $\overline{DoA}$ was worse (61.8±4.4% for self-paced, and 44.2±13.8% for rapid trials) due to the decreased peak torques values on the prosthetic limb, of 0.13±0.01 Nm/kg and 0.23±0.07 Nm/kg (self-paced and rapid), respectively. Peak hip torque asymmetry was statistically significant regardless of condition. Stool height was statistically significant for peak hip torques during rapid sit-to-stand trials and self-paced stand-to-sit trials. During rapid sit-to-stand trials, the $\overline{DoA}$ increased as stool height increased (see Fig. 6A), and in self-paced stand-to-sit trials, the peak hip torque on the intact limb decreased for higher stool heights (see Fig. 6B).

The peak knee torque during self-paced trials was 1.19±0.06 Nm/kg on the intact side and 0.46±0.03 Nm/kg on the prosthesis side. The $\overline{DoA}$ was 44.59±1.52% for the self-paced trials. Rapid sit-to-stand trials had similar values, where the intact limb had a peak knee torque of 1.13±0.46 Nm/kg, and the prosthesis side had an average of 0.09±0.01 Nm/kg with a $\overline{DoA}$ of 42.0±2.74% for the rapid trials. For stand-to-sit, the average peak knee torque during self-paced trials was 0.90±0.03 Nm/kg on the intact side and 0.75±0.06 Nm/kg on the prosthesis side. For self-paced trials, there was an average $\overline{DoA}$ of 9.32±4.7%. During rapid trials, the intact peak knee torque stayed close to the self-paced trials (0.92±0.57 Nm/kg), where the prosthesis side decreased (0.57±0.09 Nm/kg), resulting in a slightly larger $\overline{DoA}$ of 23.6±7.72% compared to the self-paced trials. Peak knee torque asymmetry was statistically significant regardless of condition.

IV. Discussion

This pilot study investigated the lower-limb kinematics and kinetics of two participants with an above-knee amputation using a powered prosthesis with a previously developed con-

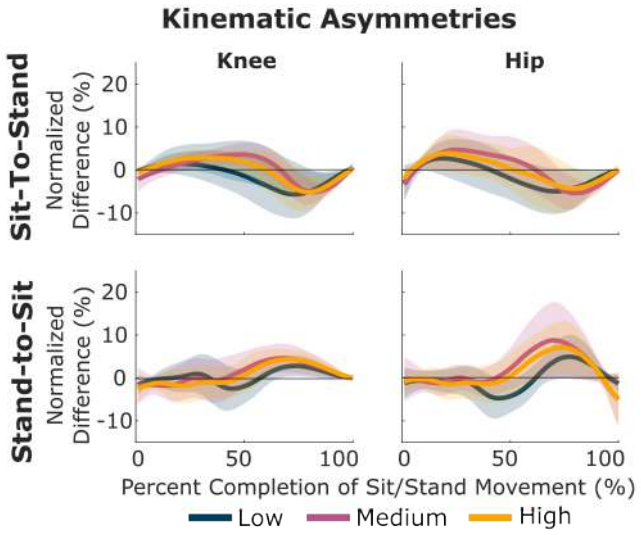


Fig. 5. Knee and hip kinematic asymmetry during sit-to-stand and stand-to-sit for self-paced trials. The normalized difference was calculated as the difference between the normalized intact and normalized prosthesis joint angles. Positive values indicate that the prosthesis side is progressing more quickly than. The shaded region represents one standard deviation from the mean.

troller [22]. We investigated asymmetries in kinematics and kinetics and compared the results to previous literature with passive and powered prostheses.

Although the kinematic profiles for the knee and the hip were similar across the prosthetic and biological sides, there was a notable difference seen in steady-state knee flexion angle during seated positions (Fig. 3A-B). While in a seated position, the biological knee is flexed greater than 100 degrees in all conditions, whereas the prosthesis side is flexed to approximately 90 degrees. The prosthetic side maximum knee flexion angle mimics the able-bodied dataset used for controller development that reaches similar maximum knee flexion angles [22], so it is possible that the difference in the biological leg is due to differences between conditions in our experiment and the dataset used for controller development. Additionally, during the trials, the fore/aft position of the feet in the frontal plane was not constrained, and because of this, the placement of the biological foot and prosthetic foot may have differed, which could have increased the knee flexion angle on the biological side.

Our kinematic asymmetry results are similar to those of Hunt et al., who investigated a powered prosthesis that provided a similar magnitude of knee torque. When using a controller with applied knee torques of up to 0.8 Nm/kg, Hunt et al. [20], found maximum kinematic peak-to-peak asymmetry values of $\sim$12%. Interestingly, the peak-to-peak kinematic asymmetry in their baseline passive prosthesis trial was $\sim$9% in the knee and $\sim$8% in the hip, the lowest of all conditions. Our self-paced and rapid trials showed similar results to both their powered and passive prosthesis kinematic asymmetries at 7.66$\pm$2.50% for the hip and 7.06$\pm$1.75% for the knee, respectively. During sit-to-stand, we saw that the prosthetic joint led the intact limb for a majority of the transition (see Fig. 5). This reflects the qualitative analyses from Welker et al. [22], who noted that their experimental phase estimate led the able-bodied data set. Additionally, during stand-to-sit, they found the opposite, where their experimental phase estimate lags behind the able-bodied data set, which is also reflected in our stand-to-sit results (see Fig. 5), showing the intact limb initially leading the stand-to-sit movement.

Although we determined significant differences between the peak torques in the knee and hip when comparing the intact and prosthesis sides, the controller still shows some improvement compared to previous passive and powered prosthesis literature. Prior work investigating the effects of a powered knee-ankle prosthesis during stand-to-sit movements found that participants produced a 0.39$\pm$0.05 Nm/kg peak knee torque on their prosthesis side with a $\overline{DoA}$ of $\sim$41.%, [27]. Our stand-to-sit peak knee torques increased compared to [27], and saw a decrease in $\overline{DoA}$ to 9.32$\pm$4.7% for self-paced trials, and 23.6$\pm$7.72% during rapid trials (Fig. 6). The improvement in peak knee torques during stand-to-sit is reflective of preliminary loading results from [22], who found an improvement of 79% for average ground reaction force loading asymmetry. Interestingly, while participants could more effectively use the controller in stand-to-sit to produce knee extension torques, they could not produce a hip extension torque on their affected side comparable to the intact side (see Fig. 4).

During the study, we also received qualitative data that may help explain the differences in asymmetry reduction during sit-to-stand and stand-to-sit. Participants reported initially struggling with stand-to-sit movements, but with training found it easier to activate the powered prosthesis by adjusting their center of mass posteriorly as the prosthesis resisted knee flexion. In contrast, to progress through the sit-to-stand motion with the controller, the biological limb likely needs to be more activated to position the user's center of mass appropriately to initiate the movement, which may have contributed to larger asymmetries.

Comparing to previous passive prosthesis research, [15] found that peak knee flexion moments for chair heights of 28 and 38 cm were $\sim$300% greater on the intact side than the prosthesis side for people with transtibial amputations wearing passive prostheses during sit-to-stand. In comparison, using the same method to calculate percent difference, the intact side produced knee torques only $\sim$60% greater compared to the prosthesis side when wearing our powered prosthesis in our study. In addition, when comparing to the first generation Power Knee as investigated in [6], our powered prosthesis saw decreased $\overline{DoA}$ metrics for both the knee and hip torques in sit-to-stand and stand-to-sit. Specifically, [6] found a $\overline{DoA}$ of 124% for the knee and 34% for hip torques during sit-to-stand, where we found a decreased $\overline{DoA}$ for the knee of $\sim$42-45%, and similar reductions in the hip (17.05$\pm$4.13% and 21.6$\pm$10.47%). Similar trends were found in stand-to-sit, with [6] reporting $\overline{DoA}$ of 87% for the knee and 45% for the hip, compared to our findings of 9.32$\pm$4.71% and 23.5$\pm$7.7% (self-paced and rapid) in the knee, and 61.8$\pm$4.41%, and

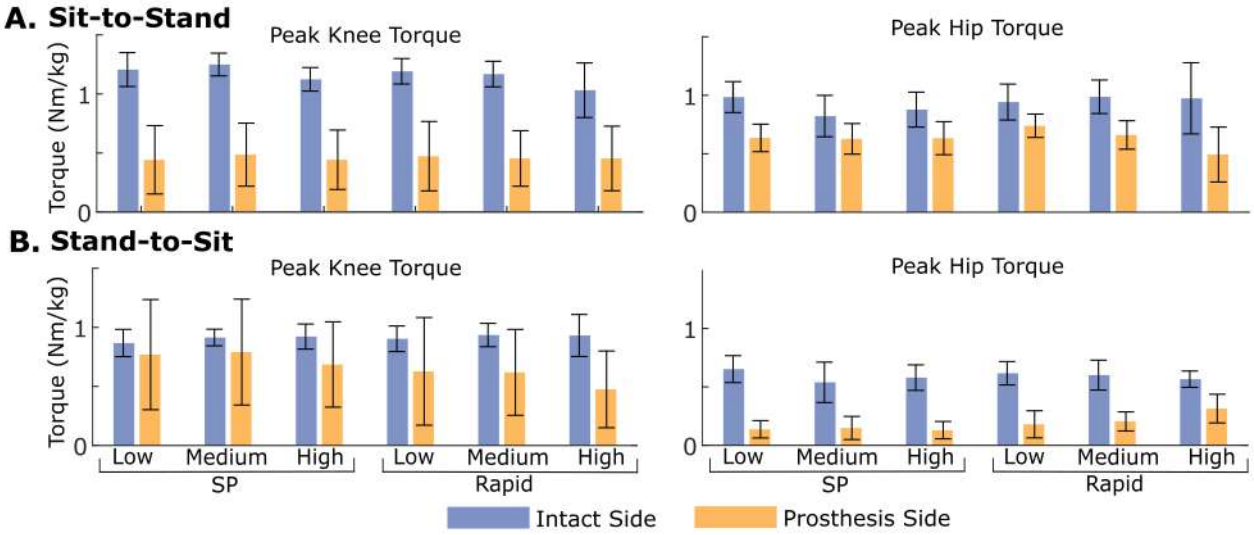


Fig. 6. Peak knee and hip extension torques were significantly different when comparing the intact and prosthesis side ($p<0.025$). Rapid paced sit-to-stand (**A.**) trials saw a significant effect due to stool height in peak hip torque extension, as seen by the decreasing peak hip torque on the prosthesis side ($p<0.025$). During self-paced stand-to-sit (**B.**) trials peak hip extension torque also experienced a significant effect due to stool height, as seen by the overall decreasing intact side hip extension torque as stool height increased ($p<0.025$). No significant effects were found on peak knee extension torques due to stool height.

$44.3\pm13.8\%$ for the hip.

Movement asymmetries, including ground reaction force loading, are known to have negative long-term effects on LLPUs. However, it is unclear what asymmetries (loading, kinematic, or kinetic) have the largest negative impact. The ground reaction force loading asymmetries found previously in [22] using the same controller indicate less uneven joint loading during sit/stand movements and, as a result, may reduce the chances of osteoarthritis. Additionally, the normalized kinematic asymmetries indicate more symmetrical movements compared to other passive and powered prostheses, which are closer to movements produced by unimpaired individuals. Although ground reaction force loading influences resulting lower-limb joint torques, the position and acceleration of the bodies in the lower-limb also have an effect that is important to quantify.

The results of this pilot study are promising but come with limitations. Due to the small sample size, the trends cannot be generalized, but they still indicate potential impact for participants when using this novel controller on a powered knee-ankle prosthesis. Additionally, comparisons across studies can be limited due to differences in participant's prescribed passive prostheses and their familiarity with powered prostheses. Each participant only had 15 minutes of training with the novel prosthesis controller. Furthermore, one participant had previous experience with a prior sit/stand controller that could affect their results and ability to use the powered prosthesis. Further work is needed to investigate the kinematic and kinetic differences between the participants' prescribed passive devices and the powered prostheses worn in this study.

V. Conclusion

This pilot study presented promising findings in kinematic and kinetic asymmetries while wearing a powered sit/stand prosthesis controller. These results reflect similar results to other powered prosthesis controllers, with decreased kinematic asymmetries and reduced $\overline{DoA}$ for both peak knee and hip torques compared to passive prostheses during sit-to-stand, and stand-to-sit, at two different speeds. Our results suggest that this controller can potentially reduce negative secondary conditions associated with long-term prosthesis use and thus improve the quality of life for LLPUs.

Acknowledgment

The authors thank the University of Michigan Locomotor Control Systems Lab for their assistance in data collection and Emily Macqueene for her assistance in data processing. This work was partially supported by the National Institute of Child Health & Human Development of the NIH under Award Number R01HD09477.

References

[1] Kathryn Ziegler-Graham et al. "Estimating the Prevalence of Limb Loss in the United States: 2005 to 2050". In: *Archives of Physical Medicine and Rehabilitation* 89.3 (Mar. 2008), pp. 422–429.

[2] Timothy R. Dillingham, Liliana E. Pezzin, and Andrew D. Shore. "Reamputation, mortality, and health care costs among persons with dysvascular lower-limb amputations". In: *Archives of Physical Medicine and Rehabilitation* 86.3 (Mar. 2005), pp. 480–486.

[3] Margrit Schaarschmidt et al. "Functional gait asymmetry of unilateral transfemoral amputees". In: *Human Movement Science* 31.4 (Aug. 2012), pp. 907–917.

[4] Kenton R. Kaufman, Serena Frittoli, and Carlo A. Frigo. "Gait Asymmetry of Transfemoral Amputees Using Mechanical and Microprocessor-Controlled Prosthetic Knees". In: *Clinical Biomechanics (Bristol, Avon)* 27.5 (Jan. 2012), p. 460.

[5] Helena Burger, Jernej Kuželički, and Črt Marinček. "Transition from Sitting to Standing after Trans-Femoral Amputation". In: *Prosthetics and Orthotics International* 29.2 (Aug. 2005), pp. 139–151.

[6] M. Jason Highsmith et al. “Kinetic asymmetry in transfemoral amputees while performing sit to stand and stand to sit movements”. In: *Gait & Posture* 34.1 (May 2011), pp. 86–91.

[7] Erik. J. Wolf et al. “Comparison of the Power Knee and C-Leg during step-up and sit-to-stand tasks”. In: *Gait & Posture* 38.3 (July 2013), pp. 397–402.

[8] Robert Gailey. “Review of secondary physical conditions associated with lower-limb amputation and long-term prosthesis use”. In: *The Journal of Rehabilitation Research and Development* 45.1 (Dec. 2008), pp. 15–30.

[9] Joseph G Wasser et al. “A Comprehensive, Multidisciplinary Assessment for Knee Osteoarthritis Following Traumatic Unilateral Lower Limb Loss in Service Members”. In: *Military Medicine* 189.3-4 (Mar. 2024), pp. 581–591.

[10] Pieter A. Struyf et al. “The Prevalence of Osteoarthritis of the Intact Hip and Knee Among Traumatic Leg Amputees”. In: *Archives of Physical Medicine and Rehabilitation* 90.3 (Mar. 2009), pp. 440–446.

[11] Christine M. McDonough and Alan M. Jette. “The Contribution of Osteoarthritis to Functional Limitations and Disability”. In: *Clinics in Geriatric Medicine* 26.3 (Aug. 2010), pp. 387–399.

[12] Philippa M. Dall and Andrew Kerr. “Frequency of the sit to stand task: An observational study of free-living adults”. In: *Applied Ergonomics* 41.1 (Jan. 2010), pp. 58–61.

[13] Jennifer Langford et al. “Physical activity participation amongst individuals with lower limb amputation”. In: *Disability and Rehabilitation* 41.9 (Apr. 2019), pp. 1063–1070.

[14] Robert L. Waters and Sara Mulroy. “The energy expenditure of normal and pathologic gait”. In: *Gait & Posture* 9.3 (July 1999), pp. 207–231.

[15] Rachel H. Teater et al. “Unilateral transtibial prosthesis users load their intact limb more than their prosthetic limb during sit-to-stand, squatting, and lifting”. In: *Clinical Biomechanics* 108 (Aug. 2023), p. 106041.

[16] Katherine E. Wagner et al. “The effect of lower-limb prosthetic alignment on muscle activity during sit-to-stand”. In: *Journal of Electromyography and Kinesiology* 51 (Apr. 2020), p. 102398.

[17] Scott L. Delp et al. “OpenSim: Open-Source Software to Create and Analyze Dynamic Simulations of Movement”. In: *IEEE Transactions on Biomedical Engineering* 54.11 (Nov. 2007). Conference Name: IEEE Transactions on Biomedical Engineering, pp. 1940–1950.

[18] Huseyin Atakan Varol, Frank Sup, and Michael Goldfarb. “Powered sit-to-stand and assistive stand-to-sit framework for a powered transfemoral prosthesis”. In: *2009 IEEE International Conference on Rehabilitation Robotics*. June 2009, pp. 645–651.

[19] Ann M. Simon et al. “Improved Weight-Bearing Symmetry for Transfemoral Amputees During Standing Up and Sitting Down With a Powered Knee-Ankle Prosthesis”. In: *Archives of Physical Medicine and Rehabilitation* 97.7 (July 2016), pp. 1100–1106.

[20] Grace R. Hunt et al. “Effect of Increasing Assistance From a Powered Prosthesis on Weight-Bearing Symmetry, Effort, and Speed During Stand-Up in Individuals With Above-Knee Amputation”. In: *IEEE Transactions on Neural Systems and Rehabilitation Engineering* 31 (2023). Conference Name: IEEE Transactions on Neural Systems and Rehabilitation Engineering, pp. 11–21.

[21] T. Kevin Best et al. “Data-Driven Variable Impedance Control of a Powered Knee-Ankle Prosthesis for Adaptive Speed and Incline Walking”. In: *IEEE transactions on robotics : a publication of the IEEE Robotics and Automation Society* 39.3 (Jan. 2023), p. 2151.

[22] Cara Gonzalez Welker, T. Kevin Best, and Robert D. Gregg. “Improving Sit/Stand Loading Symmetry and Timing Through Unified Variable Impedance Control of a Powered Knee-Ankle Prosthesis”. In: *IEEE transactions on neural systems and rehabilitation engineering* 31 (2023), pp. 4146–4155.

[23] Toby Elery et al. “Design and Validation of a Powered Knee-Ankle Prosthesis with High-Torque, Low-Impedance Actuators”. In: *IEEE transactions on robotics : a publication of the IEEE Robotics and Automation Society* 36.6 (July 2020), p. 1649.

[24] Jonas Vantilt et al. “Model-based control for exoskeletons with series elastic actuators evaluated on sit-to-stand movements”. In: *Journal of NeuroEngineering and Rehabilitation* 16.1 (June 2019), p. 65.

[25] Apoorva Rajagopal et al. “Full-Body Musculoskeletal Model for Muscle-Driven Simulation of Human Gait”. In: *IEEE Transactions on Biomedical Engineering* 63.10 (Oct. 2016). Conference Name: IEEE Transactions on Biomedical Engineering, pp. 2068–2079.

[26] Andrea M. Willson et al. “Full Body Musculoskeletal Model for Simulations of Gait in Persons with Transtibial Amputation”. In: *Computer methods in biomechanics and biomedical engineering* 26.4 (May 2022), p. 412.

[27] Grace R. Hunt et al. “Can a powered knee-ankle prosthesis improve weight-bearing symmetry during stand-to-sit transitions in individuals with above-knee amputations?” In: *Journal of NeuroEngineering and Rehabilitation* 20.1 (May 2023), p. 58.

PRISM: Parameter Recovery Identification from Synthetic Modeling

Adriana Cancrini[1,2*], Bruno Borghi[1,2], Naveed Reza Aghamohammadi[1,2], Arturo Ramirez[1,2], Courtney Celian[2] and James L. Patton[1,2*]

***Abstract*— Identifying parameters of human motor learning dynamics remains an open-ended question despite significant research in the field. While robotics and system identification offer tools for modeling dynamical systems with precision, few studies have investigated persistent excitation of human dynamics to produce accurate models. Here, we tested a forward-inverse method to estimate joint stiffness and damping as well as feedback gains in reaching when disturbed. Planar arm movements were first simulated with a synthetic model, then regression was used to identify gains, and the most crucial trial conditions (task and disturbance) were identified as those that brought the most accurate information about the gain parameters. Our results indicate that a set of 40 movements performed under specific perturbation conditions yielded the best parameter estimation ($R^2 = 0.97$). Such technique employs simulated or digital twin methods to best estimate the arm's control properties, offering a framework to optimize the experimental design and paving the way for more individualized approaches.**

I. INTRODUCTION

Gaining insight into motor learning is a challenging aim that requires more than generic approaches. One of the main limitations in this field is the lack of personalized learning models that account for individual differences and tailored needs. Current protocols often rely on repetitive exercises and generic frameworks that might not always be adequate to address individual differences in sensory-motor contributions [1]. To improve outcomes, a more customized approach is needed that integrates sensory feedback input, such as muscle and vision, into the dynamics of movement. This would reduce the number of repetitive movements required, optimize treatment time and, in the end, lead to enhanced and tailored learning programs.

Sensory feedback plays an essential role in motor recovery [2], [3] by providing crucial information about errors caused by external disturbances or intrinsic variability within the motor system [4]. Rapid corrective responses to errors during reaching are primarily produced by two main mechanisms: muscle stretch-dependent motor responses [5], [6], and visuomotor responses, the latter of which adapt based on shifts in the visual position of the hand [7]–[9]. Vision is used to guide the detection of movement targets, but signals from muscles also play an essential role in monitoring the position and motion of the limbs and facilitating smooth and coordinated actions. These feedback pathways provide rapid and accurate reactions to unexpected disturbances, making their identification crucial for modeling effective motor control dynamics. Several studies have contributed significantly by modeling sensory integration [10]–[12], demonstrating that different types of feedback contribute uniquely to the planning of reaching movements [13]. Although each feedback mechanism plays a role in compensating for external perturbations, their precise weighting values, contributions, and differences remain unclear. Intrinsic differences in sensory filtering characteristics and coordinate reference frames may distinguish their roles in motor control [14]. Given the pivotal role of sensory feedback, the first step in developing a personalized learning model is to accurately identify the sensory input gains and establish the experimental requirements necessary for identifying these contributions. Here, we present Parameter Recovery Identification from Synthetic Modeling (PRISM), a methodological framework designed to find the optimal experimental conditions necessary for accurately identifying gain parameters in sensorimotor models. We employ synthetic data in simulation to create known prior data, allowing us to explore and understand the mathematical inversion methods seen in system identification. Next, we perform an inversion process to identify important model parameters such as sensory feedback gains (Fig. 1). To refine our identification methods, we test various sensory perturbations and tasks, enabling a more accurate determination of model parameters.

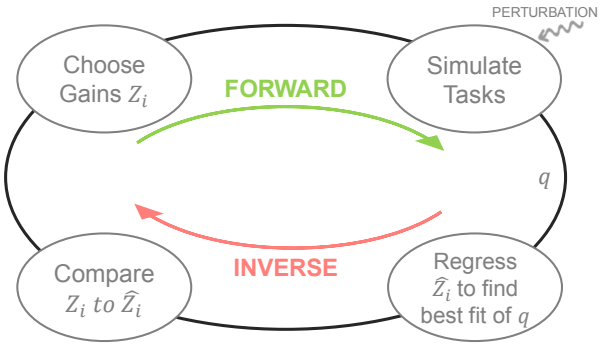


Fig. 1. Overview of the forward-inverse process. The forward process begins with selecting sensory feedback gains (Z_i), simulating tasks with perturbations, and generating system outputs (q). The inverse process involves using regression to estimate feedback gains ($\hat{Z}_i$) that best fit the observed outputs. Finally, the estimated gains are compared with the initial gains (Z_i) to evaluate model accuracy and refine the process.

Supported by the National Institute of Health (NIH) grant R01NS053606

[1]Richard and Loan Hill Department of Biomedical Engineering, University of Illinois Chicago, Chicago, IL, USA

[2]Robotics Lab at Center for Neural Plasticity, Shirley Ryan AbilityLab, Chicago, IL, USA

*Correspondence: acancr2@uic.edu, pattonj@uic.edu

By identifying these optimal conditions, we can simplify the experimental process, reducing both the physical effort required from participants and the overall costs associated with data collection. This approach aims to enhance the customization of rehabilitation protocols, enabling a more precise and efficient recovery process tailored to individual sensory profiles. Central to this effort is the development of a prior mathematical model that can identify and provide optimal experimental conditions and designs.

II. METHODS

A. Biomechanical model

We simulated the 2D planar reaching movement of a human arm using a second-order linear biomechanical system (Fig. 2), described as:

$$M(q)\ddot{q} + C(q,\dot{q})\dot{q} + G(q) = \tau_{ff} + \tau_{fb} + \tau_{ext} \quad (1)$$

where q is a point in the configuration space, $\dot{q}$ and $\ddot{q}$ its first- and second-time derivatives [15]. The vector $G(q)$ represents the contribution of gravity to the joint torque. This term becomes null when the gravity field acts orthogonally to the trajectory, as in the case of a horizontal, planar movement. On the other hand, the mass-inertia and Coriolis matrices $M(q)$, $C(q,\dot{q})$ respectively, are in the form:

$$M(q) = \begin{bmatrix} I_1 + I_2 + b + a + c + d + e & L_2 + a + e \\ L_2 + a + e & I_2 + e \end{bmatrix}$$

$$C(q,\dot{q}) = \begin{bmatrix} -L_1 M_2 R_2 (2\dot{q}_1\dot{q}_2 + \dot{q}_2^2)\sin(q_2) \\ L_1 M_2 R_2 \dot{q}_1^2 \sin(q_2) \end{bmatrix} \quad (2)$$

where:

$$a = L_1 L_2 M_2 \cos(q_2), \quad b = \frac{L_1^2 M_1}{4} + L_1^2 M_2,$$

$$c = \frac{L_2^2 M_2}{4}, \quad d = L_2 M_2 R_2 \cos(q_2), \quad e = M_2 R_2^2,$$

where the state vector is $\mathbf{s} = [q_1, q_2, \dot{q}_1, \dot{q}_2]^\top$, L represents the length of the links, M is the mass of each link, I denotes the moment of inertia, and R is the distance from the joint axis to the center of mass of each link.

The right side of (1) models the external and control torques acting on the system. If during the movement trajectory, the subject is required to apply force while maintaining the desired trajectory, the muscles will produce additional torque τ_{ext}. This torque will be equal in magnitude to those generated by the external forces acting on the limb. A feedforward control mechanism τ_{ff} is also considered. This component, computed through inverse dynamics, tries to predict the required torques for a desired motion trajectory, minimizing the reliance on feedback correction and ensuring smoother and more accurate movements. We added a feedback torque τ_{fb} to simulate the presumed control mechanisms from the central nervous system, enabling adaptive response during movement. This feedback control is modeled using a linear approximation of joint stiffness and damping characteristics, along with visual feedback gains.

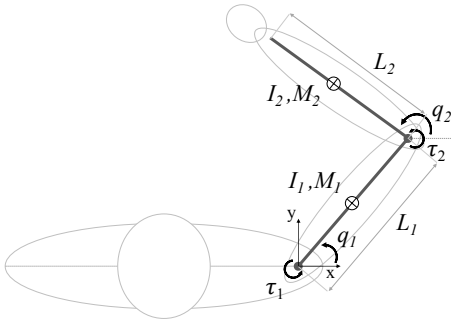


Fig. 2. Experimental apparatus for simulating arm trajectories in the horizontal plane.

This control component is analyzed in detail and expanded to account for the specific sensory channels considered in this study: muscle and vision. Equation (3) describes the sensory feedback torque τ_{fb} as the summation of all sensory contributions, providing a comprehensive model of how sensory inputs affect motor control. In particular, the feedback torque is the result of summing the individual sensory inputs, defined by the term Z_i, which represents the sensory impedance components (e.g., muscle *m* and vision *v*). This term involves the properties of stiffness, damping, and visual feedback gains collectively.

$$\tau_{fb} = \sum_{i=1}^{N_{senses}} Z_i \chi(\delta) = Z_m \chi + \eta'_m + Z_v T \chi(\delta_v) + \eta'_v \quad (3)$$

The state matrix $\chi(\delta)$ captures the joint position and velocity errors, defined as the difference between the current and ideal positions over time ((4) for the expanded version). The ideal trajectory is based on the minimum jerk model, which minimizes the rate of acceleration change (jerk) to produce smooth, natural movements commonly observed in human motor behavior [16]. In this context, δ represents the sensory response delay. It can be observed that muscle feedback has zero delay [17], reflecting the near-instantaneous response of muscles to force generation and positional changes. In contrast, vision introduces a delay, which is modeled as 70 ms [18], corresponding to the time required for visual information to be processed by the brain and integrated into motor control pathways. Incorporation of this delay is crucial in accurately modeling how vision contributes to motor learning and control. Further examination of (3) reveals that the operator T is a transformation matrix that converts signals from the cartesian coordinate system, where visual input is defined, into the joint coordinate domain where feedback is applied. Finally, η' represents the noise added to the system, modeled as Gaussian white noise, with zero mean and constant variance (10^{-3}) across all frequencies, representing random disturbances in sensory signals. To ensure model robustness while accurately capturing sensory input variability, the noise is controlled by an appropriate signal-to-noise ratio. In our implementation, white noise was specifically added to velocity components, as this induces a Brownian process in position, aligning with the assumption that human movement exhibits stochastic drift over time [19].

We can break down (3) as follows.

$$\tau_{fb} = K_m(q_d - q) + B_m(\dot{q}_d - \dot{q} + \eta_m) + \\ + J(q)^\top K_v(x_d - x) + J(q)^\top B_v(\dot{x}_d - \dot{x} + \eta_v) \quad (4)$$

Equation (4) [20], [21] shows how the terms Z_m and Z_v, which represent the sensory impedance components, are divided into components dependent on both position (K) and velocity (B). All position and velocity-dependent gains are defined as 2×2 symmetric matrices that are modeled as constant with respect to joint configuration [22]. This approach simplifies the dynamic model while still providing an accurate representation of feedback responses. Equation (5) details the sensory gain matrices.

$$K_m = \begin{bmatrix} K_{ss} & K_{se} \\ K_{es} & K_{ee} \end{bmatrix} \frac{\text{Nm}}{\text{rad}}, \quad K_v = \begin{bmatrix} K_{xx} & K_{xy} \\ K_{yx} & K_{yy} \end{bmatrix} \frac{\text{N}}{\text{m}}, \\ B_m = \begin{bmatrix} B_{ss} & B_{se} \\ B_{es} & B_{ee} \end{bmatrix} \frac{\text{Nms}}{\text{rad}}, \quad B_v = \begin{bmatrix} B_{xx} & B_{xy} \\ B_{yx} & B_{yy} \end{bmatrix} \frac{\text{Ns}}{\text{m}}. \quad (5)$$

In this model, muscle operates within the joint domain, specifically involving shoulder (S) and elbow (E) joints. On the other hand, vision is represented in the cartesian coordinate domain, which refers to the external spatial coordinates (XY) used to describe the movement of the limb in the environment. In this context, vision gains influence the model by modulating the response to errors between the perceived and actual hand motion. In Table I, the reference values used in the simulation model are detailed. Values from previous studies [22], [23] were used, with visual gains selected also to maintain system stability. The ultimate goal is for these values to be customizable, allowing the model to reflect the individual characteristics of different subjects.

TABLE I

MECHANICAL PARAMETERS OF THE SIMULATED HUMAN ARM

Upper Arm	
Mass	1.930 kg
Center of mass	0.165 m
Length	0.330 m
Inertia	0.0141 kg·m^2
Forearm	
Mass	1.520 kg
Center of mass	0.190 m
Length	0.340 m
Inertia	0.0188 kg·m^2
K_m	$\begin{bmatrix} /15 & /6 \\ /6 & /16 \end{bmatrix}$ N·m / rad
B_m	$\begin{bmatrix} /2.3 & /0.9 \\ /0.9 & /2.4 \end{bmatrix}$ N·m·sec / rad
K_v	$\begin{bmatrix} /120 & /30 \\ /30 & /50 \end{bmatrix}$ N / m
B_v	$\begin{bmatrix} /6 & /2 \\ /2 & /5 \end{bmatrix}$ N·sec / m

B. Measurement setup and perturbation signal

The simulated movements are 20 cm in length, which provides sufficient time and space to apply external perturbations and observe their effects on motor control. Movement directions follow a random walk pattern to ensure variability, and the workspace is defined as the entire range of space reachable by the hand under standard conditions. The model simulates at a frequency of 100 Hz. External perturbations play a critical role in the analysis and control of dynamic systems, especially in the context of system identification. When a system is subjected to external forces or disturbances, its response can reveal key properties about its underlying dynamics, allowing for better understanding and fine-tuning of the system's parameters. The idea of persistent excitation becomes particularly important in this context: using input signals with a rich enough frequency spectrum to stimulate all modes of a dynamic system is crucial for ensuring that the system's response contains enough information to identify any unknowns in the model accurately [24]. For this reason, different input signals have been systematically designed to obtain reliable and informative responses from the system: single-double step signal, amplitude-modulated Pseudo-Random Binary Sequence (PRBS), and chirp signal [25], [26]. These signals were implemented as external force perturbations and/or visual distortions (Fig. 3). A detailed explanation can be found below.

- *Single-double step.* This approach was used to create visual distortions by inducing sudden cursor jumps and simulating visually induced motor perturbations. These signals dictate the movement pattern of the cursor (which represents the hand position) and are characterized by abrupt shifts following either a single-step (one abrupt change) or double-step (two changes) pattern. The cursor's displacement occurred in random directions and covered distances ranging from 2 to 8 cm. These jumps would require participants to adjust their motor commands to maintain the desired trajectory (Fig. 3, panel A).

- *Amplitude-modulated PRBS.* A binary signal that switches randomly between predefined values was used to design external perturbations. This signal modulated a force applied to the system, with amplitudes randomly chosen between 5 and 15 N. The direction of the force was also varied randomly, creating controlled but unpredictable disturbances (Fig. 3, panel B).

- *Chirp signal.* A sinusoidal waveform with a frequency that gradually increases over time was used to design both external forces and visual distortions. For the external forces, the amplitude varied randomly between 5 and 15 N, while the frequency was chosen within a range of 0.5 to 3 Hz, aiming to excite low-frequency dynamics. For the visual distortions, the same frequency range was used, with continuous cursor shifts ranging from 2 to 8 cm (Fig. 3, panel C).

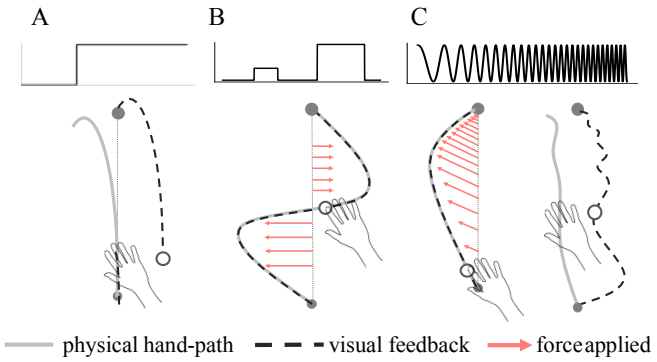


Fig. 3. The figure illustrates the application of three types of signals - a single-double step signal (A), a Pseudo-Random Binary Sequence (PRBS) signal (B), and a chirp signal (C) - which were used to simulate perturbations to the system in the form of external forces and/or visual distortions. In the first row, the waveforms of these signals are displayed. The second row shows an example output trajectory when the corresponding perturbation is applied. The solid gray line represents the hand path, the dashed line indicates the visual feedback, and the arrows depict the external forces.

C. Identification strategy

In our model, the first step included the generation of a dataset of 100,000 unique movements, each described by one of the perturbations listed above, with specified starting points and targets. The breakdown of movements by perturbation type is approximately equal, with each category accounting for about $\frac{1}{4}$ of the total number one-fourth of the total. Additionally, the structure of each perturbation was randomly selected, meaning that even when the same type of perturbation was applied, parameters such as amplitude, frequency, and duration varied across different movements. We used an incremental *play the winner* approach to estimate sensory feedback gains effectively. We began by selecting a random subset of 5 movements and fitted the model by solving a system of equations that included both muscle and vision inputs. To analyze the output data, we applied linear regression with Ridge regularization, trying to prevent overfitting and ensure smooth and reliable parameter estimates. This process was repeated 100 times, each time with a different random subset of 5 movements. The subset that achieved the highest accuracy (*winner*), as measured by the coefficient of determination comparing the estimated gains to the prior initial guess established at the beginning of the simulation, was selected. To this winning set, 5 additional movements from the remaining pool were added, and the expanded set of 10 movements was analyzed using the same process. At each stage, a new subset of movements was added to the winning set from the previous iteration. This iterative process of selection and expansion was repeated progressively increasing the size of the subset to 10 movements and reaching a total number of considered movements equal to 120. It was observed that adding movements beyond this number did not alter the results, and the analysis was therefore halted upon reaching a clear plateau (Fig. 4). By focusing on subsets that showed the best accuracy at each stage, this strategy allowed the model to refine the identification of the sensory feedback parameters more effectively. It also ensured that the most informative movements were prioritized, avoiding redundant or less meaningful data. This approach allowed us to explore how the quantity and quality of movements impact the accuracy of parameter estimation and identify when adding more movements no longer improved the fit. To ensure the robustness of the identified sensory feedback gains and to avoid the risk of overfitting, an additional validation step was implemented. After analyzing the quality of the fit for gain identification during each iteration, the best-performing set of gains was selected. This set was then used to predict the trajectories of 30 unseen perturbed and unperturbed movements that were not included in the training data. Although the perturbations were of the same general type, they were defined differently—exhibiting, for instance, higher amplitudes or longer durations—compared to those used during training. The predicted trajectories were compared to those generated using the initial dataset of gains, and the coefficient of determination was calculated based on this comparison. Unlike the previous step, where R^2 measured the model's fit to the training data, this evaluation focuses on how well the identified gains generalize to new, untrained movements. By shifting the validation metric to trajectory prediction, this step provides a more precise assessment of the model's ability to capture the underlying dynamics of motor control.

III. RESULTS

Fig. 4 provides a general overview of the synthetic model analysis, illustrating the relationship between the number of movements considered and the model's ability to identify sensory feedback gains (goodness of fit). In panel Fig. 4.A, the light-gray solution represents the overall performance using the *play the winner* strategy described earlier. Initially, as the number of movements increased, the coefficient of determination improved, indicating that additional data enhanced the model's ability to explain variance in sensory feedback gains. However, this improvement decreased over time, and the curve eventually reached a plateau. This plateau suggests that adding more movements beyond a certain point provides only marginal improvements in predictive accuracy. Focusing on the primary outcome of our analysis, the dark-gray solution highlights the best-performing set of movements for each quantity considered. The analysis identified the optimal set of 40 movements as producing the highest accuracy.

At this stage, it is important to address the potential for overfitting, particularly given that the analysis relied on training data and the sensory feedback gains themselves. Overfitting occurs when the model captures noise or specific details in the training data rather than generalizable patterns, reducing its effectiveness when applied to new scenarios. To evaluate and mitigate overfitting, the coefficient of determination was calculated by comparing model-predicted trajectories with actual test trajectories. For validation, as described before, a set of 30 test movements -not included in the training process- was used. Using the best-performing

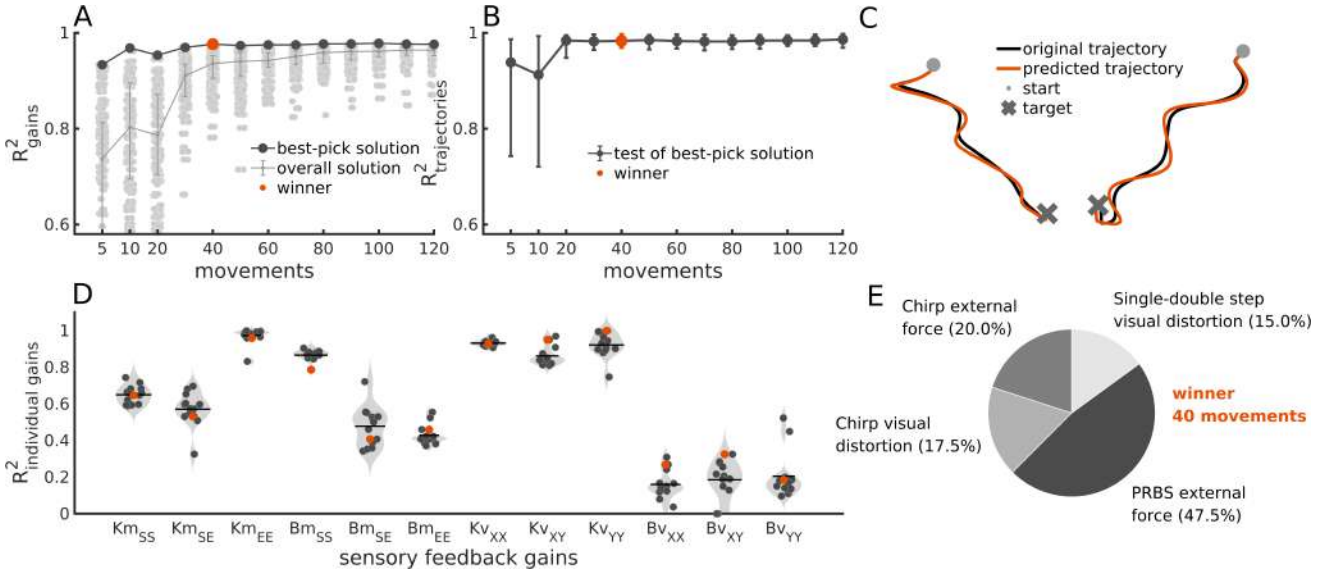


Fig. 4. Overview of the synthetic model analysis. Panel A shows the optimal set of 40 movements achieving the highest accuracy. Panel B confirms the model's generalizability with high R^2 values on unseen test movements. Panels C and D detail trajectory comparisons and the accuracy of individual sensory feedback gains, highlighting velocity-dependent vision gains as the most challenging. Panel E illustrates the distribution of the optimal set across perturbation types, with PRBS forces being the most effective.

gains identified during the iterative process (Fig. 4.A), the model predicted the test trajectories. These predictions were then compared against trajectories generated using the initial guessed gains. This validation process was applied exclusively to unseen movements in order to evaluate the model's generalizability. The results displayed in Fig. 4.B, show that the coefficient of determination remained consistently high and stable across the selected range of movements. This stability confirms that the model accurately captured the dynamics without overfitting, ensuring reliable predictions in new scenarios.

Fig. 4.C presents examples of trajectory comparisons, showing both the predicted paths (generated using the estimated gains) and the original model-generated paths (referred to as original). At this stage, our primary goal is to assess the accuracy of the identification process for each sensory feedback gain, enabling a detailed evaluation of how well each component was estimated. Fig. 4.D provides a breakdown of performance for each best pick, presenting the accuracy results for individual gains. This visualization highlights and shows how the identification process varied across different components. Interestingly, the velocity-dependent vision gains were the most challenging to identify. Additionally, the gains highlighted in red represent those included in the best-performing set, which achieved the highest overall accuracy in the previous analysis. This best set establishes the optimal conditions for reliable parameter estimation. Fig. 4.E provides a detailed illustration of how the selected set of movements, which enables the best parameters identification, is distributed across the various perturbation types. This distribution provides valuable insights into which types of perturbations were more effective and which were less represented in achieving accurate parameter estimation. As can be seen, an external force following a Pseudo-Random Binary Sequence profile resulted as the most effective in enhancing the accuracy of parameter identification. In summary, the optimal set that best identifies the sensory feedback gains consists of 40 movements, distributed as follow: 47.5% PRBS external force, 20% Chirp external force, 15% Single-double step visual distortion, 17.5% Chirp visual distortion. Within this design, the various impedances—such as muscle stiffness, damping, vision-dependent position and velocity—are identified with the following percentages of accuracy: Km_{SS} (65%), Km_{SE} (53%), Km_{EE} (96%), Bm_{SS} (79%), Bm_{SE} (41%), Bm_{EE} (46%), Kv_{XX} (93%), Kv_{XY} (95%), Kv_{YY} (99%), Bv_{XX} (27%), Bv_{XY} (33%), Bv_{YY} (19%).

IV. DISCUSSION

This work supports the importance of developing a solid mathematical model to guide data collection, optimize experimental sessions, and enhance their effectiveness. PRISM aims to address a critical gap in neurorehabilitation: the lack of robust generative models capable of predicting outcomes and prescribing personalized interventions. By replacing qualitative observations with mathematically driven, quantitative models, this approach allows for a systematic exploration of optimal conditions to improve identification strategies. Although advancements in technology, such as robotics, have revolutionized rehabilitation, a major challenge remains: the development of effective software to fully leverage these tools. Current methods often lack inverted models—mathematical frameworks designed to be directly tested and optimized for guiding applications [27]. These models have the potential to contribute significantly to both general training and

neurorehabilitation [28], [29]. By utilizing individual subject data, they can predict the outcomes of interventions, identify the most effective treatment strategies, and determine the conditions necessary for improving motor function or accelerating recovery. In this way, PRISM represents a step toward more personalized, data-driven, and effective approaches in neurorehabilitation. This strategy differs from traditional identification methods in that the focus is on recovering the underlying parameters driving the synthetic model rather than just assessing the quality of fit. The main goal is to identify the minimum but most informative set of movements that allows for accurate sensory feedback gain identification. Identifying the specific types of perturbations and conditions necessary to accurately determine these gains represents the main aspect of this work. This approach balances between maximizing data precision and information with minimal effort and exercise. Once this first step of parameter identification is accomplished, it will form the basis for the development of an individualized intervention that will involve customized exercises aimed at achieving the best possible outcomes without extra repetitions that can cause disengagement in patients and physical exhaustion. This work is related to surrogate models and digital twin approaches that are increasingly being used in complex systems for simulating, predicting, and optimizing outcomes. Within neurorehabilitation, these frameworks assure powerful tools for modeling responses of individual subjects and optimization of therapies.

Focusing on the results obtained, there is still room for improvement in identifying sensory feedback gains, especially those related to velocity. It can be assumed that velocity-dependent gains are linked with position-dependent components, which may lead to collinearity in the parameter estimation process. Changes in one gain could be masked or partially compensated by adjustments in the other, making it challenging to isolate and clearly identify the specific impact of velocity-dependent gains on system behavior. Additionally, the current *play the winner* strategy may favor similar tasks due to its random selection process, which can bias gain identification toward frequently explored perturbations. Future versions could include a diversity measure in task selection to promote a broader exploration of the perturbation space. Furthermore, introducing new, targeted external perturbations may better stimulate the system. However, these perturbations must also be translatable to real-world scenarios and practically implementable. While their selection does not affect simulations, it is crucial to determine whether they could be disruptive and inadvertently alter natural movement patterns in reaching tasks. The final goal is to develop a protocol design that can be directly used as an experiment. This requires striking a balance between creating perturbations that maximize system stimulation and ensuring their feasibility in real-world contexts, bridging the gap between theoretical precision and practical usability. Future work will also prioritize validating the proposed model in real-world settings to transition from synthetic simulations to practical applications. The synthetic model's output —designed and based on specific individual's parameter— will serve as the input and experimental design for identifying sensory gains. While the aforementioned experiments are derived from synthetic data with assumed gain values, real-world environments introduce additional variability that may challenge the model assumptions. One such challenge is the role of inertia. In the current model, inertia is solely attributed to the human arm, with external forces applied by an ideal force source. However, in practical implementations, the inertia and damping of the robotic system can be comparable to those of the human, complicating the estimation of human dynamics. A critical step will, therefore, be to assess whether the model remains robust under these conditions and whether the initially hypothesized gain space accurately reflects reality. The real-world application will use an upper-limb robotic device, b.u.r.t. [30], in combination with the augmented reality interface LookinGlass [31], which enhances user immersion. This setup will allow the robotic system to gather precise position data and apply controlled forces to participants, while a virtual environment, developed using the Unity game engine, will provide interactive visual feedback.

Our model, while providing a solid framework for understanding sensory gain identification, can be further enriched with elements that better reflect real-world motor dynamics. In particular, it does not explicitly incorporate reflex components, as its primary focus is on voluntary control mechanisms. However, reflexes play a crucial role in motor control by enabling rapid corrections to perturbations and enhancing movement stability. Extending the model to include reflex contributions would allow for a more comprehensive representation of motor responses. Additionally, refining the framework to incorporate multiple sensory modalities could further enhance its applicability in neurorehabilitation. By integrating diverse sensory inputs, we aim to explore how specific excitation methods can optimize system parameter identification. These advancements will refine the model, making it more adaptable to individual needs and more effective for tailoring interventions in complex, multi-modal systems. Ultimately, this work represents a step toward developing robust, data-driven methodologies that enhance neurorehabilitation strategies by closing the gap between theoretical models and their practical application. By integrating these approaches, it aims to improve the effectiveness of rehabilitation techniques in real-world settings.

ACKNOWLEDGMENT

We would like to thank the rest of the Robotics Lab at the Shirley Ryan AbilityLab and the Richard and Loan Hill Department of Biomedical Engineering at the University of Illinois Chicago. No conflicts of interest, financial or otherwise, are declared by the authors.

REFERENCES

[1] B. Kollen, G. Kwakkel, and E. Lindeman, "Functional recovery after stroke: a review of current developments in stroke rehabilitation research", in Review of Recent Clinical Trials, vol. 1, pp. 75–80, 2006.

[2] M. F. Bittmann and J. L. Patton, "Forces that supplement visuomotor learning: A 'sensory crossover' experiment", in IEEE Transactions on Neural Systems and Rehabilitation Engineering, vol. 25, no. 8, pp. 1109–1116, 2017, doi: 10.1109/TNSRE.2016.2613443.

[3] P. N. Parmar, F. C. Huang, and J. L. Patton, "Simultaneous coordinate representations are influenced by visual feedback in a motor learning task", in Annu. Int. Conf. IEEE Eng. Med. Biol. Soc., vol. 2011, pp. 6762–6768, 2011, doi: 10.1109/IEMBS.2011.6091668.

[4] K. P. Cross, D. J. Cook, and S. H. Scott, "Rapid online corrections for proprioceptive and visual perturbations recruit similar circuits in primary motor cortex", in eNeuro, vol. 11, no. 2, pp., 2024, doi: 10.1523/ENEURO.0083-23.2024.

[5] T. Kimura and H. Gomi, "Temporal development of anticipatory reflex modulation to dynamical interactions during arm movement", in J. Neurophysiol., vol. 102, no. 4, pp. 2220–2231, 2009, doi: 10.1152/jn.90907.2008.

[6] I. Kurtzer, J. A. Pruszynski, and S. H. Scott, "Long-latency responses during reaching account for the mechanical interaction between the shoulder and elbow joints", in J. Neurophysiol., vol. 102, no. 5, pp. 3004–3015, 2009, doi: 10.1152/jn.00453.2009.

[7] L. B. Bagesteiro, F. R. Sarlegna, and R. L. Sainburg, "Differential influence of vision and proprioception on control of movement distance", in Exp. Brain Res., vol. 171, pp. 358–370, 2006.

[8] F. Sarlegna, et al., "Target and hand position information in the online control of goal-directed arm movements", in Exp. Brain Res., vol. 151, pp. 524–535, 2003.

[9] J. A. Saunders and D. C. Knill, "Humans use continuous visual feedback from the hand to control both the direction and distance of pointing movements", in Exp. Brain Res., vol. 162, pp. 458–473, 2005.

[10] Z. Gharamani, D. M. Wolpert and M. I. Jordan, "Computational models ofsensorimotor integration", In: Self-Organization, Computational Maps and Motor Control, edited by Morasso PG and Sanguineti V. Amsterdam: North-Holland, 1997, p. 117–147.

[11] Y. Rossetti, M. Desmurget and C. Prablanc, "Vectorial coding of movement: vision, proprioception, or both?", J Neurophysiol 74: 457–463, 1995.

[12] R. J. van Beers, A.C. Sittig and JJDvd Gon, "Integration of proprioceptive andvisual position-information: an experimentally supported model", J Neuro-physiol 81: 1355–1364, 1999.

[13] S. J. Sober and P. N. Sabes, "Multisensory integration during motor planning", J Neurosci 23: 6982– 6992, 2003.

[14] R. A. Scheidt, M. A. Conditt, E. L. Secco, and F. A. Mussa-Ivaldi, "Interaction of visual and proprioceptive feedback during adaptation of human reaching movements", in J. Neurophysiol., vol. 93, no. 6, pp. 2701–2712, 2005.

[15] N. Hogan, "An organizing principle for a class of voluntary movements", in J. Neurosci., vol. 4, no. 11, pp. 2745–2754, 1984.

[16] T. Flash and N. Hogan, "The Coordination of Arm Movements: An Experimentally Confirmed Mathematical Model", in Journal of Neuroscience, vol. 5, pp. 1688–1703, 1985.

[17] F. Izzi, A. Mo, S. Schmitt, A. Badri-Spröwitz and D.F.B Haeufle, "Muscle prestimulation tunes velocity preflex in simulated perturbed hopping", Scientific reports, 13(1), 4559, 2023.

[18] K. P. Cross, D. J. Cook, and S. H. Scott, "Rapid Online Corrections for Proprioceptive and Visual Perturbations Recruit Similar Circuits in Primary Motor Cortex", in eNeuro, vol. 11, no. 2, 2024.

[19] F. Tessari, J. Hermus, R. Sugimoto-Dimitrova and N. Hogan, "Brownian processes in human motor control support descending neural velocity commands", in Sci Rep 14, 8341, 2024.

[20] J. Hermus, J. Lachner, D. Verdi and N. Hogan, "Exploiting Redundancy to Facilitate Physical Interaction", in IEEE Transactions on Robotics, vol. 38, no. 1, pp. 599-615, Feb. 2022, doi: 10.1109/TRO.2021.3086632.

[21] M.E. Huber, C. Folinus and N. Hogan, "Visual perception of joint stiffness from multijoint motion", in Journal of neurophysiology, 122(1), 2019.

[22] F. A. Mussa-Ivaldi, N. Hogan, and E. Bizzi, "Neural, mechanical, and geometric factors subserving arm posture in humans", in J. Neurosci., vol. 5, no. 10, pp. 2732–2743, 1985, doi: 10.1523/JNEUROSCI.05-10-02732.1985.

[23] R. Shadmehr and F. A. Mussa-Ivaldi, "Adaptive representation of dynamics during learning of a motor task", in Journal of Neuroscience, vol. 14, no. 5, pp. 3208–3224, 1994, doi: 10.1523/JNEUROSCI.14-05-03208.1994.

[24] L. Ljung, "System identification: Theory for the user (2nd ed.)", 1999, Prentice Hall PTR.

[25] R. E. Kearney, R. B. Stein, and L. Parameswaran, "Identification of intrinsic and reflex contributions to human ankle stiffness dynamics", in IEEE Transactions on Biomedical Engineering, vol. 44, no. 6, pp. 493–504, 1997.

[26] M. Min, T. Paavle and J. Ojarand, "Time-frequency analysis of biological matter using short-time chirp excitation", 2011 20th European Conference on Circuit Theory and Design (ECCTD), 2011, pp. 298-301, doi: 10.1109/ECCTD.2011.6043345.

[27] K. A. Thoroughman and R. Shadmehr, "Learning of action through adaptive combination of motor primitives", in Nature, vol. 407, no. 6805, pp. 742–747, 2000.

[28] R. A. Scheidt, J. B. Dingwell, and F. A. Mussa-Ivaldi, "Learning to move amid uncertainty", in Journal of Neurophysiology, vol. 86, no. 2, pp. 971–985, 2001.

[29] D. J. Reinkensmeyer, et al., "Computational neurorehabilitation: modeling plasticity and learning to predict recovery", in Journal of NeuroEngineering and Rehabilitation, vol. 13, no. 1, 2016.

[30] W. T. Townsend, D. Wilkinson, A. Jenko, J. Leland, A. Ananthanarayanan, and J. Patton, "Multi-active-axis, non-exoskeletal rehabilitation device", Nov. 20 2018, uS Patent 10,130,546.

[31] J. Patton, "New VR Technologies for Sensorimotor Rehabilitation", in Japanese Society for Medical and Biological Engineering: Supplement, 2013, doi: 10.11239/jsmbe.51.M-99.

First steps of creating a simulation environment in OpenSim to design a control method for a novel soft robotic exoskeleton

Réka Kiss
Faculty of Information Technology and Bionics
Pázmány Péter Catholic University
Budapest, Hungary
kiss.reka@itk.ppke.hu

Sándor Földi
Faculty of Information Technology and Bionics
Pázmány Péter Catholic University
Budapest, Hungary
foldi.sandor@itk.ppke.hu

Attila Répai
Jedlik Innovation Ltd.
Budapest, Hungary
repai.attila@hallgato.ppke.hu

Ádám Makk
András Pető Faculty
Semmelweis University
Budapest, Hungary
makk.adam@semmelweis.hu

György Cserey
Faculty of Information Technology and Bionics
Pázmány Péter Catholic University
Budapest, Hungary
cserey.gyorgy@itk.ppke.hu

Miklós Koller
Faculty of Information Technology and Bionics
Pázmány Péter Catholic University
Budapest, Hungary
koller.miklos@itk.ppke.hu

***Abstract*—Movement coordination disorders can originate from congenital abnormalities, traumatic injuries, or severe infections. These conditions can manifest in various ways, such as hypertonia, hypotonia, and involuntary movements, significantly impairing an individual's ability to perform daily tasks. This research focuses on the development of a soft exoskeleton designed to enhance the quality of life for individuals with cerebral palsy, particularly those affected by athetosis – a condition marked by involuntary, fluctuating muscle tone and associated balance challenges. The exoskeleton aims to provide conductive education (also known as the Pető method) for maintaining motor functions and facilitating precise movements, thereby contributing to the social and professional integration of individuals living with mobility disorders.**

This manuscript emphasizes the simulation phase of the exoskeleton development, which supports the physical design process through numerous iterative cycles. During the research, we utilized three different movement data sources, we developed a whole and a partial simulated model (reduced degree-of-freedoms) of our real exoskeleton, and investigated two different control methods in simulation. At the end of the day we achieved a qualitatively similar behavior in simulation what we produced with the physical exoskeleton at its current development stage.

***Index Terms*—control design, soft exoskeleton, OpenSim**

I. Introduction

Neural disorders remain a significant focus of modern medicine, particularly in treatment and rehabilitation. While robotic solutions have shown success in addressing well-defined diseases with deterministic mechanisms, such as Parkinson's disease [1], they often fall short in managing non-deterministic conditions requiring complex regulation. This is particularly important in conductive education, where conductors (therapeutic specialists) work to facilitate motor learning and development. For neural disorders with motor impairments, precise symptom characterization is crucial, particularly through motion capture and analysis. Techniques combining cameras and inertial measurement units (IMUs) provide detailed tracking of complex movements, addressing limitations of single-sensor systems [2], [3]. Additionally, sensor fusion techniques improve accuracy and reliability by compensating for issues such as gyroscopic drift or limited field of view, enabling the precise mapping of motion trajectories [4]. Biomechanical simulators like OpenSim further enhance analysis by simulating muscle activations and joint forces, offering a deeper understanding of motion mechanics without extensive physical trials [5].

Soft robotic systems, such as cable-driven exoskeletons, are becoming increasingly popular due to their ability to combine functionality with user comfort, ensuring effective therapy over extended periods [6], [7]. However, challenges such as soft tissue artifacts and sensor displacement during movement underscore the need for robust correction methodologies to maintain accuracy in real-world applications [8]. These advancements reflect the ongoing trend toward integrated, adaptive systems that prioritize precise motion tracking and user-specific customization [9], [10], [11].

Athetosis, a specific type of cerebral palsy, exemplifies the complexities of non-deterministic motor disorders. It arises from disrupted cortical control, typically due to damage to the basal ganglia, resulting in involuntary, unpredictable move-

The project EKÖP-24-2-PPKE-10 is funded by the National Research Development and Innovation Office within the framework of the University Research Grant Programme.
Project no. 2020-1.1.5-GYORSÍTÓSÁV-2021-00022 has been implemented with the support provided by the Ministry of Culture and Innovation of Hungary from the National Research, Development and Innovation Fund, financed under the 2020-1.1.5-GYORSÍTÓSÁV funding scheme.
This work was supported by the Ministry of Culture and Innovation of Hungary from the National Research, Development and Innovation Fund, financed under the TKP2021-NKTA funding scheme (project no. TKP2021-NKTA-66).

ments [12]. These movements often intensify during voluntary actions, significantly impairing tasks requiring fine motor control. While the muscles themselves function normally, the inability to regulate movement at the neural level creates significant challenges for therapeutic interventions.

This research focuses on leveraging OpenSim, a biomechanical simulation environment, to support the iterative development of a physical soft exoskeleton designed to address the needs of individuals with athetosis. OpenSim's ability to model multibody dynamics and simulate muscle activations enables the creation of highly customized solutions. Multibody systems treat the body as interconnected segments – bones, muscles, and joints – that interact dynamically to produce motion, making them ideal for analyzing complex biomechanical tasks. OpenSim employs this methodology to model the human musculoskeletal system, enabling precise analysis of joint forces, muscle activations, and motion dynamics. Beyond this, OpenSim supports the integration of experimental data, such as motion capture and electromyographic signals, and provides tools for simulating movement under various conditions. To meet individual needs, OpenSim models can be customized to reflect specific anatomical and functional requirements. Achieving such a high degree of personalization often involves using the software's API, which enables developers to extend functionality and create tailored workflows, ensuring the exoskeleton meets the unique challenges posed by athetosis.

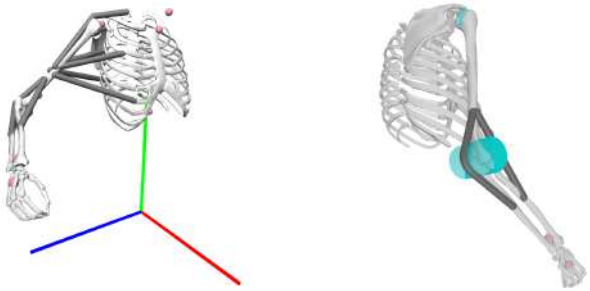
II. Methodology

A. Exoskeleton models

The goal of this research is to develop a soft exoskeleton that supports motion coordination and quality of life for individuals with athetosis. The exoskeleton utilizes lightweight paracord lines (Paracord 350 and 550), which are tensioned or relaxed to produce the required forces for movement, routed through sleeves that guide their paths for stability, and adjusted by motors to generate supportive forces for arm movements. Currently, the device interacts with the arm at seven distinct points, though in the current physical version only four motors actively control two primary movements: elbow flexion-extension and shoulder flexion-extension. The current sensory feedback system of the exoskeleton measures the tension in the inflexible cords, which provides an estimate of the system's operational state.

To refine the exoskeleton's functionality, the system was modeled and simulated in OpenSim. The `ClutchedPathSpring` actuator was identified as the most suitable option, as it mimics the real system by applying forces only when needed, allowing free movement otherwise. The actuators were attached at anatomically appropriate points on the simulated model, in line with the physical design of the exoskeleton (Fig. 1a). To guide the cords along specific paths and prevent intersection with bones during elbow flexion, wrap objects were used to ensure realistic tension distribution. In particular, a cylindrical wrap object was positioned perpendicular to the elbow joint, aligned with both the flexor and extensor paths, mimicking the setup of the physical prototype.

To match the physical settings, the complex 7-actuator model was simplified to a 2-actuator version, using only the elbow actuators (extensor and flexor, acting as agonist and antagonist actuators), as only these actuators currently have the required tension-producing ability and measurement accuracy in the physical system (Fig. 1b). The other actuators are under development and will be integrated into simulations upon reaching the necessary performance standards.



(a) Exoskeleton model in the simulation environment equipped with 7 actuators.

(b) Simplified 2-actuator system along with the additional cylindrical wrap object.

Fig. 1: Exoskeleton models in simulation

B. Data sources

In this research phase, three different data sources were investigated one after the other till the qualitative reproduction of the hardware's behavior.

To characterize the unique movement patterns associated with athetosis, a series of measurements were conducted at the András Pető Faculty of Semmelweis University (commonly known as the Pető Institute), using the Xsens MVN AWINDA (Xsens Technologies B.V., Enschede, Netherlands) motion capture system (research ethics approval ETT TUKEB IV/8514-3/2021/EKU, IV/8515-3/2021/EKU, participators' informed consent was also collected). The recorded data were subsequently processed and visualized in OpenSim, revealing that the underlying movements frequently exceeded the joint range limits defined in the simulation, primarily due to the involuntary and abnormal motions typical of individuals with athetosis. Furthermore, the lack of consistent, followable motion planes and the absence of reliable reference trajectories presented additional challenges for utilizing the data in a 2-actuator system. It should also be noted that in most of the cases, the required Xsens system calibration protocol cannot be carried out, as the subjects could not remain still for 10 seconds and could not walk around during the calibration stage. Thus, the quality of the recorded data was mostly bad. These complexities rendered the real Xsens data unsuitable for tasks such as testing control algorithms for reference exercises in our early stage, as they necessitated overly complex regulatory models.

To simplify the analysis and gain better control over input variables, synthetic data was generated for use in simulations.

These datasets were designed to meet specific requirements: the motions were confined to a single plane, avoided extreme joint angles, and included both smooth and perturbed trajectories to simulate tremors. The synthetic data incorporated variability in both amplitude and phase to emulate realistic motion patterns without exceeding the constraints of the simulation. Joint angle trajectories, primarily focused on elbow flexion-extension, were generated using MATLAB (R2022b, The Mathworks Inc., Natick, Massachusetts). The resulting `.mot` files acted as inverse kinematics outputs, storing the motion as joint angle data over time.

The baseline motion consisted of a smooth flexion-extension movement between 32° and 82°, chosen to reflect a part of natural range of motion for the elbow, to respect the current dynamical range of the real hardware while avoiding extreme joint angles that could lead to simulation errors.

Tremors were introduced by combining sinusoidal and cosine components with varying amplitudes and phases, designed to mimic irregular, non-deterministic movements characteristic of athetosis. The parameters were tuned to qualitatively replicate the athetosis tremor patterns observed in the real Xsens data, though projected in 2D and focused solely on the elbow joint. The amplitude of the perturbations ranged between 0.15° and 1.98°, while the phase values varied randomly within 0.28 to 0.42 radians (16.043° and 24.064°, respectively). Using these rules, five distinct movements were generated for the simulations. One served as a baseline, representing smooth elbow flexion and extension without perturbations. The remaining four included tremors: one with a single larger tremor applied at the midpoint of the motion and three with moderate tremors distributed at the beginning, middle, and end of the movement. In the rest we will refer to these as *synthetic data*. Using the *synthetic data*, `Computed Muscle Control` (`CMC`) was run in OpenSim to determine the muscle excitations required for the model to accurately track the input kinematics.

The third data source in this study is real-measurement based, synthetically aligned (for the simulations, afterwards referred as *real&synthetic*). One of the authors was the subject of these recordings. Before the measurement, he was verbally informed about the circumstances, and he participated voluntarily. The actuator length data was recorded and used with slight scaling in the simulated replication. The three movements in this set consisted of a baseline measurement (smooth movement), an involuntary movement recording with multiple instances of sudden jerks (with a constant-toned actuator tension without intervention), and a third movement recording also with involuntary movements, but with activated physical exoskeleton in order to prevent the sudden and intensive direction changes. During these measurements, the arm moved from a straight position (Fig. 2a) to a flexed state (Fig. 2b), with the jerks noted near the fully flexed point. The goal was to return the arm to its original position after each movement. Beyond the actuator length-change recordings, we also recorded surface electromyographic (sEMG) data with built-in acceleration informations at the sites of the biceps, triceps and hand (Cometa MiniWave Waterproof, Cometa Systems Srl., Bareggio (MI), Italy). The input data for the simulations were generated based on the flexor length changes with slight scaling applied on it.

C. Controls in simulation

In this research phase, we have examined two different control strategies. The first one is in connection with the *synthetic data* source, a pure PD-controller on the basis of the joint angles. The second one is in relation with the *real&synthetic* source, realizing multiple control rules with PD-extension to well align with the physical systems built-in control. (The exact control mechanism of the physical system is based on the patent of the driving mechanism (Patent no. US9933055B2).)

As the first control strategy, the elbow actuator controller implemented in this study is a custom controller class derived from the OpenSim `Controller` class. As a result, the new elbow controller inherits basic control functionalities, such as updating the connected actuator set, without requiring additional development. Its primary purpose is to adjust the elbow joint's flexion angle to match a reference value, accounting for the current angle and its deviation from the desired position. Based on the control signal calculated by a proportional-derivative (PD) controller, the appropriate actuator is activated. Depending on the output, actuators either tighten or loosen (as the two actuators produce opposing motions, activation is determined by the sign of the control signal). Additionally, the controller ensures that the control signal remains within specified bounds (the `ClutchedPathSpring` actuator accepts control signals between 0 and 1).

The first version of the control simulation not only integrated the custom controller into the system but also implemented movement based on muscle activations using the `ControlSetController` class. These calculations were performed by the `Manager` class in OpenSim. This manages the simulation workflow, including the integration of dynamic models, and dynamically adjusts time step size during the simulation based on the motion's complexity and specified settings, ensuring both accuracy and stability. Outputs include kinematic and dynamic variables, providing detailed insights into the model's behavior under dynamic conditions.

After achieving a functional 2-actuator system in simulation, we aimed to validate the simulation by comparing it with the current physical device, this is the second control strategy. For this purpose, the elbow controller was modified to operate based on actuator length, as this was the only built-in numerical value that could be directly measured for evaluation.

III. Evaluation

A. Results

The simulations were performed on a Microsoft Surface Pro 3 laptop (Intel Core i5-4300U, 8GB RAM, 256 GB SSD, Windows 10 Pro). The *synthetic data* used in the simulations, including tremors, and the corresponding reference data were each 5 seconds long. The runtime of the `CMC` for each measurement ranged from 2 to 4 hours, using only elbow flexion,



(a) Initial straight position of the arm. The image also shows the flexor cord (a thin black cord on the forearm) and the EMG sensors positioned on the biceps.



(b) Almost fully flexed state of the arm. The Figure also shows the hand EMG, placed on the hand.

Fig. 2: Snapshots from the physical measurement

with other joints fixed to reduce computational time. The runtime of the C++ simulation (first control strategy) depended mainly on the integration settings (e.g., maximum step size and accuracy) and the frequency of output data logging, with a simplified configuration resulting in a simulation time of 2–3 minutes. The measurements *real&synthetic* (generated from the physical system) lasted approximately 15–30 seconds. The `CMC` ran the optimization for approximately 10–14 hours, while the C++ simulation (second control strategy) ran for 6–8 minutes.

As we analyzed the *synthetic data* in the context of the first control strategy, the baseline movement of it (the smooth movement without any perturbations) served as reference value for the control signal. The different alterations (in phase and in amplitude) helped the detailed examination of the dynamic characteristics of the controller. The tuning of the PD parameters were performed knowing that the control signal should remain in the range $[0, 1]$ while effectively smoothing dynamic movements without overshooting. This also required the correct parametrization of the simulator's integrator, as different integrators showed varying abilities to maintain stable muscle activation values and to track dynamic movements. It was also found that the more detailed the simulation, the smaller the steps required to compute the error signals, enabling faster and more accurate convergence.

The selected PD parameters for the analyses were: $P = 1.0$, $D = 0.4$. The integrator (`Manager` class) used the `RungeKuttaMerson` method with an accuracy of $10^{\propto 5}$, a minimum step size of $10^{\propto 7}$, and a maximum step size of 10^{0}. The PD parameter settings were determined empirically by testing 10 different parameter pairs. Although the coefficients did not significantly impact the final result, smoother solutions were preferred for better control of the physical device. This was demonstrated in Fig. 3, which shows a section of the smoothing performed using three different PD coefficient pairs.

The impact of different smoothings were analyzed from the viewpoint of the elbow flexion angle, determined by

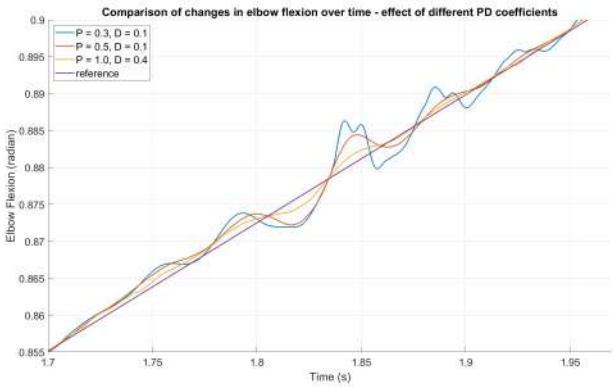


Fig. 3: Comparison of elbow flexion angles smoothed using three different PD coefficients. Among the movement paths shown in the figure, the simulation with parameters marked in yellow (P = 1.0, D = 0.4) proved to be the most effective in terms of mean square error (MSE), compared to the reference signal (purple). The mean square errors for each trajectory are: $3.528632 \times 10^{\propto 6}$ (blue), $7.126799 \times 10^{\propto 6}$ (red), $3.947505 \times 10^{\propto 7}$ (yellow), respectively.

the `Manager` class' calculations, utilizing the precalculations of the `CMC` modul. Fig. 4 illustrate the outcomes of these analyses.

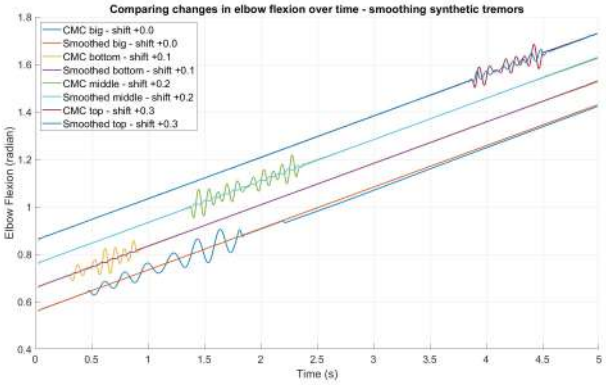


Fig. 4: Comparisons of the generated movement (performed during `CMC`) and the smoothed movement in simulations. The results are shifted along the y-axis to better visualize the differences.

In the case of the *real&synthetic* source, the actuator length data was recorded. As described earlier, here the second control strategy was utilized with the modified elbow controller.

Testing revealed that the uncertainty in the flexion-extension movement at the elbow joint is 6–8 degrees, as the current sensory feedback system of the exoskeleton measures the tension in the inflexible cords. Meanwhile, the useful length-change in cord length measurements for the flexor cord is approximately 8–10 cm, and around 5 cm for the extensor cord. Similar range of length-changes are observed at the shoulder joint, though precise measurements are still being

finalized. Additionally, the spatial accuracy of the wrist was assessed using an Azure Kinect depth camera, which provided a positional accuracy of 5–10 cm, with 3–5 cm of this variability attributed to the limits of the Kinect system itself.

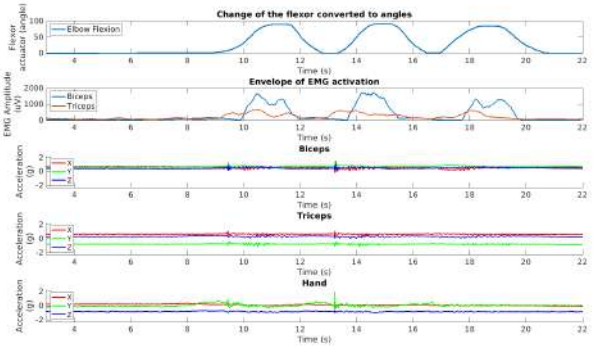


Fig. 5: The results of the baseline movement, during which no actuation was performed by the flexor. The figure illustrates the elbow angles (derived from the flexor), the EMG activation of the biceps and triceps, as well as the acceleration data from the three EMG sensors placed on the arm.

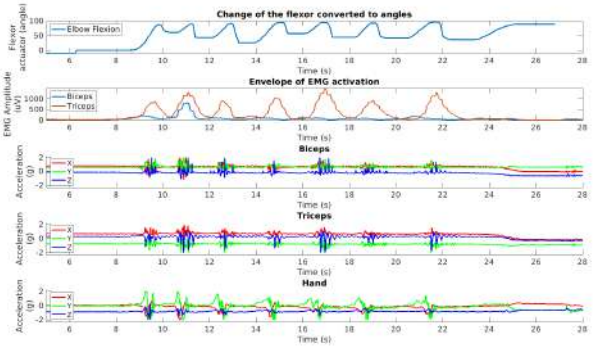


Fig. 6: Results of the involuntary movements measured with the physical soft-exoskeleton model. The figure shows the elbow angles, the EMG activation of the biceps and triceps, and also the acceleration of the three sensors.

The evaluation and visualization of the physical measurements indicate that the flexor can effectively alter the trajectory of the arm. Biceps EMG signals (Fig. 6) were lower compared to the baseline measurement (Fig. 5), which suggests that the arm was not moving. Despite this, movement is still observed, as indicated by accelerometer data and changes in elbow angle, which occurred due to the flexor's exertion of force.

Furthermore, Fig. 7 and Fig. 8 demonstrate that the simulation on *real&synthetic* data source with the second control strategy (using the custom controller designed to replicate the physical system) can effectively adjust the arm's position under the given parameters and working conditions. The system operates similarly to the physical counterpart, as activation occurs only in response to unhealthy/twitching movements.

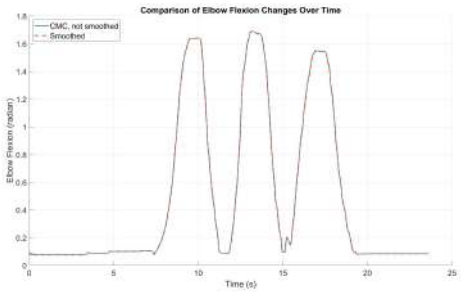


Fig. 7: The simulation of healthy movement showed no unusual behavior. The actuator required no adjustments.

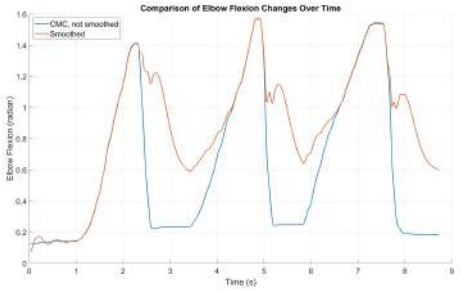


Fig. 8: When twitching was detected during the simulation, the actuator was activated and smoothed the movement.

B. Discussion

Based on the results, it can be concluded that the exoskeleton model is effective at smoothing movements. Various types of tremors were examined during the simulations in *synthetic data* source, and significant smoothing was achieved in all cases of the first control strategy. For larger phase tremors, the system proved particularly effective ($MSE = 3.528632 \cdot 10^{\propto 7}$), while for smaller phase tremors, the system achieved smoothing with an error approximately an order of magnitude higher ($MSE_{bottom} = 1.328081 \cdot 10^{\propto 6}$, $MSE_{middle} = 2.579348 \cdot 10^{\propto 6}$, $MSE_{top} = 1.484697 \cdot 10^{\propto 5}$). This discrepancy is mainly attributed to the simplicity of the controller and to the PD params initially set for larger tremors.

The effectiveness of smoothing was also analyzed based on smaller tremors, focusing on the ratio of the agonist-antagonist actuator moment arm and elbow flexion angle. Both visual observations and computed mean square errors indicated that the elbow extensor actuator exerted greater force in an extended elbow state compared to a flexed state when using the same control signal. This suggests that changes in the moment arm significantly impact actuator performance, which is an important consideration for fine-tuning controller parameters. (A more elaborated tendon system description in the *synthetic data* case with the help of its Jacobian (moment arm matrix, angular-dependent tendon length derivatives with respect to the angles) could lead to an enhanced control with gradient search to have the necessary actual tendon tightening, as presented eg. in [13], but it was out-of-scope for this phase.)

However, simulations controlled purely by muscle activations did not always follow the desired movement accurately. The observed drift was likely due to inaccuracies in the computed muscle activations. The `CMC` optimizer selects the best solution from the viable alternatives. Poorly chosen parameters can lead to cumulative deviations from the desired trajectory, resulting in significant discrepancies, which can be seen in the `CMC` output file. Reviewing and adjusting these errors can provide valuable insights into the accuracy of the computed muscle activations. An example is the `lookahead window`, which represents the foresight on the target movement path. Although optimizing this would likely improve simulation accuracy, it would also increase the required simulation time.

Talking about the physical system (which has different direct and indirect state variables), one issue identified is that the system cannot detect all movements accurately, especially when the arm moves in subspaces the cord-based sensing cannot capture. To address this, the moment arm of the extensor cord at the elbow joint was modified (increased) to support effective force application, and the integration of an IMU-based sensor system has been proposed. The other actuators at the physical level are still under development, their integration into the simulations will follow once their performance reaches the necessary standards, which would help us in future research to focus on incorporating synthetic 3D data. At the software level there are no obstacles to implement this, as all seven actuators have been constructed in the exoskeleton model, and the `ControlSetController` can control all muscle data. After validating the 3D system, real movements recorded at the Pető Institute is likely to become integrable into the simulation environment.

The developed simulation system shows promise for advancing the physical device as it can help to determine the optimal placement and orientation of actuators on the exoskeleton. It also allows consideration of factors like the mass of model components during the simulation. From a control perspective, refining real-time feedback with IMU sensors and adapting parameters based on patient characteristics or movement type could significantly enhance system performance.

IV. Conclusion

The aim of this research was to develop an exoskeleton model that operates similarly to the physical version, allowing the control system to be tested and improved for the physical exoskeleton. Actuators were integrated to closely replicate the functionality of cable-driven motion support, similar to how cables shorten and release through a sleeve mechanism. The validation of the exoskeleton model was carried out through simulations and later compared with physical measurements.

`Computed Muscle Control` (`CMC`) calculations were used in the simulation to determine muscle activations. These formed the basis for dynamic simulations, where movements were controlled using the predefined muscle activations, implemented through the `Manager` class.

Several simulations were performed using synthetic data and physical measurements, which allowed testing different aspects of the simulation system, including tremor smoothing and movement tracking, and the working principle of the physical system. The results of these simulations demonstrated that the developed system was capable of effectively smoothing tremors, supporting the conclusion that the exoskeleton model and simulation system can efficiently support movement coordination and attenuate tremors. The next steps involve parallel developments with the physical exoskeleton, as well as integrating 3D data, which will be accompanied by creating and theoretically designing a more complex controller to ensure that the exoskeleton model can provide optimal support for users in real environments.

References

[1] Chan, P. Y., Ripin, Z. M., Halim, S. A., Arifin, W. N., Yahya, A. S., Eow, G. B., ... & Wong, C. K., "Motion characteristics of subclinical tremors in Parkinson's disease and normal subjects", Scientific Reports, 12(1), 4021, 2022, doi: 10.1038/s41598-022-07957-z.

[2] L. Wade, L. Needham, P. McGuigan, and J. Bilzon, "Applications and limitations of current markerless motion capture methods for clinical gait biomechanics," PeerJ, vol. 10, p. e12995, 2022, doi: 10.7717/peerj.12995.

[3] M. Al Borno, J. O'Day, V. Ibarra, J. Dunne, A. Seth, A. Habib, C. Ong, J. Hicks, S. Uhlrich, and S. Delp, "OpenSense: An open-source toolbox for inertial-measurement-unit-based measurement of lower extremity kinematics over long durations," J. NeuroEng. Rehabil., vol. 19, pp. 1–12, February 2022, doi: 10.1186/s12984-022-01001-x.

[4] Y. Tian, X. Meng, D. Tao, D. Liu, and C. Feng, "Upper limb motion tracking with the integration of IMU and Kinect," Neurocomputing, vol. 159, pp. 207–218, July 2015, doi: 10.1016/j.neucom.2015.01.071.

[5] A. Seth, J. L. Hicks, T. K. Uchida, A. Habib, C. L. Dembia, J. J. Dunne, C. F. Ong, M. S. DeMers, A. Rajagopal, M. Millard, S. R. Hamner, E. M. Arnold, J. R. Yong, S. K. Lakshmikanth, M. A. Sherman, J. P. Ku, and S. L. Delp, "OpenSim: Simulating musculoskeletal dynamics and neuromuscular control to study human and animal movement," PLOS Comput. Biol., vol. 14, p. e1006223, July 2018, doi: 10.1371/journal.pcbi.1006223.

[6] M. Xiloyannis, D. Chiaradia, A. Frisoli, and L. Masia, "Physiological and kinematic effects of a soft exosuit on arm movements," J. NeuroEng. Rehabil., vol. 16, February 2019, doi: 10.1186/s12984-019-0495-y.

[7] A. Zeiaee, R. Soltani-Zarrin, R. Langari, and R. Tafreshi, "Design and kinematic analysis of a novel upper limb exoskeleton for rehabilitation of stroke patients," in 2017 International Conference on Rehabilitation Robotics (ICORR), July 2017, pp. 759–764, doi: 10.1109/ICORR.2017.8009339.

[8] M. Zabat, A. Ababou, N. Ababou, and R. Dumas, "IMU-based sensor-to-segment multiple calibration for upper limb joint angle measurement—a proof of concept," Med. Biol. Eng. Comput., vol. 57, pp. 2449–2460, August 2019, doi: 10.1007/s11517-019-02033-7.

[9] Y. Ganesan, S. Gobee, and V. Durairajah, "Development of an Upper Limb Exoskeleton for Rehabilitation with Feedback from EMG and IMU Sensor," Procedia Comput. Sci., vol. 76, pp. 53–59, 2015, doi: 10.1016/j.procs.2015.12.275.

[10] F. Fei, S. Xian, X. Xie, C. Wu, D. Yang, K. Yin, and G. Zhang, "Development of a Wearable Glove System with Multiple Sensors for Hand Kinematics Assessment," Micromachines, vol. 12, p. 362, March 2021, doi: 10.3390/mi12040362.

[11] L. H. Zhu, C. Cui, Z. Dong, T. Jiamin and C. Xu, "Modelling and Control of Cable Driven Exoskeleton for Arm Rehabilitation," Journal of Mechanisms and Robotics, pp. 1–17, 2024, doi: 10.1115/1.4067305.

[12] L. Zoltan, "Spasztikus cerebralis paretikus tanulok felso vegtagi mozgasainak fejlodese," unpublished, 2022. [Online]. Available: https://ppk.elte.hu/dstore/document/170/lenart_zoltan_disszertacio.pdf. Accessed: Oct. 21, 2022.

[13] P. Polcz, K. Schäffer, and M. Koller, "Posture estimation for a high degree of freedom anthropomorphic tendon-based hand model – A simulation experiment," in 22nd European Control Conference (ECC), pp. 591-596., 2024, doi: 10.23919/ECC64448.2024.10590845.

Analysis of Different Sensor Modalities for Movement Classification in Physical Therapy

Sebastian Dill[1]*, Luise Herrmann[1]*, Arjang Ahmadi[2], Martin Grimmer [2,3], Dennis Haufe[2], Yanhua Zhao[1], Maziar Sharbafi[2] and Christoph Hoog Antink[1]

***Abstract*— This study investigates feature analysis and feature fusion from different sensor modalities for the task of identifying movement errors in physiotherapeutic exercises, using squats as a case study. Incorrectly performed exercises can lead to injuries, underscoring the need for accurate monitoring tools. In an experiment, ten participants performed squats in three variations: correct execution, forward lean, and lateral tilt. To identify movement patterns, we evaluated muscle activation through electromyography (EMG), kinematic data through Motion Capture (MoCap) and joint angles from video footage through MediaPipe Pose. Distinct movement patterns were identified for the erroneous variations: forward lean altered hip and knee angles, while lateral tilt caused asymmetries in posture. In the EMG signal, deviations in the activity of distinct muscles correlated clearly with specific erroneous movements. Activation in the Gluteus Maximus was higher for the forward lean, while activity in the Quadriceps was lower. For the lateral tilt, a clear difference between left and right muscle activation was visible. Signal processing techniques extracted key features, such as muscle activation peaks and joint angle deviations, that we used to discern between the different squat types with a decision tree model. MoCap-based features offered the highest precision when used on their own, but fusing different sensor modalities achieved the best results. Although the video-based classifications were less accurate, its cost-effectiveness and ease-of-use suggest potential for home rehabilitation. Future research should enhance marker-less technologies and enable real-time feedback for broader applications.**

I. INTRODUCTION

Physiotherapy plays a vital role in the rehabilitation process, helping patients recover their health and improve their quality of life [1], [2]. Rehabilitation programs are typically designed and guided by medical professionals to meet individual needs. Traditionally, physiotherapists supervise patients during their rehabilitation exercises to ensure proper execution and prevent errors that could worsen the condition or cause additional injuries [3], [4]. While this personalized approach is highly effective, it is also resource-intensive, requiring therapists to dedicate substantial time to individual patients, which limits efficiency.

Therefore, in recent years, a wide variety of sensors have been used in the attempt to make sensor-based physiotherapy possible [5][6][7]. They can generally be divided into contact-based (obtrusive) sensors and contactless (unobtrusive) sensors. Contact-based sensors have to be attached directly to the patient, which typically necessitates the involvement of an expert for proper placement, making their use both complex and costly. Since the signal quality depends highly on the contact to the subject's body, they are also less suitable for applications involving extensive movement. Examples for contact-based sensors that are often used in physiotherapy include Electromyography (EMG), which directly assesses the electrical activity of the muscles and marker-based Motion Capture (MoCap), which provides highly accurate 3D pose information that can be used to calculate the subject's kinematics.

Contactless sensors are more versatile and can be used by the patients themselves, even at home. Typical contactless at-home sensors include marker-less MoCap through cameras (both red-green-blue (RGB) and depth cameras like the Microsoft Kinect) and radar [8]. These sensor are cheaper than marker-based MoCap or EMG, while also giving the user more freedom to perform the movement [9]. The 3D human pose estimation (HPE) library MediaPipe Pose [10], which is based on the BlazePose model [11], is particularly popular due to its higher computational efficiency and ease of use compared to other methods, and the fact that it is open-source. The downside is that systems based on contactless sensors tend to reach their limits when recording complex movement patterns, especially in terms of accuracy [12] and need calibration and extensive data processing.

Combinations of contact-based and contactless sensors have been used to assess the causes of movement disorders as early as 2000, when Harlaar et al. introduced the SYBAR system for combined recording of video, EMG and force plate data [13]. At that time, however, the analysis was still performed manually by clinicians who used the recorded data to support their decision. Since then, the integration of multiple data sources has proven to offer significant advantages, particularly in gait and running analysis [2]. More recent studies have explored the relationships between different sensing modalities, such as estimating joint angles from EMG data [14].

In this work, we will utilize three types of sensors, namely marker-less MoCap via camera, marker-based MoCap and surface EMG (sEMG) sensors, to collect data of a squat as an typical physiotherapeutic exercise. Squats were chosen

*Sebastian Dill and Luise Herrmann contributed equally as shared first authors.

[1]Sebastian Dill, Luise Herrmann, Yanhua Zhao and Christoph Hoog Antink are with KIS*MED (AI Systems in Medicine), Technische Universität Darmstadt, Darmstadt, Germany. dill@kismed.tu-darmstadt.de

[2]Arjang Ahmadi, Martin Grimmer, Dennis Haufe and Maziar Sharbafi are with Lauflabor (Locomotion Laboratory), Centre for Cognitive Science, Technische Universität Darmstadt, Darmstadt, Germany.

[3]Institute of Automatic Control and Mechatronics, Technische Universität Darmstadt, Darmstadt, Germany

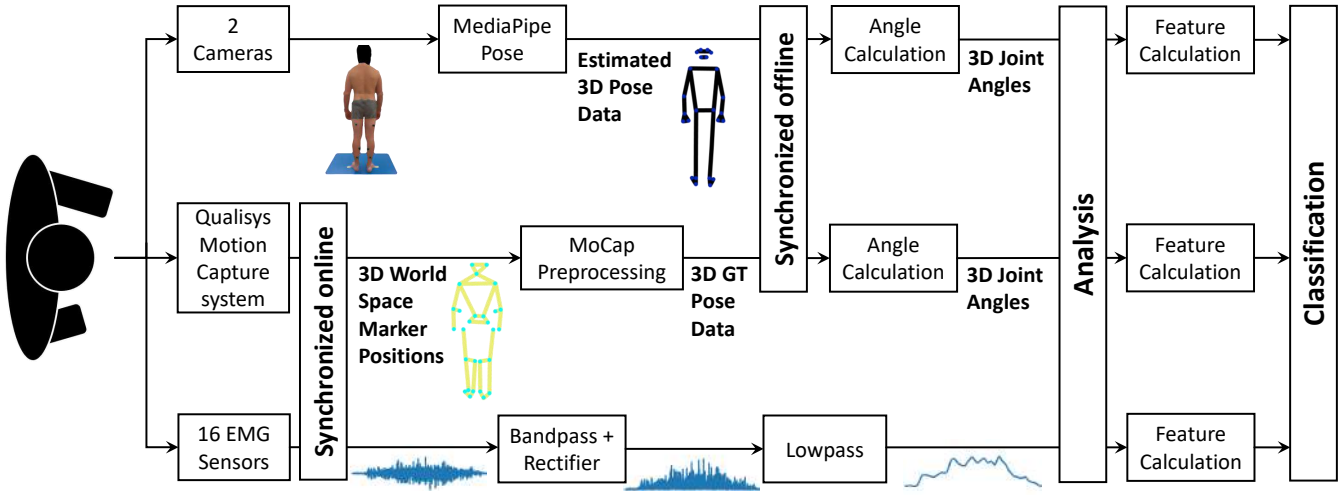


Fig. 1: Flowchart depicting the overall data collection and processing. Three different sensing modalities form three different data paths: Video, MoCap and surface EMG. Each of these paths have their own processing and synchronization. Then the data gets analyzed visually and in a correlation analysis. Finally we calculate features like maximum angle changes and mean muscle activities used in a classification.

for their advantages as a standardized exercise with a slow and controlled movement pattern, making them particularly suitable for detailed movement analysis. We will calculate features like maximum angle changes and mean muscle activities and investigate, which features show significant changes when the exercise execution is wrong. We also analyse the correlation between data from different sensors to explore potential to replace contact-based with contactless sensors. A decision tree model will be employed to differentiate between correctly and incorrectly performed squats, providing insights into the effectiveness of sensor-based error detection. Overall, we wanted to explore three main questions: 1. How effective are contactless sensors compared to contact-based sensors at identifying movement errors in the context of physiotherapy? 2. How much does a combination of sensor modalities improve the identification of movement errors? 3. Can cross-sensor correlations be identified that indicate proportionality between different sensor modalities? Specifically, we hope to find indications that it could be possible to estimate sEMG signals from camera recordings.

II. METHODS

The goal of this work is to compare different sensing modalities, namely sEMG, marker-based MoCap and marker-less MoCap with MediaPipe Pose, to evaluate their suitability for movement classification in physical therapy. To achieve this, we created a custom dataset comprising ten healthy male subjects (mean age = 22.8±3 years; height = 1.79±0.07 m; mass = 74.8±12.8 kg) performing squats in both correct and incorrect variations. The subjects were equipped with 16 different sEMG sensors and were recorded by two video cameras and a motion capture system. We feed the image streams of both cameras into two distinct instances of the MediaPipe Pose framework [11] to receive two sets of 3D human pose joint estimations. From these estimations as well as the ground truth (GT) MoCap data, we calculated relevant joint angles. Following a visual inspection of the data, features were extracted from all sensor signals for use in a classification task. The methodology for each step is detailed in the subsequent sections, while an overview of the entire approach is illustrated in Fig. 1.

A. Experiment and Dataset

A comprehensive description of the dataset and recording setup can be found in [15]; therefore, only a brief overview will be provided here.

Ten participants took part in three different experiments, each involving thirty repetitions of a squat. In experiment one (E1), the squat was performed correctly, as defined by the following criteria:

- Shoulder-width stance with parallel or slightly V-shaped feet.
- Heels remain on the floor throughout the exercise.
- The spine remains straight throughout the exercise.
- Both legs are loaded symmetrically, i.e. the centre of the body should not deviate from the centre of the feet.

In the other experiments, the exercise was performed incorrectly, recreating typical errors identified by an expert: In the second experiment (E2), the participants bend forward excessively during the squat, which also causes rounding of the back in some cases. In the third experiment (E3), the participants shift their weight heavily to the right side, resulting in asymmetry.

The subjects were recorded by two phone cameras (1080×1920 pixels and at 30 frames per second (fps)). The phones were placed upon tripods at a height of approximately 130 cm and are positioned perpendicularly to each other and to the ground, such that cam_1 has a lateral view of the

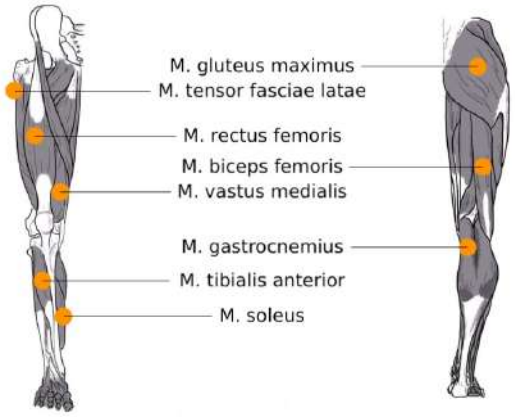


Fig. 2: sEMG sensor placement on major lower limb muscles. Abbreviations and muscle functions are provided in Table I.

TABLE I: Overview of Muscle Functions for all recorded muscles

Muscle	**Abbr.**	**Main function**
M. biceps femoris	BCF	hip extension, knee flexion
M. gastrocnemius	GAS	ankle plantarflexion
M. gluteus maximus	GLM	hip extension, external rotation and abduction, trunk extension
M. rectus femoris	RCF	hip flexion, knee extension
M. soleus	SOL	ankle plantarflexion
M. tensor fasciae latae	TFL	hip flexion, internal rotation and abduction
M. tibialis anterior	TA	ankle dorsiflexion, foot inversion
M. vastus medialis	VAS	knee extension

subject, while cam_2 has a frontal view of the subject. The videos are used to extract marker-less MoCap data through the MediaPipe Pose library, as described later in section II-B. To provide GT kinematic data, the participants were also recorded using a marker-based MoCap system (Qualisys, 31 markers, 11 cameras). The system is able to triangulate the 3D position of each marker with sub-millimeter precision. To quantify muscle activation timing and amplitude, surface electromyography (Delsys Trigno Avanti Sensor [16]) was used. The sensors were positioned on key muscles involved in squat movements, including the biceps femoris (thigh extension, pelvic extension), gastrocnemius (plantar flexion, slight calf flexion), and gluteus maximus (thigh extension, pelvic extension). An overview over the recorded muscles and the corresponding positions of the sEMG markers can be seen in Fig. 2, with a short explanation of their functions being given in Table I.

While the sEMG and MoCap data were recorded synchronously, the two sets of MoCap data extracted from the videos had to be synchronized to this data. To synchronize the three different joint position streams, an overall movement metric M was calculated by summing up the difference over the hip and shoulder joint coordinates between each frame. Although the pose data from all three recordings are represented in different coordinate systems, all three systems share a common axis that is vertical to the ground. This axis also corresponds to the direction with the largest range of movement, as all exercises are stationary. Therefore only this axis was considered when calculating M. The so-calculated movement metrics are normalized and correlated to determine the offset.

All participants voluntarily provided written informed consent before participation in this study. The study was conducted in accordance with the Declaration of Helsinki, and approved by the Ethics Committee of Technical University Darmstadt (protocol code EK 43/2023, date of approval: 11.07.2023).

B. MediaPipe Pose

We present a brief overview of the BlazePose model, which is utilized by MediaPipe and therefore serves as the baseline for the video-based motion capture. MediaPipe's output consists of x-y-z image coordinates of 33 different joint position. The x and y axis span the image plane, while the z axis is pointed perpendicularly away. The z-coordinate estimation is different than the estimation of the x- and y-coordinate as it is not located within the image plane. It is therefore less reliable as 3D pose estimation from monocular inputs presents an ill-posed problem, as multiple 3D predictions can correspond to the same 2D projection. MediaPipe addresses this issue by fitting their 2D projection to an internal model of a human [11]. The best fit is selected for depth estimation. We compare the 3D coordinates provided from MediaPipe both on the frontal and the lateral camera to the contact-based MoCap.

C. Motion capture and video processing

After running MediaPipe Pose on the two video streams, we receive three different sets of 3D Pose data: The GT MoCap data, the estimated data from the frontal camera and the estimated data from the lateral camera. All contain the positions of all relevant joints in a 3D world space. For each of these sets of joint positions, four different angles, relevant to the squat exercise were calculated, both for the left and right side of the body: The ankle angle connects middle toe, knee and heel. The knee angle connects hip, knee and heel. The hip angle connects shoulder, hip and knee. Finally, we define a symmetry angle that connects either the left or right shoulder to both knees. A visualization of the angles is shown in Fig. 3. The initial three angles were calculated using the three-dimensional coordinates, whereas the symmetry angle was projected onto the frontal plane (2D) in order to minimize the influence of noise.

From the angles, a series of features were extracted. To ensure comparability, we did not consider absolute angles, but instead focused on absolute angle change. Subsequently, the maximum angle change was extracted for each repetition. Additionally, for the two symmetry angles, the maximum difference between the left and right was extracted.



Fig. 3: Ankle, knee, hip and symmetry angles (from left to right).

D. sEMG Data Processing

The processing of the sEMG data involves the following stages: pre-processing, normalisation, feature extraction and methods for temporal adjustment and averaging.

In the preprocessing step, the data underwent filtering with a bandpass filter of the fourth order within the physiological spectrum with a low-cut frequency of 20 Hz and a high-cut frequency of 450 Hz. The data was then rectified and filtered once more with a second-order low-pass filter with a cutoff frequency of 6 Hz. It is important to consider that the amplitude of the sEMG is dependent on muscle properties, electrode placement, and the electrode-skin conductivity. Therefore, the signals were rescaled through a min-max-normalization.

As the data was recorded in sets of 10 repetitions, it was also necessary to split the data into the individual repetitions. For this, the sEMG signals were used. All muscles were examined in regards to noisiness, where a signal was considered to have low noise when the signal-to-noise (SNR) ratio was below 0dB. At least three muscles with low noise were selected per trial and then summed up to form one reference muscle. In this reference muscle, the initial and final timestamps of each repetition could be identified by a minimum in muscle activation. Since all other data streams were synchronized with the sEMG signal, the timestamps identified for the individual repetitions in the sEMG data could also be employed to divide the MoCap data. Additionally, the data was also normalized in length to 1,000 time steps per repetition through linear interpolation.

In the final step, several features were extracted. These included the peak amplitude (the maximum value of the filtered signal), the integral (total muscle activity) from the filtered and filtered plus normalised signals, and the mean and standard deviation for each muscle in each experiment.

E. Classification model

To analyze the meaningfulness of the different sensor modalities in general and the features specifically, we used two distinct sets of decision tree models to classify the different movement types. The first set of models was designed to identify the differences between the correct (as performed in E1) and incorrect (as performed in E2 and E3) execution of the squat. The second set of models was constructed with the objective of differentiating between experiments E1, E2, and E3, thus being more suitable to identify which specific errors were committed by the participants. Overall, from the three sensor modalities five groups of features were extracted. Group one and two consists of 16 features per repetition, namely the peaks and integrals of the sEMG signals of all 16 sensors, respectively. Groups three to five consist of 8 features each, namely the peaks of the knee, hip, ankle and symmetry angles of the contact-based MoCap, the contactless MoCap based on cam_1 and the contactless MoCap based on cam_2, respectively. An individual tree was trained, tuned and evaluated for each of these groups, as well as for combinations of feature groups.

The models were validated using a leave-one-out approach, whereby the model was trained on all subjects except one and then tested on the remaining subject.

III. RESULTS AND DISCUSSION

The initial stage of the analysis involved an exploratory visual examination of the sEMG data and the joint angles to see which sensor data might be a good predictor for bad exercise quality. Subsequent correlation analyses highlighted possible correlations between the characteristics of the various experiments and sensors, which indicates relation between the contact-based and contactless sensors. Finally, a decision tree model was trained to investigate which features and sensor combinations are particularly suitable for classifying movement errors.

A. Data Analysis

sEMG-Data: To gain an initial understanding of the data, a preliminary examination was conducted to identify any notable patterns in muscle activity. Fig. 4 shows typical results for subject S7 of the VAS and GLM, both for the right and left leg.

In E1 a symmetrical activation of all muscles was found, as exemplified in Fig. 4 for the VAS and GLM. In comparison to that, in E2 a general reduction in muscle activity, especially in the RCF and TA, accompanied by compensatory increases in activation of the hip muscles (GLM) was found. E3 reveals asymmetry in muscle activation, with the right-side muscles consistently showing higher activation levels than their left-side counterparts, most notably in the TFL and GLM.

MoCap-Data: While participants exhibited varying movement patterns, some showed more consistent movements, while others demonstrated greater variability across the different angles and trials. Fig. 5 shows typical results of a single participant with more consistent movement for the left knee angle, left hip angle and the symmetry angle difference. Even though general statements are not that easily made, some trends emerged with regard to the various angles and trials for all subjects.

The change in the ankle angle demonstrated consistent patterns with peak dorsiflexion occurring at 50 percent of the movement cycle. However, smaller peaks were observed in E2, and greater variance was evident in E3, which is likely attributable to balance issues. As anticipated, during the squat, the knee angle flexes, resulting in a positive angle change, and then extends, returning to its starting position. The most notable changes occur during the mid-cycle. In comparison to the results of E1, which demonstrated a correct movement pattern, E2 exhibited a reduced range of

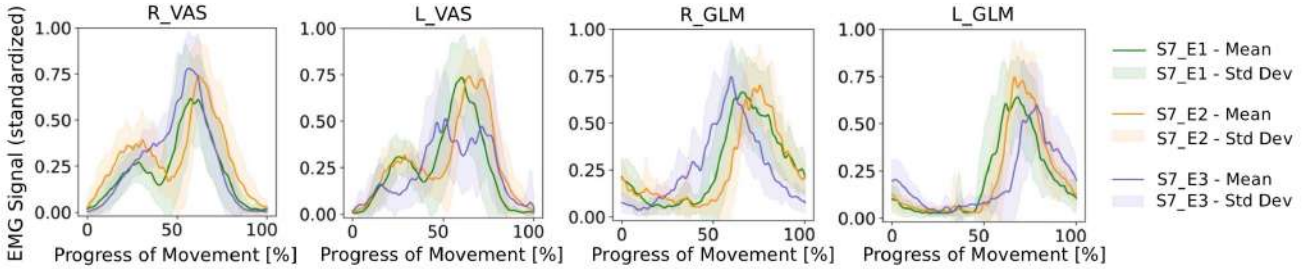


Fig. 4: Standardized sEMG signal of select muscles for subject S7, from left to right: right vastus medialis, left vastus medialis, right gluteus maximus, left gluteus maximus. Presented are the mean values and standard deviations over all 30 repetitions of each experiment.

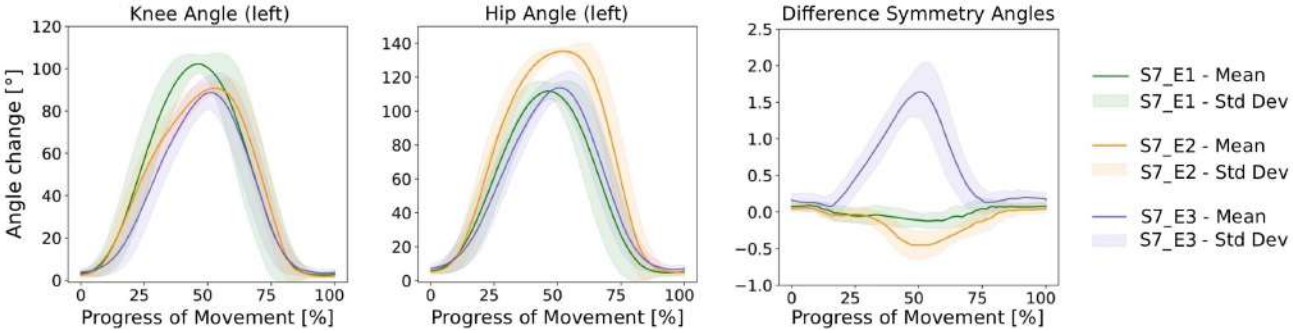


Fig. 5: Absolute angle change in degrees for subject S7, as calculated from the GT MoCap data. From left to right: left knee angle, left hip angle, difference between the left and right symmetry angles. Presented are the mean values and standard deviations over all 30 repetitions of each experiment.

motion in the knee angle. In contrast, in E3, the range of motion on the right side was found to be greater than that on the left. The hip angle is connected to the knee angle; thus, in E2, the angle undergoes greater changes and reaches a higher peak due to the forward lean. Moreover, the asymmetry observed in E3 can be seen to manifest similarly in the hip angle. Regarding the symmetry angle, the difference remains nearly zero in Experiments 1 and 2. However, in E3, a noticeable difference emerges, with the right side showing significant asymmetry due to the side lean.

Marker-less MoCap: The marker-less MoCap data that can be seen in Fig. 6, exhibits comparable outcomes to those observed in the MoCap data, although certain constraints do exist. The data from the MediaPipe system demonstrates greater variability and is more susceptible to noise. Additionally, it exhibits lower peaks in general and irregular signal shapes. With regard to the perspectives, the two perspectives also display differences. While cam_1 (lateral view) is more effective at detecting movement in the sagittal plane, such as forward motions (E2), cam_2 (frontal view) is considerably more precise in detecting abduction/adduction and symmetry (E3). However, cam_2 is less reliable when limbs overlap, which happens at 50% of the movement cycle, when the squat reaches its lowest point.

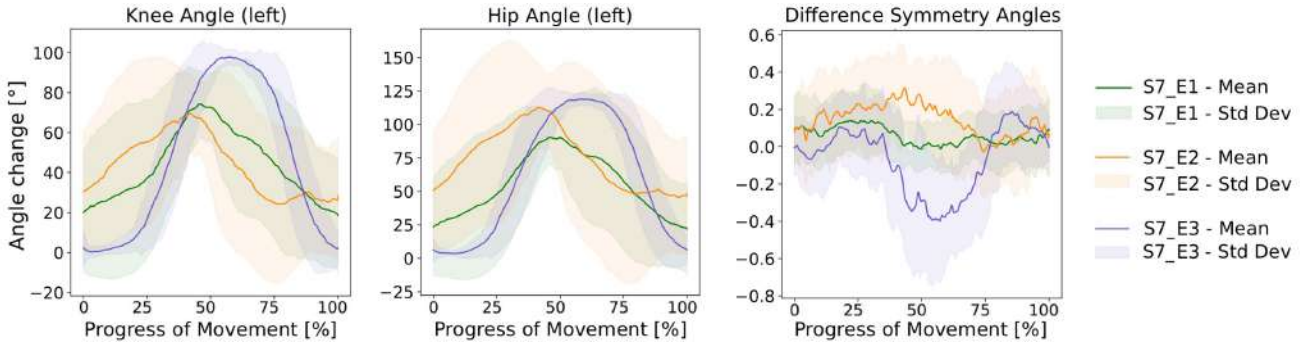
B. Correlation Analysis

The objective of the correlation analysis was to examine the relationships between the various measurement parameters. In the initial phase of the analysis, a comparison was conducted between the muscle activation of different subjects in order to ascertain the degree of similarity in their performance across the experiment. The subject displaying the most consistent results (S7) was selected as the reference. In E1, a high correlation was observed for all muscles (median 0.85), with the exception of the GAS (0.11) and BCF (0.44). In Experiments 2 and 3, considerably weaker correlations were observed (median for E2 is 0.65 and for E3 is 0.72), indicating that when errors were made in the movement, the subjects exhibited individual compensation patterns.

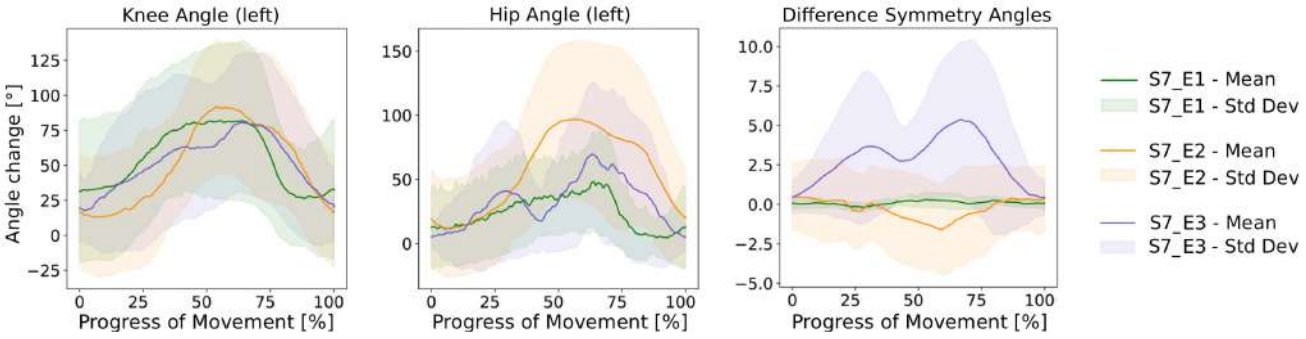
A particularly intriguing aspect was the correlation comparison between specific muscles and joint angles. In this instance, four combinations were examined: VAS and RCF with the knee angles, and GLM with hip and symmetry angles. All correlation coefficients can be seen in Table II. No significant correlations (all correlations $\leq$0.4) were observed between GLM and hip/symmetry angles. Conversely, higher correlations were evident between both knee angles and VAS (mean correlation over all experiments of 0.67) and RCF (mean correlation over all experiments of 0.82) across all experiments. This suggests the potential to estimate muscle activity from camera-based kinematic observations.

C. Movement Classification

The results for the classification based on feature group 2 (integrals of sEMG signals) were very poor and are therefore excluded from the further analysis. For the remaining monomodal feature groups, the results of the binary classification



(a) cam_1 (lateral view)



(b) cam_2 (frontal view)

Fig. 6: Comparison of absolute angle changes for subject S7, calculated from video-based MoCap extracted from cam_1 (lateral view) and cam_2 (frontal view). From left to right: left knee angle, left hip angle, difference between the left and right symmetry angles. Presented are the mean values and standard deviations over all 30 repetitions of each experiment.

TABLE II: Correlation coefficients between selected angles and sEMG signals, calculated for each Experiment.

Correlation	**E1**	**E2**	**E3**	**Mean**
Knee Angle (L), VAS (L)	0.60	0.73	0.42	0.58
Knee Angle (L), RCF (L)	0.81	0.79	0.77	0.79
Knee Angle (L), GAS (L)	-0.042	-0.12	-0.31	-0.158
Knee Angle (R), VAS (R)	0.64	0.77	0.85	0.755
Knee Angle (R), RCF (R)	0.82	0.81	0.90	0.84
Knee Angle (R), GAS (R)	-0.21	-0.27	0.22	-0.0867
Hip Angle (L), GLM (L)	-0.12	-0.13	-0.25	-0.1667
Hip Angle (R), GLM (R)	-0.22	-0.19	-0.28	-0.23
Symmetry Angle (L), GLM (L)	-0.17	-0.19	-0.25	-0.20
Symmetry Angle (R), GLM (R)	-0.28	-0.25	0.33	0.0267

(correct/incorrect) are given in Table IIIa. The table also shows the results for the combination of the features from cam_1 and cam_2. When evaluating the trees trained on these mono-modal feature groups, the trees trained on MoCap and sEMG peaks demonstrated the most optimal results, with the MoCap peaks also exhibiting the highest precision of all features. It can, therefore, be concluded that both are reliable to discern correct and incorrect movements. The results obtained from the MediaPipe angle peaks were found to be less reliable. It is noteworthy that cam_2 demonstrated superior performance compared to cam_1, indicating that the frontal view may be more advantageous in this context. The confusion matrices for the three-class-classification differentiating between error types, are given in Table IV. Overall,

TABLE III: Binary classification performance of the decision trees trained on feature groups 1 (sEMG peaks), 3 (MoCap angle peaks), 4 (cam_1 angle peaks) and 5 (cam_2 angle peaks) as well as combinations of the feature groups. *Mean* relates to the mean over all subjects, while MIN and MAX denote the lowest and highest value achieved for a single subject.

(a) Binary classification performance for mono-modal feature groups.

Feature	**sEMG**	**MoCap**	**cam_1**	**cam_2**	**cam_1 + cam_2**
F1-Score mean	0.80	0.90	0.59	0.77	0.81
F1-Score MIN	0.62	0.67	0.40	0.62	0.60
F1-Score MAX	0.91	1.00	0.75	0.89	0.98
Sensitivity mean	0.82	0.90	0.60	0.78	0.82
Specificity mean	0.79	0.90	0.56	0.75	0.81

(b) Binary classification performance for multi-modal feature group combinations.

Feature	**sEMG + MoCap**	**sEMG + cam_1**	**sEMG + cam_2**	**sEMG + cam_1 + cam_2**
F1-Score mean	0.89	0.79	0.86	0.81
F1-Score MIN	0.67	0.54	0.73	0.54
F1-Score MAX	1.00	0.95	0.99	0.98
Sensitivity mean	0.90	0.81	0.86	0.83
Specificity mean	0.89	0.78	0.86	0.80

this classification showed similar trends to the binary classification but performed consistently worse. However, we can

TABLE IV: Confusion matrices for different classification methods for the classification of the three experiments, aggregated over all subjects. Slight deviations in the absolute numbers occur because of minor errors by individual subjects like repeating one exercise eleven times instead of ten or stepping outside of the visible area of a camera.

(a) sEMG-Based Classification

		Predicted		
		E1	**E2**	**E3**
True	**E1**	217	59	25
	E2	51	203	45
	E3	26	65	208

(b) MoCap-Based Classification

		Predicted		
		E1	**E2**	**E3**
True	**E1**	223	71	7
	E2	46	234	19
	E3	10	0	289

(c) cam_1-Based Classification

		Predicted		
		E1	**E2**	**E3**
True	**E1**	122	46	133
	E2	49	177	73
	E3	119	46	124

(d) cam_2-Based Classification

		Predicted		
		E1	**E2**	**E3**
True	**E1**	203	70	28
	E2	64	201	28
	E3	23	30	226

gain some insights into what causes wrong classifications. For example, we can see that the classification based on the lateral view of cam_1 struggles with differentiating between E1 and E3. This is expected as the main difference between the two movements happens in the plane perpendicular to the camera.

In the subsequent phase, classification models were trained based on multiple feature groups, with a focus on multi-modal classification. Table IIIb shows the mean evaluation metrics over all leave-one-out iterations for these decision trees. This step resulted in an overall improvement in the performance of the model. In particular, the combination of the sEMG and MoCap peaks demonstrated a maximum F1-score of 1 and a mean F1-score across all subjects of 0.89. Additionally, the model was presented with both camera perspectives simultaneously, which also exhibited an improvement compared to the results with only one camera perspective. Due to the nature of monocular 3D pose estimation, this improvement is expected. However, combining the features of both cameras and the sEMG did not improve the results further. This might be explained by the high number of features, which might be too many for our rather small model to handle. Overall, our results suggest that the integration of muscle data with visual information can enhance the accuracy of the model.

IV. CONCLUSION

In response to the questions raised in the introduction, the following results were obtained: sEMG data displayed a high contribution to correctly identifying movement errors. For the squat, the vastus medialis and gluteus maximus were of particular importance. The results of the decision tree analysis shows that a multi-modal feature fusion improves error recognition further, when angle features are calculated from contact-based MoCap data. While results based on features calculated from camera data are overall worse, we could see the same improvement when combining these features with sEMG data. Overall, the angle features calculated on the contactless MoCap do not contribute as much, they still proved to contain additional information relevant for the task. We could also show correlation between different sensor modalities, indicating potential to derive muscle activity from joint angles. In further studies we want to investigate the possibility to fully replace contact-based sensors with contactless ones.

ACKNOWLEDGMENT

The authors gratefully acknowledge financial support provided by the Hessian Ministry for Digital Strategy and Development [Hessisches Ministerium für Digitale Strategie und Entwicklung, Distr@l-Förderlinie 2, "SG4smartmedication", 21_0038_2A], as well as TU Darmstadt's Forum for Interdisciplinary Research [FiF - Forum interdisziplinäre Forschung, "BYouTrain", 2023#6].

REFERENCES

[1] J. Grifka, *Orthopädie Unfallchirurgie*. Berlin [Heidelberg] Springer Spektrum, 2 ed., 2021.

[2] V. Wank, *Biomechanik der Sportarten: Grundlagen der Sportmechanik und Messtechnik-Fokus Leichtathletik*. Berlin [Heidelberg] Springer Spektrum, 2021.

[3] W. Pschyrembel, *Pschyrembel Klinisches Wörterbuch*. De Gruyter, 261 ed., 2007.

[4] B. H. Jones, D. N. Cowan, and J. J. Knapik, "Exercise, training and injuries," *Sports Medicine*, vol. 18, no. 3, pp. 202–214, 1994.

[5] L. M. S. d. Nascimento, L. V. Bonfati, M. L. B. Freitas, J. J. A. Mendes Junior, H. V. Siqueira, and S. L. Stevan Jr, "Sensors and systems for physical rehabilitation and health monitoring—a review," *Sensors*, vol. 20, no. 15, p. 4063, 2020.

[6] R. J. Cotton and J. Rogers, "Wearable monitoring of joint angle and muscle activity," in *2019 IEEE 16th International Conference on Rehabilitation Robotics (ICORR)*, pp. 258–263, 2019.

[7] L. et al., "A systematic review of the applications of markerless motion capture (mmc) technology for clinical measurement in rehabilitation," *Journal of NeuroEngineering and Rehabilitation*, vol. 20, no. 57, 2023.

[8] J. M. Fernandes, J. S. Silva, A. Rodrigues, and F. Boavida, "A survey of approaches to unobtrusive sensing of humans," *ACM Computing Surveys (CSUR)*, vol. 55, no. 2, pp. 1–28, 2022.

[9] K.-C. S. Melissa T. Parks, Zhuo Wang, "Current low-cost video-based motion analysis options for clinical rehabilitation: A systematic review," *American Physical Therapy Association*, vol. 99, p. 1405–1425, 2019.

[10] "Mediapipe pose landmark detection guide." `https://ai.google.dev/edge/mediapipe/solutions/vision/pose_landmarker`. Accessed: 2024-10-14.

[11] V. Bazarevsky, I. Grishchenko, K. Raveendran, T. Zhu, F. Zhang, and M. Grundmann, "Blazepose: On-device real-time body pose tracking," 2020.

[12] S. Dill, A. Rösch, M. Rohr, G. Güney, L. D. Witte, E. Schwartz, and C. H. Antink, "Accuracy evaluation of 3d pose estimation with mediapipe pose for physical exercises," *Current Directions in Biomedical Engineering*, vol. 9, no. 1, pp. 563–566, 2023.

[13] H. et al., "The sybar system: Integrated recording and display of video, emg and force plate data," *Behavior Reserch Methods*, vol. 32, pp. 11–16, 2000.

[14] S. P. Sitole and F. C. Sup, "Continuous prediction of human joint mechanics using emg signals: A review of model-based and model-free approaches," *IEEE Transactions on Medical Robotics and Bionics*, vol. 5, no. 3, pp. 528–546, 2023.

[15] S. Dill, A. Ahmadi, M. Grimmer, D. Haufe, M. Rohr, Y. Zhao, M. Sharbafi, and C. H. Antink, "Accuracy evaluation of 3d pose reconstruction algorithms through stereo camera information fusion for physical exercises with mediapipe pose," *Sensors*, vol. 24, no. 23, 2024.

[16] "DELSYS trigno avanti sensor." `https://delsys.com/trigno-avanti/`. Accessed: 2024-12-05.

Estimating Thorax and Shoulder Motion Using Magnetic-Free Quaternion-Based Functional Sensor-to-Segment Calibration

Sergio A. Salinas, *Student Member, IEEE,* Mahshad Berjis, *Student Member, IEEE,*
Katarina Grolinger, *Senior Member, IEEE,* and Ana Luisa Trejos, *Senior Member, IEEE*

***Abstract*— Wearable rehabilitation robots rely on accurate sensing of body motion. While 9-axis inertial sensors are commonly used to measure motion, signal interpretation can be challenging for upper-limb rehabilitation due to complex and unpredictable joint movements. Other studies have addressed these inaccuracies by attaching three sensor units and using magnetometer data. However, these sensors are often used near actuators that produce ferromagnetic disturbances. Therefore, the objective of this work is to develop a methodology for estimating thorax and shoulder motion using only the orientation data from two sensors, estimated by the internal fusion of accelerometer and gyroscope data. The proposed methodology involves a functional sensor-to-segment calibration that includes performing Principal Component Analysis on the data obtained during specific functional movements to identify the primary axes of rotation. The calibration aligns the sensor coordinate system with the anatomical reference frame of the body segment. Furthermore, the methodology estimates the rotation between the global coordinate systems of the sensor units. Through an experimental evaluation and a comparison with a reference sensor system, the tracking error was 4.07°–5.14° for shoulder orientation and 1.28°–3.88° for thorax orientation. The results provide a solution for tracking thorax and shoulder motion, without using the magnetometer, supporting the development of upper-limb rehabilitation robots.**

I. Introduction

For wearable rehabilitation robots to function reliably, accurate sensing of body motion is essential. This is particularly important in upper-limb rehabilitation, where joint movements are complex and unpredictable [1], [2]. Biomechanical models paired with joint angle measurements, provide a means for detecting upper limb motion. These accurate joint measurements can then be used as inputs to rehabilitation robots, in order to support patients according to their needs.

This work is supported in part by the Natural Sciences and Engineering Research Council (NSERC) of Canada under grant RGPIN-2020-05648, by a Bell-Western 5G grant, by the Canadian Foundation for Innovation (CFI), by the Ontario Research Fund (ORF), by the Canada Research Chairs Program under File #950-233069 and under file CRC-2022-00078, by scholarships awarded to S. Salinas from the Transdisciplinary Training Award from the Bone and Joint Institute at Western University, the Danny Ho Software Engineering Scholarship, and the Colombian Ministry of Science, Technology, and Innovation.

S. A. Salinas and K. Grolinger are with the Department of Electrical and Computer Engineering (ECE), Western University, London, ON, Canada, ssalina@uwo.ca, kgroling@uwo.ca,

M. Berjis is with the School of Biomedical Engineering (BME), Western University, London, ON, Canada, mberjis@uwo.ca,

A. L. Trejos is with the ECE and the BME, Western University, London, ON, Canada, (phone: +1-519-661-2111 ext. 89281), atrejos@uwo.ca.

Various techniques are available to measure joint angles. The traditional method involves using a goniometer to assess the range of motion. However, this approach is prone to human error and is not suitable for measuring movement when the body is in constant motion. Camera-based methods offer an alternative for measuring joint angles during dynamic movements. However, this method can be costly, restricts the patient to a specific location, and its accuracy is affected by marker occlusions [3]. Wearable sensors, on the other hand, enable the study of human biomechanics outside of the laboratory. Currently, inertial measurement units (IMUs) are the most commonly used and promising devices for measuring joint angles in wearable technology [3]. Unlike camera-based methods, which require users to remain in a monitored location, wearable sensors can be attached to the body without the need for external devices. This allows users to seamlessly engage in their regular activities [2].

IMUs are nine-degree-of-freedom sensors that typically include a tri-axial accelerometer, gyroscope, and magnetometer. When these components are used individually to reconstruct human movement, errors can arise: accelerometers are susceptible to noise, gyroscopes can drift over time, and magnetometers may be influenced by magnetic disturbances from closely placed metals and electronic devices such as laptops, cell phones, or actuators that form part of the wearable rehabilitation device [4]. To address these issues, sensor fusion algorithms—such as the Kalman-based filters [5] and Madgwick filter [6]—are commonly employed to integrate data from the different components.

Recent advancements in IMU sensors feature embedded processors that calculate quaternions as output. This built-in functionality allows developers to focus on enhancing other aspects of the system, as the latest fusion algorithms have become more reliable. Quaternions represent rotations in four-dimensional space, eliminating the gimbal lock problem associated with three-dimensional Euler angles [7]. Additionally, combining multiple rotations is more computationally efficient when using quaternions [2], which is beneficial for real-time applications.

A. Sensor-to-Segment Calibration

IMUs are available in a compact form that can be attached to a body segment of interest. However, mounting inertial sensors on the body presents additional challenges because, if the sensors are not properly aligned with the body's bony structures, the reconstruction of human biomechanics from inertial sensor readings can be inaccurate [3].

Sensor-to-segment calibration refers to the process of aligning the coordinate system of an IMU with the anatomical reference frame of the body segment to which it is attached [3]. Accurate sensor-to-segment calibration is essential for reliable biomechanical analysis, especially in rehabilitation, sports performance, and clinical assessment applications. If misalignments are not taken into account, the resulting data can lead to significant inaccuracies in movement reconstruction [7], [8].

In the literature, various assumptions for upper-limb sensor-to-segment alignments have been made. In some papers, the reconstruction assumes that the sensor is perfectly aligned with the body segment [3].

Although this assumption simplifies the reconstruction, fully aligning the sensor with the axis of the segment is almost impossible. Previous studies have shown that the alignment of the IMU sensor with the humerus on the upper arm is particularly difficult, causing the estimated shoulder angles to be inaccurate [8]. Another approach is using predefined static postures to calibrate the sensor to the segment [9]. However, this requires the participant to be exactly in the predefined poses. In reality, it is difficult to ensure that the participant can accurately hold multiple static postures.

B. Functional Calibration

Functional calibration is another method used for sensor-to-segment calibration, in which the participant's specific joint axes are estimated using the angular velocity during rotation around a known anatomical axis (e.g., elbow flexion, shoulder flexion). During functional calibration, the axis of rotation can be determined either by averaging the gyroscope values obtained from multiple repetitions [10], or by using Principal Component Analysis (PCA) [11]–[13]. PCA is a statistical method that identifies the direction of maximum variance in the data.

To find the anatomical axes, identifying two axes is sufficient, as the third axis can be determined by using the cross product of the first two axes, or by using the gravity vector. Mainly, functional calibration methods in the literature for finding the two axes generally fall into one of two categories: 1) using rotation around only one anatomical axis, combined with the gravity vector read from the accelerometer, to determine the longitudinal axis of the body segment [8], [14]; or 2) using two functional movements, which is possible if the joint has more than one degree of freedom.

Despite the feasibility of functional calibration, there is still a need to improve the sensor-to-segment calibration process for the shoulder, as most methods developed in the literature are either not applicable or have not been tested on complex joints. Instead, these methods are often designed for joints with two degrees of freedom, such as the elbow [15], or one degree of freedom, such as the knee [16].

C. Shoulder Motion Measurement

Shoulder rotation (humerothoracic angles), with three degrees of freedom, can be estimated based on the relative orientation of the thorax and upper arm. Therefore, to determine shoulder rotation, it is necessary to perform sensor-to-segment alignment for both the thorax and the upper arm (humerus) [7], [11], [17]. Several studies in the literature have performed functional calibration for both the thorax and the upper arm. In these studies, an additional sensor was placed on the forearm to measure elbow flexion, which was used to calibrate one of the humeral axes. This resulted in a total of three sensors used for shoulder angle estimation. Unless a model for the entire upper limb is required, this approach is inefficient. When only the shoulder and thorax are studied, two IMU sensors are sufficient to find the relative angles between the two segments.

Galinski et al. [10] proposed a framework in which only data from two IMU sensors located on the thorax and the upper arm were used for sensor-to-segment calibration. To identify two axes of the humerus, participants performed flexion–extension and abduction–adduction of the shoulder. However, for the thorax, the sensor was aligned using only a static pose. Since this method has only been tested on a benchmark setup, it is unclear how the misalignment of the thorax segment with the gravity vector was compensated. Additionally, most of the developed methodologies assumed that ferromagnetic disturbances from the devices were minimal. However, in applications of IMU sensors for robotic devices, this assumption may not hold, as the sensors are often located near metallic supports used in these devices. It is necessary to further assess whether the IMU sensor-to-segment alignment in the presence of ferromagnetic disturbances still allows for correct shoulder orientation estimation, especially for long-duration measurements [17], [18].

To address the aforementioned issues, the objective of this work is to develop a methodology for estimating thorax and shoulder orientations using magnetometer-free, functional sensor-to-segment calibration with two IMU sensors located on the thorax and the upper arm.

II. Methodology for Estimating Thorax and Shoulder Orientations

A diagram of the proposed sensor-to-segment calibration approach is presented in Fig. 1. The purpose is to calculate the misalignment between one sensor and its respective segment (${}^{Seg(i)}q_{S(i)}$) and the rotation between the global coordinate reference systems of two inertial sensors (${}^{WS(i-1)}q_{WS(i)}$), where the i–sensor is attached to the i–segment and the $(i-1)$–sensor is attached to the $(i-1)$–segment. $WS(i)$ represents the global coordinate reference systems of the i–sensor and $WS(i-1)$ represents the global coordinate reference systems of the $(i-1)$–sensor. The notation ${}^{k}q_{j}$ corresponds to a normalized quaternion that represents the orientation of frame j with respect to frame k.

This methodology can be applied to any pair of segments connected by a two/three-degrees-of-freedom joint, such that one sensor is placed on each segment and two one-axis functional movements are recorded. The anatomical axes of rotation are determined by applying PCA to the functional

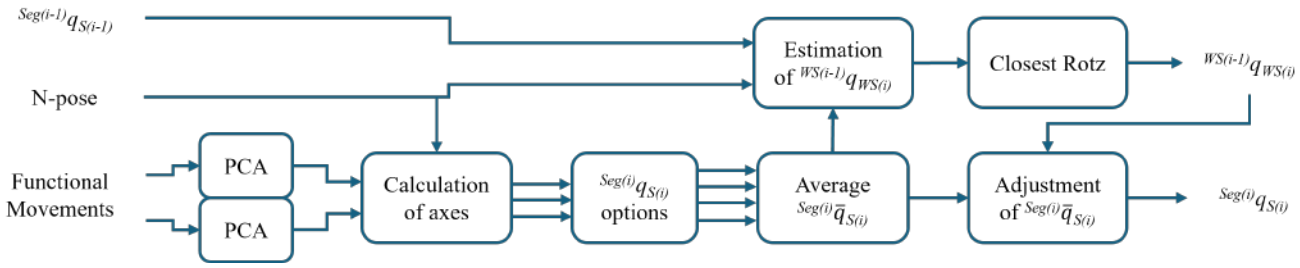


Figure 1. Sensor-to-segment calibration methodology proposed to calculate the misalignment between one sensor and its respective segment (${}^{Seg(i)}q_{S(i)}$), as well as the rotation between the global coordinate reference systems of two inertial sensors (${}^{WS(i-1)}q_{WS(i)}$), where the i–sensor is attached to the i–segment, while $(i\ /\ 1)$–sensor is attached to the $(i\ /\ 1)$–segment. Orientation data from the i–sensor, recorded during two one-axis functional movements of the i–segment and an N-pose, are used to calculate two axes of segment rotation through Principal Component Analysis (PCA). The N-pose data also help to determine the gravity vector observed by the i–sensor. Then, four options of ${}^{Seg(i)}q_{S(i)}$ are obtained using the two rotation axes and the gravity vector through orthonormalization via cross products. An average (${}^{Seg(i)}\bar{q}_{S(i)}$) of these four options, the misalignment between the $(i\ /\ 1)$–sensor and the $(i\ /\ 1)$–segment (${}^{Seg(i-1)}q_{S(i-1)}$), and orientation data from both sensors recorded during an N-pose, are used to obtain an initial estimation of ${}^{WS(i-1)}q_{WS(i)}$. The closest rotation around the z-axis of the sensors is used to refine this estimation. Finally, the result of ${}^{WS(i-1)}q_{WS(i)}$ is used to adjust ${}^{Seg(i)}\bar{q}_{S(i)}$, leading to a better estimation of ${}^{Seg(i)}q_{S(i)}$.

movement data. Similar to the approach described in the literature [16], [19], the angular velocity of the segment of interest is used to calculate the 3D vector around which the rotation occurs, corresponding to the first principal component ($PC1$) [16]. The angular velocity is estimated using quaternion data from the segment during one-axis functional movements. A third axis is computed using data from a static pose, such as the standing neutral pose (N-pose), with the arms neutrally placed alongside the body. Then, all of the possible combinations of misalignment orientation ${}^{Seg(i)}q_{S(i)}$ from the i–sensor to the underlying i–segment are identified. These combinations are averaged and then adjusted to finalize the sensor-to-segment calibration. The methodology was used in this study for estimating thorax and shoulder orientations.

A. Sensor-to-Thorax Calibration

The thorax is the first segment ($Seg1$) of interest with one inertial sensor attached to it. As shown in Fig. 2.a., the coordinate system (T), linked to the thorax, changes its orientation as a function of the thorax motion. Its z axis is the inferior–superior axis perpendicular to the transverse plane, the y axis is the anterior–posterior axis perpendicular to the frontal plane, and the x axis is the medio–lateral axis perpendicular to the sagittal plane. The orientation of T is measured with respect to a global reference coordinate system of the body (WT). This reference frame corresponds to the sagittal, frontal, and transverse planes when the participant is in an initial N-pose. The vertical axis pointing up is defined as the positive z axis, the sagittal axis from the back to the front of the body is defined as the positive y axis, and the frontal axis from left to right is defined as the positive x axis.

The IMU attached to the thorax is represented in Fig. 2.b by a box with a reference coordinate system ($S1$). The orientation of $S1$ is measured by this IMU with respect to its own global reference coordinate system ($WS1$). Data coming from this sensor is represented as ${}^{WS1}q_{S1}$. The z

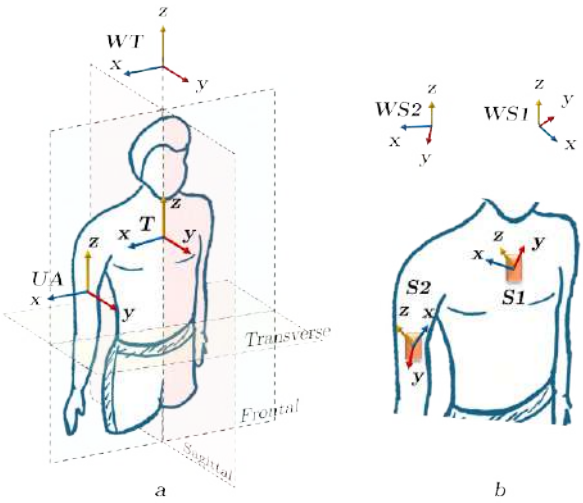


Figure 2. a. Body planes and axes of the global reference coordinate system of the body (WT) and the coordinate system (T) that moves with the thorax. b. Global reference coordinate systems of sensors ($WS1$, $WS2$) and the orientation of the thorax and upper arm sensors ($S1$ and $S2$).

axis of $WS1$ points against gravity; when the magnetometer is used, the y axis points towards the Earth's north, or when the magnetometer is not used, it points in another heading direction defined by the fusion algorithm built into the sensor [20]; finally, the x axis is computed by the same algorithm to obtain an orthonormal $WS1$.

1) Rotation axes: During functional thorax forward flexions (FF), mainly rotations around the x axis of T are expected. Similarly, large rotations around the y axis of T are expected during functional thorax lateral flexions and extensions (LFE). $S1$-orientation data collected during these functional movements are used to estimate the rotation axes of the thorax (v_{FF} and v_{LFE}, correspondingly). These axes correspond to the first principal component of PCAs, which is obtained using $S1$-orientation data. Because of the complexity of the human body structures and variations in the functional movements during the experiments, v_{FF} and

v_{LFE} are close to being aligned to the T axes, but they are not orthogonal.

2) Sensor-to-thorax misalignment options: These anatomical axes, and a third axis calculated using the z axis of $WS1$ (this axis is related to the gravity vector [20]), are used to produce four options for the sensor-to-thorax misalignment ${}^{T}q_{S1}$. As proposed by Vries et.al. [11], the thorax forward flexion axis v_{FF} and the gravity vector measured by $S1$ (g_{S1}) are used to produce the first option. g_{S1} is computed using the mean orientation of the $S1$ data while holding the N-pose (${}^{WS1}\bar{q}_{S1,Np}$), and the rotation of a vector through quaternion products [21], as shown in Equation 1.

$$[0, g_{S1}] = {}^{S1}\bar{q}_{WS1,Np} \otimes [0, z^{\mathcal{T}}_{WS1}] \otimes {}^{WS1}\bar{q}_{S1,Np}, \quad (1)$$

where ${}^{\mathcal{T}}$ represents transpose operation, $\otimes$ denotes the quaternion product, and $z_{WS1} = [0, 0, 1]^{\mathcal{T}}$ represents the z axis of $WS1$.

The first option of ${}^{T}q_{S1}$ is obtained by representing the rotation matrix ${}^{T}R_{S1,1}$ as a quaternion. The following equations are applied to build this matrix:

$$y_T = g_{S1} \times v_{FF}, \quad (2)$$

$$z_T = v_{FF} \times y_T, \quad (3)$$

$${}^{T}R_{S1,1} = \left[v_{FF}, \frac{y_T}{\|y_T\|}, \frac{z_T}{\|z_T\|} \right]^{\mathcal{T}}, \quad (4)$$

where y_T is an estimation of the y axis of T that is orthogonal to v_{FF}, z_T is an estimation of the z axis of T that is orthogonal to v_{FF} and y_T, $\times$ is a vector cross product, and $\|.\|$ represents the vector norm.

To compute the second option ${}^{T}R_{S1,2}$, a similar process is repeated but using v_{LFE} instead of v_{FF} and assuming it points in the direction of the y axis of the T coordinate frame, as shown by the following equations:

$$x_T = v_{LFE} \times g_{S1}, \quad (5)$$

$$z_T = x_T \times v_{LFE}, \quad (6)$$

$${}^{T}R_{S1,2} = \left[\frac{x_T}{\|x_T\|}, v_{LFE}, \frac{z_T}{\|z_T\|} \right]^{\mathcal{T}}, \quad (7)$$

where x_T is an estimation of the x axis of T that is orthogonal to v_{LFE}, and z_T is an estimation of the z axis of T that is orthogonal to v_{LFE} and x_T. Note that the result of this z_T is different from the z_T presented in Equation 3.

The third and fourth options, ${}^{T}R_{S1,3}$, ${}^{T}R_{S1,4}$, are calculated using only the rotation axes v_{FF} and v_{LFE}. Instead of using the gravity vector to estimate the z axis, a cross product between the anatomical axes is applied. For example, ${}^{T}R_{S1,3}$ is obtained with the following vectors being substituted on the right side of Equation 4:

$$z_T = v_{FF} \times v_{LFE}, \quad (8)$$

$$y_T = z_T \times v_{FF}. \quad (9)$$

These four options are used to compute the rotation average ${}^{T}\bar{q}_{S1}$, which is an estimation of the sensor-to-thorax misalignment ${}^{T}q_{S1}$.

3) Solutions for ${}^{T}q_{S1}$ and ${}^{WT}q_{WS1}$, and thorax orientation: Knowing that the orientation of T can be estimated using Equation 10, an estimation of ${}^{WT}q_{WS1}$ is calculated using ${}^{T}\bar{q}_{S1}$, the sensor data during the N-pose ${}^{WS1}\bar{q}_{S1,Np}$, and assuming that the thorax is approximately vertical during that N-pose so that ${}^{WT}q_T \approx [1, 0, 0, 0]$, which represents no rotation. The resulting equation for this estimation is shown in Equation 11.

$${}^{WT}q_T = {}^{WT}q_{WS1} \otimes {}^{WS1}q_{S1} \otimes {}^{S1}q_T \quad (10)$$

$${}^{WT}\hat{q}_{WS1} = [1, 0, 0, 0] \otimes {}^{T}\bar{q}_{S1} \otimes {}^{S1}\bar{q}_{WS1,Np} \quad (11)$$

Here, ${}^{WT}q_{WS1}$ is the constant rotation between the global reference coordinate systems of the thorax and its inertial sensor, ${}^{WS1}q_{S1}$ is a vector of quaternions that corresponds to the sensor orientation data, and ${}^{S1}q_T$ is the conjugate of ${}^{T}q_{S1}$, which is constant if the sensor is firmly attached during the measurements.

Due to the z axes of both WT and $WS1$ point up, ${}^{WT}q_{WS1}$ is a constant that corresponds to a rotation around those z axes. However, the first estimation of this rotation ${}^{WT}\hat{q}_{WS1}$ does not necessarily meet this constraint. Similar to Slade et.al. [22], the closest rotation about the z axis to this estimation is selected as the solution for ${}^{WT}q_{WS1}$. Using this result and manipulating Equation 11, ${}^{T}\bar{q}_{S1}$ is adjusted to obtain the solution for ${}^{T}q_{S1}$. With these two solutions, Equation 10, and data from the sensor ${}^{WS1}q_{S1}$, the thorax orientation is computed.

B. Sensor-to-Upper Arm Calibration

The upper arm is the second segment ($Seg2$). As shown in Fig. 2.a., the coordinate system (UA) linked to the upper arm changes its orientation as a function of the upper arm motion. Its z axis corresponds to the shoulder internal–external rotation axis, the y axis coincides with the shoulder abduction–adduction axis, and the x axis with the shoulder flexion–extension axis.

The IMU attached to the upper arm is represented in Fig. 2.b by a box with a reference coordinate system ($S2$). The orientation of $S2$ is measured by this IMU with respect to its own global reference coordinate system ($WS2$) and it is represented as ${}^{WS2}q_{S2}$. Same as $WS1$, the z axis of $WS2$ points against gravity; when the magnetometer is used the y axis points towards the Earth's north, or when the magnetometer is not used it points in another heading direction defined by the fusion algorithm integrated with the sensor [20]; and the x axis is computed by the same algorithm to obtain an orthonormal $WS2$. It is important to note that $WS1$ and $WS2$ have different orientations even when estimated using magnetometer data [7], [23]. However, the constant rotation between the global reference coordinate systems of the two inertial sensors ${}^{WS1}q_{WS2}$ is a rotation about their z axes.

1) Rotation axes: During functional shoulder flexions and extensions (FE), mainly rotations around the x axis of UA are expected. Similarly, large rotations around the y axis of UA are expected during functional shoulder abductions (Abd). $S2$-orientation data collected during these functional movements are used to estimate the rotation axes of the upper arm (v_{FE} and v_{Abd}, correspondingly). These axes correspond to the first principal component of PCAs, which is obtained using $S2$-orientation data. Because of the complexity of the shoulder and the variations in the functional movements during the experiments, v_{FE} and v_{Abd} are close to be aligned to the UA axes, but they are not orthogonal.

2) Sensor-to-upper arm misalignment options: The same procedure followed for the thorax is used to compute the four options for the sensor-to-upper arm misalignment ${}^{UA}q_{S2}$. The gravity vector g_{S2} is calculated using the mean orientation of the $S2$ data while holding the N-pose (${}^{WS2}\bar{q}_{S2,Np}$), and replacing the number 1 by 2 in Equation 1.

The first option of ${}^{UA}q_{S2}$ is obtained by representing the rotation matrix ${}^{UA}R_{S2,1}$ as a quaternion. The following equations are applied to build this matrix:

$$y_{UA} = g_{S2} \times v_{FE}, \tag{12}$$

$$z_{UA} = v_{FE} \times y_{UA}, \tag{13}$$

$${}^{UA}R_{S2,1} = \left[v_{FE}, \frac{y_{UA}}{\|y_{UA}\|}, \frac{z_{UA}}{\|z_{UA}\|} \right]^{\mathcal{T}}, \tag{14}$$

where y_{UA} is an estimation of the y axis of UA that is orthogonal to v_{FE}, and z_{UA} is an estimation of the z axis of UA that is orthogonal to v_{FE} and y_{UA}.

Note that Equations 12 to 14 are the same as Equations 2 to 4, replacing names and numbers of super- and sub-scripts. Therefore, the same approach is followed to find the second option ${}^{UA}R_{S2,2}$, using Equations 5 to 7, v_{Abd} instead of v_{LFE}, and g_{S2} instead of g_{S1}.

The third and fourth options, ${}^{UA}R_{S2,3}$, ${}^{UA}R_{S2,4}$ are calculated using the axes v_{FE}, v_{Abd}, and the estimation of the z axis of UA through the cross product $v_{FE} \times v_{Abd}$. The procedure is the same as explained in Section II-A.2 to find ${}^{T}R_{S1,3}$ and ${}^{T}R_{S1,4}$.

The four options of ${}^{UA}R_{S2}$ are used to compute the rotation average ${}^{UA}\bar{q}_{S2}$, which is an estimation of the sensor-to-upper arm misalignment ${}^{UA}q_{S2}$.

3) Solutions for ${}^{UA}q_{S2}$ and ${}^{WS1}q_{WS2}$, and shoulder orientation: The shoulder orientation is estimated as the relative orientation between the thorax and the upper arm [7], [24]. The following equation is used to calculate that orientation:

$$\begin{aligned} {}^{T}q_{UA} = {}^{T}q_{S1} \otimes {}^{S1}q_{WS1} \otimes {}^{WS1}q_{WS2} \\ \otimes {}^{WS2}q_{S2} \otimes {}^{S2}q_{UA}, \end{aligned} \tag{15}$$

where ${}^{S1}q_{WS1}$ is the conjugate of the $S1$ orientation ${}^{WS1}q_{S1}$, ${}^{WS2}q_{S2}$ is the $S2$ orientation, and ${}^{S2}q_{UA}$ is the conjugate of ${}^{UA}q_{S2}$.

One estimation of ${}^{WS1}q_{WS2}$ is calculated using Equation 16, the sensor-to-thorax misalignment obtained in Section II-A.3 (${}^{T}q_{S1}$), the rotation average ${}^{UA}\bar{q}_{S2}$, data of $S1$ orientation and $S2$ orientation during the N-pose (${}^{WS1}\bar{q}_{S1,Np}$ and ${}^{WS2}\bar{q}_{S2,Np}$, respectively), and assuming that the thorax is approximately aligned to the upper arm during that N-pose so that ${}^{T}q_{UA} \approx [1,0,0,0]$.

$$\begin{aligned} {}^{WS1}\hat{q}_{WS2} = {}^{WS1}\bar{q}_{S1,Np} \otimes {}^{S1}q_{T} \otimes [1,0,0,0] \\ \otimes {}^{UA}\bar{q}_{S2} \otimes {}^{S2}\bar{q}_{WS2,Np} \end{aligned} \tag{16}$$

This rotation ${}^{WS1}\hat{q}_{WS2}$ does not necessarily meet the constraint of being a rotation around z axis. Therefore the closest rotation about the z axis to this estimation is selected as the solution for ${}^{WS1}q_{WS2}$ [22]. Using this result and manipulating Equation 16, ${}^{UA}\bar{q}_{S2}$ is adjusted to obtain a final solution for ${}^{UA}q_{S2}$.

Finally, the shoulder orientation can be computed using the solutions from the sensor-to-thorax and the sensor-to-upper arms calibrations, the orientation of the sensors, and Equation 15.

C. Thorax and Shoulder Motion Representation

Although a quaternion approach is optimal for computing calculations, a more interpretable representation of thorax movements can be obtained by following the recommendations from the International Society of Biomechanics (ISB) for reporting human joint motion [24]. Accordingly, the Euler sequence XY'Z" was selected for thorax motion representation (please note that the x, y, and z axes used in this study correspond to z, x, and y axes, respectively, in the ISB convention).

In terms of shoulder angle representations, the ISB recommends the Euler sequence YX'Y" [24]. However, this sequence causes gimbal lock issues when the arm is around 0° or 90° abduction [25]. Therefore, an approach that switches between Euler sequences XY'Z" and YX'Z" was developed for representing shoulder angles. The first sequence was applied when the shoulder orientation presented a larger amplitude on the x axis. Rotations around this axis represent shoulder flexions and extensions (see Fig. 2.a). In contrast, the sequence YX'Z" was used when the shoulder orientation presented a larger amplitude on the y axis, since rotations around this axis represent shoulder abductions. In both sequences, the last rotation, i.e., the rotation around the z axis, represents shoulder internal and external rotations.

III. Experimental Setup

To test the performance of the proposed methodology, two sets of IMUs were placed on the participant's body. The first set used a BNO055-based system, which is inexpensive but able to calculate orientation in quaternions. To compare the accuracy, Xsens (Movella, USA) IMUs were also located on the same segments, as they have shown to have comparable results to the optical measurement systems [7].

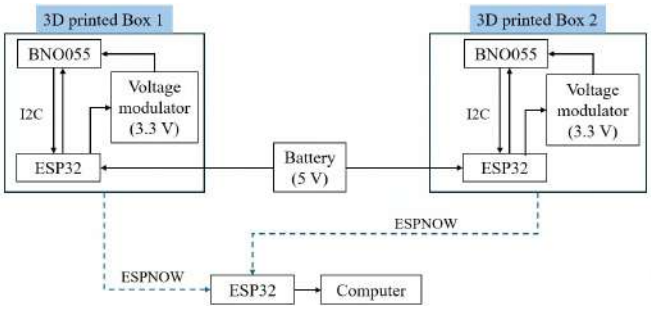


Figure 3. Block diagram of the system designed to capture IMU data. Solid lines represent the wired connections, and dashed lines represent the wireless connections.

A. BNO055-based system

The designed system included two small 3D-printed boxes; one to be placed on the thorax and the other on the upper arm. Both of the boxes had the same source of power from a 5-Volt battery that was placed on the back of the participant. Each box included a BNO055 sensor wired to an ESP32 microcontroller to receive and transfer sensor data using I2C communication. Data were captured at a sampling frequency of 60 Hz. To provide participants with greater mobility, a receiver ESP32 was connected to the lab computer, and the sensor readings were wirelessly transmitted to the lab computer using the peer-to-peer communication protocol of the ESP32 microcontrollers, ESP-NOW [26]. This method was selected for its suitability in transmitting small data packets, such as sensor readings, while maintaining low power consumption.

Fig. 3 illustrates the components used in this system and how they were connected. The BNO055 is a nine-degree-of-freedom absolute orientation IMU breakout board with built-in fusion algorithms. It offers various operating modes that allow the inclusion or exclusion of measurements from the gyroscope or magnetometer. In this study, to ensure that the quaternion outputs were based solely on accelerometer and gyroscope readings (*i.e.*, magnetometer data were not used in the quaternion calculation), the BNO055 was configured to operate in "IMU mode" [21]. Before placing the sensors on the body, both sensors were attached to a flat board to perform the calibration procedure as recommended by the manufacturer [20].

B. Xsens Motion Capture System

The Xsens system used for this experiment included wireless sensor units (called MTw, and composed of a 3D accelerometer, a 3D gyroscope, and a 3D magnetometer) and a data acquisition system (Awinda station), where the data of the sensors were synchronized at a sampling frequency of 60 Hz and sent to the host computer. This system was calibrated according to the procedure explained in the manual [27]. The Xsens sensors were stabilized by keeping them static on a desk once they were put into measurement mode.

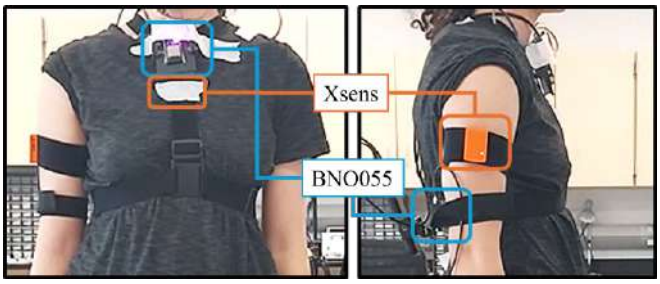


Figure 4. Placement of the inertial sensors from the two systems.

C. Data Recording

As shown in Fig. 4, one sensor of each system was placed on the sternum for tracking the thorax orientation and another sensor was used for tracking the upper arm, with the Xsens strapped to the lateral medial side and the BNO055 strapped to the posterior distal side. Orientation data were simultaneously collected by both systems while the participant stood in a static N-pose (shown in Fig. 2) for ten seconds, followed by ten functional movement repetitions of the thorax or upper arm. The thorax movements were forward flexions and lateral flexion–extensions; whereas, the upper arm movements were consequences of shoulder flexion–extensions and shoulder abduction–adductions.

IV. Results

The sensor-to-thorax and the sensor-to-upper arm calibrations were performed using the data collected during the experiment. The same methodology was applied to both systems (Xsens and BNO055). Then, the solutions for ${}^{WT}q_{WS1}$, ${}^{T}q_{S1}$, ${}^{WS1}q_{WS2}$, and ${}^{UA}q_{S2}$, were replaced into Equations 10 and 15 in order to calculate thorax and shoulder angles, as described in Section II-C. The root-mean-square error (RMSE) was used to report the differences in the resulting angles for the thorax and shoulder.

A. Thorax Motion

As shown in Fig. 5, patterns of thorax angles from both systems are comparable. The RMSEs were 3.88° in the forward flexion axis, 1.28° in the lateral flexion–extension axis, and 1.93° in the rotation axis.

B. Shoulder Motion

The results for the shoulder angles are shown in Fig. 6. It shows the decomposition of the shoulder orientation in flexion–extension, abduction, and internal–external rotations. As in the thorax, the patterns of the results from both systems are comparable. The RMSEs were 4.11° in the flexion–extension axis, 4.07° in the abduction axis, and 5.14° in the rotation axis.

V. Discussion

The sensor-to-segment alignment calibration presented in this paper was applied to the thorax and upper arm body segments to estimate the thorax and shoulder orientations. In this work, comparable results were obtained from angles estimated using the magnetometer-free system developed

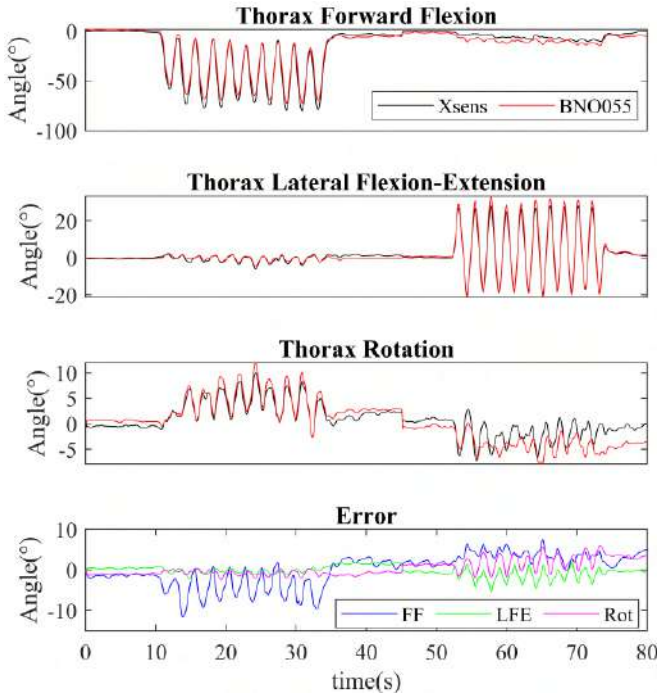


Figure 5. Comparison of the thorax motion angles obtained from both systems (Xsens and BNO055). FF: thorax forward flexion, LFE: thorax lateral flexion–extension, and Rot: thorax rotation.

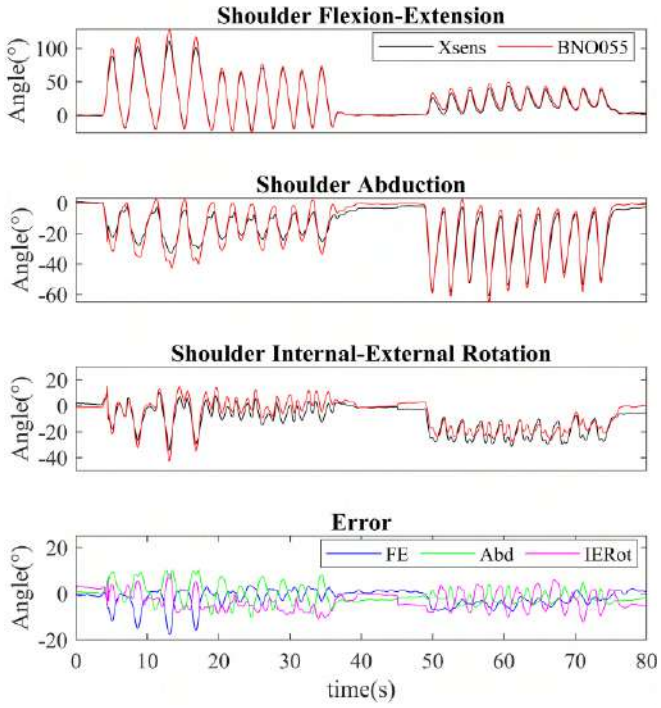


Figure 6. Comparison of the shoulder motion angles obtained from both systems (Xsens and BNO055). FE: shoulder flexion–extension, Abd: shoulder abduction, and IERot: shoulder internal–external rotation.

TABLE I

COMPARISON OF RMSE VALUES WITH SIMILAR STUDIES

	Thorax			Shoulder		
	FF	**LFE**	**Rot**	**FE**	**Abd**	**IERot**
Li. et. al. [18]	1.21°	0.76°	2.09°	3.5°	3.76°	5.44°
Zhu. et. al [7]	-	-	-	6.4°	3.8°	2.8°
This work	3.88°	1.28°	1.93°	4.11°	4.07°	5.14°

with BNO055 sensors and those obtained using the Xsens system, which included a magnetometer. Avoiding the use of the magnetometer is especially important when integrating sensors with wearable soft robots for rehabilitation applications, as the proximity of the sensor to the robot would cause interference with the orientation estimations.

A significant benefit of the proposed approach is that the methodology can be performed using only sensor orientation data. This is useful when the fusion algorithm integrated with the IMU sensors performs the sensor orientation estimations.

The estimated thorax and shoulder angles in this study were compared with other methodologies in the literature (summarized in Table I). Zhu et al. [7] utilized a third sensor on the forearm to estimate the humerus transverse axis during the functional movement of elbow flexion–extension. They used all three components of the IMU, assuming the readings were unaffected by magnetic disturbances. Compared to Zhu et al.'s methodology, the method proposed here achieved a similar RMSE for Abd estimation but had a 2° lower error in FE estimation. However, the method proposed in this paper showed a higher error in internal–external rotation (IERot) estimation. This higher error can be due to soft tissue artifacts [28], or that the wires from the BNO055 battery created variable torque, which was not present in the Xsens system.

Li et al. [18] excluded the magnetometer from their measurements and proposed a sensor-to-segment calibration combining one camera with IMUs to compensate for heading errors. The methodology proposed in this paper achieved comparable RMSE for all shoulder angle estimations, LFE, and thorax axial rotation (Rot). However, the error for FF was about 2° higher. This higher error was potentially caused by the BNO055 sensor moving during the FF, while the Xsens sensor remained stationary as it was taped directly to the skin.

VI. CONCLUSION

This study introduces a novel methodology for angle estimation using a magnetometer-free, low-cost system with two IMU sensors that measure thorax and shoulder angles. A significant advantage of this approach is its reliance solely on gyroscope and accelerometer data, making it more robust in environments with magnetic disturbances. The use of PCA for functional calibration ensures that the sensor coordinate system is accurately aligned with the anatomical reference frame of the body segment, thereby improving the accuracy of motion estimation.

The experimental results demonstrated that the proposed system could achieve comparable accuracy to a high-end

Xsens system, with RMSEs of 4.07°–5.14° for shoulder orientation and 1.28°–3.88° for thorax orientation. These results highlight the potential of the proposed methodology to provide reliable motion tracking without the need for magnetometers and based on only two sensor units.

Future work should focus on several key areas to further enhance the performance and applicability of the system. First, improving the attachment of IMU sensors to the body will help reduce movement artifacts and improve measurement accuracy. Also, expanding the experimental evaluation to include a larger and more diverse participant pool and adding more complex tasks, such as dynamic exercises and activities of daily living, will provide a more comprehensive assessment of the robustness and generalizability of the system. Additionally, comparing the estimated angles with the optical motion capture systems that are considered the "gold standard" will be essential. The next steps will be to integrate this system with wearable rehabilitation robots and conduct long-term studies.

The proposed magnetometer-free, quaternion-based functional sensor-to-segment calibration method represents a significant advancement in the field of wearable motion tracking. By providing accurate and reliable motion estimation with a low-cost and robust system, this methodology has the potential to enhance the development and deployment of upper-limb wearable rehabilitation robots, ultimately improving patient outcomes and advancing the area of rehabilitation technology.

ACKNOWLEDGEMENT

The authors thank Dr. Michael Naish and Niloufar Ahmadian for sharing some equipment used in the trials, as well as other members of the Wearable Biomechatronics Laboratory. The code and data are available at https://github.com/SASalinas/Magnetic-Free-Quaternion-Based-Functional-S2S-Calibration/tree/main.

REFERENCES

[1] L. Uhlenberg and O. Amft, "Where to mount the IMU? Validation of joint angle kinematics and sensor selection for activities of daily living," *Frontiers in Computer Science*, vol. 6, pp. 1 347 424-1–15, 2024.

[2] U. G. Longo, S. De Salvatore, *et al.*, "Motion tracking algorithms based on wearable inertial sensor: A focus on shoulder," *Electronics*, vol. 11, no. 11, pp. 1741-1–12, 2022.

[3] Z. Fang, S. Woodford, *et al.*, "Conversion of upper-limb inertial measurement unit data to joint angles: A systematic review," *Sensors*, vol. 23, no. 14, pp. 6535-1–24, 2023.

[4] D. Álvarez, J. C. Alvarez, *et al.*, "Upper limb joint angle measurement in occupational health," *Computer Methods in Biomechanics and Biomedical Engineering*, vol. 19, no. 2, pp. 159–170, 2016.

[5] L. Truppa, E. Bergamini, *et al.*, "Magnetic-free quaternion-based robust unscented Kalman filter for upper limb kinematic analysis," *IEEE Sensors Journal*, vol. 23, no. 3, pp. 3212–3219, 2022.

[6] S. Madgwick *et al.*, "An efficient orientation filter for inertial and inertial/magnetic sensor arrays," *Report x-io and University of Bristol (UK)*, vol. 25, pp. 113–118, 2010.

[7] K. Zhu, J. Li, *et al.*, "IMU shoulder angle estimation: Effects of sensor-to-segment misalignment and sensor orientation error," *IEEE Transactions on Neural Systems and Rehabilitation Engineering*, vol. 31, pp. 4481–4491, 2023.

[8] B. Bouvier, S. Duprey, *et al.*, "Upper limb kinematics using inertial and magnetic sensors: Comparison of sensor-to-segment calibrations," *Sensors*, vol. 15, no. 8, pp. 18 813–18 833, 2015.

[9] M. Zabat, A. Ababou, *et al.*, "IMU-based sensor-to-segment multiple calibration for upper limb joint angle measurement—a proof of concept," *Medical & Biological Engineering & Computing*, vol. 57, pp. 2449–2460, 2019.

[10] D. Galinski and B. Dehez, "Evaluation of initialization procedures for estimating upper limb kinematics with marg sensors," in *2012 4th IEEE RAS & EMBS International Conference on Biomedical Robotics and Biomechatronics (BioRob)*, Rome, Italy, 24–27 June, 2012, pp. 1801–1806.

[11] W. De Vries, H. Veeger, *et al.*, "Functionally interpretable local coordinate systems for the upper extremity using inertial & magnetic measurement systems," *Journal of Biomechanics*, vol. 43, no. 10, pp. 1983–1988, 2010.

[12] M. Nazarahari, A. Noamani, *et al.*, "Sensor-to-body calibration procedure for clinical motion analysis of lower limb using magnetic and inertial measurement units," *Journal of Biomechanics*, vol. 85, pp. 224–229, 2019.

[13] M. Lorenz, B. Taetz, and G. Bleser, "An approach to magnetometer-free on-body inertial sensors network alignment," *IFAC-PapersOnLine*, vol. 53, no. 2, pp. 15 982–15 989, 2020.

[14] G. Ligorio, E. Bergamini, *et al.*, "A wearable magnetometer-free motion capture system: Innovative solutions for real-world applications," *IEEE Sensors Journal*, vol. 20, no. 15, pp. 8844–8857, 2020.

[15] H. J. Luinge, P. H. Veltink, and C. T. Baten, "Ambulatory measurement of arm orientation," *Journal of Biomechanics*, vol. 40, no. 1, pp. 78–85, 2007.

[16] M. Zandbergen, "Estimating 3D orientation of a body segment during running using a single gyroscope," in *Moving forwards by going outside: Inertial measurement unit-based monitoring of running biomechanics*. Enschede, The Netherlands: University of Twente, 2021, ch. 5, pp. 131–142.

[17] P. Ertzgaard, F. Öhberg, *et al.*, "A new way of assessing arm function in activity using kinematic exposure variation analysis and portable inertial sensors–a validity study," *Manual Therapy*, vol. 21, pp. 241–249, 2016.

[18] T. Li and H. Yu, "Upper body pose estimation using a visual–inertial sensor system with automatic sensor-to-segment calibration," *IEEE Sensors Journal*, vol. 23, no. 6, pp. 6292–6302, 2023.

[19] T. McGrath, R. Fineman, and L. Stirling, "An auto-calibrating knee flexion-extension axis estimator using principal component analysis with inertial sensors," *Sensors*, vol. 18, no. 6, pp. 1882–1899, 2018.

[20] B. Sensortec, "BNO055: Intelligent 9-axis absolute orientation sensor datasheet," *BST-BNO055-DS000-18*, 2021.

[21] A. Rajkumar, F. Vulpi, *et al.*, "Wearable inertial sensors for range of motion assessment," *IEEE sensors journal*, vol. 20, no. 7, pp. 3777–3787, 2019.

[22] P. Slade, A. Habib, *et al.*, "An open-source and wearable system for measuring 3D human motion in real-time," *IEEE Transactions on Biomedical Engineering*, vol. 69, no. 2, pp. 678–688, 2021.

[23] P. Picerno, A. Cereatti, and A. Cappozzo, "A spot check for assessing static orientation consistency of inertial and magnetic sensing units," *Gait & Posture*, vol. 33, no. 3, pp. 373–378, 2011.

[24] G. Wu, F. C. Van der Helm, *et al.*, "ISB recommendation on definitions of joint coordinate systems of various joints for the reporting of human joint motion—Part II: shoulder, elbow, wrist and hand," *Journal of Biomechanics*, vol. 38, no. 5, pp. 981–992, 2005.

[25] M. Lavaill, S. Martelli, *et al.*, "The effects of anatomical errors on shoulder kinematics computed using multi-body models," *Biomechanics and Modeling in Mechanobiology*, vol. 21, no. 5, pp. 1561–1572, 2022.

[26] R. Pasic, I. Kuzmanov, and K. Atanasovski, "ESP-NOW communication protocol with ESP32," *Journal of Universal Excellence*, vol. 6, no. 1, pp. 53–60, 2021.

[27] Xsens, "MTw awinda user manual: Mtw hardware, mt manager, awinda protocol," *MW0502P*, 2018.

[28] A. G. Cutti, A. Giovanardi, *et al.*, "Ambulatory measurement of shoulder and elbow kinematics through inertial and magnetic sensors," *Medical & biological engineering & computing*, vol. 46, pp. 169–178, 2008.

Deep-Learning Control of Lower-Limb Exoskeletons via simplified Therapist Input

Lorenzo Vianello[1], Clément Lhoste[2], Emek Barış Küçüktabak[7], Matthew R. Short[1,4], Levi Hargrove[5,6], Jose L. Pons[1,3,4,6]

***Abstract*— Partial-assistance exoskeletons hold significant potential for gait rehabilitation by promoting active participation during (re)learning of "normal" walking patterns. Typically, the control of interaction torques in partial-assistance exoskeletons relies on a hierarchical control structure. These approaches require extensive calibration due to the complexity of the controller and user-specific parameter tuning, especially for activities like stair or ramp navigation. To address the limitations of hierarchical control in exoskeletons, this work proposes a three-step, data-driven approach: (1) using recent sensor data to probabilistically infer locomotion states (landing step length, landing step height, walking velocity, step clearance, gait phase), (2) allowing therapists to modify these features via a user interface, and (3) using the adjusted locomotion features to predict the desired joint posture and model stiffness in a spring-damper system based on prediction uncertainty. We evaluated the proposed approach with two healthy participants performing treadmill walking and stair ascent/descent at varying speeds, with and without external modification of the gait features through a user interface. Results showed a variation in kinematics according to the gait characteristics and a negative interaction power (-2.1 $\pm$ 1.6W for the hip and -0.6 $\pm$ 1.4W for the knee joints) suggesting exoskeleton assistance across the different conditions.**

I. Introduction

Lower-limb exoskeletons are valuable tools in rehabilitation for individuals with gait impairments. Clinically, these exoskeletons can be classified into two categories: full-assistance and partial-assistance [1]. Full-assistance exoskeletons are intended for patients with significant motor impairments who cannot ambulate independently, providing fully autonomous leg movement without requiring user input. They are usually controlled using position control strategies [2]. In contrast, partial-assistance exoskeletons are more appropriate for patients with mild to moderate impairments, as they support movement while still requiring the patient's active participation [3].

This paper focuses on partial-assistance exoskeletons, which have greater potential in rehabilitation settings as they consider the patient's volitional movements in the control loop. These exoskeletons use approaches like haptic guidance [4] or resistance through error augmentation [5] to promote the (re)learning of walking patterns, depending on the patient's functional ability.

Both of these strategies, assistance and resistance, depend significantly on the control of interaction torques between the user and the exoskeleton. This is typically achieved through a hierarchical structure comprising high-, mid-, and low-level controls [6]. High-level control determines desired interaction torques for specific activities, such as walking on flat surfaces, stairs, or ramps. Mid-level control estimates various states within an activity, like swing and stance phases during walking, and adjusts the desired interaction torque accordingly [7]. Finally, low-level control compensates for the exoskeleton's dynamics and generates motor commands based on the profiles selected in high- and mid-level control.

To provide patients partial-assistance during ambulatory activities, desired interaction torques are typically rendered using virtual springs and dampers, characterized by stiffness and damping parameters, which are attached to reference joint positions. This necessitates the identification of many control parameters specific to each activity and phase of locomotion. As many of these parameters are also user-dependent, this can result in lengthy calibration periods for a single session of therapy. This issue has been well-documented for active prosthetic devices [8], but few studies have quantified the time spent calibrating lower-limb exoskeleton controllers. This is likely due to a reliance on predefined trajectories for generating exoskeleton assistance profiles, which reduces the time and complexity of parameter selection, but limits the degree of parameter customization for individual users. Moreover, most research has concentrated on overground walking, with minimal investigation into scenarios involving stairs and ramps [1].

One potential solution to reduce controller complexity and calibration time is to employ data-driven methods that relate sensor readings with command outputs [9]–[11]. However, these approaches offer limited flexibility for personalization and adjustment of desired behaviors. For example, a therapist may require a progressive increase in foot clearance for a patient during a session of training. Additionally, therapists do not typically conceptualize adjustments in terms of gait cycle kinematics (e.g., trajectories or stiffness/damping parameters). Instead, they focus on clinically relevant features that are easier to interpret, such as step length, time, speed, or height.

[1] Legs and Walking Lab of Shirley Ryan AbilityLab, Chicago, IL, USA
[2] Rehabilitation Engineering Laboratory, ETH Zürich, CH
[3] Center for Robotics and Biosystems of Northwestern University, Evanston, IL, USA
[4] Department of Biomedical Engineering, Northwestern University, Evanston, IL, USA
[5] Neural Engineering for Prosthetics and Orthotics Lab of Shirley Ryan AbilityLab, Chicago, IL, USA
[6] Department of Physical Medicine and Rehabilitation, Northwestern University, Chicago, IL, USA
[7] Honda Research Institute, San Jose, CA (USA)
This work was conducted when E.B. Küçüktabak and C. Lhoste were with the Northwestern University and Shirley Ryan AbilityLab.

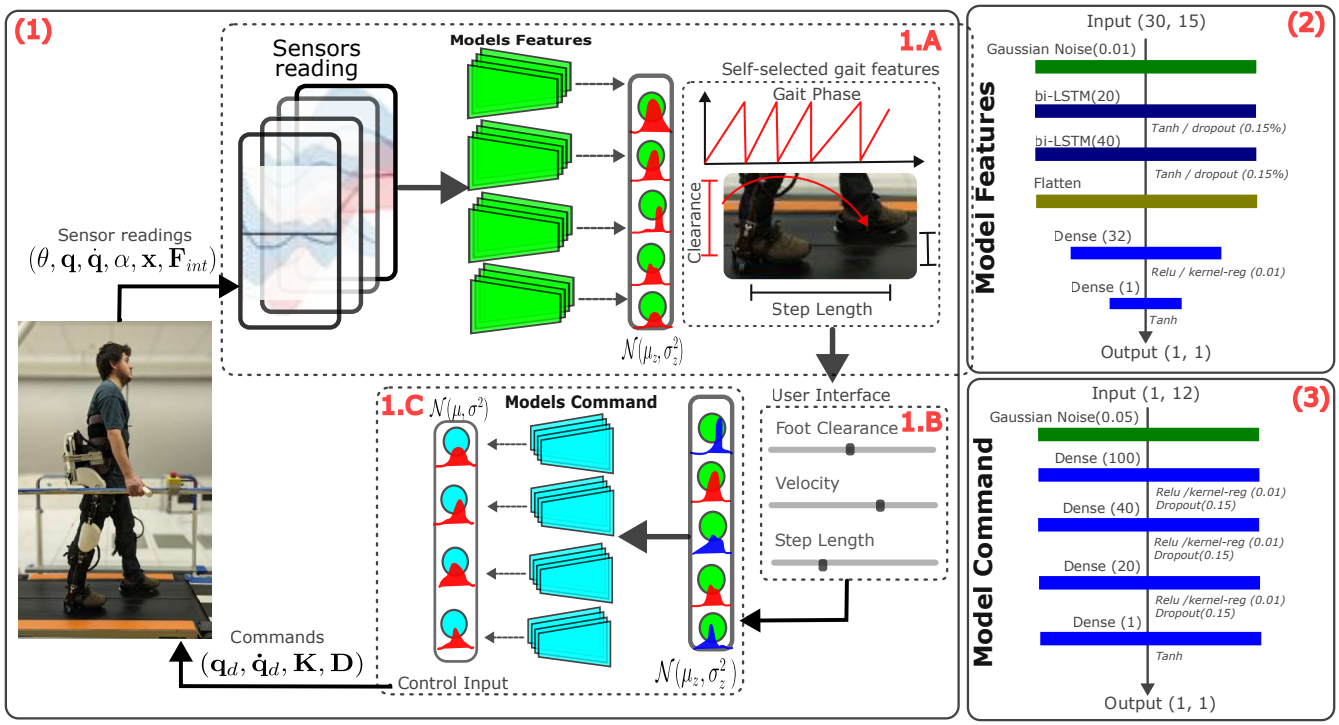


Fig. 1. (1) Data-driven controller:(1.A) Sensor readings are passed to multiple deep-learning models to estimate representative features of the walking pattern. Thes resulting features are fitted to a normal distribution to consider the uncertanty of the locomotion pattern; (1.B) User interface allows to modify the self-selected locomotion features to allow the therapist to adapt the locomotion depending on the needs of each patient; (1.C) The resulting modified features are passed to a combination of models to regress the desired joint configuration of the exoskeleton. At the same time, the uncertainty of the prediction is propagated and used to model the stiffness of the impedance controller of the exoskeleton. Impedance parameters are passed to the low-level controller of the exoskeleton as commanded input. (2) Structure of the feature extractors models. (3) Structure of the command predictor models.

For this reason, in this work, we propose a three-step data-driven approach to substitute the hierarchical structure of an exoskeleton controller (Fig. 1). In step (1) we probabilistically regress a short-term history of sensor readings (encoders, force sensors, foot-plate sensors) with a minimal set of clinically relevant gait features, namely step length, and height (to distinguish across ascending/descending surfaces), walking velocity, step clearance, gait phase; in step (2) we allow an operator (e.g., a physical therapist) to modify the self-selected gait features using a user interface and, finally in step (3) we probabilistically regress the current locomotion features to the desired joint posture of the exoskeleton, using prediction uncertainty to model the impedance in a spring-damper system connecting the user and exoskeleton.

II. METHODS

In this section, we present the structure of the proposed approach. In Sec.II-A, we present the hardware used. In Sec. II-B, we present how we collected data for training the deep-learning models. In Sec. II-C, we define the structure of the two consecutive models implemented to regress sensor readings and gait features and, subsequently, gait features with command inputs. Finally, Sec. II-D presents the real-time use of the proposed approach and the walking tests performed for validation.

A. Exoskeleton

We validated the proposed approach on a commercially available lower-limb exoskeleton (ExoMotus-X2, Fourier Intelligence, Singapore). The exoskeleton system has four active degrees of freedom (DoF) bilaterally at the hip and knee, and two passive DoFs at the ankle (Fig. 1). The following sensors are used to monitor both the exoskeleton's state and its interaction with the user [12]: joint encoders measure the positions of the knee and hip angles (θ) while strain gauges estimate interaction torque (τ_{int}) at each joint. An Inertial Measurement Unit (IMU) on the backpack measures the orientation of the trunk (θ_{bp}), while force-sensitive resistor (FSR) footplates measure ground reaction forces to quantify the weight distribution of the user (α). Communication between motors and sensors is achieved using CAN protocol. The controller is implemented on a ROS and C++ based open-source platform called the CANOpen Robot Controller (CORC) [13]; motor torque commands and sensor readings were updated at 333 Hz. The exoskeleton was controlled using an impedance controller that models the desired interaction torque passed to the exoskeleton internal controller, described in [12]:

$$\tau_{\text{int}}^{*} = K(\boldsymbol{\theta} - \boldsymbol{\theta}_d) + D(\dot{\boldsymbol{\theta}} - \dot{\boldsymbol{\theta}}_d), \tag{1}$$

where $K, D, \boldsymbol{\theta}_d, \dot{\boldsymbol{\theta}}_d$ are respectively the stiffness, damping, and the reference position and velocities returned by the data-

driven controller as discussed in Sec. II-D.

B. Data collection and processing

We collected data from nine healthy participants (5 males, 4 females, age 29.8±6.8, height 1.74±0.08 m, weight 70±10.6 kg) to train the deep-learning model. The Institutional Review Board of Northwestern University approved this study (STU00212684), and all procedures followed the Declaration of Helsinki. Participants performed various ambulatory activities while wearing the exoskeleton in two different controller conditions: haptic transparency (i.e., no assistance) [12] and state machine approach (i.e., non-zero assistance). In the state machine approach, the high-level controller was modeled using a remote (to switch between walking, ramps, or stairs). In the middle-level controller, the locomotion activities were split into four phases (early-stance, late-stance, early-swing, late-swing). For each of these phases, an equilibrium angle was selected and passed to an impedance controller. For each controller condition, participants performed five repetitions of overground walking (6 meters), three repetitions of stairs and ramps, both ascending and descending.

Data was processed offline to extract the *gait-phase* ($\boldsymbol{gp}$) for both legs, a continuous value from $[0, 100]$ indicating progression between consecutive heel strikes. To consider the periodicity of the gait phase, we transformed this value to its polar representation ($\boldsymbol{c}^{gp} = \cos(2\pi\frac{\boldsymbol{gp}}{100}), \boldsymbol{s}^{gp} = \sin(2\pi\frac{\boldsymbol{gp}}{100})$) [14]. The horizontal and vertical foot position relative to the stance foot ($x_k, z_k | k \in [0, 100]$) was calculated via forward kinematics and used to estimate descriptive features of the gait for each stride. The following features were extracted: landing step-height, landing step-length, step-clearance, and step-velocity. *Landing step-height* ($\boldsymbol{h}$) is the vertical position of the forward foot at the end of the stride ($\boldsymbol{h} = z_{100}$), this feature changes significantly when transitioning to a new locomotion mode (e.g. from overground walking to stairs) and is positive in the case of ascending and negative in descending strides. *Landing step-length* ($\boldsymbol{l}$) is the horizontal position of the forward foot at the end of the stride ($\boldsymbol{l} = x_{100}$) and represents the distance of the performed stride. *Step clearance* ($\boldsymbol{c}$) is the maximum vertical position reached from the feet during the stride $\boldsymbol{c} = \max_{[0,100]}(z_k)$. *Step-velocity* ($\boldsymbol{v}$) is the ratio between the step-length and the time required to execute the step ($\boldsymbol{v} = \frac{x_100}{\Delta t}$). All of these features were calculated for both the left and right gait phases. Robot state $\boldsymbol{q} = (\theta, \dot{\theta}, \theta_{bp}, \tau_{int}, \alpha, x_{l,r}, z_{l,r})$ and gait features $\boldsymbol{f} = (\boldsymbol{c}^{gp}_{l,r}, \boldsymbol{s}^{gp}_{l,r}, \mathbf{h}_{l,r}, \mathbf{l}_{l,r}, \mathbf{c}_{l,r}, \mathbf{v}_{l,r}) \in \mathbb{R}^{12}$ were normalized and sampled to convert from the data logging frequency to 100 Hz. Following these procedures, all data were divided in time windows of 300 ms [15] with a step size of 50ms.

C. Machine Learning Controller

In this section, we will present the two ML-based models designed to reduce the complexity of the hierarchical structure. The controller uses a data-driven approach to extract locomotion parameters representing a normative population without additional calibration procedures. Moreover, it allows therapists to modify movement execution in real-time, allowing safer and more structured adaptability to the specific needs of each patient.

Our approach is based on two consecutive neural networks (NN): (1) a Features Extractor Model (FEM), and (2) a Command Predictor Model (CPM). Both models provide probabilistic estimates of the output, enhancing the predictions with information about the associated uncertainty.

a) Features Extractor Model: Our FEM (Fig. 1.1.A) is based on two bidirectional Long Short-Term Memory (bi-LSTM) networks. The model uses a time window W of robot states ($x_1(t) = [\boldsymbol{q}_{t-T_W}, ..., \boldsymbol{q}_{t-t_1}, \boldsymbol{q}_t]$) as input and returns the current features representation of the step $y_1(t) = \hat{\boldsymbol{f}}_t$ as an output. These features represent the current locomotion intention of the user wearing the exoskeleton; we define them as *self-selected* to distinguish them from those selected by the therapist.

The architecture of the FEM is displayed in Fig. 1.A: the model receives a time-window W of dimension 30 of sensor readings and foot positions with a resulting dimension of the input $(30, 15)$. Gaussian noise (standard deviation of 0.01) is used in the first layer to introduce variability to the input data (x_t), allowing better generalization. Two bi-LSTM layers allow the model to learn dependencies between the different time steps in the window of data. The output of the second bi-LSTM model is flattened and passed to two consecutive dense layers that transform the features extracted from the bi-LSTMs to a single value representing each feature independently. A *Tanh* activation function is used to bound features in the range of $[-1, 1]$. Each feature is regressed using an independent model to avoid correlation across features. Hyperparameters were selected using a heuristic approach. The model was trained with the ADAM optimizer, employing the MSE loss function to quantify and minimize the difference between the predicted and actual values. Training proceeded for 100 epochs with early stopping, using batches of 256 samples.

b) Command Predictor Model: The second model (Fig. 1.1.C) receives as input the ground truth features extracted as described in Sec. II-B ($x_2(t) = \boldsymbol{f}_t$) and returns the expected joint kinematics $y_2(t) = (\hat{\boldsymbol{\theta}}_t, \hat{\dot{\boldsymbol{\theta}}}_t)$ as an output. Data augmentation was applied before training by weighted interpolation of both features and kinematics based on the features' Euclidean distances to create a more evenly distributed feature space. For example, we interpolated features from stair ascending and overground walking to generate intermediate feature values, such as moderate step heights.

The structure of the Command Predictor Model is displayed in Fig. 1.C. The model receives input of dimensionality $(1, 12)$ containing the current features and applies Gaussian noise (standard deviation of 0.01) in the first layer to introduce variability. Then, four consecutive dense layers with reduced dimensions, dropout, and kernel regularization transform the features to a single value representing either the joint position or velocity. Also, in this case, a *Tanh* activation function is used to bound the output in the range of $[-1, 1]$

and then rescaled in the same domain of the kinematics values. Each feature is regressed using an independent model to avoid correlation across features. Hyperparameters were selected using a heuristic approach. A training procedure similar to those of the Feature extraction models was applied.

c) Probabilistic estimation: To have a probabilistic estimation in both layers of the process, six independent NN were trained in parallel using six randomly selected subsets of users. This allows us to estimate and utilize the uncertainty of the predictions. For instance, in the early phases of the swing movement, there will be more uncertainty about the resulting foot placement, resulting in uncertainty in the joint kinematics. With a probabilistic estimation of the features followed by the kinematics, we can model this uncertainty. To propagate the uncertainty across the two phases, we used a Monte-Carlo approach similar to [16]: the normal distribution is used to randomly sample N values from the distribution which are passed to the model as a unique batch; the batch of output was fitted to a normal distribution and propagated to the next step of the framework.

All models presented were trained using TensorFlow (v2.15.0, Google) and converted to TensorFlow Lite (v2.13.0, Google) for real-time inference.

D. Real-time inference and validation

a) Real-time inference: The structure of the real-time inference is displayed in Fig. 1. A Python script performing these inferences runs in parallel to the exoskeleton controller running in C++; the two programs communicate through ROS. The script (python3 `concurrent.futures`) calls the multiple FEM Lite models in parallel. The outcome of this first phase (Fig. 1.1.A) is a batch of inferences of $\hat{\boldsymbol{f}}_i | i \in (0, 6)$. The mean and the standard deviation of the extracted features are calculated by fitting the prediction using a normal distribution ($\hat{\boldsymbol{f}} \sim \mathcal{N}(\mu_f, \sigma_f^2)$). At this point (Fig. 1.1.B), the operator (or therapist) can choose to manually change one of the features using a simplified interface designed using ROS `rqt`. This choice is implemented as the self-selected mean of the features (μ_f). Another parameter that can be manually adjusted is an increment δ, which is added to the mean of the gait phase. This adjustment results in an anticipation of the user's movement by δ instants, enabling the exoskeleton to deliver proactive assistance[1].

The distribution $\hat{\boldsymbol{f}} \sim \mathcal{N}(\mu_f, \sigma_f^2)$ is used to sample a normally distributed batch of features and passed to the CPM model. Also, in this case, the inference on multiple CPM Lite models is executed in parallel and the multiple outputs are fitted to a second normal distribution representing the expected δ future joint kinematic and its uncertainty $(\hat{\boldsymbol{\theta}}, \hat{\dot{\boldsymbol{\theta}}}) \sim \mathcal{N}(\mu_{\boldsymbol{\theta},\dot{\boldsymbol{\theta}}}, \sigma^2_{\boldsymbol{\theta},\dot{\boldsymbol{\theta}}})$. These values are passed as references to the exoskeleton controller (Eq. 1). In particular, the desired angle and velocity were chosen as equal to the mean of the prediction $\boldsymbol{\theta}_d, \dot{\boldsymbol{\theta}}_d = \mu_{\boldsymbol{\theta}}, \mu_{\dot{\boldsymbol{\theta}}}$, while stiffness and damping parameters were selected proportional to the inverse of the standard deviation similarly to [17]:

$$\boldsymbol{K} = \boldsymbol{K}_S(1 - \frac{\sigma_{\boldsymbol{\theta}}}{\sigma_{\max}}) \quad \text{with } \frac{\sigma_{\boldsymbol{\theta}}}{\sigma_{\max}} > 0, \tag{2}$$

$$\boldsymbol{D} = \boldsymbol{D}_S(1 - \frac{\sigma_{\dot{\boldsymbol{\theta}}}}{\sigma_{\max}}) \quad \text{with } \frac{\sigma_{\dot{\boldsymbol{\theta}}}}{\sigma_{\max}} > 0 \tag{3}$$

where $\sigma_{\max}$ was selected as the maximal uncertainty across the validation set while we assigned $K_S = [80, 60]$ Nm/rad, $D_S = [8, 6]$ Nm·s/rad for the hip and knee joints. These values were selected in line with previous work identifying impedance parameters during walking [9], [18]. The full inference process takes approximately 20ms, corresponding to a frequency of about 50Hz. The exoskeleton controller updates its reference whenever a new inference is available, while continuously streaming sensor readings at a frequency of approximately 333Hz.

b) Validation: The proposed framework was validated on two healthy participants external to the dataset used to train the two models. Participants gave informed consent for their participation. The study protocol was conducted in accordance with the Declaration of Helsinki and approved by the institutional review board of Northwestern University (STU00212684). The two users performed 15 minutes of treadmill walking and five iterations of stairs ascending and descending. We tested various parameters (i.e., changes in operator-selected features, changes in treadmill speed) to validate the proposed approach by manually changing these parameters during the 15 minutes of walking.

III. Results and Discussion

In this section, we present and discuss the results collected in this study. First, we evaluate the offline performance of the two models (FEM and CPM). Next, we present online results demonstrating the proposed controller's ability to assist user locomotion across different locomotion patterns. The results are evaluated using joint kinematics and interaction power metrics for two users.

Fig. 3 displays the prediction of gait features for two of the nine users used to develop the FEM and CPM model (seven users for training, two users for validation). The mean absolute error for the features is around a few centimeters (step height 3.1 ± 5.0cm, step length 2.6 ± 2.0cm, step velocity 1.6 ± 1.1cm/s, step clearance 2.7 ± 1.9cm). Nonetheless, as shown in Fig. 3, the prediction exhibits oscillations caused by uncertainty during the early-swing phase. Moreover, a limitation of the current approach is the need to identify a set of gait features that adequately capture the complexity of the walking pattern while maintaining clinical relevance. Walking patterns are highly subjective and can vary even for the same user, as shown by a moderate regression accuracy (R^2=0.68) between the predicted and desired joint kinematics on the validation set using the CPM. In preliminary tests, we included additional user characteristics (e.g., body weight and height) and features derived using auto-regressive techniques. However, these modifications did not result in additional variance explained (R^2=0.68). To

[1]It is important to note that δ is a-dimensional because it represents an increment of the gait phase and additional attention is needed to keep the resulting gait phase in the range [0, 100].

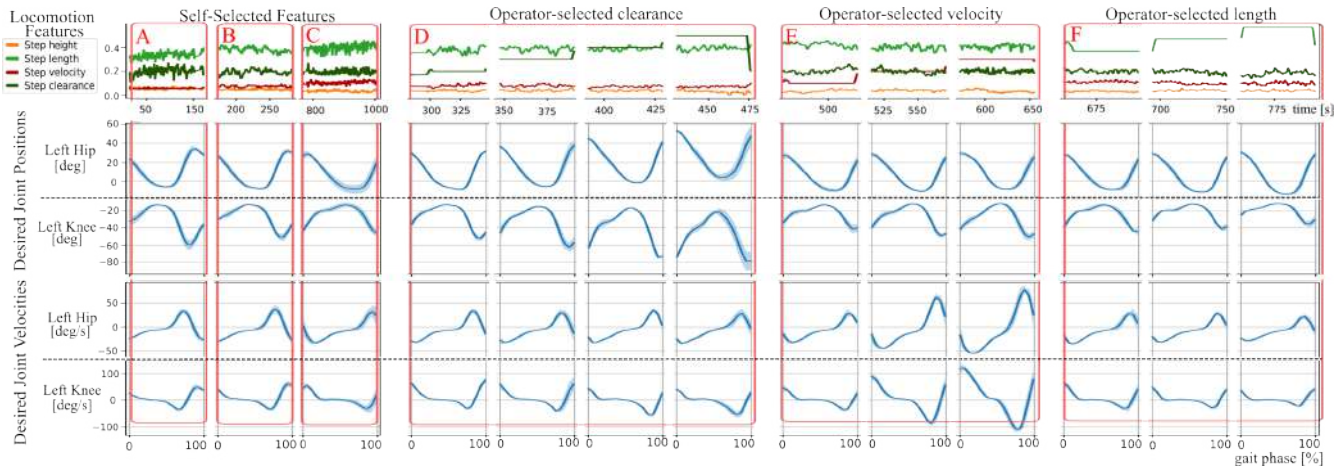


Fig. 2. Example of walking pattern for a single subject. In order, the five rows show: the implemented features (self-selected or operator-selected) over time [s], the reference position for the left hip and left knee, and the reference velocities for left hip, and left knee over the left stride percentage [%]. During the trial the user performed: (A) walking with exoskeleton controlled in transparency (self-selected features are not used to close the control loop) with treadmill velocity equal to 0.14 m/s; (B) Self-selected features used to close the loop of the controller; (C) walking with self-selected features on the treadmill at 0.19 m/s; (D) Operator-selected step clearance; (E) Operator-selected step velocity (at the same time increasing the treadmill velocity to 0.19 m/s); (F) Operator-selected step length.

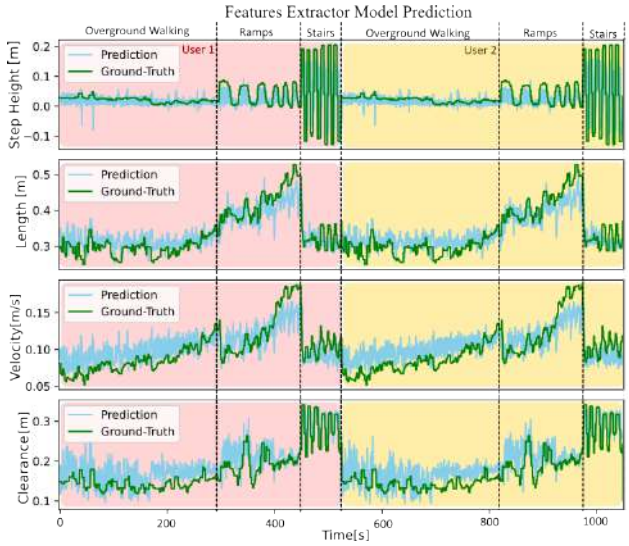


Fig. 3. Example of gait feature prediction. The plot displays the ground truth (in green) and the prediction of the Features Extractor Model (in blue) for two users in the training dataset over time (in seconds). Each user (user 1 in pink, user 2 in yellow) performed in order overground walking, ramps (both ascending and descending), and stairs(both ascending and descending). In order top-down the following features are displayed: step height, step length, step velocity, and step clearance.

address this, we adopted a probabilistic approach (II-C.0.c) for real-time prediction, which models the uncertainty in gait phases where variability is more prominent. This uncertainty was then used to adapt the compliance of the exoskeleton controller. Future research should focus on integrating additional locomotion features to further enhance the model's predictive capabilities.

Fig. 2 displays an example of a healthy user performing 15 minutes (for a total of 300 strides) of treadmill walking in different conditions. During the first three minutes (Fig.2.A), the user walked at a constant velocity of 0.14 m/s with their self-selected gait pattern while the exoskeleton was controlled in transparency. This first period of walking allows us to verify that the FEM can predict the gait features in an open loop. After predicting these self-selected gait features, we provide closed-loop control by using these features as input to the CPM (Fig.2.B). The user then walked for two minutes with exoskeleton assistance provided towards their self-selected features. We can observe that closing the loop of the controller (passing from A to B) resulted in an increased step-length (row 1 light-green plots) and step-velocity (row 1 red plot). This is likely due to the assistance the user receives during the movement. A similar trend can be observed in the following three minutes in which the velocity of the treadmill was increased to 0.19 m/s to validate its effect on the self selected features (Fig.2.C).

After testing the self-selected features, the operator manually selected the features to evaluate their effects on the participants' walking patterns. Shown in Fig.2.D, we observe how increasing the step-clearance results in a larger range of motion (ROM) in all kinematic trajectories (θ_d) for both the hip (second row) and the knee (third row). In a similar way, in Fig. 2.E, we observe the impact of increasing the step-speed, corresponding to an increase in the joint velocities ($\dot{\theta}_d$) both for the hip (fourth row) and the knee (fifth row). To account for the increased speed of the user, the velocity of the treadmill was increased from 0.14 m/s to 0.19 m/s and kept constant until the end of the experiment. Finally, in Fig. 2.F, the step length was increased. This resulted in an increased ROM for the hip joint angle (θ_d) and a smaller ROM for the knee angle, likely due to smaller knee flexion during swing movement to increase step-length.

Fig.4 shows the distribution of the joint configurations (hip and knee joint) of the two users across the different gait features. We observed that all features impact both the spatial

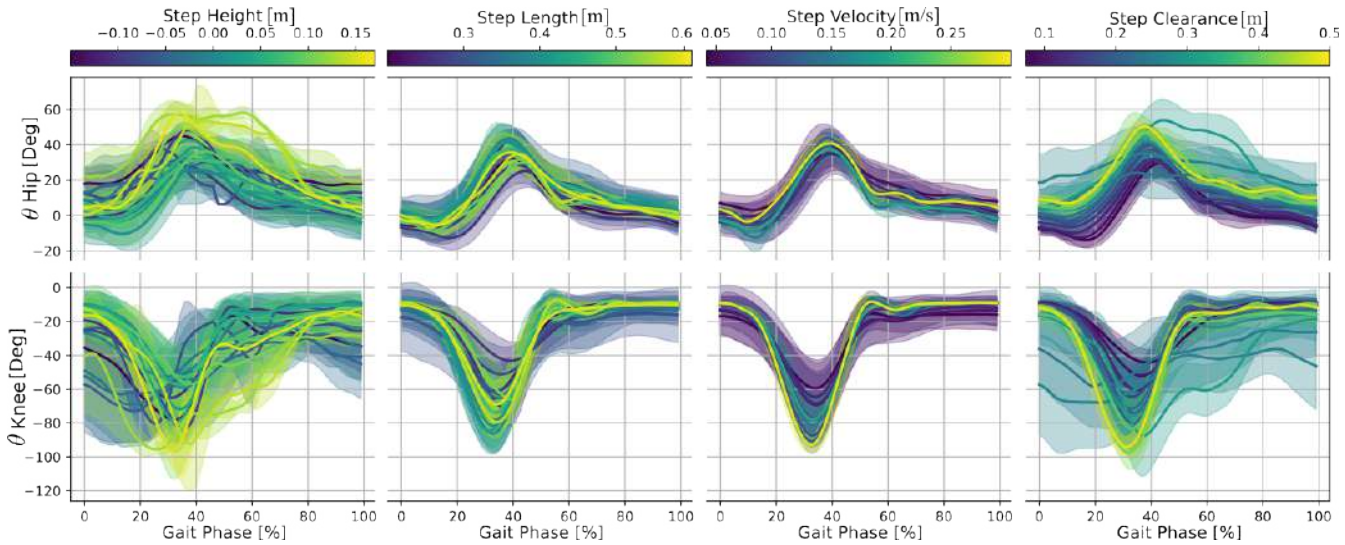


Fig. 4. Joint kinematic across gait features (both self-selected and operator-selected): The two rows display respectively the hip and knee joint angles (left and right grouped). Each column represents with a different color code the distribution of the joint kinematic for each gait feature (step-height, step-length, step-velocity, step-clearance). On the top of each column are displayed the color bars for each gait feature. The trend was grouped based on similarities in gait features and is presented using the mean and standard deviation.

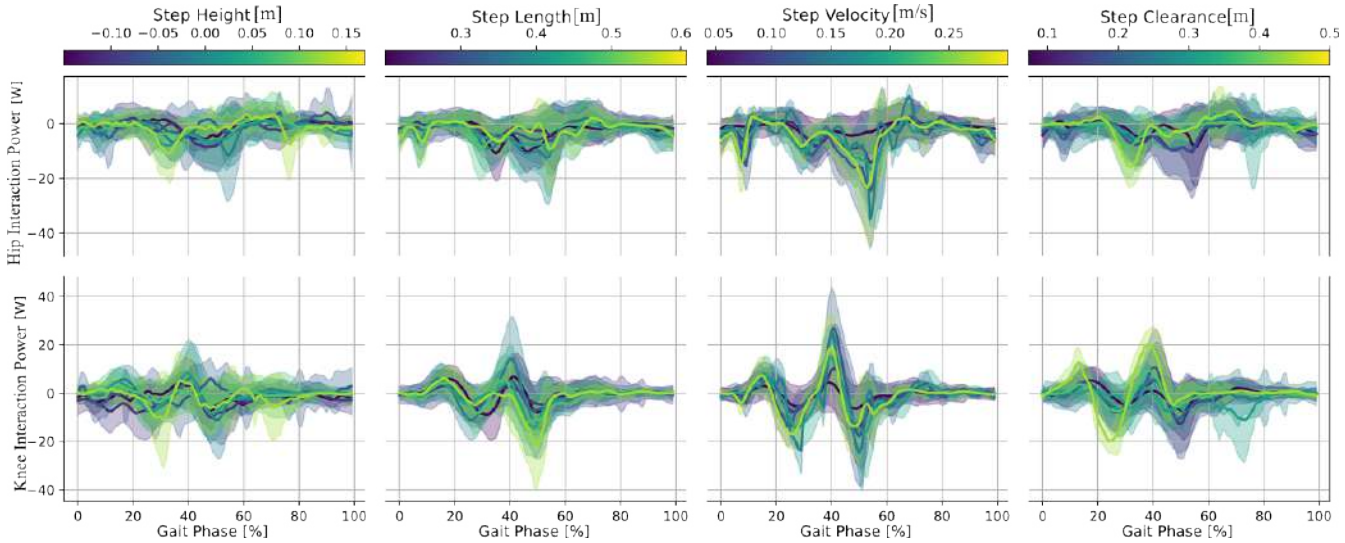


Fig. 5. Joint power across gait features (both self-selected and operator-selected): The two rows display the hip and knee joint power (left and right grouped). Each column display with a different color code the distribution of the desired joint kinematic for each gait feature (step-height, step-length, step-velocity, step-clearance).On the top of each column are displayed the color bars for each gait feature. The trend was grouped based on similarities in gait features and is presented using the mean and standard deviation. Negative joint power means exoskeleton assistance to the user while positive joint power represents resistance to the user.

and temporal aspects of the walking pattern. For instance, the step length highly influences the ROM (an increase to a step length of 0.34 m results in a increase of ROM of 20° for the hip and 40° for the knee). During these preliminary experiments, we observed an under-damped behavior of the exoskeleton during the early-stance phase (around 60% of the gait phase). This behavior could be due to two reasons: the impact of training data of stairs (after heel strike during stairs, the knee is more extended than in level-ground walking) or the independence in prediction across joint positions and velocities resulting in uncorrelated stiffness and damping parameters as they were calculated independently (Eq. 2). Further investigation is required to address these limitations.

Fig. 5 displays the interaction power ($\tau_{int} \cdot \dot{\theta}$), calculated as a product of the interaction torque and joint velocities. This metric represents the amount of assistance (negative values) or resistance (positive values) that the exoskeleton applied to the user. This metric is displayed for the two joints (hip and knee, grouped) across the two rows, and varying the gait features (across columns). For the hip joint, the interaction power is negative (assistive torque) in most conditions (mean interaction power ($\pm$ std) in all gait phases -2.05 $\pm$ 1.6W. For

the knee, the joint interaction power is also negative (-0.6 $\pm$ 1.39W) in most of the gait phase with two peaks of negative interaction power during the swing phase in knee flection (around 30% of the gait phase) and during both hip and knee extension (around 50-55% of the gait phase). This suggests that, during swing, the robot is actively assisting the user to execute the movement. On the other hand, two positive peaks were observed at the beginning of the early-swing and the beginning of the late-swing (respectively around 15% and 40% of the gait cycle). This can be due to several factors, but most importantly the users were blinded to the gait features manually selected by the operator and thus the nature of the assistance provided. Consequently, they were not aware of how much they should flex the knee during the swing phase. Moreover, they performed each activity for a few minutes, resulting in a limited time to adapt to each condition. Therefore, longer validation sessions are likely required to prove the efficacy of minimizing the interaction power across users.

IV. Conclusions

In this work, we present a three-step data-driven approach designed to replace the hierarchical structure of traditional exoskeleton controllers. The first step involves probabilistically mapping a short-term history of sensor data (including encoders, force sensors, and foot-plate sensors) to a minimal set of clinically relevant gait features: step length, height (to differentiate ascending and descending surfaces), walking velocity, step clearance, and gait phase. These features can either be applied directly or adjusted by an operator/therapist via a user interface to customize the user's locomotion. The final step uses probabilistic regression to map the current locomotion features to the desired joint posture of the exoskeleton, leveraging prediction uncertainty to adapt the impedance of a spring-damper system linking the user and the device. This adaptive compliance enhances safety, limiting large desired interaction torques when the prediction of the user's behavior is less accurate. Validation on two healthy users across diverse gait activities demonstrated the ability of the proposed approach to detect user intent and provide assistance accordingly, generating predominantly negative interaction power between the user and the exoskeleton. Future work will explore the selection of additional clinically relevant features in collaboration with therapists to ensure that they align with practical rehabilitation needs. Additionally, more extensive studies involving patient populations (e.g., stroke, spinal cord injury) are necessary to evaluate the impact of these assistive strategies on individuals with gait impairments.

Acknowledgment

This work was supported by the National Science Foundation / National Robotics Initiative (Grant No: 2024488). We would like to thank Tim Haswell for his technical support on the hardware improvements of the ExoMotus-X2 exoskeleton.

References

[1] R. Baud, A. R. Manzoori, A. Ijspeert, and M. Bouri, "Review of control strategies for lower-limb exoskeletons to assist gait," *Journal of NeuroEngineering and Rehabilitation*, vol. 18, no. 1, pp. 1–34, 2021.

[2] T. Vouga, R. Baud, J. Fasola, M. Bouri, and H. Bleuler, "Twiice—a lightweight lower-limb exoskeleton for complete paraplegics," in *2017 International Conference on Rehabilitation Robotics (ICORR)*. IEEE, 2017, pp. 1639–1645.

[3] N. L. Tagliamonte, F. Sergi, G. Carpino, D. Accoto, and E. Guglielmelli, "Human-robot interaction tests on a novel robot for gait assistance," in *2013 IEEE 13th international conference on rehabilitation robotics (ICORR)*. IEEE, 2013, pp. 1–6.

[4] J. de Miguel-Fernández, J. Lobo-Prat, E. Prinsen, J. M. Font-Llagunes, and L. Marchal-Crespo, "Control strategies used in lower limb exoskeletons for gait rehabilitation after brain injury: a systematic review and analysis of clinical effectiveness," *Journal of NeuroEngineering and Rehabilitation*, vol. 20, no. 1, Feb. 2023.

[5] E. Basalp, P. Wolf, and L. Marchal-Crespo, "Haptic training: Which types facilitate (re)learning of which motor task and for whom? answers by a review," *IEEE Transactions on Haptics*, vol. 14, no. 4, pp. 722–739, 2021.

[6] M. Kim, A. M. Simon, and L. J. Hargrove, "Seamless and intuitive control of a powered prosthetic leg using deep neural network for transfemoral amputees," *Wearable Technologies*, vol. 3, 2022.

[7] C. Lhoste, E. B. Küçüktabak, L. Vianello, L. Amato, M. R. Short, K. M. Lynch, and J. L. Pons, "Deep-learning estimation of weight distribution using joint kinematics for lower-limb exoskeleton control," *IEEE Transactions on Medical Robotics and Bionics*, pp. 1–1, 2024.

[8] A. M. Simon, K. A. Ingraham, N. P. Fey, S. B. Finucane, R. D. Lipschutz, A. J. Young, and L. J. Hargrove, "Configuring a powered knee and ankle prosthesis for transfemoral amputees within five specific ambulation modes," *PloS one*, vol. 9, no. 6, p. e99387, 2014.

[9] T.-H. Huang, S. Zhang, S. Yu, M. K. MacLean, J. Zhu, A. Di Lallo, C. Jiao, T. C. Bulea, M. Zheng, and H. Su, "Modeling and stiffness-based continuous torque control of lightweight quasi-direct-drive knee exoskeletons for versatile walking assistance," *IEEE Transactions on Robotics*, vol. 38, no. 3, pp. 1442–1459, 2022.

[10] T. K. Best, C. G. Welker, E. J. Rouse, and R. D. Gregg, "Data-driven variable impedance control of a powered knee–ankle prosthesis for adaptive speed and incline walking," *IEEE Transactions on Robotics*, 2023.

[11] D. D. Molinaro, K. L. Scherpereel, E. B. Schonhaut, G. Evangelopoulos, M. K. Shepherd, and A. J. Young, "Task-agnostic exoskeleton control via biological joint moment estimation," *Nature*, vol. 635, no. 8038, pp. 337–344, 2024.

[12] E. B. Küçüktabak, Y. Wen, S. J. Kim, M. R. Short, D. Ludvig, L. Hargrove, E. J. Perreault, K. M. Lynch, and J. L. Pons, "Haptic transparency and interaction force control for a lower limb exoskeleton," *IEEE Transactions on Robotics*, vol. 40, pp. 1842–1859, 2024.

[13] J. Fong, E. B. Küçüktabak, V. Crocher, Y. Tan, K. M. Lynch, J. L. Pons, and D. Oetomo, "Canopen robot controller (corc): An open software stack for human robot interaction development," in *Wearable Robotics: Challenges and Trends*. Cham: Springer International Publishing, 2022, pp. 287–292.

[14] M. Kim and L. J. Hargrove, "A gait phase prediction model trained on benchmark datasets for evaluating a controller for prosthetic legs," *Frontiers in Neurorobotics*, vol. 16, p. 1064313, 2023.

[15] F. Labarrière, E. Thomas, L. Calistri, V. Optasanu, M. Gueugnon, P. Ornetti, and D. Laroche, "Machine learning approaches for activity recognition and/or activity prediction in locomotion assistive devices—a systematic review," *Sensors*, vol. 20, no. 21, 2020.

[16] L. Vianello, J.-B. Mouret, E. Dalin, A. Aubry, and S. Ivaldi, "Human posture prediction during physical human-robot interaction," *IEEE Robotics and Automation Letters*, vol. 6, no. 3, pp. 6046–6053, 2021.

[17] G. Franzese, A. Mészáros, L. Peternel, and J. Kober, "Ilosa: Interactive learning of stiffness and attractors," *arXiv preprint arXiv:2103.03099*, 2021.

[18] A. Ortlieb, R. Baud, T. Tracchia, B. Denkinger, Q. Herzig, H. Bleuler, and M. Bouri, "An active impedance controller to assist gait in people with neuromuscular diseases: Implementation to the hip joint of the autonomyo exoskeleton," in *2018 7th IEEE International Conference on Biomedical Robotics and Biomechatronics (Biorob)*, 2018.

Brain biomarkers for assessing practice of robotic arm reaching movements using a head-controlled interface

Anna L. Packy*, Isabelle M. Shuggi*, Hyuk Oh, Rodolphe J. Gentili
*Co-first author

Abstract—**Limited efforts have examined the cognitive-motor processes as individuals learn to operate upper-limb assistive devices that improve interactions in their environment (e.g., prostheses, head-controlled devices). Prior work mainly focused on performance without examining cerebral cortical dynamics via brain biomarkers to assess the level of practice during the learning of such assistive devices. Specifically, it was suggested that EEG biomarkers like low- and high-beta spectral power are related to learning as they assess memory formation and attentional mechanisms. Therefore, this work examines how sensorimotor performance, and low-/high-beta spectral power are influenced as individuals without disabilities practice reaching movements with a simulated robotic effector executed via a head-controlled interface. Results revealed faster and straighter reaching movements. Additionally, as individuals progressed from early to late practice, the movement planning stage revealed an elevation of frontal, central and parietal low-beta power and an attenuation of high-beta power in the temporal region. These spectral modulations may reflect an internal model memory encoding process of the novel sensorimotor mapping imposed by this interface throughout practice which ultimately enables improved reaching performance. This work could inform patients' cognitive-motor processes when learning to control assistive systems and provide biomarkers for monitoring practice during rehabilitation.**

I. Introduction

An important characteristic of the human cognitive-motor system is its ability to process information to learn new sensorimotor skills when facing changes in the body or environment [1]. As such, a large body of work has examined the underpinning cognitive-motor mechanisms of upper-extremity performance when individuals without disabilities practice a new motor task [2-4; for review see 5]. In contrast, a limited effort has investigated the cerebral cortical dynamics underlying performance changes in a rehabilitation context where individuals must learn to operate upper-limb assistive devices (e.g., prostheses, exoskeletons, head-controlled systems) [6-7]. In such a context, while prior efforts have examined cortical dynamics when individuals perform using assistive technologies, these studies did not focus on practice [8-10]. Furthermore, although previous work investigated performance when individuals learn to operate assistive devices such as upper-limb prostheses [11-13] or a head-controlled robotic device [14-18] the cerebral cortical dynamics were not analyzed. However, the assessment of both behavioral performance and cortical dynamics is important. For instance, while the performance can improve during practice, an absence of refinement of cortical dynamics would indicate that the brain is still engaging substantial resources to execute the task. Thus, the understanding of the cognitive-motor processes engaged during sensorimotor learning is a key element to identifying progress in patients operating assistive systems more comprehensively, beyond behavior analysis alone and, as such, their examinations are critical from both a theoretical and a practical standpoint [19-21].

A possible approach to examine the cerebral cortical dynamics underlying sensorimotor learning is to derive electroencephalography (EEG) biomarkers. In particular, multiple prior efforts revealed that the changes in spectral power in the beta frequency bandwidth could serve as a biomarker to index sensorimotor learning [19, 22-25]. Namely, it was suggested that a greater level of low-/high-beta or broadband beta power has been associated with improved performance during learning [19, 26-27]. Specifically, it was suggested that an elevation of beta power during practice indicates that: i) learning processes would take place through changes in cortical pathways resulting in memory formation [19, 22-23, 26] and ii) there is a refinement of attentional mechanisms, especially in the frontal regions [23, 27].

Although interesting, the examination of these EEG biomarkers in a context where individuals learn how to control assistive systems is limited. From a computational standpoint when individuals learn to operate an assistive device (e.g., upper-limb prosthesis; head-controlled robotic arm) they must encode a sensorimotor mapping via a human-body machine interface which involves body parts that are used differently from their traditional functions and thus are not well-suited to execute the tasks [14, 16, 28-29]. An example of such a human-body machine interface is a head-controlled robotic arm which requires individuals to encode a sensorimotor mapping between their limited angular head motion and the spatial displacements of the robotic end-effector. This unusual sensorimotor map requires the use of neck muscles which have a limited communication channel making them not naturally suited for executing accurate reaching movements [30-31]. As such, the encoding of this unnatural sensorimotor mapping to control the device requires, like many assistive systems, practice from participants [14-16, 32-34].

Therefore, by combining behavioral performance and EEG biomarkers, this study aimed to examine the cognitive-motor processes underlying practice of a novel sensorimotor

A. L. Packy (apacky@umd.edu) and I. M. Shuggi (ishuggi@terpmail.umd.edu) are with the Neuroscience and Cognitive Science Program, University of Maryland, College Park.

H. Oh (hyukoh@umd.edu) and R. J. Gentili (phone: 301-405-2490; fax: 301-405-5578; e-mail: rodolphe@umd.edu) are with the Department of Kinesiology, University of Maryland, College Park.

mapping by individuals to control a head-controlled robotic effector with limited head motion. We predicted that from early to late practice, individuals will exhibit improved reaching movement performance with the robotic effector along with an elevation of low-beta and high-beta power. This work has the potential to inform the cognitive-motor processes and provide biomarkers when individuals learn to use assistive robotic systems.

II. Methods and Materials

A. Participants

Eighteen individuals without disabilities, right-handed, participants (10 female, 8 male; age range: 18-35 years) with no prior experience of using head-motion controlled systems were recruited from the University of Maryland, College Park. All participants provided written informed consent before participation, in accordance with the Institutional Review Board of the University of Maryland.

B. Task

Participants used a human-body machine interface to complete a reaching task. The goal was to move the end-effector of a two-dimensional virtual robotic arm with two degrees of freedom to a spatial target by employing limited head motion. The effector and targets were displayed on a 21-inch screen approximately 24 inches away from the participants. An infrared sensor was placed on the participant's forehead and tracked head movements using a motion capture system captured at 100Hz (Optotrak™ 3020, NDI). The overall system was configured to operate at a sampling rate of 100 Hz. Participants were able to move their head in eight directions: vertical (pitch), horizontal (yaw), and combinations of these axes, to control the end-effector using a closed-loop inverse kinematic algorithm using a proportional integral control system. The movement velocity of the end-effector was proportional to the magnitude of the head displacement (Fig.1) (for further details, see [15]).

Each participant conducted a calibration phase to determine their range of head motion and a "dead zone" threshold below where no movement was registered. After calibration, participants completed a brief familiarization phase to become acquainted with the interface. Then, they practiced reaching movements by moving the robotic arm to 200 randomly appearing targets, equidistant to the pervious, as fast and as straight as possible [14,16]. After practice, participants executed a transfer task which, for clarity and conciseness, is not reported here.

For each reaching trial, a red target appeared in a random location within the workspace. Participants were required to maintain their head in the central position (i.e., within the dead zone) and take their time to plan the upcoming movement to reach this target. Unknown to the participants, this pre-movement period lasted at least two seconds, after which the target turned green when the participant initiated their movement. Upon reaching the green target, the participant was required to remain at the target for two seconds before the target disappeared and the next appeared. Due to the different mechanisms between planning and execution, if the participant moved outside of the central location before the two seconds elapsed, the target turned black and stayed black until the participant returned to the center position and restarted the trial [2]. Target onset, movement onset, and target reached events were tracked using MATLAB R2014a (The MathWorks, Inc.).

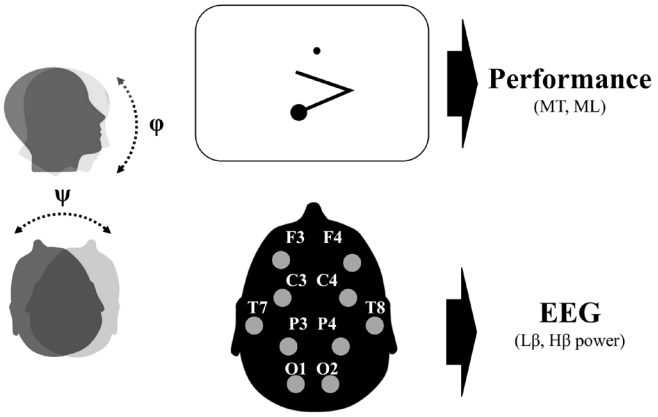


Figure 1. Experimental set-up to study cognitive-motor processes as individuals practice reaching movements with the robotic end-effector in 2D (X,Y) controlled via limited head motions (pitch (φ) and yaw (ψ)). During practice the EEG was collected to derive the low-beta (Lβ) and high-beta (Hβ) spectral power along with performance. MT: Movement Time; ML: Movement Length.

Both the kinematics of the end-effector and EEG signals were continuously recorded throughout the task. EEG signals were sampled at 1000 Hz using a 64-electrode 10-10 actiCAP (Brain Products GmbH). A 10 degrees of freedom inertial measurement unit (IMU), MTw (Xsens Technologies B.V.), was placed on the participant's forehead to capture head movements at 100 Hz for EEG movement artifact removal. For all trials, events were marked within the EEG signals to identify the start (movement onset) and end (target was reached) of the robotic arm movement for subsequent EEG analysis during both the late portion of the movement planning (-1 to 0 sec before movement onset) as well as execution (movement onset to target reached) [2]. The practice period (200 trials) lasted approximately one hour.

C. Data Processing

All data were processed using MATLAB R2014a. The movement time (MT) and length (ML) assessed motor performance of the robotic end-effector and were averaged for the early (50 first trials) and late (50 last trials) practice period [14-16]. The MT was defined as the time elapsed between the movement onset and the reaching of the target. The ML was calculated as the path travelled by the robotic end-effector during the movement.

The EEG signals were processed using EEGLAB v13 [35]. First, EEG signals were band-pass filtered between 3 and 40 Hz with an eighth-order Butterworth filter. EEG channels were manually inspected to reject and interpolate any bad channels. Following interpolation, the signals were down-sampled to 500 Hz (to compare to the up-sampled IMU data; see later). A second-order blind identification (SOBI) independent component analysis (ICA) was performed [36]. Artifacts related to eye, muscle, and channel noise were identified and removed by manual inspection. Head motion artifacts during the execution stage were removed using an ICA approach informed by the IMU data in line with

previous work [36-38]. The infrared system was employed only to control the end effector. In addition to the linear acceleration and angular velocity acquired by the IMU, linear velocity and angular acceleration were employed to identify motion artifacts. These four kinematic signals were filtered using a band-pass eighth-order Butterworth filter between 1 and 10 Hz. This filtered IMU data was up-sampled to 500 Hz to match the down-sampled EEG data and then decomposed into independent components with the SOBI ICA. The EEG components correlated with the IMU components within the lag range from -10 to 10 milliseconds were identified as motion artifacts and removed.

Power spectra in the low-beta (14-22 Hz) and high-beta (23-35 Hz) bands were computed from the Welch's power spectral density for channels over the left and right frontal (F3, F4), central (C3, C4), temporal (T7, T8), parietal (P3, P4), and occipital (O1, O2) regions for both the movement planning and execution stages. The average power values were computed for early and late practice periods. Spectral EEG metrics were naturally log-transformed before conducting statistical analysis.

D. Statistical Analysis

The performance metrics MT and ML were compared between early and late practice periods by means of paired t-test or Wilcoxon signed-rank test depending on whether the data were normally distributed or not, respectively, in which normality was assessed using the Shapiro-Wilk test.

The changes of EEG power from the early to the late practice period during both the movement planning and execution stages were examined using a 2 PERIOD (Early Practice, Late Practice) × 2 HEMISPHERE (Left, Right) × 5 REGION (Frontal, Central, Temporal, Parietal, Occipital) repeated measure ANOVAs conducted separately for the low-beta and high-beta frequency bandwidth. If the sphericity (assessed with the Mauchly test) was violated, the Greenhouse-Geisser correction was applied, and the p-value was reported with the corrected degrees of freedom. Whenever necessary, the Tukey's HSD test was employed for post-hoc analysis. Whenever appropriate the partial-eta squared (η_P^2) and Cohen's d effect sizes were reported. All criterion alpha levels were set to $p < 0.05$.

III. RESULTS

A. Motor Performance

The results revealed that MT ($z = 2.678$; $p = 0.007$; $d = 0.522$) and ML ($t(17) = 3.027$; $p = 0.008$; $d = 0.705$) decreased as practice progressed (Fig. 2).

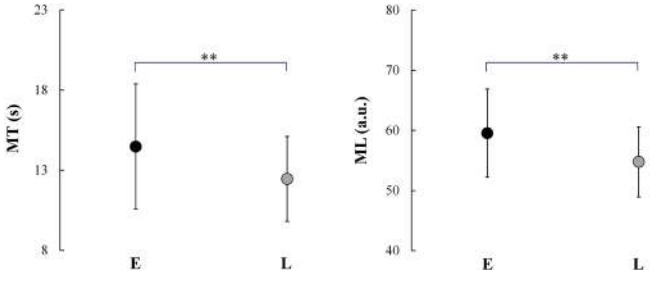


Figure 2. Changes in performance from the early (black filled circles) and late (gray filled circles) practice period. MT: Movement time; ML: Movement length; E: Early practice period; L: Late practice period; ***: $p<0.001$; **: $p<0.01$; *: $p<0.05$.

B. Spectral Power in the low- and high- beta band

For the movement planning stage, the results revealed a PERIOD × REGION interaction effect for the low-beta ($F(1.502, 25.533) = 6.414$, $p = 0.010$, $\eta_P^2 = 0.274$) as well as the high-beta ($F(1875, 31.877) = 7.351$, $p = 0.003$, $\eta_P^2 = 0.302$) power. No other effects were detected ($p > 0.050$).

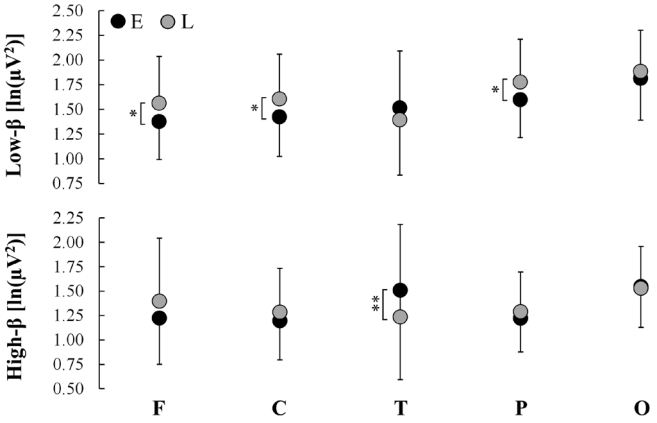


Figure 3. Changes in EEG low-beta (top row) and high-beta (bottom row) power from early (black filled circles) to late (gray filled circles) practice period during the planning stage and for each cortical region (average of left and right hemispheres of each region). ***: $p<0.001$; **: $p<0.01$; *: $p<0.05$. F: Frontal, C: Central, T: Temporal, P: Parietal, O: Occipital.

The post-hoc analysis revealed that, from the early to the late practice period, the low-beta power increased in the frontal ($p = 0.022$; $d = 0.442$), central ($p = 0.028$; $d = 0.419$) and parietal ($p = 0.034$; $d = 0.424$) regions during the movement planning stage (Fig. 3, top). In addition, the same post-hoc analysis revealed that the high-beta power in the temporal region was attenuated from early to late practice period in the planning stage ($p = 0.002$; $d = 0.315$) (Fig. 3, bottom). For the movement execution stage, the results did not reveal any main or interaction effect for both the low-beta and high-beta power ($p > 0.05$ for all comparisons) (Fig. 4).

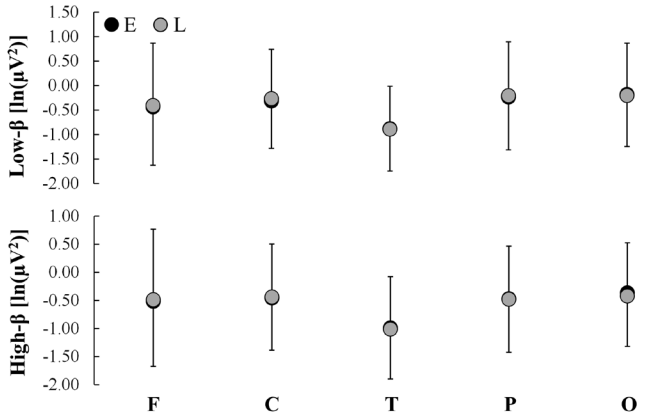


Figure 4. Changes in EEG low-beta (top row) and high-beta (bottom row) power from the early (black filled circles) to the late (gray filled circles) practice period during the movement execution stage and for each cortical region (average left and right hemispheres of each region). F: Frontal, C: Central, T: Temporal, P: Parietal, O: Occipital. ***: $p<0.001$; **: $p<0.01$; *: $p<0.05$.

IV. Discussion

This study investigated the neural correlates underlying practice reaching movements through a head-controlled virtual robotic arm. Overall, participants exhibited improved performance, with faster and straighter reaching movements, from the early to the late practice period. These behavioral improvements were accompanied by an elevation of low-beta power in the frontal, central and parietal regions along with an attenuation of high-beta power in the temporal region during the movement planning stage.

The observation that practice led individuals to produce faster and straighter reaching movements with the robotic end-effector is consistent with prior studies which revealed enhanced performance when individuals were trained to control assistive systems such as upper-limb prostheses [11-12] and head-controlled devices [14-16]. Importantly, performance enhancements were also accompanied by an elevation of low-beta power in the frontal, central and parietal regions. These changes are consistent with the notion that the increased power in this frequency range suggests a successful encoding in memory of sensorimotor information and a reduction of attention [19, 22-23, 26-27, 39]. Thus, a possible mechanism is that throughout practice, individuals have encoded in their memory an internal model of the new sensorimotor map imposed by the assistive device, resulting in an elevation of the low-beta power in the central and parietal regions [24, 40-41]. These central and parietal regions are well-known to be involved in sensorimotor processing and sensory integration contributing to the formation of internal representations [42-44]. In addition, the elevation of frontal low-beta power may suggest that, as individuals progress through practice, attentional mechanisms are being refined [23, 27, 45].

Although other interpretations could be considered, the decrease in high-beta power in the temporal regions over practice could be associated with the enhanced engagement of memory systems in the early stages of learning [46-48]. It is likely that further training would be needed for the individuals to reach a more advanced skill level [47]. While previous work in adaptation of reaching tasks identified an increase of beta power during movement execution (e.g., [49]), this was not observed here. This difference may be explained by the novel and unusual nature of the sensorimotor mapping imposed by the head-controlled system which may require a longer practice time to observe the emergence of cortical changes during the execution stage.

Therefore, this work confirms and extends prior work by suggesting that the changes in low- and high-beta power could serve as possible brain biomarkers in a clinical context to assess the practice level of individuals when they learn to control an assistive device. For example, in the cases of a high-level spinal cord injury, the cortical dynamics of patients could be assessed whenever possible to monitor their brain activity as they practice head motion to control end-effectors or more generally various assistive systems (e.g., robotic arms, computer cursors, wheelchair joysticks). Such cortical monitoring along with behavioral assessment can more comprehensively inform the training approach deployed by the therapists as their patients learn to operate the assistive device to (re-)engage with their environment for regaining autonomy.

V. Conclusion

This work suggests that the modulation of low-beta and high-beta power would reflect the advancement of the encoding in memory of an internal model of a novel sensorimotor map while individuals practice reaching movements using a head-controlled robotic effector. Thus, these spectral power dynamics could possibly provide brain biomarkers to track the changes in cerebral cortical dynamics along with performance as sensorimotor learning progresses. Beyond these findings, this work has limitations. First, the participants involved in this work were individuals without disabilities and as such this work should be extended by considering a clinical population (e.g., patients with high-level spinal cord injury). Also, while the regional activity as employed here is informative, future work should also consider cerebral cortical connectivity to capture neural network communication which could further inform the cognitive-motor processes when individuals learn to control an assistive device. In addition, the efficacy index combining performance and cortical dynamics as well as the effect of a prolonged practice period on cortical dynamics should also be examined [15,16]. Despite these limitations, this work has the potential to contribute and to inform the monitoring and retraining of individuals with disabilities who must learn to control assistive technology devices to be able to interact again with their environment using the underlying neural mechanisms for targeted biomarkers.

References

[1] R. Magill, & D. Anderson, "Motor Learning and Control: Concepts and Applications". McGraw Hill New York, 12th ed., 2024.

[2] R. J. Gentili, T. J. Bradberry, H. Oh, B. D. Hatfield, and J. L. Contreras Vidal, "Cerebral cortical dynamics during visuomotor transformation: Adaptation to a cognitive-motor executive challenge," Psychophysiology, vol. 48, no. 6, pp. 813–824, Oct. 2010. doi:10.1111/j.1469-8986.2010.01143.x

[3] R. J. Gentili et al., "Evolution of cerebral cortico-cortical communication during visuomotor adaptation to a cognitive-motor executive challenge," Biological Psychology, vol. 105, pp. 51–65, Feb. 2015. doi:10.1016/j.biopsycho.2014.12.003

[4] E. M. Reuter, A. Booms, and L. A. Leow, "Using EEG to study sensorimotor adaptation," Neuroscience & Biobehavioral Reviews, vol. 134, p. 104520, Mar. 2022. doi:10.1016/j.neubiorev.2021.104520

[5] B. Hatfield et al., "The Cognitive and Affective Neuroscience of Superior Athletic Performance," pp. 487–512, Jun. 2020, doi: 10.1002/9781119568124.ch23.

[6] R. Casas et al., "Home-based therapy after stroke using the hand spring operated movement enhancer (handsome II)," Frontiers in Neurorobotics, vol. 15, Dec. 2021. doi:10.3389/fnbot.2021.773477

[7] J. A. Borrell et al., "Prosthetic home intervention induces cortical plasticity in pediatrics with congenital limb reduction," Brain Communications, vol. 6, no. 4, 2024. doi:10.1093/braincomms/fcae044

[8] S. Deeny, C. Chicoine, L. Hargrove, T. Parrish, and A. Jayaraman, "A simple ERP method for quantitative analysis of cognitive workload in myoelectric prosthesis control and human-machine interaction," PLoS one, vol. 9, no. 11, Nov. 2014. doi:10.1371/journal.pone.0112091

[9] J. V. V. Parr, G. Gallicchio, N. R. Harrison, A. K. Johnen, and G. Wood, "All talk? challenging the use of left-temporal EEG alpha

oscillations as valid measures of verbal processing and Conscious Motor Control," Biological Psychology, vol. 155, p. 107943, Sep. 2020. doi:10.1016/j.biopsycho.2020.107943

[10] J. Gonzalez, H. Soma, M. Sekine, and W. Yu, "Psycho-physiological assessment of a prosthetic hand sensory feedback system based on an auditory display: A preliminary study." Journal of Neuroengineering and Rehabilitation, BioMed Central, https://doi.org/10.1186/1743-0003-9-33

[11] C. Bloomer, S. Wang, and K. Kontson, "Kinematic analysis of motor learning in upper limb body-powered bypass prosthesis training," PLoS one, vol. 15, no. 1, Jan. 2020. doi:10.1371/journal.pone.0226563

[12] H. Bouwsema, C. K. van der Sluis, and R. M. Bongers, "The role of order of practice in learning to handle an upper-limb prosthesis," Archives of Physical Medicine and Rehabilitation, vol. 89, no. 9, pp. 1759–1764, Sep. 2008. doi:10.1016/j.apmr.2007.12.046

[13] E. de Boer et al., "Intermanual transfer effects in below-elbow myoelectric prosthesis users," Archives of Physical Medicine and Rehabilitation, vol. 97, no. 11, pp. 1924–1930, Nov. 2016. doi:10.1016/j.apmr.2016.04.021

[14] I. M. Shuggi, H. Oh, P. A. Shewokis, and R. J. Gentili, "Mental workload and motor performance dynamics during practice of reaching movements under various levels of task difficulty," Neuroscience, vol. 360, pp. 166–179, 2017

[15] I. M. Shuggi, et al., "Motor performance, mental workload and self-efficacy dynamics during learning of reaching movements throughout Multiple Practice Sessions," Neuroscience, vol. 423, 232–248, 2018. https://doi.org/10.1016/j.neuroscience.2019.07.001

[16] I. M. Shuggi, P. A. Shewokis, J. W. Hermann, and R. J. Gentili "Changes in motor performance and mental workload during practice of reaching movements: a team dynamics perspective," Experimental Brain Research, vol. 236, pp. 433–451, 2018. https://doi.org/10.1007/s00221-017-5136-8

[17] N. Rudigkeit and M. Gebhard, "Amicus—a head motion-based interface for control of an assistive robot," Sensors, vol. 19, no. 12, p. 2836, Jun. 2019. doi:10.3390/s19122836

[18] N. Rudigkeit and M. Gebhard, "Amicus 2.0—system presentation and demonstration of adaptability to personal needs by the example of an individual with progressed multiple sclerosis," Sensors, vol. 20, no. 4, p. 1194, Feb. 2020. doi:10.3390/s20041194

[19] T. W. Boonstra, A. Daffertshofer, M. Breakspear, and P. J. Beek, "Multivariate time–frequency analysis of electromagnetic brain activity during Bimanual Motor Learning," NeuroImage, vol. 36, no. 2, pp. 370–377, Jun. 2007. doi:10.1016/j.neuroimage.2007.03.012

[20] F. Torres, S. T. Puente, and A. Úbeda, "Assistance robotics and Biosensors," Sensors, vol. 18, no. 10, p. 3502, Oct. 2018. doi:10.3390/s18103502

[21] L. A. Wheaton, "Neurorehabilitation in upper limb amputation: Understanding how neurophysiological changes can affect functional rehabilitation," Journal of NeuroEngineering and Rehabilitation, vol. 14, no. 1, May 2017. doi:10.1186/s12984-017-0256-8

[22] C. Andreou et al., "Theta and high-beta networks for feedback processing: A simultaneous EEG–fMRI study in healthy male subjects," Translational Psychiatry, vol. 7, no. 1, Jan. 2017. doi:10.1038/tp.2016.287

[23] L. Bogaerts, C. G. Richter, A. N. Landau, and R. Frost, "Beta-band activity is a signature of statistical learning," The Journal of Neuroscience, vol. 40, no. 39, pp. 7523–7530, Aug. 2020. doi:10.1523/jneurosci.0771-20.2020

[24] S. Dyck and C. Klaes, "Training-related changes in neural beta oscillations associated with implicit and explicit motor sequence learning," Scientific Reports, vol. 14, no. 1, Mar. 2024. doi:10.1038/s41598-024-57285-7

[25] P. M. Fitts, & M. I. Posner, "Human performance". In Human performance. Brooks/Cole, 1967.

[26] B. Pollok, D. Latz, V. Krause, M. Butz, and A. Schnitzler, "Changes of motor-cortical oscillations associated with motor learning," Neuroscience, vol. 275, pp. 47–53, Sep. 2014. doi:10.1016/j.neuroscience.2014.06.008

[27] C. Moisello et al., "Practice changes beta power at rest and its modulation during movement in healthy subjects but not in patients with Parkinson's disease," Brain and Behavior, vol. 5, no. 10, Sep. 2015. doi:10.1002/brb3.374

[28] F. A. Mussa-Ivaldi, M. Casadio, Z. C. Danziger, K. M. Mosier, and R. A. Scheidt, "Sensory motor remapping of space in human–machine interfaces," Progress in Brain Research, pp. 45–64, 2011. doi:10.1016/b978-0-444-53752-2.00014-x

[29] M. Casadio, R. Ranganathan, and F. A. Mussa-Ivaldi, "The body-machine interface: A new perspective on an old theme," Journal of Motor Behavior, vol. 44, no. 6, pp. 419–433, Nov. 2012. doi:10.1080/00222895.2012.700968

[30] R. J. Jagacinski and D. L. Monk, "Fitts' law in two dimensions with hand and head movements," Journal of Motor Behavior, vol. 17, no. 1, pp. 77–95, Mar. 1985. doi:10.1080/00222895.1985.10735338

[31] S. K. Card, J. D. Mackinlay, and G. G. Robertson, "A morphological analysis of the design space of input devices," ACM Transactions on Information Systems, vol. 9, no. 2, pp. 99–122, Apr. 1991. doi:10.1145/123078.128726

[32] E. F. LoPresti and D. M. Brienza, "Adaptive software for head-operated computer controls," IEEE Transactions on Neural Systems and Rehabilitation Engineering, vol. 12, no. 1, pp. 102–111, Mar. 2004. doi:10.1109/tnsre.2003.822762

[33] M. R. Williams and R. F. Kirsch, "Evaluation of head orientation and neck muscle EMG signals as command inputs to a human–computer interface for individuals with high tetraplegia," IEEE Transactions on Neural Systems and Rehabilitation Engineering, vol. 16, no. 5, pp. 485–496, Oct. 2008. doi:10.1109/tnsre.2008.2006216

[34] M. R. Williams and R. F. Kirsch, "Evaluation of head orientation and neck muscle EMG signals as three-dimensional command sources," Journal of NeuroEngineering and Rehabilitation, vol. 12, no. 1, p. 25, 2015. doi:10.1186/s12984-015-0016-6

[35] A. Delorme and S. Makeig, "EEGLAB: An open source toolbox for analysis of single-trial EEG dynamics including independent component analysis," Journal of Neuroscience Methods. Methods, vol. 134, no. 1, pp. 9–21, 2004.

[36] K. Onikura, Y. Katayama, and K. Iramina, "Evaluation of a method of removing head movement artifact from EEG by independent component analysis and filtering," Advanced Biomedical Engineering, vol. 4, no. 0, pp. 67–72, 2015. doi:10.14326/abe.4.67

[37] I. Daly, M. Billinger, R. Scherer, and G. Muller-Putz, "On the automated removal of artifacts related to head movement from the EEG," IEEE Transactions on Neural Systems and Rehabilitation Engineering, vol. 21, no. 3, pp. 427–434, May 2013. doi:10.1109/tnsre.2013.2254724

[38] B. H. Kim, J. Chun, and S. Jo, "Dynamic motion artifact removal using inertial sensors for Mobile BCI," 2015 7th International IEEE/EMBS Conference on Neural Engineering (NER), pp. 37–40, Apr. 2015. doi:10.1109/ner.2015.7146554

[39] S. Scholz, S. L. Schneider, and M. Rose, "Differential effects of ongoing EEG beta and theta power on memory formation," PLoS one, vol. 12, no. 2, Feb. 2017. doi:10.1371/journal.pone.0171913

[40] H. Tan, C. Wade, and P. Brown, "Post-movement beta activity in sensorimotor cortex indexes confidence in the estimations from internal models," The Journal of Neuroscience, vol. 36, no. 5, pp. 1516–1528, Feb. 2016. doi:10.1523/jneurosci.3204-15.2016

[41] A. B. Nelson et al., "Beta oscillatory changes and retention of motor skills during practice in healthy subjects and in patients with Parkinson's disease," Frontiers in Human Neuroscience, vol. 11, Mar. 2017. doi:10.3389/fnhum.2017.00104

[42] D. Purves, Neuroscience. Sunderland, Mass: Sinauer Associates, Publishers, 2004.

[43] M. I. Sereno and R.-S. Huang, "Multisensory maps in parietal cortex," Current Opinion in Neurobiology, vol. 24, pp. 39–46, Feb. 2014. doi:10.1016/j.conb.2013.08.014

[44] D. McNamee and D. M. Wolpert, "Internal models in biological control," Annual Review of Control, Robotics, and Autonomous Systems, vol. 2, no. 1, pp. 339–364, May 2019. doi:10.1146/annurev-control-060117-105206

[45] S. Nougaret et al., "Low and high beta rhythms have different motor cortical sources and distinct roles in movement control and spatiotemporal attention," PLOS Biology, vol. 22, no. 6, Jun. 2024. doi:10.1371/journal.pbio.3002670

[46] K. Edagawa and M. Kawasaki, “Beta phase synchronization in the frontal-temporal-cerebellar network during auditory-to-motor rhythm learning,” Scientific Reports, vol. 7, no. 1, Feb. 2017. doi:10.1038/srep42721

[47] A. Pavlova et al., “Learning of new associations invokes a major change in modulations of cortical beta oscillations in human adults,” Psychophysiology, vol. 60, no. 8, Mar. 2023. doi:10.1111/psyp.14284

[48] Y. Chen and X. Huang, “Modulation of alpha and beta oscillations during an n-back task with varying temporal memory load,” Frontiers in Psychology, vol. 6, Jan. 2016. doi:10.3389/fpsyg.2015.02031

[49] E. Tatti et al., “Frontal increase of beta modulation during the practice of a motor task is enhanced by Visuomotor Learning,” Scientific Reports, vol. 11, no. 1, Aug. 2021. doi:10.1038/s41598-021-97004-

A Task-Agnostic Knee Exoskeleton for Reducing Osteoarthritis Pain Across Activities of Daily Life: A Pilot Study

Nikhil V. Divekar*, Ernesto Hernandez Hinojosa*, Jiefu Zhang, and Robert D. Gregg

***Abstract*— Patellofemoral osteoarthritis is a prevalent musculoskeletal disorder characterized by knee pain during physically demanding activities like stair climbing and sit-to-stand transitions. These movements require high knee extension torques, leading to increased quadriceps activation and patellofemoral joint compression, which aggravates pain. While external torque assistance at the knee joint could theoretically reduce joint loads, traditional exoskeletons have not proven effective in managing osteoarthritis due to their rigid actuation, cumbersome attachments, and inadequate control systems. We address these limitations by modifying a commercial post-operative knee brace with a highly-backdrivable actuator and adapting a task-agnostic torque-assist controller, originally designed for lifting and carrying tasks, to accommodate osteoarthritis patients. In pilot trials with four participants with patellofemoral osteoarthritis, our device facilitated substantial reductions in both pain and perceived difficulty across daily activities including stair/ramp navigation, walking, and sit-to-stand transitions. Across all participants and tasks, pain and difficulty were reduced by 0.82 and 0.57 points, respectively (on a scale of 0 to 4). Electromyography revealed decreased quadriceps activation, varying by participant and task. These preliminary findings motivate future research on backdrivable knee exoskeletons as a novel conservative treatment for patellofemoral osteoarthritis.**

I. Introduction

Knee osteoarthritis (OA) is a highly prevalent musculoskeletal disorder affecting ∼14% of American adults [1]. OA can afflict one or more of the three knee joint compartments (medial, lateral, and patellofemoral), with over 24% of knee OA cases being isolated patellofemoral and 40-59% being multi-compartmental [2]–[4]. Physical therapies focus on strengthening the quadriceps to address knee instability and muscle force imbalances between the medial and lateral quadriceps heads [5], [6]. However, pain often limits patients to low joint torque activities like walking, causing them to avoid more demanding tasks such as stair climbing. This restricts general mobility and perpetuates a negative cycle of inactivity, muscle weakness, and OA progression [7].

Conventional unloader knee braces help realign tibiofemoral joint spaces by balancing force distribution between medial and lateral sides. While this alleviates pain in these compartments, these braces cannot address pain from quadriceps muscle action. This muscle action increases compressive forces primarily at the patellofemoral joint [8], [9]. Patellofemoral pain therefore intensifies during activities like stair/ramp climbing and sit-stand [10], which require high knee extension torques and thereby high quadriceps forces. This source of pain inspired the recent design of tri-compartmental unloading knee braces that use springs to help reduce forces and torques in the knee [11]. However, these devices cannot add or remove net energy during human locomotion, making them inadequate for challenging daily activities like climbing up or down stairs [12]. Moreover, the spring can cause a hindrance during swing knee flexion. These limitations highlight the need for a new class of *powered* knee unloaders that can provide a small fraction of biological torque to reduce patellar and quadriceps tendon forces across various activities of daily living (ADLs).

Recent attempts at using knee exoskeletons to relieve pain and increase physical performance in OA patients have shown promise but still face significant challenges. Both the Keeogo and ROAM Ascend exoskeletons require large backpacks and have usability issues related to comfort, weight, and noise [13], [14]. The pneumatically powered Ascend [14] is bulky and, similar to spring-based knee unloaders, does not support knee flexion during late stance and early swing. Moreover, the highly-geared Keeogo [13] was unable to induce acute benefits for knee osteoarthritis patients, likely due to the lengthy user adaptation needed for the task recognition-based controller.

We previously developed a task-agnostic knee exoskeleton to support the quadriceps during lifting-lowering and multi-terrain carrying tasks [15]. This design integrates a backdrivable, quasi-direct drive actuator with a post-operative knee brace, providing high control bandwidth, precise current-based torque control, energy regeneration, quiet operation, and impact compliance [16]–[19]. The exoskeleton features a task-agnostic controller that automatically modulates virtual springs, dampers, and gravity and inertia compensation to assist various activities. Unlike end-to-end neural networks, our controller uses predictable, bounded components with interpretable parameters that can be optimized for biomimetic assistance and fine-tuned for specific applications like OA. This approach also enables seamless task transitions while maintaining natural movement patterns. The exoskeleton reduced quadriceps effort in unimpaired individuals across six key activities: level walking, ramp and stair ascent/descent, and lifting-lowering tasks. These results suggest this technology could similarly reduce quadriceps-induced loads on the patellofemoral compartment to relieve knee OA pain.

This paper presents the deployment and pilot evaluation of our task-agnostic knee exoskeleton for relieving knee

This work was supported by the National Institute of Biomedical Imaging and Bioengineering of the NIH under Award Number R01EB031166. The content is solely the responsibility of the authors and does not necessarily represent the official views of the NIH.

The authors are with the Department of Robotics, University of Michigan, Ann Arbor, MI 48109, USA. *Authors contributed equally. Contact: {ndivekar, ehdz, zjiefu, rdgregg}@umich.edu

OA pain across the primary activities of daily life. Firstly, we refined our prior controller [15] to support sit-stand transitions rather than lifting-lowering tasks. Secondly, we simplified the brace setup used in [15] by removing the medial thigh plate to prevent unwanted knee forces from strap tightening. Finally, we evaluated the exoskeleton's effectiveness in reducing pain and difficulty across various activities in four participants with patellofemoral-dominant knee OA. Results showed *acute* reductions in both perceived pain and task difficulty, along with participant- and task-dependent reductions in peak and mean quadriceps activation. By providing targeted, backdrivable assistance when needed, this exoskeleton represents a potentially significant advance in non-invasive knee OA management, with implications for improving mobility and patient quality of life.

II. Methods

A. Controller Modifications

Fig. 1 shows a high-level summary of the task-agnostic bilateral knee controller, which was originally developed for lifting-lowering and multi-terrain carrying in [15] and adapted here for supporting knee OA participants. Briefly, the controller consists of core torque bases that are heuristically modified to form task-specific stance torque bases and general (task-invariant) swing torque bases. Next, for stance, task sensitization or multiplication with functions sensitive to certain task characteristics (such as terrain slope) provide task-adaptive stance torque functions. Last, taking the convex sum of the stance and swing torque bases based on the ground reaction force (GRF) unifies them into the final task-adaptive knee torque function.

Here, the "lifting-lowering spring", which was designed to generally support symmetric closed chain squat-like motions, was modified to support sit-stand transitions ("Sit-Stand spring" in Fig. 1). Based on user feedback, the modification essentially involved suppressing the spring torque more for small knee flexion angles. Furthermore, compared to [15], we have an additional basis function for assisting leg clearance ("Swing boost" in Fig. 1). This function supplements the gravity compensation basis by applying knee flexion torques based on the sagittal thigh angle (a commonly used signal for phase-based controllers [20]).

B. Hardware Implementation

The controller was implemented on modified bilateral knee modules of the modular lower-limb exoskeleton system M-BLUE [15], [19]—see Fig. 2. Briefly, this bilateral exoskeleton configuration uses two highly-backdrivable commercial actuators (T-Motor AK80-9, DEPHY driver), each comprising a high-torque pancake motor and an internal 9:1 planetary gearset resulting in a very low reflected friction and inertia (92.1 kg·cm^2). We bypassed the motor driver's default thermal limits and implemented a thermal model-based torque limiter [21], allowing short (1-2 s) bursts of higher peak torques (limited to 25 Nm). We also implemented a ground reaction force sensor (IEE Sense) based on a matrix of force sensitive resistors. An inertial measurement unit (3DM-GX5

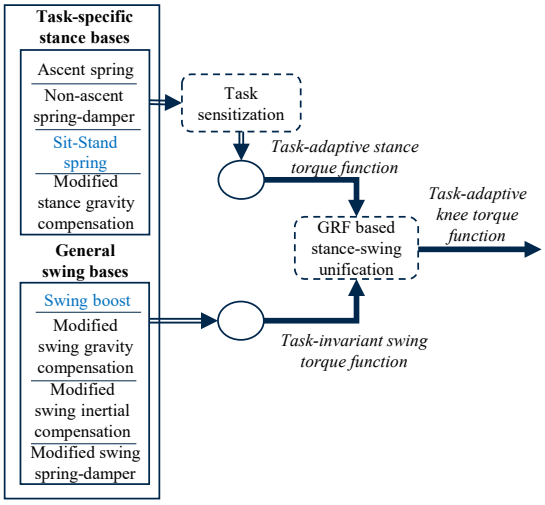


Fig. 1. High-level summary of the task-adaptive knee controller—adapted from [15]. Basis functions that were added or modified are shown in blue.



Fig. 2. Modified bilateral knee exoskeleton for knee OA users.

AHRS, Microstrain) is directly attached to each leg segment (four total) to measure the orientation and angular velocity of both thighs and shanks. The controller for each leg runs on a single board computer (Raspberry Pi 5 8GB, Raspberry Pi Foundation) at 300 Hz with wireless communication to share sensor feedback between legs. The system is powered by two 24 V, 2 Ah powertool battery (Kobalt 24-V Lithium Battery, Kobalt). The total mass of the system is 4.6 kg.

Each actuator is mounted on an off-the-shelf knee brace (T Scope Knee, Breg). We modified the brace setup used in [15] to better suit knee OA participants. Essentially, we removed the medial thigh beam of the brace to allow tightening of the thigh and shank straps with minimal stress on the knee joint in the frontal plane. While this modification makes torque transfer to the human slightly less efficient, it greatly improved comfort of our participants. For user safety, a remote emergency stop switch was implemented to cut off battery power to the motor.

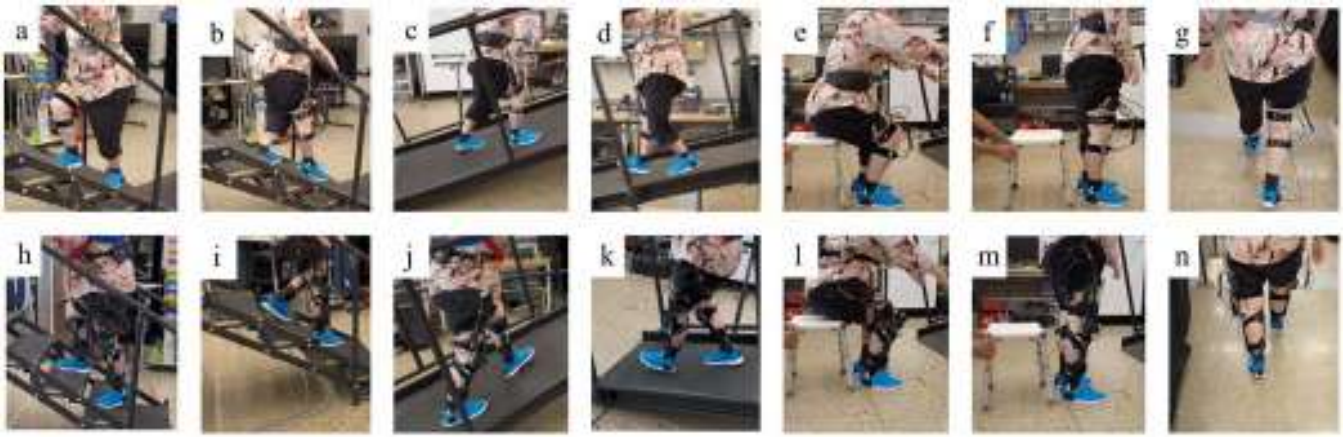


Fig. 3. Participant performing the seven different tasks with both conditions: (a-g) depict the participant without exoskeleton assistance (Bare condition), while (h-m) show the participant performing the same tasks with exoskeleton assistance (Exo condition). The tasks include: (a, h) stair ascent, (b, i) stair descent, (c, j) ramp ascent, (d, k) ramp descent, (e, l) sit-to-stand descent, (f, m) sit-to-stand ascent, and (g, n) level walking.

C. Experimental Design

TABLE I
SUBJECT INFORMATION

	Sex	Age	Weight (kg)	Height (m)
Subj. 1	F	70	94	1.6
Subj. 2	M	81	83	1.83
Subj. 3	F	65	73	1.57
Subj. 4	F	53	52	1.63

The study was approved by the University of Michigan's Institutional Review Board (HUM00201957). We enrolled four participants with pre-eminent pain at the patellofemoral joint—assessed via a questionnaire, sometimes including their x-ray reports. Participants were selected based on self-reported regular pain during walking, which worsened during stair climbing, ensuring they met the study's criteria for patellofemoral OA-related symptoms. The participant information is provided in Table I. All participants gave written consent before participating.

The study involved assessing the effect of our controller/exoskeleton on pain, difficulty, and quadriceps activation levels in a multi-activity test. The activities comprised level ground walking (LW), ramp ascent (RA), ramp descent (RD), stairs ascent (SA), stairs descent (SD), sit-to-stand (STS-A), and stand-to-sit (STS-D); performed on a multi-terrain circuit composed of a level 10 m level walkway, a 3.7-m ramp inclined at 15°, a five-step staircase with a 7 inches (18 cm) step height, and a height adjustable stool.

Before the test, participants attended a separate acclimation session lasting approximately 2-3 hours. During this session, they performed different tasks with the exoskeleton under different levels of assistance (LoA), until they were confident with the device. After acclimation we acquired important gait parameters without the exoskeleton for each activity in our multi-terrain circuit (Fig. 3) for the purpose of applying experimental controls. We acquired the maximum knee extension velocity in stance for ascent (ramp and stairs) and sit-stand transitions, resembling the protocol in [15]. Because OA participants exhibit high intra-subject variance in peak knee velocity during descent tasks (ramp and stairs) and level-ground walking, we instead acquired the time to complete these activities—resembling the average speed for each activity. These parameters served as experimental controls for both the Bare and Exo conditions during the subsequent test visit.

The test visit, which lasted approximately 3-4 hours, was conducted in two conditions: no exoskeleton (Bare) and active exoskeleton (Exo), with the order of the conditions alternated between subsequent participants. In the Exo condition, the level of assistance was kept the same for all participants to fully utilize the peak torque of the actuators. Subjects performed each activity multiple times until obtaining at least 10 gait/task cycles with peak velocities/average speeds within $\pm 10\%$ of their baseline values.

D. Data Collection and Analysis

Pain and difficulty were assessed for each activity using a modified Western Ontario and McMaster Universities Arthritis Index (WOMAC) questionnaire [22], in which participants rate their perceived pain and difficulty on a scale of 0-4, corresponding to "None", "Slight", "Moderate", "Very", and "Extremely". Participants completed the questionnaire at the end of each task trial, following all repetitions of a specific task under a given condition (e.g., after all Exo stair climbing repetitions, all Bare ramp descent repetitions, etc.).

Quadriceps effort was assessed using surface electromyography (EMG). After appropriate skin preparation, we taped three wireless electrodes (Delsys, Massachusetts, USA) onto the participant's right lower limb over the vastus medials oblique (VM), vastus lateralis (VL), and rectus femoris (RF) to assess muscle activation. EMG data was parsed into individual task/gait cycles using the knee angle for sit-stand activities and the FSR for gait activities. Each muscle's EMG was demeaned, bandpass filtered (20 - 200 Hz), and smoothed with a moving 125 ms window RMS filter with 50% overlap. EMG was normalized to the maximum muscle activation level observed during the test.

We then calculated the mean and peak muscle activation for each muscle, taking the difference between the Exo and Bare conditions. Specifically, the peak EMG difference for each muscle/activity was calculated by normalizing the peak EMG of each trial in the Exo condition relative to the Bare condition, using the formula

$$\text{Normalized Peak EMG} = \frac{\text{Exo Peak} - \text{Bare Peak}}{\text{Bare Peak}}$$

Finally, per our previous work [15], the three muscles were lumped together using a weighted average based on each muscle's cross-sectional area to acquire the overall quadriceps mean and peak activations for each activity.

III. Results

Participants reported an average pain reduction of 0.82 points across all tasks and conditions when using the exoskeleton (Fig. 4, Table II). Subject 1 reported a single-point reduction in pain for the stairs and ramp tasks. No changes were observed for other tasks. Subject 2 experienced pain reductions across all tasks except LW and STS-A, where pain remained unchanged. Subject 3 noted relief in all tasks except SD in which pain increased by one point. Subject 4 reported no change in SA, SD, and RA, but observed pain reductions in all other tasks, with the largest reduction of 2 points in STS-D.

TABLE II
PAIN DIFFERENCE (EXO MINUS BARE)

	SA	SD	RA	RD	STS-D	STS-A	LW	Avg.
Subj. 1	-1	-1	-1	-2	0	0	0	-0.71
Subj. 2	-1	-1	-1	-2	-1	-2	0	-1.14
Subj. 3	-2	1	-1	-2	-1	0	0	-0.71
Subj. 4	0	0	0	-1	-2	-1	-1	-0.71
Avg.	-1	-0.25	-0.75	-1.75	-1	-0.75	-0.25	-0.82

Task difficulty decreased by an average of 0.57 points with exoskeleton use (Fig. 4, Table III). Subject 1 reported single-point decreases in difficulty for SA, RA, RD, and STS-A, but found STS-D more difficult with a single-point increase. Other tasks remained unchanged. Subject 2 found all tasks easier except level walking, which became slightly more difficult (single-point increase)—notably this participant had the highest reduction in difficulty of 3 points for STS-A. Subject 3 observed the greatest reduction in difficulty for SA of 2 points, followed by single-point reductions for RA and RD. Sit-to-stand and level walking tasks showed no change, while SD became slightly harder with a single-point increase. Subject 4 reported single-point decreases in SA, STS-D, and level, while RD was slightly more difficult (1 point increase).

The ensemble-averaged EMG activity and torque applied by the exoskeleton (normalized to the task cycle percentage) are presented for each of the seven locomotor tasks in Fig. 5. The plots illustrate how muscle activation patterns differ between the Bare (red) and Exo (blue) conditions and highlight the timing and magnitude of exoskeleton assistance torque (black) throughout the task cycle. Table IV presents

TABLE III
DIFFICULTY DIFFERENCE (EXO MINUS BARE)

	SA	SD	RA	RD	STS-D	STS-A	LW	Avg.
Subj. 1	-1	0	-1	-1	1	-1	0	-0.43
Subj. 2	-1	-1	-2	-1	-1	-3	1	-1.14
Subj. 3	-2	1	-1	-1	0	0	0	-0.43
Subj. 4	-1	0	0	1	-1	0	-1	-0.29
Avg.	-1.25	0	-1	-0.5	-0.25	-1	0	-0.57

the mean EMG differences between the Bare and Exo conditions, where negative values indicate reduced muscle activation with the exoskeleton. Subject 1 experienced decreased activation in most tasks (the across task average change was -1.7%), especially in STS-A having the highest change of -6.8%. Subject 2 showed mixed responses, with slight reductions in RA and STS-A, but slight increases in all other tasks—the across task average change was 1.1%. Subject 3 consistently showed reductions, most notably in STS-A, with only level showing an increase—the across task average change was -3.1%. In contrast, Subject 4 exhibited increased activation across all tasks (3.9% change on average). Overall, the data suggests that the exoskeleton may provide benefits in reducing the mean activation during activities that involve greater muscle exertion, like sit-to-stand transitions with an average reduction of -3.1% across all participants.

TABLE IV
MEAN EMG DIFFERENCE (% CHANGE RELATIVE TO BARE)

	SA	SD	RA	RD	STS-D	STS-A	LW	Avg.
Subj. 1	**-3.2**	**-0.4**	**-0.8**	0.2	**-3.4**	**-6.8**	2.4	**-1.7**
Subj. 2	3.7	1.3	**-2.4**	**-0.8**	3.9	**-1.4**	3.2	1.1
Subj. 3	0.3	**-0.8**	**-1.4**	**-1.7**	**-1.2**	**-5.2**	3.2	**-1**
Subj. 4	0.9	3.4	7.2	2.5	1.2	1.1	11.1	3.9
Avg.	0.4	0.9	0.7	0.0	0.1	**-3.1**	5.0	0.6

Table V highlights changes in peak EMG activation. Subject 1 exhibited the highest peak EMG change of -13.8% observed in STS-A—the across task average change was -2.2%. Subject 2 exhibited peak EMG increase in all tasks except STS-A—the across task average change was 2.2%. Subject 3 exhibited peak EMG reductions in all tasks except level—the across task average change was -3.3%. Subject 4 exhibited peak EMG reductions in SA and STS-A, but increases in all other tasks—the across task average change was was 5.5%. Overall, there were peak EMG reductions for SA, RD, and STS-A. Notably, STS-A had the highest and most consistent change with -8.5%.

TABLE V
PEAK EMG DIFFERENCE (% CHANGE RELATIVE TO BARE).

	SA	SD	RA	RD	STS-D	STS-A	LW	Avg.
Subj. 1	**-9.8**	0.6	1.4	**-3.6**	3.5	**-13.8**	6.1	**-2.2**
Subj. 2	6.5	0.8	0.6	0.8	2.0	**-0.8**	5.7	2.2
Subj. 3	**-5.5**	**-5.3**	**-0.4**	**-2.3**	**-0.3**	**-10.3**	1.2	**-3.3**
Subj. 4	**-0.9**	5.4	14.5	1.2	15.6	**-9.0**	11.5	5.5
Avg.	**-2.4**	0.4	4.0	**-1.0**	5.2	**-8.5**	6.1	0.5

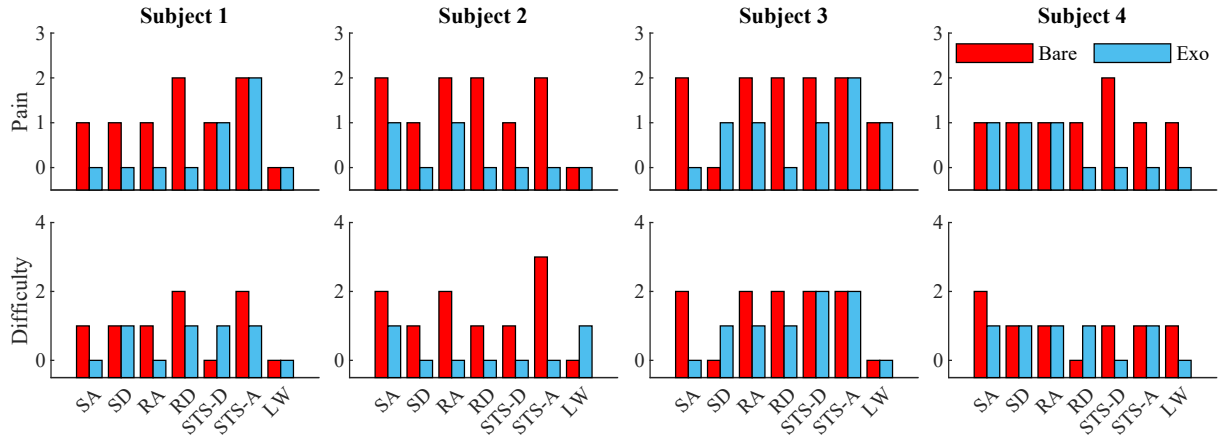


Fig. 4. Perceived pain and difficulty scores during tasks with and without the exoskeleton. The top row illustrates the perceived pain scores reported by the four participants across the seven locomotor tasks: stair ascent (SA), stair descent (SD), ramp ascent (RA), ramp descent (RD), sit-to-stand descent (STS-D), sit-to-stand ascent (STS-A), and level walking (LW). Each bar compares the Bare condition (red bars) with the Exo condition (blue bars). The bottom row displays the corresponding perceived difficulty scores for the same participants and tasks, with the same comparison between the Bare and exoskeleton conditions. The data highlight individual variability in the reported pain and difficulty changes, showcasing task-specific and participant-specific responses to exoskeleton assistance.

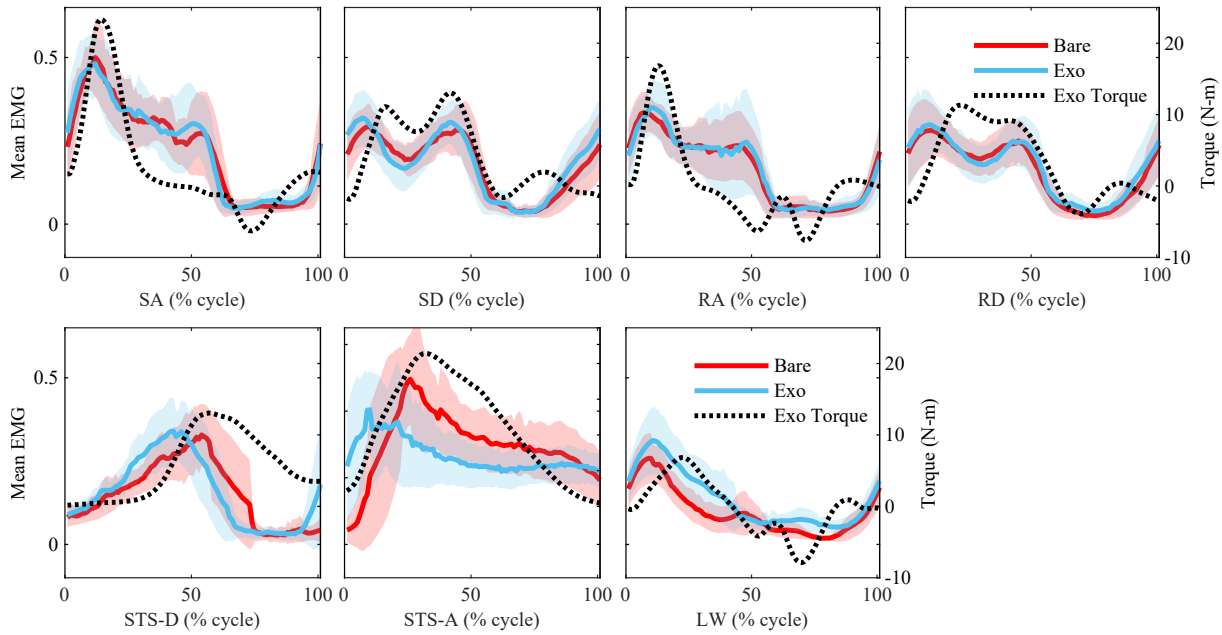


Fig. 5. Mean EMG activation and exoskeleton torque during task cycles. Each plot represents one of the seven locomotor tasks: stair ascent (SA), stair descent (SD), ramp ascent (RA), ramp descent (RD), sit-to-stand descent (STS-D), sit-to-stand ascent (STS-A), and level walking (LW). The red curve shows the mean EMG activation during the Bare condition, while the blue curve shows the mean EMG activation during the exoskeleton-assisted condition. Overlaid on each plot is the mean torque applied by the exoskeleton (black curve), illustrating the relationship between exoskeleton assistance and muscle activation throughout the task cycle.

IV. Discussion

Our study's key finding was that our knee exoskeleton provided *acute* benefits for predominantly patellofemoral OA participants, consistently lowering both their pain levels and the difficulty they experienced during various activities. Traditional unloader knee braces aim to reduce joint loading, but fall short in addressing pain caused by quadriceps muscle action, a limitation that our device directly targets. Unlike spring-based braces, which cannot adjust output torque based on kinematics and ground reaction forces, our system dynamically modulates assistance to inject energy when needed. This is achieved with backdrivable actuators and an intuitive controller that modulates virtual springs, dampers, and gravity-inertia compensation across a range of tasks. This adjustability simplifies tuning and enhances end-user adoption, offering a versatile and practical solution for knee assistance. Moreover, this study addresses the shortcomings of other knee exoskeletons, such as Keeogo and ROAM Ascend. While Keeogo can benefit individuals with knee OA after prolonged use, it has not provided acute benefits, likely due to its highly geared actuators and task-specific controller.

A. Pain and Difficulty Reductions

The most substantial pain reduction was observed during RD, with an average decrease of 1.75 points across participants. This may be attributed to the exoskeleton's capacity to assist the knee in decelerating the body's center of mass, thereby reducing the demand on the quadriceps [23]. In contrast, level walking showed minimal pain reduction, likely due to the lower baseline pain levels typically associated with this activity and its reduced reliance on quadriceps engagement. Unexpectedly, Subject 2 reported increased pain during stair descent. We attribute this to extended loading phases that arise due to hesitancy in utilizing exoskeleton assistance on the riskiest task.

The perceived difficulty of tasks generally correlated with pain levels, although exceptions were observed. For instance, Subject 1 experienced no change in pain during STS-D yet reported an increase in difficulty, suggesting that non-pain-related factors, such as balance or coordination, may have influenced their perception. Similarly, Subject 4 perceived a reduction in pain during RD but noted an increased difficulty, further emphasizing the multifaceted nature of these metrics.

B. Muscle Activity Trends

Muscle activation data revealed notable trends, particularly for STS-A, which exhibited the most pronounced reductions in both mean and peak EMG levels across participants. This aligns with expectations, as the task involves high joint loading and a large range of motion, making it particularly amenable to the exoskeleton's assistive torque. Subjects 1 and 3 showed substantial reductions in peak quadriceps activation during STS-A, SA, and RD, reflecting effective exoskeleton support in mitigating muscular demand. Conversely, Subjects 2 and 4 exhibited less consistent EMG reductions, potentially due to individual differences in balance, motor coordination, or limited acclimatization to the device. These results contrast with our earlier findings in younger, unimpaired users [15], where we observed more consistent reductions in muscle effort. This disparity may indicate that OA participants optimize additional factors, including pain, that influence muscle activation patterns, or they may simply require more acclimation time because older age slows motor adaptation to exoskeletons [24]. Previous work suggests that extended training periods may improve device integration and motor adaptation, thereby enhancing efficacy [25].

An intriguing observation is that pain reduction occurred in some cases despite increases in muscle activation. This challenges the hypothesis that higher quadriceps EMG levels directly correlate with increased joint forces and exacerbated patellofemoral pain. Some studies investigating the neural adaptations with exoskeletons [26], suggest that increased activation may reflect altered muscle recruitment patterns rather than increased joint loading. Future work should further explore the mechanisms underlying pain relief and the complex relationship between muscle activation and joint forces in patients with knee OA.

C. Study Limitations and Future Work

Several limitations of this study warrant discussion. First, the exoskeleton's maximum assistive torque was capped at 25 Nm due to motor constraints, which may have limited its effectiveness for users requiring greater support. This may have been exacerbated by removing the medial thigh plate from the exoskeleton in [15] (to prevent a structural moment in the frontal plane), which may have reduced the effective transmission of assistive torque to the user. Second, task-specific constraints on peak knee extension velocity, particularly during SA, RA, and STS movements, may have introduced variability in kinematic patterns, complicating EMG comparisons across conditions. Developing more precise gait kinematic constraints could improve alignment of muscle activation patterns in future studies, particularly for level walking and descent tasks. Lastly, the potential influence of muscle co-contraction on EMG data should be considered. Co-contraction may have contributed to apparent increases in muscle activation, particularly in tasks requiring stabilization or balance. Incorporating antagonist muscle activation measurements in future analyses could provide a more comprehensive understanding of the exoskeleton's impact on joint loading and pain perception. Future research should focus on addressing the aforementioned limitations while investigating long-term effects, acclimatization processes, and optimization of control strategies for broader clinical and biomechanical applications. Furthermore, future studies should involve larger, more diverse populations to increase the statistical power of these findings.

V. Conclusion

This study provides compelling evidence that backdrivable knee exoskeletons can provide acute reductions in pain and difficulty during a range of locomotor tasks. By addressing several critical limitations of conventional and modern knee-assistive devices, our approach offers new insights into improving knee function and alleviating discomfort. While we cannot definitively link reduced muscle activation to decreased pain, results show the exoskeleton helps users perform previously challenging tasks more comfortably. For example, this relief may enable individuals with OA to engage in physical activities that would otherwise be too painful, fostering muscle strength and potentially slowing the progression of OA. As such, the exoskeleton represents a promising alternative treatment for knee OA. By offering targeted assistance when needed, backdrivable exoskeletons may offer a significant advancement in the non-invasive management of knee OA, with the potential to improve mobility and enhance the quality of life for patients. Further research with larger sample sizes is needed to validate these findings.

References

[1] L. Murphy, T. A. Schwartz, C. G. Helmick, J. B. Renner, G. Tudor, G. Koch, A. Dragomir, W. D. Kalsbeek, G. Luta, and J. M. Jordan, "Lifetime risk of symptomatic knee osteoarthritis," *Arthritis Care & Research*, vol. 59, no. 9, pp. 1207–1213, 2008.

[2] R. Duncan, G. Peat, E. Thomas, L. Wood, E. Hay, and P. Croft, "Does isolated patellofemoral osteoarthritis matter?" *Osteoarthritis and Cartilage*, vol. 17, no. 9, pp. 1151–1155, Sep. 2009.

[3] R. C. Duncan, E. M. Hay, J. Saklatvala, and P. R. Croft, "Prevalence of radiographic osteoarthritis—it all depends on your point of view," *Rheumatology*, vol. 45, no. 6, pp. 757–760, Jun. 2006.

[4] R. D. Heekin and A. A. Fokin, "Incidence of Bicompartmental Osteoarthritis in Patients Undergoing Total and Unicompartmental Knee Arthroplasty: Is the Time Ripe for a Less Radical Treatment?" *The Journal of Knee Surgery*, vol. 27, pp. 77–82, Jul. 2013.

[5] S. C. O'Reilly, A. Jones, K. R. Muir, and M. Doherty, "Quadriceps weakness in knee osteoarthritis: the effect on pain and disability," *Annals of the Rheumatic Diseases*, vol. 57, no. 10, pp. 588–594, Oct. 1998.

[6] S. Amin, K. Baker, J. Niu, M. Clancy, J. Goggins, A. Guermazi, M. Grigoryan, D. J. Hunter, and D. T. Felson, "Quadriceps strength and the risk of cartilage loss and symptom progression in knee osteoarthritis," *Arthritis & Rheumatism*, vol. 60, no. 1, pp. 189–198, 2009.

[7] J. Dekker, P. Tola, G. Aufdemkampe, and M. Winckers, "Negative affect, pain and disability in osteoarthritis patients: the mediating role of muscle weakness," *Behaviour Research and Therapy*, vol. 31, no. 2, pp. 203–206, Feb. 1993.

[8] J. Heino Brechter and C. M. Powers, "Patellofemoral stress during walking in persons with and without patellofemoral pain," *Medicine and science in sports and exercise*, vol. 34, no. 10, pp. 1582–1593, Oct. 2002.

[9] G. B. Salsich, J. H. Brechter, D. Farwell, and C. M. Powers, "The Effects of Patellar Taping on Knee Kinetics, Kinematics, and Vastus Lateralis Muscle Activity During Stair Ambulation in Individuals With Patellofemoral Pain," *Journal of Orthopaedic & Sports Physical Therapy*, vol. 32, no. 1, pp. 3–10, Jan. 2002.

[10] A. R. Budarick, B. E. MacKeil, S. Fitzgerald, and C. D. Cowper-Smith, "Design Evaluation of a Novel Multicompartment Unloader Knee Brace," *Journal of Biomechanical Engineering*, vol. 142, no. 014502, Nov. 2019.

[11] C. A. McGibbon, S. Brandon, E. L. Bishop, C. Cowper-Smith, and E. N. Biden, "Biomechanical Study of a Tricompartmental Unloader Brace for Patellofemoral or Multicompartment Knee Osteoarthritis," *Frontiers in Bioengineering and Biotechnology*, vol. 8, Jan. 2021.

[12] N. Fukutani, H. Iijima, T. Aoyama, Y. Yamamoto, M. Hiraoka, K. Miyanobu, M. Jinnouchi, E. Kaneda, T. Tsuboyama, and S. Matsuda, "Knee pain during activities of daily living and its relationship with physical activity in patients with early and severe knee osteoarthritis," *Clinical Rheumatology*, vol. 35, no. 9, pp. 2307–2316, Sep. 2016.

[13] C. McGibbon, A. Sexton, A. Jayaraman, S. Deems-Dluhy, E. Fabara, C. Adans-Dester, P. Bonato, F. Marquis, S. Turmel, and E. Belzile, "Evaluation of a lower-extremity robotic exoskeleton for people with knee osteoarthritis," *Assistive Technology*, vol. 34, no. 5, pp. 543–556, Sep. 2022.

[14] ROAM, "Press," 2024. [Online]. Available: https://www.roamrobotics.com/press

[15] N. V. Divekar, G. C. Thomas, A. R. Yerva, H. B. Frame, and R. D. Gregg, "A versatile knee exoskeleton mitigates quadriceps fatigue in lifting, lowering, and carrying tasks," *Science Robotics*, vol. 9, no. 94, Sep. 2024.

[16] S. Seok, A. Wang, M. Y. Chuah, D. J. Hyun, J. Lee, D. M. Otten, J. H. Lang, and S. Kim, "Design Principles for Energy-Efficient Legged Locomotion and Implementation on the MIT Cheetah Robot," *IEEE/ASME Transactions on Mechatronics*, vol. 20, no. 3, pp. 1117–1129, Jun. 2015.

[17] G. Kenneally, A. De, and D. E. Koditschek, "Design Principles for a Family of Direct-Drive Legged Robots," *IEEE Robotics and Automation Letters*, vol. 1, no. 2, pp. 900–907, Jul. 2016.

[18] H. Zhu, C. Nesler, N. Divekar, V. Peddinti, and R. D. Gregg, "Design principles for compact, backdrivable actuation in partial-assist powered knee orthoses," *IEEE/ASME Transactions On Mechatronics*, vol. 26, no. 6, pp. 3104–3115, 2021.

[19] C. Nesler, G. Thomas, N. Divekar, E. J. Rouse, and R. D. Gregg, "Enhancing voluntary motion with modular, backdrivable, powered hip and knee orthoses," *IEEE robotics and automation letters*, vol. 7, no. 3, pp. 6155–6162, 2022, publisher: IEEE.

[20] S. Rezazadeh, D. Quintero, N. Divekar, E. Reznick, L. Gray, and R. D. Gregg, "A phase variable approach for improved rhythmic and non-rhythmic control of a powered knee-ankle prosthesis," *IEEE Access*, vol. 7, pp. 109 840–109 855, 2019.

[21] J. Lin, G. C. Thomas, N. V. Divekar, V. Peddinti, and R. D. Gregg, "A Modular Framework for Task-Agnostic, Energy Shaping Control of Lower Limb Exoskeletons," *IEEE Transactions on Control Systems Technology*, vol. 32, no. 6, pp. 2359–2375, Nov. 2024.

[22] E. M. K. Roos, L.S Lohmander, "WOMAC Osteoarthritis Index: Reliability, validity, and responsiveness in patients with arthroscopically assessed osteoarthritis," *Scandinavian Journal of Rheumatology*, vol. 28, no. 4, pp. 210–215, Jan. 1999.

[23] X. Hu, N. T. Pickle, A. M. Grabowski, A. K. Silverman, and S. S. Blemker, "Muscle eccentric contractions increase in downhill and high-grade uphill walking," *Frontiers in bioengineering and biotechnology*, vol. 8, 2020.

[24] A. Lakmazaheri, S. Song, B. B. Vuong, B. Biskner, D. M. Kado, and S. H. Collins, "Optimizing exoskeleton assistance to improve walking speed and energy economy for older adults," *Journal of NeuroEngineering and Rehabilitation*, vol. 21, no. 1, p. 1, Jan. 2024.

[25] K. L. Poggensee and S. H. Collins, "How adaptation, training, and customization contribute to benefits from exoskeleton assistance," *Science Robotics*, vol. 6, no. 58, Sep. 2021.

[26] S. Tortora, L. Tonin, S. Sieghartsleitner, R. Ortner, C. Guger, O. Lennon, D. Coyle, E. Menegatti, and A. D. Felice, "Effect of Lower Limb Exoskeleton on the Modulation of Neural Activity and Gait Classification," *IEEE Transactions on Neural Systems and Rehabilitation Engineering*, vol. 31, pp. 2988–3003, 2023.

Design Evaluation of a Passive Ankle Exoskeleton for Gait Training

Mac Camardo[1,3], Leah O'Shea[3], Valentino Wilson[1,3], Courtney Celian[3], Adith V. Srivatsa[1,3], Myunghee Kim[2], James L. Patton[1,3]

[1] Richard and Loan Hill Department of Biomedical Engineering, University of Illinois Chicago, Chicago, IL
[2] Department of Mechanical & Industrial Engineering, University of Illinois Chicago, Chicago, IL
[3] Robotics Lab, Shirley Ryan AbilityLab, Chicago, IL

***Abstract*— Stroke survivors often experience severe gait impairments that reduce mobility and independence, highlighting the need for innovative and practical rehabilitation solutions. Many existing devices are limited by their high cost, complexity, or invasive nature, making them inadequate for widespread use in clinical and at-home settings. To address these challenges, we introduce the LegExoNET, a passive lower-limb exoskeleton capable of providing both assistance and resistance in ankle dorsiflexion and plantarflexion. During mechanical testing, the torques applied by the device decrease non-linearly with a decrease in ankle angle. The device's lightweight, modular design ensures versatility and accessibility, establishing the LegExoNET as a promising tool for enhancing gait rehabilitation and promoting motor learning. Future work will include expanding to a multi-joint device while incorporating additional functions such as leg propulsion assistance.**

Keywords*— *Passive Exoskeleton, Ankle, Elastic Torque, Dorsiflexion, Plantarflexion, Stroke Rehabilitation

I. INTRODUCTION

Stroke is one of the leading causes of long-term disability [1]. Survivors oftentimes experience abnormal movement pattern and muscles weakness, that manifest into long-term gait impairments [2], [3]. This can hinder mobility and independence, increases fall risk, and promotes compensatory movements resulting in future orthopedic injury.

Gait devices targeted towards stroke are often costly, invasive, and tethered to complex systems, falling short in promoting lasting motor recovery. Functional electrical stimulation, a widely used method for addressing gait impairments like foot drop, relies on sensor technology to determine stimulation timing but can lead to muscle fatigue, potentially limiting its effectiveness in addressing the main causes of movement deficits [5], [6], [7]. Motor-powered exoskeletons can assist in proper foot clearance, but these devices are complex with various sets of motors, electrical sensors, and cables [4], [8]. Plus, they do not require the user's muscles to exert significant effort in moving the limb or ankle, limiting muscle engagement and strength development. Passive ankle exoskeletons have been attempted before, but they are often bulky, provide limited functionality, and lack adaptability for rehabilitation applications. Many designs rely on fixed stiffness mechanisms or pre-set resistance levels, restricting their ability to dynamically adjust torque output based on user needs. Additionally, these devices often require complex attachment mechanisms or rigid structures that limit ease of use [9], [10], [11]. Other commercial devices tend to keep the ankle in a fixed position to stabilize movement, which does little to facilitate functional recovery [12]. There is a critical need for innovative rehabilitation solutions that promote functional recovery through adaptive motor learning strategies.

Skill acquisition is a function of assistance and error augmentation (EA) and occurs during the progression from guidance and assist-as-needed training to independent practice where errors are deliberately increased to enhance learning [13]. Motor learning can occur when assistance is reduced, and difficulty is increased through error amplification. In clinical practice, physical therapists often use resistance bands to target poor eccentric control by manually assisting limb advancement during the swing phase, which is an example of transitioning between these stages [13]. The inclusion of this concept in innovative rehabilitation solutions has the potential to address the essential clinical need for adaptive motor learning strategies that promote functional recovery through tailored error feedback and skill progression.

Our solution is the LegExoNET (Exoskeletal Network for Elastic Torque) a novel, passive lower-limb exoskeleton designed to enhance rehabilitation through various applications, one of such that we describe in this paper is the use of assistance. The LegExoNET acts as an exotendon, storing elastic energy during movement and releasing it to aid propulsion while allowing for free and natural limb motion [14]. It may compensate for deficits like foot drop, provide support against gravity, and promote adaptive motor learning by exaggerating movement errors when desired. The LegExoNET has a lightweight, modular design that allows for stacked elastic elements, enabling greater torque output, adjustability, and seamless integration with the user's natural movement. In this paper, we will explore the design, modeling framework, and mechanical performance of the

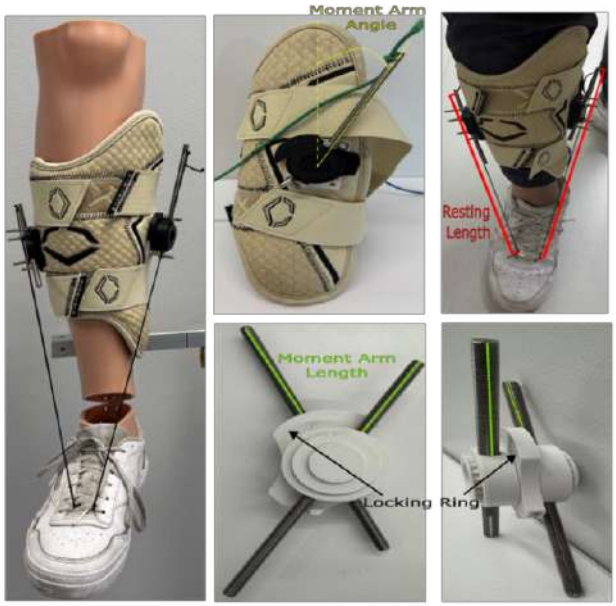


Fig. 1. Architecture of the LegExoNET

LegExoNET based on previously discussed concepts and optimization [15], [16], [17], [18].

II. METHODS

A. LegExoNET Design

The current LegExoNET design aims to achieve two primary functions to enhance rehabilitation: (1) challenge users to stabilize against exaggerated ankle dorsiflexion and a change in leg propulsion forces during the swing phase of gait; and (2) assist users in a movement when needed, facilitating controlled and adaptive engagement.

The LegExoNET is composed of a spring network system of elastic bands that run from the user's shank to a distal point of the user's shoe, attached by threaded rods. The threads allow for seamless adjustability of the moment arm during real-time adjustments. The threaded rods insert into a polylactic acid 3D printed indexed mechanism, which allows the moment arm to pivot freely in 18° increments, allowing granularity for the moment arm angle. A locking mechanism secures the moment arm in place with a locking ring. This configuration allows for real-time adjustments of the moment arm length and angle, and resting length of the elastic bands (Fig. 1). All components are secured to a rigid structure that attaches to the user's shank to ensure stability of the components.

The LegExoNET also includes a unique feature of stacked tension elements, which can increase the elastic torque produced by the spring network system. This enhancement allows for greater support and adaptability, making it highly effective in addressing various levels of resistance across different training applications.

We can achieve the different configurations via our graphical user interface that allows clinicians or patients to adjust the design and structure of the device in real-time, where the therapist is able to adjust the parameters and then held static when the user walks in it. The use of this interface is to obtain the settings for the moment arm length, moment arm angle (theta), and resting length of the bungee based on the user characteristics of height, weight, and device mode. The two modes that are tested in this study are assistance, the elastic band is stretched taut, and no-assistance, the elastic band is at full slack. The use of passive springs (elastic bands) ensures that the device is lightweight, portable, and safe to operate. Moreover, the device does not require any charging or rebooting, providing a convenient and accessible solution for individuals with motor impairments.

B. Theoretical Framework

The mechanics of the LegExoNET device are defined by the torques (τ) generated through the interaction of spring elements with the joint. These torques are calculated as the vector product of the spring element's moment arm (ρ) and the applied force (F), as shown in the equation:

$$\tau = \rho \times F \tag{1}$$

where ρ is determined by the distance between the attachment points on the proximal (X_o) and distal (X_i) segments of the limb. F_s is the force exerted by the spring element, governed by Hooke's Law:

$$F_s = -k(l - l_o) \tag{2}$$

where, k is the spring constant, l is the current length of the spring, and l_o is the slack length of the spring. This spring force function can be replaced by a more complex, nonlinear function to account for different impedance properties, such as those encountered in elastic cords.

In the LegExoNET, multiple spring elements can be combined in "stacks", where each individual spring creates a torque τ_i based on the joint angle θ_s, the attachment points (X_o, X_i), and the spring's impedance function. The total torque produced by all the stacked elements is the sum of their individual torques:

$$\tau_{total} = \sum_{i=1}^{n} \tau_i \tag{3}$$

where n is the number of stacked spring elements. Each of these spring elements contributes to the desired movement or resistance by applying torque that is a nonlinear function of the joint angle and the spring's characteristics, including its slack length, l_o.

To optimize the system, a quadratic cost function minimization approach is used. The goal is to minimize the difference between the desired torque output and the actual torque produced by the system at a set of test points within the configuration space. This is expressed as:

$$Minimum\ Cost = \sum_{k=0}^{N_{Test\ Points}} (\widehat{\tau_k} - \tau_k)^2 + R^2 \tag{4}$$

where $\widehat{\tau_k}$ is the desired torque at test point k, τ_k is the actual torque produced by the system at point k, $N_{Test\ Points}$ is the

number of points used for testing within the configuration space, and R is a regularization term that increases the cost function to penalize undesirable configurations, such as springs that are too long or that may cause unintended attachment penetration or mechanical issues like structural failure.

Additionally, constraints on the spring's geometry, such as limiting the slack length to ensure appropriate tension is maintained during the movement. This approach ensures that the optimization not only produces the desired functional output but also guarantees that the device operates within safe and feasible physical limits.

C. Mechanical Testing

To quantify the mechanical performance of the LegExoNET, we conducted a controlled mechanical test using a mannequin leg model. This test aimed to experimentally determine the torque produced by the device as it interacts with a dynamic ankle joint.

A Mark-10 force sensor (Johnson Scale & Balance Co., USA) was mounted next to the leg and was aligned with the line of action of the device's moment arm (Fig. 2). The moment arm attachment on the force sensor was designed to rotate dynamically, allowing it to freely move as the ankle was manually moved through dorsiflexion and plantarflexion. The dynamic rotation of the moment arm attachment on the force sensor ensured that the force measurement accurately reflected the torque output at various points in the range of motion.

Human motion video analysis software (Kinovea, France) was used to analyze the angle and bungee length change during all trials. The results from this test can help validate the device's ability to deliver appropriate torque for assisting or resisting ankle movements. The data can also inform future adjustments to the bungee cord stiffness or resting length for optimal performance.

III. Results

A. Mechanical Testing

Fig. 3 displays the relationship between ankle torque and angular displacement across each of the three trials. In the photo, the ankle angle is displayed as the teal angle dimension and the spring length is in orange. The overall trend

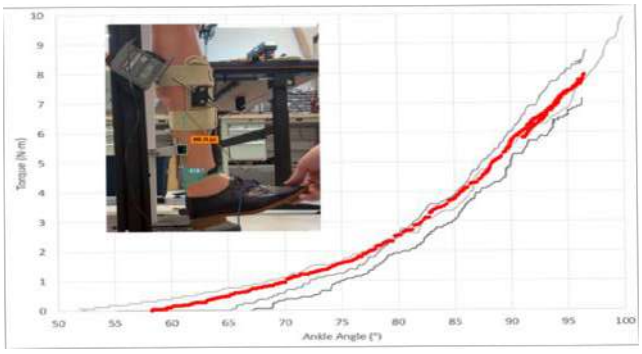


Fig. 3. Torque vs. Angle of the Ankle During Plantarflexion



Fig. 2 Mechanical Testing Experimental Setup

(displayed in red on the graph) demonstrates a consistent pattern of increasing torque with increasing angle. It is important to note that the measured torques were not normalized for mass, so the absolute torque values reported reflect the raw mechanical output of the device.

IV. Discussion

A. Mechanical Test

The torque-angle graph and the response of the leg mannequin model demonstrate a nonlinear relationship, where the bungee cords apply increasing resistance during plantarflexion. This progressive tensioning suggests that plantarflexion range of motion may be restricted, potentially leading to reduced plantarflexor muscle activity. Additionally, based on the observed response of the mannequin model, we noted that upon tension release, the stored energy in the bungee cords facilitated dorsiflexion. This recoil effect after peak plantarflexion (when tension is highest) suggests that the device may assist dorsiflexion by reducing the effort required by the tibialis anterior (TA), potentially offloading the dorsiflexor muscles.

One primary concern when experimenting with bungee cords is the elastic material fatigue over time. Repeated stretching and relaxation of the elastic bands could potentially lead to material degradation, reducing their stiffness and altering the torque output. This effect, known as hysteresis, could result in inconsistent assistance or resistance, especially after prolonged use.

B. Clinical Applications

The advantage of the LegExoNET is its potential ability to be tailored by the user to deliver a wide range of therapeutic forces, whether for assistance or restorative outcomes [20]. One such force includes error augmentation (EA); a training mechanism that employs perturbations or

resistance to intentionally amplify biomechanical errors, which can enhance the feedback provided to the user [21]. This approach increases corticospinal excitability, muscle activity, altered kinematics, and interlimb coordination; ultimately aiming to improve motor learning and movement control [22], [23]. EA creates opportunities for error feedback, which is crucial for refining motor skills. The effectiveness of this mechanism relies on a functional cerebellum, as it plays a key role in developing an "internal model" that enables predictive feedforward adaptations to movement [24]. As errors are introduced, the internal model can be updated based on feedback until the movement error is reduced. Counter intuitively, the temporary introduction of errors can lead to long-term improvements in movement efficiency and control.

The LegExoNET's adaptability may replace the need for therapists to manually apply resistance bands for error augmentation in gait therapy, making it ideal for both clinical and at-home use. We developed a framework that allows us to adaptively modify the torque applied by the LegExoNET device at different points in the gait cycle. This adaptability may enable us to either decrease or increase muscle activity as needed, creating personalized assistance or resistance tailored to an individual's rehabilitation needs while promoting motor learning during gait training.

C. *Future Work and Limitations*

We plan to conduct clinical trials with both able-bodied participants and stroke survivors. Once IRB approval is officially obtained, the device will be tested for its ability to improve gait symmetry and motor learning in stroke survivors. Additionally, we will incorporate EMG analysis to evaluate muscle activation patterns, providing further insight into how the device influences muscular engagement and motor adaptation during gait rehabilitation.

We also plan to collaborate with physical therapists to refine the device and incorporate real-time feedback to further optimize its functionality and usability. This also will lead us to implement a multi-joint network system that can assist with knee and hip torques along with the ankle.

Next iterations of this assistive device could improve by fine-tuning configurations through optimization algorithms to better control where assistance or resistance is applied based on the individual needs of the patient. For instance, optimized configurations could provide targeted assistance during push-off to address plantarflexion weakness or during swing to prevent foot drop resulted from dorsiflexion weakness. Similarly, controlled resistance could be implemented to promote muscle strengthening or motor learning. By incorporating human-in-the-loop optimization techniques, the device could adjust its settings to maximize therapeutic outcomes. These configurations would need to be manually adjusted based on the user's specific needs. The LegExoNET offers a flexible, adjustable approach to assist and enhance gait, allowing for more dynamic and customizable support without restricting natural joint movement.

A limitation of our study was that we focused on a single torque profile configuration, rather than exploring multiple configurations to fully demonstrate the device's adaptability. Future work will expand on this by testing various moment arm and elastic element configurations to verify the range of torques that can be achieved throughout the gait cycle with our device.

V. Conclusion

The LegExoNET device shows potential as both an assistive and restorative device to improve performance of activities of daily living (ADLs). It may help mitigate gait impairments experienced by individuals with neurological impairments. Future designs hope to restore function by strengthening muscles involved in gait, particularly through its customizable resistance and error augmentation features, which promote adaptive motor learning. Initially designed for stroke survivors with hemiparesis, the LegExoNET may also extend its applications to include individuals with spinal cord injuries (SCI), muscular dystrophy, and other neurological diagnoses, helping them achieve greater independence and stability during movement. Its versatility also makes it an ideal training tool for physical therapists, where it provides safe, effective support without requiring constant clinical supervision.

VI. Acknowledgments

We would like to thank the Robotics Lab at the Shirley Ryan AbilityLab, the Richard and Loan Hill Department of Biomedical Engineering at the University of Illinois Chicago and the Rehabilitation Robotics Laboratory at the University of Illinois Chicago. This study was funded by NIDLRR grant 90REGE0005-01 Collaborative Machines Enhancing Therapies (COMET). The authors declare that there are no conflicts of interest.

VII. References

[1] CDC, "Stroke Facts," Stroke. Accessed: Nov. 08, 2024. [Online]. Available: https://www.cdc.gov/stroke/data-research/facts-stats/index.html

[2] H.-S. Kim *et al.*, "Primary and secondary gait deviations of stroke survivors and their association with gait performance," *J. Phys. Ther. Sci.*, vol. 28, no. 9, p. 2634, Sep. 2016, doi: 10.1589/jpts.28.2634.

[3] H. Abe, A. Michimata, K. Sugawara, N. Sugaya, and S.-I. Izumi, "Improving gait stability in stroke hemiplegic patients with a plastic ankle-foot orthosis," *Tohoku J. Exp. Med.*, vol. 218, no. 3, pp. 193–199, Jul. 2009, doi: 10.1620/tjem.218.193.

[4] E. M. Gutierrez-Farewik, R. Wang, Y. Liu, and X. Zhang, "Soft ankle exoskeleton to counteract dropfoot and excessive inversion," *Front. Neurorobotics*, vol. 18, Aug. 2024, doi: 10.3389/fnbot.2024.1372763.

[5] "Walkaide FES – AxioBionics, LLC." Accessed: Nov. 08, 2024. [Online]. Available: https://www.axiobionics.com/walkaide-fes/

[6] J. Malešević, L. Konstantinović, G. Bijelić, and N. Malešević, "Smart Protocols for Physical Therapy of Foot Drop Based on Functional Electrical Stimulation: A Case Study," *Healthcare*, vol. 9, no. 5, p. 502, Apr. 2021, doi: 10.3390/healthcare9050502.

[7] B. Dreibati, C. Lavet, A. Pinti, and G. Poumarat, "Influence of electrical stimulation frequency on skeletal muscle force and fatigue," *Ann. Phys. Rehabil. Med.*, vol. 53, no. 4, pp. 266–277, May 2010, doi: 10.1016/j.rehab.2010.03.004.

[8] M. Zorkot, L. H. Dac, E. Morya, and F. L. Brasil, "G-Exos: A wearable gait exoskeleton for walk assistance," *Front. Neurorobotics*, vol. 16, Nov. 2022, doi: 10.3389/fnbot.2022.939241.

[9] A. C. Inc, "ABBY™ AFO Ankle Foot Orthosis | Anatomical Concepts, Inc." Accessed: Feb. 19, 2025. [Online]. Available: https://www.anatomicalconceptsinc.com/abby-articulating-ankle-foot-orthosis-afo

[10] X. Wu, A. Ide, K. Osawa, K. Nakagawa, L. Yuge, and E. Tanaka, "Development of a motorless walking assistive device for foot flexions with instant torque output in gait cycle," *J. Adv. Mech. Des. Syst. Manuf.*, vol. 17, no. 4, 2023, doi: 10.1299/jamdsm.2023jamdsm0053.

[11] E. Etenzi, R. Borzuola, and A. M. Grabowski, "Passive-elastic knee-ankle exoskeleton reduces the metabolic cost of walking," *J. NeuroEngineering Rehabil.*, vol. 17, no. 1, p. 104, Jul. 2020, doi: 10.1186/s12984-020-00719-w.

[12] "SaeboStep Foot Drop Brace | Best Soft AFO - Stroke," Saebo. Accessed: Nov. 08, 2024. [Online]. Available: https://www.saebo.com/products/saebostep

[13] T. G. Hornby, "Potential Utility of Providing High Intensity, Variable Step Training for Improving Locomotion in Patients Across Neurological Disorders," Chicago, IL, Jun. 05, 2014.

[14] A. J. van den Bogert, "Exotendons for assistance of human locomotion," *Biomed. Eng. OnLine*, vol. 2, no. 1, p. 17, Oct. 2003, doi: 10.1186/1475-925X-2-17.

[15] B. Malizia, M. Jacobsorr, P. Ryali, M. Kim, and J. L. Patton, "Theoretical Development of a Knee-Ankle ExoNET to Supplement Muscle Function," in *2022 9th IEEE RAS/EMBS International Conference for Biomedical Robotics and Biomechatronics (BioRob)*, Aug. 2022, pp. 1–6. doi: 10.1109/BioRob52689.2022.9925522.

[16] B. Malizia, P. Ryali, and J. Patton, "Passive Exotendon Spring Elements can replace Muscle Torque during Gait," in *2020 8th IEEE RAS/EMBS International Conference for Biomedical Robotics and Biomechatronics (BioRob)*, Nov. 2020, pp. 773–778. doi: 10.1109/BioRob49111.2020.9224297.

[17] Srivatsa, Adith V *et al.*, "Abnormal Synergies and Muscle Weakness Identified in Stroke Survivors via Wrist Position Probability Distributions," presented at the International Conference on Rehabilitation Robotics (ICORR), Chicago, IL, USA: IEEE, May 2025, p. Accepted. doi: pending.

[18] V. Wilson *et al.*, "Structural Optimization of a Passive ExoNET for Forearm Supination," in *International Conference on Rehabilitation Robotics (ICORR)*, Chicago, IL, USA: IEEE, May 2025, p. Accepted. doi: Pending.

[19] A. Schmitz, A. Silder, B. Heiderscheit, J. Mahoney, and D. G. Thelen, "Differences in lower-extremity muscular activation during walking between healthy older and young adults," *J. Electromyogr. Kinesiol. Off. J. Int. Soc. Electrophysiol. Kinesiol.*, vol. 19, no. 6, pp. 1085–1091, Dec. 2009, doi: 10.1016/j.jelekin.2008.10.008.

[20] K. Hohl, PT, DPT, NCS, "High Intensity Gait Training: Error Augmentation," May 09, 2022.

[21] G. Severini, "A Perspective on the Use of Error Augmentation in Robot-Assisted Gait Training of StrokeSurvivors," in *Converging Clinical and Engineering Research on Neurorehabilitation III*, L. Masia, S. Micera, M. Akay, and J. L. Pons, Eds., Cham: Springer International Publishing, 2019, pp. 153–156. doi: 10.1007/978-3-030-01845-0_30.

[22] T. Lam, K. Luttmann, A. Houldin, and C. Chan, "Treadmill-based locomotor training with leg weights to enhance functional ambulation in people with chronic stroke: a pilot study," *J. Neurol. Phys. Ther. JNPT*, vol. 33, no. 3, pp. 129–135, Sep. 2009, doi: 10.1097/NPT.0b013e3181b57de5.

[23] D. S. Reisman, A. J. Bastian, and S. M. Morton, "Neurophysiologic and rehabilitation insights from the split-belt and other locomotor adaptation paradigms," *Phys. Ther.*, vol. 90, no. 2, pp. 187–195, Feb. 2010, doi: 10.2522/ptj.20090073.

[24] A. J. Bastian, "Learning to predict the future: the cerebellum adapts feedforward movement control," *Curr. Opin. Neurobiol.*, vol. 16, no. 6, pp. 645–649, Dec. 2006, doi: 10.1016/j.conb.2006.08.016.

Theoretical Evaluation of DE-AFO-1550: a Comfortable Robotic Ankle Exoskeleton for Children with Cerebral Palsy Powered by Advanced Stacked Dielectric Elastomer Actuators

1st Mobina Masaei
Department of Biomechanics
University of Nebraska Omaha
Omaha, NE
mmasaeikoroyeh@unomaha.edu

2nd Vahid Mohammadi
Department of Biomechanics
University of Nebraska Omaha
Omaha, NE
vmohammadi@unomaha.edu

3rd Mohammad Tajdani
Independent Researcher
University of Tehran
Tehran, Iran
mohammadtajdani@gmail.com

4th Ahad Behboodi
Department of Biomechanics
University of Nebraska Omaha
Omaha, NE
abehboodi@unomaha.edu

***Abstract*— Cerebral palsy (CP), the most prevalent motor disorder in children, significantly impairs gait, often due to deficiencies in ankle control. Traditional ankle-foot orthoses (AFOs) used in CP management provide passive support but restrict natural ankle motion, resulting in muscle atrophy and limited adaptability. Powered AFOs, while offering propulsion assistance, are frequently bulky and uncomfortable, hindering long-term use. We designed an innovative, biomimetic AFO in our most recent study. Named DE-AFO, this device employs artificial muscles made from an electroactive polymer actuator called dielectric elastomer (DEA) to assist ankle movements in the sagittal plane. DE-AFO features a gait-phase detection controller that synchronizes the artificial muscles with the user's natural gait cycle, mimicking the behavior of biological muscles while maintaining a lightweight, compact, and silent design. This study builds upon the initial DE-AFO model by incorporating the latest version of the commercially available and stacked configuration of DEA (SDEA-1550), which offers enhanced force and displacement capabilities. Testing was expanded to include three participants with spastic diplegic CP to theoretically test and evaluate the updated DE-AFO's (DE-AFO-1550's) effectiveness in compensating for ankle moment deficits. The DE-AFO-1550 could fully compensate for dorsiflexion deficits (100%) during the swing phase and address 75% of plantarflexion deficits during the pre-swing. These findings highlight the DE-AFO-1550's potential as a next-generation, user-centered robotic AFO, capable of significantly improving mobility and quality of life for individuals with CP.**

Keywords—Cerebral Palsy, AFO, Exoskeleton, Dielectric Elastomer, Artificial Muscle

I. INTRODUCTION

Cerebral palsy (CP) represents the most common movement disorder among children, with an observed prevalence of approximately 2 to 3 cases per 1,000 in the general population [1]. Among the primary challenges in CP are deficiencies in ankle control, which significantly impact gait and contribute to instability, slower gait speeds, and increased risks of falls and injuries [2]. Gait generally stabilizes by age four, highlighting the importance of early detection and intervention for optimal motor development [3]. Over time, mobility often declines in individuals with CP, impacting their independence, physical activity levels, and social engagement [4]. Additionally, inactivity due to gait impairments increases the risks of secondary health issues, such as cardiovascular disease, and is associated with a higher mortality rate [5], [6].

Traditional ankle-foot orthoses (AFOs) are frequently prescribed for individuals with spastic CP due to their capacity to provide passive support. However, these devices are predominantly rigid and cumbersome, resulting in restricted ankle mobility and limited active muscle engagement. This design not only diminishes natural movement but also contributes to muscle atrophy and skin discomfort. Furthermore, these orthoses may inhibit sensory feedback and adaptive motor control during ambulation, consequently impacting the overall mobility and stability of the user [7], [8]. In contrast, powered AFOs have been engineered to actively generate torque, specifically aiding the plantarflexor muscles in facilitating the forward propulsion of the center of mass during walking [9], [10], [11], [12]. Despite these advancements, the majority of current models operate using DC motors [13], [14] or pneumatic actuators [15], [16], [17], which are generally ill-suited for proximity to the human body due to their rigid and inflexible structures. This rigidity may further restrict natural joint movement, potentially causing pressure sores and discomfort, similar to the issues commonly observed with traditional AFOs. Additionally, the bulky, heavy, and noisy nature of these powered AFOs reduces user comfort and acceptance, thereby hindering their broader commercialization.

Cable-driven exoskeletons powered by DC motors have recently gained attention as more compact and flexible alternatives for AFOs, with devices like ReWalk Restore [18] and Biomotume [19] exemplifying this trend. Despite improved comfort, these systems are still cumbersome to wear and visually conspicuous. In an innovative direction, Park et al. introduced a bio-inspired soft AFO powered by pneumatic actuators, designed to closely mimic the natural muscular structure of the ankle joint. This design supported movement in both the sagittal plane (plantarflexion/dorsiflexion) and the frontal plane (eversion/inversion) [15]. However, current

pneumatic AFOs face limitations, including a substantial weight of approximately 2.5 kg and acoustic noise levels around 65 dB [20], [21], nearing the annoyance threshold of 70 dB (comparable to a washing machine) [22]. These drawbacks emphasize the urgent need for the development of actuators that are soft, lightweight, quiet, and compact, which closely replicate the characteristics of biological muscles. This advancement is essential for improving both the functionality and user comfort of AFO designs.

Soft electroactive polymer actuators, particularly dielectric elastomer actuators (DEAs), present a fast, efficient, and quiet alternative to traditional actuation methods. Renowned for their muscle-like properties, DEAs are increasingly recognized as one of the most promising candidates for soft actuator technologies.

Structurally, DEAs operate as compliant capacitors, comprising a thin elastic dielectric layer sandwiched between two flexible, conductive electrodes. When a DC voltage is applied across the electrodes, electrostatic forces—known as Maxwell pressure—act on the dielectric, compressing it in the thickness direction. This compression results in lateral expansion, generating displacement, force, and mechanical output (Fig. 1A). The simplicity of this mechanism not only allows DEAs to replicate the behavior of natural muscles but also provides significant design flexibility.

Among DEA designs, the stacked dielectric elastomer actuator (SDEA) configuration, developed by Kovacs et al. [23], is a powerful and versatile actuator that most closely resembles human skeletal muscle. This advanced actuator is created by stacking multiple thin, enhanced DEA layers, with each layer functioning similarly to a sarcomere within skeletal muscle (Fig. 1B). This SDEA configuration achieves impressive performance, generating 32 N of isometric force and 15% strain while lifting a 1.1 kg load [24]. We pioneered the benchmark testing of the mechanical properties of these actuators [25], [26]. Since SDEA mimics key characteristics of natural muscle, including the ability to contract longitudinally, provide flexibility, and generate forces and displacements similar to those produced by biological muscles, we referred to it as "artificial muscle".

Guided by insights from customer discovery supported by the NSF I-Corps (project #1906128) [27], we developed DE-AFO, a robotic AFO designed to prioritize user comfort and provide targeted plantarflexion (PF) assistance, two features identified as top priorities by AFO users and physical therapists. At the core of the DE-AFO's functionality is a finite state machine controller and advanced artificial muscles [28]. This setup enables the DE-AFO to detect the timing and direction of the assistive moment required in the sagittal plane and activate the corresponding set of artificial muscles. These muscles are strategically aligned in parallel with the natural action line of the ankle's biological muscles, enhancing their ability to support and facilitate natural ankle movement. To further enhance gait biomechanics, the DE-AFO includes a metatarsal joint, which facilitates a natural foot position during the push-off phase of gait (Fig. 2A), a significant advancement over traditional AFO designs.

For the initial theoretical evaluation of our design, we used ankle moment data from one representative child with CP

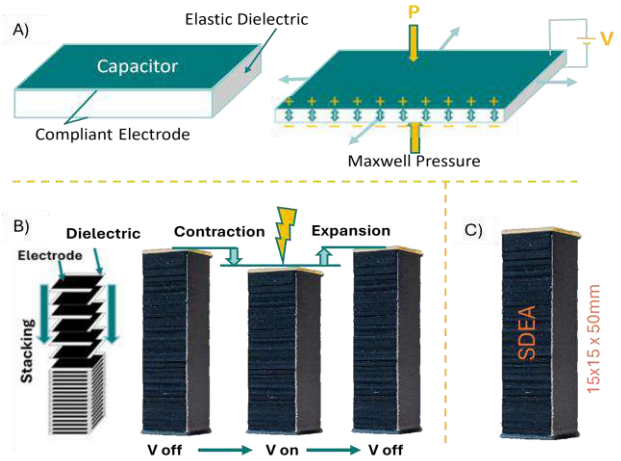


Fig. 1. A) Elastic Capacitor and Maxwell pressure creating displacement. B) Stacked dielectric elastomer actuator (SDEA) configuration consists of multiple layers of elastic capacitors. C) a real SDEA consists of about 2500 layers of capacitors.

(CP01) and seven typically developing (TD) children (Table 1). The results showed that the DE-AFO could compensate for 68% of the subject's PF deficit during the pre-swing phase and fully address the dorsiflexion (DF) deficit during the swing phase [28].

This original DE-AFO model employed CT-SDEAs, which we benchmark tested [25] and was capable of generating 3.3% strain and 10N of force (0.037 MPa of stress). In light of the substantial improvement in the stress and strain capabilities of the latest version of SDEA, the main objective of this study was to evaluate the performance of the DE-AFO powered by the latest SDEA in three children with CP following the similar analysis we reported for the previous version of the actuator [28].

II. Methods

A. Participants

Ankle moment data from three children with CP and seven TD children, originally collected in a separate study, were integrated into this analysis [29]. Participant details are summarized in Table 1. Two participants were recruited from a study approved by the University of Delaware Institutional Review Board (IRB) and registered on ClinicalTrials.gov (NCT05233748). Additionally, one participant from a separate study, approved under the IRB protocol 20459, was included in our analysis. Informed consent and assent were obtained from all participants.

For data collection, participants walked on a treadmill with reflective markers placed on anatomical landmarks of the lower limbs. Gait dynamics were recorded using a motion capture system (Motion Analysis Corporation, Santa Rosa, CA, USA) at a sampling rate of 128 Hz and two force plates (Bertec, Columbus, OH, USA) at 3200 Hz. The collected gait kinematics and kinetics were processed in Visual 3D (C-Motion Inc., Germantown, MD, USA).

B. Original DE-AFO Design

In the original DE-AFO design (Fig. 2), we employed SDEAs from CTsystems (model CT25.0-15-15-71, Compliant Transducer Systems, Dubendorf, Switzerland) as

the motor units of the artificial muscles that powered the device. To mimic the structure of biological muscle fibers, the SDEAs were arranged in series to form artificial myofibrils, enabling the actuator to achieve the required length shortening. Additionally, the force generation capability can be further enhanced by configuring multiple artificial myofibrils in parallel. As an example, a 1 × 3 artificial muscle consists of three SDEAs connected in series to form one artificial myofibril. Based on the manufacturer's report and our benchmark test results, each CT-SDEA can produce a force of 10N and a displacement of 1.17mm [25]. As a result, the 1 × 3 artificial muscle can achieve a displacement that is three times greater than that of an individual CT-SDEA, equals to 3.53mm, and 10N of force [28]. Our DE-AFO device incorporated two sets of 1 × 3 artificial muscles medially and laterally for dorsiflexion assistance and another two for plantarflexion, termed dorsiflexor and plantarflexor artificial muscles, respectively (Fig. 2A). Each artificial myofibril weighed 33.9 g (with each SDEA contributing 11.3 g), resulting in a total mass of 135.6 g for all the artificial muscles in the design. The overall weight of the DE-AFO was approximately 1250 g, which includes 900 g for electronics and 200 g for the mechanical structure.

Table 1. Detailed information on participants' age, gender, height, weight, Gross Motor Function Classification System (GMFCS), and self-selected walking speed (SSWS).

	Age (yrs)	Gender	Height (m)	Weight (kg)	GMFCS	SSWS (m/s)
TD01	16	M	1.78	71.92	-	0.8
TD02	10	M	1.46	32.55	-	0.8
TD03	10	F	1.46	31.95	-	1.2
TD04	12	F	1.59	43.25	-	1.25
TD05	12	F	1.47	36.42	-	1
TD06	14	F	1.55	52.61	-	1.1
TD07	13	F	1.73	56.29	-	1.1
CP01	12	M	1.37	25.89	I	0.9
CP02	12	M	1.52	41.50	II	0.75
CP03	13	F	1.31	32.13	III	0.45

C. *Theoretical Analysis, and Augmented DE-AFO Design*

To evaluate the theoretical performance of the DE-AFO, we examined its ability to compensate for ankle moment deficits in a representative child with CP. The deficit was calculated by subtracting the sagittal plane ankle moment of the CP subject, normalized to body mass, from the normative ankle moment of TD children. The normative data was generated by averaging the sagittal plane ankle moments of seven TD subjects, with each moment averaged over 30 gait cycles and normalized to body mass. To quantify the ankle moment deficit, we determined the difference between the normative TD data and the ankle moment of the CP child. Subsequently, the sagittal plane ankle moment generated by the DE-AFO was computed and compared with the identified deficit. This analysis allowed us to assess the forces required to restore ankle function closer to normative levels and evaluate the DE-AFO's effectiveness in generating the necessary compensatory forces [28].

While the DF requirements were adequately met using two artificial muscles, the initial configuration for PF assistance proved insufficient. To address this, the plantarflexor artificial muscles were replaced with a 4 × 3 configuration consisting of four 1 × 3 artificial myofibrils connecting together (Fig. 2B). This modification increased the system's capacity to approximately 68% of the required PF moment, enabling the DE-AFO to generate near-typical ankle moments and significantly improving functional outcomes for the user. However, the addition of these muscles increased the device's bulk, a drawback noted during user feedback.

D. *DE-AFO Powered by the Latest SDEA: DE-AFO-1550*

In this study, we integrated the latest version of SDEAs, produced by Dätwyler Schweiz AG (Schattdorf, Switzerland), as motor units in our updated DE-AFO. We named these actuators SDEA-1550, reflecting their dimensions of 15 × 15 × 50 mm. Accordingly, for the purposes of clarity, the DE-AFO powered by these SDEAs is referred to as DE-AFO-1550. In our previous research, we evaluated the axial stress and strain capabilities of SDEA-1550 [26]. Our findings demonstrated that the new SDEAs exhibited significant advancements in strain and stress capabilities, with improvements exceeding 200% compared to previous models. In particular, force generation has increased from 10N to 25.84 N, and displacement has risen from 3.3% to 11%,

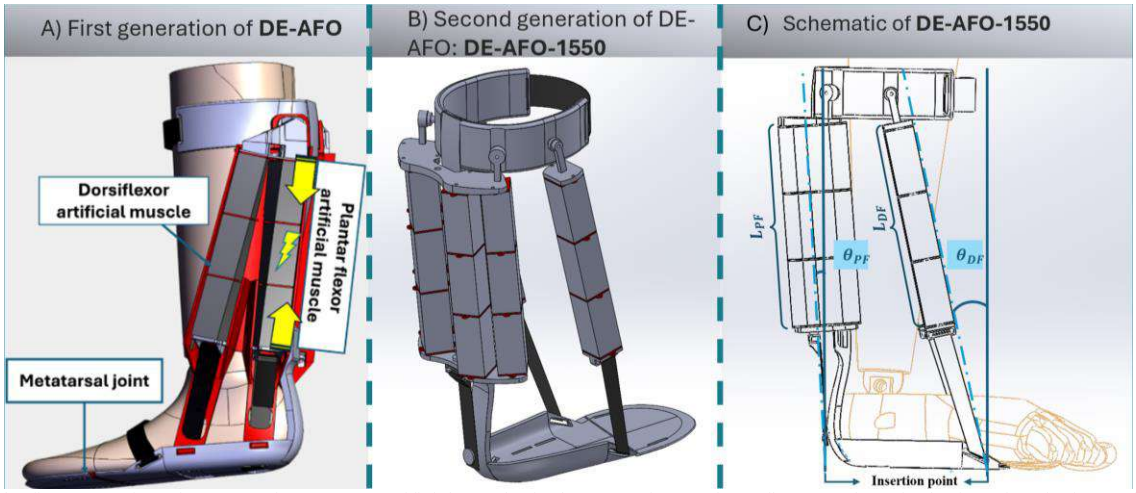


Fig. 2. A) The first generation of DE-AFO features two artificial muscles in the rear acting as plantarflexors and two in the front functioning as dorsiflexors. B) The second version of DE-AFO utilizes four artificial muscles in the rear to provide additional plantarflexion (PF) force, specifically designed to assist children with cerebral palsy (CP). C) Schematic of the DE-AFO-1550. θ_{DF} and θ_{PF} indicate the dorsiflexor and plantarflexor artificial muscles angle to the vertical axis, respectively. L_{DF} and L_{PF} represent the length of dorsiflexor and plantarflexor artificial muscles.

surpassing typical stress values of human biceps [26]. Each myofibril of SDEA-1550 weighs 42 g, totaling 252 g for all of its artificial muscles.

The aim of this paper was to quantify the capabilities of the DE-AFO-1550 in compensating for ankle moment deficits in real-life scenarios. Using the same theoretical procedure applied in evaluating the original design of the DE-AFO, we expanded the analysis by including ankle moment data from two additional CP subjects, CP02 and CP03 (Table 1). By analyzing ankle moment data from those three CP subjects and comparing it with normative data from TD counterparts, we identified the specific PF and DF forces required to compensate for the observed deficiencies. Additionally, by averaging the ankle moments of the CP subjects, we created a virtual subject, CP_{AVG} (Fig. 3C), to represent the collective performance of the DE-AFO-1550 in compensating for ankle moment deficits in children with CP.

For simplicity, we focused on Pre-swing for the PF force and the Swing period for the DF force calculation, where the most assistance is often required.

E. DE-AFO-1550's Ankle Moment and Force Generation Calculation

The averaged ankle moment deficit was calculated by subtracting the observed ankle moment in CP subjects (τ_{CP}) (Fig. 3B) from the TD counterparts (τ_{TD}) (Fig. 3A) which is depicted in Fig. 3D. We calculated the torque deficiency (τ_{Diff}) using the following equation:

$$\tau_{Diff} = \tau_{TD} - \tau_{CP} \tag{1}$$

Fig. 4 provides a detailed comparison of each participant's deficiency, the desired force, and the maximum force generated by the artificial muscles for both DF and PF under real-world conditions. For DF, forces are applied anterior to the ankle joint, while for PF, forces are applied posterior to the ankle joint. The moment arm (MA) of the dorsiflexor artificial muscle (MA_{DF}) and plantarflexor artificial muscle (MA_{PF}) at the insertion point on the footplate were calculated using "(2)" and "(3)":

$$MA_{DF} = L_{Shank} \times \tan(\theta_{DF}) \tag{2}$$

$$MA_{PF} = L_{Shank} \times \tan(\theta_{PF}) \tag{3}$$

Here, θ_{DF} and θ_{PF} represents the angle between the artificial muscles and the superior-inferior axis at their insertion point. Using the ankle angle (θ_{Ankle}), we calculated the length of the front actuators, L_{DF}, and length of rear actuators, L_{PF}, using the following equations (Fig. 2C):

$$L_{DF} = \sqrt{L_{Shank}^2 + MA_{DF}^2 - 2 * L_{Shank} * MA_{DF} * \cos(\theta_{Ankle})} \tag{4}$$

$$L_{PF} = \sqrt{L_{Shank}^2 + MA_{PF}^2 - 2 * L_{Shank} * MA_{PF} * \cos(\theta_{Ankle})} \tag{5}$$

Angles at which forces are applied during walking relative to the footplate:

$$\sin(\theta_{DF}) = \frac{L_{Shank} * \sin(\theta_{Ankle})}{L_{DF}} \tag{6}$$

$$\sin(\theta_{PF}) = \frac{L_{Shank} * \sin(\theta_{Ankle})}{L_{PF}} \tag{7}$$

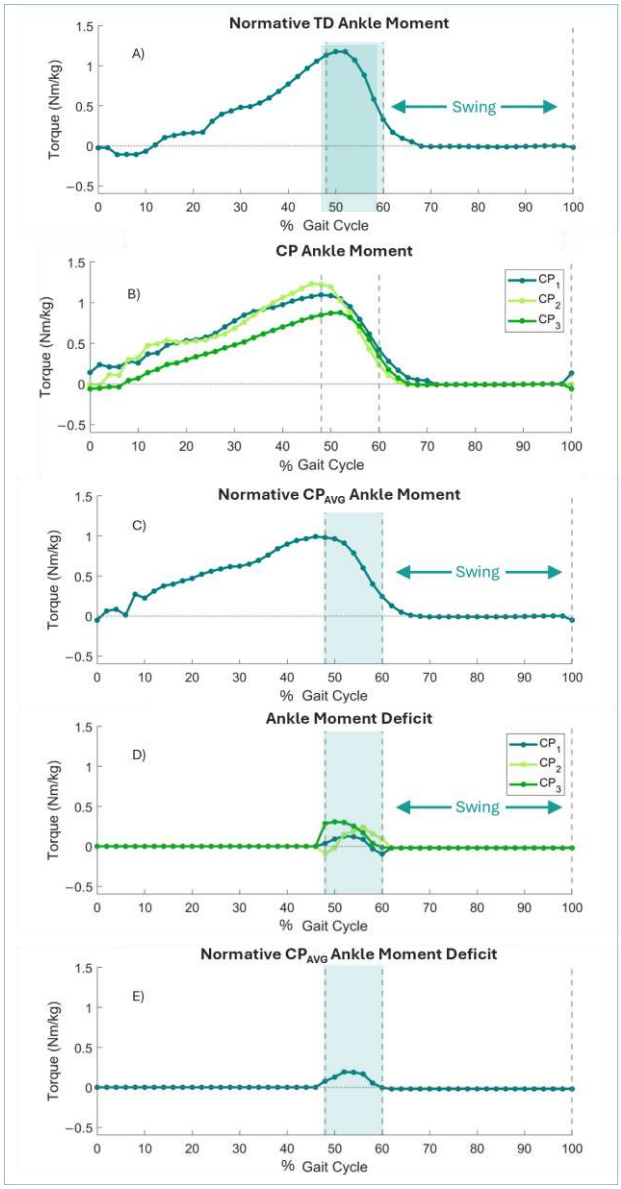


Fig. 3. Ankle dynamic. A) The normative sagittal plane ankle moment for typically developing (TD) children, normalized to body mass, was calculated as the average from seven TD participants. B) Normative ankle moment in the sagittal plane for each child with cerebral palsy (CP), and C) the average of them (CP_{AVG}). D) Ankle moment deficit of each CP subject individually. E) The averaged ankle moment deficit of the CP group was calculated by subtracting CP ankle moments from the TD result.

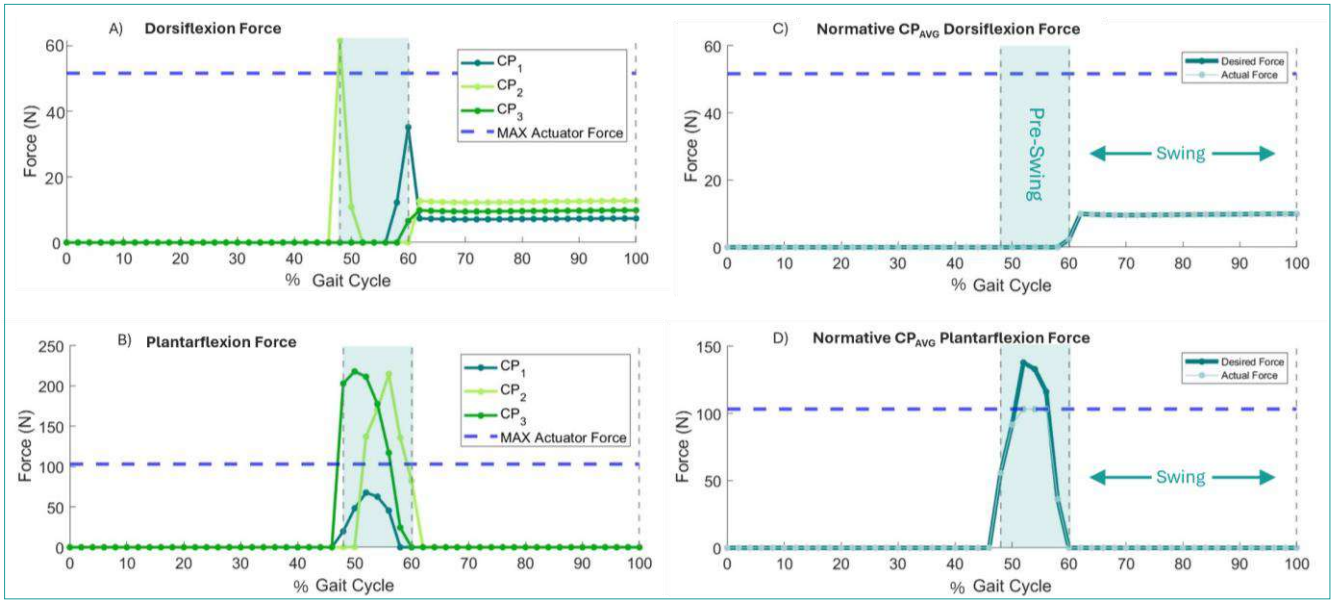


Fig. 4. A) Dorsiflexion force and B) Plantarflexion force deficiencies of each child with cerebral palsy (CP) compared to the maximum actuator force. Average of the Desired force vs actual C) Dorsiflexion Force, and D) Plantarflexion force generated by the artificial muscles of DE-AFO-1550. The dashed line shows the exoskeleton's maximum Dorsiflexion force (51.7 N) and Plantarflexion force (103.5 N).

Desired forces for dorsiflexor and plantarflexor actuators were calculated as follows:

$$F_{DF} = \frac{\tau_{Exo}}{sin(\theta_{DF}) * L_{DF}} \tag{8}$$

$$F_{PF} = \frac{\tau_{Exo}}{sin(\theta_{PF}) * L_{PF}} \tag{9}$$

III. Results

Dorsiflexion Assistance: The system achieves complete compensation for the required DF force throughout most of the swing phase in CP01 and CP03 (Fig. 4A). Specifically, the design generates 51.7 N of DF force (Table 2), significantly exceeding the desired 10 N (Fig. 4C), demonstrating the capability to provide robust support and ensure proper ankle function during this phase of the gait cycle. Furthermore, the device compensates for 84% of the required DF force in CP02, further highlighting its effectiveness.

Additionally, the DE-AFO-1550's DF force generation continued during the swing phase of the gait based on each individual's foot weight and the straight line during the swing phase, ensuring adequate foot clearance throughout the gait cycle (Fig. 4). The DE-AFO-1550 was capable of fully compensating the CP_{AVG}'s DF force deficit (100%).

Plantarflexion Assistance: The maximum force required to assist plantarflexor muscles during the pre-swing phase was calculated as 138 N (Fig. 4D). To achieve a balance between functional support and minimizing bulk around the shank, the DE-AFO-1550's modularity was leveraged to configure four artificial muscles, each capable of generating 25.84 N, resulting in a combined output of 103.5 N. This represents the full compensation of PF deficiency in CP01, 48.2% in CP02, and 47.5% in CP03 (Fig. 4B). The DE-AFO-1550 was capable of generating 75% of the desired PF force of CP_{AVG} which was deemed sufficient for providing meaningful assistance.

Table 2. Shows the dorsiflexion (DF) and plantarflexion (PF) deficit of each representative subject. The maximum capacity of the exoskeleton (Exo) in generating DF and PF forces along with the percentage of deficit compensation achieved by the device are provided.

	CP01	CP02	CP03	CP_{AVG}
DF (N)	35.2	61.5	9.8	10
PF (N)	67.7	214.8	218	138
Max DF Exo (N)	51.7			
Max PF Exo (N)	103.5			
Compensated DF Force (%)	100	84.06	100	100
Compensated PF Force (%)	100	48.2	47.5	75

IV. Conclusion

In this study, we aimed to theoretically evaluate the capabilities of the DE-AFO-1550, a DE-AFO powered by the latest commercially available SDEA (SDEA-1550), in compensating for ankle moment deficits observed in real-life cases of children with CP. By leveraging real-world ankle moment data, the DE-AFO-1550 demonstrated meaningful compensation for dorsiflexion (100%) and plantarflexion (75%) deficits during the swing and pre-swing phases of gait, respectively, showcasing its potential to restore ankle function closer to normative levels. The DE-AFO-1550 incorporates an innovative, lightweight design that adds only 116.4 grams compared to its predecessor, resulting in a total weight of 0.5 kg for the mechanical structure and artificial muscles. Moreover, its strain rate has increased significantly from 660 %/s to 2500 %/s, making it a compelling alternative to traditional AFOs.

Future work will focus on refining the DE-AFO-1550's design by optimizing its bulk by coupling the elastic pushing force of the SDEAs with their active contractile force to magnify DE-AFO's force and displacement in the sagittal plane. Additionally, we will leverage the self-sensing capabilities of SDEAs to develop effective control strategies

for modulating DE-AFO's displacement. Further down the line, clinical trials will be necessary to validate the device's real-world effectiveness and expand its applications to broader populations requiring mobility assistance.

The DE-AFO-1550 and its motor units, the SDEAs, establish a solid foundation for the development of innovative exoskeletons, with potential applications in humanoid robots [30]. This advancement holds the promise of significantly improving the field of rehabilitation robotics and enhancing the quality of life for individuals with neuromotor disorders.

ACKNOWLEDGMENT

This study received support from the National Institutes of Health (NIH) through Grants P20GM109090 and P20GM152301. We also extend our sincere gratitude to the Venture Development Center at the University of Delaware and its Blue Hen Proof of Concept program for their invaluable assistance in the DE-AFO project. Their funding and resources have been instrumental in advancing our research and development efforts.

REFERENCES

[1] M. Oskoui, F. Coutinho, J. Dykeman, N. Jetté, and T. Pringsheim, "An update on the prevalence of cerebral palsy: a systematic review and meta-analysis," *Dev. Med. Child Neurol.*, vol. 55, no. 6, pp. 509–519, Jun. 2013.

[2] A. Aboutorabi, M. Arazpour, M. Ahmadi Bani, H. Saeedi, and J. S. Head, "Efficacy of ankle foot orthoses types on walking in children with cerebral palsy: A systematic review," *Ann. Phys. Rehabil. Med.*, vol. 60, no. 6, pp. 393–402, Nov. 2017.

[3] D. Sutherland, "The development of mature gait," *Gait Posture*, vol. 6, no. 2, pp. 163–170, Oct. 1997.

[4] R. J. Palisano, L.-J. Kang, L. A. Chiarello, M. Orlin, D. Oeffinger, and J. Maggs, "Social and Community Participation of Children and Youth With Cerebral Palsy Is Associated With Age and Gross Motor Function Classification," *Phys. Ther.*, vol. 89, no. 12, pp. 1304–1314, Dec. 2009.

[5] J. M. Ryan *et al.*, "Mortality due to cardiovascular disease, respiratory disease, and cancer in adults with cerebral palsy," *Dev. Med. Child Neurol.*, vol. 61, no. 8, pp. 924–928, Aug. 2019.

[6] P. G. Mcphee, E. A. Claridge, S. G. Noorduyn, and J. W. Gorter, "Cardiovascular disease and related risk factors in adults with cerebral palsy: a systematic review," *Dev. Med. Child Neurol.*, vol. 61, no. 8, pp. 915–923, Aug. 2019.

[7] H.-J. Appell, "Muscular Atrophy Following Immobilisation: A Review," *Sports Med.*, vol. 10, no. 1, pp. 42–58, Jul. 1990.

[8] J. F. M. Geboers, J. H. Van Tuijl, H., "EFFECT OF IMMOBILIZATION ON ANKLE DORSIFLEXION STRENGTH," *Scand. J. Rehabil. Med.*, vol. 32, no. 2, pp. 66–71, Jun. 2000.

[9] M. Moltedo, T. Bacek, K. Junius, B. Vanderborght, and D. Lefeber, "Mechanical design of a lightweight compliant and adaptable active ankle foot orthosis," in *2016 6th IEEE International Conference on Biomedical Robotics and Biomechatronics (BioRob)*, Singapore, Singapore: IEEE, Jun. 2016, pp. 1224–1229.

[10] K. E. Gordon, G. S. Sawicki, and D. P. Ferris, "Mechanical performance of artificial pneumatic muscles to power an ankle–foot orthosis," *J. Biomech.*, vol. 39, no. 10, pp. 1832–1841, Jan. 2006.

[11] J. A. Blaya and H. Herr, "Adaptive control of a variable-impedance ankle-foot orthosis to assist drop-foot gait," *IEEE Trans. Neural Syst. Rehabil. Eng.*, vol. 12, no. 1, pp. 24–31, Mar. 2004.

[12] K. A. Shorter, G. F. Kogler, E. Loth, W. K. Durfee, and E. T. Hsiao-Wecksler, "A portable powered ankle-foot orthosis for rehabilitation," *J. Rehabil. Res. Dev.*, vol. 48, no. 4, p. 459, 2011.

[13] J. Ward, T. Sugar, A. Boehler, J. Standeven, and J. R. Engsberg, "Stroke Survivors' Gait Adaptations to a Powered Ankle–Foot Orthosis," *Adv. Robot.*, vol. 25, no. 15, pp. 1879–1901, Jan. 2011.

[14] J. Kim, S. Hwang, R. Sohn, Y. Lee, and Y. Kim, "Development of an Active Ankle Foot Orthosis to Prevent Foot Drop and Toe Drag in Hemiplegic Patients: A Preliminary Study," *Appl. Bionics Biomech.*, vol. 8, no. 3–4, pp. 377–384, 2011.

[15] Y.-L. Park *et al.*, "Design and control of a bio-inspired soft wearable robotic device for ankle–foot rehabilitation," *Bioinspir. Biomim.*, vol. 9, no. 1, p. 016007, Jan. 2014.

[16] S. Galle, P. Malcolm, W. Derave, and D. De Clercq, "Adaptation to walking with an exoskeleton that assists ankle extension," *Gait Posture*, vol. 38, no. 3, pp. 495–499, Jul. 2013.

[17] K. Z. Takahashi, M. D. Lewek, and G. S. Sawicki, "A neuromechanics-based powered ankle exoskeleton to assist walking post-stroke: a feasibility study," *J. NeuroEngineering Rehabil.*, vol. 12, no. 1, p. 23, 2015.

[18] L. N. Awad, A. Esquenazi, G. E. Francisco, K. J. Nolan, and A. Jayaraman, "The ReWalk ReStore™ soft robotic exosuit: a multi-site clinical trial of the safety, reliability, and feasibility of exosuit-augmented post-stroke gait rehabilitation," *J. NeuroEngineering Rehabil.*, vol. 17, no. 1, p. 80, Dec. 2020.

[19] "Robotics for Rehabilitation| Biomotum Inc. | United States." Accessed: Oct. 15, 2023. [Online]. Available: https://www.biomotum.com/

[20] M. K. Boes, M. Islam, Y. David Li, and E. T. Hsiao-Wecksler, "Fuel efficiency of a Portable Powered Ankle-Foot Orthosis," in *2013 IEEE 13th International Conference on Rehabilitation Robotics (ICORR)*, Seattle, WA, USA: IEEE, Jun. 2013, pp. 1–6.

[21] S. J. Kim, H. Chang, J. Park, and J. Kim, "Design of a Portable Pneumatic Power Source With High Output Pressure for Wearable Robotic Applications," *IEEE Robot. Autom. Lett.*, vol. 3, no. 4, pp. 4351–4358, Oct. 2018.

[22] "CDC. What Noises Cause Hearing Loss?" [Online]. Available: https://www.cdc.gov/hearing-loss/causes/index.html

[23] G. Kovacs, L. Düring, S. Michel, and G. Terrasi, "Stacked dielectric elastomer actuator for tensile force transmission," *Sens. Actuators Phys.*, vol. 155, no. 2, pp. 299–307, Oct. 2009.

[24] G. Kovacs, S. M. Ha, S. Michel, R. Pelrine, and Q. Pei, "Study on core free rolled actuator based on soft dielectric EAP," presented at the The 15th International Symposium on: Smart Structures and Materials & Nondestructive Evaluation and Health Monitoring, Y. Bar-Cohen, Ed., San Diego, California, Mar. 2008, p. 69270X.

[25] A. Behboodi and S. C. K. Lee, "Benchmarking of a Commercially Available Stacked Dielectric Elastomer as an Alternative Actuator for Rehabilitation Robotic Exoskeletons," in *2019 IEEE 16th International Conference on Rehabilitation Robotics (ICORR)*, Toronto, ON, Canada: IEEE, Jun. 2019, pp. 499–505.

[26] V. Mohammadi, S. Mohammadi Ghalehney, M. Tajdani, S. C. K. Lee, and A. Behboodi, "Evaluating Stacked Dielectric Elastomer Actuators as Soft Motor Units for Forming Artificial Muscles in Biomimetic Rehabilitation Robots," *Actuators*, vol. 13, no. 10, p. 381, Sep. 2024.

[27] A. Behboodi, "NSF Award Search: Award # 1906128 - I-Corps: Soft Ankle Foot Orthosis Using Artificial Muscle, DEAFO." [Online]. Available: https://www.nsf.gov/awardsearch/showAward?AWD_ID=1906128

[28] V. Mohammadi, M. Tajdani, M. Masaei, S. Mohammadi Ghalehney, S. C. K. Lee, and A. Behboodi, "DE-AFO: A Robotic Ankle Foot Orthosis for Children with Cerebral Palsy Powered by Dielectric Elastomer Artificial Muscle," *Sensors*, vol. 24, no. 12, p. 3787, Jun. 2024.

[29] A. Behboodi, N. Zahradka, H. Wright, J. Alesi, and Samuel. C. K. Lee, "Real-Time Detection of Seven Phases of Gait in Children with Cerebral Palsy Using Two Gyroscopes," *Sensors*, vol. 19, no. 11, p. 2517, Jun. 2019.

[30] V. Mohammadi, M. Hosseini, F. Jafari, and A. Behboodi, "RoboMan: An Adult-Sized Humanoid Robot with Enhanced Performance, Inherent Stability, and Two-Stage Balance Control to Facilitate Research on Humanoids," *Robotics*, vol. 13, no. 10, p. 146, Sep. 2024.

Measuring Upper Extremity Loading in Passive Exoskeleton-Assisted Gait: A Case Study

Robert Pastor[1], Michal Gloger[1], and Pavel Klouček[2]

***Abstract*— This study investigates upper extremity loading during exoskeleton-assisted walking with the UNILEXA passive exoskeleton using an instrumented platform walker. The goal was to assess upper limb weight-bearing and its implications for rehabilitation. Data were collected from two participants performing walking and standing tasks. During steady walking, the average vertical load on the walker was approximately 30% of body weight, while standing maneuvers showed peaks up to 90%. These results demonstrate that, despite the passive nature of the UNILEXA exoskeleton, upper extremity loading remains within acceptable limits, suggesting its suitability for safe and effective rehabilitation.**

I. INTRODUCTION

Individuals with spinal cord injury (SCI) often rely on assistive devices, such as walkers or crutches, in combination with orthoses or exoskeletons, to facilitate ambulation and rehabilitation [1], [2]. While these devices are essential for mobility, they place significant demands on the upper extremities, particularly the shoulders, as they bear a substantial portion of body weight during movement [2]. Prolonged or excessive loading of the shoulders can lead to secondary complications, including glenohumeral instability, impingement syndrome, rotator cuff injuries, and degenerative joint diseases, significantly affecting the long-term quality of life for individuals with SCI [2], [3]. These risks underscore the importance of optimizing assistive device design and use to reduce upper limb strain while maintaining functional mobility.

Although force plates are commonly used to measure ground reaction forces in gait analysis, they pose a logistical challenge when combined with a platform walker, because the walker wheels create an additional contact point that can invalidate force-plate measurements. To address this, we aimed to capture upper limb load during UNILEXA-assisted walking by developing an instrumented platform walker that isolates the forces transmitted through the user's arms.

Instrumented walkers and crutches are capable of measuring a range of parameters related to gait and rehabilitation. There have been multiple instrumented assistive devices developed to assess upper extremity reaction forces for patients with walking impairments. Most of the articles in literature use instrumented walkers [4], [5], [6], [7], [8], [9], [10], [11], [12], [13], [14] or instrumented crutches [7], [12], [15], [16], [17], [18], [19], [20], [21], though other approaches—such as force sensors built into footwear [22]—have also been explored . Across these studies, researchers have employed various measurement methods when instrumenting walkers. While some researchers use load cells [6], [7], [17], [23] , some chose a more cost effective solution with strain gauges [4], [5], [9], [10], [12], [13], [18], [19], [20] or force sensitive resistors [14], [16], [21]

Haubert et al. [7] compared three-dimensional shoulder joint forces during assisted ambulation using crutches versus a front-wheeled walker in individuals with incomplete spinal cord injuries. They observed significantly greater superior shoulder joint forces and rates of loading during crutch walking compared to walker-assisted gait, despite similar walking velocities. Their findings underscore the need to consider shoulder joint demands when selecting assistive devices for individuals with upper extremity weakness or pain.

Bachschmidt et al. [4], [5] developed a six-degree-of-freedom force-sensing walker to characterize upper extremity kinetics and kinematics during assisted gait. The system utilized strain gauges and finite element modelling to address structural cross-talk and measure forces and moments applied by each hand independently. Their work revealed significant upper extremity demands during walker-assisted gait, emphasizing the need for optimized walker designs to improve efficiency and user safety.

A. Objective of the Study

The previous research in the literature has primarily focused on the instrumentation of front-wheeled walkers and walking frames. To the authors' knowledge, there has been no previous research involving instrumented platform walkers, sometimes referred to as walking tables with forearm support.

In this article, we aim to assess the weight distribution on a platform walker during walking with the UNILEXA exoskeleton. Because the lateral motion of a platform walker can invalidate force-plate measurements when the walker rests on the plates, we developed an instrumented platform walker to measure upper extremity weight-bearing and weight transfer between the walker and the exoskeleton. This device seeks to offer further insight into upper extremity forces during a gait cycle with lower-limb assistive devices.

This paper serves two purposes: (1) to describe the design and calibration of the novel instrumented platform walker and (2) to present an initial feasibility study involving two individuals with SCI. While the small sample precludes broad statistical generalization, the results provide preliminary evidence regarding upper extremity loading when using the UNILEXA exoskeleton with a platform walker.

[1]R. Pastor and M. Gloger are with MEBSTER s.r.o.
[2]P. Klouček is with VÚTS a.s.

II. MATERIALS AND METHODS

A. Instrumented Walker

The walker, originally a FOLLO FUTURA AS model, was extensively modified to allow detailed force measurement . Initially, we intended to instrument the original walker frame to avoid excessive modifications, but it was not rigid enough to allow precise force measurements and avoid excessive crosstalk between the force sensors. Therefore, the walker was modified with a welded frame featuring four support sliders for height adjustment. The handles and armrests were attached to two 25 mm thick aluminum plates, with four three-axis Kistler piezoelectric force sensors (model 9027C) installed between them. The system has a measurement range of 10 kN per sensor. This setup ensured the stability of the measurement system under various load conditions. Fig. 1 shows an image of the instrumented walker.

Measurements were acquired using a Dewetron DEWE-2602 analyzer at a sampling rate of 1 kHz, ensuring high temporal resolution for capturing the dynamic behavior during activities. Data processing was conducted using FlexPro software, with additional filtering applied to reduce noise and account for minor signal drift.

The walker was transformed into a dynamometer system capable of measuring forces and moments in six degrees of freedom. The force sensors were mounted at four key locations on the walker (front left, front right, rear left, and rear right) to capture forces in the three orthogonal directions (X, Y, and Z). Fig. 2 provides a top-down view of the sensor placement with dimensions. The dynamometer system was designed to isolate these forces and measure moments with minimal crosstalk, using strategic placement and calibration protocols.

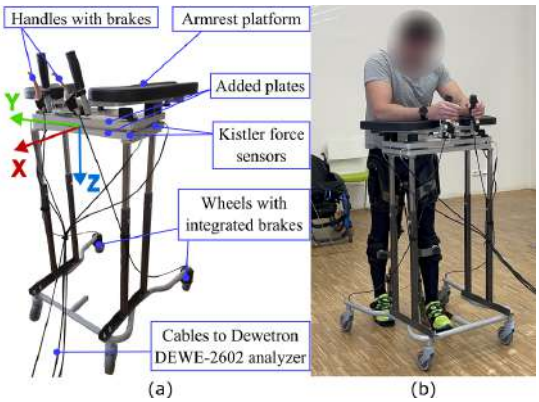


Fig. 1. a) Parts of the instrumented walker. b) Participant P01 with UNILEXA and the instrumented walker.

B. Calibration

Sensor preloading was crucial to ensure accuracy and reduce crosstalk between sensors. To achieve this, we placed standardized weights (10 kg and 20 kg) directly over each sensor axis, as well as in intermediate positions offset from the centre, thereby testing various load distributions. Because

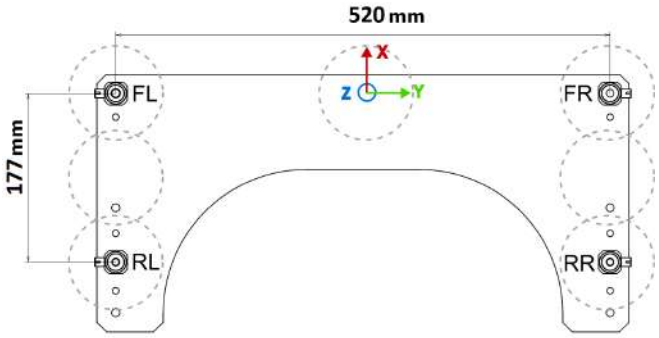


Fig. 2. Top-down view of walker platform. Sensors positions (FR-Front left, FR-Front right, RL-Rear left, RR-Rear right. The coordinate frame for force calculations are shown by the X and Y arrows. Dashed circles show the locations used for calibration with known weights.

of the symmetric construction, we performed small adjustments to the manufacturer-provided calibration constants to minimize measurement deviations. The final calibration ensured that the measured force matched the known weight within approximately 5%. Lateral calibration was verified by tensioning each sensor axis with a calibrated force gauge, confirming minimal influence from sensor preloads. These steps reduced crosstalk and yielded a linear response across the load range. Data were sampled at 1 kHz and processed in FlexPro. A 10 Hz low-pass Butterworth filter was then applied to remove high-frequency noise, consistent with typical gait analysis practices.

C. Experiment Setup

The laboratory setup was designed to simulate a straightforward and repeatable walking task. A 6-meter length was marked on the floor, and participants began from a designated starting point. Each participant walked the measured 6 meters, performed a 180 turn, and then walked back to the starting point. The setup was inspired by the 10-Meter Walk Test (10MWT), where typically the middle 6 meters are measured, with an additional 2 meters for acceleration and 2 meters for deceleration. However, in our case, we omitted the classic 2-meter sections for acceleration and deceleration due to equipment limitations—specifically, the numerous cables attached to the instrumented walker. This omission was not critical, as walking with the UNILEXA exoskeleton and a platform walker is not a very dynamic movement, and typical acceleration or deceleration phases are less applicable. The gait cycle itself includes moments when the participant is moving at zero velocity. Despite these modifications, the results should still be comparable with other studies involving the 10MWT with SCI patients, exoskeletons, or orthoses.

D. Participants

The participants were individuals with SCI and were recruited based on their prior experience with the UNILEXA exoskeleton. Participant P01 is a regular user of the device and has the exoskeleton in his home, where he uses it

for exercise. Participant P02 is in her early days of using the exoskeleton and used it for 3 previous session with a physiotherapist. The measurements were conducted as part of their normal visit with our physiotherapist, during which they would typically walk in a similar manner. For this study, they used the instrumented walker, which was the same type as their usual platform walker but equipped with additional sensors for force measurement. Both participants were less than two years post-injury (Time After Onset, TAO), with an American Spinal Injury Association (ASIA) score of A and a lesion level at T7. No control group was included, as the study aimed to document upper extremity loading in SCI individuals using their usual assistive devices. Participants were fully briefed on the study's aims and procedures and signed informed consent before taking part in the measurements. Table I presents the demographics of the participants involved in the study.

TABLE I

DEMOGRAPHIC DATA OF PARTICIPANTS.

Participant ID	Sex	Age	Weight [kg]	Height [cm]	Lesion	AISA	TAO
P01	M	37	95	190	T7	A	2Y
P02	F	45	68	173	T7	A	2Y

E. Data Acquisition

The height of the instrumented walker was adjusted so that each subject's elbow rested comfortably on the armrest while maintaining an upright posture. Following the initial standing maneuver, subjects were instructed to briefly suspend their full body weight on the walker. The resulting force was recorded and used as a reference for the subject's body weight, with the exoskeleton weight (9 kg) subtracted from the measured value.

Participant P01 completed the 6-meter walk test 8 times, whereas participant P02 completed it fully only once before fatigue occurred. As this measurement was included as part of their normal physiotherapy session, we did not ask the participants to push themselves beyond their comfortable exercise level. We also plan to use this case study as a guide for future studies that will take user fatigue levels into consideration. Participant P01 performed the trials in sets of 2; walking 6 m, rotating, walking back, and then resting for 15 minutes before repeating the trials.

The duration of each walking trial was measured using a stopwatch. The stopwatch was started when the participant began their first step and stopped when the front wheels of the walker crossed the six-meter mark.

F. Data Processing

The measured force data were cropped based on the recorded stopwatch times. The mean and standard deviation for each trial were calculated using the NumPy Python library. The data for the stand-up plot were synchronized using a common inflection point on the force curve

III. RESULTS

A. Standing Up

The forces recorded during standing showed significant vertical load on the walker. Seven instances of standing up were recorded for participant P01, Fig. 3 shows the force curves on the walker synchronized with the time of standing up from the wheelchair. Participant P02 showed a similar trend, but with proportionally lower forces due to their lower body weight.

Both participants demonstrated that nearly their entire body weight was momentarily transferred through the walker during the standing motion, with approximately 90% of the body weight contributing to a peak in vertical force. Fig. 4 presents selected standing force curves for each participant, normalized by their body weight. The data indicate that placing the hands on the walker armrests transfers roughly 20% of the participant's weight to the walker. This force peaks during the stand up and decreases after the knees of the UNILEXA exoskeleton are locked. For the more experienced participant (P01), the vertical force ultimately drops to about 40% of body weight. At this point, the user begins relying less on the walker as they shift more of their weight to their legs, which are supported by the exoskeleton's structure.

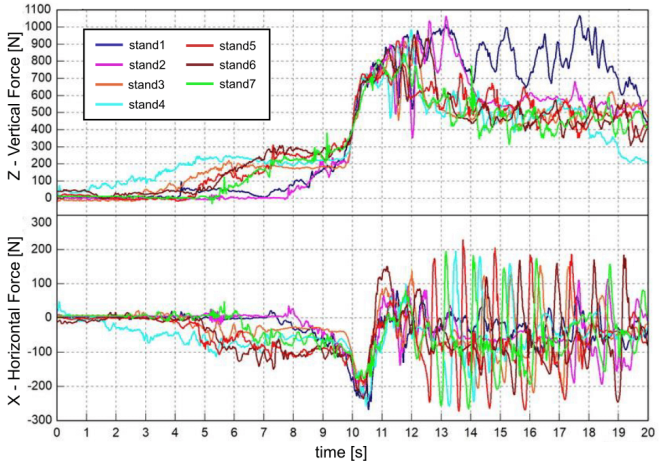


Fig. 3. Force curves on the walker synchronized with the standing-up motion for participant P01.

B. Weight Shifting and Hanging

During weight shifting exercises, a test was conducted in which the participant transferred weight between legs while using the walker for support. The results showed an asymmetrical force distribution depending on which leg bore the weight. Fig. 5 displays the forces during the balancing exercise and full weight hanging, which were then used for body weight data normalization. The figure shows the net force in the Z direction as the sum of all sensors, as well as separate sums from the left and right sensor pairs to illustrate weight shifting during the balancing exercise.

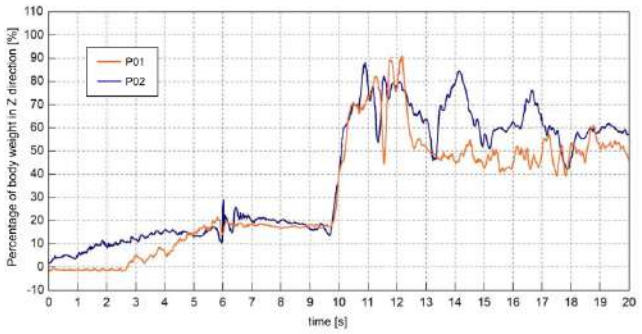


Fig. 4. Selected force curves (not averaged) showing vertical load on the walker for both participants during the standing maneuver, normalized to percentage of BW.

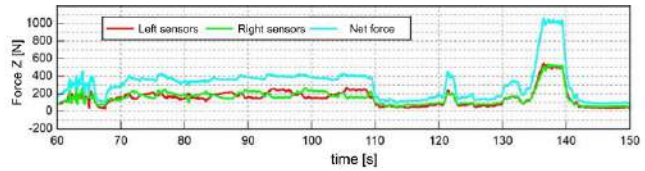


Fig. 5. Balancing exercise (from 70 to 110 s) and full body-weight hanging (from 135 to 140 s) with participant P01

C. Walking

The participants walked for six meters, then rotated 180 degrees, and walked back the same length. Fig. 8 shows one of the recorded trials with participant P01. The first six meters are shown between 170 and 300 seconds, then the participant rotated until 350 seconds, and then walked back. A detailed plot of the first six meters from this trial is shown in Fig. 9, and a detailed view of the rotation is shown in Fig. 10.

For participant P01, the average load on the walker was measured to be approximately 30% of body weight. During the trials, a gradual increase in walker load was observed, with an average of 27.8% Body Weight (BW) transferred to the walker during the first walk and 35.3% BW during the last walk. This increase can likely be attributed to a rising level of fatigue over the course of the trials. Table II lists the walking time, along with the maximum, minimum, mean, and standard deviation of the weight supported by the walker, expressed as a percentage of body weight for participant P01. The data in the table are visualized in Fig. 6 and Fig. 7. An interesting observation from the time measurements is that, since the trials were performed in sets of two, the first walk in each set was always significantly slower than the second. The participant increased their comfortable walking speed during the trial but, after resting for 15 minutes, resumed at a slower pace.

D. Turning

Turning introduced significant lateral forces, which were captured during trials. During a 6-meter walk with a turn, forces in the lateral direction fluctuated based on the turning direction and how the users manoeuvred the walker. Fig. 10 shows a relatively stable load in the Z direction, fluctuating slightly around 350 N, but at the same time a frequent load transfer between the left and right sides. In the X and Y directions, a sustained application of lateral loads is evident, which induces a moment to rotate the walker.

TABLE II

SUMMARY OF WALKING TRIALS (P01)

Trial	Time [s]	Min [%BW]	Max [%BW]	Mean [%BW]	SD [%BW]
Walk1	2:51	8.4	49.6	27.8	8.0
Walk2	2:00	13.4	50.9	29.8	7.5
Walk3	2:20	17.0	56.6	32.4	8.7
Walk4	1:34	12.7	56.4	33.0	9.0
Walk5	2:16	12.3	53.9	30.7	8.7
Walk6	1:44	10.3	53.7	32.9	9.3
Walk7	2:12	15.9	54.9	34.1	8.6
Walk8	2:00	13.1	57.6	35.3	9.2

TABLE III

SUMMARY OF WALKING TRIALS (P02)

Trial	Time [s]	Min [%BW]	Max [%BW]	Mean [%BW]	SD [%BW]
Walk1	3:26	18.1	77.5	51.7	9.9

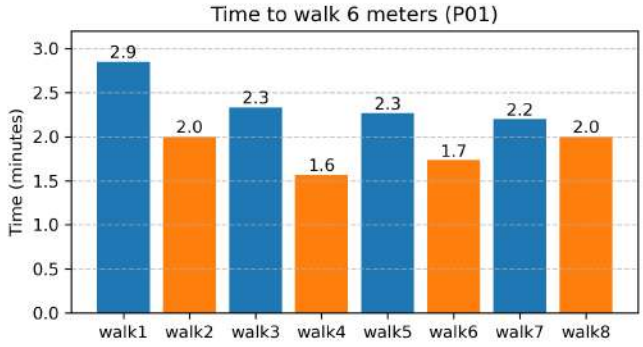


Fig. 6. A bar graph displaying walking times for each trial. Blue bars indicate a walk immediately following a rest pause, after which the participant rotates 180 degrees and walks back, represented by orange bars.

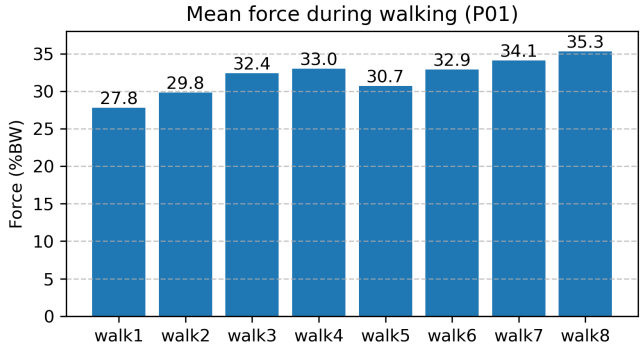


Fig. 7. A bar graph visualizing the mean of the walker load (as a percentage of body weight) for each trial.

IV. DISCUSSION

This study provides a case study of upper extremity loading during walking with the UNILEXA passive exoskeleton,

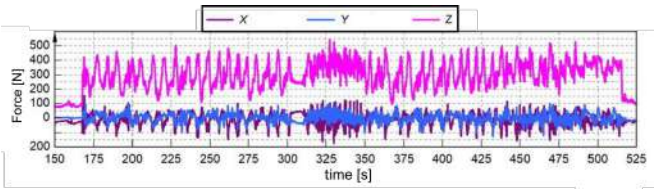


Fig. 8. The net force exerted by participant P01 during a full walking trial (walk3), showing the initial 6-meter walk, 180-degree rotation, and return path.

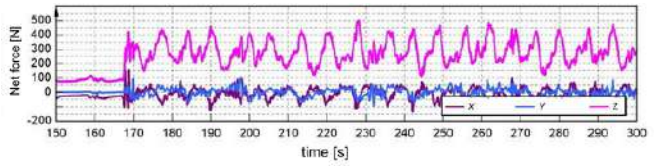


Fig. 9. Forces during the initial 6-meter segment of the walk3 trial for participant P01.

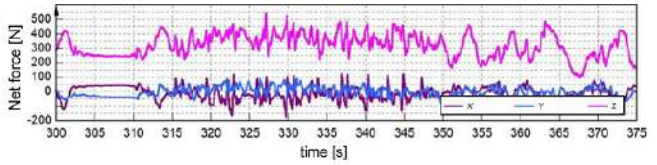


Fig. 10. Lateral and vertical forces on the walker during a 180-degree turn (walk3), showing load distribution changes.

using an instrumented platform walker. Our data reveal an average vertical load of approximately 30% of body weight during steady walking, with peaks reaching up to 90% during standing maneuvers. This peak corresponds to the participant's mass above the knees—the portion they must lift to engage the knee locks—after which they can relax as the exoskeleton supports the lower limbs. Additionally, we observed a gradual increase in upper limb loading across successive walking trials, likely attributable to user fatigue. These results suggest that, even with the UNILEXA exoskeleton being a passive device, users are not excessively overloading their upper extremities during ambulation.

The observed upper extremity load of 30% for participant P01 aligns closely with values reported in walker-assisted gait studies. For instance, Simoneau et al. [13] measured upper limb efforts in walking frames and found comparable loading values in the range of 25–35% of body weight depending on walker height and handle positioning. In contrast, Haubert et al. [7] observed significantly higher shoulder forces during crutch-assisted ambulation, often exceeding 50% of body weight due to concentrated loading on fewer contact points. These findings highlight the advantage of platform walkers in distributing forces more evenly, potentially reducing shoulder joint strain compared to crutches. However, participant P02—who was using the exoskeleton for only the second time—exhibited a mean load of 51.7% BW, more akin to crutch ranges, suggesting that limited proficiency may lead to greater reliance on the walker. A longer-term study would be needed to confirm whether additional training reduces this upper extremity load to levels closer to participant P01's or other walker users. Importantly, the relatively moderate loading observed overall supports the conclusion that the UNILEXA exoskeleton, when used with a platform walker, enables safe and controlled gait without excessive strain on the user's upper limbs.

During the standing motion, peak loads in our study reached 90% of body weight for a brief moment. This is consistent with observations by Khuna et al. [3], who noted that high upper extremity forces during sit-to-stand transitions are critical for stability but pose risks of shoulder overuse injuries. While these forces are momentarily high, the exoskeleton appears to effectively assist users in stabilizing themselves post-transition, reducing prolonged upper extremity strain. In participant P01's trials (Fig. 3), the initial stands involved slower knee locking—likely due to the legs needing an initial stretch or warm-up—which kept more weight on the walker for longer. Once the knees could lock more readily, the force on the walker dropped sooner.

V. CONCLUSION

This study demonstrates that the combination of the UNILEXA passive exoskeleton and a platform walker allows for safe ambulation without excessive upper extremity loading. The average upper limb load of 30% of body weight during walking is within acceptable ranges reported in previous walker studies and significantly lower than loads observed with crutch-assisted gait. Because platform walker use is the primary modality with UNILEXA, these results suggest that it supports efficient weight distribution and may reduce the risk of overuse injuries to the upper extremities. Nonetheless, further studies are needed to determine whether these findings generalize to other methods of ambulation with the exoskeleton, such as parallel bars, frame walkers, or crutches.

As a case study with two participants, the findings are not generalizable to the broader SCI population. Future studies should involve larger sample sizes and direct comparisons with other assistive devices to validate these results and better understand the relative benefits of the UNILEXA exoskeleton and platform walkers in SCI rehabilitation. Additionally, further refinement of sensor calibration protocols is necessary to minimize crosstalk and enhance measurement accuracy during dynamic tasks. Despite these limitations, the preliminary findings highlight the potential of this device combination for effective and safe rehabilitation.

ACKNOWLEDGEMENT

This work was carried out at the expense of MEBSTER s.r.o. The authors would like to thank Pavel Klouček for his contributions to data collection and processing.

CONFLICT OF INTEREST

This research was conducted as part of the development of the UNILEXA exoskeleton, manufactured by Company MEBSTER, which provided the devices and oversight during the measurements. The measurement and initial data analysis

were performed by VUTS, with further analysis and interpretation conducted by the authors.

REFERENCES

[1] F. Rasouli and K. B. Reed, "Walking assistance using crutches: A state of the art review," *Journal of Biomechanics*, vol. 98, p. 109489, Jan. 2020.

[2] T. Q. Lee and P. J. McMahon, "Shoulder biomechanics and muscle plasticity: Implications in spinal cord injury," *Clinical Orthopaedics and Related Research*, vol. 403, p. S26–S36, Oct. 2002.

[3] L. Khuna, L. Mato, P. Amatachaya, T. Thaweewannakij, and S. Amatachaya, "Increased lower limb loading during sit-to-stand is important for the potential for walking progression in ambulatory individuals with spinal cord injury," *Malaysian Journal of Medical Sciences*, vol. 26, no. 1, p. 99–106, 2019.

[4] R. Bachschmidt, G. Harris, and G. Simoneau, "Development of a force sensing walker for rehabilitation," in *Proceedings of 17th International Conference of the Engineering in Medicine and Biology Society*, ser. IEMBS-95, vol. 2. IEEE, 1995, p. 1267–1268.

[5] R. Bachschmidt, G. Harris, and Simoneau, "Walker-assisted gait in rehabilitation: a study of biomechanics and instrumentation," *IEEE Transactions on Neural Systems and Rehabilitation Engineering*, vol. 9, no. 1, p. 96–105, Mar. 2001.

[6] R. Gerena, P. VanDeventer, A. Vistamehr, C. Conroy, P. Freeborn, H. Govin, E. Fox, and J. Aceros, "Wireless instrumented walker for remote rehabilitation monitoring," in *2015 IEEE Virtual Conference on Applications of Commercial Sensors (VCACS)*. IEEE, Mar. 2015, p. 1–7.

[7] L. L. Haubert, D. D. Gutierrez, C. J. Newsam, J. K. Gronley, S. J. Mulroy, and J. Perry, "A comparison of shoulder joint forces during ambulation with crutches versus a walker in persons with incomplete spinal cord injury," *Archives of Physical Medicine and Rehabilitation*, vol. 87, no. 1, p. 63–70, Jan. 2006.

[8] A. Hojjati Najafabadi, S. Amini, and F. Farahmand, "Using a saddle-assistive device equipped with mechanical orthosis for walking of the person with incomplete spinal cord injury," *Proceedings of the Institution of Mechanical Engineers, Part H: Journal of Engineering in Medicine*, vol. 235, no. 9, p. 1088–1095, May 2021.

[9] Y. Hu, D. Ming, Y. Wang, Y. Wong, B. Wan, K. Luk, and J. Leong, "Three-dimensional dynamical measurement of upper limb support during paraplegic walking," in *The 26th Annual International Conference of the IEEE Engineering in Medicine and Biology Society*, ser. IEMBS-04, vol. 4. IEEE, 2004, p. 4944–4947.

[10] M. Khodadadi, M. A. Baniasad, M. Arazpour, F. Farahmand, and H. Zohoor, "Designing instrumented walker to measure upper-extremity's efforts: A case study," *Assistive Technology*, vol. 31, no. 5, p. 267–275, Apr. 2018.

[11] L. Khuna, L. Mato, P. Amatachaya, T. Thaweewannakij, and S. Amatachaya, "Increased lower limb loading during sit-to-stand is important for the potential for walking progression in ambulatory individuals with spinal cord injury," *Malaysian Journal of Medical Sciences*, vol. 26, no. 1, p. 99–106, 2019.

[12] E. Melis, R. Torres-Moreno, H. Barbeau, and E. Lemaire, "Analysis of assisted-gait characteristics in persons with incomplete spinal cord injury," *Spinal Cord*, vol. 37, no. 6, p. 430–439, Jun. 1999.

[13] G. Simoneau, G. Hambrook, R. Bachschmidt, and G. Harris, "Quantifying upper extremity efforts when using a walking frame," in *Pediatric Gait: A New Millennium in Clinical Care and Motion Analysis Technology*, ser. PG-00. IEEE, 2000, p. 210–216.

[14] H. S. Ter, S. Parasuraman, M. A. khan, and I. Elamvazuthi, "Walking-assisted gait in rehabilitation," *Procedia Computer Science*, vol. 76, p. 257–263, 2015.

[15] M. Febrer-Nafría, R. Pallarès-López, B. J. Fregly, and J. M. Font-Llagunes, "Prediction of three-dimensional crutch walking patterns using a torque-driven model," *Multibody System Dynamics*, vol. 51, no. 1, p. 1–19, Jun. 2020.

[16] D. B. Fineberg, P. Asselin, N. Y. Harel, I. Agranova-Breyter, S. D. Kornfeld, W. A. Bauman, and A. M. Spungen, "Vertical ground reaction force-based analysis of powered exoskeleton-assisted walking in persons with motor-complete paraplegia," *The Journal of Spinal Cord Medicine*, vol. 36, no. 4, p. 313–321, Jul. 2013.

[17] F. L. Haufe, R. H. Hassani, R. Riener, and P. Wolf, "The insight crutches: Analyzing the role of arm support during robot-assisted leg movements," *IEEE Robotics amp; Automation Magazine*, vol. 27, no. 1, p. 103–113, Mar. 2020.

[18] M. Lancini, M. Serpelloni, and S. Pasinetti, "Instrumented crutches to measure the internal forces acting on upper limbs in powered exoskeleton users," in *2015 6th International Workshop on Advances in Sensors and Interfaces (IWASI)*. IEEE, Jun. 2015, p. 175–180.

[19] P. S. Requejo, D. P. Wahl, E. L. Bontrager, C. J. Newsam, J. K. Gronley, S. J. Mulroy, and J. Perry, "Upper extremity kinetics during lofstrand crutch-assisted gait," *Medical Engineering amp; Physics*, vol. 27, no. 1, p. 19–29, Jan. 2005.

[20] A. J. Smith, B. N. Fournier, J. Nantel, and E. D. Lemaire, "Estimating upper extremity joint loads of persons with spinal cord injury walking with a lower extremity powered exoskeleton and forearm crutches," *Journal of Biomechanics*, vol. 107, p. 109835, Jun. 2020.

[21] J. Wade, M. Beccani, A. Myszka, E. Bekele, P. Valdastri, P. Flemming, M. de Riesthal, T. Withrow, and N. Sarkar, "Design and implementation of an instrumented cane for gait recognition," in *2015 IEEE International Conference on Robotics and Automation (ICRA)*. IEEE, May 2015, p. 5904–5909.

[22] M. Raaben, H. Holtslag, R. Augustine, R. Van Merkerk, B. Koopman, and T. Blokhuis, "Technical aspects and validation of a new biofeedback system for measuring lower limb loading in the dynamic situation," *Sensors*, vol. 17, no. 3, p. 658, Mar. 2017.

[23] M. Kumprou, P. Amatachaya, T. Sooknuan, P. Arayawichanon, T. Thaweewannakij, and S. Amatachaya, "The utility of upper limb loading device in determining optimal walking ability in ambulatory individuals with spinal cord injury," *Hong Kong Physiotherapy Journal*, vol. 41, no. 01, p. 55–63, Jan. 2021.

An Anatomically Accurate Biomimetic Robotic Hand with Textile Connective Tissues

Benedek J. Tasi†*, Dávid L. Pelyva†, Dávid Holló†, Zsófia Nguyen, Boróka G. Molnár,
Balázs Kráz, Márton I. Klenczner, Veronika Kiss, Balázs I. Formanek, Márton B. Naszlady
Faculty of Information Technology and Bionics
Pázmány Péter Catholic University
Budapest, Hungary
*benedek.tasi@itk.ppke.hu

***Abstract*—Artificial hands are developed and employed widely for solving challenges in present-day robotics, with an increasing number of such systems being integrated into our daily lives. For humanoid or human-centric applications in medical or industrial sectors demanding increased naturality, biomimetics offers a promising approach. However, replicating biological structures and functions to the detail commonly results in excessive complexity in both design and production, preventing widespread adoption. This work presents a biomimetic hand developed with the use of modern procedural design methods and additive and textile production technologies, evaluated with a modular actuator frame through grasp and gesture demonstrations and finger trajectory analysis. The results aim to exemplify how leveraging these advancements may enable the creation of naturally compliant robotic devices with intricate functionality, while simultaneously satisfying the industrial requirements for robustness, cost-effectiveness and production scalability, therefore bringing the universal applicability of such systems within reach.**

***Index Terms*—biomimetics, robotic hand, humanoid robotics, prosthetics, textile technology, 3D braiding**



Fig. 1. The Anatomically Accurate Biomimetic Hand with various layers of covering (textile skin, underlying hard covering and removed covers).

I. Introduction

Replicating hand functionality is one of the most widely investigated cornerstones of present-day robotic development efforts. The efficiency and application versatility of teleoperated or autonomous humanoid robots largely depend on the abilities and dexterity of their hands, while the manipulator designs of industrial and collaborative robotics have long been borrowing ideas from living systems to solve various gripping tasks [1]. In the upper-limb prosthetics industry, increasing embodiment is considered a key factor in combating high abandonment rates [2] [3], for which a high degree of human-likeness is desired in both function and aesthetics.

The motivation to design better anthropomorphic hands is therefore understandably high, with a wide range of devices being developed for an even wider range of applications [4]. However, in terms of replicating all the intricacies that make our hand such a versatile tool, existing solutions are still approximate at best. This can be mainly attributed to the conventional methods of mechanics and robotics that still drive most design approaches, and which are usually based on greatly simplifying the complex biomechanical structures for the sake of adhering to the often strict constraints of volume and power, while also having to ensure scalable production.

This either leads to highly simplified, elementary mechanical behavior, as can be observed in most upper-limb prostheses or soft robotic hands (which are widely researched but are less common in the industry due to their fragility); or necessitates integrating numerous sensors, actuators and overly complex assemblies to attain higher levels of dexterous functionality. In both cases, however, the compliance and tactility, or to put it more generally, the human-like nature of the movements suffers the consequences, keeping the solutions at a distance from the ideal of the biological hand.

Highly biomimetic approaches in both structural design and material composition have been experimented with to address this problem [5] [6], as closely replicating the hard and soft tissues and biomechanics of our anatomy using hybrid systems of rigid and soft robotic components inherently promises increased performance in this respect. Yet, these often face durability issues due to the popular choices for soft materials

†Equal contribution.

Project no. TKP2021-NKTA-66 has been implemented with the support provided by the Ministry of Technology and Industry of Hungary from the National Research, Development and Innovation Fund, financed under the TKP2021-NKTA funding scheme.

Cadaveric studies were conducted in accordance with the approval of the local ethics committee (ETT-TUKEB, Reference No. IV/3633- 1 /2021/EKU).

(such as rubber and silicon), and share the inherent complexity of biological systems, being composed of layers upon layers of interconnected tissues, leading to challenging design and production problems and time-consuming assembly processes.

Nevertheless, the potential functional improvements this approach promises are quite significant, as the fields of both humanoid and medical robotics are advancing rapidly, and are in need of more naturalistic solutions towards improved integration into both user body-image and society. Its widespread adoption could very possibly depend on whether the two most pressing issues, those of durability and production efficiency, can be solved.

With the advancement of technology, however, all this is becoming possible. Procedural methods allow us to design modeling processes instead of mere parts, with a well-construed system being capable of algorithmically synthesizing elaborate, organic geometries based on descriptive data. Additive manufacturing has long been accessible to assist in their realization, while the digitalization of textile technologies is also rapidly emerging, carrying within the potential for producing and integrating components that are soft, flexible and strong at once. This paper proposes a robotic hand and methods developed for its design and production, to exemplify leveraging these advances towards improving both durability and manufacturability, while avoiding any significant reduction in the functional delicacy and complexity that embody the primary values of biomimicry.

II. Biomechanical Structure

Out of all prehensile solutions evolved by nature, the feature that makes our hand with the opposable thumb most distinctive is its remarkable versatility, characterized primarily by two factors: adaptiveness and dexterity. While the former is a consequence of soft tissues surrounding a rigid skeletal frame enabling our fingers to compliantly wrap around any object, the latter can be directly attributed to our intricate ability to coordinate our joint movements.

A. Parametrically Generated Skeleton

Biomechanical systems are generally based on articulating joints, characterized by contacting convex and concave surfaces of various shapes gliding and rolling about each other. These have several beneficial properties compared to traditional couplings used in mechanical constructs, which together effectuate the movement characteristics of biological organisms human perception deems ”natural”.

First and foremost, their movement trajectories are not constrained around one or more fixed axes, but follow the curvature of the articulating surfaces instead, allowing for specialized motion trajectories in each joint, and highly variable ranges of motion (RoM) across each degree of freedom (DoF). Second, the stiffness of the joints varies across the different stages of the motion, as a result of the ligaments becoming tensioned due to the distances changing between their attachment points, contributing to dynamic stabilization and further DoF constraints to reinforce grasping.

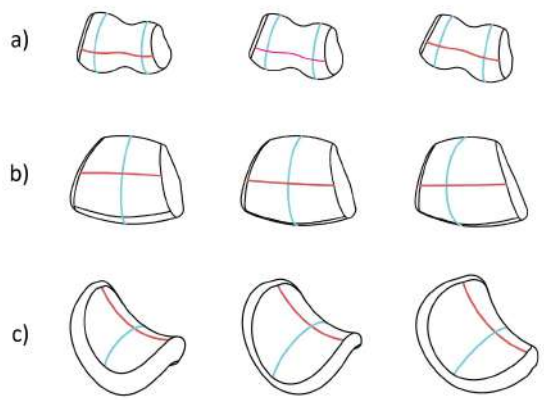


Fig. 2. Articulating joint head geometries generated by the developed procedural modeling algorithm, showing varying parameters for conical obliqueness in ginglymoid (a), tilting range of motion in condyloid (b), and rotation curvatures in saddle-shaped (c) joints.

Such influences are clearly exemplified by the prehensile center-oriented conical obliqueness at the flexed interphalangeal (IP) joints, by the second, tilting DoF of condyloid metacarpophalangeal (MCP) joints becoming almost entirely constrained in flexion except for slight pronation-supination, and by the opposition-enhancing automatic axial rotation arising during flexion in the saddle-shaped trapeziometacarpal (TMC) joint of the thumb [7].

As small as each of these features seem on their own, their cumulative effect is quite significant - articulating joints are one of the primary enablers of adaptive grasping capabilities of the human hand, synergizing with the soft tissues to allow our fingers to envelop objects in a much more compliant manner than any conventional robotic gripper to date, no matter how anthropomorphic they might be on the outside.

Recognizing these advantages, several experimental designs were attempted in the past to integrate these articulation-related characteristics into robotic systems without resorting to over-simplification [8] [9] [10]. However, due to the complex nature of the joint surface geometries, these are usually based on pre-existing skeletal mesh models acquired mostly via medical imaging. The results can be highly natural and effective, but the method is very difficult to scale, as control over properties or functional parameters is virtually non-existent - each joint variant would have to be designed manually, constantly bearing the consequences of the heuristic approach.

Therefore, to realize such integration while respecting the need for design controllability, a procedural articulating joint generator was developed using the 3D design and scripting capabilities of the PTC Creo 11 CAD environment, for the automated modeling of anatomically correct surfaces from just a few key parameters (joint size, desired movement ranges and distortions, etc), based on extensive literature research and cadaveric studies. The system allows for deep personalization by taking input parameters based on measurements or the analysis of 3D scans or medical images, and as shown in Fig. 2, it is capable of generating each joint type occurring in the

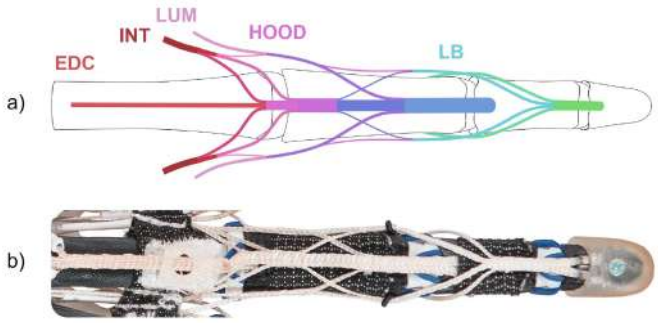


Fig. 3. Color-coded schematic drawing of the tendinous system's anatomical structure with key functional segments identified (a), and its braided realization attached to a long finger (b).

fingers, with inherent degrees of freedom, naturally oblique movement axes and optimized surface geometries.

The generator outputs production-ready skeletal components, with all features required for mechanical assembly already included. In the current prototyping process, an abrasion-resistant, self-lubricating material (igus iglidur i150) was used via easily accessible FDM technology. Joint ligaments were realized by simply threading elastic ropes (Paracord, elastic cord) through holes made in their anatomical attachment points, to retain the variable stiffness property.

B. 3D Braided Tendon Network

The movement of the joints in each human finger is controlled by the interplay of six extrinsic and intrinsic muscles on average (nine in case of the thumb). Instead of directly attaching to the bones, however, these form an elaborate branching structure commonly referred to as the finger extensor system [11] [12] [13], through which each muscle is connected to several areas across multiple phalanges. The geometry of this network accentuates the synergistic-antagonistic behavior of the muscles - generally, each of them has a primary role, but their effects are largely dependent on the actual joint positions, and the level of contraction in specific other muscles.

A prime example for this is the threefold role of the interosseous (INT) muscles [14]. When operating independently, they are the dedicated actuators of finger tilting, but their synchronous contraction causes the full extension of the IP joints via the lateral bands (LB) of the network when the MCP joint is kept extended by the long extensor (EDC). When the MCP is flexed, however, the interossei pull downward upon the so-called extensor hood enveloping the base of the proximal phalanx instead, resulting in a significant enhancement to flexion strength due to their optimal lever arm. In this state, their independent contraction is unable to activate finger tilting due to the constraints of the MCP joint, eliciting slight axial rotation instead. Besides reinforcing our movements, the interossei act as a modifiers on the effects of the forearm muscles. Because of their presence, the EDC does not need to have a direct extending effect on the IP joints - it is allowed to be kept taut while the long flexors (FDP and FDS) activate, resulting in our ability to reliably perform the "claw-finger" posture - the interossei thus effectively allow us to indirectly "turn off" our flexors' influence on our MCP joints.

Similar in behavior but opposite in effect, the lumbrical (LUM) muscles have an increased lever arm acting upon the LB while bypassing the hood structure, so they are used to redistribute the forces of the long flexors and extensors towards flexing the MCP and extending the IP joints simultaneously. This enables the formation of the "beak hand" posture, and has a significant role in delicate manipulation tasks.

The effects of the intrinsics are even more prominent in the thumb [15], where they are responsible for the independent control of adduction, abduction, pronation and supination at both the TMC and MCP joints. Their activity ensures a smooth and controllable transition between flexion-extension and opposition-anteposition.

These example interactions show that intrinsic muscles act as dynamic switches on the activity of the stronger extrinsics, able to redirect their effects to enable or reinforce certain movements at will. The interconnections of the tendinous network contribute greatly to our natural finger tones and trajectories, resulting in dexterous functionality becoming severely impaired when deliberately omitting these features from artificial hands, as is often the case.

Attempts at replicating this intricate system all face the same challenge: producing such complex, branching geometry that also shares the most important property of biological tendons: high load-bearing capacity. Several methods have been tried during the recent years [16] [17] [18], supporting the endeavor by achieving significantly increased human-likeness, but each had to make a costly tradeoff: the tendon system either has an elaborate fabrication and assembly process involving time-consuming manual steps such as crimping, gluing or knotting, or it is simple in production but remains hindered by its fragility, like laser-cut silicone components.

In search of a solution eliminating these issues, a custom 3D braiding environment was developed, capable of producing branching rope structures quickly and effectively due to a visual and script-based design and control system and automated patterning capacities. The machinery is based on variation braiding technology [19], which essentially entails a matrix of conventional fixed-track maypole rope-braider [20] units interconnected by switches capable of adjusting the pathways the yarn carriers take, changing the patterns of the produced braids on the fly. This allows for the realization of homogeneous 3D structures with high tensile strength, without significant weak points or obstructions at branch junctions.

The tendinous systems for our hand prototype were produced using this method, as multi-branching constructs of polyester multifilament fibers, the braided microstructure of which adequately mimics the tenacity and behavior of collagenous connective tissue. As shown in Fig. 3, the braided network was designed to include all anatomical substructures, with the intent of accurately replicating the biomechanics of the flexor, extensor, interosseous and lumbrical tendons, while satisfying requirements for both load-bearing and simple, scalable production.

C. Covering Soft Tissues

Biological tendons are guided along the fingers in synovial tendon sheaths, acting as pulleys to redirect muscle torque to the target phalanx regions. Similar ligamentous structures assist in holding the palmar bones together. As shown in Fig. 4/a, these are replicated separately for each phalanx as simple pull-on sleeves of bilayered, semi-elastic, UHMWPE (ultra-high molecular weight polyethylene) reinforced nylon fabric to maintain ease of assembly. An additional laminated UHMWPE layer envelops the tendons to ensure low friction and high tensile strength, while the simple sewing pattern enables quick bulk-manufacturing on any conventional sewing machine.

Fat and muscle pads are equally essential for truly compliant grasping - these were realized experimentally as lightweight, 3D printed, elastic lattice structures of spatially varying density, designed and optimized in the implicit 3D modeling and simulation software nTopology for assisting flexion and bulging in the appropriate areas during grasping, analogous to the functionality of palmar creases. The palmar, thenar and hypothenar padding-complex is shown in Fig. 4/b.

Soft, removable skin is sewn in a long, layered glove pattern with insets at the joints to facilitate wrinkling and reduce wear and tear, used for protection and for holding the lattice padding in place. The glove is made using a thin spacer-mesh fabric material to provide further padding and a comfortable texture.

III. Actuator System

In terms of motorization, it is important to address that different target use cases have different requirements. The electrophysiological control interfaces currently available on the prosthetics market are unable to acquire and supply delicate control signals, and device volume is also severely constrained, so the placement of multiple motors for each finger would be infeasible. True dexterity is not on the table - grasping versatility and reliability are, alongside ergonomic factors such as weight, aesthetics and compactness. Therefore, the goal in prosthetic hand development is to restore grasping performance, while simplifying the actuator system as much as possible. In humanoid or telerobotic systems, space and weight are much less limiting constraints, while dexterous functionality can be fully utilized owing to the employment of advanced autonomous or wearable control interfaces. Replicating the intricate capabilities of the biological hand by increasing the number of controllable DoF thus becomes a focus point.

The purpose of the presented biomimetic system is to provide a platform with exceedingly human-like functionality, easily configurable for various applications. The described biomechanical structure is therefore effectively able to fulfill the requirements of both environments: in the case of complex manipulation tasks, each tendon can be connected to actuators while still exploiting certain antagonistic relations to reduce the total number of motors in the system, while in cases where the need for compactness dominates, it is sufficient to actuate only the primary flexors and extensors - the extensor network, alongside a number of elastic interconnections (Fig. 5/a) can passively ensure partially maintaining their reinforcing effects,

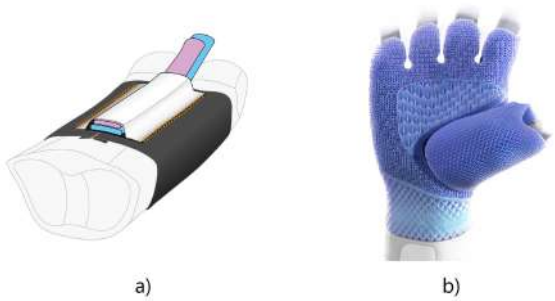


Fig. 4. The tendon sheath and pulley of the hand prototype realized as a simple, sewn pull-on sleeve (a), and the palmar fat and muscle tissues mimicked by selectively compliant, varying-density lattice structures (b).

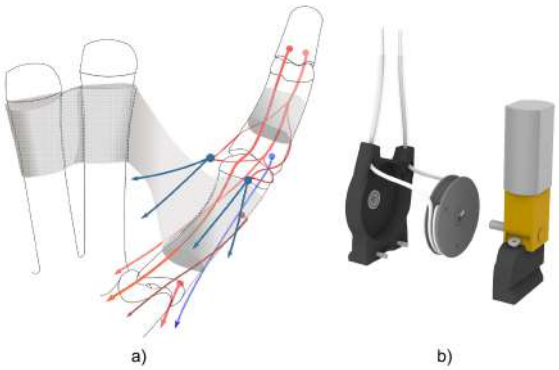


Fig. 5. Anatomical model of the thumb actuator tendons based on [7] (a). In our compact frame, tendons in blue are passivated by elastic connections, while in the extended version, all can be actuated. Exploded view of a single actuator unit with its antagonistic tendon-driving winch mechanism (b).

and enabling a highly adaptive grasping performance due to their contributions to finger tone and natural trajectories.

To demonstrate the extensive capabilities of this biomechanical system, a modular forearm frame and actuation system was developed. It can be configured for single or double-layered construction, each layer capable of housing 6 actuators, with the rotatable wrist area holding room for up to 4 more. High-power, N50 and coreless 12V DC micromotors with worm gearboxes of various gear ratios (range of 100-300:1) are used with winch drums of variable sizes to allow setting the extents of tendon speed and displacement, while attaining high gripping forces and even higher holding torques (Fig. 5/b). The motors are mounted by dovetail joints, ensuring easy removal and reconfigurability. The tendons are connected to the motor housings by PTFE tubes, realizing a Bowden mechanism. Each motor is capable of driving 2 tendons, formulating an antagonistic relation between them.

The electronic control unit is centered around an STM32 MCU, with a dedicated FPGA chip for processing the magnetic encoder signals of each motor, and capabilities to indirectly estimate applied load via motor current measurements. The system can be powered by 2-6 cells of 2900 mAh Li-ion batteries, and can communicate with external IoT agents through the Bluetooth (BLE 4.2) module of an ESP chip, rendering both versions completely wireless and portable.

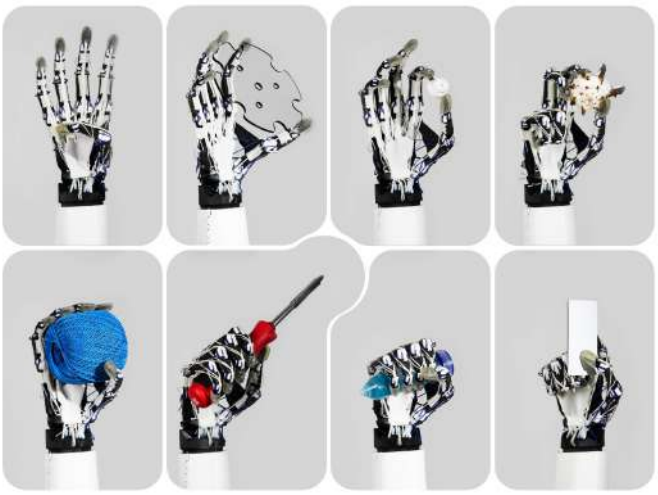


Fig. 6. The Biomimetic Hand performing selected classified grasps [23] and demonstrating maximal thumb opposition, capabilities available in both compact and extended actuator configurations.



Fig. 7. The hand demonstrating finger tilting, claw and beak hand postures, enabled by the intrinsic activity of the extended actuator system.

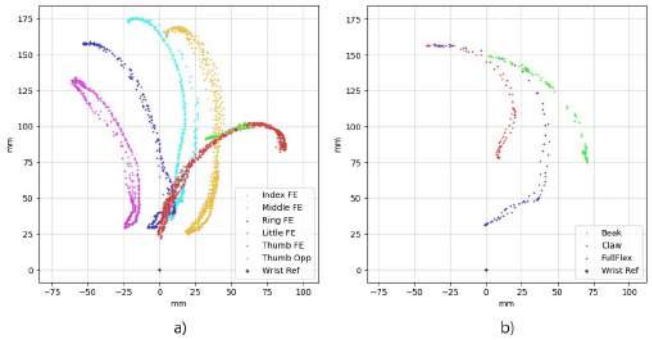


Fig. 8. Color-coded fingertip trajectories: latero-frontal projection of full flexion and extension of each digit and thumb opposition using the compact actuator frame (a), and lateral view of the ring finger's advanced trajectories enabled by the extended frame (b).

IV. Results and Evaluation

The developed hand has 17 active and 12 passive DoF in its joints, including thumb opposition and wrist movements. The speed and strength of its fingers were evaluated using a 120 FPS camera and a Tinius Olsen 5ST universal testing machine equipped with a 5kN load cell, averaged across 10-10 repetitions. It has a closing speed of $\sim$0.5s and a grip strength of $\sim$15N during the full flexion of each individual finger, with further reinforcement possible by the simultaneous activity of the independent intrinsics in the extended system. The load-bearing capacity of the braided tendons at different cross-sectional areas was also examined, and the breaking load was found to be $\sim$20kg for the thinnest (lumbrical, 0.9 mm^2), and $\sim$170kg for the thickest (flexor, 8.4 mm^2) segment.

Besides reinforcing that biomimetic hands are able to reach operating speeds and forces similar to anthropomorphic robotic hands built by more conventional methods, these tests also show that the tensile properties of artificial tendons produced via braiding can possibly match those of their biological counterparts, with both cross-sectional areas and breaking stresses falling into the same magnitude [21].

Two variants of a modular actuator system were constructed: the smaller version aimed at prosthetics houses 7 motors, 1 for each finger's flexion-extension, and additional 1-1 for thumb opposition and wrist rotation. This allows for independent finger control along natural trajectories susceptible to passive influences, resulting in the fingers wrapping compliantly around any object obstructing their path with sufficient resistance. Independent intrinsic muscle control and active finger tilting is lost as a tradeoff, but the stability and adaptivity of grasping is still significantly increased due to the human-like nature of the biomechanical construction. With such a low number of actuators, the complete, life-sized compact system weighs 1.2kg, less than the average human forearm [22]. With the hand itself weighing below 300g, and the battery pack (currently 300g) being highly variable, the frame is light enough to be considered adaptable for prosthetic use-cases.

The extended version for humanoid or telerobotic applications has a less strictly constrained, but still favorable total weight of 1.45kg, and 16 motors contained within the forearm, with the potential to allow for independent flexor and extensor activities, and a fully actuated thumb capable of traversing its complete biological workspace. Intrinsic muscles are antagonistically coupled, enabling active finger tilting, alongside a fully actuated 3 DoF wrist. Besides having similar, highly adaptive grasping capabilities, this version is built to truly exploit the biomimetic design towards realizing human-like dexterous capabilities.

The functional capabilities of the hand were evaluated by performing the GRASP taxonomy [23] as demonstrated in Fig. 6, using a manual, button-based controller configured to drive individual and/or simultaneous motor activity as needed. Using the compact actuator system, the hand was capable of performing 28 out of 33 classified grasps, with the only exceptions requiring controlled finger tilting and independent intrinsic muscle activity (these being: adduction grip, tripod variation, inferior pincer, light tool, and parallel extension). The extended actuator frame, however, enabled the hand to perform all listed grasps, and also to produce the claw and beak postures (Fig. 7) made possible by the active intrinsics (attainable by extensor-flexor synergy enabled by the presence of the interossei, and independent or extensor-assisted lumbrical actuation respectively).

Fingertip trajectories were also analyzed via motion tracking over video captured by a single camera setup. A stable reference marker was placed at the palm and a moving marker

at the tip of each finger. Recordings were taken of individual finger activities with 5 uninterrupted repetitions at 25 FPS. In Fig. 8/a, trajectories were projected to 2D and plotted for each digit's full flexion-extension and separate thumb opposition using the compact actuator configuration, while in Fig. 8/b the additionally performable claw and beak finger trajectories were isolated using our extended setup.

The results show high repetition accuracy with trajectories visibly and generally comparable to cadaveric measurements [24], with highly similar full flexion and extension sweeps. This shows a clear improvement on reliability in mechanical performance without regard to directionality, despite the vastly different volar and dorsal tendon configurations, demonstrating the effectiveness of our anatomically inspired methods in replicating natural motion characteristics.

V. Conclusion and Future Work

In this work, a life-sized biomimetic hand was developed and prototyped, with 3D printed bones and articulations generated by a procedural algorithm based on key parameters, 3D braided tendons produced by a custom variation braider, and textile-reinforced soft tissues. The biomechanical significance of the included articulations and tendinous components was explained from an anatomical perspective, and a modular actuation frame was designed and realized in a compact and an extended version with varying levels of muscular inclusion, each targeted at applications requiring different levels of dexterity. Capabilities were evaluated through grasp and gesture demonstrations and finger trajectory analysis, to highlight the advanced functions and natural compliance enabled by the mimicry of anatomical structures and degrees of freedom.

The results aim to highlight that by today, design and manufacturing methods have advanced to a level that makes the production of such geometrically and functionally complex systems feasible. Combining procedural design with 3D printing enables the quick and efficient realization of customizable organic functional structures. Textile solutions can be leveraged to include advantages of soft robotics, while maintaining high durability. And owing to the ongoing digitalization of advanced technologies such as 3D braiding leading to less time-consuming assembly processes, cost-efficient and scalable production is also within reach, supporting the integrability of biomimetic systems across a wide spectrum.

In future work, advanced control algorithms will be implemented to coordinate actuator co-activity for the automated control of complex movements. The mechanical capabilities of the model will be further evaluated and improved, including performance when connected to actual prosthetic and teleoperation interfaces, and iterations on the initial padding and skin designs for enhancing grasping robustness. Finally and most importantly, successive developments on skeletal modeling and textile/fiber-engineering will be carried out to further enhance the design and production efficiency of such highly biomimetic devices, towards increasing the presence and recognition of intuitively natural robotic platforms in both medical and industrial settings.

References

[1] Nguyen, V. P., Dhyan, S. B., Mai, V., Han, B. S., Chow, W. T. (2023). Bioinspiration and biomimetic art in robotic grippers. Micromachines, 14(9), 1772.

[2] Salminger, S., Stino, H., Pichler, L. H., Gstoettner, C., Sturma, A., Mayer, J. A., ... Aszmann, O. C. (2022). Current rates of prosthetic usage in upper-limb amputees–have innovations had an impact on device acceptance?. Disability and Rehabilitation, 44(14), 3708-3713.

[3] Biddiss, E., Chau, T. (2007). Upper-limb prosthetics: critical factors in device abandonment. American journal of physical medicine rehabilitation, 86(12), 977-987.

[4] Piazza, C., Grioli, G., Catalano, M. G., Bicchi, A. (2019). A century of robotic hands. Annual Review of Control, Robotics, and Autonomous Systems, 2(1), 1-32.

[5] Mattar, E. (2013). A survey of bio-inspired robotics hands implementation: New directions in dexterous manipulation. Robotics and Autonomous Systems, 61(5), 517-544.

[6] Tasi, B. J., Koller, M., Cserey, G. (2019). Design of the anatomically correct, biomechatronic hand. arXiv preprint arXiv:1909.07966.

[7] I. A. Kapandji, (1982) The Physiology of the Joints, Volume One, Upper Limb, 5th ed., Churchill Livingstone, Edinburgh, London, Melbourne and New York, 164-281.

[8] Xu, Z., Todorov, E., Dellon, B., Matsuoka, Y. (2011, May). Design and analysis of an artificial finger joint for anthropomorphic robotic hands. 2011 IEEE International Conference on Robotics and Automation (pp. 5096-5102). IEEE.

[9] Hockings, N., Iravani, P., Bowen, C. R. (2014, November). Artificial ligamentous joints: methods, materials and characteristics. 2014 IEEE-RAS International Conference on Humanoid Robots (pp. 20-26). IEEE.

[10] Faudzi, A. A. M., Ooga, J., Goto, T., Takeichi, M., Suzumori, K. (2017). Index finger of a human-like robotic hand using thin soft muscles. IEEE robotics and Automation Letters, 3(1), 92-99.

[11] Clavero, J. A., Golanó, P., Farinas, O., Alomar, X., Monill, J. M., Esplugas, M. (2003). Extensor mechanism of the fingers: MR imaging–anatomic correlation. Radiographics, 23(3), 593-611.

[12] Crampton Harris, J. R., RUTLEDGE JR, G. L. (1972). The functional anatomy of the extensor mechanism of the finger. JBJS, 54(4), 713-726.

[13] Schultz, R. J., Furlong II, J., Storace, A. (1981). Detailed anatomy of the extensor mechanism at the proximal aspect of the finger. The Journal of hand surgery, 6(5), 493-498.

[14] Schreuders, T. A. R., Brandsma, J. W., Stam, H. J. (2007). The intrinsic muscles of the hand. Physikalische Medizin, Rehabilitationsmedizin, Kurortmedizin, 17(01), 20-27.

[15] Gupta, S., Michelsen-Jost, H. (2012). Anatomy and function of the thenar muscles. Hand clinics, 28(1), 1.

[16] Xu, Z., Todorov, E. (2016, May). Design of a highly biomimetic anthropomorphic robotic hand towards artificial limb regeneration. 2016 IEEE International Conference on Robotics and Automation (ICRA) (pp. 3485-3492). IEEE.

[17] Xu, Z., Matsuoka, Y., Deshpande, A. D. (2015, December). Crocheted artificial tendons and ligaments for the anatomically correct testbed (ACT) hand. 2015 IEEE International Conference on Robotics and Biomimetics (ROBIO) (pp. 2449-2453). IEEE.

[18] Wilkinson, D. D., Weghe, M. V., Matsuoka, Y. (2003, September). An extensor mechanism for an anatomical robotic hand. 2003 IEEE international conference on robotics and automation (Cat. No. 03CH37422) (Vol. 1, pp. 238-243). IEEE.

[19] Emonts, C., Grigat, N., Merkord, F., Vollbrecht, B., Idrissi, A., Sackmann, J., Gries, T. (2021). Innovation in 3D braiding technology and its applications. Textiles, 1(2), 185-205.

[20] Kyosev, Y. (2014). Braiding technology for textiles: Principles, design and processes. Elsevier.

[21] Weber, J. F., Agur, A. M. R., Fattah, A. Y., Gordon, K. D., Oliver, M. L. (2015). Tensile mechanical properties of human forearm tendons. Journal of Hand Surgery (European Volume), 40(7), 711-719.

[22] Clauser, C. E., Mc Conville, J. T., Young, J. W. (1969). Weight, volume, and center of mass of segments of the human body (No. AMRL-TR-69-70).

[23] Feix, T., Romero, J., Schmiedmayer, H. B., Dollar, A. M., Kragic, D. (2015). The grasp taxonomy of human grasp types. IEEE Transactions on human-machine systems, 46(1), 66-77.

[24] R. A. Chase and W. L. White, "Functional Anatomy of the Hand," Stanford Anatomy. [Online]. Available: https://youtu.be/9V1ZzAiB1rY?t=1588.

Evaluating the Relationship between Motor and Cognitive Impairment and Lesion Size and Location Post-Stroke Using CT Scans*

Reem M. Azar[1], Natalia Stroutinsky Sobotka[2], Pamela Cacchione[3], Rochelle J. Mendonca[4], Michelle J. Johnson, *Member, IEEE*[5]

Abstract— **With stroke being the leading cause of disability worldwide, there is a need to improve current rehabilitative care. Stroke causes brain damage in the form of a lesion, resulting in both cognitive and motor deficits. Clinicians often rely on functional behavior to determine treatment directions; however, behavioral deficit may not represent the neural damage. Understanding how the neural damage influences the behavioral impairments with stroke subjects could allow clinicians to provide a more personalized therapeutic plan. Focusing on global accessibility, CT-scans were used to image the lesion given that it is an affordable imaging modality that is used world-wide. Eleven chronic stroke patients were mapped into functional groups by their motor and cognitive behavior and their CT-scans was used to quantify lesion volume and define how the volume location mapped unto the whole brain areas at different granular levels. Our main findings were that lesion size may not be a good indicator of behavioral deficit. These results suggest that assessing brain areas more granularly may show larger differences in behavior.**

I. Introduction

Stroke is one of the most common causes of death and disability worldwide, with annual treatment costs reaching approximately 53 billion dollars in America alone [1]. In an ischemic stroke, blockage of a cerebral artery leads to reduced blood flow and oxygen in the brain. The loss of blood (and oxygen) leads to a cascade of events that eventually lead to neural cell death. Like wounds in other systems in the body, the immune system will clean up the damage in the brain and lead to the formation of a lesion (which can result in both motor and cognitive deficits). To assess this damage clinically, medical professionals typically use either Computerized Tomography (CT) or Magnetic Resonance Imaging (MRI) [2,3]. While MRI offers superior tissue contrast, CT scans remain the more globally accessible and cost-effective option for stroke diagnosis and assessment [2]. Since CT scan primarily visualizes changes in tissue density, the damaged area may not be clear in the early acute stage of stroke as the cell clean-up process is still underway. While several studies have assessed lesion size and location and behavior using CT scans, these studies focus on relationships between specific regions of interests and outcome behaviors, rather than exploring the whole brain [4-6]. The limitation of this approach is that there may be regions of the brain that are overlooked. Since the brain is deeply interconnected, any disruption in any brain networks due to stroke may lead to deficits in both motor and cognitive performance. Upper limb impairments are often more severe than lower limb impairments, mainly due to most strokes involving the middle cerebral artery, which mostly spares the lower limb [7-10]. Studies show that 77% of stroke survivors have upper limb motor deficits and about 40% also have at least mild cognitive deficits [11]. Despite this, there are few studies that look at the prevalence of concurrent motor and cognitive deficits, but of the studies that have, they found that motor performance is affected by cognition and low/moderate cognition can mask high motor performance [12-14].

The literature has also extensively shown that there is a relationship between brain structure and function [15,16]. Many studies focus on correlating lesion metrics to behavioral outcomes using a dichotomized metric (i.e., good vs. severe) of a single assessment, which is not effective since there is evidence that both cognitive and motor impairments result from stroke. Robotic-based rehabilitation typically relies on decreasing motor impairment and assumes that these changes arise from use-dependent brain plasticity. It is not always clear who is the best candidate for robot-based therapy or what is the best treatment strategy. There is an urgent need to improve robot-assisted rehabilitation devices to ensure that patients are getting the most appropriate and personalized therapeutic plan. Given that cognitive impairment can mask motor performance, it is essential to understand the effect lesion metrics have on motor and cognitive behavior post-stroke.

In this paper, we explore the relationship between structure and function in stroke patients. We deployed a validated lesion segmentation approach to harness neural features from retrospective CT scans and explore their relationship to both motor and cognitive behavior acquired

*Research reported in this publication is supported by the core National Institute of health (NIH) Eunice Kennedy Shriver National Institute of Child Health and Human Development under NIH-funded under the award numbers R42HD104325 and R42HD104325-03S1. This work is also made possible by the NIH-funded T32 grant (Training in Musculoskeletal Research) under the award number T32AR007132-48, the Penn Fontaine Society, and the Penn Departments of Bioengineering and Physical Medicine and Rehabilitation.

[1]Reem M. Azar is a PhD Student in Bioengineering at the University of Pennsylvania (610-573-9423; e-mail: razar@seas.upenn.edu)

[2]Natalia Stroutinsky Sobotka is an occupational therapist with the Pennsylvania Medicine Rehabilitation Center.

[3]Dr. Pamela Cacchione is a Professor of Geropsychiatric Nursing at the University of Pennsylvania.

[5]Dr. Rochelle J. Mendonca is an Assistant Professor in the Department of Rehabilitation and Regenerative Medicine/Programs in Occupational Therapy at Columbia University

[5]Dr. Michelle J. Johnson is an Associate Professor at the University of Pennsylvania with a primary appointment in Physical Medicine and Rehabilitation and secondary appointments in Bioengineering and Mechanical Engineering and Applied Mechanics (email:johnmic@pennmedicine.upenn.edu)

from clinical assessments of 11 stroke subjects. We seek to 1) confirm that we can acquire lesion metrics from CT scans and 2) explore the relationship between lesion features (size and location) and motor and cognitive behavior in stroke subjects.

II. METHODS

A. Participant Screening

Participants were primarily recruited from an urban hospital comprehensive stroke center and from inpatient/outpatient rehabilitation centers (CBR/GSPP). To be included in the study, participants were at least 3 months post-stroke with a confirmed ischemic stroke diagnosis, including a diagnosis of hemiparesis. Patients had to have a CT scan that can be accessed retrospectively. All patients had to be able to provide informed consent. All participants must present with some motor impairment and function, with a Fugl-Meyer UE score between 15 and 60. Furthermore, their upper arm manual muscle strength scores must be greater than 1 and their upper arm spasticity less than 4 based on the Modified Ashworth scale. Patients must also present with less than 33 on the NeuroQoL Depression measure. Eleven patients (57.4 ± 10.3 years) were included in this study, with 9 patients identifying as male and 2 subjects identifying as female. Table 1 shows their demographic data.

B. CT Scan Selection

The lesion development studies have shown that a stroke lesion evolves over time until the stroke becomes chronic (>three months) [17,18]. After initial injury, the lesion will appear bigger in volume due to swelling, however, the size will eventually settle into its chronic phase with the formation of the glial scar. To the knowledge of these authors, only one study to date has assessed behavior and lesion metrics at the acute and chronic time points. This study suggests that research collected from one time point of stroke may be applicable to other timepoints (with aphasia specifically). Although the results cannot be generalized to all human behaviors, there is other evidence in the literature that suggests that initial lesion volume can predict behavior [15,16]. For the purposes of this study, chronic scans were selected when available and acute scans were used otherwise.

C. Lesion Segmentation

Currently, the gold standard for lesion identification is through manual segmentation [19] by using digital imaging and communications in medicine, DICOM files. A lesion is a hypodense area on the CT scan that appears on multiple z-slices (indicating a volumetric loss). To manually segment the lesions, we followed the guidelines published from Liew et al., 2018 [20]. We used ITK-SNAP, an interactive tool developed for medical imaging segmentation, to create the lesion masks [19, 21]. The Montreal Neurological Institute (MNI) is the standard template used in literature, and it was developed from 152 young adult healthy MR brain scans, making these templates larger on average than brains of stroke patients [22]. To register individual brains to a uniform space, Rorden et al., 2012 developed an age specific template from CT images that can be accessed easily through the Statistical Parametric Mapping (SPM Version 12) Clinical toolbox in MATLAB [23]. Since the SPM Clinical toolbox relies on average size brains, we used an atlas that matched the SPM template dimensions (157 X 189 X 136). To ensure proper template matching, images were normalized using the following bounding box:

-90, -126, -72

90, 90, 108

There is an array of brain atlases to choose from. Since we are analyzing the whole brain, we limited ourselves to atlases that can label the whole brain, covering both cortical and subcortical areas. To accomplish the goal of capturing Brodmann areas and subcortical brain regions, we used the Automated Anatomical Labeling Atlas 3 (AAL 3). The AAL is one of the most widely used atlases in neuroimaging studies, and the AAL 3 is the most updated version of this atlas [24, 25]. The AAL 3 provides structural parcellations of some subcortical brain nuclei (such as the thalamus), giving us an opportunity to examine extensive subcortical involvement in the future. The AAL3 used matched bounding box parameters of the SPM12 toolbox.

D. Whole Brain Analysis

The brain is complex, and thus can be analyzed at various levels. We analyzed the brain in an increasingly granular function. At a broad level, the brain is divided into the right and left-brain hemispheres. The two hemispheres are mostly symmetrical, however, there are some asymmetries that may lead to differences in function [26]. At the next level of division, we will explore the involvement of depth levels of the brain. The brain is divided into cortical, subcortical, and brain stem regions (technically, the brain stem is not a part of the cerebrum, but it is a vital territory of the nervous system that can be affected by stroke). The next level of division of the brain are the lobes of the cerebrum, which are traditionally four lobes (frontal, parietal, temporal, and occipital). The brain anatomy goes beyond the cerebrum with both the cerebellum and brain stem, which are considered two separate lobes. With an increased understanding of the brain, more lobes have been established: insula and limbic lobes, however, the existence and boundaries of the limbic lobe are not universally accepted [27].

Lastly, the most granular division we looked at is seven main brain networks that each have evolving functions. Importantly, few brain areas deal with specifically either

TABLE I. PARTICIPANT DEMOGRAPHICS

ID	*Age*	*Sex*	*Race*
001	39	M	Asian
003	56	M	White
005	35	M	Black or African American
007	48	M	Black or African American
008	24	F	White
009	51	F	Black or African American
010	70	M	Black or African American
012	47	M	White
013	49	M	White
023	59	M	White
047	40	M	Black or African American

domain, however, five areas are mostly *correlated* with cognitive functions (temporal and junction lobes, Default Mode Network (DMN), Dorsal Attention Network (DAN), and Salience Network (SAN). The temporal lobe is mainly involved with communication and sensing the world. The junction lobe represents areas that do not fall in any specific lobe, and these areas are mainly involved in communicating between different brain areas. The SAN is mainly involved in executive functioning and processing of stimuli and communicated with the DMN. The DMN is mainly involved in memory processing and memory retrieval, as well as resting-state activity, which is essential for overall brain function. Lastly, the DAN mainly processes visual stimuli to focus attention.

E. Clinical Assessments

The clinical assessments used in research settings are different than those acquired by therapists in hospital settings. To save time and acquire general motor and cognitive impairment status, clinicians prefer short and rapid assessment and may not use the research state of the art. To assess cognitive impairment, Montreal Cognitive Assessment (MoCA) was used. The MoCA is used to measure impairment in visuospatial/executive function, naming, memory, attention, language, abstraction, delayed recall, and orientation [28]. Specifically, the MoCA has been used in patients with stroke to measure cognitive impairment and was able to detect more people who had chronic stroke when compared to other state-of-the-art assessments, with a maximum score of 30 [28]. The Fugl-Meyer upper extremity (FM-UE) scale is a widely used and stroke-specific measure of both upper extremity impairment [29]. The FM-UE is the most used scale to measure post stroke upper extremity impairment within research settings [30]. The FM UE assesses reflex activity, movement control, and muscle strength, with a maximum score of 66. Certified and trained individuals scored clinical assessments.

F. Functional Subgroups

Clinical score cut offs for motor and cognitive assessments determine motor and cognitive functional status. These functional subgroups distinguished between high to low motor and cognitive function. An FM -UE score of 48 and below was used as the cutoff for moderate-to-low UE function and a cutoff score of 26 and below was used to indicate moderate-to-low cognitive function [31]. To simplify the labeling, we divided the groups into high and low function. We can then classify the subjects into four functional subgroups: high motor/high cog, high motor/low cog, low motor/high cog, and low motor/low cog. Figure 1 illustrates the functional subgroup stratifications.

III. RESULTS

All data were collected under guidance and with approval from the University of Pennsylvania Internal Review Board (IRB) from two approved studies: 849090 and 823511. The images were all acquired retrospectively using the electronic, medical records system used by the Penn Medicine Hospital Group. Given the small sample size, all results presented are to show potential relationships. Table 1 shows subject demographics.

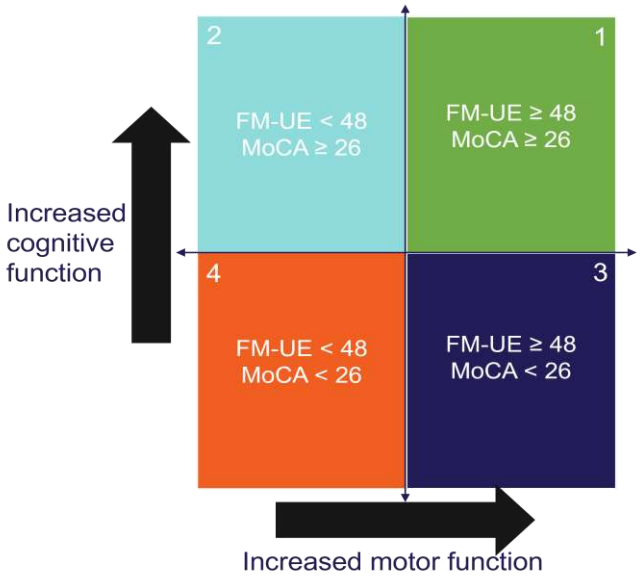


Figure 1: Motor and cognitive cut off scores that define the functional subgroups

A. Functional Subgroups

Table 2 displays UE-FM and MoCA scores for each participant as well as their functional grouping. Figure 2 displays each participant in their functional subgroup. Due to the small sample size, there is not an even distribution of subjects across the groups. There is *one subject with low motor and low cognitive function and no subjects in the group with low motor and high cognitive function*. Subject 23 lays right on the cutoff point between high and low cognitive function, being categorized as a person with high cognitive function.

B. Overall Lesion Segmentation Results

We were able to successfully extract and normalize lesion features from CT scans for eleven subjects. The same individual segmented all scans blindly (without indication of where the lesions were). All images were traced in the axial brain view. Figure 3 shows the lesion development of a subject with a large stroke: the lesion mask is in red. This subject has a mostly cortical stroke with minimal extension into subcortical areas. All subjects' brains and respective lesions masks were normalized according to the method described above. These scans display warping since they are normalized to a general space, with smaller slice thickness.

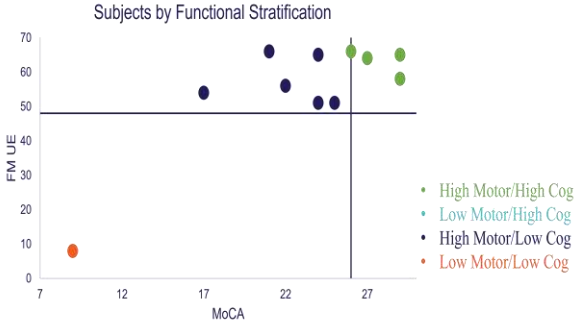


Figure 2: The functional subgroup division of our population

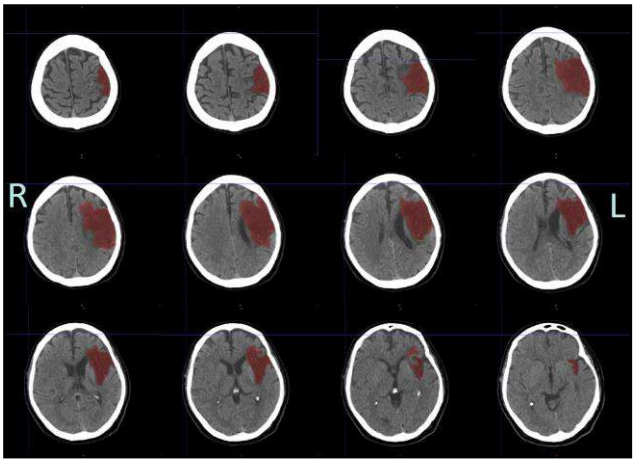


Figure 3: Subject 23's lesion development in axial view. The lesioned area is marked in red.

As mentioned, acute scans were used when chronic scans were not available, which was the case for four of the eleven subjects (subjects 001, 003, 010, and 012). Identifying the stroke lesions from CT scan was not always possible. For example, the CT scan for subject 001 showed a clear stroke, while the other three did not have clear lesions. One subject (subject 010) had MR scans available for cross analysis. These MR scans showed that the lesion was located dorsally right on the brain's surface. It is most likely that the scanner did not pick up the lesions at the surface.

C. *Lesion Size*

Table 2 presents the lesion volumes per subject, and there is no indication that there is a relationship between volume and motor and cognitive deficit in our population. The person with the most severe behavioral deficits had a small stroke (Subject 007) and the person with the largest stroke had high motor and cognitive function (Subject 023).

D. *Lesion Location*

Of the nine subjects with visible lesions, seven (77.8%) presented with left-hemisphere strokes and two (22.2%) with right-hemisphere strokes. All subjects (100%) exhibited contralateral motor impairment, where upper extremity deficits occurred on the opposite side of the lesion location. There were *no clear* differences in groups and hemisphere involvement.

At the next level of analysis, brain depth, after overlaying the atlas, initial analysis showed no lesions in the brain stem region. However, further analyses showed that there were indeed subjects with stroke damage, however, atlas coverage of subcortical areas was a limiting factor (fig. 4). Navigating to the red arrows on the side-by-side figures, there is a cerebellar stroke that the AAL3 did not capture in its overlay. There were also no differences among the functional groups in both cortical and subcortical involvement.

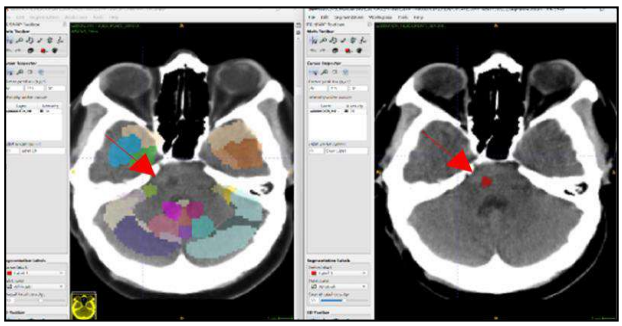


Figure 4: Subject 012 atlas overlay and lesion mask side-by-side

There is indication that the parietal, temporal, and junction areas have varying involvement among the three groups (as the low motor, high cog group had no subjects), with the high motor/low cog group displaying the greatest involvement in these areas (fig. 5 (a)). Importantly, the low motor/low cog group did not display lesion involvement in these lobes.

At the brain network level, both low cog groups displayed higher involvement in the Salience Network when compared to the other groups (fig. 5 (b)). The low motor/low cog subject displayed about 2mL of lesion involvement in the salience network, which is around thirty percent of the entire lesion size. The high motor/high cog group had lesions impacting this network.

IV. Discussion

The two goals with this study were to confirm that we can acquire lesion metrics from CT scans (at varying timepoints) and explore the relationship of lesion metrics to both motor and cognitive behavior. To our knowledge, there are no studies that look at whole brain analysis and combined motor and cognitive assessments, as we do in this study.

We were able to successfully acquire lesion metrics from one subject with only an acute scan, but were unsuccessful in acquiring lesion metrics from the other two subjects. One of the two subjects had an MR scan, where we were able to find that the small stroke was on the brain's surface. Due to the slice thickness used in CT scans, it is most likely that the scanner did not capture the small lesion. This limitation is present regardless of scan time point, but without a chronic CT scan for this subject, we cannot confirm that the lack of visible lesion was not due to the scan time point. The other subject that lacked a visible lesion did not have other scans available, so we cannot confirm the existence of a lesion.

Our study corroborated previous findings in the literature

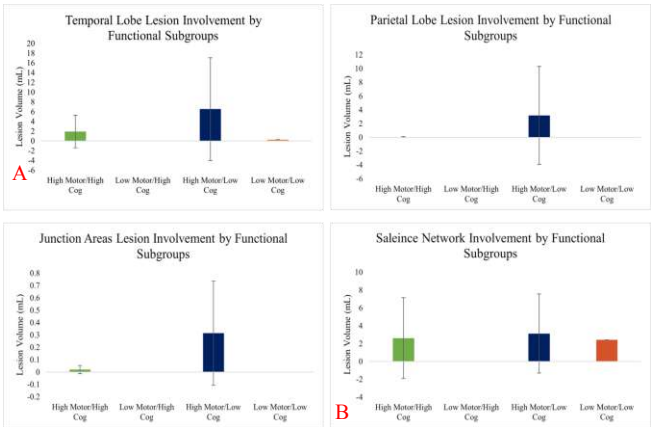


Figure 5: Lesion involvement results. A) Lesion involvement in the Temporal, Parietal, and Junction Lobes across the four groups. B) Lesion involvement in the Salience Network across the four groups.

TABLE II. CLINICAL ASSESSMENT AND LESION CHARACTERISTICS FOR THE PARTICIPANTS

ID	*Lesion Volume (mL)*	*FM*	*MoCA*	*Group*	*Scan Time*	*Lesion Location*
001	1.257	65	24	3	Acute	L
003	0	65	29	1	Acute	NA
005	0.584	51	24	3	Chronic	R
007	7.292	8	9	4	Chronic	L
008	0.232	58	29	1	Chronic	L
009	0.715	64	27	1	Chronic	R
010	0	56	22	3	Acute	NA
012	0.058	51	25	3	Acute	L
013	140.1	54	17	3	Chronic	L
023	167.095	66	26	1	Chronic	L
047	50.772	66	21	3	Chronic	L

that lesion size alone is not an indicator of function [32]. Inversely, the subject (Subject 007) with the most severe impairment had a subcortical lesion with involvement in the temporal, insular, and basal ganglia domains. Given this subject's severe motor impairment, we expected that this person would have some involvement of the motor cortex (cortical lobe), however, we are not surprised by the result since the basal ganglia and insula are involved in facilitating motor functions, rather than executing them (motor cortex). Additionally, this person has aphasia, meaning it is possible that their cognitive score is not indicative of their cognitive function, but rather, their ability to understand and communicate (due to the aphasia).

In this study, we took a gradual approach to assessing lesion location involvement in behavior. The brain is interconnected and brutely dividing areas to correlate with just motor and cognitive functions is difficult at broad levels in the brain, however, the gradual digging deeper in our analysis allows us to ensure we do not miss general findings. Given that both hemispheres are involved in both motor and cognitive tasks, we were not surprised to find that there is no indication of a relationship between hemispheres and resulting behavior. Similarly, we were not surprised that at different cortical depths, there was no relationship indicated between brain area and behavior. We were limited in assessing the brain stem region since the atlas did not capture those brain areas. When we continued to look more granularly and identified brain areas (temporal and junction lobes) that are more involved in cognitive functions, the high motor/low cognitive group had lesions in these areas. In other words, we found that the group that had high motor/lower cog function had lesion involvement in brain areas involved in cognitive function. We did not see similar involvement in the low motor/low cog group, however, given the potential effect of aphasia on the MoCA, it is possible his low MoCA score is not indicative of his actual cognitive function.

When we looked even deeper at brain networks, we identified three brain networks involved in mainly cognitive functions: Default Mode Network, Salience Network, and Dorsal Attention Network. Our results showed that both low cognitive functioning groups had lesions in the salient network (SAN). Interestingly, subject 23 (high motor/high cognitive group) had some involvement in the SAN. Subject 23 (fig 3) had a largely cortical stroke and presented with a MoCA of 26 and FM of 66, indicating high motor and high cognitive function. This subject has regained full motor function, while retaining mild cognitive deficit, specifically in the visuospatial/executive domain, supporting the previous literature that mostly cortical strokes display larger behavior recovery post therapy [33]. Given that his deficit is in the executive functioning domain, we are not surprised that he has lesion involvement in the SAN. This finding suggests that we should look beyond the raw assessment scores and investigate the specific motor and cognitive domains.

Another interesting finding is that the high motor/low cog function group had more involvement of the parietal cortex than the other groups. This result is unexpected considering how deeply woven the parietal cortex is with motor cortex. At the same time, the parietal cortex is also deeply connected with cognitive areas (sensory processing). This finding further corroborates that there is a need to look at individual brain areas based on functional domains (Brodmann Areas). During the lesion segmentation process, we also found that several subjects with a lesion had no overlap with the AAL3 (subjects 008, 009, and 012). Although these subjects had visible lesions, their lesion involvement across all brain areas was zero. This result is due to lack of overlap with the atlas used. Although the AAL3 is one of the most used and developed whole brain atlases, it has low coverage of the cerebellum and brain stem areas. It also has incomplete coverage of the whole brain, often missing borders.

This work targets structural changes in the brain post stroke, however, there is evidence of reorganization of the brain post stroke [34]. Brain plasticity involves synaptic remodeling and reorganizing, which cannot be visually detected using a CT scan. One non-invasive technique that can detect neuroplasticity post-stroke is an electroencephalogram (EEG), which measures electrical activity in the brain. EEG can detect brain plasticity post-stroke by detecting changes in electrical activity across the brain regions [35]. Understanding brain reorganization post-stroke by using tools such as EEG would enhance our current work of understanding lesion location's role in behavior post-injury.

The biggest limitation of our study is the current sample size. With our current sample size, we could not perform any

correlation analyses, severely limiting the impact of this work. We also were limited in the number of subjects with motor impairment, with only one subject meeting the criteria for low motor function. While we used the gold standard assessments for measuring motor and cognitive impairments, we place aphasic patients at an extreme disadvantage. In future considerations, we will use the MoCA for people with aphasia.

V. Conclusion

In this paper, we explore relationships between structure and function between the brain and behavior leveraging affordable tools. Although our small sample size cannot provide correlational data between brain area and behavior, we demonstrate that there is a need to continue this work. Our results show that there may be a relationship between lesion location and behavior.

Financial Conflicts of Interest

Dr Michelle J Johnson and Dr. Rochelle Mendonca who are the PI and/or Co-I leading this study has a patent that uses devices inspired by the device being evaluated through this research. The PI is a co-founder of Recupero Robotics LLC should appear before the acknowledgment.

Acknowledgment

We would like to acknowledge the members at the Rehabilitation Robotics Lab and Recupero, LLC.

References

[1] D.N. Wheatley, "Diffusion, perfusion and the exclusion principles in the structural and functional organization of the living cell: reappraisal of the properties of the 'ground substance'." *J Exp Biol*, vol. 206, no. 12, pp. 1955-6, 2003.

[2] Saini et al., "Computer tomography for prediction of cognitive outcomes after ischemic cerebrovascular events." *J Stroke Cerebrovasc Dis*, vol. 23, no. 7, pp. 1921-7, 2014.

[3] Chalela et al., "Magnetic resonance imaging and computed tomography in emergency assessment of patients with suspected acute stroke: a prospective comparison." *Lancet*, vol. 369, no. 9558, pp. 293-8, 2007.

[4] Yeganeh Doost et al., "Bimanual motor skill learning and robotic assistance for chronic hemiparetic stroke: a randomized controlled trial." *Neural Regen Res*, vol. 16, no. 8, pp. 1566-73, 2021.

[5] Ernst et al. "Impact of Ischemic Lesion Location on the mRS Score in Patients with Ischemic Stroke: A Voxel-Based Approach." *AJNR Am J Neuroradiol*, vol. 39, no. 11, pp. 1989-94, 2018.

[6] Bogousslavsky et al., "Loss of psychic self-activation with bithalamic infarction. Neurobehavioural, CT, MRI and SPECT correlates." *Acta Neurol Scand*, vol. 83, no. 5, pp. 309-16, 1991.

[7] F.N. Shelton and M.J Reding, "Effect of lesion location on upper limb motor recovery after stroke." *Stroke*, vol. 32, no. 1, pp. 107-12, 2001.

[8] T. E. Nogles and M.A. Galuska, "Middle Cerebral Artery Stroke." *StatPearls*, 2023.

[9] G.R. de Freitas, G. Devuyst G, G. van Melle, and J. Bogousslavsky, "Motor strokes sparing the leg: different lesions and causes." *Arch Neurol*, vol. 57, no. 4, pp. 513-8, 2000.

[10] R. Schneider and J.C. Gautier, "Leg weakness due to stroke. Site of lesions, weakness patterns and causes." *Brain*, vol. 117, no. 2, pp. 347-54, 1994.

[11] M. Balkaya M and S. Cho, "Optimizing functional outcome endpoints for stroke recovery studies." *J Cereb Blood Flow Metab*, vol. 39, no. 12, pp. 2323-42, 2019.

[12] L. Cengic, V. Vuletic, M. Karlic, M. Dikanovic, V. Demarin, "Motor and cognitive impairment after stroke." *Acta Clin Croat*, vol. 50, no. 4, pp. 463-7, 2011.

[13] K.D. Bui, M.J. Johnson, "Designing robot-assisted neurorehabilitation strategies for people with both HIV and stroke." *J Neuroeng Rehabil*, vol. 15, no. 1, pp. 75, 2018.

[14] T. Ohzuno andS. Usuda, "Cognitive-motor interference in post-stroke individuals and healthy adults under different cognitive load and task prioritization conditions." *J Phys Ther Sci*, vol. 31, no. 3, pp. 255-60, 2019.

[15] M.H. Schieber, "Somatotopic gradients in the distributed organization of the human primary motor cortex hand area: evidence from small infarcts." *Exp Brain Res*, vol. 128, no. 1-2, pp. 139-48, 1999.

[16] V.S. Hedna, S. Jain, O. Rabbani, S.E. Nadeau, "Mechanisms of arm paresis in middle cerebral artery distribution stroke: pilot study." *J Rehabil Res Dev*, vol. 50, no. 8, pp. 1113-22, 2013.

[17] L.M. Allen, A.N. Hasso, J. Handwerker, H. Farid, "Sequence-specific MR imaging findings that are useful in dating ischemic stroke." *Radiographics*, vol. 32, no. 5, pp1285-97, 2012.

[18] Brott et al., "Measurements of acute cerebral infarction: lesion size by computed tomography." *Stroke*, vol. 20, no. 7, pp. 871-5, 1989.

[19] Liew et al., "A large, curated, open-source stroke neuroimaging dataset to improve lesion segmentation algorithms." *Sci Data*, vol. 9, no. 1, pp. 320, 2022.

[20] Liew et al., "A large, open source dataset of stroke anatomical brain images and manual lesion segmentations." *Sci Data*, vol. 5, 2018.

[21] P.A. Yushkevich and G. Gerig. ITK-SNAP: An Intractive Medical Image Segmentation Tool to Meet the Need for Expert-Guided Segmentation of Complex Medical Images. *IEEE Pulse*, vol. 8, no. 4, pp. 54-7, 2017.

[22] Horn et al., "Probabilistic conversion of neurosurgical DBS electrode coordinates into MNI space." *Neuroimage*, vol. 150, pp. 395-404, 2017.

[23] C. Rorden, L. Bonilha, J. Fridriksson, B. Bender, H.O. Karnath, "Age-specific CT and MRI templates for spatial normalization." *Neuroimage*, vol. 61, no. 4, pp. 957-65, 2012.

[24] E.T. Rolls, C.C. Huang, C.P. Lin, J. Feng, M. Joliot, "Automated anatomical labelling atlas 3." *Neuroimage*, vol. 206, 2020.

[25] Tzourio-Mazoyer et al., "Automated anatomical labeling of activations in SPM using a macroscopic anatomical parcellation of the MNI MRI single-subject brain." *Neuroimage*, vol. 15, no. 1, pp. 273-89, 2002.

[26] S. Ocklenburg, O. Gunturkun, "Hemispheric asymmetries: the comparative view." *Front Psychol*, vol. 3, pp. 5, 2012.

[27] M.W. Kortz, K.O. Lillehei, "Insular Cortex." *StatPearls*, 2023.

[28] S.T. Pendlebury, J. Mariz, L. Bull, Z. Mehta, P.M. Rothwell, "MoCA, ACE-R, and MMSE versus the National Institute of Neurological Disorders and Stroke-Canadian Stroke Network Vascular Cognitive Impairment Harmonization Standards Neuropsychological Battery after TIA and stroke." *Stroke*, vol. 43, no. 2, pp. 464-9, 2012.

[29] B. Singer and J. Garcia-Vega, "The Fugl-Meyer Upper Extremity Scale." *J Physiother*, vol. 63, no. 1, pp. 53, 2017.

[30] Woytowicz et al., "Determining Levels of Upper Extremity Movement Impairment by Applying a Cluster Analysis to the Fugl-Meyer Assessment of the Upper Extremity in Chronic Stroke." *Arch Phys Med Rehabil*, vol. 98, no. 3, pp. 456-62, 2017.

[31] Nasreddine et al., "The Montreal Cognitive Assessment, MoCA: a brief screening tool for mild cognitive impairment." *J Am Geriatr Soc*, vol. 53, no. 4, pp. 695–9, 2005.

[32] S.J. Page, L.V. Gauthier, & S. White, "Size doesn't matter: cortical stroke lesion volume is not associated with upper extremity motor impairment and function in mild, chronic hemiparesis." *Archives of phys med and rehab*, vol. 94, no. 5, pp. 817–821, 2013.

[33] Edwardson et al., "Reduced Upper Limb Recovery in Subcortical Stroke Patients With Small Prior Radiographic Stroke." *Front Neurol*, vol. 10, pp. 454, 2019.

[34] Z. Kou and A. Iraji, "Imaging brain plasticity after trauma." *Neural regeneration research*, vol. 9, no. 7, pp. 693–700, 2014.

[35] P. Manganotti, M. Ajčević, and A. Buoite Stella, "EEG as a marker of brain plasticity in clinical applications." *Handbook of Clinical Neurology*, vol. 184, pp. 91–104, 2022.

Using a robotic device to quantify the impact of conventional gait training on ankle proprioception after stroke

Christopher A. Johnson
Rancho Los Amigos National Rehab Center
Rancho Research Institute
Downey, CA, USA
johnson4@uci.edu

Piyashi Biswas
Department of Biomedical Engineering
University of California Irvine Irvine, CA, USA
piyashib@uci.edu

Jill See
Department of Rehabilitation Services
University of California at Irvine Medical Center
Orange CA, USA
jsee@hs.uci.edu

Olivia Briendel
Department of Rehabilitation Services
University of California at Irvine Medical Center
Orange CA, USA
obriende@hs.uci.edu

Vicky Chan
Department of Rehabilitation Services
University of California at Irvine Medical Center
Orange CA, USA
vchan2@hs.uci.edu

Lucy Dodakian
Department of Rehabilitation Services
University of California at Irvine Medical Center
Orange CA, USA
ldodak@hs.uci.edu

Po T. Wang
Henry Samueli School of Engineering
University of California, Irvine, Irvine CA, USA
ptwang@hs.uci.edu

Zoran Nenadic
Department of Biomedical Engineering
University of California Irvine Irvine, CA, USA
znenadic@uci.edu

Steven C. Cramer
School of Medicine
Department of Neurology, University of California Los Angeles
Los Angeles CA, USA
sccramer@mednet.ucla.edu

An Do
School of Medicine
Department of Neurology, University of California Irvine Irvine, CA, USA
and@hs.uci.edu

David J. Reinkensmeyer
Department of Mechanical and Aerospace Engineering
Department of Anatomy and Neurobiology
University of California Irvine Irvine, CA, USA
dreinken@uci.edu

***Abstract*— Ankle proprioception is important for gait control and is often impaired after stroke. It is currently unclear if conventional gait training can improve ankle proprioception. Here we used a novel robotic device, Ankle Measuring Proprioceptive Device (AMPD), to quantify key aspects of ankle proprioception before and after four weeks of gait training delivered to 24 individuals who were in the chronic phase of stroke. We implemented two assessments with AMPD to quantify passive and active and dynamic/static proprioception. For the Crisscross assessment, AMPD moved the ankles past each other and the participants pushed a button to indicate when the ankles passed each other, thereby testing passive, dynamic proprioception. For the Joint Position Reproduction (JPR) assessment, AMPD moved the impaired ankle in a random pattern and the participant tracked with their unimpaired ankle, thereby testing active, dynamic proprioception. We also incorporated static periods into JPR to quantify static position sense. At baseline, active and passive ankle proprioception errors, as well as static and dynamic errors, were significantly increased compared to age-matched controls and were moderately correlated. Gait training improved only static ankle position sense, with greater improvement for more severely impaired individuals. These findings suggest that stroke damages multiple aspects of ankle proprioception in an interrelated manner. In contrast, conventional gait training improved only static ankle proprioception ability. This suggests a need for an array of training methodologies to comprehensively retrain ankle proprioception.**

Keywords— stroke, ankle proprioception, gait therapy, robotic

I. Introduction

An estimated one in four people worldwide will experience a stroke in their lifetime [1], with ~60% of survivors experiencing frequent falls, balance limitations, reduced walking speeds, asymmetric gait, and motor coordination problems [2], [3], [4]. In a recent survey, improving walking and balance ability was the top priority of 589 people post-stroke [5]. Therefore, understanding the causes of gait impairment and how best to target those causes is a key goal in rehabilitation research.

One of the most significant contributors to gait impairment after stroke is foot drop, which is caused by a reduced ability to actively dorsiflex the ankle during the swing phase of gait. Weakness of the impaired ankle, present in ~30% of people post-stroke [6], strongly predicts reduced gait velocity [7], [8]. However, sensory deficits of the lower extremity are also common after stroke, occurring in about a third to half of people [9], [10]. Poor lower extremity proprioception has been linked to poor gait [11], [12], reduced balance ability [9], [11], [13], falls [9], [11], and decreased endurance [14], with ankle proprioception being a strong predictor of balance ability in chronic stroke [13]. This predictive ability makes sense from a theoretical perspective, as the body's feedback control systems and learning systems depend on accurate sensory information. Thus, treating both the motor and sensory aspects of ankle function is important goal for gait

rehabilitation after stroke.

However, conventional gait rehabilitation mostly focuses on motor related capabilities, such as active range of motion, strength, endurance, and overall walking [15]. Currently, it is unclear if conventional gait training improves proprioceptive impairment, with some studies reporting that conventional gait therapy significantly improved ankle proprioception [16], [17] and other reporting no improvements in ankle proprioception [18], [19]. These mixed results could arise because the exercises performed during conventional gait training do not sufficiently challenge the proprioceptive system, and/or the proprioception assessments used are not sensitive enough.

To the latter point, a recent review through empirical evidence highlighted that measure of proprioceptive accuracy are characterized by method-specificity [20]. This review found no studies reporting significant correlations between different errors measured with different proprioceptive tests. Of note, however, these studies primarily focused on populations of young, unimpaired individuals.

Here, we sought to quantify the effect of conventional gait training on ankle proprioception in chronic stroke, we well as whether proprioceptive errors measured with different assessments correlate after stroke. We used a robotic device to improve objectivity and sensitivity of proprioception testing, and used it to implement tests of passive, active, dynamic, and static ankle proprioception.

II. Methods

A. Participants

The people with stroke studied here were the control participants in a clinical trial of brain-computer interface, functional electrical stimulation for foot drop [21]. An extensive list of the inclusion and exclusion criteria followed are in Biswas et al.[21], however a subset of the inclusion criteria most relevant to the current study were: (1) age 18-80 years, (2) radiologically confirmed stroke more than 26 weeks prior, (3) gait velocity < 0.8 m/s, (4) presence of foot-drop, and (5) walk > 10 m with or without assistive device at a supervised level. Control participants received conventional gait therapy.

For comparison, we also recruited age-matched controls who had not experienced a stroke and evaluated their ankle proprioception. The University of California, Irvine Internal Review Board approved the procedures and participants provided informed consent.

B. Ankle Measuring Proprioceptive Device (AMPD)

For this study we used two versions of the Ankle Measuring Proprioceptive Device (AMPD, Figure 1). Both versions are platform-based robots that have the ability to individually adjust each foot pedal's impedance state to be either rigid (in which case the ankle position is controlled by a linear motor) or transparent (in which case the linear actuator is not connected to the ankle). For more details on the AMPD robots see [22].

To assess ankle proprioception with AMPD, participants sat in an upright position with the hip and knee bent at 90 degrees such that the shank was perpendicular to the ground, the center of the lateral malleolus was aligned to the rotational shaft, and the feet were adjusted to hip width (Figure 1). AMPD records seating parameters with sensors so they can be repeated.

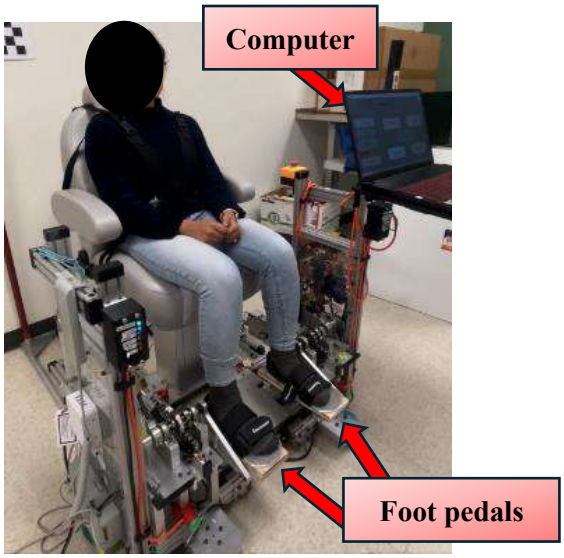


Figure 1. A picture of a volunteer seated in the correct position in AMPD. Both foot pedals can be driven robotically or moved freely by the participant, depending on whether a rack and pinion is engaged between a linear motor and the pedals.

C. Crisscross Assessment of Ankle Proprioception

The Crisscross test of proprioception is a novel test of passive proprioception sense developed by our laboratory initially for the fingers [22]. Crisscross measures the ability to predict the moment that two, passively moved, body parts cross. Key features of Crisscross are it: does not require the participant to have active movement ability and is thus a test of passive proprioception sense; requires detection of both movement speed and position to anticipate the crossing moment; does not require memorization; and focuses on self-observation of the movement of related body parts obviating the need for internal coordinate transformations into visual space. In initial studies employing Crisscross with the fingers, we found it was sensitive to aging [15] and presence of a prior stroke [5]. It also predicted the ability to benefit from robotic finger training [4].

To implement Crisscross for the ankles, both foot pedals of AMPD were placed in their rigid mode and then AMPD moved the left and right ankles in opposing directions, creating a crossing event (Figure 2 top). For each ankle crossing trial, participants were instructed to press a handheld button when they perceived their ankles to be at the same angular position.

Before starting the Crisscross test, a licensed physical therapist assessed each participant's passive range of motion (ROM) by manually moving each ankle to a comfortable dorsiflexion and plantarflexion position within the robot, with the robot in transparent mode. The maximum dorsiflexion and plantarflexion positions for both ankles were recorded and used as the range of motion for the test. The crossing

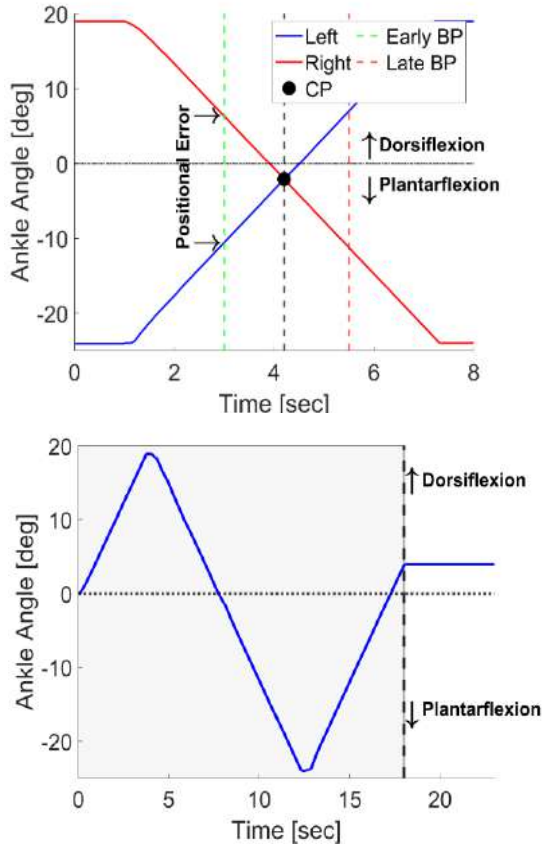


Figure 2. Examples of ankle trajectories for Crisscross and JPR. Left: A single crossing position (denoted by black circle) during the Crisscross test generated by 2AMPD. Right: The impaired ankle trajectory of a single JPR dynamic (before dotted black line) and static period (after dotted black line). **CP** = Crossing Position

workspace for both ankles was set to be identical and equal to the workspace of the ankle with the smallest passive ROM. Once the workspace was set, we divided it into five distinct zones to ensure a uniform distribution of crossings: extreme plantarflexion (>60% PF), moderate plantarflexion (60-20% PF), neutral position (20% PF - 20% DF), moderate dorsiflexion (20-60% DF), and extreme dorsiflexion (>60% DF). Next, the assessment was explained, and participants experienced an example test that consisted of four crossings with vision of the ankles, verbally confirming that they understood the test. Subsequently, participants performed 10 ankle-crossing trials with their vision occluded by a lapboard. Crossing speed (4-8 deg/sec) and position were pseudorandomized.

D. Joint Position Reproduction (JPR) Assessment

JPR is a common methodology in proprioceptive testing in which one joint is moved and then the participant is asked to replicate the movement with the same joint or another joint. For this study we implemented a contralateral JPR test that did not require memorization. To implement JPR, we set one foot pedal to be in rigid mode and the other to be in transparent mode. AMPD then guided the passive, impaired ankle through a predetermined motion, while the participant actively moved their unimpaired ankle to match the impaired side. We designed the test to have two parts, dynamic and static periods. Dynamic periods consisted of AMPD driving the impaired ankle at a constant velocity (5°/s) through its available dorsiflexion and plantarflexion range. Dynamic periods were randomly interrupted by static periods where the robot stopped moving the ankle at a pseudo-random set of positions. Participants were instructed to match the angular position of the stationary impaired ankle by making fine adjustments with their unimpaired ankle for as long as they wished, pushing a button when finished. The robot initiated a dynamic period after they pushed the button. Participants first completed an example JPR test with vision of the ankles that consisted of two dynamic and static periods, verbally confirming that they understood the test. Then, with vision occluded by the lapboard, they completed four dynamic and four static periods.

E. Conventional Gait Therapy

Participants received conventional gait therapy three times a week for four weeks in two-hour sessions. Activities were customized by a physical therapist and included passive/active range of motion, resistance, balance, and overground walking exercises. Participants were asked to refrain from engaging in outside physical therapy during the study.

F. Data Analysis

For Crisscross, proprioceptive error was defined as the absolute angular difference between the left and right ankles at the moment of button press. If a participant did not push the button a trial, this trial was excluded from analysis.

For the dynamic period of the JPR test, proprioceptive error was define as the average of the absolute angular differences between the ankles throughout the movement period. For the static period, proprioceptive error was calculated as the absolute angular difference between the impaired and unimpaired ankles at the moment of button press.

Statistical analyses were conducted using Matlab R2023. Proprioceptive errors for each proprioceptive assessment were normally distributed (Shapiro Wilks, $p > 0.05$), so we used parametric tests, including two-tailed student t-tests for comparisons between baseline and end of therapy proprioceptive error, and Pearsons's correlation. An alpha of 0.05 was considered significant.

III. Results

We used a robotic device to quantify ankle proprioceptive ability in 24 people in the chronic phase of stroke, before and after they received 24 hours of conventional gait training over 4 weeks. Table 1 provides a clinical overview of the participants.

Table 1. Baseline characteristics of the participants with a stroke.

	Average ± SD
Age	59.8 ± 12.4
Months Post Stroke	42 ± 32
NIH Stroke Severity Scale [0 42]	7.0 ± 3.2
Lower Extremity Fugl Meyer [0 34]	19.0± 5.3
10M Walk Test (m/s)	0.45 ± 0.22
Sex M/F	10/14

A. *Effect of Stroke on Baseline Ankle Proprioception*

At baseline, stroke participants demonstrated significantly greater errors in all proprioceptive tasks compared to the age-matched unimpaired adults (t-test, $p < 0.01$). Specifically, the stroke group produced an average error of $17.2° \pm 7.2°$ for the Crisscross test, and $12.9° \pm 8.0°$ and $11.7° \pm 5.7°$ for JPR static and JPR dynamic test, respectively. In contrast, the age-matched controls produced an average error of $9.3° \pm 3.5°$ for the Crisscross test, $6.8° \pm 2.9°$ and $6.7° \pm 2.4°$ for JPR static and JPR dynamic test. For each proprioceptive measure, 42%, 33%, and 46% of the stroke participants had a mean proprioceptive error greater than 2 standard deviations (SD) of the age-matched participants. Crisscross error was moderately correlated with JPR static and JPR dynamic error (Fig. 3).

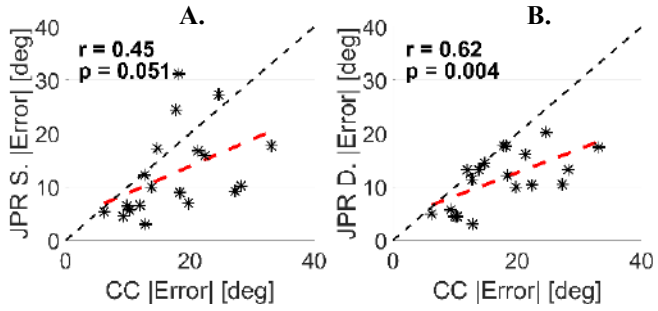


Figure 3. Relationships between average absolute Crisscross error (x-axis) and JPR static and dynamic error (y-axis) at baseline. Red, dashed lines show linear fits. Black, dashed lines represent a slope of 1.

B. *Effect of Conventional Gait Therapy on Proprioception*

The average change from baseline to end of therapy for Crisscross, JPR static, and JPR dynamic errors was $0.7° \pm 5.5°$, $-3.3° \pm 6.5°$ and $-1.0° \pm 3.5°$, respectively. None of these changes were significant ($p > 0.05$), although the reduction in JPR static error approached significance ($p = 0.07$). When we plotted baseline versus end-of-therapy errors for each participant (Fig. 4), for JPR static error we noticed that one individual's EOT proprioceptive error was 2 SD than the mean for the group. Removing this outlier, we found that the change in JPR static error from baseline to end-of-therapy was significant ($p = 0.04$) .

We defined a threshold for identifying impaired proprioception as 2 SDs of the age-matched error found in uninjured participants and found it to be 12.5° for JPR static error. The six individuals with a baseline JPR static error exceeding 12.5° demonstrated significant improvement at the end of therapy assessment, reducing their error by an average of $9.0° \pm 3.2°$ ($p = 0.005$). Moreover, the six participants showed significantly greater improvement compared to stroke participants within the two standard deviations of the age-matched error ($1.0° \pm 1.4°$, $p < 0.001$). Individuals with greater than 2 SD of Crisscross or JPR dynamic error did not reduce their error, however (Fig. 4 left and right).

IV. Discussion

We assessed the ankle proprioception of 24 participants in the chronic phase of stroke using two robotic proprioceptive assessments (Crisscross and JPR) before and after a four-week gait therapy program that incorporated conventional treatment exercises. We found that, as a group, the stroke participants had significantly impaired ankle proprioception at baseline, and that different types of proprioception (active vs. passive) were moderately correlated. Although conventional gait therapy did not significantly improve Crisscross error or JPR dynamic error, it did result in a significant improvement in JPR static error when we applied a standard outlier removal. Notably, the participants with the poorest static ankle position sense at baseline showed a significantly greater improvement in static error by the end of the therapy assessment. We will now discuss these results as well as directions for future research.

A. *Ankle Proprioception after Stroke*

It was not surprising to us that ankle proprioception was impaired after stroke, as several studies have reported this finding (e.g., [23], [24]). However, to our knowledge, this study was one of the first to test multiple aspects of ankle proprioception after stroke and find that they are moderately correlated. Many tests for assessing proprioception have been developed using manual techniques, simple mechanical technologies, or robots [20], [25]. A recent review counted

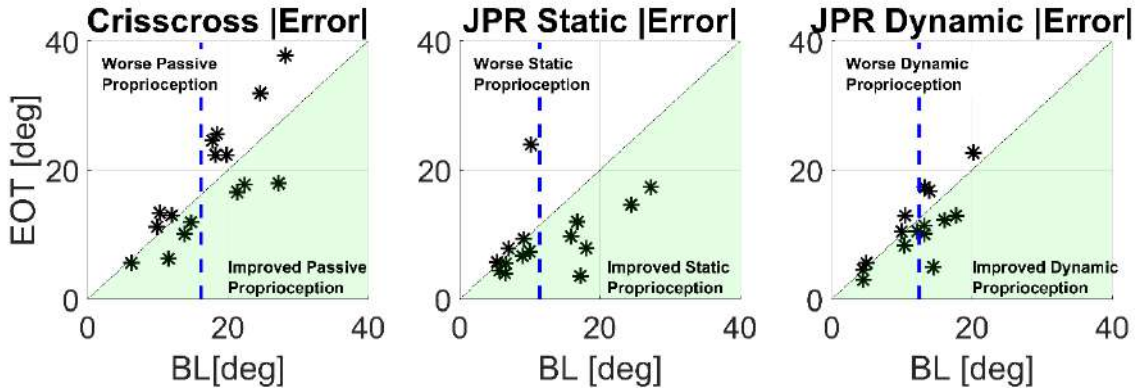


Figure 4. Robotic proprioceptive measures at baseline (x-axis) and end of therapy (y-axis). The dotted blue lines represent a threshold for detecting substantially impaired proprioception, defined as a mean error greater than 2 SDs of the error age-matched controls, for each proprioception assessment. EOT: End of Therapy; BL: Baseline

over 1,300 different types of proprioceptive measurements [20], and highlighted that results obtained with one method rarely generalize to another method. However, the studies analyzed in that review focused primarily on populations that were either young unimpaired individuals [26], [27], [28] or individuals with peripheral nervous system damage [29], [30]. Here, we found "method generalizability" for people with stroke.

A possible explanation for generalization of proprioception assessments is that similar neuroanatomical substrates and computational processes are involved in performing each assessment. Both Crisscross and JPR assessments share components of movement discrimination, movement speed and direction sense, and interhemispheric communication. Considering interhemispheric communication alone, stroke causes connectivity abnormalities between hemispheres [31], resulting in heightened influence of the contralesional hemisphere in motor tasks [4], [32]. Perhaps this altered relationship affected the sensory processing needed for both Crisscross and JPR, causing their errors to be correlated.

B. Response of Ankle Proprioception Ability to Gait Therapy

Ankle proprioception ability did not significantly improve following four weeks of conventional gait training for Crisscross and JPR dynamic error. This suggests that conventional therapy may not sufficiently challenge the dynamic aspects of proprioception required for these assessments, such as predicting angular positions and speeds during continuous motion. A recent meta-analysis of proprioceptive learning found that it is task-specific [33].

For proprioceptive training, a common strategy is to remove visual input so that participants cannot compensate with vision. This was not a focus of the conventional gait training used here. Further, exercises that require a person to make conscious and repeated judgments about limb position and movement are also not commonly employed in conventional gait training.

The stroke participants significantly improved only their JPR static error. The conventional gait therapy implemented for this study incorporate balance exercises at slow speeds under weight-bearing conditions, potentially enhancing static proprioceptive sense.

When we focused on the subset of individuals with particularly poor static angle proprioception ability (defined as > 2D of control error for the JPR test), we found that they improved their ankle proprioception more, compared to the individuals with smaller baseline errors. These individuals may simply have had greater room for improvement, but it is notable to use that poor ankle proprioception does not mean poor relearning ability, in contrast to the motor system for which it has been observed that the most severely impaired individuals respond less to training [34]. Future research should focus on identifying the neuroplastic responses that help proprioception improve, potentially providing new targets for rehabilitation.

V. Conclusion

By using a robotic device to implement two types of proprioceptive assessments, this study provided novel insights into sensory impairment and training after stroke. Stroke impairs ankle proprioception in a way that affects both dynamic and static, and passive and active proprioceptive ability, in a coordinated way. Conventional gait training does not appear to be an effective way to retrain ankle proprioception ability, except maybe static position sense.

These results suggest a need for an array of training methodologies and technologies that can work together to comprehensively retrain ankle proprioception. We believe it is crucial to address not only motor impairment but also sensory impairment to optimize rehabilitation outcomes after stroke. Conventional gait therapy could be supplemented with targeted proprioceptive exercises to facilitate comprehensive sensory motor recovery. Robotic devices can not only play a role in improving proprioception assessment but also proprioception training for example by replacing visual elements of training games with robotically-driven, proprioceptive elements [35].

VI. References

[1] V. L. Feigin *et al.*, "Global, regional, and national burden of stroke and its risk factors, 1990–2019: a systematic analysis for the Global Burden of Disease Study 2019," *Lancet Neurol*, vol. 20, no. 10, pp. 795–820, 2021, doi: https://doi.org/10.1016/S1474-4422(21)00252-0.

[2] J. W. Sturm, H. M. Dewey, G. A. Donnan, R. A. L. Macdonell, J. J. McNeil, and A. G. Thrift, "Handicap After Stroke: How Does It Relate to Disability, Perception of Recovery, and Stroke Subtype?," *Stroke*, vol. 33, no. 3, pp. 762–768, Mar. 2002, doi: 10.1161/hs0302.103815.

[3] K. K. Patterson *et al.*, "Gait Asymmetry in Community-Ambulating Stroke Survivors," *Arch Phys Med Rehabil*, vol. 89, no. 2, pp. 304–310, Feb. 2008, doi: 10.1016/j.apmr.2007.08.142.

[4] G. Poomalai, S. Prabhakar, and N. Sirala Jagadesh, "Functional Ability and Health Problems of Stroke Survivors: An Explorative Study," *Cureus*, Jan. 2023, doi: 10.7759/cureus.33375.

[5] A.-S. Rudberg *et al.*, "Stroke survivors' priorities for research related to life after stroke," *Top Stroke Rehabil*, vol. 28, no. 2, pp. 153–158, Feb. 2021, doi: 10.1080/10749357.2020.1789829.

[6] C. Peishun, Z. Haiwang, L. Taotao, G. Hongli, M. Yu, and Z. Wanrong, "Changes in Gait Characteristics of Stroke Patients with Foot Drop after the Combination Treatment of Foot Drop Stimulator and Moving Treadmill Training," *Neural Plast*, vol. 2021, pp. 1–5, Nov. 2021, doi: 10.1155/2021/9480957.

[7] B. F. Mentiplay, B. Adair, K. J. Bower, G. Williams, G. Tole, and R. A. Clark, "Associations between lower limb strength and gait velocity following stroke: A systematic review," *Brain Inj*, vol. 29, no. 4, pp. 409–422, Apr. 2015, doi: 10.3109/02699052.2014.995231.

[8] P. Y. Lin, Y. R. Yang, S. J. Cheng, and R. Y. Wang, "The Relation Between Ankle Impairments and Gait Velocity and Symmetry in People With Stroke," *Arch Phys Med Rehabil*, vol. 87, no. 4, pp. 562–568, Apr. 2006, doi: 10.1016/J.APMR.2005.12.042.

[9] T. Gorst *et al.*, "The prevalence, distribution, and functional importance of lower limb somatosensory impairments in chronic stroke survivors: a cross sectional observational study," *Disabil Rehabil*, vol. 41, no. 20, pp. 2443–2450, Sep. 2019, doi: 10.1080/09638288.2018.1468932.

[10] L. A. Connell, N. B. Lincoln, and K. A. Radford, "Somatosensory impairment after stroke: frequency of different deficits and their recovery," *Clin Rehabil*, vol. 22, no. 8, pp. 758–767, Aug. 2008, doi: 10.1177/0269215508090674.

[11] T. Gorst, J. Freeman, K. Yarrow, and J. Marsden, "Assessing lower limb position sense in stroke using the gradient discrimination test (GradDT™) and step-height discrimination test (StepDT™): a reliability and validity study," *Disabil Rehabil*, 2018, doi: 10.1080/09638288.2018.1554008.

[12] A. L. Hsu, P. F. Tang, and M. H. Jan, "Analysis of impairments influencing gait velocity and asymmetry of hemiplegic patients after mild to moderate stroke," *Arch Phys Med Rehabil*, vol. 84, no. 8, pp. 1185–1193, Aug. 2003, doi: 10.1016/S0003-9993(03)00030-3.

[13] J.-E. Cho and H. Kim, "Ankle Proprioception Deficit Is the Strongest Factor Predicting Balance Impairment in Patients With Chronic Stroke," *Arch Rehabil Res Clin Transl*, vol. 3, no. 4, p. 100165, Dec. 2021, doi: 10.1016/J.ARRCT.2021.100165.

[14] M. J. Lee, S. L. Kilbreath, and K. M. Refshauge, "Movement detection at the ankle following stroke is poor," *Australian Journal of Physiotherapy*, vol. 51, no. 1, pp. 19–24, Jan. 2005, doi: 10.1016/S0004-9514(05)70049-0.

[15] A. Guzik, M. Drużbicki, and A. Wolan-Nieroda, "Assessment of two gait training models: conventional physical therapy and treadmill exercise, in terms of their effectiveness after stroke.," *Hippokratia*, vol. 22, no. 2, pp. 51–59, 2018.

[16] P. O. MCKEON, C. D. INGERSOLL, D. C. KERRIGAN, E. SALIBA, B. C. BENNETT, and J. HERTEL, "Balance Training Improves Function and Postural Control in Those with Chronic Ankle Instability," *Med Sci Sports Exerc*, vol. 40, no. 10, pp. 1810–1819, Oct. 2008, doi: 10.1249/MSS.0b013e31817e0f92.

[17] J. E. Aman, N. Elangovan, I. L. Yeh, and J. Konczak, "The effectiveness of proprioceptive training for improving motor function: A systematic review," *Front Hum Neurosci*, vol. 8, no. JAN, p. 119864, Jan. 2015, doi: 10.3389/FNHUM.2014.01075/ABSTRACT.

[18] L. Connell, N. Lincoln, and K. Radford, "Somatosensory impairment after stroke: frequency of different deficits and their recovery," *Clin Rehabil*, vol. 22, no. 8, pp. 758–767, Aug. 2008, doi: 10.1177/0269215508090674.

[19] C.-H. Lee, Y. Kim, and B.-H. Lee, "Augmented reality-based postural control training improves gait function in patients with stroke: Randomized controlled trial," *Hong Kong Physiotherapy Journal*, vol. 32, no. 2, pp. 51–57, Dec. 2014, doi: 10.1016/j.hkpj.2014.04.002.

[20] Á. Horváth, E. Ferentzi, K. Schwartz, N. Jacobs, P. Meyns, and F. Köteles, "The measurement of proprioceptive accuracy: A systematic literature review," *J Sport Health Sci*, Apr. 2022, doi: 10.1016/J.JSHS.2022.04.001.

[21] P. Biswas *et al.*, "A single-center, assessor-blinded, randomized controlled clinical trial to test the safety and efficacy of a novel brain-computer interface controlled functional electrical stimulation (BCI-FES) intervention for gait rehabilitation in the chronic stroke population," *BMC Neurol*, vol. 24, no. 1, p. 200, 2024, doi: 10.1186/s12883-024-03710-3.

[22] C. A. Johnson and D. J. Reinkensmeyer, "Assessing Ankle Proprioception using a Novel Robotic Device: Generalizability, Parameter Sensitivity, and Predictive Power for Stroke Rehabilitation," United States -- California, 2024. [Online]. Available: https://www.proquest.com/dissertations-theses/assessing-ankle-proprioception-using-novel/docview/3087880464/se-2?accountid=14509

[23] Y. Mao, Z. Gao, H. Yang, and C. Song, "Influence of proprioceptive training based on ankle-foot robot on improving lower limbs function in patients after a stroke," *Front Neurorobot*, vol. 16, Oct. 2022, doi: 10.3389/fnbot.2022.969671.

[24] K.-H. Kim and S.-H. Jang, "Effects of Task-Specific Training after Cognitive Sensorimotor Exercise on Proprioception, Spasticity, and Gait Speed in Stroke Patients: A Randomized Controlled Study," *Medicina (B Aires)*, vol. 57, no. 10, p. 1098, Oct. 2021, doi: 10.3390/medicina57101098.

[25] J. Han, G. Waddington, R. Adams, J. Anson, and Y. Liu, "Assessing proprioception: A critical review of methods," Mar. 01, 2016, *Elsevier B.V.* doi: 10.1016/j.jshs.2014.10.004.

[26] N. Elangovan, A. Herrmann, and J. Konczak, "Assessing Proprioceptive Function: Evaluating Joint Position Matching Methods Against Psychophysical Thresholds," *Phys Ther*, vol. 94, no. 4, p. 553, Apr. 2014, doi: 10.2522/PTJ.20130103.

[27] D. Kiran, M. Carlson, D. Medrano, and D. R. Smith, "Correlation of three different knee joint position sense measures," *Physical Therapy in Sport*, vol. 11, no. 3, pp. 81–85, Aug. 2010, doi: 10.1016/J.PTSP.2010.06.002.

[28] L. Li, Z.-Q. Ji, Y.-X. Li, and W.-T. Liu, "Correlation study of knee joint proprioception test results using common test methods".

[29] A. De Jong, S. L. Kilbreath, K. M. Refshauge, and R. Adams, "Performance in different proprioceptive tests does not correlate in ankles with recurrent sprain," *Arch Phys Med Rehabil*, vol. 86, no. 11, pp. 2101–2105, Nov. 2005, doi: 10.1016/j.apmr.2005.05.015.

[30] B. Arnold, C. L. Docherty, B. L. Arnold, S. M. Zinder, K. Granata, and B. M. Gansneder, "Relationship between two proprioceptive measures and stiffness at the ankle," *Journal of Electromyography and Kinesiology*, vol. 14, pp. 317–324, 2004, doi: 10.1016/S1050-6411(03)00035-X.

[31] M. Allegra, C. Favaretto, N. Metcalf, M. Corbetta, and A. Brovelli, "Stroke-related alterations in inter-areal communication," 2021, doi: 10.1016/j.nicl.2021.102812.

[32] A. K. Rehme and C. Grefkes, "Cerebral network disorders after stroke: evidence from imaging-based connectivity analyses of active and resting brain states in humans," *J Physiol*, vol. 591, no. 1, pp. 17–31, Jan. 2013, doi: 10.1113/jphysiol.2012.243469.

[33] H. G. Seo, S. J. Yun, A. J. Farrens, C. A. Johnson, and D. J. Reinkensmeyer, "A Systematic Review of the Learning Dynamics of Proprioception Training: Specificity, Acquisition, Retention, and Transfer," *Neurorehabil Neural Repair*, Oct. 2023, doi: 10.1177/15459683231207354/ASSET/IMAGES/LARGE/10.1177_15459683231207354-FIG4.JPEG.

[34] M. R. Senesh and D. J. Reinkensmeyer, "Breaking Proportional Recovery After Stroke," *Neurorehabil Neural Repair*, vol. 33, no. 11, pp. 888–901, Nov. 2019, doi: 10.1177/1545968319868718.

[35] D. S. Reinsdorf, E. E. Mahan, and D. J. Reinkensmeyer, "Proprioceptive Gaming: Making Finger Sensation Training Intense and Engaging with the P-Pong Game and PINKIE Robot," in *2021 43rd Annual International Conference of the IEEE Engineering in Medicine & Biology Society (EMBC)*, 2021, pp. 6715–6720. doi: 10.1109/EMBC46164.2021.9631041.

Development of an Affordable Self-Stretching Passive Device for Treatment and Assessment of Spastic Wrist and Fingers Post-Stroke

Jacob Kim [1], Reem Azar [2], Nova Meng [3], Michelle J. Johnson, Member, IEEE [4]

Abstract— **Stroke, a condition in which blood flow has been restricted to parts of the brain, has been known to cause spasticity, a condition in which the muscles abnormally tense up through an overactivation of the stretch reflex. One low-cost solution to this problem is the use of self-operated passive stretching devices that can be operated with minimal assistance. The goal of this project was to develop and evaluate a new self-stretching wrist and finger device using an iterative design cycle. The device was designed with the following two stretching mechanisms: a rotating dial and an inflatable grip. Three stages of the device prototypes were developed: early, late, and final. After each stage, a usability survey was conducted with a group of healthy controls to rate 0-10 in criteria of overall comfort, unexpected pain, upper arm muscle tension, and device security of the arm. After, design changes were made to address common feedback. In the end, we saw that prioritizing the reduction of pain, decrease of unnecessary upper arm muscle tension, and increase of device security of the arm proved to be valuable measures of increasing overall device comfort. In addition, electromyography (EMG) data was collected with a healthy control subject to verify that the device was able to properly initiate the wrist flexors and extensors through the flexion and extension movement, and that each muscle group was isolated properly to their respective movements through the device.**

I. Introduction

Stroke occurs when blood supply to a region of the brain has been interrupted or reduced, preventing the brain tissue from receiving proper oxygen and nutrient supply from the brain [1]. Hemiplegia is the most common sequela of stroke that is described as a one-sided paralysis of the body. Damage in the upper motor neurons (UMN), which can be caused by stroke, multiple sclerosis, or spinal cord injury, will lead to a loss of lower motor neuron (LMN) inhibition. This lack of balance can lead to the muscles being tight, stiff, and resistant to movement, causing hypertonicity and exaggerated reflexes (hyperreflexia), often leading to the velocity dependent spasticity [2].

Unfortunately, while physical therapy is still a widely used practice in treating spasticity, a recent study found that about 33% of the 500 post-stroke patients studied did not receive any physical therapy, while about 50% of them did not receive occupational therapy. Even worse, those who received any therapy had only 6 to 8 sessions, while certain minority populations received disproportionately lower amounts of therapy in general [3].

One solution to address accessibility to physical rehabilitation is technology-assisted therapy. State-of-the-art spasticity assessment devices such as the Neuroflexor, Portable Spasticity Assessment Device (PSAD) utilizes electromyography (EMG) to quantify muscle activity throughout stretching motions while applying external force [4,5]. As for therapy devices, various options exist such as the Saebo flex, FlintRehab music glove, and the Saeboglove exist that functions as a glove that can also stretch each finger individually [6]. While many of these devices offer a unique method of treating or assessing spasticity, its price often stands as an obstacle for many low resource areas. Thus, one of the main objectives is to ensure that the price of the prototype will be much lower than its state-of-the-art alternatives.

The overall structure of the paper will follow a 4-step systematic design and analysis plan as seen in figure 1. Ultimately, the purpose of this technical proof-of-concept paper is to describe the iterative development process of the device through its multiple stages of usability testing and confirm the device's ability to properly activate the wrist flexors and extensors through EMG.

II. Passive Self-Stretching Spasticity Device

Our design goals were to create a self-operable passive device to treat and assess spasticity in the wrist and fingers. The device was required to support two essential stretching motions: wrist flexion/extension and finger flexion/extension (fig 2).

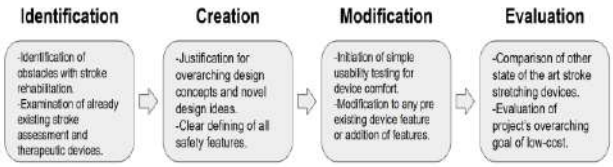


Figure 1. Flow chart of the paper's systematic plan

*Research reported in this publication is supported by the core National Institute of health (NIH) Louis Stokes Alliances for Minority Participation (LSAMP) under the award number NSF 24-563. This work is also made possible by the NIH-funded T32 grant (Training in Musculoskeletal Research) under the award number T32AR007132-48, the Penn Fontaine Society, and the Penn Departments of Bioengineering and Physical Medicine and Rehabilitation.

[1] Jacob Kim is a undergraduate student in Neuroscience at the University of Pennsylvania (714-323-3966; e-mail: dracob@sas.upenn.edu)

[2] Reem M. Azar is a PhD Student in Bioengineering at the University of Pennsylvania (610-573-9423; e-mail: razar@seas.upenn.edu)

[3]Nova Meng is a graduate with a B.S. in Bioengineering at the University of Pennsylvania (e-mail: nmeng@seas.upenn.edu)

[4]Dr. Michelle J. Johnson is an Associate Professor at the University of Pennsylvania with a primary appointment in Physical Medicine and Rehabilitation and secondary appointments in Bioengineering and Mechanical Engineering and Applied Mechanics (email:johnmic@pennmedicine.upenn.edu)

To stretch the wrist, we relied on a rotating dial system as seen in figure 2A. in which the center of rotation would be placed around the wrist joint, while the dial moves alongside the flexed or extended wrist from a -90° to +90°, with 0° being the wrist positioned straight alongside the forearm. Thus, patients would be able to use a screw to lock their wrist at a certain angle during stretching, while moving their wrist manually by pushing a tab connected to the rotating platform. This rotation system did not stray away from other common wrist stretching devices in the field, but it did emphasize specifically isolating the flexion and extension movement from other motions such as supination or pronation [7]. Figure 3 shows the flexed and extended configurations.

To stretch the fingers, we relied on an inflatable grip system as seen in figure 2B in which patients would grasp a deflated ball that is able to be inflated using a pressure bulb. Though the implementation of an inflatable grip as a mechanism of stretching provided a novel factor to this design, it was based on pneumatic systems that existed in other fields of rehabilitation [8]. As the ball inflates, the hand gripping the ball would also open and extend the fingers. As the ball deflates, the spastic stretch would force the fingers to flex and close the hand. Figure 4 shows the grip handle in two different configurations.

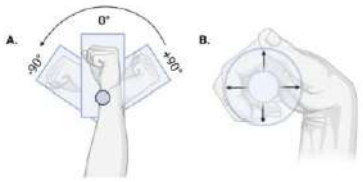


Figure 2. Diagrams for the isolated movements of the device. A) Wrist flexion and extension based on a rotating dial mechanism with the axis of rotation based on the wrist joint. B) Opening and closing of the fingers based on an expanding and deflating grip

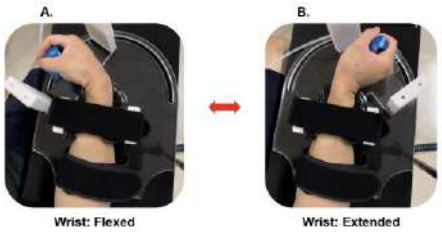


Figure 3. Device at flexed and extended configurations. A) At a negative angle, the wrist is flexed B) At a positive angle, the wrist is extended

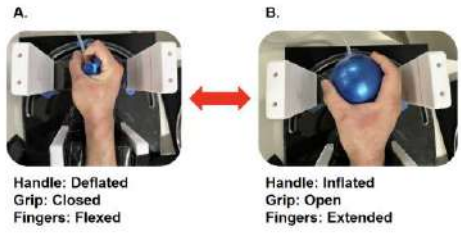


Figure 4. Grip in different configurations: A) The deflated grip allows the grip to close and the fingers to flex. B) The inflated grip opens the hand and extends the fingers.

A. Design Philosophies

Throughout the design process, multiple factors regarding spasticity, usability, and comfort were considered. However, we prioritized two requirements for the device's operability: independent operation and built-in safety.

Previous iterations of the wrist dial consisted of using a stepper system, in which wrist flexion and extension was only allowed in increments of +5° or -5°. However, we noticed that this design not only made the operation of the device much more difficult but the stretching process much more rigid. Instead, we diverted our design to a free moving 180° dial, with users being able to secure their wrist at any angle. Although wrist stretching devices in the field have varying degrees on just how much the wrist can flex or extend, we determined that 180° proved to be enough range of motion for the wrist to fully extend or flex [9,10]. We also realized that providing a free range of motion for the wrist would be beneficial for most patients, as it spastic limbs may not have been able to move 5° at a time.

Since the device allows for a free range of motion for wrist extension and flexion, users can stretch their wrists freely, it is inherently safe. Since patients are in full control of their wrist with no added force, the likelihood from injury is minimal to none while being able to operate the device independently without external assistance.

The inflatable grip was designed to allow spastic patients to easily operate and adapt to the device. Due to the grip's malleable nature, patients can freely adjust their fingers while the handle expands into a ball. Additionally, as the ball deflates, the spastic fingers dig into the silicone grip, allowing for not only a comfortable grip but also a complete flexion of the fingers. The handle is entirely operated by a simple hand pump, which makes the entire operation easily operable with the other non-spastic arm, which most spastic patients are able capable of [11].

The degrees of freedom provided were enclosed in a structure that would secure the forearm and allow the user to correctly place their wrist and fingers into the proper testing and treatment position each use. Figure 5 shows the three evolutions of the device. To ensure that users can use the device for long periods of time while the device remains suitable for variable degrees of spasticity, it was essential that any muscle tension should be incurred only in the proper stretching zone of the wrist extensors and flexors.



Figure 5. Pictures of early, late, and final stage prototypes

Additionally, certain patients of high spasticity may experience higher levels of discomfort during stretching sessions, so the upper arm should be as comfortable as possible without incurring any additional tension [12]. We wanted to avoid any room for the wrist to supinate or pronate, as well as any other external movements that could allow for compensation of muscle groups. Only through securing the wrist and forearms properly could proper motions be performed through the proper muscle groups, allowing for the affected spastic muscle groups to stretch rather than unaffected muscle groups compensating and alleviating activation [13].

B. Device Safety

Throughout the development of the device, it was important to note that the safety mechanisms were built-into the overall design of the device rather than being an external compartment.

Safety of the device was maintained through its self-moving mechanism, meaning all and any component of the device would move directly by the user, without the interference of any movement from the device. We ensured that the device would not contain any motorized or spring-loaded compartments, with both the dial and hand pump operable through the unaffected arm. We also ensured that the device would not contain any sharp edges through proper sanding of the acrylic, while ensuring that variable padding sizes would be available for small, medium, and large so that padding would not constrict the user's arm excessively. Additionally, the silicone ball and the support structures were tested for structural and material stability by loading excessive pressure / forces physically as well as increasing the overall infill and construction durability throughout the design process.

III. Method

A. Usability Testing

The device went through three development stages. At the end of each stage users were asked to experience the device and provide feedback. Usability surveys were given to healthy users to evaluate factors that affect the device's comfort. In this survey, subjects were asked to rate their experiences on a scale of 0-10 in the criteria shown in Figure 6. At each stage 5 new healthy subjects were interviewed and asked to report their scores anonymously, with a total of 15 participants.

It is essential to note that all data collected was deidentified and no personal health information was collected at all. An IRB exemption has been submitted under category 3, and future studies relating to this project will be enrolled under existing IRB as a modification to IRB protocol #849090. The purpose of the usability tests is not to represent a comprehensive usability test, but rather as a design aid. Although the device is meant for post-stroke patients, we wanted to focus on safety and usability of the device. Prior to testing with a sensitive population, we wanted to ensure our device was usable with a healthy population. While post-stroke patients would face different usability concerns compared to healthy subjects, we wanted to improve the overall usability and comfort of the device, which would translate to post-stroke patients as well. In the future, we plan to confirm that the usability features we added with healthy subjects will benefit the usability of post-stroke patients as well.

In the survey, overall comfort was the overarching criteria that encompassed three subcategories of usability: pain, muscle tension, and device security. Most obviously, pain is an important criterion of usability that helps us prioritize any design failures. Muscle tension, more specifically, unnecessary upper arm tension, was chosen as a key criterion for usability because a wrist and finger stretching device should not incur any tension in the upper arm, most importantly in the biceps, triceps, and deltoids. Device security was also chosen as one of the categories of usability as we wanted to prioritize the device's effectiveness in promoting the correct flexion and extension movement [14].

Alongside the survey, subjects were asked to give feedback on potential design improvements. After each round of surveys, design changes were made to address these concerns.

B. Muscle Activation Testing

After the finished development of the final stage prototype as seen in figure 7, EMG data was collected to analyze if the device was able to properly activate the wrist flexors and extensors, mainly the respective carpi radialis muscle groups. Although we understand that muscle activation will vary between healthy and post-stroke users, the current stage of the project aims to confirm that the device's movements can elicit the necessary muscle groups.

The user was seated comfortably in a chair with the device on their right arm and was asked to perform the flexion and extension movement through the device. The user was instructed to perform their maximal flexion and extension movements in 5 second intervals, starting out with a 10 second baseline of no movement. Raw surface EMG data was from 8 muscles of the upper limb using two four-channel sensor motes (Trigno Quattro, Delsys, Inc., Natick, MA, USA). The selected muscle groups were the biceps, posterior deltoid, anterior deltoid, middle deltoid, triceps, wrist flexors, wrist extensors, and brachioradialis.

To remove any low frequency noise, the raw EMG data was first put through a high pass filter at 10 Hz to remove any low frequency noise. Baseline offset was removed by subtracting the median of the overall signal and the resulting signal was then rectified to correct for negative values. The signal was then passed through an envelope with a window size of 80 to smooth the data for better visualization. A rolling window outlier removal method was applied with a window size of 100 and a threshold of three standard deviations away from the mean of the window. Lastly, for each subject, each of the eight channels was individually normalized to the highest signal value recorded for that channel across all ROM trials for that particular subject. Collected EMG data was then plotted in respect to activation (mV) to trial time (seconds) with the data normalized to the max muscle activation per muscle group.

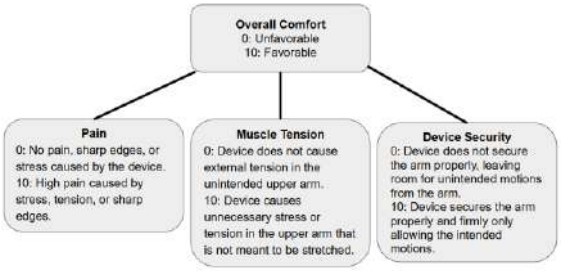


Figure 6. Flowchart of survey questions. The measured criterias were: Overall Comfort, Pain, Muscle Tension, and Device Security



Figure 7. Picture of how the user was seated for EMG collection process

IV. Results And Discussion

A. *Usability Surveys and Improvements*

Although iterations between early, late, and final stage prototypes differed in some respects, each usability survey added a key design change. Figure 9 shows that the Early-Stage Prototype had an average assessment value of 2.6 (comfort), 0.4 (pain), 7.6 (muscle tension), and 2.6 (device security).

One feedback pointed towards the fact that although the device did not cause pain, too much muscle tension was present in the upper arm, most notably the deltoids and biceps. To address this, extended elbow padding was added for an increase in arm security and alleviating unnecessary shoulder tension. This way, users could put the entire weight of their arm onto the device without having to use any force from the shoulders (fig 8 (a)).

We believe that extending the elbow padding prevented the user from exerting any additional forces to keep their arms placed within the device – a design choice that seems to be prevalent in many other arm therapeutic devices [9, 15]. This ultimately helps reduce activation of the upper arm – most notably the triceps, biceps, and deltoids – which may be a priority for higher spastic patients who may need to focus on stretching their wrist and fingers rather than exerting needless energy to simply keep their arm placed within the device – a common design trend in upper limb spasticity assessment devices [10].

Figure 9 shows that the Late-Stage Prototype had an average assessment value of 8 (comfort), 0.2 (pain), 1 (muscle tension), and 9.2 (device security). After making these changes, the user experience improved. This finding helps us understand that reducing muscle tension and pain in the shoulder and elbow muscles and increasing comfort in terms of the secure positioning of the wrist is crucial to designing a more sustainable stretching device. To address this, detachable padding was added for patient variability in wrist sizes for a comfortable and tighter fit. This way, the user's wrists could be properly secured without leaving room for movement (fig 8 (b)). We believe that limiting pronation and supination movement from the flexion and extension movement will allow for proper targeting of the flexor and extensor carpi radialis, aiding in focused stretch rather than the compensation of nearby unaffected muscle groups [16].

Figure 9 shows that the Final Stage Prototype had an average of 9.6 (comfort), 0.06 (pain), 0.4 (muscle tension), and 9.4 (device security). We noticed that subjects were much more comfortable with the more permanent materials (abs plastic / acrylic) used in the final stage prototype as well as the extra stability and reinforcement provided. In addition, subjects found the device much more comfortable to use as well as operate, all while causing very minimal to no pain or unnecessary tension in the upper arm. To address this, we slanted the arm rest, improving overall ergonomics and reducing tension in elbow, biceps, and triceps for longer periods of time. This way, users did not have to exert any force to keep their arm placed within the device (fig 8 (c)). We believe that allowing patients to place their forearms in a slanted slope will allow for a more natural stretching position, in which instead of a 90° elbow joint the user can orient a smaller or larger angle at the elbow, alleviating any tension at the elbow joint. This helps the user focus on the stretching of the wrist and fingers without interference from fatigue or pain from the elbow joint.

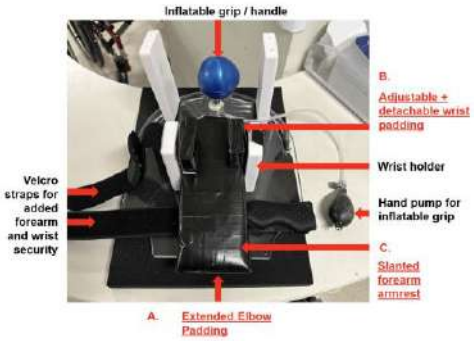


Figure 8. Labeled picture of the final stage prototype. Red and underlined features are key additions added after a usability testing stage.

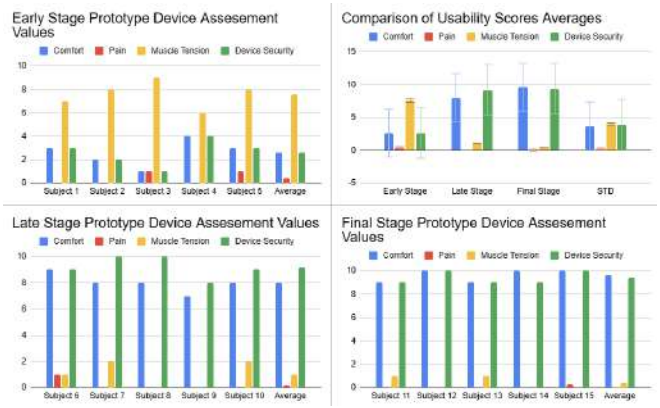


Figure 9. Early, Late, Final and Averages of de-identified pilot usability testing

As seen with Figure 9, each design addition and usability surveys, the device was able to improve its overall comfort through the minimization of pain, decreasing of unnecessary upper arm muscle tension, and increase of device security of the forearm, meaning that the users were able to stretch comfortably and securely without invoking the activation of the biceps or triceps, which are not included in the intended stretching muscles.

B. EMG Data

From the preliminary EMG data, we noticed distinct peaks of flexor and extensor activation between the movements. As seen in figure 10 C, the extensor carpi radiales was first shown to activate for around 5 seconds after the 10 second baseline, which was followed by another 5 second activation of the flexor carpi radialis. This activation pattern of around 5 seconds per movement and muscle group correlates to our movement, as the patient was instructed to first extend then flex their wrists then continue alternating from one motion to the other.

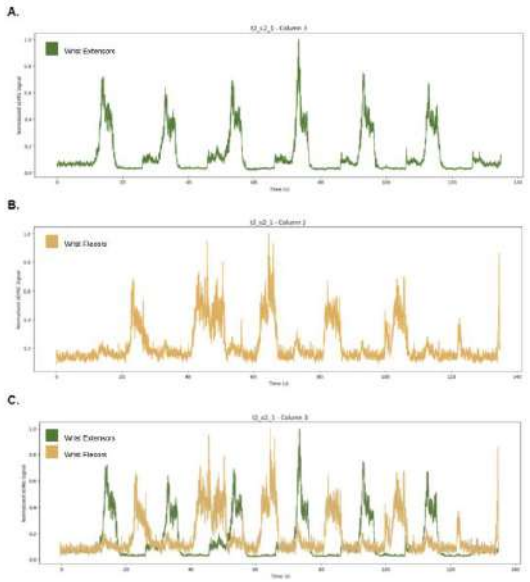


Figure 10. EMG data collected from healthy control during wrist flexion/extension movement. A) muscle activation recorded for wrist extensor. B) muscle activation recorded for wrist flexor. C) Combined extensor + flexor muscle activation data.

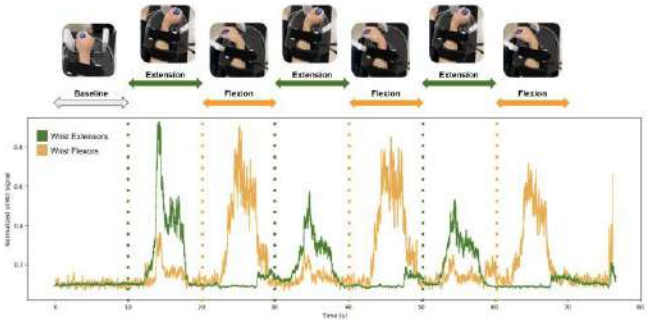


Figure 11. Labeled digram of EMG data representing matching muscle activation (extensor/flexor) and motion performed (extension/flexion).

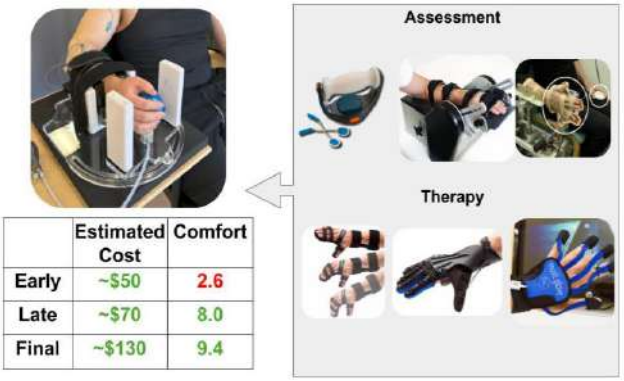
We were able to confirm that the device was able to properly elicit the correct muscle group activation with its corresponding movement. When the user was extending their wrist through the device the extensors were able to activate, while the flexors activated when the user flexed the wrist (fig 11). We also confirmed that the device was able to activate the muscle groups significantly above the baseline recordings, which was the first 10 seconds of the data collection in which there was no movement from the user in a relaxed position.

C. State of the Art Comparison

While the device is still in its early stages of development, the initial purpose of the device was to serve as a low-cost assesement and therapeutic device.

Since the device relies on a passive system that is controlled manually, price is one of the main advantages comapared to some of the state-of-the-art hand spasticity devices. We set out cost threshold to be $780, which was the reported mean total cost of physcial rehabilitation in a study conducted in a cash-based physical therapy clinic by Pulford et Al. [17]. All stages of the prototype had estimated costs to be under the threshold with our final prototype costing around $130, which is significantly less than other types of hand-spasticity devices such as the Saebo Hand Spasticity Treatment Kit (~$335) [18].

Another design advantage to our passive system is its emphasis on self-operability. Our inflatable handle system allows for the user to sllide in their fist through a soft silicon pillar, without having to individually correct the positioining of their fingers as seen in figure 3a. This feature is advantageous compared to the more common glove design, in which users may have much more difficulty putting the glove over their spastic fingers indivdually. Additionaly, common spasticity glove devices such as FlintRehab music glove and the Saeboglove all cost much more than our prototype (~$350-499) [19, 20].



	Estimated Cost	Comfort
Early	~$50	2.6
Late	~$70	8.0
Final	~$130	9.4

Figure 12. Table of estimated cost per prototype and state of the art stroke therapeutic and assesement devices.

V. Conclusion

This paper documents the development of the device through its key early, late, and final stages as well as a verification of the device's ability to properly activate the correct muscle groups. Key requirements considered were that the device be self-operable, affordable, and usable as both a therapeutic and assessment tool. This was achieved. The device's passive system does not rely on any electronics or motors ultimately allow for the device to not only be affordable but safe and easy to operate, showing its novelty in the field of pre-existing devices that traditionally utilize electronic systems [4,9]. Thus, we determined that the safety of the device was adequate and that only hazards were from improper set up of the device.

Additionally, EMG data of the device in-use showed that the device was able to stretch the proper flexor / extensor muscle groups but also compatibility with the commonly used EMG system as an assessment tool for spasticity as well. This shows that the device can work both in-home and in the clinic both as a therapeutic or assessment tool. In the future, we want to test out the muscle activation of post-stroke patients as well, analyzing the differences that may occur from compensation as well as velocity-dependent stretch.

Future directions of the device will focus on the attachment of additional sensors (potentiometer, pressure sensor, load cell) to further help analyze spasticity in a quantitative manner. Although the device will maintain its low cost and independent operation, the attachment of potentiometer and pressure sensors will help us understand the exact pressure enacted by a spastic hand and the velocity of the wrist. Finally, the continued development of this device can also serve as a vital treatment and assessment options for spasticity in low-resource areas – not just in the clinic, but in the home as well.

Acknowledgment

Additionally, this study has been submitted for IRB exemption under Category 3, while any future studies have been submitted for IRB protocol #849090.

We would like to thank the University of Pennsylvania School of Engineering and Applied Science Office of Diversity, Equity, and Inclusion (ODEI) for their support of this project as well as members at the Rehabilitation Robotics Lab.

References

[1] A. Bersano and L. Gatti, "Pathophysiology and Treatment of Stroke: Present Status and Future Perspectives," *International Journal of Molecular Sciences*, vol. 24, no. 19, Art. no. 19, Jan. 2023.

[2] "Frontiers | New insights into the pathophysiology of post-stroke spasticity." Accessed: Oct. 21, 2024.

[3] "Rehabilitation Therapy Doses Are Low After Stroke and Predicted by Clinical Factors | Stroke." Accessed: Nov. 21, 2024.

[4] W. Mahmoud, M. Haugland, A. Ramos-Murguialday, H. Hultborn, and U. Ziemann, "Measuring resistance to externally induced movement of the wrist joint in chronic stroke patients using an objective hand-held dynamometer," *Clin Neurophysiol Pract*, vol. 8, pp. 97–110, May 2023.

[5] A. Andringa, E. van Wegen, I. van de Port, G. Kwakkel, and C. Meskers, "Measurement Properties of the NeuroFlexor Device for Quantifying Neural and Non-neural Components of Wrist Hyper-Resistance in Chronic Stroke," *Front Neurol*, vol. 10, p. 730, Jul. 2019.

[6] N. A. Lannin *et al.*, "Upper limb motor training using a Saebo™ orthosis is feasible for increasing task-specific practice in hospital after stroke," *Aust Occup Ther J*, vol. 63, no. 6, pp. 364–372, Dec. 2016.

[7] Garratt, B. J. (2009). *The development of a wrist rehabilitation device for movement therapy* (Bachelor of Engineering dissertation, University of Southern Queensland).

[8] M. U. A. Khan, A. Ali, R. Muneer, and M. Faisal, "Pneumatic artificial muscle-based stroke rehabilitation device for upper and lower limbs," *Intel Serv Robotics*, vol. 17, no. 1, pp. 33–42, Jan. 2024.

[9] K. Kawamura *et al.*, "Quantitative measurement of resistance force and subsequent attenuation during passive isokinetic extension of the wrist in patients with mild to moderate spasticity after stroke," *J Neuroeng Rehabil*, vol. 19, no. 1, p. 110, Oct. 2022.

[10] Krogt, Hanneke & Kouwijzer, Ingrid & Klomp, Asbjorn & Meskers, Carel & Arendzen, Hans & Groot, Jurriaan H.. (2019). Loss of selective wrist muscle activation in post-stroke patients. Disability and Rehabilitation. 42. 1-9. 10.1080/09638288.2018.1509241.

[11] E. H. Kim, M. C. Jang, J. P. Seo, S. H. Jang, J. C. Song, and H. M. Jo, "The Effect of a Hand-Stretching Device During the Management of Spasticity in Chronic Hemiparetic Stroke Patients," *Ann Rehabil Med*, vol. 37, no. 2, pp. 235–240, Apr. 2013.

[12] L. Black and D. Gaebler-Spira, "Nonsurgical Treatment Options for Upper Limb Spasticity," *Hand Clinics*, vol. 34, no. 4, pp. 455–464, Nov. 2018.

[13] D. Xu et al., "Development of a Reconfigurable Wrist Rehabilitation Device with an Adaptive Forearm Holder," 2018 IEEE/ASME International Conference on Advanced Intelligent Mechatronics (AIM), Auckland, New Zealand, 2018, pp. 454-459.

[14] G. F. Garcia, R. S. Gonçalves, and G. Carbone, "A Review of Wrist Rehabilitation Robots and Highlights Needed for New Devices," *Machines*, vol. 12, no. 5, Art. no. 5, May 2024.

[15] Y. Leng *et al.*, "Alterations of Elastic Property of Spastic Muscle With Its Joint Resistance Evaluated From Shear Wave Elastography and Biomechanical Model," *Front Neurol*, vol. 10, p. 736, 2019.

[16] C. Bütefisch, H. Hummelsheim, P. Denzler, and K. H. Mauritz, "Repetitive training of isolated movements improves the outcome of motor rehabilitation of the centrally paretic hand," *J Neurol Sci*, vol. 130, no. 1, pp. 59–68, May 1995.

[17] K. Pulford, B. Kilduff, W. J. Hanney, M. Kolber, X. Liu, and R. Miller, "Service Utilization and Costs of Patients at a Cash-Based Physical Therapy Clinic," *Health Care Manag (Frederick)*, vol. 38, no. 1, pp. 37–43, 2019.

[18] Saebo, "Hand Spasticity Treatment Kit," [Online]. Available: https://www.saebo.com/products/spasticity-treatment-kit.

[19] Saebo, "SaeboGlove," [Online]. Available: https://www.saebo.com/products/saeboglove. [Accessed: Feb. 22, 2025].

[20] Flint Rehab, "MusicGlove Hand Therapy," [Online]. Available: https://www.flintrehab.com/product/musicglove-hand-therapy

A case study of Error Fields: A three-dimensional personalized robotic therapy

1st Naveed Reza Aghamohammadi*[1,2], 2nd Courtney Celian[1], 3rd Victoria Wojcik[1,2], 4th Bruno Borghi[1], 5th Arturo Ramirez[1,2], 6th Adriana Cancrini[1,2], 7th James L. Patton*[1,2]

1 : Robotics Lab, Center for Neural Plasticity, Shirley Ryan AbilityLab, Chicago, IL, USA

2 : Richard and Loan Hill Department of Biomedical Engineering, University of Illinois at Chicago, Chicago, IL, USA

Correspondence: nagham2@uic.edu, pattonj@uic.edu

***Abstract*—Treating post-stroke individuals with physical devices (mechanoceuticals) has produced mild but significant recovery. While it is widely recognized that therapy should focus on movement error, there is currently no model of relearning that can inform the design of longer-term treatment. We present a case study dubbed Error Fields, a personalized robotic therapy for stroke survivors, based on a mathematical model of each person's unique response to error, used to diagnose and address specific deficits. After three days of Error Fields treatment, errors significantly decreased compared to baseline demonstrated by shift in error distributions. In contrast, three days of practice with the robotic system without treatment showed no significant error reduction. Comparing Error Fields sessions to null treatment sessions also revealed significant improvements in error levels.**

***Index Terms*—Personalized Robotic Neurorehabilitation, Stroke Neurorehabilitation, Models of Motor Re-learning**

I. Introduction

Learning is a critical mechanism for post-stroke motor recovery, yet the ability to relearn movement skills varies greatly among individuals. Rehabilitation robotics offers tools that enhance motor recovery, and have shown benefits when used in upper-extremity retraining in the stroke population even in isometric conditions [1]. However, most systems strictly guide the user, which limits exploration, prevents mistakes, and lack personalization for each stroke survivor's specific movement impairments [2]–[6]. This highlights the need for techniques that allow individuals to experience and correct their own errors which can promote learning, adaptation, and neuroplasticity [7]–[9].

Error augmentation (EA) has emerged as a promising strategy to enhance relearning by amplifying movement errors to drive adaptation and has shown significant potential [7]–[10], in upper-extremity rehabilitation [11]. However, EA does not account for individual differences in how people respond to errors; thus, personalized training tailored to each person's error sensitivity is crucial. Building on this principle, we developed a customized technique called Error Fields (EF) training, where users learn by leveraging their own errors. This approach employs a statistical model based on a individual's movement errors, which is inverted to amplify their most frequent errors for targeted training [12]. Preliminary results from our planar-reaching experiment showed that EF training reduces error magnitude in healthy participants compared to those undergoing error augmentation or null treatment [12]. Also EF has been implemented in 3D for neuro-typical subjects undergoing a haptic curl force fields shown that subjects who recieved EF had higher error reduction commpared to null treatment [13]. Despite these advances, planar robotic training lacks the sensory richness and functional relevance of real-world 3D actions. [14]. By contrast, immersive 3D training systems promote natural variability in arm movements—a key driver of motor learning [15], [16]. While EF training has demonstrated superior learning outcomes in planar tasks [12], it has not yet been tested in 3D settings or with stroke survivors. In this study, we evaluated EF training in a 3D robotic reaching task with a single stroke survivor. We hypothesized that EF treatment would reshape error distributions, leading to a significant reduction in errors across sessions. Additionally, we hypothesized that EF training would increase kinematics of subjects affected arm and improve clinical outcomes.

II. Methods

This is a case example of a clinical trial, here we narrate enrollment and protocol policies of the clinical trial.

A. Apparatus

We used the Barret Upper-Extremity Robotic Trainer (Burt®) [17] (Fig. 1a,b), which provides real-time, 3D haptic feedback and forces for unrestricted upper-extremity movements. We also used our in-house made LookingGlass 3D augmented reality system [18]–[20] (Fig. 1a,c) and active shutter 3D glasses that allow the stereoscopic representation of virtual objects, as well as a view of the subject's hands and arms through a semi-silvered mirror. We used Unity® software to provide a real-time graphical interface with the Burt® and monocular cues to the depth [21] (Perspective, Occlusion, Shadow, Relative Height, Texture Gradient) in the scene (Fig. 1a). We matched the viewpoints across subjects to the scene (Fig. 1a) by calibrating the seating and head position to the LookingGlass system as well as the stereoscopic camera system in Unity. The calibration ensured that the cursor (the green object in Fig. 1a) always matched the subject's hand position. We also provided gravity compensation to cancel the weight of subjects arms. We also used Movisense® *Move 4* accelerometer device [22] strapped to the subject's wrist for at-home observation of their arm kinematics.

B. Enrollment

Experimental protocols were approved by the Northwestern University Institutional Review Board (STU0021500). Informed consent was obtained. Eligible participants had to be at least 8 months post-stroke, hemiparetic with some elbow and shoulder movement, and not concurrently receiving any upper-extremity therapy or enrollment in another research study. Subjects were excluded if they have the following conditions: bilateral paresis, Severe tactile deficits using the Two-Point Discrimination Test, Severe proprioceptive deficits using the proprioception screen, Severe spasticity (Modified Ashworth ¿3), Aphasia, cognitive impairment, or affective dysfunction that would influence the ability to perform the experiment, Visual deficits (BIVABA confrontation testing, Snellen eye test, Stereo Fly Test, Star Cancellation Test), diffuse/multiple lesion sites or multiple stroke events, Botox injection to the affected upper extremity within the previous 4 months and Inability to provide an informed consent.

C. Protocol

A cross-over design study in which each participant receives both EF and null treatment is chosen to account for the effect of subject inter-variability. In this study, participants complete a total of 9 visits across nine weeks (Fig. 1e) and participant is randomly assigned to one of 2 groups; Group 1 completes the reaching experiment with Error Fields (EF) applied in visits 5-7, and simple practice (Sham) applied in visits 2-4. Group 2 receives the opposite treatment (Sham in visits 5-7, EF applied in visits 2-4). Upper extremity evaluations are to be completed by a licensed occupational therapist at visits 1 (baseline), 8 (post), and 9 (follow-up) using the Upper Extremity Fugl-Meyer Test (UEFM), Action Research Arm Test (ARAT) and Box and Block Test (BBT) [23].

Subject practice successive 10-cm-long reaches, using a cursor with diameter of 0.5 cm terminating at sphere targets with diameter of 2 cm witin a fixed-size constrained 3D random walk goal-directed reaching pattern (Fig. 1d) in a $20 \times 20 \times 20$ cm box. Subjets were given 5 seconds to complete a reach. Four "Practiced" directions (d_0, d_1, d_2, d_3) as shown in Fig. 1d are seen for the majority of the experiment schedule (Fig. 1f). In order to test generalization of learning we have the subject perform reaching in the unpracticed directions (d_4, d_5, d_6, d_7) which are 180^o opposites of practiced directions (Fig. 1d) in two *"Un-Practiced"* phases of experiment schedule (Fig. 1f). We calibrate the extreme bounds of target positions (Fig. 1d) to a subject's existing movement range such that regardless of handedness the center of medial-lateral axis is in front of the subject's sternum. We believe such a design allows for a true unbiased assessment of any 3D treatment across a subjects existing range of motion.

The most pure evidence for changes in the feedforward motor plan are reportedly observed within the first 300 milliseconds of a volitional movement [24], [25], before visual and proprioceptive feedback has reached the motor cortex. Our primary interest is in assessing changes in the feedforward motor plan, we require a parameter that monotonically increases to track movement progress and detect movement onset in real-time. We selected the path distance of the movement trajectory instead of time because path distance reflects the subject's volitional intent, whereas time is an external metric that can complicate onset detection and movement tracking. We chose for a 10 cm reach, the path distance threshold values of 5 mm and 105 mm based on the aggregates of pilot data from both healthy and stroke subjects, we call this the "launch window". To detect onset in real-time, we set this rule: onset of movement is detected when path distance is bigger than 5 mm and speed is bigger than 3 mm/s. Subject is allowed to plan movements before executing them. At end of the reach, visual and auditory feedback are provided for half a second based on the subjects maximum speed during the launch window. If subjects maximum speed is inside the acceptable range $[0.1976\ m/s\ ,\ 0.5138\ m/s]$ a "good" visual and auditory feedback was presented, other feedbacks in similar fashion are presented for "Slow" and "Too-Fast" reaches. These values were determined based on pilot data of post-stroke subjects for 10 cm reaches. The experiment schedule consists of 7 phases with 590 movement trials (Fig. 1f):

Familiarization phase (#1): subjects are familiarized with the environment and robot making reaches in practiced directions with 10 repeat-per-directions (RPD), data from this phase is not used in analysis.

Baseline phases (#2-3): are placed to make pre-training assessment of error levels for both practiced and un-practiced directions, each of these phases have 5 RPD.

"Evaluation" phase (#4): which has 30 RPD with practiced directions was used to create a statistical profile of movement errors for each path distance during the launch window of movements.

"Training" phase (#5): when a subject is under the "Error Fields" condition they receive EF therapy force (60 RPD, practiced directions). No force catch trials are used to assess learning(16 RPD with a 1/5 chance).

Null phases (#6-7): are placed to make post-training assessment of error levels be made in practiced and un-practiced directions, each of these phases have 5 RPD.

D. Error Definitions

Three types of movement errors were analyzed, all represented in an error vector ($\mathbf{e}(t)$): Extent Error ($\mathbf{e}_{ext}(t)$), Horizontal ($\mathbf{e}_{hor}(t)$) and Vertical ($\mathbf{e}_{ver}(t)$). Errors (Fig. 1g) are described in Error reference frame $[E]$ and where t is path distance. Horizontal and Vertical errors represent the real-time distances of hand position from ideal line connecting start to target positions. Extent Error ($\mathbf{e}_{ext}(t)$) is defined as the difference in position between the ideal hand position, i.e. $x_{MJ}(t)$ described along x-axis of direction frame $[i]$ for a direction d_i according to Flash and Hogan's minimum jerk profile [26], and the projection of the actual hand position on the ideal line. The ideal time of a reach is 650 milliseconds, and extent error measures lead or lag error of subjects in reaching targets. To calculate errors, we first transformed

robot end-effector position $\mathbf{x}(t)$ described in left-handed Unity reference frame $[U]$ (Fig. 1g) to right-handed frame $[i]$ for movement direction d_i described in $[U]$, origin of $[i]$ is strapped to ideal start position $\mathbf{x}_S$ and its x-axis points towards target $\mathbf{x}_T$. Homogeneous transform $\rho_i(t) = T_{iU}\mathbf{x}(t)$ was used where T_{iU} consisted of rotation R_{iU} and translation $\mathbf{p}_{iU}$. Rotation is given by $\mathrm{R}_{iU} = [\mathrm{d}_i, -<\mathrm{d}_i \times \mathrm{g}>, <(-\mathrm{d}_i \times \mathrm{g}) \times \mathrm{d}_i>]^\top$ in which g is the gravity vector described in $[U]$ and $<>$, $\times$ and $^\top$ are unit vector, cross product and transpose operators respectively. Translation is given by $\mathbf{p}_{iU} = -\mathbf{x}_S$. Values of second and third components of ρ_i vector equal values of horizontal and vertical errors. To calculate Extent error $\mathbf{e}_{ext}(t)$, we strapped origin of $[E]$ to $x_{MJ}(t)$:

$$\mathbf{e}(t) = \begin{bmatrix} \mathbf{e}_{ext}(t) \\ \mathbf{e}_{hor}(t) \\ \mathbf{e}_{ver}(t) \end{bmatrix} = \begin{bmatrix} \mathrm{I} & \mathbf{p}_{Ei}(t) \\ \mathbf{0}^\top & 1 \end{bmatrix} \rho_i(t) = T_{Ei}(t) T_{iU} \mathbf{x}(t) \tag{1}$$

where $\mathbf{p}_{Ei}(t) = [-x_{MJ}(t), 0, 0]^\top$. An ideal movement description in $[U]$ follows minimum jerk trajectory and traverses on ideal line connecting $\mathbf{x}_S$ to $\mathbf{x}_T$ (orange trace in Fig 1h), such movement described in $[i]$ traverses along x-axis from 0 to 0.1 according to $x_{MJ}(t)$, however in the error frame $[E]$, an ideal movement trajectory always remains stationary at origin of $[E]$. This is the basis of ideal error distribution Q described in $[E]$ and defined by $Q \sim \mathcal{N}(\mathbf{0}_{3\times1}, \mathbf{0}_{3\times3})$ where $\mathcal{N}(\mu, \Sigma)$ signifies multivariate Gaussian distribution with mean vector μ and covariance matrix Σ.

E. Treatment Forces

During the Evaluation phase (Fig. 1f), errors were profiled during the launch window, according to direction and path distance, to construct a path-distance-dependent ensemble statistic 3-dimensional Multivariate Gaussian distribution of errors for each direction according to the distribution function:

$$p = \frac{1}{\sqrt{(2\pi)^3|\Sigma|}} exp((\mathrm{e}-\mu)^\top \Sigma^{-1}(\mathrm{e}-\mu)) \tag{2}$$

where μ and Σ are ensemble mean and covariance of all movements belonging to direction $\mathbf{d}_i$ during the Evaluation phase. This creates a set of pre-training distributions for each path distance during launch window, we denote that set as $\mathbf{P} = \{P(t) \sim \mathcal{N}(\mu(t), \Sigma(\mathrm{t})) \ \forall \ t\}$. Fig. 1h shows an instance of such distribution for direction d_1 at a path distance during the launch window shown in Unity refrence frame $[U]$ where the yellow dots represent mean of error vector i.e. $\mu(t)$ and yellow ellipsoid shows uncertainty of error i.e. $\Sigma(t)$ for intermittent exposure trial in the Evaluation phase. Fig. 1h also shows ideal movement trajectory $x_{MJ}(t)$ (orange dots) from start to target, and black dot-traces here show error vectors $\mathbf{e}(t)$. During the Training Phase, a therapeutic force vector will be applied during launch. For Error Fields this will be $\mathbf{f}_{EF}(t) = \lambda p(t)\mathbf{e}(t)$ described in $[E]$. λ is a direction-dependent constant corrective gain such that the overall force applied to the subjects hand never exceeds 20 N. Transform T_{UE} were used to apply forces to subject hand in $[U]$ which is shown in Fig. 1h as solid black arrows for a trial at end of training, note that EF force are clearly along direction of error vectors $\mathbf{e}(t)$ and are augmenting error. Sham treatment has no therapeutic force. EF force effectively applies more forces when instantaneous Mahalanobis distance i.e. $(\mathrm{e}-\mu)^\top \Sigma^{-1}(\mathrm{e}-\mu)^\top$ between error $\mathbf{e}$ and pre-training distribution $\mathcal{N}(\mu, \Sigma)$ is small which pushes likelihood of error p closer to 1, meaning subject is repeating a movement error. We hypothesized that by applying EF, post-training error distributions denoted by $\mathbf{R} = \{R(t) \ \forall \ t\}$ would shift away from pre-training error distributions and move closer to ideal distribution Q at origin of Error frame $[E]$ signaling motor learning.

F. Analysis

1) Error Distribution Analysis: Since EF primarily uses distribution of errors along a movement direction to apply therapy forces, we also created a novel assessment to quantify shifting of distributions. We measured distance of all distributions in the pre-training set $\mathbf{P}$ from the ideal distribution Q. We chose Wasserstein-2 distance metric for multivariate Gaussian distributions [27] with considers mean and variability to calculate distance between two distributions. Since we always want to calculate distance of an error distribution from ideal distribution Q, the equation of Wasserstein-2 distance simplifies to $W_2(P(t), Q) = \sqrt{||\mu_{P(t)}||^2 + \mathrm{Tr}(\Sigma_{P(t)})}$. Essentially distance is squared root of sum of squared norm of mean and summation of all error variances. We calculated such distances for all members of pre-training set and post-training set. We declare the subject has "learned" if distances of pre-training distribution from ideal distribution are higher than those of post-training distributions. We declare a worsening for the reverse situation.

2) Trial-to-Trial Error Reduction: : We used following metrics for each trial: "Maximum Error Amplitude" i.e. $max(||\mathbf{e}(t)||) \ \forall \ t$ & "Launch Deviation Angle" is angle between the vector starting at position of movement onset and position at first speed peak and the ideal line. We used median bootstrapping with replacement (1,000 iterations) to estimate errors. We then compared overall error levels and error reduction across sessions under EF and Sham using bootstrapped error estimates.

3) At-Home Kinematics Analysis: We performed signal conditioning on acceleration by wavelet de noising, removing mean and passing through a band-pass filter ($[0.5\ 12]\ Hz$). We then analyzed distributions of acceleration and calculated differences across histogram counts.

III. Results

We enrolled a 55-year-old male with hemi-paretic chronic stroke who was left-hand affected but right-hand dominant.

A. Error Distributions Improved After Error Fields

Fig. 2a shows the medians of error distribution distances in pre- and post-training for each practiced direction. Although on some treatment visits post-training distances were higher than pre-training distances, the overall trend demonstrates an

error reduction and shifting of error distribution towards the ideal distribution. To be specific distances of distributions at the end of EF treatment week were significantly closer to ideal than distances of distributions on baseline visit by 1.5 cm (Kruskal-Wallis $p = 0.02$, $df = 1$, $F = 5.3$, $CI = [0.6, 7.4]$). Fig. 2a also shows that subject retained learning when we compare pre-training distances at baseline visit to pre- distances on treatment visit 4 which is the begin of Sham treatment week (Kruskal-Wallis $p = 0.0209$, $df = 1$, $F = 5.3$, $CI = [0.61, 7.3]$). However when we compare distances of distributions from baseline to end of Sham treatment week, no significant difference is observed (Kruskal-Wallis $p = 0.185$, $df = 1$, $F = 2.08$, $CI = [-0.89, 5.89]$) signaling that simple repetitions were not enough. A significant difference in distribution distances was observed when baseline and post evaluation visits are compared (Kruskal-Wallis $p = 0.02$, $df = 1$, $F = 5.332$, $CI = [0.6, 7.39]$), this shows overall improvement due to both treatment and getting better at task.

B. EF treatment week shows superior Error reduction

We analyzed maximum error amplitude and launch deviation angle using bootstrapping, due to page limitation we only present results for maximum error amplitude, launch deviation angle results showed very similar patterns. Fig. 3 shows that analysis across difference section of experiment schedule. The comparison plots 3b,e,h,k show comparisons of error levels within EF treatment week, comparisons 3d,g,j,m show comparisons of error levels within Sham treatment week and comparisons 3c,f,i,l show comparisons of error reduction under EF and sham treatments. Comparisons in Fig. 3c,f,i,l show that Error Fields has significantly higher reduction than Sham treatment when comparing baseline phase to null phase (Kruskal-Wallis $p < 1 \times 10^{-10}$, $df = 1$, $F = 418$, $CI = [477, 579]$). Also EF treatment had significantly higher error reduction than sham when comparing early training to late training (Kruskal-Wallis $p < 1 \times 10^{-10}$, $df = 1$, $F = 49$, $CI = [130, 231]$) although this was to be expected given that EF augments some errors. Comparing baseline and null phases in the un-practiced directions show EF treatment had lower reduction compared to Sham treatment (Kruskal-Wallis $p < 1 \times 10^{-10}$, $df = 1$, $F = 385$, $CI = [-557, -456]$). Another interesting find is that when comparing late-evaluation to null phase, EF also had lower error reduction compared to Sham (Kruskal-Wallis $p < 1 \times 10^{-10}$, $df = 1$, $F = 385$, $CI = [-557, -456]$). To save space, we are not presenting statistics of within-week error levels, although significant lines drawn on Fig. 3.

C. At-Home Changes of Kinematics

Fig. 2b,c,d show log-normalized distribution of subject's acceleration after baseline visit, visit 4 (end of EF treatment week) and visit 7 (end of Sham treatment week). Fig. 2e shows difference between counts on each bin between end of EF treatment and Baseline visit, Fig. 2f and g which show differences in counts from baseline to end of EF week and Sham week respectively, all show worsening in histogram counts. We cannot determine if reduction of acceleration is result of practice with robot or not.

TABLE I
CLINICAL SCORES

Evaluation Visit	ARAT	UEFM	BBT
Baseline	7/57	17/66	0/150
Post	6/57	17/66	0/150
Follow-Up	7/57	17/66	0/150

D. Clinical Assessments show no change

No changes are seen in the clinical scores (table I).

IV. DISCUSSION

This study is part of larger blinded, randomized controlled trial, and compares the reduction of movement errors, shifting of error distributions and across 2 training conditions each with 3 sessions: Error Fields personalized therapy, and null treatment (Sham) while practicing three dimensional reaches. Although the results generally support the effectiveness of the Error Fields treatment over simple practice, this support is not without reservations. For example reduction of distances of error distributions evaluated by our Wasserstein distance analysis, from begin of EF week compared to its end (Fig. 2a) although positive (apprx. 5 mm) is not significant. Also the overall decrease of distances could be at least partly due to practice. This will be further scrutinized when we analyze performance of other subjects who receive Sham treatment first and EF treatment later. Also distribution analysis of subject's kinematics while at home, provides mixed results. Although improvements attributed to EF or practice were observed, they did not reach the Minimum Clinically Important Difference (MCID), as indicated in table I. However this study is meant to assess feasibility of this EF treatment for stroke subjects rather than a longitudinal investigation. In Fig. 3e, the reduction in errors for the EF condition was smaller compared to the Sham condition when late-evaluation were compared against the null phase. This may be because the three EF therapy sessions occurred earlier in time, possibly allowing improvement by pure practice during the EF evaluation week. By the time the Sham sessions took place, these improvements had likely stabilized, resulting in a smaller relative reduction in error levels for the EF condition. Also, when comparing the un-practiced baseline to the un-practiced null phase, EF displayed a lower reduction in errors (Fig. 3l). This could be due to the fact that the un-practiced directions were opposite of those that had been practiced, and EF treatment was administered only to practiced directions. As a result, the generalization of learning to un-practiced directions was negatively affected.

Overall, these preliminary findings from just stroke survivor validate the foundations for our larger study with our novel personalized robotic treatment and we anticipate stronger trends and analysis to be presented when the results of our larger clinical trial are presented.

ACKNOWLEDGMENT

This work is supported by the National Institute of Health (NIH) under grant R01NS053606. We would like to thank the rest of the Robotics Lab at the Shirley Ryan AbilityLab and Biomedical Engineerig department at University of Illinois at Chicago. No conflicts of interest, financial or otherwise, are declared by the authors.

REFERENCES

[1] A. Ramirez, N. R. Aghamohammadi, C. Celian, A. Cancrini, B. Borghi, and Patton, James L, "Do Motor Skills Learned in Isometric Training Generalize to Unpracticed Workspaces?" in *International Conference on Rehabilitation Robotics (ICORR)*. Chicago, IL, USA: IEEE, May 2025, p. Accepted.

[2] S. Tesfazgi, A. Lederer, J. F. Kunz, A. J. Ordóñez-Conejo, and S. Hirche, "Personalized rehabilitation robotics based on online learning control," *arXiv preprint arXiv:2110.00481*, 2021.

[3] L. Masia, M. Casadio, P. Giannoni, G. Sandini, and P. Morasso, "Performance adaptive training control strategy for recovering wrist movements in stroke patients: a preliminary, feasibility study," *Journal of neuroengineering and rehabilitation*, vol. 6, pp. 1–11, 2009.

[4] V. Klamroth-Marganska, J. Blanco, K. Campen, A. Curt, V. Dietz, T. Ettlin, M. Felder, B. Fellinghauer, M. Guidali, A. Kollmar *et al.*, "Three-dimensional, task-specific robot therapy of the arm after stroke: a multicentre, parallel-group randomised trial," *The Lancet Neurology*, vol. 13, no. 2, pp. 159–166, 2014.

[5] S. Dalla Gasperina, V. Longatelli, M. Panzenbeck, B. Luciani, A. Morosini, A. Piantoni, P. Tropea, F. Braghin, A. Pedrocchi, and M. Gandolla, "Agree: an upper-limb robotic platform for personalized rehabilitation, concept and clinical study design," in *2022 International Conference on Rehabilitation Robotics (ICORR)*. IEEE, 2022, pp. 1–6.

[6] T. G. Hornby, D. J. Reinkensmeyer, and D. Chen, "Manually-assisted versus robotic-assisted body weight- supported treadmill training in spinal cord injury: what is the role of each?" pp. 214–221, 2010.

[7] J. L. Patton, M. E. Stoykov, M. Kovic, and F. A. Mussa-Ivaldi, "Evaluation of robotic training forces that either enhance or reduce error in chronic hemiparetic stroke survivors," *Experimental brain research*, vol. 168, pp. 368–383, 2006.

[8] F. Abdollahi, S. V. Rozario, R. V. Kenyon, J. L. Patton, E. Case, M. Kovic, and M. Listenberger, "Arm control recovery enhanced by error augmentation," in *2011 IEEE International Conference on Rehabilitation Robotics*. IEEE, 2011, pp. 1–6.

[9] F. Abdollahi, E. D. Case Lazarro, M. Listenberger, R. V. Kenyon, M. Kovic, R. A. Bogey, D. Hedeker, B. D. Jovanovic, and J. L. Patton, "Error augmentation enhancing arm recovery in individuals with chronic stroke: a randomized crossover design," *Neurorehabilitation and neural repair*, vol. 28, no. 2, pp. 120–128, 2014.

[10] D. J. Lin, S. P. Finklestein, and S. C. Cramer, "New directions in treatments targeting stroke recovery," *Stroke*, vol. 49, no. 12, pp. 3107–3114, 2018.

[11] Y. Wei, P. Bajaj, R. Scheidt, and J. Patton, "Visual error augmentation for enhancing motor learning and rehabilitative relearning," in *9th International Conference on Rehabilitation Robotics, 2005. ICORR 2005.* IEEE, 2005, pp. 505–510.

[12] N. R. Aghamohammadi, M. F. Bittmann, V. Klamroth-Marganska, R. Riener, F. C. Huang, and J. L. Patton, "Error fields: personalized robotic movement training that augments one's more likely mistakes," *Scientific Reports*, vol. 15, no. 1, p. 4201, 2025.

[13] B. Borghi, N. R. Aghamohammadi, A. Cancrini, A. Ramirez, C. Celian, and J. L. Patton, "Personalized Robotic Training on a Planar Reaching Task," in *International Conference on Rehabilitation Robotics (ICORR)*. Chicago, IL, USA: IEEE, May 2025, p. Accepted.

[14] N. Wenk, K. A. Buetler, and L. Marchal-Crespo, "Virtual reality in robotic neurorehabilitation," in *Virtual reality in health and rehabilitation*. CRC Press, 2020, pp. 41–60.

[15] R. J. Van Beers, P. Haggard, and D. M. Wolpert, "The role of execution noise in movement variability," *Journal of neurophysiology*, vol. 91, no. 2, pp. 1050–1063, 2004.

[16] K. Sutter, L. Oostwoud Wijdenes, R. J. van Beers, and W. P. Medendorp, "Movement preparation time determines movement variability," *Journal of Neurophysiology*, vol. 125, no. 6, pp. 2375–2383, 2021.

[17] W. T. Townsend, D. Wilkinson, A. Jenko, J. Leland, A. Ananthanarayanan, and J. Patton, "Multi-active-axis, non-exoskeletal rehabilitation device," Nov. 20 2018, uS Patent 10,130,546.

[18] J. J. Patton, "New vr technologies for sensorimotor rehabilitation," *Transactions of Japanese Society for Medical and Biological Engineering*, vol. 51, no. Supplement, pp. M–99, 2013.

[19] F. Porta, C. Celian, and J. L. Patton, "Upper extremity functional rehabilitation for stroke survivors using error-augmented visual feedback: Interim results," in *2021 43rd Annual International Conference of the IEEE Engineering in Medicine & Biology Society (EMBC)*. IEEE, 2021, pp. 1318–1324.

[20] C. Celian, M. Verardi, and J. Patton, "Visual error augmentation during bimanual therapy in individuals post stroke," *Archives of Physical Medicine and Rehabilitation*, vol. 103, no. 12, p. e91, 2022.

[21] B. L. Schwartz and J. H. Krantz, *Sensation and perception*. Sage Publications, 2018.

[22] S. Härtel, J.-P. Gnam, S. Löffler, and K. Bös, "Estimation of energy expenditure using accelerometers and activity-based energy models—validation of a new device," *European Review of Aging and Physical Activity*, vol. 8, pp. 109–114, 2011.

[23] T. Platz, C. Pinkowski, F. van Wijck, I.-H. Kim, P. Di Bella, and G. Johnson, "Reliability and validity of arm function assessment with standardized guidelines for the fugl-meyer test, action research arm test and box and block test: a multicentre study," *Clinical rehabilitation*, vol. 19, no. 4, pp. 404–411, 2005.

[24] R. S. Woodworth, "Accuracy of voluntary movement." *The Psychological Review: Monograph Supplements*, vol. 3, no. 3, p. i, 1899.

[25] E. R. F. Crossman and P. Goodeve, "Feedback control of hand-movement and fitts' law," *The Quarterly Journal of Experimental Psychology*, vol. 35, no. 2, pp. 251–278, 1983.

[26] T. Flash and N. Hogan, "The coordination of arm movements: an experimentally confirmed mathematical model," *Journal of neuroscience*, vol. 5, no. 7, pp. 1688–1703, 1985.

[27] D. Dowson and B. Landau, "The fréchet distance between multivariate normal distributions," *Journal of multivariate analysis*, vol. 12, no. 3, pp. 450–455, 1982.

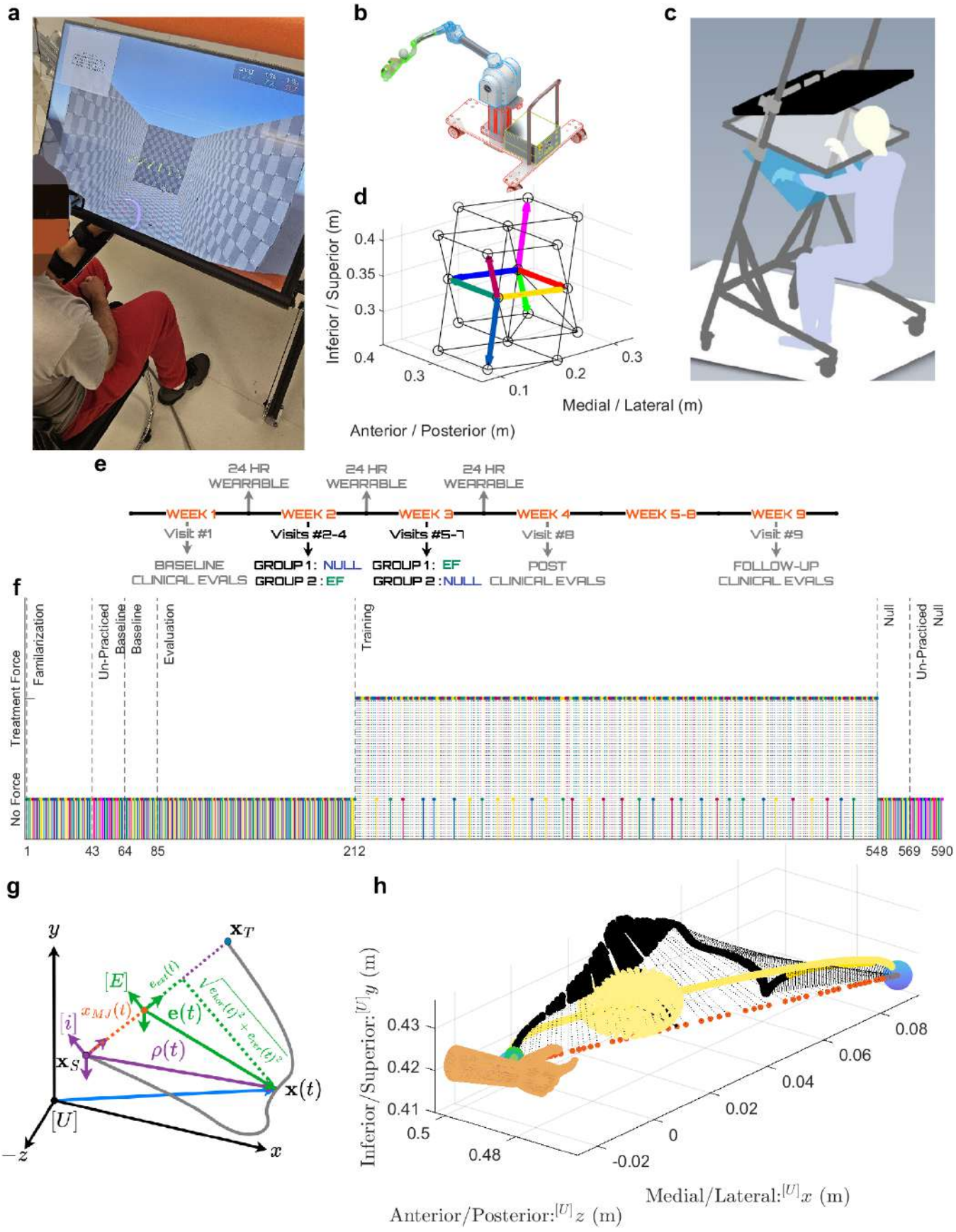


Fig. 1. (a) Subject reaching with Unity scene (b) Burt® robot (c) LookinGlass AR system (d) Targets & directions of experiment (e) Sessions protocol (f) experiment protocol (g) positions, reference frames and error vector (h) A trial at end of training: pre-training error mean and distributions (yellow dots and ellipsoid) and EF forces applied (black solid arrows)

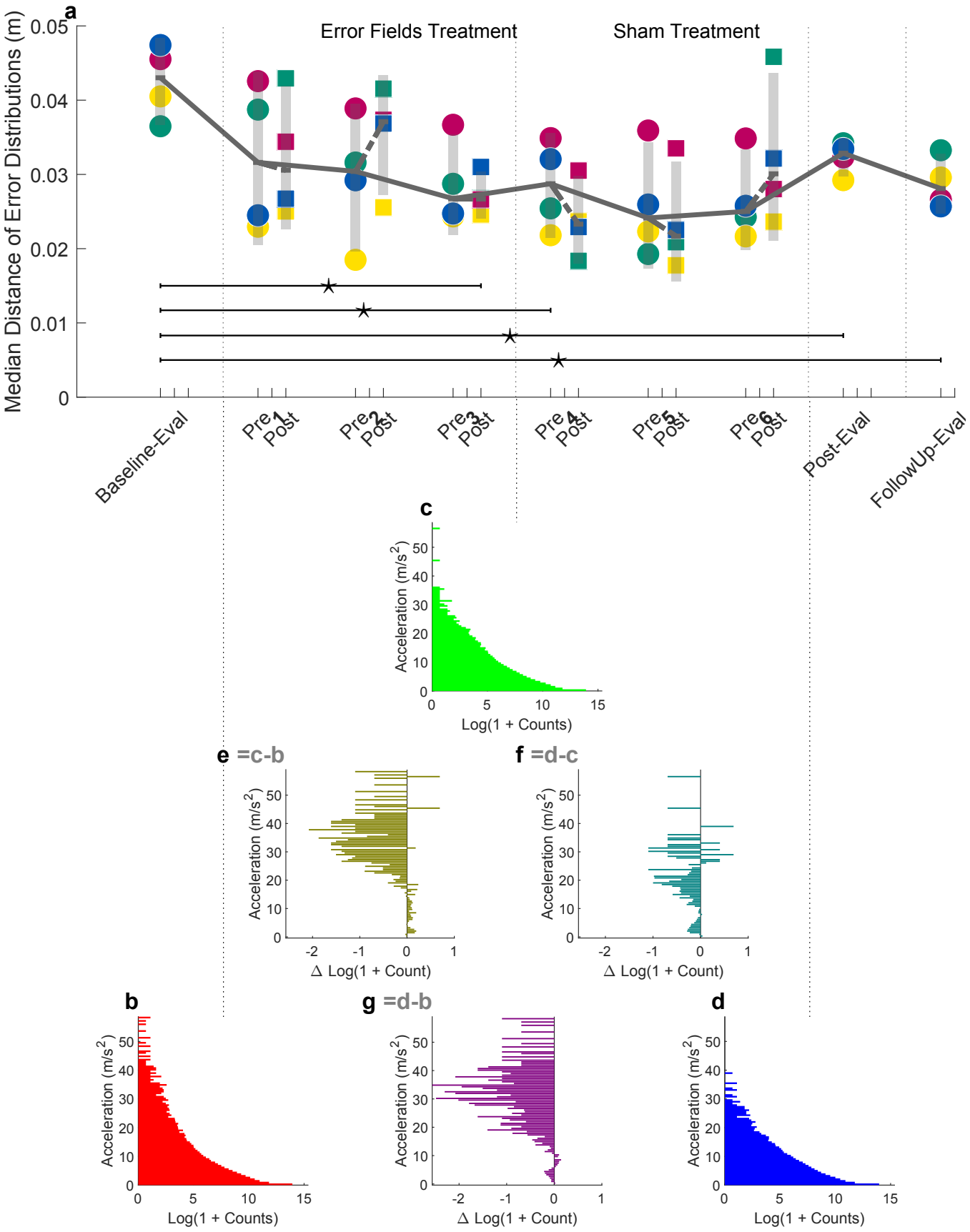


Fig. 2. EF treatment reduced error by reducing distance of error distribution and ideal distribution (a) median of error distribution, direction colors follow that of Fig. 1), circles for pre-trainig, squares for post-traing (b-d) acceleration distribution of subject at home (e-g) differences of counts of acceleration distributions

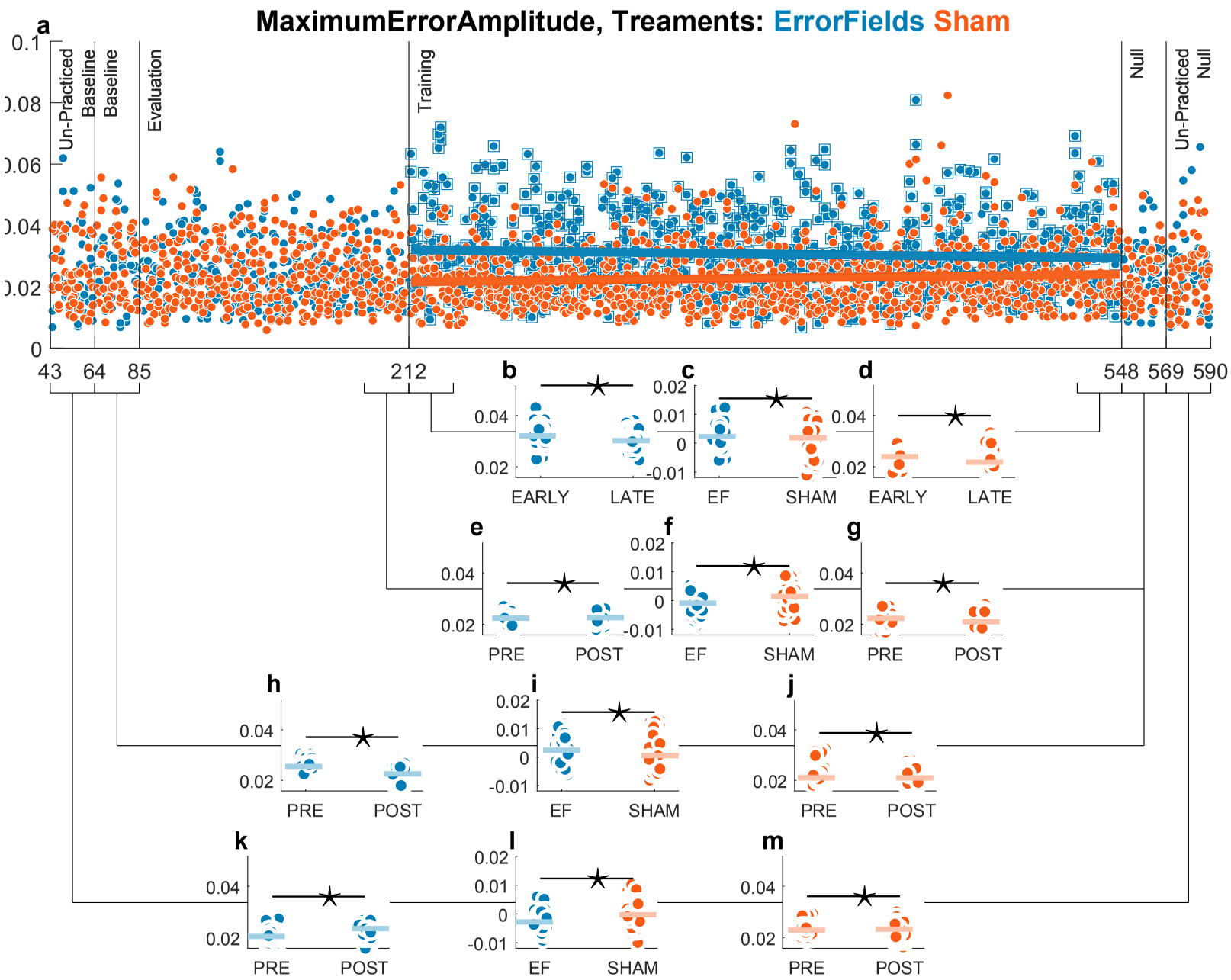


Fig. 3. Error Fields has superior redction compared to Sham treatment (a) maximum error amplitude for ErrorFields and Sham, solid traces show exponential decay model fits to trials in training (b-m) error level comparisons (same color) and error reduction comparisons

Personalized Robotic Training on a Planar Reaching Task

Bruno Borghi[1,2,3*], Naveed Reza Aghamohammadi[1,2], Adriana Cancrini[1,2], Arturo Ramirez[1,2], Courtney Celian[1], James Patton[1,2*]

***Abstract*— Based on recent advancements in neuro-adaptive control, we evaluated a novel iterative algorithm for generating customized training forces. The objective was to study the motor adaptation required to compensate for robot-generated perturbations during an upper-limb reaching task. We hypothesized that the adaptation process would induce changes in the brain's feed-forward command, dynamically reshaping the neuromuscular system to refine movement patterns and result in trajectory alterations. The results indicate that after a training period with these robot-generated forces, trajectories undergo modifications due to internal model adaptation, leading to improved performance measured in terms of position error. This experiment explores motor learning in different directions and compares two conditions: 1) curl force field, a velocity-dependent perturbation applied to deviate trajectories, and 2) Error Field force, a customized force specifically designed to address and correct trajectory errors. The findings highlight the effectiveness of the Error Field force in enhancing motor learning and show the potential of customized robotic perturbation forces for improving motor performance in personal activities and advancing neurorehabilitation techniques.**

I. INTRODUCTION

Robot-assisted training offers significant potential for enhancing motor skills and facilitating rehabilitation by providing highly accurate, sustained practice over long periods of time, automatically measuring progress, and producing a wide range of forces and motions. All of these can be implemented to facilitate learning, including the recovery of multi-joint arm coordination, which is frequently lost after stroke, spinal cord injury, or traumatic brain injury.

This study investigates how robot-generated forces, that augment errors based on individual trajectory deviation patterns, can enhance motor adaptation in upper-limb movements. We hypothesize that participants trained with the Error Field (EF) force will exhibit greater error reduction compared to training without it. This study employs an Error Field paradigm where the system collects real-time kinematic data from the participant's movements and generates forces designed to disturb the arm motion during the reaching task exercises [1], [2]. Conducted with 10 neurotypical subjects, it serves as a preliminary investigation for a larger study involving a broader range of reaching points and a stroke survivor population, along with [2] and [3]. Previous research suggest that subjects learn an internal model of the perturbing force field rather than simply learning an appropriate temporal sequence of muscle activation [4], [5]. The first experimental evidence of internal models in motor learning emerged from studies on reaching movements in force fields. These experiments revealed that subjects gradually developed the ability to predict and cancel the applied forces along their trajectories [6]. Furthermore, when the force field was suddenly removed the subjects exhibited after-effects, unintended deviations that provided evidence of an induced internal model adaptation [7]. These after-effects demonstrate that individuals do not simply react to perturbations but learn to predict their functional form, altering the dynamics of the controlled system [6].

In this study, we investigated how the customized Error Field force enhances motor learning in the upper limb, focusing on the two forces applied during the experiment:

1) *Curl force field:* A velocity-dependent perturbation that scales with movement speed to simulate spasticity-related motor impairments in the neurotypical population [8].
2) *Error Field force (EF):* A force based on the subject's trajectory errors, where the robot identifies hand deviations from the ideal path and applies force according to the error distribution. The EF paradigm operates on the principle that emphasizing errors during training enhances learning more effectively than directly correcting them [9].

The concept of error is central to this work and is defined as the deviation of the actual movement trajectory from the ideal trajectory during the experiment. The analysis focuses on the error amplitude (also known as extent error), which represents the difference between the hand's position at each time instant and the ideal trajectory profile, defined by the minimum jerk model [10][11].

II. MATERIALS AND METHODS

The experiment involved reaching tasks where participants were asked to reach a target appearing on the screen with their dominant hand while holding the end effector of the BURT robot, seen in Fig. 1.

A. Participants

Ten subjects ranging in age from 22 to 30 years participated in the study (9 right-handed and 1 left-handed). The inclusion criteria were that participants had to be 18 years or older, had no history of stroke, and were capable of providing informed consent. The exclusion criteria were

Supported by the National Institute of Health (NIH) grant R01NS053606

[1]Robotics Lab at Center for Neural Plasticity, Shirley Ryan AbilityLab, Chicago, IL, USA

[2]Richard and Loan Hill Department of Biomedical Engineering, University of Illinois Chicago, Chicago, IL, USA

[3]Dipartimento di Elettronica, Informazione e Bioingegneria, Politecnico di Milano, Milano, Italia

*Correspondence: bborghi@sralab.org, jpatton@sralab.org

participants with severe medical conditions, impairments in upper extremity movement, range of motion, strength, or coordination, or visual deficits that could have impacted the experiment. This study was approved by the Northwestern Institutional Review Board (STU00215000), and participants provided written informed consent.

B. BURT robot

The study employed the b.u.r.t.® upper-extremity robotic training (BURT) [12], a three-degrees-of-freedom robotic arm that provides real-time 3D haptic feedback and forces. This design transmits torque to the joints through a system of cables connected to motors, all of which are located at the robot's base. Its lightweight design and high backdrivability ensures efficient force transmission and control [13]. The system is user-friendly, easy to access and offers a large adjustable range of motion. The measurement apparatus involved the participant sitting on a chair placed in the same position relative to the screen and robot, with always the same head positioning with respect to the LookinGlass for consistency (Fig. 1).

C. LookinGlass

LookinGlass is the name of the augmented reality interface used with the BURT and was employed to project the reaching task game in a three-dimensional view [14], [15]. The system consists of two coupled panels: the top panel is a 3D television that generated the image, while the bottom panel is a see-through mirroring glass, allowing the user to see their hand behind it (Fig. 1). A pair of active 3D glasses enabled the perception of the 3D image. The main advantages of this system are its portability, ease of setup, and adjustability to the user's height, making it versatile for various applications.

D. Experimental protocol

The experiment involved a planar reaching task with a series of targets positioned within a defined 20 cm squared workspace, aligned horizontally in front of the user's chest, allowing free arm movement. Targets were sequentially generated using a random walk pattern, constraining movements to two sets of three directions, classified as practiced and unpracticed. These directions, visible in the colored radial arrows in Fig. 1, Fig. 2 and Fig. 3, represented the minimum number of movement directions to ensure adequate plane exploration. The experiment consisted of 560 trials, with each requiring a straight 10 cm hand movement from a starting position to a target. To mitigate muscle fatigue and maintain performance, every 15th trial there was a rest period with no movement required, lasting up to a minute and a half. The 560 trials were divided into nine phases, each serving a distinct purpose in the study, as detailed below and visualized in Fig. 2.

1) *Familiarization:* This phase consisted of the first 32 movements in the practiced directions, exploring the workspace without any applied forces. It allowed the participant to get familiar with the robot and the visual interface.
2) *Unpracticed Intermittent Exposure:* Involved 32 movements in the unpracticed directions. A curl force was applied intermittently to one randomly selected movement in each group of five consecutive movements.
3) *Baseline:* Consisted of 16 reaching movements in the practiced directions, without any perturbation forces.
4) *Intermittent Exposure:* 160 trials in the practiced directions with the curl force applied to one randomly selected trial in each group of five consecutive trials.
5) *Training:* This phase differentiated the EF and Control group protocols as follows: in the EF group, the EF force was applied in addition to curl force in 190 randomly selected trials, while the simple curl force trials were still present across the phase. Additionally, some trials had no force applied. In contrast, the Control group received only the curl force, with no EF force applied.
6) *Post Force-On:* 16 trials in the practiced directions with the curl force always on.
7) *Unpracticed Post Force-On:* 16 movements in the unpracticed directions with the curl force always on.
8) *Post Force-Off:* 16 trials in the practiced directions with no force.
9) *Unpracticed Post Force-Off:* 16 trials in the unpracticed directions with no force applied, marking the end.



Fig. 1. Experimental set-up showing the participant holding the BURT's robotic handle while performing the task, displayed on the LookinGlass screen via 3D glasses. The multi-colored radial arrows on the right represent movement directions performed during the experiment, with blue, yellow, and red for practiced directions and green, orange, and purple for unpracticed directions. The bottom right plot shows a subject's reaching trial example with forces on, with the hand icon marking the start position, the trajectory ending at the target position, a dashed line for the ideal path, and the actual movement shown.

E. Intervention

The robot program was developed in Unity game engine, providing both a graphical front-end and algorithm back-end. In order to perform the experiment correctly, subjects were instructed to perform the 10 cm target reaching movement with a quick launch speed to prevent unnatural muscle contraction, which could affect the feed-forward motor command essential to the study. Then a color-based visual feedback at the target indicated whether their peak launch speed fell within the 0.28–0.44 m/s desired range, where range values have been determined from aggregate of pilot data based on the velocity-dependent curl force magnitude produced. During the experiment participants first experience a velocity-dependent curl force field, designed to simulate the spasticity-related conditions by inducing velocity-triggered trajectory deviations resembling involuntary muscle contraction. They were randomly assigned to two groups: the Control group, which received only the curl force field, and the Error Field (EF) group, which experienced both the curl force field and the additional EF (training) force. Initially, the curl force field was applied intermittently in a semi-randomized pattern, while during the training phase, it was consistently applied to most movements. The curl force field f_C was calculated as follows:

$$f_C = B\dot{x} = \begin{bmatrix} 0 & 0 & -\lambda \\ 0 & 0 & 0 \\ \lambda & 0 & 0 \end{bmatrix} \begin{bmatrix} \dot{x_1} \\ \dot{x_2} \\ \dot{x_3} \end{bmatrix} \tag{1}$$

where λ is a constant value that regulates the environment's viscosity (calibrated to ensure the total generated force does not exceed 20 Newtons), and $\dot{x}$ represents the velocity, obtained as a derivative of the position along the three spatial directions. When the curl force field is applied during a specific trial, it remains active for the entire duration of the movement. Since this force depends on velocity, it is unpredictable because when you first visualize the target and prepare to start the movement, the velocity and thus the force is zero, preventing the upper-limb's pre-compensation and consequent involuntary contraction.

The Error Field force $f_T(t)$ is defined as follows:

$$f_T(t) = \lambda p(t) e(t) \tag{2}$$

and unlike the curl force field, it is not velocity-dependent but instead it is proportional to the probability of error $p(t)$, the error matrix $e(t)$ and the viscosity factor λ, based on [1], [2], [16]. The Error Field force is intended to affect only the feed-forward component of the movement, and is therefore applied exclusively during the launch phase, approximated as the first 300 milliseconds following the movement onset in [17], [18].

F. Data analysis

Data analysis was performed in Matlab (MathWorks, Inc., Natick, MA), generating a file for each subject with detailed movement data, including timing, phase, arm position, target coordinates, velocities, applied forces, and trajectory errors. The analysis focused on error amplitude, measuring hand deviation from the ideal trajectory, as it effectively captures both position and velocity. Particularly, it was analyzed only the launch phase (first 300 ms from movement onset), in order to study the feed-forward control. To avoid skewing results computing the averages with near-zero values at movement onset, it was considered in the analysis only the maximum value of the errors. A decrease in error amplitude across trials would support the motor adaptation hypotesis, reflecting improved accuracy with practice in particular during the Training phase. The statistical analyses performed involved a paired t-test and a non-parametric bootstrap, with a 95% confidence interval and an α value of 0.05, with normally-distributed data.

III. RESULTS

The EF group exhibited a significantly higher error reduction during the Training phase compared to the Control group (black dots/circles in Fig. 3, early vs late training comparison), along with significantly larger induced after-effects (Fig. 4), demonstrating the efficacy of the exercise in enhancing motor control and validating the benefits of EF treatment for neuromuscular adaptation. The following sections present the key research questions and corresponding analyses to assess the effectiveness of the Error Field (EF) force.

A. Does the curl force field cause error?

To mimic the spasticity-related conditions observed in patients with motor deficits, we applied a velocity-dependent curl force. Its effectiveness was validated by the direct effects, which are errors increase when participants first encountered the perturbation, particularly observable during the Intermittent Exposure phases when the force field was intermittently activated. The amplified error amplitude in these phases, visible in the circled-dots in Fig. 2, highlights the perturbation's impact on movement trajectories.

B. Does the Error Field cause larger error reduction?

To evaluate whether the Error Field (EF) group exhibited greater learning due to the additional EF force during training, we analyzed error amplitude across trials. As shown in Fig. 3, the EF group (filled dots) demonstrated a greater error reduction during the Training phase compared to the Control group (circles). This reduction was significantly higher for the EF group (1.2 cm average) than for the Control group (0.27 cm average) across all movement directions (statistical p-value < 0.05), as seen in the early vs. late-training comparison (black dots vs. black circles).

Focusing on specific directions in the Training phase in Fig. 3 for the EF group, the forward direction (blue) showed a clear and substantial reduction in error, far outpacing the trend observed in the Control group, where performance actually worsened across the phase. In the back-right direction (yellow), the EF group demonstrated a high and fast error reduction, clearly visible in the descending regression curve. Interestingly, the Control group also exhibited a similar

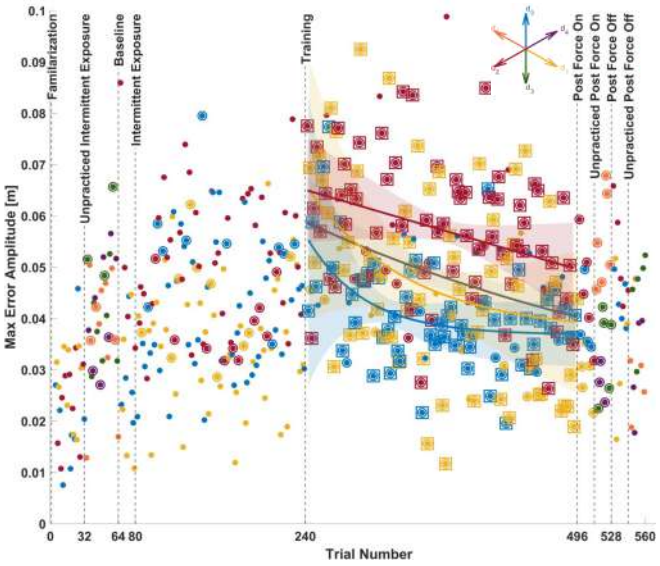


Fig. 2. Plot of the maximum error amplitude during the movement launch of each trial throughout the experiment, collected from one EF group subject. Each dot represents the maximum error per trial, with colors for directions and shape for the condition: simple dot (no perturbation), dot with a circle (curl force applied), and dot with both a circle and square (curl force + training force). During the Training phase, four exponential regression curves depict error trends, with shaded areas for standard deviation. The black curve represents the regression fit across all directions.

trend, despite being exposed only to the curl force field and expected to adapt less than the EF group. This suggested that the training force did not significantly enhance error reduction in the back-right direction. Therefore, the back-left direction, which showed the highest error amplitude on average, did not exhibit any error reduction throughout the training phase, indicating no learning in that direction. However, this result may have been influenced by one particular subject in the EF group, whose error in the back-left direction dramatically increased during the training phase, altering the overall trend for the group. This subject was treated the same as all other participants and was not excluded as an outlier, which may have influenced the overall tendency of the EF group in the back-left direction, especially given the small group sizes and high inter-subject variability. Fig. 2 clearly shows that the EF subject analyzed there demonstrated a noticeable error reduction in this direction (red), a pattern also observed in other subjects of the same group. This highlights the limited statistical power of studies with small sample sizes, which are highly susceptible to inter-subject variability.

Another effect of motor adaptation is illustrated in Fig. 4, which depicts the distribution of error with speed in the context of the speed-accuracy trade-off, originally introduced by Fitts' law [19]. The observed decreasing accuracy with increasing speed validates this principle. A comparison of force-on trials in the pre- and post-training phases (Intermittent Exposure and Post Force On) further highlights this effect. In fact, the top two subplots in that figure show that the EF group (left subplot) achieved greater accuracy improvements after training, particularly in trials within the targeted launch peak speed. This suggests that training with the Error Field force enhanced motor adaptation to the curl force field, resulting in more refined movement patterns under the spasticity-simulated condition, where the force field remained active in all analyzed trials. In other words, participants achieved higher accuracy in the presence of simulated spasticity. Additionally, trajectory rose plots reveal that the EF group demonstrated greater accuracy, with reduced movement deviations, especially in directions associated with higher learning, such as back-right and forward. While both groups showed similar accuracy improvements in the forward direction, the EF group exhibited a more pronounced improvement in the back-right direction. However, in the back-left direction, results were skewed by that one EF subject whose performance unexpectedly declined across training, disproportionately influencing the data for that direction.

Fig. 3 illustrates the pre- and post-training error data, during the Intermittent Exposure and Post Force On phases. This analysis revealed that the control group showed no improvement in terms of error amplitude, as the median error increased from pre- to post-training. In contrast, the Error Field group maintained a steady median error, which decreased slightly, though not enough to conclude a significant reduction.

C. Does training affect unpracticed directions?

Another critical aspect of motor adaptation was assessing the training's effects on unpracticed directions, which provided valuable insights into generalization, a key indicator of learning [8]. While the Training phase focused solely on the standard directions, subjects were also required to perform movements in unpracticed directions during both pre- and post-training scenarios. The Unpracticed phases shown in Fig. 2 (Unpracticed Intermittent Exposure, Unpracticed Post Force On and Unpracticed Force Off) illustrated a small but notable averaged reduction in error for these unpracticed directions, pointing toward potential generalization effects. However, the observed improvements were limited, likely due to the induced after-effects immediately following the sudden removal of the force field. These afte-effects deviated the trajectories and influenced the results, masking the potential benefits of training. A longer post-training phase with forces-off would have been ideal to allow the induced trajectory deviations to wash out and provide a clearer picture of how movement precision improved in unpracticed directions, offering stronger evidence of generalization and the lasting impact of training.

D. After-effects and washout

The experimental protocol included several no-force trials, even during the first phases with the forces on like Intermittent Exposure phase and Training phase. These no-force trials, particularly in the final phases of the experiment, were crucial for assessing residual changes in the internal model

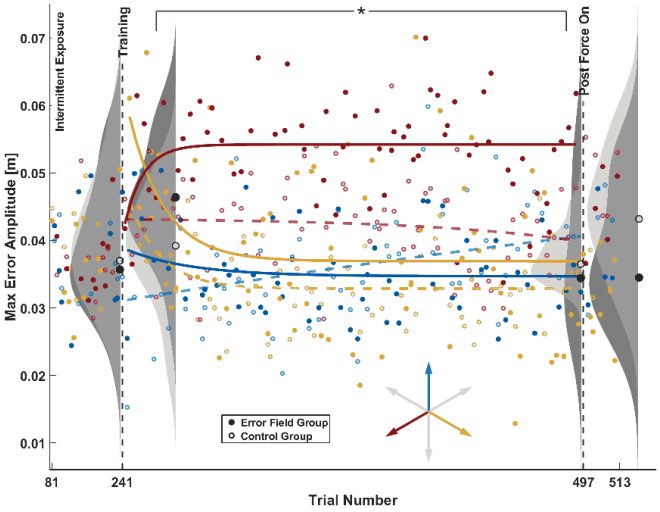


Fig. 3. Maximum error amplitude during the launch phase for all subjects across pre-training, training, and post-training. Each dot represents the median maximum error per trial, showing overall trends for each group. Solid dots and solid lines indicate the Error Field group, while semi-transparent circles and dashed-lines represent the Control group, with exponential regression fits. Colors differentiate the directions, with black dots/circles representing direction-independent analysis. The background shows a distribution analysis comparing pre- vs. post-training and early vs. late training. A horizontal line with an asterisk marks significant error reduction differences between groups.

induced by the training forces. By comparing these trials to their corresponding pre-training phases, any observed differences in error behavior could be attributed to the influence of the forces on the internal model, demonstrating the presence of after-effects as a phenomenon of anticipation of the force with an adjustment in the feed-forward joint torques [7]. This phenomenon was illustrated in Fig. 4, revealing a clear increase in error, manifested as a decline in accuracy, during the no-force trials between the pre- and post-training phases. This trend suggested the presence of after-effects and a shift in behavior consistent with the expected internal model adaptation. Notably, these after-effects were significantly bigger in the Error Field group compared to the Control group, as shown in the bottom plots of Fig. 4 (statistical p-value < 0.05). Comparing the Baseline and Post Force Off phases, identical no-force conditions before and after training, the blue dots (Baseline) showed higher accuracy than the red dots (Post Force Off) for the Error Field group (bottom-left subplot). The related rose plot, which displayed the median movement trajectories for all subjects in the practiced directions, further highlighted this effect. In the Error Field group, the post-training trajectories hooked in the opposite direction of the pre-training trend for some directions, strongly indicating induced after-effects. This decline in accuracy and the hooked trajectory could be attributed to the internal model adaptations to the training forces, supporting our hypothesis. However, the limited number of no-force trials at the end may have prevented washout of the after-effects, preventing re-adaptation.

IV. DISCUSSION

This research explores an adaptive training approach in robot-assisted motor learning, focusing on implicit learning through repeated hand-reaching movements under perturbing forces. These forces initially disrupt task performance, increasing execution error and prompting the motor control system to adapt and compensate for them. Over time, this adaptation resulted in improved movement trajectories as the participants learned to better control the movements after practice. The terms motor learning and motor adaptation are used interchangeably in this study, as in [5], described as the motor system continuously updating its model of the environment to compensate for external perturbations. This method targeted the nervous system to generate new motor commands, recalibrate control mechanism and enhance performance under force disturbances. This adaptive trick effectively encourages motor system adjustments, demonstrating the potential for improving motor learning outcomes. Furthermore, the study provides empirical support for existing theories of force-field adaptation and feed-forward control [7], [16], [8], applying them to practical, robot-assisted interventions.

Despite validating the main hypothesis, certain uncertainties remain. Specifically, the curl force field simulates spasticity-related motor impairments by introducing a velocity-dependent distortion, serving as a preliminary model. However, spasticity varies across individuals due to complex factors, such as afferent input to spinal motor neurons, which our model does not account for. Nonetheless, as shown by the direct effects in the Intermittent Exposure phases, the curl force field fulfilled its intended purpose of creating an unpredictable velocity-dependent perturbation. Additionally, the EF force was designed to act within the first 300 milliseconds of movement to minimize feedback contributions from the nervous system. Although the duration may have been sufficient for spinal reflexes to influence outcomes [7], [20], synchronization challenges arose due to differing frequencies between Unity's internal clock and the robot's controller clock, leading to minor delays in force application. While these delays were small, on the order of a few milliseconds, they compensated across sampling periods, ensuring no significant impact on the study's findings.

This experiment assumes that the small number of participants minimizes the impact of variability, though individual differences in movement execution and musculoskeletal biomechanics introduce inherent variability. Variations in arm configuration affect muscle usage and responses to applied forces, ranging from no reaction (the ideal scenario) to stiffness adaptations that alter mechanical properties. Different body biomechanics introduce mass, inertia, and strength variability between subjects, while handedness adds another source of uncertainty since a left-handed subject has a different arm biomechanical alignment with the movement directions compared to a right-handed subject. Additionally, the hour-long duration may cause fatigue, leading participants to adjust their posture, such as changing the distance

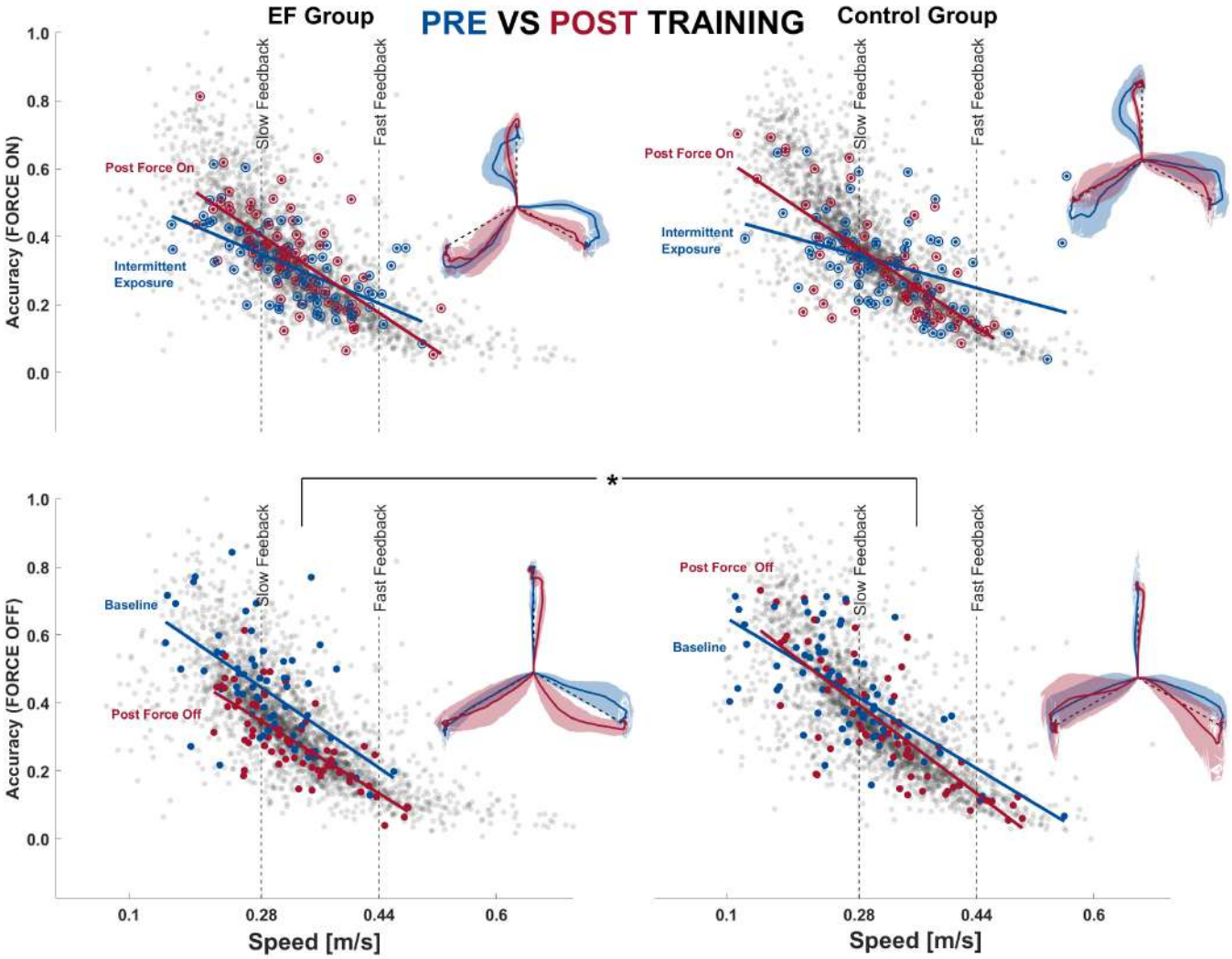


Fig. 4. Speed vs Accuracy trade-off plot shows that after training with the EF force, the EF group improved their reaching accuracy under the curl force disturbance and experienced higher after-effects when it was suddenly turned off. This figure shows the distribution of maximum error amplitude during launch relative to speed, comparing pre- and post- training for EF (left side) and Control (right) groups. The upper plots compare pre- and post-training under the curl force, while the lower plots show the same for no-force conditions. Each subplot includes trajectory plots illustrating movement deviations due to training. The x-axis represents speed, with vertical dashed lines marking the feedback range for slow and fast movements. The y-axis shows accuracy, scaled from 0 (the worst performance across all the trials for all the subjects) to 1 (the best), obtained as the inverse of error amplitude in a logarithmic scale. A horizontal black line with an asterisk marks statistical significance. Red and blue indicate pre- and post- training phases only and are not associated with movement direction.

between the elbow and body, further influencing movement patterns. These factors underscore the complexity introduced by individual-specific characteristics, such as arm configuration, force perception, and fatigue-induced adjustments. Recognizing and accounting for these influences is essential for accurately interpreting the results within the context of the experiment. The results obtained confirmed the main hypothesis, as shown in the previous sections. The EF force is effective, it induces a higher error by deviating the hand's trajectory when they are first interfaced, and then going on with the trials and familiarizing with the forces (conscious or not about the presence of a robot-generated perturbation) the subject starts to improve the performances and the error decreases. In Fig. 3 and the individual case in Fig. 2, we observed that the back-right movement shows a greater potential for learning, as indicated by a larger and faster reduction in error during the Training phase. Similarly, the forward movement also shows evidence of motor learning, and it exhibits the most significant discrepancy in learning rates between the two groups. This difference in learning can be attributed to the fact that anterior-posterior movements are more frequently performed in daily life, when we reach to grab objects on the table for example, making individuals more proficient at executing them and thus more resistant to perturbations. Additionally, the greater error observed in the back-left movement can be explained by the biomechanics of arm movement described by the stiffness ellipsoid: movements along the forearm's longitudinal axis tend to have

higher stiffness, while those perpendicular to it exhibit lower stiffness, making them more susceptible to the effects of perturbations [21].

Robot-assisted training offers the advantage of repeated, monitored practice over extended periods, progressively improving movement accuracy. Previous studies [22], [23] have demonstrated success in using robotics for rehabilitation, assessment, and training. Adaptive training serves as a promising addition to rehabilitation strategies. While conflicting methods exist for treating stroke and brain injuries, some advocating for assistance in error reduction in reaching movements and others for resistance, objective testing using robotic tools is still lacking. It remains unclear whether assistive or resistive forces are more effective, with this study focusing on the latter approach.

The significance of incorporating implicit learning through robot-assisted approaches is striking. This methodology enables individuals to acquire skills with reduced attention and motivation compared to explicit practice methods like pattern tracing. Notably, the concept of applying implicit learning techniques is now being explored in a preliminary manner within the context of post-stroke rehabilitation [24]. The process of implicit learning occurs unconsciously, without explicit awareness of what has been learned [25], and often does not demand full conscious attention. Moreover, the recall of implicitly acquired knowledge tends to be more automatic in nature [26]. Implicit learning is associated with distinct neural pathways [27], [23] that have evolved earlier than the brain regions involved in explicit learning [28]. To conclude, the personalized robotic training implemented in this study may provide an efficient way to induce motor learning that can be used as a guidance for rehabilitation, sport training or other general physical activities that involves motor control.

ACKNOWLEDGMENT

We would like to thank the Robotics Lab at Shirley Ryan AbilityLab, DEIB at Politecnico di Milano and BME department at University of Illinois Chicago. No conflicts of interest, financial or otherwise, are declared by the authors.

REFERENCES

[1] M. E. Fisher, F. C. Huang, V. Klamroth-Marganska, R. Riener, and J. L. Patton, "Haptic error fields for robotic training," in *2015 IEEE world haptics conference (WHC)*. IEEE, 2015, pp. 434–439.

[2] N. R. Aghamohammadi, C. Celian, V. Wojicik, B. Borghi, A. Ramirez, A. Cancrini, and J. L. Patton, "A case study of Error Fields: A three-dimensional personalized robotic therapy." Chicago, IL, USA: IEEE, May 2025, p. Accepted.

[3] A. Ramirez, N. R. Aghamohammadi, C. Celian, A. Cancrini, B. Borghi, and Patton, James L, "Do Motor Skills Learned in Isometric Training Generalize to Unpracticed Workspaces?" in *International Conference on Rehabilitation Robotics (ICORR)*. Chicago, IL, USA: IEEE, May 2025, p. Accepted.

[4] M. A. Conditt, F. Gandolfo, and F. A. Mussa-Ivaldi, "The motor system does not learn the dynamics of the arm by rote memorization of past experience," *Journal of Neurophysiology*, vol. 78, no. 1, pp. 554–560, 1997.

[5] F. Gandolfo, F. A. Mussa-Ivaldi, and E. Bizzi, "Motor learning by field approximation." *Proceedings of the National Academy of Sciences*, vol. 93, no. 9, pp. 3843–3846, 1996.

[6] S. M.-I. Reza Shadmehr, *Biological learning and control*. MIT press, 2012.

[7] J. L. Patton and F. A. Mussa-Ivaldi, "Robot-assisted adaptive training: custom force fields for teaching movement patterns," *IEEE Transactions on Biomedical Engineering*, vol. 51, no. 4, p. 636–646, 2004.

[8] R. Shadmehr and F. A. Mussa-Ivaldi, "Adaptive representation of dynamics during learning of a motor task," *Journal of neuroscience*, vol. 14, no. 5, pp. 3208–3224, 1994.

[9] J. L. Patton, M. E. Stoykov, M. Kovic, and F. A. Mussa-Ivaldi, "Evaluation of robotic training forces that either enhance or reduce error in chronic hemiparetic stroke survivors," *Experimental brain research*, vol. 168, pp. 368–383, 2006.

[10] T. Flash and N. Hogan, "The coordination of arm movements: an experimentally confirmed mathematical model," *Journal of neuroscience*, vol. 5, no. 7, pp. 1688–1703, 1985.

[11] R. Shadmehr and S. P. Wise, *The computational neurobiology of reaching and pointing: a foundation for motor learning*. MIT press, 2004.

[12] W. T. Townsend, D. Wilkinson, A. Jenko, J. Leland, A. Ananthanarayanan, and J. Patton, "Multi-active-axis, non-exoskeletal rehabilitation device," Nov. 20 2018, uS Patent 10,130,546.

[13] T. Ishida and A. Takanishi, "A robot actuator development with high backdrivability," in *2006 IEEE Conference on Robotics, Automation and Mechatronics*, 2006, pp. 1–6.

[14] E. Hajissa, C. Celian, K. O. Thielbar, F. Kade, Y. A. Majeed, and J. L. Patton, "Stroke rehabilitation with distorted vision perceived as forces," in *2019 IEEE 16th International Conference on Rehabilitation Robotics (ICORR)*. IEEE, 2019, pp. 644–647.

[15] J. J. Patton, "New vr technologies for sensorimotor rehabilitation," *Transactions of Japanese Society for Medical and Biological Engineering*, vol. 51, no. Supplement, pp. M–99, 2013.

[16] N. R. Aghamohammadi, M. F. Bittmann, V. Klamroth-Marganska, R. Riener, F. C. Huang, and J. L. Patton, "Error fields: personalized robotic movement training that augments one's more likely mistakes," *Scientific Reports*, vol. 15, no. 1, p. 4201, 2025.

[17] E. R. F. Crossman and P. Goodeve, "Feedback control of hand-movement and fitts' law," *The Quarterly Journal of Experimental Psychology*, vol. 35, no. 2, pp. 251–278, 1983.

[18] R. S. Woodworth, "Accuracy of voluntary movement." *The Psychological Review: Monograph Supplements*, vol. 3, no. 3, p. i, 1899.

[19] P. M. Fitts, "Cognitive aspects of information processing: Iii. set for speed versus accuracy." *Journal of experimental psychology*, vol. 71, no. 6, p. 849, 1966.

[20] N. Hogan, "Mechanical impedance of single-and multi-articular systems," *Multiple muscle systems: Biomechanics and movement organization*, pp. 149–164, 1990.

[21] D. W. Franklin, G. Liaw, T. E. Milner, R. Osu, E. Burdet, and M. Kawato, "Endpoint stiffness of the arm is directionally tuned to instability in the environment," *Journal of Neuroscience*, vol. 27, no. 29, pp. 7705–7716, 2007.

[22] P. S. Lum, C. G. Burgar, D. E. Kenney, and H. M. Van der Loos, "Quantification of force abnormalities during passive and active-assisted upper-limb reaching movements in post-stroke hemiparesis," *IEEE Transactions on Biomedical Engineering*, vol. 46, no. 6, pp. 652–662, 1999.

[23] H. I. Krebs, N. Hogan, M. L. Aisen, and B. T. Volpe, "Robot-aided neurorehabilitation," *IEEE transactions on rehabilitation engineering*, vol. 6, no. 1, pp. 75–87, 1998.

[24] J. Patton, F. Mussa-Ivaldi, and W. Z. Rymer, "Altering movement patterns in healthy and brain-injured subjects via custom designed robotic forces," in *2001 Conference Proceedings of the 23rd Annual International Conference of the IEEE Engineering in Medicine and Biology Society*, vol. 2. IEEE, 2001, pp. 1356–1359.

[25] C. A. Seger, "Implicit learning." *Psychological bulletin*, vol. 115, no. 2, p. 163, 1994.

[26] R. A. Magill, "Knowledge is more than we can talk about: Implicit learning in motor skill acquisition," *Research Quarterly for Exercise and Sport*, vol. 69, no. 2, pp. 104–110, 1998.

[27] S. T. Grafton, E. Hazeltine, and R. B. Ivry, "Abstract and effector-specific representations of motor sequences identified with pet," *Journal of Neuroscience*, vol. 18, no. 22, pp. 9420–9428, 1998.

[28] A. S. Reber, F. F. Walkenfeld, and R. Hernstadt, "Implicit and explicit learning: individual differences and iq." *Journal of experimental psychology: Learning, memory, and cognition*, vol. 17, no. 5, p. 888, 1991.

Advancing Soft Rehabilitation Robotics: Evaluating the Stress and Strain Generation Capabilities of Stacked Dielectric Elastomer Actuators (SDEAs)

Sahel Mohammadi Ghalehney
Department of Biomechanics
University of Nebraska Omaha
Omaha , USA
smohammadi@unomaha.edu

Vahid Mohammadi
Department of Biomechanics
University of Nebraska Omaha
Omaha , USA
vmohammadi@unomaha.edu

Mohammad Tajdani
Independent Researcher
University of Tehran
Tehran , Iran
mohammadtajdani@gmail.com

Ahad Behboodi
Department of Biomechanics
University of Nebraska Omaha
Omaha , USA
abehboodi@unomaha.edu

***Abstract*— To improve exoskeleton acceptability, there is increasing interest in soft actuators that operate safely near the human body. Dielectric elastomer actuators (DEAs) are particularly promising due to their silent operation and high energy density. In this study, we evaluate the stress and strain generation capabilities of the latest version of commercially available stacked dielectric elastomer actuators (SDEA-1550s) for rehabilitation robotics. This demand for soft, lightweight, and noiseless actuators is especially critical in pediatric applications, where current systems often lack a natural feel and suffer from low user acceptance. We investigated the pushing and pulling forces of SDEAs under two conditions: isometric contraction and free-standing. In isometric tests, peak forces reached 32.82 N and 28.75 N at 1200 V for compressive (pulling) force and tensile (pushing) force, respectively. In the free-standing setup at 800 V, the actuators achieved 1.61 mm of displacement in 0.038 seconds, with a peak strain rate of 4232.4 %/s, demonstrating rapid contraction. Notably, this study reports, for the first time, the capability of SDEAs to generate bidirectional force—both actively (pulling) and passively (pushing)—further differentiating their performance from other alternative actuators. These results highlight the enhanced stress and strain generation of SDEAs, reinforcing their potential as artificial skeletal muscles. Their integration into rehabilitation robotics—including biomimetic exoskeletons—aims to improve functionality and user experience, particularly in pediatric rehabilitation.**

Keywords— Rehabilitation robotics, Stacked dielectric elastomer actuators (SDEAs), Actuator performance, Artificial skeletal muscles

I. INTRODUCTION

Soft robotics represents a transformative advancement in rehabilitation robotics and exoskeleton design, enabling safer and more adaptive human-robot interactions [1]. The development of actuators that replicate natural muscle movements is critical for enhancing mobility and functionality in individuals with musculoskeletal impairments. Various types of soft actuators have gained attention in this context, including pneumatic actuators, hydraulic systems [2], flexible pumps [3,4], shape memory polymers [5], gel-based actuators [6,7], paper-based soft robots [9], and dielectric elastomer actuators (DEAs) [8-11].

Conventional actuators, such as servo motors and pneumatics, are often bulky, acoustically noisy, and heavy, which can hinder user comfort and compliance in orthotics and rehabilitation robotics. For better adoption of these systems, it is crucial to prioritize natural feel, which is characterized by lightweight, quiet operation, softness, and form factor resembling natural skeletal muscles. Accessibility also plays a key role in the development of such devices. Dielectric elastomer actuators (DEAs), which can be configured as artificial skeletal muscles [12], can potentially replace conventional actuators or augment their performance and natural feel in rehabilitation and assistive robotics. DEAs exhibit significant properties, including power efficiency, high cycle life, and low energy consumption. They provide a lightweight, soft, and silent alternative, enhancing the natural feel and overall user experience in rehabilitation robotics [13,14]. DEAs are mechanically compliant capacitors consisting of two stretchable electrodes sandwiching an elastic dielectric [15]. Upon applying DC voltage to the electrodes, electrostatic forces, through a phenomenon called Maxwell pressure, compress the dielectric, the elastomer, and thereby compress it longitudinally and expand its area [16,17]. DEAs typically require high voltages in the kilovolt range to generate sufficient electrostatic forces for effective actuation, presenting practical challenges. However, as capacitive devices, DEAs draw minimal current (under 10 mA), allowing for safe operation, below 20 mA per Underwriters Laboratories (UL) Safety Standard, despite their high voltage requirements [18]. Their performance is influenced by viscoelastic effects, where increasing strain and strain rate lead to higher internal stress, slowing response time and complicating precise control. [19]. Despite these drawbacks, there has been limited exploration of DEAs in rehabilitation

Table 1. Reported Mechanical Properties of CT-SDEA and SDEAs-1550 at 1200 V [22].

	CT_SDEA	SDEA-1550
Max Force (N)	10.01 ±0.2 N	25.84 ±1.5
Max Strain (%)	3.3 %	10.9 %
Shortening (mm)	1.3 ± 0.8	5.46 ± 0.48
Stress (Kpa)	35	111
Dimension (mm^3)	39 × 17 × 17	15 × 15 × 50
Weight (gr)	11.3	14



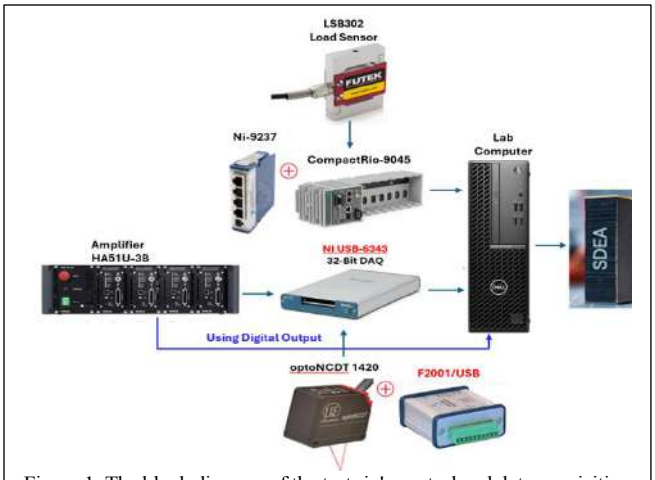


Figure 1. The block diagram of the test rig's control and data acquisition system is shown. NI MAX was utilized to manage the HV amplifier, which powered the SDEAs, and to capture force data through the NI 9237 module. Displacement measurements were directly recorded using a laser displacement sensor, with data acquisition handled via the Micro-Epsilon SensorTOOL software.

robotics, and research remains preliminary. Recently, the introduction of stacked dielectric elastomer actuators (SDEAs) has opened new opportunities for their application as "artificial skeletal muscles" in rehabilitation robots and powered exoskeletons.

Kovacs et al. [20] developed an SDEA configuration which closely mimics the properties of human skeletal muscles more effectively than other soft actuators. This design features multiple layers of thin DEAs stacked together, where each layer functions like a sarcomere in a myofibril. The original design of these tensile actuators was able to generate 32 N of isometric force and 15% strain while supporting an 11 N load. These outstanding performances led to the commercialization of SDEAs, making them the first commercially available DEAs [21]. We assessed the electromechanical characteristics of these commercially available SDEAs to determine their suitability for rehabilitation robotics, particularly in applications requiring numerous repetitive contractions to assist individuals with musculoskeletal impairments [22]. The earlier actuators demonstrated a high cycle life exceeding 50 million cycles, as reported by the manufacturer, making them well-suited for such applications. The earlier version exhibited a swift electromechanical delay of 21 ms and a strain rate of 660% per second, delivering a force of 21.74 N with a power-to-mass ratio of 426 W/kg [21]. Additionally, they achieved a longitudinal strain of 3.3% while consuming only 39 µA in steady-state operation. The combination of quick response times, minimal electromechanical delay, and high strain rates suggests their suitability for integration into closed-loop control systems. Furthermore, their robust force output, rapid response, high power-to-mass ratio, and low energy requirements underscore their potential for exoskeleton applications [20, 21]. These features position SDEA as an emerging viable option for creating artificial skeletal muscles, particularly in biomimetic rehabilitation robots.

Recently, SDEA manufacturing quality has improved substantially; thus, we assessed the latest commercial SDEAs (which we call SDEA-1550) and compared them with earlier versions from CTsystems (refer to Table 1). The SDEA-1550 actuator evaluated in this study is commercially available and manufactured by, Dätwyler Schweiz AG (Schattdorf, Switzerland) [23]. Our analysis revealed significant improvements in strain and stress performance, with stress values increasing by over 300%, to 111KPa, approaching levels comparable to human biceps. The data, collected for both single SDEA and 1x3 configurations, indicated enhanced responsiveness under high-voltage conditions. These advancements in muscle-like properties—such as longitudinal contraction, softness, and silent operation—further validate SDEAs as promising alternatives to biological muscles, highlighting their potential for next-generation rehabilitation robots [22].

Here, we shared the second round of these assessment results. Our experiments measured key performance indicators, including maximum pulling and pushing forces. In our testing setup, when the actuator is compressed, it exerts a pulling force on the attached force sensor, and when it expands, it exerts a pushing force. To clarify, we consistently refer to these as compressive (pulling) force and tensile (pushing) force throughout the manuscript. This manuscript presents the first evaluation of SDEA's capability to generate tensile force by leveraging its inherent elastic properties. Additionally, we evaluated the active and passive force generation under varying extension and compression levels using the Length-Tension analysis.

II. Method

A. Testing Setup

The performance of the SDEA-1550 was evaluated under two distinct conditions: isometric contraction and free-standing. A specially designed test rig, reported in [22] was utilized for this assessment, comprising the following components and is shown in (Fig. 1):

1) An aluminum mainframe, 2) A laser displacement sensor, 3) A load cell, 4) Precision translation stages, 5) High-Voltage (HV) fast amplifier, 6) National Instruments (NI) data acquisition (DAQ) boards

A laser displacement sensor (model ILD 142025 from Micro-Epsilon, Ortenburg, Germany) and F2001/USB, were used to measure the longitudinal contraction displacement of the actuators, providing high precision with a resolution of 1 µm to ensure accurate readings. These measurements were recorded using Micro-Epsilon's sensorTOOL software (version 1.12.0.1370).

A load cell (model LSB302 from FUTEK Advanced Sensor Technology, Inc., Irvine, CA, USA) was used to measure both active and passive forces, with a maximum capacity of 25 lb. The force data were obtained through an H-Bridge Input Module (NI 9237 from National Instruments, Austin, TX, USA), which was connected to a National Instruments compact RIO (cRIO-9045).

Three precision translation stages, each with a graduation of 10 µm and an axial load capacity of 102 N, are featured in the test setup. These stages allowed for precise positioning of the load cell, ensuring accurate alignment and load application (Fig. 2a).

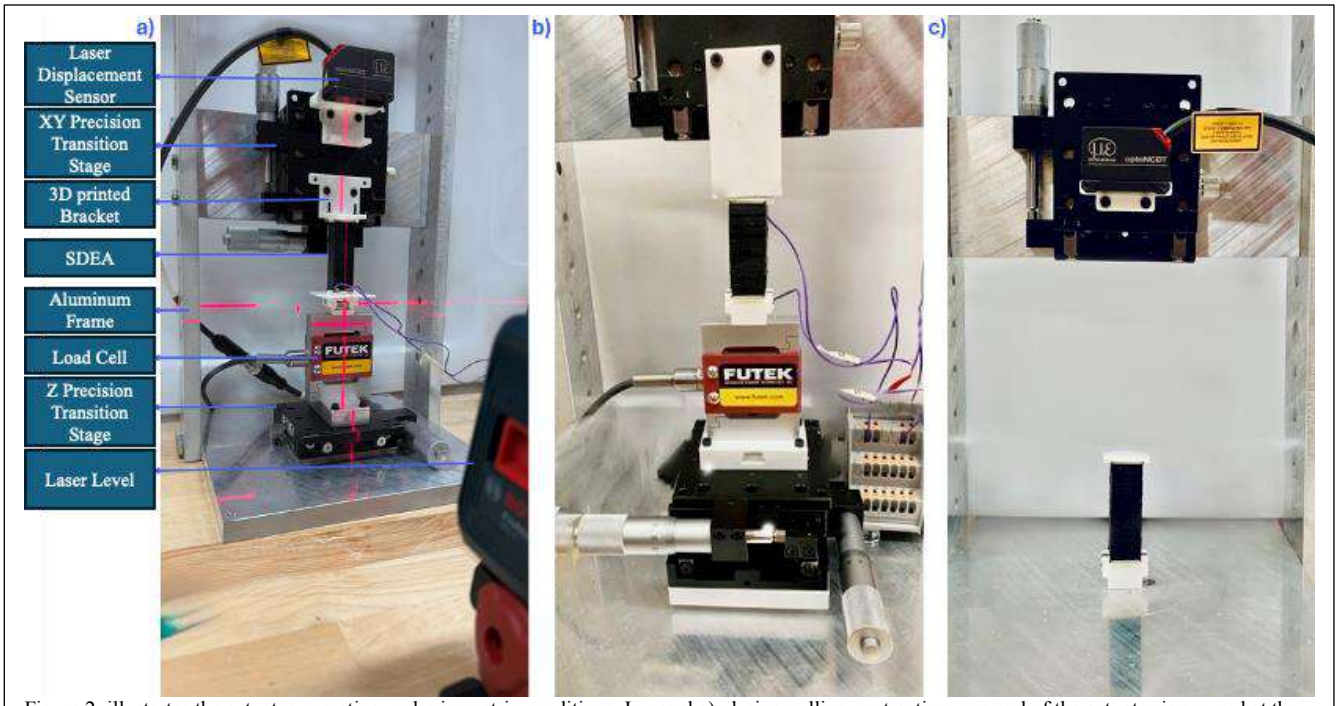


Figure 2. illustrates the actuator operating under isometric conditions. In panel a), during pulling contraction, one end of the actuator is secured at the bottom, and the other end is connected to a load cell. In panel b), for pushing contraction, the actuator's end is attached to a load cell, while the other end remains unanchored until voltage is applied. c) a free-standing configuration. An actuator is secured at the base and subjected to 1200 volts. The resulting contraction is then measured with the aid of a laser displacement sensor.

A High-Voltage (HV) fast amplifier (model HA51U-1.6P10-3 from hivolt.de, Hamburg, Germany) was employed to supply the necessary driving voltage to the CT-SDEAs, with a slew rate of 80 V/µs. The HV amplifier was controlled via an NI DAQ Data Acquisition board (NI USB-6343 from National Instruments, Austin, TX, USA).

NI MAX (version 2024 Q2) was used to generate control voltages ranging from 0.625 to 7.5 V, which were then amplified to a range of 100 to 1200 V by the HV amplifier, with a 1:160 amplification ratio.

The integration of these high-precision sensors and advanced data acquisition systems enabled a thorough assessment of the SDEAs' performance across various loading conditions, providing comprehensive insights into their operational capabilities and characteristics.

1) Isometric Condition

In this test, the length of the actuators was kept constant throughout the measurements. This testing setup was used to measure the blocked force for both compressive (pulling) and tensile (pushing) forces (Fig. 2a, b).

In our earlier research we measured the compressive force generation of the SDEA-1550 for 10 samples, (Fig. 3) [23]. For these measurements, the SDEAs were maintained at their rest length of 50 mm, under no compression or extension at the beginning of each trial. The SDEAs were mounted vertically, with one end fixed to a rigid frame and the other end attached to a load cell. Precise alignment was ensured using three precision translation stages: two for adjustments along the X and Y axes at the top and one for Z-axis adjustments at the base (Fig. 2a). Additionally, a Cross-Line Laser (Bosch GLL 2) was used to assist with precise vertical and horizontal alignment [22]. Forces generated at various activation voltages from 0V to 1200V were recorded by the load cell. To measure the tensile (pushing) force, the length of the activated actuator (the length after the application of voltage) was kept constant throughout the measurement. The activation voltage used was the same as that applied during the compressive (pulling) force measurements.

This setup ensured accurate measurement of the tensile force. The Y-axis translation stage was first adjusted to position the actuator neutrally, free from tension or compression. Upon applying voltage, the actuator compressed. Next, the load cell was lowered, using the translation stage until it touched the top endplate of the actuator without compressing it further. To ensure that no external force was applied during this process, the load cell output was continuously monitored while the upper endplate of the actuator made contact with the load cell. Upon releasing the voltage, the elastomer layers of the actuator attempted to return to their initial, non-compressed form, generating a substantial amount of passive/elastic force. This force was recorded by the load cell while blocking any movement. The peak compressive force generated by the SDEAs at activation voltages ranging from 23.15 N to 28.75 N was examined and reported [22].

Length-tension relationship: To assess the length-tension characteristics of the SDEA, we measured the force generation while the actuator was compressed and extended at various levels. The actuator was incrementally adjusted to different lengths, covering a range from 95.5% to 105% of the original length, to simulate both compression and extension. The passive (elastic) force was recorded at each length without applying any activation voltage. Note that as the actuator passive changes length, the elastic components (dielectric elastomers) want to return back to their original

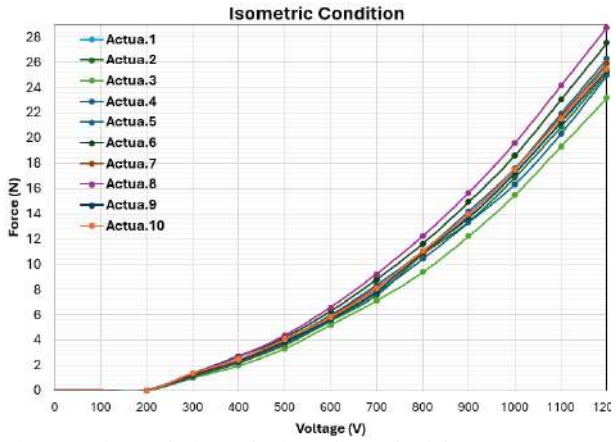


Figure 3. The graph shows the force that each of the 10 actuators can generate in isometric condition at voltages up to 1200 V [21].

forms. Subsequently, the active force was determined by applying voltage and subtracting the baseline passive force from the total generated force. This approach provided a comprehensive view of the SDEA-1550's ability to generate force under various compressive and tensile loads. This is crucial for applications where artificial muscles must replicate the force modulation required for varying load-bearing tasks, such as assisting ankle motion during gait [17,23].

2) Free-Standing condition (measuring strain-rate)

In the free-standing condition (Fig. 2c), the actuator was securely fixed in a vertical orientation by screwing its lower endplate to the base of the test rig's mainframe to maintain stability throughout the test. At the same time, the upper endplate was free to move. In our earlier research, we measured the displacement for each applied voltage in both single SDEA and 1x3 configurations using a laser displacement sensor [22]. The results showed that at 1200 V, displacements ranged from -6.15 mm to -4.4 mm, with an average displacement of -5.45 ± 0.47 mm for the single SDEA and 16.44 mm for the 1x3 configuration [22]. For the current study, we measure the time required to achieve maximum displacement (strain), and the strain rate (mm/s) at 1200 V to assess contraction speed. The strain rate is calculated using the recorded charge time and the measured maximum longitudinal strain. The laser displacement sensor positioned directly above the SDEAs, beaming on the upper endplate, to measure the displacement (Fig. 2c).

III. Results

Isometric condition: The compressive force generation measured in our previous study [22] and the measured tensile force at various voltages are shown in Fig. 4. The results demonstrate that both forces increased quadratically as the voltage rose from 0 to 1200 V, in agreement with the theoretical Maxwell pressure-voltage relationship, Equation (1). Notably, at 800 V, the SDEA-1550 generated a force comparable to the maximum force output of CT-SDEA at 1200 V, highlighting its improved force efficiency at lower voltages. At 1200 V, the maximum operating voltage (refer to Table 1), the highest recorded performance was achieved, with the tensile force reaching 32.824 N and the compressive force peaking at 28.75 N. This trend follows the theoretical Maxwell stress model, which predicts that force generation scales quadratically with applied voltage. Equation (1) describes this parabolic relationship between Maxwell pressure (P) and voltage (V), where ε and ε₀ represent the polymer's permittivity and vacuum permittivity, respectively, and d denotes the thickness of the dielectric material [22].

$$P = \varepsilon\varepsilon_0 \left(\frac{V}{d}\right)^2 \quad (1)$$

Strain-rate under free-standing conditions at 1200V: (Fig. 5a) presents displacement (mm) versus time (seconds) for five actuators, illustrating their rapid response characteristics under free-standing conditions. All actuators achieve 30% of their full displacement within approximately 0.038 seconds, demonstrating high responsiveness and rapid acceleration, which is crucial for applications requiring quick movements. Subsequently, the actuators reach 80% of their full displacement in around 1.48 seconds, highlighting their efficiency in achieving significant motion promptly. The displacement then progresses through 90% and 100% at a reduced rate, eventually reaching a steady state as internal resistance counteracts the applied force. Across all tested actuators, the final displacement values show minor variations, ranging between 4.95 mm and 5.15 mm. (Fig. 5b) depicts the strain rate (%/s) as a function of strain reported as a percentage of the resting length over time (%). The strain rate peaks at 20% displacement, reaching 8935 %/s, corresponding to the rapid initial phase observed in (Fig. 5a). Beyond 20%, the strain rate gradually decreases to a steady 3%/s at 100%, attributed to material resistance. This trend emphasizes the actuator's transition from rapid contraction to stable motion, which is essential for maintaining controlled, consistent movement across the full displacement range.

The Length-Tension curve (Fig. 6) shows the active and passive force generation capability of the SDEA under different levels of extension/compression. Although small, the more extended the SDEA, the less force it could generate. The SDEA showed a substantial passive force under compression and extension due to the elasticity of the dielectric layers, i.e., silicone elastomer (Fig. 6, grey trace). The passive force ranged (-14.9 N to 13.85 N) at 5%

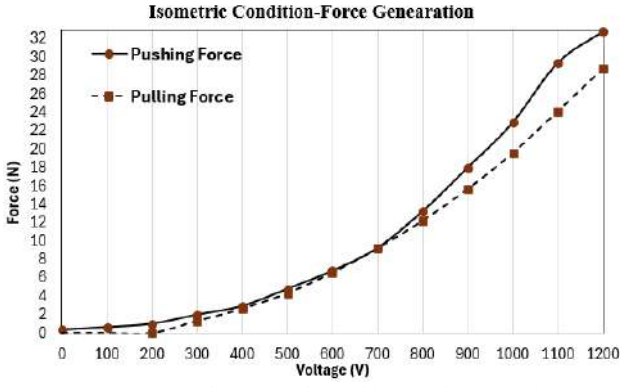


Figure 4. Isometric Condition, tensile (pushing), and compressive (pulling) force generation at voltages up to 1200 V.

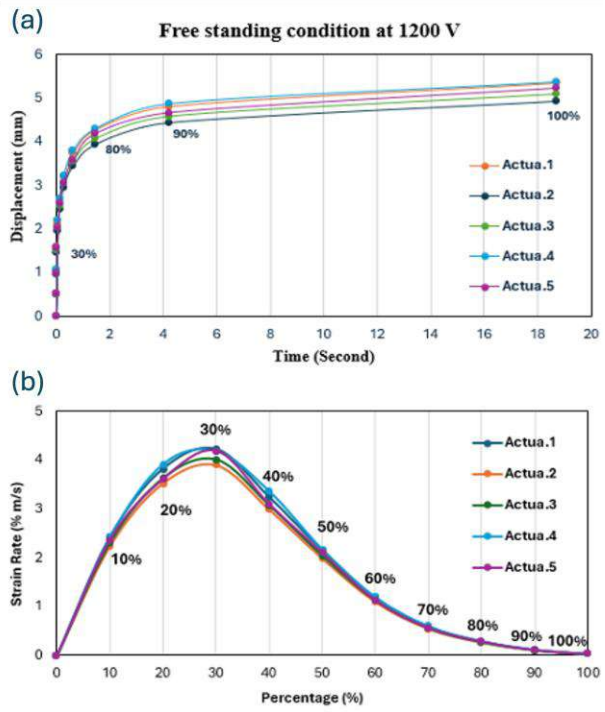


Figure 5. (a) Displacement over time, and (b) strain rate of the actuator as a function of displacement percentage under 1200 V.

compression and extension, respectively. along with the maximum total force (25.55 N)

IV. Discussion

The objective of this research was to assess the stress and strain generation capabilities of SDEA-1550 as a potential actuator for use in rehabilitation devices. Our tests, conducted under both free-standing and isometric conditions, highlighted the key performance metrics of SDEAs, including their ability to generate substantial tensile forces and their rapid response within the first 80% of displacement. These characteristics are particularly crucial for rehabilitation applications, such as lower-limb exoskeletons designed to enhance walking performance. Isometric testing demonstrated parabolic increases in both compressive and tensile forces as the voltage increased, with peak forces of 32.82 N and 28.75 N recorded at 1200 V, respectively. This strong force generation can be coupled to amplify joint moments and range of motion, making SDEAs well-suited for exoskeleton applications.

Additionally, SDEAs balance high stress, moderate strain, and rapid response, while maintaining long-term durability. Their commercial availability and exceptionally long cycle life (up to 70M cycles) provide them ideal for prosthetic limbs, rehabilitation robotics, and orthotic devices [20]. Furthermore, their muscle-like compliance and silent operation enhance user comfort, making them particularly suitable for exoskeletons and orthotic devices [12]. The layered composite structure enables them to withstand cyclic tensile loads while maintaining structural integrity, where applied voltage generates Maxwell stress, leading to contractive motion. Since the dielectric film only experiences compressive stress, tensile failure is prevented, enhancing fatigue resistance essential for long-term use. Compared to other soft actuators, such as hydraulically amplified self-healing electrostatic (HASEL) actuators and PVC gel actuators, SDEAs offer significant advantages. HASEL actuators provide high force and strain rates, but their extremely high voltage requirement (up to 40 kV) and snap-through behavior complicate integration into wearable rehabilitation devices. Additionally, their shorter cycle life (158k cycles) limits their long-term reliability. PVC gel actuators, while operating at lower voltages, exhibit moderate force and strain output but require bulky packaging, which reduces their practicality for compact rehabilitation applications. Their shorter lifespan (170k cycles) also poses limitations [12].

SDEAs demonstrate their suitability for rehabilitation robotics by providing biomimetic movement. The passive force, which varies with actuator length, can be effectively utilized in agonist-antagonist configurations, mimicking the elastic components of muscles. This feature, representing the elastic components in the Hill muscle model [22], is particularly beneficial when actuators work in parallel with muscles to augment their function, requiring performance that closely resembles natural muscle behavior. Furthermore, the minimal variation in active force generation across compressed and extended states highlights the reliability of SDEAs under varying load conditions. Leveraging their substantial force output to magnify displacement through mechanical linkages further enhances their versatility, making SDEAs ideal for a wide range of rehabilitation applications, including walking assistance [16], upper extremity prosthetics and orthotics [24,25], and even humanoid robots [26].

Our findings demonstrate that SDEAs can be a viable alternative to conventional actuators for wearable rehabilitation devices. We are currently applying SDEAs in the design of dielectric elastomer-powered ankle-foot orthoses (DE-AFOs) for children with cerebral palsy (CP), Fig. 7 [16]. These biomimetic exoskeletons aim to promote natural ankle motion by providing mechanical assistance during walking.

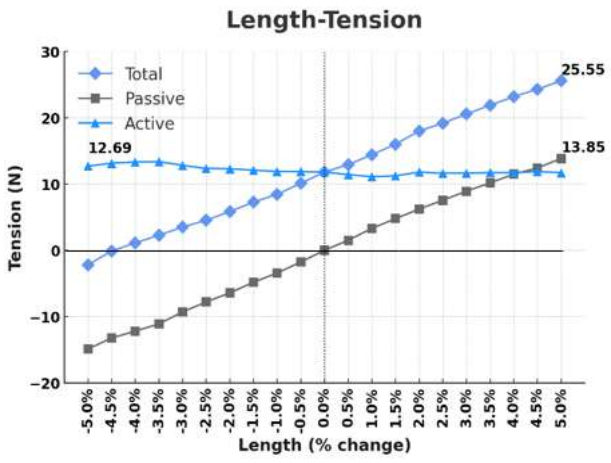


Figure 6. The Length-Tension curve illustration of the active and passive force generation of a representative SDEA during compression and extension. The 0.0% point represents the actuator's normal length, with positive values indicating extension and negative values indicating compression, emphasizing the role of material elasticity in force generation.

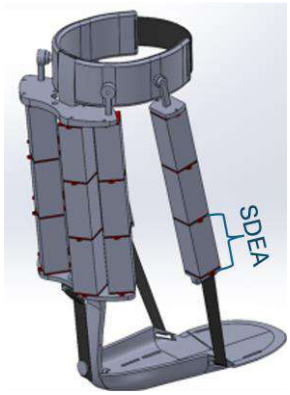


Figure 7. Our robotic ankle foot orthosis, DE-AFAFO, is powered by SDEA-based artificial muscles [16].

V. Conclusion

In conclusion, this study evaluated the tensile force generation, strain rate, and length-tension curve of commercially available SDEAs to determine their suitability for rehabilitation robotics. The SDEAs exhibited favorable characteristics, particularly in elastic (pushing) force generation, making them viable options for forming artificial muscles in robotic exoskeletons. Future work should focus on configuring SDEA-based artificial muscles, measuring their mechanical properties, and exploring control strategies for modulating the strain and stress of SDEAs and the resultant artificial muscles.

Acknowledgment

This study received support from the National Institutes of Health (NIH) through Grants P20GM109090 and P20GM152301.

Reference

[1] M. Duduta, R. J. Wood, and D. R. Clarke, “Multilayer dielectric elastomers for fast programmable actuation without prestretch,” Advanced Materials, 2016. DOI: 10.1002/adma.201601842.

[2] R. Kobayashi, H. Nabae, and K. Suzumori, “Large torsion thin artificial muscles tensegrity structure for twist manipulation,” IEEE Robotics and Automation Letters, vol. 8, no. 3, pp. 1207–1214, 2023. DOI: 10.1109/LRA.2023.3236889.

[3] V. Cacucciolo, J. Shintake, Y. Kuwajima, S. Maeda, D. Floreano, and H. Shea, “Stretchable pumps for soft machines,” Nature Communications, 2019. DOI: 10.1038/s41586-019-1479-6.

[4] Z. Mao, T. Iizuka, and S. Maeda, “Bidirectional electrohydrodynamic pump with high symmetrical performance and its application to a tube actuator,” Sensors and Actuators: A Physical, vol. 332, 2021, p. 113168. DOI: 10.1016/j.sna.2021.113168.

[5] W. Miao, X. Liu, Y. Zhao, Y. Zhu, and L. Sun, “On-demand shape memory polymer via light regulated topological defects in a dynamic covalent network,” Nature Communications, 2020. DOI: 10.1038/s41467-020-18116-1.

[6] X. Meng, L. Shi, L. Yao, Y. Zhang, and L. Cui, “Fe (III) clusters modified Bi12O17Cl2 nanosheets photocatalyst for boosting photocatalytic performance through interfacial charge transfer effect,” Colloids and Surfaces A, vol. 594, 2020, p. 124658. DOI: 10.1016/j.colsurfa.2020.124658.

[7] Z. Mao, M. Kuroki, Y. Otsuka, and S. Maeda, “Contraction waves in self-oscillating polymer gels,” Extreme Mechanics Letters, vol. 39, 2020, p. 100830. DOI: 10.1016/j.eml.2020.100830.

[8] H. Shigemune, Y. Ogasawara, K. Asaka, and S. Maeda, “Printed paper robot driven by electrostatic actuator,” IEEE Robotics and Automation Letters, vol. 2, no. 2, pp. 1001–1008, 2017. DOI: 10.1109/LRA.2017.2658942.

[9] N. Hosoya, H. Masuda, and S. Maeda, “Balloon dielectric elastomer actuator speaker,” Applied Acoustics, vol. 148, pp. 238–245, 2019. DOI: 10.1016/j.apacoust.2018.12.032.

[10] A. Wiranata, Y. Ishii, N. Hosoya, and S. Maeda, “High-frequency, low-voltage oscillations of dielectric elastomer actuators,” Applied Physics Express, vol. 15, 2022, p. 011002. DOI: 10.35848/1882-0786/ac3d41.

[11] A. Wiranata, Y. Ishii, N. Hosoya, and S. Maeda, “Simple and reliable fabrication method for polydimethylsiloxane dielectric elastomer actuators using carbon nanotube powder electrodes,” Advanced Engineering Materials, vol. 23, 2021, p. 2001181. DOI: 10.1002/adem.202001181.

[12] A. Behboodi, J. F. Alesi, and S. C. K. Lee, “An artificial skeletal muscle for use in pediatric rehabilitation robotics,” in Soft Robotics in Rehabilitation, 1st ed., Elsevier, 2021, pp. 241–258. DOI: 10.1016/B978-0-12-818538-4.00008-3.

[13] Y. Peng, X. Li, L. Chen, Z. Zhang, and H. Wang, “Funabot-suit: A bio-inspired and McKibben muscle-actuated suit for natural kinesthetic perception,” Biomimetic Intelligence and Robotics, vol. 3, 2023, p. 100127. DOI: 10.1016/j.birob.2023.100127.

[14] H. Shigemune, K. Asaka, Y. Ogasawara, and S. Maeda, “Dielectric elastomer actuators with carbon nanotube electrodes painted with a soft brush,” Actuators, vol. 7, no. 3, 2018, p. 51. DOI: 10.3390/act7030051.

[15] H. Herr and R. Kornbluh, “New horizons for orthotic and prosthetic technology: Artificial muscle for ambulation,” in Electroactive Polymer Actuators and Devices (EAPAD), Proc. SPIE, vol. 5385, 2004, p. 1117. DOI: 10.1117/12.544510.

[16] V. Mohammadi, M. Tajdani, M. Masaei , S. Mohammadi Ghalehney, S. C. K. Lee, and A. Behboodi, “DE-AFO: A robotic ankle foot orthosis for children with cerebral palsy powered by dielectric elastomer artificial muscle,” Sensors, vol. 24, 2024, p. 3787. DOI: 10.3390/s24123787.

[17] D. P. Allen, J. Shintake, H. Shea, and S. Maeda, “Mechanical simplification of variable-stiffness actuators using dielectric elastomer transducers,” Actuators, vol. 8, no. 2, 2019, p. 44. DOI: 10.3390/act8020044.

[18] S. Pourazadi, A. Shagerdmootaab, H. Chan, M. Moallem, and C. Menon, "On the electrical safety of dielectric elastomer actuators in proximity to the human body," *Smart Materials and Structures*, vol. 26, no. 11, pp. 115007, 2017. DOI: 10.1088/1361-665X/aa89b1.

[19] D. P. Allen, J. Shintake, H. Shea, and S. Maeda, “Towards an ankle-foot orthosis powered by a dielectric elastomer actuator,” Mechatronics, vol. 76, 2021, p. 102551. DOI: 10.1016/j.mechatronics.2021.102551.

[20] G. Kovacs, L. Düring, S. Michel, and G. Terrasi, “Stacked dielectric elastomer actuator for tensile force transmission,” Sensors and Actuators A: Physical, vol. 155, 2009, pp. 299–307. DOI: 10.1016/j.sna.2009.08.027.

[21] A. Behboodi, S. C. K. Lee, “Benchmarking of a commercially available stacked dielectric elastomer as an alternative actuator for rehabilitation robotic exoskeletons,” in Proceedings of the IEEE 16th International Conference on Rehabilitation Robotics (ICORR), Toronto, Canada, June 24–28, 2019, pp. 499–505. DOI: 10.1109/ICORR.2019.8779471.

[22] V. Mohammadi, S. Mohammadi Ghalehney, M. Tajdani, S. C. K. Lee, and A. Behboodi, “Evaluating stacked dielectric elastomer actuators as soft motor units for forming artificial muscles in biomimetic rehabilitation robots,” Actuators, vol. 13, 2024, p. 381. DOI: 10.3390/act13100381.

[23] F. Fallahtafti, K. Samson, Z. Salamifar, J. Johanning, I. Pipinos, and S. A. Myers, "Enhancing walking performance in patients with peripheral arterial disease: An intervention with ankle-foot orthosis," *International Journal of Cardiology*, vol. 407, p. 131992, 2024. DOI: 10.1016/j.ijcard.2024.131992.

[24] A. Behboodi, C. DeSantis, J. Lubsen, S. C. K. Lee , “A mechanized pediatric elbow joint powered by a de-based artificial skeletal muscle, ” 2020 42nd annual international conference of the IEEE Engineering in Medicine & Biology Society (EMBC). IEEE, 2020.

[25] A. Behboodi, S. C. K. Lee, S. A. Binder-Macleod, H. Wright, “Modular artificial skeletal muscle actuators and exoskeletons powered thereby,” U.S. Patent Application Publication, No. US20210121355A1, Apr. 29, 2021.

[26] V. Mohammadi, M. Hosseini, F. Jafari, and A. Behboodi, “RoboMan: An Adult-Sized Humanoid Robot with Enhanced Performance, Inherent Stability, and Two-Stage Balance Control to Facilitate Research on Humanoids,” *Robotics*, vol. 13, no. 10, p. 146, Sep. 2024. DOI: 10.3390/robotics13100146.

Markerless Motion Capture Enhances Clinical Assessments: Preliminary Validation with the Box and Blocks Test

Andria Farrens[1], Vicky Chan[2], Luis Garcia-Fernandez[1], Ziqiang "Joe" Zhu[3], Jun Min Kim[3], Matthew Karl Farrens[3] and Samuel T. King[3]

***Abstract*— Precision rehabilitation, therapy tailored to patient-specific impairments, is hindered by the low resolution of clinical assessments and the limited uptake of high resolution technological solutions that are too cumbersome for regular use. To address this, we developed C-MoRe, a phone-based system that applies computer vision to clinical assessments to produce quantitative metrics of upper extremity motor function. We tested C-MoRe in 7 chronic stroke participants performing the Box and Block Test (BBT), which scores the number of blocks participants can transfer over a divider in 1 minute. We used ML models to identify assessment and hand landmarks, and developed a custom algorithm to autoscore the assessment and quantify movement duration, amplitude, and velocity during grasping and transfer movements. Our algorithm had high fidelity in block counting (98.4% accuracy) and identifying task movement phases (ICC>0.99) compared to human raters. Movement velocity, grasp, and transfer duration were sensitive to functional differences between limbs, and grasp duration was significantly related to finger proprioception, a known predictor of therapy outcomes. Thus, C-MoRe can provide meaningful, quantitative measures of movement quality in BBT, and its simplicity may enable widespread use and the creation of large databases needed for predictive modeling.**

Keywords: computer vision, clinical assessments, stroke, proprioception, upper extremity

I. Introduction

One in four people will experience a stroke in their lifetime, and more than half of survivors are left with lasting motor impairments. Although there are numerous therapy options available, we have a limited understanding of the factors that mediate recovery. This lack of specificity, paired with the heterogeneous nature of stroke, has resulted in varied, sub-optimal (<50%) patient outcomes [1], [17].

Outcomes may be improved through tailored patient-specific rehabilitation, which can be achieved using machine learning (ML) and AI to create predictive models of how patients will respond to different therapy options. However, such modeling is limited by the relatively low resolution of commonly used clinical assessments that rate deficits as "absent, partial, or severe". Robots and motion capture technology can more accurately capture heterogeneity between patients via quantitative metrics of sensorimotor function (speed, smoothness, range of motion, strength). However, these tools have seen limited clinical adoption due to their high cost and the technical expertise and time required to use the systems [2].

[1]Mechanical Engineering Department, UC Irvine, California, USA farrensa@uci.edu, [2]Physical Therapy, UC Irvine, California, USA [3] Computer Science Department, UC Davis, California, USA

Advances in computer vision provide a solution to these issues, by offering a simple way to integrate kinematic analysis into existing clinical assessments without the need for a cumbersome marker set. Computer vision has been successfully used in the Fugl-Meyer Assessment and the Unified PD Rating Scale ([3], [14], and was found to increase assessment accuracy and consistency compared to assessment by clinicians alone. In this work, we incorporated computer vision in the Box and Block Task (BBT), a widely used assessment of upper extremity function in stroke, used for its ease of administration and functional relevance [18], [19]. Performance in this task is strongly linked to hand proprioception—the sense of position and movement—which is a predictor of responsiveness to robotic hand therapy [18].

In BBT, participants transfer as many blocks over a wooden divider as possible within one minute, and are scored by the total number of blocks successfully transferred. Kinematic analysis of BBT can provide greater detail regarding the source of patients' motor impairments. Previous research identified grasping and transfer duration, movement amplitude and speed as meaningful metrics of hand and shoulder function [4], [13]. Proprioception, which is believed to impair grasping ability, may be similarly quantifiable through kinematic assessment of block grasping. Previous groups report a high fidelity between markerless and standard motion capture analysis for these metrics, making them good candidates for computer-vision applications [8].

Given its relevance, other groups have incorporated sensors into the BBT assessment for clinical applications. However, these solutions all rely on specialized equipment, such as sensorized blocks [12], the Microsoft Kinect [16], virtual reality or a haptic robot [4], [5], which all require maintenance and costs that pose barriers to clinical uptake. Instead, our solution relies on widely available camera phones.

We present here the initial findings of our camera-vision based system for **C**linical **Mo**tor **Re**covery assessment (C-MoRe) tested in seven chronic stroke participants. We used an open-source, real-time hand-tracking model (MediaPipe Hand [6]), in combination with machine learning (ML), to develop an algorithm to autoscore the BBT assessment and perform kinematic analysis of hand movement. We hypothesized that 1) C-MoRe would be able to autoscore the BBT assessment with errors below the minimal clinically important difference (5 blocks), 2) that kinematic metrics (speed, movement amplitude) would be sensitive to hemiparetic effects of stroke, and 3) that grasping metrics would be associated with measures of finger proprioception.

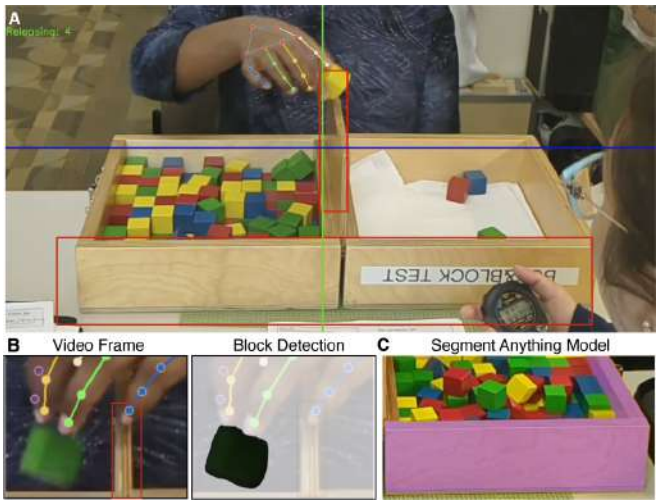


Fig. 1: A. Video frame showing ML annotations during BBT. The annotations show our hand landmark detection, box detection (red rectangles), task phase detection (green text) and task boundaries used for our scoring algorithm (blue and green lines). B: Preliminary block detection results, indicating future feasibility. C. Segment Anything Model identification of the front edge of the BBT box (pink highlight) used to convert pixels to meters

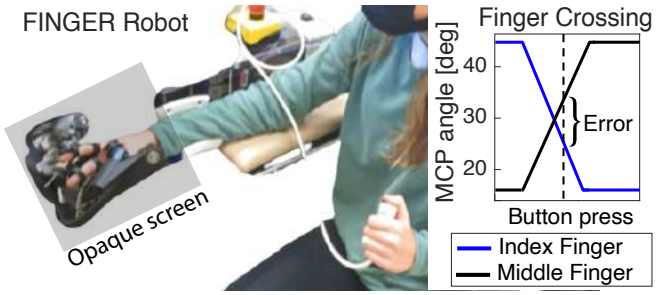


Fig. 2: Crisscross task on the FINGER robot. FINGER crosses the index and middle fingers of the affected hand in an alternating pattern with view of the hand blocked by an opaque screen. Participants must push a button at perceived finger crossing. Proprioception is quantified by the absolute error between MCP finger joints at button press.

II. Materials and Methods

A. Participants

Seven stroke survivors (59 ± 9.5 years, 2 female, 7 right-handed, 4 right-side impaired) with chronic stroke (mean: 34.9, range: [7.2, 95.2] months post stroke, 3 ischemic) were included in our study. Participants were recruited from the U.C. Irvine stroke survivor database, regional hospitals and stroke support groups. All visits took place at U.C. Irvine, and participants gave informed consent in accordance with the UCI Institutional Review Board.

The data was collected as part of a larger clinical trial on robotic hand therapy using the FINGER robot [18]. For this paper, we analyzed data from participants' 1-month post-therapy visit. During this visit, each participant performed BBT with their unaffected arm first, followed by their affected arm. Participants were instructed to transfer as many blocks as possible within one minute, crossing the center divider with their hand on every transfer. The center divider of the box was aligned to the center-line of the patient's torso and set at mid-torso height. The task was filmed on either a Pixel 7a (N=4) or an iPhone 13 mounted on a phone tripod for stability. The field of view was centered to the midline of the assessment box, and angled downward to include full view of the blocks (Fig. 1).

Following BBT performance, participants' proprioception was assessed using the Crisscross task on the FINGER robot (Fig. 2). In the crisscross task, the FINGER robot crossed the index and middle fingers of the affected hand in an alternating pattern with vision of the hand occluded. Participants were tasked with pushing a button when they felt their fingers were overlapped; performance was quantified as the absolute error between the metacarpal phalangeal (MCP) finger joints at button press. Average performance was measured across 20 crossings that had a movement amplitude of 30 deg and crossing speeds that varied randomly from trial-to-trial between 8-18 deg/s. Crisscross has a high degree of correlation to BBT, and is predictive of therapy outcomes following robotic therapy [9], [10], [18].

B. Experimental Protocol

C. Camera-Vision Markerless Motion Capture

Our goals were to automate the BBT assessment to autoscore the task, and to capture more fine-grained kinematic metrics that provide deeper insight into the individual's functional impairments. To acheive these goals, C-MoRe uses a commodity mobile device to capture videos of an individual performing BBT, and computer vision algorithms to detect the individual's hand, the box, and individual blocks on each frame of the video. By detecting and localizing these objects, we were able to use an algorithm to identify grasp, transfer and release phases of the task for autoscoring and kinematic analysis (Section II-D). As a general principle, we use off-the-shelf ML models as much as possible, reserving custom ML for tasks that do not have suitable off-the-shelf models necessary for our overall algorithm. We additionally favor deep learning ML to provide more flexibility in dealing with variations between different participants.

1) Hand Landmark Detection: Our first ML task was to detect and localize hands within the video using hand landmark detection [7] to infer transitions between distinct phases of picking up, transferring and releasing a block. We chose to use the hand landmark detection model from Media Pipe [6], which identifies hands in each frame, and then detects the wrist joint, all joints for all five fingers and all of the fingertips (Fig. 1).

The Media Pipe hand landmark detector worked well, but required a few adjustments to ensure accurate results. We found that for regular speed videos, rapid movements caused the hand to be blurred in the frames and the model

would struggle to accurately identify hand landmarks (at one point assigning a "finger" to the veins in the neck of the participant). Switching to capturing videos in "slow motion" (1/4 speed) removed the blurring and solved the problem.

We also found that we needed to crop the videos in post-processing so that the hands were large enough relative to the overall video for detection to work. To implement this in real-time, we plan to have a user interface that will instruct the therapist to align the assessment kit to a stenciled outline on the screen in order to standardize the camera field of view.

2) Box and Blocks Detection: Our second ML task was to detect and localize the BBT test kit within the video using object detection ML [20]. In particular, we detected the divider in between the two halves of the box and used this information to calculate when an individual transfers a block by virtue of their fingertips crossing the divider (Fig. 1). We also detected the front edge of the box, used for detection of when an individual attempts to grab a block. For this task, we used a pre-trained EfficientNet-lite0 object detector [15] and transfer learning to refine the detector to this specific task. To train our divider detection model, we labeled 152 frames from videos outside of our test set videos, and these labeled images served as training data for our custom model.

We also developed a custom object detection model to identify blocks during transfer. We have developed a model that can detect falling blocks in images (Fig. 1B) with a detection accuracy of 93%. However, at the time of this submission the model is still being refined and will be included in future manuscripts.

3) Converting Pixels to Meters: When processing video frames, all landmarks are recorded in pixel-space. However, to calculate speed and other meaningful metrics, as well as to standardize measurements between participants, pixels must be converted to meters. To do this, object within the video field of view that has a known fixed size must be identified, and can be used to calculate how to convert pixels to meter. We decided to use the front edge of the BBT tesk kit as all BBT sets are built to the same standardized dimensions.The challenge in performing this conversion is in localizing objects precisely enough for this calculation to be accurate. In our first version of this algorithm, we used the custom box object detector (Section II-C.2), and although it detected the front edge of the box accurately, the detected bounding box was too loose to support accurate transformations. Therefore, we chose to use the Segment Anything Model [11] to segment the image into different objects (Figure 1C). The output from this model is an annotation for each pixel about whether it is part of the same object. With this data, we use heuristics to identify the front edge of the box and an algorithm to calculate the number of pixels in the far right front edge of the box. We used the fact that the front edge of the box is 10.16 cm tall to effectively convert pixels to meters.

4) ML Training and Refinement: We focus our accuracy assessment on the end-to-end task of BBT automation, evaluating the entire system – ML, signal processing, and algorithms – as a whole (Section III). For the custom ML that we trained, we employed standard ML training best practices, including rigorous train/test separation, cross-validation during training, early stopping and model selection, and learning rate tuning to ensure the quality of each individual model. However, our quantitative measures focus on the system as a whole and the most clinically relevant measures for how we envision the system being used.

D. Signal processing

Currently, kinematic analysis is done offline by transforming frame-by-frame hand landmarks into continuous landmark signals measured across time. To define relevant features of the task workspace, we used the box detection ML to define the bounds of the center divider and the box, including the top, bottom and horizontal positions in the plane. Due to landmark detection errors and instances of spurious hands being detected, we created a signal preprocessing algorithm to reject outliers. We used a 1 second sliding window to detect local outliers due to signal dropout and a spline fill to address discontinuities. If the signal jumped outside of the reasonable workspace, defined by the borders of the box, the signal was removed from further processing. This occurred rarely (4 total instances), when the therapist's hand or the participant's other hand were misidentified in the video.

For kinematic analysis, we defined hand position as the average location across all the hand landmarks. Hand velocities were calculated by differentiating the hand position signal, and then filtering with a 4th order low-pass (Fc =1 Hz) butterworth filter using filtfilt in MATLAB. We defined finger "tips" and "touch" signals as the maximum and minimum values, respectively, across all distal finger landmarks (DIP joints, finger tips). The tips signal was used to identify all instances in which any finger tip crossed over the center divider, and the touch signal was used to identify grasping periods. All other analysis was based on the average hand position and velocity.

The algorithm first identified all potential crossing events and worked outward from each event. Potential crossing events were defined as the instance the "tips" signal exceeded the center dividers leading edge and height, until the "tips" re-crossed over the center divider. For crossing event detection, we reduced the leading edge and height of the divider by 0.5 cm to create a search buffer to enable detection of all potential crossing events (see vertical red box in Fig. 1).

We searched outwards from each potential crossing event to identify the time instances of transfer initiation, grasp initiation, and block release times. Transfer initiation was identified by searching backwards from the crossing event to identify the first local minimum ($<$15 cm/s) in vertical hand velocity. Release times were identified by searching forward from the transfer onset to the end of the potential crossing event for reversals in absolute hand velocity of 15 cm/s or greater. If multiple reversals were observed, and the crossing duration was normal ($<$2 s) we took the reversal closest to the crossing onset; for abnormally long crossings we selected the reversal closest to the end of the crossing.

To identify grasp initiation, we searched between the end of the previous crossing event to the instant of transfer initiation (search range) to identify all potential grasping periods. Potential grasping periods were defined from the instant the touch signal fell below the average position and velocity in the search range and persisted until the vertical displacement exceeded 4 cm. Within the grasp region, grasp initiation was defined as the first local minimum in vertical hand velocity prior to transfer initiation. If there were multiple potential grasp regions, then grasp attempts, transfer attempts and subsequent releases were identified for each region following the logic described above, and were counted toward attempted block transfers.

E. Automated Review

Potential crossing events in which the fingertips did not exceed the full height or leading edge of the divider were rejected as failed attempts, and not counted toward the number of block transfers. Crossings in which the finger "tips" did not cross within 0.1 cm of the divider top or leading edge or had velocity reversals prior to crossing onset were flagged for review by the proctoring assessor. All other events were considered as successful transfers and counted towards the total score.

F. Ground Truth Video Scoring

To create a set of ground truth metrics, the videos were hand scored by two of the authors and checked for consistency. We quantified the number of blocks successfully transferred, attempted grasps and attempted transfers. Successful transfers were counted only when participants fully transferred a block over the divider, such that their fingertips crossed the divider center line and the block fell on the other side of the divider. If participants transferred more than one block at a time, it was counted as a single block, consistent with clinical scoring. Grasp attempts were counted as each time a participant touched a block, and transfer attempts were counted each time the participant imposed a vertical velocity on a block.

To determine the duration of grasp and transfer phases of task performance, we identified the time instance of grasp initiation as the time instant the participant touched any block within the box, transfer initiation as the time instant of imposed vertical movement on the block, and block release as the time instant the block had an independent velocity or separation from the hand.

1) Kinematic Performance Metrics: Using the task events identified by both C-MoRe and the ground truth video scoring, we calculated participants' grasp duration as the difference between grasp initiation and transfer initiation, and transfer duration as the difference between transfer initiation time and block release. Using C-MoRe kinematics, we further defined the movement extent (sum of x and y displacement) and velocity (peak, avg) of the hand during the grasp phase and the transfer phase of movement.

G. Statistical Analysis

To validate our results, we quantified the percent accuracy and the maximum error in the number of blocks scored by C-MoRe compared to the ground truth scoring. For BBT, performance variation below 5 blocks is considered to be below minimal clinically important difference (MCID); as such, maximum errors must be below 5, and ideally, 0. To compare results between the ground truth and C-MoRe metrics, we calculated the interclass correlation between grasp, transfer, and release times, and performed a paired t-test between the calculated grasp and transfer durations calculated with C-MoRe compared to human-evaluators. Kinematics measured by C-MoRe were compared using t-tests to previously reported data in the literature [8], [13].

To determine the sensitivity of these metrics to the effects of stroke, we used paired t-tests to compare performance between the affected and unaffected hands. All participants suffered from upper-extremity hemiparesis, which should be observable as reduced performance in the affected limb. We further explored the relationship between our metrics and proprioception, because proprioception has been shown to explain 30% of the variability in BBT scores and is predictive patient outcomes following robotic rehabilitation of the hand [18]. To test the relationship between proprioception and performance in BBT, we performed an exploratory Spearman's correlational analysis between grasping and transfer phases of BBT and proprioception, and compared the performance of participants with impaired proprioception to non-impaired proprioception via Wilcoxon rank sum testing.

III. Results

A. Comparison to ground truth measures

Without review, C-MoRe had an average accuracy of 94.7%, with a maximum error of 7 blocks which exceeded our desire tolerance. However, with assessor review of automatically flagged trials, C-MoRe had an average accuracy of 98.4%, with a maximum error of 3 blocks, within our desired tolerance range (Tbl. I). Under these conditions C-MoRe performed suitably, with 100% accuracy in 11 of the 14 assessments.

C-MoRe and the ground truth task event times had an excellent agreement (all ICC$>$0.998). The mean estimation error was 146 $\pm$ 313 ms for grasp onset times, 128 $\pm$ 155 ms for transfer onset times, and 106 $\pm$ 107 ms for release times. In line with these results, there was no significant difference between estimation of grasp (difference mean $\pm$ std: 366 $\pm$ 1660 ms, p$>$0.42) or transfer durations (difference mean $\pm$ std: 174 $\pm$ 568 ms, p$>$0.27).

B. Kinematic Analysis

1) Comparison to standard motion capture: Hand movement extent had an average horizontal and vertical movement extent of 19.6 $\pm$ 7 cm, and 24 cm $\pm$ 8 cm respectively, and an average peak velocity of 137.35 $\pm$ 21.8 cm/s. Previous studies that used gold standard motion capture of the hand during the Box and Blocks assessment in stroke participants reported average movement ranges of 26 cm $\pm$

Subject	Side	Hand	PCE	R	F	Score	Raw	Final
CONK	U	D	73	2	5	70	71	70
FRAP	U	N	52	3	5	49	49	49
LEDU	U	N	56	0	3	55	56	55
MASR	U	N	83	9	6	74	74	74
RUPD	U	N	58	1	7	57	57	57
SARS	U	D	58	13	8	45	45	45
ZHAE	U	D	76	10	14	65	66	65
CONK	A	N	10	7	1	4	5	4
FRAP	A	D	55	2	6	46	53	49
LEDU	A	D	49	1	1	48	48	48
MASR	A	D	65	8	1	55	57	57
RUPD	A	D	6	4	2	4	5	4
SARS	A	N	19	3	0	14	16	16
ZHAE	A	N	37	1	2	36	36	36

TABLE I: Algorithm performance for participants' dominant/nondominant (D/N) affected/ unaffected (A/U) hands. Includes potential crossing events (PCE) detected, events rejected (R), and events flagged (F) for review. Ground truth scores (Score) are compared to the algorithms (raw) and (final) scores after review.

4 cm for horizontal movements and 21.6 $\pm$ 2 cm for vertical movements, and average peak vertical velocities of 150.7 $\pm$ 24.1 cm/s [13]. Using the reported standard deviations and two-sample t-tests, our results are not significantly different from reported values.

2) Sensitivity of selected metrics to effects of Stroke: To identify the sensitivity of our kinematic metrics to hemiparesis (unilateral weakness) secondary to stroke, we compared participants' movement extent and velocity between the affected and non-affected limbs (Fig. 3). Across participants, average velocity of the affected hand was significantly slower during both the transfer (mean difference $\pm$ std: 6.5 $\pm$ 10 cm/s, p<0.012) and grasp phases (mean difference $\pm$ std: 6.5 $\pm$ 10 cm/s, p<0.015) of the task, consistent with known effects of slowed movement speed with stroke. There was also a trend towards larger movement extent in the affected limb compared to the non-affected limb consistent with reduced movement efficiency, although these differences did not reach significance (mean difference $\pm$ std, grasping: 6.5 $\pm$ 10 cm, p<0.13; transfer: $\pm$ 19 cm, p<0.11). In line with these results, we observed increased grasp and transfer durations in the affected limb compared to the unaffected limb (mean difference $\pm$ std, grasp: 3 $\pm$ 4 s, p = 0.1, transfer, 0.7 $\pm$ .57 s p<0.007).

We further performed these comparisons at the individual level, to provide participants with feedback about the relative performance of their affected hand to their non-affected hand. In line with the known heterogeneity of stroke, not all participants exhibited deficits in the same categories. Two participants had significant deficits in movement efficiency but not speed, two had deficits only in speed, two had deficits in both movement efficiency and speed, and one had no comparative difference between sides (FRAP, Tbl. 1). The variability between subjects highlights the potential utility of such an assessment in identifying patient-specific deficits.

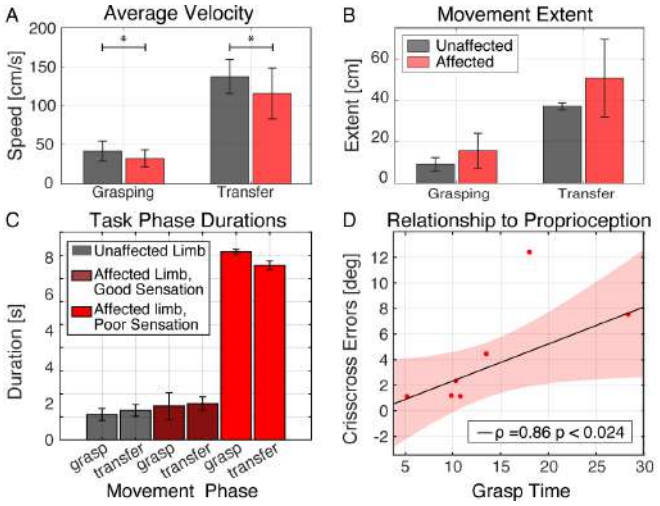


Fig. 3: Top: Hand kinematics during the grasp and transfer phases of movement. Velocity metrics (A) had the greatest sensitivity to effects of hemiparesis, while (B) differences in movement extent did not reach significance. (C) Comparison of grasp and transfer phases of movement for the unaffected limb and the affected limb, broken down by intact and impaired proprioception. (D) Correlation between grasp duration and finger proprioception

C. Relationship to Proprioception

Proprioception had no relationship to any kinematic measure nor transfer duration. However, grasp duration, which effectively combines the observed increases in movement extent and reduced velocity during grasping, showed a significant relationship to proprioception (Fig. 3, spearman's ρ = 0.86, p <0.024). The relationship between grasp duration and proprioception was stronger than its relationship to BBT Score (ρ = -0.56, p=0.21). Interestingly, individuals with poor proprioception tended to have grasp durations that were longer than their transfer durations, while individuals with intact proprioception showed the opposite trend (Wilcoxon rank sum test, p = 0.057). For the unaffected limb, which is assumed to have intact proprioception, all participants had average grasp durations that were shorter than their transfer duration. This suggests that the ratio of grasp duration to transfer duration may be a surrogate measure to identify proprioceptive deficits.

IV. Discussion

We have shown that C-MoRe, a phone-based system that uses computer vision to autoscore the Box and Block task, had an average accuracy of 94.7% and achieved an accuracy of 98.4% with assessor review of flagged trials. The algorithm primarily suffered from false positives due to block dropping and collisions, issues that will be fixed once block detection is fully implemented. Trial flagging was robust, and identified numerous instances that the human evaluators missed in which the participants fingers did not fully cross the divider. Consequently, we intend to add real-

time functionality to C-MoRe, to provide participants with auditory feedback each time their fingers cross the central divider to help prevent unintentional block tossing.

C-MoRe results had excellent agreement with ground truth task event times and produced kinematic metrics within expected ranges [8], [13]. Our kinematic metrics were sensitive to the effects of stroke, identifying group level differences in movement velocity between limbs, and subject-specific deficits in movement efficiency, velocity, and the relative duration of block grasping time to transfer time. We identified that grasp and transfer durations–which are not subject to any potential kinematic mis-estimation– were robust features of movement performance that were related to proprioception both at the group and individual level, providing a potential new avenue to identify proprioceptive deficits. The variability observed between subjects reflects known heterogeneity in stroke, and highlights the utility of such an assessment in more accurately quantifying patient-specific deficits.

Hand scoring took over an hour per video, and standard motion capture is similarly time intensive and requires specialized equipment. While other sensorized BBT solutions exist that capture similar features as C-MoRe, our system has the advantage that it only requires a commodity phone and no specialized equipment like [4], [5], [12], has higher accuracy compared to [16], and perfect fidelity to the standard assessment. As such, C-MoRe provides a rapid, simple method for quantitative assessment of movement in BBT.

Our kinematic analysis results are limited primarily by our sample size, and require additional test-retest reliability and direct comparison to gold standard motion capture metrics. In addition to validation, next steps will be to create a system that can process frames from the camera of a mobile device in real time, which will make the system easier for clinicians to adopt and employ in the field, and enable the opportunity to provide real time auditory feedback of block crossing.

V. Conclusion

Here we present C-MoRe, a phone-based system that implements computer vision during BBT for autoscoring and kinematic analysis. Our results show that we can effectively enhance the Box and Block clinical assessment of upper extremity motor function to produce sensitive, functionally meaningful measures of movement speed, extent and duration using only a camera phone and a tripod for stabilization, enabling potential widespread clinical uptake.

Acknowledgment

This work was supported by NIH R01HD062744.

References

[1] Adriana Daniela Banyai and Cornel Brișan. Robotics in Physical Rehabilitation: Systematic Review. *Healthcare (Switzerland)*, 12(17), 2024.

[2] Courtney Celian, Veronica Swanson, Maahi Shah, Caitlin Newman, Bridget Fowler-King, Sarah Gallik, Kaitlin Reilly, David J. Reinkensmeyer, James Patton, and Miriam R. Rafferty. A day in the life: a qualitative study of clinical decision-making and uptake of neurorehabilitation technology. *Journal of NeuroRehabilition*, 18(1):1–12, 2021.

[3] Guillem Cornella-barba, Andria J Farrens, Christopher A Johnson, Luis Garcia-fernandez, Vicky Chan, and David J Reinkensmeyer. Using a Webcam to Assess Upper Extremity Proprioception : Experimental Validation and Application to Persons Post Stroke. *Sensors*.

[4] Ying Dong, Xiaoyu Liu, Min Tang, Hongqiang Huo, Duo Chen, Zhixin Wu, Ran An, and Yubo Fan. A haptic-feedback virtual reality system to improve the Box and Block Test (BBT) for upper extremity motor function assessment. *Virtual Reality*, 27(2):1199–1219, 2023.

[5] Gauthier Everard, Yasmine Otmane-Tolba, Zélie Rosselli, Thomas Pellissier, Khawla Ajana, Stéphanie Dehem, Edouard Auvinet, Martin Gareth Edwards, Julien Lebleu, and Thierry Lejeune. Concurrent validity of an immersive virtual reality version of the Box and Block Test to assess manual dexterity among patients with stroke. *Journal of NeuroRehabilition*, 19(1):1–11, 2022.

[6] Google, Inc. Hand landmarks detection.

[7] Tomasz Grzejszczak, Michal Kawulok, and Adam Galuszka. Hand landmarks detection and localization in color images. *Multimedia Tools and Applications*, 75:16363–16387, 2016.

[8] Robyn M. Hansen, Sara L. Arena, and Robin M. Queen. Validation of upper extremity kinematics using Markerless motion capture. *Biomedical Engineering Advances*, 7(May):100128, 2024.

[9] Morgan L. Ingemanson, Justin B. Rowe, Vicky Chan, Eric T. Wolbrecht, Steven C. Cramer, and David J. Reinkensmeyer. Use of a robotic device to measure age-related decline in finger proprioception. *Experimental Brain Research*, 234(1):83–93, 2016.

[10] Morgan L. Ingemanson, Justin R. Rowe, Vicky Chan, Jeff Riley, Eric T. Wolbrecht, David J. Reinkensmeyer, and Steven C. Cramer. Neural Correlates of Passive Position Finger Sense After Stroke. *Neurorehabilitation and Neural Repair*, 33(9):740–750, 2019.

[11] Alexander Kirillov, Eric Mintun, Nikhila Ravi, Hanzi Mao, Chloe Rolland, Laura Gustafson, Tete Xiao, Spencer Whitehead, Alexander C Berg, Wan-Yen Lo, et al. Segment anything. In *Proceedings of the IEEE/CVF International Conference on Computer Vision*, pages 4015–4026, 2023.

[12] Sucheta V. Kolekar, Yashasvi Yathish Bangera, Aneesha Acharya K, Madhushankara M, and Vrinda Acharya. Fine motor assessment using automated box and block test. *Cogent Engineering*, 11(1):–, 2024.

[13] Kimberly Kontson, Ian Marcus, Barbara Myklebust, and Eugene Civillico. Targeted box and blocks test: Normative data and comparison to standard tests. *PLoS ONE*, pages 1–15, 2017.

[14] Winnie W.T. Lam, Yuk Ming Tang, and Kenneth N.K. Fong. A systematic review of the applications of markerless motion capture (MMC) technology for clinical measurement in rehabilitation. *Journal of NeuroRehabilition*, 20(1):1–26, 2023.

[15] Renjie Liu. Higher accuracy on vision models with efficientnet-lite, 2020.

[16] Edwin Daniel Oña, Alberto Jardón, and Carlos Balaguer. The Automated Box and Blocks Test an Autonomous Assessment Method of Gross Manual Dexterity in Stroke Rehabilitation. In Yang Gao, Saber Fallah, Yaochu Jin, and Constantina Lekakou, editors, *Towards Autonomous Robotic Systems*, pages 101–114, Cham, 2017. Springer International Publishing.

[17] H. Rodgers, H. Bosomworth, Hermano I. Krebs, Frederike van Wijck, Denise Howel, Nina Wilson, L. Aird, Natasha Alvarado, Sreeman Andole, David L. Cohen, J. Dawson, Cristina Fernandez-Garcia, T. Finch, Gary A. Ford, Richard Francis, Steven Hogg, N. Hughes, Christopher I. Price, L. Ternent, Duncan L. Turner, Luke Vale, S. Wilkes, and Lisa Shaw. Robot assisted training for the upper limb after stroke (RATULS): a multicentre randomised controlled trial. *The Lancet*, 394(10192):51–62, 2019.

[18] Justin B. Rowe, Vicky Chan, Morgan L. Ingemanson, Steven C. Cramer, Eric T. Wolbrecht, and David J. Reinkensmeyer. Robotic Assistance for Training Finger Movement Using a Hebbian Model: A Randomized Controlled Trial. *Neurorehabilitation and Neural Repair*, 31(8):769–780, 2017.

[19] Manoj Sivan, Rory J. O'Connor, Sophie Makower, Martin Levesley, and Bipinchandra Bhakta. Systematic review of outcome measures used in the evaluation of robot-assisted upper limb exercise in stroke. *Journal of Rehabilitation Medicine*, 43(3):181–189, 2011.

[20] Zhong-Qiu Zhao, Peng Zheng, Shou-tao Xu, and Xindong Wu. Object detection with deep learning: A review. *IEEE transactions on neural networks and learning systems*, 30(11):3212–3232, 2019.

Reciprocal Learning of Intent Inferral with Augmented Visual Feedback for Stroke

Jingxi Xu*,[1], Ava Chen*,[2], Lauren Winterbottom[3], Joaquin Palacios[2], Preethika Chivukula[4], Dawn M. Nilsen[3,5], Joel Stein[3,5], and Matei Ciocarlie[2,5]

***Abstract*— Intent inferral, the process by which a robotic device predicts a user's intent from biosignals, offers an effective and intuitive way to control wearable robots. Classical intent inferral methods treat biosignal inputs as unidirectional ground truths for training machine learning models, where the internal state of the model is not directly observable by the user. In this work, we propose reciprocal learning, a bidirectional paradigm that facilitates human adaptation to an intent inferral classifier. Our paradigm consists of iterative, interwoven stages that alternate between updating machine learning models and guiding human adaptation with the use of augmented visual feedback. We demonstrate this paradigm in the context of controlling a robotic hand orthosis for stroke, where the device predicts *open*, *close*, and *relax* intents from electromyographic (EMG) signals and provides appropriate assistance. We use LED progress-bar displays to communicate to the user the predicted probabilities for *open* and *close* intents by the classifier. Our experiments with stroke subjects show reciprocal learning improving performance in a subset of subjects (two out of five) without negatively impacting performance on the others. We hypothesize that, during reciprocal learning, subjects can learn to reproduce more distinguishable muscle activation patterns and generate more separable biosignals.**

I. Introduction

Developing intuitive, user-driven methods for interfacing robotic devices with humans offers the potential to restore or enhance movement capabilities that are lost after neuromotor injuries such as stroke. Approaches that infer intent with the use of electromyography (EMG) and other biosignal data can encourage users to practice integrating the impaired limb in daily activities [1], which in turn can facilitate neuroplasticity to improve motor function [2].

Recent advances in machine learning (ML) can infer intent from EMG even when the strength of muscle activation is insufficient to move the limb [3], [4], [5]. However, neuromotor impairments after stroke include abnormal muscle coactivation and diminished capacity to generate consistent EMG patterns. Such abnormalities in biosignal generation increase with volitional effort when attempting to use the arm [6], [7], which in turn increases the challenge of intent inferral as a control method for robot-assisted movement.

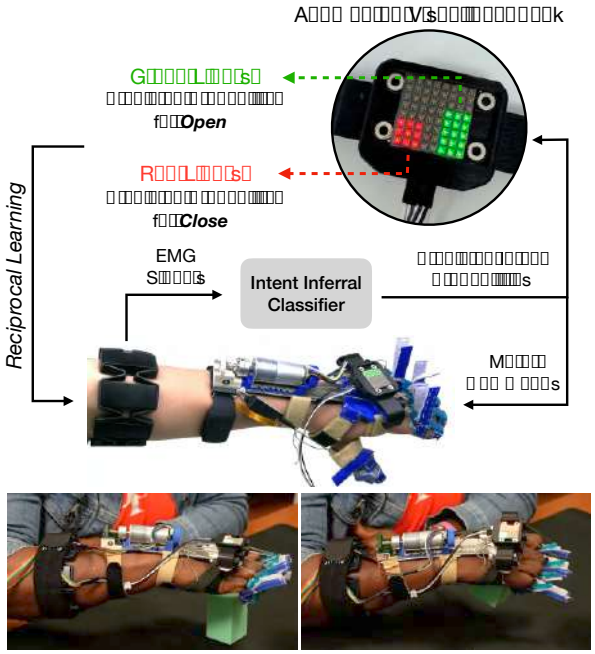


Fig. 1. **Reciprocal learning with robotic hand orthosis and augmented visual feedback.** Our hand orthosis assists stroke survivors in opening the hand when an *open* intent is detected from EMG signals, and allows the hand to close when it detects the *close* intent. Augmented feedback consists of LED display bars corresponding to the predicted probabilities of *open* and *close* from the intent classifier running on the orthosis. Subjects use visual feedback to adapt to the intent inferral model during reciprocal learning practice. The bottom row shows a stroke survivor using our device with augmented feedback for a functional pick-and-place task.

Typical intent inferral methods take in user intents as unidirectional ground truths, but wearable interfaces are inherently bidirectional systems. Humans modify their control inputs in response to sensory feedback of device behavior, such as whether the device moves according to expectations [8]. Device developers have sought to provide augmented feedback, or feedback in addition to intrinsic human sensing, to communicate information about biosignals that are not directly observable in order to aid human adaptation. Augmented feedback can compensate for reduced proprioception associated with sensory impairments after stroke [9], and when applied to EMG signals can offer insights into muscle coactivations [10]. Multiple groups [11], [12] have suggested augmented feedback of biosignals as a potential modality

This work was supported in part by the National Institutes of Health: National Institute of Neurological Disorders and Stroke under grant R01NS115652, and Eunice Kennedy Shriver National Institute of Child Health and Human Development under award F31HD111301.

*These authors have contributed equally to this work.

[1]J. Xu is with the Department of Computer Science, Columbia University, New York, NY 10027, USA. jxu@cs.columbia.edu

[2]A. Chen, J. Palacios, and M. Ciocarlie are with the Department of Mechanical Engineering, Columbia University, New York, NY 10027, USA. {ava.chen, matei.ciocarlie}@columbia.edu

[3]L. Winterbottom, D. M. Nilsen, and J. Stein are with the Department of Rehabilitation and Regenerative Medicine, Columbia University Irving Medical Center, New York, NY 10032, USA.

[4]P. Chivukula is with the Department of Biomedical Engineering, Columbia University, New York, NY 10027, USA.

[5] Co-Principal Investigators

to mediate co-adaptive learning and enable personalized control, such as human and device simultaneously adjusting control parameters in response to the other agent's behavior. However, co-adaptation in practical deployments such as physically assistive devices or rehabilitative interventions has yet to be realized for non-able-bodied users.

Our approach uses bidirectional intent inferral on a robotic device to dynamically encourage greater separability of control input patterns by stroke-impaired users, instead of solely relying on static thresholding of physiological or kinematic signals [13]. Furthermore, we can immediately deploy this approach for robot-assisted movement. We treat the human as a dynamic co-learner alongside the classifier algorithm, prompting each to update their understanding of the other's behavior. The combination of an adaptive classification algorithm and augmented feedback can increase the coherence of sensory input and action output, which in turn helps users develop greater automaticity when controlling the hand. In reciprocal learning, the user learns to generate better biosignals for ML models while practicing actively using the hand. In summary, our main contributions are as follows:

- We introduce a novel paradigm for training EMG-based intent inferral, consisting of interwoven sessions that alternate between updating ML models based on human biosignal generation and encouraging human exploration and adaptation to models with the use of augmented feedback.
- As far as we know, this bidirectional training system is a completely unexplored area in the context of upper-limb rehabilitation after stroke. We are the first to use augmented feedback to communicate the inner state of the learning model running on a wearable robotic orthosis as it assists hand movement.
- Our results demonstrate that reciprocal learning leads to better predictions for intent inferral on a subset of stroke subjects by aiding in the generation of more separable muscle activation patterns and biosignals.

II. Related Work

a) EMG Intent Inferral for Stroke: ML offers a data-driven approach to learn personalized human motor pattern classification. Many works have demonstrated robust EMG control of exoskeletons by healthy users and amputees [1], [11], [12]; however, the interpretation of biosignals from stroke-impaired users is a challenge. The majority of works on intent inferral for stroke use supervised [3], [14] or semi-supervised [4] learning approaches to train models on an initial dataset for later use during that same session, but these paradigms are vulnerable to severe shifts in distribution due to scarce data and time available for training. Recent works have sought to generalize intent inferral to enable few-shot transfer from data trained on a cohort of stroke survivors [15], [16], or have attempted to expand the data available from a single training session with a given stroke subject by use of synthetic data generation [17]. However, these methods expect muscle activation inputs to not substantially change as the user attempts to repeat movements. Impaired users who are unable to execute, and therefore are unable to observe, movements due to muscle weakness after stroke generate highly variable and inconsistent EMG patterns [14] that are prone to drift.

b) Interactive Learning with Augmented Feedback: Augmented feedback describes methods that provide the user with information on biosignals by sources outside the body. Visual augmented feedback, such as the use of computer displays or indication lights embedded on a device, has extensive support for improving rates of human motor adaptation beyond performing the task alone [18], and has long been deployed in EMG-based rehabilitation regimens for stroke [19]. Providing continuous, real-time concurrent feedback with human actions has widely shown benefit for stroke-impaired users to interactively learn mappings between different movement behaviors and resulting muscle activation patterns [20], [21]. In these works, augmented feedback is used to reinforce already-learned activation-movement mappings against fixed thresholds; instead, we use augmented feedback to train paretic users to practice movement capabilities that the user does not already possess.

Other research [11] combined augmented feedback with task-specific training to develop new control inputs. Seo et al. [22] altered flexor synergies in healthy subjects using EMG signal-guided conditioning on an isometric task. Silversmith et al. [23] used co-adaptation to enable a paralyzed subject to add additional control dimensions to a brain-computer interface. However, our reciprocal learning paradigm uniquely co-trains adaptation in the context of physical devices and movement. Simon et al. [24] developed a video-guided protocols to teach and recalibrate control of a myoelectric prosthesis, but relied on the user's ability to perform consistent muscle contractions and self-regulate force modulation with residual proprioception. To our knowledge, no previous works have tackled the challenge of mediating highly-variable intent signaling and adaptation between devices and users.

III. Reciprocal Learning Paradigm

The ultimate goal of this project is to develop algorithms that can infer discrete intent (one of {*open*, *relax*, *close*}) from EMG signals generated by stroke-impaired users attempting to move their hands, so that our robotic device can provide appropriate assistance. If the predicted intent is *open*, the robot extends the user's fingers to open the hand; if the predicted intent is *close*, the robot releases to allow the user to use their own strength to close the hand; if the predicted intent is *relax*, the robot simply maintains the previous state.

The classical way to train intent inferral algorithms is completely unidirectional. A researcher would issue cues to open, close, or relax the hand to a user wearing the device, then would record the real-time EMG signals and label the data using the provided cues as ground truth intent. In this unidirectional process, ML models learn personalized patterns through the labeled dataset and generate predictions. Although the user can observe the robot opening or closing,

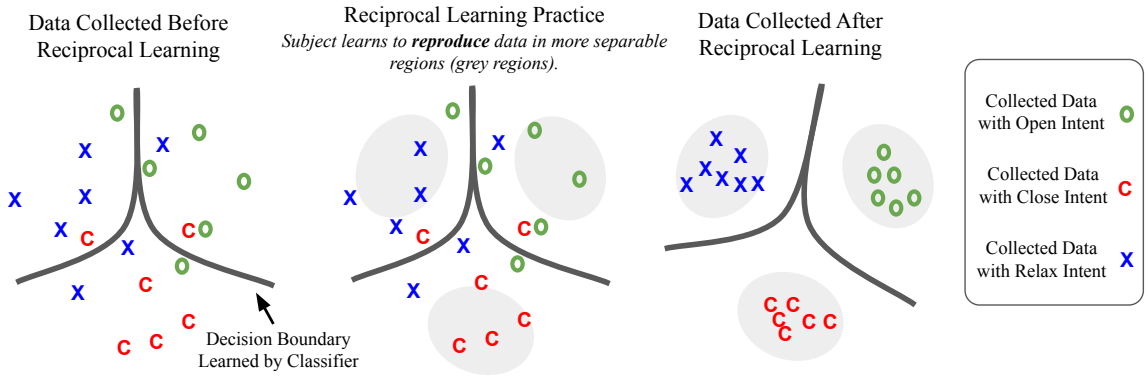


Fig. 2. **The goal of reciprocal learning is to guide the subject in generating more separable signals.** Before reciprocal learning practice, the collected data are more diverse for each intent, making it difficult for the classifier to learn a perfect decision boundary. During reciprocal learning practice, the subject adapts to the intent inferral classifier and learns to generate data in more separable regions. After reciprocal learning practice, we retrain the classifier using the newly generated more separable data. This figure is intended to illustrate the concept, and does not show EMG signals collected from real subjects; separability data from real stroke subjects will be shown in Fig. 4.

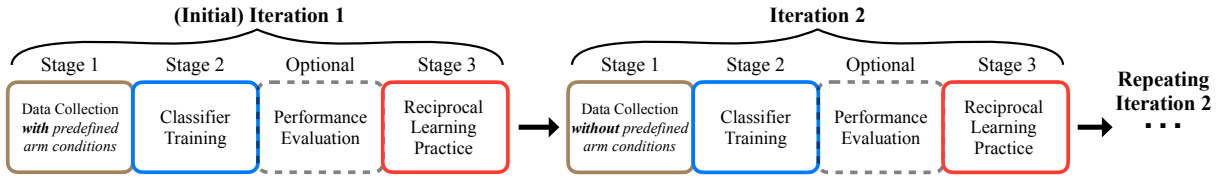


Fig. 3. **Reciprocal learning paradigm.** An iteration consists of data collection, classifier training, performance evaluation, and reciprocal learning practice.

they do not have knowledge about the underlying ML predictions or EMG signals that led to the robot taking action.

Our approach aims for a different bidirectional paradigm, dubbed reciprocal learning. We hypothesize that by providing insights about the internal state of the model in an intuitive and self-explanatory way, a user can adapt to the behavior of the classifier and reproduce more distinguishable control inputs. This idea is illustrated conceptually in Fig. 2.

Reciprocal learning is an iterative process and can have a potentially unlimited number of iterations (shown in Fig. 3). Each iteration consists of multiple stages, listed below:

- **Stage 1: Data Collection.** We collect a labeled dataset from a subject by providing verbal cues of *open*, *relax* and *close* while simultaneously recording EMG signals.
- **Stage 2: Classifier Training.** We train an intent inferral classifier using the collected dataset. This is where one direction of the learning happens—the ML model learns from the subject through the labeled dataset.
- **Optional: Performance Evaluation.** The purpose of this optional stage is to use any metric of our choice to track the performance of the trained intent inferral classifiers across iterations.
- **Stage 3: Reciprocal Learning Practice.** We run the learned intent inferral classifiers on the orthosis and provide the augmented visual feedback to communicate the inner state of the ML model that is not directly observable. The subject practices to generate distinguishable biosignals for *open* and *close* intents, using augmented feedback as guidance. This is where the opposite direction of learning happens—the subject explores and adapts to the ML model.
- **Repeat...** We continue to the next iteration, and collect a new batch of data from the subject who has supposedly learned to produce more distinguishable EMG signals.

IV. Methods and Implementation

Having described our general concept and approach, we now expand on the method and implementation of each stage.

A. Data Collection

In the data collection stage of each iteration, we collect a labeled dataset by providing verbal cues for subjects to open, close, and relax the hand. We simultaneously record the EMG signals and the given verbal cues as ground truth intent labels. The EMG armband (Myo, Thalmic Labs) has eight electrodes encircling the forearm. It streams filtered and rectified 8-channel surface EMG signals at 50Hz.

Note that the arm conditions under which the data is collected differ between the first iteration and the following iterations. A *condition* is a particular combination of hand position and whether the orthosis is actively providing assistance. In the initial iteration, the orthosis has no existing classifiers to run and thus no augmented visual feedback (see Sec. IV-C for details on the feedback mechanism) to provide. The subject has not done any reciprocal learning practice and thus has not found any muscle activations that consistently generate distinguishable EMG signals. As a result, we collect data from a diverse set of predefined arm conditions in the hope that this set provides enough diversity of muscle activation patterns such that one of them or interpolation between them is easily reproducible and separable.

The four different arm conditions of the initial iteration are as follows. (1) *Arm on table, motor off*: the assisted arm of the subject rests on the table, and the motor of the orthosis is disengaged, providing no physical assistance to the subject. (2) *Arm on table, motor on*: the assisted arm of the subject rests on the table, and the motor of the orthosis is engaged, allowing the device to provide active grasp assistance to the user. (3) *Arm off table, motor off*: the subject keeps their arm raised to shoulder level for the duration of data collection, and the motor is disengaged, providing no physical assistance to the subject. (4) *Arm off table, motor on*: the subject keeps their arm raised to shoulder level for the duration of data collection, and the motor of the orthosis is engaged, allowing the device to provide active hand-opening assistance.

For each condition, we collect two recordings, one for training and the other one held out for testing. A *recording* is defined to be a continuous and uninterrupted recorded sequence of EMG signals. For each recording, we instruct the subject to open and close their hand 3 times. Each verbal cue lasts for 5 seconds, with a *relax* cue between each *open* and *close* cue. As we have not yet trained a user orthosis controller, to collect data for motor-on conditions we manually command the orthosis to move approximately 1 second after the verbal cue.

In the data collection stage of the following iterations, there are no more predefined arm conditions. The orthosis runs the trained classifier, providing both active assistance and augmented visual feedback at a 5 Hz operational rate. The subject's goal is to reproduce the muscle activation patterns learned in the reciprocal learning practice of the previous iteration. We collect four recordings: two for training and the other two for testing.

B. Classifier Training

In each classifier training stage, we train a Linear Discriminant Analysis (LDA) classifier. We choose LDA because it is fast, trackable, and widely used in biomedical research [3], [4], [15], [17]. In the optional performance evaluation stage, we evaluate the performance of the classifiers both qualitatively and quantitatively (see Sec. VI for details).

The classifiers take in a single time step of an 8-channel, 50Hz EMG signal. We clip the signal to $[0, 1000]$ and then normalize it to $[-1, 1]$. Prediction on a single step is noisy, so during online inference we apply a median filter of window size 20 to the predicted probabilities of *relax*, *open*, and *close* over time. This median filter reduces unwanted oscillations in predictions when changing intents.

C. Reciprocal Learning Practice

Our augmented visual feedback consists of two progress-bar displays mounted on the dorsal side of the hand orthosis so that the subject can observe them comfortably during reciprocal learning, as shown in Fig. 1. The relative heights of the green and red LED bars correspond to the model's predicted probabilities for *open* and *close* intents, respectively.

In the reciprocal learning practice stage, we ask the subject to practice opening and closing their hands guided by the augmented visual feedback. We run the trained classifier on the device to provide appropriate assistance. In this stage, we instruct the subject to trigger different device states (*open* and *close*) by maximizing the respective green or red LED bars.

This is the exploration stage, where the subject adapts to the behavior of the device, and tries to discover and reinforce the muscle activation pattern that is easily reproducible and distinguishable. In this stage, the subject uses augmented visual feedback to learn to generate more separable EMG signals for each intent. This idea is conceptually illustrated in Fig. 2. Reciprocal learning practice essentially helps the subject locate the EMG subspace that is both reproducible and separable (i.e., far from the *decision boundary* learned by the classifier of the previous iteration). Then, in the next iteration, the subject can reproduce data in these more separable regions, leading to new retrained classifiers that can more accurately predict user intent.

V. Experimental Setup

We tested reciprocal learning in single-session experiments with five stroke subjects, and compared intent inferral accuracies from two iterations. Reciprocal learning supports multiple iterations; however, here we only complete two iterations due to session time constraints. We leave the study of reciprocal learning with more iterations as future work.

A. Subjects

We recruited stroke survivors who presented with chronic hemiparesis and moderate muscle tone defined as Modified Ashworth Scale (MAS) scores ≤ 2 in the upper extremity. Our subjects can fully close their hands but are unable to completely extend their fingers without assistance. The passive range of motion in the fingers is within functional limits. Testing was approved by the Columbia University Institutional Review Board (IRB-AAAS8104) and was performed in a clinical setting under the supervision of an occupational therapist. See Table I for details on subjects.

Our subjects have different degrees of hand impairment severity, as measured on the Fugl-Meyer scale for upper extremity (FM-UE). Subjects S1, S2, and S3 have no active finger extension (minimal observable movement) and lower corresponding FM-UE scores (27, 26, 26, respectively), whereas S4 and S5 have some residual active finger extension capacity (limited observable movement) and higher corresponding FM-UE scores (50, 47, respectively).

B. Hardware

Our hand orthosis [25], [26] is a robotic exotendon device with a forearm EMG armband and LED visual displays,

TABLE I
Subject information.

Subject ID	Age	Gender	FM-UE
S1	46	Male	27
S2	48	Male	26
S3	53	Female	26
S4	31	Male	50
S5	53	Male	47

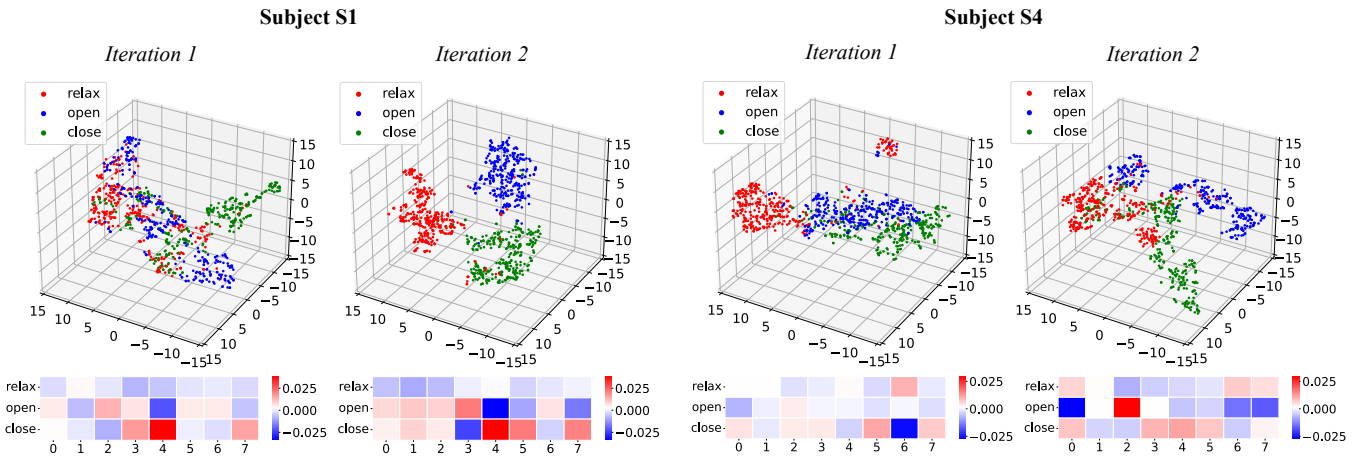


Fig. 4. **Reciprocal learning results on two stroke subjects. Top:** comparing data separability. After reciprocal learning, clusters associated with each intent become more easily separable. **Bottom:** LDA classifier weights visualization indicating a specific EMG electrode (0 through 7) is negatively (blue) or positively (red) associated with a specific intent. Reciprocal learning strengthens such associations, which helps separability.

TABLE II

MEAN INTENT INFERRAL ACCURACY.

Subject	S1	S2	S3	S4	S5
Iteration 1	0.61	0.69	**0.70**	0.86	**0.82**
Iteration 2	**0.88**	**0.71**	0.68	**0.94**	0.80

TABLE III

VARIANCE OF LDA WEIGHTS FOR THE OPEN INTENT.

Subject	S1	S2	S3	S4	S5
Iteration 1	7.8e/6	1.0e/4	8.8e/4	1.1e/4	1.0e/4
Iteration 2	**2.5e/4**	**4.6e/4**	**1.2e/3**	**2.8e/4**	**2.0e/4**

as shown in Fig. 1. The device assists hand opening by extending all digits simultaneously. It does not directly assist finger flexion and relies on human strength for hand closing.

When operating under user control, the device acts on streaming *open* and *close* predictions at approximately 5 Hz to move to preset hand poses. The user is able to countermand the device mid-motion by generating an opposing intent input. *Relax* predictions do not change device state.

VI. RESULTS AND DISCUSSION

A. Intent Inferral Accuracy

During the performance evaluation stage of each iteration, we use the test set to compute the classifier's per-timestep intent inferral accuracy against the ground truth labels. Table II reports the mean accuracies across samples. While the intent inferral accuracies for S2, S3, and S5 remain similar across the first two iterations, we observe an accuracy improvement for S1 and S4, from 0.61 to 0.88 and from 0.86 to 0.94, respectively. Augmented visual feedback during reciprocal learning practice may have helped S1 and S4 generate more consistent and distinguishable muscle activation patterns, creating more separable intent signals. As a result, the data collected after the first reciprocal learning practice become easier to classify. We note that S1 has more limited hand movement capacity compared to S4 (also reflected by their intent inferral accuracy). This suggests that whether reciprocal learning can improve intent inferral accuracy may not depend on stroke subjects' residual hand function.

One possibility for why reciprocal learning does not improve performance across all subjects is the randomness of exploration in the practice stage. Although the prescribed arm conditions during the data collection stage of the first iteration provide data variance, due to the variation of impairment across stroke subjects, it is not guaranteed that the initial dataset is diverse enough to contain reproducible and distinguishable muscle activation patterns for all intents. In addition, even though the initial dataset collected with predefined arm conditions contains many activation patterns, due to randomness of exploration, it is not guaranteed for a subject to successfully locate or reproduce a specific pattern.

While advancing the proposed paradigm to have a positive effect on most participants is obviously desirable and is the focus of our future work, we believe that an approach that improves performance on a subset of participants without hindering performance on the others can also have practical usefulness. Furthermore, a detailed study of the differences between cases showing successes versus more limited effects can suggest future areas of exploration.

B. Data Separability

We further investigate the data of subjects S1 and S4 to show how reciprocal learning may lead to biosignals with more discriminative information for classifying intent. We visualize 1000 randomly sampled 8D EMG signals for each intent before and after the reciprocal learning practice in 3D space using t-distributed stochastic neighbor embedding (t-SNE) [27], as shown in Fig. 4. Each data point is labeled using its ground truth label, which is only available during training. After reciprocal learning, the data clusters associated with each intent improve in separability, which could explain the increased classification accuracy and lend support to the hypothesis that reciprocal learning may help some subjects generate signals that are more easily interpretable by intent inferral algorithms.

We also visualize the LDA weights associated with each EMG electrode in Fig 4 to show the spatial distribution of predicted intents on the forearm. Positive values (red) mean that muscle activity under that particular electrode is positively associated with a specific intent, while negative values (blue) mean that muscle activity contributes negatively to that intent. We notice that after reciprocal learning practice, the weights (especially for the *open* intent) become more diverse, meaning that the positive weights are more positive, and the negative weights are more negative. In fact, the variance of the 8D weights for the *open* intent increases consistently for all subjects, as shown in Table III. These results suggest that subjects have stronger muscle activation patterns after reciprocal learning practice and explain improvements in intent inferral accuracy from another angle.

VII. Conclusion

We propose a novel bidirectional reciprocal learning paradigm that co-trains stroke-impaired users with intent inferral algorithms. We achieve reciprocal learning through augmented visual feedback in the form of LED progress-bar displays, which communicate the probabilities of the *open* and *close* intents predicted by the classifier. Our paradigm consists of iterative and interwoven stages of training the machine learning models and human exploration and adaptation to the classifiers. By using the augmented visual feedback of the classifier internal state as guidance, a subset of our stroke subjects learn to modulate muscle activation and generate more separable EMG signals, leading to better intent inferral performance, while the performance of the other subjects is not adversely affected. Future work includes conducting detailed studies of reciprocal learning involving multiple iterations, exploring the factors that influence a subject's ability to find consistent and reproducible muscle activation patterns during reciprocal learning practice, and finally to translate acquired skills across tasks and contexts of use.

References

[1] S. Luo, Q. Meng, S. Li, and H. Yu, "Research of intent recognition in rehabilitation robots: a systematic review," *Disabil. Rehabil. Assist. Technol.*, vol. 19, no. 4, pp. 1307–1318, 2024.

[2] B. R. Ballester, M. Maier, R. M. San Segundo Mozo, V. Castañeda, A. Duff, and P. F. M J Verschure, "Counteracting learned non-use in chronic stroke patients with reinforcement-induced movement therapy," *J. Neuroeng. Rehabil.*, vol. 13, no. 1, p. 74, 2016.

[3] C. Meeker, S. Park, L. Bishop, J. Stein, and M. Ciocarlie, "EMG pattern classification to control a hand orthosis for functional grasp assistance after stroke," in *IEEE Int. Conf. Rehabil. Robot.*, 2017.

[4] J. Xu, C. Meeker, A. Chen, L. Winterbottom, M. Fraser, S. Park, L. M. Weber, M. Miya, D. Nilsen, J. Stein, and M. Ciocarlie, "Adaptive semi-supervised intent inferral to control a powered hand orthosis for stroke," in *IEEE Int. Conf. Robot. Autom.*, 2022.

[5] X. Zhang and P. Zhou, "High-density myoelectric pattern recognition toward improved stroke rehabilitation," *IEEE Trans. Biomed. Eng.*, vol. 59, no. 6, pp. 1649–1657, 2012.

[6] A. Chen, K. Lee, L. Winterbottom, J. Xu, C. Lee, G. Munger, A. Deli-Ivanov, D. M. Nilsen, J. Stein, and M. Ciocarlie, "Volitional control of the paretic hand post-stroke increases finger stiffness and resistance to robot-assisted movement," in *IEEE Int. Conf. Biomed. Robot. Biomechatron.*, 2024.

[7] A. J. Barry, D. G. Kamper, M. E. Stoykov, K. Triandafilou, and E. Roth, "Characteristics of the severely impaired hand in survivors of stroke with chronic impairments," *Top. Stroke Rehabil.*, vol. 29, no. 3, pp. 181–191, 2022.

[8] C. E. Proulx, M. T. Louis Jean, J. Higgins, D. H. Gagnon, and N. Dancause, "Somesthetic, visual, and auditory feedback and their interactions applied to upper limb neurorehabilitation technology: A narrative review to facilitate contextualization of knowledge," *Front. Rehabil. Sci.*, vol. 3, p. 789479, 2022.

[9] M. L. Ingemanson, J. R. Rowe, V. Chan, E. T. Wolbrecht, D. J. Reinkensmeyer, and S. C. Cramer, "Somatosensory system integrity explains differences in treatment response after stroke," *Neurology*, vol. 92, no. 10, pp. e1098–e1108, 2019.

[10] Z. A. Wright, W. Z. Rymer, and M. W. Slutzky, "Reducing abnormal muscle coactivation after stroke using a myoelectric-computer interface: A pilot study," *Neurorehabil. Neural Repair*, vol. 28, no. 5, pp. 443–451, 2014.

[11] M. M. Madduri, S. A. Burden, and A. L. Orsborn, "Biosignal-based co-adaptive user-machine interfaces for motor control," *Curr. Opin. Biomed. Eng.*, vol. 27, p. 100462, 2023.

[12] X. Hu, A. Song, H. Zeng, Z. Wei, H. Deng, and D. Chen, "Bridging human-robot co-adaptation via biofeedback for continuous myoelectric control," *IEEE Robot. Autom. Lett.*, vol. 8, no. 12, p. 8573, 2023.

[13] A. Cisnal, P. Gordaliza, J. Pérez Turiel, and J. C. Fraile, "Interaction with a hand rehabilitation exoskeleton in emg-driven bilateral therapy: Influence of visual biofeedback on the users' performance," *Sensors*, vol. 23, no. 4, p. 2048, 2023.

[14] S. W. Lee, K. M. Wilson, B. A. Lock, and D. G. Kamper, "Subject-specific myoelectric pattern classification of functional hand movements for stroke survivors," *IEEE Trans. Neural Syst. Rehabil. Eng.*, vol. 19, no. 5, pp. 558–566, 2010.

[15] P. L. La Rotta, J. Xu, A. Chen, L. Winterbottom, W. Chen, D. Nilsen, J. Stein, and M. Ciocarlie, "Meta-learning for fast adaptation in intent inferral on a robotic hand orthosis for stroke," in *2024 IEEE/RSJ Int. Conf. Intel. Robot. Sys.*, 2024.

[16] H. Sarwat, A. Alkhashab, X. Song, S. Jiang, J. Jia, and P. B. Shull, "Post-stroke hand gesture recognition via one-shot transfer learning using prototypical networks," *J. Neuroeng. Rehabil.*, vol. 21, p. 100, 2024.

[17] J. Xu, R. Wang, S. Shang, A. Chen, L. Winterbottom, T.-L. Hsu, W. Chen, K. Ahmed, P. L. La Rotta, X. Zhu, D. M. Nilsen, J. Stein, and M. Ciocarlie, "ChatEMG: Synthetic data generation to control a robotic hand orthosis for stroke," *IEEE Robot. Autom. Lett.*, vol. 10, no. 2, pp. 907–914, 2024.

[18] R. Wang, S. Zhang, J. Zhang, Q. Tong, X. Ye, K. Wang, and J. Li, "Electromyographic biofeedback therapy for improving limb function after stroke: A systematic review and meta-analysis," *PLoS One*, vol. 19, no. 1, p. e0289572, 2024.

[19] S. L. Wolf, "Electromyographic biofeedback applications to stroke patients. a critical review," *Phys. Ther.*, vol. 63, no. 9, p. 1448, 1983.

[20] C. Jian, L. Deng, H. Liu, T. Yan, X. Wang, and R. Song, "Modulating and restoring inter-muscular coordination in stroke patients using two-dimensional myoelectric computer interface: a cross-sectional and longitudinal study," *J. Neural Eng.*, vol. 18, no. 3, 2021.

[21] L. Rinaldi, L.-F. Yeung, P. C.-H. Lam, M. Y. C. Pang, R. K.-Y. Tong, and V. C. K. Cheung, "Adapting to the mechanical properties and active force of an exoskeleton by altering muscle synergies in chronic stroke survivors," *IEEE Trans. Neural Syst. Rehabil. Eng.*, vol. 28, no. 10, pp. 2203–2213, 2020.

[22] G. Seo, J.-H. Park, H.-S. Park, and J. Roh, "Developing new inter-muscular coordination patterns through an electromyographic signal-guided training in the upper extremity," *J. Neuroeng. Rehabil.*, vol. 20, no. 1, p. 112, 2023.

[23] D. B. Silversmith, R. Abiri, N. F. Hardy, N. Natraj, A. Tu-Chan, E. F. Chang, and K. Ganguly, "Plug-and-play control of a brain-computer interface through neural map stabilization," *Nat. Biotechnol.*, vol. 39, no. 3, pp. 326–335, 2021.

[24] A. M. Simon, B. A. Lock, and K. A. Stubblefield, "Patient training for functional use of pattern recognition-controlled prostheses," *J. Prosthet. Orthot.*, vol. 24, no. 2, pp. 56–64, Apr. 2012.

[25] S. Park, C. Meeker, L. M. Weber, L. Bishop, J. Stein, and M. Ciocarlie, "Multimodal sensing and interaction for a robotic hand orthosis," *IEEE Robot. Autom. Lett.*, vol. 4, no. 2, pp. 315–322, 2018.

[26] A. Chen, L. Winterbottom, S. Park, J. Xu, D. M. Nilsen, J. Stein, and M. Ciocarlie, "Thumb stabilization and assistance in a robotic hand orthosis for post-stroke hemiparesis," *IEEE Robot. Autom. Lett.*, vol. 7, no. 3, pp. 8276–8282, 2022.

[27] L. Van der Maaten and G. Hinton, "Visualizing data using t-SNE." *J. Mach. Learn. Res.*, vol. 9, no. 11, 2008.

Optimizing Locomotor Task Sets for Training a Biological Joint Moment Estimator

Jimin An[1], Changseob Song[1], Eni Halilaj[1] and Inseung Kang[1]

***Abstract*— Accurate estimation of a user's biological joint moment from wearable sensor data is vital for improving exoskeleton control during real-world locomotor tasks. However, most state-of-the-art methods rely on deep learning techniques that necessitate extensive in-lab data collection, posing challenges in acquiring sufficient data to develop robust models. To address this challenge, we introduce a locomotor task set optimization strategy designed to identify a minimal, yet representative, set of tasks that preserves model performance while significantly reducing the data collection burden. In this optimization, we performed a cluster analysis on the dimensionally reduced biomechanical features of various cyclic and non-cyclic tasks. We identified the minimal viable clusters (i.e., tasks) to train a neural network for estimating hip joint moments and evaluated its performance. Our cross-validation analysis across subjects showed that the optimized task set-based model achieved a root mean squared error of 0.29±0.06 Nm/kg. This performance was significantly better than using only cyclic tasks ($p<0.05$) and was comparable to using the full set of tasks. Our results demonstrate the ability to maintain model accuracy while significantly reducing the cost associated with data collection and model training. This highlights the potential for future exoskeleton designers to leverage this strategy to minimize the data requirements for deep learning-based models in wearable robot control.**

***Index Terms*— Exoskeleton, Deep Learning, Biological Joint Moment Estimation, Dimensionality Reduction, Cluster Analysis**

I. Introduction

Lower-limb exoskeletons have been shown to enhance human mobility, thereby improving quality of life [1]. These robotic systems can augment users and enhance gait performance, for example, by reducing energy expenditure in healthy individuals [2] and improving spatiotemporal gait metrics in patient populations [3]. Among different lower-limb exoskeletons, hip exoskeletons present a particularly compelling value proposition due to the critical role of the hip in generating substantial mechanical power during locomotion. Unlike the ankle joint, which benefits from an efficient muscle-tendon mechanism, the hip is mechanically less efficient, requiring greater muscle work (i.e., energy) to complete locomotor tasks [4].

Control strategies for robotic exoskeletons have significantly advanced over the past decade. Initially relying on heuristic, rule-based controllers utilizing onboard wearable sensors [5], [6], recent approaches now directly leverage the user's physiological state, such as biological joint moments, to control the exoskeleton more effectively [7]. Biological torque controllers directly estimate the user's biological joint moments and apply a reshaped, scaled envelope as the assistance profile [8]. This method leverages deep learning techniques with wearable sensing as model input and has demonstrated notable performance benefits [9]. The range of activities that can be assisted by exoskeletons has expanded significantly, progressing from simple continuous walking [10], [11] to dynamic transitions between locomotion modes [9], [12], and now including various non-cyclic movements [13], [14]. These advancements could enable more natural hip exoskeleton assistance during daily locomotor tasks.

However, a significant bottleneck of deep learning approaches is their data-intensive nature, requiring large datasets that comprehensively represent various activities, along with ground-truth joint moments obtained through motion capture. Studies have demonstrated that user-independent models typically require data from at least a dozen participants completing multiple tasks [15], with some relying on even larger groups and more diverse tasks [9]. While comprehensive datasets are essential for ensuring reliable model performance across various activities, the associated costs and resources are substantial. Furthermore, for patient populations, such data collection can be even more challenging due to physical limitations, time constraints, and logistical barriers. These challenges highlight the necessity for an automated solution that reduces the burden of data collection while not compromising model performance.

Few studies have verified that optimal model performance can be achieved with data from a reduced set of tasks [13], [14]. These studies employed an iterative forward task selection approach, incrementally adding tasks to the training dataset until further additions no longer improved model performance. While these results suggest that a full dataset is not always necessary during training, they do not clarify which tasks are most relevant and useful or explain why certain tasks are more effective in developing user-independent joint moment estimators. Without a deeper analysis beyond model performance, these approaches provide limited insight into the relationships between tasks and their biomechanical relevance. This gap emphasizes the need for a systematic approach to identify a minimal task set that ensures reliable model training and performance while reducing data collection requirements.

Given the similarities among human movement profiles across various locomotor tasks, collecting data with finely discretized task separation may not always be necessary. Instead, grouping tasks based on shared biomechanical features might be a better strategy for improving efficiency and

[1]J. An, C. Song, E. Halilaj, and I. Kang are with the Department of Mechanical Engineering, Carnegie Mellon University, Pittsburgh, PA 15213, USA. Corresponding author: Jimin An (jimina@andrew.cmu.edu).

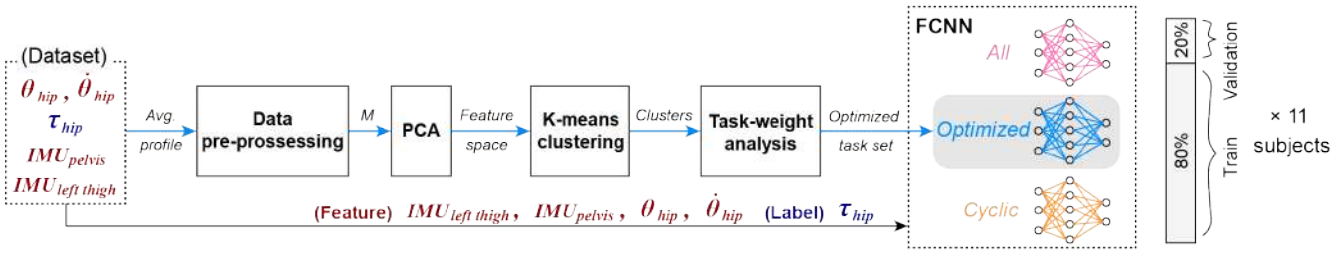


Fig. 1: Task Selection and Model Training. Average joint moment, angle, and velocity profiles were used for principal component analysis (PCA), k-means clustering, and task-weight analysis to determine a smaller optimized set of tasks that were representative of the full set. The time-series data for each training dataset condition (all tasks, optimized tasks, and cyclic tasks) were used for the fully connected neural network (FCNN) model training with leave-one-subject-out cross-fold validation.

applicability in various contexts. Prior studies have applied dimensionality reduction and clustering methods to biomechanical data analysis for applications such as locomotion phase classification [16], [17], kinematic pattern recognition [18], gait differentiation [19], and movement analysis [20], [21]. Building on prior literature, grouping tasks using a clustering approach based on shared biomechanical features offers a systematic solution for identifying redundant tasks that provide similar information. By selecting representative tasks from each cluster and training the model on these tasks, we can significantly reduce data collection efforts while preserving essential biomechanical patterns needed for accurate joint moment estimation.

In this work, we propose a strategy for optimizing locomotor task selection through clustering analysis. We hypothesized that a model trained on an optimized task set would achieve hip joint moment estimation comparable to a model trained on the full dataset. Our underlying rationale is that the latent space representation of these tasks likely exhibits significant overlap for certain tasks due to their shared biomechanical features. To test this hypothesis, we trained a neural network using three different datasets to evaluate the effectiveness of our task set reduction: 1) the full set of tasks, 2) an optimized reduced set of tasks, and 3) only cyclic tasks. The model estimated hip joint moments using sensor data commonly available for hip exoskeletons, such as encoders and inertial measurement units. Our study results contribute to the field by demonstrating that a biological torque controller for hip exoskeletons can be developed using data from fewer tasks, while also identifying key tasks for future data collection efforts.

II. Methods

A. Dataset and Data Pre-Processing

We used an open-source biomechanics dataset of 12 healthy young individuals (7 males, 5 females, age of 21.8±3.2 years, height of 176.7±8.6 cm, and weight of 76.9±14.4 kg) performing various locomotor tasks [22]. These tasks included 10 cyclic and 17 non-cyclic tasks. The dataset included kinematics (joint angles and velocities), kinetics (ground reaction forces, joint moments, and joint power), and wearable sensor data. For dimensionality reduction, we focused on unilateral hip joint angles, velocities, and moments in the sagittal plane. These features, combined with pelvis and thigh inertial measurement unit (IMU) data, were also used to train a user-independent model for hip moment estimation in exoskeletons.

We used principal component analysis (PCA) to reduce the dimension of our data. We constructed an input matrix, M, through a pre-processing pipeline (Fig. 1). The unilateral hip joint moment, angle, and velocity, pre-segmented and averaged by gait or movement cycle, were linearly interpolated to standardize their lengths while preserving overall patterns. These processed vectors were concatenated to represent the biomechanical features for each subject-task combination, and all such vectors were aggregated to form the matrix, M. During this process, seven non-cyclic tasks (meander, poses, push, obstacle walk, start stop, tug of war, and twister) were excluded due to their atypical movement profiles, which could not be segmented into uniform gait or movement cycles. The remaining tasks were categorized into eight cyclic and 12 non-cyclic tasks. We excluded data from one subject due to insufficient cyclic task trials, ensuring balanced task representation and minimizing potential biases in analyses.

B. PCA, Clustering, and Task Selection

By reducing high-dimensional biomechanical data, PCA [21] enhanced the interpretability of relationships among task datasets. We derived principal components and assessed their explained variance to determine the optimal number of components. This process balanced variance representation and component counts, ensuring an adequate representation of the data's variability for the clustering process.

We applied k-means clustering [17] to group tasks by biomechanical feature similarities in the PCA-derived feature space (Fig. 1). We first performed a silhouette score analysis to determine the number of clusters. The silhouette score measures both inter-cluster and intra-cluster distances, indicating how well-defined the clusters are [23]. The K (i.e., number of clusters) that yielded the highest silhouette score was selected as the optimal K.

Since each cluster contained different types of tasks, we developed a task-weight analysis to calculate, R, the representativeness of a task for a cluster using Eq. 1,

$$R = \frac{A}{B} \times \frac{A}{C} \times \frac{S}{11} \times w \quad (1)$$

where A is the number of a specific task's data points in a cluster, B is the total number of data points in that cluster, C is the total number of data points for that task across all clusters, and S is the number of unique subjects contributing task data in the cluster. w is a weight assigned to each task based on its popularity in the research field and the ease of collecting task data. Using Eq. 1, we accounted for the proportion of data, the diversity of subjects, and the difficulty associated with data collection in our task selection process. The representative tasks for each cluster identified through this analysis constituted our set of optimized tasks for model training.

C. Optimized Task Set Performance Validation

We implemented a fully connected neural network (FCNN) using PyTorch (Python v3.8) to predict a unilateral hip joint moment from IMU, joint angle, and joint velocity data. The network architecture was comprised of an input layer, three hidden layers, and an output layer. The input layer had a 14-dimensional feature vector corresponding to the input features (Fig. 1). Each hidden layer contained 50 nodes. We applied batch normalization after each linear transformation to enhance training stability and convergence speed. We used the rectified linear unit activation function followed by a dropout layer with a rate of 0.2. The output layer was a single node that returned the unilateral hip joint moment. The hyperparameters for each condition, including the learning rate (lr), dropout rate (dr), and batch size (bs), were sequentially tuned. The selected values are as follows: lr = 0.001, dr = 0.1, and bs = 128 for the all-task; lr = 0.001, dr = 0.1, and bs = 32 for the optimized-task; and lr = 0.001, dr = 0.4, and bs = 32 for the cyclic-task. Training proceeded for up to 100 epochs, with early stopping applied if the validation loss did not improve for 10 consecutive epochs to prevent overfitting and unnecessary computations.

To further address the data imbalance between cyclic and non-cyclic tasks, we applied bootstrapping. In our approach, for each training batch, we first separated the data into two groups: cyclic and non-cyclic tasks. We then computed the sample counts for each group. Recognizing that the minority group (typically the non-cyclic tasks) contained fewer samples, we applied bootstrapping to this group—repeatedly sampling with replacement—to match the sample size of the majority group. By doing so, we generated a balanced training set in which both cyclic and non-cyclic tasks were equally represented. This method ensures a balanced training set, reduces bias toward the majority class, and introduces variability that may enhance generalization.

We conducted leave-one-subject-out cross-validation for training and testing (Fig. 1). For each iteration, the entire dataset from one subject was left out, and the remaining data was filtered based on predefined task conditions (all tasks, optimized tasks, or cyclic tasks). The filtered data was then split into 80% training and 20% validation sets. After training, the left-out subject's data was used for testing. Model performance was evaluated using root mean squared error (RMSE) and the coefficient of determination (R^2). RMSE assessed the accuracy of the model's predicted hip joint moment values, while R^2 evaluated the model's ability to track the characteristic pattern of the hip joint moment profile. We computed the average RMSE and R^2 for each training condition across all cross-validation folds as the final metric of the model performance.

We performed statistical analyses to evaluate the differences among the three conditions. A one-way analysis of variance (ANOVA) was conducted to test for overall differences in RMSE and R^2 values across conditions with the significance level set to 0.05. If significant differences were identified, post-hoc pairwise comparisons with a Bonferroni correction were performed to determine which specific conditions differed.

III. Results

A. PCA and Clustering Results

The first three principal components accounted for 41.79%, 18.04%, and 10.21% of the variance, respectively (Fig. 2a). By projecting the original data onto these top three principal components, a three-dimensional representation of the biomechanical latent space of a total of 70.04% of explained variance was generated (Fig. 3a). This reduced-dimensional space served as the foundational coordinate system for our clustering analysis.

The optimal cluster number for our dataset was eight with a silhouette score of 0.38 (Fig. 2b). Using the clustering result (Fig. 3b) and task-weight analysis, the representativeness of each task, R, was computed (Table 1). The task with the highest R score in each cluster was selected as the representative task for the cluster. Among these eight tasks, three were cyclic tasks (normal walk, stairs up, and stairs down) and five were non-cyclic tasks (lunges, jump, cutting, sit to stand, and lift weight). These tasks were our training dataset for the optimized-task model. The other two conditions were trained with 1) all tasks, which included all 20 different tasks and 2) cyclic tasks, which included all eight cyclic tasks.

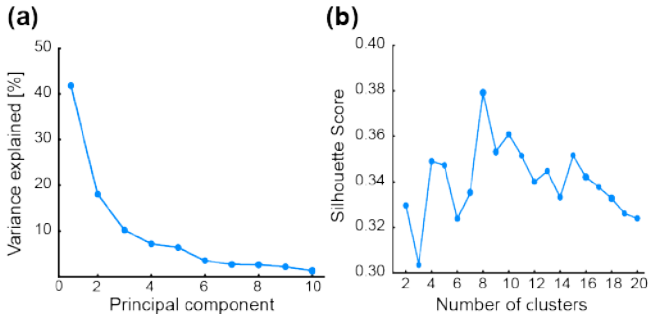


Fig. 2: PCA and K-means Clustering Parameter Selection. (a) We used the first three principal components since they explained over 70% of the variance. (b) The Silhouette method revealed that K = 8 yielded the best silhouette score, indicating it as the optimal number of clusters for our dataset.

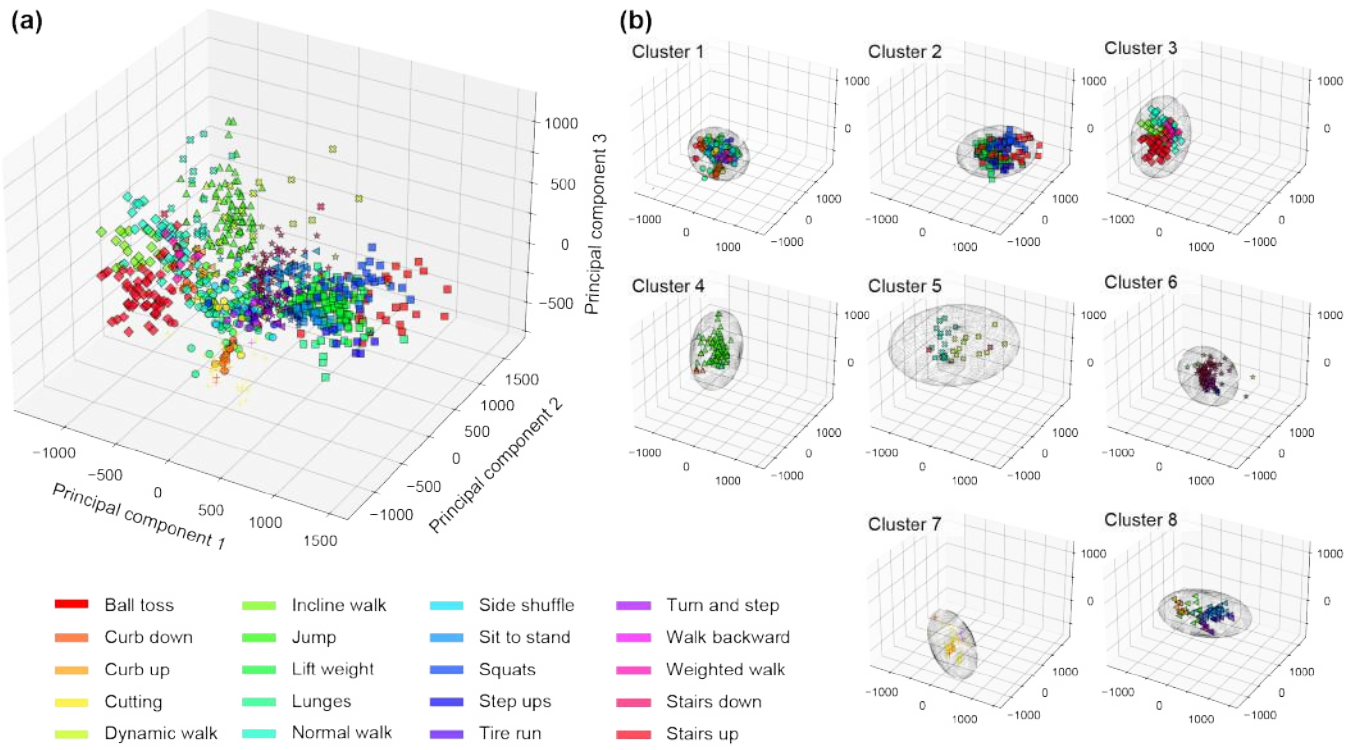


Fig. 3: PCA and K-means Clustering Results. (a) All biomechanical feature data represented in the reduced dimensions. Each task mode is colored differently and each cluster is marked in a different marker shape. (b) Separate plots for each cluster, with the ellipsoid representing the space of 99% confidence for each cluster.

TABLE I
Cluster Task-Weight Analysis

Clusters	Task	$\frac{A}{B}$	$\frac{A}{C}$	$\frac{S}{11}$	w	R
Cluster 1	Lunges	0.172	0.470	1.000	0.9	0.07280
	Dynamic Walk	0.128	0.523	1.000	0.9	0.06011
	Tire Run	0.122	1.000	1.000	0.9	0.11000
Cluster 2	Lift Weight	0.406	0.977	1.000	0.8	0.31715
	Lunges	0.165	0.530	1.000	0.9	0.07880
	Ball Toss	0.151	0.941	1.000	0.8	0.11365
Cluster 3	Stairs Up	0.438	0.914	0.909	1.0	0.36387
	Normal Walk	0.298	0.493	1.000	1.0	0.14672
	Incline Walk	0.182	1.000	1.000	1.0	0.18182
Cluster 4	Jump	0.906	0.755	1.000	0.9	0.61547
	Curb Down	0.047	0.167	0.273	0.8	0.00171
	Dynamic Walk	0.024	0.045	0.182	0.9	0.00018
Cluster 5	Normal Walk	0.531	0.233	0.727	1.0	0.08998
	Dynamic Walk	0.406	0.295	0.818	0.9	0.08838
	Stairs Down	0.031	0.017	0.091	1.0	0.00005
Cluster 6	Stairs Down	0.528	0.950	0.909	1.0	0.45581
	Walk Backward	0.287	0.939	1.000	0.9	0.24268
	Dynamic Walk	0.056	0.136	0.364	0.9	0.00248
Cluster 7	Cutting	0.686	0.795	1.000	0.8	0.43672
	Curb Down	0.137	0.292	0.455	0.8	0.01456
	Curb Up	0.137	0.292	0.545	0.8	0.01747
Cluster 8	Sit to Stand	0.393	0.500	1.000	0.9	0.17679
	Jump	0.167	0.137	0.727	0.9	0.01497
	Turn and Step	0.143	0.600	1.000	0.8	0.06857

Three tasks with the highest R values in each cluster and their task-weight analysis: columns, in order, represent (1) task data proportion within the cluster, (2) task data allocated to the cluster relative to its total, (3) subject diversity rate of the task in the cluster, (4) data collection difficulty weight, and (5) representativeness score.

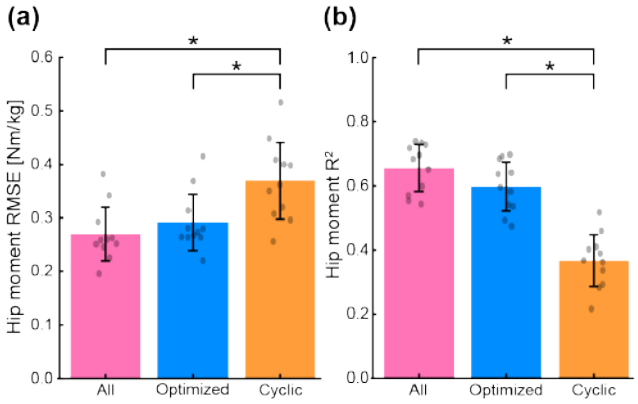


Fig. 4: Model Performance. (a) The all-task and optimized-task models outperformed the cyclic-task model, with significantly lower root mean squared errors (RMSEs). (b) Similarly, the optimized-task model showed higher R^2 compared to the cyclic task model, but similar performance compared to the all-task model. Gray dots represent values from 11 models per condition. * indicates a statistical difference from the cyclic tasks model ($p<0.05$).

B. Neural Network Performance

The optimized-task model performed better than the cyclic-task model and as well as the all-task model. The optimized model achieved an average RMSE of 0.29±0.06 Nm/kg and R^2 of 0.60±0.08 (Fig. 4). The all-task model had an average RMSE of 0.27±0.05 Nm/kg and R^2 of 0.66±0.08 . The cyclic-task model presented an average RMSE of 0.37±0.07 Nm/kg and R^2 of 0.37±0.08 . The

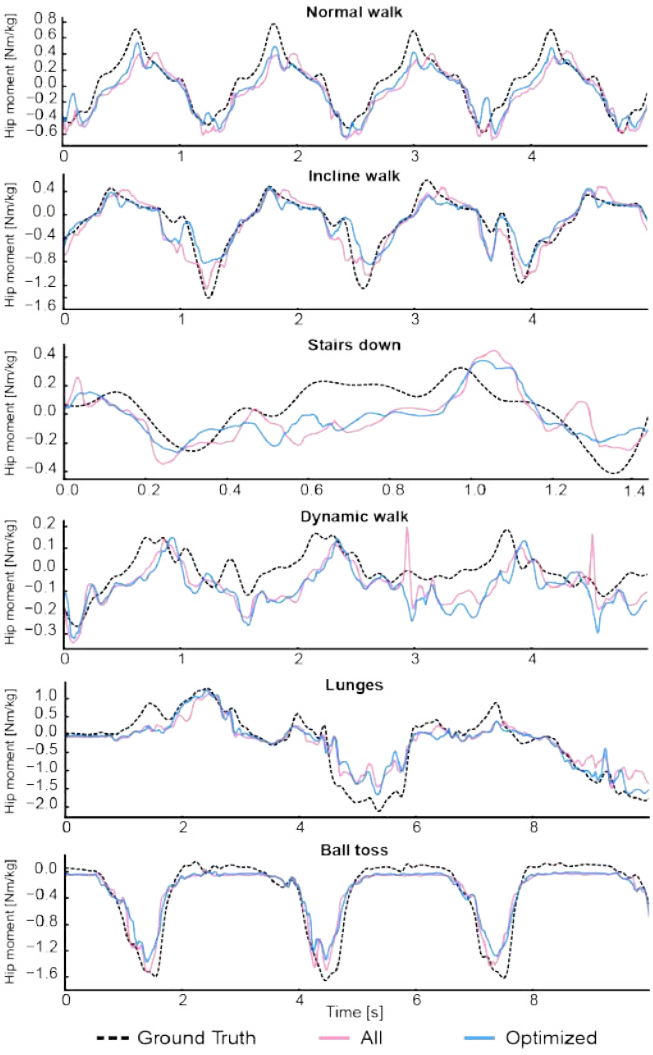


Fig. 5: Qualitative Performance Evaluation. Ground truth and estimated hip joint moments for the optimized-task (skyblue) and all-task (pink) models on four cyclic and two non-cyclic tasks using leave-out subject data with median RMSE performance. Ground truth is shown as a black dashed line. Both models follow the ground truth trend in similar performance.

models trained with all tasks and optimized tasks had lower RMSEs compared to the model trained with all cyclic tasks, by 26.52±6.48% and 20.40±6.70%, respectively ($p<0.05$). The optimized-task model was not different, by both RMSE and R^2, compared to the all-task model. The ground truth versus predicted hip joint moments of the optimized-task and all-task model are depicted for two cyclic and one non-cyclic tasks from both the included (normal walk, stairs down and lunges) and excluded task sets (incline walk, dynamic walk and ball toss), serving as representative examples of each task type (Fig. 5).

IV. Discussion

As hypothesized, the model trained on the optimized task set achieved comparable performance to the model trained on the entire dataset in hip joint moment estimation (Fig. 4). This finding validates the effectiveness of the task set optimization approach we used. Notably, the optimized-task model outperformed the cyclic-task model in RMSE and R^2 metrics, even though both sets contained the same number of tasks. This result highlighted the importance of including non-cyclic tasks in training data. It also presented the advantage of task optimization over relying solely on cyclic tasks for training a biological joint moment estimator.

The comparison of model predictions supports our argument that the optimized-task model performs comparably to the all-task model (Fig. 5). Both models were tested on a leave-out subject whose data showed median RMSE performance with the optimized task model. Despite its median performance, the model produced predictions nearly equivalent to those of the all-task model. Furthermore, when predictions were poorly executed, both models underperformed. This suggests that these difficulties are not stemming from the training tasks but from the limitation of using an FCNN and the inherent challenges of predicting non-cyclic tasks using only kinematic data. Overall, these results imply that developing a user-independent hip joint moment estimator is feasible with reduced task data. This approach could streamline future exoskeleton controller design by reducing data collection and training demands, facilitating the deployment of hip exoskeletons for daily activities.

Compared to a previous hip joint torque estimation using the same dataset, our optimized task model demonstrated comparable accuracy [22]. The study trained temporal convolutional networks (TCN) with kinematic sensor inputs (pelvis and thigh IMUs, hip angle, and velocity) and achieved an RMSE of 0.280 Nm/kg and an R^2 of 0.56 [22]. Using an FCNN, our model achieved similar performance, likely due to the exclusion of seven non-cyclic tasks with atypical movements. Although these excluded tasks were more challenging to predict accurately, the task set we included remains diverse compared to datasets limited to only treadmill or cyclic tasks. This comparison indicated the effectiveness of our task optimization and demonstrated that model performance is maintained even with fewer task data.

Furthermore, our approach of grouping tasks into clusters based on biomechanical features proved successful, offering a foundation for interpretable task relationships. The previous study applied a forward task selection algorithm and suggested that their ten tasks were sufficient to achieve optimal model performance [22]. Three of their tasks (sit-to-stand, normal walk, and jumping) overlapped with our optimized tasks. Their inclusion of some tasks that we excluded may have caused these distinct results. Nevertheless, this comparison highlighted the potential of our method to optimize task selection for model training through a more interpretable and biomechanics-grounded approach. From our clustering result, we can see that tasks were grouped with similarly performed tasks (Table 1). For instance, Cluster 3 predominantly included cyclic tasks focused on ascending movements (stairs up, incline walk, and normal walk), while Cluster 2 comprised non-cyclic and propulsive tasks (lift weight, lunges, and ball toss). These results demonstrated that our method provided a more intuitive understanding of task relationships compared to black box, performance-

driven approaches. Thus, our proposed approach was not only cost-efficient but also more interpretable, making it a practical alternative for task selection in model training.

While our study presented promising results, it has several limitations. First, compared to the previous studies that used more complex models like long short-term memory (LSTM) networks [24] or TCN [8], we opted for a simple FCNN. While the neural network architecture was intentionally kept simple to serve as a controlled variable in this study, a more complex model might better capture the intricate relationships between tasks within each cluster. Such models could also more effectively highlight the impact of task selection optimization. Future research could explore architectures like LSTM or TCN and fine-tune such models to investigate their potential advantages in this context. Second, the dataset used in this study exhibited an imbalanced number of trials for each task, which could influence the outcomes of the optimization process. Although a task-weight analysis formula was employed to mitigate these effects, ensuring an equal number of data points for each task in future datasets could further enhance the quality and reliability of the PCA and k-means clustering. Finally, this study used data only from healthy participants. Our approach relied on biomechanical profile similarities, which limits its effectiveness in individuals with significant differences, such as patient populations. Severe differences (e.g., crouch gait or stiff knee) may degrade the task optimization process and, consequently, model performance. Further research with more diverse subjects is needed to refine the approach for patient applications.

V. Conclusion

In this work, we presented a method to optimize task selection for a user-independent hip joint moment estimator. We identified the most representative tasks for model training by leveraging dimensionality reduction and clustering techniques on biomechanical features. The model trained on these optimized tasks achieved comparable performance to the model trained on the full dataset. These findings underscore the robustness of our approach and provide a pathway for future research on hip exoskeleton controller development with minimal training efforts.

References

[1] G. S. Sawicki, O. N. Beck, I. Kang, and A. J. Young, "The exoskeleton expansion: improving walking and running economy," *J. Neuroeng. Rehabil.*, vol. 17, p. 25, Feb. 2020.

[2] P. Slade, M. J. Kochenderfer, S. L. Delp, and S. H. Collins, "Personalizing exoskeleton assistance while walking in the real world," *Nature*, vol. 610, pp. 277–282, Oct. 2022.

[3] Y.-T. Pan *et al.*, "Effects of bilateral assistance for hemiparetic gait post-stroke using a powered hip exoskeleton," *Ann. Biomed. Eng.*, vol. 51, pp. 410–421, Feb. 2023.

[4] G. S. Sawicki, C. L. Lewis, and D. P. Ferris, "It pays to have a spring in your step," *Exerc. Sport Sci. Rev.*, vol. 37, pp. 130–138, July 2009.

[5] G. M. Bryan *et al.*, "Optimized hip-knee-ankle exoskeleton assistance reduces the metabolic cost of walking with worn loads," *J. Neuroeng. Rehabil.*, vol. 18, p. 161, Nov. 2021.

[6] A. J. Young, J. Foss, H. Gannon, and D. P. Ferris, "Influence of power delivery timing on the energetics and biomechanics of humans wearing a hip exoskeleton," *Frontiers in Bioengineering and Biotechnology*, vol. 5, 2017.

[7] G. M. Gasparri, J. Luque, and Z. F. Lerner, "Proportional joint-moment control for instantaneously adaptive ankle exoskeleton assistance," *IEEE Transactions on Neural Systems and Rehabilitation Engineering*, vol. 27, no. 4, pp. 751–759, 2019.

[8] D. D. Molinaro, I. Kang, J. Camargo, M. C. Gombolay, and A. J. Young, "Subject-independent, biological hip moment estimation during multimodal overground ambulation using deep learning," *IEEE Transactions on Medical Robotics and Bionics*, vol. 4, no. 1, pp. 219–229, 2022.

[9] D. D. Molinaro, I. Kang, and A. J. Young, "Estimating human joint moments unifies exoskeleton control, reducing user effort," *Science Robotics*, vol. 9, no. 88, p. eadi8852, 2024.

[10] M. S. B. Hossain, Z. Guo, and H. Choi, "Estimation of lower extremity joint moments and 3d ground reaction forces using imu sensors in multiple walking conditions: A deep learning approach," *IEEE Journal of Biomedical and Health Informatics*, vol. 27, no. 6, pp. 2829–2840, 2023.

[11] W. Meng *et al.*, "Optimized impedance control of a lightweight gait rehabilitation exoskeleton based on accurate knee joint torque estimation," *IEEE Transactions on Medical Robotics and Bionics*, vol. 6, no. 4, pp. 1648–1657, 2024.

[12] H. Dinovitzer, M. Shushtari, and A. Arami, "Accurate real-time joint torque estimation for dynamic prediction of human locomotion," *IEEE Transactions on Biomedical Engineering*, vol. 70, no. 8, pp. 2289–2297, 2023.

[13] K. L. Scherpereel, D. D. Molinaro, M. K. Shepherd, O. T. Inan, and A. J. Young, "Improving biological joint moment estimation during real-world tasks with emg and instrumented insoles," *IEEE Transactions on Biomedical Engineering*, vol. 71, no. 9, pp. 2718–2727, 2024.

[14] D. D. Molinaro *et al.*, "Task-agnostic exoskeleton control via biological joint moment estimation," *Nature*, vol. 635, pp. 337–344, Nov. 2024.

[15] T. Sun *et al.*, "Influence of number of subjects and number of trials on biomechanical variable estimation via deep-learning models and wearable imus during drop landings," *IEEE Sensors Journal*, pp. 1–1, 2025.

[16] Y. Lu, H. W. 0010, F. Hu, B. Zhou, and H. Xi, "Effective recognition of human lower limb jump locomotion phases based on multi-sensor information fusion and machine learning," *Med. Biol. Engineering and Computing*, vol. 59, no. 4, pp. 883–899, 2021.

[17] P. Santikan, W. Tangwongcharoen, and W. Kimpan, "Define stance and swing pattern of gait cycle using motion sensor and k-mean clustering," in *2022 19th International Conference on Electrical Engineering/Electronics, Computer, Telecommunications and Information Technology (ECTI-CON)*, pp. 1–4, 2022.

[18] C. Malloggi *et al.*, "Kinematic patterns during walking in children: Application of principal component analysis," *Human Movement Science*, vol. 80, p. 102892, 2021.

[19] S. M. Reid, R. B. Graham, and P. A. Costigan, "Differentiation of young and older adult stair climbing gait using principal component analysis," *Gait Posture*, vol. 31, no. 2, pp. 197–203, 2010.

[20] V. Andel *et al.*, "Whole-body movement analysis using principal component analysis: What is the internal consistency between outcomes originating from the same movement simultaneously recorded with different measurement devices?," *Front. Bioeng. Biotechnol.*, vol. 10, p. 1006670, Nov. 2022.

[21] X. Wang, N. O'Dwyer, and M. Halaki, "A review on the coordinative structure of human walking and the application of principal component analysis," *Neural Regen. Res.*, vol. 8, pp. 662–670, Mar. 2013.

[22] K. L. Scherpereel, D. D. Molinaro, O. Inan, M. Shepherd, and A. Young, "A human lower-limb biomechanics and wearable sensors dataset during cyclic and non-cyclic activities," *Sci. Data*, vol. 10, p. 924, Dec. 2023.

[23] P. J. Rousseeuw, "Silhouettes: A graphical aid to the interpretation and validation of cluster analysis," *Journal of Computational and Applied Mathematics*, vol. 20, pp. 53–65, 1987.

[24] M. Mundt *et al.*, "A comparison of three neural network approaches for estimating joint angles and moments from inertial measurement units," *Sensors*, vol. 21, no. 13, 2021.

Guided training with visual feedback can improve direct electromyography control of prosthetic ankles and sit-to-stand performance: A case study

Joshua R. Tacca*, Austin L. Mituniewicz*, Brendan Driscoll†, Elizabeth D. Buxton‡,
Michael D. Lewek*§, and He (Helen) Huang*
*Lampe Joint Department of Biomedical Engineering, UNC-Chapel Hill and NC State University, Raleigh, USA
†Department of Electrical and Computer Engineering, NC State University, Raleigh, USA
‡Department of Rehabilitation Therapies, UNC Hospitals, Chapel Hill, USA
§Department of Health Sciences, UNC-Chapel Hill, Chapel Hill, USA

***Abstract*—Direct electromyography (EMG)-controlled prostheses can allow people with amputation (PWA) to directly control their prosthetic ankle. This versatile control can assist with a variety of activities of daily life (ADL), including rising from and sitting down into a chair (i.e., sit-to-stand (S2S)). However, direct EMG control may be limited by a PWA's ability to activate their residual muscles. Physical therapy training with visual feedback may allow PWA to better utilize direct EMG-controlled prostheses. One PWA (transtibial) completed four training sessions with physical therapy guidance and visual feedback of their dorsiflexor and plantarflexor EMG during S2S tasks using a direct EMG-controlled prosthesis. They returned two weeks after the fourth training session and repeated S2S tasks without physical therapist guidance or visual feedback. We found that as the training progressed, residual EMG activation became more similar to the intact limb and was retained when feedback was removed. We also found that S2S movement was smoother (less jerk) during the retention session compared to the first training session. Our results demonstrate the potential of physical therapy with visual feedback to improve PWA's utilization of direct EMG-controlled ankle prostheses and performance in tasks related to ADL.**

I. Introduction

Powered ankle prostheses have been developed to mimic biological ankle muscles with the goal to improve function and mobility of people with lower-limb amputation (PWA) [1]. Most powered ankle prostheses utilize autonomous control, which is well-suited for cyclic tasks such as walking; however, these schemes do not allow PWA to directly control their device and typically require individual states and tasks to be pre-programmed [2]. Recently, researchers have developed methods to decode user intent and utilize neural signals to control powered ankle prostheses [2], [3], [4], [5], [6], [7], [8]. Neural control can allow for greater task versatility and is better suited to non-cyclic tasks than autonomous control [2]. One neural control strategy is direct electromyography (EMG) control, where signals from sensors placed on residual muscles are used to control the prosthesis directly and are proportional to the dynamics of the prosthesis [2]. Previous studies have demonstrated that PWA using direct EMG-controlled prostheses were able to adapt their prosthesis control to a wide range of tasks and improve balance during perturbations [3], [4].

While direct EMG control of powered ankle prostheses has shown promising results, it may be limited by a PWA's ability to activate their residual muscles. Different PWA exhibit varied activation patterns with their residual muscles, such as different levels of co-activation between the gastrocnemius (GAS) and tibialis anterior (TA) muscles and varied performance in generating desired activation patterns [9], [10]. While calibration methods can account for different levels of co-activation [11], there is still potential for PWA to improve their ability to generate desired, discrete activation patterns.

Feedback can be used to help PWA activate their residual muscles and control direct EMG prostheses. In Huang et al. [8], PWA using a direct EMG controlled prosthesis during walking were able to adapt their activation patterns and increase prosthetic push-off when visual feedback was given, but this adaptation was not retained when the visual feedback was removed. One research group developed a novel amputation surgery that maintains proprioceptive feedback from residual antagonistic muscles [4], [7]. PWA with the surgery exhibited less residual muscle co-activation and better utilized the EMG-controlled prosthesis during gait tasks such as walking on slopes, stairs, and obstacles compared to those without the surgery [4]. However, tying EMG-controlled prosthesis benefits to a surgical intervention may limit accessibility.

Alternatively, guided training may help PWA utilize direct EMG control [12], [13]. In a case study, one PWA completed a five-day training protocol with a direct EMG prosthesis that included tasks such as moving a rocker board, arm raises, forward reach, load transfer, and sit-to-stand (S2S) [12], changing their EMG activation strategy between the start and end of training [12]. Moreover, their performance in the load transfer task, requiring between limb synchronization, improved across training days [12]. This study demonstrated the potential for training with joint-level and whole-body movements to improve PWA's ability to utilize direct EMG prostheses for a range of tasks.

This study is funded by a National Institutes of Health Research Project grant (NIH: 5R01HD110519-02).

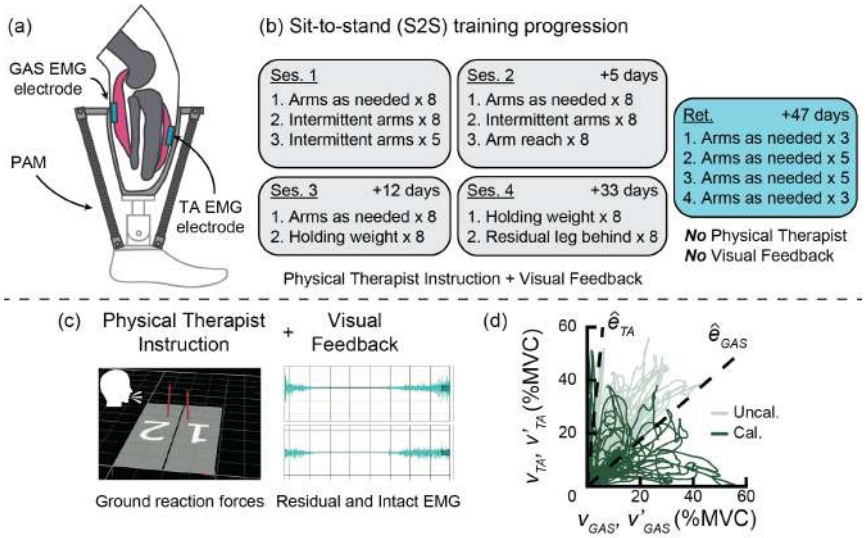


Fig. 1. (a) Diagram of the EMG-controlled powered prosthesis used. (b) Diagram of the sit-to-stand (S2S) training progression. For the first four sessions physical therapist instruction and visual feedback were given while the participant completed S2S trials. The difficulty of the S2S trials were varied to facilitate training. For the retention session, no physical therapist instruction or visual feedback were provided. The number of trials, cycles per trial, and days since the first session are indicated. This case study is a subset of a larger study and additional tasks were performed during sessions (Ses.) 1–4. In addition to S2S, the participant completed a joint-level visual feedback task during Ses. 1–2, squats during Ses. 1–4, arm raises during Ses. 2–4, rocker board during Ses. 3–4, stool stepping during Ses. 4, and stop and go walking during Ses. 4. (c) Physical therapist instruction and visual feedback given during sessions 1–4. (d) Uncalibrated (light green) GAS (v_{GAS}) and TA (v_{TA}) activation during the calibration task. Unit vectors ($\hat{e}_{GAS}$, $\hat{e}_{TA}$) that bound the uncalibrated control input space were used as a basis for the calibrated control signals (dark green, v'_{GAS}, v'_{TA}).

One important and ubiquitous activity of daily life (ADL) is sitting down and getting up from a chair [14], which can be challenging for PWA [15], [16]. Non-amputees activate the muscles surrounding the ankle during the S2S. For example, when rising from a chair the TA activates at the onset of movement contributing to forward motion of the body's center of mass while the GAS is activated later in ascension contributing to postural adjustments [17]. Given that passive prostheses cannot mimic these functions, PWA using these devices often compensate with their intact limb during S2S, exemplified by greater intact limb ground reaction forces and knee moments [16]. Direct EMG-controlled prostheses that can mimic the function of the muscles that surround a biological ankle have the potential to improve S2S performance through improved joint control for more symmetric joint motion. Therefore, the goal of the case study was to examine how a PWA controls a direct EMG prosthesis to perform S2S tasks and determine how guided physical therapy training with visual feedback could help the participant develop residual neural control activation that matches the intact limb and improve performance in the S2S. Moreover, we examined if the EMG activation strategies and task performance were retained after physical therapy instruction and visual feedback were removed.

II. Methods

One participant with unilateral, transtibial amputation (1 female, age: 29 years of age, height: 1.64 m, mass: 76.8 kg, time since amputation: 18 years, cause of amputation: cancer, K-level: 4 [19]) gave informed, written consent to participate in the study to the Institutional Review Board of North Carolina State University. This case study is a subset of a larger clinical study related to use of direct EMG-controlled prostheses for postural control and stability (NIH: 5R01HD110519-02).

A. Powered prosthesis

1) Design and sensing: The participant used a powered prosthesis with pneumatic artificial muscles (PAMs) (Fig. 1a) [3], [6]. The prosthesis has two PAMs in the front to control dorsiflexion and two PAMs in the back to control plantarflexion. Bipolar, low profile, neo-natal surface electrodes (Ambu Neuroline, Columbia, MD, USA) were placed on the residual TA and GAS muscles, inside the socket.

2) Signal processing and control: Residual muscle EMG (Ambu Neuroline 715, Ballerup, Denmark) were recorded in real-time at 1000 Hz (Motion Lab Systems MA-400, Lake Elsinore, CA, USA) and used as control inputs (v_{GAS}, v_{TA}) for the PAMs (dSPACE, Paderborn, Germany) [3]. In real-time, EMG were first high-pass filtered (100 Hz), then rectified, and finally low-pass filtered (2 Hz) using a custom Simulink model (Mathworks, Natick, MA, USA) [3]. Post-tuning and calibration, described below, the processed EMG signals (0-10 V) were sent to proportional pressure regulators (MAC 36 series valve and PPC36A pressure regulator, Wixom, MI, USA) to modulate PAM internal pressure (0 to 90 psi) [3].

3) Calibration and tuning: We calibrated control signals to lines of co-activation exhibited by the participant at the beginning of each session (Fig. 1d). To determine the co-activation, the participant completed a one minute visual feedback task in which they moved a cursor through a grid on

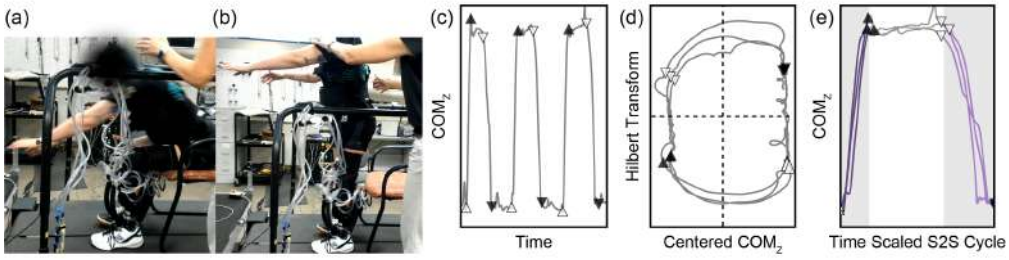


Fig. 2. Participant beginning (a) and (b) ending a S2S ascent. (c) Time series data from the vertical (i.e. "Z") component of the participant's CoM. Up and down pointing triangles indicate the beginning (open) and end (filled) of S2S ascent and descent periods, respectively. (d) These event locations were determined from the Hilbert transformed phase portrait of CoM_Z [18]. In this phase portrait (x-axis inverted), the first S2S cycle begins in the bottom right quadrant and proceeds counter-clockwise. (e) COM_Z data normalized to the time between ascent beginning and descent ending events. The shaded regions on the left and right depict the average ascent and descent sections of these cycles, respectively, and are highlighted in each cycle by purple.

a computer screen representing their control input space [9]. The processed, but not yet calibrated, control signals from the residual GAS and TA controlled horizontal and vertical cursor movement, respectively. As the cursor moved through the grid, the squares of the grid changed colors. The participant was asked to move the cursor as close to the x- and y-axes as possible, which corresponds to isolated activation from one muscle without activation from its antagonist. We determined the "natural" co-activation of the GAS and TA anterior muscles as the unit vectors of the lines that bound the participant's control input space ($\hat{e}_{GAS}$, $\hat{e}_{TA}$) (Fig. 1d). We calculated the calibrated control inputs (v'_{GAS}, v'_{TA}) using (1):

$$\begin{pmatrix} v'_{GAS} \\ v'_{TA} \end{pmatrix} = K^{-1} * \begin{pmatrix} v_{GAS} \\ v_{TA} \end{pmatrix} = \rceil \hat{e}_{GAS} \quad \hat{e}_{TA} \rceil^{-1} \begin{pmatrix} v_{GAS} \\ v_{TA} \end{pmatrix} \tag{1}$$

where K^{-1} is the inverse calibration matrix (Fig. 1d). We then manually set gains and baseline values that were multiplied and added, respectively, to v'_{GAS} and v'_{TA} [3], [6]. Gains were adjusted such that a maximum contraction during sitting for each muscle resulted in a 8–9 V signal which corresponds to 72–81 psi generated by the pressure regulators [3]. Adding constant offset values (2–3 V) established baseline prosthetic ankle stiffness.

B. Measurements and processing

1) EMG: Bilateral EMG were recorded from TA and GAS muscles at 1000 Hz. For analysis, EMG were demeaned, bandpass-filtered (fourth-order Butterworth , 10-350 Hz), rectified, and low-pass filtered (fourth-order Butterworth, 6 Hz).

2) Kinematics and kinetics: A 12-camera motion capture system (Vicon, Oxford, UK) recorded reflective motion capture markers placed on the anterior superior iliac spines, posterior superior iliac spines, and iliac crests at 100 Hz, while a dual-belt, force-measuring treadmill (Bertec, Columbus, OH, USA) measured ground reaction forces (GRFs) at 1000Hz. In analysis, marker data were low-pass filtered (7 Hz).

C. Protocol

First, a certified prosthetist fit and aligned the participant's socket to the pneumatic ankle prosthesis. Then on separate days, the participant completed four pre-training evaluation sessions, as part of the larger study. The participant completed postural control tasks using their own passive prosthesis and the pneumatic ankle prosthesis for two sessions each. After that, they completed five training sessions with a physical therapist using the pneumatic prosthesis on separate days at least 5 days apart. The training sessions consisted of joint-level and body-level tasks (e.g. joint-level visual feedback tasks, squats, stop and go walking) [9], [12], performing S2S tasks during each of the five sessions (Ses. 1–4 and Ret.; Fig. 1b).

1) S2S training protocol and feedback: The participant maximally contracted (MVC) the TA and GAS of both legs in sitting and standing three times each. We calibrated the control inputs and tuned the prosthesis controller gains based on the process described above. For the first four sessions, the participant completed S2S tasks with physical therapy guidance and visual feedback (Fig. 1b). They completed 5–8 S2S trials per task and 2–3 tasks per session. The physical therapist provided instructions regarding S2S performance and use of the prosthesis. For example, the physical therapist instructed the participant to bear weight symmetrically between the two limbs and contract the muscles in a smooth, controlled manner. The physical therapist progressed S2S difficulty. Variations of the S2S included utilizing the chair arm rests with one or two arms, not using the arm rests, reaching arms forward throughout the task, holding a 5 lb weight, and staggering the feet to target the residual limb (Fig. 1b). During these tasks, the participant was given visual feedback of GRFs and EMG from both legs (Fig. 1c). To determine if the participant retained any training benefits, she returned for a fifth session where she completed four S2S tasks without physical therapist guidance, visual feedback, and minimal arm rest use.

D. Data analysis and outcome measures

1) Determining S2S ascent and descent: To analyze the ascent and descent periods of the S2S independently, we sectioned the trials based on the body center of mass (CoM). We estimated CoM from marker data and a model of the pelvis in Visual3D (HAS-Motion, Kingston, Canada). To accommodate variations in S2S cycle duration and position extrema, CoM data was sectioned using a procedure similar to [20]. Briefly, this process created phase portraits for each trial and utilized

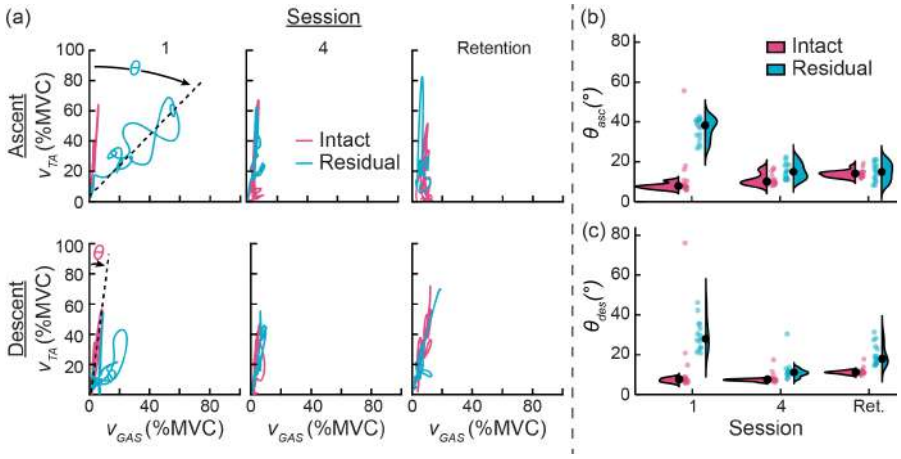


Fig. 3. (a) Representative S2S ascent (top) and descent (bottom) TA-GAS activation spaces, normalized to MVC, from the intact (red) and residual (blue) limbs during training session 1 (left), training session 4 (middle), and the retention session (right). The angle θ measures the amount of co-activation during the section. (b, c) θ of the intact (red) and residual (blue) limbs, their probability distributions, and medians (black symbol) for both ascent (b, θ_{asc}) and descent (c, θ_{des}) from all trials in each session.

the Hilbert transform method due to the data's non-sinusoidal nature [18]. The horizontal axis for each trial consisted of the CoM's vertical component, centered by its extrema, while the vertical axis was created from the imaginary portion from the Hilbert transform of the centered CoM position (Fig. 2c) [18]. Horizontal axis crossings from the resulting phase portraits occur at S2S superior and inferior midpoints (Fig. 2a,b) and vertical axis crossing midway through descent and ascent. Hence, the first passing of the phase angle across the phasal midpoints between axis crossings (i.e. 45, 135, 225, and 315°) approximate the beginning and ending of S2S ascent and descent (Fig. 2b-d). To avoid distortion from the Hilbert transform [21], data from the first and last 100 samples from a trial were not considered in this report.

2) EMG: EMG data were normalized to their respective MVCs (maximum value from sitting and standing MVC trials) and segmented into sections. To quantify the EMG activation strategy used during ascent and descent, we computed limb and ascent/descent-specific principal component analyses (PCA) (Fig. 3a). The angle of the PCA (θ) represents the relative contribution of the GAS and TA muscles where 0° signifies only TA activation and 90° signifies only GAS activation (Fig. 3a). PCA inputs were post-processed TA and GAS activity normalized to MVC. θ was acquired by calculating the cosine similarity between $[0, 1]^T$ and the first eigenvector of the covariance matrix.

3) CoM jerk: To quantify S2S performance, we computed CoM jerk because of the emphasis placed on task smoothness by the physical therapist and that smoother motion is a sign of improved control [22]. To account for differences in S2S duration and speed, we calculated the log transformation of normalized, integrated CoM [22]. To do this, we first took the third derivative of the CoM magnitude timeseries (2).

$$jerk = \left(\frac{\mathrm{d}^3 ||CoM||}{\mathrm{d}t^3} \right) \tag{2}$$

Next, data were sectioned into ascent and descent portions using the method described above. The squared jerk was integrated, multiplied by its duration (T) to the 5^{th}, and then divided by the square of its CoM magnitude amplitude (A). We log-normalized the result to get unit-less, log-normalized, integrated square jerk (NJ) (3).

$$NJ = \log_e \left(\frac{T^5}{A^2} \int jerk^2 dt \right) \tag{3}$$

For the CoM jerk, we analyzed data from the first trial in session 1, the first trial in session 4, and the second trial during the retention session (Fig. 1b). We chose to analyze data from the first trial on session 1 and 4 because those were the S2S tasks that were most similar between the first and last training days. We chose to analyze data from the second trial on the retention day as it was the first complete trial (trial 1 only had 3 repetitions).

EMG and COM jerk were analyzed descriptively given that the current study is a case study of one participant.

III. Results

On the first training day, in both the ascent and descent periods of S2S, the participant primarily activated their intact TA and displayed little co-activation (Fig. 3a). However, the residual muscles exhibited considerably more co-activation (Fig. 3a). During session 1, the median intact side θ_{asc} and θ_{des} were 7.84° and 7.68°, respectively (Fig. 3b-c). While, the median residual side θ_{asc} and θ_{des} were 38.29° and 28.01°, respectively (Fig. 3b-c). By session 4, the participant was able to activate their residual TA during S2S without GAS co-activation, better matching their intact limb strategy (Fig. 3a). The median intact θ_{asc} and θ_{des} from this session were 10.06° and 7.58°, respectively (Fig. 3b-c). Similarly, the median residual θ_{asc} and θ_{des} were 15.01° and 11.18°, respectively (Fig. 3b-c). The EMG activation pattern was retained two weeks following the final training session during S2S tasks

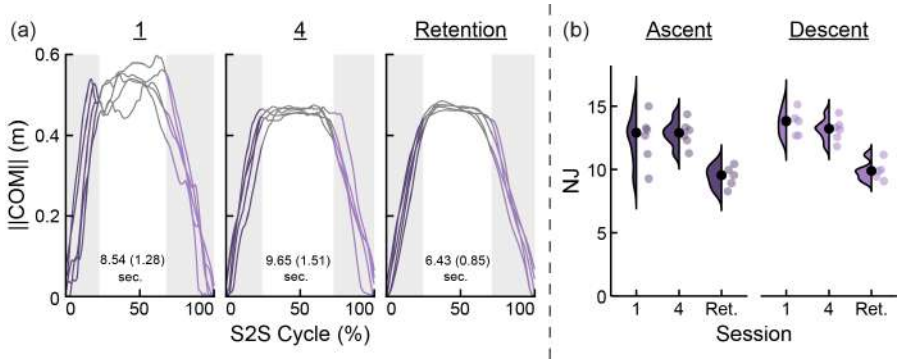


Fig. 4. (a) CoM Magnitudes of the S2S cycles analyzed during training session 1 (left), training session 4 (middle), and the retention session (right). The participant held a weight during session 4 S2S tasks. Shaded gray areas on the left and right show the average ascent and descent periods, while dark and light purple parts of the lines indicate these respective sections for each cycle. The average cycle time and trial standard deviation are displayed at the bottom of each plot. (b) Log scale normalized jerk (NJ; purple symbols), their probability distributions, and medians (black symbols) of the ascent (left) and descent (right) S2S sections.

without physical therapist instruction or visual feedback (Fig. 3a). During the retention session, the median θ_{asc} and θ_{des} of the intact limb were 14.10° and 11.28°, respectively (Fig. 3b-c). Similarly, the median θ_{asc} and θ_{des} of the residual limb were 14.92° and 17.90°, respectively (Fig. 3b-c).

CoM smoothness during the ascent of the S2S was almost equivalent during sessions 1 and 4, but the CoM smoothness improved relative to the training sessions on the retention day (Fig. 4a). Median NJ during ascent was 12.92, 12.91, and 9.54 during session 1, session 4, and the retention session, respectively (Fig. 4b). Similarly, during descent, the smoothness of the CoM was almost equivalent during sessions 1 and 4, but improved during the retention session (Fig. 4a). Median NJ during descent was 13.83, 13.24, and 9.89 during session 1, session 4, and the retention session, respectively (Fig. 4b).

IV. Discussion

Direct EMG control of powered prostheses allows people with limb amputation to directly control their prosthetic ankle, making it versatile to a wide range of tasks, but it can be limited by a participant's ability to activate their residual muscles. Our results indicate that guided physical therapy with visual feedback during training not only improves PWA's ability to control residual muscle activity, but also this ability is retained up to two weeks later without prior training aids. In the first training session, the participant displayed considerable co-activation between residual shank muscles but not intact muscles during both the ascent and descent S2S phases. In the final training and retention sessions, their intact and residual EMG co-activation patterns became more similar and were dominated by TA activation. This corresponds with non-amputee EMG activity during S2S. A study that measured EMG from eight lower limb and torso muscles of non-amputees found that the TA contributed 29% of the total activation during S2S ascent, while the GAS contributed 5% [23]. Furthermore, the training protocol seemed to affect S2S performance. Despite the increase in difficulty in S2S trials between session 1 and session 4 (holding 5 lb. weight in session 4), NJ was similar during S2S ascent and descent in session 4 compared to session 1. We also found that NJ decreased in the retention session compared to the other sessions. A reduction in NJ or an increase in "smoothness" of the movement implies that the participant was able to make a more controlled ascent and descent. The licensed physical therapist who conducted the training noted that the participant demonstrated improved ability to initiate the S2S task, attain and sustain postural stability in standing, and maintain control when descending onto the chair. Our result demonstrates the potential for direct EMG control to improve PWA's ability to stand up from a chair or sit down, an important ADL.

Our findings could have potential implications beyond S2S. Huang et al. found that without visual feedback, PWA using a direct EMG-controlled prosthesis walked with lower peak prosthetic power than with visual feedback [8]. Similarly, Song et al. found that PWA who had a novel surgery that provided proprioceptive feedback exhibited 187% greater peak prosthetic ankle power compared to the control group when both walked with a direct EMG-controlled prosthesis [4]. Their results suggest that without proprioceptive feedback, PWA were unable to fully capitalize on the EMG-controlled prosthesis. However, Stafford et al. reported that PWA walking with a direct EMG controlled prosthesis more than once a week helped maintain familiarity and improved EMG adaption [5]. Likewise, we found that even without physical therapist guidance and visual feedback, the control of residual EMG activation was retained in our participant at two weeks after training. Perhaps, training on a variety of tasks, progressing task difficulty, and utilizing visual feedback of muscle activation are key to the successful direct EMG-controlled prostheses use.

Our study had several limitations. First, this was a case study of one young, highly active participant who had never used EMG-controlled prostheses prior to the study. PWA's ability to activate residual muscles varies [10] and it is possible that the improvements observed throughout this case study represent larger changes than could be expected for other participants.

Second, we prioritized the physical therapy protocol and training flexibility over experimental control. The variation in the S2S tasks adds a potential confounding variable when comparing between sessions. Nevertheless, since the S2S tasks in session 4 were more challenging than in session 1, we speculate that we may have observed an improvement in NJ in session 4 compared to session 1 if the S2S tasks had been controlled. In future studies, we would like to examine the effects of the training protocol with a larger sample size and examine other important ADLs such as stop and go walking, turning, reaching, and rising up on toes. To evaluate independent effects of the EMG-controlled prosthesis and the training, we plan to recruit two groups of PWA: one group using their own passive prosthesis and the other using the EMG-controlled prosthesis.

V. Conclusion

One participant with lower limb amputation using a direct EMG-controlled prosthesis completed a 4-session training protocol with physical therapist instruction and visual feedback. As the training progressed, the participant was able to adapt their residual EMG activation so that it more closely matched their intact limb during S2S tasks. These residual EMG activation patterns were retained when physical therapy instruction and visual feedback were removed. Moreover, the participant improved S2S performance in the retention session compared to the first session. Our findings suggest that physical training that includes visual feedback, varies tasks to encourage use of the residual limb, and progresses in difficulty is a promising strategy to improve PWA's utilization of direct EMG-controlled prostheses.

Acknowledgment

The authors thank Avery Murray, Pinar Onal, Xiaolu Bai, and Benjamin Killen for their help with data collections.

References

[1] H. M. Herr and A. M. Grabowski, "Bionic ankle–foot prosthesis normalizes walking gait for persons with leg amputation," *Proceedings of the Royal Society B: Biological Sciences*, vol. 279, no. 1728, pp. 457–464, Feb. 2012.

[2] A. Fleming, N. Stafford, S. Huang, X. Hu, D. P. Ferris, and H. H. Huang, "Myoelectric control of robotic lower limb prostheses: a review of electromyography interfaces, control paradigms, challenges and future directions," *Journal of Neural Engineering*, vol. 18, no. 4, p. 041004, Jul. 2021.

[3] A. Fleming, W. Liu, and H. H. Huang, "Neural prosthesis control restores near-normative neuromechanics in standing postural control," *Science Robotics*, vol. 8, no. 83, p. eadf5758, Oct. 2023.

[4] H. Song, T.-H. Hsieh, S. H. Yeon, T. Shu, M. Nawrot, C. F. Landis, G. N. Friedman, E. A. Israel, S. Gutierrez-Arango, M. J. Carty, L. E. Freed, and H. M. Herr, "Continuous neural control of a bionic limb restores biomimetic gait after amputation," *Nature Medicine*, vol. 30, no. 7, pp. 2010–2019, Jul. 2024.

[5] N. E. Stafford, E. B. Gonzalez, and D. P. Ferris, "Walking Ankle Biomechanics of Individuals With Transtibial Amputations Using a Prescribed Prosthesis and a Portable Bionic Prosthesis Under Myoelectric Control," *IEEE Transactions on Neural Systems and Rehabilitation Engineering*, vol. 32, pp. 3036–3047, 2024.

[6] S. Huang, J. P. Wensman, and D. P. Ferris, "An Experimental Powered Lower Limb Prosthesis Using Proportional Myoelectric Control," *Journal of Medical Devices*, vol. 8, no. 024501, Mar. 2014.

[7] T. R. Clites, M. J. Carty, J. B. Ullauri, M. E. Carney, L. M. Mooney, J.-F. Duval, S. S. Srinivasan, and H. M. Herr, "Proprioception from a neurally controlled lower-extremity prosthesis," *Science Translational Medicine*, vol. 10, no. 443, p. eaap8373, May 2018.

[8] S. Huang, J. P. Wensman, and D. P. Ferris, "Locomotor Adaptation by Transtibial Amputees Walking With an Experimental Powered Prosthesis Under Continuous Myoelectric Control," *IEEE Transactions on Neural Systems and Rehabilitation Engineering*, vol. 24, no. 5, pp. 573–581, May 2016.

[9] S. Huang and H. Huang, "Voluntary Control of Residual Antagonistic Muscles in Transtibial Amputees: Reciprocal Activation, Coactivation, and Implications for Direct Neural Control of Powered Lower Limb Prostheses," *IEEE Transactions on Neural Systems and Rehabilitation Engineering*, vol. 27, no. 1, pp. 85–95, Jan. 2019.

[10] ——, "Voluntary Control of Residual Antagonistic Muscles in Transtibial Amputees: Feedforward Ballistic Contractions and Implications for Direct Neural Control of Powered Lower Limb Prostheses," *IEEE Transactions on Neural Systems and Rehabilitation Engineering*, vol. 26, no. 4, pp. 894–903, Apr. 2018.

[11] R. R. Posh, E. C. Barry, J. P. Schmiedeler, and P. M. Wensing, "Lower-Limb Myoelectric Calibration Postures for Transtibial Prostheses," *IEEE Transactions on Neural Systems and Rehabilitation Engineering*, vol. 32, pp. 1210–1220, 2024.

[12] A. Fleming, S. Huang, E. Buxton, F. Hodges, and H. H. Huang, "Direct continuous electromyographic control of a powered prosthetic ankle for improved postural control after guided physical training: A case study," *Wearable Technologies*, vol. 2, p. e3, Jan. 2021.

[13] A. Fleming, W. Liu, and H. Huang, "Neural Coherence of Homologous Muscle Pairs During Direct EMG Control of Standing Posture in Transtibial Amputees," in *Converging Clinical and Engineering Research on Neurorehabilitation IV*, D. Torricelli, M. Akay, and J. L. Pons, Eds. Cham: Springer International Publishing, 2022, vol. 28, pp. 139–143.

[14] P. M. Dall and A. Kerr, "Frequency of the sit to stand task: An observational study of free-living adults," *Applied Ergonomics*, vol. 41, no. 1, pp. 58–61, Jan. 2010.

[15] B. J. Hafner, S. J. Morgan, D. C. Abrahamson, and D. Amtmann, "Characterizing mobility from the prosthetic limb user's perspective: Use of focus groups to guide development of the Prosthetic Limb Users Survey of Mobility," *Prosthetics and Orthotics International*, vol. 40, no. 5, pp. 582–590, Oct. 2016.

[16] R. H. Teater, D. N. Wolf, K. A. McDonald, and K. E. Zelik, "Unilateral transtibial prosthesis users load their intact limb more than their prosthetic limb during sit-to-stand, squatting, and lifting," *Clinical Biomechanics*, vol. 108, p. 106041, Aug. 2023.

[17] M. M. Khemlani, J. H. Carr, and W. J. Crosbie, "Muscle synergies and joint linkages in sit-to-stand under two initial foot positions," *Clinical Biomechanics*, vol. 14, no. 4, pp. 236–246, May 1999.

[18] P. F. Lamb and M. Stöckl, "On the use of continuous relative phase: Review of current approaches and outline for a new standard," *Clinical Biomechanics*, vol. 29, no. 5, pp. 484–493, May 2014.

[19] E. M. Balk, A. Gazula, G. Markozannes, H. J. Kimmel, I. J. Saldanha, L. J. Resnik, and T. A. Trikalinos, *Lower Limb Prostheses: Measurement Instruments, Comparison of Component Effects by Subgroups, and Long-Term Outcomes*, ser. AHRQ Comparative Effectiveness Reviews. Rockville (MD): Agency for Healthcare Research and Quality (US), 2018. [Online]. Available: http://www.ncbi.nlm.nih.gov/books/NBK531523/

[20] A. L. Mituniewicz, V. Nalam, and H. H. Huang, "A Novel Approach to Assess Coordination in People with Transtibial Amputations Using Continuous and Event Relative Phase," Rochester, NY, Sep. 2024.

[21] P. Ippersiel, R. Preuss, and S. M. Robbins, "The Effects of Data Padding Techniques on Continuous Relative-Phase Analysis Using the Hilbert Transform," Aug. 2019.

[22] N. Hogan and D. Sternad, "Sensitivity of Smoothness Measures to Movement Duration, Amplitude and Arrests," *Journal of motor behavior*, vol. 41, no. 6, pp. 529–534, Nov. 2009.

[23] A. I. Cuesta-Vargas and M. González-Sánchez, "Differences in Muscle Activation Patterns during Sit to Stand Task among Subjects with and without Intellectual Disability," *BioMed Research International*, vol. 2013, no. 1, p. 173148, 2013.

Mantis shrimp-inspired quasi passive ankle-foot prosthesis*

Siavash Gitifar, Sy Nguyen, and Hwan Choi, *Member, IEEE.*

Abstract— **The biological ankle joint adjusts stiffness to adapt to changing walking speed and environments. However, commercial passive ankle-foot prostheses lack the ability to adjust stiffness, which causes gait issues. While powered prostheses can address these problems, they require large actuators, making them heavy, bulky, and energy insufficient. In this study, we introduce a quasi-passive, variable-stiffness ankle-foot prosthesis that employs unique characteristics of mantis shrimp's saddle spring. Mantis shrimps employ the saddle spring's energy storing and return mechanism to effectively punch their prey with their appendages. To integrate this saddle spring, we developed governing equations for parameterizing the geometry of the saddle spring. From the parameterization, the curvature and thickness of the saddle spring were optimized to match the biological ankle stiffness in normal walking speed. The moment arm of the saddle spring is then optimized to provide a range of biological ankle stiffness for slow to fast walking speeds. A theoretical model of the saddle spring is validated with experimental bench tests. The designed saddle spring can adjust dorsiflexion stiffness of the prosthesis from 8.63 to 18.43 Nm/° for a 100 kg user. The stiffness adjustment time from the lowest to highest stiffness is 0.3 sec. Our prosthesis shows a promising ability to provide prompt user-specific stiffness in daily living while maintaining compact, lightweight, and energy efficiency.**

I. Introduction

Approximately one million individuals in the United States are living with lower-limb amputations, and this number is expected to double by 2050 due to causes such as accidents and chronic illnesses, including obesity and diabetes [1]. The majority of lower-limb amputees utilize commercially available passive prostheses, generally manufactured with carbon-fiber, glass fiber, or other composite materials, which mimics spring-like behavior [2]. Although passive prostheses are affordable, lightweight, and compact, these designs impose significant limitations on the daily life of their users (e.g., uneven terrain or fast walking) [3]. Passive prostheses increase the risk of falls, decrease walking speed, and restrict users to a limited range of self-determined speeds, frequently leading to a walking speed that is half of a normal person's speed [4]. Moreover, the metabolic expenditure for users of passive prostheses is higher compared to able-bodied individuals [5], and activities such as ascending and descending stairs, as well as traversing the sloping surfaces, become considerably more difficult [6,7]. Prolonged usage of passive prostheses may result in side effects including backache, knee pain, and postural deformities, due to the asymmetrical gait cycle [8].

The issues faced by amputees mostly result from the lack of a functional lower limb, particularly the ankle joint. The biological ankle joint is essential for ensuring stability during the stance phase by adjusting the level of stiffness and facilitating moving forward during the push-off phase [9]. For example, ankle stiffness increases with an increase in walking speed. Biological ankle stiffness dynamically adjusts to diverse walking conditions, improving stability and efficiency over various terrains. On incline surfaces, such as ramps, increased ankle stiffness enhances control and facilitates propulsion by stabilizing the foot during push-off. Meanwhile, when traversing soft ground, stiffness generally reduces according to the terrain's instability, enabling the ankle to absorb and adjust to uneven forces [10,11]. The lack of joint stiffness adjustment capability in the passive prostheses considerably affects amputees' walking, daily activities, and overall quality of life [12].

Quasi-passive prosthesis, which use actuators to adjust stiffness, have been proposed as an alternate way to adapt different walking speeds and environments such as slop, soft ground, and stairs [13]. People with lower limb amputation can increase stability and reduce energy expenditure by using quasi-passive prosthesis that provides a suitable stiffness of the biological ankle joint while dynamically changing stiffness in response to walking demands [14]. These enhancements aim to improve amputees' quality of life by offering better control and reduced reliance on electrical power.

The variable stiffness prosthetic ankle-foot [15] uses an elastic cantilever beam to adjust stiffness by changing the slider's position. This design is compact and lightweight. However, it includes a rigid forefoot, limiting its ability to mimic the natural flexibility of the human foot, and requires continuous motor operation to adjust stiffness, resulting in a slow response. The Pro-Flex Pivot [16], with shear thickening fluid damper-spring system to vary stiffness through changing the damping ratio, also faces challenges with energy dissipation, and reducing efficiency in energy storage and return. The 2-degrees of freedom (DOF) Ankle foot prosthesis [17] uses two linear actuators to adjust stiffness. This design requires continuous motor operation, resulting in large battery demands. Quasi-passive variable stiffness prosthesis presented in [18] has multiple carbon fiber blades, and a locking mechanism uses solenoid as actuator. While lightweight, this quasi-passive variable stiffness mechanism is a high-profile design with discrete stiffness values, lacking the fine adjustment seen in a biological ankle.

This paper introduces a novel quasi-passive ankle-foot prosthesis inspired by the mantis shrimp, known for its rapid and powerful predatory strikes. The mantis shrimp utilizes a saddle-shaped elastic structure as a spring to store energy before striking, thereby amplifying the generated force [19,20]. Similarly, the proposed study employs a saddle-shaped elastic shell, named the "saddle spring", which functions as the prosthesis's spring element. This design addresses critical limitations of existing quasi-passive

*Research is supported by the National Science Foundation (NSF) under Grant No. 2231032. (Corresponding Author: Hwan Choi.)

The authors are with the department of Mechanical and Aerospace Engineering, University of Central Florida, Orlando, FL32816, USA (e-mail: siavash.gitifar@ucf.edu, sy.nguyen@ucf.edu, hwan.choi@ucf.edu).

prostheses by offering: (1) an adjustable stiffness with wider range to accommodate various walking speeds, sprinting, and running; (2) rapid stiffness adjustments within a single swing phase; and (3) an energy-efficient, self-locking mechanism that minimizes battery consumption. The paper presents the device's design, parameterization and optimization of the saddle spring, experimental testing, and an analysis of the results, demonstrating the effectiveness of the proposed approach.

II. Methods

A. Design of Mantis Shrimp-inspired Ankle-Foot Prosthesis (MSAFP)

The overall design of the ankle-foot prosthesis is shown in Fig. 1. The saddle spring is positioned between the upper and lower fixtures, which are capable of rotating around the central shaft that connects the adapter to the foot plate. The rotation of the upper fixture is driven by a worm-bevel gear system with a 60:1 ratio, powered by a DC motor (DCX 22 L, 10W, Maxon, Sachseln, Switzerland). The footplate is fabricated from Delrin, a strong and lightweight plastic material that offers sufficient mechanical strength while reducing overall weight compared to metal alternatives. This mechanism allows the saddle spring to rotate around the central shaft, enabling adjustments to the distance between the edge of the saddle spring and the central shaft. The distance between the saddle spring and hinge joint is defined as the moment arm, with the hinge joint functioning as the ankle joint.

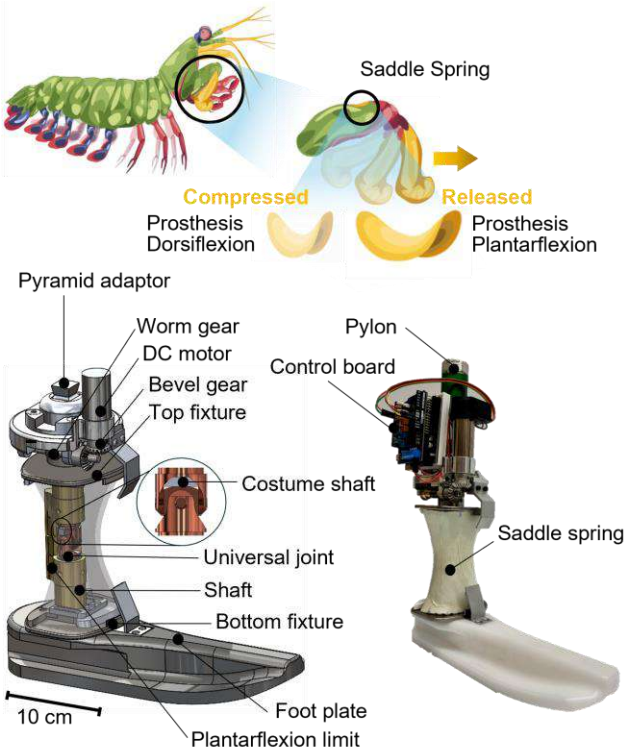


Fig. 1. Mantis Shrimp-inspire Ankle-Foot Prosthesis (MSAFP)

Utilizing the worm-bevel gear system, the proposed design can lock the saddle spring at the desired orientation and maintain stiffness without being affected by the induced torque on the transverse plane caused by the saddle spring's curvature, thereby enhancing energy efficiency. A custom-designed shaft pin was used to restrict the universal joint's degrees of freedom in the frontal plane, effectively converting it into a hinge joint in the sagittal plane. This design allows for future modifications to analyze the effects of inversion and eversion. The overall stiffness of the prosthesis adjusts as the saddle spring rotates. This hinge joint not only supports the user's load but also allows for bending to accommodate the saddle spring's movement. In addition, two stoppers are designed on the back side of the prosthesis in the sagittal plane to limit plantar flexion to a maximum of 5°, while dorsiflexion is constrained to 20° to ensure a controlled range of motion suitable for walking conditions [21]. These stoppers utilize rubber pants to prevent foot flapping and cancelling noise when two stoppers touch each other.

The prosthesis features an adjustable stiffness mechanism controlled by the rotation of the saddle spring. The design is compact and lightweight, with a height of 25 cm (including the DC motor) and a weight of 2 kg (excluding the battery), making it suitable for lower-limb amputees with varying residual limb lengths. The mechanism enables rapid stiffness adjustments, transitioning from minimum to maximum stiffness faster than the duration of the swing phase, ensuring quick responsiveness and adaptability.

B. Parameterization of saddle spring

The parameterization objective is to enable precise control over the saddle spring's curvature along the sagittal and transverse planes, which directly affects stiffness. Transforming the geometry to cylindrical coordinates allows direct curvature adjustments via defined parameters. The saddle spring's geometry is represented by Eq. 1.

$$\frac{x^2}{a} - \frac{y^2}{b} = z \tag{1}$$

Here, x, y, and z represent spatial coordinates, respectively, while a and b control the magnitudes of curvature along the sagittal and transverse planes, respectively. The level of stiffness of the saddle spring depends on its material properties and curvature on the sagittal plane [22]. To directly adjust curvature in different orientations, the Cartesian geometry is transformed into cylindrical coordinates, as shown in Eq. 2-4. This allows for targeted manipulation of moment arm via parameters in cylindrical terms.

$$x = c \cdot R \cdot cos(e\theta) \tag{2}$$

$$y = d \cdot R \cdot sin(f\theta) \tag{3}$$

$$R = \sqrt{z^2 + h} \tag{4}$$

Where R, θ, and z represent the radius, angle, and height in cylindrical coordinates. Parameters c and d scale the radius along the sagittal and transverse axes, respectively, while e and f adjust curvature orientation, and h controls flatness.

C. Stiffness calculation of saddle spring

The design optimization of the saddle spring aims to (1) minimize the height to accommodate different limb lengths and (2) achieve a stiffness range comparable to that of the biological ankle, which varies from 8.87 Nm/° to 14.91 Nm/° for a 100 kg prosthetic foot user [23]. This ensures the

prosthesis can deliver the required stiffness across different walking speeds.

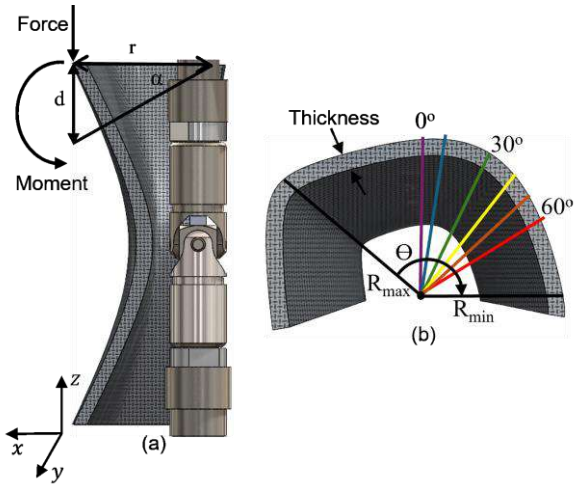


Fig. 2. Side and top view of saddle spring

Target stiffness is achieved by adjusting the moment arm and the saddle spring's thickness, as shown in Fig. 2 while maintaining identical curvatures in sagittal plane. Using the first-order shear deformation theory (FSDT) [24], we calculated stiffness values by integrating stress distributions over the thickness of saddle spring [25]. The saddle spring's radius of curvature along the sagittal (R_u) and transverse (R_h) planes are functions of the scaling parameters c and d. These equations are given as follows:

$$R_u = cR \tag{5}$$

$$R_h = dR \tag{6}$$

To model the saddle spring's stiffness properties, we calculate the extensional, coupling, and bending stiffness matrices A_{ij}, B_{ij}, and D_{ij}, which represent resistance to deformation under varying loads. These matrices are defined as follows:

$$A_{ij} = \int_{-t/2}^{t/2} Q_{ij}\left(1+\frac{f}{R_u}\right)\left(1+\frac{f}{R_h}\right)df \tag{7}$$

$$B_{ij} = \int_{-t/2}^{t/2} f\,Q_{ij}\left(1+\frac{f}{R_u}\right)\left(1+\frac{f}{R_h}\right)df \tag{8}$$

$$D_{ij} = \int_{-t/2}^{t/2} f^2\,Q_{ij}\left(1+\frac{f}{R_u}\right)\left(1+\frac{f}{R_h}\right)df \tag{9}$$

Here, the matrix A_{ij} integrates extensional stiffness across the spring thickness, the coupling matrix B_{ij} incorporates displacement fields and stiffness coefficients, and the bending matrix D_{ij} includes curvature effects. Where Q_{ij} is the transformed material stiffness coefficient for each layer, t is the shell thickness, and f is the displacement element in direction of thickness. The material stiffness coefficient Q_{ij} for each layer of saddle spring defines the material stiffness of each layer in terms of its elastic properties, allowing multi-layered material stiffness calculation, as shown in Eq. 10:

$$Q_{ij} = \begin{cases} \dfrac{E_s}{1-\nu_{st}\nu_{ts}} & i = j \\ \dfrac{\nu_{st}E_t}{1-\nu_{st}\nu_{ts}} & i \neq j \end{cases} \tag{10}$$

Where E_s and E_t are the young's modulus in sagittal and transverse plane, ν_{st} is Poisson's ratio. The subscripts i and j denote different layers in the system, referring to their respective load and stiffness components. Also, the sagittal and transverse planes are represented by the subscripts s and t, respectively. In Eqs. 11-13, S, V, and W are the global displacement components of both in-plane and out-of-plane components in the sagittal, transverse, and frontal plane, respectively.

$$S(u,h,f,t) = s(u,h,t) + f\phi_u(u,h,t) \tag{11}$$

$$V(u,h,f,t) = v(u,h,t) + f\phi_h(u,h,t) \tag{12}$$

$$W(u,h,f,t) = w(u,h,t) \tag{13}$$

The displacement field components s, v, and w are defined along the u-, h-, and thickness f -directions, respectively. The terms ϕ_u and ϕ_h represent the rotations of the saddle spring normal with respect to the u- and h-axes. Then, the corresponding normal, shear, and curvature strains are calculated for u-direction in Eqs. 14-16, respectively. The same method (Eq. 14-16) can be used to calculate the corresponding normal, shear, and curvature strains in other directions.

$$\varepsilon_u = \frac{\partial S}{\partial u} \tag{14}$$

$$\gamma_{uh} = \frac{\partial S}{\partial h} + \frac{\partial V}{\partial u} \tag{15}$$

$$k_u = -\frac{\partial^2 w}{\partial u^2} \tag{16}$$

ε_u, γ_{uh}, and k_u represent the corresponding normal, shear, and curvature strains in u-direction, respectively. s, v, and w defined along the u, h, and f-direction. To evaluate the spring's mechanical response, the strain energy U_S is calculated, combining force, moment, and shear across the entire geometry:

$$U_S = \tfrac{1}{2}\int_0^L \int_0^\pi \big(F_u\varepsilon_u + F_h\varepsilon_h + F_{uh}\gamma_{uh} + M_u k_u + M_h k_h + M_{uh}k_{uh} + Q_u\gamma_{uf} + Q_h\gamma_{hf}\big)(R_u)(R_h)\,dh\,du \tag{17}$$

In this equation, F, M, and Q are force, moment, and shear resultants, respectively, while ε, γ, and k represent the corresponding normal, shear, and curvature strains. Together, these terms represent stresses on the saddle spring. The stiffness matrix k is derived from applying the variational principle to the total strain energy U_S. L is the maximum height in sagittal plane. This matrix incorporates axial, bending, and shear forces, as follows:

$$k_{ij} = \int_0^L \int_0^\Pi \left(A_{ij}\frac{\partial U_S}{\partial u} + B_{ij}\frac{\partial^2 U_S}{\partial u^2} + D_{ij}\frac{\partial^3 U_S}{\partial u^3}\right) R_u R_h\,dh\,du \tag{18}$$

This matrix is assembled for the entire saddle spring domain and accounts for both classical and elastic boundary conditions through the inclusion of artificial springs, which simulate various boundary conditions by setting stiffness values to zero (free) or infinity (fixed). To address various

boundary conditions, each displacement function is expanded in a modified Fourier series:

$$u(u,h,t) = \sum_{m=0}^{M^*} \sum_{n=0}^{N^*} A_{mn}^{s} cos\left(\frac{m\Pi u}{L}\right) cos(nh) + \sum_{m=0}^{M^*} \sum_{n=0}^{N^*} a_{ln} p_l(u)\, cos(nh) \quad (19)$$

M^*, and N^* representing the highest orders of the terms in the series used to approximate the displacement functions in u, and h directions. The circumferential wave number is represented with n, and m in each direction. A_{mn}^{s} is the double Fourier cosine coefficient, a_{ln} represent the corresponding coefficients of the auxiliary function. The auxiliary function $p_l(u)$ is chosen to remove discontinuities at boundary points, ensuring continuity of displacement and its derivatives. Boundary conditions are simulated by adjusting artificial spring stiffness along the boundary. The governing equation system is transformed into an eigenvalue problem:

$$([k] - \omega^2[M])[G] = 0 \quad (20)$$

where $[k]$ and $[M]$ are the stiffness and mass matrices, ω is the natural frequency, and $[G]$ is the displacement vector. This equation is solved to obtain the eigenvalues and eigenvectors, representing the saddle spring's stiffness and modal characteristics. Finally, the overall stiffness matrix of the saddle spring in three-dimension coordinate, calculated based on the presented method in this section (Eq. 20). The entire stiffness of the prosthesis is calculated by converting the force-displacement stiffness of the saddle spring to geometry of the prosthesis (Eq. 20). Where M, r, and F are moment, moment arm, and vertical force, respectively. α , d, and r represent rotation angle, vertical displacement, and moment arm, respectively.

$$M = rF \quad (21)$$

$$\alpha = tan^{-1}\left(\frac{d}{r}\right) \quad (22)$$

D. Optimization of saddle spring

A nonlinear optimization identifies optimal values for thickness and height of saddle spring based on normal walking speed, then moment arm of the saddle spring, constrained to match biological ankle stiffness from slow to fast walking speed with using MATLAB's SQP algorithm [26]. The scaling factors of saddle spring's radius (parameters c, and d in Eqs. 5 and 6), and thickness of the saddle spring (t in Eq. 7) are selected as optimization variables. The objective function is formulated to minimize the discrepancy between the saddle spring's stiffness range to match the biological ankle. Specifically, it is defined as:

$$J = \sum_{i=1}^{N} \left| k_{Saddle\ spring,i} - k_{Target,i} \right| \quad (23)$$

$k_{Saddle\ spring,i}$, and $k_{Target,i}$ represent the computed stiffness of the saddle spring, and the biological ankle stiffness at the same speed, respectively. The curvature and thickness of the saddle spring is optimized based on the appropriate stiffness for normal walking speed. Then, the moment arm (r) optimized to cover the stiffness range needed for slow to fast walking speed. Thus, the cost function for optimization was set as the absolute difference between the stiffness of the saddle spring and the target stiffness of the human ankle. To determine the overall prosthetic stiffness in slow walking speed (mild stiffness) and fast walking speed (rigid stiffness).

As walking speed increases, biological ankle stiffness increases. Based on the saddle spring's parameterization and optimization (sections B and C), the saddle spring is designed to match stiffness at normal walking speed, with further adjustments of the moment arm, the mechanism covering the stiffness range from slow to fast walking speeds. The saddle spring's radius is constrained between 20 and 40 mm, with thickness ranging from 2-5 mm. Material properties of the glass fiber saddle spring are defined as 12700 Mpa, 2.48×10^{-9} ton/mm^3, and 0.22 for the young's modulus, density and Poisson's ratio, respectively [27].

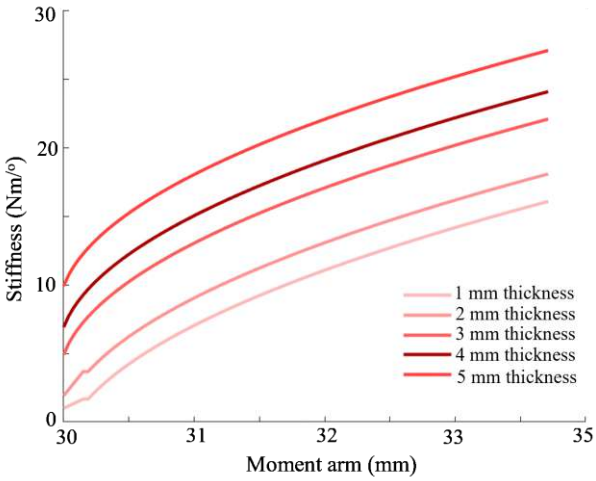


Fig. 3. Optimization of saddle spring

The stiffness-moment arm relationship for different thicknesses of the saddle spring, as shown in Fig. 3, highlights the impact of saddle spring's thickness on stiffness. Thinner saddle springs (1 mm and 2 mm) exhibit lower stiffness ranges. For instance, the 1 mm thickness provides a stiffness range of approximately 5 to 12 Nm/° across the moment arm range, while the 2 mm thickness achieves slightly higher values, ranging from about 7 to 15 Nm/°. Conversely, the 5 mm thickness yields the highest stiffness, ranging from 10 to 30 Nm/°. Therefore, the 4 mm thickness was chosen as the optimal configuration, offering a stiffness range of 8 to 25 Nm/°, which aligns well with the functional requirements of variable stiffness mechanisms, ensuring sufficient adaptability across different walking speeds.

E. Saddle spring bending test

The saddle spring is secured with two stoppers to prevent horizontal sliding, as shown in Fig. 4, replicating the boundary conditions of its fixtures in the prosthesis. A 30 mm diameter metal tip of the universal testing machine (313 tabletop dual column universal testing machine, TestResources, Shakopee, MN) was positioned on the top edge of the saddle spring to apply a vertical force of 1000 N at a constant rate of 100 N/s, ensuring compatibility with ISO 10328 [28]. The vertical force and displacement were calibrated before each test, with data recorded at 50 Hz. Static tests were conducted for different saddle spring orientations from 0° to 180° with 10° increments to evaluate the stiffness. Each test was repeated three times per orientation to assess stiffness changes, with experimental values collected based on the machine's measurements.

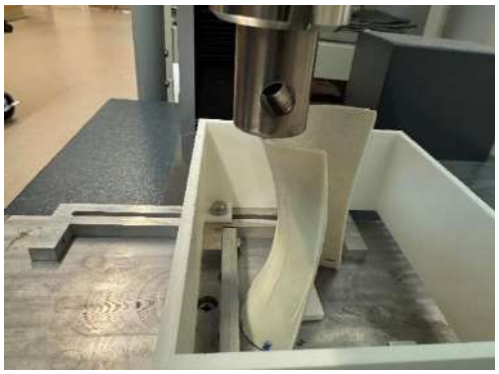


Fig. 4. Static bench test of experimental setup

III. Results

The saddle spring has variable stiffness at different orientations, with simulation results aligning closely with experimental data (Fig. 5). The stiffness of the saddle spring decreases as the moment arm shortens, making the system more compliant compared to configurations with a greater moment arm. From this analysis, the stiffness range of the designed saddle spring can be estimated to be from 8.63 to 18.46 Nm/° which meets the biological stiffness range [22].

Table 1 demonstrates that the saddle spring's stiffness decreases with increasing orientation angles, both in experimental and calculation results, indicating greater compliance at higher angles. The calculation closely matches experimental values, with root mean square error (RMSE) 1.2 to 3.89, suggesting that the model is fairly accurate across orientations. The lowest error occurs at 10° is 1.2, which indicates that the calculation performs best at mid-range orientations.

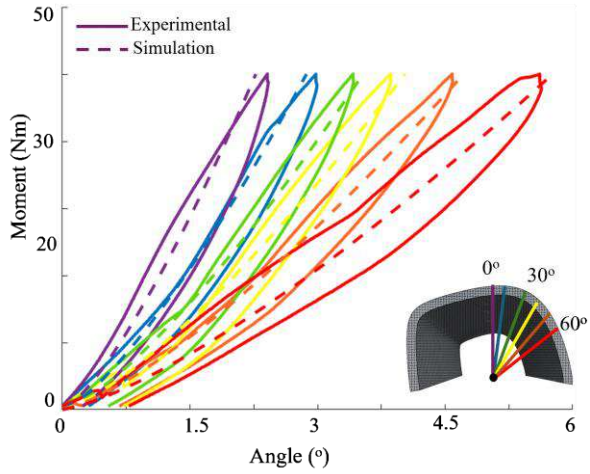


Fig. 5. Experiment and simulation stiffness. The color variation in the figure represents different orientations of the saddle spring, with the vertical purple line in the top view marking the origin (0°). Blue, green, yellow, orange, and red lines correspond to orientations of 10°, 30°, 40°, 50°, and 60°, respectively. Solid lines indicate experimental test results, while dashed lines represent simulation results for different saddle spring orientations.

MSAFP can adjust stiffness by rotating the saddle spring from 0° to 180° within 0.3 seconds. This speed is sufficient enough to change any level of stiffness within the swing phase duration that is approximately 0.4 seconds. This responsiveness enables real-time adaptation to gait changes.

TABLE 1 STIFFNESS ERROR BETWEEN CALCULATION AND EXPERIMENT

Saddle spring orientation	Stiffness (Nm/°)		
	Experiment	*Calculation*	*RMSE*
0°	18.46	19.62	1.69
10°	16.97	18.51	1.20
30°	14.47	13.86	1.60
40°	12.19	11.18	2.35
50°	9.63	9.05	2.78
60°	8.63	7.85	3.89

IV. Discussion

The MSAFP can adjust stiffness to accommodate a variety of walking speeds from slow to fast by altering the orientation of the saddle spring. This suggests that the prosthesis can deliver suitable stiffness for daily usage. The discrepancy between experimental and calculation occurs because the saddle spring is more balanced under load in the central region, whereas at the edges, slips occur during loading due to the uneven balance of the saddle spring (Fig. 5). Additionally, the edges are regions of high stress concentration, which can result in localized plastic deformation. Furthermore, the sharp edges of the saddle spring exacerbate stress distribution, contributing to the observed discrepancies.

The error between calculation and experimental values can come from manufacturing imperfections, such as uneven layer thickness or inconsistent material distribution across the saddle spring. Notably, fiber orientation, which has a significant impact on the quality of glass fiber, is designed based on the material stiffness coefficients (Q_{ij}) and elastic modulus [29,30]. Moreover, the discrepancy could stem from simplified material assumptions, such as linear elasticity, which fail to capture the complex responses observed during static tests. Also, the small slip during experiments leads to a higher experimental value compared to theoretical analysis. Furthermore, the universal testing machine may apply forces over a broader region of the saddle spring shell rather than targeting specific in theorical model.

In terms of energy storage and return in the saddle spring, the area of hysteresis increases as the saddle spring rotates from 0° to 60°. This is because the saddle spring's edge is more compliant than the center, resulting in more stored energy. Saddle spring is a specific type of hyperboloid shell. Previous studies [22] demonstrated that the curvature of hyperbolic paraboloid shells significantly influences their overall stiffness. Specifically, as the curvature decreases the stiffness of shell increases. In the MSAFP mechanism, the curvature on the sagittal plane of the saddle spring can be adjusted to reduce energy loss.

Future research will focus on refining the saddle spring design to better align with the biological ankle's stiffness profile over a wider range of walking, sprinting, and running speeds. For the current development, we optimized the thickness and moment arm of saddle spring to find the stiffness range for different walking speeds. Optimization of curvatures on the sagittal plane in addition to thickness and moment arm can be explored to maximize the range of stiffness and reduce the size of saddle spring and make it compact. Further optimizations using finite element analyses can also be

considered for the saddle spring's structural durability, as well as the hysteresis of energy storage and return.

In the MSAFP design, components such as the top fixture, bottom fixture, and bottom part support (which secures the bottom shaft to the footplate) are currently made of steel, with a combined mass of 0.573 kg. These components can be replaced with aluminum without compromising performance using finite element analyses. Employing aluminum can reduce the weight of MSAFP by approximately 0.2 kg, resulting in the total weight of the MSAFP, including the DC motor, of 1.8 kg.

V. Conclusion

Our MSAFP utilizes a novel saddle spring mechanism to adapt prosthetic foot stiffness across different walking speeds. The design is compact, fast respond, lightweight, and energy-efficient, with a responsive adjustment mechanism that operates within the swing phase duration. By consuming energy only during stiffness adjustments, the prosthesis minimizes power usage, enhancing its practicality for everyday use. Additionally, the mechanism is customizable to meet the unique needs of each prosthetic user and can accommodate running stiffness ranges, expanding its applicability.

Acknowledgment

The authors would like to thank Michael Carroll, Michael Varro, and Scott Anderson for their clinical advice on the prosthetic device design and saddle spring fabrication in this research project.

References

[1] K. Ziegler-Graham, E. J. MacKenzie, P. L. Ephraim, T. G. Travison, and R. Brookmeyer, “Estimating the prevalence of limb loss in the united states: 2005 to 2050,” Arch. Phys. Med. Rehabil., vol. 89, no. 3, pp. 422–429, 2008

[2] G. K. Klute, C. F. Kallfelz, and J. M. Czerniecki, “Mechanical properties of prosthetic limbs: Adapting to the patient,” Rehabil. Res. Develop., vol. 38, no. 3, pp. 299–307, 2001.

[3] D. J. Farris and G. S. Sawicki, “The mechanics and energetics of human walking and running: A joint level perspective,” J. R. Soc. Interface, vol. 9, no. 66, pp. 110–118, Jan. 2012.

[4] E. G. Gonzalez, P. J. Corcoran, and L. R. Rodolfo, “Energy expenditure in B/K amputees: Correlation with stump length,” Archs. Phys. Med. Rehabil., vol. 55, pp. 111–119, 1974.

[5] R. L. Waters and S. Mulroy, “The energy expenditure of normal and pathologic gait,” Gait Posture, vol. 9, no. 3, pp. 207–231, 1999.

[6] V. Struchkov and J. G. Buckley, “Biomechanics of ramp descent in unilateral trans-tibial amputees: Comparison of a microprocessor controlled foot with conventional ankle-foot mechanisms,” Clin. Biomech., vol. 32, pp. 164–170, Feb. 2016.

[7] L. Fradet, M. Alimusaj, F. Braatz, and S. I. Wolf, “Biomechanical analysis of ramp ambulation of transtibial amputees with an adaptive ankle foot system,” Gait Posture, vol. 32, no. 2, pp. 191–198, 2010.

[8] R. Gailey, K. Allen, J. Castles, J. Kucharik, and M. Roeder, “Review of secondary physical conditions associated with lower-limb amputation and long-term prosthesis use,” J. Rehabil. Res. Dev., vol. 45, no. 1, pp. 15–30, 2008.

[9] H. Charkhkar, B. P. Christie, and R. J. Triolo, “Sensory neuroprosthesis improves postural stability during sensory organization test in lowerlimb amputees,” Sci. Rep., vol. 10, no. 1, p. 6984, Dec. 2020.

[10] E. A. Hedrick, P. Malcolm, J. M. Wilken, and K. Z. Takahashi, “The effects of ankle stiffness on mechanics and energetics of walking with added loads: A prosthetic emulator study,” J. Neuroeng. Rehabil., vol. 16, Nov. 2019, Art. no. 148.

[11] K. Xie, Y. Lyu, X. Zhang, and R. Song, “How compliance of surfaces affects ankle moment and stiffness regulation during walking,” Frontiers in Bioengineering and Biotechnology, p. 759, 2021.

[12] M. Song, W. Chen, S. Guo, Z. Li, J. Rasmussen, S. Bai. “Design, simulation and kinematic verification of a multi-loop ankle-foot prosthetic mechanism,” IEEE Robotics and Automation Letters. Jul. 2023.

[13] M. J. Major, M. Twiste, L. P. J. Kenney, and D. Howard, “The effects of prosthetic ankle stiffness on ankle and knee kinematics, prosthetic limb loading, and net metabolic cost of trans-tibial amputee gait,” Clin. Biomech., vol. 29, no. 1, pp. 98–104, Jan. 2014.

[14] M. K. Shepherd, A. F. Azocar, M. J. Major, and E. J. Rouse, “Amputee perception of prosthetic ankle stiffness during locomotion,” J. Neuroeng. Rehabil., vol. 15, no. 1, pp. 1–10, 2018.

[15] M. K. Shepherd and E. J. Rouse, “The VSPA foot: A quasi-passive ankle-foot prosthesis with continuously variable stiffness,” IEEE Trans. Neural Syst. Rehabil. Eng., vol. 25, no. 12, pp. 2375–2386, Dec. 2017.

[16] H. Tryggvason, F. Starker, A. L. Armannsdottir, C. Lecomte, and F. Jonsdottir, ‘‘Speed adaptable prosthetic foot: Concept description, prototyping and initial user testing,’’ IEEE Trans. Neural Syst. Rehabil. Eng., vol. 28, no. 12, pp. 2978–2986, Dec. 2020.

[17] E. A. Rogers, M. E. Carney, S. H. Yeon, T. R. Clites, D. Solav, and H. M. Herr, “An ankle-foot prosthesis for rock climbing augmentation,” IEEE Trans. Neural Syst. Rehabil. Eng., vol. 29, pp. 41–51, Oct. 2020.

[18] E. Rogers-Bradley, S. H. Yeon, C. Landis, and H. M. Herr, ‘Design and Evaluation of a Quasi-Passive Variable Stiffness Prosthesis for Walking Speed Adaptation in People With Transtibial Amputation’, IEEE/ASME Transactions on Mechatronics, vol. 29, no. 1, pp. 335–346, Feb. 2024.

[19] S. A. M.Tadayon, Z. Wang, and A. Miserez, “Biomechanical design of the mantis shrimp saddle: A biomineralized spring used for rapid raptorial strikes,” Science, vol. 8, no. 26, pp. 271–282, Oct. 2018.

[20] B. Zhang, X. Peng, Z. Mu, S. Niu, Z. Han, L. Ren, “The Super Tough Saddle of Mantis Shrimp Derived from Strain Transformation Between Helical Fibers and Interlaminar Fibrils,” Advanced Functional Materials, no. 16, Apr. 2024.

[21] Ugbolue, U. C., Robson, C., Donald, E., Speirs, K. L., Dutheil, F., Baker, J. S.,Gu, Y. Joint angle, range of motion, force, and moment assessment: responses of the lower limb to ankle plantarflexion and dorsiflexion. Applied Bionics and Biomechanics, 2021.

[22] T. Mensch, E. Delesky, R. Learsch, K. Foster, S. Yeturu, W. Srubar, G. Miyake, “Mechanical evaluation of 3D printed biomimetic non-Euclidean saddle geometries mimicking the mantis shrimp,” Bioinspiration & biomimetics. no. 1, Jul. 2021.

[23] A.-R. Akl, A. Baca, J. Richards, and F. Conceição, “Leg and lower limb dynamic joint stiffness during different walking speeds in healthy adults,” Gait Posture, vol. 82, pp. 294–300, Oct. 2020.

[24] RP. Shimpi, HG. Patel, H. Arya, “New first-order shear deformation plate theories,” pp. 523–533, 2007.

[25] T. Ye, G. Jin, Y. Zhang. “Vibrations of composite laminated doubly-curved shells of revolution with elastic restraints including shear deformation, rotary inertia and initial curvature,” Composite Structures. pp. 202–225, Dec. 2015.

[26] R. Fletcher, “The sequential quadratic programming method,” in Nonlinear Optimization, G. Di Pillo and F. Shoen, Eds. Berlin, Germany: Springer-Verlag, 2010.

[27] https://www.spsco.com/by-product-type

[28] J. Tabucol, T. M. Brugo, M. Povolo, M. Leopaldi, M. Oddsson, R. Carloni, and A. Zucchelli, ‘‘Structural FEA-based design and functionality verification methodology of energy-storing-and-releasing prosthetic feet,’’ Appl. Sci., vol. 12, no. 1, p. 97, Dec. 2021.

[29] Mortazavian S, Fatemi A. Effects of fiber orientation and anisotropy on tensile strength and elastic modulus of short fiber reinforced polymer composites. Composites part B: engineering. 2015 Apr 1;72:116-29.

[30] Sabuncuoglu B, Tanabi H, Soete J, Lomov SV. Micro-CT analysis of deviations in fiber orientation and composite stiffness near the microvascular channels embedded in glass-fiber reinforced composites. Composite Structures. 2020 Apr 1;237:111896.

User Preferences and Information Gaps for AI-Assisted Selection of Engineered Devices for Home Rehabilitation after Stroke

Juan C. Perez-Ibarra, Luis Garcia-Fernandez, Andria J. Farrens, Miriam Bender, Jay J. Han, David J. Reinkensmeyer, *Senior Member, IEEE*

Abstract— **There has been a proliferation of engineered devices for movement rehabilitation, but their uptake remains sporadic. Using a mixed-methods approach with qualitative interviews and quantitative surveys, we asked nine post-stroke individuals to identify their information needs and to inform the design of an AI-powered decision support system to help select devices for home movement training after stroke. Key themes that emerged were: 1) difficulties finding information about device efficacy and motivational features and 2) openness to being helped by an AI chatbot. In a follow-up ranking exercise, participants indicated that the decision support system should provide information on the frequency of use required to get a benefit, ease of use, and the amount of expected benefit. They also highly rated potential features such as being able to provide personal information for customized recommendations, ask questions, and receive non-sales-driven guidance. In parallel, we analyzed 67 FDA-listed devices for movement rehabilitation. Of those with cost information, 43% were under $1,000, and 45% had insurance reimbursement. We emailed companies to get more data about motivational features and expected efficacy, but only 30% responded. These results confirm that post-stroke users have numerous devices available for home therapy but face substantial barriers to obtaining the information they want. Further, they are enthusiastic about using an AI chatbot to help find devices.**

I. Introduction

In 2021, more than 3 billion people worldwide were living with neurological conditions, representing about 43% of the world's population [1]. Stroke, in particular, remains one of the world's leading causes of long-term disability, with about 15 million people affected annually and half requiring long-term rehabilitation [2]. In response to the increasing demand for neurorehabilitation, the past three decades have seen a rapid increase in the development of neurorehabilitation technologies [3-4]. Innovations such as robotic therapy devices, sensor-based gaming systems, exoskeletons, brain-computer interfaces (BCIs), and functional electrical stimulation (FES) systems hold the promise of semi-automated therapy, increased user engagement, and more precise data for decision-making in treatment. Considering the case of rehabilitation robotics, the number of academic publications since 2001 has grown consistently due to the proliferation of both engineering and clinical studies [3-5]. The number of companies offering engineered rehabilitation devices also grew during this period. Despite this growth, clinical uptake of rehabilitation technology is sporadic. Key barriers include high costs, perceived complexity, and limited awareness of evidence-based benefits [6-8]. Both clinicians and patients struggle to find useful and trustworthy information that helps them select devices.

Our working hypothesis is that recent advances in AI could power a decision support system to help potential users of advanced rehabilitation technology make informed choices, reducing one barrier to uptake. In this paper, we report efforts toward gaining insight into how to develop such a system, focusing on two preliminary objectives of identifying user informational needs and gaps in available information. We have adopted a user-centric approach to ensure that the voices and needs of individuals with neurological impairments are central to the design and development of the proposed system. In this initial phase, we focus on post-stroke individuals as primary end-users, with the perspectives of other stakeholders, such as clinicians, planned for future studies. This paper describes the results of interviews followed by quantitative surveys of nine post-stroke individuals regarding the proposed system. In parallel, we sought to curate user-relevant information in a database of commercially available devices.

II. Methods

A. Interviews and surveys to gain insight into the informational needs and preferences of people post-stroke

Participants: We recruited nine individuals in the chronic phase of stroke from ongoing clinical trials of rehabilitation technologies at our institution; participant characteristics are shown in Table I.

Eight of the nine individuals participated in interviews (Group 1, see questions in Table II) and four in a pilot test of a survey comprised of a ranking exercise (Group 2, see Table III). All participants provided informed consent, and the Institutional Review Board of UC Irvine approved the study.

*This study was supported in part by the National Center for Research Resources and the National Center for Advancing Translational Sciences, National Institutes of Health (grant number 1UM1TR004927).

J. C. Perez-Ibarra is with the Departments of Physical Medicine and Rehabilitation, and Mechanical and Aerospace Engineering, University of California at Irvine, Irvine, CA, 92697 USA (e-mail: jperezib@uci.edu).

L. Garcia-Fernandez and A. J. Farrens are with the Department of Mechanical and Aerospace Engineering, University of California at Irvine, Irvine, CA, 92697 USA (e-mail: garciaf7@uci.edu; farrensa@uci.edu).

J. J. Han is with the Department of Physical Medicine and Rehabilitation, University of California at Irvine, Irvine, CA, 92697 USA (e-mail: jayjhan@hs.uci.edu).

M. Bender is with the Sue & Bill Gross School of Nursing, University of California at Irvine, Irvine, CA, 92697 USA (e-mail: miriamb@uci.edu).

D. J. Reinkensmeyer is with the Departments of Physical Medicine and Rehabilitation, Anatomy and Neurobiology, Biomedical Engineering, and Mechanical and Aerospace Engineering, University of California, Irvine, CA 92697 USA (e-mail: dreinken@uci.edu).

TABLE I. PARTICIPANT CHARACTERISTICS

ID	Gender	Age	Time post-stroke	Group 1	Group 2
SARS	Female	47	11 months	Yes	No
MASR	Male	68	10 months	Yes	No
RUPD	Male	62	2 years	Yes	No
LEDU	Male	61	13 months	Yes	No
CONK	Female	62	8 years	Yes	No
ZHAE	Male	46	8 months	Yes	Yes
BUIT	Female	60	13 years	Yes	Yes
SCHJ	Male	27	5 years	Yes	Yes
SIHR	Male	67	6 years	No	Yes

Interview Methods: Author A.F. conducted all interviews. Table II shows that the interview included questions about recovery, barriers to accessing and following rehabilitation advice, experiences using rehabilitation devices or apps, preferences for device recommendations, familiarity with artificial intelligence, and interest in AI-driven support systems. While not explicitly based on a single theoretical model, the questions were developed using a user-centered design approach, and they align with principles from the Technology Acceptance Model (TAM), particularly regarding perceived usefulness and ease of use [9-10]. Our analytical approach was guided by a constructivist paradigm, recognizing that individual experiences and social contexts shape attitudes. Therefore, we conducted an inductive thematic analysis, allowing themes to emerge organically from the data rather than being pre-defined. The analysis followed a summative content analysis approach, where we identified key themes based on the frequency and depth of participant responses. Two independent researchers developed a codebook (see the Results section) and coded the data separately, followed by consensus-building to refine the themes. Future studies will implement reliability assessments.

Survey Methods: We developed a quantitative survey based on the results of the interviews (Table III). The survey has two parts: ranking information preferences for a decision support system and ranking software feature preferences for the system. The same investigator who conducted the interviews briefly explained our intent of building a database and website to help stroke survivors compare and select rehabilitation devices. Participants were then presented with a list of nine potential types of information that such a website could provide about devices (e.g., ease of use, risks, and expected benefits; see Table III). They were asked to categorize each item into one of three levels of importance: most important (followed by ranking the top 3), medium importance, and lower importance. Following this, participants rated the importance of eight website features (e.g., personalized recommendations, chatbot functionality, accessibility on mobile devices) using a 10-point Likert scale, where 1 denoted "not important" and 10 "very important." A 3-point scale was used for ranking information priorities to simplify prioritization, while a 10-point scale allowed for finer granularity in assessing user preferences.

TABLE II. INTERVIEW QUESTIONS

1	What questions do you have regarding your recovery and rehabilitation?
2	How do you currently find information about your recovery? Internet, books, podcasts, primary care doctors, occupational therapists, friends/family, support groups?
3	What current barriers do you face regarding your recovery and finding resources to help?
4	Do you face barriers trying to follow the advice you've been given regarding your recovery (time, motivation, inability to perform suggested activities, conflicting advice)?
5	What have you done since your stroke that has been most helpful towards your recovery?
6	Have you used any devices or apps to help with your recovery? If yes, how did you learn about the device, how long did you use it, and what was your impression of its usability and usefulness?
7	Would you be interested in a customized system with a chatbot designed to answer your rehabilitation/stroke recovery questions?
8	What is your familiarity with AI/ChatGPT?
9	Would you be interested in device recommendations? If so, are you more interested in active devices (actuated gloves, home-based robotic tools, still devices), passive devices (weights, splints, hand exercisers, etc.), or computer or phone-based training apps?
10	Do you have any concerns about using high-tech devices (safety, useability, cost)?
11	What price range of devices would you want to have recommended?
12	Are you more interested in devices, recommendations on their use, or recommendations on general health/exercise?
13	What kind of information/vetting would you like to be provided with device recommendations (research articles, FDA approval, user reviews?)
14	Would you like the interface to be primarily optimized for computer or phone-based, or both?
15	What concerns do you have about the useability of such a system?

TABLE III. SURVEY QUESTIONS

Part 1. **Information the website should provide about the devices** (select three as most important, three as medium, and three lower)	
[ ]	Information about how easy each device is to use.
[ ]	Risks such as discomfort or pain
[ ]	How often and for how long do I need to use it to get a benefit?
[ ]	What amount of benefit can I expect?
[ ]	Information about what motivational features the device offers*
[ ]	Videos of people using the devices
[ ]	User reviews
[ ]	Information about scientific studies that support its effectiveness
[ ]	Return policy
Part 2. **How the website should help you find devices** (rate 1 to 10)	
[ ]	Ask me for personal information about my impairments and my goals so it can make personalized recommendations for what device would be best for me.
[ ]	Suggest devices in a way that's easy for me to compare them.
[ ]	Allow me to ask questions like a chatbot.
[ ]	Be accessible on my phone.
[ ]	Guide me through the selection process.
[ ]	Allow me to search without guiding me or asking me questions.
[ ]	Connect me with other people who are using a device I am interested in to help me make my decision.
[ ]	Connect me with a salesperson from the company that makes the device so I get more information.

* These could be things like progress tracking, social networks, gamification, goal setting with feedback, or motivational messages.

TABLE IV. FDA PRODUCT CODES RELEVANT TO OUR DATABASE

Code	Description
HCC	Device, Biofeedback
GZI	Stimulator, Neuromuscular, External Functional
ISD	Exerciser, Measuring
LXJ	Interactive Rehabilitation Exercise Devices
QKC	Interactive Rehabilitation Exercise Devices, Prescription Use
ION	Exerciser, Non-Measuring
PKS	Exerciser, Non-Measuring For Stroke Rehabilitation
BXB	Exerciser, Powered
JFA	Exerciser, Finger, Powered
QOL	EEG-Driven Upper Extremity Powered Exerciser
IPF	Stimulator, Muscle, Powered

B. Identifying informational gaps for a curated database of rehabilitation devices

We also developed a preliminary database of engineered rehabilitation devices suitable for home use. As part of this development effort, we sought to obtain information about each device related to the expressed needs and interests of the survey/interview participants.

Methods to develop the database: We conducted a structured search using online databases, manufacturer websites, and online marketplaces for rehabilitation devices. The search focused on FDA-approved devices suitable for home use and targeted those recovering from stroke. Devices were included if they addressed movement rehabilitation. The FDA classifies medical devices using a "product code." By searching the FDA's Product Code Classification database using keywords like "rehabilitation devices" and "stroke rehabilitation," we created a list of potential product codes to search for relevant devices (see Table IV). Then, we searched two FDA databases (the Establishment Registration & Device Listing database and the Premarket Notifications (510(k)s) database) using those product codes. We examined each device's online information to identify those that referenced or demonstrated applicability for stroke rehabilitation at home. We collected data on functionality, clinical validation, usability, and pricing if it was available.

Methods to obtain further information directly from manufacturers: Information available on websites was limited. We, therefore, contacted device manufacturers to supplement the website information and gain insights into areas of interest specific to end users. To do this, we sent a standardized email to solicit specific information identified as important by users in the interviews described above but often not available on product websites. We asked about:

- **Pricing and Return Policy:** We asked manufacturers to provide detailed pricing information for their devices, including whether they offered a return policy.
- **Ease of Use:** We asked about the device's ease of operation, specifically whether it required supervision, the level of independence users could achieve, and any reports of discomfort or pain. We inquired about the proportion of customers who used the device at home.
- **Usage Requirements:** We sought clarification on the recommended usage frequency and duration per week to achieve noticeable benefits. We also asked to share any supporting scientific studies validating their effectiveness.

TABLE V. PRELIMINARY DATABASE STRUCTURE

Field	Description
Name	The commercial name of the device
Manufacturer	The company that produces the device.
Website	Official website of the device or manufacturer.
Description	A summary of the device and intended use.
FDA Code	The classification code assigned by the FDA. Indicating the device category.
Year of Approval	The year the device received FDA approval.
Country	The country where the manufacturer is based.
Price	The retail price of the device, when available.
Price Per Year	Annual cost, applicable if the device is subscription-based or rented.
Insurance Coverage	Whether the device can be reimbursed or partially covered by insurance.
Return Policy	The availability of a return policy for the device.
Home Usability	An indication of whether the device can be used in a home-based setting.
Trained Body Parts	The specific body parts that the device targets (e.g., hand, arm, ankle, leg, torso).
Ease of Use	A summary of the ease of operation of the device.
Usage Requirements for Benefit	Recommended usage frequency and duration to achieve benefits. Expected size of benefits.
Clinical Evidence	Summaries of clinical studies.
Motivational Features	Does it contain features such as progress tracking, gamification, social networks, or feedback?

- **Motivational Features:** We asked companies to describe features to motivate users, such as progress tracking, gamification, social networks, or feedback.

We analyzed the replies from the companies for response rate and time, the replier's job title, answer format (i.e., whether companies answered by email or suggested a call or demo), and the presence of motivational features. We populated a database with the information obtained (Table V) for future use with the planned AI.

III. RESULTS

We asked individuals in the chronic phase post-stroke to identify their informational needs for selecting engineered devices to continue their rehabilitation at home. We also developed a preliminary database of FDA-approved, home-based rehabilitation devices and attempted to populate the database with answers to those informational needs.

A. Interview results

The eight participants interviewed reported facing challenges in their recovery, including time constraints (7/8), physical limitations (5/8), and transportation issues (4/8), highlighting the need for at-home therapy options. Participants expressed strong interest in a range of at-home rehabilitation tools. We briefly highlight several key themes related that emerged:

1. **Difficulties in finding reliable information:** They reported the use of a variety of sources for rehabilitation information, including the Internet, support groups, healthcare providers, books, and social media. However, 7/8 expressed difficulty finding reliable information.

TABLE VI. CODEBOOK: THEMATIC ANALYSIS OF USER INTERVIEWS

Theme	Code	Freq. (n/8)
Challenges in recovery	Time constraints	7/8
	Physical limitations	5/8
	Transportation issues	4/8
Difficulties in finding reliable information	Struggles to find trustworthy sources	7/8
	Difficulty assessing device efficacy	4/8
	Unclear treatment options	3/8
Desirable features in the devices	Motivation-enhancing features	7/8
	Community support	3/8
	Progress tracking	4/8
	Gamification	4/8
Openness to AI-based Chatbots	Low familiarity with AI chatbots	1/8
	Interest in AI chatbot for rehab support	7/8
	Preference for phone-based app	3/8
	Preference for computer-based access	3/8
Experience with home-based rehabilitation devices	Use of simple hand exercisers/stretchers	7/8
	Positive reception of engineered devices	4/8
	Use of fitness apps for tracking	2/8

2. **Desire to identify devices with motivational features:** Obtaining information about the motivational features of devices was mentioned as a key interest of participants (7/8). They mentioned community support (3/8), progress tracking (4/8), and gamification as desirable (4/8).
3. **Openness to AI Chatbots:** While familiarity with AI chatbots like ChatGPT was low (1/8), 7/8 patients expressed interest in using an AI chatbot for rehabilitation support, indicating a desire for accessible, interactive assistance in their recovery. Three participants preferred it on a phone-based app, while three on a computer.

Regarding home use of devices, participants used simple hand exercisers and stretchers (4/8) but viewed them as having mixed effectiveness (1/4). Mechatronic and sensor-based devices were well-received (4/8) despite some frustration (1/4) with technical difficulties. Some appreciated fitness apps like Garmin and Strava for tracking progress (2/8). Table VI provides the codebook for these analyses.

B. *Survey results*

Based on the interview themes, we created a survey that was conducted on four individuals. First, participants ranked the importance of eight types of device-related information. The most highly ranked attributes were the frequency of use required to achieve benefits (mean rating: 3.0), followed closely by information about ease of use (2.75) and the amount of benefit that can be expected (2.75) (Fig. 1a). Moderately important was information about risks such as discomfort or pain (2.25) and motivational features (2.25). Lower-ranked attributes were user reviews and scientific data on effectiveness (both 1.75), videos of people using the devices (1.5), and return policies (1.0). Second, participants rated the importance of eight potential features of a decision support system on a scale from 1 (least important) to 10 (most important). The highest-rated feature was the ability of the system to ask for personal information to make personalized recommendations (mean rating: 9.75, Fig 1b). Chatbot functionality and guidance through the selection process both received ratings of 9.5. Additional high-priority features included comparing suggested devices easily (9.25)

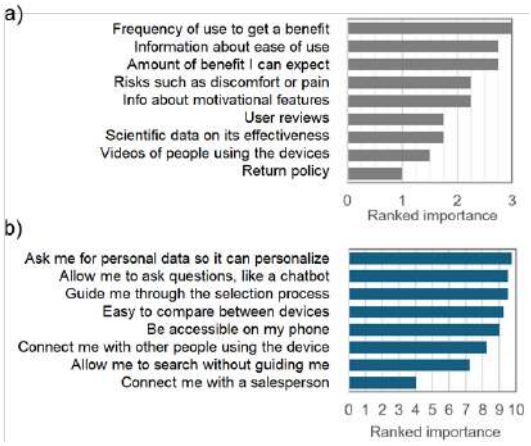


Figure 1. **Overview of survey results.** a) Participants ranked eight types of information about the devices using a 3-level scale: most (3), medium (2), and lower importance (1). Bars represent the mean rating for each category. b) Participants ranked the importance of eight potential features of the decision support system using a 10-point Likert scale, where 1 represented "not important" and 10 "very important." The graph shows the mean rating.

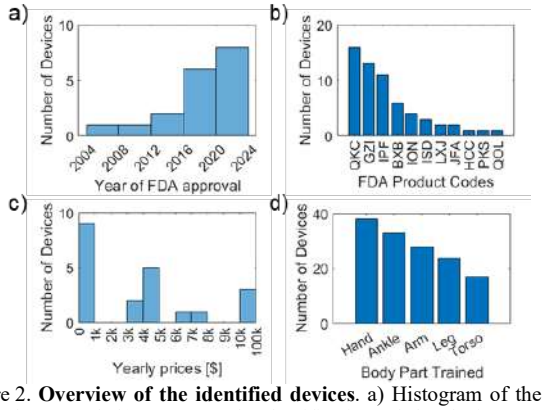


Figure 2. **Overview of the identified devices**. a) Histogram of the FDA's year of approval. b) FDA's code classification of the devices. c) Yearly expenses, including subscription, purchase, and leasing models. d) The body part targeted by the device (some devices target more than one part).

and mobile accessibility (9.0). Lower-rated features included the ability to search without guidance (7.25) and to connect with other users of the same device (8.25). The lowest-rated feature was connecting with a salesperson, with a 4.0 score.

C. *Database generation results*

From the FDA website, we identified 67 FDA-approved devices suitable for home use after stroke. Fig. 2 summarizes several observations about these devices. Notice that we could not obtain information for all 67 devices for each observation. Most devices for which we found approval dates were approved after 2016 (Fig. 2a). The most common FDA codes were 24% QKC (Interactive Rehabilitation Exercise Devices, Prescription Use), 19% GZI (Stimulator, Neuro-muscular), 16% IPF (Stimulator, Muscle, Powered), and 9% BXB (Exerciser, Powered), highlighting a focus on interactive and neuromuscular stimulation devices (Fig 2b). Device costs ranged from $60 to $70,000, with 43% under $1,000 (Fig. 2c) and about 13% offering subscription models. Only 45% of devices were covered by insurance, and 50% had a return policy. 94% had at least one supporting research paper, though the extent of validation varied widely. Most devices targeted the hand (57%) and ankle (49%), often as part of whole-arm and whole-leg training (Fig. 2d).

We sent emails to the 41 companies that manufactured the 67 devices requesting further information relevant to the specific interests of individuals post-stroke we identified in our surveys. 15 (37%) companies replied to our email inquiry, ten of them within 2 days and the rest within 8 days (no further companies responded over the next several weeks). Ten companies (67%) answered our questions via email, and 5 (33%) suggested a follow-up call instead. We set up meeting times with 2 of those 5 companies, bringing the total to 12 responding companies. All 12 companies provided information on the pricing and return policy, eight about ease of use, nine about usage requirements (e.g., recommended usage frequency and duration per week to achieve noticeable benefits), and 10 provided information about motivational features. From these, all 10 reported that their devices use progress tracking, five use goal-setting features, and eight provided feedback. Five reported gamifications on their devices, and 3 included social network tools. Regarding the roles of the individuals who replied to our inquiry, 33% of the responses were sent by C-suite executives (e.g., CEO, COO), 33% by sales representatives, 13.3% by clinical specialists, and the remaining 20% comprising managers, customer support staff, and automated replies.

IV. Discussion

We asked people post-stroke about their rehabilitation device information needs. We also attempted to catalog available devices for home rehabilitation after a stroke. Three key takeaways from this process are as follows. First, there is a large and growing array of engineered devices available for home rehabilitation movement therapy after stroke. Yet, users encounter significant barriers in identifying those that meet their needs. Second, users prioritize information about motivational features and dose-response efficacy, but reliable information is difficult to find. Third, users expressed openness to AI-powered chatbots as tools to guide them in the device selection process. We discuss these results now, followed by an analysis of limitations and future directions.

A. The current rehabilitation therapy device informational landscape is challenging to navigate

People post-stroke expressed difficulty finding relevant information about rehabilitation devices to continue home therapy. They told us that they used Internet searches, support groups, healthcare providers, books, and social media but felt that these sources were incomplete. When we attempted to collate devices for them, we also experienced significant barriers. With online searching, we were not confident that we were finding all the relevant devices, although we found some websites with more comprehensive listings of devices or companies (e.g., https://www.neurorehabdirectory.com/ or https://iisart.org/). AbleData, a comprehensive database, had been discontinued.

We thus turned to the general FDA medical device database but found it difficult to use. The process we eventually developed was an iterative process of finding FDA Product Codes related to the devices we were interested in, then searching several FDA databases for all the devices listed with those codes, then searching the devices' manufacturer's websites online to check if they were relevant for our database, then finding that some of those manufacturer's had more than one device, trying to locate those other devices in the FDA databases, all the while trying to expand the list of relevant codes and repeat this process. Even with this process, we are uncertain if we have found all relevant products. Nevertheless, we found 67 devices, which confirmed that a significant number of device options are now available for people post-stroke.

Finding specific information that people post-stroke want about these devices was even more difficult. Users highlighted, for example, that they desired information about motivational features (such as gamification, social support, and progress tracking) as well as ease-of-use features of devices. They also wanted information about potential outcomes and the effort required to achieve them. When we emailed companies to ask for this information, only 30% responded. Response content and level of detail varied, and there was no standardized way to compare features such as ease of use or expected dose response. These difficulties highlight the need for a concerted effort to collate information, coupled with an effort to define expectations, formats, and sources for information important to users.

B. People post-stroke see value in a personalized and guided search paradigm

In the interviews, people post-stroke expressed openness to "chatbots" to aid in decision-making. In the follow-up survey, when we asked them to rate specific potential design features, they highly rated features amenable to a chatbot approach, including being able to provide personal information to obtain customized recommendations, being able to ask questions, and being guided through the selection process. The only feature they rated as undesirable was being connected to a salesperson. This seems to suggest that the participants envision a chatbot as a way to get personalized information with reduced sales pressure or bias.

C. Limitations and Future Directions

The findings discussed above must be considered within the context of several limitations of this pilot study. The sample size was small (N=9), potentially limiting the observations' generalizability. However, prior studies suggest that a sample size of 6–12 participants is often sufficient for thematic saturation in qualitative research [11]. Consistent with this, while we did not formally assess thematic saturation, themes such as the difficulty in finding reliable device information and interest in AI-powered support were consistently reported across participants. Additionally, the study participants were residents of Orange County, California, an affluent and technology-oriented locale. This may account for the limited concern with pricing information and the openness to new technologies, including chatbots. Future work will expand the sample size and participant diversity to enhance the generalizability of the findings. A formal saturation analysis will also be conducted in future work to determine whether additional participants will introduce new insights.

The device search process remains a work in progress. Finding more devices or obtaining more responses from companies may alter the results. Future work will incorporate an early health technology assessment (eHTA) approach [12], including expert validation and direct user testing, to improve the database reliability.

We have begun developing an AI-powered decision support system that will integrate various features to guide people through selecting a device from the database, with a key component being a customized, retrieval-augmented, LLM-based chatbot. It will offer real-time, personalized guidance, addressing the need for accessible and customized device recommendations. While alternative methods such as static informational websites or clinician-guided consultations could also provide such information, a chatbot component allows users to ask specific questions and receive tailored responses dynamically, offering a scalable, low-cost, and 24/7 available interactive solution that aligns with the preferences of the study participants. This hybrid approach leverages the strengths of both structured information delivery and interactive AI-driven assistance.

We aim to leverage the potential of LLMs to process large amounts of information and to generate texts readable by populations of diverse backgrounds. The development of this system will require extensive feedback, not only from people with stroke to tune the way the chatbot interacts with them, but also from various stakeholders, including clinicians, scientists, industry, payors, and healthcare providers, to verify and be involved in vetting the collected information. An LLM has the potential to make information available in different languages and for individuals with different educational levels. In our next steps, we will refine the system's design, compare the chatbot's effectiveness with other approaches, and integrate additional stakeholder perspectives, including clinicians and caregivers, to ensure a well-rounded approach to rehabilitation technology selection.

Users highlighted the importance of motivational features in the devices they are looking for. This suggests that rehabilitation device companies could potentially increase the perceived value of their products by incorporating these features and highlighting them in detail. Likewise, users emphasized the importance of ease-of-use information. In the future, ease-of-use could be quantified and made publicly available using a standardized metric such as the System Usability Scale [13].

A third interest was for information about expected benefits and the amount of device use required to obtain that benefit. This is perhaps the most challenging information to provide, as the "dose-response" curve of movement training after stroke remains a debated topic and almost certainly depends on various patient baseline characteristics. Research data from clinical studies may be available for some devices. Those studies' main findings and results can be extracted and included in the information displayed. However, explanations of the relevance and implications of research data for predicting practical benefits to specific individuals are often written in technical language, which can be difficult for most people to understand. LLMs can be used to translate technical information into non-specialist language. Nevertheless, developing ways to measure and convey dose-response information should be a priority if companies seek to satisfy the consumers' interests.

V. Conclusion

This study describes our initial efforts to understand the rehabilitation therapeutic device informational needs of individuals post-stroke and their preferences for how an automated system might help meet those needs. The results confirm that people post-stroke have numerous engineered devices available to continue home rehabilitation therapy. However, they encounter substantial barriers to obtaining the information they want about these devices, particularly regarding motivational features and expected benefits. Finally, they are enthusiastic about the features an AI chatbot could provide in helping them find devices, including customizing to their individual needs, answering questions, and providing guidance.

Acknowledgment

We want to thank the individuals with stroke who participated in this study.

References

[1] J. D. Steinmetz, et al., Global, regional, and national burden of disorders affecting the nervous system, 1990–2021: a systematic analysis for the Global Burden of Disease Study 2021. The Lancet Neurology, 2024, 23(4), 344-381.

[2] Feigin, V. L., Abate, M. D., Abate, Y. H., Abd ElHafeez, S., Abd-Allah, F., Abdelalim, A., ... & Arifin, H. (2024). Global, regional, and national burden of stroke and its risk factors, 1990–2021: a systematic analysis for the Global Burden of Disease Study 2021. The Lancet Neurology, 23(10), 973-1003.

[3] Y. Zhang, X. Liu, X. Qiao, Y. Fan. Characteristics and Emerging Trends in Research on Rehabilitation Robots from 2001 to 2020: Bibliometric Study J Med Internet Res 2023;25:e42901

[4] Reinkensmeyer, D. J., & Dietz, V. (Eds.). (2016). Neurorehabilitation technology (Vol. 106). 2016 New York: Springer.

[5] Zuccon, G., Lenzo, B., Bottin, M., & Rosati, G. "Rehabilitation robotics after stroke: a bibliometric literature review." Expert Review of Medical Devices, 2022, 19(5), 405-421.

[6] Celian, C., et al., "A day in the life: a qualitative study of clinical decision-making and uptake of neurorehabilitation technology." J Neuroeng and Rehab, 2021, 18, 1-12.

[7] Mitchell, J., Shirota, C., & Clanchy, K. "Factors that influence the adoption of rehabilitation technologies: a multi-disciplinary qualitative exploration." J NeuroEng and Rehab, 2023, 20(1), 80.

[8] Hughes, A. M., Burridge, J. H., Demain, S. H., Ellis-Hill, C., Meagher, C., Tedesco-Triccas, L., ... & Swain, I. (2014). Translation of evidence-based assistive technologies into stroke rehabilitation: users' perceptions of the barriers and opportunities. BMC health services research, 14, 1-12.

[9] Davis, F. D. (1989). Technology acceptance model: TAM. Al-Suqri, MN, Al-Aufi, AS: Information Seeking Behavior and Technology Adoption, 205(219), 5.

[10] De Cicco, R., Iacobucci, S., Aquino, A., Romana Alparone, F., & Palumbo, R. (2021, November). Understanding users' acceptance of chatbots: an extended TAM approach. In International Workshop on Chatbot Research and Design (pp. 3-22). Cham: Springer International Publishing.

[11] IJzerman, M. J., Koffijberg, H., Fenwick, E., & Krahn, M. (2017). Emerging use of early health technology assessment in medical product development: a scoping review of the literature. Pharmacoeconomics, 35, 727-740.

[12] Guest, G., Bunce, A., & Johnson, L. (2006). How many interviews are enough? An experiment with data saturation and variability. Field methods, 18(1), 59-82.

[13] Brooke, J. (1996). SUS: A quick and dirty usability scale. Usability evaluation in industry, 189(3), 189-194.

A home-based suite of sensors for monitoring and improving upper extremity proprioception after stroke

Guillem Cornella-Barba, Callen S. Zimmer, Shusuke Okita, and David J. Reinkensmeyer, *Senior Member, IEEE*

***Abstract*— Proprioception assessment and training are theoretically important in stroke rehabilitation because proprioception impairment contributes to reduced upper extremity (UE) function and is a promising predictor of the effectiveness of movement therapy. Currently, however, there are few tools available for home-based monitoring and training of proprioception. Here, we describe three tools that we are developing for UE proprioception rehabilitation that are suitable for home use. OpenPoint uses a webcam to automate UE proprioception assessment via a classic neurologic test: finger-to-finger pointing. Proprio gamifies proprioception training by embedding the finger-to-finger pointing test within a video game similar to GuitarHero. Diversify is an app on a smartwatch that provides feedback about the diversity of arm proprioceptive states associated with the variety of arm postures that an individual experiences throughout the day. We describe here the design of each system as well as preliminary testing results.**

I. INTRODUCTION

Over 50% of individuals who have had a stroke experience proprioception deficits in their upper extremities (UE) [1], [2]. These deficits are associated with reduced UE function [3], which makes sense in light of the crucial role proprioception plays in both the control [4] and learning of movement [5]. However, despite the functional importance and widespread nature of proprioception impairments, it has been reported that only 1% of rehabilitation clinicians are evaluating proprioception, as indicated by a recent survey of 431 clinicians [6]. If clinicians do assess it, they typically rely on coarse clinical scales.

Several studies have also suggested that proprioceptive impairment is one of the most powerful predictors of treatment response. For example, an analysis of data from the EXCITE trial of constraint-induced movement therapy (CIMT) found that, compared to people with intact proprioception, participants with impaired UE proprioception had a 20% probability of achieving a clinically meaningful outcome [7]. In our own work, proprioceptive deficits of the finger were the strongest predictor of the ability to benefit from an intensive course of robotic hand movement training [8]. Proprioception therefore can potentially play a crucial role in rehabilitation robotics and assistive technology, as tracking proprioceptive deficits could help tailor rehabilitation therapies and enhance assistive interventions.

Beyond assessing proprioception, retraining it is also of interest. In addition to stroke, there are other conditions that impair proprioception such as orthopedic injuries [9], spinal cord injury [10], Parkinson's disease [11], neuropathies [12], and genetic conditions [13]. Proprioception training is possible in a broad range of disease conditions [14]. Proprioceptive learning shows similar properties to motor learning, including training specificity, fast/slow learning dynamics, retention, and transfer [15]. Despite this, there are few technologies available to help with proprioceptive learning, particularly in the home environment.

The goal of the work described in this paper is to harness recent advances in computer vision and wearables to provide new tools to assess and retrain UE proprioception after stroke. We describe three novel technologies. OpenPoint [16] leverages computer vision for UE proprioceptive assessment. Proprio [17] is an innovative serious game that also leverages computer vision but for the purpose of gamifying finger proprioception training. Diversify [18] is a smartwatch application designed to sense forearm movement diversity.

II. METHODS

A. OpenPoint: A webcam-based proprioceptive assessment

The fundamental aim of the OpenPoint proprioception assessment is to automate the measurement of proprioceptive accuracy by returning the distance error between finger landmarks during a finger-to-finger pointing task using a webcam and hand tracking technology (Fig. 1). As described below, we have tested OpenPoint with sixteen post-stroke survivors and eighteen age-matched adults without neurologic impairments. The user is directed to hold their impaired hand (the "target hand") against their torso with the aid of a pillow or sling, if needed, as this is an attainable position for most individuals with stroke arm impairments, and it also puts the target hand out of view. The user then views a live video of themselves as a mirror image on the computer screen, and OpenPoint uses the MediaPipe library [19] to capture the keypoints on both hands, including the fingertips (Fig. 1).

*Development of this application was partly supported by the App Factory to Support Health and Function of People with Disabilities funded by a grant from the National Institute on Disability, Independent Living and Rehabilitation Research (NIDILRR) in the U.S. Department of Health and Human Services to the Shepherd Center (Grant #90DPHF0004). Also funded by NIH #R01HD062744; NIDILRR #90REGE0010; and NIDILRR RERC #90REGE0005.

G. Cornella-Barba is with the Department of Mechanical and Aerospace Engineering, University of California Irvine, Irvine, CA, USA cornellg@uci.edu

C. S. Zimmer is with the Department of Mechanical and Aerospace Engineering, University of California Irvine, Irvine, CA, USA zimmerc@uci.edu

S. Okita is with the Max Näder Center for Rehabilitation Technologies and Outcomes Research, Center for Bionic Medicine, Shirley Ryan AbilityLab, Chicago, IL, USA. He is also with the Department of Physical Medicine and Rehabilitation, Northwestern University, Chicago, IL, USA sokita@sralab.org

D. J. Reinkensmeyer is with the Department of Mechanical and Aerospace Engineering, and the Department of Anatomy and Neurobiology, University of California Irvine, Irvine, CA, USA dreinken@uci.edu

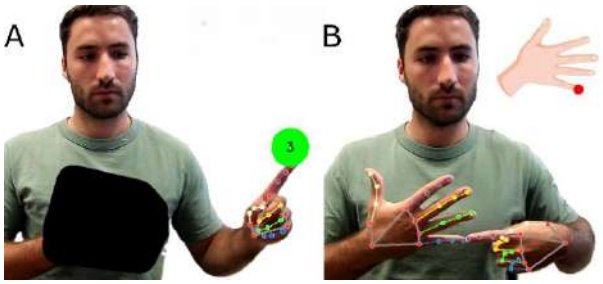


Figure 1. The OpenPoint proprioception assessment. A live video, obtained by a webcam, is shown to the user. (A): The user rests their impaired hand (the "target hand") on their torso. MediaPipe [19] tracks hand landmarks, and a polygon is used to obscure the target hand. The user raises their pointing finger to the green target. After a three-second countdown, the software displays a target on a cartoon fingertip. (B): After receiving the visual cue, the user points to the target fingertip. OpenPoint measures pointing error when movement stops. Note: the polygon is removed in B to show tracking but remains present during actual use of the system.

To obscure the hand, an opaque polygon is drawn over the target hand. To perform a pointing trial, the user raises their pointing index finger to a green start target. After a three-second countdown, a cartoon hand appears on the screen, highlighting a randomly chosen target finger. The user attempts to touch that finger by pointing to their target hand. OpenPoint detects when the pointing movement is complete and identifies the pointing error in the frontal plane, scaling it by measured hand size to convert it to centimeters. If a user is unable to extend the fingers of the target hand, OpenPoint allows for the target point to be set to the MCP or PIP joints.

To prove that OpenPoint is a valid way to test for proprioceptive impairment after stroke, sixteen people (54.0 ± 12.8 years, 11 male, 15 right-handed, 9 right-side impaired) in the chronic phase post-stroke (2381 ± 1499 days post stroke, 9 ischemic) performed 30 pointing movements to fingers on their hemiparetic hand [16]. Participants were grouped based on the severity of motor impairment using the Upper Extremity Fugl-Meyer (UEFM) score [20]: 3 had severe impairment (UEFM<30), 5 had moderate impairment (30≤UEFM<50), and 8 had mild impairment (UEFM≥50).

For comparison, a group of eighteen older users (62.3 ± 8.7 years, 6 male, 16 right-handed) with no neurological or visual deficits also performed the task. This group also performed several other testing conditions, one of them being pointing to a fake hand (a hand-shaped cardboard attached to a stick). This condition removed proprioceptive input from the target hand to test if OpenPoint's accuracy depends on it. We expected worse performance in unimpaired individuals due to the loss of proprioception from the target hand. We also tested OpenPoint's validity by examining whether its measured error correlated with finger proprioceptive error measured with a previously validated robotic proprioceptive assessment, the Crisscross assessment [21], where participants try to identify when their fingers pass each other as the robot moves them.

B. Proprio: a proprioceptive training game

The aim of Proprio is to gamify the finger-to-finger pointing task from OpenPoint, transforming it into a proprioceptive training tool. Proprio [17] is a rhythm-based game, inspired by GuitarHero, where players try to hit streaming notes to the beat of a song as the notes move over a visual target on the screen (Fig. 2).

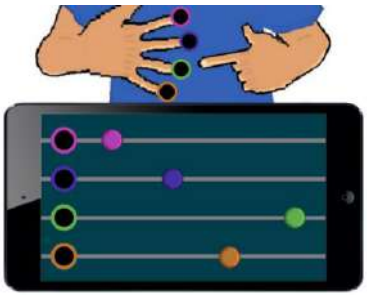


Figure 2. Proprio is a smart phone app available on the Apple Store that gamifies proprioceptive training. This figure shows the main gameplay scene on the phone. Players use the index finger of their pointing hand to touch the fingertips of their target hand, with each fingertip representing a different string. As notes move leftward across the screen, players try to point to the correct fingertip in time with the note. Successfully hitting a note on time earns the player a point https://apps.apple.com/us/app/proprio/id6630381452

Players use their pointing hand's index fingertip to touch the fingertips on their target hand as with OpenPoint. Each finger corresponds to a note travelling down a different string on a guitar. When the pointing distance error between fingertips falls below a certain threshold radius, the target note is considered a "hit," indicating good proprioceptive accuracy. For people post-stroke with limited finger extension, targets can be set at the PIP or MCP joints. Game difficulty can also be adjusted by choosing songs with varying note speeds. Players receive visual feedback based on their performance, aiming to hit as many correct notes as possible.

During Proprio's development, we conducted four rounds of user-centered testing: first, with 10 non-impaired young participants using the Windows beta version. Second, the same 16 post-stroke participants who had tested OpenPoint also tested the Windows game, and those same 16 also tested the beta iOS version later. In the fourth round, 10 additional impaired participants tested the finalized version, which is now available on the Apple Store (ID: 6630381452). Feedback from each round improved usability; we assessed usability using the System Usability Scale (SUS) [22].

As a pilot test of Proprio's effectiveness for proprioceptive learning, we invited the same 16 post-stroke participants that had previously used OpenPoint to play the game using both hands as the target for three 30-minute sessions: a baseline, 24 hours later, and one week later. The percentage of notes hit correctly for both target hands was normalized relative to the participant's score from the 3rd session to identify the gain in gameplay ability. We additionally used OpenPoint to assess proprioceptive accuracy by calculating each session's pointing error and normalizing it to the errors from the 1st session. OpenPoint requires a similar pointing ability as gameplay in Proprio, but the tasks are not identical, and so using OpenPoint allowed us to test generalizability of proprioceptive pointing ability to a related task.

C. Diversify: A wearable sensing app to encourage exploration of UE proprioceptive states

Due to spasticity and sensory-motor deficits, people with severe to moderate hemiparesis after stroke tend to adopt characteristic arm postures [23], and use their arm [24] and hand [25] less throughout the day. Challenge and new experiences are important for motor learning [26].



Figure 3. The Diversify app vibrates and provides visual feedback when the wearer moves their arm in a diverse and vigorous way in a one-minute epoch.

We hypothesized that movement stagnation limits recovery, and that Diversify, a smartwatch app (Fig. 3), will help people explore a more diverse set of arm postures in their daily life through wearable feedback, improving their "quality of movement experience" ("QOME") [27], [28]. From a proprioceptive training perspective, more diverse arm postures should cause a greater variety of proprioceptive input to the brain, helping maintain or expand proprioceptive representations in sensory areas under the "use-it-or-shrink-it" principle of somatosensory representations [29].

To provide a tool to test this hypothesis, we developed a new way to measure the variety of forearm posture that can be accessed from a smartwatch, the kurtosis of the forearm's tilt angle, which is calculated using its accelerometers [27]. Kurtosis is a widely recognized statistical metric used to assess the "peakedness" of distributions. Lower kurtosis values indicate greater movement diversity. Thus, our goal is to use kurtosis as the primary outcome measure for assessing the effectiveness of Diversify in promoting varied arm postures. In [27] we confirmed that people with greater impairment post-stroke exhibit lower forearm postural kurtosis throughout the day, and that different movement activities produce different values of kurtosis with seven unimpaired participants [18]. However, our hypothesis that promoting movement diversity feedback will enhance rehabilitation outcomes using wearables remains untested.

Providing real-time feedback of movement diversity is non-trivial because the computational demand of calculating kurtosis increases as the buffer sample size increases. Building upon the research presented in [30] we developed an innovative algorithm called "Rolling Sample Kurtosis" (RSK) [18]. We conducted an offline comparison of the execution speed of RSK to the speed of a conventional iterative kurtosis calculation, and to Python's SciPy kurtosis implementation. We chose a Samsung watch (Fig. 3) for implementing real-time RSK due to its low cost, API, and versatility. We attached the watch to the wrist of a custom-designed robot arm with three motors [18], which helped us simulate human-like movements with predetermined levels of movement diversity, and created an interface that notifies the wearer when they achieve diverse periods of movement.

III. RESULTS

A. OpenPoint: A webcam-based, proprioceptive assessment

OpenPoint quantifies finger-to-finger pointing skill. To determine if OpenPoint was sensitive to UE proprioceptive impairment after stroke, we compared proprioceptive pointing error between a group of people post-stroke (45±13 UEFM score) to an age-matched group as described more fully in [16].

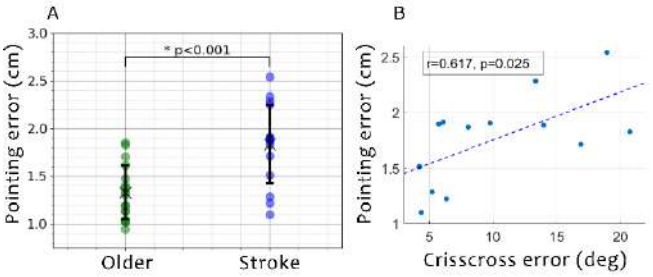


Figure. 4. Results from using the OpenPoint proprioception assessment to assess proprioceptive pointing error after stroke. (A): Pointing errors for older and stroke groups. The stroke group had significantly larger pointing errors ($p<0.001$). The error bars represent the standard deviation (SD) of the pointing errors. (B): The pointing error from the OpenPoint assessment had a moderate correlation with the angular error in finger proprioception measured by the Crisscross assessment. Adapted from [16].

We found a significant increase in pointing error after stroke (Fig. 4A, t-test, $p<0.001$). 53% of stroke survivors showed mean pointing errors exceeding two standard deviations from the older group. The pointing error in the OpenPoint assessment showed a moderate Pearson correlation with the finger proprioception error obtained through the robotic Crisscross assessment (Fig. 4B, $r=0.62$, $p=0.025$) after stroke, showing concurrent validity of the two proprioception assessments. For the unimpaired group, we also replaced their real hand with a fake hand, thereby removing proprioceptive input from the target hand. Pointing to the fake hand (2.97±1.25 cm) caused significantly higher errors compared to pointing to the real hand (1.33±0.28 cm). This verifies that OpenPoint accuracy depends on proprioceptive information from the target hand.

B. Proprio: a proprioceptive training game

Proprio gamifies finger-to-finger pointing. To determine if gameplay with Proprio improves proprioceptive accuracy, 16 individuals post-stroke played Proprio for 30 minutes in 3 sessions conducted in the laboratory. They switched which hand was the target and which was the pointing hand halfway through the session; 9/16 participants were able to do this. We also evaluated their UE proprioceptive ability using OpenPoint, allowing us to test the generalizability of any proprioceptive pointing ability gains achieved through practice with Proprio to a related but different pointing task (Fig. 5B).

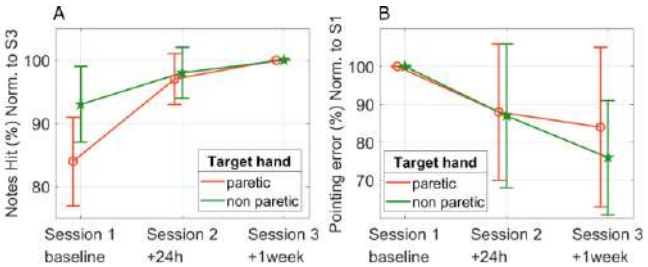


Figure 5. Results from testing the Proprio proprioceptive training game with 16 individuals poststroke. (A): The percentage of notes hit in each of the three sessions, normalized to percentage of notes hit in the 3rd session. The target hand is indicated by the orange line when it was the paretic hand, and by the green line when it was the non-paretic hand. (B): The pointing error across three sessions, measured with OpenPoint. We normalized each participant's error to that of the 1st session. Six participants with a more severe UE motor impairment were limited to using their paretic hand as the target, as they were unable to point with it. Consequently, only nine data samples were available for the non-paretic target hand.

Proprio's participants improved the quantity of notes they effectively hit with both hands throughout all the study, with the improvement from Session 1 to Session 2 being significant (Fig. 5A, $p<0.001$ when using the paretic hand as the target hand and $p=0.03$ for using the non-paretic hand as the target). Participants retained their skill from Session 2 to Session 3. Participants also reduced their proprioceptive pointing error (Fig. 5B), for both the paretic ($p=0.02$) and non-paretic ($p=0.01$) hands as measured with the OpenPoint assessment system from Session 1 to 3.

Ten individuals with stroke installed the Proprio app on their smartphone and used it at home for a week. They rated the usability of the app 76.5%±18% on the SUS, which can be described as "good" usability [31].

C. Diversify: A wearable sensing app to encourage exploration of UE proprioceptive states

Diversify is the smartwatch app we are developing to track forearm movement diversity. As we showed previously [27], individuals with more severe arm impairment after stroke exhibit significantly decreased forearm postural diversity, quantified with kurtosis (Fig. 6A). To allow real-time calculation of kurtosis on a smartwatch, we implemented the rolling-sample kurtosis algorithm on a Samsung smartwatch, as more fully described in [18]. The RSK algorithm greatly boosted computation speed across buffer sizes. For instance, it achieved a reduction in processing time that was approximately 200 times faster than the optimized SciPy kurtosis function for sample sizes under 3000, allowing execution in less than ten milliseconds [18]. We used a robotic arm to simulate a human arm trajectory and establish the ground truth of kurtosis. The results showed a strong correlation with the predicted kurtosis values derived from the watch tilt angles using RSK, with correlation coefficients of $r^2 = 0.99$, $p = 0.0001$ for slow motor speeds, and $r^2 = 0.86$, $p = 0.0078$ for faster speeds [18].

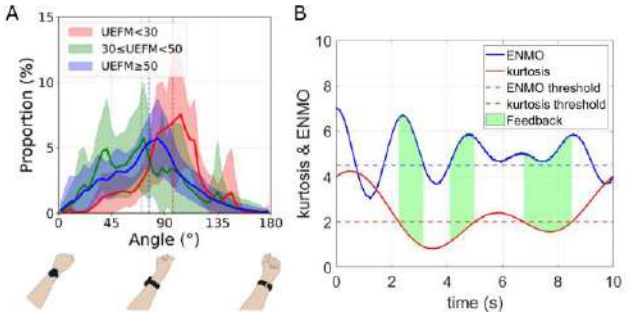


Figure 6. Results supporting the development of Diversify, a smartwatch app for providing wearable feedback on forearm postural diversity. (A): Results from 22 participants with chronic stroke who wore a 3-axis accelerometer on the wrist for one day, adapted from [27] under the (Creative Commons Attribution 4.0 International Public License). The orientation of the forearm relative to gravity and the distribution of the wrist accelerometer's tilt angle. The red, green, and blue lines represent the means of distribution for severely, moderately, and mildly impaired groups, as measured by the UEFM score. The severely impaired group (red) showed forearm postural "stagnation" with a more peaked distribution, quantified by a higher value of kurtosis. The shaded areas represent the confidence interval for each group. (B): Graph illustrating how the Diversify app works. When movement intensity (measured with ENMO [32]) exceeds a custom threshold, and movement diversity (measured with kurtosis) falls short of another threshold, the watch vibrates and provides visual feedback (Fig. 3)

We are using this information to design the Diversify app for Samsung smartwatches for daily use by individuals post-stroke. Initially, Diversify estimated forearm postural diversity for moving windows of 1 minute using RSK and then vibrated and provided an encouraging message if the kurtosis value in that window fell below an adjustable threshold, indicating high diversity. In pilot testing, however, we found it is possible to create low kurtosis values (i.e. high diversity) by holding the forearm statically in two disparate tilt states. Since we desire activity and diversity, we incorporated a conventional algorithm for movement vigor (ENMO, [32]) along with the diversity algorithm. The app now provides a vibration and congratulatory message when a one-minute epoch of movement is both vigorous and diverse (see Fig. 3 and Fig. 6B). We are preparing now to clinically test Diversify.

IV. DISCUSSION

These results represent steps toward designing home-based sensors for monitoring and improving upper extremity proprioception after stroke. OpenPoint automates the quantification of pointing errors for a finger-to-finger pointing test of proprioception ability using the MediaPipe computer vision library. We showed that pointing error measured with OpenPoint is increased after stroke, depends on proprioceptive input form the target hand, and is correlated with an independent, robotic measure of finger proprioception. Proprio automates game-based proprioceptive training. Our findings suggest that playing Proprio may help improve proprioception accuracy after stroke, as measured with OpenPoint, but further studies with larger populations and a broader range of proprioceptive outcome measures are needed to confirm its effectiveness. Finally, we presented pilot study data supporting the development of Diversify, a novel watch application that provides wearable feedback about the diversity of arm postural states achieved throughout the day. We found that more severely impaired individuals post-stroke show less forearm movement diversity throughout their day, and that is it possible to measure diversity with kurtosis in real-time using the RSK algorithm. We briefly discuss each approach including directions for future research.

A. OpenPoint

A review conducted recently [33] identified 1,346 methodologies for testing proprioception, with 42 studies specifically focusing on pointing to proprioceptive targets. In clinical practice, a common approach to assess UE proprioception involves instructing patients to close their eyes and attempt to touch their nose with a fingertip from various starting positions [34]. Another method involves asking patients to identify specific fingers by pointing [35]. We integrated similar methodologies into OpenPoint to assess pointing errors.

Despite being quick and equipment-free, clinical proprioception assessments face challenges such as poor resolution due to binary scoring, inconsistent results among assessors, lack of normative benchmarks, and limited sensitivity. Motion tracking systems [36] and robots [37], [38], [39] have been used to quantify proprioceptive, but their high costs and limited portability are barriers to clinical use. A few mobile phone-based applications have been developed for more practical and cost-effective proprioception

assessment [40], but they focus on joint angle reproduction and use the phone as an electronic goniometer.

Recent advancements in open-source, deep learning-based motion capture techniques like OpenPose [41] and MediaPipe [19] have improved human movement sensing without the need for body markers. We used MediaPipe Hands to develop OpenPoint, a smartphone-compatible hand-tracking application suitable for proprioceptive assessment.

One possible limitation is that, despite placing the target hand out of view, users could potentially "cheat" by looking down at their hand, introducing a confounding effect. To address this, we present visual stimuli on the screen, focusing attention on the display and away from the hand, but it would also be possible to use MediaPipe to try to detect "cheating".

We found that OpenPoint pointing errors increased when participants pointed to a fake hand; thus, the errors depend on the presence of proprioceptive signals from the target hand. OpenPoint also successfully detected increased proprioceptive pointing errors in individuals with chronic stroke. OpenPoint pointing error measured after stroke also moderately correlated with finger proprioception error measured with an independent, previously validated technique (Crisscross), suggesting concurrent validity. These findings support OpenPoint's potential for use in clinical settings for identifying UE proprioceptive deficits. Future work could also seek to automate other proprioception tests for different joints or limbs using computer vision.

B. Proprio

To our knowledge, there are few technologies for home-based training of UE proprioception, including a lack of smartphone-based approaches focused on proprioceptive training [42]. Our goal for Proprio was to design a gamified app to enhance engagement and adherence to training in at-home rehabilitation scenarios, aiding people post-stroke in retraining their UE proprioceptive skills.

In the pilot study described here, we found that the Proprio game is both learnable and retainable, supporting the idea that serious games could be effective for sensory rehabilitation. The reduction in pointing error measured with a separate assessment technique, i.e. OpenPoint, supports the hypothesis that training with Proprio enhances sensory-motor integration and precision [14], [15]. The iterative design process successfully addressed user requirements, as users found the system user-friendly and well-integrated. Although the system received a SUS rating above the standard usability benchmark, some users indicated a need for technical guidance, highlighting opportunities for further improvement. Future research will test whether extended use of Proprio at home improves UE proprioception using a wider variety of outcome measures and whether this improvement translates to improved UE use and function.

C. Diversify

Wearable sensors such as smartwatches and activity trackers are widely accessible and increasingly being used in physical rehabilitation [43], but they generally measure only the quantity of movement, like step counts or UE movements [44]. Quantifying the "quality of movement experience" (QOME), for example by describing the diversity or complexity of movement periods [27], might be valuable in neurologic rehabilitation, but this idea still needs to be tested. Considering the human somatosensory system, it is known that experiencing diverse physical activity sustains and expands cortical representations, while a lack of activity diminishes them [29].

We previously established a measure of forearm postural diversity based on kurtosis [27]. In a study with unimpaired individuals, we measured a diverse set of movement activity using the kurtosis of the wrist's tilt angle distribution [18]. Our findings indicate that various movement activities yield a broad spectrum of kurtosis values, suggesting that encouraging diverse movement could enhance UE movement diversity. The Diversify app may potentially encourage people to seek out vigorous and diverse movement activities.

To make Diversify possible, we developed a recursive algorithm (i.e. RSK) for real-time kurtosis calculation, reducing the kurtosis computation speed to a range suitable for a smartwatch [18]. Future research should investigate whether setting daily movement diversity goals and rewarding people with smartwatch feedback when they achieve periods of vigorous and diverse UE movement is effective at restoring proprioceptive ability and promoting UE use and function.

V. CONCLUSION

We presented three novel sensor systems for monitoring and improving UE proprioception after stroke. Each is potentially highly accessible since they depend only on webcams, smartphones, and smart watches. The three sensor systems could be used together to train and assess proprioception. We envision other proprioceptive assessments and games could also be implemented in a similar way with computer vision and smartwatches, expanding the toolset available to therapists and people post-stroke for engaging in proprioceptive training

REFERENCES

[1] M. L. Ingemanson *et al.*, "Neural Correlates of Passive Position Finger Sense After Stroke," *Neurorehabil Neural Repair*, vol. 33, no. 9, pp. 740–750, Sep. 2019, doi: 10.1177/1545968319862556.

[2] L. Connell, N. Lincoln, and K. Radford, "Somatosensory impairment after stroke: frequency of different deficits and their recovery," *Clin Rehabil*, vol. 22, no. 8, pp. 758–767, Aug. 2008, doi: 10.1177/0269215508090674.

[3] D. Rand, "Proprioception deficits in chronic stroke—Upper extremity function and daily living," *PLOS ONE*, vol. 13, no. 3, p. e0195043, Mar. 2018, doi: 10.1371/journal.pone.0195043.

[4] U. Proske and S. C. Gandevia, "The Proprioceptive Senses: Their Roles in Signaling Body Shape, Body Position and Movement, and Muscle Force," *Physiological Reviews*, vol. 92, no. 4, pp. 1651–1697, Oct. 2012, doi: 10.1152/physrev.00048.2011.

[5] J. D. Wong, D. A. Kistemaker, A. Chin, and P. L. Gribble, "Can proprioceptive training improve motor learning?," *Journal of Neurophysiology*, vol. 108, no. 12, pp. 3313–3321, Dec. 2012, doi: 10.1152/jn.00122.2012.

[6] J. E. Hoh, M. R. Borich, T. M. Kesar, D. S. Reisman, and J. A. Semrau, "Limitations in utilization and prioritization of standardized somatosensory assessments after stroke: A cross-sectional survey of neurorehabilitation clinicians," *Topics in Stroke Rehabilitation*, vol. 31, no. 1, pp. 29–43, Jan. 2024, doi: 10.1080/10749357.2023.2200304.

[7] S.-W. Park, S. L. Wolf, S. Blanton, C. Winstein, and D. S. Nichols-Larsen, "The EXCITE Trial: Predicting a Clinically Meaningful Motor Activity Log Outcome," *Neurorehabil Neural Repair*, vol. 22, no. 5, pp. 486–493, Sep. 2008, doi: 10.1177/1545968308316906.

[8] M. Ingemanson, J. Rowe, V. Chan, E. Wolbrecht, D. Reinkensmeyer, and S. Cramer, "Somatosensory system integrity explains differences in treatment response after stroke," *Neurology*, vol. 92, p.

10.1212/WNL.0000000000007041, Feb. 2019, doi: 10.1212/WNL.0000000000007041.

[9] L. Sharma, "Proprioceptive impairment in knee osteoarthritis," *Rheumatic Disease Clinics*, vol. 25, no. 2, pp. 299–314, May 1999, doi: 10.1016/S0889-857X(05)70069-7.

[10] "Balance, gait, and falls in spinal cord injury - ScienceDirect." Accessed: Nov. 17, 2024.

[11] J. Konczak *et al.*, "Proprioception and Motor Control in Parkinson's Disease," vol. 41, no. 6, pp. 543–552, Nov. 2009, doi: 10.3200/35-09-002.

[12] A. Nardone, M. Grasso, and M. Schieppati, "Balance control in peripheral neuropathy: Are patients equally unstable under static and dynamic conditions?," *Gait & Posture*, vol. 23, no. 3, pp. 364–373, Apr. 2006, doi: 10.1016/j.gaitpost.2005.04.002.

[13] A. T. Chesler *et al.*, "The Role of PIEZO2 in Human Mechanosensation," *New England Journal of Medicine*, vol. 375, no. 14, pp. 1355–1364, Oct. 2016, doi: 10.1056/NEJMoa1602812.

[14] L. Winter, Q. Huang, J. V. L. Sertic, and J. Konczak, "The Effectiveness of Proprioceptive Training for Improving Motor Performance and Motor Dysfunction: A Systematic Review," *Front. Rehabil. Sci.*, vol. 3, Apr. 2022, doi: 10.3389/fresc.2022.830166.

[15] H. G. Seo, S. J. Yun, A. J. Farrens, C. A. Johnson, and D. J. Reinkensmeyer, "A Systematic Review of the Learning Dynamics of Proprioception Training: Specificity, Acquisition, Retention, and Transfer," *Neurorehabil Neural Repair*, vol. 37, no. 10, pp. 744–757, Oct. 2023, doi: 10.1177/15459683231207354.

[16] G. Cornella-Barba, A. J. Farrens, C. A. Johnson, L. Garcia-Fernandez, V. Chan, and D. J. Reinkensmeyer, "Using a Webcam to Assess Upper Extremity Proprioception: Experimental Validation and Application to Persons Post Stroke," *Sensors*, vol. 24, no. 23, Art. no. 23, Jan. 2024, doi: 10.3390/s24237434.

[17] C. S. Zimmer, "Proprio: A Computer-Vision-Based App for Upper Extremity Proprioception Training," UC Irvine, 2024. Accessed: Aug. 30, 2024.

[18] G. Cornella-Barba, S. Okita, Z. Li, and D. J. Reinkensmeyer, "Real-Time Sensing of Upper Extremity Movement Diversity Using Kurtosis Implemented on a Smartwatch," *Sensors*, vol. 24, no. 16, Art. no. 16, Jan. 2024, doi: 10.3390/s24165266.

[19] F. Zhang *et al.*, "MediaPipe Hands: On-device Real-time Hand Tracking," Jun. 17, 2020, *arXiv*: arXiv:2006.10214. doi: 10.48550/arXiv.2006.10214.

[20] J. See *et al.*, "A Standardized Approach to the Fugl-Meyer Assessment and Its Implications for Clinical Trials," *Neurorehabil Neural Repair*, vol. 27, no. 8, pp. 732–741, Oct. 2013, doi: 10.1177/1545968313491000.

[21] C. A. Johnson, D. S. Reinsdorf, D. J. Reinkensmeyer, and A. J. Farrens, "Robotically quantifying finger and ankle proprioception: Role of range, speed, anticipatory errors, and learning," in *2023 45th Annual International Conference of the IEEE Engineering in Medicine & Biology Society (EMBC)*, Jul. 2023, pp. 1–5. doi: 10.1109/EMBC40787.2023.10340566.

[22] J. Brooke, "SUS: A 'Quick and Dirty' Usability Scale," in *Usability Evaluation In Industry*, CRC Press, 1996.

[23] H. Hefter, W. H. Jost, A. Reissig, B. Zakine, A. M. Bakheit, and J. Wissel, "Classification of posture in poststroke upper limb spasticity: a potential decision tool for botulinum toxin A treatment?," *International Journal of Rehabilitation Research*, vol. 35, no. 3, p. 227, Sep. 2012, doi: 10.1097/MRR.0b013e328353e3d4.

[24] R. R. Bailey, J. W. Klaesner, and C. E. Lang, "Quantifying Real-World Upper-Limb Activity in Nondisabled Adults and Adults With Chronic Stroke," *Neurorehabil Neural Repair*, vol. 29, no. 10, pp. 969–978, Nov. 2015, doi: 10.1177/1545968315583720.

[25] D. Schwerz de Lucena, J. Rowe, V. Chan, and D. J. Reinkensmeyer, "Magnetically Counting Hand Movements: Validation of a Calibration-Free Algorithm and Application to Testing the Threshold Hypothesis of Real-World Hand Use after Stroke," *Sensors (Basel)*, vol. 21, no. 4, p. 1502, Feb. 2021, doi: 10.3390/s21041502.

[26] O. Shusuke and D. J. Reinkensmeyer, "Forearm Postural Diversity and Complexity: Targets for Wearable Feedback after Stroke," presented at the American Society of Neurorehabilitation, Charleston, South Carolina, Mar. 2023.

[27] S. Okita, D. Schwerz de Lucena, and D. J. Reinkensmeyer, "Movement Diversity and Complexity Increase as Arm Impairment Decreases After Stroke: Quality of Movement Experience as a Possible Target for Wearable Feedback," *IEEE Transactions on Neural Systems and Rehabilitation Engineering*, vol. 32, pp. 2961–2970, 2024, doi: 10.1109/TNSRE.2024.3439669.

[28] J. W. Krakauer *et al.*, "Comparing a Novel Neuroanimation Experience to Conventional Therapy for High-Dose Intensive Upper-Limb Training in Subacute Stroke: The SMARTS2 Randomized Trial," *Neurorehabil Neural Repair*, vol. 35, no. 5, pp. 393–405, May 2021, doi: 10.1177/15459683211000730.

[29] S. Lissek *et al.*, "Immobilization Impairs Tactile Perception and Shrinks Somatosensory Cortical Maps," *Current Biology*, vol. 19, no. 10, pp. 837–842, May 2009, doi: 10.1016/j.cub.2009.03.065.

[30] Z. Li and J. Galdames-Retamal, "On IoT-Friendly Skewness Monitoring for Skewness-Aware Online Edge Learning," *Applied Sciences*, vol. 11, no. 16, Art. no. 16, Jan. 2021, doi: 10.3390/app11167461.

[31] A. Bangor, P. T. Kortum, and J. T. Miller, "An Empirical Evaluation of the System Usability Scale," *International Journal of Human–Computer Interaction*, vol. 24, no. 6, pp. 574–594, Jul. 2008, doi: 10.1080/10447310802205776.

[32] K. Bakrania *et al.*, "Intensity Thresholds on Raw Acceleration Data: Euclidean Norm Minus One (ENMO) and Mean Amplitude Deviation (MAD) Approaches," *PLOS ONE*, vol. 11, no. 10, p. e0164045, Oct. 2016, doi: 10.1371/journal.pone.0164045.

[33] Á. Horváth, E. Ferentzi, K. Schwartz, N. Jacobs, P. Meyns, and F. Köteles, "The measurement of proprioceptive accuracy: A systematic literature review," *Journal of Sport and Health Science*, vol. 12, no. 2, pp. 219–225, Mar. 2023, doi: 10.1016/j.jshs.2022.04.001.

[34] K. Bo, "Finger nose proprioception test (case study)," *Clinical Medicine*, vol. 19, no. 3, Supplement, p. s20, Jun. 2019, doi: 10.7861/clinmedicine.19-3s-s20.

[35] A. Benton and B. Cohen, "Right-Left Discrimination and Finger-Localization in Normal and Brain Injured Subjects," *Proceedings of the Iowa Academy of Science*, vol. 62, no. 1, pp. 447–451, Jan. 1955.

[36] W. G. Darling, B. I. Zuck, L. Mikhail, and J. Adhikari, "Proprioceptive acuity for landmarks on the hand and digits," *Exp Brain Res*, vol. 242, no. 2, pp. 491–503, Feb. 2024, doi: 10.1007/s00221-023-06761-z.

[37] J. B. Rowe, V. Chan, M. L. Ingemanson, S. C. Cramer, E. T. Wolbrecht, and D. J. Reinkensmeyer, "Robotic Assistance for Training Finger Movement Using a Hebbian Model: A Randomized Controlled Trial," *Neurorehabil Neural Repair*, vol. 31, no. 8, pp. 769–780, Aug. 2017, doi: 10.1177/1545968317721975.

[38] H. Taheri, J. B. Rowe, D. Gardner, V. Chan, D. J. Reinkensmeyer, and E. T. Wolbrecht, "Robot-assisted Guitar Hero for finger rehabilitation after stroke," *Annu Int Conf IEEE Eng Med Biol Soc*, vol. 2012, pp. 3911–3917, 2012, doi: 10.1109/EMBC.2012.6346822.

[39] D. S. Reinsdorf, E. E. Mahan, and D. J. Reinkensmeyer, "Proprioceptive Gaming: Making Finger Sensation Training Intense and Engaging with the P-Pong Game and PINKIE Robot," in *2021 43rd Annual International Conference of the IEEE Engineering in Medicine & Biology Society (EMBC)*, Nov. 2021, pp. 6715–6720. doi: 10.1109/EMBC46164.2021.9631041.

[40] Q. Mourcou, A. Fleury, B. Diot, C. Franco, and N. Vuillerme, "Mobile Phone-Based Joint Angle Measurement for Functional Assessment and Rehabilitation of Proprioception," *BioMed Research International*, vol. 2015, no. 1, p. 328142, 2015, doi: 10.1155/2015/328142.

[41] Z. Cao, G. Hidalgo, T. Simon, S.-E. Wei, and Y. Sheikh, "OpenPose: Realtime Multi-Person 2D Pose Estimation Using Part Affinity Fields," *IEEE Transactions on Pattern Analysis and Machine Intelligence*, vol. 43, no. 1, pp. 172–186, Jan. 2021, doi: 10.1109/TPAMI.2019.2929257.

[42] K. Valdes, E. Gendernalik, J. Hauser, and M. Tipton, "Use of mobile applications in hand therapy," *Journal of Hand Therapy*, vol. 33, no. 2, pp. 229–234, Apr. 2020, doi: 10.1016/j.jht.2019.10.003.

[43] S. F. M. Toh, K. N. K. Fong, P. C. Gonzalez, and Y. M. Tang, "Application of Home-Based Wearable Technologies in Physical Rehabilitation for Stroke: A Scoping Review," *IEEE Transactions on Neural Systems and Rehabilitation Engineering*, vol. 31, pp. 1614–1623, 2023, doi: 10.1109/TNSRE.2023.3252880.

[44] J. E. Sasaki, D. John, and P. S. Freedson, "Validation and comparison of ActiGraph activity monitors," *Journal of Science and Medicine in Sport*, vol. 14, no. 5, pp. 411–416, Sep. 2011, doi: 10.1016/j.jsams.2011.04.003.

A Customizable Fitting Protocol for the Body-Machine Interface

Fiona A. Neylon[1,2], Andrew Thompson[1,2], Rachel Kalvakota[2],
Corinne Fischer[2], Fabio Rizzoglio[1,2], Lee Miller[1,2], and Brenna D. Argall[1,2]

***Abstract*— In this work, we present a case study evaluation that compares two methods of fitting the Body-Machine Interface (BoMI) to an individual with cervical spinal cord injury for the purpose of operating a robotic arm in 6-D. A BoMI is a control interface created by recording body movements and mapping them to the controls of a device or machine, and has shown promise for individuals with motor impairments whose access to standard interfaces is otherwise limited. Results from this case study show a one-size-fits-all placement strategy is not a sufficient fitting method for an individual with severe upper extremity limitations. However, when a flexible fitting protocol informed by a clinical evaluation is applied, we see improvement in two key categories: (1) success in map fitting and (2) robot task results. Informed by the case study analyses, we develop a *novel* method to customize and fit the BoMI to users in a way that is analogous to how commonly used assistive technologies are fit clinically: the BoMI Customization Evaluation (BCE). This new method of customization is determined from a physical evaluation conducted by a clinician in conjunction with participant feedback and BoMI engineers. Deployment of this novel method within a full evaluation study is underway. The current work focuses on the evolution to this protocol.**

I. Introduction

Individuals living with cervical spinal cord injury (cSCI) depend on a variety of assistive technologies to perform activities of daily living (ADL). The commonly used powered wheelchair employs low-dimensional control (2-D) to achieve increased mobility [1]. The less commonly used robotic arm requires high-dimensional control (e.g., 6-D) to assist those with upper extremity limitations with feeding, picking-and-placing objects, or opening doors [2].

For those with cSCI, their assistive technologies (ATs) are not traditionally out-of-the-box ready. Users undergo fittings, calibrations, and customization options with clinicians. For a powered wheelchair, components of the chair such as seating interfaces, suspension mechanisms, and driving interfaces are written into a prescription [3]. For a sip/puff interface, the user undergoes a calibration protocol to construct a mapping from their respiration pressure signals to device controls. However, to the knowledge of the authors, an analogous prescriptive fitting protocol informed by clinical metrics does not exist for the Body-Machine Interface (BoMI).

We address this gap by designing the BoMI Customization Evaluation (BCE)—a prescriptive fitting protocol for the BoMI. A BoMI is a control interface created by recording body movements and mapping them to the controls of a device or machine. It has shown promise for individuals with motor impairments whose access to standard interfaces is otherwise limited [4]. We motivate the final BCE design through a case study evaluation of two BoMI fitting protocols, in which an individual with cSCI operates a robotic arm in 6-D. The contributions of this work are the following:

- A case study evaluation of two evolutions of BoMI fitting protocols to a person with cSCI for the purpose of robotic arm operation.
- The identification of a collection of considerations and guidelines when fitting wearable interfaces, such as the BoMI, to individuals with cSCI.
- A prescriptive fitting protocol for a BoMI to persons with upper-extremity mobility limitations: the BoMI Customization Evaluation (BCE).

In Section II, we present related background and describe the current gap in BoMI fitting protocol. We then present the evolution of our three approaches to fitting the BoMI in Section III. We setup our case study experimental protocol and evaluation metrics in Section IV and discuss the results in Section V. We summarize our takeaways and future work in Sections VI and VII.

II. Background & Related Work

For people both with and without injury, the use of interfaces to send a control signal to a device is a daily phenomenon; even pressing a button for an elevator is an example of a control interface. For those with cSCI and resultant upper and lower extremity impairments, the dependence on control interfaces is more significant. The interfaces accessible to them vary in operation, type, and issued signal depending on their injury level.

Common non-invasive interfaces used by cSCI individuals include joysticks, head arrays, sip/puffs (SNPs), and micro light switches (MLSs) [5]. The joystick, at most a 3-D interface, becomes limited or completely inaccessible to those with severe paralysis. Alternatives such as head arrays (2-D), SNPs (1-D), and MLSs (1-D) issue even lower dimensional signals. Moreover, when using traditional interfaces for higher-dimensional control, such as a robotic arm (6-D), there is a dimensionality mismatch between the issued signals and the device's control space.

One solution to this mismatch is the use of *modal control*—the partitioning of the control space into subsets, with *mode-switch* actions that change the operational mode of the interface in order to access the various subsets [6]. The added hurdle of mode switching can increase the mental and physical load on the user, and accordingly also the difficulty of simple ADL tasks [7].

[1]Northwestern University, Evanston, IL., USA
[2]Shirley Ryan AbilityLab, Chicago, IL., USA

A challenge when designing and fitting ATs to people with cSCI is how the same injury can manifest as very different movement capabilities [8], lending customization to be a desired feature. The aforementioned interfaces are commercially available in part due to their limited customization options. For the joystick, handle interfaces can be changed—for example to a T-bar for high cSCI individuals—but this modification reduces the input space from 3-D to 2-D. Moreover, any 1-D or 2-D interface requires significant mode switching when controlling high-dimensional devices—furthering the cognitive load.

The BoMI provides an alternative solution to address the dimensionality mismatch between ATs and their control interfaces, while maintaining the capability of customization to meet users where *they* are physically. The BoMI uses sensors to capture and translate body motions to control signals; common methods include capturing body kinematics via Inertial Measurement Units (IMUs) or cameras, and muscle signals via electromyography [4], [9], [10]. There is preliminary evidence that BoMIs are able to issue sufficiently high control signals to obviate the need for mode switching during robotic arm operation [11].

III. Body-Machine Interface Fitting

We present in this section an evolution of three BoMI fitting methods. In Method 1 (Sec. III-A), customization of the BoMI focuses on sensor placement and selection from a menu of vetted motion prompts. *Motion prompts* are body motions that are collected during calibration to obtain the parameters of the BoMI map, and which will be executed to operate the robotic arm. Method 2 (Sec. III-B) is a flexible approach, fitting the sensors and prompts based on the movement capabilities of the participant.

A case study comparison of these two methods then drives the development the third method. Method 3 (Sec. III-C) is a prescriptive approach which combines input from three parties—clinicians, BoMI engineers, and the user—in a collaborative effort to customize the BoMI.

Our target population is individuals with cSCI with a complete (ASIA A) lesion at C3-6 or an incomplete injury (ASIA B, C, or D) lesion in the cervical cord. These are individuals who have limitations in hand and manipulation ability, but also the potential to execute six distinct upper-body movements: that is, individuals who would benefit from the use of an assistive robotic arm, and would potentially be able to operate it without mode switching.

A. Method 1: Fixed Procedure

Method 1 fits a predetermined configuration of prompts and sensor placements to a user. As a default, the shoulder (up/down and forwards/backwards) and arm (elbow abduction/adduction) prompts are paired with empirically determined sensor placements limited to the shoulders (front/back) and arms (upper/fore). These default prompts are chosen as upper body joint motions that our target population are expected to be able to perform [12].

With the user in their seated rest position, we record a dataset as they execute the motion prompts. If the user is unable to reproduce a prompt, we replace it with a head prompt—defined as head up/down, left/right, up-right(UR)/down-left(DL), up-left(UL)/down-right(DR), or tilt right/left. These configurations are hypothesized to decrease the likelihood of generating an invalid map—a map wherein the user does not have access to all the required control dimensions.

B. Method 2: Flexible Procedure

Method 2 takes a flexible fitting approach to the BoMI that does not use a default configuration; instead, the configuration is defined via the range of motion (ROM) of the user. The user undergoes a clinical evaluation which assesses areas of the body to define the ROM. The results inform a fitting with the user, clinicians, and experimenters.

The user is asked to perform common upper extremity (UE) motions that they are expected to have access to based on the results of the ROM exam. Experimenters select six visually distinct movements—with visually appreciable motion and with limited similarity. Formally, these are motions in which extremities follow a rotation around orthogonal axes bisecting a common joint, which allow for conscious isolation between the six motions during execution. IMUs then are fit to the user's UEs with placements able to record the selected prompts.

C. Method 3: BoMI Customization Evaluation (BCE)

Method 3, the prescriptive approach, comprises two phases: (1) physical examination and (2) collaborative fitting.

Physical Examination. The first phase is comprised of a clinical evaluation protocol plus an evaluation framework that categorizes cervical and UE movements based on potential sensor placements. This evaluation framework ultimately facilitates the identification of viable sensor placements and the assessment of the movement quality at each placement.

Clinical Protocol. The clinical evaluation incorporates measurements of UE active range of motion (AROM) and utilizes a modified version of the International Standards for Neurological Classification of Spinal Cord Injury (ISNCSCI) [12] in an effort to provide insights into the users' residual motor abilities. The ISNCSCI provides an objective framework to quantify injury levels, thereby facilitating consistent comparisons among users. To enhance user comfort and minimize unnecessary procedures, modifications are made to the ISNCSCI, substituting the anal testing component with a self-report questionnaire [13]. This study targets individuals with injuries at or above the C8 level, so the sensory assessment concludes at T2, while the motor assessment is unaltered.

Movement Categorization. The movement scoring framework begins with a Manual Muscle Test (MMT) to the cervical and bilateral UE regions, reflective of any movement eligible for IMU placement. Unlike the MMT scale used in the ISNCSCI, the 5-point MMT scale used is a variation that is more sensitive to lower strength levels, which is relevant data when selecting optimal sensor placement [14]. This scale defines 0 as having no muscle contraction and 5 as normal muscle contraction with full motion in a gravity plane against maximum resistance. A score of 2 on the ISNCSCI

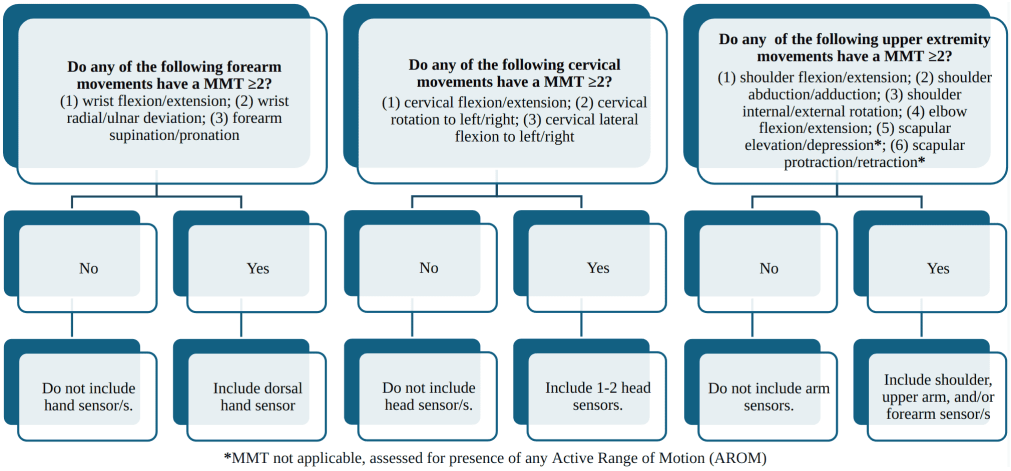


Fig. 1: Flowchart directing the sensor placement based on the movement score in each region.

MMT rubric requires full ROM in a gravity-eliminated plane, while a score of 2 on the updated scale only requires some motion. This provides a more nuanced scoring for someone who does not have full ROM, typical of our target population.

The MMT motions are divided into categories based on sensor placement, presented in Figure 1. For example, the eligibility of a hand sensor placement is determined by evaluating wrist flexion/extension, radial/ulnar deviation, and forearm supination/pronation. If the MMT score is 2 or greater for any movement in the sensor category, it qualifies as a valid sensor placement.

Collaborative Fitting. In the second phase, the clinician presents the list of valid sensor locations and the corresponding movements with above-threshold MMT scores. The BoMI developers choose six visually distinct movements: with appreciable motion and limited similarity (as in Section III-B). Experimenters ask the user to execute the prompts and visually inspect if appreciable motion is achieved on their body. The user then is asked if these prompts are comfortable and non-strenuous. If the user responds 'no', the prompt is either swapped out for an alternative high-scoring motion prompt in the same region, or the user may alter the execution of the motion to be within their comfort level. Once the motions are finalized, developers pre-assign each prompt to a specific robot control dimension.

IV. Experimental Protocol

Here we overview the experimental protocol for case study evaluations of BoMI fitting Methods 1 and 2, the results of which motivate the creation of the BCE.

A. Participant Profile

We compare Methods 1 and 2 with respect to BoMI fitting and operation by a 68 year-old male with a self-reported cSCI injury level at C2. The onset of injury was approximately 4 years ago after suffering from a spinal stroke post heart attack. Since his diagnosis, he uses a powered wheelchair daily controlled by a T-bar joystick, and self-assesses being 'comfortable' controlling his device. Participant also self-assesses experience controlling a wheelchair with a head array, but 'not experienced' controlling a robotic arm. The participant gave his informed, signed consent to participate in the experiment which was approved by the Northwestern University Institutional Review Board.

B. Hardware & Software

The experimental BoMI consists of 6 IMU sensors that capture body motions predefined according to the fitting procedure (Method 1 or 2). The 24-D quaternion signals issued from the IMUs ($\mathbf{q}_{[1\times 24]}$) are mapped via supervised learning to a 6-D robot end-effector control space ($\mathbf{v}_{[1\times 6]} = [\dot{x}, \dot{y}, \dot{z}, \dot{\phi}_x, \dot{\phi}_y, \dot{\phi}_z]$).

Specifically, a k-nearest neighbors classifier ($k = 50$) is used to predict the probability of each of the pre-selected prompts ($\Gamma^{[1\times 6]}$) given the user's movement as captured by the IMUs (Algorithm 1). The robot control dimension associated with the most likely prompt is selected for execution. The magnitude of the robot motion is determined from Principal Component Analysis (PCA) maps derived *a priori* for each of the 6 prompts from the calibration data ($\mathscr{D}$, described in Section IV-D); the first principal axis of the associated PCA map is used to determine the amplitude of the control signal for the selected control dimension.

The IMUs are the x-io Technologies x-IMU3 (Bristol, UK). The robotic arm is the 7-DoF UFactory xArm7 (Shenzhen, China) with associated ROS2 Humble packages. The experimental pipeline runs on a Lenovo ThinkStation P3 Tower (64GB RAM, 13th Gen Intel™ Core i9-1300 x32 processor) running Ubuntu 22.04. Hardware is commanded and data is logged using Open Robotics ROS2 Humble.

C. Data Collection

From fitting Method 1, we construct Configuration C_1 (Figure 2). Sensor placements are front of the shoulders (1/2), upper arms (3/4), and sides of the head (5/6). The prompts and map to robot controls for C_1 are: (1) Head R/L $\rightarrow x$, (2) R shoulder forwards/backwards $\rightarrow y$, (3) R shoulder up/down $\rightarrow z$, (4) L shoulder up/down $\rightarrow \phi_x$, (5) Head up/down $\rightarrow \phi_y$, and (6) L shoulder forwards/backwards $\rightarrow \phi_z$.

From Method 2, we construct configuration C_2 (Figure 2). Sensor placements for this configuration are front of the

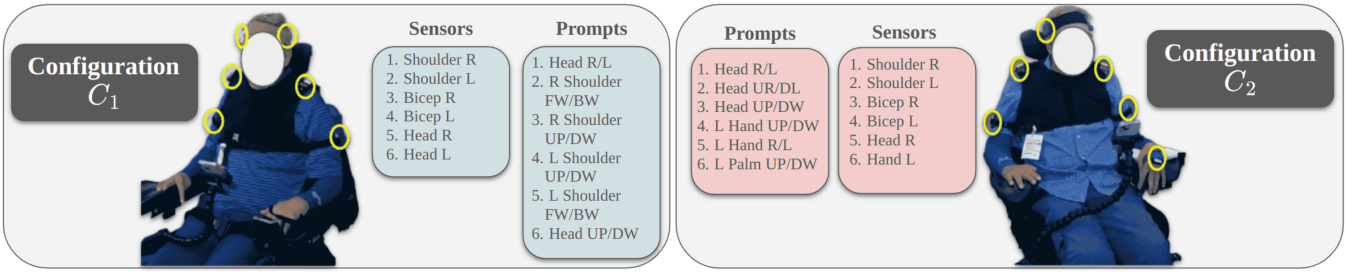


Fig. 2: Experimental setup showing the prompts and sensor placements for configuration 1 (C_1) and configuration 2 (C_2)

Algorithm 1 BoMI Mapping Using KNN and PCA

Input: 24-D quaternion input $\mathbf{q}^{[1\times 24]}$ and $\mathscr{D}$
Ouput: 6-D control signal $\mathbf{v}^{[1\times 6]}$
Step 1: Calibration (Offline)
for each motion prompt $\gamma_i \in \Gamma^{[1\times 6]}$ **do**
Derive PCA map $\mathbf{PCA}_i$ from $\mathscr{D}_i$
end for
Step 2: Motion Prediction (Run-time)
Use k-nearest neighbors (KNN, $k = 50$) to predict the probability vector

$$\mathbf{p} = \mathrm{KNN}(\mathbf{q}) \quad \text{where } \mathbf{p} \in [0,1]^{1\times 6}$$

Identify Highest Probability Index

$$i^* = \arg\max_i p_i$$

Step 3: Compute Velocity Vector (Run-time)
Reduce the 24-D signal to 1-D using the first principal axis of $\mathbf{PCA}_{i^*}$:

$$a = \mathbf{q} \cdot \mathbf{PCA}_{i^*,1}$$

Compute the final control signal:

$$\mathbf{v} = [0,\ldots,a,\ldots,0]$$
$$\uparrow$$
i^*th position

shoulders (1/2), upper arms (3/4), side of the head (5), and top of the left hand (6). The prompts and map to robot controls for C_2 are: (1) Head R/L $\rightarrow x$, (2) Head UR/DL $\rightarrow y$, (3) head up/down $\rightarrow z$, (4) L hand up/down $\rightarrow \phi_x$, (5) L palm up/down $\rightarrow \phi_y$, and (6) L hand right/left $\rightarrow \phi_z$.

For this analysis, we focus on 4 study sessions: 3 sessions under C_1 ($C_1^{S_1}$, $C_1^{S_2}$, and $C_1^{S_3}$) and 1 session under C_2 ($C_2^{S_1}$), which define the divide between the two different fitting protocols. We focus on these sessions to highlight the immediate effects of changing to a BoMI configuration informed by a clinical evaluation. For the three C_1 sessions, each session occurred within 4 days of each other. The C_2 session occurred 16 days later. This is due to the presence of 3 *wash* sessions (defined in Section IV-E) that occurred under the C_1 fitting method, in which the C_1 map became unusable as a result of physiological changes in the participant—specifically, reduced ROM due to a gap in physical therapy.

D. Calibration

Each session begins with a calibration phase. The participant executes directed motion prompts to generate the dataset $\mathscr{D}$ for map computation. This is done in a cyclic fashion, where each prompt is executed in sequence 6 times. A sequential approach, in comparison to repeated iterations, is expected to better reflect the control signals the user issues during teleoperation, and also to mitigate the biased accumulation of IMU drift across the recording (sampling at 50Hz).

E. 6-D GUI Validation

Next, a 6-D GUI task is used to validate the map—ensuring that the participant has isolated control of each of the required dimensions (Figure 3a). The GUI is a circular figure divided into 6 equally spaced wedges with a different color arc located in the center of the wedge [15]. Each arc begins in a grey zone of the wedge which defines the *deadzone* of the control space that maps to the bodily rest position of the user. The colored arc moves in accordance to the magnitude of the velocity control signal issued by the user and returns to the *deadzone* when no signal is being issued.

To validate, the experimenter instructs the participant to execute a body prompt. If the correct arc displaces in the correct direction, the signal is considered valid. A valid map is defined as the user being able to issue intended and correct signals using the defined body motions in both the positive and negative directions for the required control dimensions, defined at a minimum to be 3-D translation. This is conducted for all 6 prompts in each direction (+/-), for 12 distinct movements total.

Wash Sessions. If instead a direction is considered invalid—incorrect or with no activation after repeated attempts—we *tare* the BoMI: the participant returns to their self-defined rest position, and we tare the IMU quaternions back to zero to eliminate any drift accumulation that might have caused poor GUI performance. We then revisit the invalid directions and ask the participant to repeat the motion.

If the map is deemed invalid—incorrect or no activation after repeated attempts in one or more of the required control dimensions—the most recent valid map (from prior sessions) is tested under the same protocol. If this map is valid, it is used, otherwise the calibration protocol is executed again. If the re-recorded map results in an invalid map, the session is a *wash* and concludes without progressing further.

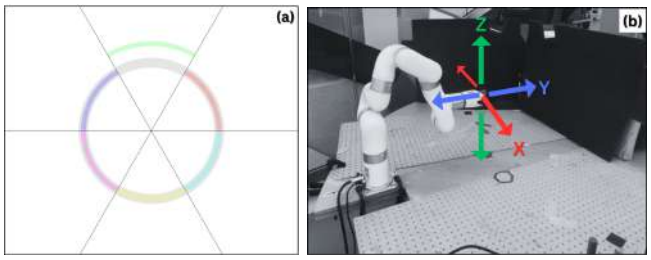


Fig. 3: Experimental setup where (a) shows the 6-D GUI validation task and (b) shows the 3-D Dimensional Freezing task.

F. 3-D Dimensional Freezing (DF)

The 3-D Dimensional Freezing (DF) task is a training task to teach users to command the robotic arm with the BoMI. For each translation dimension, the user practices how to independently move the robot end-effector in one dimension at a time in a center-out-reaching fashion (Figure 3a). During these reaches, the robot motion is restricted to only move in the training dimension, effectively filtering out all spurious BoMI commands and allowing only those that achieve motion in the intended robot dimension to pass through. We ask the participant to complete 3 reaches in a row for each robot control dimension.

G. Metrics

Expert Comparison. A common method used to evaluate reaching tasks is to define an 'expert' or desired trajectory and compare reaching trials [16]. To analyze the DF trials, we define an expert trajectory for each center-out reaching translation dimension. This expert trajectory is defined as a time series of end-effector positions as a result of a synthetic velocity control signal roll-out on the robot. For all trajectories, a moving window average ($N = 10$) is used to filter out mechanical noise from the profile of the end-effector positions, sampled at 100 Hz.

We use Dynamic Time Warping (DTW) to quantify the similarity between the participant trajectories and the expert trajectory. DTW lends itself to being useful for comparing time series profiles where events occur during a window of time—this algorithm has been used to compare trajectories [17]. We use the Fast Distance Dynamic Time Warping method from the DTAIDistance Python package [18].

Trajectory Characteristics. We also examine a number of *trajectory characteristics*. Three main characteristics we look for in a reach are, relative to the end-effector start position, (1) the presence of a departure path due to a positive velocity signal, (2) a turnaround, and (3) a return path due to a negative velocity signal. The presence of each indicate the user, at a rudimentary level, is able to not only access all areas of the control space for that dimension, but is also able to purposefully elicit the correct sequence of commands that would allow them to complete the task as asked.

We construct a scoring paradigm that looks for this sequence of events, or partial sequence at any point during the reach. We assign a score of 1 if the characteristic: (1) is present, (2) in the correct direction, and (3) occurs in the proper sequence of events (departure→turnaround→return).

TABLE I: Summary of trajectory characteristics.

	Characteristic	$C_1^{S_1} - C_1^{S_3}$	$C_2^{S_1}$
X Reaches	*Departure*	3.0 ± 0.0	3.0
	Turn around	3.0 ± 0.0	3.0
	Return	3.0 ± 0.0	3.0
Y Reaches	*Departure*	1.7 ± 1.2	3.0
	Turn around	1.3 ± 1.2	2.0
	Return	1.0 ± 0.8	2.0
Z Reaches	*Departure*	2.3 ± 0.9	3.0
	Turn around	2.0 ± 0.8	3.0
	Return	1.0 ± 0.8	3.0

The characteristic otherwise is assigned a score of 0.

Cross-talk. We finally look to the raw signals issued by the user during teleoperation. For every set of dimensional reaches and each timestep of each reach, we count the commands issued in every control dimension. This is to analyze *cross-talk*—in which unintended control dimensions are accessed due to prompt similarity.

With limited mobility, there are limited body sites to choose from for the motion prompts. When a single mobility site needs to be overloaded with multiple distinct motion prompts, the possibility of *cross-talk* is present. This introduces an optimization problem when fitting the BoMI, wherein we choose sites to maximize movement activation while minimizing crosstalk between prompts. An example of *cross-talk* would be if a third motion prompt combines two motion prompts off-axis (e.g., head up/down, left/right, and up-right/down-left). Within the latent space of the map, the user might have to pass through a region of one of the first two prompts before reaching the more defined and separated area of the third prompt, and within this region inadvertent commands would be issued.

Map & Experimental Metadata. In addition to robot task data, map and experimental metadata is considered to assess how reliable the fit is between days. We measure this by calculating (1) the percentage of wash sessions across all sessions, (2) the average number of calibration recordings per session, and (3) the number of modifications along with the intensity of the modification.

V. Results

We present the results of the metrics described in Section IV-G; this includes results from the 3-D DF task and metadata from the maps collected over the sessions.

A. Robot Task Results

Trajectory Characteristics. Table I summarizes the breakdown of the presence of each trajectory characteristic during each session. The end-effector trajectories for the corresponding reaches are shown in Figure 4.

Comparing the two fitting protocols, the y reaches improve by greater than 50% under C_2; notably, none of the characteristics are present in $C_1^{S_3}$. In z under C_1 the participant has difficulty obtaining a turn-around or return path; for these

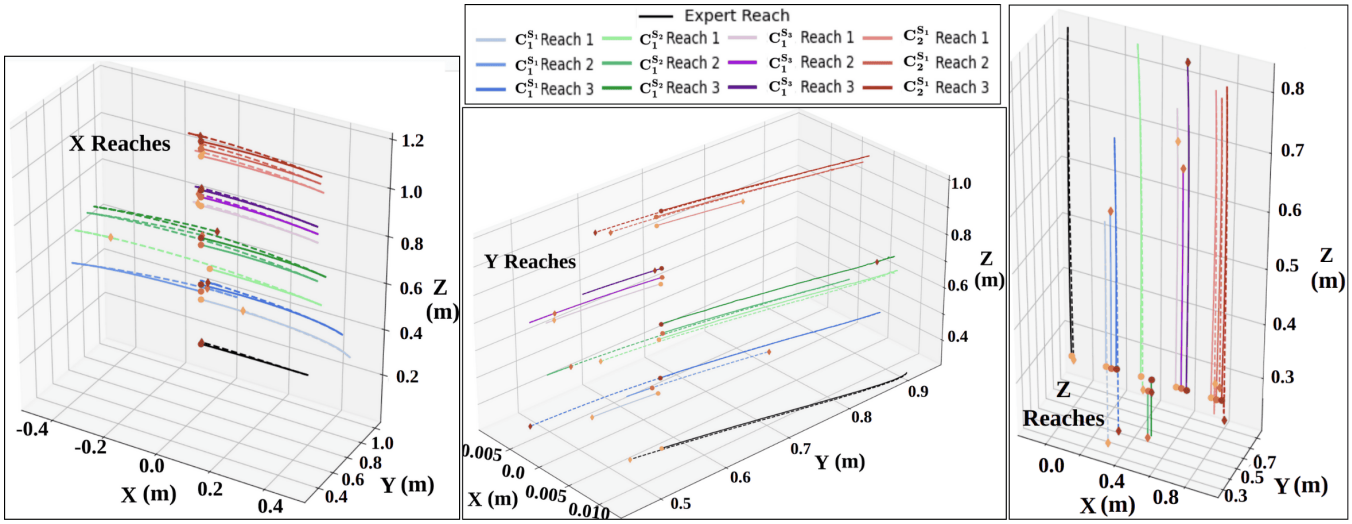


Fig. 4: Comparison of robot end-effector positions for $C_1^{S_1}$-$C_1^{S_3}$ and $C_2^{S_1}$. Reaches under C_1 are blue/green/purple, and under C_2 are red, with the expert trajectory in black. Motion prior to the first turnaround is presented as solid lines, and post turnaround as dashed lines. Start (yellow circle) and end (yellow diamond) positions indicated for each trajectory. Reaches are offset for visibility: by 0.03m within a single session, and by 0.2m between sessions.

two characteristics, there is greater than 130% increase with C_2. By contrast, for the x reaches (unchanged dimension), the presence of these characteristics is stable across all sessions and configurations.

Expert Comparison. In Figure 5, we see the mean DTW distance for each type of dimensional reach between C_1 and C_2. Comparing the two changed dimensions, y and z, there is an immediate ∼45% reduction in the DTW distance for each dimension (5.30 ± 1.02m to 2.84 ± 0.55m for y, and 8.93 ± 1.44m to 5.04 ± 0.21m for z) following the configuration change, $C_1^{S_3}$ and $C_2^{S_1}$.

While not statistically significant (Wilcoxon non-parametric statistical t-test), these reductions do indicate that the changes in configuration positively impacted robot operation performance. In the z dimension, performance under C_1 progressively erodes across sessions, while performance in the y dimension is consistently inferior to that under C_2. All sessions under C_1 furthermore display higher variability than C_2, in both dimensions y and z.

By contrast, for the unchanged x dimension, the DTW averages were comparatively similar between C_1 and C_2

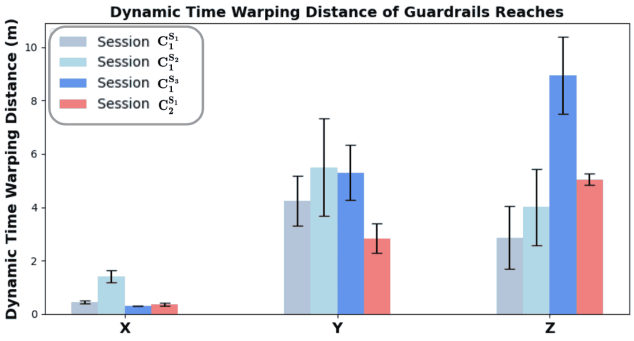


Fig. 5: Average DTW distance computed across reaches for $C_1^{S_1}$-$C_1^{S_3}$ and the $C_2^{S_1}$. The blue-toned bars indicate sessions under C_1 and the red-toned bars indicate sessions under C_2.

(0.31 ± 0.01m and 0.38 ± 0.06m, respectively), and are smaller overall. These results underline the suitability of the BoMI motion prompt affiliated with x dimension robot control, and also confirm that the change from C_1 to C_2 did not impact the operability of this motion prompt.

For C_2 we also see the average distance traversed is comparatively closer to the expert reach, in each of dimensions x (expert: 0.79m, C_2 : 0.97 ± 0.08m, C_1: 1.23 ± 0.32m), y (expert: 0.74m, C_2 : 0.45 ± 0.24m, C_1: 0.38 ± 0.25m), and z (expert: 1.15m, C_2 : 1.15 ± 0.08m C_1: 0.54 ± 0.34m).

Cross-talk. In Figure 6, we compare the commands issued under configurations $C_1^{S_3}$ and $C_2^{S_1}$. Specifically, for each intended control dimension, we tally the number of (positive/negative) commands issued all control dimensions.

We see for C_2, there is more *cross-talk*. This is not surprising with C_2 because the body prompt for y activation (head UR/DL) is a combination of the body prompts for x (head R/L) and z (head UP/DW). The user therefore likely needed to pass through a latent space region corresponding to x or z to reach y area. The body, specifically the upper body, is highly coupled which means that *cross-talk* (between prompts and, accordingly, control signals) is a natural feature of the BoMI that users need to learn how to manage.

We also, however, see more correct y and z signals issued under C2. These signals additionally are more balanced in the ratio of positive to negative signals, indicating reliable access to dimensions in both the positive and negative directions.

B. Map & Experimental Metadata

Our analysis so far has focused on 4 study sessions, to dive deep into the impact of the configuration change from $C_1 \rightarrow C_2$. We now zoom out for a moment, and examine metadata from all sessions with this participant, including *wash* sessions and continued sessions with C_2. The total number of sessions is 17: 8 under C_1 and 9 under C_2.

Wash Sessions. Looking at all of the maps recorded over all

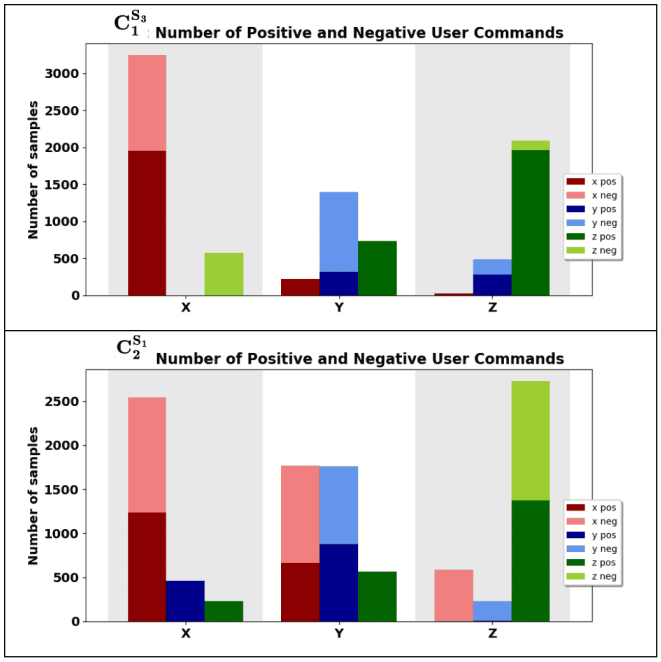


Fig. 6: Comparison of user signals commanded under C_1 and C_2. More *cross-talk* between dimensions is evident in $C_2^{S_1}$ than $C_1^{S_3}$, however the signals in y and z also are more correct and more balanced. (No crosstalk would have only a red bar in x, only a blue in y, and only a green in z.)

17 attempted sessions, for each configuration two metrics are calculated: (1) percentage of wash sessions of the attempted sessions and (2) average number of maps recorded per session. With C_1 we see 37.5% of the attempted sessions end in a *wash* protocol; for C_2 that number is 0.0%. The number of recorded maps per session is reduced from an average of 1.9 recordings per session to 1.1 recordings per session. Both of these metrics signal an informed approach to fitting the BoMI results in a more reliable mapping mechanism that is more robust to day-to-day variation. This not only eases the burden on experimenters and clinicians, but also on the user.

Moreover, while the evaluation of the BCE protocol is beyond the scope of this paper, we note that it has since been deployed in a total of 67 sessions across 8 participants, *none* of which has ended in a *wash* session.

Modifications. It is expected that unforeseen modifications will need to be made to the BoMI between users, as modifications made to ATs are not uncommon in the field [19]. Between C_1 and C_2, the physical and environmental modifications made in order to get the BoMI to work on a given day changed, including number and type.

Across all 17 sessions, we catalog 3 types of modifications: (1) removing wheelchair armrests, (2) providing limb support, and (3) restraining limbs. If the same type of modification is applied to both sides of the body, we count it as 2 modifications.

For C_1, 4 modifications were applied: (1/2) removing right/left armrest, and (3/4) restraining the right/left arm to wheelchair armrest. There was also a lack of consistency in whether a modification actually resulted in any appreciable difference in the map validity. In comparison, the only modification for C_2 during the 9 attempted sessions was the support of the left wrist to elevate the hand. This modification not only was less invasive compared with modifications made in C_1, but also was applied to every session as it positively impacted map validity.

VI. Discussion

For this work, we consider both the quantitative robot task data and the map metadata to provide insights into assessing the fit of each configuration (Section VI-A). We also compile our observations from this case study into guidelines for those working with wearable interfaces similar to the BoMI on individuals with cSCI (Section VI-B). Our on-going and future work will continue to evaluate the BCE, in a multi-session user study with the cSCI population.

A. Quantitative Results

This case study marks a milestone in the experimental development for properly fitting the BoMI. When trying to implement Method 1 on an AROM-restricted participant, the interface was unreliable and, at times, completely unusable. Once we took a flexible approach with Method 2, we not only saw *immediate* improvement in the day-to-day fitting and calibration process, but we also saw improvement in robot task performance. The inconsistencies and low yield of desired characteristics in the y and z dimensions in the DF task improved immediately in the first session with C_2.

It is suspected that motor learning of the interface was not the cause of this improved performance: in Figure 5, $C_1^{S_1} \rightarrow C_1^{S_3}$ in fact was moving farther away from the expert trajectory, prior to the switch to C_2. The lack of statistical significance in these results is hypothesized to be due to a small sample size ($N = 3$). Finally, the consistent trajectory characteristics across the x reaches indicated the x dimension was properly fitted from the beginning.

B. cSCI Wearable Considerations

The AT field expects modifications to fully meet the user. The reliability of these modifications requires an open dialog between clinicians, developers, and the user. The flexibility built into our mapping paradigm, taring protocol, and choice of hardware are vital to meeting these needs. The mapping paradigm has parameters, such as *deadzone* size, to algorithmically tune the sensitivity per participant. The taring protocol is the key to combating drift accumulation in the IMUs, which becomes even more vital when working with the relatively low-variance samples enacted by lower-ROM movements. The use of appropriate hardware and filtering methods enables the capture of these low-variance signals, in turn allowing for accurate mapping. These three components introduce robustness into a system that interfaces with a population with high physiological variability.

The need for stability in the user/device relationship is all the more pressing when any physical instability will manifest in the interface; because the stability of a wearable interface is tied to the stability of the user's body. Creating a system that is robust to instabilities results in a more learnable system by minimizing stochastic components of the user map. For example, our cSCI population requires

frequent pressure breaks and additional personal needs that cause changes in the position of the IMU and overall postural positioning. The user should be able to do these things, re-tare the interface, and resume operation as normal. Artifacts such as *cross-talk*, a present and unavoidable consequence of working with a population with limited sites for appropriate sensor placement, becomes more predictable and learnable to the user when the system is reliable and robust.

VII. Conclusions

The value of designing ATs that are inherently customizable lies in their ability to meet the diverse needs of individuals with varied motor abilities. Traditional interfaces to control ATs often fail to address the full spectrum of user needs due to their fixed design, which limits adaptability and accessibility. We have presented an evolution of protocols that fit a Body-Machine Interface (BoMI) to a person with cervical spinal cord injury (cSCI) for the purpose of 6-D robotic arm control. A case study comparison of the first two protocols has demonstrated the benefit of introducing flexibility into the fitting protocol, with improvements in the day-to-day fitting and calibration process as well as in robot task performance. We also have introduced the BoMI Customization Evaluation (BCE): a user-centric fitting approach that includes a clinical evaluation and combines input from three parties—clinicians, BoMI developers, and the user—in a collaborative effort to customize the BoMI to ensure that both the clinical and functional requirements of the technology are met. The evaluation of the BCE within a multi-session study with cSCI users is on-going, with promising preliminary results.

Acknowledgments

The authors would like to thank Lucy Ammon and Divyanka Thakur for their assistance in running study sessions and data analysis. Funding for this work was provided by the National Institute of Biomedical Imaging and Bioengineering (NIBIB) under Award Number R01-EB024058. The content is solely the responsibility of the authors and does not necessarily represent the official views of the NIH.

References

[1] J. Florio, U. Arnet, A. Gemperli, T. Hinrichs, and SwiSCI study group, "Need and use of assistive devices for personal mobility by individuals with spinal cord injury," *Journal of Spinal Cord Medicine*, vol. 39, no. 4, pp. 461–470, 2016.

[2] V. Maheu, P. S. Archambault, J. Frappier, and F. Routhier, "Evaluation of the jaco robotic arm: Clinico-economic study for powered wheelchair users with upper-extremity disabilities," in *Proceedings of the IEEE International Conference on Rehabilitation Robotics (ICORR)*, 2011.

[3] E. Michael, T. Sytsma, and R. E. Cowan, "A primary care provider's guide to wheelchair prescription for persons with spinal cord injury," *Topics in Spinal Cord Injury Rehabilitation*, vol. 26, no. 2, pp. 100–107, 2020.

[4] M. Casadio, R. Ranganathan, and F. A. Mussa-Ivaldi, "The body-machine interface: a new perspective on an old theme," *Journal of Motor Behavior*, vol. 44, no. 6, pp. 419–433, 2012.

[5] K. Cezat, "Power wheelchair alternative drive controls in spinal cord injury," 2019.

[6] J. D. Simon and S. K. Mitter, "A theory of modal control," *Information and Control*, vol. 13, p. 316353, 1968.

[7] H. Tijsma, F. Liefhebber, and J. Herder, "A framework of interface improvements for designing new user interfaces for the manus robot arm," in *Proceedings of IEEE International Conference on Rehabilitation Robotics (ICORR)*, 2005.

[8] R. Parasuraman and V. Riley, "Humans and automation: Use, misuse, disuse, abuse," *Human Factors*, vol. 39, no. 2, p. 230253, 1997.

[9] M. MacChini, F. Schiano, and D. Floreano, "Personalized telerobotics by fast machine learning of body-machine interfaces," *IEEE Robotics and Automation Letters*, vol. 5, no. 1, pp. 179–186, 2020.

[10] E. B. Thorp, F. Abdollahi, D. Chen, A. Farshchiansadegh, M.-H. Lee, J. P. Pedersen, C. Pierella, E. J. Roth, I. S. Gonzales, and F. A. Mussa-Ivaldi, "Upper body-based power wheelchair control interface for individuals with tetraplegia," *IEEE Transactions on Neural Systems and Rehabilitation Engineering*, vol. 24, no. 2, pp. 249–260, 2015.

[11] S. Chau, S. Aspelund, R. Mukherjee, M.-H. Lee, R. Ranganathan, and F. Kagerer, "A five degree-of-freedom body-machine interface for children with severe motor impairments," in *Proceedings of the International Conference on Intelligent Robots and Systems (IROS)*, 2017.

[12] R. Rupp, F. Biering-Sørensen, S. P. Burns, D. E. Graves, J. Guest, L. Jones, M. S. Read, G. M. Rodriguez, C. Schuld, K. E. Tansey-MD, K. Walden, and S. Kirshblum, "International Standards for Neurological Classification of Spinal Cord Injury: Revised 2019," *Topics in Spinal Cord Injury Rehabilitation*, vol. 27, no. 2, pp. 1–22, 2021.

[13] L. A. Harvey, G. Weber, R. Heriseanu, and J. L. Bowden, "The diagnostic accuracy of self-report for determining s4-5 sensory and motor function in people with spinal cord injury," *Spinal Cord*, vol. 50, no. 2, p. 119122, 2012.

[14] N. A. Roman, R. S. Miclaus, C. Nicolau, and G. Sechel, "Customized manual muscle testing for post-stroke upper extremity assessment," *Brain Sciences*, vol. 12, no. 4, p. 457, 2022.

[15] A. Thompson, F. Rizzoglio, F. A. Neylon, D. R. Barsoum, L. E. Ammon, M. N. McCune, L. Miller, and B. Argall, "An evolution of assistive robot control to meet end-user ability," *Companion of the International Conference on Human-Robot Interaction (HRI)*, 2024.

[16] J. L. Patton, M. E. Stoykov, M. Kovic, and F. A. Mussa-Ivaldi, "Evaluation of robotic training forces that either enhance or reduce error in chronic hemiparetic stroke survivors," *Experimental Brain Research*, vol. 168, no. 3, pp. 368–383, 2006.

[17] N. Vaughan and B. Gabrys, "Comparing and combining time series trajectories using dynamic time warping," *Procedia Computer Science*, vol. 96, p. 465474, 2016.

[18] W. Meert, K. Hendrickx, T. V. Craenendonck, H. B. Pieter Robberechts, and J. Davis., "DTAIDistance," 2022, DTAIDistance (Version v2). Zenodo. [Online]. Available: http://doi.org/10.5281/zenodo.5901139

[19] L. Aflatoony and S. Kolari, "One size doesnt fit all: On the adaptable universal design of assistive technologies," *Proceedings of the Design Society*, vol. 2, p. 12091220, 2022.

An Extensible Platform for Measurement and Modification of Muscle Engagement During Upper-Limb Robot-Facilitated Rehabilitation

Ajay Anand, Chad A. Berghoff*, Carson J. Wynn*, Evan Cole Falconer*, Gabriel Parra*, Jono Jenkens*, Caleb J. Thomson, W. Caden Hamrick, Jacob A. George, and Laura A. Hallock

***Abstract*—Populations with upper-limb neuromotor disabilities could greatly benefit from robot-mediated therapy, but the heterogeneity of these disorders, combined with unresolved questions around neuroplasticity mechanisms, hinders the standardized prescription of effective rehabilitation tasks and corresponding robot behaviors. Building on consensus that active neuromuscular engagement is vital for therapy, we introduce a novel, extensible rehabilitation robot platform to directly measure (and, ultimately, modify) user engagement at the muscle level. The system integrates surface electromyography to monitor muscle activation patterns during isometric tracking tasks in all 6 dimensions of hand exertion — beyond the planar constraints of most systems. Usability testing with 13 healthy and 2 post-stroke participants demonstrates the system's utility in analyzing motor behavior across varying poses, trajectories, and impairment levels. Preliminary results indicate that pose and task selection significantly impact activation patterns, highlighting the rehabilitative potential of systems that support motion along all axes and at multiple user poses and guiding our own planned augmentations of the platform (personalized controllers, additional sensing, etc.). To facilitate broader research into muscle activation–force relationships and address the scarcity of open-source upper-limb motor behavior data, we have released all collected data and analysis code as part of the OpenRobotRehab project on SimTK (`simtk.org/projects/openrobotrehab`) alongside this publication.**

***Index Terms*—rehabilitation robotics, human–robot interaction, biomechanics, surface electromyography (sEMG), user-centered design**

I. Introduction

Many patient populations, including individuals recovering from stroke or spinal cord injury, and those with cerebral palsy, multiple sclerosis, and other congenital or acquired neuromotor disorders, could benefit significantly from high-intensity motor therapy. In the context of a global shortage of therapists and caregivers [1], robot-mediated therapy is a promising method to rehabilitate such impairments [2]–[6]. However, the heterogeneity of individuals' motor behaviors and their evolution over time poses a significant challenge, and there remains no consensus on how rehabilitation robots should behave to optimize therapeutic outcomes — for example, when to provide assistance or resistance, and when to augment motion errors or correct them.

One rare point of consensus is that patients should be *actively engaged* in therapy, rather than passively moved by a device or therapist, which is key to inducing the neural plasticity that facilitates motor recovery [7]. While a number of rehabilitation robot control paradigms (detailed in section II below) have evolved to incentivize this engagement, they do not generally adapt to the muscle-level engagement actually observed in an individual user, and whether that engagement is healthy or pathological, nor do they leverage the full 6 dimensions (3 positional and 3 rotational) of possible effort at the hand. To address this gap, we propose a novel robotic rehabilitation system to directly measure and assess muscle-level engagement, and, ultimately, modify that engagement by prescribing personalized trajectories and robot behaviors across both positional and rotational axes. This paper presents the first steps toward the creation of this system. Specifically, our contributions include:

- development of a novel, extensible, proof-of-concept rehabilitation platform enabling muscle activation measurement (via surface electromyography, or sEMG), during isometric, force- and torque-based trajectory tracking tasks, robustly designed for future expansion (to include varied robot controllers and additional sensing modalities);
- a pilot, open-source data set, including all collected sensing and performance data, from 15 individuals (13 healthy and 2 post-stroke), at multiple poses, performing a variety of trajectory tracking tasks on this novel platform, enabling detailed examination of the relationship between applied 6D hand forces and torques and patterns of muscle engagement; and
- preliminary analyses of this force/torque–engagement relationship in this pilot cohort, as well as this cohort's subjective impressions of the system and protocol, motivating our planned augmentations of the system and highlighting the need for expanded research into the impacts of rehabilitation task selection on motor activation patterns.

The open-source data set noted above, as well as additional platform details and analysis code, has been made available as part of the OpenRobotRehab project on SimTK (`simtk.org/projects/openrobotrehab`).

*These authors contributed equally to this work.

This work was supported by the Department of Mechanical Engineering and the Office of Undergraduate Research at the University of Utah, as well as the Office of The Director (OD), Eunice Kennedy Shriver National Institute Of Child Health & Human Development (NICHD), and National Institute Of Dental & Craniofacial Research (NIDCR) of the National Institutes of Health (NIH) under Award Number DP5OD029571 awarded to J.A.G.

The authors are with the Departments of Mechanical Engineering, Electrical and Computer Engineering, Biomedical Engineering, Physical Medicine & Rehabilitation, and Mathematics, the Kahlert School of Computing, the Utah Center for Neural Interfaces, the Craig H. Neilsen Rehabilitation Hospital, and the Robotics Center at the University of Utah, Salt Lake City, UT 84112, USA. Correspondence should be directed to {`ajay.anand`, `laura.hallock`}`@utah.edu`.

The study protocol employed in this work was approved by the University of Utah Institutional Review Board under Protocols IRB_00154923 and IRB_00098851 and written informed consent was obtained from each study participant.

II. Related Work & Context

Several control paradigms have evolved to motivate engagement during robot-mediated rehabilitation, including "assistance as needed" (AAN) [8], "intent-triggered" [8], and "dynamic difficulty adjustment" (DDA) [9] frameworks; however, these systems are all vulnerable to user laziness through their reliance on error signals and/or insufficiently comprehensive in their ability to adjust to individuals' diverse motor strategies and pathologies. Consequently, to date, no clinical trials of rehabilitation robots employing these paradigms have shown improvements in functional outcomes [10]–[13], for ambiguous reasons, illustrating the critical need for comprehensive, personalized models of individuals' neuromusculoskeletal engagement and how it changes under different robot control paradigms. Without such insights, we cannot systematically provide effective, engaging rehabilitation, nor can we quantify the efficacy of the control paradigms we already have.

Alongside these control schemes, muscle synergy analysis [14] has emerged as a promising approach to close this modeling gap by quantifying neuromotor behavior (and post-stroke impairment) and offering a window into how motor control is reorganized following neurological injury [15], [16]. Unlike traditional clinical assessments that primarily rely on kinematic performance or subjective scoring, synergy-based metrics capture the underlying coordination patterns of muscle activations, providing a more mechanistic understanding of motor deficits [17], [18]. However, while synergy-based assessments offer detailed neurophysiological insights, their direct integration into clinical rehabilitation — and particularly, into rehabilitation robotics — remains limited, and further validation and standardization is required to achieve widespread adoption of synergy-based paradigms in stroke rehabilitation protocols [17], [19].

To address this gap, we propose a novel sEMG-based rehabilitation paradigm that leverages these synergy analysis breakthroughs, including recent advancements demonstrating sEMG's potential in identifying muscle synergies to quantify post-stroke impairment [18]–[22]. Rather than employing the standard AAN-style assistance discussed above to enable users to complete specific tasks, we aim to prescribe tasks and robot behaviors to directly enhance user engagement and reduce pathological synergies at the neuromuscular level. Furthermore, because natural motion is not restricted to a single axis, we propose a system that can measure and rehabilitate motion along all 6 (positional and rotational) axes of hand action, a feature not prevalent in the planar rehabilitation systems that dominate the field of physical rehabilitation [23], [24] or in the anthropomorphic robots used for social rehabilitation [25].

The remainder of this paper presents the first steps toward such a system — one that enables this proposed engagement-centric control paradigm in all 6 dimensions — including hardware and software development of a (to begin, isometric) rehabilitation platform (section III); collection of pilot activation data from both healthy and impaired individuals completing a variety of multidimensional trajectory tracking tasks (section IV); preliminary analyses of those individuals' motor strategies and experiences using the platform (section V); and the resulting implications for future rehabilitation system design (section VI). While a full analysis of synergistic motor behavior is beyond the scope of this initial paper, we ultimately aim to perform such analyses on our collected data to inform future work on directly altering pathological synergies via robot intervention.

III. Rehabilitation Platform Design

In this section, we detail both hardware and software aspects of our proof-of-concept rehabilitation platform, as outlined in Figures 1 and 2, respectively. This section delineates both current capabilities and planned expansions (informed by the motor rehabilitation literature and our pilot data analysis in section V, as noted). Detailed system information, including firmware and software versions and configurations, can be found in the data release accompanying this paper.

A. Hardware

Our rehabilitation platform hardware consists of the following elements and associated capabilities:

1) Rehabilitation Robot: The core of our rehabilitation platform is an LBR iiwa 14 R820 7-degree-of-freedom cobot (KUKA AG, Augsburg, Germany), shown in Figure 1(f). The handle and force torque sensor (described below) through which the user interacts with the rehabilitation system are mounted to the cobot's end effector. This setup allows the robot to locate the interface at any point in space to accommodate different user poses and limb geometries. The robot currently serves as a static "jig" for isometric rehabilitation tasks, but will be augmented in future iterations of the system to move, and be moved, by the human user according to various robot control strategies (e.g., error correction or augmentation, resistance or assistance).

2) Force Torque Sensor & Handle: A SensONE 6-axis force torque sensor (Bota Systems AG, Zürich, Switzerland), shown in Figure 1(a), is used to measure the forces and torques applied to the end effector of the robot through a custom-built, ergonomic handle. In the future, additional handles will be designed to support varying user capabilities (e.g., under-wrist bracing for those unable to lift their arm, wrist attachments for those unable to grasp).

3) Surface EMG: Muscle activation data are collected from 8 key muscles of the arm — shown in Figure 1(e) — using two Trigno Quattro 4-channel sensor motes, controlled through a Trigno Base Station (Delsys, Inc., Natick, MA, USA), at 1000 Hz. Data are currently visualized and logged for motor pattern analysis via the software system described below; future iterations of the platform will use this data within the system control loop to adapt parameters of the game and robot behavior based on the user's muscle activations. We also aim to expand the platform to support additional sEMG channels and placements to enable even more comprehensive examination of muscle activation strategies in the arm and hand.

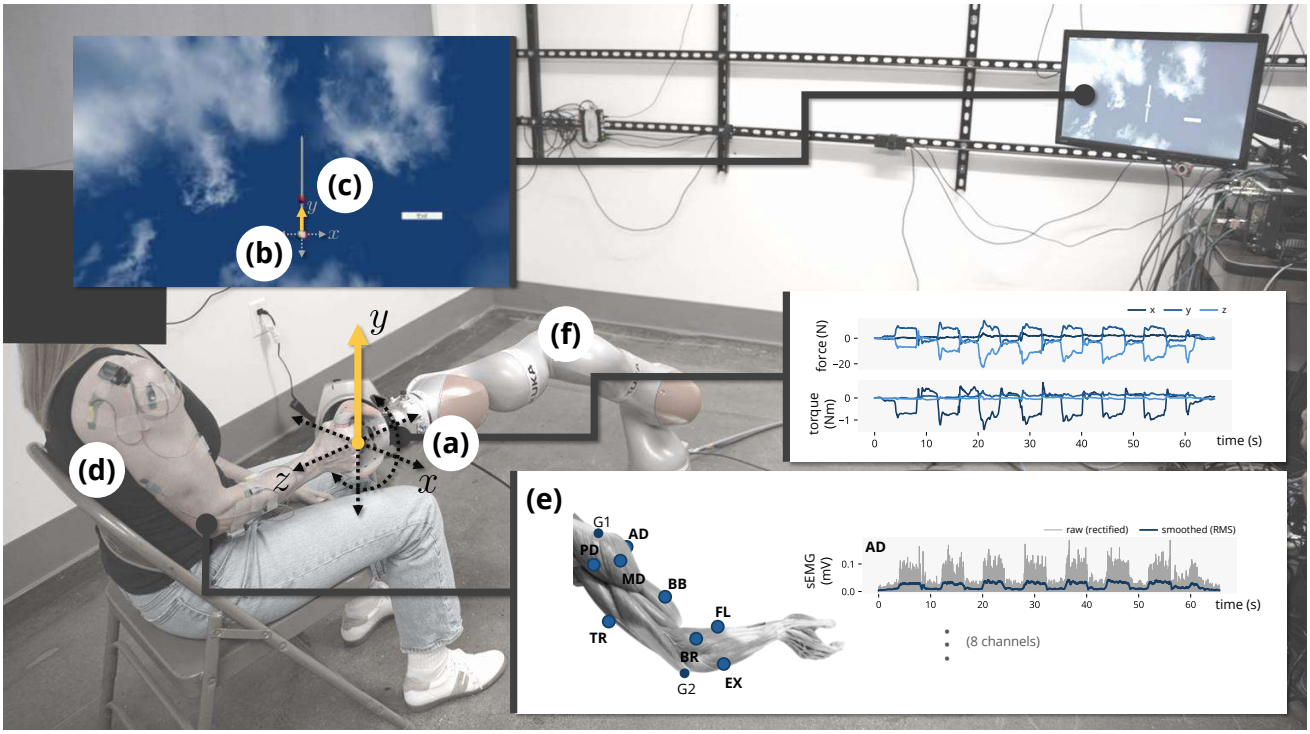


Fig. 1. Motor rehabilitation platform enabling measurement of muscle engagement during trajectory tracking tasks. Users exert forces and torques on load cell (a) through the attached handle, which are then mapped to x–y coordinates of on-screen avatar (b) to allow users to follow red target ball (c) through different trajectories, while surface electromyography (sEMG) electrodes (d) placed on key muscles of the arm (e) record muscle activations. The system currently supports isometric rehabilitation tasks at arbitrary poses — robot (f) remains static — but will be expanded in the future to support a variety of robot controllers. Surface EMG electrode placements: anterior deltoid (AD), middle deltoid (MD), posterior deltoid (PD), and biceps brachii (BB), grounded at the acromion (G1); triceps brachii (long head, TR), brachioradialis (BR), wrist flexors (FL), and wrist extensors (EX), grounded at the olecranon (G2).

B. Software

The hardware elements above, when networked together, enable the user to play a force-based trajectory tracking rehabilitation game while muscle activations are recorded for analysis. Details of this software and the platform's associated network architecture, as well as our plans for future expansion, are described below.

1) Rehabilitation Game: The platform's rehabilitation game, consisting of varied trajectory tracking tasks, is developed in Unity (Unity Software Inc., San Francisco, CA, USA). To play, users exert forces and torques on the above-described handle. These values are then linearly mapped to the (x, y) position of a small ball avatar (Figure 1(b)). Users are instructed to follow the position of a red target ball (Figure 1(c)) as it traverses a displayed trajectory. The specific mapping between 6-axis force/torque values and on-screen avatar positions, as well as the number of repetitions before the game ends, varies by trajectory and is documented in Table I, enabling examination of motor behavior under a wide variety of isometric exertions. Current trajectories and mappings are designed to span the space of forces and torques required during activities of daily living (ADLs), while the goal remains displayable on a 2D screen; future iterations of the system will use a virtual and/or augmented reality headset to display 3D trajectories, enabling even more complexity in game tasks (and, thus, motor behaviors).

2) Network Architecture: The rehabilitation game and hardware sensors are integrated across two desktop computers through a ROS2 network (Open Source Robotics Foundation, Inc., San Jose, CA, USA), as detailed in Figure 2. To enable integration with this network, sEMG data are routed through the Trigno Control Utility (TCU) (Delsys, Inc., Natick, MA, USA) to Motive 3.1 software and then through the associated NatNet SDK (NaturalPoint, Inc. DBA OptiTrack, Corvallis, OR, USA). To facilitate this data transfer, a Delsys Trigger Module is subordinated to an OptiTrack OptiHub controller, allowing recording start/stop signals to be passed down the system from the Motive software to the Trigno Quattro modules. All sensor data and game state information, as well as freeform typed investigator notes, are aggregated into a single time-synced recording ("rosbag") and stored locally, such that all sensor data streams can be accessed for analysis and full trial playback as desired.

Note that sensor data from, and control interfaces to, the rehabilitation robot have not yet been implemented; the current platform allows the end effector of the robot to be positioned at arbitrary locations using its associated pendant controller, but no robot data is collected or used in the current software system. In the future, we will leverage the robot's native ROS2 interfaces to both control robot behavior and log its associated kinematic and dynamic data.

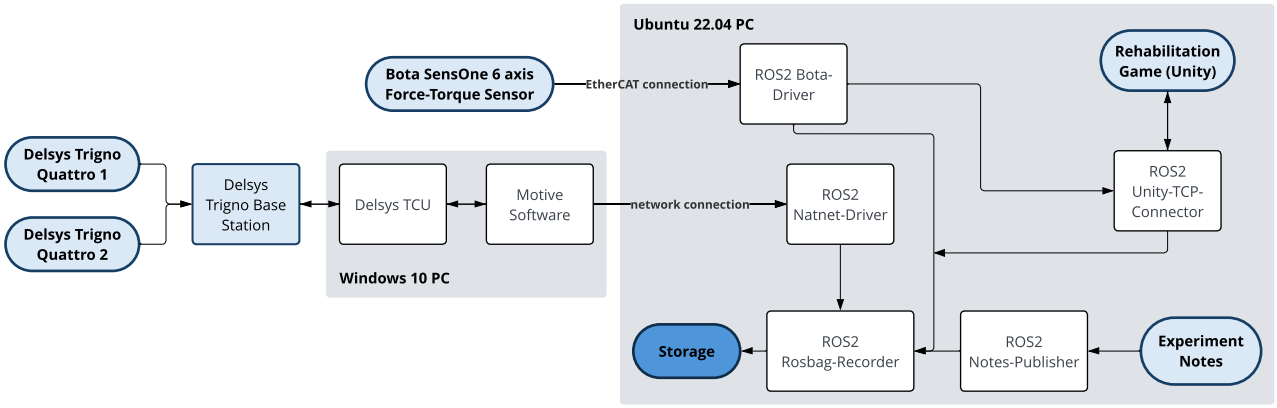


Fig. 2. Software architecture of motor rehabilitation platform. Delsys Trigno sEMG sensor motes, Bota SensOne force torque sensor, Unity rehabilitation game, and typed investigator input are networked via Delsys Trigno Control Utility (TCU), OptiTrack Motive software, and ROS2 network to enable time-synced streaming and storage of muscle activation, force/torque, and game state data, as well as typed investigator notes.

TABLE I
TRAJECTORY TRACKING TASKS & MAPPINGS

Goal Trajectory	Input	Output (Game)	Repetitions
x-axis	x-axis force	x coordinate	7
y-axis	y-axis force	y coordinate	7
z-axis	z-axis force	y coordinate	7
torque	z-axis torque	x coordinate	5
circle (CW[1])	(x, y)-axis force	(x, y) coordinate	3
circle (CCW[2])	(x, y)-axis force	(x, y) coordinate	3
spline 1 (CCW[2])	(x, y)-axis force	(x, y) coordinate	3
spline 2 (CW[1])	(x, y)-axis force	(x, y) coordinate	3

Screenshots of each trajectory are included with data release.
[1]clockwise [2]counter-clockwise

IV. PILOT DATA SET COLLECTION

To illustrate the capabilities of the above rehabilitation platform, assess users' subjective impressions of the system, and provide initial data with which to study variations in human motor strategies, data were collected from a pilot cohort of healthy and post-stroke participants as they performed various isometric trajectory tracking tasks in multiple poses.

Preliminary findings on observed muscle activation patterns and how they vary across individuals and rehabilitation tasks, as well as subjective participant feedback, follow in section V. In addition, to help alleviate the dearth of open-source data sets of this type, the complete data set, including raw and processed force torque and sEMG values, game performance data, and complete subject demographic information, has been released with this paper for further exploration by our own and other research groups.

A. Participant Demographics

Data were collected from 13 healthy individuals and 2 stroke survivors, for a total of 15 participants.[1] The 13 healthy individuals included 7 male individuals and 6 female, 9 right-handed individuals and 4 left-handed, of ages 29.5 ± 14.0 (mean $\pm$ standard deviation, min 20, max 70). Of the two stroke survivor participants, both in the chronic phase of pediatric stroke, the first was female, age 24, right-side hemiparetic, and reports being right-handed prior to her stroke. The second was male, age 34, left-side hemiparetic, and does not report handedness prior to neurological injury. Both stroke survivors exhibited mild spasticity (2 and 1, respectively, at the hand on the Modified Ashworth Scale [26]) and mild decreases in muscle strength (4/4 and 4+/4+, respectively, for flexion and extension of the wrist on the Manual Muscle Testing scale [27]).[2]

B. Study Procedures

The following section, alongside Figure 3, details the procedures used in pilot data set collection from the above participants.

1) Consent & Subjective Data Collection: After providing written informed consent on arrival, each participant completed an intake survey to obtain their baseline affect using the Self-Assessment Manikin (SAM) [28]. The SAM was also completed at the experiment midpoint and after all core experiments were completed, alongside Likert-scale [29] and free-response assessments of comfort, fatigue, motivation, and platform usefulness. Notes on participant feedback when conversing during experiments were also recorded by investigators for inclusion in subjective analysis.

2) Participant Sensorization: After completing the intake survey, participants were instrumented with 8 sEMG electrodes on key muscles of the arm, as described in section III and shown in Figure 1(d)–(e). For all healthy participants, the right arm was sensorized and subsequently used to play the rehabilitation games, allowing us to compare cohorts of dominant-hand users and lightly "impaired" non-dominant

[1]Two additional healthy participants also completed the study (male, left-handed, age 33 and male, right-handed, age 23), but their data was erroneously not recorded due to network issues, so their demographics are not included in the aggregate statistics above, nor is their partial sensor and performance data included in subsequent analyses or data release. As they performed the same experimental tasks, however, their feedback is included in the subjective platform impressions discussed in section V-F.

[2]For additional demographic data, broken down by subject, see the full open-source data release.

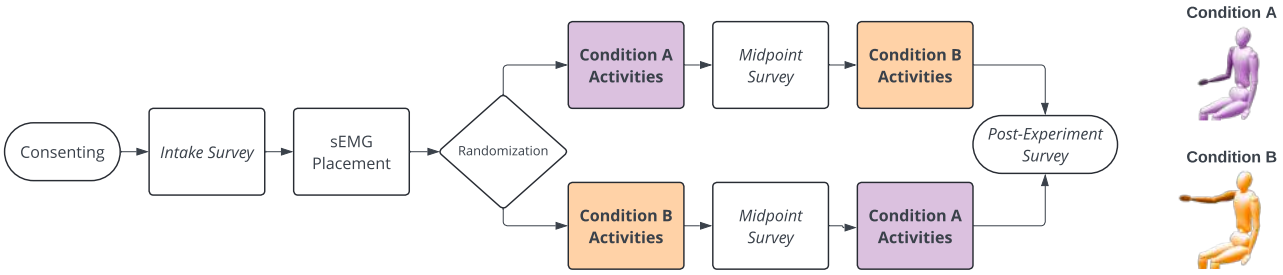


Fig. 3. Experimental flow during collection of pilot data set. Participants were consented and surveyed, then completed trajectory tracking tasks at two ADL-inspired poses (Conditions A and B) in randomized order before providing final survey feedback.

users. For post-stroke participants, the paretic arm was sensorized and tested, as it is the primary target for rehabilitation.[3]

Participants' skin was first cleaned and lightly abraded with alcohol wipes to remove dead skin, then electrodes adhered using Trigno adhesives (Delsys, Inc., Natick, MA, USA) and reinforced using transparent "transpore" surgical tape. Electrodes were precisely positioned using the protocol described in our supplemental data release, then manually adjusted by the investigator by real-time inspection of the signal traces to pick up data from the desired muscles with minimal noise.

3) Core Experimental Activities: Once instrumented with sEMG sensors, participants were seated comfortably upright, feet planted (as able), in a stationary, armless chair at the rehabilitation platform described in section III. The robot end effector was then moved to allow the participant to grasp the handle at one of two poses, illustrated in Figure 3: Condition A (right upper arm comfortably adducted (vertical), right elbow flexed $\sim 90°$ with forearm parallel to the floor) or Condition B (shoulder flexed forward slightly above horizontal and slightly externally rotated, elbow almost fully extended). These two poses were selected to span a workspace useful during activities of daily living, and their order was randomized per-participant, as shown in Figure 3, to avoid the confounding effects of fatigue when analyzing muscle activations across conditions.

Once posed, participants completed the 8 trajectory tracking tasks detailed in Table I. For each task, participants were first allowed to practice following the displayed trajectory as many times as desired, then verbally confirm that they were ready to begin the real trial, at which point data was collected for the listed number of trajectory repetitions. Participants were required to rest for at least 2 min between the first 3, the subsequent 3, and the final 2 tasks to avoid excessive fatigue, and were encouraged to request additional breaks as needed.

After completing all tasks in their first assigned condition, participants completed the midpoint survey, investigators reposed the robot to the second condition, and all tasks were repeated at this new pose using the same protocol. Participants then completed the post-experiment survey, were desensorized, and exited the study.

[3]Note that the second stroke survivor was the only participant for which we measured data from the left arm. This participant completed the same (non-mirrored) rehabilitation tasks, which means that some trajectory tracking tasks are not precisely equivalent in terms of required motor strategy. For our preliminary analyses in section V, we primarily treated this discrepancy as a source of noise, except where noted as impacting overall findings.

C. Data Post-Processing & Release

At study completion, data were cleaned and post-processed for release and further analysis. Trial data was first clipped to include the precise data between start and end timestamps of each rehabilitation task. Next, each channel of sEMG data (pre-rectified by the software pipeline) was smoothed with a 400-sample RMS filter. To remove artifacts caused by (reasonably rare) bumped wires and non-isometric motions, the mean value of each channel, for each subject across all activities and conditions, was calculated, and any data points more than 4 standard deviations greater than this mean were saturated at this value. Each sEMG signal was then normalized to the maximum value of this outlier-reduced signal (in practice, this saturating value), again calculated per-subject across all activities and conditions.[4]

These processed data (alongside raw rectified sEMG signals) have been released for open-source analysis with this paper and are used in our preliminary analyses below.

V. Preliminary Analyses of Task-Dependent Muscle Engagement

Ultimately, we aim to augment the rehabilitation platform described in section III to prescribe poses, trajectories, and robot behaviors to induce desired patterns of muscle engagement in individual device users. In this section, we leverage the data set above to gain preliminary insights on how altering poses and trajectories generates changes in motor behavior, and how these changes vary across impairment levels. We also briefly discuss participants' subjective impressions of our system and suggested enhancements. These analyses not only inform our plans for future system development, but suggest promising directions for further study of upper-limb motor behavior by the wider rehabilitation community.

The analyses below constitute only a small fraction of those enabled by the collected data set. We outline our own plans for its future exploration in section V-E, and encourage other

[4]Note that we normalized to this maximum value because in the context of multi-joint motions, the more standard maximum voluntary contraction (MVC) value becomes poorly defined, as well as potentially hazardous to test in certain impaired populations.

teams to perform their own to support their own rehabilitation system development.

A. Muscle Activation Metric: Area Under the Curve

For our initial analyses comparing muscle activations across poses, trajectory tracking tasks, and impairment levels, we used the area under the curve (AUC) of each processed sEMG signal trace, normalized by trace length, as an aggregate measure of a given muscle's level of activation over the length of the trial. In the future, we aim to employ richer analysis methods to describe the time-dependent and synergistic aspects of the observed data, as discussed in section V-E below.

B. Pose-Dependent Engagement

To explore the relationship between kinematic pose and muscle activation pattern, we examined the AUC-quantified level of activation for each muscle, aggregated across all participants, for each experimental condition (i.e., pose), for each of the trajectory tracking tasks. In general, we found that for the same trajectory, Condition B (arm lifted) elicited an increase in activation of the shoulder muscles (PD, AD, and MD), but had inconsistent impact on arm and wrist muscles, as is expected from the active arm gravity compensation required by that pose. Figure 4 shows illustrative data from the y-axis task, in which this relationship is demonstrated. This trajectory-independent finding suggests that in future rehabilitation systems, the body pose during each activity can be employed as a variable to directly modulate muscle activations toward rehabilitatively desirable patterns.

C. Trajectory-Dependent Engagement

We explored the relationship between task trajectory and muscle activation in an analogous manner, again aggregating AUC-quantified activations for each muscle across all participants and observing relative levels of activation during each activity. Given the wide variety of muscle exertions required to generate each trajectory's varied, time-dependent forces and torques, a plethora of different patterns can be observed; for this first exploratory study, we present a single exemplar result, shown in Figure 5, that illustrates the manner in which different types of trajectories reliably induce changes in specific muscle activations. Even this simple result, which only scratches the surface of the rich patterning observed, supports the idea that prescribed motions can be strategically designed to target specific muscle groups, further enabling the development of more individualized robotic rehabilitation therapies.

D. Engagement Across Impairment Levels

Both healthy and (mildly impaired) post-stroke participants were sufficiently able to complete all trajectory tracking tasks[5] to generate associated muscle activations, confirming the feasibility of system usage by those with motor impairment. Using

[5]Qualitatively, our post-stroke and healthy participants performed comparably well; a full quantitative analysis of tracking performance (described in section V-E as future work) is beyond the scope of this paper.

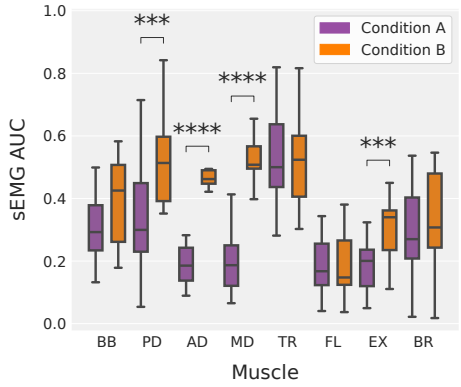


Fig. 4. Cumulative activations of each of the 8 arm muscles (calculated as area under the sEMG curve (AUC), as detailed in section V-A), aggregated across all participants, during the y-axis trajectory tracking task across both tested pose conditions (shown in Figure 3). Adjusting from Condition A (arm low) to Condition B (arm high) caused a largely consistent increase in activation of the muscles required to lift the arm (PD, AD, and MD), across this and all other trajectories, suggesting that pose can be used to selectively modulate muscle activations for rehabilitative purposes. In the activity shown, PD, AD, and MD all showed statistically significant differences across conditions (as calculated via Wilcoxon signed-rank statistical test, reported as $*p < 0.05$, $**p < 0.01$, $***p < 0.001$, $****p < 0.0001$). An addition statistical difference was observed in EX, but was not observed consistently across other unreported trajectories. Statistical annotations displayed via [30].

the same AUC-quantified activation from previous analyses, post-stroke and healthy participants (including left-handed participants using their right hand) exhibited similar motor strategies, as illustrated during the y-axis activity[6] in Figure 6. The one exception is that one stroke survivor exhibited almost no activation of the brachioradialis (BR), which may be the result of nonuse by the participant or of sensor malfunction.[7] Despite this similarity, however, investigators qualitatively observed characteristic compensatory motions in both post-stroke participants (as well as in our age-70 left-handed participant), including various rotations of the torso and lifting and flexing of the shoulder and elbow. This discrepancy suggests the need for more sophisticated sensing (including motion capture and/or inertial measurement sensing to capture joint angles and torso pose) and analyses (discussed below in section V-E) to describe these pathologies, at least in the mildly impaired individuals tested, as well as additional data collection from post-stroke individuals to enable non-anecdotal findings.

E. Future Isometric Analyses

The data collected during this study, though limited to isometric exertions, constitute a novel archive with which to study patterns of motor behavior across individuals as they engage with the end effector of rehabilitation robots. The

[6]Note that while this task is right/left symmetric and thus the data presented are directly comparable for both stroke survivors, this is not true for other task plots included with data release; analyses of these supplementary plots must account for this discrepancy.

[7]Erratic behavior of this electrode was observed by investigators during the trial in our otherwise-reliable sEMG system, and it is unclear whether this was the result of true motor behavior or sensor failure, a question we will explore during expanded future data collection.

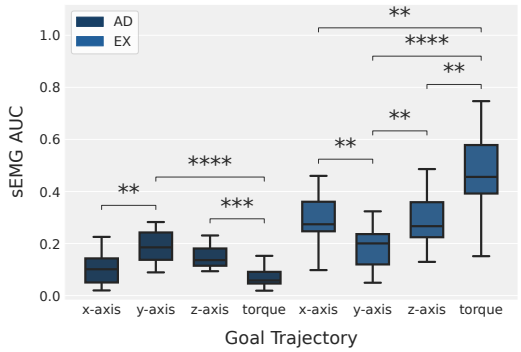


Fig. 5. Cumulative activations of the AD and EX arm muscles, aggregated across all participants, during the 4 single-axis trajectory tracking tasks in pose Condition A. The choice of trajectory — x-axis, y-axis, z-axis, or (z-axis) torque — substantially influenced the activation of both the shoulder flexor (AD) and the wrist extensor (EX). Specifically, movements typically associated with the AD, such as forward and upward motions at the shoulder (y- and z-axis tasks), demonstrated significantly increased activation patterns when compared with x-axis force and z-axis torque (as calculated via Kruskal-Wallis statistical test, reported as $^*p < 0.05$, $^{**}p < 0.01$, $^{***}p < 0.001$, $^{****}p < 0.0001$). Similarly, tasks requiring twisting movements at the wrist (here, the torque task) showed significantly increased EX activation compared with the non-twisting x-, y-, and z-axis tasks. Significant differences were also observed, to a lesser degree, among EX activations in the non-twisting tasks. These observed patterns provide evidence that force- and torque-requiring trajectories can be combined to independently modulate desired muscle activations. Statistical annotations displayed via [30].

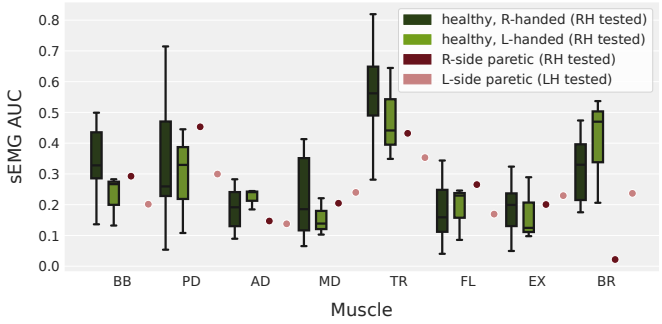


Fig. 6. Cumulative activations of each of the 8 arm muscles, during the y-axis trajectory tracking task in pose Condition A, for aggregated healthy right-handed and left handed participants (all completing the tasks with the right arm) and for individual post-stroke participants (completing the tasks with their paretic arm). Both healthy and post-stroke participants effectively completed the tasks, confirming the feasibility of system usage in the target population. Aside from consistent nonuse of the brachioradialis (BR) by one stroke survivor (which may also be the result of technical malfunction), post-stroke participants exhibited similar motor behavior to that of healthy individuals as evaluated by this metric, despite qualitative observation of compensatory motions, suggesting the need for more sophisticated temporal analyses and/or additional sensing to describe these pathological movements.

preliminary analyses above examine only a single aspect of this patterning, leveraging the same aggregate AUC measure of muscle activation to begin elucidating which muscles are activated under what circumstances, and neglect many aspects of these signals (including time- and co-dependence) that are key to fully understanding both healthy and pathological motion. In the future, we aim to employ tools like statistical parametric mapping [31] and synergy analysis [18] to assess and describe the observed motor behavior in its full temporal richness.

In addition, the analyses above compare muscle activation levels regardless of task performance: while participants largely followed each assigned trajectory, they varied in both how much they deviated from the assigned path and the extent to which they exerted forces and torques in "null" dimensions that did not impact cursor movement for a given task.[8] Future analyses will probe these relationships more deeply by explicitly relating activations to observed forces (through both data-driven methods and physiology-based modeling systems [32]) and examining the relationship between displayed and executed trajectories.

F. Subjective Impressions of the Platform

Both quantitative and qualitative analysis of subject feedback showed a largely positive impression of the system, which participants described as "fun" to use and largely "responsive" to their desired motions. Several participants provided concrete feedback on system improvements, which we will implement in the next version of the platform and should be considered in the development of future rehabilitation systems generally (including the need for a more comfortable and supportive chair, and for a larger screen to capture a wider field of view, reducing visual distractions and enhancing focus). Participants also emphasized the importance of maintaining cognitive engagement through interactive and engaging activities. One participant noted that their engagement in the activity contributed to lower levels of habitual pain, underscoring the potential therapeutic benefits of enhanced engagement beyond the motor neuroplasticity we explicitly target with this system.

Unsurprisingly, due to the additional gravity compensation required, participants found pose Condition B significantly more fatiguing, as measured by Likert scale feedback at the midpoint survey after all tasks at a single experimental condition had been completed.[9] This statistical finding was further supported by subjective remarks, with multiple participants reporting that Condition B was more challenging. Notably, one participant remarked that while Condition B was more difficult compared with Condition A, its difficulty was comparable to that of a traditional rehabilitation therapy session, indicating that the protocol overall was not prohibitively fatiguing for those with only mild impairment. To allow those with more severe motor impairment to use the platform in the future, we aim to incorporate gravity compensation systems through wrist-supporting end effectors and supportive robot controllers.

[8] An example of the latter can be seen in the force torque traces in Figure 1: accomplishing the displayed y-axis task required force only in the y direction (upward and downward), but this participant also exerted substantial force along the z axis (in and out) that was disregarded by the game but is definitionally reflected in the observed muscle activation.

[9] Of the 17 participants who completed the study, 8 were randomized to perform tasks at pose Condition A first, while 9 performed Condition B first. A Wilcoxon rank-sum statistical test indicated that Condition B was statistically more fatiguing than Condition A ($p = 0.05$). No significant differences were found across the intake, mid-point, and post-experiment surveys on the valence, arousal, and dominance scales of the Self-Assessment Manikin (SAM) or the Likert scale used to assess participant comfort.

VI. Conclusions & Future Work

The neurorehabilitation field is still contending with many foundational questions around neuroplasticity, rehabilitation task prescription, and device control. There is thus a great need for improved tools to explore large cohorts of patients in standardized, replicable, extensible, and clinically interpretable ways, and to do so during natural, multidimensional motion. This paper presents our first step toward such a tool: a modular, robust framework to enable wide ranging, controller-agnostic study of these questions and precise quantification of motor behavior across all isometric dimensions of the end effector workspace. We look forward to expanding this system's capabilities in all the ways detailed throughout this paper in order to address these questions — and, ultimately, provide more effective neuromotor therapy — and invite the wider rehabilitation and neuromechanics communities to leverage our data to do the same.

Acknowledgment

The authors thank Adam Losser, for his invaluable assistance in data collection, and Ethan Berry, for his essential support in configuring Motive software to stream sEMG data to the ROS2 network.

References

[1] V. Lin, X. Zhang, and P. Dixon, "Occupational therapy workforce in the United States: Forecasting nationwide shortages," *PM&R*, vol. 7, no. 9, pp. 946–954, 2015.

[2] G. Kwakkel, R. C. Wagenaar, T. W. Koelman, G. J. Lankhorst, and J. C. Koetsier, "Effects of intensity of rehabilitation after stroke: A research synthesis," *Stroke*, vol. 28, no. 8, pp. 1550–1556, 1997.

[3] M. Mekki, A. D. Delgado, A. Fry, D. Putrino, and V. Huang, "Robotic rehabilitation and spinal cord injury: A narrative review," *Neurotherapeutics*, vol. 15, no. 3, pp. 604–617, 2018.

[4] N. A. Malik, F. A. Hanapiah, R. A. A. Rahman, and H. Yussof, "Emergence of socially assistive robotics in rehabilitation for children with cerebral palsy: A review," *International Journal of Advanced Robotic Systems*, vol. 13, no. 3, p. 135, 2016.

[5] T. T. Lewis, H. Kim, A. Darcy-Mahoney, M. Waldron, W. H. Lee, and C. H. Park, "Robotic uses in pediatric care: A comprehensive review," *Journal of Pediatric Nursing*, vol. 58, pp. 65–75, 2021.

[6] K. Mannella, A. C. Cudlip, and M. W. R. Holmes, "Adaptations in muscular strength for individuals with multiple sclerosis following robotic rehabilitation: A scoping review," *Frontiers in Rehabilitation Sciences*, vol. 3, 2022.

[7] N. Hogan, H. I. Krebs, B. Rohrer, J. J. Palazzolo, L. Dipietro, S. E. Fasoli, J. Stein, R. Hughes, W. R. Frontera, D. Lynch *et al.*, "Motions or muscles? Some behavioral factors underlying robotic assistance of motor recovery," *Journal of Rehabilitation Research & Development*, vol. 43, no. 5, 2006.

[8] A. A. Blank, J. A. French, A. U. Pehlivan, and M. K. O'Malley, "Current trends in robot-assisted upper-limb stroke rehabilitation: Promoting patient engagement in therapy," *Current Physical Medicine and Rehabilitation Reports*, vol. 2, no. 3, pp. 184–195, 2014.

[9] M. Pezzera and N. A. Borghese, "Dynamic difficulty adjustment in exergames for rehabilitation: A mixed approach," in *IEEE SeGAH*, 2020, pp. 1–7.

[10] L. De Iaco, J. M. Veerbeek, J. C. F. Ket, and G. Kwakkel, "Upper limb robots for recovery of motor arm function in patients with stroke: A systematic review and meta-analysis," *Neurology*, vol. 103, no. 2, p. e209495, 2024.

[11] P. Feys, K. Coninx, L. Kerkhofs, T. De Weyer, V. Truyens, A. Maris, and I. Lamers, "Robot-supported upper limb training in a virtual learning environment: A pilot randomized controlled trial in persons with MS," *Journal of NeuroEngineering & Rehabilitation*, vol. 12, no. 1, p. 60, 2015.

[12] M. Gandolfi, N. Valè, E. K. Dimitrova, S. Mazzoleni, E. Battini, M. D. Benedetti, A. Gajofatto, F. Ferraro, M. Castelli, M. Camin, M. Filippetti, C. De Paoli, E. Chemello, A. Picelli, J. Corradi, A. Waldner, L. Saltuari, and N. Smania, "Effects of high-intensity robot-assisted hand training on upper limb recovery and muscle activity in individuals with multiple sclerosis: A randomized, controlled, single-blinded trial," *Frontiers in Neurology*, vol. 9, 2018.

[13] S. Adar, D. Keskin, Ü. Dündar, H. Toktaş, H. Yeşil, S. Eroğlu, N. Eyvaz, E. Beştaş, and A. Demircan, "The effect of robotic rehabilitation on hand functions and quality of life in children with cerebral palsy: A prospective randomized controlled study," *American Journal of Physical Medicine & Rehabilitation*, pp. 10–1097, 2024.

[14] C. Alessandro, I. Delis, F. Nori, S. Panzeri, and B. Berret, "Muscle synergies in neuroscience and robotics: From input-space to task-space perspectives," *Frontiers in Computational Neuroscience*, vol. 7, p. 43, 2013.

[15] A. J. McMorland, K. D. Runnalls, and W. D. Byblow, "A neuroanatomical framework for upper limb synergies after stroke," *Frontiers in Human Neuroscience*, vol. 9, p. 82, 2015.

[16] F. J. Valero-Cuevas, *Fundamentals of Neuromechanics*. Springer, 2016.

[17] L. Dipietro, H. I. Krebs, S. E. Fasoli, B. T. Volpe, J. Stein, C. Bever, and N. Hogan, "Changing motor synergies in chronic stroke," *Journal of Neurophysiology*, vol. 98, no. 2, pp. 757–768, 2007.

[18] J.-H. Park, J.-H. Shin, H. Lee, J. Roh, and H.-S. Park, "Relevance of upper limb muscle synergies to dynamic force generation: Perspectives on rehabilitation of impaired intermuscular coordination in stroke," *IEEE TNSRE*, vol. 31, pp. 4851–4861, 2023.

[19] D. J. Berger and A. d'Avella, "Myoelectric control and virtual reality to enhance motor rehabilitation after stroke," *Frontiers in Bioengineering and Biotechnology*, vol. 12, p. 1376000, 2024.

[20] P. Konrad, *The ABC of EMG – A Practical Introduction to Kinesiological Electromyography*. Noraxon Inc. USA, 2005.

[21] B. Rodríguez-Tapia, I. Soto, D. M. Martínez, and N. C. Arballo, "Myoelectric interfaces and related applications: Current state of EMG signal processing – A systematic review," *IEEE Access*, vol. 8, pp. 7792–7805, 2020.

[22] S. Facciorusso, E. Guanziroli, C. Brambilla, S. Spina, M. Giraud, L. M. Tosatti, A. Santamato, F. Molteni, and A. Scano, "Muscle synergies in upper limb stroke rehabilitation: A scoping review," *European Journal of Physical and Rehabilitation Medicine*, vol. 60, no. 5, p. 767, 2024.

[23] E. L. Waters, R. J. Mendonca, P. Z. Cacchione, and M. J. Johnson, "TheraDyad: Feasibility of an affordable robot for multi-user stroke rehabilitation," in *IEEE BioRob*, 2024, pp. 1498–1503.

[24] A. Scibilia, A. Prini, T. Dinon, N. Pedrocchi, and M. Caimmi, "Over three decades of upper-limb robotic neurorehabilitation: Drawing conclusions and future work," in *IEEE CASE*, 2024, pp. 1303–1310.

[25] A. T. Nguyen, A. Anand, and M. J. Johnson, "Exploring EEG Responses During Observation of Actions Performed by Human Actor and Humanoid Robot," in *IEEE BioRob, 2024*, pp. 1795–1801.

[26] R. W. Bohannon and M. B. Smith, "Interrater reliability of a modified Ashworth scale of muscle spasticity," *Physical Therapy*, vol. 67, no. 2, pp. 206–207.

[27] J. Mendell and J. Florence, "Manual muscle testing," *Muscle & Nerve*, vol. 13, pp. S16–S20, 1990.

[28] M. M. Bradley and P. J. Lang, "Measuring emotion: The Self-Assessment Manikin and the Semantic Differential," *Journal of Behavior Therapy and Experimental Psychiatry*, vol. 25, no. 1, pp. 49–59.

[29] R. Likert, "A technique for the measurement of attitudes," *Archives of Psychology*, 1932.

[30] F. Charlier, "trevismd/statannotations: v0.5," Oct 2022. [Online]. Available: https://doi.org/10.5281/zenodo.7213391

[31] M. A. Robinson, J. Vanrenterghem, and T. C. Pataky, "Statistical parametric mapping (SPM) for alpha-based statistical analyses of multi-muscle EMG time-series," *Journal of Electromyography and Kinesiology*, vol. 25, no. 1, pp. 14–19, 2015.

[32] K. R. Saul, X. Hu, C. M. Goehler, M. E. Vidt, M. Daly, A. Velisar, and W. M. Murray, "Benchmarking of dynamic simulation predictions in two software platforms using an upper limb musculoskeletal model," *Computer Methods in Biomechanics and Biomedical Engineering*, vol. 18, no. 13, pp. 1445–1458, 2015.

Biomechanical Effects of Varying Transcutaneous Spinal Cord Stimulation Amplitude during Walking in Individuals with Spinal Cord Injury: A Case Series

Annika Pfister
Department of Electrical & Computer Engineering, University of Washington
Seattle, WA USA
apfist8@uw.edu

Soshi Samejima
Department of Rehabilitation Medicine, University of Washington
Seattle, WA USA

Chet T. Moritz
Departments of Electrical & Computer Engineering, Rehabilitation Medicine, and Neurobiology & Biophysics, University of Washington
Seattle, WA USA

Kimberly A. Ingraham
Department of Electrical & Computer Engineering, University of Washington
Seattle, WA USA
kingra@uw.edu

***Abstract*— Transcutaneous spinal cord stimulation (tSCS) is a promising neuromodulation strategy with the potential to enhance locomotor rehabilitation for individuals with spinal cord injury. To maximize the effectiveness of this technique, it is crucial to select the optimal stimulation amplitude during a rehabilitation session. But, current tuning methods are time-consuming and subjective, relying on trial-and-error, clinician observations, and participant feedback. To improve this process, there is a need to define quantitative relationships between stimulation amplitude and measurable biomechanical metrics. In this study, we present a case series that includes two participants with motor-incomplete spinal cord injury walking with tSCS programmed to provide different stimulation amplitudes. We measured spatiotemporal parameters, electromyography, and inverse kinematics during overground walking with tSCS. Our results indicate that gait speed, stride length, and electromyography outcomes (e.g., muscle co-activation) systematically change with stimulation amplitude. This research is valuable in advancing our understanding of how stimulation amplitude relates to walking biomechanics. In the future, this knowledge will be used to design real-time, adaptive tSCS tuning methods for use in rehabilitation.**

Keywords—transcutaneous spinal cord stimulation, spinal cord injury, walking, biomechanics, neuromodulation

I. Introduction

Spinal cord injury (SCI) is a heterogenous condition, wherein spinal cord damage can impact both efferent and afferent nervous signals. This injury can result in partial or complete loss of motor, sensory, and autonomic function [1]. A common effect of SCI is reduced mobility, which in turn can lead to secondary health complications such as loss of bone density, and impaired cardiovascular function that may further impact quality of life [1], [2].

The majority of people with SCI (67%) have incomplete injuries [3], which indicates some capacity for recovery. However, impacted functions and symptoms vary greatly between individuals and across level and severity of injury. Prior research indicates that walking is a high priority for people with SCI, particularly for individuals with incomplete SCI [4], [5], [6], [7]. Thus, restoring walking is a valuable rehabilitation target for people with incomplete SCI.

Standard approaches for functional rehabilitation of walking include a variety of activity-based therapies such as bodyweight-supported treadmill training, functional electrical stimulation, and locomotor training [8]. However, rehabilitation outcomes for individuals with incomplete SCI are mixed, and many do not achieve their functional goals [9], [10].

One emergent technology that has the potential to improve rehabilitation outcomes for individuals with SCI is transcutaneous spinal cord stimulation (tSCS) [11]. tSCS is a neuromodulation technique that delivers pulsed electrical stimulation via surface electrodes placed on the skin over the spinous processes. Unlike surgically implanted epidural spinal stimulators, tSCS is non-invasive, which makes it accessible, customizable, and easy to use during outpatient rehabilitation.

Transcutaneous spinal cord stimulation can be combined with activity-based therapies, such as overground walking, bodyweight-supported treadmill training, and exoskeleton walking [12], [13]. Previous research demonstrated that adding tSCS to locomotor rehabilitation can improve walking function compared to locomotor rehabilitation alone, and improvements are sustained for at least several months after stimulation [14]. It is thought that the electrical stimulation delivered by tSCS increases the excitability of the primary afferent fibers in the spinal cord. This enables neural signals that may still propagate along residual spinal cord tracts to facilitate voluntary control of lower extremities [12]. tSCS is also hypothesized to contribute to activity-based neural plasticity, which may promote recovery within a rehabilitation session and over a broader recovery timeframe [12], [15].

Presently, tSCS implementation in rehabilitation research is still both novel and experimental. A clinician could spend significant time during a session "tuning" the tSCS stimulation for an individual participant. While frequency and waveform properties (e.g., pulse width) are often held constant based on objective values derived from prior experiments [16], the amplitude of stimulation is often tuned subjectively. Clinicians may evaluate the participant's range of motion, walking speed, and/or voluntary movement at different stimulation amplitudes before deciding on a final amplitude [14]. Further, once a stimulation amplitude is set, it is often held constant for the duration of the session.

Funding for this study was provided by Wings for Life.

However, neuromotor recovery, particularly under the influence of neuromodulation, can be nonlinear and dynamic. Therefore, shifting away from conventional fixed-amplitude stimulation towards personalized, adaptive amplitude modulation may improve functional outcomes.

One significant barrier to designing adaptive tSCS tuning paradigms is that there are currently no quantitative metrics that define "optimal" stimulation. Publications typically only report the final stimulation amplitude for a training session and do not specify any changes made to amplitude during the session, which makes it difficult to define the tuning process [13]. Trial-and-error visual observation of locomotion at different stimulation amplitudes is inherently subjective and requires an experienced clinician. Clinicians also rely on qualitative participant feedback about how different amplitudes feel for stimulation tuning. This process can take a significant portion of each session to optimize just once, let alone multiple times per session. Therefore, to successfully implement adaptive tSCS algorithms, there is a need to understand the relationship between stimulation amplitude and measurable biomechanical or physiological signals.

The goal of this study was to determine how spatiotemporal gait parameters, electromyography, and gait kinematics systematically vary as a function of tSCS amplitude during overground walking. In this paper, we present a case series with two adult participants with motor-incomplete cervical SCI walking overground using a sweep of tSCS amplitudes. In the future, this knowledge can be used to refine protocols for tSCS-mediated locomotor rehabilitation programs, improving treatment efficiency. This work is a crucial first step towards the development of real-time adaptive tSCS tuning algorithms for locomotor rehabilitation that can maximize functional walking recovery for adults with motor-incomplete SCI.

II. Methods

A. Participants

Two participants with chronic (>1 year) motor-incomplete SCI were recruited for this study. Participant 1 (P1; female, 59 years old) has spinal cord injury level C5-6 with American Spinal Injury Association Impairment Scale (AIS, [17]) grade D, 15 years post-injury. P1 uses a powered wheelchair as her primary means of mobility in the community, and uses no mobility aids at home. Participant 2 (P2; male, 49 years old) has spinal cord injury level C6 with AIS grade C, 18 years post-injury. P2 uses a manual wheelchair as his primary means of mobility. Participants gave informed written consent to participate in this protocol, which was approved by the University of Washington Institutional Review Board (Study #00003070).

B. Experimental Protocol

We used the experimental SpineX SCONE device to deliver tSCS (SpineX, Northridge, CA). We placed electrodes on the T11-12 and L1-L2 spinous processes, with ground electrodes placed bilaterally over the anterior iliac crests [14]. Stimulation was delivered via 30 Hz biphasic rectangular 1 ms pulses, with a 10 kHz carrier frequency [11]. At the beginning of each session, a trained physical therapist assessed the participant and determined their 'preferred' stimulation amplitude based on visually observed changes in voluntary movements.

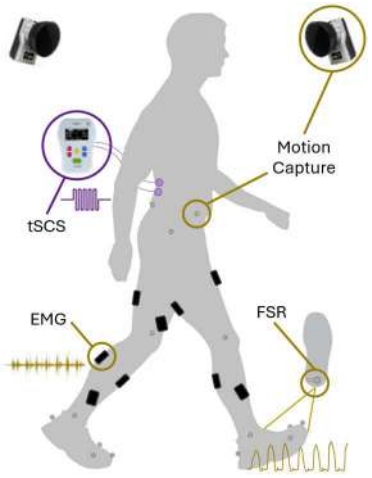


Figure 1. Summary of experimental setup. We applied transcutaneous spinal cord stimulation (tSCS) over a participant's lumbar spine. We measured muscle activity using electromyography (EMG), foot contacts using force-sensitive resistors (FSR), and kinematics using motion capture.

Each participant completed a single experimental session. Participants were asked to perform overground walking passes across a 9m walkway at a variety of stimulation amplitudes. Participants wore a safety harness that provided no bodyweight support. P2 completed his session using a two-wheeled walker as a mobility aid. Participants walked at their self-selected walking speed for all trials.

The number of trials and the stimulation amplitudes we tested varied between participants to accommodate for stamina and different participant needs. P1 completed 35 walking trials and P2 completed six (one pass per trial). We selected stimulation amplitudes for each participant above and below their clinician-preferred value. We also repeated some stimulation amplitudes to examine changes across a single session. Participants started and ended the session walking with no stimulation (0 mA) as a baseline. The stimulation amplitude protocol for each participant is shown in Table 1.

TABLE I. Stimulation Amplitude Conditions

Stimulation amplitude (# of trials)	
Participant 1	***Participant 2***
0 mA (4)	0 mA (1)
80 mA (2)	120 mA (1)
100 mA (2)	140 mA (1)
120 mA (2)	160 mA (1)
140 mA (4)	120 mA* (1)
160 mA (2)	0 mA* (1)
180 mA (3)	
200 mA (2)	
100 mA* (2)	
120 mA* (2)	
140 mA* (2)	
160 mA* (4)	
0 mA* (4)	
35 total trials	6 total trials

*Indicates repeated condition

C. Data Collection

We collected lower-limb motion data using a 12-camera optical motion capture system (Qualisys AB, Gothenburg, SE). Thirty-nine (39) markers were placed on the lower limbs according to the modified Helen-Hayes model. We measured muscle activity using electromyography (EMG) (Delsys Inc,

Natick, MA). We collected EMG data bilaterally from six muscles: tibialis anterior (TA), medial gastrocnemius (MG), soleus (SOL), biceps femoris (BF), rectus femoris (RF), and vastus medialis (VM). EMG sensors were placed in accordance with SENIAM guidelines [18]. We captured foot strikes using four force-sensitive resistors (FSR) (Delsys Inc, Natick, MA) placed on the plantar surface of each foot. We captured motion capture data at 120 Hz for P1, 100 Hz for P2 and EMG and FSR data at 2000 Hz. All data were synchronously collected using Qualisys Track Manager (QTM; v2019.3).

D. Data Processing and Analysis

We labeled motion capture marker trajectories in QTM using a combination of Automatic Identification of Markers (AIM) models and manual labeling. We exported labeled trajectories and performed inverse kinematics analysis via OpenSim (Stanford, CA) using the Gait 2392 model scaled to each participant. We then exported these trajectories to MATLAB (Mathworks, Natick, MA) and used the FSR data from the mid-heel to perform stride segmentation. We averaged the kinematic trajectories across strides within a stimulation condition. All subsequent analyses were conducted using MATLAB.

For each trial, we calculated average gait speed by measuring the distance traveled by the sacral marker (as an approximation of center of mass) divided by the total trial time. We performed linear regression and calculated Pearson's correlation coefficient (r) for gait speed vs. stimulation amplitude and gait speed vs. trial. We calculated stride length as the distance traveled by the heel marker from 0-100% of the gait cycle for each leg per stride.

For the EMG data, we applied an ACSR filter [19] to remove stimulation artifact with window size of 300 ms at 50% window overlap. Due to limited quiet standing data, training data for the filter was selected as 0.4 seconds of quiet EMG data for each trial. After stimulation artifact removal, EMG data were bandpass filtered (2nd order Butterworth 20-450 Hz), rectified, and lowpass filtered (2nd order Butterworth 5 Hz). We segmented the filtered EMG data by stride using the FSR signal, and calculated the area under the curve (AUC) for each stride. We performed linear regression between the AUC and stimulation amplitude for each muscle.

We also analyzed the joint-probability density (JPD) for the TA and SOL agonist-antagonist muscles to evaluate changes in co-activation across stimulation amplitudes [20]. We performed JPD analyses using all strides from all trials at each stimulation amplitude. We normalized the filtered EMG signals by the 99th percentile of the peak EMG amplitude for each muscle. We then created the JPD by creating a 2-dimensional histogram between the amplitude of the TA and the amplitude of the SOL. We divided the data into four quadrants (Q1-Q4) with the designation between quadrants set at 20% of the maximum amplitude of each muscle. The total number of data points in Q2 and Q4 represent alternation between TA and SOL activation; the total number of data points in Q1 represents co-activation of TA and SOL. We calculated the percentage of data points in Q2 and Q4 as well as the percentage of data points in Q1 for each stimulation amplitude. We repeated these analyses for both legs.

III. RESULTS

The clinician-preferred stimulation amplitude was 140 mA for P1 and 120 mA for P2, determined through a combination of clinical observation and conversation.

A. Spatiotemporal Parameters

For P1, we observed a negative correlation between gait speed and trial number (r = -0.6) (Fig. 2), with a linear regression R^2 = 0.36. Gait speed did not strongly correlate with stimulation amplitude for P1 (r = -0.02, R^2 = 0.0). For P2, the correlation between gait speed and trial number was r = -0.37 (R^2 = 0.13), and between gait speed and stimulation amplitude was r = 0.77 (R^2 = 0.59).

We compared average gait speed between the repeated stimulation conditions for each participant (Fig. 3). For P1, we found that, on average, gait speed decreased by 11.8% (0.4%) [mean (SD)] from first to second repetition for no stimulation, 100, 120, and 140 mA conditions. We observed only a 0.5% decrease in gait speed between repetitions for the 160 mA condition. For P2, there was a 32% decrease in gait speed from the first to second repetition of the no stimulation condition, and there was a 2% *increase* in gait speed for the 120 mA condition.

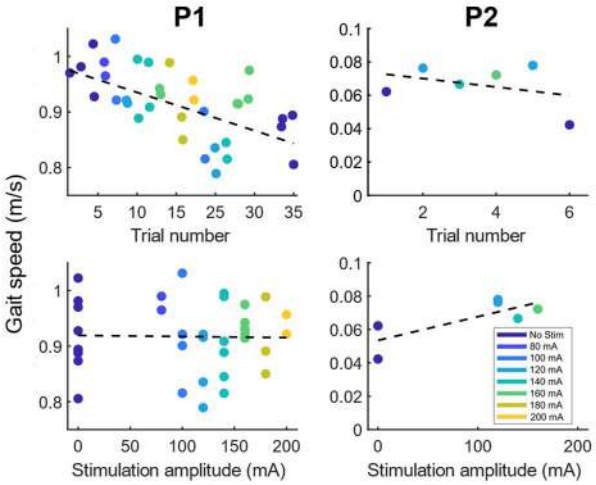


Figure 2. Gait speed across session and stimulation amplitudes. Each data point represents the mean gait speed for one walking pass. Different colors correspond to different stimulation amplitudes. The dashed black line shows a linear regression model for each plot. Please note the different y-axes used to best visualize the data.

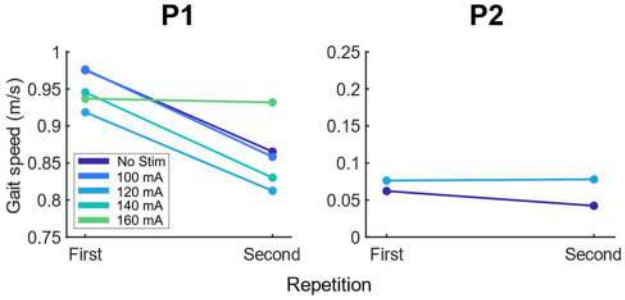


Figure 3. Comparison of gait speed between first and second repetitions of stimulation amplitude conditions. The colored lines depict different repeated stimulation amplitude conditions. Each data point shows the average gait speed calculated across all trials for that condition. Please note the different y-axes used to best visualize the data.

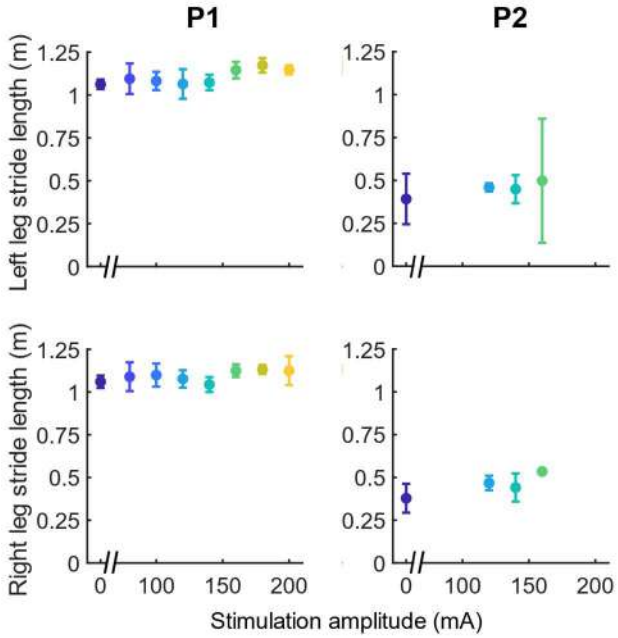


Figure 4. Stride length as a function of stimulation amplitude. Data for P1 (left column) and P2 (right column) are shown for both left (top row) and right (bottom row) legs. Each data point indicates the average stride length calculated over all strides collected for a given amplitude condition. The error bars indicate the 95% confidence interval.

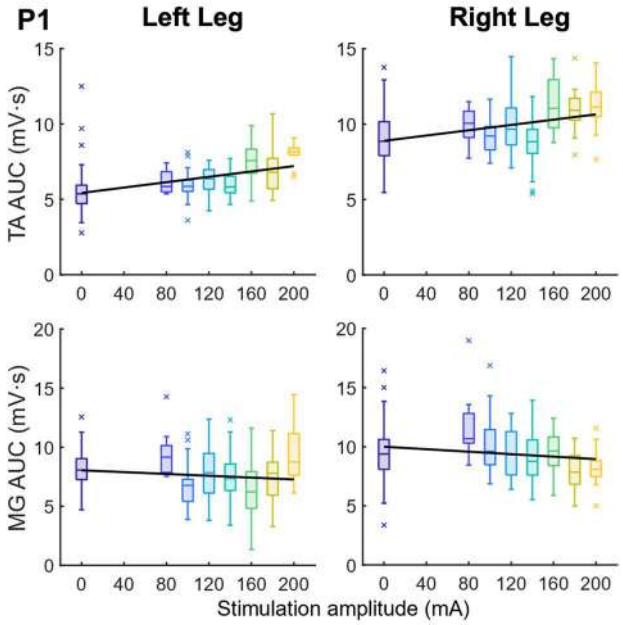


Figure 5. EMG area under the curve (AUC) across stimulation amplitudes for Participant 1. Tibialis anterior (TA, top) and medial gastrocnemius (MG, bottom) AUC distributions for left and right legs as a function of stimulation amplitude. Each boxplot shows the distribution across all strides collected for a given amplitude condition. The solid black lines show the linear regression models fit to the data.

For P1, we observed a longer mean stride length for both left and right legs at higher stimulation amplitudes (>160 mA) compared to no stimulation (Fig 4). For 160, 180, and 200 mA conditions, P1's average stride length (across both legs) increased by 0.08 (0.02) m (7.6% change) compared to no stimulation. For the 80, 100, 120, and 140 mA conditions, P1's average stride length (across both legs) increased by 0.01 (0.01) m (1.5% change) compared to no stimulation. We observed a similar trend for P2, whose average stride length (across both legs) increased by 0.09 (0.04) m (23% change) compared to no stimulation for 100, 120, and 140 mA conditions.

B. Electromyography (EMG)

The muscles with the highest positive and negative correlations between EMG area under the curve (AUC) and stimulation amplitude for P1 were for the tibialis anterior (TA) and medial gastrocnemius (MG), respectively (Fig. 5). The TA had $R^2 = 0.18$, $r = 0.43$ for the left leg and $R^2 = 0.10$, $r = 0.32$ for the right leg. The MG had $R^2 = 0.01$, $r = -0.11$ for the left leg, and $R^2 = 0.02$, $r = -0.16$ for the right leg. All other muscles for P1 had correlations $|r| < 0.12$.

A representative joint probability density (JPD) plot for P1's 180 mA condition is shown in Figure 6. For this analysis, more points in quadrant Q1 indicates increased co-activation of the muscles, while more points in quadrants Q2 and Q4 indicates less co-activation of the agonist-antagonist (TA-SOL) pair. We found that for P1, the lowest-co-activation (i.e., the largest percentage of points in Q2 and Q4) occurred during the 180 mA condition (74.6%).

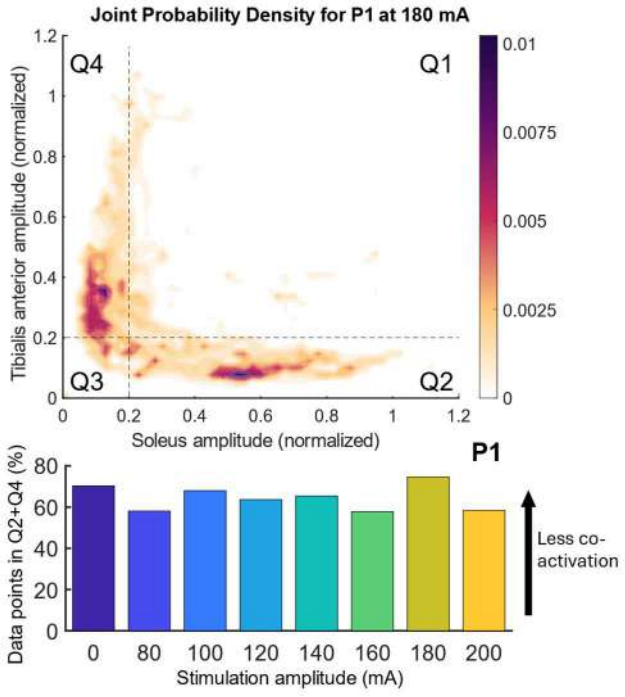


Figure 6. Joint probability density (JPD) between agonist-antagonist muscle pair (tibialis anterior and soleus) for Participant 1. *Top:* A representative JPD is shown for P1 during the 180 mA condition. A higher percentage of points in quadrants Q2 and Q4 (*i.e.,* the plot is more 'L-shaped') indicate less co-activation. *Bottom:* The percent of data points in Q2 and Q4 across all stimulation conditions for P1.

For P2, we did not examine linear regressions for EMG AUC or generate JPD plots due to the small number of strides and conditions that P2 completed.

C. *Inverse Kinematics*

Overall, inverse kinematics at the ankle, knee, and hip did not appear to meaningfully change at different stimulation amplitudes for either participant (Fig. 7).

IV. Discussion

Here, we document our preliminary findings on how walking biomechanics vary as a function of transcutaneous spinal cord stimulation (tSCS) amplitude for two individuals with motor-incomplete cervical spinal cord injury (SCI). While both participants were able to complete walking passes at different stimulation amplitudes above and below the clinician-preferred value, Participant 1 (P1) completed significantly more conditions (35 trials at 8 different amplitudes) than Participant 2 (P2) (6 trials at 4 different amplitudes). In this study, we observed relationships between spatiotemporal gait parameters, muscle activity and stimulation amplitude, but did not observe noticeable changes in kinematics when tSCS amplitude was varied.

We observed that gait speed had a slight positive correlation with increasing stimulation amplitude for P2, but were surprised that P1 did not have a similar trend, as prior studies have shown that participants with SCI are able to walk faster with tSCS than without [14]. However, when we examined the relationship between gait speed and trial number (i.e., time) for P1, we found a moderate negative correlation (Fig. 2). We found a similar relationship for P2, albeit less striking. This overall trend suggests that fatigue may be playing a dominant role in the participants' choice of walking speed. When examining Figure 2, we noticed that walking trials 28-31 (160 mA, green) for P1 do not appear to follow this overall downward trend. In fact, when we examined how gait speed compared between repeated amplitude conditions, we saw that P1's gait speed was essentially unchanged for the 160 mA condition, while it decreased by 11.8% (on average) for all other amplitudes (Fig 3.). We observed a similar phenomenon in P2, whose gait speed decreased by 31% in the repeated no stimulation condition, but actually increased slightly (2%) in the repeated 120 mA condition. This suggests that there may exist some optimal stimulation amplitude that can counteract the effects of fatigue.

We observed increased stride length at sufficiently high stimulation amplitudes (Fig. 4), which agrees with prior studies that have also reported this phenomenon [13], [14]. Because P1 completed more conditions across a wider range of amplitudes, we can see that there appears to be a 'threshold' of stimulation amplitude required before observable changes in stride length may occur. For P1, it appears this threshold is

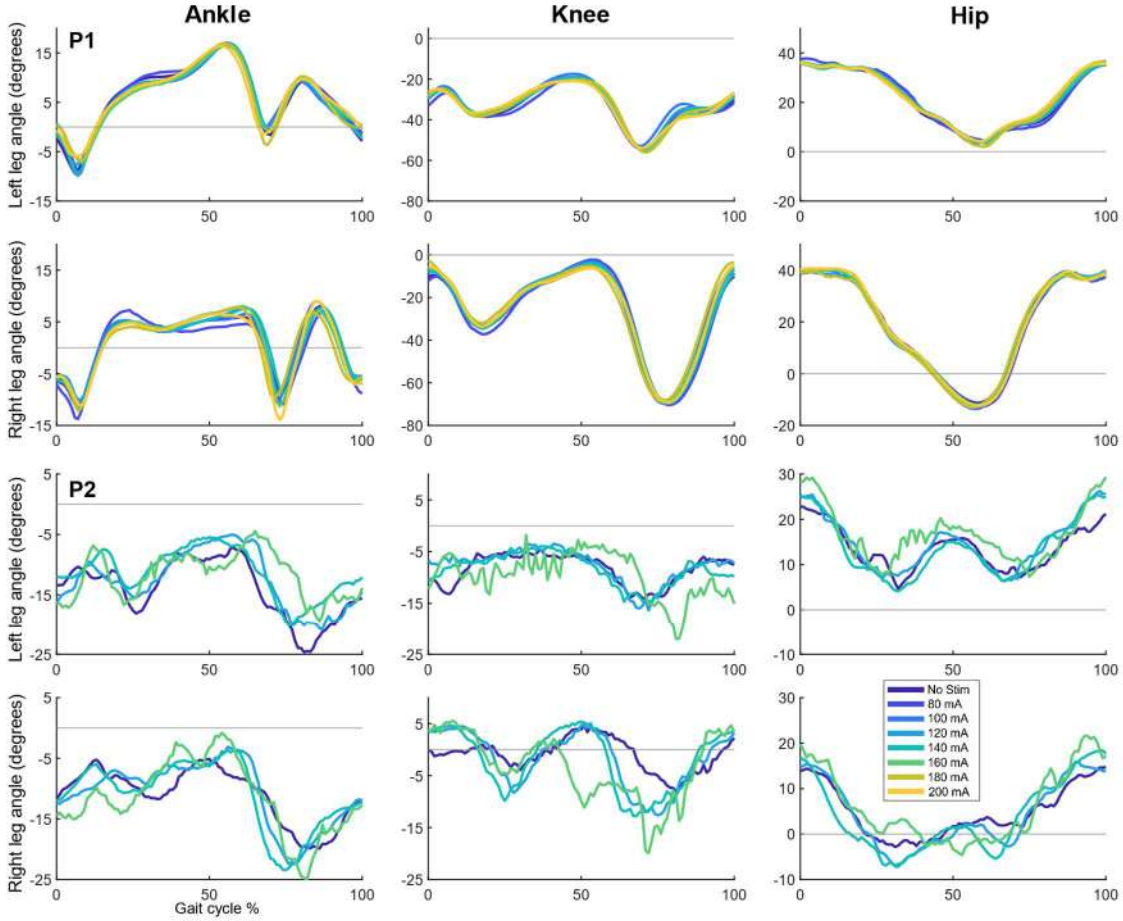


Figure 7: Mean inverse kinematics trajectories. Mean ankle, knee, and hip angle traces across stimulation amplitudes for P1 (5-18 strides per condition) and P2 (2-6 strides per condition). Grey lines indicate zero degrees for each plot.

around 140 mA. For P2, we saw the same increase in stride length for all amplitudes conditions tested. Because we could not continue to increase stimulation for either participant, we do not yet know if there exists a higher amplitude for which stride length would decrease again.

Our analysis of EMG data for P1 indicates that different muscles respond differently to changes in stimulation amplitude. We observed an overall increase in TA activity (but an overall decrease in MG activity) with increasing stimulation amplitude. However, in the absence of clinical data that describe the muscles' strength, tone, or spasticity, we cannot definitively conclude that these results correspond to "improved" or "worsened" biomechanics. The joint probability densities between the TA and SOL (Fig. 6) indicate that for certain stimulation amplitudes (i.e., 180 mA), P1 displayed more normative agonist-antagonist coordination compared to the other stimulation conditions.

We did not observe noticeable changes in overall gait kinematics between stimulation conditions (Fig. 7). It has previously been shown that adults with SCI have higher kinematic variability during overground walking compared to nondisabled adults [21]. This may have contributed to less distinction between kinematic joint angle outcomes across stimulation amplitudes. We have not yet quantified the role that fatigue may have played on kinematics.

Our results highlight the challenges inherent in determining an individual's "optimal" stimulation amplitude. For example, if the objective was to maximize walking speed or increase stamina, the optimal amplitude for P1 may be 160 mA. Alternatively, if the goal was to maximize stride length or minimize muscle co-activation, 180 mA provides better results for P1. Furthermore, we cannot discount the clinician-preferred amplitude of 140 mA for P1, which was determined through holistic observation and conversations with the participant about their qualitative experience of ease of walking at different stimulation amplitudes. In the future, having easy-to-obtain quantitative outcome measures that can supplement clinical expertise could accelerate the tuning process and provide clinicians with additional data to support their decision-making.

This case series was limited by its small sample size and small number of trials per participant. In the future, we seek to expand this protocol to more individuals with SCI across multiple sessions to determine population trends and further elucidate the multi-dimensional factors that underlie choosing the optimal stimulation amplitude. With this knowledge, we plan to design real-time adaptive tuning algorithms for tSCS that can enhance locomotor rehabilitation for adults with SCI.

ACKNOWLEDGMENT

We thank our research participants for their time and contribution to this work. We also acknowledge Rich Henderson, Siddhi Shrivastav, Zijie Jin, and Siena Villancio-Wolter for their assistance with data collection and analysis.

REFERENCES

[1] C. S. Ahuja *et al.*, "Traumatic spinal cord injury," *Nat. Rev. Dis. Primer*, vol. 3, no. 1, pp. 1–21, Apr. 2017.

[2] G. Forte *et al.*, "Exoskeletons for Mobility after Spinal Cord Injury: A Personalized Embodied Approach," *J. Pers. Med.*, vol. 12, no. 3, Art. no. 3, Mar. 2022.

[3] National Spinal Cord Injury Statistical Center (NSCISC)., "Facts and Figures at a Glance. 2023 SCI Data Sheet." 2023. [Online]. Available: https://www.nscisc.uab.edu/

[4] K. D. Anderson, "Targeting Recovery: Priorities of the Spinal Cord-Injured Population," *J. Neurotrauma*, vol. 21, no. 10, pp. 1371–1383, Oct. 2004.

[5] P. L. Ditunno, M. Patrick, M. Stineman, and J. F. Ditunno, "Who wants to walk? Preferences for recovery after SCI: a longitudinal and cross-sectional study," *Spinal Cord*, vol. 46, no. 7, Art. no. 7, Jul. 2008.

[6] L. A. Simpson, J. J. Eng, J. T. C. Hsieh, and D. L. Wolfe and the Spinal Cord Injury Rehabilitation Evidence (SCIRE) Research Team, "The Health and Life Priorities of Individuals with Spinal Cord Injury: A Systematic Review," *J. Neurotrauma*, vol. 29, no. 8, pp. 1548–1555, May 2012.

[7] N. P. Thorogood *et al.*, "Spinal Cord Injury Community Personal Opinions and Perspectives on Spinal Cord Stimulation," *Top. Spinal Cord Inj. Rehabil.*, vol. 29, no. 2, pp. 1–11, Mar. 2023.

[8] E. Swaffield *et al.*, "Perspectives of people living with a spinal cord injury on activity-based therapy," *Disabil. Rehabil.*, vol. 44, no. 14, pp. 3632–3640, Jul. 2022.

[9] G. Scivoletto, F. Tamburella, L. Laurenza, M. Torre, and M. Molinari, "Who is going to walk? A review of the factors influencing walking recovery after spinal cord injury," *Front. Hum. Neurosci.*, vol. 8, Mar. 2014.

[10] C. Morawietz and F. Moffat, "Effects of locomotor training after incomplete spinal cord injury: a systematic review," *Arch. Phys. Med. Rehabil.*, vol. 94, no. 11, pp. 2297–2308, Nov. 2013.

[11] C. Moritz *et al.*, "Non-invasive spinal cord electrical stimulation for arm and hand function in chronic tetraplegia: a safety and efficacy trial," *Nat. Med.*, vol. 30, no. 5, pp. 1276–1283, May 2024.

[12] S. Samejima, R. Henderson, J. Pradarelli, S. E. Mondello, and C. T. Moritz, "Activity-dependent plasticity and spinal cord stimulation for motor recovery following spinal cord injury," *Exp. Neurol.*, vol. 357, p. 114178, Nov. 2022.

[13] R. Henderson *et al.*, "Transcutaneous Spinal Stimulation Improves Exoskeleton Assisted Walking in Spinal Cord Injury: A Pilot Study," presented at the American Physical Therapy Association (APTA) Combined Sections Meeting, Boston, MA, Feb. 15, 2024.

[14] S. Samejima *et al.*, "Multisite Transcutaneous Spinal Stimulation for Walking and Autonomic Recovery in Motor-Incomplete Tetraplegia: A Single-Subject Design," *Phys. Ther.*, vol. 102, no. 1, p. pzab228, Jan. 2022.

[15] J. V. Lynskey, A. Belanger, and R. Jung, "Activity-dependent plasticity in spinal cord injury," *J. Rehabil. Res. Dev.*, vol. 45, no. 2, pp. 229–240, 2008.

[16] K. Gelenitis *et al.*, "Non-invasive Transcutaneous Spinal Cord Stimulation Programming Recommendations for the Treatment of Upper Extremity Impairment in Tetraplegia," *Neuromodulation Technol. Neural Interface*, Jul. 2024.

[17] T. T. Roberts, G. R. Leonard, and D. J. Cepela, "Classifications In Brief: American Spinal Injury Association (ASIA) Impairment Scale," *Clin. Orthop.*, vol. 475, no. 5, pp. 1499–1504, May 2017.

[18] H. J. Hermens, B. Freriks, C. Disselhorst-Klug, and G. Rau, "Development of recommendations for SEMG sensors and sensor placement procedures," *J. Electromyogr. Kinesiol. Off. J. Int. Soc. Electrophysiol. Kinesiol.*, vol. 10, no. 5, pp. 361–374, Oct. 2000

[19] M. Kim *et al.*, "A Novel Technique to Reject Artifact Components for Surface EMG Signals Recorded During Walking With Transcutaneous Spinal Cord Stimulation: A Pilot Study," *Front. Hum. Neurosci.*, vol. 15, 2021, Accessed: Nov. 16, 2023. [Online]. https://www.frontiersin.org/articles/10.3389/fnhum.2021.660583

[20] P. Gad, *et al.*, "Transcutaneous Spinal Neuromodulation Reorganizes Neural Networks in Patients with Cerebral Palsy," *Neurotherapeutics*, vol. 18, no. 3, pp. 1953–1962, Jul. 2021.

[21] W. J. Sohn, A. Q. Tan, H. B. Hayes, S. Pochiraju, J. Deffeyes, and R. D. Trumbower, "Variability of Leg Kinematics during Overground Walking in Persons with Chronic Incomplete Spinal Cord Injury," *J. Neurotrauma*, vol. 35, no. 21, pp. 2519–2529, Nov. 2018.

Development of multimodal EEG-EMG human machine interface for hand-wrist rehabilitation: A preliminary study

Minki Kim, SeongHyeon Jo, Hyeonseung Cho, Seungmin Ye, Yeongtae Kim, Hyung-Soon Park *

Abstract— **Patients with neurological disorders, such as stroke, often undergo upper limb motor impairments, severely limiting their ability to perform activities of daily living (ADL). Wearable robots have been developed to provide intensive and precise repetitive training for upper limb rehabilitation. Effective rehabilitation requires aligning robotic assistance with patient movement intention to promote brain plasticity. Additionally, robotic assistance must accommodate the complex, coordinated upper limb motions required for ADL tasks, including not only isolated hand movements but also integrated hand and wrist actions. This paper presents a multimodal human-machine interface (HMI) for integrated hand-wrist rehabilitation using both EEG and EMG signals. A three-degrees-of-freedom (3-DOF) soft wearable robot, combining a robotic hand glove and forearm skin brace, was designed to assist coordinated hand and wrist movements during reaching and grasping. EEG signals classified rest and grasp states using a Riemannian geometry approach, while EMG signals from three forearm muscles detected reaching onset to trigger the wrist adjustment. Preliminary tests with four healthy participants demonstrated 85% accuracy in EEG-based classification and sufficient EMG amplitude for motion onset detection. Future studies will expand participant testing to improve system robustness and evaluate its effectiveness for stroke rehabilitation.**

I. INTRODUCTION

Stroke, a common neurological disorder caused by blocked or ruptured brain blood vessels, often results in upper limb motor impairments, affecting up to two-thirds of post-stroke patients [1]. The motor function disabilities lead to spasticity and flexion in the hand, wrist, and forearm, which significantly limit their ability to perform essential activities of daily living (ADL) tasks, thereby reducing the quality of life [2]. To address these deficits, robot-assisted rehabilitation therapy has emerged as a promising approach, offering high-intensive repetitive training [3]. This approach facilitates task-oriented training by incorporating repetitive, goal-oriented tasks that enhance upper limb function in stroke patients while reducing the workload of physical therapists [4], [5]. In recent decades, wearable robotic systems have evolved from rigid exoskeletons [6], [7] to soft wearable robots [8], [9], [10], [11], which are lightweight, portable, and fabricated soft materials, making them more suitable for long-term use in intensive rehabilitation tasks. In this work, we propose a soft wearable robot designed for grasping assistance, aimed at task-oriented stroke rehabilitation.

To effectively support upper limb rehabilitation of post-stroke, robotic assistance should account for the coordinated and complex movements of the hand, wrist, and forearm. Many existing assistive robots, however, focus on isolated rehabilitation of either the hand or the wrist [12]. Most wearable robotic systems designed for ADL-oriented training target hand movements alone, as they are directly associated with task completion [13]. Nevertheless, the biomechanical interdependence of the hand and wrist—where hand muscle tendons traverse the wrist to control finger movements—makes wrist posture critical to finger range of motion (RoM) and stiffness [14]. Consequently, many hand rehabilitation robots require additional passive wrist support or therapist intervention to address spasticity-related forearm postures. To facilitate natural movement in ADL tasks, robotic systems should assist both the hand and wrist in coordination. Although some robots have attempted simultaneous hand-wrist support [6], [7], [15], achieving compactness while restoring both functions remains a challenge. Thus, our wearable robot is designed to assist both the hand and wrist during object grasping.

Active participation in rehabilitation is essential for promoting natural, intuitive movements and inducing brain plasticity [16]. Passive repetitive tasks, even with robot assistance, may aid in restoring motor function but do not guarantee recovery of the damaged neural systems in stroke patients. Emerging evidence suggests that closed-loop rehabilitation systems, based on the Hebbian rule, effectively enhance brain plasticity and require patient-initiated movement intent to actuate robotic systems [17]. Developing human-machine interfaces (HMI) that facilitate active participation is therefore essential for effective rehabilitation, a concept applied to this work as well.

For decoding motor intention, electromyography (EMG) and electroencephalography (EEG) are widely employed in upper limb rehabilitation HMIs [18], [19]. EEG-based brain-machine interfaces (BMI) classify motor intentions to execute motion, while EMG detects direct muscle activation during arm movement. However, EEG suffers from low signal-to-noise ratio (SNR) and non-stationarity, whereas EMG signals exhibit high inter-individual variability and degradation in patients with severe spasticity. To overcome these issues, multimodal EEG-EMG HMIs combine both modalities [19], [20], [21], but most merge EEG and EMG

*This research was supported by the Bio & Medical Technology Development Program of the National Research Foundation (NRF) funded by the Korean government (MSIT) under Grant RS-2024-00397674.

M. Kim, S.-H. Jo, H. Cho, S. Ye, and Y. Kim are with the Department of Mechanical Engineering, Korea Advanced Institute of Science and Technology (KAIST), Daejeon, 34141, Korea (e-mail: 1minki6@kaist.ac.kr; sh.jo@kaist.ac.kr; hs.cho@kaist.ac.kr; yesmin@kaist.ac.kr; yeongtaekim@kaist.ac.kr)

H.-S. Park is with the Department of Mechanical Engineering, Korea Advanced Institute of Science and Technology (KAIST), Daejeon, 34141, Korea (phone: +82-42-350-3078; fax: +82-42-350-5038; e-mail: hyungspark@kaist.ac.kr)

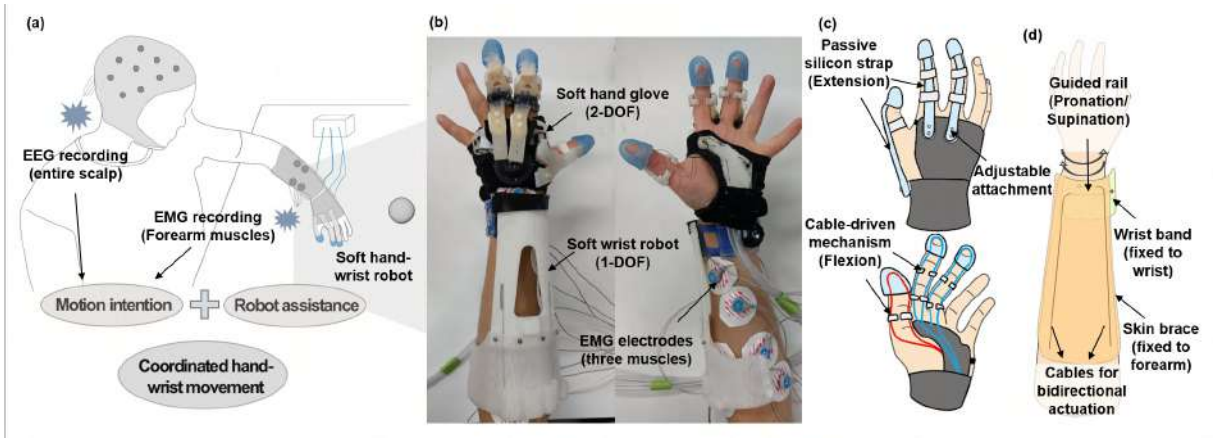


Fig. 1. Schematic of the multimodal EEG-EMG human machine interface for hand-wrist rehabilitation. (a) Conceptual overview of the proposed system, (b) Dorsal and palmar views of 3-DOF soft wearable hand-wrist robot integrated with EMG electrodes, (c) Soft hand glove mechanism demonstrating finger/thumb flexion-extension, (d) Soft wrist robot enabling bidirectional actuation for wrist pronation-supination.

into a single classification, overlooking the sequential coordination needed for grasping. In particular, effective grasping necessitates forearm-wrist adjustment before hand closure, which many existing systems difficult to accommodate [22], [23]. This study proposes a sequential multimodal EEG-EMG HMI system, where EMG detects reaching intent to induce preemptive wrist adjustment, followed by EEG-based grasp/rest classification, ensuring natural movement transitions for robotic stroke rehabilitation.

This study aims to develop a multimodal HMI that utilizes EEG and EMG data for coordinated hand-wrist rehabilitation using a wearable robot (Fig. 1 (a)). The proposed motion intention recognition algorithm facilitates smooth transitions from rest to grasp. EEG signals were recorded from 19 sponge electrodes placed across the entire scalp to classify grasp and rest states. EMG signals, collected from three forearm muscles, detected reaching intent to adjust wrist posture before grasping. The hand-wrist wearable robot (Fig. 1 (b)), integrating a soft hand glove and forearm skin brace, provides independent assistance for finger/thumb flexion-extension and wrist pronation-supination, forming a three-degrees-of-freedom (3-DOF) system. EEG and EMG data were collected from four healthy subjects performing a grasping task with the wearable robot. The feasibility of the system is evaluated for its potential application in stroke rehabilitation beyond this preliminary study.

II. Materials and Methods

A. Soft wearable hand-wrist assistive robot

For hand movement assistance, a modified version of the high-DOF soft-robotic glove originally developed in [11], [24] was utilized to suit the specific requirements of this study. The original glove was designed for versatile in-hand manipulation to support activities of daily living (ADL) for patients with neurological disorders. Its actuation mechanism employed a bioinspired design: active cable-driven exotendons routed along the palmar side facilitated flexion, while passive elastic exotendons on the dorsal side maintained extended postures.

To enhance wearability and focus on grasping assistance, we simplified both the actuation mechanism and the structural design of the glove. The original glove assisted individual finger movements, but in this study, the soft hand glove design was simplified to involve only the thumb, index, and middle fingers, which play primary roles in various grasping postures. This decision improved wearability by reducing system weight and bulk while retaining effective functional grasping of various objects, including spheres, cylinders, and thin plates. The two cables routed on the index and middle fingers were bundled and connected to a single actuator so that two fingers could make flexion or extension simultaneously. Consequently, the number of actuating motors was reduced from eight to two (2-DOF): one motor drives the extension of two fingers, and the other facilitates thumb extension, as highlighted in Fig. 1 (c). Additionally, two passive elastic tendons for the thumb enable both extension and opposition movements, supporting natural grasping postures.

The soft wearable wrist robot employed for wrist motion assistance is based on the low-profile forearm skin brace developed in [25]. This wrist robot comprises a wristband and cuff that rotate relative to each other along a guided rail to achieve wrist pronation and supination. The guided rail and the associated cables were designed to mimic the pronation and supination, which result from the rotation of the radius bone around the ulna. A single motor is required to drive two cables aligned with the guided rail, enabling bidirectional rotation of the wrist motion (Fig. 1 (d)).

The soft hand glove and soft wrist robot were simply integrated without structural interference, allowing independent motion of the hand and wrist. As the wristband of the skin brace and the glove's proximal portion do not overlap, wrist pronation/supination and finger flexion/extension can be actuated freely. Both components shared a cable-driven mechanism, enabling simultaneous assistance during reach-

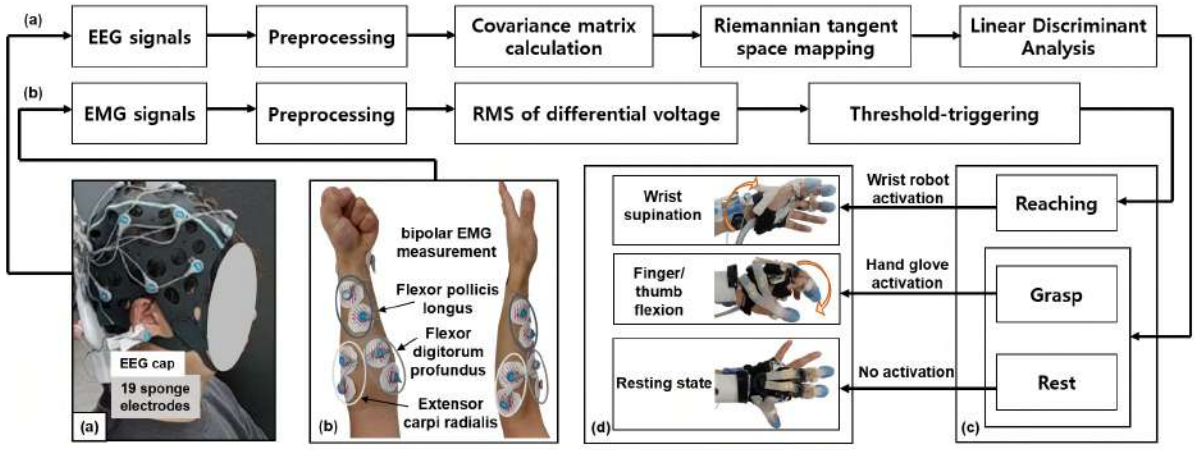


Fig. 2. Flowchart of the signal processing in the multimdoal EEG-EMG motion intention recognition system. (a) EEG-based grasp/rest classification using a Riemannian geometry approach, (b) EMG signal processing using RMS amplitude for reaching detection, (c) Robotic assistance based on motion intention recognition, (d) Photos depicting the corresponding induced movements.

ing and grasping. The integrated wearable robot consisted of a three-DOF structure: two for the soft glove and one for wrist robot with a combined weight of approximately 250g (110g for the glove and 140g for the forearm skin brace).

- Soft hand glove (Fig. 1 (c)): Assists index/middle finger and thumb flexion/extension (2-DOF) for grasping.
- Soft wrist robot (Fig. 1 (d)): Assists wrist supination/pronation (1-DOF) for wrist adjustment before grasping.
- Soft hand-wrist wearable robot (Fig. 1 (b)): Integrate both components (3-DOF) for coordinated hand-wrist assistance.

B. EEG-EMG signals acquisition and processing

EEG and EMG data were independently collected through the same acquisition module (Mindd Scan, Ybrain). For the EEG measurement, 20 electrodes, including a reference channel, were positioned in accordance with the international 10-20 system. The EEG signals were sampled at 500 Hz and preprocessed using a 60 Hz notch filter to remove noise, a high-pass filter with a cutoff frequency of 2 Hz, and a low-pass filter with a cutoff frequency of 50 Hz. For EMG measurement, signals were sampled at 1000 Hz using a bipolar electrode configuration. Commercial electrodes (Monitoring Electrode, 3M) were attached in pairs to the forearm skin over targeted muscles. As illustrated in Figure 2, eight electrodes were used: two as references placed on non-muscular regions and six arranged in three pairs to acquire surface EMG (sEMG) signals from three muscles in the forearm. The recorded EMG signals were processed using a fifth-order bandpass Butterworth filter with cutoff frequencies of 1 Hz and 60 Hz.

After preprocessing, the Ledoit-Wolf Shrinkage method was applied to calculate the covariance of EEG signals collected from 19 channels. The EEG data were then mapped onto the Riemannian manifold and expressed T in tangent space using the following equation for further analysis, where C_r refers to the mean covariance matrix, while C_i is the estimated covariance matrix for each trial. A linear discriminant analysis (LDA) algorithm was implemented to classify the subject's intention as either the rest or the grasp based on these features (Fig. 2 (a)).

$$T = \log(C_r^{\frac{-1}{2}} C_i C_r^{\frac{-1}{2}}) \tag{1}$$

For EMG signals, the root mean square (RMS) value was computed from the difference signals of paired electrodes using a 200 ms sliding window with a 50% overlap. The extracted RMS amplitude was directly used as a feature to determine threshold values (Fig. 2 (b)), triggering the soft wearable robot's actuation for wrist adjustment during reaching. This multimodal system was configured to distinguish between grasp and rest intentions using EEG data, and to sequentially assist grasping after facilitating reaching by utilizing distinct EMG signals observed during the reaching phase prior to grasping an object (Fig. 2 (c) and 2 (d)).

C. Experimental protocol

A pilot experiment was conducted to collect EEG and EMG data for developing the motion intention algorithm and validating the multimodal EEG-EMG HMI system (Figure 3). The study was approved by the Institutional Review Boards of KAIST (KH2024-227), and all participants provided written informed consent. Four healthy participants were recruited, with EEG and EMG sensors placed at designated positions (Figure 3 (c)). EEG channel impedances were adjusted below 50 kΩ using saline-soaked sponge electrodes. EMG electrodes were positioned on the extensor carpi radialis (wrist movement), flexor pollicis longus (thumb flexion), and flexor digitorum profundus (finger flexion) in a bipolar configuration, with reference electrodes on the wrist.

Subjects wore the hand-wrist robot and followed visual cues displayed on a computer (Fig. 3 (a)), including 'Grasp,' 'Rest,' and a preparatory '+' signal. Each trial began with a 2s '+' cue, followed by a 5s 'Grasp' phase, another 2s '+',

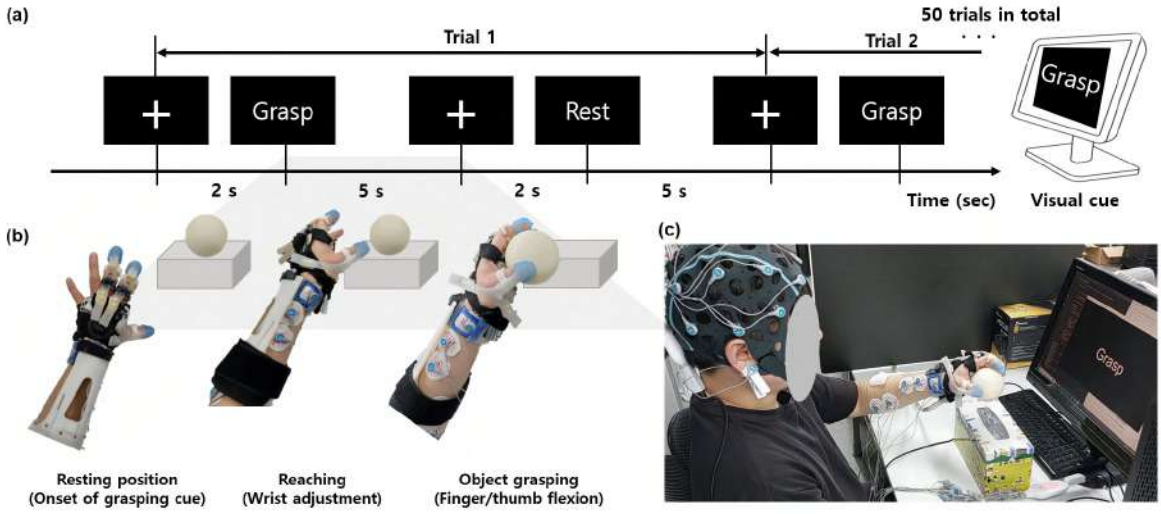


Fig. 3. Experimental protocol for data collection. (a) Visual cues presented to guide subject movement, (b) Sequential snapshots of hand-wrist movements during the grasp phase, from rest to reaching and grasping, (c) Experimental setup with EEG and EMG sensors worn by a subject using the wearable robot.

and a 5s 'Rest' phase. During grasping, subjects reached for and grasped a spherical object at a set height, then released it upon the 'Rest' cue, returning to the initial posture with their hands open and wrists neutral on a table (Fig. 3 (b)). Each session included 50 trials, with a 3-minute break after 25 trials to reduce fatigue.

III. RESULT

Following data collection from the four subjects, offline analyses were conducted to evaluate the proposed multimodal EEG-EMG motion intention detection system. Figure 4 presents the EEG-based classification results for grasp and rest states. The Receiver Operating Characteristic (ROC) curve achieved an Area Under the Curve (AUC) of 0.93 (Fig. 4 (a)). The confusion matrix (Fig. 4 (b)) indicates 338 correct predictions, yielding an accuracy of 84.5%, precision of 83.9%, and a recall of 85.5%. Pseudo-real-time validation using a 500 ms time window demonstrated stable classification performance (Fig. 4 (c)), where the blue line represents predicted classes (1: Grasp, 0: Rest) and red dots indicate true labels. Figure 5 illustrates EMG activity from hand-wrist muscles during grasp and rest states collected from the four subjects. The RMS amplitudes of flexor pollicis longus, flexor digitorum profundus, and extensor carpi radialis were averaged across sessions, highlighting distinct activation patterns for wrist and finger movements during grasping cue.

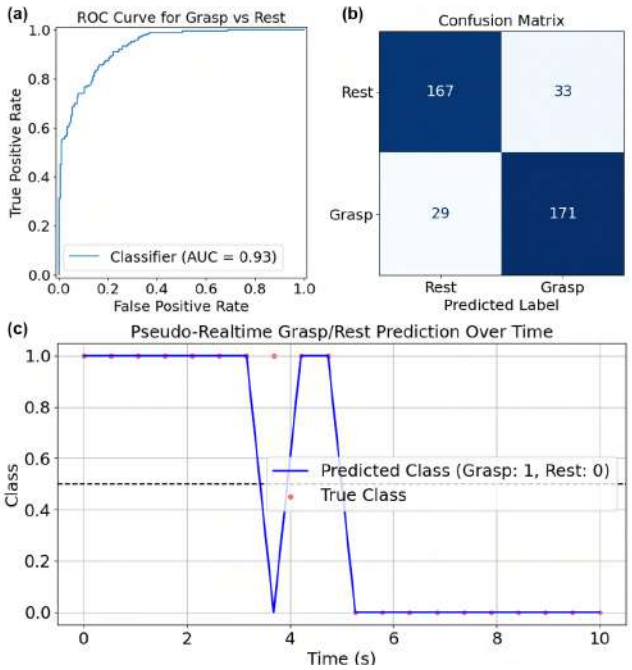


Fig. 4. Experimental results of developed EEG-based grasp/rest classification algorithm, (a) ROC curve for grasp/rest binary classification, (b) Confusion matrix showing classification accuracy, (c) Grasp/rest state predictions in a pseudo-real-time testing environment.

IV. DISCUSSION

This study presents a multimodal EEG-EMG-based motion intention recognition system integrated with a 3-DOF soft wearable hand-wrist robot. Unlike conventional EEG-EMG HMIs that fuse both modalities into a single decision model, our system integrates EEG and EMG independently to recognize distinct phases of the grasping task. EEG classified grasp and rest states for grasping the object, while EMG detected reaching onset, allowing for preemptive wrist adjustment before grasping. This sequential approach promotes natural movement transitions, as hand and wrist movements are inherently interconnected [14]. Given their biomechanical interdependence, proper wrist orientation is essential for optimizing distal hand RoM and executing stable grasps. Since stroke patients often exhibit inwardly flexed elbow, wrist, and clenched fists [26], this HMI system extends rehabilitation support beyond the isolated hand function to

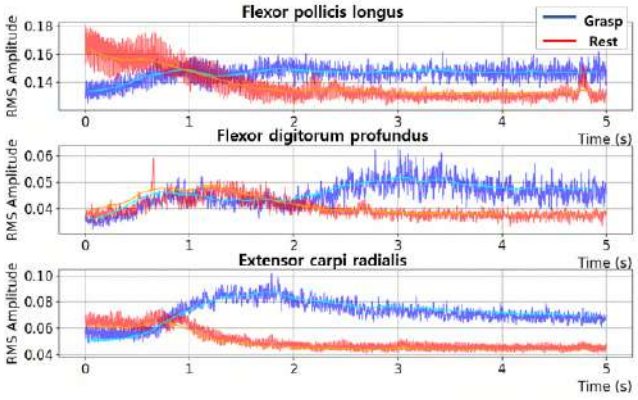


Fig. 5. Measured EMG activity during grasp and rest states. RMS amplitudes overlaid on rectified raw EMG signals for three muscles: (top) flexor pollicis longus, (middle) flexor digitorum profundus, (bottom) extensor carpi radialis.

facilitate coordinated upper limb recovery.

The EEG binary classification algorithm was developed by transformation from Euclidean space to Riemannian space using signals recorded from 19 channels. While prior studies often employ fewer channels focused on the motor cortex for motor intention or execution, we opted for full-scalp coverage to enhance robustness across individuals, particularly for future applications in stroke patients with varying neural activation patterns. Our EEG-based motion intention recognition demonstrated comparable classification performance, with an AUC of 0.93 and an accuracy of 84.5% according to the confusion matrix. Though this study primarily presents offline validation results as a preliminary investigation, a pseudo-real-time test was conducted to bridge the transition from offline to real-time implementation. By randomly selecting the grasp/rest task sessions from the offline pilot dataset, we generated a pseudo-real-time environment and achieved over 80% accuracy when classifying every 0.5 seconds (Fig. 4 (c)). This result aligns with existing literature, where EEG-based motor intention detection using pre-recorded real-time test sets reported accuracies of 87% [27], and multi-class motor imagery classification studies achieved 84% accuracy [28]. These findings suggest that our algorithm is viable for real-time application, as its classification performance is comparable to prior studies [29].

EMG signals were analyzed independently from EEG-based grasp/rest classification to detect the reaching phase, enabling preemptive wrist posture adjustments. As shown in Fig. 5, wrist extensor activation peaked 1–2 seconds after the grasp cue, while finger flexors exhibited an initial response alongside wrist extensors, followed by a second, greater activation around 3 seconds before declining. This activation pattern marks the reaching phase, allowing for wrist supination assistance before grasping by setting subject-specific activation thresholds. We employed 6 bipolar EMG signals to enhance detection reliability across diverse activation patterns, ensuring robust classification across individuals despite the relatively large number of channels. Notably, the thumb flexor (flexor pollicis longus) lacked a distinct peak during grasping but exhibited an initial peak during the rest cue, gradually decreasing over time. This suggests redundancy in reaching detection, and such redundant channels may be excluded in further studies while maintaining detection robustness in stroke patients.

The soft hand-wrist robot was designed with lightweight, compactness, and adjustability in mind to enhance wearability. By assisting only two fingers, the design reduces weight to under 250g, while a simplified cable routing guide minimizes its footprint on the palmar side, preserving thumb RoM and enabling quick donning/doffing. Although excluding the ring and little fingers may reduce grip strength [30], this wearable robot prioritizes functional grasping over maximizing grip force. As the thumb, index, and middle fingers play dominant roles in various grasping tasks, the soft glove supports various hand postures beyond power grasp, such as lateral pinch and precision grip, facilitating diverse ADL tasks. To accommodate varying hand sizes and levels of spasticity, passive elastic exotendons feature adjustable attachment points for personalized anchoring on the dorsal hand. The wrist robot, equipped with a BOA lacing system and soft silicone materials, provides a secure, customizable fit for different wrist and forearm dimensions. These design considerations contribute to comfortable, long-term rehabilitation with reduced physical and mental fatigue.

Overall, the proposed multimodal EEG-EMG HMI system offers advantages for stroke rehabilitation. Its soft and lightweight design supports long-term use while enabling coordinated hand-wrist-forearm assistance, promoting natural movement patterns. Unlike conventional robots focused solely on hand grasping, this system adjusts wrist posture during reaching to cover a broader range of upper limb motion, addressing post-stroke impairments like inwardly flexed elbows, wrists, and clenched fists. The motion intention recognition model effectively integrates EEG for grasp/rest classification and EMG for reaching detection, allowing wrist pronation before grasping. This multimodal approach enhances functional grasping compared to single-modality systems.

However, the system also has limitations. First, the current model was only validated on a small sample of healthy participants. Stroke patients show high variability in EMG due to muscle weakness and spasticity, requiring individual calibration processes to detect reaching accordingly. The EEG classification algorithm must also be adjusted to accommodate weaker motor-related EEG responses in stroke patients. Second, the wearable robot only supports pronation-supination, lacking flexion-extension, which is important for natural reaching. Third, the system lacks object and hand posture recognition, limiting adaptability to different grasping tasks, despite the soft glove can support various grasping postures like lateral pinch, or tripod grip. Integrating a vision-based object recognition system [31] could enhance adaptive grasping postures.

Future work will expand testing to stroke patients and refine the motion intention algorithm based on patient-specific neural and muscular responses. The vision-based

object detection system may further improve grasping adaptability. The system will be evaluated for its impact on motor function recovery and neuroplasticity through task-oriented rehabilitation for mild to moderate stroke patients.

V. ACKNOWLEDGMENT

The authors thank YBrain for providing the EEG and EMG acquisition module used in this study.

REFERENCES

[1] H. Nakayama, H. S. Jørgensen, H. O. Raaschou, and T. S. Olsen, "Recovery of upper extremity function in stroke patients: the copenhagen stroke study," *Archives of physical medicine and rehabilitation*, vol. 75, no. 4, pp. 394–398, 1994.

[2] S. M. Hatem, G. Saussez, M. Della Faille, V. Prist, X. Zhang, D. Dispa, and Y. Bleyenheuft, "Rehabilitation of motor function after stroke: a multiple systematic review focused on techniques to stimulate upper extremity recovery," *Frontiers in human neuroscience*, vol. 10, p. 442, 2016.

[3] W. H. Chang and Y.-H. Kim, "Robot-assisted therapy in stroke rehabilitation," *Journal of stroke*, vol. 15, no. 3, p. 174, 2013.

[4] P. Langhorne, J. Bernhardt, and G. Kwakkel, "Stroke rehabilitation," *The Lancet*, vol. 377, no. 9778, pp. 1693–1702, 2011.

[5] C. Zhang, C. W. Li-Tsang, and R. K. Au, "Robotic approaches for the rehabilitation of upper limb recovery after stroke: a systematic review and meta-analysis," *International Journal of Rehabilitation Research*, vol. 40, no. 1, pp. 19–28, 2017.

[6] H. T. Peters, S. J. Page, and A. Persch, "Giving them a hand: wearing a myoelectric elbow-wrist-hand orthosis reduces upper extremity impairment in chronic stroke," *Archives of physical medicine and rehabilitation*, vol. 98, no. 9, pp. 1821–1827, 2017.

[7] E. Pezent, C. G. Rose, A. D. Deshpande, and M. K. O'Malley, "Design and characterization of the openwrist: A robotic wrist exoskeleton for coordinated hand-wrist rehabilitation," in *2017 international conference on rehabilitation robotics (ICORR)*. IEEE, 2017, pp. 720–725.

[8] H. Choi, B. B. Kang, B.-K. Jung, and K.-J. Cho, "Exo-wrist: A soft tendon-driven wrist-wearable robot with active anchor for dart-throwing motion in hemiplegic patients," *IEEE Robotics and Automation Letters*, vol. 4, no. 4, pp. 4499–4506, 2019.

[9] B. B. Kang, H. Choi, H. Lee, and K.-J. Cho, "Exo-glove poly ii: A polymer-based soft wearable robot for the hand with a tendon-driven actuation system," *Soft robotics*, vol. 6, no. 2, pp. 214–227, 2019.

[10] T. Bützer, O. Lambercy, J. Arata, and R. Gassert, "Fully wearable actuated soft exoskeleton for grasping assistance in everyday activities," *Soft robotics*, vol. 8, no. 2, pp. 128–143, 2021.

[11] D. H. Kim, Y. Lee, and H.-S. Park, "Bioinspired high-degrees of freedom soft robotic glove for restoring versatile and comfortable manipulation," *Soft robotics*, vol. 9, no. 4, pp. 734–744, 2022.

[12] I. Aprile, M. Germanotta, A. Cruciani, S. Loreti, C. Pecchioli, F. Cecchi, A. Montesano, S. Galeri, M. Diverio, C. Falsini *et al.*, "Upper limb robotic rehabilitation after stroke: a multicenter, randomized clinical trial," *Journal of Neurologic Physical Therapy*, vol. 44, no. 1, pp. 3–14, 2020.

[13] C. Liu, J. Lu, H. Yang, and K. Guo, "Current state of robotics in hand rehabilitation after stroke: a systematic review," *Applied Sciences*, vol. 12, no. 9, p. 4540, 2022.

[14] E. Peña Pitarch, *Virtual human hand: Grasping strategy and simulation*. Universitat Politècnica de Catalunya, 2008.

[15] M. Dragusanu, M. Z. Iqbal, T. L. Baldi, D. Prattichizzo, and M. Malvezzi, "Design, development, and control of a hand/wrist exoskeleton for rehabilitation and training," *IEEE Transactions on Robotics*, vol. 38, no. 3, pp. 1472–1488, 2022.

[16] A. A. Blank, J. A. French, A. U. Pehlivan, and M. K. O'Malley, "Current trends in robot-assisted upper-limb stroke rehabilitation: promoting patient engagement in therapy," *Current physical medicine and rehabilitation reports*, vol. 2, pp. 184–195, 2014.

[17] A. Jackson and J. B. Zimmermann, "Neural interfaces for the brain and spinal cord—restoring motor function," *Nature Reviews Neurology*, vol. 8, no. 12, pp. 690–699, 2012.

[18] N. A. Bhagat, A. Venkatakrishnan, B. Abibullaev, E. J. Artz, N. Yozbatiran, A. A. Blank, J. French, C. Karmonik, R. G. Grossman, M. K. O'Malley *et al.*, "Design and optimization of an eeg-based brain machine interface (bmi) to an upper-limb exoskeleton for stroke survivors," *Frontiers in neuroscience*, vol. 10, p. 122, 2016.

[19] H. Yang, J. Wan, Y. Jin, X. Yu, and Y. Fang, "Eeg-and emg-driven poststroke rehabilitation: a review," *IEEE Sensors Journal*, vol. 22, no. 24, pp. 23 649–23 660, 2022.

[20] R. Leeb, H. Sagha, R. Chavarriaga, and J. del R Millán, "A hybrid brain–computer interface based on the fusion of electroencephalographic and electromyographic activities," *Journal of neural engineering*, vol. 8, no. 2, p. 025011, 2011.

[21] S. Jo, J. H. Jung, M. J. Yang, Y. Lee, S. J. Jang, J. Feng, S.-H. Heo, J. Kim, J.-H. Shin, J. Jeong *et al.*, "Eeg-emg hybrid real-time classification of hand grasp and release movements intention in chronic stroke patients," in *2022 International Conference on Rehabilitation Robotics (ICORR)*. IEEE, 2022, pp. 1–6.

[22] O. Lambercy, L. Dovat, H. Yun, S. K. Wee, C. W. Kuah, K. S. Chua, R. Gassert, T. E. Milner, C. L. Teo, and E. Burdet, "Effects of a robot-assisted training of grasp and pronation/supination in chronic stroke: a pilot study," *Journal of neuroengineering and rehabilitation*, vol. 8, pp. 1–12, 2011.

[23] S. Ambike, F. Paclet, V. M. Zatsiorsky, and M. L. Latash, "Factors affecting grip force: anatomy, mechanics, and referent configurations," *Experimental brain research*, vol. 232, pp. 1219–1231, 2014.

[24] Y. Lee and H.-S. Park, "Design optimization of a soft robotic rehabilitation glove based on finger workspace analysis," *Biomimetics*, vol. 9, no. 3, p. 172, 2024.

[25] H. Su, K.-S. Lee, Y. Kim, and H.-S. Park, "A soft, wearable skin-brace for assisting forearm pronation and supination with a low-profile design," *IEEE Robotics and Automation Letters*, vol. 7, no. 4, pp. 12 078–12 085, 2022.

[26] A. Opheim, A. Danielsson, M. A. Murphy, H. C. Persson, and K. S. Sunnerhagen, "Upper-limb spasticity during the first year after stroke: stroke arm longitudinal study at the university of gothenburg," *American journal of physical medicine & rehabilitation*, vol. 93, no. 10, pp. 884–896, 2014.

[27] H. J. Choi, S. Das, S. Peng, R. Bajcsy, and N. Figueroa, "On the feasibility of eeg-based motor intention detection for real-time robot assistive control," in *2024 IEEE International Conference on Robotics and Automation (ICRA)*. IEEE, 2024, pp. 5592–5599.

[28] N. Sharma, A. Upadhyay, M. Sharma, and A. Singhal, "Deep temporal networks for eeg-based motor imagery recognition," *Scientific Reports*, vol. 13, no. 1, p. 18813, 2023.

[29] V. Benzy, A. Vinod, R. Subasree, S. Alladi, and K. Raghavendra, "Motor imagery hand movement direction decoding using brain computer interface to aid stroke recovery and rehabilitation," *IEEE transactions on neural systems and rehabilitation engineering*, vol. 28, no. 12, pp. 3051–3062, 2020.

[30] J. Methot, S. J Chinchalkar, and R. S Richards, "Contribution of the ulnar digits to grip strength," *Canadian Journal of Plastic Surgery*, vol. 18, no. 1, pp. 10–14, 2010.

[31] E. Rho, H. Lee, Y. Lee, K.-D. Lee, J. Mun, M. Kim, D. Kim, H.-S. Park, and S. Jo, "Multiple hand posture rehabilitation system using vision-based intention detection and soft-robotic glove," *IEEE Transactions on Industrial Informatics*, 2024.

Design and Evaluation of a Solar-Powered Modular Robotic Object Maneuvering Assistance System

S. M. Mizanoor Rahman, *Member, IEEE*

***Abstract*—We present the design and evaluation of a solar-powered robotic object maneuvering (reaching, grasping and manipulating) system for assistance to sick, weak, and disabled people. The system is 0.78m long and 0.4kg heavy. The structure is made of lightweight PLA material. The front side of the system (device) acts as an end-effector, which is made of a 2-parallel jaw gripper actuated by a servomotor via a spur gear mechanism. Additional components can be attached to the inner sides of the jaws to help the gripper adjust its gripping strategies with objects of different shapes, sizes and surface textures. The back side of the device includes a rectangular groove that holds electronics circuit components such as the Arduino board, wires, batteries, etc. A solar panel is placed on the groove, which can harvest solar energy and charge the batteries to power the electronics circuit. A rotary potentiometer placed on the handle is connected to the Arduino board, which is used as a haptic input knob to control the servomotor for opening and closing the jaw-type gripper. We present the CAD model and the proof-of-concept physical prototype of the system. We experimentally evaluate the prototype for its performance (technical specifications) and human-robot interactions using healthy subjects. The results show that the system can assist humans maneuvering objects of different shapes and surface textures and produce satisfactory human-robot interactions. The proposed system can assist sick, weak and disabled people in maneuvering objects in their daily activities, facilitate people needing upper arm rehabilitation and thus significantly improve their quality of life (QoL) even in remote areas where electricity is scarce or unavailable.**

I. INTRODUCTION

Accident, age, sickness, etc. can reduce the abilities of human upper arms for object maneuvering (reaching, grasping and manipulating) in their daily activities [1]. Consequently, they depend on others for their daily activities, which imposes burdens on family members and/or caregivers. They also need assistive technologies to assist them in maneuvering objects for their daily activities. Considering this need, researchers proposed numerous object maneuvering assistance devices to assist people in this situation [1]-[4]. However, some existing devices are purely or mainly mechanical devices [1]-[3]. We believe that suitable robotic (mechatronic) devices used for maneuvering assistance and rehabilitation support may be more convenient, useful, user-friendly and effective [4]. The literature shows several robotics-based maneuvering devices, but their designs are complex in nature, and they are expensive for users with limited financial abilities [5]-[6].

Therefore, robotic devices that are inexpensive and that are easy to use and control are still in demand. The shape, size and weight of the devices are very important for effective, ergonomic and satisfactory performance of the devices. Researchers emphasized anthropomorphic or human-like appearance and design of robotic object maneuvering assistance devices [7]-[8]. They argued that robotic assistance devices for object maneuvering that use human-like design and/or working principles may be robust and dexterous like humans [8]. The literature shows that large sizes of the devices are inconvenient for use, and heavy weights of the devices can create fatigue in users, which may reduce usability of the devices and hinder their long-time use [9]. Modularity in the design may help mitigate this problem partly [9]. However, modular design of robotic object maneuvering assistance devices has not received much attention yet.

Supplying power to robotic object maneuvering assistance devices is a challenging task, and it becomes extremely challenging to operate assistive devices in remote areas that either lack electricity or electricity is scarce there [10]. Use of large batteries to power the devices increases size, weight and cost of the devices. Therefore, it is realized that application of solar energy to power robotic object maneuvering assistance devices may be more reasonable, economic, ergonomic and convenient for the users [10]. However, solar energy cannot be used directly to operate robotic assistance devices for object maneuvering. Appropriate methods and strategies of harvesting and storing solar energy as well as converting solar energy to useful electric power are required to operate robotic assistance devices for object maneuvering powered by solar energy [10]. Innovative design considerations for the robotic assistance devices are also required for this purpose [9]. However, the literature does not show significant attention towards developing robotic object maneuvering assistance devices powered by solar or renewable energy [10].

A comprehensive evaluation scheme should be developed and applied to evaluate robotic object maneuvering assistance devices to ensure that they meet technical performance requirements (technical specifications) and gain target user satisfaction [11]. We need novel evaluation schemes that are comprehensive in the nature and that address the evaluations from multifarious aspects such as evaluation of key performance indicators (KPI), assessment of interactions between the devices and their users, etc. A few performance evaluation schemes have been proposed in the literature for

S. M. M. Rahman is with the Mechanical Engineering Program at The Pennsylvania State University, 120 Ridge View Drive, Dunmore, PA 18512, USA (e-mail: mrahman@psu.edu; Tel.: +1-570-963-2588).

robotic object maneuvering assistance devices [11]-[12]. However, these evaluation schemes do not seem to be comprehensive for holistic evaluations of the devices.

Considering the above background and motivation, the objective of this paper is to propose a simple, lightweight, easy to use, low-cost, anthropomorphic, solar-powered and modular object maneuvering assistance robotic device for sick, weak and disabled people and for people needing upper arm rehabilitation support. We here present the innovative electro-mechanical design of such an assistance device, describe its prototype and present the evaluation results for the prototype device after evaluating the device following a novel, innovative and comprehensive evaluation scheme.

II. Design of the Robotic Object Maneuvering Assistance Device

We developed a 3-dimensionl CAD model of the solar-powered robotic object maneuvering (reaching, grasping and lifting) assistance device, as shown in Fig.1. As shown in the figure, the front side of the device includes an end-effector for grasping objects. The end-effector is designed with a 2-parallel jaw-type gripping mechanism that can be used to grip objects by the end-effector of the device. The two jaws are attached to 2 spur gears. One gear is the driver, the other gear is the driven. The axis of the driver gear is colinearly aligned with the shaft of a servomotor, which can actuate the gear mechanism. When the servomotor rotates, it rotates the gears that creates linear inward and outward motions of the jaws, which help grasp an object by the device for its maneuvering [3]. The inward and outward movement directions of the jaws can be controlled through controlling the direction of rotation of the servomotor via a rotary potentiometer placed at the other end of the device [4]. The linear speeds of the jaws are proportional to the rotational speeds of the servomotor, if we ignore nonlinearities in the mechanism [3], [9].

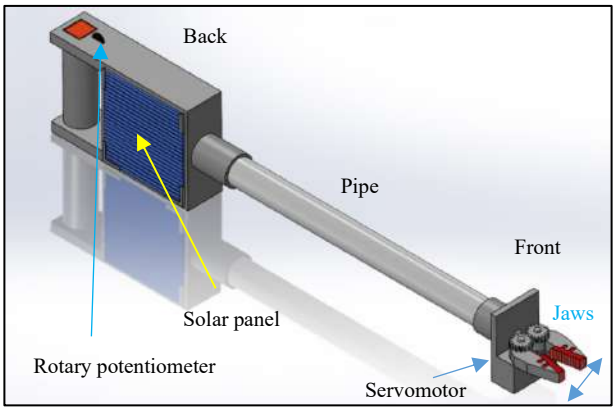
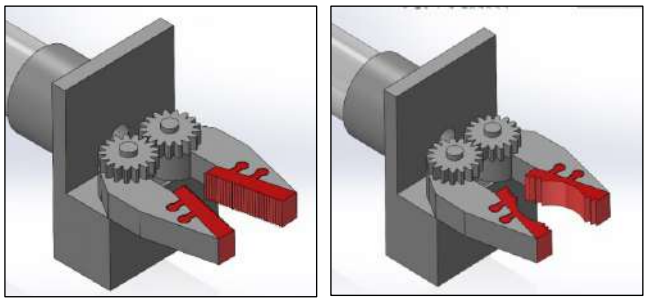


Fig.1 Design of the solar-powered robotic object maneuvering assistance device.

Gripping arrangements and strategies at the inner sides of the jaws can be adjusted by attaching two different gripping attachments or modules (the red components at the front of the device as shown in Fig. 1). This is shown using enlarged views in Fig.2. The attachments can change the surface roughness of the inner sides of the jaws. Such changes of surface roughness can facilitate grasping of objects with different shapes, sizes and surface textures. It can happen because the changes in surface roughness of the inner jaws can change the grip force requirements for maneuvering objects of different shapes, sizes and textures with the device [9]. The arrangement in Fig. 2 (a) can be used when grasping rectangular objects with smooth surfaces. The arrangement in Fig. 2 (b) can be used when grasping circular objects with smooth surfaces. These attachments (modules) can be attached and detached conveniently considering the target objects to be grasped and maneuvered, which adds modularity to the design [9]. The attachments can be removed (detached) for grasping rectangular or circular objects with rough or not-so-smooth surfaces.



(a) (b)

Fig.2 Adjustable modular gripping mechanisms. Attachments at the inner surface of the jaws for gripping (a) rectangular objects with smooth surfaces, and (b) circular objects with smooth surfaces.

As the back side of the device shows in Fig. 1, we used a rotary potentiometer (the black half-circular component) as a haptic input knob of the system. The rotary potentiometer is connected to an Arduino board. There is a groove at the back side of the device (it is covered with the blue solar panel in Fig.1). The inner view of the groove is shown separately in Fig.3. As Fig.3 shows, the groove can accommodate the Arduino board and other necessary electronic and electric components such as batteries, wires, etc. The solar panel is placed on the groove that acts as the lid of the groove. The solar panel can be used to harvest solar energy in remote areas where electricity is scarce or not available [10]. Required number of small batteries can be connected to the solar panel to store the harvested solar energy, and then the electronics

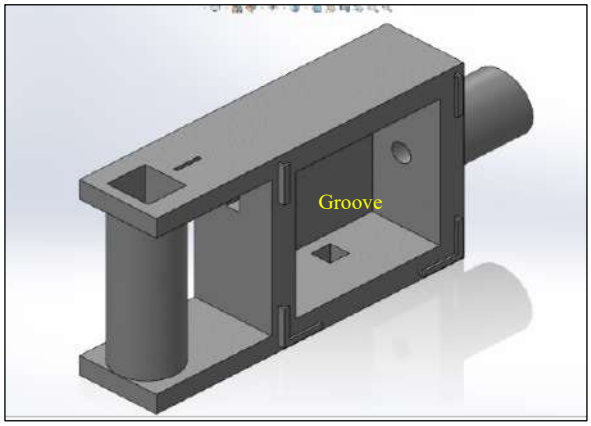


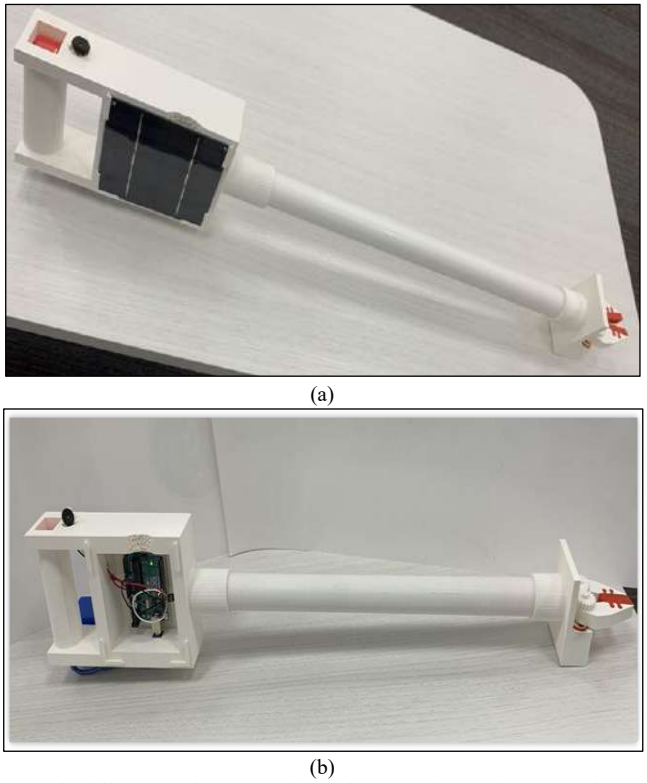
Fig.3 The groove at the back side of the device to contain electronic and electric circuit components.

can be powered by the batteries [10]. The front and back sides of the device are rigidly connected via a pipe-like structure. The servomotor placed at the front of the device is also connected to the Arduino board using a wire (placed inside the pipe), and the servomotor can also be powered by the batteries placed inside the groove at the back of the device.

The design uses lightweight PLA material to 3D print the structure of the device as Figs.1-3 show [9]. The device was 0.78m long, which could make it feasible to grasp different objects from a distant location [1]. The weight of the device was designed to be approximately 0.4kg [9].

III. Development of the Proof-of-Concept Device

We developed a physical prototype of the design demonstrated in Fig.1. Fig.4(a) shows the assembled view of the physically developed robotic reaching and grasping assistance device, where the electronics circuit is covered with the solar panel. Fig. 4(b) exposes the electronics circuit of the fully assembled device. A battery holder could be accommodated inside the groove, or it could be attached to the structure of the device. The batteries could be charged with the solar energy harvested using the solar panel to supply power to the electronics circuit. PLA plastic material was used to 3D-print the structure of the device to make it lightweight (less than a pound) [9].



(a)

(b)

Fig.4 The fully assembled views of the robotic reaching and grasping device: (a) with a solar panel covering the electronics circuit, (b) without the solar panel exposing the electronics circuit.

Fig. 5 shows the mechatronics design of the solar-powered reaching and grasping device [10]. The solar panel was connected to a battery via a charge/solar controller, and then it was connected to an Arduino and shield board, which was used to control the electronics of the device. The solar panel was used to harvest solar energy and to store the energy in the battery to power the electronics. We connected the rotary potentiometer (analog input) to a 3.3V input port (analog) and the ground terminal of the Arduino board. We connected the servomotor (placed at the end-effector) to a 3-pin extension wire, and then we connected it to the 5V port (digital output) and the ground terminal of the Arduino board. The force and position sensors used for experimental purposes could be connected to the Arduino board as well. The Arduino board was connected to a computer with the Arduino IDE. Note that the Arduino board could be powered using either the power from electric line or the battery power. We used the Arduino IDE to develop code in C++ to control the electronics circuit.

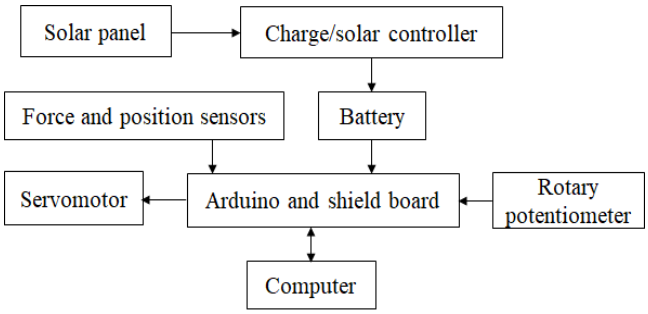


Fig.5 The mechatronics design of the solar-powered robotic reaching and grasping assistance device.

IV. Performance Evaluation of the Device

A. Experiments

The literature shows that different researchers emphasized different criteria when evaluating object maneuvering assistance and rehabilitation robotic devices [11]-[17]. We here accumulated the evaluation approaches of technical performance specifications and of human-robot interactions based on a comprehensive set of criteria [18]. We conducted a series of experiments of the physical reaching and grasping robotic device to evaluate its performance and interactions based on the evaluation scheme and tried to justify the design and applications of the device, as follows.

(1) Experiment 1: Solar Energy Harvest Test

We exposed the solar panel to the direction of the sun in a sunny day from 11am to 2pm to harvest solar energy and charge the battery. The charge of the battery was measured using a digital multimeter. The amount of charge obtained in the battery was a measure of the harvested solar energy assuming no loss of energy occurred in the conversion or harvesting process [10]. We charged two batteries separately and connected them in series to power the circuit depending on the total power requirement of the circuit.

(2) Experiment 2: Input-Output Displacement Relationships

As Fig. 6 shows, a human subject opened and closed the jaws of the gripper (end-effector) by rotating the rotary potentiometer attached onto the back side of the device

counterclockwise using the thumb finger of the right hand. A horizontal ultrasonic sensor was used at a distant position to measure the opening lengths of the jaws of the gripper (termed as output displacements) for approximately 90 degrees, 180 degrees, 270 degrees and 360 degrees of counterclockwise rotations of the rotary potentiometer (termed as input displacements) separately [1], [3]. We also used a stopwatch to separately measure the time the human subject took to complete 90 degrees, 180 degrees, 270 degrees and 360 degrees of rotations of the rotary potentiometer. Those times were termed as input times. We used another stopwatch to measure the duration of time starting from when the subject started to rotate the rotary potentiometer to when the jaws of the end effector ended the linear displacement. This time was termed as the output time. The difference between the input and output times was considered as the time delay between the input displacement and the output displacement. We determined the time delay of the system for 90 degrees, 180 degrees, 270 degrees and 360 degrees of rotations of the rotary potentiometer separately [4].

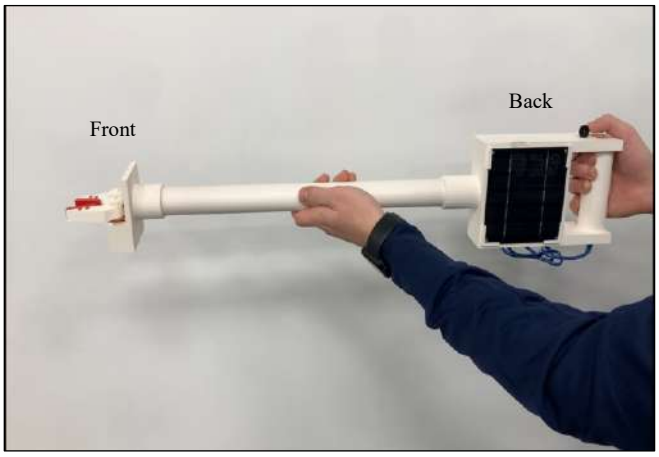


Fig.6 A subject opens and closes the jaws of the gripper (end-effector) by rotating the rotary potentiometer counterclockwise using the thumb finger of the right hand. It is a two-handed or one-handed (dominant hand) operation.

(3) Experiment 3: Input-Output Force Relationships

A foil strain gauge type force sensor was pasted on the rotary potentiometer. The force sensor was used to measure the tangential force applied by the human subject to rotate the potentiometer counterclockwise to operate the device (input force). Another foil strain gauge type force sensor was pasted on the inner side of a jaw of the end effector to measure the grip force (output force) to grasp and lift an object using the device. In an experiment, a human subject rotated the rotary potentiometer 360 degrees counterclockwise to grasp and lift 4 different types of objects using the device such as a rectangular object with a smooth surface, a rectangular object with a rough surface, a circular object with a smooth surface and a circular object with a rough surface separately. We adjusted the gripping mechanism for the objects considering the shapes and surface textures (roughness) of the objects by attaching and detaching additional attachments inside the jaws as introduced in Fig.2. The input and output forces for each object were recorded and analyzed separately [18].

(4) Experiment 4: User Study

A human subject rotated the rotary potentiometer 360 degrees counterclockwise to grasp and lift 4 different types of objects using the device such as a rectangular object with a smooth surface, a rectangular object with a rough surface, a circular object with a smooth surface and a circular object with a rough surface separately. Same as the above, we adjusted the gripping mechanism for the objects considering the shapes and surface textures (roughness) of the objects by attaching and detaching additional attachments inside the jaws as introduced in Fig.2. We recorded whether the subject was able to grasp and lift each object using the device successfully to calculate the success rate for each type of object [18].

At the end of the experiment, the subject completed a set of questionnaires to evaluate human-robot interactions (HRI) based on his/her interactions with the device for grasping and lifting objects [13], [18]. We developed the questionnaires reflecting relevant HRI criteria and the subject evaluated each of the HRI criteria using a 7-point Likert scale, 1 being the least favorable HRI and 7 being the most favorable HRI [18]. The physical HRI (pHRI) criteria were anthropomorphism (whether the use of the device resembled object maneuvering using a biological human hand in terms of configuration and biomechanics of the hand) [7], haptically perceived heaviness of the device where the least heaviness would be the best [9], symbiosis (how the human subject and the device depended on each other for the object maneuvering operation) [18], adaptability (how the human felt when using the same device to grasp objects of different types) [15], coordination (how the human users coordinated and balanced the input-output relationships especially the force and position relationships) [17], ease of use (how easy the human felt when maneuvering the objects using the assistance device) [18], naturalness (how the human user felt when maneuvering objects using the device compared to when maneuvering the same objects without using the device, i.e., using the biological hand only) [1], and intuitiveness (whether the human user was intuitive in using the device for potential future maneuvering of objects) for grasping and lifting objects using the device [14]. The cognitive HRI (cHRI) criterion was the user trust in the device for its application, which was also evaluated using the above-mentioned Likert scale [16], [18], [19].

Another measure of cHRI was the cognitive workload of the subject for grasping and lifting each object. The subject completed the NASA-TLX to report cognitive workload [20]. In total, 10 subjects participated in this user study separately. The subjects received instructions on experiment procedures. The ethical standards for human subject tests were maintained following the IRB principles.

B. Experiment Results

(1) Experiment 1 (Solar Energy Harvest Test) Results

Table I shows voltages contained in a rechargeable battery for different time periods. The voltages were produced by the solar panel, which were to be used to power the device for its operations. The results thus prove the potential of the device for its applications in remote areas that lack electricity or where electricity is scarce [10].

Table I: Solar Energy Harvest Test Results

Time periods (trials)	Solar panel voltage (V)	Battery voltage (V)
11:00am-11:30am	4.16	3.32
11:31am-12:00pm	4.28	3.44
12:01pm-12:30pm	4.36	3.52
12:31pm-1:00pm	4.47	3.61
1:01pm 1:30pm	4.62	3.74

(2) Experiment 2 (Input-Output Displacement Relationships) Results

Table II shows the input-output displacement relationships results (the mean displacements with standard deviations in parentheses). The opening and closing lengths of the jaws (at the front side of the device) for different angles of rotations of the rotary potentiometer (at the back of the device) showed that it was possible for the users (subjects) to successfully open and close the jaws of the end-effector. The jaws were actuated by the servomotor which was haptically controlled via the rotary potentiometer [4]. The results thus proved the potentiality of the grasping and lifting device for its intended use by handicapped, sick, weak and disabled people for assistance in reaching, grasping and lifting objects in their daily household activities [1]-[4].

The time delays in the operations of the device (difference between input and output times) were also small as Table III shows, which proved efficient and synchronized operations of the device between the input (rotation of the rotary potentiometer) and the output (linear movements of the jaws of the end-effector) [3]. However, the time delays could be further reduced by providing trainings to the users, improving the quality of the rotary potentiometer and reducing nonlinearities in the mechanisms of the end-effector (e.g., reducing backlash of the gear pair, reducing friction, etc.) [9].

Table II: Input-Output Displacement Relationships Results

Output displacements (mm)	Input displacements (degrees)			
	90	180	270	360
	12.72 (0.13)	25.86 (0.33)	38.18 (0.74)	51.44 (1.09)

Table III: Time delays in the operations of the device

Time (s)	Input displacements (degrees)			
	90	180	270	360
Input	0.51 (0.03)	0.96 (0.04)	1.48 (0.06)	1.92 (0.08)
Output	0.78 (0.04)	1.28 (0.07)	1.93 (0.05)	2.21 (0.03)

(3) Experiment 3 (Input-Output Force Relationships) Results

Table IV shows the input-output force relationships results. The results show that the device was able to amplify the input forces significantly, which were sufficient to grasp and lift objects of different shapes and surface features. The results also show that the device needed to apply slightly larger magnitude of forces to maneuver circular and smooth surface objects than rectangular and rough surface objects [4].

Table IV: Input-Output Force Relationships Results

Mean measured forces (N)	Test conditions (objects)			
	Rectangular-smooth	Rectangular-rough	Circular-smooth	Circular-rough
Input force	0.11 (0.02)	0.10 (0.015)	0.12 (0.01)	0.11 (0.03)
Output force	2.96 (0.07)	2.88 (0.03)	3.19 (0.05)	3.08 (0.04)

(4) Experiment 4 (User Study) Results

Table V shows the success rates for grasping different types of objects [18]. The results reveal that the device was capable of maneuvering objects successfully. Fig.7 shows the HRI evaluation results for the device [13]. The results show high level of effectiveness in HRI for maneuvering objects using the device. As the HRI results show, the subjects haptically perceived the device as a less heavy or lightweight device for the targeted applications. Low heaviness of the device should not generate high fatigue in users if they use the device for long duration, which can make the device suitable for old, disabled and weak persons [9]. We conducted analysis of variance (ANOVA) for the results in Fig. 7, which showed that variations in HRI scores between subjects were statistically non-significant (p= 3.79, p>0.05). Such statistical results indicate that the results were consistent even though we used a small number of subjects [18].

Table VI shows that the operations of the device did not create high level of cognitive workload in the users, which proved user-friendliness of the device [20]. The results in Table VI show that the shape and surface roughness slightly impacted the cognitive workload of the users. We see that the circular objects with smooth surfaces created slightly higher cognitive workloads in users compared to rectangular objects with rough surfaces [20]. The ANOVA results showed that the cognitive workload percentages between objects were statistically significant (p = 0.0018, p<0.05), but the cognitive workload percentages between subjects were not statistically significant (p = 5.13, p>0.05). Such statistical results indicate

Table V: Success rate (%) for grasping different types of objects using the device

Test conditions (objects)			
Rectangular-smooth	Rectangular-rough	Circular-smooth	Circular-rough
100%	100%	100%	100%

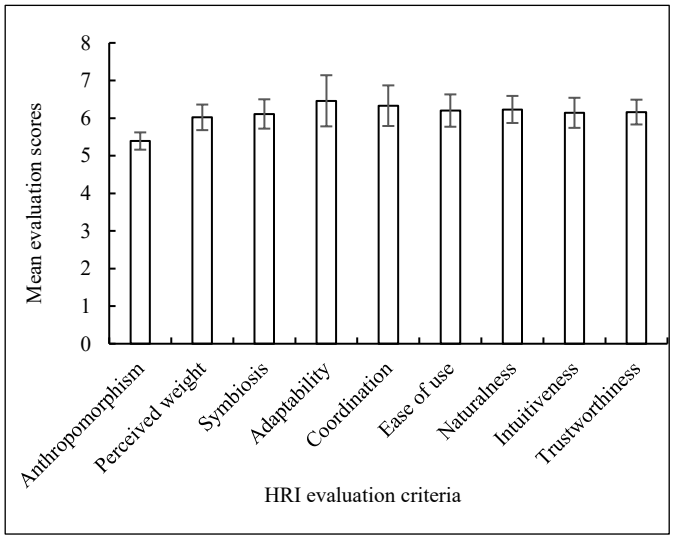


Fig.7 HRI evaluation results for grasping and lifting objects using the device.

Table VI: Total cognitive workload (%) of users for grasping and lifting different types of objects using the device

Test conditions (objects)			
Rectangular-smooth	Rectangular-rough	Circular-smooth	Circular-rough
24.61 (2.38)	22.42 (2.63)	28.24 (2.89)	26.58 (1.76)

that the results were consistent even though we used a small number of subjects [18]. The statistical results also proved that shapes and surface conditions of objects can impact the cognitive workload of human users when maneuvering objects using the robotic assistance device [20].

V. Conclusions and Future Research Directions

We presented the design and prototype evaluation of a novel robotic object maneuvering assistance system powered by solar energy for assisting sick, weak and disabled people. The evaluation results showed that the system was able to satisfy the technical requirements in object maneuvering operations. The results also showed that the system was able to produce satisfactory and effective human-robot interactions. The design of the system included a novel adjustable gripping mechanism, which added modularity to the design. The system was designed to be powered with solar energy, which made it suitable for use in remote areas lacking electricity. Similar robotic assistance devices are not so common in the literature. Thus, the proposed design is important, and it advances the state-of-the-art contributions in this research area. We propose to use the device as a personal assistance tool to improve the quality of life (QoL) of people with sickness, weaknesses, and disabilities needing upper arm rehabilitation support.

In the future, we will reduce the weight and size of the device. We will examine the effectiveness of the force input using a force sensor instead of the position input of the potentiometer to control the motor. We will maximize the energy efficiency (the time required to fully charge the battery and the maximum duration the device can be operated with a fully charged battery). We will apply a PID control of the opening and closing motions of the grippers so the objects can be grasped with more accurate opening lengths of the jaws. An RGB-D camera will be attached to the end-effector, which will be used to implement a Convolutional Neural Networks (CNN) algorithm to enhance accuracy in detecting and grasping arbitrary objects. A suitable collision avoidance strategy based on an intelligent motion control algorithm will be proposed to avoid collisions while grasping objects. We will conduct a clinical study using many sick and disabled patients to verify and validate the results for sick and disabled people and to confirm the generality of the results.

Research Ethics Statement:

The author applied responsible conduct of research (RCR) and followed relevant IRB principles with human subjects. Informed consent was received from the subjects.

References

[1] Y. Itaguchi, "Toward natural grasping with a tool: effects of practice and required accuracy on the kinematics of tool-use grasping," *Journal of Neurophysiology*, 2020, 123:5, 2024-2036.

[2] C. L. A. Gomes, R. O. Cacho, V. T. B. Nobrega, *et al.,* "Low-cost equipment for the evaluation of reach and grasp in post-stroke individuals: a pilot study," *BioMed Eng OnLine* 19, 14 (2020).

[3] B. Zheng, C. MacKenzie, "Kinematics of reaching and grasping with a tool," *in Proc. of the Human Factors and Ergonomics Society Annual Meeting*, 2007, 51. 10.1177/154193120705101917.

[4] Á. A. Pálsdóttir, M. Mohammadi, B. Bentsen and L. N. S. A. Struijk, "A dedicated tool frame-based tongue interface layout improves 2D visual guided control of an assistive robotic manipulator: A design parameter for tele-applications," *IEEE Sensors Journal*, vol. 22, no. 10, pp. 9868-9880, May15, 2022.

[5] Y. Xu, H. Zhang, L. Cao, X. Shu and D. Zhang, "A shared control strategy for reach and grasp of multiple objects using robot vision and noninvasive brain–computer interface," *IEEE Transactions on Automation Science and Engineering*, vol. 19, no. 1, pp. 360-372, 2022.

[6] M. Sierotowicz *et al*., "EMG-driven machine learning control of a soft glove for grasping assistance and rehabilitation," *IEEE Robotics and Automation Letters*, vol. 7, no. 2, pp. 1566-1573, April 2022.

[7] A. Kargov *et al*., "Development of an anthropomorphic hand for a mobile assistive robot," *9th International Conference on Rehabilitation Robotics (ICORR 2005)*, Chicago, IL, USA, 2005, pp.182-186.

[8] H. Yamazaki, M. Nishiyama and K. Watanabe, "A fiber-optic mechanoreceptor in a finger-shaped end effector for human-like tactile sensing," *IEEE Sensors Journal*, vol. 17, no. 16, pp. 5123-5129, 2017.

[9] S. M. M. Rahman, "Design of a modular knee-ankle-foot-orthosis using soft actuator for gait rehabilitation," In: Natraj, A., Cameron, S., Melhuish, C., Witkowski, M. (eds) *Towards Autonomous Robotic Systems. TAROS 2013. Lecture Notes in Computer Science*, vol 8069. Springer, Berlin, Heidelberg, pp.195-209, 2014.

[10] S. M. M. Rahman, "Modeling and analysis of a dynamic smart solar panel system for harvesting solar energy in remote areas," In: Yang, XS., Sherratt, S., Dey, N., Joshi, A. (eds) *Proc. of Ninth Int. Congress on Information and Communication Technology. ICICT 2024, Lecture Notes in Networks and Systems*, vol 1002, Springer, 2024, pp.581-591.

[11] X. Wu, B. Gong, H. Yang, X. Liu, Y. Fang, "Performance evaluation of a traditional Chinese medicine massage robot based on multi-information fusion," *IEEE Access*, vol. 12, pp. 150564-150573, 2024.

[12] A. Khan, D. Joshi, B. Mukherjee, "Design and psychophysical validation of a slip induction device for sensorimotor evaluation of prehensile grip," *IEEE Sensors Journal*, vol.24, no.15, pp.24750-24757, 2024.

[13] L. Zongxing, Z. Jie, Y. Ligang, C. Jinshui and L. Hongbin, "The human–machine interaction methods and strategies for upper and lower extremity rehabilitation robots: A review," *IEEE Sensors Journal*, vol. 24, no. 9, pp. 13773-13787, May 1, 2024.

[14] C. Dune, C. Leroux and E. Marchand, "Intuitive human interaction with an arm robot for severely handicapped people - A one click approach," *IEEE 10th International Conference on Rehabilitation Robotics*, Noordwijk, Netherlands, 2007, pp. 582-589.

[15] A. Garzás-Villar, C. Boersma, A. Derumigny, A. Zgonnikov, L. Marchal-Crespo, "Personality traits modulate the effect of haptic guidance during robotic-assisted motor training," *2024 10th IEEE RAS/EMBS International Conference for Biomedical Robotics and Biomechatronics,* Heidelberg, Germany, 2024, pp.1023-1028.

[16] S. Li, Z. Wang, X. Yin, Z. Pang and X. Yan, "Rehabilitation evaluation of upper limb motor function for stroke patients based on belief rule base," *IEEE Transactions on Neural Systems and Rehabilitation Engineering*, vol. 32, pp. 241-248, 2024.

[17] D. Copaci, N. Pernalete, Á. G. Ortiz and D. B. Rojas, "Proposed eye-hand correlation assessment system: A novel approach for evaluating coordination," *IEEE Access*, vol. 12, pp. 3926-3935, 2024.

[18] S. M. M. Rahman, "Performance metrics for human-robot collaboration: an automotive manufacturing case," *2021 IEEE Int. Workshop on Metrology for Automotive*, Italy, 2021, pp. 260-265.

[19] A. Gul, L. D. Turner and C. Fuentes, "An exploratory analysis of trust in socially assistive robot interactions with unpaid carers of older adults," *IEEE International Conference on Robot and Human Interactive Communication*, Pasadena, CA, USA, 2024, pp. 1630-1637.

[20] A. Kalatzis, V. G. Prabhu, L. Stanley and M. P. Wittie, "Effect of augmented reality user interface on task performance, cognitive load, and situational awareness in human-robot collaboration," *2023 32nd IEEE International Conference on Robot and Human Interactive Communication (RO-MAN)*, Busan, Korea, 2023, pp. 1252-1259.

A Novel Elastic Model for Exoskeleton-User Coupling Interfaces

Christian Mele[1], David Choi[2], Katja Mombaur[3] and James Tung[4]

***Abstract*— Current research on physical human-robot interactions (pHRI) in wearable assistive robots, such as lower-limb exoskeletons, primarily focuses on improving net force estimates at each interface to improve robot controller performance. Consequently, estimating force distribution along physical interfaces of wearable robots, crucial for user safety and comfort, has been largely overlooked. We propose a novel computational model that uses interface geometry and strapping tension as inputs, and predicts the static pressure field generated during the user donning process by treating the supporting surface as an elastic foundation. Accuracy of the proposed computational method was validated by comparing the estimated static pressure field of a commercially available interface to experimental data. While measured pressure magnitudes were significantly lower than model prediction, likely due to a combination of assumptions and limitations associated with model design, similar loading patterns were observed. Identifying regions of high pressure from simulation and similar patterns allow for reliable scaling to reduce inaccuracies, and may be used to inform design. Further refinements of the proposed model will provide a valuable tool for developing more comfortable and safer interfaces for wearable robots.**

I. Introduction

The coupling interface is the location, or surface(s), at which forces and torques are transmitted from the device to user [1]–[4]. The coupling interface is critical for functional performance of exoskeleton (exo) devices in transmitting controlled forces from actuators, or stored energy from passive components, to the user. User safety is directly tied to the coupling interface by joining the user to the device for assistance, support, and preventing of user-device separation, as well as the potential complications and risks from improper or ineffective coupling [1]–[8].

The H3 exoskeleton (Technaid, Spain), pictured in Figure 1, left, is a 6-DoF assistive lower-limb exoskeleton with coupling interfaces typical to assistive wearable exoskeletons [1], [2]. While there exists a range of interface designs for coupling the user to the exo, most comprise of a soft convex hull interface, rigid surface, and a "strap" or hook-and-loop system that fixes and holds the user in position [1], [2], [9]. An example coupling interface is shown in Figure 1, right.

*This work was completed with support from NSERC

[1]Christian Mele is with the Dept. of Systems Design Engineering, University of Waterloo, Waterloo, Canada cmele@uwaterloo.ca

[2]David Choi is with the Dept. of Mechanical & Mechatronics Engineering, University of Waterloo, Waterloo, Canada bj2choi@uwaterloo.ca

[3]Katja Mombaur with the Institute for Anthropomatics and Robotics, Karlsruhe Institute of Technology, Karlsruhe, Germany katja.mombaur@kit.edu

[4]James Tung is with the Dept. of Systems Design Engineering, University of Waterloo, Waterloo, Canada james.tung@uwaterloo.ca

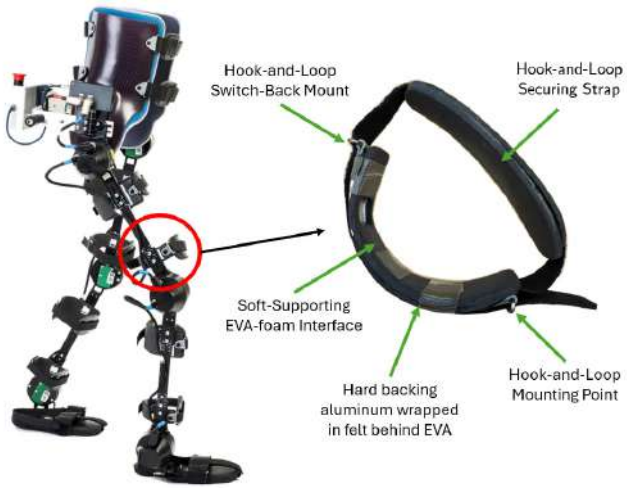


Fig. 1. The H3 Exoskeleton, (Technaid, Spain) alongside the lower thigh coupling interface as seen from a top-down view. Points of interest critical to the function of the device, and user comfort are highlighted. This interface is characterized by the convex hull shape and soft supporting interface overlaid a rigid hard-backed surface. It has a hook-and-loop strap for securing.

The coupling interface directly influences compliant and restrictive motion at the interface. Excessive or improperly designed pressures and misalignments caused by them can lead to musculoskeletal and/or skin injuries [1]–[4], [6]–[8], [10]. The risk of pressure injuries, such as ulcers and bruising, increases with large and/or prolonged applied normal and shear forces to the skin, and has been shown to occur during exo use [1], [3], [4], [10], [11].

Research on physical human robot interaction (pHRI), specifically interface pressure and coupling interface design for exos is centered on sensorisation and linear modeling approaches [1], [2], [9], [12]. Sensor-based approaches often use single value readings as metrics associated with coupling interface effects, complicated by a lack of user variable control or consideration, which makes tying sensor-based findings to design features of the coupling interface challenging [1]. Model-based approaches have focused primarily on force and torque vectors necessary for rigid-body dynamics and control [1], [2], [12]–[14]. Compliant single linear spring elements have been utilised, but are currently incapable of correlating predicted results to coupling interface design. Recent advancements examine how initial donning pressures influence kinetics; however, these have not yet impacted coupling interface design for exoskeletons [15], [16].

Elastic foundations, which have been implemented in robotics and assistive devices to model complex geometric interactions between biomechanical interfaces [17]–[20],

may be useful in relating coupling interface geometry to pressure fields. The objective of this paper is to describe a proposed algorithm implementing elastic foundations for modeling static donning pressures of the exo coupling interface for evaluation and design. The algorithm and the formulation of the supporting elastic foundation interfaces are described, then validated against experimental evaluation of a mannequin and an isolated H3 exo coupling interface.

II. The Coupling Model Algorithm

A. Model Overview

The methods presented are a framework for utilization and analysis with an elastic foundation model that may be applied to exoskeleton coupling interfaces to determine initial donning indentation depth and pressure distributions prior to interface fabrication. A flow chart of the algorithm used that highlights the implementation of the elastic foundation model in localizing pressures can be seen in Figure 2.

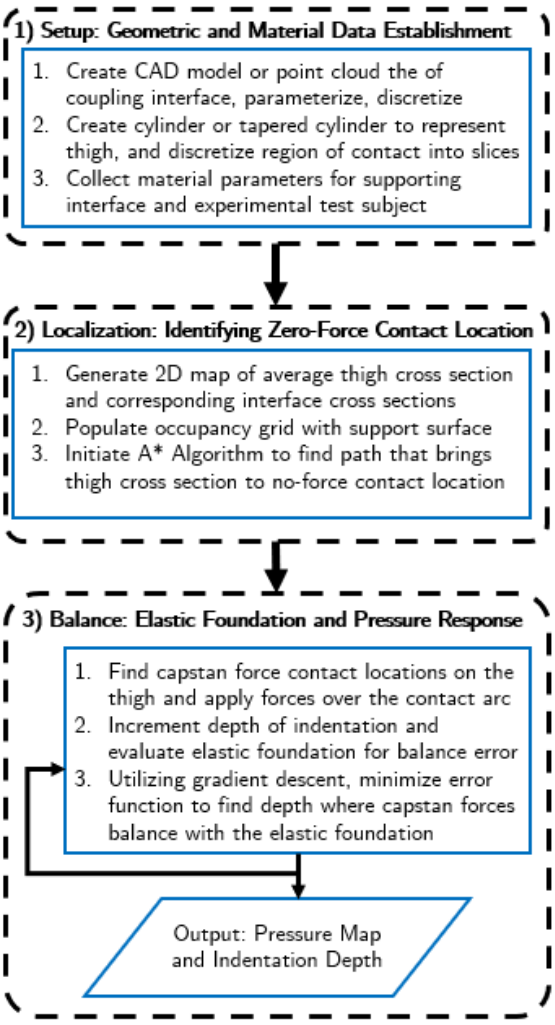


Fig. 2. Flowchart highlighting the three distinct phases of the algorithm to determine coupling surface interactions.

The H3 Exoskeleton was selected as the testing interface. An example of the coupling interface is shown in Figure 1, right. It is a rigid metal supporting surface with an ethylene-vinyl acetate (EVA) foam soft supporting surface. This algorithm is designed to be applied to coupling interfaces with similar mechanical composition.

B. Interface Surface Mechanical Properties

Elastic foundation models implement constants informed by material properties. ISO 3386-1:1986 [21] for cellular flexible materials in compression was selected to inform compression testing evaluation. The H3 Exoskeleton uses a generic non-labeled ethylene vinyl acetate (EVA) closed cell foam as a supporting interface, and was sampled for evaluation.

Two 50mmx50mm samples with the same thickness as the H3 supporting EVA surface (5 mm) was evaluated in compression up to 100N in quasi static loading conditions [22]. Young's modulus was found (0.7629 MPa) from the initial linear elastic region [22]. The plateau region of EVA foam was not able to be characterized due to hardware limitations. Figure 3, showcases the experimental setup, and stress-strain. The Poisson's ratio is assumed negligible for open-cell foams from collapse under compression [22].

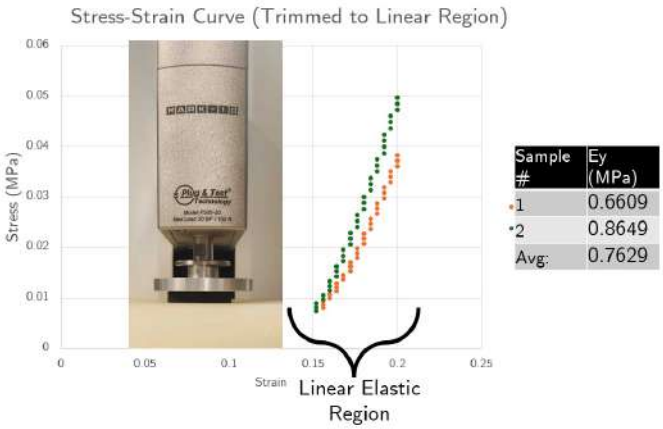


Fig. 3. Material testing setup and linear elastic compression region for the EVA foam used by the H3 exoskeleton on the coupling interface. Region of no-load strain was removed to highlight the linear elastic region.

A mannequin limb was used in the experimental evaluation to reduce the number of compliant interfaces that must be simulated. The mannequin thigh, as such, was assumed and treated as rigid, and was not characterized.

C. Defining Interface and Indenter Geometry

Interface geometry can be broken into stacked slices that represents the coupling interface in the cross-sectional transverse plane. These slices are treated as uncoupled to limit interface interactions to 2 dimensions. The thickness of the selected slices can vary; however, for simple interfaces, such as the H3 interfaces with no variation with height (Figure 1), then the driving factor for slice thickness should be height variation along the length of user limb.

Coupling interface geometry for the H3 exoskeleton was found by reconstructing the interface in SolidWorks. With

a CAD model, the surface may be cut and the transverse outer edge converted into a point cloud using DXF files. The point cloud is then converted into an equivalent high-dimensional spline and points are interpolated to achieve a minimum segment length between points (1 mm). Figure 4 highlights the example curvature.

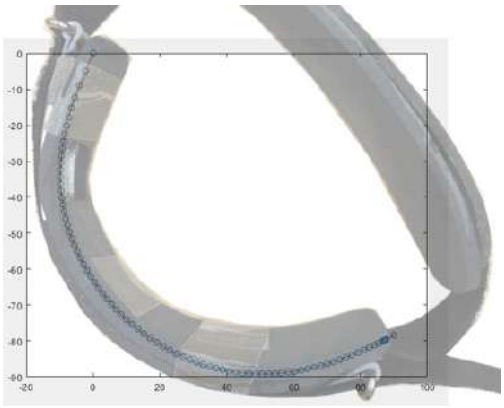


Fig. 4. Equivalent spline for the H3 coupling interface. Interfaces with variation in curvature along interface height require additional splines.

The indenting surface represents the user's limb, in this case a mannequin. The CAD mannequin was sliced along the center of the contact region and the same process was followed as the interface to retrieve a point cloud thigh cross section. To simplify the process, an assumed cylinder or tapered cylinder may be chosen if no particular user cross section can be used.

D. Identifying Zero-Force Contact of Body Segment

Initial no force contact locations are the points or curves where two bodies may be adjacent in contact without applied force [23]. The initial zero-force contact location determines where indentation and pressure begins for elastic foundations. Considering exoskeleton donning is difficult to perform, known initial configurations may be hard to find, and selecting a random location for initial contact may not be representative of the use case.

A heuristic method for initial contact configuration is proposed to determine initial zero-force contact. When aiding someone into the device, it is assumed the objective is to situate the user securely within the convex hull. In the case of the H3 Exoskeleton where no clear goal location can be identified, the furthest outside points of the surface are selected, seen in Figure 5, left.

Using these assumptions, an A-star path algorithm is proposed. With the center of the simulated limb cross section as the control point, the objective is to find the location/position closest to the objective goal within the convex hull. Each thigh slice is stored in cylindrical coordinates and referenced to prevent overlap. A visualization of an example trajectory path and grid configuration can be seen in Figure 5.

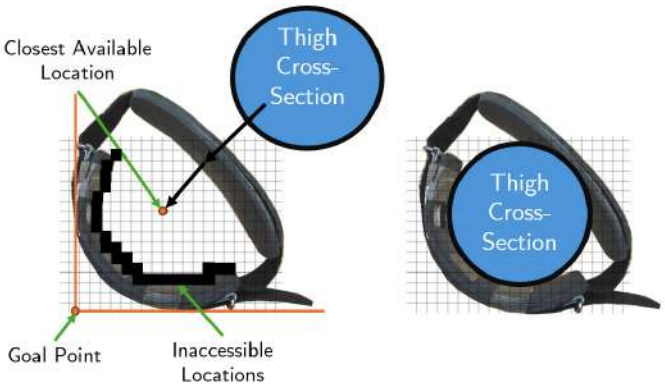


Fig. 5. Visualization of the A* algorithm as it has been applied to the H3 exoskeleton. Without a clear inflection point, the most extreme outer points have been defined as the goal for zero force contact.

E. Estimating Net Strapping Force

The hook-and-loop strap on the coupling interface provides securing forces that act as input forces for the elastic foundation reaction. During donning, a range of applied tensions is expected at different coupling interfaces, and between donning sessions. Evaluating a range of strapping tensions is necessary to systematically evaluate coupling interface performance.

For interfaces with a securing soft surface that wraps around the user's limb, like hook-and-loop straps, a generalized capstan clamping approach may be used [24]. Capstan forces relate tension in a rope-like material to a change in curvature. The governing equations for capstan forces are shown in eq. 1, and visualized in Figure 6, left. T is the tension in the rope, $d\Theta$ is a slice of the curvature, and dN is the force normal to the surface curvature.

$$dN = T * d\Theta \tag{1}$$

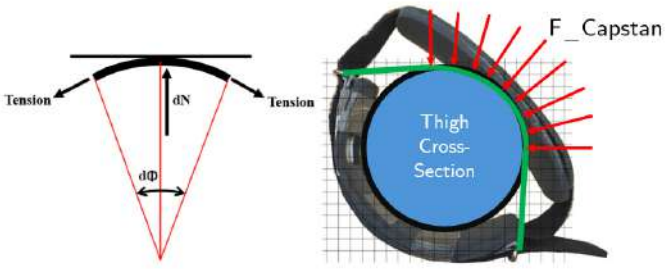


Fig. 6. Visualization of capstan forces applied to the thigh.

Capstan force values may be found within the local coordinate system by "wrapping" curvature from the loop mount location to the simulated thigh, around the surface, and to the terminal loop. The length of the curvature arc on the thigh is determined by locating the tangent line between the strap mounting locations and simulated thigh cross section. An example of the strap securing configuration in simulation can be found in Figure 6, right. Strapping tension varies along the

contacting surface, influenced by the relative friction between the two surfaces. A coefficient of $mu = 0.15$ was selected, from frictional properties between Nylon - the surface of the mannequin thigh [25].

F. Elastic Foundation Formulation

Elastic foundations are simplified representations of complex contact mechanics problems into analogous spring and shear layer representations [17]–[20]. Two elastic foundations, Winkler and Pasternak, were implemented with the assumption that only the EVA foam interface was compliant.

The Winkler foundation is the simplest elastic foundation approximation. The pressure-displacement relationship is defined in eq. 2, where k, the foundation modulus, is analogous to the spring constant and p, is the applied force. Figure 7 illustrates the Winkler foundation.

$$p\left(x,y\right) = kw\left(x,y\right) \tag{2}$$

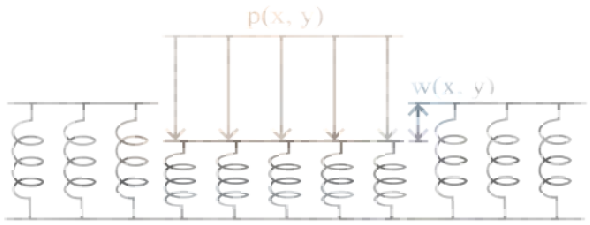


Fig. 7. Example of a Winkler foundation with discrete uncoupled springs.

The Pasternak foundation has a shear layer over top of the springs that allows for forces to be transmitted transversely and deform adjacent springs. The load-deflection relationship for the Pasternak foundation is given by eq. 3, where G is a modified shear modulus, visualized in Figure 8.

$$p\left(x,y\right) = kw\left(x,y\right) - G\nabla^2 w\left(x,y\right) \tag{3}$$

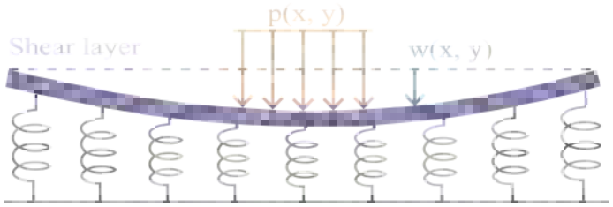


Fig. 8. Example of a Pasternak Foundation

The two constants k and G are typically calculated as a function of the foundation's material properties [17]. The relationships are as follows in eq. 4 and eq. 5:

$$k = \frac{E_{Young}}{(H * (1 - v^2))} \tag{4}$$

$$G_{foundation} = \frac{G_{shear} * H_{Hetenyi}}{6} \tag{5}$$

Where:

- H - Width of the supporting interface
- $H_{Hetenyi}$ - The depth of the shear layer [17].
- v - Poisson's ratio - zero for EVA foam

Using the depth of indentation in the two principal global coordinate directions as control variables (X,Y), an optimization approach may be implemented to find the relative position of the limb cross section to satisfy the goal condition minimizing error in eq. 6:

$$\min_{\delta} \quad \left(P - \sum_{n=-a}^{a} p_i \Delta x\right)^2 \tag{6}$$

Where P denotes the total applied force from capstan forces and p denotes the reaction of the elastic foundation for any individual cell summed over the contact region. Only compressive interactions are observed, and it is assumed that no friction or sticking is present at the interface. For the Pasternak foundation, an additional constraint must be solved for the point of separation on surfaces.

When the elastic foundation is mapped to the support interface, each segment of the spline is assigned an elastic element normal to the rigid backing. Elastic foundation resistance is determined first in the local coordinate system using cylindrical coordinates and relative indentation depth.

Depth of indentation is determined by overlapping indenter point clouds, with the supporting interface cells. Indentation depth is found by the normal of the relative slope between points, as seen in Figure 9. If multiple particles fall underneath a contact arc, depth of contact is averaged for that cell. All forces are then summed and used in eq. 6.

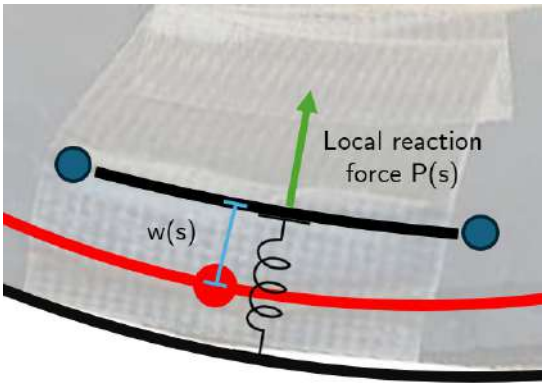


Fig. 9. Visualization of the particle calculation underneath.

The user thigh is then shifted based on a gradient descent approach scaled to the error from an initial small guess, with a small learning rate ($\gamma = 0.05$) to avoid large oscillations or overshooting. The final position and elastic foundation force vectors are used to determine pressure normal to the interface that balances the applied capstan forces.

G. Validation of Algorithm

To validate the relative accuracy and effectiveness of this algorithm in predicting interface pressure, a single isolated

coupling interface from the H3 Exoskeleton (Figure 1, right) and a mannequin leg, is shown in Figure 10. Testing was performed upright to avoid introducing gravitational forces. Regions of contact and orientation were marked and measured for replication in simulation.

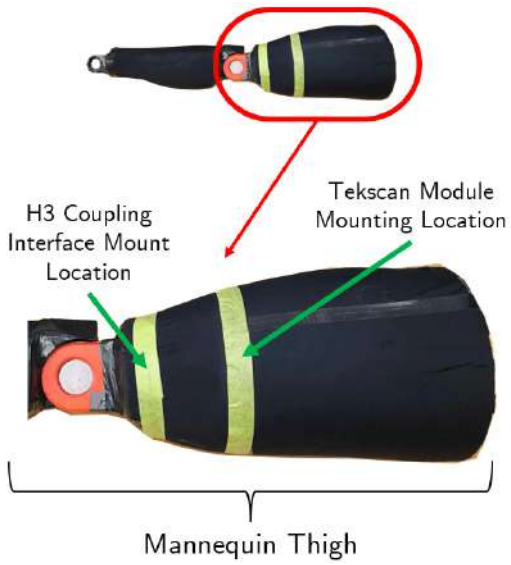


Fig. 10. Mannequin leg utilised for experimental evaluation. Made of rigid PLA, with 3D geometry drawn from scanning. Locations of sensor mounting and strap mounting are marked with green tape.

The pressure sensor used, Tekscan-MDL 9811E, comprises of 96 individual FSRs over a 203.2 by 76.2 mm area. The sensor was secured to the mannequin to avoid crimping and/or creasing, within the marked region of contact, seen in Figure 10 and Figure 11, and calibrated for zero load. A comparison of peak, average, and general trends in pressure will be analyzed, with details in subsequent sections.

A range of applied tension force values was evaluated using a handheld load cell. Three tests ranging from 30 to 50 Newtons was evaluated, tested, and collected with the Tekscan sensors. The experimental setup in Figure 11 shows 3 angles to indicate relative positions relative to the mannequin, sensor, and H3 coupling interface.



Fig. 11. Experimental setup of mannequin, H3 coupling interface and Tekscan sensor. The strap was held in place between tests to keep the cross-sectional area consistent between uses.

III. Results

Results include experimental and simulated pressure maps. Data is presented within the surface frame respective to the Tekscan (for experimental results). The Tekscan was limited to mounting to the thigh without crimping or folding excessively due to the securing hook-and-loop strap during donning. The pressure map generated from simulation is oriented to the surface of the coupling interface.

A. Experimental Pressure Values and Relationships

Peak and average pressures were evaluated over active Tekscan cells covered by the coupling interface. The pressure maps taken from the Tekscan sensor were averaged over a labeled collection period. An example of the collection, and processing can be seen in Figure 12.

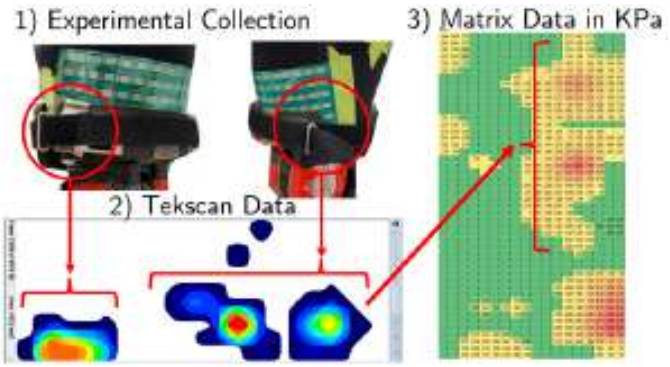


Fig. 12. Experimental setup and collection. Corresponding resulting Tekscan measurement for 50N pull test (maximum load), and the processed average data for the load in a matrix format for analysis.

Values for analysis from the Tekscan data include average observed pressure, peak pressures, and total active area. Table I contains the values for each of the three tests.

TABLE I
EXPERIMENTAL DATA COLLECTED FROM THE TEKSCAN MDL SENSOR

Test–Pull (Newtons)	Peak Pressure (KPa)	Average Pressure (Kpa)	Total active area/ Number of cells
27-29	76.58	14.99	27.7%
39-41	70.34	12.3	39.1%
48-52	82.34	12.36	62.5%

Notably, average pressure remain relatively stationary with increasing applied force, while surface area increases. Peak pressure does rise in the final test with a large increase in surface area. Surface area changes dominate the pattern of applied tension over this small sample size.

B. Simulated Elastic Foundation Pressures

Table II, contains the Winkler pressure information, and Table III contains the Pasternak pressure information. Each method of defining the coupling interface remained relatively similar, with small differences in pressure, where the Pasternak foundation had increased contact depth. The Winkler

spring for normal indentation depth was the primary driving constant in pressure during simulation. Raised points at the edges generated the most pressure at the edges of the convex hull, primarily due to a mismatch in overlapping curvature.

TABLE II

SIMULATED WINKLER FOUNDATION PRESSURES.

Test–Pull Newtons	Peak Pressure (KPa)	Average Pressure (Kpa)	Total active area/ Number of cells
28	295.35	115.19	47.66%
40	350.03	143.02	53.13%
50	395.28	168.47	55.47%

TABLE III

SIMULATED PASTERNAK FOUNDATION PRESSURES.

Test–Pull Newtons	Peak Pressure (KPa)	Average Pressure (Kpa)	Total active area/ Number of cells
28	295.23	112.47	48.44%
40	350.40	138.54	54.69%
50	395.27	165.51	56.25%

An example of an overlapping contact arc may be seen below in Figure 13 for a balanced Capstan - Elastic Foundation equilibrium. This point cloud informs the elastic foundation response using cylindrical coordinate overlap.

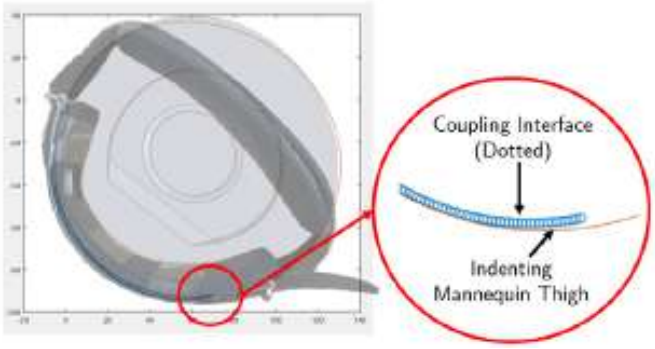


Fig. 13. Point cloud representation of overlapping support surface and thigh indenter equilibrium. The blue dotted surface represents the coupling interface, while the orange outline visualizes the contact of the thigh.

C. Comparison

Measured Tekscan peak and average pressure magnitudes were significantly lower than both Pasternak and Winkler model predictions across all three test-pull conditions. Measured total active area was also smaller than predicted model results, except at the highest pull condition. Trends in average active area were similar with increasing pull magnitude. Trends in measured average pressure, which were observed to decrease with increased pull magnitude, did not correspond to predicted model results. Discrepancies in model performance will be addressed in the next section.

A graph comparing the pattern of pressure loading along the surface is shown in Figure 14. As a result of treating the thigh cross section as an extruded cylinder at the point of contact, each simulated cell is treated as in contact with the interface at the coupling point along the length of the thigh. The lack of a vertical pressure gradient is explained by the assumption of no variation in the vertical contact direction.

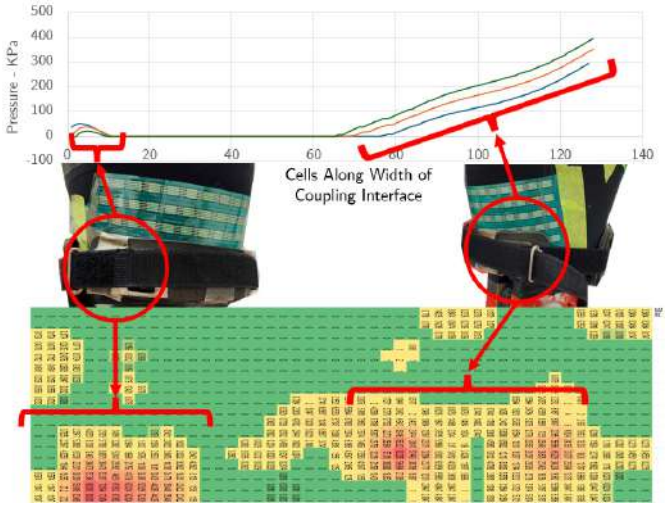


Fig. 14. Visual comparison of the simulated pressure map from the algorithm (top) and the Tekscan heatmap (bottom) pressure locations (red indicates high load). The top graphic showcases the low (28N), middle (40N) and high (50N), strap tension conditions. The active area of the Tekscan is 62.5% while the experimental predicted area is 56.25%. Brackets highlight pressure regions and their respective area on the experimental setup.

IV. DISCUSSION

This paper proposes a novel computational model utilizing interface geometry and strapping tension to predict the support surface static pressure field generated by elastic foundations during the donning process. Accuracy of the proposed computational method was validated by comparing measured and simulated pressure fields. While measured pressure magnitudes were significantly lower than model predictions, likely due to model assumptions, similar patterns in pressure magnitude and spatial distribution were observed.

A. Performance and application

Contact between a user and the robotic coupling interface is a complex system. Factors such as friction, shearing, relative geometric positions and configurations alter the conditions and define modes of contact. With increasing strapping tension, experimental peak and average pressures follow a similar pattern, decreasing in magnitude before increasing at the final strapping tension, while total active area increases with applied tension.

Discrepancies in pressure-area behavior is potentially attributable to unmeasured shear and friction forces shifting or rotating the coupling interface on the thigh. Once shifting is initiated, the configuration of contact, and relative depth of contact may shift as a combination of rotational and translational forces. Shifting may cross regions of larger

peak pressure before settling into an area with increased contact, but not necessarily increased pressure. Regions of peak pressure on the Tekscan are correlated with raised surfaces on the mannequin thigh and outer edges of the H3 interface overlapping, seen in Figure 14, highlighted in red. Differences in location and magnitude of pressure between experimental and simulation results may be influenced by the placement of the Tekscan sensor on the mannequin, while simulation evaluates the coupling interface surface, resulting in a mismatch of surface normal slope.

Simulation of the coupling interface yielded pressure magnitudes higher than measured results. While not ideal, loading patterns appear similar when examining overlapping regions of contact at raised surfaces, and the location of regions of no contact. In Figure 12, the regions of no contact are represented similarly in the simulated data with two distinct regions of peaking pressure. The major distinction between the two is the relatively small peak force on the left of Fig. 14, mismatching the experimental values in the same region. Discontinuation in force on the right of Fig. 14 (bottom) was not modeled, likely due to the simplifications made for the interface curves and the prevention of sliding or bunching of material. Pressure magnitudes in the current iteration of this model are not useful for design (i.e., exact values), but are typically difficult to use when designing for a wide user population. Relative ratios of peak and gradient pressures are more informative of mechanical interaction, and may be used to inform design. Additional limitations exist in the inability to model frictional and shear pressures, major factors in skin injury and static-dynamic interaction that limit the applicability of this model currently.

The Pasternak and Winkler foundation performed relatively similarly, attributable to the contact depth being shallow, and the curvature of the thigh and the supporting interface being relatively similar. Hence, the contributions of the Pasternak shear layer are relatively small compared to the Winkler foundation in this contact configuration.

B. Experimental Study Limitations

Limitations in experimental validation may contribute to the differences observed in evaluation. Due to limitations of the Tekscan MDL sensor, placing it directly on the coupling interface was not possible without damaging the sensor. By measuring on the user's thigh, it is harder to match geometric features with heightened normal pressure, both due to the potential for mismatched surface curvature and positioning. In the experimental setup, the coupling interface was removed from the exoskeleton frame. When tension was applied through the strap, rotational motion occurred which may have displaced the strap relative to the Tekscan. While the test mannequin possessed similar geometry to an actual user's thigh, the material was rigid, not compliant. Future validation should include a compliant cross-section to better represent user application of this model.

C. Model Limitations

Implementing hyper-elastic material models over linear elastic constants may improve soft material responses [17]. Currently moment forces, frictional/tangential shear effects, and time-dependent (viscous) components are not accounted for in the foundation. Frictional forces may allow additional surfaces that contribute very little in this current iteration (i.e., with little indentation depth) to contribute to resisting motion. Considering measured average pressure stagnated despite an increasing applied tension may be attributed to friction, and including these contribution via modeling represents a promising approach for improvement.

Material properties primarily influence elastic foundation equations, and can be changed by utilizing more accurate and improved material testing methods. EVA and other open-cell foams have a plateau region of loading that was not accounted for [17]. Including neo-Hookean governing models [17], [22], may potentially explain the experimental pressure to increasing area relationship. Additionally, reactions with respect to the mannequin are relatively simple due to rigid assumptions, but contact with users will include compliant interaction that is currently not accounted for.

Interface and indenter geometry is defined by the desired complexity of the simulation. In the current implementation, a simplified approach is examined. Concessions were made in simplifying the mannequin thigh to a single average curve. Future works utilizing scanning techniques, or curves from CAD models as opposed to approximations, are warranted to investigate the influence of higher geometrical accuracy.

Localization required the most heuristic assumptions to be made on how a coupling interface may come into contact with a user donning the device. It was assumed that, with a visual goal target, a clinician would move the limb towards that goal/point. A clear inflection point such as a "U" hull, or in the case of this simulation the points closest to the outermost surface edges in the global coordinate space. Limitations of this approach are pronounced when considering how some configurations that would be achieved in practice, may only be achieved by applying pressure to move past regions of high friction, or elastic resistance that would be avoided in purely zero-force localization.

Capstan forces rely heavily on the curvature of the wrapping surface, highlighting the influence relative surface-indenter orientation has on the model. Changing initial orientation of the thigh cross section and supporting surface will alter where tangency is, the applied forces, and what geometry of the thigh intersects with the coupling interface. Improvements in the approach to how the elastic foundation is optimized may still be made. Shifting, or jumping, over regions of peak pressure with smaller contact areas, into configurations that rely more heavily on friction to balance with larger surface areas may be the cause of the pressure-area relationship found in experimentation. Using global optimization techniques to search for minima past the first equilibrium may locate more accurate contact configurations.

V. Conclusion and Future Work

Assistive lower-limb exoskeletons provide assistance and rehabilitation in gait, posture and balance to those affected by mobility impairments. The coupling interface is a critical component of an exoskeleton's functionality and, until recently, has not been the focus of design and research in exoskeleton development. Initial pressures and coupling interface composition directly influence the kinetics and kinematics of exoskeleton-user interactions [1], [15], [16], and excessive pressures, and steep pressure gradients, can influence the formation of skin injuries [1], [10], [11]. This knowledge of exoskeleton interaction, and skin injury, highlights the need for an increased focus on the coupling interfaces between user and device in exoskeleton research.

The algorithm presented herein models the initial donning pressure and deformation map for a coupling interface. Using this algorithm, initial pressure, risky areas and an evaluation of trends in coupling interactions may be identified. With future work and improvements to the model the goal becomes applying this model in the evaluation and optimization of novel interface designs for exoskeletons.

Utilizing interface and user-subject geometry coupled with compliant elastic foundations, this algorithm determines static pressure field interactions during donning. After localizing the subjects in 3D space for no-force contact locations, capstan forces are applied to determine initial securing conditions which balance with the elastic foundation. This generates a pressure field that describes general patterns of pressure and areas of contact for exo donning.

As a preliminary algorithm, future work is needed to improve the applicability of this algorithm to alternative coupling interface designs, dynamic loading conditions and expanded out to include the entire exoskeleton. With additional contributions, the goal would be to create an environment where adjustments to interface geometric design, placement location, and materials would be controlled for idealized interactions in exoskeletons.

References

[1] S. Massardi, D. Rodriguez-Cianca, D. Pinto-Fernandez, J. C. Moreno, M. Lancini, and D. Torricelli, "Characterization and Evaluation of Human–Exoskeleton Interaction Dynamics: A Review," Sensors, vol. 22, no. 11, p. 3993, Jan. 2022, doi: 10.3390/s22113993.

[2] C. Siviy et al., "Opportunities and challenges in the development of exoskeletons for locomotor assistance," Nature Biomedical Engineering, pp. 1–17, Dec. 2022, doi: 10.1038/s41551-022-00984-1.

[3] Y. He, D. Eguren, T. P. Luu, and J. L. Contreras-Vidal, "Risk management and regulations for lower limb medical exoskeletons: a review," Medical Devices: Evidence and Research, vol. Volume 10, pp. 89–107, May 2017, doi: 10.2147/mder.s107134.

[4] A. S. Gorgey, "Robotic exoskeletons: The current pros and cons," World Journal of Orthopedics, vol. 9, no. 9, pp. 112–119, Sep. 2018, doi: 10.5312/wjo.v9.i9.112.

[5] A. Schiele and F. C. T. van der Helm, "Kinematic Design to Improve Ergonomics in Human Machine Interaction," IEEE Transactions on Neural Systems and Rehabilitation Engineering, vol. 14, no. 4, pp. 456–469, Dec. 2006, doi: 10.1109/tnsre.2006.881565.

[6] R. Mallat, M. Khalil, G. Venture, V. Bonnet, and S. Mohammed, "Human-Exoskeleton Joint Misalignment: A Systematic Review," Oct. 2019, doi: 10.1109/icabme47164.2019.8940321

[7] J. Bessler-Etten, L. Schaake, G. B. Prange-Lasonder, and J. H. Buurke, "Assessing effects of exoskeleton misalignment on knee joint load during swing using an instrumented leg simulator," Journal of NeuroEngineering and Rehabilitation, vol. 19, no. 1, Jan. 2022, doi: 10.1186/s12984-022-00990-z.

[8] Stefano Massardi et al., "Relevance of hazards in exoskeleton applications: a survey-based enquiry," Journal of Neuroengineering and Rehabilitation, vol. 20, no. 1, May 2023, doi: 10.1186/s12984-023-01191-y.

[9] M. del C. Sanchez-Villamañan, J. Gonzalez-Vargas, D. Torricelli, J. C. Moreno, and J. L. Pons, "Compliant lower limb exoskeletons: a comprehensive review on mechanical design principles," Journal of NeuroEngineering and Rehabilitation, vol. 16, no. 1, May 2019, doi: 10.1186/s12984-019-0517-9.

[10] R. B. van Dijsseldonk, I. J. W. van Nes, A. C. H. Geurts, and N. L. W. Keijsers, "Exoskeleton home and community use in people with complete spinal cord injury," Scientific Reports, vol. 10, no. 1, p. 15600, Sep. 2020, doi: 10.1038/s41598-020-72397-6.

[11] Al Aboud AM, Manna B. Wound Pressure Injury Management.. In: StatPearls. Treasure Island (FL): StatPearls Publishing; 2024 Jan-. Available from: www.ncbi.nlm.nih.gov/books/NBK532897.

[12] R. Baud, A. R. Manzoori, A. Ijspeert, and M. Bouri, "Review of control strategies for lower-limb exoskeletons to assist gait," Journal of NeuroEngineering and Rehabilitation, vol. 18, no. 1, Jul. 2021, doi: 10.1186/s12984-021-00906-3.

[13] P. Manns, M. Sreenivasa, M. Millard, and K. Mombaur, "Motion Optimization and Parameter Identification for a Human and Lower Back Exoskeleton Model," IEEE Robotics and Automation Letters, vol. 2, no. 3, pp. 1564–1570, Jul. 2017, doi: 10.1109/lra.2017.2676355.

[14] D. Shi, W. Zhang, W. Zhang, and X. Ding, "A Review on Lower Limb Rehabilitation Exoskeleton Robots," Chinese Journal of Mechanical Engineering, vol. 32, Aug. 2019, doi: 10.1186/s10033-019-0389-8.

[15] K. Langlois et al., "Investigating the Effects of Strapping Pressure on Human-Robot Interface Dynamics Using a Soft Robotic Cuff," IEEE Transactions on Medical Robotics and Bionics, vol. 3, no. 1, pp. 146–155, Feb. 2021, doi: 10.1109/tmrb.2020.3042255.

[16] A. Schiele and F. C. T. van der Helm, "Influence of attachment pressure and kinematic configuration on pHRI with wearable robots," Applied Bionics and Biomechanics, vol. 6, no. 2, pp. 157–173, Jul. 2009, doi: 10.1080/11762320902879961.

[17] D. Younesian, A. Hosseinkhani, H. Askari, and E. Esmailzadeh, "Elastic and viscoelastic foundations: a review on linear and nonlinear vibration modeling and applications," Nonlinear Dynamics, vol. 97, no. 1, pp. 853–895, May 2019, doi: 10.1007/s11071-019-04977-9.

[18] Y. Gonthier, J. McPhee, C. Lange, and J.-C. Piedbœuf, "A Contact Modeling Method Based on Volumetric Properties," Volume 6: 5th International Conference on Multibody Systems, Nonlinear Dynamics, and Control, Jan. 2005, doi: 10.1115/detc2005-84610.

[19] M. W. Hast, B. G. Hanson, and J. R. Baxter, "Simulating contact using the elastic foundation algorithm in OpenSim," Journal of Biomechanics, vol. 82, pp. 392–396, Jan. 2019, doi: 10.1016/j.jbiomech.2018.11.025.

[20] D. A. Dillard, B. Mukherjee, Preetika Karnal, R. C. Batra, and J. Frechette, "A review of Winkler's foundation and its profound influence on adhesion and soft matter applications," Soft Matter, vol. 14, no. 19, pp. 3669–3683, May 2018, doi: 10.1039/c7sm02062g.

[21] Polymeric materials, cellular flexible — Determination of stress-strain characteristics in compression, ISO 3386-1:1986, 1986.

[22] H. Chen, D. Sun, L. Gao, X. Liu, and M. Zhang, "Mechanical Behavior of Closed-Cell Ethylene-Vinyl Acetate Foam under Compression," Polymers, vol. 16, no. 1, p. 34, Jan. 2024, doi: 10.3390/polym16010034.

[23] V. L. Popov, CONTACT MECHANICS AND FRICTION : physical principles and applications. 2018.

[24] K. Jayawardana, "A Generalisation of the Capstan Equation and a Comparison Against Kikuchi and Oden's Model for Coulomb's Law of Static Friction," arXiv (Cornell University), Jan. 2020, doi: 10.48550/arxiv.2012.13353.

[25] M. Watanabe, M. Karasawa, and K. Matsubara, "The frictional properties of nylon," Wear, vol. 12, no. 3, pp. 185–191, Sep. 1968, doi: 10.1016/0043-1648(68)90525-5.

Multi-modal Muscle Activation Modeling using Koopman Operator Linearization for an Ankle Exoskeleton

Noor Hakam[1], Mayank Singh[2], Nitin Sharma[1, 2]
[1]Lampe Joint Department of Biomedical Engineering
North Carolina State University & the University of North Carolina at Chapel Hill
Raleigh, NC 27606 USA
Email: nzhakam@ncsu.edu, nsharm23@ncsu.edu
[2]Department of Electrical Engineering
North Carolina State University
Raleigh, NC 27606 USA
Email: msingh25@ncsu.edu

***Abstract*—Gait impairments impact mobility and quality of life, necessitating intelligent rehabilitation devices that utilize dynamic models to improve the human-machine interaction and provide effective assistance. This study presents a data-driven model that integrates Koopman operator linear estimations with fused surface electromyography (sEMG) and ultrasound (US) imaging for estimating volitional ankle torque throughout the gait cycle. The Koopman operator estimates the nonlinear, phase-dependent dynamics of ankle motion, while the fusion of sEMG and US signals enhances muscle activation predictions by combining electrical and morphological insights. This framework demonstrates the potential to improve state and volitional torque estimation accuracy, laying the groundwork for individualized exoskeleton assistance and enhanced gait rehabilitation strategies.**

I. Introduction

Gait impairments precipitated from neurological disorders or injuries present profound challenges for mobility, independence, and quality of life [1], [2]. For many with these impairments, regaining the ability to walk independently, minimizing gait abnormalities, and increasing walking speed and endurance are primary goals [3]. As such, the use of devices that emphasize muscle activation while aiding in movement completion is highly encouraged.

Exoskeletons are one such type of wearable device that have emerged as promising tools to support individuals with various types of gait impairments [4], [5], [6], [7], [8]. In this paper, we specifically focus on those that impact the critical role that the ankle plays in walking. Ankle "push-off" during the late stance phase and prolonged foot lift during the swing phase are both vital features of a energy efficient gait cycle that are often heavily impacted by neurological impairments [9], [10], [11]. Ankle exoskeletons capable of assisting with plantarflexion and dorsiflexion are therefore especially useful in gait rehabilitation.

An exoskeleton with a model of the user's volitional capabilities can estimate how much joint torque needs to be compensated to complete the gait cycle. Accurate modeling of voluntary ankle torque is challenging due to the nonlinear, phase-dependent dynamics of walking. The application of Koopman operator theory (KOT) offers a modeling solution to the complexities of gait. KOT transforms nonlinear dynamics into a higher-dimensional space, enabling a linear approximation of gait across stance and swing phases [12], [13]. Such linearization techniques simplify the computational demands of real-time control and improve the scalability of predictive models in response to dynamic changes in human gait. Theoretically, a Koopman operator is infinite-dimensional and can linearly describe the evolution of the system's observables. Therefore, to compute a practical estimation, we use extended dynamic mode decomposition (EDMD), which approximates a finite-dimensional Koopman operator using data-driven methods.

To enhance the EDMD model's ability to predict volitional torque, this study incorporates real-time muscle activation signals derived from multi-modal sources: ultrasound (US) imaging and surface electromyography (sEMG). Torque contributions during walking are dynamic, influenced by complex physiological factors such as muscle fatigue, activation levels, and coordination with other joint movements [14], [15]. Traditionally, sEMG has been the primary modality for estimating muscle activation by recording electrical activity in muscle fibers, but it has notable limitations, including susceptibility to noise and difficulty in accessing deep muscle layers [16]. Ultrasound imaging, conversely, provides a direct visualization of muscle morphology, offering higher spatial resolution and the ability to capture mechanical aspects of muscle contractions which are correlated with force generation [17], [18], albeit at a lower sampling frequency.

By combining sEMG and US imaging data, this study leverages the complementary strengths of these two modalities. Ultrasound-derived echogenicity can assess deeper muscles (e.g., the soleus) and has shown potential to monitor changes in muscle architecture that reflect activation and fatigue levels [17], [18]. When fused with sEMG signals,

which provide a high-frequency electrical assessment of superficial muscle activity, the combined data allow for a more comprehensive and robust estimation of muscle activation states. This integration improves the fidelity of volitional torque estimates, which is particularly critical for gait assistance applications where accurate prediction of user intent is essential for seamless interaction with the exoskeleton. Furthermore, by employing a sequential multirate observer, this framework mitigates the mismatch in sampling rates between the low-sampled US signals and high-sampled sEMG signals, providing continuous and accurate volitional torque estimates suitable for real-time control applications.

The primary contribution of this study is an a Koopman operator linear estimation of gait dynamics utilizing fused US and sEMG muscle activation signals. The proposed data-driven model of ankle dynamics and muscle activation data aims to lay the groundwork for individualized optimal assistance, fostering natural gait patterns and reducing unnecessary dependency on robotic support.

II. Problem Formulation

A. Ankle Joint Dynamics

During a gait cycle, ankle movement can be modeled as continuous dynamics within the swing and stance phases, with a discrete transition event between the two phases [19]. Therefore, these dynamics, modeled as a switched system to account for the transition, is expressed as

$$\begin{bmatrix} J^P\ddot{\theta} + f^P(\theta,\dot{\theta}) \\ J^D\ddot{\theta} + f^D(\theta,\dot{\theta}) \end{bmatrix} = \begin{cases} \tau^P + \tau^m + \tau^{ext} & t \in t_{st} \\ \tau^D + \tau^m, & t \in t_{sw} \end{cases} \quad (1)$$

where $\zeta = P, D$ represents the ankle dynamics driven by ankle plantarflexors during the stance phase, timed as $t_{st} \coloneqq [T_{start}, t_{stance}]$, and ankle dorsiflexors during the swing phase, timed as $t_{sw} \coloneqq [t_{swing}, T_{end}]$, respectively. $J^\zeta \in \mathbb{R}^+$ is the unknown inertia term of the foot along the dorsiflexion and plantarflexion axis of rotation, and θ, $\dot{\theta}$, and $\ddot{\theta} \in \mathbb{R}$ denote the angular position, angular velocity, and angular acceleration, respectively. $f^\zeta(\theta,\dot{\theta})$ is composed of the musculoskeletal viscosity torque term, musculoskeletal elasticity, and the gravitational term acting on the ankle. The explicit definitions of these functions can be obtained from [20], [21]. τ^{ext} is the external plantarflexion torque caused by the ground reaction forces.

The torque driven by the exoskeleton motor is given as

$$\tau^m(t) \quad = \quad K_m i(t), \quad (2)$$

where $K_m \in \mathbb{R}^+$ is a constant motor gain and $i(t) \in \mathbb{R}$ is the controlled current. The volitional ankle torque is described by

$$\tau^\zeta \quad = \quad r^\zeta(\theta) F_m \eta_1^\zeta(\theta) \eta_2^\zeta(\dot{\theta}) a^\zeta, \quad (3)$$

where $r^\zeta(\theta) \in \mathbb{R}^+$ represents the gait phase-specific moment arm for the muscle tendon force, which is a function of the joint position. The explicit functional form is described in [22]. The moment arm is a continuously differentiable, positive, and bounded function with a bounded first-order time derivative. $F_m \in \mathbb{R}^+$ represents the constant maximum isometric muscle contraction force at the equilibrium position. Variables $\eta_1^\zeta(\theta)$, $\eta_2^\zeta(\dot{\theta})$ denote the force-length and force-velocity fascicle terms [23], and both are continuously differentiable, non-zero, positive, and bounded functions.

For each phase t_{st} and t_{sw}, we can rewrite the system dynamics in (1) by selecting $\theta_1 = \theta$ and $\theta_2 = \dot{\theta}$.The equivalent state space representation for can be formulated as

$$\dot{x} = \begin{cases} f^P(x) + g^P(x,u^P), & \forall\ t \in t_{st} \\ f^D(x) + g^D(x,u^D), & \forall\ t \in t_{sw} \end{cases} \quad (4)$$

where $\dot{x} = \begin{bmatrix} \dot{\theta}_1 & \dot{\theta}_2 & \dot{a}^\zeta \end{bmatrix}^T$, $f^\zeta(x) \in \mathbb{R}^3$ are the system dynamics, and $g^\zeta(x,u^\zeta) \in \mathbb{R}^3$ are the actuation dynamics.

We can define an indicator function σ_k based on the gait phase time intervals for the stance and swing phases as

$$\sigma_k = \begin{cases} 0, & \forall\ t \in t_{st} \\ 1, & \forall\ t \in t_{sw} \end{cases}, \quad (5)$$

where the phase indicator σ_k takes the value 0 for the stance phase and 1 for the swing phase.

Using a zero order hold, these dynamics can then be discretized as

$$\begin{aligned} x_{k+1} \quad = \quad & (1-\sigma_k)\left(f^P(x_k) + g^P(x_k, u_k^P)\right) \\ & +\sigma_k\left(f^D(x_k) + g^D(x_k, u_k^D)\right) \end{aligned} \quad (6)$$

B. Muscle Activation and Ultrasound Echogenicity

Now discretized, the variable $a_k^\zeta \in [0,\ 1]$ from (3), which denotes the muscle activation level can be described by

$$a_k^\zeta = \delta^\zeta Y_k^{\zeta,emg} + (1-\delta^\zeta) Y_k^{\zeta,us} + v_k^\zeta \quad (7)$$

where $Y_k^{\zeta,\,emg}, Y_k^{\zeta,\,us} \in \mathbb{R}$ are the normalized measurements from the sEMG linear envelope and US imaging-derived echogenicity described in [24]. $\delta \in [0,\ 1]$ is a weighting variable, and v_k^ζ is a net additive white Gaussian noise signal. Echogenicity measurements from US images are defined by our previous work [18] , which has detailed methods for estimating real-time muscle activation during walking. At sampling instant k, echogenicity is calculated as

$$echo_k = \frac{1}{N_A N_L} \sum_{x=1}^{N_A} \sum_{y=1}^{N_L} I_k(x_{pos},\, y_{pos}), \quad (8)$$

where $N_A, N_L \in \mathbb{R}^+$ represent the number of pixels along axial and lateral directions of the region of interest, respectively. The term $I_k(x_{pos},\, y_{pos}) \in \mathbb{R}$ represents the US intensity information at the pixel location $(x_{pos},\, y_{pos})$ on the

image at sampling instant k from the logarithmically compressed imaging signals after the beamforming procedure.

C. Koopman Operator Framework

We consider the dynamics in (6) where the controlled state $x_k \in \mathcal{X}$ and input $u_k \in \mathcal{U}$ are sampled to form a finite set, $\mathcal{N}_c$. The Koopman operator acts on a function space $\mathcal{F}$ of mapping from $\mathcal{X}$ into $\mathbb{R}$, referred to as observables. The Koopman operator, $\mathcal{K}$, is an infinite-dimensional linear operator that models the time-based evolution of a composite function $\Lambda(x_k) \in \mathbb{R}$, which act as the $Koopman\ observables$, forward in time. Koopman operators are parameterized by x_k, u_kas follows:

$$\mathcal{K}\Lambda(x_k) \quad = \quad \Lambda(f(x_k, u_k)), \qquad \Lambda \in \mathcal{F} \tag{9}$$

where $\mathcal{K}$ maps observables $\Lambda(x_k)$ to the original state space dynamics in (6). A subspace is Koopman-invariant if

$$\mathcal{K}\Lambda \quad \in \quad \mathcal{F}, \quad \forall \Lambda \in \mathcal{F},\ \forall u \in \mathcal{U} \tag{10}$$

A dictionary of observables, $\chi : \mathcal{X} \to \mathbb{R}^{\mathcal{N}}$ is Koopman-invariant if its elements span a Koopman-invariant subspace. Since evaluation of the dictionary often involves "lifting" of the original state vector to a higher dimensional space, $\chi(x_k)$, the new state is commonly referred to as the lifted state. $\chi(x_k)$ is composed of the original states or nonlinear functions of the state that are $Lipschitz$ continuous. The extension to non-autonomous systems has been researched extensively recently, see [25], [26], [27]. For a non-autonomous system, the equivalent to (9) is given as

$$\mathcal{K}(\Lambda(x_k, u_k)) \quad = \quad \Lambda(f(x_k, u_k),\ h(x_k, u_k))\ \forall \Lambda \in \mathcal{F} \tag{11}$$

While this operator accurately describes a nonlinear system through an infinite-dimensional linear system, it is practically infeasible to implement. For practical feasibility, the infinite-dimensional operator, $\mathcal{K}$, is approximated using a finite dimensional operator, defined as $\tilde{\mathcal{K}}$, which is usually calculated using Extended Dynamic Mode Decomposition (EDMD) [25].

To derive the Koopman operators for each phase, we collect time-series data snapshots of the state data as $\{x_k\}_{k=1}^{M}$ where x_k represents the state at time step k, and control input data as $\{u_k^{\zeta}\}_{k=1}^{M}$, where u_k^{ζ} represents the control input at time step k during the stance and swing phases. We define the Koopman observable in lifted space, $\Psi_k(x, u^{\zeta}) \in \mathbb{R}^W$, to set up an EDMD problem. We can predict the linear evolution of the Koopman observable vector using

$$\Psi_{k+1}(x, u^{\zeta}) \quad = \quad \tilde{\mathcal{K}}\Psi_k(x, u^{\zeta}), \tag{12}$$

where $\tilde{\mathcal{K}}$ is the finite-dimensional Koopman operator approximation which maps the lifted-state observables forward in time. Using the state and control time-series snapshots, we populate the lifted-space data matrices with $M \in \mathbb{N}$ samples as

$$\begin{array}{rl} \mathcal{D}^{\zeta}{}_k & = [\Psi(x_1, u_1) \quad \Psi(x_2, u_2) \quad \cdots \quad \Psi(x_{M\circledast 1}, u_{M\circledast 1})] \\ \mathcal{D}^{\zeta}{}_{k+1} & = [\Psi(x_2, u_2) \quad \Psi(x_3, u_3) \quad \cdots \quad \Psi(x_M, u_M)] \end{array} \tag{13}$$

where $\mathcal{D}^{\zeta}{}_k,\ \mathcal{D}^{\zeta}{}_{k+1} \in \mathbb{R}^{W \times M}\ \forall\, k = 1, \ldots, M$, are the collected observable block snapshots from kinematic state measurements for each gait phase. The Koopman observable data matrix dynamically evolves as

$$\mathcal{D}^{\zeta}{}_{k+1} = \tilde{\mathcal{K}^{\zeta}}\mathcal{D}^{\zeta}{}_k, \tag{14}$$

where $\mathcal{D}^{\zeta}{}_k = \Psi_k(x, u^{\zeta}) = \begin{bmatrix}\Psi_x(x_k) & \Psi_u(u_k)\end{bmatrix}^T$. To obtain the control state and control flow maps in the lifted space, the approximated Koopman operator$\tilde{\mathcal{K}}$ can be further subdivided as

$$\tilde{\mathcal{K}^{\zeta}} = \begin{bmatrix}\tilde{\mathcal{K}}_{xx} & \tilde{\mathcal{K}}_{xu} \\ \tilde{\mathcal{K}}_{ux} & \tilde{\mathcal{K}}_{uu}\end{bmatrix}, \tag{15}$$

where $\tilde{\mathcal{K}}_{xx}$ represents the influence of the state observables, $\Psi_x(x_k)$, on the future state observables, and $\tilde{\mathcal{K}}_{xu}$ represents the influence of the control observables, $\Psi_u(u_k)$, on the future state observables. The terms $\tilde{\mathcal{K}}_{ux}, \tilde{\mathcal{K}}_{uu}$ in (15) refer to mappings that evolve the observations on control, which are ignored here. To determine the Koopman operator for each phase, $\zeta = \{P - stance\ phase,\ D - swing\ phase\}$, we set up a least-squares regression problem minimizing the error between the observed next step data, $\mathcal{D}_{k+1}$, and the prediction from $\tilde{\mathcal{K}^{\zeta}}\mathcal{D}_k$. The problem is formulated as

$$\begin{aligned} \tilde{\mathcal{K}^{\zeta}} \quad = \quad & \arg\min_{\tilde{\mathcal{K}}} \sum_{k=0}^{M\circledast 1} \left\| \begin{bmatrix}\Psi_x(x_{k+1}) \\ \Psi_u(u_{k+1})\end{bmatrix} \right. \\ & \left. - \begin{bmatrix}\tilde{\mathcal{K}}^{\zeta}_{xx} & \tilde{\mathcal{K}}^{\zeta}_{xu} \\ \tilde{\mathcal{K}}^{\zeta}_{ux} & \tilde{\mathcal{K}}^{\zeta}_{uu}\end{bmatrix} \begin{bmatrix}\Psi_x(x_k) \\ \Psi_u(u_k)\end{bmatrix} \right\|^2. \end{aligned}$$

The least-squares solution for $\tilde{\mathcal{K}}$ is given as

$$\tilde{\mathcal{K}^{\zeta}} = FG\ , \tag{16}$$

where

$$\begin{aligned} F &= \frac{1}{M}\sum_{k=0}^{M\circledast 1} \mathcal{D}_{k+1}\mathcal{D}_k^T, \\ G &= \frac{1}{M}\sum_{k=0}^{M\circledast 1} \mathcal{D}_k\mathcal{D}_k^T, \end{aligned} \tag{17}$$

where Moore-Penrose pseudoinverse G is utilized. Using the indicator function in (5) and the phase-based Koopman operator, the ankle motion dynamics during a complete gait cycle can then be represented as

$$\begin{aligned} \begin{bmatrix}\Psi_x(x_{k+1})\end{bmatrix} \quad = \quad & (1-\sigma_k)\begin{bmatrix}\tilde{\mathcal{K}}^P_{xx} & \tilde{\mathcal{K}}^P_{xu}\end{bmatrix}\begin{bmatrix}\Psi_k(x, u^P)\end{bmatrix} \\ & +\sigma_k\begin{bmatrix}\tilde{\mathcal{K}}^D_{xx} & \tilde{\mathcal{K}}^D_{xu}\end{bmatrix}\begin{bmatrix}\Psi_k(x, u^D)\end{bmatrix}. \end{aligned} \tag{18}$$

To obtain the prediction dynamics for the original state in (4), we compute the flow map between lifted-space observables $\Psi_k(x, u)$ and original state dynamics x_k. To recover x_k, we can describe the mapping between K$\Psi_k(x, u)$ and

x_k as $x_k = C\Psi_k(x,u)$, where $C \in \mathbb{R}^{3\times P}$ is obtained by solving the following least-squares problem:

$$\arg\min_{C} \quad \sum_{k=0}^{M\infty 1} \frac{1}{2}||C\Psi_k(x,u) - x_k||^2. \tag{19}$$

By solving (19) and substituting $\Psi_k(x,u) = C^{\infty 1}x_k$ into the lifted-space flow map (12), we obtain the linear prediction model for phase-based ankle motion dynamics during a complete gait cycle as

$$x_{k+1} = \tilde{A}^{\zeta}x_k + \tilde{B^{\zeta}}u_k^{\zeta}, \tag{20}$$

where

$$\tilde{A}^{\zeta} \quad = \quad C\tilde{\mathcal{K}}_{xx}^{\zeta}C^{\infty 1};\ \tilde{B}^{\zeta} = C\tilde{\mathcal{K}}_{xu}^{\zeta}C^{\infty 1}. \tag{21}$$

Using the indicator function, σ_k, the combined state dynamics can be written as

$$\begin{aligned} x_{k+1} \quad &= \quad (1-\sigma_k)\left(A^P x_k + B^P u_k^P\right) \\ &\quad +\sigma_k\left(A^D x_k + B^D u_k^D\right), \end{aligned} \tag{22}$$

where $x_k \in \mathbb{R}^3$ is the original state vector as described in (6), A^P, $A^D \in \mathbb{R}^{3\times 3}$,$B_1$, $B_2 \in \mathbb{R}^{6\times 2}$ are the Koopman operator-based linear state space mappings, and u_k^P, $u_k^D \in \mathbb{R}$ are the control inputs for assisting ankle plantarflexion and dorsiflexion during a gait cycle.

III. Experimentation Validation of the Proposed Koopman Approach

A. Experimental procedure

This treadmill walking study was conducted with approval from the Institutional Review Board (IRB) at NC State University (IRB #20602). A 24-year-old able-bodied female participant (height: 168 cm) without neuromuscular disabilities or walking difficulties was recruited. She walked at 0.5 m/s on a treadmill (Bertec, Columbus, OH, USA) outfitted with load cells measuring ground reaction forces (GRF) at 1000 Hz while wearing a bidirectional, cable-driven ankle exoskeleton. The walking speed was intentionally chosen to approximate the reduced walking speeds commonly observed in individuals undergoing rehabilitation for neuromuscular disorders. This selection aimed to create gait conditions more representative of clinical populations while maintaining experimental control.

The ankle exoskeleton was not closed-loop controlled; it provided pre-determined sinusoidal torques synchronized to the participant's gait cycle, matched to the GRF period at the specified walking speed. Two sEMG sensors (DELSYS, Natick, MA, USA) were placed on the medial gastrocnemius and tibialis anterior to record muscle electrical signals at 1000 Hz. Offline processing included filtering, rectifying, and normalizing the signals to create the sEMG linear envelope.

An ultrasound probe (L7.0SC Prodigy Probe, S-Sharp, Taipei, Taiwan) was affixed to the participant's shank above the tibialis anterior to capture US images at 992 Hz. Offline, echogenicity from the US images was calculated and normalized to derive muscle activation. Twenty reflective markers for motion capture (Vicon Motion System Ltd., Los Angeles, CA, USA) were placed on the pelvis and lower limbs to measure kinematic data, including ankle angle and torque. Fig. 1 shows the placement of the US, sEMG sensors, and motion capture markers during the experimental procedure.



Fig. 1. Sensor set-up for the treadmill walking experiments. (A) sEMG sensors are placed on the plantarflexors (medial gastrocnemius) and dorsiflexors (tibialis anterior) and an US probe is placed on the dorsiflexors only. (B) After wearing the cable-driven ankle exoskeleton, the motion capture markers are placed on the lower limbs.

The participant walked for 30 seconds with exoskeleton assistance. Data acquisition, including sEMG, US imaging, GRF, and exoskeleton motor output, was implemented in Matlab's Simulink Real-Time environment (R2019b, MathWorks, Natick, MA, USA) on a Speedgoat target machine (Bern, Switzerland). Motion capture and GRF data were collected separately at 100 Hz and time-synchronized offline. From the recorded data, 23 seconds representing 12 complete gait cycles were extracted for analysis.

Seeing as the lowest sampling rate for the data collected for offline processing was 100 Hz, all data was downsampled to that frequency. This was done to avoid interpolating the data to the higher frequency since the lower sampling frequency more closely reflects the rate of real-time processing. As well, US data was only collected from the dorsiflexors, therefore δ^P from (7) was set to 1, which made the muscle activation measurement for plantarflexion entirely based on the sEMG sensor data from the medial gastrocnemius. δ^D was chosen at values of $1.00, 0.90, 0.80, ..., 0.00$ in different model iterations to evaluate the benefit of increasing the weight of the echogenicity measurements on the model accuracy.

B. Ankle Exoskeleton

The ankle exoskeleton is comprised of an actuation module, a push-pull cable, and an end-effector unit. All components required for the exoskeleton are portable, except for the power supply. The actuation module consists of a brushless EC motor (EC 90 flat, Maxon, Switzerland), a servo controller (ESCON 50/8, Maxon, Sachseln, Switzerland), a threaded ball screw and ball nut (Thomson Linear, Radford, VA, USA), a linear magnetic shaft encoder (LinACE InAxis,

TABLE I
RMSE VALUES FOR THE VALIDATED STATES, ESTIMATED USING EDMD MODEL

δ^D	1.00	0.90	0.80	0.70	0.60	0.50	0.40	0.30	0.20	0.10	0.00
q	0.228	0.242	0.214	0.202	0.201	0.236	0.226	0.234	0.253	0.241	0.238
$\dot{q}$	0.146	0.146	0.145	0.145	0.144	0.144	0.143	0.144	0.146	0.146	0.146

RLS, Ljubljana, Slovenia), and a microcontroller with PWM functionality (Arduino Uno, Torino, Italy). The motor sits upright at the hip, within 3D printed housing. When the motor rotates, the ball nut, connected to the push-pull cable, moves upwards or downwards, pushing and pulling the ankle to produce plantarflexion and dorsiflexion. The magnetic shaft encoder measures the movement of the ball nut – an analog for the ankle joint angle. The maximum motor torque is 1.56 Nm. The device has a total mass of 3 kg, with most of that centered at the hip-worn actuation module. The actuation module was secured to the participant using a standard utility belt.

IV. KOOPMAN PREDICTION RESULTS

The Koopman operator framework was used to model (6) for the entire experimental cycle. The first 5 seconds were designated as training data, after which the remaining time was used for validation. A root-mean-squared-error (RMSE) value was calculated for each of the validated states. This modeling process was performed for 11 datasets. Each dataset differed only in the a^D value, calculated using different sensor fusion weights δ^D. The RMSE values for validated states q and $\dot{q}$ are shown in Table I. Underlined values represent the sEMG sensor fusion weight (δ^D) that produced the best possible RMSE for the evaluated state. Among all the EDMD modeled states, the best average performance for q was demonstrated when $\delta^D = 0.60$ (shown in Fig. 2) and the worst performance was demonstrated when$\delta^D = 0.20$ (shown in Fig. 3). RMSE values for $\dot{q}$ had relatively low variance.

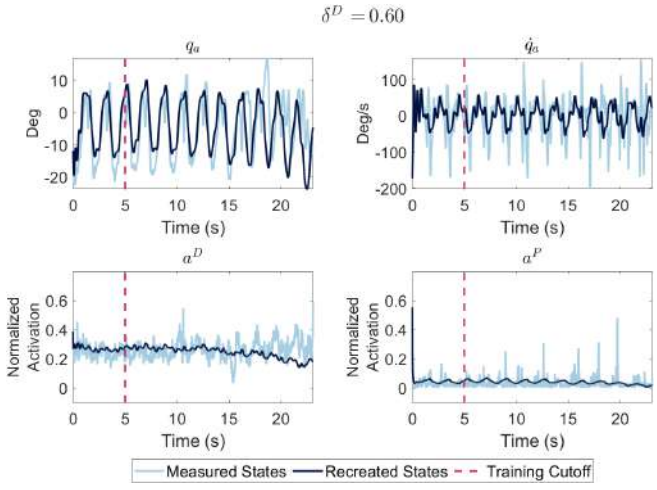


Fig. 2. The measured and recreated states from the EDMD model in the dataset with the best q RMSE value.

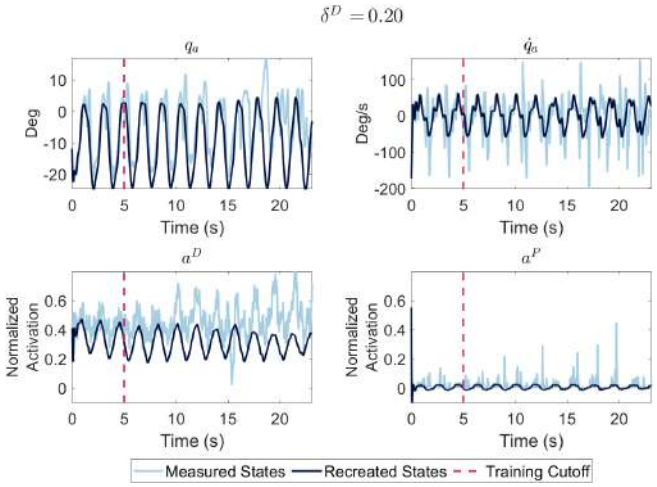


Fig. 3. The measured and recreated states from the EDMD model in the dataset with the worst q RMSE value.

V. DISCUSSION

The results demonstrate that the proposed Koopman operator framework, combined with fused US and sEMG signals, effectively models the nonlinear, phase-dependent dynamics of ankle motion during gait. By leveraging the complementary strengths of US and sEMG, the framework achieved accurate estimations of muscle activation, particularly for the dorsiflexors, with peak performance observed at a sensor fusion weight of $\delta^D = 0.60$. This configuration yielded the lowest RMSE for q. Notably, models relying exclusively on sEMG ($\delta^D = 1.00$) or US imaging ($\delta^D = 0.00$) demonstrated higher RMSE values, highlighting the limitations of single-modality approaches in comprehensively estimating muscle activation dynamics. However, the differences in RMSE across various δ^D values were relatively small, suggesting that the fusion framework is robust across a range of weight configurations.

The results indicate that while the model accurately captures overall gait trends, it struggles to reproduce high peaks and extreme values in the validated states. Highly transient periods or abrupt state changes during, for instance, peak force production, may not captured by basis functions since they represent particularly high frequency data or may be filtered out and smoothed during sensor processing. Introducing higher-order polynomial or expanding the set of Koopman observables could improve the model's ability to track extreme values.

A key limitation of this study is that experiments were conducted on a single young, able-bodied participant. While this approach allowed for a controlled comparison of the

EDMD model across various sensor fusion weights, it does not account for inter-individual variability that may be particularly common among populations with neuromuscular impairments, who remain the ultimate intended clinical population. It is well established that neurological impairment often alter muscle activation patterns, gait kinematics, and torque production, which may impact the performance of any model. Additionally, muscle fatigue and compensatory strategies that are more prevalent in clinical populations were not accounted for in this study. For improved generalizability, our future work will be trained on a wider dataset with participants of varying levels of ability and increased variability in peak torque production.

The immediate next step in this research is to perform the same analysis for sensor weights in combined US and sEMG measurements for modeling plantarflexor muscle activation. To strengthen the findings, future work should include statistical analyses to quantify the significance of performance differences across δ^{ζ} values and conduct sensitivity analyses to evaluate the framework's robustness under varying gait speeds or load conditions. Additionally, assessing the real-time feasibility and computational efficiency of the Koopman-based model would demonstrate its applicability for exoskeleton control. Overall, the integration of Koopman operator theory with fused US and sEMG data presents a promising avenue for individualized gait modeling, offering enhanced accuracy and adaptability for potential exoskeleton applications.

REFERENCES

[1] I. G. L. van de Port, G. Kwakkel, I. van Wijk, and E. Lindeman, "Susceptibility to deterioration of mobility long-term after stroke: a prospective cohort study," *Stroke*, vol. 37, pp. 167–171, Jan. 2006.

[2] L. I. Iezzoni, E. P. McCarthy, R. B. Davis, and H. Siebens, "Mobility Difficulties Are Not Only a Problem of Old Age," *Journal of General Internal Medicine*, vol. 16, no. 4, pp. 235–243, 2001.

[3] L. A. Simpson, J. J. Eng, J. T. Hsieh, and D. L. Wolfe, "The health and life priorities of individuals with spinal cord injury: A systematic review," *Journal of neurotrauma*, vol. 29, pp. 1548–1555, May 2012.

[4] T.-H. Hsu, C.-L. Tsai, J.-Y. Chi, C.-Y. Hsu, and Y.-N. Lin, "Effect of wearable exoskeleton on post-stroke gait: A systematic review and meta-analysis.," *Annals of physical and rehabilitation medicine*, vol. 66, p. 101674, Feb. 2023.

[5] B. Chen, B. Zi, Z. Wang, L. Qin, and W.-H. Liao, "Knee exoskeletons for gait rehabilitation and human performance augmentation: A state-of-the-art," *Mechanism and Machine Theory*, vol. 134, pp. 499–511, Apr. 2019.

[6] R. S. Calabrò, A. Naro, M. Russo, P. Bramanti, L. Carioti, T. Balletta, A. Buda, A. Manuli, S. Filoni, and A. Bramanti, "Shaping neuroplasticity by using powered exoskeletons in patients with stroke: a randomized clinical trial," *Journal of NeuroEngineering and Rehabilitation*, vol. 15, p. 35, Apr. 2018.

[7] J. Zhang, P. Fiers, K. A. Witte, R. W. Jackson, K. L. Poggensee, C. G. Atkeson, and S. H. Collins, "Human-in-the-loop optimization of exoskeleton assistance during walking," *Science*, vol. 356, pp. 1280–1284, June 2017.

[8] K. Z. Takahashi, M. D. Lewek, and G. S. Sawicki, "A neuromechanics-based powered ankle exoskeleton to assist walking post-stroke: a feasibility study," *Journal of NeuroEngineering and Rehabilitation*, vol. 12, p. 23, Feb. 2015.

[9] L. Miller, A. McFadyen, A. C. Lord, R. Hunter, L. Paul, D. Rafferty, R. Bowers, and P. Mattison, "Functional Electrical Stimulation for Foot Drop in Multiple Sclerosis: A Systematic Review and Meta-Analysis of the Effect on Gait Speed," *Archives of Physical Medicine and Rehabilitation*, vol. 98, pp. 1435–1452, July 2017.

[10] T.-w. P. Huang, K. A. Shorter, P. G. Adamczyk, and A. D. Kuo, "Mechanical and energetic consequences of reduced ankle plantarflexion in human walking," *The Journal of Experimental Biology*, vol. 218, pp. 3541–3550, Nov. 2015.

[11] W. Shin, D. Nam, B. Ahn, S. J. Kim, D. Y. Lee, S. Kwon, and J. Kim, "Ankle dorsiflexion assistance of patients with foot drop using a powered ankle-foot orthosis to improve the gait asymmetry," *Journal of NeuroEngineering and Rehabilitation*, vol. 20, p. 140, Oct. 2023.

[12] M. Singh and N. Sharma, "Data-driven model predictive control for drop foot correction," in *2023 American Control Conference (ACC)*, pp. 2615–2620, IEEE, 2023.

[13] M. Singh, K. Lambeth, N. Hakam, and N. Sharma, "Ultrasound-informed recursive koopman model predictive control for gait assistance," in *2025 American Control Conference (ACC)*, pp. 2615–2620, IEEE, 2025.

[14] Y. Giat, J. Mizrahi, and M. Levy, "A musculotendon model of the fatigue profiles of paralyzed quadriceps muscle under FES," *IEEE Trans. Biomed. Eng.*, vol. 40, no. 7, pp. 664–674, 1993.

[15] E. M. Arnold, S. R. Ward, R. L. Lieber, and S. L. Delp, "A Model of the Lower Limb for Analysis of Human Movement," *Annals of Biomedical Engineering*, vol. 38, pp. 269–279, Feb. 2010.

[16] Y. Zheng, M. Chan, J. Shi, X. Chen, and Q. Huang, "Sonomyography: Monitoring morphological changes of forearm muscles in actions with the feasibility for the control of powered prosthesis," *Medical Engineering & Physics*, vol. 28, no. 5, pp. 405–415, 2006. Publisher: Elsevier.

[17] Q. Zhang, A. Iyer, K. Lambeth, K. Kim, and N. Sharma, "Ultrasound echogenicity as an indicator of muscle fatigue during functional electrical stimulation," *Sensors*, vol. 22, no. 1, p. 335, 2022.

[18] Q. Zhang, N. Fragnito, J. R. Franz, and N. Sharma, "Fused ultrasound and electromyography-driven neuromuscular model to improve plantarflexion moment prediction across walking speeds," *Journal of NeuroEngineering and Rehabilitation*, vol. 19, p. 86, Aug. 2022.

[19] M. Singh, N. Hakam, and N. Sharma, "Koopman-based model predictive control for ankle dorsiflexion and plantarflexion assistance via fes," *IEEE Transactions on Neural Systems and Rehabilitation Engineering*, vol. 40, no. 1, pp. 318–327, 2024.

[20] N. Sharma, K. Stegath, C. M. Gregory, and W. E. Dixon, "Nonlinear neuromuscular electrical stimulation tracking control of a human limb," *IEEE Trans. Neural Syst. Rehabil. Eng.*, vol. 17, no. 6, pp. 576–584, 2009.

[21] N. Sharma, S. Bhasin, Q. Wang, and W. Dixon, "RISE-based adaptive control of a control affine uncertain nonlinear system with unknown state delays," *IEEE Trans. on Autom. Control*, vol. 57, no. 1, pp. 255–259, 2012.

[22] N. Kirsch, N.and Alibeji and N. Sharma, "Nonlinear model predictive control of functional electrical stimulation," *Control Eng. Practice*, vol. 58, pp. 319–331, 2017. Publisher: Elsevier.

[23] H. Hatze, "A myocybernetic control model of skeletal muscle," *Biological Cybernetics*, vol. 25, no. 2, pp. 103–119, 1977. Publisher: Springer.

[24] Q. Zhang, K. Lambeth, Z. Sun, A. Dodson, X. Bao, and N. Sharma, "Evaluation of a Fused Sonomyography and Electromyography-Based Control on a Cable-Driven Ankle Exoskeleton," *IEEE Transactions on Robotics*, vol. 39, pp. 2183–2202, June 2023.

[25] J. L. Proctor, S. L. Brunton, and J. N. Kutz, "Generalizing koopman theory to allow for inputs and control," *SIAM Journal on Applied Dynamical Systems*, vol. 17, no. 1, pp. 909–930, 2018.

[26] M. Korda and I. Mezić, "Optimal construction of koopman eigenfunctions for prediction and control," *IEEE Transactions on Automatic Control*, vol. 65, no. 12, pp. 5114–5129, 2020.

[27] G. Mamakoukas, M. L. Castano, X. Tan, and T. D. Murphey, "Derivative-based koopman operators for real-time control of robotic systems," *IEEE Transactions on Robotics*, vol. 37, no. 6, pp. 2173–2192, 2021.

Do Motor Skills Learned in Isometric Training Generalize to Unpracticed Workspaces?

Arturo Ramirez[1,2*], Naveed Reza Aghamohammadi[1,2] , Courtney Celian[1]
Adriana Cancrini[1,2], Bruno Borghi[1], James L. Patton[1,2*]

***Abstract*— Previous studies have looked at the potential for using visual feedback from isometric forces to illicit movement learning without actually moving. We investigate the potential of isometric movement training further by investigating the generalization of motor skills learned through isometric training to unconstrained movement. Using the Barret Upper-Extremity Robotic Trainer as both a position control device and a force clamp, participants engaged in an isometric reaching task with simulated movement arm dynamics feedback. The simulated movement was displayed on an augmented reality display that occludes the arm to increase immersion and belief of movement. We studied planar-targeted reaching in the presence and absence of a velocity-dependent curl field and evaluated if skills acquired in isometric reaching using robotic constraints transfer effectively to free-reaching tasks in an unpracticed and practiced workspace. Our results demonstrated an ability to transfer motor skills in the practiced workspace which supports previous findings in literature; however, motor skills in an unpracticed workspace showed increase performance in the presence of the curl field but no signs of an after effect in the absence of the field. This finding shows promise of generalization of isometric movement training in unpracticed workspaces, and further studies are needed.**

I. Introduction

The amount and type of rehabilitation an individual receives after a stroke can significantly impact their recovery and functional gains. Patients benefit from repetitive physical and mental exercises, such as mental rehearsal, progressive resistance force training, and repetitive motion therapy [1], [2]. Error augmentation has also shown promise as a therapeutic approach, where task errors are intentionally amplified, requiring participants to make greater corrections rather than receiving assistance [3]–[6]. However, many stroke survivors experience severe weakness or spasticity, making it difficult to perform the recommended therapeutic activities or generate sufficient volitional movement to benefit from error augmentation [1]. This difficulty increases their risk of long-term disabilities, including "learned non-use," reduced mobility, and persistent spasticity [7]. Ensuring that individuals with varying levels of movement ability can participate in repetitive exercises is essential for optimizing recovery outcomes. For patients with greater impairments, force-modulated training and constraint-induced movement therapy have proven effective in mitigating learned non-use [1], [2], [8], [9]. Isometric movement training has emerged as a potential solution to address these rehabilitation challenges, though its effectiveness in transferring training benefits to real-world movements remains under explored.

Understanding how skills learned in constrained environments transfer to free movement is critical for determining the viability of isometric training as a therapeutic approach. Previous work by Melendez-Calderon et al. (2017) demonstrated that dynamic motor skills acquired through isometric training could transfer to free-reaching movements [10]. In their study, participants performed isometric tasks within a single workspace using a simulated environment where an avatar represented arm movements based on force output, enabling training in velocity-dependent force fields. The participants exhibited positive transfer effects, suggesting that isometric learning can induce sensorimotor adaptations applicable to unrestricted movement conditions.

Building upon this research, the present study employs a similar isometric reaching protocol while introducing tests in a second, unpracticed workspace. Investigating generalization to unpracticed workspaces is essential for establishing isometric reaching as a viable rehabilitation approach. Since isometric training is inherently confined to a single workspace, its effectiveness depends on whether the acquired skills can transfer to new movement contexts required for daily function. We hypothesize that dynamic motor skills learned through isometric training will transfer within the practiced workspace and, critically, will also generalize to the unpracticed workspace, reinforcing the potential of isometric training for real-world rehabilitation.

II. Methods

A. Participants

Four healthy adults (two males, two females) aged 25–55, with no prior experience in isometric training, were recruited. All participants were right-handed, and their data and informed consent were collected in accordance with the Declaration of Helsinki and Northwestern University's Institutional Review Board (STU00220740).

B. Experimental Setup

Our experiment utilizes a robotic arm, an augmented reality display, and an arm simulation. The robotic arm used is the Barrett Upper Extremity Robotic Trainer (Burt®) [11] (Fig. 1) from Barrett Technologies. The Burt® is a 3-DOF robotic manipulator that provides real-time end-effector

[1]Richard and Loan Hill Department of Biomedical Engineering, University of Illinois Chicago, Chicago, IL, USA
[2]Robotics Lab at Center for Neural Plasticity, Shirley Ryan AbilityLab, Chicago, IL, USA
*Correspondence: aramire4@uic.edu, pattonj@uic.edu
Supported by the National Institute of Health (NIH) under grant R01NS053606

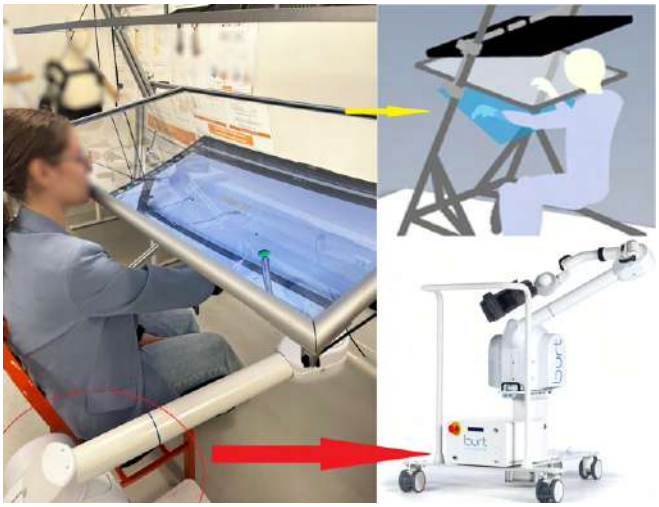


Fig. 1. Example of the experimental setup used for data collection. The yellow arrow indicates the LookinGlass augmented reality display, while the red arrow highlights the Burt® robotic arm

tracking, haptic feedback, and force generation, which are used to generate perturbations and maintain a force clamp during isometric training. A key feature of the Burt® is its full back-drivability, ensuring user safety.

The augmented reality display is the Looking Glass, which consists of an angled display and a semi-silvered screen. Unlike systems that require head tracking, the Looking Glass eliminates latency and the need for additional devices attached to the user [3], [12]–[16] (Fig. 1).

We developed the virtual arm simulation using Unity software, which provides visual feedback in real time to the participant. A virtual cursor (0.3 cm in diameter) was aligned with the end effector of the Burt® to ensure accurate spatial feedback.

C. Force Clamp

To perform isometric training,the participant's hand is clamped in place using the robot handle which applies forces to maintain the hand at a desired location. These forces are generated by a virtual spring with resting length of zero, whose origin is located at the starting position of the workspace. The equation governing the spng force is as follows.

$$F_{\text{spring}} = -F \cdot \hat{F} = -\rho \cdot k \cdot \begin{bmatrix} \sin(\phi)\cos(\theta) \\ \sin(\phi)\sin(\theta) \\ \cos(\phi) \end{bmatrix} \tag{1}$$

Where:

$$\rho = \|r\|, \quad \theta = \tan^{-1}\left(\frac{r_y}{r_x}\right), \quad \phi = \cos^{-1}\left(\frac{r_z}{\|r\|}\right) \tag{2}$$

$$r = RobotPosition - SpringOrigin \tag{3}$$

An additional damping force is applied to the user to mitigate the spring's oscillatory behavior and ensure stable positioning.

$$\mathbf{F}_{\text{applied}} = \mathbf{F}_{\text{spring}} + c \cdot (\mathbf{v} \cdot \hat{\mathbf{F}}) \tag{4}$$

Where c is the damping coefficient (dampeningCoeff), and $\mathbf{v} \cdot \hat{\mathbf{F}}$ represents the velocity component aligned with the direction of the spring force

Since the Burt® robot lacks a force sensor, the force clamp serves as a proxy for measuring user-applied forces. It is assumed that the force exerted by the robot to hold the user in place is equal and opposite to the force applied by the user:

$$\mathbf{F}_{\text{ext}} = -\mathbf{F}_{\text{applied}} \tag{5}$$

D. Isometric Framework

The virtual arm simulation is modeled using the dynamic equation below. This experiment involves a planar reaching task, where the arm is represented as a two-link, two-degree-of-freedom system with revolute joints at the shoulder and elbow. The mass,length and moment of inertia were determined for an average person of 1.75 m in height and 70 kg in weight [17].

$$M(q)\ddot{q} + C(q,\dot{q})\dot{q} + G(q) = J(q)^T * (\mathbf{F}_{Vf} + \mathbf{F}_{ext}) + \tau_{fb} \tag{6}$$

Where:

$M(q)$ is the mass matrix.
$C(q,\dot{q})$ is the Coriolis and centripetal matrix.
$G(q)$ is the gravitational torque vector.
$J(q)^T$ is the transpose of the Jacobian.
$\mathbf{F}_{Vf}$ is the virtual force applied to the end effector.
$\mathbf{F}_{ext}$ is the external force applied by the user.
τ_{fb} is the feedback torque.

In the presence of a curl field, the virtual force is given by:

$$\mathbf{F}_{Vf} = \mathbf{F}_{curl} = \dot{\mathbf{X}} \cdot \begin{bmatrix} 0 & 25 \\ -25 & 0 \end{bmatrix} \tag{7}$$

Feedback torque is determined using an equilibrium point controller in the joint domain. The desired joint angles are calculated based on the minimum jerk trajectory from starting point to target as the ideal path and transformed to joint angles using inverse kinematics. The controller is defined as:

$$\tau_{fb} = \lambda \left(K_p(q - q_{\text{desired}}) + K_d(\dot{q} - \dot{q}_{\text{desired}})\right) \tag{8}$$

The scaling factor λ is velocity-dependent to prevent high feedbacks at low velocities:

$$\lambda = \begin{cases} 1, & |\dot{x}| \geq 0.8\,\text{m/s} \\ \frac{|\dot{x}|}{0.8}, & |\dot{x}| < 0.8\,\text{m/s} \end{cases} \tag{9}$$

Joint stiffness K_p is torque-dependent derived from empirical data gathered from published work [18]:

$$K_p = \begin{bmatrix} 10.8 + 3.18|\tau_{\text{Fext1}}| & 2.83 + 2.15|\tau_{\text{Fext2}}| \\ 2.51 + 2.34|\tau_{\text{Fext2}}| & 8.67 + 6.18|\tau_{\text{Fext2}}| \end{bmatrix} \tag{10}$$

Joint damping K_d is proportional to K_p and inversely related to joint velocity magnitude [10], [19]:

$$K_d = \frac{0.42}{\sqrt{\dot{q}^T(\dot{q}+1)}} K_p \tag{11}$$

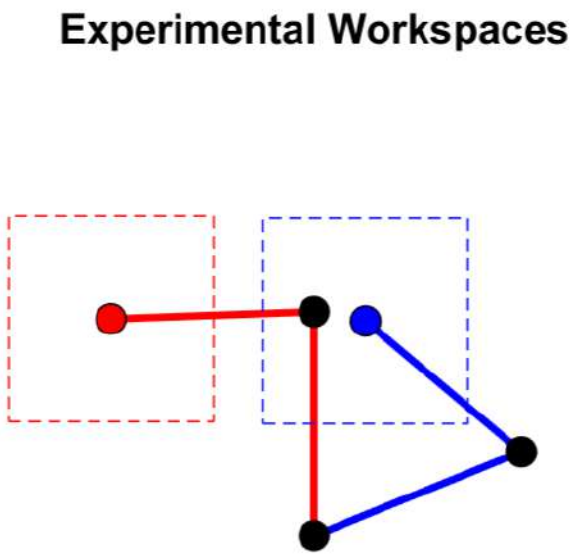


Fig. 2. Visual representation of the two workspaces. The blue workspace is the practiced workspace centered at elbow angle 118° and shoulder angle 22°. The red is the unpracticed workspace centered at elbow angle 92° and shoulder angle 90°

This feedback model incorporates torque-dependent joint stiffness and damping, ensuring realistic responses during isometric tasks. The velocity-dependent scaling factor λ prevents feedback from driving the simulation when minimal input is provided by the user.

E. Protocol

The experiment consisted of 445 trials of 15 cm center-out reaches (4 cm targets) across 15 phases in two workspaces as seen in Fig.2. The practiced workspace had three target directions (90°, 210°, 330°) and additional catch trials in unpracticed directions to take into consideration generalization within the workspace (30°, 150°, 270°). The unpracticed workspace featured only the three practiced directions. Table 1 summarizes the phases with "c" for catch trials, "*" denoting key analysis phases, yellow highlighting the unpracticed workspace, and blue highlighting phases in the isometric condition.

Participants received 150-second rest periods every 75 trials to minimize fatigue. During each reach, they received continuous feedback on their movement speed via a color-coded cursor system: - **Yellow**: Movement time below 550 ms (too fast). - **Green**: Movement time between 550 ms and 850 ms (ideal). - **Red**: Movement time over 850 ms (too slow).

If participants reached the target within the ideal time window (550–850 ms), they received a **positive reinforcement** in the form of a green explosion visual effect and a rewarding auditory cue. If they missed the ideal time, a **negative auditory cue** was provided as feedback. The color feedback and positive reinforcement were implemented to enhance extrinsic motivation, promoting learning and encouraging proper reaching during trials [20].

TABLE I. Table 1: Experimental Design

Phase	Name (# of Trials)
1*	Unpracticed Workspace Baseline (6)
2	Unpracticed Workspace Intermittent Exposure (Forces Off) (12)
2c*	Unpracticed Workspace Intermittent Exposure (Forces On) (12)
3*	Baseline (15)
4	Intermittent Exposure (Forces Off) (30)
4c*	Intermittent Exposure (Forces On) (24)
5	Familiarization (15)
6*	Baseline (15)
7	Intermittent Exposure (Virtual Forces Off) (30)
7c*	Intermittent Exposure (Virtual Forces On) (18)
8	Early Training (Virtual Forces On) (21)
8c	Early Training (Virtual Forces Off) (15)
9	Training (Virtual Forces On) (72)
9c	Training (Virtual Forces Off) (6)
10*	Late Training (Virtual Forces On) (15)
10c*	Late Training (Virtual Forces Off) (24)
11	Unpracticed Workspace Test (Free Motion) (15)
12	Refresh (Virtual Forces On) (15)
13*	Transfer Test Unpracticed Workspace (Forces On) (15)
14*	Transfer Test (Forces On) (30)
14c*	Transfer Test (Forces Off) (15)
15	Post Training (Free) (15)

F. Data Collection and Analysis

The position and velocity of the robotic end effector and the arm cursor were recorded for each trial. During isometric conditions, since the robotic end effector remains stationary, the position and velocity of the arm cursor were used to analyze trajectories and error metrics. The primary error metric was the maximum perpendicular distance, defined as the maximum deviation of the arm cursor from the ideal straight-line path between the starting point and the target for each trial:

$$d = \pm \frac{ax_1 + by_1 + c}{\sqrt{a^2 + b^2}} \tag{12}$$

where a, b, and c represent the coefficients of the line equation, and (x_1, y_1) represents the arm cursor's position.

To compare phases, the Kolmogorov-Smirnov test was used first to assess data normality. If both datasets were normally distributed, a paired t-test was conducted. For non-normal datasets, a non-parametric Wilcoxon signed-rank test was performed. A significance level of $\alpha = 0.05$ was applied for all comparisons, and p-values were reported to indicate the statistical outcomes.

III. Results

We hypothesized that skills learned in isometric training will transfer to unconstrained reaching tasks in the practiced workspace and will also show generalizability to the unpracticed workspace. We consider transfer of learning to be an increase in performance in unconstrained reaching while under the effects of a velocity-dependent curl field and a decrease in performance in the null condition after training. The maximum perpendicular error of each subject at every phase were plotted as shown in Fig. 3. Trend lines were then computed to determine if individual subjects were responding similarly to the protocol. In the isometric training phases (phases 8-10) there is a clear downward trend that

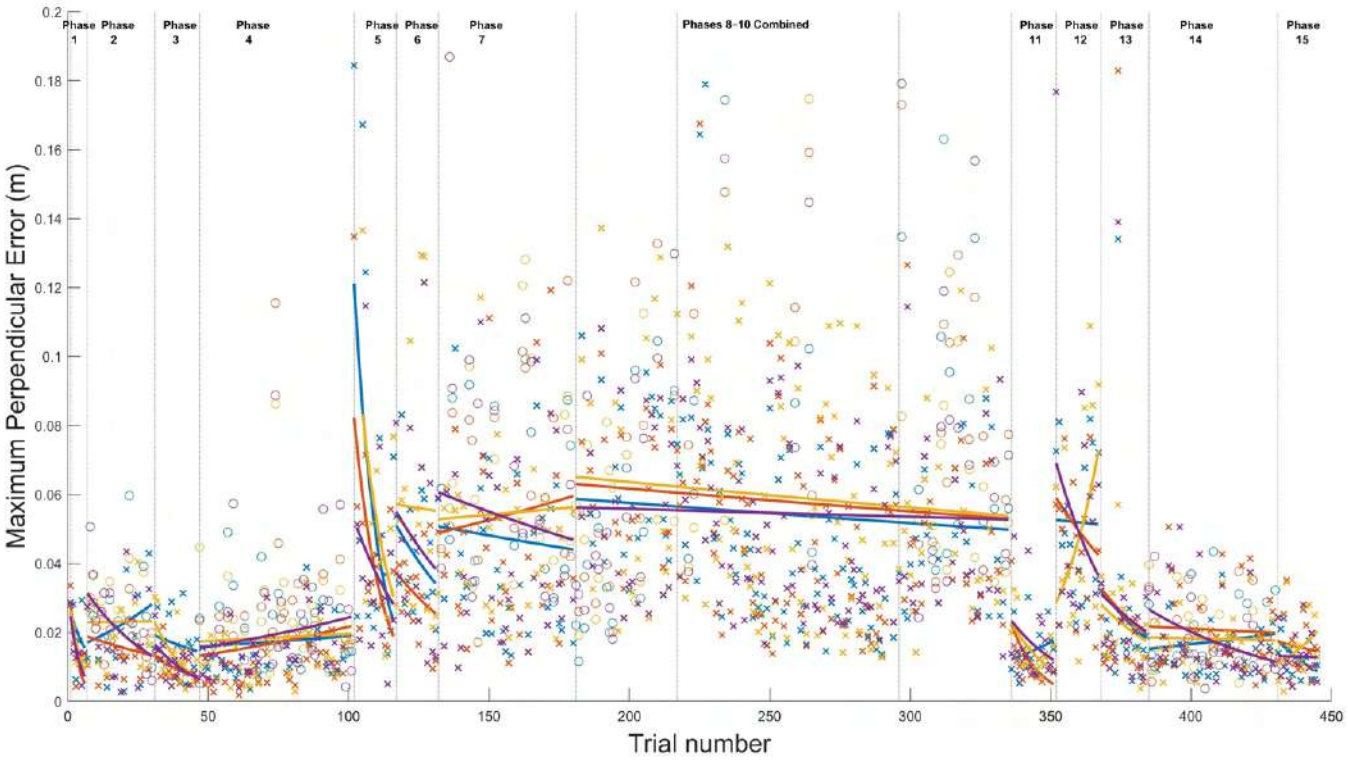


Fig. 3. Perpendicular Error (m) for all subjects (n=4) across all experiment phases. Blue represents S1, orange represents S2, yellow represents S3, and purple represents S4. Solid lines depict data fits for each subject, excluding catch trials. Catch trials are indicated by open circles, while main phase data points are marked with Xs.

suggests that the participants were getting better at navigating the virtual curl field in the isometric condition.

This experiment analyzed the movement trajectories in various phase. The individual trajectories of key phases were shown in Fig. 4, blue trajectories correspond to conditions without the velocity-dependent curl field, while red trajectories illustrate movements with the presence of the force field. These plots further support the trending argument of adaptation as after effects, as denoted by blue trajectories in Post-Training for both unconstrained and constrained appear to produce more perpendicular error when compared to the blue trajectories in Pre-Training. There appears to be little to no after effects present in the unpracticed workspace post-isometric training.

To evaluate performance changes under a virtual velocity-dependent curl field during isometric conditions, we compared the initial exposure to the field (phase 7c) with late training (phase 10), where learning was expected. A Wilcoxon signed-rank test revealed that errors during late training were significantly lower than during initial exposure ($p = 4.0721 \times 10^{-4}$). To assess the aftereffects of learning, we compared the isometric baseline (phase 6) with the catch trials of late training (phase 10c). The errors in the catch trials were significantly higher than those in the baseline ($p = 5.3518 \times 10^{-7}$), indicating substantial aftereffects.

The impact of isometric training on unconstrained reaching performance in a velocity-dependent curl field was examined by comparing initial exposure pre-training (phase 4c) with a test phase post-training (phase 14). This comparison revealed a significant reduction in perpendicular errors ($p = 2.7317 \times 10^{-5}$) following training. For aftereffects in unconstrained reaching, the baseline (phase 3) was compared with the post-training test phase (phase 14c). This showed an increase in errors ($p = 2.7317 \times 10^{-5}$) after training.

To explore the generalization of isometric training to an unpracticed workspace, we analyzed performance and aftereffects. There were no significant aftereffects(phase 1 vs 11) in the unpracticed workspace post-training ($p = 0.3313$); however, performance under the curl field(phase 2c vs 13) showed significant improvement ($p = 0.0260$). A summary of all these comparison can be seen in Fig. 5

IV. Discussion

The results of this experiment provide insights into the adaptation and generalization of motor control under the influence of a velocity-dependent curl field, particularly in the isometric condition. Statistical analyses and trajectory evaluations revealed distinct trends supporting the occurrence of learning and adaptation, though with limitations in generalizing learned behaviors to unpracticed workspaces.

A. Adaptation and Learning in the Isometric Condition

Participants demonstrated a progressive adaptation to the curl field during isometric training (phases 8–10), as evidenced by a downward trend in the maximum perpendicular error during training. This improvement suggests that participants refined their ability to navigate the virtual environment

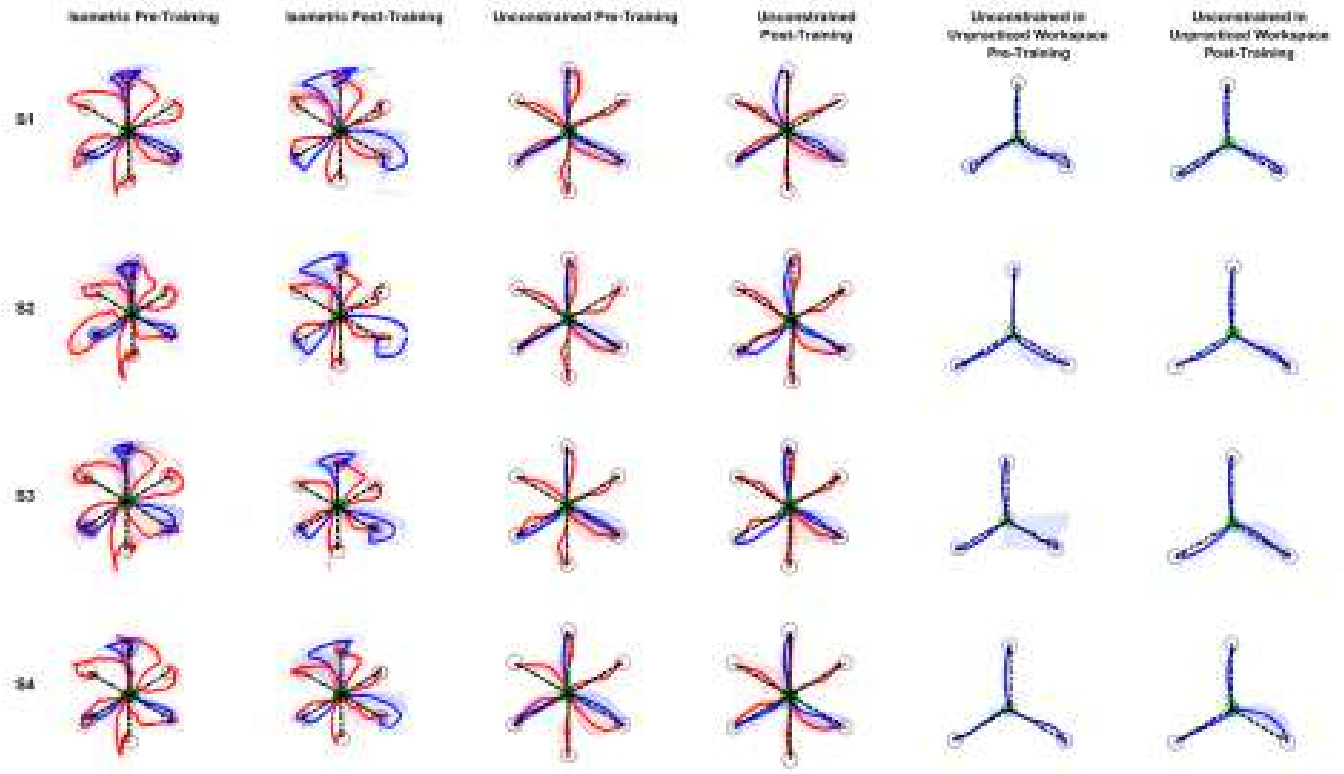


Fig. 4. Movement trajectories of key phases in the experiment. Blue trajectories represent movements without a velocity-dependent curl field, and red represents movements with the force field. Green circles indicate movement onset, darker lines represent the ensemble average trajectory and the shaded regions is the standard deviation.

despite the perturbation. While improvement in performance alone does not necessarily indicate learning or adaptation,the presence of aftereffects, indicated by higher errors during catch trials compared to the baseline, supports the belief that participants internalized the curl field dynamics and had some level of motor learning and adaptation. These findings align with previous studies showing that repeated exposure to perturbations facilitates the development of compensatory strategies and altered internal models. [21]–[24]

B. Impact on Unconstrained Reaching Performance

Isometric training positively influenced performance in unconstrained reaching tasks, as shown by the reduction in perpendicular errors under the unconstrained curl field from pre- to post-training. This implies that the abilities gained during isometric training remain present once unconstrained. Furthermore, the increased errors observed in the post-training test phase without the force field, compared to the unconstrained baseline, suggest that dynamic skills learned in isometric condition were transferred to the unconstrained arm dynamics. This observation supports the assertion by Dr. Melendez-Calderon that dynamic skills are transferable from isometric learning, although the extent of their generalizability remains unclear [10], [25].

C. Generalization to an Unpracticed Workspace

The analysis of performance and aftereffects in the unpracticed workspace provide insights into the limits of isometric training. The absence of significant changes in maximum perpendicular error when testing for aftereffects suggests that the learned dynamics in the trained workspace did not transfer to the unpracticed workspace. This result suggests that the internalized model of the curl field was either postural dependent or could be due the workspace torque being too dissimilar for proper generalization to occur as seen in literature [26].. Nevertheless, the significant improvement in performance under the curl field in the unpracticed workspace still suggests some degree of generalization. Participants were able to apply their learned strategies to perform better in the curl field, even in a novel spatial context. This increase in performance could be due to the re-weighting of visual feedback in the isometric condition, allowing participants to respond effectively to the visual cue of the curl field as opposed to the environmental forces being applied [27]. The literature also suggests that adaptation can be generalized due to the CNS creating and storing generalized control strategies from visually perceived kinematic coordinates [28]–[30]

D. Implications and Future Directions

These findings have important implications for the design of rehabilitation protocols and motor learning paradigms. The demonstrated ability of isometric training to improve performance in unconstrained tasks suggests its potential as a safe and effective training paradigm, especially for individuals with motor impairments. However, the limited generalization of aftereffects to unpracticed workspaces im-

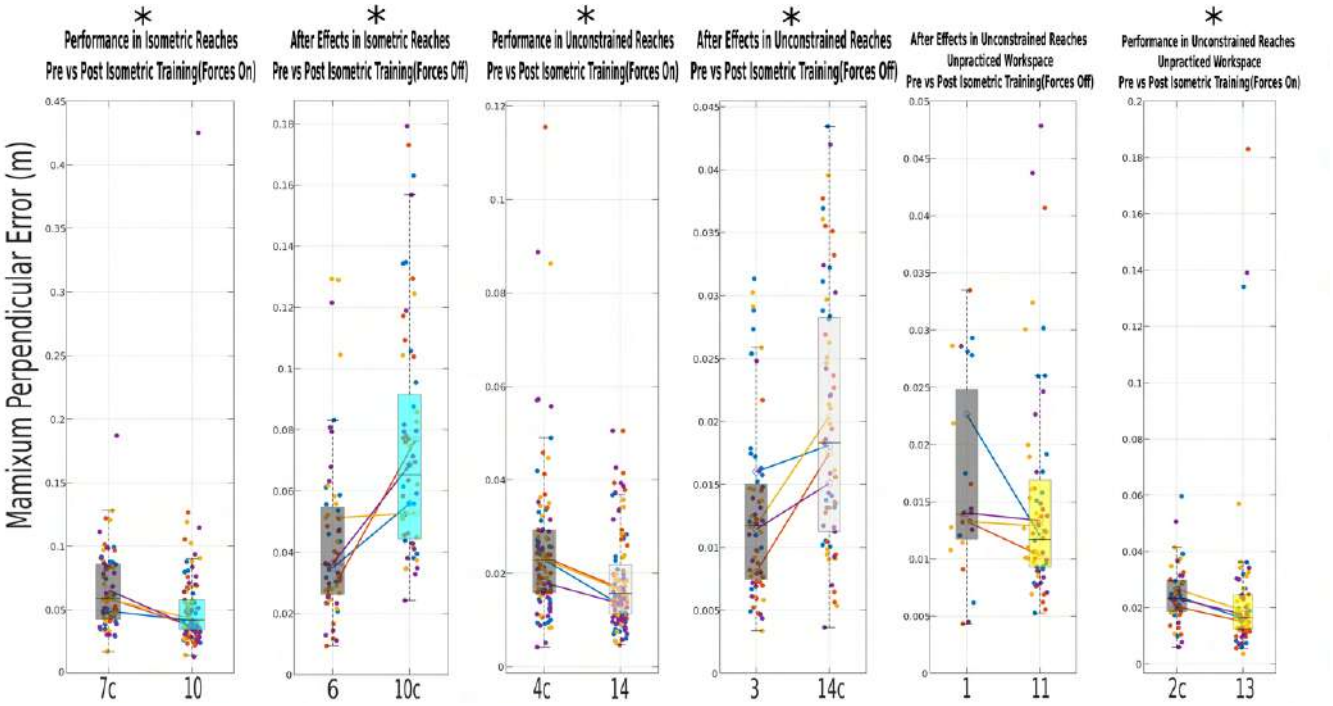


Fig. 5. Key phase comparisons are shown with gray box plots representing pre-training phases and colored box plots representing post-training phases. Box plot colors follow the same convention as the table: blue represents phases in the isometric condition, white represents unconstrained in the practiced workspace and yellow represents unconstrained phases in the unpracticed workspace. Solid lines indicate the medians for individual subjects, and asterisks above the plots denote p-values less than 0.05, indicating statistical significance.

plies the need for more robust isometric trainings that spans multiple workspaces which limits it effectiveness. Future studies should investigate the mechanisms underlying the observed workspace-specific adaptation and explore strategies to enhance generalization. There is the possibility that this training protocol did not provide sufficient time in the isometric training condition to fully learn the curl field in and a further analyses on the dynamics of the learning needs to be done to ensure steady state was reached. The rose plots suggest that learning and adaptation did not fully occur since there are still curling effects evident in late training when the expected trajectory should be close to straight. Recent study has shown that the difficulty in a task can affect the potential to encode and internalize adaptations, by increasing the speed of the targeted reaches we could potentially increase the amount of learning internalized [31]. Additionally, examining the neural systems responsible for adaptation and generalization in isometric conditions could provide valuable insights into the underlying processes and inform the development of more effective training approaches. Another future direction could be updating the arm simulation, which currently utilizes a linear torque stiffness relationship, to be more dynamic by implementing a personalized model of the user from reaching data collected using techniques like PRISM [32].

E. Study Limitations

A primary limitation of this study is the small sample size, which limits the generalizability of our findings. Future research recruiting a larger participant pool is necessary to support any observed trends on the transfer of dynamic skills and generalization. Another limitation of this study is that a bug was observed in the isometric condition in the forward direction. This bug was a misaligned ideal position for the forward direction which caused the torque feedback to apply a force toward the left of the target. This bug could have limited the amount of learning observed since it made reaching to the target much more difficult in this direction as opposed to the other two.

F. Conclusion

In summary, this study demonstrates the efficacy of isometric training in facilitating motor adaptation and improving performance in dynamic reaching tasks. While the adaptation was robust and accompanied by significant aftereffects, the limited generalization to unpracticed workspaces highlights the need for further investigation into strategies to enhance transfer. These findings still highlight the potential of isometric training as a tool for motor skill enhancement and rehabilitation and supports literature on the dynamic skills acquired from isometric conditions.

V. Acknowledgment

We would like to thank the Robotics Lab at the Shirley Ryan AbilityLab ,the Richard and Loan Hill Department of Biomedical Engineering at the University of Illinois Chicago and Dr. Melendez-Calderon. No conflicts of interest, financial or otherwise, are declared by the authors. This work was supported by the National Institute of Health (NIH) under grant R01NS053606.

REFERENCES

[1] G. E. Francisco and J. R. McGuire, "Poststroke spasticity management," vol. 43, no. 11, pp. 3132–3136. [Online]. Available: https://www.ahajournals.org/doi/10.1161/STROKEAHA.111.639831

[2] A. J. Butler and S. J. Page, "Mental practice with motor imagery: Evidence for motor recovery and cortical reorganization after stroke," vol. 87, no. 12, pp. 2–11. [Online]. Available: https://linkinghub.elsevier.com/retrieve/pii/S000399930601272X

[3] F. Abdollahi, M. Corrigan, E. D. Lazzaro, R. V. Kenyon, and J. L. Patton, "Error-augmented bimanual therapy for stroke survivors," vol. 43, no. 1, pp. 51–61, publisher: IOS Press. [Online]. Available: https://www.medra.org/servlet/aliasResolver?alias=iospress&doi=10.3233/NRE-182413

[4] N. R. Aghamohammadi, C. Celian, V. Wojicik, B. Borghi, A. Ramirez, A. Cancrini, and J. L. Patton, "A case study of error fields: A three-dimensional personalized robotic therapy." IEEE, p. Accepted.

[5] N. R. Aghamohammadi, M. F. Bittmann, V. Klamroth-Marganska, R. Riener, F. C. Huang, and J. L. Patton, "Error fields: personalized robotic movement training that augments one's more likely mistakes," vol. 15, no. 1, p. 4201. [Online]. Available: https://www.nature.com/articles/s41598-025-87331-x

[6] B. Borghi, N. R. Aghamohammadi, A. Cancrini, A. Ramirez, C. Celian, and J. L. Patton, "Personalized robotic training on a planar reaching task," in *International Conference on Rehabilitation Robotics (ICORR)*. IEEE, p. Accepted.

[7] E. Taub, G. Uswatte, V. W. Mark, and D. M. M. Morris, "The learned nonuse phenomenon: implications for rehabilitation," vol. 42, no. 3, pp. 241–256.

[8] S. Kagawa, T. Koyama, M. Hosomi, T. Takebayashi, K. Hanada, F. Hashimoto, and K. Domen, "Effects of constraint-induced movement therapy on spasticity in patients with hemiparesis after stroke," vol. 22, no. 4, pp. 364–370.

[9] E. Taub, N. E. Miller, T. A. Novack, E. W. Cook, W. C. Fleming, C. S. Nepomuceno, J. S. Connell, and J. E. Crago, "Technique to improve chronic motor deficit after stroke," vol. 74, no. 4, pp. 347–354.

[10] A. Melendez-Calderon, M. Tan, M. F. Bittmann, E. Burdet, and J. L. Patton, "Transfer of dynamic motor skills acquired during isometric training to free motion," vol. 118, no. 1, pp. 219–233. [Online]. Available: https://www.physiology.org/doi/10.1152/jn.00614.2016

[11] W. T. Townsend, D. Wilkinson, A. JENKO, J. LELAND, A. ANANTHANARAYANAN, and J. Patton, "Multi-active-axis, non-exoskeletal rehabilitation device," patenteu 3 049 041A4. [Online]. Available: https://patents.google.com/patent/EP3049041A4/ko

[12] J. J. Patton, "New VR technologies for sensorimotor rehabilitation." [Online]. Available: https://doi.org/10.11239/jsmbe.51.M-99

[13] F. Porta, C. Celian, and J. L. Patton, "Upper extremity functional rehabilitation for stroke survivors using error-augmented visual feedback: Interim results," in *2021 43rd Annual International Conference of the IEEE Engineering in Medicine & Biology Society (EMBC)*, vol. 17. IEEE, pp. 1318–1324. [Online]. Available: https://ieeexplore.ieee.org/document/9630799/

[14] J. Patton, Yejun Wei, C. Scharver, R. Kenyon, and R. Scheidt, "Motivating rehabilitation by distorting reality," in *The First IEEE/RAS-EMBS International Conference on Biomedical Robotics and Biomechatronics, 2006. BioRob 2006.*, vol. 427. IEEE, pp. 869–874. [Online]. Available: http://ieeexplore.ieee.org/document/1639200/

[15] E. Hajissa, C. Celian, K. O. Thielbar, F. Kade, Y. A. Majeed, and J. L. Patton, "Stroke rehabilitation with distorted vision perceived as forces," in *2019 IEEE 16th International Conference on Rehabilitation Robotics (ICORR)*, pp. 644–647, ISSN: 1945-7901. [Online]. Available: https://ieeexplore.ieee.org/document/8779410

[16] E. Hajissa, A. Shah, and J. L. Patton, "Visual limit-push training alters movement variability," vol. 65, no. 10, pp. 2162–2167, conference Name: IEEE Transactions on Biomedical Engineering. [Online]. Available: https://ieeexplore.ieee.org/document/8233203

[17] S. Plagenhoef, F. G. Evans, and T. Abdelnour, "Anatomical data for analyzing human motion," vol. 54, no. 2, pp. 169–178. [Online]. Available: http://www.tandfonline.com/doi/abs/10.1080/02701367.1983.10605290

[18] H. Gomi and R. Osu, "Task-dependent viscoelasticity of human multijoint arm and its spatial characteristics for interaction with environments," vol. 18, no. 21, pp. 8965–8978, publisher: Society for Neuroscience. [Online]. Available: https://www.jneurosci.org/lookup/doi/10.1523/JNEUROSCI.18-21-08965.1998

[19] K. P. Tee, E. Burdet, C. M. Chew, and T. E. Milner, "A model of force and impedance in human arm movements," vol. 90, no. 5, pp. 368–375, publisher: Springer Science and Business Media LLC. [Online]. Available: https://link.springer.com/10.1007/s00422-004-0484-4

[20] D. P. M. v. V. R. Fellow and G. Wulf, "Extrinsic feedback for motor learning after stroke: What is the evidence?" publisher: Taylor & Francis. [Online]. Available: https://www.tandfonline.com/doi/full/10.1080/09638280500534937

[21] J. L. Patton, M. E. Stoykov, M. Kovic, and F. A. Mussa-Ivaldi, "Evaluation of robotic training forces that either enhance or reduce error in chronic hemiparetic stroke survivors," vol. 168, no. 3, pp. 368–383. [Online]. Available: http://link.springer.com/10.1007/s00221-005-0097-8

[22] P. Dizio and J. R. Lackner, "Motor adaptation to coriolis force perturbations of reaching movements: endpoint but not trajectory adaptation transfers to the nonexposed arm," vol. 74, no. 4, pp. 1787–1792. [Online]. Available: https://www.physiology.org/doi/10.1152/jn.1995.74.4.1787

[23] R. Shadmehr and F. A. Mussa-Ivaldi, "Adaptive representation of dynamics during learning of a motor task," vol. 14, no. 5, pp. 3208–3224, publisher: Society for Neuroscience Section: Articles. [Online]. Available: https://www.jneurosci.org/content/14/5/3208

[24] D. M. Wolpert, Z. Ghahramani, and M. I. Jordan, "An internal model for sensorimotor integration," vol. 269, no. 5232, pp. 1880–1882. [Online]. Available: https://www.science.org/doi/10.1126/science.7569931

[25] A. Melendez-Calderon, E. Rodrigues, K. Thielbar, and J. Patton, "Movement therapy without moving — first results on isometric movement training for post-stroke rehabilitation of arm function," in *2017 International Conference on Rehabilitation Robotics (ICORR)*. IEEE, pp. 106–110. [Online]. Available: https://ieeexplore.ieee.org/document/8009230/

[26] N. Malfait, P. L. Gribble, and D. J. Ostry, "Generalization of motor learning based on multiple field exposures and local adaptation," vol. 93, no. 6, pp. 3327–3338, publisher: American Physiological Society. [Online]. Available: https://journals.physiology.org/doi/full/10.1152/jn.00883.2004

[27] R. A. Scheidt, M. A. Conditt, E. L. Secco, and F. A. Mussa-Ivaldi, "Interaction of visual and proprioceptive feedback during adaptation of human reaching movements," vol. 93, no. 6, pp. 3200–3213, publisher: American Physiological Society. [Online]. Available: https://journals.physiology.org/doi/full/10.1152/jn.00947.2004

[28] E. Burdet, K. P. Tee, I. Mareels, T. E. Milner, C. M. Chew, D. W. Franklin, R. Osu, and M. Kawato, "Stability and motor adaptation in human arm movements," vol. 94, no. 1, pp. 20–32, publisher: Springer Science and Business Media LLC. [Online]. Available: http://link.springer.com/10.1007/s00422-005-0025-9

[29] D. Wolpert, Z. Ghahramani, and M. Jordan, "Are arm trajectories planned in kinematic or dynamic coordinates? an adaptation study," vol. 103, no. 3. [Online]. Available: http://link.springer.com/10.1007/BF00241505

[30] P. Bourdin, M. Martini, and M. V. Sanchez-Vives, "Altered visual feedback from an embodied avatar unconsciously influences movement amplitude and muscle activity," vol. 9, no. 1, p. 19747. [Online]. Available: https://www.nature.com/articles/s41598-019-56034-5

[31] S. Kim, J. Kwon, J.-M. Kim, F. C. Park, and S.-H. Yeo, "On the encoding capacity of human motor adaptation," vol. 126, no. 1, pp. 123–139. [Online]. Available: https://journals.physiology.org/doi/10.1152/jn.00593.2020

[32] A. Cancrini, B. Borghi, N. R. Aghamohammadi, A. Ramirez, C. Celian, and J. L. Patton, "PRISM: Parameter recovery identification from synthetic modeling," in *International Conference on Rehabilitation Robotics (ICORR)*. IEEE, p. Accepted.

Efficient Multi-Positioned Training for Regression-Based Myoelectric Control: Exploring Transformer Models with Transfer Learning

Shriram Tallam Puranam Raghu
Institute of Biomedical Engineering
University of New Brunswick
Fredericton, Canada
stallam@unb.ca

Heather E. Williams
Institute of Biomedical Engineering
University of New Brunswick
Fredericton, Canada
heather.williams@unb.ca

Erik Scheme
Institute of Biomedical Engineering
University of New Brunswick
Fredericton, Canada
escheme@unb.ca

***Abstract*—State-of-the-art upper-limb myoelectric prostheses are typically controlled using classification-based models that *do not* offer simultaneous control of wrist and hand movements (degrees of freedom or DOFs). Regression-based alternatives are being studied because they *do* offer simultaneous DOF control, yielding more natural movements, but generally require longer training routines. We investigated methods to reduce the training burden for regression-based myoelectric control. Five different methods to train regression models were tested using electromyographic (EMG) data collected from the forearms of 10 able-bodied participants. First, models were either trained traditionally with data from elbows at 90° position, with data from 3 limb positions, or trained by few-shot learning (with fewer data from 3 limb positions). Then, transfer learning was employed to pre-train models using data from all other users, with the models subsequently fine-tuned using either traditional or few-shot learning with new end-user data. The resulting five models were evaluated using linear regressor-, Convolutional Neural Network-, and Transformer-based approaches. Interestingly, the transfer learning pre-trained model in conjunction with few-shot fine-tuning achieved the second-highest median R^2 of 0.76 across all participants. Our findings offer a proof of concept for regression-based myoelectric control of multiple DOFs that may more closely resemble natural limb function.**

***Index Terms*—myoelectric control, electromyography, regression, transformers, transfer learning, few-shot learning**

I. Introduction

Together, the human hand and wrist allow us to perform many activities of daily living. The hand, whose function is to manipulate, grip, and grasp, is comprised of complicated joints. The wrist is responsible for orienting the hand in space and includes three degrees of freedom (DOFs): 1) flexion/extension, 2) abduction/adduction, and 3) pronation/supination. These DOFs allow the wrist and hand to perform movements at the same time with varied velocities. Replicating these simultaneous movements with proportional control across multiple limb positions remains a challenge for the prosthetics field.

State-of-the-art myoelectric prostheses aim to restore lost function after amputation. These devices capture and use electromyographic (EMG) signals generated by the muscles of a user's residual limb. Signals are captured by electrodes embedded in its socket, and are then interpreted by its controller to initiate user-intended actions such as a hand open/close and wrist rotation [1], with variations in movement velocity offered proportionally to the user's muscle contraction strength [2].

To initialize a pattern recognition model for use, a user must first perform a series of muscle contractions, known as a training routine [1]. A prosthetic hand that is capable of opening and closing, for instance, normally needs to be trained for three distinct movement scenarios: hand open, hand close, and no movement (rest). For each such scenario, the user is prompted to contract their residual limb muscles in unique and consistent manners. Afterwards, the controller's trained model is ready to interpret new incoming EMG signals during daily device use.

Pattern recognition models for upper limb prosthesis control are typically controlled using classification-based models, which repeatedly classify short time windows of movements. Notably, these models *do not* offer simultaneous control of multiple wrist and hand movements because they can only output one class decision at a time, and as such, do not yield smooth movements.

Regression-based models, however, *do* offer simultaneous control of multiple DOFs [3], and arguably yield smoother and more natural movements. Rather than training distinct classes as with classifiers, regressors are employed to build models that map EMG data to the continuous proportional level of activation of each DOF (e.g. an output may be 50% hand open *and* 30% wrist pronation). To enable robust simultaneous and independent DOF control, regressors require training routines that involve a series of repeated dynamic movements, with users instructed to contract their muscles through a desired range of motion. Because this training typically includes combinations of DOFs, and variations within each, regressors require longer training routines than classifiers, which can be burdensome for the user.

Another challenge in myoelectric control is that unexpected changes in EMG signals can cause even well-trained models to degrade due to confounding factors [4]. Inherently,

Research supported by the Natural Sciences and Engineering Research Council of Canada (Grants RGPIN 2020-04776 and ALLRP 570710-2021).

changes in the position of the upper arm during daily device use are known to alter forearm EMG signals. These positional changes pose problems when a model is only trained with the user's arm at their side, elbow bent at $90°$, and their prosthetic hand out in front (that is, in one limb position, as is common) [5]. It has been shown that when training routines are performed in varied limb positions, confounding factors are mitigated and more reliable control results are obtained. Fortunately, machine learning models can now handle EMG data from multiple limb positions and yield performance that is robust to changes in input signals [4]. Multi-limb position training, however, increases the time and effort associated with model training [6].

The use of transfer learning approaches has been shown to reduce the duration of model training by users [7], [8]. This is particularly relevant for multi-limb position training routines and when repeated dynamic and simultaneous muscle contractions are required for training a regression-based model. With transfer learning, a model is initially pre-trained using a large amount of EMG data from other individuals to become the starting point for a new user's device control. The new user's model is then fine-tuned using a smaller amount of training data specific to their muscle activations. Although Ameri *et al.* previously investigated the use of regression with transfer learning to potentially reduce the effect of electrode shift [9], no studies have investigated whether the technique can provide accurate control in multiple limb positions and if it can reduce training burden in regression-based control.

In this work, we investigate the potential of transfer learning to reduce the training burden inherent to regression-based myoelectric control across limb positions. We evaluate this potential by comparing the performance of three regressors: a transformer, a convolutional neural network (CNN), and a linear regressor (LR). The transformer and CNN regressors were evaluated both with and without transfer learning, while the LR served as a baseline. Our evaluation focused on the impact of transfer learning on model performance and the feasibility of reducing user-specific calibration data. We explored whether transfer learning can enable accurate and proportional simultaneous control of wrist and hand devices that are robust to changes in limb position and minimize the required user training. While transformers have recently been explored for myoelectric control [10], and the robustness of regression-based models to limb position variations has been examined [11], the application of transfer learning to regression models for multi-degree-of-freedom control across limb positions remains an open question. This work aims to address this gap and determine the viability of transfer learning with advanced regression architectures, such as transformers and CNNs, for next-generation upper limb prosthesis controllers.

II. Methods

A. Participants

Ten participants without upper-body pathology or recent neurological or musculoskeletal injuries were recruited. Their median age was 23.5 years (range: 21–32), 3 participants were male, 7 were female, 8 were right-handed, 2 were left-handed, 5 had some experience with pattern recognition, and the remaining 5 had no experience. Each participant provided written informed consent. Approval of all ethical and experimental procedures and protocols was granted by the University of New Brunswick's Research Ethics Board (REB #2024-082) and performed in accordance with the Declaration of Helsinki.

B. Equipment

Six Delsys Trigno electrodes (Natick, USA) were affixed to the participants' right forearm, spaced equidistantly around the area of maximum muscle bulk, as shown in Fig. 1A. EMG signals were recorded with a sampling rate of 2000 Hz. A custom Python script captured streamed data from the electrodes and simultaneously displayed participant instructions.

C. EMG Data Collection

Participants followed onscreen instructions to ensure that they executed similarly paced continuous wrist and hand motions within their range of muscle contraction intensity capabilities.

Muscle Contractions: Participants elicited both single- and multi-DOF forearm muscle contractions for a period of 4 seconds each, by performing oscillations between extremes of the DOFs, as illustrated in Fig. 1B and described below.

Single-DOF muscle contractions included:

- Forearm muscles at rest, followed by oscillations between hand open and close
- Forearm muscles at rest, followed by oscillations between forearm pronation and supination

Multi-DOF muscle contractions included:

- Forearm muscles at rest, followed by oscillations between hand open & forearm pronation and hand close & forearm supination
- Forearm muscles at rest, followed by oscillations between hand close & forearm pronation and hand open & forearm supination

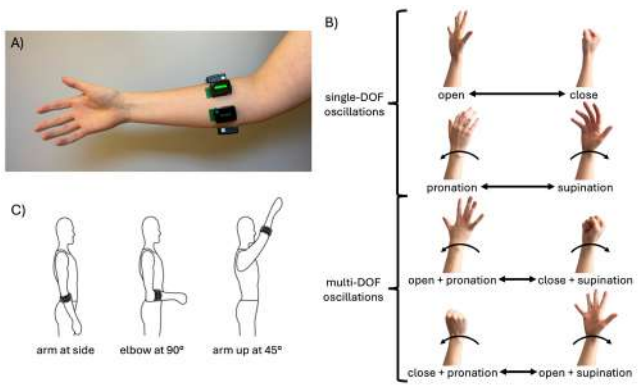


Fig. 1. A) Placement of EMG electrodes, equidistant around the forearm of each participant, over the area of maximum muscle bulk, and with hand at rest, B) single- and multi-DOF oscillating muscle contractions performed, and C) limb positions in which contractions were performed.

Limb Positions: Participants repeated the above-mentioned single- and multi-DOF oscillating muscle contractions in three limb positions, as illustrated in Fig. 1C and described below.

- With the participant's arm at their side (a total of 60 seconds of rest and 12 repetitions of each oscillation)
- With their elbow bent at $90°$ (a total of 80 seconds of rest and 16 repetitions of each oscillation)
- With their arm up $45°$ from vertical (a total of 60 seconds of rest and 12 repetitions of each oscillation)

D. Data Pre-Processing

The EMG data from the six forearm electrodes were filtered using 4^{th}-order zero-phase filters: a highpass filter with a cutoff of $20\,\text{Hz}$ and a lowpass filter with a cutoff of $450\,\text{Hz}$. Additionally, a notch filter at $60\,\text{Hz}$ was used to remove power-line interference. Data were segmented into overlapping windows with a $13.5\,\text{ms}$ increment (chosen based on the communication protocol of the Delsys electrodes). For the CNN regressor and the LR, the window length was set to $150\,\text{ms}$, which is optimal for EMG pattern recognition tasks [12]. For the transformer regressor, the window length was set to $32\,\text{ms}$. The log amplitude spectrum of each window was then computed for each window, yielding spectral feature vectors. For the CNN, each spectral vector was reshaped and presented as a 'Frequency Bin x Channel' image. Finally, for the LR, these spectral vectors served as inputs. For the transformer, 32 consecutive spectral vectors were presented as a sequence. In all cases, the spectral vectors were standardized to have zero mean and unit variance. An example spectrogram across the 6 channels is illustrated in Fig. 2.

E. Control Model Implementation

In previous prosthesis control studies, temporal classifiers such as long short-term memory (LSTM) regressors have shown promise. These classifiers can learn the dynamics of how EMG signals vary over time to yield improved predictive performance, as evidenced by real-time experimentation [13], [14]. Inspired by these results, a temporal transformer regressor was implemented in this current study to evaluate its suitability for regression-based control. For comparative purposes, a CNN regressor and an LR were also implemented.

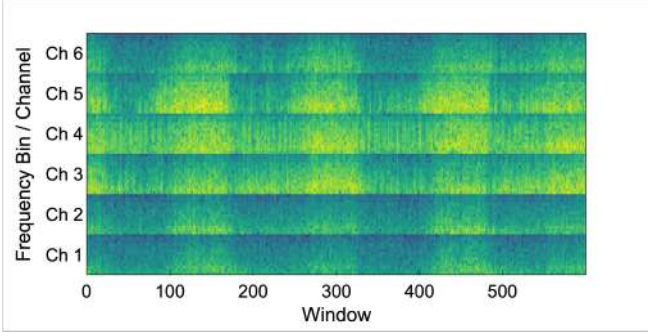


Fig. 2. An example spectrogram across the 6 channels (Ch). The y-axis shows the frequency bins in each of the 6 channels, and the x-axis shows the EMG data windows.

1) Transformer Regressor: Learnable positional encoding [15] prepared the captured EMG data for input to the transformer regressor's architecture. The architecture consisted of 4 encoder layers, each of which included a 64-dimension key space and 2 attention heads. The feedforward dimension within these layers was also 64. A dropout rate of 0.5 was applied within the encoder layers. A multilayer perceptron (MLP) with three layers followed these encoder layers, each with 128 units. Layer normalization and rectified linear unit (ReLU) activation were used throughout the MLP. A final linear layer used the MLP outputs to produce regression-based model predictions.

2) CNN Regressor: To ensure a fair comparison, the CNN regressor's architecture was kept similar to that of the transformer, with the 4 encoder layers replaced with 4 convolution blocks. Each block consisted of a 2D convolution layer, a batch normalization layer, and a ReLU activation layer. Each convolution layer had 64 filters, with a size of 3x3. The first three convolution blocks also included a 2D maximum pooling layer, with a pooling size of 2x1 and a stride of 2x1.

3) Linear Regressor (LR): LR has been established as a baseline in the literature [16]. In this work, LR was implemented on a per-DOF basis and the coefficients were obtained using ordinary least squares [16].

4) Description of Five Regression-Based Models: The EMG data were divided into 3 categories: training, validation, and testing. Specifically, five models were developed and validated, with each differing based on the data with which they were trained. Testing data were extracted from 5 seconds of rest and the final 4 occurrences of each oscillation performed in all 3 limb positions. Of the remaining EMG data, 75% were used for training of all models and 25% were used for validation of all models.

Models 1–3: The first three models were trained in a within-subject fashion, using data only from the active participant.

1) ***Standard Model (SM):*** A model trained with a total of 15 seconds of rest and 4 DOF oscillations (2 single-DOF, 2 multi-DOF) performed 12 times each, with the elbow bent at $90°$ (as per standard pattern recognition-based training routines [17]).
2) ***Full Model (FM):*** A model trained with the first 5 seconds of rest and the 4 DOF oscillations performed 4 times each in 3 limb positions (with the amount of resulting data equal to that of the SM, as less data were used per limb position).
3) ***Few-Shot Model (FSM):*** A model trained with the first 5 seconds of rest and the 4 DOF oscillations performed only once in 3 limb positions (as with the FM, but with only a single repetition of each DOF oscillation [18]).

Note that additional EMG data were collected with the elbow bent at $90°$ (as detailed in Section II-C) to facilitate training of both the SM and FM using the same amount of data.

Models 4–5: Two additional models were trained in a transfer learning fashion. Each model was pre-trained using the data from the nine other participants (15 seconds of rest and 12 seconds of each oscillation in 3 limb positions, as in the FM, per participant). The models were then adapted for the (10^{th}) participant under test by replacing their final layers and fine-tuning them using that participant's data. Subsequently, all previous layers were unfrozen and further trained using the same data. The two models with transfer learning included:

4) ***Pre-Trained Standard Model (PT-SM):*** A pre-trained model, fine-tuned for the new participant using data consistent with the SM.
5) ***Pre-Trained Few-Shot Model (PT-FSM):*** A pre-trained model, fine-tuned for the new participant using less data consistent with the FSM.

Note that LR transfer learning models were not tested, as LR is not conducive to this kind of knowledge transfer.

F. Exploration of Single-DOF vs Multi-DOF Training

To enable robust simultaneous and independent control of multiple DOFs with regression, a trained model must be equipped to handle combinations of DOFs. Researchers often assume that these combinations are implicitly learned by the models using training data only from single DOF activations [17]. In this work, we explicitly explored this assumption by comparing the transformer regressor trained with: 1) single-DOF data only, 2) multi-DOF data only, and 3) both single *and* multi-DOF data. To do so, we mimicked the FM training approach, but modified the inclusion of the DOF oscillations accordingly.

G. Performance Evaluation

Since regression can be used to control two DOFs simultaneously at varying speeds, each window was labelled with two values: one that represented the hand open/close DOF and one that represented the forearm pronation/supination DOF. Each value ranged from -1 (full hand close or full forearm pronation) to 1 (full hand open or full forearm supination), where 0 represents rest.

This data labelling scheme was based on slight modifications to a "squared proportional control" approach presented in a previous work [19]. Pilot testing of the models in an online, user-in-the-loop target acquisition test confirmed that the approach yielded a higher fidelity of control during low proportional control values (leading to an improved user experience). The labelling modifications introduced in this study included the establishment of low and high thresholds to define the shape of the target shown in Fig. 3. The low threshold was set to encourage the model to eliminate unwanted jitter during rest. It is worth noting that though many regression studies do not explicitly incorporate this threshold in labelling, they do set a threshold as a post-processing step to eliminate jitter [20]. By establishing a low threshold in labelling, our work both eliminated the need for a post-processing step and allowed each model to inherently handle hand-at-rest conditions. Furthermore, establishing a high threshold should enable users to achieve maximum speeds without overexertion during prolonged use. Although these modifications have only a minor impact on the offline results presented in this preliminary work, our experience suggests that they may be important for supporting goal-oriented online control.

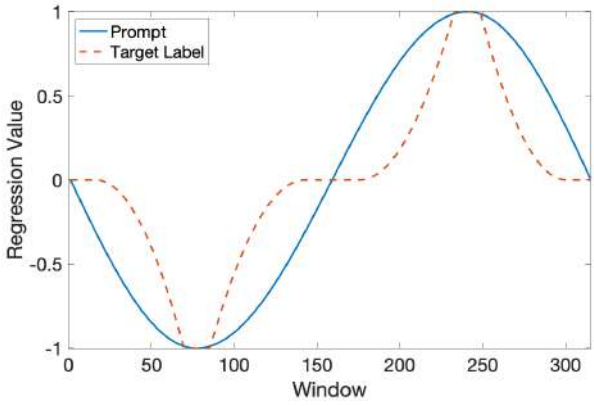


Fig. 3. Labelling scheme outcomes. The solid blue line represents the prompt displayed to the user and the dashed orange line shows the corresponding target label for the given window.

The performance of the models was evaluated by computing the coefficient of determination, R^2, values between the predictions and target labels assigned to the test data.

Finally, to identify any differences between the control models under investigation, a one-way repeated measures analysis of variance (RMANOVA) was performed on the median R^2 values across all limb positions. Data were normally distributed. When the resulting controller effects were deemed significant (that is, when the Greenhouse-Geisser-corrected p-value was less than 0.05), pairwise comparisons (t-tests) between the controllers were conducted. Pairwise comparisons were considered significant when the Šidák-corrected p-value was less than 0.05.

III. Results

Fig. 4A depicts the R^2 values by regressor (transformer, CNN, and LR) as averaged across all limb positions. When comparing within model types (SM, FM, and FSM), the statistical comparison revealed both the transformer and CNN outperformed the LR in all 3 cases. Specifically, the transformer outperformed the LR with $p<0.001$ in 3 all cases and Cohen's $d>0.401$; while the CNN outperformed the LR with $p<0.001$ in 3 all cases and $d>0.3670$.

Fig. 4B illustrates the transformer regressor's R^2 values when tested in each of the three limb positions. A high median R^2 value (close to 1) indicated that a model type was a good fit for the data. Overall, the FM predictably resulted in the highest median R^2 (0.80) across all participants. However, the PT-FSM yielded a close second-highest median R^2 of 0.76.

When comparing the 5 different model types within the transformer regressor, as depicted in Fig. 4C, the statistical

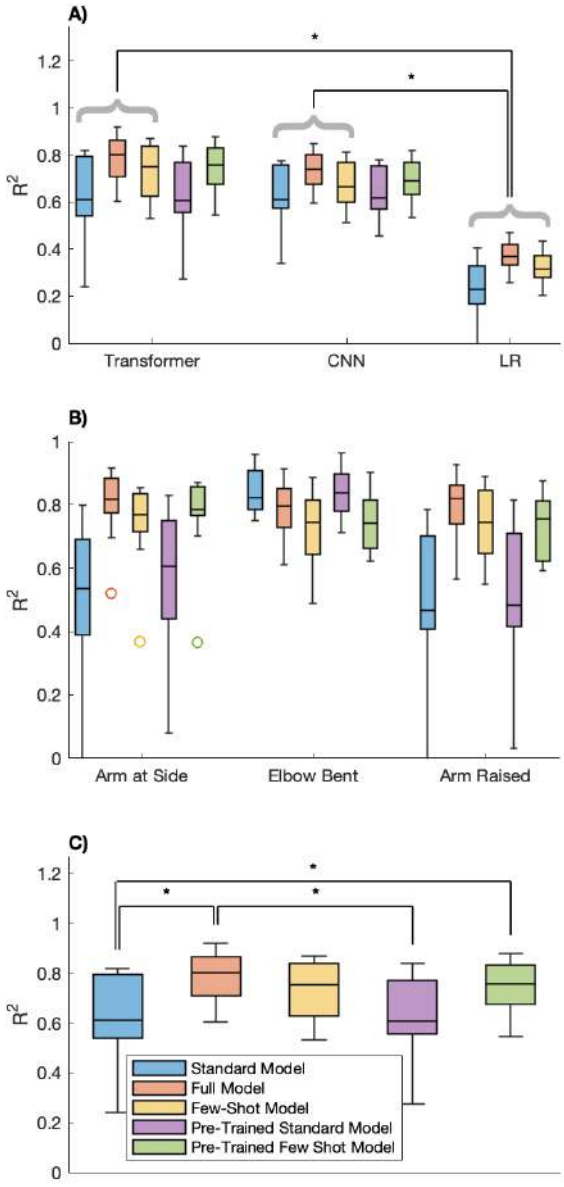


Fig. 4. Box plots illustrating R^2 values for each of the five control models investigated, with results presented A) by regressor (transformer, CNN, and LR), each across all limb positions, with statistical significances between regressors, and B) the transformer regressor in each limb position, and C) the transformer regressor across all limb positions, with statistical significances between models. * denotes p-value < 0.05. Note that in panel A), curly brackets indicate that statistical comparisons were performed on each type of model (i.e., Standard Model vs Standard Model, etc.).

comparison revealed that the R^2 values of the FM was significantly better than the SM (p=0.006, d>0.178) and the PT-SM (p=0.015, d>0.156). Furthermore, the PT-FSM performed significantly better than the SM (p=0.033, d>0.135). Notably, the FM was not significantly different from the FSM or the PT-FSM.

Fig. 5 illustrates the R^2 values of the FM when training a transformer with single- *or* multi-DOF data, or with both single *and* multi-DOF data. The highest median R^2 value (0.80) across all participants was achieved when the FM was trained with single data *and* multi-DOF datasets. Performance dropped significantly when using only the multi-DOF (p<0.001, d>0.173) or single-DOF (p<0.001, d>0.261) data. Training with only multi-DOF, however, was significantly better (p=0.047, d>0.088) than only training with the single-DOF cases.

IV. Discussion

The human arm can perform combined movements in multiple limb positions; for instance, reaching overhead to grasp an object while slowly rotating the wrist. Regression-based myoelectric control models can yield simultaneous control of multiple DOFs and independent speed control to better mimic the function and movements of an intact upper limb [3]. This control, however, comes at the expense of longer training routines that introduce user burden. Additionally, control models that predict movements across multiple limb positions can further increase training durations. For these and other reasons, classifiers remain more commonly implemented for upper limb prosthesis control, with model training conducted in a simple bent elbow position [17]. The findings from this work suggest that a shift to the use of regressors and multi-limb position training for myoelectric control is feasibly on the horizon, through the use of transfer learning and FSM approaches.

Our research capitalized on the positive attributes of transformers to implement regression-based myoelectric prosthesis control. Transformers are deep learning networks that have emerged as an architecture used for natural language processing and computer vision applications [21]. Their ability to capture long-term relationships and contextual patterns in time series signals has opened new opportunities for control that uses EMG data. This study demonstrated that regression models (as implemented using a transformer) can successfully provide accurate movement predictions across varied limb positions (when trained with data from each position).

Our results also indicated that although both transformers and CNNs significantly outperformed the LR, the transformer was slightly (though not significantly) better than the CNN. Still, the transformer exhibited larger improvements, as evidenced by the larger Cohen's d values. Our findings corroborate results in the broader literature that demonstrate the efficacy of temporal models when employed for EMG pattern recognition [22], [13].

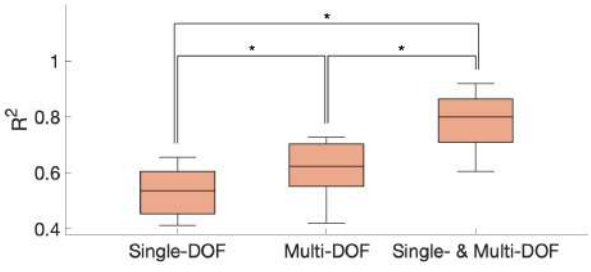


Fig. 5. Box plots illustrating R^2 values when training the transformer (FM) with single- or multi-DOF data, or both single and multi-DOF data. * denotes p-value < 0.05.

Recall that our work considered whether single- or multi-DOF training datasets (or both) provided regression-based models with the necessary data to yield accurate movement predictions. The FM was found to perform the best when trained with both single- and multi-DOF muscle contractions. This same training requirement was expected to hold true for all five models implemented through this study's transformer regressor. As such, the research findings and discussion that follow are based on this combined single- and multi-DOF training approach.

The transformer regressors outperformed the LR and the CNN while using a window that is $\approx 5\text{x}$ shorter in duration. This observation suggests that using a large window size is not a requirement when employing temporal models, likely as they are able to leverage temporal information across windows. Indeed, further pilot testing revealed that there were minimal differences in performance when increasing the window length from $32\,\text{ms}$ to $150\,\text{ms}$ for the transformer. On the other hand, this same testing revealed a significant reduction in performance for both LR and CNN regressors when decreasing the window length, further reinforcing our hypothesis that the temporal information learned across windows by the transformer alleviates the need for large window lengths.

We also compared the predictive accuracy and data fit of the five transformer models under investigation in this study. The models ranked as follows, from best to worst: 1) FM (R^2=0.80), 2) PT-FSM (R^2=0.76), 3) FSM (R^2=0.72), 4) PT-SM (R^2=0.61), and 5) SM (R^2=0.61).

As anticipated, the FM (trained with 5 seconds of rest and 4 of each oscillation performed in 3 limb positions) was top-ranked. It took a total of 3.45 minutes of training time to capture its required EMG data. Surprisingly, the PT-FSM (pre-trained by 9 participants who performed 5 seconds of rest and 4 of each oscillation in 3 limb positions, and then fine-tuned to a new 10^{th} participant) was a close second. It took only 1.05 minutes of retraining time to capture its participant-specific data—a 2.4-minute, 70% decrease in collection time versus the FM. The PT-FSM also did *not* have a significantly different median R^2 value versus the FM. Together, these findings demonstrated that transfer learning can indeed reduce the amount of training data required for regression-based models, without sacrificing model predictive accuracy.

Our work also reinforced that training a model in more than one limb position positively impacts overall device control performance. Consider that the lowest-ranked SM (trained with 15 seconds of rest before each of 4 oscillations performed 12 times, with the elbow bent at 90° as per standard pattern recognition-based training routines [17]), performed the best when tested in the same limb position in which it was trained. Conversely, it performed poorly in all other limb positions. This finding aligns with the literature surrounding the confounding factor of the limb position effect, which identifies that device control performance degrades in untrained limb positions [4]. This current work, therefore, concurs with recommendations that regression-based control solutions should be trained across multiple limb positions.

In addition, this study allowed us to consider alternative means of reducing the training burden. Interestingly, the third-ranked FSM performed favourably, even *without* implementing transfer learning. This finding supports the notion that few-shot models eliminate the need for long data collection sessions, as reported by Godoy *et al.* [18]. In their study, a few-shot approach is recommended for scenarios where data are scarce, collected in different sessions, or collected for several users. Consider that in this work, the FSM was trained with limited EMG data (trained with 5 seconds of rest and only 1 of each oscillation performed), but that the data included signals from three limb positions (that is, a richer training dataset was captured). Despite the limited training samples in each limb position, the few-shot transformer model performed well when compared to the FM. This particular finding suggests that few-shot learning is a promising means of reducing training burden, and reaffirms that more variability in training is more important than simply more data.

Finally, it is noteworthy that the targets used to train and test the models in this work were a modified version of the prompted sinusoid, as shown in Fig. 3. While this labelling scheme had minimal impact on the findings of this offline study (the re-labelling was applied equally to both the training and testing labels, providing a consistent mapping that the models could learn), our empirical observations suggest that it more accurately reflects user behaviours when responding to sinusoidal prompts. Furthermore, pilot results from our ongoing work using the models presented herein and similar models for online control, suggest that users may prefer the finer distinction between slow and fast movements afforded by such mappings. Regardless, the potential impacts of user compliance in regression training [23] and how best to map these models to control outputs is an interesting area worthy of further research.

V. Conclusions

This work uncovered promising methods to reduce lengthy and burdensome training routines inherent to regression-based myoelectric prosthesis control solutions, that are trained across multiple limb positions. These methods include the adoption of transformer regressors, transfer learning techniques, and a few-shot model approach. We recognize that our work is offline and as such, these results may not fully explain subsequent real-world control experience. Consequently, the next steps should include real-time testing of the control methods presented. We also recognize that the EMG data collected in this research results from isotonic muscle contractions, whereas isometric contractions are used to control actual myoelectric prostheses. Future work should confirm whether the control methods that we investigated yield similar results under real-use conditions. Finally, we acknowledge that only ten participants without amputation were recruited for this study. We recommend the work be repeated using more participants, as well as with those who

have limb loss to confirm results. Despite some limitations, this work is a valuable proof of concept that lays the foundation for exciting new myoelectric prosthesis control opportunities, with device movements approaching those of a healthy human wrist and hand—that is, with simultaneous control of multiple DOFs, executed at varied speeds, and performed reliably in multiple limb positions.

REFERENCES

[1] E. Scheme and K. Englehart, "Electromyogram pattern recognition for control of powered upper-limb prostheses: State of the art and challenges for clinical use," *Journal of Rehabilitation Research & Development*, vol. 48, no. 6, p. 643–59, 2011.

[2] A. M. Simon, K. Stern, and L. J. Hargrove, "A comparison of proportional control methods for pattern recognition control," in *2011 Annual International Conference of the IEEE Engineering in Medicine and Biology Society*, 2011, pp. 3354–7.

[3] A. D. Roche, H. Rehbaum, D. Farina, and O. C. Aszmann, "Prosthetic myoelectric control strategies: A clinical perspective," *Current Surgery Reports*, vol. 2, p. 44, 2014.

[4] Y. Geng, P. Zhou, and G. Li, "Toward attenuating the impact of arm positions on electromyography pattern-recognition based motion classification in transradial amputees," *Journal of NeuroEngineering and Rehabilitation*, vol. 9, no. 1, p. 74, 2012.

[5] E. Scheme, A. Fougner, O. Stavdahl, A. D. C. Chan, and K. Englehart, "Examining the adverse effects of limb position on pattern recognition based myoelectric control," in *2010 Annual International Conference of the IEEE Engineering in Medicine and Biology*, Buenos Aires, Argentina, 2010.

[6] H. E. Williams, J. Günther, J. S. Hebert, P. M. Pilarski, and A. W. Shehata, "Composite recurrent convolutional neural networks offer a position-aware prosthesis control alternative while balancing predictive accuracy with training burden," in *2022 International Conference on Rehabilitation Robotics (ICORR)*, Rotterdam, the Netherlands, 2022.

[7] C. Prahm, A. Schulz, B. Paaßen, J. Schoisswohl, E. Kaniusas, G. Dorffner, B. Hammer, and O. Aszmann, "Counteracting electrode shifts in upper-limb prosthesis control via transfer learning," *IEEE Transactions on Neural Systems and Rehabilitation Engineering*, vol. 27, no. 5, pp. 956–62, 2019.

[8] S. Tam, M. Boukadoum, A. Campeau-Lecours, and B. Gosselin, "Intuitive real-time control strategy for high-density myoelectric hand prosthesis using deep and transfer learning," *Nature*, vol. 11, p. 11275, 2021.

[9] A. Ameri, M. A. Akhaee, E. Scheme, and K. Englehart, "A deep transfer learning approach to reducing the effect of electrode shift in emg pattern recognition-based control," *IEEE Transactions on Neural Systems and Rehabilitation Engineering*, vol. 28, no. 2, p. 370–9, 2020.

[10] R. V. Godoy, G. J. G. Lahr, A. Dwivedi, T. J. S. Reis, P. H. Polegato, and M. Becker, "Electromyography-based, robust hand motion classification employing temporal multi-channel vision transformers," *IEEE Robotics and Automation Letters*, vol. 7, no. 4, p. 10200–7, 2022.

[11] H. E. Williams, A. W. Shehata, K. Y. Cheng, J. S. Hebert, and P. M. Pilarski, "Myoelectric prosthesis control using recurrent convolutional neural network regression mitigates the limb position effect," *bioRxiv*, 2024.

[12] L. H. Smith, L. J. Hargrove, B. A. Lock, and T. A. Kuiken, "Determining the optimal window length for pattern recognition-based myoelectric control: Balancing the competing effects of classification error and controller delay," *IEEE Transactions on Neural Systems and Rehabilitation Engineering*, vol. 19, no. 2, pp. 186–92, 2011.

[13] S. T. P. Raghu, D. T. MacIsaac, and E. J. Scheme, "Self-supervised learning via VICReg enables training of EMG pattern recognition using continuous data with unclear labels," *Computers in Biology and Medicine*, vol. 185, p. 109479, 2025.

[14] S. T. P. Raghu, D. MacIsaac, and E. Scheme, "Self-supervised representation learning with augmentations of continuous training data improves the feel and performance of myoelectric control," *arXiv*, 2024.

[15] G. Zerveas, S. Jayaraman, D. Patel, A. Bhamidipaty, and C. Eickhoff, "A transformer-based framework for multivariate time series representation learning," in *Proceedings of the 27th ACM SIGKDD Conference on Knowledge Discovery & Data Mining*, ser. KDD '21. New York, NY, USA: Association for Computing Machinery, 2021, pp. 2114–24.

[16] J. M. Hahne, F. Bießmann, N. Jiang, H. Rehbaum, D. Farina, F. C. Meinecke, K.-R. Müller, and L. C. Parra, "Linear and nonlinear regression techniques for simultaneous and proportional myoelectric control," *IEEE Transactions on Neural Systems and Rehabilitation Engineering*, vol. 22, no. 2, pp. 269–79, 2014.

[17] H. E. Williams, A. W. Shehata, M. R. Dawson, E. Scheme, J. S. Hebert, and P. M. Pilarski, "Recurrent convolutional neural networks as an approach to position-aware myoelectric prosthesis control," *IEEE Transactions on Biomedical Engineering*, vol. 69, no. 7, p. 2243–55, 2022.

[18] R. V. Godoy, B. Guan, F. Sanches, A. Dwivedi, and M. Liarokapis, "Electromyography based gesture decoding employing few-shot learning, transfer learning, and training from scratch," *IEEE Access*, vol. 1, p. 104142–54, 2023.

[19] E. Scheme, B. Lock, L. Hargrove, W. Hill, U. Kuruganti, and K. Englehart, "Motion normalized proportional control for improved pattern recognition-based myoelectric control," *IEEE Transactions on Neural Systems and Rehabilitation Engineering*, vol. 22, no. 1, pp. 149–57, 2014.

[20] L. H. Smith, T. A. Kuiken, and L. J. Hargrove, "Linear regression using intramuscular EMG for simultaneous myoelectric control of a wrist and hand system," in *2015 7th International IEEE/EMBS Conference on Neural Engineering (NER)*, 2015, pp. 619–22.

[21] B. Núñez Montoya, E. Valarezo Añazco, S. Guerrero, M. Valarezo-Añazco, D. Espin-Ramos, and C. Jiménez Farfán, "Myo transformer signal classification for an anthropomorphic robotic hand," *Prosthesis*, vol. 5, no. 4, p. 1287–300, 2023.

[22] E. Eddy, E. Campbell, S. Bateman, and E. Scheme, "Big data in myoelectric control: large multi-user models enable robust zero-shot EMG-based discrete gesture recognition," *Frontiers in Bioengineering and Biotechnology*, vol. 12, 2024.

[23] C. Morrell, E. Campbell, and E. Scheme, "Exploring user compliance in the training of regression-based myoelectric control," in *Myoelectric Controls Symposium*, Fredericton, 2024.

A First Design of the Inertially Correct Testbed Arm Platform for Testing of Wearable Devices

William White[1], Jonathan Hong[1], Scott Uhlrich[1], and Edoardo Battaglia[1]

***Abstract*— Wearable systems for rehabilitation and assistive applications presents significant challenges related to personalization to individual size and shapes of the users' limbs, which can often turn design into a slow and challenging trial and error process. Additionally, because of the limited amount of body shapes and sizes that can be tested in research settings, wearable systems risk being ill-suited when it comes to adapting to individual users, and can be perceived as difficult or uncomfortable to interact with. In this paper we propose to address this challenge through the design of simple and relatively low-cost physical simulators. In this first iteration we offer a proof of concept of this approach with the Inertially Correct Arm, a physical prototype that is designed to have the shape and inertia properties consistent with anthropometric data on the average arm for male population and is intended as a tool to aid development of a soft arm-swing exosuit. In addition to the inertia properties, we tested a few different configurations for damping obtained through deformable pads compressed between plates at fixed distances, and compared the results of free swinging from a 90 degree shoulder elevation from the ICT with results from human participants, as quantified by dynamic time warping distances. Our results show that the system follows human data more closely when a higher level of joint resistance is present.**

I. INTRODUCTION

There is an ever-increasing number of people with physical disabilities – around 16% of people in the world according to World Health Organization figures [1], with comparable numbers in the United States [2], [3] and Europe [4]. The number of people affected by pathologies that cause severe impairment, such as stroke, Parkinson's disease or other neurological disorders has been increasing steadily every year [5]–[7]. Overall, recent estimates suggest that one in three people in the world will be in the position to benefit from rehabilitation services because of an illness or injury at some point in their lives [8]. It is no surprise then that research on devices that can help facilitate this type of therapy and/or provide assistance for people with disabilities have garnered a strong interest, with applications in therapy for both lower and upper limb [9]–[15].

A particular class of robots used in assistance and rehabilitation are wearable robots, which generally take the form of exoskeletons or exosuits that are kinematically coupled to the users' limbs [9], [10], [12], [16]. This class of systems has proven to be versatile in its ability to not only provide rehabilitation for a variety of conditions, but also be used in applications augmenting the capabilities of healthy individuals [15], [17], [18]. However, their design presents unique challenges, related to the fact that actuators, links and sensing elements are coupled to the limbs of the user, leading to the necessity for the system to be able to apply any desired mechanical action in a way that can adapt to different shapes and sizes, and is safe for the user. This problem has been approached with a variety of designs, from systems that only apply forces to the lower arm, [19], to systems that connect directly to the upper limb and solve the challenge created by the tighter coupling with a more careful kinematic design [16]. However, the coupling between the user and the wearable system always has to be kept in mind, and is subject to the specific body size of the user.

This leads to challenges in the design of new systems, where modeling is generally followed by a trial and error process and careful testing. While this was done for many systems in the state of the art, it tends to be time consuming. Additionally, safety is not the only requirement for a wearable system. In [20] Sugawara et al. reported an abandonment rate of around 19% for assistive devices from a survey of 1390 users, with the rate being higher for orthoses and prostheses, and discomfort while using the device being reported as one of the leading causes for abandonment. This is consistent with a more general trend of abandonment of wearable devices that has been observed across different applications [21], [22]. It would then be helpful to be able to automate part of the testing process with evaluation on bodies of different shapes and sizes.

In this paper we proposed a first iteration of an approach to streamline this design process by building physical simulators. Specifically, we introduce the Inertially Correct Testbed arm (ICT), an upper limb physical simulator that is designed to have inertia properties consistent with the average human arm for a male user, which we named taking inspiration from the Anatomically Correct Testbed hand introduced in [23]. We will describe the design rationale and process, the physical construction of the prototype, and a test where we compare kinematic data for a passive fall movement from a 90 degree shoulder extension for both human participants and the ICT with deformable pads with different levels of contact force, to simulate passive friction/damping that is naturally present in the human body, for an intended application as a test platform for an arm swing soft exosuit [24].

II. CONCEPT

Construction of physical simulators of the human body is relatively under-explored in the state of the art, and is for the most part represented by simplified models in

[1]William White, Johnathan Hong, Scott Uhlrich, and Edoardo Battaglia are with the Department of Mechanical Engineering University of Utah, 201 Presidents' Cir, Salt Lake City, UT 84112 USA william.white@utah.edu

medical trainers and mannequins [25]–[27]. For what concerns biomechanical simulations, very powerful tools are available in software simulation, such as OpenSim [28], which enable analysis of motion as well as muscle activity and musculoskeletal models of varying complexity. However, while these simulation tools can offer important insights, they were not designed to test wearable devices and robots, and as such can be helpful in defining models that can be considered in the design, but offer limited support for simulation of the devices themselves. Some physical simulators with more advanced features do exist, but they are generally targeted for specific application, e.g. the study of kinematics and motor control in human hands [23], [29].

The motivation behind this work comes from ongoing work on development of a soft arm swing exosuit for gait rehabilitation [24], for which we felt the need for a physical platform to evaluate different ways of attaching our system to the arm and/or different types of controllers. This informs the design requirements that we set out to meet in this work, specifically: (i) we focus on simulations of passive arm movements, since muscular activity in arm swing, while present, is very limited, leading in general to very compliant behavior in the arm [30]; (ii) the arm simulator should have inertia properties close to those of a human arm; (iii) the physical simulator should have mechanical properties at the joints comparable to those of a human arm in a relaxed state; and (iv) given that the long term goal is to have different personalized physical simulators for a variety of body shapes, the system should be able to be fabricated in a relatively simple and low-cost way.

For what concerns (ii), we referred to anthropometric data collected by Plagenhoef et al. in [31] where authors collected data on weight and center of mass position for different body parts in both men and women, and reported them as a percentage of body weight and limb length. The arm simulator designed in this work is intended to represent the arm of a man weighting 153 pounds (approximately 69.4 kg). Point (iii) is more challenging, both because modeling of mechanical properties of joints is difficult, and because building adjustable mechanical damping systems to mimic them is non-trivial. In this work we evaluate the potential effectiveness of using deformable rubber pads with different levels of compressions to simulate this aspect. In the next section we report the design details for our proposed system.

III. System Design

A. Hardware

The Inertially Correct Testbed arm (ICT) was built in three distinct parts as shown in Figure 1: upper arm, lower arm, and hand. Each of these segments were constructed using silicone, to simulate human tissue, and 3D printed plastic support elements, simulating the bone. The target weight (see Table I), center of mass (COM), and moment of inertia of each segment was determined using the previously mentioned work from Plagenhoef at al. [31], and the weight was confirmed with a scale on the physical prototype (Table I).

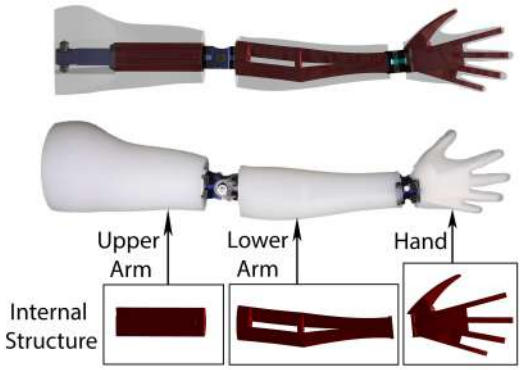


Fig. 1: Side view of the Inertialy Correct Testbed arm (ICT) and the obscured internal structural elements.

TABLE I: Estimated [31] and Actual Mass of the Inertialy Correct Arm. Weights were obtained using a digital scale with a resolution of $\pm$1g and a maximum measurement weight of 15 kg.

	Upper (g)	**Lower (g)**	**Hand (g)**	**Arm (total) (g)**
Nominal	2255	1298	451	4004
Actual	2285	1371	455	4106

In order for the ICT to better aid in the testing of ergonomic exoskeletons we molded a flexible silicone, EcoFlex 00-30 with a 1:1 ratio, into the shape of a human arm. A mold was created by segmenting a mesh rendering of a human arm in three segments as described above. The mesh was then modified to accommodate the joints for each segment (top of Figure 1). The joints were not contained within the siliconesil to prevent the silicone material properties from affecting the baseline elasticity and damping of the joints. By using silicone to construct the majority of the ICT we were able to evenly distribute the weight of each arm segment while still maintaining a coarse approximation of the compliant behavior of human arm tissue.

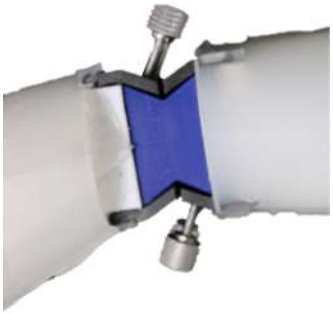


Fig. 2: Dovetail clamp and joint connections.

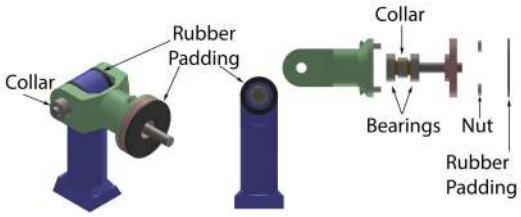
While the silicone makes the ICT durable and aids in ergonomic design, it would not be able to maintain the proper structure of each arm segment on its own. Custom designed rigid structures, intended to simulate the bones, were constructed from polylactic acid (PLA) using a 3D printer (see Fig. 1). These rigid structures serve a few

different purposes: they are used to create attachment points for the joints between each segment, they provide support for the silicone and maintain the shape of the ICT, and they have a geometry designed to place the center of mass for each limb at the location suggested by [31]. Because the mechanical properties and density of PLA are not the same as human bone, the supports were not modeled as human bones, but had a custom structure to both have better structural integrity and cause the overall system to have inertia properties comparable to those reported in [31].

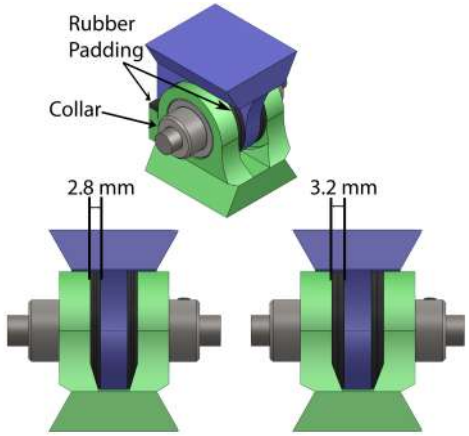
The process described so far covers inertia properties of the arm, but to build a system that has equivalent mechanical properties and kinematic behavior we will also need to have appropriate stiffness, damping and friction at the joints. To facilitate iterative testing towards these desirable properties, the connection point between each arm segment utilizes a dovetail clamp (Figure 2). This solid aluminum clamp is fastened to each segment by the use of a screw and nut. Joints are held in place by the pressure exerted by the screws, but can easily slide out of the clamp when unscrewed.

In this first design for the system, we focused on a simplified model for the shoulder joint. Upper limb and arm exoskeletons typically use a ball-and-socket joint mechanism for the components that are attached to the shoulder [16]. While this is the solution that we had considered originally, we opted for a simplified two degrees of freedom (d.o.f.) design for this first iteration for the following reasons: (i) commercially available ball-and-socket joint mechanisms typically have limited range of motion; (ii) while the kinematics of the shoulder joint is often approximated as a ball-and-socket joint, this is also a simplified model that does not match the kinematic behavior of a human shoulder [32]; and (iii) for our intended application, we are mostly concerned with arm swing movement. For these reasons, we decided to implement a simplified shoulder joint with two d.o.f. to provide flexion and abduction, but not rotation. As we mentioned in the previous section and as we will show in the evaluation section, the main focus in this work was to evaluate a few different levels of damping for the arm joint, and compare passive kinematic behavior with the behavior of human arms in passive arm swing movement. Given the modular design for the connections, the joints can be swapped out and replaced easily, and the design of a more complex and anatomically correct shoulder joint is left for future work.

Figure 3a shows the current simplified shoulder joint, which is comprised of two parts: an inner *I* and outer *U* shaped piece. The *I* component uses two sealed 8 mm stainless steel ball bearings stacked in series to reduce friction caused by ab/adduction of the ICT. Similarly, in order to reduce friction in the flexion degree of freedom, the *U* was designed with a chamber containing two more bearings held in place by a cap fastened as shown in Figure 3a. An 8 mm 1040 carbon steel rotary shaft mounted perpendicular to the ground was inserted into the *U*'s bearings and held in place using a stainless steel screw collar. A similar shaft was used to connect the *I* and *U* components through the bearings in *I* with screw collars mounted on the outside of the *U*.



(a) 2-DOF U-joint.



(b) 1-DOF axial joint in the highest (left) and lowest (right) friction configuration.

Fig. 3: ICT shoulder joint (a) and elbow joint (b). Each joint has rubber disks separating the inner (blue) and outer (green) components. The amount of friction between components can be adjusted by changing the distance between components. Spacing between components is measured from the most compressed state, 2.8 mm apart, to the least compressed state, 3.2 mm apart.

The elbow was built as a single axis joint with a limited range of rotation (Figure 3b). Similar to the ICT's shoulder, the elbow is comprised of an inner and outer piece. A single bearing is placed in the inner piece parallel to the two bearings in the outer piece. These bearings are placed on either side of the outer piece and the assembly revolves around a shaft passed through the bearings. The shaft is held in place by a pair of screw collars on either side of the outer piece. To prevent the elbow from rotating further than desired a flat platform was placed on the back of each piece. This platform was then padded using Viton rubber to prevent jarring stops. Finally, unlike the shoulder and elbow the wrist joint was built as a solid block, made from the same PLA as the other joints. This was done to reduce the complexity of the design as we assumed that the wrist would have little affect on ICT.

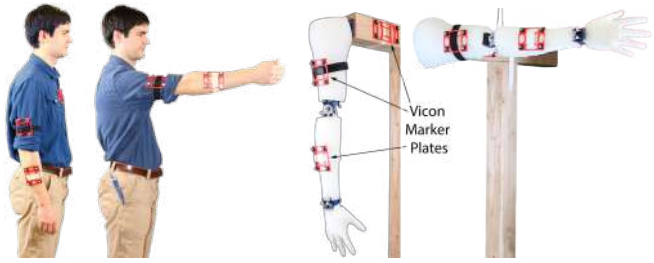
Friction between joint components was added through the use of pairs of 1.6 mm thick Viton rubber washers. These washer were placed on both inside and outside joint components as well as between the shoulder's *U* component and the mounting block (see Figure 3 for a visualization of the elbow). By altering the amount of space between

each set of washers we were able to change the amount of resistance in each joint, both through increased friction and change in the properties of the pad through compression. This will cause the ICT to lose energy as it is swinging, with the goal of making it behave more similarly to a human arm. Viton rubber was chosen for its durability and high frictional coefficient which allowed for greater damping. The space was set to vary from a minimum level of resistance where the pads were barely touching (visualized for the elbow on the bottom-right drawing of Figure 3), to the highest possible pressure that we were able to achieve with the loading system (which corresponded to a 0.4 mm deformation of the pad as measured with a caliper). An additional intermediate level was considered, for a total of three levels of resistance on each joint (which we will refer to as low, medium and high resistance throughout the paper). Since we are interested in evaluating the system for arm swing movement, we considered only changes to the elbow and shoulder flexion/extension (or elevation) joints, for a total of nine possible configurations.

IV. Evaluation

A. Experimental Setup

We performed a user study with human participants to compare the kinematics of arms swinging freely with those of the different configurations of the Inertially Correct Testbed arm (ICT). For this study, we recruited eight healthy males (mean and standard deviation: age = 26.1 ± 4.4, height = 179.1 ± 8.1 cm, weight = 73.5 ± 11.5 Kg). Prior to the study, the subjects gave written informed consent to participate. The study was approved by the Institutional Review Board of the University of Utah under IRB number 00154923.



(a) (b)

Fig. 4: We evaluated the ICT in an arm swing task by comparing kinematic data from participants dropping their arm from a 90 degrees angle (a) with the same data measured on the ICT, which was raised and released using an elastic cable held by one of the experimenters.

Kinematics were measured by a 12-camera motion capture system (Vero, VICON, Oxford, UK) for both human participants and the ICT, with a sampling frequency of 100Hz. In order to track motion during the experiment, mounting plates were designed to place markers for the Vicon motion capture system. These plates were made with a platform at each corner and curved slightly to better fit on a human arm. The Vicon markers were attached to the platform with double sided tape. To help reduce the effect the plates might have on the motion of the arm, as much material as possible was removed without the structure collapsing. Elastic straps were then threaded through the platform allowing it to be attached to the participants' arm. An equivalent setup was used for the ICT, with four reflective markers on the lower-arm, upper-arm, and cross beam which served as its "chest" area (Figure 4b). For the ICT, we tested different combinations of levels of damping/friction for the shoulder and elbow by varying the amount of pressure applied between rubber pads as described in Section III, with three levels of resistance being considered for each joint (low, medium and high), for a total of nine possible configurations.

For both human participants and the ICT, each trial consisted of lifting the arm to 90° shoulder elevation, with the elbow joint being perfectly straight, and then letting the arm drop and swing freely until it came to rest. To facilitate consistency, human participants were instructed to do this by pulling their arm forward and straight in front of them as much as they could comfortably, while keeping their torso straight and still, and were asked to be fully relaxed when they let their arm drop. They were also instructed to wear relatively light clothes (such as a t-shirt or a button down shirt), to prevent potential added resistance that could come from thick clothing. For the ICT, an experimenter used a cable wrapped around the elbow joint to lift it to 90° shoulder elevation. This ensured that the elbow joint was straight before the arm was dropped, and also facilitated consistency in maintaining the correct elevation since the experimenter could feel the direction and amount of the force being applied by the weight of the ICT. A single session of ten repetitions was done for each participant and each ICT joint configuration.

B. Data Processing

Experimental data were analyzed using MATLAB (The MathWorks, Inc. Massachusetts, USA) and the R Project for Statistical Computing (version 4.4.1). Specifically, joint angles were calculated in MATLAB from marker data, and a joint angle trajectory for the shoulder elevation was calculated for each session. Joint angle data was then segmented to identify each of the ten repetitions in each session, leading to ten segments for each participant/ICT configuration. The segmentation was accomplished by selecting as start for each trial the sample where the joint angle was decreasing from a peak value, and as end the second local minimum in the oscillatory behavior. Figure 5 shows a plot of a full session (i.e., ten trials) for one of the participants and one of the ICT configurations, with segmented trials colored in red.

For each ICT configurations, and for each of the segmented trials, dynamic time warping as implemented in the R package `dtw` [33] was used to calculate the distance from each segmented trial from each participant. Dynamic time warping can be used to compare signals that have different lengths in time, by identifying an alignment between two time series that deforms them on the time axis to minimize the distance between them. The choice for the start and end

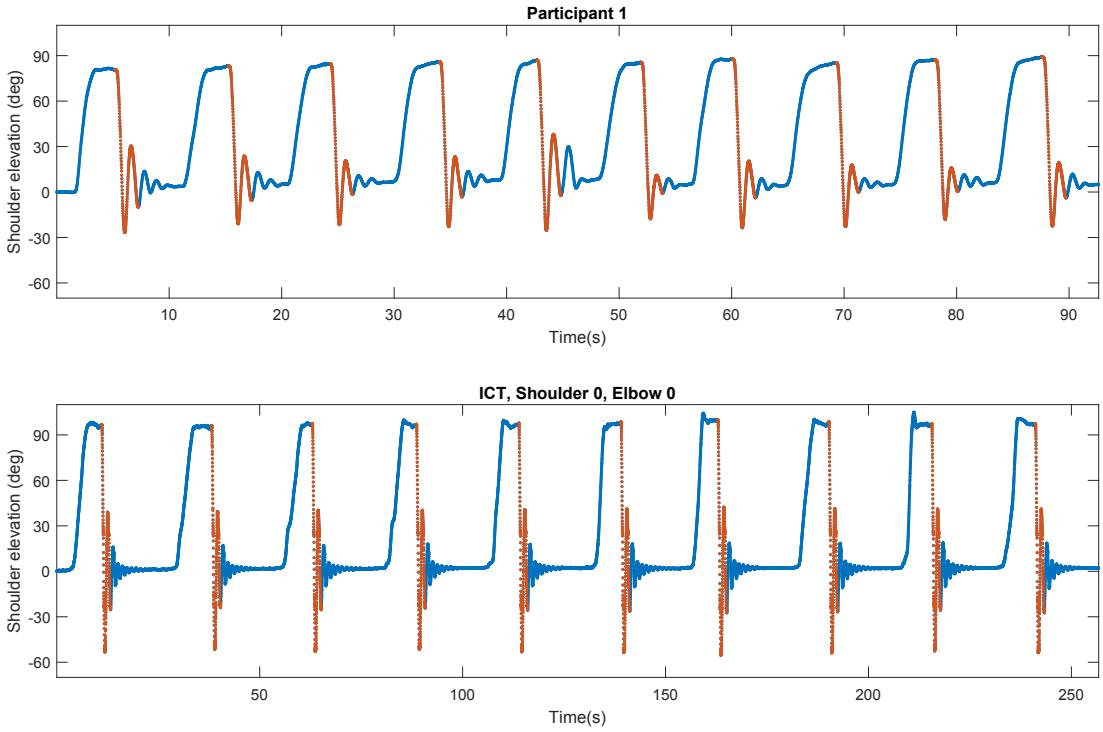


Fig. 5: Representative plots for human (top) and Inertially Correct Testbed arm (bottom). Segmented trials are shown in red.

of the segmentation was done to make such comparison meaningful: in general, systems with lower damping and friction will keep oscillating for a longer amount of time, but a difference can already be seen in the amplitude of the first few peaks, and using segments were the same oscillations are present for all systems considered will allow to match points in the time series with dynamic time warping more organically. The dynamic time warp distances for each pair of segmented trials were calculated using the ICT segment as query and human participant segment as reference, with an asymmetric step pattern to ensure one-to-one alignment, normalized with respect to the length of the ICT segment sequence according to standard practices in application of dynamic time warping [34]–[36].

C. Results

We compared dynamic time warping distances between ICT and participant trajectories for different levels of damping and friction at the joints, obtained by compressing deformable rubber pads with three different levels of pressure (low, medium and high) as described in Section III. Figure 6 shows box plots for the main effects from each joint on average data across all participants. It can be seen that lower levels of resistance are associated to higher distances between ICT and human trajectories (which is reasonable, since the ICT arm is under-damped when both joints are set at a low level of resistance). This effect seems quite pronounced for the resistance at the shoulder joint (especially for what concerns the low level of resistance), while it appears to be much smaller for the elbow joint.

We performed statistical analysis to better evaluate these effects. We first ran a two-way ANOVA for main effects and interaction from both joint resistances, but examination of a QQ plots of residuals suggested strong non-normal behavior. As a consequence of that, we ran instead the non-parametric equivalent Scheirer–Ray–Hare Test, which showed a very strong significant effect for the shoulder joint ($H(2, 63) = 28.7, p < 10^{-16}$) and non-significant effects for the elbow joint and interaction ($H(2, 63) = 1.52, p = 0.468$ and $H(4, 63) = 0.318, p = 0.989$ respectively). We followed up this result with a post-hoc Dunn test with Bonferroni correction for the p-values, which showed a significant difference between high and low ($p_{adj} = 4.78 \times 10^{-7}$) and between medium and low ($p_{adj} = 0.00106$), but not between medium and high ($p_{adj} = 0.285$).

These results suggest that the rubber pads that we used, while helpful when compared to the plain joints, are limited in their ability to get the ICT to a level of damping comparable to that of a human arm, or at least suffer from diminishing returns. A qualitative insight into this can be obtained from looking at a few of the segmented trials, extracted from three participants and the high/high and low/low ICT configurations, respectively (Figure 7). The trials from participants 6, 1 and 5 show different levels of damping (which could be ascribed to individual differences, either in their biomechanics or the state of relaxation that

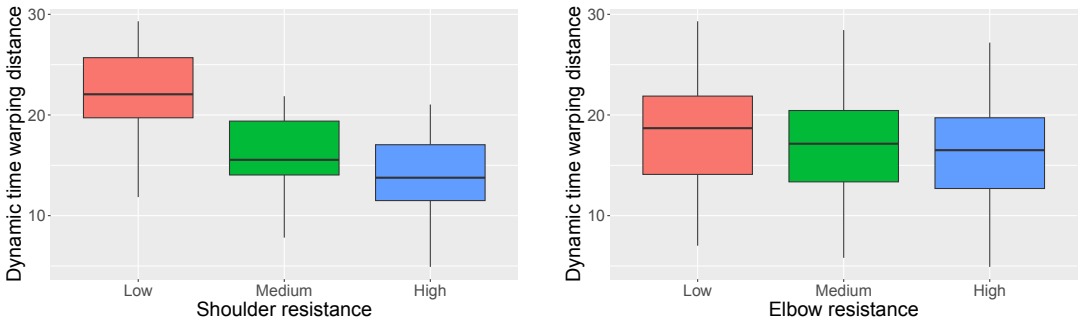


Fig. 6: Box plots showing the effect on overall dynamic time warping distance for the shoulder flexion/extension joint of different levels of resistance at the shoulder (left) and the elbow (right).

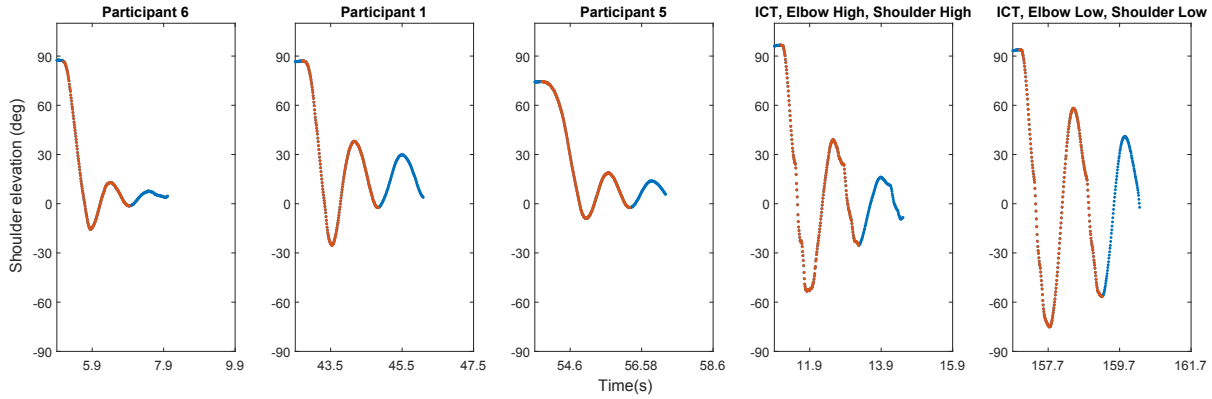


Fig. 7: Segments from individual trials from participants 1, 5 and 6, and from the high/high and low/low configurations of the ICT arm. Segmented data is shown in red.

they were able to achieve when dropping their arm). Of the two ICT trials, the high/high configuration is closer to trials from all participants, and appears relatively similar to the trial from participant 1. However, some irregularities in the trajectory for both ICT trials can be observed, which could be caused by the friction from the pad.

V. CONCLUSIONS

In this paper we have introduced a first prototype of the Inertially Correct Testbed (ICT) arm, which is intended to replicate inertia properties of a human arm for applications in test and evaluations of wearable devices for rehabilitation and assistive applications. In this first iteration of the design, we limited the scope to evaluation of kinematics in a free arm swing movement, evaluating the effect of applying deformable rubber pads with different level of pressure (obtained by changing the spacing between the pads) on differences between kinematic in a pool of human participants and the ICT. Results show that adding tightened pads at the shoulder improves the result significantly when compared to no damping, although some differences in the kinematics remain. We also showed a qualitative comparison of individual trials from two participants and two ICT configurations, which indicate that differences can be qualitatively smaller for some participants, but also highlighted some irregularities in the trajectory of the ICT which we believed to be cause by friction from the pad.

The fact that the trajectories were qualitatively similar is encouraging for what concerns our first intended application as a tool to support development of the arm swing device introduced in [24]. However, the joint resistance in the simulator might still not be sufficient to match human kinematics at a general level. Aside from the limited scope, which is for now focused on evaluation of arm swing movement, this work also has some limitation related to the fact that we are defining inertia property of the arm based on a percentage of body weight, which is in general an approximation. Still, the fact that we are able to obtain trajectories that are qualitatively similar for some participants even with the coarse solution that was tested to simulate damping is encouraging.

Future work will focus on evaluating alternative solutions to dampen the joint. We reached the limit of what can be achieved with Viton rubber, but softer material could improve performance in terms of matching human kinematics. Additionally, we are planning to start testing the arm swing exosuit introduced in [24] to refine controller design, and will complement traditional first evaluations with healthy participants with bench testing on this platform. Long term, a more anatomically correct design for the shoulder would also be desirable, and together with including actuation to simulate muscle tension could lead to applications with a broader scope.

REFERENCES

[1] D. Sakellariou, E. S. Rotarou, and C. B. Peterson, "Leadership and governance to achieve disability inclusive health systems: guidance for self-assessment." *Copenhagen: WHO Regional Office for Europe; 2024. Licence: CC BY-NC-SA 3.0 IGO.*, 2024.

[2] C. for Disease Control and Prevention, "Disability and health data system," Available from: http://dhds.cdc.gov, May 2023.

[3] A. Houtenville and S. Bach, "Annual report on people with disabilities in america: 2024." *Institute on Disability, University of New Hampshire*, 2024.

[4] A. Timmis, N. Townsend, C. P. Gale, A. Torbica, M. Lettino, S. E. Petersen, E. A. Mossialos, A. P. Maggioni, D. Kazakiewicz, H. T. May, *et al.*, "European society of cardiology: cardiovascular disease statistics 2019," *European heart journal*, vol. 41, no. 1, pp. 12–85, 2020.

[5] C. Marras, J. Beck, J. Bower, E. Roberts, B. Ritz, G. Ross, R. Abbott, R. Savica, S. Van Den Eeden, A. Willis, *et al.*, "Prevalence of parkinson's disease across north america," *NPJ Parkinson's disease*, vol. 4, no. 1, p. 21, 2018.

[6] V. L. Feigin, E. Nichols, T. Alam, M. S. Bannick, E. Beghi, N. Blake, W. J. Culpepper, E. R. Dorsey, A. Elbaz, R. G. Ellenbogen, *et al.*, "Global, regional, and national burden of neurological disorders, 1990–2016: a systematic analysis for the global burden of disease study 2016," *The Lancet Neurology*, vol. 18, no. 5, pp. 459–480, 2019.

[7] C. W. Tsao, A. W. Aday, Z. I. Almarzooq, C. A. Anderson, P. Arora, C. L. Avery, C. M. Baker-Smith, A. Z. Beaton, A. K. Boehme, A. E. Buxton, *et al.*, "Heart disease and stroke statistics—2023 update: a report from the american heart association," *Circulation*, vol. 147, no. 8, pp. e93–e621, 2023.

[8] A. Cieza, K. Causey, K. Kamenov, S. W. Hanson, S. Chatterji, and T. Vos, "Global estimates of the need for rehabilitation based on the global burden of disease study 2019: a systematic analysis for the global burden of disease study 2019," *The Lancet*, vol. 396, no. 10267, pp. 2006–2017, 2020.

[9] B. Chen, H. Ma, L.-Y. Qin, F. Gao, K.-M. Chan, S.-W. Law, L. Qin, and W.-H. Liao, "Recent developments and challenges of lower extremity exoskeletons," *Journal of orthopaedic translation*, vol. 5, pp. 26–37, 2016.

[10] R. Gopura, D. Bandara, K. Kiguchi, and G. K. Mann, "Developments in hardware systems of active upper-limb exoskeleton robots: A review," *Robotics and Autonomous Systems*, vol. 75, pp. 203–220, 2016.

[11] R. Bertani, C. Melegari, M. C. De Cola, A. Bramanti, P. Bramanti, and R. S. Calabrò, "Effects of robot-assisted upper limb rehabilitation in stroke patients: a systematic review with meta-analysis," *Neurological Sciences*, vol. 38, pp. 1561–1569, 2017.

[12] L. N. Awad, J. Bae, K. O'donnell, S. M. De Rossi, K. Hendron, L. H. Sloot, P. Kudzia, S. Allen, K. G. Holt, T. D. Ellis, *et al.*, "A soft robotic exosuit improves walking in patients after stroke," *Science translational medicine*, vol. 9, no. 400, p. eaai9084, 2017.

[13] J. M. Veerbeek, A. C. Langbroek-Amersfoort, E. E. Van Wegen, C. G. Meskers, and G. Kwakkel, "Effects of robot-assisted therapy for the upper limb after stroke: a systematic review and meta-analysis," *Neurorehabilitation and neural repair*, vol. 31, no. 2, pp. 107–121, 2017.

[14] C.-Y. Chu and R. M. Patterson, "Soft robotic devices for hand rehabilitation and assistance: a narrative review," *Journal of neuroengineering and rehabilitation*, vol. 15, pp. 1–14, 2018.

[15] M. A. Gull, S. Bai, and T. Bak, "A review on design of upper limb exoskeletons," *Robotics*, vol. 9, no. 1, 2020. [Online]. Available: https://www.mdpi.com/2218-6581/9/1/16

[16] B. Kim and A. D. Deshpande, "An upper-body rehabilitation exoskeleton harmony with an anatomical shoulder mechanism: Design, modeling, control, and performance evaluation," *The International Journal of Robotics Research*, vol. 36, no. 4, pp. 414–435, 2017.

[17] J. van der Vorm, R. Nugent, and L. O'Sullivan, "Safety and risk management in designing for the lifecycle of an exoskeleton: A novel process developed in the robo-mate project," *Procedia Manufacturing*, vol. 3, pp. 1410–1417, 2015, 6th International Conference on Applied Human Factors and Ergonomics (AHFE 2015) and the Affiliated Conferences, AHFE 2015. [Online]. Available: https://www.sciencedirect.com/science/article/pii/S2351978915003054

[18] M. P. De Looze, T. Bosch, F. Krause, K. S. Stadler, and L. W. O'sullivan, "Exoskeletons for industrial application and their potential effects on physical work load," *Ergonomics*, vol. 59, no. 5, pp. 671–681, 2016.

[19] R. Vertechy, A. Frisoli, A. Dettori, M. Solazzi, and M. Bergamasco, "Development of a new exoskeleton for upper limb rehabilitation," in *2009 IEEE International Conference on Rehabilitation Robotics*. IEEE, 2009, pp. 188–193.

[20] F. M. A. André T. Sugawara, Vinícius D. Ramos and L. R. Battistella, "Abandonment of assistive products: assessing abandonment levels and factors that impact on it," *Disability and Rehabilitation: Assistive Technology*, vol. 13, no. 7, pp. 716–723, 2018, pMID: 29334475. [Online]. Available: https://doi.org/10.1080/17483107.2018.1425748

[21] H. Lee and Y. Lee, "A look at wearable abandonment," in *2017 18th IEEE International Conference on Mobile Data Management (MDM)*. IEEE, 2017, pp. 392–393.

[22] K. J. Fietkiewicz and A. Ilhan, "Annoyed to discontinue: factors influencing (dis) continuance of using activity tracking wearables," in *Human-Computer Interaction. Interaction Techniques and Novel Applications: Thematic Area, HCI 2021, Held as Part of the 23rd HCI International Conference, HCII 2021, Virtual Event, July 24–29, 2021, Proceedings, Part II 23*. Springer, 2021, pp. 372–389.

[23] A. D. Deshpande, J. Ko, D. Fox, and Y. Matsuoka, "Anatomically correct testbed hand control: Muscle and joint control strategies," in *2009 IEEE International Conference on Robotics and Automation*, 2009, pp. 4416–4422.

[24] J. Prime, J. Liechty, H. Zhang, J. Abbott, and E. Battaglia, "An exosuit to assist with arm swing in pathological gait," in *2023 IEEE World Haptics Conference (WHC) - Work in Progress paper*. Accepted for publication, IEEE, 2023.

[25] L. M. Sutherland, P. F. Middleton, A. Anthony, J. Hamdorf, P. Cregan, D. Scott, and G. J. Maddern, "Surgical simulation: a systematic review," *Annals of surgery*, vol. 243, no. 3, pp. 291–300, 2006.

[26] K. R. Rosen, "The history of medical simulation," *Journal of critical care*, vol. 23, no. 2, pp. 157–166, 2008.

[27] Y. Okuda, E. O. Bryson, S. DeMaria Jr, L. Jacobson, J. Quinones, B. Shen, and A. I. Levine, "The utility of simulation in medical education: what is the evidence?" *Mount Sinai Journal of Medicine: A Journal of Translational and Personalized Medicine: A Journal of Translational and Personalized Medicine*, vol. 76, no. 4, pp. 330–343, 2009.

[28] S. L. Delp, F. C. Anderson, A. S. Arnold, P. Loan, A. Habib, C. T. John, E. Guendelman, and D. G. Thelen, "Opensim: open-source software to create and analyze dynamic simulations of movement," *IEEE transactions on biomedical engineering*, vol. 54, no. 11, pp. 1940–1950, 2007.

[29] J. A. Tigue, W. B. Rockwell, K. B. Foreman, and S. A. Mascaro, "Investigating the effects of flexor tendon shortening on active range of motion after finger tendon repair," *The Anatomical Record*, vol. 305, no. 5, pp. 1231–1244, 2022.

[30] P. Meyns, S. M. Bruijn, and J. Duysens, "The how and why of arm swing during human walking," *Gait & posture*, vol. 38, no. 4, pp. 555–562, 2013.

[31] S. Plagenhoef, F. G. Evans, and T. Abdelnour, "Anatomical data for analyzing human motion," *Research quarterly for exercise and sport*, vol. 54, no. 2, pp. 169–178, 1983.

[32] R. Krishnan, N. Björsell, E. M. Gutierrez-Farewik, and C. Smith, "A survey of human shoulder functional kinematic representations," *Medical & biological engineering & computing*, vol. 57, pp. 339–367, 2019.

[33] T. Giorgino, "Computing and visualizing dynamic time warping alignments in r: the dtw package," *Journal of statistical Software*, vol. 31, pp. 1–24, 2009.

[34] P. Tormene, T. Giorgino, S. Quaglini, and M. Stefanelli, "Matching incomplete time series with dynamic time warping: an algorithm and an application to post-stroke rehabilitation," *Artificial intelligence in medicine*, vol. 45, no. 1, pp. 11–34, 2009.

[35] S. N. Rai, P. J. Trainor, F. Khosravi, G. Kloecker, and B. Panchapakesan, "Classification of biosensor time series using dynamic time warping: applications in screening cancer cells with characteristic biomarkers," *Open access medical statistics*, pp. 21–29, 2016.

[36] B. Debnath, M. O'brien, M. Yamaguchi, and A. Behera, "A review of computer vision-based approaches for physical rehabilitation and assessment," *Multimedia Systems*, vol. 28, no. 1, pp. 209–239, 2022.

Quantifying the Sense Agency: A Forced Choice Paradigm for Assessing Intentional Binding During Upper Limb Movements

Momchil Gavrilov[1] Katherine A. Jordan[2] Weiwei Zhou[3] Wilsaan M. Joiner[4] Daniel Blustein[5] Jonathon Schofield[6]

***Abstract*—The sense of agency is the perceptual experience of authoring our volitional actions. It is a valuable framework for assessing perceptions of control and the quality of interaction for users operating assistive devices. Intentional binding (IB) is a quantitative measure of the sense of agency where individuals perceive temporal compression between a volitional action and its sensory outcome. IB has been investigated during simple button press actions, but little work extends findings to gross whole-limb movements that are more relevant to assistive or rehabilitative robotics. This study develops and examines the feasibility of a novel, high-resolution approach for assessing IB using a forced two-choice discrimination paradigm. We designed a target acquisition task that required movement of the whole upper limb. Eight participants discriminated time durations between pairs of auditory tones coinciding with paired active and passive movements executed on a Kinarm. Participants reported which movement had a shorter time interval between tones while we varied time delays across movements and trials. We fit psychometric curves to participant responses and achieve a high-resolution estimate of IB biases while also providing a new slope dimension of analysis for IB experiences. The median bias across participants was -36.2ms (IQR: 145.1). We measured IB biases in whole limb movements with high resolution using this method and share its implications for assistive device design.**

***Index Terms*—Embodiment, Agency, Intentional Binding, Bias, Evaluation Metrics, Implicit, Psychopysics, Psychometrics, Interface, Human-Machine interface, Control, Motor Control**

*This work was supported by the Vision Science Training Program: Cornea to Cortex training grant (5T32EY015387-22) and the National Science Foundation, Mind, Machine, and Motor Nexus program grant (221190)

[1]Momchil Gavrilov is with the Department of Biomedical Engineering at the University of California, Davis, 1 Shields Avenue, United States of America mggavrilov@ucdavis.edu

[2]Katherine A. Jordan is with the Department of Neuroscience at the University of California, Davis ,1 Shields Avenue, United States of America kajordan@ucdavis.edu

[3]Weiwei Zhou is with the Department of Neuroscience, Physiology, and Biology at the University of California, Davis, 1 Shields Avenue, United States of America wzho@ucdavis.edu

[4]Wilsaan M. Joiner is with the Faculty of Neuroscience, Physiology, and Biology at the University of California, Davis, 1 Shields Avenue, United States of America wmjoiner@ucdavis.edu

[5]Daniel Blustein is with the Department of Psychology at Acadia University, Wolfville, 15 University Ave, Nova Scotia, Canada daniel.blustein@acadiau.ca

[6]Jonathon Schofield is with the Faculty of Mechanical Engineering at the University of California, Davis, 1 Shields Avenue, United States of America jschofield@ucdavis.edu

I. Introduction

Driven by advances in mechatronics and neuroengineering, many modern assistive and rehabilitative devices (such as limb prostheses, powered orthoses, exoskeletons, and others) are seeing rapid technological transformations. However, the literature reporting on methods for evaluating the effectiveness of human-machine interactions within these technologies has lagged [1]. Contemporary evaluation metrics are needed to keep pace with this evolution which will better define functional capabilities and reveal unmet clinical and user needs. Evaluating devices relative to the sense of embodiment the user may form during robotic operation has recently become an area of growing interest across numerous fields [2], [3]. The sense of embodiment is the perceptual experience of ownership over our body and actions [4]. It offers a new dimension to assess relevant perceptual aspects of human-machine interactions with assistive technologies [5]. For example, in upper limb prostheses, high abandonment rates may be associated with a poorly formed sense of embodiment [6], [7], [8]. Thus, evaluating embodiment may offer possibilities toward improved perception of prosthesis control, forgiveness of control errors, and ultimately improved patient outcomes [6], [7], [8].

Three constituent components underpin the sense of embodiment: (1) the **sense of ownership** defining our perception that our body (or body parts) belongs to ourselves; (2) the **sense of agency** which defines the sense of authorship one has over the volitional actions they perform with their body; and (3) **body localization** which defines the perception of the environment and space immediately surrounding the body in which it can interact with the external world [5]. The sense of agency is of particular value for many rehabilitation and assistive robotic technologies. It offers an insightful avenue to assess user perceptions of controlling their body when assisted by the device. We can further break down the sense of agency into internal and external representations, where **internal agency** refers to perceptions of controlling actions and experiencing the sensory consequences in our own body, and **external agency** refers to the perceptions of controlling events and their sensory consequence in the environment that surrounds the body [4]. Most prior work has focused on evaluating external agency [9]. Although this certainly carries value in assessing

human-machine interactions, quantifying the internal sense of agency is particularly relevant to many assistive technologies aiming to seamlessly integrate with human natural sensory-motor control loops, for example, bionic prostheses or neuro-integrated exoskeleton control.

Implicit and explicit methods define two categories of metrics used to quantify the components of embodiment including the sense of agency. **Explicit methods**, such as questionnaires or survey sets, directly probe conscious perceptions of authoring the sensory outcomes of volitional actions. Such methods are typically easily implemented in most experimental paradigms and are well -validated well in numerous applications. However, they are susceptible to biases, including social desirability and impression management, that can jeopardize their reliability [10], [11], [12]. In contrast, **implicit methods** quantify indirect correlates to the sense of agency outside of human conscious control; some examples include changes in skin conductance, time perception, and histamine responses [13]. They offer the advantage of consistent results that are difficult to bias, making them reliable for retesting and tracking patient changes [13]. However, validating implicit methods as correlates to aspects of embodiment can be challenging since there is uncertainty in the causal or correlative relationships they may have [13], [14]. Nevertheless, such measures offer an important dimension of analysis to quantify the sense of agency that may form when operating assistive technologies more completely.

One prominent implicit method used to assess the sense of agency is **intentional binding**. Intentional binding describes the phenomenon where the perceived time between a volitional action and its sensory outcomes becomes compressed as the participant experiences a strong sense of agency compared to when the sense of agency is absent [11], [14], [15]. Intentional binding is most commonly measured using either a Libet clock paradigm or direct estimation of temporal intervals [12], [14]. In the Libet clock approach, participants estimate time intervals by observing the position of a rotating clock hand. Discrepancies between the actual time interval and the reported clock position quantify intentional binding effects [14]. However, there are limitations with this approach, including potential biases resulting from the requisite high attentional demands [14], [16], [17]. Direct temporal interval estimation can overcome some of the limitations of the Libet clock by having participants state their perceived time delay between experiment events without needing to monitor a clock [14]. However, direct interval estimation has a natural limitation since the small time intervals commonly used in intentional binding protocols can be difficult for participants to estimate. This limitation can introduce inconsistency in participant responses to reoccurring delay intervals and make the method more subjective, hurting its reliability.

Overcoming the challenges above, Steele et al. 2022 proposed a forced choice discrimination task to quantify intentional binding effects and remove participant inconsistency inherent in direct temporal interval estimations [9]. This paradigm involved presenting participants with a 1-degree-of-freedom cursor-to-target task, which they executed using a mouse, and then a passive replica of the same task executed by the computer. By having participants first actively control the cursor and then passively watch the same movement, this paradigm carefully controlled for the sense of agency that may form over the movement. Participants reported the movement task they perceived as taking longer while an adaptive staircase adjusted their passive movement durations to converge on a delay value where participants could no longer differentiate between active and passive movements. The converged value is a high-resolution quantification of their intentional binding bias [9]. This novel paradigm provides an effective framework to determine an implicit measure of the sense of agency while reducing subjectivity in interval estimation tasks. However, how it may scale to larger whole-limb movements relevant to rehabilitation and assistive technologies is unknown. Providing participants with proprioceptive cues associated with whole-limb motion could influence the sense of agency and would be more transferable to assistive devices aiming to restore dexterity or mobility. Whole-body limb movements can also translate to studies investigating the internal sense of agency and provide a more holistic assessment tool for researchers, clinicians, and device developers. Therefore, our current work aims to leverage the Steele et al. 2022 framework to develop and examine the feasibility of a protocol that quantifies intentional binding with high resolution across whole-limb movements.

II. Methods

Protocol Design

Our protocol incorporated the Kinarm Robot (End-Point Lab, Kingston, Canada) (Fig. 1A), a robotic apparatus with two handles that accurately tracks arm motion kinematics and can actively replicate arm movements using onboard motors. In our protocol, participants played a computer game by moving one of the robot handles to control the position of a cursor—a white dot that tracked the occluded handle/hand position.

Participants were seated at a table with the Kinarm and instructed to grasp the right handle of the robot with their right hand (Fig. 1B). The horizontal Kinarm screen, positioned 60 centimeters above the table, provided visual instructions, targets, and cursor position. The screen occluded the view of the table, Kinarm handle, and arms to participants (Fig. 1B and C). They rested their left hand on the table over two mechanical buttons that they used for reporting their perceptual decisions (described below).

We programmed the KinArm to (1) record active movements, in which the participant actively moved their arm, and (2) perform passive movements, where the handle moved the arm of the participant. Each trial consisted of a pair of movements: one active, followed by one passive replicating the previous active movement (Fig. 1D). There were no significant differences in the velocity profiles of active and passive movements. We restricted movements to the y-axis – which traced a line in the sagittal plane of the participant as they sat

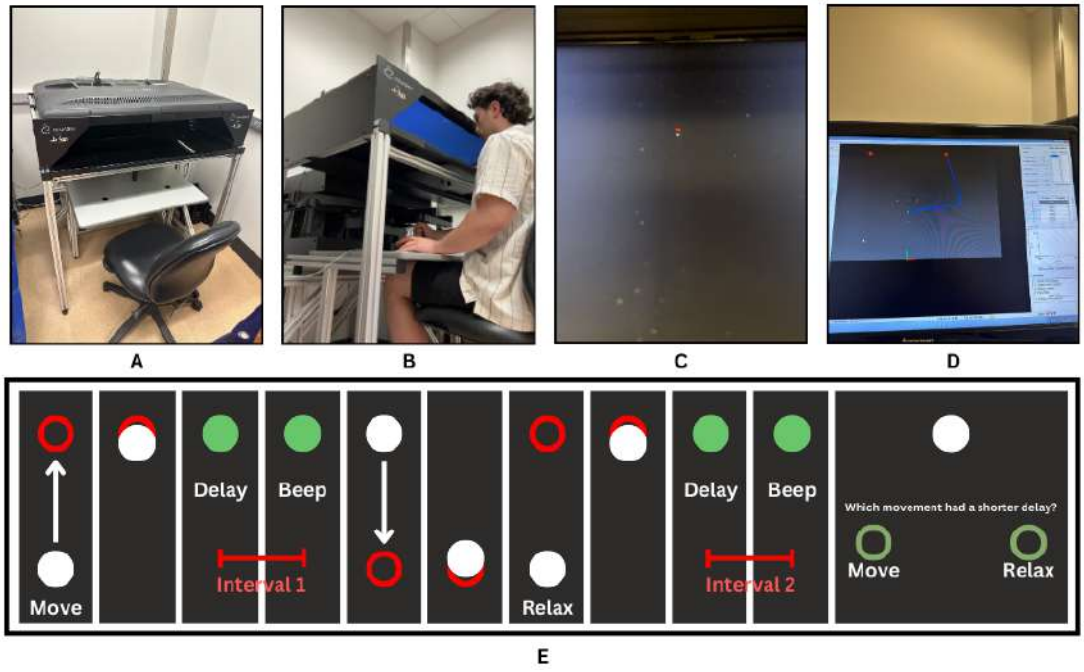


Fig. 1. Overview of experiment. A. The experimental setup with the Kinarm equipment, chair, screen, and table. B. User interacting with the Kinarm experimental setup, holding the right handle with their right hand and their left hand on the buttons while watching the screen for instructions. C. User view of the experimental screen. They move the white cursor to the red target. D. Experimenter view showing the user's execution of the task, allowing for monitoring of participant compliance. E. Sequence of one experimental trial with an active movement followed by a passive movement modulated by a delay. The participant then selects the faster trial (i.e. the smaller interval between tones).

facing the device (Fig. 1B). The participants were encouraged to move at an average velocity ranging between 13-22cm/s and received feedback from our cursor color scheme. When participants reached the target, the cursor would momentarily change to one of three colors: green, indicating that their motion was within the 13-22cm/s velocity range; red, if they were above the velocity range; yellow, if they were below the velocity range. We selected the velocity range to standardize the test between participants and limit the peak velocities they experienced from the passive movements.

We instructed participants that their goal was to achieve the highest possible accuracy on an audio acuity task, and . Participantsthey were blindnaive to the true purpose of the experiment, and we told them that the test measured their audio acuity. We did this to avoid placebo biases in their reporting . We required participants to use the buttons to select which of two-time intervals—presented as delays between auditory tones—they perceived as shorter. Participants first engaged in the active movement task, followed by the passive movement task. The active movement began with the onset of participant motion, triggering the first tone. The participant would then advance the handle to position their cursor within a circular target 12 centimeters away in the positive y-axis direction from the starting position, and after a variable time delay (described below), the second tone played. Once they completed the movement, participants returned the cursor to the starting position (Fig. 1E). The passive motion followed the same procedure except that the onset of motion started one second after the participant reached the starting position and the robot positioned the cursor within the circular target. After each active-passive pair of movements, participants reported whether the active or passive task had a shorter time interval between the tones.

We randomly perturbed the time intervals between the arrival of the cursor at the target and the second tone sounding using a set of 11 possible values. The first (active) movement always included a fixed delay of 400 ms, while the second (passive) movement had a randomly selected delay between 0 ms and 800 ms, chosen from the set of 11 values: 0 ms, 100 ms, 200 ms, 300 ms, 350 ms, 400 ms, 450 ms, 500 ms, 600 ms, 700 ms, 800 ms. Each perturbation value was presented 12 times during the experiment (132 trials total) and four times per block (44 trials per block).

Feasibility Testing

We obtained human testing ethics approval through the UC Davis Institutional Review Board (IRB ID: 1336438-7). To examine the feasibility of our protocol, we recruited eight participants. They ranged between 18-24 years of age with an average age of 20.4 years and standard deviation of 2.06 years. 5/8 were female, and 7/8 were right-handed. All subjects were healthy, taking no medication for neurological impairments, and provided informed consent prior to participation.

To examine the feasibility of our protocol and its ability to quantify intentional binding effects during whole arm movements, all 8 participants completed a full set of 132 trials with the Kinarm task, as described above. We processed the

collected data from the Kinarm using the Bkin_Toolbox_3.8 in MATLAB Software (MathWorks, Natick, USA). We used the Psignifit toolbox (Heiko Schütt, AG, NIP, University of Tübingen) to fit a psychometric curve based on how participants responded in the paired active-passive movement comparison trials. If a participant reported that active movements had shorter delays than passive movements, the 50% threshold of their psychometric curve (on the y-axis) would be shifted in the negative time direction (on the x-axis), indicating a negative time bias. The opposite is true for positive time biases. We then quantified this time bias for each participant to determine if there was an overall negative intentional binding value. This would suggest that our method has intentional binding effects that align with the literature and show that participants perceive active movement conditions and their sensory consequences (intervals between auditory tones) as shorter.

III. Results

Fig. 2 shows an example of a psychometric curve fit using the Psignifit toolbox on an example participant. The x-axis denotes each perturbation level: the passive movement delay minus active movement delay at each trial. The percentage of responses for a shorter active movement compared to total responses represents the y-axis: active responses divided by total responses. The data points shown in blue represent the percent-of-active-movement-responses at each perturbation level. The best fit psychometric curve is represented by the black trace, and the line where the curve inflects, the 50% y-axis point, intersecting the x-axis, indicates participant bias.

Fig. 3 illustrates the psychometric curves for all 8 participants with an average intentional binding curve, shown in red. The average curve was calculated by averaging the Percent-of-active-responses for all participants at each perturbation level and fitting a curve based on the averaged data. Each participant demonstrated a bias that we interpolated to a high degree of resolution from their psychometric curve. A Shapiro-Wilk normality test showed that the biases did not follow a normal distribution. The average bias of the group was -44.0 ms with a standard deviation of +77.3ms, but it would be best to report the median -36.2 ms and an interquartile range 145.1 ms since the data is not normally distributed. We used the sign test to determine that our distribution does not differ significantly from a distribution with a 0ms median ($p = 0.73$). The reason for choosing a sign test is the continuous nature of our bias values and the non-parametric nature of the test.

Unexpectedly, our psychometric curve results presented high variability in participant slopes. We quantified participant slopes by taking the x-axis value at 50% accruacy (bias) and subtracting it from their x-axis value at 75% accuracy. This strategy quantifies the amount an experimenter needs to increase the delay of the passive movement time interval to have participants consistently report that active movements had shorter time intervals. The median amount of time an experimenter would need to increase the passive movement in our group to get the above behaviour is 230ms (IQR: 109.6ms). The range of this threshold varies highly betwen participants, with one participant only needing a 99.8ms increase from their bias value as another needed a 429.9ms increase to respond consistently. Although an aggregated cohort-wide intentional binding effect was statistically not discernable across our cohort, our feasibility results clearly illustrate the potential to identify individual participant variations in intentional binding responses.

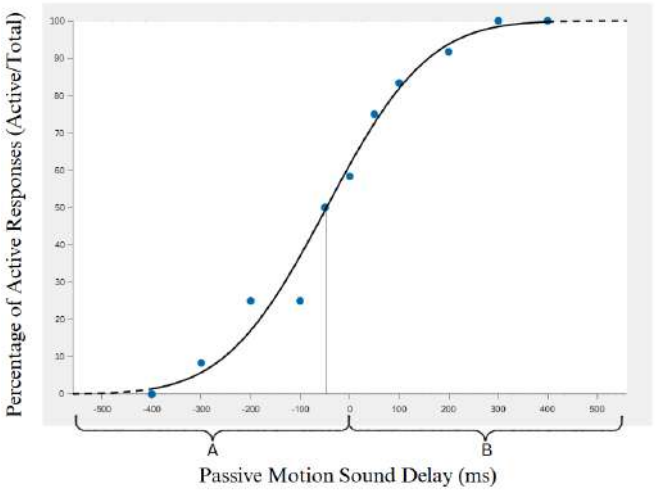


Fig. 2. An example of a participant's psychometric curve. Each data point, in blue, represents the percentage that the participant reported perceiving a shorter delay in the active movement (y-axis) at each perturbation level (x-axis). The psychometric curve was fit using the Psignifit toolbox. The line going from the curve's 50% y-axis value to the x-axis represents the participant's bias. The intersection point is the bias value: -48ms. (A) Represents the perturbation levels where the time interval between the tones of the active movement is shorter than the time interval between the tones of the passive movement. (B) Represents the opposite, where the time interval between the tones of the active movement is shorter than the time interval between the tones of the passive movement. The zero point on the x-axis represents the perturbation level where there is no difference between the active and passive time intervals.

IV. Discussion

In this work, we developed and demonstrated the feasibility of a forced two-choice discrimination movement paradigm to assess intentional binding effects during whole-limb movements with high interpolative resolution and reliability. Such an approach builds on the body of literature on implicit agency measures, which typically benefit from minimal attentional demands, consistency, impression management, and social desirability biases [9], [12], [13], [14]. Our results extend this work by offering a protocol that incorporates whole limb movements and the possibility of quantifying intentional binding biases with high resolution. This approach holds promise to be less biased and more informative for developing human-machine interfaces compared to direct interval estimation and the Libet clock.

One advantage of our method is the high-resolution interpolation of the 50% inflection point of participant psychometric curves to determine intentional binding bias. The inflection

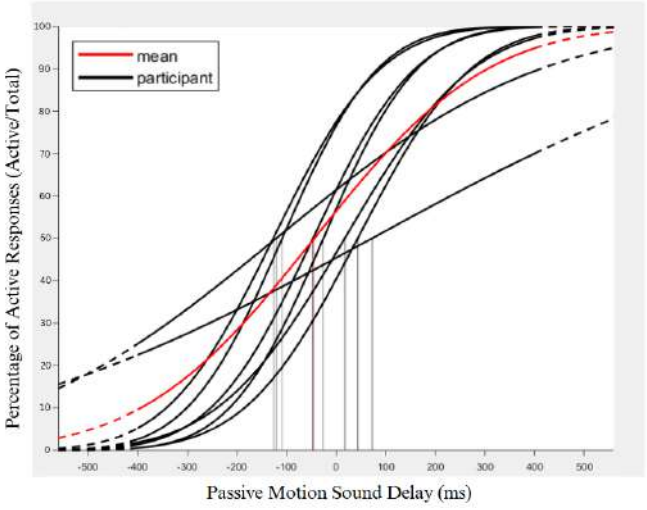


Fig. 3. Psychometric curves evaluating participant intentional binding biases based on active/passive movement voting at different delay intervals. Black curves represent individual participant voting (N = 8), red curve represents average voting of group. Biases are selected at the 50% inflection point of each curve - both individual and average. Median bias = -36.2 ms (IQR: 145.1 ms), Sign Test p-value = 0.73. The median threshold from the 50% inflection point to the 75% consistent response point is 230ms.

point indicates the time delay value at which participants cannot differentiate between the delays of the active and passive movements. In our design, a negative bias value indicates that the participant frequently reported a shorter delay following the active movement, supporting the intentional binding theory. Conversely, a positive bias value suggests that the participant frequently reported the passive movement having a shorter delay. Our results demonstrate a net-negative intentional binding bias with -44.0ms at the average, aligning with existing literature [18]. Two of our eight participants reported an average, positive, intentional binding bias, which can also be seen in well-established methods [19]. Our data did not reveal a statistically significant group bias in either the negative or positive direction which is expected since we are only reporting information on eight participants. We propose that studies with larger cohorts would provide greater power to characterize group behavior in our novel protocol. Toward this goal, this work was to develop a whole-limb intentional binding protocol, and our feasibility testing demonstrated the ability to quantify individual participant biases with high resolution.

One of the more exciting contributions of this work is the new possibility to examine the slope of individual and group-based psychometric curves to quantify intentional binding effects. These slopes quantified individual precision during the experiment. Participants who reported consistently on similar trials will have steeper slopes and smaller threshold values than participants who reported inconsistently during the experiment. We can see in Fig. 3 that two participants had shallower slopes and larger threshold values compared to the other six. We can not provide a specific explanation for why this occurred, but our protocol offers the advantage of quantifying these individual precision differences. This slope parameter provides a new dimension for assessing intentional binding and can be used to offer richer data for quantifying differences in the sense of agency.

As an example of how the slope can provide a richer analysis in agency assessments, intentional binding bias appeared to be independent of the psychometric curve slopes in our experimental cohort (Fig. 3). Although we require larger sample sizes to assess the relationships between the variables confidently, we can see that participants with steep slopes had variable biases and participants with shallow slopes also had variable biases. This result suggests that the slope metric carries additional information and may allow for further characterization of intentional binding and agency experiences.

A valuable aspect of our protocol is its natural translation into the fields of rehabilitation and robotics. For example, this work may be relevant to researchers, clinicians, and device developers interested in quantifying the sense of agency of whole limb movements using myoelectric prostheses, exoskeletons, or other assistive devices. We used a single degree of freedom whole-limb task (straight line reaching) to reduce the complexity of our experimental variables, but this does not need to be the case. Our methods can be replicated directly using the Kinarm or adapted for different tasks such as lower limb, fine, or dexterous movements. Although the Kinarm was locked to a straight line trajectory, participants were free to move their arm in complex ways to hit the target. This is in contrast to many other methods which use less complex movements such as button presses and computer-mouse clicks [9], [14]. We further suggest that our paradigm may be readily modified beyond this one degree of freedom to provide further insight into less kinematically constrained applications.

Our paradigm also offers the advantage of being adaptable to more clinically relevant applications. For example, intentional binding protocols have been developed [20] and used to assess user perceptions of prosthetic control and feedback techniques [21]. In this context, direct time interval estimates have been employed to examine binding between a virtual prosthesis first contacting a grasped object and auditory cues played shortly after this event. Our paradigm could be readily integrated by modifying the prosthesis grasping action into two control conditions: one in which the user actively controls the prosthesis and another in which they view a replay of that action. Participants would then indicate which sequence of events, from the prosthesis's first contact with the object to the auditory tone, they perceived as occurring over a shorter time interval. By varying the delay between contact and the tone, we could obtain a precise estimate of intentional binding biases, directly aligning with our active/passive paradigm described above. Beyond prosthetic limbs, this approach could be extended to various clinical and assistive-device applications by incorporating both passive and active control along with strategically timed sensory events. This would enable precise estimation of intentional binding biases, offering valuable insights into improving user perceptions.

Our study does include some limitations. Given that our goal was to develop a protocol and examine its feasibility, our sample size of N=8 limits our ability to extend our results more broadly to describe group-based results. However, given the demonstrated potential to capture individual participant differences, we argue that work with larger cohort sizes is warranted to develop data sets reflective of normative and affected populations. Such follow-up work has potential impactful implications beyond rehabilitative and assistive robotic applications to provide quantitative insights into a variety of conditions in which patients present with an atypical sense of agency and intentional binding biases, such as schizophrenia, Parkinson's disease, Tourette's disorder, and cortico-basal syndrome [22], [23].

ACKNOWLEDGMENT

The authors of this paper would like to thank the UC Davis Institutional Review Board for approving our study and letting us develop our methods. We would also like to thank the SONA recruiting system and the wonderful participants who gave their time to make this possible.

REFERENCES

[1] J. R. Siegel, M. A. Battraw, E. J. Winslow, M. A. James, W. M. Joiner, and J. S. Schofield, "Review and critique of current testing protocols for upper-limb prostheses: a call for standardization amidst rapid technological advancements," *Front. Robot. AI*, vol. 10, Nov. 2023, doi: 10.3389/frobt.2023.1292632.

[2] R. L. Hybart and D. P. Ferris, "Embodiment for Robotic Lower-Limb Exoskeletons: A Narrative Review," *IEEE Trans. Neural Syst. Rehabil. Eng.*, vol. 31, pp. 657–668, 2023, doi: 10.1109/TNSRE.2022.3229563.

[3] M. Pazzaglia and M. Molinari, "The embodiment of assistive devices—from wheelchair to exoskeleton," *Phys. Life Rev.*, vol. 16, pp. 163–175, Mar. 2016, doi: 10.1016/j.plrev.2015.11.006.

[4] S. Gallagher, "Philosophical conceptions of the self: implications for cognitive science," *Trends Cogn. Sci.*, vol. 4, no. 1, pp. 14–21, Jan. 2000, doi: 10.1016/S1364-6613(99)01417-5.

[5] J. S. Schofield, M. A. Battraw, A. S. R. Parker, P. M. Pilarski, J. W. Sensinger, and P. D. Marasco, "Embodied Cooperation to Promote Forgiving Interactions With Autonomous Machines," *Front. Neurorobotics*, vol. 15, p. 661603, Apr. 2021, doi: 10.3389/fnbot.2021.661603.

[6] R. Bekrater-Bodmann, "Factors Associated With Prosthesis Embodiment and Its Importance for Prosthetic Satisfaction in Lower Limb Amputees," *Front. Neurorobotics*, vol. 14, p. 604376, 2020, doi: 10.3389/fnbot.2020.604376.

[7] A. W. Shehata, M. Rehani, Z. E. Jassat, and J. S. Hebert, "Mechanotactile Sensory Feedback Improves Embodiment of a Prosthetic Hand During Active Use," *Front. Neurosci.*, vol. 14, p. 263, Mar. 2020, doi: 10.3389/fnins.2020.00263.

[8] C. Stiegelmar, D. Blustein, J. Sensinger, J. Hebert, and A. Shehata, "TOWARDS QUANTIFYING THE SENSE OF AGENCY AND ITS CONTRIBUTION TO EMBODIMENT OF MYOELECTRIC PROSTHESES," *Myoelectric Controls Symp.*, Jul. 2020, doi: 10.57922/mec.27.

[9] R. Steele, A. Shehata, J. Sensinger, J. Hebert, and D. Blustein, "A PSYCHOPHYSICAL APPROACH TO MEASURE THE SENSE OF AGENCY," *Myoelectric Controls Symp.*, Aug. 2022, doi: 10.57922/mec.1978.

[10] Z. Barlas and S. Obhi, "Freedom, choice, and the sense of agency," *Front. Hum. Neurosci.*, vol. 7, Aug. 2013, doi: 10.3389/fnhum.2013.00514.

[11] N. Braun *et al.*, "The Senses of Agency and Ownership: A Review," *Front. Psychol.*, vol. 9, Apr. 2018, doi: 10.3389/fpsyg.2018.00535.

[12] P. I. Cornelio Martinez, E. Maggioni, K. Hornbæk, M. Obrist, and S. Subramanian, "Beyond the Libet Clock: Modality Variants for Agency Measurements," in *Proceedings of the 2018 CHI Conference on Human Factors in Computing Systems*, in CHI '18. New York, NY, USA: Association for Computing Machinery, Apr. 2018, pp. 1–14. doi: 10.1145/3173574.3174115.

[13] 'J. L. Segil, L. M. Roldan, and E. L. Graczyk, "Measuring embodiment: A review of methods for prosthetic devices," *Front. Neurorobotics*, vol. 16, Dec. 2022, doi: 10.3389/fnbot.2022.902162

[14] J. W. Moore and S. S. Obhi, "Intentional binding and the sense of agency: A review," *Conscious. Cogn.*, vol. 21, no. 1, pp. 546–561, Mar. 2012, doi: 10.1016/j.concog.2011.12.002.

[15] E. A. Caspar, A. De Beir, P. A. Magalhaes De Saldanha Da Gama, F. Yernaux, A. Cleeremans, and B. Vanderborght, "New frontiers in the rubber hand experiment: when a robotic hand becomes one's own," *Behav. Res. Methods*, vol. 47, no. 3, pp. 744–755, Sep. 2015, doi: 10.3758/s13428-014-0498-3.

[16] S. Imaizumi and Y. Tanno, "Intentional binding coincides with explicit sense of agency," *Conscious. Cogn.*, vol. 67, pp. 1–15, Jan. 2019, doi: 10.1016/j.concog.2018.11.005.

[17] D.-W. Dai and P.-J. (Brown) Hsieh, "High perceptual load attenuates the magnitude of intentional binding for audiovisual events," *J. Vis.*, vol. 24, no. 10, p. 414, Sep. 2024, doi: 10.1167/jov.24.10.414.

[18] J. Liu *et al.*, "Common intentional binding effects across diverse sensory modalities in touch-free voluntary actions," *Conscious. Cogn.*, vol. 123, p. 103727, Aug. 2024, doi: 10.1016/j.concog.2024.103727.

[19] K. Suzuki, P. Lush, A. K. Seth, and W. Roseboom, "Intentional Binding Without Intentional Action," *Psychol. Sci.*, Apr. 2019, doi: 10.1177/0956797619842191.

[20] J. S. Schofield, C. E. Shell, Z. C. Thumser, D. T. Beckler, R. Nataraj, and P. D. Marasco, "Characterization of the Sense of Agency over the Actions of Neural-machine Interface-operated Prostheses," *JoVE J. Vis. Exp.*, no. 143, p. e58702, Jan. 2019, doi: 10.3791/58702.

[21] P. D. Marasco *et al.*, "Illusory movement perception improves motor control for prosthetic hands," *Sci. Transl. Med.*, vol. 10, no. 432, p. eaao6990, Mar. 2018, doi: 10.1126/scitranslmed.aao6990.

[22] M. D. Luzio *et al.*, "Sense of Agency and Its Disturbances: A Systematic Review Targeting the Intentional Binding Effect in Neuropsychiatric Disorders.," *Eur. Psychiatry*, vol. 67, no. S1, pp. S622–S622, Apr. 2024, doi: 10.1192/j.eurpsy.2024.1290.

[23] A. Koreki *et al.*, "Altered sense of agency in schizophrenia: the aberrant effect of cardiac interoceptive signals," *Front. Psychiatry*, vol. 15, Sep. 2024, doi: 10.3389/fpsyt.2024.1441585.

Day-to-Day User Adaptation to a Robotic Ankle-Foot Prosthesis

Sina Miri, Michael Jacobson, Matthew J. Major, Myunghee Kim*

Abstract— **Adaptation in locomotion of lower limb amputees is essential for effective interaction with assistive devices such as robotic ankle-foot prostheses (AFP), which can provide personalized assistance. Bayesian Optimization (BO) and Human-in-the-Loop (HIL) optimization frameworks have been utilized to personalize device parameters based on user feedback; however, these methods may not always fully consider the dynamic nature of human adaptation. This study investigates day-to-day adaptation to a robotic ankle-foot prosthesis by modeling socket pressure distributions across different AFP stiffness conditions using Gaussian processes. We performed a secondary analysis on data from three unilateral transtibial amputees who participated in a four-day experimental protocol involving discrete parameter sweeps and HIL optimization using BO. Gaussian process models were constructed from data collected on the discrete sweep day and the HIL optimization day. Comparative analyses using Kullback–Leibler (KL) divergence and a mean absolute error (MAE) loss metric revealed subject-specific shifts in optimal stiffness values and changes in the pressure landscape between the two days. The average KL divergence was 1.15, and the MAE loss was 0.59, suggesting adaptations in gait and limb dynamics. These findings suggest the importance of using adaptation in a short time period and personalization methods may need to not only optimize device parameters based on static performance snapshots but also accommodate the dynamic shifts that occur as users adapt over time.**

Keywords—Adaptation, Prosthesis, Human-Robot interaction, Human-in-the-loop

I. Introduction

The development of assistive devices, including powered prostheses and exoskeletons, has made significant progress toward improving mobility and reducing the physical effort required for walking in individuals with motor impairments [1], [2], [3], [4], [5], [6], [7]. These devices often rely on the integration of physiological and non-physiological signals to achieve user-specific adaptations through human-in-the-loop (HIL) optimization. This systematic approach involves iteratively tuning device parameters based on real-time user feedback [8], [9], [10]. Historically, metabolic cost has been the primary feedback metric for optimization [6]. However, recent studies have explored alternative or proxy measures, including muscle activity [11], electrocardiogram (ECG) [12], ground reaction forces, foot pressure distributions [3], [5], and user subjective preferences [1]. While these advances have improved device personalization, successful outcomes depend on the user's ability to adapt to and effectively utilize the device.

Adaptation is a critical process that enables users to effectively interact with assistive devices. It involves the modification of neural, muscular, and biomechanical patterns to optimize device utilization and improve overall performance during activities such as walking [3], [13]. This process is essential for aligning the user's motor strategies with the mechanical assistance provided by the device [4], [7].

In human locomotion, adaptation reflects the central nervous system's ability to modify walking patterns in response to environmental or mechanical perturbations, ensuring stability and efficiency [14]. Experimental setups such as split-belt treadmills demonstrate how individuals adjust gait kinematics, such as step length [15], stride time [16], and interlimb coordination [17], to accommodate new constraints [18]. These adjustments rely on both reactive and predictive mechanisms, integrating sensory feedback and feedforward control to restore symmetry over time [18], [19]. Individuals with motor impairments, including stroke survivors, also demonstrate the capacity for locomotor adaptation, though adaptation rates and extents vary with baseline asymmetries [18].

The ability to adapt gait kinematics is also influenced by sensory inputs and cognitive processes. For instance, visual feedback has been shown to enhance gait adaptation by providing real-time cues that help individuals correct deviations in their walking patterns [20]. This approach allows wearable device users to optimize their gait to the assistance, thereby reducing the metabolic cost of walking [21]. Visual feedback can also enhance the adaptation process by guiding users toward target gait patterns [4]. Additionally, the effectiveness of training and customization in exoskeleton use demonstrates the relationship between motor learning and adaptation, with gradual exposure to variable assistance profiles resulting in sustained reductions in energy expenditure [13]. Studies have shown that adaptation to assistive devices can also result in changes in gait kinematics, kinetics, and muscle activity [21], [22].

*Research supported by National Science Foundation (CBET-2340519) and US Department of Veterans Affairs (I21RX004077-01A1).

Sina Miri is with the Department of Mechanical and Industrial Engineering, University of Illinois at Chicago, Chicago, IL 60607 USA (smiri2@uic.edu).
Michael Jacobson is with the Department of Mechanical and Industrial Engineering, University of Illinois at Chicago, Chicago, IL 60607 USA (mjacob38@uic.edu).
Matthew J. Major is with the Department of Physical Medicine & Rehabilitation, Northwestern University and Jesse Brown VA Medical Center, Chicago IL 60611 USA (matthew-major@northwestern.edu).
Myunghee Kim (corresponding author) is with the Department of Mechanical and Industrial Engineering, University of Illinois at Chicago, Chicago, IL 60607 USA (myheekim@uic.edu , 312.996.3601).

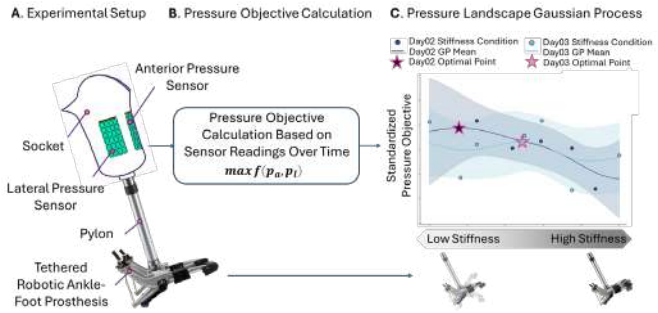


Figure 1. Experimental setup, (A) Ankle-Foot prosthesis and socket pressure sensors. (B) Pressure cost objective calculation using. (C) Modeling the pressure landscape using Gaussian process

The extent and rate of adaptation are influenced by the amount and type of training provided. Research has emphasized the importance of prolonged exposure to device assistance in achieving stable adaptation [13]. Long-term adaptation, often observed over weeks or months, involves gradual recalibration of sensorimotor pathways and the nervous system's ability to integrate device assistance into walking patterns. Studies have shown that repeated exposure to robotic assistance facilitates durable changes in motor control and gait dynamics, enabling users to achieve smoother and more energy-efficient movements over time [13], [23]. In contrast, short-term adaptation occurs over hours or days and typically involves rapid adjustments to device parameters or environmental changes [24], [25], [26]. While these initial adjustments can result in notable improvements in gait symmetry and efficiency, they may lack the permanence of long-term adaptations unless reinforced by consistent practice [27]. Despite these findings, the interplay between short-term adaptation mechanisms and their contribution to long-term changes remains underexplored, particularly in the context of how device parameters modulate the adaptation process [28].

One of the conventional indicators of adaptation is the kinematic changes observed during gait [29]. Socket pressure has been well established as a measure in lower limb amputee studies. This can give insights into interfacial load transfer [30], support action of friction [31] and external moments acting on this interface [32]. Studies suggest relationships between socket pressure and muscle activation [33] as well as gait characteristics [34].

In this study, we used Gaussian processes (GP) to model the distribution of socket pressure as a function of the prosthetic stiffness parameter across multiple experimental days. GPs can be thought of as a probabilistic model for distributions over functions, generalizing the multivariate Gaussian distribution to continuous domains [35]. This approach allowed us to infer the nonlinear relationships between stiffness and pressure using limited data collected during human subject experiments [36].

In robotics research, the Kullback–Leibler (KL) divergence is employed as a quantitative measure to detect changes in kinematic behavior or overall task performance [37], [38]. A high KL divergence value between the probability distributions of expected and observed kinematic data indicates significant deviations, which may signify alterations in movement patterns, anomalies, or shifts in robot behavior [37]. Therefore, a high KL divergence during learning from demonstration may reveal that the robot's actions are not accurately replicating expert demonstrations, highlighting discrepancies in kinematic replication [39].

Another metric for the change in user gait pattern is the Mean Absolute Error (MAE) [40]. This metric quantifies the absolute average discrepancy between the models' central tendency predictions, providing a straightforward measure of divergence in their mean predictions without incorporating uncertainty. In addition to KL divergence, we calculated the MAE-based loss metric to capture the absolute differences in mean predictions between two GP models [41]. We have extended these measures to analyze alterations in human kinematics, particularly in the context of assessing adaptation using Gaussian process regression of the activity [42], [43].

We hypothesized that adaptation effects to the assistive robotic ankle-foot prosthesis could be captured through changes in the socket pressure landscape observed over two different experimental days. To describe these effects, we used explicit measures, including shifts in the optimal pressure distribution point, and quantitative metrics such as KL divergence and MAE loss metric to assess the differences in socket pressure patterns.

We conducted a four-day study with three unilateral transtibial amputees using a robotic ankle-foot prosthesis emulator. Pressure objective was obtained from the pressure sensors implemented in the socket from the last two days of experimental protocol. GP models were built to analyze the relationship between AFP stiffness landscape and socket pressure objective. Quantitative metrics were calculated based on the two GP models.

II. Methods

A. Socket pressure data collection and pressure objective calculation

We have used two pressure maps (9811E sensor, Tekscan, USA) on the anterior and lateral sides of the socket as shown in Fig.1.A. Building on this, we developed a novel pressure objective function that utilizes socket interface pressure to determine the optimal stiffness parameter by maximizing this function during Bayesian Optimization.

$$\max f(p_a, p_l) = \left(\frac{\sum_{t=1}^{T} \left(\sum_{i=1}^{n} p_a(i,t) \cdot \omega_a + p_l(i,t) \cdot \omega_l \right)}{\frac{1}{T} \left(\sum_{t=1}^{T} \max_i p_a(t) + \sum_{t=1}^{T} \max_i p_l(t) \right)} \right) \quad (1)$$

Equation (1) defines the cost function being maximized in the optimization process. Here, $p_a(i,t)$ and $p_l(i,t)$ represent the pressure values in the anterior and lateral regions at cell i and time t, respectively. The summation $\sum_{t=1}^{T}$ aggregates the pressure data over the time period T. Weights ω_a and ω_l are applied to $p_a(i,t)$ and $p_l(i,t)$, respectively, to reflect the relative importance of these pressures in the overall objective function. In the denominator, the term $\frac{1}{T}$ averages the

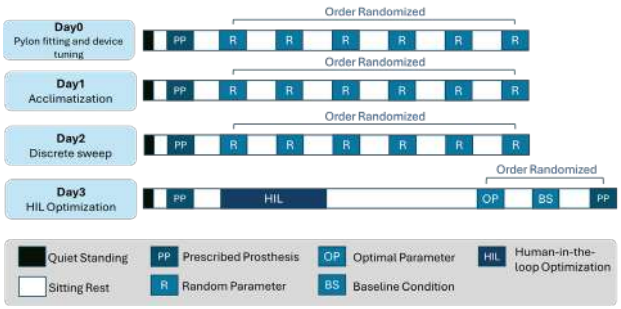


Figure 2. Experimental protocol, Day 0: Confirm fit, determine preferred speed, fit pylon, tune neutral angle, walk under multiple stiffness conditions. Days 1 (Acclimatization) & 2 (Discrete Sweep): After baseline standing and walking with the prescribed prosthesis, participants complete repeated walking trials at varying stiffness conditions with rests in between. Day 3 (HIL Optimization): After baseline measurements, participants undergo real-time iterative optimization of prosthesis parameters, followed by validation walking trials at the optimized and baseline and prescribed prosthesis conditions.

maximum pressure values over the time period T. Specifically, $\max_i p_a(t)$ and $\max_i p_l(t)$ denote the maximum pressures observed in the anterior and lateral regions at each time point t. Summing these maximum values over T provides an aggregate measure of the peak pressures in each region. The objective function expresses the cumulative and peak pressures of pressure-intolerant zones of the residual limb, enabling the selection of the optimal stiffness parameter that minimizes pressure-related discomfort.

B. Robotic ankle-foot prosthesis and controller design

We utilized a tethered robotic ankle-foot prosthesis emulator, powered by off-board system (Humotech, Pittsburgh, USA) and a real-time control system, to enable dynamic adjustments of control parameters such as stiffness and push-off energy during walking [44]. The control system was structured into low-, mid-, and high-level controllers: the low-level controller managed linear torque and position tracking, the mid-level controller generated desired ankle trajectories based on gait phases and the selected stiffness parameter, and the high-level controller employed HIL Bayesian optimization to continuously optimize stiffness in real-time. The emulator achieved a plantarflexion peak torque of 250 Nm with a control bandwidth exceeding 10 Hz [5].

C. Experimental protocol

The study included three unilateral transtibial amputees—two males and one female—aged 59, 47, and 45 years (mean ± SD: 50.33 ± 7.57 years) and weighing 98.88 kg, 56.7 kg, and 66.9 kg (74.16 ± 22.02 kg). These participants were recruited to optimize ankle-foot prosthesis parameters for enhanced mobility and comfort using a HIL optimization approach. The experimental protocol spanned four days which is shown in Fig.2. On Day 0, after informed consent and screening by a research prosthetist, participants stood upright for up to 3 minutes, followed by at least 2 minutes of seated rest, then walked with their prescribed prosthesis for up to 5 minutes to determine their preferred walking speed. A brief rest was provided before pylon fitting and device calibration. With the prosthesis emulator's neutral plantarflexion angle tuned for comfort, participants then walked for up to 5 minutes at their preferred speed for approximately six different stiffness conditions, with a minimum of 2 minutes of seated rest between conditions. Informed consent was obtained from all participants prior to the study, and the study protocol was approved by the University of Illinois at Chicago Institutional Review Board (STUDY 2019-0087).

During Days 1 and 2, participants performed discrete parameter sweeps. Each day began with standing for up to 3 minutes, followed by at least 2 minutes of rest, then walking with their prescribed prosthesis for up to 5 minutes. After a minimum 10-minute rest, participants completed about six different stiffness conditions, each lasting up to 5 minutes of walking at their preferred speed, with a minimum of 5 minutes res t between conditions.

On Day 3, the baseline routine was repeated (stand up to 3 minutes, rest at least 2 minutes, walk with prescribed prosthesis up to 5 minutes, then rest at least 10 minutes) before conducting HIL optimization using Bayesian optimization. Participants walked for up to 18 minutes while prosthesis parameters were iteratively adjusted based on participant feedback. After a minimum of 10 minutes rest, a validation session was performed: participants walked up to 5 minutes each at the optimized condition, a baseline condition, and with their prescribed prosthesis, with at least 5 minutes of rest between conditions.

D. Gaussian process modeling

The dataset used in this study was obtained from day 2 discrete sweep conditions and day 3 HIL explored parameters. A single-parameter GP was constructed based on the different robotic ankle-foot prosthesis stiffness parameters and measured pressure objective during day 2 and day 3 shown in Fig.1.C. The independent variable, stiffness, served as the input feature, while the dependent variable, standardized pressure objective, was treated as the response variable. Stiffness parameters were scaled using global Min-Max normalization to ensure values were in the range [0,1] for both days. Data preprocessing and normalization were implemented using custom Python scripts.

A Gaussian Process is a non-parametric Bayesian approach to regression that defines distribution over functions. For a given input x, the GP defines a prior over the possible values of the function $f(x)$. The GP is fully specified by its mean function $\mu(x)$ and covariance function $k(x, x')$:

$$f(x) \sim GP(\mu(x), k(x, x')) \tag{2}$$

The covariance function, also known as the kernel, encapsulates our assumptions about the function $f(x)$. We employed the Squared Exponential (SE) kernel with Automatic Relevance Determination (ARD):

$$k(x, x') = \sigma_f^2 exp(-\frac{1}{2}\sum_{d=1}^{D}\frac{(x_d - x_d')^2}{{l_d}^2}) \tag{3}$$

Where σ_f^2, l_d and D are the output variance (output scale), the lengthscale parameter and dimensionality of the input space respectively.

To model observation noise, we assume that the observed responses y are related to the latent function $f(x)$ via Gaussian noise:

$$y = f(x) + \epsilon, \epsilon \sim N(0, \sigma_n^2 I) \quad (4)$$

Where σ_n^2 represents the noise variance, and I is the identity matrix. To ensure numerical stability during optimization, the noise variance σ_n^2 is constrained to be greater than 10^{-5}.

The GP models were trained by maximizing the Exact Marginal Log-Likelihood (MLL), which serves as the objective function for hyperparameter optimization. The MLL for a GP with training data $D = \{X, y\}$ is given by:

$$log\ p(\ y \mid X\ ) = -\frac{1}{2} y^\top K^{-1} y - \frac{1}{2} log \mid K \mid - \frac{n}{2} log 2\pi \quad (5)$$

Where $K = K_f + \sigma_n^2 I$ is the covariance matrix with K_f derived from the SE kernel, and n as the number of training observations.

To optimize the hyperparameters, we employed the Adam optimizer, a stochastic gradient descent method that adapts the learning rate for each parameter. Each GP model was trained over 500 epochs. Throughout training, key hyperparameters, the lengthscale l_d, output scale σ_f^2, and noise variance σ_n^2, were recorded to monitor convergence and assess the optimization trajectory.

E. Post training model comparison analysis

To quantitatively assess the similarity or dissimilarity between the GP models for day 2 and day 3 for each subject we employed the Kullback-Leibler (KL) Divergence and MAE loss metrics. We also showed the optimal point of each GP.

The KL Divergence between two Gaussian distributions $N(\mu_1, \sigma_1^2)$ and $N(\mu_2, \sigma_2^2)$ is mathematically defined as:

$$KL(N_1 \parallel N_2) = \frac{1}{2}\left(log\left(\frac{\sigma_2^2}{\sigma_1^2}\right) + \frac{\sigma_1^2 + (\mu_1 - \mu_2)^2}{\sigma_2^2} - 1\right) \quad (6)$$

We generated 100 equally spaced test points X_{test} within the normalized stiffness range [0,1] to sample the parameter space comprehensively.

The KL Divergence was calculated at each test point to quantify the divergence between the two predictive distributions. An overall comparison metric was derived by computing the mean of the KL Divergence values across all test points, providing a singular measure of the models' similarity across the stiffness range.

In addition to KL Divergence, we used an MAE loss metric to capture the absolute differences in mean predictions between the two GP models.

For each test point in X_{test}, the mean predictions μ_1 and μ_2 from GP Model 1 and GP Model 2 were extracted.

$$MAE\ Loss = \frac{1}{D}\sum_{x \in D} |\mu_1 - \mu_2| \quad (7)$$

The MAE loss value was computed across all test points to provide an aggregate measure of the models' prediction differences. To identify the optimal stiffness value that maximizes the standardized pressure objective for each GP model, we performed an optimal point calculation based on the posterior mean predictions in both GP models. Using the same set of 100 uniformly spaced test points X_{test} within the normalized stiffness range [0,1], we evaluated the posterior distributions of both GP models with the posterior mean predictions $\mu_1(x)$ and $\mu_2(x)$. The optimal stiffness value for each model was identified by locating the test point with the highest posterior mean prediction:

$$Optimal\ Point = arg \max_{x \in X_{test}} \mu(x) \quad (8)$$

III. RESULTS

We modeled the pressure objective across different stiffness values of the robotic ankle-foot prosthesis. All hyperparameters (σ_f^2, l_d and, σ_n^2) converged within 500 epochs. Fig.3 presents the experimental results. Subject-specific analyses revealed shifts in optimal stiffness values between the discrete sweep day and the HIL day.

For Subject 1, the optimal point shifted from the low stiffness region during the discrete sweep day to the mid-stiffness region on the HIL day. Subject 2's optimal point transitioned from the high stiffness region to the low stiffness region during the HIL day, indicating a complete shift. Subject 3

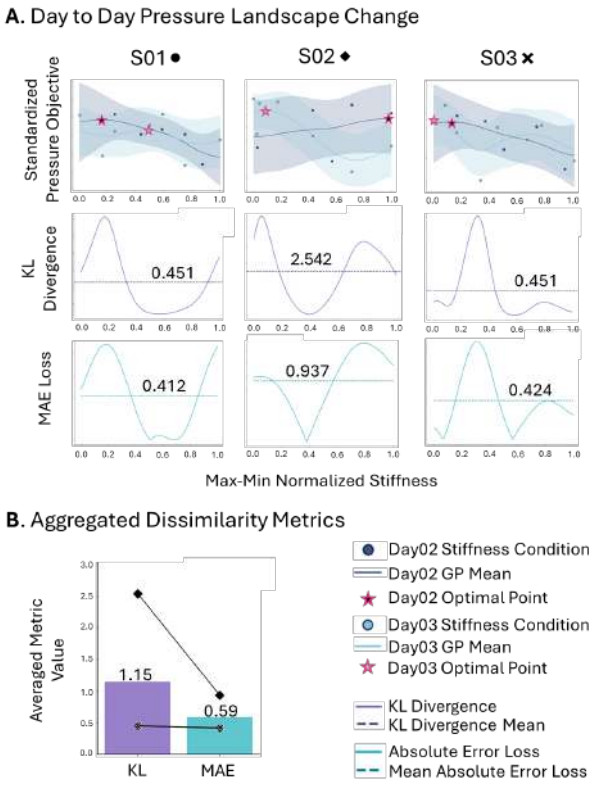


Figure 3. Experimental results. (A) Day 2 and 3 pressure landscape, KL Divergence and MAE loss of participants (shown in columns respectively). (B) Aggregated dissimilarity metrics results

exhibited a minor shift toward a lower stiffness region from the discrete sweep day to the HIL day. The averaged KL divergence values over the test points were 0.451 for Subject 1, 2.542 for Subject 2, and 0.451 for Subject 3 (mean = 1.15). A KL divergence value close to 0 indicates high similarity between the two GP models' predictions and uncertainties at that stiffness level.

The MAE loss values were 0.412 for Subject 1, 0.937 for Subject 2, and 0.424 for Subject 3 (mean = 0.59).

IV. Discussion and Conclusion

In this study, we hypothesized that users would adapt their gait patterns when using a robotic ankle-foot prosthesis (AFP) during experimental days, as evidenced by changes in socket interface pressure distributions each day. We performed secondary data analysis on three individuals with transtibial amputation. Our findings, derived from modeling the pressure landscape using Gaussian Process (GP) regressions across different AFP stiffness settings, revealed day-to-day shifts in optimal stiffness values. This adaptation effect was further supported by the observed non-zero, positive mean values of Kullback-Leibler (KL) divergence (mean = 1.15) and MAE loss metric (mean = 0.59). These results collectively indicate ongoing day-to-day changes in the underlying socket pressure landscape, suggesting that users adapted their gait patterns to accommodate the AFP over the short term.

The socket pressure objective in this study represents the distribution of forces exerted between the prosthetic socket and the residual limb in anterior and lateral directions. We used GP regression to model this pressure objective across different stiffness ranges of the AFP system. This approach allowed us to model the nonlinear relationships between AFP stiffness and socket pressure using limited data collected during human subject experiments [36]. The resulting pressure landscape provides a holistic view of the user's response to the AFP. Day-to-day changes in the pressure landscape under varying stiffness parameters indicate that users adapt their limb and gait dynamics to the device, even over short periods. This adaptation may be oriented toward optimizing loading [45] and efficiency [46]. These results align with the notion that adaptation to robotic devices involves constructing an internal model of the locomotor task [42], [43] and are consistent with findings that prolonged interaction with assistive devices leads to improved personalization of gait characteristics [5], [6].

Beyond the general adaptation effects, we also observed subject-specific patterns. Subject 2 significantly altered the optimal point, while others exhibited only minor changes. Subject 2 also showed a change in the pressure landscape, indicated by an averaged KL divergence of 2.542 and an MAE loss of 0.937. Perhaps, one of the factors of this inter-subject variability is that since subjects walked at their preferred speeds, the number of steps taken within the fixed time window varied, potentially influencing the training dosage [47], [48]. Research also suggests that adaptation to a new device does not follow a uniform trajectory [49], and training protocols must also account for individual characteristics [50]. This variability suggests the importance of personalization, ensuring that assistive devices are tailored to each user's unique adaptation patterns for optimal effectiveness.

Bayesian optimization frameworks are well suited for personalizing assistive robots due to their non-parametric, sample-efficient, and noise-tolerant characteristics [36], [51]. BO-based Human-in-the-Loop (HIL) optimization frameworks use GP models to describe the prior and posterior distributions [51] as they iteratively tune device parameters based on the objective cost. However, current BO-based methods often focus on objective functions, such as metabolic cost or gait symmetry, without fully accounting for the dynamic nature of adaptation. Instead, they tend to treat these changes as noise, overlooking the effect of human-robot co-adaptation [4], [52]. Previous research has also emphasized the need for adaptive HIL strategies that account for time-varying user-device interactions [4], [52]. Such frameworks can be extended to incorporate adaptive metrics, ensuring that device performance evolves alongside the user's changing needs and adaptation [6], [7].

A potential limitation of this study arises from the differences of data collection protocols on the discrete sweep Day and HIL-explored parameters. Future research with a similar protocol across days with a larger group of participants can be planned to provide a more comprehensive overview of short-term adaptation to assistive devices and solutions offered by personalization methods.

Acknowledgment

The authors would like to extend their thanks to the members of the Rehabilitation Robotics Lab for their invaluable support and contributions throughout the course of this project.

References

[1] A. Alili *et al.*, "A Novel Framework to Facilitate User Preferred Tuning for a Robotic Knee Prosthesis," *IEEE Trans. Neural Syst. Rehabil. Eng.*, vol. 31, pp. 895–903, 2023.

[2] Xiaorong Zhang, Ding Wang, Qing Yang, and He Huang, "An automatic and user-driven training method for locomotion mode recognition for artificial leg control," in *2012 Annual International Conference of the IEEE Engineering in Medicine and Biology Society*, San Diego, CA: IEEE, Aug. 2012, pp. 6116–6119.

[3] Y. Feng, C. Mao, W. Zhang, and Q. Wang, "Gait-Symmetry-Based Human-in-the-Loop Optimization for Unilateral Transtibial Amputees With Robotic Prostheses," *IEEE Trans. Med. Robot. Bionics*, vol. 4, no. 3, pp. 744–753, Aug. 2022.

[4] B. L. Fylstra *et al.*, "Human-prosthesis cooperation: combining adaptive prosthesis control with visual feedback guided gait," *J. NeuroEngineering Rehabil.*, vol. 19, no. 1, p. 140, Dec. 2022.

[5] M. Jacobson *et al.*, "Foot contact forces can be used to personalize a wearable robot during human walking," *Sci. Rep.*, vol. 12, no. 1, p. 10947, Jun. 2022.

[6] J. Zhang *et al.*, "Human-in-the-loop optimization of exoskeleton assistance during walking," *Science*, vol. 356, no. 6344, pp. 1280–1284, Jun. 2017.

[7] T.-C. Wen *et al.*, "The personalization of stiffness for an ankle-foot prosthesis emulator using Human-in-the-loop optimization," in *2020 IEEE/RSJ IROS*, Las Vegas, NV, USA: IEEE, Oct. 2020, pp. 3431–3436.

[8] J. Lee, S. Miri *et al.*, "Biosignal-integrated robotic systems with emerging trends in visual interfaces: A systematic review," *Biophys. Rev.*, vol. 5, no. 1, p. 011301, Mar. 2024.

[9] P. Slade *et al.*, "On human-in-the-loop optimization of human–robot interaction," *Nature*, vol. 633, no. 8031, pp. 779–788, Sep. 2024.

[10] W. Felt *et al.*, "'Body-In-The-Loop': Optimizing Device Parameters Using Measures of Instantaneous Energetic Cost," *PLOS ONE*, vol. 10, no. 8, p. e0135342, Aug. 2015.

[11] H. Jeong *et al.*, "Muscle coordination and recruitment during squat assistance using a robotic ankle–foot exoskeleton," *Sci. Rep.*, vol. 13, no. 1, p. 1363, Jan. 2023.

[12] J. Kim *et al.*, "Soft wearable flexible bioelectronics integrated with an ankle-foot exoskeleton for estimation of metabolic costs and physical effort," *Npj Flex. Electron.*, vol. 7, no. 1, p. 3, Jan. 2023.

[13] K. L. Poggensee *et al.*, "How adaptation, training, and customization contribute to benefits from exoskeleton assistance," *Sci. Robot.*, vol. 6, no. 58, p. eabf1078, Sep. 2021.

[14] L. A. Malone *et al.*, "How does the motor system correct for errors in time and space during locomotor adaptation?," *J. Neurophysiol.*, vol. 108, no. 2, pp. 672–683, Jul. 2012.

[15] D. S. Reisman *et al.*, "Repeated Split-Belt Treadmill Training Improves Poststroke Step Length Asymmetry," *Neurorehabil. Neural Repair*, vol. 27, no. 5, pp. 460–468, Jun. 2013.

[16] D. S. Reisman *et al.*, "Split-Belt Treadmill Adaptation Transfers to Overground Walking in Persons Poststroke," *Neurorehabil. Neural Repair*, vol. 23, no. 7, pp. 735–744, Sep. 2009.

[17] D. S. Reisman *et al.*, "Interlimb Coordination During Locomotion: What Can be Adapted and Stored?," *J. Neurophysiol.*, vol. 94, no. 4, pp. 2403–2415, Oct. 2005.

[18] L. A. Malone *et al.*, "Spatial and Temporal Asymmetries in Gait Predict Split-Belt Adaptation Behavior in Stroke," *Neurorehabil. Neural Repair*, vol. 28, no. 3, pp. 230–240, Mar. 2014.

[19] G. Torres-Oviedo *et al.*, "Locomotor adaptation," in *Progress in Brain Research*, vol. 191, Elsevier, 2011, pp. 65–74.

[20] Y. A. Sekhavat *et al.*, "Projection-Based AR: Effective Visual Feedback in Gait Rehabilitation," *IEEE Trans. Hum.-Mach. Syst.*, vol. 48, no. 6, pp. 626–636, Dec. 2018.

[21] M. Kim *et al.*, "Visual guidance can help with the use of a robotic exoskeleton during human walking," *Sci. Rep.*, vol. 12, no. 1, p. 3881, Mar. 2022.

[22] I. Sanz-Pena *et al.*, "Computer Interface for Real-Time Gait Biofeedback Using a Wearable Integrated Sensor System for Data Acquisition," *IEEE Trans. Hum.-Mach. Syst.*, vol. 51, no. 5, pp. 484–493, Oct. 2021.

[23] S. Galle *et al.*, "Adaptation to walking with an exoskeleton that assists ankle extension," *Gait Posture*, vol. 38, no. 3, pp. 495–499, Jul. 2013.

[24] J. Wolpaw *et al.*, "Adaptive plasticity in the primate spinal stretch reflex: evidence for a two-phase process," *J. Neurosci.*, vol. 4, no. 11, pp. 2718–2724, Nov. 1984.

[25] A. J. Bastian *et al.*, "Understanding sensorimotor adaptation and learning for rehabilitation," *Curr. Opin. Neurol.*, vol. 21, no. 6, pp. 628–633, Dec. 2008.

[26] A. R. Luft *et al.*, "Stages of Motor Skill Learning," *Mol. Neurobiol.*, vol. 32, no. 3, pp. 205–216, 2005.

[27] S. M. Morton *et al.*, "Cerebellar Contributions to Locomotor Adaptations during Splitbelt Treadmill Walking," *J. Neurosci.*, vol. 26, no. 36, pp. 9107–9116, Sep. 2006.

[28] S. Huang *et al.*, "Locomotor Adaptation by Transtibial Amputees Walking With an Experimental Powered Prosthesis Under Continuous Myoelectric Control," *IEEE Trans. Neural Syst. Rehabil. Eng.*, vol. 24, no. 5, pp. 573–581, May 2016.

[29] E. C. Prinsen *et al.*, "Adaptation Strategies of the Lower Extremities of Patients With a Transtibial or Transfemoral Amputation During Level Walking: A Systematic Review," *Arch. Phys. Med. Rehabil.*, vol. 92, no. 8, pp. 1311–1325, Aug. 2011.

[30] P. Laszczak *et al.*, "A pressure and shear sensor system for stress measurement at lower limb residuum/socket interface," *Med. Eng. Phys.*, vol. 38, no. 7, pp. 695–700, Jul. 2016.

[31] M. Zhang *et al.*, "Frictional action at lower limb/prosthetic socket interface," *Med. Eng. Phys.*, vol. 18, no. 3, pp. 207–214, Apr. 1996

[32] S. I. Wolf *et al.*, "Pressure characteristics at the stump/socket interface in transtibial amputees using an adaptive prosthetic foot," *Clin. Biomech.*, vol. 24, no. 10, pp. 860–865, Dec. 2009.

[33] J. H. Hong *et al.*, "Relationship between socket pressure and EMG of two muscles in trans-femoral stumps during gait," *Prosthet. Orthot. Int.*, vol. 29, no. 1, pp. 59–72, Apr. 2005.

[34] A. Mai *et al.*, "Effect of Prosthetic Foot on Residuum-Socket Interface Pressure and Gait Characteristics in an Otherwise Healthy Man With Transtibial Osteomyoplastic Amputation," *JPO J. Prosthet. Orthot.*, vol. 24, no. 4, pp. 211–220, Oct. 2012.

[35] M. Seeger, "GAUSSIAN PROCESSES FOR MACHINE LEARNING," *Int. J. Neural Syst.*, vol. 14, no. 02, pp. 69–106, Apr. 2004.

[36] M. Kim *et al.*, "Human-in-the-loop Bayesian optimization of wearable device parameters," *PLOS ONE*, vol. 12, no. 9, p. e0184054, Sep. 2017.

[37] Y. Ariki *et al.*, "Latent Kullback-Leibler control for dynamic imitation learning of whole-body behaviors in humanoid robots," in *2016 IEEE-RAS 16th International Conference on Humanoid Robots (Humanoids)*, Cancun, Mexico: IEEE, Nov. 2016, pp. 946–951.

[38] T. Matsubara *et al.*, "Latent Kullback Leibler Control for Continuous-State Systems using Probabilistic Graphical Models," 2014.

[39] J. Ho *et al.*, "Generative Adversarial Imitation Learning," in *Advances in Neural Information Processing Systems*, Curran Associates, Inc., 2016. Accessed: Dec. 07, 2024.

[40] X. Lu *et al.*, "Application of Isokinetic Dynamometry Data in Predicting Gait Deviation Index Using Machine Learning in Stroke Patients: A Cross-Sectional Study," *Sensors*, vol. 24, no. 22, p. 7258, Nov. 2024.

[41] E. Snelson *et al.*, "Warped Gaussian Processes," in *Advances in Neural Information Processing Systems*, MIT Press, 2003. Accessed: Dec. 07, 2024.

[42] R. Shadmehr *et al.*, "Adaptive representation of dynamics during learning of a motor task," *J. Neurosci.*, vol. 14, no. 5, pp. 3208–3224, May 1994.

[43] M. Kawato, "Internal models for motor control and trajectory planning," *Curr. Opin. Neurobiol.*, vol. 9, no. 6, pp. 718–727, Dec. 1999.

[44] S. H. Collins *et al.*, "An ankle-foot prosthesis emulator with control of plantarflexion and inversion-eversion torque," in *2015 IEEE International Conference on Robotics and Automation (ICRA)*, May 2015, pp. 1210–1216.

[45] D. J. Sanderson *et al.*, "Lower extremity kinematic and kinetic adaptations in unilateral below-knee amputees during walking," *Gait Posture*, vol. 6, no. 2, pp. 126–136, Oct. 1997.

[46] J. M. Finley *et al.*, "Learning to be economical: the energy cost of walking tracks motor adaptation," *J. Physiol.*, vol. 591, no. 4, pp. 1081–1095, Feb. 2013.

[47] K. S. Thomas *et al.*, "The impact of speed and time on gait dynamics," *Hum. Mov. Sci.*, vol. 54, pp. 320–330, Aug. 2017.

[48] S. W. Ducharme *et al.*, "Association between stride time fractality and gait adaptability during unperturbed and asymmetric walking," *Hum. Mov. Sci.*, vol. 58, pp. 248–259, Apr. 2018.

[49] R. J. van Beers, "How Does Our Motor System Determine Its Learning Rate?," *PLOS ONE*, vol. 7, no. 11, p. e49373, Nov. 2012.

[50] C. Giang *et al.*, "Motor improvement estimation and task adaptation for personalized robot-aided therapy: a feasibility study," *Biomed. Eng. OnLine*, vol. 19, no. 1, p. 33, May 2020.

[51] Y. Ding, M. Kim ,"Human-in-the-loop optimization of hip assistance with a soft exosuit during walking," *Sci. Robot.*, vol. 3, no. 15, p. eaar5438, Feb. 2018.

[52] C. G. Welker, A. S. Voloshina, V. L. Chiu, and S. H. Collins, "Shortcomings of human-in-the-loop optimization of an ankle-foot prosthesis emulator: a case series," *R. Soc. Open Sci.*, vol. 8, no. 5, p. rsos.202020, 202020, May 2021.

Biomechanical Analysis of Repetitive Lifting with Passive Exosuit Assistance: Preliminary Results

Ronak Vyas[1], Francesco Travascio[2], Vineet Vashista[1*]

***Abstract*— Repetitive lifting tasks, common in labor-intensive industries, are a significant contributor to work-related musculoskeletal disorders (WMSDs) and chronic lower back pain (LBP). The continuous physical strain associated with these tasks leads to the accumulation of fatigue, which can reduce performance and increase the risk of injury over time. This study evaluates the impact of passive back exosuit assistance on muscle activation and fatigue during repetitive lifting tasks. Surface electromyography (sEMG) and biomechanical assessments were conducted to analyze kinematics and key muscle groups under two conditions: with and without exosuit support. Preliminary findings indicate that passive exosuit assistance reduces muscle activation levels in the back and lower limbs, effectively mitigating fatigue during repetitive lifting. These results highlight its potential to enhance workplace safety and alleviate the physical demands of repetitive lifting tasks, providing valuable insights into ergonomic innovations aimed at minimizing fatigue-related risks in demanding environments.**

I. INTRODUCTION

Repetitive lifting is a common occupational activity, especially in labor-intensive sectors such as manufacturing, construction, and logistics. Workers in these settings often handle tasks that involve lifting and carrying loads for extended durations, which exposes them to significant physical strain. This prolonged exertion is a major contributor to work-related musculoskeletal disorders (WMSDs), which account for a substantial proportion of workplace injuries globally [1], [2]. Lower back pain (LBP), a prevalent manifestation of WMSDs, has been linked to over 30% of occupational injuries and is often the result of repetitive load-bearing tasks combined with poor postures and inadequate recovery time [3], [4]. These demands not only affect worker efficiency but also lead to chronic health conditions that compromise long-term well-being.

The continuous nature of lifting tasks gradually affects the body's biomechanics, particularly the musculoskeletal system [5]. Persistent engagement of muscles without sufficient recovery leads to fatigue, which diminishes the system's ability to generate necessary force during lifting. Unlike acute injuries, which are often associated with sudden trauma, the fatigue induced by repetitive lifting evolves over time. It can alter movement patterns, prompting workers to adopt compensatory strategies that increase strain on adjacent muscle groups and joints [6]. For example, studies indicate that during fatiguing tasks, individuals often transition to postures involving greater trunk flexion, placing additional mechanical demands on the lower back [7], [8]. Over prolonged periods, such compensatory mechanisms can exacerbate the risk of developing severe musculoskeletal conditions, including muscle imbalances, tendinitis, or even herniated discs [9], [10].

Ergonomic advancements have led to the development of assistive devices such as back exosuits, which are designed to reduce physical strain and support proper biomechanics during manual lifting [21]. Broadly classified into active and passive systems, these exosuits have been studied for their ability to reduce load on the lumbar spine, enhance postural control, and delay the onset of muscle fatigue [22]. Passive exosuits utilize mechanical components like springs or elastic bands to provide support without external power sources, whereas active systems incorporate powered actuators for adaptive and dynamic assistance[23]. Research in this domain has demonstrated that both types of systems have the potential to alleviate strain during repetitive lifting tasks [11], [12].

While several studies have examined the role of exosuits in improving lifting efficiency, fewer have focused on their direct relationship with muscle fatigue [33]. Preliminary findings suggest that exosuits can redistribute the mechanical load from fatigued muscle groups to other structures, thereby preserving functional performance. For instance, passive exosuits have been shown to reduce electromyographic (EMG) activity in the lower back muscles during repetitive tasks, indicating delayed fatigue onset. However, there is limited data on how these devices influence compensatory movements, postural adaptations, and overall musculoskeletal health over prolonged usage. Understanding this relationship is critical for optimizing exosuit designs to effectively prevent fatigue-related injuries.

The primary objective of this research is to investigate the effects of repetitive loading on biomechanical changes in kinematics and activation patterns of back muscles, quadriceps, and hamstring muscle groups of the lower limb. This study aims to quantify the impact of continuous lifting over time, emphasizing shifts in posture and their influence on muscle fatigue during manual material handling tasks. To address these objectives, we designed an experimental protocol involving repetitive lifting tasks under two configurations: one with passive back exoskeletal assistance and

[1]Ronak Vyas and Vineet Vashista are with the Department of Mechanical Engineering, Indian Institute of Technology Gandhinagar (IITGN), India. Email: ronak.v@iitgn.ac.in.

[2]Francesco Travascio is with the Department of Mechanical and Aerospace Engineering, University of Miami, Coral Gables, FL 33146, USA. Email: f.travascio@miami.edu.

*Vineet Vashista is the corresponding author. Email: **vineet.vashista@iitgn.ac.in**.

one without. Passive exosuit assistance is hypothesized to influence kinematics by reducing the range and frequency of compensatory movements, which could otherwise amplify strain on fatigued muscle groups. Additionally, the exosuit is expected to modulate muscle activation patterns, potentially redistributing the mechanical load and delaying the onset of fatigue. A preliminary study was conducted with four participants, where surface electromyography (sEMG) data analysis and kinematic assessments were used to evaluate the influence of exosuit assistance on muscle engagement, fatigue development, and postural adjustments throughout the lifting protocol. This research provides foundational insights into the interaction between exosuit support, muscle fatigue, and biomechanical adaptations during repetitive lifting.

II. Methods

In this section we are presenting our system design, experimental protocol and data analysis procedure.

A. Exosuit Design

The Exosuit provides upper body support and includes a Taylor's Brace (TB), a detachable moment arm, a mid-thigh segment with thigh cuffs, and elastic and non-elastic straps for passive actuation, refer Fig. 1. The elastic straps link the thigh cuffs to a flat release buckle system, enabling easy stiffness adjustments without removing the suit. The elastic bands, with stiffness levels up to 850N/mm, are connected to non-elastic nylon straps via an adjustable side buckle, offering flexibility for different users [20]. The nylon strap connects to load cell (LC1), routed over a pulley in the moment arm assembly, with its other end linked to two nylon straps from shoulder-anchored buckles. Inside the TB, a padded compressive load cell (LC2) is secured with Velcro, using a stitched female strip on the TB and a glued male strip on the LC2 casing to ensure comfort and prevent pinching at the lower back. The elastic strap assists the buttocks during squatting or bending, providing torque to aid lifting, while distributing the spinal load between the trunk, shoulders, and thighs. The moment arm assembly consists of a pocketed base and a flanged-base arm, positioned 45 degrees from the back and measuring 16 cm to reduce device-to-body forces and improve comfort [13]. The arm is securely held in the pocketed base by a catcher lock and can be removed easily by disengaging the lock. The pocketed base is fixed to aluminum strips at the L5-S1 joint on the TB. The exosuit is adjustable for heights varying between 152 cm and 165 cm, which represent the average heights of Indian females and males, respectively, based on NFHS trends [34].

B. Experimental Procedure

Four healthy male participants (age 21.25±0.83 years and an average weight of 72.5±7.54 kg) with no history of spinal disorders or injuries volunteered for the study. None of the participants had a history of musculoskeletal disorders in the past six months. Before the experiment, the participants were briefed about the procedure, and signed informed consent was obtained in accordance with the institute's ethics committee (study approval no: IEC/VV/2021/013).

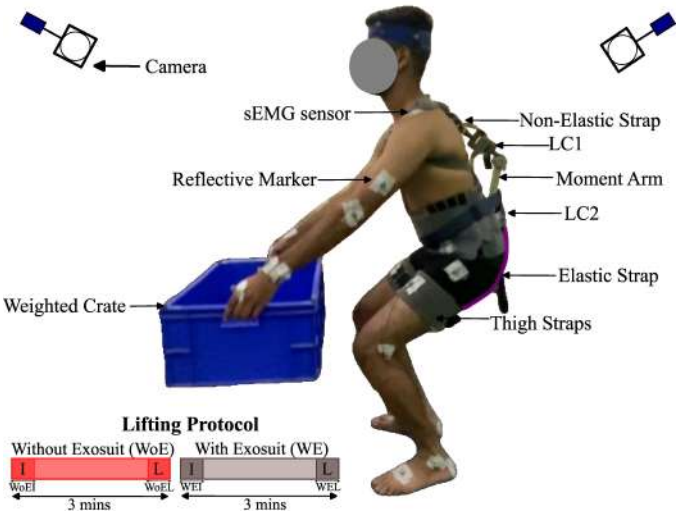


Fig. 1: The repetitive lifting experimental setup. A full-body, 37-marker model was used to track human motion with an eight-camera motion capture system, while participants lifted an 8 kg weighted crate. Eight surface EMG (sEMG) sensors were placed on specific muscles to capture muscle activity during the task. The setup includes Load Cell 1 (LC1) in the moment arm assembly and Load Cell 2 (LC2) on the inner side of the Taylor's Brace (TB), along with elastic and non-elastic straps for actuation and support. The lifting protocol comprised with exosuit and without exosuit.

The experimental setup, shown in Fig. 1, involved repetitive lifting and lowering of a weighted crate. Muscle activity was recorded using eight surface electromyography (EMG) sensors (model SX230, Biometrics, Newport, UK) placed on the multifidus, erector spinae, latissimus dorsi, and trapezius muscles of the back, as well as the rectus femoris and biceps femoris of both lower limbs. The EMG signals were sampled at 1000 Hz. Sensor placement and skin preparation adhered to SENIAM standards [17]. Additionally, 37 reflective markers full-body lumbar spine (FBLS) model was applied to analyze kinematics [18], with data collected via a motion capture system (Vicon, Oxford, UK).

C. Repetitive Lifting Protocol

In this study, the Recommended Weight Limit (RWL) was calculated using the NIOSH Lifting Equation, which takes into account factors such as horizontal, vertical, and distance multipliers, along with frequency, coupling, and asymmetry adjustments [18]. The actual load lifted was 8 kg at a rate of 10 lifts per minute over 3 minutes. Based on these parameters, the Lifting Index (LI) was determined as the ratio of the actual load to the RWL, where an LI exceeding 1 indicates a moderate to severe injury risk. The methodology and calculations adhered to the guidelines outlined in [16].

The experiment involved repetitive lifting and lowering tasks performed both without exosuit (WoE) and with exosuit (WE), refer Fig. 1. The lifting order was randomized, ensuring that either the exosuit or the non-exosuit condition could be conducted first, thus minimizing any potential bias in the

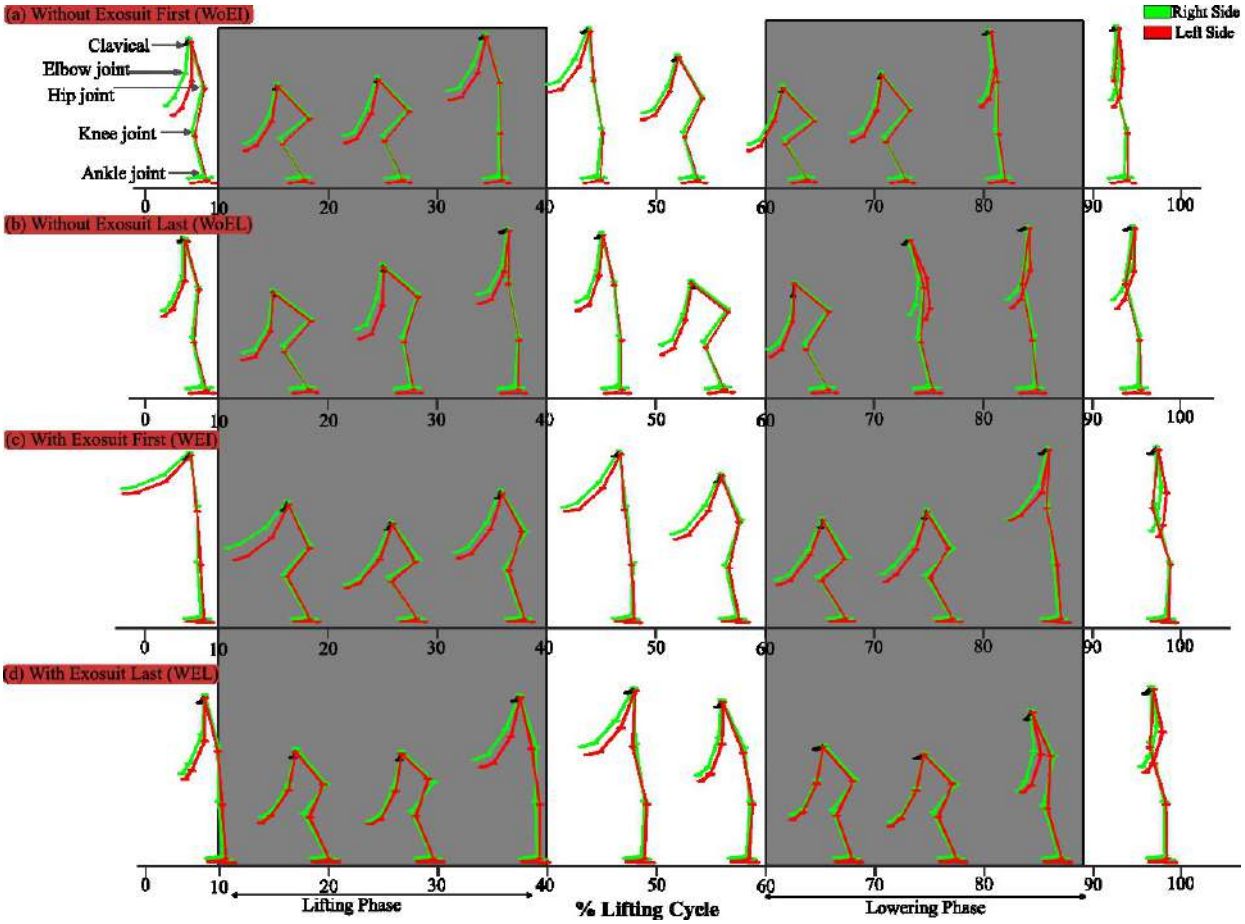


Fig. 2: The sagittal plane stick diagrams of a representative participant's repetitive lifting cycles under the without-exo first, without-exo last, with-exo first, and with-exo last conditions. The diagrams show the right side (green) and left side (red) joint movements. The highlighted regions represent the lifting and lowering of the load during each cycle.

results. To further prevent the influence of fatigue or muscle soreness, participants were given one full day of rest between sessions. This rest period helped to mitigate any confounding factors, ensuring that the results from each session were not influenced by prior performance or muscle fatigue.

D. Data Analysis

Joint angle trajectories, including peak hip and knee flexion, were analyzed during the first and last lifting cycles for both conditions: "without exosuit" (WoEI for the first cycle, WoEL for the last cycle) and "with exosuit" (WEI for the first cycle, WEL for the last cycle), refer to Fig. 1. Electromyography (EMG) signals were band-pass filtered (20–400 Hz), and root mean square (RMS) values were calculated using a 125 ms sliding window. Values were normalized (nRMS) based on the maximum voluntary isometric contraction (MVIC) method, as outlined in [13]. Muscle fatigue was analyzed using processed EMG signals, with the power spectral density (PSD) estimated using Welch's method. The median frequency (MDF) was computed for 1-second epochs, and the starting MDF values for each muscle were normalized for consistency across conditions. Linear regressions were applied to the MDF data points, allowing comparison of fatigue trends over time for each muscle under both conditions, as detailed in [14], [15].

III. Results

Repetitive lifting under two conditions, without exosuit (WoE) and with exosuit (WE), revealed notable kinematic differences during the lifting (10–40%) and lowering (60–90%) phases. As shown in Fig. 2(a-d), trunk, hip, and knee flexion varied across four conditions: Without Exosuit First (WoEI), Without Exosuit Last (WoEL), With Exosuit First (WEI), and With Exosuit Last (WEL). Further, distinct patterns of hip and knee flexion were observed in the joint angle trajectories, see Fig. 3, further support these findings.

A. Joint Kinematics

Without Exosuit (WoE): A noticeable increase in trunk flexion was observed in WoEL compared to WoEI, particularly during the lifting phase (around 20%), as shown in Figs. 2(a) and (b). The hip joint showed reduced extension and increased flexion during lifting, while knee flexion decreased during lowering (60–90% of the cycle). These adaptations, evident in the stick diagrams, Figs. 2(a) and (b), and are further supported by distinct patterns of peak hip and knee

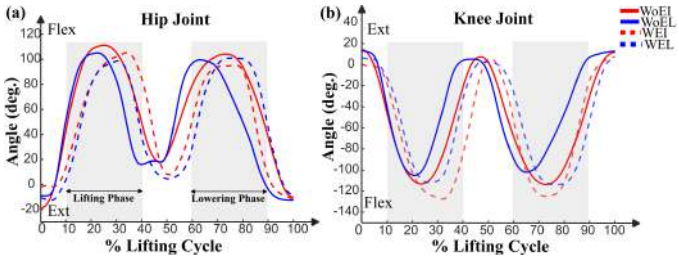


Fig. 3: (a-b) Representative participants' right leg hip and knee joint kinematics in the sagittal plane. Solid lines represent without exosuit (WoEI and WoEL), and dashed lines represent with exosuit (WEI and WEL). Highlighted regions indicate the lifting and lowering phases of the cycle.

flexion observed in joint angle trajectories Fig. 3(a) and (b), highlighting progressive kinematic adaptations across cycles.

With Exosuit (WE): During the initial lifting cycle with exosuit assistance (WEI), less trunk flexion was observed around 20% of the lifting phase compared to the last cycle (WEL), as shown in Figs. 2(c) and 2(d). This observation suggests that the exosuit in WEI assists in maintaining a more upright posture during the lift. During the lowering phase, trunk flexion was reduced by around 70% in WEL compared to WEI, indicating postural adjustments introduced by the exosuit over time. Consequently, these differences are evident with less hip flexion and controlled knee flexion observed in Fig. 3(a) and 3(b), highlighting the role of the exosuit in facilitating more efficient and controlled movement patterns during repetitive lifting.

Without Exosuit (WoEI) vs With Exosuit (WEI) - First Cycle: In the initial lifting cycle, WoEI showed greater trunk flexion (around 20%) than WEI, as seen in Figs. 2(a) and 2(c), suggesting that the exosuit helps maintain a more upright posture in WEI. The WEI condition also demonstrated more controlled hip and knee flexion during lifting (20–40%) and lowering (60–80%) phases. The joint angles during lifting in WEI showed smoother and more controlled flexion patterns in the hip and knee, as illustrated in Figs. 3(a) and 3(b), compared to the more abrupt and inconsistent flexion observed in WoEI. During the lowering phase, the WEI condition enabled smoother, more controlled hip and knee extension, as further highlighted in the joint angle trajectories, refer to Fig. 3(a) and 3(b), while the WoEI condition exhibited abrupt and uneven movements.

Without Exosuit (WoEL) vs With Exosuit (WEL) - Last Cycle: In the last lifting cycle, the WEL condition showed reduced trunk flexion and more controlled hip and knee movements during both the lifting (20–40% of the cycle) and lowering phases (60–80% of the cycle) compared to WoEL, as seen in Figs. 2(b) and 2(d). The WoEL condition exhibited greater variability in joint movements, while the WEL condition promoted smoother and more consistent motion patterns, highlighting exosuit assistance. Joint angle data in Fig. 3 further highlights these distinctions.

Kinematic analysis across participants: Peak flexion angles of the hip and knee joints demonstrated distinct patterns between conditions with and without exosuit assistance, see Figs. 4(a) and 4(b). During the lifting and lowering phases, hip flexion was higher in the conditions without exosuit assistance (WoEI and WoEL), indicating greater reliance on the hip joint to compensate for the absence of external support, see Fig. 4(a). In contrast, with exosuit assistance (WEI and WEL), hip flexion was reduced, reflecting the exosuit's ability to alleviate the demand on the hip joint. In the case of knee flexion, an opposing trend was observed. Without the exosuit (WoEI and WoEL), knee flexion was slightly lower, suggesting a compensatory strategy that relied more heavily on the hip, see Fig. 4(b). However, with exosuit assistance (WEI and WEL), knee flexion increased, reflecting a more coordinated and balanced engagement of the hip and knee joints. This increased knee flexion allowed for a greater range of motion, facilitating improved posture and motion efficiency during the lifting and lowering tasks.

B. EMG Analysis

Muscle Activation: Repetitive lifting tasks revealed distinct differences in muscle activation levels under the two conditions: without exosuit (WoE) and with exosuit (WE). Figure 5(a) highlights these variations by presenting the mean activation levels of the targeted muscle groups. Essentially, a general reduction in muscle activation was observed across all muscle groups when participants performed tasks with exosuit support. The Multifidus and Erector Spinae muscles exhibited a marked decrease in activation levels, suggesting that the exosuit effectively alleviated the workload on these muscles. On the other hand, while the Latissimus Dorsi and Trapezius muscles showed similar trends of reduced activation, the extent of reduction was more pronounced in lower limb muscles, such as the Rectus Femoris and Biceps Femoris. Consequently, the overall muscular demand during lifting tasks appeared to be redistributed and diminished with exosuit assistance.

Muscle Fatigue: The regression slopes derived from the median frequency (MDF) analysis, representing muscle fatigue under the two conditions, as shown in Fig. 5(b). Without exosuit, fatigue slopes were generally more negative, indicating a greater accumulation of fatigue over time. In contrast, with the exosuit, fatigue slopes tended to be closer to zero, reflecting a reduction in fatigue accumulation. Notably, the Multifidus and Erector Spinae muscles substantially improved fatigue resistance when using the exosuit. Similarly, the Trapezius and lower limb muscles exhibited less fatigue with exosuit support. Essentially, these findings highlight the exosuit's capacity to enhance muscle endurance during repetitive lifting tasks.

IV. Discussion and Conclusion

In this study, we aimed to investigate the biomechanical effects of repetitive lifting, focusing on kinematics, muscle activation, and fatigue. Our experimental protocol assessed these factors under two conditions: with and without passive back exosuit assistance. The findings revealed notable differences in kinematic and muscle activation patterns between the two conditions. Notably, distinct postural strategies emerged during both the lifting and lowering phases, with

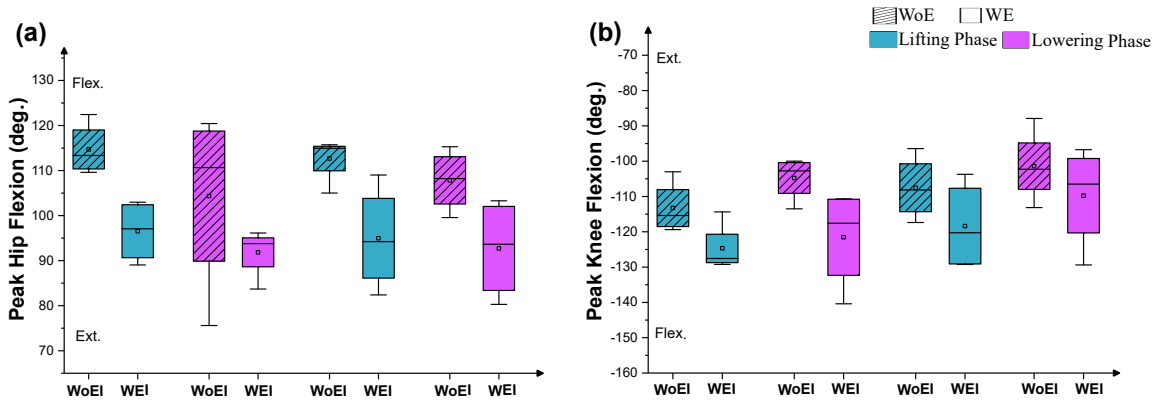


Fig. 4: (a) Peak hip flexion and (b) peak knee flexion while lifting and lowering the load for four participants under two conditions: without exosuit (WoE) and with exosuit (WE) during the first and last cycles of repetitive lifting.

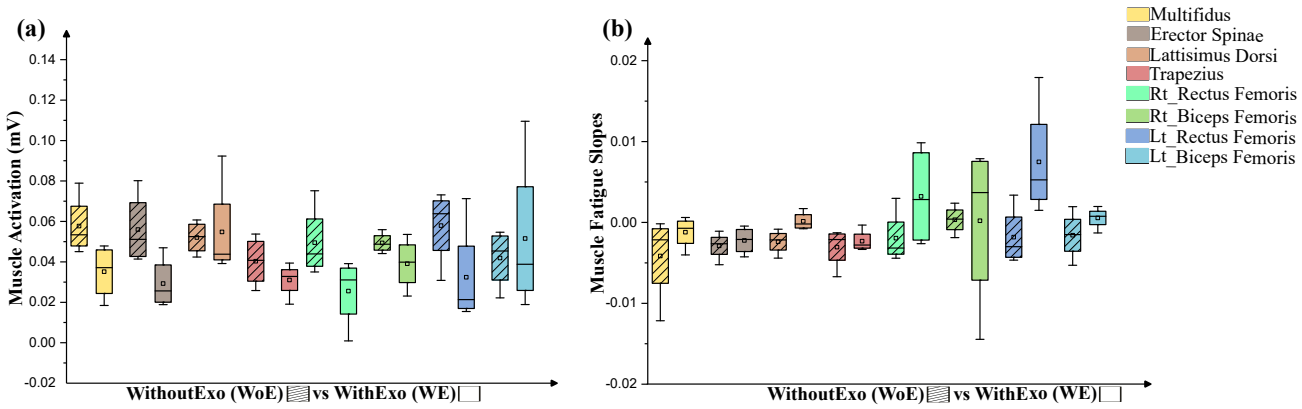


Fig. 5: (a) Muscle activation and (b) muscle fatigue results for four participants under two conditions: without exosuit (WoE) and with exosuit (WE). The targeted muscles include the Multifidus, Erector Spinae, Latissimus Dorsi, Trapezius, and lower limb muscles (Right/Left Rectus Femoris and Biceps Femoris). Activation values represent mean values, while fatigue values are represented by regression slopes from median frequency (MDF) analysis.

the exosuit playing a crucial role in reducing compensatory movements and improving movement efficiency. These results highlight the potential of passive exosuit assistance in enhancing lifting performance by reducing biomechanical strain and improving movement efficiency, with implications for improving worker safety and reducing fatigue during repetitive lifting tasks.

A key observation in this study was the reduction in muscle activation levels, particularly in the Multifidus and Erector Spinae muscles, when participants used the passive exosuit. This reduction highlights the exosuit's role in alleviating physical demands on spinal stabilizers, thereby decreasing overall muscular strain. Similar trends have been reported in previous research, where the use of passive back exosuits during lifting tasks resulted in decreased lumbar extensor muscle activation [13], [26], [27]. These findings emphasize the role of passive back exosuits in improving biomechanical efficiency and reducing the risk of musculoskeletal strain during physically demanding tasks.

The observed decrease in fatigue accumulation, as evidenced by median frequency regression slopes tending to remain closer to zero, further emphasizes the exosuit's role in enhancing muscle endurance during repetitive lifting tasks. By reducing the physical demands on stabilizing lower back muscles, the exosuit delays fatigue onset, thereby mitigating compensatory movements that can elevate strain on other muscle groups and joints [21], [31]. This aligns with the study's objective to investigate fatigue-related biomechanical adaptations, demonstrating that passive exosuits not only promote more efficient and ergonomic movement patterns but also reduce the risk of musculoskeletal injuries. These benefits contribute to safer and more sustainable lifting practices, supporting findings from prior research indicating that minimizing fatigue enhances both immediate task performance and long-term musculoskeletal health [32], [33]. Consequently, these results show that passive exosuits can improve work efficiency in tasks involving repetitive lifting.

In the current experiments, preliminary results revealed notable biomechanical adaptations introduced by exosuit assistance, largely driven by the repetitive nature of the lifting task. Without the exosuit, participants developed a stooped posture, characterized by increased trunk flexion and reduced knee involvement, as a compensatory response to the repeated demands of the task. This pattern heightened strain on lower back stabilizers, accelerating fatigue onset and exacerbating biomechanical inefficiencies [24], [25]. Over

time, these fatigue-driven compensations increased the risk of injury [28], [29]. In contrast, with exosuit assistance, participants maintained a more upright posture and better joint coordination, redistributing the repetitive workload across joints and alleviating strain on the spinal stabilizers. This delayed fatigue accumulation, supporting more efficient task execution and reducing deviations from optimal posture. These findings highlight the importance of passive exosuits in mitigating the cumulative strain caused by repetitive lifting tasks, enhancing long-term safety and performance.

While this study provides valuable insights into the potential of passive exosuits in enhancing ergonomic outcomes and reducing muscle fatigue during repetitive lifting tasks, it is important to acknowledge its limitations. The findings are based on a small sample size and lack comprehensive statistical analysis, necessitating further research to validate and expand upon these results. Direct measurements of muscle fatigue and biomechanical adaptations are essential for deeper understanding. Overall, this study underscores the utility of exosuits in occupational and rehabilitation settings, promoting worker safety, efficiency, and long-term musculoskeletal health.

ACKNOWLEDGMENT

This work was partially supported by the Gujarat Council on Science and Technology under project number GUJCOST/STI/2023-24/340 and the Life Science Research Board under project number LSRB/01/15001/LSRB-399/LS&BD/2023.

REFERENCES

[1] MF Antwi-Afari, Heng Li, DJ Edwards, EA Pärn, Joonoh Seo, and Arnold Yu Lok Wong, "Biomechanical analysis of risk factors for work-related musculoskeletal disorders during repetitive lifting task in construction workers," *Automation in Construction*, vol. 83, pp. 41–47, 2017.

[2] lexander Magora. Investigation of the relation between low back pain and occupation. IMS Indust Med Surg, 11:465–471, 1970.

[3] Bruce P Bernard and Vern Putz-Anderson. Musculoskeletal disorders and workplace factors: a critical review of epidemiologic evidence for work-related musculoskeletal disorders of the neck, upper extremity, and low back. NIOSH Publication, 1997.

[4] Laura Punnett and David H Wegman. Work-related musculoskeletal disorders: the epidemiologic evidence and the debate. Journal of electromyography and kinesiology, 14(1):13–23, 2004.

[5] Sean Gallagher and John R Heberger. Examining the interaction of force and repetition on musculoskeletal disorder risk: a systematic literature review. Human factors, 55(1):108–124, 2013.

[6] Roger M Enoka and Jacques Duchateau. Muscle fatigue: what, why and how it influences muscle function. The Journal of physiology, 586(1):11–23, 2008.

[7] Kevin P Granata and William S Marras. Relation between spinal load factors and the high-risk probability of occupational low-back disorder. Ergonomics, 42(9):1187–1199, 1999.

[8] P Dolan and MA Adams. Repetitive lifting tasks fatigue the back muscles and increase the bending moment acting on the lumbar spine. Journal of biomechanics, 31(8):713–721, 1998.

[9] Stuart McGill. Low back disorders: evidence-based prevention and rehabilitation. Human Kinetics, 2015.

[10] David G Allen, Graham Douglas Lamb, and H Westerblad. Skeletal muscle fatigue: cellular mechanisms. Physiological reviews, 88(1):287–332, 2008.

[11] Jean Theurel and Kevin Desbrosses. Occupational exoskeletons: overview of their benefits and limitations in preventing work-related musculoskeletal disorders. IISE Transactions on Occupational Ergonomics and Human Factors, 7(3-4):264–280, 2019.

[12] Pranav Madhav Kuber and Ehsan Rashedi. Product ergonomics in industrial exoskeletons: potential enhancements for workforce efficiency and safety. TheoreTical issues in ergonomics science, 22(6):729–752, 2020.

[13] Siddharth Bhardwaj, Akshayraj B Shinde, Randheer Singh, and Vineet Vashista. Manipulating device-to-body forces in passive exosuit: An experimental investigation on the effect of moment arm orientation using passive back-assist exosuit emulator. Wearable Technologies, 4:e17, 2023.

[14] Farina, Dario, Marco Gazzoni, and Roberto Merletti. "Assessment of low back muscle fatigue by surface EMG signal analysis: methodological aspects." Journal of Electromyography and Kinesiology 13.4 (2003): 319-332.

[15] Merletti, Roberto, Marco Knaflitz, and Carlo J. De Luca. "Myoelectric manifestations of fatigue in voluntary and electrically elicited contractions." Journal of applied physiology 69.5 (1990): 1810-1820.

[16] Thomas R Waters, Vern Putz-Anderson, and Arun Garg. Applications manual for the revised niosh lifting equation. DHHS (NIOSH) Publication No. 94-110, 1994.

[17] Hermie J Hermens, Bart Freriks, Catherine Disselhorst-Klug, and Günter Rau. Development of recommendations for semg sensors and sensor placement procedures. Journal of electromyography and Kinesiology, 10(5):361–374, 2000.

[18] M. E. Raabe, A. M. W. Chaudhari, An investigation of jogging biomechanics using the full-body lumbar spine model: Model development and validation. J. Biomech. 49, 1238–1243 (2016).

[19] Waters, Thomas R., et al. "Efficacy of the revised NIOSH lifting equation to predict risk of low back pain due to manual lifting: expanded cross-sectional analysis." Journal of Occupational and Environmental Medicine 53.9 (2011): 1061-1067.

[20] Bhardwaj, Siddharth, et al. "Passive exosuit emulator for material handling applications." IEEE Robotics and Automation Letters 7.3 (2022): 7605-7611.

[21] Ali, Athar, et al. "Systematic review of back-support exoskeletons and soft robotic suits." Frontiers in bioengineering and biotechnology 9 (2021): 765257.

[22] Fritzsche, Lars, et al. "Assessing the efficiency of exoskeletons in physical strain reduction by biomechanical simulation with AnyBody Modeling System." Wearable technologies 2 (2021): e6.

[23] Davoudi Kakhki, Fatemeh, et al. "Evaluating the Efficacy of a Passive Exoskeleton for Enhancing Ergonomics in Manufacturing." Applied Sciences 14.13 (2024): 5810.

[24] Washmuth, Nicholas B., Abby D. McAfee, and C. Scott Bickel. "Lifting techniques: why are we not using evidence to optimize movement?." International Journal of Sports Physical Therapy 17.1 (2022): 104.

[25] Vecchio, L. Del. "Choosing a lifting posture: squat, semi-squat or stoop." MOJ Yoga Phys. Ther 2 (2017): 56-62.

[26] van Sluijs, Rachel M., et al. "A method to quantify the reduction of back and hip muscle fatigue of lift-support exoskeletons." Wearable Technologies 4 (2023): e2.

[27] Schwartz, M., et al. "Using passive or active back-support exoskeletons during a repetitive lifting task: influence on cardiorespiratory parameters." European Journal of Applied Physiology 122.12 (2022): 2575-2583.

[28] McGill, Stuart M. "The biomechanics of low back injury: implications on current practice in industry and the clinic." Journal of biomechanics 30.5 (1997): 465-475.

[29] Marras, William S., and Kevin P. Granata. "Changes in trunk dynamics and spine loading during repeated trunk exertions." Spine 22.21 (1997): 2564-2570.

[30] Quirk, D. Adam, et al. "Evaluating adaptiveness of an active back exosuit for dynamic lifting and maximum range of motion." Ergonomics 67.5 (2024): 660-673.

[31] Rodzak, Katherine, et al. "Can back exosuits simultaneously increase lifting endurance and reduce musculoskeletal disorder risk?." Authorea Preprints (2024).

[32] Pesenti, Mattia, et al. "Towards a functional performance validation standard for industrial low-back exoskeletons: State of the art review." Sensors 21.3 (2021): 808.

[33] Lamers, Erik P., et al. "Low-profile elastic exosuit reduces back muscle fatigue." Scientific Reports 10.1 (2020): 15958.

[34] Deaton, Angus. "Height, health, and inequality: the distribution of adult heights in India." American Economic Review 98.2 (2008): 468-474.

Where Is My Hand? Assessing Visuo-Tactile Integration of Hand and Shoulder After Virtual Reality Training Using a Body-Machine Interface

Lucas R. L. Cardoso[1], Harriet Dempsey-Jones[1], Antonio P. L. Bo[1,2], Vanesa Bochkezanian[3], Arturo Forner-Cordero[4], Alejandro Melendez-Calderon[1,5,6]

***Abstract*— Immersive virtual reality (VR) has potential for enhancing rehabilitation in clinical populations, such as individuals with stroke, but many face usability challenges. A promising approach involves a Body-Machine Interface using shoulder movements to control a virtual hand, potentially altering body perception. Investigating bodily illusions is crucial for expanding therapeutic applications. This study examines how a single VR motor-training session, using shoulder movements to control a virtual hand, affects brain representations of the real hand and shoulder. The Crossmodal Congruency Test (CCT) was adapted to assess the visuo-tactile interaction between the shoulder and hand in neurotypical participants before and after VR training. Nine participants controlled the virtual hand with shoulder movements, while eight used their fingers, both receiving shoulder tactile feedback. No significant differences were found in hand-to-shoulder visuo-tactile integration. The results suggest that the Body-Machine Interface may not alter bodily representations of the hand and shoulder, or that tactile feedback alone could elicit changes. Although the results did not fully meet expectations, the study provided valuable insights and identified methodological limitations for future research.**

I. Introduction

In recent years, immersive virtual reality (VR) has been proposed as a tool to enhance rehabilitation practices [1]. However, despite the appeal of its immersive components and gaming elements, many individuals with conditions such as stroke or spinal cord injury face usability challenges [2], including difficulty holding controllers, pressing buttons, or using modern finger-tracking systems, which are often incompatible with non-standard hand gestures.

One promising approach to enable VR interaction for individuals with hand impairments is a Body-Machine Interface [3], which leverages alternative body parts, such as the shoulder, to control hand movements in VR [4]. However, it is still unclear how such a Body-Machine interface influences an individual's perception of their body.

If the avatar's hand, controlled by shoulder movements, is perceived as an extension of the user's actual hand (a phenomenon known as embodiment [5]), how might this control strategy affect body representation for both body parts? Could it alter interactions with the real shoulder and hand or induce neurophysiological adaptations? These questions remain largely unexplored.

Previous research showed that after prolonged training (20 sessions) with a robotic hand controlled by forearm muscle signals, participants exhibited significant body representation adaptations [6]. However, embodiment has been shown to occur almost instantaneously in illusory or immersive VR environments [5]. This study investigates how a single VR motor-training session using shoulder movements to control a virtual hand affects body representations of the real hand and shoulder.

Body representations in the brain are linked to the size of the peripersonal space (PPS)—the space around a body part where sensory stimuli are integrated. Research has shown that reaction times to tactile stimuli on the fingers are influenced by concurrent visual input within the hand's PPS. This visuo-tactile integration can assess whether objects, such as tools [7] or virtual avatars [5], [8], are incorporated into the PPS, reflecting changes in body representation.

In a prior study, we adapted this paradigm by applying tactile stimuli to the shoulder while presenting visual distractors near a virtual hand [9], aiming to measure hand-to-shoulder visuo-tactile integration. These regions are thought to be naturally connected, as suggested by brain models of bodily representation [10] and PPS interactions between body parts like the hand and foot [11]. We hypothesize that testing this paradigm before and after VR training, where shoulder elevation controls the virtual hand's pinch, will strengthen cross-body part interaction.

Although preliminary results showed no significant hand-to-shoulder interaction [9], in the present study, we modified the VR protocol by pairing virtual touches to the index finger or thumb with corresponding vibrations at distinct shoulder locations. This addition compensates for the previous reliance on proprioceptive feedback alone by introducing artificial tactile feedback.

Building on prior findings, this study examines how tactile feedback affects hand-to-shoulder PPS interactions. To obtain preliminary data before expanding to a larger cohort, we adopted a fixed-order design to minimize variability and identify trends while keeping the sample size manageable. We hypothesize that pairing tactile feedback over the trapezius with virtual index or thumb touches enhances visuo-tactile integration between the shoulder and hand.

*L.R.L. Cardoso was supported by The University of Queensland Research Training Program Scholarship.

[1]School of Electrical Engineering & Computer Science, The University of Queensland, Australia

[2]Department of Mechanical, Electrical & Chemical Engineering, Oslo Metropolitan University, Norway

[3]Faculty of Health & Medical Sciences, The University of Adelaide, Australia

[4]Department of Mechatronics, University of São Paulo, Brazil

[5]School of Health & Rehabilitation Sciences, The University of Queensland, Australia

[6]Jamieson Trauma Institute, Metro North Health, Australia

Correspondence: l.ribeirolopescardoso@uq.edu.au or alej.melendez@uq.edu.au

II. Materials and Methods

A. Participants

We recruited 21 right-handed, English-speaking adults (18–65) from the university community. Inclusion required the ability to perform 30 minutes of seated upper-limb movements, while exclusion criteria included neurological conditions (e.g., stroke, spinal cord injury) or inability to provide informed consent. The protocol was approved by the University of Queensland's Ethics Committee (2022/HE002234). All participants were naive to the experimental conditions and provided informed consent.

Three participants were in the pilot phase were excluded from analysis, and one withdrew due to technical issues, leaving 17 for analysis (*Finger* group: $n = 8$, 22–35 years, 2 women; *Shoulder* group: $n = 9$,21–37 years, 1 woman). Demographics were similar between groups, with comparable age, handedness, and sleep assessments.

B. Experimental setup

Participants were seated comfortably (Figure 1A), and four vibrotactile motors (LRAs; LV101040A, Jinlong Machinery) were placed on the front and back of the right shoulder and on the tips of the right index finger and thumb, secured with hypoallergenic medical tape. The shoulder LRAs were positioned to align with the C4 dermatome. The LRAs were controlled with a custom-made *Haptic Box* integrating an Arduino Nano 33 BLE, a custom PCB, and a DRV2605 motor driver (Texas Instruments). This box also integrated input from two push buttons for participants to indicate perceived vibration locations during the CCT using their left (non-tested) hand, which rested on the desk with the two buttons under their index finger and thumb, mirroring the right hand receiving stimuli.

Shoulder elevation was tracked using OpenCV in Python with a webcam detecting two ArUco tags: one fixed on the chair and another on the participant's right scapula (Figure 1B). The system operated at 44 FPS, with tag distance increasing as the shoulder was raised. Both groups, including *Finger*, performed calibration as in [9]. Unlike our previous study, which used Inertial Measurement Units (IMUs) with a Kalman Filter for shoulder tracking [9], this study employed three IMUs (Avanti, Delsys) on the right Trapezius, upper arm, and forearm solely to record shoulder activity. Shoulder engagement during VR training was estimated from the Trapezius IMU as the highest roll angle within each trial.

Participants received instructions about the experimental protocol, prior to wearing a VR headset (Oculus Quest 2, Meta, USA) and noise-isolating headphones. The VR environment was developed in Unity 3D (2022.3.26f1) and displayed a tracked virtual hand in a fixed pinching posture (Figure 1A inset).

C. Experimental protocol

After providing consent, participants completed baseline demographic forms, the Epworth Sleepiness Scale (ESS), the Pittsburgh Sleep Quality Index (PSQI), and the Edinburgh Handedness Inventory. The EES and PSQI assessments were included to consider potential fatigue due to poor sleep. Figure 2 illustrates the experiment phases, which included a VR-based motor training task and Cross-Modal Congruency Test (CCT) phases, followed by subjective reports to assess participants' phenomenological experience. The latter consisted of (1) a six-item Ownership subscale from a standardized embodiment questionnaire [13], which assessed virtual hand ownership on a 7-point Likert scale; and (2) the NASA-TLX, which measured workload on a 0–20 scale to evaluate task load differences affecting CCT performance. CCT blocks lasted 5–6 min, VR training 10–15 min (*Shoulder* group longer due to motor learning), with total session time under 90 min.

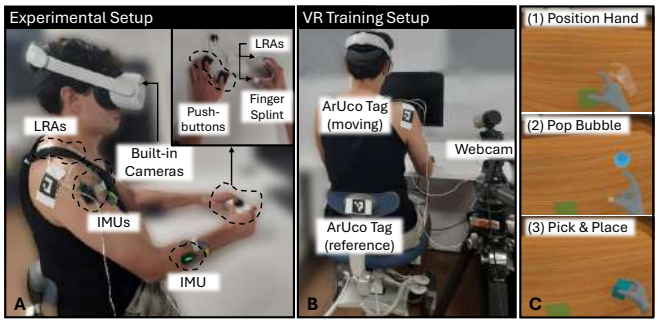


Fig. 1. **Experimental Setup.** A) Hand tracking via the headset's cameras; IMUs record shoulder activity. The Haptic Box, with four vibrotactile motors (LRAs), supports H2H and H2S implementations, and the tactile feedback during the VR training, with shoulder-mounted devices vibrating upon virtual touch. B) Shoulder elevation (only for the *Shoulder* group) is tracked using ArUco tags and a webcam. C) The VR task involves three stages: hand-shadow alignment, bubble popping, and block placement to start the next trial.

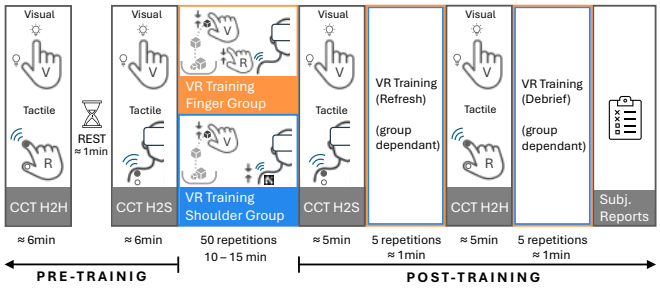


Fig. 2. **Experimental Design.** Two groups controlled a virtual pinch: *Finger* (fingers) and *Shoulder* (shoulder movements). Both received vibrotactile feedback on the shoulder during VR training. In the CCT, visual distractors appeared near the virtual hand, with tactile stimuli applied to the real hand (H2H) or shoulder (H2S). Assessments occurred *pre* and *post* training. Letters inside the hand indicate real (R) or virtual (V) body parts.

During VR training, participants interacted with objects using their virtual index finger or thumb, following a three-stage trial: (1) aligning the virtual hand with a shadow cue, (2) popping a bubble, and (3) picking and placing a block to complete the trial (Figure 1C). Training emphasized successful execution over speed. *Shoulder* and *Finger* groups experienced distinct VR training conditions. The *Finger* group controlled the virtual hand using real index-thumb movements (enabled by the Oculus Quest's vision-based hand tracker), while the *Shoulder* group used scapular elevation/relaxation (enabled by the real-time tracking of

the ArUco Tags). To maintain a similar hand shape across groups during VR training, all participants, regardless of their group, held a piece of foam with their middle, ring, and little fingers. In addition, participants in the *Shoulder* group wore a custom-fitted finger splint on the index finger and thumb to ensure a fixed curved posture between these digits. Both received vibrotactile feedback on the trapezius when touching virtual objects, but only the *Shoulder* group experienced a visuo-proprioceptive link between their shoulder and pinch motions.

CCT, described in detail in section II-D, was assessed *pre* and *post* training, using the two types, H2H (*virtual* Hand to *real* Hand) and H2S (*virtual* Hand to *real* Shoulder). The study followed a 2 (test stage: pre, post) × 2 (test type: H2H, H2S) design. To obtain preliminary data from a limited cohort while minimizing variability, we fixed the order of conditions across participants to ensure that any observed effects were not influenced by order-related differences. This approach allowed us to identify trends more clearly before introducing counterbalancing in a future full study. In the pre-stage, we ran the CCT H2H first to mitigate potential effects of the embodiment of the virtual hand, based solely on visual feedback. In the post-stage, the CCT H2S was administered immediately after the VR training to prevent potential washout effects.

The sequence was (Figure 2): pre-training CCT H2H, pre-training CCT H2S (after a short break), VR training (50 trials), post-training CCT H2S, and post-training CCT H2H (after a brief 5-trial refresh). Breaks minimized interference, and a final 5-trial VR session ensured subjective questionnaires reflected the training rather than CCT.

Each CCT block (H2H pre, H2S pre, H2S post, H2H post) had 60 trials (30 congruent, 30 incongruent) and 8 no-go trials (see section II-D). Before H2H pre and H2S pre, participants completed 10 Target-Only trials (no visual distractors) to learn vibration-button mapping and 20 Familiarization trials (with visual distractors, reaction times not analyzed), including 2 no-go trials. The CCT used the same VR environment, displaying a fixation sphere (15mm diameter) that turned green for 1–1.5s to signal trial start. After each trial, it flickered at 36Hz [15]—green for correct, red for incorrect. A stopwatch appeared if response time exceeded 1500ms [15]. Visual distractors (blue spheres, 15mm diameter) flickered at 36Hz for 200ms [15] near the index finger or thumb. All participants, regardless of the group, wore a custom-fitted finger splint on their right index finger and thumb, and held a piece of foam with their middle, ring, and little fingers, to maintain hand shape.

D. Crossmodal Congruency Test

To access the visuo-tactile integration between the shoulder and hand, we used an adaptation of a psychophysiological assessment, Crossmodal Congruency Test (CCT) [12].

In the classical CCT, participants rapidly discriminate between two tactile stimuli at distinct body locations (e.g., index finger and thumb) while ignoring visual distractors near one location. The test includes congruent trials, where tactile and visual stimuli coincide, and incongruent trials, where they differ [12]. Reaction times are typically slower in incongruent trials, a difference termed the Crossmodal Congruency Effect (CCE) [8], [12], [14], [15]. This effect is amplified when tactile and visual stimuli are spatially close, a phenomenon known as *Spatial Modulation*, which is used to study tool incorporation [16].

In our adaptation, *CCT H2S* (*virtual* Hand to *real* Shoulder), tactile stimuli were applied to the shoulder, while visual distractors appeared near the virtual hand. We also tested the classical (but virtual) *CCT H2H* (*virtual* Hand to *real* Hand), where tactile stimuli were applied to the real hand.

CCE and Spatial Modulation were calculated as:

$$CCE = \frac{\sum_{n=1}^{N} RT_{incong}}{N} - \frac{\sum_{n=1}^{M} RT_{cong}}{M} \quad (1)$$

and

$$Spatial\ Modulation = CCE_{H2H} - CCE_{H2S} \quad (2)$$

where RT_{incong} and RT_{cong} are reaction times (RTs, in seconds) for incongruent and congruent trials, occurring N and M times, respectively. RTs were measured as the duration between the vibration stimulus (shoulder or fingers) and the button press (contralateral index or thumb).

H2S results indicate (virtual) hand to (real) shoulder visuo-tactile integration, while H2H reflects integration between the virtual and real hand. Comparing CCEs between H2S and H2H provides insights into Spatial Modulation, as H2H involves co-localized stimuli, whereas H2S spatially separates them.

The protocol includes *no-go* trials, where the finger and thumb visual distractors appear simultaneously, prompting participants to withhold responses to maintain attention and prevent eye closure. Visual feedback after each trial categorizes responses as correct, incorrect (green or red sphere between index and thumb), or too slow (a stopwatch in the same size and location as the sphere).

E. Data analysis

Analyses were conducted using MATLAB® 2022a and GraphPad Prism. Trials with reaction times between 200–1500ms were included [14], [15].

Given the study's exploratory nature, we used the Least Significant Difference (LSD) method [17] to identify trends for future research. Normality was assessed via Shapiro-Wilk tests, with non-parametric tests (Mann-Whitney and Wilcoxon signed-rank) used when assumptions were unmet.

To validate CCT data, a repeated measures ANOVA examined adaptation effects across the last five correct trials, followed by Tukey's post-hoc tests. Spatial Modulation variance was assessed using Pitman-Morgan's and Levene's tests.

Demographic variables (age, handedness, sleepiness, VR practice, shoulder engagement) were compared using independent t-tests. Subjective reports were analyzed with the Mann-Whitney test.

Statistical significance is denoted as $*$ ($p \leq 0.05$) and $**$ ($p \leq 0.01$).

III. Results

The results indicated successful adaptation to VR training for both groups, but no significant group differences in CCE, Spatial Modulation, or subjective ownership reports.

A. Validity of the CCT Data

In target-only trials, all participants exceeded 80% accuracy, confirming task comprehension.

Reaction time analysis of the last five correct trials per CCT block, including pre-stage Target Only and Familiarization blocks (Figure 3), showed a significant block effect in incongruent trials ($F(3.68, 58.92) = 11.45, p < 0.0001$), but not in congruent trials ($F(2.95, 47.21) = 2.154, p = 0.1069$).

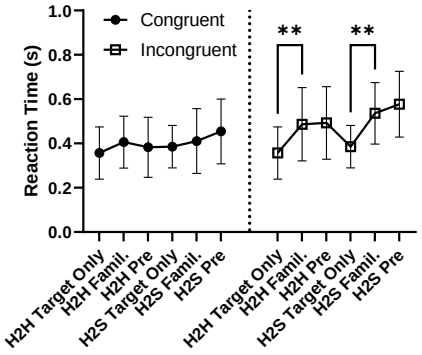


Fig. 3. **Adaptation During CCT.** Mean reaction times for the last five correct trials, segmented by congruency type.

Tukey's test showed visual distractors significantly increased reaction times in incongruent trials for H2H ($t(16) = -4.25, p = 0.0067$) and H2S ($t(16) = -4.97, p = 0.0016$), but no other consecutive block comparisons were significant, indicating stabilization post-familiarization.

False alarm rates in no-go trials (7%) align with previous studies [14], supporting data validity.

B. VR Training

The graph in Figure 4 shows *time per trial* fitted to an exponential function and *shoulder movement amplitude*, measured as the highest roll angle from the IMU on the Trapezius muscle. These metrics indicate participants' adaptation during VR training.

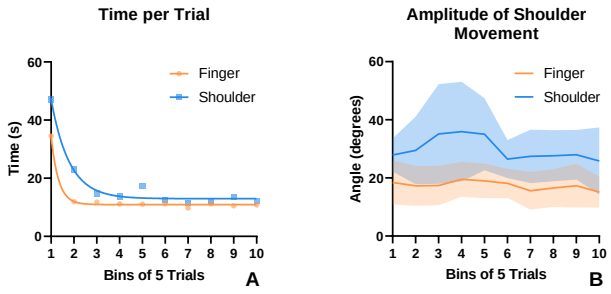


Fig. 4. **Adaptation During VR Training.** A) Average trial time for *Finger* and *Shoulder* groups, binned in sets of 5 trials. Solid lines show exponential least squares fits. B) Mean shoulder engagement, measured as the highest roll angle from the accelerometer.

The *Finger* group started with 12 seconds lower trial time and had a faster decay constant ($\tau = 0.80$) than the *Shoulder* group ($\tau = 0.32$). No significant difference was found in the last five bins' average trial times ($t(15) = -1.99, p = 0.064$), indicating both groups effectively learned to control virtual pinching.

The *Shoulder* group had significantly higher shoulder engagement than the *Finger* group ($t(12) = -3.39, p = 0.005$), consistent with their control modality.

C. Reaction Times and Crossmodal Congruency Effect

Trials with too-fast, too-slow, or incorrect responses were excluded (20, 0.5%, and 184, 4.5%, respectively). Exclusions were similar across groups, with 10 too-fast and 10 too-slow in each, and incorrect responses resulted in 79 exclusions for the Finger group and 105 for the Shoulder group.

Wilcoxon signed-rank tests on average reaction times showed significant differences ($p < 0.05$) in all CCT stages, trial types, and participant groups (Figure 5A). For between-group CCE analyses, no significant effects were found: stage ($F(2.16, 32.45) = 1.78, p = 0.181, \eta_p^2 = 0.11, 1 - \beta = 0.15$); group ($F(1, 15) = 2.07, p = 0.171, \eta_p^2 = 0.16, 1 - \beta = 0.42$); or interaction ($F(3, 45) = 0.76, p = 0.521, \eta_p^2 = 0.05, 1 - \beta = 0.07$).

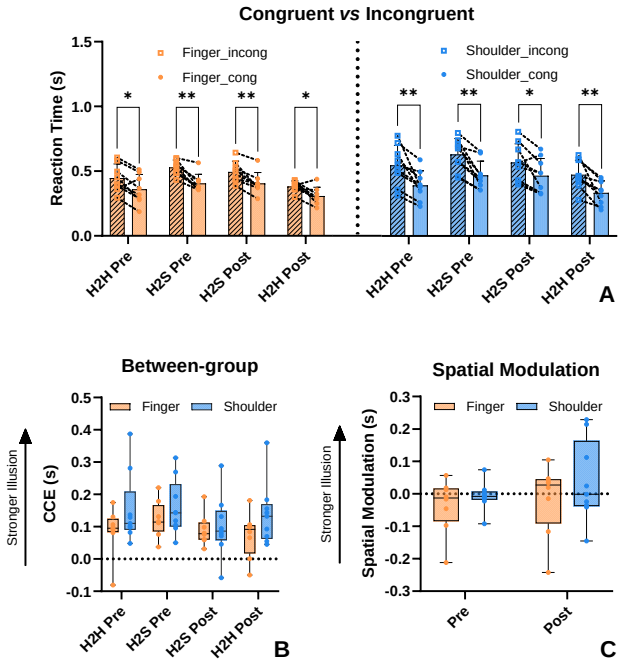


Fig. 5. **Summary of Reaction Times, CCE and Spatial Modulation Across Stages and Groups.** A) The reaction times for congruent and incongruent trials, with error bars representing the standard deviation. B) The between-group comparison for the CCE. Greater values mean stronger illusion (or visuo-tactile integration). C) The bottom-right panel shows Spatial Modulation results. Greater values mean stronger illusion.

D. Spatial Modulation

Results for Spatial Modulation are shown in Figure 5C. Wilcoxon signed-rank and Mann-Whitney tests (pre vs. post within- and between-group) were not significant: stage ($F(1, 15) = 0.86, p = 0.369, \eta_p^2 = 0.05, 1 - \beta = 0.07$);

group ($F(1,15) = 1.78$, $p = 0.202$, $\eta_p^2 = 0.09$, $1-\beta = 0.11$); interaction ($F(1,15) = 0.11$, $p = 0.744$, $\eta_p^2 = 0.01$, $1-\beta = 0.05$).

Homogeneity tests found no variance difference in the *Finger* group ($t(6) = 0.70, p = 0.511$), but a significant difference in the *Shoulder* group ($t(7) = 4.15, p = 0.0043$), with an 8.4-fold variance increase post-training.

E. Subjective Reports

For both subjective assessments (Ownership and NASA-TLX), no significant group differences were found across all questions and dimensions (Figure 6).

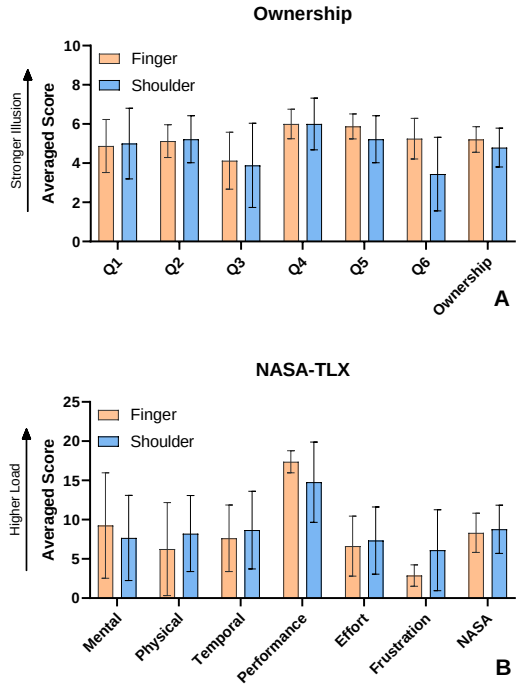


Fig. 6. **Results from the Subjective Reports.** A) Results from the Ownership questionnaire, where higher values indicate a stronger illusion of ownership in VR. B) The NASA Task Load Index scores for the Finger and Shoulder groups, with higher values indicating greater physical or cognitive load experienced during the VR training.

IV. Discussion

Interacting with VR via a Body-Machine Interface, using body parts like the shoulder to control hand movements in virtual environments, provides a valuable solution for clinical applications, such as for individuals with stroke or spinal cord injury. By inducing VR illusions to alter body perception, the technology's therapeutic potential extends beyond assistive use.

This study explores how a single VR motor-training session, using shoulder movements to control a virtual hand, affects body representations of the real hand and shoulder in neurotypical participants. Building on previous work [9], we address the lack of tactile feedback during VR training. The aim was to examine hand-to-shoulder visuo-tactile integration in two groups: one using shoulder movements to control the virtual hand's pinch and the other using finger movements. Finger tracking, used in both VR training for the *Finger* group and all CCT blocks, improves upon our prior setup, where participants held a controller to detect hand movements.

We adapted the Crossmodal Congruency Test (CCT) to assess visuo-tactile interaction and the relationship between the PPS of the shoulder and hand. The main variables were the Crossmodal Congruency Effect (CCE), reflecting the difference in reaction times between congruent and incongruent trials, and the Spatial Modulation of the CCE, quantified as the difference between the CCE for the virtual and real hand (CCT H2H) and the virtual hand and real shoulder (CCT H2S). CCT blocks (H2H and H2S) were performed pre- and post-VR training to assess the intervention's impact.

A. Incongruent vs Congruent Trials

We expected longer reaction times in incongruent trials, resulting in a positive CCE. For the *Shoulder* group, we hypothesized an increased CCE H2S post-training, indicating enhanced hand-to-shoulder visuo-tactile integration, with no changes in CCE H2H. To control for practice effects, we analyzed CCT adaptations (Section III-A). Our results showed significantly higher reaction times for incongruent trials. However, as shown in Figure 5B, some participants had negative CCEs, consistent with previous studies [8], [15]. Further analysis is needed to investigate potential causes, including outliers (e.g., attentional deviations) affecting the global mean.

B. Changes in CCE and Spatial Modulation

For the *Finger* group, we expected no change in CCE H2S (pre vs. post) as passive shoulder feedback alone (actile feedback, but no active movement engagement) was insufficient for integration, but anticipated an increase in CCE H2H due to active finger engagement. In the *Shoulder* group, we hypothesized an increase in CCE H2S due to both shoulder feedback and active movement, and a higher post CCE H2S compared to the *Finger* group. We expected CCE H2H in the *Shoulder* group to remain stable (or decrease) due to lack of active finger engagement, while the *Finger* group was expected to show a larger post CCE H2H. Finally, we predicted increased Spatial Modulation post-training in the *Shoulder* group, but no change in the *Finger* group.

Contrary to expectations, no statistical differences were found within or between groups. While the small sample size limits conclusions, these findings suggest two possibilities: (1) a lack of hand-to-shoulder visuo-tactile integration in both groups, or (2) equivalent integration in both groups, indicating shoulder tactile feedback alone could induce changes without active movement. This may be due to visual feedback dominating the embodiment effect, as prior research suggests visual dominance in body ownership and perceptual integration [19]. The virtual hand's visual representation may have strongly influenced ownership, overshadowing tactile feedback and motor control effects.

Data showed a visual trend toward reduced CCE post-training, particularly in the *Shoulder* group, suggesting both methods reduced hand-to-shoulder integration. An alterna-

tive explanation is increased participant awareness of VR elements, reducing the illusion effect over time. This aligns with findings that CCE is lower for naturalistic hands than non-naturalistic ones [5].

Regarding Spatial Modulation, trends were consistent with expectations. The significant pre-post change in variance in the *Shoulder* group suggests a differential intervention effect. Further investigations are needed to explore this.

While results didn't fully align with expectations, this study has provided valuable insights, helping us identify methodological limitations and areas for improvement in future iterations.

C. Subjective Reports

The lack of between-group differences in the Ownership questionnaire suggests that both groups experienced a similarly high sense of ownership over the virtual hand, regardless of the effector used, aligning with the CCE and Spatial Modulation results. Similarly, the NASA-TLX scores indicated comparable motor and cognitive load, as well as performance perception, suggesting that the *Shoulder* group found the new motor skill intuitive and easy to acquire.

D. Limitations and Future Work

This experiment has several limitations. First, it is underpowered due to small group sizes. While studies with groups of $N \leq 10$ have been conducted [8], our power analysis indicates that at least 30 participants are needed for 80% power. Increasing the sample size would reduce variability and improve power. However, adjustments to the experimental design could also help. Of the 15 studies reviewed using CCE as the primary outcome, only one compared two groups [18], highlighting inter-subject variability as a limitation. Future studies could adopt a within-subject design to mitigate this. Additionally, more robust methods, such as gaze tracking available in other VR headsets, could replace the no-go trials to control attentional deviation.

In our setup, participants discriminated between tactile stimuli on the front or back of their shoulder, with the right hand positioned with the index finger distal and the thumb proximal. However, the left hand mirrored the right, introducing a confounding factor that disrupted tactile stimuli and enhanced visual distractors, potentially affecting response accuracy. Using foot pedals, as in classical CCT implementations [12], would address this issue.

Similarly, although the tactile stimuli and finger positioning during the CCT were both normal to the coronal plane, this alignment was not maintained during training, as participants could grip in any direction. This variability may have influenced the assimilation of virtual touches to the respective shoulder locations. Future implementations should ensure that grip positioning consistently aligns with tactile placement during training.

Additionally, our CCT protocol may be susceptible to a washout effect, limiting the capture of lasting VR practice effects. In studies measuring tool incorporation, interleaving CCT trials with tool-use trials enhances retention [16]. Since our protocol separated VR practice from post-training CCT, the effects may have diminished. Future research should incorporate "active CCT" to strengthen retention.

Finally, our design did not control for visual feedback, which could have influenced results. This may have limited our ability to isolate the effects of hand-to-shoulder integration in VR. Future studies should include a control group with an abstract hand avatar to better isolate these effects.

REFERENCES

[1] D. Brouwer *et al.*, "Virtual reality in functional neurological disorder: A theoretical framework and research agenda for use in the real world," *BMJ Neurology Open*, vol. 6, no. 2, p. e000622, 2024.

[2] M. M. T. E. Kouijzer, C. J. Klein, M. V. K. Janssen, and S. M. H. Van der Staal, "Implementation of virtual reality in healthcare: A scoping review on the implementation process of virtual reality in various healthcare settings," *Implementation Science Communications*, vol. 4, no. 1, p. 67, 2023.

[3] M. Casadio, R. Ranganathan, and F. A. Mussa-Ivaldi, "The body-machine interface: A new perspective on an old theme," *J. Mot. Behav.*, vol. 44, no. 6, pp. 419–433, 2012.

[4] E. Losanno *et al.*, "A virtual reality-based protocol to determine the preferred control strategy for hand neuroprostheses in people with paralysis," *IEEE Transactions on Neural Systems and Rehabilitation Engineering*, 2024.

[5] M. Marucci *et al.*, "Rewiring the evolution of the human hand: How the embodiment of a virtual bionic tool improves behavior," *iScience*, 2024.

[6] F. Marini *et al.*, "Crossmodal representation of a functional robotic hand arises after extensive training in healthy participants," *Neuropsychologia*, vol. 53, pp. 178–186, 2014.

[7] L. E. Miller *et al.*, "Sensing with tools extends somatosensory processing beyond the body," *Nature*, vol. 561, no. 7722, pp. 239–242, 2018.

[8] S. Shokur *et al.*, "Assimilation of virtual legs and perception of floor texture by complete paraplegic patients receiving artificial tactile feedback," *Sci. Rep.*, vol. 6, no. 1, p. 32293, 2016.

[9] L. R. L. Cardoso, A. Melendez-Calderon, V. Bochkezanian, A. Forner-Cordero, and A. P. L. Bo, "Towards visual-tactile integration of shoulder and hand using immersive virtual reality," *2023 45th Annu. Int. Conf. IEEE Eng. Med. Biol. Soc. (EMBC)*, pp. 1–4, 2023.

[10] E. M. Gordon *et al.*, "A somato-cognitive action network alternates with effector regions in motor cortex," *Nature*, vol. 617, no. 7960, pp. 351–359, 2023.

[11] T. Schicke, F. Bauer, and B. Röder, "Interactions of different body parts in peripersonal space: how vision of the foot influences tactile perception at the hand," *Exp. Brain Res.*, vol. 192, pp. 703–715, 2009.

[12] F. Pavani, C. Spence, and J. Driver, "Visual capture of touch: Out-of-the-body experiences with rubber gloves," *Psychol. Sci.*, vol. 11, no. 5, pp. 353–359, 2000.

[13] T. C. Peck and M. Gonzalez-Franco, "Avatar embodiment: A standardized questionnaire," *Front. Virtual Reality*, vol. 1, pp. 575943, 2021, doi: 10.3389/frvir.2021.575943.

[14] R. Zopf, G. Savage, and M. A. Williams, "Crossmodal congruency measures of lateral distance effects on the rubber hand illusion," *Neuropsychologia*, vol. 48, no. 3, pp. 713–725, 2010.

[15] A. Cataldo, M. Di Luca, O. Deroy, and V. Hayward, "Touching with the eyes: Oculomotor self-touch induces illusory body ownership," *iScience*, vol. 26, no. 3, 2023.

[16] N. P. Holmes, "Does tool use extend peripersonal space? A review and re-analysis," *Experimental Brain Research*, vol. 218, pp. 273–282, 2012.

[17] D. J. Saville, "Multiple comparison procedures: the practical solution," *The American Statistician*, vol. 44, no. 2, pp. 174–180, 1990.

[18] D. Blustein *et al.*, "Crossmodal congruency effect scores decrease with repeat test exposure," *PeerJ*, vol. 7, p. e6976, 2019.

[19] A. Melendez-Calderon, M. Tan, M. F. Bittmann, E. Burdet, and J. L. Patton, "Transfer of dynamic motor skills acquired during isometric training to free motion," *Journal of Neurophysiology*, 118(1), 219-233, 2017.

Evaluating Convolution Neural Network Architecture for Neural Drive Decoding from High-Density Surface Electromyography

Jirui Fu[1,2], Helen J. Huang[1,2,3], and Yue Wen[1,2]

***Abstract*—Prior studies demonstrated encouraging results in the application of convolution neural network models (CNN), one-dimensional (1D CNN), or three-dimensional (3D CNN) convolutional layers to decode the neural drive to muscles from high-density surface electromyography (HD-sEMG) signals. However, the impact of the dimensionality (1D or 3D) of the convolutional layers on the performance of the deep CNN models using the same dataset has yet to be investigated. This study assesses the performance of 3D CNNs and 1D CNNs in extracting the neural drive as a cumulative spike train (CST) under various window sizes and step sizes that are critical parameters in decoding neural drives. Experimental HD-sEMG dataset sourced from the gastrocnemius medialis muscle of three participants, alongside the corresponding neural drive decoded using the convolution kernel compensation (CKC) algorithm, was employed to train and validate the 1D and 3D CNN models. We compared the F1 score and correlation coefficient between the CST from CKC and those from both 1D and 3D CNN models, revealing that 1D CNN performs more effectively with larger sliding window sizes (80 or 120 samples) with a peak F1 score of 0.84 and a correlation of 0.94. In contrast, 3D CNN achieves peak F1 score (0.83) and correlation (0.92) with smaller sliding window sizes (20 or 40 samples), indicating reduced latency in using 3D CNN to decode neural drives. Both models experience a performance decline as the step size increases. Furthermore, this research evaluates the computational cost of 1D and 3D CNN models, finding that the 3D CNN model requires significantly more computational resources (938G FLOPs) than the 1D CNN model (60G FLOPs). The results elucidate significant distinctions between CNN architectures and identify optimal parameters and model selection for precise and real-time neural drive decoding.**

***Index Terms*—Neural interface, motor unit, high-density electromyography, deep learning, convolutional neural networks.**

I. Introduction

Surface electromyogram (sEMG) signals represent the electrical activity of motor units (MUs) and are recorded non-invasively by placing electrodes on the skin. Based on the number of reference electrodes, sEMG signals can be categorized as bipolar sEMG in which each channel has a specific reference electrode, or high-density sEMG (HD-sEMG), in which all channels on the HD-sEMG grid share a single reference electrode [1]. Compared to bipolar sEMG, HD-sEMG provides both temporal and spatial information, enabling the decomposition of signals into MU spike trains for estimating neural drive to muscles. Neural drive estimation is used in wearable robotics for tasks like predicting wrist kinematics for prosthesis control [2], estimating finger extension forces for exoskeletons [3], employing an attention-based hybrid CNN-RNN for hand gesture estimation [4], and using a physics-informed CNN for muscle force estimation from EMG signals [5], highlighting the need for precise methods to extract neural drive from HD-sEMG signals.

The conventional methods to decode neural drive always employed the blind source separation (BSS) algorithm, such as gradient CKC algorithm [6], [7], FastICA-based frameworks [8], or a CKC-FastICA algorithm [9]. While these approaches have advanced MU spike train decomposition, they often lack the capability for real-time estimation due to the variability and complexity of HD-sEMG signals, limiting their use in wearable robotic systems. To overcome these limitations, CNNs have been explored for their ability to automatically extract spatial and temporal features from HD-sEMG signals. For instance, 1D CNNs have demonstrated success in estimating neural drive across varying contraction intensities and joint angles [10], [11]. Building on this success, 3D CNN models leverage the spatial features of HD-sEMG electrodes to simultaneously capture spatial and temporal features, improving accuracy and robustness [12].

Despite these advancements, gaps remain in the current research. No studies have directly benchmarked the performance of 1D CNN models and 3D CNN models in neural drive estimation from HD-sEMG signals using the same dataset and protocol which hinders the systematic evaluation of their strengths and weaknesses. Additionally, the characteristics of HD-sEMG signals that influence the accuracy and computational cost of 3D CNNs in neural drive estimation, such as window size and step size, still need further exploration.

To address these challenges, this paper provides a comparison of 1D CNN and 3D CNN architectures for neural drive decoding from HD-sEMG signals using the same dataset. The study evaluates the effect of window size and step size on the performance of 1D and 3D CNN models in decoding neural drives and investigates their computational costs for potential real-time applications. The findings aim to guide the design of robust CNN architectures for real-time neural drive estimation thereby advancing their application in wearable robotics and rehabilitation.

In the following sections, the protocol used to collect the HD-sEMG signals, the framework of the 1D and 3D CNN

[1] Department of Mechanical and Aerospace Engineering at the University of Central Florida, FL, USA.

[2] Disability, Aging, and Technology (DAT) Cluster at the University of Central Florida, FL, USA.

[3] Biionix Cluster at the University of Central Florida, FL, USA.

architectures to decode neural drive from HD-sEMG signals, and the pipeline to prepare HD-sEMG signals for the training of 1D and 3D CNN are described (Section II) The protocol to train and validate the CNN model is illustrated (Section III), and the preliminary result are presented (Section IV). Finally, the insight from experimental results, as well as the challenges and future extensions are discussed (Section V and VI).

II. Methods

A. Collection of HD-sEMG Dataset

1) Participants: This study used a subset of experimental data from a previously published study [13]. Three participants (mean $\pm$ SD; age 34 ± 8 years, height 178 ± 6 cm, body mass 76 ± 7 kg) with no recent lower leg injuries participated in this study. The data collection was approved by the University of Queensland ethics committee (Approval No. 2013001448) and adhered to the Declaration of Helsinki. Informed consent was obtained.

2) Experimental Procedures: Participants laid prone on a custom-made dynamometer, knees fully extended and ankles at $10°$ plantar flexion (Fig. 1(a)), to measure ankle joint torque. After a warm-up, they performed three maximum voluntary contractions (MVC) for $3-5$ s with 120 s rest. Submaximal contractions followed at 10 %, 30 %, and 50 % MVC each for 5 s (ramp-up), $15-20$ s (plateau), and 5 s (ramp-down), with $60-120$ s rest to minimize fatigue, using MVC torque for feedback (Fig. 1(c)).

3) Collection of HD-sEMG Signals: HD-sEMG signals were recorded from the gastrocnemius medialis (GM) muscle using a 64-electrode grid (13×5, 8 mm distance; SpesMedica, Italy; Fig. 1(d)), aligned with muscle fascicles via ultrasound. Skin was prepped with shaving and cleaning. The grid was secured with adhesive and elastic bands. Signals were recorded in mono-polar mode, band-pass filtered ($10-900$ Hz), and digitized at 2048 Hz using OT Bioelettronica's system (Fig. 1(b)).

4) Motor Unit Decomposition: We used the CKC algorithm to decompose the HD-sEMG signals into MU spike trains [7]. The CKC algorithm was implemented in the DEMUSE tool software (v4.9; University of Maribor, Slovenia) developed on MATLAB (The Matkworks Inc, Natick, Massachusetts, USA). Before the decomposition, the HD-sEMG signals were filtered by a band-pass filter (Butterworth 2nd order, 20-500 Hz) to remove the artifacts. After the decomposition of the HD-sEMG signals, all of the identified MU spike trains were visually inspected and manually edited when a false positive (FP: labeled artifact) or a false negative (FN: non-labeled discharge) was observed by an experienced operator. Only then MUs with a pulse-to-noise ratio (PNR) $>$ 30 db and at least 150 spikes per contraction segment were selected to ensure high sensitivity (> 90 %) and low false-positive rates (< 2 %) for further analysis. The processed HD-sEMG signals and the decomposed MU spike trains were used to train and validate the deep CNN models [13].

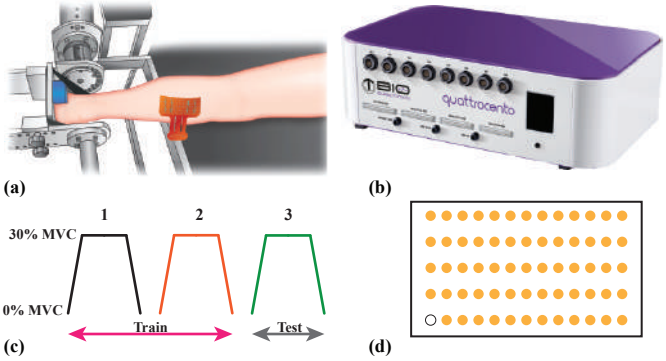


Fig. 1: (a) The participant performed a sub-maximal plantar flexion in a custom ankle dynamometer, and a grid of 64 high-density electrodes was placed over the GM muscle [13]; (b) The OT-Bioelettronica HD-sEMG acquisition system; (c) To this end, torque feedback was displayed, and three contractions were performed for each intensity level; (d) The arrangement of electrodes for the 13×5 HD-sEMG electrode grid used to collect HD-sEMG signals.

B. Structure of the Deep Convolutional Neural Network for Neural Drive Decoding

1) 1D CNN Architecture for Decoding Neural Drive: This study investigated two types of CNN models for decoding neural drive to muscles from HD-sEMG signals (Fig. 2). The architecture of the 1D CNN model was adopted from the work in [13], and the model consisted of two serially connected convolutional blocks followed by multi-head outputs that included four heads, each with two dense layers (Fig. 3(a)). Each convolutional block contained two one-dimensional convolutional layers, each followed by a rectified linear unit (ReLU) activation function to introduce non-linearity (Fig. 3(a)). After the activation function of the second convolutional layer, max pooling was applied with a kernel size of 2 and a stride size of 2. This operation reduced the spatial dimensions of the feature maps while retaining the most prominent features, enhancing computational efficiency and robustness to spatial variations. To prevent overfitting, a dropout layer was added at the end of each convolutional block, randomly deactivating 50 % of the neurons in the output feature map. The input channel of the first convolutional layer processed the 64-channel HD-sEMG signals with 64 input channels and 128 output channels. The size of the input and output channels of the rest convolutional layers is 128, and the kernel size of each convolutional layer is 3.

After the convolutional blocks, a flatten layer was used to convert the feature maps into a vector, preparing them for input to the dense layers. The number of parallel dense layers matched the number of spikes the CNN could detect from the input HD-sEMG signals. Based on findings from [10], four parallel dense layers were chosen for their optimal performance.

Each dense layer head consisted of two fully connected layers. The first fully connected layer took the flattened feature

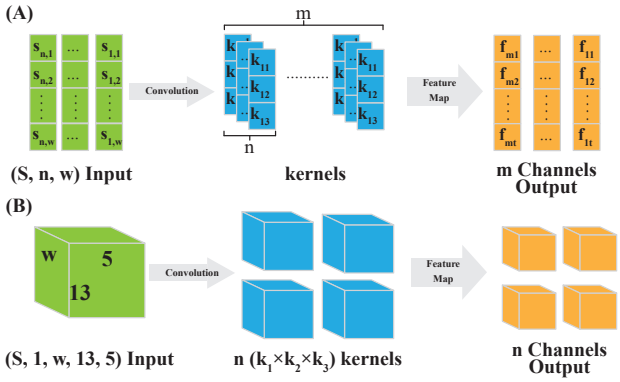


Fig. 2: (a) The mechanism of 1D CNN architecture in which the number of input channels equals the number of HD-sEMG channels and the length of each channel equals the size of the sliding window. (b) The mechanism of the 3D CNN architecture.

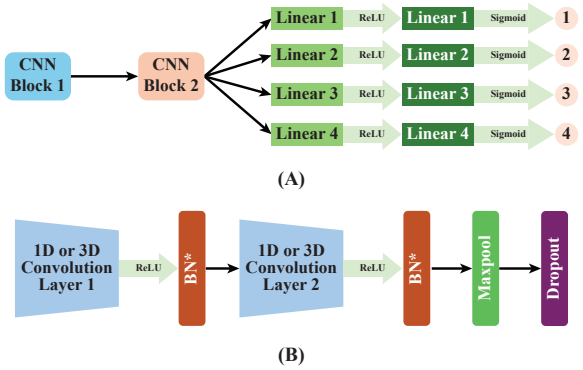


Fig. 3: (a) The architecture of the 3D CNN model. The number of input channels equals the number of HD-sEMG channels and the shape of each channel equals the size of the sliding window. (b) The network structure in each CNN block. Note that only the 3D CNN model includes the batch normalization layers (BN*).

map as input, with its shape determined by the input HD-sEMG signals. This layer had 128 neurons, defining both its output size and input size for the second fully connected layer. A ReLU activation function was applied between the layers to introduce non-linearity. Finally, a Sigmoid activation function was used after the second layer to constrain outputs to the range $[0, 1]$. We rounded the neural network output greater than 0.5 to 1 and interpreted it as a spike [13].

2) 3D CNN Architecture for Decoding Neural Drive: The second CNN architecture was a three-dimensional extension of the 1D CNN architecture (Fig. 2(b) and Fig. 3(b)). Different from the 1D CNN architecture, the 3D CNN architecture implemented 3D convolutional layers with 32 kernels in each layer and each kernel with a size of 3. Additionally, other modifications were made to improve the performance of 3D CNN. First of all, a batch normalization layer was added to the output of each 3D convolutional layer after the activation function. The purpose of batch normalization was to stabilize and accelerate training, reduce internal covariate shifts, and improve generalizability which has been widely used on 2D- and 3D CNNs [14]. Additionally, padding of two elements was applied to the input of each convolutional layer. This ensured that the spatial dimensions of the input feature maps were preserved after convolution, retaining edge information and enabling consistent output sizes across layers. Furthermore, the input channels of the first layer differed from the 1D CNN architecture; for the 3D CNN model, the reshaped HD-sEMG signals resulted in a single input channel, while subsequent layers had equal input and output channels set to 32. Aside from these modifications, another minor modification was the max-pooling algorithm which was replaced by the 3D max-pooling algorithm to adapt to the 3D CNN blocks.

C. Data Preparation

To prepare the dataset for 1D and 3D CNN models, we normalized HD-sEMG signals to a range -1 to 1 to preserve spatiotemporal information and generated the cumulative spike train (CST) by summing MU spike trains. We then segmented the HD-sEMG signals and CST with a sliding window method from [13]. The window size and step size were denoted as WS and SS respectively (Fig. 4), defining the width of the sliding window and the overlap between consecutive windows. Moreover, the CST (specifically the number of identified spikes) was used to label the corresponding HD-sEMG signals, and they were used to train the deep CNN models.

Therefore, a batch of HD-sEMG windows after segmentation by sliding window method was directly used to train the 1D CNN model, in which each window consists of a $64 \times w$ matrix, where 64 corresponds to the number of HD-sEMG channels and w to the width of sliding window.

In contrast, the 3D CNN model required a three-dimensional tensor input. Given the 13×5 electrode configuration of the HD-sEMG grid, with one corner electrode absent which reflects the spatial arrangement of the HD-sEMG grid.

The segmented HD-sEMG signal was reshaped to a $w \times 13 \times 5$ tensor for the 3D CNN model. Firstly, the segmented HD-sEMG signal ($64 \times w$) was zero-padded at index 0 to become a $65 \times w$ array. Then, the padded $65 \times w$ array was reshaped to a $13 \times 5 \times w$ tensor to preserve the spatial information coded in the electrode location. Finally, the $13 \times 5 \times w$ tensor was permuted to a $w \times 13 \times 5$ so the depth of the input equals the width of the sliding window because we found this setting achieved the best performance.

III. Experiment

A. Training and Validation Protocol

A three-fold cross-validation methodology was employed to train and validate the 1D CNN and 3D CNN models, aiming to ensure their robustness. Unlike traditional random splits, we treated each contraction as an independent fold. The model was trained on two contractions and validated on the third to evaluate performance. This process was repeated three times,

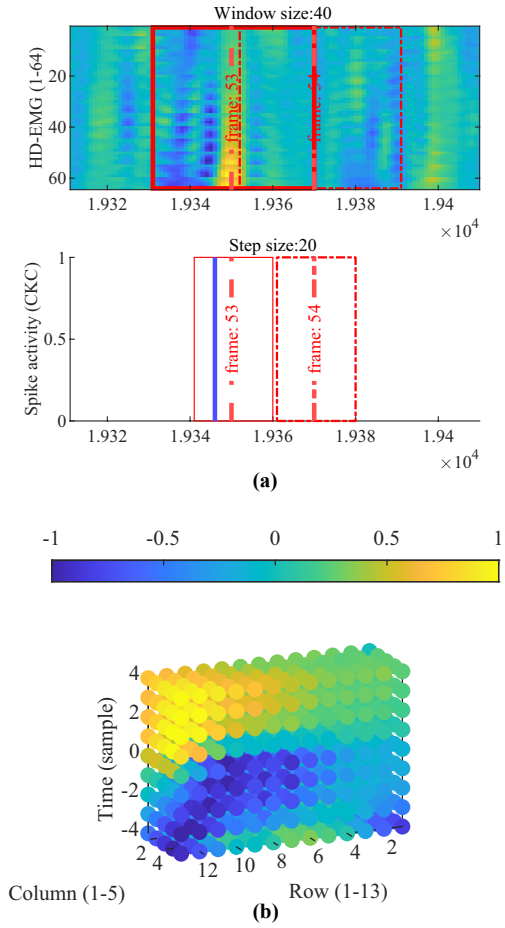


Fig. 4: (a) The sliding window approach to segment the HD-sEMG signals and the CST, as this figure shows, a sliding window with a window size of w (red box) samples the HD-sEMG signals along the temporal axis. The distance between consecutive windows is the step size (top); Segmentation of the CST using the same step size (bottom); The y-axis of this figure represents the channel of HD-sEMG signal while the x-axis represents the number of samples. (b) A segment of reshaped HD-sEMG signals for the 3D CNN model.

with each contraction used as the validation set once. The overall performance was calculated as the average across the three validation runs.

The training and validation were performed on the workstation equipped with an NVIDIA RTX 4090 graphics card. During training, a batch size of 64 was used to optimize the computational process. The training process was configured to stop after 200 epochs. Training timestamp and F1 score for each epoch were recorded for post-analysis. The model achieving the highest F1 score during training was saved. For validation, this best-performing model was loaded and evaluated on the validation data segment to predict the CST. The detected CST and the time required for each inference were recorded for further analysis.

B. Evaluation Criteria

This study focuses on evaluating the impact of CNN architectures on decoding the neural drive from HD-sEMG signals, with a specific emphasis on the ability of CNN to identify the CST. For this purpose, the F1 score was adopted as the primary performance metric which provides a comprehensive measure of the network's ability to accurately decode the neural drive in the form of CST.

Additionally, the neural drive decoded by the CNN model was compared with the neural drive decoded by the CKC algorithm. This comparison calculated the Pearson correlation coefficient (PCC) between the smoothed CSTs from the CNN model and the CKC algorithm.

Finally, we also investigated the inference time of the 3D and 1D CNN models which is the average processing time of the CNN models to decode neural drive from a window of HD-sEMG signal.

IV. Results

A. Evaluation of 3D CNN and 1D CNN Models for Decoding Neural Drive

Table I presents an in-depth analysis of the F1 scores achieved by both the 1D CNN and the 3D CNN. This analysis elucidates how varying the window and step sizes can impact the accuracy of neural drive decoding. For the 1D CNN model, the optimal F1 score of 0.84 was attained with a configuration comprising a window size of 120 combined with a step size of 20. A robust performance range, approximately from 0.79 to 0.82, was consistently observed when utilizing step sizes of 5 and 10 across the majority of window sizes tested. Conversely, employing larger step sizes such as 40 significantly compromised performance, particularly in scenarios involving smaller windows (e.g., yielding a mere 0.33 with a window size of 20). On the other hand, the 3D CNN model reached its peak F1 score of 0.83 with a step size of 10 and a window size of either 40 or 20. Consistent performance was delivered with smaller step sizes, notably 5 and 10, across various window sizes. In contrast, larger step sizes like 40 induced substantial declines in performance, especially with smaller window sizes (e.g., achieving only 0.39 with a window size of 20).

B. Evaluation of CST Estimation by CNN Models versus CKC Algorithm

An in-depth analysis of the correlation results, as summarized in Tables II, reveals that both 3D CNN and 1D CNN models achieved maximum correlation values of 0.92

TABLE I: F1 Score for 3D CNN and 1D CNN Models under various window sizes (WS) and step sizes (SS)

F1 score WS / SS	20	40	80	120
5	0.82 (0.79)	0.81 (0.79)	0.79 (0.79)	0.74 (0.77)
10	0.83 (0.80)	0.83 (0.82)	0.80 (0.82)	0.80 (0.83)
20	0.76 (0.71)	0.80 (0.82)	0.78 (0.82)	0.74 (0.84)
40	0.39 (0.33)	0.65 (0.58)	0.57 (0.66)	0.54 (0.66)

with the CKC algorithm when evaluated using smaller step sizes of 5 and 10 samples. However, the models demonstrated distinct performance trends based on window sizes. Specifically, 1D CNN exhibited superior correlation performance at larger window sizes, demonstrating its capability to capture temporal dependencies over extended durations. In contrast, 3D CNN showed greater effectiveness at smaller window sizes (20 and 40 samples), probably benefiting from its ability to exploit both spatial and temporal features. For a direct visual comparison of the CST decoded by the CNN models and the CKC method, we selected a combination of window size and step size that the 3D and 1D CNN trained with HD-sEMG dataset segmented by this window-step size that have marginal differences in the correlations of CST as shown in Table II. According to Table II, we selected a window size of 40 and a step size of 10. These CST results were smoothed using a Hanning window of 400 ms to facilitate comparison. The corresponding visualization of CST is shown in Figures 5(a) and (b), respectively.

C. Evaluation of Computational Load and real-time efficacy of 1D CNN and 3D CNN Models

Additionally, this work examined the computational cost and real-time efficacy of the 1D CNN and 3D CNN models for neural drive decoding. The computational cost was assessed by computing the FLOPs (Floating-point operations) of both 1D CNN and 3D CNN using the optimal window size and step size as determined by the F1 score in Table I. The 3D CNN model, when trained and validated with HD-sEMG data segmented using the optimal window sizes of 20 or 40 samples, exhibited an average of 938G FLOPs. In contrast, these metrics for the 1D CNN model, trained and validated with HD-sEMG data segmented using an optimal window size of 120 samples, manifested as 60G FLOPs.

Furthermore, real-time efficacy was assessed via inference time, defined as the duration required for the neural network model to decode the neural drive with a sample of HD-sEMG signal ($1\times64\times w$ for 1D CNN, $1\times1\times w\times13\times5$ for 3D CNN). Similar to the FLOPS, inference time calculations for both the 3D CNN and 1D CNN, trained and validated with the HD-sEMG dataset segmented by the optimal window size as per Table I, were conducted. Consequently, the average inference time for the 3D CNN trained on HD-sEMG signals segmented by 20 or 40 samples is 4.3 ms, whereas for the 1D CNN trained on signals segmented by 120 samples, it is 1.28 ms.

TABLE II: The Correlation Coefficient of CST Estimated by 3D CNN or 1D CNN and the CKC under various window sizes (WS) and step sizes (SS)

PCC: WS / SS	20	40	80	120
5	0.98 (0.96)	0.97 (0.97)	0.97 (0.98)	0.97 (0.97)
10	0.97 (0.96)	0.97 (0.97)	0.96 (0.96)	0.98 (0.96)
20	0.96 (0.94)	0.97 (0.97)	0.95 (0.96)	0.95 (0.96)
40	0.88 (0.91)	0.94 (0.95)	0.94 (0.92)	0.93 (0.93)

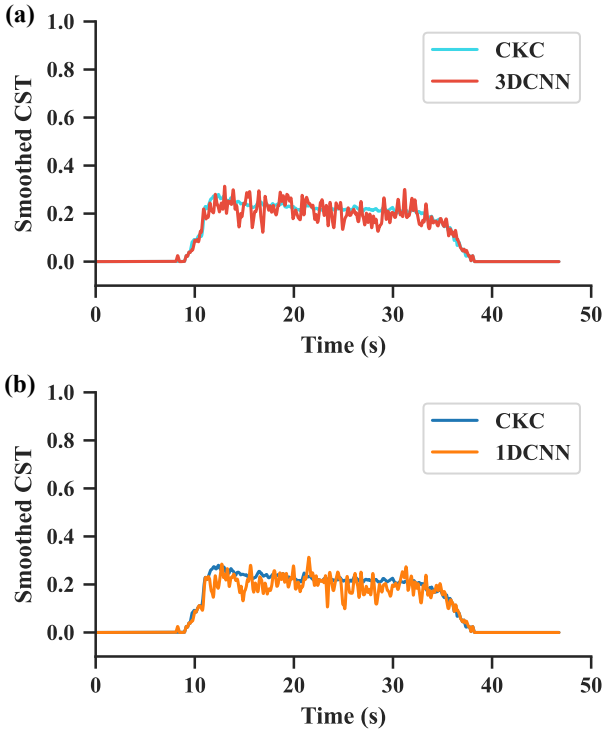


Fig. 5: The smoothed CSTs estimated by the 3D CNN (a) and 1D CNN (b) vs the CSTs identified by the CKC algorithm. Note: the window size and step size combination was selected from Table II which reaches the best correlation coefficient.

V. Discussion

This study investigates the impact of the dimensionality (1D or 3D) of the convolutional layers on the performance of decoding neural drive from HD-sEMG signals using the same dataset by comparing their decoding accuracy (F1 score), computational cost (FLOPs), and real-time efficacy (inference time).

The results of this study reveal that both the 1D CNN and 3D CNN models can effectively decode the neural drive from HD-sEMG signals, with performance contingent upon step size and window size parameters. The 1D CNN model achieved a marginally superior peak F1 score (0.84) compared to the 3D CNN model (0.83), with the optimal configuration determined as a window size of 120 and a step size of 20. This finding indicates the particular efficacy of the 1D CNN model when extensive sliding window size is accessible. Nevertheless, its performance exhibits a decline with increased step sizes, particularly for smaller windows, underscoring the necessity of balancing input granularity to maintain accuracy. In contrast, the 3D CNN model demonstrated resilience at smaller step sizes (5 and 10), reaching its peak performance (0.83) with a step size of 10 and a window size of 20 or 40 (Table I). This advantage highlights the ability of the 3D CNN model to decode neural drive when a brief window size is necessary (less latency). Nonetheless, the 3D CNN

model exhibits greater sensitivity to larger step sizes, with more abrupt performance declines compared to the 1D CNN model, thus restricting its applicability in contexts where larger sliding window size is required.

The CST correlation analysis further emphasize the strengths and limitations of both models. While both achieve high correlations with CST from CKC at smaller step sizes (5 and 10), the 1D CNN model sustains higher correlations at larger step sizes, indicating greater robustness. The 3D CNN model excels in exploiting spatiotemporal features at small window sizes, achieving peak correlations comparable to those of the 1D CNN model.

Visual comparisons of smoothed CSTs underscore the fidelity of both models in extracting the neural drive in the form of CST, generating CSTs analogous to those decoded by the CKC algorithm, which is the benchmark for CST decoding. By employing optimal window and step size configurations (WS120-SS20 for the 1D CNN model and WS40-SS20 for the 3D CNN model [window size-step size]), both models proficiently capture CST. These findings emphasize the criticality of application-specific trade-offs between accuracy, efficiency, and parameter sensitivity when choosing between 1D and 3D CNN models for neural drive decoding.

However, a significant limitation of the 3D CNN is its exceedingly high computational cost (938G FLOPs) compared to the 1D CNN (60G FLOPs). The substantial computational cost of 3D CNN could hinder its implementation on devices with limited computational resources, such as embedded computers on exoskeletons or prosthetics. Moreover, high computational cost hinders its real-time efficacy. According to the results, the 3D CNN exhibits worse inference time while using a much smaller window size (20 or 40 samples) than the 1D CNN models (120 samples), contrary to our hypothesis that the 3D CNN would have better real-time efficacy than the 1D CNN due to its superior F1 score under smaller window size. Therefore, with respect to the current structure of 3D CNN and 1D CNN models, the 1D CNN should be more suitable for real-time neural drive decoding even if it performs suboptimally compared to 3D CNN under small window size conditions. And further studies should focus more on the development of lightweight 3D CNN models that consume less computational power than current architecture.

VI. Conclusion

This study examined the influence of convolutional layer architecture (either 1D or 3D) on neural drive decoding performance by assessing the two different CNN models—namely, the 1D CNN and the 3D CNN—using an identical dataset. The investigation focused on distinguishing the 1D and 3D CNN models in terms of accuracy, computational cost, and real-time efficacy. The findings indicated that the 1D CNN model exhibits greater potential for real-time applications due to its reduced computational cost and shorter inference time. Conversely, additional research is necessary to decrease the computational cost of the 3D CNN model, thereby enhancing its performance in real-time applications.

References

[1] D. Farina, R. Merletti, and R. M. Enoka, "The extraction of neural strategies from the surface emg," *Journal of applied physiology*, vol. 96, no. 4, pp. 1486–1495, 2004.

[2] T. Kapelner, I. Vujaklija, N. Jiang, F. Negro, O. C. Aszmann, J. Principe, and D. Farina, "Predicting wrist kinematics from motor unit discharge timings for the control of active prostheses," *Journal of neuroengineering and rehabilitation*, vol. 16, pp. 1–11, 2019.

[3] Y. Zheng and X. Hu, "Real-time isometric finger extension force estimation based on motor unit discharge information," *Journal of neural engineering*, vol. 16, no. 6, p. 066006, 2019.

[4] Y. Hu, Y. Wong, W. Wei, Y. Du, M. Kankanhalli, and W. Geng, "A novel attention-based hybrid cnn-rnn architecture for semg-based gesture recognition," *PloS one*, vol. 13, no. 10, p. e0206049, 2018.

[5] J. Zhang, Y. Zhao, F. Shone, Z. Li, A. F. Frangi, S. Q. Xie, and Z.-Q. Zhang, "Physics-informed deep learning for musculoskeletal modeling: Predicting muscle forces and joint kinematics from surface emg," *IEEE Transactions on Neural Systems and Rehabilitation Engineering*, vol. 31, pp. 484–493, 2022.

[6] A. Holobar and D. Zazula, "Multichannel blind source separation using convolution kernel compensation," *IEEE Transactions on Signal Processing*, vol. 55, no. 9, pp. 4487–4496, 2007.

[7] A. Holobar and Z. Demjan, "Gradient convolution kernel compensation applied to surface electromyograms," in *International Conference on Independent Component Analysis and Signal Separation*. Springer, 2007, pp. 617–624.

[8] M. Chen and P. Zhou, "A novel framework based on fastica for high density surface emg decomposition," *IEEE Transactions on Neural Systems and Rehabilitation Engineering*, vol. 24, no. 1, pp. 117–127, 2015.

[9] F. Negro, S. Muceli, A. M. Castronovo, A. Holobar, and D. Farina, "Multi-channel intramuscular and surface emg decomposition by convolutive blind source separation," *Journal of neural engineering*, vol. 13, no. 2, p. 026027, 2016.

[10] Y. Wen, S. J. Kim, S. Avrillon, J. T. Levine, F. Hug, and J. L. Pons, "A deep cnn framework for neural drive estimation from hd-emg across contraction intensities and joint angles," *IEEE Transactions on Neural Systems and Rehabilitation Engineering*, vol. 30, pp. 2950–2959, 2022.

[11] Y. Wen, S. Avrillon, J. C. Hernandez-Pavon, S. J. Kim, F. Hug, and J. L. Pons, "Toward a generalizable deep cnn for neural drive estimation across muscles and participants," *Journal of Neural Engineering*, vol. 20, no. 1, p. 016006, 2023.

[12] M. Talke *et al.*, "Using supervised deep learning for real-time motor unit decomposition of high-density surface electromyography signals," Master's thesis, Aalto University, 2022.

[13] Y. Wen, S. Avrillon, J. C. Hernandez-Pavon, S. J. Kim, F. Hug, and J. L. Pons, "A convolutional neural network to identify motor units from high-density surface electromyography signals in real time," *Journal of neural engineering*, vol. 18, no. 5, p. 056003, 2021.

[14] S. Ioffe and C. Szegedy, "Batch normalization: Accelerating deep network training by reducing internal covariate shift," 2015. [Online]. Available: https://arxiv.org/abs/1502.03167

Normalizing Task-Oriented Human-Robot Interaction for Large-Scale Virtual Environments

Burak Balta*, Khandaker Nusaiba Hafiz*, and Jonathan Realmuto

***Abstract*—Physical simulation platforms, including haptic manipulanda and robotic rehabilitation systems, enable controlled human-robot interaction, but variability in users' physical attributes impacts consistency across individuals. Here, we present a method to standardize user effort in a physical tracking task, a common paradigm in rehabilitation and motor learning, where participants interact with a manipulator simulating a virtual environment. In addition to optimizing the initial configuration and scaling of the task trajectory, we analyze the effect of different scaling factors on the robot's virtual stiffness matrix, the impedance parameter that largely determines the effort required during the task. Simulations of nine virtual participants with varying heights and masses show that allometric scaling of robot's virtual stiffness by a factor of $(\mathrm{m}/\mathrm{h})^{2/3}$ best minimizes effort disparities. These findings advance the development of adaptive physical simulation platforms for rehabilitation, training, human motor control experiments, and human-robot collaboration.**

***Index Terms*—Physical Human-Robot Interaction, Haptics, Human Motor Control.**

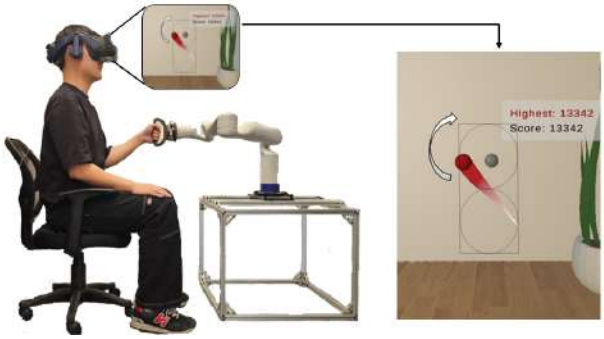


Fig. 1: Large-scale physical simulator integrating a virtual reality (VR) headset with a 7-DOF manipulator. During a task, the human participant interacts with the manipulator's end-effector. Task-space impedance control enables programming the end-effector's behavior for various simulated environments, including the virtual-spring environment explored in this work. This setup supports immersive and controlled experimentation with dynamic force rendering.

I. Introduction

Physical simulation platforms, including kinesthetic haptic manipulanda, provide an adjustable virtual environment that is mechanically rendered at the human-robot interaction point [1]. These systems have become essential tools for motor control research [2], [3], and neurorehabilitation where they enable patient-centered interventions, post-surgery recovery, and address limitations of traditional therapy, including high resource demands and geographic constraints [4], [5]. These devices have evolved from simple assistive tools to adaptive systems capable of modulating impedance and force feedback based on user interaction [6], [7]. Advances in virtual reality and robotic-assisted neuromotor therapy further expand rehabilitation possibilities, facilitating engaging and interactive treatments that improve motor function, cognition, and user motivation [8]. However, disparities in user effort and task difficulty due to individual physical differences remain a challenge in standardizing human-robot interaction.

Human-robot interaction plays a crucial role in these physical simulation systems and enables intuitive and adaptive interaction between humans and robotic devices. Impedance control is the dominant method for regulating the robot's response to user interaction [9]. Prior research has demonstrated benefits of variable impedance control in enhancing compliance, adaptability, and safety. A learning-based time-varying impedance controller has been shown to autonomously adjust robot stiffness based on human input [10]. Biomechanics-driven methods to adapt robot impedance for improved interaction comfort have also been explored [11]. Another approach leverages learning-based variable impedance frameworks, enabling robotic arms to adapt stiffness and damping from human demonstrations, improving trajectory accuracy and compliance across diverse tasks [12]. While these advancements allow robots to dynamically adjust to user input, they do not account for differences in body size and strength, leading to inconsistencies in task difficulty and effort.

Adaptive techniques are widely used in virtual reality to personalize user experience, dynamically adjusting task difficulty and parameters based on individual progress and physical characteristics. This is particularly crucial in rehabilitation, where patient needs vary widely. Adaptive virtual reality has been shown to enhance motor skill development, balance training for post-stroke patients, and real-time feedback for para-athletes by tailoring exercises to individual capabilities [13], [14], [15]. Integrating biosignal feedback further improves engagement by allowing virtual reality systems to adjust exercises based on brain and muscle activity [16]. Systematic reviews indicate that adaptive virtual reality enhances user engagement and therapeutic effectiveness compared to static systems, but standardization remains a challenge [17], [18]. Such adaptive strategies have yet to be fully leveraged in physical simulation platforms, where variability in user attributes can similarly impact task difficulty and effort. Addressing this gap requires normalization techniques that ensure consistent interaction dynamics across diverse users.

Normalization in physical performance assessments ensures

*These authors contributed equally. This research was supported by NSF award CMMI 2221315. All authors are with Bionic Systems Laboratory, Mechanical Engineering Department of University of California, Riverside, USA, 92521. Email: burak.balta@email.ucr.edu, nusaiba.hafiz@email.ucr.edu, jrealmut@ucr.edu.

fair comparisons by accounting for body size differences. Allometric scaling is widely used to adjust strength and movement data, making them independent of body mass [19]. Standardized methods recommend normalizing muscle torque by body mass, muscle force and power by body mass$^{2/3}$, and body-weight-supported exercises by body mass$^{-1/3}$ [20]. Studies comparing different normalization techniques suggest that body weight is the most effective parameter for adjusting muscle strength, particularly in sports such as baseball pitching [21]. While some research supports height-based normalization [22], other findings indicate that weight provides more accurate adjustments [23].

While previous research has explored adaptive impedance control and task customization in human-robot interaction, existing methods primarily focus on optimizing performance, compliance, or user comfort rather than ensuring standardized task difficulty across individuals of varying body sizes. Current approaches do not explicitly normalize human effort in physical interaction tasks, leading to variability in perceived difficulty based on participant anthropometrics. In contrast, this work introduces a novel allometric scaling strategy, scaling the robot's virtual stiffness by $(m/h)^{2/3}$, to ensure that participants experience a consistent level of effort regardless of their mass and height. Additionally, we scale the task trajectory based on participants' height to ensure that extreme task points remain within each participant's reachable workspace. We further propose adjustments to the participant distance from the robot, and initial human and robot poses, tailoring them to individual physical attributes. Together, these three normalizations, robot impedance, task trajectory, and initial interaction configuration, ensure fairness and consistency, allowing all participants to face comparable challenges regardless of their physical differences. To the best of our knowledge, this is the first study that systematically applies biomechanical scaling principles to adjust robot impedance for standardizing task effort in human-robot interaction, bridging a critical gap in the design of adaptive physical simulation platforms for rehabilitation, motor learning, and collaborative robotics.

II. Dynamic Model of the Human-Robot Interaction

We model the human-robot interaction as a coupled dynamical system with virtual stiffness and damping between the human hand and the robot's end-effector [24]. The model integrates the dynamic properties of both the human and the robot, including inertia, Coriolis effects, and gravitational forces, into a unified representation. Virtual stiffness and damping terms enforce the kinematic constraint between the hand and end-effector. This approach eliminates the need for differential-algebraic equations that arise in analytical coupling models, thereby reducing computational complexity while preserving fidelity. In this framework, the robot is controlled by a task-space impedance controller with a fixed equilibrium, emulating spring-like behavior to provide a compliant response to external forces. Meanwhile, the human is modeled as a task-space proportional-derivative controller, designed to follow the desired trajectory.

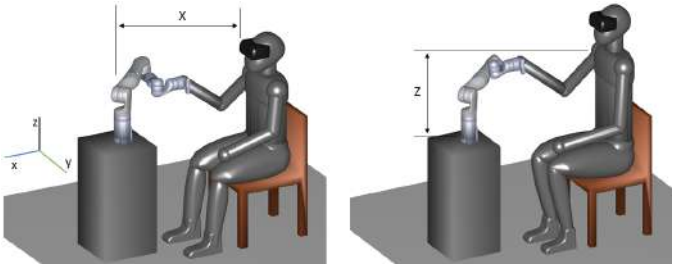


Fig. 2: Two individuals with different heights in our simulation, highlighting the variation in shoulder positions determined by height and optimization.

The human arm is modeled with three revolute joints at the shoulder (allowing for flexion-extension, abduction-adduction, and internal-external rotation) and one revolute joint at the elbow (for flexion-extension). This configuration was implemented as a two-link four-joint rigid body system, where the links corresponds to the upper arm and forearm segments, and the joints replicate the shoulder and elbow motions. The model includes a fixed base to represent the participant's body, providing a realistic dynamic representation of human upper limb movement. The length and mass of the arm segments were calculated using standard anthropometric ratios based on the participant's height and weight, with segment lengths as proportions of height and masses as proportions of body weight [25].

The coupled human-robot dynamics are expressed as:

$$\begin{bmatrix} M_h(q_h) & 0 \\ 0 & M_r(q_r) \end{bmatrix} \begin{bmatrix} \ddot{q}_h \\ \ddot{q}_r \end{bmatrix} + \begin{bmatrix} C_h(q_h, \dot{q}_h) & 0 \\ 0 & C_r(q_r, \dot{q}_r) \end{bmatrix} \begin{bmatrix} \dot{q}_h \\ \dot{q}_r \end{bmatrix} + \begin{bmatrix} g_h(q_h) \\ g_r(q_r) \end{bmatrix} = \begin{bmatrix} \tau_h \\ \tau_r \end{bmatrix} + \begin{bmatrix} J_h(q_h)^\top \mathcal{F}_{r,h} \\ J_r(q_r)^\top \mathcal{F}_{h,r} \end{bmatrix}, \quad (1)$$

where M_h, M_r are the inertia matrices for the human and robot; C_h, C_r the Coriolis matrices for the human and the robot; τ_h, τ_r the joint torques for the human and robot; g_h, g_r the gravitational torques for the human and robot; J_h, J_r the Jacobian matrices for the human and robot; $\mathcal{F}_{r,h}$, $\mathcal{F}_{h,r}$ the interaction wrenches applied to the human and robot. The interaction wrenches are formulated as:

$$\mathcal{F}_{h,r} = K_c(\mathcal{S}_{r,h} - \mathcal{S}_{r,h,0}) - K_d\left(J_r(q_r)\dot{q}_r - J_h(q_h)\dot{q}_h\right) \quad (2)$$

$$\mathcal{F}_{r,h} = K_c(\mathcal{S}_{h,r} - \mathcal{S}_{h,r,0}) - K_d\left(J_h(q_h)\dot{q}_h - J_r(q_r)\dot{q}_r\right) \quad (3)$$

where K_c is the coupling stiffness matrix, K_d the coupling damping matrix, $\mathcal{S}_{h,r}$ the screw vector representing the difference between the human and robot end-effectors relative to the human, $\mathcal{S}_{r,h}$ the screw vector representing the difference between the robot and human end-effectors relative to the robot, and $\mathcal{S}_{h,r,0}$, $\mathcal{S}_{r,h,0}$ the screw vectors representing the initial differences (e.g., at the start of the simulation). The screws are formulated as follows (see, e.g., [26]):

$$[\mathcal{S}_{i,j}] = \log(T_i^{-1} T_j) \quad (4)$$

where T_i, T_j are the homogeneous transformation matrices for i^{th} and j^{th} end-effectors, log is the matrix logarithm, and $[\mathcal{S}_{i,j}]$

is the matrix representation of the screw between the i^{th} and j^{th} end-effectors. A matrix representation of the screw is given by:

$$[\mathcal{S}] = \begin{bmatrix} [\omega] & v \\ 0 & 0 \end{bmatrix} \tag{5}$$

with $[\omega]$ the skew-symmetric matrix representation of the unit angular velocity and v unit linear velocity. The skew-symmetric matrix is:

$$[\omega] = \begin{bmatrix} 0 & -\omega_z & \omega_y \\ \omega_z & 0 & -\omega_x \\ -\omega_y & \omega_x & 0 \end{bmatrix}. \tag{6}$$

Then the screw vector is:

$$\mathcal{S} = \begin{bmatrix} \omega_x & \omega_y & \omega_z & v_x & v_y & v_z \end{bmatrix}^T. \tag{7}$$

The human tracking controller is formulated as:

$$\tau_h = J_h(q_h)^\top (K_{p,h}\mathcal{S}_{h,d} - K_{d,h}J_h(q_h)\dot{q}_h) + g_h(q_h) \tag{8}$$

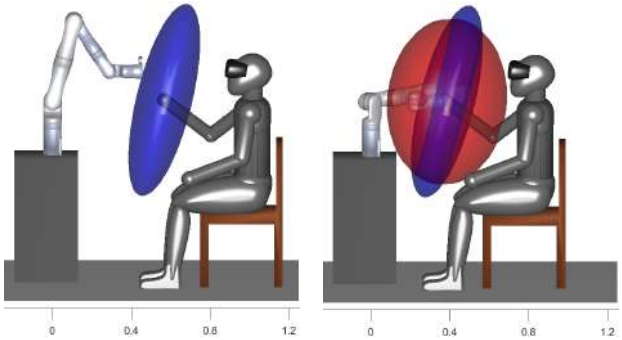
with $K_{p,h}$ the human's proportional gain matrix, $\mathcal{S}_{h,d}$ the screw representing the error from the desired transformation T_d, K_d the derivative gain matrix, and g_h the gravitational torque. The robot impedance controller is formulated in a similar way:

$$\tau_r = J_r(q_r)^\top (K_{p,r}\mathcal{S}_{r,d_0} - K_{d,r}J_r(q_r)\dot{q}_r) - b\dot{q}_r + g_r(q_r) \tag{9}$$

where $K_{p,r}$ the robot's stiffness impedance parameter, $\mathcal{S}_{r,d_0}$ the screw representing the deviation from the center of the desired trajectory, $K_{d,r}$ the robot's damping impedance parameters, b joint damping coefficient which models friction in the motors (and enhances the stability of the simulation), and g_r the gravitational torque which provides gravity compensation. The impedance controller is designed to emulate spring-like behavior, providing a compliant response to external forces with the equilibrium fixed at the center of the trajectory. In this way, the task can be interpreted as trajectory tracking in a spring-like environment with the springs zero-force point at the center of the trajectory. The human arm joint states were directly available in the simulation, the Jacobian was computed analytically from the kinematic chain, and the gain matrices in were determined for the mean participant and iteratively tuning for stability.

III. Normalizing the Configuration

Our method configures the initial pose of both the human and robot, and the task trajectory, with all parameters tailored to the participant's height and mass for normalized interaction. The human shoulder position is defined in Cartesian coordinates x, y, z, where $y = 0$ ensured lateral alignment with the robot, z represented the shoulder height relative to the robot's base, and x was determined through optimization. Figure 2 highlights participants with two different heights, demonstrating that their shoulder positions vary in the x and z coordinates. This difference is critical for identifying the interaction point, as the shoulder position influences the participant's reachable workspace and determines the optimal location for interaction. Tailoring the interaction to these variations ensures comfortable and efficient task execution for participants of different body dimensions.



(a) human arm pose (b) robot pose

Fig. 3: Initial pose for human arm, chosen as the maximum manipulability of the hand, and of robot end-effector, chosen as the minimum ratio of the longest to the shortest axis of the translational manipulability ellipsoid.

Our first aim is to maximize the human's manipulability at the initial arm pose, and therefore we use Yoshikawa's manipulability index [27], $\mu_h = \sqrt{\det(J_{v,h}J_{v,h}^T)}$, where $J_{v,h}$ is the 3×4 matrix corresponding to the translation part of the human's Jacobian matrix. This approach ensures that the arm starts and operates in a posture that provides the greatest flexibility and agility for task execution [28].

The optimization for arm joint angles were performed using MATLAB's `fmincon` function to solve constrained nonlinear optimization problems. While our methodology shares similarities with ergonomic human-robot collaboration research, particularly in optimizing human arm manipulability, our objective differs. Prior work primarily aims to enhance comfort and efficiency in collaborative manipulation tasks [29], whereas we focus on standardizing task effort based on participant anthropometrics. The optimization of human arm manipulability serves a critical role in our study by ensuring that all participants begin the task in a biomechanically neutral, high-dexterity posture. This removes postural biases, allowing a direct evaluation of how impedance scaling affects effort across individuals with different body sizes. The objective function was set as the negative of the manipulability metric, effectively maximizing manipulability. The optimizer adjusted four revolute joints: three at the shoulder (flexion-extension, abduction-adduction, and internal-external rotation) and one at the elbow (flexion-extension). The resulting joint angles (q) for all the participants' starting arm pose are as follows (in rad):

- Abduction/adduction of the shoulder: $q_1 = -0.0137$;
- Flexion/extension of the shoulder: $q_2 = 0.6613$;
- Rotation of the humerus: $q_3 = 0$;
- Flexion/extension of the elbow: $q_4 = -1.3670$.

Next, we aim to maximize the robot's freedom of motion at the point of contact by minimizing the ratio of the longest axis ($\sqrt{\lambda_1}$) to the shortest ($\sqrt{\lambda_3}$) axis of the robot's translational manipulability ellipsoid ($\mu_r = \sqrt{\lambda_1/\lambda_3}$). This approach encourages an isotropic ellipsoid, improving the

robot's dexterity and adaptability during dynamic interactions. Additionally, the optimization determines the optimal position of the human participant along the x-axis, x_c. The constraints ensured precise alignment of the robot's end-effector with the human's end-effector to enable effective interaction, while also maintaining realistic robot configurations by adhering to joint limits. The optimization problem for the parameter vector $\mathbf{x}$ was formulated as:

$$\min_{\mathbf{x}} \ \mu_r \tag{10}$$
$$\text{subject to:} \quad \underline{\mathbf{x}} \leq \mathbf{x} \leq \bar{\mathbf{x}}$$

with the parameter vector $\mathbf{x} = [q_1, \ \cdots \ q_7, \ x_c]$, which includes the 7 robot joint angles and the human-robot interaction point x_c, along the x-axis. The initial pose of the robot for human-robot collaboration is found using a global optimization process, combining MATLAB's `patternsearch` and `fmincon` within a loop. To select the starting points for the optimization, we used a multi-start approach. This ensured that the optimization began from multiple diverse initial configurations, increasing the likelihood of finding a globally optimal solution. The outputs of the two optimizers for human and robot poses determined the interaction point, e.g., the center of the trajectory, which is defined by the coordinates x_c, z_c, ($y_c = 0$) as shown in Fig. 3. Only x_c is a parameter in the optimization, since z_c is determined based on the participant's height.

We also scale the desired human trajectory based on the person's height:

$$p_d(t) = \begin{bmatrix} x_c \\ A_y \sin(2t) \\ z_c + A_z \sin(t) \end{bmatrix}, \tag{11}$$

where, p_d is the task space desired position of the hand, A_y and A_z are the amplitudes of sinusoidal motion along the y and z axes and are expressed as percentages of the individual's height. Here, we choose $A_y = 0.06 \cdot h$ and $A_z = 0.12 \cdot h$, where h is the participant's height. This scaling ensures that the task trajectory is customized to the participant's reach limits, maintaining consistent effort across participants with varying physical attributes. The values were arrived at through an iterative process, ensuring that the task trajectory was challenging yet achievable for participants. Note that in this work, we do not consider a desired orientation of the human hand, only the translational position p_d.

The final component used to ensure a consistent and standardized experience for participants of varying physical attributes during human-robot interactions is scaling of the robot's stiffness matrix $K_{p,r}$. Human biomechanics, such as limb length, body mass, and muscle strength, vary significantly with height and weight, and these factors can influence the perceived stiffness and overall interaction dynamics. By normalizing the stiffness matrix using these scaling factors, we aim to account for individual differences in physical characteristics, thereby improving the fairness, reproducibility, and biomechanical relevance of the experimental conditions across

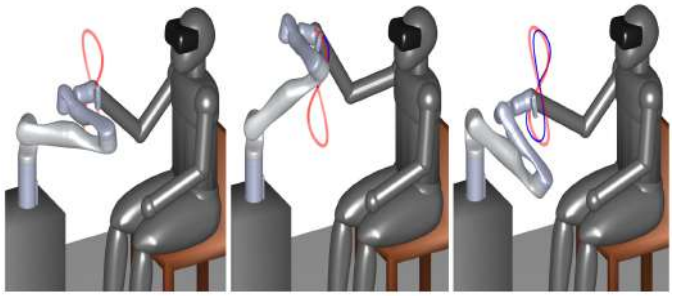


Fig. 4: A sequence of the human-robot interaction task at three different time instances. The task involves tracking a moving target in a figure-eight pattern. The robot acts as a spring-like environment, providing compliant resistance to the human participant.

participants. Since the proper scaling is unknown, we systematically explore common biomechanical relationships that could influence human-robot interaction dynamics. We compare the following scalings: mass (m), mass power $2/3$ ($m^{2/3}$), height (h), inverse height ($1/h$), mass divided by height (m/h) and mass divided by height power $2/3$ ($(m/h)^{2/3}$). We apply the scaling as follows: $K_{p,r}(P) = \alpha(P) K^0_{p,r}$, where $\alpha(P)$ is the scaling factor for participant P, and $K^0_{p,r}$ is the nominal stiffness matrix, which is found for the averaged sized participant first. The scaling factor $\alpha(P)$ is determined by the participant's height and mass as described above. The results of this analysis will provide insights into the impact of these scaling strategies on the human-robot interaction dynamics, helping to optimize the experimental setup for participants with diverse physical attributes.

In contrast, the human controller gains are kept constant to maintain consistency in modeling human motor control. Unlike the robot's stiffness matrix, which directly interacts with and needs to adapt to the participant's physical characteristics for standardization, the human gains reflect the inherent neuromuscular properties and motor control strategies. These properties are relatively stable across individuals. Keeping these gains constant ensures the experimental focus remains on how variations in the robot's stiffness matrix influence the interaction, without introducing additional variability from altering human control parameters.

IV. Results

To account for variations in participant height and mass, we considered three different heights: 1.54 m, 1.74 m (average

TABLE I: Simulation parameters.

Parameter	**Value/Description**
$K_{h,p}$	$10^6 \cdot \text{diag}([0,0,0,1,1,1])$
$K_{h,d}$	$500 \cdot I_6$
$K_{r,p}(h = 1.73, m = 73)$	$1.5{\cdot}10^5{\cdot}\text{diag}([0.01, 0.01, 0.01, 1, 1, 1])$
$K_{r,d}$	$1000 \cdot \text{diag}([0.01, 0.01, 0.01, 1, 1, 1])$
K_c	$2.8 \cdot 10^6 \cdot I_6$
K_d	$10^5 \cdot I_6$
T	2π
dt	0.01

height), and 1.94 m, representing a range of possible participant statures. For each height, a nominal corresponding body mass was determined using a body-mass index (BMI) of 24.1, a standard value representing average body composition. This calculation resulted in masses of 57.2 kg for 1.54 m, 73.0 kg for 1.74 m, and 90.8 kg for 1.94 m. To capture a diverse range of participants, we considered nine profiles by permuting the three different masses among the three heights.

For all nine virtual participants, we simulated the human-robot interaction task using our optimization method in conjunction with each of the six scaling factors for the robot's stiffness $K_{p,r}$, a nominal simulation, where the placement and configuration of the robot was chosen as the optimal configuration for an average-sized participant, and a case where the robot's stiffness matrix was not scaled. All simulations were integrated using an implicit solver with variable order method (`ode15s` in MATLAB) with a time step of 0.01 s. The simulation parameters are shown in Table I and a sequence of one of the simulations at three different time instances is shown in Fig. 4.

For each simulation we calculated the human effort as the total norm of the human joint torque over the entire simulation and then normalized by mass times height (mh) of the individual. The rational for normalization is to produce a dimensionless magnitude that can be compared across participants. Since torque has units of $N \cdot m$, a reasonable normalization factor would be mgh and g can be dropped since it is common to all participants. Our main outcome measure, the effort ratio, was defined as the human effort for each participant normalized by the human effort required for the average-sized participant minus 1, thus positive values indicate higher effort than the average-sized participant while negative values indicate lower effort.

The results of this analysis are shown in Fig. 5. The scaling strategies demonstrate noticeable changes in the effort distribution, highlighting how adjustments affect task difficulty for participants with diverse body compositions. Our optimization method with the scaling factor of $(m/h)^{2/3}$ shows the most consistent effort ratio across participants, indicating an effective strategy for standardizing the task effort across individuals with varying physical attributes.

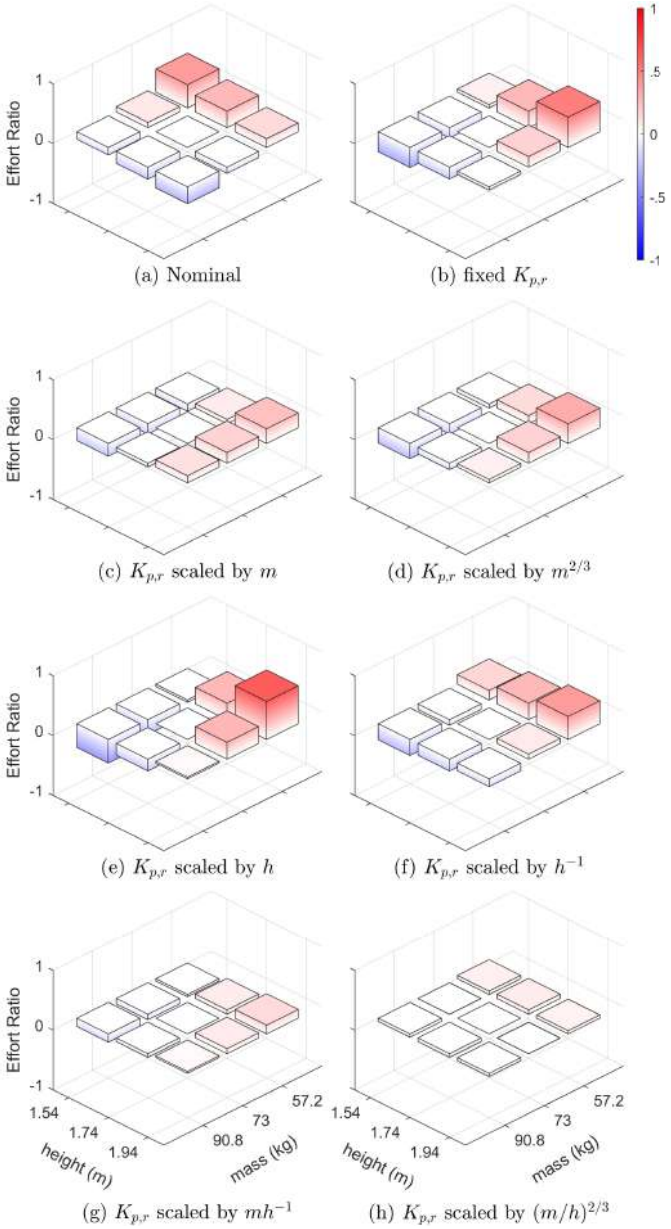


Fig. 5: Human effort ratio for different scaling of $K_{p,r}$ for all virtual participants.

V. Discussion

Our goal was to ensure equitable task difficulty and physical effort across participants with varying attributes. Differences in participant height and weight significantly influence their reachability and exertion capabilities, leading to disparities in task performance and overall experience. To address this, our approach involves standardizing key interaction parameters: the initial poses of both human and robot and the task trajectory. For humans, having the same initial pose across subjects ensures consistent task difficulty, while optimizing the robot's initial pose improves its efficiency. The interaction must balance human accessibility and robot reachability, ensuring seamless interaction. This alignment sets the foundation for smooth task execution and effective human-robot interaction.

Additionally, we observed that tailoring the robot's stiffness matrix $K_{p,r}$ based on the participant's physical attributes (height and mass) further normalizes the effort across individuals, promoting fairness in the interaction. There is a noticeable variation in effort across participants in the nominal configuration (Fig. 5a), with taller and heavier individuals experiencing lower effort. Our optimization method with a fixed $K_{p,r}$ (Fig. 5b) reduces this disparity but causes lower-mass and taller subjects to exert more effort than others, leading to an imbalance in effort distribution. Scaling $K_{p,r}$ by mass (Fig. 5c) produces moderate normalization across participants with different masses but same height. This adjustment reduces the robot's resistance for subjects with lesser mass, who would otherwise experience excessive effort. The robot's

gain should also be scaled inversely with height, as taller participants follow larger trajectories; if not, it would apply greater resistance to them. As observed, mass-inverse-height scaling (Fig. 5g) effectively balances the effort ratio across all participants. Initially, we used a power of 1 for both mass and height, but Jaric et al. [20] showed that muscle strength scales with $m^{2/3}$. While their work only considers mass, height also plays a role in our task by influencing reachability and interaction dynamics. Directly measuring individual muscle strength would be impractical for large-scale studies and may not generalize well across populations. Instead, we apply the same allometric scaling principle to both mass and height, resulting in $(m/h)^{2/3}$, which achieves the most consistent effort ratio across individuals (Fig. 5h). While non-physical factors such as experience and reflexes may influence task performance, our approach ensures that the baseline physical effort remains standardized, independent of these variations. These findings highlight the importance of customizing stiffness parameters in human-robot interaction.

VI. Conclusion

We developed a method to standardize human-robot interactions during physical tracking in a virtual environment, optimizing key interaction parameters to ensure equitable task difficulty and effort across participants with varying physical attributes. Our findings highlight the need for individualized task configurations experiments to enhance fairness and user experience. By tailoring the robot's stiffness matrix and optimizing interaction parameters, we can reduce physical disparities, enabling participants with varying body compositions to perform tasks with comparable difficulty and effort. Future research should explore the physiological and cognitive effects of these adjustments, as well as their impact on long-term engagement and task performance. Factors such as neuromuscular control strategies, muscle strength, experience, skills, and reflexes may also influence task difficulty and should be considered. Our approach offers a framework for designing inclusive systems that adapt to diverse participant needs, paving the way for broader adoption of physical simulators in rehabilitation, training, and entertainment.

References

[1] I. S. Howard, J. N. Ingram, and D. M. Wolpert, "A modular planar robotic manipulandum with end-point torque control," *Journal of neuroscience methods*, vol. 181, no. 2, pp. 199–211, 2009.

[2] R. Shadmehr and J. W. Krakauer, "A computational neuroanatomy for motor control," *Experimental brain research*, vol. 185, pp. 359–381, 2008.

[3] E. Burdet, R. Osu, D. W. Franklin, T. E. Milner, and M. Kawato, "The central nervous system stabilizes unstable dynamics by learning optimal impedance," *Nature*, vol. 414, no. 6862, pp. 446–449, 2001.

[4] A. C. Lo, P. D. Guarino, L. G. Richards, J. K. Haselkorn, G. F. Wittenberg, D. G. Federman, R. J. Ringer, T. H. Wagner, H. I. Krebs, B. T. Volpe *et al.*, "Robot-assisted therapy for long-term upper-limb impairment after stroke," *New England Journal of Medicine*, vol. 362, no. 19, pp. 1772–1783, 2010.

[5] P. Maciejasz, J. Eschweiler, K. Gerlach-Hahn, A. Jansen-Troy, and S. Leonhardt, "A survey on robotic devices for upper limb rehabilitation," *Journal of neuroengineering and rehabilitation*, vol. 11, pp. 1–29, 2014.

[6] H. I. Krebs, N. Hogan, M. L. Aisen, and B. T. Volpe, "Robot-aided neurorehabilitation," *IEEE transactions on rehabilitation engineering*, vol. 6, no. 1, pp. 75–87, 1998.

[7] E. L. Waters and M. J. Johnson, "Motor learning in robot-based haptic dyads: A review," *IEEE Transactions on Haptics*, 2024.

[8] K. Baur, A. Schättin, E. D. de Bruin, R. Riener, J. E. Duarte, and P. Wolf, "Trends in robot-assisted and virtual reality-assisted neuromuscular therapy: a systematic review of health-related multiplayer games," *Journal of neuroengineering and rehabilitation*, vol. 15, pp. 1–19, 2018.

[9] N. Hogan, "Impedance control: An approach to manipulation," in *1984 American control conference*. IEEE, 1984, pp. 304–313.

[10] M. Sharifi, V. Azimi, V. K. Mushahwar, and M. Tavakoli, "Impedance learning-based adaptive control for human–robot interaction," *IEEE Transactions on Control Systems Technology*, vol. 30, no. 4, pp. 1345–1358, 2021.

[11] F. Zahedi and H. Lee, "Biomechanics-based user-adaptive variable impedance control for enhanced physical human–robot interaction using bayesian optimization," *Advanced Intelligent Systems*, p. 2400333, 2024.

[12] F. Zhong, L. Hu, and Y. Chen, "Robot variable impedance control and generalizing from human–robot interaction demonstrations," *Mathematics*, vol. 12, no. 23, p. 3840, 2024.

[13] D. Kumar, A. González, A. Das, A. Dutta, P. Fraisse, M. Hayashibe, and U. Lahiri, "Virtual reality-based center of mass-assisted personalized balance training system," *Frontiers in bioengineering and biotechnology*, vol. 5, p. 85, 2018.

[14] F. Hong, L. Wang, and C. Z. Li, "Adaptive mobile cloud computing on college physical training education based on virtual reality," *Wireless Networks*, pp. 1–24, 2023.

[15] R. M. Carrera, C. Tao, and S. K. Agrawal, "Designing and analyzing in-place motor tasks in virtual reality with goal functions," *IEEE Transactions on Neural Systems and Rehabilitation Engineering*, 2024.

[16] L. Wang, S. Du, H. Liu, J. Yu, S. Cheng, and P. Xie, "A virtual rehabilitation system based on eeg-emg feedback control," in *2017 Chinese Automation Congress (CAC)*. IEEE, 2017, pp. 4337–4340.

[17] M. Zahabi and A. M. Abdul Razak, "Adaptive virtual reality-based training: a systematic literature review and framework," *Virtual Reality*, vol. 24, no. 4, pp. 725–752, 2020.

[18] P. H. B. Correia, "Adaptive virtual reality solutions: A literature review," in *Proceedings of the 26th Symposium on Virtual and Augmented Reality*, 2024, pp. 1–10.

[19] S. Jaric, "Muscle strength testing: use of normalisation for body size," *Sports medicine*, vol. 32, pp. 615–631, 2002.

[20] S. Jaric, D. Mirkov, and G. Markovic, "Normalizing physical performance tests for body size: aproposal for standardization," *The Journal of Strength & Conditioning Research*, vol. 19, no. 2, pp. 467–474, 2005.

[21] W. J. Hurd, B. F. Morrey, and K. R. Kaufman, "The effects of anthropometric scaling parameters on normalized muscle strength in uninjured baseball pitchers," *Journal of sport rehabilitation*, vol. 20, no. 3, pp. 311–320, 2011.

[22] M. Kasović, P. Sagat, Z. Kalčik, L. Štefan, A. Hubinák, and P. Krška, "Allometric normalization of handgrip strength in older adults: Which body size parameter is the most appropriate?" *BMC Sports Science, Medicine and Rehabilitation*, vol. 15, no. 1, p. 18, 2023.

[23] T. Xu, X. Li, D. Wang, Y. Zhang, Q. Zhang, J. Yan, J. Jiang, W. Liu, and J. Chen, "Hand grip strength should be normalized by weight not height for eliminating the influence of individual differences: findings from a cross-sectional study of 1,511 healthy undergraduates," *Frontiers in Nutrition*, vol. 9, p. 1063939, 2023.

[24] J. Wang, C. M. Gosselin, and L. Cheng, "Modeling and simulation of robotic systems with closed kinematic chains using the virtual spring approach," *Multibody System Dynamics*, vol. 7, pp. 145–170, 2002.

[25] P. De Leva, "Adjustments to zatsiorsky-seluyanov's segment inertia parameters," *Journal of biomechanics*, vol. 29, no. 9, pp. 1223–1230, 1996.

[26] K. Lynch, *Modern Robotics*. Cambridge University Press, 2017.

[27] T. Yoshikawa, "Manipulability of robotic mechanisms," *The international journal of Robotics Research*, vol. 4, no. 2, pp. 3–9, 1985.

[28] J. Jacquier-Bret, P. Gorce, and N. Rezzoug, "The manipulability: a new index for quantifying movement capacities of upper extremity," *Ergonomics*, vol. 55, no. 1, pp. 69–77, 2012.

[29] G. Chiriatti, A. Bottiglione, and G. Palmieri, "Manipulability optimization of a rehabilitative collaborative robotic system," *Machines*, vol. 10, no. 6, p. 452, 2022.

Real-Time Estimation of Intended Lower-Limb Motion for Assist Robots

Satsuki Kugai
Dept. of Mechanical Engineering
Kyushu University
Fukuoka, Japan
kugai.satsuki.347@s.kyushu-u.ac.jp

Satoshi Nishikawa
Dept. of Mechanical Engineering
Kyushu University
Fukuoka, Japan
nishikawa@mech.kyushu-u.ac.jp

Kazuo Kiguchi
Dept. of Mechanical Engineering
Kyushu University
Fukuoka, Japan
kiguchi@mech.kyushu-u.ac.jp

***Abstract*— Motion assist robots have been studied to assist human motion for elderly, disabled, injured persons. The motion assist robots can be classified into two types: wearable robots which are directly attached to the user's body and external robots which assist the user's motion from the outside of the user. It is important for those robots to estimate motion intention of users in real-time to assist their daily motion effectively. This paper presents a method to estimate human lower-limb motion intention and its motion phase in real-time for the motion assist robots. By detecting motion phase in addition to the intended motion in real-time, the robots can figure out when and how human motion are assisted even in the middle of the motion. In the proposed method, integrated information about human physical and biological data and the surrounding environment are used to estimate the motion intention and its phase. Damping neuron has been applied in the artificial neural networks for the intended motion estimation and also for the motion phase estimation. Furthermore, changing velocity from the output of the artificial neural network is considered to figure out the intended motion in early stage. Experimental results show that lower-limb motion and its phase are effectively estimated with the proposed method. Furthermore, it is shown that the motion phase is correctly estimated even if the user gives up the intended motion during the motion.**

Keywords—real-time estimation, human motion intention, motion phase estimation, motion assist robots

I. INTRODUCTION

Motion assist robots have been studied to assist human motion for elderly, disabled, and injured persons [1]-[5]. The motion assist robots can be classified into two types: wearable robots which are directly attached to the user's body [1]-[3] and non-wearable external robots which assist the user's motion from the outside of the user [4][5]. It is important for the motion assist robots to automatically assist the user to perform movements according to the user's intention appropriately and safely. In addition, it is important to estimate the series of whole target motion for the robots which assist the user's motion as necessary from the outside of the user like a human assistant. Therefore, recognizing the user's motion intention at an early stage and planning appropriate assistance to achieve the user's intended motion is necessary for appropriate and effective assistance by the motion assist robots. By estimating the user's intended motion and its phase in the early stage of the motion, the assist robot can provide appropriate assist for the user as necessary. In that case, the robot will be able to support the users properly to complete the intended motion even if they give up the intended motion in the middle of the motion.

Although many studies have been performed to estimate human motion [6]-[8], those methods may not be applied for the user's intended motion estimation for the motion assist robots since the intended motion and the actually generated motion are different sometimes especially in the case of elderly or disabled persons. Furthermore, the intended motion must be estimated in real time without time delay to assist the motion with the robots. The intended motion estimation is basically derived from information that reflects user's intention, such as skin surface electromyography (sEMG) and Electroencephalography (EEG) [9]-[13]. By using sEMG, body acceleration information can be taken into account in advance so that the intended motion can be estimated in real time at an early stage of the motion [10][11]. Furthermore, several studies on real-time estimation have employed artificial neural network to conduct real-time estimation, examining the relationship between the time required for estimation and its accuracy [10][12]. Accurate estimation at the start of a motion allows the robot to proper support the user's intended motion like a human assistant. In the case of motion phase estimation, however, few estimation methods that represent the motion phase as a percentage from 0 to 100% have been studied [14]. Therefore, further study is required realize more accurate early estimation of the intended motion and its motion phase simultaneously.

This paper proposes a method for real-time estimation of intended motion and its motion phase for nine types of daily human lower-limb movements. The proposed method estimates the intended motion and its phase using artificial neural networks (ANNs) that can learn high-dimensional nonlinear relationships based on integrated data from human body motion captured via motion capture systems, electromyogram (EMG) signals, and environmental information. The proposed method is a modified method of our previous study [14]. Intended motion and its phase estimations have been performed in our previous studies, applying damping neurons to the ANN for motion phase estimation to appropriately accelerate or decelerate the output. In the modified method, the motion intention estimation

This work was supported by JST [Moonshot R&D] [Grant Number JPMJMS2034].

model takes into account the change from the output of the ANN to estimate the intended motion earlier at the early stage. By introducing the change of the outputs of the ANNs, the first and second candidate motions alternate more quickly, enabling estimation earlier in the early stage. In the phase estimation, although one ANN was used for all estimations in our previous method, the specific ANN is used for each motion in the modified method to learn specific motion phase of each motion accurately. Therefore, a separate ANN is used for each motion to specifically train and estimate the phases.

In the case of motion assist robots, especially the external robots, it is sometimes important to start assisting the user's motion even during the movement if the user requires help of the robots. In order to allow the robot to assist the user even though the user gives up the intended motion in the middle of the movement, the effectiveness of the proposed method under those situations is evaluated for the first time. This evaluation is extremely important in assessing the feasibility of introducing a robot, since it assumes a scenario where robotic assistance is required. Experiments have been carried out to evaluate the effectiveness of the proposed method.

II. PROPOSED METHOD

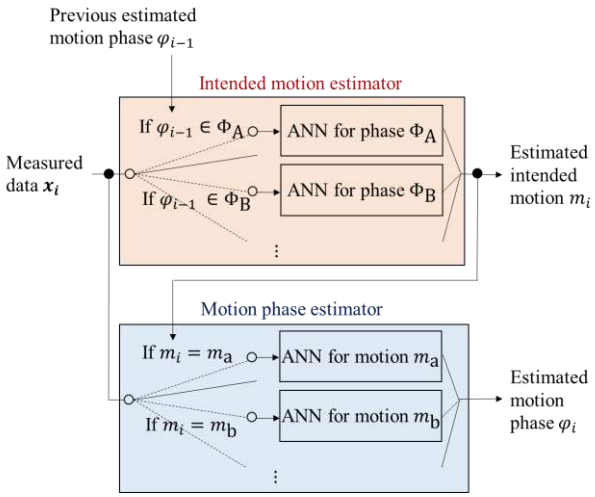


Fig 1 Estimation system for intended motion estimation and phase estimation

In this paper, the input information for estimating the intended motion and phase includes various parameters. These are the 2D position, velocity, and acceleration in the sagittal plane of knee, ankle, heel, and toe of the user's supporting and swinging leg, and both shoulders. If both legs are stationary, the leg that moved most recently is considered the swing leg. Additionally, the input data include lower limb joint angles, the Zero Moment Point (ZMP), and the relative position between the swing leg's toe and the nearest obstacle. The time series information of the swing leg position and 8 sEMG signals (the rectus femoris, biceps femoris, gastrocnemius, and tibialis anterior of both the swing and supporting legs) are also used as important input information. Here, the coordinates are defined as x-direction in the sagittal plane horizontal direction and y-direction in the vertical upward direction, with user's waist as the origin.

The output from intended motion estimator for the intended motion estimation is the estimated daily lower-limb activity (stand up, sit down, squatting, descending, ascending, push, step, standing still, and sitting still), and the output from the motion phase estimator is the numerical value from the start to the end of the activity, expressed between 0 and 1.

This paper proposes a method for real-time estimation of human lower-limb intended motion and their phases. The proposed method consists of two estimators: the intended motion estimator and the motion phase estimator (Fig. 1). Each estimator consists of ANNs. The input for both estimators is the measured data x_i at time step i, the output of the intended motion estimator is the estimated intended motion m_i, and the output of the motion phase estimator is the estimated motion phase φ_i. The ANN for each estimator is switched among multiple ANNs depending on estimation results of intended motion or phase. The ANNs of intended motion estimator is provided for each phase range and switched based on the motion phase (φ_{i-1}) estimated by the motion phase estimator. The ANNs of motion phase estimator is provided for each motion and switched based on the intended motion (m_i) estimated by the intended motion estimator.

As in previous work [14], damping neurons are applied to ANNs for motion intention estimation and phase estimation in order to effectively learn the dynamic characteristics [15]. Damping neurons can effectively learn the dynamic characteristics of the input data.

A. Intended Motion Estimation

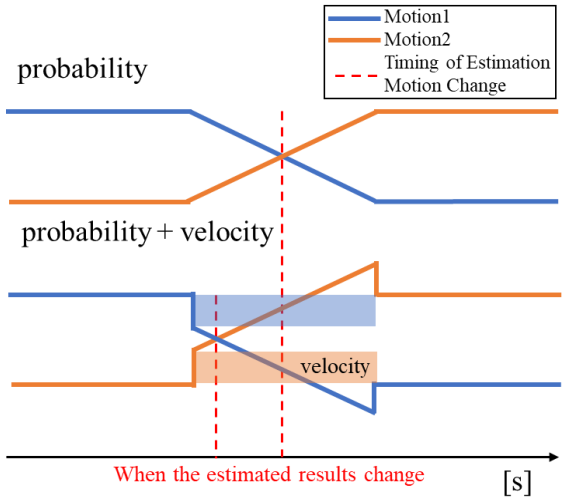


Fig 2 Timing of intended motion estimation considering change of output

For the intended motion estimation, two kinds of ANNs, *i.e.*, a standard ANN and an early estimation ANN, are prepared. For early estimation, we propose a method to ascertain the intended motion in the early phase by considering the change of the ANN output.

In intended motion estimation, during the early phase of a motion transition, the movement often resembles the previous motion. As a result, it is more likely to be misclassified as the previous motion, leading to lower

estimation accuracy compared to the middle phase of the motion. In this study, by adding the time variation of the estimation result, the second and first candidates of the estimated motion are alternated earlier, and the estimation is performed earlier (Fig. 2). The equation that takes into account the time variation of the output from the ANN is written below.

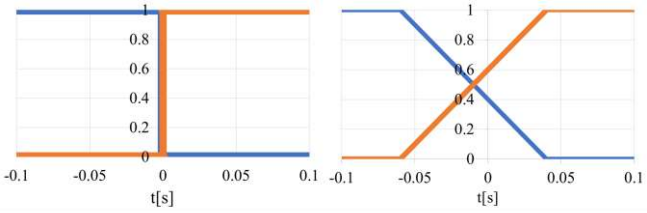
$$z = y + c_v\dot{y} \tag{1}$$

where y is the output of the ANN, $\dot{y}$ is the time variation of y, c_v is a constant, and z is an estimate considering the change.

For the neurons in the output layer of the ANN for motion intention estimation, damping neurons are used in order to effectively learn the dynamic characteristics included in sEMG and other input data. The output equation of the damping neuron is shown below.

$$y = f_x(w_x x) + w_v f_v(\dot{f}_x(w_x x)) \tag{2}$$

where x is the input signal to the neuron and f is the activation function. This damping neurons is used in the output layer of the intended motion estimation model .



(a) Regular labeling (b) Labeling in this method

Fig. 3 Intended motion labeling method

Figure 3 shows the labeling method. Usually, the labels are switched between 0 and 1 as shown in Fig. 3 (a). However, in Fig. 3 (b), the labeling is designed so that the rate of probability increase or decrease gradually before the operation is switched.

B. Maintaining the Integrity of the Specifications

In the motion phase estimation, the progression of a motion from start to end is represented by values ranging from 0 to 1. This real-time estimation of movement phases enables external robots to assist with the remaining phases of movement, even if a user, such as an elderly person, stops moving partway through the target movement.

To effectively learn the dynamic characteristics contained in sEMG, etc., damping neurons are also applied to the neurons in hidden layer 3 and the output layer of the phase estimation model. Additionally, a separate motion phase estimation model for each motion is developed and the results of intended motion estimation is utilized to select the appropriate phase estimation model for a given motion.

III. EXPERIMENTS

To evaluate the effectiveness of the proposed method for estimating intended motion and its phase, the lower limb movements shown in Fig. 4 and the continuous movements ("descending to step," "stand up to step," and "step to ascending") were performed 10 times each. The sEMG data and position data were measured during the movements. The sEMG data at the rectus femoris, biceps femoris, tibialis anterior, and gastrocnemius muscles on both sides were measured with 2000Hz using Noraxon's Ultium system. The data were processed using RMS with a sampling size of 200. Positional data of joint positions of the lower-limbs, shoulders, obstacles, and chairs were measured with 2000Hz using Natural Point's Opti Track system.

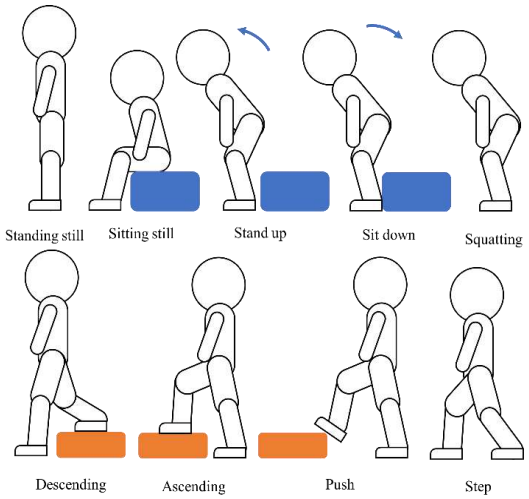


Fig 4 Motion of collected data

The subjects were three young adults, and the experiment collected movement data as "young individuals" and as "pseudo-elderly" subjects wearing aging simulation suits (Sanwa Seisakusho, Model Number 4562363578061), respectively. The aging simulation suit restricts the range of motion by applying resistance to each joint and simulates the difficulty of lifting the legs by adding weights. The "young adult" movements were performed at three different speeds, "slow," "normal," and "fast," while the "pseudo-elderly" movements were performed at two different speeds, "slow" and "normal. In this study, data from all subjects and all speeds were trained together. The experiments were performed based on a protocol approved by the Ethics Committee of the Faculty of Engineering, Kyushu University. Movements were defined as the period during which the foot or waist was in motion. For stair descent, stair ascent, and step, the movement was defined as the time from the start of foot movement to the change between the swing leg and the supporting leg. Table 1 shows the number of neurons in the hidden and output layers of each ANN used in this study. K-fold (K = 5) cross-validation was conducted. Phase estimation was also performed for ANNs without damping neurons to investigate the effect of damping neurons.

The error functions for the motion intention estimation and the motion phase estimation model were the squared errors as shown below:

$$E = \frac{1}{2}K_x e^2 + \frac{1}{2}K_v \dot{e}^2 \tag{3}$$

where K_x is the coefficient of error, K_v is the coefficient of velocity error, e is the estimated phase error, and the optimization algorithm is Adam.

Table 1 Number of neurons in each layer of ANN

		hidden layer 1	hidden layer 2	hidden layer 3	output layer
Intended motion	nodes	80	50	30	10
	activation function	tanh	tanh	tanh	tanh
	damping	without	without	without	with
Phase	nodes	80	50	10	1
	activation function	tanh	tanh	tanh	
	damping	without	without	with	with

Table 2 Average motion time

	young individual			pseudo-elderly	
	slow [s]	normal [s]	fast [s]	slow [s]	normal [s]
Stand up	1.54	1.06	0.82	1.88	1.32
Sit down	1.70	1.50	1.17	2.19	1.64
Squatting	1.67	1.20	1.03	1.80	1.25
Descending	0.93	0.68	0.53	1.15	1.01
Ascending	0.87	0.65	0.51	1.01	0.81
Push	1.73	1.38	1.20	1.90	1.48
Step	0.92	0.77	0.49	0.93	0.73

Table 2 shows the average time from the beginning to the end of each movement (while heel, toe or hip is moving).Table 3 shows the average accuracy rate per phase for the proposed Estimation System, early estimation ANN, and standard ANN. Table 4 presents the intended motion estimation accuracy for each motion, calculated for every 10% phase interval, using the proposed estimation system (early estimation ANN is applied to less than 20% of the phases). Figures 5 and 6 show the phase estimation with and without damping neurons, and the phase estimation results when the error equation (3) is the average or minimum. Table 5 shows the average and minimum phase estimation errors equation (3) with and without damping neurons, respectively. Figure 7 shows the estimation results when the user gave up the intended motion in the middle of the motion. In addition, the horizontal position of the shoulder relative to the heel position (set as the origin) and the time at which its maximum value is reached, representing the timing of giving up, are shown in a graph.

Table 3 Average of Accuracy rate of each motion

phase	standard ANN	early estimation ANN	Estimation system
0-10%	0.9136	0.9485	0.9383
10-20%	0.9567	0.9633	0.9611
20-30%	0.9622	0.9640	0.9656
30-40%	0.9668	0.9679	0.9729
40-50%	0.9770	0.9740	0.9823
50-60%	0.9804	0.9754	0.9825
60-70%	0.9795	0.9769	0.9849
70-80%	0.9730	0.9687	0.9787
80-90%	0.9394	0.9247	0.9507
90-100%	0.7416	0.6678	0.7335
0-100%	0.9381	0.9318	0.9441
Standing still	0.9204	0.9105	0.8963
Sitting stil	0.9144	0.9032	0.9033

Table 4 Accuracy rate of each motion with the proposed Estimation system

	Stand up	Sit down	Squatting	Descending	Ascending	Push	Step	Standing still	Sitting stil
0-10%	0.9680	0.9726	0.9492	0.9703	0.8737	0.9135	0.9212		
10-20%	0.9775	0.9823	0.9649	0.9717	0.9290	0.9720	0.9306		
20-30%	0.9831	0.9911	0.9679	0.9622	0.9413	0.9836	0.9300		
30-40%	0.9861	0.9968	0.9896	0.9511	0.9605	0.9793	0.9471		
40-50%	0.9881	0.9908	0.9934	0.9801	0.9815	0.9714	0.9706		
50-60%	0.9889	0.9919	0.9913	0.9759	0.9848	0.9665	0.9781	0.8963	0.9033
60-70%	0.9839	0.9939	0.9937	0.9794	0.9802	0.9820	0.9813		
70-80%	0.9759	0.9867	0.9917	0.9708	0.9659	0.9811	0.9789		
80-90%	0.9526	0.9715	0.9913	0.9087	0.8954	0.9860	0.9491		
90-100%	0.5824	0.7115	0.9910	0.7121	0.6539	0.6994	0.7843		
0-100%	0.9371	0.9584	0.9824	0.9368	0.9147	0.9429	0.9362		

IV. DISCUSSION

Table 3 demonstrates that the proposed estimation system (Fig. 1) effectively leverages the advantages of both standard ANN and early estimation ANN for its predictions. In the early phase of operation (0-10%), the early estimation ANN has 3.5% higher estimation accuracy than the standard ANN. In the proposed estimation system, by using the early estimation ANN for phases less than 20% and the standard ANN for phases above 20%, the accuracy up to phase 10% was 2.5% higher than that using the standard ANN, and from 90 to 100% was 6.6% higher than that using the early estimation ANN. By using phase estimates, it is possible to improve accuracy at the phase 0-10% without significantly reducing accuracy at the phase 90-100%, thereby achieving an overall improvement in accuracy.

Table 5 Phase errors

	Without damping		With damping	
	average	minimum	average	minimum
Stand up	0.02600	0.00439	0.01985	0.00103
Sit down	0.00626	0.00133	0.00889	0.00058
Squatting	0.02235	0.00556	0.01920	0.00125
Descending	0.04401	0.00674	0.04393	0.00247
Ascending	0.04225	0.00823	0.04023	0.00409
Push	0.02234	0.00421	0.01884	0.00174
Step	0.04720	0.00492	0.04626	0.00452

Table 4 shows that the accuracy of the phase 0-10% is 87.3% or better, and the accuracy of the phase 10-80% is 92.9% or better. While the accuracy of ascending, push, and step estimation is mostly below 93% during the phase 0-20%, the accuracy for stand up, sit down, squatting and descending, is 96% or higher, except for the phase 0-10% of squatting. This may be due to the similarity of the initial operation of descending, push, and step.

The experimental results shown in Table 5, Fig. 5 and Fig. 6 show that damping neurons effectively works for the accurate phase estimation. Table 5 shows that the use of damping neurons reduced the errors for all items except sit down, and for stand up, the errors equation (3) were reduced by 23.7%. In addition, the estimation results shown in Figs. 5 and 6 show that the one with the minimum error follows the correct phase from the initial stage of motion to the end of motion. It was also confirmed that, on average, the estimated phase was accurately tracked in the motion of push, squatting,

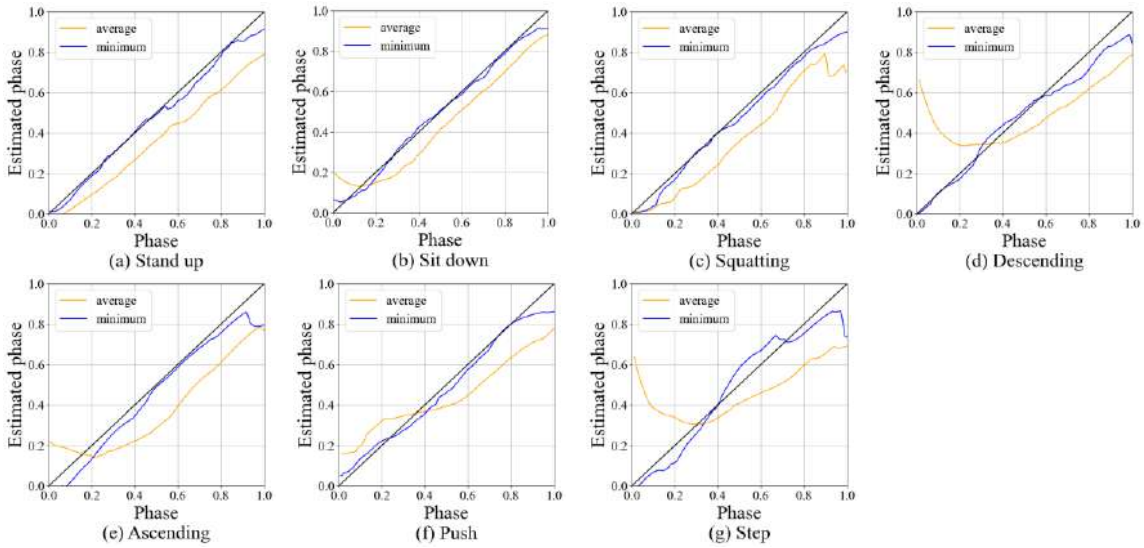


Fig. 5 Motion phase estimation results with damping neuron

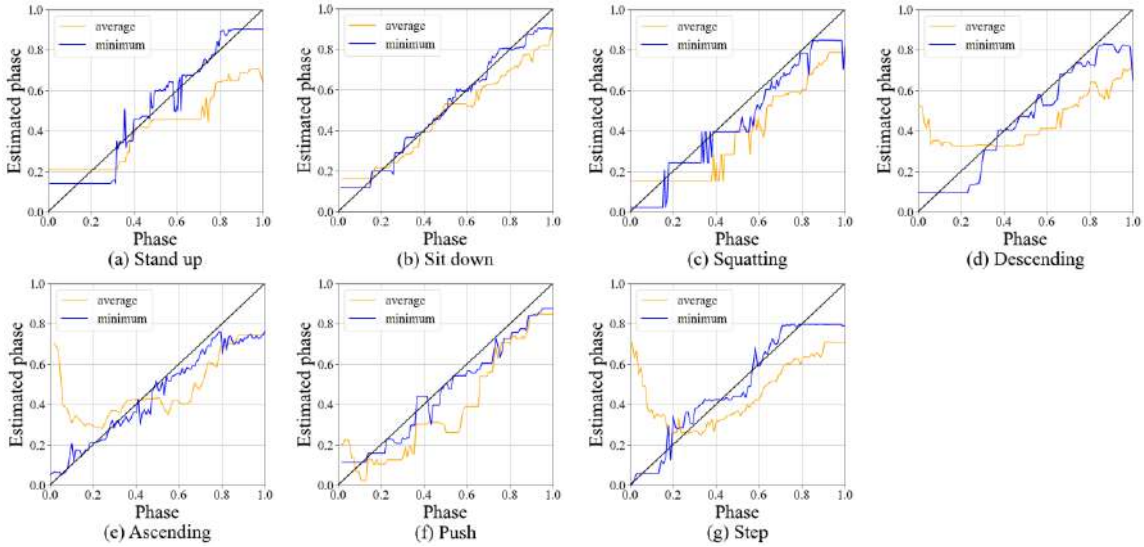


Fig. 6 Motion phase estimation results without damping neuron

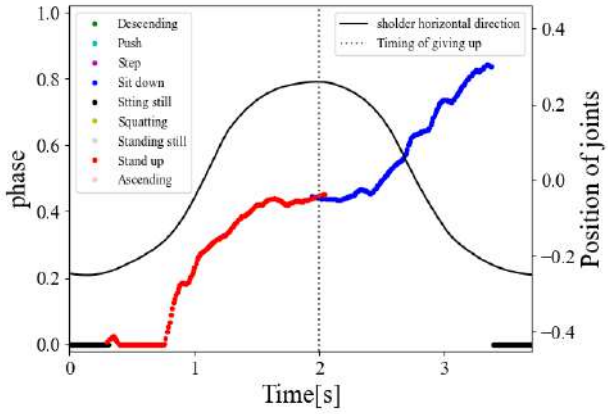


Fig.7 Motion estimation and phase estimation results when the intended motion is changed

sit down, and stand up. The damping neurons effectively accelerate the output moderately and suppress excessive changes, thereby improve the estimation accuracy. However, for descending, step, and ascending, the error was more than twice as large as for the other movements, as shown in Table 5, and a large phase was estimated, especially in the early phase of the movement.

Figure 7 demonstrates that motion estimation is possible even when the intended motion is changed in the middle of the movement. Around the timing when the intended motion was changed, the estimated motions alternate between sit down and standing up. It was observed that before and after this point, the respective motion was estimated accurately. Additionally, the phase estimation shows less gradient around the timing when the intended motion was changed, indicating that the motion was performed more slowly and its motion phase was properly estimated during this period.

V. CONCLUSION

In this paper, we proposed a method for real-time estimation of the intended motion and its motion phase for nine types of daily human lower limb movements, such as sit down, stand up, and so on. The proposed method consists of two estimators: the intended motion estimator and the motion phase estimator. Each estimator, based on the conditions, is accompanied by multiple switched ANNs. For intended motion estimation, both a standard ANN and an early estimation ANN are provided. The early estimation ANN performs its function by taking changes into account. For phase estimation, ANNs were prepared for each movement and damping neurons were applied to all of them. Experimental results show that the proposed method is effective in simultaneously estimating the intended motion of the lower limb and its phase. Furthermore, it is confirmed that the proposed method can be applicable even if the intended motion is changed in the middle of the motion. For future studies, it is suggested to incorporate actual elderly individuals or persons with disabilities into the experiments, rather than relying on simulated elderly scenarios, in order to enhance the applicability and reliability of the findings.

REFERENCES

[1] A. B. Zoss, H. Kazerooni, and A. Chu, "Biomechanical design of the Berkeley Lower Extremity Exoskeleton (BLEEX)," IEEE/ASME Transactions on Mechatronics, vol. 11, no. 2, pp. 128–138, 2006, doi: 10.1109/TMECH.2006.871087.

[2] H. Kawamoto and Y. Sankai, "Power Assist System HAL-3 for Gait Disorder Person," Lecture Notes in Computer Science (including subseries Lecture Notes in Artificial Intelligence and Lecture Notes in Bioinformatics), vol. 2398, pp. 196–203, 2002, doi: 10.1007/3-540-45491-8_43.

[3] K. Kiguchi and Y. Yokomine, "Perception-Assist with a Lower-Limb Power-Assist Robot for Sitting Motion," in Proc. of 2015 IEEE Int. Conf. on Systems, Man, and Cybernetics, pp. 2390–2394, 2016, doi: 10.1109/SMC.2015.418.

[4] M. Takeda, K. Sato, Y. Hirata, T. Katayama, Y. Mizuta, and A. Koujina, "Standing, Walking, and Sitting Support Robot Based on User State Estimation Using a Small Number of Sensors," IEEE Access, vol. 9, pp. 152677–152687, 2021, doi: 10.1109/ACCESS.2021.3127275.

[5] T. Mukai et al., "Development of a nursing-care assistant robot RIBA that can lift a human in its arms," in Proc. of 2010 IEEE/RSJ Int. Conf. on Intelligent Robots and Systems, pp. 5996–6001, 2010, doi: 10.1109/IROS.2010.5651735.

[6] M. Baccouche, F. Mamalet, C. Wolf, C. Garcia, and A. Baskurt, "Sequential Deep Learning for Human Action Recognition," in Human Behavior Understanding, pp. 29–39, 2011.

[7] P. Wang, W. Li, P. Ogunbona, J. Wan, and S. Escalera, "RGB-D-based human motion recognition with deep learning: A survey," Computer Vision and Image Understanding, vol. 171, pp. 118–139, 2018, doi: 10.1016/j.cviu.2018.04.007.

[8] J. Beil, I. Ehrenberger, C. Scherer, C. Mandery, and T. Asfour, "Human Motion Classification Based on Multi-Modal Sensor Data for Lower Limb Exoskeletons," in Proc. of 2018 IEEE Int. Conf. on Intelligent Robots and Systems, pp. 5431–5436, 2018, doi: 10.1109/IROS.2018.8594110.

[9] H. A. Varol, F. Sup, and M. Goldfarb, "Multiclass real-time intent recognition of a powered lower limb prosthesis," IEEE Trans Biomed Eng, vol. 57, no. 3, pp. 542–551, 2009, doi: 10.1109/TBME.2009.2034734.

[10] X. Shi, P. Qin, J. Zhu, M. Zhai, and W. Shi, "Feature Extraction and Classification of Lower Limb Motion Based on sEMG Signals," IEEE Access, vol. 8, pp. 132882–132892, 2020, doi: 10.1109/ACCESS.2020.3008901.

[11] K. Kiguchi and Y. Hayashi, "An EMG-based control for an upper-limb power-assist exoskeleton robot," IEEE Trans on Systems, Man, and Cybernetics, Part B: Cybernetics, vol. 42, no. 4, pp. 1064–1071, 2012, doi: 10.1109/TSMCB.2012.2185843.

[12] J. Ryu, B. H. Lee, and D. H. Kim, "sEMG signal-based lower limb human motion detection using a top and slope feature extraction algorithm," IEEE Signal Process Lett, vol. 24, no. 7, pp. 929–932, 2016, doi: 10.1109/LSP.2016.2636320.

[13] T. C. Bulea, S. Prasad, A. Kilicarslan, and J. L. Contreras-Vidal, "Sitting and standing intention can be decoded from scalp EEG recorded prior to movement execution," Front Neurosci, vol. 8, Art. no. 376, 2014, doi: 10.3389/fnins.2014.00376.

[14] K. Hayashida, S. Nishikawa, and K. Kiguchi, "Estimation of human intended motion and its phase for human-assist systems," in Proc. of 2022 IEEE Int. Conf. on Systems, Man and Cybernetics, pp. 1531–1536, 2022, doi: 10.1109/SMC53654.2022.9945330.

[15] K. Kiguchi and T. Fukuda, "Neural network controllers for robot manipulators application of damping neurons," Advanced Robotics, vol. 12, no. 3, pp. 191–208, 1997, doi: 10.1163/156855398X00145

Examining Postural Responses to Perturbations in 3D: A Pilot Study

Rhet O. Hailey *Student Member, IEEE* and Chad G. Rose *Member, IEEE*

***Abstract*— Affecting muscle spasticity, strength, and coordination, stroke results in alterations to muscle control and ability to compensate from unexpected perturbations. Post-stroke, upper extremity movements are heavily modified from perturbations, which increase the difficulty of activities of daily living (ADLs). Postural responses from upper extremity perturbations in healthy and stroke populations have been examined in movements constrained to 2D planar motion, and may provide insight as an assessment tool to help inform therapists to better structure rehabilitation training regimens towards individualized health care for improved long-term outcomes. However, implications on constraining motion in the horizontal plane are not clear and may reduce the generalizability of the findings to the movement through unconstrained 3D space necessary for ADLs. In this paper, we explore the effects of joint perturbations on the elbow and shoulder in unconstrained, gravity-compensated position holding tasks. We present a metric-diverse, dynamic task framework building upon previous 2D experiments designed to better assess rehabilitative efforts in movement trajectories with applied gravity compensation in three dimensional space aimed towards the generalizability of 3D motion. Results suggest that motion of multi-DoF joints display varied movement qualities in 3D space with robotic gravity compensation when compared to constrained planar movements.**

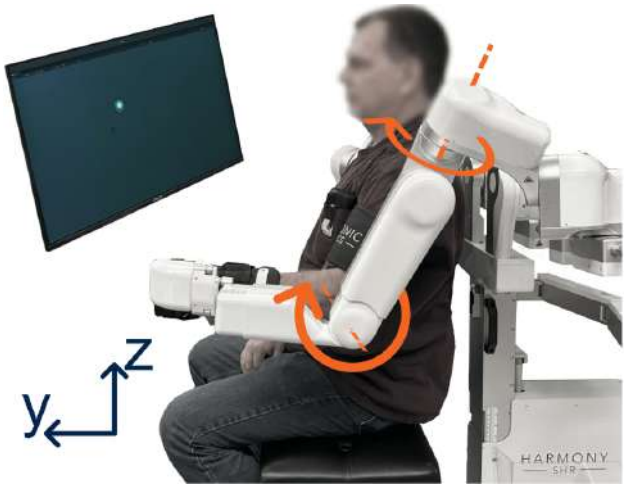


Fig. 1. The Harmony exoskeleton, a bimanual upper body exoskeleton with joint level impedance control, applies a model-based gravity compensation torque to participants to replace planar constraints on movement and enable analysis of unconstrained, 3D postural responses to joint torque perturbations in shoulder and elbow rotation. Task visual feedback of target position of the end-effector is shown on screen.

I. INTRODUCTION

Over the last 30 years, stroke incidents have increased by 70%, which can create long term motor and proprioceptive impairments leading to physical, mental, and cognitive decline [1]. In recent years, robot-assisted therapy methods have been shown as a promising avenue in combination with traditional rehabilitation therapies [2], [3]. Exoskeletons enable high resolution data acquisition for increased assessment metrics to improve robotics, control, and rehabilitative research. Robotic exoskeletons geared towards stroke rehabilitation use multiple control strategies to provide assistance to the wearer. Most common control strategies aim to assist the user to uncover neural pathways for the re-learning of a new subset of movement patterns such as gravity compensation, assist-as-needed or other control methods [4]–[7]. Upper extremity exoskeletons, such as the Harmony Exoskeleton (Fig. 1) can be used for task-based interventions with high levels of repetition to mimic the repeatability of locomotion tasks similar to lower extremity gait mechanics.

Given that many lower-extremity movements are centered around walking locomotion under different loading conditions, any unknown disturbances in locomotion can lead to trips or fall episodes that can lead to increased complications especially in an impaired population. During gait rehabilitation, a common therapy method is to emulate trip episodes in a safe environment to train kinematic compensation tactics and response [8], [9]. Through a mechanical perturbance in gait biomechanics, bipedal movements are analyzed to assess rehabilitative improvements post-stroke via a double treadmill with muscle usage, kinetic and kinematic responses, and movement quality.

With most upper-extremity trajectories being acyclic and moving in free space without the loading body weight and maintaining being upright, task compensation and improvement creates added difficulties to observe rehabilitative improvements. Without the cyclical loading of bipedal locomotion, upper-extremity recovery and rehabilitation has not fully utilized perturbance response for movement recovery and improvement. From stroke, damage to the cortical regions of the brain results in erratic motions with inappropriate muscle coordination patterns [1], [10]. In addition to kinematic measures of movement quality on reaching or pointing movements (e.g., [11], [12]) where the robot is transparent, motor function assessment modalities have been proposed where the robot applies torque perturbations to elicit response movements [13]–[15] with other works examining the role of perturbations at measuring proprioceptive function [16]. Bourke et al. demonstrated the use of joint perturbations

*This work was supported by NSF Grant 2230971 and the Samuel Ginn College of Engineering at Auburn University. All authors are in the Wearable and Bio-Robotics Lab, Department of Mechanical Engineering, Auburn University, Auburn, AL 36849. rhet.hailey@auburn.edu

to assess stroke in planar tasks in an acute stroke population [17]. This study was restricted to a planar task space and a subacute stroke population with a focus on the correlation between assessment modalities. Planar restraints may impact the interpretation of movement results and the generalizability to ADLs. Testing postural joint perturbations in three dimensions may expose new insight into into human movement and compensation.

In this paper, we examine the impact of removing the planar constraint on this motor function assessment. Specifically, we examined the motion in the directions perpendicular to the plane of perturbation, and present the results for a healthy cohort and a single participant with chronic stroke. Section II introduces the experimental methods and metrics. The results presented in Section III are discussed in Section IV, along with the limitations of the study and direction for future work before concluding in Section V.

II. Methods

A reaching perturbance assessment framework has been designed to assess kinematic compensation modalities correcting for unknown task disturbances in patients with chronic-stroke in unconstrained free space. This assessment framework is possible through the use of the Harmony Exoskeleton and its three-dimensional gravity compensation abilities to remove the wearer's arm-load weight [4]. Outlined in Fig. 2, this framework provides useful insight to the differences between constrained, planar tasks and movement in free-space [17].

A. Experimental Setup

The perturbation experimental assessment was performed using the Harmony exoskeleton, a bi-manual upper-extremity exoskeleton. Seen in Fig. 1, the Harmony exoskeleton promotes proper scapulohumeral rhythm focused on stroke rehabilitation through series elastic actuators [18], [19]. The 14-degree of freedom (DoF) exoskeleton allows for free movement through three dimensional space that may be obfuscated by arm weight via the added robotic gravity compensation.

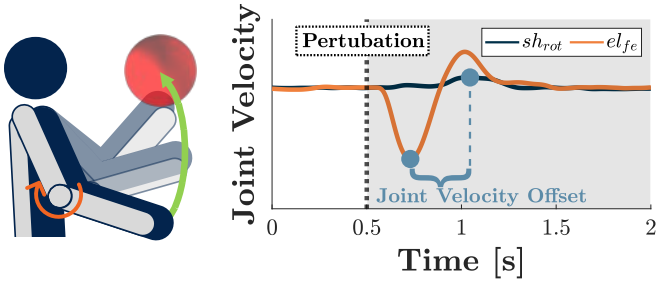


Fig. 2. Exemplary graphic of movement task wearing the Harmony Exoskeleton in unconstrained, gravity supported 3D space for an elbow perturbation. Participants were instructed to maintain end-effector position in the target location (sphere) and were perturbed by a joint torque at random intervals. The plot on the right shows the joint velocity of shoulder internal/external rotation (blue) and elbow flexion/extension (orange). The black line indicates perturbation onset while the two highlighted points show the peak joint velocity, with the time difference between the two resulting in the joint velocity offset time.

In this assessment, user arm weights were calculated and fine tuned during each session. All participants were within 5-95% of normal human sizes to fit inside the Harmony exoskeleton. Participants were tasked with maintaining hand position at a target goal held in front of them with a radius of 1 cm. Visual feedback of hand end-effector point position was shown in computer simulation using Unity-3D where users were given a green light within the target bounds via an isometric viewpoint of the target goal. During this assessment, joint perturbations were applied at the shoulder for internal-external rotation at ± 2 Nm and ± 1 Nm at the elbow for flexion-extension and is shown in a diagram in Fig. 2. As per the joints laid in out Kim 2017, these constant torques were applied in the Harmony Exoskeleton at J4 for shoulder internal-external rotation and J6 for elbow flexion-extension [19]. Perturbation order was decided randomly per each trial for a total of 9 blocks of 8 perturbations, which allowed for 2 identical perturbations per each block set. Prior to each joint torque, a delay of 1.75-2.25 seconds occurred before a constant torque was applied for 3 seconds followed by a 5 seconds wait period before the next perturbation. Prior to assessment, participants were given the opportunity to interact with the visual feedback simulation and an individual perturbation block.

B. Data Acquisition & Statistical Analysis

All data was recorded directly on board the Harmony Exoskeleton at 200 Hz for joint angles, joint torques, and end-effector position. During post-processing, all differentiated data was filtered via a 4^{th} order Butterworth low pass filter with a 6 Hz cutoff frequency [20]. All movements were segmented at perturbation onset for the entire 3 seconds. Metric data was tested for normality via the Shapiro-Wilk test. Following, a Wilcoxon signed rank one-sided test between healthy and impaired populations was used to evaluate the assessment metrics used in this 3D perturbation task [21]. Resultant assessment metrics were considered significant with a $p-\text{value} < \alpha = 0.05$.

C. Performance Metrics

Following the guidelines set out by Bourke et. al, the following task assessment metrics were quantified: Posture speed ($|\text{cm/s}|$), acceleration time (s), return time (s), endpoint error (cm), maximum displacement error (cm), and joint velocity offset (s) [17]. Posture speed was quantified as the 95^{th} percentile of the median hand speed for the first 0.5s before perturbation onset, which indicated difficulty to maintain target position. Acceleration time is quantified as the peak velocity in hand speed post-perturbation onset. Return time was the time taken to return back to the target volume if the hand position ever left the target range. Endpoint error was the mean error after returning to the target volume. Joint velocity offset was the difference between peak elbow and shoulder rotation joint velocities where a positive value indicates the elbow joint moving first. Fig. 2 shows an example trajectory highlighting the joint velocity offset time.

D. Participant Demographics

Ten healthy participants and one impaired participant were recruited as volunteers to participate in this preliminary assessment study. All demographic information was self reported and is shown below in Table I. Target impaired population met the following criteria: (1) post-stroke $>$ 6 months with chronic symptoms of impairment (2) age between 18 and 65, (3) body dimensions within the 5-95% range of mean sizes [21]. The impaired participant (S1) suffered from an ischemic stroke in the occipital lobe in the right hemisphere resulting in left side sensorimotor impairments. S1 is 25 months post onset and requires assistance in ADLs with a modified Rankin Score (mRS) of 3 and a Fugl-Meyer Upper Extremity (FM-UE) score of 36. Ten participants are right hand dominant and one left hand dominant. The impaired participant used their affected, left hand for the study. This protocol was approved by the Auburn University IRB protocol #22-559 MR 2301.

TABLE I
PARTICIPANT DEMOGRAPHICS

	Age (yr)	Weight (lb.)	(M/F)	FM-UE	mRS
Healthy	27.5 ± 9.1	170.5 ± 43.3	(9/2)	-	-
Stroke	54	250	(M)	36	3

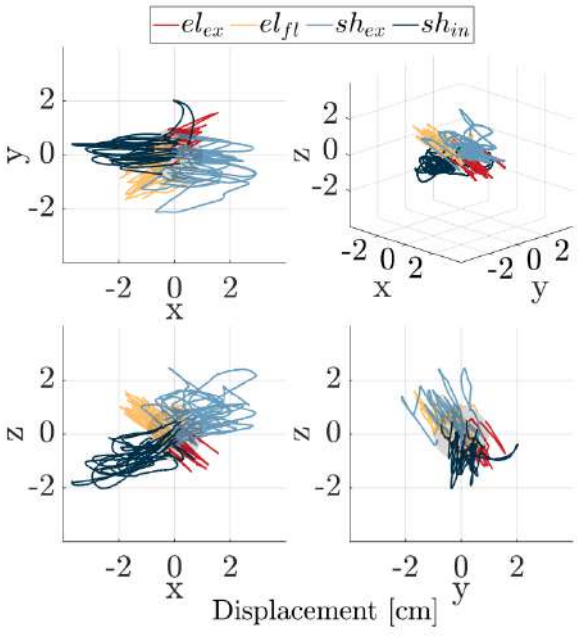


Fig. 3. Shown above is healthy example of individual reaching motions from perturbation onset until target return in centimeters. The top left has a top-down view of the transverse plane (X-Y) with an isometric view on the top right. The bottom graphs show planar representation of the Z-deviation of these reaching trajectories of the frontal plane (X-Z) and the sagittal plane (Y-Z) respectively. Hand trajectories are color coded by perturbed joint. Trajectories that did not escape the target volume were excluded.

III. RESULTS

A set of performance were outlined previously to assess upper-extremity movements in unconstrained 3D space. Fig. 3 shows the individual hand trajectories for an entire trial of a healthy participant. Multiple planar views are given to give better viewpoint to understand the underlying tasks dynamics. It is evident from the plots that the perturbations at the elbow encouraged near-parallel movements as the trajectories are in line at every viewpoint. In contrast, shoulder perturbed movements generated more non-parallel trajectories when returning to the target volume. Given the unconstrained nature of the upper extremities, shoulder flexion and extension and the high DoF in the shoulder joint, it is a natural response that the shoulder shows increased trajectory curvature in a reaction to a 1DoF perturbation.

In response to mechanical perturbations, the means and standard deviations of the healthy participants population and S1 are shown in Table II. When comparing the mean results of S1 to healthy participants, all values were shown to be statistically significant with all p-values $< \alpha = 0.05$. Most significantly, the acceleration time was much higher in the S1 with a mean difference of 0.4s. The return time of hand to the target also was increased in S1 by 0.4s. Joint velocity offset was the most significantly different showing that the elbow joint angle peak velocity occurred after the shoulder rotation peak velocity. Following the expected results for this assessment task, S1 performed worse and took more time all with much higher deviation throughout the task.

Compared to a healthy participant, S1 showed less variance in repeated movements. Fig. 4 shows the difference in individuals trajectories and the variance plots between trials for a shoulder internal perturbation. It is important to note in Fig. 4 that S1 showed slower hand speeds and joint velocities than the healthy example, H1, which remained consistent across all healthy participants. After perturbation onset, the H1 showed intent to reduce z-error without overshooting the target while S1 consistently overshot the z-error after each perturbation, taking longer to return to the target volume. Interestingly, it can be seen that the joint velocity of shoulder flexion and extension was activated as compensation without direct influence on the joint space.

IV. DISCUSSION

These results provide healthy movement quality baseline, which can be used when establishing the motor function of impaired populations, and lead towards development of individualized assessment profiles.

A. Unconstrained 3D Movements

Compared with planar movements, 3D trajectories move in an unconstrained manner, with much more potential for deviation and lack of precise repeatability. Free space allows for less generalizability in movement assessment, even more obscured with the added spasticity of post-stroke patients.

Given the expected outcome, S1 performed statistically significantly different in all assessment metrics except for endpoint error, which was statistically insignificant. Since endpoint error was the mean error after returning to the target volume, it is expected that there be little to no

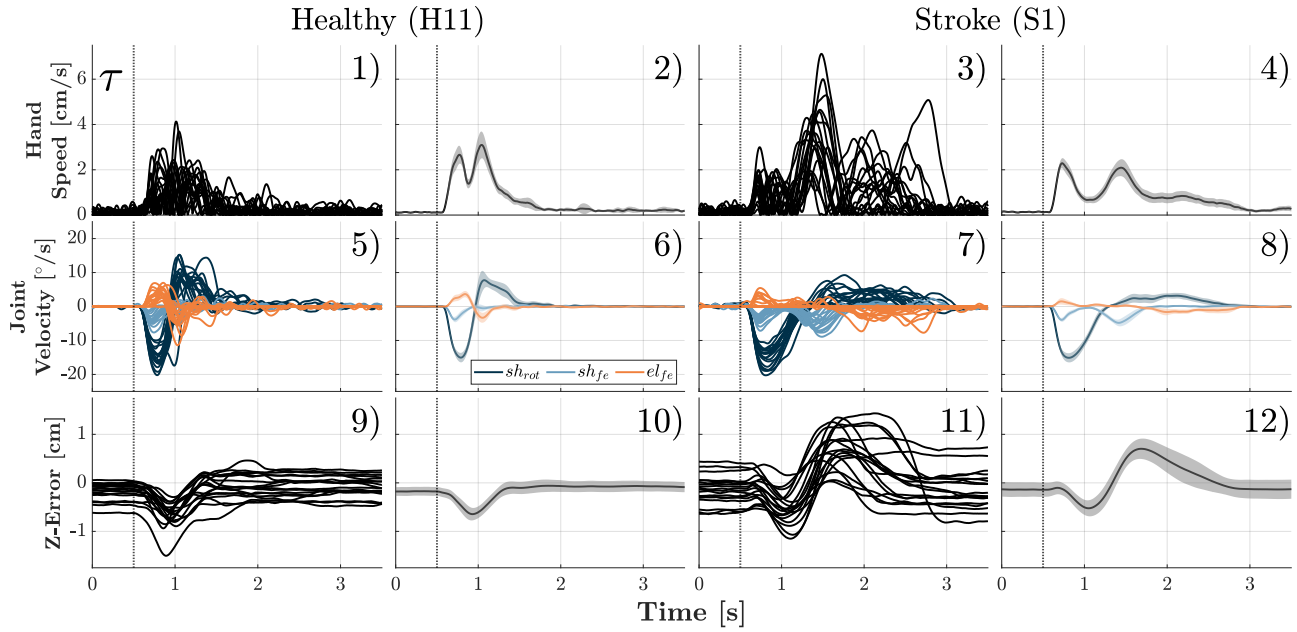


Fig. 4. Healthy movements from a single, age-matched participant, H11, (left columns) and S1 (right columns) for hand speed (1-4), joint velocity (5-8), and height deviation (9-12) from perturbation onset (gray vertical line) for the entire 3 seconds of applied perturbation torque. This data is shown from a shoulder internal rotation perturbation. For each set of columns, the left most column represents individual movements while the right most column showcases movement mean and variance.

difference as the data implies. As well, the mean return time is skewed since all individual reaches that did not leave the target volume were excluded from this metric. Due to the faster, more erratic movements, S1 showed far less controlled movement capabilities in the affected arm. S1 had much higher deviations in performance from the increased spasticity from chronic stroke. S1 showed increase in posture speed, which indicates difficulty of maintaining hand position inside the target volume. However, S1 was always able to return back to the target. Instructed to hold the hand out in front of them, all healthy participants held their hands at breast height, but S1 did not have the range of motion to achieve this same target position, and thus gravitated back towards the same position from increased stiffness and lack of volitional control.

From Fig. 5, S1's assessment metrics may be seen overlaid healthy participants for all perturbations types. For the healthy participants, all movements that did not leave the target volume were not assessed and withheld from the metric data to reject falsely positive data points, which slightly skews the data for the return time and endpoint error. Even in unconstrained space with added gravity compensation, volitional movements must still overcome some added inertia that the robotic exoskeleton provides in order to maintain the impedance controlled gravitational assistance.

Planar motions of elbow compared to the spatially curved trajectories of shoulder movements suggests that the added DoF at the shoulder reduce repeatability of exact movements and make assessment of shoulder movement far more difficult in 3D space. Focusing on flexion, extension, and

TABLE II
COMPARISON OF ASSESSMENT METRICS FOR HEALTHY (H) AND STROKE (S1) PARTICIPANTS

	H	S	p
Posture Speed $[\frac{cm}{s}]$	0.59 ± 0.31	0.77 ± 0.26	$2.5e-06$
Accel. Time $[s]$	0.46 ± 0.33	0.90 ± 0.57	$2.7e-10$
Return Time $[s]$	0.87 ± 0.48	1.37 ± 0.57	$4.4e-13$
Joint ω Offset [s]	0.13 ± 0.41	0.48 ± 0.56	$9.3e-06$
Endpoint Error $[cm]$	0.63 ± 0.19	0.60 ± 0.20	$4.1e-01$
Max. Disp. $[cm]$	1.87 ± 0.54	2.48 ± 1.15	$2.2e-04$
Z-Deviation $[cm]$	0.06 ± 0.33	0.13 ± 0.41	$2.2e-04$

internal and external rotation, shoulder biomechanics in one plane do not react in the same plane in both healthy and impaired participants to postural perturbations. Shown in Fig. 3, shoulder flexion and extension perturbations result in spatially curved trajectories in unconstrained space.

B. Limitations

The presented study had a few limitations in the experiment design which may reduce the generalizability of the findings. One limitation in perturbation-based assessments is the difficulty in separating volitional control responses from those potentially generated through increasing joint impedance through co-contraction. In our experiment, joint torques were relatively low (1 and 2 Nm) and applied smoothly via impedance control from the Harmony Exoskeleton.

Another concern is that the joint axes, and therefore the joint torques applied by the exoskeleton may not exactly

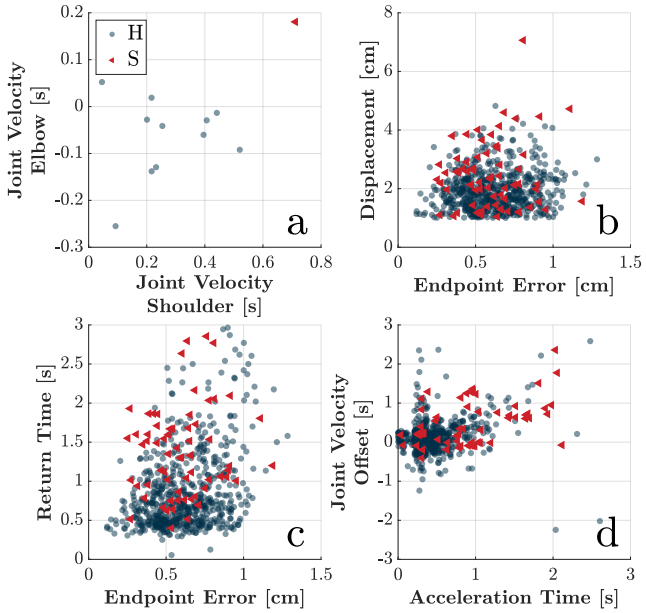


Fig. 5. Participant task performance of healthy participants compared to S1. In these plots, healthy data is shown with blue points while S1 data is shown shown as red triangles. a.) mean joint velocity offset is shown compared between the perturbed joints. Positive values in time indicate that the elbow peak velocity occurred later than the shoulder peak joint velocity. b.) maximum displacement vs. endpoint error c.) return time vs. endpoint error d.) joint velocity offset vs. deceleration time.

mirror the joint axes of the wearer. However, prior work with the Harmony Exoskeleton has shown high quality mapping between robot and human joints when donned correctly [22]–[24] suggesting that misalignments can be minimized, and the consideration of Cartesian space or otherwise normalized metrics (e.g., hand speed) are robust to misalignments.

Next, the target position was ambiguously suggested to be a comfortable position with the elbow, shoulder flexion, shoulder abduction and shoulder flexion. As such, this user-selected comfortable position may have resulted in slightly different orientations between participants, resulting in changes to passive joint properties or other biomechanical features. However, it is reasonable to assume that the volitional control examined in this study was not significantly impacted. As mentioned earlier, this may have resulted in a type 1 error with S1 have significantly better endpoint error given that the S1 had a reduced range of motion and control of the affected hand. This may have resulted in a decrease of positional error with a lack of overall movement and compensation abilities.

Next, the healthy cohort was not age-matched to the single chronic stroke participant, potentially reducing the validity of the direct comparison of trajectories. Further, the use of a single impaired participant reduces the potential generalizability of the findings. However, even in this preliminary pilot study, the results motivate further examination and comparison of the traditionally explored 2D planar arm movements with unconstrained, 3D movements.

While the model-based gravity compensation approach implemented in this study [4], [19] is feedforward, which can introduce errors in the amount of gravity compensation as a function of position, the relatively small workspace used in this study should prevent potential inaccuracies in the model from significantly impacting the results.

Most healthy participants raised concern about the visual feedback simulation in regards to the depth perception of the hand position and the target size and how this effects the assessment task. Participants also had visual feedback of the robot and hand in addition to the computer simulation for depth. Future work could address this limitation by adding a second view of the task in the transverse plane, or by using an immersive display (i.e., VR headset) to more effectively render depth.

C. Future Work

Future studies look to increase participant population. As one impaired participant is not indicative of an entire population, results suggest further investigation into three dimensional postural perturbations. Alongside current metric assessments, a unit force will be applied at the end-effector to investigate postural responses to complex upper-extremity disturbances. This will reduce complications that may arise from joint misalignment with the activation of multiple joints at once to study multi-DoF curvature.

An additional consideration in this study was the use of gravity compensation to replace the planar constraint of prior works. However, it may be the case that gravity compensation may reveal improved motor function obscured by the strength required to perform unassisted movements [4], [25]. Future studies should seek to understand the potential interactions between gravity compensation, sensorimotor impairment, and the metrics presented here.

Ultimately, this framework could identify movement quality shifts from the assessment to be used in real time in accordance with robotic rehabilitation. Given user postural responses to perturbations, an online agent could help clinicians in the assessment and suggest rehabilitative exercises in 3D space.

V. Conclusion

Robotic devices such as exoskeletons have unique interaction and measurement capabilities towards understanding, rehabilitating, and assessing sensorimotor function. Prior studies of the sensorimotor responses to mechanical perturbations have focused on planar upper extremity motion. However, in this work we showed that motions of multi-DoF joints such as the shoulder display different movement qualities than single DoF joints when the planar movement constraint is replaced with gravity compensation (of robot and human arm). These 3D perturbation metrics provide insight into movement quality in pre-defined tasks and could provide objective feedback in real time in a standardized task design for potential human in the loop solutions. These pilot results from one impaired participant suggest that future study is needed to explore the implications and correlation

of our findings on motor function and assessments, as well as sensory assessments both with and without gravity compensation in 3D space.

REFERENCES

[1] C. W. Tsao, A. W. Aday, Z. I. Almarzooq *et al.*, "Heart disease and stroke statistics—2023 update: a report from the american heart association," *Circulation*, vol. 147, no. 8, pp. e93–e621, 2023.

[2] J. W. Krakauer, T. Kitago, J. Goldsmith *et al.*, "Comparing a novel neuroanimation experience to conventional therapy for high-dose intensive upper-limb training in subacute stroke: The SMARTS2 randomized trial," *Neurorehabilitation and Neural Repair*, vol. 35, no. 5, pp. 393–405, 2021.

[3] D. J. Reinkensmeyer, "Breaking Proportional Recovery After Stroke," *Neurorehab. and Neural Repair*, vol. 33, no. 11, pp. 875–969, 2019.

[4] R. Hailey, A. C. De Oliveira, K. Ghonasgi, B. Whitford, R. K. Lee, C. G. Rose, and A. D. Deshpande, "Impact of Gravity Compensation on Upper Extremity Movements in Harmony Exoskeleton," in *International Conference on Rehabilitation Robotics (ICORR)*. IEEE, 2022.

[5] Z. A. Wright, E. Lazzaro, K. O. Thielbar, J. L. Patton, and F. C. Huang, "Robot Training With Vector Fields Based on Stroke Survivors' Individual Movement Statistics," *IEEE Trans. on Neural Sys. and Rehab. Eng.*, vol. 26, no. 2, pp. 307–323, 2017.

[6] K. Ghonasgi, R. Mirsky, N. Bhargava, A. M. Haith, P. Stone, and A. D. Deshpande, "Kinematic coordinations capture learning during human–exoskeleton interaction," *Scientific reports*, vol. 13, no. 1, p. 10322, 2023.

[7] I. Scott, C. G. Rose, and A. D. Deshpande, "A novel velocity-based controller to avoid synergistic movement after stroke," in *2024 10th IEEE RAS/EMBS International Conference for Biomedical Robotics and Biomechatronics (BioRob)*. IEEE, 2024, pp. 1491–1497.

[8] L. M. Nashner, "Adaptation of human movement to altered environments," *Trends in Neurosciences*, vol. 5, pp. 358–361, 1982.

[9] M. Qiao and D. L. Jindrich, "Compensations during unsteady locomotion," *Integrative and Comparative Biology*, vol. 54, no. 6, pp. 1109–1121, 06 2014.

[10] P. Raghavan, "Upper limb motor impairment after stroke," *Physical Medicine and Rehabilitation Clinics*, vol. 26, no. 4, pp. 599–610, 2015.

[11] O. Celik, M. K. O'Malley, C. Boake, H. S. Levin, N. Yozbatiran, and T. A. Reistetter, "Normalized movement quality measures for therapeutic robots strongly correlate with clinical motor impairment measures," *IEEE Transactions on Neural Systems and Rehabilitation Engineering*, vol. 18, no. 4, pp. 433–444, 2010.

[12] S. Balasubramanian, A. Melendez-Calderon, A. Roby-Brami, and E. Burdet, "On the analysis of movement smoothness," *Journal of neuroengineering and rehabilitation*, vol. 12, pp. 1–11, 2015.

[13] S. H. Scott and K. Park, "Method and apparatus for assessing sensorimotor performance," Jan. 10 2023, US Patent 11,547,325.

[14] K. Park, B. R. Ritsma, S. P. Dukelow, and S. H. Scott, "A robot-based interception task to quantify upper limb impairments in proprioceptive and visual feedback after stroke," *Journal of NeuroEngineering and Rehabilitation*, vol. 20, no. 1, p. 137, 2023.

[15] M. Zbytniewska, M. Siegenthaler, C. M. Kanzler, J. Hermsdörfer, R. Gassert, and O. Lambercy, "Design and preliminary evaluation of a perturbation-based robot-assisted assessment of hand sensorimotor impairments," in *2020 8th IEEE RAS/EMBS International Conference for Biomedical Robotics and Biomechatronics (BioRob)*. IEEE, 2020, pp. 721–726.

[16] M. D. Rinderknecht, O. Lambercy, V. Raible, I. Büsching, A. Sehle, J. Liepert, and R. Gassert, "Reliability, validity, and clinical feasibility of a rapid and objective assessment of post-stroke deficits in hand proprioception," *Journal of neuroengineering and rehabilitation*, vol. 15, pp. 1–15, 2018.

[17] T. C. Bourke, A. M. Coderre, S. D. Bagg, S. P. Dukelow, K. E. Norman, and S. H. Scott, "Impaired corrective responses to postural perturbations of the arm in individuals with subacute stroke," *J. of NeuroEngineering and Rehabilitation*, vol. 12, no. 1, p. 7, Jan. 2015.

[18] B. Kim and A. D. Deshpande, "Controls for the shoulder mechanism of an upper-body exoskeleton for promoting scapulohumeral rhythm," in *2015 IEEE International Conference on Rehabilitation Robotics (ICORR)*. IEEE, 2015, pp. 538–542.

[19] ——, "An upper-body rehabilitation exoskeleton harmony with an anatomical shoulder mechanism: Design, modeling, control, and performance evaluation," *The International Journal of Robotics Research*, vol. 36, no. 4, pp. 414–435, 2017.

[20] S. D. Uhlrich, A. Falisse, Ł. Kidziński, J. Muccini, M. Ko, A. S. Chaudhari, J. L. Hicks, and S. L. Delp, "Opencap: Human movement dynamics from smartphone videos," *PLoS computational biology*, vol. 19, no. 10, p. e1011462, 2023.

[21] A. C. de Oliveira, C. G. Rose, K. Warburton, E. M. Ogden, B. Whitford, R. K. Lee, and A. D. Deshpande, "Exploring the capabilities of harmony for upper-limb stroke therapy," in *2019 IEEE 16th International Conference on Rehabilitation Robotics (ICORR)*. IEEE, 2019, pp. 637–643.

[22] A. C. de Oliveira, K. Warburton, Y. Yun, E. M. Ogden, J. Sulzer, and A. D. Deshpande, "Arm kinematics estimation with the harmony exoskeleton," in *2017 International Symposium on Wearable Robotics and Rehabilitation (WeRob)*. IEEE, 2017, pp. 1–2.

[23] A. C. De Oliveira and A. D. Deshpande, "Assessment of upper-body movement quality in the cartesian-space is feasible in the harmony exoskeleton," *IEEE Transactions on Human-Machine Systems*, vol. 53, no. 6, pp. 985–995, 2023.

[24] A. C. De Oliveira, J. S. Sulzer, and A. D. Deshpande, "Assessment of Upper-Extremity Joint Angles Using Harmony Exoskeleton," *IEEE Transactions on Neural Systems and Rehabilitation Engineering*, vol. 29, pp. 916–925, 2021, publisher: Institute of Electrical and Electronics Engineers Inc.

[25] T. Krabben, G. B. Prange, B. I. Molier, A. H. Stienen, M. J. Jannink, J. H. Buurke, and J. S. Rietman, "Influence of gravity compensation training on synergistic movement patterns of the upper extremity after stroke, a pilot study," *Journal of neuroengineering and rehabilitation*, vol. 9, pp. 1–12, 2012.

Reimagining Assistive Walkers: An Exploration of Challenges and Preferences in Older Adults

Victory A. Aruona[1], Sergio D. Sierra M.[1], Nigel Harris[1], Marcela Munera[1], Carlos A. Cifuentes[1]

***Abstract*— The well-being of older adults relies significantly on maintaining balance and mobility. As physical ability declines, older adults often accept the need for assistive devices. However, existing walkers frequently fail to consider user preferences, leading to perceptions of imposition and reduced acceptance. This research explores the challenges faced by older adults, caregivers, and healthcare professionals when using walkers, assesses their perceptions, and identifies their needs and preferences. A holistic approach was employed, using tailored perception questionnaires for older adults (24 participants), caregivers (30 participants), and healthcare professionals (27 participants), all of whom completed the survey. Over 50% of caregivers and healthcare professionals displayed good knowledge, positive attitudes, and effective practices regarding walkers. However, over 30% of participants perceived current designs as fall risks, citing the need for significant upper body strength, potentially affecting safety and movement. More than 50% highlighted the importance of incorporating fall detection, ergonomic designs, noise reduction, and walker ramps to better meet user needs and preferences.**

I. Introduction

Mobility is fundamental for performing essential tasks and actively participating in societal life, allowing older adults to live more independently [1]. In 2017, the global population over 60 years old was 962 million, and it is forecast to double again by 2050, reaching 2.1 billion [2]. With the rising life expectancy among older adults, more of them are facing mobility issues that may require assistance with daily tasks [3], [4].

Loss of physical mobility makes full participation in desired activities more complicated and could prevent social involvement [5]. The impact of limited mobility on mental health, the risk of falls, disability, hospitalization, and mortality rates cannot be understated, as indicated by studies [6]–[8]. Therefore, mobility plays a pivotal role in fostering independence, social engagement, and overall well-being as individuals age [9], [10].

Assistive technologies can enhance autonomy, safety, and quality of life of the ageing population [11]. Among these technologies, assistive walkers stand out for their potential to improve ambulation and promote physical activity [12]. For instance, walkers are used indoors by 22% and outdoors by 44% of older adults in the UK [13]. This category of devices includes canes, standard walkers, and wheeled walkers.

*This work was supported by the UKRI Medical Research Council [grant number MR/Y010620/1], EPSRC, and FARSCOPE CDT.

[1]All authors are with the Bristol Robotics Laboratory , University of the West of England, Bristol, UK. victory2.aruona@live.uwe.ac.uk, {sergio.sierramarin, nigel2.harris, marcela.munera, carlos.cifuentes}uwe.ac.uk

While mobility devices have been shown to boost independence, foster social participation, and improve the quality of life in older adults [14], the use of assistive walkers presents its own set of challenges. Despite some studies suggesting that walking aids may prevent falls in older individuals [15], the association remains poorly understood [16]. This is because walking aids can alter gait patterns by preventing normal arm swing, changing posture, decreasing gait speed, and increasing standing time [17]. Difficulty in navigating stairs, destabilizing biomechanical effects, upper limb pain, and an increased risk of falling are among the potential drawbacks [18], [19].

Moreover, assistive walkers frequently fail to satisfy the needs of older adults, and this misalignment between their needs and the adoption of these technologies stymies their capacity to achieve independence [20]. For instance, canes and wheeled walkers may fall short in providing adequate support during essential sit-to-stand transfers that are crucial for daily activities [21]. Several studies have examined older adults' experiences and satisfaction with mobility aids. The study in [22] found high user satisfaction with rollators and manual wheelchairs. However, differences were noted in how users assessed the usefulness and characteristics of each device. The systematic review in [23] analysed 45 studies to assess the usability of rollators, focusing on aspects such as ease of use, comfort, and safety. Using a deductive approach, they found that while these factors were frequently discussed, areas like repairs, servicing, and durability received less attention. The study highlights the lack of dedicated research on rollators' usability and calls for future user-centred, participatory studies to improve satisfaction and evaluation in assistive mobility device design.

Thus, understanding the challenges faced by older adults using assistive walkers, analysing their perspectives, and examining the insights of healthcare professionals and caregivers are essential steps towards the development of more effective, user-centric solutions. This study explores the challenges encountered by older adults using assistive walkers to enhance gait activities. We aim to analyse older adults' perspectives on the features they desire in an ideal assistive walker, aligning future advancements with their unique requirements and preferences. Additionally, we explore the perspectives of healthcare professionals and caregivers, who possess valuable first-hand experience with the mobility difficulties faced by older adults. This approach aims to bridge the gap between existing assistive walker technologies and the evolving needs of the ageing population.

TABLE I
CHARACTERISTICS OF THE OLDER ADULTS

Participants	n = 24, 6 Male, 18 Female
Age Mean (SD)	88.67 (6.64) years
Weight Mean (SD)	75.98 (6.90) kg
Health conditions	
Vision Problems	79.0 %
Hearing problems	58.0 %
Mobility difficulty	92.0 %
Health conditions affecting mobility	
Arthritis	42.0 %
Osteoporosis	5.0 %
Parkinson disease	8.0 %
Paralysis	8.0 %
Knee and hip condition	42.0 %
Stroke	8.0 %

II. MATERIALS AND METHODS

This section outlines the perception questionnaires for older adults, healthcare professionals, and caregivers.

A. Demographics

Information about the older adults' demographics was recorded (See Table I). The information from healthcare professionals and caregivers, including job titles and experience, was included in the questionnaire.

B. Knowledge, Attitude, and Practice (KAP)

According to [24], the KAP standardized questionnaire measures a population's knowledge, attitudes, and practices, identifying the initial misconceptions, beliefs, and behaviours in relation to a specific health-related topic. This questionnaire also provides information on needs, issues, and barriers related to technology. The questionnaire aimed to gather information from health professionals and caregivers regarding their knowledge base, overall perception, and everyday activities using assistive walkers. Questions were phrased as statements and graded on a 5-point Likert scale ranging from -2 (strongly disagree) to 2 (strongly agree).

C. Closed-Ended Questions

The functionality and limitations of conventional assistive walkers (CAWs) were assessed using a series of statements that were developed following a literature review. A 5-point Likert scale was used. Questions aimed at assessing the walker's effectiveness, safety, comfort, stability, and support for daily activities, mobility, and transitions both indoors and outdoors. Questions also included perceptions of fall risk, navigation support, user-friendliness, complexity, movement limitations, and physical effort required.

D. Open-Ended Questions

The open-ended questions evaluated the features of CAWs that older adults consider necessary. These questions also collected suggestions, perceived drawbacks and benefits, ideas for improvement, and overall perceptions from caregivers and healthcare professionals. Questions assessed preferences, concerns, and ideal walker features. Moreover, questions inquired about perceptions of familiar walkers, emphasizing limitations faced and proposed enhancements.

E. Research setting and protocol

The study was conducted in two private residential care homes in south-west England, selected for their high number of older adults using assistive walkers and participants' cognitive abilities. Caregivers and physiotherapists with relevant experience were recruited from these homes, while additional caregivers and healthcare professionals were recruited from other facilities and institutions. All participants provided informed consent after reviewing the consent statement. They then submitted demographic information and completed the survey. Ethical approval was granted by the University of West of England's Ethics Committee.

F. Participant Recruitment

The study included older adults selected using non-random convenience sampling. Medical information regarding memory function was reviewed with the physiotherapist prior to interviews. Inclusion criteria were: (1) aged 75 or older, (2) living in residential or home care settings, (3) requiring mobility assistance and having visited a hospital for related issues, (4) relying on a walker for daily transportation, or (5) prescribed a walker. Exclusion criteria included: (1) inability to walk and (2) cognitive impairment.

The study also included physiotherapists, occupational therapists, and general practitioners with experience working with older adults, as well as caregivers providing support to individuals using assistive walkers. Inclusion criteria were: (1) providing care to older adults, (2) working in care homes, and (3) at least six months of experience in elderly care. Exclusion criteria included: (1) no experience attending to older adults.

G. Data Analysis

The study employed a mixed methods approach to explore participants' perceptions towards the use of CAWs among older adults. The primary focus was qualitative, aiming to capture the depth and richness of participants' experiences and preferences through open-ended questions. To complement the qualitative insights, a Likert scale was utilized to quantify the levels of agreement with specific statements related to assistive walkers. Responses were summarized by examining the percentage of agreement, neutrality, and disagreement, providing a comprehensive view of participants attitude and preference.

III. RESULTS

Data were collected from a total of 81 participants (24 older adults, 30 caregivers and 27 clinicians). The outcomes from the KAP survey, the closed-ended and the open-ended questions, are discussed as follows.

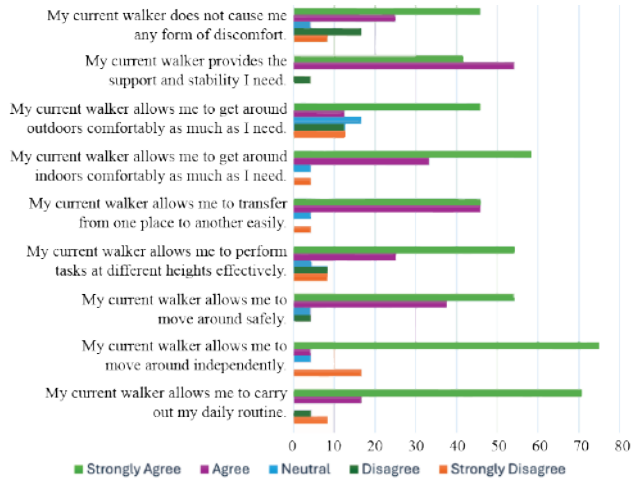


Fig. 1. Older adult's opinions on the functionalities of the assistive walkers

A. Older Adults

A total of 24 older adults took part in the study. Table I details their characteristics; most participants had a visual or hearing impairment, with arthritis and/or hip or knee problems affecting their mobility. Figure 1 presents older adults' opinions on the assistive walker's functionalities. Most older adults perceive their current walkers as effective tools for maintaining daily routines and ensuring independent mobility, with 88% and 96% respectively agreeing with these statements. However, opinions on specific aspects of walker use are more varied. While 79% feel safe using their walkers, concerns persist regarding stability and comfort, with 21% questioning safety and 25% experiencing discomfort. Walkers are generally considered effective for indoor use, as 91% of users report comfort within their homes. Outdoor usability is less favourable, with only 59% finding their walkers suitable for external environments. Additionally, while 79% agree that their walkers help in performing tasks at different heights, and 92% find them useful for easy transfers, there are still notable percentages of users who disagree.

B. Healthcare professionals and Caregivers

A total of 30 caregivers and 27 healthcare professionals took part in the study. Regarding work experience in elderly care, approximately 60% of caregivers had more than 2 years' experience and 78% of healthcare professionals had more than 2 years' experience. Regarding the number of older adults being cared for, 64% of caregivers cared for more than 10 older adults while 59% of clinicians attended to more than 10 older adults.

Figure 2, Figure 3 and Figure 4 present the level of agreement of healthcare professionals to the KAP questions. As expected, Figure 2 shows that health professionals have a high level of knowledge, with 50% and above agreement with the statements in this category, but with some uncertainty around safety precautions and prescribing. Figure 3 shows health professionals' attitudes, which are overwhelmingly positive, with 75% and above agreement with most statements in this category, reflecting a positive attitude to the

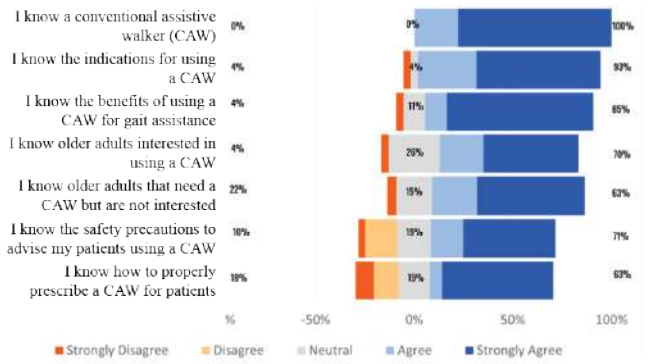


Fig. 2. Knowledge of healthcare professionals regarding the use of an assistive walker. Percentages show total disagreement, neutral and agreement.

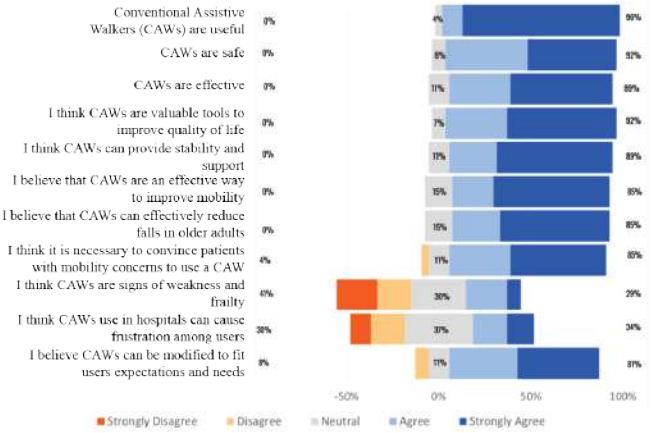


Fig. 3. Attitude of healthcare professionals regarding the use of an assistive walker. Percentages show total disagreement, neutral and agreement.

use of assistive walkers. However, there is 50% neutral agreement with statements "I think assistive walkers serve as a sign of weakness and frailty" and "I think CAWs used in hospital settings can cause frustration among users". Figure 4 explores practice, there is 50% and above agreement with statements in this category showing good practice by these respondents on the usage of assistive walkers. However, there is 50% neutral agreement with statements "I have a procedure for evaluating patients requiring a CAW", "I perform regular follow up on mobility improvements with patients who use a CAW", and "I have observed older adults are reluctant to use a CAW due to fear".

Figure 5 shows there is 50% and above agreement to the statements in knowledge, highlighting a strong foundational knowledge of caregivers regarding using an assistive walker. Figure 6 shows there is 100% agreement with most statements in attitude, reflecting a positive attitude to the use of assistive walkers. However, there was a 25% mixed perception with the statement "I think assistive walkers serve as a sign of weakness and frailty". Figure 7 shows 75% agreement with statements in this practice showing good practice by these respondents on the usage of assistive walkers. However, 50% of respondents were neutral on whether older adults avoid CAWs due to usage factors or design.

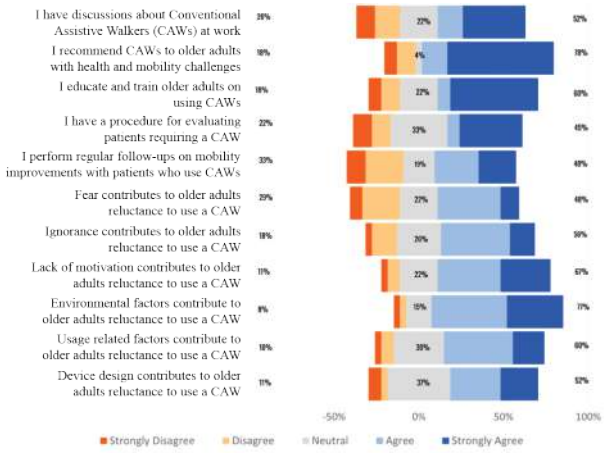


Fig. 4. Practice of healthcare professionals regarding the use of an assistive walker. Percentages show total disagreement, neutral and agreement.

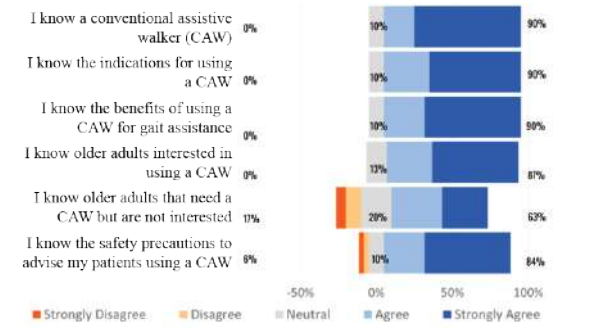


Fig. 5. Knowledge of caregivers regarding the use of an assistive walker. Percentages show total disagreement, neutral and agreement.

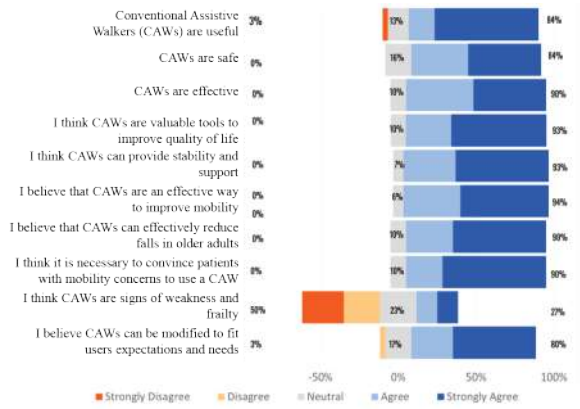


Fig. 6. Attitude of caregivers regarding the use of an assistive walker. Percentages show total disagreement, neutral and agreement.

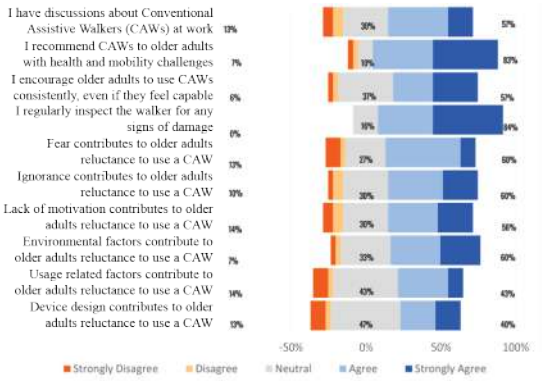


Fig. 7. Practice of caregivers regarding the use of an assistive walker. Percentages show total disagreement, neutral and agreement.

C. Limitations of assistive walkers

The analysis of perceptions revealed diverse concerns and satisfaction levels. While 55% of older adults feel safe using walkers, 37% of both older adults and caregivers, along with 33% of healthcare professionals, perceive walkers as fall risks due to stability issues. A major gap identified is the lack of navigation systems, highlighted by 96% of older adults, suggesting a need for technological enhancements. Usability is generally rated positively, with 80% of older adults, 60% of caregivers, and 59% of healthcare professionals finding walkers easy to use, though some complexity remains for 21% of older adults. Movement restrictions are less of a concern for older adults, but some caregivers and healthcare professionals disagree, indicating design adaptability needs. The physical effort required to use walkers is noted by 42% of older adults and 40% of caregivers, pointing to the need for ergonomic improvements to enhance safety and ease of use.

D. Perception of Older adults, Caregivers and Healthcare professionals towards the use of an assistive walker

The result shows consistent preference of assistive walkers across all groups. Common challenges included fear of falling, difficulty navigating tight spaces, and usage challenges relating to size, noise, and brakes. To mitigate this, more than 50% of each group recommended the need for innovative features such as navigation systems, ergonomic designs, and threshold ramps. Above 50% of caregivers and healthcare professionals also noted the need for additional safety and convenience features including alarm buttons, user-friendly brakes, and fall detection systems. Additionally, over 50% of healthcare professionals advised the inclusion of noise reduction features and enhanced device designs[1].

IV. Discussion

Most caregivers and healthcare professionals demonstrated a strong understanding, positive outlook, and proficient usage of these walkers, emphasizing their significance for older adults. The respondent groups expressed concerns about the frequent falling incidents related to the walker usage, with older adults sharing their experiences of falling while transferring and navigating with the walker. Older adults and caregivers blamed walker deficiencies, such as wheel issues and poor brakes. However, healthcare professionals attributed falls to poor balance and cognitive impairments, this was particularly problematic in cognitively impaired patients, as also stated in previous studies by [25], [26]. This implies

[1]See complementary material with perception answers: here

there would be benefit in incorporating cognitive assistance features into these walkers to facilitate smoother transfers.

Healthcare professionals reported walkers to be heavy, requiring so much strength and effort, further exacerbating the issues and increasing the risk of falling which supports a study by [27]. Both older adults and caregivers reported that the walkers were not enough to support their weight, causing discomfort, pain, and psychological distress. This statement is consistent with [28] indicating that individuals with a much higher weight find it difficult to move around comfortably. In addition, caregivers reported that the noise from the walkers, particularly from the wheels and brakes, could cause discomfort, stress, and agitation, leading to reluctance to use the walkers.

All respondents' groups expressed concerns about walkers' limited manoeuvrability in certain situations, like stairs, narrow doorways, and thresholds. The walker's size, including width, length, and height, significantly affects its ability to move effectively in confined spaces [29]. Older adults reported getting stuck while taking turns or negotiating tight corners, while caregivers confirmed experiencing this with the older adults they care for. This situation can be particularly challenging in places like bathrooms or crowded areas, where precise navigation is crucial for the user's safety and convenience [30], [31].

The results from this research have outlined additional features:

A. Smart Design

Integrating an alarm function allows users to access emergency assistance quickly, especially during outdoor falls where pendant alarms may fail. While studies [32], [33] highlight the importance of such features, their feasibility depends on factors such as cost, power consumption, and user familiarity with GPS-enabled devices. Simplified interfaces and low-maintenance designs could enhance adoption among older adults.

Assisting users in navigating unfamiliar environments, detecting obstacles, and guiding posture, this feature could improve walker interaction. However, implementation must balance functionality with ease of use, ensuring it does not increase device complexity or require high technological literacy.

Measuring grip force could support fall risk assessments and intervention. Older adults showed strong interest in this feature (85% approval). However, maintenance and battery requirements must be considered to ensure long-term usability. Studies [34] indicate stability benefits, but further evaluation is needed to confirm cost-effectiveness.

B. Ergonomic Design

An ergonomically designed walker should accommodate various user heights and body types, promoting optimal posture while reducing physical effort. Features like adjustable size, wheels, and brakes [35] could enhance stability on uneven terrain. However, adjustable mechanisms must be intuitive to prevent usability barriers.

C. Mechanical Design

Integrating noise reduction features, such as noise-absorbing materials in wheels and brakes, could dampen vibrations and improve user experience. Additionally, an attachable threshold ramp could aid smoother transitions over door thresholds [36]. While these features enhance accessibility, factors such as added weight, durability, and maintenance requirements must be considered to avoid potential trade-offs that could deter usage.

D. Limitations

Older adults and some caregivers preferred in-person surveys, while clinicians and other caregivers preferred virtual formats. This approach, while ensuring broader participation, is not believed to have biased the findings. Older adults were recruited exclusively from two private care homes, while caregivers and healthcare professionals came from these homes and other institutions. Variations in knowledge, attitudes, and practices (KAP) may exist; however, they likely reflect normal professional differences. The use of non-random convenience sampling, based on availability and willingness to participate, and the exclusive focus on care home residents may have introduced bias. Future studies should aim for a broader sample, including older adults living independently and participants from more diverse cultural and socioeconomic backgrounds to enhance generalizability.

The study's applicability is also constrained by its sample size of 81 participants, though this remains one of the largest studies of its kind. Additionally, the questionnaire did not explicitly differentiate between various types of assistive devices (e.g., canes, standard walkers, wheeled walkers), which may have led to overly broad conclusions. Future research should refine the survey design to distinguish between device types and provide more targeted recommendations. Furthermore, our survey design did not incorporate reverse semantic questions, which are often used to assess response reliability. While we mitigated this by structuring the survey clearly and ensuring logical consistency in responses, we acknowledge that incorporating additional validation techniques could strengthen data robustness, particularly for older adult respondents.

Finally, some inconsistencies in user perceptions, such as differing views on navigation systems, highlight the diverse needs of assistive walker users. Our study aimed to capture a broad spectrum of experiences; however, these discrepancies suggest that additional segmentation or subgroup analysis may be beneficial in future research. Additionally, since our findings rely primarily on self-reported data, they may be influenced by subjective biases. Incorporating observational or experimental methods in future studies could provide a more comprehensive understanding of the real-world effectiveness and limitations of assistive walker designs.

V. Conclusions

This study establishes a foundation for designing improved assistive walkers tailored to the specific needs of older adults. The positive attitudes and knowledge among healthcare

professionals and caregivers highlight the potential of these devices to enhance the quality of life for the elderly. By integrating advanced features such as GPS-enabled alarms, internal navigation systems, and grip force sensors, walkers can become safer, more user-friendly, and better address existing limitations.

This research emphasizes the importance of adaptability in walker design to meet the diverse needs of older adults. A user-centred approach, including real-world testing, is critical to creating devices that genuinely improve mobility and independence. Future research should explore integrating advanced technologies, ergonomic designs, and noise reduction features while increasing sample sizes by including independently living older adults.

REFERENCES

[1] N. I. on Aging, *Maintaining mobility and preventing disability are key to living independently as we age*, 2020.

[2] U. Nations, *World population ageing - highlights*, Department of Economic and Social Affairs - Population Division (ST/ESA/SER.A/397), 2017.

[3] E. Jaul and J. Barron, "Age-related diseases and clinical and public health implications for the 85years old and over population," *Frontiers in Public Health*, vol. 5, 2017.

[4] S. Abdi *et al.*, "Correction to: Understanding the care and support needs of older people: A scoping review and categorisation using the who international classification of functioning, disability and health framework (icf)," *BMC Geriatrics*, vol. 20, no. 1, p. 23, 2020.

[5] R. E. Cowan *et al.*, "Recent trends in assistive technology for mobility," *Journal of NeuroEngineering and Rehabilitation*, vol. 9, no. 1, p. 20, 2012.

[6] D. Lee and S. H. Tak, "Barriers and facilitators of older adults' usage of mobility devices: A scoping review," *Educational Gerontology*, vol. 49, no. 2, pp. 96–108, 2023.

[7] J. C. Davis *et al.*, "Mobility is a key predictor of change in well-being among older adults who experience falls: Evidence from the vancouver falls prevention clinic cohort," *Archives of Physical Medicine and Rehabilitation*, vol. 96, no. 9, pp. 1634–1640, 2015.

[8] S. Musich *et al.*, "The impact of mobility limitations on health outcomes among older adults," *Geriatric Nursing*, vol. 39, no. 2, pp. 162–169, 2018.

[9] E. Pantelaki, E. Maggi, and D. Crotti, "Mobility impact and well-being in later life: A multidisciplinary systematic review," *Research in Transportation Economics*, vol. 86, p. 100 975, 2021.

[10] A. L. Rosso *et al.*, "Mobility, disability, and social engagement in older adults," *Journal of Aging and Health*, vol. 25, no. 4, pp. 617–637, 2013.

[11] C. Bäccman and L. Bergkvist, "Welfare technology and user experience: A study of seniors' expectations on and first impressions of a robotic shower," in *Proceedings of the Annual Hawaii International Conference on System Sciences*, vol. 2019-January, 2019.

[12] R. Fomiatti *et al.*, "A systematic review of the impact of powered mobility devices on older adults' activity engagement," *Physical & Occupational Therapy in Geriatrics*, vol. 31, no. 4, pp. 297–309, 2013.

[13] C. Löfqvist *et al.*, "Use of mobility devices and changes over 12 months among very old people in five european countries," *Aging Clinical and Experimental Research*, vol. 19, no. 6, pp. 497–505, 2007.

[14] S. T. Boerema *et al.*, "Value-based design for the elderly: An application in the field of mobility aids," *Assistive Technology*, vol. 29, no. 2, pp. 76–84, 2017.

[15] W. C. Graafmans *et al.*, "Daily physical activity and the use of a walking aid in relation to falls in elderly people in a residential care setting," *Zeitschrift Fur Gerontologie Und Geriatrie*, vol. 36, no. 1, pp. 23–28, 2003.

[16] J. A. Stevens *et al.*, "Unintentional fall injuries associated with walkers and canes in older adults treated in u.s. emergency departments," *Journal of the American Geriatrics Society*, vol. 57, no. 8, pp. 1464–1469, 2009.

[17] H. (Liu *et al.*, "Comparison of gait characteristics between older rolling walker users and older potential walker users," *Archives of Gerontology and Geriatrics*, vol. 48, no. 3, pp. 276–280, 2009.

[18] H. Bateni and B. E. Maki, "Assistive devices for balance and mobility: Benefits, demands, and adverse consequences," *Archives of Physical Medicine and Rehabilitation*, vol. 86, no. 1, pp. 134–145, 2005.

[19] S. M. Bradley and C. R. Hernandez, "Geriatric assistive devices," *American Family Physician*, vol. 84, no. 4, pp. 405–411, 2011.

[20] J. Soar, L. Yu, and L. Al-Hakim, "Older people's needs and opportunities for assistive technologies," in *The Impact of Digital Technologies on Public Health in Developed and Developing Countries: 18th International Conference, ICOST 2020 Hammamet, Tunisia, June 24–26, 2020 Proceedings*, vol. 12157, 2020, pp. 404–414.

[21] K. Schmidt *et al.*, "The myosuit: Bi-articular anti-gravity exosuit that reduces hip extensor activity in sitting transfers," *Frontiers in Neurorobotics*, vol. 11, 2017.

[22] K. Samuelsson and E. Wressle, "User satisfaction with mobility assistive devices: An important element in the rehabilitation process," *Disability and Rehabilitation*, vol. 30, pp. 551–558, 7 Jan. 2008, ISSN: 0963-8288.

[23] M. Schmucker *et al.*, "The usability of rollators as part of the human-centred quality of mobility devices: A systematic narrative literature review," *Disability and Rehabilitation: Assistive Technology*, vol. 20, pp. 268–285, 2 Feb. 2025, ISSN: 1748-3107.

[24] C. Andrade *et al.*, "Designing and conducting knowledge, attitude, and practice surveys in psychiatry: Practical guidance," *Indian Journal of Psychological Medicine*, vol. 42, no. 5, pp. 478–481, 2020.

[25] B. O'Neill, K. Moran, and A. Gillespie, "Scaffolding rehabilitation behavior using a voice-mediated assistive technology for cognition," *Neuropsychological Rehabilitation*, vol. 20, no. 4, pp. 509–527, 2010.

[26] L. Nilsson *et al.*, "Driving to learn in a powered wheelchair: The process of learning joystick use in people with profound cognitive disabilities," *The American Journal of Occupational Therapy*, vol. 65, no. 6, pp. 652–660, 2011.

[27] Y. Sakano *et al.*, "Factors influencing the use of walking aids by frail elderly people in senior day care centers," *Healthcare*, vol. 11, no. 6, p. 858, 2023.

[28] N. Mali *et al.*, "Safety concerns in mobility-assistive products for older adults: Content analysis of online reviews," *Journal of Medical Internet Research*, vol. 25, e42231, 2023.

[29] S. B. Thies *et al.*, "Are older people putting themselves at risk when using their walking frames?" *BMC Geriatrics*, vol. 20, no. 1, p. 90, 2020.

[30] K. A. Nickerson, K. Diaz, and B. C. Muir, "Circumstances of falls among older adult walker users in long-term care and the associated walker design deficits," *Assistive Technology*, vol. 36, no. 3, pp. 248–253, 2024.

[31] L. Sloot and V. Komisar, "Real-life movement analysis: Circumstances of falls involving walkers in frail older persons living in long-term care," *Gait Posture*, vol. 97, S256–S257, 2022.

[32] M. D. Messaoudi, B.-A. J. Menelas, and H. Mcheick, "Review of navigation assistive tools and technologies for the visually impaired," *Sensors*, vol. 22, no. 20, p. 7888, 2022.

[33] A. Cullen *et al.*, "Wearable and portable gps solutions for monitoring mobility in dementia: A systematic review," *Sensors*, vol. 22, no. 9, p. 3336, 2022.

[34] F. C. Krafft *et al.*, "Young individuals are more stable and stand more upright when using rollator assistance during standing up and sitting down," *Frontiers in Bioengineering and Biotechnology*, vol. 10, 2022.

[35] R. H. Wang *et al.*, "Power mobility with collision avoidance for older adults: User, caregiver, and prescriber perspectives," *Journal of Rehabilitation Research and Development*, vol. 50, no. 9, pp. 1287–1300, 2013.

[36] S. B. Thies *et al.*, "Evaluation of a novel biomechanics-informed walking frame, developed through a knowledge transfer partnership between biomechanists and design engineers," *BMC Geriatrics*, vol. 23, no. 1, p. 734, 2023.

Amplifying Human Strength Through a Virtual Sprung Inertia

Anthony Petrakian, Zachary Bucknor-Smartt, Crystal Q. Scott, and Gray C. Thomas

***Abstract*—While better known for their ability to work autonomously in structured tasks, robots have the potential to aid human workers in unstructured tasks via force control. More specifically, cobots and exoskeletons that physically interact with human operators can amplify human strength by feeding back measurements of their interaction forces, agnostic to the task the operator is performing. However, due to limited control bandwidth and coupled human–robot dynamics, naive force-feedback can easily result in instability similar to pilot-induced oscillation in planes. Controllers that amplify strength while also guaranteeing some stability properties have become the standard approach in the space, often at the cost of the user's perception of a transparent system. This paper 1) extends a previously theorized virtual-mass-based exoskeleton controller to a strength-amplifying robot arm, 2) theoretically and experimentally demonstrate the improved stability properties that result from the inclusion of the virtual mass term, 3) identifies the robot's end-effector compliance and self-deflection transfer functions, and 4) determines the extent to which the robot can reliably measure the stiffnesses of a spring-box apparatus in order to better understand its ability to identify human mechanical impedance.**

I. INTRODUCTION

In demanding physical tasks, such as in rehabilitative healthcare, robots have the potential to assist or replace humans, with recent focus shifting toward assistive collaboration between humans and robots [1]. Unlike the inherently unsafe nature of older position-based control schemes [2], modern robot force sensing allows for safer physical contact in human-robot interaction. The main challenge is then to control the robot to work with humans in a desirable manner.

The paradigm of collaborative robots or "cobots" builds toward this challenge from an autonomous robotics baseline. Cobots are robots designed to share a workspace with humans, and are usually able to apply control schemes such as impedance control to ensure only safe levels of force are applied in the event of an unexpected collision or intentional handoff [3], [4]. However, since they are autonomous, they must reliably understand their role in the interaction or risk unwanted and unexpected behavior that interferes with the human. While studies have tried to design architectures that can sense/anticipate unexpected human behavior and plan accordingly, it remains a difficult task [5]. Even more difficult is helping the human operator to understand what the robot thinks is going on; a lack of transparency can understandably make the cobot a suspicious coworker.

For less structured and more physical tasks like those associated with rehabilitative environments and patient care, simple dynamic robot behaviors offer to be simpler for the operator to understand and rely less on complex robot decision making. Some assistive exoskeletons, for example, are attached to and directly positioned by the human as they provide assistive torque according to gravitational load of a known weight [6], acceleration of a known inertia [7], or a virtual potential energy function [8]. This removes the understanding component of the task from the robot's responsibilities, and allows for greater flexibility for the human, provided that they can anticipate the exoskeleton's behavior in new tasks. This assumes that the patient has some capability to perform self-movement, with the general goal to reduce the load/effort the patient needs to apply. However, these approaches are not suited for interacting with the general environments posed in rehabilitative healthcare settings, since they cannot distinguish between identical poses with different amounts of environmental interaction forces. This problem motivates the inclusion of force sensors to allow amplification of human strength in a truly task-agnostic way [9].

Feedback control of the human–robot interaction force can allow a human operator to perceive amplified strength in manipulation tasks, at least at frequencies within the

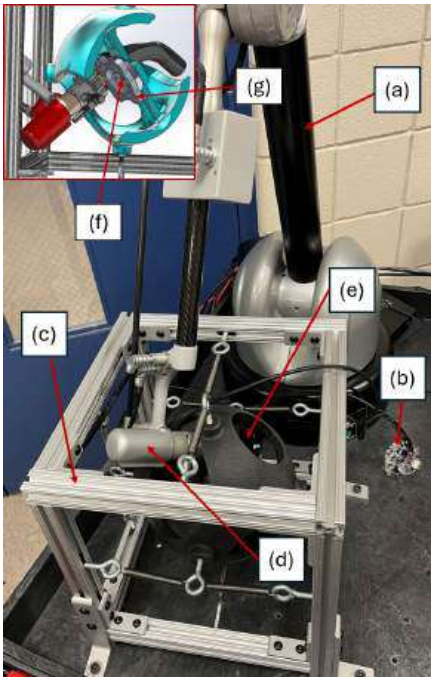


Fig. 1. The experimental setup, comprising: (a) the Haption Virtuose 6D TAO™ High Force Robotic Manipulator, (b) Sunrise Instruments (SRI) 6-axis force/torque sensor breakout board, (c) the spring-box frame, as well as the springs that attach the black sphere to the frame, (d) the end-effector of the robot arm, attached in the center of the spring-box to the black sphere, (e) the handle of the robot arm, (f) the force/torque sensor, and (g) the interface between the handle and the end-effector where the force/torque sensor is held.

*This work supported by Texas A&M Experiment Station, the Texas Governor's University Research Initiative, and the Texas A&M Chancellor's University Research Initiative

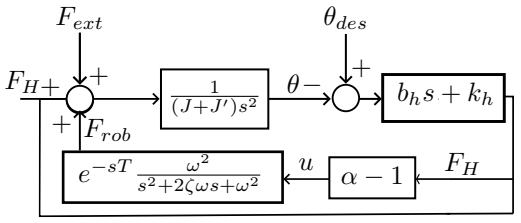


Fig. 2. Control Block Diagram: Naive Force-Feedback Controller

bandwidth of the control [9]. However, practical implementations have tended to be low and sluggish in order to avoid instabilities in the control algorithm [10]. These instabilities (uncontrolled oscillations, etc.) are in large part due to a coupling between the exoskeleton and the human's mechanical impedance behavior [11], [12], [13], which are not unlike those found in pilot-induced oscillation [14]. Unfortunately, the human element is hard to model; they are not linear and their stiffness can change due to muscle co-contraction, fatigue, and pose [15]. Adapting to this changing behavior has required extra sensors for muscle activation and subject-specific training [16]. This means any stiffness measurements made can potentially be unreliable since they are dependent on the conditions under which the measurements occurred. Thus, even if a stiffness model is taken into account in designing the controller, amplification robots based on only force sensors are sensitive to uncontrollable stiffness changes [13], pushing designers toward low-bandwidth, conservative control tunings [17].

In this paper, we implement a controller that both amplifies human strength and adds a virtual inertia to reduce sensitivity to operator stiffness. While virtual inertia has been used before in controllers, using it for the purposes of force feedback/strength amplification is novel to this paper. More specifically, we 1) extend a previously theorized virtual-mass based energy-shaping controller approach [18] to a MIMO strength-amplifying robot arm application, 2) theoretically and experimentally demonstrate the improved stability properties that result from the inclusion of the virtual mass term, 3) identify the robot's end-effector compliance and self-deflection transfer functions, 4) validate a testing apparatus that can mimic human stiffness in multiple directions, thus allowing for experimental determination of a multi-degree-of-freedom stiffness model, and 5) experimentally validate the controller design and the robot's ability to infer the dynamics of the human surrogate. The controller is validated through comparison with a naive force-feedback approach to demonstrate the superior performance under stability constraints.

II. METHODS

A. CONTROLLER DESIGN

This paper considers two controller structures for comparison. The first, the *Naïve Controller* (Fig. 2), uses unfiltered force feedback to amplify user strength and serves as a control group in our experiment. The second, the *Virtual-Mass Controller* (Fig. 4), applies our proposed innovation and serves as an experimental group in our experiment. Both controllers interact with the same fundamental robot physics.

1) Plant Model: We consider a 1-DOF linearized translational idealization of our system in which the mass of the robot, J, and any supported object, J', are acted upon by an external force, F_{ext}, a sensed human interaction force, F_H, and a robot force F_{rob}. This model is similar to the tuning model used in [17]. Applying Newton's laws, the dynamics can be written as

$$(J + J')\ddot{\theta} = F_{rob} + F_{ext} + F_H, \tag{1}$$

where θ represents the position of the robot's end-effector, and all the forces are reflected to act in the end-effector frame.

Since the robot torque is an imperfect input that is subject to bandwidth limits, we also consider an actuator limiting transfer function,

$$\eta(s) = e^{-sT}\frac{\omega^2}{s^2 + 2\zeta\omega s + \omega^2}, \tag{2}$$

where e^{-sT} represents a time delay, and the other term is a second-order low-pass filter with critical frequency ω (bandwidth of the actuating system) and damping ratio ζ. This bandwidth limit is representative of the lowest frequency issue of the many potential bandwidth limiting effects we have not modeled, for example: electrical dynamics in the electric motor, or mechanical dynamics in the cable-drives of the robot. Including the actuator limitations, the robot force is

$$F_{rob} = \eta(s)u, \tag{3}$$

where u is the desired robot force, the input used by the feedback controller.

Thus, we consider this *open-loop* system, Σ_{open} to have three inputs (F_{ext}, F_H, and u) and one output (θ). Connecting a model for human behavior, we obtain a *human-included* system, Σ_{human}. For this purpose, we use a simple human impedance model,

$$F_H = (k_h + b_h s)(\theta_{des} - \theta), \tag{4}$$

where k_h and b_h is a human perturbation-response stiffness and damping respectively, and θ_{des} is a human desired position. The parameters k_h and b_h are not necessarily known at any given time, and are assumed to be arbitrary/allowed to take on any reasonable (positive) value. We neglect to use an inertial term, as it is only relevant at higher frequencies and is typically a very small value relative to the stiffness and damping. This system Σ_{human} is also three-input, one-output, with inputs F_{ext}, θ_{des}, and u, with output F_H.

2) Naïve Controller: The naïve force-feedback strength amplification controller is simple,

$$u = (\alpha - 1)F_H, \tag{5}$$

where $\alpha > 1$ is the intended amplification rate (Fig. 2). This amplification rate reflects the closed-loop dynamics resulting from the approximation $\eta(s) \approx 1$,

$$(J + J')\ddot{\theta} = F_H + (\alpha - 1)F_H + F_{ext} = \alpha F_H + F_{ext}, \tag{6}$$

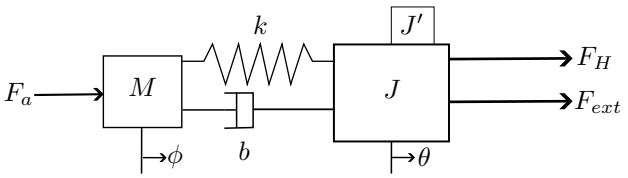


Fig. 3. FBD showing the dynamical system that would be achieved by the Virtual-Mass Controller under ideal actuation assumptions ($\eta(s) \approx 1$). The system features a virtual mass M coupled to the physical masses $J + J'$ by a virtual spring and damper. An amplification force $F_a = (\alpha - 1)F_H$ is applied to the virtual mass rather than to the physical mass in order to avoid amplification at high frequencies.

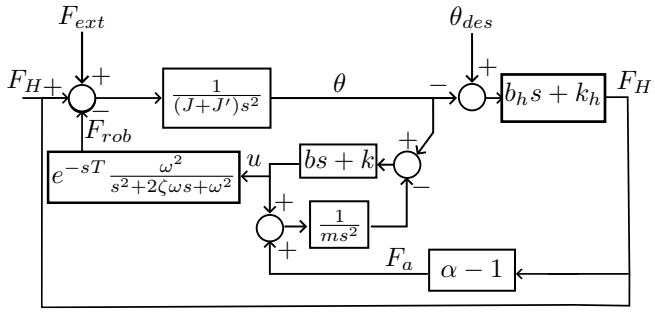


Fig. 4. Control Block Diagram: Virtual-Mass Based Controller

which shows F_H amplified by a factor of α. Naturally, such ideal behavior is not achievable with a more realistic $\eta(s)$ consideration, since it implies a meaningful change to the system dynamics at all frequencies.

3) Virtual-Mass Controller: It was previously theorized that an energy-shaping controller for exoskeletons could achieve an energetically passive mechanical interface for the human-side of an amplification behavior by simulating some specialized virtual dynamics that are coupled to the physical robot [18]. These virtual dynamics included a second copy of the robot's inertia, coupled to the physical robot by virtual springs, where the virtual inertia felt an amplified version of the human interaction force. However, the concept was only evaluated in a planar simulation of a lower-body exoskeleton with ground-contact sensing.

This paper explores a similar virtual-mass based controller for this robot arm model (Fig. 3). The dynamics of the virtual mass are denoted

$$M\ddot{\phi} = F_a + k(\theta - \phi) + b(\dot{\theta} - \dot{\phi}), \tag{7}$$

where M is the virtual mass, ϕ is the position of the virtual mass, k is the virtual spring rate, b is a virtual damper, and F_a is the ideal amplification force $F_a = (\alpha - 1)F_H$. This virtual system then imparts a force F_{rob} on the physical system using the control input u (*i.e.,* it is filtered by the actuator limitation transfer function),

$$u = k(\phi - \theta) + b(\dot{\phi} - \dot{\theta}), \tag{8}$$

resulting in a two input, one output closed loop system known as $\Sigma_{virt\ con}$ (Fig. 4), with inputs F_{ext} and θ_{des} and output F_H.

4) Steady-State Analysis: Steady-state analysis shows that this new system preserves the desired amplification behavior at low frequencies. Let $\dot{\phi} = \dot{\theta} = \ddot{\theta} = \ddot{\phi} = 0$, and (1), (2), (3), (7), and (8) reduce to

$$\begin{cases} 0 = F_{ext} + F_H + k(\phi - \theta) \\ F_a = k(\phi - \theta) \end{cases}, \tag{9}$$

where $F_a = (\alpha - 1)F_H$. The resulting steady state force balance is

$$0 = F_{ext} + \alpha F_H, \tag{10}$$

as expected. The human force required to balance the arbitrary external load is therefore reduced by a factor α, and environment-side perceptions of human strength magnified by α.

5) Stability Analysis: Whether it's rehabilitation or industrial work, an unstable control system can cause unintended harm or injury to the user. Due to the human-robot interaction in strength amplification, it is important to ensure stability of the system when a human operator is present in the control loop. The goal of this section is to show that the virtual mass controller improves the potentially attainable ratio without compromising stability.

To determine the stability of the system, we consider the two input one output system,

$$\theta(s) = G_H(s)F_H(s) + G_{ext}(s)F_{ext}(s). \tag{11}$$

Assuming θ_{des} is zero, the transfer function between the human input and theta is,

$$\theta = -H(s)F_H, \text{ where } H(s) = \frac{1}{b_h s + k_h}. \tag{12}$$

Substituting (12) into (11), we attain a closed-loop SISO system experienced by the environment,

$$\theta = (1 + H^{-1}(s)G_H(s))^{-1}G_{ext}F_{ext}. \tag{13}$$

This indicates that looking at the phase margin of the open-loop transfer function $H^{-1}(s)G_H(s)$ is enough to determine stability for the closed-loop system. In this case, the phase margin is

$$PM = \angle G_H(j\omega_c) - \angle H(j\omega_c) + 180^\circ, \tag{14}$$

where ω_c is the crossover frequency such that $\|H^{-1}(j\omega_c)G_H(j\omega_c)\| = 1$.

We use Simulink (Mathworks, Natick, MA) to model the naïve and virtual mass controller approaches, with the time-delay approximated by a first-order Padé approximation and the robot actuation bandwidth represented by a second-order low-pass filter (Fig. 5). The system parameters of the simulation are found in table I. The model does not include the human feedback in order to assess the open-loop properties. For consistency, the time-delay and bandwidth for the virtual mass simulation are the same as for the naïve approach. Picking $m = (\alpha - 1)J$ ensures the virtual mass and real mass have the same acceleration in response to human inputs, since the force due to the human that the virtual mass feels is amplified by $(\alpha - 1)$.

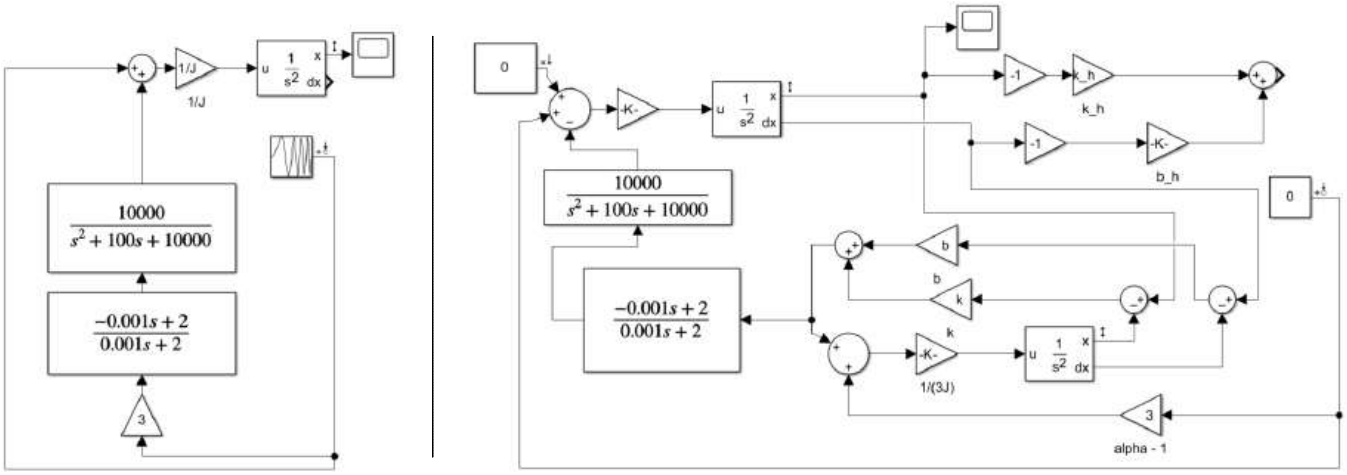


Fig. 5. Simulink model of naïve controller (left), Simulink model of virtual-mass controller (right). The model on the right shows the human model in the upper right to demonstrate how it would be included in a simulation, although it is shown to be not closed in order to assess the open-loop bode plots. The inputs are set to zero, as their value does not matter for forming the bode plots.

TABLE I
SIMULATION PARAMETERS

Parameter	Value
Strength Amplification Ratio, α	4
Time Delay, t_d	1 ms (0.001 s)
Low Pass Filter Frequency, ω_c	100 rad/s ($\approx$ 16 Hz)
Robot Inertia (including unmodeled inertia), J	15 kg
Virtual Mass, $m = (\alpha - 1)J$	45 kg
Virtual Stiffness, k	4500 N/m
Virtual Damping, b	450 N·s/m

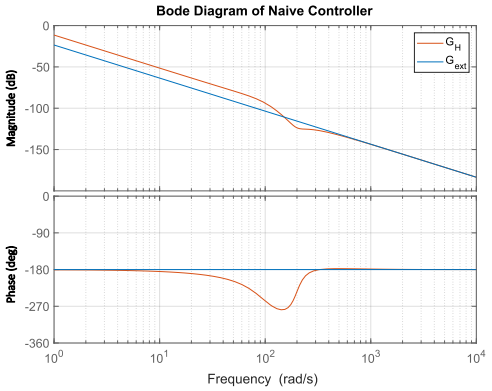


Fig. 6. Bode Plot of Naive Controller

The Bode plot of the naïve controller system (Fig. 6) shows both the $G_{ext}(s)$ and $G_H(s)$ transfer functions. The phase of the human-side integral admittance, $G_H(s)$, for the naïve controller is either at or below $-180°$ for the entire frequency range, with a significant phase drop to $\approx -275°$ around the actuation limit/bandwidth ($\approx$ 16 Hz). The reason for the phase drop is that at frequencies past the actuation bandwidth, the system must tend towards its natural dynamics $\frac{1}{(J+J')s^2}$. This means the transfer function representing G_H ($\frac{X}{F_H}$) must end up following the natural dynamics, and thus

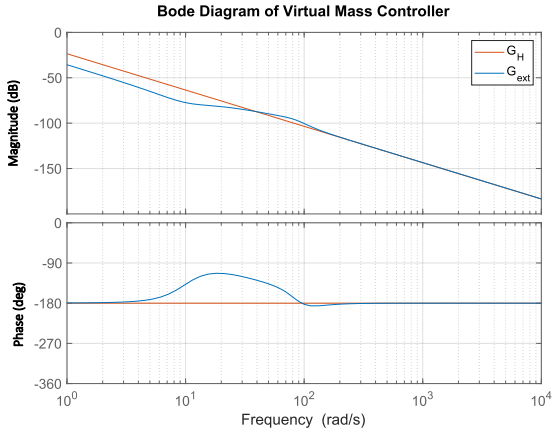


Fig. 7. Bode Plot of Virtual Mass Controller

requires a rapid drop in magnitude and phase in order to meet this requirement, as shown in the Bode plot.

Evaluating the PM from (14) for this model shows that the closed-loop SISO system risks instability if the human does not have damping, and is unstable for crossover frequencies near 16 Hz even *with* significant human damping. Past experiments have shown that it can be feasible for the system to be stable if the amplification ratio is small and the human stiffness is also very small (i.e. the operator is holding on loosely), however for practical purposes it is not usable.

In contrast, the Bode plot for the virtual mass controller (Fig. 7), shows a $G_H(s)$ transfer function with a constant phase of $-180°$, or a close approximation thereof. Rather than dropping below $-180°$ phase like in the naïve controller, the phase for the human transfer function remains at a constant $-180°$, which indicates passivity. Calculating the PM from (14) with this shows that the PM will always be positive, even with the slightest human damping. This means that the controller will remain stable under any positive k_h and b_h values in the human impedance model. However, this

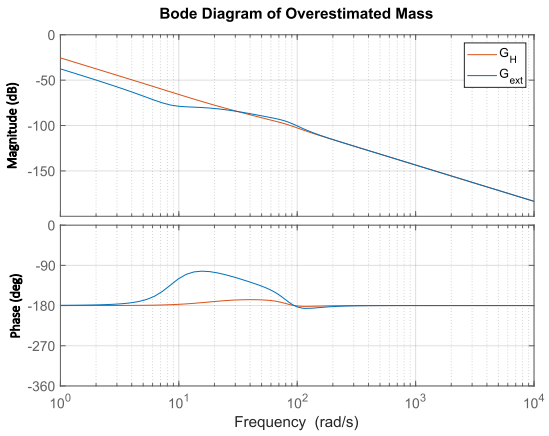


Fig. 8. Bode Plot of Overestimated Mass

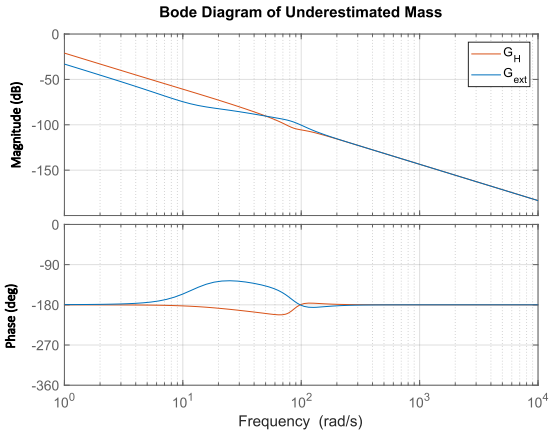


Fig. 9. Bode Plot of Underestimated Mass

comes with the assumption that J can be predicted perfectly and m chosen appropriately. The problem setup assumed an unknown inertia J', so it is instructive to see what happens if the inertia $J + J'$ is either underestimated or overestimated in the calculation of m.

Overestimation of m (Fig. 8) maintains the positive phase margin of the system and guarantees stability of the closed-loop SISO system due to the increase in phase of the human transfer function. However, underestimation (Fig. 9) causes a noticeable phase drop below $-180°$ in the $G_H(s)$ transfer function, although the phase drop is not as severe as that of the naive controller. Thus, over-estimating the inertia parameter m appears to be the conservative choice. Another consideration is the slight dip below $-180°$ that the G_{ext} transfer function exhibits in the bode plots. While this is not a passive transfer function, that doesn't necessarily mean that it will exhibit unstable behavior. Since the non-passivity is due to a combination of time delay and a low-pass filter (acting as an actuation bandwidth filter), it can be shown that the passivity requirements can be relaxed for these types of systems [19].

It is instructive to think of the physics behind what is happening. In the naive control approach, the human-side force relative to the environmental force and the robot inertia is amplified. As shown in (Fig. 6), this causes a phase drop below $-180°$ since the artificially attenuated robot inertia must act like its natural dynamics after a certain frequency.



Fig. 10. A side view of the spring box apparatus

In the virtual mass approach, by carefully choosing the acceleration (Fig. 7), the inertia of the robot relative to the human-side remains unchanged while still amplifying the human-side force relative to the environmental force. This is why the plots in (Fig. 6) and (Fig. 7) appear switched. This maintains the stability of the closed-loop system force-feedback system. For the overestimated and underestimated robot inertia cases, they have the effect of artificially adding and decreasing the robot inertia respectively. This is why there is a small potential for instability in the underestimated case. However, the phase drop is much smaller than the naive controller and is thus less likely to be unstable. With these results, the next step is to apply these two controllers in an experiment to validate the stability analysis.

B. HARDWARE DESIGN

During this study, we deploy strength amplification controllers on the 6 degree of freedom Haption Virtuose 6D TAO™ High Force robotic manipulator (Fig. 1). Due to its low gear ratios and backdriveability, the manipulator can provide force control at its end-effector. We modify the Haption arm end-effector by integrating a 6-axis force-torque sensor between two 3D-printed plates. The plates interface with the Haption arm end-effector handle and the remaining components of the end-effector joint. This modification enables the force-torque sensor to differentiate between applied loads at the handle where the human grasps, and the end of the end-effector joint. Care was taken to ensure no force leakage could occur between the interface of the force torque sensor and the end-effector components by creating gaps between the force torque sensor and the opposing human and environment sides of the apparatus. This analysis ensured that

under maximum deflection, the two end-effector plates never collided, resulting in corrupted system identification data.

Since a major facet of strength amplification involves the coupling between the human and the robot, testing a controller can be difficult and is subject to the availability of human testing. However, this coupling is one of the major factors responsible for the instability from force-feedback, so it is necessary to have in order to test controllers in a realistic setting. One potential solution to this is to design an apparatus that can simulate human stiffness in a multiple-degree-of-freedom fashion. Not only does this allow for testing without relying on human test subjects, but it provides an avenue for testing how different stiffness values affect the controller.

We use an adjustable, spring-loaded end effector mount to simulate human arm stiffness in response to force input. Our "spring box" apparatus (Fig. 10) includes a 3D-printed PLA mount interfaces with the force torque sensor and handle on the human side. The exterior of the mount is equipped with six eye bolts secured by heat-set inserts, with each eye bolt supporting two extension springs. The springs are secured to corresponding eye bolts a long cube-shaped frame constructed from aluminum extrusion. This makes it easy to change out the springs and allows for easier testing.

In total, twelve springs in tension hold the mount in a centered equilibrium within the frame. The springs are configured such that four are oriented along each Cartesian axis. Both the spring box and the Haption arm are affixed to the same ground surface, ensuring a rigid base. The spring box was evaluated using sets of springs with rates of $k_1 = 175.13\frac{N}{m}$, $k_2 = 437.817\frac{N}{m}$, $k_3 = 893.146\frac{N}{m}$, $k_4 = 1821.31\frac{N}{m}$, and $k_5 = 4220.55\frac{N}{m}$ which provide total spring stiffness values of $4k_n$ in each Cartesian direction.

C. SYSTEM IDENTIFICATION

We empirically identified a multi-degree-of-freedom model of the human–robot coupling dynamics using system identification. Since robot position measurements cannot be trusted in calculating the estimated stiffness of the spring box due to self-deflection of the robot, we estimated a model of this self-deflection using a chirp test with a locked end-effector. The end-effector was affixed to the table using a special purpose variant handle, and a chirp of desired end-effector frame force was applied in each Cartesian direction.

The derived compliance matrix, C_γ, is then

$$C_\gamma(\omega) = R(\omega)F_l(\omega)^{-1}, \tag{15}$$

where R is the robot's recorded position, and F_l is the measured force via the 6-axis force-torque sensor, all as a function of frequency. After performing the locked test in all three directions, a matrix C'_γ of bode plots (Fig. 11) characterizes the compliance, and matrix inversion yields a low-frequency stiffness.

With this robot compliance model, similar chirp tests using the spring box were performed to quantify the robot's ability to measure the mechanical impedance of the environment or human. The spring box compliance matrix, C_S, can be calculated in a similar manner to C_γ, now with a subtractive term $(R - C_\gamma F_s)$ to extract the true end-effector position as the spring box emulates human contact,

$$C_S(\omega) = (R(\omega) - C_\gamma(\omega)F_s(\omega))F_s(\omega)^{-1}, \tag{16}$$

where R is the robot's recorded position, and F_s is the measured force via the 6-axis force-torque sensor in the spring box test. Inverting the matrix of compliance bode plots C'_S to achieve K'_S then yields the spring box stiffness matrix, where the low-frequency response of the system represents the spring box stiffnesses mentioned previously (Fig. 6, 7).

Performing system identification on the spring box with $k_1 = 175.13\frac{N}{m}$, $k_2 = 437.817\frac{N}{m}$, and $k_3 = 893.146\frac{N}{m}$ produces the following predicted stiffness matrices:

$$K_{1\,(N/m)} = \begin{bmatrix} 171.55 & 43.275 & 15.240 \\ 8.87 & 214.37 & 43.4172 \\ 36.11 & 87.028 & 217.57 \end{bmatrix} \tag{17}$$

$$K_{2\,(N/m)} = \begin{bmatrix} 257.392 & 64.877 & 63.574 \\ 125.749 & 526.829 & 137.478 \\ 282.815 & 71.431 & 538.710 \end{bmatrix} \tag{18}$$

$$K_{3\,(N/m)} = \begin{bmatrix} 2030.453 & 716.413 & 1659.375 \\ 235.748 & 1398.485 & 481.472 \\ 914.981 & 3536.165 & 3350.282 \end{bmatrix} \tag{19}$$

By comparing each predicted stiffness matrix with the theoretical expected stiffness matrix given by $K_i = diag(k_i, k_i, k_i)$, a Frobenius-norm error vector can be used to provide a quantitative accuracy of the prediction for each of the three tested spring stiffnesses.

$$\text{Error_Vector} = \begin{bmatrix} K_1 \text{ Error} \\ K_2 \text{ Error} \\ K_3 \text{ Error} \end{bmatrix} = \begin{bmatrix} 42.09\% \\ 55.75\% \\ 319.85\% \end{bmatrix}. \tag{20}$$

We believe the large error is most likely due to bandwidth limits in the force and position sensing, as the motion of the end-effector in the apparatus during testing is too small to have any noticeable coupling effects from the springs.

III. CONTROLLER VALIDATION EXPERIMENT

Using the spring box apparatus shown in (Fig. 10) to mimic the human stiffness shown in the control block diagrams (Fig. 2, 4), an experiment was carried out to compare the naive force-feedback controller compared to the virtual-mass based controller. The main goal of the experiment was to test stability. The amplification ratio α was chosen to be 1.5, a fairly small amount (at least for small forces). This value was picked to demonstrate that even at small amplification ratios, the naive force-feedback controller can go unstable very fast. For the virtual-mass controller, the parameter values are: $m = 5$, $k = 500$, $b = 100$.

The experiment was performed by applying the controller while the robot arm was attached to the spring box apparatus. The experimental setup is shown in (Fig. 1). After a short time, the robot arm was perturbed by a small force, and the corresponding displacement in the perturbed direction was measured. This allowed for experimentally determining stability.

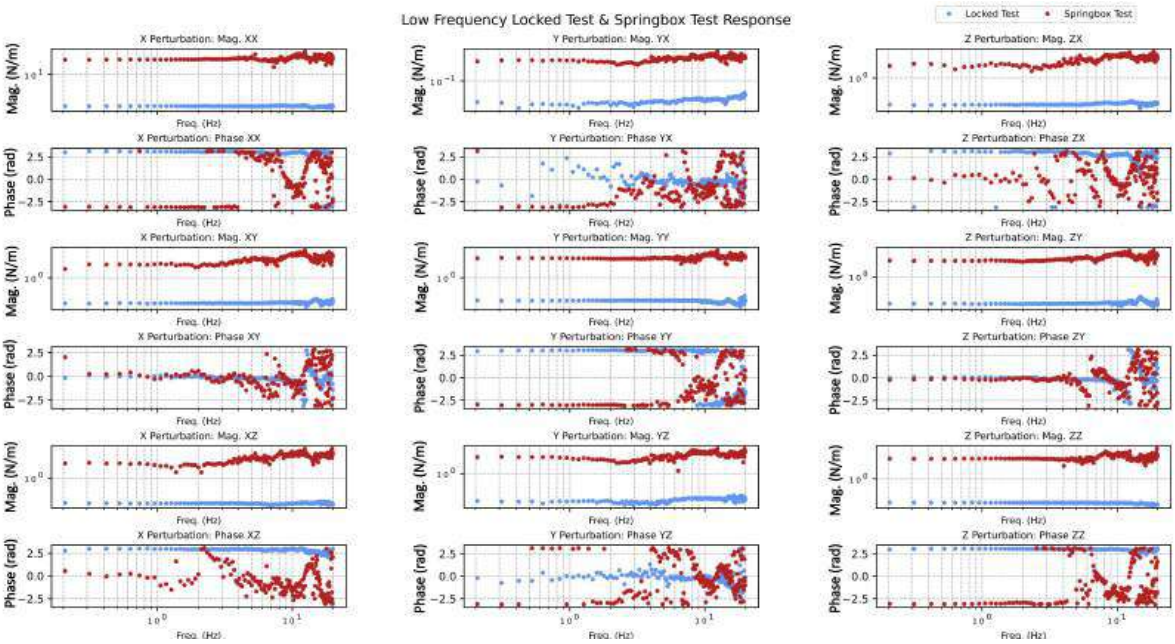


Fig. 11. Stiffness matrix of bode plots overlaying the results of the locked test as compared to the spring box test.

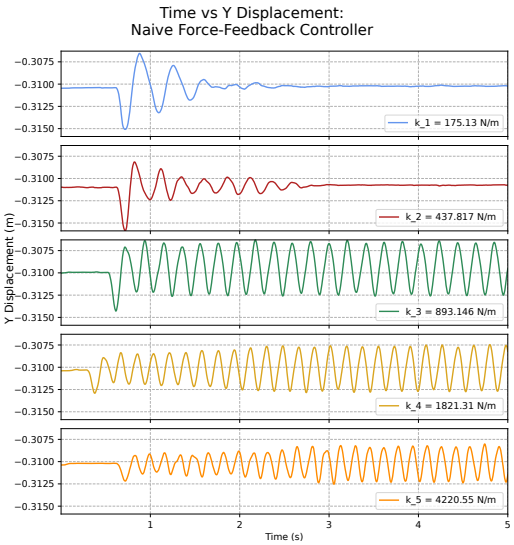


Fig. 12. Time series data of naïve force feedback control results for spring box spring constants of: k = (175.13, 437.817, 893.146, 1821.31, 4220.55) $\frac{N}{m}$ in order of top to bottom.

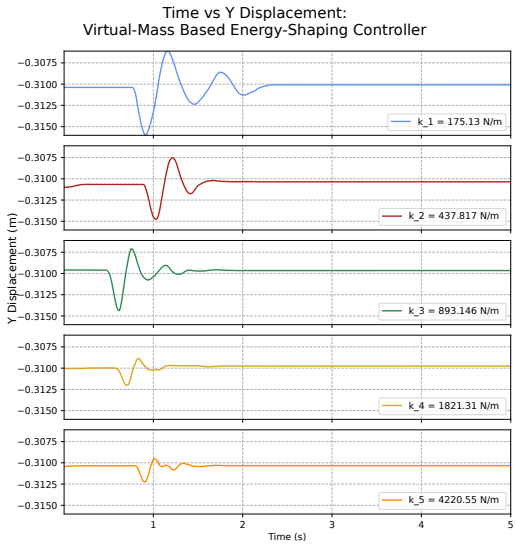


Fig. 13. Time series data of virtual-mass based force feedback control results for spring box spring constants of: k = (175.13, 437.817, 893.146, 1821.31, 4220.55) $\frac{N}{m}$ in order of top to bottom.

IV. RESULTS

The naïve controller was destabilized by increasing spring stiffness (Fig. 12), whereas the virtual-mass controller was not (Fig. 13). The naïve controller appears stable at $\alpha = 1.5$ for the first two stiffnesses ($< 500N/m$), but sustains persistent or slowly-growing oscillations for the higher stiffness configurations of the apparatus. This demonstrates that the stability of the naïve controller is dependent on the stiffness of the human surrogate. In contrast, the virtual-mass controller shows clearly decaying perturbation responses for all five tested configurations of the apparatus (Fig. 13). As the spring box stiffness increased, the robot arm returned to its original position faster, which is expected of the mass-like theoretical behavior of this port (see $G_H(s)$ in Fig. 7). In comparison to the naive force-feedback tests, the virtual-mass controller showed much less oscillatory behavior for the two plots which were stable for both controllers, which is consistent with our predictions of improved phase margin.

V. DISCUSSION

Theoretically and in a simple experiment, the use of a virtual mass to reduce the environment-side admittance

reduces sensitivity to human stiffness in comparison to increasing the human-side admittance with the naïve control. Increasing the controller's estimate of the inertia furthermore allows conservative decreases in both admittances, while decreasing the controller's mass estimate smoothly transitions back toward human-side admittance increase. Notably, this result is achieved in the absence of virtual damping, a reliance on friction in the robot (none modeled in simulation), or minimum damping requirements sought from the human. While it is easy to override the dynamics of the human with a damping-based admittance controlled robot—one that only moves as fast as the human is willing to push—the approach presented here builds on an energy-conservative backdrivable robot and, with an appropriate mass estimate, does not alter the human-side dynamics of the robot relative to that behavior.

The experimental validation was, however, superficial in relation to the simulation. Only five springs were tested physically, whereas a simulated bode plot implies a stability result with all possible springs through the phase margin criterion. Future testing could reach further toward this goal if a second robot arm were available to perform frequency-domain system identification on the first arm's closed-loop behavior. In relation to the hardware, the compensation for parasitic robot compliance and torque actuation bandwidth relied on a simplifying linearization, which would need to be extended to appropriately compensate these effects throughout the workspace of the robot, and this would be a pre-condition to realistic testing with a human performing a manipulation task.

The accuracy of measurement toward the spring apparatus deteriorated for the higher stiffness configurations. This is a natural result of the increased sensitivity to the robot's imperfect compliance model when measuring stiffnesses higher than the robot's own stiffness.

Both experiment and theory stopped short of an analysis of the amplified human in feedback with a set of realistic environments. However, practical experiments suggest that interacting with the table, other humans, or small objects on the table is unlikely to destabilize either of the two tested controllers if the human grasping the handle does not. In other words, if the controller is stable under the human feedback loop, then it seems to be stable under the environmental feedback loop as well. Empirical validation of such properties might make use of yet a third robot arm for environment-side perturbation.

REFERENCES

[1] S. Robla-Gómez, V. M. Becerra, J. R. Llata, E. González-Sarabia, C. Torre-Ferrero, and J. Pérez-Oria, "Working together: A review on safe human-robot collaboration in industrial environments," *IEEE Access*, vol. 5, pp. 26 754–26 773, 2017.

[2] M. Vasic and A. Billard, "Safety issues in human-robot interactions," in *2013 IEEE International Conference on Robotics and Automation*, 2013, pp. 197–204.

[3] C. Taesi, F. Aggogeri, and N. Pellegrini, "Cobot applications—recent advances and challenges," *Robotics*, vol. 12, no. 3, 2023. [Online]. Available: https://www.mdpi.com/2218-6581/12/3/79

[4] B. G. C. Lima, E. Ferrentino, P. Chiacchio, and M. Vento, "Assistive force control in collaborative human-robot transportation," in *2023 32nd IEEE International Conference on Robot and Human Interactive Communication (RO-MAN)*, 2023, pp. 2646–2651.

[5] O. C. Görür, B. Rosman, F. Sivrikaya, and S. Albayrak, "Social cobots: Anticipatory decision-making for collaborative robots incorporating unexpected human behaviors," in *Proceedings of the 2018 ACM/IEEE International Conference on Human-Robot Interaction*, ser. HRI '18. New York, NY, USA: Association for Computing Machinery, 2018, p. 398–406. [Online]. Available: https://doi.org/10.1145/3171221.3171256

[6] K. Shi, J. Yang, Z. Hou, and H. Yu, "Design and evaluation of a four-dof upper limb exoskeleton with gravity compensation," *Mechanism and Machine Theory*, vol. 201, p. 105746, 2024. [Online]. Available: https://www.sciencedirect.com/science/article/pii/S0094114X24001733

[7] H. Kazerooni, J.-L. Racine, L. Huang, and R. Steger, "On the control of the berkeley lower extremity exoskeleton (bleex)," in *Proceedings of the 2005 IEEE International Conference on Robotics and Automation*, 2005, pp. 4353–4360.

[8] J. Lin, N. V. Divekar, G. C. Thomas, and R. D. Gregg, "Optimally biomimetic passivity-based control of a lower-limb exoskeleton over the primary activities of daily life," *IEEE Open Journal of Control Systems*, vol. 1, pp. 15–28, 2022.

[9] H. Kazerooni and J. Guo, "Human Extenders," *Journal of Dynamic Systems, Measurement, and Control*, vol. 115, no. 2B, pp. 281–290, 06 1993. [Online]. Available: https://doi.org/10.1115/1.2899068

[10] B. Makinson, "Research and development prototype for machine augmentation of human strength and endurance. hardiman i project," 1971. [Online]. Available: https://api.semanticscholar.org/CorpusID:107783740

[11] H. Kazerooni, "Human-robot interaction via the transfer of power and information signals," *IEEE Transactions on Systems, Man, and Cybernetics*, vol. 20, no. 2, pp. 450–463, 1990.

[12] B. He, H. Huang, G. C. Thomas, and L. Sentis, "A complex stiffness human impedance model with customizable exoskeleton control," *IEEE Transactions on Neural Systems and Rehabilitation Engineering*, vol. 28, no. 11, pp. 2468–2477, 2020.

[13] S. P. Buerger and N. Hogan, "Complementary stability and loop shaping for improved human–robot interaction," *IEEE Transactions on Robotics*, vol. 23, no. 2, pp. 232–244, 2007.

[14] D. T. McRuer, "Pilot-induced oscillations and human dynamic behavior," Tech. Rep., 1995.

[15] N. Hogan, "Adaptive control of mechanical impedance by coactivation of antagonist muscles," *IEEE Transactions on Automatic Control*, vol. 29, no. 8, pp. 681–690, 1984.

[16] H. Huang, H. F. Cappel, G. C. Thomas, B. He, and L. Sentis, "Adaptive compliance shaping with human impedance estimation," in *2020 American Control Conference (ACC)*, 2020, pp. 5131–5138.

[17] G. C. Thomas, O. Campbell, N. Nichols, N. Brissonneau, B. He, J. James, N. Paine, and L. Sentis, "Formulating and deploying strength amplification controllers for lower-body walking exoskeletons," *Frontiers in Robotics and AI*, vol. 8, p. 720231, 2021.

[18] G. C. Thomas and R. D. Gregg, "An energy shaping exoskeleton controller for human strength amplification," in *2021 60th IEEE Conference on Decision and Control (CDC)*, 2021, pp. 1419–1425.

[19] G. C. Thomas, J. S. Mehling, J. Holley, and L. Sentis, "Phase-relaxed-passive full state feedback gain limits for series elastic actuators," *IEEE/ASME Transactions on Mechatronics*, vol. 26, no. 1, pp. 586–591, 2021.

sEMG-Based Assessment of Engagement in VR-Integrated BALANSens Ankle Rehabilitation

Elif Hocaoglu*
Living Robotics Laboratory
Electrical and Electronics Engineering
Research Institute for Health Sciences and Technologies (SABITA)
Istanbul Medipol University
Istanbul, Türkiye

Mahmut Beyaz
Living Robotics Laboratory
Electrical and Electronics Engineering
Istanbul Medipol University
Istanbul, Türkiye

Mennat Allah Tarek Ahmed
Living Robotics Laboratory
Department of Biomedical Engineering
Istanbul Medipol University
Istanbul, Türkiye

Ayse Gurluk
Physiotherapy and Rehabilitation Department
Istanbul Medipol University
Istanbul, Türkiye

Ramazan Unal
Human-Centred Design Laboratory
Mechanical Engineering
Ozyegin University
Istanbul, Türkiye

Pınar Kaya
Physiotherapy and Rehabilitation Department
Istanbul Medipol University
Istanbul, Türkiye

***Abstract*—This study investigates participant engagement with various types of virtual reality (VR)-integrated passive ankle robotic rehabilitation offered by the BALANSens platform, using surface electromyography (sEMG) signals to quantitatively assess involvement. The low adherence rates in robotic rehabilitation, often due to the monotonous nature of exercises, highlight the importance of enhancing patient motivation. VR is shown to improve patient engagement by providing immersive and interactive therapy environments, ultimately increasing training time, reducing dropout rates, and enhancing motivation. The role of VR in robotic rehabilitation is further explored through a comparison of motivation-related outcomes across different rehabilitation modalities, such as robot-assisted gait training and upper limb rehabilitation, where VR demonstrates increased patient engagement. Additionally, the study evaluates the cognitive demands of VR during active ankle therapy. By combining subjective self-reports with psychophysiological measurements, including sEMG, the study seeks to offer a comprehensive analysis of how VR-integrated rehabilitation influences patient motivation and adherence. The results are expected to contribute valuable insights into the design of more engaging and effective robotic rehabilitation systems, highlighting the need for dynamic and stimulating therapy environments to sustain long-term patient commitment.**

***Index Terms*—Effective rehabilitation, robotic rehabilitation, surface electromyography signals, virtual reality environment**

I. Introduction

The effectiveness of robotic rehabilitation for musculoskeletal disease is frequently compromised by poor patient adherence to therapy protocols. Studies indicate that adherence rates in clinical settings can be as low as 50% [1]. A key factor contributing to these low adherence rates is a lack of motivation, often driven by the repetitive and monotonous nature of rehabilitation exercises.

Virtual reality (VR) environments play a crucial role in robotic rehabilitation by providing immersive, interactive settings that enhance patient engagement and motivation during therapy. The effect of a semi-immersive VR environment on robot-assisted gait training (RAGT) is evaluated by comparing motivation-related outcomes between a VR group and a control group. The VR group demonstrates increased training time, a lower dropout rate, and higher acceptability, indicating enhanced motivation [2]. Moreover, the use of a semi-immersive VR environment in post-stroke rehabilitation is analyzed by comparing the intrinsic motivation inventory (IMI) scores between a control group and an intervention group. Patients in the VR group showed slightly higher motivation scores and positive reactions to VR therapy, as observed through video recordings [3]. A self-designed and validated questionnaire measures patient engagement in a non-immersive VR environment during upper limb rehabilitation. The results indicated high engagement levels, with patients demonstrating strong flow, presence, and low distraction during VR-based therapy [4].

Beyond its integration with robotic rehabilitation, the features and design elements of VR directly impact an individual's adherence to therapy. A self-designed questionnaire is utilized to evaluate the user experience of patients undergoing ankle rehabilitation with the Rutgers ankle rehabilitation robot in various VR environments [5], [6]. The questionnaire assesses the quality of the VR environment, patient fatigue, and overall enjoyment of incorporating VR into therapy, with patients consistently expressing strong agreement regarding

This study was supported by the Scientific and Technological Research Council of Türkiye (TUBITAK) under Grant Number 122E246.

The authors would like to thank the member of the Living Robotics Laboratory, Hafiz Muhammad Bilal for his support in controlling the 3-RPS manipulator of BALANSens.

*Corresponding author (e-mail: ehocaoglu@medipol.edu.tr)

their enjoyment of VR-based rehabilitation. Along the same line, the experiences of children with cerebral palsy using the PedPot Home, a home-based ankle rehabilitation robot, were assessed through a questionnaire aligned with the Home Exercise Program (HEP) Adherence Theory and the PYTHEIA scale. The results indicated that while the integrated game initially increased motivation, it decreased over time due to its repetitive nature, highlighting the need for alternative forms of challenge to maintain engagement [7].

Subjective self-reports, such as post-experiment questionnaires, are commonly used to assess user experience due to their broad relevance and ease of statistical analysis [8]. However, these methods are prone to biases, such as social masking or the inability of participants to effectively articulate their emotions. To address these limitations, psychophysiological measurements, which capture the body's electrophysiological activity (e.g., electrocardiogram (ECG), electromyography (EMG), and electrodermal activity (EDA)), have been increasingly utilized as complementary techniques [9]. While facial EMG is commonly used to analyze emotional states, the relationship between muscle activity in other body regions and emotional or motivational states remains underexplored.

The literature demonstrates that sEMG signals can serve as an effective biofeedback method within VR interfaces, not only enhancing patient motivation and compliance but also improving awareness of the rehabilitation process. Additionally, this approach enables therapists to quantitatively assess the patient's progress [10], [11]. Previous studies report that fun and game-based rehabilitation tasks yield more effective results compared to traditional physiotherapy exercises [12], [13]. Motor skills acquired through game-based training in a virtual reality (VR) environment are utilized more effectively in daily activities. To maximize therapeutic effectiveness, a high number of repetitions, continuous supervision, clear rewards, and long-term application are required. Hence, maintaining motivation is considered essential for enhancing patient engagement and treatment effectiveness. These movements should be performed in an interactive environment that supports cognitive, motor, and emotional components [10].

Studies integrating EMG-based assessments with surveys on motivation are limited. In this context, the effects of EMG-controlled video games on muscle activation and motivation in individuals with upper limb amputation are particularly examined [10]. It is reported that maximum voluntary contraction values increase before training (6,8%) and in the follow-up session (7,1%). Assessment with the IMI records high scores in interest, perceived competence, choice, and usefulness subscales, while low scores are observed in pressure and tension. Survey responses indicate that video game use during training maintains patient engagement, enhancing motivation, exercise intensity, and adherence throughout rehabilitation.

When a stroke patient moves their limbs, the automatic and active tracking of each movement phase indicates that the patient can place their limbs. This means that patients with good sensory input can fire the correct motor units to move. In this study, muscle activation changes during passive movement while playing games are measured using sEMG signals of healthy individuals. This aims to determine the development of the ability to actively and automatically engage in movement during passive motion when the game is visually challenging [14].

Active joint movement increases the potential for motor control development, supports motor learning processes, and enhances neuroplasticity by encouraging greater participation in rehabilitation [15]. The relationship between motor learning and neuroplasticity is directly related to how challenging, meaningful, and specific the exercises are. A high number of repetitions performed during a targeted muscle movement (e.g., gait training) can lead to lasting changes in the brain [16]. In this context, rehabilitation involving active movements integrated with technologies like VR increases neuroplasticity by encouraging patients to focus more on their movements and participate more in the treatment [16], [17].

Evaluating muscle activation with EMG during both passive and active movements allows for the objective assessment of the effectiveness of VR-based rehabilitation programs and motor learning [17]. The aim of this study is to assess and compare muscle activation and motivation levels during passive and active ankle dorsiflexion and plantarflexion movements, both with and without VR, as well as during monotonous and engaging VR games. Additionally, the effects of two different VR scenarios with slow and fast speeds on motivation are included in the study results. In this context, the effects of VR under different scenarios and speeds are thoroughly examined.

II. Methodology

The evaluation encompasses both passive and active ankle therapy on the BALANSens platform, with a focus on task-specific VR design and sEMG signal detection.

A. BALANSens Robotic Platform

The BALANSens robotic platform features a 3-degree-of-freedom (3-DOF) parallel manipulator utilizing a revolute-prismatic-spherical (RPS) configuration, tailored for lower limb and balance rehabilitation and assistance with multiple feedback modalities within the I-BAR framework [18], [19]. Its design connects the upper and lower platforms via prismatic joints, which are motorized, and passive revolute and spherical joints [20], [21]. The complete BALANSens system, as depicted Fig. 1 has been specifically engineered to support rehabilitation objectives effectively. The range of motion (RoM) of the 3-RPS robot can be adjusted to the upper limit of each participant, ensuring safe interaction during the evaluation.

B. Design of Virtual Reality Environment

According to Ryan and Deci [22], motivation can be either intrinsic, where an activity is pursued for its inherent enjoyment, or extrinsic, where the activity is performed to achieve an external outcome. Unlike intrinsic motivation, extrinsic motivation is often perceived as less fulfilling, as individuals may

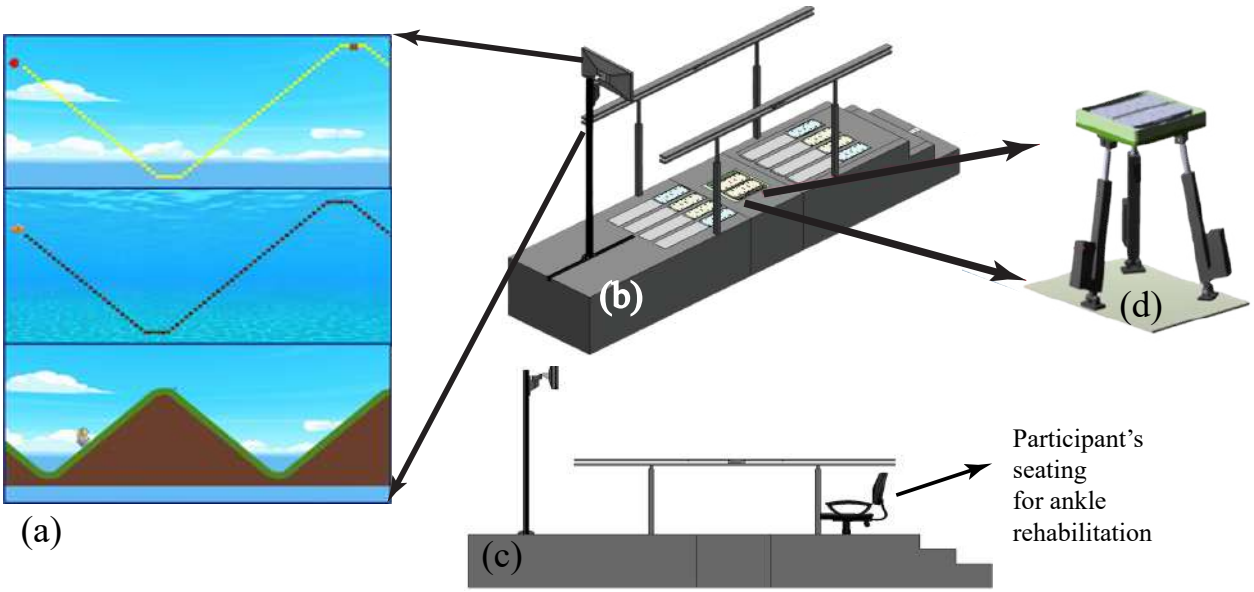


Fig. 1. BALANSens Platform with VR feedback (a) Designed games for passive ankle rehabilitation (b) Isometric view of BALANSens platform (c) Rear view of BALANSens platform, prepared for ankle rehabilitation (d) 3RPS parallel manipulator

engage in such activities with reluctance or disinterest, driven only by obligation. In the context of VR-based rehabilitation, patients' motivation is typically extrinsic—they participate in the game not for its enjoyment but as part of their therapy. The challenge, then, is to encourage patients to engage in the activity without feeling coerced. This can be achieved by making the activity sufficiently interesting [22].

The focus shifts to how VR environments can be designed to captivate patients' interest. Mader et al. [23] proposed a model outlining key criteria for creating therapeutic games. According to their framework, two essential features are challenge and variability. *Challenge* is defined as the uncertainty a player feels about their ability to achieve their goals, while *variability* encompasses curiosity—either cognitive, which reflects how much new information a player can acquire, or sensory, which pertains to the diversity in the game's presentation. To sustain motivation, the model emphasizes that challenge levels must be carefully calibrated to avoid frustration or boredom, and the environment must incorporate sufficient variability to maintain long-term engagement.

In VR environments designed for rehabilitation and motor recovery, maintaining an appropriate challenge level is crucial, as initial failure may lead players to attribute their performance to poor motor abilities, reducing engagement and participation [24]. Moreover, providing patients with feedback on their progress plays a key role in sustaining their motivation. What's more, a *flow state*, defined as a condition where an individual is fully immersed, focused, and satisfied with an activity, is considered crucial for enhancing patient performance in rehabilitation. In such a state, the VR environment should include clear goals, minimal distractions, appropriate difficulty, feedback, and a reward system to foster focus and satisfaction. From the therapist's perspective, the expectations closely align with the benefits of VR for the patients. Therapists value gaming features such as ease of setup, clear patient instructions, and easily interpretable feedback [25].

In accordance with the design criteria outlined in the literature, the VR environments in this study are purposefully crafted to meet these standards using the Unity game development platform. During ankle rehabilitation, participants perform dorsiflexion (DF) and plantarflexion (PF) to control a VR proxy, such as a bird, which collects objects like coins placed along a specific trajectory. This trajectory is designed to align with the RoM limits of the ankle.

C. Real-time sEMG Recording and Conditioning

sEMG signals are collected in real-time with Biosignal Plux© EMG sensors. The electrodes are placed on the tibialis anterior muscle and gastrocnemius muscles responsible for DF and PF of the ankle, respectively. sEMG signals are relayed to MATLAB through the lab streaming layer communication protocol, operating at a sampling rate of 2000 Hz. The acquired signal undergoes processing with a fourth-order Butterworth filter, employing cutoff frequencies of 20 Hz and 500 Hz to isolate the desired frequency range. The absolute value of the signal is computed to capture its full energy. Additionally, a moving average window is applied to further refine the signal. After normalization, the signal's energy is assessed using both the Hamming window method and a traditional energy evaluation approach. The energy method provides a representation of the signal's energy in the time domain but does not account for the irregular distribution of amplitude in sEMG signals, which often exhibit random structures. Energy deviation is employed to gain a deeper understanding of the signal's characteristics. This deviation is exposed by dividing the signal into smaller segments, with each segment

representing the variation in energy distribution over time. In this study, the Hamming-windowed sEMG energy feature vector is extracted to analyze muscular energy over time. The signal is divided into three segments, each multiplied by a window function, smoothing the signal by suppressing the edges and enhancing the center. The energy of each windowed segment serves as a feature, with the number of windows determining the feature vector size. Overlapping regions, set to three-tenths of the window length, are included to capture finer signal details [26]. Finally, both energy features are employed to construct sEMG feature vectors, which are utilized to gauge the participant's engagement in the rehabilitation process.

D. Experimental Procedure

The assessment of participants' engagement and cognitive contribution to therapy facilitated by VR environments is conducted in two main sessions. In the first session, engagement during passive ankle therapy is analyzed based on sEMG analyses, focusing on the immersive and interactive qualities of the VR environment, with additional insights derived from questionnaire responses. The second session emphasizes active participation in ankle therapy, integrating sEMG-based evaluations with questionnaire results to provide a comprehensive analysis.

In this experiment, seven healthy volunteers (three women, aged 20, 26, and 42 and four men, aged 22, 26, 29, and 30) participated, with informed consent obtained prior to the experiment following approval from the Institutional Review Board (IRB) of Istanbul Medipol University. During the experimental procedures, participants are positioned in a prolonged seated posture with knee support. A physiotherapist determines the normative RoM for ankle DF and PF using a baseline goniometer. Accordingly, the RoM of the 3-RPS manipulator for DF and PF is set individually for each participant to prevent neuromuscular issues, such as tendon strain or muscle fatigue. The hypothesis of the experiment was withheld from the participants. During the experiment, the participant sits on a chair with their foot strapped to the moving platform of the 3-DOF manipulator. The robot's rotational motion is used to train the participant's DF and PF RoMs.

In the first session, the participant's foot is strapped to the manipulator and follows the VR proxy passively with position control. This session consists of three subsessions, each lasting 3 minutes, with a 1-minute break in between. The order of the sessions is randomized for each volunteer. The subsessions include passive ankle rehabilitation without VR, monotonous VR-based passive ankle rehabilitation, and passive ankle rehabilitation with a relatively entertaining VR experience. In the second session, the manipulator's impedance control is activated, requiring the subject to interact and move the VR proxy. This session consists of two subsessions, each lasting 2 minutes, with a 1-minute break in between. The difficulty level of the tasks varies between the two subsessions, with the challenge being increased by a faster trajectory flow in the second subsession. An illustration of the experiment is available at the following link: https://youtu.be/AdOYldMuLgg. After each subsession, the volunteers are given a questionnaire to score the games.

III. Results

The sEMG-based evaluation of participants' engagement with the VR environment is illustrated in Fig. 2. During the experiment, sEMG signals are recorded from the Tibialis Anterior and Gastrocnemius muscles, which are responsible for DF and PF functions, respectively. A Student's t-test is performed to assess statistical significance between groups. As shown in Fig. 2(a) and (b), the results from the entertaining VR feedback condition demonstrate a statistically significant difference compared to both the monotonous VR condition and the non-VR condition. Additionally, the comparison between the non-VR and monotonous VR conditions is found to be marginally significant, with a p-value ranging between 0.05 and 0.1. These findings suggest that participants exhibit greater engagement with VR-based rehabilitation, even when no physical interaction is required, as the visual component alone appears to be sufficient to enhance their involvement. Immediately following each experiment, participants are presented with the IMI questionnaire [27] to evaluate the VR environment across dimensions of intrinsic motivation, including interest/enjoyment, perceived competence, effort, perceived choice, tension/pressure, and value/usefulness. Notably, the interest/enjoyment scores show a significant increase, rising from an average of 2 (out of 7) in the non-VR condition to an average of 5.87 (out of 7) in the enjoyable VR condition. This score is directly correlated with the EMG-based findings, supporting the conclusion that the participant's engagement with the game can be demonstrated through sEMG feature.

In the literature, it is well-established that EMG amplitude increases with greater effort. However, the extent to which engagement in the game contributes to EMG energy remains unclear. Building on the findings of the first session, the correlation we established between questionnaire results and sEMG feature is also investigated in the context of the active ankle rehabilitation experiment. In this session, the VR environment remains constant, but the difficulty level is adjusted by increasing the speed of the game (i.e., the trajectory to be followed in the VR environment). sEMG normalization is performed based on each participant's maximum contraction level during the session. Results from both muscle groups reveal a significant increase in sEMG energy across all participants, with a t-test confirming the statistical significance of differences between the subsessions. Following the experiment, participants are presented with the same questionnaire. The interest/enjoyment scores increased from an average of 6.2 (out of 7) in the easy task to 6.7 (out of 7) in the challenging task condition. Similarly, the effort scores rose from 4.2 (out of 7) in the easy task to 4.8 (out of 7) in the challenging task. These findings indicate that the sEMG features correlate with both effort exertion and participant engagement.

IV. Discussion

In this study, the implementation of VR environment with both passive and active rehabilitation provides a critical

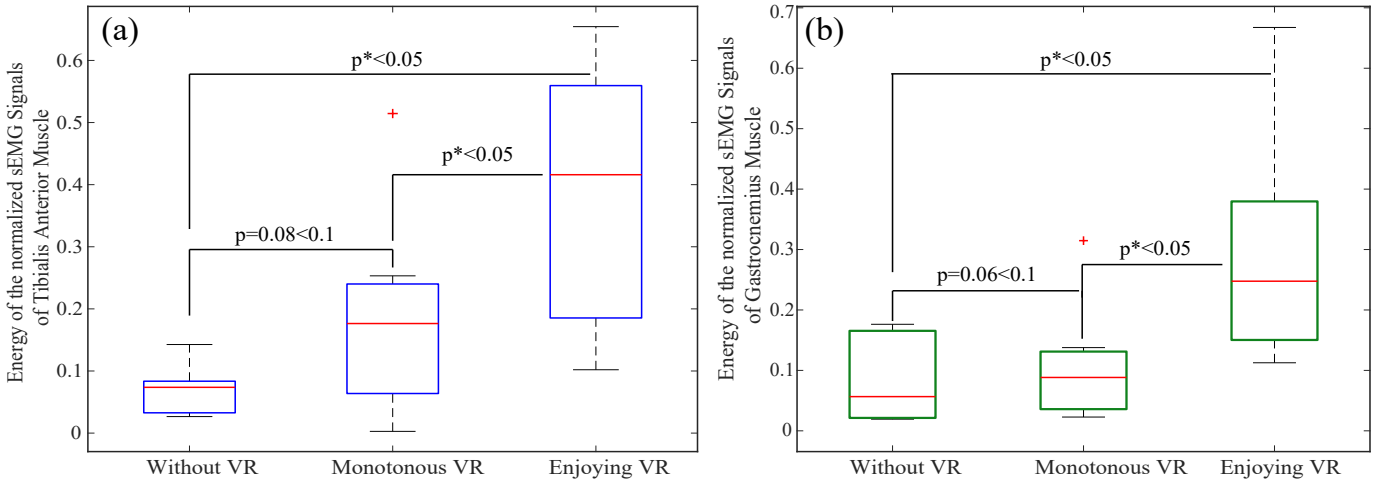


Fig. 2. Experimental evaluation of the participants during passive ankle rehabilitation with BALANSens (a) sEMG features from Tibialis Anterior muscle (b) sEMG features from Gastrocnemius muscle

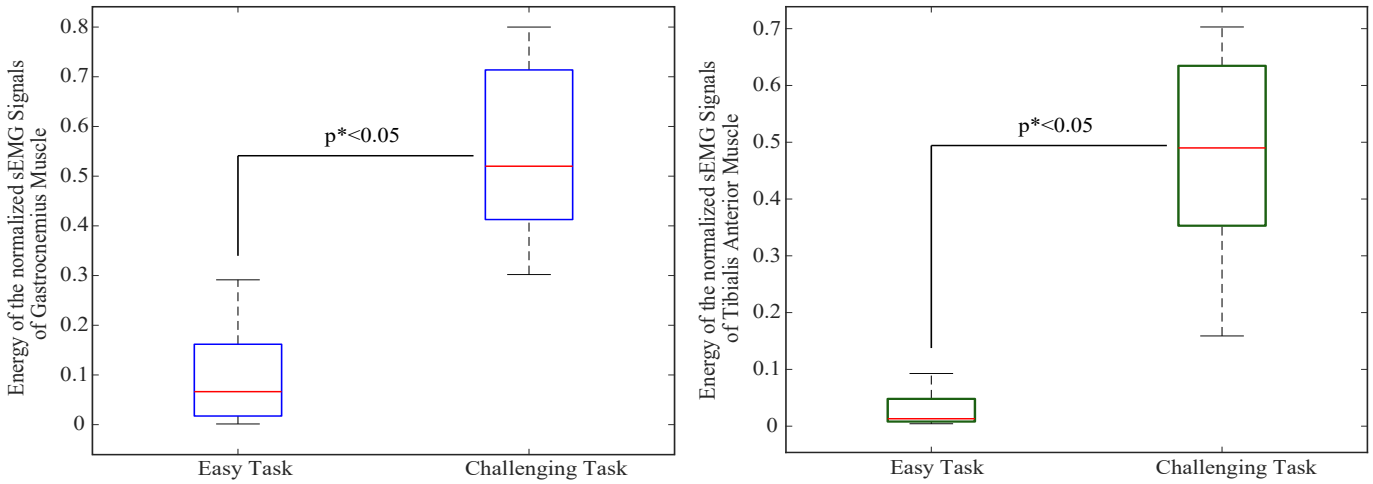


Fig. 3. Experimental evaluation of the participants during active ankle rehabilitation with BALANSens (a) sEMG features from Tibialis Anterior muscle (b) sEMG features from Gastrocnemius muscle

foundation for evaluating the effects of different intervention methods. While passive rehabilitation in monotonous VR environments may lead to low engagement, incorporating active movements can enhance participants' interest [16]. In our study, higher energy features of sEMG signals are recorded during passive movements with VR compared to movements without VR. Enjoying and challenging VR environments can foster active participation, yielding significant effects on motor control, muscle strength, and the neuromuscular system. Similarly, energetic EMG signals are observed during active ankle therapy with VR, enabling the assessment of participants' engagement in the rehabilitation process.

One of the primary advantages of VR technology in neurological rehabilitation is its ability to provide goal-oriented and highly repetitive training opportunities. VR creates enriched learning environments that support problem-solving, complex task execution, and the acquisition of new skills in individuals with stroke. Offering an alternative to the monotonous structure of traditional therapies, VR-based interventions are perceived by patients as more engaging and enjoyable. These attributes encourage a higher frequency of repetitions and improve adherence to treatment programs.

VR technology is effective in improving motor skills, balance, gait disorders, and cognitive functions (such as attention, memory, executive functions, and dual-task performance) in individuals with stroke. While VR enhances motivation and participation, monotonous environments can diminish motivation and reduce task duration. In contrast, engaging VR applications improve attention and performance, support neuroplasticity and motor control, and optimize learning by tailoring task difficulty to individual capacity. Excessive difficulty, however, can hinder effectiveness. Although traditional methods are effective, they often fall short in boosting motivation. VR addresses this gap by promoting interaction with the environment and supporting gains in range of motion (ROM) and muscle strength. In this study, it is observed that

games enriched with enjoyable elements and cognitive tasks led to higher muscle activation—and thus greater participation—compared to monotonous games. Such an observation is quantitatively evaluated by means of sEMG characterization.

The combined use of motivation surveys and sEMG features offers a valuable approach to evaluating rehabilitation processes both behaviorally and physiologically. The literature demonstrates that motivation positively influences muscle activity and task performance. Examining the relationship between these metrics can provide a more comprehensive understanding of VR's effectiveness in rehabilitation. Future research explores the impact of VR scenarios on motivation and sEMG outcomes to develop more personalized rehabilitation programs.

V. Conclusion

As the study is limited to healthy individuals, the generalizability of the findings to pathological populations remains uncertain. The sEMG and motivation responses of healthy individuals may not fully reflect the processes of neuroplasticity in patient groups, where these processes operate differently. Furthermore, only short-term effects have been evaluated, and it is unclear whether these findings will translate into functional improvements over the long term. Therefore, additional studies focusing on patient populations and long-term effects are needed.

A key strength of this study is determining individuals' level of engagement during passive movement using both the motivation questionnaire and sEMG data. The combined use of these two outcome measures provides a significant contribution to the literature by emphasizing the importance of individual adaptation and physiological responses in rehabilitation processes. The study may serve as a pioneering example of how VR applications can be an effective tool in personalized passive and active treatment plans.

Our research will expand to include a larger cohort of healthy individuals and stroke patients, with preliminary findings undergoing validation through data and survey evaluations collected from an expanded sample. These refined results will be presented to offer deeper insights into the effectiveness of the EMG-driven evaluation in assessing VR-mediated engagement during the rehabilitation process.

References

[1] K. Kingston, D. Jenkins, and G. Kingston, "Promoting adherence to rehabilitation through supporting patient well-being: A self-determination perspective," *Essentials of exercise and sport psychology: An open access textbook*, pp. 759–782, 2021.

[2] J. Bergmann, C. Krewer, P. Bauer, A. Koenig, R. Riener, and F. Müller, "Virtual reality to augment robot-assisted gait training in non-ambulatory patients with a subacute stroke: a pilot randomized controlled trial." *European journal of physical and rehabilitation medicine*, vol. 54, no. 3, pp. 397–407, 2017.

[3] P. Epure and M. B. Holte, "Analysis of motivation in virtual reality stroke rehabilitation," in *Interactivity, Game Creation, Design, Learning, and Innovation: 6th International Conference, ArtsIT*. Springer, 2018, pp. 282–293.

[4] S. S. Esfahlani, T. Thompson, A. D. Parsa, I. Brown, and S. Cirstea, "Rehabgame: A non-immersive virtual reality rehabilitation system with applications in neuroscience," *Heliyon*, vol. 4, no. 2, 2018.

[5] J. E. Deutsch, J. Latonio, G. C. Burdea, and R. Boian, "Post-stroke rehabilitation with the rutgers ankle system: A case study," *Presence*, vol. 10, no. 4, pp. 416–430, 2001.

[6] M. Girone, G. Burdea, M. Bouzit, V. Popescu, and J. Deutsch, "Orthopedic rehabilitation using the "rutgers ankle" interface," in *Medicine Meets Virtual Reality 2000*. Ios Press, 2000, pp. 89–95.

[7] M. M. Schladen and et.al., "Toward evaluation of the subjective experience of a general class of user-controlled, robot-mediated rehabilitation technologies for children with neuromotor disability," in *Informatics*, vol. 7, no. 4. MDPI, 2020, p. 45.

[8] R. L. Mandryk, M. S. Atkins, and K. M. Inkpen, "A continuous and objective evaluation of emotional experience with interactive play environments," in *Proceedings of the SIGCHI conference on Human Factors in computing systems*, 2006, pp. 1027–1036.

[9] A. E. Gaffey and M. M. Wirth, *Psychophysiological Measures*. Dordrecht: Springer Netherlands, 2014, pp. 5181–5184.

[10] N. A. Hashim, N. A. A. Razak, H. Gholizadeh, and N. A. A. Osman, "Video game–based rehabilitation approach for individuals who have undergone upper limb amputation: Case-control study," *JMIR Serious Games*, vol. 9, p. e17017, 2021.

[11] C. L. Toledo-Peral and et al, "Virtual/augmented reality for rehabilitation applications using electromyography as control/biofeedback: Systematic literature review," *Electronics*, vol. 11, p. 2271, 2022.

[12] R. Armiger and R. Vogelstein, "Air-Guitar Hero: A real-time video game interface for training and evaluation of dexterous upper-extremity neuroprosthetic control algorithms," in *IEEE BioCAS*, 2008.

[13] L. R. Swanson and D. M. Whittinghill, "Intrinsic or Extrinsic? Using Videogames to Motivate Stroke Survivors: A Systematic Review," *Games for Health Journal*, vol. 4, no. 3, pp. 253–258, Jun. 2015.

[14] G. V. M. N. Hanphode and S. Kanase, "The effectiveness of constraint-induced movement therapy and placing technique of bobath on upper limb function in hemiparetic individual," *Indian Journal of Public Health Research and Development*, vol. 10, no. 7, p. 25, January 2019.

[15] H. Sveistrup, "Motor rehabilitation using virtual reality," *Journal of NeuroEngineering and Rehabilitation*, vol. 1, no. 1, pp. 1–9, 2004.

[16] K. Chance-Larsen, "Ten guiding principles for movement training in neurorehabilitation," *OpenPhysio Journal*, vol. 2020, January 2020.

[17] J. H. R. Pelletier and D. Bourbonnais, "Addressing neuroplastic changes in distributed areas of the nervous system associated with chronic musculoskeletal disorders," *Phys. Ther.*, vol. 95, no. 11, pp. 1582–1591, November 2015.

[18] T. Ersoy, P. Kaya, E. Hocaoglu, and R. Unal, "I-BaR: integrated balance rehabilitation framework," *Frontiers in Neurorobotics*, vol. 18, p. 1401931, 2024.

[19] H. Bilal, E. Hocaoglu, R. Unal, and P. Kaya, "An overview of integrated balance rehabilitation (I-BaR) framework," in *International Conference on NeuroRehabilitation (ICNR)*, 2024.

[20] T. Ersoy and E. Hocaoglu, "A 3-DoF robotic platform for the rehabilitation and assessment of reaction time and balance skills of MS patients," *PLoS ONE*, vol. 18, p. 0280505, 2023.

[21] T. Ersoy, P. Kaya, E. Hocaoglu, and R. Unal, "Design of BalanSENS: Functional evaluation in ankle preparation phase," *Journal of Bionic Engineering*, vol. 21, 2024.

[22] R. M. Ryan and E. L. Deci, "Intrinsic and extrinsic motivations: Classic definitions and new directions," *Contemporary educational psychology*, vol. 25, no. 1, pp. 54–67, 2000.

[23] S. Mader, S. Natkin, and G. Levieux, "How to analyse therapeutic games: the player/game/therapy model," in *Entertainment Computing Conference-ICEC 2012*. Springer, 2012, pp. 193–206.

[24] D. R. Ferreira, C. K. Baptista, B. da Silva Rodrigues, B. C. Siqueira, S. M. Blascovi-Assis, and A. G. Corrêa, "Development and test of a serious game for dorsiflexion and plantarflexion exercises of the feet," *Journal on Interactive Systems*, vol. 12, no. 1, pp. 58–68, 2021.

[25] C. Hamilton, M. Lovarini, M. van den Berg, A. McCluskey, and L. Hassett, "Usability of affordable feedback-based technologies to improve mobility and physical activity in rehabilitation: a mixed methods study," *Disability and Rehabilitation*, vol. 44, no. 15, pp. 4029–4038, 2022.

[26] D. Toledo-Pérez, J. Rodríguez-Reséndiz, R. Gómez-Loenzo, and J. Jauregui-Correa, "Support Vector Machine-Based EMG Signal Classification Techniques: A Review," *Applied Sciences*, vol. 9, no. 20, p. 4402, 2019.

[27] E. L. Deci and R. M. Ryan, *Intrinsic motivation and self-determination in human behavior*. Springer Science & Business Media, 2013.

Curating User-Defined Interface Maps For Robot Teleoperation

Demiana R. Barsoum[1,2], Michelle H. Zhang[1], Larisa Y.C. Loke[1,2], and Brenna D. Argall[1,2]

***Abstract*— The interfaces used to operate assistive robots typically employ fixed, predefined maps to associate interface-level commands to robot control commands. User-defined control maps instead consider an individual's preferences and capabilities, moving away from a one-size-fits-all mapping paradigm. This work presents novel methods for (1) eliciting user-defined control maps, (2) identifying and addressing issues in control signal data that arise from such a user-centered design, and (3) methodologies to filter erroneous signals and construct synthetic data in an effort to address these issues. We experimentally evaluate our proposed methods by conducting a user study that elicits user-defined, interface-level commands for controlling a powered wheelchair and a robotic arm through four control interfaces. Our results highlight the differing suitability of user-defined, data-driven control maps for the various interface-platform pairings, and provide an analysis of the errors generated during dataset definition and the impact of our postprocessing methods.**

I. Introduction

Assistive robots—such as robotic arms and powered wheelchairs—play a crucial role in improving quality of life for many individuals living with motor impairments. By enhancing manipulation and mobility capabilities, these technologies advance user ability to complete daily functions with independence.

When an individual is fitted for an assistive device, an accompanying control interface—such as a joystick, head array, or sip/puff—is chosen and customized to best meet their needs and abilities. However, the limitations of such interfaces can render assistive devices difficult or unintuitive for users to control. A leading cause for the abandonment of assistive devices is lack of adaptability and configurability [1], which forces users to conform to interfaces and control schemes that do not adequately adapt to meet their individual needs. Research on device customization typically focuses on the interface hardware, including novel sensor setups and more diverse input options [2]. By contrast, less attention is given to the customization of control mappings used by interfaces that are the standards for assistive device control in clinical and real-world settings.

When a user actuates an interface, there is *noise* and *bias* associated with their issued control signals that is shaped by their physiology, psychology, and preferences. For example, handedness may result in biases in joystick actuation. Due to these noise and bias patterns, the ability of an individual to use an interface depends heavily on the alignment between their behavioral patterns and those expected by the control mapping. This dependence can restrict the accessibility of an interface for users whose behaviors do not align well with predefined expectations.

[1]Northwestern University, Evanston, IL., USA
[2]Shirley Ryan AbilityLab, Chicago, IL., USA

Interface control maps moreover can be unintuitive to operate, and require extensive practice before users are able to control devices effectively [3]. We posit that to investigate the noise and preference patterns in user control signal data is useful not only for identifying these patterns, but also for uncovering improved methods able to accommodate individual differences within the control interface design. Such an analysis ultimately might enable the creation of interfaces that are more accessible to a wider range of users.

In this paper, we propose and evaluate methods for constructing task-agnostic, user-defined control maps for robot teleoperation that adapt interface operation to the unique capabilities and preferences of a given user. This work makes the following contributions:

(1) We present a protocol for constructing datasets of task-agnostic interface use, for the purpose of generating customized interface maps for teleoperation.

(2) We design methods to identify, quantify, and filter artifacts that arise in datasets generated from user-defined, data-driven control interface design.

(3) We introduce an approach for generating synthetic data from users' verbal statements to capture their intended control mappings.

(4) We evaluate our proposed methods by conducting a participant study that elicits user-defined, interface-level commands for controlling a powered wheelchair and a robotic arm through four control interfaces (Fig. 1).

The rest of the paper is organized as follows. Section II outlines related literature. Section III details the proposed data processing methods. Section IV presents the user data collection pipeline, including experimental setup and protocol. Results and discussion are presented in Section V, including limitations and avenues for future work in Section VI, with conclusions presented in Section VII.

II. Background

In this section, we present a summary of related literature on teleoperation control and customization.

A. Control Interfaces and User Customization

Assistive devices and robots can be teleoperated using a variety of accessible interfaces such as joysticks, sip/puffs, eye gaze trackers, head arrays, brain-computer interfaces, body-movement interfaces, tongue-controlled interfaces, and lip-controlled interfaces, as well as customized setups and multi-interface systems.

Customization of these interfaces is a widely researched topic [4]–[6]. Joystick handles, for example, can be re-

designed to allow control using wrist movements [7], accommodating users with limited or no hand motion. Interfaces such as the sip/puff and MouthPadˆ (Augmentalˆ, California, USA) are designed for individuals with upper body paralysis. While their actuation mechanisms are accessible, the learning curve for using accessible interfaces to operate assistive devices and robots can be high [5], particularly as many issue lower-dimensional signals than the device being controlled and, as a result, use modal control paradigms (mode switching) [8].

B. Control Mappings for Teleoperation

Teleoperation is an attractive means of controlling assistive devices because it allows users to remain maximally in control, preserving user agency. However, the mismatch between a user's physical capabilities and the input requirements of standardized control mechanisms can hinder effective device operation, leading to frustration, fatigue [4], and device abandonment [1]. Work in the design of control maps that explicitly aim to address such a mismatch is overviewed here.

In detail, the mapping from interface actuation signal ϕ (e.g., joystick deflection) to machine control command u (e.g., joint or end-effector velocity) is typically static and defined *a priori* by experts (system engineers or assistive technology technicians). There is work that investigates instead learning user-preferred mappings for intuitive robot control [9], where the learned mapping is task-dependent. Customizing standard control maps to accommodate users' characterized physiological variability is also explored [10], using an approach that relies on a predefined baseline map. Other work aims to explicitly model discrepancies between intended ϕ_i and measured ϕ_m interface commands [11], where discrepancies might arise due to physiological factors such as fatigue or motor impairment, or an incomplete understanding of the robot system. All of these works evaluate a single combination of interface and platform.

In this paper, we propose a methodology for the design of *user-defined* control maps that are *task-agnostic* and leverage knowledge of intended interface commands—by capturing user biases and preferences— to postprocess noisy and scarce data. We also evaluate this methodology on multiple interfaces, operating two robot platforms.

III. Technical Methods

In this section, we provide an overview of our proposed methods for constructing datasets for the purpose of learning user-defined interface maps.

We first present a methodology to elicit users' preferred interface commands for task-agnostic robot actions (Sec. III-A). However, a dataset gathered from examples of human-issued interface commands and associated robot motion labels can be prone to data sparsity and inconsistencies between the human's intended versus issued interface commands (Sec. III-B). We therefore propose a suite of data processing tools that aim to address these potential pitfalls (Sec. III-C and Sec. III-D). In particular, our methods leverage verbal descriptions from the user of their intended interface commands, which we convert to automated scripts



Fig. 1: Experimental Hardware. Robot platforms (*top, left to right*): Sunrise Quickie powered wheelchair and Kinova JACO robotic arm. Control Interfaces *(bottom, left to right)*: 3-axis Joystick, Sip/Puff, 3-switch Head Array, and x-IMU3 sensors.

that generate both *filtered data* that refines the raw signals and *synthetic data* based on the user's vocalized intent.

A. User-Defined Control Interface Maps

We consider a user-defined interface-level command to represent the user's intended actuation of an interface to produce an observed robot motion. These commands can be continuous, discrete, or both, depending on the control interface. Continuous signals can be interpreted proportionally, while discrete signals, such as button presses, only provide an indicator of activation without magnitude. An "intuitive" control map has previously been defined [9] to have the following properties:

- Proportional: The system's response scales with the command's input intensity.
- Reversible: Opposing interface actuations (e.g., left-right deflection) correspond to inverse commands.
- Consistent: Users can remember the correspondence between interface actuations and system controls, and reliably issue them.

In this work, we prompt users to issue their preferred interface-level command ϕ in response to observed robot motion a. We furthermore propose a data collection protocol that *annotates* this data with vocalizations of their intended interface-level commands—capturing complete, unfiltered interface interactions, including noise and incorrectly issued (unintended) commands that may diminish the quality of the data. The purpose of these intent annotations is to provide a means for repairing such artifacts.

While such an approach leaves the control design in the hands of the user, it can also result in violations of the aforementioned properties of an intuitive control map, as well as artifacts in the data that pose considerable challenges for model training. These challenges ultimately inform our data postprocessing and synthetic data generation methods (Secs. III-C, III-D).

B. Implications of User Design

The usage characteristics of a given interface, combined with the user's understanding of its control method, leave

TABLE I: Discrepancies observed in user-defined datasets and proposed methods to handle these issues.

Artifact	Sources	Data Processing Techniques
Incorrect Command	(1) Unfamiliar with interface (2) Struggle to actuate interface (3) Forget how to issue a command or how to actuate the interface	(a) Replace with synthetic data (b) Replace with correct data from user (c) Remove from dataset
One-to-Many Command	(1) Issue similar (or identical) signals for different robot actions	(a) Replace with synthetic data
Data Sparsity	(1) Insufficient training data for command (2) Similar signals for different robot actions	(a) Add synthetic data (b) Add copies of raw user data
Noisy Signal	(1) User actuation behavior (2) Environmental interference	(a) Replace with synthetic data (b) Replace with correct data from user

a distinct imprint on the signal intended for robot control. This imprint can be beneficial if it helps produce a control mapping tailored to the user's unique behavior, or it can be problematic if the user develops inefficient or inconsistent control patterns. Additionally, the inherent variability in allowing users to design their own control maps may result in unusual or unpredictable control signals.

In this work, we identify four *categories of user-induced dataset artifacts*, along with their potential sources, summarized in Table I. We highlight potential strategies for mitigating issues that arise from these artifacts in the *Data Processing Techniques* column.

Furthermore, we identify and define five notable *types of actuation error* that can result from these artifacts and contribute to the aforementioned dataset challenges. To do so, we first define an interface channel to be an independent input signal of a control interface. Each channel is activated through an actuation mechanism: for example, joystick deflection, head array button press, or sip/puff respiration. Channels can be discrete or continuous in value. The types of actuation error then are defined as follows:

(1) Incorrect Activation: At least one intended channel is activated but in the wrong direction, or at least one unintended channel is activated with a magnitude greater than or equal to that of the intended channel(s).

(2) Additional Channel Activation: The intended channel(s) is activated, but there are also nonzero signals in one or more extraneous channels with magnitudes lower than those of the intended activations.

(3) Missing Channel Activation: The intended channel is not activated for a substantial portion of the command duration.

(4) Transient Zero: At least one intended channel momentarily reports zero activation when it is expected to have a consistent nonzero value.

(5) Leading/Trailing Zero: An intended channel exhibits periods of zero activation, as a result of the user pausing before and/or after issuing a command.

In our implementation, the groundtruth intended channels are derived (Sec. III-C) from a user's vocalized annotations.

C. Methodology for Filtering

Here, we present our methodology for identifying and filtering out the aforementioned dataset artifacts based on the error type. We propose a ***filtering methodology*** that *removes* instances of:

(1) Incorrect activation.

(2) No channel activation, which includes missing channel activations, transient zeros, and leading/trailing zeros.

In order to determine signal correctness, we leverage user annotations of intended interface signals. Specifically, our data collection protocol (Sec. III-A) annotates examples of interface→robot control mappings with vocalizations of the intended interface command. Our application of this filtering methodology is coarse and applies only to:

(1) Signal *absence* or *incorrect sign* on intended channels.

(2) Signal *presence* on unintended channels.

Notably, such an application may not catch all errors—incorrect patterns of interface activations, for example, will be missed. However, the likelihood that it filters correct signals will also be minimized.

D. Methodology for Synthetic Data Generation

Next, we present our methodology for generating synthetic data to rectify dataset artifacts. We propose a ***synthetic data generation methodology*** that *replaces* instances of:

(1) Signal *absence* or *incorrect sign* on intended channels.

Notably, this replacement approach retains unintended channel activations, as well as commands whose magnitudes differ from those of the intended signals, in order to preserve real-world variability and noise to enrich the dataset.

For a user annotation to be eligible for synthetic data generation, it must meet the following criteria:

(1) Non-varying in magnitude.

(2) No intended transient zeros (patterns).

As with our filtering methodology, such an application will not generate data for all annotations: only straightforward and unambiguous intended inputs will qualify. We leave the interpretation of more complex annotations and input patterns to future work.

To generate synthetic data, we define replacement rules for the three most common interfaces used to operate powered wheelchairs: joystick, head array, and sip/puff. We build these synthetic representations by hand, according to the following prescription:

(1) **Joystick Mapping**: The joystick interface utilizes a three-axis control scheme, denoted as $[x, y, z]$. Based on the deflection direction, the joystick mapping translates to the corresponding channel activations as follows:

- **Forward**: [0.0, 1.0, 0.0]
- **Backward**: [0.0, -1.0, 0.0]
- **Left**: [1.0, 0.0, 0.0]

- **Right**: [-1.0, 0.0, 0.0]
- **Twist Left (Counterclockwise)**: [0.0, 0.0, 1.0]
- **Twist Right (Clockwise)**: [0.0, 0.0, -1.0]

(2) **Head Array Mapping**: The head array interface consists of multiple pads that once pressed map to specific channel activations:

- **Back Pad**: [1, 0, 0, 0]
- **Right Pad**: [0, 1, 0, 0]
- **Left Pad**: [0, 0, 1, 0]
- **Chin Switch**: [0, 0, 0, 1]

(3) **Sip/Puff Mapping**: The sip/puff interface maps to continuous values based on respiration pressure. The range for a user is based on their intent vocalizations:

- **Sipping**: Ranges from 0.0 to 1.0
- **Puffing**: Ranges from -1.0 to 0.0

These rules are applied to data that meet the replacement criteria defined above.

IV. Experimental Procedure

In this section, we overview the details of our evaluation study in which participants observe the movements of a robotic wheelchair and a robotic arm, and are asked to vocalize, practice, and issue their intended interface-level commands corresponding to the movements.

A. Participants

A total of ten participants without motor impairment (6 female, 4 male) and with ages ranging from 23 to 52 years (mean 30.1$\pm$8.18) were recruited for this study. Participants gave their informed, signed consent to participate in the experiment, which was approved by Northwestern University's Institutional Review Board (STU00217536). None of the participants had prior experience with powered wheelchair driving. One participant (F, 25) had experience operating robotic arms, but not the robotic arm used in this study.

Each volunteer participated in two study sessions, during which a single robot platform was operated. The order of platform presentations was random and approximately balanced across participants (6 of 10 interacted with the robotic wheelchair in the first session).

B. Hardware

Two robotic platforms and a total of four control interfaces are utilized in the study (Fig. 1).

Robot Platforms. The first robot platform is a robotic wheelchair, built atop a Sunrise (Arizona, USA) Quickie Q500M base. Platform control is achieved through the LUCI ROS 2 SDK [12]. The wheelchair is a differential drive robot, which operates in 2-D, allowing for translational (forward/backward) and rotational (spinning) movement.

The second robot platform is a Jaco Gen2 robotic arm from Kinova Robotics (Quebec, Canada). Platform control is achieved through the Kinova SDK [13]. The Jaco is a 7-DoF non-anthropomorphic robotic arm with a 3-finger gripper—offering 6-D control (3-D translation and 3-D rotation) in task space.

Participants have no control over the motion of the robots during the study. All movements (Sec. IV-C) are prerecorded and controlled by the experimenters.

Control Interfaces. Three of the four interfaces—joystick, sip/puff, and switch-based head array—are commercial standards for powered wheelchair operation, selected to encompass a broad range of dimensionality, continuity, and actuation mechanisms. The fourth interface is not a commercial standard, but offers a richer input space to better match the higher-dimensional output space of a robotic arm. It uses a set of n inertial measurement unit sensors (IMUs) to track the upper body motions of participants, where n is determined based on the movements chosen by the participant (e.g., two-arm versus one-arm motions).

- Joystick. A 3-axis joystick (CH Products, California, USA) with 3 axes of deflection and 12 buttons.
- Sip/Puff. A 1-D USB Sip/Puff Breeze Switch (Origin Instruments, Texas, USA) that is operated via respiration and outputs a continuous-valued pressure signal.
- Head Array. A 3-switch FUSION Proportional and Digital head array with a chin switch (Adaptive Switch Laboratories, Inc., Texas, USA) that detects head taps to the back, left, and right pads and chin presses to the chin switch. This interface is used with the ASL ATOM Wireless Mouse Emulator which converts pad and button activations into discrete mouse inputs for data recording on a computer.
- IMU Sensors. The IMU-based motion tracking interface consists of x-IMU3 sensors (x-io Technologies Limited, Bristol, UK) attached to the participant via x-IMU3 elasticated straps. Each IMU outputs a 4-D (quaternion) velocity signal, corresponding to the motion of the participant body part to which it is affixed.

Participants are free to issue commands over any number and combination of channels on the given interface in use.

C. Study Protocol

Setup for Wheelchair. During the powered wheelchair session, each participant is seated in the wheelchair and asked to physically actuate the joystick, head array, and sip/puff interfaces. The head array is positioned for optimal activation. Participants observe 8 prerecorded, task-agnostic robot motions: *forward, backward, clockwise-spot-turn, counterclockwise-spot-turn, forward-clockwise, forward-counterclockwise, backward-clockwise,* and *backward-counterclockwise.*

Setup for Robotic Arm. During the robotic arm session, each participant is seated a safe distance from the arm and asked to physically actuate the joystick, sip/puff, and IMU interfaces. Participants are presented with 12 prerecorded, task-agnostic robot motions: *forward, backward, left, right, up, down, roll-clockwise, roll-counterclockwise, pitch-up, pitch-down, yaw-left*, and *yaw-right*.

Study Procedure. The study consists of two phases that are repeated for each interface:

(1) *Familiarization*. Participants are instructed on all avail-

able channel activations of the given interface.[1]

(2) *Map Data Collection*. Participants observe the prerecorded robot motions, presented as reversible pairs (e.g., forward/backward) in a randomized order that is balanced across participants. (The presentation order within the pairs themselves is also randomized and balanced.) For each observed motion:

- Participants first verbalize the interface-level command they would like to associate with the observed motion and are encouraged to practice issuing this command through the interface.
- Participants issue the interface-level command they have verbalized. To help anchor their command, the prerecorded robot motion is repeated as they issue their intended command through the interface.

Control signal data from the interface is recorded during both steps, including practice. For the sip/puff interface, visual feedback in the form of a pressure signal plot is provided.

D. Datasets

We generate *six* datasets based on our data processing methodologies presented in Section III:

- *Raw*: User's issued interface actuation signals.
- *Filtered*: Refines the raw signals according to the methodology described in Section III-C.
- *Synthetic*: Contains data generated based on the user's intended interface commands according to the methodology described in Section III-D.
- *Synth-raw*: Union of raw and synthetic datasets.
- *Synth-filtered*: Union of filtered and synthetic datasets.
- *Balanced*: Upsamples the raw signals to ensure all classes have the same number of samples as the most populated class in that raw dataset.

The *Synth-raw* formulation expands the size of the dataset while preserving the richness of the raw user interface-level commands. By retaining the inherent noise of the raw signals, the machine learning model is encouraged to tolerate variability and identify underlying patterns within the data. By contrast, the *Synth-filtered* formulation removes this noise.

We also compare the performance of our synthetic data generation method against state-of-the-art techniques:

- *SoTA-cont:* Random noise augmentation [14] by adding Gaussian noise to the raw signals ($\mu = 0, \sigma^2 = 0.05$).
- *SoTA-disc:* A Conditional Generative Adversarial Network (CGAN) [15].

While random noise augmentation is broadly deployed throughout the field, it is not suitable for discrete inputs. We therefore train a CGAN on the set of $\{(\phi_m^t,\ a^t)\}$ pairs for the head array interface. By conditioning both the generator and discriminator on a^t, the CGAN is able to produce meaningful synthetic data that mirrors the original dataset and is contextually relevant to the robot's actions.

We thus generate seven datasets (six based on our methodologies and one SoTA) for each interface-robot combination, with one notable exception: the IMU Sensors. None of the data generated using the IMU Sensors interface met the eligibility criteria for our Filtering or Synthetic Data Generation methodologies (Sec. III-C and III-D). Thus, only *raw* datasets are generated for this interface.

E. Machine Learning Algorithms

We select a subset of open-source machine learning algorithms to assess the viability of our proposed dataset generation methods using the open-source package PyCaret [16], which uses Scikit-learn [17] for the implementation and automated hyperparameter tuning of multiple algorithms.

Given the structure of our data, $(\phi_m^t,\ a^t)$, which includes robot motion labels, we focus on a supervised learning approach. We frame our problem as a classification task, requiring each model to predict a probability distribution over robot action labels given an interface signal input, and outputting the highest probability action. We explore a total of 16 machine learning algorithms, ranging from simple and lazy such as K-Nearest Neighbors (KNN) to more complex architectures such as Neural Networks (NN)—plus a chance classifier baseline that predicts a random label. Our selection spans a diverse range of capabilities, including models suited for high-dimensional data (e.g., Gaussian Naive Bayes [18]) and those effective for handling complex, high-variance data (e.g., ensemble methods [19]).

We implement a Feed-Forward Neural Network using TensorFlow and Keras [20], while our CGAN is implemented in PyTorch [21]. The hyperparameters for these two models, which are not included in PyCaret, are detailed in Table II.

To build and validate our models, we perform an 80/20 split into training and testing sets for each dataset. We conduct 10-fold cross-validation on the training set and take the best-performing of these to be our model, which is then evaluated on the holdout test set data. The results in Section V report on this test set performance.

TABLE II: Neural Network and CGAN model parameters and training hyperparameters.

Machine Learning Model	**Hyperparameters**	
Neural Network (NN)	activation function	relu & softmax
	loss function	CCE
	learning rate	0.001
	epoch	200
	optimizer	'Adam'
Conditional Generative Adversarial Network (CGAN) (Generator only)	activation function	relu & softmax
	loss function	BCE
	learning rate	0.001
	epoch	5000
	optimizer	'Adam'

F. Analysis Methods

To evaluate the performance of our models across the different datasets, we use both entropy and accuracy. *Entropy*, H, quantifies the level of uncertainty in a prediction. Lower entropy values indicate reduced uncertainty in the model. The

[1]For robotic arm sessions, prior to interface familiarization, participants additionally are presented with the prerecorded robot arm motions (which are more complex and unfamiliar).

following equation [22], modified to include normalization, is used to calculate H:

$$H_{\text{norm}}(X) = -\frac{1}{\log_2(n)} \sum_{i=1}^{n} p(x_i) \log_2 p(x_i)$$

where n is the number of class labels for each robot platform.

For each prediction, we compute H on the probability estimates for the most likely class label, classifying the prediction into one of four categories: (a) correct and certain, (b) wrong and certain, (c) correct and uncertain, and (d) wrong and uncertain. We define a second performance metric, *certain-accuracy*, which accounts for both model certainty and accuracy, using the formula:

$$\textit{Certain-Accuracy} = \frac{|a|}{|a| + |b|}$$

We define a baseline threshold for whether a model is predicting with certainty to be the entropy of a random classifier, which varies by participant-platform-interface-dataset type combination. All models' entropy values are compared to this threshold.

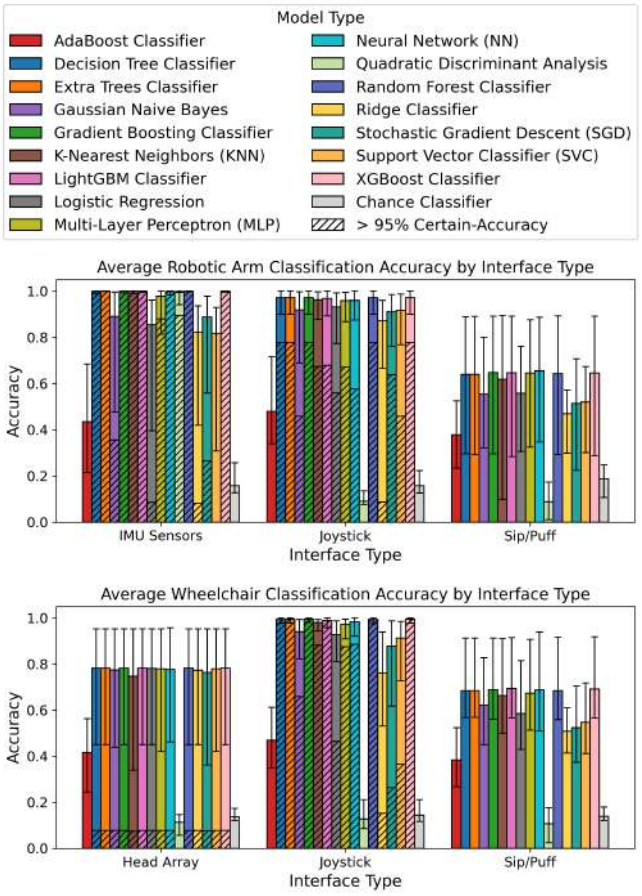


Fig. 2: Average model accuracy across all participants (S01-S10) for the robotic arm (top) and robotic wheelchair (bottom) platforms, clustered by interface type. For each bar (interface-platform-model combination), the proportion of participants whose model demonstrated a certain-accuracy greater than 95% is indicated with hatch lines.

V. Results and Discussion

We first evaluate the performance of a suite of machine learning models trained and tested on the raw datasets. For models that fall below a performance threshold of 60% prediction accuracy, we analyze the impact of our postprocessing methodologies. We also quantify the types of actuation errors (Sec. III-C) observed in the raw datasets.

A. Performance of Models

For each classification algorithm, Figure 2 shows the average accuracy aggregated across all 10 participants grouped by interface type for each robotic platform. These results indicate that multiple algorithms are able to successfully learn control map models for the joystick and IMU sensors interfaces, while all algorithms struggle to learn models for the sip/puff and head array interfaces. This struggle is evident in both the overall accuracy and the certain-accuracy demonstrated by the resulting models.

Notably, the sip/puff and head array interfaces offer less complex—lower-dimensional and/or discrete—input signals, which introduces challenges such as data sparsity and one-to-many command mappings (if participants develop difficult-to-disambiguate patterns to compensate for limited input options). By contrast, the IMU sensors interface offers the richest input signals and achieves the highest performance of all interface-platform combinations, with multiple algorithms demonstrating perfect accuracy.

Table III summarizes the algorithms that are high-performing on the raw datasets.[2] Here, the determination of *high performance* is a prediction accuracy that exceeds the 95% threshold, when averaged across all participants.

Of these 10 algorithms, 9 are high-performing on half of the interface-platform combinations. Among these, 6 are ensemble methods—Decision Tree, Extra Trees, Gradient Boosting, LightGBM, Random Forest, and XGBoost—which combine predictions from multiple weak models with high variance to produce a single prediction with low variance. Such an approach appears to be well-suited to the high variability, low sample volume, and sparsity present in our datasets. The remaining algorithms that are high-performing but are *not* ensemble methods are the Neural Network, Multi-Layer Preceptron (MLP), and K-Nearest Neighbor algorithms, all of which are able to model highly nonlinear decision boundaries.

B. Analysis of Methodologies

We analyze the impact of our postprocessing methodologies on *prediction accuracy* and *prediction certainty* for participants whose (*raw*) models are low-performing, meaning they achieve less than 60% prediction accuracy. For raw datasets that are already high-performing, postprocessing methodologies are of limited utility. We assess prediction certainty through a measure of entropy, where lower entropy correlates with lower uncertainty. Two platform-interface combinations meet this low performance criteria: **robotic arm & sip/puff** (participants S04, S08, and S09) and **wheelchair & head array** (participants S05 and S10).

[2]Four algorithms are never high-performing on any dataset, so they are omitted from this table: AdaBoost, Gaussian Naive Bayes, Ridge Classification, and Stochastic Gradient Descent (SGD).

TABLE III: High Performance Algorithms on the Raw Datasets.

Platform	Interface	Decision Tree	Extra Trees	Gradient Boosting	KNN	LightGBM	MLP	NN	Quadratic Discriminant Analysis	Random Forest	XGBoost
Robotic Arm	IMU Sensors	✓	✓	✓	✓	✓	✓	✓	✓	✓	✓
Robotic Arm	Joystick	✓	✓	✓	✓	✓	✓	✓		✓	✓
Robotic Arm	Sip/puff										
Wheelchair	Head Array										
Wheelchair	Joystick	✓	✓	✓	✓	✓	✓	✓		✓	✓
Wheelchair	Sip/puff										

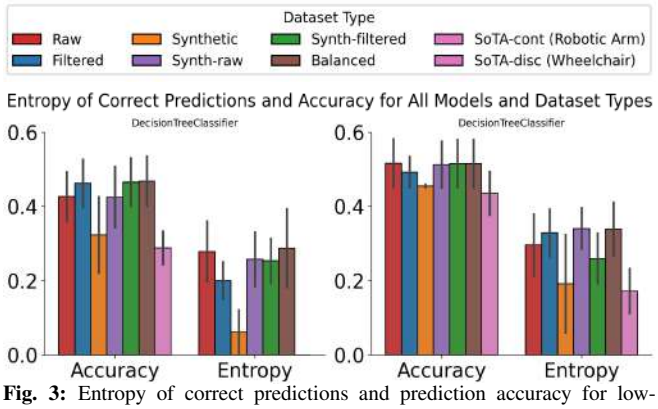


Fig. 3: Entropy of correct predictions and prediction accuracy for low-performance (lower than 60% accuracy) models trained and tested on the raw datasets: robotic arm & sip/puff (*left*, participants S04, S08, and S09) and wheelchair & head array (*right*, participants S05 and S10).

Only these five participant-platform-interface combinations are evaluated in the following postprocessing methodology analysis.

Figure 3 presents the entropy of correct predictions and prediction accuracy for each low-performance platform-interface combination, averaged over the five participants. For presentation clarity, only one representative algorithm is shown (Decision Tree Classifier); results for all algorithms are summarized next.

For the robotic arm & sip/puff combination shown in Figure 3, only one methodology noticeably reduces entropy without a sacrifice in prediction accuracy (in fact, accuracy slightly improves): our *Filtered* methodology. Across all tested machine learning algorithms, 62.5% (10 of 16) exhibit this trend of decreasing entropy while preserving or slightly increasing accuracy with the *Filtered* methodology, in comparison to the raw dataset. Additionally, 10 (of 16) exhibit this trend with the *Synth-filtered* methodology, and 1 (of 16) with *Synth-raw*.

Any other methodologies that reduce entropy do so at the cost of prediction accuracy, while other methodologies that preserve prediction accuracy do so without reducing entropy. Notably, the SoTA (*SoTA-cont*) and the standard data postprocessing technique of upsampling (*Balanced*) exhibit this trend for only *one* algorithm; in all other cases, our postprocessing methodologies outperform both the SoTA and standard postprocessing technique.

For the wheelchair & head array combination shown in Figure 3, it is also the case that only one methodology noticeably reduces entropy without a sacrifice in prediction accuracy: our *Synth-filtered* methodology. This trend again holds across 62.5% (10 of 16) of the tested machine learning algorithms. Additionally, 2 (of 16) exhibit this trend with the *Synthetic* methodology, and 1 (of 16) with each of *Filtered* and *Synth-raw*.

Notably, for this platform-interface combination, *neither* the SoTA (*SoTA-disc*) nor the standard data postprocessing technique of upsampling (*Balanced*) ever exhibit this trend for *any* algorithm. Our collective postprocessing methodologies thus outperform both the SoTA and standard postprocessing technique.

C. Quantifying Errors

For interfaces that meet our criteria for filtering (joystick, sip/puff, head array), we quantify actuation errors as defined in Section III-B. Errors are tallied for each participant, and the aggregated counts are reported in Figure 4. An illustration of selected individual participant error counts and types is also provided for the robotic arm & joystick combination—showcasing the variability in errors across participants. Note that a single actuation can contribute to multiple error categories (e.g., both "wrong command" and "missing activation").

The most frequent errors across all interfaces are **incorrect activation** and **leading/trailing zeros**. As expected, given the challenges of using the sip/puff device, **incorrect activation** errors are more prevalent for this interface. For head array, a notable number of **missing channel** errors are observed, likely due to suboptimal device positioning that can hinder a user's ability to issue simultaneous commands.

VI. Limitations and Future Work

A major limitation of this work is that our method was evaluated solely using data from people without motor impairment. In practice, motor impaired users may experience interface actuation difficulties unique to their conditions that were unobserved in the data we collected, and could affect the performance of our methodologies.

Future work will extend this work to end-users, evaluating how user-defined interface maps can be customized to their specific interfaces, needs, and preferences. We will also evaluate the utility of these user-defined control maps when used for robotic teleoperation. For the sip/puff interface, where a clear method for filtering data is currently lacking due to user variations in definitions for Φ, future efforts will explore better methods to filter noise both online (real-time) and offline (post-hoc), as well as investigate practical strategies for synthesizing data. While user-driven design is important, due to artifacts that can arise, a more collaborative design process will also be explored where researchers provide feedback on the feasibility of preferred commands.

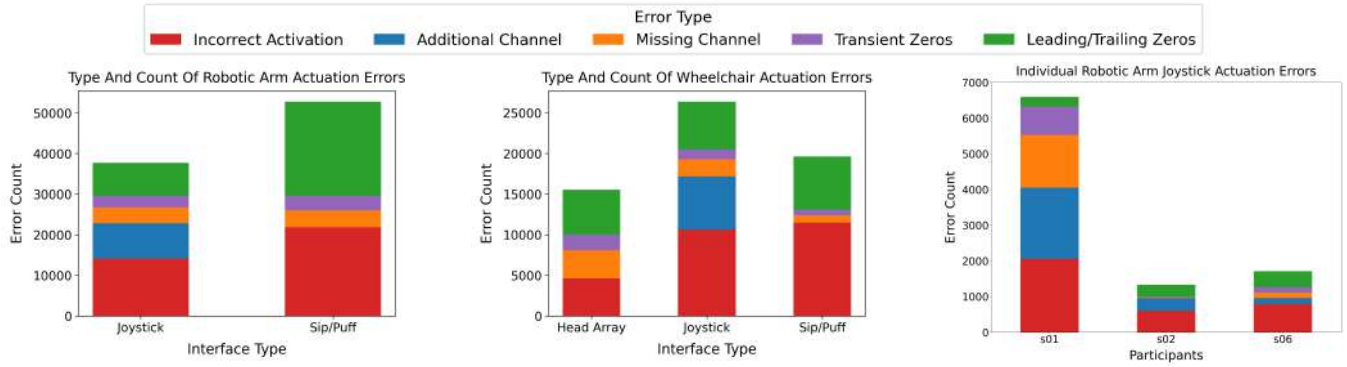


Fig. 4: Aggregated counts and types of actuation errors in the raw dataset for each platform-interface combination meeting the filtering criteria (Sec. III-C), tallied across all participants (left and center) and showcasing the variability between individual participants (right).

VII. Conclusions

In this work, we presented methods for curating user-defined interface control maps, addressing challenges in user-centered design, and filtering actuation errors to enhance dataset quality. Our experimental work evaluated, in a participant study, user-defined interface maps for two robotic platforms and four control interfaces. The performance of a suite of machine learning models on this data showed that multiple algorithms were able to successfully learn maps derived from raw joystick and IMU sensor signals. For platform-interface combinations that struggled to learn mappings between interface-level commands and robot actions, training on datasets curated via our postprocessing methodologies was demonstrated to decrease uncertainty. These results underscore the differing suitability of user-defined, data-driven control maps for various interface-platform combinations. By enhancing adaptability and personalization in assistive device control, this work contributes to more user-customized robotic teleoperation systems.

Acknowledgment

The authors would like to thank Corinne Fischer, OTR/L, Occupational Therapist at the Shirley Ryan AbilityLab, for assisting with sessions. Funding for this work was provided by the National Science Foundation under Grant CMMI-2208011. Any opinions, findings, and conclusions or recommendations expressed in this material are those of the authors and do not necessarily reflect the views of the National Science Foundation.

References

[1] A. T. Sugawara, V. D. Ramos, F. M. Alfieri, and L. R. Battistella, "Abandonment of assistive products: assessing abandonment levels and factors that impact on it," *Journal of Disability and Rehabilitation: Assistive Technology*, vol. 13, no. 7, p. 716–723, 2018.

[2] C. L. Fall *et al.*, "Wireless semg-based body–machine interface for assistive technology devices," *Journal of Biomedical and Health Informatics*, vol. 21, no. 4, p. 967–977, 2016.

[3] Y. M. L. R. Silva, W. C. S. S. Simões, E. L. M. Naves, T. F. Bastos Filho, and V. F. De Lucena, "Teleoperation training environment for new users of electric powered wheelchairs based on multiple driving methods," *IEEE Access*, vol. 6, 2018.

[4] I. Mougharbel, R. El-Hajj, H. Ghamlouch, and E. Monacelli, "Comparative study on different adaptation approaches concerning a sip and puff controller for a powered wheelchair," in *Proceedings of the IEEE Science and Information Conference*, 2013.

[5] H. S. Grewal, A. Matthews, R. Tea, V. Contractor, and K. George, "Sip-and-puff autonomous wheelchair for individuals with severe disabilities," in *Proceedings of the IEEE Ubiquitous Computing, Electronics & Mobile Communication Conference (UEMCON)*, 2018.

[6] S. Pozzi and S. Bagnara, "Individuation and diversity: the need for idiographic hci," *Journal of Theoretical Issues in Ergonomics Science*, vol. 14, no. 1, p. 1–21, 2013.

[7] H. D. Shin *et al.*, "Customized power wheelchair joysticks made by three-dimensional printing technology: A pilot study on the environmental adaptation effects for severe quadriplegia," *International Journal of Environmental Research and Public Health*, vol. 18, p. 7464, 2021.

[8] L. V. Herlant, R. M. Holladay, and S. S. Srinivasa, "Assistive teleoperation of robot arms via automatic time-optimal mode switching," in *Proceedings of the International Conference on Human-Robot Interaction (HRI)*, 2016.

[9] M. Li, D. P. Losey, J. Bohg, and D. Sadigh, "Learning user-preferred mappings for intuitive robot control," in *Proceedings of the IEEE International Conference on Intelligent Robots and Systems (IROS)*, 2020.

[10] A. Thompson, L. Y. Loke, and B. Argall, "Control interface remapping for bias-aware assistive teleoperation," in *Proceedings of the IEEE International Conference on Rehabilitation Robotics (ICORR)*, 2022.

[11] M. N. Javaremi, L. Y. Loke, and B. Argall, "Experimental validation of interface-aware assistance for 7-dof robot arm teleoperation," in *International Symposium on Experimental Robotics*, 2023.

[12] C. Prather, A. Ernst, and R. Dasgupta, "luci-ros2-sdk," https://github.com/lucimobility/luci-ros2-sdk.git, 2022.

[13] Kinova, "kinova-ros," https://github.com/Kinovarobotics/kinova-ros.git, 2022.

[14] M. Momeny *et al.*, "Learning-to-augment strategy using noisy and denoised data: Improving generalizability of deep cnn for the detection of covid-19 in x-ray images," *Journal of Computers in Biology and Medicine*, vol. 136, p. 104704, 2021.

[15] M. Mirza, "Conditional generative adversarial nets," *arXiv preprint arXiv:1411.1784*, 2014.

[16] M. Ali *et al.*, *PyCaret: An open source, low-code machine learning library in Python*, 2020, pyCaret version 1.0.0.

[17] F. Pedregosa *et al.*, "Scikit-learn: Machine learning in Python," *Journal of Machine Learning Research*, vol. 12, pp. 2825–2830, 2011.

[18] L. Chen and S. Wang, "Automated feature weighting in naive bayes for high-dimensional data classification," in *Proceedings of the 21st ACM international conference on Information and knowledge management*, 2012, pp. 1243–1252.

[19] D. Pedro, "A unified bias-variance decomposition and its applications," in *Proceedings of the 17th International Conference on Machine Learning*, 2000, pp. 231–238.

[20] M. Abadi *et al.*, "TensorFlow: Large-scale machine learning on heterogeneous systems," 2015, software available from tensorflow.org. [Online]. Available: https://www.tensorflow.org/

[21] J. Ansel *et al.*, "PyTorch 2: Faster Machine Learning Through Dynamic Python Bytecode Transformation and Graph Compilation," in *Proceedings of the International Conference on Architectural Support for Programming Languages and Operating Systems (ASPLOS)*, 2024.

[22] C. E. Shannon, "A mathematical theory of communication," *The Bell System Technical Journal*, vol. 27, 1948.

Design of a Pneumatic Splint for Forearm Fracture Immobilization

Tristan McCarty[1], Jared Dube[1], Omar O'Mari[1], Christopher Rico[1], Adam Farha[1], Mark McHugh[1], Robert McKee[1], Konstantinos Karydis[2], Elena Kokkoni[1*]

***Abstract*— This paper introduces a pneumatic splint design for managing distal radius and ulna fractures which are injuries commonly occurring in adults. The proposed design capitalizes on the advantages of pneumatically-actuated splints while mitigating airflow complications associated with conventional designs. The designed splint comprises two primary components: 1) a pressure cuff that wraps around the forearm and inflates to apply pressure on the injury site, and 2) a forearm support platform that combines all the different components together to contribute to forearm immobilization. Modeling and simulation results that informed the design selection process are presented, offering insights on component selection and system integration. Results demonstrate the preliminary feasibility of the proposed design and provide pointers toward the fabrication of a prototype in future work.**

I. Introduction

Upper extremity injuries are a significant public health concern, with forearm fractures being among the most frequently observed in hospital trauma units worldwide [1], [2]. Prompt stabilization is crucial for healing (e.g., reducing the time it takes for the injury to heal completely, avoiding further injury, etc.), but factors like heavy patient loads and long waiting times can hinder timely intervention [3], [4]. This can lead to a delayed union, characterized by slower-than-normal bone healing, or non-union, characterized by a complete failure of the bone to heal [5]–[7]. Consequently, patients may experience persistent pain, swelling, and functional limitations, impacting their quality of life and incurring significant healthcare costs [3], [4]. Addressing the impact of delayed stabilization on fracture healing is essential for optimizing patient care and improving outcomes.

Splints provide initial stabilization to the injured area while the patient is transported to the hospital for advanced treatment. Gypsum-based plaster of Paris splints have been the cornerstone of fracture management for centuries, with historical references dating back to the 18th century [8], [9]. While other materials (e.g., fiberglass) have emerged as an alternative, gypsum remains the most economical and versatile material for immobilization due to its adaptability and cost-effectiveness [8], [9]. Such splints offer quick and easy application. However, their rigid nature, poor ventilation, and potential for improper fit can increase the risk of complications, such as compartment syndrome. This serious condition occurs when pressure within a muscle compartment builds to dangerous levels, restricting blood flow and potentially leading to tissue damage [9]–[11]. Lastly, while effective for many fractures, traditional splints may not be ideal for acute fractures requiring complete immobilization [12].

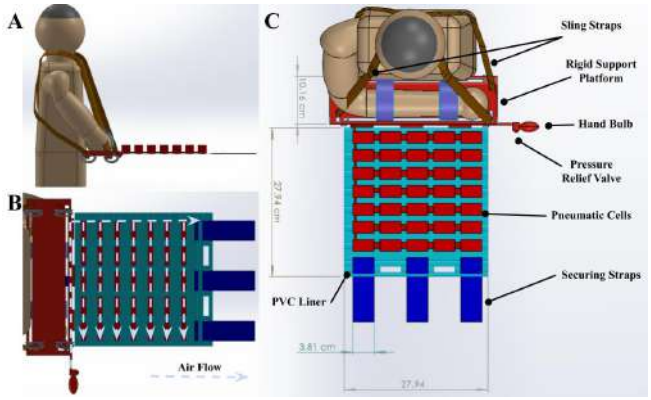


Fig. 1: Schematic views illustrating the cross sling design, rigid support platform for the arm, actuator placement, as well as the direction of airflow within the pressure cuff; the distribution of the inflatable components is visible too. (A) Side view of the double D-rings and sling being worn. (B) The bottom view with the pressure cuff is shown unrolled to clearly present the cutouts within the PVC cuff liner. (C) Top view showing how the pneumatic flow occurs between the hand pump and pneumatic cells.

The limitations of traditional splinting methods have driven the development of unconventional alternatives, such as pneumatic splints. These splints, often constructed from vinyl, Polyvinyl Chloride (PVC), or polyurethane, offer a unique approach to fracture immobilization [13], [14]. Once wrapped around the injured body segment and secured with straps, air is pumped into the splint until it becomes firm, providing compressive support to the fracture site. This pressure contributes to reduced pain, stiffness, inflammation, and swelling [15]. Pneumatic splints are highly adaptable, accommodating a wide range of adult body segment sizes through adjustable inflation. While pneumatic splints offer an innovative approach to fracture immobilization, they also present certain limitations. Excessive continuous pressure from full inflation can potentially compromise blood flow to the injured extremity [16]. Additionally, the development and application of pneumatic splints have primarily focused on fractures of the lower extremities [17], [18]. As such, the potential of pneumatic splints for treating forearm fractures remains largely unexplored.

This paper proposes a new design of a pneumatic splint for fracture management. The trauma of interest for this splint design is a distal fracture or a fracture isolated to either the radius or ulna, which are common sites of fractures in adults [19], [20]. Our design leverages the benefits of

[1] Dept. of Bioengineering, University of California, Riverside. [2] Department of Electrical and Computer Engineering, University of California, Riverside. * Corresponding Author, Email: elenak@ucr.edu

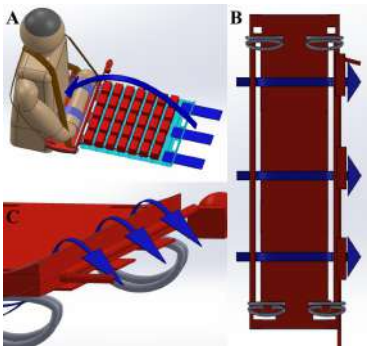


Fig. 2: CAD illustration of the process of securing the pressure cuff around the arm. (A) The cuff is wrapped over the arm. (B) The straps are inserted into the rail slot closest to the body and under the rigid support platform. (C) The straps are inserted into the opposite slot and pulled away from the body to create a tight fit around the arm.

pneumatic splints while addressing limitations such as airflow complications associated with traditional and existing models. A mechanical valve is designed to maintain adequate forearm pressure, thereby aiming to reduce the incidence of delayed union and non-union. Manually-operated pumps are also included to maintain adequate pressure and mitigate potential blood flow restrictions. The various components of our design are evaluated through simulations, encompassing pressure, immobilization, and lifetime assessments. The following sections provide information on the design and simulation results for each component.

II. Approach

The proposed pneumatic splint design comprises two main components: (1) Pressure Cuff, and (2) Support Platform. These components contain various sub-components intended to work in synergy to provide effective fracture immobilization (Fig. 1). The pressure cuff wraps around the forearm and is secured with safety straps (Fig. 2). An interconnected manually-operated hand pump is used to inflate a system of pneumatic cells within the cuff, exerting pressure on the forearm. A spring-loaded pressure relief valve regulates the air pressure within the cells, releasing excess air as needed. The rigid support platform keeps the injured forearm fixed, minimizing movement and reducing the risk of further damage. Lastly, the sling supports the weight of the forearm and stabilizes the shoulder and elbow joints during application.

Our approach to the proposed design is twofold, focusing on component and material selection, as well as interfacing of the different components, to ensure a non-intrusive, adjustable, and user-friendly solution for fracture immobilization. Soft pneumatic actuators are selected for pressure application on the skin over rigid alternatives to enhance patient comfort and device adaptability. This approach aligns with recent trends in wearable device design, where pneumatic actuators are increasingly favored due to their low mass, high power-to-weight ratio, inherent safety, affordability, and ease of fabrication [21]–[25]. Additionally, a hand-operated pump offers several advantages over electrical control boards or inflation by a user directly blowing into a tube. It allows the professional or user to precisely regulate pressure, providing a sense of control and agency during injury management [26]. By utilizing atmospheric air for inflation (rather than human breath), moisture and bacterial buildup are minimized, reducing infection risk and extending the device's lifespan. Complex electrical components are eliminated, simplifying the design, lowering overall costs, and thus improving accessibility.

Building upon this foundation, the choice of PVC as the primary material for the splint further enhances the device's aim. PVC's antimicrobial properties (e.g., resistance to bacterial and fungal growth) facilitate disinfection through various methods, including alcohol rinse, and soap and water [27]. This variation in sanitation methods allows for appropriate cleaning of the device in both clinical and at-home settings. PVC also offers a favorable combination of mechanical properties: high tensile strength for durability, compressibility for adaptability to different limb shapes, elasticity for comfortable fit, and thermoplasticity [27]. Additionally, PVC's radiolucency allows for medical imaging (i.e. x-ray) without the need for removal, facilitating diagnostic procedures [28]. The proposed compact device design, enabled by PVC's properties, further enhances its portability and storage. The cost of parts, including the hand pump, would round up to be around 10$ per splint, making it economically feasible and as such accessible for all medical emergency units. The proposed device design can be scaled to accommodate both adult and pediatric needs.

The subsequent sections provide detailed information on the design of each component of the pneumatic splint, incorporating results from modeling and simulation to achieve optimal design parameters, such as material properties, reaction forces, and expected lifespan. The analyses were performed in AutoCAD (AutoDesk, San Francisco, CA) and COMSOL (COMSOL Multiphysics, Burlington, MA).

III. Design

A. Pressure Cuff

The cuff provides the primary stabilizing pressure to the affected area of the forearm. It consists of pneumatic cells, interconnected tubing, a pressure relief valve, and straps (Fig. 1). The cells are arranged in seven parallel rows each containing five cells connected in series with each other. Each cell measures about 4.6 cm by 3.3 cm and is designed based on a 12-gauge PVC sheet and separated from adjacent cells by 0.6 cm spacing. The multi-cell design, with spaced-out cells, facilitates ventilation around the forearm, mitigating heat accumulation at the injury site. The cuff design has a rectangular shape measuring 30.5 cm in length, to comfortably wrap around the forearm, and 26.7 cm in width, to accommodate the forearm segment's length. When deflated, the design allows for compact storage, folding to a size of about 35.6 cm x 10.2 cm x 2.5 cm. Its dimensions are based on the 50th percentile forearm measurements of 20-year-old individuals (32.3 cm for females; 34.7 cm for males [29]), ensuring a proper fit for many adults. However, it may not be suitable for individuals under 18 (females) or

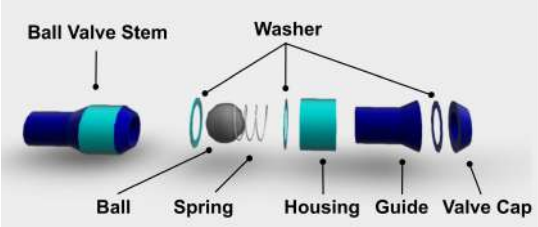


Fig. 3: CAD visualization of the pressure relief valve to regulate internal pressure without involving any electronic components.

15 (males), as their smaller forearm dimensions could cause the pneumatic cells to overlap when the cuff is wrapped around the forearm.

The pneumatic cells inflate in response to positive pressure input from the manual pump integrated into the splint. Air flows from the pump through tubing and into the cuff's network of cells (Fig. 1). Within each row, air progresses sequentially from one cell to the next, inflating all five cells. This design might lead to varying pressure distribution throughout the cuff, with cells farther from the primary air source experiencing lower pressure, or taking longer to inflate. To optimize pressure distribution, inflation time, and user effort, each cell incorporates a small cavity. This cavity allows for efficient inflation, reducing the required pumping effort by minimizing the volume of air needed to achieve the desired pressure without compromising the device's overall volume. To be effective, there should be no more than 20 mmHg air pressure build-up within the cells [30]. A spring-loaded pressure relief valve working synergistically with the manual pump is designed to regulate pneumatic pressure, releasing excess air if the aforementioned critical value is exceeded (Fig. 3). Simulations guided the design of the individual cells to ensure they could generate the necessary forces for this application.

B. Forearm Support Platform

The forearm support platform acts as a means to balance between providing uniform pressure around the forearm while also having a rigid surface to support the weight of the forearm. The rectangular support platform is designed to be out of a 12-gauge PVC sheet measuring 35.6 cm x 27.9 cm. It houses the pump, tubing, double D-rings with screws, and two straps. Sling straps going around the body and over the neck hold the weight of the forearm while stabilizing the elbow and shoulder joints. The double D-rings and screws secure the straps to the support platform, allowing the user to wrap the cuff around the forearm and fasten it securely. The straps are designed to be made out of 6-gauge PVC. Padding is also added to the support platform for comfort. Sling straps have a cross design, which was selected following a series of simulations. The model was created so that the sling straps were 2.54 cm wide and 76.2 cm long.

IV. Simulation Analysis and Results

This section presents the results of modeling and simulation, which informed the design selections presented before.

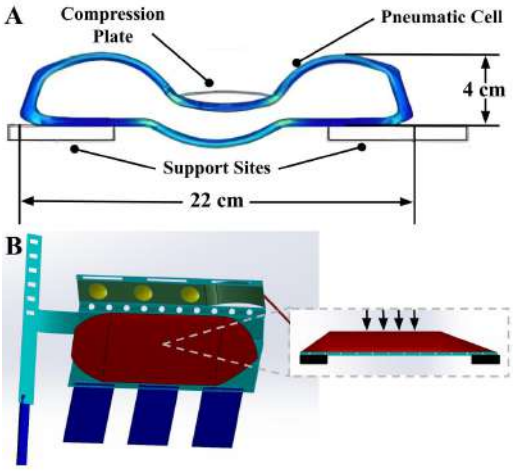


Fig. 4: (A) Compression testing of a single 22 cm pneumatic cell when placed directly on the injury and secured using two straps at the wrist and elbow areas. (B) CAD visualization of an earlier pressure cuff design version. The inset displays a cross-sectional view of the single pneumatic cell. Arrows represent the forces applied by the compression plate during simulation testing.

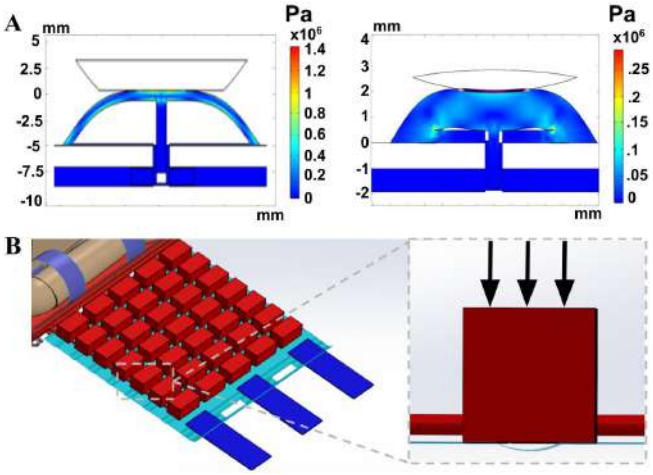


Fig. 5: (A) Compression testing on one of the individual pneumatic cells within the pressure cuff for different cell wall thicknesses. (B) CAD visualization of the pressure cuff. The inset displays a cross-sectional view of a single pneumatic cell. Arrows represent the forces applied by the compression plate during simulation testing.

A. Forearm Immobilization Afforded by Different Pneumatic Actuation System and Support Platform Selections

Simulations evaluated the appropriateness of different setups to lead to immobilization of the affected area of the forearm. A first set of simulations considered the use of a single (larger) pneumatic cell placed on top of the affected area and secured in place using two straps around the arm. Figure 4 visualizes this condition for the case of a 22-cm-long actuator. The two ends remained fixed, and a load (shown as a 'compression plate') was used in COMSOL as a means to emulate the reaction force exerted from the forearm to the inflated cell. Results show that the cell would deform too much and would be thus unable to apply the

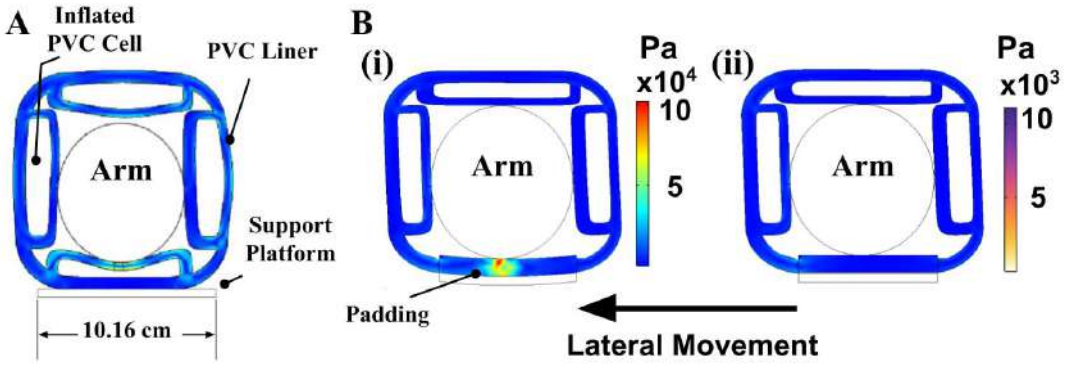


Fig. 6: Cross-sectional views of different iterations of multi-cell splints wrapped around the forearm. (A) 4-cell design where an inflatable cell is placed on top of rigid support platform at the bottom of the forearm. (B) 3-cell design, where the bottom cell is replaced with soft padding. Within this iteration, we considered (i) curved and (ii) flat platforms, and assessed which one can provide better immobilization with respect to lateral movements of the forearm.

proper pressure onto the forearm.

We also assessed the effect of cell wall thickness on pressure applied to the cell when fully inflated and in contact with a compressive plate (modeling the contact with the forearm). Two test cases are shown in Fig. 5. The first case (Fig. 5A) corresponds to one extreme case of a thin (approximately 0.75 mm) wall cell acting upon a flat surface. It can be seen that the pressure is applied relatively uniformly over the cell's wall, with high values at the center point of contact with the plate. In the second case (Fig. 5B), a thicker cell (12-gauge) with a thin indentation at its bottom (approximately 0.5 mm) was considered. The analysis in the second case reveals a smaller maximum pressure overall. The maximum values are also observed at the cell's indentation, and not at the point of contact with the arm (top part of cell). The use of a curved compressive plate (which is closer to the actual type of contact with the forearm) further demonstrates that such a design might be preferred over thin-wall cells.

Given that a single cell placed on top of the forearm does not yield satisfactory performance, we then considered multiple inflatable cells connected with each other via PVC liner and wrapped around the forearm. The performance of several different iterations was analyzed. First, we considered a 4-cell design that employs long, thick-wall cells placed along the top, bottom, and side parts of the forearm (Fig. 6A). The bottom cell is supported by a rigid support platform since earlier results (Fig. 4) showed that support over the two ends alone does not yield satisfactory performance. Results show that while this design approach is in principle feasible, it was still unable to apply sufficient pressure to the affected area since the bottom support cell yielded as pressure increased, eventually failing to immobilize the forearm (note the gap between the top cell and arm).

The follow-on iteration then featured removing the bottom inflatable cell and replacing it with soft non-actuated backing (for comfort) directly situated upon the rigid plate. An early design iteration visualizing this design is shown in Fig. 7. Figure 6B depicts a cross-section view. Within this iteration, we considered two subcases, one with a flat rigid support and

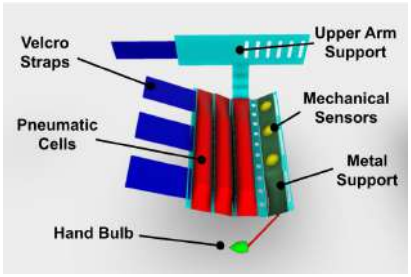


Fig. 7: Early iteration of the design for the pneumatic splint, visualizing an initial 3-cell design.

one with a curved design, in an effort to test immobilization with respect to lateral movement (i.e. motion along the horizontal plane in terms of the forearm's frontal plane shown in Fig. 6B). One main distinction between the two is in terms of manufacturing; a flat sheet is more directly obtainable and requires minimal machining, whereas a curved sheet would need additional processing (heating and possibly pressing) to be molded in the right shape, thus increasing costs. However, simulated force testing revealed that a curved rigid support platform can lead to higher pressure exerted onto the splint by the forearm's lateral movement which in turns results to higher resistance to arm motion and hence successful forearm immobilization as compared to when a flat rigid support platform was selected.

In our final design, we elected to make two revisions to the above down-selected characteristics (namely: curved rigid support platform with soft padding at the bottom of the arm and thick-wall pneumatic cells warped around the forearm and connected with each other and the platform via PVC liner). The first one involves splitting each long cell to multiple shorter ones (here we elected seven cells to facilitate manufacturing of a physical prototype). Using more distributed cells instead of a single one can yield faster pressurization and a more uniform application of pressure as the splint inflates. In addition, if desired, advanced pneumatic control systems can be deployed for actuating different cells at different rates, e.g., by using microfluidics [31]. The

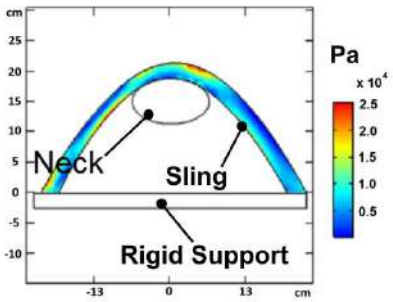


Fig. 8: Simulation on material stress distribution over a single-loop sling as depicted. Force is applied to the two ends via the rigid support, and the neck is simulated as a rigid plate. High stress points around the neck area in the sling imply that a higher pressure will be applied to the user's neck.

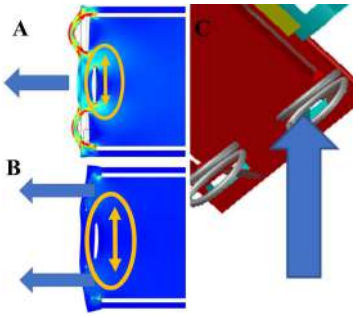


Fig. 9: Material stress in response to regular use load applied via the sling. Stress when the double-d rings are mounted on (A) the outer side of the cut-out slot and (B) the inner side. (C) Detailed view on the placement of the double-d rings used to connect the rigid support with the sling onto the rigid support platform.

second revision involves increasing the number of cells wrapped around the arm while keeping the platform as is. We elected to use five cells (from three shown before) to increase surface contact with the arm and lead to improved arm stabilization and comfort. Each of the five actuators 'lines' is operated in parallel, with the seven components within each line to be actuated in series (cf. Fig. 1).

B. Pressure Distribution on the Body via the Sling

We also sought to understand how the combined weight of the arm and the device should be distributed to the rest of the patient's body, and specifically at the back of the neck. Simulations showed that a direct application of a sling around the neck and connected to the two ends of the support platform would lead to large stress values (Fig. 8). As such, we elected to use a secondary sling that also wraps around the back, to reduce the load on the neck.

C. Structural Integrity

The last set of simulation experiments considered studying points of failure (in terms of structural weaknesses) of the splint. We specifically considered cracks in the rigid support of the splint. The rationale is that even if (some of) the individual cells fail, the use of multiple ones as proposed adds redundancy and can hence expand usage although some cells may have failed. However, cracks in the rigid support platform can propagate fast since the applied pressure at the platform is, in general, larger, and were thus modeled.

Recall that the proposed rigid support has cut-out slots for the sling and the sling straps to attach to (Fig. 9). When the splint is in use, these are the points of large forces being applied to the rigid support. The side slots are used to mount the double D-rings. We tested the difference in the stress applied to the rigid plate when placing the rings on the outer (Fig. 9A) over the inner (Fig. 9B) side of the slots. It can be directly verified that there is significantly higher material stress when forces are applied to the rings places on the outer side, which led to the decision to place the rings on the inner side, as detailed in Fig. 9C).

We also investigated how small cracks occurring around the slots would propagate to the rest of the platform under loading (via the sling when the device is in use, as before) over different usage cycles. Results are depicted in Fig. 10. The crack growth rate with and without rails shows that the rails significantly increase the rate of crack growth propagation (note the orders of magnitude difference). Hence, small cracks can still lead to material failure if the rails are present.

V. Discussion

This paper presents the design and validation of a pneumatic splint for forearm fracture immobilization. While not intended for long-term rehabilitation, this splint offers a promising solution for stabilizing injuries during transport to a medical facility. Our design approach offers key advantages in ease of use, affordability, and low production cost, significantly undercutting the price of the most expensive modern-day materials being used for splints [32]. The model was rigorously tested via simulation to evaluate its core components. Results demonstrate the feasibility of this design and its potential to effectively immobilize fractures in a simulated environment.

Previous work with pneumatic splints have highlighted their effectiveness at providing stability to injury sites by conforming to the arm of the user, as opposed to forcing the injury to conform to the splint [13]. Additionally, positive feedback has been received from clinicians regarding the effectiveness and ease of use for multiple fracture types, but long-term patient comfort has been an issue [13], [33], [34]. As these splints conform to the injury site uniformly with high pressure, problems with maceration and blood flow restriction to the injury site have arisen while steps have not been taken to ensure sufficient ventilation and proper pressure regulation [35]. Our work aimed to address these issues by integrating a grid-like network of interconnected pneumatic cells in a pressure cuff with a built-in user-friendly pump to inflate and a novel mechanical pressure relief valve to deflate. To the best of our knowledge, this is the first pneumatic splint designed for forearm fracture immobilization. Future steps involve the construction of the physical prototype, and assessing its maximum lifetime, applied pressure, and user comfort.

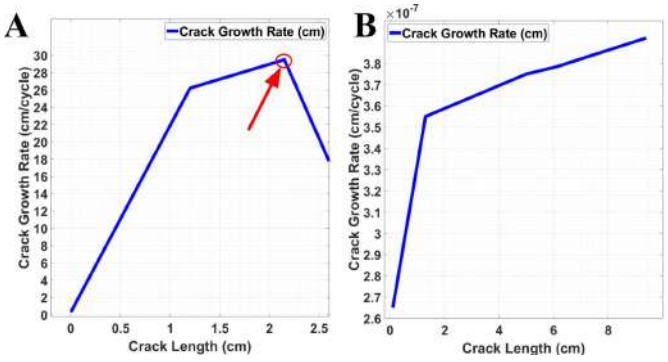


Fig. 10: Simulation testing of the propagation of a crack under a sample stress of 0.3 MPa via the sling (A) with and (B) without the side railings.

REFERENCES

[1] D. Ootes, K. T. Lambers, and D. C. Ring, "The epidemiology of upper extremity injuries presenting to the emergency department in the United States," *Hand*, vol. 7, no. 1, pp. 18–22, 2012.

[2] S. Soerensen, P. Larsen, L. R. Korup, A. A. Ceccotti, M. B. Larsen, J. T. Filtenborg, K. P. Weighert, and R. Elsoe, "Epidemiology of distal forearm fracture: A population-based study of 5426 fractures," *Hand*, vol. 19, no. 1, pp. 24–29, 2024.

[3] C. James, R. Denholm, and R. Wood, "The cost of keeping patients waiting: retrospective treatment-control study of additional healthcare utilisation for UK patients awaiting elective treatment," *BMC Health Services Research*, vol. 24, no. 1, p. 556, 2024.

[4] J. Valenzuela-Moss, K. Antoniak, N. Sarkisova, C. VandenBerg, J. Yang, D. Ryan, and R. Y. Goldstein, "Delay in time to physical therapy after orthopaedic treatment," *Journal of the Pediatric Orthopaedic Society of North America*, vol. 5, no. 4, p. 649, 2023.

[5] D. J. Hak, D. Fitzpatrick, J. A. Bishop, J. L. Marsh, S. Tilp, R. Schnettler, H. Simpson, and V. Alt, "Delayed union and nonunions: Epidemiology, clinical issues, and financial aspects," *Injury*, vol. 45, 2014.

[6] M. Bhandari, K. Fong, S. Sprague, D. Williams, and B. Petrisor, "Variability in the definition and perceived causes of delayed unions and nonunions: A cross-sectional, multinational survey of orthopaedic surgeons," *Journal of Bone and Joint Surgery*, vol. 94, 2012.

[7] Y. Liu, Z. Jia, M. P. Akhter, X. Gao, X. Wang, X. Wang, G. Zhao, X. Wei, Y. Zhou, X. Wang, C. W. Hartman, E. V. Fehringer, L. Cui, and D. Wang, "Bone-targeting liposome formulation of salvianic acid a accelerates the healing of delayed fracture union in mice," *Nanomedicine: Nanotechnology, Biology, and Medicine*, vol. 14, 2018.

[8] P. Hernigou, "Plaster of paris: the orthopaedic surgeon heritage," *International Orthopaedics*, vol. 40, 2016.

[9] B. Szostakowski, P. Smitham, and W. Khan, "Plaster of paris–short history of casting and injured limb immobilzation," *The Open Orthopaedics Journal*, vol. 11, 2017.

[10] J. M. Kistler, A. M. Ilyas, and J. J. Thoder, "Forearm compartment syndrome: Evaluation and management," *Hand Clinics*, vol. 34, 2018.

[11] R. P. Wilder and S. Sethi, "Overuse injuries: Tendinopathies, stress fractures, compartment syndrome, and shin splints," *Clinics in Sports Medicine*, vol. 23, 2004.

[12] H. D. Stewart, A. R. Innes, and F. D. Burke, "Functional cast-bracing for Colles' fractures. a comparison between cast-bracing and conventional plaster casts," *The Journal of Bone & Joint Surgery British Volume*, vol. 66, no. 5, pp. 749–753, 1984.

[13] R. Letts and D. Hobson, "The vacuum splint: an aid in emergency splinting of fractures," *Canadian Medical Association Journal*, vol. 109, no. 7, p. 599, 1973.

[14] D. Sasaki, T. Noritsugu, and M. Takaiwa, "Development of active support splint driven by pneumatic soft actuator (assist)," in *IEEE International Conference on Robotics and Automation (ICRA)*, 2005, pp. 520–525.

[15] P. T. McKnight and F. L. Schomburg, "Air pressure splint effects on hand symptoms of patients with rheumatoid arthritis," *Archives of Physical Medicine and Rehabilitation*, vol. 63, 1982.

[16] A. M. Stirling, J. M. McBride, E. K. Merritt, and A. R. Needle, "Nervous system excitability and joint stiffness following short-term dynamic ankle immobilization," *Gait and Posture*, vol. 59, 2018.

[17] M. K. Dodds, A. Daly, K. Ryan, and L. D'Souza, "Effectiveness of 'in-cast' pneumatic intermittent pedal compression for the pre-operative management of closed ankle fractures: A clinical audit," *Foot and Ankle Surgery*, vol. 20, 2014.

[18] D. E. Yeung, X. Jia, C. A. Miller, and S. L. Barker, "Interventions for treating ankle fractures in children," *Cochrane Database of Systematic Reviews*, vol. 2016, 4 2016.

[19] S. M. Lamont, A. M. Steffensmeier, T. W. Harman, and D. W. Martineau, "A qualitative study assessing information on the internet compared with AAOS guidelines for the treatment of distal radius fractures," *Orthopedics*, vol. 43, pp. E79–E86, 2020.

[20] J. C. Kyriakedes, E. Y. Tsai, D. S. Weinberg, C. C. Yu, H. A. Hoyen, K. Malone, and B. T. Bafus, "Distal radius fractures: AAOS appropriate use criteria versus actual management at a level i trauma center," *Hand*, vol. 13, no. 2, pp. 209–214, 2018.

[21] C. Thalman and P. Artemiadis, "A review of soft wearable robots that provide active assistance: Trends, common actuation methods, fabrication, and applications," *Wearable Technologies*, vol. 1, p. e3, 2020.

[22] H. Majidi Fard Vatan, S. Nefti-Meziani, S. Davis, Z. Saffari, and H. El-Hussieny, "A review: A comprehensive review of soft and rigid wearable rehabilitation and assistive devices with a focus on the shoulder joint," *Journal of Intelligent & Robotic Systems*, vol. 102, pp. 1–24, 2021.

[23] P. Maeder-York, T. Clites, E. Boggs, R. Neff, P. Polygerinos, D. Holland, L. Stirling, K. Galloway, C. Wee, and C. Walsh, "Biologically inspired soft robot for thumb rehabilitation," *Journal of Medical Devices*, vol. 8, no. 2, pp. 20 933–20 935, 2014.

[24] P. H. Nguyen, C. Sparks, S. G. Nuthi, N. M. Vale, and P. Polygerinos, "Soft poly-limbs: Toward a new paradigm of mobile manipulation for daily living tasks," *Soft Robotics*, vol. 6, no. 1, pp. 38–53, 2019.

[25] E. Kokkoni, Z. Liu, and K. Karydis, "Development of a soft robotic wearable device to assist infant reaching," *Journal of Engineering and Science in Medical Diagnostics and Therapy*, vol. 3, no. 2, p. 021109, 2020.

[26] B. Li, A. Baraldi Cunha, S. M. Kriner, and M. A. Lobo, "Playskin AirTM: A pediatric pneumatic exoskeleton for children with upper extremity disabilities," in *Proceedings of the 2022 ACM International Symposium on Wearable Computers*, 2022, pp. 123–126.

[27] C. E. Wilkes, J. W. Summers, C. A. Daniels, and M. T. Berard, *PVC handbook*. Hanser Munich, 2005, vol. 184.

[28] W. Li, B. Belmont, J. M. Greve, A. B. Manders, B. C. Downey, X. Zhang, Z. Xu, D. Guo, and A. Shih, "Polyvinyl chloride as a multimodal tissue-mimicking material with tuned mechanical and medical imaging properties," *Medical physics*, vol. 43, no. 10, pp. 5577–5592, 2016.

[29] C. D. Fryar, M. D. Carroll, Q. Gu, J. Afful, and C. L. Ogden, "Anthropometric reference data for children and adults: United States, 2015-2018," 2021.

[30] H. V. Nielsen, "External pressure-blood flow relations during limb compression in man," *Acta Physiologica Scandinavica*, vol. 119, no. 3, pp. 253–260, 1983.

[31] S. Hoang, K. Karydis, P. Brisk, and W. H. Grover, "A pneumatic random-access memory for controlling soft robots," *Plos one*, vol. 16, no. 7, p. e0254524, 2021.

[32] C. Ekanayake, J. Gamage, P. Mendis, and P. Weerasinghe, "Revolution in orthopedic immobilization materials: A comprehensive review," *Heliyon*, vol. 9, no. 3, 2023.

[33] M. H. Moen, T. Bongers, E. Bakker, A. Weir, W. Zimmermann, M. Van der Werve, and F. Backx, "The additional value of a pneumatic leg brace in the treatment of recruits with medial tibial stress syndrome; a randomized study," *BMJ Military Health*, vol. 156, no. 4, pp. 236–240, 2010.

[34] M. D. Kerstein, "Utilization of an air splint after below-knee amputation," *American Journal of Physical Medicine & Rehabilitation*, vol. 53, no. 3, pp. 119–126, 1974.

[35] M. Ginsberg, J. M. Miller, and G. C. McElfatrick, "The use of inflatable plastic splints," *JAMA*, vol. 200, no. 2, pp. 180–181, 1967.

Robotic Individualized Driving Evaluation (RIDE): Design and Preliminary Evaluation

Tim D. Yang[1,2], *Student Member, IEEE*, Laura Rice[1], Seth Hutchinson[3,4], *Fellow, IEEE*, and Yih-Kuen Jan[1]

***Abstract*— Power wheelchair driving entails safety risks, including tips and collisions. Thus, driving assessments are important to safeguard both drivers and their surroundings. However, current driving assessments are deterministic, whereas driving itself is stochastic due to individual and environmental uncertainty. Moreover, disabilities magnify this uncertainty. In this study, a robotic wheelchair was used for a novel function: stochastic assessment of PWC driving. The Robotic Individualized Driving Evaluation (RIDE) is a stochastic assessment that contrasts with deterministic assessments by accounting for individual differences via assessment profiles. The robotic wheelchair acquired the information needed for the stochastic model, and a probabilistic risk score was formulated. The purpose of this preliminary study was to test the effect of assessment profiles within and between driving tasks. Within tasks, there were significant differences in RIDE risk between the profiles. Between tasks, there were significant differences in the new stochastic RIDE metrics but not in the conventional deterministic metrics. Results demonstrated potential for this novel use of robotic wheelchairs to support personalized assessment and training in power mobility rehabilitation.**

I. INTRODUCTION

Power wheelchairs (PWCs) increase autonomy in people with severe mobility impairments [1] insofar as the user can drive effectively. However, functional steering is "extremely difficult" for many PWC users [2]. Day-to-day usage entails safety risks, including tips and collisions [3]. Thus, PWC assessments are used to ensure the safety of both the users and their surroundings. Clinicians perform a comprehensive evaluation of the client's personal and environmental factors. This iterative process of in-clinic evaluations and at-home trials [4] includes clinical ratings and measurements.

Clinical ratings target various levels of the International Classification of Functioning, Disability, and Health [5] (e.g., function [6], activity [7], participation [8]–[10], and environment [11], [12]). Clinical measurements target either wheelchair trajectory (e.g., driving duration, driving error, driving variability, driving speed, and driving acceleration) or human performance (e.g., information processing capacity, reaction time, fatigue, target accuracy, joystick activations, and joystick directional variability) or both [13]–[17].

However, driving contains complexities that are difficult to formalize with ratings and measurements. Driving is a dynamic, stochastic, and nonlinear process [18] involving real-time adaptation mediated by personal and environmental factors. Individual differences in motor skill, cognitive skill, visual acuity, etc., inject uncertainty into the driving process, and disabilities magnify that uncertainty which in turn influences the optimal driving strategy. For example, whereas an unimpaired driver might choose the most efficient trajectory in a given scenario, an impaired driver (i.e., with higher uncertainty in driving control) might instead choose a less efficient trajectory in favor of more safety. By measurements, the impaired driver chose a worse plan (e.g., longer driving time). In practice, they demonstrated good decision-making by accounting for their impairment. These contextual driving decisions are difficult to formalize with ratings and measurements. While a rating may account for some context, it lacks in objectivity and granularity. While a measurement may be objective and granular, it lacks in context.

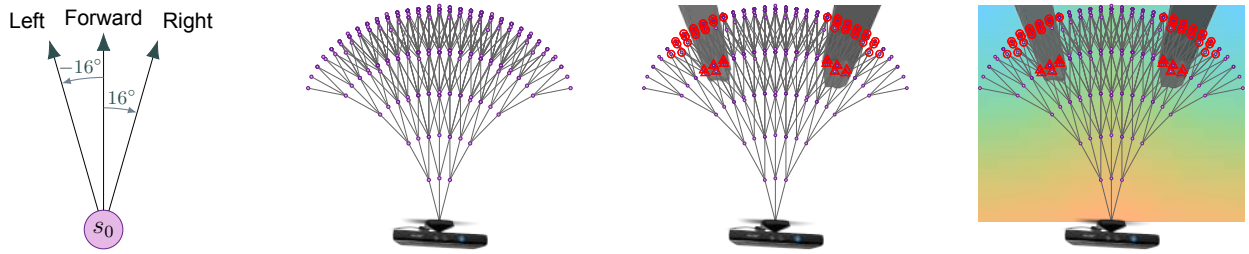
Stochastic analysis can complement measurement statistics by objectively accounting for contextual differences. A stochastic model can balance task objectives against personal and environmental factors [19]. In this study, a robotic wheelchair was used for a novel function: stochastic assessment of PWC driving. The Robotic Individualized Driving Evaluation (RIDE) was developed on the basis of a Markov model and was configurable via assessment profiles, represented internally as Markov transition models. The robotic wheelchair acquired the information needed for the model, and a probabilistic risk score was formulated. In practice, a clinician would use their expertise to determine a suitable RIDE profile befitting their client's individual differences. The resulting RIDE score would then represent a personalized measure of driving risk. In this preliminary study, the purpose was to test the effect of RIDE profiles within and between driving tasks. It was hypothesized that:

1) within tasks, there will be significant differences in stochastic metrics between assessment profiles; and
2) between tasks, there will be significant differences in stochastic metrics but not deterministic metrics.

TABLE I
MARKOV DECISION PROCESS (MDP) FORMULATION

		Driving	Implementation
State	$s \quad S$	Position	Directed acyclic graph
Action	$a \quad A(s)$	Heading	Rigid body dynamics
Reward	$R(s)$	Environment	Infrared depth point cloud
Transition	$P(s'\|s,a)$	Uncertainty	Assessment profiles

[1]Department of Health and Kinesiology, University of Illinois Urbana-Champaign, Urbana, IL 61801, USA
[2]Siebel School of Computing and Data Science, University of Illinois Urbana-Champaign, Urbana, IL 61801, USA
[3]School of Interactive Computing, Georgia Institute of Technology, Atlanta, GA 30332, USA
[4]Institute for Robotics and Intelligent Machines, Georgia Institute of Technology, Atlanta, GA 30332, USA



(a) Actions (b) States (c) Environment (d) Rewards

Fig. 1. Markov decision process components. (a) The action space consists of left-, for-, and rightward actions. (b) The state space is formed by propagating actions into a 3-branch, 6-depth directed acyclic graph. (c) The state graph is overlaid on a point cloud with two obstacles. (d) The point cloud is further overlaid on a Markov reward function that penalizes obstacles based on proximity and directness of path.

II. SYSTEM DESIGN

The RIDE algorithm was based on a first-order Markov decision process (MDP) [20], consisting of a set of states (i.e., wheelchair positions), set of actions (i.e., wheelchair headings), probability distribution of movement transitions (i.e., movement uncertainty), and reward function (i.e., environmental cues) (Table I). These components were used to model PWC driving as a sequence of MDP decisions, accounting for differences in driving skill and environmental context. Driving risk was determined by contrasting the driver's observed actions with the MDP's computed actions.

A C300 power wheelchair (Permobil, Inc., Lebanon, TN) was robotized, although computational navigation functionality was not used; the participants retained full driving control, as the purpose of the study was to assess their own driving. The robotic wheelchair facilitated the capture and extraction of information needed for the MDP—i.e., the driver's actions and the environment's context.

To capture the driver's actions, an Arduino Mega 2560 R3 (Smart Projects SRL, Strambino, Italy) was interfaced with the joystick's microcontroller board to intercept `FORE_AFT` and `LEFT_RIGHT` voltages. The model's action space $A(s)$ (Fig. 1a) consisted of three discrete actions: left ($-16°$), forward ($0°$), and right ($16°$). These actions were propagated into the state space S (Fig. 1b): a directed acyclic graph with three branches and six levels. To determine the driver's action $a \in A(s)$ in a given state s, the PWC heading was computed. The turning of a PWC is actuated via differential steering, in which new headings are based on relative wheel torques. For example, the PWC actuates a right turn by increasing the left wheel's velocity relative to the right wheel's velocity. In this study, joystick excursions were used to ascertain the wheel velocities, which in turn were used to compute the PWC headings:

$$\begin{array}{ccccccc} \text{Joystick} & & \text{Wheel} & & \text{PWC} & & \text{MDP} \\ \text{excursion} & \mapsto & \text{velocities} & \mapsto & \text{heading} & \mapsto & \text{action} \\ (r,\theta) & & \langle \mathbf{v}_L, \mathbf{v}_R \rangle & & \theta & & a \in A(s) \end{array}$$

Joystick excursions fell within eight regions, each with its own excursion-velocity mapping. The regions were bounded by the polar angles 0, ϕ_1, $\frac{\pi}{2}$, $\pi - \phi_1$, π, $\pi + \phi_2$, $\frac{3\pi}{2}$, and $-\phi_2$ (Fig. 2a). The boundary angles and output velocities were parameterized by five constants, which were derived from empirical testing on the standard speed setting of the indoor driving profile. The linear velocities were computed from angular velocities based on the PWC's wheel radius. Using the resultant wheel velocity tuple, the PWC heading θ was computed via rigid body dynamics (Fig. 2b),

$$\theta = \frac{v_L - v_R}{2Af_s} \tag{1}$$

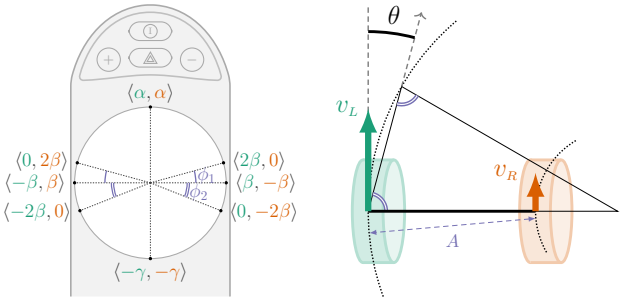
where v_L and v_R were the wheel velocities, A was the axle length, and f_s was the sampling frequency.

To capture the environment's context, the headrest was retrofitted with a Kinect (Microsoft Corporation, Redmond, WA), containing a depth sensor with 11-bit depth, $57°$ horizontal field of view, $43°$ vertical field of view, and $4\,\mathrm{m}$ radial distance. Each depth image was transformed into a point cloud of obstacles onto which the state graph was overlaid (Fig. 1c). The reward function $R(s)$ (Fig. 1d) was then used to determine the reward value at each graph node. Obstacle nodes and their descendent nodes were penalized inversely by the distance from the driver,

$$R(s) = \lambda\sqrt{(x_{\max} - |x_s|)^2 + (y_{\max} - |y_s|)^2}, \quad \lambda < 0 \tag{2}$$

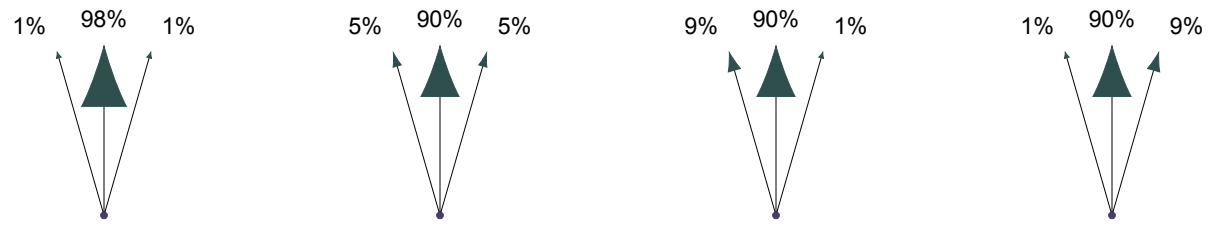
where x_s and y_s were the coordinates of state s, and λ was a negative penalty coefficient. Thus, $R(s)$ was scaled both for proximity and directness of path to the driver.

The joystick data and depth images were acquired simultaneously using MATLAB (The MathWorks, Inc., Natick, MA) at sampling frequencies of 2 Hz and 10 Hz, respectively.



(a) Wheel Velocities v_L, v_R (b) Wheelchair Heading θ

Fig. 2. Heading derivation. (a) Wheel velocities were first extracted from joystick excursions using a microcontroller board. (b) Wheelchair heading was then computed from the wheel velocities using rigid body dynamics.



(a) Unimpaired (b) Bilateral (c) Unilateral Left (d) Unilateral Right

Fig. 3. The four assessment profiles for the stochastic model. The profiles were represented internally as Markov transition models. (a) The unimpaired profile contained 2% overall variability. (b)–(d) The bilateral and unilateral assessment profiles each contained 10% overall variability.

III. EXPERIMENT DESIGN

A. Protocol

The experiment was conducted in a university building hallway. Two driving tasks were defined per [7]:

1) turn left 90° while moving forward and
2) turn right 90° while moving forward.

To prevent interference from passersby, the hallway was cordoned off for the duration of the protocol. Three healthy participants completed the experiment. The impairment level of the participants was not relevant, as the purpose of the study in this preliminary stage was to test the effect of assessment profiles versus tasks. Each participant was a right-handed joystick user and was given time to acclimate to the wheelchair and joystick before performing the experimental task. Each task was repeated twice with brief resting periods in between. The joystick data and depth images were extracted from the robotic wheelchair for offline analysis.

B. Data Analysis

For each driving trial, two deterministic and four stochastic metrics were analyzed. The deterministic metrics included driving duration and joystick variability per [15]. The stochastic metrics included four RIDE risk scores (i.e., one per profile) computed from the Markov model.

Markov decisions were optimized into a policy of actions maximizing the driver's expected utility according to the Bellman equation,

$$U(s) = R(s) + \gamma \max_{a \in A} \sum_{s' \in S} P(s'|s,a)U(s'), \quad 0 < \gamma < 1 \quad (3)$$

where $U(s)$ was the utility value for state s, $R(s)$ was the reward for state s, γ was a discount factor, and $P(s'|s,a)$ was the transition model for transitioning to state s' given the current state s and action a.

For PWC driving, a transition model with higher or lower variability suggests a driver with stronger or milder impairments, respectively. This transition model $P(s'|s,a)$ can be viewed as an *assessment profile*. In practice, a healthcare provider could use their clinical expertise to determine a suitable profile befitting their client's individual differences. In this study, four basic profiles were used (Fig. 3) as a preliminary test of the system:

1) unimpaired (1% left and 1% right variability),
2) bilateral (5% left an 5% right variability),
3) unilateral-left (9% left and 1% right variability), and
4) unilateral-right (1% left and 9% right variability).

For each profile, an optimal policy was computed numerically via backward induction [21].

For each optimal policy, a RIDE risk score was formulated under the rationale that suboptimal decisions are not inherently risky and do not necessarily preclude functional driving. Mathematically, a deviation simply means that the driver can no longer achieve the highest possible utility. Functionally, the impact could range from trivial to substantial. The severity of a deviation can be quantified in terms of the expected utility difference. Thus, at the root node of each graph, the observed actions and computed actions were compared by their respective expected utilities. RIDE risk Γ was defined as the inverse hyperbolic sine (IHS) [22] of the relative error,

$$\Gamma(t) = \sinh^{-1}\left(\frac{\hat{U}(t) - U(t)}{U(t)}\right) \quad (4)$$

where $\hat{U}(t)$ and $U(t)$ were the observed and computed utilities, respectively, at time t. Thus, when the observed action matched the computed action at a given time t, the RIDE risk evaluated to zero; otherwise, riskier mismatches evaluated to higher values. The IHS transformation was chosen to dampen the effect of runaway scores (e.g., 2,000% risk is not pragmatically different from 200% risk).

Data analysis was performed in GNU Octave.

C. Statistical Analysis

RIDE risk was normalized to the interval $[0, 1]$. Based on the Shapiro-Wilk test and quantile-quantile visualization, it was determined that the data were not normally distributed. Thus, nonparametric comparisons were used. All tests were conducted using $\alpha = .05$.

1) Within Tasks: RIDE risk was compared between the four assessment profiles using the Kruskal-Wallis one-way analysis of variance. Given a significant difference across profiles, the Conover-Iman test with Holm-Bonferroni correction was used for post hoc pairwise comparisons.

2) Between Tasks: RIDE risk, driving durations, and joystick variabilities were compared using the Wilcoxon signed-rank test.

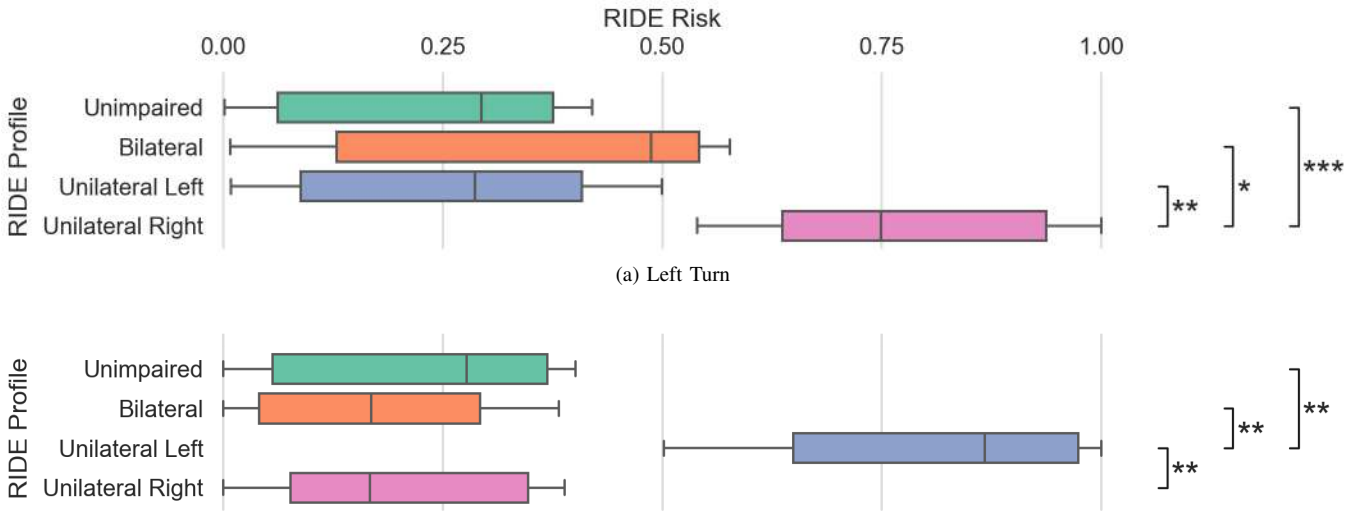


Fig. 4. Intra-task comparisons of driving risk across assessment profiles. (a) For the left turn task, risk from the unilateral-right profile was significantly higher than that of the unimpaired, bilateral, and unilateral-left profiles. Other differences were not significant. (b) For the right turn task, risk from the unilateral-left profile was significantly higher than that of the unimpaired, bilateral, and unilateral-right profiles. Other differences were not significant. Abbreviations: * ($p < .05$), ** ($p < .01$), *** ($p < .001$), RIDE (Robotic Individualized Driving Evaluation)

Statistical analysis was performed in Python using the `pandas`, `scipy`, and `scikit-posthocs` libraries.

IV. RESULTS

A. Intra-Task

1) Left Turn: There was a significant difference in RIDE risk across the four assessment profiles ($p = .003$). Post hoc comparisons (Fig. 4a) indicated that the RIDE risk from the unilateral-right assessment profile (median[IQR], $0.75[0.64 - 0.94]$) was significantly higher than that of the unimpaired profile ($0.29[0.06 - 0.38]$, $p < .001$), bilateral profile ($0.49[0.13 - 0.54]$, $p = .021$), and unilateral-left profile ($0.29[0.09 - 0.41]$, $p = .002$). Other differences were not significant.

2) Right Turn: There was a significant difference in RIDE risk across the four assessment profiles ($p = .008$). Post hoc comparisons (Fig. 4b) indicated that the RIDE risk from the unilateral-left assessment profile ($0.87[0.65 - 0.97]$) was significantly higher than that of the unimpaired profile ($0.28[0.06 - 0.37]$, $p = .003$), bilateral profile ($0.17[0.04 - 0.29]$, $p = .001$), and unilateral-right profile ($0.17[0.08 - 0.35]$, $p = .003$). Other differences were not significant.

B. Inter-Task

1) Stochastic: For the unilateral-left assessment profile, there was a significant difference in RIDE risk between the left turn task ($0.29[0.09 - 0.41]$) and right turn task ($0.87[0.65 - 0.97]$, $p = .031$). For the unilateral-right assessment profile, there was a significant difference in RIDE risk between the left turn task ($0.75[0.64 - 0.94]$) and right turn task ($0.17[0.08 - 0.35]$, $p = .031$). For the unimpaired and bilateral assessment profiles, there were no significant differences in RIDE risk between tasks (Table II).

2) Deterministic: There were no significant differences in either driving duration or joystick variability between tasks (Table II).

V. DISCUSSION

In this paper, the design and preliminary results of RIDE are presented. RIDE uses a robotic wheelchair to assess PWC driving stochastically. In integrating context from the driver and environment, this stochastic approach complements deterministic assessments by providing a more standardized method for personalization. Individual differences are configurable via the model's assessment profiles.

Clinical profiles are routinely used for diagnosis, prognosis, and treatment throughout the healthcare industry, from internal medicine [23] to sports medicine [24] to rehabilitation medicine [25]. Clinical decisions are made with a breadth of information, including client demographics, biomedical measurements, clinical ratings, etc. Healthcare providers develop clinical recommendations through the lens of the client's profile. In this study, the profile-based design mirrors this approach. RIDE computes risk through the lens of a given assessment profile. It was hypothesized that PWC driving actions would yield significantly different RIDE risk scores as viewed through different assessment profiles.

Within tasks, experimental testing indeed revealed significant differences between certain profiles. For a given directional task, significantly higher RIDE risk was observed under the contradirectional profile but not the ipsidirectional profile. This result was likely due to the turning strategy adopted by the participants (Fig. 5). In preparing for a turn, they tended to anticipate the turn by executing a wider arc—bringing themselves closer to the contradirectional wall—prior to executing the turn. Under most circumstances (i.e., bilateral, ipsidirectional, or no impairment), this would be a reasonable driving plan and would not cause significant

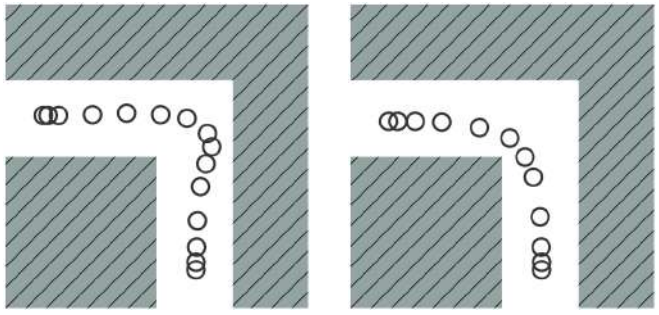
TABLE II
INTER-TASK COMPARISONS FOR STOCHASTIC AND DETERMINISTIC METRICS

	Metric	Profile	Left Turn Task		Right Turn Task		
			Mdn	(IQR)	Mdn	(IQR)	p
Stochastic	RIDE Risk	Unimpaired	0.29	(0.06–0.38)	0.28	(0.06–0.37)	.844
		Bilateral	0.49	(0.13–0.54)	0.17	(0.04–0.29)	.219
		Unilateral Left	0.29	(0.09–0.41)	0.87	(0.65–0.97)	**.031***
		Unilateral Right	0.75	(0.64–0.94)	0.17	(0.08–0.35)	**.031***
Deterministic	Driving Duration (s)	N/A	9.00	(8.25–10.50)	9.50	(9.00–10.00)	.655
	Joystick Variability (°)	N/A	7.02	(6.79–8.62)	7.11	(5.28–9.08)	.844

Abbreviations: * ($p < .05$), IQR (interquartile range), Mdn (median), N/A (not applicable), RIDE (Robotic Individualized Driving Evaluation)

risk. However, under a contradirectional assessment profile, this wider trajectory (Fig. 5a) represents a significantly increased risk of colliding with the contradirectional wall. The stochastic model developed in this study accounted for this context via the given assessment profile. If the driver had instead taken a more direct line to the corner (Fig. 5b), the ipsidirectional profile would instead have yielded the highest RIDE risk. This profile-based approach enables clinicians to perform standardized assessments that account for impairment context. Furthermore, the robotic assessment could be performed in clients' homes and communities to provide targeted risk assessments of their daily environments. Thus, RIDE could serve as a clinical decision support tool to assess clients' needs within individual and environmental contexts.

Stochastic models can leverage context to extract more meaning from deterministic metrics. However, stochastic assessment has yet to be used for power mobility, although it has been used in the related field of power seating [26]. In conventional wheelchair seating practice, seating pressures are measured to screen for pressure ulcer risk. Since conclusive thresholds for pressure ulcer formation have yet to be determined [27], stochastic gradient descent has been used to predict pressure ulcer risk by integrating interface pressure measurements with clinical context (i.e., pressure ulcer history) [26]. In the present study, stochastic modeling was also used to assess risk via contextual profiles. It was hypothesized that the deterministic metrics would not detect significant differences between PWC driving tasks, whereas the stochastic RIDE model—given context via assessment profiles—would detect significant differences.



(a) Representative (b) Hypothetical

Fig. 5. Representative and hypothetical trajectories for the left turn task. (a) A representative trajectory from one driving trial, in which the participant anticipated the turn by executing a contradirectional arc. (b) A hypothetical trajectory, in which the driver takes a more direct path around the corner.

Between tasks, experimental testing indeed revealed significant differences in stochastic metrics but not deterministic ones. This result highlighted the contextless nature of traditional measurements. For example, a more direct turning trajectory (Fig. 5b) may not be ideal in all contexts, despite being superior by deterministic measurements (e.g., lower driving duration and joystick variability). Consider a PWC user, Alice, with advanced cervical dystonia. Her chin tends to point down toward her right shoulder, causing her field of vision to be rotated rightward. Even with seating adjustments and physical therapy, her postural condition will unlikely resolve in the near future. Thus, her reduced leftward perception constitutes a unilateral-left impairment. For Alice, the more direct trajectory (Fig. 5b) represents a significantly increased risk of collision with the corner. The more roundabout trajectory (Fig. 5a)—despite its higher driving duration and joystick variability—would represent a more optimal decision. The RIDE model would account for Alice's condition and could complement deterministic metrics to provide a more contextual, client-centered assessment.

Beyond assessment, training is needed to address identified barriers. For example, trainees of the Wheelchair Skills Training Program have seen improvements in PWC driving performance [28]. However, the improvements were modest and transient. To boost efficacy, robotics-based stochastic assessment may be able to identify personalized hotspots for more targeted training. This computational approach could also reveal hidden risks. For example, for wheelchair seating, stochastic modeling revealed potential underappreciation of the coccygeal region in predicting pressure ulcer risk [26]. For PWC driving, stochastic modeling could reveal analogous insights on previously underappreciated risks and barriers. Furthermore, because RIDE leverages a robotic wheelchair, the training could potentially occur remotely. Robotic assessment could allow PWC users to continue self-paced training at home so that skill improvements could be better retained over time.

There were limitations to this study. In terms of system design, all obstacles were treated equally. Future work should distinguish between different obstacle types and their respective threat levels. In terms of experiment design, the sample size was small. Future work should include more participants so that more diverse driving strategies and trajectories can be observed. Additionally, the study participants did not present

with disabilities since this was a preliminary test of the robotic system and assessment profiles. Future work will assess the drivers, so the sample should include people with disabilities. Lastly, only two driving tasks were included. Future work should include a higher quantity and variety of tasks, especially to test the bilateral and ipsidirectional profiles.

VI. CONCLUSION

The RIDE model brings a personalized approach to power mobility clinical practice. It represents a novel use of robotic wheelchairs: stochastic assessment of PWC driving. In contrast to deterministic metrics, this stochastic approach accounts for individual and environmental differences. Clinicians can use configurable RIDE profiles to perform standardized assessments that account for impairment context and, in turn, provide more targeted training to enhance functional independence in PWC users.

REFERENCES

[1] B. E. Dicianno, A. Gaines, D. M. Collins, and S. Lee, "Mobility, assistive technology use, and social integration among adults with spina bifida," *American Journal of Physical Medicine and Rehabilitation*, vol. 88, no. 7, pp. 533–541, 2009.

[2] L. Fehr, W. E. Langbein, and S. B. Skaar, "Adequacy of power wheelchair control interfaces for persons with severe disabilities," *Journal of Rehabilitation Research and Development*, vol. 37, no. 3, pp. 353–360, 2000.

[3] S. Evans, C. Neophytou, L. de Souza, and A. O. Frank, "Young people's experiences using electric powered indoor-outdoor wheelchairs (EPIOCs)," *Disability and Rehabilitation*, vol. 29, no. 16, pp. 1281–1294, 2007.

[4] P. Guerette, D. Tefft, and J. Furumasu, "Pediatric powered wheelchairs," *Assistive Technology*, vol. 17, no. 2, pp. 144–158, 2005.

[5] World Health Organization, *International Classification of Functioning, Disability, and Health (ICF)*. Geneva: World Health Organization, 2001.

[6] J. Furumasu, P. Guerette, and D. Tefft, "Relevance of the Pediatric Powered Wheelchair Screening Test for children with cerebral palsy," *Developmental Medicine and Child Neurology*, vol. 46, pp. 468–474, 2004.

[7] R. L. Kirby, J. Swuste, D. J. Dupuis, D. A. MacLeod, and R. Monroe, "The Wheelchair Skills Test," *Archives of Physical Medicine and Rehabilitation*, vol. 83, no. 1, pp. 10–18, 2002.

[8] T. Mills, M. B. Holm, E. Trefler, M. Schmeler, S. Fitzgerald, and M. Boninger, "Development and consumer validation of the Functional Evaluation in a Wheelchair (FEW) instrument," *Disability and Rehabilitation*, vol. 24, no. 1-3, pp. 38–46, 2002.

[9] W. B. Mortenson, W. C. Miller, and J. Miller-Pogar, "Measuring wheelchair intervention outcomes: Development of the wheelchair outcome measure," *Disability and Rehabilitation: Assistive Technology*, vol. 2, no. 5, pp. 275–285, 2007.

[10] W. C. Miller, J. Garden, and W. B. Mortenson, "Measurement properties of the wheelchair outcome measure in individuals with spinal cord injury," *Spinal Cord*, vol. 49, no. 9, pp. 995–1000, 2011.

[11] D. Dawson, R. Chan, and E. Kaiserman, "Development of the power mobility indoor driving assessment for residents of long-term care," *Canadian Journal of Occupational Therapy*, vol. 61, no. 5, pp. 239–299, 1994.

[12] L. Letts, D. Dawson, I. Bretholz, *et al.*, "Reliability and validity of the power-mobility community driving assessment," *Assistive Technology*, vol. 19, no. 3, 154–63, quiz 127, 2007.

[13] R. A. Cooper, D. K. Jones, S. G. Fitzgerald, M. Boninger, and S. J. Albright, "Analysis of position and isometric joysticks for powered wheelchair driving," *IEEE Transactions on Biomedical Engineering*, vol. 47, no. 7, pp. 902–910, 2000.

[14] B. E. Dicianno, D. M. Spaeth, R. A. Cooper, S. G. Fitzgerald, and M. L. Boninger, "Advancements in power wheelchair joystick technology: Effects of isometric joysticks and signal conditioning on driving performance," *American Journal of Physical Medicine and Rehabilitation*, vol. 85, no. 8, pp. 631–639, 2006.

[15] G. U. Sorrento, P. S. Archambault, F. Routhier, D. Dessureault, and P. Boissy, "Assessment of joystick control during the performance of powered wheelchair driving tasks," *Journal of NeuroEngineering and Rehabilitation*, vol. 8, p. 31, 2011.

[16] B. E. Dicianno, H. Mahajan, A. S. Guirand, and R. A. Cooper, "Virtual electric power wheelchair driving performance of individuals with spastic cerebral palsy," *American Journal of Physical Medicine and Rehabilitation*, vol. 91, no. 10, pp. 823–830, 2012.

[17] H. Hoenig, M. Morgan, C. Montgomery, L. R. Landerman, and K. Caves, "One size does not fit all-mobility device type affects speed, collisions, fatigue, and pain," *Archives of Physical Medicine and Rehabilitation*, vol. 96, no. 3, pp. 489–497, 2015.

[18] M. C. Nechyba and Y. Xu, "Human control strategy," *IEEE Control Systems*, vol. 17, no. 5, pp. 48–61, 1997.

[19] R. S. Sutton and A. G. Barto, *Reinforcement learning: An introduction*, 2nd ed. Cambridge, MA: MIT Press, 2018.

[20] R. Bellman, "A Markovian decision process," *Journal of Mathematics and Mechanics*, vol. 6, no. 5, pp. 679–684, 1957.

[21] S. J. Russell and P. Norvig, *Artificial intelligence: A modern approach*, 3rd ed. Upper Saddle River, NJ: Prentice Hall, 2010.

[22] J. B. Burbidge, L. Magee, and A. L. Robb, "Transformations to handle extreme values of the dependent variable," *Journal of the American Statistical Association*, vol. 83, no. 401, pp. 123–127, 1988.

[23] Y. Dong, J. Wang, S. Zhu, H. Zheng, C. Wang, and P. Zhao, "Clinical profiles and diagnostic challenges in 1158 children with rare hepatobiliary disorders," *Pediatric Research*, vol. 89, no. 1, pp. 238–245, 2021.

[24] S. Ren, D. J. Corwin, C. C. McDonald, D. Fedonni, C. L. Master, and K. B. Arbogast, "Age-related variations in clinical profiles for children with sports- and recreation-related concussions," *Diagnostics*, vol. 14, no. 18, 2024.

[25] G. Yavuzer, A. Küçükdeveci, T. Arasil, and A. Elhan, "Rehabilitation of stroke patients: Clinical profile and functional outcome," *American Journal of Physical Medicine and Rehabilitation*, vol. 80, no. 4, pp. 250–255, 2001.

[26] T. D. Yang and Y.-K. Jan, "Nonnegative matrix factorization for the identification of pressure ulcer risks from seating interface pressures in people with spinal cord injury," *Medical and Biological Engineering and Computing*, vol. 58, no. 1, pp. 227–237, 2020.

[27] J. Reenalda, M. Jannink, M. Nederhand, and M. IJzerman, "Clinical use of interface pressure to predict pressure ulcer development: A systematic review," *Assistive Technology*, vol. 21, no. 2, pp. 76–85, 2009.

[28] R. L. Kirby, W. C. Miller, F. Routhier, *et al.*, "Effectiveness of a wheelchair skills training program for powered wheelchair users," *Archives of Physical Medicine and Rehabilitation*, vol. 96, no. 11, 2017–2026.e3, 2015.

Integration of a Gripper-Equipped Humanoid Social Robot for EEG-Monitored Action Observation Paradigms

Anh T. Nguyen, *Member, IEEE*[1], Hao Zhang[2], Tian Tan[2], Mohammad Abrar[1], Yuxin Zhang[3], and Michelle J. Johnson, *Member, IEEE*[4]

***Abstract*— Action Observation (AO) therapy leverages the mirror neuron system (MNS) and may support motor recovery in neurorehabilitation. In this study, we integrated Flo v2, a humanoid robot equipped with grippers and object detection system, into an AO therapy paradigm with electroencephalography (EEG) monitoring. Flo v2's enhanced design enables the execution of upper-limb actions, either transitive (involving object interaction such as grasping a cup) or intransitive (gesture-based without object manipulation such as waving). The robot control is synchronized with EEG recording to facilitate the investigation of cortical responses during AO tasks. We also conducted a case study to assess of the upgraded robot system's feasibility. Three healthy participants observed and imitated robot-performed actions, where the robot actor was in person or on videos. Exploratory analyses of EEG signals examined sensorimotor mu event-related desynchronization (ERD) during video-based and in-person AO tasks. Results indicated stronger responses during bimanual and transitive AO in the in-person settings. However, individual variability in cortical responses was evident, with one subject showing less pronounced ERD patterns, and that comparisons of mu ERDs across different types of action in video-based AO settings were inconsistent among subjects. Flo v2's enhancements demonstrated its feasibility as a tool for robot-mediated AOE therapy and highlighted potential for further neurorehabilitation research.**

I. INTRODUCTION

Action observation (AO) therapy enhances upper-extremity motor function in individuals recovering from neurological conditions like stroke [1]. It leverages the mirror neuron system (MNS), which activates during the observation and execution of motor acts, facilitating motor learning through motor cortex and parietofrontal region activation [2], [3]. MNS activation supports cortical reorganization, aiding motor recovery in stroke survivors [4]. EEG can measure cortical responses during AO to assess motor recovery through sensorimotor mu rhythm (8–13 Hz) suppression [3], [5], [6].

Factors such as the human-like appearance of the agent and types of actions in visual stimuli during AO affect neural responses in the MNS [7]. Several studies used different types of robots, such as robotic arms [8], [9] and humanoid robots [10], [11] in AO paradigms and analyzed the MNS responses to actions performed by robots versus by humans [12]. The MNS shows varying responses to human and robot actions, with generally stronger activation for human agents in simple movements [8], [13], [14]. However, complex and goal-oriented actions elicit similar MNS responses to both agents, particularly in the parietal and premotor regions [15], [16], [17], [10]. These findings suggest that the potential use of robots for neurorehabilitation such as AO therapy. Regarding the concept of transitivity during AO, transitive actions involve interaction with objects in the peripersonal space (e.g., grasping a ball), while intransitive actions are simple hand-arm movements that do not involve objects (e.g., waving). Human MNS typically displays greater responses in frontal and parietal MNS and motor cortex to transitive than intransitive actions [18], [19]. EEG studies indicate that MNS responses to transitive actions of the human hand induce greater mu suppression in the C3 channel compared to intransitive actions [20].

Although the neuromodulatory effects of transitivity in human actions have been widely studied, only a few studies have explored this concept in the context of observing robot actions. Gazzola et al. identified significant differences in fMRI activity in the premotor and parietal areas when observing transitive versus intransitive robot arm movements [8]. However, an EEG study by Oberman et al. found no such effect of object versus non-object robot arms actions using mu suppression in C3 and C4 [9]. These mixed results highlight the need for further research to clarify how different types of robot-performed actions influence cortical responses. Furthermore, previous studies examining transitivity have primarily utilized robot arms rather than full humanoid robots. Compared to simpler robot arms, robots embodying a human-like form can perform complex, full-body movements that more closely resemble human motor patterns, potentially leading to stronger neural responses during AO. This highlights a gap in understanding how actions performed by humanoid robots influence MNS activation during AO.

The Flo robot, a custom-designed humanoid social robot developed in the Rehabilitation Robotics Lab at the Univer-

This work was supported by the Department of Physical Medicine and Rehabilitation at the University of Pennsylvania and by the Eunice Kennedy Shriver National Institute of Child Health & Human Development of the National Institutes of Health (NIH) (Award Number F31HD102165) and the Vingroup Scholarship Program for Master's and Ph.D. Degrees Overseas Study. The content does not necessarily represent the views of the NIH.

[1] Anh T. Nguyen and Mohammad Abrar are with Department of Bioengineering, University of Pennsylvania, Philadelphia, PA, USA tuna28ng,moabrar@seas.upenn.edu

[2] Hao Zhang and Tian Tan are with Department of Electrical and Systems Engineering, University of Pennsylvania, Philadelphia, PA, USA shzyh,tiantan@seas.upenn.edu

[3] Yuxin Zhang was with the Rehabilitation Robotics Lab, University of Pennsylvania, Philadelphia, PA, USA and is now with Department of Mechanical and Aerospace Engineering, University of California, Davis, Davis, CA, USA eyxzhang@ucdavis.edu

[4]Dr. Michelle J. Johnson is an Associate Professor with Department of Physical Medicine and Rehabilitation and Deparment of Bioengineering. She directs the Rehabilitation Robotics Lab (A GRASP Lab), University of Pennsylvania, Philadelphia, PA, USA johnmic@pennmedicine.upenn.edu

sity of Pennsylvania, features an expressive facial interface and articulate upper limbs to demonstrate upper extremity tasks [21], [22]. Initially designed as part of a telerehabilitation system, Flo enables remote interaction between clinicians and patients while facilitating demonstration of rehabilitation activities [23]. Previous studies found Flo effective in comparison to traditional telepresence method [24] and has potential use for exploring MNS activation during AO tasks [11]. This proof-of-concept paper presents the latest advancements in Flo robot (Flo version 2), aimed at improving its suitability for AO therapy, and a case study to assess the use of upgraded system in AO paradigms and investigate the neurophysiological effects of observing various robot actions using EEG.

II. FLO V2: ENHANCEMENTS FOR AO THERAPY

A. Design Objectives

The improvements aimed to provide Flo with a more human-like appearance and movement capability, optimizing its potential to engage patients effectively. Specifically, the design sought to increase the robot's ability to perform both transitive and intransitive actions. The addition of an automated object detection and grasping system aimed to streamline its manipulation with objects. These advancements collectively aim to create a reliable, user-friendly platform that aligns with the therapeutic needs of AO therapy, potentially supporting motor recovery after stroke through enriched and interactive robot-mediated therapy.

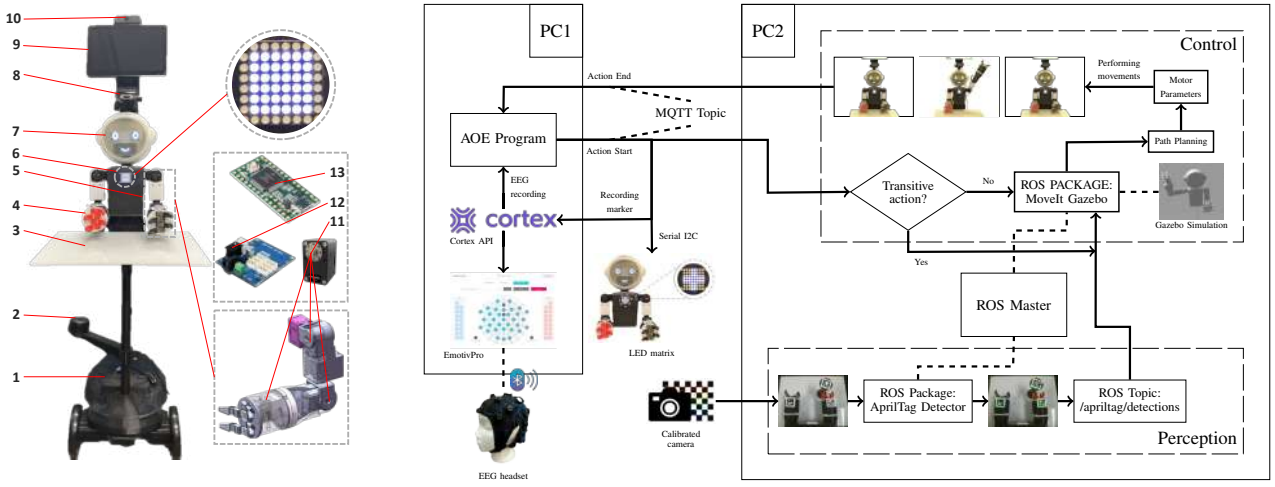
Moreover, Action Observation and Execution (AOE) program was developed to integrate EEG recording with real-time robot control, allowing precise synchronization between observed actions and recorded brain activity. This integration enables the examination of cortical responses to robot-assisted AO therapy. Fig. 1(a) shows the Flo v2 system hardware set-up and Fig. 1(b) shows control of the robot integrated with the EEG-monitored AOE experiment. Details of the robot's development, including hardware and software specifications, are available in our GitHub repository.

B. Hardware Developments

1) Humanoid Arms and Grippers: Each arm offers four DYNAMIXEL-driven DOF in Fig. 1(a), closely resembling basic human joint configurations. The lower arm section accommodates a quick-change mechanism in Fig. 2(a) that simplifies gripper swaps. Inspired by the Yale OpenHand project [25], each gripper employs a single motor and a fishing-line tendon system in Fig. 2(b) to flexibly grasp common household objects.

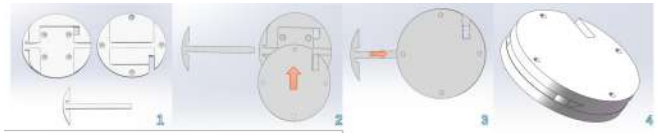
2) Face and Chest LED Matrix System: Flo v2's LED system includes a 16×8 matrix for the mouth, two 8×8 matrices for the eyes, and an 8×8 chest matrix, maintaining the interactive design of the previous version [21]. A Teensy 3.2 microcontroller integrated with ROS enables real-time facial expression adjustments via serial communication. The LED matrices are embedded in a translucent black urethane screen for effective light transmission and contrast while concealing internal components.

The chest LED matrix is of the same type as used in the AOE program (described in section II-E), capable of displaying predefined patterns such as a fixation cross,

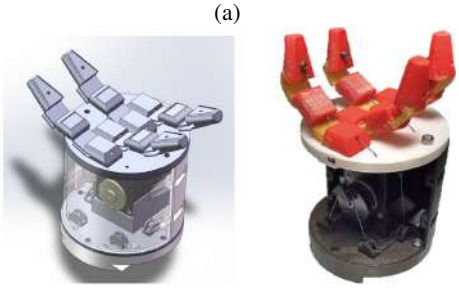


(a) (b)

Fig. 1: a) The Flo v2 robotic system includes: 1. Ohmnilab base; 2. LIDAR; 3. Tray; 4. Gripper; 5. Arm; 6. Chest LED matrix; 7. Face LED matrices; 8. RGB Camera; 9. Ohmnilab screen; 10. Ohmnilab camera; 11. DYNAMIXEL motors; 12. U2D2 Power Hub; and 13. Teensy 3.2. (b) The software architecture follows a step-by-step flow. Initially, the AOE program on PC1 starts an action, triggering the system workflow. If the action is identified as a transitive action involving an object on the tray, PC2 utilizes data provided by the perception module, specifically AprilTag detections, to plan and control the robot to execute the action. If the action is not transitive, it will be performed by the robot without additional planning for grasping. Simultaneously, PC1 controls the chest LED matrix, synchronizing with the AOE experiment to provide precise markers on EEG recording linked to the subject's actions.

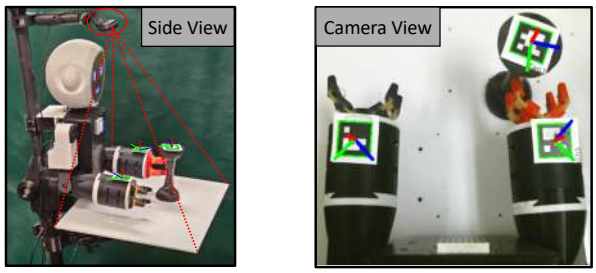


(a)



(b)

Fig. 2: (a) Quick-change mechanism and (b) Gripper design



(a) (b)

Fig. 3: Automated grasping system: (a) Side view showing the camera's vision range indicated by the red dotted lines; (b) Camera view displaying detected AprilTags.

a triangle, a square (Fig. 1(a)) , or remaining in an off state. These visuals provide supplementary feedback, further enhancing Flo v2's expressive capabilities.

3) Telepresence Base: The social robot Flo v2 is mounted on the Ohmnilab telepresence robot, which can be controlled using ROS and equipped with both a camera and LIDAR sensor for remote-controlled navigation and obstacle detection.

C. Automated Grasping and Object Detection System

1) Tray and Camera Setup: Flo v2 is capable of performing automated grasping actions, which allows Flo v2 to perform more actions. To achieve this, Flo v2 is equipped with a 42.4 cm × 32.3 cm tray used for placing objects that need to be grasped. An RGB camera positioned 43 cm above the tray offers a top-down view, enabling precise identification of the objects' locations for grasping.

2) AprilTag System: Each object placed on the tray is fitted with a 2.4 cm × 2.4 cm AprilTag. The AprilTags serve as visual fiducial markers, allowing the camera system to detect and identify the objects' positions. This setup, shown in Fig. 3(a), ensures that Flo v2 can efficiently locate and grasp objects autonomously. Figure 3(b) shows the arrangement of April Tags on each gripper and on an object.

3) Object Localization and Grasping Process: Object localization and grasping in Flo v2 involve detecting AprilTags attached to objects using a top-mounted RGB camera. Once the object is identified and its position determined, the coordinates are transmitted to the control system. Using the ROS framework, the robot plans a path to accurately position its gripper, ensuring precise object grasping with real-time adjustments for reliable manipulation.

D. Software Development and System Architecture

The software architecture is illustrated in Fig. 1 (b).

1) Robot Control System: We import the Unified Robotic Description Format (URDF) model of the robot into the Gazebo simulation environment, perform path planning and collision detection through ROS Noetic MoveIt, and convert angle data of each joint into motor data and send it to each motor via USB. While driving the real-world robotic arm, arm motion is also represented in the Gazebo simulation.

2) Visual LED Control System: To implement visual markers during the AOE experiment, we utilized a Teensy 3.2 microcontroller programmed via the Arduino IDE. The microcontroller was designed to control the patterns of the chest LED matrix, including a fixation cross, a triangle, and a square. These patterns serve as visual stimuli, synchronized with the EEG recording. Serial communication using I2C protocol was established between the Teensy and the AOE program, enabling real-time control of the chest LED. The program sends commands through a serial interface to the microcontroller to display or turn off specific patterns.

3) Camera Calibration and AprilTag Detection: To localize the real robot arm end-effector and determine the 6-DOF position of various objects (e.g., a cup, a dumbbell, a hairbrush), camera calibration is first performed using a checkerboard pattern with a size of 8x6 inner corners and each square measuring 0.0245 meters to obtain intrinsic parameters, such as the focal lengths f_x and f_y, and the principal point coordinates c_x and c_y. This is achieved using the `camera_calibration` package in ROS [26].

After camera calibration, we use the ROS package `apriltag_ros` [27] to detect AprilTags attached to the objects. This package identifies the AprilTags in the scene and publishes their 3D pose (position and orientation), as well as their respective IDs, enabling accurate positioning and tracking of the tagged objects.

To further calculate the physical distance D from the camera to the detected tag, we developed a custom ROS package named `apriltag_detector`. This package uses the intrinsic camera parameters obtained from the calibration process. According to the pinhole camera model, the distance is calculated by $D = (f \times s)/w$, where f represents the focal length, s is the actual size of the AprilTag, and w is the perceived width of the tag in the image (measured in pixels). The `apriltag_detector` package then publishes the final 3D coordinates, pose, and calculated distance of the detected tag to a ROS topic (`/apriltag/detections`). These data are subsequently used in the robot control system for manipulation tasks.

E. AOE Experiment Program

The AOE experiment program is designed to facilitate the execution of a series of robot actions while recording EEG data using the Cortex API [28]. The program initiates by establishing a connection to the Cortex service and creating a recording session (Fig. 1(b)). During the session, markers are injected at specific points to annotate events, such as the presentation of stimuli or the execution of actions. The Cortex API is used to manage the recording session, inject markers, and handle session-related callbacks.

In parallel, the program utilizes the MQTT protocol to communicate movement commands to the robot's control system. Each action in the sequence is randomized, and the corresponding movement number is published to a predefined MQTT topic. This enables the robot to receive real-time movement instructions synchronized with the experimental protocol. The program includes a simple GUI for controlling the experiment and offering visual feedback to the operator. Overall, the integration of the Cortex API and MQTT allows for precise synchronization, facilitating the coordination between EEG data recording and robotic control.

F. Specifications and Performance Testing

1) Gripper Payload Testing: The payload capacity of Flo v2's gripper was measured in two directions: along the gripper's axis (horizontal) and perpendicular to it (vertical). An NLB-500 analog force gauge was used for both measurements. For horizontal force, the gripper grasped a model object connected to the gauge via rope, and force was applied until detachment. For vertical force, the gripper held the object while downward force was applied until detachment. The average payload capacities, calculated over five trials, were as follows: 328.34 g (horizontal) and 356.9 g (vertical) for the left gripper, and 259.0 g (horizontal) and 326.3 g (vertical) for the right gripper.

2) Range of Motion and Capabilities: To determine the workspace, we used the robot's URDF model to generate approximately 20,000 reachable points for each arm. These points were then validated using MoveIt to ensure they were free of collisions with the robot itself or the environment. The collision-free points were visualized as a point cloud in RViz, providing a clear representation of the arm's spatial capabilities. The robot arm's modified DH parameters are shown in Table I. Figure 4 shows the robot arm's configuration with coordinate frames (X_i, Y_i, Z_i) established according to the modified DH parameters in Table I, along with key dimensions between joints.

The workspace of Flo v2's arms, shown in Fig. 5, represents the spatial extent of reachable points for each arm. The workspace accommodates a range of unimanual and bimanual actions. Unimanual actions include intransitive movements such as overhead arm raise and waving, as well as transitive actions like lifting objects or using tools. Bimanual actions include intransitive tasks such as clapping or synchronous shoulder movements, as detailed in Table II. This study focused on unimanual transitive and intransitive actions, with bimanual intransitive actions included for comparison. Bimanual transitive actions were not intentionally excluded but were beyond the study's scope.

Joint i	θ_i(Angle)	d_i(along z_{i-1})	a_i(along x_i)	α_i(around x_i)
1	θ_1	40 mm	0 mm	0
2	θ_2	0 mm	0 mm	$\pi/2$
3	θ_3	117 mm	0 mm	$-\pi/2$
4	θ_4	0 mm	0 mm	$\pi/2$
End-effector	–	151.14 mm	0 mm	0

TABLE I: Modified DH parameters of the robot arm

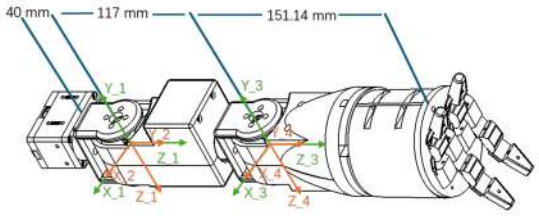


Fig. 4: Modified DH parameters and robot arm coordinates



Fig. 5: Visualization of the Flo v2 robot's arm workspace from front, side, and top views, with white dots indicating reachable points and range of motion for various actions.

Arm Configuration	Action Type	Action Examples
Unimanual	Intransitive	Overhead arm raise, Forward punching, Waving, Shoulder abduction/adduction
	Transitive	Lifting a dumbbell, Drinking from a cup, Using a hairbrush
Bimanual	Intransitive	Clapping, Synchronous and Alternating shoulder abduction/adduction, Alternating forward punching

TABLE II: Types of action the robot can perform.

3) System Limitations and Future Upgrades: Despite the robot's capability to autonomously grasp objects, the current system requires manual placement of objects onto the tray. Furthermore, during intransitive actions, objects on the tray may obstruct the robot's movements, necessitating manual removal of the objects. To address these limitations, we plan to upgrade the tray system by enabling it to lower when objects are not required, thereby preventing interference, and raise when objects are needed for grasping. This improvement aims to achieve fully automated object grasping and seamless operation in all action types.

In addition, the Flo v2 system currently relies on two separate PCs to manage its operations: one for controlling

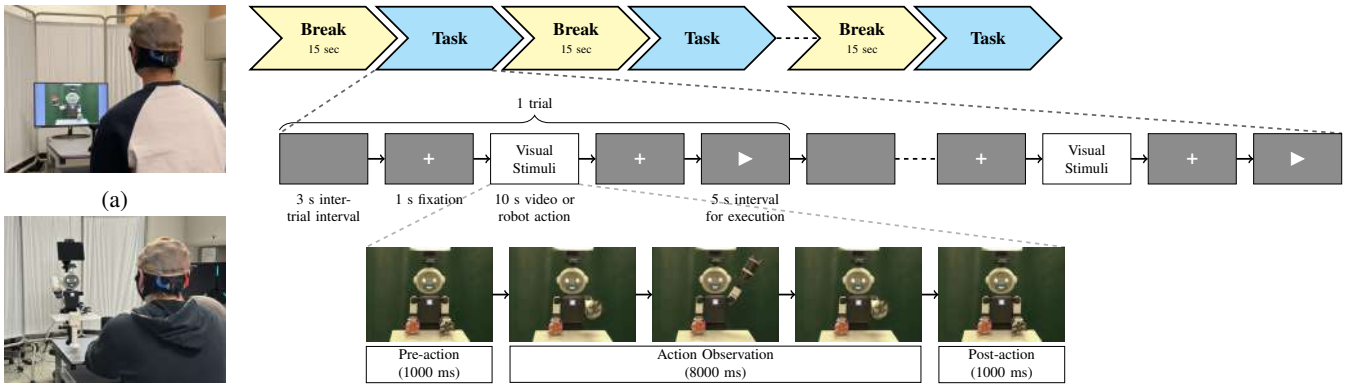


Fig. 6: Experimental setup of (a) video-based and (b) in-person robot AOE experiments. (c) Block design of AOE experiments.

the robot and another for handling EEG recording and data synchronization. This setup increases complexity, introduces potential latency in data communication, and complicates portability and deployment in new environments. To address this, we plan to containerize the entire system using Docker, which will enable the deployment of all required software on a single PC through modular ROS Docker containers.

III. EVALUATING FLO V2 IN AO THERAPY

A. Experimental Design and Protocol

This case study recruited three right-handed participants, ages 23 to 24, with no history of neurological or psychiatric disorders, to explore the neurophysiological effects of observing various robot-performed actions on the mirror neuron system (MNS). This study was approved by the University of Pennsylvania Institutional Review Board (IRB No. 830126) on June 29, 2021.

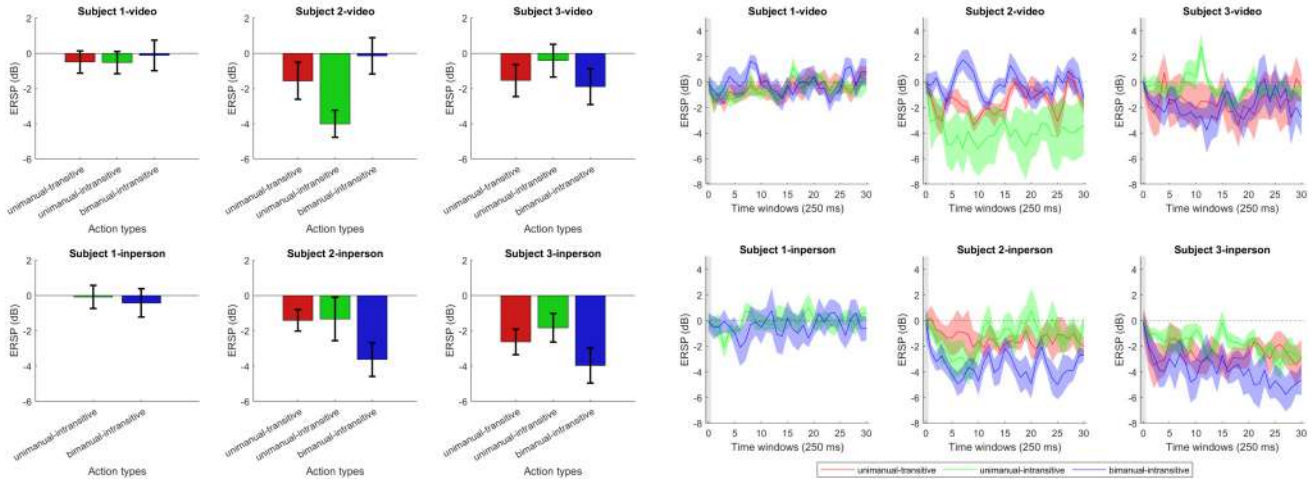
Participants completed two experiments in order: a video-based and an in-person robot action observation and execution (AOE) experiment. In the video-based experiment (Fig. 6(a)), pre-recorded videos of actions performed by the Flo v2 robot were presented as visual stimuli using the open-source software PsychoPy[29]. In the in-person experiment (Fig. 6(b)), the Flo v2 robot performed actions directly, with the LED matrix on its chest indicating task stages, and the system was administered by the aforementioned AOE program. For both experiments, participants observed 10-second arm actions of different types (i.e., seven unimanual actions for each arm and four bimanual actions, see Table II) consisting of a 1000 ms stationary pre-action, an 8000 ms action observation interval, and a 1000 ms stationary post-action. Each stimulus was repeated four times and presented in a counterbalanced block design (Fig. 6c), each block contained a sequence of trials. Each trial began with a 1000 ms fixation cross, followed by the stimulus, another 1000 ms fixation cross, and a 5000 ms action execution interval indicated by a triangle shape. The video-based experiment included six blocks of 12 trials each. In the in-person experiment, the first six blocks featured the 12 intransitive actions including four unimanual actions for each arm and four bimanual actions, and the final six blocks each featured one of the six transitive actions (i.e, two for each arm).

To control for perceptual differences between 2D and 3D settings, participants were positioned 150 cm away from the monitor or robot. Videos were recorded in an allocentric perspective using an APS-C camera with a 30 mm focal length (equivalent to a 45 mm full-frame focal length, close to the ”normal” human perspective of 50 mm [30]) and displayed full-screen on a 27-inch monitor, approximating the size of the in-person robot (40 cm height). Before the experiments, participants received training on AOE tasks with sample videos. They were instructed to focus and keep their hands still while observing the fixation cross and the videos, and later mirror the observed actions during the execution phase.

B. EEG Data Acquisition and Processing

The EEG data were recorded using the Emotiv EPOC Flex system (Emotiv Inc., San Francisco, U.S.A.), equipped with 32 Ag-AgCl electrodes arranged according to the International 10–20 system. EEG data acquisition was managed through Emotiv Pro software, which facilitated real-time communication with the PsychoPy platform during the video-based experiment and with the AOE program during the in-person experiment via the Cortex API.

Off-line pre-processing and analysis were conducted using EEGLAB toolbox [31] in MATLAB. EEG data were filtered (1–40 Hz) and channels with artifacts (sudden shifts, excessive noise, or voltage amplitude) were visually removed. The data were re-referenced to the average, interpolating removed channels, and cleaned with Independent Component Analysis (ICA) to eliminate muscular, ocular, or cardiac artifacts. Data segments were created with epochs starting at the onset of visual stimuli, rejecting those with amplitudes exceeding 100 μV. To calculate the event-related desynchronization (ERD), fixation cross intervals were used as the baseline. Time-frequency analyses were conducted for all trials, assessing the sensorimotor mu (8-13 Hz) ERDs relative to baseline power, averaged across action types and channels (C3 and C4), separately for condition, and experiment.



(a) Mean ERD values during AO

(b) Individual ERD time courses during AO

Fig. 7: Mean mu ERD values and time courses during AO tasks for each condition, including three action types (unimanual transitive, unimanual intransitive, and bimanual intransitive) and two experiments (video-based and in-person robot).

C. Results

For the included EEG data across experiments (video-based and in-person robot), an average of $87.89 \pm 6.89\%$ of AO epochs were retained after preprocessing. The Bluetooth connection between EEG headset and PC1 during collection of EEG for transitive action stimuli during the in-person experiment for Subject 1 was disrupted by environmental electromagnetic interference, leading to missing data on transitive robot actions.

Overall, all subjects showed ERDs in mu band, indicated by negative values of event-related spectral perturbation (ERSP), during AO across all conditions (Fig. 7(a)), and patterns of mu ERDs were consistent across the time course of the task (Fig. 7(b)). Subject 1 showed less visible ERD patterns compared to others. Examining the Power Spectral Density (PSD) in the alpha range (8–13 Hz) of this subject also found flatter and less defined patterns compared to others. Among the other two subjects, except for the data from Subject 2 during video-based AO, data from Subject 2 during in-person AO and data from Subject 3 during both AO conditions showed the strongest mu ERDs for bimanual actions and stronger mu ERDs induced by observation of unimanual transitive actions compared to unimanual intransitive ones.

D. Discussion

The Flo v2 robot was able to perform transitive actions, which is an upgrade from Flo's previous version. The integration with the AOE program to facilitate EEG acquisition and real-time synchronization with robot actions helped conduct EEG-based investigation of cortical responses during robot-performed AOE tasks. The case study demonstrates the feasibility of integrating Flo v2 into AO paradigms. All subjects exhibited mu band ERDs; however, there was variability among participants, in which one subject displayed less pronounced ERD patterns than the others. The pilot results in other two subjects revealed that the strongest values of mu ERD were observed during the observation of bimanual actions for both subjects in the in-person experiment. This finding aligns, in part, with Vuckovic et al.'s EEG study, which demonstrated that motor execution of a bimanual task elicited significantly stronger mu ERD compared to unimanual tasks [32]. While Vuckovic et al. focused on motor execution, our study extends this understanding to the domain of action observation, suggesting that observing bimanual actions may engage similar sensorimotor processes as those activated during their execution. Comparing the effects of unimanual transitive and intransitive actions, the latter induced stronger mu ERDs in both Subject 2 and 3 particularly in the in-person experiment. This agrees with findings from the previous EEG study [20] as well as the meta-analyses of functional neuroimaging studies on MNS activation [18], [19]. However, these findings were limited to the in-person experiment; the video-based experiment showed variability in mu ERDs among subjects (e.g., Subject 2 showed the strongest mu ERD for unimanual intransitive actions, while Subject 3 showed the strongest mu ERD for bimanual actions). To validate these findings and investigate the efficacy of these systems in clinical populations, larger sample sizes are essential for further research. Additionally, future studies could incorporate test-retest analysis to assess EEG response reliability across sessions and utilize insights on neural predictors of human-robot interaction [33] to create personalized rehabilitation protocols that adapt to individual cognitive and neural profiles.

ACKNOWLEDGMENT

We thank the National Institutes of Health for funding this research through grant F31-HD102165. Additionally, we appreciate Michael Sobrepera and Ajay Anand for their contributions to the robot system development.

REFERENCES

[1] L. R. Borges, A. B. Fernandes, J. O. dos Passos, I. A. O. Rego, and T. F. Campos, "Action observation for upper limb rehabilitation after stroke," *Cochrane Database of Systematic Reviews*, no. 8, 2022.

[2] G. Rizzolatti, L. Fogassi, and V. Gallese, "Neurophysiological mechanisms underlying the understanding and imitation of action," *Nature reviews neuroscience*, vol. 2, no. 9, pp. 661–670, 2001.

[3] J. J. Q. Zhang, K. N. K. Fong, N. Welage, and K. P. Y. Liu, "The Activation of the Mirror Neuron System during Action Observation and Action Execution with Mirror Visual Feedback in Stroke: A Systematic Review," *Neural Plasticity*, vol. 2018, p. 2321045, 2018.

[4] S. L. Small, G. Buccino, and A. Solodkin, "Brain repair after stroke—a novel neurological model," *Nature Reviews Neurology*, vol. 9, pp. 698–707, Dec. 2013.

[5] I. C. Brunner, J. S. Skouen, L. Ersland, and R. Grüner, "Plasticity and response to action observation: a longitudinal fmri study of potential mirror neurons in patients with subacute stroke," *Neurorehabilitation and neural repair*, vol. 28, no. 9, pp. 874–884, 2014.

[6] N. A. Fox, M. J. Bakermans-Kranenburg, K. H. Yoo, L. C. Bowman, E. N. Cannon, R. E. Vanderwert, P. F. Ferrari, and M. H. Van IJzendoorn, "Assessing human mirror activity with EEG mu rhythm: A meta-analysis.," *Psychological bulletin*, vol. 142, no. 3, p. 291, 2016.

[7] D. Kemmerer, "What modulates the mirror neuron system during action observation?: Multiple factors involving the action, the actor, the observer, the relationship between actor and observer, and the context," *Progress in Neurobiology*, vol. 205, p. 102128, 2021.

[8] V. Gazzola, G. Rizzolatti, B. Wicker, and C. Keysers, "The anthropomorphic brain: the mirror neuron system responds to human and robotic actions," *Neuroimage*, vol. 35, no. 4, pp. 1674–1684, 2007.

[9] L. M. Oberman, J. P. McCleery, V. S. Ramachandran, and J. A. Pineda, "EEG evidence for mirror neuron activity during the observation of human and robot actions: Toward an analysis of the human qualities of interactive robots," *Neurocomputing*, vol. 70, no. 13-15, pp. 2194–2203, 2007.

[10] B. A. Urgen, M. Plank, H. Ishiguro, H. Poizner, and A. P. Saygin, "EEG theta and mu oscillations during perception of human and robot actions," *Frontiers in neurorobotics*, vol. 7, p. 19, 2013.

[11] A. T. Nguyen, A. Anand, and M. J. Johnson, "Exploring eeg responses during observation of actions performed by human actor and humanoid robot," in *2024 10th IEEE RAS/EMBS International Conference for Biomedical Robotics and Biomechatronics (BioRob)*, pp. 1795–1801, IEEE, 2024.

[12] A. Wykowska, T. Chaminade, and G. Cheng, "Embodied artificial agents for understanding human social cognition," *Philosophical Transactions of the Royal Society B: Biological Sciences*, vol. 371, no. 1693, p. 20150375, 2016.

[13] Y. F. Tai, C. Scherfler, D. J. Brooks, N. Sawamoto, and U. Castiello, "The human premotor cortex is' mirror'only for biological actions," *Current biology*, vol. 14, no. 2, pp. 117–120, 2004.

[14] N. Miura, M. Sugiura, M. Takahashi, Y. Sassa, A. Miyamoto, S. Sato, K. Horie, K. Nakamura, and R. Kawashima, "Effect of motion smoothness on brain activity while observing a dance: An fmri study using a humanoid robot," *Social neuroscience*, vol. 5, no. 1, pp. 40–58, 2010.

[15] E. S. Cross, R. Liepelt, A. F. de C. Hamilton, J. Parkinson, R. Ramsey, W. Stadler, and W. Prinz, "Robotic movement preferentially engages the action observation network," *Human brain mapping*, vol. 33, no. 9, pp. 2238–2254, 2012.

[16] A. Kupferberg, M. Iacoboni, V. Flanagin, M. Huber, A. Kasparbauer, T. Baumgartner, G. Hasler, F. Schmidt, C. Borst, and S. Glasauer, "Fronto-parietal coding of goal-directed actions performed by artificial agents," *Human brain mapping*, vol. 39, no. 3, pp. 1145–1162, 2018.

[17] A. P. Saygin, T. Chaminade, H. Ishiguro, J. Driver, and C. Frith, "The thing that should not be: predictive coding and the uncanny valley in perceiving human and humanoid robot actions," *Social cognitive and affective neuroscience*, vol. 7, no. 4, pp. 413–422, 2012.

[18] S. Caspers, K. Zilles, A. R. Laird, and S. B. Eickhoff, "ALE meta-analysis of action observation and imitation in the human brain," *Neuroimage*, vol. 50, no. 3, pp. 1148–1167, 2010.

[19] P. G. Enticott, H. A. Kennedy, J. L. Bradshaw, N. J. Rinehart, and P. B. Fitzgerald, "Understanding mirror neurons: Evidence for enhanced corticospinal excitability during the observation of transitive but not intransitive hand gestures," *Neuropsychologia*, vol. 48, pp. 2675–2680, July 2010.

[20] D. Arnstein, F. Cui, C. Keysers, N. M. Maurits, and V. Gazzola, "μ-Suppression during Action Observation and Execution Correlates with BOLD in Dorsal Premotor, Inferior Parietal, and SI Cortices," *The Journal of Neuroscience*, vol. 31, p. 14243, Oct. 2011.

[21] M. J. Sobrepera, E. Kina, and M. J. Johnson, "Designing and Evaluating the Face of Lil'Flo: An Affordable Social Rehabilitation Robot," in *2019 IEEE 16th International Conference on Rehabilitation Robotics (ICORR)*, (Toronto, ON, Canada), pp. 748–753, IEEE, June 2019.

[22] M. J. Sobrepera, V. G. Lee, and M. J. Johnson, "The design of Lil'Flo, a socially assistive robot for upper extremity motor assessment and rehabilitation in the community via telepresence," *Journal of Rehabilitation and Assistive Technologies Engineering*, vol. 8, pp. 1–26, Apr. 2021.

[23] M. J. Sobrepera and M. J. Johnson, "Designing Arms for Lil'Flo, a Socially Assistive Rehabilitation Robot," in *Biomedical Engineering Society Annual Meeting 2019*, (Philadelphia, PA), Biomedical Engineering Society, Oct. 2019.

[24] M. J. Sobrepera, V. G. Lee, S. Garg, R. Mendonca, and M. J. Johnson, "Perceived Usefulness of a Social Robot Augmented Telehealth Platform by Therapists in the United States," *IEEE Robotics and Automation Letters*, vol. 6, pp. 2946–2953, Apr. 2021.

[25] R. R. Ma, L. U. Odhner, and A. M. Dollar, "A modular, open-source 3D printed underactuated hand," in *2013 IEEE International Conference on Robotics and Automation*, (Karlsruhe, Germany), pp. 2737–2743, IEEE, May 2013.

[26] ROS Wiki, "camera_calibration." `https://wiki.ros.org/camera_calibration`.

[27] E. Olson, "AprilTag: A robust and flexible visual fiducial system," in *Proceedings of the IEEE International Conference on Robotics and Automation (ICRA)*, pp. 3400–3407, IEEE, May 2011.

[28] "Cortex api."

[29] J. Peirce, J. R. Gray, S. Simpson, M. MacAskill, R. Höchenberger, H. Sogo, E. Kastman, and J. K. Lindeløv, "Psychopy2: Experiments in behavior made easy," *Behavior research methods*, vol. 51, pp. 195–203, 2019.

[30] R. Modrak and B. Anthes, *Reframing photography: theory and practice*. Taylor & Francis, 2011.

[31] A. Delorme and S. Makeig, "EEGLAB: an open source toolbox for analysis of single-trial EEG dynamics including independent component analysis," *Journal of neuroscience methods*, vol. 134, no. 1, pp. 9–21, 2004.

[32] A. Vuckovic, S. Pangaro, and P. Finda, "Unimanual versus bimanual motor imagery classifiers for assistive and rehabilitative brain computer interfaces," *IEEE Transactions on Neural Systems and Rehabilitation Engineering*, vol. 26, no. 12, pp. 2407–2415, 2018.

[33] F. Bossi, C. Willemse, J. Cavazza, S. Marchesi, V. Murino, and A. Wykowska, "The human brain reveals resting state activity patterns that are predictive of biases in attitudes toward robots," *Science robotics*, vol. 5, no. 46, p. eabb6652, 2020.

Personalized Range of Motion Scaled Wrist Pointing for Robotic-Based Motor Impairment Assessment

Elijah Rice
Dept. of Mechanical Engineering
Rice University
Houston, United States
er72@rice.edu

Marcia K. O'Malley
Dept. of Mechanical Engineering
Rice University
Houston, United States
omalleym@rice.edu

***Abstract*—Movement smoothness is a commonly employed metric of motor impairment in stroke patients due to a strong correlation with Fugl-Meyer Assessment score, and because it can be assessed with functional-oriented tasks like wrist pointing. Robotic assessments of wrist-pointing tasks typically use targets located at fixed points in the workspace, which can exceed the range of motion (ROM) of stroke patients who exhibit severe motor impairment. We hypothesize that movement smoothness assessed based on movements that do not reach visual targets may conflate assessment of movement smoothness with ROM. We propose that scaling the locations of wrist pointing targets for wrist flexion-extension and radial-ulnar movements from a ROM assessment will better reflect movement characteristics. In this paper, we analyze wrist-pointing movements for fixed and ROM-scaled target locations. We evaluate wrist-pointing performance in both conditions for 8 neurologically-intact participants whose wrist ROM was constrained with a wrist brace simulating ROM deficits present after stroke. Results show that failing to reach targets during wrist pointing has a significant negative impact on movement smoothness. Additionally, scaling target placement to ROM increases the proportion of targets reached while producing practically equivalent movement smoothness to successfully reached fixed target locations. These findings support incorporation of ROM-scaled target placement into movement smoothness assessment.**

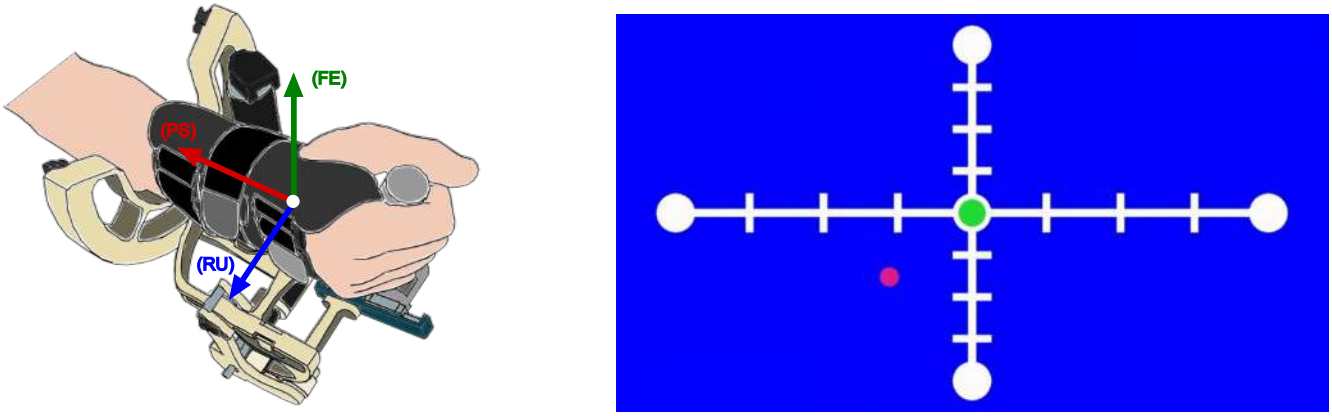
***Index Terms*—exoskeleton, movement smoothness, robotic assessment, stroke rehabilitation.**

I. Introduction

Stroke is the leading cause of long-term disability. In the United States, 9.4 million people are estimated to have had a stroke, cumulatively costing 56.5 billion dollars. By 2030, it is projected that another 3.4 million adults in the US will have had a stroke [1]. Rehabilitation is important to reduce impairment and restore quality of life and independence in the stroke population. Objective motor impairment assessments are useful tools to assess motor recovery after stroke and to determine therapy protocols that have the potential to promote rehabilitation. Robotic assessments of motor impairment provide an objective basis for assessment through precise measurement of kinematic and dynamic quantities of movement [2]. Comparatively, clinical assessments typically rely on a series of clinician-evaluated ordinal scales that require specialized training to administer. Further, these assessments can introduce subjective variability in evaluations between clinicians [3]. Despite the benefits of robotic assessment and rehabilitation, which are often performed in tandem [4], they remain underutilized in rehabilitation [5], [6]. One reason could be the potential that robotic measures of motor impairment, such as movement smoothness, have poor construct validity. In other words, the tasks used to assess movement smoothness could mischaracterize the observed motor impairment such as if movement smoothness was impacted by range of motion (ROM), limiting the ability of these metrics to accurately quantify motor impairment.

Movement smoothness is a commonly used metric in robotic assessment of upper limb functionality [2]. Prior work suggests that movement smoothness increases with stroke recovery as sub-movements become blended [7], and movement smoothness has been shown to positively correlate with clinical assessments of stroke [8], [9]. Tasks for assessing movement smoothness typically consist of goal-directed movements performed through planar reaching or point-to-point movement. These assessments typically use either fixed placement of targets, or they scale the placement of targets according to an individual's range of motion (ROM). Across prior studies, there is a lack of consistency in implementation of fixed or scaled targets during robotic assessment. The impact of the decision to fix or scale the placement of targets on movement smoothness remains unexplored in the literature. Understanding the impact of fixed and scaled targets on movement smoothness is the first step toward improving assessment of motor impairment by determining which paradigm provides smoothness measurements that are more strongly correlated with motor recovery.

We hypothesize that using a fixed placement of targets in the robot's workspace that may exceed an individual's ROM could conflate assessment of their movement smoothness with ROM. ROM impairment in the upper limb is a frequent motor deficit of in movement disorders such as stroke [10]. If an individual is unable to reach all fixed placement targets during goal-directed movements, the assessed movement smoothness may not accurately reflect their movement characteristics. This coupling would negatively impact the construct validity of movement smoothness assessment since its intent is to gauge motor coordination. We additionally hypothesize that scaling target placement to an individual's



(a) (b)

Fig. 1: (a) In the study, neurologically-intact participants donned a wrist brace to simulate the ROM deficits common to stroke survivors. The image shows the neutral wrist position of the OpenWrist robotic device, which has 3 serial revolute joints aligning with the anatomical degrees of freedom (DOF) passing through the wrist: pronation-supination (PS), flexion-extension (FE), and radial-ulnar (RU) deviation. In the current study, only FE and RU axes were used for the wrist pointing task. (b) Participants view a series of target locations and their current location on a computer monitor. The red circle is the participant's current location, computed from the FE and RU joint angles of the OpenWrist. The current target location is indicated by a green circle. During wrist pointing, users made goal directed movements by visually overlapping the red circle representing their wrist orientation with the green circle representing the target position.

ROM could decouple ROM from assessment of movement smoothness by ensuring that targets lie within an individual's reachable workspace.

In this study, we evaluate the aforementioned hypotheses to determine the effects of these two target placement methods on the construct validity of movement smoothness assessment. To this end, we conduct an experiment where neurologically-intact individuals perform wrist ROM assessments and wrist pointing tasks in a wrist and forearm exoskeleton, the OpenWrist [11]. Participants perform these tasks with and without a wrist brace donned to simulate the ROM deficits of stroke survivors. The choice to use neurologically-intact individuals wearing a wrist brace limits additional motor deficits, such as poor coordination, that frequently accompany stroke and could confound movement smoothness assessment [10]. To evaluate these hypotheses, our experiment addresses three aims: First, we seek to quantify the effect of constraining wrist motion with a wrist brace. Second, we quantify the percent of successful (complete) target acquisitions with a wrist brace donned with and without ROM-scaled target placement. Third, we quantify the effect of target location on movement smoothness measured via spectral arc length (SPARC). The outcomes of this experiment are used to inform guidelines for the creation of future movement smoothness assessments.

II. Methods

We conducted a series of experiments to assess the effect of limited range of motion on movement smoothness when performing goal-directed reaching movements with the wrist. Neurologically-intact participants performed point-to-point reaching movements using the Rice OpenWrist [11] to move a cursor on a screen to various target locations. Participants used both wrist flexion-extension (FE) and radial-ulnar (RU) deviation to reach targets. We constrained movements using a wrist brace, and we varied the mapping of the user's range of motion to the various target locations. Our dependent variable was movement smoothness, which was quantified by the metric spectral arc length (SPARC) [7].

A. Participants

Eight neurologically-intact participants (5 female, 3 male) with an age range of 20-30 years old ($\mu = 25.8$ yr, $\sigma = 3.5$ yr) with limited or no experience with wrist pointing tasks were enrolled in the experiment. Participants were right-hand dominant or ambidextrous (7 right-handed, 1 ambidextrous). Each participant completed the experiment and provided informed consent in compliance with Rice University's Institutional Review Board, protocol number IRB-FY2023-48.

B. Apparatus

The device used in this study was the OpenWrist, a serial manipulator for wrist rehabilitation and assessment [11]. This exoskeleton contains three revolute joints that facilitate three degrees of freedom of wrist movement: forearm pronation-supination (PS) (locked during this experiment), wrist flexion-extension (FE), and wrist radial-ulnar (RU) deviation (Fig. 1a). An additional linear slider on the hand grip allows for passive movement to abate joint misalignment. Prior studies on the movement impedance of the OpenWrist have validated it as a measurement device when using spectral arc length to assess movement smoothness [12]. Control of the OpenWrist and measurement of joint angles were executed using C++ and a Q8 USB data acquisition device (Quanser) running at a sampling rate of 200 Hz. Wrist FE and RU deviation joint angles were measured with a resolution of 0.0094º and 0.0070º respectively, using Broadcom HEDL-5540 A11 optical encoders on each of the Maxon DC motors driving each joint. Velocity of each joint was estimated through the Q8's instantaneous velocity

estimator. The OpenWrist has a wrist FE ROM of 1.2217 rad (70º) in flexion and 1.1345 rad (65º) in extension, along with a RU ROM of 0.6109 rad (35º) in radial deviation and 0.6981 rad (40º) in ulnar deviation.

To mitigate misalignment of participants' anatomical wrist joint axes with the OpenWrist, the device orientation was adjusted for each participant. Participants were instructed to maintain comfortable standing posture while the OpenWrist's height was adjusted via a standing desk to rest the participant's elbow on the OpenWrist's elbow support with both shoulders level. Afterwards, the participants were guided to adjust their position in the OpenWrist to achieve neutral forearm pronation-supination, 90 degrees of elbow flexion, and slight shoulder abduction. To limit deviation in grip or forearm position during the experiment, the hand and forearm of each participant was secured to the OpenWrist with self-adhering medical tape. Alignment of the participant and device joint axes was maintained through verbal feedback aimed at minimizing compensatory movements throughout the experiment.

To visually guide ROM assessment and wrist pointing, a graphical user interface (GUI) was used to display FE and RU deviation joint angles (Fig. 1b). Output from the optical encoders was scaled by a constant factor to map FE and RU deviation to the x and y axes, respectively.

C. Task Description

Participants were asked to manipulate the OpenWrist handle to move the cursor on the screen. The tasks comprised an assessment of their ROM and an evaluation of movement smoothness (measured with SPARC) as they completed wrist pointing movements to various targets in the workspace.

1) ROM Assessment: The purpose of ROM assessment was to capture the maximum and minimum joint angles of each participant in wrist flexion-extension (FE) and radial-ulnar (RU) deviation. Assessment consisted of 2 blocks, the first to assess FE ROM and the second RU deviation ROM. Each block was comprised of 3 trials, each with a duration of 20 seconds. Participants began each trial with their wrist in a neutral position (0º FE, 0º RU deviation). During each trial, participants were asked to sweep back and forth as far as they could in the FE or RU direction while the other DOF was held in a fixed location (via active PD control on the joint). Absolute minimum and maximum joint angles during the trial blocks were selected for each joint axis.

2) Wrist Pointing: The purpose of the wrist pointing tasks was to measure the completion or incompletion of each goal-directed wrist movement along with movement smoothness. Assessment consisted of 3 identical blocks of 40 trials of wrist pointing movements. The number of blocks and trials was determined from pilot testing to provide a sufficient number of trials for data analysis while mitigating mental and physical fatigue. Participants began each block with their wrist in a neutral position (0º FE, 0º RU deviation) and targets on the GUI then alternated between being placed away from neutral and returning to neutral. They were instructed to acquire each target within 6 seconds by moving directly to the visual target. If targets were acquired within 6 seconds, the trial was counted as complete and the next target appeared. Conversely, if a target was not acquired within 6 seconds, the trial was counted as incomplete and the next target appeared. The 6 second time window was determined from pilot testing to provide ample time to reach targets while minimizing buildup of fatigue in participants trying to reach targets outside of their wrist ROM.

D. Target Location Scaling

For the wrist pointing with fixed target locations, target positions were distributed within a square 2D coordinate space extending 0.4 rad (22.9º) in the positive and negative FE and RU deviation axes. During ROM-scaled target placement phases, the target locations used in fixed target placement were scaled according to minimum and maximum joint angles in FE and RU deviation. To calculate the position of the ROM-scaled targets, the fixed placement target positions were scaled to 75 percent of minimum and maximum joint angles assessed during the brace-on phase for ROM assessment (1).

$$\theta_{scaled} = 0.75 \cdot \theta_{fixed} \cdot \frac{0.8}{\theta_{max} - \theta_{min}} + \frac{\theta_{max} - \theta_{min}}{2} \quad (1)$$

The 75 percent scaling was chosen to limit changes in movement smoothness resulting from increased stiffness experienced close to wrist ROM limits with the brace donned.

E. Experiment Design

The experiment consisted of two phases of ROM assessment (R) that varied the brace-on condition (B1-on or B0-off) and four phases of wrist pointing (W) that varied the brace-on condition (B1-on or B0-off) and target placement method (S-scaled or F-fixed) to address our three aims.

To address our first aim, ROM assessment was conducted in two conditions, one with the brace on (RB1) and one with the brace off (RB0), to determine the effect of the wrist brace on ROM. Wrist pointing was conducted with the wrist brace off (WB0F) and wrist brace on (WB0S) to determine the effect of the wrist brace on movement smoothness, measured via SPARC. Additionally, the wrist brace-on condition of ROM assessment was used to determine the appropriate scaling factors for target placement during wrist pointing. To address our second aim, we quantify the number of targets achieved in the brace-on condition during wrist pointing with both ROM-scaled (WB1S) and fixed (WB1F) target placements. To address our third aim, we evaluate movement smoothness for four different conditions. First, we evaluate the effect of target location on SPARC (WB0S vs. WB0F). Then, we evaluate the effect of target completion on SPARC (WB1S vs. WB1F).

The phases and conditions of the experiment were presented in four different orders (O1, O2, O3, and O4) in a counterbalanced manner to mitigate the effects of training on the average performance of each section across the participants (see Table I). Participants were evenly distributed among the 4 experiment orders. Counterbalancing between

the brace-on (B1) and brace-off (B0) wrist pointing conditions was not implemented due to observed difficulties during pilot testing in reproducing ROM limitations due to donning and doffing of the wrist brace. Prior to starting the experiment, participants completed a familiarization period for wrist pointing tasks comprised of one WB1S block and one WB1F block. A short break was provided between phases 3 and 4 to minimize participant fatigue.

TABLE I: Experiment Phase Orders

Order	Brace On			Brace Off		
	1	2	3	4	5	6
O1	RB1	WB1S	WB1F	RB0	WB0S	WB0F
O2	RB1	WB1F	WB1S	RB0	WB0S	WB0F
O3	RB1	WB1S	WB1F	RB0	WB0F	WB0S
O4	RB1	WB1F	WB1S	RB0	WB0F	WB0S

[R-ROM assessment, W-Wrist pointing, B1-Brace on, B0-Brace off, S-scaled target locations, F-Fixed target locations]

Brace-on ROM assessment was implemented first for each order since the ROM value for constrained wrist pointing movements was needed to calculate the ROM-scaled target placement. To minimize brace donning and doffing, all brace-on conditions were conducted first, followed by all brace-off conditions. This approach served to address observed issues with ROM measurement reproducibility during pilot testing after repeat donning and doffing of the wrist brace.

F. Data Analysis

Movement smoothness for each of the individual wrist pointing trials was calculated using SPARC [7]. While many metrics to quantify movement smoothness exist, SPARC performs favorably in simulations of harmonic disturbance, change in movement duration and distance, and measurement noise [13]. SPARC calculates movement smoothness as the negative arc length of the Fourier magnitude spectrum within a selected frequency range:

$$SPARC = -\int_0^{\omega_c} \left[\left(\frac{1}{\omega_c} \right)^2 + \left(\frac{d\hat{V}(\omega)}{d\omega} \right)^2 \right]^{\frac{1}{2}} d\omega \quad (2)$$

where $\hat{V}$ is the normalized Fourier magnitude spectrum of the velocity profile (3), and ω_c is the cutoff frequency (4) with a max of 10 Hz.

$$\hat{V} = \frac{A(\omega)}{A(0)} \quad (3)$$

$$\omega_c \triangleq min\ \{w_c^{max}, min\ \{\omega, \hat{V}(r) < \overline{V}\ \forall\ r > \omega\ \}\ \} \quad (4)$$

As movements become less smooth, the number of the peaks in the normalized Fourier magnitude spectrum increase. These additional peaks indicate more distinct sub-movements and increase the magnitude of the negative arc length.

Statistical analysis of the practical equivalence of movement smoothness distributions was performed using a Region of Practical Equivalence (ROPE) test [14]. To conduct this test a ROPE was defined. Any difference in measurment falling within the ROPE was considered negligible. We selected ROPE values to be 0.2 times the standard deviation of the test data, assuming that an effect size of ≤ 0.2 is small or negligible, based on recommendations from Cohen [14]. We used a 95% credible interval for these tests.

Statistical comparison of the difference in movement smoothness distributions was performed with a Mann-Whitney U test [15]. A p-value less than 0.05 was chosen as the standard for establishing significance.

III. Results and Discussion

We analyzed wrist ROM in FE and RU deviation with and without the wrist brace, achievement of targets during wrist pointing, and movement smoothness measured with SPARC during wrist pointing. These data highlight and address our three aims. First, we quantify the effect of restricting wrist motion with a wrist brace. Second, we quantify the effect of scaling target placement on successful target acquisition during wrist pointing with a wrist brace donned. Third, we quantify the effect of target location and wrist motion constraint on movement smoothness.

We compared wrist ROM in FE and RU deviation assessed during RB0 (brace on) and RB1 (brace off). Then, we compared the effect of donning the wrist brace on movement smoothness during WB1S and WB0S. The data presented in Table II suggest that the wrist brace was effective in constraining wrist motion.

TABLE II: Mean ROM for Wrist FE and RU Deviation

	FE Min	FE Max	RU Min	RU Max
RB0	-0.474 rad	0.574 rad	-0.428 rad	0.496 rad
RB1	-0.842 rad	0.962 rad	-0.727 rad	0.563 rad

It should be noted that some participants saturated the ROM of the OpenWrist during ROM assessment, preventing discernment of the actual amount by which the wrist brace reduced ROM.

The effect of the wrist brace on movement smoothness was evaluated using the distribution of movement smoothness for complete target acquisitions during WB1S and WB0S as shown in Fig. 2. Incomplete target acquisition trials were omitted from the comparison, since we hypothesized that movement smoothness would be altered for trials in which the targets were not successfully acquired.

Mean SPARC values for the wrist brace on versus off conditions were similar, but the distribution of SPARC values for these two conditions were significantly different with a p-value less than 0.001. Therefore, while the wrist brace effectively constrained wrist movements, there was a significant difference in movement smoothness between the conditions.

Next, we evaluated the effect of target placement scaling on the percent of successful target acquisitions during wrist pointing (WB1F vs. WB1S), with results presented in Fig. 3. The mean percentage of target locations reached during fixed and ROM-scaled target location wrist pointing was 92.3 % and 98.2 %, respectively. For some participants, the ROM

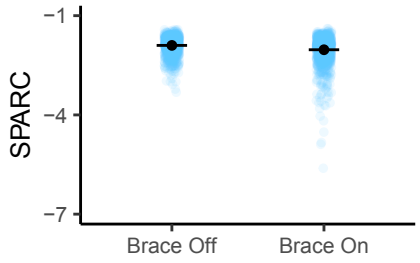


Fig. 2: SPARC values for successful target acquisition movements during WB1S and WB0S. Mean values of SPARC for brace off and brace on target acquisitions were -1.899 and -2.073, respectively.

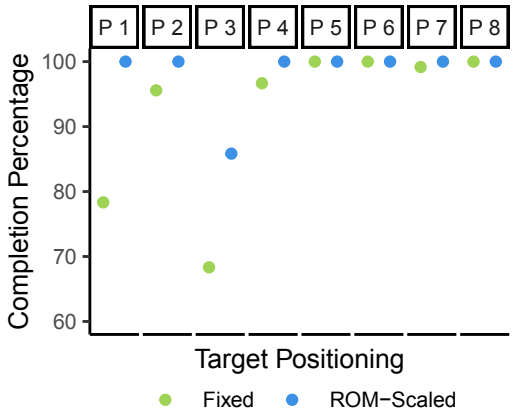


Fig. 3: Percentage of targets reached during WB1F and WB1S for each participant (P1 to P8). P1 and P2 completed the experiment in order O1, P3 and P4 in O2, P5 and P6 in O3, and P7 and P8 in O4 (Table I).

constraints imposed by the brace during both conditions were insufficient to prevent complete target acquisition of any targets. However, scaling target location to ROM improved the percentage of targets reached for participants who were unable to acquire all fixed location targets and had not saturated the mechanical constraints of the OpenWrist.

One participant (P3) exhibited incomplete target acquisitions despite implementation of ROM-scaled target locations. It was noted during the experiment that the proportion of their ROM in combined wrist FE and RU deviation (diagonal movement) to their assessed wrist ROM along the FE and RU axes was lower than other participants. Differences in the shape of their wrist ROM and that of the average wrist ROM defined by Crisco, et. al [16] are likely responsible for their 85.3 % target completion during WB1S. Even with scaled target locations, the corners of the rectangular bounds of the target pattern (as seen in Fig. 4) could exceed their wrist ROM. It is possible that saturation of the mechanical ROM of the OpenWrist by some participants limited additional cases of wrist ROM shape mismatch. Failure to acquire targets due to wrist ROM shape mismatch could be minimized by scaling a target pattern that more closely reflects the wrist ROM defined by Crisco, et. al [16]. Alternatively, replacement of both the FE and RU ROM assessments with a circumduction task that captures a continuous wrist ROM profile could be used to map target placement to a personalized wrist ROM.

To examine the effect of both target locations and ROM-scaling on task completion, the location and number of target incompletions during WB1F and WB1S were evaluated. Sample results for participant 1 are shown in Fig. 4.

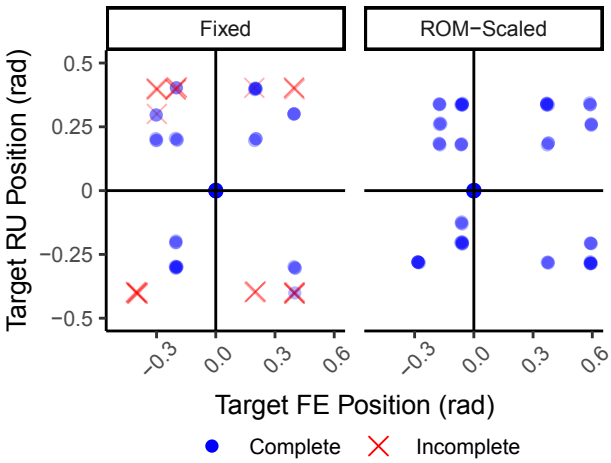


Fig. 4: 3 blocks of 40 trials each are plotted for both wrist pointing conditions. Participant 1 reached 78.3 % of fixed target locations and 100 % of ROM-scaled target locations.

For wrist pointing with fixed target locations, there was a higher proportion of task incompletion for target locations that were farther from the center (diagonally located). When wrist pointing was performed with scaled target locations in both the FE and RU directions, there was an increase in the number of successful target acquisitions.

Finally, we compared the effect of scaling target locations on movement smoothness calculated with SPARC (using data from WB0F and WB0S). The distribution of SPARC measures from successful (complete) target acquisition trials is shown in Fig. 5.

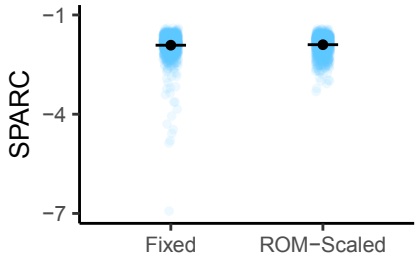


Fig. 5: Mean values of SPARC for target acquisition of fixed and ROM-scaled target locations were -1.914 and -1.899 respectively.

Using the ROPE (region of practical equivalence) test, we showed that the two distributions were practically equivalent when targets where successfully acquired. Thus, during wrist pointing, movement smoothness measured from ROM-scaled

target locations can be used in place of movement smoothness measured from fixed target locations.

To compare the effects of target incompletion on movement smoothness, the distribution of movement smoothness measured from complete and incomplete target acquisition during WB1S and WB1F are shown in Fig. 6.

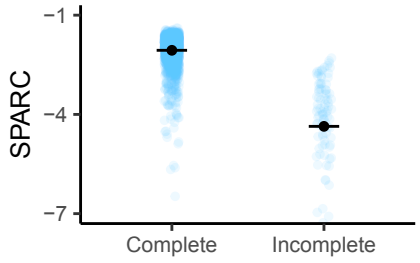


Fig. 6: Mean values of SPARC for complete and incomplete target acquisition were -2.062 and -4.361 respectively.

Differences in movement smoothness distributions were assessed with a Mann-Whitney U test, resulting in a p-value of 0.008 which met the criteria for statistical significance. This supports our hypothesis that the use of goal-directed movements with target locations placed outside of an individual's workspace conflate assessment of movement smoothness with ROM.

Based on our findings, we propose that movement smoothness assessments should implement target locations that are scaled to an individual's ROM. Given that assessments for determining ROM are common among robotic assessments of upper limb functionality [2], the barrier for implementing ROM-scaled target locations is relatively low. Additionally, we recommend that the pattern of targets used for goal-directed movements should reflect the shape of the average individual's ROM. Future work should investigate whether improvements in the construct validity of movement smoothness assessments from ROM-scaled target locations improves how well movement smoothness tracks functional recovery.

IV. Conclusion

Movement smoothness is a commonly used metric for gauging motor impairment during robotic assessments of upper limb functionality employed in rehabilitation. Heterogeneity of placement methods for target locations in goal-directed movements used in movement smoothness assessment calls into question the effect of target location. In this paper, we evaluated the effects of target location and completion on movement smoothness and target completion with and without ROM-scaled target locations. Neurologically-intact individuals donned a wrist brace to simulate ROM-limitations of individuals with stroke, limiting the additional motor deficits that frequently accompany stroke. The wrist brace was found to be effective for constraining wrist ROM in FE and RU deviation, but imposed slight, significant changes in movement smoothness. As expected, we found that failure to reach targets due to ROM limitations had a significant effect on movement smoothness, worsening the construct validity of movement smoothness assessment. Scaling target locations with ROM increased the proportion of targets acquired, while producing practically equivalent movement smoothness to complete target acquisition of fixed target locations. Based on these findings, we conclude that target locations for movement smoothness assessments should be scaled according to an individual's ROM.

References

[1] S. S. Martin, A. W. Aday, Z. I. Almarzooq, C. A. Anderson, P. Arora, C. L. Avery, C. M. Baker-Smith, B. Barone Gibbs, A. Z. Beaton, A. K. Boehme *et al.*, "2024 heart disease and stroke statistics: a report of us and global data from the american heart association," *Circulation*, vol. 149, no. 8, pp. e347–e913, 2024.

[2] S. Balasubramanian, R. Colombo, I. Sterpi, V. Sanguineti, and E. Burdet, "Robotic assessment of upper limb motor function after stroke," *American journal of physical medicine & rehabilitation*, vol. 91, no. 11, pp. S255–S269, 2012.

[3] E. D. Hernandez, C. P. Galeano, N. E. Barbosa, S. M. Forero, Å. Nordin, K. S. Sunnerhagen, and M. Alt Murphy, "Intra-and inter-rater reliability of fugl-meyer assessment of upper extremity in stroke," *J Rehabil Med*, vol. 51, no. 9, pp. 652–659, 2019.

[4] R. Colombo, F. Pisano, S. Micera, A. Mazzone, C. Delconte, M. C. Carrozza, P. Dario, and G. Minuco, "Robotic techniques for upper limb evaluation and rehabilitation of stroke patients," *IEEE transactions on neural systems and rehabilitation engineering*, vol. 13, no. 3, pp. 311–324, 2005.

[5] P. Maciejasz, J. Eschweiler, K. Gerlach-Hahn, A. Jansen-Troy, and S. Leonhardt, "A survey on robotic devices for upper limb rehabilitation," *Journal of neuroengineering and rehabilitation*, vol. 11, pp. 1–29, 2014.

[6] H. M. Qassim and W. Wan Hasan, "A review on upper limb rehabilitation robots," *Applied Sciences*, vol. 10, no. 19, p. 6976, 2020.

[7] S. Balasubramanian, A. Melendez-Calderon, A. Roby-Brami, and E. Burdet, "On the analysis of movement smoothness," *Journal of neuroengineering and rehabilitation*, vol. 12, pp. 1–11, 2015.

[8] M. Saes, M. I. Mohamed Refai, J. van Kordelaar, B. L. Scheltinga, B.-J. F. Van Beijnum, J. B. Bussmann, J. H. Buurke, P. H. Veltink, C. G. Meskers, E. E. van Wegen *et al.*, "Smoothness metric during reach-to-grasp after stroke: part 2. longitudinal association with motor impairment," *Journal of neuroengineering and rehabilitation*, vol. 18, pp. 1–10, 2021.

[9] O. Celik, M. K. O'Malley, C. Boake, H. S. Levin, N. Yozbatiran, and T. A. Reistetter, "Normalized movement quality measures for therapeutic robots strongly correlate with clinical motor impairment measures," *IEEE Transactions on Neural Systems and Rehabilitation Engineering*, vol. 18, no. 4, pp. 433–444, 2010.

[10] C. A. Yarosh, D. S. Hoffman, and P. L. Strick, "Deficits in movements of the wrist ipsilateral to a stroke in hemiparetic subjects," *Journal of neurophysiology*, vol. 92, no. 6, pp. 3276–3285, 2004.

[11] E. Pezent, C. G. Rose, A. D. Deshpande, and M. K. O'Malley, "Design and characterization of the openwrist: A robotic wrist exoskeleton for coordinated hand-wrist rehabilitation," in *2017 international conference on rehabilitation robotics (ICORR)*. IEEE, 2017, pp. 720–725.

[12] C. G. Rose, E. Pezent, C. K. Kann, A. D. Deshpande, and M. K. O'Malley, "Assessing wrist movement with robotic devices," *IEEE transactions on neural systems and rehabilitation engineering*, vol. 26, no. 8, pp. 1585–1595, 2018.

[13] M. I. Mohamed Refai, M. Saes, B. L. Scheltinga, J. van Kordelaar, J. B. Bussmann, P. H. Veltink, J. H. Buurke, C. G. Meskers, E. E. van Wegen, G. Kwakkel *et al.*, "Smoothness metrics for reaching performance after stroke. part 1: which one to choose?" *Journal of neuroengineering and rehabilitation*, vol. 18, pp. 1–16, 2021.

[14] J. Cohen, *Statistical power analysis for the behavioral sciences*. routledge, 2013.

[15] P. E. McKnight and J. Najab, "Mann-whitney u test," *The Corsini encyclopedia of psychology*, pp. 1–1, 2010.

[16] J. J. Crisco, W. M. Heard, R. R. Rich, D. J. Paller, and S. W. Wolfe, "The mechanical axes of the wrist are oriented obliquely to the anatomical axes," *JBJS*, vol. 93, no. 2, pp. 169–177, 2011.

Modeling and Estimation of Stiffness Imposed by Cable-based Exosuits

Randheer Singh[1] and Vineet Vashista[2]

Abstract— **Cable-based exosuits are one of the prevalent choices for rehabilitation, among others. These exosuits are redundant in nature and are capable of imposing a desired joint torque along with a specific impedance simultaneously due to redundancy. The exosuit imposed impedance majorly depends on the geometric routing of the cables and tension in cables. Therefore, the resulting stiffness and damping imposed onto humans could be different from what is intended for a musculoskeletal system of generalized anthropometry. Thus, modeling and estimating the impedance imposed by a cable-based exosuit is of utmost importance for the design and development of efficient and effective rehabilitation exosuits. The current work developed a framework to estimate stiffness imposed by a passive cable-based exosuit onto a human arm. To test the framework, an experiment was conducted on two participants, and the joint space and task space stiffness was estimated using the developed framework. The results indicate that during the design of routing, the geometry is more important than the cable tension. Furthermore, for the same cable routing, the imposed stiffness differed in magnitude for both participants. The developed framework can be even more beneficial in the design of complex and nonintuitive cable routing.**

I. INTRODUCTION

The human musculoskeletal system enables the desired motion of a limb by planning the trajectory and generating the necessary joint dynamics (i.e., torques and impedance) [1]. However, musculoskeletal disorders arising from neural and motor disability can potentially compromise this capability [2], [3]. Rehabilitation, by applying external dynamics to the disabled limb, is one of the most conventional approaches to improve motor and neural control. Recently, robot-based rehabilitation has also shown potential for the motor recovery of disabled limbs, along with conventional physiotherapy [4]–[8]. The robot imposes predefined dynamics onto the targeted limb, mimicking a physical interaction similar to a physiotherepist.

The rehabilitation robots typically apply force and torque either depending on the limb's task space trajectory or based on a particular joint's biological reference torque depending on body weight. Similarly, in other cases, the dynamics is imposed based on joint kinematics to impose a predefined impedance on the particular joint [4], [5], [7], [9]–[11]. The two categories of robots, rigid link and cable-based exosuits [12], are the most widely used for rehabilitation. The cable-based exosuits are redundant and can impose diverse impedances onto human limbs for the same joint torque due to redundancy. The imposed stiffness and damping could vary due to the different anthropometry of the user, the type of cable routing, the magnitude of tensions in the cables, and the impedance of the cable passive elements [13].

Furthermore, depending on the physiological parameters, each human perceives the imposed dynamics differently since the segment lengths would result in different moment arms. Eventually,the resulting stiffness and damping imposed onto humans could differ from what is intended for a musculoskeletal system of generalized anthropometry. Moreover, the type of imposed dynamics plays an important role since humans adapt differently when subjected to the same magnitude of external torques, but different impedances (i.e., stiffness and damping) are imposed [14]–[16]. Therefore, estimating the imposed external dynamics as impedance during a physical interaction is vital for designing efficient and effective rehabilitation solutions. However, modeling exosuit-imposed dynamics as impedance has not been fully explored, and very little work has been done to estimate the imposed external dynamics as impedance [17] during the physical interaction of the human arm.

The objective of the current work was to develop a framework to model and estimate the exosuit imposed stiffness and map it to the human arm anatomical joints. To achieve this, a passive exosuit is used to apply different force fields onto the arm during planar motion. The exosuit is capable of altering the imposed dynamics by allowing to have different routings of the cables. Further, an experiment was performed on two participants to test the developed framework, and the imposed stiffness was quantified and mapped onto the arm anatomical joints.

II. METHODS

The current study aims to model and estimate the dynamics imposed by a cable-based exosuit during physical interaction tasks. A passive exosuit is used to achieve it, which applies force on the arm segments that eventually result in joint torques and impedance onto the arm. It is worth noting that throughout the remainder of the article, the impedance should only be understood as the imposed stiffness by the exosuit as damping and inertia are ignored due slow movement and low weight of the exosuit.The imposed stiffness by the passive exosuit onto the human arm was estimated by utilizing a redundant system stiffness formulation to model the imposed stiffness [13]. Human experiments were performed with a passive exosuit to mimic a physical interaction task for the human arm.

[1]Randheer Singh is with the Department of Mechanical Engineering, Indian Institute of Technology Gandhinagar, Palaj, Gandhinagar, India randheers@iitgn.ac.in

[2]Vineet Vashista is with the Department of Mechanical Engineering, Indian Institute of Technology Gandhinagar, Palaj, Gandhinagar, India vineet.vashista@iitgn.ac.in

A. Experimental Setup

The passive exosuit contains a table-based platform that consists of mounted grooved pullies through which the cables are routed. A typical steel cable is connected at one end onto the human arm through a polypropylene brace and passes over the pullies. The cable is connected to a spring and a constant weight at the other end, as shown in Fig.1. The cable routings are used in four configurations: C1, C2, C3, and C4, as depicted in Table I. The system resembles a passive exosuit since the cables can be routed in any of the configurations mentioned in Table I. The kinematics is recorded using the motion capture system (vicon, UK), and the external force exerted by the cables during the interaction trials is recorded using the load cell sensors (Futek, USA).

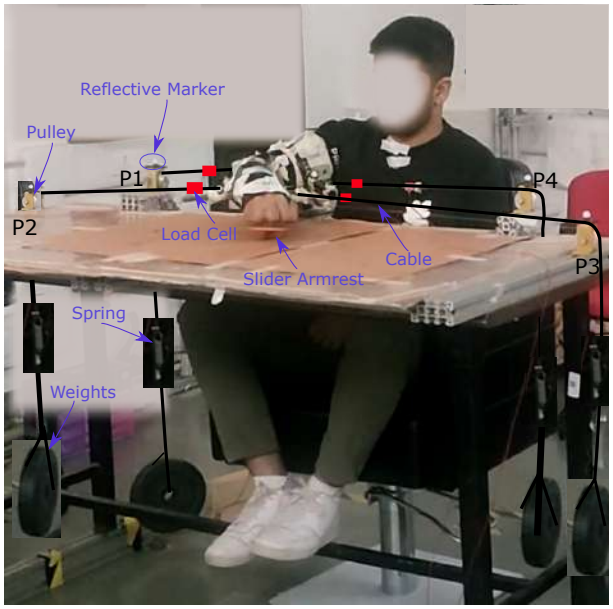


Fig. 1. A representative picture of the participant for configuration C1. The cables attached to the arm brace pass through a pully and eventually terminate with a spring in series holding a weight. Also, load cells are connected in series to measure the cable tensions.

The cable routings are chosen to impose diverse stiffness on the human arm, as shown in Fig. 2. The two of the routings, C3 and C4, are single-joint intervention routings, and the other two, C1 and C2, are multijoint routings, as shown in TableI.

TABLE I

CONFIGURATION DEFINITION BASED ON THE CABLES USED IN THE EXOSUIT EMULATOR

Configuration ID	Cables used	Affecting Joints
C1	All	both
C2	only 2 and 3	both
C3	only 1 and 2	only Shoulder
C4	only 5	only Elbow

B. Imposed Dynamics Modeling

The mathematical formulation of the imposed stiffness is modeled assuming the exosuit is a serial chain multibody system having two serially connected rigid links. The link lengths are assumed equal to the arm limb segments and the joints coincide with the arm joints. The cables, along with the springs, are considered actuators of this redundant system. In the remainder of the article, the exosuit manipulator refers to a two-link serial chain cable-driven manipulator. The dynamics of such a system can be derived using the Lagrangian approach [18], [19].

$$\frac{d}{dt}\Big(\frac{dL}{d\dot{\theta}_i}\Big) - \frac{\partial L}{\partial \theta_i} = \tau_i, i = 1, ..., n \tag{1}$$

Where L represents the Lagrange, θ_i is the generalized coordinate, and τ_i is external joint torque at i^{th} joint. Now, the joint torques generated at i^{th} joint by j^{th} cable having a tension, T_j, can be represented by Eq. (2).

$$\tau_i^c = \Big(\hat{l}_j \cdot \frac{\partial \vec{r}_j}{\partial \theta_j}\Big) T_j, where \;\; \vec{l}_j = \vec{M}_j - \vec{r}_j \tag{2}$$

M_j in Eq. (2) represents the pulley position, r_j represents the location of connection point of j^{th} cable on i^{th} link, and T_j represents the force applied by the j^{th} cable. Now, for the current system *m* cables and *n* joints, the mapping between joint torques and cable tension is given by Eq. (3).

$$\underbrace{\begin{bmatrix}\tau_1\\ \tau_2\\ \vdots\\ \tau_n\end{bmatrix}}_{\tau} = \underbrace{\begin{bmatrix}(\hat{l}_1 \cdot \frac{\partial \vec{r}_1}{\partial \theta_1}) & (\hat{l}_2 \cdot \frac{\partial \vec{r}_2}{\partial \theta_1}) & \cdots & (\hat{l}_m \cdot \frac{\partial \vec{r}_m}{\partial \theta_1})\\ (\hat{l}_1 \cdot \frac{\partial \vec{r}_1}{\partial \theta_2}) & (\hat{l}_2 \cdot \frac{\partial \vec{r}_2}{\partial \theta_2}) & \cdots & (\hat{l}_m \cdot \frac{\partial \vec{r}_m}{\partial \theta_2})\\ \vdots & \vdots & \vdots & \vdots\\ (\hat{l}_1 \cdot \frac{\partial \vec{r}_1}{\partial \theta_n}) & (\hat{l}_2 \cdot \frac{\partial \vec{r}_2}{\partial \theta_n}) & \cdots & (\hat{l}_m \cdot \frac{\partial \vec{r}_m}{\partial \theta_n})\end{bmatrix}}_{A} \underbrace{\begin{bmatrix}T_1\\ T_2\\ \vdots\\ T_m\end{bmatrix}}_{T} \tag{3}$$

$$\tau = AT \tag{4}$$

The term τ is a $n \times 1$ column vector representing joint torques imposed by the passive exosuit during the interaction, and T is a $m \times 1$ column vector representing cable forces of the exosuit. Notably, for the current analysis, m depends on the configuration and has values 4, 2, 2, 1, respectively, for the configurations C1, C2, C3, and C4.

Since the task is planar, for simplifying the data representations, the imposed joint stiffness is represented only for shoulder elevation (ElvAngle) and elbow flexion/extension (EFE) degrees of freedom, resulting in a two 2×2 matrix in the joint space. For the remainder of the article, the shoulder will refer to the shoulder elevation degree of freedom. The elbow will refer to the elbow flexion-extension degree of freedom, and the stiffness should be interpreted as the exosuit imposed stiffness.

$$\begin{bmatrix}d\tau_s\\ d\tau_e\end{bmatrix} = \begin{bmatrix}K_{SS} & K_{SH}\\ K_{ES} & K_{EE}\end{bmatrix} \begin{bmatrix}d\theta_s\\ d\theta_e\end{bmatrix} \tag{5}$$

$$d\tau = \mathbf{K}_{\theta \mathbf{Exo}} d\theta \tag{6}$$

$\mathbf{K}_{\theta Exo}$ is an exosuit imposed multi-joint stiffness matrix that relates the imposed joint torque, $d\tau$, and angular deflection, $d\theta$. Elements K_{SS} and K_{EE} in Eq. (5) represent the imposed

shoulder and elbow joint stiffness. From the relation between A and τ in Eq. (3), we get Eq. (7). Further, using Eq. (6), Eq. (7) can be re-written as in Eq. (8).

$$d\tau = (dA)T + A(dT) \tag{7}$$

$$\mathbf{K}_{\theta\mathbf{Exo}} d\theta = (dA)T + A(dT) \tag{8}$$

$$dT = k_c dl \tag{9}$$

The cable stiffness can be expressed as in Eq. (9). Here, *dl* is a differential change in cable length resulting due to changes in cable tension, *dT*. k_c is a $m \times m$ diagonal cable stiffness matrix holding the spring stiffness values of each cable, k_c, along the diagonal. Subsequently, k_c for each spring can be estimated experimentally.

$$dl = -A^T(d\theta) \tag{10}$$

$$\mathbf{K}_{\theta\mathbf{Exo}} d\theta = (dA)T - Ak_cA^T d\theta \tag{11}$$

$$\mathbf{K}_{\theta\mathbf{Exo}} = \underbrace{\left[\frac{dA}{d\theta_1}T \quad \frac{dA}{d\theta_2}T \quad \cdots \quad \frac{dA}{d\theta_7}T\right]}_{\kappa_d} - \underbrace{Ak_cA^T}_{\kappa_c} \tag{12}$$

Equation 10 presents the relation between changes in cable length. *dl*, with change in joint angles, $d\theta$. By using Eq. (10) and (9), Eq (7) can be re-written as Eq. (11). Further, dividing both sides by $d\theta$ results in the expression for the imposed joint stiffness of the modeled multibody system as in Eq. (12). The matrix κ_d represents the effect of the rate of moment arm and cable tensions, and κ_c represents the effect of the spring stiffness and geometry on the overall joint stiffness $\mathbf{K}_{\theta\mathbf{Exo}}$ respectively.

The resistance required at the joints to resist this external perturbation can be written by equation (13),

$$dF = \mathbf{k_x} dx \tag{13}$$

using the virtual work principle as in Eq. (14), the endpoint force and the corresponding joint torques can be related.

$$\tau = \mathbf{J^T} F_{ext} \tag{14}$$

Where $\mathbf{J}$ is the exosuit manipulator Jacobian and F_{ext} is the external force at the endpoint of the exosuit manipulator. Subsequently, the task space stiffness of the model can be written using the Jacobian transformation from joint space to task space as represented in Eq. (15).

$$\mathbf{K}_{\mathbf{xExo}} = J^{\propto T}\left[\mathbf{K}_{\theta\mathbf{Exo}} - (\frac{\partial J^T}{\partial \theta})F_{ext}\right]J^{\propto 1} \tag{15}$$

$$\mathbf{K}_{\mathbf{xExo}} = \mathbf{J}^{\propto\mathbf{T}}\left[\mathbf{K}_{\theta\mathbf{Exo}}\right]J^{\propto 1} \tag{16}$$

For the case of no external force, F_{ext}, on the manipulator, the imposed task space stiffness of the arm model can be obtained from Eq. (16)

The passive exosuit system had springs in series along with the constant weight. The stiffnesses of the springs were estimated by hanging the weight and measuring the corresponding deflection. The passive exosuit cables 1, 2, 3, 4, and 5 have spring stiffness of $550, 460, 460, 550, 275$ N/m, respectively.

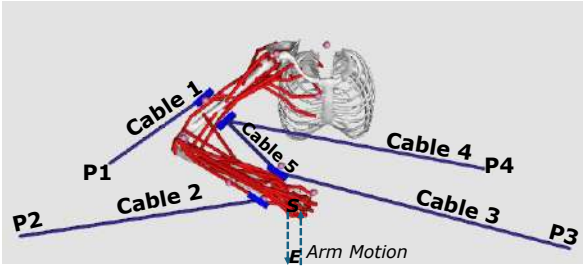


Fig. 2. The cables of the exosuit are modeled as muscles in OpenSim 4.1 to estimate the three-dimensional moment arm matrix and its derivative.

C. Estimation of Cable Moment Arms

An upper limb musculoskeletal model has been used to estimate the three-dimensional moment arms of the exosuit cables onto the arm anatomical joints and their derivatives during the task [20]. The flow of the data is depicted in Fig 3. A generic model is scaled used to estimate the joint kinematics of the arm using the standard inverse kinematics tool available in OpenSim [21]. During the experiment, the pulley position,and the point where the cables connect to the human arm were also recorded using reflective markers to determine cable force direction. Also, the cables were modeled as muscle and added to the scaled musculoskeleton model using an XML editor to estimate the approximate moment arms during the motion and are depicted in Fig.2. Only moment arms were estimated, and no dynamic analyses were performed in the OpenSim tool.The moment arms are extracted from the OpenSim 4.1 using the MATLAB (MathWorks, Natick, Massachusetts, USA) API method [22]. Also, the derivatives of the moment arm are numerically computed using a custom Matlab script using the central difference formula. Once these two quantities are computed, the structure matrix A and the derivative of the structure matrix with the joint coordinates $\frac{dA}{dq_i}$ are determined, and eventually, the three-dimensional imposed joint stiffness can be evaluated from the equation (12).

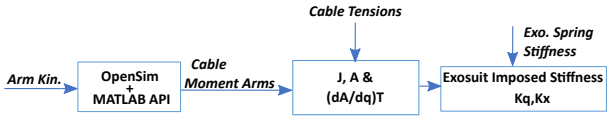


Fig. 3. The flowchart explaining the process to estimate exosuit imposed stiffness from the experimental data

D. Experimental protocol

The experiment was conducted on two healthy male participants (mean age: 28 years; weight: 67.5 kg; height: 171 cm). Participants were informed about the experimental procedure and signed a written consent form approved by the Institute Ethics Committee of the Indian Institute of Technology Gandhinagar (Identifier number: IEC/VV/2021/013) before participation. The participants were asked to sit in the chair, torso was firmly fixed to chair to avoid compensatory movement.Participant was instructed to trace a straight line

drawn on the table (to maintain uniformity of motion across participants) while the passive exosuit was connected to the human arm, as depicted in Fig 2. All the configurations were used in a random sequence, with different configurations in each trial, resulting in a total of four trials for each participant. The cable routing used for each configuration is depicted in Table I. The participants were instructed to trace a marked straight line on the table, reach the end point E, and return back to the starting point S as shown in Fig. 2 constituting a lap. Five such laps were performed by each participant, and the data was analyzed only for the third lap of each trial for each participant.

III. Results

All the trajectory samples are normalized and represented in a 0% to 100% range, as shown in Fig 4, where 0% is at the start of the trajectory, 50% is at the point E (fully extended arm) in Fig. 2, and 100% refers to the reaching back to the start point. The estimated joint stiffness and task space stiffness imposed by the passive exosuit onto the human arm at a single point (i.e., the $50\%^{th}$ Trajectory corresponding to point E in Fig. 2) for both the subjects and all the configurations are represented in Tables II and III, respectively.

TABLE II

Joint stiffness imposed by the passive exosuit onto the human arm. The values are at the 50% of the trajectory

	P1 :$K_{\theta Exo}(Nm/rad)$	**P2:** $K_{\theta Exo}(Nm/rad)$
C1	$\begin{bmatrix} /209.7240 & /101.3796 \\ /101.7724 & /53.6666 \end{bmatrix}$	$\begin{bmatrix} /106.2269 & /58.7875 \\ /57.2850 & /33.0859 \end{bmatrix}$
C2	$\begin{bmatrix} /185.7969 & /102.1495 \\ /102.3850 & /56.4579 \end{bmatrix}$	$\begin{bmatrix} /100.0407 & /60.8073 \\ /59.1132 & /35.3615 \end{bmatrix}$
C3	$\begin{bmatrix} /17.6669 & /0.0000 \\ /0.0000 & /0.0000 \end{bmatrix}$	$\begin{bmatrix} /6.0788 & /0.0000 \\ /0.0000 & /0.0000 \end{bmatrix}$
C4	$\begin{bmatrix} /0.0000 & /0.0000 \\ /0.0000 & /1.9121 \end{bmatrix}$	$\begin{bmatrix} /0.0000 & 0.0000 \\ 0.0000 & /2.6704 \end{bmatrix}$

The element $(1,1)$, $(2,2)$ and diagonal terms of the joint stiffness matrix denoted in Table II represent the shoulder elevation angle and elbow flexion-extension and coupling terms, respectively. Similarly, the elements $(1,1)$, $(2,2)$ and diagonal terms of the task stiffness matrix denoted in Table III represent the lateral and anterior-posterior(Ant-Post) and coupling terms, respectively. As expected during the single joint intervention configurations, $C3$ and $C4$ have no coupling terms in the imposed joint stiffness matrix; however, the imposed task space matrix has coupling terms for the same.

The joint stiffness can be divided into two components κ_C and κ_D representing the effect of cable tensions and geometry, respectively, as defined in the equation (12). The contribution of the cable tensions is much less as compared to the contribution of the geometry of the cable routings, as shown in Fig.4(a)-(f). This is due to the fact that dA/dq terms have very little magnitude, and even a higher magnitude of the cable tensions would result in less contribution to total joint stiffness as compared to the κ_C.

TABLE III

Task stiffness imposed by the passive exosuit onto the human arm. The values are at the 50% of the trajectory

	P1 :$K_{xExo}(N/m)$	**P2:** $K_{xExo}(N/m)$
C1	$\begin{bmatrix} /20.4199 & 114.4939 \\ 88.2816 & /19.9199 \end{bmatrix}$	$\begin{bmatrix} /36.6288 & 14.7282 \\ /3.4024 & 51.2419 \end{bmatrix}$
C2	$\begin{bmatrix} /5.5510 & 81.4191 \\ 61.0320 & 26.6057 \end{bmatrix}$	$\begin{bmatrix} 18.3495 & /20.1117 \\ /35.3627 & 58.6005 \end{bmatrix}$
C3	$\begin{bmatrix} /40.2956 & 18.4938 \\ 15.8039 & 10.8469 \end{bmatrix}$	$\begin{bmatrix} /33.5169 & 27.6373 \\ 28.7943 & /6.1885 \end{bmatrix}$
C4	$\begin{bmatrix} /30.1460 & 16.7266 \\ 16.7266 & /8.9128 \end{bmatrix}$	$\begin{bmatrix} /66.2173 & 38.7086 \\ 38.7086 & /22.0125 \end{bmatrix}$

The configurations C1 and C2 have four cables and two cables attached, respectively, but impose a similar magnitude of joint stiffness. Even though the C1 configuration has four weights attached to the arm as compared to C2, where only two weights are attached to the arm. Configuration C2 also imposes higher task space stiffness as compared to C1 for both participants in either direction, as shown in Fig. 5(a)-(f). This is due to the reason that in configuration C1, cables 1 and 4 are connected to the upper arm and do not have a larger moment arm, resulting in less contribution to the imposed joint stiffness, as shown in Fig. 4.

The single joint intervention routings (C3 and C4) do not impose coupling on the joints directly, as shown in Figs. 4(c) and (d); however, the task space stiffness contains coupling terms due to the coupled nature of the cartesian kinematics, as shown in Figs. 5(c) and (d). Hence, the participant perceives a coupled force field in task space during the task, even during the single joint intervention configurations (i.e., C3 and C4) were not intended to be coupled physically.

IV. Discussion

The primary objective of this study was to develop a computational framework for estimating the stiffness imposed by a cable-based exosuit onto human arm during physical interaction and map it to arm anatomical joints. The framework was successfully implemented and tested on two participants to analyze the role of geometrical stiffness κ_c and cable tension κ_d in determining joint stiffness. The results indicate that geometrical stiffness contributes more significantly to total joint stiffness than cable tension [13], and that imposed impedance varies based on user anthropometry. These findings demonstrate the effectiveness

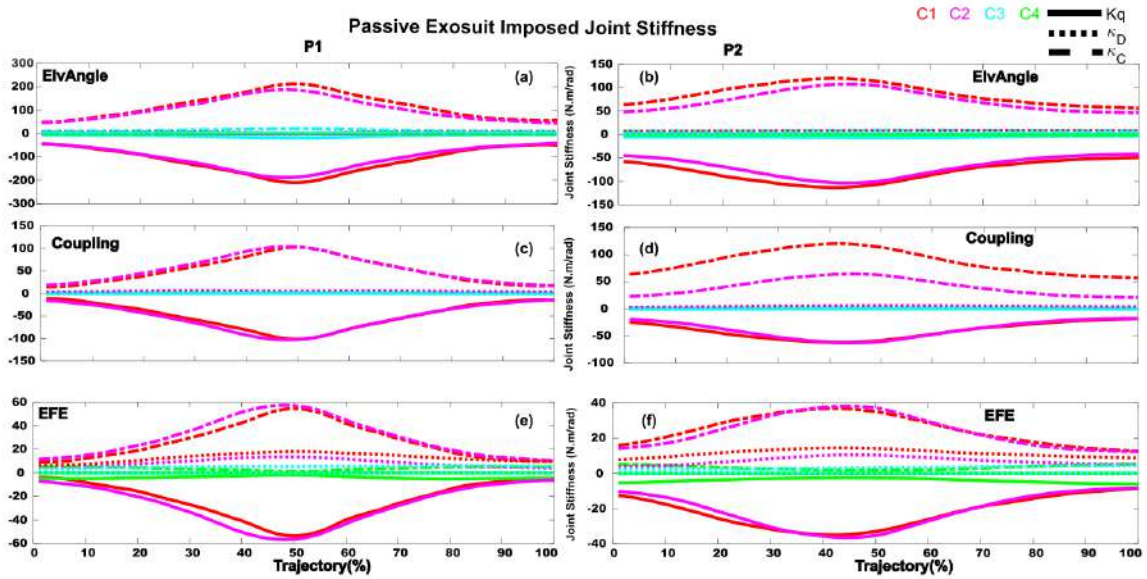


Fig. 4. Imposed joint stiffness by the passive exosuit onto the human arm. The values of κ_C are plotted using the dashed line, and the values of κ_D are represented using the dash-dot line. The configurations are denoted by the color of the configuration ID (i.e.,$C1, C2, C3$ and $C4$). The total joint stiffness is plotted using the solid line.

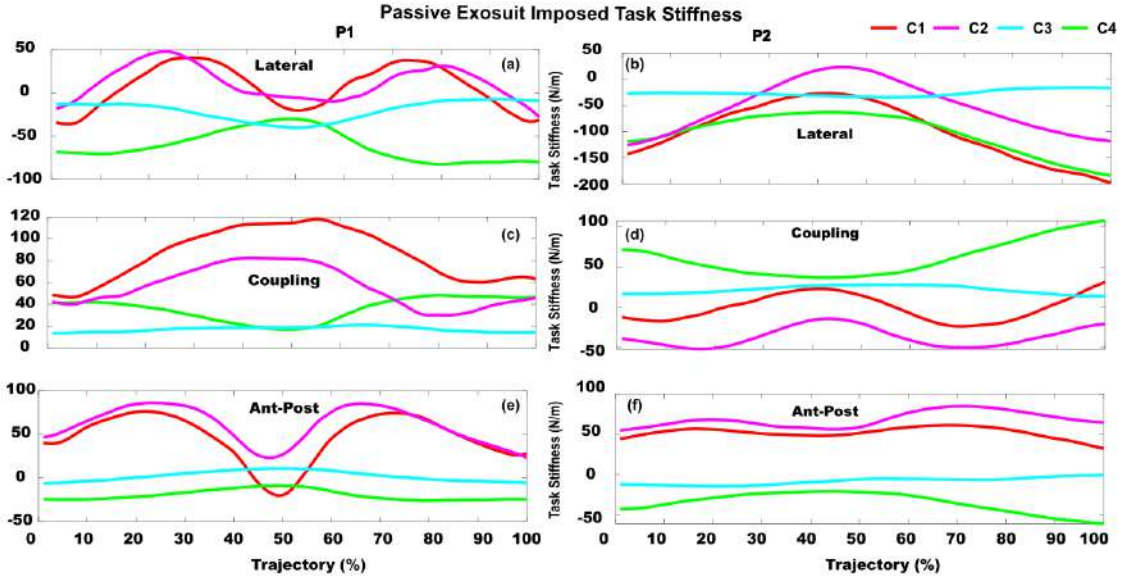


Fig. 5. Imposed task space stiffness by the passive exosuit onto the human arm. The configurations are denoted by the color of the configuration ID (i.e.,$C1, C2, C3$, and $C4$). The total task space stiffness is plotted using the solid line.

of the developed framework in quantifying exosuit-imposed stiffness changes.

The results show that configuration C2 imposes more stiffness in task space than C1, even though during the C1 configuration, the applied weight on the arm is double that of C2. This would probably be due to the cable tension having very little contribution to joint stiffness and cable routing having a larger effect on the imposed stiffness. So, Configuration C2 could potentially be a better option for imposing more stiffness in cartesian space. This also indicates that during the design of cable-based exosuits, the geometric routing should be given priority over the cable tensions.The single joint intervention routings do not impose coupling on the joints, as shown in Figs. 4(c) and (d); however, the task space stiffness has coupling terms due to the coupled nature of the cartesian kinematics, as shown in Figs. 5(c) and (d). The force field perceived by the participant would be of a coupled nature. This is important from a rehabilitation paradigm design perspective because the participant would react to the imposed dynamic

depending on what the participant perceives in the task space.

The framework also maps the stiffness imposed by the exosuit onto the arm anatomical joints . This mapping helps interpret the interaction force field in terms of imposed impedance. The results indicate that for identical configurations for participants 1 and 2, the exosuit imposed different joint stiffness on the arm joints .The difference would mean that the shoulder would be stiffer for P1 as compared to P2 during the same trajectory and the same exosuit, and if this were not to be taken care of, it would potentially result in different adaptions among the users [13], [17]. This would even strengthen the notion that the dynamics to be imposed onto participants by any cable-based exosuit should be modeled beforehand for all the participants and rehabilitation/intervention paradigms should be designed accordingly.Additionally, this framework holds significant potential for rehabilitation applications. Understanding how users perceive task-space stiffness is essential for designing motor training interventions that are tailored to individual needs. The ability to account for variations in stiffness due to geometric and anthropometric differences ensures that exosuits can be personalized to person spacific and joint specific inverventions.By accounting for variations in stiffness resulting from both geometric and anthropometric differences, the framework enables personalized exosuit designs that can be tailored to individual-specific and joint-specific rehabilitation interventions.

The framework was tested on only two participants, limiting the generalizability of the findings and future studies should include a larger and more diverse sample . Additionally, the framework was evaluated on passive exosuits with simple cable routings, and its application to active exosuits with dynamic control mechanisms remains unexplored. Future research should focus on integrating the framework into real-time control systems to enable dynamic, impedance-informed adjustments, enhancing human-exosuit interaction and performance [13].

ACKNOWLEDGMENT

This work was partially supported by the Gujarat Council on Science and Technology under project number GUJCOST/STI/2023-24/340.

REFERENCES

[1] Meghan E. Huber, Charlotte Folinus, and Neville Hogan. Visual perception of joint stiffness from multijoint motion. *Journal of Neurophysiology*, 122:51–59, 2019.

[2] Khadijeh Moulaei, Abbas Sheikhtaheri, Mansour Shahabi Nezhad, AliAkbar Haghdoost, Mohammad Gheysari, and Kambiz Bahaadinbeigy. Telerehabilitation for upper limb disabilities: a scoping review on functions, outcomes, and evaluation methods. *Archives of Public Health*, 80(1), August 2022.

[3] Steff Doumen, Luca Sorba, Peter Feys, and Lisa Tedesco Triccas. Efficacy and dose of rehabilitation approaches for severe upper limb impairments and disability during early acute and subacute stroke: A systematic review. *Physical Therapy*, 103(4), January 2023.

[4] Paweł Maciejasz, Jörg Eschweiler, Kurt Gerlach-Hahn, Arne Jansen-Troy, and Steffen Leonhardt. A survey on robotic devices for upper limb rehabilitation. *Journal of neuroengineering and rehabilitation*, 11(1):1–29, 2014.

[5] Md Rasedul Islam, Brahim Brahmi, Tanvir Ahmed, Md Assad-Uz-Zaman, and Mohammad Habibur Rahman. Exoskeletons in upper limb rehabilitation: A review to find key challenges to improve functionality. *Control Theory in Biomedical Engineering*, pages 235–265, 2020.

[6] Julie Bernhardt and Jan Mehrholz. Robotic-assisted training after stroke: Ratuls advances science. *The Lancet*, 394(10192):6–8, 2019.

[7] Abolfazl Mohebbi. Human-robot interaction in rehabilitation and assistance: a review. *Current Robotics Reports*, 1:131–144, 2020.

[8] Sk. Khairul Hasan, Subodh B. Bhujel, and Gabrielle Sara Niemiec. Emerging trends in human upper extremity rehabilitation robot. *Cognitive Robotics*, 4:174–190, 2024.

[9] Ying Mao and Sunil Kumar Agrawal. Design of a cable-driven arm exoskeleton (carex) for neural rehabilitation. *IEEE transactions on robotics*, 28(4):922–931, 2012.

[10] Bongsu Kim and Ashish D Deshpande. An upper-body rehabilitation exoskeleton harmony with an anatomical shoulder mechanism: Design, modeling, control, and performance evaluation. *The International Journal of Robotics Research*, 36(4):414–435, 2017.

[11] Dohyeon Pyeon, Jungmin Ahn, Dong Hyun Kim, Sangheui Cheon, Guyeol Jeong, and Kyu-Jin Cho. A cable-driven exosuit for bidirectional upper limb resistance exercises. *IEEE Robotics and Automation Letters*, 9(11):9613–9620, November 2024.

[12] Muhammad F. Shah, Shahid Hussain, Roland Goecke, and Prashant K. Jamwal. Mechanism design and control of shoulder rehabilitation robots: A review. *IEEE Transactions on Medical Robotics and Bionics*, 5(4):780–792, November 2023.

[13] N. S. S. Sanjeevi and Vineet Vashista. Stiffness modulation of a cable-driven serial-chain manipulator via cable routing alteration. *Journal of Mechanisms and Robotics*, 15(2), June 2022.

[14] E. H. F. van Asseldonk, B. Koopman, and H. van der Kooij. Locomotor adaptation and retention to gradual and sudden dynamic perturbations. In *2011 IEEE International Conference on Rehabilitation Robotics*, pages 1–5, 2011.

[15] Iahn Cajigas, Alexander Koenig, Giacomo Severini, Maurice Smith, and Paolo Bonato. Robot-induced perturbations of human walking reveal a selective generation of motor adaptation. *Science Robotics*, 2(6):eaam7749, 2017.

[16] Sanjeevi Nakka and Vineet Vashista. External dynamics dependent human gait adaptation using a cable-driven exoskeleton. *IEEE Robotics and Automation Letters*, 8(9):6036–6043, Sep. 2023.

[17] Sung-Sik Yun, Keewon Kim, Jooeun Ahn, and Kyu-Jin Cho. Body-powered variable impedance: An approach to augmenting humans with a passive device by reshaping lifting posture. *Science Robotics*, 6(57), August 2021.

[18] Shih-Feng Chen and Imin Kao. Conservative congruence transformation for joint and cartesian stiffness matrices of robotic hands and fingers. *The International Journal of Robotics Research*, 19(9):835–847, September 2000.

[19] Siavash Rezazadeh and Saeed Behzadipour. Workspace analysis of multibody cable-driven mechanisms. *Journal of Mechanisms and Robotics*, 3(2), March 2011.

[20] Katherine R Saul, Xiao Hu, Craig M Goehler, Meghan E Vidt, Melissa Daly, Anca Velisar, and Wendy M Murray. Benchmarking of dynamic simulation predictions in two software platforms using an upper limb musculoskeletal model. *Computer methods in biomechanics and biomedical engineering*, 18(13):1445–1458, 2015.

[21] Scott L Delp, Frank C Anderson, Allison S Arnold, Peter Loan, Ayman Habib, Chand T John, Eran Guendelman, and Darryl G Thelen. Opensim: open-source software to create and analyze dynamic simulations of movement. *IEEE transactions on biomedical engineering*, 54(11):1940–1950, 2007.

[22] Scripting with Matlab - OpenSim Documentation - OpenSim — opensimconfluence.atlassian.net. `https://opensimconfluence.atlassian.net/wiki/spaces/OpenSim/pages/53089380/Scripting+with+Matlab`. [Accessed 06-12-2024].

Learning-based Estimation of Forward Kinematics for an Orthotic Parallel Robotic Mechanism

Jingzong Zhou,[1,†] Yuhan Zhu,[1,†] Xiaobin Zhang,[1,†] Sunil Agrawal,[2] and Konstantinos Karydis[1]

***Abstract*— This paper introduces a 3D parallel robot with three identical five-degree-of-freedom chains connected to a circular brace end-effector, aimed to serve as an assistive device for patients with cervical spondylosis. The inverse kinematics of the system is solved analytically, whereas learning-based methods are deployed to solve the forward kinematics. The methods considered herein include a Koopman operator-based approach as well as a neural network-based approach. The task is to predict the position and orientation of end-effector trajectories. The dataset used to train these methods is based on the analytical solutions derived via inverse kinematics. The methods are tested both in simulation and via physical hardware experiments with the developed robot. Results validate the suitability of deploying learning-based methods for studying parallel mechanism forward kinematics that are generally hard to resolve analytically.**

I. Introduction

Cervical spondylosis, a common source of neck pain caused by degenerative changes that start in the intervertebral discs, has been significantly affecting people over 30 years of age [1]. A study in testing the efficacy of intermittent cervical traction in patients with chronic neck pain has shown that 26% to 71% of the adult population experience an episode of neck pain in their lifetime [2]. Although neck pain has been reported to lead to a lesser degree of disability compared to back pain, the quality of life of patients is still severely affected by chronic symptoms [3]. To mitigate the long-term impact, effective management is thus crucial. Typical medical management includes pharmacological and rehabilitation components, with physical therapy playing a pivotal role for the latter [4]. A randomized clinical study that involved 60 patients with neck pain lasting for at least six months revealed that patients receiving physical therapy demonstrated greater improvement in pain relief and functional outcomes than those solely with drug treatment [5]. Controlled clinical trials have substantiated that extension traction as part of cervical spine rehabilitation can improve patients' quality of life [6]. To enhance accessibility and convenience, an assistive wearable neck brace presents a promising alternative for therapy. Such a device could offer patients consistent treatment and minimize the need to visit the hospital frequently.

Traction exercise neck braces, developed as a treatment for cervical spondylosis, aim to adjust the cervical vertebra structure to alleviate related neck pain [7]. Because of spatial restrictions in the head-neck region, parallel robots are particularly well-suited to deliver appropriate motion support while employing a compact structure. A notable example is a three-chain parallel robotic neck brace whereby each chain contains three joints (two revolute [R] and one spherical [S]) arranged in series (RRS) [8]. This design provides an assist-as-needed moment around the head-neck area, ensuring both safety and efficacy in a head movement training task [8]. Similarly, a study of a three degree-of-freedom (DoF) neck brace used a three-chain-RPUR parallel mechanism,[1] which was developed to relieve pain in the cervical spine by delivering an upward traction force [9].

However, operating a parallel robot can pose great challenges because of the complexity of its forward kinematics [10] and the often-times complete absence of closed-form analytical solutions. The intricate geometry and highly nonlinear dynamics of such robots result in non-unique solutions in most cases [11]. Although numerical solvers are commonly employed, their computational inefficiency may limit more widespread applicability, especially when in need to perform online computation on edge hardware [12]. Further, the solution of forward kinematics is often attained indirectly by solving inverse kinematics first and then inverting them locally, as demonstrated in studies with a two degree-of-freedom spatial parallel mechanism [13]. Motivated by these challenges, our work aims to employ data-driven methods to solve the forward kinematics based on solutions obtained from inverse kinematics.

One data-efficient yet powerful learning-based family of methods for robotic systems is Koopman operator theory, which has been gaining attention owing to its capacity to enable real-time learning and support data-driven control [14]. The Koopman operator is not nearly as data-intensive as most other machine learning techniques and takes much less time to train, making it a suitable candidate method for hardware with lower computation capabilities and requiring a higher update frequency. Koopman operator theory, along with methods to estimate the operator from data (such as the Extended Dynamic Mode Decomposition with control (EDMDc) [15]), has been applied in the modeling and control of various robotic systems [16]. Notable examples include the modeling and control of a tail-actuated robotic fish [17], trajectory control for micro-aerial vehicles [18], dynamics estimation for spherical robots [19], and model extraction for soft systems [20]. Koopman operator theory

† These authors contributed equally. [1] Dept. of Electrical and Computer Engineering, University of California, Riverside, 900 University Ave, Riverside, CA 92521, USA. Email:{jzhou227, yzhu275, xzhan548, karydis}@ucr.edu. [2] Dept. of Mechanical Engineering, Columbia University, 500 W. 120th Street #510, New York, NY 10027, USA. Email:sa3077@columbia.edu.

[1] Recall that P stands for a prismatic joint and U for a universal one.

has also been applied to the trajectory tracking control of a three-soft-fingered mechanism for zero-shot grasping [21].

Deep neural networks provide a promising alternative to capture the non-linear relationship between the inputs (in the joint space) and the outputs (in the cartesian space) in forward kinematics [11], [22], [23]. The depth of deep neural networks can be flexibly adjusted, allowing different layers to capture varying levels of complexity in forward kinematics [24]. Some works have focused on deploying neural network-based methods for estimating the forward kinematics of various parallel mechanisms. For instance, Dehghani et al. proposed to solve the forward kinematics of parallel robot HEXA with a multilayer perceptron (MLP) [25], while Lee et al. used MLP as an estimator to capture the input-output relationship of the Stewart platform [26]. The Radial Basis Function (RBF) network was used in a hybrid robot for learning forward kinematics [12]. Prado et al. applied baseline neural networks to solve the forward kinematics of a wearable parallel robot [11].

In this paper, we first design and fabricate a three-chain Revolute-Revolute-Universal-Revolute (3-RRUR) parallel robot to provide traction support for patients who suffer from cervical spondylosis. The use of the RRUR structure for each chain is motivated by the need to enlarge the workspace compared to an earlier related work that used a Revolute-Prismatic-Universal-Revolute (RPUR) structure [13]. The inverse kinematics is first solved analytically (Section II) to generate data which are in turn used to train two distinct learning-based methods considered herein. Then, forward kinematics is estimated using the Koopman operator (Section III) and a recurrent neural network (RNN; Section IV). Extensive testing in simulation and via physical experiments (Section V) demonstrate the feasibility of both learning-based methods and offer insights as to when one method might be preferred over the other. This work provides a key step toward porting data-driven methods into robotic orthotics and establishes a basis for more Koopman operator-based methods to be investigated within this context. The contributions are summarized as follows:

- A 3-RRUR parallel robot is designed to support patients who suffer from cervical spondylosis. The physical and kinematics models are described in detail.
- Two data-driven methods, the Koopman operator and an RNN, and an analytical method, are deployed to solve the forward kinematics in simulation. To the best of the authors' knowledge, this is the first attempt to utilize the Koopman operator on a 3-RRUR parallel robot.
- A physical prototype of the parallel robot is fabricated and tested in the real world with the analytical method.

II. Analytical Kinematic Analysis

A. Physical Structure of the 3-RRUR Parallel Robot

The physical structure of the developed parallel robot is shown in Figure 1. The robot is composed of three chains. A kinematic description of each chain is shown in Figure 2. The joint centers in each chain are represented as S_i, K_i, Q_i, and E_i, $(i = 1, ..., 3)$ for joints $R_{1,i}$, $R_{2,i}$, U_i, and $R_{3,i}$, respectively. Each chain has five DoFs and provides one constraint to the end-effector frame, P. In total, the end-effector frame has three independent DoFs, which can be controlled by three rotary motors located on the first revolute joint of each chain, attaching them to the base plate characterized by frame O. In each chain, the axes of the first two revolute joints and one axis of the universal joint are chosen to be perpendicular to the plane in which the chain operates. The intersection of the other axis of the U_i joint and the axis of the third revolute joint $R_{3,i}$ is denoted by point A_i. Intersection points A_1, A_2 and A_3 form an intermediate plane. With the particular choice of geometric constraints, A_1 and A_3 stay in the same plane XZ ($^OA_{1y} = 0$, $^OA_{3y} = 0$), while A_2 stays in plane YZ ($^OA_{2x} = 0$).

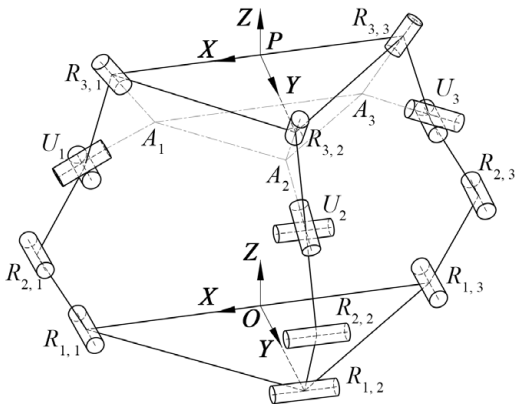


Fig. 1. Diagram of the developed 3-RRUR parallel robot.

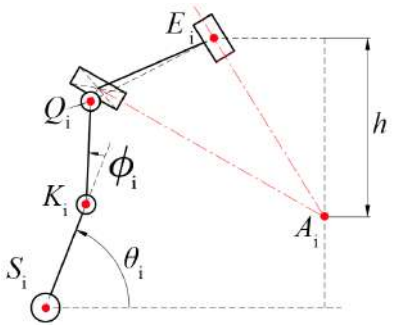


Fig. 2. Chain structure diagram of 3-RRUR parallel robot

B. Inverse Kinematics

Since the end-effector has three DoFs that can be independently controlled, we choose those DoFs that are directly related to head-neck motion as input to inverse kinematics. The three main head orientations to be supported by the mechanism are shown in Figure 3. The chosen DoFs are the z-translation, z_p, flexion/extension, β, and lateral bending, γ. The rest of the DoFs of the end-effector are accommodated based on the constraints once the aforementioned actuated DoFs obtain valid values. Here we choose Space-three 3-1-2 rotation matrix (1) to express the rotation between the base



Fig. 3. Description of three orientations of the head-neck aligned with the fixed base frame shown in Figure 1: (i) axial rotation, (ii) lateral bending, (iii) flexion and extension.

frame O and end-effector frame P, that is

$$R_O^P = \begin{bmatrix} s_\alpha s_\beta s_\gamma + c_\gamma c_\alpha & c_\alpha s_\beta s_\gamma - c_\gamma s_\alpha & c_\beta s_\gamma \\ s_\alpha c_\beta & c_\alpha c_\beta & -s_\beta \\ s_\alpha s_\beta c_\gamma - s_\gamma c_\alpha & c_\alpha s_\beta c_\gamma + s_\gamma s_\alpha & c_\beta c_\gamma \end{bmatrix} . \quad (1)$$

Each coordinate of A_i in the base frame can be written as

$${}^O A_i = [x_p, y_p, z_p]^T + R_O^P({}^P A_i) \ , \quad (2)$$

where $[x_p, y_p, z_p]^T$ represents the origin of the end-effector frame expressed in the base frame. Further, we have ${}^P A_1 = [r_A, 0, -h]^T$, ${}^P A_2 = [0, r_A, -h]^T$, and ${}^P A_3 = [-r_A, 0, -h]^T$. The axial rotation of the end-effector is equal to zero. Then,

$${}^O A_1 = \begin{bmatrix} x_p \\ y_p \\ z_p \end{bmatrix} + R_O^P({}^P A_1) = \begin{bmatrix} x_p + r_A c_\gamma - h c_\beta s_\gamma \\ y_p + h s_\beta \\ z_p - r_A s_\gamma - h c_\beta c_\gamma \end{bmatrix} \quad (3)$$

$${}^O A_2 = \begin{bmatrix} x_p \\ y_p \\ z_p \end{bmatrix} + R_O^P({}^P A_2) = \begin{bmatrix} x_p + r_A s_\beta s_\gamma - h c_\beta s_\gamma \\ y_p + r_A c_\beta + h s_\beta \\ z_p + r_A s_\beta c_\gamma - h c_\beta c_\gamma \end{bmatrix} \quad (4)$$

$${}^O A_3 = \begin{bmatrix} x_p \\ y_p \\ z_p \end{bmatrix} + R_O^P({}^P A_3) = \begin{bmatrix} x_p - r_A c_\gamma - h c_\beta s_\gamma \\ y_p + h s_\beta \\ z_p + r_A s_\gamma - h c_\beta c_\gamma \end{bmatrix} \quad (5)$$

where h and r_A are design constants of the parallel robot; h stands for the distance between plane $A_1A_2A_3$ and plane $E_1E_2E_3$, while r_A stands for the radius formed by circle $A_1A_2A_3$. Considering the geometry constraints, the x-translation, x_p, and y-translation, y_p, are expressed as

$$x_p = h c_\beta s_\gamma - r_A s_\beta s_\gamma \ , \quad (6)$$

$$y_p = -h s_\beta \ . \quad (7)$$

To solve for the joint variables θ_i and ϕ_i for each chain, we use

$$||{}^O Q_i(\theta_i, \phi_i) - {}^O E_i||^2 = l_{Q_i E_i}^2 \ , \quad (8)$$

$$||{}^O Q_i(\theta_i, \phi_i) - {}^O A_i||^2 = l_{Q_i A_i}^2 \ . \quad (9)$$

where $l_{Q_iE_i}$ and $l_{Q_iA_i}$ are design constants of the parallel robot, and ${}^O Q_i(\theta_i, \phi_i)$, $i = 1, ..., 3$, represent the joint coordinates in the base frame.

C. Forward Kinematics

Three sets of equations (each containing two functions f_1 and f_2) can be found after resolving the inverse kinematics. We can write these as follows (detailed expressions of those equations can be found in the appendix).

$$f_1(\theta_i, \phi_i, z_p, \beta, \gamma) = 0 \text{ and } f_2(\theta_i, \phi_i, z_p, \beta, \gamma) = 0 \ . \quad (10)$$

The unknown variables now are ϕ_1, ϕ_2, ϕ_3, z_p, β, and γ. Concerning the safety during the usage of the mechanism, we do not expect the mechanism to have "inward" or "elbow up" postures ($\theta_i < 90°$). Therefore, we are only interested in the solutions with $\theta_i > 90°$ from the inverse kinematics. Thus, those solutions from inverse kinematics should match the forward kinematics. Further, θ_i joint values obtained from the inverse kinematics, when sent as input to forward kinematics, should produce the same end-effector pose as in the inverse kinematics. To circumvent the complex procedure of solving the forward kinematics directly, data-driven approaches are introduced in the following sections.

III. Koopman-based Kinematics Estimation

A. Koopman Operator Overview

The Koopman operator efficiently learns the system's dynamics by lifting the original states to a latent space and capturing the flow of the lifted states (observables) with a finite number of linear functions. For an unforced system $x_{t+1} = f(x_t)$ with flow $\Phi(t, x)$ and complex-valued observables $\varphi \in \mathcal{F}$, the continuous time Koopman operator $\mathcal{K} : \mathcal{F} \to \mathcal{F}$ is defined as $(\mathcal{K}\varphi)(\cdot) = \varphi \circ \Phi(t, \cdot)$. Being linear, the Koopman operator can be characterized by its eigenvalues and eigenfunctions. A function ϕ is an eigenfunction of $\mathcal{K}$ if $(\mathcal{K}\varphi)(\cdot) = e^{\lambda t}\phi(\cdot)$, with λ being the corresponding eigenvalue [27]. The time-varying observable $\psi(t, x) = \mathcal{K}\varphi(x)$ is the solution of the PDE [28],

$$\begin{matrix} \frac{\partial \psi}{\partial t} = \mathcal{L}_f \psi \\ \psi(0, x) = \varphi(x_0) \end{matrix} \ , \quad (11)$$

where x_0 is the initial condition for the unforced system and $\mathcal{L}_f$ is the Lie derivative with respect to f.

A vector-valued observable $\mathrm{g}(\cdot)$ may be expressed in terms of Koopman eigenfunctions ϕ_i as $\mathrm{g}(\cdot) = \sum_{i=1}^{\infty} \phi_i(\cdot) v_i$, where v_i denote the Koopman modes. Koopman modes are obtained from the projection of the observable on the span of Koopman eigenfunctions. Then,

$$\mathcal{K}\mathrm{g}(\cdot) = \mathcal{K} \sum_{i=1}^{\infty} \phi_i(\cdot) v_i = \sum_{i=1}^{\infty} \mathcal{K}\phi_i(\cdot) v_i = \sum_{i=1}^{\infty} \lambda_i \phi_i(\cdot) v_i \ . \quad (12)$$

B. Implementation

Herein, the Koopman operator is utilized to learn the mapping from the motor angles, $\theta_1, \theta_2, \theta_3$, to end-effector angles β and γ, and translation z_p. The x- and y-translations can be then computed by (6) and (7). Suppose there are M sets of motor angles and corresponding end-effector poses. Let $X = [x_1, x_2, ..., x_M]$ denote the M motor angle states, where $x_j = [\theta_{j1} \quad \theta_{j2} \quad \theta_{j3}]^T, j = 1, 2, ..., M$, and

$Y = [y_1, y_2, ..., y_M]$ denote the corresponding M end-effector poses, where $y_j = [\beta_j \quad \gamma_j \quad z_{pj}]^T, j = 1, 2, ..., M$. For the lifting function design, which plays a crucial part in approximating the true system propagation model, we set

$$\begin{aligned}\Psi(x_j) =&(1, \theta_{j1}, \theta_{j1}^2, \sin\theta_{j1}, \cos\theta_{j1}) \otimes \\ &(1, \theta_{j2}, \theta_{j2}^2, \sin\theta_{j2}, \cos\theta_{j2}) \otimes \\ &(1, \theta_{j3}, \theta_{j3}^2, \sin\theta_{j3}, \cos\theta_{j3}) \ ,\end{aligned} \tag{13}$$

where $\otimes$ stands for the Kronecker product. Note that this is a minimal dictionary. A larger dictionary consisting of more complex operations may increase prediction accuracy at the expense of increasing complexity. Construction of the dictionary is out of the scope of this paper; we refer the interested reader to [29] for a detailed analysis of how to construct such a dictionary based on an underlying system's kinematic information. The Koopman operator can be numerically approximated from data using EDMDc [15]. It entails the minimization of the total residual between the prediction and ground truth in the Koopman state, i.e.

$$J = \frac{1}{2}\sum_{j=1}^{M}(\Psi(y_j) - K\Psi(x_j))^2 \ . \tag{14}$$

This least-squares problem 14 can be solved by truncated singular value decomposition (SVD) as

$$K \triangleq G^{\dagger}A \ , \tag{15}$$

where

$$G = \frac{1}{M}\sum_{j=1}^{M}\Psi^*(x_j)\Psi(x_j) \tag{16}$$

$$A = \frac{1}{M}\sum_{j=1}^{M}\Psi^*(x_j)\Psi(x_{j+1}), \tag{17}$$

with $\dagger$ denoting the pseudoinverse and $*$ denoting the conjugate transpose operations, respectively.

With K in (15), the following equations are obtained

$$\begin{cases} v_n = (w_n^* B)^T \\ \lambda_n \xi_n = K\xi_n, \\ \varphi_n = \Psi\xi_n \end{cases} \tag{18}$$

where ξ_n is the n-th eigenvector, w_n is the n-th left eigenvector of K, and B is the matrix of appropriate weighting vectors so that $x = (\Psi B)^T$. By plugging expressions (18) back to (12) we can then describe the evolution of the system using the estimated Koopman operator.

IV. RNN-based Kinematics Estimation

A. RNN Overview

RNNs are a class of deep neural networks designed for sequential data processing and temporal modeling. Unlike feedforward networks, RNNs have a recurrent structure that allows information from previous time steps to be recorded and used in the current computation. This is achieved through feedback connections in the hidden layers, enabling RNNs to capture dependencies over time. The hidden state h_t at time step t is updated using $h_t = f(W_h h_{t-1} + W_x x_t + b)$ where f is a nonlinear activation function, W_h and W_x are weight matrices, x_t is the input, and b is the bias. In the context of solving the forward kinematics of parallel robots, RNNs offer a distinct advantage due to their ability to model the inherent dependencies between joint variables and the resulting end-effector poses.

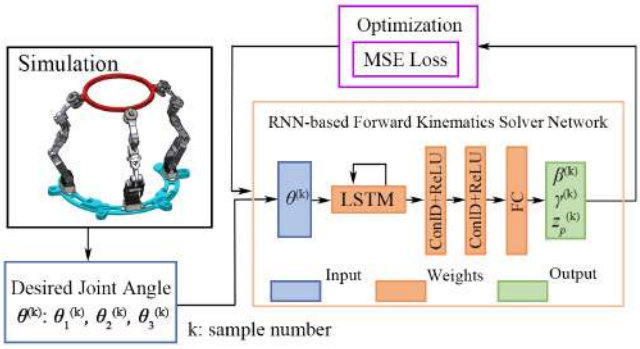


Fig. 4. The RNN-based architecture considered herein.

B. Implementation

The employed RNN architecture is shown in Figure 4. The *RNN-based Forward Kinematics Solver Network* module receives the three motor angles as inputs and outputs the flexion angle (β), lateral bending angle (γ), and the z-translation (z_p) of the end-effector. Training data were generated using the analytical inverse kinematic solver. The inputs and outputs from the analytical inverse kinematic solver were flipped and fed into the network.

V. Experimental Testing and Results

Validation and testing were formulated into two parts; simulations and physical experiments. Simulations aim to assess the accuracy of predicting the end-effector pose from the active joint variables using the Koopman operator-based and RNN-based estimators. To establish a ground truth for validation, a trajectory of end-effector positions and orientations was generated from inverse kinematics. This trajectory serves as a benchmark to evaluate the performance of both methods. A dataset consisting of 248,790 samples was created for training. A distinct set of 802 samples was used for testing. Simulations with the Koopman Operator and the RNN-based estimator (including training and testing) were performed on an Intel Core i7-11800H processor @2.3GHz with RTX3060 Mobile GPU with 6GB of VRAM.

Results for the Koopman operator-based and RNN-based estimator are shown in Figures 5 and 6, respectively. It takes just 28.08 sec to train the Koopman operator. The average MSE in predicted trajectory positions is 3.24 (base units in mm), while the average MSE in predicted trajectory orientations is only 0.06 (base units in deg). The RNN was trained for 50 epochs with a total training time of 455.55 sec. The model achieved a trajectory translation MSE of 0.0062 (base units in mm) and orientation MSE of 0.0035 (base units in deg). Additionally, the testing performance yielded an $\mathbf{R}^2$-score of 0.9974, indicating a high level of accuracy

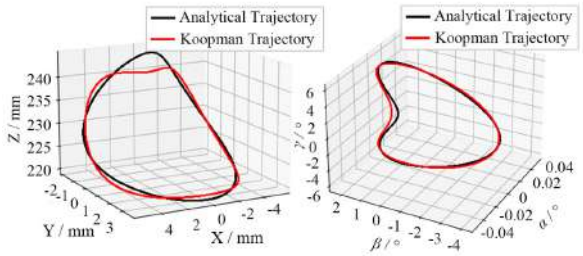


Fig. 5. Predicted end-effector position (left) and orientation (right) in simulation using the Koopman operator-based estimator.

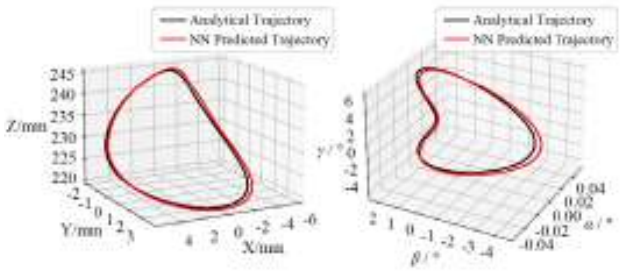


Fig. 6. Predicted end-effector position (left) and orientation (right) in simulation using the RNN-based estimator.

in the model's predictions. Overall, both methods' feasibility was shown in the simulated testing.

When comparing the two methods, we observe a notable trade-off between accuracy and computational efficiency. The RNN-based method achieves a significantly lower trajectory prediction error compared to that estimated via the Koopman operator. However, this improved performance comes at the cost of computational efficiency since the RNN-based method requires approximately 10 times more training time to reach this level of accuracy. This highlights a critical consideration in selecting the appropriate method based on the specific requirements of accuracy and computational efficiency in practical applications. Deviations from the desired trajectory were observed in the predicted position (Figure 5). However, the overall trajectory form is maintained. In addition, the prediction accuracy depends to a certain extent on the selection of the Koopman dictionary; a more extended dictionary could help rectify this.

Physical experiments considered the same ground truth trajectory as in the simulation testing. The latter was applied to the fabricated 3-RRUR parallel robot prototype (Figure 7). End-effector frame $E_1E_2E_3$, base frame $S_1S_2S_3$, and link $S_iK_iQ_iE_i$ $(i = 1, ..., 3)$ are 3D-printed with PLA basic material (Bambu Labs). Joints S_i are formed by LX16A bus servomotors. Joints K_i, Q_i, E_i are revolute joints formed by binding barrels with 304 stainless steel phillips head and deep groove ball bearings. The physical trajectory data were captured by an 8-camera Optitrack motion capture system at 100Hz. Key dimensions of the prototype include: $r_A = 85.04\,\text{mm}$, $r_S = 141\,\text{mm}$, $r_E = 120\,\text{mm}$, $h = 48.51\,\text{mm}$, $l_{Q_iA_i} = 66.56\,\text{mm}$, $l_{Q_iE_i} = 85.06\,\text{mm}$, $l_{K_iS_i} = 83.925\,\text{mm}$, $l_{K_iQ_i} = 83.925\,\text{mm}$, $l_{E_iA_i} = 59.76\,\text{mm}$.

Results of the captured trajectory and desired trajectory are shown in Figure 8. The overall trajectory trend was followed by the feedforward trajectory computed analytically. However, deviations and, at times, large offsets were observed as well. Two likely sources caused these errors. First, differences in assumptions used in the mathematical model and the real physical prototype (for instance the geometry constraints of A_i) cannot be fully achieved because of the deformation of each link. Second, fabrication errors, especially those causing friction in the revolute joints and collision of links on each chain $S_iK_iQ_iE_i$, can all contribute to cumulative errors in the end-effector motion.

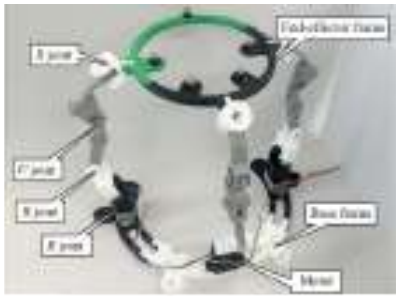


Fig. 7. Fabricated prototype of the proposed 3-RRUR parallel robot. In each chain, the first R joint that is connected to the base frame is actuated via a servomotor, whereas all other joints are passive and forced to move as determined by the geometry constraints.

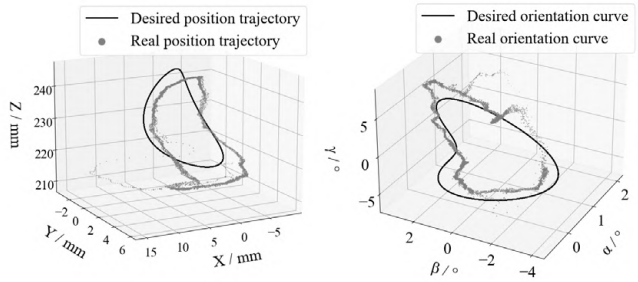


Fig. 8. Comparison between desired trajectory and the experimentally-obtained one collected via motion capture.

VI. Conclusion

A 3-RRUR parallel robot was designed as a means to provide traction support for patients who suffer from cervical spondylosis. To address the challenge in forward kinematics analysis associated with the parallel mechanism structure, an analytical method for solving inverse kinematics, which can often be solved directly in contrast to forward kinematics, was studied to generate a dataset for data-driven model training. Then, a Koopman operator-based method and an RNN-based method were introduced to resolve the forward kinematics of the robot. The prediction accuracy from the RNN-based estimator is noticeably higher than that of the Koopman operator, while the Koopman operator can be much more quickly and easily deployed and updated online, without the need for large computational resources. Lastly, a fabricated prototype of the proposed 3-RRUR parallel robot was designed to validate the results of the same trajectory presented in the two data-driven methods. This work offers a basis to support porting data-driven methods into robotic orthotics. Future directions of research include online model learning via the Koopman operator to control the mechanism,

as well as design and fabrication improvements to make the motion of the physical prototype smoother.

ACKNOWLEDGMENT

The authors would like to thank Dr. Zhichao Liu for offering his assistance with the experiments.

APPENDIX

We list below the closed-form expressions for the forward kinematics of the developed mechanism. Let r_E be the diameter of the circle spanned by points E_1, E_2, E_3 and r_S the diameter of the circle spanned by points S_1, S_2, S_3. The two kinematic constraints in chain $S_1K_1Q_1E_1$ are

$$f_1 : (a_{11} + z_{11})^2 + (a_{21} - z_{21})^2 = a_{31} \ , \qquad (19)$$

$$f_2 : (a_{41} + z_{11})^2 + (a_{51} - z_{21})^2 = a_{61} \ , \qquad (20)$$

where $a_{11} = x_p + r_E c_\gamma - r_S$, $a_{21} = z_p - r_E s_\gamma$ $a_{31} = l_{QE}^2 - y_E^2$, $a_{41} = x_p + r_A c_\gamma - h c_\beta s_\gamma - r_S$, $a_{51} = z_p - r_A s_\gamma - h c_\beta c_\gamma$, $a_{61} = l_{Q_1A_1}^2$, $z_{11} = l_{K_1S_1} c_{\theta_1} + l_{K_1Q_1} c_{\theta_1+\phi_1}$, and $z_{21} = l_{K_1S_1} s_{\theta_1} + l_{K_1Q_1} s_{\theta_1+\phi_1}$.

The two kinematic constraints in chain $S_2K_2Q_2E_2$ are

$$f_1 : (a_{12} + z_{12})^2 + (a_{22} - z_{22})^2 = a_{32} \ , \qquad (21)$$

$$f_2 : (a_{42} + z_{12})^2 + (a_{52} - z_{22})^2 = a_{62} \ , \qquad (22)$$

where $a_{12} = y_p + r_E c_\beta - r_S$, $a_{22} = z_p + r_E s_\beta c_\gamma$, $a_{32} = l_{Q_2E_2}^2 - (x_p + r_E s_\beta s_\gamma)^2$, $a_{42} = r_A c_\beta - r_S$, $a_{52} = z_p + r_A s_\beta c_\gamma - h c_\beta c_\gamma$, $a_{62} = l_{Q_2A_2}^2$, $z_{12} = l_{K_2S_2} c_{\theta_2} + l_{K_2Q_2} c_{\theta_2+\phi_2}$, and $z_{22} = l_{K_2S_2} s_{\theta_2} + l_{K_2Q_2} s_{\theta_2+\phi_2}$.

The two kinematic constraints in chain $S_3K_3Q_3E_3$ are

$$f_1 : (a_{13} - z_{13})^2 + (a_{23} - z_{23})^2 = a_{33} \ , \qquad (23)$$

$$f_2 : (a_{43} - z_{13})^2 + (a_{53} - z_{23})^2 = a_{63} \ , \qquad (24)$$

where $a_{13} = x_p - r_E c_\gamma + r_S$, $a_{23} = z_p + r_E s_\gamma$, $a_{33} = l_{Q_3E_3}^2 - y_E^2$, $a_{43} = x_p - r_A c_\gamma - h c_\beta s_\gamma + r_S$, $a_{53} = z_p + r_A s_\gamma - h c_\beta c_\gamma$, $a_{63} = l_{Q_3A_3}^2$, $z_{13} = l_{K_3S_3} c_{\theta_3} + l_{K_3Q_3} c_{\theta_3+\phi_3}$, and $z_{23} = l_{K_3S_3} s_{\theta_3} + l_{K_3Q_3} s_{\theta_3+\phi_3}$.

REFERENCES

[1] A. I. Binder, "Cervical spondylosis and neck pain," *Bmj*, vol. 334, no. 7592, pp. 527–531, 2007.

[2] P. Borman, D. Keskin, B. Ekici, and H. Bodur, "The efficacy of intermittent cervical traction in patents with chronic neck pain," *Clinical rheumatology*, vol. 27, pp. 1249–1253, 2008.

[3] A. Popescu and H. Lee, "Neck pain and lower back pain," *Medical Clinics*, vol. 104, no. 2, pp. 279–292, 2020.

[4] D. Mazanec and A. Reddy, "Medical management of cervical spondylosis," *Neurosurgery*, vol. 60, no. 1, pp. S1–43, 2007.

[5] E. Aslan Telci and A. Karaduman, "Effects of three different conservative treatments on pain, disability, quality of life, and mood in patients with cervical spondylosis," *Rheumatology international*, vol. 32, pp. 1033–1040, 2012.

[6] P. A. Oakley, N. N. Ehsani, I. M. Moustafa, and D. E. Harrison, "Restoring cervical lordosis by cervical extension traction methods in the treatment of cervical spine disorders: a systematic review of controlled trials," *Journal of physical therapy science*, vol. 33, no. 10, pp. 784–794, 2021.

[7] L.-X. Xiao, C.-S. Liu, S.-Z. Zhong, and W.-H. Huang, "Effect of a traction exercise neck brace on cervical spondylopathy radiculopathy: a clinical study and finite element analysis," *Evidence-Based Complementary and Alternative Medicine*, vol. 2021, no. 1, p. 8825150, 2021.

[8] H. Zhang, B.-C. Chang, and S. K. Agrawal, "Using a robotic neck brace for movement training of the head–neck," *IEEE Robotics and Automation Letters*, vol. 4, no. 2, pp. 846–853, 2019.

[9] P. Kulkarni and S. K. Agrawal, "Design and validation of a novel robotic neck brace for cervical traction," *IEEE/ASME Transactions on Mechatronics*, 2024.

[10] Z. Pandilov and V. Dukovski, "Comparison of the characteristics between serial and parallel robots." *Acta Technica Corviniensis-Bulletin of Engineering*, vol. 7, no. 1, 2014.

[11] A. Prado, H. Zhang, and S. K. Agrawal, "Artificial neural networks to solve forward kinematics of a wearable parallel robot with semi-rigid links," in *IEEE International Conference on Robotics and Automation (ICRA)*, 2021, pp. 14 524–14 530.

[12] R. Kang, H. Chanal, T. Bonnemains, S. Pateloup, D. T. Branson, and P. Ray, "Learning the forward kinematics behavior of a hybrid robot employing artificial neural networks," *Robotica*, vol. 30, no. 5, pp. 847–855, 2012.

[13] J. Zhou, P. Kulkarni, X. Zhao, and S. K. Agrawal, "Design of a traction neck brace with two degrees-of-freedom via a novel architecture of a spatial parallel mechanism," *Robotica*, pp. 1–14, 2024.

[14] L. Shi, M. Haseli, G. Mamakoukas, D. Bruder, I. Abraham, T. Murphey, J. Cortes, and K. Karydis, "Koopman operators in robot learning," *arXiv preprint arXiv:2408.04200*, 2024.

[15] M. Korda and I. Mezić, "Linear predictors for nonlinear dynamical systems: Koopman operator meets model predictive control," *Automatica*, vol. 93, pp. 149–160, 2018.

[16] L. Shi, Z. Liu, and K. Karydis, "Koopman operators for modeling and control of soft robotics," *Current Robotics Reports*, vol. 4, no. 2, pp. 23–31, 2023.

[17] G. Mamakoukas, M. L. Castano, X. Tan, and T. D. Murphey, "Derivative-based koopman operators for real-time control of robotic systems," *IEEE Transactions on Robotics*, vol. 37, no. 6, pp. 2173–2192, 2021.

[18] L. Shi, H. Teng, X. Kan, and K. Karydis, "A data-driven hierarchical control structure for systems with uncertainty," in *IEEE Conference on Control Technology and Applications (CCTA)*, 2020, pp. 57–63.

[19] I. Abraham, G. De La Torre, and T. D. Murphey, "Model-based control using koopman operators," *arXiv preprint arXiv:1709.01568*, 2017.

[20] D. Bruder, C. D. Remy, and R. Vasudevan, "Nonlinear system identification of soft robot dynamics using koopman operator theory," in *IEEE International Conference on Robotics and Automation (ICRA)*, 2019, pp. 6244–6250.

[21] L. Shi, C. Mucchiani, and K. Karydis, "Online modeling and control of soft multi-fingered grippers via koopman operator theory," in *IEEE 18th International Conference on Automation Science and Engineering (CASE)*, 2022, pp. 1946–1952.

[22] P. R. Kumar and B. Bandyopadhyay, "The forward kinematic modeling of a stewart platform using nlarx model with wavelet network," in *IEEE International Conference on Industrial Informatics*, 2013, pp. 343–348.

[23] Z. Geng and L. Haynes, "Neural network solution for the forward kinematics problem of a stewart platform," in *IEEE International Conference on Robotics and Automation*, 1991, pp. 2650–2651.

[24] R. A. Janik and P. Witaszczyk, "Complexity for deep neural networks and other characteristics of deep feature representations," *arXiv preprint arXiv:2006.04791*, 2020.

[25] M. Dehghani, M. Ahmadi, A. Khayatian, M. Eghtesad, and M. Farid, "Neural network solution for forward kinematics problem of hexa parallel robot," in *American Control Conference*, 2008, pp. 4214–4219.

[26] L. H. Sang and M.-C. Han, "The estimation for forward kinematic solution of stewart platform using the neural network," in *IEEE/RSJ International Conference on Intelligent Robots and Systems. Human and Environment Friendly Robots with High Intelligence and Emotional Quotients*, vol. 1, 1999, pp. 501–506.

[27] J. Nathan Kutz, J. L. Proctor, and S. L. Brunton, "Applied koopman theory for partial differential equations and data-driven modeling of spatio-temporal systems," *Complexity*, no. 1, p. 6010634, 2018.

[28] A. Surana, "Koopman operator based observer synthesis for control-affine nonlinear systems," in *IEEE 55th Conference on Decision and Control (CDC)*, 2016, pp. 6492–6499.

[29] L. Shi and K. Karydis, "Acd-edmd: Analytical construction for dictionaries of lifting functions in koopman operator-based nonlinear robotic systems," *IEEE Robotics and Automation Letters*, vol. 7, no. 2, pp. 906–913, 2021.

Assessing Personalized FES Patterns for Gait Rehabilitation in a Clinical Setting

Nicolas Feppon, Amine Metani, Samer Mohammed, *Senior Member, IEEE*

***Abstract*—Functional electrical stimulation (FES) for motor and neurological rehabilitation produces patient-dependent functional responses influenced by the individual's pathology and clinical profile. Given this inherent variability in patient responses, it is essential to personalize FES gait rehabilitation parameters to enhance the rehabilitation outcomes effectively. To optimize these parameters for gait neurorehabilitation, appropriate metrics are needed. In this preliminary case study, we assess if selected metrics can comprehensively evaluate the effectiveness of FES gait patterns with different degrees of personalization for specific post-stroke patients in the context of a clinical rehabilitation routine. These metrics do not only reflect the immediate orthotic effects, but also gait parameters that indicate rehabilitation progress and improved treatment outcomes. We analyzed data collected during rehabilitation of three post-stroke hemiplegic individuals with NeuroSkin, a multichannel textile FES system with embedded movement sensors and dry electrodes. We evaluated different stimulation patterns using metrics related to kinematic, spatio-temporal, postural, and asymmetry aspects of gait. Some metrics identified modest overall improvements between default and personalized stimulation patterns: walking speed (+0.63cm/s) and stride length (+0.41cm). However, patient-dependent analysis revealed substantial improvements which differed between patients across walking speed (+3.3cm/s), stride length (+4.7cm) and metrics reflecting asymmetry and postural control, as well as kinematic trajectories. We argue that these metrics should be integrated in FES-aided gait assessments. However, it remained difficult to identify which metrics should be primarily considered when optimizing an FES strategy, given heterogeneous improvements and limitations of the current framework.**

***Index Terms*—Functional Electrical Stimulation, Artificial Intelligence, Stroke, Motor Handicap, Neurological Rehabilitation, Neuroprosthesis, Personalized assistance**

I. Introduction

Functional Electrical Stimulation (FES) is used for motor rehabilitation following neurological injuries or diseases, such as stroke, spinal cord injuries or multiple sclerosis [1] [2]. To generate reliable functional movements, these systems must address various challenges, both related to the characteristics of FES and the redundancies of the neuromusculoskeletal system. Muscle fibers fatigue more quickly than with voluntary contractions induced by the central nervous system (CNS), and fatigue dynamics vary from patient to patient [1] [3]. Additionally, intensive FES can be painful, further limiting the intensity of muscle contractions. Electromechanical delay, which is the time between motor neuron activation and the initiation of muscle contraction [4], differs between patients. FES-induced movement is subject to variations in both muscle response and neural response [4]. Finally, inter-subject variability of nerves and motor points locations also limits the reproducibility of stimulation responses across patients. To address these variabilities, FES systems should be capable of adjusting to these characteristics, adapting parameters and timings of stimulation to each patient.

Stroke, a vascular cerebral injury that disrupts brain circuits due to impaired blood supply, often results in hemiplegia and gait impairments. FES therapies are widely used for post-stroke rehabilitation [5] and one of the highest priorities after stroke is gait rehabilitation. However, variability in patient conditions complicates the standardization of FES therapies, as the severity of gait deficits dictates rehabilitation options, and gait impairments vary based on the stroke's anatomic localization [6]. Factors such as fatigue, sensory function, and spasticity levels further influence rehabilitation protocols [7].

Human gait is a complex coordinated movement, which depends on an array of components to make it functional: support and forward propulsion of the center of gravity, balance of the center of gravity as it transitions between limbs, controlling knee and toe paths for toe clearance and foot placement and controlling coordination [8]. These components can also be categorized across dimensions, which have been found to explain most of gait's variability: Pace, Rhythm, Variability, Asymmetry and Postural control [9]. Gait analysis is used in rehabilitation to analyze gait impairments and measure rehabilitation outcomes. Spatiotemporal metrics of gait measure spatial and temporal differences between various gait events [10], while kinematic metrics measure displacements and trajectories of key anatomical points of interest. Gait phase represents the progression of the gait cycle, with 0% at heel strike, 60% at toe-off, and 100% at the next heel strike, providing a standardized framework for monitoring the cycle's progression. In neurorehabilitation robotics, the orthotic effect of the system on the gait is often evaluated using metrics from gait analysis: mean square error on joint angle trajectories [11], spatio temporal parameters [12] and walking speed [12] [13], and the clinically widespread 10-meter walk test [14] related to walking speed.

FES has demonstrated effects on high-level gait parameters, such as walking speed and spatiotemporal metrics, as well as physiological cost index in stroke patients [2] [15]. For

N. Feppon is with the laboratory LISSI, Université Paris-Est Créteil, Creteil, France and the company Kurage, Lyon, France.

A. Metani is with the company Kurage, Lyon, France and Laboratoire de Physique, Univ. Lyon, ENS de Lyon, CNRS, Lyon, France

S. Mohammed is with the laboratory LISSI, Université Paris-Est Créteil, Creteil, France.

This work was supported by Kurage.

example, the review of Kottink et al., which evaluated orthotic effect after FES therapy, found an aggregate improvement of 0.13m/s in walking speed [15]. Street et al. found an orthotic effect of 0.10m/s [14]. These changes stem from FES-induced alterations in lower limb dynamics, as stimulation parameters directly influence muscle contraction patterns. The timing, profile, and amplitude of stimulation (referred to as "patterns" in this study) significantly impact gait kinematics, as evidenced through gait analysis metrics [16]. Given FES's role as a precision tool for inducing gait changes, reliable and precise evaluation metrics are crucial for determining optimal patient-specific modifications.

In the context of a long term rehabilitation, a rehabilitation system or therapy should not only produce an orthotic effect, but also a therapeutic one. FES aided therapy should aim to improve the patient's gait pattern, promoting better ambulation, autonomy, and general quality of life. FES is shown to have therapeutic effects [2], but the relationship between short-term robotic and FES interventions and long-term functional improvements remains unclear [17] and the therapeutic effect of FES remains not fully understood [1]. Individualized optimal pathways for gait improvement and rehabilitation using FES have yet to be established. However, it is necessary to have metrics which can evaluate instantaneous orthotic improvements of gait, but also indicate the best directions of orthotic changes for optimal rehabilitation. One way to do this is to evaluate the gait using metrics that are correlated with good rehabilitation outcomes. These can for example be found in literature-based predictors of rehabilitation outcomes. Good trunk control and balance as well as a greater range of motion of the hip at initial assessment are strong predictors of successful rehabilitation [18]. Additionally, walking speed is closely linked to quality of life and autonomy [19]. In stroke specifically, walking speed can serve as an indicator of the patient's clinical profile [14] and stage of rehabilitation.

Past studies have evaluated instantaneous orthotic effects of FES on patient's gait, as well as the long term therapeutic effects [14] [16] [2]. However, there is a need to evaluate FES patterns in the context of continued FES therapies, where a particular instantaneous orthotic effect can translate into different therapeutic effects over the long term. FES-aided gait should be evaluated continuously using an appropriate set of metrics to inform on how adequate a particular pattern is for the clinical profile of a patient, and how to optimize a FES-aided rehabilitation.

In this preliminary study, spatiotemporal metrics, metrics related to the gait dimensions of pace, asymmetry and postural control as well as kinematics will be evaluated on gait aided by different FES patterns. Spatiotemporal metrics will include gait speed, stance and swing durations, stride length and duration, double support duration and ratio. Asymmetry of swing phase and hip movement jerk will be evaluated as measures of asymmetry and postural control. Regarding gait kinematics, joint angle trajectories will be evaluated. This study conducts a preliminary evaluation of these metrics in post-stroke FES-aided gait, hypothesizing that they constitute essential parameters for characterizing the adequacy and efficacy of FES stimulation patterns for a specific patient. Through a series of three case studies, we evaluate a condition without stimulation and two conditions with a default and a personalized stimulation pattern using outcome measures that assess orthotic effects and measures wich are predictors of rehabilitation improvements. Through this analysis, we investigate the metrics' capacity to characterize gait enhancements. The condition with personalized stimulation is calibrated to be adapted to a patient's particular clinical profile and response to FES therapy.

II. Materials & Methods

We realized a retrospective analysis of the gait metrics data acquired by the Neuroskin device to compare the effects of different stimulation patterns. We compared the gait data of stroke patients with autonomous or assisted walking capacity under FES assistance provided by the Neuroskin device, across two stimulation conditions using gait analysis metrics.

Authorization to use the data was obtained from the National Commission for Data Protection and Privacy (CNIL: 22451530, MR-004). Patients were informed and gave their consent for data collection and analysis.

A. Experimental protocol

1) Functional electrical stimulation device: The commercial electrical stimulation device Neuroskin (Kurage, Lyon, France) was used for this study. Neuroskin integrates an 8 channels functional electrical stimulator (3F Fit Fabricando Faber, Belgrade, Serbia) [20], seven Inertial Measurement Units (IMUs, MikroE ICM-42688-P, Belgrade, Serbia) distributed on the back of the pelvis and the legs (3 on each leg: on the thigh, on the shank and on the foot), and Sateco SXTSC pressure sensors (Sateco AG, Schwerzenbach, Switzerland) integrated in a sole or shoe (4 sensors per side). Dry electrodes (Nanoleq, Rumlang, Switzerland) are integrated in a tight garment which is worn by the patient and connected to the stimulator. Electrodes are positioned on average motor point locations of patients, to induce contraction of 6 muscles or muscle groups on each leg: quadriceps, tibialis anterior, fibularis, gluteus maximus, hamstring and gastrocnemius. See Figure 1 for a depiction of the Neuroskin system.



Fig. 1. Neuroskin functional electrical stimulation device (Kurage, Lyon, France) with its main components

For a FES therapy session with Neuroskin, a practitioner first calibrates intensities for each muscle group individually, by selecting the stimulation for each muscle, increasing intensity, stimulating and going over this process until the patient feels discomfort. The last intensity is set as the maximum stimulation intensity. During the session, the device automatically stimulates patients as they walk, with timings based on the gait phase. The stimulation intensity is controlled as a percentage of the previously set maximal intensities, and can be adjusted globally throughout the session.

For all conditions, the default FES parameters for frequency and pulse width of the Neuroskin are used: frequency is set to 40Hz for all muscles, pulse width is set to 400 microseconds for quadriceps, gluteus and hamstrings, 250 microseconds for gastrocnemius, and 200 microseconds for tibialis and fibularis.

2) Data collection: We collected data from 1 minute walking bouts, on level ground, at a self-selected comfortable speed, under 3 different conditions:

1) walk without stimulation,
2) walk with stimulation using default stimulation patterns,
3) walk with stimulation using personalized stimulation patterns

"Default stimulation patterns" refers to the default stimulation algorithm of Neuroskin without personalization, "personalized stimulation patterns" refers to the condition with personalized gait phase prediction of Neuroskin and with stimulation parameters set by an expert. These modalities are detailed in section II-B.

The maximal stimulation intensities for each muscle were calibrated according to the recommended usage guidelines for Neuroskin in FES therapies (see section II-A1). For each patient, the session began with the condition without stimulation. The order of the subsequent conditions was specific to each patient: 1-2-3 for patient 1, 1-3-2 for patient 2, and 1-3-2 for patient 3. Before beginning the first of the two stimulation conditions, the patient walked for a period with stimulation controlled by the Neuroskin stimulation algorithm, to become accustomed to the stimulation levels. During this time, the stimulation intensities were gradually increased for all muscles (as described in section II-A1) to the maximum level acceptable for the patient. This stimulation intensity was then selected for all stimulation conditions and is reported in Table I for each patient. The two modalities used in the personalized stimulation condition are described in the section II-B2. For the first of these modalities, a configuration change was necessary to switch between the default and personalized gait phase prediction models, and involves using data from the patient's gait over 10 consecutive steps in a straight line without stimulation, which is then used for finetuning of the gait phase prediction model. Secondly, a physiotherapist adjusted the stimulation parameters (intensity and timing in gait phase domain) to further optimize the patient's walking pattern. To accomplish this, the patient walked for a few minutes while the physiotherapist modified the relevant parameters. Once an optimal configuration was identified, the personalized stimulation condition was conducted. The chosen parameters are reported in Table I.

TABLE I
INCLUDED PATIENTS WITH HEMIPARETIC SIDE AND DETAILS OF STIMULATION PARAMETERS USED.

Patient number	**Time since stroke, Hemiparetic side**	**Patient information (Gender, Age, Weight)**	**Stimulation intensities for default stimulation condition**	**Stimulation timings[1] and intensities for personalized stimulation condition**
1	88 months, right	M, 61, 88kg	quad: 0mA tib: 45mA fib: 45mA glut: 0mA hams: 0mA gas: 0mA	quad: 0mA. 80-5% tib: 45mA. 60-10% fib: 45mA. 60-10% glut: 0mA. 0-30% hams: 0mA. 60-70% gas: 0mA. 40-60%
2	93 months, left	M, 64, 76kg	quad: 27.5mA tib: 30mA fib: 25mA glut: 32mA hams: 27mA gas: 30mA	quad: 27.5mA. 80-5% tib: 30mA. 60-10% fib: 25mA. 60-10% glut: 32mA. 0-30% hams: 33mA.60-100% gas: 30mA. 40-60%
3	49 months, right	M, 77, 83kg	quad: 38.5mA tib: 42mA fib: 47mA glut: 35mA hams: 42mA gas: 38mA	quad: 38.5mA. 73-5% tib: 42mA. 52-10% fib: 47mA. 60-10% glut: 35mA. 0-30% hams: 42mA. 60-74% gas: 13mA. 46-60%

[1] Stimulation timings are given as beginning and end of stimulation, expressed as a percentage of predicted gait phase.

Distance markers were placed at 0 and 10m on the ground. For each condition, the patient started from behind the first marker, and was asked to walk straight, passing both distance markers. After reaching the second marker, the patient was asked to turn around and walk back to the first marker. The time was recorded each time the patient passed a marker.

3) Participants: 3 chronic stroke patients were included in this preliminary study. These patients were undergoing rehabilitation with the Neuroskin in their usual rehabilitation location in France. They were stimulated only on their paretic side. Detailed information for each patient, along with the stimulation parameters, is provided in Table I. In the third column, stimulation intensities for the default stimulation condition are given. The default stimulation timings for this condition are given in Figure 2. The final column of Table I describes the parameters (intensities and timings) for the personalized stimulation condition. "quad" stands for quadriceps, "hams" for hamstring, "tib" for tibialis, "gas" for gastrocnemius, "glut" for gluteus and "fib" for fibularis.

4) Metrics & data processing: Metrics reflecting spatiotemporal, kinematic, postural and asymmetry aspects of gait were computed to assess the gait resulting from the stimulation patterns. Kinematic metrics were computed: hip, knee and ankle joint angle trajectories were calculated using the algorithms described below and range of motion of the hip was computed. Following spatiotemporal metrics were computed: walking speed, cadence, stance and swing time and ratio, and double support time and ratio). Metrics related

to postural control and asymmetry were also calculated: asymmetry in swing phase duration and hip movement jerkiness. Cadence, stance and swing durations were calculated from gait events (heelstrike and toe-off) which were detected using a threshold-based method on signals from pressure sensors. Joint angles were calculated from the IMU data with the use of the Versatile Quaternion-based Filter algorithm [21] for IMU orientation estimation and Quaternion Management Toolbox [22]. They were segmented into single gait cycles using the heelstrike events. Walking speed was calculated with the distance marks and the recorded time. Stride length was calculated using the distance, and the number of strides extracted from gait events. Asymmetry was calculated as a measure of right and left swing phase duration discrepancies, as defined in the work of Rössler et al. [23]. Postural sway jerkiness was used as a measure of trunk control and calculated as defined in the work of Kim et al. [24]. Parts of the conditions where there was no straight walking were excluded from the analysis.

B. Stimulation conditions

1) Stimulation with default stimulation patterns: The stimulation is controlled by an algorithm developped by Kurage. In this algorithm, a neural network predicts the gait phase percentage from IMU data (gyroscope and accelerometer data) in real time. The gait phase percentage represents the gait cycle and is 0 at heel strike, and increases from 0 to 100 in a gait cycle. The neural network was trained on a dataset of 193 stroke patients. The default stimulation rules are predefined and indexed on the real time predicted gait phase percentage (Figure 2). The default stimulation was used in the second condition of the experimental protocol, named "default stimulation patterns".

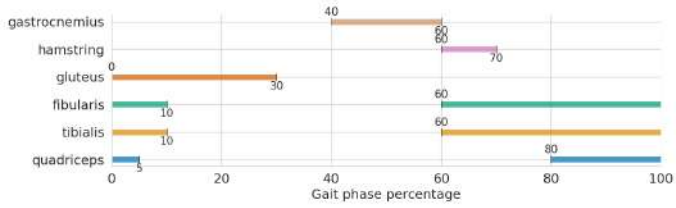


Fig. 2. Default stimulation rules used in the Neuroskin device for the 6 targeted muscle groups. Stimulation is applied based on gait phase percentage. The color bars show when stimulation is active for each muscle.

2) Stimulation with personalized stimulation patterns: In the condition "personalized stimulation patterns", two functionalities were used for personalizing the stimulation patterns: personalization through finetuning of the gait phase prediction model to the patient and when needed as assessed by an expert physiotherapist, the change of FES parameters (timings expressed as a percentage of gait phase and intensities). These modalities are explained below.

The gait phase real time estimation can be adapted to the user's specific gait by finetuning of the gait phase prediction model to the data recorded on the gait of the patient. This allows to better predict gait phase and therefore more accurately time stimulation based on the defined percentages of stimulation, but it does neither affect the stimulation intensities nor the beginning and end percentages.

Finetuning is a common method in Deep learning to leverage the paradigm of transfer learning, where a neural network is firstly trained on a large corpus of data, with underlying characteristics and subsequently trained again on data on a different task. The goal with this procedure is reducing training time and improving accuracy by limiting overfitting. An example of this adaptation, for patient number 1 is shown in Figure 3. In part (a) of this figure, the predicted gait phase percentage (in %) is shown in relation to normalized real gait cycle duration (in %). The solid line represents the median predicted gait phase percentage values, with the shaded areas indicating the first and third quartiles. The dashed line represents the gait phase percentage detected by gait events, which is the target for the neural network prediction and can be considered the true gait phase percentage. In part b, the default muscle stimulation rules based on the predicted gait phase percentage are shown, with the lower and upper quartiles for the beginning and end of stimulation shown in lighter shades. Here, we can observe that the start and the end of stimulation in gait cycle duration for each muscle are not accurate (comparing to the default stimulation rules in Figure 2, the median beginning of stimulation is off target for most muscles, maximally by 11% for gluteus), and there is considerable variability (mean interquartile range across muscles is 9.3%). We are able to compare values of beginning and end of stimulation in gait cycle duration and predicted gait phase because the dashed line representing true gait phase is linear in this case. In parts c and d where the personalized stimulation is used, we observe that the gait phase estimation is more accurate (maximal offset for median beginning or end is 3%) with reduced variability (mean interquartile range is 2.7%). As a result, stimulation is more accurately timed, closer to the defined start and end gait cycle percentage values and with smaller variability.

The second modality used in the personalized stimulation condition was expert adaptation of FES parameters. The FES system also integrates functionalities to manually change the following parameters: timings of the stimulation rules for each muscle in gait phase domain (as a percentage), impulse width for each channel and frequency for bilateral pairs of muscles. This procedure is useful for further adapting stimulation patterns to suit individual patients or specific exercises, using the expert knowledge of medical staff and physiotherapists. In this study, the timings in gait phase domain and intensities of stimulation were adapted.

III. Results

We analyzed the metrics described in Section II-A4 across all conditions and patients. Mean results and standard deviations are given in Table II. Metrics showing most important variations are shown in Figure 4, which displays patient-specific outcomes relative to normative ranges (green bands), taken from [23] and [24]. Overall patient responses did not

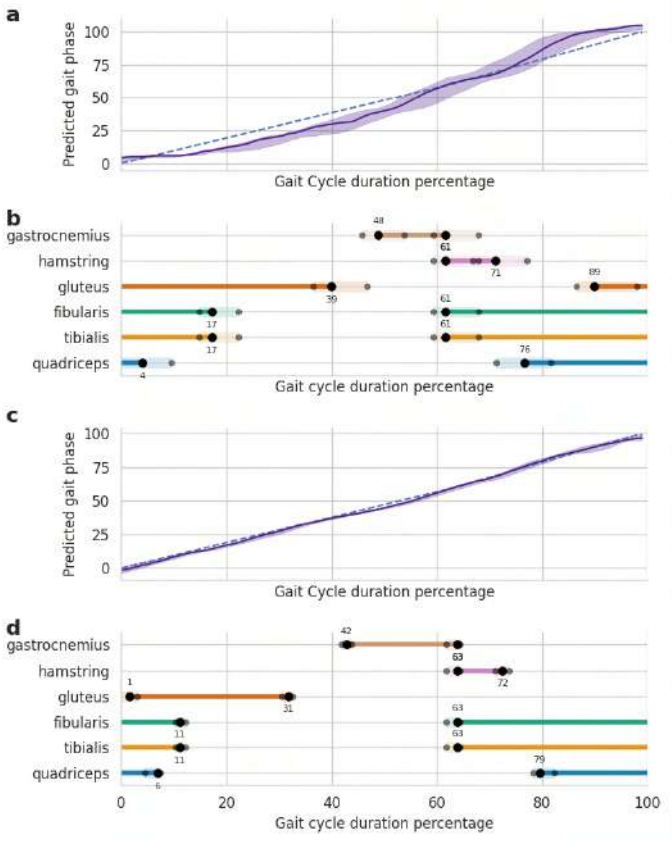


Fig. 3. Stimulation patterns personalization through finetuning for patient 1. **a.** Gait phase estimation using Kurage default stimulation shown in violet as a percentage of gait cycle, against normalized gait cycle duration. The dashed line represents true gait phase percentage as calculated using gait events. **b.** Median muscle stimulation rules with the default stimulation patterns, applied based on gait phase percentage. Quartiles are shown in shaded colors **c.** Gait phase estimation using Kurage personalized stimulation model shown in violet as a percentage of gait cycle, against normalized gait cycle duration. **d.** Median muscle stimulation rules for personalized model, applied based on gait phase. Quartiles are shown in shaded colors.

show substantial trends of metric variations between conditions when considering the mean. However individual patient responses analysis indicates heterogeneous results between no stimulation, default stimulation, and personalized stimulation conditions.

To facilitate understanding results in a clinical context, clinically relevant changes are given for following metrics: the minimal clinically important difference (MCID) for stroke patients is 10cm/sec for gait speed [25] and 5.81° for hip ROM [26]. For other spatiotemporal metrics and to the best of our knowledge, MCID values have not been established yet in the literature, therefore minimum detectable change (MDC) values are given. MDC values are 8.58 for cadence and 11.96 cm for stride length [27]. To the best of our knowledge, MDC or MCID values for asymmetry in gait phase duration and hip movement jerkiness have not been established. Firstly, the conditions without stimulation and with default stimulation are compared. The comparison revealed improvements in asymmetry (-2.6%), walking speed (+2.59cm/s), and stride length (+5.16cm), but with considerable standard deviations across patients: 4.2%, 7.5cm/s and 9.5cm respectively. Double support ratio (+2.7%) and postural sway (+14.77$cm^2 * s^{\propto 5}$) increased, with standard deviations of the difference between the conditions of 1.2% and 19.8$cm^2 * s^{\propto 5}$ respectively. This indicates deviation from double support ratio normative values and reduced trunk control, respectively. However, increased double support ratio may indicate increased stability. The increased postural sway is primarily attributed to patient 1, who also exhibits important gait asymmetry under stimulated conditions. It should be noted that this patient was only stimulated on the ankle dorsiflexor muscles.

Personalized stimulation yielded modest additional improvements in walking speed (+0.63cm/s) compared to default stimulation, with a standard deviation of 2.34cm/s. Hip range of motion on the left hemiparetic patient increased by 3.44° from default to personalized stimulation, which is an increase of 12% or reduction of 30% of the gap to healthy values. Postural sway and double support ratio continued to increase further away from normative values. Other spatiotemporal parameters remained largely unchanged between all conditions (maximum variations for individual patients: cadence ±1 step/min; stance duration ±0.04s; swing duration ±0.02s; stride duration ±0.02s). Hip range of motion for the right side hemiparetic patients also did not show substantial changes (±1,54°).

Kinematic trajectories improved between conditions without stimulation and with default stimulation mainly for 2 patients, correcting the main gait deficit of each patient, with an additional improvement for one patient with personalized stimulation. Individual patient responses on evaluated metrics varied substantially across conditions. Given this heterogeneity, patient-level analysis provides additional meaningful insights.

Patient 1 had right-side hemiplegia and exhibited ankle dorsiflexion impairment. Dorsiflexor stimulation improved swing phase ankle dorsiflexion and reduced compensatory knee flexion through enhanced ground clearance, resulting in improved walking speed and stride length. The timing of hip flexion aligned better with normative values. However, asymmetry increased with stimulation. The personalized stimulation condition improved further plantarflexion at toe-off and further enhanced walking speed (+3.3cm/s, +4.7%), though gait asymmetry (+11.4%) and postural sway (+44$cm^2 * s^{\propto 5}$, +45.5%) continued to increase.

Patient 2 presented with left hemiplegia, characterized by impaired ankle dorsiflexion with phase delay and a beginning of genu recurvatum, evidenced by minimal knee flexion during stance phase (Figure 6). The patient exhibited a compensatory strategy by throwing his leg forward which resulted in a slight phase lead in knee angle trajectory. Default stimulation application slightly resolved the knee flexion phase lead, contributing to improved gait symmetry, as can be seen on Figure 4. However, there was no substantial improvement in ankle joint trajectories, and a decrease in walking speed (-6.5cm/s, -12%). For the personalized stimulation condition, the physiotherapist increased stimulation intensity and advanced onset timing for hamstring stimulation to address both the knee

TABLE II
RESULTS ON ALL METRICS ACROSS STIMULATION CONDITIONS[1]: MEAN AND STANDARD DEVIATION

Condition	Without stimulation	Default stimulation	Personalized stimulation
Cadence (steps/min)	**49.0** (8.89)	48.33 (6.81)	48.0 (7.55)
Left stance duration (s)	0.98 (0.19)	**0.98** (0.15)	1.00 (0.15)
Right stance duration (s)	**0.73** (0.14)	0.76 (0.11)	0.78 (0.16)
Left swing duration (s)	**0.36** (0.02)	0.35 (0.02)	0.35 (0.05)
Right swing duration (s)	0.27 (0.1)	**0.28** (0.09)	0.27 (0.1)
Mean stance duration (s)	**0.86** (0.16)	0.88 (0.12)	0.9 (0.15)
Mean swing duration (s)	**0.37** (0.06)	0.36 (0.05)	0.35 (0.06)
Left stance ratio (%)	**72.5** (3.79)	73.5 (2.65)	74 (1.53)
Right stance ratio (%)	72 (5.51)	**72** (4.36)	74 (6.66)
Stride duration (s)	**1.23** (0.2)	1.24 (0.17)	1.25 (0.2)
Double support duration (s)	**0.48** (0.12)	0.51 (0.09)	0.53 (0.11)
Double support ratio (%)	**38.33** (4.5)	41.0 (3.0)	42.33 (4.6)
Walking Speed (cm/s)	49.18 (12.5)	51.77 (17.1)	**52.39** (18.9)
Mean stride length (cm)	60.09 (14.8)	65.24 (26.0)	**65.65** (26.0)
Range of motion left hip (deg)	29.26	28.17	**31.61**
Range of motion right hip (deg)	28.38 (1.4)	**29.73** (0.21)	28.41 (0.01)
Asymmetry swing (%)	19.38 (11.0)	**16.78** (13.7)	17.86 (22.4)
Postural sway jerkiness (cm^2/s^5)	**54.97** (43.8)	69.74 (37.9)	80.81 (63.7)

[1] Reported values in the table are mean values and standard deviation is shown in brackets. Metrics concerning one specific side were calculated only on hemiparetic sides. Standard deviation is not given for left hip ROM, since there is only 1 patient. For each metric, the closest result to normative values across the three conditions is shown in bold. Normative healthy values are taken from [23] and [24].

flexion phase advance and genu recurvatum. Personalized stimulation improved slightly further knee flexion phase lead which translated to an improved hip range of motion (+12% or reduction of 30% of the gap to healthy values) and maximal hip flexion angle, yielding additional symmetry improvements (-3.6% in asymmetry or reduction of 34% of the gap to healthy values), but did not show other meaningful improvements in ankle movement control. The small improvements on this patient with stimulation conditions could be due to the fact that the speed of this patient was initially quite high with a short stride length, making FES orthotic changes smaller due to delays in neuromuscular responses.

Patient 3, a chronic stroke patient with right-side hemiplegia, presented ankle dorsiflexion impairment and gastrocnemius spasticity, leading to excessive plantarflexion during swing and toe-off phases (Figure 5). The patient compensated with exaggerated knee flexion to achieve ground clearance, resulting in gait asymmetry and right stance instability. Default stimulation patterns improved swing phase dorsiflexion. These modifications yielded enhanced walking speed (+2.2cm/s, +6.3%) and reduced asymmetry (-2.3%, reduction of 46% of the gap to healthy values) through improved heel strike (Figure 4). The personalized stimulation patterns incorporated parameter adjustments done by the physiotherapist: reduced gastrocnemius stimulation to mitigate spasticity, advanced timing of quadriceps and tibialis anterior activation and extended hamstring stimulation duration. This parameterization resulted in a slightly reduced knee flexion, sign of less ground clearance necessity, and improved slightly dorsiflexion angle at toe off, as seen on joint angle trajectories. This manifested in increased stride length (+4.7cm, +9.3%) and better postural control (-12.5$cm^2 * s^{\propto 5}$, getting into healthy values range).

These results indicate that the metrics showing improvement from default to personalized stimulation differ from patient to patient: for some patients, there was an improvement on asymmetry (patient 2 getting closer to normative healthy values with -3.6%, patient 1 getting into the range of healthy values) and postural control (patient 3 getting into healthy values range) and walking speed decreased or stagnated (-2.6cm/s for patient 2, stagnation for patient 3), and for others, the inverse occured (increase of asymmetry and postural sway, with increase in walking speed, +3.3cm/s or +4.7%, for patient 1). In this situation, it is difficult to identify what is the more relevant metric to consider for FES pattern optimization. However, the most relevant and informative assessed metrics in this preliminary study were walking speed, stride length, kinematic analyses and hip ROM and metrics reflecting postural sway and asymmetry, which all give information on the possible rehabilitation improvements of patients. Especially, we see that metrics revealing macro-level dimensions of gait like pace, asymmetry and postural control were as important as more precise measures of kinematic changes, which can explain changes in macro-level measures of gait.

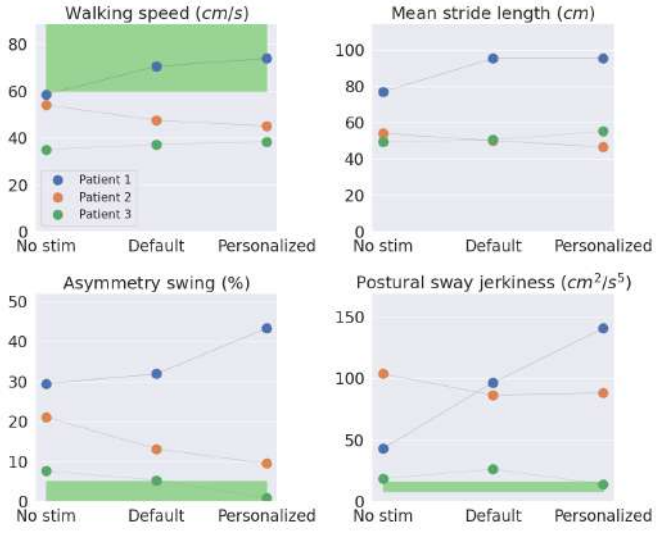


Fig. 4. Changes in gait metrics across stimulation conditions, on most relevant metrics. Green areas represent normative healthy values. For mean stride length, the normative values are above the chart. For postural sway, a pathological gait is generally indicated by a higher hip movement jerk than a healthy gait. Normative healthy values are taken from [23] and [24].

IV. DISCUSSION

Although a small improvement in gait speed and left hip range of motion was found when comparing default stimulation to personalized stimulation, no clinically significant overall improvement was observed across metrics. It is important to note that this study evaluates immediate orthotic

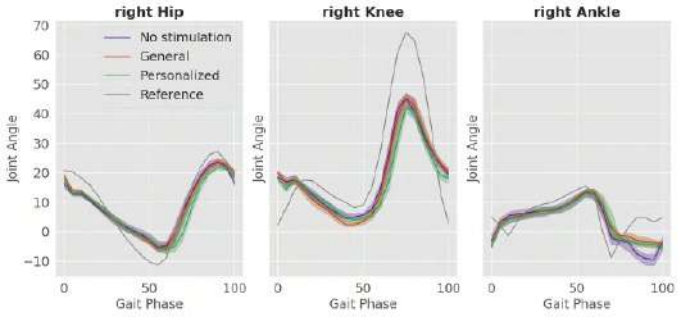


Fig. 5. Joint angles for all conditions of stimulation for patient 3. Only paretic side is shown. The median is shown in plain color, and translucid colors show the lower and higher quartiles. The reference of joint angles trajectory is shown in grey.

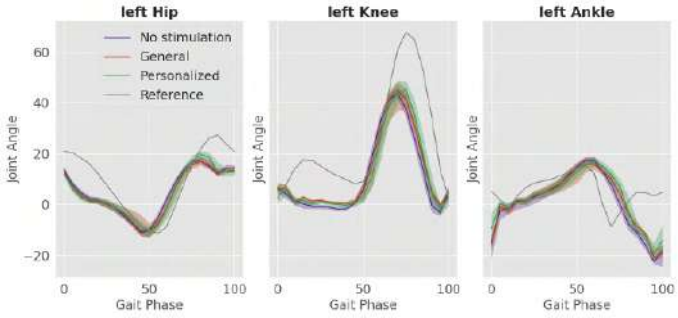


Fig. 6. Joint angles for all conditions of stimulation for patient 2. Only paretic side is shown. The median is shown in plain color, and translucid colors show the lower and higher quartiles. The reference of joint angles trajectory is shown in grey.

effects, while clinically significant improvements may emerge over the course of prolonged FES therapy. For example, we observed that improvements in gait kinematics for patient 2 did not translate to increased walking speed when evaluating the orthotic effect, but could eventually translate to improvements along a therapy. Individual analysis revealed different patient-specific gains, with small additional improvements with personalized stimulation, which was specifically tailored to address each patient's primary gait impairment, subsequently impacting other gait metrics.

This preliminary study shows small improvements due to personalized FES on gait, and while not being clinically meaningful overall, some patient-specific improvements can be noted. These discrepancies between patients indicate the need for a more general framework to understand how improvements manifest for some patients on some metrics but not for others. This framework needs to better take into account the clinical profiles and current rehabilitation status and needs of patients, to inform on which aspects of gait should be primarily improved. It is possible that optimal rehabilitation for some patients may require improvements in certain metrics while accepting temporary degradation in others to facilitate overall gait enhancement. Evaluation of gait in the light of more theoretical frameworks of gait, like biomechanical frameworks of gait would be useful. These open questions relate to gaps in the understanding of poststroke recovery [28].

Our selection of metrics and their implications merits a more detailed discussion. Walking speed, while commonly used, represents a macro-level measure that does not describe the qualitative aspects of gait within gait cycles and patients may increase speed with a more pathological gait. Walking speed should therefore not be the sole metric for FES-aided gait evaluation. Additionally, the use of reference trajectories for joint angles presents another methodological challenge, especially for stroke patients, as there is no universal optimal gait pattern [29]. This could introduce bias when evaluating patients' gait against standardized references.

While these preliminary results suggest that the chosen metrics are relevant for evaluating different FES stimulation patterns, and that personalized stimulation can enhance gait patterns beyond default stimulation, several limitations should be noted. Firstly, the current personalization process only influences stimulation timings within the gait cycle by small percentages and does not account for the muscle response to stimulation, so orthotic differences can be expected to be small. Additionally, the expert setting of FES parameters is constrained by time limitations, and high inter-operator variability, which could result in suboptimal and heterogeneous parameterization. This highlights potential future directions. There is a clear need for automated, more detailed parameterization of FES patterns. Secondly, the retrospective analysis done in this preliminary study limits the possibilities in terms of applied FES patterns and evaluated metrics: in a clinical context, no specific intervention could be planned, which limited the design of this preliminary study.

All the aspects discussed above show that this preliminary study, while showing promising results, requires extension to a larger prospective patient population and the evaluation of additional metrics relevant to FES-based gait rehabilitation, while better taking into account clinical profiles of patients and embedding them in a clinical gait rehabilitation framework. Further work in this direction is currently in progress.

V. Conclusion and Perspectives

This study evaluated FES in gait rehabilitation for three post-stroke patients, comparing gait parameters under three conditions: non stimulated gait, default FES-assisted gait, and personalized FES-assisted gait. The personalized stimulation condition incorporated patient-specific parameter adjustments by an expert physiotherapist, as well as finetuning of the stimulation algorithm. Analysis revealed modest improvements in speed, stride length, and asymmetry between non stimulated and default stimulation conditions, while the transition from default to personalized stimulation showed a small mean speed improvement. However, individual patients exhibited notable improvements across distinct metrics, indicating that therapeutic responses vary according to each patient's clinical profile, specific gait impairments, and individual-optimal rehabilitation pathways. Future research should validate these findings through a larger prospective cohort study to integrate FES-aided gait evaluation into a comprehensive clinical rehabilitation framework, later potentially enabling exploration of

AI-based methods for dynamic parameter adaptation tailored to individual patient profiles and clinical needs.

ACKNOWLEDGMENT

The authors gratefully acknowledge the physiotherapists Marwan Al Khoury and Nikola Babic for their FES parameters optimization in personalized stimulation conditions, Baptiste Moreau for code support, MD. Perrine Séguin for assistance with data usage approval and Kurage for providing the Neuroskin and technical infrastructure.

Declaration of potential conflicts of interest: NF's doctoral studies are financed by the company Kurage. AM is a cofounder and the chief scientific officer of Kurage.

REFERENCES

[1] M. Milosevic, C. Marquez-Chin, K. Masani, M. Hirata, T. Nomura, M. R. Popovic, and K. Nakazawa, "Why brain-controlled neuroprosthetics matter: Mechanisms underlying electrical stimulation of muscles and nerves in rehabilitation," *BioMedical Engineering OnLine*, vol. 19, p. 81, Dec. 2020.

[2] G. Andreopoulou, G. Busselli, T. Street, C. Bulley, R. Safari, M. L. van der Linden, and J. Burridge, "Is functional electrical stimulation effective in improving walking in adults with lower limb impairment due to an upper motor neuron lesion? An umbrella review," *Artificial Organs*, vol. 48, pp. 210–231, Mar. 2024.

[3] D. B. Popović and T. Sinkjær, eds., *Control of Movement for the Physically Disabled*. London: Springer London, 2000.

[4] A. Sena, H. Kavianirad, S. Endo, E. Burdet, and S. Hirche, "The gap in functional electrical stimulation," 3rd Workshop on Closing the Reality Gap in Sim2Real Transfer for Robotics, 2022.

[5] "Impact case studies. research excellence framework 2014 [internet].." https://impact.ref.ac.uk/casestudies/CaseStudy.aspx?Id=43853. Accessed: 2025-02-15.

[6] V. A. Stanhope, B. A. Knarr, D. S. Reisman, and J. S. Higginson, "Frontal plane compensatory strategies associated with self-selected walking speed in individuals post-stroke," *Clinical Biomechanics*, vol. 29, pp. 518–522, May 2014.

[7] S. A. Moore, P. Boyne, G. Fulk, G. Verheyden, and N. A. Fini, "Walk the Talk: Current Evidence for Walking Recovery After Stroke, Future Pathways and a Mission for Research and Clinical Practice," *Stroke*, vol. 53, pp. 3494–3505, Nov. 2022.

[8] J. H. Carr and R. B. Shepherd, *Stroke Rehabilitation: Guidelines for Exercise and Training to Optimize Motor Skill*. Edinburgh {: Butterworth-Heinemann, 1st ed., reprinted ed., 2009.

[9] S. Lord, B. Galna, and L. Rochester, "Moving forward on gait measurement: Toward a more refined approach," *Movement Disorders*, vol. 28, pp. 1534–1543, Sept. 2013.

[10] J. Perry, *Gait Analysis: Normal and Pathological Function, Second Edition*. Thorofare: SLACK, Incorporated, 2nd ed ed., 2010.

[11] D. Pinto-Fernandez, D. Torricelli, M. D. C. Sanchez-Villamanan, F. Aller, K. Mombaur, R. Conti, N. Vitiello, J. C. Moreno, and J. L. Pons, "Performance Evaluation of Lower Limb Exoskeletons: A Systematic Review," *IEEE Transactions on Neural Systems and Rehabilitation Engineering*, vol. 28, pp. 1573–1583, July 2020.

[12] M. Roberts, D. Mongeon, and F. Prince, "Biomechanical parameters for gait analysis: A systematic review of healthy human gait," *Physical Therapy and Rehabilitation*, vol. 4, no. 1, p. 6, 2017.

[13] G. Cicirelli, D. Impedovo, V. Dentamaro, R. Marani, G. Pirlo, and T. R. D'Orazio, "Human Gait Analysis in Neurodegenerative Diseases: A Review," *IEEE Journal of Biomedical and Health Informatics*, vol. 26, pp. 229–242, Jan. 2022.

[14] T. Street, I. Swain, and P. Taylor, "Training and orthotic effects related to functional electrical stimulation of the peroneal nerve in stroke*," *Journal of Rehabilitation Medicine*, vol. 49, no. 2, pp. 113–119, 2017.

[15] A. I. Kottink, L. J. Oostendorp, J. H. Buurke, A. V. Nene, H. J. Hermens, and M. J. IJzerman, "The Orthotic Effect of Functional Electrical Stimulation on the Improvement of Walking in Stroke Patients with a Dropped Foot: A Systematic Review," *Artificial Organs*, vol. 28, pp. 577–586, June 2004.

[16] T. Aout, M. Begon, B. Jegou, N. Peyrot, and T. Caderby, "Effects of Functional Electrical Stimulation on Gait Characteristics in Healthy Individuals: A Systematic Review," *Sensors*, vol. 23, p. 8684, Oct. 2023.

[17] L. Gerez, S. Micera, R. Nuckols, and T. Proietti, "Assessment of wearable robotics performance in patients with neurological conditions," *Current Opinion in Neurology*, Oct. 2024.

[18] C. Selves, G. Stoquart, and T. Lejeune, "Gait rehabilitation after stroke: Review of the evidence of predictors, clinical outcomes and timing for interventions," *Acta Neurologica Belgica*, vol. 120, pp. 783–790, Aug. 2020.

[19] J. J. Eng and P.-F. Tang, "Gait training strategies to optimize walking ability in people with stroke: A synthesis of the evidence," *Expert Review of Neurotherapeutics*, vol. 7, pp. 1417–1436, Oct. 2007.

[20] L. Popović-Maneski and S. Mateo, "MotiMove: Multi-purpose transcutaneous functional electrical stimulator," *Artificial Organs*, vol. 46, pp. 1970–1979, Oct. 2022.

[21] D. Laidig and T. Seel, "VQF: Highly accurate IMU orientation estimation with bias estimation and magnetic disturbance rejection," *Information Fusion*, vol. 91, pp. 187–204, Mar. 2023.

[22] D. Laidig, "Quaternion-based inertial motion tracking toolbox." https://github.com/dlaidig/qmt. Accessed: 2024-11-15.

[23] R. Rössler, J. Wagner, R. Knaier, N. Rommers, R. W. Kressig, A. Schmidt-Trucksäss, and T. Hinrichs, "Spatiotemporal gait characteristics across the adult lifespan: Reference values from a healthy population – Analysis of the COmPLETE cohort study," *Gait & Posture*, vol. 109, pp. 101–108, Mar. 2024.

[24] K. J. Kim, Y. Gimmon, J. Millar, and M. C. Schubert, "Using Inertial Sensors to Quantify Postural Sway and Gait Performance during the Tandem Walking Test," *Sensors*, vol. 19, p. 751, Feb. 2019.

[25] S. Perera, S. H. Mody, R. C. Woodman, and S. A. Studenski, "Meaningful Change and Responsiveness in Common Physical Performance Measures in Older Adults," *Journal of the American Geriatrics Society*, vol. 54, pp. 743–749, May 2006.

[26] A. Guzik, M. Drużbicki, L. Perenc, A. Wolan-Nieroda, A. Turolla, and P. Kiper, "Establishing the Minimal Clinically Important Differences for Sagittal Hip Range of Motion in Chronic Stroke Patients," *Frontiers in Neurology*, vol. 12, p. 700190, Sept. 2021.

[27] M. Geiger, A. Supiot, D. Pradon, M.-C. Do, R. Zory, and N. Roche, "Minimal detectable change of kinematic and spatiotemporal parameters in patients with chronic stroke across three sessions of gait analysis," *Human Movement Science*, vol. 64, pp. 101–107, Apr. 2019.

[28] C. Grefkes and G. R. Fink, "Recovery from stroke: Current concepts and future perspectives," *Neurological Research and Practice*, vol. 2, p. 17, Dec. 2020.

[29] S. Armand, F. Moissenet, G. De Coulon, and A. Bonnefoy-Mazure, "Identifying and understanding gait deviations: Critical review and perspectives," *Movement & Sport Sciences - Science & Motricité*, no. 98, pp. 77–88, 2017.

Hybrid Actuation Paradigm in Back-Assist Exoskeleton for Symmetric Loading Conditions - A Feasibility Study

Arpeet Dhal[1], Teja Krishna Mamidi[1], Vineet Vashista[1*]

***Abstract*— The mandates of safety standards in manual material handling tasks have spurred the development and commercialization of many back-assist exoskeletons. These devices prevent back pain injuries by redistributing the applied loads, reducing the effort and fatigue in heavy and repetitive loading tasks. The majority of them employ passive and active actuation paradigms. The passive ones are known for better transparency and energy efficiency, while the active ones provide a higher degree of assistance and quickly adapt to task severities. The present work investigates the feasibility of a hybrid actuation paradigm for load-carriage under symmetric loading conditions. The preliminary results suggest that the proposed modifications to an existing passive exoskeleton effectively economize energy expenditure and improve adaptability.**

quasipassive, exoskeleton, load-carriage, hybrid actuation.

I. Introduction

Low back pain due to manual material handling tasks is a common problem in occupational settings [1], [2]. Specifically, lifting performed using wrong postures or heavy loads and repetitively was reported to be the primary cause of this ailment [3]. In order to ensure safety and promote preventive measures, guidelines, including recommended lifting weight limits [4], and techniques [5] were formulated. Further, personal protective equipment such as back braces and exoskeletons are promising alternative solutions, but assessment of their benefits is still ongoing [6].

Many back-assist exoskeletons were developed in the past for commercial and research purposes [7]. Among these, the *passive* devices provide assistance by redistributing the biomechanical energy over a lifting cycle using mechanical restoring elements [8]. In contrast, the *active* ones use an external energy resource such as electric, hydraulic, and pneumatic actuators to augment human effort [9].

Although passive devices are lighter, energy-efficient, and cost-effective, they have limited adaptability to task and environment variability. Hence, the current work explores the benefits of hybrid actuation paradigms [10], wherein external energy resources are only employed to alter the mechanics of passive exoskeletons. In particular, the passive Back-ASsist Exosuit (BASE) proposed in [11] was considered for improvement.

[1]Arpeet Dhal, Teja Krishna Mamidi, and Vineet Vashista are with the Department of Mechanical Engineering, Indian Institute of Technology Gandhinagar, Gujarat 382355, India. Emails: dhalarpeet100@gmail.com, teja.mamidi@iitgn.ac.in, vineet.vashista@iitgn. ac.in. ORCIDs: 0009-0000-7716-4992, 0000-0002-2191 -2581, 0000-0001-6776-7431.

[*]Vineet Vashista is the corresponding author.

The preliminary studies with the BASE emulator involved finding the appropriate design to minimize muscle effort, reduce the device-to-body forces, and improve comfort for squat lifting/lowering tasks [12]. The limitations of this recommended design considered for mitigation in this work include the following. Eliminate manual adjustments of stiffness bands to match task severity. Alleviate the device-to-body forces on the shoulder during the pretension of the stiffness band. Therefore, in the current study, the following modifications are made to transform the passive device into a hybrid one for enhanced transparency and adaptability.

- An algorithm to detect different phases of the lifting cycle was developed using a thigh-mounted IMU.
- Inclusion of control and actuation units to attain the desired cable tension profiles during the phases of pre-tension and release (see Section III-B) while adapting to the task severity and reducing the device-to-body forces on shoulders.
- A load-bearing element was introduced to support the reaction forces from stretching the stiffness band and reduce the energy expenditure of the actuator.

The proposed phase detection algorithm is unique as it only uses the data from a single gyroscope's axis and bio-signatures for classification. In the past, multiple sensors with learning techniques were used for such purposes [13], [14]. Further, research incorporating hybrid actuation paradigms in back-assist exoskeletons is very limited [15].

The rest of the paper is organized as follows. The details pertinent to the passive and hybrid back-assist exoskeletons are presented in Sections II and III, respectively. Section IV presents the preliminary results and discussions. Finally, the conclusions are presented in Section V.

II. Passive Exoskeleton

The optimal configuration for the moment arm of the BASE emulator from [12] is adopted in this work to demonstrate the mechanics of the passive exoskeleton. Its design, different phases of the lifting task, and the profile of device-to-body force on shoulders during a typical lifting cycle are described first. It is then followed by the motivation to explore a hybrid paradigm for better user comfort and adaptive assistance.

As depicted in Fig. 1(a), the passive exoskeleton comprises Taylor's back brace with an additional base plate to mount the lever arm at a specific orientation. An inextensible nylon strap attached at the shoulders connects the load cell with another strap passing over the lever arm. Subsequently, the

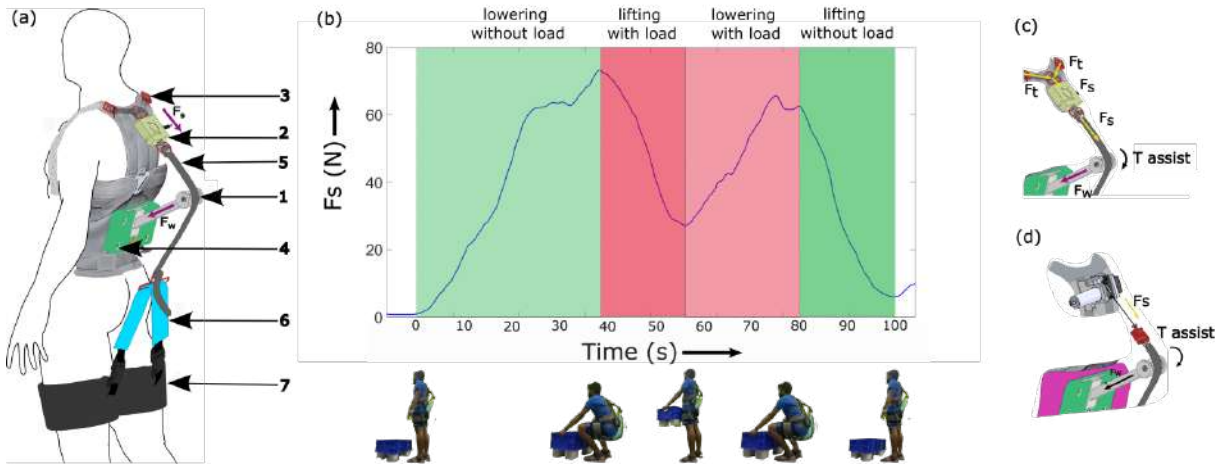


Fig. 1. (a) Schematic of a passive back-assist exoskeleton. 1: Moment Arm, 2: S-beam Load Cell, 3: Taylor's Brace, 4: Fixture for Moment Arm, 5: Non-extensible Cable, 6: Stiffness Band, 7: Thigh Straps, (b) Variation of assistive force F_s with different phases of the task involving lowering and lifting with/without load, (c) An inset depicting the shoulder straps balancing the assistive force F_s in a passive configuration, (d) An inset showing the actuator unit balancing the assistive force F_s in the hybrid design.

nylon strap is coupled with an elastic stiffness band clipped to the thigh braces.

The working principle of the exoskeleton is as follows. Initially, as the person donning the exoskeleton starts to squat, the stiffness band stretches, storing the kinetic energy till the lowest position. Later, when the person starts to stand with/without the load, the potential energy stored in the stiffness band augments the motion to reach the highest position, thereby reducing muscle efforts [8]. Also, it provides an alternative path for load transfer from the shoulders to the thighs through the mechanical components, reducing the joint loadings.

As shown in Fig. 1(b), a complete cycle of the task would involve a sequence of four phases, namely, lowering without load, lifting with load, lowering with load, and lifting without load. The forces F_s measured by the load cell would gradually increase when lowering and decrease when lifting due to the extension and shortening of the stiffness band, respectively. Further, as depicted in depicted in Fig. 1(c), these forces would create an assistive moment T_{assist} about the lumbosacral joint and the device-to-body forces including the tensile forces F_t at the shoulder and the compressive force F_w at the lumbosacral joint [12].

The modulation of assistance to match varying task severity could be achieved by replacing the elastic band with a higher/lower stiffness band or manually increasing/decreasing the pretension after donning. In the former approach, frequent donning and doffing are needed to meet the needs of dynamic task severity scenarios. In the latter, along with discomforting and unnecessary device-to-body interactions (e.g., shoulder pull) when standing, manual interruptions with frequent adjustments are warranted. Hence, in the current study, the modulation of assistance is attempted using a hybrid actuation paradigm, ensuring transparency and energy-efficient modifications.

III. Hybrid Exoskeleton

The modifications to the design of the passive exoskeleton are elucidated first. Next, a gait event detection algorithm is described using the signature of the sagittal plane angular velocity of the right thigh during lifting tasks. Finally, the control architecture, followed by preliminary results, is presented.

A. Design

The hybrid exoskeleton additionally features actuation, locking, and control units.

1) Actuation Unit: This unit modulates the assistive forces by adjusting the pretension of the stiffness band to ensure transparency in the phases of non-intervention and achieve the desired levels of assistance during interventions. Hence, it alleviates the need for manual interruptions to change the stiffness band and accounts for changes in the task severity to some extent. Further, as shown in Fig. 1(d), it replaces the nylon straps connected to the shoulders in the passive exoskeleton. Consequently, the device forces, i.e., reaction force, will now be distributed through Taylor's brace instead of being concentrated at the shoulders, enhancing the user's comfort.

A Faulhaber BP4 3274 BLDC motor with a built-in encoder and a custom pulley attached to its shaft constitutes the actuator unit, as depicted in Fig. 2(b). The two-stage custom pulley has a drum for winding and unwinding the cable next to a pawl for engaging and disengaging with a ratchet of the locking mechanism described below.

2) Locking Unit: In order to conserve energy expenditure of the portable exoskeleton and promote passive transparency, the actuation unit is only used when the required assistive forces are minimal, i.e., in the initiation of lowering and termination of lifting. In the remaining phases of the task, the assistive load is transferred to a load-bearing element through the pawl and ratchet mechanism.

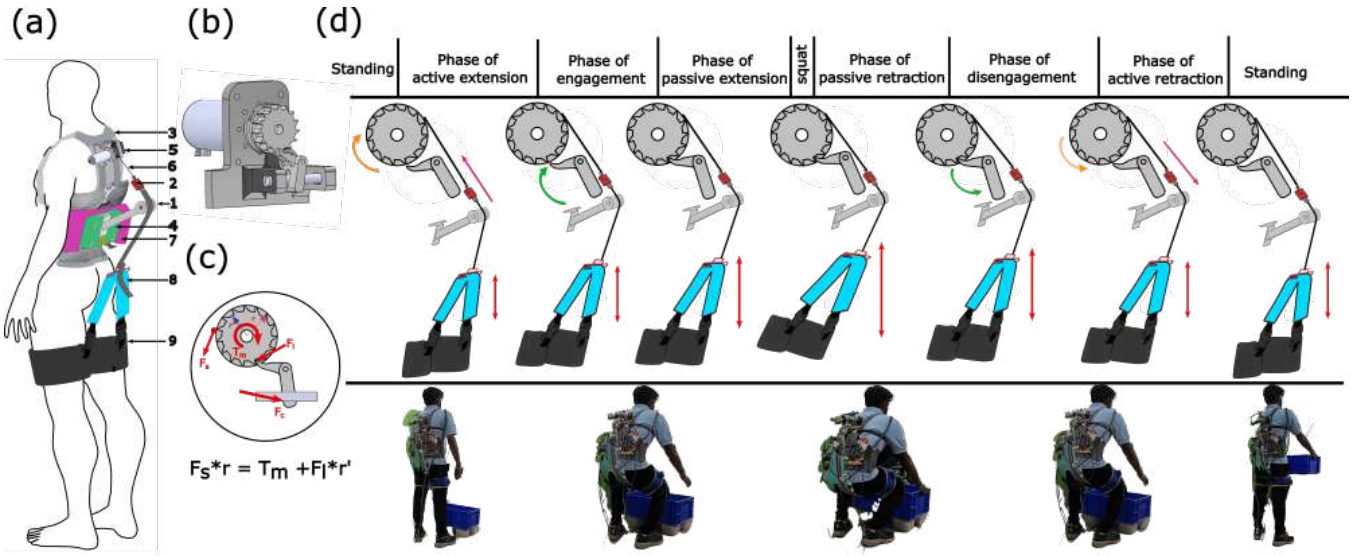


Fig. 2. (a) Schematic of a hybrid back-assist exoskeleton. 1: Moment Arm, 2: S-beam Load Cell 3: Taylor's Brace, 4: Fixture for Moment Arm, 5: Actuator Unit, 6: Inextensible Cable, 7: Control Unit, 8: Stiffness Band, 9: Thigh Straps, (b) Actuation and locking units, (c) An overlay of forces acting on different elements (including the load-bearing element) when engaging the pawl. (d) A classification of different phases of the load carriage cycle to aid in designing the control inputs. The actuator's rotation is denoted in orange, the servo's rotation in green, the cable movement in purple, and the extent of stiffness band deflection in red.

The ratchet forms the distal part of the custom pulley in the actuation unit. It was designed to engage with the pawl and transfer the load to a load-bearing element (a steel rod fixed to the motor mount) when required. The pawl is attached to an MG995 metal gear servo motor for engagement and disengagement with the ratchet at the appropriate phases using position control. Since the servo cannot support the loads experienced during the task (shown in Fig. 1), the pawl engages with the load-bearing element. As depicted in Fig. 2(c), a pawl extension makes contact with a steel rod, preventing it from moving further even when the cable pulls the ratchet to rotate anti-clockwise, acting as an anchor to support deflections of the stiffness band. Eventually, the load-bearing element would transfer the reaction forces to the back brace. Hence, with this design, the energy the BLDC motor requires to maintain the pulley position is economized. The forces experienced by the ratchet F_l can be determined from the assistive force F_s and the torque applied by the actuator T_m using the relation specified in Fig. 2(c). Subsequently, this information can be used to choose the appropriate dimensions of the load-bearing element.

3) Control Unit: The NI myRIO micro controller forms a central component that integrates the inputs from an Adafruit BNO085 IMU and an S-beam load cell to control actuation and locking at appropriate gait cycle phases. Apart from these, the control unit includes a motor motion manager and a load cell amplifier.

B. Load-carriage Phase Classifier

The signature of variations in the angular velocity of the thigh (ω_t) in the sagittal plane was used to detect different phases of the load-carriage task [16]. One of the axes of the gyroscope in an IMU, aligned with the front axis, is used for this purpose. The IMU is mounted on the thigh brace using an elastic strap. The data was collected with a sampling frequency of 200 Hz, and a moving average window of 100 samples was used to alleviate the noise.

The zero crossings and peaks of the signature determine the transition between phases. In order to avoid false detection of zero crossings, a threshold ϵ_t, i.e., a value close to zero (30 deg/s), was used in this work. The choice of ϵ_t predominantly depends on the sensor's sensitivity to small variations of the thigh motion in a static posture and is typically independent of the user. The peaks (p_i) and valleys (v_i) are identified by instances where a change in the sign of slope, i.e., $\dot{\omega}_t$, occur. As shown in Fig. 4, the following phases are detected in a sequence.

- Phase 1 $[\epsilon_t < \omega_t < \omega_t(p_1)]$: As the wearer squats without load, the angular velocity increases and reaches a local maximum.
- Phase 2 $[\omega_t(p_1) < \omega_t < \epsilon_t]$: As the wearer continues squatting without load and rests near the ground, the angular velocity decreases from a local maximum to zero.
- Phase 3 $[-\epsilon_t > \omega_t > \omega_t(v_1)]$: As the wearer picks up the load and starts lifting, the angular velocity decreases from zero to a local minimum.
- Phase 4 $[\omega_t(v_1) > \omega_t > -\epsilon_t]$: As the wearer continues moving and stands with the load, the angular velocity increases from a local minimum to zero.

The wearer would squat, leave the load, and stand up to complete one cycle. Hence, the detection of Phases 5-8 is similar to that of Phases 1-4 mentioned above.

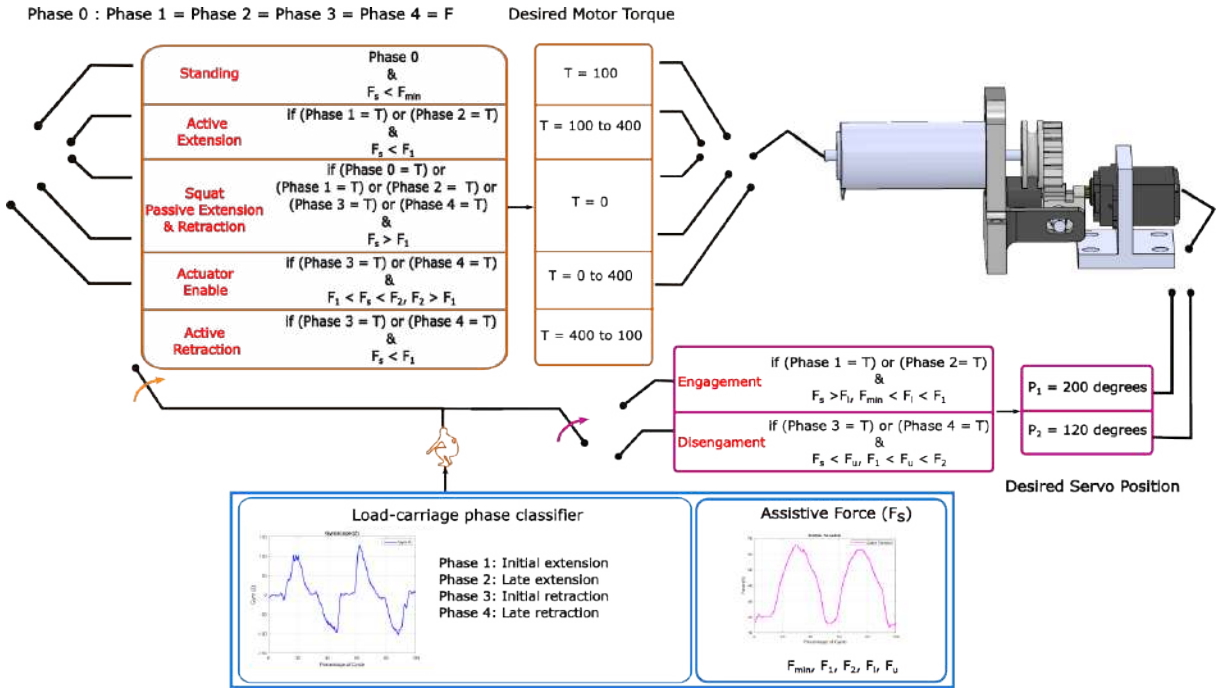


Fig. 3. Schematic of the control inputs to the actuators based on the phases of load-carriage task and the assistive force.

C. Control Architecture of Hybrid Exoskeleton

The phases identified from the signature of ω_t in Section III-B and the values of assistive force F_s, the engagement, and release of the locking unit and operation of the actuator unit are performed using the algorithms shown in Fig. 3. As shown in Fig. 2(d), a typical load carriage task would undergo the following phases twice in a cycle.

- Standing: A wearer is ideal in an upright posture.
- Phase of Active Extension: As the wearer starts to squat, the actuator starts applying the torque in a controlled manner to reach the desired assistive force.
- Phase of Engagement: As the assistive force increases beyond a specified threshold, the servo motor engages the pawl, and the actuator shuts off.
- Phase of Passive Extension: As the wearer continues squatting, the stiffness band expands with the assistive forces supported by the load-bearing element.
- Squat: A wearer halts in the squatting posture.
- Phase of Passive Retraction: As the wearer moves up, the stiffness band restores and the load-bearing element continues to support the assistive force.
- Actuator Enable: As the assistive force reduces beyond a threshold, the actuator is enabled to be ready with the necessary supporting torque.
- Phase of Disengagement: Once the actuator is enabled, the servo motor disengages the pawl, and the actuator supports the assistive force to prevent the slackness before reaching the upright posture.
- Phase of Active Retraction: As the wearer moves up, the actuator gradually reduces the assistive force to a minimum value.

In this work, the high-level control involves determining the desired motor torques and servo positions based on the inputs from IMU and load cell. The low-level torque control is governed by a PI controller of the motion manager using the feedback of motor input current and the servo positions through pulse width modulation. A typical variation of the desired control inputs during a load-carriage cycle is shown in Fig. 4.

IV. Results and Discussions

The developed exoskeleton was tested in two modes: passive and active. The details of the pilot studies with one male participant (31 years, 167 cm height, and 73 Kg weight) and their outcomes are presented below. The participant was informed about the experiment and signed a written consent approved by the Institute Ethics Committee of the Indian Institute of Technology Gandhinagar (Identifier number: IITGN/IEC/2023-24/71).

1) Passive: The purpose of this study is to demonstrate that the proposed locking unit is effective, i.e., it is capable of supporting the assistive force. For this purpose, first, the actuator achieves an assistive force of 20 N. Subsequently, the pawl is engaged, and the actuator is disabled. The pawl is kept engaged when the wearer performs the load-carriage task with a 10 kg payload.

The variation of the assistive force F_s and the actuator torque T are depicted in Fig. 5. It can be seen that the assistive force is non-zero, and its variation is similar to that of the passive exoskeleton in Fig. 1(b), indicating no slippage during the task. Also, with effective locking, the actuator does not draw current to support the assistive force.

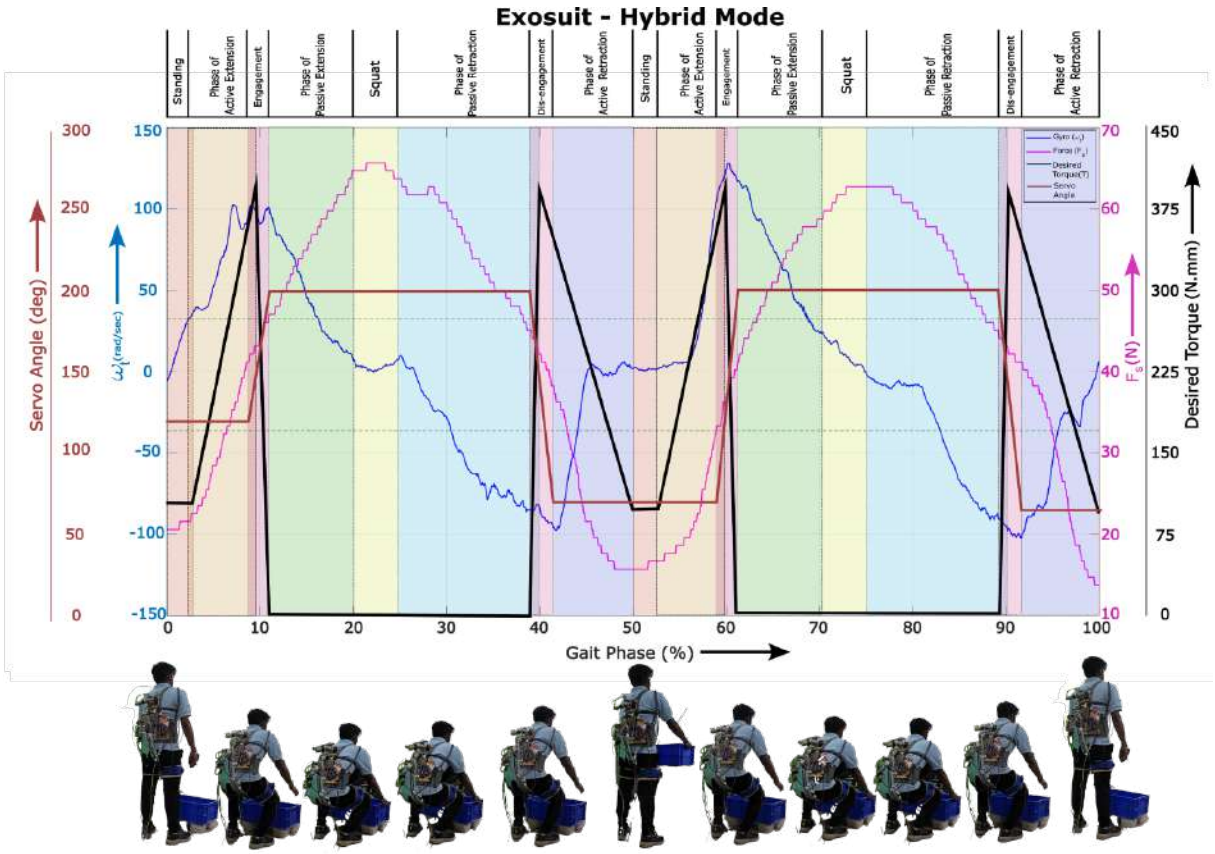


Fig. 4. A depiction of desired actuation torques and servo positions for typical variations of the thigh's angular velocity and assistive force during a load-carriage cycle.

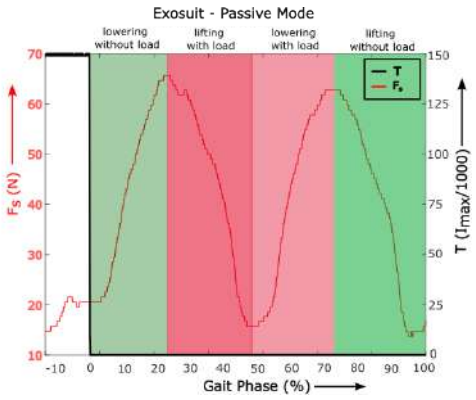


Fig. 5. Changes in the assistive force during a load-carriage gait cycle when the pawl is engaged with the ratchet and the load-bearing element.

2) Active: The typical torque requirements of an actuator to support the assistive forces in a gait cycle were investigated in this study. For this purpose, the actuator's shaft was ensured to be stationary using position control. Subsequently, the wearer was asked to perform the load-carriage task with a 10 kg payload.

As depicted in Fig. 6, the measured actuator torque varies in proportion to the assistive load. For an initial pretension of 20 N, the peak torque requirement is 80% of the rated torque, i.e., 0.65 N-m. Such loads on the actuator could be avoided with the proposed hybrid actuation strategy. Further, the zero crossings of ω_t match with the local minimum and maximum values of the assistive loads, indicating that the standing and stooping postures are identified correctly.

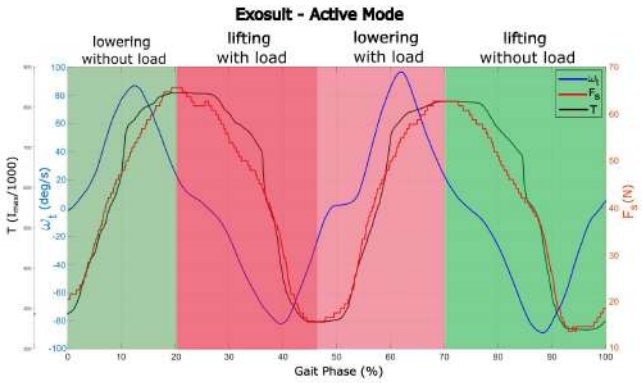


Fig. 6. Changes in the torque requirement, assistive force, and angular velocity for the load-carriage cycle when the actuator acts as a stationary anchoring point.

In essence, this work features a simple and effective classifier to detect different phases of the load-carriage task

as opposed to the ones in the past [13], [14], often requiring multiple sensors and learning-based classifiers. The proposed classifier is tested for squat lifting tasks and may not work for the cases of stooping involving minimal thigh movement. In such cases, the input to the classifier could be changed to signatures of cable tension from the load cell or angular velocity from an additional sensor placed on the trunk.

Although increasing the force F_s would increase the assistive moment at the lumbosacral joint, it would also amplify the device-to-body forces [12]. It is unwarranted to subject the participant to such forces when assistance is not required, e.g., the pretension during standing in the passive designs. Therefore, the proposed hybrid design avoids such scenarios by gradually increasing the assistive forces only when the participant starts lowering, i.e., the phase of active extension. Further, the electrical energy consumption of the actuator is kept minimal by transferring the load to the load-bearing element once the desired pretension is achieved.

Hence, the proposed hybrid design improves the user's comfort by reducing unnecessary device-to-body forces while providing the required assistance in an energy-efficient manner when compared to the active and passive paradigms [6]. These improvements were realized by the appropriate design of the actuation unit and the introduction of the locking unit. In the current work, only a qualitative and limited quantitative assessment were performed. A full-scale study with multiple participants are to be performed to establish the robustness of these units.

V. Conclusions

The feasibility of using a hybrid actuation paradigm in back-assist exoskeleton for symmetric loading conditions in squatting load-carriage tasks is investigated. An existing passive exoskeleton, BASE, is considered for improvement in this study. In order to improve user comfort, an actuation unit was developed to avoid unnecessary device-to-body forces at the shoulder and modulate the provided assistance to match the task severity. A locking unit was introduced to conserve the energy expended by the actuator and exploit the advantage of passive transparency. Further, a load-carriage phase detection algorithm is developed to provide appropriate control signals to the actuation and locking unit. In the present work, different components of the proposed actuation paradigm are examined. In the near future, experiments, including longitudinal studies, are yet to be conducted to comment on the efficacy of the proposed actuation paradigm.

ACKNOWLEDGMENT

This work was partially supported by the Life Science Research Board under project number LSRB/01/15001/LSRB-399/LS&BD/2023.

References

[1] Kristen Iker and Sara E. Luckhaupt. Low back pain among workers: The problem and what to do about it, 2019.

[2] Gautam M. Shetty, Shikha Jain, Harshad Thakur, and Kriti Khanna. Prevalence of low back pain in india: A systematic review and meta-analysis. *Work*, 73:429–452, 2022.

[3] Pieter Coenen, Vincent Gouttebarge, Aafje S A M van der Burght, Jaap H van Dieën, Monique H W Frings-Dresen, Allard J van der Beek, and Alex Burdorf. The effect of lifting during work on low back pain: A health impact assessment based on a meta-analysis. *Occupational and Environmental Medicine*, 71:871–877, 2014.

[4] Thomas R. Waters, Vern Putz-Anderson, and Arun Garg. *Applications manual for the revised NIOSH lifting equation*. Number (NIOSH) 94-110 (Revised 9/2021) in DHHS publication. 2021.

[5] Robin Burgess-Limerick. Squat, stoop, or something in between? *International Journal of Industrial Ergonomics*, 31:143–148, 2003.

[6] Mohamed I. Mohamed Refai, Alejandro Moya-Esteban, Lynn van Zijl, Herman van der Kooij, and Massimo Sartori. Benchmarking commercially available soft and rigid passive back exoskeletons for an industrial workplace. *Wearable Technologies*, 5:e6, 2024.

[7] Stefano Toxiri, Matthias B. Näf, Maria Lazzaroni, Jorge Fernández, Matteo Sposito, Tommaso Poliero, Luigi Monica, Sara Anastasi, Darwin G. Caldwell, and Jesús Ortiz. Back-support exoskeletons for occupational use: An overview of technological advances and trends. *IISE Transactions on Occupational Ergonomics and Human Factors*, 7:237–249, 2019.

[8] Erik P. Lamers, Aaron J. Yang, and Karl E. Zelik. Feasibility of a biomechanically-assistive garment to reduce low back loading during leaning and lifting. *IEEE Transactions on Biomedical Engineering*, 65:1674–1680, 2018.

[9] Stefano Toxiri, Andrea Calanca, Jesús Ortiz, Paolo Fiorini, and Darwin G. Caldwell. A parallel-elastic actuator for a torque-controlled back-support exoskeleton. *IEEE Robotics and Automation Letters*, 3:492–499, 2018.

[10] Simona Crea, Philipp Beckerle, Michiel De Looze, Kevin De Pauw, Lorenzo Grazi, Tjaša Kermavnar, Jawad Masood, Leonard W. O'Sullivan, Ilaria Pacifico, Carlos Rodriguez-Guerrero, Nicola Vitiello, Danijela Ristić-Durrant, and Jan Veneman. Occupational exoskeletons: A roadmap toward large-scale adoption. methodology and challenges of bringing exoskeletons to workplaces. *Wearable Technologies*, 2:e11, 2021.

[11] Siddharth Bhardwaj, Akshayraj B. Shinde, Randheer Singh, and Vineet Vashista. Passive exosuit emulator for material handling applications. *IEEE Robotics and Automation Letters*, 7:7605–7611, 2022.

[12] Siddharth Bhardwaj, Akshayraj B. Shinde, Randheer Singh, and Vineet Vashista. Manipulating device-to-body forces in passive exosuit: An experimental investigation on the effect of moment arm orientation using passive back-assist exosuit emulator. *Wearable Technologies*, 4:e17, 2023.

[13] Steven D. Hlucny and Domen Novak. Characterizing human box-lifting behavior using wearable inertial motion sensors. *Sensors*, 20(8):2323, 2020.

[14] Mattia Pesenti, Giovanni Invernizzi, Julie Mazzella, Marco Bocciolone, Alessandra Pedrocchi, and Marta Gandolla. Imu-based human activity recognition and payload classification for low-back exoskeletons. *Scientific Reports*, 13:1184, 1 2023.

[15] Gijoon Song, Junyoung Moon, Jehyeok Kim, and Giuk Lee. Development of quasi-passive back-support exoskeleton with compact variable gravity compensation module and bio-inspired hip joint mechanism. *Biomimetics*, 9(3), 2024.

[16] Mathias Blandeau, Romain Guichard, Rémy Hubaut, and Sébastien Leteneur. IMU positioning affects range of motion measurement during squat motion analysis. *Journal of Biomechanics*, 153:111598, 2023.

Development of a Soft, Spring-like Finger Tendon Exo-Glove Design with a Four-Output Cable-Driven Linear Servomechanism

Lauren Gan[1], Oscar Vazquez[1], Nicholas Dalton[3], Zhuwei Qin[2], Xiaorong Zhang[2], and David Quintero[1]

***Abstract*—Powered hand exoskeletons offer a viable solution to improve the quality of life for individuals experiencing hand paralysis caused by cardiovascular diseases (e.g., stroke). While hand rehabilitation exoskeleton gloves aid in regaining hand functionality, enabling users to perform a variety of active daily living tasks for independent living remains challenging. This paper presents the Rehabilitative Tendon Actuated Control Hand Exo-Glove, a lightweight, soft exo-glove that uses spring-like finger tendons driven by four actuated rack and pinion transmission for finger flexion and extension. Force validation experiments measured fingertip forces during actuation, with average values of 4.95 N (thumb), 4.66 N (index), 6.61 N (middle), and 3.89 N (ring). The exo-glove achieves a maximum hand grasping force of 21 N, an open/close grasping time of 1.2 seconds, and successfully handles objects up to 450 g. These performance metrics meet healthy hand grasping criteria while offering a lighter and more affordable solution compared to other exo-gloves with large, complex set of actuator design components.**

I. INTRODUCTION

Millions of Americans experience mobility impairment, particularly in the hand or arm, from musculoskeletal disorders to cardiovascular diseases such as stroke [1]. Hand impairment weakens finger muscle movements and disrupts biomechanical coupling, limiting hand grasping capabilities [2]. Effective hand rehabilitation requires consistent and repetitive therapy, which has been shown to improve hand function and strength [3]. A Powered hand exoskeleton (e.g., exo-glove) is a rehabilitation device designed to assist with hand grasping using motorized actuators to control finger flexion and extension, combined with sensors for intelligent control. In general, exo-gloves implement force or position control schemes, using sensors such as electromyography [4], electroencephalogram [5], or force myography [6] to detect user grasping intent. However, exo-gloves face significant challenges due to their reliance on wearable sensors. Sensor placement, calibration, and signal interference can compromise accuracy and responsiveness, especially in dynamic, real-world environments.

School of Engineering in Mechanical Engineering[1] and Computer Engineering[2] at San Francisco State University, San Francisco, CA 94132. Department of Mechanical Engineering[3], University of California, Berkeley, CA 94720.

This work was supported by the California State University's Program for Education and Research in Biotechnology (CSUPERB) New Investigator Award and Dr. Kenneth Fong Translational Research Award. The content is solely the responsibility of the authors and does not necessarily represent the official views of the funding source. Corresponding authors e-mail: {laurenmgan},{ovazquez1},{qdavid}@sfsu.edu.

In recent years, soft robotic approaches in exo-glove designs have significantly reduced device weight and improved user conformity compared to rigid, heavier mechanisms that are overly constrained [7]. Manufactured from complaint and flexible materials, soft exo-gloves adapt comfortably to the hand's musculoskeletal structure, making them practical for daily use. Soft exo-gloves typically use one of two actuation methods for hand manipulation. The first relies on pneumatic or hydraulic systems, where fluidic chambers with ridges expand from air or hydraulic pressure to control finger movement [8]. The second approach uses tendon or cable-driven actuation, routing cables through soft material straps and Teflon tubing to reduce friction during force transmission [9], [10]. Typically, Bowden cables are commonly employed for a push-pull linear motion along the fingers to adjust joint displacement. A notable contribution in cable-driven, soft exo-glove designs is the Exo-Glove Poly (EGP) II in [11], a polymer-based design with cable routing along both the dorsal and palmar side of the hand. The EGP II only supports three-finger actuation for the thumb, index, and middle finger in grasping objects. Although limited to three digits, the EGP II and similar designs highlight the potential of cable-driven soft exo-gloves in rehabilitation, suggesting that further investigation in different design alternatives can improve hand grasping and enhance user dexterity.

This paper presents the Rehabilitative Tendon Actuated Control Hand (REACH) Exo-Glove, a novel polymer-based, tendon-driven exo-glove designed to improve hand conformity and multi-finger functionality. Conventional cable-driven, soft exo-gloves often experience structural deformation from forces exerted by the actuator transmission [12]. The REACH Exo-Glove addresses this issue using a cable-driven linear servo actuation system that delivers strong holding force and independent finger actuation for various grasping tasks. The design introduces two key innovations. First, the exo-glove features a flexible crisscross membrane, manufactured from thermoplastic polyurethane (TPU) material, which conforms to the finger with a low profile and functions similarly to a scissor-lift mechanism, allowing efficient elongation. Second, the exo-glove incorporates a lightweight servomechanism with a custom-built four rack and pinion linear drive system, fabricated through additive manufacturing. This replaces heavier, off-the-shelf direct drive linear actuators. Theoretical kinematics and force analyses confirmed that the REACH Exo-Glove

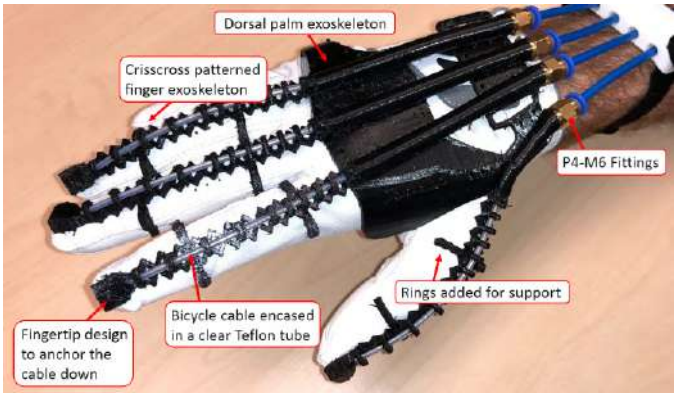


Fig. 1. REACH Exo-Glove design features a crisscross pattern, flexible cable routing structure from additive manufacturing malleable material, to enhance finger flexion. Ring anchors along the middle and proximal phalanges support the routing, ensuring efficient tendon movement.

achieves the required cable travel for producing hand flexion and extension while generating sufficient fingertip forces for grasping objects. Experimental measurements validated these findings by comparing the exo-glove's range of motion and fingertip forces to the desired specifications. A preliminary user study further evaluated the exo-glove's performance, assessing its ability to perform multi-finger grasping tasks with objects of various shapes and sizes.

II. REACH EXO-GLOVE DESIGN AND FINGER FORCE MODELING

A. Design Overview

Assistive exo-gloves must enable users to pinch and grasp objects of various shapes and sizes, while remaining comfortable, easily movable, and capable of generating sufficient force for flexion and extension. The design goals for this exo-glove include cable-driven flexion and extension actuation, full hand open/close grasping in under 4 seconds, and ability to manipulate objects of varying weights and diameters [13]. For activities daily living (ADLs) and hand rehabilitation, each finger should produce a target force of up to 5 N [14]. Full hand grasping force between 10-15 N is satisfactory for essential ADLs [15], though some existing exo-gloves exceed these values [16], [17]. Based on these benchmarks, the REACH Exo-Glove was designed to deliver approximately 5 N per finger, achieving a combined grasping force of over 20 N.

The REACH Exo-Glove actuates finger flexion and extension to enhance hand movement performance. To ensure proper alignment and user comfort, the exoskeleton body is sewn onto a lightweight spandex golf glove with breathable mesh (FINGER TEN Men's Golf Glove). The tendon-drive system positions actuators remotely, reducing the on-hand weight and improving wearability. This design prioritizes both rehabilitation and assistive applications, while maintaining user comfort. Additive manufacturing techniques (i.e., 3D printing) was employed to accelerate production, allow easily modified design components for different users adjustments,

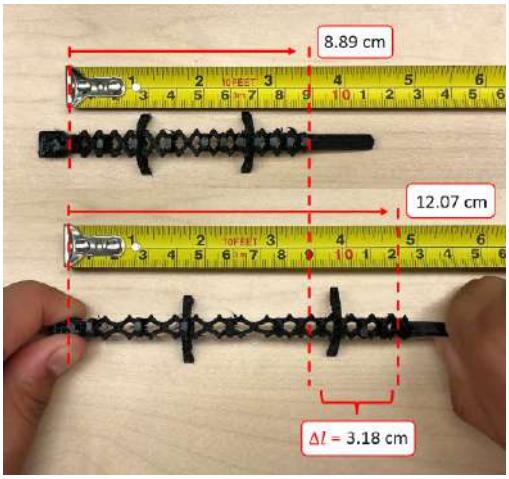


Fig. 2. The crisscross design along the finger body mimics a scissor mechanism, enabling spring-like actuation with up to 35% elongation, achieving 3.18 cm of extension during flexion.

and reduce the weight of the system. This was utilized for the finger tendon design (Fig. 1) and the custom rack and pinion gear train design (Fig. 3).

B. Elastic Finger Body and Cable Actuation Design

In Fig. 1, the exterior finger body design features a crisscross pattern at the base to enable vertical extension and compression. This structure is made from TPU material (85A NinjaFlex), which reduces costs while maintaining favorable properties for flexion and extension. This novel tendon design incorporates complaint, spring-like flexibility, as demonstrated in Fig. 2, allowing the structure to retract toward its equilibrium distance. Further, the semi-circular rings positioned on the middle and proximal phalanx provide additional support, ensuring the cable remains in a designated linear path for proper actuation parallel to the fingers. Loops extend from the crisscross base to guide the cabling. To minimize friction, a thin Teflon tube (4 mm outer diameter, 2 mm inner diameter) is placed along the finger body, trimmed to length, and slid over a 1.5 mm diameter Bowden cable. The Bowden cable provides the necessary strength and stiffness for push-pull actuation from the linear servomechanism. The cable is then threaded through the loops and anchored at each fingertip by crimping an end cap, which is securely sewn to the box-like fingertip structure and the glove. As the cable transitions from the sheath and routed through the dorsal palm exoskeleton (see Fig. 1), the cable is held in place using a crimp, that is then mounted to the connectors (PC4-M6 straight fittings) onto the servobox. The dorsal palm body mounting structure is made from TPU material and designed to naturally conform as a contour fit to the hand. This brace design is fabricated separately from the finger actuators, but integrates into the exoskeleton through sewn connections. Holes (1.5 mm in diameter) are distributed throughout the exoskeleton to facilitate this assembly.

C. Gear Transmission and Servobox

The finger flexion and extension entailed a back-drivable push-pull effect of the singular cable by way of linear motion. To provide the linear travel for the cable-driven mechanism, a rack and pinion actuator servobox was designed using polylactic acid polymer (PLA) material. The weight for the servobox is 704±2g, which includes four sets of a two-stage 2:1 gear train system, one gear transmission for each servo motor to actuate the thumb, index, middle, and ring finger independently. The little finger is not independently actuated, i.e. there is no servo motor designated for this finger. This is reasonable to exclude a dedicated actuator system for the little finger as for the human hand muscular structure [18], the ring and little share intertwined tendons. As observed during the execution of most grasping tasks, the little finger is excluded from having independent motion. For the motor selection, we opted for a higher torque servo motor (FT6335M, 360°, 35 kg/cm rated torque, 7.4V), which is 55 x 20 x 43 mm (L x W x H) and weighs 67±1g. Each independent actuated finger has its servo motor connected to the rack and pinion. The gear train comprises a spur, pinion, and linear rack, with motion transmitted from the servo motor pinion gear (see Fig. 3).

The gears used in this system are spur gears with full-depth involute-shaped teeth. The following values were chosen based on tooth system: 20° pressure angle and 1.5 mm module. Gear pitch diameters were kept below a size of 50 mm to ensure the overall size of the servomechanism would remain small for a compact servobox. Gear 3 is the pinion gear which makes it the largest gear in the system to ensure the linear travel of the rack is enough for flexion. Once the number of teeth and pitch diameters for spur gears have been selected and checked with consistent pitch circle values, gear ratios, and interference, force analysis is carried out.

The free-body diagram illustrating the gear train and the forces acting on each gear is depicted in Fig. 4. Numbering for gears begin at 1 while the shafts are denoted with the alphabet, starting with a, while F and T correspond to force and torque. Subscripts indicate the force or torque of one object against another, e.g. F_{a1} is the force of shaft a against gear 1 (spur pinion). Superscripts indicate whether the force is in the tangential or radial direction [19]. As the force we are concerned with is the force of the rack, the output force will be the value of F_{34}, as it is the pinion force transmitted to the rack. Recall, all diagonal forces must be resolved into tangential and radial forces, as seen with F_{32}, where the angle is equivalent to the pressure angle, ϕ. The rack gear is made to be as long as necessary; the length of the rack is simply dependent on the circumference of the pinion gear, therefore it is found through the simple equation $2\pi r$ and then multiplied by the control angle ratio to 360°, representing one full revolution, to get the linear travel.

The force exerted by the rack comes out to be:

$$F^t{}_{34} = \frac{2T_{b3}}{d_3} \tag{1}$$

where $F^t{}_{34}$ is the tangential force of the rack (gear 4) as it transmits the force acting on the pinion (gear 3), T_{b3} is the torque of shaft b against the pinion, and d_3 is the pinion's pitch diameter. This comes from the transmitted load equation, where the transmitted load W_t is set equal to the tangential force F^t. The tangential force is the important to recognize here as using the radial component would not be accurate because it transmits no power; thus $F^t{}_{34} = F_{34}$. F^t can be plugged into the equation for torque and W_t, where $T = (d/2)W_t$. As for working out the free-body diagram, the torques and forces acting upon the gears were calculated through first working out gear 1. Since gear 1 is the input from the motor, the gear will share torque and RPM values based on the motor used. Also, gears 2 and 3 share the same shaft, so T_{3b} is equivalent to T_{b4} where T_{3b} is solved using the equations for transmitted load and torque. After assigning measurements to the respective gears and referencing equations modeling gear force relations, F_{34} is estimated to be 9.23 N.

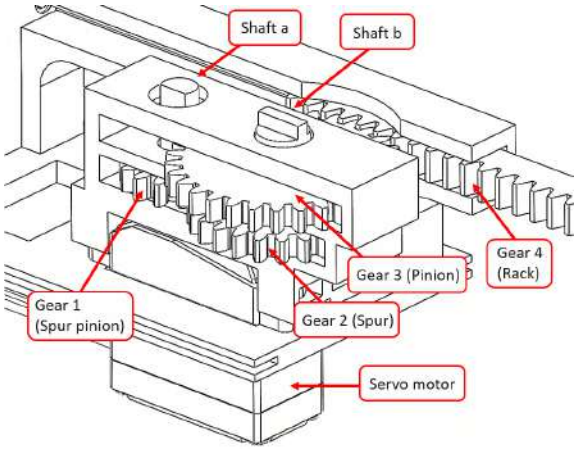


Fig. 3. Rack and pinion gear train attached to servo motor to translate rotary motion to linear motion to actuate the Bowden cables for flexion and extension.

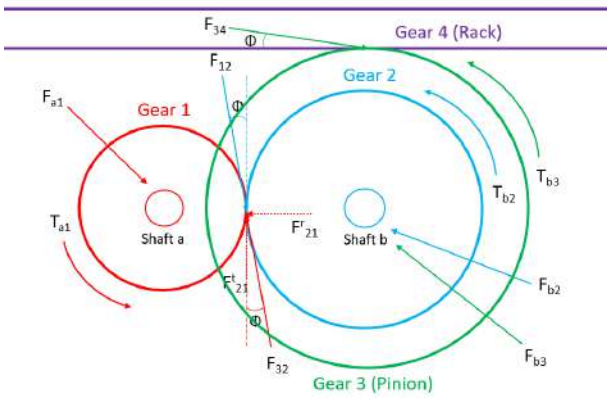


Fig. 4. Diagram of gear force resolutions per gear. Gear 1 (spur pinion) drives gear 2 (spur), where gear 2 and gear 3 (pinion) share the same shaft, and gear 4 (rack) shares the same force output as gear 3.

D. Force Estimation Using Kinematics

Kinematic calculations to estimate force were carried out a total of four times, one per actuated finger. The process of obtaining the force and torque at the fingertips is outlined as follows. The input torque at the servo spline is given by the relationship $T = k_t i(t)$, where k_t is the motor torque constant, and $i(t)$ represents the load current with respect to time as measured by the current sensors. There are four INA219 DC current sensors being used, one for each servo motor, to continuously monitor load current. This measured current is directly related to the torque generated by the servo motor. To account for the interaction between the motor and the rack and pinion, the linear force exerted by the rack is derived from the torque and can be expressed as:

$$F_{\text{rack lin}} = \frac{k_t i(t) N}{r_s} \tag{2}$$

where N is the total gear ratio of the system and r_s is the radius of the servo spline.

The linear force $F_{\text{rack lin}}$ of the rack is equal to the input force applied to the actuation cable, which is routed to the finger tip. As the cable travels through a Teflon tube, friction between the cable and the tube becomes a factor, reducing the effective force transmitted to the joints. Therefore, the output force from the cable, $F_{\text{cable out}}$, is adjusted for the frictional losses and can be expressed as:

$$F_{\text{cable out}} = \frac{k_t\, i(t)\, N}{r_s} - \mu_{\text{PTFE}}\, m_c\, g \tag{3}$$

with μ_{PTFE} representing the coefficient of friction for Teflon tubes (0.05-0.1 range). m_c refers to the mass of the cable and g is the gravitational constant. (9.81 m/s^2).

Once the force has been adjusted for friction, it is transmitted through the cable to the fingertip. To estimate the force at the fingertip, we modeled the fingers as a 2-link rigid body for the thumb and a 3-link rigid body for the index, middle, and ring fingers. In this model, measured joint angles were incorporated to approximate the finger's trajectory as the cable force flexed the finger, ultimately transmitting force to the fingertip. The metacarpophalangeal (MCP), proximal interphalangeal (PIP), distal interphalangeal (DIP), and interphalangeal (IP) joints were measured while a subject wore the glove as it was actuated to its maximum closing position. Based on the adjusted output force and the finger joint configuration, the fingertip force was then computed. Using geometric forward kinematics, the force at the fingertip, F_{tip}, is represented as:

$$F_{\text{tip}} = F_{\text{cable out}} \qquad _i = 1^n \ \cos\theta_i \tag{4}$$

where θ_i is the angle at a specific joint i, and k corresponds to the number of joints involved in finger flexion. As the cable moves the finger joints, the force is transferred sequentially through the joints, decreasing slightly based on the cosine of the angle θ_i at each joint. These angle reductions reflect the mechanical advantage (or disadvantage) of each joint as the finger moves through its range of motion.

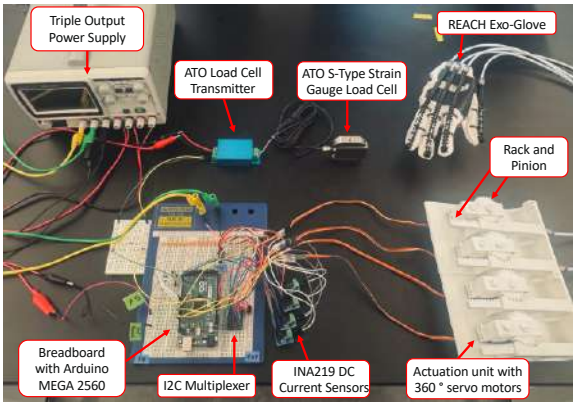


Fig. 5. Overall testing setup, where currently the prototype is actuated using a benchtop servobox connected to the microcontroller.

By summing the forces applied at each joint, we can approximate the force exerted by the finger. This iterative computation builds on the output force at each joint, which is influenced both by the cable's frictional losses and the joint angles, providing an estimate of the total force transmitted to the fingertip during actuation.

III. EXPERIMENTAL RESULTS AND DISCUSSION

A. Experimental Hardware Setup & Protocol

The derived kinematic equation was implemented in the system and validated through the experimentation that was approved by the Institutional Review Board (IRB) at San Francisco State University. Fig. 5 shows the experimental hardware setup of the power source supplying 7.4 V, 24 V, and 5 V to the high-torque servo motors, the INA219 current sensors, and the ATO load cell transmitter, respectively. The tests utilized an Arduino Mega 2560 microcontroller to control the servo motors and measure the sensor readings measurements. During bench-top testing, the actuators housed in the servobox are placed on a table beside the user as tasks are performed. For each test, three trials were carried out, with data recorded during three phases: (1) Rest - a single finger moved from a fully open rest position to a closed position by servo actuation, (2) Press - the finger maintained a fully closed position while pressing on a load cell for five seconds, and (3) Rest - the finger returned from the fully closed position, back to the open resting position. During testing, the subject placed a single finger over the load cell, keeping their wrist and palm flat on the table and fully relaxed for the entire process.

B. Fingertip Force Experiment Validation

The results shown in Fig. 6 compare the forces applied to the load cell by each finger to the predicted force for the thumb, index, middle, and ring fingers. The load cell measurements serve as the ground truth, capturing the actual compression forces, while the predicted forces are derived from a kinematic equation implemented in the control system. This comparison validates the accuracy and consistency of the force prediction algorithm. The load cell forces have smaller standard deviations across all fingers, indicating greater consistency in the

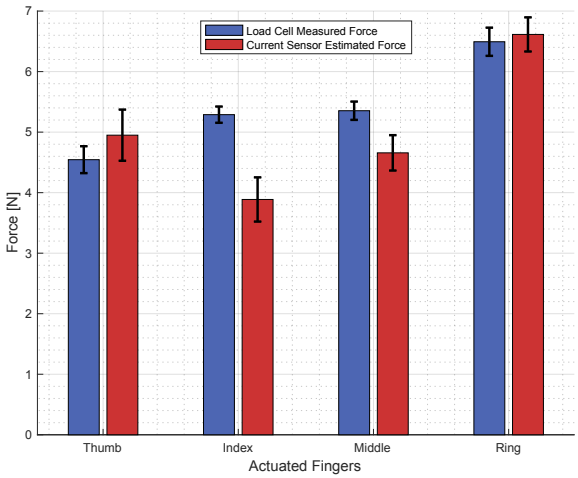


Fig. 6. Validation of Force Estimation Algorithm Using Measured Load Cell Forces as Ground Truth References Compared to Predicted Forces Across Individually Actuated Fingers for Five Trials Each .

measured data compared to the predicted forces. The thumb and ring fingers show the closest alignment between predicted and measured forces, with small absolute errors. Conversely, the index and middle fingers exhibit larger absolute errors, with predicted forces falling short the measured values. These results show the effectiveness of the prediction algorithm for certain fingers, as well as areas for further improvement.

Initially it was stated that a target of 5 N force per finger was desired. This goal was only achieved by the index, middle, and ring fingers, achieving measured forces of 5.29 N, 5.35 N, and 6.49 N, respectively. Overall, the ring finger produced the highest average force, while the thumb produced the lowest average force. The index and middle fingers exhibited similar average forces, indicating more consistent measurements. These results suggest that the load cell measurements provide reliable ground truth values for validation.

The ring finger maintained the highest average predicted force, aligning reasonably well with the measured force but showing a slightly higher standard deviation. Similarly, the thumb's predicted average force closely matches its measured value, but the standard deviation increases, indicating more variability in predictions. The index and middle fingers, however, show significant underestimations in predicted forces, with average values of 3.89 N and 4.66 N, respectively, and larger standard deviations of 0.37 N and 0.29 N. These predicted values fall short of the measured values for the index and middle fingers, which are 5.29 N and 5.35 N, respectively.

The observed discrepancies, particularly for the index and middle fingers, can be attributed to the cable routing and actuation mechanics. The cables routed over the fingers are fixed at the fingertips, creating a stiffer load for the servos to drive. However, this stiffness causes the index and middle fingers to twist as they flex forward during actuation. As a result, the fixed portion of the cable at the fingertips shifts, reducing the force pushing back against the servo motors. This reduction in force leads to a drop in the measured load



Fig. 7. The exo-glove grasped a variety of different sized objects and weights that include: a.) glue stick, b.) plastic ball, c.) hand sanitizer bottle, d.) plastic bottle, e.) aluminum bottle, and f.) spray bottle

TABLE I
AVERAGE FORCE APPLIED PER OBJECT

Object	Diameter (mm)	Weight (g)	Force (N)
Glue stick	20	16	9
Toy capsule	49	14	13
Hand sanitizer	51	119	18
Plastic bottle	64	408	19
Aluminum bottle	74	447	21
Spray bottle	35	119	–

current, which is directly used to estimate fingertip forces. Therefore the predicted forces for the index and middle fingers fall short of the actual measured forces from the load cell. This mechanical behavior highlights a key limitation in the current system design and explains the larger absolute errors observed for these fingers. Addressing variability across fingers. Could prob be written better. Also considering length, the index and middle fingers were more prone to cable stiffness as the cable is required to actuate along a longer distance. Traveling within the housing tube, greater friction force is present compared to the thumb.

Pinch and grasping tests were conducted to assess the forces applied to objects ranging from 20 to 74 mm in diameter and

weighing $\leq$ 450 g. For objects requiring a full-hand grasp, such as the hand sanitizer, plastic bottle, aluminum bottle, and spray bottle, the motors were actuated to the closed-hand position. The glue stick and toy capsule required a two-finger and three-finger pinch, respectively. Therefore, only the servo motors for those fingers were actuated to the closed-hand position. Because of this, the finger placement was dependent on the shape of the object being held. As it can be seen in Fig. 7, object f, the spray bottle, was unsuccessful. Despite providing sufficient force, the glove was not able to provide the required range of motion to grasp the spray bottle's neck. There was an approximate 10 mm gap between the glove and the bottle's surface, so it can be assumed that the minimum diameter an item must be for successful grasping is over 45 mm. Table I presents the diameter, weight, and average force per object.

IV. CONCLUSION

This paper introduces the REACH Exo-Glove, a proposed assistive exo-glove with four finger independent control. The fingers flex and extend by translating servo motors' rotary motion into linear travel in this tendon-drive approach. The glove implements a finger exoskeleton body designed for optimal flexion/extension and a servobox printed using PLA due to its low density. In efforts to advance the system proposed within this paper and upon conducting further research, the glove is planned to be integrated with additional sensors, such as to provide haptic feedback, or precise finger positions via inertial measurement unit sensors. Additional experiments on the glove's grasping will be conducted with a closed-loop control scheme and a variety of objects to determine the force required to grasp a variety of common household items. While the ergonomic design attempts to minimize strain, further redesigns will be carried out to simplify the glove's assembly process and improve user experience. The main priority of this project lies within making the glove more functional and available for future testing and research. The results obtained support the validity of using additive manufacturing for actuator design. Although the glove currently lacks a control interface and has yet to be integrated with all desired sensors, this four finger exo-glove provides a promising functional device that can allow for expansion in the biomedical engineering research field with the current lack of information about exo-gloves with this exact methodology approach.

REFERENCES

[1] "Disability impacts all of us infographic," May 2023. [Online]. Available: https://www.cdc.gov/ncbddd/disabilityandhealth/infographic-disability-impacts-all.html

[2] M. H. Schieber, C. Lang, K. Reilly, P. McNulty, and A. Sirigu, "Selective activation of human finger muscles after stroke or amputation," *Progress in motor control: a multidisciplinary perspective*, pp. 559–575, 2009.

[3] B. French, L. H. Thomas, J. Coupe, N. E. McMahon, L. Connell, J. Harrison, C. J. Sutton, S. Tishkovskaya, and C. L. Watkins, "Repetitive task training for improving functional ability after stroke," *Cochrane database of systematic reviews*, no. 11, 2016.

[4] N. Ho, K. Tong, X. Hu, K. Fung, X. Wei, W. Rong, and E. Susanto, "An emg-driven exoskeleton hand robotic training device on chronic stroke subjects: task training system for stroke rehabilitation," in *2011 IEEE international conference on rehabilitation robotics*. IEEE, 2011, pp. 1–5.

[5] L. Randazzo, I. Iturrate, S. Perdikis, and J. d. R. Millán, "mano: A wearable hand exoskeleton for activities of daily living and neurorehabilitation," *IEEE Robotics and Automation Letters*, vol. 3, no. 1, pp. 500–507, 2017.

[6] M. R. U. Islam and S. Bai, "Effective multi-mode grasping assistance control of a soft hand exoskeleton using force myography," *Frontiers in Robotics and AI*, vol. 7, p. 567491, 2020.

[7] H. In, B. B. Kang, M. Sin, and K.-J. Cho, "Exo-glove: A wearable robot for the hand with a soft tendon routing system," *IEEE Robotics & Automation Magazine*, vol. 22, no. 1, pp. 97–105, 2015.

[8] P. Polygerinos, S. Lyne, Z. Wang, L. F. Nicolini, B. Mosadegh, G. M. Whitesides, and C. J. Walsh, "Towards a soft pneumatic glove for hand rehabilitation," in *2013 IEEE/RSJ International Conference on Intelligent Robots and Systems*. IEEE, 2013, pp. 1512–1517.

[9] M. Delph, S. Fischer, P. Gauthier, C. Martinez-Luna, E. Clancy, and G. Fischer, "A soft robotic exomusculature glove with integrated semg sensing for hand rehabilitation," *IEEE ... International Conference on Rehabilitation Robotics : [proceedings]*, vol. 2013, pp. 1–7, 06 2013.

[10] L. Gerez, J. Chen, and M. Liarokapis, "On the development of adaptive, tendon-driven, wearable exo-gloves for grasping capabilities enhancement," *IEEE Robotics and Automation letters*, vol. 4, no. 2, pp. 422–429, 2019.

[11] B. B. Kang, H. Choi, H. Lee, and K.-J. Cho, "Exo-glove poly ii: A polymer-based soft wearable robot for the hand with a tendon-driven actuation system," *Soft Robotics*, vol. 6, no. 2, p. 214–227, Apr 2019.

[12] U. Jeong, i. In, H. Lee, B. B. Kang, and K.-J. Cho, "Investigation on the control strategy of soft wearable robotic hand with slack enabling tendon actuator," in *2015 IEEE International Conference on Robotics and Automation (ICRA)*, 2015, pp. 5004–5009.

[13] H. K. Yap, J. H. Lim, F. Nasrallah, and C.-H. Yeow, "Design and preliminary feasibility study of a soft robotic glove for hand function assistance in stroke survivors," *Frontiers in Neuroscience*, vol. 11, Oct. 2017. [Online]. Available: http://dx.doi.org/10.3389/fnins.2017.00547

[14] J.-M. Dávila-Vilchis, J. C. Ávila Vilchis, A. H. Vilchis-González, and LAZ-Avilés, "Design criteria of soft exogloves for hand rehabilitation-assistance tasks," *Applied Bionics and Biomechanics*, vol. 2020, p. 1–19, Aug. 2020. [Online]. Available: http://dx.doi.org/10.1155/2020/2724783

[15] K. Matheus and A. M. Dollar, "Benchmarking grasping and manipulation: Properties of the objects of daily living," in *2010 IEEE/RSJ International Conference on Intelligent Robots and Systems*. IEEE, Oct. 2010, p. 5020–5027. [Online]. Available: http://dx.doi.org/10.1109/IROS.2010.5649517

[16] B. B. Kang, H. Lee, H. In, U. Jeong, J. Chung, and K.-J. Cho, "Development of a polymer-based tendon-driven wearable robotic hand," in *2016 IEEE International Conference on Robotics and Automation (ICRA)*. IEEE, 2016, pp. 3750–3755.

[17] S. Cheon, D. Kim, S. Kim, B. Kang, J. Lee, H. Gong, S. Jo, K.-J. Cho, and J. Ahn, "Single emg sensor-driven robotic glove control for reliable augmentation of power grasping," *IEEE Transactions on Medical Robotics and Bionics*, vol. PP, pp. 1–1, 12 2020.

[18] S. Kilbreath and S. Gandevia, "Limited independent flexion of the thumb and fingers in human subjects." *The Journal of Physiology*, vol. 479, no. 3, pp. 487–497, 1994.

[19] R. G. Budynas and J. K. Nisbett, *Chapter 13 Gears - General*, 9th ed. McGraw-Hill, 2011, p. 674–709.

Variable Power Assistance Robotic Manipulation System for Upper Arm Rehabilitation

S. M. Mizanoor Rahman, *Member, IEEE*

***Abstract*—We present a 1DOF power assist robotic system that can be used by stroke patients for upper arm rehabilitation. An object can be tied with the power assist robotic system, and a human patient can lift the object vertically up and lower it down continuously. The power assist robotic system provides power assistance to the human in lifting and lowering the object. The amount of power assistance could be changed, which could change the haptically perceived heaviness of the object and vice versa. Therefore, the stroke patient could adjust the perceived heaviness of the object at different stages of rehabilitation progress considering the abilities of the patient to lift and lower the object with the assist system at different stages of rehabilitation. We developed a model to quantity power assistance levels and implemented a psychophysical method to compute power assistance for different perceived heaviness of the object. In an experiment, we evaluated the performance of the power assist robotic system based on a novel evaluation scheme using healthy subjects. The results showed that the subjects were able to realize the variations in the power assistance levels due to variations in the perceived heaviness of the object. The human-robot interaction (HRI) evaluation results showed satisfactory interactions between human subjects and the power assist system. The proposed device can be used by stroke patients for free motion upper arm rehabilitation, which can improve their quality of life (QoL).**

I. INTRODUCTION

Stroke patients are encouraged to receive training using rehabilitation devices, especially robotic devices to fully or partially recover the impacts of stroke [1]. The literature shows separate robotic devices for upper arm and lower arm rehabilitation [2]-[3]. For upper arm rehabilitation, it seems to be important that the robotic rehabilitation devices that provide power assistance to stroke patients may be more effective for rehabilitation training compared to the robotic rehabilitation devices that do not provide power assistance to the patients [4]. This is because the power assist devices can reduce burdens of the users/patients and augment their capabilities and performance [4]. Therefore, the use of power-assisted robotic rehabilitation devices, especially devices for upper arm rehabilitation received attention and priority [5]. However, most of the state-of-the-art power assist devices for upper arm rehabilitation are wearable, and the patients may need to bear the weight of the devices [6].

S. M. M. Rahman is with the Mechanical Engineering Program at The Pennsylvania State University, 120 Ridge View Drive, Dunmore, PA 18512, USA (e-mail: mrahman@psu.edu; Tel.: +1-570-963-2588).

We believe that a power assist robotic device that allows stroke patients to manipulate objects freely may be more advantageous and effective for robotics-based upper arm rehabilitation. However, the literature does not show such a free manipulation type power assisted robotic rehabilitation device for the upper arm.

We also believe that changes in power assistance levels through changes in the perceived haptic heaviness of the manipulated object may impact the rehabilitation process significantly [7]. For example, a patient may need more power assistance at the initial stage of rehabilitation training because the patient does not have enough strength to manipulate a heavy object. On the other hand, the patient can gain strength after receiving rehabilitation training and then he/she may be able to manipulate comparatively heavier objects, i.e., he/she may need less power assistance. Therefore, we believe that investigation on such a variable power assistance system that can adjust the power assistance levels with the rehabilitation progress of patients could be a new research direction. However, such initiatives are not so evident in the literature. We proposed such a power assist robotic system for object manipulation for industrial load handling purposes [8]. However, its prospects for upper arm stroke rehabilitation were not investigated.

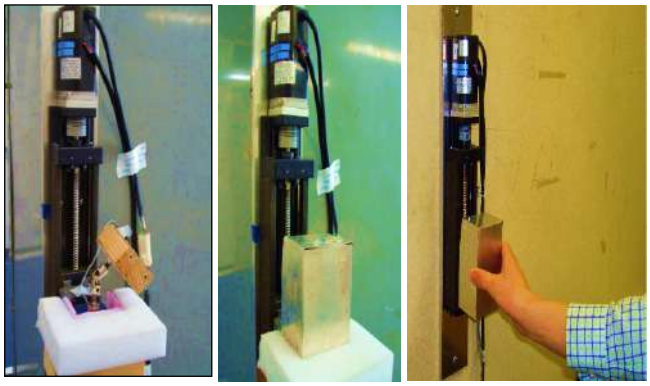
Therefore, in this paper, as a preliminary initiative, we proposed a simple 1DOF power assist robotic system that a stroke patient (here, healthy human subjects) could use to freely manipulate an object (lift an object up and lower it down) tied with the power assist system to receive power assistance at the time of rehabilitation training. We changed the power assistance levels and observed how the changes impacted the feelings and interactions of the patient (here, healthy human subjects) with the power assist system.

II. THE PROTOTYPE POWER ASSIST ROBOTIC SYSTEM

We developed a physical model of the power assist robotic system, as presented in Fig.1(a)-(c) [9]. This is a proof-of-concept prototype of the system. This is a 1DOF system that the patient could use to manipulate (lift and lower down) objects tied with the system for rehabilitation training. We used an AC servomotor with an encoder at its top, and attached it colinearly with a ball screw mechanism, and attached the entire system to a wall, as Fig.1 (a) shows. We used a load cell type force sensor to sense the force applied by the human/patient. We attached the force sensor to the ball nut of the ball screw system. Then, the force sensor was tied to one end of a universal joint. The other end of the universal joint was tied to a rectangular wooden

(resin) cube. This is shown in Fig.1(a). We then used an aluminum sheet (thickness: 0.0005m) to build a rectangular box with a cap by bending it. It was a small box with size 0.06 x 0.05 x 0.12m. Then, we placed the box through the wooden cube, which looked like as presented in Fig.1(b) [9].

Fig.1(c) shows how it looked like when a patient (a human subject) grasped the object and lifted it up and lowered it down with the system [9]. The ball screw output the linear motion of the object from the rotary input motion of the servomotor. The object (box) could be placed on a foam to protect it from possible vibration to be generated when the box would touch the bottom surface (Fig.1(b)). The self-weight of the object was negligible, which was 0.016 kg. The object was manipulated with the power assist system, and we named it 'power-assisted object (PAO)'. The power assist system was connected to a computer through interfaces. This was the configuration of the prototype power assist system used in the experiments, as follows.



(a) (b) (c)

Fig.1 Different steps of constructing the physical power assist robotic system model.

III. DYNAMICS AND CONTROL OF THE ASSIST SYSTEM

Based on the physical model shown in Fig.1(c), we derived a simple dynamics model for lifting and lowering an object with the power assist robotic system as presented in (1). In (1), f_a denotes the linear force applied by the actuator (servo motor), f_h denotes the linear force applied onto the object by the human user (the patient), F denotes the force that can be generated due to the friction in the mechanical drive (ball screw) system, m denotes the mass value of the object that we may use in the control system of the power assist system (virtual mass) for the object to be manipulated with the assist system, g denotes the gravitational acceleration, K denotes the viscosity of the mechanical drive or ball screw sliding mechanism, and x_d can be used to denote the desired linear displacement of the object manipulated with the power assist robotic system, which we call the 'desired displacement' [9].

$$m\ddot{x}_d + K\dot{x}_d + mg + F = f_h + f_a \tag{1}$$

We want that patients should manipulate objects with the power assist system freely. By free manipulation, we here mean that the hand of the user (patient) may not need to be tied with the object during manipulation of the object with the power assist robotic system. Therefore, considering the free motion dynamics [9], we can ignore the actuator or motor force (it exists, but human patient may not realize it), viscosity, friction and any other types of disturbances to keep the model in (1) simple. This assumption results in a new and simpler dynamics model of the power assist robotic system as presented in (2).

$$m\ddot{x}_d + mg = f_h \tag{2}$$

Our experience shows that the weight of an object visually perceived by a human differs from the weight of the same object perceived haptically by a human user if the object is manipulated with a power assist robotic system [9]. This happens because a power assist robotic system reduces the haptically perceived wight of an object [9]. A human user (patient) may not be able to realize this difference, and as a result the human may apply an incorrect force to the object to manipulate it with the power assist robotic system. The chance of such an error in human force programming is higher in the beginning of the use of the power assist robotic system by patients because the patients are not familiar with the exact behaviors of the system.

This erroneous force application can seriously impact the motion of the assist system, which may cause injuries and accidents to the patients [9]. As an attempt to mitigate this effect, a psychophysical hypothesis is adopted that the mass parameter used in the inertial force in (2) may be different from the mass parameter used in the gravitation force in (2), which results in a newer dynamics model as shown in (3). For (3), we use the assumptions that $m_1 \neq m_2 \neq m$, $m_1 \ll m, m_2 \ll m, m_1\ddot{x}_d \neq m_2 g$. We derived a simple admittance type feedback position control of the power assist robotic system for object manipulation by patients based on (3), as shown in Fig.2. This control is simple, but it is a novel control method in the sense that it reflects patient psychology in term of potential mismatch between the visual and haptic weight perceptions of the manipulated object [9].

$$m_1\ddot{x}_d + m_2 g = f_h \tag{3}$$

IV. MODEL TO COMPUTE POWER ASSISTANCE

We propose a computational model as in (4) to compute the power assistance amount for lifting and lowering an object with the developed power assist robotic system, shown in Fig.1. In (4), *PAA* stands for power assistance amount, and *PAW* stands for power assisted weight or haptically perceived heaviness of object manipulated with the power assist robotic system for an arbitrary value of m_2 [9]. As the model shows, it is expected that changes in m_2 mainly change the *PAA* because the changes in *PAW* also depend on m_2.

$$PAA = m_2 - PAW \tag{4}$$

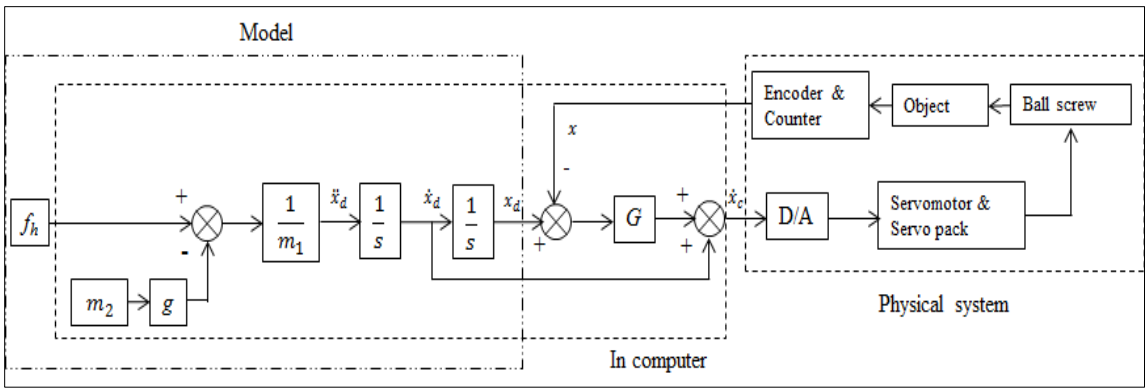


Fig.2 The admittance type feedback position control system for the power assist robotic system for object manipulation. Here, G denotes feedback gain, x is the actual displacement, x_d is the desired displacement, x_c is the commanded displacement, D/A is digital to analog converter [9].

V. EXPERIMENTS

A. Subjects

We recruited 24 human subjects (15 engineering graduate students, 9 engineering undergraduate students; 22 males, 2 females) to conduct the experiments. The ages of the subjects were from 21 years to 34 years with mean 24.39 years and standard deviations ± 4.63. The subjects received written instructions of the experimental procedures. The procedures were also verbally explained to each subject separately. We collected written consent from each student (subject) for their voluntary participation to the experiments. The study plan was approved by the ethical committee of the university. The subjects did not report major health problems. Therefore, the subjects were considered as healthy subjects.

B. Experiments Design

We conducted two independent experiments using the healthy subjects we recruited. In the first experiment (Experiment 1), we investigated whether the human subjects could feel the changes in power assistance provided by the power assist robotic system and the amount of strength the subjects needed to manipulate the object with the power assist system for each level of power assistance. In the second experiment (Experiment 2), we investigated human subjects' physical and cognitive interactions with the power assist robotic system for different levels of power assistance provided by the power assist robotic system. We believe that those investigations were very necessary for the power assist robotic system for its suitability as an upper arm free motion rehabilitation device for stroke patients. It was necessary to use actual stroke patients in clinical trials to evaluate the proposed rehabilitation device. However, unavailability of stroke patients motivated us to use healthy subjects to evaluate the proposed design in lieu of stroke patients. We believe that the results obtained through using healthy subjects would help prove the effectiveness of the proposed device in principle, which could tell about the prospect of the device for its potential use by actual stroke patients [1].

C. Experimental Procedures

For Experiment 1, we implemented the proposed admittance type feedback position control system (as presented in Fig.2) using MATLAB/Simulink. We selected the ode4 solver (Runge-Kutta; fixed-step) with the sample time (fundamental) as 0.001s. We see in the computational model in (4) that m_1 values have no influences on the power assistance provided by the system though m_1 values were observed to influence the system kinematics such as velocity and accelerations of the assist system [9]. Therefore, we used an arbitrary value m_1=0.50 in the control system in Fig.2 because such a value was observed producing the optimal kinematics of the assist system [10]. We see in (4) that m_2 values can influence the computed values of power assistance and we found in our previous research that m_2 values influenced haptically perceived weights and power assistances [10]. Therefore, we selected a combination of m_2 values heuristically (based on our experiences with the proposed assist system), which is presented in Table I.

Table I: The m_2 values selected to be used in the control system

m_2 values (kg)										
0.1	0.15	0.20	0.25	0.50	0.75	1.0	1.25	1.5	1.75	2.0

At the time of the experiment, we randomly selected a m_2 value from the set of values given in Table I and used the value to implement the control system shown in Fig.2. We then randomly selected a human subject. The human subject lifted the object tied with the power assist robotic system and lowered it down and again lifted it up and then released the object. Then, the subject lifted different reference weights (known weights) separately using the dominant hand and in this way compared the perceived haptic weight (heaviness) of the object manipulated with the power assist robotic system with that of the reference weights, and thus psychophysically estimated the perceived haptic weight of the object manipulated with the power assist robotic system [10]. This weight was named "power-assisted weight or *PAW*" of the object manipulated with the power assist system for that value of m_2. In this procedure, we conducted the experiment for each value of m_2 shown in Table I for

each of the 24 subjects separately. Each subject also subjectively rated how much hand strength he/she needed to manipulate the object with the power assist system for some selected values of m_2 such as 0.1kg (the lowest value), 1.0kg (the moderate value) and 2.0kg (the highest value) using a 7-point Likert scale, where 1 indicated the least amount of strength needed and 7 indicated the most amount of strength needed to manipulate the object [11]. We here believe that the lower the needed strength, the higher the assistance provided by the system.

For Experiment 2, we repeated Experiment 1 procedures as the above for all subjects. However, we used only 3 values of m_2 such as 0.1kg (the lowest value), 1.0kg (the moderate value) and 2.0kg (the highest value). At the end of the manipulation of the object with the power assist system, each subject responded to a set of questionnaires regarding assessing his/her interactions with the power assist system for object manipulation. We developed the questionnaires reflecting relevant human-robot interaction (HRI) criteria and each subject evaluated each of the HRI criteria using a 7-point Likert scale, 1 being the least favorable HRI and 7 being the most favorable HRI [12]-[13]. The physical HRI (pHRI) criteria [13] that we used were adaptability (how the human subjects were adapted his/her grasp configurations and grasp locations on the object) [14], coordination (how the human subjects maintained a balance between the forces they applied to the object for its manipulation and the resulted motion or kinematics of the manipulated object) [15], safety (how safe the human subjects felt when manipulating the object with the power assist system) [16], ease of use (how easy it was for the subjects to manipulate the object) [17], naturalness (how normal or natural the subjects felt when manipulating the object with the power assist system freely) [18], and intuitiveness (whether the human subjects were intuitive and enthusiastic in using the system for potential future manipulation of objects) [19].

We also used cognitive HRI (cHRI) criteria to assess the cognitive HRI of the human subjects [13]. Two cHRI criteria were the human subject's trust in the device for its intended application [20], and the subject's situation awareness at the time of object manipulation using the power assist system [21]. The subjects assessed those two criteria separately using the Likert scale [11], [13]. Another measure of cHRI was the cognitive workload of subjects for grasping and manipulating the object [22]. Each subject completed the NASA-TLX to report his/her cognitive workload [22]. All the subjects participated in Experiment 2 separately.

VI. EXPERIMENTAL RESULTS

A. Results of Experiment 1

We used the m_2 value and the mean of the corresponding *PAW* value to calculate *PAA* for each m_2 value using (4). The results are shown in Table II. The results in Table II show that the *PAW* values were almost 40% of the m_2 values [10]. This empirical relationship reveals that the power assist robotic system can reduce the haptically perceived heaviness of the manipulated object to approximately 40% of the true weight (m_2 value) of the object. The obtained results can be interpreted in such a way that the power assistance amount (*PAA*) is the amount of reduction of the true weight of the object due to the contribution (assistance) of the robotic system [9]. This can mean that more reduction in the weight haptically perceived by the user can result in more power assistance amount, and vice versa. Higher amount of power assistance should be the usual expectation of the users. The results thus prove that the human subjects can feel or realize the changes in the power assistance provided by the power assist robotic system through changes in the haptic weights.

Table II: Different m_2 values, the corresponding *PAW* values, and the computed *PAA* values

m_2 (kg)	*PAW (kg)*	*PAA (kg)*
0.10	0.04	0.06
0.15	0.06	0.09
0.20	0.08	0.12
0.25	0.10	0.15
0.50	0.20	0.3
0.75	0.30	0.45
1.0	0.40	0.6
1.25	0.50	0.75
1.50	0.60	0.90
1.75	0.70	1.05
2.0	0.80	1.2

Fig.3 shows that the human subjects needed to apply more hand strength (hand power) to manipulate the object with the power assist robotic system when the true weight (m_2 values) increased, and vice versa. The human users, especially stroke patients may not possess a high amount of hand strength at the early stages of rehabilitation. However, stroke patients can recover gradually and thus can apply more hand strength gradually and thus the stroke patients can manipulate heavier objects and obtain higher amount of power assistance gradually. Thus, this device can help stroke patients pursue a gradual rehabilitation process adjusting with the need of the power assistance amount of the system at different stages of rehabilitation progress [1].

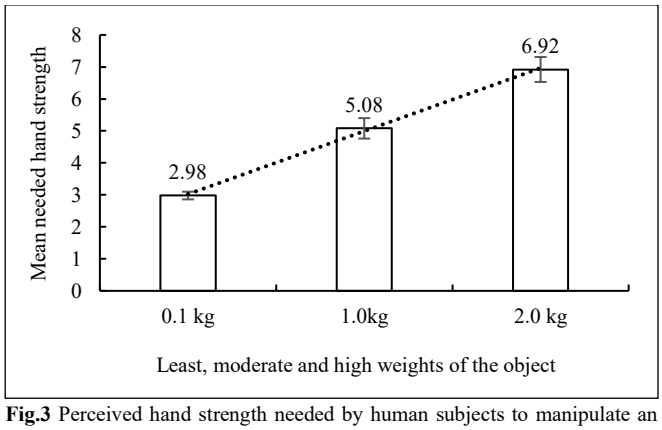


Fig.3 Perceived hand strength needed by human subjects to manipulate an object with the power assist system for different virtual weights of the object. Here, the less strength needed to manipulate the object is considered as the better.

B. Results of Experiment 2

We analyzed the displacement profile and the velocity profile for a trial for manipulating the object with the power

assist robotic system by a human subject for the m_2 value equal to 0.10kg, which showed that smooth displacement and velocity were generated when manipulating the object with the power assist robotic system. The smooth kinematics indicated that the power-assisted manipulation was safe for the users because unsafe manipulation could generate severe vibrations that could make the kinematics unsmooth or fluctuating [10].

Fig.4 shows the pHRI assessment results for different m_2 values (least, moderate and highest values) [13]. The results show that the pHRI effectiveness was the highest for the least m_2 value, and it decreased as the m_2 values increased. It happened probably due to the reason that the higher m_2 values increased the haptically perceived weights that reduced the pHRI. Therefore, an optimum m_2 value would need to be determined for optimal rehabilitation experience [10]. We conducted an analysis of variance (ANOVA) for the results presented in Fig.4, which showed that variations in the pHRI scores between the subjects were statistically nonsignificant (p = 4.82, p>0.05). However, variations in the pHRI scores between different m_2 values were statistically significant (p = 0.00039, p<0.05).

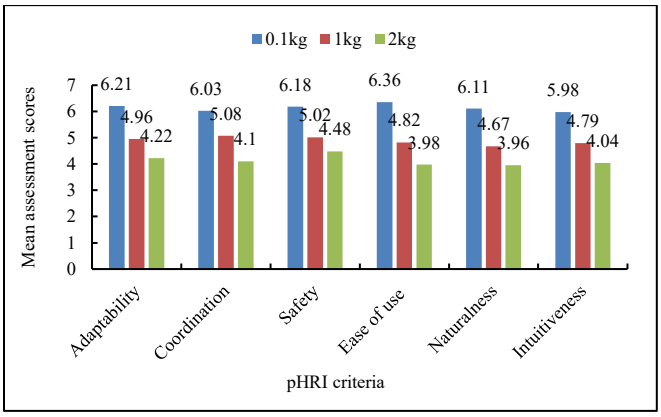


Fig.4 The pHRI assessment results for different m_2 values (kg).

Fig.5 shows the cHRI (trust, situation awareness) assessment results for different m_2 values (least, moderate and highest values). Like the pHRI results, the cHRI results also show that the cHRI effectiveness was the highest for the least m_2 value, and it decreased as the m_2 values increased. It happened probably due to the reason that the higher m_2 values increased the haptically perceived weights that reduced the cHRI effectiveness [13]. Especially, higher haptic weights for greater m_2 values might force the human subjects to concentrate more on adapting and coordinating with manipulation complexities caused by higher perceived weights and corresponding unfavorable kinematics of object manipulation [14]-[15], which might reduce human trust in the assist system as well as lower situation awareness [20]-[21]. It means that the humans needed to pay more attention to manipulating the object for higher haptic weights. As a result, humans were not able to be highly aware of the entire working environment. We conducted an analysis of variance (ANOVA) for the results presented in Fig. 5, which showed that the variations in cHRI scores between the subjects were statistically nonsignificant (p = 6.33, p>0.05). However, the variations in cHRI scores between different m_2 values were statistically significant (p = 0.00687, p<0.05) [13].

Fig.6 shows the cHRI (cognitive workload) assessment results for different m_2 values (least, moderate and highest values) [22]. The results show that the cognitive workload was the least for the least m_2 value, and the cognitive workload increased as m_2 values increased. Note that least cognitive workload is the best [22]. Those results might occur because the human subjects needed more efforts and physical and mental demands when the haptic weights increased, and the corresponding kinematics became more unfavorable when m_2 values increased. Human subjects had more pressure on maintaining time and performance for unfavorable kinematics due to higher m_2 values that caused frustration [23]. All those situations increased the cognitive workload for increased m_2 values [22]. We conducted an analysis of variance (ANOVA) for the results in Fig. 6, which showed that variations in cognitive workload scores between subjects were statistically nonsignificant (p =18.48, p>0.05). However, variations in cognitive workload scores between different m_2 values were statistically significant (p = 0.000824, p<0.05) [13], [24].

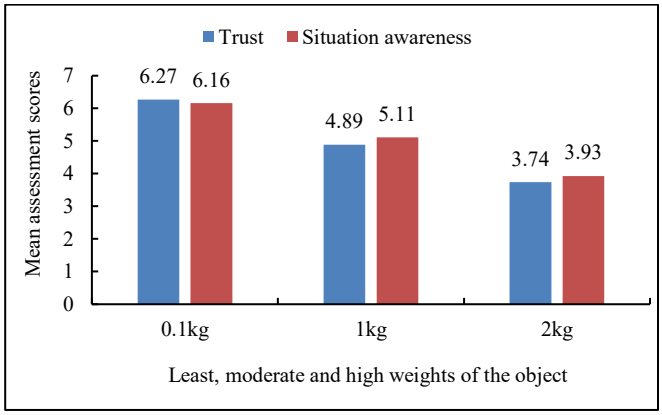


Fig.5 The cHRI (trust and situation awareness) assessment results for different m_2 values.

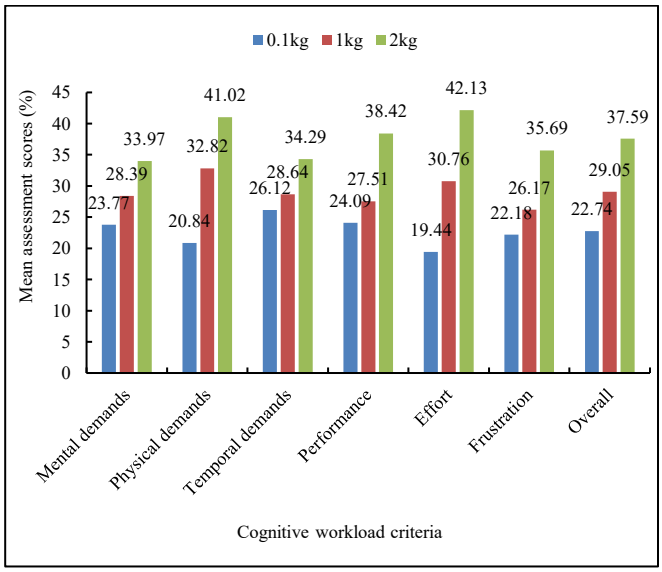


Fig.6 The cHRI (cognitive workload) assessment results for different m_2 values (kg).

VII. CONCLUSIONS AND FUTURE RESEARCH

We developed a 1DOF simple and small power assist robotic system so that stroke patients could manipulate an object tied with the power assist system freely, which could facilitate their free motion rehabilitation training by providing variable power assistance in object manipulation. We also applied a psychological cue (weight perception) to adjust the control of the system following psychophysical approaches to enhance safety and adaptability of the assist device for stroke patients. The evaluation results show that the device can provide variable power assistance at different conditions, which can help stroke patients adjust the power assistance amount with their hand strengths at different stages of rehabilitation progress. We also evaluated the effectiveness of interactions of healthy subjects with the device and the results show that the interactions were effective and satisfactory. Those results using healthy subjects indicate the possibility that similar results may be obtained if the device is used by stroke patients.

In the future, we will derive more advanced control methods that can further enhance safety and adaptability of the system for stroke patients. We will conduct a clinical study using stroke patients to verify and validate the results that we obtained herein using healthy human subjects.

ACKNOWLEDGMENT

The author conducted the experiments when the author was with Mie University, Tsu, Mie, Japan. The author expresses his thanks to Mie University for the support he received at that time for this research.

Research Ethics Statement:

The author followed necessary ethical principles while working with the human subjects for this research. Informed consent was received from the subjects.

REFERENCES

[1] M. Baysa, S. Lund and Y. -L. Han, "Exploring a novel rehabilitation soft robot design for stroke patients with clenched fists," *2024 10th International Conference on Mechatronics and Robotics Engineering (ICMRE)*, Milan, Italy, 2024, pp. 28-32.

[2] A. Scibilia, A. Prini, T. Dinon, N. Pedrocchi and M. Caimmi, "Over three decades of upper-limb robotic neurorehabilitation: drawing conclusions and future work," *2024 IEEE 20th International Conference on Automation Science and Engineering (CASE)*, Bari, Italy, 2024, pp. 1303-1310.

[3] E. R. S. Serafini *et al*., "Gait training-based motor imagery and EEG neurofeedback in Lokomat: A clinical intervention with complete spinal cord injury individuals," *IEEE Transactions on Neural Systems and Rehabilitation Engineering*, vol. 32, pp. 1896-1905, 2024.

[4] A. Umemura, Y. Saito and K. Fujisaki, "A study on power-assisted rehabilitation robot arms operated by patient with upper limb disabilities," *2009 IEEE International Conference on Rehabilitation Robotics*, Kyoto, Japan, 2009, pp. 451-456.

[5] J. Huang, W. Huo, W. Xu, S. Mohammed and Y. Amirat, "Control of upper-limb power-assist exoskeleton using a human-robot interface based on motion intention recognition," *IEEE Transactions on Automation Science and Engineering*, vol. 12, no. 4, pp. 1257-1270, Oct. 2015.

[6] Z. Tang, Z. Cui, H. Wang, P. Liu, X. Xu and K. Yang, "A 4-DOF exosuit using a hybrid EEG-based control approach for upper-limb rehabilitation," *IEEE Journal of Translational Engineering in Health and Medicine*, vol. 12, pp. 622-634, 2024.

[7] S. M. M. Rahman, "Trustworthy power assistance in object manipulation with a power assist robotic system," *2019 SoutheastCon*, Huntsville, AL, USA, 2019, pp. 1-6.

[8] S. M. M. Rahman and R. Ikeura, "Cognitive feedforward learning control for object manipulation with a power assist robotic system," *2021 IEEE 2nd International Conference on Human-Machine Systems (ICHMS)*, Magdeburg, Germany, 2021, pp. 1-7.

[9] S. M. M. Rahman, "Machine learning-based cognitive position and force controls for power-assisted human–robot collaborative manipulation" *Machines* 9, no. 2: 28, 2021.

[10] S. M. M. Rahman, R. Ikeura, M. Nobe and H. Sawai, "Controlling a power assist robot for lifting objects considering human's unimanual, bimanual and cooperative weight perception," *IEEE International Conference on Robotics and Automation*, Anchorage, AK, USA, 2010, pp. 2356-2362.

[11] M. L. Schrum, M. Johnson, M. Ghuy, M. Gombolay, "Four years in review: statistical practices of Likert scales in human-robot interaction studies," *in Proc. of 2020 ACM/IEEE International Conference on Human-Robot Interaction*, 2020, pp.43-52.

[12] L. Zongxing, Z. Jie, Y. Ligang, C. Jinshui and L. Hongbin, "The human–machine interaction methods and strategies for upper and lower extremity rehabilitation robots: A review," *IEEE Sensors Journal*, vol. 24, no. 9, pp. 13773-13787, May 1, 2024.

[13] S. M. M. Rahman, "Performance metrics for human-robot collaboration: an automotive manufacturing case," *IEEE International Workshop on Metrology for Automotive (MetroAutomotive)*, Bologna, Italy, 2021, pp. 260-265.

[14] A. T. Khan, D. Joshi and B. Mukherjee, "Design and psychophysical validation of a slip induction device for sensorimotor evaluation of prehensile grip," *IEEE Sensors Journal*, vol. 24, no. 15, pp. 24750-24757, Aug.1, 2024.

[15] D. Copaci, N. Pernalete, Á. G. Ortiz and D. B. Rojas, "Proposed eye-hand correlation assessment system: A novel approach for evaluating coordination," *IEEE Access*, vol. 12, pp. 3926-3935, 2024.

[16] C. Nielsen, M. Mathiesen, J. Nielsen and L. C. Jensen, "Changes in heart rate and feeling of safety when led by a rehabilitation robot," *2019 14th ACM/IEEE International Conference on Human-Robot Interaction (HRI)*, Daegu, Korea (South), 2019, pp. 580-581.

[17] J. Schmidtler, K. Bengler, F. Dimeas and A. Campeau-Lecours, "A questionnaire for the evaluation of physical assistive devices (QUEAD): Testing usability and acceptance in physical human-robot interaction," *2017 IEEE International Conference on Systems, Man, and Cybernetics (SMC)*, Banff, AB, Canada, 2017, pp. 876-881.

[18] Y. Itaguchi, "Toward natural grasping with a tool: effects of practice and required accuracy on the kinematics of tool-use grasping," *Journal of Neurophysiology*, 2020, 123:5, 2024-2036.

[19] C. Dune, C. Leroux and E. Marchand, "Intuitive human interaction with an arm robot for severely handicapped people - A one click approach," *IEEE 10th International Conference on Rehabilitation Robotics*, Noordwijk, Netherlands, 2007, pp. 582-589.

[20] A. Gul, L. D. Turner and C. Fuentes, "An exploratory analysis of trust in socially assistive robot interactions with unpaid carers of older adults," *2024 33rd IEEE International Conference on Robot and Human Interactive Communication (ROMAN)*, Pasadena, CA, USA, 2024, pp. 1630-1637.

[21] O. Ruiz-Celada, A. Dalmases, I. Zaplana and J. Rosell, "Smart perception for situation awareness in robotic manipulation tasks," *IEEE Access*, vol. 12, pp. 53974-53985, 2024.

[22] A. Kalatzis, V. G. Prabhu, L. Stanley and M. P. Wittie, "Effect of augmented reality user interface on task performance, cognitive load, and situational awareness in human-robot collaboration," *2023 32nd IEEE International Conference on Robot and Human Interactive Communication (RO-MAN)*, Busan, Korea, Republic of, 2023, pp. 1252-1259.

[23] S. M. M. Rahman, "Cyber-physical-social system between a humanoid robot and a virtual human through a shared platform for adaptive agent ecology," *IEEE/CAA Journal of Automatica Sinica*, vol. 5, no. 1, pp. 190-203, Jan. 2018.

[24] S. M. M. Rahman and R. Ikeura, "Weight-prediction-based predictive optimal position and force controls of a power assist robotic system for object manipulation," *IEEE Transactions on Industrial Electronics*, vol. 63, no. 9, pp. 5964-5975, Sept. 2016.

EPIC-Tech - Engineering and Physiotherapy Interdisciplinary Collaboration with Technology: A case study

Camila Shirota, Jacquelin Donovan, Catherine Cave, Sami A. Kaab, Alejandro Melendez-Calderon

Abstract— **We present a case study investigating the impact of integrating a novel rehabilitation device (Andago) into physiotherapy services of a public hospital in Australia. A 3-month baseline of usual therapy was compared to a 3-month trial which involved an implementation team consisting of a physiotherapist and a rehabilitation engineer supporting a new rehabilitation device being used in clinical practice. Therapists were free to use the Andago for therapy. The patient progressed from non-ambulatory during baseline to walking with single-person assistance by trial end. There was a higher proportion of therapy dedicated to walking when comparing baseline to trial phases, and when comparing Andago and usual therapy within the trial phase. However, therapists reported increased perceived strain and fatigue during Andago-assisted sessions. Therapist engagement with the Andago was moderate, with the device utilized in approximately one out of five sessions per week. The implementation team enabled safe and supported uptake of the novel device which was valued by the case study participant and their therapist. Findings suggest the Andago's potential to enhance gait training but highlight the need to address usability challenges and staff burden to optimize integration and adoption in clinical practice. We believe this can be addressed by better integration of clinically-oriented engineers in the delivery of rehabilitation services.**

I. Introduction

Rehabilitation technologies have the potential to support the delivery of therapy. Electromechanical gait training devices in combination with physiotherapy increase the chance of regaining independent walking ability for patients after stroke [1]. However, the adoption of rehabilitation technologies in clinic is still limited [2, 3]. Many factors affect the clinical adoption of rehabilitation technologies [4], including training requirements, limited technical support, difficulty in evaluating different technology-based options when initial investment is high, and a history of technology not meeting the needs of patients and therapists. Although clinical physiotherapists already manage many of these issues, it is typically not within their scope of practice. In contrast, these issues are within scope of rehabilitation engineers, who can play a crucial role in addressing these challenges. For instance, they can collaborate with therapists to translate clinical goals into technology-enabled training programs, allowing therapists to focus on patient care without the added concern of adjusting and operating a variety of devices. They can also establish robust technical support to ensure therapists have access to assistance when needed, reducing the burden of limited support and high training requirements. Furthermore, engineers can facilitate the evaluation of different technology-based options by conducting thorough assessments that consider clinical/user needs and technical specifications. They can help therapists make informed decisions, even when faced with high initial investments (e.g., device cost). Lastly, by actively engaging with both patients and therapists during the design and implementation phases, engineers can ensure that the technologies developed truly meet the needs of end-users, addressing the historical issues of technology not aligning with the reality of service delivery. A collaborative approach where rehabilitation engineers become an integral part of clinical rehabilitation teams, could foster more effective and efficient adoption of technologies. Fortunately, new models of cooperation between rehabilitation stakeholders [5, 6] are gaining ground and demonstrating positive outcomes.

Our goal is to establish a targeted approach to implementing new technology in rehabilitation services–which is currently fragmented and does not fully exploit potential synergies across disciplines (e.g. physical therapy and clinical rehabilitation engineers). An alliance between rehabilitation engineers and therapists could address some of the challenges in clinical adoption of technology, resulting in better rehabilitation outcomes for patients. To test this concept, we pilot the introduction of a novel device to the therapy team within a public hospital. Here, we describe the protocol for our study, and elaborate on the journey of one case study–with the purpose of discussing insights into the factors that can facilitate successful technology adoption in an inpatient rehabilitation hospital.

II. Methods

The selected device for this pilot trial was the Andago (Hocoma, Switzerland)–a medically-certified robotic device that provides adaptable body weight support to allow users to

* This research project was partly supported by a seed grant from The Hopkins Centre – a joint initiative of Department of Rehabilitation, Metro South Health and Griffith University; and The University of Queensland's UQ AI Collaboratory. The NIISQ Agency provided funding to The Hopkins Centre to support and conduct research activities that aim to improve the health and quality of life outcomes for NIISQ participants. The Motor Accident Insurance Commission (MAIC) has also provided funding to The Hopkins Centre and the Jamieson Trauma Institute to support and conduct research activities that aim to improve the treatment and rehabilitation of people injured in motor vehicle crashes.

C. Shirota is with The Hopkins Centre, Griffith University, Australia (c.shirota@griffith.edu.au).

J. Donovan and C. Cave are with the Princess Alexandra Hospital, Metro South Health, Australia

S.A. Kaab was with The Hopkins Centre, Griffith University, Australia, and the School of Electrical Engineering and Computer Science, The University of Queensland, Australia

A. Melendez-Calderon is with the School of Electrical Engineering and Computer Science, and the School of Health and Rehabilitation Sciences, The University of Queensland, Australia; and the Jamieson Trauma Institute, Metro North Health, Queensland, Australia (alej.melendez@uq.edu.au)

practice standing, balance and walking tasks safely in overground conditions. The Andago has been assessed for usability and acceptance in inpatient neurorehabilitation populations [7-9], and the short set-up times and overall high satisfaction by patients and therapists suggest it is a promising adjunct to conventional overground gait therapy. Thus, it provides an ideal use-case to test the overall concept of a therapist-engineer alliance more broadly, with decreased concern for the usability of the technology itself being a confounding factor [10].

The Andago was a novel device for the rehabilitation services involved in this study, and unknown to the physiotherapy clinicians other than those on the research team (JD and CC). Research team members (CS, JD, CC, AMC) were trained to operate the device, in a train-the-trainer model.

A. Participants

The study took place at the Geriatric and Rehabilitation Unit and the Brain Injury Rehabilitation Unit of the Princess Alexandra Hospital (Brisbane, Australia). Inclusion criteria for patient participants included being an inpatient over 18 years of age; eligible to use the Andago (<2.00 m and <135 kg); eligible for standing, stepping, and/ or overground gait and balance training with need for bodyweight support or falls prevention mechanism; and adequate English, cognition and communication skills (or legal guardian) to provide consent. The study was approved by local ethics committees (HREC/2023/QMS/99869, GU Ref No: 2024/024). All participants provided consent prior to study enrolment. Participants were enrolled in the study as they became eligible to participate (e.g., became inpatients or started gait training), and exited the study as they were discharged from hospital or at the end of the study period(s).

B. Protocol

The study was split into two phases of 12 weeks: a baseline and a trial phase, with 8 weeks in between. In the baseline phase, patients followed treatment as usual. Within the clinical settings of this study, the included services aim for at least one physiotherapy session of 60 min per day for every inpatient. In the trial phase, the treating team had access to an Andago as an option to be used as part of therapy. The Andago was available for use as part of a clinic that was offered for 4-half days/ week, organized and staffed by an implementation support team of one advanced physiotherapist and one rehabilitation engineer (both from the research team). Bookings were available for 45-60 min, and limited to 2x/ week per patient due to patient numbers and clinic capacity. Andago sessions were led by the patient's treating therapist, who could refer to the implementation team members for support as needed (e.g., clinical reasoning, device operation, troubleshooting). The implementation support team further managed scheduling, communication with clinical teams, therapist training, ensured the device was ready for use (e.g., charging, cleaning between patients, storage), and overall safety during use.

C. Data collection and analysis

Patient demographics–such as age, condition, and date of admission–were collected at study entry. To compare the effect of therapy during the study phases, we chose assessments and outcome measures that were familiar to and routinely used by the clinical teams and thus more easily integrated into the patient workflow. Patient outcomes were collected at study entry and exit, including functional measures (i.e., Functional Ambulation Category - FAC, a global summary of physical function using the Clinical Outcome Variables Scale - COVS [11], a summary of staff physical assistance required for several mobility tasks including transfers and walking, 10-meter walk test and quiet balance measures).

As part of the study, the participating patients' treating physiotherapist documented every therapy session. This included the number and experience of staff that delivered the session (junior – new graduates, senior, and advanced – e.g., specialists and leads of clinical service teams); estimates of the amount of time spent standing, stepping, walking, and total exercise time. Standing, stepping and walking were recorded as discrete items, for example, standing time did not include any time associated with stepping or walking tasks. Therapists also recorded the estimated number of sit-to-stands and steps, and distances walked; the levels of physical strain and fatigue perceived by staff to deliver each session; and any factors that might have impacted therapy. Physical data sheets were given to therapists every Monday and collected every Friday.

During the trial phase, research team members also documented every Andago session. Similar to the usual therapy session documentation, it included the number and experience of staff who delivered the session; estimates of the amount of time spent standing, stepping, walking, and total exercise time; the number of sit-to-stands and steps, and distances walked; and the levels of physical strain and fatigue of staff to deliver each session. Total exercise time and walking distance were taken as measured by the Andago. Patients and clinicians were invited to semi-structured interviews at the end of the trial phase to provide their perspectives as participants in this study.

We separated session data between days with and days without therapy, to understand what affects the delivery of regular therapy. All session data were averaged across the session types (i.e., baseline, trial without Andago, and trial with only Andago). We used these data to better understand what types of activities are completed during therapy sessions, staffing utilized and service delivery-related outcomes (e.g., number of sessions delivered, session duration). To compare sessions between study phases while minimizing external factors, we identified 2 participants who were enrolled in both phases of the study. We selected the longest enrolled participant for this case study.

III. Results

This case study is about a 60-year-old male (1.75 m, 71.5 kg), who had multiple strokes over the course of one admission (right MCA followed by meningitis and a right cerebellar stroke over 5 weeks). He had type-2 diabetes, vasculitis, hypertension, and gastro-oesophageal reflux disease comorbidities. He was admitted to rehabilitation 3.5 weeks after his second stroke. When admitted to the physiotherapy service, he had 4 mobility goals for discharge: transferring (e.g., from bed to chair) independently, standing

independently at a rail for 5 min, walking with a mobility aid (e.g., walker, walking stick) and assistance of 1 person for 20 m, and accessing the community with a wheelchair and assistance of 1 person. This patient joined the baseline phase (36 days post-last stroke) for its last 7 weeks, the trial phase for the full 12 weeks, and was discharged a few weeks later. The patient's outcomes improved throughout these periods (TABLE I.); notably, he was unable to walk at baseline entry and progressively improved to require the assistance of only 1 person at exit of the trial phase.

TABLE I. PARTICIPANT ENTRY AND EXIT DATA. IMPROVEMENTS DURING STUDY PERIODS ARE INDICATED IN **BOLD**.

Function/ Outcome	**Timepoint**			
	Baseline Entry 27/3/24	***Baseline Exit 17/5/24***	***Trial Entry 18/7/24***	***Trial Exit 04/10/24***
Transfers[a]	1x SBA	1x SBA	1x SBA	1x SBA
Standing	2x A	**1x A**	1x A	**1x SBA**
Walking	-	**3x A**	2x A	**1x A**
Stairs, 10MWT, balance	-	-	-	-
COVS[b]	26	**28**	32	**34**
FAC[c]	0	0	0	**1**

[a]number and type of assistance required: SBA=stand-by-assist (i.e., patient is not touched but person is nearby in case of e.g., loss of balance or safety risk); A=assist; -=unable.

[b]Clinical Outcome Variables Scale, from 13 (lowest) to 91 (highest) physical function.

[c]Functional Ambulation Category, from 0 (requires 2+ assistance) to 5 (independent) walking ability.

During the baseline study phase, a total of 39 sessions were documented. 6 sessions were not delivered due to public holidays (n=4), staffing issues (n=1), or other therapies (n=1). 4 sessions were affected by other therapies (n=2), medical procedures (n=1), or staffing issues (n=1), resulting in shorter sessions. 7 extra therapy sessions (i.e., second therapy session for the day) were delivered by physiotherapy assistants.

During the trial study phase, 63 sessions were documented. 13 sessions were not delivered due to public holidays (n=1), patient doing other activities (such as discharge planning, n=4), staffing issues (n=2), patient issues (n=2), other therapies (n=2), and not specified (n=2). 24 sessions were shortened by other therapies (n=18), other activities (n=3), Andago (n=2), and staffing issues (n=1). 14 sessions were with the Andago only.

On average, during the baseline phase on days where therapy was delivered, the patient received 65.2 min of therapy, with approximately 1/3 of the time spent on gait-related activities (Fig. 1). During the trial phase, therapy lasted 42.0 min on average per day, with increased portions focused on gait-related training (39% without Andago and 66% in Andago-only sessions). There was a decrease in standing time and repetitions, a slight increase in stepping time with increased number of steps, and a clear increase in walking time and walked distances between the baseline and trial phases, and sessions without and with the Andago.

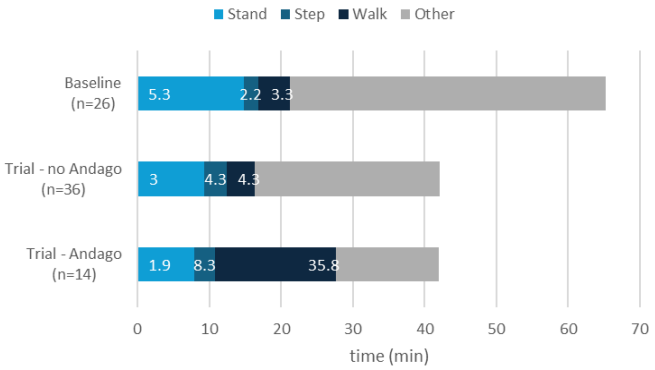


Figure 1. Breakdown of physiotherapy sessions: average dose and intensity of activities per therapy day. Numbers inside bars indicate number of sit-to-stands, number of steps, or distances walked (in m).

Baseline sessions required, on average, 1.5 staff per session to deliver therapy (Fig. 2), while trial phase sessions required approximately 1.2 staff with or without the Andago. Trial sessions had relatively more senior staff. Note that the Andago implementation team had dedicated advanced physiotherapists.

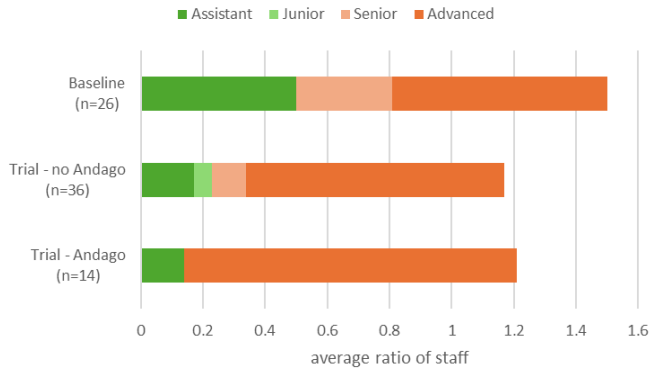


Figure 2. Staff required to deliver therapy (n=number of sessions): average number of staff and their level of experience per session.

Staff perceived baseline phase sessions (Fig. 3) more straining than trial sessions overall (average 1.36) and similarly fatiguing (average 0.94). Andago sessions were associated with the highest perceived strain and fatigue, and trial phase non-Andago sessions with the lowest strain and fatigue.

Regarding the patient's and therapist's perspectives, based on preliminary analysis of the interviews, the case-study patient stated that the Andago helped him balance, he felt more in control, and he was able to do more with the Andago than when free walking with his therapist. The therapist was initially unsure about the suitability of the device to the patient but saw therapeutic and psychological benefits once initiated, they found implementation staff support allowed them to focus on the patient during Andago sessions, and the implementation team were able to support the service more widely by providing expertise to address issues with other existing technologies that were otherwise not being used.

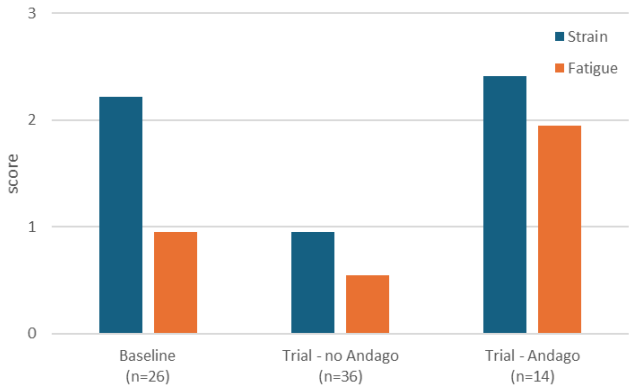


Figure 3. Staff perceived strain and fatigue delivering sessions. Scale from 0 (least) to 10 (most).

IV. Discussion

This case study illustrated the potential benefits of integrating a novel rehabilitation technology, in this case the Andago, into routine inpatient neurorehabilitation care in a model supported by a clinician and a rehabilitation engineer. Specifically, the patient was able to increase the amount of walking training compared to usual care sessions. During the trial phase, the amount of walking was remarkably higher in sessions using the Andago compared to without; but this came at the expense of staff perceiving higher strain and fatigue to deliver therapy.

Despite the expectation that a body-weight support device would decrease the physical demands of gait-related training on therapists, the treating therapist perceived it to be more physically straining and fatiguing than usual therapy. The most likely reason for this result was the much larger number of steps and walking distance achieved within the device compared to usual therapy, in combination with the physical build of the device impacting on the therapist's access to the patient's leg and preferred methods of facilitation. Although the Andago is not counter-indicated for patients that require leg facilitation to walk, this may have negatively impacted therapists' perceptions of the device. With further time and use, therapists may be able to develop different strategies to facilitate leg movements in less straining and fatiguing ways. Furthermore, it is possible that gait-related (and thus most physically strenuous) activities were mostly reserved for the Andago sessions, which is supported by the increased walking times and distances in these sessions when compared to sessions without the Andago. Despite the treating therapist's increase in fatigue and strain, the overall physical assistance of a second person for therapy reduced. In particular, as described by the therapist in a post-trial interview, during Andago training the second assistant was required to do very limited manual handling compared to their requirements completing similar gait tasks without the Andago. It could be that less overall staffing during Andago sessions resulted in higher strain and fatigue for each individual therapist. Although strain and fatigue scores were overall low (< 2.5 out of 10), the increased perceived physical effort could keep therapists from using devices. Indeed, usability issues are often cited as barriers to the adoption of technology in clinical settings.

Many of the changes observed in this study are due to the patient's improvement during their inpatient stay. For example, the length of therapy sessions and number of staff decreased between the baseline and trial phases, which could reflect more resources (in the form of staffing and extra sessions) afforded to this patient during the baseline phase due to his high level of functional impairment, which was not needed in the trial phase as he improved. This is supported by a higher proportion of the trial sessions dedicated to gait-related activities, which also shifted from standing to walking. This difference is even more evident when comparing concurrent trial phase sessions with and without the Andago, suggesting the device was not only appropriate and useful for this patient, but also enabled higher intensity gait intervention provision as reported in [9].

As a first pilot study of the EPIC-Tech model, we were interested in whether and how much therapists would engage in using a new piece of technology as part of their therapy. As such, therapists were able to decide whether their patients would benefit from the device (Andago), and schedule its use accordingly. For this case study in particular, the treating therapist chose to use it for roughly 1 session out of 5 in a week rather than the 2 that were available to them. This could be due to competing workload demands and challenges aligning with Andago clinic times from the treating therapist, who also had managerial responsibilities. This highlights an organizational obstacle to device implementation, which requires more careful consideration should we expect increased adoption and use of ever more complex devices.

Despite best intentions to deliver at least 1 physiotherapy session per day, many sessions were missed or shortened due to other activities. Notably, issues were mostly at the organizational (e.g., staffing and other therapies), and patient (e.g., prioritization of other activities) levels [3, 12]. We believe that the presence of the dedicated therapist and rehabilitation engineer to support the use of the novel device avoided the appearance of issues related to technological factors (e.g., usability, technical issues). Notably, the device was always set up for every clinic, any device errors that occurred during sessions were quickly resolved on-the-spot, and no sessions needed to be modified due to device-related issues. Such practical issues are rarely considered in research studies but are critical in implementation of technologies into clinical practice, and should be further studied.

A. *Limitations and future work*

While this is only a single case study, we aimed at reporting clinically relevant insights into how rehabilitation technologies may impact therapy delivery. Our team has collected data from 25 participants, and is in the process of fully analyzing the pooled data. In our ongoing analysis, we will not only examine the service delivery outcomes and Andago training data, but also incorporate patient and staff experiences from semi-structured interviews, as well as discussing key considerations such as workflow integration and organizational readiness.

V. Acknowledgment

Authors acknowledge Mr. W Mitchell for his valuable contributions to this research, as a colleague researcher and as a consumer representative; and Dr. R Bell, Director of the

Brain Injury Rehabilitation Services at the Princess Alexandra Hospital for supporting this study.

REFERENCES

[1] J. Mehrholz, S. Thomas, J. Kugler, M. Pohl, and B. Elsner, "Electromechanical-assisted training for walking after stroke," *Cochrane database of systematic reviews,* no. 10, 2020.

[2] S. Letourneau, E. T. Zewdie, Z. Jadavji, J. Andersen, L. M. Burkholder, and A. Kirton, "Clinician awareness of brain computer interfaces: a Canadian national survey," *J Neuroeng Rehabil,* vol. 17, no. 1, p. 2, Jan 6 2020, doi: 10.1186/s12984-019-0624-7.

[3] C. Jacob, A. Sanchez-Vazquez, and C. Ivory, "Social, Organizational, and Technological Factors Impacting Clinicians' Adoption of Mobile Health Tools: Systematic Literature Review," *JMIR Mhealth Uhealth,* vol. 8, no. 2, p. e15935, Feb 20 2020, doi: 10.2196/15935.

[4] S. Curtis, L. Sheehan, E. Buchman, and S. Bhattacharjya, "Clinicians' perspectives and usage of rehabilitation technology: a survey," *Disabil Rehabil Assist Technol,* pp. 1-8, Nov 21 2023, doi: 10.1080/17483107.2023.2284365.

[5] S. Oh, T. Hodson, M. Kendall, C. Shirota, and E. Kendall, "A technology-focused service within a rehabilitation setting: exploring the experiences and current technology demands of people with disabilities," *Disability and Rehabilitation: Assistive Technology,* vol. 19, no. 5, pp. 2000-2009, 2024/07/03 2024, doi: 10.1080/17483107.2023.2244001.

[6] E. Kendall *et al.*, "HabITec: a sociotechnical space for promoting the application of technology to rehabilitation," *Societies,* vol. 9, no. 4, p. 74, 2019.

[7] D. Marks *et al.*, "The Andago for overground gait training in patients with gait disorders after stroke-results from a usability study," *Physiother Res Rep,* vol. 2, no. 2, pp. 1-8, 2019.

[8] A. Fay, E. Synott, E. McDaid, and E. Barrett, "A comparison of the immediate effects of the Andago over ground body weight support trainer versus over ground walking on selected gait parameters in a post-acute rehabilitation population," *Physiother Theory Pract,* pp. 1-11, Jan 2 2023, doi: 10.1080/09593985.2022.2162834.

[9] S. S. Tay *et al.*, "Effectiveness of Adjunct Robotic Therapy With a Patient-Guided Suspension System for Stroke Rehabilitation Using a 7-Days-a-Week Model of Care: A Comparison With Conventional Rehabilitation," *Arch Rehabil Res Clin Transl,* vol. 3, no. 3, p. 100144, Sep 2021, doi: 10.1016/j.arrct.2021.100144.

[10] H. J. A. van Hedel, I. Rosselli, and S. Baumgartner-Ricklin, "Clinical utility of the over-ground bodyweight-supporting walking system Andago in children and youths with gait impairments," *J Neuroeng Rehabil,* vol. 18, no. 1, p. 29, Feb 8 2021, doi: 10.1186/s12984-021-00827-1.

[11] Shirley Ryan Ability Lab. Rehabilitation Measures Database [Online] Available: https://www.sralab.org/rehabilitation-measures

[12] T. Greenhalgh *et al.*, "The NASSS-CAT Tools for Understanding, Guiding, Monitoring, and Researching Technology Implementation Projects in Health and Social Care: Protocol for an Evaluation Study in Real-World Settings," *JMIR Research Protocols,* vol. 9, no. 5, 2020, doi: 10.2196/16861.

Engineering Synthetic Soft Tissue for Accurate Human-Exoskeleton Interaction Testing

1st Massimo Cenciarini
ME Dept. and IRIS-UPC
Universitat Politècnica de Catalunya
Barcelona, Spain
massimo.cenciarini@upc.edu

2nd Giorgia Mariuzzo
University of Padova
Padova, Italy, and
ME Dept. and IRIS-UPC
Universitat Politècnica de Catalunya
Barcelona, Spain

3rd Stefano Massardi
DIMI, University of Brescia
Brescia, Italy, and,
BioRobotics Group
Centre for Automation and Robotics (CAR), CSIC-UPM, Madrid, Spain

4th David Rodriguez-Cianca
BioRobotics Group
Centre for Automation and Robotics (CAR), CSIC-UPM, Madrid, Spain

5th Diego Torricelli
BioRobotics Group
Centre for Automation and Robotics (CAR), CSIC-UPM, Madrid, Spain

***Abstract*—In the field of wearable robotics, assessing physical human-exoskeletons interaction (pHEI) is of critical importance in the development of wearable assistive devices. However, in the early stages of development of such devices, involving human testing could raise safety and ethical concerns. To address those limitations, we developed an active dummy leg named Leg Replica. Yet, the realism for pHEI was not adequate when mimicking soft-tissue behavior (compression and shear). The work presented here focused on identifying synthetic soft tissue simulants to enhance the fidelity of the Leg Replica, resulting in responses under compressive and shear stresses similar to those observed in human subjects.**

A novel approach is proposed in this work as a testing method for mechanical characterization of compressive and shear stresses of human soft tissues that is coherent with the specific application of wearable lower limb exoskeletons. The testing methodology was applied to 10 human subjects as well as the Leg Replica enhanced with three different platinum-catalyzed silicone material of varying hardness and thickness. One of the tested materials, with a thickness of 3 cm, demonstrated a mechanical behavior under compression and shear stresses comparable to that observed in human tissue. This study demonstrates the ability of the proposed methodology to objectively benchmark the adequacy of the Leg Replica combined with a new tissue simulant to mimic the biomechanical behavior of the human leg.

***Index Terms*—physical Human-Exoskeleton Interaction, Soft Tissue Biomechanics, Synthetic Tissue Simulants, Evaluation methods, Exoskeleton Benchmarking, Biomimetics, Wearable Robotics, Assistive Technologies**

I. Introduction

Robotic assistive devices such as lower extremity exoskeletons have been developed for the past four (4) decades, but only in the last 10–15 years they have received a great interest both from the scientific and industrial community. Such devices can range from different target contexts: healthcare, industrial, and consumer applications [1]. This rapid development of such wearable devices led to an increased number of available options seeking to reach the market [2].

In a previous work from our group, the critical problem faced by the community regarding the lack of a systematic benchmarking framework to quantitatively assess and compare these technologies was pointed out [3], which is crucial when considering any device to reach the market [4].

To fill this gap, a sensorized robotic dummy limb of a human leg (hereon referred to as Leg Replica) was developed and fabricated to provide a standard and reproducible test-bed that can be used to study multiple aspects of physical human-exoskeletons interaction (pHEI) without the need of involving human individuals, particularly in the initial phases of the development of wearable robotic assistive devices. Details of the Leg Replica can be found in [5]. A benchmarking methodology to study pHEI based on the Leg Replica was recently proposed [3], in which a soft silicon layer was placed between the exoskeleton and the dummy leg rigid outer shells to mimic human soft tissues. The presence of a soft layer between the Leg Replica and the exoskeleton is not only to reduce noncontact area resulting from the rigid outer shells (made of ABS thermoplastic polymer), but also to guarantee that the Leg Replica itself serves as a realistic benchmarking platform for testing wearable lower-limb assistive devices. Indeed, the ability of the soft tissue simulant to follow the movements imposed by the exoskeleton without slippage is a crucial requirement to ensure high fidelity of human soft tissue mechanics and an effective evaluation of the exoskeleton performance. In our previous work, the mechanical properties associated with the soft tissue composition found in the human leg were obtained using a 1.3 cm-thick layer of a platinum-catalyzed silicone (EcoFlex OO-30™, Smooth-On Inc., Macungie, PA, USA).

The work presented here aimed to identify a synthetic

This work was supported by the research initiation grants to Lecturers "ALECTORS-2023" as described in the agreement CG/2023/08/07, of October 25, 2023, of the UPC Governing Council and also by the project EXOSAFE, awarded by the COVR European Project under grant agreement No. 779966.

simulant material that would improve the human likeness of the Leg Replica regarding human soft tissues in terms of mechanical behavior when wearing an exoskeleton. In the process of selecting the synthetic simulant, a novel application-oriented testing method for mechanical characterization of the overall compressive and shear stresses of the thigh has been developed. The specific procedures originated from the consideration that proper development and characterization of synthetic simulants (material + thickness), followed by comparisons with human tissue properties, can be challenging. Additionally, this process requires specialized knowledge and potentially collaboration with experts in the field, and it is application-specific. The proposed tests aim to provide a basic characterization that is compatible with the aim of measuring the exoskeleton mechanical load to the human leg consisting of compression and shear stresses applied to the human soft tissue by the cuffs and straps used to secure wearable lower limb exoskeletons around the human leg. Without a detailed knowledge of the material's intrinsic properties, our goal was to find a synthetic material that would behave, at macroscopic level, like human tissue under compression and also how much displacement the simulant would allow in response to tangential forces oriented longitudinally without any slippage of the straps. To our knowledge, no similar characterization tests have been reported in the literature.

This approach was necessary because, on the market, there are many commercially available materials labelled as skin tissue simulants, however the properties required to replicate tissue behavior vary based on the specific application. Consequently, a material that effectively simulates tissue behavior for one application might not perform as well in another. It is crucial that material selection is carried out through tests tailored to the specific application context.

The paper is structured as follows. Section II describes the methodology adopted for this evaluation. Then, results are presented and discussed in Section III and Section IV, respectively. Section V offers concluding remarks from the work presented.

II. Materials and Methods

The main aim of this work is to characterize the mechanical properties of human soft tissues at the macroscopic level, with a focus on the specific application of mobility assistive devices such as exoskeletons. This characterization is a necessary step to find the requirements for a soft tissue layer to be added to an existing Leg Replica [5] and make it an effective benchmarking device to emulate the human leg for wearable exoskeleton R&D and to investigate pHEI. Therefore, in this section, an application-specific method is presented that aims to characterize the mechanical properties of human limbs in the context of wearable lower-limb exoskeletons. Specifically, the method includes two tests to characterize the macroscopic compressive (1) and shear (2) stresses of the thigh. These tests are conducted both on the Leg Replica thigh together with the simulant material and on a sample of 10 human subjects to establish a reliable comparison. Moreover, as the Leg Replica was designed as a left side leg, all testing procedures were conducted on the left leg of human subjects.

A detailed description of these tests is provided later in subsections II-B and II-C.

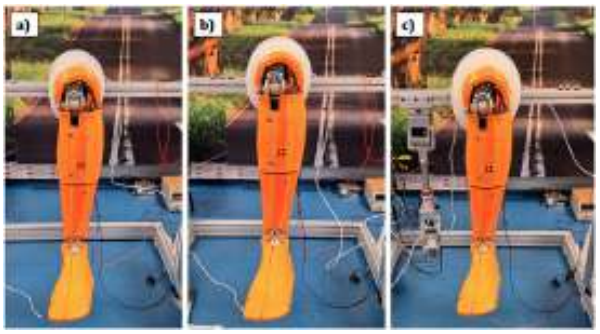


Fig. 1. Sample materials applied on the Leg Replica thigh. The different thicknesses for each of the three materials included in the present work: (a) 1-cm, (b) 2-cm and (c)-3 cm.

A. Experimental procedures

Ten (10) healthy subjects (6m; 4f) were enrolled in the study. All participants provided written informed consent prior to enrollment. The study protocol was approved by CSIC's Ethics Committee (approval 185/2023). The human research was conducted ethically in accordance with the World Medical Association Declaration of Helsinki. From each subject, anthropometric and demographic measurements were taken including: age (24$\pm$3 years; mean$\pm$1SD), height (172$\pm$6 cm), weight (63.2$\pm$7.6 kg), BMI (21.4$\pm$2.1 kg/m^2), leg circumference at the strap (interface) location for the shank (29.7$\pm$2 mm), for thigh at the Distal location (43.4$\pm$3 mm) and at the Proximal location (52.4$\pm$4 mm). BMI was calculated based on subjects' height and weight [6].

Three sample materials were selected for testing on the Leg Replica: the previously used Ecoflex OO-30™ [3], a softer variant from the same product line, Ecoflex OO-10™, and an even softer version created by adding 10% by weight of Silicone Thinner™ to Ecoflex OO-10™, referred to as OO-10T. Ecoflex OO-30™ and OO-10™ have a hardness of 00-30 and 00-10, respectively. Hardness is not available for the OO-10T material. Each material was produced in three different thicknesses: 1, 2, and 3 cm resulting in a total of nine (9) samples. Each sample was placed onto the Leg Replica's thigh segment, as shown in Fig. 1. For both Compression and Displacement tests, all human participants and the Leg Replica wore identical leggings for consistency in the measured outcomes of these experiments. The leggings composition consisted of polyester, polyamide, and elastane.

B. Compression test

The assessment of the static compression that is exerted by the straps on the soft tissue was indirectly estimated by measuring the torque required to secure the exoskeleton strap to the thigh and the consequent reduction in the perimeter of this securing strap.

A torsional dynamometer (STS103, Sealey Ltd, Bury St Edmunds, England) was used to indirectly measure the

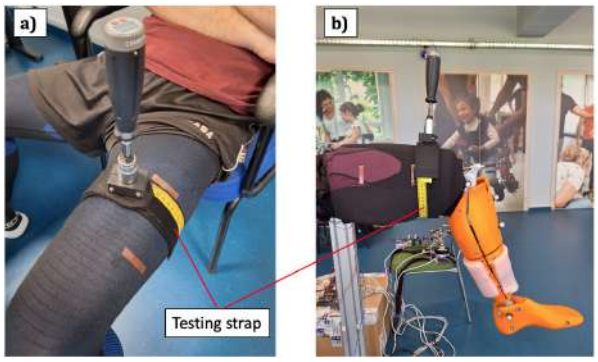


Fig. 2. Compression tests setup on a) Human thigh ("Proximal" location) and b) Leg Replica thigh ("Distal" location)

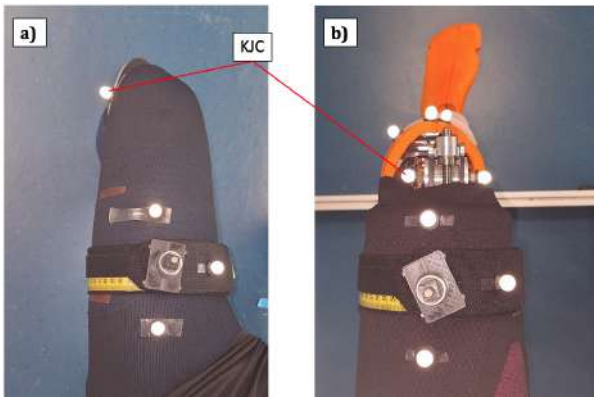


Fig. 3. Displacement test setup on a) human thigh ("Proximal" location) and b) Leg Replica thigh ("Distal" location). Location of the KJC is highlighted.

compressive forces applied to the leg tissues by measuring the torque required to turn the BOA dial used to tighten the strap around the leg. A custom adapter transfered the torque from the dynamometer to the dial. This provides an indirect estimation of the compressive mechanical characteristics of the human soft tissues in the thigh, which in turn represents the reference for the Leg Replica + soft tissue simulant.

The experimental protocol for compression testing included the steps described below. Human participants were instructed to keep their muscles as relaxed as possible during the whole experimental procedure. The first step is to identify the subjects' knee joint center of rotation (KJC). The second step is to apply adhesive tape markers along the longitudinal axis of the thigh, at distances of 125 mm ("Distal") and 239 mm ("Proximal") from the KJC. The placement of these tapes allowed the correct positioning of the straps with respect to the KJC for applying the compression stresses on the thigh. These distances correspond to the locations of the attachments (cuffs and straps) along the thigh segment of the exoskeleton used in [3]. The testing strap, consisting of a 5-cm wide strap (QuickFit Strap 2" (50mm), with BOA® dial, Click Medical LLC, Steamboat Springs, USA, OK1420-130-05) to which a conventional sewing measuring tape, was attached to determine leg circumference and changes in circumference resulting from the compression. The third step requires fitting the strap tightly around the thigh to ensure a snug fit while minimizing compression of the underlying tissue (see Fig. 2 for details). To ensure a snug fit, preliminary tests established a minimum threshold torque of 0.20 Nm corresponding to the reference baseline state of zero tissue compression. This normalization was intended to ensure estimation of mechanical properties of the leg soft tissues under compression only. The fourth step started after reaching the 0.20 Nm value, and in this step the strap was gradually tightened using the dynamometer in increments of 0.05 Nm. At each increment, tightening was paused to measure and record the reduction in circumference due to the compression. Tightening stopped when reaching a maximum torque value of 0.60 Nm to prevent discomfort and any pain suffered by the volunteers. Steps 3 to 4 of this procedure were performed for a total of three times in both the distal and proximal locations on all 10 human subjects, as well as on the Leg Replica with the three synthetic tissue simulants described earlier II. The number of runs per body site was limited to three to prevent fatigue while ensuring enough repetitions to account for intra-subject variability.

C. Displacement test

The second test consisted in the evaluation of the maximum displacement permitted by the soft tissues in the thigh. This evaluation was conducted by applying shear stress along the thigh's longitudinal axis. As for the Compression test, participants were instructed to keep their muscles as relaxed as possible. The first and second steps are identical to those of the Compression test, including the identification of the subjects' KJC and placement of adhesive tape markers at the Proximal and Distal locations (see II-B).

The longitudinal position of two (2) reflective markers was included in this test:

A reference marker placed on the subject's KJC (visible in Fig. 3) was assumed as static during the procedure.

The second marker was placed in the middle of the testing strap's width to measure the maximum displacement allowed by the tissue softness with respect to the KJC. This marker is referred to as "interface marker".

The other two markers shown in Fig. 3 were not included in the protocol of this test.

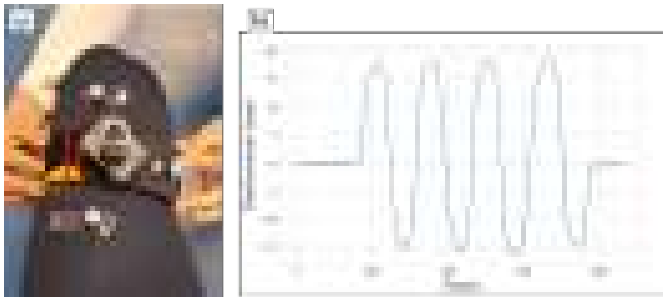


Fig. 4. Detail of the tangential motion applied to the testing strap. In a) the red arrow show the directions of the motion when applying the tangential force. In b) the relative displacement of the interface marker placed on the strap with respect to the KJC is shown over time [frame] for subject 8 in the Proximal location during the 5th run of the test.

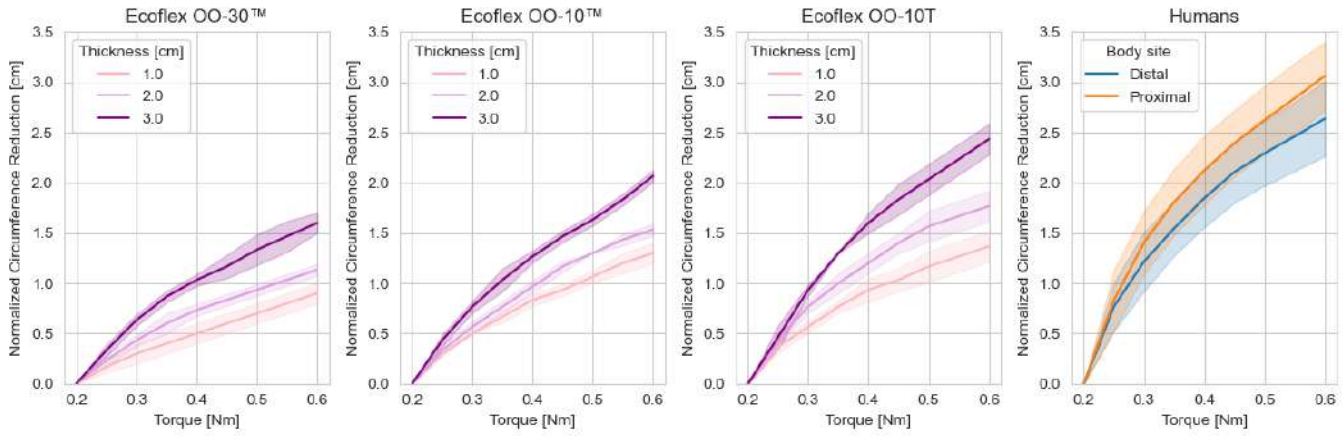


Fig. 5. Circumference reduction-Torque characteristics extracted for each material (OO-30, OO-10, OO-10T) and the considered thickness (1.0, 2.0, or 3.0 [cm]) combining the two locations in the first three plots; and for humans at both distal and proximal location in the fourth plot. Shaded areas represent the standard deviation calculated on different trials for the Leg Replica and different subjects for human tests.

This setup is illustrated in Fig. 3 for both human subjects and the Leg Replica. In the third step, the strap was tightened around the thigh using the dynamometer until a torque value of 0.60 Nm was reached. Preliminary testing determined that this value prevents discomfort for the large majority of individuals while preventing sliding of the strap during the test. The fourth step, consisted of manually displacing the strap from its resting position until the maximum displacement was reached along the longitudinal direction of the thigh (see Fig. 4 for details). The motion consisted of applying a shear stress to the strap first towards the proximal direction, then towards the distal direction, and finally returning it to the resting position. This alternating motion was repeated four times (Fig. 4b)). The experimenter ensured that the strap moved along the thigh with no occurrence of slippage between the strap and the thigh. The fourth step was performed for a total of five (5) times, always starting and ending in the resting position for both the Proximal and Distal locations.

Marker displacements relative to the KJC were recorded using an optoelectronic motion capture system (VICON, Oxford, UK) with a sampling rate of 100 sample/s and accuracy of 0.2 mm. This test was carried out on both human subjects and the Leg Replica. Quantifying the maximum displacement permitted by the soft tissue in the human thigh allowed an estimation of the shear mechanical characteristics under similar conditions to when an exoskeleton is strapped around the leg and in turn represents the reference characteristics for the Leg Replica + soft tissue simulant.

D. Data analysis

The normalized circumference reduction with respect to the dynamometer torque reading estimated the compression of the soft tissue under the strap. The normalized circumference reduction was defined as the difference between the circumference reduction of the thigh at any particular torque reading minus the circumference reduction measured at 0.20 Nm (zero-compression). Therefore, it always starts from 0 cm, and it increases as the applied torque increases.

The displacement metric developed to characterize the response to shear stress was based on the position of the interference marker with respect to the KJC marker along the thigh's longitudinal direction (see Figs. 3 and 4 for details). The position was normalized by the distance at rest. The displacement was estimated as maximum range using the 4 peaks in both directions (distally and proximally) and these were referred to as absolute maximum and minimum displacements allowed by the soft tissue at each location. Some variability across cycles can occur and to avoid bias in the results the 4 peaks were not averaged across cycles.

The statistical analysis performed on the results of human testing were carried out using Python within the DataSpell environment. The Shapiro-Wilk normality test was performed to confirm the normality distribution assumption, justifying the use of ANOVA and T-tests for determining the significance of subject-specific factors. Paired T-tests were performed to test a significant effect of the strap location along the thigh. For the weight, height, and circumference at rest (no strap) the Pearson correlation analysis was performed to evaluate the correlation between the results and factors related to body size. The α-value=0.05 was used to test for significance.

III. Results

A. Compression test

The behavior of the human soft tissues in response to compression is shown in Fig. 5. In this figure, the Normalized Circumference Reduction is plotted vs the applied torque to the BOA dial. It can be seen that, in general, the behavior of the reduction is larger at the Proximal location than in the Distal (closer to the knee joint). This difference resulted to be significant ($p<0.05$) for torque values greater than 0.25 Nm. Therefore, the results from the two locations can't be combined, and have to be treated separately, specifically regarding any further analysis aimed at evaluating the statistical influence of the other factors. However, this is not the case for the soft tissue simulant and that is why there is no distinction of body site, but only the material and its thickness. The

effect of gender on compression was tested using an ANOVA and no significant effect of gender was found ($p>0.05$) for both locations. The Person correlation analysis performed on weight, height, and the circumference at rest (no strap) showed weak correlation with values always less than 0.5 and in most cases close to 0 across all the torque values and the two locations. Age did not show to be correlated, as the Pearson-coefficients ranged between 0.04 and 0.31.

When the performance of the simulants is compared to that of the human tissues, all simulants exhibited a greater compression stiffness than the human reference, which reached a Normalized Circumference Reduction of 2 to 3.5 cm at 0.6 Nm. The only sample that achieved this level of reduction was the Ecoflex OO-10T with a thickness of 3 cm, which reached a circumference reduction of 2.5 cm. Additionally, this simulant consistently exhibits the highest circumference reduction and closeness to the human values, followed by Ecoflex OO-10™, with Ecoflex OO-30™ showing the least reduction across all thicknesses (see Fig. 5).

B. Displacement test

In Fig. 4-b) a sample data of the motion resulted from the shear stresses applied is provided. Displacement results were averaged across repetitions and for the humans also across subjects (are provided in (Fig. 6). Minor differences were observed between the displacement results at the Proximal and Distal locations on the Leg Replica. Consequently, the results for soft tissue simulants are presented according to varying thicknesses, while for human subjects, the results are separated by location. The key findings of the displacement test are collected in this figure, illustrating the maximum range of motion of the interface marker. In general, the displacement was significantly higher at the Proximal than the Distal location ($p<0.05$). Therefore, the results from the two locations had to be treated separately and any further analysis evaluating the statistical influence of the other factors should be performed separately. The correlation analysis performed on weight, height, the circumference at rest (no strap), and age showed weak correlation with values between 0.13 and 0.27 in magnitude across all repetitions and the two locations.

The average displacement of the interface marker in humans was about 2.6 cm and 1.6 cm at the Proximal and the Distal location, respectively. On the Leg Replica, the Ecoflex OO-10T being the softest and most compliant among the three material types, it is the only material that allowed displacement ranges comparable to. It is worth noting that the Ecoflex OO-10T consistently exhibited the highest displacement range, followed by Ecoflex OO-10™, with Ecoflex OO-30™ showing the smaller displacement across all thicknesses.

IV. Discussion

The present study aimed to address the challenge of characterizing the overall (macroscopic) behavior of soft tissues in human and dummy limbs. Specifically, the replication of human tissue behavior by means of a rigid dummy leg in combination with a layer of synthetic soft tissue simulants

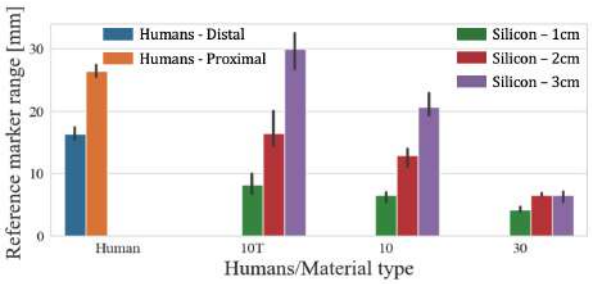


Fig. 6. Bar plots showing the average displacement results of the interface marker at the Distal and Proximal locations for the 10 subjects and also for each simulant material (OO-30, OO-10, OO-10T) for the three different thickness values (1, 2, or 3 [cm]). Error bars represent 1 SD.

was set forth. Addressing properly this task requires systematic testing of materials under various conditions plus assessing human soft tissue characteristics is inherently challenging. Moreover, the existing literature describing human soft tissue behavior under external stress shows high variability depending on body location, age, sex, and training level of individuals. Taking these aspects into account, we designed general tests that capture key macroscopical mechanical characteristics highly related to the effects of a wearable exoskeleton attached to a limb. The primary effects identified were the degree of tissue compression and the natural limit of skin displacement under the effect of shear stress. These tests are not intended to provide an exhaustive and precise analysis of the materials considered, but rather to establish benchmarking methods and metrics tailored to the use case of an exoskeleton strapped to a limb.

In section III it has been presented the outcomes of the compression and displacement tests to assess the mechanical properties of soft tissues at two locations (Proximal and Distal) of the thigh segment. Results included the application of the proposed methodology to human volunteers and also to the Leg Replica with each of the three synthetic tissue simulants and each of the three different thicknesses.

The compression test results in humans, Fig. 5, illustrate an upward trend of the Normalized Circumference Reduction at both locations. This indicates that as torque increases, the reduction in circumference also increases. This is expected because higher torque generally implies greater compression of the tissue. Additionally, results showed that the tissue behavior was found to be significantly different between the Distal and the Proximal locations. Specifically, the proximal site consistently shows a greater reduction in circumference compared to the distal site at all torque levels. This suggests that the proximal body site is more compressible, which is expected in humans due to differences in tissue composition and in the volume of soft tissue surrounding the bone at the two locations. The proximal site, being thicker and fleshier, is expected to be more compressible as supported by the data. Thus, the increased compressive effects at the proximal site are consistent with its anatomical characteristics and the expected physiological response to higher torque levels (see Fig. 5). Lastly, the curves exhibit an almost asymptotic behav-

ior, which aligns with expectations. Initially, tissues compress more easily, but as the compression (torque) increases, tissues approach their maximum compression limit. Therefore, further increases in torque yield minimal additional compression. This effect would be even more pronounced with higher torque values, but ethical limitations prevented testing beyond certain compression levels.

In the compression test results, the comparison of performance between the three simulants and the human tissue showed a strong influence of the simulant thickness across all three materials. As thickness increased from 1 to 3 cm, an increase in Normalized Circumference Reduction was observed for the same torque (see Fig. 5). Hence, in general, for the three synthetic simulants included in this study, increasing thickness enhances compressibility. Among all material types and levels of thickness, the 3-cm Ecoflex OO-10T combination emerged as the only candidate to achieve compression values comparable to those observed in human tissues. Even though human tissue exhibited greater compression characteristics than the tested simulants for the three levels of thickness, the 3-cm Ecoflex OO-10T is the only one for which the displayed curves almost coincided with those of the human tissue. Therefore, it can be concluded that the 3-cm Ecoflex OO-10T combination is a suitable simulant for mimicking human soft tissue compressive behavior when applied to the Leg Replica. It is worth noting that thickness was limited to 3 cm to maintain the overall size of the Leg Replica within the range of average human leg circumference. Additionally, an excessive thickness of the soft tissue simulant layer would hinder exoskeleton mounting. Considering the trend in the data presented, a higher thickness would have allowed to obtain results overlapping with those obtained in human testing.

When considering the results obtained from the displacement test and comparing the performance of the three simulants with the outcomes of the human testing, the influence of the thickness on the displacement for the simulant materials is evident for all three simulant materials (see Fig. 6). As thickness increases from 1 to 3 cm, all materials showed an increased displacement range. Additionally, the results indicated that the human displacement range at the Proximal location was matched only by the OO-10T material with a 3 cm thickness, while at the Distal location, a smaller displacement range was observed in humans, and it could be achieved by a minimum 2 cm layer of the OO-10T and a 3 cm layer of EcoFlex OO-10™.

Concluding, it has to be acknowledged that the simulant thickness is much lower than the overall thickness of the thigh, for example. However, this work tried to verify the feasibility of replicating the mechanical behavior observed in human when wearing an exoskeleton by simply adding a layer of soft tissue simulant.

V. Conclusions

The research presented here focused on identifying and testing materials to enhance the human likeness of the Leg Replica, enabling better benchmarking of lower limb exoskeletons. The aim was to replicate the behavior of human soft tissues under compression and shear stresses, simulating conditions similar to those when an exoskeleton is attached to the human leg. To achieve this, a new application-oriented testing methodology was developed and proposed. It provided a way to assess mechanical properties of the human leg that are meaningful for benchmarking wearable exoskeletons by including compression and displacement tests simulating conditions resulting from exoskeleton straps. Three different platinum-catalyzed silicone materials of varying hardness and thickness were tested using this methodology when placed around the rigid Leg Replica, and their performance was compared to human results. The performance of all three materials, met or exceeded human tissue results in some cases. Among them, the Ecoflex OO-10T was the most effective, particularly in the 3 cm thickness, achieving similar results to those of humans. This material closely matched human soft tissue behavior in both tests, highlighting the importance of both material properties and design parameters (e.g. thickness). These findings contribute positively to the development of benchmarking systems like the Leg Replica for evaluating exoskeleton designs. The Ecoflex OO-10T placed on the Leg Replica enables more accurate testing of human-exoskeleton interactions, enhancing reliability and performance validation.

In conclusion, while remarkable progress was made, further refinement is needed to fully replicate human tissue behavior. Future investigations should identify materials with better performance; extend testing of a wider age range; include movement disorder individuals; and investigate materials that mimic the complex properties of human tissues (i.e. anisotropy and viscoelasticity). Improved materials replicating these characteristics would significantly enhance benchmark devices like the Leg Replica even further.

Acknowledgment

The authors would like to thank Laia Piulachs and Erin H. Hovendon for their technical assistance.

References

[1] A. Kohli, H. Makad, N. Parekh, S. Pandey, D. Sawant, and R. Terkar, "Comparative study and analysis of lower extremity exoskeletons," in *2021 5th International Conference on Intelligent Computing and Control Systems (ICICCS)*. IEEE, 2021, pp. 889–894.

[2] B. Chen, H. Ma, L.-Y. Qin, F. Gao, K.-M. Chan, S.-W. Law, L. Qin, and W.-H. Liao, "Recent developments and challenges of lower extremity exoskeletons," *J. Orthop. Transl.*, vol. 5, pp. 26–37, 2016.

[3] S. Massardi, D. Rodriguez-Cianca, M. Cenciarini, D. C. Costa, J. M. Font-Llagunes, J. C. Moreno, M. Lancini, and D. Torricelli, "Systematic evaluation of a knee exoskeleton misalignment compensation mechanism using a robotic dummy leg," in *2023 International Conference on Rehabilitation Robotics (ICORR)*, 2023, pp. 1–6.

[4] D. Torricelli, A. J. Del Ama, J. Gonzalez, J. Moreno, A. Gil, and J. L. Pons, "Benchmarking lower limb wearable robots: Emerging approaches and technologies," in *Proc. of the 8th ACM International Conference on Pervasive Technologies Related to Assistive Environments*, 2015, pp. 1–4.

[5] M. Dežman, S. Massardi, D. Pinto-Fernandez, V. Grosu, C. Rodriguez-Guerrero, J. Babič, and D. Torricelli, "A mechatronic leg replica to benchmark human–exoskeleton physical interactions," *Bioinspiration & Biomimetics*, vol. 18, no. 3, p. 036009, 2023.

[6] F. Q. Nuttall, "Body mass index: obesity, bmi, and health: a critical review," *Nutrition today*, vol. 50, no. 3, pp. 117–128, 2015.

Prosthetic Control by Learning: A Multi-Agent Cooperative Game Framework

Haofei Hou, Wenduo Zhu, Lecheng Ruan, and Qining Wang, *Senior Member, IEEE*

***Abstract*—Lower-limb powered prostheses traditionally rely on structured, phase-based controllers designed for specific movement patterns, limiting their adaptability to diverse human motions. This paper presents that powered prosthetic control is a cooperative multi-agent game between the human user and the prosthetic device, as both agents must coordinate their actions actively and adapt their policy reciprocally for successful prosthetic motions. Based on this insight, we develop a model-free reinforcement learning framework that enables the prosthesis to adapt to diverse human movement patterns through cooperative policy learning. Preliminary results in the simulator demonstrate that our framework can generate human-like motions across both walking and complex tasks, establishing the effectiveness of viewing prosthetic control through the lens of multi-agent cooperation. This work opens new possibilities for developing more intuitive and versatile prosthetic systems that naturally synchronize with human movement intentions.**

***Index Terms*—Powered Prostheses, Multi-agent Reinforcement Learning, Cooperative Game**

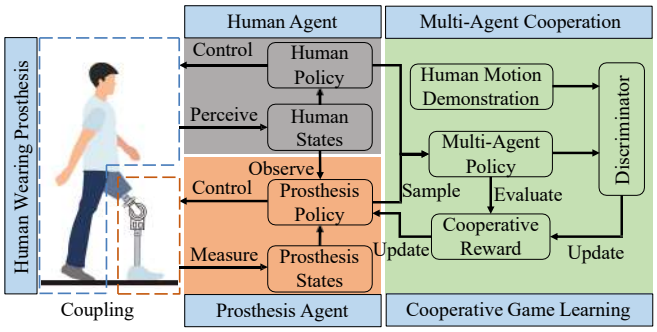


Fig. 1. **Framework.** Human wearing prosthesis can be regarded as a coupled system with two agents. The human agent has its own closed-loop controls, which runs independently but only observed. The prosthesis can be controlled, but the control goal is to achieve human-prosthesis collective optimality. By introducing the multi-agent game formulation, the prosthetic controller can be searched globally from a model-free reinforcement learning framework.

I. Introduction

Lower-limb amputation significantly impacts mobility and independence, affecting millions of people globally. Powered prostheses have emerged as a transformative solution, employing sophisticated controllers to restore natural movement patterns and enhance the quality of life [1]. Recent advances in control strategies have demonstrated remarkable improvements in walking efficiency and user satisfaction [2], [3], while expanded motion ranges and support for natural aperiodic movements have fostered improved body-prosthesis integration [4].

Traditional prosthetic control approaches primarily rely on phase-based methods, where the prosthetic follows predetermined trajectories or execution patterns based on walking gait thresholds [5], [6], which can be directly measured [7], [8] or indirectly estimated [9]. Representative frameworks include state machine control [10], [11], [12] and echo control [13]. Given their well-structured nature, research efforts have focused mainly on tuning control parameters and optimizing predetermined trajectories [14]. Recently, reinforcement learning has been successfully integrated into these frameworks for tuning structured prosthetic controllers, leading to improved control performance in prosthetic walking [15], [16], [17].

However, structured prosthetic controllers are inherently limited by their design for specific movement types. Since successful prosthetic control must comply with human motion, the interaction policy is typically embedded within the control logic and controller structure [18]. The explicit description of such human-prosthesis interaction remains challenging, which explains why existing works predominantly focus on periodic, symmetric motions like walking and running [19], [20]. Yet, the broader vision of rehabilitation engineering extends beyond walking capabilities to fully reconstruct mobility for individuals with disabilities. This necessitates prosthetic controllers that can adapt to diverse movement patterns rather than rely solely on well-structured policies for specific movements. This challenge parallels developments in bipedal robotics, where model-free reinforcement learning (RL) has been explored for policy generation in non-cyclic motions and universal control frameworks [5], [6], [21], achieving diverse movements and robust generalization [22].

Nevertheless, policy learning for complex prosthetic movements remains largely unexplored. A fundamental distinction between prostheses and bipedal robotics lies in the unique human-prosthesis relationship. Unlike fully autonomous systems with self-contained control objectives, prosthetic control involves continuous interaction with an independent, uncontrolled human agent. This interaction creates a dynamic environment where both the user and prosthesis must actively coordinate their actions through mutual force interactions to

This work was supported by the National Natural Science Foundation of China (No. 52475001). Haofei Hou and Wenduo Zhu contributed equally to this work. (Corresponding authors: Lecheng Ruan and Qining Wang.)

Haofei Hou, Wenduo Zhu, and Lecheng Ruan are with the College of Engineering, Peking University, Beijing 100871, China.

Qining Wang is with the Department of Advanced Manufacturing and Robotics, College of Engineering, and the Institute for Artificial Intelligence, Peking University, Beijing, 100871, China, also with the Schoool Rehabilitation Sciences and Engineering, University of Health and Rehabilitation Sciences, Qingdao, 266071, China, and also with Peking University Third Hospital, Beijing, 100191, China.

achieve cooperative optimal performance, as shown in Fig.1. This inherent interdependence naturally frames the human-prosthesis system as a fully cooperative multi-agent game, where success depends on the synchronized actions of both agents.

In this paper, we present a novel framework that explicitly models the human-prosthesis relationship as a cooperative multi-agent game. We validated our framework on the left knee and ankle prosthetic control. Our approach leverages model-free RL to develop control strategies that accommodate diverse movement patterns. First-stage results demonstrate that the proposed framework can generate human-like motion across walking and complex tasks. Our results establish the effectiveness of viewing prosthetic control through the lens of multi-agent cooperation, offering a promising direction for developing more intuitive and versatile prosthetic systems.

Key contributions of this paper can be concluded in the following three aspects:

1) A formal characterization of prosthetic control as a cooperative multi-agent system.
2) A novel model-free reinforcement learning framework for prosthetic control on diverse movement patterns.
3) Validation of the framework's effectiveness across different movement patterns.

II. Methodology

A. Notations

The human-prosthesis coupling system is modeled with a markov decision process (MDP) [23], defined by a tuple $\langle \mathcal{S}, \mathcal{A}, \mathcal{T}, r, \gamma \rangle$, where $\mathcal{S} = \mathcal{S}_h \times \mathcal{S}_p$ represents the system joint state space of human and prosthesis, $\mathcal{A} = \mathcal{A}_h \times \mathcal{A}_p$ is the joint action space of human and prosthesis, $\mathcal{T} : \mathcal{S} \times \mathcal{A} \to \mathcal{S}$ is the transition function, $r : \mathcal{S} \times \mathcal{A} \to \mathbb{R}$ is the reward function, and $\gamma \in [0, 1)$ is the discount factor. At each time step t, the global state in the environment is s_t, state of human is represented by s_t^h, and the state of prosthesis is s_t^p,

$$s_t = \text{concat}(s_t^h, s_t^p) \in \mathcal{S}, \tag{1}$$

where $\text{concat}(\cdot, \cdot)$ represents the concatenation operation. The joint action a_t is executed in the environment. The human's action a_t^h is sampled from the policy $\pi^h(a_t^h|s_t)$.

$$a_t = \text{concat}(a_t^h, a_t^p) \in \mathcal{A}. \tag{2}$$

Human and prosthesis actions (states) are concatenated into a unified action (state) for the entire system. Joint action at iteration k is sampled from the joint policy $\pi_k = \pi_k^h \times \pi_k^p$. A key feature of a human-centric system is that the human model is observable but not directly controllable. Similarly, the prosthesis's action a_t^p is sampled from the policy $\pi^p(a_t^p|s_t)$. Collaboration is realized through the joint state s_t, joint action a_t, and joint reward r_t. The joint reward is defined as:

$$r_t = r(s_t, a_t) \in \mathbb{R}. \tag{3}$$

The reward is determined by the global state of the human-prosthesis system rather than being limited to the prosthesis's state.

The transition function obtained through simulation inherently models mechanisms such as the interactions between humans and prostheses (*e.g.*, motion constraints, and mechanisms). Through this modeling, we aim to enable RL strategies to learn the mechanisms of human-prosthesis interaction.

B. Human-Prosthesis Cooperative Game Model

The goal of the human-prosthesis coupled system is to collectively generate a satisfactory motion. When written in an optimization form, the whole coupled system can be optimized as

$$\max_{\pi} J(\pi) = \mathbb{E}_{s_0}[Q_\pi(s_0, a_0)], \tag{4}$$

where $Q_\pi(s_0, a_0)$ refers to the action value function of the whole system at the starting episode instance (s_0, a_0) and the notation $\mathbb{E}_x[f(x)]$ represents the expected value of $f(x)$ given the random variable x. However, as a cooperative game, we only have access to the control policy of the prosthesis π^p. Therefore, the reward function of the whole coupled human-prosthesis system needs to be optimized within the search for prosthetic control policy, as

$$\max_{\pi^p} J(\pi) = \mathbb{E}_{s_0}[Q_\pi(s_0, a_0)|\pi^h]. \tag{5}$$

This multi-agent cooperative game optimization can be investigated using the decomposed forms of the advantage function [23]. Define the state value function $V_\pi(s_t)$ as

$$V_\pi(s_t) = \mathbb{E}_{a_{t:\infty} \sim \pi}[\sum_{i=t}^{\infty} \gamma^{i-t} r(s_i, a_i)|\pi^h], \tag{6}$$

and action value function $Q_\pi(s_t, a_t)$ as

$$Q_\pi(s_t, a_t) = \mathbb{E}_{a_{t+1:\infty} \sim \pi}[\sum_{i=t}^{\infty} \gamma^{i-t} r(s_i, a_i)|\pi^h], \tag{7}$$

respectively. The advantage function can then be calculated as

$$A_\pi(s_t, a_t) = Q_\pi(s_t, a_t) - V_\pi(s_t). \tag{8}$$

The human-prosthesis system is then decoupled using multi-agent advantage decomposition and the sequential policy update scheme [23]. Define action value function for the human model $Q_\pi^h(s_t, a_t^h)$ as

$$Q_\pi^h(s_t, a_t^h) = \mathbb{E}_{a^p \sim \pi^p}[Q_\pi(s_t, (a_t^h, a^p))], \tag{9}$$

advantage function for the human model $A_\pi^h(s_t, a_t^h)$ as

$$A_\pi^h(s_t, a_t^h) = Q_\pi^h(s_t, a_t^h) - V_\pi(s_t), \tag{10}$$

and advantage function for prosthesis $A_\pi^p(s_t, a_t^h, a_t^p)$ as

$$A_\pi^p(s_t, a_t^h, a_t^p) = Q_\pi(s_t, a_t) - Q_\pi^h(s_t, a_t^h). \tag{11}$$

It is easy to know that multi-agent global advantage can be decomposed into two subsystem advantage functions as follows,

$$A_\pi(s_t, a_t) = A_\pi^h(s_t, a_t^h) + A_\pi^p(s_t, a_t^h, a_t^p). \tag{12}$$

We can also perform decomposition of the policy as

$$\begin{cases} L^h_{\pi_k}(\pi^h_{k+1}) = \mathbb{E}_{s,a^h\sim\pi^h_{k+1}}[A^h_{\pi_k}(s,a^h)] \\ L^p_{\pi_k}(\pi^h_{k+1},\pi^p_{k+1}) = \mathbb{E}_{s,a^h\sim\pi^h_{k+1},a^p\sim\pi^p_{k+1}}[A^p_{\pi_k}(s,a^h,a^p)], \end{cases} \tag{13}$$

where $L^h_{\pi_k}$ and $L^p_{\pi_k}$ are surrogate optimization functions of the two subsystems.

We can obtain from multi-agent trust region policy optimization (TRPO) theorem [23], [24] that

$$\begin{aligned} J(\pi_{k+1}) \geq J(\pi_k) + L^h_{\pi_k}(\pi^h_{k+1}) - C\mathrm{D}^{\max}_{\mathrm{KL}}(\pi^h_k,\pi^h_{k+1}) \\ + L^p_{\pi_k}(\pi^h_{k+1},\pi^p_{k+1}) - C\mathrm{D}^{\max}_{\mathrm{KL}}(\pi^p_k,\pi^p_{k+1}) \end{aligned} \tag{14}$$

holds universally, where

$$C = \frac{4\gamma \max_{s,a}|A_{\pi_k}(s,a)|}{(1-\gamma)^2}, \tag{15}$$

and KL-Divergence is defined as

$$\mathrm{D}^{\max}_{\mathrm{KL}}(\pi_k,\pi_{k+1}) = \max_s \mathrm{D}_{\mathrm{KL}}(\pi_k(\cdot|s),\pi_{k+1}(\cdot|s)). \tag{16}$$

Therefore, the prosthetic control policy can be updated by

$$\pi^p_{k+1} = \arg\max_{\pi^p}(L^p_{\pi_k}(\pi^h_{k+1},\pi^p) - C\mathrm{D}^{\max}_{\mathrm{KL}}(\pi^p_k,\pi^p)). \tag{17}$$

When assuming that the human policy evolves in a way for the human-prosthesis cooperation, *i.e.*, $L^h_{\pi_k}(\pi^h_{k+1}) \geq C\mathrm{D}^{\max}_{\mathrm{KL}}(\pi^h_k,\pi^h_{k+1})$, we can guarantee a monotonic improvement of the prosthesis policy as $J(\pi_{k+1}) \geq J(\pi_k)$.

C. Policy Update from Reinforcement Learning

Equ. 17 provides a theoretical optimization method, however, issues with convergence and computational cost make it challenging to solve. Therefore, we introduce the proximal policy optimization (PPO)-clip algorithm to perform reinforcement learning optimization [25].

We can get an estimator $\hat{A}(s,a)$ of the advantage function $A_{\pi_k}(s,a)$ by generalized advantage estimation (GAE) [24].

$$\hat{A}(s,a) = \sum_{i=0}^{T}(\gamma\lambda)^i[r_{t+i} + \gamma V(s_{t+i+1}) - V(s_{t+i})], \tag{18}$$

where T, λ, γ is trajectory horizon length hyper-parameter, GAE smoothing parameter and discount factor in MDP formulation. PPO optimizes the policy π^p_{k+1} by maximizing the PPO-clip objective [25].

$$\begin{aligned} \pi^p_{k+1} = \arg\max_{\pi_p} \Big\{ L^{\mathrm{PPO}}_{\pi^p_k}(\pi^p) = \mathbb{E}_{s,a\sim\pi_k}\Big[\min\Big(\\ \frac{\pi^p(a^p|s)}{\pi^p_k(a^p|s)}\hat{A}(s,a), \mathrm{clip}(\frac{\pi^p(a^p|s)}{\pi^p_k(a^p|s)}, 1\pm\epsilon)\hat{A}(s,a)\Big)\Big]\Big\}. \end{aligned} \tag{19}$$

To better learn human motion postures and dynamics and achieve more natural prosthetic control, we optimized the reward design to reflect human movements captured by motion capture.

Discriminator $D(s)$ is trained to predict whether a given state s is sampled from the human demonstrations $\mathcal{M}$ or generated by running the policy π [26]. The discriminator should result in a small score close to 0 for generated samples and a big score close to one for real samples from human demonstration. This is based on the assumption that real whole-body human motion demonstrates an upper bound for human-prosthesis cooperation.

With human motion prior (HMP) [26], reward function r_t can regularly updated as

$$r_t = -log\Big]1 - D_k(s_t)\big), \tag{20}$$

where $D_k(s)$ is the current discriminator.

The following objective is used to get updated discriminator

$$D_{k+1} = \arg\min_D \big\{-\mathbb{E}_{m\sim d_{\mathcal{M}}} log\big(D(m)\big) - \mathbb{E}_{m\sim d_{\pi_k}} log\big(1-D(m)\big)\big\}, \tag{21}$$

where $d_{\mathcal{M}}$ and d_{π_k} represent the probability of observing a state m in dataset $\mathcal{M}$ and when following policy π_k.

III. Simulation Setup

A. Environment

We established a human-prosthesis hybrid model in IsaacGym for verification of the control policy. The full-body model consists of 28 degrees-of-freedom (DoF): 14 DoF for the lower limb and 14 DoF for the upper body. The prosthesis is modeled as a four-DoF system, including 1 DoF for the knee joint and 3 DoF for the ankle joint: dorsiflexion-plantarflexion, inversion-eversion, and internal-external rotation.

The state vector s_t refers to the global state in Sec. II-A, which includes joint angles and global positions, joint angular velocities, linear velocities, and environmental interaction data (*e.g.*, ground contact forces). The action vector a_t specifies the target angles for all joints. A PD controller computes joint torques τ^m_t based on the target angles a_t:

$$\tau^m_t = g\cdot\left[k_p\cdot(a_t-\theta_t) + k_d\cdot(a_t-\theta_t)'\right]. \tag{22}$$

where τ^m_t is the motor output torque, g is the gear ratio, k_p is the stiffness (proportional gain), k_d is the damping coefficient (derivative gain), and θ_t is the current joint angle. These torques are applied to the joints based on the motor dynamics model as described in Equ. 23, while the IsaacGym physics engine simulates the system's transition function $\mathcal{T}$, updating the model's state accordingly by

$$\tau^m_t - \tau^l_t = J\cdot\theta''_t - k_d\cdot\theta'_t, \tag{23}$$

where τ^l_t is the load torque on the joint and J is the moment of inertia. Each episode is set to last up to 300 steps during training, with each step lasting 1/45 of a second.

B. Human Model and Demonstrations

We employ a human model π^h derived from AMP [26], a reinforcement learning-based bipedal controller, enabling dynamic and realistic simulations of human movements. This approach facilitates the study of complex control tasks. Human demonstrations are derived from motion capture data, rather than simulations, for both the human model and human motion prior, which are sourced from the Human3.6M dataset [27].

Since the specific mechanism of how the human adapts to the prosthesis is unknown, we train the human model firstly

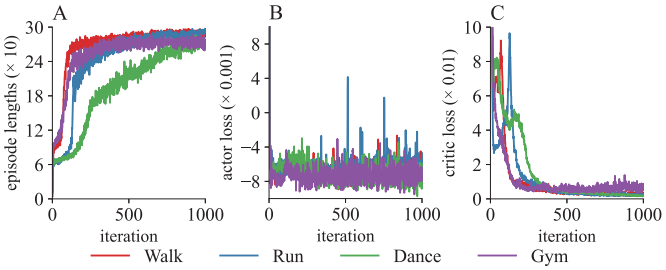


Fig. 2. **Learning Convergence.** The x-axis represents training iteration. (A) Episode length converges to approximately 300. (B) Actor loss stabilizes near zero. (C) Critic loss also approaches zero as training progresses.

and then freeze its parameters, *i.e.*, $\pi^h_{k+1} = \pi^h_k = \pi^h_0$. Therefore, it follows that $L^h_{\pi_k}(\pi^h_{k+1}) = 0 \geq C\mathrm{D}^{\max}_{\mathrm{KL}}(\pi^h_k, \pi^h_{k+1}) = 0$.

During the AMP training process for the human model, we also obtain a discriminator D_h, which serves as ground truth for analyzing the similarity between the actions of the human-prosthesis system and natural human motion.

C. Tasks and Metrics

We validate our method by testing the control of a left knee-ankle prosthesis across various tasks, including walking, running, dancing, and gymnastics. These tasks highlight the ability of our method to generate versatile and natural motion, which is demonstrated through detailed evaluations, analyses, and showcases.

The actions span a spectrum of complexity, from simple motions like walking and running to moderately complex activities like dancing and intricate movements like gymnastics. Walking involves a basic gait where one foot remains on the ground at all times while running features a quicker pace with phases where neither foot touches the ground. In the dance task, both hands are raised high, and the feet alternate ground contact while the body propels one foot to spin in the air for a full rotation. Gymnastics include high knee lifts, stretches, and balance-holding movements.

To validate our prosthetic control strategy (referred to as *Ours*), we use the human model (bipedal controller, referred to as *HC*) as our reference. The human controllers are trained to mimic the real motion of humans, thus conducting full cooperation of humans and prostheses. It performs similarly to the role of ground truth but is degraded to a certain extent as it is still a data-driven model, which only captures the distribution of human motion in a statistical sense.

We sampled 4,096 episodes and conducted two experiments: one tested the algorithm's generalization ability across various complex motions, and the other compared the system-generated motions from the perspective of gait symmetry with the human model to analyze the prosthetic controller's adaptability to humans. In the former experiment, we calculated the average normalized episode length ($\bar{T}_{\mathrm{n}}$), which measures policy robustness on different motions to prove our algorithm's generalization ability. In the ablation study, the mean discrimination score ($\sigma(\bar{D}_h)$) is calculated, which evaluates the similarity between the agent's motion and natural human behavior to show how our prosthetic controller can help people with disabilities achieve natural and human-like motion.

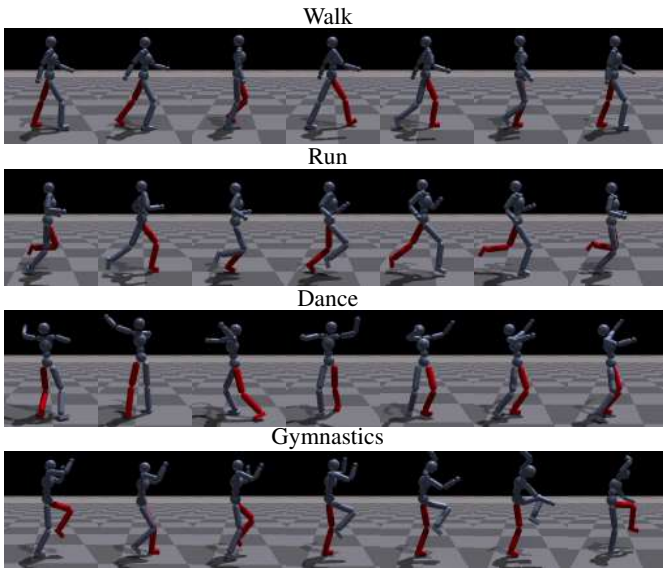


Fig. 3. **Showcases of the proposed prosthetic control.** The prosthetic control policy obtained from RL search can perform stable action in diverse types of motions, such as walk, run, dance, and gymnastics. The prosthesis part is represented in red in the simulation, including the left knee and left ankle.

TABLE I
EFFECTIVENESS TO PERFORM VARIOUS MOTION TASKS ($\bar{T}_{\mathrm{N}}$)

	HC	*Ours*
walk	99.2	96.7
run	98.8	98.4
dance	95.5	91.8
gymnastics	92.0	94.9

IV. RESULTS

A. Convergence

During the 1,000 training epochs, all networks, including the actor network (policy π^p_θ) and the critic network (value V_ϕ), successfully converged. The training losses and episode lengths stabilized and fluctuated within a small range, consistently approaching the specified maximum episode length. Detailed training metrics are shown in Fig. 2.

B. Generalization to Various Motion Tasks

As mentioned earlier, we trained a bipedal controller on the whole human model to mimic the real human motion, as a ground truth reference to our prosthetic controller. Tab. I presents the performance of our control policy across various motion tasks, in comparison with the mimic controller of real human motion. The results show that our proposed prosthetic control policy demonstrates comparable capability on various motion tasks, including periodic motions such as walking and running, and complex tasks like dancing and gymnastics. The average normalized episode length is

TABLE II
EFFECTS OF REWARD UPDATES (RU) ON SIMILARITY TO REAL HUMAN MOTION ($\sigma(\bar{D}_h)$)

	w/ RU	w/o RU
walk	20.5	16.1
run	15.2	11.2
dance	35.7	31.4
gymnastics	38.7	35.1

used to measure controller effectiveness. Unit difference in $\bar{T}_{\text{n}}$ indicates a performance reduction of only about 0.067 seconds in the whole trajectory, which has an almost negligible impact on performance in complex tasks. Key frames of the human-prosthesis system's motion were captured for visual demonstration, as shown in Fig. 3. These results, obtained without early stopping, highlight the system's stability and generalization across diverse types of motions.

C. Similarity to Human Motions

The reward updates in the proposed pipeline not only introduce a reference for the effectiveness of human-prosthesis cooperation but also create a chance to incorporate motion features of real human data as a prior in the policy search. Therefore, the proposed method shall have better similarity to normal human walking than the policy without reward updates. Such results are shown in Tab. II. It is easy to witness that when reward updates are removed, the motion diverges more from the real human motion reference. The policy search can easily get stuck in a local optimum focusing only on stability without coordinating with human motion. Some examples are demonstrated in Fig. 4. These results demonstrated the importance of human motion prior to helping our prosthetic controller achieve natural and human-like movements, and thus the effectiveness of incorporating reward updates in the pipeline.

V. DISCUSSION

The gait pattern of able-bodied individuals is often considered the ideal reference for amputees, as these patients typically aim to regain normal movement abilities [28]. Research has shown that imitating the gait of able-bodied individuals can significantly improve the mobility of amputees, reduce energy consumption, and lower the risk of secondary musculoskeletal injuries [29]. Some studies have designed 3-DoF ankle-foot prostheses and demonstrated that traditional 1-DoF transtibial prostheses, due to their limited degrees of freedom, tend to cause gait asymmetries and lack the ability to generate human-like motion [30], [31]. To achieve a gait more similar to that of a human, we hypothesize that an ankle prosthesis should possess motion capabilities akin to those of a human ankle.

Creating a universal model for individuals with disabilities is challenging because of significant gait variation between individuals and the impact of the prosthesis used. Our current model, based on the gait of an able-bodied individual with one leg amputated, partially captures the movement of individuals

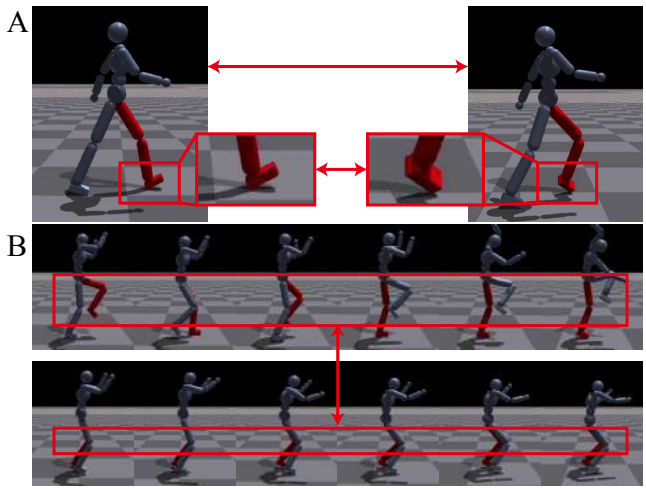


Fig. 4. **Effect of reward updates.** The reward updates in the proposed pipeline not only introduce a reference for the effectiveness of human-prosthesis cooperation but also create a chance to incorporate motion features of real human data as a prior in the policy search. (A) shows the anomaly of the ankle prosthesis joint arises when the reward update is turned off. (B) shows that the policy in gymnastics is stuck in a local optimum for stability, preventing the successful completion of the movement, when the reward update is turned off.

with disabilities. Our framework decouples the human model from prosthetic control, allowing for continuous refinement and customization. This flexibility offers the potential for better modeling of amputees as advancements in game modeling, musculoskeletal techniques, and new motion datasets emerge. In addition, several challenges may arise during implementation, including the variability of human motion, computational burdens, sensor accuracy, and system complexity.

For future work, we aim to improve the generalization of our method and implement our framework in real-world settings. The emergence of advanced musculoskeletal models [32], [33], high-performance sensors with enhanced accuracy [34], continuous advancements in prosthetic hardware [35], [36], and automated structural planning methods [37], [38] are progressively paving the way for practical applications. A significant challenge remains in regaining trust after unexpected movements, which could potentially be addressed through real-time environmental information acquisition to predict and prevent anomalous motions. Moreover, implementing motion constraints may help restore user confidence in the system's reliability and safety.

VI. CONCLUSION

This study models the human-prosthesis system as a multi-agent cooperative game, to capture the reciprocal adaptation nature of this human-robot hybrid system. We introduce a model-free RL on this formulation and enables the prosthetic control under complex and diverse movement patterns. The cooperative game model decouples prosthetic motion from human and thus provides an adaptive solution to non-cyclic complex motions such as dancing and gymnastics. The reward updating helps develop adaptive, personalized prosthetic

devices that better align with natural human movement patterns. These developments represent a significant step toward enhancing motor capabilities in individuals with mobility impairments and advancing the field of rehabilitation robotics.

REFERENCES

[1] K. A. Samuelsson, O. Töytäri, A.-L. Salminen, and Å. Brandt, "Effects of lower limb prosthesis on activity, participation, and quality of life: a systematic review," *Prosthetics and orthotics international*, vol. 36, no. 2, pp. 145–158, 2012.

[2] Y. Lv, J. Xu, H. Fang, X. Zhang, and Q. Wang, "Data-mined continuous hip-knee coordination mapping with motion lag for lower-limb prosthesis control," *IEEE Transactions on Neural Systems and Rehabilitation Engineering*, vol. 30, pp. 1557–1566, 2022.

[3] S. Gao, J. Mai, J. Zhu, and Q. Wang, "Mechanism and controller design of a transfemoral prosthesis with electrohydraulic knee and motor-driven ankle," *IEEE/ASME Transactions on Mechatronics*, vol. 26, no. 5, pp. 2429–2439, 2021.

[4] A. Mohebbi, "Human-robot interaction in rehabilitation and assistance: a review," *Current Robotics Reports*, vol. 1, no. 3, pp. 131–144, 2020.

[5] M. Windrich, M. Grimmer, O. Christ, S. Rinderknecht, and P. Beckerle, "Active lower limb prosthetics: a systematic review of design issues and solutions," *Biomedical engineering online*, vol. 15, pp. 5–19, 2016.

[6] M. R. Tucker, J. Olivier, A. Pagel, H. Bleuler, M. Bouri, O. Lambercy, J. d. R. Millán, R. Riener, H. Vallery, and R. Gassert, "Control strategies for active lower extremity prosthetics and orthotics: a review," *Journal of neuroengineering and rehabilitation*, vol. 12, pp. 1–30, 2015.

[7] Y. Feng and Q. Wang, "Combining push-off power and nonlinear damping behaviors for a lightweight motor-driven transtibial prosthesis," *IEEE/ASME Transactions on Mechatronics*, vol. 22, no. 6, pp. 2512–2523, 2017.

[8] B. Chen, Q. Wang, and L. Wang, "Adaptive slope walking with a robotic transtibial prosthesis based on volitional emg control," *IEEE/ASME Transactions on Mechatronics*, vol. 20, no. 5, pp. 2146–2157, 2015.

[9] H. Vallery, R. Ekkelenkamp, M. Buss, and H. Van Der Kooij, "Complementary limb motion estimation based on interjoint coordination: experimental evaluation," in *2007 IEEE 10th International Conference on Rehabilitation Robotics*. IEEE, 2007, pp. 798–803.

[10] S. K. Au, J. Weber, and H. Herr, "Powered ankle–foot prosthesis improves walking metabolic economy," *IEEE Transactions on robotics*, vol. 25, no. 1, pp. 51–66, 2009.

[11] Q. Wang, K. Yuan, J. Zhu, and L. Wang, "Walk the walk: A lightweight active transtibial prosthesis," *IEEE Robotics Automation Magazine*, vol. 22, no. 4, pp. 80–89, 2015.

[12] W. Zhu, J. Mai, and Q. Wang, "Effects of modulation coefficient adjustment on energy regeneration of damping torque controlled transtibial prosthesis," in *2022 9th IEEE RAS/EMBS International Conference for Biomedical Robotics and Biomechatronics (BioRob)*, 2022, pp. 1–6.

[13] W. J. Wang, J. Li, W. D. Li, and L. N. Sun, "An echo-based gait phase determination method of lower limb prosthesis," *Advanced Materials Research*, vol. 706, pp. 629–634, 2013.

[14] H. Xia, M. Pi, L. Jin, R. Song, and Z. Li, "Human collaborative control of lower-limb prosthesis based on game theory and fuzzy approximation," *IEEE Transactions on Cybernetics*, 2024.

[15] R. Wu, J. Zhong, B. Wallace, X. Gao, H. Huang, and J. Si, "Human-robotic prosthesis as collaborating agents for symmetrical walking," *Advances in Neural Information Processing Systems*, vol. 35, pp. 27 306–27 320, 2022.

[16] X. Gao, J. Si, Y. Wen, M. Li, and H. H. Huang, "Knowledge-guided reinforcement learning control for robotic lower limb prosthesis," in *2020 IEEE international conference on robotics and automation (ICRA)*. IEEE, 2020, pp. 754–760.

[17] X. Gao, J. Si, Y. Wen, M. Li, and H. Huang, "Reinforcement learning control of robotic knee with human-in-the-loop by flexible policy iteration," *IEEE Transactions on Neural Networks and Learning Systems*, vol. 33, no. 10, pp. 5873–5887, 2021.

[18] J. Mendez, S. Hood, A. Gunnel, and T. Lenzi, "Powered knee and ankle prosthesis with indirect volitional swing control enables level-ground walking and crossing over obstacles," *Science Robotics*, vol. 5, no. 44, p. eaba6635, 2020.

[19] G. Fu, W. Zhu, H. Wang, Y. Huang, J. Zhu, L. Ruan, and Q. Wang, "A robotic transtibial prosthesis with equilibrium-adjustable parallel springs to improve energy efficiency in slope walking," *IEEE/ASME Transactions on Mechatronics*, pp. 1–12, 2024.

[20] A. H. Shultz, B. E. Lawson, and M. Goldfarb, "Running with a powered knee and ankle prosthesis," *IEEE Transactions on Neural Systems and Rehabilitation Engineering*, vol. 23, no. 3, pp. 403–412, 2015.

[21] F. Peng, H. Wen, C. Zhang, B. Xu, J. Li, and H. Su, "Adaptive robust force position control for flexible active prosthetic knee using gait trajectory," *Applied Sciences*, vol. 10, no. 8, p. 2755, 2020.

[22] Y. Yang, K. Caluwaerts, A. Iscen, T. Zhang, J. Tan, and V. Sindhwani, "Data efficient reinforcement learning for legged robots," in *Conference on Robot Learning*. PMLR, 2020, pp. 1–10.

[23] J. G. Kuba, R. Chen, M. Wen, Y. Wen, F. Sun, J. Wang, and Y. Yang, "Trust region policy optimisation in multi-agent reinforcement learning," *arXiv preprint arXiv:2109.11251*, 2021.

[24] J. Schulman, P. Moritz, S. Levine, M. Jordan, and P. Abbeel, "High-dimensional continuous control using generalized advantage estimation," *arXiv preprint arXiv:1506.02438*, 2015.

[25] J. Schulman, F. Wolski, P. Dhariwal, A. Radford, and O. Klimov, "Proximal policy optimization algorithms," *arXiv preprint arXiv:1707.06347*, 2017.

[26] X. B. Peng, Z. Ma, P. Abbeel, S. Levine, and A. Kanazawa, "Amp: Adversarial motion priors for stylized physics-based character control," *ACM Transactions on Graphics (ToG)*, vol. 40, no. 4, pp. 1–20, 2021.

[27] C. Ionescu, D. Papava, V. Olaru, and C. Sminchisescu, "Human3. 6m: Large scale datasets and predictive methods for 3d human sensing in natural environments," *IEEE transactions on pattern analysis and machine intelligence*, vol. 36, no. 7, pp. 1325–1339, 2013.

[28] Y. Wen, M. Li, J. Si, and H. Huang, "Wearer-prosthesis interaction for symmetrical gait: A study enabled by reinforcement learning prosthesis control," *IEEE Transactions on Neural Systems and Rehabilitation Engineering*, vol. 28, no. 4, pp. 904–913, 2020.

[29] K. De Pauw, B. Serrien, J.-P. Baeyens, P. Cherelle, S. De Bock, J. Ghillebert, S. Bailey, D. Lefeber, B. Roelands, B. Vanderborght *et al.*, "Prosthetic gait of unilateral lower-limb amputees with current and novel prostheses: a pilot study," *Clinical Biomechanics*, vol. 71, pp. 59–67, 2020.

[30] D. G. K. Madusanka, L. N. S. Wijayasingha, K. Sanjeevan, M. A. R. Ahamed, J. C. W. Edirisooriya, and R. A. R. C. Gopura, "A 3dof transtibial robotic prosthetic limb," in *7th International Conference on Information and Automation for Sustainability*, 2014, pp. 1–6.

[31] S. Alfayad, F. B. Ouezdou, and F. Namoun, "New 3-dofs hybrid mechanism for ankle and wrist of humanoid robot: Modeling, simulation, and experiments," *Journal of Mechanical Design*, vol. 133, no. 2, p. 021005, 01 2011.

[32] Y. Lu, Y. Huang, R. Yang, Y. Wang, Y. Ikegami, Y. Nakamura, and Q. Wang, "A human-prosthesis coupled musculoskeletal model for transtibial amputees," *IEEE Transactions on Biomedical Engineering*, 2025.

[33] W. Jin, J. Liu, Q. Zhang, X. Zhang, Q. Wang, J. Xu, and H. Fang, "Forward dynamics simulation of a simplified neuromuscular-skeletal-exoskeletal model based on the cma-es optimization algorithm: framework and case studies," *Multibody System Dynamics*, pp. 1–34, 2024.

[34] S. Zhao, Z. Yu, Z. Wang, H. Liu, Z. Zhou, L. Ruan, and Q. Wang, "A learning-free method for locomotion mode prediction by terrain reconstruction and visual-inertial odometry," *IEEE Transactions on Neural Systems and Rehabilitation Engineering*, 2023.

[35] W. Zhu, Z. Ju, G. Fu, L. Ruan, and Q. Wang, "Design of a mode-switchable elastic actuator towards interactive robotic applications," in *International Conference on Intelligent Robotics and Applications*. Springer, 2024, pp. 133–146.

[36] S. Gao, C. Yang, H. Chen, X. He, L. Ruan, and Q. Wang, "Bioinspired origami-based soft prosthetic knees," *Nature Communications*, vol. 15, no. 1, p. 10855, 2024.

[37] Y.-Z. Shi, H. Hou, Z. Bi, F. Meng, X. Wei, L. Ruan, and Q. Wang, "AutoDSL: Automated domain-specific language design for structural representation of procedures with constraints," in *Proceedings of the 62nd Annual Meeting of the Association for Computational Linguistics (Volume 1: Long Papers)*, Aug. 2024, pp. 12 177–12 214.

[38] Y.-Z. Shi, F. Meng, H. Hou, Z. Bi, Q. Xu, L. Ruan, and Q. Wang, "Expert-level protocol translation for self-driving labs," in *Advances in Neural Information Processing Systems*, vol. 37, 2024, pp. 47 488–47 529.

Low-Rank Adaptation for Transformers in Dynamic Hand Gesture Recognition Using High-Density Surface Electromyography

Jirou Feng, Xingce Bao, Won Dong Kim, Kun Wang, and Jung Kim

***Abstract*— Dynamic hand gesture recognition (HGR) is critical for real-time prosthetics and neural robotics applications, where high-density surface electromyography (HD-sEMG) signals provide valuable insights into muscle activity. However, adapting machine learning models to new users while maintaining high accuracy and computational efficiency presents a significant challenge, mainly when dealing with individual variability in muscle signals. This study investigates the application of Low-Rank Adaptation (LoRA) in transformer-based models for dynamic HGR tasks. By incorporating LoRA into a pre-trained generalized transformer model, we explore its effectiveness in adapting to new subjects with varying rank values (r = 32, 64, 96) and different HD-sEMG signal window sizes (100 ms, 200 ms). Our experimental results demonstrate that LoRA achieves high accuracy during the dynamic phase of hand gestures and improves computational efficiency by reducing training parameter size. It is a promising solution for scalable and robust transformer-based systems in dynamic HGR. Furthermore, the ability to adapt quickly to new subjects with minimal retraining could make this approach particularly valuable for real-world applications.**

I. Introduction

Hand gestures offer a natural and intuitive way to facilitate communication, making them vital in human-to-human and human-to-machine interactions [1]. Hand gesture recognition (HGR) is crucial in developing advanced prosthetics, neurorobotics, and human-robot interaction (HRI), offering innovative and non-invasive control methods [2]. Surface electromyography (sEMG) signals are recorded non-invasively using sensors placed on the skin, detecting the electrical activity generated by the motor units of muscles [3]. These signals provide valuable information for decoding distinctive and consistent patterns, effectively classifying the user's motion intention. sEMG-based gesture recognition can be a real-time myoelectric control for bionic limbs [4], [5]. High-density surface electromyography (HD-sEMG) has garnered significant attention in recent years. It involves recording signals using a large number of electrodes arranged in a two-dimensional (2D) array. This dense electrode configuration captures muscle activity over time while providing a spatial (topological) representation of the underlying muscle group [6]. This wealth of information offers significant advantages over traditional bipolar sEMG, paving the way for next-generation neural interfaces with enhanced accuracy, sensitivity, and robustness [7].

Most existing studies primarily focus on the plateau phase of muscle contraction—a steady-state phase observed during highly controlled and instructed tasks, where the signal does not reflect dynamic contractions. Focusing solely on this steady segment limits temporal resolution, delays reactions, and increases the likelihood of misclassification during transient phases, thereby reducing the practicality and intuitiveness of the system. Dynamic hand gesture recognition leverages the benefits of electromechanical delay (EMD) [8] to predict hand gestures before their complete execution, enabling more proactive recognition during transitional phases.

sEMG-based HGR is commonly achieved through pattern recognition (PR), which typically involves two key stages: feature extraction and classification. Traditional machine-learning algorithms, such as linear discriminant analysis (LDA) [9], support vector machine (SVM), and k-nearest neighbors (kNN) [10] have been extensively explored in this context. For HD-sEMG, increasing the number of electrodes and gestures requires extracting more features, which increases the complexity of the feature extraction process. With the power of deep neural networks (DNNs), convolutional Neural Networks (CNNs) are among the most commonly used DNN architectures for HGR tasks, as HD-sEMG signals are often represented as HD-sEMG images [11], [12], [13]. While CNNs excel at extracting spatial features, they are less effective at extracting temporal features from sequential sEMG data. Recurrent Neural Networks (RNNs), such as Long Short-Term Memory (LSTM) networks, have been employed in recent studies [14], [15], [16] for capturing the temporal dynamics of sEMG signals. However, the sequential nature of LSTM's structure processes data step by step, leading to a time-consuming process.

Transformer neural network architecture introduces a self-attention mechanism to eliminate the need for recurrence or convolution [17]. This architecture enables parallel data processing and has widespread application in natural language processing and computer vision. Previous studies have introduced transformer-based models for HGR using both sparse sEMG [18], [19] and HD-sEMG signals [20], [21], achieving improved accuracy in decoding sEMG for hand movement classification.

The significant variability in sEMG signals between individuals makes it challenging for models to generalize

This project was supported by Robot Industrial Core Technology Development Project (20018157) funded by the Ministry of Trade, Industry and Energy (MOTIE, South Korea).

Jirou Feng, Won Dong Kim, and Jung Kim are with the Department of Mechanical Engineering, Korea Advanced Institute of Science and Technology (KAIST), 34141, Daejeon, Republic of Korea (e-mail: fengjirou@kaist.ac.kr; kwd92@kaist.ac.kr; jungkim@kaist.ac.kr)

Xingce Bao is with École Polytechnique Fédérale de Lausanne (EPFL), Lausanne, Switzerland (e-mail: xingce.bao@alumni.epfl.ch)

Kun Wang is with the Cho Chun Shik Graduate School of Mobility, Korea Advanced Institute of Science and Technology (KAIST), 34141, Daejeon, Republic of Korea (e-mail: walkerwang@kaist.ac.kr)

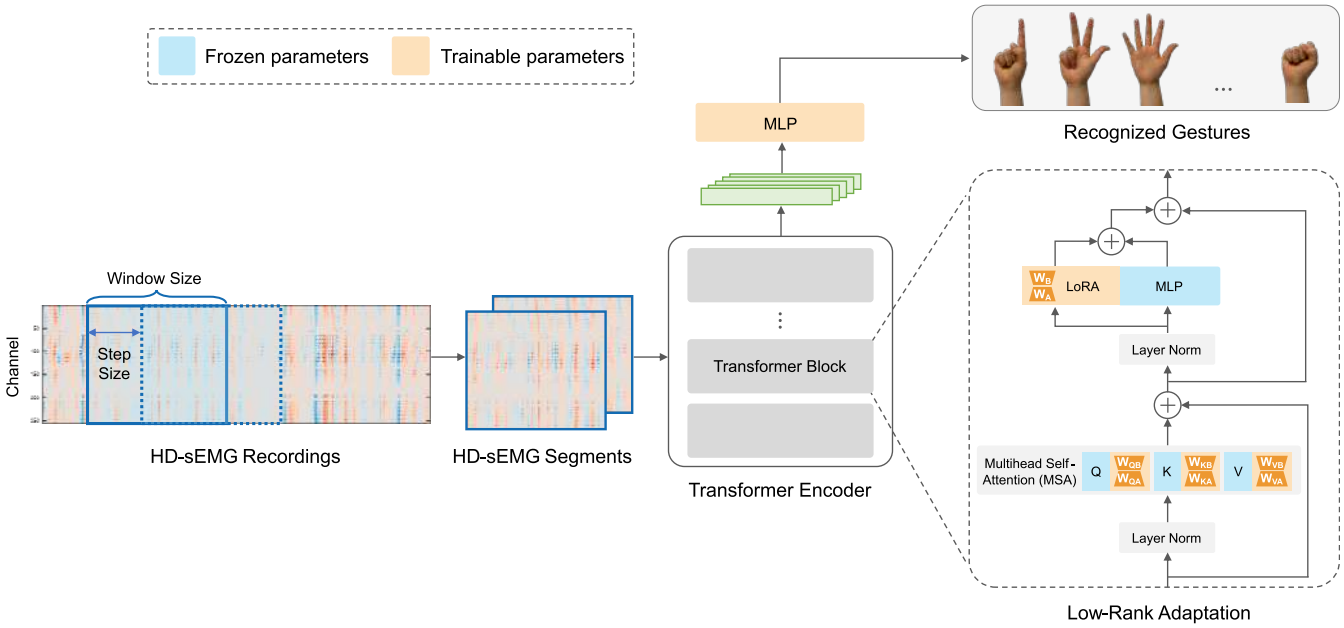


Fig. 1. Illustration of the Low-Rank Adaption (LoRA) of transformer models for hand gesture recognition using HD-sEMG signals

across subjects. Since each person's muscle structure and neurological activity can produce distinct sEMG patterns, directly applying a model trained on one subject to another typically results in poor performance. This variability necessitates using transfer learning to adapt the model to new subjects with limited data. The adaptation methods have gained traction, focusing on tuning only a small subset of parameters, reducing overfitting and computational burdens. One such method, Low-Rank Adaptation (LoRA) [22], optimizes only the low-rank matrices representing changes in the model's weight matrices, leaving the original weights unchanged. LoRA is computationally efficient and well-suited for transfer learning. Fig. 1 illustrates the LoRA of transformer models for hand gesture recognition using HD-sEMG signals.

In this paper, we are the first to investigate applying LoRA to transformers for HD-sEMG-based dynamic hand gesture recognition cross-subject transfer learning. We investigated the recognition accuracy on different ranks of LoRA and the effect of different window sizes of HD-sEMG signal segments. By leveraging pre-trained models and adapting them using LoRA, we can efficiently generalize across different subjects with minimal retraining. This approach reduces computational costs while maintaining acceptable recognition performance for a new user. It effectively solves HD-sEMG-based HGR tasks with diverse subjects and limited data.

II. Materials and Methods

A. HD-sEMG Datasets

In this study, we aim to evaluate the performance of LoRA of transformers on the dynamic phases of sEMG signals, a scenario relevant to real-world prosthesis control. We utilize the publicly available HD-sEMG dataset *Hyser*, precisely its pattern recognition (PR) sub-dataset, which includes 34 hand gestures covering various finger and wrist movements, as shown in Fig. 2(a). The PR dataset was collected from the right hand of 20 able-bodied subjects, consisting of 12 males and 8 females, with an average age of 26.55 ± 4.43 years. The HD-sEMG signals were recorded using four 8×8 electrode arrays, with two arrays placed on the extensor and flexor muscles of the subject's forearm, as shown in Fig. 2(b). A total of 256 channels of HD-sEMG signals were captured using the Quattrocento amplifier (OT Bioelettronica, Torino, Italy) at a sampling rate of 2048 Hz. Subjects were instructed to perform two trials for each gesture: three dynamic repetitions (a 1-second transition from hand resting to the target gesture) and a maintenance task (holding the gesture for 4 seconds). This study focuses on the dynamic transition phase for early gesture prediction, resulting in six repetitions per gesture. Fig. 2(c) presents an example signal plot from several representative channels, capturing the 1-second execution of a dynamic hand gesture. The *Hyser* PR dataset includes recordings from two sessions conducted on separate days. In this work, the variance of each subject on different days is not focused on; all experiments were conducted using data from session 1.

B. Signal Preprocessing

The PR dataset was processed with a 10–500 Hz 8th-order Butterworth band-pass filter and a notch filter to attenuate powerline interference at 50 Hz and its harmonic components up to 400 Hz. To enhance the quality of the recorded signals, outlier channels were identified using a threshold of 3 standard deviations from the root mean square of the signal and were replaced with the average values of the

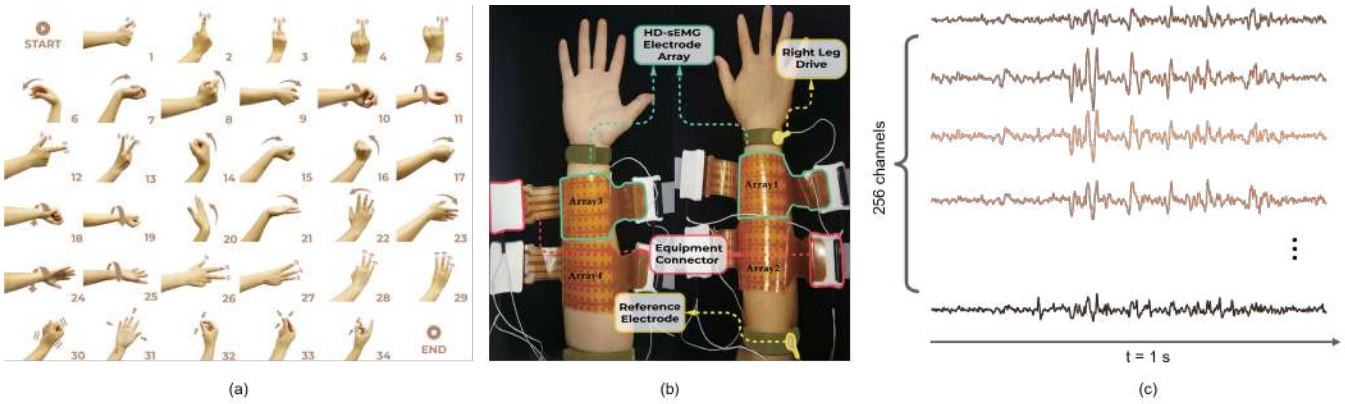


Fig. 2. *Hyser* pattern recognition (PR) dataset. (a) Involved 34 gestures, including finger and wrist movements. (b) HD-sEMG electrode array placement on the forearm. (c) Example plot illustrating recorded sEMG signals during a dynamic hand gesture. Images (a) and (b) are adapted from [23] under a Creative Commons license.

neighboring channels [24]. The initial 0.25 seconds of each 1-second signal were excluded to account for reaction time in each repetition. The z-score normalization was applied using the mean and standard deviation of the training data [25]. The signals were then segmented with a 100 ms (200 data samples) and 200 ms (400 data samples) sliding window and a 10 ms (20 data samples) stride, following commonly adopted standards from previous studies to meet real-time requirements.

III. Model Architecture

This section describes the transformer architecture that processes HD-sEMG signals for cross-subject transfer learning. The HD-sEMG segments are processed by a transformer encoder to capture temporal dependencies and contextual information. To facilitate efficient adaptation to new subjects, we apply LoRA, which allows model fine-tuning with minimal computational cost. For the final classification, an MLP head with a Softmax activation is used, and the model is optimized using cross-entropy loss to predict class probabilities. We will elaborate on these parts below.

A. Transformer Encoder

We utilize the original transformer architecture [17] and process the HD-sEMG signal segments, which are segmented into M overlapped windows. Each window represents a fixed-length signal segment with a slight overlap between consecutive windows to ensure continuity and capture temporal dependencies. These windows will be fed into transformers independently. Each input will have a size of $R^{N\times D}$, where N denotes the window length and D denotes the channel size.

The encoder consists of L stacked Transformer blocks that generate the contextualized encoding sequence $z_L \in R^{N\times D}$. Each block is composed of two key components:

- **Multihead Self-Attention (MSA):** This module applies a self-attention operation to the input z_{i-1} after normalization, followed by a residual connection:

$$z'_i = \text{MSA}(\text{Norm}(z_{i-1})) + z_{i-1}. \tag{1}$$

- **Multi-Layer Perceptron (MLP):** This module applies a feed-forward network to the output of the MSA after normalization, followed by another residual connection:

$$z_i = \text{MLP}(\text{Norm}(z'_i)) + z'_i. \tag{2}$$

In the self-attention mechanism, the queries Q_i, keys K_i, and values V_i are computed as:

$$Q_i = z_0 W_i^Q, \quad K_i = z_0 W_i^K, \quad V_i = z_0 W_i^V, \tag{3}$$

where W_i^Q, W_i^K, and W_i^V are learnable parameters. The attention output for each head is computed as:

$$\text{Attn}_i(Q, K, V) = \text{softmax}\left(\frac{QK^T}{\sqrt{D}}\right)V. \tag{4}$$

Finally, the outputs from all attention heads are concatenated and transformed using a learnable weight matrix $W \in R^{D\times D}$:

$$\text{MSA}(z_L) = [\text{head}_1, \ldots, \text{head}_L]W. \tag{5}$$

These operations work together to progressively refine the contextual information from the patches, ultimately producing the enriched embedding sequence z_L.

B. LoRA Adaptation

LoRA is an efficient method for adapting large pre-trained models to new tasks without updating the entire set of model parameters. Rather than fine-tuning all the parameters of a model, LoRA approximates the weight update with a low-rank decomposition. Specifically, the weight update ΔW is expressed as the product of two low-rank matrices A and B:

$$\Delta W = AB^T, \tag{6}$$

where $A \in R^{d\times r}$ and $B \in R^{r\times d}$, with r being a user-defined rank that is typically much smaller than d, the dimensionality of the weight matrix. This decomposition reduces the number of parameters that need to be updated, resulting in significant computational and memory savings.

The key idea behind LoRA is that the weight update ΔW can be introduced into the pre-trained weight matrix W_0 as follows:

$$W = W_0 + \Delta W = W_0 + AB^T. \tag{7}$$

This means that only the low-rank matrices A and B are trained during fine-tuning, which substantially reduces the number of parameters that need to be updated compared to traditional fine-tuning, where all parameters in W_0 are adjusted.

LoRA achieves this by introducing trainable low-rank matrices into specific parts of the model architecture, such as the attention layers in transformers. For instance, in the case of the self-attention mechanism, the attention weight matrices W_Q, W_K, W_V are adapted using LoRA. The update to the query, key, and value matrices in a self-attention layer can be written as:

$$W_Q = W_{Q0} + A_Q B_Q^T \tag{8}$$

$$W_K = W_{K0} + A_K B_K^T \tag{9}$$

$$W_V = W_{V0} + A_V B_V^T \tag{10}$$

where W_{Q0}, W_{K0}, W_{V0} are the original pre-trained weight matrices, and A_Q, A_K, A_V and B_Q, B_K, B_V are the learnable low-rank matrices for each respective weight matrix.

In this paper, we utilize LoRA to facilitate subject transfer learning for EMG-based models. When adapting to a new subject, LoRA allows us to update only the low-rank matrices A and B in the attention layers, enabling the model to efficiently learn the specific characteristics of the subject's data without the need for retraining the entire model. This approach minimizes computational overhead by focusing on low-rank updates while preserving the general knowledge from the pre-trained weights. As a result, LoRA enhances the model's ability to generalize to new subjects, making it a resource-efficient method for subject-specific adaptation in scenarios with limited computational resources. By leveraging LoRA, we can rapidly adapt to diverse subjects, ensuring that the model remains accurate and efficient even as the subject's data differs from the original training set.

C. Transfer Learning

Our transfer learning strategy employs LoRA for cross-subject model adaptation. As illustrated in Fig. 3, the approach comprises two stages: pretraining and calibration. During the pretraining stage, we aggregate data from multiple subjects to develop a generalized model. When introducing a new subject, we use LoRA to fine-tune the model with minimal parameter adjustments. This approach allows us to adapt the model to the new subject's specific characteristics efficiently, while maintaining the core knowledge from the initial training. This LoRA-based transfer learning strategy enables precise model customization with minimal computational overhead, ensuring effective learning across diverse datasets.

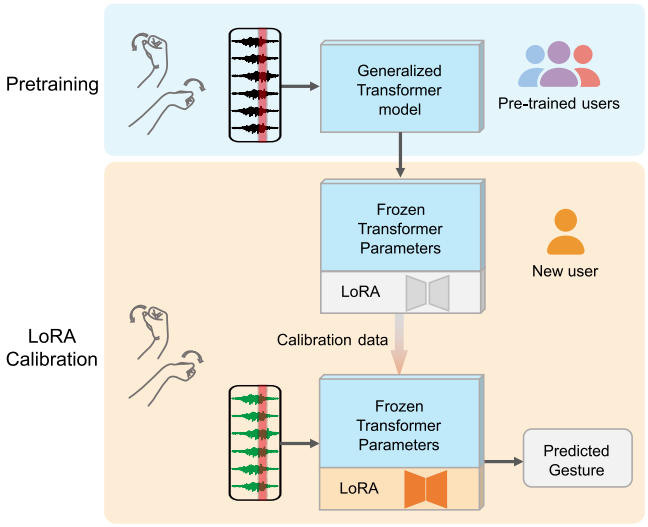


Fig. 3. Illustration of cross-subject transfer learning with LoRA

IV. Experiments and Results

A. Pre-trained Generalized Transformer Model

We employed subjects 1 through 10 to establish a generalized pre-trained model. The training set comprised repetitions $\{1, 2, 3, 4\}$, while repetitions $\{5, 6\}$ were the validation set to optimize the model's performance. All networks are implemented in Python, and computations are performed on an RTX 4090. Through hyperparameter tuning, the transformer encoder is configured with three layers (L = 3), each featuring an MSA with two heads, each of dimension 64. The MLP hidden layer size in the classifier is set to 128. Dropout rates of 0.3 are applied to both the classifier and the transformer encoder. The generalized model achieved an accuracy of 88.04% when trained on subjects 1–10 together.

To effectively assess the model's transfer learning capabilities, we used subjects 11 through 20 as new test subjects for transfer learning. For these subjects, we conducted experiments to analyze results from various combinations of calibration repetitions, specifically assessing the outcomes when using repetition sets $\{1\}$, $\{1, 2\}$, $\{1, 2, 3\}$, and $\{1, 2, 3, 4\}$. The test set remained consistent across all evaluations, utilizing repetitions $\{5, 6\}$ to ensure a standardized measure of the model's performance.

B. Evaluation of LoRA with Different Ranks

In the adaptation experiments, we first evaluated the performance of LoRA under different rank configurations. Table I presents the recognition accuracy (Acc.) and calibration time (Time) for different rank values ($\{32, 64, 96\}$) across varying calibration data sizes (1 to 4 repetitions). The results reveal distinct patterns regarding the impact of rank values and calibration data sizes on recognition performance and calibration time.

For recognition accuracy, higher rank values consistently yield better performance across all calibration data sizes. For example, with 4 repetitions, the accuracy increases from

TABLE I

TRAINABLE PARAMETERS AND AVERAGE RECOGNITION ACCURACY FOR 10 NEW SUBJECTS ACROSS VARYING RANK VALUES AND AMOUNTS OF CALIBRATION DATA (200 MS WINDOW SIZE).

Training Strategy		**Acc. [%] /Time [s]**	**Calibration Data Sizes**				**#Trainable Parameters**
			1 Rep	2 Reps	3 Reps	4 Reps	
LoRA (different Rank)	32	Acc.	50.53±6.18	61.54±6.99	67.71±7.02	75.76±6.79	295,330
		Time	69.9	127.4	187.5	234.0	
	64	Acc.	53.10±7.45	64.12±7.53	69.17±6.83	77.62±7.36	555,378
		Time	70.1	122.7	184.9	234.9	
	96	Acc.	54.12±8.47	66.38±7.46	72.27±7.10	80.29±6.46	811,426
		Time	68.1	124.3	184.4	239.2	
Subject-specific model without transfer learning		Acc.	58.50±13.63	63.35±14.23	69.25±13.73	72.18±12.17	929,122
		Time	52.31	98.49	147.12	181.99	

75.76% for rank 32 to 77.62% for rank 64, and further to 80.29% for rank 96. This improvement reflects the greater capacity of models with higher ranks to generalize from calibration data. Calibration time, on the other hand, is primarily influenced by the calibration data size rather than the rank value. For all ranks, the calibration time increases almost linearly with the number of repetitions, from approximately 70 seconds with 1 repetition to around 239 seconds with 4 repetitions. The minor variations in calibration time across rank values (e.g., 234.0 s for rank 32, 234.9 s for rank 64, and 239.2 s for rank 96 with 4 repetitions) suggest that the computational overhead associated with increasing rank is negligible in this context.

These results emphasize the importance of calibration data in improving accuracy while demonstrating that the time required for calibration is mainly independent of the rank value. Rank 64 offers a strong balance between accuracy and model complexity, achieving significant performance gains over rank 32 with only a moderate increase in trainable parameters. Although rank 96 achieves slightly better accuracy, the marginal improvement suggests diminishing returns, making rank 64 a practical choice for balancing performance and computational demands in real-world applications.

In Table 1, we also provide the results for individual subject-specific models without using LoRA. The results show that using a pre-trained model with LoRA, under the same training data size, can improve accuracy while reducing the training parameter size.

C. Evaluation of LoRA with Different HD-sEMG windows size

Figure 4 illustrates the recognition accuracy across different rank values ($r = 32, 64, 96$) and calibration data sizes (1 to 4 repetitions) for two HD-sEMG window sizes: 100 ms and 200 ms. The Wilcoxon signed-rank test was conducted in this study. Asterisks (*) are used to indicate statistical significance with respect to p-values: 1) $p > 0.05$ is considered not significant (ns); 2) * denotes $0.01 < p \leq 0.05$; 3) ** denotes $0.001 \leq p \leq 0.01$. Across all rank values and calibration data sizes, the recognition accuracy is consistently higher when using a 200-ms window compared to a 100-ms window. For instance, with $r = 96$ and 4 repetitions, the accuracy for the 200ms window reaches approximately 80.29%, whereas it is noticeably lower (around 75.38%) for the 100ms window. This pattern suggests that the 200 ms window provides richer temporal information, enabling the model to better capture relevant features for recognition tasks.

These results show the importance of window size in determining recognition performance. While a larger window (200 ms) generally yields better accuracy, practical considerations such as real-time constraints and computational overhead must be taken into account when selecting the appropriate window size for specific applications.

V. CONCLUSIONS

This paper presents an effective hand gesture recognition approach leveraging LoRA to enhance model adaptability

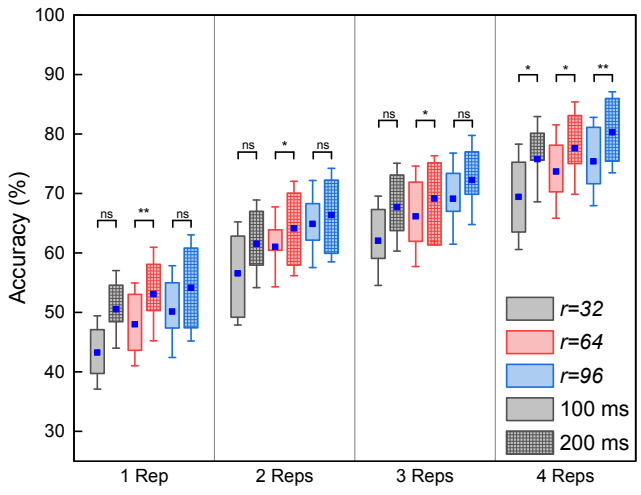


Fig. 4. Recognition accuracy boxplots of HGR performance for 10 new subjects with 100 ms and 200 ms HD-sEMG window size. Blue squares represent the average values.

for HD-sEMG signals. By aggregating data from multiple subjects during the pre-training phase, we developed a generalized model that efficiently customizes learning when introducing new subjects through the adjustment of a limited set of low-rank matrices. This method not only significantly reduces computational overhead but also ensures that the model rapidly adapts to new data characteristics, maintaining its efficiency and accuracy. Experimental results validate the reliability and flexibility of LoRA across different subjects, providing a strong foundation for future applications in gesture recognition, particularly in human-robot interaction and biomedical devices. The promising outcomes of this study position the LoRA approach as a valuable tool in advancing gesture recognition technology to meet increasing demands.

REFERENCES

[1] T. Song, H. Zhao, Z. Liu, H. Liu, Y. Hu, and D. Sun, "Intelligent human hand gesture recognition by local–global fusing quality-aware features," *Future Generation Computer Systems*, vol. 115, pp. 298–303, 2021.

[2] C. Gentile and E. Gruppioni, "A perspective on prosthetic hands control: From the brain to the hand," *Prosthesis*, vol. 5, no. 4, pp. 1184–1205, 2023.

[3] D. Farina, R. Merletti, and R. M. Enoka, "The extraction of neural strategies from the surface emg," *Journal of applied physiology*, vol. 96, no. 4, pp. 1486–1495, 2004.

[4] A. Jaramillo-Yánez, M. E. Benalcázar, and E. Mena-Maldonado, "Real-time hand gesture recognition using surface electromyography and machine learning: A systematic literature review," *Sensors*, vol. 20, no. 9, p. 2467, 2020.

[5] A. Ameri, M. A. Akhaee, E. Scheme, and K. Englehart, "Real-time, simultaneous myoelectric control using a convolutional neural network," *PloS one*, vol. 13, no. 9, p. e0203835, 2018.

[6] A. Holobar and D. Farina, "Noninvasive neural interfacing with wearable muscle sensors: Combining convolutive blind source separation methods and deep learning techniques for neural decoding," *IEEE signal processing magazine*, vol. 38, no. 4, pp. 103–118, 2021.

[7] S. Tam, M. Boukadoum, A. Campeau-Lecours, and B. Gosselin, "Intuitive real-time control strategy for high-density myoelectric hand prosthesis using deep and transfer learning," *Scientific Reports*, vol. 11, no. 1, p. 11275, 2021.

[8] P. R. Cavanagh and P. V. Komi, "Electromechanical delay in human skeletal muscle under concentric and eccentric contractions," *European journal of applied physiology and occupational physiology*, vol. 42, pp. 159–163, 1979.

[9] S. Kyeong, W. Shin, M. Yang, U. Heo, J.-r. Feng, and J. Kim, "Recognition of walking environments and gait period by surface electromyography," *Frontiers of Information Technology & Electronic Engineering*, vol. 20, no. 3, pp. 342–352, 2019.

[10] S. An, J. Feng, E. Song, K. Kong, J. Kim, and H. Choi, "High-accuracy hand gesture recognition on the wrist tendon group using pneumatic mechanomyography (pmmg)," *IEEE Transactions on Industrial Informatics*, vol. 20, no. 2, pp. 1550–1561, 2023.

[11] A. R. Asif, M. Waris, S. Gilani, M. Jamil, H. Ashraf, M. Shafique, and I. Niazi, "Performance evaluation of convolutional neural network for hand gesture recognition using emg," *Sensors*, vol. 20, 03 2020.

[12] J. Chen, S. Bi, G. Zhang, and G. Cao, "High-density surface emg-based gesture recognition using a 3d convolutional neural network," *Sensors*, vol. 20, p. 1201, 02 2020.

[13] H. Jeong, J. Feng, and J. Kim, "2.5 d laser-cutting-based customized fabrication of long-term wearable textile semg sensor: from design to intention recognition," *IEEE Robotics and Automation Letters*, vol. 7, no. 4, pp. 10 367–10 374, 2022.

[14] T. Sun, Q. Hu, J. Libby, and S. F. Atashzar, "Deep heterogeneous dilation of lstm for transient-phase gesture prediction through high-density electromyography: Towards application in neurorobotics," *IEEE Robotics and Automation Letters*, vol. 7, no. 2, pp. 2851–2858, 2022.

[15] A. Toro-Ossaba, J. Jaramillo-Tigreros, J. C. Tejada, A. Peña, A. López-González, and R. A. Castanho, "Lstm recurrent neural network for hand gesture recognition using emg signals," *Applied Sciences*, vol. 12, no. 19, 2022. [Online]. Available: https://www.mdpi.com/2076-3417/12/19/9700

[16] Y. Hu, Y. Wong, W. Wei, Y. Du, M. Kankanhalli, and W. Geng, "A novel attention-based hybrid cnn-rnn architecture for semg-based gesture recognition," *PloS one*, vol. 13, no. 10, p. e0206049, 2018.

[17] A. Vaswani, "Attention is all you need," *Advances in Neural Information Processing Systems*, 2017.

[18] S. Zabihi, E. Rahimian, A. Asif, and A. Mohammadi, "Trahgr: Transformer for hand gesture recognition via electromyography," *IEEE Transactions on Neural Systems and Rehabilitation Engineering*, 2023.

[19] Y. Liu, X. Li, L. Yang, and H. Yu, "A transformer-based gesture prediction model via semg sensor for human-robot interaction," *IEEE Transactions on Instrumentation and Measurement*, 2024.

[20] M. Montazerin, S. Zabihi, E. Rahimian, A. Mohammadi, and F. Naderkhani, "Vit-hgr: vision transformer-based hand gesture recognition from high density surface emg signals," in *2022 44th Annual International Conference of the IEEE Engineering in Medicine & Biology Society (EMBC)*. IEEE, 2022, pp. 5115–5119.

[21] Q. Hu, G. A. Azar, A. Fletcher, S. Rangan, and S. F. Atashzar, "Vit-mdhgr: Cross-day reliability and agility in dynamic hand gesture prediction via hd-semg signal decoding," *IEEE Journal of Selected Topics in Signal Processing*, 2024.

[22] E. J. Hu, Y. Shen, P. Wallis, Z. Allen-Zhu, Y. Li, S. Wang, and W. Chen, "Lora: Low-rank adaptation of large language models," *CoRR*, vol. abs/2106.09685, 2021. [Online]. Available: https://arxiv.org/abs/2106.09685

[23] X. Jiang, X. Liu, J. Fan, X. Ye, C. Dai, E. A. Clancy, M. Akay, and W. Chen, "Open access dataset, toolbox and benchmark processing results of high-density surface electromyogram recordings," *IEEE Transactions on Neural Systems and Rehabilitation Engineering*, vol. 29, pp. 1035–1046, 2021.

[24] J. Fan, X. Jiang, X. Liu, X. Zhao, X. Ye, C. Dai, M. Akay, and W. Chen, "Cancelable hd-semg biometric identification via deep feature learning," *IEEE Journal of Biomedical and Health Informatics*, vol. 26, no. 4, pp. 1782–1793, 2022.

[25] G. A. Azar, Q. Hu, M. Emami, A. Fletcher, S. Rangan, and S. F. Atashzar, "A deep learning sequential decoder for transient high-density electromyography in hand gesture recognition using subject-embedded transfer learning," *IEEE Sensors Journal*, vol. 24, no. 9, pp. 14 778–14 791, 2024.

Enhancing Comfort and Repeatability of Human-Robot Attachment Systems: Comparison of a Compliant Orthosis for BLUE SABINO

Emile C. Johnson, Joel C. Perry, Christopher K. Bitikofer
Assistive Robotics Lab, Mechanical Engineering Department
University of Idaho
Moscow, ID, USA
john1816@vandals.uidaho.edu, jperry@uidaho.edu, bitikofer@uidaho.edu

***Abstract*— The human-robot attachments (HRA) connecting humans to exoskeleton robots should facilitate user independence, efficient donning/doffing, maintain user-robot-kinematic alignment using interfaces that are sufficiently rigid, comfortable to wear, and (with the aid of the exoskeleton) accommodate dexterous human motion. This report presents a proof-of-concept comparison of an innovative self-aligning, size-adjustable HRA system designed for the upper arm. A novel discretely contracting orthosis adjusted by a dial ratcheting cable mechanism was fabricated from flexible and semi-rigid plastics to improve support and rigidity. Experiments comparing this new design to an existing rigid HRA design for the BLUE SABINO are conducted to characterize suitability in terms of ability to maintain kinematic alignment and to distribute interaction forces evenly on the user's arm. Piezoelectric force-sensitive-resistor sensors embedded in an elastic sleeve are used to measure human/orthosis interface forces at 8 Locations distributed on the circumference of the arm interface. Kinematic alignment was assessed for 5th-percentile female to 95th-percentile male sizes using 3D-printed mock arm cross sections. Laser alignment experiments found that the proposed device reduced arm center to orthosis center misalignment magnitude by up to 11.5 mm for 5th percentile male arm circumference vs. the existing design. Force measurements are inconclusive but indicate the potential to alter force distribution while being adequately adjustable and usable with repeatable settings.**

Keywords—human-robot interaction, orthosis design, rehabilitation robotics, compliant mechanism design.

I. INTRODUCTION

Stroke is a significant cause of physical disability, affecting approximately 1.3 million people annually [1]. Arm and hand impairments are the most common long-term consequence of stroke [2]. Traditional physical therapy is effective [3] but labor-intensive and expensive. Aging populations [4] and a limited supply of skilled therapists [5] have inspired the development of robotic solutions to decrease therapy labor requirements, investigate factors that promote recovery, and simultaneously assess and train users [6]–[10]. Research efforts have increasingly sought exoskeleton solutions that can simultaneously assist and train the upper limb and provide features such as gravity support and motion guidance [8], [11]. A growing body of evidence suggests that patient engagement is critical to recovery, with patients benefiting most from higher-intensity/longer-duration therapy and training protocols that continually adapt assistance according to patient performance [12]. Extended-duration therapies necessitate a design focus on the comfort and functionality of human-robot attachment systems to maintain users' motivation to undergo challenging therapy and work within clinical settings' inherent time constraints [13].

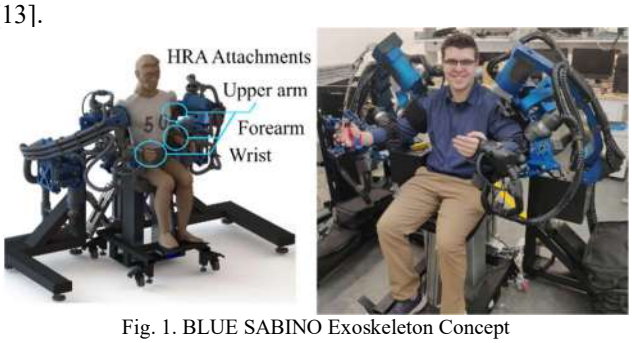


Fig. 1. BLUE SABINO Exoskeleton Concept

BLUE SABINO (BiLateral Upper-extremity Exoskeleton for Simultaneous Assessment of Biomechanical and Neuromuscular Output) (Figure 1) [14] is an 18-degree-of-freedom rehabilitative exoskeleton currently being developed at the University of Idaho. BLUE SABINO was developed with three HRA interfaces per arm, achieving size adaptability via 3D-printed sliding orthoses. However, kinematic misalignment between user and exoskeleton joints can still occur when users' arms are significantly above or below the 50th percentile. In addition, BLUE SABINO is intended to provide gravity assistance for users whose neurological impairment limits their ability to support the weight of their arm independently. In such cases, pressure at the orthotic interfaces can be concentrated, particularly around interface edges, and become uncomfortable. This is typically alleviated by including foam layers and large rounds on interface edges to distribute pressure, but foam inserts can reduce the precision of user-robot kinematic alignment. Furthermore, BLUE SABINO's primary force control uses force sensors between the HRA interfaces and the exoskeleton structure. The readings acquired by these sensors are affected by the rigidity of the HRA connection to the user. Therefore, consistency of exoskeleton measurements may be

influenced by the repeatability of donning aspects such as strap tensioning and user alignment. This project focuses on designing an alternate HRA system for devices like BLUE SABINO to improve kinematic misalignment, force distribution, and repeatability of orthosis securement to the upper limb.

II. Background

A. Compliance and Rigidity in HRA Systems

The dynamics of human-robot interaction must be designed to enable precise and repeatable control of interaction force and position [15]. Furthermore, human and robot joints should remain aligned during use since misalignment creates undesired interaction forces that can be uncomfortable or present a hazard to the user, depending on magnitude [16]. Stiff attachment constraints between the user and robot are desirable to facilitate high force transmission bandwidth, enforce alignment, and improve the accuracy of human joint angle estimation. On the other hand, some level of compliance in HRA is required. The complexity of human kinematics requires exoskeleton designs to approximate human's natural motion, meaning that even high-DOF devices inevitably suffer some degree of misalignment that is taken up in HRA [17]. Additionally, connection interfaces along the limb must account for the internal structure of the limb, including bony and fleshy areas, which change shape depending on joint positions. How to appropriately balance compliance vs rigidity in HRA connections remains an open question, so adjustable HRA devices that provide measurable and repeatable connection stiffness are needed.

B. HRA Designs State-of-the-Art

Traditional HRA designs use U-shaped cuffs and fabric straps to achieve size adjustability but often favor too much compliance, resulting in large or small users being poorly aligned with devices without significant care and attention from operators. Zimmerman et al. [18] proposed a design that included self-centering features, significantly improving reported user comfort and perceived device controllability. Simultaneously, growing attention is being placed on soft manipulators, including cable and pneumatically actuated components, to control force while manipulating objects precisely. Leveraging compliance in the design of HRA components for exoskeletons can enable improved control of the interfaces along with a better ability to align the user and exoskeleton joints. This is because a compliant orthosis can achieve far more adaptability in terms of geometry than a rigid shell. Further, compliance in the HRA can be designed to spread interaction forces more intentionally to enhance comfort and optimize overall rigidity.

III. Methods

A. Technical Requirements

To investigate the efficacy of a compliant HRA system design, a prototype orthosis was developed for the upper arm. Major design criteria were as follows:

1) Adjustability:

High-performance rehabilitative exoskeletons are multi-user devices, and it is therefore necessary to accommodate a large population range. The time required to fit devices to users by changing components or adjusting sizes in clinical applications should be limited. BLUE SABINO supports subjects sized approximately from the 5th-percentile female to 95th-percentile male; thus, the proposed orthosis design must accommodate at least this range. The corresponding diameter range for the upper arm is 70mm – 110mm [19].

2) Self-Centering:

Proper joint alignment enables repeatable human-robot interaction (HRI) measurement, essential to safe exoskeleton control [20]. On BLUE SABINO, the upper arm orthosis is located near the shoulder above the elbow. Angular alignment of the arm's long axis and center alignment on the upper-arms remote center of rotation locate the user's shoulder concerning the device, so the ability of the upper arm HRA to maintain this alignment is critical.

3) User Independence

Poor usability of assistive devices has been shown to lead to lower user acceptance rates and increased treatment abandonment [21], [22]. Patients who have suffered strokes often struggle to move their hands and limbs through small openings due to reduced motor control [3]. For this reason, the orthosis design should allow donning in a fully open configuration (rather than bypassing the arm through a closed loop) and have a method of securing and adjustment that can be easily performed with one hand.

4) Discrete Control/Repeatable

To optimize the balance between user comfort and attachment stiffness, the tightness of the orthosis must be quickly and incrementally adjustable. The design must allow fast and repeatable tensioning so that data collected over several sessions remains comparable and captures relevant information on user improvement rather than being overshadowed by misalignment effects. Finally, a readout of tension level is desirable to assist in repeatably setting (or adjusting) settings for desired patient comfort.

5) Comfortable

To enable extended therapy sessions, the orthosis must be comfortable for the user [23]. It's also vital that the HRA impedes patient movement as little as possible while using the exoskeleton [17]. Comfort is a subjective measurement, but objective measurements of force distribution from the orthosis can be used to evaluate comfort and transparency of the device.

B. Proposed solution

A cuff design has been developed with eight 3D-printed PLA linkages, connected in an octagon via a 3D-printed TPU outer shell (Figure 2). These linkages have cabling run through 4 channels, which are fed through a custom-made dual ratcheting dial. This outer shell maintains gaps between the linkages, so when the cabling is pulled, the walls of the

gaps are pushed inwards, and the mechanism contracts, reducing the overall diameter of the cuff.

The cuff is 100 mm long to adequately and comfortably distribute pressure on the upper arm. It can be opened, allowing donning/doffing without requiring a user to maneuver their arm through closed loops. It is secured via two cable loops, which wrap on embedded posts near the dual ratcheting system.

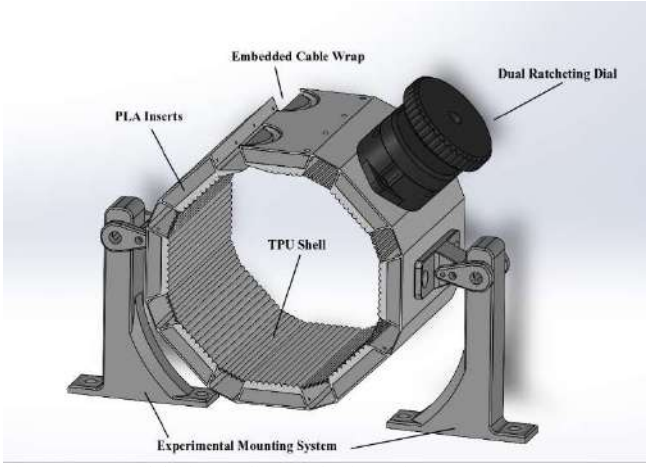


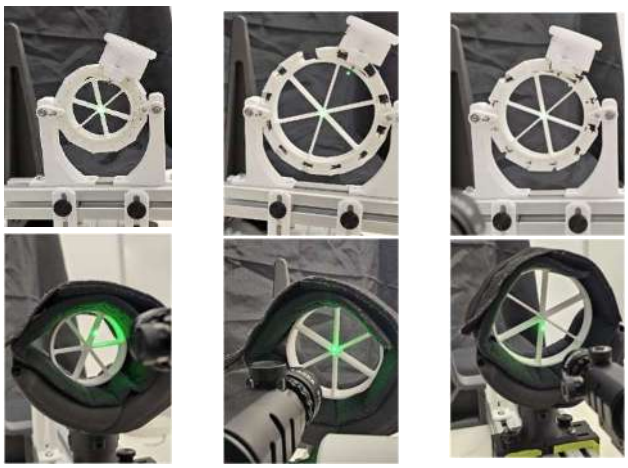
Fig. 2: CAD model of Compliant Orthosis Design

C. Experimental Evaluation

To establish initial evaluations of the prototype design, experimental comparisons are conducted with the prototype-compliant design and the present rigid shell orthosis from the BLUE SABINO exoskeleton. These tests evaluate 1) arm center to HRA center alignment, 2) Force distribution between the orthosis and user interface, and 3) volunteer-reported comfort while wearing each orthosis for a short time. Alignment data were collected with printed/molded arm mocks to facilitate direct center measurements. Force and comfort measures were collected from five healthy volunteers (one m, 4 f, ages 18 to 21). Participants provided written, informed consent, and tests were conducted according to protocol approved by the University of Idaho's Institutional Review Board (IRB #22-093).

1) Self-Centering Evaluation via Laser Scope

A laser alignment setup was constructed to measure the ability of orthoses to center a user's arm and differing diameter settings. The setup consists of a laser scope mounted in line with the orthosis. The orthosis was loaded with a mold-cast synthetic arm section, representing a 50th-percentile male bicep, with a marked center to which the laser was aligned. The orthosis was then loaded with circular 3D-printed pieces representing the 5th-percentile female (70mm diameter),
50th-percentile male (95mm diameter), and 95th-percentile male (110mm diameter) upper arms. The absolute planar distance between the marked center of these 3D-printed pieces and the laser point was measured to the nearest 0.1 mm using digital calipers (Fig 3).


Fig 3: Kinetic Alignment of Compliant (Top) and Solid Orthosis, using 5th (Right), 50th (Center), and 95th (Left) percentile cross section.

2) Force Distribution and User Reported Short Duration Comfort

a) Force Distribution

A testing apparatus arm band (Fig 4) containing an array of eight FlexiForce [24] piezoelectric sensors was created to measure the forces exerted at discrete points around the arm. The sensors were held in place by fabric loops to maintain equal spacing around the arm while the elastic arm band stretches to the accommodate diameter size variations as necessary (Fig 4).

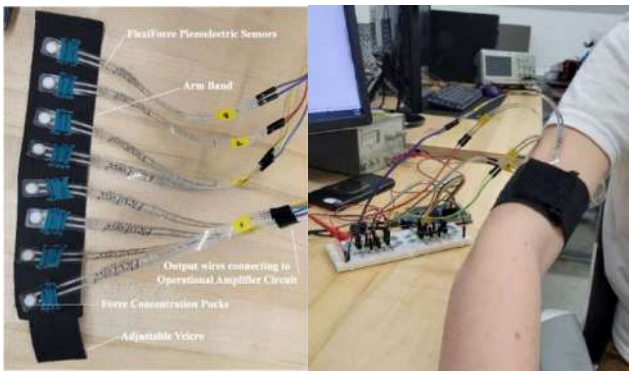


Fig 4. Arm Band FSR Testing apparatus with FlexiForce sensors while not worn (LEFT) and fit to a subject's upper arm (RIGHT).

Comfort was evaluated using this testing apparatus to measure pressure across the orthosis and identify high-pressure areas and overall pressure distribution. Participants wore the armband before donning the orthosis, and baseline force data was collected over 30 seconds. Once in the orthosis (Fig 5), force data was again collected over a period of one minute.

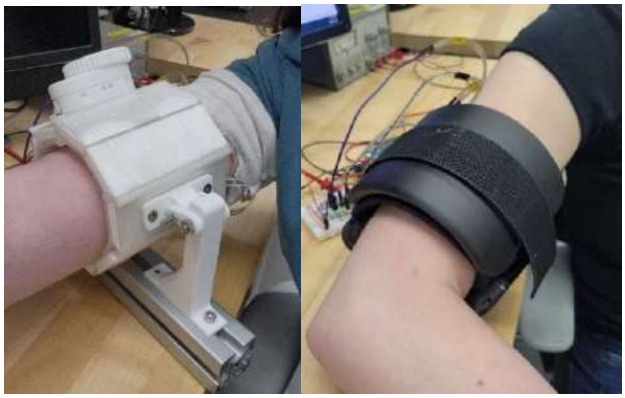


Fig 5. Participants secured in the prototype compliant orthosis (LEFT) and BLUE SABINO's solid orthosis (RIGHT) while collecting interaction force data.

b) Sensor Calibration and Data Processing

The piezoelectric sensors used generate a nonlinear output based on the force applied. Thus, calibration curves were generated for each sensor to map voltage readings to measured force. To this end, each sensor was incrementally placed under load using weights from 5 grams to 500 grams using a hanging force concentrator (Fig 6).



Fig 6. Sensor Calibration using hanging weight and force concentrator

The output voltages were recorded, and using MATLAB's "lsqcurvefit," a nonlinear least squares regression was applied to fit the a model of form :

$$y_N = p_1 e^{-p_2 x} + p_3$$

This model and the generated fit parameters provide a map that converts measured voltage readings from each sensor to force in (Newtons). The resulting calibrations were validated by applying various known weights and having MATLAB output the weights based on the corresponding calibration curve.

3) Comfort evaluation

Following the force distribution analysis, the patients were asked to evaluate the comfort of each orthosis using the Likert scale seen in Table 1. Patients were then encouraged to describe the comfort or discomfort further and what features they felt contributed to it and this feedback was also recorded.

TABLE I. COMFORT EVALUATION LIKERT SCALE

1	2	3	4	5
Very Uncomfortable	Somewhat Uncomfortable	Neutral	Somewhat Comfortable	Totally Comfortable

IV. RESULTS

Table II shows the misalignment measured from the laser scope to the center of the respective 3D printed section. The measurements are for the proposed flexible orthosis and the current solid design for 5th, 50th, and 95th percentile arm diameters.

TABLE II. MEASURED MISALIGNMENT

Device	**5th % (mm)**	**50th % (mm)**	**95th % (mm)**	**Average (mm)**
Flexible Orthosis	0.0	0.0	0.0	0.0
Solid Orthosis	11.5	2.7	10.3	8.2

Figures 7 and 8 illustrate forces measured during patient testing using the piezoelectric sensors on polar plots where 90 degrees (top) corresponds with the topmost point of the orthosis during experiments. The force between the points is estimated using MATLAB's "interp1" spline interpolation tool.

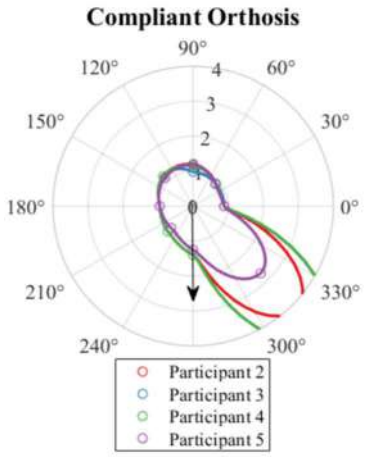


Fig. 7: Force Distribution for Compliant Orthosis

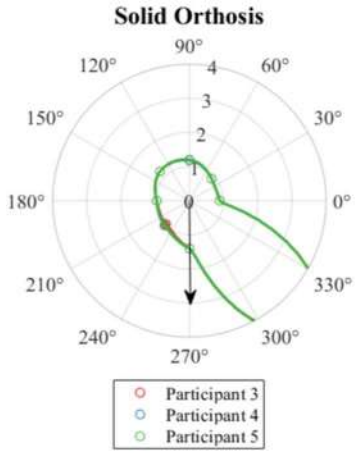


Fig. 8: Force Distribution for Solid Orthosis

Table III shows the results from the comfort evaluation using the Likert scale (Table I). The table includes participant data for solid and compliant orthoses and displays the total force measured and their arm circumference. Participant 1 had data recorded, but it was deemed unusable due to their arm size being under the 5th percentile.

TABLE III. CASE STUDY WITH 5 PARTICIPANTS

Participant	Upper arm diameter (mm)	Total Force (N) - Solid	Solid Orthosis Likert	Total Force (N) - Compliant	Compliant Orthosis Likert
2	76.4	N/A	3	11.75	4
3	89.1	12.64	4	12.48	4
4	87.5	12.68	4	12.65	4
5	90.7	12.68	N/A	9.93	N/A

V. DISCUSSION

The alignment comparison results demonstrate that the prototype design can better maintain proper center alignment across the necessary size range. Further testing with the prototype mounted to an exoskeleton is required to evaluate user-to-exoskeleton joint center alignment differences in a realistic application. The force distribution results are less conclusive, with both the solid and compliant designs achieving very similar levels of force and similar profiles. Indicating an issue with the data collection system. In both cases, FSRs under the arm experienced significantly more loading due to gravity, making it difficult to discern other differences. The comfort results are comparable to the current solid orthosis design. Still, some participants mentioned that the solid orthosis made the force concentrator bumps more noticeable than the compliant orthosis, indicating that the compliant orthosis.

VI. CONCLUSION

This project introduced a novel, compliant Human-Robot Attachment system for BLUE SABINO and other similar applications. A novel force testing apparatus and method of comparing orthotic systems has also been proposed through a proof-of-concept upper arm orthosis. The orthosis design proposed fulfills crucial requirements of adaptability from 5th to 95th percentile subjects, self-centering, independent usability, discrete control, and repeatability. These developments aim to further the work towards rehabilitative exoskeletons and highlight an often-overlooked feature of such systems.

VII. FUTURE WORK

The proposed HRA design will continue to be developed, with special care taken on the usability and comfort aspects of the design. Further design iteration is planned to and will consider the addition of a 3-point contact HRA using the developed compliant technology. It is planned to refine the force measurement systems for higher accuracy and develop a simple readout of the total force on the user. Further testing will be done to time the donning and doffing speed with untrained and trained participants to further determine independent usability. These HRA designs will then be applied to BLUE SABINO, and further testing will cover ADLs (Activities of Daily Living). Motion capture systems will be used on the exoskeleton to measure if/how the misalignment changes while in movement. If these orthosis designs are deemed successful and valuable for BLUE SABINO, they will be integrated across the other HRAs.

ACKNOWLEDGMENT

The authors would like to thank the University of Idaho Office of Undergraduate Research for awarding a Summer Undergraduate Research Fellowship to develop this project and to the DeVlieg Scholars Fund for supporting continuing work during the school year.

REFERENCES

[1] V. L. Feigin et al., "Global, regional, and national burden of stroke and its risk factors, 1990–2019: a systematic analysis for the Global Burden of Disease Study 2019," Lancet Neurol., vol. 20, no. 10, pp. 795–820, Oct. 2021, doi: 10.1016/S1474-4422(21)00252-0.

[2] L. Alrabghi et al., "Stroke types and management," Int. J. Community Med. Public Health, vol. 5, no. 9, p. 3715, Aug. 2018, doi: 10.18203/2394-6040.ijcmph20183439.

[3] P. Langhorne, J. Bernhardt, and G. Kwakkel, "Stroke rehabilitation," The Lancet, vol. 377, no. 9778, pp. 1693–1702, May 2011, doi: 10.1016/S0140-6736(11)60325-5.

[4] H. Ritchie and M. Roser, "Age Structure," Our World Data, Sep. 2019, Accessed: Jan. 25, 2023. [Online]. Available: https://ourworldindata.org/age-structure

[5] T. Platz, L. Schmuck, S. Roschka, and J. Burridge, "Arm Rehabilitation," in Clinical Pathways in Stroke Rehabilitation: Evidence-based Clinical Practice Recommendations, 2021, pp. 97–121. doi: 10.1007/978-3-030-58505-1_7.

[6] W. H. Chang and Y.-H. Kim, "Robot-assisted Therapy in Stroke Rehabilitation," J. Stroke, vol. 15, no. 3, pp. 174–181, Sep. 2013, doi: 10.5853/jos.2013.15.3.174.

[7] C. M. L. Hughes, P. Tommasino, A. Budhota, and D. Campolo, "Upper Extremity Proprioception in Healthy Aging and Stroke Populations, and the Effects of Therapist- and Robot-Based Rehabilitation Therapies on Proprioceptive Function," Front. Hum.Neurosci., vol. 9, 2015, Accessed: Jan. 26, 2023. [Online]. Available: https://www.frontiersin.org/articles/10.3389/fnhum.2015.00120

[8] R. A. R. C. Gopura, D. S. V. Bandara, K. Kiguchi, and G. K. I. Mann, "Developments in hardware systems of active upper-limb exoskeleton robots: A review," Robot. Auton. Syst., vol. 75, pp. 203–220, Jan. 2016, doi: 10.1016/j.robot.2015.10.001.

[9] L. Santisteban, M. Térémetz, J.-P. Bleton, J.-C. Baron, M. A. Maier, and P. G. Lindberg, "Upper Limb Outcome Measures Used in Stroke Rehabilitation Studies: A Systematic Literature Review," PLoS ONE, vol. 11, no. 5, p. e0154792, May 2016, doi: 10.1371/journal.pone.0154792.

[10] R. Colombo et al., "Robotic techniques for upper limb evaluation and rehabilitation of stroke patients," IEEE Trans. Neural Syst. Rehabil. Eng., vol. 13, no. 3, pp. 311–324, Sep. 2005, doi: 10.1109/TNSRE.2005.848352.

[11] E. T. Wolbrecht, V. Chan, D. J. Reinkensmeyer, and J. E. Bobrow, "Optimizing Compliant, Model-Based Robotic Assistance to Promote Neurorehabilitation," IEEE Trans. Neural Syst. Rehabil. Eng., vol. 16, no. 3, pp. 286–297, Jun. 2008, doi: 10.1109/TNSRE.2008.918389.

[12] V. Bartenbach, "Constraints caused by lower extremity exoskeletons," Ph.D. dissertation, Dept. Health Sci. Technol., ETH Zurich, Zurich, Switzerland, 2017. [Online]. Available: https://doi.org/10.3929/ethz-b-000161421

[13] J. T. Meyer, S. O. Schrade, O. Lambercy, and R. Gassert, "User-centered Design and Evaluation of Physical Interfaces for an Exoskeleton for Paraplegic Users," in 2019 IEEE 16th International Conference on Rehabilitation Robotics (ICORR), Jun. 2019, pp. 1159–1166. doi: 10.1109/ICORR.2019.8779527.

[14] C. K. Bitikofer, S. R. Parra, R. Maura, E. T. Wolbrecht, and J. C. Perry, “BLUE SABINO: Development of a BiLateral Upper-Limb exoskeleton for simultaneous assessment of biomechanical and neuromuscular output,” Machines, vol. 12, no. 9, p. 617, Sep. 2024, doi: 10.3390/machines12090617.

[15] N. Jarrasse and G. Morel, “Connecting a human limb to an exoskeleton,” IEEE Transactions on Robotics, vol. 28, no. 3, pp. 697–709, Jun. 2012. doi:10.1109/tro.2011.2178151

[16] Y. Akiyama, Y. Yamada, K. Ito, S. Oda, S. Okamoto, and S. Hara, "Test method for contact safety assessment of a wearable robot -analysis of load caused by a misalignment of the knee joint-," in 2012 IEEE RO-MAN: The 21st IEEE International Symposium on Robot and Human Interactive Communication, Sep. 2012, pp. 539–544. doi: 10.1109/ROMAN.2012.6343807.

[17] N. JarrassÃ© et al., “Robotic exoskeletons: A perspective for the rehabilitation of arm coordination in stroke patients,” Frontiers in Human Neuroscience, vol. 8, Dec. 2014. doi:10.3389/fnhum.2014.00947

[18] Y. Zimmermann et al., "Human–Robot Attachment System for Exoskeletons: Design and Performance Analysis," IEEE Trans. Robot., vol. 39, no. 4, pp. 3087–3105, Aug. 2023, doi: 10.1109/TRO.2023.3268587.

[19] "National aerospace and space administration: Anthropometry and biomechanics", Apr. 2022, [online] Available: https://msis.jsc.nasa.gov/sections/Section03.htm

[20] “Human-Exoskeleton Joint Misalignment: A Systematic review,” IEEE Conference Publication | IEEE Xplore, Oct. 01, 2019. https://ieeexplore.ieee.org/document/8940321

[21] J. Gantenbein, J. Dittli, J. T. Meyer, R. Gassert, and O. Lambercy, “Intention detection strategies for robotic upper-limb orthoses: A scoping review considering usability, daily life application, and User Evaluation,” Frontiers in Neurorobotics, vol. 16, Feb. 2022. doi:10.3389/fnbot.2022.815693

[22] A. T. Sugawara, V. D. Ramos, F. M. Alfieri, and L. R. Battistella, “Abandonment of assistive products: Assessing abandonment levels and factors that impact on it,” Disability and Rehabilitation: Assistive Technology, vol. 13, no. 7, pp. 716–723, Jan. 2018. doi:10.1080/17483107.2018.1425748

[23] D. Patel et al., “Optimizing Children’s hand orthosis design: A study on contact pressure distribution using FSR sensors,” Materials & Design, vol. 251, p. 113679, Mar. 2025. doi:10.1016/j.matdes.2025.113679

[24] Tekscan, https://www.tekscan.com/sites/default/files/FLX-Datasheet-A201-RevI.pdf (accessed Feb. 22, 2025).

Structural Optimization of a Passive ExoNET for Forearm Supination

Valentino Wilson[1,2*], Partha Ryali[1,2], Leah O'Shea[1], Adith Srivatsa[1,2], Mac Camardo[1,2], Courtney Celian[1] and James L. Patton[1,2]

***Abstract*— Impairments in forearm supination are a common consequence of stroke, impeding essential activities of daily living and hand-object interactions. To address this, we present a forearm ExoNET—a novel, passive, wearable device designed to both assist and improve forearm supination for stroke survivors and others with movement deficits by generating clinician-defined, multijoint torque patterns using elastic actuators. Guided by torque deficit measurements from a custom-designed diagnostic device and driven by a mathematical model and structural optimization algorithm, the forearm ExoNET can be customized in real time to meet individual needs, providing configurations that deliver both assistive and therapeutic applied torque fields. Initial results demonstrate that the diagnostic device effectively identifies supination torque deficits in stroke survivors, while the optimization algorithm achieves strong predictive accuracy (R^2 = 0.987) in designing ExoNET configurations to counteract these deficits. These findings underscore the forearm ExoNET's potential to support active supination across the full range of motion, offering a low-cost, accessible solution with significant promise for improving upper-limb rehabilitation outcomes.**

I. INTRODUCTION

Forearm supination is essential for hand positioning during many activities of daily living, such as reaching, grasping, and manipulating objects. Reductions in forearm range of motion impair the ability to position the hand effectively [1] and diminish strength [2] during these tasks. After a stroke, individuals often experience motor impairments that compromise their ability to supinate the forearm, making tasks such as turning a doorknob, using utensils, or picking up objects challenging [3]. These impairments are part of broader sensorimotor deficits caused by stroke, which not only limit functional arm use but often result in compensatory strategies that lead to muscle imbalances and injury [4], [5]. Compounding these challenges, stroke survivors frequently exhibit abnormal joint coordination and altered muscle synergies across the upper limb [6], which can disrupt functional movement and limit precise motor control, further affecting forearm and hand positioning. Decreased arm use can exacerbate these challenges by leading to learned non-use, a vicious cycle of impairment that further diminishes muscle strength and gives rise to secondary effects such as contracture [7]. While large-scale arm therapy studies, such as the EXCITE [8] and ICARE trials [9], demonstrated improvements on clinical scores, substantial deficits persisted, particularly in resolving impairments that critically affect bimanual tasks—many of which depend on forearm supination. Therapeutic efforts to remediate the forearm and wrist, while promising, do not lead to recovery, thereby leaving many adults with life-long deficits [10].

Rehabilitation technology has predominantly focused on hand location rather than hand orientation [11], creating a significant gap in practical supination-supporting devices. Many existing solutions, such as the Bi-Manu-Track [12] and Haptic Knob [13], are large, non-wearable robotic systems, impractical for use during daily activities. While more portable options exist—such as the fabric-based helical actuator developed by Realmuto and Sanger [14] and the pneumatically powered sleeve by Park et al. [15]—they depend on external air supply systems, limiting real-world applicability. Other devices, such as the CRUX exotendon suit [16], use motors and a cable-driven system for active assistance but focus on general upper-limb augmentation rather than targeted supination support, lacking task-specific torque modulation. A more targeted solution is the guided double-rod active exoskeleton by Dezman et al. [17], which offers pronation/supination assistance in a compact form. However, such active devices rely on powered actuation—batteries, motors, and control algorithms—resulting in increased cost, complexity, and power dependence. Despite these advances, the field still lacks a system that is simultaneously wearable, inexpensive, lightweight, easy to use, and unintimidating for both users and clinicians.

The forearm ExoNET (Exoskeletal Network for Elastic Torque) presented here addresses these limitations and seeks to fill this critical gap. We present an alternative approach to motorized systems: the use of spring elements without a rigid skeleton. Such passive exoskeletal devices have excitingly been shown to assist walking [18] and running [19], but effective wearable units have yet to be developed for the forearm. The forearm ExoNET is a passive, wearable device designed specifically to support forearm supination by using a network of elastic actuators that can be configured to generate clinician-specified torque patterns. Instead of relying on software-based control, the ExoNET utilizes hardware-encoded torque generation, where actuator configurations are pre-programmed through structural optimization of material properties, geometry, and attachment points. This design enables targeted torque delivery while allowing the system to recycle energy efficiently, without the need for motors, controllers, sensors, or external power. The first realization

Research is supported by NIDILRR RERC Grant 90REGE0017.

[1]All authors are with the Robotics Lab, Center for Neural Plasticity, Shirley Ryan AbilityLab, Chicago, IL, USA.

[2]Valentino Wilson, Partha Ryali, Adith Srivatsa, Mac Camardo, and James L. Patton are with the Richard and Loan Hill Department of Biomedical Engineering, University of Illinois Chicago, Chicago, IL, USA.

[*]Valentino Wilson is corresponding author, viwilso2@uic.edu.

of the ExoNET concept was the MARIONET (Moment Arm Adjustment for Remote Induction of Net Effective Torque), a device that modulates generated torque by adjusting the moment arm [20], [21]. This approach introduced a novel method for delivering torque to a joint, which has since been applied in various systems utilizing diagonal tension elements [21], [22], [23]. These applications include counteracting the effects of gravity during upper extremity reaching tasks [24], [25], [26] and supplementing muscle torque during gait [27], [28]. The forearm ExoNET represents the next evolution of this system, advancing the concept as a logical progression in its development.

The forearm ExoNET is configurable as both 1) an assistive orthotic that facilitates forearm supination and hand positioning for everyday tasks, and 2) a therapeutic device that strengthens supinator muscles and fosters motor coordination. The device can uniquely combine these functions by first providing resistance throughout the user's active range of motion, then transitioning to assistance upon reaching their movement limit (Fig. 1), thus encouraging active engagement while ensuring full supination. Prior research supports this approach, demonstrating that structured modulation of resistance during movement can enhance functional performance and facilitate motor learning [29]. To maximize its effectiveness, the ExoNET can be optimized to provide personalized support for each user's torque deficits. A custom-designed diagnostic tool measures a user's peak supination torque at multiple discrete angles, which are then compared to a neurotypical average to quantify these deficits. The arrangement of the elastic actuators is then tailored to meet each user's needs through a structural optimization model. Each tension element generates a sinusoidal torque profile that functions mathematically as a basis function, which can be linearly combined to achieve any desired torque profile through tuning via optimization [24].

By using passive elastic elements, the forearm ExoNET is lightweight, portable and safe to operate by a wide range of users. Its passive elastic actuators eliminate the need for complex controls, making the device simple and intuitive to operate. The simplicity of the device's design enables clinicians, care partners, and users to adjust its structure in real time. The ExoNET's passive design, simple construction, and user-centered approach make it affordable ($50 to manufacture) and accessible, reducing barriers to advanced rehabilitation technology and offering significant potential to enhance users' quality of life.

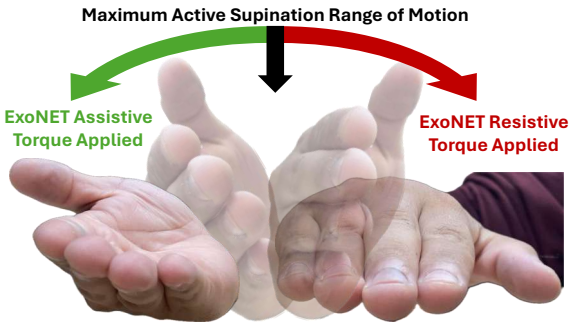


Fig. 1. Torque delivery mechanics of the forearm ExoNET. The device resists active supination and transitions to assistance at the maximum range. This dynamic response promotes muscle engagement while enabling full supination, highlighting its combined assistive and therapeutic capabilities.

In this paper, we outline the theoretical model of the forearm ExoNET, detailing the optimization algorithm for user-specific configurations, and present initial results demonstrating its potential for use in clinical settings.

II. METHODS

A. Device Actuation and Mathematical Representation

The forearm ExoNET can comprise two types of actuators—helical bungee cords and shutter springs—designed to create stable and unstable equilibrium states for controlled assistance and resistance during supination. The device's 3D-printed forearm and wrist bands, made of Thermoplastic Polyurethane (TPU), anchor the actuators to the body and are positioned distal to the elbow and proximal to the wrist, respectively. For simulation and optimization, the forearm is modeled as a frustum with elliptical cross-sections at the proximal and distal ends to accurately capture its tapered geometry. This representation enables precise modeling of actuator force vectors and torque generation.

1) Helical Bungee Actuator: The helical bungee actuator provides a stable equilibrium, offering consistent assistance or resistance across the full supination range (Fig. 2(g), blue curve). It is helically wrapped between the forearm and wrist bands (Fig. 2(a)) to optimize force transfer to the wrist through precisely oriented force vectors, thereby maximizing torque efficiency. The actuator is offset from the skin to enhance user comfort, and its length can be adjusted in real time to allow for fine-tuning of the applied torque magnitude to align with specific therapeutic objectives. This actuator can also be integrated with other types to balance stability and bias movement toward either assistance or resistance.

The actuator is mathematically modeled as a series of discrete spring segments along a helical path around the forearm (Fig. 2(e)). Each segment is treated as an individual spring with unique characteristics, allowing for variations in spring stiffnesses and resting lengths. This segmented approach provides a more accurate representation of the actuator's wrapping mechanics, enhancing the model's ability to simulate realistic behavior. The helical path of the bungee actuator is defined using parametric equations (1) that specify the positions of discrete points (nodes) along the helix. The helix is characterized by an average radius (r), axial distance between attachment points (h), number of helical turns (n), and angular change along the helix (u).

$$\begin{cases} x(u) = r\cos(u), \\ y(u) = r\sin(u), \quad u \in [0, 2\pi] \\ z(u) = \frac{h}{2\pi n}u, \end{cases} \tag{1}$$

To maintain this helical configuration, the actuator's trajectory is influenced by the height difference between the wrist and forearm attachment points ($h_{\text{w_mnt}}$, $h_{\text{f_mnt}}$) and their respective angular offsets ($\theta_{\text{w_mnt}}$, $\theta_{\text{f_mnt}}$), which define

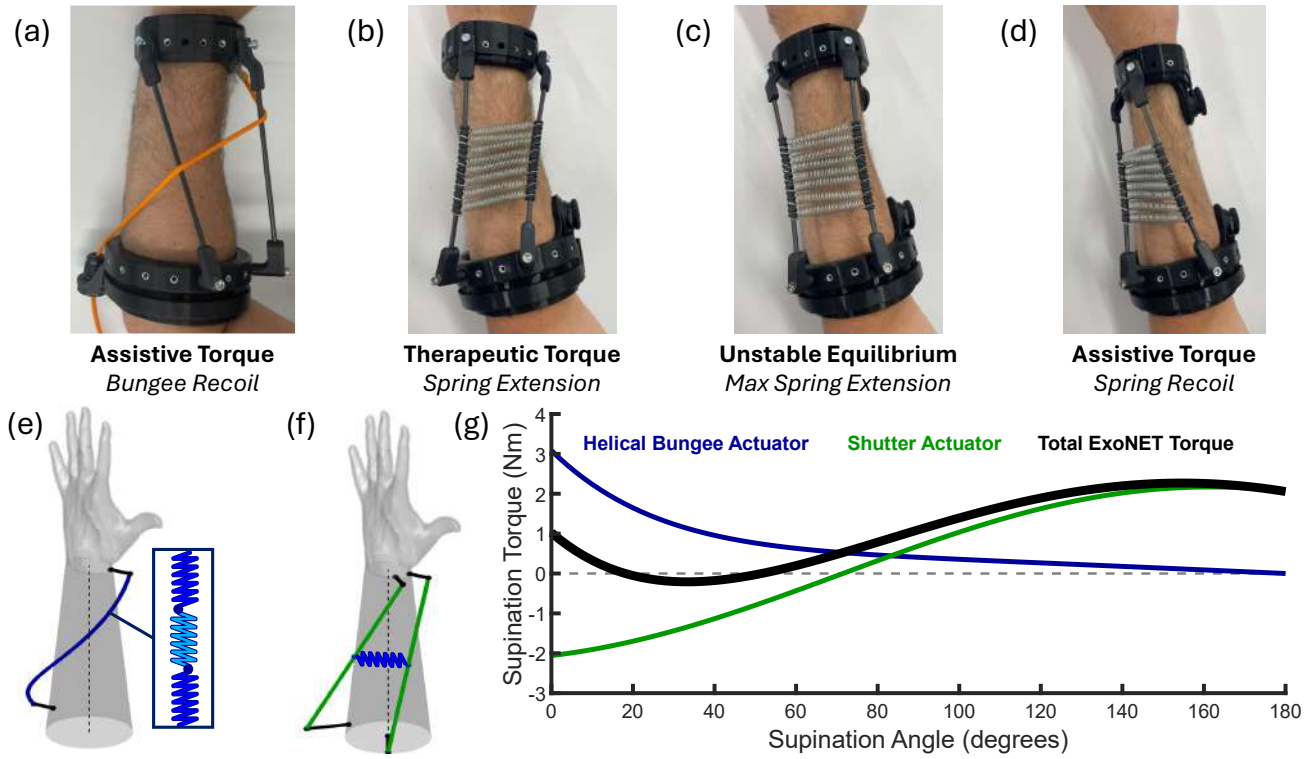


Fig. 2. Functionality of the forearm ExoNET actuators. (a) The helical bungee actuator, wrapped around the forearm, provides stable assistance across the full supination range. (b) Tension springs in the shutter actuator generate resistance within the user's active supination range. (c) The shutter actuator transitions from resistance to assistance, creating an unstable equilibrium. (d) Assistance is provided as supination exceeds the active range. (e) The helical bungee model consists of discrete spring segments, improving the accuracy of its wrapping mechanics and torque-delivering capacity. (f) The shutter actuator is modeled as rigid rods connected by an arbitrary number of tension springs. (g) Torque profiles for the helical bungee (blue) and shutter actuator (green) can be summed to create more complex torque profiles (black).

the rotational positioning of the bungee cord. These factors determine the actuator's wrapping trajectory, which is recalculated dynamically at each rotation step based on the updated attachment positions at the wrist and forearm. The helical pitch and number of turns are modulated by these attachment constraints, ensuring a structured, repeatable path rather than following the shortest straight-line route.

2) Shutter Actuator: Inspired by the mechanics of a camera shutter, the shutter actuator consists of two or more rigid fiberglass rods connected by tension springs. These rods function as mechanical extensions of the forearm, mimicking the behavior of the radius and ulna during supination while being offset with distinct origin and insertion points on the forearm and wrist band. Mathematically, the actuator is modeled as a system of rigid rods connected by tension springs, spanning between the forearm and wrist bands to reflect its physical configuration (Fig. 2(f)).

As the user initiates supination, the springs stretch, generating a resistive torque that increases with rotation (Fig. 2(b)). This resistance encourages muscle engagement, promoting active effort and progressive strengthening. However, the system exhibits a nonlinear torque response due to a mechanically encoded transition point. As supination progresses, the attachment geometry shifts the mechanical advantage of the springs, reaching a critical rotation angle at which the springs stop stretching and begin contracting instead (Fig. 2(c)). This reverses the torque contribution, causing the actuator to transition from providing resistance to offering assistance, facilitating the final phase of supination (Fig. 2(d)). This behavior arises from the nonlinear kinematic relationship between forearm rotation and spring extension, which is governed by the attachment locations and initial spring tension. The transition point represents a passive instability, where the effective moment arm changes sign, making further supination easier rather than harder. As a result, the shutter actuator seamlessly integrates resistive and assistive phases within a single motion, supporting both therapeutic strengthening and functional completion of supination (Fig. 2(g), green curve). While preliminary testing suggests that this approach is feasible, further controlled experiments are needed to quantify how this nonlinear torque profile influences rehabilitation outcomes.

B. Theoretical Model of Torque Generation

The core of the forearm ExoNET's functionality lies in the torque generated by each elastic actuator. The torque ($\boldsymbol{\tau}$) produced by each actuator is a product of the spring element's moment arm ($\boldsymbol{\rho}(\alpha)$) and force ($\boldsymbol{F}$):

$$\boldsymbol{\tau} = \boldsymbol{\rho}(\alpha) \times \boldsymbol{F} \tag{2}$$

The moment arm ($\boldsymbol{\rho}(\alpha)$) is governed geometrically by:

$$\boldsymbol{\rho}(\alpha) = \begin{bmatrix} 0 \\ 0 \\ L_{\text{forearm}} \end{bmatrix} - h_{\text{w_mnt}} \sin(\beta) \begin{bmatrix} \cos(\theta_{\text{w_mnt}} \pm \alpha) \\ \sin(\theta_{\text{w_mnt}} \pm \alpha) \\ \lambda \end{bmatrix} \tag{3}$$

and is a function of the actuator attachment point at the wrist ($h_{\text{w_mnt}}$), the wrist mount angle around the forearm's longitudinal axis ($\theta_{\text{w_mnt}}$), the wrist rotation angle (α), the fixed inclination angle of the forearm relative to the horizontal (β), and the fractional position of the attachment along the forearm length (λ). The spring force ($\boldsymbol{F}$) was initially modeled as a linear function using Hooke's Law but was later generalized to account for nonlinear elastic properties, thus improving accuracy in torque estimation. Given the inherent nonlinearity of the helical bungee, its force-displacement behavior was characterized experimentally using a load cell (Mark-10 Corporation, USA). Bungee cord samples were incrementally stretched while recording the applied force, generating tension-stretch curves to capture the actuator's nonlinear stiffness (Fig. 3). A smooth, differentiable function was fitted to the measured data to ensure accurate representation in the computational model. For compatibility with most optimization algorithms, this function was constrained to be C^2-continuous. This empirical characterization ensured that the torque predicted by our models was validated against real-world measurements obtained during benchtop testing.

Torque deficit profiles are often highly complex, making it impractical for a single spring or ExoNET element to produce the desired torque. However, by using combinations of ExoNET elements (where n represents the total number of elastic elements in the system), we can leverage their behavior as basis functions. This approach allows us to sum the torque profiles of each element to achieve complex, user-specific torque profiles:

$$\boldsymbol{\tau}_{\text{total}} = \sum_{i=1}^{n} \boldsymbol{\tau}_i \tag{4}$$

C. Diagnostic Tool

A custom-designed diagnostic tool is critical for assessing individual supination torque deficits, enabling precise customization of the forearm ExoNET to address each user's unique needs (Fig. 4). To establish a representative baseline, supination torque profiles are collected from neurotypical participants and averaged. This baseline serves as a reference for quantifying torque deficits in stroke survivors. The resulting individualized torque deficit profiles are then used as primary inputs to the structural optimization algorithm, guiding the ExoNET's configuration.

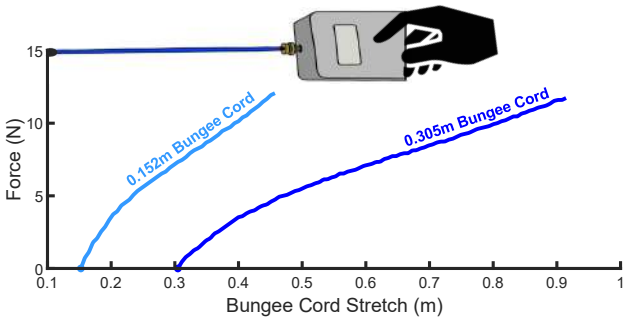


Fig. 3. Bungee cord tension-stretch relationship. (Top) Experimental setup where a load cell incrementally applies a controlled tensile force to the bungee cord. (Bottom) Experimentally derived tension-stretch curves for the same bungee cord at different resting lengths, demonstrating nonlinear elastic behavior. These data inform the computational model to ensure accurate torque predictions for ExoNET optimization.

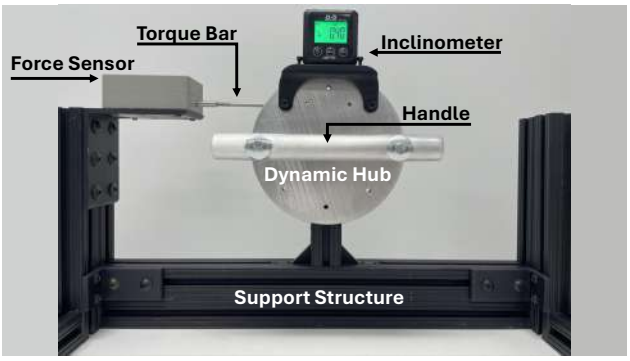


Fig. 4. Diagnostic tool user-specific supination assessment. The tool measures supination torque at discrete angles (0°, 45°, 90°, 135°, 180°) using the Dynamic Hub connected to a force sensor via the Torque Bar. When the Torque Bar is disengaged, the Dynamic Hub acts as a free-rotating disc, enabling active supination range measurement via a digital inclinometer. This data informs the forearm ExoNET optimization algorithm, tailoring torque assistance and resistance to each user's therapeutic needs.

The diagnostic device employs a Dynamic Hub connected to a force sensor via a Torque Bar to measure peak supination torque at multiple discrete angles (0°, 45°, 90°, 135°, 180°). Participants are instructed to exert their maximum supination effort at each angle, with the device recording peak torque output at each tested position. When the torque bar is disengaged from the hub, the system transitions into a free-rotating disc, allowing the measurement of the user's active supination range of motion. This dual functionality facilitates comprehensive assessments, including (1) manual muscle testing, quantifying the maximum torque the user can generate at multiple discrete angles across the full supination range, and (2) active supination range of motion, defining the functional range within which the ExoNET must operate effectively. To account for muscle synergies between pronation/supination ability and elbow flexion/extension, these tests are conducted at 0°and 90°of elbow flexion. The resulting data provides a quantifiable profile of the user's supination capacity and torque deficits through a structured, reproducible evaluation. This information serves as a foundational input for the ExoNET's optimization framework, ensuring that the device delivers targeted assistance or resistance where it is most needed.

D. Optimization Cost Function and Constraints

A multi-step constrained optimization algorithm was implemented to tailor the forearm ExoNET's design parameters for each user. The goal of this approach is to minimize the discrepancy between the user's specific torque deficit profile (desired torque) and the torque profiles generated by the ExoNET across the user's forearm range of motion (0-180°). The optimization adjusts variables such as number of actuators, actuator attachment points, spring stiffnesses, and other mechanical properties, ensuring that the ExoNET's

output precisely meets each user's therapeutic needs. The loss function (i.e., cost function) is defined as:

$$\arg\min \left(\sum_{\theta \in \Theta} \left[T_{\text{desired}}(\theta) - T_{\text{ExoNET}}(\theta, p) \right]^2 + Q \right) \quad (5)$$

where Θ denotes the discrete supination angles for torque measurements, $T_{\text{desired}}(\theta)$ is the desired torque from the user's measured torque deficit profile, and $T_{\text{ExoNET}}(\theta, p)$ is the torque generated by the forearm ExoNET at supination angle (θ) with the given parameters (p). Q is a regularization term that enforces soft constraints to ensure practical device configurations, as detailed below:

1) Number of Actuators Constraint: To encourage simpler and less cumbersome ExoNET designs, the optimization enforces a penalty term proportional to the number of actuators in the system:

$$Q_{\text{actuators}} = \lambda_{\text{actuators}} \cdot N_{\text{actuators}} \quad (6)$$

where $\lambda_{\text{actuators}}$ is a weighting factor that controls the impact of this penalty on the total cost.

2) Actuator Length Constraint: To promote safety and feasibility, actuator lengths are constrained within acceptable physical limits. If an actuator's length (L_i) exceeds its maximum allowed length ($L_{\max,i}$) or falls below its minimum allowed length ($L_{\min,i}$), a penalty is incurred:

$$Q_{\text{lengths}} = \lambda_{\text{lengths}} \sum_i \big[\max(0, L_i - L_{\max,i})^2 + \max(0, L_{\min,i} - L_i)^2 \big] \quad (7)$$

where λ_{lengths} is a weighting factor for length penalties, with squared terms imposing disproportionately higher penalties for larger violations.

3) Collision Avoidance Constraint: To prevent actuators from intersecting with the user's forearm (modeled as a frustum with elliptical ends), a penalty is applied when collisions are detected. The penalty is proportional to the degree of intersection:

$$Q_{\text{collision}} = \lambda_{\text{collision}} \cdot N_{\text{collisionPoints}} \quad (8)$$

where $N_{\text{collisionPoints}}$ is the number of points along the actuator that intersect the forearm, and $\lambda_{\text{collision}}$ controls the severity of the penalty.

The total regularization term (Q) is the sum of these individual penalties:

$$Q = Q_{\text{actuators}} + Q_{\text{lengths}} + Q_{\text{collision}} \quad (9)$$

E. Structural Optimization for Personalized Torque

The optimization process employs user-specific diagnostic data—including active supination range of motion and measured torque deficits—to define actuator configurations that minimize the loss function. This ensures the ExoNET delivers tailored assistance or resistance, enhancing user supination effectively. The model optimizes 70 design parameters used to configure the forearm ExoNET. These parameters can be broadly categorized into three groups: (1) actuator geometry, which includes attachment angles, distances, and the number of actuators; (2) spring properties, such as stiffnesses, resting lengths, and helical path characteristics; and (3) feasibility constraints, which ensure physical realism by preventing actuator collisions and enforcing practical attachment limits. Adjustments in actuator geometry modify moment arms, directly shaping the torque profile across the supination range, while spring properties influence the tension-stretch relationship and the magnitude of delivered torque. Collectively, these parameters drive the ExoNET's optimization process, ensuring the device is configured to address user-specific torque deficits. To address the complex, multimodal cost landscape, we implemented a stochastic optimization strategy, comprising two main phases.

1) Constrained Optimization with Multiple Initial Guesses: We used MATLAB's *fmincon* function within a custom loop to initiate multiple optimization runs from randomly generated initial parameter sets within defined bounds. This approach diversifies explored solutions and reduces the likelihood of the algorithm becoming trapped in local minima.

2) Simulated Annealing Refinement: After identifying the best solution from the initial runs, we applied a simulated annealing algorithm to further refine the actuator parameters. During each iteration, the parameters were perturbed, and the acceptance of the new configuration was determined by the Metropolis criterion [30] which follows a probabilistic rule for accepting worse solutions to escape local minima.

$$P_{\text{accept}} = \begin{cases} 1, & \text{if } \Delta C \leq 0 \\ \exp\left(-\frac{\Delta C}{kT}\right), & \text{if } \Delta C > 0 \end{cases} \quad (10)$$

Here, $\Delta C = C_{\text{new}} - C_{\text{current}}$ is the change in cost, k is the Boltzmann constant (set to 1 for normalization), and T is the current temperature. A random number between 0 and 1 determines acceptance based on P_{accept}, allowing occasional acceptance of worse solutions to escape local minima. The temperature (T) decreases according to a cooling schedule (e.g., exponential decay), gradually reducing the likelihood of accepting higher-cost solutions and enabling the algorithm to converge toward a global minimum.

F. Participant Characteristics and Neurotypical Baseline

The Northwestern University Institutional Review Board (Chicago, IL) approved this study (STU00218538) and served as the IRB of record. A reliance agreement was established with the University of Illinois Chicago research ethics authority (STUDY2023-1215). The study was conducted in accordance with the Declaration of Helsinki, with written informed consent obtained from all participants.

A single hemiparetic male with chronic stroke (more than 8 months), who is right-hand affected and dominant, was enrolled in the study. Baseline clinical outcome measures were collected, which included the Action Research Arm Test (ARAT, 25/57), Fugl-Meyer Upper Extremity (FMUE, 30/66), and Box and Blocks Test (BBT, unaffected hand: 35 blocks and affected hand: 20 blocks). The subject's supination capacity and torque-generating capability were assessed using the diagnostic tool, which measured active

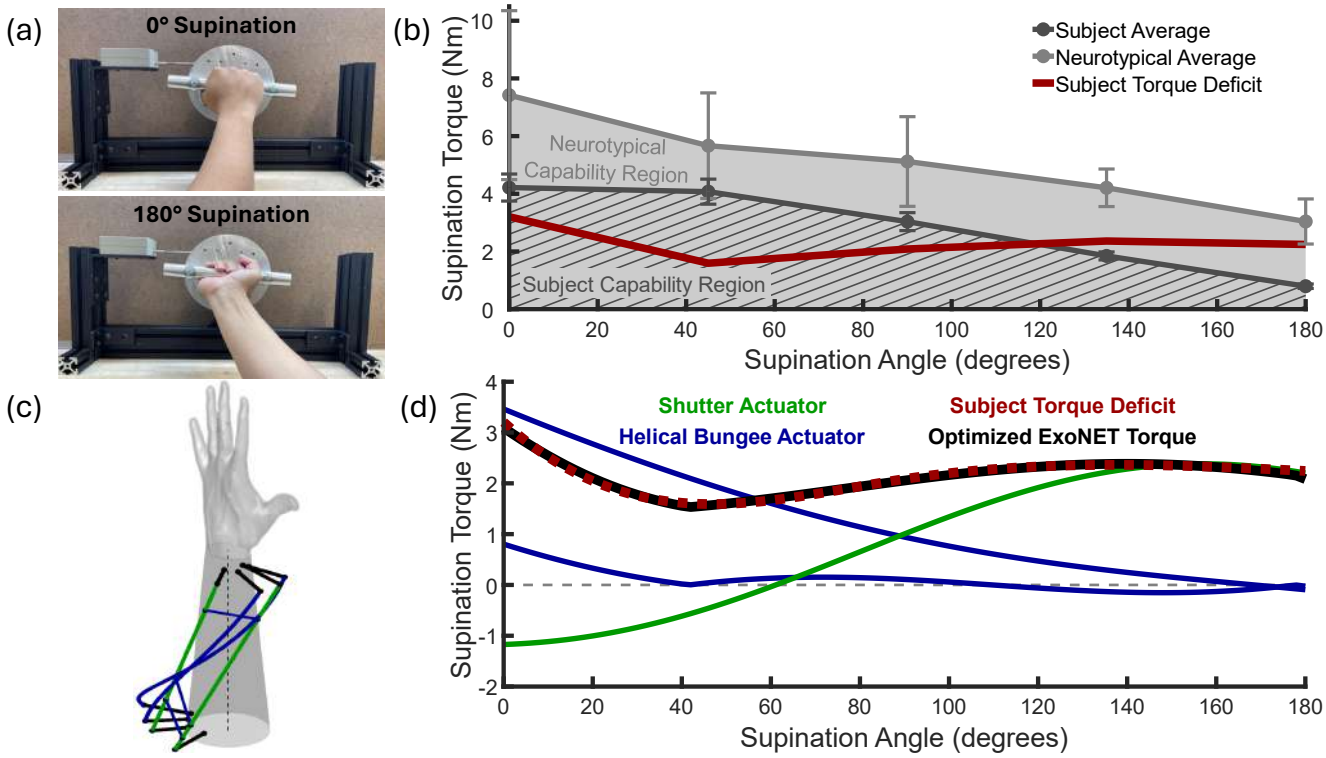


Fig. 5. Experimental results demonstrating the forearm ExoNET's personalized torque delivery. (a) Hand orientation during diagnostic testing at 0°and 180°of supination. (b) The subject's torque deficit profile (red) was correctly identified by comparing their torque ability curve (dark gray) with a neurotypical baseline (light gray). (c) Optimization results predicting actuator configurations tailored to the subject's specific torque needs. (d) Simulated torque output from the ExoNET (black), demonstrating targeted assistance in regions of limited strength and precise alignment with the subject's torque deficit profile (red), achieving a predictive accuracy of $R^2 = 0.987$ and a root mean square error (RMSE) of $0.039Nm$.

supination range of motion and maximum voluntary torque production at discrete angles across the forearm's range of motion (0°, 45°, 90°, 135°, 180°). Examples of hand orientation during testing are illustrated in Fig. 5(a).

All torque measurements were taken three times per individual, and each individual's three torque profiles were averaged to generate a single profile. At each discrete angle, both supination and pronation torque production were recorded to assess whether the subject exhibited total weakness in either motion. To establish a representative neurotypical baseline, supination torque profiles were collected from four neurotypical research team members (three female, one male), and then averaged. The subject's averaged torque profile was subsequently compared against the neurotypical baseline to quantify their torque deficit. This comparison was completed through direct subtraction of the subject's torque profile from the neurotypical average.

III. RESULTS

The subject exhibited sufficient strength in both pronation and supination, with no signs of total weakness, confirming the suitability of their data for optimization. Additionally, across three trials (n=3), the subject demonstrated an average active supination range of motion of 161°at 90°of elbow flexion and 147°at 0°of elbow flexion. The subject's supination torque measurements were compared with those of four neurotypical individuals to generate an individualized torque deficit profile. This deficit profile highlighted specific regions of weakness and asymmetry in the subject's supination torque generation, particularly around 90°of supination (Fig. 5(b)). This result directly guided the optimization of the forearm ExoNET configuration to address the subject's unique torque requirements.

The computational model successfully utilized the subject's individualized torque deficit profile to predict actuator configurations tailored to their specific needs (Fig. 5(c)). The optimization process involved 500 runs (4,595,065 function evaluations), during which an optimal solution was identified (Fig. 5(d), black). The resulting configuration combined the summed torque contributions of two helical bungee actuators (Fig. 5(d), blue) and three shutter springs connected to two shutter rods (Fig. 5(d), green), aligning with the subject's torque deficit profile to provide consistent assistance of varying magnitudes across all areas of weakness. Table I presents a representative subset of the 70 parameters optimized for the forearm ExoNET. These parameters were selected to illustrate the diversity of design variables involved in the optimization process, including actuator attachment points, stiffness values, and lengths. While these parameters contribute to defining the torque profile, no formal analysis was conducted to determine their relative influence compared to other optimized variables. As shown in Fig. 5, the ExoNET's simulated torque outputs closely aligned with the subject's torque deficit profile, achieving a predictive accuracy of $R^2 = 0.987$ and a root mean square

TABLE I
SUBSET OF OPTIMIZED PARAMETERS FOR THE FOREARM EXONET
(SUBSET OF 70 TOTAL PARAMETERS)

Parameter	Actuator Type	Value
Unstretched Length (m)	Helical Bungee	0.29, 0.22
Stiffness (N/m)	Helical Bungee	465, 352
Wrist Attachment (°)	Helical Bungee	235, 264
Forearm Attachment (°)	Helical Bungee	126, 96
Stiffness (N/m)	Shutter Spring	485, 212, 326
Spring Location Along Rod 1 (%)	Shutter Spring	15, 79, 7
Spring Location Along Rod 2 (%)	Shutter Spring	36, 82, 21
Wrist Attachment (°)	Shutter Rod	248, 198
Forearm Attachment (°)	Shutter Rod	174, 133

error (RMSE) of $0.039Nm$. This alignment ensures precise, targeted assistance to enhance functional supination while avoiding unnecessary torque in unaffected regions.

Preliminary testing was conducted to gain initial user insights into the comfort and perceived benefits of the forearm ExoNET. During this testing, the subject provided anecdotal feedback, noting that the device was comfortable and that they recognized its potential benefits. Additionally, they described an unexpected sensation of weightlessness at the elbow, suggesting a potential secondary effect of the device. This observation has prompted further investigation to determine its underlying cause and whether it may have therapeutic implications for users of the ExoNET.

IV. DISCUSSION

The results outlined in this study suggest that the diagnostic tool can effectively quantify supination deficits and that the computational model can generate user-specific actuator configurations for the forearm ExoNET in a single subject with chronic stroke. While findings from this single-subject study demonstrate the feasibility of using a structural optimization algorithm to design passive actuator configurations for targeted supination torque profiles, additional testing with a larger cohort is needed. Further validation is required to assess the diagnostic tool's reliability and evaluate the ExoNET's therapeutic impact in a clinical setting. This tailored approach demonstrates substantial promise for customizing rehabilitation strategies to address the unique needs of individual subjects, ultimately supporting improved upper-limb functionality post-stroke. To translate this technology into clinical application, the next step is to implement the optimized actuator configurations into the forearm ExoNET and test the device on a user. This will be critical for validating model predictions and refining device performance. Additionally, refining the computational model itself remains an essential step to ensure accurate optimization of actuator configurations for user-specific needs.

The computational model provides a promising initial framework for designing the forearm ExoNET, enabling a cost-effective, data-driven approach to creating personalized devices for individuals with supination torque deficits. By aligning the ExoNET's torque delivery with the user's torque deficit profile, the model aims to provide targeted support where it is most needed, integrating resistance and assistance within a single motion. These findings suggest that the forearm ExoNET has the potential to address the gap in accessible, user-specific supination-supporting devices. However, while preliminary results demonstrate feasibility in a single-subject study, further validation with a larger, more diverse cohort is necessary to determine the model's generalizability and clinical effectiveness.

While the model demonstrates strong predictive capabilities, physical validation of the forearm ExoNET remains a crucial next step. Future work will focus on constructing and testing the device based on the model's predictions to evaluate its real-world performance. Limitations in the current model will be addressed to improve its mathematical representation of the physical system. For example, incorporating contact forces and refining the helical bungee actuator's wrapping mechanics to account for variable spring/segment expansion could improve the model's accuracy and applicability. Although further validation is required, the approach used to model the helical bungee actuator in this study may offer insights for improving musculoskeletal modeling tools such as OpenSim [31], which currently rely on simplified geometric representations to approximate how muscles interact with bones and neighboring structures [32].

Similarly, modeling the shutter actuator rods as deformable beams rather than rigid components could enhance the accuracy of force and torque predictions, allowing for energy storage and transfer that facilitates supination or modifies spring torque contributions. Expanding the model to include pronation torque and additional upper-limb motions would further broaden its applicability to other impairments, such as those associated with C7 spinal cord injuries. Incorporating real-time feedback mechanisms and conducting longitudinal studies to evaluate motor learning, functional recovery, and quality of life will be essential to ensuring the device's long-term therapeutic benefits.

V. CONCLUSIONS

This study presents a novel framework for addressing supination deficits in individuals with motor impairments, leveraging user-specific diagnostic data and computational optimization to guide the design of the forearm ExoNET. The model demonstrates the ability to accurately approximate desired torque profiles, compensating for deficits and facilitating the full range of supination motion. This approach represents a shift from software-based control to hardware-encoded torque generation, emphasizing simplicity and accessibility without sacrificing functionality. While these results provide a promising foundation, future work will focus on implementing the optimized actuator configurations into the forearm ExoNET and evaluating its safety, usability, and therapeutic efficacy in clinical settings. If successful, the forearm ExoNET could significantly enhance the accessibility and effectiveness of stroke rehabilitation therapies.

ACKNOWLEDGMENT

We would like to thank the rest of the Robotics Lab at the Shirley Ryan AbilityLab and the Richard and Loan Hill Department of Biomedical Engineering at the University of Illinois Chicago. The authors declare that there are no conflicts of interest.

REFERENCES

[1] N. Flinn, "A Task-Oriented Approach to the Treatment of a Client With Hemiplegia," *The American Journal of Occupational Therapy*, vol. 49, no. 6, pp. 560–569, June 1995.

[2] L. G. Richards, B. Olson, and P. Palmiter-Thomas, "How Forearm Position Affects Grip Strength," *The American Journal of Occupational Therapy*, vol. 50, no. 2, pp. 133–138, Feb. 1996.

[3] H. S. Nam, W. H. Lee, H. G. Seo, Y. J. Kim, M. S. Bang, and S. Kim, "Inertial Measurement Unit Based Upper Extremity Motion Characterization for Action Research Arm Test and Activities of Daily Living," *Sensors*, vol. 19, no. 8, p. 1782, Apr. 2019.

[4] L. Ada, C. M. Dean, and F. H. Mackey, "Increasing the amount of physical activity undertaken after stroke," *Physical Therapy Reviews*, vol. 11, no. 2, pp. 91–100, June 2006.

[5] R. W. Teasell, N. C. Foley, S. K. Bhogal, and M. R. Speechley, "An Evidence-Based Review of Stroke Rehabilitation," *Topics in Stroke Rehabilitation*, vol. 10, no. 1, pp. 29–58, Apr. 2003.

[6] Srivatsa, Adith V, *et al.*, "Abnormal Synergies and Muscle Weakness Identified in Stroke Survivors via Wrist Position Probability Distributions," in *International Conference on Rehabilitation Robotics (ICORR)*. Chicago, IL, USA: IEEE, May 2025, p. Accepted.

[7] E. Taub and G. Uswatte, "Constraint-Induced Movement Therapy: A New Family of Techniques with Broad Application to Physical Rehabilitation–A Clinical Review," *J. Rehabil. Res. Dev.*, 1999.

[8] S. L. Wolf, *et al.*, "Effect of Constraint-Induced Movement Therapy on Upper Extremity Function 3 to 9 Months After Stroke: The EXCITE Randomized Clinical Trial," *JAMA*, vol. 296, no. 17, p. 2095, Nov. 2006.

[9] C. J. Winstein, *et al.*, "Effect of a Task-Oriented Rehabilitation Program on Upper Extremity Recovery Following Motor Stroke: The ICARE Randomized Clinical Trial," *JAMA*, vol. 315, no. 6, p. 571, Feb. 2016.

[10] A. Houwink, R. H. Nijland, A. C. Geurts, and G. Kwakkel, "Functional Recovery of the Paretic Upper Limb After Stroke: Who Regains Hand Capacity?" *Archives of Physical Medicine and Rehabilitation*, vol. 94, no. 5, pp. 839–844, May 2013.

[11] R. Rätz, F. Conti, R. M. Müri, and L. Marchal-Crespo, "A Novel Clinical-Driven Design for Robotic Hand Rehabilitation: Combining Sensory Training, Effortless Setup, and Large Range of Motion in a Palmar Device," *Front. Neurorobot.*, vol. 15, p. 748196, Dec. 2021.

[12] S. Hesse, G. Schulte-Tigges, M. Konrad, A. Bardeleben, and C. Werner, "Robot-assisted arm trainer for the passive and active practice of bilateral forearm and wrist movements in hemiparetic subjects11An organization with which 1 or more of the authors is associated has received or will receive financial benefits from a commercial party having a direct financial interest in the results of the research supporting this article." *Archives of Physical Medicine and Rehabilitation*, vol. 84, no. 6, pp. 915–920, June 2003.

[13] O. Lambercy, L. Dovat, R. Gassert, E. Burdet, C. L. Teo, and T. Milner, "A Haptic Knob for Rehabilitation of Hand Function," *IEEE Trans. Neural Syst. Rehabil. Eng.*, vol. 15, no. 3, pp. 356–366, Sept. 2007.

[14] J. Realmuto and T. Sanger, "A robotic forearm orthosis using soft fabric-based helical actuators," in *2019 2nd IEEE International Conference on Soft Robotics (RoboSoft)*. Seoul, Korea (South): IEEE, Apr. 2019, pp. 591–596.

[15] S.-H. Park, J. Yi, D. Kim, Y. Lee, H. S. Koo, and Y.-L. Park, "A Lightweight, Soft Wearable Sleeve for Rehabilitation of Forearm Pronation and Supination," in *2019 2nd IEEE International Conference on Soft Robotics (RoboSoft)*. Seoul, Korea (South): IEEE, Apr. 2019, pp. 636–641.

[16] S. Lessard, *et al.*, "CRUX: A compliant robotic upper-extremity exosuit for lightweight, portable, multi-joint muscular augmentation," in *2017 International Conference on Rehabilitation Robotics (ICORR)*. London: IEEE, July 2017, pp. 1633–1638.

[17] M. Dezman, T. Asfour, A. Ude, and A. Gams, "Exoskeleton Arm Pronation/Supination Assistance Mechanism With A Guided Double Rod System," in *2019 IEEE-RAS 19th International Conference on Humanoid Robots (Humanoids)*. Toronto, ON, Canada: IEEE, Oct. 2019, pp. 559–564.

[18] S. H. Collins, M. B. Wiggin, and G. S. Sawicki, "Reducing the energy cost of human walking using an unpowered exoskeleton," *Nature*, vol. 522, no. 7555, pp. 212–215, June 2015.

[19] R. Nasiri, A. Ahmadi, and M. N. Ahmadabadi, "Reducing the Energy Cost of Human Running Using an Unpowered Exoskeleton," *IEEE Trans. Neural Syst. Rehabil. Eng.*, vol. 26, no. 10, pp. 2026–2032, Oct. 2018.

[20] J. Sulzer, M. Peshkin, and J. Patton, "MARIONET: An exotendon-driven rotary series elastic actuator for exerting joint torque," in *9th International Conference on Rehabilitation Robotics, 2005. ICORR 2005.* Chicago, IL: IEEE, 2005, pp. 103–108.

[21] J. L. Patton, M. A. Peshkin, and J. S. Sulzer, "Cable Driven Joint Actuator and Method," U.S. Patent US9 597 217B2, Mar., 2017.

[22] R. Van Ham, B. Vanderborght, M. Van Damme, B. Verrelst, and D. Lefeber, "MACCEPA, the mechanically adjustable compliance and controllable equilibrium position actuator: Design and implementation in a biped robot," *Robotics and Autonomous Systems*, vol. 55, no. 10, pp. 761–768, Oct. 2007.

[23] I. Vanderniepen, R. Van Ham, M. Van Damme, R. Versluys, and D. Lefeber, "Orthopaedic rehabilitation: A powered elbow orthosis using compliant actuation," in *2009 IEEE International Conference on Rehabilitation Robotics*. Kyoto, Japan: IEEE, June 2009, pp. 172–177.

[24] P. Ryali, T. Carella, D. McDermed, V. Perizes, F. Huang, and J. Patton, "A Theoretical Framework for a Network of Elastic Elements Generating Arbitrary Torque Fields," in *2020 8th IEEE RAS/EMBS International Conference for Biomedical Robotics and Biomechatronics (BioRob)*. New York City, NY, USA: IEEE, Nov. 2020, pp. 286–291.

[25] P. Ryali, *et al.*, "Evaluation of a passive wearable arm ExoNET," *Front. Robot. AI*, vol. 11, p. 1387177, July 2024.

[26] C. Celian, P. Ryali, V. Wilson, and A. Srivatsa, "A wearable anti-gravity supplement to therapy does not improve arm function in chronic stroke: a randomized trial," arXiv preprint arXiv:2405.04707, 2024.

[27] B. Malizia, P. Ryali, and J. L. Patton, "Passive Exotendon Spring Elements can Replace Muscle Torque during Gait," Master's thesis, University of Illinois at Chicago, Chicago, IL, 2021.

[28] M. Camardo, *et al.*, "Design Evaluation of a Passive Ankle Exoskeleton for Gait Training," in *International Conference on Rehabilitation Robotics (ICORR)*. Chicago, IL, USA: IEEE, May 2025, p. Accepted.

[29] N. R. Aghamohammadi, M. F. Bittmann, V. Klamroth-Marganska, R. Riener, F. C. Huang, and J. L. Patton, "Error fields: personalized robotic movement training that augments one's more likely mistakes," *Scientific Reports*, vol. 15, no. 1, p. 4201, Feb. 2025.

[30] N. Metropolis, A. W. Rosenbluth, M. N. Rosenbluth, A. H. Teller, and E. Teller, "Equation of State Calculations by Fast Computing Machines," *The Journal of Chemical Physics*, vol. 21, no. 6, pp. 1087–1092, June 1953.

[31] S. L. Delp, *et al.*, "OpenSim: Open-Source Software to Create and Analyze Dynamic Simulations of Movement," *IEEE Trans. Biomed. Eng.*, vol. 54, no. 11, pp. 1940–1950, Nov. 2007.

[32] D. Ao, G. Li, M. S. Shourijeh, C. Patten, and B. J. Fregly, "EMG-Driven Musculoskeletal Model Calibration With Wrapping Surface Personalization," *IEEE Trans. Neural Syst. Rehabil. Eng.*, vol. 31, pp. 4235–4244, 2023.

A Novel Template-Matching Method for Extracting Gait Cycles from Underfoot Pressure Data

Grange M. Simpson, Kylee North, Sonny T. Jones, Ashley N. Dalrymple

***Abstract*— The isolation of gait cycles from underfoot pressure data is a critical step in human movement analysis, yet existing methods require either expensive equipment or substantial manual effort. We present a generalizable, low-resource algorithm for parsing gait cycles from wearable underfoot pressure sensor data across multiple walking terrains. Compared to a ground-truth dataset manually marked and verified by an expert, our algorithm achieved similar accuracy with significantly reduced processing time. For a dataset of 577 steps, our algorithm parsed gait cycles in 41 seconds with only one false negative, whereas three naïve manual parsers required an average of 29 minutes, with total errors ranging from 6 to 33 gait cycles. The algorithm also outperformed threshold-based parsing, which produced 49–362 false positives, depending on the threshold value. By improving computational efficiency with accuracy, this method enables scalable gait cycle detection in real-world applications, expanding the feasibility of automated gait analysis beyond controlled laboratory environments.**

***Index Terms*— Gait Analysis, Walking, Underfoot Pressure, Ground Reaction Force, Rehabilitation**

I. Introduction

Advances in gait analysis and rehabilitation technology, such as wireless sensors, motion capture, exoskeletons, and gait assistance devices, have created a growing demand for efficient, high-quality data analysis methods. A critical component of gait analysis is isolating complete individual gait cycles. Historically, gait analysis has relied on motion capture systems in controlled laboratory settings, but the field is rapidly shifting toward wearable sensors that enable data collection in real-world environments [1]–[3]. This shift presents new challenges, particularly the need for generalizable data reduction and analysis techniques to parse individual gait cycles effectively. The ability to automatically parse gait cycles is particularly challenging when gait data are collected in variable walking environments or with populations that have motor impairments [4].

Gait data from wearable underfoot pressure sensors exhibit substantial variability due to changing walking speeds, terrains, and patient footwear in both healthy individuals and those with motor deficits from musculoskeletal or neurological conditions [5], [6]. These factors complicate the development of standardized analysis pipelines to identify key events, such as the transition from swing to stance phase (i.e., heel strike, marked by the onset of loading), which is critical for parsing gait cycles. Existing pipelines to parse gait cycles, including manual labeling, thresholding, and neural networks [7]–[9], are resource-intensive and have notable limitations. Access to gait experts who can dedicate the time necessary to manually mark large datasets is often limited, leaving the task to naïve parsers. Manual labeling is prone to human bias, time-consuming, and difficult to generalize across datasets and applications [10]. Thresholding entails setting a minimum value to indicate the onset of limb loading [9]. It is prone to false positives with variable pressure, shuffling, or bumping of the foot, requiring the use of catch statements to exclude missteps. Neural networks require large pre-labeled training datasets, extensive computational power, and expertise in machine learning [7]. Previous work has applied a template-based approach to angular velocity signals, but the template was made for waveforms across the entire gait cycle, limiting its generalizability [4].

This work introduces a novel template-matching framework forefficient, generalizable, low-resource gait cycle parsing. A semi-automated approach allows users to mark the onset of limb loading in a subset of data via an intuitive graphical user interface (GUI). After the parser marks the onset of loading, a shape template is generated, capturing the characteristic pressure pattern at the transition from the swing to stance phase. This allows the algorithm to identify similar events across the dataset. This template-matching method was compared to standard methods of parsing gait cycles, including manual labeling by experts and naïve researchers, and thresholding. By overcoming the limitations of existing gait cycle parsing methods, this template-matching framework offers a simple yet scalable and transferable solution for isolating gait cycles, which supports the growing needs of locomotor and rehabilitation research and real-world gait applications.

II. Methods

A. Participants and Data Acquisition

Four male participants with no known neuromuscular deficits were recruited for this study after providing written informed consent following the University of Utah Institutional Review Board (IRB00171076). Participants were 31, 19, 27, and 25 years of age (mean weight = 182.25 ± 17.90 lbs).

A wireless pressure insole containing 235 embedded pressure sensors (XSensor High-Resolution Intelligent Insoles Pro, Calgary, AB, Canada) was placed in each shoe and

We thank the Departments of Biomedical Engineering and Physical Medicine and Rehabilitation for funding this study. We also thank our participants for volunteering their time.

G. M. Simpson (corresponding author e-mail grange.simpson @utah.edu), K. North, S.T. Jones are with the Department of Biomedical Engineering, University of Utah, Salt Lake City, UT, USA. A.N. Dalrymple (corresponding email ashley.dalrymple@utah.edu) is with the Departments of Biomedical Engineering and Physical Medicine and Rehabilitation, University of Utah, Salt Lake City, UT, USA.

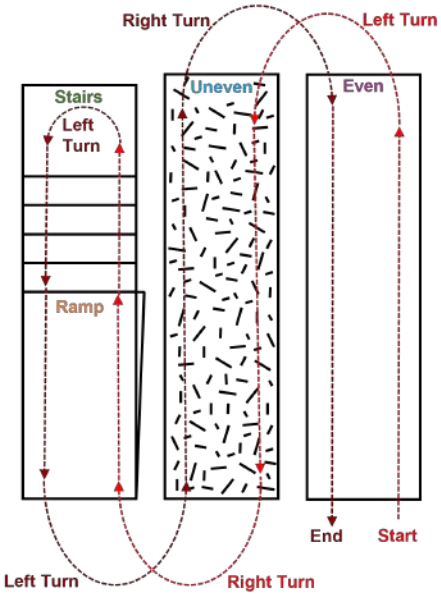


Fig. 1. Walking track containing different types of terrains (7.3m long).

sampled at 33 Hz. A custom GUI built in Python (version 3.8.1, Python Software Foundation, Wilmington, DE) and ran on a desktop computer with an Intel Core i7 CPU and 32 GB of RAM. The GUI controlled the hardware and data collection and data were saved for subsequent offline analysis.

B. Data Collection Experimental Protocol

To evaluate our framework on a dataset reflecting the complexity of real-world walking, participants navigated a mixed-terrain track at a self-selected pace. The mixed-terrain track consisted of even ground, uneven ground, up and down ramps, upstairs, downstairs, and left and right turns (Fig. 1). Each participant completed seven trials: four mixed-terrain trials traversing all types of terrain arranged in the track and three terrain-specific trials on stairs, ramps, and uneven ground to increase the number of steps for each of these terrains. Transitions between types of terrain were manually marked. A mixed-terrain dataset was constructed from all participant data. Manually marked terrain transitions were used to generate five datasets per participant: two datasets combining even ground, turns, and uneven ground; one combining even and uneven ground; one combining even ground and stairs; and one combining even ground and ramps. Of the 20 datasets (five datasets from each of the four participants), two were excluded from analysis due to technical issues, leaving 18 datasets for testing the manual and automatic parsing methods. Pressure values from each insole were normalized to the participant's weight and the area of the individual sensor cell.

C. Establishing the Ground Truth of Gait Cycle Parsing

Underfoot pressure data were upsampled by a factor of 60 from 33 Hz to 1980 Hz to increase the resolution for selecting the onset of limb loading and smoothed using a Savitzky-Golay filter (3rd order, window size = 93, derivative order = 1, rate = 1). This onset of limb loading is an inflection point in the pressure data and defined as the lowest point before a sharp positive increase in slope due to initial ground contact at the transition from swing to stance phase. Pressure profiles from each dataset were visualized for manual marking of the inflection points using a custom GUI (Python, PyQT5 library). At typical walking speeds, each gait cycle is approximately 60% stance phase and 40% swing phase [11]–[13]. The stance phase is characterized by a single or double peak, whereas during swing phase, the underfoot pressure is zero. Gait cycles with noisy or incomplete steps from shuffling, sharp turns, or tripping were excluded if they visually lacked: distinct single or double peaks, a roughly 60/40 stance-to-swing ratios, and/or near-zero pressure values during swing. All 18 datasets were manually marked, based on the above rules, by an individual with 3+ years of experience with underfoot pressure data. The experienced individual's work was validated by a gait researcher with over 6 years of experience analyzing underfoot pressure data. These cross-checked inflection points served as the ground truth for gait cycle parsing. The total number of complete gait cycles was 577.

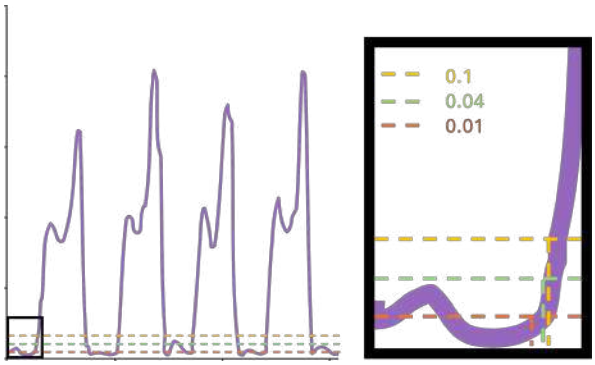


Fig. 2. Three different thresholds were applied to remove low-level noise between gait cycles. Higher thresholds removed more noise but also truncated the signal, affecting the accuracy of loading onset detection.

D. Naïve Manual Gait Cycle Parsing

To simulate naïve junior researchers manually parsing gait data, three independent researchers with no prior experience in gait analysis were recruited. Each naïve parser received instructions for using the GUI, the three criteria defining a complete gait cycle, and a reference of marked inflection points on a set of 10 gait cycles. Each researcher independently marked the same 18 datasets using the GUI. All marked points were saved in a Python dictionary and categorized by dataset for later analysis.

E. Thresholding Algorithm

Thresholding is a widely used automated method for identifying inflection points in gait data [4]. Thresholds are typically set as a multiple of the standard deviation of the background (noise) signal, or manually selected by leveraging knowledge of the particular data, making this method subjective. Thresholding often results in false positives and

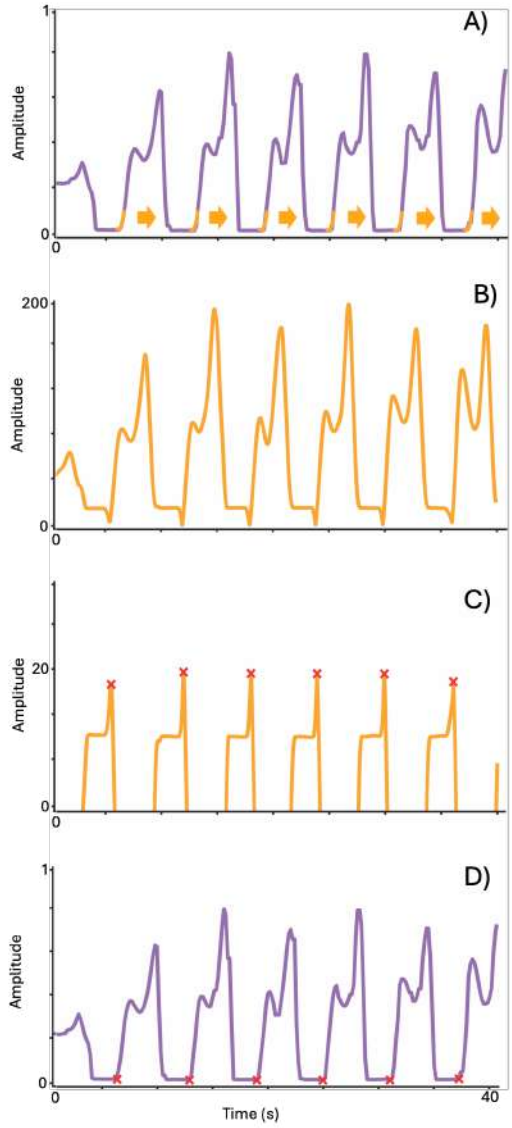


Fig. 3. Template matching algorithm flow chart. A) Iterating the template across the underfoot pressure signal to obtain the sum of the absolute difference between the raw signals and the template. B) The result of the sum of the absolute difference between the raw signals and the template. The sharp troughs indicate the point where the template best overlaps with the raw signal at the inflection point. C) Reflected signal from B about the horizontal axis, isolating the region near the peak overlap between the raw signal and the template, for each step. The peak represents the timepoint of maximum overlap (i.e., the inflection point) and is marked by a red X. D) Found inflection points mapped back onto the underfoot pressure signal, indicated by a red X.

inaccurate marking of the time of loading onset. To evaluate these limitations on parsing gait cycles, three different thresholds were tested. As gait data were normalized between 0 and 1, a low threshold of 0.01, a medium threshold of 0.04, and a high threshold of 0.1 [4] were used (Fig. 2). For each of the three thresholds, underfoot pressure values below the thresholds were set to zero, and time points where transitions from 0 to a value greater than zero were marked as inflection points. No additional programming statements were added to remove false positives or adjust positioning of the marked inflection points.

F. Template-Matching Algorithm

A total of 577 manually marked inflection points from ground truth parsing were grouped into their respective datasets (18 total). For each marked inflection point, a 200-point array was created by extracting 100 points before (including the inflection point) and 100 points after from the underfoot pressure data. These 200-point arrays were averaged within each dataset to generate a template representing the inflection point for that dataset. The final template was created by taking the average of all template arrays across all 18 datasets. The template was matched to the underfoot pressure signal by iterating the 200-point window across the signal (Fig. 3A). At each window position, the similarity between the template and the signal was quantified using the sum of absolute differences (Equation 1), producing a waveform of these differences (Fig. 3B).

$$\sum |(\textit{200 points underfoot pressure}) - \textit{template}| \quad (1)$$

Regions where the template best matched the signal appeared as pronounced troughs in the difference waveform, corresponding to the points of minimum difference (Fig. 3B). To identify these troughs, the difference signal was inverted and shifted upward by 10% of its maximum value (Fig. 3C). This transformation ensured that regions far from an inflection point remained below zero. As the transformed signal rose above zero, values were stored in a buffer until it returned below zero. The index of the maximum value within each buffer was identified as the location of the template match. Identified maxima were then mapped back onto the underfoot pressure signal to mark the inflection points (Fig. 3D). Access the full open-source pipeline on GitHub [14].

G. Template-Matching Algorithm Using Subsets of the Ground Truth Inflection Points

Given the impracticality of manually parsing all inflection points, we investigated whether fewer inflection points could still yield reliable template-based parsing. Templates using 50% (282) and 25% (112) of the total ground truth inflection points were created. A 10-fold validation was performed by randomly selecting a subset of inflections points from the full dataset, building a template from these subsets, and evaluating that template's performance relative to the 100% template for each of the 10 iterations.

H. Comparing Performance of the Template-Matching Algorithm, Thresholding, and Naïve Manual Parsers

The performance of the template-matching algorithm, thresholding, and naïve researcher manual parsing were evaluated by calculating their proximity of the marked inflection points to the ground truth, as well as the number of false positives and negatives in relation to the ground truth. Comparing the location of the inflection points relative to the expert gait data (ground truth) allows for the assessment of error related to the loss of loading data at the onset and the subsequent addition of that loading data to the end of the following step. A closest-pair algorithm was used to calculate the proximity of each method's inflection points to the ground truth. The closest-pair algorithm iterated through all ground

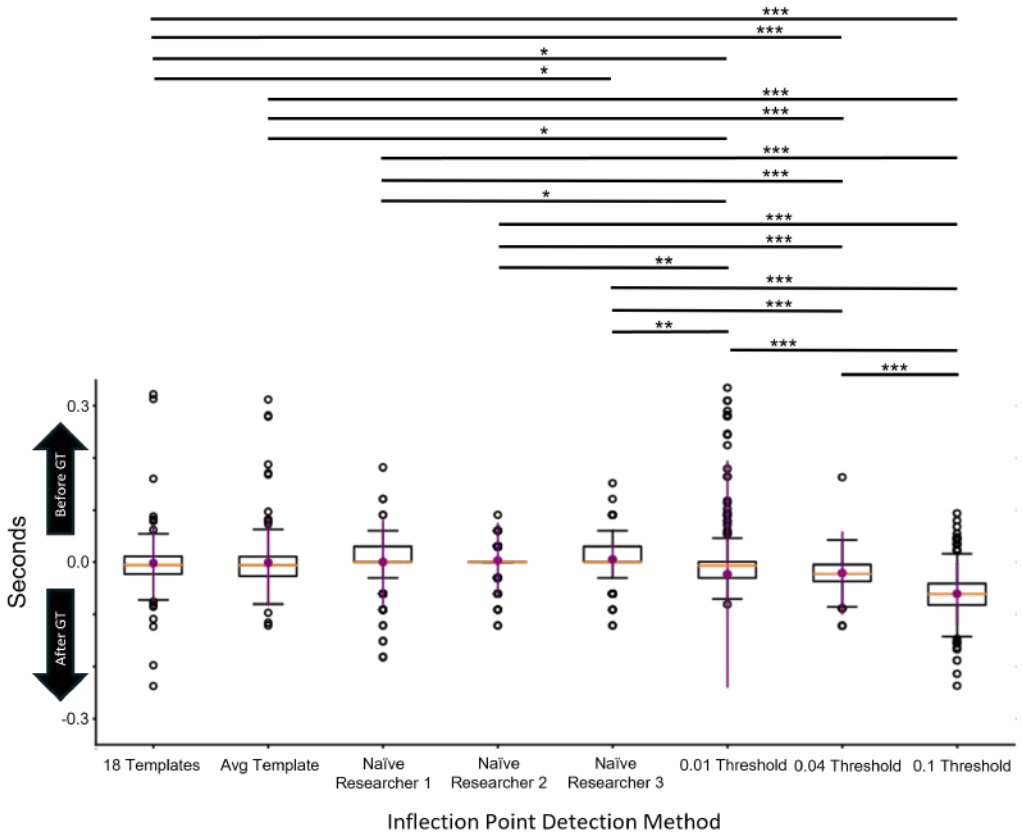


Fig. 4. Box and whisker plots of differences in inflection point location relative to the ground truth for all non-ground truth methods. Zero on the y-axis represents a perfect match with the location of the ground-truth dataset. A positive value indicates the detected inflection point occurred before the point in the ground truth. A negative value indicates the detected inflection point was after the point in the ground truth. The orange line represents the median, the box represents the first and third quartiles, and the whiskers represent the maximum and minimum for each. *p $<$ 0.05; **p $<$ 0.01; ***p $<$ 0.001.

truth inflections points, identifying the non-ground inflection point from either the template, thresholding, or naïve parsers. For each closest-pair value, the index difference between the ground truth and non-ground truth inflection point was determined. The closest-pair algorithm was also used to determine the number of false positives and false negatives of the non-ground truth methods. For example, if the naïve researcher identified 17 inflection points, and the ground truth parser identified 19, the closest pairs algorithm matched 17 points, indicating two false negatives. False positives were calculated as the total number of additional steps from the ground truth.

I. Performance of a Mean Template Built from 18 Different Templates

Building a separate template for each of the 18 datasets is not the most efficient way to parse the data. A more efficient method is to build a template that can capture the inflection points from all 18 datasets that have different cadences, step lengths, and types of terrains. To assess the performance of this mean template, all 577 inflection points were used to construct 577 templates which were then averaged to create one mean template. This mean template was then iterated across all 18 datasets identical to the methods described in section G.

J. Statistical Analysis

Normality was assessed using the Anderson-Darling test (Python's *anderson* function from the scipy.stats library). The data were nonparametric; therefore, a Kruskal-Wallis multi-group test was performed using the scipy.stats library's *kruskal* function to compare the time difference in the detection of the inflection point between all detection methods. Multiple comparisons with a Bonferroni correction were performed using Python's statsmodels.stats. *multicomp* function. The performance of the 50% and 25% templates were compared to the 100% template. For each iteration of the 10-fold validation, the Kruskal-Wallis test was performed to compare the difference in inflection point location from the ground truth for all templates. For all comparisons, a significance level less than or equal to 0.05 was considered significant.

III. Results

A. Number of Marked Inflection Points Compared to Ground Truth

Table I summarizes the total number of marked inflection points, false positives, false negatives, and the mean and standard deviation of the time between the marked inflection points and the ground truth.

TABLE I

PERFORMANCE STATISTICS FOR EACH NON-GROUND TRUTH DATASET IN RELATION TO THE GROUND TRUTH

	Marked Inflection Points #	False Positives	False Negatives	Mean Inflection Point Difference from Ground Truth (ms)	Std Inflection Point Difference from Ground Truth (ms)
18 Templates	606	28	1	-1.8	75
10x Random 50% Template	606	28	1	-1.8	73.6
10x Random 25% Template	606	28	1	0.4	76.2
Average Template	605	27	1	-1	81.2
Threshold = 0.01	939	362	0	-23	217.8
Threshold = 0.04	633	56	0	-20.8	80
Threshold = 0.1	626	49	0	-60.6	59.1
Naïve Researcher 1	544	0	33	0.4	81.3
Naïve Researcher 2	560	0	17	3.3	72
Naïve Researcher 3	571	0	6	5.3	34.5

B. Time of Marked Inflection Points Compared to Ground Truth

All methods differed significantly from the higher threshold ($p < 0.001$). The lower and medium thresholds were each different from all other methods ($p < 0.030$), except each other. Additionally, the template made of the 18 individual datasets differed from the naïve researcher 3 ($p = 0.040$). See Fig. 4. The naïve researchers marked inflection points approximately 5 ms or less before the actual onset from the ground truth (Fig. 4; Table I). For the thresholding method, all thresholds resulted in delayed detection of the inflection point, with the highest threshold resulting the largest delay (60.6 ms). The template-matching method detected the inflection point with a delay of less than 2 ms from the ground truth, accounting for less than 0.2% of a typical gait cycle duration (which is typically 1 second) [11]–[13]. The template-matching algorithm required on average 41 seconds to analyze all 18 datasets, the thresholding method required on average 22 seconds, and the manual parsers required 29 ± 2 minutes.

C. Performance of the Template-Matching Algorithm Built Using Subsets of Steps

Templates were built using a subset of steps: 50% and 25% of the total dataset containing 577 steps. The subsets of steps used for the reduced templates were randomly extracted from the full dataset 10 different times. For each 10-fold validation, the time difference of the detected inflection point between the reduced templates and the template from the full data set were compared.

The time differences ranged from -2.3 ms to 0.59 ms and -10.7 to 7.7 ms for the 50% and 25% templates, respectively. The p-values from the Kruskal-Wallis test ranged from 0.12 to 0.96, meaning that the difference in the detected time of the inflection points for the 50% template was not statistically different from the full template. However, the p-values for the 25% template ranged from 0.012 to 0.46, meaning that the time differences were sometimes statistically different.

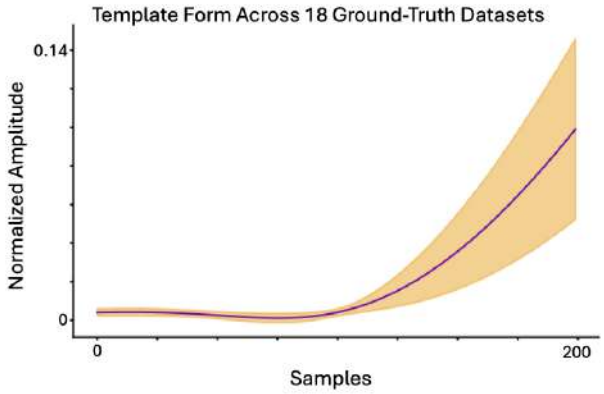


Fig. 5. Mean (± standard deviation) template shape of all templates across the 18 datasets.

IV. DISCUSSION

This work presents a novel template-matching framework that provides a low-resource, efficient, and accurate solution for gait cycle parsing across multiple terrains. Our approach is more efficient than manual parsing and more accurate than thresholding techniques, making it a practical tool for parsing large-scale gait datasets. By testing the algorithm on varying walking terrains, we demonstrated its potential for real-world applications, where traditional gait parsing methods struggle. This novel template-matching approach overcomes key limitations of existing methods and offers a transferable and accessible solution for parsing gait data in both controlled and uncontrolled settings.

Thresholding identifies the onset of loading when pressure surpasses a predefined minimum value. While computationally efficient, thresholding techniques inherently involve a trade-off between false positives and timing accuracy. This was evident in our study, as shown in Table I and Fig. 2. A lower threshold (0.01, or 1% of full scale) detected loading onset more accurately than higher thresholds (-23 ms mean difference from ground truth) but resulted in 362 false positives. In contrast, a higher threshold (0.1, or 10% of full scale) reduced false positives to 49 but introduced greater timing errors, delaying loading onset detection by -60.6 ms. This trade-off demonstrates that while increasing the threshold reduces false positives, it also shifts the detected inflection point later in the gait cycle, leading to loss of early loading pressure information. However, even at the lowest threshold, the timing of the onset of loading was significantly different compared to the template matching algorithm (Fig. 4). To mitigate false positives, researchers often implement dataset-specific catch statements to exclude misclassified steps. However, these custom rules limit generalizability across datasets which include shuffling, foot bumps, or other transient pressure fluctuations as steps. In contrast, the template-matching algorithm automatically differentiated true gait cycles from transient fluctuations, reducing false positives without custom rules.

In contrast to thresholding, which is prone to false positives, manual parsing effectively eliminates this issue but is more susceptible to false negatives. In our study, all three

naïve manual parsers exhibited fewer total errors (6–33) compared to thresholding (49–362 false positives; Table I, highlighting the relative accuracy of human annotation. The template-matching algorithm performed similarly to the naïve manual parsers, with total errors ranging from 27 to 28. Additionally, the timing of the marked inflection point, as measured by the mean difference from the ground truth in milliseconds, was statistically different between only 1 of the 3 naïve parsers when compared to the 18 template-matching algorithm and showed no statistical difference when compared to the average template algorithm (see Fig. 4). The inconsistencies among the naïve researchers highlight the limitations associated with human non-experts, which is problematic with these large-scale datasets.

The template-matching algorithm retains the strengths of manual parsing while maintaining speed (29 minutes for manual parsing compared to 41 seconds for the template-matching algorithm). With the template-matching approach, a user selects a subset of data to generate a template, which is then used to automatically identify the onset of gait cycles. This method also benefits from the low-resource nature of thresholding techniques but with improved accuracy. Additional fine-tuning of the template matching algorithm is possible using a shift parameter that enables adjustment of the height of the inverted sum absolute value signal (Fig. 3).

A limitation of the template-matching approach is the reliance on a high-quality and consistent dataset. Parsing the 577 steps with an average template constructed from all18 datasets was not significantly different in performance compared to the template made from the average of the 18 templates specific to each dataset. This demonstrates the feasibility of a generalizable template for parsing multiple datasets. There are key are some key considerations to keep in mind before using building a generalizable template. Fig. 5 displays the mean and standard deviation from the 18 different templates. There is little variability in the template values before the inflection point, and large variability in the template slope after the inflection point. Care should be taken during template construction to capture the variability in slope data after the inflection point. Cross validation, as performed here, helps to avoid biases from data sampling when constructing the template.

To further refine the template-matching algorithm, future work will involve performance testing on a larger and more diverse population, including variability in age and sex, and test its generalizability on data collected from people with gait impairments. We plan to investigate the feasibility of using the template matching algorithm for other applications and signals, specifically live or real-time parsing of data, angular velocity, reflex responses, or electrocardiography.

V. Conclusion

With this novel template-matching algorithm, large volumes of gait data can be efficiently and accurately parsed to meet the demand of modern gait analysis and rehabilitation technology development. This method successfully detected individual gait cycles from underfoot pressure data collected from participants walking across varying types of terrain. This will enable researchers to expand their gait analysis capabilities to a larger scale and beyond highly controlled laboratory settings to more variable real-world settings.

References

[1] S. D. Uhlrich, A. Falisse, Kidziński, J. Muccini, M. Ko, A. S. Chaudhari, J. L. Hicks, and S. L. Delp, "OpenCap: Human movement dynamics from smartphone videos," *PLOS Computational Biology*, vol. 19, no. 10, p. e1011462, Oct. 2023, publisher: Public Library of Science. [Online]. Available: https://shorturl.at/Gsak1

[2] A. Torres-Pardo, D. Pinto-Fernández, M. Garabini, F. Angelini, D. Rodriguez-Cianca, S. Massardi, J. Tornero, J. C. Moreno, and D. Torricelli, "Legged locomotion over irregular terrains: state of the art of human and robot performance," *Bioinspiration & Biomimetics*, vol. 17, no. 6, p. 061002, Oct. 2022, publisher: IOP Publishing. [Online]. Available: https://dx.doi.org/10.1088/1748-3190/ac92b3

[3] K. North, G. Simpson, W. Geiger, A. Cizik, D. Rothberg, and R. Hitchcock, "Predicting the Healing of Lower Extremity Fractures Using Wearable Ground Reaction Force Sensors and Machine Learning," *Sensors*, vol. 24, no. 16, p. 5321, Jan. 2024, number: 16 Publisher: Multidisciplinary Digital Publishing Institute. [Online]. Available: https://www.mdpi.com/1424-8220/24/16/5321

[4] V. N. Bobić, M. D. Djurić-Jovièić, S. M. Radovanović, N. T. Dragaević, V. S. Kostić, and M. B. Popović, "Challenges of Stride Segmentation and Their Implementation for Impaired Gait," in *2018 40th Annual International Conference of the IEEE Engineering in Medicine and Biology Society (EMBC)*, Jul. 2018, pp. 2284–2287, iSSN: 1558-4615. [Online]. Available: https://ieeexplore.ieee.org/abstract/document/8512836

[5] Y. Moon, J. Sung, R. An, M. E. Hernandez, and J. J. Sosnoff, "Gait variability in people with neurological disorders: A systematic review and meta-analysis," *Human Movement Science*, vol. 47, pp. 197–208, Jun. 2016. [Online]. Available: https://www.sciencedirect.com/science/article/pii/S0167945716300306

[6] K. North, G. M. Simpson, A. R. Stuart, E. N. Kubiak, T. J. Petelenz, R. W. Hitchcock, D. L. Rothberg, and A. M. Cizik, "Early postoperative step count and walking time have greater impact on lower limb fracture outcomes than load-bearing metrics," *Injury*, vol. 54, no. 7, p. 110756, Jul. 2023. [Online]. Available: https://www.sciencedirect.com/science/article/pii/S0020138323003881

[7] Z. Zhang, Z. Wang, H. Lei, and W. Gu, "Gait phase recognition of lower limb exoskeleton system based on the integrated network model," *Biomedical Signal Processing and Control*, vol. 76, p. 103693, Jul. 2022. [Online]. Available: https://www.sciencedirect.com/science/article/pii/S1746809422002154

[8] A. N. Dalrymple, D. A. Roszko, R. S. Sutton, and V. K. Mushahwar, "Pavlovian control of intraspinal microstimulation to produce over-ground walking," *Journal of Neural Engineering*, vol. 17, no. 3, p. 036002, May 2020, publisher: IOP Publishing. [Online]. Available: https://dx.doi.org/10.1088/1741-2552/ab8e8e

[9] A. N. Dalrymple, D. G. Everaert, D. S. Hu, and V. K. Mushahwar, "A speed-adaptive intraspinal microstimulation controller to restore weight-bearing stepping in a spinal cord hemisection model," *Journal of Neural Engineering*, vol. 15, no. 5, p. 056023, Aug. 2018, publisher: IOP Publishing. [Online]. Available: https://shorturl.at/16mZy

[10] "Gait Cycle - an overview | ScienceDirect Topics." [Online]. Available: https://www.sciencedirect.com/topics/engineering/gait-cycle

[11] "Gait Analysis: Normal and Pathological Function," *Journal of Sports Science & Medicine*, vol. 9, no. 2, p. 353, Jun. 2010. [Online]. Available: https://www.ncbi.nlm.nih.gov/pmc/articles/PMC3761742/

[12] Y. Liu, K. Lu, S. Yan, M. Sun, D. K. Lester, and K. Zhang, "Gait phase varies over velocities," *Gait & Posture*, vol. 39, no. 2, pp. 756–760, Feb. 2014. [Online]. Available: https://www.sciencedirect.com/science/article/pii/S0966636213006437

[13] F. Hebenstreit, A. Leibold, S. Krinner, G. Welsch, M. Lochmann, and B. M. Eskofier, "Effect of walking speed on gait sub phase durations," *Human Movement Science*, vol. 43, pp. 118–124, Oct. 2015. [Online]. Available: https://www.sciencedirect.com/science/article/pii/S0167945715300117

[14] "Garangatang/Gait_cycle_template_matching." [Online]. Available: https://github.com/Garangatang/Gait$_{C}ycle_{T}emplate_{M}atching$

Robotic Assessment of Cognitive and Motor Impairment in Adults with Sickle Cell Disease

Joana Opong-Duah[1], Arushi Mittal[2], Erica Waters[3], Farzana Sayani[4], Suzanne Sall[5], Frances Shofer[6], Michelle J. Johnson[7]

***Abstract*— For decades, Sickle Cell Disease (SCD) research has explored the influence of the disease in many domains of functioning throughout childhood. As medical advancements have increased the lifespan of those living with SCD, it is crucial to also evaluate the effects of the disease in adulthood. This paper investigates the relationship between cognition and physical abilities in adults with and without Sickle Cell Disease. We present a preliminary analysis identifying the influence of one domain over the other, focusing on the way cognitive impairment may worsen motor function. To determine this, we employ the Haptic TheraDrive one-degree-of-freedom robot as an objective measure to assess performance, and we compare the results to a battery of clinical assessments. SCD participants were frequency matched to healthy controls to investigate the cognitive and motor functions affected by SCD. There were not many significant differences between groups across cognitive and motor domains, partly due to a small sample size. We did identify significant impairments in elements of working memory. We also found that motor performance could have been impacted by SCD-related pain and stiffness affecting robotic score.**

I. Introduction

Sickle Cell Disease (SCD) is considered one of the most prevalent monogenic disorders in the world. In the United States (US) alone, there are about 100,000 individuals living with SCD [1]. A critical protein in our red blood cells responsible for oxygen transport to our tissues is hemoglobin. Beta Hemoglobin or β-globin, a subunit of that protein, is where the mutation causing SCD occurs. In the β-globin, there is a substitution in the base nucleotides; this mutation causes a replacement of the amino acids, switching from glutamic acid to valine, thus producing HbS or sickle hemoglobin. This change in amino acids causes polymerization, which forms fibers that reshape the red blood cells. These fibers "sickle" the red blood cells, giving them the 'C' shape commonly associated with this disease, thus the name Sickle Cell [1,2]. SCD is a hereditary condition and can manifest in various subtypes, including the three most common: Sickle Cell Anemia (HbSS), Sickle Cell-Hemoglobin C (HbSC), and S-Beta Thalassemia ($HbS\beta^{+}$-Thalassemia/ $HbS\beta^{0}$-Thalassemia). Some people are carriers of the trait but do not suffer from complications of SCD itself, Sickle Cell Carrier (HbAS) [3]. HbSS occurs when both parents pass along the sickle gene to their child, as it is the homozygous inheritance of the gene mutation. This subtype represents the most severe cases of SCD and is the most prevalent, accounting for 70-75% of SCD cases globally [4]. In the US and the UK, HbSC accounts for about 30% of SCD cases and is the second most common disease variation [5].

Some studies have found past evidence of neurocognitive and motor impairments across the lifespan of the SCD population when compared to controls. Structural changes to the red blood cells can lead to many physical issues. These changes often cause repeated vessel occlusion, leading to a variety of impairments, including painful episodes and chronic anemia, which lead to organ and tissue damage, delayed growth, a compromised immune system, and, in many cases, stroke or infarction [6,7]. Approximately 11% of SCD patients have clinically apparent strokes before the age of 20; by the time they reach 45 years old, this number jumps to 24% [8]. These strokes have been thought to account for some impairments identified in domains of executive functioning, such as processing speed, visuospatial function, and attention, which in the past, has been measured by the Wechsler Adult Intelligence Scale-Third Edition (WAIS-III), symbol digit coding, and the Montreal Cognitive Assessment (MoCA) [1][9]. Physical assessments used in past literature have included the 6-minute walk test and Grip Strength, observing significantly lower performance in SCD participants than controls.

Due to a lack of research and understanding, SCD had once been considered a black pediatric disease, with many patients dying in childhood from disease complications [10]. Given the commonality of stroke in childhood, there was and still is a significant emphasis on providing consistent and extensive care for children living with SCD. However, this initiative has failed to follow patients once they age out of

[1] Joana Opong-Duah is a research assistant in the Rehabilitation Robotics Lab at the University of Pennsylvania joana.opongduah@gmail.com

[2] Arushi Mittal is an undergraduate student in Bioengineering and Electrical Engineering at the University of Pennsylvania arushim@seas.upenn.edu

[3] Erica Waters is a PhD candidate in Mechanical Engineering and Applied Mechanics at the University of Pennsylvania waterica@seas.upenn.edu

[4] Farzana Sayani is an Associate Professor, Temerity Faculty of Medicine at the University of Toronto in the Division of Medical Oncology and Hematology and an Adjunct Associate Professor at the Perelman School of Medicine at the University of Pennsylvania in the Department of Medicine, Division of Hematology-Oncology Farzana.sayani@uhn.ca

[5] Suzanne Sall is a psychologist at the University of Pennsylvania in the Department of Medicine, Division of Hematology-Oncology suzanne.sall@pennmedicine.upenn.edu

[6] Frances Shofer is the Director of Epidemiology & Biostatistics in the Department of Emergency Medicine at the University of Pennsylvania Perelman School of Medicine shofer@pennmedicine.upenn.edu

[7] Michelle J. Johnson is an Associate Professor at the University of Pennsylvania with a primary appointment in Physical Medicine and Rehabilitation and secondary appointments in Bioengineering and Mechanical Engineering and Applied Mechanics johnmic@pennmedicine.upenn.edu

pediatric care at 18, leaving a significant gap in the literature that explores the effects of SCD in adulthood. The lack of research about the effects of SCD on daily function and quality of life in adults also means there is little to no research on the possibility and usefulness of rehabilitation in this age group. As medicine has advanced and the lifespan expectancy of SCD patients has increased, there is a significant need for continued diagnostic and rehabilitation efforts in this population.

Assistive technologies have been used to objectively measure cognitive and motor impairment in adults with stroke and other brain injuries. The Haptic TheraDrive, a one-degree-of-freedom robot, was initially created to provide affordable therapy and assess upper arm function in stroke survivors. It can also be used to provide an affordable and objective measure of impairment in various populations. This robotic system utilizes multiple computerized assessments to identify impairments. This study explores the role of the Haptic Theradrive as an objective and accurate assessment tool for the cognitive and motor impairments of SCD in adults. Our efforts are aimed at identifying the cognitive and motor impairments associated with SCD and adding to the literature. This paper is also focused on understanding the relationship between clinical assessments and robotic tasks and identifying whether increasing the cognitive aspect of robotic tasks interferes with SCD participants' motor performance. To consider both objectives, we have matched SCD patients to healthy controls and compared their results across both clinical and robotic assessments.

II. Methods

A. Study Design/ Setting

This study was implemented at the Rehabilitation Robotics Lab located in Philadelphia, PA, at the Penn Medicine-Rittenhouse Rehabilitation and Acute-Care Facility. All SCD participants were recruited from the Penn Medicine Comprehensive SCD Program, while all healthy controls were recruited from the Penn Medicine iConnect database and the community. After determining eligibility, participants were invited to the lab and consented. The University of Pennsylvania Institutional Review Board (IRB) approved this study (#854019). After giving consent, participants performed a battery of four cognitive, four motor, and two robotic assessments. Assessments were split into two sections: the clinical and the robotic portion. These could all be performed in one day, or participants could choose to split the sections over two days, within 7 days of each other.

B. Participants

Inclusion criteria for this study detailed that all adults over the age of 18 with or without SCD, any race, gender, and education level were welcomed. Due to chronic pain commonly associated with this disease, participants were not excluded based on pain levels. Instead, pain for all participants was recorded before and throughout the trials. Exclusionary criteria for all subjects prevented adults with a history of stroke or silent infarct from participating. SCD participants were excluded from the study if they had experienced a vaso-occlusive pain crisis within the 7 days leading up to pre-screening or if they were experiencing a vaso-occlusive pain crisis at the time of the pre-screening as well. Other exclusionary criteria for both groups included a Montreal Cognitive Assessment (MoCA) score of less than 18, drug and/or alcohol abuse, or a depression score greater than nine as measured by the Patient Health Questionnaire-9 (PHQ-9).

A total of 19 adults were recruited and completed the study protocol. Ten participants were living with SCD, and 9 were healthy controls. Of the 19, one person was excluded due to an inability to focus on completing the tasks asked of them during the study protocol. Their matched pair was removed from this data set for the purpose of having paired data included in this paper. Another participant's clinical data was eligible to remain in the study but, due to extreme shoulder pain in one arm, was unable to complete the robot assessments in a standardized way. In this case, their data and the matched control's data were also removed from this paper for one arm. The last participant had not yet been placed into a matched pair, so their data was also removed. Table I outlines the demographics of the final groups discussed in this paper. Of the 16 participants, 12 were female, 14 were Black, and 15 had over a high school education. In this study, pairs were made based on age, gender, and education level. We had aimed for a total of 10 pairs and were able to present the data of eight matched pairs (Table I).

D. Assessments

Participants were contacted to complete the pre-screen forms with a study Research Assistant, which included the PHQ-9 and two of the Patient-Reported Outcomes Measurement Information System (PROMIS) Pain Intensity/ Pain Interference short forms. The PHQ-9 was used as a measurement of depression in this study population. This assessment is commonly used across many populations as a valid measure of depression, with nine questions that are based on the Diagnostic and Statistical Manual of Mental Disorders- Fourth Edition (DSM-IV) criteria [11]. The PROMIS Pain Interference and Pain Intensity Scales were used to assess pain details within the seven days before recruitment. These valid measures have previously been used in the adult SCD population alongside the Adult Sickle Cell Quality of Life Measurement Information System (ASCQ-Me) [12][13]. Due to consistent pain associated with

TABLE I. Demographic Data

		SCD Participants n=8	***Control Participants n=8***
Age		42.4 ± 14.8	41.9 ± 16.6
		n	n
Gender	Female	6	6
	Male	2	2
Education	<12 Years	0	1
	12-16 Years	6	1
	>16 years	2	6
Race	White/Caucasian	1	0
	Asian	0	1
	Black/African American	7	7

SCD, we monitored pain levels throughout the study. During the clinical and robotic trials, every participant was asked to rate any pain using the Visual Analog Scale (VAS). During the robot session, we also recorded the level of effort to complete the assessments using the BORG Rating of Perceived Exertion Scale (Table III).

Cognitive assessments included the MoCA, Color Trails I & II (CT), Hopkins Verbal Learning (HPVL), and Digit Symbol Coding (DS). The MoCA test was used to assess multiple domains of functioning, including visuospatial/executive function, naming, memory, attention, language, abstraction, delayed recall, and orientation. Scoring less than 18 out of 30 indicates moderate to severe cognitive impairment, while a score of 26 and above is indicative of normal functioning [14]. Color Trails I & II are a set of assessments used to test for visuospatial functioning, attention, motor speed, and mental flexibility. For these tests, a higher score indicates poorer performance [15]. Hopkins Verbal Learning is an assessment focused on immediate recall, delayed recall, recognition index, and retention, which means that the more words a participant can remember, the better their score [16]. Digit Symbol Coding is used primarily to test for processing speed alongside attention. The more symbols a participant can quickly and accurately match to its specified number, the higher their score and the better their performance [17].

Motor assessments for this study included Box & Blocks (BB), Grip Strength (GS), Grooved Pegboard (GP), and the 10m Walk. The box & blocks assessment is used primarily to determine the level of gross motor skills in participants; higher scores signify better gross motor function [18]. In the grooved pegboard assessment, participants were asked to complete this task as quickly as possible to assess fine motor skills and executive functioning. A lower time could demonstrate normal functioning in both domains, as defined in the literature [19]. The Grip strength test assesses upper body strength and has been used in past research as a measure of impaired development [20]. As for the 10m Walk, this test was used to determine lower limb ability across participants. A shorter time on this assessment demonstrates better lower limb usability [21].

All participants were placed in standardized seating next to the robotic arm (Fig. 1), where they then completed two computerized games using the Haptic TheraDrive robot [22]. The Trajectory Tracking (TT) motor task is mainly used to assess upper limb performance. However, it also holds a cognitive element as participants are expected to learn the assessment and improve accuracy as they complete all 15 trials. This assessment required participants to push and pull the Haptic Theradrive robot arm forward and backward, controlling a small cursor on the screen that moves left and right in correspondence. Participants saw a semi-opaque box on the screen that followed a vertical sinusoidal path. To score well in this task, one must stay within the moving box, controlling the cursor to remain as accurate as possible. Participants completed a total of 15 trials that were about 15 seconds each, not including the 1-3 practice trials every participant completed (Fig. 2- left).

For the Spatial Span (SS) Motor-cognitive task, participants were shown a 3x3 grid of squares (Fig. 2 right). They were asked to move the robotic arm back at the start of each of the 18 trials. Once they have moved into position, a pattern of squares on the screen will flash in green. When the green stops, they were to use the robotic arm to repeat the pattern exactly as they witnessed it, in order. If they matched the pattern correctly, the next trial would be one square longer; if they were incorrect, it would be one tile shorter. All participants started with a pattern of two squares and tried to work their way up to the maximum of seven squares in a trial. Participants were asked to complete 18 trials in total.

One assessment was completed only by the SCD participants, which was the ASCQ-Me. This test is specifically used to assess SCD's physical, emotional, and social impact on daily living. For this study, the survey was used to understand how SCD patients feel and function in their day-to-day lives. This questionnaire was created by the American Institutes for Research (AIR) and the National Heart, Lung, and Blood Institute (NHLBI) and can be compared to the generalized results of the PROMIS scales as a more SCD-focused survey [11][23].

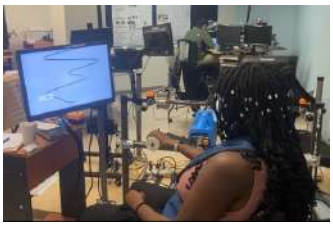


Figure 1. *Participant's position with the Haptic TheraDrive Arm*

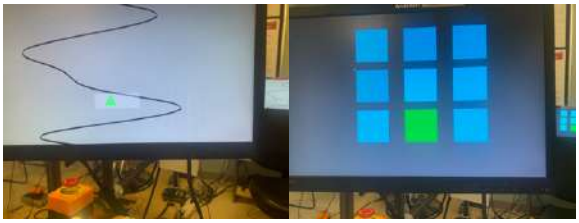


Figure 2. Robotic Assessments *(Left-TT, Right-SS)*

E. Statistical Methods

For the Trajectory Tracking task, we calculated four metrics: Root Mean Square Error (RMSE), Normalized Distance Traversed (ND), Mean Absolute Velocity (MAV), and Spectral Arc Length (SPARC) (Fig.5) for both groups. RMSE was defined as the root mean square error between the angular trajectory that the participant travels and the desired trajectory. A higher RMSE indicates greater error and worse performance. ND is defined as the total angular distance traveled by the participant divided by the distance required to travel the desired trajectory. An ND value close to 1 indicates that the participant moved as much as the task required. An ND value of less than 1 indicates that the participant did not move enough, and a value greater than 1

indicates that the participant moved more than the desired trajectory. MAV was calculated by finding the mean of the absolute value of angular velocity. A higher MAV indicates faster movements. Finally, we calculate smoothness using SPARC [24]. A more negative SPARC value indicates a less smooth movement. For the spatial span task, we calculate a task-specific metric, mean sequence length, and two kinematic metrics, MAV and SPARC. Mean Sequence Length is defined as the mean length of the displayed sequence across all trials. MAV and SPARC are defined for Spatial Span the same as for Trajectory Tracking. For the Spatial Span task, the mean sequence length is the primary metric reported (Fig.6).

To analyze and visualize the robotic assessment data, Python scripts were developed to process the raw data and generate meaningful charts. The graph in Fig. 3 was created to compare the position of the robot handle over time in TT, highlighting the differences between the actual and desired movement paths. All graphs were presented as participant pairs through the example of Participant 5 and Participant 13. To generate these plots, the time points for each trial were averaged across all trials for each participant, creating one averaged trial that was then compared to the desired path. The processed data was then visualized using Matplotlib, enabling a clear representation of movement performance. For the SS task, the data was processed to plot the sequence length distribution as a histogram, which displayed the frequency of different sequence lengths completed during the task (Fig. 4). This figure's analysis and visualization aided in the interpretation of performance patterns across the participant pairs.

In Table II, we were also able to run a Wilcoxon Signed-Rank Test to properly compare the SCD and Controls' Z-Scores on the Hopkins Verbal Learning assessment, Box & Blocks, Grooved Pegboard, and Grip Strength after calculating the raw means and standard deviations displayed.

In Fig. 5, an analysis of variance was used in repeated measures where the trial number was the repeated measure. Like many of the results in this study, these analyses did not display significant differences between groups. However, it does provide us with interesting and unexpected visuals about the similarities and differences in performance based on other factors.

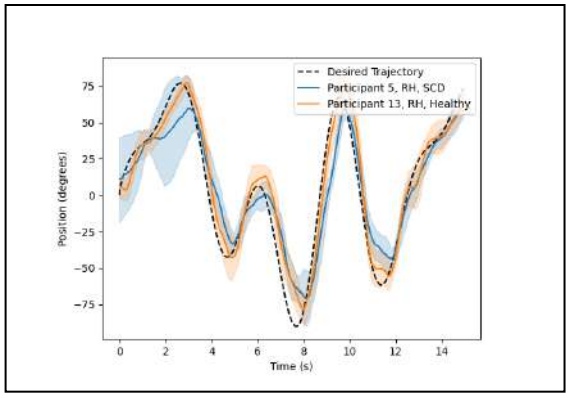


Figure 3. Trajectory Tracking Actual vs Desired Trajectories of a Pair

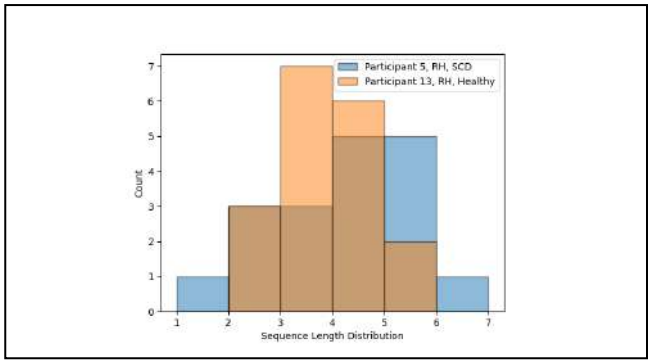


Figure 4. Spatial Span Actual vs Desired Trajectories of a Pair

III. Results

TABLE II. Clinical Assessment Raw Score Data

Assessment	*SCD Participants n=8*	*Control Participants n=8*
Box & Blocks (Dominant Hand) (mean ± SD)	59.2 ± 8.5	61.5 ± 10.0
Box & Blocks (Non-Dominant Hand) (mean ± SD)	59.8 ± 7.4	60.5 ± 9.2
MoCA (mean ± SD)	25.3 ± 2.8	24.3 ± 2.5
Color Trails 1 (mean ± SD)	40.7 ± 13.9	37.9 ± 13.9
Color Trails 2 (mean ± SD)	72.4 ± 13.4	73.0 ± 20.9
Hopkins Verbal Learning (Delayed Recall)*	6.38 ± 2.13	8.88 ± 1.89
Hopkins Verbal Learning (Retention)*	67.6 ± 17.2	83.8 ± 12.3

*Statistically Significant p-value

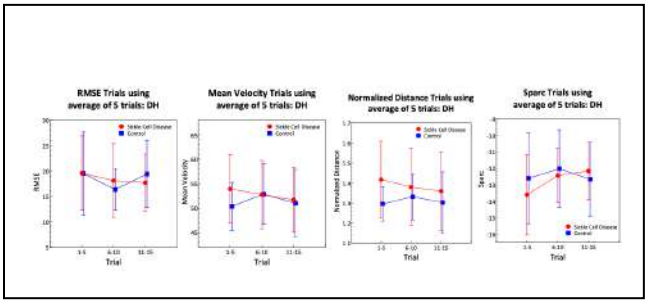


Figure 5. Trajectory Tracking Results of SCD Participants and Healthy Controls For Dominant Hand (DH)

A. Example Robotic Tasks

Figs. 3 and 4 display examples of paired Trajectory Tracking and Spatial Span results. Participant 5 was a 60-year-old female SCD volunteer. They scored in the normal cognitive function range with a MoCA score of 27 and a CT2 T-score above 60. Participant 13 was a 65-year-old female control displaying mild-normal cognitive impairment with a MoCA of 20 and a CT2 T-score of 59.

The dotted line in Fig. 3 represents the desired trajectory presented to all participants while completing the task. The example trajectories of the two participants indicate the average path taken by them across 15 trials. In this case, we see that the SCD participant averaged better along the desired trajectory as opposed to the healthy subject. The highlighted regions depict the standard deviations of each participant.

In Fig. 4, the Y-axis shows us the number of instances, and the X-axis shows us the number of squares in a pattern. For this pair, we can see that both participants were able to reach up to a pattern of five squares at some point during their 18 trials. However, the SCD participant was able to remember the pattern of five squares five times, compared to the healthy control, who only reached a pattern of five, twice. This could indicate that the SCD participant had better working memory function when compared to their healthy control, which was unexpected.

We identified three clinical assessments as comparable to the results of the robotic assessments. The MoCA for overall cognitive function and Color Trails 1 & 2 (CT1, CT2) served as different measures of executive function and were used in comparison to the Spatial Span Task. The box & blocks were used as a measure of gross motor function, which was necessary to adequately use the robotic arm for both TT and SS. Table II displays the raw clinical assessment data of all participants. The significant differences identified were between the groups in the HPVL- Delayed Recall and Retention with p-values of 0.016.

TABLE III. ROBOTIC ASSESSMENT DATA

Assessment	***SCD Participants n=8***	***Control Participants n=8***
Average Pain (Trajectory Tracking)	1.53 ± 2.6	0.63 ± 1.0
Average Pain (Spatial Span)	1.49 ± 2.4	0.13 ± 0.35
Average Exertion (Trajectory Tracking)	2.95 ± 2.13	1.85 ± 1.4
Average Exertion (Spatial Span)	2.1 ± 1.24	1.25 ± 0.82
Average RMSE	18.5 ± 8.8	18.0 ± 7.3
Average SPARC	-12.8 ± 3.18	-12.1 ± 2.9
Mean Absolute Velocity	52.0 ± 10.1	53.4 ± 8.6
Normalized Distance	1.36 ± 0.27	1.36 ± 0.2
Mean Sequence Length	4.17 ± 1.05	3.72 ± 0.90

IV. DISCUSSION

A. Key Results

Many of the clinical assessments did not present significant results, which was expected based on past literature. This is in part due to the small sample size of this study as well as the possibility that adults with SCD have lived with deficits for years and have learned to adapt to life with these impairments. The significant differences noticed in Delayed Recall and Retention were, however, an expected result, as memory is one of the domains often described as being impacted by SCD, [25]. In trials and our preliminary analyses, it was clear that as participants were completing the assessments, our results would be much closer than originally expected.

Based on the SPARC results (Fig. 5- right), our SCD participants seemed to have a mean smoothness that started lower but improved throughout the 15 trials, whereas the controls were higher throughout the first 10 trials and dropped at the last five. Based on past literature, we hypothesized that our SCD participants would indicate pain levels greater on average than the controls (Table III). The potential for pain was an expected risk factor of using the robot. However, if a subject already reports chronic pain, we were interested in seeing how additional pain would impact performance. For example, could chronic pain lead to a quicker onset of fatigue? We believed the additional pain could have prevented SCD participants from performing consistently or as well as their healthy counterparts. The presented MAV results could potentially support this belief. Fig. 5 depicts the SCD participants' steady decrease in their velocity, which was an expected result versus the controls who increased in velocity before tapering off in their dominant hand (DH). When looking at RMSE (Fig. 5- left), we expected to see a decrease in scores as participants completed the trajectory-tracking task. This would indicate improved learning of the task and a participant's ability to adjust to the robotic arm movement. In this study, we saw that both groups showed some learning, and the healthy controls seemed to learn faster in the first six trials. This result is somewhat mirrored in the ND scores, as, on average, the controls were able to move in a more consistent manner than the SCD subjects. If SCD participants were experiencing pain or fatigue, their accuracy would take a hit, as the speed of the task did not change during the 15 trials. In Fig. 6, we see how close the SCD group and controls were scoring in their average number of sequences. Fig.6 shows that the SCD participants were able to memorize more sequences of the pattern than the controls. Results such as this have been an interesting example of SCD participants outperforming their healthy control when, by all accounts, the result should be flipped. This brings to question what other factors may not have been considered in the assessment of the SCD group. One belief we had was that medications that SCD participants have been taking for years to reduce anemia symptoms, such as hydroxyurea and folic acid, could help SCD subjects live relatively symptom-free lives, therefore allowing for more freedom to perform as "healthy" participants themselves. Much of the literature explains that the subtype of SCD that someone has, or in other words the genotype they live with, determines the severity of the disease and, in turn, the level of impact in daily life. Our study suggests this may not always be the case. Instead, we hypothesize that based on our population and their recorded genotypes, sometimes those with even the HbSC type of the disease can experience symptoms as severe as those who are HbSS. We can infer from the results of this study that some motor impairment is apparent and has

affected participant performance in the Trajectory-Tracking task. Along with the SCD groups' individually reported pain levels at the end of the robotic trial, this was an expected result. What we have observed in the Spatial Span results shows that although there were significant impairments in long-term memory (Table II), the same may not be true for short-term memory. Based on the literature reviewed, while working memory has been identified as a common domain of impairment in SCD subjects, it has not been specified whether it's long or short-term memory that is impacted.

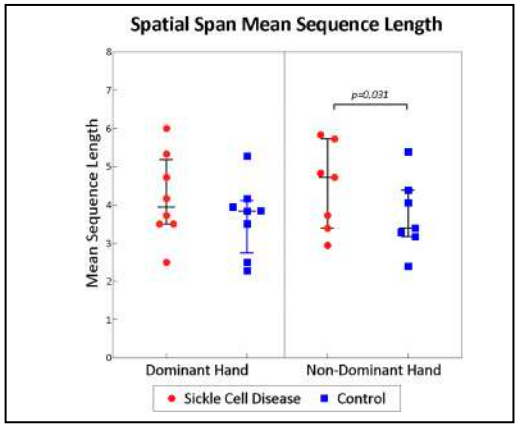


Figure 6. Mean Sequence Length Results of The Spatial Span Task Between Groups

B. Limitations

The major limitation of this study is the small sample size. With this sample size, we were unable to identify many significant differences between our SCD and control groups. Future directions for this research include growing our sample to create stronger arguments and supporting data.

Financial Conflicts of Interest

Dr. Michelle J Johnson, who is the PI and/or Co-I leading this study, has a patent that uses devices inspired by the device being evaluated through this research. The PI is a co-founder of Recupero Robotics LLC and should appear before the acknowledgment.

Acknowledgment

We would also like to acknowledge Dr. Laura Stubbs and the University of Pennsylvania School of Engineering Office of Diversity, Equity, and Inclusion for their continued support of this project, as well as the Penn Medicine Comprehensive Sickle Cell Disease Program and other members of the Rehabilitation Robotics Lab and Recupero, LLC.

References

[1] T. Sahu, B. Pande, M. Sinha, R. Sinha, and H. K. Verma, "Neurocognitive Changes in Sickle Cell Disease: A Comprehensive Review," *Ann. Neuro.*, 29(4), p.255, Jul. 2022,.

[2] S. Farooq and F. D. Testai, "Neurologic Complications of Sickle Cell Disease," *Curr. Neurol. Neurosci. Rep.*,19,(4), p.17, Apr. 2019.

[3] CDC, "About Sickle Cell Disease," Sickle Cell Disease (SCD). Accessed: Nov. 17, 2024. [Online]. Available: https://www.cdc.gov/sickle-cell/about/index.html

[4] D. C. Rees, V. A. M. Brousse, and J. N. Brewin, "Determinants of severity in sickle cell disease," *Blood Rev.*, vol. 56, p. 100983, Nov. 2022.

[5] L. H. Pecker, B. A. Schaefer, and L. Luchtman-Jones, "Knowledge Insufficient: The Management of Haemoglobin SC Disease," *Br. J. Haematol.*, 176(4), p.515, Dec.2016.

[6] "(PDF) Sickle cell disease: current treatment and emerging therapies." Accessed:Sep.07,2024.Online].Available:https://www.researchgate.net/publication/337819453_Sickle_cell_disease_current_treatment_and_emerging_therapies

[7] M. Rhodes *et al.*, "Growth Patterns in Children with Sickle Cell Anemia during Puberty," *Ped. Blood Cancer*, 53(4), p.635–641, Oct. 2009.

[8] K. Ohene-Frempong *et al.*, "Cerebrovascular Accidents in Sickle Cell Disease: Rates and Risk Factors," *Blood*, 91(1), p.288–294, Jan. 1998.

[9] M. L. Early *et al.*, "The Montreal cognitive assessment as a cognitive screening tool in sickle cell disease: Associations with clinically significant cognitive domains," *Br. J. Haematol.*, 198(2), p.382–390, Jul. 2022.

[10] S. Chaturvedi and M. R. DeBaun, "Evolution of sickle cell disease from a life-threatening disease of children to a chronic disease of adults:The last 40 years," *Am. J. Hematol.*,91(1), p.5–14, Jan. 2016.

[11] K. Kroenke, R. L. Spitzer, and J. B. Williams, "The PHQ-9: validity of a brief depression severity measure," *J. Gen. Intern. Med.*,16(9), p.606–613, Sep. 2001.

[12] S. Keller, M. Yang, M. J. Treadwell, and K. L. Hassell, "Sensitivity of alternative measures of functioning and wellbeing for adults with sickle cell disease: comparison of PROMIS® to ASCQ-Me^{SM}," *Health Qual. Life Outcomes*, 15(1), p.117, Jun. 2017.

[13] "Anxiety, Depression, Pain Intensity and Interference in Adult Patients with Sickle Cell Disease | Blood | American Society of Hematology."Accessed:Nov.17,2024.[Online].Available:https://ashpublications.org/blood/article/128/22/1312/96158/Anxiety-Depression-Pain-Intensity-and-Interference

[14] Z. S. Nasreddine *et al.*, "The Montreal Cognitive Assessment, MoCA: a brief screening tool for mild cognitive impairment," *J. Am. Geriatr. Soc.*, 53(4), p.695–699, Apr. 2005.

[15] "(PDF) Color Trails Test: Normative Data and Criterion Validity for the Greek Adult Population," ResearchGate. Accessed: Nov.17, 2024. [Online].Available:https://www.researchgate.net/publication/51113381_Color_Trails_Test_Normative_Data_and_Criterion_Validity_for_the_Greek_Adult_Population

[16] R. H. B. Benedict, D. Schretlen, L. Groninger, and J. Brandt, "Hopkins Verbal Learning Test – Revised: Normative Data and Analysis of Inter-Form and Test-Retest Reliability," *Clin. Neur.*12(1),43–55, Feb. 1998.

[17] S. Joy, E. Kaplan, and D. Fein, "Speed and memory in the WAIS-III Digit Symbol--Coding subtest across the adult lifespan," *Arch. Clin. Neuropsychol. Off. J. Natl. Acad. Neuropsy.*, 19(6),p.759–767, Sep. 2004.

[18] V. Mathiowetz, G. Volland, N. Kashman, and K. Weber, "Adult norms for the Box and Block Test of manual dexterity," *Am. J. Occup. Ther. Off. Publ. Am. Occup. Ther. Assoc.*, 39(6), 386–391, Jun.1985.

[19] K. A. Tolle, A. M. Rahman-Filipiak, A. C. Hale, K. A. K. Andren, and R. J. Spencer, "Grooved Pegboard Test as a measure of executive functioning," *Appl. Neuropsy. Adult*, Feb. 2019, Accessed: Jan. 08, 2023. [Online].Available:https://www.tandfonline.com/doi/full/10.1080/23279095.2018.1559165

[20] C. I. Oyedeji, K. Hall, A. Luciano, M. C. Morey, and J. J. Strouse, "The Sickle Cell Disease Functional Assessment (SCD-FA) tool: a feasibility pilot study," *Pilot Feas.*,8, p.53, Mar.2022.

[21] "Sickle Cell Disease - How Sickle Cell Disease May Affect Your Health | NHLBI, NIH." Accessed: Nov. 17, 2024. [Online]. Available: https://www.nhlbi.nih.gov/health/sickle-cell-disease/health-effects

[22] K. D. Bui, C. A. Wamsley, F. S. Shofer, D. L. Kolson, and M. J. Johnson, "Robot-based assessment of HIV-related motor and cognitive impairment for neurorehabilitation," *medRxiv*, p.2020., Nov. 2020.

[23] O. Cooper *et al.*, "Psychometric analysis of the adult sickle cell quality of life measurement information system (ACSQ-Me) in a UK population," *Health Qual. Life Outcomes*, 17(1), p. 74, Apr. 2019.

[24] S. Balasubramanian, A. Melendez-Calderon, A. Roby-Brami, and E. Burdet, "On the analysis of movement smoothness," *J. NeuroEng. Rehabil.*,12(1), p.112, Dec. 2015.

[25] M. C. Kral, R. T. Brown, and G. W. Hynd, "Neuropsychological Aspects of Pediatric Sickle Cell Disease," *Neuropsyc. Rev.* 11(4), p.179–196, Dec. 2001.

Interactive Gait Rehabilitation Through Gamified Real-Time Biofeedback and Adaptive Hip Exoskeleton Assistance: A Preliminary Evaluation

Mariya Tohfafarosh, Neethan Ratnakumar, *Student Member, IEEE,* Lorenzo Zurzolo, Sergei Adamovich, *Member, IEEE,* Xianlian Zhou*, *Member, IEEE*

***Abstract*— This paper presents the design and functional evaluation of an interactive rehabilitation system that integrates a hip exoskeleton with a game-based environment for targeted gait rehabilitation. The system offers real-time visualization of full-body motion tracking and biofeedback, including electromyography (EMG) based muscle activation feedback. Users control an anatomical avatar within a task-based gameplay interface, where the avatar mirrors their motion and displays muscle activation through dynamic, red-shaded overlays corresponding to real-time EMG signals. To assess the system's functionality, a healthy subject participated in a study involving treadmill walking at 0.25 m/s slower than their self-selected speed. The subject navigated a forest environment to collect virtual apples while using two stiffness-based hip control modes: an in-phase assistive mode and an out-of-phase resistive mode. The assistive mode reduced muscle activation, while the resistive mode increased muscle activation for strength training. Additionally, the system supports post-processing of collected data for further analysis, enabling visualization of kinematics, exoskeleton torques, and EMG patterns. Users can customize rehabilitation parameters to tailor the experience to their needs. The results demonstrate the system's potential as an interactive, feedback-driven rehabilitation platform, showcasing its biofeedback capabilities and adaptability.**

Keywords—gamified rehabilitation, assistive technology, biomechanical feedback, myofeedback

I. Introduction

Movement disabilities, whether chronic or temporary, can arise from various medical conditions and injuries, including neurological events, motor impairments, congenital disorders, trauma affecting the lower body, or common post-operative conditions such as those following joint replacement surgery. Approximately, 12.2% of individuals in the United States experience significant challenges in walking or climbing stairs [1]. This limited mobility not only impacts their quality of life but also heightens their risk of secondary health complications [2]. As a result, effective rehabilitation strategies are critically needed. However, hospital-based physiotherapy is often costly and logistically challenging, which can lead to inconsistent patient participation and slower recovery.

Successful rehabilitation requires a highly personalized approach, with recovery plans tailored to each patient's specific condition, type of impairment, personal goals, and individual circumstances. This underscores the need to follow three main principles: first, rehabilitation exercises should be designed to sustain patient motivation; second, they must be adaptable to the patient's needs; and third, patient performance should be objectively evaluated, for instance, comparing movements against an ideal reference model [3]. Gamified approaches, with real-time biofeedback and customizable features, have emerged as valuable tools to engage patients and meet these principles. Specifically, incorporating motion and electromyographic (EMG) feedback into these programs provides additional benefits.

Real-time motion feedback is a critical component in rehabilitation gaming, offering patients immediate insights into their movements. This instantaneous feedback enables individuals to adjust their posture, refine motor skills, and improve task execution, thus fostering enhanced motor learning [4]. By guiding patients toward real-time corrections, motion feedback not only enhances therapy effectiveness but also accelerates recovery and contributes to sustained long-term improvements. Furthermore, such feedback increases patient motivation, making rehabilitation more engaging and impactful [5]. Integrating motion feedback allows clinicians to track and evaluate patient performance seamlessly, proving its value in both clinical and home-based therapy settings.

Combining motion feedback with biofeedback modalities like muscle EMG creates a more interactive and immersive rehabilitation experience, addressing both physical and psychological recovery dimensions. Studies, such as those by Giggins et al [6], emphasize the importance of virtual reality and real-time feedback in improving functional outcomes for post-stroke patients and Parkinson's patients by offering tailored, actionable insights during therapy sessions and helps the patients to preserve their motivation during the rehabilitation process.

EMG feedback offers real-time insights into muscle activity, motivating, and empowering patients to adjust their movements and enhance motor control. Studies have shown that EMG feedback training can be effective in improving muscle strength, pain reduction, functionality, and joint range of motion in the context of sports and orthopedic rehabilitation [7, 8]. Additionally, evidence suggests that EMG biofeedback therapy also significantly improves limb function after stroke, particularly in the short term [9, 10]. For example, Intiso et al. [11] show the effectiveness of EMG feedback in increasing muscle strength in the tibialis anterior which plays a critical role in avoiding foot drop during gait. By delivering personalized myofeedback, EMG complement gamified

All authors are with the Department of Biomedical Engineering, New Jersey Institute of Technology Newark, NJ, USA (*: corresponding author; e-mail: alexzhou@njit.edu)

This work was supported in part by NIH grants R01NS085122 and R01HD058301, and NIDILRR funded Rehabilitation Engineering Research Center, grant 90RE5021 and 90REGE0025.

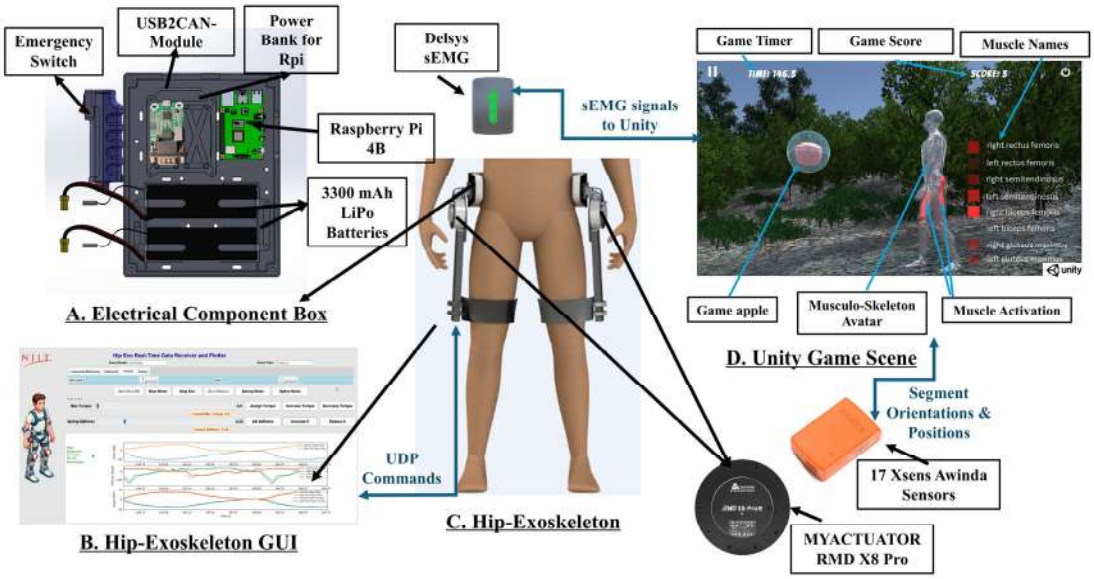


Fig. 1. The gaming system framework. (A) The electrical component box. (B) The hip exoskeleton is controlled through a custom app. This allows for interactively changing stiffness values and observe various parameter plots. (C) The hip exoskeleton is powered by two RMD X8 PRO motors. (D) The game scene receives data from the EMGs and the IMUs.

strategies, boosting patient motivation and facilitating neuromuscular re-education. The same systems can also be applied to sports training [12].

Repetitive and targeted gait movements, on the other hand, also play a pivotal role in fostering neuroplasticity, enabling the brain to establish new neural connections critical for relearning walking patterns and achieving functional recovery [13]. Exoskeletons can assist in facilitating these repetitive movements, particularly when a patient's strength or coordination is insufficient to sustain the intensity needed for effective therapy. We believe that integrating gamified strategies, EMG biofeedback, and advanced technologies like lower-limb robotic exoskeletons will foster neuroplasticity through repetitive, targeted movements, making gait rehabilitation more effective and personalized for individuals regaining mobility. To advance this vision, we developed an interactive rehabilitation framework that combines a Unity-3D based gaming system with a backdrivable hip exoskeleton. This system incorporates real-time multimodal feedback, including inertial measurement unit (IMU) based motion tracking, visualization of muscle activation via surface electromyography (sEMG) sensors, and dynamically adapts gameplay based on patient performance, providing tailored visual and physical guidance.

By reducing physical strain and metabolic energy consumption, hip exoskeletons enable patients to participate in extended rehabilitation sessions, promoting consistent progress. Studies have shown that the metabolic cost of walking is significantly reduced while wearing a hip-only exoskeleton compared to unassisted walking [14], which could help improve endurance and overall participation in therapy. In addition to these assistive benefits, hip exoskeletons can provide resistive training by targeting key hip muscles, effectively aiding in muscle strengthening stability [15, 16]. Our framework integrates these features into a rehabilitation gaming system designed to explore its potential for clinical and home-based use. It aims to provide a cost-effective and accessible approach to support motor recovery and contribute to long-term rehabilitation outcomes.

II. Gaming System Framework

Over the past decade, gamification has advanced significantly in healthcare, showing positive impacts through engaging experiences, progress tracking, and accessible technology, while gaining widespread adoption across various fields [17]. Our approach builds on this progress by integrating a realistic Unity-3D game environment with a backdrivable, size-adjustable hip exoskeleton for targeted gait rehabilitation exercises. The following subsections provide a detailed overview of the system's components, including the game environment and the hip exoskeleton. The Unity game serves as the central component of the system, incorporating motion sensors to track movement and EMG sensors to monitor muscle activation, delivering real-time biofeedback to the user. The hip exoskeleton complements these elements by actively interacting with the user and providing self-tailored assistance or resistance during rehabilitation tasks. Together, these components form a cohesive framework for effective gait rehabilitation, as illustrated in Fig. 1.

A. Game Functionality and Sensor Integration

The game environment primarily features an avatar within a flexible setting, where tasks, surroundings, and gameplay elements can be adjusted as needed, to make rehabilitation both engaging and effective. Unlike traditional rehabilitation tools, the game integrates dynamic and immersive gameplay elements to captivate users while addressing specific therapeutic goals. The avatar is an anatomically accurate human model, composed of 3D meshes of skin, bones, muscles, and other anatomical structures. This high fidelity human anatomic avatar model provides superior realism

compared to typical skin avatars or stick figures employed in most games [18, 19] and offers in-depth exploration of its musculoskeletal behavior through visualization of muscle activation and 3D deformation with tracked motion.

The avatar's whole-body movements are dynamically tracked through synchronization with the Xsens MVN system, which employs 17 Xsens Awinda IMU sensors (Xsens Technologies B.V., Netherlands) [20]. Real-time movement data tracked by the sensors, including segment orientation and position, is transmitted to the Unity-Xsens MVN Live plug-in through UDP network protocol, allowing integration of the subject's real-time actions within the game environment. To measure muscle activation, wireless Delsys Trigno Avanti sEMG sensors (Delsys Inc., MA, USA) are placed on selected lower leg muscles of the subject, namely Rectus Femoris, Biceps Femoris (Long Head), Gluteus Maximus, and Semitendinosus. These sensors wirelessly transmit real-time sEMG signals to the Delsys API using a proprietary radio frequency protocol, and subsequently to Unity. In Unity, the signals are normalized in real time using a z-score method.

To establish a baseline, the subject first walks on a treadmill at their normal walking speed for 30 seconds. During this baseline period, sEMG data is recorded, and the mean and standard deviation of the signals are calculated. These baseline values are then used to continuously compute the z-score of the real-time EMG data during gameplay. To ensure precise synchronization across all components, the Xsens motion capture system and sEMG data acquisition are simultaneously triggered by the exoskeleton's graphical user interface (GUI). This synchronization mechanism is essential for preserving the temporal integrity of multimodal data streams, enabling accurate alignment of muscle activation (sEMG) and body motion (Xsens) data within the Unity environment.

The normalized EMG signals, representing muscle activation levels, are visualized on corresponding 3D muscle models in Unity. A gradient color map is used for rendering, with shades transitioning from lighter, more transparent red (indicating lower activation) to darker, more intense, and opaque red (indicating higher activation), as shown at the bottom of Fig. 2.

B. Hip Exoskeleton Integration

The hip exoskeleton utilized in this study is adapted from the open-source OpenExo design [21], with several key modifications to enhance performance. These include the use of a more powerful motor, the MyActuator RMD X8 Pro V2, with a nominal torque of 13 Nm. The original electronic components were replaced with a Raspberry Pi 4B (RPi), a USB-C to Controller Area Network (CAN) module to facilitate communication between the RPi and the motors, and a handheld emergency safety switch. The exoskeleton is powered by two 3300 mAh LiPo batteries for extended duration operations. Additionally, some structural components were replaced to accommodate the motor's increased torque. The total weight of the exoskeleton is approximately 7 kg. Fig. 3 illustrates multiple views of the exoskeleton device.

The hip exoskeleton currently operates in two distinct stiffness modes: an in-phase assistive and another out-of-phase resistive mode. The exoskeleton is controlled by a GUI that communicates with the RPi on the exoskeleton. The GUI

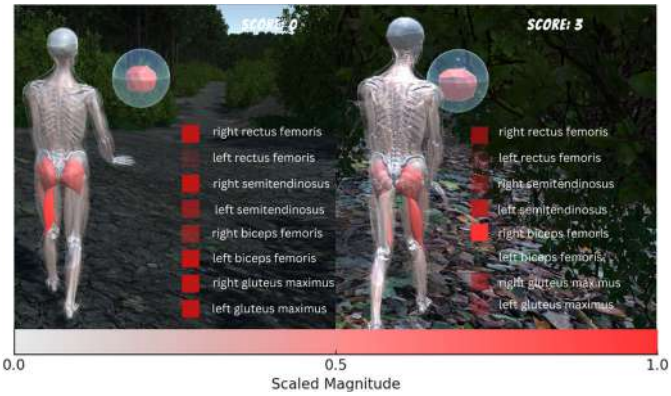


Fig. 2. Snapshots of the game scene show different time instants and viewing angles of the game when the subject approaches the apple. Muscle activations are shown with a list of color-coded boxes and shaded on the muscles of the avatar. The color bar at the bottom maps the normalized muscle EMG (between 0 and 1) to the rendering color of the 3D muscle mesh.



Fig. 3. Front, side, and back views of the hip exoskeleton CAD assembly and as worn by subjects.

allows users or researchers to adjust stiffness levels, control motor operation (start/stop), and trigger the recording of data, including encoder measured joint angles and velocities, commanded motor torques, sEMG, and Xsens motion capture data. Additionally, the GUI provides real-time visualization of trajectories for joint angles, velocities, and torques, enhancing user interaction and data monitoring, as illustrated in Fig. 1B.

1) Stiffness based assistive mode (in-phase)

Modulating hip exoskeleton stiffness has been extensively utilized in gait rehabilitation, as the inability to tune natural hip joint stiffness is believed to contribute to gait impairments. For example, the GEMS-H (Samsung Electronics, Suwon, South Korea) exoskeleton has been used in this mode to study the induced gait changes in healthy populations [22]. Additionally, it has demonstrated significant improvements in walking speed and endurance in older adults using a more complex delayed feedback approach [23].

In our work, we configured our exoskeleton to simulate a virtual torsional spring between the thighs, governed by the following control law [22, 24]:

$$\tau_R = -\tau_L = k\,\theta_{REL} \quad (1)$$

Here k is the stiffness and θ_{REL} is the relative angle between the encoder measured left and right hip angles (θ_L - θ_R). The torque was limited to 15 Nm for safety reasons and filtered by

a low pass filter to avoid sharp fluctuations caused by encoder noise. This control follows the trend of biological hip torques approximately and operates in phase with the relative hip angle to provide a naturalistic assistive force.

2) Stiffness based resistive mode (out-of-phase)

The resistive mode opposed the subject's gait movement by applying torque off-phase to the hip joints. The torque magnitude was calculated similarly to the stiffness-based assistance, but with a reversed direction. For safety reasons, the torque was also limited to 15 Nm.

III. Experimental Procedure & Data Processing

A set of preliminary experiments were carried out to demonstrate the feasibility of the gaming system. A healthy adult (male, weight 97 kg, height 180 cm, age 32 years-old) took part in the pilot test under the NJIT approved protocol (# 2305033091). Delsys Trigno Avanti EMG sensors were attached to four hip muscles per leg (Gluteus Maximus, Biceps Femoris (Long Head), Semitendinosus and Rectus Femoris). The maximum voluntary contraction (MVC) for each muscle was recorded by performing specific isometric exercises against resistance, ensuring maximal effort for each target muscle group. The subject was also equipped with the 17 IMU sensors required for the full body motion feedback.

The subject participated in the game while wearing the exoskeleton under an unassisted zero torque walking condition (No Torque), as well as the in-phase and out-of-phase hip exoskeleton conditions detailed in Section II. sEMG, IMU and exoskeleton data were continuously recorded during each trial, which lasted for two minutes each. The walking speed was set to 0.25 m/s lower than the self-selected speed (when not wearing the exoskeleton) to account for dual-tasking demands, as concurrent gameplay and treadmill walking may increase cognitive load and compromise gait stability.

A. Unity Game Setup

The game was designed to simulate an engaging forest environment where the subject's avatar collects scattered apples by navigating through varied terrains. A USB Joystick (Retro Games Ltd., UK) was used to allow the subject to turn the avatar to the left or right during gameplay, which was performed on a treadmill (AC5000, SCIFIT Systems, Inc., OK, USA).

This setup enables the game to be played in confined spaces, such as at home or in small rehabilitation facilities, while the subject explores a large, unconfined environment within the game. The game environment was displayed on a large screen in front of the subject, providing real-time feedback on their movements and interactions with the virtual world. Fig. 2 shows the game setup and game environment details. Fig. 4 depicts the data collection setup, including a screenshot of the subject walking on the treadmill and playing the game while wearing the exoskeleton.

B. Data Post-processing

The raw EMG signals were postprocessed using a multi-step filtering approach to obtain a clean and meaningful signal envelope for analysis. First, the signals underwent a fourth-order Butterworth bandpass filter with a passband of 50–450 Hz to isolate the EMG frequency range and remove low-



Fig. 4. Data collection setup showing the treadmill control, joystick, and screen (top) and a subject playing the game on the (bottom).

frequency motion artifacts and high-frequency noise. Following this, the processed signals were rectified, and a sixth-order Butterworth low-pass filter with a 6 Hz cutoff frequency was applied to extract the smoothed signal envelope. The signals were then finally normalized by the corresponding MVCs.

Virtual markers for each trial were exported in C3D format using Xsens Analyze Pro. Since a normal gait cycle is defined as beginning and ending with a heel strike [25], the trajectory of the virtual heel marker was used to segment the trials into individual gait cycles for further analysis. The mean trajectory and standard deviation (SD) across all cycles were calculated for muscle activations, hip joint angles, and exoskeleton torques, with the results plotted as mean ± SD for each variable.

IV. Results and Discussion

We conducted functionality tests on the gaming system integrated with the hip exoskeleton. This system provided real-time, semi-immersive feedback on the subject's gait and navigation, displaying dynamic, red-shaded overlays of muscle activation intensity and coordination which could enhance understanding of muscle engagement during training. In the game, the subject navigated a forest-based environment, to collect virtual apples while walking on a treadmill. The apple-picking task was scored based on the user's accuracy and efficiency in navigating the environment, creating an additional layer of motivation and challenge. The system also allowed the subject to adjust rehabilitation parameters in real time, such as switching between assistive and resistive modes and modifying stiffness levels to match their needs. The overall operational smoothness of the system was high, with minimal latency between user motion and avatar response. Beyond real-time feedback, the system also supports post-processing of collected data, enabling detailed analysis of the subject's gait adaptation and muscle coordination under various training modes and conditions.

To illustrate the muscle activation results, we present data from representative activations of two hip muscles per leg as depicted in Fig. 5: the Gluteus Maximus and Rectus Femoris on the left leg, and the Biceps Femoris and Semitendinosus on the right leg, under assistive, no torque, and resistive modes. The results reveal that the Gluteus Maximus (Left) displays relatively consistent activation across all modes. The Rectus Femoris (Left) shows smaller activation in the assistive mode compared to the no torque and resistive modes, suggesting reduced engagement when assistance is provided. For the Biceps Femoris (Right), the resistive mode leads to noticeably higher activation, highlighting increased muscle engagement with resisting torques. Similarly, the Semitendinosus (Right)

demonstrates significantly higher activation in the resistive mode, while assistive and no torque modes exhibit comparable and lower levels of activity.

Fig. 6 shows the right hip joint angle and torque trajectories under the no-torque, assistive, and resistive conditions. The results illustrate that, as expected, the hip torque in the assistive mode aligns in phase with the hip angle, providing support during flexion and reducing extension effort. In contrast, the resistive mode generates out-of-phase torque, opposing the natural motion to encourage muscle engagement, particularly during extension.

Notably, the resistive mode also led to a noticeable increase in the peak extension angle compared to the no-torque and assistive conditions, likely due to the subject compensating for the opposing force and a slight tilt of the waistbelt due to large torque (close to 15 Nm). Across all conditions, the trajectories of both the hip angle and torque are relatively smooth, demonstrating the system's ability to deliver consistent and controlled assistance or resistance during gait.

Moreover, walking in the resistive mode was perceived as noticeably harder compared to the no-torque condition by the subject. However, in the assistive mode, the subject did feel a notable reduced effort compared to the no-torque condition. The overall experience of the subject was positive, with him describing the gaming system as interactive and stimulating.

The gaming system could benefit from testing across a broader range of populations, including both healthy individuals and specific patient groups. Post-stroke patients are a promising focus, as the system may help normalize spastic muscle contractions [26] through EMG feedback, while also promoting neural plasticity and enhancing motor control. Similarly, children with cerebral palsy could experience enhanced gait performance and mobility. By functioning as a strengthening intervention, the system has the potential for widespread application across various age groups and medical conditions[27]. The present system utilizes proprietary Xsens software and IMUs for motion capture and data transfer. Alternatively, we can replace it with the real-time OpenSim inverse kinematics (IK) method, where kinematics may be tracked using inexpensive IMUs or other markerless mocap devices, such as depth cameras or video based systems, making it a cost-effective solution that can also be used in out-of-the-lab conditions [28]. While our system integrates biofeedback, gamification, and an exoskeleton to enhance gait rehabilitation, its holistic nature makes it challenging to determine the individual contribution of biofeedback. Understanding its specific role is essential not only for optimizing system effectiveness but also for ensuring the right balance between feedback complexity and user comprehension to prevent cognitive overload. Future studies could systematically remove certain components and evaluate their impact on rehabilitation outcomes, helping refine the system for better therapeutic benefits and usability. Moreover, future enhancements could further boost user immersion and system functionality. Based on internal user feedback, we identified that the exoskeleton's weight and design caused some discomfort. We plan to integrate a mixed- reality platform , such as Microsoft HoloLens, to create a more realistic and interactive environment. This would allow users

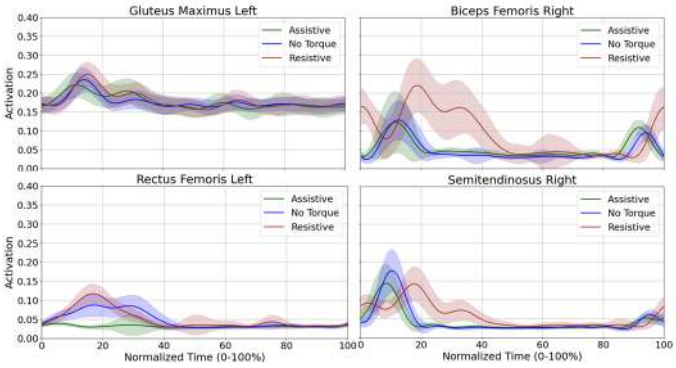


Fig. 5. Mean±SD muscle activations for left Gluteus Maximus and Rectus Femoris as well as right hamstrings.

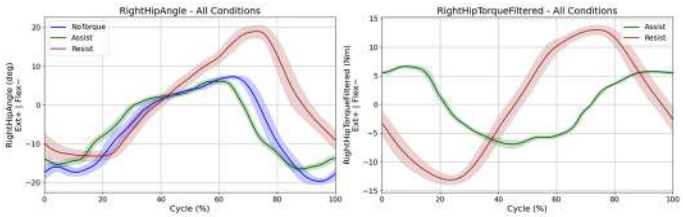


Fig. 6. Right hip joint angles and hip exoskeleton assistive torques for different exoskeleton conditions.

to move naturally and unrestrictedly without the need for a joystick, replacing it with head rotation to control movement. This approach will foster more lifelike interactions and enrich the therapeutic experience. Additionally, we plan to integrate instrumented pressure insoles such as OpenGo (Moticon GmbH, Munich, Germany) [29] or loadsol (novel GmbH, Munich, Germany) [30] in our rehabilitation gaming system. These insoles will provide real-time feedback on the estimated center of pressure (COP) position and vertical ground reaction force within the Unity game. This feedback will enable patients to monitor their walking, identify asymmetries or abnormal COP movements, and detect improper foot placement that could lead to imbalance or impede rehabilitation progress [31, 32].

V. Conclusion

We designed and conducted a preliminary evaluation of a gaming system integrated with a hip exoskeleton, intended as an interactive and adaptive tool for gait rehabilitation. The system incorporates motion feedback, with a high-fidelity avatar that mirrors the user's movements in real-time using IMU sensors, alongside EMG-based biofeedback to enhance engagement, muscle coordination, and gait improvement. Preliminary tests with a single user showed the system to be highly engaging, with the hip exoskeleton and effectively modulating activation levels in the major hip muscles. Activation was reduced in the assistive mode and increased in the resistive mode. We believe this system has significant potential to improve rehabilitation outcomes by providing personalized, motivating, and effective therapy for users.

Acknowledgment

The authors would like to thank Erick Nunez for their contributions to the prototype implementation and system setup.

REFERENCES

[1] Centers for Disease Control and Prevention. " Disability and Health Data System (DHDS)." https://dhds.cdc.gov (accessed Nov. 14, 2024).

[2] C. M. M. de Brito, L. R. Battistella, and M. L. C. Guarita, "Challenges and complications of immobility," *Topics in cognitive rehabilitation in the TBI Post-Hospital Phase,* pp. 25-33, 2018.

[3] D. Avola, L. Cinque, G. L. Foresti, and M. R. Marini, "An interactive and low-cost full body rehabilitation framework based on 3D immersive serious games," *Journal of biomedical informatics,* vol. 89, pp. 81-100, 2019.

[4] A. Moinuddin, A. Goel, and Y. Sethi, "The Role of Augmented Feedback on Motor Learning: A Systematic Review," (in eng), *Cureus,* vol. 13, no. 11, p. e19695, Nov 2021, doi: 10.7759/cureus.19695.

[5] N. M. Tuah, F. Ahmedy, A. Gani, and L. N. Yong, "A Survey on Gamification for Health Rehabilitation Care: Applications, Opportunities, and Open Challenges," *Information,* vol. 12, no. 2, p. 91, 2021. [Online]. Available: https://www.mdpi.com/2078-2489/12/2/91.

[6] O. M. Giggins, U. M. Persson, and B. Caulfield, "Biofeedback in rehabilitation," (in eng), *J Neuroeng Rehabil,* vol. 10, p. 60, Jun 18 2013, doi: 10.1186/1743-0003-10-60.

[7] T. Haab, P. Leinen, and P. Burkey, "Role and effectiveness of surface EMG feedback in sports and orthopedic rehabilitation: a systematic review," *Exploration of Musculoskeletal Diseases,* vol. 2, no. 5, pp. 391-407, 2024.

[8] E. H. Hinton *et al.*, "Real-Time Visual Kinematic Feedback During Overground Walking Improves Gait Biomechanics in Individuals Post-Stroke," (in eng), *Ann Biomed Eng,* vol. 52, no. 2, pp. 355-363, Feb 2024, doi: 10.1007/s10439-023-03381-0.

[9] R. Wang *et al.*, "Electromyographic biofeedback therapy for improving limb function after stroke: A systematic review and meta-analysis," *PLoS One,* vol. 19, no. 1, p. e0289572, 2024.

[10] L. Y. Liu, S. Sangani, and A. Lamontagne, "A real-time visual feedback protocol to improve symmetry of spatiotemporal factors of gait in stroke survivors," in *2017 International Conference on Virtual Rehabilitation (ICVR)*, 19-22 June 2017 2017, pp. 1-2, doi: 10.1109/ICVR.2017.8007527.

[11] D. Intiso, V. Santilli, M. Grasso, R. Rossi, and I. Caruso, "Rehabilitation of walking with electromyographic biofeedback in foot-drop after stroke," *Stroke,* vol. 25, no. 6, pp. 1189-1192, 1994.

[12] M. Hribernik, A. Umek, S. Tomažič, and A. Kos, "Review of Real-Time Biomechanical Feedback Systems in Sport and Rehabilitation," *Sensors,* vol. 22, no. 8, p. 3006, 2022. [Online]. Available: https://www.mdpi.com/1424-8220/22/8/3006.

[13] H. Nedergård, A. Arumugam, M. Sandlund, A. Brändal, and C. K. Häger, "Effect of robotic-assisted gait training on objective biomechanical measures of gait in persons post-stroke: a systematic review and meta-analysis," *Journal of NeuroEngineering and Rehabilitation,* vol. 18, no. 1, p. 64, 2021/04/16 2021, doi: 10.1186/s12984-021-00857-9.

[14] P. W. Franks, G. M. Bryan, R. M. Martin, R. Reyes, A. C. Lakmazaheri, and S. H. Collins, "Comparing optimized exoskeleton assistance of the hip, knee, and ankle in single and multi-joint configurations," *Wearable Technologies,* vol. 2, p. e16, 2021, Art no. e16, doi: 10.1017/wtc.2021.14.

[15] E. Kim, S.-H. Lee, D. Kim, J. Yu, H.-J. Lee, and Y.-H. Kim, "A wearable hip exoskeleton for anaerobic exercise in healthy adults," *Scientific Reports,* vol. 14, no. 1, p. 26424, 2024.

[16] W. Cao *et al.*, "Development and Evaluation of a Hip Exoskeleton for Lateral Resistance Walk Exercise," *IEEE/ASME Transactions on Mechatronics,* vol. 28, no. 4, pp. 1966-1974, 2023, doi: 10.1109/TMECH.2023.3273717.

[17] L. Sardi, A. Idri, and J. L. Fernández-Alemán, "A systematic review of gamification in e-Health," *Journal of Biomedical Informatics,* vol. 71, pp. 31-48, 2017/07/01/ 2017, doi: https://doi.org/10.1016/j.jbi.2017.05.011.

[18] G. F. Muñoz, R. A. M. Cardenas, and F. Pla, "A kinect-based interactive system for home-assisted active aging," *Sensors,* vol. 21, no. 2, p. 417, 2021.

[19] A. Winkler, J. Won, and Y. Ye, "Questsim: Human motion tracking from sparse sensors with simulated avatars," in *SIGGRAPH Asia 2022 Conference Papers*, 2022, pp. 1-8.

[20] M. Paulich, M. Schepers, N. Rudigkeit, and G. Bellusci, "Xsens MTw Awinda: Miniature wireless inertial-magnetic motion tracker for highly accurate 3D kinematic applications," *Xsens: Enschede, The Netherlands,* pp. 1-9, 2018.

[21] J. R. Williams *et al.*, "OpenExo: An Open-Source Modular Exoskeleton to Augment Human Function," *bioRxiv,* p. 2024.10.02.616295, 2024.

[22] J. Lee, M. E. Huber, and N. Hogan, "Applying Hip Stiffness with an Exoskeleton to Compensate Gait Kinematics," *IEEE Transactions on Neural Systems and Rehabilitation Engineering,* pp. 1-1, 2021, doi: 10.1109/TNSRE.2021.3132621.

[23] C. Jayaraman *et al.*, "Modular hip exoskeleton improves walking function and reduces sedentary time in community-dwelling older adults," *Journal of NeuroEngineering and Rehabilitation,* vol. 19, no. 1, p. 144, 2022/12/30 2022, doi: 10.1186/s12984-022-01121-4.

[24] T. Zhang, Y. Li, C. Ning, and B. Zeng, "Development and adaptive assistance control of the robotic hip exoskeleton to improve gait symmetry and restore normal gait," *IEEE Transactions on Automation Science and Engineering,* vol. 21, no. 1, pp. 799-809, 2022.

[25] M. Jacquelin Perry, "Gait analysis: normal and pathological function," *New Jersey: SLACK,* 2010.

[26] S. Li, "Spasticity, Motor Recovery, and Neural Plasticity after Stroke," (in eng), *Front Neurol,* vol. 8, p. 120, 2017, doi: 10.3389/fneur.2017.00120.

[27] E.-Y. Park and W.-H. Kim, "Meta-analysis of the effect of strengthening interventions in individuals with cerebral palsy," *Research in Developmental Disabilities,* vol. 35, no. 2, pp. 239-249, 2014/02/01/ 2014, doi: https://doi.org/10.1016/j.ridd.2013.10.021.

[28] D. Stanev *et al.*, "Real-Time Musculoskeletal Kinematics and Dynamics Analysis Using Marker- and IMU-Based Solutions in Rehabilitation," *Sensors,* vol. 21, no. 5, p. 1804, 2021. [Online]. Available: https://www.mdpi.com/1424-8220/21/5/1804.

[29] T. Stöggl and A. Martiner, "Validation of Moticon's OpenGo sensor insoles during gait, jumps, balance and cross-country skiing specific imitation movements," *Journal of sports sciences,* vol. 35, no. 2, pp. 196-206, 2017.

[30] K. E. Renner, D. B. Williams, and R. M. Queen, "The Reliability and Validity of the Loadsol® under Various Walking and Running Conditions," *Sensors,* vol. 19, no. 2, p. 265, 2019. [Online]. Available: https://www.mdpi.com/1424-8220/19/2/265.

[31] J. Kim, S. Jung, and C. Song, "The Effects of Auditory Feedback Gait Training Using Smart Insole on Stroke Patients," *Brain Sciences,* vol. 11, no. 11, p. 1377, 2021. [Online]. Available: https://www.mdpi.com/2076-3425/11/11/1377.

[32] S. Neumann *et al.*, "Accuracy, concurrent validity, and test–retest reliability of pressure-based insoles for gait measurement in chronic stroke patients," (in English), *Frontiers in Digital Health,* Original Research vol. 6, 2024-April-03 2024, doi: 10.3389/fdgth.2024.1359771.

Developing a methodology for quantifying infant interaction with a robotic toy*

McKenzie E. Davis[1], O. Francis Sowande[2], Julie Skorup[3], Melanie Segado[4], Frances Shofer[5], Laura A. Prosser[6], Michelle J. Johnson[7], *Member, IEEE*

***Abstract*— Preterm infants are at increased risk for developmental delays and disability such as cerebral palsy. When these delays are detected early, movement training can significantly improve patients' quality of life. Instrumented toys have the potential to solve the pressing need for easily accessible, inexpensive diagnostic tools for infant development. While many studies have focused on developing toys for sensor-based assessment, the body of work dedicated to developing quantitative measurements from this data is minimal and has several limitations. Using a consistent and novel video coding methodology, a case study of 18 preterm and full-term infants' videotaped interactions with the Play and Neuro Development Assessment (PANDA) Gym, an affordable, mechatronic, and sensor-based play environment, were analyzed. The coding methodology was able to quantify infant interactions with the PANDA toy and differences between preterm and full-term infants, but future analysis of involuntary interactions and a larger sample size are needed to determine whether results are consistent with expected developmental milestones.**

I. Introduction

Cerebral palsy (CP) is the main chronic condition causing disability in childhood [1]. CP results from perinatal brain lesions such as those seen following preterm birth [2], and risk of cerebral palsy increases with decreasing birthweight and gestational age [3, 4]. Cerebral palsy is non-curable, and no mechanisms are in place for healing or recovery [2], but movement training can significantly improve quality of life for individuals with CP. It is important for movement training to begin as early as possible, as the first year of life is a crucial period for the establishment of the key neural circuits that support the development of normal motor function in humans [2]. However, many children are not diagnosed with cerebral palsy until around 2 years of age [5]. Thus, there is a need for earlier detection of deviation from the typical course of development, as earlier interventions can leverage the greater neuroplasticity seen in younger infants and improve developmental outcomes for infants with CP [6].

Instrumented toys have demonstrated potential to solve the need for accessible, inexpensive diagnostic tools for infant development, and a significant amount of work has been done to improve these toys to the point of serving as tools for assessment. For example, a sensorized ball designed by Campolo et al. used quantum tunneling composites to detect grasping patterns during manipulation [7]. Tenzer et al. developed a versatile, low-cost, and sensitive tactile sensor using commercial off-the-shelf MEMS barometers [8] and Takada et al. used a waterproof mobile device's built-in barometer to measure touch force [9]. Additionally, Ramanathan et al. designed a set of 8 instrumented toys outfitted with Physilog 6 commercial off-the-shelf wearable motion sensors [10]. Further studies demonstrate potential for the use of these toy measurements as clinical indicators for infant development. For example, Serio et al. developed a soft, horseshoe-shaped sensorized, wireless toy, and found that typically developing infants could produce unimanual (one-handed) and bimanual (two-handed) grasps detectable by the sensors [11]. Udayagiri et al. have also worked toward developing a toy leveraging soft lossy force sensors from optical fibers to gather play interaction data and were able to identify distinct interaction types using machine learning analysis [12].

However, there have been minimal studies dedicated to evaluating interactions with toys and developing quantitative measurements. Kather et al. successfully used manual video coding to quantify the frequency and duration of toy interactions and found that preterm infants gazed at the toys with similar frequency as full-term infants, but infants born full-term physically engaged more frequently and for longer durations with the robotic toys than infants born preterm [13]. However, there are significant challenges with manual video coding – it is time-consuming, is prone to user bias and inconsistency, and it can be difficult to capture complex behaviors. Additionally, despite its ability to output quantitative measures of infant interaction, it is hard to relate

*Research supported by the Department of Physical Medicine and Rehabilitaton at the University of Pennsylvania and by the Eunice and Keneedy Shriver National Institue of Child Health & Human Development of the National Institutes of Health (NIH) under award numbers R01HD097686 and R21HD084327.

[1]McKenzie E. Davis is an undergraduate student in Bioengineering at the University of Pennsylvania (240-585-0702; email: davismck@seas.upenn.edu)

[2]O. Francis Sowande is a PhD student in Mechanical Engineering and Applied Mechanics at the University of Pennsylvania.

[3]Julie Skorup is a physical therapist with the Division of Physical Medicine and Rehabilitation Team at Children's Hospital of Philadelphia.

[4] Dr. Melanie Segado is a postdoctoral researcher at the University of Pennsylvania.

[5] Dr. Frances Shofer is the Director of Epidemiology & Biostatistics and Adjunct Professor of Emergency Medicine, Occupational Medicine, and Physical Medicine and Rehabilitation at the University of Pennsylvania Perelman School of Medicine.

[6] Dr. Laura A. Prosser is an Associate Professor at the University of Pennsylvania with a primary appointment in Pediatrics and a research scientist with the Division of Physical Medicine and Rehabilitation Team at Children's Hospital of Philadelphia.

[7] Dr. Michelle J. Jonhson is an Associate Professor at the University of Pennsylvania with a primary appointment in Physical Medicine and Rehabilitation and secondary appointments in Bioengineering and Mechanical Engineering and Applied Mechanics (email: johnmic@pennmedicine.upenn.edu)

manual video coding outputs to clinical measures due to limited camera views and obstructions.

This study aims to address the issues with manual video coding by developing a consistent, novel methodology for coding interactions with toys that can be used on larger datasets and in the future, to train a machine learning algorithm. To address the issue of limited camera views and obstructions with manual coding, multiple camera angles were used. This paper reports the protocol for establishing the interaction labels and the coding methodology. Additionally, it outlines a preliminary study to verify the methodology is sensitive to babies' age, term status (preterm vs. full-term) and its impact on their motor performance and presents initial results using this system.

II. Development of Coding Protocol

To develop the interaction classifications (Table 1), a literature review was performed of previous manual video coding studies and clinical movement definitions for observed motor behaviors. Kather et al. used "touch" and "grasp" interactions for upper body classifications, "touch" and "kick" for lower body classifications, "mouth" if the infant placed a piece of the toy in their mouth, "gaze" if the infant's eyes locked on the toy, and "involuntary" interactions if the infant interacted with the toy unintentionally [13]. However, Kather's classifications neglected to mention reaching behavior [13]. Additionally, a literature review of infant motor milestones was conducted. The 14 classifications used in this study are more robust and specific than previous studies, and they are consistent with developmental milestones expected for babies aged 1-6 months – gazing, touching, kicking, reaching, and grasping [14]. Additionally, unimanual, bimanual, unilateral (one-legged) and bilateral (two-legged) interactions were coded separately, given that as infants get older, unimanual interactions increase while bimanual interactions decrease [15].

TABLE I. Parent Codes: High Level Interaction Descriptions

Movement Classification	Interaction Description
Involuntary	Any unintentional contact with toy with any body part; toy does not appear to be the direct target & the infant was not looking at the toy
Gaze	Direct eye contact with toy; determined by pupil direction and head angle
Voluntary Reach	Any intentional reach for the toy with one or both arms or legs without touch, kick, or grasp event
Voluntary Touch	Preceded by reach, any contact of the toy with one or both hands or feet
Voluntary Kick	Preceded by leg reach, one or both feet intentionally contact toy with greater force than a touch
Voluntary Grasp	Preceded by arm or leg reach, one or both hands or feet intentionally come into contact with the toy and at least three fingers cup/close around the toy
External Movement	Any movement of the toy caused by a non-infant entity (ex. parents moving the toy, toy movement caused by the baby rolling off the mat)
Baby Off Mat	Baby was off mat for any reason (i.e., rolled off mat, removed by parents)

A. Interaction Classification

A total of 7 parent codes were used (Table 1) and 14 voluntary interaction codes were used (Table 2), along with Involuntary Interaction and Gaze. Each video was also coded for emotion – positive, neutral, or negative (Table 3). The code "Pre/Post Trial" was used to indicate portions of the video where the cameras may have been recording, but the two-minute trial had either started or ended.

TABLE II. Voluntary Interaction Codes

Parent Code	Code
Voluntary Kick	Unilateral Kick
	Bilateral Kick
Voluntary Touch	Bilateral Leg Touch
	Unilateral Leg Touch
	Bimanual Arm Touch
	Unimanual Arm Touch
Voluntary Grasp	Bilateral Leg Grasp
	Unilateral Leg Grasp
	Bimanual Arm Grasp
	Unimanual Arm Grasp
Voluntary Reach	Bilateral Leg Reach
	Unilateral Leg Reach
	Bimanual Arm Reach
	Unimanual Arm Reach

TABLE III. Emotion Codes

Emotion	Description
Negative or Crying	Baby crying or otherwise visibly upset
Positive	Baby smiling or otherwise visibly happy
Neutral	Emotion not positive or negative

B. Coding of Interactions

MAXQDA (Verbi Software, 2024) was leveraged to assign codes to video segments. The videos were separated into two-second frames, and codes were manually assigned by the investigator if the interaction was observed at any point during the frame. Interactions were coded in two-second frames to reduce subjectivity by eliminating the need to determine an exact time point when the interaction began. If an interaction began in a previous frame but continued into the current frame (i.e. the infant touched the toy and sustained contact), the interaction was still coded in the current frame. If an interaction occurred twice in a frame (i.e., the infant touched the toy, removed their hand, and touched the toy again), the interaction was coded twice. This protocol was preliminarily implemented with 18 infants, a subset of the 90 enrolled in the study. The goal was to understand the sensitivity of some of the key metrics of age and motor delay and to identify challenges in applying this methodology to the rest of the infant population.

III. METHODS

A. Participants

This study was approved by the Institutional Review Boards (IRBs) of the University of Pennsylvania and the Children's Hospital of Philadelphia. Informed consent was obtained from parents of all infants. Infants born preterm and full-term (at least 36 completed weeks of gestation) between the ages of 1-6 months were eligible for participation. Infants born full-term were excluded if they had a history of any neurologic, orthopedic, cardiac, or genetic condition. Infants born preterm were born after 24–35 weeks of gestation. Ninety infants were enrolled in the study. Of the 18 infants analyzed in the case study, 12 were full-term and 6 were born preterm and had motor delay as determined by the AIMS and TIMP clinical assessment measures (Table 4). The ages of the preterm infants were corrected for prematurity by subtracting the number of weeks born before 40 weeks of gestation from their age to provide a more accurate assessment of developmental milestones.

B. The Play and Neuro Development Assessment (PANDA) Gym

The Play and Neuro Development Assessment (PANDA) gym (Figure 1) is a low-cost, portable instrumented play environment designed to measure infant interactions in high and low resource settings. The system uses a pressurized mat, a sensor-based panda-shaped toy, and 7 GoPro cameras positioned to give different views of the interaction. The toy contains a 9 DOF internal measurement unit (IMU), touch sensors on the face and the ears, and NeoPixel lights in the ears. The panda shape was chosen because for several months after birth, infants prefer toys with high black-and-white contrast, and the overall shape is symmetrical and circular, allowing for safe interaction [16].

TABLE IV. CASE STUDY DEMOGRAPHIC DATA

Infant #	***Full-term/Preterm***	***Corrected age (months)***	***Sex***
221	Full-term	1	Male
219	Full-term	1	Female
52	Preterm	1	Female
16	Full-term	2	Male
61	Full-term	2	Female
50	Preterm	2	Male
13	Full-term	3	Female
31	Full-term	3	Female
64	Preterm	3	Female
32	Full-term	4	Female
45	Full-term	4	Male
72	Preterm	4	Female
23	Full-term	5	Male
19	Full-term	5	Male
55	Preterm	5	Female
20	Full-term	6	Female
28	Full-term	6	Female
63	Preterm	6	Male

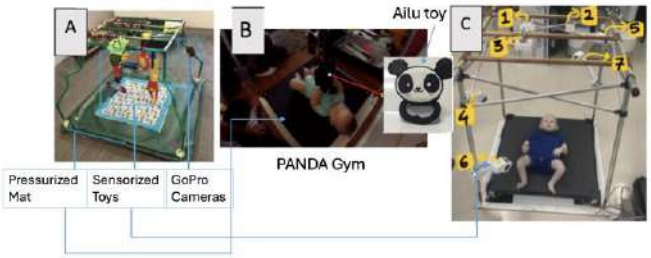


Figure 1: A: PANDA GYM version 1, B: Current set-up of PANDA gym, C: Seven GoPro camera set-up in current gym.

C. Data Acquisition

Static calibration, with an ArUco board placed lying down on the mat, and dynamic calibration, with the board moving around slowly within view of the cameras, were performed to collect the cameras' extrinsic and intrinsic parameters. Then, data was recorded of the gym with nothing inside to collect baseline data for the sensors. Infant data acquisition lasted a total of six minutes in two-minute intervals– infants were first placed supine on the mat with no toy. Next, the toy was placed near their arms (tilted so they could see the face) and at their feet (within kicking distance) in randomized order. Rest breaks were not given between trials unless the baby was upset, and trials resumed once the baby calmed down. Infants were encouraged to engage with the toy through the built-in sounds and lights. Most trials occurred at infants' homes; some trials on preterm infants were performed at the Children's Hospital of Philadelphia. Some preterm infants who were recruited from the NICU required supplemental oxygen at the time of testing. Equipment was arranged so that it did not disturb the infants' ability to engage with the toy. This analysis will focus only on the toy at arms and toy at feet conditions, totaling 4 minutes of interaction time.

D. Video Coding Protocol

MAXQDA (VERBI Software, 2024) was leveraged to assign interactions to the corresponding two-second frames of videos with the toy at arms and toy at feet. Videos from camera 7 were analyzed, and camera 4 videos were used to verify interactions with the back of the toy. Infants were coded in randomized order. Individual interactions were initially classified as involuntary, voluntary, or gaze—with voluntary interactions further classified by extremity and unimanual/bimanual or unilateral/bilateral nature. Interactions were classified as voluntary when the infant's interaction occurred with clear intent, often accompanied by a gaze interaction to confirm said intent. Simultaneous interactions were often observed, and the videos were coded accordingly. For example, if an infant were to intentionally grasp the toy with one arm while simultaneously touching it

with both feet and one hand (Figure 2), "Voluntary Unimanual Arm Grasp", "Voluntary Unimanual Arm Touch", "Voluntary Bilateral Leg Touch", and "Gaze" would be coded for the two-second interval. Frequency of each interaction was calculated for each trial.



Figure 2: In this image, Infant 28 (left) simultaneously performs a unimanual arm touch, bilateral leg touch, and unimanual arm grasp while gazing at the toy. The two-second coded segment is shown at right.

E. Data Analysis & Processing

Once each video was coded, the MAXQDA "Codes" output was generated (Table 5). For each video, the output included the parent code, code, how many video segments were coded the percentage of total interactions each code represents, and information about the coder(s). Emotion and Pre/Post Trial codes were removed from the frequency and percent of coded segments calculations. Then, the frequency of each interaction for each infant was compiled to analyze trends.

TABLE V. EXAMPLE MAXQDA OUTPUT: INFANT 28

Parent Code	*Code*	*# of Coded Segments*	*% Coded Segments*
Pre/Post Trial	Pre/Post Trial	1	0.99
Emotion: Neutral	Emotion: Neutral	1	0.99
Gaze	Gaze	58	38.41
Involuntary Interaction	Involuntary Interaction	2	1.32
Voluntary Grasp	Bimanual Arm Grasp	4	2.65
Voluntary Grasp	Unimanual Arm Grasp	17	11.26
Voluntary Grasp	Unilateral Leg Grasp	1	0.66
Voluntary Reach	Unimanual Arm Reach	3	1.99
Voluntary Reach	Bimanual Arm Reach	1	0.66
Voluntary Touch	Unimanual Arm Touch	37	24.50
Voluntary Touch	Unilateral Leg Touch	8	5.3
Voluntary Touch	Bilateral Leg Touch	5	3.31
Voluntary Touch	Bimanual Arm Touch	13	8.61

IV. RESULTS

Table 6 reports the combined MAXQDA output for each infant across both toy trials (toy at arms and at feet). Figure 3 shows how this total number of interactions varied by age and infant group (full-term versus preterm with motor delay).

Across the 18 infants, a total of 1,652 motor and gaze interactions were coded. 1,424 (86.2%) of these interactions were voluntary, while 228 were involuntary (Table 6). As full-term infants got older, the percentage of involuntary interactions decreased significantly while the percentage of voluntary interactions increased (Table 6). This trend was not seen in preterm infants – the percentage of involuntary interactions remained high (50-100%). A two-way ANOVA was done by age and term (preterm vs. full-term) on the percentage of voluntary movements, and a significant difference was found by age ($P=0.002$) and term ($P=<0.0001$). On average, full-term infants interacted with the toy more when the toy was at their arms (average = 75.33 interactions) compared to when the toy was at their legs (average = 52 interactions). Preterm infants interacted with the toy more when it was at their legs (average = 18.5 interactions) than at their arms (average = 2.16 interactions).

Additionally, as full-term infants got older, they interacted with the toy more frequently (Figure 3). This trend was not seen in preterm infants – frequency of interactions with the toy among preterm infants were similarly low regardless of age. Despite this, infants interacted with the toy frequently. Of the 18 infants, only 1 of preterm infant (Infant 64) did not voluntarily interact with the toy.

TABLE VI. TOTAL VOLUNTARY & INVOLUNTARY INTERACTIONS BY INFANT

Infant #	*Adjusted Age (mo)*	*Term*	*Tot. Voluntary Interactions (%)*	*Tot. Involuntary Interactions (%)*
221	1	Full-term	16 (59%)	11 (41%)
219		Full-term	3 (10%)	26 (90%)
52		Preterm	1 (13%)	7 (87%)
16	2	Full-term	3 (19%)	13 (81%)
61		Full-term	40 (83%)	8 (17%)
50		Preterm	2 (6%)	31 (94%)
13	3	Full-term	32 (52%)	30 (48%)
31		Full-term	70 (93%)	5 (7%)
64		Preterm	0 (0%)	17 (100%)
32	4	Full-term	104 (99%)	1 (1%)
45		Full-term	182 (98%)	4 (2%)
72		Preterm	4 (21%)	15 (79%)
23	5	Full-term	269 (99%)	4 (1%)
19		Full-term	248 (96%)	9 (4%)
55		Preterm	1 (3%)	34 (97%)
20	6	Full-term	190 (98%)	4 (2%)
28		Full-term	253 (99%)	2 (1%)
63		Preterm	6 (50%)	6 (50%)
Total			1,424 (86.2%)	228 (13.8%)

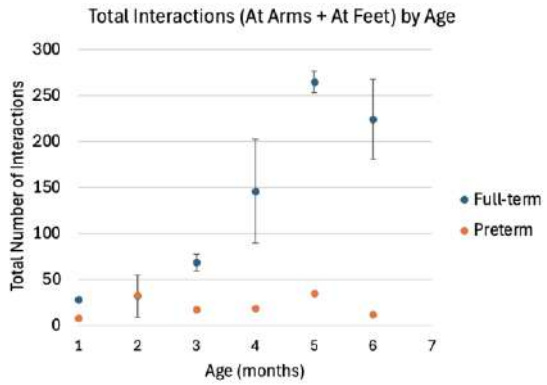


Figure 3: Total arm and leg interactions (voluntary and involuntary, with standard deviation bars) with PANDA toy by age. No standard deviation bars included for preterm infants, as only 1 preterm infant was analyzed per month.

Figure 4 shows the emergence of arm and leg interactions by age. The mean number of voluntary arm interactions across all ages was 30.4 for full-term infants and 0.16 for preterm motor delayed infants. Arm interactions increased with age for full-term infants, peaking at 5-months. The mean number of voluntary leg interactions across ages for full-term infants was 21.25 and 0.66 for preterm motor delayed infants. Leg interactions also increased with age for full-term infants, peaking at 5 months. In full-term infants, arm interactions emerged at two months and leg interactions emerged at three months. In preterm infants with motor delay, similar trends were not observed. Arm interactions emerged at 5 months in preterm infants, but the six-month-old infant did not interact with the toy with their arms. Leg interactions emerged at 1 month, but the 3,4-, and 5-month-old infants did not interact with the toy using their legs.

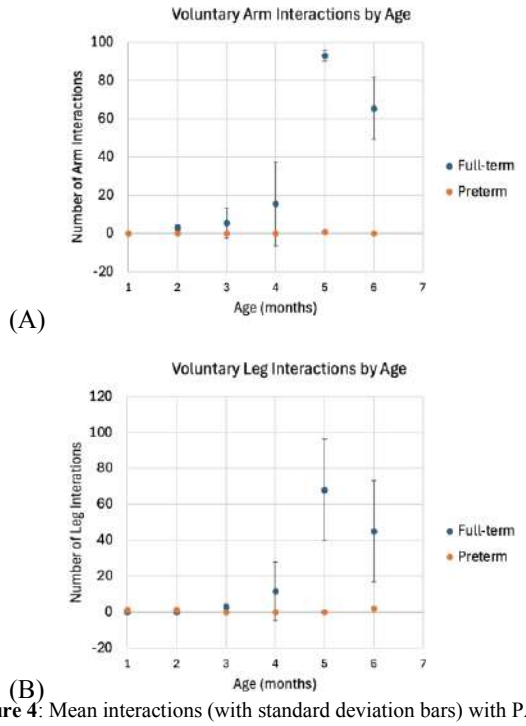


Figure 4: Mean interactions (with standard deviation bars) with PANDA toy by infant group and age: A) Total number of unimanual/bimanual arm touch and grasp interactions; B) Total number of unilateral/bilateral leg touch and kick interactions. No standard deviation bars included for preterm infants, as only 1 preterm infant was analyzed per month.

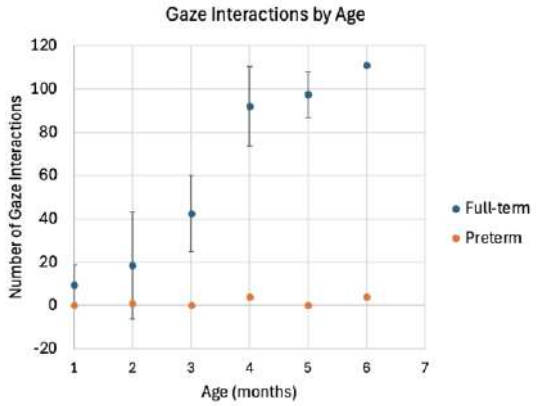


Figure 5: Mean gaze interactions (with standard deviation bars) with PANDA toy by infant group and age. No standard deviation bars included for preterm infants, as only 1 preterm infant was analyzed per month.

Figure 5 shows gaze interactions by infant group and age. Gaze interactions were coded regardless of whether the toy was engaged. The mean number of gaze interactions was 61.8 for full-term infants and 1.5 for preterm motor delayed infants. Out of arm, leg, and gaze interactions, gaze interactions emerged first in full-term infants - at one month. Gaze interactions increased with age for full-term infants, peaking at six months. The trend was not clear in the preterm infants with motor delay. Although gaze interactions emerged at two months, both the 3- and 5-month-old infants did not gaze at the toy.

V. Discussion

The PANDA gym successfully evoked motor and gaze interactions and the coding methodology successfully quantified differences between full-term and preterm infants – suggesting that it is sufficiently sensitive to metrics of age and motor delay. Building on the work of Kather et al. [13], infants in this study were correctly age-matched and differences were still seen among the two infant populations. The interaction codes were specific enough that all interactions seen in the videos were adequately described by one of the codes. Critically, coding in two-second intervals simplified the process of separating out interactions. However, the process of manual annotation is still time-consuming, and may benefit from the integration of automated object and gesture recognition tools from computer vision to scale to larger datasets.

Based on the literature on infant milestones, it was expected that as infants got older, their interactions with the toy would increase. In full-term infants, leg interactions emerged at three months. This is supported by the literature, which states that by three months old, infants should be able to touch toys with their feet [14]. Leg interactions peaked at five months, which was unexpected, given that the literature suggests interactions should continually increase as infants get older. However, this may be an artifact of the small sample size and high degree of inter-subject variability.

In full-term infants, arm interactions emerged at two months. This is about 1-2 months earlier than expected by the

literature, which expects infants to begin reaching for toys using their arms at around 3-4 months of age [14]. Additionally, "feet-reaching" typically precedes hand-reaching by a month or more [17], so the emergence of arm interactions before leg interactions was unexpected. However, typical infant milestones represent averages and the 50th percentile for age, so individual variation is expected. Additionally, involuntary interactions were not separated out into arm and leg interactions – if involuntary interactions were separated into upper and lower limb, it is expected that the high percentage of involuntary interactions seen at 1 and 2 months would be lower limb interactions. Similar to leg interactions, arm interactions peaked at five months, which was unexpected, as the literature expects interactions to continue increasing with age.

In full-term infants, gaze interactions emerged at one month. This is at least one month earlier than expected given the literature, which states that at two months old, typically developing infants should be able to follow large, highly contrasting objects such as toys with their eyes [14] and that purposeful gazing becomes more sophisticated around four to six months of age [18]. Preterm infants gazed at the toy with much less frequency than full-term infants.

Here we show that our coding methodology can yield insights into infant motor development using a small sample. However, due to the time-consuming nature of manual video coding, only 18 of the 90 infants were included in this case study. The limited sample size, and the use of only 1 preterm infant from each age group, limits a more robust analysis. Additionally, manual video coding is subject to an element of qualitative judgment and potential error, especially when quantifying gaze interactions. Despite the small sample size, the patterns observed are largely consistent with the literature, suggesting that the coding methods are suitable for quantifying infant/toy interactions if scalability is addressed.

VI. Conclusion

This study presents a novel methodology for coding infant interactions with a robotic toy. Going forward, the coding of involuntary interactions will be separated into upper and lower limb at a minimum, with the goal of eventually using the same 14 codes used for voluntary interactions for involuntary interactions. This revised coding methodology will be applied to the larger infant population in the study, and inter-rater reliability studies will be conducted to verify that the methodology is sufficiently standardized. Future work will focus on increasing scalability. State of the art approaches from computer vision, such as pre-trained vision transformers, are ideally suited to overcoming scalability limitations by automating the process of coding toy interactions. No direct comparison was made; however, we anticipate that manually coded labels could be used to train a supervised learning algorithm to automatically quantify infant interactions with the PANDA toy from video, thus providing a low-cost, efficient, and scalable method of evaluating infant motor development at home.

Acknowledgment

We would like to acknowledge study participants and their caregivers for their time and effort to participate in this research. We would also like to acknowledge the members of the Rehabilitation Robotics Lab PANDA Gym development team, the Children's Hospital of Philadelphia, and Dr. Prosser's clinical team including Noor Ruwaih for coordinating the data collection with infants. Additionally, we thank the University of Pennsylvania School of Engineering and Applied Science's First Year Exposure to Research in STEM program and Michaile Rainey for supporting undergraduate research.

References

[1] Institute of Medicine (US) Committee on Understanding Premature Birth and Assuring Healthy Outcomes, Preterm Birth: Causes, Consequences, and Prevention. in The National Academies Collection: Reports funded by National Institutes of Health. Washington (DC): National Academies Press (US), 2007. Accessed: Mar. 17, 2024. [Online]. Available: http://www.ncbi.nlm.nih.gov/books/NBK11362/

[2] A. G. Allievi, T. Arichi, A. L. Gordon, and E. Burdet, "Technology-aided assessment of sensorimotor function in early infancy," Front Neurol, vol. 5, p. 197, 2014.

[3] M. C. Allen, "Neurodevelopmental outcomes of preterm infants," Current Opinion in Neurology, vol. 21, no. 2, p. 123, Apr. 2008.

[4] M. J. Platt, "Outcomes in preterm infants," Public Health, vol. 128, no. 5, pp. 399–403, May 2014.

[5] "What are the early signs of cerebral palsy? | NICHD - Eunice Kennedy Shriver National Institute of Child Health and Human Development." Accessed: Mar. 17, 2024. [Online]. Available: https://www.nichd.nih.gov/health/topics/cerebral-palsy/conditioninfo/signs

[6] H. Kuo et al., "Hand Use and Grasp Sensor System in Monitoring Infant Fine Motor Development," Arch Rehabil Res Clin Transl, vol. 4, no. 3, p. 100203, Sep. 2022.

[7] D. Campolo et al., "Design of a Sensorized Ball for Ecological Behavioral Analysis of Infants," in Proceedings 2007 IEEE International Conference on Robotics and Automation, Apr. 2007, pp. 1529–1534.

[8] Y. Tenzer, L. P. Jentoft, and R. D. Howe, "Inexpensive and Easily Customized Tactile Array Sensors using MEMS Barometers Chips," 2012.

[9] "A Technique for Touch Force Sensing using a Waterproof Device's Built-in Barometer | Proceedings of the 2017 CHI Conference Extended Abstracts on Human Factors in Computing Systems." Accessed: Mar. 15, 2024. [Online]. Available: https://dl.acm.org/doi/10.1145/3027063.3053130

[10] V. Ramanathan et al., "The Design and Development of Instrumented Toys for the Assessment of Infant Cognitive Flexibility," Sensors (Basel), vol. 23, no. 5, p. 2709, Mar. 2023, doi: 10.3390/s23052709.

[11] S. M. Serio, F. Cecchi, T. Assaf, C. Laschi, and P. Dario, "Design and development of a sensorized wireless toy for measuring infants' manual actions," IEEE Trans Neural Syst Rehabil Eng, vol. 21, no. 3, pp. 444–453, May 2013, doi: 10.1109/TNSRE.2013.2255066.

[12] R. Udayagiri et al., "Towards an AI-driven soft toy for automatically detecting and classifying infant-toy interactions using optical force sensors," Front. Robot. AI, vol. 11, Mar. 2024, doi: 10.3389/frobt.2024.1325296.

[13] Kather, C., Shofer, F. S., Park, J. I., Bogen, D., Pierce, S. R., Kording, K., Nilan, K. A., Zhang, H., Prosser, L. A., & Johnson, M. J. (2023). Quantifying interaction with robotic toys in pre-term and full-term infants. *Frontiers in pediatrics*, *11*, 1153841.

[14] R. J. Gerber, T. Wilks, and C. Erdie-Lalena, "Developmental Milestones: Motor Development," Pediatrics In Review, vol. 31, no. 7, pp. 267–277, Jul. 2010.

[15] V. Goyal et al., "Quantifying infant physical interactions using sensorized toys in a natural play environment," in 2017 International Conference on Rehabilitation Robotics (ICORR), Jul. 2017, pp. 882–887.

[16] U. C. P. S. Commission and J. A. Therell, Age determination guidelines: Relating children's ages to toy characteristics and play behavior. Consumer Product Safety Commission, 2002.

[17] J. C. Galloway and E. Thelen, "Feet first: object exploration in young infants," Infant Behavior and Development, vol. 27, no. 1, pp. 107–112, Feb. 2004.

[18] . Piek J. Infant motor development. Human Kinetics (2006). 18–31.

Non-invasive spatiotemporal spinal cord stimulation paired with force perturbations improves balance in individuals post-stroke: a pilot study

Ming Wu
Department of Biomedical Engineering
University of Illinois Chicago
Chicago, USA
mingwu9@uic.edu

Shijun Yan
Legs and Walking Lab

Shirley Ryan AbilityLab,
Chicago, USA
syan@sralab.org

Weena Dee
Legs and Walking Lab
Shirley Ryan AbilityLab
Chicago, USA
wdee@sralab.org

Hyosok Lim
Legs and Walking Lab

Shirley Ryan AbilityLab,
Chicago, USA
hlim@sralab.org

Velarie Pech
Legs and Walking Lab
Shirley Ryan AbilityLab
Chicago, USA
vpech@sralab.org

Iram Hameeduddin
Department of Biomedical Engineering
University of Illinois Chicago
Chicago, USA
ihamee2@uic.edu

***Abstract*— The goal of this study was to determine the feasibility of applying targeted force perturbations paired with spatiotemporal transcutaneous spinal cord stimulation during walking for improving balance in individuals post-stroke. Five individuals with chronic stroke (> 6 months) were recruited and completed 6 sessions (3 times/week) of balance training paired with spatiotemporal spinal cord stimulation. Balance was assessed pre, post 2 weeks of training, and follow-up, i.e., 2 weeks after the end of training. Results indicated that individuals post-stroke could tolerate the force perturbations applied to the pelvis paired with spatiotemporal spinal cord stimulation during walking. Further, individual post-stroke showed improvements in balance, assessed using the Dynamic Gait Index and Berg Balance Scale scores, after targeted force perturbation balance training paired with spatiotemporal spinal cord stimulation, although this was not significant due to the small sample size. Results from this study suggest that it was feasible to improve balance in individuals post-stroke using targeted pelvis force perturbations paired with spatiotemporal spinal cord stimulation during walking.**

Keywords*— *stroke, balance, spatiotemporal spinal cord stimulation, walking, lateral force perturbation.

I. INTRODUCTION

While clinical significance of falls in individuals post-stroke is widely acknowledged, current fall prevention programs are not very effective in preventing falls in many stroke survivors [1-3]. One of the possible reasons for this is that the motor skills obtained from current conventional balance interventions, such as voluntary stepping or perturbation-based standing balance training [4], may not be effectively transferred to most real-life fall circumstances, of which most occur during walking for community-dwelling stroke survivors [3]. The ability to execute a successful reactive protectivestepping is very crucial for balance recovery and avoiding falls [5], particularly when the magnitude of the perturbation is large [6]. However, many individuals post-stroke demonstrate impairments in reactive stepping, such as slow initiation, reduced step length and reduced foot clearance [7]. There is, therefore, a critical need to develop a new intervention approach to improve the ability of reactive stepping, particularly stepping of the paretic leg (as the majority of fallers landed sideways, toward the paretic side [8]), during dynamic activities, such as walking, which is expected to reduce falls in stroke survivors [9].

Perturbation-based balance training has been shown to reduce falls in healthy older adults [10], although the evidence of reducing falls in individuals post-stroke is still unclear [11, 12]. One of possible reasons may be due to the lack of focusing on improving key impairments of the paretic leg, e.g., the impairments in reactive stepping of the paretic leg during walking, particularly in the frontal plane. For instance, most current perturbation-based balance trainings are conducted during standing [13, 14] or focus on perturbations acting in the sagittal plane [15, 16], which may have limited transfers to balance control in the frontal plane [17].

On the other hand, neuromodulation, such as non-invasive direct current brain stimulation, has been used to improve the efficacy of gait training in individuals post-stroke, although there is still insufficient evidence to recommend this treatment [18]. Previous animal studies [19, 20] indicate that electrical epidural spinal cord stimulation may engage large myelinated fibers associated with proprioceptive and cutaneous feedback circuits, and the recruitment of these fibers may raise the excitability of spinal circuits [21] and activate central pattern generating networks [22, 23]. Clinical application of spinal epidural stimulation through continuous, non-modulated stimulation patterns has been used to improve walking in humans with spinal cord injury [22, 24, 25]. However, this continuous stimulation has two major limitations in the clinical application of spinal cord neuromodulation therapies [26]. First, the spatial location of electrical stimulation is confined to single spinal cord segments [22]. Second, the temporal structure of electrical stimulation is a non-modulated pattern that remains constant during locomotor execution regardless of the state of leg movement [22, 24]. Thus, while this continuous stimulation may increase the general excitability of the spinal circuits, it may

be less effective in addressing subject-specific deficits of gait through dynamic movement execution [27].

Results from previous studies suggest that the production of locomotion involves activation of spatiotemporal distributed motoneurons [28, 29], which are continuously adjusted through sensory feedback [30]. For individuals post-stroke, the disruption of descending pathways toward the paretic side may alter this task-dependent modulation of sensorimotor feedback circuits [31, 32]. Consequently, increasing the general excitability of the spinal cord through continuous stimulation may be insufficient to target the specific impairments of the paretic leg. Thus, electrical spinal neuromodulation that integrates spatial selectivity and temporal structure matching the natural dynamics of motoneuron activation may be more effective in improving motor performance of the paretic leg [26].

Clinical application of spatiotemporal epidural spinal electrical stimulation has shown improvements in walking function in people with spinal cord injury [33, 34]. Recent studies indicated that non-invasive transcutaneous spinal stimulation may activate the same neural structures as epidural spinal stimulation [35, 36]. In particular, results from previous studies suggested that multi-electrode configuration may improve muscle recruitment selectivity through non-invasive transcutaneous spinal cord stimulation [37]. Thus, there is a clear need to determine whether targeted force perturbations paired with spatiotemporal transcutaneous spinal cord stimulation during walking can improve reactive stepping of the paretic leg and result in improvements in balance in individuals post-stroke. The goal of this pilot study was to determine the feasibility of applying targeted force perturbations paired with spatiotemporal transcutaneous spinal cord stimulation during walking for improving balance in individuals post-stroke. We hypothesized that it would be feasible to apply controlled lateral perturbation forces to the pelvis during walking paired with spatiotemporal spinal cord stimulation to improve motor control of reactive paretic stepping, resulting in improvements in balance in individuals post-stroke.

II. Method

A. Participants

Five individuals post chronic stroke (> 6 months) were recruited in this pilot study (average age: 66.0 ± 7.0 years old; and average time post stroke: 11.2 ± 4.1 years, 1 female), see Table 1.

The inclusion criteria were: 1) 21-75 years old; 2) a single unilateral, supratentorial stroke of either ischemic or hemorrhagic etiology, confirmed by radiographic imaging; 3) weakness/paresis of the affected leg; and 4) ability to stand and walk (>10 m) without physical assistance and with the use of assistive devices or ankle-foot orthoses as needed.

Exclusion criteria were: 1) brainstem or cerebellar stroke; 2) a score of <24 on the Mini Mental State Examination [38]; 3) other neurological conditions, cardiorespiratory/metabolic disorders, or orthopedic conditions that affect ambulatory ability; 4) uncontrolled hypertension (systolic >200 mg Hg, diastolic >110 mm Hg); 5) botulinum toxin injection within the prior 6 months; 6) inability to tolerate 30 min of treadmill walking with sitting breaks. The Northwestern University Medical School Institutional Review Board approved all procedures and all participants signed an informed consent document before data collection.

B. Apparatus

A custom designed cable-driven robotic system, which was mounted over a treadmill (Woodway, Waukesha, WI, USA), was used to apply controlled lateral perturbations to the pelvis during treadmill walking (Figure 1), which has been reported previously [39]. In brief, the cable-driven robotic system was composed of 2 nylon-coated stainless-steel cables (in diameter 2mm) driven by 2 motors (AKM 43H, Kollmorgen, Radford, VA) through cable spools, which were mounted on an aluminum frame that was located at the two sides of the treadmill. In this study, we used only one pair of a motor and a cable spool at one side to apply controlled lateral perturbation forces to the pelvis toward the paretic side, depending on which side of each participant was affected.

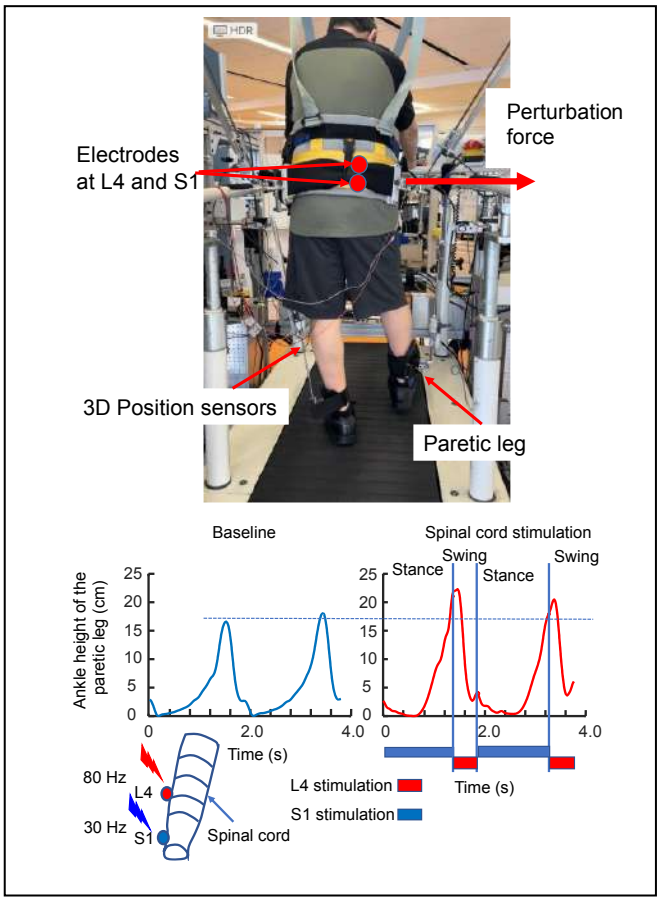


Fig. 1. Cable-driven robotic system paired with spatiotemporal transcutaneous spinal stimulation, which was applied to the L4 during swing phase of the paretic leg (80Hz) and to S1 during stance phase of the partic leg (30Hz). Ankle height of the paretic leg with spatiotemporal stimulation and without stimulation (baseline) during treadmill walking. Red curves indicate an increased step height of the paretic leg with the application of spatiotemporal spinal cord stimulation.

In addition, a set of customized 3-dimensional position sensors was attached to ankles through straps to collect ankle position signals, and another set of position sensors was attached

to the pelvis through a waist belt to measure pelvis position signals, see Fig 1. Specifically, each position sensor consisted of a detector rod and 3 potentiometers (one linear and two rotational potentiometers). One end of the rod was attached at the subject's ankle through a strap and the other end of the rod was attached to a fixed frame located at both sides of treadmill through a U joint. Two rotational potentiometers (P2201, Southborough, MA) were used to measure the angular displacement of the detector rod in the anterior-posterior and mediolateral directions. One linear potentiometer (SP-2, Celesco, Chatsworth, CA) was used to measure the length of telescopic detector rod. We used the positional signals from these 3 potentiometers to calculate the ankles and pelvis 3D trajectories. The robotic system was controlled by a custom-written program in LabVIEW (National Instrument, Austin, TX, USA) on a personal computer. The controller used ankle position signals to trigger the pelvis perturbations force at targeted phase of gait, i.e., starting at the early swing phase of the paretic leg for 300 ms.

Spatiotemporal transcutaneous spinal stimulation was delivered using a current stimulator (DS8R, Digitimer, UK), electrode selector, and a custom designed controller. The controller detected the gait events based on the ankle position signals, which were recorded using a set of custom designed 3D position sensors, and delivered the electrical currents to the electrodes at targeted phase of gait, which was controlled by a PC through a custom LabVIEW program. The ankle position signals were used to trigger electrical stimulations at targeted phase of gait (e.g., stance phase and swing phase of the paretic leg) through an electrode selector (D188, Digitimer, UK), which was controlled by a custom LabVIEW program. Two self-adhesive round electrodes (5cm in diameter, cathode) were placed ~2cm laterally from midline of spinal cord at the level of L4 and S1 spinous processes on the paretic leg side as active electrodes. In particular, we attached electrodes at ~2cm laterally toward the paretic side from the midline of the spinal cord in order to selectively target specific motoneurons pools [40]. Two round electrodes (5cm in diameter, anode) were placed on the anterior superior iliac spine on both sides as references.

TABLE I. PARTICIPANTS INFORMATION.

	Age	Sex	Time post stroke (y)	Weak side	Brace	AD
Sub 1	58	M	14	Right	AFO	RW
Sub 2	77	M	14	Left	None	None
Sub 3	66	M	12	Right	None	None
Sub 4	63	F	4	Left	AFO	Hemiwalker
Sub 5	66	M	12	Left	AFO	Tripod cane

AD: assistance device; RW: reverse Walker.

C. Experimental protocol

The participants trained 3 times/week for two weeks. They walked on a treadmill for 40 minutes excluding setup time although short sitting breaks were allowed during the training session in each visit. An overhead harness was used for protection only and no body weight support was provided. The treadmill speed was set at the subject's comfortable speed and was gradually increased during the course of training. Blood pressure and heart rate were monitored during training and were maintained below 220/110 mm Hg and 85% of age-predicated maximum heart rate, respectively.

The magnitude of the force was set at ~8% of body weight, which was adjusted depending on the tolerance of each subject and gradually increased during the course of training sessions. In order to make the perturbation force less predictable, the perturbation force was randomly applied in one step within every 5 steps of the paretic leg, which was determined based on our pilot study. The rating of perceived exertion (RPE) [41] was monitored during the course of training and the targeted RPE was 12 to 16.

We applied electrical stimulation on spinal cord at the level of L4 and S1 spinous processes during swing and stance phases of the paretic leg, respectively, to target leg flexor and extensor muscles, based on the results of previous epidural stimulation studies [34]. In particular, a higher frequency (e.g., 80 Hz) and a lower frequency (e.g., 30 Hz) of stimulation was applied during the swing phase and stance phase, targeting the paretic leg flexor and extensor muscles, respectively, as the motor neurons innervating these muscles exhibit distinct preferential activation frequencies, based on previous studies in animals [26] and in humans with spinal cord injury [34]. The electrical stimulations were filled with a carrier frequency of 9.5 kHz. The stimulation intensity was determined based on the tolerance of pain of each participant, with the average intensity of stimulation was 25.7±1.2 mA across participants. The stimulation intensity was reduced as needed if participant felt discomfortable.

Dynamic balance, the primary outcome measure, was assessed using Dynamic Gait Index (DGI) [42], Berg Balance Scale (BBS), and endurance (i.e., 6-minute walking distance), secondary outcome measures, were evaluated at pre and post 2 weeks of balance training, and follow up, i.e., 2 weeks after the end of training. DGI was used as the primary outcome measure because that scores have discrimination in the prediction of falls in stroke survivors and the probability that stroke survivors with a DGI score of $\leqslant$ 16.5 will experience a fall is 3.8 times higher than those with a DGI score of > 16.5.

D. Data analysis

The normality of outcome measures of interest was examined using Kolmogorov-Smirnov test. Given the data were not normally distributed, Kruskal-Wallis test was used to examine the changes of variables across three time points (pre, post and follow up) with significance noted at $p < 0.05$. Multiple comparisons were corrected for with Bonferroni correction, again with significance noted at $p < 0.05$. In addition, Cohen's d was used to calculate effect size, where 0.2 was considered a small effect, 0.5 a medium effect, and 0.8 a large effect [43].

III. RESULTS

Five participants completed all the training and assessment sessions with no dropout in this pilot study. All participants could tolerate the force perturbations applied to the pelvis and spinal cord electrical stimulation during walking. Further, as shown in Fig 2, the average DGI score increased from 12.6 ± 5.5, baseline, to 13.2 ± 5.3, post perturbations balance training

paired with spatiotemporal spinal cord stimulation, and further increased to 14.0 ± 4.7 at 2 weeks follow up test, the effect size d = 0.3, although this was not significant (Kruskal-Wallis ANOVA, $p > 0.05$, n = 5) due to small sample size. In addition, the average BBS score increased from 38.8 ± 12.7, baseline, to 40.8 ± 12.0, post balance training paired with spinal cord stimulation, and was 40.6 ± 11.7 at 2 weeks follow up test, the effect size d = 0.2, although this was not significant due to the small sample size (Kruskal-Wallis ANOVA, $p > 0.05$, n = 5). The 6 minutes walking distance increased from 187.1 ± 124.9 m, baseline, to 197.9 ± 130.9 m, post balance training, and was 193.7 ± 134.3 m at 2 weeks follow up test, the effect size was d = 0.1, and this was not significant ($p > 0.05$).

IV. Discussion

We have tested the feasibility of applying targeted lateral force perturbations paired with spatiotemporal spinal cord stimulation during walking for improving balance, particularly dynamic balance, in individuals post-stroke. We found that individuals post-stroke could tolerate the robotic perturbation force paired with spatiotemporal spinal cord electrical stimulation with the dropout rate of 0. We also found that individual post-stroke showed improvements in balance, which was assessed using the DGI and BBS scores, after force perturbation balance training paired with spatiotemporal spinal cord stimulation, although this was not significant due to the small sample size.

Given the impairments in motor control of the paretic leg and/or dyscoordination between the two legs often experienced by people with stroke, many individuals post-stroke show impairments in reactive stepping with the paretic leg [44]. Impairments in reactive stepping with the paretic leg may be one of key factors contributing to the falls in individuals post-stroke. In this study, the application of targeted perturbation forces might force individuals post-stroke to take a reactive stepping using the paretic leg during walking. Repetitive practice in this manner may lead to reinforcement of this stepping strategy, which is consistent with use-dependent synaptic plasticity [45].

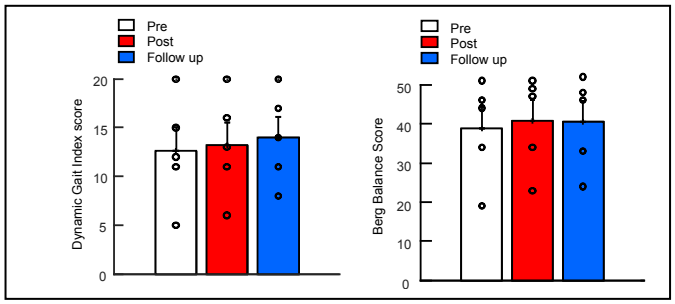


Fig. 2. Dynamic Gait Index (left column) scores and Berg Balance Scale (right column) per and post robotic balance training paired with non-invasive spatiotemporal spinal cord stimulation and follow up, i.e., 2 weeks after the end of training. Data shown are average of scores across participants (n = 5) and standard error.

In particular, the application of spatiotemporal spinal cord stimulation paired with targeted force perturbation balance training might facilitate the motor learning of reactive stepping with the paretic leg in individuals post-stroke. Specifically, in this study, electrical stimulation was applied at the L4 and S1 segments during swing phase and stance phase of the paretic leg, respectively, which might enhance afferents inputs of hip flexors and dorsiflexors during swing, and hip extensors and plantarflexors during stance, respectively. In particular, a higher stimulation frequency (i.e., 80 Hz) was applied during swing phase, and a lower stimulation frequency (i.e., 30 Hz) was applied during stance phase of the paretic leg, which may be more effective in recruiting flexors and extensors, respectively. The application of the spatiotemporal spinal cord stimulation, which may induce enhanced afferents inputs that are more consistent with the natural patterns of neural activity during walking, may have led to improved motor control of paretic leg in individuals post-stroke through use-dependent neural plasticity.

The results of this study need to be interpreted with caution due to the following limitations. First, while this study was a pilot feasibility study, the sample size was small. Further studies with a large cohort of participants are needed to obtain a confirmed conclusion. Second, we had no control group in this pilot study. We do not know whether this approach is more effective than the conventional balance training approaches in improving balance in individuals post-stroke. Further studies are needed to determine the effect of targeted pelvis force perturbations paired with spatiotemporal spinal cord stimulation through randomized controlled studies. Third, because the dosage of intervention was small, i.e., only 6 training sessions, the functional gains in balance were small. We expect to see greater functional gains in balance through a greater dosage of balance training. Fourth, the functional gains in balance in individuals post-stroke after the intervention might be due to the application of both repeated force perturbations and spatiotemporal spinal cord stimulation. Thus, further studies are needed to determine the functional gains in balance induced by the perturbation force and/or the spatiotemporal spinal cord stimulation during walking.

In conclusion, results from this study indicated that it was feasible to improve balance in individuals post-stroke using targeted force perturbations paired with spatiotemporal spinal cord stimulation during walking. Perturbation induced repeated practice of reactive stepping with paretic leg during walking when paired with spatiotemporal spinal cord stimulation might induce improvements in balance, particularly dynamic balance, in individuals post-stroke.

ACKNOWLEDGMENT

This was supported by NIH/NICHD, R01HD082216. We thank Mr. Jack Snodgrass' assistance in the development of the controller of spatiotemporal spinal cord electrical stimulation system.

References:

[1] F. Yang, J. Lees, C. Simpkins, and A. Butler, "Interventions for preventing falls in people post-stroke: A meta-analysis of randomized controlled trials," *Gait Posture,* vol. 84, pp. 377-388, Feb, 2021.

[2] G. S. Verheyden, V. Weerdesteyn, R. M. Pickering, D. Kunkel, S. Lennon, A. C. Geurts, and A. Ashburn, "Interventions for preventing falls in people after stroke," *Cochrane Database Syst Rev,* vol. 2013, no. 5, pp. CD008728, May 31, 2013.

[3] V. Weerdesteyn, M. de Niet, H. J. van Duijnhoven, and A. C. Geurts, "Falls in individuals with stroke," *J Rehabil Res Dev,* vol. 45, no. 8, pp. 1195-213, 2008.

[4] A. Schinkel-Ivy, A. H. Huntley, A. Aqui, and A. Mansfield, "Does Perturbation-Based Balance Training Improve Control of Reactive Stepping in Individuals with Chronic Stroke?," *J Stroke Cerebrovasc Dis,* vol. 28, no. 4, pp. 935-943, Apr, 2019.

[5] P. Salot, P. Patel, and T. Bhatt, "Reactive Balance in Individuals With Chronic Stroke: Biomechanical Factors Related to Perturbation-Induced Backward Falling," *Phys Ther,* vol. 96, no. 3, pp. 338-47, Mar, 2016.

[6] B. E. Maki, and W. E. McIlroy, "The role of limb movements in maintaining upright stance: the "change-in-support" strategy," *Phys Ther,* vol. 77, no. 5, pp. 488-507, May, 1997.

[7] A. Mansfield, J. S. Wong, W. E. McIlroy, L. Biasin, K. Brunton, M. Bayley, and E. L. Inness, "Do measures of reactive balance control predict falls in people with stroke returning to the community?," *Physiotherapy,* vol. 101, no. 4, pp. 373-80, Dec, 2015.

[8] D. Hyndman, A. Ashburn, and E. Stack, "Fall events among people with stroke living in the community: circumstances of falls and characteristics of fallers," *Arch Phys Med Rehabil,* vol. 83, no. 2, pp. 165-70, Feb, 2002.

[9] A. Mansfield, E. L. Inness, J. S. Wong, J. E. Fraser, and W. E. McIlroy, "Is impaired control of reactive stepping related to falls during inpatient stroke rehabilitation?," *Neurorehabil Neural Repair,* vol. 27, no. 6, pp. 526-33, Jul-Aug, 2013.

[10] Y. C. Pai, T. Bhatt, F. Yang, and E. Wang, "Perturbation training can reduce community-dwelling older adults' annual fall risk: a randomized controlled trial," *J Gerontol A Biol Sci Med Sci,* vol. 69, no. 12, pp. 1586-94, Dec, 2014.

[11] A. Mansfield, A. Aqui, C. J. Danells, S. Knorr, A. Centen, V. G. DePaul, A. Schinkel-Ivy, D. Brooks, E. L. Inness, and G. Mochizuki, "Does perturbation-based balance training prevent falls among individuals with chronic stroke? A randomised controlled trial," *BMJ Open,* vol. 8, no. 8, pp. e021510, Aug 17, 2018.

[12] S. Handelzalts, M. Kenner-Furman, G. Gray, N. Soroker, G. Shani, and I. Melzer, "Effects of Perturbation-Based Balance Training in Subacute Persons With Stroke: A Randomized Controlled Trial," *Neurorehabil Neural Repair,* vol. 33, no. 3, pp. 213-224, Mar, 2019.

[13] E. L. Inness, A. Mansfield, B. Lakhani, M. Bayley, and W. E. McIlroy, "Impaired reactive stepping among patients ready for discharge from inpatient stroke rehabilitation," *Phys Ther,* vol. 94, no. 12, pp. 1755-64, Dec, 2014.

[14] L. A. Wojcik, D. G. Thelen, A. B. Schultz, J. A. Ashton-Miller, and N. B. Alexander, "Age and gender differences in single-step recovery from a forward fall," *J Gerontol A Biol Sci Med Sci,* vol. 54, no. 1, pp. M44-50, Jan, 1999.

[15] S. Dusane, and T. Bhatt, "Can prior exposure to repeated non-paretic slips improve reactive responses on novel paretic slips among people with chronic stroke?," *Exp Brain Res,* vol. 240, no. 4, pp. 1069-1080, Apr, 2022.

[16] V. Esmaeili, A. Juneau, J. O. Dyer, A. Lamontagne, D. Kairy, L. Bouyer, and C. Duclos, "Intense and unpredictable perturbations during gait training improve dynamic balance abilities in chronic hemiparetic individuals: a randomized controlled pilot trial," *J Neuroeng Rehabil,* vol. 17, no. 1, pp. 79, Jun 17, 2020.

[17] B. W. Dijkstra, F. B. Horak, Y. P. Kamsma, and D. S. Peterson, "Older adults can improve compensatory stepping with repeated postural perturbations," *Front Aging Neurosci,* vol. 7, pp. 201, 2015.

[18] J. A. Chamorro-Hinojosa, F. Molina-Rueda, and M. Carratala-Tejada, "Transcranial Direct Current Stimulation in the Treatment of Gait Disturbance in Post-Stroke Patients: An Overview of Systematic Reviews," *Sensors (Basel),* vol. 23, no. 23, Nov 21, 2023.

[19] U. S. Hofstoetter, S. M. Danner, B. Freundl, H. Binder, W. Mayr, F. Rattay, and K. Minassian, "Periodic modulation of repetitively elicited monosynaptic reflexes of the human lumbosacral spinal cord," *J Neurophysiol,* vol. 114, no. 1, pp. 400-10, Jul, 2015.

[20] Y. P. Gerasimenko, I. A. Lavrov, G. Courtine, R. M. Ichiyama, C. J. Dy, H. Zhong, R. R. Roy, and V. R. Edgerton, "Spinal cord reflexes induced by epidural spinal cord stimulation in normal awake rats," *J Neurosci Methods,* vol. 157, no. 2, pp. 253-63, Oct 30, 2006.

[21] V. R. Edgerton, G. Courtine, Y. P. Gerasimenko, I. Lavrov, R. M. Ichiyama, A. J. Fong, L. L. Cai, C. K. Otoshi, N. J. Tillakaratne, J. W. Burdick, and R. R. Roy, "Training locomotor networks," *Brain Res Rev,* vol. 57, no. 1, pp. 241-54, Jan, 2008.

[22] C. A. Angeli, V. R. Edgerton, Y. P. Gerasimenko, and S. J. Harkema, "Altering spinal cord excitability enables voluntary movements after chronic complete paralysis in humans," *Brain,* vol. 137, no. Pt 5, pp. 1394-409, May, 2014.

[23] S. M. Danner, U. S. Hofstoetter, B. Freundl, H. Binder, W. Mayr, F. Rattay, and K. Minassian, "Human spinal locomotor control is based on flexibly organized burst generators," *Brain,* vol. 138, no. Pt 3, pp. 577-88, Mar, 2015.

[24] M. R. Carhart, J. He, R. Herman, S. D'Luzansky, and W. T. Willis, "Epidural spinal-cord stimulation facilitates recovery of functional walking following incomplete spinal-cord injury," *IEEE Trans Neural Syst Rehabil Eng,* vol. 12, no. 1, pp. 32-42, Mar, 2004.

[25] C. A. Angeli, M. Boakye, R. A. Morton, J. Vogt, K. Benton, Y. Chen, C. K. Ferreira, and S. J. Harkema, "Recovery of Over-Ground Walking after Chronic Motor Complete Spinal Cord Injury," *N Engl J Med,* vol. 379, no. 13, pp. 1244-1250, Sep 27, 2018.

[26] N. Wenger, E. M. Moraud, J. Gandar, P. Musienko, M. Capogrosso, L. Baud, C. G. Le Goff, Q. Barraud, N. Pavlova, N. Dominici, I. R. Minev, L. Asboth, A. Hirsch, S. Duis, J. Kreider, A. Mortera, O. Haverbeck, S. Kraus, F. Schmitz, J. DiGiovanna, R. van den Brand, J. Bloch, P. Detemple, S. P. Lacour, E. Bezard, S. Micera, and G. Courtine, "Spatiotemporal neuromodulation therapies engaging muscle synergies improve motor control after spinal cord injury," *Nat Med,* vol. 22, no. 2, pp. 138-45, Feb, 2016.

[27] E. M. Moraud, M. Capogrosso, E. Formento, N. Wenger, J. DiGiovanna, G. Courtine, and S. Micera, "Mechanisms Underlying the Neuromodulation of Spinal Circuits for Correcting Gait and Balance Deficits after Spinal Cord Injury," *Neuron,* vol. 89, no. 4, pp. 814-28, Feb 17, 2016.

[28] S. Yakovenko, V. Mushahwar, V. VanderHorst, G. Holstege, and A. Prochazka, "Spatiotemporal activation of lumbosacral motoneurons in the locomotor step cycle," *J Neurophysiol,* vol. 87, no. 3, pp. 1542-53, Mar, 2002.

[29] G. Cappellini, Y. P. Ivanenko, N. Dominici, R. E. Poppele, and F. Lacquaniti, "Migration of motor pool activity in the spinal cord reflects body mechanics in human locomotion," *J Neurophysiol,* vol. 104, no. 6, pp. 3064-73, Dec, 2010.

[30] O. Kiehn, "Locomotor circuits in the mammalian spinal cord," *Annu Rev Neurosci,* vol. 29, pp. 279-306, 2006.

[31] S. Li, G. E. Francisco, and P. Zhou, "Post-stroke Hemiplegic Gait: New Perspective and Insights," *Front Physiol,* vol. 9, pp. 1021, 2018.

[32] R. Kitatani, K. Ohata, Y. Aga, Y. Mashima, Y. Hashiguchi, M. Wakida, A. Maeda, and S. Yamada, "Descending neural drives to ankle muscles during gait and their relationships with clinical functions in patients after stroke," *Clin Neurophysiol,* vol. 127, no. 2, pp. 1512-1520, Feb, 2016.

[33] J. Aguilar, F. Pulecchi, R. Dilena, A. Oliviero, A. Priori, and G. Foffani, "Spinal direct current stimulation modulates the activity of gracile nucleus and primary somatosensory cortex in anaesthetized rats," *J Physiol,* vol. 589, no. Pt 20, pp. 4981-96, Oct 15, 2011.

[34] F. B. Wagner, J. B. Mignardot, C. G. Le Goff-Mignardot, R. Demesmaeker, S. Komi, M. Capogrosso, A. Rowald, I. Seanez, M. Caban, E. Pirondini, M. Vat, L. A. McCracken, R. Heimgartner, I. Fodor, A. Watrin, P. Seguin, E. Paoles, K. Van Den Keybus, G. Eberle, B. Schurch, E. Pralong, F. Becce, J. Prior, N. Buse, R. Buschman, E. Neufeld, N. Kuster, S. Carda, J. von Zitzewitz, V. Delattre, T. Denison, H. Lambert, K. Minassian, J. Bloch, and G. Courtine, "Targeted neurotechnology restores walking in humans with spinal cord injury," *Nature,* vol. 563, no. 7729, pp. 65-71, Nov, 2018.

[35] U. S. Hofstoetter, B. Freundl, H. Binder, and K. Minassian, "Common neural structures activated by epidural and transcutaneous lumbar spinal cord stimulation: Elicitation of posterior root-muscle reflexes," *PLoS One,* vol. 13, no. 1, pp. e0192013, 2018.

[36] J. S. Calvert, M. L. Gill, M. B. Linde, D. D. Veith, A. R. Thoreson, C. Lopez, K. H. Lee, Y. P. Gerasimenko, V. R. Edgerton, I. A. Lavrov, K. D. Zhao, P. J. Grahn, and D. G. Sayenko, "Voluntary Modulation of Evoked Responses Generated by Epidural and Transcutaneous Spinal Stimulation in Humans with Spinal Cord Injury," *J Clin Med,* vol. 10, no. 21, Oct 24, 2021.

[37] N. Bryson, L. Lombardi, R. Hawthorn, J. Fei, R. Keesey, J. D. Peiffer, and I. Seanez, "Enhanced selectivity of transcutaneous spinal cord stimulation by multielectrode configuration," *J Neural Eng,* vol. 20, no. 4, Jul 25, 2023.

[38] M. F. Folstein, S. E. Folstein, and P. R. McHugh, ""Mini-mental state". A practical method for grading the cognitive state of patients for the clinician," *J Psychiatr Res,* vol. 12, no. 3, pp. 189-98, Nov, 1975.

[39] M. Wu, T. G. Hornby, J. M. Landry, H. Roth, and B. D. Schmit, "A cable-driven locomotor training system for restoration of gait in human SCI," *Gait Posture,* vol. 33, no. 2, pp. 256-60, Feb, 2011.

[40] J. S. Calvert, G. A. Manson, P. J. Grahn, and D. G. Sayenko, "Preferential activation of spinal sensorimotor networks via lateralized transcutaneous spinal stimulation in neurologically intact humans," *J Neurophysiol,* vol. 122, no. 5, pp. 2111-2118, Nov 1, 2019.

[41] G. Borg, "Perceived exertion as an indicator of somatic stress," *Scand J Rehabil Med,* vol. 2, no. 2, pp. 92-8, 1970.

[42] A. Shumway-Cook, and M. Woollacott, *Motor control: theory and practical applications*, Baltimore, MD: Williams & Wilkins, 1995.

[43] J. Cohen, *Statistical Power Analysis for the Behavioral Sciences*, 2nd Edition ed., New York: Routledge, 1988.

[44] B. Lakhani, A. Mansfield, E. L. Inness, and W. E. McIlroy, "Compensatory stepping responses in individuals with stroke: a pilot study," *Physiother Theory Pract,* vol. 27, no. 4, pp. 299-309, May, 2011.

[45] D. Hebb, *The organization of behavior: A neuropsychological theory*, New York: Wiley, 1949.

[46] E. Formento, K. Minassian, F. Wagner, J. B. Mignardot, C. G. Le Goff-Mignardot, A. Rowald, J. Bloch, S. Micera, M. Capogrosso, and G. Courtine, "Electrical spinal cord stimulation must preserve proprioception to enable locomotion in humans with spinal cord injury," *Nat Neurosci,* vol. 21, no. 12, pp. 1728-1741, Dec, 2018.

Recovr Glove: Accessible Hand Exoskeleton for Stroke Rehabilitation and Everyday Aid

*1st Sharon Zheng
Mechanical Engineering and Applied Mathematics Department
University of Pennsylvania
Phildelphia, USA
sharonzh@seas.upenn.edu

*2nd Nova Meng
Bioengineering Department
University of Pennsylvania
Phildelphia, USA
nmeng@seas.upenn.edu

***Abstract*—Each year, over 7 million stroke survivors experience upper limb dysfunction, often losing the ability to perform essential hand movements like finger extension and contraction for grasping. Exoskeletons offer a promising solution for rehabilitating gross hand function, providing controlled, repetitive movements and personalized exercises. However, existing models struggle with affordability, usability, and integration into daily life. This paper presents Recovr Glove, a cost-effective, user-friendly exoskeleton glove aimed at improving gross hand function recovery. Recovr features passive extension and active contraction mechanisms, adaptable to varying levels of spasticity. By capturing surface electromyography (sEMG) signals from the flexor digitorum profundus muscle, responsible for grasping, it enables cognitive control of hand movements. We evaluated the Recovr Glove across four parameters: grip strength, extension strength, contraction angle, and object grasping. In motor response testing, Recovr achieved 95% accuracy, with reliable rotation and an average delay of 0.49 seconds ± 0.41. During contraction tests, the grasp strength was an average of 55.21 ± 5.68 N. Extension testing, using a spring scale on each finger, showed an adjustable average force range of 0.1 to 5.5 N for the pinky and from 0.7 to 7.7 N for the thumb, depending on rubber band tension.**

***Index Terms*—Stroke Rehabilitation, Electromyography, Hand Spasticity**

I. Introduction

In the United States alone, there are over 7 million stroke survivors, and more than 80% experience significant loss of hand functionality [1]. This impairment often leads to a loss of independence, reduced quality of life, and increased financial strain on individuals and their families [2].

Early access to an effective rehabilitation regimen is crucial for maximizing the potential to regain hand function following a stroke [3]–[6]. Rehabilitation therapies, such as constraint-induced movement therapy, aim to restore motor skills through repetitive, targeted exercises. However, patients with moderate to severe impairments often face significant challenges in fully engaging with these therapies due to limited motor function [7]. These difficulties are further exacerbated by the high costs and time commitments associated with therapy. As a result, these barriers can lower adherence rates and hinder the overall effectiveness of rehabilitation [8].

Several devices on the market, including the SaeboGlove, SYREBO, Emovo Grasp, and Hand of Hope, have demonstrated efficacy in improving gross hand motor function [9]. In addition, academic innovations such as the FlexoGlove [10] and AirExGlove [11] focus on features like portability - allowing patients to move freely while wearing the device - and customizability - allowing users to modify glove features based on individual needs. Despite these advancements, current designs are often limited by a lack of tactile sensing, insufficient portability such as the inclusion of a tethered control system, high costs, and inadequate customizability (Table 1) [12]. These limitations hinder accessibility and reduce their effectiveness for daily living activities [13]. Additionally, many of the devices on the market, such as ExoFlex and AirExGlove do not aid in the reconstitution of the cognitive motor link due to the lack of direct muscle-controlled feedback and sensory input [14].

This paper introduces Recovr Glove, a customizable and cost-effective exoskeleton glove designed to address these deficiencies. Recovr integrates forearm surface electromyography (sEMG) signals to control hand grasping and releasing. By providing real-time sensory feedback to the user during movements, Recovr stimulates neural pathways that are crucial for motor control, promoting neuroplasticity. This process helps retrain the brain's motor-cognitive pathways, encouraging the re-establishment of functional connections and enabling the restoration of fine motor skills essential for activities of daily living [15] [16]. Concerns regarding the viability of sEMG signals in stroke survivors with limited muscle activity are addressed by studies demonstrating their effectiveness in rehabilitation and assistive technologies, even in cases of diminished muscle strength [17]–[19]. Our design leverages sensory-motor feedback loops to promote neuroplasticity and retrain motor-cognitive pathways, facilitating functional recovery and aiding activities of daily living (ADLs) [20].

II. Recovr Glove System Design

This section outlines the design architecture of the Recovr system, including customized mechanical features, sEMG signal acquisition and processing, software implementation, hardware integration, and attention to affordability in the overall design.

Recovr Glove only aids in gross grasping and extension motions of the hand and not individual finger control. The device is meant for patients who struggle with grasping motions where fine-tuned movements are typically only regained after the gross movements have been achieved [21]. The purpose

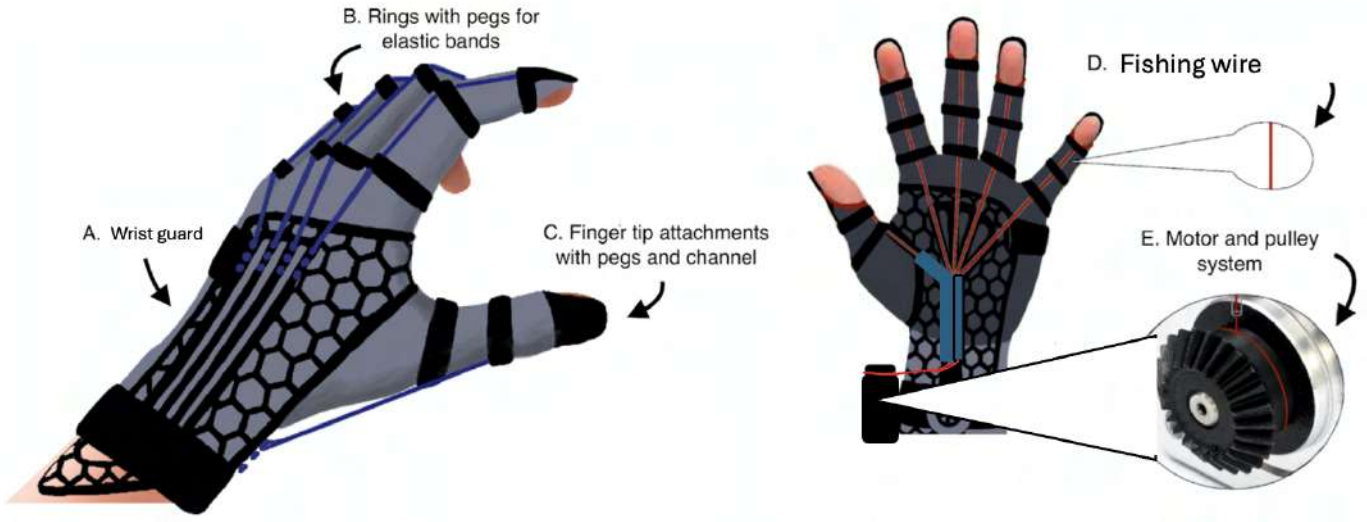


Figure 1: A) Removable wrist guard with adjustable straps, pegs for elastic band attachment, and channel for fishing wire. B) Rings with pegs sewn into gloves for reliable extension. Each ring has two components sewn together via elastic cords. C) Finger tip attachments with pegs for elastic bands. Contains a channel for fishing wire to loop through. D) Fishing wire for contraction. E) Pulley and motor system to control fishing wires for contraction or extension.

Table 1: Comparison of Hand Rehabilitation Solutions

Feature	SYREBO	SaeboGlove	FlexoGlove	AirExGlove	ExoFlex	Our Solution
Mode of Actuation	Pneumatic	Tension Bands	Linear Actuator via Motor	Pneumatic	Linear Actuator via Motor	Linear Actuator via Motor
Aids in Flexion and/or Extension	Both	Extension only	Both	Both	Both	Both
Cost (USD)	550	399	>199.99**	N/A*	N/A*	148.72
Control	Mirroring Unaffected Hand	Passive Control	EMG	Remote Controlled	Touchpad Control	sEMG
Adaptable	No	No	No	Yes	No	Yes
Portable	No	Yes	Yes	Yes	Yes	Yes
Tactility	No	Yes	No	No	No	Yes
Purpose	Muscle Training	Resistive Muscle Development	Resistive Muscle Development and Everyday Use	Resistive Muscle Development	Muscle Training	Resistive Muscle Development and Everyday Use

Comparison of the prominent exoskeleton gloves on the market to Recovr Glove, evaluated across several key criteria.

*Price not listed.
**Utilizes MyoBand, which is priced at $199.99. This price does not include 3D printing and customization costs.

of the Recovr Glove is to both aid in rehabilitation through motor recovery and aid in everyday activities. Rehabilitation focuses on strengthening gross motor skills as a foundation for fine motor control, while the support function aims to assist individuals in performing routine tasks despite their motor impairments. Therefore, the Recovr Glove was designed for both comfort of use and sEMG integration for easy wear and effective retraining of the neuromotor connection [22]–[24].

A. Custom Mechanical Design

The mechanical design can be seen in Figure 1. It consists of a fabric glove with sewn-in rings, a 3D-printed PLA wrist guard, a pulley system, and a 3D-printed enclosure housing the electronics. The wrist guard is sized and molded to the user's hand during the manufacturing process. It utilizes a honeycomb structure to minimize weight while maintaining structural integrity. Adjustable elastic bands are secured to pegs on the back of the glove, allowing users to fine-tune resistance by looping the bands around the pegs. This supports gradual increases in resistance as hand extension improves. The fishing wire is threaded through the rings on the front of the glove and connected to an elastic band to create a dampening system, such that the elastic bands would snap before over-contraction. The fishing wires are actuated by a motor, actively controlling the contraction of all five phalanges.

A pulley cover is included to maintain a consistent fishing wire pathway and ensure user safety. The speed of the DC motor can be pre-configured to provide personalized contraction support. Additionally, two fabric straps were sewn onto the wrist guard design and hook-and-loop fasteners were attached to the straps. The electronics enclosure is approximately $6\times4\times4$ inches in size and incorporates a curved side to ensure comfort when belted around the user's hips (Figure 2). The entire product weighs approximately 2.13 pounds, making it lightweight and highly portable - ideal for supporting everyday tasks and facilitating rehabilitation.

B. sEMG Processing

We created our own sEMG filter circuit as it minimizes the cost significantly relative to commercially available sEMG

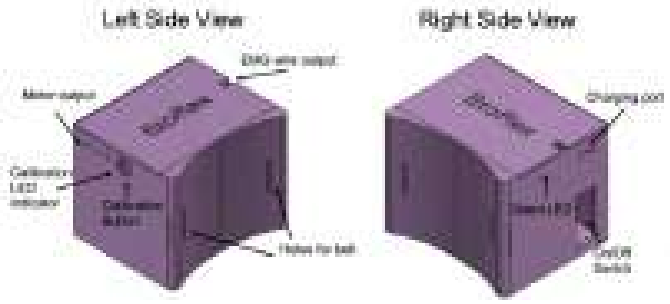


Figure 2: CAD of Electronics Enclosure

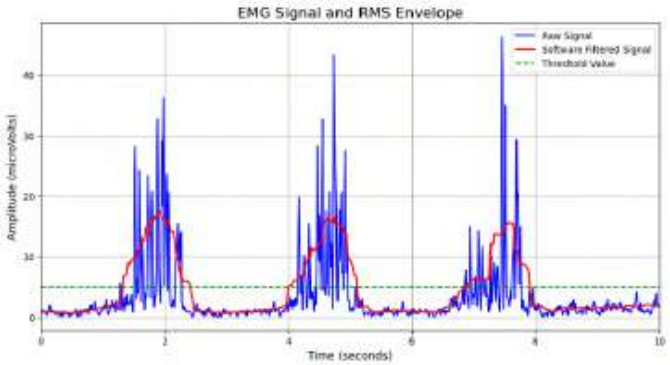


Figure 3: The hardware filtered sEMG signal (blue), recorded for 10 seconds, shows three distinct peaks, each representing a forearm flex. The red signal indicates post-software filtering with a 30-sample rolling average. When the red signal exceeds the green threshold, the motor triggers hand contraction; when it falls below, the motor releases the hand to its original position.

circuits. Raw sEMG signal was collected at a baud rate of 9600 and passed through a passive high-pass filter with a cutoff frequency of 0.16 Hz to eliminate any potential fluctuations caused by the DC component [25]. The signal then went through a differential amplifier, which both amplified the signal and converted the three-lead sEMG input into a two-lead output with respect to the ground signal. The signal was then passed through a buffer to prevent signal backflow, followed by a Sallen-Key bandpass filter designed to isolate frequencies between 50 Hz and 160 Hz [26]. Afterward, the signal was processed by a full-wave rectifier and finally passed through a non-inverting amplifier to further enhance its amplitude. Figure 3 showcases the unfiltered and filtered sEMG signal. The hardware and software processing did not create any noticeable delay in the signal response.

C. Software

The embedded software calculates a threshold by averaging sEMG data collected during the first five seconds of use, during which the forearm is slightly flexed. Therefore the threshold would be significantly above baseline for an individual but below the amplitude of an active flex. Subsequently, a rolling average of the EMG signal, computed over a window size of 30 samples (120ms), is continuously compared to this threshold. If the rolling average exceeds the threshold, the microcontroller drives the motor in one direction to initiate contraction; if it falls below the threshold, the motor is driven in the opposite direction to enable extension. If the encoder count exceeds a pre-configured value corresponding to a comfortable contraction or extension position, the motor halts to prevent over-contraction.

Table 2: Overall Recovr Glove Cost

Item	Cost ($)
Athletic Glove	4.53
Basic Electric Components	14.56
Basic Materials	1.80
EMG Electrode Leads + Stickers	30.99
ESP32C3 Microcontroller	8.00
Lipo Batteries	41.97
12V CB Motor + Encoder	38.90
3D Printed Components	7.97
Total Cost	**148.72**

D. Hardware

Recovr uses electrodes connected to the forearm to acquire sEMG signals, which are initially processed by passive and active filters before being sent to an ESP32C3 microcontroller. This microcontroller controls a brushed DC motor (12V, 5.5A stall current) with encoders that winds and unwinds fishing wire, actively regulating the contraction and passively allowing the rubber bands to control the extension of the hand. Zebco Omniflex Monofilament Fishing Line was used for its strength and flexibility.

E. Affordability

Recovr was designed with accessibility in mind, prioritizing both user comfort and affordability. A detailed cost breakdown of all the physical components of Recovr is provided in Table 2. Current gloves on the market typically exceed $300. To minimize costs, we incorporated a single motor, utilized 3D printing for cost-effective production, and minimized the use of expensive electronic components by employing software filtering. The bulk purchasing of many components could further reduce costs in mass production. However, it is important to note that this cost calculation does not include manufacturing expenses, which could significantly increase the final unit price.

III. Recovr Glove Performance Evaluation

This study focuses on evaluating the functionality and design of Recovr. As such, all experiments were conducted solely to assess the device's technical performance, usability, and effectiveness in simulated scenarios. The following methods were designed to validate its functionality and ensure its readiness for future clinical studies.

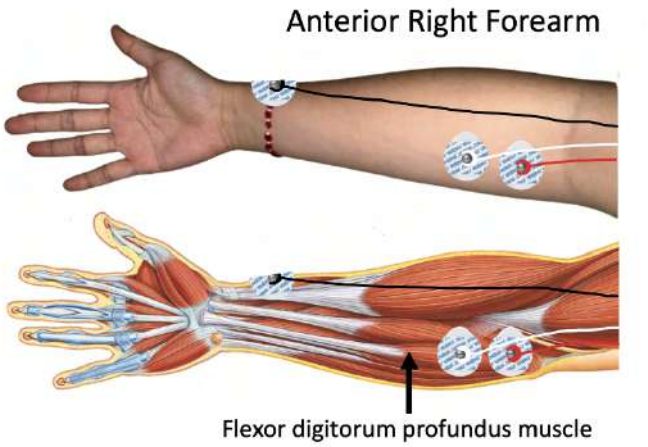


Figure 4: Positive and negative electrodes are placed on the flexor digitorum profundus muscle of the dominant arm to detect sEMG signals. Ground is placed towards the wrist for signal comparison.

Loops/Peg	Thumb	Index	Middle	Ring	Pinky
1	0.8	0.6	0.7	0.3	0.1
2	2.7	2.0	2.2	1.8	0.9
3	4.1	3.9	3.8	3.0	2.8
4	5.8	5.0	6.2	4.8	4.0
5	6.8	6.0	6.6	5.5	4.7
6	7.5	6.2	7.2	6.7	5.6

Table 3: Average Tensile Force Measurements (N) Per Phalange

A. Data Collection

Electrodes were placed on the dominant forearm (Figure 4) to read the sEMG signal and to control the motor. The Recovr glove was fitted to a wooden hand model for testing and evaluation. The device was turned on and the calibration was done by lightly flexing the forearm for approximately 5 seconds, indicated by a blinking LED easily visible to the user near the top of the box before testing began.

1) Grip Strength Testing: We evaluated Recovr's grip strength by contracting the glove around a pneumatic dynamometer squeeze bulb before using its surface area to convert from pressure to force. We conducted three contraction trials and measured an average grip force of approximately 55.21 ± 5.68 N, under full contraction. This makes sense as motor gearbox torque limit is 5 kg-cm with the pulley being a distance of 0.3 inches from the motor shaft.

2) Tensile Force Testing (N): We evaluated the tensile force exerted by the elastic bands wrapped around the hand to determine if they provide sufficient force to assist the fingers into an extended position. The evaluation involved measuring the force applied to a wooden finger as it was moved from a relaxed to a contracted position using a stationary spring scale.

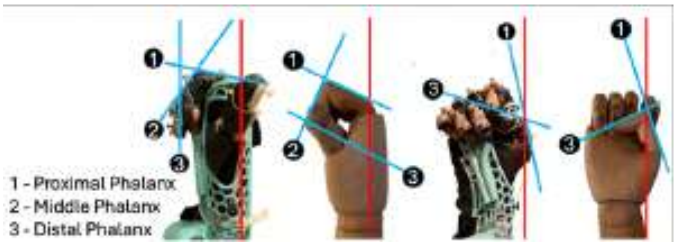


Figure 5: Side and front view of contraction angle of each finger comparing a hand model wearing Recovr to the model hand not wearing Recovr.

The tensile force of the elastic bands required to achieve finger contraction was recorded during testing.

Our measurements indicated that the elastic bands' applied forces ranged from approximately 0.1 N to 5.6 N for the pinky and 0.8 to 7.5 N for the thumb (Table 3).

3) Contraction Angle Analysis: We evaluated the constraints that Recovr may impose on hand movement by conducting an experiment where the wooden hand model was used to form a fist, both with and without wearing gloves. Images were taken from the front of the hand, and from the side (Figure 5). An online protractor was used to measure the angle of the index and thumb phalanx that dictate the shape of a fist relative to the back of the hand. It can be assumed that the other phalanges bend at similar angles as the index when forming a fist. These measurements were taken for both conditions—gloved and ungloved. The percentage difference between these measurements was then calculated. The thumb distal phalanx showed the most impairment, with a percent difference of 22.91%, whereas the index proximal phalanx showed the least at 8.45% (Table 4). This assessment shows that the glove does impair some joint contractions especially in the distal phalanx. Future iterations of the device therefore would need to be altered to allow for a higher range of motion. Although, it can be noted that the wooden glove model is not entirely accurate to a real hand's anatomy and therefore the results are only an indication of actual performance.

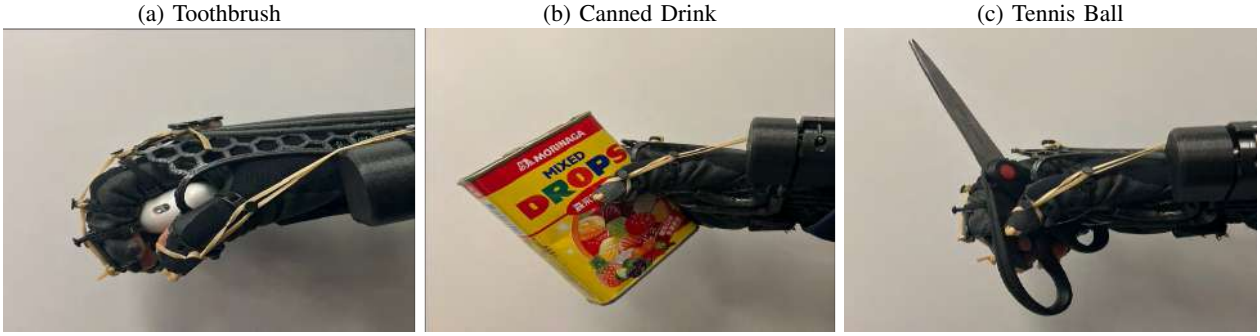
	Proximal Phalanx	Middle Phalanx	Distal Phalanx
Index			
With glove	74	144	180
Without glove	68	158	221
Percent Difference	8.45%	9.27%	20.45%
Thumb			
With glove	14	-	85
Without glove	17	-	107
Percent Difference	19.35%	-	22.91%

Table 4: Joint angles (in degrees) for index and thumb with and without glove using the wooden hand model.

4) Object Grasping: The glove with the wooden hand model was activated via sEMG to grasp and lift six distinct objects vertically: a can, a wire stripper, a multimeter, a



(a) Toothbrush (b) Canned Drink (c) Tennis Ball



(d) AirPods (e) Candy Container (f) Scissor

Figure 6: Object grasping assessment with a variety of objects that one may encounter in daily life.

toothbrush, a cube, and an AirPods case (Figure 6). These objects were deliberately selected to represent a diverse range of shapes from cylinders to spheres to irregular shapes as well as a range of sizes in order to reflect the variety of items individuals typically encounter in daily life. The model hand successfully grasped and lifted each object, maintaining a secure hold at various heights without the objects falling.

5) Motor Response Accuracy: The motor response accuracy was evaluated by instructing when to initiate and stop flexion. A total of 30 trials were conducted with the hand model. These sessions were recorded on camera to measure the latency between the onset of the sEMG signal and the activation of the motor for contraction through post analysis of the videos recorded at 30 fps and converted to seconds. The analysis indicated an average delay of 0.49 ± 0.41 seconds. Additionally, the motor reliably halts upon reaching the pre-configured contraction or extension position. However, in some instances, motor noise caused initial movement in the opposite direction before correcting itself, resulting in 95% accuracy for the motor moving in the intended direction initially.

IV. Discussion

The evaluation of Recovr demonstrates its potential as an effective assistive and rehabilitative device while identifying areas for refinement. The design incorporates key features that aim to balance adaptability, functionality, and user safety. This study provides a systematic assessment of Recovr's capabilities and limitations, offering insights into its current performance and areas for future development.

Recovr's ability to adjust the intensity of grip strength is a critical feature for user adaptability. In our grip strength testing, we observed that Recovr produced an average grip force of approximately 55.21 ± 5.68 N during full contraction. This is more than the maximum force of 20N to sufficiently grasp day-to-day objects for vertical lifting [27], [28].

Moreover, the tensile forces exerted by the elastic bands further highlight Recovr's customizability. By adjusting elastic tension, the device achieved a range of forces from 0.1 to 7.5 N per finger, with potential for higher forces through the use of high-tension elastic bands. This range is consistent with external research, which suggests that a total force between 3.4 N and 12.6 N may be necessary to extend the fingers, depending on the user's level of spasticity [29]. These results demonstrate that the elastic bands are capable of providing adequate assistance for finger extension. This adaptability enables the device to be tailored to individual user needs, including those with spastic clenched fist deformity, where increased resistance must be overcome to facilitate functional hand opening and movement [30].

Contraction angle analysis revealed minimal movement restrictions imposed by Recovr, where the overall limitation was less than 30% for all fingers when not wearing the glove vs. wearing the glove. Although the wooden hand model may have restrictions as previously mentioned, these restrictions did not impede basic grasping tasks, and thus indicates that the glove does not severely limit hand movement and is effective in gross function rehabilitation. Although the performance could be improved with thinner rings that still maintain structural integrity.

The ability to maintain functional grasping, despite minor

movement restrictions, suggests that Recovr's design can be adjusted to provide either increased support for users with severe hand impairments or greater flexibility for those with higher levels of hand mobility. Additionally, Recovr is capable of accommodating a variety of object shapes and sizes. This adaptability is particularly relevant in rehabilitation contexts, where patients often progress through different stages requiring varying levels of assistance.

Further developments may also include obtaining regulatory approval for clinical testing on stroke rehabilitation patients, addressing feedback from subjects and improving motor response. We believe these implementations would not increase costs significantly, if at all.

V. Conclusion

Recovr Glove offers a promising solution for stroke rehabilitation by integrating surface electromyography (sEMG) control with both passive extension and active contraction mechanisms. Our design allows for customization of both fit and support level, making it adaptable to varying degrees of spasticity. Recovr is portable, and user-friendly, ensuring comfort and ease of use during daily activities. Its affordability potential for personalized therapy make it a promising tool for improving hand function and quality of life in stroke survivors. In our preliminary characterization of Recovr, we found that the glove has the ability to effectively support both hand contraction and extension during gross grasping movements. The lack of testing on post-stroke individuals highlights the need for further evaluation, ideally through long-term use by stroke survivors, to draw more robust conclusions about the glove's rehabilitative effectiveness. We plan to conduct additional clinical testing with post-stroke individuals to refine its performance in real-world rehabilitation settings.

ACKNOWLEDGMENT

We want to thank the Bioengineering Department and the George H. Stephenson Foundation Educational Laboratory & Bio-MakerSpace at the University of Pennsylvania for funding this project and providing endless support.

References

[1] S. A. Foundation, "Stroke facts & statistics," 2023. Accessed: 2023-07-11.

[2] T. Ingwersen *et al.*, "Long-term recovery of upper limb motor function and self-reported health: results from a multicenter observational study 1 year after discharge from rehabilitation," *Neurological Research and Practice*, vol. 3, Dec. 2021.

[3] M. Yagi *et al.*, "Impact of rehabilitation on outcomes in patients with ischemic stroke," *Stroke*, vol. 48, pp. 740–746, Mar. 2017.

[4] N. Liu *et al.*, "Randomized controlled trial of early rehabilitation after intracerebral hemorrhage stroke," *Stroke*, vol. 45, pp. 3502–3507, Dec. 2014.

[5] E. R. Coleman *et al.*, "Early rehabilitation after stroke: a narrative review," *Current Atherosclerosis Reports*, vol. 19, Nov. 2017.

[6] S. A. Maulden, J. Gassaway, S. D. Horn, R. J. Smout, and G. DeJong, "Timing of initiation of rehabilitation after stroke," *Archives of Physical Medicine and Rehabilitation*, vol. 86, pp. 34–40, Dec. 2005.

[7] Z.-S. Hosseini, H. Peyrovi, and M. Gohari, "The effect of early passive range of motion exercise on motor function of people with stroke: A randomized controlled trial," *Journal of Caring Sciences*, 2019.

[8] K. Jack, S. M. McLean, J. K. Moffett, and E. Gardiner, "Barriers to treatment adherence in physiotherapy outpatient clinics: a systematic review," *Manual Therapy*, vol. 15, no. 3, pp. 220–228, 2010.

[9] C. E. Proulx, J. Higgins, and D. H. Gagnon, "Occupational therapists' evaluation of the perceived usability and utility of wearable soft robotic exoskeleton gloves for hand function rehabilitation following a stroke," *Disability and Rehabilitation: Assistive Technology*, vol. 18, no. 6, pp. 953–962, 2021.

[10] A. Mohammadi, J. Lavranos, P. Choong, and D. Oetomo, "Flexo-glove: A 3d printed soft exoskeleton robotic glove for impaired hand rehabilitation and assistance," in *2018 40th Annual International Conference of the IEEE Engineering in Medicine and Biology Society (EMBC)*, pp. 2120–2123, 2018.

[11] A. Stilli *et al.*, "Airexglove — a novel pneumatic exoskeleton glove for adaptive hand rehabilitation in post-stroke patients," in *2018 IEEE International Conference on Soft Robotics (RoboSoft)*, pp. 579–584, 2018.

[12] S. Handelzalts, G. Ballardini, C. Avraham, M. Pagano, M. Casadio, and I. Nisky, "Integrating tactile feedback technologies into home-based telerehabilitation: Opportunities and challenges in light of covid-19 pandemic," *Frontiers in Neurorobotics*, vol. 15, Feb. 2021.

[13] D. G. E. K. Jian, Chan and b. . C. l. . S. y. . . p. . . d. . I. T. Kok Kheng, title = Wearable Hand Exoskeleton for Activities of Daily Living

[14] "Understanding the role of the primary somatosensory cortex: Opportunities for rehabilitation," *Neuropsychologia*, vol. 79, pp. 246–255, 2015. Special Issue: Sensory Motor Integration.

[15] N. Bolognini, C. Russo, and D. J. Edwards, "The sensory side of post-stroke motor rehabilitation," *Restorative Neurology and Neuroscience*, vol. 34, no. 4, pp. 571–586, 2016.

[16] Q. Meng, "A survey on semg control strategies of wearable hand exoskeleton for rehabilitation," *2017 2nd Asia-Pacific Conference on Intelligent Robot Systems (ACIRS)*, pp. 165–169, 2017.

[17] K. M. Steele, C. Papazian, and H. A. Feldner, "Muscle activity after stroke: Perspectives on deploying surface electromyography in acute care," *Frontiers in Neurology*, vol. 11, 2020.

[18] G. Francisco, J. Chae, H. Chawla, *et al.*, "Electromyogram-triggered neuromuscular stimulation for improving the arm function of acute stroke survivors: A randomized pilot study," *Archives of Physical Medicine and Rehabilitation*, vol. 79, no. 5, pp. 570–575, 1998.

[19] M. Jochumsen, I. K. Niazi, M. Zia ur Rehman, *et al.*, "Decoding attempted hand movements in stroke patients using surface electromyography," *Sensors*, vol. 20, no. 23, p. 6763, 2020.

[20] I. J. Hubbard, M. W. Parsons, C. Neilson, and L. M. Carey, "Task-specific training: evidence for and translation to clinical practice," *Occupational Therapy International*, vol. 16, pp. 175–189, Sep. 2009.

[21] J. M. Wagner *Clinical Neurophysiology*, vol. 118, pp. 164–176, 2007.

[22] O. Armagan, F. Tascioglu, and C. Oner, "Electromyographic biofeedback in the treatment of the hemiplegic hand: A placebo-controlled study," *American Journal of Physical Medicine & Rehabilitation*, vol. 82, pp. 856–861, Nov. 2003.

[23] W. Hj and P. Cim, "EMG biofeedback for the recovery of motor function after stroke (review)," 2009. Publication details (e.g., journal or publisher) not fully specified.

[24] M. Lyu *et al.*, "Training wrist extensor function and detecting unwanted movement strategies in an EMG-controlled visuomotor task," in *International Conference on Rehabilitation Robotics (ICORR)*, pp. 1549–1555, 2017.

[25] M. Boyer, L. Bouyer, J. S. Roy, and A. Campeau-Lecours, "Reducing noise, artifacts and interference in single-channel emg signals: A review," *Sensors (Basel, Switzerland)*, vol. 23, no. 6, p. 2927, 2023.

[26] S. Bhatlawande, S. Shilaskar, M. Kinge, and A. Mahajan, "Expert system for real time arm movement recognition based on surface emg signal," *Springer Professional*, 2023. Retrieved February 11, 2025.

[27] Y. Hiramatsu *et al.*, "Control of precision grip force in lifting and holding of low-mass objects," *PLOS ONE*, 2015.

[28] H. Khamis, B. Xia, and S. J. Redmond, "Real-time friction estimation for grip force control," in *2021 IEEE International Conference on Robotics and Automation (ICRA)*, pp. 1608–1614, 2021.

[29] S. Kim, J. Lee, and J. Bae, "Analysis of finger muscular forces using a wearable hand exoskeleton system," *Journal of Bionic Engineering*, vol. 14, no. 4, pp. 680–691, 2017.

[30] S. Balakrishnan and A. B. Ward, "The diagnosis and management of adults with spasticity," in *Handbook of Clinical Neurology*, vol. 110, pp. 145–160, Elsevier, 2013.

Digital Design Workflow for Individualized 2-DOF Ankle Exoskeletons

Hunter M. Schmidt, Andy Li, Aytac Teker, Mariana H. Rocha, Biruk A. Gebre,
Karen J. Nolan, Kishore Pochiraju and Damiano Zanotto

***Abstract*— Gait rehabilitation programs aid individuals recovering from brain injury or severe lower-leg trauma. While robotic exoskeletons may offer advantages over traditional exercise-based interventions, their high cost and lack of personalized fit limit their clinical utility. In this paper, we present a new efficient design workflow for individualized 2-DOF ankle exoskeletons. The anatomical orientations of the talocrural and subtalar joints are estimated by utilizing a functional calibration procedure and then embedded and implemented into the ankle exoskeleton. The exoskeleton is fabricated using affordable additive manufacturing processes to conform to the user's leg morphology. This creates a personalized design that encapsulates the envelope of the ankle joint complex motion. By achieving this without the need for kinematic redundancy, we aim at maintaining a lightweight design with reduced mechanical complexity. Early tests with two healthy individuals indicate the feasibility of the proposed approach.**

***Index Terms*— Personalized Ankle Exoskeleton, Robot-Assisted Gait Training, Functional Calibration.**

I. Introduction

The ankle is capable of motion across all three planes (frontal, sagittal, transverse) of the body. On top of this triplanar motion, the joint axes of the ankle are very complex, spanning two non-orthogonal articulations (talocrural and subtalar) [1]. There is currently no consensus on how to identify the orientation of the talocrural and subtalar joints in a non-invasive manner. Additionally, the talocrural joint has been shown to have high interpersonal variability [2]. These characteristics of the ankle joint contribute to the difficulty of creating a robotic orthosis that does not inhibit the ankle's range of motion. Conventional "one-size-fits-all" powered ankle-foot orthoses (AFOs) and ankle exoskeletons can cause discomfort due to excessive rubbing against the wearer's skin. This excessive movement of the exoskeleton relative to the patient's body is caused by misalignment between the exoskeleton joint axis and the anatomical joint axis [3], [4]. One of the primary complaints documented with patient satisfactory surveys regarding AFOs is that they are not comfortable [5]. This may cause the patient to refrain from wearing their AFO. Therefore, it is critical to prioritize user comfort when wearing the AFO and to minimize the AFO's affect of altering the ankle's natural motion during walking tasks.

Two main approaches have been introduced in recent years for reducing misalignments: soft exosuits and multi-degree-of-freedom (DOF) exoskeletons. Soft exosuits are a relatively new addition to the robotic orthosis field. These devices assist two or more limbs without rigidly connecting to them. Hence, they do not introduce misalignment because movement is constrained solely by the anatomical joint. However, the anatomical joint must bear all the forces and torques applied by the device, which limits the magnitude of forces and torques that the exosuit can exert. Most existing ankle exosuits, such as the design by Awad, Bae, and colleagues, are single-DOF devices [6], [7]. Over a decade ago, Park and colleagues introduced the first two-DOF, pneumatically actuated ankle exosuit [8]. However, their innovative design was tethered and its use was limited to ankle mobilization exercises. More recently, Xia *et al.* developed a soft, lightweight ankle exosuit capable of actuating the ankle joint in both the sagittal and frontal planes [9]. This design consists solely of a foot and calf brace. While it demonstrated success in reducing drop foot and stabilizing ankle inversion and eversion, it was tested only at a slow walking speed of 0.7 m/s. Zhang *et al.* designed a two-DOF soft ankle exosuit that includes a foot brace, calf brace, and waist strap [10]. This device was tested primarily during seated ankle movements, with limited testing conducted during walking.

Multi-DOF ankle exoskeletons include two-DOF devices that use the additional joint to better accommodate the range of motion of the ankle, and three-DOF devices wherein kinematic redundancy is leveraged to compensate for joint misalignment between the orthosis axes and the human joints. Several two-DOF powered AFOs have been proposed in attempt to match the two anatomical joints of the ankle. Carberry *et al.* [11] created a symmetric powered exoskeleton with two-DOFs. Elery *et al.* [12] created a spring-powered, lateral, two-DOF AFO. Both designs involve two orthogonal joints for ankle rotation on the sagittal and frontal planes. This allows for an increased range of motion compared with traditional single-DOF AFOs, but prevents foot rotations on the transverse plane. Agrawal *et al.* [13] created a two-DOF AFO with the talocrural and subtalar joints oriented based on the average orientations of the anatomical joints [1]. While this subject-agnostic approach improved the ranges of motion about both joints, large inter-subject variability might restrict its applicability [3]. The design was also relatively bulky, which may negatively impact the wearer's natural gait [14].

H. M. Schmidt, A. Li, and D. Zanotto (dzanotto@stevens.edu) are with the WRS Lab., Stevens Inst. of Technology, Hoboken, NJ 07030, USA.

M. H. Rocha, A. Teker, B. A. Gebre, and K. Pochiraju are with the PROOF Lab., Stevens Inst. of Technology, Hoboken, NJ 07030, USA.

K. J. Nolan is with Human Performance and Engineering Research, Kessler Foundation, West Orange, NJ 07052, USA and Rutgers-NJMS, Newark, NJ 07103, USA.

Similarly, Lee *et al.* [15] created a two-DOF AFO with both joints aligned with the average anatomical joint orientation. Here, a poly-centric linkage joint was placed at the talocrural exoskeleton joint. This aligns the talocrural joint very well, but can make it difficult to actuate this joint due to its increased mechanical complexity. The subtalar joint is also still not aligned with the anatomical joint.

Dežman *et al.* [16] introduced a multi-DOF exoskeleton with three DOFs to accommodate the complex nature of the ankle joint. The redundant design effectively captures the full range of motion of the ankle joint, including compensation for the movement of the ankle joint center of rotation. Notably, it is one of the few designs validated for walking tasks beyond straight-line walking. This is critical for the final phases of rehabilitation to allow for a more seamless transition back into daily life. Although the redundant AFO is effective in mitigating misalignment between the human leg and the orthosis, it increases the mechanical complexity of the AFO, as well as its distal mass, thereby increasing the inertia reflected at the hip joint, which may hamper the wearer's natural gait patterns [14].

In this paper, we introduce an efficient design method for generating fully-constrained, two-DOF personalized ankle exoskeletons. The resulting design (Fig. 1) features two joints, with their alignment calibrated to the average orientations of the wearer's own talocrural and subtalar axes, estimated during functional movements. Compared to a traditional single-DOF design, we show that this approach substantially mitigates misalignment when performing in-place movements and ambulatory tasks, though slight residual misalignment persists due to the inherent movement of the ankle joint center of rotation. To develop this design, the orientation of the two joints on the exoskeleton must be personalized to the user. To this end, we modified the functional calibration technique first introduced by van den Bogert *et al.* [17] and enhanced by Leitch *et al.* [18], to find the orientation of the wearer's anatomical joint axes. The estimated joint axes are then fed into an automated design workflow recently introduced by our team at Stevens Institute of Technology, which generates a subject-tailored AFO model from 3D scans of the wearer's lower leg [19], [20]. The AFO is then fabricated using affordable additive manufacturing processes. To validate the proposed design method, we carried out preliminary tests with healthy individuals who performed several motor tasks using unpowered AFOs.

The remainder of this paper is organized as follows: Section II describes the functional calibration methods used to obtain the subject-specific joint orientations. Section III describes the design workflow that generates personalized Ankle Units. Section IV details the process of fabricating the AFO. Section V describe the experimental validation for preliminary testing of the non-actuated, personalized two-DOF AFO while Section VI summarizes the results from these tests. Lastly, the paper is concluded in Section VII.

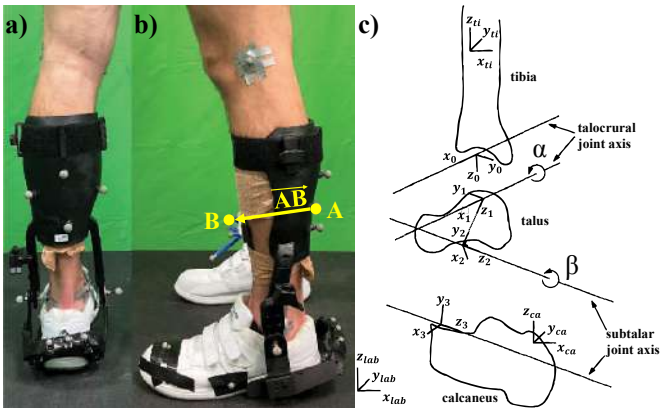


Fig. 1. **(a-b)** Posterior and lateral views of individualized 2-DOF ankle exoskeleton and the marker setup used for validation. **(c)** Twelve-parameter kinematic model of the ankle joint complex (adapted from [17]), with dorsiflexion-plantarflexion (D-P) and inversion-eversion (I-E) rotations labeled as α and β, respectively. This model was used for the functional calibration of the D-P and I-E axes.

II. Ankle Joint Functional Calibration

A. Anatomy of the Ankle Joint Complex

The ankle joint can be modeled by three rigid bodies connected by two non-orthogonal hinge joints (Fig. 1-c). The tibia (shank) is connected to the talus by the talocrural joint. This joint is primarily responsible for the dorsiflexion-plantarflexion (D-P) movement. Due to the orientation of the talocrural joint, it also enables motion across the other biological planes, however this motion is deemed to be negligible compared to the D-P motion [1]. The subtalar joint connects the talus and the calcaneus and is responsible for the coupled motion of inversion-eversion (I-E) and abduction-adduction of the foot. Similarly, this has a small component of D-P motion, but it is also deemed negligible [1].

B. Related Work on Functional Calibration

Functional calibration techniques enable the accurate localization of anatomical joints through sequences of single-axis motions [21], [22]. The functional calibration technique utilized in this work builds upon the method introduced by van den Bogert *et al.* [17]. This method utilizes the ankle joint complex model described in Sec. II-A, wherein the distances and orientations between the shank, the two joints, and the foot are described by a twelve-parameter kinematic model using the Denavit-Hartenberg (DH) convention. For calibration, subjects were instructed to raise their foot while keeping their leg straight, and performed several motions across the range of the D-P and I-E joints [17]. A least-squares optimization was used to find the model parameters, with the initial guess based on the location of the malleoli [17]. While this method produced repeatable results for a single subject, the estimated orientations of the D-P and I-E axes did not match across subjects, highlighting the need for subject-specific models.

Leitch *et al.* expanded upon van den Bogert's method by incorporating additional functional movements into the model, beyond the foot-raised motions, and by performing

walking tasks to validate the model [18]. The additional functional movements included tasks where the subject stood with their foot "planted" on the floor [18]. They also determined the optimal locations for the reflective markers on the shank and the shoe that resulted in the best model fit. While their results confirmed high inter-subject variability in the D-P and I-E axes, emphasizing the need for subject-specific calibration, they also showed that the difference in model fit between the foot-raised and foot-planted calibrations, as evaluated on the walking dataset, were minimal, concluding that both could be used.

C. Modified Functional Calibration Method

The functional calibration method summarized in Sec. II-B was adapted to align with the goal of developing a new personalized two-DOF AFO prototype. Data was collected using an optical motion capture system (Vero 2.2, Vicon Motion Systems, Oxford, U.K.) with 9 cameras, and a split-belt instrumented treadmill (Bertec, Columbus, OH). Four reflective markers on the shank and four on the shoe were placed as in [18] (Fig. 1-a,b). Additionally, two markers were placed at the knee (lateral and medial femoral condyles) and two were placed at the ankle (medial and lateral malleoli) to enable the integration of the results from the functional calibration procedure with the automated AFO design workflow described in Sec. III. Subjects performed nine *foot-raised* and seven *foot-planted* ankle motions, similar to [18], with each motion being repeated three times. The foot-raised motions were dorsiflexion and plantarflexion with the foot in neutral, inverted, and everted positions followed by inversion and eversion with the foot in neutral, dorsiflexed, half-plantarflexed, and full-plantarflexed positions and lastly circular motion in the clockwise and counter-clockwise directions. The foot-planted motions were calf raises with the foot neutral, inverted, and everted followed by quarter squats with the foot neutral, inverted, and everted and lastly swaying side to side. Subsequently, subjects walked for 90 seconds on the treadmill at 1 m/s.

A genetic algorithm (GA) was utilized in place of the least-squares method used in [17], [18] to find the optimal set of twelve DH model parameters (Fig. 1-c) based on the data collected from the foot-raised and foot-planted motions. GA is an evolutionary algorithm that employs heuristic search strategies to solve complex global optimization problems, even in the presence of multiple local minima, without requiring gradient information. The optimization procedure was conducted on a 4.5 GHz AMD Ryzen Threadripper PRO 5975WX with 32 cores, using the `ga` function from MATLAB (The Mathworks Inc., Natick, MA). Appropriate upper and lower bounds were set on each of the twelve DH parameters to constrain the search range to anatomically meaningful values. Additionally, the following GA settings were used, based on preliminary tests: max generations - 3000, population size - 800, function tolerance - 10^{-6}, max stall generations - 60, elite count 40, cross over fraction - 0.9. In line with [17], [18], the difference between the measured coordinates of each foot marker and the corresponding coordinates estimated by the DH model was computed for each foot marker, at each timestamp. The root-mean-square (RMS) difference between measured and predicted coordinates was then selected as the cost function for GA.

III. Personalized Design Workflow

The personalized AFO design workflow is based on shape/size information obtained from a 3D scan of the wearer's leg. It builds upon our previous work in [20], but integrates calibrated D-P and I-E axes derived from the procedure described in Sec. II-C. After the user completes the functional calibration movements, the shank and shoe markers are removed, so that a 3D scan can be captured of the lower leg in neutral pose, with only two markers on the femoral condyles and two on the malleoli. Those four markers serve as reference points for the AFO design, and to locate the calibrated D-P and I-E axes in the coordinate frame of the AFO model.

Similar to [20], the workflow uses five tools implemented in Python and Open3D to derive the AFO design directly from the 3D scan, with minimal manual input (Fig. 2). First, the calibrated D-P axis is imported into Open3D, and virtual markers are added onto the medial and lateral intersections between the calibrated D-P axis and the surface of the user's leg as determined from the point cloud. The *marker detector* identifies the position of the femoral condyles markers and defines anatomical axes based on those two markers and the virtual D-P markers. The *mapper* extracts from the point cloud the portion of the calf surface that is relevant to the design of the AFO shank bracket. The *mesher* tool uses the Poisson Reconstruction Algorithm to produce a triangle mesh from the point cloud. The *slicer* computes a set of closed curves by slicing the mesh with a set of planes orthogonal to the longitudinal axis of the shank and applying a desired thickness determined by strength and kinematic constraints. Next, the *solid generator* creates a 3D object by connecting the contour curves with triangles. This procedure creates a personalized shank bracket that fits the user's calf precisely and aligns with the calibrated D-P axis. More details about the five tools can be found in [20].

The shoe bracket assembly, which includes a gimbal and a main shoe bracket anchored on the user's shoe (Fig. 2), is created following a similar approach. First, the calibrated I-E axis is imported into the model, Next, medial and lateral dropdown links are added to connect the shank bracket to the shoe bracket assembly. These dropdown links allow the shoe bracket assembly to rotate with respect to the shank link about the calibrated D-P axis. The distal ends of the dropdown links are rigidly connected to the gimbal. A curved rail-slider mechanism connects the gimbal to the main shoe bracket, allowing for rotations of the latter about the I-E axis. This mechanism was chosen to avoid a physical joint lying directly on the I-E axis, i.e., above the dorsal foot or posterior to the calcaneous. The posterior location is undesirable due to potential interferences with the ground at initial contacts (heel strikes). The dorsal location results

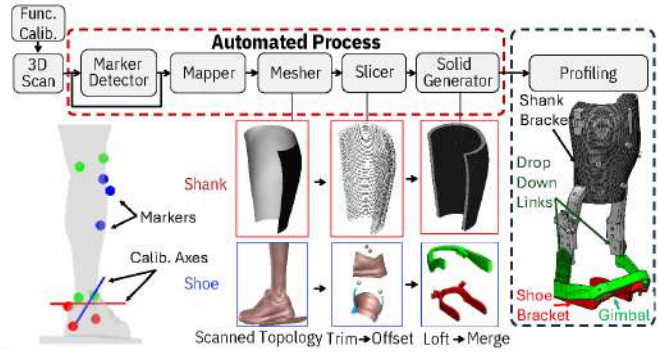


Fig. 2. Digital design workflow to generate personalized shank and shoe brackets for the two-DOF AFO, from a 3D point cloud augmented with the D-P and I-E axes extimated via functional calibration.



Fig. 3. Personalized two-DOF AFO prototype: sagittal plane (top) and frontal plane (bottom) motions.

in cumbersome designs and makes it harder to don/doff the AFO [13]. Conversely, the gimbal-like design allows most AFO components to be located medially and laterally to the hindfoot, enabling rotation about the I-E axis without compromising the ease of donning and doffing the AFO.

IV. AFO Fabrication

Two passive (non-actuated) AFOs were fabricated to evaluate the feasibility of the calibration method and the personalized design workflow (Fig. 3). The two test subjects were healthy male adults in their early-to-mid twenties. The study was approved by the U.S. Army Office of Human Research Oversight (OHRO) under protocol E03214.1a-1, and both participants provided written informed consent. Personalized shank and shoe bracket assemblies were produced using carbon fiber-PLA (CF-PLA) with fused deposition modeling (FDM) 3D printing technology, resulting in a total weight of 0.7 kg for the entire two-DOF AFO structure. In a prior study [23], we demonstrated that the AFO components have a substantial safety factor against anticipated compressive loads. A torque wrench was used to apply simulated D-P assistive torques to the assembly, while the AFO shank was secured to a 3D printed model of the subject's leg. The AFO assembly failed above 60 Nm [23], significantly exceeding the maximum assistive torque of 18 Nm [20]. A 3-mm soft foam layer, contoured to match the inner curvature of the shank via laser-cutting technology, was positioned as a cushioning interface between the shank module and the wearer's skin. The shank was secured to the wearer's shinbone with a wide Velcro strap to ensure comfort.

The shoe bracket assembly, entirely fabricated from CF-PLA, connects the gimbal to the main shoe bracket through a curved rail-slider mechanism. The rail piece comprises two curved sub-rails with identical circular cross-sections, offset from each other to enhance stiffness. The slider piece features two hooks designed with tolerances to snap into place on the rail and slide smoothly over the circular sub-rails during use. Silicone-based lubricant was applied between the hooks and the rails to minimize friction. This specific lubricant was selected for its effectiveness and its non-irritating properties on the skin. For evaluation purposes, a locking mechanism was incorporated into each slider-rail sub-assembly. This mechanism allows a bolt to be inserted into both components, creating a rigid connection between the gimbal and the main shoe bracket and thereby preventing relative I-E rotations between the two pieces.

V. Experimental Validation

For both study participants, the accuracy of the functional calibration method was quantified as the RMS difference between the measured and predicted coordinates of the foot markers during the 90-second walking task collected during the functional calibration procedure (but not used for calibration).

Additional tests were conducted to evaluate the personalized two-DOF AFO design. To this end, each participant was asked to perform two types of motion tasks: a set of 9 foot-raised ankle motions (two repetitions each), identical to the functional calibration movements described in [17], followed by a 90-second treadmill walking bout at 1 m/s. These tasks were repeated under two conditions: with the AFO having a locked I-E axis (1DOF-AFO), and with the AFO having both D-P and I-E axes enabled (2DOF-AFO). During these tests, reflective markers were placed on the AFO and on the participant's lower leg and shoe, as shown in Fig. 1-a,b. These markers were used to evaluate the ranges of motion about the D-P and I-E axes, as well as the relative displacements between the AFO structure and the wearer's leg. D-P and I-E ranges of motions were quantified using the calibrated axes for each subject. Relative displacements between the AFO structure and the human leg were evaluated in terms of maximum percent changes in the distance between markers attached to the AFO shank bracket and the human lower leg (i.e., markers A and B in Fig. 1-b), as described by Langlois *et al.* [24]. Compared to the 1DOF-AFO condition, we hypothesized that the 2DOF-AFO would enable extended D-P and I-E ranges of motion. Additionally, we hypothesize that the 1DOF-AFO condition would result in larger relative displacements, indicative of misalignment between AFO joints and human articulation [24].

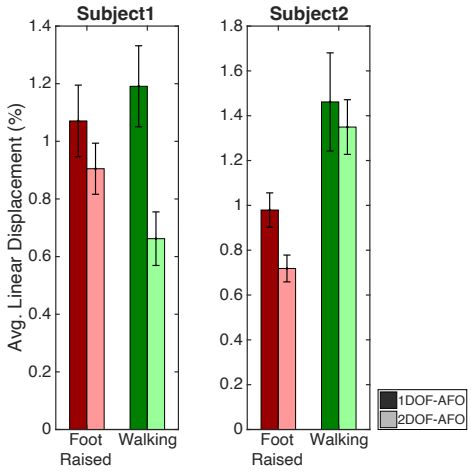


Fig. 4. Relative displacements between the AFO structure and the human leg during foot-raised tasks and treadmill walking task, under the 1DOF-AFO and 2DOF-AFO conditions, averaged across all repetitions/gait cycles. Error bars indicate ±1SE.

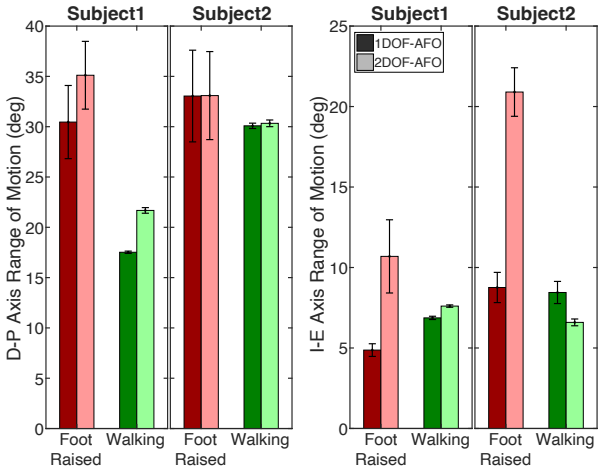


Fig. 5. Ranges of motion about D-P (left) and I-E (right) axes during foot-raised tasks and treadmill walking task, under the 1DOF-AFO and 2DOF-AFO conditions, averaged across all repetitions/gait cycles. Error bars indicate ±1SE.

VI. Results

A. Evaluation of Functional Calibration Method

To confirm convergence of the GA to a global optimum, the optimization procedure was run three times for each study participant. It took approximately 45 minutes for the optimization procedure to converge. Variations in each of the estimated DH parameters across all repetitions never exceeded ±0.25 rad and ±7.5 mm for angular and linear parameters, respectively, with over half remaining within ±0.15 rad and ±2.5 mm. These relatively small variations indicated that the method can converge in a single run – an evident advantage of the proposed GA-based approach over previous implementations that relied on non-linear least-squares optimization [17], [18], which is prone to falling into local minima and thus requires careful trial-and-error tuning [18]. Residuals (evaluated on the calibration dataset) were within ±0.3 mm for all 12 DH parameters, in line with previous works [17], [18]. The RMS difference between measured and predicted coordinates was 2.77 mm and 3.23 mm for the two participants, again aligned with previous works [18].

Figure 4 indicates the relative displacements between the AFO structure and the human leg during foot-raised tasks and treadmill walking tasks. For both participants, there was a noticeable reduction in these relative displacements when both DOFs were enabled (2DOF-AFO condition), indicating better fit.

Figures 5 illustrates the range of motion (ROM) of the ankle measured about the D-P and I-E axes during foot-raised tasks and treadmill walking tasks. The 2DOF-AFO configuration consistently enabled larger ROM during foot-raising tasks across individuals, though differences in D-P ROM between the two configurations were minimal for the second subject. The discrepancies in the I-E ROM was likely due to anatomical inter-subject variability. This finding suggests that the personalized two-DOF AFO design effectively encapsulates more of the range of motion of the ankle joint complex compared to the single-DOF configuration. For the treadmill walking task, the 2DOF-AFO condition resulted in increased D-P and I-E ROM for subject 1, while subject 2 exhibited a slight increase in D-P ROM and a noticeable decrease in I-E ROM. This discrepancy might be attributed to the nature of the walking task, which does not require significant ankle motion in the frontal plane.

VII. Discussion and Conclusion

In this paper, we introduced a novel design workflow for a personalized two-DOF AFO with both joints aligned with the anatomical D-P and I-E joints of the user. By building off of previous functional calibration algorithms, we developed an efficient GA-based optimization procedure capable of accurately estimating the twelve parameters modeling the wearer's ankle joint complex. Additionally, by leveraging the personalized shank and shoe bracket design workflow from our previous work [20], we integrated the calibrated joint axes into an AFO structure that conforms to the morphology of the wearer's leg. Unlike recently proposed multi-DOF AFO designs [16], [25], the proposed AFO encompasses a considerable portion of the range of motion of the ankle joint complex without relying on kinematic redundancy. This approach enables efficient fabrication while maintaining a lightweight, simple, and affordable design. However, it requires additional lead time—approximately 30 minutes for functional calibration and 15 minutes for leg scans—to generate personalized shank and shoe brackets.

When unlocked, the AFO I-E axis was successful in reducing relative displacements between the wearer's shank and the AFO structure during in-place foot-raised tasks and walking, indicating that the two-DOF version of our AFO more accurately aligns with the anatomical joints and may reduce user discomfort [24]. Similarly, the increased range of motion for foot-raised tasks with both DOFs unlocked demonstrates that the design encapsulates the ankle complex

motion well. The mixed results obtained during treadmill walking warrant further investigation, but can be contributed to the fact that treadmill walking does not require significant ankle motion in the frontal plane.

The preliminary validation of the AFO design was conducted with a small number of able-bodied subjects and a limited set of motion tasks. Expanding the scope to include a broader range of ambulatory tasks and testing the prototype on a larger sample will be essential to confirm the findings. Collecting data from ambulatory tasks performed without the AFO will also provide valuable insights for comparing the ROM of the D-P and I-E axes to baseline values. The single-DOF configuration still permitted some movement about the I-E axis, even when that axis was mechanically locked, suggesting that the current locking mechanism should be improved before future tests. Additionally, the AFO was non-actuated in this study. Given the serial configuration of the D-P and I-E axes in the design, we do not anticipate significant spurious forces or moments along the I-E axis resulting from the application of assistive torques about the D-P axis. However, further testing with an actuation unit [20] will be necessary to validate this hypothesis.

ACKNOWLEDGMENT

This work was supported by the U.S. National Science Foundation under Grant CMMI-1944203 and by the US Department of Defense, through the Peer Reviewed Orthopaedic Research Program (PRORP), under Award No. W81XWH-22-1-0193. Opinions, interpretations, conclusions and recommendations are those of the author and are not necessarily endorsed by the US Department of Defense.

REFERENCES

[1] M. Nordin and V. H. Frankel, "Basic biomechanics of the musculoskeletal system," *Lippincott Williams & Wilkins google scholar*, vol. 4, 2012.

[2] L. Claassen, P. Luedtke, D. Yao, S. Ettinger, K. Daniilidis, A. M. Nowakowski, M. Mueller-Gerbl, C. Stukenborg-Colsman, and C. Plaass, "The geometrical axis of the talocrural joint—suggestions for a new measurement of the talocrural joint axis," *Foot and Ankle Surgery*, vol. 25, no. 3, pp. 371–377, 2019.

[3] R. L. Andrade, J. Figueiredo, P. Fonseca, J. P. Vilas-Boas, M. T. Silva, and C. P. Santos, "Human-robot joint misalignment, physical interaction, and gait kinematic assessment in ankle-foot orthoses," *Sensors*, vol. 24, no. 1, p. 246, 2023.

[4] D. Zanotto, Y. Akiyama, P. Stegall, and S. K. Agrawal, "Knee joint misalignment in exoskeletons for the lower extremities: Effects on user's gait," *IEEE Transactions on Robotics*, vol. 31, no. 4, pp. 978–987, 2015.

[5] K. Malkin, J. Dawson, R. Harris, G. Parfett, P. Horwood, C. Morris, and G. Lavis, "A year of foot and ankle orthotic provision for adults: prospective consultations data, with patient satisfaction survey," *The Foot*, vol. 18, no. 2, pp. 75–83, 2008.

[6] L. N. Awad, J. Bae, K. O'Donnell, S. M. M. D. Rossi, K. Hendron, L. H. Sloot, P. Kudzia, S. Allen, K. G. Holt, T. D. Ellis, and C. J. Walsh, "A soft robotic exosuit improves walking in patients after stroke," *Science Translational Medicine*, vol. 9, no. 400, p. eaai9084, 2017.

[7] J. Bae, C. Siviy, M. Rouleau, N. Menard, K. O'Donnell, I. Geliana, M. Athanassiu, D. Ryan, C. Bibeau, L. Sloot, P. Kudzia, T. Ellis, L. Awad, and C. J. Walsh, "A lightweight and efficient portable soft exosuit for paretic ankle assistance in walking after stroke," in *2018 IEEE Int. Conf. on Robotics and Automation (ICRA)*, 2018, pp. 2820–2827.

[8] Y.-L. Park, B. rong Chen, N. O. Pérez-Arancibia, D. Young, L. Stirling, R. J. Wood, E. C. Goldfield, and R. Nagpal, "Design and control of a bio-inspired soft wearable robotic device for ankle–foot rehabilitation," *Bioinspiration Biomimetics*, vol. 9, no. 1, p. 016007, jan 2014.

[9] H. Xia, J. Kwon, P. Pathak, J. Ahn, P. B. Shull, and Y.-L. Park, "Design of a multi-functional soft ankle exoskeleton for foot-drop prevention, propulsion assistance, and inversion/eversion stabilization," in *2020 8th IEEE RAS/EMBS Int. Conf. for Biomedical Robotics and Biomechatronics (BioRob)*, 2020, pp. 118–123.

[10] X. Zhang, Y.-X. Liu, R. Wang, and E. M. Gutierrez-Farewik, "Soft ankle exoskeleton to counteract dropfoot and excessive inversion," *Frontiers in Neurorobotics*, vol. 18, p. 1372763, 2024.

[11] J. Carberry, G. Hinchly, J. Buckerfield, E. Tayler, T. Burton, S. Madgwick, and R. Vaidyanathan, "Parametric design of an active ankle foot orthosis with passive compliance," in *2011 24th Int. Symposium on Computer-Based Medical Systems (CBMS)*, 2011, pp. 1–6.

[12] T. Elery, E. Reznick, S. Shearin, K. McCain, and R. D. Gregg, "Design and initial validation of a multiple degree-of-freedom joint for an ankle-foot orthosis," *Journal of Medical Devices*, vol. 16, no. 2, p. 021001, 2022.

[13] A. Agrawal, V. Sangwan, S. K. Banala, S. K. Agrawal, and S. A. Binder-Macleod, "Design of a novel two degree-of-freedom ankle-foot orthosis," *Journal of Mechanical Design*, 2007.

[14] X. Jin, Y. Cai, A. Prado, and S. K. Agrawal, "Effects of exoskeleton weight and inertia on human walking," in *2017 IEEE Int. Conf. on Robotics and Automation (ICRA)*, 2017, pp. 1772–1777.

[15] T. Lee, I. Kim, and Y. S. Baek, "Design of a 2dof ankle exoskeleton with a polycentric structure and a bi-directional tendon-driven actuator controlled using a pid neural network," in *Actuators*, vol. 10, no. 1. MDPI, 2021, p. 9.

[16] M. Dežman, C. Marquardt, and T. Asfour, "Ankle exoskeleton with a symmetric 3 dof structure for plantarflexion assistance," in *2024 IEEE Int. Conf. on Robotics and Automation (ICRA)*, 2024, pp. 3227–3233.

[17] A. J. van den Bogert, G. D. Smith, and B. M. Nigg, "In vivo determination of the anatomical axes of the ankle joint complex: an optimization approach," *Journal of biomechanics*, vol. 27, no. 12, pp. 1477–1488, 1994.

[18] J. Leitch, J. Stebbins, and A. B. Zavatsky, "Subject-specific axes of the ankle joint complex," *Journal of biomechanics*, vol. 43, no. 15, pp. 2923–2928, 2010.

[19] B. A. Gebre, R. Nogueira, S. Patidar, R. Belle-Isle, K. Nolan, K. Pochiraju, and D. Zanotto, "Efficient digital modeling and fabrication workflow for individualized ankle exoskeletons," in *ASME Int. Mechanical Engineering Congress and Exposition*, vol. 85598. American Society of Mechanical Engineers, 2021, p. V005T05A068.

[20] M. T. Eraky, A. Li, M. H. Rocha, A. Teker, B. A. Gebre, K. J. Nolan, K. Pochiraju, and D. Zanotto, "A novel personalized ankle exoskeleton with co-located sea for gait training," in *2024 10th IEEE RAS/EMBS Int. Conf. for Biomedical Robotics and Biomechatronics (BioRob)*, 2024, pp. 1715–1720.

[21] J. Favre, R. Aissaoui, B. Jolles, J. de Guise, and K. Aminian, "Functional calibration procedure for 3d knee joint angle description using inertial sensors," *Journal of Biomechanics*, vol. 42, no. 14, pp. 2330–2335, 2009.

[22] G. Ligorio, D. Zanotto, A. Sabatini, and S. Agrawal, "A novel functional calibration method for real-time elbow joint angles estimation with magnetic-inertial sensors," *Journal of Biomechanics*, vol. 54, pp. 106–110, 2017.

[23] M. Hernandez, A. Teker, M. T. Eraky, A. Li, B. A. Gebre, D. Zanotto, and K. Pochiraju, "Optimized design workflow for patient-customized composite orthotics," *Proceedings of the 39th American Society for Composites Technical Conf.*, vol. 1, no. 188632, 2024.

[24] K. Langlois, M. Moltedo, T. Bacek, C. Rodriguez-Guerrero, B. Vanderborght, and D. Lefeber, "Design and development of customized physical interfaces to reduce relative motion between the user and a powered ankle foot exoskeleton," in *2018 7th IEEE Int. Conf. on Biomedical Robotics and Biomechatronics (Biorob)*, 2018, pp. 1083–1088.

[25] K. Pruyn, R. Murray, L. Gabert, and T. Lenzi, "Autonomous powered ankle exoskeleton improves foot clearance and knee hyperextension after stroke: A case study," *IEEE Transactions on Medical Robotics and Bionics*, pp. 1–1, 2024.

An Offline Reinforcement Learning-Based Auto-Tuning Framework for Continuous Impedance Control in Powered Prostheses

Woolim Hong[1], Abbas Alili[2], and He (Helen) Huang[1]

***Abstract*— A continuous impedance control framework has recently gained attention in powered prosthesis control for its ability to mimic human behavior by smoothly and continuously modulating joint impedance. While recent advancements in tuning this framework have enabled more personalized control for walking, the manual tuning process remains time-intensive and empirical, limiting its scalability and adaptability. To address this challenge, we propose a reinforcement learning (RL)-driven framework for offline tuning, focusing on stiffness parameters that play a critical role in shaping knee kinematics during walking. A Gaussian Process Regression (GPR)-based Continuous Stiffness-Kinematics (CSK) model was developed to predict knee kinematics based on stiffness parameters, trained and validated using experimental data from four participants. Leveraging the Deep Deterministic Policy Gradient (DDPG) algorithm, we optimized stiffness parameters in offline, significantly reducing the need for manual adjustments. Validation results confirmed the reliability of the CSK model in capturing the relationship between stiffness parameters and knee kinematics, as well as the feasibility of the RL framework for offline tuning. This study demonstrates the potential of RL-driven tuning to enhance prosthesis control for walking within a continuous impedance control framework. Future work will focus on integrating offline-trained policies into an online human-in-the-loop framework, enabling adaptive and personalized real-time control while extending functionality to a broader range of ambulation tasks.**

I. Introduction

A recent study estimated that over 2 million individuals in the United States are living with limb loss, with this number projected to increase by 145% by 2060 due to the rising prevalence of vascular diseases and diabetes [1]. Lower-limb amputation profoundly impacts individuals both physically and psychologically, increasing the risk of falls and injuries while also restricting their ability to participate in daily activities and engage with their communities [2], [3]. For decades, powered prostheses (i.e., robotic prostheses) have been studied to restore a more natural gait and enable enhanced mobility in dynamic scenarios such as navigating ramps [4], [5] and stairs [6], [7]. These advanced devices have demonstrated significant potential, offering improved functionality alongside clinical benefits such as enhanced symmetry [8], [9], reduced metabolic energy expenditure [10], and greater overall mobility [11].

Impedance control is a widely used approach for controlling powered prostheses due to its compliant behavior, which allows adaptation to varied terrains and facilitates safe locomotion [12]–[14]. Traditional impedance control frameworks typically feature 4–5 discrete states, each governed by specific impedance parameters, including stiffness, damping, and equilibrium angle. These parameters are fine-tuned based on user feedback, clinical observations, or the requirements of specific tasks such as ramps or stair navigation [15]–[17]. However, the piecewise nature of these frameworks often results in reduced accuracy and mechanical jerkiness in prosthesis control [18], [19]. In contrast, humans control their movements by continuously modulating joint impedance during locomotion [20]–[22], making continuous impedance control a promising alternative for powered prosthesis control. This approach offers a more human-like control strategy, enabling smoother and more natural movements [5], [23]. A key challenge, however, lies in estimating human joint impedance in a continuous manner. Previous studies using perturbation systems have empirically estimated human ankle joint impedance, identifying a certain trend throughout the gait cycle [24], [25]. Building on these findings, researchers introduced linearly varying joint impedance parameters for prosthesis control, including stiffness and damping [23], [26]. More recently, data-driven methods have been developed to derive joint impedance and directly apply it to powered prosthesis control [5], [19]. For example, Best et al. used constrained convex optimization to generate a continuously varying impedance model—encompassing stiffness, damping, and equilibrium angle—achieving global optimality across various slopes and walking speeds [5]. This method has been further extended to accommodate sit/stand [9] and stair ascent/descent [7], demonstrating its versatility and effectiveness in enhancing prosthesis functionality.

Although generalized models are versatile, they lack the adaptability required for personalization, as their parameters are predetermined through offline optimization and fail to account for individual differences in physiological traits and preferences [27]. Specifically, these models are often derived from data collected from able-bodied (AB) individuals, which may not adequately represent the physiological differences between AB and amputee populations. As a result, adjustments are necessary to address the unique needs of amputees more effectively. Personalization is crucial for delivering tailored assistance to individuals when controlling powered prostheses [14], [28], particularly considering that

This work was supported by the National Science Foundation (NSF #2211739) and by the National Institute on Disability, Independent Living, and Rehabilitation Research (NIDILRR #90ARHF0004 and #90SFGE0050).

[1]Woolim Hong and He (Helen) Huang are with the UNC/NCSU Joint Department of Biomedical Engineering, North Carolina State University, Raleigh, NC 27695, USA, and also with the University of North Carolina at Chapel Hill, Chapel Hill, NC 27599, USA. whong3@ncsu.edu, hhuang11@ncsu.edu

[2]Abbas Alili is with the Department of Electrical and Computer Engineering, North Carolina State University, Raleigh, NC 27695, USA. aalili@ncsu.edu

approximately 68% of amputees use a prosthesis for at least seven hours per day [2]. Despite its importance, the personalization of continuous impedance control remains largely unexplored. A key challenge lies in effectively characterizing continuous impedance curves with a reasonable number of adjustable parameters. Reducing the dimensionality of these parameters is crucial, as higher-dimensional parameter spaces demand significant tuning effort, making manual or automatic adjustments impractical [29]. This challenge is further amplified when accounting for multiple joints (e.g., knee-ankle prostheses) or diverse ambulation modes (e.g., slope and stair walking), where the tuning burden and computational cost become overwhelming. To address this, our previous work introduced the use of Principal Component Analysis (PCA) to parameterize continuous impedance functions, streamlining the personalization process for powered prostheses [30], [31]. Despite inherent individual variability, human locomotion shares common physiological traits [32], [33], making PCA an effective tool for capturing these shared characteristics in joint impedance functions. Through PCA, we identified six principal components (PCs)—two each for stiffness, damping, and equilibrium angle—and used their weights as tuning parameters. This approach enabled the personalization of impedance functions for powered prosthesis control by tuning the given parameters to achieve the target knee kinematics [31]. However, while this significantly simplified the tuning dimension, manual adjustments remain inefficient, and automated tuning processes are becoming increasingly necessary. Reinforcement learning (RL) presents a promising approach for automatic prosthesis tuning. RL-based methods can dynamically learn and adjust tuning policies in real time, optimizing performance by adapting parameters as needed. These methods have demonstrated both feasibility and robustness, effectively fine-tuning prosthesis control as the wearer-prosthesis system evolves [34]–[36].

To the best of our knowledge, auto-tuning within the continuous impedance control framework has yet to be explored. This study aims to address this gap by implementing RL to automate the tuning process for continuous impedance control. Specifically, we focus on offline training and validating the trained RL policy to achieve a target knee profile. The main contributions of this work are (1) developing an RL-based auto-tuning scheme for a continuous impedance control framework, (2) conducting offline training to establish an initial policy, and (3) validating the performance of the offline-trained RL policy.

II. Methods

A. Continuous Impedance Control Framework

Knee joint impedance was determined through convex optimization by aligning the generated torque $\hat{\tau}$ from the impedance controller (1) with the human knee joint torque τ obtained from Camargo et al., which was based on data from 20 AB individuals [37].

$$\hat{\tau} = f_K(\phi) \cdot (\theta - f_{EQ}(\phi)) + f_D(\phi) \cdot \dot{\theta} \tag{1}$$

where $f_K(\phi)$, $f_D(\phi)$, and $f_{EQ}(\phi)$ represent the knee stiffness, damping, and equilibrium angle functions, respectively. The phase variable $\phi \in [0, 1]$ denotes the user's gait phase within the gait cycle, while θ and $\dot{\theta}$ correspond to the measured human knee angle and velocity. The stiffness and damping functions were modeled as fourth-order polynomials, while the equilibrium angle function was defined as a sixth-order polynomial, as given in (2). The polynomial coefficients for stiffness, damping, and equilibrium angle–denoted as k_i, d_i, and e_i, respectively–were estimated via convex optimization [30].

$$f_K(\phi) = \sum_{i=0}^{4} k_i \phi^i,\ f_D(\phi) = \sum_{i=0}^{4} d_i \phi^i,\ f_{EQ}(\phi) = \sum_{i=0}^{6} e_i \phi^i \tag{2}$$

Each individual's stiffness ($f_K(\phi)$), damping ($f_D(\phi)$), and equilibrium angle ($f_{EQ}(\phi)$) functions can be obtained through offline optimization. While gait patterns vary across individuals, there are shared characteristics due to fundamental human gait traits [32], [33]. To capture these shared gait features from 20 AB individuals, we employed PCA to reduce the dimensionality of the impedance functions by identifying key components that account for most of the variance [4], [38]. These PCs were extracted during the offline process, and their corresponding weights are used as tuning parameters for fine-tuning of the impedance functions. We selected the first two PCs for each impedance function (PC_1, PC_2), as they capture the majority of variance. The impedance functions can then be reconstructed using these two PCs and their associated coefficients, as shown in (3).

$$\begin{aligned} f_K(\phi) &= K_1 \cdot PC_1^k(\phi) + K_2 \cdot PC_2^k(\phi) \\ f_D(\phi) &= D_1 \cdot PC_1^d(\phi) + D_2 \cdot PC_2^d(\phi) \\ f_{EQ}(\phi) &= E_1 \cdot PC_1^{eq}(\phi) + E_2 \cdot PC_2^{eq}(\phi) \end{aligned} \tag{3}$$

Our earlier findings revealed that stiffness parameters play a more significant role than damping parameters in influencing knee kinematics [31]. Building on this insight, this study focuses on implementing an RL-driven offline tuning framework exclusively for stiffness parameters K_1 and K_2.

B. Data-Driven Continuous Stiffness-Kinematics Model

To develop an offline RL training model for the continuous impedance control framework, it is crucial to establish the relationship between stiffness parameters (inputs) and knee kinematics from the prosthesis (outputs). To achieve this, we employed Gaussian Process Regression (GPR) to construct the Continuous Stiffness-Kinematics (CSK) model, enabling dynamic prediction of knee kinematics based on the stiffness parameters K_1 and K_2, as illustrated in Fig. 1. GPR was chosen for its ability to adapt flexibly to complex, nonlinear relationships between stiffness parameters and knee kinematics while providing a robust solution with high predictive accuracy, even with relatively limited data.

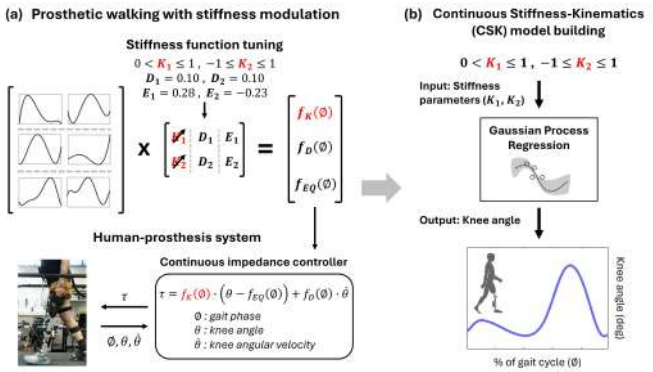


Fig. 1. Building the Continuous Stiffness-Kinematics (CSK) model using Gaussian Process Regression (GPR): (a) Data collection from prosthetic walking: During walking, the stiffness parameters (K_1 and K_2) were modulated, and the resulting knee kinematics were recorded from four participants. (b) Model construction: Using the collected prosthetic walking data, the CSK model was developed via GPR, with stiffness parameters as inputs and knee kinematics as outputs.

1) Data collection: As shown in Fig. 1a, the CSK model was trained using walking experiment data collected from four participants: three AB individuals and one transfemoral amputee (all male, 31.5±3.35 years, 171.4±2.82 cm, 72.6±5.90 kg). A powered knee prosthesis prototype, controlled by the continuous impedance controller, was used for the experiments [31]. All participants were given sufficient training time to ensure they could walk comfortably with the prosthesis. Safety measures included handrails on both sides of the treadmill and a ceiling-mounted harness for fall prevention. Written informed consent was obtained from all participants, and the study protocol was reviewed and approved by the Institutional Review Board (IRB) of North Carolina State University (#24356). Each participant walked for over 30 combinations of K_1 and K_2, with each trial lasting 30 seconds, during which knee kinematics were recorded; the AB participants used an adapter to walk with the prosthesis, while the amputee participant used his daily-use socket to connect to the prosthesis. The stiffness parameters were varied within the range of $0< K_1 \leq 1$ and $-1\leq K_2 <1$, while the damping and equilibrium parameters were held constant at (D_1, D_2) = (0.10, 0.10) and (E_1, E_2) = (0.28, -0.23), respectively.

2) CSK model training: To prevent overfitting to specific participants or experimental conditions, we trained the GPR model on experimental data from four participants and performed 3-fold cross-validation. Using sets of stiffness parameters (K_1, K_2) and PCs, the knee stiffness functions (3) were calculated to serve as the input dataset for the CSK model and the corresponding measured knee kinematics served as the output dataset (see Fig. 1b). A sparse Gaussian Process model was implemented using MATLAB's $fitrgp$ function (R2024b, MathWorks, Natick, MA, USA) to ensure computational efficiency for real-time applications and minimize training and prediction times [39]. Additionally, automatic hyperparameter optimization was performed during training to enhance the CSK model's predictive accuracy and performance.

C. RL Framework for Offline Tuning

In our previous work, we demonstrated that tuning stiffness parameters in continuous impedance control effectively achieves the desired knee profile. [31]. However, manual tuning is inherently empirical and time-intensive, making the process challenging. To overcome this limitation, we propose an RL-based approach for tuning the stiffness parameters of a continuous impedance controller. This study focuses specifically on offline training, leveraging the CSK model to identify an optimal policy adaptable to different participants, as depicted in Fig. 2.

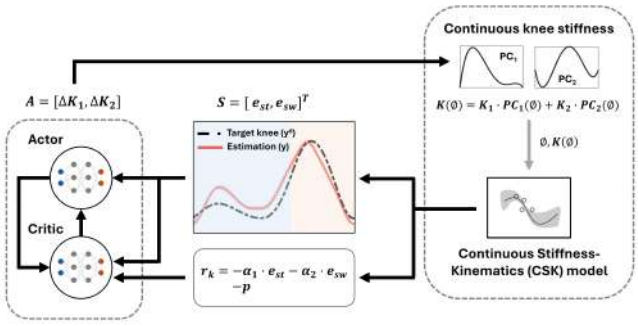


Fig. 2. Offline training process of the RL agent. The RL agent is trained offline to tune the stiffness parameters (K_1 and K_2) using the state variable (S), action variable (A), and reward (r_k). Knee kinematics are predicted using the CSK model based on the given stiffness parameters.

1) RL framework design: The RL framework optimizes two stiffness parameters (K_1 and K_2) by updating them every four gait cycles within each episode. To encourage exploration, these parameters are randomized at the start of each episode within a predefined range. The state variables, $S \in R^2$, are derived from the root-mean-square errors (RMSEs) between the predicted knee kinematics (y) and the desired knee kinematics (y^d) during the stance (e_{st}) and swing (e_{sw}) phases. The action variables, $A \in R^2$, represent updates to the stiffness parameters, defined as (4):

$$S = [e_{st}, e_{sw}], \quad A = [\Delta K_1, \Delta K_2] \tag{4}$$

where $e_{st} = \sqrt{\sum_{i=1}^{N_{st}} \frac{(y_i - y_i^d)^2}{N_{st}}}$ and $e_{sw} = \sqrt{\sum_{j=1}^{N_{sw}} \frac{(y_j - y_j^d)^2}{N_{sw}}}$, with N_{st} and N_{sw} representing the number of data points in the stance and swing phases, respectively.

2) Reward function design: The reward function, r_k, for each update step k, is designed to penalize errors and prevent undesirable conditions:

$$r_k = -\alpha_1 \cdot e_{st} - \alpha_2 \cdot e_{sw} - p \tag{5}$$

where p, the penalty term, is defined as:

$$p = \begin{cases} 100, & \text{if } K < 0 \text{ or y} < \text{-}10^\circ \\ 0, & \text{otherwise.} \end{cases} \tag{6}$$

The coefficients α_1 and α_2 are set to 0.6 and 0.4, respectively, to prioritize minimizing stance phase errors, which are more critical and perceptible than swing phase errors [27]. In the reward function, the first two terms penalize stance and swing errors, while the penalty term prevents negative stiffness values and excessive knee hyperextension; a penalty is applied when the knee angle exceeds -10° to ensure a safety margin of 2°, considering the prosthesis hardware constraint of -12° for hyperextension.

3) Actor-Critic network design: The RL model was trained using the Deep Deterministic Policy Gradient (DDPG) algorithm, including two neural networks [40]:

- Actor network – Maps the input state vector S to an action vector $A(\mu(S))$.
- Critic network – Estimates the long-term discounted reward $Q(S, A)$ using the Bellman equation.

Both networks were implemented and trained using MATLAB's Reinforcement Learning Toolbox (R2024b, MathWorks, Natick, MA, USA). In the actor network, the state input is passed through two fully connected layers, each with 250 neurons, followed by ReLU activation and batch normalization layers to enable nonlinear transformations. The final action output layer applies a $tanh$ activation to constrain actions to the range $[-1, 1]$, followed by a scaling layer to match the stiffness parameter range. The critic network takes two inputs: the state vector (S) and the action vector (A). Each input is processed separately through fully connected layers with 250 neurons, followed by batch normalization and ReLU activation. These processed inputs are combined and passed through an additional fully connected layer with batch normalization, ReLU activation, and a final output layer.

4) RL training workflow: At the start of training, the weights of the actor (μ) and critic (Q) networks were randomly initialized. Target networks (μ' and Q') were also created with identical structures and initialized weights: $\theta^{\mu'}$ and $\theta^{Q'}$. Training was conducted up to 1,000 episodes, with stiffness parameter sets randomized at the start of each episode. During each update step k, the knee kinematics were predicted using the CSK model based on the current stiffness parameters. The state vector S_k and reward r_k were computed as defined in (5). The actor network generated the action vector A_k, augmented with a noise vector N_m from an Ornstein-Uhlenbeck process to promote exploration [40]:

$$A_k = \mu(S_k) + N_m. \tag{7}$$

A minibatch of N transitions was sampled randomly from a replay buffer for network weight updates:

- Critic update: The critic weights were updated by minimizing the loss function (8):

$$L_Q = \frac{1}{N}\sum_i (y_i - Q(S_i, A_i|\theta^Q))^2. \tag{8}$$

where y_i, derived from the Bellman equation (9), represents the target value, and γ is the discount factor:

$$y_i = r_i + \gamma Q'(S_{i+1}, \mu'(S_{i+1})). \tag{9}$$

- Actor update: The actor weights were updated to maximize the long-term discounted reward using the policy gradient optimization (10):

$$\nabla_{\theta^\mu} J = \frac{1}{N}\sum_i \nabla_A Q(S_i, \mu(S_i)) \nabla_{\theta^\mu} \mu(S_i). \tag{10}$$

- Target network update: The target actor ($\theta^{Q'}$) and critic ($\theta^{\mu'}$) weights were updated using a soft update rule (11):

$$\theta^{Q'} = \tau \cdot \theta^{Q} + (1-\tau)\cdot\theta^{Q'}, \;\; \theta^{\mu'} = \tau \cdot \theta^{\mu} + (1-\tau)\cdot\theta^{\mu'}. \tag{11}$$

III. Results and Discussion

A. CSK Model Validation

To validate the trained CSK model, we computed the RMSE for both the training and testing datasets to assess potential overfitting and evaluate the model's generalization ability. Figure 3a presents the RMSE results for the training and testing sets across three folds: 3.4193±1.4224 for training and 3.5348±0.9372 for testing. The model exhibited consistent predictive performance across folds, with training and testing RMSE values remaining within a similar range, suggesting less likely overfitting. The error bars represent the standard deviation across the three folds, reflecting the variability in prediction accuracy. Figure 3b illustrates the predicted knee kinematics over the gait cycle for each fold. The solid lines represent the mean predicted trajectory, while the shaded regions indicate the standard deviation, capturing variability in predictions across different participants and stiffness conditions. The results confirm that the CSK model generalizes well across different participants and varying stiffness parameters, capturing the variations in knee kinematics. These findings demonstrate the robustness and flexibility of the CSK model, indicating its suitability for offline RL tuning in continuous impedance control for powered prostheses.

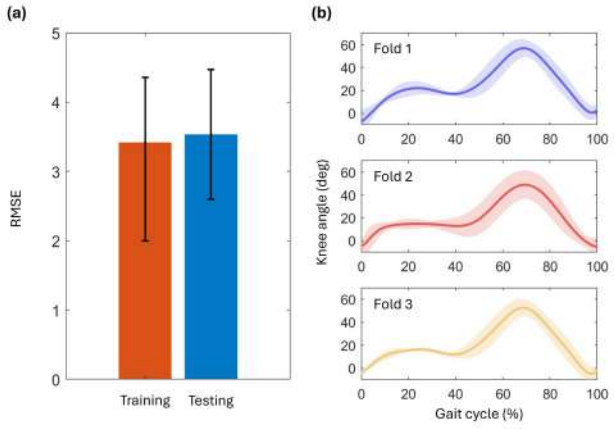


Fig. 3. Validation of the CSK model. (a) RMSE comparison between the training and testing datasets. (b) Predicted knee kinematics over the gait cycle for each fold. The solid lines represent the mean trajectory, while the shaded regions denote the standard deviation.

B. Offline RL Framework Validation

The RL training phase converged after 421 episodes during offline learning, requiring approximately 21 minutes on an NVIDIA Quadro P620 GPU, as shown in Fig. 4a. The training process automatically stopped upon meeting the convergence criterion, defined as the average reward stabilizing within the range [-7,0] over 15 consecutive steps. This stopping criterion was heuristically determined, balancing fast convergence and minimizing the error between the target and predicted knee kinematics. As further shown in Fig. 4a, after 48 episodes, the average reward began staying between -13 and -10, nearing the stopping threshold but not meeting it. If a lower threshold (e.g., -10) had been set, convergence would have been faster, but this study prioritized minimizing the error with respect to the target kinematics. The stiffness variations in the final episode are given in Fig. 4b, resulting in the optimized stiffness parameters: $K_1 = 0.235$ and $K_2 = 0.190$, with a final average reward of -6.9755.

Figure 4c presents the RMSE (vs. target knee) across different tuned parameters, including (1) the offline RL-tuned stiffness parameter set, (2) the initial parameter setting (from optimization [31]), (3) RMSE results from previous studies [31]. The offline RL-tuned parameter set achieved an RMSE of 6.7569, showing a notable improvement over the initial condition (8.2179 RMSE). This demonstrates that RL effectively optimized the stiffness parameters, generating knee kinematics that closely match the target profile. The offline RL-tuned model was also compared with RMSE values reported for a transfemoral amputee (TF01) and AB participants (AB01, AB02) in [31]. Notably, the offline RL-tuned model (6.7569 RMSE) performed better than AB01 (6.808±0.667 RMSE) but the error was slightly higher than AB02 (5.857±0.710 RMSE); TF01 showed the lowest RMSE (5.580±1.021). Compared to both AB individuals and the transfemoral amputee, the RL-tuned model achieved a competitive performance range, indicating that it can generalize well without requiring manual tuning.

C. Limitations and Future Directions

While the data-driven CSK model exhibited reasonable accuracy in predicting knee kinematics based on continuous knee stiffness, it does not fully capture the complex dynamics of the human-prosthesis system. Further improvements could be achieved by collecting additional experimental data or incorporating a digital twin environment to simulate prosthetic walking. Additionally, although the offline-trained policy provides safety boundaries and facilitates faster convergence, the RL policy might shift when a human interacts with the powered prosthesis in real-world scenarios. To address these limitations, we plan to integrate an online RL-tuning phase using a human-in-the-loop framework, complementing the offline tuning presented in this study. The RL formulation and stopping criteria will be further refined to balance convergence speed and tuning performance for real-time online learning. Furthermore, we aim to extend the proposed framework to optimize damping and equilibrium angle parameters, enabling the system to support a broader range of ambulation

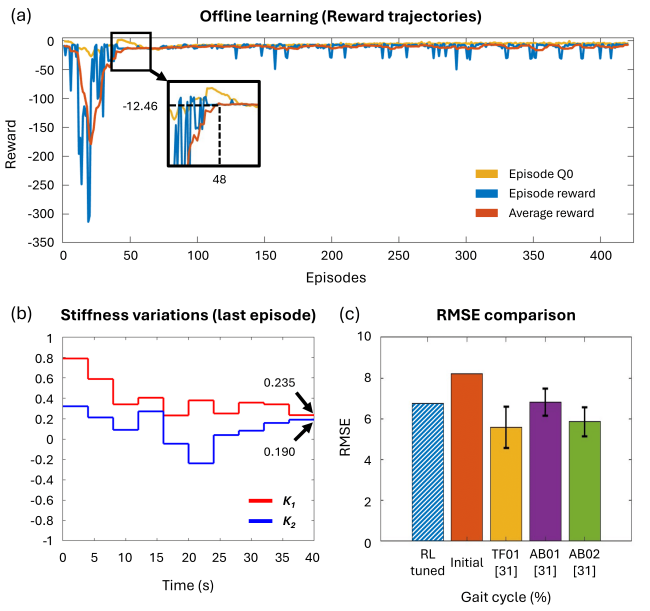


Fig. 4. Offline RL tuning result. (a) Reward trajectories during training until convergence. (b) Stiffness variations in the last episode, resulting in the optimized stiffness parameters: $K_1 = 0.235$ and $K_2 = 0.190$. (c) RMSE comparison between the target and the knee profiles across different tuned parameters, including the offline RL-tuned stiffness parameters, the initial parameter setting, and previously reported results from one amputee and two AB individuals in [31].

tasks, such as slope and stair navigation. The proposed framework has the potential to scale to multi-joint prostheses (e.g., knee-ankle prostheses) by utilizing multi-agent RL to personalize the controller, enhancing coordination between the prosthesis and the user.

IV. Conclusion

This study introduced an RL-driven framework for offline tuning of continuous impedance control in powered knee prostheses, with a specific focus on stiffness parameters, which were identified as significant in our previous work. Using the GPR-based CSK model, we successfully established a predictive relationship between stiffness parameters and knee kinematics, validated with experimental data from both able-bodied and amputee participants. The RL framework, built on the DDPG algorithm, demonstrated the feasibility of optimizing stiffness parameters in an offline setting, reducing reliance on the time-intensive manual tuning process. The results highlight the potential of this approach to effectively personalize powered prostheses within a continuous impedance control framework while providing a foundation for future studies. Future efforts will integrate the offline-trained policies into a real-time human-in-the-loop framework, enabling adaptive and personalized prosthesis control for a wide range of ambulation tasks.

References

[1] J. A. Rivera, K. Churovich, A. B. Anderson, and B. K. Potter, "Estimating recent us limb loss prevalence and updating future projections," *Archives of Rehabilitation Research and Clinical Translation*, p. 100376, 2024.

[2] T. Pohjolainen, H. Alaranta, and M. Kärkäinen, "Prosthetic use and functional and social outcome following major lower limb amputation," *Prosthetics and Orthotics International*, vol. 14, no. 2, pp. 75–79, 1990.

[3] C. Gauthier-Gagnon, M.-C. Grisé, and D. Potvin, "Enabling factors related to prosthetic use by people with transtibial and transfemoral amputation," *Archives of Physical Medicine and Rehabilitation*, vol. 80, no. 6, pp. 706–713, 1999.

[4] N. Anil Kumar, S. Patrick, W. Hong, and P. Hur, "Control framework for sloped walking with a powered transfemoral prosthesis," *Frontiers in Neurorobotics*, vol. 15, p. 790060, 2022.

[5] T. K. Best, C. G. Welker, E. J. Rouse, and R. D. Gregg, "Data-driven variable impedance control of a powered knee–ankle prosthesis for adaptive speed and incline walking," *IEEE Transactions on Robotics*, 2023.

[6] H. Zhao, J. Reher, J. Horn, V. Paredes, and A. D. Ames, "Realization of stair ascent and motion transitions on prostheses utilizing optimization-based control and intent recognition," in *2015 IEEE International Conference on Rehabilitation Robotics (ICORR)*. IEEE, 2015, pp. 265–270.

[7] R. J. Cortino, T. K. Best, and R. D. Gregg, "Data-driven phase-based control of a powered knee-ankle prosthesis for variable-incline stair ascent and descent," *IEEE Transactions on Medical Robotics and Bionics*, 2023.

[8] C. Jayaraman, S. Hoppe-Ludwig, S. Deems-Dluhy, M. McGuire, C. Mummidisetty, R. Siegal, A. Naef, B. E. Lawson, M. Goldfarb, K. E. Gordon *et al.*, "Impact of powered knee-ankle prosthesis on low back muscle mechanics in transfemoral amputees: A case series," *Frontiers in neuroscience*, vol. 12, p. 134, 2018.

[9] C. G. Welker, T. K. Best, and R. D. Gregg, "Data-driven variable impedance control of a powered knee-ankle prosthesis for sit, stand, and walk with minimal tuning," in *2022 IEEE/RSJ International Conference on Intelligent Robots and Systems (IROS)*. IEEE, 2022, pp. 9660–9667.

[10] E. D. Ledoux and M. Goldfarb, "Control and evaluation of a powered transfemoral prosthesis for stair ascent," *IEEE Transactions on Neural Systems and Rehabilitation Engineering*, vol. 25, no. 7, pp. 917–924, 2017.

[11] B. J. Hafner and R. L. Askew, "Physical performance and self-report outcomes associated with use of passive, adaptive, and active prosthetic knees in persons with unilateral, transfemoral amputation: Randomized crossover trial." *Journal of Rehabilitation Research & Development*, vol. 52, no. 6, 2015.

[12] F. Sup, A. Bohara, and M. Goldfarb, "Design and control of a powered transfemoral prosthesis," *The International Journal of Robotics Research*, vol. 27, no. 2, pp. 263–273, 2008.

[13] A. M. Simon, K. A. Ingraham, N. P. Fey, S. B. Finucane, R. D. Lipschutz, A. J. Young, and L. J. Hargrove, "Configuring a powered knee and ankle prosthesis for transfemoral amputees within five specific ambulation modes," *PloS One*, vol. 9, no. 6, p. e99387, 2014.

[14] H. Huang, D. L. Crouch, M. Liu, G. S. Sawicki, and D. Wang, "A cyber expert system for auto-tuning powered prosthesis impedance control parameters," *Annals of Biomedical Engineering*, vol. 44, no. 5, pp. 1613–1624, 2016.

[15] J. Yuan, X. Bai, A. Alili, M. Liu, J. Feng, and H. Huang, "Finding a natural fit: A thematic analysis of amputees' prosthesis setting preferences during user-guided auto-tuning," in *Proceedings of the Human Factors and Ergonomics Society Annual Meeting*, vol. 67, no. 1, 2023, pp. 2591–2597.

[16] F. Sup, H. A. Varol, and M. Goldfarb, "Upslope walking with a powered knee and ankle prosthesis: initial results with an amputee subject," *IEEE Transactions on Neural Systems and Rehabilitation Engineering*, vol. 19, no. 1, pp. 71–78, 2011.

[17] B. E. Lawson, H. A. Varol, A. Huff, E. Erdemir, and M. Goldfarb, "Control of stair ascent and descent with a powered transfemoral prosthesis," *IEEE Transactions on Neural Systems and Rehabilitation Engineering*, vol. 21, no. 3, pp. 466–473, 2012.

[18] F. Sup, H. A. Varol, J. Mitchell, T. J. Withrow, and M. Goldfarb, "Preliminary evaluations of a self-contained anthropomorphic transfemoral prosthesis," *IEEE/ASME Transactions on Mechatronics*, vol. 14, no. 6, pp. 667–676, 2009.

[19] N. Anil Kumar, W. Hong, and P. Hur, "Impedance control of a transfemoral prosthesis using continuously varying ankle impedances and multiple equilibria," in *2020 IEEE International Conference on Robotics and Automation (ICRA)*. IEEE, 2020, pp. 1755–1761.

[20] N. Hogan, "Impedance control: An approach to manipulation," in *1984 American Control Conference*, 1984, pp. 304–313.

[21] J. Mizrahi, "Mechanical impedance and its relations to motor control, limb dynamics, and motion biomechanics," *Journal of Medical and Biological Engineering*, vol. 35, pp. 1–20, 2015.

[22] V. Joshi, E. J. Rouse, E. S. Claflin, and C. Krishnan, "How does ankle mechanical stiffness change as a function of muscle activation in standing and during the late stance of walking?" *IEEE Transactions on Biomedical Engineering*, vol. 69, no. 3, pp. 1186–1193, 2021.

[23] W. Hong, "Transfemoral prosthesis control for inclined walking using impedance control and bezier polynomial based optimization," Master's thesis, Texas A&M University, College Station, TX, USA, 2017.

[24] E. J. Rouse, L. J. Hargrove, E. J. Perreault, and T. A. Kuiken, "Estimation of human ankle impedance during the stance phase of walking," *IEEE Transactions on Neural Systems and Rehabilitation Engineering*, vol. 22, no. 4, pp. 870–878, 2014.

[25] H. Lee, E. J. Rouse, and H. I. Krebs, "Summary of human ankle mechanical impedance during walking," *IEEE Journal of Translational Engineering in Health and Medicine*, vol. 4, pp. 1–7, 2016.

[26] N. P. Fey, A. M. Simon, A. J. Young, and L. J. Hargrove, "Controlling knee swing initiation and ankle plantarflexion with an active prosthesis on level and inclined surfaces at variable walking speeds," *IEEE Journal of Translational Engineering in Health and Medicine*, vol. 2, pp. 1–12, 2014.

[27] A. Alili, V. Nalam, M. Li, M. Liu, J. Feng, J. Si, and H. Huang, "A novel framework to facilitate user preferred tuning for a robotic knee prosthesis," *IEEE Transactions on Neural Systems and Rehabilitation Engineering*, 2023.

[28] D. Quintero, E. Reznick, D. J. Lambert, S. Rezazadeh, L. Gray, and R. D. Gregg, "Intuitive clinician control interface for a powered knee-ankle prosthesis: A case study," *IEEE Journal of Translational Engineering in Health and Medicine*, vol. 6, pp. 1–9, 2018.

[29] Y. Wen, J. Si, X. Gao, S. Huang, and H. H. Huang, "A new powered lower limb prosthesis control framework based on adaptive dynamic programming," *IEEE Transactions on Neural Networks and Learning Systems*, vol. 28, no. 9, pp. 2215–2220, 2016.

[30] W. Hong and H. H. Huang, "Towards personalized control for powered knee prostheses: Continuous impedance functions and pca-based tuning method," in *2023 International Conference on Rehabilitation Robotics (ICORR)*, 2023, pp. 1–6.

[31] W. Hong, A. Naseri, and H. H. Huang, "Toward online personalization of continuous impedance control for powered knee prostheses," 2024.

[32] A. McIntosh, K. Beatty, L. Dwan, and D. Vickers, "Gait dynamics on an inclined walkway," *Journal of Biomechanics*, vol. 39, no. 13, pp. 2491–2502, 2006.

[33] D. A. Winter, *Biomechanics and Motor Control of Human Movement*, 4th ed. Wiley, 2009.

[34] Y. Wen, X. Gao, J. Si, A. Brandt, M. Li, and H. H. Huang, "Robotic knee prosthesis real-time control using reinforcement learning with human in the loop," in *International Conference on Cognitive Systems and Signal Processing*. Springer, 2018, pp. 463–473.

[35] M. Li, Y. Wen, X. Gao, J. Si, and H. Huang, "Toward expedited impedance tuning of a robotic prosthesis for personalized gait assistance by reinforcement learning control," *IEEE Transactions on Robotics*, vol. 38, no. 1, pp. 407–420, 2021.

[36] X. Tu, M. Li, M. Liu, J. Si, and H. H. Huang, "A data-driven reinforcement learning solution framework for optimal and adaptive personalization of a hip exoskeleton," in *2021 IEEE International Conference on Robotics and Automation (ICRA)*, 2021, pp. 10 610–10 616.

[37] J. Camargo, A. Ramanathan, W. Flanagan, and A. Young, "A comprehensive, open-source dataset of lower limb biomechanics in multiple conditions of stairs, ramps, and level-ground ambulation and transitions," *Journal of Biomechanics*, vol. 119, p. 110320, 2021.

[38] N. Anil Kumar, W. Hong, and P. Hur, "Control of a transfemoral prosthesis on sloped terrain using continuous and nonlinear impedance parameters," in *2021 IEEE International Conference on Robotics and Automation (ICRA)*. IEEE, 2021, pp. 3219–3225.

[39] N. Thatte, N. Srinivasan, and H. Geyer, "Real-time reactive trip avoidance for powered transfemoral prostheses," *Robotics Systems and Sciences (RSS)*, 2019.

[40] T. Lillicrap, "Continuous control with deep reinforcement learning," *arXiv preprint arXiv:1509.02971*, 2015.

UP-CARE: An Upper Limb Portable Cable Assistive Recovery Exoskeleton for Elbow Movement Assistance

Jarren Bachiller Berdal, Ryan Jason Hartnett, and David Quintero

***Abstract*— Each year, many stroke survivors experience upper limb paralysis, negatively affecting their ability to perform activities of daily living. Powered assistive exoskeletons can help restore these abilities, promoting independence and improving their quality of life. While upper limb assistive devices show promise, challenges still remain in developing a lightweight and portable system for broad patient use. This paper presents the Upper limb Portable Cable Assistive Recovery Exoskeleton (UP-CARE) a lightweight, portable robotic exoskeleton designed to assist elbow movement. UP-CARE features a brushless DC motor whose torque is amplified through a two stage planetary gearbox and dual-pulley cable system made with high strength additive manufacturing materials. By leveraging 3D printing, the actuator design achieved a 52% weight reduction as compared to conventional off-the-shelf gear transmissions, while promoting design modularity and an increase in accessibility. UP-CARE has a total mass of 4.75 kg, with only 0.62 kg resting directly on the user's arm. Its high torque to weight ratio makes it suitable for portable assistive rehabilitation. Preliminary subject testing demonstrated accurate elbow position tracking up to 90°, while producing an average elbow joint torque of 18.9 Nm. The performance indicate that UP-CARE can support the assistive needs of elbow flexion/extension, helping stroke survivors regain independent living.**

I. INTRODUCTION

Nearly 800,000 people in the United States experience a stroke each year due to traumatic brain injury or cardiovascular disease [1]. Recent studies show that 70% of stroke survivors develop arm muscle weakness, preventing them from articulating solely, or a combination of, their shoulder, elbow, wrist, or hand, under their own physical power [2]. This impairment leads to both mental and physical hardships, significantly reducing their quality of life [3]. Elbow augmentation in particular is critical for performing activities of daily living (ADLs), such as drinking water or picking up objects [4]. To regain a sense of independence and improve their quality of life, stroke survivors may turn to robot-assistive devices, such as exoskeletons, in order to perform ADLs [5], [6].

Exoskeleton advancements over the past few decades have demonstrated that upper limb devices can enhance a patient's independence and quality of life [7], [8]. Various prime mover approaches have been developed to assist upper limb impairments and support ADLs movements. Pneumatic actuators use compressed air to drive an exoskeleton joint movement, offering a high force-to-weight ratio, low-cost implementation, and inherent system compliance for user safety [9]. However, their delayed response time and reliance on an air reservoir limit their suitability for portable exoskeletons. Hydraulic actuators provide high power density by compressing fluid but suffer from bulky designs and complex hydraulic plumbing, hinders portability [10], [11]. Electric motors are commonly used to actuate upper limb exoskeletons due to their precise control. When paired with a transmission system, they can generate the high torque required for various ADLs. Further, cable-driven systems powered by high-torque motors and pulley systems, can elevate a user's impaired arm. [12].

An emerging area of research focuses on integrating additive manufacturing, or 3D printing, into medical robotics technologies [13]. Fused Deposition Modeling (FDM) and Stereolithography Apparatus (SLA) 3D printers have become industry standards due to their affordability and accessibility, driven by a growing consumer market. These technologies enable rapid prototyping of medical devices [14]. 3D printing has facilitated the creation of strong structural components for exoskeletons, such as rigid links, and allowed the development of complex geometries for pneumatic actuators [13], [15]. Lopez Garcia et al. (2019) showcased the potential of 3D printed components in gearbox transmissions, while Urs et al. (2022) demonstrated the durability and performance of 3D printed transmissions, rivaling those of metal gearboxes [16], [17].

This paper introduces the Upper limb Portable Cable Assistive Recovery Exoskeleton (UP-CARE), a mobile, modular actuation system designed to assist elbow movement in stroke patients. UP-CARE emphasizes lightweight portability and customization by leveraging 3D printing with off-the-shelf (OTS) components, facilitating rapid fabrication and easy accessibility. The system targets elbow impairment and incorporates a brushless DC motor (BLDC), coupled with a custom 3D printed two stage planetary gearbox (TSPG) with a 19:1 gear reduction to deliver an average torque of 18.9 Nm during preliminary tests, exceeding the healthy human elbow joint torque requirement of 17 Nm [18]. The use of 3D printing reduced the TSPG's weight by 52% compared to traditional metal 19:1 planetary gear transmissions. The complete UP-CARE system, including the actuator, backpack, mounting platform, and dual-pulley system has a totals 4.75 kg, promoting portability and ease of transport. Preliminary subject tests consist of position tracking and frequency response evaluation, demonstrated

Authors are with the School of Engineering in Mechanical Engineering, San Francisco State University, San Francisco, CA 94132.

This work was supported by the San Francisco State University (SFSU) Dr. Ken Fong Translational Research Fund. The content is solely the responsibility of the authors and does not necessarily represent the official views of the funding source. Corresponding authors e-mail: jberdal@mail.sfsu.edu, hartnett@sfsu.edu,qdavid@sfsu.edu.

the system's ability to control the user's elbow joint while delivering the necessary torque. These results validate UP-CARE as a proof-of-concept and showcase the potential of 3D printing in developing a lightweight, portable exoskeleton for patients with arm muscle weakness.

II. METHODS

The UP-CARE portable assistive exoskeleton is designed for both clinical and home care setting, focusing on lightweight construction and user accessibility. The design leverages 3D printing to fabricate key components of the actuator and backpack platform, reducing weight while maintaining structural integrity. The combination of 3D printed elements with OTS components facilitates rapid manufacturing, easy accessibility, and cost-effective assembly. The system consists of two primary sub-assemblies: the backpack mounting platform and the UP-CARE actuator, as shown in Figure 1. The backpack mounting platform houses the motor control driver and mechanical actuator. The UP-CARE actuator includes the BLDC motor, custom multistage transmission, and dual-pulley system. The complete UP-CARE exoskeleton weighs 4.75 kg, ensuring portability without compromising performance.

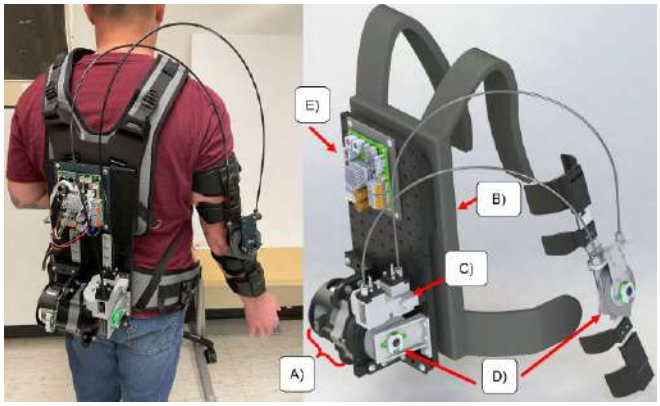


Fig. 1. Photo of human wearing the UP-CARE device (left). UP-CARE CAD assembly (right) with main components consisting of A) brushless DC motor paired with TSPG, B) custom backpack platform mount, C) idler tensioner system, D) Dual-pulley system & encoders: TSPG output pulley (left arrow) and elbow joint pulley (right arrow), and E) Copley Nano NPS motor driver.

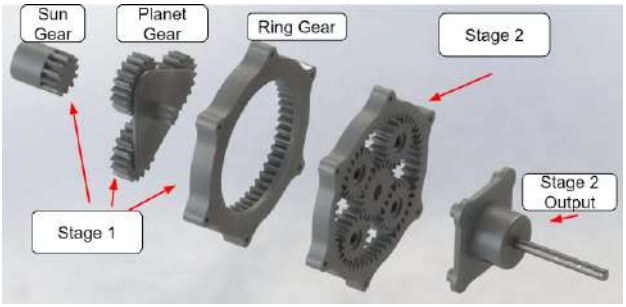


Fig. 2. Image of UP-CARE's 3D printed two stage planetary 19:1 reduction gearbox

A. UP-CARE Actuator

1) Transmission and DC Motor: The UP-CARE's actuator uses a Maxon EC 90 400W BLDC motor, delivering continuous torque of 1.29 Nm when supplied with 9.5 A. Previous studies from Vrije Universiteit Brussel highlight the viability of 3D printed gearbox transmissions [16]. In addition, researchers from the University of Michigan further analyze the use of 3D printed transmissions in quasi-direct actuators for legged robot (8-15 kg), revealing that moderate ratio gearboxes (1:1 to 30:1) that can handle intensive use over extended periods of time (420,000 strides) and perform comparable to metal gearboxes [17]. These findings support the integration of 3D-printed elements in UP-CARE to achieve a lightweight, high-torque transmission without sacrificing durability [19].

The custom TSPG features a 19:1 reduction ratio, selected to meet the torque demands of 8 to 17 Nm for ADLs involving motions close to and away from the body [18]. Additionally, 3D printing allows rapid development of custom gear ratios, allowing adaptations tailored to individual user needs. The theoretical torque produced by our BLDC amplified by a 19:1 TSPG, neglecting efficiency losses, would output a continuous torque of 24.5 Nm. However, based on efficiencies of 95% and 77% for similar TSPG [20] and cable driven exoskeleton systems [21], respectively, the UP-CARE system should achieve a continuous joint torque of 18 Nm. This validates our choice to meet the minimum joint torque requirement for elbow actuation, while accounting for an approximate efficiency of 73%, consistent with reported literature.

The sun gear, planet gears, planet carrier, and ring gear of the TSPG (Figure 2) were fabricated using SLA due to its high dimensional accuracy and superior layer bonding strength [22]. Formlabs Tough 2000 resin was selected for its ductile characteristic under tensile, compressive, and rotational loads [23]. Components were printed with a five-degree offset from the X-Y plane to reduce shear between print layers, followed by a post-curing to enhance mechanical strength. [23]. The sun gear connects to the BLDC motor via a knurled brass threaded insert, pressure-fitted with epoxy. This allows a set screw to secure the motor's D-profile output shaft. The second stage carrier outputs torque through a high carbon steel D-profile shaft, chosen for its rigidity and durability to withstand the joint torque demands of ADLs. The resulting 3D printed TSPG achieves a 52% reduction in weight at 301 g in comparison to an OTS metal 19:1 TSPG transmission (Maxon Group, Model: 223085) at 620 g.

2) Dual-pulley System and Elbow Brace: The UP-CARE device employs a close cable configuration for its dual-pulley system, enabling bidirectional push-pull cable movements to transmit torque efficiently [24]. Similar to the TSPG, the dual-pulley system is 3D printed, allowing torque transfer from the actuator to the user's elbow. Each push and pull cable runs through separate channels around the pulley without interference. The cables wrap in opposite directions and are anchored into precision grooves on the pulley's sides,

180° apart, using cable crimps for secure fastening. The driving pulley mounts directly onto the TSPG's output shaft via set screws, while steel cables connect it to the driven pulley, which integrates with a commercial arm brace. To introduce compliance and maintain pretension, a 19 Nm spring is incorporated as a series elastic element with each cable on the driven pulley [25]. This setup enhances safety and smoothens force transmission during elbow actuation.

Slack is inherent in the configuration of the close cable dual-pulley system, requiring proper tensioning to ensure effective torque transfer. To address this, the UP-CARE device integrates a custom 3D printed idler tensioner system, created using FDM (see Figure 1). The idler tensioner body is printed from polylactic acid (PLA) material, chosen for its ease of printing and rigidity. The adjustable idlers are made from polyethylene terephthalate glycol (PETG), selected for its superior mechanical strength and durability. Idlers were printed in the same orientation as the TSPG gears with a 60% infill gyroid pattern [26], [27], to balance strength and weight. Tension is adjusted by rotating a bolt located on top of the tensioner body, which presses the idler against the steel cable, increasing tension and eliminating slack.

UP-CARE includes a hard form factor elbow brace from Orthomen for its accessibility and cost-effectiveness [28]. The elbow brace provides a range of motion (ROM) from $0°$ to $110°$, meeting the minimum 80° ROM required for common ADLs involving elbow flexion and extension [29]. Total weight on the user's arm is 0.62 kg.

3) Backpack and Actuator Mounting Platform: An OTS harness from EGO Electronics (see Figure 1), allows the mounting platform and attached actuation system to be transported by a user [29]. The lightweight, adjustable harness is chosen for its durability and capability to carry heavy loads comfortably. UP-CARE's mounting platform was fabricated in two pieces with PLA filament, chosen for high strength property, connects the actuator to the EGO harness. To reduce weight, a 20% gyroid pattern infill is applied and two metal rods are inserted in the platform for added rigidity between the two pieces. One side of the platform contains mounting brackets designed to interface with the EGO harness. The other side is modeled after an optical board, allowing for easy attachment of the full actuator system. The optical board-like mounting platform enhances system modularity, enabling the attachment of multiple actuators to expand UP-CARE's functionality for future integration to assist additional arm joints (e.g., shoulder).

B. Electronics

UP-CARE uses Samesky (formerly CUI) AMT10 series rotary incremental encoders for position sensing feedback with resolution of 2048 counts per revolution. They are attached to the output of the TSPG driving pulley and the elbow brace driven pulley at the elbow joint (Figure 1). To monitor and measure cable pretension, 10-kΩ sliding potentiometers mounted at the elbow joint pulley track changes in spring compression. Using the measured displacement and the known spring constant, the system calculates the corresponding cable pretension force. A dSPACE MicroLabBox provided the real-time control development programmed in MATLAB/Simulink and provide data acquisition at 1 kHz to send analog control commands to the Copley Nano NPS-180-30-D motor driver (Figure 3). UP-CARE operates while tethered to an DC power supply (Keysight, N5766A/861) set at 35 V/28 A during each experiment. A 20.4 mF capacitor is connected in parallel with a Copley motor driver from the power supply for a low noise voltage/current draw to the driver.

III. PRELIMINARY EXPERIMENTATION AND RESULTS

A. Experimental Setup and Protocol

Preliminary experimental tests to assess the performance of UP-CARE consists of two experiments to the quantify system's accuracy and determine the device's controller bandwidth. A single-patient and a single test run methodology have been seen in literature [30], [31], allows for analyzing the mechanical system response before scaling to a larger sample of trials. Given the need for user-specific tuning, a case study approach provides meaningful feedback while reducing ethical and logistical constraints. UP-CARE uses a position-based proportional-derivative (PD) controller, custom-tuned for each wearer. Elbow joint position and velocity serve as feedback inputs to operate the system during experiments. The experimentation was approved by the Institutional Review Board (IRB) at San Francisco State University.

- Experiment I involves six tests tracking $90°$ positive and negative minimum jerk trajectory command with a maximum velocity of $35°$ per second which is 27% the velocity needed during ADLs [32]. A 5'7" male subject, weighing 89.6 kg (197 lbs), with no prior injuries, volunteered for the experiment. Before each test, the subject's arm is positioned perpendicular to the level floor and initialized at $0°$. Subject was allowed to rest shoulder vertically in their natural position. Experiment I employs a single-patient study to provide preliminary validation of UP-CARE's design and supply insight of its initial performance. The subject wore UP-CARE system and stood beside the power supply. A solid-state relay is placed in series for an emergency stop button and is positioned near the user's free hand.
- Experiment II evaluated a $15°$ magnitude position with frequency response sweep up to 100 Hz. UP-CARE was mounted on a table with a table fixture without a human subject. The arm brace was placed on a mount at a $45°$ offset from vertical and initialized at $0°$ (Figure 3).

B. Results

The UP-CARE system utilization of a position PD controller in Experiment I yield an average root mean square error (RMSE) of $8.29 \pm 2.11°$ across six trials as seen in Figure 4. During the user trajectory tracking, the average current draw is 10 A, peaking at 28 A. Using the BLDC motor torque constant of 0.136 Nm/A with an estimated

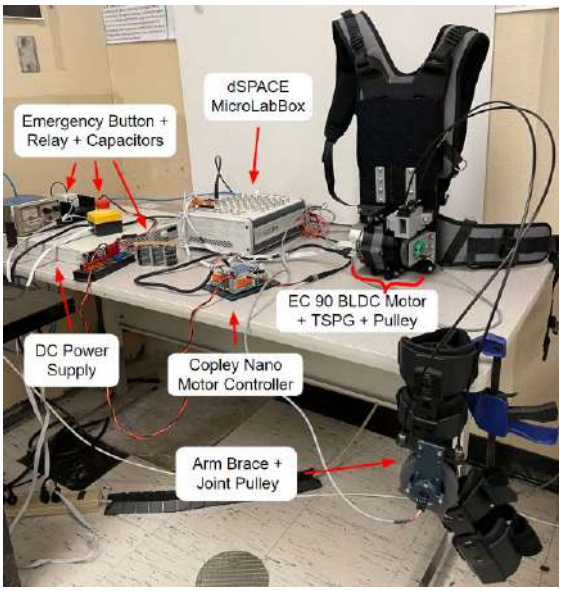


Fig. 3. Photo of experimental test setup for Experiment I & Experiment II frequency response test.

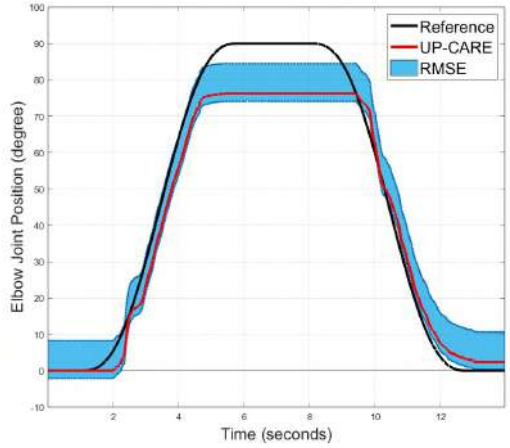


Fig. 4. Six trial average of system response of a bidirectional 90° minimum jerk trajectory command while lifting user's arm.

73.2% efficiency for the system based on similar actuators [20], [21], the derived average and peak torque throughout the six trials was 19 Nm and 53 Nm, respectively.

Experiment II consisting of a position chirp frequency response commands the elbow joint to actuate between 0° and 15° while varying frequency from 0 to 100 Hz. Figure 5 shows the results from Experiment II of a bode magnitude and phase plots, producing a closed-loop bandwidth (magnitude at -3 dB) at 2 Hz.

IV. Discussion

The UP-CARE system's RMSE position tracking performance is comparable to other cable assistive devices as shown in [33], [34]. Results from Experiment I demonstrate the UP-CARE system is able to achieve the ADLs torque

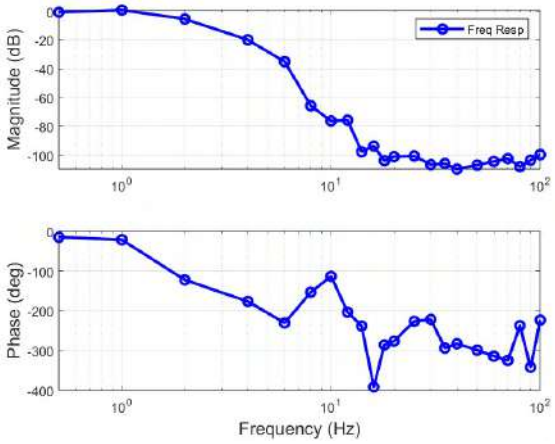


Fig. 5. Response of a 15° 100 Hz chirp frequency sweep with a 45° offset from vertical

performance requirement of 17 Nm for elbow flexion and extension [18]. With an estimated peak torque of 52.96 Nm, UP-CARE is able to output higher torque, exceeding commensurate systems such as [11], [34], [35]. In addition, UP-CARE's actuator can achieve a higher force output per weight of a nominal torque of 3.97 Nm/kg compared to other portable devices at 1.78 Nm/kg and 3.59 Nm/kg [36], [33]. From Experiment II, UP-CARE system's control scheme is able to perform while peaking at a bandwidth of 2 Hz, meeting the ADLs minimum bandwidth metric for therapeutic and assistive operation [33], [34]. Further more, UP-CARE's control bandwidth is higher than portable cable driven systems such as those seen in [34] and [36] using traditional controllers.

A. Limitations and Future Works

Though 3D printed transmissions are expected to be less durable when compared to metal gearboxes, a new study sheds light on the potential of 3D printed transmissions to perform similarly to metal gearboxes [17]. Urs et al. 2022 characterizes 3D printed gearboxes for legged robots. Their study observed a 3D printed actuator perform 420,000 cycles with minimal wear and backlash [17]. Power efficiency of the 3D printed transmission is elevated during high speeds and low torque applications, similar to other actuators in the literature [37]. Urs et al. concludes 3D printed actuator transmissions can deliver high torques and have properties that allow for impact mitigation, such as low output mechanical impedance and low resistance to external loads applied by the user. Thus, they are suitable for wearable robotic applications. 3D printing allows cost savings for rapid manufacturing of customizable actuators tailored to meet the performance requirements for each use case [17], [15]. To further increase durability of UP-CARE TSPG and other components, higher grade materials such as Nylon can replace the Formlabs Tough 2000 resin.

Incorporating the idler tensioner system has advantages and disadvantages. This system can easily apply tension

needed for a close cable pulley configuration and reduce slack [24]. Disadvantages to the idler tensioner is the added inertia and friction the system has to overcome to operate in conjunction with nonlinearities, such as convergent, bifurcation, and bistable states which may occur during operation. To solve these nonlinearities, a torque controller may need to be derived and implemented into the system [24]. Some approaches to minimize error include model based advance control schemes such as feed-forward to achieve greater precision in trajectory response trials [35]. Investigating frictional backlash in the TSPG and accounting for hysteresis effects in the steel cabling can also provide better performance [38].

UP-CARE's modular portable platform can support multiple UP-CARE actuators to address other areas of impairments such as the shoulder, hand, or wrist as seen in [35]. The next iteration of the system will include an embedded system controller on the backpack, a smaller motor driver, and an optimized battery pack to allow the user to roam without being tethered to a power source. In addition, UP-CARE will develop various assistance modes and controllers to allow more user control. Intuitive control operation for user could be improved by employing a deep machine learning algorithm to control the elbow using surface electromyography signals, force transducers, and an inertial measurement unit [39], [40], [41].

V. CONCLUSIONS

This paper delivers a proof of concept of UP-CARE as a functional elbow impairment assistive device for clinical and in-home care. The UP-CARE actuator, consisting of a TSPG and a dual-pulley system, is manufactured using 3D printed and OTS parts. The use of 3D printed and OTS components allows for ease of accessibility, enabling rapid production, and adaptability for UP-CARE to be tailored to meet each patient's own assistance needs. The proposed exoskeleton meets the minimum requirements to deliver 17 Nm of torque to assist elbow flexion and extension ADLs and operates within the therapeutic and assistive movements bandwidth of 2 Hz. The device's light-weight and modular features with the UP-CARE actuator and backpack platform place it among the higher torque output to weight ratio portable exoskeletons, suitable for stroke patient's various needs for in home assistance.

REFERENCES

[1] CDC, "Stroke Facts | cdc.gov," Sept. 2023. [Online]. Available: https://www.cdc.gov/stroke/facts.htm

[2] R. Allison, L. Shenton, K. Bamforth, C. Kilbride, and D. Richards, "Incidence, Time Course and Predictors of Impairments Relating to Caring for the Profoundly Affected arm After Stroke: A Systematic Review," *Physiother. Res. Int.*, vol. 21, no. 4, pp. 210–227, Dec. 2016. [Online]. Available: https://onlinelibrary.wiley.com/doi/10.1002/pri.1634

[3] P. Maciejasz, J. Eschweiler, K. Gerlach-Hahn, A. Jansen-Troy, and S. Leonhardt, "A survey on robotic devices for upper limb rehabilitation," *Journal of neuroengineering and rehabilitation*, vol. 11, pp. 1–29, 2014.

[4] N. A. Abd Razak, N. A. Abu Osman, H. Gholizadeh, and S. Ali, "Biomechanics principle of elbow joint for transhumeral prostheses: comparison of normal hand, body-powered, myoelectric & air splint prostheses," *Biomedical engineering online*, vol. 13, pp. 1–12, 2014.

[5] D. Zengin-Metli, S. Özbudak-Demir, İ. Eraktaş, V. Binay-Safer, and T. Ekiz, "Effects of robot assistive upper extremity rehabilitation on motor and cognitive recovery, the quality of life, and activities of daily living in stroke patients," *Journal of Back and Musculoskeletal Rehabilitation*, vol. 31, no. 6, pp. 1059–1064, 2018.

[6] C. Ochieze, S. Zare, and Y. Sun, "Wearable upper limb robotics for pervasive health: A review," *Progress in Biomedical Engineering*, vol. 5, no. 3, p. 032003, 2023.

[7] J. S. Khan, M. Mohammadi, J. Rasmussen, S. Bai, and N. Lotte Andreasen Struijk, "A review on the design of assistive cable-driven upper-limb exoskeletons and their experimental evaluation," in *2022 IEEE International Conference on Systems, Man, and Cybernetics (SMC)*. Prague, Czech Republic: IEEE, Oct. 2022, pp. 59–64. [Online]. Available: https://ieeexplore.ieee.org/document/9945523/

[8] P. Maciejasz, J. Eschweiler, K. Gerlach-Hahn, A. Jansen-Troy, and S. Leonhardt, "A survey on robotic devices for upper limb rehabilitation," *J NeuroEngineering Rehabil*, vol. 11, no. 1, p. 3, Dec. 2014. [Online]. Available: https://jneuroengrehab.biomedcentral.com/articles/10.1186/1743-0003-11-3

[9] X. Gao, Y. Sun, L. Hao, H. Yang, Y. Chen, and C. Xiang, "A new soft pneumatic elbow pad for joint assistance with application to smart campus," *IEEE Access*, vol. 6, pp. 38 967–38 976, 2018.

[10] M. Bolignari, G. Moretti, and M. Fontana, "Design and Experimental Characterisation of a Hydrostatic Transmission for Upper Limb Exoskeletons," in *2018 IEEE/RSJ International Conference on Intelligent Robots and Systems (IROS)*. Madrid: IEEE, Oct. 2018, pp. 2768–2773. [Online]. Available: https://ieeexplore.ieee.org/document/8593639/

[11] A. Otten, C. Voort, A. Stienen, R. Aarts, E. Van Asseldonk, and H. Van Der Kooij, "LIMPACT:A Hydraulically Powered Self-Aligning Upper Limb Exoskeleton," *IEEE/ASME Trans. Mechatron.*, vol. 20, no. 5, pp. 2285–2298, Oct. 2015. [Online]. Available: https://ieeexplore.ieee.org/document/7044558

[12] Y. Wang, A. Zahedi, Y. Zhao, and D. Zhang, "Extracting Human-Exoskeleton Interaction Torque for Cable-Driven Upper-Limb Exoskeleton Equipped With Torque Sensors," *IEEE/ASME Trans. Mechatron.*, vol. 27, no. 6, pp. 4269–4280, Dec. 2022. [Online]. Available: https://ieeexplore.ieee.org/document/9733396/

[13] B. W. K. Ang and C.-H. Yeow, "Design and modeling of a high force soft actuator for assisted elbow flexion," *IEEE Robotics and Automation Letters*, vol. 5, no. 2, pp. 3731–3736, 2020.

[14] S. F. Iftekar, A. Aabid, A. Amir, and M. Baig, "Advancements and Limitations in 3D Printing Materials and Technologies: A Critical Review," *Polymers*, vol. 15, no. 11, p. 2519, May 2023. [Online]. Available: https://www.mdpi.com/2073-4360/15/11/2519

[15] Triwiyanto, L. F. Wakidi, W. Caesarendra, A. Rizal, A. A. Ahmed, and V. Abdullayev, "A review of 3d printing technology for the development of exoskeletons for upper limb rehabilitation," in *International Conference on Electronics, Biomedical Engineering, and Health Informatics*. Springer, 2023, pp. 643–663.

[16] P. Lopez Garcia, S. Crispel, T. Verstraten, E. Saerens, B. Vanderborght, and D. Lefeber, "Customizing planetary gear trains for human limb assistance and replication," *MATEC Web Conf.*, vol. 287, p. 01014, 2019. [Online]. Available: https://www.matec-conferences.org/10.1051/matecconf/201928701014

[17] K. Urs, C. E. Adu, E. J. Rouse, and T. Y. Moore, "Design and Characterization of 3D Printed, Open-Source Actuators for Legged Locomotion," in *2022 IEEE/RSJ International Conference on Intelligent Robots and Systems (IROS)*. Kyoto, Japan: IEEE, Oct. 2022, pp. 1957–1964. [Online]. Available: https://ieeexplore.ieee.org/document/9981940/

[18] D. Meijering, R. G. Duijn, A. Murgia, A. L. Boerboom, D. Eygendaal, M. P. van den Bekerom, S. K. Bulstra, M. Stevens, and R. J. Vegter, "Elbow joint biomechanics during adl focusing on total elbow arthroplasty-a scoping review," *BMC musculoskeletal disorders*, vol. 24, no. 1, p. 42, 2023.

[19] J. B. Berdal, R. Lile, and D. Quintero, "CARE: Cable Assistive Rehabilitation Elbow Exoskeleton for Arm Movement Assistance," in *2023 IEEE International Conference on Systems, Man, and Cybernetics (SMC)*. Honolulu, Oahu, HI,

USA: IEEE, Oct. 2023, pp. 4313–4318. [Online]. Available: https://ieeexplore.ieee.org/document/10394153/

[20] Z. Qin, Y.-T. Wu, A. Eizad, K.-H. Lee, and S.-K. Lyu, "Design and evaluation of two-stage planetary gearbox for special-purpose industrial machinery," *Journal of Mechanical Science and Technology*, vol. 33, pp. 5943–5950, 2019.

[21] Y. Shi, M. Guo, H. Zhong, X. Ji, D. Xia, X. Luo, and Y. Yang, "Kinetic walking energy harvester design for a wearable bowden cable-actuated exoskeleton robot," *Micromachines*, vol. 13, no. 4, p. 571, 2022.

[22] R. Zou, Y. Xia, S. Liu, P. Hu, W. Hou, Q. Hu, and C. Shan, "Isotropic and anisotropic elasticity and yielding of 3D printed material," *Composites Part B: Engineering*, vol. 99, pp. 506–513, Aug. 2016. [Online]. Available: https://linkinghub.elsevier.com/retrieve/pii/S1359836816309052

[23] "Resin Family: Tough and Durable." [Online]. Available: https://formlabs.com/materials/tough-durable/

[24] J. Sanjuan, A. D. Castillo, M. A. Padilla, M. C. Quintero, E. Gutierrez, I. P. Sampayo, J. R. Hernandez, and M. H. Rahman, "Cable driven exoskeleton for upper-limb rehabilitation: A design review," *Robotics and Autonomous Systems*, vol. 126, p. 103445, 2020.

[25] M. d. C. Sanchez-Villamañan, J. Gonzalez-Vargas, D. Torricelli, J. C. Moreno, and J. L. Pons, "Compliant lower limb exoskeletons: a comprehensive review on mechanical design principles," *Journal of neuroengineering and rehabilitation*, vol. 16, pp. 1–16, 2019.

[26] M. T. Sepahi, H. Abusalma, V. Jovanovic, and H. Eisazadeh, "Mechanical properties of 3d-printed parts made of polyethylene terephthalate glycol," *Journal of Materials Engineering and Performance*, vol. 30, pp. 6851–6861, 2021.

[27] A. Pandžić, D. Hodžić, and A. Milovanović, "Effect of infill type and density on tensile properties of pla material for fdm process," in *Proceedings of the 30th DAAAM International Symposium*. DAAAM International, 2019, pp. 545–554.

[28] "Post OP Elbow Brace," Feb. 2023. [Online]. Available: https://www.orthomen.com/products/rom-arm-elbow-brace

[29] D. H. Gates, L. S. Walters, J. Cowley, J. M. Wilken, and L. Resnik, "Range of Motion Requirements for Upper-Limb Activities of Daily Living," *The American Journal of Occupational Therapy*, vol. 70, no. 1, pp. 7 001 350 010p1–7 001 350 010p10, Jan. 2016. [Online]. Available: https://research.aota.org/ajot/article/70/1/7001350010p1/6119/Range-of-Motion-Requirements-for-Upper-Limb

[30] L. Grazi, E. Trigili, G. Proface, F. Giovacchini, S. Crea, and N. Vitiello, "Design and experimental evaluation of a semi-passive upper-limb exoskeleton for workers with motorized tuning of assistance," *IEEE Transactions on Neural Systems and Rehabilitation Engineering*, vol. 28, no. 10, pp. 2276–2285, 2020.

[31] B. W. Gasser, D. A. Bennett, C. M. Durrough, and M. Goldfarb, "Design and preliminary assessment of vanderbilt hand exoskeleton," in *2017 International Conference on Rehabilitation Robotics (ICORR)*, 2017, pp. 1537–1542.

[32] F. Amirabdollahian, R. Loureiro, and W. Harwin, "Minimum jerk trajectory control for rehabilitation and haptic applications," in *Proceedings 2002 IEEE International Conference on Robotics and Automation (Cat. No.02CH37292)*, vol. 4, 2002, pp. 3380–3385 vol.4.

[33] N. Lotti, M. Xiloyannis, G. Durandau, E. Galofaro, V. Sanguineti, L. Masia, and M. Sartori, "Adaptive Model-Based Myoelectric Control for a Soft Wearable Arm Exosuit: A New Generation of Wearable Robot Control," *IEEE Robot. Automat. Mag.*, vol. 27, no. 1, pp. 43–53, Mar. 2020. [Online]. Available: https://ieeexplore.ieee.org/document/8963852/

[34] Q. Wu, X. Wang, B. Chen, and H. Wu, "Design and Fuzzy Sliding Mode Admittance Control of a Soft Wearable Exoskeleton for Elbow Rehabilitation," *IEEE Access*, vol. 6, pp. 60 249–60 263, 2018. [Online]. Available: https://ieeexplore.ieee.org/document/8489867/

[35] H. H. Cheng, T. M. Kwok, and H. Yu, "Design and Control of the Portable Upper-limb Elbow-forearm Exoskeleton for ADL Assistance," in *2023 IEEE/ASME International Conference on Advanced Intelligent Mechatronics (AIM)*. Seattle, WA, USA: IEEE, June 2023, pp. 343–349. [Online]. Available: https://ieeexplore.ieee.org/document/10196165/

[36] M. Xiloyannis, L. Cappello, K. D. Binh, C. W. Antuvan, and L. Masia, "Preliminary design and control of a soft exosuit for assisting elbow movements and hand grasping in activities of daily living," *Journal of rehabilitation and assistive technologies engineering*, vol. 4, p. 2055668316680315, 2017.

[37] U. H. Lee, C.-W. Pan, and E. J. Rouse, "Empirical characterization of a high-performance exterior-rotor type brushless dc motor and drive," in *2019 IEEE/RSJ International Conference on Intelligent Robots and Systems (IROS)*, 2019, pp. 8018–8025.

[38] T. Do, T. Tjahjowidodo, M. Lau, T. Yamamoto, and S. Phee, "Hysteresis modeling and position control of tendon-sheath mechanism in flexible endoscopic systems," *Mechatronics*, vol. 24, no. 1, pp. 12–22, Feb. 2014. [Online]. Available: https://linkinghub.elsevier.com/retrieve/pii/S0957415813002237

[39] A. Foroutannia, M.-R. Akbarzadeh-T, and A. Akbarzadeh, "A deep learning strategy for EMG-based joint position prediction in hip exoskeleton assistive robots," *Biomedical Signal Processing and Control*, vol. 75, p. 103557, May 2022. [Online]. Available: https://linkinghub.elsevier.com/retrieve/pii/S1746809422000799

[40] J.-L. Ren, Y.-H. Chien, E.-Y. Chia, L.-C. Fu, and J.-S. Lai, "Deep Learning based Motion Prediction for Exoskeleton Robot Control in Upper Limb Rehabilitation," in *2019 International Conference on Robotics and Automation (ICRA)*. Montreal, QC, Canada: IEEE, May 2019, pp. 5076–5082. [Online]. Available: https://ieeexplore.ieee.org/document/8794187/

[41] S. Luo, G. Androwis, S. Adamovich, E. Nunez, H. Su, and X. Zhou, "Robust walking control of a lower limb rehabilitation exoskeleton coupled with a musculoskeletal model via deep reinforcement learning," *J NeuroEngineering Rehabil*, vol. 20, no. 1, p. 34, Mar. 2023. [Online]. Available: https://jneuroengrehab.biomedcentral.com/articles/10.1186/s12984-023-01147-2